CD-ROM Proceedings

W. Gutkowski and
T. A. Kowalewski (Eds.)

MECHANICS OF 21st CENTURY



PART 1

International Union of
Theoretical and Applied Mechanics

Springer Academic Publishers

PREFACE

The 21st International Congress of Theoretical and Applied Mechanics (ICTAM04) took place August 15 – 21, 2004, in Warsaw, Poland. It was organized by Polish National Committee of IUTAM, Institute of Fundamental Technological Research of the Polish Academy of Sciences (IPPT PAN) and Warsaw University of Technology. The Congress venue was the main building of Warsaw University of Technology.

The idea of congresses devoted to mechanics, can be traced back to a conference on problems of fluid mechanics in Innsbruck, 1922. It was organized by four individuals, whose names, are and will, remain very well known to next generations of scientists, C. W. Oseen, T. Levi-Civite, T. von Kármán, and L. Prandtl. This conference was so fruitful, that the organizers decided to arrange similar meetings in the future, every four years, and to extend the scope of the future meetings to include solid mechanics. Hence a series of meetings started eighty years ago with the 1st ICTAM held in Delft, Netherlands.

From the meetings of the Congress Committee sprang the idea of a more permanent organization to look out for the world interests in the mechanical sciences. Thus, IUTAM, the International Union of Theoretical and Applied Mechanics, was formed on September 26, 1946. In 1947 IUTAM became a member of ICSU, the International Council of Scientific Unions, itself founded in 1931. The highest authority of IUTAM is the General Assembly, with delegates from the Adhering Organizations, each of which is affiliated with a national learned society in a given country.

W. Gutkowski
T.A. Kowalewski

Scientific Program

Contemporary mechanics poses both, the fundamental problems from the area of pure science, and its strong links with modern technology. It spreads over such areas of our knowledge as oceanography, physical chemistry, biology, medicine, geophysics and astrophysics. Hence, any conclusions deduced in the framework of mechanics, are likely to have a value for other fields. We may easily find prove of it in the scientific program of the ICTAM04. It consists of plenary opening and closing lectures, sectional lectures, mini-symposia, and contributed papers presented in lecture and seminar presentation sessions. These were intended to cover all aspects of mechanics.

All contributed papers were peer reviewed. Recommendations had been received from Pre-selection Committees of the National Committees of the nine countries: Canada, France, Germany, Japan, PR China, Poland, Russia, UK and USA. Moreover, recommendations had been received from the Chairs of the Mini-Symposia and of the Pre-nominated Sessions with classifications of the papers submitted within the topics of their Symposia/Sessions. Finally, the International Papers Committee paid careful attention to the above recommendations. Accordingly, of the 2086 eligible submissions 1574 contributions were invited by the IPC for their presentation. The total number of submitted and accepted papers represents a quite substantial enhancement relative to the previous congresses, providing evidence of vitality of the contemporary mechanics.

This volume of Proceedings consists of a book with full texts of invited talks and attached CD-ROM with Extended Summaries of 1225 papers presented during the Congress by authors[1]. We have tried to assemble the paper volume with an extensive index of names and papers collected on the CD-ROM. We hope that this volume – pre-ordered at the Congress in record numbers – will be found useful not only as a document of the event but to asses achievements and new paths of research in mechanics of 21st Century.

[1] From 1273 papers presented during the Congress we exclude multiple presentations and those given by proxy.

Codes used for Lectures and Sessions

Throughout the book and CD-ROM all papers are coded using letters and numbers denoting appropriate session code, presentation type, presenting author's ID, presentation day, time and lecture room. Following codes are used to mark sessions:

OL, **CL** - Opening and Closing Lectures

SL - Sectional Lectures

MS - Mini-Symposia

Pre-nominated Sessions:

FM - Fluid Mechanics

SM - Solid Mechanics

FSM - Topics involving Fluid and Solid Mechanics

Plenary and Contributed Papers

Opening Lecture *(page 112)*

Leen van Wijngaarden (Netherlands)

Interplay Between Air and Water

Closing Lecture *(page 113)*

Kazimierz Sobczyk (Poland)

Stochastic Dynamics of Engineering Systems

Sectional Lectures

Symbol	Title	Presenting Author
SL1 *(page 115)*	Multibody dynamics: bridging for multidisciplinary applications	Jorge Ambrosio
SL2 *(page 118)*	Rapid formation of strong gradients and diffusion in the transport of scalar and vector fields	Konrad Bajer
SL3 *(page 120)*	Near-critical point hydrodynamics and microgravity	Daniel A. Beysens
SL4 *(page 122)*	Suspensions: From Micromechanics to Macroscopic Behavior	John F. Brady
SL5 *(page 123)*	Nanoscale mechanics of biological materials	Huajian Gao
SL6 *(page 126)*	Variational and multiscale methods in turbulence	Thomas J. R. Hughes
SL7 *(page 130)*	Non-Newtonian fluid mechanics using molecular theory	Roland Keunings

SL8 *(page 132)*	Nonlinear dynamics in ocean engineering	Edwin Kreuzer
SL9 *(page 134)*	A bridge between the micro- and mesomechanics of laminates, fantasy or reality	Pierre J. Ladeveze
SL10 *(page 136)*	Turbulence and large-eddy simulations	Marcel Lesieur
SL11 *(page 138)*	Probability phenomena in perturbated dynamical systems	Anatoly Neishtadt
SL12 *(page 140)*	Mechanics of rubberlike solids	Raymond W. Ogden
SL13 *(page 142)*	Some issues in active vibration control of smart structures	Andre Preumont
SL14 *(page 144)*	Ocean circulation and its influence on climate	Peter B. Rhines
SL15 *(page 146)*	Microviscoelasticity of cells: cells as viscoplasctic bodies	Erich Sackmann
SL16 *(page 148)*	Electrokinetics & electrohydrodynamics in microfluids	D. A. Saville
SL17 *(page 149)*	Problems in astrophysical fluid dynamics	Edward Spiegel
SL18 *(page 151)*	Scaling in quasi-2D turbulence expreiments in a rotating flow	Harry L. Swinney

Mini Symposia

Symbol	Session subject	Responsible Chairs
MS1 *(page 15)*	Smart materials and structures	N. Sottos (USA), J. Holnicki-Szulc (Poland)
MS2 *(page 16)*	Tissue, cellular and molecular biomechanics	P. Janmey (USA), D. Barthes-Biesel (France), A. Hoger (USA)
MS3 *(page 17)*	Mechanics of thin films and nanostructures	K. Kim (USA), Z. Suo (USA), H. Jensen (Denmark)
MS4 *(page 18)*	Microfluids	P. Tabeling (France), R. Adrian (USA), J. Santiago (USA)
MS5 *(page 19)*	Microgravity flow phenomena	J. Legros (Belgium), G. Neitzel (USA), I. Alexander (USA)
MS6 *(page 20)*	Atmosphere and ocean dynamics	J. Sommeria (France), M. McIntyre (UK)

Pre-Nominated Sessions – Topics involving both fluid mechanics and solid mechanics

Symbol	Session subject	Responsible Chairs
FSM1 *(page 21)*	Acoustics	T. Geers (USA), N. Peake (UK)
FSM2 *(page 22)*	Chaos in fluid and solid mechanics	I. Mezic (USA), G. Rega (Italy)
FSM3 *(page 23)*	Continuum mechanics	K. Rajagopal (USA), G. Saccomandi (Italy)
FSM4 *(page 24)*	Fluid-structure interaction	J. Grue (Norway), M. Paidoussis (Canada)
FSM5 *(page 24)*	Mechanics of foams and cellular materials	S. Hilgenfeldt (Netherlands), D. Weaire (Ireland)
FSM6 *(page 25)*	Multiscale phenomena in mechanics	A. Carpinteri (Italy), C. Miehe (Germany)
FSM7 *(page 26)*	Education in mechanics	R. Engel (USA), B. Karihaloo (UK)

Pre-Nominated Sessions – Fluid Mechanics

Symbol	Topic	Responsible Chairs
FM1 *(page 27)*	Biological fluid dynamics	M. Gharib (USA), F. van de Vosse (Netherlands)
FM2 *(page 28)*	Boundary layers	P. Duck (UK), A. Kluwick (Austria)
FM3 *(page 28)*	Combustion and flames	N. Peters (Germany), P. Wolanski (Poland)
FM4 *(page 29)*	Complex and smart fluids	B. Khusid (USA), A. Yarin (Israel)
FM5 *(page 30)*	Compressible flow	H. Hornung (USA)
FM6 *(page 31)*	Computational fluid dynamics	L. Kleiser (Switzerland), W. Schroeder (Germany)
FM7 *(page 32)*	Convective phenomena	G. de Vahl Davis (Australia), K. Zhang (UK)
FM8 *(page 33)*	Drops and bubbles	J. Eggers (UK), A. Prosperetti (USA)
FM9 *(page 34)*	Environmental fluid dynamics	H. Huppert (UK), R. Narasimha (India)
FM10 *(page 35)*	Experimental methods in fluid mechanics	A. Leder (Germany), J. Westerweel (Netherlands)
FM11 *(page 36)*	Flow control	J. Freund (USA), M. Gad-el-Hak (USA)
FM12 *(page 36)*	Flow in porous media	A. Mojtabi (France), V. Nikolaevskiy (Russia)
FM13 *(page 37)*	Flow instability and transition	P. Huerre (France), P. Monkewitz (Switzerland)

FM14 *(page 39)*	Flow in thin films	N. Aksel (Germany), V. Shkadov (Russia)
FM15 *(page 39)*	Fluid mechanics of materials processing	F. Dupret (Belgium), R. Moreau (France)
FM16 *(page 40)*	Fluid mechanics of suspension	R. Bonnecaze (USA), E. Guazzelli (France)
FM17 *(page 41)*	Granular flows	R. Behringer (USA), I. Goldhirsch (Israel)
FM18 *(page 42)*	Low-Reynolds-number flow	R. Davis (USA), C. Pozrikidis (USA)
FM19 *(page 42)*	Magnetohydrodynamics	P. Davidson (UK), A. Thess (Germany)
FM20 *(page 43)*	Multiphase flows	S. Balachandar (USA), J. Magnaudet (France)
FM21 *(page 44)*	Solidification and crystal growth	M. Glicksman (USA), M. Worster (UK)
FM22 *(page 45)*	Stirring and mixing	H. Aref (USA), E. Villermaux (France)
FM23 *(page 46)*	Topological fluid mechanics	P. Boyland (USA), K. Ohkitani (Japan)
FM24 *(page 47)*	Turbulence	O. Metais (France), R. Moser (USA)
FM25 *(page 48)*	Vortex dynamics	E. Krause (Germany), G. van Heijst (Netherlands)
FM26 *(page 49)*	Waves	W. Melville (USA), V. Shrira (UK)

Pre-Nominated Sessions – Solid Mechanics

Symbol	Topic	Responsible Chairs
SM1 *(page 50)*	Computational solid mechanics	T. Belytschko (USA), P. Wriggers (Germany)
SM2 *(page 52)*	Contact and friction mechanics	I. Goryacheva (Russia), A. Klarbring (Sweden), G. Szefer (Poland)
SM3 *(page 54)*	Control of structures	F. Chernousko (Russia), S. Pellegrino (UK)
SM4 *(page 54)*	Damage mechanics	M. Chrzanowski (Poland), P. Steinmann (Germany)
SM5 *(page 55)*	Dynamic plasticity of structures	N. Jones (UK), T. Wierzbicki (USA)
SM6 *(page 56)*	Elasticity	R. Kienzler (Germany), L. Wheeler (USA)
SM7 *(page 57)*	Experimental methods in solid mechanics	I. Emri (Slovenia), J. Freire (Brazil)
SM8 *(page 57)*	Fatigue	J. Dominguez (Spain), K. Reifsnider (USA)
SM9 *(page 58)*	Fracture and crack mechanics	D. Gross (Germany), A. Needleman (USA)
SM10 *(page 59)*	Functionally graded materials	R. Batra (USA), G. Paulino (USA)
SM11 *(page 60)*	Impact and wave propagation	A. Norris (USA), K. Wilmanski (Germany)
SM12 *(page 62)*	Material instabilities	D. Bigoni (Italy), H. Petryk (Poland)
SM13 *(page 62)*	Mechanics of composites	S. Adali (South Africa), N. Fleck (UK)

SM14 *(page 64)*	Mechanics of phase tranformations (jointly with IACM)	F. Fischer (Austria), A. Molinari (France)
SM15 *(page 65)*	Mechanics of porous materials	W. Ehlers (Germany), J. Huyghe (Netherlands)
SM16 *(page 66)*	Mechatronics	W. Schiehlen (Germany), M. Tomizuka (USA)
SM17 *(page 66)*	Multibody dynamics	M. Geradin (Italy), F. Pfeiffer (Germany)
SM18 *(page 68)*	Plasticity and viscoplasticity	E. van der Giessen (Netherlands), P. Perzyna (Poland)
SM19 *(page 69)*	Plates and shells	H. Mang (Austria), E. Ramm (Germany)
SM20 *(page 70)*	Rock mechanics and geomechanics	Z. Mroz (Poland), I. Vardoulakis (Greece)
SM21 *(page 70)*	Solid mechanics in manufacturing	B. Heimann (Germany), T. Inoue (Japan)
SM22 *(page 70)*	Stability of structures	Z. Gaspar (Hungary), S. Kyriakides (USA)
SM23 *(page 71)*	Stochastic micromechanics	Y. Brechet (France), Y. Shibutani (Japan)
SM24 *(page 72)*	Structural optimization	K. Choi (USA), J. Herskovits (Brazil)
SM25 *(page 73)*	Structural vibrations	I. Blekhman (Russia), K. Popp (Germany)
SM26 *(page 75)*	Vehicle dynamics	S. Iwnicki (UK), R. Sharp (UK)
SM27 *(page 76)*	Viscoelasticity and creep	A. Cocks (UK), N. Ohno (Japan)

Mini Symposium MS1
Smart materials and structures

Chair: **N. Sottos (USA)**

Co-Chair(s): **J. Holnicki-Szulc (Poland)**

Introductory Lectures

Paper ID	Title	Authors
MS1I_10680 (page 153)	Elastic Wave Propagation Development for Structural Health Monitoring	Wieslaw M. Ostachowicz
MS1I_10722 (page 156)	A Way to Search for Smart Materials with Unprecedented Physical Properties	Richard D. James
MS1I_13010 (page 157)	Autonomic Healing of Polymers and Composites	Scott R. White, Nancy R. Sottos, Jeffrey S. Moore, Eric N. Brown, Alan Jones, Joseph Rule

Contributed Papers

Paper ID	Title	Authors
MS1S_10136 (page 159)	Composite Plates with Active Fibres	Mieczyslaw S. Kuczma
MS1L_10784 (page 161)	Transient Eigenstrains Without Incremental Displacements in a Hyperelastic Body	Hans Irschik, Uwe Pichler
MS1S_10821 (page 163)	Shape Fixity and Shape Recovery of Shape Memory Polymer and their Applications	Hisaaki Tobushi, Ryosuke Matsui, Tsuyoshi Takada, Shunichi Hayashi
MS1S_10985 (page 165)	Vibration Control of Stiffened Plates with Integrated Piezoelectrics	Jin-Young Jung, Ji-Hwan Kim
MS1L_11685 (page 167)	Stress Effects on Ferroelectric Thin Film Patterning, Properties and Performance	N. R. Sottos, T. Berfield, R. Ong, D. A. Payne
MS1L_11731 (page 169)	A Novel Approach to the Application of Ferroelectric Thin Films to Micro - actuation	Kaushik Bhattacharya
MS1S_11752 (page 171)	A Geometrically Non-Linear Finite Shell Element with Piezoelectric Layers	Sven Lentzen, Ruediger Schmidt
MS1S_11810 (page 173)	Piezodiagnostics a New SHM Method and its Potential Engineering Applications	Jan Holnicki-Szulc, Przemyslaw Kolakowski, Anita Orlowska, Andrzej Swiercz, Dariusz Wiacek, Tomasz G. Zielinski
MS1S_11857 (page 175)	Thermal - Induced Fracture of Electroded Piezoelectric Composites	Cun-Fa Gao, Masayuki Ishihara, Naotake Noda
MS1S_12011 (page 177)	Thermal Buckling of Active Composite Plates with Shape Memory Alloy Fibers	Rivka Gilat, Jacob Aboudi
MS1S_12016 (page 179)	Study of Non - Linear Magnetomechanical Constitutive Relations of Ferromagnetic Materials	Daining Fang, Xue Feng, Yongping, Keh-Chih Hwang
MS1S_12018 (page 181)	Optimum Control of Thermoelastic Deformation in a Smart Composite Disk	Fumihiro Ashida, Theodore R. Tauchert
MS1L_12027 (page 183)	SMA Hybrid Composites: Self - healing, Self - Stiffening and Shape Control Simulations	Catherine L. Brinson, Deborah Burton, Xiujie Gao
MS1S_12147 (page 185)	Active Control of FGM Plates Using Distributed Piezoelectric Sensors and Actuators	V. Balamurugan, S. Narayanan
MS1S_12552 (page 187)	On a Model of Layered Piezoelectric Beams Including Transverse Interactions Between Different Layers	Corrado Maurini, J. Pouget, F. dell'Isola
MS1L_12637 (page 189)	Ultrasonic Characterization of Phase Transformation in NiTi Wire During Thermomechanical Loading	Michal Landa, Petr Sedlak, Frantisek Marsik, Petr Sittner, Vaclav Novak

MS1L_12786 (page 191)	Upper and Lower Bounds of Electric Induction Intensity Factors for Multiple Piezoelectric Cracks by the BEM	Mitsunori Denda, Mayur Mansukh
MS1L_13007 (page 193)	Direct Identification of the State Equation in Complex Nonlinear Systems	Sami F. Masri, John P. Caffrey, Thomas K. Caughey, Andrew W. Smyth, Anastasios G. Chassiakos
MS1L_13011 (page 195)	Self-Healing Polymer Composites for Extended Fatigue Life	Eric N. Brown, Alan S. Jones, Scott R. White, Nancy R. Sottos
MS1L_13015 (page 197)	The Concept of Multifoldig and Its Experimental Validation	Jan Holnicki-Szulc, Piotr Pawlowski

Mini Symposium MS2
Tissue, cellular and molecular biomechanics

Chair: **P. Janmey (USA)**

Co-Chair(s): **D. Barthes-Biesel (France), A. Hoger (USA)**

Introductory Lectures

Paper ID	Title	Authors
MS2I_10709 (page 199)	Molecular Mechanics of Cytoskeletal Components	Christoph F. Schmidt, M. Atakhorrami, K. Addas, G.H. Koenderinck, F. C. MacKintosh, J. X. Tang
MS2I_10933 (page 201)	Tissue Mechanics	Susan S. Margulies
MS2I_12811 (page 202)	Elastic Interactions of Biological Cells	Samuel Safran, Alice Nicolas, Ulrich Schwarz

Contributed Papers

Paper ID	Title	Authors
MS2L_10627 (page 203)	Micromechanics of Cytoskeletal Actin Networks	Erik Van der Giessen, Patrick Onck
MS2L_10670 (page 205)	Residual Stress Fields in Soft Tissues	Anders Klarbring, Tobias Olsson, Jonas Staalhand
MS2L_10689 (page 207)	From Individual Cells To Complex Tissues - an Immersed Boundary Approach	Katarzyna A. Rejniak
MS2S_10838 (page 209)	Travelling Waves in a Model of Skin Pattern Formation	Kazimierz Piechor, Bogdan Kazmierczak
MS2L_10988 (page 211)	Mechanics of Deep Penetration of Soft Solids	Norman Fleck, Oliver Shergold
MS2S_11102 (page 213)	Mechanics of Elastic and Viscous Magnetic Filaments	Andrejs Cebers, I. Javaitis
MS2S_11148 (page 215)	Intracellular Control Mechanisms of Cardiac Contraction & Energetics	Samuel Sideman
MS2L_11581 (page 217)	Mechanics of Venus' flytrap Closure	Yoel Forterre, Jan Skotheim, Jacques Dumais, L. Mahadevan
MS2L_11808 (page 219)	Approximations of Stiffness Tensor of Bone - Determining and Accuracy	Jaroslaw Piekarski, K. Kowalczyk-Gajewska, J.H. Waarsing, M. Mazdziarz
MS2L_11866 (page 221)	Theory of Polymorphism in Bacterial Flagella	Srikanth V. Srigiriraju, Thomas R. Powers
MS2L_11961 (page 222)	Hydrodynamic Interaction Between Two Bioartifical Capsules in Shear Flow	Arnaud Morel, Etienne Lac, Dominique Barthes-Biesel
MS2L_12031 (page 224)	Stress and Strain in a Yeast Cell under High Hydrostatic Pressure	Christoph Hartmann, Antonio Delgado

MS2S_12059 (page 227)	Models of Hair Cell Bundle Functioning	Alexander V. Kondrachuk, Vasyl P. Lukomsky, Ivan S. Gandzha
MS2L_12064 (page 229)	Measuring the Mechanical Properties of Soft Biological Tissues	Edoardo Mazza, Alessandro Nava, Davide Valtorta
MS2S_12100 (page 231)	Anisotropic Hyperelastic and Pseudo-hyperelstic Materials and Applications to Soft Tissue Modelling	Stanislaw Jemiolo, Jozef Joachim Telega
MS2S_12192 (page 233)	Molecular Dynamics Study of Permeation Process of Small Molecules Through A Lipid Bilayer	Taisuke Sugii, Shu Takagi, Yoichiro Matsumoto
MS2L_12315 (page 235)	Modeling of Periodic Load Effects in Bone Tissue Adaptation	Tomasz Lekszycki
MS2S_12453 (page 237)	A Particle Method Computer Simulation of Blood Flow	Ken-ichi Tsubota, Shigeo Wada, Takami Yamaguchi
MS2L_13049 (page 239)	Wrinkling and Buckling of Isotropic Biological Tissues	Luigi Gambarotta, Roberta Massabo, Vittoria Villa

Mini Symposium MS3
Mechanics of thin films and nanostructures

Chair: **K.S. Kim (USA)**

Co-Chair(s): **Z. Suo (USA), H.M. Jensen (Denmark)**

Introductory Lectures

Paper ID	Title	Authors
MS3I_11070 (page 241)	Mechanics of Thin Film Structures	Henrik Myhre Jensen
MS3I_11594 (page 243)	Mechanics of Nanostructures	Rodney S. Ruoff
MS3I_12132 (page 244)	A Hybrid Molecular/continuum Analysis of IFM Experiments on a Self-assembled Monolayer	Kenneth. M. Liechti, M. Wang, J. M. White, P. J. Rossky, R. M. Winter

Contributed Papers

Paper ID	Title	Authors
MS3L_10105 (page 246)	Thermomechanical Continuum Representation of Atomistic Deformation at Arbitrary Time and Size Scales	Min Zhou
MS3L_10699 (page 247)	Ratcheting-induced Wrinkling of an Elastic Film on a Metal Layer Under Cyclic Temperatures	Rui Huang, S.H. Im
MS3L_11122 (page 249)	Atomistic study of Size Effect in Torsion Tests of Nanowire	Akihiro Nakatani, Hiroshi Kitagawa
MS3L_11260 (page 251)	Solid Mechanics Methods in Nano-technologies	Elena A. Ivanova, Anton M. Krivtsov, Nikita F. Morozow, Boris Semenov
MS3L_11279 (page 253)	Microstructural and Atomistic Simulation for Deformation of Nano-grained Metals	Yang Wei
MS3S_11444 (page 255)	Energy-based Approach to Limit States in Nanostructures. Calculation of the Critical Values of Energy from Firt Principles	Kinga Nalepka, Pawel Nalepka, Ryszard B. Pecherski
MS3L_11474 (page 257)	Size-dependent Elastic State of Embedded Nano-inclusions & Quantum Dots	Pradeep Sharma, Lewis Wheeler
MS3S_11599 (page 259)	Fracture Criterious for Bridged Crack: from Macro to Nanoscale	Mikhail N. Perelmuter
MS3S_12181 (page 261)	Investigation of Wave Propagation in Multiwall	Sha Fenghuan, Zhao Longmao, Yang Guitong

MS3S_12251 (page 263)	Homogenisation Models of Carbon Nanocomposites Mechanical Properties	Aleksander Muc, Malgorzata Chwal
MS3S_12314 (page 265)	Micro - and Nano - mechanics of Carbon Nanotubes Composites	Xi - Qiao Feng, Dong - Li Shi, Y. Huang, Keh - Chih Hwang
MS3L_12384 (page 267)	Characterization of MEMS Materials	Jurg Dual, Gerd Simons, Jacqueline Vollmann
MS3L_12386 (page 269)	An Analytical Model of Oxide Rumpling as the Mechanism Leading to Failure in Thermal Barrier Coatings	Daniel S. Balint, John W. Hutchinson
MS3S_12432 (page 271)	Instabilities of Composite Materials Reinforced by Nano-Fibres : a Re-examination of Elastic Buckling	Raymond Parnes, Alexander Chiskis
MS3L_12486 (page 273)	Interfacial Adhesion of PZT Ferroelectric Thin Films Determined by Nano - Indentation Method	X. J. Zheng, Y. C. Zhou
MS3S_12627 (page 275)	A Cellular Automaton for Modelling Evolution of Heteroepitaxial Systems	Simon P. A. Gill
MS3L_12705 (page 277)	Mechanical Behaviour of Nano Grained Metals	Aman Haque, Taher Saif
MS3S_12718 (page 279)	Effective Thermoelastic Properties of Nanocomposites with Prescribed Random Orientation of Nanofibers	Ajit Roy, V. A. Buryachenko
MS3L_12778 (page 281)	Nano-scale Planar Field Projection of Atomistic Decohesion of Crystalline Solids	SeungTae Choi, Kyung-Suk Kim

Mini Symposium MS4
Microfluids

Chair: **P. Tabeling (France)**

Co-Chair(s): **R.J. Adrian (USA), J. Santiago (USA)**

Introductory Lectures

Paper ID	Title	Authors
MS4I_12960 (page 283)	Slip, Patterns, and other small Things in Microfluidic Systems	Patrick Tabeling, A. Dodge, P. Joseph, C. Jullien, L. Menetrie, H. Willaime
MS4I_12961 (page 287)	Electrokinetic Flow Instabilities in Microfluidic Systems	Juan G. Santiago
MS4I_12976 (page 288)	Miniaturization of Explosive Technology and Microdetonics	D. Scott Stewart

Contributed Papers

Paper ID	Title	Authors
MS4L_10723 (page 290)	Plane Poiseuille Flow in a Rarefied Gas with General Boundary Conditions	Carlo Cercignani, M. Lampis, S. Lorenzani
MS4S_10971 (page 292)	Water Flows in Copper and Quartz Nanochannels	Anna Kucaba-Pietal, Z. Walenta, Z. Peradzynski
MS4L_11437 (page 294)	A Second-order Slip Model for Early-transition-regime Flows	Nicolas G. Hadjiconstantinou
MS4L_11604 (page 296)	Direct Measurement and Simulation of Apparent Slip Velocities in Sub-micron-scale Flows	Peter Huang, Kenneth S. Breuer
MS4L_11607 (page 298)	Theoretical and Experimental Study of Microchannel Blockage Phenomena	Eiichiro Yamaguchi, Ronald J. Adrian
MS4L_11777 (page 300)	Induced-Charge Electro-Osmosis: Theory and Microfluidic Applications	Todd M. Squires, Martin Z. Bazant

MS4S_12047 (page 302)	Using Microfluidics to Investigate Reaction-diffusion Phenomena in Simple Flows	Laure Menetrier, Fridolin Okkels, Charles N. Baroud, Jean-Baptiste Salmon, Patrick Tabeling
MS4S_12130 (page 304)	Magnetic Particles Aggregation in the Presence of a Hydrodynamic Shear	Guillaume Degre, Edouard Brunet, Fridolin Okkels, Patrick Tabeling
MS4S_12536 (page 306)	Chaotic Mixing and Resonances in a Microfluidic System	Arash Dodge, Caroline Jullien, Fridolin Okkels, Patrick Tabeling
MS4L_12673 (page 308)	An Accurate Velocity Profile Measurement System for Microfluidics : A Direct Measurement of the Slip Length	Pierre Joseph, Patrick Tabeling
MS4L_12966 (page 310)	Tunable Microfluidic Bubble Generator	Piotr Garstecki, Howard A. Stone, George M. Whitesides

Mini Symposium MS5
Microgravity flow phenomena

Chair: **J.C. Legros (Belgium)**

Co-Chair(s): **P. Neitzel (USA), J.I.D. Alexander (USA)**

Introductory Lectures

Paper ID	Title	Authors
MS5I_10598 (page 312)	Foams, Films and Surfaces in Microgravity	Denis Weaire, S. Cox
MS5I_10714 (page 313)	Collisional Granular Flows with and without Gas Interactions in Microgravity	Haitao Xu, Michel Y. Louge
MS5I_11133 (page 314)	Microgravity and Microscale Fluid Mechanics	George M. Homsy

Contributed Papers

Paper ID	Title	Authors
MS5S_10958 (page 315)	Hydrodynamic Effect of Slow Phase Transitions in Microgravity	Eleonora K. Bevza, O.O. Kochubey, D.V. Yevdokymov
MS5S_10980 (page 317)	Heat Transfer Due to High Frequency Vibration: a New Approach for Achieving Thermally Optimum Geometry Under Microgravity Conditions	M. C. Charrier Mojtabi, Y. P. Razi, K. Maliwan, A. Mojtabi
MS5S_11483 (page 319)	Thermocapillary Convection in Liquid Bridges and Annuli	Bok-Cheol Sim, Abdelfattah Zebib
MS5L_11757 (page 321)	Mathematical Models of Microconvection for Isothermally Incompressible and Weakly Compresible Liquids	Vladislav V. Pukhnachov, Olga N. Goncharova
MS5L_11843 (page 323)	Onset of Oscillations in High-Prandtl Thermocapillary Liquid Bridges: Linear-stability Analysis vs. Experiment	Ermakov M.K.
MS5L_12402 (page 325)	Spherical Two-phase Interface in a Near-critical Fluid. Gradient Approach	Anatoly M. Vorobev, D.V. Lyubimov, T.P. Lyubimova
MS5L_12427 (page 327)	Transition to Chaotic Marangoni Convection in Liquid Bridge	Shevtsova V., Melnikov D., Legros J. C.
MS5L_12447 (page 329)	Capillary Pressure of a Liquid Between Uniform Spheres Arranged in a Square-packed Layer	J. Iwan D. Alexander, Lev A. Slobozhanin, Stephen H. Collicott
MS5L_12651 (page 331)	Recent Advances in Permanent Noncoalescence and Nonwetting	G. Paul Neitzel, Pasquale Dell'Aversana, Peter Nagy, Maria-Isabel Carnasciali
MS5S_12765 (page 333)	The Stability of Connected Pendant Drops	Lev A. Slobozhanin, J. Iwan D. Alexander

Mini Symposium MS6
Atmosphere and ocean dynamics

Chair: **J. Sommeria (France)**
Co-Chair(s): **M.E.McIntyre (UK)**

Introductory Lectures

Paper ID	Title	Authors
MS6I_10716 (page 334)	Wave Vortex Interactions in the Atmosphere and Oceans; with Applications to Climate	Onno Bokhove
MS6I_10803 (page 336)	Assimilation of Observations into Numerical Models	Olivier Talagrand
MS6I_10987 (page 338)	Transport And Mixing in the Atmosphere	Peter Haynes

Contributed Papers

Paper ID	Title	Authors
MS6L_10261 (page 340)	Modelling Oceanographic Coastal Currents in Small-scale and Large-scale Laboratory Experiments	Peter J. Thomas, Paul F. Linden, David Marah
MS6L_10513 (page 342)	Near-surface Turbulence in a Neutral Planetary Boundary Layer: Comparison of LES with the CASES'99 Experiment Observations	Pierre Carlotti, Philippe Drobinski, Jean-Luc Redelsperger, Rob K. Newsom, Robert M. Banta
MS6L_10634 (page 344)	Meridional Flow of Source Driven Grounded Abyssal Flow in a Wind Driven Basin with Topography	Gordon E. Swaters
MS6L_10977 (page 346)	Remote Recoil and Wave Capture: Wave--vortex Interactions in Atmosphere-Ocean Models	Oliver Buehler, Michael McIntyre
MS6L_11152 (page 348)	Anisotropic Large - Scale Turbulence on Giant Planets and in the Ocean	B. Galperin, S. Sukoriansky, H. Nakano
MS6S_11336 (page 350)	Strong Vortex Insteractions in Quasi-Geostrophic Flows	Jean N. Reinaud, David G. Dritschel, Ross R. Bambrey
MS6L_11499 (page 352)	Turbulent Horizontal Convection and the Global Thermohaline Circulation of the Oceans	Ross Griffiths, Graham Hughes, Julia Mullarney
MS6L_11547 (page 354)	Instability of Gravity Driven Coastal Current in a Turntable Experiment	Thivolle-Cazat, Sommeria J.
MS6L_11585 (page 356)	Intrusive Gravity Currents in a Stratified Ambient - novel Theoretical Results and Insights	Marius Ungarish
MS6S_11732 (page 358)	Irreversible Transition to a State with Higher Entropy Production in Oceanic General Circulation	Shinya Shimokawa, Hisashi Ozawa
MS6L_11829 (page 360)	Interactions of Planar Waves with a Baroclinic Vortex	Moulin Frederic, Flor Jan-Bert
MS6S_11942 (page 362)	A New Spectral Closure Model of Turbulent Flows with Stable Stratification and Its Application to Atmospheric SBLS	Semion Sukoriansky, Boris Galperin, Veniamin Perov
MS6S_12035 (page 364)	Roll Vortices in the Atmospheric Boundary Layer	Dieter Etling, Micha Gryschka
MS6L_12104 (page 366)	Spontaneous Generation of Inertia-gravity Waves by Balanced Motion	Jacques Vanneste
MS6S_12140 (page 368)	The Energy Cycle of the Tropical Madden-Julian Oscillations seen through Wavelets	Jun-Ichi Yano
MS6L_12157 (page 370)	Wave Capture and Wave-vortex Duality	Oliver Buhler, Michael E McIntyre
MS6S_12169 (page 371)	A New Theory For Convection In Rapidly Rotating Spherical Systems	Keke Zhang, Xinhao Liao

MS6S_12194 (page 373)	Vortex-based Models of Quasigeostrophic Turbulence	Takeshi Miyazaki, Qin Wei, Yingtai Li
MS6L_12210 (page 375)	Generation of Internal Waves in the Deep Ocean by Barotropic Tides	Jonas Nycander
MS6L_12294 (page 377)	Instability of Corotating Vertical Vortices in a Stratifield Fluid : Why Strongly Stratifield Turbulence is not Similar to 2D Turbulence	Pantxika Otheguy, Paul Billant, Jean-Marc Chomaz
MS6S_12408 (page 379)	Laboratory and Numerical Modelling of Exchange Flows	Kanarska Yuliya, Maderich Vladimir
MS6S_12463 (page 381)	Wave---mean Flow Interaction in Coupled Atmosphere--ice--ocean Systems	Alastair D. Jenkins
MS6L_12494 (page 384)	Multiple Jet Formation in a Convectively Driven Flow on a Beta - plane	Peter L. Read, Yasuhiro H. Yamazaki, Stephen R. Lewis, Paul D. Williams, Joel Sommeria, Henri Didelle
MS6S_12601 (page 386)	Intermittency in Stratified Turbulence Produced by Breaking Internal Gravity Waves	Pascale Bouruet-Aubertot, Joel Sommeria, Christophe Koudella
MS6S_12722 (page 388)	Measurements of the Influence of Ocean Surface Kinematics on Air-sea Heat Fluxes	Farbice Veron, W. Ken Melville
MS6S_12776 (page 390)	Linear Waves and Baroclinic Instability in an Inhomogeneous-density Layered Primitive-equation Ocean Model	Francisco J. Beron-Vera, M. J. Olascoaga, J. Zavala-Garay
MS6S_13017 (page 392)	Simulation of Sea Surface Temperature Trends Under Severe Wind Forcing With a Full Atmosphere-Ocean Coupled Model	Arnaldo Longhetto, Roberto Purini, Claudio Cassardo, Nicola Loglisci, Silvia Ferrarese, Renzo Richiardone

Pre-nominated Session FSM1
Acoustics

Co-Chair(s): **T. Geers (USA)**
N. Peake (UK)

Paper ID	Title	Authors
FSM1S_10294 (page 394)	Dissipative Effects on Propagation of the Acoustic Solitary Waves	N. Sugimoto, M. Masuda, K. Yamashita, H. Horimoto
FSM1L_10907 (page 396)	An Empirical 'lower bound' on Free-Shear-Flow Noise	Jonathan B. Freund, Mingjun Wei
FSM1L_11249 (page 398)	Special Short Wave Finite Elements for Flow Acoustics	Jeremy Astley, Pablo Gamallo
FSM1S_11337 (page 400)	Wave Propagation in and Sound Emission from a Sandwich Plate Under Heavy Fluid Loading	Sergey Sorokin
FSM1L_11373 (page 402)	3-D Structural Acoustics Modeling with HP-Adaptive Finite Elements	David S. Burnett, Mario Zampolli
FSM1S_11508 (page 404)	The Low - Temperature Acoustical and Thermal Properties of Materials due to the Dynamics of Linear Topological Defects	Dmitry V. Churochkin, Vladimir Osipov
FSM1L_11561 (page 406)	Shock Leakage Through a Vortex-Laden Mixing Layer Causing Jet Screech	Takao Suzuki, Sanjiva K. Lele
FSM1S_11896 (page 408)	Transmission of Elastic Waves and Localised Modes in Composite Structures	Natasha V. Movchan, Alexander B. Movchan
FSM1S_11973 (page 409)	Arbitrarily Wide-Angle Wave Equations and their Applications to Unbounded Domain Modeling and Subsurface Imaging	Murthy N. Guddati, A. Homayoun Heidari, Keng-Wit Lim
FSM1S_12149 (page 411)	Ultrasonic Travel - Time Technique for Diagnostic of Grid - Generated Turbulence	Tatiana A. Andreeva, William W. Durgin

FSM1S_12180 (page 413)	The Acoustics of Two - Dimensional Leapfrogging Vortex Interactions	Jeff D. Eldredge
FSM1L_12477 (page 415)	A Theoretical Model for Resonances in Flow Past a Cavity	E. J. Kerschen, J. O. Alvarez, A. Tumin
FSM1L_12497 (page 417)	Structure of Sonic Booms in a Medium with Multiple Relaxation Modes	Paul W. Hammerton, M. E. Johnson
FSM1S_12516 (page 419)	Gas Oscillations in a Closed Tube at Resonance	Alexander Alexeev, Chaim Gutfinger
FSM1S_12527 (page 421)	The Effect of Viscosity on the Propagation of Acoustic Waves Through Fine Cylindrical Meshes	Iain D. J. Dupere, Ann P. Dowling, Tian J. Lu
FSM1S_12533 (page 423)	Modelling of Hydrophone Based on a DFB Fiber Laser	Lars V. Hansen, F. Kullander
FSM1S_12555 (page 425)	Numerical Analysis of the Texture and Acousto-Elastic Properties of Prestressed Polycrytalline Aggregate	Jozef Lewandowski
FSM1S_12586 (page 427)	Measurements and Calculations Related to Curve Squealing in the Railway System	Rossano Stefanelli, Juerg Dual, Eric Cataldi-Spinola, Mathias Goetsch
FSM1S_12643 (page 429)	Acoustic Wave Propagation Through a Random Array of Dislocations	Agnes Maurel, Jean F. Mercier, Fernando Lund
FSM1S_12691 (page 431)	Distributed Parameter Control of a 2D Acoustic Helmholtz Problem on a Halfspace	George Biros, Seong-Won Na, Loukas F. Kallivokas
FSM1S_12717 (page 433)	Frequency- and Directionality- Continuation Schemes for Scatterer Shape Detection in Acoustics	Seong-Won Na, Loukas F. Kallivokas

Pre-nominated Session FSM2
Chaos in fluid and solid mechanics

Co-Chair(s): **I. Mezic (USA)**
G. Rega (Italy)

Paper ID	Title	Authors
FSM2S_10070 (page 435)	Nonlinear Dynamics of Parametrical Excited Two - Degrees - of - Freedom Flexible Pendulum	Amir A. Zadpoor
FSM2L_10252 (page 437)	Nonlinear Dynamics of High - Speed Milling	Gabor Stepan, Tamas Insperger, Robert Szalai
FSM2L_10499 (page 439)	The Effect of Smoothing on Bifurcation and Chaos Computations in Non - Smooth Mechanics	John S. Hogan
FSM2S_10823 (page 441)	Attractor and Pattern Control in Nonlinear Media by Localized Defects	Sergey Vakulenko, Bogdan Kazmierczak
FSM2L_11183 (page 443)	A Set - Valued Force Law For Spatial Coulomb - Contensou Friction	Remco I. Leine, Christoph Glocker
FSM2S_11241 (page 445)	Chaotic Attractors with Long Regular Sequences	Ugo Galvanetto
FSM2S_11302 (page 447)	Reduction of Multidimensional Flow to Low Dimensional Map for Piecewise Smooth System Experiencing Chaos	Ekaterina E. Pavlovskaia, Marian Wiercigroch
FSM2L_11363 (page 449)	Numerical Detection and Continuation of Sliding Bifurcations in a Dry - Friction Oscillator	M. di Bernardo, Piotr Kowalczyk, P. Piiroinen
FSM2S_11416 (page 451)	On Generating Chaotic Dynamics in Nonlinear Vibrating Systems	Elzbieta Tyrkiel
FSM2S_11512 (page 453)	Chaos in Wave Front Propagation in Heterogeneous Media	Anatoly V. Chigarev, Yuri V. Chigarev, Aleksander Brostovich, Larysa N. Bialiatskaya

FSM2L_11535 (page 455)	Low - Dimensional Chaotic Dynamics in Dripping Faucets	Ken Kiyono, Tomoo Katsuyama
FSM2S_12014 (page 457)	Influence of Remaining Chaos on Convergence of Solutions in Time Delayed Feedback Controlled Duffing System	Kohei Yamasue, Takashi Hikihara
FSM2L_12129 (page 459)	A Dynamical Systems Analysis of the Overturning of Rigid Blocks	Stefano Lenci, Giuseppe Rega
FSM2S_12468 (page 461)	On the Nonlinear Dynamics of Multicomponent Dynamical Systems	Igor Mezic
FSM2S_12482 (page 463)	Short-Time Dynamical Behavior of Fluids at the Atomic Scale	Theodoros E. Karakasidis, Antonios B. Liakopoulos
FSM2L_12674 (page 465)	Nonlinear Dynamics of Axially Moving Viscoelastic Strings Based on Translating Eigenfunctions	Li-Qun Chen, Neng-Hui Zhang
FSM2L_12927 (page 467)	Nonlinear Oscillators with Time Delays	Zbigniew Peradzynski, Jacek Kurzyna
FSM2L_12972 (page 469)	Non - Linear Oscillator Under Random Renewal - Driven Trains of Impulses	Radoslaw Iwankiewicz, Matilde R. Sotera

Pre-nominated Session FSM3
Continuum mechanics

Co-Chair(s): **K.R. Rajagopal (USA)**
G. Saccomandi (Italy)

Paper ID	Title	Authors
FSM3S_11096 (page 471)	Pseudo - Rigid Bodies Viewed as Globally Constrained Continua	James Casey
FSM3S_11140 (page 473)	Constitutive Equations of Mesoelastic Deformation	Lev Steinberg
FSM3L_11227 (page 475)	Nonlinear Response of Magnetoelastic Solids	Luis A. Dorfmann, Ray W. Ogden
FSM3S_11247 (page 477)	Application of Continuum Mechanics in the Textile Fabrics	Bohuslav Striz, Brigita Kolcavova Sirkova, Jaroslava Richterova
FSM3L_11347 (page 479)	Generalized Continuum Mechanics: Three Paths	Gerard A. Maugin
FSM3L_11515 (page 481)	Deformation of Solder Joints Under Current Stressing: Experimental Measurement and Numerical Simulation	Hua Ye, Cemal Basaran, Douglas C. Hopkins, Darrel Frear
FSM3S_11638 (page 483)	Viscoelastic Fluid Flows in a Falling Cylinder Viscometer and the Evaluation of Shear Viscosity	Victor M. Tigoiu
FSM3S_11642 (page 485)	Fundamental Inequalities for the Bounds on the Effective Transport Coefficients of Two--Phase Media	Stanislaw Tokarzewski, Jozef Joachim Telega, J. Gilewicz
FSM3S_11704 (page 487)	On the Source of Singularities in Mechanics	Glenn B. Sinclair
FSM3L_11818 (page 490)	Extended Polar Decompositions for Finite Plane Strain	Michael A. Hayes, Philippe S. Boulanger
FSM3S_11840 (page 492)	Nonlinear Waves in Elastic Solids	Wlodzimierz Domanski
FSM3L_11950 (page 494)	Explicit Secular Equations for Surface and Interface Waves in Anisotropic Solids	Michel Destrade
FSM3S_12392 (page 496)	Views on Material Forces in Multiplicative Elastoplasticity	A. Menzel, P. Steinmann
FSM3S_12406 (page 498)	Affine Symmetry in Mechanics of Discrete and Continuous Systems	Jan J. Slawianowski

Pre-nominated Session FSM4
Fluid-structure interaction

Co-Chair(s): **J. Grue (Norway)**
M.P. Paidoussis (Canada)

Paper ID	Title	Authors
FSM4S_10520 (page 500)	Coupled Frequancies of a Fluid-Structure Interaction Cylindrical System	Elena Gavrilova
FSM4S_10826 (page 502)	Fluid Structure Interaction in Multiphase Mixing Vessel	Matej Vesenjak, Zoran Ren, Matjaz Hribersek
FSM4S_10911 (page 504)	Piston Impact Onto the Boundary of Two - Layer Fluid	Tatiana I. Khabakhpasheva
FSM4L_11078 (page 506)	Nonlinear Dynamics of Pinned-Pinned Cylinders in Axial Flow	Michael P. Paidoussis, Yahya Modarres-Sadeghi, Christian Semler
FSM4S_11668 (page 508)	Interaction of Oscillating Flow with a Pair of Side - By - Side Square Cylinders	Ming-Jyh Chern, Ji-Zen Lu
FSM4L_11736 (page 510)	The Hydroelastic Destabilisation of Finite Compliant Panels	Anthony D. Lucey
FSM4L_11758 (page 512)	Water - Surface Dynamics Among a Periodic Array of Floating Bodies Subject to Regular Incident Waves	Hiroshi Kagemoto, Motohiko Murai
FSM4L_11801 (page 514)	The Mixing Layer Instability of Wind Over a Flexible Crop Canopy	Charlotte Py, Emmanuel de Langre, Bruno Moulia
FSM4S_11833 (page 516)	An Updated Arbitrary - Lagrangian - Eulerian Description in Continuum Mechanics and Its Application to Nonlinear Fluid-Structure Interaction Dynamics	J. T. Xing, W. G. Price
FSM4S_11912 (page 518)	Slender Body Theory Approach to Nonlinear Ship Motions	Edwin J. Kreuzer, Wolfgang M. Sichermann
FSM4S_11986 (page 520)	Inverse Magnus Force in Free Molecular Flow	Andrzej Herczynski, Patrick Weidman
FSM4L_12175 (page 522)	Fast Multipole Algorithm for Wave Response Analysis of Floating Structures	Tomoaki Utsunomiya, Eiichi Watanabe
FSM4S_12521 (page 524)	Effect of an Oscillating Cylinder on a Neighbouring Cylinder Wake	Y. Yang, Y. Zhou, Z. Guo
FSM4L_12557 (page 526)	Disturbed-Laminar Flow Over an Oscillating Cylinder	John R. Chaplin, Dominique Mouaze
FSM4L_12956 (page 528)	PIV Experiments on Vortex Induced Vibrating Cylinders at High Reynolds Numbers	John Grue, Odin Gramstad, Arnaud Sanchis
FSM4S_13050 (page 530)	Influence of the Circular Cylinder Cross-Sectrion Variation on the Near Wake Behaviour	Oualli Hamid, Hanchi Samir, Boubdallah Ahcene, Radomir Askovic

Pre-nominated Session FSM5
Mechanics of foams and cellular materials

Co-Chair(s): **S. Hilgenfeldt (Netherlands)**
D.L. Weaire (Ireland)

Paper ID	Title	Authors
FSM5L_10597 (page 532)	Bubble Shapes in Foams: The Importance of Being Isotropic	Sascha Hilgenfeldt, Andrew M. Kraynik, Douglas A. Reinelt, John M. Sullivan
FSM5L_11095 (page 533)	Mechanics of Bidimensional Liquid Foams	Benjamin Dollet, Francois Graner, Catherine Quilliet, Miguel Aubouy, Florence Elias

FSM5L_11240 (page 535)	Average N-hedra as Descriptors of 3D Network Cells	Martin E. Glicksman
FSM5S_11292 (page 537)	Modelling the Round-off and the Tensile/Compressive Failure Behaviour of Plant and Vegetable Tissues	H. X. Zhu
FSM5L_11605 (page 539)	On the Crushing Response of Open Cell Foams	Lixin Gong, Stelios Kyriakides
FSM5L_11663 (page 541)	A Statistical Mechanics Theory of Random Honeycomb and Open - Cell Foam Structures	Alfonso H. W. Ngan
FSM5L_12052 (page 543)	Dissipation in 2D Foam Flow	Isabelle Cantat, Renaud Delannay
FSM5L_12212 (page 545)	Surfactant and Protein Foams : Differences in Drainage and Rheology	Arnaud Saint-Jalmes, Sebastien Marze, Dominique Langevin
FSM5L_12373 (page 546)	Determining Stress During Finger Propagation in 2D Foams	Adrian D. Staicu, Bas van Gelder, Sascha Hilgenfeldt
FSM5S_12395 (page 547)	Thermal Flow through Brazed Woven Screens	J. Tian, T.J. Lu, H.P. Hodson, D.T. Queheillalt, H.N.G. Wadley
FSM5L_12435 (page 549)	Drainage of Emulsion and Foam Films in Scheludko - Exerowa Cells	J. Coons, P. Halley, S. McGlashan, T. Tran - Cong
FSM5L_12578 (page 551)	Shear - Induced Normal Stress Differences in Aqueous Foams	Vincent Labiausse, Sylvie Cohen-Addad, Reinhard Hohler
FSM5L_12851 (page 553)	The Dispersion of Particles within Foams	S.J. Neethling, H.T. Lee, J.J. Cilliers
FSM5S_12986 (page 555)	Iinvestigation of Foam Development in Porous Media Using X-Ray Computed Tomography	Quoc P. Nguyen, Peter K. Currie, Pacelli L. J. Zitha
FSM5L_13033 (page 557)	Nucleation of Cracks in Two - Dimensional Periodic Cellular Material	Michael Ryvkin, Moshe Fuchs, Fabian Lipperman

Pre-nominated Session FSM6
Multiscale phenomena in mechanics

Co-Chair(s): **A. Carpinteri (Italy)**
C. Miehe (Germany)

Paper ID	Title	Authors
FSM6S_10399 (page 559)	Simulations of Micro - and Nano - Channel Flows by a Dissipative Particle Dynamics Method	Justyna Czerwinska, Nikolaus A. Adams
FSM6L_11224 (page 560)	Multi - Scaling Approach in the Mechanics of Disordered Materials	Alberto Carpinteri, Simone Puzzi
FSM6S_11237 (page 562)	Grad - Type Expansion About Nonequilibrium States for the Relaxion - Time Approximation of the Boltzmann - Peierls Equation	Zbigniew Banach, Wieslaw Larecki
FSM6S_11340 (page 564)	Two - Scale Simulations of Epitaxial Surfaces	Heike Emmerich, Christof Eck
FSM6L_11471 (page 566)	A Geometrical Theory of Discrete Dislocations in Lattices, with Applications to Dislocation Dynamics and Crystal Plasticity	M. P. Ariza, M. Ortiz
FSM6L_11476 (page 568)	Stress - Defect Interactions at Molecular / Continuum Scales	Mathieu Bouville, Krishna Garikipati, Michael Falk
FSM6L_11806 (page 570)	Deterministic Size Effect in the Strength of Cracked Quasi - Brittle Structures	B. L. Karihaloo, H. M. Abdalla, Q. Z. Xiao
FSM6L_11830 (page 572)	Multi - Scale Second - Order Computational Homogenization of Heterogeneous Materials	V. Kouznetsova, M. G. D. Geers, W. A. M. Brekelmans

FSM6L_11862 (page 574)	Jumping of a Spinning Spheroid	Yutaka Shimomura, Michal Branicki, Keith Moffatt
FSM6S_12040 (page 576)	Characteristics of Orientation and Grain - Size Distributions	Luca Placidi, Kolumban Hutter
FSM6S_12078 (page 578)	Numerical Homogenization of a Locally Hyperelastic Constitutive Law	Antoine Gloria, Claude Le Bris
FSM6L_12112 (page 580)	Multiscale Analyses of Granular Media at Finite Strains Based on Micro - Macro Transitions with Different Boundary Constraints	Joachim Dettmar, Christian Miehe
FSM6L_12113 (page 582)	Exploitation of Incremental Energy Minimization Rinciples in Computational Multiscale Analyses of Inelastic Solids	Christian Miehe
FSM6S_12118 (page 584)	Non - Convex Homogenization of Inelastic Composites with Interaction of Material and Structural Instabilities on Different Scales	Martin Becker, Christian Miehe
FSM6L_12334 (page 586)	Physical Modeling of Fracture Mechanics in Complex Materials	Fabrizio Cleri, Luciano Colombo, Pier G. Gabrielli, Mariella Ippolito, Alessandro Mattioni
FSM6S_12336 (page 588)	Analysis of a Variational Method Coupling Discrete and Continuum Machanics	Xavier Blanc, Claude Le Bris, Frederic Legoll

Pre-nominated Session FSM7
Education in mechanics

Co-Chair(s): **R. Engel (USA)**
B. Karihaloo (UK)

Paper ID	Title	Authors
FSM7L_10003 (page 590)	Toys and Games in Mechanics Education	Hassan Aref
FSM7L_10016 (page 592)	African Institute for Mathematical Sciences: a Capacity Building Initiative in Which IUTAM Has an Active Involvement	H. K. Moffatt
FSM7L_10226 (page 594)	On Mechanics/Engineering Science Education	Carl T. Herakovich
FSM7S_11724 (page 595)	Mechanics - a New Internet Tutor	Aleksandr Kositsyn
FSM7S_11765 (page 596)	Teaching Mechanics as an Engineering Science in China	Yilong Bai
FSM7S_11869 (page 598)	Education and Tutorial on Fluid Mechanics on the Basis of Computer Laboratory	Vasily P. Yaremchuk, Mikhail K. Ermakov, Sergei A. Nikitin, Vadim I. Polezhaev
FSM7S_12259 (page 600)	Education in Mechanics in Latvia Higher Schools	Vitauts Tamuzs, Janis Viba
FSM7L_12467 (page 602)	Multiimedia Fluid Mechanics: a Flexible Educational Tool for Teaching and Learning Fluid Mechanics	G. M. Homsy, K. S. Breuer
FSM7S_12488 (page 604)	Simulator, Nohguchi Bottle, of Soil Liquifaction for Education	Yasuaki Nohguchi
FSM7S_12603 (page 606)	Mechanics Education in Sweden	Anders Bostrom
FSM7L_12642 (page 608)	Rigid Body Dynamics: Student Misconceptions and Their Diagnosis	D. L. Evans, Gary L. Gray, Francesco Costanzo, Phillip Cornwell, Brain P. Self
FSM7L_12752 (page 610)	Web-Based Instructional Units for Teaching Mechanics	Kamal B. Rojiani, Rakesh K. Kapania, Yong Y. Kim, Jing Li

Pre-nominated Session FM1
Biological fluid dynamics

Co-Chair(s): **M. Gharib (USA)**
F. van de Vosse (Netherlands)

Paper ID	Title	Authors
FM1L_10132 (page 614)	Mechanics of the Bounding Flight Revisited	Takeshi Sugimoto
FM1S_10741 (page 616)	Deformation of Vesicles Flowing Through a Capillary	Victoria Vitkova, Maud Mader, Thomas Podgorski
FM1L_11013 (page 618)	How to Breathe in a Liquid-Filled Lung: Symmetry of Airway Reopening	Charles N. Baroud, Matthias Heil
FM1S_11187 (page 620)	Computational Exploration of Liver Acinus Microstructure	H. P. Rani, Tony W. H. Sheu, P. C. Liang
FM1L_11441 (page 622)	Bacterium Swimming Motion Close to a Wall	Tomonobu Goto, Kousou Nakata, Yukio Magariyama, Masaharu Nishimura
FM1L_11851 (page 624)	A CFD Study of the Effects of Physiological Vessel Wall Motion on Oxygen Transport in Coronary Arteries	Maheshwaran K. Kolandavel, Ernst-Torben Fruend, Erik M. Pedersen, Steffen Ringgaard, Peter G. Walker
FM1L_11900 (page 626)	In Vivo PIV Measurement in the Embryonic Chicken Heart	Peter Vennemann, Kenneth T. Kiger, Beerend P. Hierck, Nicolette T. C. Ursem, Timo L. M. Ten Hagen, Jerry Westerweel
FM1S_11908 (page 628)	A Model of Plankton Dynamics Coupled with a LES of the Surface Mixed Layer	David M. Lewis
FM1S_11943 (page 630)	Self - Propulsion of an Oscillatory Wing	Adrian S. Carabineanu
FM1L_12063 (page 632)	Bioirrigation in Marine Sediments: Ecological Conclusions from Numerical Modelling	Oleksiy S. Galaktionov, Filip J. R. Meysman, Jack J. Middelburg
FM1L_12124 (page 634)	Direct Numerical Simulation of Red Blood Cell Flow and Aggregation	Cyrus K. Aidun, E-Jiang Ding
FM1L_12295 (page 636)	Three - Dimensional Airway Reopening - Finite - Reynolds - Number Effects	Andrew L. Hazel, Matthias Heil
FM1L_12400 (page 638)	Cell Permeabilisation and Transport Focused Around Oscillating Microbubbles	Philippe Marmottant, Sascha Hilgenfeldt, Michel Versluis, Han Gardeniers, Albert van den Berg, Detlef Lohse
FM1S_12409 (page 640)	Computational Model of Selected Transport Processes in an Infant Incubator	Maciej K. Ginalski, Andrzej J. Nowak
FM1L_12423 (page 642)	Red Blood Cell Dynamics, Deformation and Rheology via Microfluidic Experiments	Manouk Abkarian, Magalie Faivre, Annie Viallat, Howard A. Stone
FM1L_12522 (page 644)	Flow in an Integrated Model of Heart and Aorta	Masanori Nakamura, Shigeo Wada, Suguru Yokosawa, Haruo Isoda, Ken-Ichi Tsubota, Takami Yamaguchi
FM1S_12655 (page 646)	In Vivo Visualization of the Water Refilling Process in Xylem Vessels Using Synchrotron X - Ray Micro - Imaging	Yang - Min Kim, Sang - Joon Lee
FM1L_12784 (page 648)	On the Issue of Optimal Trans - Mitral Flow	M. Gharib, E. Rambod, A. Kheradvar, D. Sahn

Pre-nominated Session FM2
Boundary layers

Co-Chair(s): **P.W. Duck (UK)**
A. Kluwick (Austria)

Paper ID	Title	Authors
FM2L_10103 (page 651)	The Development (and Suppression) of Very Short-Scale Instabilities in Buoyant Boundary Layers	James P. Denier, Peter W. Duck, Jian Li
FM2L_10275 (page 653)	3D Distributed Boundary - Layer Receptivity to Non - Stationary Free - Stream Vortices in Presence of Surface Roughness	V. I. Borodulin, A. A. Fedenkova, A. V. Ivanov, Y. S. Kachanov, V. Y. Komarova
FM2S_10948 (page 655)	Extending the Generalized Logarithmic Law to the Wall	Matthias M. Buschmann, Mohamed Gad-el-Hak
FM2S_11017 (page 657)	Sub - and Supersonic Shapes without Separation and Cavitation	Ihor Nesteruk
FM2L_11083 (page 659)	Non - Unique Quasi - Equilibrium Turbulent Boundary Layers	Bernhard Scheichl, Alfred Kluwick
FM2L_11084 (page 661)	Near Critical Unsteady Three - Dimensional Triple Deck Flows	Stefan Braun, Alfred Kluwick
FM2S_11210 (page 663)	Long Layers Exhibiting Local Jumps, in Industrial and Biomedical Applications	Frank T. Smith
FM2S_11339 (page 664)	Secondary Instability of Stationary Vortex Packets in a Swept Wing Boundary Layer	Valery G. Chernoray, Alexander V. Dovgal, Victor V. Kozlov, Lennart Loefdahl
FM2L_11397 (page 666)	Discontinuous Solutions of the Boundary - Layer Equations	Anatoly I. Ruban
FM2S_11479 (page 668)	Boundary Layer Development in Unsteady Flows	Andrei Camyshev, Andrei Kolyshkin, Inta Volodko
FM2S_11780 (page 670)	New Numerical Method for Complex Interacting Flows	Vladimir B. Zametaev, Marina A. Kravtsova
FM2L_11887 (page 672)	Why do Dolphins Have Cutaneous Ridges?	Peter W. Carpenter, Reza Ali
FM2S_11984 (page 674)	Two - Fluid Jets and Wakes	Patrick Weidman, Andrzej Herczynski, Georgy Burde
FM2S_12030 (page 676)	The Trailing Edge Problem for Mixed Convection Flow Past a Horizontal Plate	Herbert Steinrueck, Ljubomir Savic
FM2S_12062 (page 678)	Experimental and Theoretical Study of Heated Coanda Jet	Tomas Vit, Frantisek Marsik
FM2L_12241 (page 680)	A Combined Numerical and Asymptotic Approach to Boundary Layer Receptivity Problems	Matthew R. Turner, P. W. Hammerton
FM2L_12320 (page 682)	Flow Along a Long Thin Cylinder	Owen. R. Tutty, A. T. Parsons, W. G. Price
FM2L_12631 (page 684)	Aspects of the Laminar-Turbulent Transition in Axisymmetric Boundary Layers	N. Vinod, Rama Govindarajan

Pre-nominated Session FM3
Combustion and flames

Co-Chair(s): **N. Peters (Germany)**
P. Wolanski (Poland)

Paper ID	Title	Authors
FM3S_10367 (page 686)	Enhancement of the Impinging Diffusion Flame by Splash Plate	Ay Su, Ying-Chieh Liu

FM3S_10747 (page 688)	Exothermic Explosions in a Slab: a Case Study of Series Summation Technique	Oluwole D. Makinde
FM3L_10918 (page 690)	A Nearly 1-D Non - Premixed Flame Near Extinction. Cell Formation and the Effect of the Direction of Bulk Flow	David Lo Jacono, Paul Papas, Moshe Matalon, Peter A. Monkewitz
FM3S_11031 (page 692)	Simulation of Flame Propagation in a Tube with Obstacles	Aidarkhan Kaltayev, Zhomart Ualiev
FM3S_11888 (page 694)	Large Eddy Simulation of Piloted and Bluff - Body Diffusion Flame	Tim Broeckhoven, Sergey Smirnov, Chris Lacor, Eduardo Brizuela
FM3S_11914 (page 696)	Influence of the Subgrid Models on Combustion Modelling	Artur Tyliszczak, William P. Jones, Andrzej Boguslawski, Stanislaw Drobniak
FM3S_12199 (page 698)	Chemical Aspects of the Flameless Oxidation Applied for GasTurbine Combustor	Yeshayahou Levy, Valery Sherbaum, Vladimir Erenburg
FM3L_12348 (page 700)	Experimental and Numerical Investigation of a Flameless Oxidation Combustor	J. Melo, A. Yadav, J. M. M. Sousa, M. Costa, P. J. Coelho, Y. Levy
FM3L_12745 (page 702)	Detonations of Hexane Vapor/Droplets - Air Mixtures	Stanislaw Cudzilo, A. Kuhl, P. Wolanski
FM3S_12843 (page 704)	Simulation of Ram Accelerator with PETN Layer	Arkadiusz Kobiera, Piotr Wolanski
FM3S_12911 (page 706)	Simple Model of a Detonating Gas for use with the Direct Monte - Carlo Simulation Technique	Zbigniew Walenta, Andrzej Teodorczyk, Waldemar Witkowski

Pre-nominated Session FM4
Complex and smart fluids

Co-Chair(s): **B. Khusid (USA)**
A. Yarin (Israel)

Paper ID	Title	Authors
FM4L_10140 (page 708)	Capillary Microfluidics for Viscoelastic Fluids	Konstantin G.Kornev, Gerardo Callegari, Alexander V.Neimark
FM4L_10753 (page 710)	Field-Induced Dielectrophoresis and Phase Separation in Suspention	Dawn J. Bennett, Boris Khusid, Conrad D. James, Paul C. Galambos, Murat Okandan, David Jacqmin, Anil Kumar, Zhiyong Qiu, Andreas Acrivos
FM4L_10932 (page 712)	Electrospinning of Nanofibers from Polymer Solutions	A. L. Yarin, E. Zussman
FM4L_11165 (page 714)	The Giant Electrorheological Effect in Suspensions of Nanoparticles	Ping Sheng, Weijia Wen, Xianxiang Huang, Shihe Yang, Kunquan Lu
FM4S_11184 (page 716)	Electrospinning of Liquid Jets	Slawomir Blonski, Anna Blasinska, Tomasz A. Kowalewski
FM4L_11209 (page 718)	Modeling DNA Separations in Self-Assembled Magnetic Arrays: Comparison of Theory and Experiment	Kevin D. Dorfman, Nicolas Minc, Claus Fuetterer, Jean-Louis Viovy
FM4S_11603 (page 720)	Contact Angle Dynamics of Droplets Impacting on Flat Substrates	Ilker S. Bayer, Constantine M. Megaridis
FM4S_11648 (page 722)	Dissipation Features at Nonlinear Pulsations of Bubbles in Viscoelastic Fluids	Semyon P. Levitsky, Jehuda Haddad
FM4L_11954 (page 724)	Break up of Polymer Solution Drop Impacting a Small Target	Aleksey Rozhkov, Bernard Prunet-Foch, Michele Vignes-Adler
FM4L_11982 (page 726)	Ferrohydrodynamic Hele-Shaw Cell Flows and Instabilities with Simultaneous DC Axial and In-Plane Rotating Magnetic Fields	Scott E. Rhodes, Juan A. Perez, Shihab M. Elborai, Se-Hee Lee, Markus Zahn

FM4L_12254 (page 728)	Spray Impact on Solid Walls of Non - Newtonian Fluids, Including Yield Stress and Thixotropic Behavior	Daniel A. Weiss, Annett Reinl, David M. Binding
FM4S_12319 (page 730)	Nanowires Assembly Using Microfluidic: an Experimental Investigation	Wael Salalha, Eyal Zussman
FM4L_12437 (page 732)	Particle Manipulation in Microfluidics: the Role of Dielectrophoresis, Electrohydrodynamics and AC Electrokinetics	Antonio Castellanos, Antonio Ramos, Antonio Gonzalez, Nicolas G. Green, Hywel Morgan
FM4S_12894 (page 734)	Non - Newtonian Effects of Ink - Jet Printed Droplets	Paul C. Duineveld, J. F. Dijksman, H. Huang
FM4S_12910 (page 736)	Conditions for Creating Thin Liquid Layers at the Contact Surface of Two Other Liquids	Agnieszka Slowicka, Zbigniew A. Walenta

Pre-nominated Session FM5
Compressible flow

Co-Chair(s): **H. Hornung (USA)**

Paper ID	Title	Authors
FM5L_10531 (page 738)	Hysteresis - Related Phenomena in Shock Wave Reflection	Mikhail Ivanov, Dmitry Khotyanovsky, Alexey Kudryavtsev, Stanislav Nikifirov, Anatoly Trotsyuk
FM5L_10789 (page 740)	Nonclassical Dynamics of Laminar Dense Gas Boundary Layers	Mats Kinell, Alfred Kluwick
FM5S_10945 (page 742)	Analytical Models for Shocks in Compressible Flow	Helmut Sobieczky
FM5S_10984 (page 744)	LDA Investigation of a Transonic Bump Flow	Holger Babinsky, Sebastien Prioris
FM5L_11049 (page 746)	Unsteady Drag Force Measurements of Shock Loaded Bodies Suspended in a Vertical Shock Tube	Kazuyoshi Takayama, Mingyu Sun, Koji Tamai, Tsutomu Saito, Hiroyuki Tanno, Joseph Falcovitz
FM5L_11072 (page 748)	Shock Wave Reflection in a Non - Circular Inlet	Beric W. Skews, Jithin A. Mohan, Nankishore Menon
FM5S_11229 (page 750)	Turbulent Effects in Type4 Shock Interactions	Josef Ballmann, F. Bramkamp, B. U. Reinartz, J. van Keuk
FM5S_11560 (page 752)	Numerical Optimization of 2D Scramjet Inlets	Susumu Hasegawa, Doyle Knight
FM5L_11730 (page 754)	The Mach Reflection of Weak Shocks	John K. Hunter, Allen M. Tesdall
FM5S_11864 (page 756)	Effect of Surface Roughness on Mach Reflection	Susumu Kobayashi, Takashi Adachi, Klaus Debatin, Torsten Schenkel, Herbert Oertel, Jr.
FM5S_12066 (page 758)	On the Theory for Subsonic, Transonic and Supersonic Flows in Water with Supercavitation	Vladimir Serebryakov, Guenter H. Schnerr
FM5S_12219 (page 760)	Interaction of Supersonic Flows in an Ejector	Vaclav Dvorak, Pavel Safarik
FM5L_12997 (page 762)	Shock Wave - Boundary Layer Interaction Control by Streamwise Vortices	Piotr Doerffer, Ryszard Szwaba
FM5S_13016 (page 764)	Correlation of Nearfield Pressure with Mixing Layer Velocity in a Supersonic Jet	Francois Coiffet, Joel Delville, Carine Fourment, Peter Jordan, Patrick Braud

Pre-nominated Session FM6
Computational fluid dynamics

Co-Chair(s): **L. Kleiser (Switzerland)**
W. Schroeder (Germany)

Paper ID	Title	Authors
FM6L_10163 (page 766)	Non - Reflecting Boundary Condition for Direct Aeroacoustic Computation	X. M. Li, Randolph C. K. Leung, Ronald M. C. So
FM6S_10857 (page 768)	Treesph Simulations of Choked Flow Systems Using Smoothed Particle Hydrodynamics	Jaime Klapp, Leonardo Di G Sigalotti, Eloy, Gonzalo
FM6S_10921 (page 770)	Poloidal - Toroidal Decomposition in Cylindrical von Karman Flow	Piotr Boronski, Laurette Tuckerman
FM6L_11348 (page 772)	On Inflow Boundary Conditions for Large Eddy Simulation of Turbulent Swirling Jets	Manuel Garcia - Villalba, Jochen Froehlich, Wolfgang Rodi
FM6S_11456 (page 774)	Numerical Simulation of the Flow over a Backward - Facing Step in a Beowulf - Class Cluster	Rubens Campregher, Aristeu da Silveira Neto, Wellington Marinho, Sergio Said Mansur
FM6S_11485 (page 776)	Development and Paractical Application of WENO Schemes for Compressible Fluid Flow Computations	Alexey N. Kudryavtsev, Dmitry V. Khotyanovsky
FM6S_11569 (page 778)	Numerical Analysis and Design Optimization of Lateral Jet Controlled Missile	Jae-Woo Lee, Byung-Young Min, Yung-Hwan Byun, Changjin Lee
FM6S_11578 (page 785)	Numerical Prediction of Energy Dissipation in Condensing	Tadeusz Chmielniak, Wlodzimierz Wroblewski, Slawomir Dykas
FM6L_11602 (page 787)	A Pressure - Correction Method for All Mach Numbers	Krista Nerinckx, Jan Vierendeels, Erik Dick
FM6S_11702 (page 789)	Numerical Computation of Compressible Viscous Flow Through a Male Rotor - Housing Gap of Screw Compressors	Jan Vimmr
FM6S_11763 (page 791)	Fast Numerical Method for the Boltzmann Equation on Nonumiform Grids	Alexei Heintz, Piotr Kowalczyk
FM6S_11937 (page 793)	Computation of Viscous Vortices with Fully Meshless Method	Lorena A. Barba, A. Leonard
FM6S_12076 (page 795)	Dirichlet/Dirichlet and Neumann/Neumann Parallel Non-Overlapping Domain Decomposition Method	Slawomir Kubacki, Andrzej Boguslawski
FM6S_12337 (page 797)	CFD Methods in Industrial Applications Vehicle External Aerodynamics and Aerodynamic Interaction of Moving Vehicles	Milan Schuster
FM6S_12356 (page 799)	A Computational Model for the Si/C/N Nanopowder	Mohamed Amara, Djamila Hourlier, Mohammed El Ganaoui
FM6S_12510 (page 802)	Numerical Error Evaluation for Tip Clearance Flow Calculations in Centrifugal Compressor	Guillaume Dufour, X. Carbonneau, P. Arbez, J. B. Cazalbou, P. Chassaing
FM6S_12565 (page 804)	Simulation of a Viscous Flow Past a Three Dimensional Obstacle Using Vortex Particles	Piotr Duszynski, Marta Pocwierz, Andrzej Styczek, Jacek Szumbarski
FM6L_12583 (page 806)	Multiscale Simulations Using Particles	Michael Bergdorff, Georges - Henri Cottet, Petros Koumoutsakos
FM6S_12618 (page 808)	Investigation of WENO Scheme for 3D Unstructured Grids	Jerzy Majewski, Robert Wieteska
FM6S_12985 (page 810)	Numerical Study of the Dynamics of Coalescence of Two Bubbles of Air in a Water Column at Rest	Jean M. Martinez, Xavier Chesneau, Belkacem Zeghmati
FM6L_13030 (page 812)	Commutator - Errors in Large - Eddy Simulation of Turbulent Flow	Bernard J. Geurts, Fedderik van der Bos, Darryl D. Holm
FM6L_13051 (page 814)	Three - Dimensional Rayleigh - Benard Instability in a Supercritical Fluid by Direct Numerical Simulation	Gilbert Accary, Isabelle Raspo, Patrick Bontoux, Bernard Zappoli

Pre-nominated Session FM7
Convective phenomena

Co-Chair(s): **G. de Vahl Davis (Australia)**
K. Zhang (UK)

Paper ID	Title	Authors
FM7L_10306 (page 816)	Cellular Compressible Magnetoconvection: a Machanism for Magnetic-Field Amplification and Structuring	Alexander V. Getling, Wolfgang Dobler
FM7S_10438 (page 818)	Scaling Laws for Thermal Convections	Martin P. King, M. Wilson
FM7S_10538 (page 820)	On Features of Magnetic Convection in Ferrofluid	Ekaterina N. Beresneva, Aleksandra A. Bozhko, Gennady Putin
FM7S_10914 (page 822)	Multiplicity of Patterns in Cylindrical Convection	Katarzyna Boronska, Laurette Tuckerman
FM7L_11053 (page 824)	Large - Scale Semi - Organized Structures in Geophysical Turbulent Convection	Tov Elperin, Nathan Kleeorin, Igor Rogachevskii, Sergej Zilitinkevich
FM7S_11160 (page 826)	Natural Convection for Anomalous Density Variation of Water - Numerical Benchmark	Tomasz Michalek, Tomasz A. Kowalewski, Bozidar Sarler
FM7S_11251 (page 828)	3D Flow Transition Behind a Heated Cylinder	Maosheng Ren, Camilo C.M. Rindt, Anton A. van Steenhoven
FM7L_11440 (page 830)	Experimental Studies of Planetary Core Convection and Dynamo Processes	Jonathan M. Aurnou
FM7S_11673 (page 832)	Penetrative Convection in Stratified Fluids: Velocity Measurements by Image Analysis	Antonio Cenedese, Massimo Miozzi, Monica Moroni
FM7S_11905 (page 838)	Experimental and Numerical Studies of Convection Flow in a Cylindrical-Conical Fermenting Tank	Heiko Meironke, J. A. Szymczyk
FM7L_11972 (page 840)	Sea Convective Motions Driven by Random Buoyancy Inputs	Bouche Vanda
FM7L_12126 (page 842)	Thermochemical Convection in Two Superimposed Miscible Viscous Fluids	Michael Le Bars, Anne Davaille
FM7L_12168 (page 844)	Nonlinear Convective Patterns in Spherical Rayleigh - Benard Systems	Xinhao Liao, Keke Zhang
FM7L_12173 (page 846)	Visualization of the Flow Structure and Temperature Field in the Region of Mixed Convection	Elzbieta Fornalik, Wolfgang Leiner, Janusz S. Szmyd, Tomasz A. Kowalewski, Hiroyuki Ozoe
FM7L_12220 (page 848)	Large Eddy Simulation of Rayleigh - Benard Convection in an Infinite Fluid Layer	Anne Sergent, P. Joubert, P. Le Quere
FM7S_12267 (page 850)	The Influence of Translational Vibration of Circular Polarization on Fluid Convection Stability and Flow Patterns	Aleksander Kozlov, Igor Babushkin, Gennady Putin
FM7L_12344 (page 852)	Thermal Buoyancy Convection in Systems with Deformable Interfaces	Dmitriy V. Lyubimov, Nicolay I. Lobov, Tanyana P. Lyubimova, Nikita A. Ospennikov, Sergey V. Shklyaev
FM7S_12730 (page 854)	Convective Phenomena in Rotating Annuli Heated on Periphery	Vladimir V. Ris, Evgueni M. Smirnov, Alexander A. Smirnovskii
FM7S_12850 (page 856)	On the Rayleigh - Benard Problem in the Continuum Limit	Avshalom Manela, Itzchak Frankel
FM7S_13005 (page 858)	The Influence of Vibration on the Onset of Marangoni Convection in Horizontal Fluid Layer	S. M. Zenkovskaya, A. L. Shleykel, V. A. Novosiadliy
FM7S_13022 (page 860)	Air Convection in a Cubic Enclosure with Laterally Shifted Electric Coil without a Gravity Field.	Tomasz Bednarz, Toshio Tagawa, Masayuki Kaneda, Hiroyuki Ozoe, Janusz S. Szmyd

Pre-nominated Session FM8
Drops and bubbles

Co-Chair(s): **J. Eggers (UK)**
A. Prosperetti (USA)

Paper ID	Title	Authors
FM8S_10580 (page 862)	Method for Solving Nonlinear Problems on Unsteady Free - Boundary Flows	Yuriy A. Semenov
FM8S_11026 (page 864)	Bubble Wall Interaction and Bubble Pairs Motion Using Potential Flow Theory	M. Moctezuma, R. Zenit, R. Lima
FM8S_11250 (page 866)	Locomotion of a Viscous Drop, Induced by the Internal Secretion: Boundary Effects	Olga M. Lavrenteva, Dina Tsemakh, Avinoam Nir
FM8L_11289 (page 868)	Theoretical Studies of Flow - Induced Coalescence	L. Gary Leal, Fabio Baldessari, Marcos Borrell, Yosang Yoon
FM8S_11299 (page 870)	Occurrence of Micro - Bubbles During the Coalescence of Two Bubbles	Teruo Kumagai, Kazuyuki Yokota, Shingo Saida, Masaki Shimizu
FM8L_11317 (page 872)	Atomization of an Undulating Liquid Sheet	N. Bremond, C. Clanet, E. Villermaux
FM8L_11330 (page 874)	Evaporation - Driven Assembly of Colloidal Particles	Eric Lauga, Michael P. Brenner
FM8L_11411 (page 876)	High-frequency Linear Viscosity of Emulsions Composed of Two Viscoelastic Fluids	Jerzy Blawzdziewicz, Eligiusz Wajnryb
FM8S_11448 (page 878)	Bubble Formation in a Co - Flowing Air - Water Stream	A. Sevilla, J. M. Gordillo, C. Martinez - Bazan
FM8L_11462 (page 880)	Molecule Configurations in a Droplet Detachment Process of a Semdilute Xanthan Solutions	Christian Wagner, Andriy Kityk
FM8S_11614 (page 882)	Spreading and Retraction of Impacting Drops	Christophe Josserand, Stephane Zaleski
FM8S_11669 (page 884)	Main Factors Controlling the Emulsification Process under Turbulent Conditions. Experiment and Data Interpretation	Slavka S. Tcholakova, Nikolai D. Denkov, Ivan B. Ivanov, Thomas Danner
FM8S_11670 (page 886)	Water Mist Behavior as Flame Supressant	M. T. Parra, F. Castro, J. M .Villafruela, C. Mendez, M. A. Rodriguez
FM8L_11723 (page 888)	Numerical Simulation of Liquid - Gas Interfaces with Applications to Atomization	Thomas Boeck, Stephane Zaleski
FM8S_11855 (page 890)	Viscous Extensional Flow and Drop Break - Off Under Gravity	Ernest O. Tuck, Yvonne M. Stokes
FM8L_11911 (page 892)	Evolution of a Pair of Spherical Bubbles Rising Side by Side at Moderate Reynolds Number	Jacques Magnaudet, Dominique Legendre
FM8S_11979 (page 894)	On the Numerical Simulation of Two Phase Liquid - Vapor Phenomena	Damir Juric, Patrick Le Quere, Virginie Daru, Marie C. Duluc
FM8L_11999 (page 896)	Cavitation Inception on Micro-particles: a Self Propelled Particle Accelerator	Manish Arora, Claus-Dieter Ohl, Knud Aage Morch
FM8S_12106 (page 898)	Level - Set Simulations of Shear Flow with Inertia Pas a Droplet Adhering to a Wall with Moving Contact Lines	Peter D. M. Spelt
FM8S_12163 (page 900)	Modelling Surface Tension Using a Ghost Fluid Technique within a Volume of Fluid Formulation	Marianne M. Francois, Douglas B. Kothe, Sharen J. Cummins
FM8S_12190 (page 902)	Dynamics of Bubble Supercompression in Organic Liquids	Robert I. Nigmatulin, Raisa Kh. Bolotnova, Nailya K. Vakhitova, Andrei S. Topolnikov
FM8S_12311 (page 904)	Hydrodynamics of Gas Bubbling through Organic Liquids	Ryszard Pohorecki, Wladyslaw Moniuk, Pawel Bielski

FM8S_12329 (page 906)	Surfactant Effects on Buoyancy - Driven Coalescence of Spherical Drops	Michael A. Rother, Alexander Z. Zinchenko, Robert H. Davis
FM8S_12388 (page 908)	Static Shapes of Levitating Viscous Drops	Laurent Duchemin, Ulrich Lange, John Lister
FM8L_12429 (page 910)	A Long-wavelength Model of Viscous Entrainment	Wendy W. Zhang
FM8S_12547 (page 912)	Entrainment of Air Bubbles During Strong Vorticity - Free - Surface Interaction	Alessandro Iafrati, Emilio F. Campana, Ulderico P. Bulgarelli
FM8S_12548 (page 914)	Spreading of Charged Microdroplets	Santiago I. Betelu, Marco A. Fontelos
FM8S_12596 (page 916)	Multiple Bubbles Dynamics Using Level Set Indirect Boundary Element Method	C. Wang, Fong Siew Wan, Khoo Boo Cheong, Hung Kin Chew
FM8L_12741 (page 918)	Low - Reynolds - Number Motion of a Drop Beween Two Parallel Plane Walls	Andrew J. Griggs, Alexander Z. Zinchenko, Robert H. Davis
FM8S_12873 (page 920)	Thermodynamic Parameters of Vapour Bubble Growth by Image Analysis	A. Zachara, J. Pakleza, S. Blonski, R. Trzcinski, T.A. Kowalewski
FM8L_13025 (page 922)	Singular Droplets	Daniel Bonn, Salima Rafai, Arezki Boudaoud

Pre-nominated Session FM9
Environmental fluid dynamics

Co-Chair(s): **H.E. Huppert (UK)**
R. Narasimha (India)

Paper ID	Title	Authors
FM9L_10366 (page 924)	The Growth and Structure of Double - Diffusive Cells Adjacent to a Side - Wall in a Salt - Stratified Enviroment	O. M. Phillips, L. Malki - Epshtein, H. E. Huppert
FM9S_10467 (page 926)	Flow and Dispersion in the Atmospheric Boundary Layer Investigation by Physical Modelling	Zbynek Janour, Klara Bezpalcova, Zdenek Zelinger
FM9S_10576 (page 928)	Experiments on Up - slope to Down - slope Transition in an Inclined Box Filled with Water	K. Dekajlo, T. A. Kowalewski, H. J. S. Fernando
FM9S_10733 (page 930)	Analysis of Double - Free Surface Flow through Gates Using Element - Free Galerkin Method	Farhang Daneshmand, Mohammad.J. Kazemzadeh - Parsi
FM9L_11164 (page 932)	Free Surface Behavior in Turbulent Open - Channel Flows	Hitoshi Miyamoto, Kenji Shimoyama
FM9L_11182 (page 934)	Integral and Laboratory Modelling of Sedimentation from Turbulent Buoyant Jets	Gregory F. Lane-Serff
FM9S_11294 (page 936)	Modified Shallow Water Equations for Inviscid Gravity Currents	Falin Chen, A. C. Ruo
FM9S_11346 (page 938)	Dam - Break Flow for Arbitrary Slope of the Bottom	R. Fernandez - Feria
FM9S_11433 (page 940)	Extended Nonlinear Theory for Topographic Rossby Waves	Oksana E. Poloukhina, Andrey A. Kurkin
FM9S_11703 (page 942)	The Propagation of Viscous Gravity Currents over a Rigid Conic Surface	A. A. Osiptsov, A. A. Barmin, O. E. Melnik
FM9L_12072 (page 943)	An Alternative Model for “Pingo” Formation in Permafrost Regions	James G. A. Croll
FM9S_12099 (page 944)	Fast Ferry Traffic as a New Forcing Factor of Enviromental Processes in Non-Tidal Sea Areas	Tarmo Soomere

FM9S_12266 (page 946)	Dynamics of Separation Zone behind the 2D Hill in Oscillating Incident Wind.	Alicja Jarza, Jaroslaw Ciechanowski
FM9S_12270 (page 948)	Effects of Curvature in Avalanche Deflecting Dams	Arne Moe, Fridtjov Irgens, Ulrik Domaas, Carl Bonnevie Harbitz
FM9S_12396 (page 950)	Lobe and Cleft Formation at the Head of a Gravity Current	J. N. McElwaine, M. D. Patterson
FM9L_12410 (page 952)	Experimental and Numerical Simulation of Dense Water Overflows on a Continental Slope	Sabine Decamp, Joel Sommeria
FM9S_12592 (page 954)	High Resolution Modelling of Atmospheric Flow over Southern Poland	Jakub Krawczyk, Miroslaw Andrejczuk, Zbigniew Piotrowski, Joanna Struzewska, Bogumil Jakubiak, Szymon Malinowski
FM9L_12626 (page 956)	Formation and Rapid Expansion of Double Diffusive Layering in Lake Nyos	Alfred Wuest, Martin Schmid
FM9S_12738 (page 958)	Joint Urban 2003 Surface Energy Budget Measurements and Analysis	J. E. Holeman, M. Princevac, S. Grossman - Clarke, S. M. Lee, H. J. S. Fernando, R. Calhoun
FM9S_12980 (page 960)	Nocturnal Temperature Inversions Under Calm Clear Conditions: an Analytical Study	A. S. Vasudeva Murthy, Saji Varghese

Pre-nominated Session FM10
Experimental methods in fluid mechanics

Co-Chair(s): **A. Leder (Germany)**
J. Westerweel (Netherlands)

Paper ID	Title	Authors
FM10S_10445 (page 962)	On the Evaporation of a Monodisperse Droplet Stream at High - Pressure	Grazia Lamanna, Han Sun, Bernhard Weigand, Davide Magatti, Pietro Micciche, Fabio Ferri
FM10L_11088 (page 965)	HPIV using Polarization Multiplexing Holography in Bacteriorhodopsin (bR)	V. S. S. Chan, W. D. Koek, D. H. Barnhart, T. A. Ooms, J. J. M. Braat, J. Westerweel
FM10S_11455 (page 967)	Time-resolved Wall Shear Stress Measurements using MEMS	Alister N. Gibson, Valery G. Chernoray, Lennart Loefdahl, Sjoerd Haasel, Goeran Stemme
FM10L_11909 (page 969)	Void Collapse and Jet Formation: The Impact of a Disk on a Water Surface.	Raymond Bergmann, Mark Stijnman, Devaraj van der Meer, Andrea Prosperetti, Detlef Lohse
FM10S_11916 (page 971)	Comprehensive Experimental and Computational Investigations of the Unsteady Flow in an Axial Flow Low Speed Compressor Stage	Andrzej S. Witkowski, Tadeusz J. Chmielniak, Miroslaw M. Majkut, Michal D. Strozik, Jacek M. Zukowski
FM10L_12070 (page 973)	Experimental Detection of the New Phenomenon of Turbulent Thermal Diffusion	Alexander Eidelman, Tov Elperin, Nathan Kleeorin, Alexander Krein, Igor Rogachevskii, Gerd Grunefeld
FM10S_12213 (page 975)	3D Vortices Structure Monitoring in Turbulent Flows by Digital Speckle Photography	Nikita A. Fomin, Andrey V. Krauklis, Elena I. Lavinskaya
FM10S_12719 (page 977)	Thermal-wave Resonator Cavity: Modelling and Applications for Water Mixtures	Anna Matvienko, Andreas Mandelis
FM10S_12855 (page 979)	Particle Image Velocimetry (PIV) for Cloud Droplets - Laboratory Investigations	Piotr M. Korczyk, Szymon P. Malinowski, Tomasz A. Kowalewski
FM10S_13048 (page 981)	Optical Diagnosis Systems for Measuring Thermofluiddynamicals Phenomena in Liquid Biosystems Under Ultra High Pressure	Antonio Delgado, Ozlem Ozmutlu, Christoph Hartmann, Albert Baars

Pre-nominated Session FM11
Flow control

Co-Chair(s): **J.B. Freund (USA)**
M. Gad-el-Hak (USA)

Paper ID	Title	Authors
FM11S_10128 (page 983)	Liquids: The Holy Grail of Microfluidics Modeling	Mohamed Gad-el-Hak
FM11S_10872 (page 984)	Active Control of Shock/Boundary Layer Interaction in Transonic Flow Over Airfoils	Ramesh K. Agarwal, Jose L. Vadillo
FM11S_11043 (page 986)	Manipulating a Vee - Shaped Bluff Body Wake Using a Fluidic Oscillator	Rong F. Huang, Kuo T. Chang
FM11L_11394 (page 988)	Response on the Near Wall Turbulence to Localized Unsteady Blowing Periodical and Dissymetric in Time	Sedat Tardu, Olivier Doche
FM11L_11636 (page 990)	Passive Control of Turbulent Flow behind a Model Vehicle for Drag Reduction Using Wake Disrupter	Dongkon Lee, Jin Choi, Woo - Pyung Jeon, Jeonglae Kim, Seonghyeon Hahn, Haecheon Choi
FM11S_11918 (page 992)	Control of Internal Supersonic Flow Separation	Andrzej Szumowski, Jan Wojciechowski
FM11L_12013 (page 994)	A Singular Value Analysis of Boundary Layer Control	Junwoo Lim, John Kim
FM11L_12068 (page 996)	Separation Control by Stationary and Time Periodic Lorentz Forces	Tom Weier, Gunter Gerbeth, Gerd Mutschke
FM11L_12156 (page 998)	On the Possibility and Prospects of Turbulent Flow Noise Control	Victor F. Kopiev
FM11S_12244 (page 1000)	Control of Flow Oscillations over a Cavity by Means of a Spanwise Cylinder	Illy Herve, Philippe Geffroy, Laurent Jacquin
FM11S_12258 (page 1002)	Synthetic Jet Actuation at the Resonance Frequency	Zdenek Travnicek, Frantisek Marsik, Tomas Vit, Pieter de Boer
FM11L_12305 (page 1004)	Optimal Energy Growth and Optimal Control of the Swept Attachment - Line Boundary Layer	Alan Guegan, Peter Schmid, Patrick Huerre
FM11L_12387 (page 1006)	Feedback Control of Vortex Shedding in a Separated Diffuser	Tim Colonius, Takao Suzuki, Douglas G. MacMartin
FM11S_12491 (page 1008)	Reduction of Aerodynamic Noise Induced by Flow over a Cavity	Seiichiro Izawa, Masafumi Kuroda, Ao-Kui Xiong, Yu Fukunishi
FM11S_12602 (page 1010)	Control of Turbulent Streaks by Active Wall Movement	Philippe Konieczny, Alexis Renotte, Bertrand Nogarede, Alessandro Bottaro
FM11L_12624 (page 1012)	Model - Based Control of Shear Flows Using Low - Dimensional Galerkin - and Vortex Models	Mark Pastoor, Rudibert King, Bernd R. Noack, Gilead Tadmor, Marek Morzynski
FM11L_12736 (page 1014)	Numerical Analysis of the Wake Control behind a Circular Cylinder with Oscillatory Rotation	Marek Morzynski, Sophie Goujon-Durand, Bernd R. Noack, Jose E. Wesfreid, Benjamin Thiria

Pre-nominated Session FM12
Flow in porous media

Co-Chair(s): **Abder Kader Mojtabi (France)**
V. Nikolaevskiy (Russia)

Paper ID	Title	Authors
FM12L_10199 (page 1016)	Numerical Investigation of Convective Regimes in a Planar Filtrational Convection Problem	Vasiliy N. Govorukhin, Igor V. Shevchenko

FM12L_10234 (page 1018)	Dissolution in Porous Media: Upscaling, Instabilities and Heterogeneity Effects	F. Golfier, B. Bazin, R. Lenormand, M. Quintard
FM12S_10548 (page 1020)	Instability and Dynamic Chaos of Non-equilibrium Filtration of Gaseous Liquid	Guzel T. Bulgakova, Mars M. Khasanov
FM12L_11059 (page 1022)	Double - Porosity Soils with Highly Conductive Inclusions: Modeling of Water Flow in Unsaturated Conditions	Jolanta Lewandowska, Adam Szymkiewicz, Jean-Louis Auriault
FM12L_11109 (page 1024)	Plastic Mass Flow of Sand Under Action of Pore Pressure Gradient	Victor N. Nikolaevskiy
FM12S_11115 (page 1026)	P - Waves Behavior at Transition from Liquid to Gas - Saturated Porous Media	Dmitry N. Mikhayalov
FM12S_11248 (page 1028)	Nonstationary Flow of Stokesian Fluid through Elastic Skeleton with Hierarchical Structure	Wlodzimierz R. Bielski, Jozef J. Telega
FM12L_11343 (page 1030)	Confined Air - liquid Drainage: Local Analysis and Invasion Percolation Model	F. Plouraboue, S. Geoffroy, F. Flukiger, O. Amyot, M. Prat
FM12S_11487 (page 1032)	A Joule-Thomson Process of a Wetting Fluid Near Saturation	Thomas Loimer
FM12L_11994 (page 1034)	Microscopic Simulations of the Dissolution of Rock Fractures	Piotr Szymczak, Anthony Ladd
FM12L_12376 (page 1036)	Fractional Model for Solute Spreading in Randomly Heterogeneous Porous Media	Kira Logvinova, Marie-Christine Neel
FM12S_12528 (page 1038)	Oscillatory Modes of Adsorption in the Flow of Multicomponent Systems	Liana Kovaleva, Marat Mavletov
FM12S_12611 (page 1040)	Extended Description of Pore Space Structure and Fluid Flow through Anisotropic Porous Materials	Mieczyslaw Cieszko
FM12L_12617 (page 1042)	Onset of Convection for a Miscible Fluid in a Porous Medium	Robert Behringer, Michael Carey, Mark Steen, Laurens Howle

Pre-nominated Session FM13
Flow instability and transition

Co-Chair(s): **P. Huerre (France)**
P.A. Monkewitz (Switzerland)

Paper ID	Title	Authors
FM13S_10185 (page 1044)	Instabilities in a Taylor - Dean Open Flow	Aomar Ait Aider, S. Skali, J. P.Brancher
FM13S_10188 (page 1046)	Shear Layer Instability and Frequency Modes Inside an Open Cavity	Francois Lusseyran, Thierry M. Foure, Celine Aschenbrenner, Yann Fraigneau
FM13L_10313 (page 1048)	Travelling Waves and Transition to Turbulence in Pipe Flow	Bruno Eckhardt, Holger Faisst
FM13S_10487 (page 1050)	Nonlinear Mechanics of Wavy Instability of Steady Longitudinal Vortices and Drag Rise in Boundary Layer Flow	J. T. C. Liu, I. G. Girgis
FM13L_10489 (page 1052)	Stability of Flow in a Rough Channel	J.M. Floryan, M. Asai
FM13L_10525 (page 1054)	Stability of Lagrangian Ideal Flows	Stephane Leblanc
FM13L_10640 (page 1056)	Instability Thresholds of Flow Between Exactly Counter - Rotating Disks	C. Nore, M. Tartar, O. Daube, L. S. Tuckerman
FM13L_10916 (page 1058)	Transient Growth in Developing Plane and Hagen Poiseuille Flow	Peter W. Duck

FM13L_11186 (page 1060)	Three-dimensional Global Modes in Spatially Varying Rayleigh-Benard-Poiseuille Convection	Denis Martinand, Philippe Carriere, Peter A. Monkewitz
FM13L_11396 (page 1062)	Elliptical Instability in a Rotating Spheroid	Laurent Lacaze, Staphane Le Dizes, Patrice Le Gal
FM13L_11461 (page 1064)	The Instability of a Localized Vortex Disturbance in Uniform Shear Flow	Jacob Cohen, Victoria Suponitsky, Pinhas Z. Bar-Yoseph
FM13L_11647 (page 1066)	Subcritical Transition to Turbulence in Plane Couette Flow	Maher Lagha, Paul Manneville
FM13L_11995 (page 1068)	Three - Dimensional Vortex Breakdown in Swirling Jets and Wakes	M. R. Ruith, P. Chen, E. Meiburg, T. Maxworthy
FM13S_12150 (page 1070)	A New Convective Instability with Growth Normal to a Boundary Layer	J.J. Healey
FM13L_12233 (page 1072)	By-pass Laminar - Turbulent Transition of the Wind - Driven Free Surface Flow	Guillemette Caulliez, Richard Dupont, Victor I. Shrira
FM13L_12250 (page 1074)	Large - Eddy Simulation of the Transitional Flow in Natural Convection in a Horizontal Annulus	Elie L. M. Padilla, Aristeu Silveira - Neto
FM13S_12280 (page 1076)	Influence of Swirl Vibrations on Flow in Long Cylinder	Denis S. Goldobin, Dmitry V. Lyubimov
FM13S_12291 (page 1078)	Nonlinear Stability of Rotating Channel Flow	M. Nagata, D.P. Wall, T. Mitsumoji
FM13L_12372 (page 1080)	On Instability Mechanisms in a Separating Boundary-layer Flow	Matthieu Marquillie, Uwe Ehrenstein, Francois Gallaire
FM13S_12381 (page 1082)	Gortler Vortex Secondary Stability: Varicose Mode	Leandro F. Souza, Marcio T. Mendonca, Marcello A. F. Medeiros, Markus J. Kloker
FM13L_12425 (page 1084)	Spiral Vortex Breakdown as a Global Mode	Michael Ruith, Francois Gallaire, Jean-Marc Chomaz, Patrick Huerre, Eckart Meiburg
FM13L_12431 (page 1086)	Computational Study of Turbulent - Laminar Bands in Couette Flow	Dwight Barkley, Laurette S. Tuckerman
FM13L_12483 (page 1088)	A Generic Mechanism for By - Pass Transition in Vortices	Arnaud Antkowiak, Pierre Brancher
FM13S_12508 (page 1090)	Global Stability of the Flow Induced by Wall Injection	Thierry Feraille, Gregoire Casalis
FM13L_12509 (page 1092)	Acoustic Field Generated by Instability Waves in the Transonic Regime	Christophe Millet, Stephane Le Dizes
FM13L_12542 (page 1094)	Nonlinear Transition of a Flow Driven by a Rotating Magnetic Field	Ilmars Grants, Gunter Gerbeth
FM13S_12711 (page 1096)	Fully Nonlinear Global Modes and Transition to Turbulence in Open Flows	Jean - Marc Chomaz
FM13S_12766 (page 1098)	Stability of Plane Poiseuille Flow and Energy Growth in the Case of a Bingham Fluid	Cherif Nouar, Nadjiba Kabouya, Jan Dusek, Aziz Salem
FM13S_13019 (page 1100)	Instability of the Far Wake Behind a Wind Turbine	Valery L. Okulov, Jens N. Sorensen

Pre-nominated Session FM14
Flow in thin films

Co-Chair(s): **N. Aksel (Germany)**
V. Shkadov (Russia)

Paper ID	Title	Authors
FM14L_10220 (page 1102)	Dynamics of a Reactive Falling Film at Large Peclet Numbers	Serafim Kalliadasis, Philip Trevelyan
FM14L_10543 (page 1104)	Long - Wave Marangoni Instability in Binary - Liquid Films with Soret Effect	Alexander Oron, Alexander A. Nepomnyashchy
FM14L_10557 (page 1106)	Solitary Waves on Liquid Film Flowing Along a Periodic Wall	M. Vlachogiannis, K. Argyriadi, V. Bontozoglou
FM14L_10642 (page 1108)	Effect of Bottom Undulations on the Stability of Film Flow Down Inclined Planes	Nuri Aksel, Andreas Wierschem
FM14L_10928 (page 1110)	Hydraulic Jumps and Resonance in Gravity - Driven Flows of Liquid in Inclined Wavy Channels: Transition and Hysteresis	Andreas Wierschem, N. Aksel
FM14L_11089 (page 1112)	Hydrodynamic Theory of De - Wetting	Jens Eggers
FM14L_11404 (page 1114)	Surfactant-Induced Fingering Phenomena in Thin Liquid Films	M. R. E. Warner, R. V. Craster, Omar K. Matar, Barry Edmonstone
FM14S_11413 (page 1116)	Linear Response of a Viscous Liquid Sheet	Norbert Alleborn, Hans Raszillier
FM14S_11477 (page 1118)	Experimental and Numerical Study of Marangoni - Natural Convection	Le Han Tan, E. Leonardi, T. J. Barber, S. S. Leong, T. A. Kowalewski
FM14L_11509 (page 1120)	Layer Thickness Distribution of Thin-Film Ink-Jet Printed Structures.	Dirkjan B. van Dam
FM14S_11739 (page 1122)	Amplification of Nonlinear Disturbances on a Falling Liquid Sheet	Takao Yoshinaga, Kentaro Kan
FM14S_12155 (page 1124)	Thin Film Flows Near Isolated Humps and Interior Corners	Gregory P. Chini, Oliver E. Jensen, John R. King
FM14L_12293 (page 1126)	Gravity - and Shear - Driven Thin Films Flow on Heated Hicrostructured Walls	Tatiana Gambaryan-Roisman, Alexander Alexeev, Peter Stephan
FM14L_12656 (page 1128)	Hydrodynamics of the Solitary Waves Travelling Down a Liquid Film	Jaroslav Tihon
FM14L_12858 (page 1130)	Transient Displacement of Viscoelastic Liquids by Air	Yiannis Dimakopoulos, John Tsamopoulos

Pre-nominated Session FM15
Fluid mechanics of materials processing

Co-Chair(s): **F. Dupret (Belgium)**
R. Moreau (France)

Paper ID	Title	Authors
FM15L_10363 (page 1132)	Analysis of Flow - Induced, Step - Bunching Instabilities During the Growth of Crystal from Liquid Solutions	Bing Dail, Yong-Il Kwon, Jeffrey J. Derby
FM15L_10860 (page 1134)	Relevance of Alfven Waves in Process Metallurgy under a High Magnetic Field	Rene Moreau, Kazuhiko Iwai, Takashi Kameyama
FM15S_11386 (page 1136)	Effect of Thermal Boundary Modulation in a Restricted Fluid Domain of a 3D Vertical Bridgman Apparatus	E. Semma, M. El Ganaoui, R. Bennacer, V. Timchenko, E. Leonardi
FM15L_11893 (page 1138)	3D Computer Simulation of Time - Depended Solutal Convection	Viatcheslav V. Kolmychkov, O. S. Mazhorova, Yu. P. Popov, P. Bontoux, M. El Ganaoui

FM15S_11903 (page 1140)	Liquid and Gas Jets Impinging on a Moving Wetted Surface	Anh V. Nguyen, Geoffrey M. Evans
FM15L_11929 (page 1142)	Convective Instabilities in Czochralski Model	V. I. Polezhaev, N. V. Nikitin, S. A. Nikitin
FM15L_12349 (page 1144)	New Possibilities for Velocity Measurements and Model Experiments in Liquid Metal Processing	Andreas Cramer, Kapil Varhsney, Gunter Gerbeth
FM15L_12591 (page 1146)	Dynamic Simulation of the Entire Crystal Growth Process: Multi - Scale Analysis of Melt Flow Transients	V. Regnier, L. Wu, B. Delsaute, F. Bioul, N. Van den Bogaert, F. Dupret
FM15S_12636 (page 1148)	Sensitive Regions and Optimal Perturbations in the Floating Zone Using the Adjoint System	Othman Bouizi, Claudine Dang Vu-Delcarte, Guillaume Kasperski

Pre-nominated Session FM16
Fluid mechanics of suspension

Co-Chair(s): **R. Bonnecaze (USA)**
E. Guazzelli (France)

Paper ID	Title	Authors
FM16S_10248 (page 1150)	Effective Viscosity of an Inhomogeneous Dilute Suspension Flowing Along a Wall	Laurentiu Pasol, Francois Feuillebois
FM16L_10361 (page 1152)	Velocity Fluctuations in Non - Brownian Suspensions Undergoing Simple Shear Flows	A. Acrivos, G. Drazer, J. Koplik, B. Khusid
FM16L_10603 (page 1154)	The Collective Dynamics of Self - Propelled Particles	Vishwajeet Mehandia, Prabhu R. Nott
FM16L_10993 (page 1156)	Microstructure of a Dilute Sedimenting Suspension	Bogdan Cichocki, Krzysztof Sadlej
FM16S_11236 (page 1158)	Sedimentation of Dilute Suspensions	B. U. Felderhof
FM16S_11409 (page 1159)	Relaxation Time for Sedimenting Spheres of a Suspension with Periodic Boundary Conditions	Maria L. Ekiel - Jezewska, Eligiusz Wajnryb
FM16L_11418 (page 1161)	Numerical Simulations of Particle Suspensions in a Rotating Flow	Jonghoon Lee, Anthony J. C. Ladd
FM16S_11431 (page 1163)	A Mode - Mode Coupling Scheme of Colloidal Electrolyte Friction	Mathieu G. McPhie, Gerhard Naegele
FM16L_11473 (page 1165)	The Effect of Different Particle Contacts on Suspension Rheology	Helen J. Wilson, Robert H. Davis
FM16L_11480 (page 1167)	Evolution of Suspension Sedimenting in a Container Bounded by Horizontal Walls	Evgeny S. Asmolov
FM16S_11588 (page 1169)	Spreading Fronts and Fluctuations in Sedimentation: Part I Experiments	Laurence Bergougnoux, Sebastien Ghicini, Elisabeth Guazzelli, John Hinch
FM16S_11725 (page 1170)	Constant Force and Constant Velosity Momentum Tracers in Concentrated Suspensions	Patrick T. Reardon, Alan L. Graham, James R. Abbott, Howard Brenner
FM16S_11749 (page 1172)	Flow of a Concentrated Suspension Down a Rough Plane	Cyril Cassar, Maxime Nicolas, Olivier Pouliquen
FM16L_11850 (page 1174)	Inertial Migration of Rigid Spherical Particles in Poiseuille Flow	J. P. Matas, J. F. Morris, E. Guazzelli
FM16L_11884 (page 1176)	Segregation of Suspended Particles in a Rotating Fluid - Filled Horizontal Cylinder - Experiment and Theory	G. Seiden, S. Lipson, M. Ungarish, J. Franklin
FM16L_11991 (page 1178)	Migration of Buoyant Mono - and Bi - Disperse Suspensions in Low Reynolds Number Pressure - Driven Pipe Flow	Jay T. Norman, Hebri V. Nayak, Roger T. Bonnecaze

FM16L_12005 (page 1180)	Dynamic Simulations of the Instability of Sedimenting Fibers	David Saintillan, Eric Darve, Eric S. G. Shaqfeh
FM16S_12056 (page 1182)	Mobility of Membrane - Trapped Particles: Protrusion into the Surrounding Fluid	Howard A. Stone
FM16L_12345 (page 1184)	Spreding Fronts and Fluctuations in Sedimentation: Part II Computer Simulations	Laurence Bergougnoux, Sebastien Ghicini, Elisabeth Guazzelli, John Hinch
FM16S_12438 (page 1185)	The Role of Cohesive Forces on the Fluidization Behavior of Fine Powders	J. M. Valverde, A. Castellanos, M. A. S. Quintanilla
FM16S_12452 (page 1187)	Single Particle Motion in Colloidal Dispersions	Ileana C. Carpen, Todd M. Squires, John F. Brady
FM16L_12574 (page 1189)	Slip and Flow in Pastes	Michel Cloitre, Roger T. Bonnecaze

Pre-nominated Session FM17
Granular flows

Co-Chair(s): **R. Behringer (USA)**
I. Goldhirsch (Israel)

Paper ID	Title	Authors
FM17L_10253 (page 1191)	Impact	Detlef Lohse, Raymond Bergmann, Rene Mikkelsen, Christiaan Zeilstra, D. van der Meer, Michel Versluis
FM17S_10371 (page 1193)	Maximum - Entropy Estimates and Virtual Thermomechanics for Granular Assemblies	J. D. Goddard
FM17L_10524 (page 1195)	Granular Column Collapse	Gert Lube, Herbert E. Huppert, R. Stephen Sparks, Mark A. Hallworth
FM17L_10959 (page 1197)	Gravity Flow of a Densely - Packed Granular Material	Jean Rajchenbach
FM17S_10969 (page 1199)	Flow Dynamics of Dense Granular Materials Subjected to Vertical Vibration	Azita Soleymani, Vesa Tanskanen, Piroz Zamankhan, William Polashenski, Jr.
FM17S_11169 (page 1201)	Particle Image Velocimetry Analysis of Granular Material Flows	Irena Sielamowicz, Slawomir Blonski
FM17L_11751 (page 1203)	Pore Pressure Relaxation During Granular Compaction	Maxime Nicolas, Max Belzons, Olivier Pouliquen
FM17L_11775 (page 1205)	Granular Flows on a Heap	Pierre Jop, Yoel Forterre, Olivier Pouliquen
FM17L_11876 (page 1207)	Collapse, Growth and Merging of Cavity Regions in a Granular Material due to Viscous Flow	O. Sano, Y. Kaneko, G. P. RajaSekhar
FM17L_11883 (page 1209)	Undulations and Ripples of a Thin Granular Layer Due to Vertical Vibration	Akiko Ugawa, Osamu Sano
FM17S_12073 (page 1211)	Species Segregation Driven by a Granular Temperature Gradient	Janine E. Galvin, Steven R. Dahl, Christine M. Hrenya
FM17L_12308 (page 1213)	Kinetics of Weakly Frictional Granular Gases	Isaac Goldhirsch, S. Henri Noskowicz, O. Bar-Lev
FM17S_12338 (page 1215)	Morphology and Scaling of Impact Craters in Granular Media	Amanda M. Walsh, John R. de Bruyn
FM17L_12399 (page 1217)	Extended Granular Temperature	Lou Kondic, Robert P. Behringer
FM17L_12445 (page 1219)	Evolution of Internal Structure of Sheared Dense Granular Flows: Crystallization and History - Dependent Final States	J. C. Tsai, J. P. Gollub

FM17S_12790 (page 1221)	Arching in Granular Media	Radoslaw L. Michalowski, Namgyu Park
FM17L_12883 (page 1223)	Transverse Motion, Segregation and Rotations in 2D Granular Flows	Renauld Delannay, Alexandre Valance, Patrick Richard, Weitao Bi, Gaelle Berton, Nicolas Taberlet
FM17L_13029 (page 1225)	Velocity Profiles During Granular Avalanches	Marc Rabaud, Sylvain Courrech du Pont, Philippe Gondret, Bernard Perrin

Pre-nominated Session FM18
Low-Reynolds-number flow

Co-Chair(s): **R.H. Davis (USA)**
C. Pozrikidis (USA)

Paper ID	Title	Authors
FM18S_10297 (page 1227)	Radially Symmetric Polar Ice Sheet Flow with Evolving Anisotropic Fabric	Ryszard Staroszczyk, Leslie W. Morland
FM18L_10565 (page 1229)	Hydrodynamic Interaction of a Spherical Particle in Poiseuille Flow Between Planar Walls	R. B. Jones
FM18S_10766 (page 1231)	Two - Layer Stagnation Point Flows	M. G. Blyth, C. Pozrikidis
FM18L_10983 (page 1233)	Free Surface Deformation in Suspensions Near a Rotating Rod	L. A. Mondy, R. R. Rao, M. M. Hopkins, S. A. Altobelli
FM18S_11300 (page 1235)	Particles Located on a Planar Free - Surface - Hydrodynamic Interactions in Quasi - Two - Dimensional System	Bogdan Cichocki, Maria L. Ekiel - Jezewska, Gerhard Naegele, Eligiusz Wajnryb
FM18L_11460 (page 1237)	Microcavitation and Detachment of a Stokes Particle in Near - Wall Slow Motion	A. N. Prokunin
FM18S_11915 (page 1239)	Flow Visualization Experiments of Cellular Stokes Flows Induced by Rotation of a Cylinder Variously Positioned Inside Channels	Emin F. Kent
FM18S_11922 (page 1241)	Many - Sphere Hydrodynamic Interactions: Weak Convective Inertia Effects	I. T. Pienkowska
FM18S_12164 (page 1243)	Viscous Eddy Structures in an Oscillating Cylinder with Sharp Corners	M. Branicki, H. K. Moffatt
FM18S_12859 (page 1245)	Transient Squeeze Flow of Viscoplastic Liquids	G. Karapetsas, N. Chatzidai, M. Pavlidis, J. Tsamopoulos
FM18S_12981 (page 1247)	Slow Rotation of a Double Sphere in a Viscous Fluid	D. Palaniappan

Pre-nominated Session FM19
Magnetohydrodynamics

Co-Chair(s): **P.A. Davidson (UK)**
A. Thess (Germany)

Paper ID	Title	Authors
FM19L_10025 (page 1249)	Migration and Interaction of two Conducting Particles Freely Immersed in a Liquid Metal	Antoine Sellier
FM19S_10235 (page 1251)	Bifurcation of Conical Magnetic Field	Vladimir Shtern
FM19L_10931 (page 1253)	Complementary Experiments at the Karlsruhe Dynamo Test Facility	Urlich Mueller, Robert Stieglitz, Sandor Horanyi, Fritz Busse

FM19L_11120 (page 1255)	Liqiud Metal Flow Under Inhomogeneous Magnetic Field	Oleg Andreev, Yurii Kolesnikov, Andre Thess
FM19L_11124 (page 1257)	Small - Scale Motion in the Core of the Earth	P. A. Davidson, F. Siso-Nadal
FM19L_11429 (page 1259)	Magnetohydrodynamic Instabilities of Astrophysical Jets	Hubert Baty, Rony Keppens, Pierre Comte
FM19L_11458 (page 1261)	Magnetohydrodynamic Motion of Toroidal Magnetic Eddies	Y. Hattori, H. K. Moffatt
FM19S_11621 (page 1263)	Fluid Dynamos and Precession Driving	J. Leorat
FM19L_11637 (page 1265)	Large Eddy Simulation of Magnetic Damping of Jet	Jungwoo Kim, Jeongyoung Park, Haecheon Choi
FM19L_11681 (page 1267)	Observations of the Magnetorotational Instability in Spherical Couette Flow	Daniel P. Lathrop
FM19S_11809 (page 1268)	Simulating the Orszag-Tang vortex using RSPH	Steinar Borve, Marianne Omang, Jan Trulsen
FM19S_11906 (page 1270)	Homogenisation of Electrically Heated Glass Melts by Lorentz Forces	U. Krieger, B. Halbedel, D. Hulsenberg, A. Thess
FM19L_12090 (page 1272)	A Model for Liquid Metal Current Limiters	Andre Thess, Yurii Kolesnikov, T. Boeck
FM19L_12107 (page 1273)	The Magnetohydrodynamic Couette Flow in a Plane and Spherical Geometries with Singular Hartmann Boundary Layers	Krzysztof A. Mizerski
FM19S_12120 (page 1275)	Mean Electromotive Force for a Ring of Helical Vortices	Raul A. Avalos-Zuniga, Franck Plunian, Karl-Heinz Radler
FM19L_12125 (page 1277)	Numerical Simulations of Dynamo Experiments	Andreas Tilgner
FM19L_12290 (page 1278)	Stability of Liquid Metal Drops Affected by High - Frequency Magnetic Fields	Vaclav Kocourek, Christian Karcher, Dietmar Schulze
FM19L_12330 (page 1280)	Quasi - Geostrophic Dynamos	Nathanel Schaeffer, Philippe Cardin
FM19S_12363 (page 1282)	Model of Gas Flow Inside a Plasma Thruster	S. Barral, Z. Peradzynski, K. Makowski, M. Dudeck
FM19S_12587 (page 1284)	Numerical Study of the Flow in a Finite Cylinder Driven by a Rotating Magnetic Field	Karel Frana, Jorg Stiller
FM19S_12605 (page 1286)	Interface Reconstruction in Cylindrical Two - Compartment - Systems Using Magnetic Field Tomography	Hartmut Brauer, Marek Ziolkowski, Milko Kuilekov, Shouqiang Men, Christian Resagk
FM19S_12613 (page 1288)	Contactless Inductive Flow Tomography: Theory and Experiment	Frank Stefani, Gunter Gerbeth, Thomas Gundrum
FM19L_12979 (page 1290)	Dynamo Action in Steady Helical Pipe Flow	Leszek Zabielski, Jonathan A. Mestel

Pre-nominated Session FM20
Multiphase flows

Co-Chair(s): **S. Balachandar (USA)**
J. Magnaudet (France)

Paper ID	Title	Authors
FM20S_10416 (page 1292)	Large - Eddy Simulation of Particle Dispersion in the Duct with Fluid Injection	Konstantin N. Volkov

FM20S_10690 (page 1294)	Sings of Flooding Instability in Inclined Liquid Films at High Pressure and Mass Transfer in High Density Gas Slugs	Maria J. F. Ferreira, Joao R. F. Guedes de Carvalho
FM20L_10843 (page 1296)	Viscous and Viscelastic Potential Flow	Daniel D. Joseph
FM20S_11189 (page 1298)	Separation and Sorting of Heavy Particles Suspended in a Fluid by Settling in a Periodic Vorticity Field	Urbano Sanchez, Maria J. Moreno
FM20S_11655 (page 1300)	Gas - Liquid Interfractial Distribution in Inclined Downward Pipe Flow	Elena Trostinetsky, Lev Shemer, Dvora Barnea
FM20S_11745 (page 1302)	Videogrametry in Fluidized Bed Reactors	Stanislaw Anweiler, Roman Ulbrich
FM20L_12092 (page 1304)	Gravity Induced Mixing of Miscible Fluids in Vertical and Inclined Tubes	Thomas Seon, Bernard Perrin, Dominique Salin, Jean-Pierre Hulin
FM20L_12139 (page 1306)	Oscillatory Motion of Freely - Moving Light Bodies: from Cylinders to Disks	P. Cordeiro Fernandes, P. Ern, F. Risso, J. Magnaudet
FM20L_12332 (page 1308)	Particle Turbulence Interaction	S. Balachandar, P. Bagchi, L. Wakaba, L. Zeng
FM20L_12342 (page 1310)	Non - Uniform Flow Hydrodynamics of Deformable Shapes	T. Miloh
FM20L_12383 (page 1312)	Mean Motion Induced in a Liquid by Rising Bubbles	Veronique Roig, Amaury Larue de Tournemine
FM20L_12397 (page 1315)	Plane Couette Flow of Dense Liquid - Particle Suspensions	Jos Derksen, Sankaran Sundaresan
FM20S_12671 (page 1317)	Simulation of Planar Wave Instabilities in Liquid - Fluidized Beds	Jos Derksen, Sankaran Sundaresan
FM20S_12886 (page 1319)	Image Processing Method in Estimation of Bubble Column's Work	Daniel Zajac, Roman Ulbrich
FM20L_13012 (page 1321)	Statistics and Preferential Distribution of Micro - Particles in Turbulent Boundary Layer: Implications for Resuspension Mechanisms	Maurizio Picciotto, Cristian Marchioli, Andrea Giusti, Alfredo Soldati

Pre-nominated Session FM21
Solidification and crystal growth

Co-Chair(s): **M. Glicksman (USA)**
M.G. Worster (UK)

Paper ID	Title	Authors
FM21S_11058 (page 1323)	Experimental Observations of Hydrate Formation in a Convection Tank	C. F. Chen, Cho Lik Chan
FM21S_11208 (page 1325)	Morphological Stability of Directional Solidification under Temperature Modulations	C. A. Chung, K. H. Ho, W. Z. Chien
FM21L_11270 (page 1327)	Nonlinear Oscillatory Convection in Mushy Layers	Peter Guba, M. Grae Worster
FM21L_11320 (page 1329)	Magnetic Resonance Imaging of Structure and Convection in Solidifying Mushy Layers	P. Aussillous, A. J. Sederman, L. F. Gladden, H. E. Huppert, M. G. Worster
FM21L_11328 (page 1331)	Solidification and Compositional Convection of a Ternary Alloy	Andrew F. Thompson, Herbert E. Huppert, M. Grae Worster, Anneli Aitta
FM21S_11331 (page 1333)	AHP Setup for Low Laminar Melt Flow Study in Crystal Growth	Michael A. Gonik, Janusz A. Szymczyk, Tomasz A. Kowalewski
FM21S_11362 (page 1335)	Optimization of the Growth Conditions of a Nd:YVO4 Cylindrical Bar	Liliana Braescu, Robert Szabo, Agneta M. Balint, Stefan Balint

FM21S_11364 (page 1337)	Front Tracking Technique on a Fixed Grid in Modelling of Binary Mixture Soldification with Natural Convection	Jerzy Banaszek, David J. Browne, Marek Rebow, Mariusz Proczek
FM21L_11926 (page 1339)	Salt Precipitation in Geothermal Reservoirs	George G. Tsypkin, Andrew W. Woods
FM21S_12276 (page 1341)	Boundary - Layer Analysis of Chimney Structures in Mushy Layers	Jacqueline Ashmore, M. Grae Worster
FM21S_12278 (page 1343)	Travelling Magnetic Field Influence on Crystal Growth by Bridgman Method	Irina S. Fayzrakhmanova, Tatyana P. Lyubimova
FM21L_12312 (page 1345)	A Semi-Sharp Phase Field Method for Quantitative Phase Change Simulations	Gustav Amberg
FM21L_12365 (page 1347)	Directional Solidification of Pb-Sn Alloys Affected by a Rotating Magnetic Field	Sven Eckert, Bernd Willers, Ulf Michel, Gustav Zouhar, Petr A. Nikrityuk, Kerstin Eckert
FM21L_12543 (page 1349)	Cell Shapes in Directional Solidification: a Global Study	Marc Georgelin, Alain Pocheau
FM21L_12743 (page 1351)	Convection Driven by Tidal Heating: Numerical Model and Parameterized Theory	Leszek Czechowski
FM21S_12768 (page 1353)	Ternary Alloy Convection in Mushy Layers: Extended Summary	Daniel M. Anderson, T. P. Schulze
FM21S_13008 (page 1355)	Convective Instabilities During Solidification of a Mushy Layer	In G. Hwang, Chang K. Choi

Pre-nominated Session FM22
Stirring and mixing

Co-Chair(s): **H. Aref (USA)**
E. Villermaux (France)

Paper ID	Title	Authors
FM22S_10130 (page 1357)	Development of the Fractal Dimension of Material Elements in Homogeneous Isotropic Turbulence Using Kinematic Simulation	F. Nicolleau, A. El Maihy
FM22L_10497 (page 1359)	Chaotic Advection in a Mixer with Changing Geometry	Stephen M. Cox, Matthew D. Finn
FM22S_10532 (page 1361)	Enhanced Mixing by Vortices	Patrice Meunier, Emmanuel Villermaux
FM22S_10896 (page 1363)	Geometric Features of High - Schmidt Number Scalar Mixing	Jörg Schumacher, Katepalli R. Sreenivasan
FM22L_11190 (page 1365)	Front Propagation in Laminar Cellular Flows : an Experimental Study	Alain Pocheau, Fabien Harambat
FM22L_11293 (page 1367)	On the Design of 3D Micromixers Having the Bernoulli Property	Stephen Wiggins, Julio M. Ottino
FM22L_12048 (page 1369)	Intermittent Distribution of Heavy Inertial Particles in Turbulent Flows	Alain Pumir, Gregory Falkovich
FM22S_12110 (page 1371)	Chaotic Stirring of Passive Fluid by a Vortex Pair in Circular Domain	Alexandre A. Gourjii, Vyacheslav V. Meleshko, GertJan F. van Heijst
FM22L_12158 (page 1373)	Chaotic Advection and Mixing in Pulsed Source - Sink Systems	Mark A. Stremler, Baratunde A. Cola
FM22S_12209 (page 1375)	On Dissipative Structures of Stirring - Grids Turbulence	L. J. Jiang, S. S. Shy, T. H. Yuan
FM22L_12257 (page 1377)	Evaluation of Transport Properties by Exchange Matrix Method	Tatyana S. Krasnopolskaya, Vyacheslav V. Meleshko

FM22L_12326 (page 1379)	Mixing Is an Aggregation Process	E. Villermaux, J. Duplat
FM22S_12415 (page 1381)	Stirring and Mixing Effects in Agglomerative Precipitation	Jerzy Baldyga, Magdalena Jasinska
FM22S_12439 (page 1383)	Resonances and Mixing in Stokes Flows	Dmitri Vainchtein, Igor Mezic, Anatoly Neishtadt
FM22L_12442 (page 1385)	Mixing in Multiconnected Planar Domains	Philip Boyland
FM22S_12545 (page 1387)	Eulerian Measures for Lagrangian Stirring in a Thermally Driven Flow	R. J. Keane, P. L. Read, G. P. King
FM22S_12610 (page 1389)	An Analysis of Mixing Process in a Static Mixer	Marek Jaszczur, Janusz Szmyd, Marcus Petermann
FM22S_12633 (page 1391)	Stirring by Blinking Rotlets in a Bounded Stokes Flow	Dennis van der Woude, Herman Clercx, GertJan van Heijst, Vyacheslav V. Meleshko
FM22S_12731 (page 1393)	Weak Inertia and Mixing Between Rough Surfaces	David Lo Jacono, Franck Plouraboué, Alain Bergeon, Pauline Assemat
FM22L_12761 (page 1395)	Active Shear Superpositon Micromixer	Frederic Bottausci, Caroline Cardonne, Igor Mezic, Carl Meinhart

Pre-nominated Session FM23
Topological fluid mechanics

Co-Chair(s): **P.L. Boyland (USA)**
K. Ohkitani (Japan)

Paper ID	Title	Authors
FM23S_10247 (page 1397)	Streamline Topology of the Nearwake of a Circular Cylinder at Low Reynolds Numbers	Morten Brons, Kristine Niss, Bo Jakobsen, Lars K. Voigt, Rune Petersen, Anders Bisgaard
FM23L_10938 (page 1399)	Eulerian - Lagrangian Analysis of Navier - Stokes Turbulence	Koji Ohkitani, Peter Constantin
FM23L_11060 (page 1401)	Topological Chaos in Simple Mixers	Matthew D. Finn, Stephen M. Cox, Helen M. Byrne
FM23S_11166 (page 1403)	Gauge Principle for Ideal Fluids and Variational Principle	Tsutomu Kambe
FM23L_11660 (page 1405)	Particle Transport by a Vortex Soliton	Yoshi Kimura, Souji Koikari
FM23L_11677 (page 1407)	Generic Hydrodynamic Instability	Robert W. Ghrist, John B. Etnyre
FM23L_12375 (page 1409)	Helicity Dynamics of Vortex Filaments	Darryl D. Holm, Samuel N. Stechmann
FM23L_12484 (page 1411)	Relation Between Mixing Efficiency and Geometrical Property of Stable Manifolds	Mitsuaki Funakoshi, Hiroshi Kawazoe
FM23S_12868 (page 1413)	Topological Aspects of the Tornado Problem	Dmytro I. Cherniy, Vyacheslav V. Meleshko, Stanislav A. Dovgiy

Pre-nominated Session FM24
Turbulence

Co-Chair(s): **Olivier Metais (France)**
R.D. Moser (USA)

Paper ID	Title	Authors
FM24L_10149 (page 1415)	Large Eddy Simulations of Decaying Rotating Turbulence	Andrzej J. Domaradzki, Xiaolong Yang
FM24L_10455 (page 1417)	Large - Eddy Simulation of Shock - Wave / Turbulent - Boundary - Layer Interaction	M. S. Loginov, N. A. Adams, A. A. Zheltovodov
FM24S_10506 (page 1419)	Experimental Study of Rotor-Stator Flows with Centripetal Fluxes	Sebastien Poncet,, Marie-Pierre Chauve, Patrice Le Gal
FM24L_10564 (page 1421)	PDF Computation of Turbulent Flows with a New Near - Wall Model	Marta Waclawczyk, Jacek Pozorski, Jean - Pierre Minier
FM24L_10937 (page 1423)	Interaction Between a Columnar Vortex and External Turbulence	Naoya Takahashi, Takeshi Miyazaki
FM24S_11116 (page 1425)	Turbulence Scalings in Supersonic Channel Flow	Rainer Friedrich, Holger Foysi, Sutanu Sarkar
FM24S_11151 (page 1427)	On the Scale Similarity in Large Eddy Simulation	F. Gallerano, G. Cannata, E. Pasero
FM24S_11161 (page 1429)	Two Scale Approach to Anisotropic Turbulence in Hel II	Tomasz Lipniacki
FM24S_11256 (page 1431)	Optimization of an Implicit Subgrid - Scale Model for LES	S. Hickel, S. Franz, N. A. Adams, P. Koumoutsakos
FM24L_11303 (page 1433)	Study of the Turbulent Energy Spectrum Build Up in an Experimental Vortex Burst	Yannis Cuypers, Agnes Maurel, Philippe Petitjeans
FM24S_11454 (page 1435)	Empirical Galerkin Models for Incompressible Flow --- Pressure-Term and 'Subgrid' Turbulence Representations	Bernd R. Noack, Paul Papas, Peter A. Monkewitz, Marek Morzynski, Gilead Tadmor
FM24S_11488 (page 1437)	Orthonormal Wavelet Analysis of CGT in Fully Developed Asymmetric Turbulent Channel Flow	Yu - Lu Liu, Jian - Bo Jiang, Xiang Qiu
FM24L_11802 (page 1439)	The Cellular Structure and Its Tracks of a H2/O2/Ar Detonation Waves	Xiangyu Hu, J. Czerwinska, N. Adams, B. C. Khoo
FM24S_11814 (page 1441)	Energy Spectrum in Rotating Turbulence	Frederic Moisy, Cyprien Morize, Marc Rabaud
FM24S_12004 (page 1443)	Three-Dimensional Turbulent Structures of Different Scales	Akira Rinoshika, Yu Zhou
FM24L_12151 (page 1445)	Inertial Similarity of Velocity Distributions in Homogeneous Isotropic Turbulence	Tomomasa Tatsumi, Takahiro Yoshimura
FM24S_12430 (page 1447)	A New Mixed Nonlinear LES Models for Boundary Layers	R.M. Kerr, P.G.Tucker
FM24L_12436 (page 1449)	Nonlinear Scale - Free Cascades and Their Stationary Spectra	Dmitri O. Pushkin, Hassan Aref
FM24L_12564 (page 1451)	3D - Measurements in an Adverse - Pressure - Gradient Turbulent Boundary Layer over Smooth and Ribbed Surfaces	Thomas Indinger, Stefan Hickel, Nikolaus A. Adams
FM24S_12652 (page 1453)	POD Analysis of Coherent Structures in Turbulent Flows	Song Fu, Min Tang, Jiang He
FM24L_12675 (page 1455)	Resonant Interactions of 3D Instability Waves in an Airfoil Boundary Layer for Harmonic and Broadband Perturbations	D. Sartorius, W. Wurz, S. Wagner, V. I. Borodulin, Y. S. Kachanov
FM24S_12740 (page 1457)	Compressibility Effects and Sound Propagation in Turbulent Channel Flow	Pierre Comte, Christophe Brun, Marie Haberkorn, Gilles Bouchet, V. Pagneux, Y. Auregan

FM24L_12757 (page 1459)	On the Structure of Turbulence and Reynolds Stress Distribution in the Bottom Boundary Layer of the Coastal Ocean	Luksa Luznik, Roi Gurka, W.A.M. Nimmo Smith, Weihong Zhu, Joseph Katz, Thomas Osborn
FM24S_12922 (page 1461)	Numerical Modelling of Small - Scale Turbulence in Clouds	Miroslaw Andrejczuk, Szymon Malinowski
FM24L_12965 (page 1463)	Impact of Pressure - Gradient Conditions on High Reynolds Number Turbulent Boundary Layers	Hassan Nagib, Chris Christophorou, Peter Monkewitz

Pre-nominated Session FM25
Vortex dynamics

Co-Chair(s): **G.J.F.van Heijst (Netherlands)**
E. Krause (Germany)

Paper ID	Title	Authors
FM25L_10683 (page 1465)	New Means of Vortex Breakdown Control	Miguel A. Herrada, Vladimir Shtern
FM25L_11391 (page 1467)	Instabilities of a Vortex Pair in a Stratified and Rotating Fluid	Paul Billant, Augustin Colette, Jean-Marc Chomaz
FM25L_11467 (page 1469)	Stability of Oceanic Vortices: a Solution to the Problem	Eugene Benilov
FM25L_11615 (page 1471)	Curvature Instability of a Vortex Ring	Yasuhide Fukumoto, Yuji Hattori
FM25S_11676 (page 1473)	Numerical Experiments on Vortex Shedding From an Oscillating Cylinder	Fernando Ponta, Hassan Aref
FM25S_11683 (page 1475)	Bifurcation of Motions of Three Vortices and Applications	Lu Ting, Denis Blackmore
FM25L_11741 (page 1477)	Strong Cyclonic Vortices over Topography on a Beta - Plane	Hung - Cheng Chen, Chin - Chou Chu, Chien - Cheng Chang
FM25L_11964 (page 1479)	Spontaneous Sign Reversals in Self-Organized States of Forced Two-Dimensional Turbulence on a Bounded Square Domain	David Molenaar, Herman J.H. Clercx, GertJan F. van Heijst
FM25S_12032 (page 1481)	A Model for the Formation of 'Optimal' Vortex Rings with Taking into Account Viscosity	Felix B. Kaplanski, Ylo A. Rudi
FM25S_12041 (page 1483)	Numerical Simulation of Vortical Flows Using a Highly Accurate Finite Difference Scheme	Katsuya Ishii, Tomonori Nihei, Shizuko Adachi
FM25L_12051 (page 1485)	The Development of an Axisymmetric Gravity Current	M. D. Patterson, J. E. Simpson, S. B. Dalziel, G. J. F. van Heijst
FM25S_12080 (page 1487)	Numerical Investigation of the Laminar - Turbulent Transition of the Flow in a Rotor - Stator Cavity	Ewa Tuliszka - Sznitko, Eric Serre, Patrick Bontoux
FM25S_12108 (page 1489)	Viscous Vertical Length Scale Selection in Stratified Fluids	Ramiro Godoy-Diana, Jean-Marc Chomaz, Paul Billant
FM25L_12161 (page 1491)	On Local Vortex Identification	Pinaki Chakraborty, S. Balachandar, Ronald J. Adrian
FM25L_12196 (page 1493)	The Modelling of The Dynamics of Hairpin Vortex Packets in Wall Turbulence	Vyacheslav V. Meleshko, Eugene I. Nikiforovich, Alexandre A. Gourjii, Ronald J. Adrian
FM25L_12275 (page 1495)	Coherent Structure of Point Vortices Influenced by Uniform Straining Flow	Marcin Kurowski, Konrad Bajer
FM25L_12690 (page 1497)	Strong Shock - Vortex Interaction a Numerical Study	W. Schroeder, O. Thomer, E. Krause
FM25L_12748 (page 1499)	Isolated Vortices over Seamounts: Laboratory Experiments and Numerical Simulations	O. U. Velasco Fuentes

FM25S_12821 (page 1501)	Three Dimensional Velocity Field of Vortices Impinging on a Wall Obtained by Scanning Particle Tracking Velocimetry	Klaus W. Hoyer
FM25L_12836 (page 1503)	Study of the Vortex Rings Interaction by 3d Vorticity Particle - In - Cell Method	Henryk Kudela, Pawel Regucki

Pre-nominated Session FM26
Waves

Co-Chair(s): **W.K. Melville (USA)**
V.I. Shrira (UK)

Paper ID	Title	Authors
FM26S_10123 (page 1505)	Nonlinear Long Waves on the Interface of a Two - Layered Horizontal Flow of Viscous Liquids	Dmitry G. Arkhipov, Georgy A. Khabakhpashev
FM26L_10245 (page 1507)	Unidirectional Steep Waves in Wave Tanks	L. Shemer, K. Goulitski, E. Kit
FM26S_10746 (page 1509)	Wave Breaking and Equilibrium Surfacewave Spectra	Tetsu Hara, Stephen E. Belcher
FM26L_10762 (page 1511)	Propagation and Interactions of Nonlinear Internal Gravity Wave Beams	T. R. Akylas, Ali Tabaei
FM26L_10861 (page 1513)	Weak - Turbulent Theory of Wind - Driven Sea	Vladimir E. Zakharov
FM26S_11126 (page 1515)	Shallow - Water Theory for Wave - Current - Bottom Interactions	Hu Huang
FM26S_11134 (page 1517)	Unsteady Undular Bore Transition in Fully Nonlinear Dispersive Wave Dynamics	Gennady El
FM26L_11144 (page 1519)	The Theory of Travelling Deformation Waves and Its Applications in Biomechanics, Engineering, and Geophysics	Anatoli I. Dobrolyubov
FM26L_11179 (page 1521)	The Spacing of Langmuir Circulation in Strong Wavy Shear	William R. C. Phillips
FM26L_11199 (page 1522)	Experiments on Rotating and Reflecting Internal Wave Beams	Thomas Peacock, Patrick Weidman, Ali Tabaei
FM26L_11230 (page 1524)	Spatio - Temporal Measurements of Capillary - Gravity Waves	Paul A. Hwang, David W. Wang, Guillemette Caulliez, Vladimir K. Makin
FM26L_11290 (page 1526)	Standing Gravity Waves in Deep Water	Gerard Iooss, Pavel Plotnikov, John F. Toland
FM26S_11345 (page 1528)	Nonlinear Three-Dimensional Free Surface Flows in Finite and Infinite Depth	Emilian Parau, Jean-Marc Vanden-Broeck, Mark J. Cooker
FM26S_11417 (page 1530)	Dynamics of Crescentwave Patterns in a Channel	D. Fructus, C. Kharif, D. Clamond, M. Francius, O. Kristiansen, J. Grue
FM26S_11468 (page 1532)	Evolution of Packets of Surface Gravitywaves over Smooth Topography	Eugene S. Benilov, Jason D. Flanagan, Colm P. Howlin
FM26L_11548 (page 1534)	Three Dimensional Gravity Water Waves	Walter Craig
FM26S_11591 (page 1536)	Sharpening and Breaking of Subharmonic Gravity Waves on Deep Water	Vasyl P. Lukomsky, Ivan S. Gandzha, Yaroslav V. Tsekhmister
FM26S_11680 (page 1538)	Short Wind Waves and Surface Wind Drift	Xin Zhang
FM26L_11746 (page 1540)	Transverse Instability of Surface Solitary Waves	Takeshi Kataoka, Michihisa Tsutahara

FM26L_11803 (page 1542)	A Lagrangian Approach to Wave - Induced Oceanic Mass Transport	Jan Erik Weber
FM26L_12087 (page 1544)	Effect of Horizontal Component of the Coriolis Force on Propagation of Near - Inertial Waves in the Ocean	Theo Gerkema, Victor I. Shrira
FM26L_12089 (page 1546)	Generalized Internal Solitary Waves and Fronts	Frederic Dias, Christophe Fochesato
FM26S_12268 (page 1548)	Intermittent Mixing by Multiscale Breaking of Wind Waves: Implications for Oil Dispersion	Igor A. Brovchenko, Vladimir S. Maderich
FM26S_12318 (page 1550)	Equatorial Wave Attractors and Inertial Oscillations	Leo R. M. Maas, Uwe Harlander
FM26L_12424 (page 1551)	Focusing of an Inertia - Gravity Wave Packet with a Baroclinic Shear Flow	Chantal Staquet, Neil R. Edwards
FM26S_12715 (page 1553)	Steep Capillary Waves in Electrified Fluid Sheets	Jean - Marc Vanden - Broeck, Demetrios Papageorgiou
FM26S_12813 (page 1555)	Bi - Directionalwaterwaves and Integrable High Order KDV Equations	Georgy I. Burde

Pre-nominated Session SM1
Computational solid mechanics

Co-Chair(s): **T. Belytschko (USA)**
P. Wriggers (Germany)

Paper ID	Title	Authors
SM1S_10270 (page 1559)	Elastic - Plastic Large Deformation Analysis of 2D Frame Structure	Chung - Yue Wang, Ren - Zuo Wang, Long - Chyuan Kang, Edward C. Ting
SM1S_10274 (page 1561)	Multiscale Analysis of Scattered Elastic Waves Based on the Lippmann - Schwinger Equation	Terumi Touhei
SM1L_10423 (page 1563)	Model Updating a Multicriteria Optimization Process in Mechanics	Hans H. Muller-Slany
SM1L_10559 (page 1565)	Experiment and Quasicontinuum Simulation of Nanoindentation of Single Crystal Copper	Yuan Lin, Shan Debin, Guo Bin
SM1L_10665 (page 1567)	A BEM Solution to Transverse Shear Loading of Beams	Evangelos J. Sapountzakis, Vasilios G. Mokos
SM1L_10728 (page 1569)	Mechanical Features of Piano Hammer Felt	Anatoli Stulov
SM1S_10829 (page 1571)	A Dual Particle Computational Method for Continua	L.D. Libersky, P.W. Randles
SM1L_11154 (page 1572)	Mesh Optimization for the Quasicontinuum Method: A Generalization of VALE	J. Knap, J. Marian, M. Ortiz
SM1S_11193 (page 1574)	Derivation of the Higher - Order Stiffness Matrix of a Space Frame Element for Geometric Nonlinear Analysis of Structrues	Jiann - Tsair Chang, I-Dang Huang
SM1S_11202 (page 1577)	The Method of Solving of Non - Stationary Coupled Problems of the Theory Thermal - Plasticity for the Rotation Shells	Pavlo A. Steblyanko
SM1L_11211 (page 1579)	A New Approach for the FE Modelling of Cohesive Cracks	Julia Mergheim, Ellen Kuhl, Paul Steinmann
SM1S_11291 (page 1581)	Effective Solution for Finite Element Problems with Nonlinear Constraints	Stanislaw A. Lukasiewicz, Hassan M. Hojjati
SM1L_11298 (page 1583)	Lingopti Project: Semi - Continuous Casting Process of Copper - Nickel Alloys	Etienne Pecquet, Ralf Volles, Jacqueline Lecomte - Beckers, Anne Marie Habraken

SM1S_11334 (page 1585)	Two Scale Finite Element Method	George Mejak
SM1S_11389 (page 1587)	Problems of Application of Hierarchical Modelling, Displacement FEM and a Posteriori Residual Error Estimation to Static and Dynamic Adaptive Analysis of Complex Structures	Grzegorz Zboinski, Maciej Jasinski
SM1S_11482 (page 1589)	Statics And Kinematics of Symmetric Swelling Viruses	Florian Kovacs, Tibor Tarnai, Simon D. Guest, Patrick W. Fowler
SM1S_11580 (page 1591)	A Numerical Approach for Large - Scale Computation CEM	Jixin Yang, Cheng Wang, Chengwu Shen
SM1L_11720 (page 1593)	Some Investigations on FM Bem in Solid Mechanics	Zhenhan Yao, Haitao Wang, Pengbo Wang
SM1L_11769 (page 1595)	Radial - Type Approximation Technique for a Space - Time Multiscale Computational Strategy	Anthony Nouy, Pierre Ladeveze
SM1L_11797 (page 1597)	An Energy Conserving Scheme for Time Dependent Problems Using the Extended Finite Element Method	J. Rethore, A. Gravouil, A. Combescure
SM1L_11817 (page 1599)	Development of a Novel 'Crack' Finite Element for Propagation Simulation	Young-Sam Cho, Sukky Jun, Seyoung Im
SM1L_12054 (page 1601)	Modelling of Static and Dynamic Processes of Nanoparticles Interaction	Alexander V. Vakhrouchev
SM1L_12101 (page 1603)	Singularities of the Four - Sided Antiprism Ring	Andras Lengyel
SM1L_12115 (page 1605)	Analysis of Evolving Deformation Microstructures in Instable Inelastic Solids Based on Energy Relaxation Methods	Ercan Guerses, Christian Miehe
SM1L_12131 (page 1607)	Microstructural Behaviour of Solder Joints	Rene L. J. M. Ubachs, Piet J. G. Schreurs, Marc G. D. Geers
SM1L_12167 (page 1609)	Molecular Mechanics Simulations of Carbon Nanostructures Using Multi-Scale Boundary Conditions	Sergey N. Medyanik, Eduard G. Karpov, Wing Kam Liu
SM1L_12177 (page 1611)	Multiscale Buckling Analyses of Corrugated Fiberboard	Hirohisa Noguchi, Nobutada Ohno, Dai Okumura
SM1L_12237 (page 1613)	Modified Error in Constitutive Relation and Its Application to Dynamic Tests with Corrupted Boundary Conditions	Pierre Feissel, Olivier Allix
SM1L_12310 (page 1615)	Geometry Based Rational Enrichment Functions for Triangular Plane Elasticity Element	Juha Makipelto
SM1S_12340 (page 1617)	Solving of Indirect Problems Using Trefftz Method	Marek S. Karas
SM1S_12351 (page 1619)	Tensor Invariants and Mechanisms of Transition to Chaos in Nonholonomic Dynamical Systems	Alexey V. Borisov, Ivan S. Mamaev
SM1S_12359 (page 1621)	Analysis of a Structural Detail Using a Two - Scale Approach	M. Cloirec, N. Moes, P. Cartraud
SM1L_12441 (page 1622)	Adaptive Discontinuous Galerkin Method for Elastodynamics on Unstructured Spacetime Grids	Reza Abedi, Shuo-Heng Chung, Yong Fan, Shripad Thite, Jeff Erickson, Robert B. Haber
SM1L_12455 (page 1624)	Continuum Mechanics and Carbon Nanotubes	Marino Arroyo
SM1L_12458 (page 1626)	Toward Convergence in Initially Rigid Cohesive Fracture Models	Chin-Hang Sam, Katerina Papoulia, Pritam Ganguly
SM1L_12534 (page 1628)	Computational Homogenisation of Microheterogeneous Materials Including Decohesion at Finite Strains	Stefan Loehnert, Peter Wriggers

SM1L_12562 (page 1631)	The Load Cases in Numerical Model of Pelvic Bone with Artificial Acetabulum	A. John, P. Orantek, J. J. Telega
SM1S_12579 (page 1633)	Shakedown Safety Criterion in Reliability Analysis	Andrzej Siemaszko
SM1S_12584 (page 1635)	A New Finite Element Formulation Based on the Theory of a Cosserat Point	E. F. I. Boerner, S. Loehnert, M. B. Rubin, P. Wriggers
SM1S_12607 (page 1637)	Arc - Length Method for Explicit Dynamic Relaxation	Ilson P. Pasqualino
SM1L_12723 (page 1639)	Modelling of Non - Uniform Deformation of Metals with Dislocation Cell Structure	E. M. Viatkina, W. A. M. Brekelmans, M. G. D. Geers
SM1S_12727 (page 1641)	The Numerical Homogenization of the Concrete Behavior	Frederic Grondin, Helene Dumontet, Abdelwahed Ben Hamida, Ghassan Mounajed, Hocine Boussa
SM1L_12737 (page 1643)	Discrete Dislocation Calculations of the Stored Energy of Cold Work	A. A. Benzerga, Yves Brechet, Alan Needleman, Erik van der Giessen
SM1S_12844 (page 1645)	Deformation Analysis of Inflated Cylindrical Membrane of Composite Material with Rubber Matrix Reinforced by Cords	Tran Huu Nam, Bohdana Marvalova
SM1L_12845 (page 1647)	Dynamic Analysis of Gradient Elastic Solids by BEM	Demosthenes Polyzos, Katerina G. Tsepoura, Dimitri E. Beskos
SM1L_12901 (page 1649)	Variable - Order Singular Boundary Element for Calculation of Three - Dimensional Stress Intensity Factors	Kian - Meng Lim, Wei Zhou, Andrew A. O. Tay
SM1L_12924 (page 1651)	Application of the Material Force Method to Structural Optimization	Swantje Bargmann, Ellen Kuhl, Harm Askes, Paul Steinmann

Pre-nominated Session SM2
Contact and friction mechanics

Co-Chair(s): **I. Goryacheva (Russia)**
A. Klarbring (Sweden), G. Szefer (Poland)

Paper ID	Title	Authors
SM2S_10211 (page 1653)	Thermocontact Interaction of Bodies of Revolution During Induction Heating	Mykola Shulzhenko, Pavlo Gontarowskiy, Yuriy Matyukhin, Mykhaylo Pantelyat, Ivo Dolezel, Bohus Ulrych
SM2S_10342 (page 1655)	Dynamic Characteristics and Monitoring of Rubbing Surfaces Quality	Victor M. Musalimov, Y. V. Lisitsin, S. V. Orlov
SM2L_10415 (page 1657)	Electric - Mechanical Beam - To-Beam Contact	Daniela P. Boso, Przemyslaw Litewka, Bernhard A. Schrefler, Peter Wriggers
SM2S_10459 (page 1659)	Contact Mechanical Analysis of Elastic Multibody Structures	Herman Parland, Antero Miettinen
SM2L_10686 (page 1661)	Existence and Uniquness of Steady State Solutions in Thermoelastic Contact With Frictional Heating	L.-E. Andersson, A. Klarbring
SM2L_10718 (page 1663)	FE Analysis of Bond for Smooth FRP Rods Embedded in Concrete	Hamid Reza Irannejad, Amir Reza Khoei
SM2S_10999 (page 1665)	Modelling of Contact of Structured Materials Based on Data from Scanning Probe Microscopy	Sergey A.Chizhik, Zygmunt Rymuza, Dmitri I. Shasholko
SM2S_11008 (page 1667)	A Universal Property of Geometrical Hardening	Graham J. Weir
SM2L_11074 (page 1669)	Contact Optimization Problems Associated with the Wear Process	Istvan Paczelt, Zenon Mroz

SM2L_11135 (page 1671)	Molecular Adhesive Contact for Indenters of Non - Ideal Shapes	Feodor M. Borodich, Boris A. Galanov
SM2L_11196 (page 1673)	Adhesive Component of the Rolling Friction Force	Irina Goryacheva, Yulia Makhovskaya
SM2L_11215 (page 1675)	Fundamental Relations for Frictional and Adhesive Nanoindentation Tests	Feodor M. Borodich, Leon M. Keer
SM2L_11365 (page 1677)	Hertz Contact at Finite Friction and Arbitrary Profiles	Bertil Storakers, Denis Elaguine
SM2S_11452 (page 1679)	Frictional Contact with Wear Diffusion	Meir Shillor, Mircea Sofonea, Jozef Joachim Telega
SM2S_11481 (page 1681)	On the Contact Thermoelastic Problem with Frictional Heating, Wear and Auto - Vibrations	Jan Awrejcewicz, Yuriy Pyryev
SM2S_11611 (page 1683)	Three-Dimensional Problem of the Contact by Doubly Connected Domain Taking into Account Roughness and Friction	Ganna Shyshkanova
SM2S_11613 (page 1685)	Evolutions of Friction Anisotropy and Heterogeneity	Alfred Zmitrowicz
SM2S_11697 (page 1687)	Inverse Problems of Thermoelasticity for Frictionally Interacting Layers	Victor Shevchuk, Anatoliy Yasinskyi
SM2S_11778 (page 1689)	Multidimensional Model of Combined Dry Friction	Alexey A. Kireenkov
SM2L_11933 (page 1691)	Numerical Modeling of Contact Fracture of Elasto - Plastic Cracked Bodies	Alexandr A. Bobylov, Yuriy A. Letser
SM2L_11987 (page 1693)	Crack - Like and Pulse - Like Modes of Frictional Sliding along an Interface Under Dynamic Shear Loading	Demirkan Coker, Alan Needleman, Ares J. Rosakis
SM2S_12082 (page 1695)	Experimental and Numerical Study of the Brick-Mortar Interface	Leila Abdou, Ramdane Ami Saada, Fekri Meftah, Ahmed Mebarki
SM2L_12086 (page 1697)	Experimental and Analytical Investigation of Rubber Friction	Markus Lindner, Matthias Kroeger, Karl Popp, Holger Blume
SM2S_12097 (page 1699)	Penalty Approximation of Impact with Coulomb Friction	Michelle Schatzman
SM2L_12246 (page 1701)	Chaotic Response of Non - Reversible Dry Friction Oscillator	Andrzej Stefanski, Jerzy Wojewoda, Marian Wiercigroch, Tomasz Kapitaniak
SM2L_12382 (page 1703)	A Dynamic Unilateral Contact Problem for a Cracked Body	Marius Cocou, Eliane Becache, Patrick Joly, Gilles Scarella
SM2S_12412 (page 1705)	A Simple Model to Account for the Locking Effect Between Two Rough Surfaces under Cyclic Loading	Larissa Gorbatikh
SM2L_12553 (page 1707)	Boundary Layers Induced by Contact of Rough Bodies	Stanislaw Stupkiewicz
SM2L_12559 (page 1709)	The Accounting of Surface Roughness in Contact of Arbitrary Shaped Bodies Using FEM	Alexandr A. Olshevsky, Alexei A. Olshevsky, Konstantin V. Shevchenko, Vladimir I. Sakalo
SM2L_12563 (page 1711)	Frictional Sliding of a Multislip System	Thibaut Putelat, John R. Willis
SM2L_12646 (page 1713)	Second - Order Cone Complementarity Formulation for Quasi-Static Incremental Frictional Contact Problem in Three - Dimensional Space	Y. Kanno, A. Pinto da Costa, J. A. C. Martins
SM2S_12773 (page 1715)	A Novel Contact Model Based on Volumetric Information	Yves Gonthier, John McPhee, Christian Lange, Jean-Claude Piedboeuf

Pre-nominated Session SM3
Control of structures

Co-Chair(s): **F. Chernousko (Russia)**
S. Pellegrino (UK)

Paper ID	Title	Authors
SM3S_10098 (page 1717)	Coupled Optimal Design of Building with TMD	Anupam S. Ahlawat, Ananth Ramaswamy
SM3L_10457 (page 1719)	Optimal Vibration Control of Guyed Masts	Bartlomiej D. Blachowski, Witold Gutkowski
SM3S_10458 (page 1721)	Time - Optimal Control of Hydraulic Manipulators	Witold Gutkowski, Pawel Holobut
SM3S_10879 (page 1723)	Surface Accuracy of Inflatable Reflector Covered with Stretched Cable	Kazuo Tanizawa, Jun Nishimura, Kazuo Yamamoto
SM3S_11036 (page 1725)	H-inf Control for Smart Multistory Building Structures	Daniela Marinova, Georgios Stavroulakis
SM3L_11163 (page 1727)	Exact Tracking Control for Nonlinear Structural and Mechanical Systems	Firdaus E. Udwdia
SM3S_11219 (page 1729)	Pre - Acting Impact Isolation Systems	Dmitry V. Balandin, Nikolai N. Bolotnik
SM3L_11243 (page 1731)	Control of Multibody Systems Moving along a Plane	F.L. Chernousko
SM3L_11265 (page 1733)	Control of Random Dynamics of a Rigid Rocking Block	Agnessa Kovaleva
SM3S_11287 (page 1735)	Suppression of Train - Induced Vibrations of Continuous Truss Bridge by Hybrid TMDs	Jong - Dar Yau
SM3L_12756 (page 1737)	Optimization of Active Control of Structural Vibration by the Beam Analogy	Walerian Szyszkowski, Manish Baweja
SM3S_13004 (page 1739)	Control of a Nonlinear Slewing Flexible Beam	Andre Fenili, L. C. Gadelha DeSouza

Pre-nominated Session SM4
Damage mechanics

Co-Chair(s): **M. Chrzanowski (Poland)**
P. Steinmann (Germany)

Paper ID	Title	Authors
SM4S_10011 (page 1741)	Stability and Creep Damage of Quasi - Brittle Materials	Noel Challamel, Christophe Lanos, Charles Casandjian
SM4L_10456 (page 1743)	Modeling of the Damage Evolution at the Granular Scale in Polycrystals under Complex Cyclic Loadings	A. Abdul-Latif, M. Chadli
SM4L_10865 (page 1745)	Continuumthermodynamic and Variationalmodeling and Simulation of Ductile Failure at Large Deformation with Application to Engineering Structures	Bob Svendsen, Frederik Reusch, Dietmar Klingbeil
SM4S_10960 (page 1747)	Material Models for Hookean Materials with Voids or Cracks	Kari Santaoja, Anniina Kuistiala
SM4L_10961 (page 1749)	Localized Necking Criterion Based on Acoustic Tensor for Materials with Anisotropic Damage	C. L. Chow, M. Jie
SM4L_10974 (page 1751)	An Elasto - Viscoplastic Model Coupled to Damage and Grain Growth to Take Account of Material Variability	Benoit Vereecke, Rene Billardon
SM4L_11228 (page 1753)	Damage and Failure of Brittle Solids	Andrzej Litewka, Leszek Szojda

SM4L_11406 (page 1755)	Numerical Analysis of Nonlocal Anisotropic Continuum Damage	Sabine Ricci, Michael Brunig
SM4L_11414 (page 1757)	Discrete Models and Their Application in Damagemechanics	Gian Antonio D'Addetta, Ekkehard Ramm
SM4L_11415 (page 1759)	A Nonlocal Plasticity - Damage Formulation Based on the Micromechanics of Defect Growth	R. H. J. Peerlings, R. A. B. Engelen, M. G. D. Geers
SM4L_11665 (page 1761)	Propagation of Cracks in Terms of Continuum Damage Mechanics	Adam Bodnar, Marcin Chrzanowski
SM4S_11779 (page 1763)	An Asymptotic Analysis of Mode I Crack in Creepnig Damaged Solids	Larisa V. Stepanova, Maria E. Phedina
SM4L_11796 (page 1765)	Damage Acquired Anisotropy in Elastic - Plastic Materials	Jacek J. Skrzypek, Halina Kuna - Ciskal, Jan Bielski
SM4L_11885 (page 1767)	A CDM Approach of Ductile Damage with Plastic Volume Changes	J.L. Chaboche, K. Saanouni, M. Boudifa
SM4L_11886 (page 1769)	Micromechanical Modelling of the Deformation and Damage of Inelastic Brittle Three - Phase Composites: Application to Fiber - Reinforced Concrete	A. Ouaar, I. Doghri, J. Fr. Thimus, F. Huge
SM4L_12021 (page 1771)	Damage Field Identification using Full - Field Displacement Measurements	Damien Claire, Francois Hild, Stephane Roux
SM4L_12036 (page 1773)	A New Energy - Based Elastoplastic Damage Model for Concrete	Jianying Wu, Jie Li
SM4L_12088 (page 1775)	Lifetime Prediction with a Damage Model Based on Mixed-Mode Microcrack Propagation	Henning Schuette
SM4L_12116 (page 1777)	A Micromechanically Based Network Model for Rubbery Polymers Incorporating Mullins - Type Stress Softening	Serdar Goektepe, Christian Miehe
SM4S_12277 (page 1779)	Computational Micro - Meso Modeling for Laminates Under Thermomechanical Fatigue and an Oxidizing Atmosphere	Lubineau Gilles, Ladeveze Pierre
SM4S_12298 (page 1781)	A Non-Associative Anisotropic Damage Model for Brittle Materials	Luigi Gambarotta, Ilaria Monetto
SM4S_12333 (page 1783)	Robust Identification of an Augmented Gurson Model for Elasto-Plastic Porous Media	Andrzej Stachurski, Zdzislaw Nowak
SM4S_12335 (page 1785)	Low Cycle Fatigue Based on Unilateral Damage Evolution	Artur Ganczarski
SM4L_12341 (page 1787)	Coupled Meso-Macro Simulation of Masonry Cracking	T.J. Massart, R.H.J. Peerlings, M.G.D. Geers
SM4L_12749 (page 1789)	Coupling Between Progressive Damage and Permeability of Concrete	George Chatzigeorgiou, Vincent Picandet, Abdelhafid Khelidj, Gilles Pijaudier-Cabot
SM4L_12913 (page 1791)	Anisotropic Damage Model for Concrete Including Unilateral Effects	V. Godard, J.-B. Leblond, P.-B. Badel

Pre-nominated Session SM5
Dynamic plasticity of structures

Co-Chair(s): **N. Jones (UK)**
T. Wierzbicki (USA)

Paper ID	Title	Authors
SM5L_11022 (page 1793)	Blast Resistance of Clamped Sandwich Beams	Vikram S. Deshpande, Norman A. Fleck
SM5L_11051 (page 1795)	Collision Between Two Deformable Structures	T. X. Yu, H. H. Ruan

SM5L_11107 (page 1797)	Counterintuitive Response of Long Circular Tubes to Axial Impact	D. Karagiozova, Norman Jones
SM5L_12043 (page 1799)	Self Similar Dynamic Expansion of a Spherical Cavity in Elastoplastic Media	Rami Masri, David Urban
SM5L_12949 (page 1800)	Numerical Investigation of Dynamic Shear Bands in Inelastic Solids as a Problem of Mesomechanics	Adam Glema, Tomasz Lodygowski, Piotr Perzyna
SM5L_12982 (page 1802)	On Non-Axisymmetric Collapse of Thin Tubes	N. K. Gupta

Pre-nominated Session SM6
Elasticity

Co-Chair(s): **R. Kienzler (Germany)**
L. Wheeler (USA)

Paper ID	Title	Authors
SM6S_10442 (page 1804)	On Invariants of the Elasticity Tensor for Orthotropic Materials	Katarzyna Kowalczyk-Gajewska, Janina Ostrowska-Maciejewska
SM6S_10972 (page 1806)	Motion and Stability of an Elastic Heavy Top	Tsolo P. Ivanov, Radijanka Savova
SM6L_11220 (page 1808)	Stability of Compressible Elastic Blocks	D M Haughton
SM6L_11523 (page 1810)	Generalized Stress Concentration Factors	Reuven Segev
SM6S_11526 (page 1812)	On Asymptotic Method of Static and Dynamic Boundary Problems Solution	Lenser A. Aghalovyan
SM6S_11901 (page 1814)	Axisymmetric Force Solution for a Semi - Infinite Cubic Solid	Charles Ruimy, Marc Dahan
SM6S_11960 (page 1816)	An Exactly Solvable Microgeometry in Torsion	Tungyang Chen
SM6S_11998 (page 1818)	A New Nonlinear Constitutive Relation for Magnetostrictive Materials	Xiaojing Zheng, Xinen Liu
SM6S_12039 (page 1820)	Nonlinear Radial Oscillations of Anisotropic Thin-Walled Cylindrical Tubes	G. H-S. Maluleke, D. P. Mason
SM6L_12122 (page 1822)	Nonlocal Eshelby Entities: a One - Dimensional Example	Marcelo Epstein, Les Sudak
SM6L_12189 (page 1825)	Analysis of Trabecular Bone as a Hierarchical Material	Iwona M. Jasiuk
SM6L_12289 (page 1827)	Investigation of Couple - Stress Effects in Elastic Bodies Under Deformation	Valery P. Matveyenko, Valery V. Korepanov, Michail A. Kulesh, Igor N. Shardakov
SM6S_12324 (page 1829)	New Analytical Approach for Investigation of Non - Stationary Dynamics of Media with Moving Inhomogeneities	Serge N. Gavrilov
SM6S_12354 (page 1831)	Agmon's Condition for Incompressible Elasticity: a Variational Formulation	Gearoid Mac Sithigh
SM6L_12434 (page 1833)	Modelling of Complex Elastic Crystals by Means of Micromorphic Gyrocontinua	Elena F. Grekova, Gerard A. Maugin
SM6S_12520 (page 1835)	Axisymmetric Problem for an Elastic Medium with a Spherical Inclusion When There Is a Crack at the Interface	Iryna V. Lebedyeva, Myhaylo A. Martynenko
SM6S_12575 (page 1837)	Truncated Elastic Wedge under Torsional Load	Vyacheslav V. Lyakh

SM6S_12685 (page 1839)	Homogenization of Triply Periodic Elastic Media with Random Imperfections	Valeriy Buryachenko
SM6S_12987 (page 1841)	On the Impact Law in Elastic Plate - Like Bodies	R. Sburlati

Pre-nominated Session SM7
Experimental methods in solid mechanics

Co-Chair(s): **I. Emri (Slovenia)**
Jose L. Freire (Brazil)

Paper ID	Title	Authors
SM7L_10492 (page 1843)	An Optical Strain Rosette/ring - Core Method Applied on Laser Weld	Wei Ren, Keyu Li
SM7L_10691 (page 1845)	Estimation of Principal Axes of Inertia	Masashi Sato, Yasusuke Jinnouchi
SM7S_11556 (page 1847)	The Whole Field Non - Destructive Optical Slicing Method in Three - Dimensional Photoelasticity	Michael N. Osipov, Vychislav K. Emelin
SM7S_11617 (page 1849)	Porous Ceramics - Experimental Research and Modelling	Sylwester Samborski, Tomasz Sadowski
SM7S_11764 (page 1851)	Critical Sensitivity in Rock Experiments	Xianghong Xu, Mengfen Xia, Fujiu Ke, Yilong Bai
SM7L_12272 (page 1853)	Phase Transitions and Mechanical Properties of Ternary Chalcogenides	Vladimir V. Shchennikov, Sergey V. Ovsyannikov, Natalya Yu. Frolova, Vsevolod V. Shchennikov
SM7L_12551 (page 1855)	SHPB Technique for Identification of Complex Modulus Under Condition of Non - Uniform Stress	S. Mousavi, U. Valdek, K. Welch, B. Lundberg
SM7S_12666 (page 1857)	IN-SITU Observation of Fatigue Crack Growth in Carbon Steel	Michal A. Miskiewicz, Zbigniew Pakiela, Krzysztof J. Kurzydlowski
SM7S_12799 (page 1859)	New Solutions in Experimental Modal Analysis of Mechanical Structures	Tadeusz Uhl, Mendrok Krzysztof, Wojciech Lisowski, Piotr Kurowski

Pre-nominated Session SM8
Fatigue

Co-Chair(s): **J. Dominguez (Spain)**
K. Reifsnider (USA)

Paper ID	Title	Authors
SM8L_10698 (page 1861)	Influence of Contact Conditions on Fretting Fatigue Under Spherical Contact	Carlos Navarro, Manolo Tur, Javier Fuenmayor, Jaime Dominguez
SM8S_11371 (page 1863)	Fatigue Investigations into a Composite Glider Structure	Miroslaw Rodzewicz, Krystyna Majorkowska - Knap
SM8L_11686 (page 1865)	A Microscopic Mechanics Model	Yi Sun, Rei Zhang, Jun Ma, Jianmin Qu
SM8S_11737 (page 1867)	Fatigue Life Prediction Considering Residual Stress Relaxation	Byeongchoon Goo, Sungyong Yang
SM8S_11920 (page 1869)	Effects of Frequency Temperature and Loading Waveform on Fatigue Crack Growth Rate in Steel 15Kh13MF	P. V. Yasniy, P. O. Maruschak
SM8L_11927 (page 1872)	Stress Concentrations Caused by Dislocations at the Free Surface	Steffen Brinckmann, Erik Van der Giessen
SM8S_12001 (page 1874)	A Study on the Effect of Residual Stress on a Fatigue Bahavior	Seung - Yong Yang, Byeongchoon Goo

SM8S_12034 (page 1876)	Probabilistic Analysis of Fatigue Crack Growth using Moment Method	Ki-Seok Kim, Hyun Moo Koh, Hae Sung Lee
SM8L_12217 (page 1878)	Energy Release Rate Approach for Delamination in a Fatigue Crack Configuration in Glare	Rene Alderliesten
SM8S_12228 (page 1880)	Modelling Fatigue Crack Growth with Time - Derivative Equations	Marion Risbet, Sylvie Pommier, Michel Clavel
SM8L_12391 (page 1882)	Characteristics of Very - High - Cycle Fatigue for a High Carbon Low Alloy Steel	Hong Youshi, Zhou Cheng - en
SM8S_12914 (page 1884)	Modelling of Short Fatigue Crack Growth in a Metal in HCF Range	D. Kocanda

Pre-nominated Session SM9
Fracture and crack mechanics

Co-Chair(s): **D. Gross (Germany)**
A. Needleman (USA)

Paper ID	Title	Authors
SM9S_10250 (page 1886)	A Fractal Cohesive Crack Model	Michael P. Wnuk
SM9S_10334 (page 1892)	Influence of Stress State on Crack - Tip Driving Force	Daniel Kujawski
SM9L_10338 (page 1894)	Branching Instability of Brittle Fracture	M. Adda - Bedia
SM9S_10419 (page 1896)	Size Effect in Tensile Fracture of Concrete - A Study Based on Lattice Model Applied to CT - Specimen	Remalli Vidya Sagar, B. K. Raghu Prasad
SM9S_10429 (page 1899)	Numerical and Experimental Study of the Plastic Zone in the Vicinity of the Crack Tip by the Optical Caustics Method	Octavian Pop, Valery Valle, Mario Cottron
SM9S_10579 (page 1901)	Thermoelastic Problems for a Bimaterial with Defects/singularities	Vera E. Petrova
SM9S_10646 (page 1903)	Dynamic Crack Analysis Under Thermal Shock	Parissa Hosseini - Tehrani, Alireza Hosseini - Godarzi
SM9L_10676 (page 1906)	Experimental Investigation on Concrete Shear Crack Extension	Huijian Li, Shengwang Hao
SM9S_10824 (page 1908)	Effect of Inter - and Intralaminar Damage on the Compressive Fracture of Hyperelastic Materials	Igor A. Guz, Maria Kashtalyan, Klaus P. Herrmann
SM9L_10864 (page 1910)	Experimental and Numerical Crack Growth in a Special Geometry	Liviu Marsavina, Dan M. Constantinescu
SM9S_10897 (page 1912)	Elastodynamics Problems in Domains with Edges	S. I. Matioukevitch, N. F. Morozov, B. A. Plamenevskii
SM9L_10910 (page 1913)	3D Microstructural Effects on Plane Strain Ductile Crack Growth	Alan Needleman, Viggo Tvergaard
SM9S_11045 (page 1915)	Weight Functions for Cracks in Piezoelectrics	Andreas Ricoeur, Meinhard Kuna
SM9S_11087 (page 1917)	Three - Dimensional Correction of Two - Dimensional Fracture Criteria Using a Constraint Factor	Rimantas Kacianauskas, Vladislav Zarnovskij, Eugenius Stupak
SM9S_11195 (page 1919)	Elastodynamic Contact Problem for Two Penny - Shaped Cracks	Oleksandr V. Menshykov
SM9L_11321 (page 1921)	Numerical Approach for Dynamic Fracture in Piezoelectric Solids	Jose Dominguez, Andres Saez, Felipe Garcia - Sanchez
SM9L_11425 (page 1923)	Finite Element Analysis of Fracture and Polarization Switching Behavior in Modified Small Punch Testing of Piezoelectric Ceramics	Yasuhide Shindo, Fumio Narita, Yasuyo Magara, Masaru Karaiwa

SM9L_11484 (page 1925)	On Crack Assessment at Bimaterial Interfaces	Axel Mueller, Joerg Hohe, Wilfried Becker
SM9S_11502 (page 1927)	Analysis of Tensile Testing of a Soft Ferromagnetic Elastic Strip Containing a Central Crack under a Magnetci Field	Daisuke Sekiya, Yasuhide Shindo, Fumio Narita, Katsumi Horiguchi
SM9S_11568 (page 1929)	A Quasi - Spherical Coordinate System and Its Application to the Determination of Vertex - Type Singularities	Hai - Tao Wang, K. Y. Sze
SM9L_11626 (page 1931)	Failure Model of Protective Coatings	Asher A. Rubinstein, Yaliang Tang
SM9S_11856 (page 1933)	Modeling of Environment Assisted Delamination I. Quasistatic Case	Alla V. Balueva
SM9S_11910 (page 1935)	The Influence of Remote Stresses on the Near Crack Tip Stress Field	Ewa Turska, Krzysztof Wisniewski
SM9S_11934 (page 1937)	The Elasto-Plastic Thin Film/Substrate Via Buckle-Driven Delamination and Crack Growth	Qunyang Li, Shouwen Yu
SM9S_11980 (page 1939)	On 3-D Thermoelastic Problems of Interfacial Cracks in a Periodic Stratified Space	Andrzej Kaczynski, Stanislaw J. Matysiak
SM9L_12044 (page 1941)	Automatic 3D Crack Growth Simulation Based on Boundary Elements	Karsten Kolk, Guenther Kuhn
SM9L_12171 (page 1943)	Massively Parallel Simulations of Dynamic Fracture and Fragmentation of Brittle Solids	Irene Arias, Jaroslaw Knap, Anna Pandolfi, Michael Ortiz
SM9S_12174 (page 1945)	the Shield Effect of Phase Transformation Stress Field at Crack Tip	Ping Wang, Zhenguo Tian, Zhiren Wang, Lijuan Zheng, Xiangzhong Bai
SM9S_12249 (page 1947)	Contact Zone Approach to the Analysis of Interface Cracks in Thermomechanically Loaded Piezoelectric Bimaterials	Klaus P. Herrmann, Volodymyr V. Loboda
SM9L_12378 (page 1949)	Interaction of Propagting Cracks and Shear Waves	Daniel Bonamy, Krishnaswamy Ravi-Chandar
SM9L_12393 (page 1951)	Disorder of the Front of a Tensile Tunnel - Crack Propagating in Some Inhomogeneous Medium	Jea - Baptiste Leblond
SM9S_12492 (page 1953)	Creep Deformation in Thermal Barrier Coatings due to the Effect of Thermal Growth Oxidation and Temperature Gradient	Y. C. Zhou, D. Wu
SM9S_12798 (page 1955)	Numerical Analysis of Strain Hardening and Pressure Sensitivity Effects on J - Integral	Abdulhamid Al - Abduljabbar
SM9L_12921 (page 1957)	Incremental Minimization Principles in Fracture and Damage Mechanics	G. A. Francfort, J. J. Marigo

Pre-nominated Session SM10
Functionally graded materials

Co-Chair(s): **R. Batra (USA)**
G.H. Paulino (USA)

Paper ID	Title	Authors
SM10L_10045 (page 1959)	Dynamic Stability of Functionally Graded Plate Under In - Plane Compression	Andrzej Tylikowski
SM10L_10135 (page 1962)	Micromechanics - Based Elastic Model for Functionally Graded Materials with Particle Interactions	Lizhi Sun, Huiming Yin, Glaucio Paulino
SM10S_10364 (page 1964)	A State Space Formalism for Piezothermoelasticity of Functionally Graded Materials	Jiann - Quo Tarn, Hsi - Hung Chang
SM10S_10501 (page 1966)	Conservation Laws of Functionally Graded Materials in Elastodynamics	Shi Weichen

SM10L_10836 (page 1968)	Transient Dynamic Crack Analysis in FGMs Under Impact Loading	Chuanzeng Zhang, Jan Sladek, Vladimir Sladek
SM10L_11177 (page 1970)	Asymptotic Ananlysis of a Stationary Crack in a Ductile Functionally Graded Material	Dhirendra V. Kubair, Philippe H. Geubelle, John Lambros
SM10S_11551 (page 1972)	The Plane Crack Problem in a Functionally Graded Orthotropic Strip	Linzhi Wu, Licheng Guo, Li Ma
SM10S_11572 (page 1974)	Frictional Slip Between a Gradient Non - Homogeneous Layer and a Half - Space in Anti - Plane Elastic Wawe Field	Gai Bing - Zheng
SM10L_11592 (page 1978)	Wave Propagation in Functionally Graded Materials	Arkadi Berezovski, Juri Engelbrecht, Gerard A. Maugin
SM10S_11671 (page 1980)	Adaptive Modelling of Microscopic Heterogeneous Medium Undergoing Large Deformation	Eduard Rohan, Vladimir Lukes
SM10L_12093 (page 1982)	Actuator and Sensor Modelling for Laminated Piezoelectric Plates	Amancio Fernandes, Joel Pouget
SM10L_12273 (page 1984)	Complex - Variable Methods Applied to Functionally - Graded Elastic Plate Problems	Arthur H. England, Anthony J. M. Spencer
SM10S_12461 (page 1986)	Study of Two - Dimensional Elasticity on FGM	Takemasa Seto, Tetsu Nishimura
SM10S_12465 (page 1988)	Three - Dimensional Transient Thermoelastic Analysis of Orthotropic Functionally Graded Rectangular Plate	Yoshihiro Ootao, Yoshinobu Tanigawa
SM10L_12594 (page 1990)	Adiabatic Shear Bands in Functionally Graded Materials	R. C. Batra, B. M. Love
SM10S_12664 (page 1992)	Nonlocal Effects in Micromechanics of Functionally Graded Composites of Random Structure	Gregory Schoeppner, Valeriy Buryachenko
SM10L_12665 (page 1994)	Topology Optimization Applied to the Design of Functionally Graded Material (FGM) Structures	Emilio Carlos Nelli Silva, Glaucio H. Paulino
SM10S_12968 (page 1996)	First Principles - Based Equations of State for Functionally Graded Materials	S. Hanagud, Xia Lu
SM10L_12978 (page 1999)	Design of FGM Bimorph Piezo - Actuators	Minoru Taya
SM10L_13018 (page 2001)	Thermoelastic Analysis of Functionally Graded Materials Submitted to Shocks	Carlos Augusto Vieira Carneiro, Fernando Alves Rochinha, Lavinia S. A. Borges

Pre-nominated Session SM11
Impact and wave propagation

Co-Chair(s): **A. Norris (USA)**
K. Wilmanski (Germany)

Paper ID	Title	Authors
SM11L_10072 (page 2003)	Surface Waves on an Impermeable Boundary of a Poroelastic Medium	Bettina Albers
SM11L_10114 (page 2005)	Bulk Solitons do not Decay in Elastic Wave Guides	Alexander M. Samsonov, Galina V. Dreiden, Irina V. Semenova
SM11L_10344 (page 2007)	Stress - Focusing Effect in a Spherical Zirconia Inclusion with Dynamically Transforming Strains	Toshiaki Hata
SM11L_10422 (page 2009)	Simultaneous Simulation of Dispersion Curves and H/V Spectra	Toshiro Maeda
SM11S_10426 (page 2011)	Nonlinear Waves in Shock - Loaded Solids	Nikolai N. Myagkov

SM11L_10612 (page 2013)	Critical Time for Acoustic Waves in Weakly Nonlinear Poroelastic Materials	Wilmanski Krzysztof
SM11S_10891 (page 2015)	Rayleigh - Like Surface Waves on a Nonlinear Layered Elastic Half Space	Semra Ahmetolan, Mevlut Teymur
SM11L_11085 (page 2017)	Non - Destructive Testing of Wood by Wave Propagation	Istvan A. Veres, Mahir B. Sayir
SM11S_11099 (page 2019)	A Two - Dimensional Analysis of Surface Acoustic Waves in Finite Anisotropic Solids with Electrodes	Ji Wang, Jingbo Lin
SM11S_11242 (page 2021)	Nonlinear Wawe Processes in a Bi - Layer	Karima R. Khusnutdinova, Roger H. J. Grimshaw
SM11L_11271 (page 2023)	Shock - Induced Surface Waves in Porous Reservoirs	G. Chao, D. M. J. Smeulders, M. E. H. van Dongen
SM11L_11360 (page 2025)	Trapping of Plastic Waves by Adiabatic Deformation	Janusz R. Klepaczko
SM11S_11377 (page 2027)	Modeling of Solitary Impulses in a Composite Material Using Wavelet Analysis	Kateryna V. Terletska
SM11S_11401 (page 2029)	Some Degenerated and Extended Wave Models of Elasto - and Hydrodynamics with Finite Velocity Disturbance Propagation	Igor Selezov
SM11S_11596 (page 2031)	Uniqueness Results for the Reflection - Transmission Problem	Angelo Morro
SM11S_11620 (page 2033)	Wave Interaction Resonances in Inhomogeneous Elastic Materials	Andres Braunbrueck, Arvi Ravasoo
SM11S_11682 (page 2035)	Acceleration Wavefronts in Random Media	Martin Ostoja - Starzewski, Jerzy Trebicki
SM11S_11812 (page 2037)	Inhomogeneous Circularly Polarized Waves in Orthorhombic Crystals	Philippe S. Boulanger, Michael A. Hayes
SM11S_11813 (page 2039)	Hidden and Driven solitons in Microstructured Media	Andrus Salupere, Juri Engelbrecht
SM11S_11853 (page 2041)	Thermo-Mechanical Wave Propagation in Materials with Internal State Variables	Witold Kosinski, Kurt Frischmuth
SM11S_11989 (page 2043)	Self - Consistent Methods in the Problem of Elastic Wave Propagation Through Matrix Composite Matrials	Sergey K. Kanaun, Valery M. Levin
SM11S_12203 (page 2045)	Waves of Deformation Propagation in Nonlinear Viscously Elastic Porous Material	Vladimir I. Erofeyev, Anton G. Pegushin
SM11L_12313 (page 2047)	Elastoplasticity of Gravel Protecting Rockfall-Endangered Steel Pipelines	Bernhard Pichler, Christian Hellmich, Herbert A. Mang
SM11L_12418 (page 2049)	Flaw Identification by Angle Beam Electromagnetic Acoustic Transducers	Shumpei Hanada, Toshihiko Sugiura
SM11L_12481 (page 2051)	Impact Fracture of Rock Materials Due to Percussive Drilling Action	Anton M. Krivtsov, Ekaterina E. Pavlovskaia, Marian Wiercigroch
SM11S_12514 (page 2053)	Dispersion and Stability Analysis of Waves in Pre - Stressed Imperfectly Bonded Layered Composites	Anil C. Wijeyewickrema, Sasikorn Leungvichcharoen
SM11L_12568 (page 2055)	On the Propagation of Solitary Waves in Microstructured Solids	Olari Ilison, Andrus Salupere
SM11L_12763 (page 2057)	Level - Sets and Mixed Approaches for Dynamic Contact Problems	Hachmi Ben Dhia, Chokri Zammali
SM11L_12772 (page 2059)	Analysis and Design of Dispersive Materials and Structures	Mahmoud I. Hussein, Gregory M. Hulbert, Richard A. Scott

Pre-nominated Session SM12
Material instabilities

Co-Chair(s): **D. Bigoni (Italy)**
H. Petryk (Poland)

Paper ID	Title	Authors
SM12L_10265 (page 2061)	Material Instabilites in Thermo - Mechanical Processes	Ahmed Benallal, Davide Bigoni
SM12S_10314 (page 2063)	Dynamical Systems Theory in Material Instabilities	Peter B. Beda
SM12S_10867 (page 2065)	An Idea and Theory of Hypothetical Device for Investigating the Localization Phenomena	Eugene I. Ryzhak
SM12L_10996 (page 2067)	Incremental Energy Minimization in Material Instaqbility Problems	Henryk Petryk, Klaus Thermann
SM12L_11254 (page 2069)	Dynamics of Perturbations and Shear Band Instabilities	Bigoni Davide, Capuani Domenico
SM12L_11277 (page 2071)	On Convexity Conditions in Spatial and Material Settings of Hyperelasticity	Paul Steinmann, Ellen Kuhl, Harm Askes
SM12L_11432 (page 2073)	Computational Characterization of Micro - to Macroscopic Mechanical Behavior of Carbon Black - Filled Rubber	Yoshihiro Tomita, Wei Lu, Yasuhiro Furutani
SM12L_11705 (page 2075)	Material Instabilities of Fiber - Reinforced Nonlinearly Elastic Solids	Jose Merodio, Ray W. Ogden
SM12L_12025 (page 2077)	Ultrastiff Elastic Composites via Negative Stiffness Inclusions, and Material Stability Implications	Walter J. Drugan
SM12S_12223 (page 2079)	Stability of Ideal Infinite Crystal Under Finite Uniform Deformation	Pavel V. Tkachev
SM12S_12419 (page 2081)	Explosive Instabilities in a Class of Hyperelastic Materials with Higher - Order Gradients	Igor Dobovsek
SM12L_12682 (page 2083)	On the Concept of “Dynamic (In)Stablility of Quasi - Static Paths”	Joao A. C. Martins, F. M. F. Simoes, A. Pinto da Costa, Isabel Coelho
SM12L_12751 (page 2085)	Strain Localization at the Brittle - Ductile Transition of the Earth's Continental Crust.	Yves M. Leroy, Frédéric Gueydan, Laurent Jolivet

Pre-nominated Session SM13
Mechanics of composites

Co-Chair(s): **S. Adali (South Africa)**
N.A. Fleck (UK)

Paper ID	Title	Authors
SM13S_10189 (page 2087)	Numerical Evaluation of Mixed Mode Delamination in a U.D. Glass/Epoxy Composite in 2D and 3D States	M. R. Khoshravan, Arash Yourdkhani
SM13L_10244 (page 2089)	Interfacial Properties of Nanowire - Polymer Composites	Ryszard Pyrz
SM13L_10347 (page 2091)	Plane Harmonic Waves in a Microperiodic Layered Thermoelastic Solid Revisited	Jozef Ignaczak
SM13L_10412 (page 2093)	Damage Progression by the Element - Failure Method (EFM) and Strain Invariant Failure Theory (SIFT)	Tong - Earn Tay, V. B. C. Tan, S. H. N. Tan
SM13S_10483 (page 2095)	Effective Properties of Solids Containing Randomly Distributed Multi-Phase Spherical Particles	Hossein M. Shodja, Farshid Roumi
SM13S_10555 (page 2097)	Porous Anisotropic Composites under Microfructures	Lidiya Nazarenko

SM13L_10667 (page 2099)	Reissner-Mindlin-Von Karman Type Plate Modle for Postbuckling Analysis of Laminated Composite Structures	Petri Kere, Mikko Lyly
SM13S_10745 (page 2101)	Three-Dimensional Transmission in Plane Layered Elastic Composites	Kanmi Aderogba
SM13L_11014 (page 2104)	Aspects of the Mechanical Response of Randomly Reinforced, Chopped Fiber Strand, Polymeric Composites	Y. Jack Weitsman, A. Ionita
SM13L_11080 (page 2107)	Computational Modeling of Deformation and Damage in Particle-Reinforced Composites	Javier Segurado, Javier LLorca
SM13L_11162 (page 2109)	Elastic Interaction of Multiple Delaminations in Laminated Structures	Martin G. Andrews, Roberta Massabo, Brian N. Cox
SM13S_11176 (page 2111)	Overall Properties of Periodic Biocomposites	Lucia Doval-Montes, Eduardo Lopez-Lopez, Federico J. Sabina, Julian Bravo-Castillero, Raul Guinovart-Diaz, Reinaldo Rodriguez-Ramos
SM13L_11180 (page 2113)	Damage Tolerance of Composite Structures with Thermal Shield	Christophe Bouvet, Sandrine Petit, Alain Bergerot, Jean-Jacques Barrau
SM13L_11387 (page 2115)	Can it Be Made? Predicting the Formability of Textile Composite Components	Mike J. Clifford, P. Harrison, A. C. Long
SM13S_11426 (page 2117)	Electroelstic Fields Concentrations and Polarization Switching by Circular Electrodes in Piezoelectric Disk Composites	Fumio Narita, Yasuhide Shindo, Masaru Karaiwa
SM13S_11457 (page 2119)	Fuzzy Set Approach to Modelling Composite Mechanical Properties	Aleksander Muc
SM13S_11507 (page 2121)	Evaluation of Linearization Procedures Sustaining Nonlinear Homogenisation Theories	Amna Rekik, Michel Bornert, Andre Zaoui, Francois Auslender
SM13L_11610 (page 2123)	Three-Dimensional Thermoelastic Analalysis of Plain Weave Glass/Epoxy Composities with Cracks at Cryogenic Temperatures	Tomo Takeda, Yasuhide Shindo, Fumio Narita
SM13L_11747 (page 2125)	Advanced Beam Model for Fiber-Bridging in Unidirectional Composite Double-Cantilever Beam Specimens	Andras Szekrenyes, Jozsef Uj
SM13L_11782 (page 2127)	Interfacial Jump Conditions in Strain-Gradient Plasticity and Relations of Hall-Petch Type	K. Aifantis, John R. Willis
SM13L_11794 (page 2128)	A Study of Particle Debonding with Anisotropy	Brian Nyvang Legarth
SM13L_11805 (page 2130)	Nonlinear Affine Extension of the Three-Phase Sphere Model	Emmanuelle Chabert, Michel Bornert, Andre Zaoui
SM13S_11895 (page 2132)	H-Convergence and Multilayering in Piezocomposites	Antoni Galka, Barbara Gambin, Jozef J. Telega, Stanislaw Tokarzewski
SM13L_12141 (page 2134)	On the Role of Inter-Granular Layers in Polycrystalline Ceramics	Tomasz Sadowski, Stephen Hardy, Eligiusz Postek
SM13L_12148 (page 2136)	A Homogenization Based Laminated Beam Theory	Jorn S. Hansen, Sergio F. M. de Almeida
SM13L_12214 (page 2138)	Compressive Strength of Fiber Composite with Porosity	Ulrik Borg
SM13S_12242 (page 2140)	Thermal Residual Stress in Al2O3/SiCnano Ceramic Composites Measured by Nanoindenter	Zhong Ling
SM13L_12321 (page 2142)	Composites with Planar Random Fiber Arrangements	Dominik Duschlbauer, Helmut J. Boehm, Heinz E. Pettermann
SM13S_12489 (page 2144)	Inclusion Dispersion: Effects on Stress and Effective Properties	Jan Schjoedt - Thomsen, Ryszard Pyrz
SM13L_12496 (page 2146)	Thermal Fatigue of MMC Induced by Laser Heating	Shiguo G. Long, Y. C. Zhou

SM13S_12531 (page 2148)	Thermo-Mechanical Stability and Vibration Analysis of Composite Shells	J. Girish, Lingadahally S. Ramachandra
SM13S_12560 (page 2150)	New Trends in Optimal Design of Composite Materials	Aleksander Muc, Marcin Trzebicki
SM13L_12576 (page 2152)	An Anisotropic Damage Model for the Prediction of the Degradation Behaviour of Novel Textile Reinforced Composites	Werner Hufenbach, Robert Boehm, Albert Langkamp
SM13S_12588 (page 2154)	Asymptotic Study of Imperfect Interfacial Bonding in Periodic Composite Materials	Igor V. Andrianov, Vladyslav V. Danishevs'kyy, Dieter Weichert
SM13S_12667 (page 2156)	T-Inclusion Regions for the Effective Transport Coefficients of Two--Phase Media	Stanislaw Tokarzewski, Antoni Galka, Barbara Gambin, Jozef J. Telega
SM13L_12680 (page 2158)	Crack Tunneling in Laminates	Akke S. J. Suiker, Norman A. Fleck
SM13S_12732 (page 2160)	Macroscopic Relations for Nonlinear Thermodiffusion in Heterogeneous Elastic Medium	Antoni A. Galka, Jozef J. Telega, Ryszard Wojnar
SM13L_12818 (page 2162)	Study of the Usability of Various Cruciform Geometries for Biaxial Testing of Fiber Reinforced Composites	Arwen Smits, D. Van Hemelrijck, T. Philippidis, A. M. van Wingerde, A. Cardon
SM13S_12970 (page 2164)	Incremental Effective Constitutive Law for Composite Material in the Form of Artificial Neural Network	Marek Lefik
SM13L_13009 (page 2166)	Analysis of Thick Laminated Panel With Piezoelectric Sensors Based on Three-Dimensional Theory of Elasticity	Ali Daneshmehr, M. Shakeri, Akbar Alibiglu

Pre-nominated Session SM14
Mechanics of phase transformations

Co-Chair(s): **F.D. Fischer (Austria)**
A. Molinari (France)

Paper ID	Title	Authors
SM14L_10046 (page 2168)	Temperature and Strain Rate Effects on TRIP Sheet Steel. Measurement of Temperature by Infrared Thermograph	Wojciech K. Nowacki, Alexis Rusinek, Stefan P. Gadaj, Janusz R. Klepaczko
SM14L_10088 (page 2170)	A Numerical Approach to Martensitic Phase Transformations	Thomas Antretter, Franz Dieter Fischer, Georges Cailletaud
SM14L_10434 (page 2172)	Macro-, Meso- and Micro - Scopic Metallo - Thermo - Mechanics	Tatsuo Inoue
SM14L_10648 (page 2174)	Multiscale Modeling of Steels assisted by Transformation - Induced Plasticity	Sergio Turteltaub, A. S. J. Suiker
SM14L_10721 (page 2176)	The Nature of Stress and Strain Fields in Shape Memory Polycrystals	Isaac Chenchiah, Kaushik Bhattacharya
SM14L_11308 (page 2178)	Shape Memory Alloy Under Strain and Stress Controlled Conditions - Thermomechanical Aspects of Martensite and Reverse Transformations	Wojciech K. Nowacki, Elzbieta A. Pieczyska, Stefan P. Gadaj, Hisaaki Tobushi, Makoto Takagi
SM14L_11325 (page 2180)	High Pressure Mechanochemistry: Conceptual Multiscale Theory and Interpretation of Experiments	Valery I. Levitas
SM14L_11393 (page 2182)	Stress-Induced Martensitic Phase Transition Front Propagation	Arkadi Berezovski, Gerard A. Maugin
SM14L_11395 (page 2184)	Modeling Martensite Transformation in the Elasto - Plastic Material at Finite Strain	Shangping Chen, V. Kouznetsova, M. G. D. Geers
SM14L_11625 (page 2186)	Modeling of the Microstructural Evolution in Cr-Mo Steels During Tempering and Hydrogen Exposure	Sabine M. Schloegl
SM14S_11837 (page 2188)	Equilibrium and Stability of Two - Phase Deformations within the Framework of Phase Transition Zones	Alexander Freidin, Yibin Fu

SM14L_11852 (page 2190)	On Modeling the Longitudial Impact of Two Shape Memory Bars	Cristian Faciu, Alain Molinari
SM14L_12077 (page 2192)	A Micromechanical Model for Single - Crystal Shape - Memory - Alloys	Thorsten Bartel, Klaus Hackl
SM14S_12121 (page 2194)	Simulation of Discontinuity Movement by Boundary Elements	Claus Oberste - Brandenburg
SM14L_12225 (page 2196)	Determination of Phase Transformation Yield Surface of Anisotropic Shape Memory Alloys	Taillard Karine, Calloch Sylvain, Bouvet Christophe, Lexcellent Christian
SM14L_12421 (page 2198)	Numerical Determination of Diffusional Transformation Induced Plasticity from Computations of Random Microstructures	Fabrice Barbe, Romain Quey, Lakhdar Taleb
SM14L_12747 (page 2200)	Numerical Analyses of the Interaction Classical Plasticity - TRIP	Salem Meftah, Fabrice Barbe, Lakhdar Taleb, Francois Sidoroff
SM14S_12881 (page 2202)	Nucleation and Motion of Phase Boundary in Shape Memory Alloy Microtubes	Qingping Sun

Pre-nominated Session SM15
Mechanics of porous materials

Co-Chair(s): **W. Ehlers (Germany)**
J.M. Huyghe (Netherlands)

Paper ID	Title	Authors
SM15L_10198 (page 2203)	Biodegradation in Porous Landfill Bodies	Tim Ricken, Reint de Boer, Veronika Ustohalova, Renatus Widmann
SM15S_10790 (page 2205)	Mandel and Cryer Problems For Fluid - Saturated Foams With Negative Poisson's Ratio	Michio Kurashige, Keiichi Sato, Kazuwo Imai
SM15L_10792 (page 2207)	Localization and Stability of Unsaturated Soil	Wolfgang Ehlers, Martin Ammann, Tobias Graf
SM15L_11119 (page 2209)	Convolution Quadrature Based Boundary Element Method for Quasi - Static Poroelasticity	Martin Schanz, Thomas Rueberg
SM15L_11194 (page 2211)	Theory and Numerics of Multicomponent Mixture Models for Soft Biological Tissues	Bernd Markert, Wolfgang Ehlers, Ayhan Acartuerk, Nils Karajan
SM15L_11463 (page 2213)	Probabilistic Homogenization of Hyperelastic Solid Foams	Joerg Hohe, Wilfried Becker
SM15L_11941 (page 2215)	Coupling Between Permeability and Damage: a Micromechanical Approach	Luc Dormieux, Djimedo Kondo
SM15L_12114 (page 2217)	Thermo - Hydro - Chemical - Mechanical Analysis of Concrete at High Temperatures	Stefano Dal Pont, B. A. Schrefler, A. Ehrlacher
SM15S_12358 (page 2219)	FE - Investigations on Shear Localizations in Granular Bodies within Hypoplasticity	Tejchman Jacek
SM15S_12518 (page 2221)	Modelling of Composites Processing Using a Two - Phase Porous Media Theory	Maciej Wysocki, Ragnar Larsson, Staffan Toll
SM15S_12566 (page 2223)	Wave Propagation in High Porosity Bones-a Cellular Model	Pakula Michal, Kaczmarek Mariusz, Jozef Kubik
SM15S_12567 (page 2225)	Soft Porous Media Model of Magnetic Fluid	Mariusz Kaczmarek, Tomasz Hornowski
SM15L_12577 (page 2227)	Mechanics of Saturated High Porosity / Soft Materials	Jozef Kubik, Mariusz Kaczmarek, Michal Pakula
SM15S_12614 (page 2229)	A Three Layer Porous Media Model of Cutaneous Circulation with Application to Mechanical Skin Irritation	Daniela Bauer, Reinhard Grebe, Alain Ehrlacher

SM15S_12713 (page 2231)	Identification of Some Chemoporoelastic Parameters of a Reactive Shale from Experimental Data	J. Sarout, E. Detournay
SM15L_12771 (page 2233)	Mesoscale Predictions for the Thermomechanics of Granular Energetic Composites	Michael W. Crochet, Keith A. Gonthier
SM15L_12903 (page 2235)	The Structure of Constitutive Laws for Powder Metallurgical Components	Alan C. F. Cocks, Csaba I. Sinka, Ludwig C. R. Schneider
SM15L_12917 (page 2238)	Experimental Characterisation and Numerical Modelling of Density Distribution in Tablets	Csaba I. Sinka, J. C. Cunningham, A. Zavaliangos
SM15L_13006 (page 2240)	Stresses and Fractures in Capillary - Porous Materials Under Drying	Stefan J. Kowalski, Jacek Banaszak

Pre-nominated Session SM16
Mechatronics

Co-Chair(s): **W.O. Schiehlen (Germany)**
M. Tomizuka (USA)

Paper ID	Title	Authors
SM16S_10510 (page 2242)	Stability Analyses of Electrostatic Torsional RF MEMS Switch	Ya - Pu Zhao, Jian - Gang Guo
SM16L_10553 (page 2244)	Improvement of Positioning Accuracy of Delta Parallel Robot	Dominique Deblaise, Cedric Baradat, Patrick Maurine, Vigen Arakelian
SM16L_10809 (page 2246)	Dynamics and Control of a Hydraulically Driven Boring Plant	Friedrich G. Pfeiffer
SM16L_10900 (page 2248)	Investigation of Powerfull and High Precision Piezoelectric Actuator for Two - Dimensional Positioning	Piotr Vasiljev, Dalius Mazeika, Genadijus Kulvietis
SM16L_11282 (page 2250)	Gain - Scheduling Control of Machine Tools with Varying Structural Flexibilities	Wim Symens, Hendrik Van Brussel, Jan Swevers
SM16L_12417 (page 2252)	A Systematic Load Identification Procedure for Parallel Robot Manipulators	Horst Schulte, Patrick Gerland
SM16S_12546 (page 2254)	Development of Positioning of Mechanisms with Piezoelectric Engines	Alfredas Busilas, Romualdas Naumavicius
SM16S_12712 (page 2256)	Hierarchical Tracking Control of Wheeled Mobile Robot	Pu - Sheng Tsai, Li - Sheng Wang, Fan - Ren Chang
SM16L_12758 (page 2258)	Rapid Prototyping of Model Based Control Algorithms for Diesel - Engines with Turbocharger	Matthias Weber, Rolf Isermann
SM16S_12929 (page 2260)	Development of High - Performance Motion Simulator for Virtual Reality Systems	Dzmitry O. Tsetserukou, Alena V. Neviarouskaya

Pre-nominated Session SM17
Multibody dynamics

Co-Chair(s): **M. Geradin (Italy)**
F. Pfeiffer (Germany)

Paper ID	Title	Authors
SM17S_10026 (page 2262)	A Geometrical Framework for Modeling and Simulation of Nonholonomic Mechanical Systems	Blajer Wojciech
SM17S_10533 (page 2264)	Research of Movement of the Mechanism Sufficient with Elastic Part	Gakhip Ualiyev, Zair G. Ualiyev
SM17S_10624 (page 2266)	Homoclinic Orbits Layering in the Coupled Rotor Nonlinear Dynamics and Chaotic Clock Models: a Paradi	Katica Stevanovic-Hedrih

SM17S_10647 (page 2268)	Design of the Rear Carriage Stabilizer of a Low - Floor Articulated Trolleybus	Pavel Polach
SM17S_10779 (page 2270)	Stabilization by Rotating Rigid Bodies for Unstable Rotation of a Rigid Body with Cavities Containing a Fluid	Yuriy N. Kononov, Tanya V. Khom'yak
SM17S_10893 (page 2272)	Simulation of Constrained Rigid and Elastic Bodies Without Constraint Equations	Oleg Dmitrochenko, Dmitry Pogorelov, Su-Jin Park, Wan-Suk Yoo
SM17L_11020 (page 2274)	Analysis of Grazing Bifurcations in Impact Microactuators	Xiaopeng Zhao, Harry Dankowicz
SM17L_11223 (page 2276)	Low Energy Control of Periodic Motions in Manufacturing	Nils Guse, Werner Schiehlen
SM17S_11352 (page 2278)	Selected Problems of Discrete - Continuous Mechanical Systems with Local Nonlinearities	Pielorz Amalia
SM17L_11361 (page 2280)	Modeling Ballast Behavior Using a Three - Dimensional Polyhedral Discrete Element Method	Gilles Saussine, Jean-Jacques Moreau, Frederic Dubois, Catherine Cholet, Claude Bohatier, Pierre-Etienne Gautier
SM17L_11375 (page 2282)	Efficient Generalized Speeds in a Recursive Formulation of Flexible Multibody Dynamics	Arun Banerjee, Mark Lemak
SM17S_11640 (page 2284)	On Approximate Jacobian Matrices in Simulation of Stiff Multibody Systems	Dmitry Pogorelov
SM17S_11674 (page 2286)	Intrinsic Formulation of Dynamics of Curvilinear Systems	Jean Lerbet
SM17S_11688 (page 2288)	Simulation of Track Ballast	Dmitry Agapov, Dmitry Pogorelov, Aleksandr Bidulya
SM17L_11700 (page 2290)	Configuration Control and Dynamic Analysis of Redundant Link - Type Manipulators	Kazuo Yamamoto, Masashi Okada, Kazuo Tanizawa
SM17S_11789 (page 2292)	A Study on the Brush Noise Reduction of a DC Motor Using Multi - Body Dynamics	Tae - Won Park, Il - Ho Jung, Jong - Whi Seo
SM17S_12029 (page 2294)	The Absolute Coordinate Formulation with Reduced Strain and Stiffening	Johannes Gerstmayr, Hans Irschik
SM17S_12071 (page 2296)	Stability Analysis of a Tethered System	J. Valverde, J. L. Escalona, J. Dominguez
SM17L_12133 (page 2298)	Simulation of Contacting Spatial Polyhedral Particles	Beate Muth, Peter Eberhard, Stefan Luding
SM17L_12134 (page 2300)	Plastic Deformation by Impacts in Multibody Systems	Robert Seifried, Werner Schiehlen
SM17S_12208 (page 2302)	A Systematic Model Reduction Method for the Control of Flexible Multibody Systems	Olivier Bruls, Pierre Duysinx, Jean-Claude Golinval
SM17S_12464 (page 2304)	Expression on the Deflection of a Flexible Thin Rod and It's Measurement	Kohichi Miura, Tetsu Nishimura
SM17S_12537 (page 2306)	Dynamic Analysis and Vibration Control of The Planar Beams Moving Along the Axial Direction	Naoki Sugano, Etsujiro Imanishi
SM17S_12539 (page 2308)	Generating Optimal Motions of Constrained Multibody Systems	Guy Bessonnet, Pascal Seguin
SM17L_12569 (page 2310)	Contact Problems in Roller Chain Drive Systems.	Sine Leergaard Pedersen
SM17L_12582 (page 2312)	Motion and Vibration Control of the Lift Mechanism of a Ladder Truck	Katsuhisa Fujita, Yasuhiro Shiono, Mitihiro Itihara, Takuro Koseki

Pre-nominated Session SM18
Plasticity and viscoplasticity

Co-Chair(s): **E. van der Giessen (Netherlands)**
P. Perzyna (Poland)

Paper ID	Title	Authors
SM18L_10064 (page 2314)	Metal Forming Processes Conditioned by Cyclic Loading. A New Challenge for the Theory of Plasticity	Zenon Mroz, Ryszard B. Pecherski
SM18S_10383 (page 2316)	Quasi Rate - Independent Viscoplastic fcc - Polycrystals	Milan Micunovic
SM18L_10393 (page 2318)	Physically Based Thermomechanical Modeling of Metals over a Wide Range of Strain Rates and Temperatures	George Z. Voyiadjis, Farid H. Abed
SM18L_10652 (page 2320)	Plastic Properties Identification With Plural Sharp Indenters	Norimasa Chiba, Nagahisa Ogasawara
SM18S_10729 (page 2322)	A Viscoplastic Model for Thermoplastic Polymers Under Uniaxial Monotonic and Cyclic Straining	Ghorbel Elhem
SM18S_10734 (page 2324)	Advanced Thermo - Visco - Plastic Constitutive Relations for Direct Applications in Numerical Analyses	Alexis Rusinek, Janusz R. Klepaczko, Ramon Zaera
SM18L_10797 (page 2326)	Calibration of Anisotropic Elastic - Plastic Models for Thin Layers and Foils in Microtechnologies: Two Novel Techniques	Massimiliano Bocciarelli, Gabriella Bolzon, Giulio Maier
SM18L_10955 (page 2328)	Simulation of Dynamic Polycrystalline Thermoelastoviscoplasticity and Fracture	John D. Clayton
SM18L_11005 (page 2330)	Assessing Different Self - Consistent Approximations by Comparison with Full - Field Simulations in Viscoplastic Polycrystals	Ricardo A. Lebensohn, Yi Liu, Pedro Ponte Castaneda
SM18L_11110 (page 2332)	Three - Dimensional Modelling of Thermo - Elasto / Viscoplastic Solids Containing Adiabatic Shear Bands	Patrice Longere, Andre Dragon, Herve Trumel, Thibaut de Resseguier, Xavier Deprince
SM18S_11185 (page 2334)	Energy Storage Rate in Non - Homogeneous Deformation	Wiera Oliferuk, Michal Maj
SM18S_11295 (page 2336)	Dynamic Behavior of Many - Dislocation Systems in Silicon	Kazuwo Imai, Shigeru Fujinuma, Michio Kurashige
SM18S_11309 (page 2338)	The Eshelby Problem for Elastic - Viscoplastic Materials	Sebastien Mercier, Alain Molinari, Nicolas Jacques
SM18S_11344 (page 2340)	Multiscale Modeling of the Structure - Property Relationship for Semicrystalline Materials	J. A. W. van Dommelen, W. A. M. Brekelmans, F. P. T. Baaijens
SM18S_11350 (page 2342)	Modeling of Viscoplastic Constitutive Equation for Polymers by Taking Into Account Strain Recovery	Mamoru Mizuno, Yukio Sanomura
SM18L_11410 (page 2344)	Thickness Dependent Yield Strength of Thin Films	Peter Gudmundson, Per Fredriksson
SM18S_11498 (page 2346)	Yield Surfaces Using an Extension of the Regularized Schmid Law to Polycrystalline Materials	Stéphane Berbenni, Patrick Franciosi
SM18L_11790 (page 2348)	Size - Effects in Void Growth	Christian F. Niordson
SM18L_11820 (page 2350)	On the Accounting of Dislocation Internal Stress in Continuum Plasticity	Amit Acharya, Anish Roy
SM18S_11930 (page 2352)	Steady - Flow of a Non - Homogeneous Bingham Material Over a Wedge	Oana Cazacu, N. D. Cristescu
SM18S_11953 (page 2354)	Modelling of Elastic - Plastic or Viscoplastic Materials Sensitive to the Type of Processes - Different Approaches	Anguel I. Baltov, Georgi B. Stoychev
SM18L_11963 (page 2356)	Strain Gradient Crystal plasticity Incorporating Grain Boundary Effects	Marc G. D. Geers, L. P. Evers, W. A. M. Brekelmans

SM18S_11975 (page 2358)	Metal Forming and Texture Development Modelling	Wiktor L. Gambin
SM18L_12058 (page 2360)	Limit and Shakedown Analysis with Decohesive Effects	Dieter Weichert, Abdelkader Hachemi
SM18L_12339 (page 2362)	A Constitutive Law for Glassy Polymers and Blends	F. Zairi, K. Woznica, M. Nait Abdelaziz, J. M. Gloaguen
SM18L_12469 (page 2364)	Development and Identification of a Probabilistic Two - Scale Model for High Cycle Fatigue Prediction	Cedric Doudard, Sylvain Calloch, Philippe Cugy, Andre Galtier, Francois Hild
SM18S_12549 (page 2366)	Modeling the Crystallographic Texture Evolution Based on the Maximum Entropy Method	T. Boehlke, A. Bertram
SM18S_12634 (page 2368)	An Elastoplastic Model for Prediction of Permanent Deformations of Unbound Granular Pavement Layers	Absamad El Abd, Pierre Hornych, Denys Breysse, Alain Denis, Cyril Chazallon
SM18S_12697 (page 2370)	Intragranular Kinematic Hardening Modelling and Validation	Maxime Sauzay
SM18L_13038 (page 2372)	Mean Field Homogenization of Elasto - (Visco) Plastic Composites: Formulation for Time - Dependent and Independent Behaviors	Issam Doghri, Olivier Pierard

Pre-nominated Session SM19
Plates and shells

Co-Chair(s): **H. Mang (Austria)**
E. Ramm (Germany)

Paper ID	Title	Authors
SM19L_10038 (page 2374)	A Cohesive Approach to Thin Shell Fragmentation	Fehmi Cirak, Michael Ortiz, Anna Pandolfi
SM19S_10071 (page 2376)	The Stress Analysis of the Multilayered Plates and Shells with Defects of the Structure	Lvov G. I., Vereshchaka S. M.
SM19L_10233 (page 2378)	Some New Thoughts on the Buckling of Thin Cylindrical Shells	Parthasarathi Mandal
SM19L_10287 (page 2380)	Continuity Conditions in Elastic Shells with Phase Transformation	Victor A. Eremeyev, Wojciech Pietraszkiewicz
SM19S_10770 (page 2382)	Analytical Solution of Bending of a Clamped Elliptical Plate Under Lateral Load and In - Plane Force	Kenzo Sato
SM19L_11021 (page 2384)	Sensitivity Analysis Concerning the Initial Postbuckling Behavior of Elastic Structures	Herbert A. Mang, Christian Schranz
SM19S_11238 (page 2386)	Meshless LBIE Formulations for Viscoelastic Thin Plates	Jan Sladek, Vladimir Sladek
SM19S_11815 (page 2388)	Effect of a 'Static' Resonance in Elastic Thin - Walled Cylinders	Vasyl L. Krasovskyy, Maryna A. Varyanychko
SM19S_11890 (page 2390)	Energy - Conserving Scheme for Nonlinear Dynamics of Shells - Numerical Examples	Jacek Chroscielewski, Izabela Lubowiecka, Wojciech Witkowski
SM19S_12224 (page 2393)	Mindlin Cylindrical Panels with Twist and Double Curvature	T. Sakiyama, C. W. Lim, X. X. Hu, H. Matsuda, C. Morita
SM19S_12328 (page 2395)	Application of the Return Mapping Algorithm to Perzyna Viscoplasticity for Plane Stress	Zdzislaw Nowak, Krzysztof Wisniewski
SM19S_12346 (page 2397)	A Perturbation Method for Nonlinear Vibrations of Structures	E. L. Jansen
SM19L_12350 (page 2399)	Nonlinear Vibrations of Shallow Shells and Thin Plates of Arbitrary Shape	Lidija V. Kurpa, Galina V. Pilgun

SM19L_12606 (page 2401)	Parallel Multilevel Solution of Large - Scale Nonlinear Shell Problems	Ekkehard Ramm, Michael Gee, Wolfgang A. Wall

Pre-nominated Session SM20
Rock mechanics and geomechanics

Co-Chair(s): **Z. Mroz (Poland)**
I. Vardoulakis (Greece)

Paper ID	Title	Authors
SM20L_10231 (page 2403)	The Material Point Method in Soil Mechanics Problems	Zdzislaw Wieckowski
SM20S_10374 (page 2405)	Dynamic Behaviours of Soils and Rocks in a Wide Pressure Range	Anatoly M. Bragov, Andrey K. Lomunov, Ivan V. Sergeichev, Leopold Kruszka
SM20L_10866 (page 2407)	Micromechanical Study of Macroscopic Friction and Dissipation in Idealised Granular Materials: The Effect of Iinterparticle Friction	N.P. Kruyt, L. Rothenburg
SM20L_11584 (page 2409)	Influence of Contact Phenomena on Structure - Subsoil Interaction: Finite Elements Method Analysis	Marcin Mazdziarz
SM20L_11667 (page 2411)	Modeling of Static Liquefaction and Evolving Failure Modes	Nathalie Boukpeti, Andrew Drescher
SM20L_11845 (page 2413)	Development of Shear Banding in Sandstone	Jeffery J. Riedel, Joseph F. Labuz
SM20S_12364 (page 2415)	On the Use of Second - Order Topological Information for Subsurface Imaging by Elastic Waves	Bojan Guzina, Ivan Chickichev
SM20L_12462 (page 2417)	Incremental Nonlinearity in Constitutive Relation for Granular Media	Yuji Kishino
SM20L_12779 (page 2419)	A High - Pressure Hish Strain Rate Elastic - Viscoplastic Model for Cementitious Materials	Martin J. Schmidt, Oana Cazacu, Mark L. Green, Nicolaie D. Cristescu
SM20S_12848 (page 2421)	The Influence of Teeth on the Earth - Working Processes	Jan Maciejewski, Andrzej Jarzebowski

Pre-nominated Session SM21
Solid mechanics in manufacturing

Co-Chair(s): **B. Heimann (Germany)**
T. Inoue (Japan)

Session Cancelled

Pre-nominated Session SM22
Stability of structures

Co-Chair(s): **Z. Gaspar (Hungary)**
S. Kyriakides (USA)

Paper ID	Title	Authors
SM22S_10378 (page 2423)	Shallow Spherical Caps Under External Pressure	J. Blachut
SM22L_10692 (page 2425)	Elastoplastic Microscopic Bifurcation and Post - Bifurcation Behavior of Periodic Cellular Solids	Nobutada Ohno, Dai Okumura, Hirohisa Noguchi

SM22L_10915 (page 2427)	Statical Models to Illustrate Special Instabilities	Zsolt Gaspar
SM22L_11097 (page 2429)	Wrinkles in Square Membranes	Yew W. Wong, Sergio Pellegrino
SM22S_11172 (page 2431)	Nonlinear Dynamic Stability of Multi - Suspended Roof Systems	Ioannis G. Raftoyiannis, George T. Michaltsos
SM22L_11174 (page 2433)	Coupling of Axisymmetric and 3D Shell Models for Non Linear Elastoplastic Buckling Prediction of Mainly Axisymmetric Shells	A. Combescure, J. C. Bauruelle, C. Baillis
SM22L_11600 (page 2435)	Dynamic Arrest of Propagating Buckles in Offshore Pipelines	Theodoro A. Netto, Stelios Kyriakides
SM22S_11653 (page 2437)	Bifurcation Buckling of Sandwich Plates and Shells in Plastic Range	Suresh C. Shrivastava
SM22L_11816 (page 2439)	On the Stability of the Sky - Hook	Alois Steindl, Hans Troger
SM22L_11939 (page 2441)	Stability of Parametrically Excited Structures: New Results	Alexander P. Seyranian
SM22S_11962 (page 2443)	A Unified Treatment for the Elastoplastic Bifurcation of Structural Elements	Philippe Le Grognec, Anh Le van
SM22L_12084 (page 2445)	Buckling and Imperfection - Sensitivity of Axially Compressed Cylindrical Shells with Compliant Cores	H. Obrecht, B. Rosenthal, P. Fuchs
SM22L_12297 (page 2447)	Stability of Shear - Flexible Frames	Esben Byskov, Ronni Dam, Thomas Frost, Lars Hulsbaek
SM22S_12420 (page 2449)	Instabilities of Initially Stressed Hyperelastic Cylindrical Membrane and Shell Under Internal Pressure	Djenane C. Pamplona, Paulo B. Goncalves, Stefane R. X. Lopes
SM22L_12558 (page 2451)	Generalised Beam Theory Formulation to Analyse the Post - Buckling Behaviour of Orthotropic Laminated Plate Thin - Walled Members	Nuno Silvestre, Dinar Camotim
SM22S_12669 (page 2453)	The Stiffness of Prestressed Frameworks: A Unifying Approach	Simon D. Guest
SM22L_12688 (page 2455)	Twist Buckling and the Foldable Cylinder: An Exercise in Origami	Giles W. Hunt, Ichiro Ario
SM22S_12931 (page 2457)	On Stability of Systems Subject to Generalized Follower Force	Roman Bogacz, Szymon Imielowski, Wlodzimierz Kurnik
SM22L_12934 (page 2459)	Dynamic Instability of a High - Speed Flexible Shaft with a Massive Disc and Follower Load.	Wlodzimierz Kurnik, Jaroslaw Weronko
SM22S_12967 (page 2461)	Secondary Bifurcations and Localisation of Buckle Patterns	Ciprian D. Coman

Pre-nominated Session SM23
Stochastic micromechanics

Co-Chair(s): **Y. Brechet (France)**
Y. Shibutani (Japan)

Paper ID	Title	Authors
SM23S_10242 (page 2463)	Creep Rupture and Fiber Breaks Accumulation in Unidirectional Composite	Andrejs Krasnikovs, Scott Case
SM23S_12380 (page 2465)	Homogenization of Plain Weave Composites with Imperfect Microstructure	Jan Zeman, Michal Sejnoha
SM23S_12571 (page 2467)	Collective Prismatic Dislocation Loops Mechanism	Yoji Shibutani, Tomohito Tsuru

Pre-nominated Session SM24
Structural optimization

Co-Chair(s): **K.K. Choi (USA)**
J. Herskowits (Brazil)

Paper ID	Title	Authors
SM24S_10048 (page 2469)	Shape Sensitivity Analysis for Fixed - Grid Analysis Based on Oblique Boundary Curve Approximation	Yoon Young Kim, Gang-Won Jang
SM24S_10052 (page 2471)	Perturbation of the Compliance Functional Due to the Apperance of a Small Cavity in an Elastic Body	Tomasz Lewinski, Jan Sokolowski
SM24L_10433 (page 2473)	Topology Optimization of Vibrating Structures with Hydrodynamic Surface Pressure Loading	Niels Olhoff, Jianbin Du
SM24L_10594 (page 2475)	A Technique for Nonsmooth Optimization Based on the Interior Point Feasible Directions Algorithm	Jose Herskovits, Wilhelm Passarel, Susana Scheimberg, Regina Burachik
SM24S_10621 (page 2477)	Nash Equilibrium in Bicriteria Structural Optimization	Timo Saksala
SM24L_10669 (page 2479)	On Shape Optimization for Eigenvalue Problems	Pauli Pedersen, Niels L. Pedersen
SM24L_11015 (page 2481)	Shape Optimisation of Railway Wheel Profile	V. L. Markine, I. Y. Shevtsov, C. Esveld
SM24L_11137 (page 2483)	Shape Optimization of Thermomechanical Structures in the Presence of Convection and Radiation Using Parallel Evolutionary Computation	Ryszard A. Bialecki, Tadeusz S. Burczynski, Adam Dlugosz, Waclaw Kus, Ziemowit Ostrowski
SM24S_11316 (page 2485)	Efficient Optimization of Transient Dynamic Problems for a Micro Accelerometer Using Model Order Reduction	Jeong Sam Han, Evgenii B. Rudnyi, Jan G. Korvink
SM24L_11349 (page 2487)	Damage Identification in Structures by Means of Thermographic Methods	Krzysztof Dems, Zenon Mroz
SM24S_11486 (page 2489)	Topological Optimization for Contact Problems	Jan Sokolowski, Antoni Zochowski
SM24S_11532 (page 2491)	Coupled Sensitivity and Design Optimization for Thermo - Structural Systems	Yuanxian Gu, Biaosong Chen, Tao Liu
SM24L_11623 (page 2493)	New Classes of Analytically Derived Optimal Topologies and Their Numerical Confirmation	George I. N. Rozvany, Janos Logo, Osvaldo M. Querin
SM24S_11634 (page 2495)	Optimal Structures for Buckling Forces and Buckling Displacements	Jacek Kruzelecki, Pawel Smas
SM24L_11744 (page 2497)	Optimization of Beam Properties with Respect to Maximum Band-Gap	Soeren Halkjaer, Ole Sigmund
SM24L_11760 (page 2499)	Optimal Layout of Two Materials within the Core Layer of a Sandwich Plate. Relaxed Formulation and Its Computiational Algorithm	Slawomir Czarnecki, Michal Kursa, Tomasz Lewinski
SM24L_11826 (page 2501)	Material Cloud Method for Topology Optimization	Su - Young Chang, Sung - Kie Youn
SM24S_11858 (page 2503)	Optimal Design of Unconstrained Damping Layer on Beams	Doo - Ho Lee, Woo - Seok Hwang
SM24L_11936 (page 2505)	On Separation of Eigenfrequencies in Two - Material Structures	Niels L. Pedersen
SM24S_12074 (page 2507)	Density Gradient Based Regularization of Topology Optimization Problems	Gregor Kotucha, Klaus Hackl
SM24S_12075 (page 2509)	New Results of Structural Optimization for Post - Buckling Behaviour	Bogdan Bochenek, Michal Zyczkowski
SM24L_12079 (page 2511)	Compliant Mechanism Design for Adaptive Trailing Edge Flaps	Thomas Buhl

SM24L_12098 (page 2513)	Structural Optimization of Composite Shell Structures Using a Discrete Constitutive Parameterization	Erik Lund, Jan Stegmann
SM24S_12185 (page 2515)	Why Parameterizing Element Connectivity for Topology Optimization?	Yoon Gil Ho, Kim Yoon Young
SM24S_12200 (page 2517)	Topology Optimization of the Geometrically Nonlinear Structures Made of Rubber - Like Material	Sami Holopainen
SM24L_12222 (page 2519)	Optimal Design of Lossy Bandgap Structures	Jakob S. Jensen
SM24S_12287 (page 2521)	Non - Gap Design Method and Test for Post - Tensioned Prestressed R.C. Structure	Li Lijuan, Liu Feng, Fu Ganqing, Lu Weiwen
SM24L_12302 (page 2523)	Design of Articulated Mechanisms with a Degree of Freedom Constraint Using Global Optimization	Atsushi Kawamoto, Mathias Stolpe
SM24S_12413 (page 2525)	Simulation of Trabecular Bone Adaptation - Creating the Optimal Structure	Michal Nowak, Marek Morzynski
SM24S_12573 (page 2527)	Optimal Design of Elasto-Plastic Structures Subjected to Normal Loads and Earthquake	Sandor Kaliszky, Janos Logo
SM24S_12628 (page 2529)	Optimal Force Action and Reaction in Structural Design and Identification	Andrzej Garstecki, Zbigniew Pozorski, Krzysztof Ziopaja
SM24S_12679 (page 2531)	DSA for Elastic - Plastic Finite Rotation Shells under Dynamic Loads	K. Wisniewski, Piotr Kowalczyk, Ewa Turska
SM24L_12789 (page 2533)	Optimization of Functionally Graded Materials with Temperature Dependent Properties. A Meshfree Solution	Florin Bobaru, Han Jiang
SM24L_12870 (page 2535)	Optimum Blank Design for Deep Drawing Using Interaction of High and Low Fidelity Simulation	Ryutaro Hino, Fusahito Yoshida, Vassili Toropov
SM24S_12916 (page 2537)	Computational Tricks for Efficient Design Sensitivity Analysis	Henrik T. Moller, Erik Lund
SM24L_13013 (page 2539)	The Concurrent Design of Materials and Structures for Cellular Materials on Efficiency of Heat Dissipation	Wang Bo, Gengdong D. Cheng

Pre-nominated Session SM25
Structural vibrations

Co-Chair(s): **I. Blekhman (Russia)**
K. Popp (Germany)

Paper ID	Title	Authors
SM25L_10166 (page 2541)	Extreme Value Distribution and Dynamic Reliability of Stochastic Structures	Jianbing Chen, Jie Li
SM25L_10408 (page 2543)	Experimental Study of Nonlinear Energy Pumping	D. Michael McFarland, Lawrence A. Bergman, Alexander F. Vakakis
SM25L_10470 (page 2545)	Nonlinear Vibrations of Jeffcott Rotor with Preloaded Snubber Ring	Evgueni E. Karpenko, Marian Wiercigroch, Ekaterina Pavlovskaia
SM25S_10656 (page 2547)	Non - Linear Stochastic Vibration Problems for the Plates with Time - Dependent Parameters	Victor Z. Gristchak, Valentin V. Lysenko
SM25S_10750 (page 2549)	A Multi - Step Transversal Linearization Method in Nonlinear Dynamics	Debasish Roy
SM25L_10863 (page 2551)	Equivalent Stochastic Linearization as an Alternative to Solving the Fokker - Planck Equation	Stephen H. Crandall
SM25L_11055 (page 2553)	Nonlinear Effects, Observed in the Process of the Liquid Flowing Out of the Vibrating Vessels: Theory, Experiment and Applications	I. I. Blekhman, L. I. Blekhman, L. A. Vaisberg, V. B. Vasilkov, K. S. Yakimova
SM25S_11066 (page 2555)	Propagation Analysis of Flexural Waves by Wavelet Transform	Akihiko Higashi, Fumihiro Mizuguchi

SM25S_11079 (page 2557)	Bifurcations of Damped Nonlinear Normal Modes: Linear Oscillator with Strongly Nonlinead Attachment	Oleg V. Gendelman
SM25L_11082 (page 2559)	Effect of Root Flexibility on the Aeroelastic Analysis of a Composite Wing Box	Gamal M. Ashawesh, Ali M. Elmabrok, Tarek A. Abdunabi, Alakrami A. Nakas
SM25L_11246 (page 2561)	Reanalysis of an SEA High - Frequency Vibration Calculation Based on the VTCR	Herve Riou, Pierre Ladeveze
SM25L_11261 (page 2563)	Active Control of Disk Brake Sqeal	Utz von Wagner, Daniel Hochlenert, Peter Hagedorn
SM25L_11273 (page 2565)	Experimental and Theoretical Modal Analysis of Three Support Rotor Test Rig Using LMS CADA-X and ABAQUS	Marcin Luczak
SM25S_11338 (page 2567)	Stability of a Rotor with Periodically Varying Angular Velocity	J. P. Meijaard
SM25S_11384 (page 2569)	Paradoxical Behaviour of Vibrating Systems Challenging Rayleigh's Theorem	Tibor Tarnai
SM25S_11494 (page 2571)	Imperfection Sensitivity of Circular Arch's Non - Linear Modes	Carlos E. N. Mazzilli, Odulpho G. P. Baracho Neto, Mario E. S. Soares, Cesar T. Sanches
SM25S_11536 (page 2573)	Optimal Shapes of Parametrically Excited Beams	Alexei A. Mailybaev, Hiroshi Yabuno, Hiroyuki Kaneko
SM25S_11679 (page 2575)	Non Trivial Effect of Strong High - Frequency Excitation on a Nonlinear Controlled System	Alexander Fidlin, Jon J. Thomsen
SM25S_11699 (page 2577)	An Aproach to Worm - Like Motion	Klaus Zimmermann, Igor Zeidis, Joachim Steigenberger, Mikhail Pivovarov
SM25S_11712 (page 2579)	Dynamics of a Rotor Rolling Along a Circular Surface	Alla D. Firsova
SM25S_11716 (page 2581)	The New Statement of Problem of Unbalance Identification	Yuri L. Mehshikov, Nikolaj V. Polyakov
SM25S_11719 (page 2583)	Vibrorheology: Main Results, New Problems	Iliya Blekhman, Ekaterina Shishkina
SM25S_11759 (page 2585)	Nonlinear Vibrations of Gear Drives	Vladimir Zeman, Miroslav Byrtus, Michal Hajzman
SM25L_11783 (page 2587)	Passive Vibration Control of a Piecewise Linear Beam System	Rob H. B. Fey, Joris H. Bonsel, Henk Nijmeijer
SM25S_11834 (page 2589)	A power Flow Mode Theory Based on Inherent Characteristics of Damping Distributions in Systems and Its Applications	Y. Xiong, J. T. Xing, W. G. Price
SM25S_11867 (page 2591)	Stability of a Spinning Disk Under a Stationary Oscillating Unit	T. H. Young, C. Y. Lin
SM25S_11904 (page 2593)	High Revolving Speed Spindles Definition Due to Transient Vibration Conditions	Mehdi S. Zangeneh, Seyed S. H. Yazdi
SM25S_12026 (page 2595)	Suppressing Self - Excited Vibrations in a Coupled Pendulum System	Fadi Dohnal, Ecker Horst
SM25L_12322 (page 2597)	The Running Behaviour of an Elastic Wheelset	Ingo Kaiser, Karl Popp
SM25L_12404 (page 2599)	Thermoelastic Relaxation in Thin Plates with Applications to MEMS and NEMS Oscillators	Andrew N. Norris, Douglas M. Photiadis
SM25S_12498 (page 2601)	Estimation of the Vibration Energy Characteristics for Joints of Constructional Elements	Jacek Cieslik
SM25S_12511 (page 2603)	Sound Radiation by the White Noise Excited Viscoelastic Shallow Shells	Marek S. Kozien, Jozef Niziol
SM25L_12535 (page 2605)	Self - Excited Stick - Slip Oscillations of Drag Bits	Thomas Richard, Christophe Germay, Emmanuel Detournay

SM25L_12593 (page 2607)	Vibration Characteristics of the Main Tower, the Byaon Temple	Yoshikazu Sugiura, Yuki Fukumoto, Toshiro Maeda
SM25S_12632 (page 2609)	Application of Extended Phase Space to Investigation of Forced Biharmonic Oscillations	Michael I. Kazakevitch, Viktorija E. Volkova
SM25S_12659 (page 2611)	Non - Linear Modelling of Earthquake Induced Pounding of Buildings	Robert Jankowski
SM25L_12694 (page 2613)	Discontinuous Transformations and Averaging for Vibro - Impact Analysis	Jon Juel Thomsen, Alexander Fidlin
SM25L_12759 (page 2615)	Experimental Analysis of Modal Interactions in the Non - Linear Vibrations of a Plate	Pedro Ribeiro
SM25L_12770 (page 2617)	Optimum Selection of Design Features of Electromechanical Drive Systems Incorporating a Control Unit	Pawel Bachorz, Arkadiusz Mezyk, Eugeniusz Switonski
SM25L_12785 (page 2619)	Mode Switching of Rain - Wind Induced Vibrations	Christian Seidel, Dieter Dinkler
SM25S_12814 (page 2621)	Regenerative Tool Chatter Near a Codimension - 2 Hopf Point	Pankaj Wahi, Anindya Chatterjee
SM25S_12842 (page 2623)	Axial Decay of Time Harmonic End Perturbation in Prestretched Hyperelastic Plates	Baruch Karp, David Durban
SM25S_12890 (page 2624)	Vibration of the Train/Track System with Two Types of Sleepers	Roman Bogacz, Czeslaw Bajer
SM25S_12977 (page 2626)	Characteristics of Vibroacoustic Signals in Diagnosing Early Stages of Defects	Stanislaw Radkowski, Jan Samsonowicz
SM25S_12984 (page 2628)	Entering the Excitation into a Mechanical System with Dynamic Eliminators of Vibration	Tadeusz Majewski, Roza Sokolowska, Vadiraja Sudhakar
SM25S_12989 (page 2630)	Frictional Auto - Oscillations under the Action of Almost Periodic and Periodic Excitations	Konstantin V. Avramov, Jan Awrejcewicz, Gayane V. Manucharyan

Pre-nominated Session SM26
Vehicle dynamics

Co-Chair(s): **S. Iwnicki (UK)**
R. Sharp (UK)

Paper ID	Title	Authors
SM26L_10701 (page 2632)	Optimal Path Following Road Vehicle Steering Control	Robin S. Sharp
SM26L_10909 (page 2634)	Simulation and Testing of a Wheelset with Induction Motor Driven Independent Wheels	B. Liang, S. D. Iwnicki, F. J. Swift
SM26L_11589 (page 2636)	Railway Vehicle Simulation Using Non - Elliptical Wheel - Rail Contact Model	Vladislav Yazykov, Dmitry Pogorelov, Georgy Mikhalchenko
SM26L_11672 (page 2638)	A Modelling Technique for Fast Computer Simulations of Configurable Vehicle Systems	Georg Rill, Cornelius Chucholowski
SM26L_11795 (page 2640)	Experimental and Theoretical Aanalysis of Freight Wagon Link Suspension	Per - Anders Joensson, Sebastian Stichel
SM26L_11832 (page 2642)	Mathematical Models and Simulation of Stick - Slip Processes in a Car Steering System	Zbigniew Lozia, Dariusz Zardecki

Pre-nominated Session SM27
Viscoelasticity and creep

Co-Chair(s): **F. Cocks (UK)**
N. Ohno (Japan)

Paper ID	Title	Authors
SM27S_10018 (page 2644)	Nonlinear Overall Viscoelastic Properties of the Random Multicomponent Media	Boris P. Maslov
SM27L_10906 (page 2646)	Sintering Simulation of Stainless Steel Powder Compacts	Rui Zhang, Renata S. Engel
SM27L_11201 (page 2648)	Characterisation of the Cyclic Behaviour of Elastic - Plastic - Creeping Bodies	Alan R. S. Ponter
SM27L_11368 (page 2650)	A Creep Continuum Damage Theory for Beams, Plates and Shells	Holm Altenbach, Konstantin Naumenko
SM27L_11506 (page 2652)	Multiscale Modeling Schemes Spanning a Large Range of Scales	Jinghong Fan, Y. He
SM27L_11827 (page 2654)	Constitutive Modeling of Rubber Components Under Small Vibration Superimposed on Large Static Deformation Considering Strain - Dependent Properties	Ji - Hyun Cho, Sung - Kie Youn, Wan - Sul Lee, Bong - Kyu Kim
SM27S_11957 (page 2656)	An Influence of Cold Work on Creep of Engineering Materials	Zbigniew L. Kowalewski
SM27S_11981 (page 2658)	Multi - Scale Model for Low - Temperature Creep of Asphalt	Roman Lackner, Andreas Jaeger, Karl Kappl, Markus Spiegl, Ronald Blab, Josef Eberhardsteiner
SM27L_12450 (page 2660)	A Model of Cyclic Viscoplasticity with Special Reference to Yield - Point Phenomena	Fusahito Yoshida

ICTAM 2004 Author Index

A

Abbott J.R.
FM16_11725 *(page 1170)*

Abdalla H.M.
FSM6_11806 *(page 570)*

Abdou L.
SM2_12082 *(page 1695)*

Abdul-Latif A.
SM4_10456 *(page 1743)*

Abdunabi T.A.
SM25_11082 *(page 2559)*

Abed F.H.
SM18_10393 *(page 2318)*

Abedi R.
SM1_12441 *(page 1622)*

Abkarian M.
FM1_12423 *(page 642)*

Aboudi J.
MS1_12011 *(page 177)*

Acartuerk A.
SM15_11194 *(page 2211)*

Accary G.
FM6_13051 *(page 814)*

Acharya A.
SM18_11820 *(page 2350)*

Acrivos A.
FM16_10361 *(page 1152)*
FM4_10753 *(page 710)*

Adachi S.
FM25_12041 *(page 1483)*

Adachi T.
FM5_11864 *(page 756)*

Adams N.A.
FM24_10455 *(page 1417)*
FM24_11256 *(page 1431)*
FM24_11802 *(page 1439)*
FM24_12564 *(page 1451)*
FSM6_10399 *(page 559)*

Adda-Bedia M.
SM9_10338 *(page 1894)*

Addas K.
MS2_10709 *(page 199)*

Aderogba K.
SM13_10745 *(page 2101)*

Adrian R.J.
FM25_12161 *(page 1491)*
FM25_12196 *(page 1493)*
MS4_11607 *(page 298)*

Agapov D.
SM17_11688 *(page 2288)*

Agarwal R.K.
FM11_10872 *(page 984)*

Aghalovyan L.A.
SM6_11526 *(page 1812)*

Ahlawat A.S.
SM3_10098 *(page 1717)*

Ahmetolan S.
SM11_10891 *(page 2015)*

Aider A.A.
FM13_10185 *(page 1044)*

Aidun C.K.
FM1_12124 *(page 634)*

Aifantis K.
SM13_11782 *(page 2127)*

Aitta A.
FM21_11328 *(page 1331)*

Aksel N.
FM14_10642 *(page 1108)*
FM14_10928 *(page 1110)*

Akylas T.R.
FM26_10762 *(page 1511)*

Al-Abduljabbar A.
SM9_12798 *(page 1955)*

Albers B.
SM11_10072 *(page 2003)*

Alderliesten R.
SM8_12217 *(page 1878)*

Alexander J.I.D.
MS5_12447 *(page 329)*
MS5_12765 *(page 333)*

Alexeev A.
FM14_12293 *(page 1126)*
FSM1_12516 *(page 419)*

Ali R.
FM2_11887 *(page 672)*

Alibiglu A.
SM13_13009 *(page 2166)*

Alleborn N.
FM14_11413 *(page 1116)*

Allix O.
SM1_12237 *(page 1613)*

Almeida S.F.M. de
SM13_12148 *(page 2136)*

Altenbach H.
SM27_11368 *(page 2650)*

Altobelli S.A.
FM18_10983 *(page 1233)*

Alvarez J.O.
FSM1_12477 *(page 415)*

Amalia P.
SM17_11352 *(page 2278)*

Amara M.
FM6_12356 *(page 799)*

Amberg G.
FM21_12312 *(page 1345)*

Ambrósio J.
SL1_11040 *(page 115)*

Ammann M.
SM15_10792 *(page 2207)*

Amyot O.
FM12_11343 *(page 1030)*

Anderson D.M.
FM21_12768 *(page 1353)*

Andersson L.-E.
SM2_10686 *(page 1661)*

Andreev O.
FM19_11120 *(page 1255)*

Andreeva T.A.
FSM1_12149 *(page 411)*

Andrejczuk M.
FM24_12922 *(page 1461)*
FM9_12592 *(page 954)*

Andrews M.G.
SM13_11162 *(page 2109)*

Andrianov I.V.
SM13_12588 *(page 2154)*

Antkowiak A.
FM13_12483 *(page 1088)*

Antretter T.
SM14_10088 *(page 2170)*

Anweiler S.
FM20_11745 *(page 1302)*

Arakelian V.
SM16_10553 *(page 2244)*

Arbez P.
FM6_12510 *(page 802)*

Aref H.
FM24_12436 *(page 1449)*
FM25_11676 *(page 1473)*
FSM7_10003 *(page 590)*

Argyriadi K.
FM14_10557 *(page 1106)*

Arias I.
SM9_12171 *(page 1943)*

Ario I.
SM22_12688 *(page 2455)*

Ariza M.P.
FSM6_11471 *(page 566)*

Arkhipov D.G.
FM26_10123 *(page 1505)*

Arora M.
FM8_11999 *(page 896)*

Arroyo M.
SM1_12455 *(page 1624)*

Asai M.
FM13_10489 *(page 1052)*

Aschenbrenner C.
FM13_10188 *(page 1046)*

Ashawesh G.M.
SM25_11082 *(page 2559)*

Ashida F.
MS1_12018 *(page 181)*

Ashmore J.
FM21_12276 *(page 1341)*

Askes H.
SM12_11277 *(page 2071)*
SM1_12924 *(page 1651)*

Askovic R.
FSM4_13050 *(page 530)*

Asmolov E.S.
FM16_11480 *(page 1167)*

Astley J.
FSM1_11249 *(page 398)*

Atakhorrami M.
MS2_10709 *(page 199)*

Aubouy M.
FSM5_11095 *(page 533)*

Auregan Y.
FM24_12740 *(page 1457)*

Auriault J.-L.
FM12_11059 *(page 1022)*

Aurnou J.M.
FM7_11440 *(page 830)*

Auslender F.
SM13_11507 *(page 2121)*

Aussillous P.
FM21_11320 *(page 1329)*

Avalos-Zuniga R.A.
FM19_12120 *(page 1275)*

Avramov K.V.
SM25_12989 *(page 2630)*

Awrejcewicz J.
SM25_12989 *(page 2630)*
SM2_11481 *(page 1681)*

B

Baaijens F.P.T.
SM18_11344 *(page 2340)*

Baars A.
FM10_13048 *(page 981)*

Babinsky H.
FM5_10984 *(page 744)*

Babushkin I.A.
FM7_12267 *(page 850)*

Bachorz P.
SM25_12770 *(page 2617)*

Badel P.-B.
SM4_12913 *(page 1791)*

Bagchi P.
FM20_12332 *(page 1308)*

Bai X.
SM9_12174 *(page 1945)*

Bai Y.
FSM7_11765 *(page 596)*
SM7_11764 *(page 1851)*

Baillis C.
SM22_11174 *(page 2433)*

Bajer C.
SM25_12890 *(page 2624)*

Bajer K.
FM25_12275 *(page 1495)*
SL2_10042 *(page 118)*

Balachandar S.
FM20_12332 *(page 1308)*
FM25_12161 *(page 1491)*

Balamurugan V.
MS1_12147 *(page 185)*

Balandin D.V.
SM3_11219 *(page 1729)*

Baldessari F.
FM8_11289 *(page 868)*

Balint A.M.
FM21_11362 *(page 1335)*

Balint D.S.
MS3_12386 *(page 269)*

Balint S.
FM21_11362 *(page 1335)*

Ballmann J.
FM5_11229 *(page 750)*

Baltov A.I.
SM18_11953 *(page 2354)*

Balueva A.V.
SM9_11856 *(page 1933)*

Bambrey R.R.
MS6_11336 *(page 350)*

Banach Z.
FSM6_11237 *(page 562)*

Banaszak J.
SM15_13006 *(page 2240)*

Banaszek J.
FM21_11364 *(page 1337)*

Banerjee A.
SM17_11375 *(page 2282)*

Banta R.M.
MS6_10513 *(page 342)*

Bar-Lev O.
FM17_12308 *(page 1213)*

Bar-Yoseph P.Z.
FM13_11461 *(page 1064)*

Baracho Neto O.G.P.
SM25_11494 *(page 2571)*

Baradat C.
SM16_10553 *(page 2244)*

Barba L.A.
FM6_11937 *(page 793)*

Barbe F.
SM14_12421 *(page 2198)*
SM14_12747 *(page 2200)*

Barber T.J.
FM14_11477 *(page 1118)*

Bargmann S.
SM1_12924 *(page 1651)*

Barkley D.
FM13_12431 *(page 1086)*

Barmin A.A.
FM9_11703 *(page 942)*

Barnea D.
FM20_11655 *(page 1300)*

Barnhart D. H.
FM10_11088 *(page 965)*

Baroud C.N.
FM1_11013 *(page 618)*
MS4_12047 *(page 302)*
SL18_10495 *(page 151)*

Barral S.
FM19_12363 *(page 1282)*

Barrau J.-J.
SM13_11180 *(page 2113)*

Bartel T.
SM14_12077 *(page 2192)*

Barthes-Biesel D.
MS2_11961 *(page 222)*

Basaran C.
FSM3_11515 *(page 481)*

Batra R.C.
SM10_12594 *(page 1990)*

Baty H.
FM19_11429 *(page 1259)*

Bauer D.
SM15_12614 *(page 2229)*

Bauruelle J.C.
SM22_11174 *(page 2433)*

Baweja M.
SM3_12756 *(page 1737)*

Bayer I.S.
FM4_11603 *(page 720)*

Bazant M.Z.
MS4_11777 *(page 300)*

Bazin B.
FM12_10234 *(page 1018)*

Bałdyga J.
FM22_12415 *(page 1381)*

Becache E.
SM2_12382 *(page 1703)*

Becker M.
FSM6_12118 *(page 584)*

Becker W.
SM15_11463 *(page 2213)*
SM9_11484 *(page 1925)*

Beda P.B.
SM12_10314 *(page 2063)*

Bednarz T.
FM7_13022 *(page 860)*

Behringer R.P.
FM17_12399 *(page 1217)*

Behringer R.
FM12_12617 *(page 1042)*

Belcher S.E.
FM26_10746 *(page 1509)*

Belzons M.
FM17_11751 *(page 1203)*

Ben Dhia H.
SM11_12763 *(page 2057)*

Ben Hamida A.
SM1_12727 *(page 1641)*

Benallal A.
SM12_10265 *(page 2061)*

Benilov E.
FM25_11467 *(page 1469)*
FM26_11468 *(page 1532)*

Bennacer R.
FM15_11386 *(page 1136)*

Bennett D.J.
FM4_10753 *(page 710)*

Benzerga A.A.
SM1_12737 *(page 1643)*

Berbenni S.
SM18_11498 *(page 2346)*

Beresneva E.N.
FM7_10538 *(page 820)*

Berezovski A.
SM10_11592 *(page 1978)*
SM14_11393 *(page 2182)*

Berfield T.
MS1_11685 *(page 167)*

Berg A. van den
FM1_12400 *(page 638)*

Bergdorff M.
FM6_12583 *(page 806)*

Bergeon A.
FM22_12731 *(page 1393)*

Bergerot A.
SM13_11180 *(page 2113)*

Bergman L.A.
SM25_10408 *(page 2543)*

Bergmann R.
FM10_11909 *(page 969)*
FM17_10253 *(page 1191)*

Bergougnoux L.
FM16_11588 *(page 1169)*
FM16_12345 *(page 1184)*

Bernardo M. di
FSM2_11363 *(page 449)*

Beron-Vera F.J.
MS6_12776 *(page 390)*

Berton G.
FM17_12883 *(page 1223)*

Bertram A.
SM18_12549 *(page 2366)*

Beskos D.E.
SM1_12845 *(page 1647)*

Bessonnet G.
SM17_12539 *(page 2308)*

Betelu S.I.
FM8_12548 *(page 914)*

Beysens D.A.
SL3_10880 *(page 120)*

Bezpalcova K.
FM9_10467 *(page 926)*

Bhattacharya K.
MS1_11731 *(page 169)*
SM14_10721 *(page 2176)*

Bi W.
FM17_12883 *(page 1223)*

Bialiatskaya L.N.
FSM2_11512 *(page 453)*

Białecki R.A.
SM24_11137 *(page 2483)*

Bidulya A.
SM17_11688 *(page 2288)*

Bielski J.
SM4_11796 *(page 1765)*

Bielski P.
FM8_12311 *(page 904)*

Bielski W.R.
FM12_11248 *(page 1028)*

Bigoni D.
SM12_10265 *(page 2061)*

Billant P.
FM25_11391 *(page 1467)*
FM25_12108 *(page 1489)*
MS6_12294 *(page 377)*

Billardon R.
SM4_10974 *(page 1751)*

Bin G.
SM1_10559 *(page 1565)*

Binding D.M.
FM4_12254 *(page 728)*

Bing-Zheng G.
SM10_11572 *(page 1974)*

Bioul F.
FM15_12591 *(page 1146)*

Biros G.
FSM1_12691 *(page 431)*

Bisgaard A.
FM23_10247 *(page 1397)*

Blab R.
SM27_11981 *(page 2658)*

Blachowski B.D.
SM3_10457 *(page 1719)*

Blachut J.
SM22_10378 *(page 2423)*

Blackmore D.
FM25_11683 *(page 1475)*

Blajer W.
SM17_10026 *(page 2262)*

Blanc X.
FSM6_12336 *(page 588)*

Blasinska A.
FM4_11184 *(page 716)*

Blekhman I.
SM25_11055 *(page 2553)*
SM25_11719 *(page 2583)*

Blekhman L.I.
SM25_11055 *(page 2553)*

Blonski S.
FM17_11169 *(page 1201)*
FM4_11184 *(page 716)*
FM8_12873 *(page 920)*

Blume H.
SM2_12086 *(page 1697)*

Blyth M.G.
FM18_10766 *(page 1231)*

Bo W.
SM24_13013 *(page 2539)*

Bobaru F.
SM24_12789 *(page 2533)*

Bobylov A.A.
SM2_11933 *(page 1691)*

Bocciarelli M.
SM18_10797 *(page 2326)*

Bochenek B.
SM24_12075 *(page 2509)*

Bodnar A.
SM4_11665 *(page 1761)*

Boeck T.
FM19_12090 *(page 1272)*
FM8_11723 *(page 888)*

Boehlke T.
SM18_12549 *(page 2366)*

Boehm H.J.
SM13_12321 *(page 2142)*

Boehm R.
SM13_12576 *(page 2152)*

Boer P. de
FM11_12258 *(page 1002)*

Boer R. de
SM15_10198 *(page 2203)*

Boerner E.F.I.
SM1_12584 *(page 1635)*

Bogacz R.
SM22_12931 *(page 2457)*
SM25_12890 *(page 2624)*

Bogaert N. van den
FM15_12591 *(page 1146)*

Boguslawski A.
FM3_11914 *(page 696)*
FM6_12076 *(page 795)*

Bohatier C.
SM17_11361 *(page 2280)*

Bokhove O.
MS6_10716 *(page 334)*

Bolotnik N.N.
SM3_11219 *(page 1729)*

Bolotnova R.Kh.
FM8_12190 *(page 902)*

Bolzon G.
SM18_10797 *(page 2326)*

Bonamy D.
SM9_12378 *(page 1949)*

Bonn D.
FM8_13025 *(page 922)*

Bonnecaze R.T.
FM16_11991 *(page 1178)*
FM16_12574 *(page 1189)*

Bonnevie Harbitz C.
FM9_12270 *(page 948)*

Bonsel J.H.
SM25_11783 *(page 2587)*

Bontoux P.
FM15_11893 *(page 1138)*
FM25_12080 *(page 1487)*
FM6_13051 *(page 814)*

Bontozoglou V.
FM14_10557 *(page 1106)*

Borg U.
SM13_12214 *(page 2138)*

Borges L.S.A.
SM10_13018 *(page 2001)*

Borisov A.V.
SM1_12351 *(page 1619)*

Bornert M.
SM13_11507 *(page 2121)*
SM13_11805 *(page 2130)*

Borodich F.M.
SM2_11135 *(page 1671)*
SM2_11215 *(page 1675)*

Borodulin V.I.
FM24_12675 *(page 1455)*
FM2_10275 *(page 653)*

Boronska K.
FM7_10914 *(page 822)*

Boronski P.
FM6_10921 *(page 770)*

Borrell M.
FM8_11289 *(page 868)*

Borve S.
FM19_11809 *(page 1268)*

Bos F. van der
FM6_13030 *(page 812)*

Boso D.P.
SM2_10415 *(page 1657)*

Bostrom A.
FSM7_12603 *(page 606)*

Bottaro A.
FM11_12602 *(page 1010)*

Bottausci F.
FM22_12761 *(page 1395)*

Boubdallah A.
FSM4_13050 *(page 530)*

Bouchet G.
FM24_12740 *(page 1457)*

Bouché V.
FM7_11972 *(page 840)*

Boudaoud A.
FM8_13025 *(page 922)*

Boudifa M.
SM4_11885 *(page 1767)*

Bouizi O.
FM15_12636 *(page 1148)*

Boukpeti N.
SM20_11667 *(page 2411)*

Boulanger P.S.
FSM3_11818 *(page 490)*
SM11_11812 *(page 2037)*

Bouruet-Aubertot P.
MS6_12601 *(page 386)*

Boussa H.
SM1_12727 *(page 1641)*

Bouvet C.
SM13_11180 *(page 2113)*
SM14_12225 *(page 2196)*

Bouville M.
FSM6_11476 *(page 568)*

Boyland P.
FM22_12442 *(page 1385)*

Bozhko A.A.
FM7_10538 *(page 820)*

Braat J. J. M.
FM10_11088 *(page 965)*

Brady J.F.
FM16_12452 *(page 1187)*
SL4_12160 *(page 122)*

Braescu L.
FM21_11362 *(page 1335)*

Bragov A.M.
SM20_10374 *(page 2405)*

Bramkamp F.
FM5_11229 *(page 750)*

Brancher J.P.
FM13_10185 *(page 1044)*

Brancher P.
FM13_12483 *(page 1088)*

Branicki M.
FM18_12164 *(page 1243)*
FSM6_11862 *(page 574)*

Braud P.
FM5_13016 *(page 764)*

Brauer H.
FM19_12605 *(page 1286)*

Braun S.
FM2_11084 *(page 661)*

Braunbrueck A.
SM11_11620 *(page 2033)*

Bravo-Castillero J.
SM13_11176 *(page 2111)*

Brechet Y.
SM1_12737 *(page 1643)*

Brekelmans W.A.M.
FSM6_11830 *(page 572)*
SM18_11344 *(page 2340)*
SM18_11963 *(page 2356)*
SM1_12723 *(page 1639)*

Bremond N.
FM8_11317 *(page 872)*

Brenner H.
FM16_11725 *(page 1170)*

Brenner M.P.
FM8_11330 *(page 874)*

Breuer K.S.
FSM7_12467 *(page 602)*
MS4_11604 *(page 296)*

Breysse D.
SM18_12634 *(page 2368)*

Brinckmann S.
SM8_11927 *(page 1872)*

Brinson C.L.
MS1_12027 *(page 183)*

Brizuela E.
FM3_11888 *(page 694)*

Broeckhoven T.
FM3_11888 *(page 694)*

Brons M.
FM23_10247 *(page 1397)*

Brostovich A.
FSM2_11512 *(page 453)*

Brovchenko I.A.
FM26_12268 *(page 1548)*

Brown E.N.
MS1_13011 *(page 195)*
MS1_13010 *(page 157)*

Browne D.J.
FM21_11364 *(page 1337)*

Bruls O.
SM17_12208 *(page 2302)*

Brun C.
FM24_12740 *(page 1457)*

Brunet E.
MS4_12130 *(page 304)*

Brunig M.
SM4_11406 *(page 1755)*

Bruyn J.R. de
FM17_12338 *(page 1215)*

Buehler O.
MS6_10977 *(page 346)*

Buhl T.
SM24_12079 *(page 2511)*

Bulgakova G.T.
FM12_10548 *(page 1020)*

Bulgarelli U.P.
FM8_12547 *(page 912)*

Burachik R.
SM24_10594 *(page 2475)*

Burczynski T.S.
SM24_11137 *(page 2483)*

Burde G.
FM2_11984 *(page 674)*
FM26_12813 *(page 1555)*

Burnett D.S.
FSM1_11373 *(page 402)*

Burton D.
MS1_12027 *(page 183)*

Buryachenko V.
MS3_12718 *(page 279)*
SM10_12664 *(page 1992)*
SM6_12685 *(page 1839)*

Buschmann M.M.
FM2_10948 *(page 655)*

Busilas A.
SM16_12546 *(page 2254)*

Busse F.
FM19_10931 *(page 1253)*

Byrne H.M.
FM23_11060 *(page 1401)*

Byrtus M.
SM25_11759 *(page 2585)*

Byskov E.
SM22_12297 *(page 2447)*

Byun Y.-H.
FM6_11569 *(page 778)*

Bławzdziewicz J.
FM8_11411 *(page 876)*

Bühler O.
MS6_12157 *(page 370)*

C

Caffrey J.P.
MS1_13007 *(page 193)*

Cailletaud G.
SM14_10088 *(page 2170)*

Calhoun R.
FM9_12738 *(page 958)*

Callegari G.
FM4_10140 *(page 708)*

Calloch S.
SM14_12225 *(page 2196)*
SM18_12469 *(page 2364)*

Camotim D.
SM22_12558 *(page 2451)*

Campana E.F.
FM8_12547 *(page 912)*

Campregher R.
FM6_11456 *(page 774)*

Camyshev A.
FM2_11479 *(page 668)*

Cannata G.
FM24_11151 *(page 1427)*

Cantat I.
FSM5_12052 *(page 543)*

Carabineanu A.S.
FM1_11943 *(page 630)*

Carbonneau X.
FM6_12510 *(page 802)*

Cardin P.
FM19_12330 *(page 1280)*

Cardon A.
SM13_12818 *(page 2162)*

Cardonne C.
FM22_12761 *(page 1395)*

Carey M.
FM12_12617 *(page 1042)*

Carlotti P.
MS6_10513 *(page 342)*

Carnasciali M.-I.
MS5_12651 *(page 331)*

Carneiro C.A.V.
SM10_13018 *(page 2001)*

Carpen I.C.
FM16_12452 *(page 1187)*

Carpenter P.W.
FM2_11887 *(page 672)*

Carpinteri A.
FSM6_11224 *(page 560)*

Carriere P.
FM13_11186 *(page 1060)*

Cartraud P.
SM1_12359 *(page 1621)*

Casalis G.
FM13_12508 *(page 1090)*

Casandjian C.
SM4_10011 *(page 1741)*

Case S.
SM23_10242 *(page 2463)*

Casey J.
FSM3_11096 *(page 471)*

Cassar C.
FM16_11749 *(page 1172)*

Cassardo C.
MS6_13017 *(page 392)*

Castellanos A.
FM16_12438 *(page 1185)*
FM4_12437 *(page 732)*

Castro F.
FM8_11670 *(page 886)*

Cataldi-Spinola E.
FSM1_12586 *(page 427)*

Caughey T.K.
MS1_13007 *(page 193)*

Caulliez G.
FM13_12233 *(page 1072)*
FM26_11230 *(page 1524)*

Cazacu O.
SM18_11930 *(page 2352)*
SM20_12779 *(page 2419)*

Cazalbou J.B.
FM6_12510 *(page 802)*

Cebers A.
MS2_11102 *(page 213)*

Cenedese A.
FM7_11673 *(page 832)*

Cercignani C.
MS4_10723 *(page 290)*

Chabert E.
SM13_11805 *(page 2130)*

Chaboche J.L.
SM4_11885 *(page 1767)*

Chadli M.
SM4_10456 *(page 1743)*

Chakraborty P.
FM25_12161 *(page 1491)*

Challamel N.
SM4_10011 *(page 1741)*

Chan V. S. S.
FM10_11088 *(page 965)*

Chang C.-C.
FM25_11741 *(page 1477)*

Chang F.-R.
SM16_12712 *(page 2256)*

Chang H.-H.
SM10_10364 *(page 1964)*

Chang J.-T.
SM1_11193 *(page 1574)*

Chang K.T.
FM11_11043 *(page 986)*

Chang S.-Y.
SM24_11826 *(page 2501)*

Chao G.
SM11_11271 *(page 2023)*

Chaplin J.R.
FSM4_12557 *(page 526)*

Charrier Mojtabi M.C.
MS5_10980 *(page 317)*

Chassaing P.
FM6_12510 *(page 802)*

Chassiakos A.G.
MS1_13007 *(page 193)*

Chatterjee A.
SM25_12814 *(page 2621)*

Chatzidai N.
FM18_12859 *(page 1245)*

Chatzigeorgiou G.
SM4_12749 *(page 1789)*

Chauve M.-P.
FM24_10506 *(page 1419)*

Chazallon C.
SM18_12634 *(page 2368)*

Chen B.
SM24_11532 *(page 2491)*

Chen C.F.
FM21_11058 *(page 1323)*

Chen F.
FM9_11294 *(page 936)*

Chen H.-C.
FM25_11741 *(page 1477)*

Chen J.
SM25_10166 *(page 2541)*

Chen L.-Q.
FSM2_12674 *(page 465)*

Chen P.
FM13_11995 *(page 1068)*

Chen S.
SM14_11395 *(page 2184)*

Chen T.
SM6_11960 *(page 1816)*

Chenchiah I.
SM14_10721 *(page 2176)*

Cheng G.D.
SM24_13013 *(page 2539)*

Cheong K.B.
FM8_12596 *(page 916)*

Chern M.-J.
FSM4_11668 *(page 508)*

Cherniy D.I.
FM23_12868 *(page 1413)*

Chernoray V.G.
FM10_11455 *(page 967)*
FM2_11339 *(page 664)*

Chernousko F.L.
SM3_11243 *(page 1731)*

Chesneau X.
FM6_12985 *(page 810)*

Chew H.K.
FM8_12596 *(page 916)*

Chiba N.
SM18_10652 *(page 2320)*

Chickichev I.
SM20_12364 *(page 2415)*

Chien W.Z.
FM21_11208 *(page 1325)*

Chigarev A.V.
FSM2_11512 *(page 453)*

Chigarev Y.V.
FSM2_11512 *(page 453)*

Chini G.P.
FM14_12155 *(page 1124)*

Chiskis A.
MS3_12432 *(page 271)*

Chizhik S.A.
SM2_10999 *(page 1665)*

Chmielniak T.
FM6_11578 *(page 785)*
FM10_11916 *(page 971)*

Cho J.-H.
SM27_11827 *(page 2654)*

Cho Y.-S.
SM1_11817 *(page 1599)*

Choi C.K.
FM21_13008 *(page 1355)*

Choi H.
FM11_11636 *(page 990)*
FM19_11637 *(page 1265)*

Choi J.
FM11_11636 *(page 990)*

Choi S.T.
MS3_12778 *(page 281)*

Cholet C.
SM17_11361 *(page 2280)*

Chomaz J.-M.
FM13_12425 *(page 1084)*
FM13_12711 *(page 1096)*
FM25_11391 *(page 1467)*
FM25_12108 *(page 1489)*
MS6_12294 *(page 377)*

Chow C.L.
SM4_10961 *(page 1749)*

Christophorou C.
FM24_12965 *(page 1463)*

Chroscielewski J.
SM19_11890 *(page 2390)*

Chrzanowski M.
SM4_11665 *(page 1761)*

Chu C.-C.
FM25_11741 *(page 1477)*

Chucholowski C.
SM26_11672 *(page 2638)*

Chung C.A.
FM21_11208 *(page 1325)*

Chung S.-H.
SM1_12441 *(page 1622)*

Churochkin D.V.
FSM1_11508 *(page 404)*

Chwał M.
MS3_12251 *(page 263)*

Cichocki B.
FM16_10993 *(page 1156)*
FM18_11300 *(page 1235)*

Ciechanowski J.
FM9_12266 *(page 946)*

Cieslik J.
SM25_12498 *(page 2601)*

Cieszko M.
FM12_12611 *(page 1040)*

Cilliers J.J.
FSM5_12851 *(page 553)*

Cirak F.
SM19_10038 *(page 2374)*

Claire D.
SM4_12021 *(page 1771)*

Clamond D.
FM26_11417 *(page 1530)*

Clanet C.
FM8_11317 *(page 872)*

Clavel M.
SM8_12228 *(page 1880)*

Clayton J.D.
SM18_10955 *(page 2328)*

Clercx H.J.H.
FM25_11964 *(page 1479)*

Clercx H.
FM22_12633 *(page 1391)*

Cleri F.
FSM6_12334 *(page 586)*

Clifford M.J.
SM13_11387 *(page 2115)*

Cloirec M.
SM1_12359 *(page 1621)*

Cloitre M.
FM16_12574 *(page 1189)*

Cocks A.C.F.
SM15_12903 *(page 2235)*

Cocou M.
SM2_12382 *(page 1703)*

Coelho I.
SM12_12682 *(page 2083)*

Coelho P.J.
FM3_12348 *(page 700)*

Cohen J.
FM13_11461 *(page 1064)*

Cohen-Addad S.
FSM5_12578 *(page 551)*

Coiffet F.
FM5_13016 *(page 764)*

Coker D.
SM2_11987 *(page 1693)*

Cola B.A.
FM22_12158 *(page 1373)*

Colette A.
FM25_11391 *(page 1467)*

Collicott S.H.
MS5_12447 *(page 329)*

Colombo L.
FSM6_12334 *(page 586)*

Colonius T.
FM11_12387 *(page 1006)*

Coman C.D.
SM22_12967 *(page 2461)*

Combescure A.
SM1_11797 *(page 1597)*
SM22_11174 *(page 2433)*

Comte P.
FM19_11429 *(page 1259)*
FM24_12740 *(page 1457)*

Constantin P.
FM23_10938 *(page 1399)*

Constantinescu D.M.
SM9_10864 *(page 1910)*

Cooker M.J.
FM26_11345 *(page 1528)*

Coons J.
FSM5_12435 *(page 549)*

Cordeiro Fernandes P.
FM20_12139 *(page 1306)*

Cornwell P.
FSM7_12642 *(page 608)*

Costa M.
FM3_12348 *(page 700)*

Costanzo F.
FSM7_12642 *(page 608)*

Cottet G.-H.
FM6_12583 *(page 806)*

Cottron M.
SM9_10429 *(page 1899)*

Courrech du Pont S.
FM17_13029 *(page 1225)*

Cox B.N.
SM13_11162 *(page 2109)*

Cox S.M.
FM22_10497 *(page 1359)*
FM23_11060 *(page 1401)*

Cox S.
MS5_10598 *(page 312)*

Craig W.
FM26_11548 *(page 1534)*

Cramer A.
FM15_12349 *(page 1144)*

Crandall S.H.
SM25_10863 *(page 2551)*

Craster R.V.
FM14_11404 *(page 1114)*

Cristescu N.D.
SM18_11930 *(page 2352)*
SM20_12779 *(page 2419)*

Crochet M.W.
SM15_12771 *(page 2233)*

Croll J.G.A.
FM9_12072 *(page 943)*

Cudziło S.
FM3_12745 *(page 702)*

Cugy P.
SM18_12469 *(page 2364)*

Cummins S.J.
FM8_12163 *(page 900)*

Cunningham J.C.
SM15_12917 *(page 2238)*

Currie P.K.
FSM5_12986 *(page 555)*

Cuypers Y.
FM24_11303 *(page 1433)*

Czarnecki S.
SM24_11760 *(page 2499)*

Czechowski L.
FM21_12743 *(page 1351)*

Czerwinska J.
FM24_11802 *(page 1439)*
FSM6_10399 *(page 559)*

D

D'Addetta G.A.
SM4_11414 *(page 1757)*

Dahan M.
SM6_11901 *(page 1814)*

Dahl S.R.
FM17_12073 *(page 1211)*

Dail B.
FM15_10363 *(page 1132)*

Dal Pont S.
SM15_12114 *(page 2217)*

Dalziel S.B.
FM25_12051 *(page 1485)*

Dam D.B. van
FM14_11509 *(page 1120)*

Dam R.
SM22_12297 *(page 2447)*

Daneshmand F.
FM9_10733 *(page 930)*

Daneshmehr A.
SM13_13009 *(page 2166)*

Danishevs'kyy V.V.
SM13_12588 *(page 2154)*

Dankowicz H.
SM17_11020 *(page 2274)*

Danner T.
FM8_11669 *(page 884)*

Daru V.
FM8_11979 *(page 894)*

Darve E.
FM16_12005 *(page 1180)*

Daube O.
FM13_10640 *(page 1056)*

Davaille A.
FM7_12126 *(page 842)*

Davide B.
SM12_11254 *(page 2069)*

Davidson P.A.
FM19_11124 *(page 1257)*

Davis R.H.
FM16_11473 *(page 1165)*
FM8_12329 *(page 906)*
FM8_12741 *(page 918)*

Debatin K.
FM5_11864 *(page 756)*

Debin S.
SM1_10559 *(page 1565)*

Deblaise D.
SM16_10553 *(page 2244)*

Decamp S.
FM9_12410 *(page 952)*

Degre G.
MS4_12130 *(page 304)*

Dekajlo K.
FM9_10576 *(page 928)*

Delannay R.
FM17_12883 *(page 1223)*
FSM5_12052 *(page 543)*

Delgado A.
MS2_12031 *(page 224)*
FM10_13048 *(page 981)*

Dell'Aversana P.
MS5_12651 *(page 331)*

Delsaute B.
FM15_12591 *(page 1146)*

Delville J.
FM5_13016 *(page 764)*

Dems K.
SM24_11349 *(page 2487)*

Denda M.
MS1_12786 *(page 191)*

Denier J.P.
FM2_10103 *(page 651)*

Denis A.
SM18_12634 *(page 2368)*

Denkov N.D.
FM8_11669 *(page 884)*

Deprince X.
SM18_11110 *(page 2332)*

Derby J.J.
FM15_10363 *(page 1132)*

Derksen J.
FM20_12397 *(page 1315)*
FM20_12671 *(page 1317)*

Deshpande V.S.
SM5_11022 *(page 1793)*

Destrade M.
FSM3_11950 *(page 494)*

Detournay E.
SM15_12713 *(page 2231)*
SM25_12535 *(page 2605)*

Dettmar J.
FSM6_12112 *(page 580)*

Di G. Sigalotti L.
FM6_10857 *(page 768)*

Dias F.
FM26_12089 *(page 1546)*

Dick E.
FM6_11602 *(page 787)*

Didelle H.
MS6_12494 *(page 384)*

Dijksman J.F.
FM4_12894 *(page 734)*

Dimakopoulos Y.
FM14_12858 *(page 1130)*

Ding E.-J.
FM1_12124 *(page 634)*

Dinkler D.
SM25_12785 *(page 2619)*

Dmitrochenko O.
SM17_10893 *(page 2272)*

Dobler W.
FM7_10306 *(page 816)*

Dobovsek I.
SM12_12419 *(page 2081)*

Dobrolyubov A.I.
FM26_11144 *(page 1519)*

Doche O.
FM11_11394 *(page 988)*

Dodge A.
MS4_12536 *(page 306)*

Doerffer P.
FM5_12997 *(page 762)*

Doghri I.
SM18_13038 *(page 2372)*

Dohnal F.
SM25_12026 *(page 2595)*

Dolezel I.
SM2_10211 *(page 1653)*

Dollet B.
FSM5_11095 *(page 533)*

Domaas U.
FM9_12270 *(page 948)*

Domanski W.
FSM3_11840 *(page 492)*

Domaradzki A.J.
FM24_10149 *(page 1415)*

Domenico C.
SM12_11254 *(page 2069)*

Dominguez J.
SM17_12071 *(page 2296)*
SM8_10698 *(page 1861)*

Dominguez J.
SM9_11321 *(page 1921)*

Dommelen J.A.W. van
SM18_11344 *(page 2340)*

Dongen M.E.H. van
SM11_11271 *(page 2023)*

Dorfman K.D.
FM4_11209 *(page 718)*

Dorfmann L.A.
FSM3_11227 *(page 475)*

Dormieux L.
SM15_11941 *(page 2215)*

Doudard C.
SM18_12469 *(page 2364)*

Doval-Montes L.
SM13_11176 *(page 2111)*

Dovgal A.V.
FM2_11339 *(page 664)*

Dovgiy S.A.
FM23_12868 *(page 1413)*

Dowling A.P.
FSM1_12527 *(page 421)*

Dragon A.
SM18_11110 *(page 2332)*

Drazer G.
FM16_10361 *(page 1152)*

Dreiden G.V.
SM11_10114 *(page 2005)*

Drescher A.
SM20_11667 *(page 2411)*

Dritschel D.G.
MS6_11336 *(page 350)*

Drobinski P.
MS6_10513 *(page 342)*

Drobniak S.
FM3_11914 *(page 696)*

Drugan W.J.
SM12_12025 *(page 2077)*

Du J.
SM24_10433 *(page 2473)*

Dual J.
FSM1_12586 *(page 427)*
MS3_12384 *(page 267)*

Dubois F.
SM17_11361 *(page 2280)*

Duchemin L.
FM8_12388 *(page 908)*

Duck P.W.
FM13_10916 *(page 1058)*
FM2_10103 *(page 651)*

Dudeck M.
FM19_12363 *(page 1282)*

Dufour G.
FM6_12510 *(page 802)*

Duineveld P.C.
FM4_12894 *(page 734)*

Duluc M.C.
FM8_11979 *(page 894)*

Dumais J.
MS2_11581 *(page 217)*

Dumontet H.
SM1_12727 *(page 1641)*

Dupere I.D.J.
FSM1_12527 *(page 421)*

Duplat J.
FM22_12326 *(page 1379)*

Dupont R.
FM13_12233 *(page 1072)*

Dupret F.
FM15_12591 *(page 1146)*

Durban D.
SM25_12842 *(page 2623)*

Durgin W.W.
FSM1_12149 *(page 411)*

Duschlbauer D.
SM13_12321 *(page 2142)*

Dusek J.
FM13_12766 *(page 1098)*

Duszynski P.
FM6_12565 *(page 804)*

Duysinx P.
SM17_12208 *(page 2302)*

Dvorak V.
FM5_12219 *(page 760)*

Dykas S.
FM6_11578 *(page 785)*

Długosz A.
SM24_11137 *(page 2483)*

E

Eberhard P.
SM17_12133 *(page 2298)*

Eberhardsteiner J.
SM27_11981 *(page 2658)*

Eck C.
FSM6_11340 *(page 564)*

Eckert K.
FM21_12365 *(page 1347)*

Eckert S.
FM21_12365 *(page 1347)*

Eckhardt B.
FM13_10313 *(page 1048)*

Edmonstone B.
FM14_11404 *(page 1114)*

Edwards N.R.
FM26_12424 *(page 1551)*

Eggers J.
FM14_11089 *(page 1112)*

Ehlers W.
SM15_10792 *(page 2207)*
SM15_11194 *(page 2211)*

Ehrenstein U.
FM13_12372 *(page 1080)*

Ehrlacher A.
SM15_12114 *(page 2217)*
SM15_12614 *(page 2229)*

Eidelman A.
FM10_12070 *(page 973)*

Ekiel-Jezewska M.L.
FM16_11409 *(page 1159)*
FM18_11300 *(page 1235)*

El Abd A.
SM18_12634 *(page 2368)*

El G.
FM26_11134 *(page 1517)*

El Ganaoui M.
FM15_11386 *(page 1136)*
FM15_11893 *(page 1138)*
FM6_12356 *(page 799)*

El Maihy A.
FM22_10130 *(page 1357)*

Elaguine D.
SM2_11365 *(page 1677)*

Elborai S.M.
FM4_11982 *(page 726)*

Eldredge J.D.
FSM1_12180 *(page 413)*

Elias F.
FSM5_11095 *(page 533)*

Elmabrok A.M.
SM25_11082 *(page 2559)*

Elperin T.
FM10_12070 *(page 973)*
FM7_11053 *(page 824)*

Emelin V.K.
SM7_11556 *(page 1847)*

Emmerich H.
FSM6_11340 *(page 564)*

Engel R.S.
SM27_10906 *(page 2646)*

Engelbrecht J.
SM10_11592 *(page 1978)*
SM11_11813 *(page 2039)*

Engelen R.A.B.
SM4_11415 *(page 1759)*

England A.H.
SM10_12273 *(page 1984)*

Epstein M.
SM6_12122 *(page 1822)*

Eremeyev V.A.
SM19_10287 *(page 2380)*

Erenburg V.
FM3_12199 *(page 698)*

Erickson J.
SM1_12441 *(page 1622)*

Ermakov M.K.
FSM7_11869 *(page 598)*
MS5_11843 *(page 323)*

Ern P.
FM20_12139 *(page 1306)*

Erofeyev V.I.
SM11_12203 *(page 2045)*

Escalona J.L.
SM17_12071 *(page 2296)*

Esveld C.
SM24_11015 *(page 2481)*

Etling D.
MS6_12035 *(page 364)*

Etnyre J.B.
FM23_11677 *(page 1407)*

Evans D.L.
FSM7_12642 *(page 608)*

Evans G.M.
FM15_11903 *(page 1140)*

Evers L.P.
SM18_11963 *(page 2356)*

F

Faciu C.
SM14_11852 *(page 2190)*

Faisst H.
FM13_10313 *(page 1048)*

Faivre M.
FM1_12423 *(page 642)*

Falcovitz J.
FM5_11049 *(page 746)*

Falk M.
FSM6_11476 *(page 568)*

Falkovich G.
FM22_12048 *(page 1369)*

Fan J.
SM27_11506 *(page 2652)*

Fan Y.
SM1_12441 *(page 1622)*

Fang D.
MS1_12016 *(page 179)*

Fayzrakhmanova I.S.
FM21_12278 *(page 1343)*

Fedenkova A.A.
FM2_10275 *(page 653)*

Feissel P.
SM1_12237 *(page 1613)*

Felderhof B.U.
FM16_11236 *(page 1158)*

Feng L.
SM24_12287 *(page 2521)*

Feng X.-Q.
MS3_12314 *(page 265)*

Feng X.
MS1_12016 *(page 179)*

Fenghuan S.
MS3_12181 *(page 261)*

Fenili A.
SM3_13004 *(page 1739)*

Feraille T.
FM13_12508 *(page 1090)*

Fernandes A.
SM10_12093 *(page 1982)*

Fernandez-Feria R.
FM9_11346 *(page 938)*

Fernando H.J.S.
FM9_10576 *(page 928)*
FM9_12738 *(page 958)*

Ferrarese S.
MS6_13017 *(page 392)*

Ferreira M.J.F.
FM20_10690 *(page 1294)*

Ferri F.
FM10_10445 *(page 962)*

Feuillebois F.
FM16_10248 *(page 1150)*

Fey R.H.B.
SM25_11783 *(page 2587)*

Fidlin A.
SM25_11679 *(page 2575)*
SM25_12694 *(page 2613)*

Finn M.D.
FM22_10497 *(page 1359)*
FM23_11060 *(page 1401)*

Firsova A.D.
SM25_11712 *(page 2579)*

Fischer F.D.
SM14_10088 *(page 2170)*

Flanagan J.D.
FM26_11468 *(page 1532)*

Fleck N.
MS2_10988 *(page 211)*
SM13_12680 *(page 2158)*
SM5_11022 *(page 1793)*

Floryan J.M.
FM13_10489 *(page 1052)*

Flukiger F.
FM12_11343 *(page 1030)*

Flór J.-B.
MS6_11829 *(page 360)*

Fochesato C.
FM26_12089 *(page 1546)*

Fomin N.A.
FM10_12213 *(page 975)*

Fontelos M.A.
FM8_12548 *(page 914)*

Fornalik E.
FM7_12173 *(page 846)*

Forterre Y.
FM17_11775 *(page 1205)*
MS2_11581 *(page 217)*

Foure T.M.
FM13_10188 *(page 1046)*

Fourment C.
FM5_13016 *(page 764)*

Fowler P.W.
SM1_11482 *(page 1589)*

Foysi H.
FM24_11116 *(page 1425)*

Fraigneau Y.
FM13_10188 *(page 1046)*

Frana K.
FM19_12587 *(page 1284)*

Francfort G.A.
SM9_12921 *(page 1957)*

Franciosi P.
SM18_11498 *(page 2346)*

Francius M.
FM26_11417 *(page 1530)*

Francois M.M.
FM8_12163 *(page 900)*

Frankel I.
FM7_12850 *(page 856)*

Franklin J.
FM16_11884 *(page 1176)*

Franz S.
FM24_11256 *(page 1431)*

Frear D.
FSM3_11515 *(page 481)*

Fredriksson P.
SM18_11410 *(page 2344)*

Freidin A.
SM14_11837 *(page 2188)*

Freund J.B.
FSM1_10907 *(page 396)*

Friedrich R.
FM24_11116 *(page 1425)*

Frischmuth K.
SM11_11853 *(page 2041)*

Froehlich J.
FM6_11348 *(page 772)*

Frolova N.Yu.
SM7_12272 *(page 1853)*

Frost T.
SM22_12297 *(page 2447)*

Fructus D.
FM26_11417 *(page 1530)*

Fruend E.-T.
FM1_11851 *(page 624)*

Fu S.
FM24_12652 *(page 1453)*

Fu Y.
SM14_11837 *(page 2188)*

Fuchs M.
FSM5_13033 *(page 557)*

Fuchs P.
SM22_12084 *(page 2445)*

Fuenmayor J.
SM8_10698 *(page 1861)*

Fuetterer C.
FM4_11209 *(page 718)*

Fujinuma S.
SM18_11295 *(page 2336)*

Fujita K.
SM17_12582 *(page 2312)*

Fukumoto Y.
FM25_11615 *(page 1471)*
SM25_12593 *(page 2607)*

Fukunishi Y.
FM11_12491 *(page 1008)*

Funakoshi M.
FM23_12484 *(page 1411)*

Furutani Y.
SM12_11432 *(page 2073)*

G

Gabrielli P.G.
FSM6_12334 *(page 586)*

Gad-el-Hak M.
FM11_10128 *(page 983)*
FM2_10948 *(page 655)*

Gadaj S.P.
SM14_10046 *(page 2168)*
SM14_11308 *(page 2178)*

Galaktionov O.S.
FM1_12063 *(page 632)*

Galambos P.C.
FM4_10753 *(page 710)*

Galanov B.A.
SM2_11135 *(page 1671)*

Gallaire F.
FM13_12372 *(page 1080)*
FM13_12425 *(page 1084)*

Gallerano F.
FM24_11151 *(page 1427)*

Galperin B.
MS6_11152 *(page 348)*
MS6_11942 *(page 362)*

Galtier A.
SM18_12469 *(page 2364)*

Galvanetto U.
FSM2_11241 *(page 445)*

Galvin J.E.
FM17_12073 *(page 1211)*

Gamallo P.
FSM1_11249 *(page 398)*

Gambarotta L.
SM4_12298 *(page 1781)*
MS2_13049 *(page 239)*

Gambaryan-Roisman T.
FM14_12293 *(page 1126)*

Gambin B.
SM13_11895 *(page 2132)*
SM13_12667 *(page 2156)*

Gambin W.L.
SM18_11975 *(page 2358)*

Ganczarski A.
SM4_12335 *(page 1785)*

Gandzha I.S.
FM26_11591 *(page 1536)*
MS2_12059 *(page 227)*

Ganguly P.
SM1_12458 *(page 1626)*

Ganqing F.
SM24_12287 *(page 2521)*

Gao C.-F.
MS1_11857 *(page 175)*

Gao H.
SL5_10772 *(page 123)*

Gao X.
MS1_12027 *(page 183)*

Garcia-Sanchez F.
SM9_11321 *(page 1921)*

Garcia-Villalba M.
FM6_11348 *(page 772)*

Gardeniers H.
FM1_12400 *(page 638)*

Garikipati K.
FSM6_11476 *(page 568)*

Garstecki A.
SM24_12628 *(page 2529)*

Garstecki P.
MS4_12966 *(page 310)*

Gaspar Z.
SM22_10915 *(page 2427)*

Gautier P.-E.
SM17_11361 *(page 2280)*

Gavrilov S.N.
SM6_12324 *(page 1829)*

Gavrilova E.
FSM4_10520 *(page 500)*

Gałka A.
SM13_11895 *(page 2132)*
SM13_12667 *(page 2156)*
SM13_12732 *(page 2160)*

Gee M.
SM19_12606 *(page 2401)*

Geers M.G.D.
FSM6_11830 *(page 572)*
SM14_11395 *(page 2184)*
SM18_11963 *(page 2356)*
SM1_12131 *(page 1607)*
SM1_12723 *(page 1639)*
SM4_11415 *(page 1759)*
SM4_12341 *(page 1787)*

Geffroy P.
FM11_12244 *(page 1000)*

Gelder B. van
FSM5_12373 *(page 546)*

Gendelman O.V.
SM25_11079 *(page 2557)*

Geoffroy S.
FM12_11343 *(page 1030)*

Georgelin M.
FM21_12543 *(page 1349)*

Gerbeth G.
FM11_12068 *(page 996)*
FM13_12542 *(page 1094)*
FM15_12349 *(page 1144)*
FM19_12613 *(page 1288)*

Gerkema T.
FM26_12087 *(page 1544)*

Gerland P.
SM16_12417 *(page 2252)*

Germay C.
SM25_12535 *(page 2605)*

Gerstmayr J.
SM17_12029 *(page 2294)*

Getling A.V.
FM7_10306 *(page 816)*

Geubelle P.H.
SM10_11177 *(page 1970)*

Geurts B.J.
FM6_13030 *(page 812)*

Gharib M.
FM1_12784 *(page 648)*

Ghicini S.
FM16_11588 *(page 1169)*
FM16_12345 *(page 1184)*

Ghorbel E.
SM18_10729 *(page 2322)*

Ghrist R.W.
FM23_11677 *(page 1407)*

Gibson A.N.
FM10_11455 *(page 967)*

Giessen E. van der
MS2_10627 *(page 203)*
SM1_12737 *(page 1643)*
SM8_11927 *(page 1872)*

Gilat R.
MS1_12011 *(page 177)*

Gilewicz J.
FSM3_11642 *(page 485)*

Gill S.P.A.
MS3_12627 *(page 275)*

Gilles L.
SM4_12277 *(page 1779)*

Ginalski M.K.
FM1_12409 *(page 640)*

Girgis I.G.
FM13_10487 *(page 1050)*

Girish J.
SM13_12531 *(page 2148)*

Giusti A.
FM20_13012 *(page 1321)*

Gladden L.F.
FM21_11320 *(page 1329)*

Glema A.
SM5_12949 *(page 1800)*

Glicksman M.E.
FSM5_11240 *(page 535)*

Gloaguen J.M.
SM18_12339 *(page 2362)*

Glocker C.
FSM2_11183 *(page 443)*

Gloria A.
FSM6_12078 *(page 578)*

Godard V.
SM4_12913 *(page 1791)*

Goddard J.D.
FM17_10371 *(page 1193)*

Godoy-Diana R.
FM25_12108 *(page 1489)*

Goektepe S.
SM4_12116 *(page 1777)*

Goetsch M.
FSM1_12586 *(page 427)*

Goldhirsch I.
FM17_12308 *(page 1213)*

Goldobin D.S.
FM13_12280 *(page 1076)*

Golfier F.
FM12_10234 *(page 1018)*

Golinval J.-C.
SM17_12208 *(page 2302)*

Gollub J.P.
FM17_12445 *(page 1219)*

Goncalves P.B.
SM22_12420 *(page 2449)*

Goncharova O.N.
MS5_11757 *(page 321)*

Gondret P.
FM17_13029 *(page 1225)*

Gong L.
FSM5_11605 *(page 539)*

Gonik M.A.
FM21_11331 *(page 1333)*

Gontarowskiy P.
SM2_10211 *(page 1653)*

Gonthier K.A.
SM15_12771 *(page 2233)*

Gonthier Y.
SM2_12773 *(page 1715)*

Gonzalez A.
FM4_12437 *(page 732)*

Goo B.
SM8_11737 *(page 1867)*
SM8_12001 *(page 1874)*

Gorbatikh L.
SM2_12412 *(page 1705)*

Gordillo J.M.
FM8_11448 *(page 878)*

Goryacheva I.
SM2_11196 *(page 1673)*

Goto T.
FM1_11441 *(page 622)*

Goujon-Durand S.
FM11_12736 *(page 1014)*

Goulitski K.
FM26_10245 *(page 1507)*

Gourjii A.A.
FM22_12110 *(page 1371)*
FM25_12196 *(page 1493)*

Govindarajan R.
FM2_12631 *(page 684)*

Govorukhin V.N.
FM12_10199 *(page 1016)*

Graf T.
SM15_10792 *(page 2207)*

Graham A.L.
FM16_11725 *(page 1170)*

Gramstad O.
FSM4_12956 *(page 528)*

Graner F.
FSM5_11095 *(page 533)*

Grants I.
FM13_12542 *(page 1094)*

Gravouil A.
SM1_11797 *(page 1597)*

Gray G.L.
FSM7_12642 *(page 608)*

Grebe R.
SM15_12614 *(page 2229)*

Green M.L.
SM20_12779 *(page 2419)*

Green N.G.
FM4_12437 *(page 732)*

Grekova E.F.
SM6_12434 *(page 1833)*

Griffiths R.
MS6_11499 *(page 352)*

Griggs A.J.
FM8_12741 *(page 918)*

Grimshaw R.H.J.
SM11_11242 *(page 2021)*

Gristchak V.Z.
SM25_10656 *(page 2547)*

Grondin F.
SM1_12727 *(page 1641)*

Grossman-Clarke S.
FM9_12738 *(page 958)*

Grue J.
FM26_11417 *(page 1530)*
FSM4_12956 *(page 528)*

Grunefeld G.
FM10_12070 *(page 973)*

Gryschka M.
MS6_12035 *(page 364)*

Gu Y.
SM24_11532 *(page 2491)*

Guazzelli E.
FM16_11588 *(page 1169)*
FM16_11850 *(page 1174)*
FM16_12345 *(page 1184)*

Guba P.
FM21_11270 *(page 1327)*

Guddati M.N.
FSM1_11973 *(page 409)*

Gudmundson P.
SM18_11410 *(page 2344)*

Guedes de Carvalho J.R.F.
FM20_10690 *(page 1294)*

Guegan A.
FM11_12305 *(page 1004)*

Guerses E.
SM1_12115 *(page 1605)*

Guest S.D.
SM1_11482 *(page 1589)*
SM22_12669 *(page 2453)*

Gueydan F.
SM12_12751 *(page 2085)*

Guinovart-Diaz R.
SM13_11176 *(page 2111)*

Guitong Y.
MS3_12181 *(page 261)*

Gundrum T.
FM19_12613 *(page 1288)*

Guo J.-G.
SM16_10510 *(page 2242)*

Guo L.
SM10_11551 *(page 1972)*

Guo Z.
FSM4_12521 *(page 524)*

Gupta N.K.
SM5_12982 *(page 1802)*

Gurka R.
FM24_12757 *(page 1459)*

Guse N.
SM17_11223 *(page 2276)*

Gutfinger C.
FSM1_12516 *(page 419)*

Gutkowski W.
SM3_10457 *(page 1719)*
SM3_10458 *(page 1721)*

Guz I.A.
SM9_10824 *(page 1908)*

Guzina B.
SM20_12364 *(page 2415)*

H

H. Kaneko
SM25_11536 *(page 2573)*

H. Yabuno
SM25_11536 *(page 2573)*

Haber R.B.
SM1_12441 *(page 1622)*

Haberkorn M.
FM24_12740 *(page 1457)*

Hachemi A.
SM18_12058 *(page 2360)*

Hackl K.
SM14_12077 *(page 2192)*
SM24_12074 *(page 2507)*

Haddad J.
FM4_11648 *(page 722)*

Hadjiconstantinou N.G.
MS4_11437 *(page 294)*

Hagedorn P.
SM25_11261 *(page 2563)*

Hahn S.
FM11_11636 *(page 990)*

Hajzman M.
SM25_11759 *(page 2585)*

Halbedel B.
FM19_11906 *(page 1270)*

Halkjaer S.
SM24_11744 *(page 2497)*

Halley P.
FSM5_12435 *(page 549)*

Hallworth M.A.
FM17_10524 *(page 1195)*

Hammerton P.W.
FM2_12241 *(page 680)*
FSM1_12497 *(page 417)*

Hanada S.
SM11_12418 *(page 2049)*

Hanagud S.
SM10_12968 *(page 1996)*

Hanchi S.
FSM4_13050 *(page 530)*

Hansen J.S.
SM13_12148 *(page 2136)*

Hansen L.V.
FSM1_12533 *(page 423)*

Hao S.
SM9_10676 *(page 1906)*

Haque A.
MS3_12705 *(page 277)*

Hara T.
FM26_10746 *(page 1509)*

Harambat F.
FM22_11190 *(page 1365)*

Hardy S.
SM13_12141 *(page 2134)*

Harlander U.
FM26_12318 *(page 1550)*

Harrison P.
SM13_11387 *(page 2115)*

Hartmann C.
MS2_12031 *(page 224)*
FM10_13048 *(page 981)*

Hasegawa S.
FM5_11560 *(page 752)*

Hata T.
SM11_10344 *(page 2007)*

Hattori Y.
FM19_11458 *(page 1261)*
FM25_11615 *(page 1471)*

Haughton D.M.
SM6_11220 *(page 1808)*

Hayashi S.
MS1_10821 *(page 163)*

Hayes M.A.
FSM3_11818 *(page 490)*
SM11_11812 *(page 2037)*

Haynes P.
MS6_10987 *(page 338)*

Hazel A.L.
FM1_12295 *(page 636)*

He J.
FM24_12652 *(page 1453)*

He Y.
SM27_11506 *(page 2652)*

Healey J.J.
FM13_12150 *(page 1070)*

Heijst G.J.F. van
FM25_12051 *(page 1485)*
FM22_12633 *(page 1391)*
FM22_12110 *(page 1371)*
FM25_11964 *(page 1479)*

Heil M.
FM1_11013 *(page 618)*
FM1_12295 *(page 636)*

Heintz A.
FM6_11763 *(page 791)*

Hellmich C.
SM11_12313 *(page 2047)*

Herakovich C.T.
FSM7_10226 *(page 594)*

Herczynski A.
FM2_11984 *(page 674)*
FSM4_11986 *(page 520)*

Herrada M.A.
FM25_10683 *(page 1465)*

Herrmann K.P.
SM9_10824 *(page 1908)*
SM9_12249 *(page 1947)*

Herskovits J.
SM24_10594 *(page 2475)*

Herve I.
FM11_12244 *(page 1000)*

Hickel S.
FM24_11256 *(page 1431)*
FM24_12564 *(page 1451)*

Hierck B.P.
FM1_11900 *(page 626)*

Higashi A.
SM25_11066 *(page 2555)*

Hikihara T.
FSM2_12014 *(page 457)*

Hild F.
SM18_12469 *(page 2364)*
SM4_12021 *(page 1771)*

Hilgenfeldt S.
FM1_12400 *(page 638)*
FSM5_10597 *(page 532)*
FSM5_12373 *(page 546)*

Hinch J.
FM16_11588 *(page 1169)*
FM16_12345 *(page 1184)*

Hino R.
SM24_12870 *(page 2535)*

Ho K.H.
FM21_11208 *(page 1325)*

Ho Y.G.
SM24_12185 *(page 2515)*

Hochlenert D.
SM25_11261 *(page 2563)*

Hodson H.P.
FSM5_12395 *(page 547)*

Hogan J.S.
FSM2_10499 *(page 439)*

Hohe J.
SM15_11463 *(page 2213)*
SM9_11484 *(page 1925)*

Hohler R.
FSM5_12578 *(page 551)*

Hojjati H.M.
SM1_11291 *(page 1581)*

Holeman J.E.
FM9_12738 *(page 958)*

Holm D.D.
FM23_12375 *(page 1409)*
FM6_13030 *(page 812)*

Holnicki-Szulc J.
MS1_11810 *(page 173)*
MS1_13015 *(page 197)*

Holobut P.
SM3_10458 *(page 1721)*

Holopainen S.
SM24_12200 *(page 2517)*

Homayoun Heidari A.
FSM1_11973 *(page 409)*

Homsy G.M.
FSM7_12467 *(page 602)*
MS5_11133 *(page 314)*

Hong Y.
SM8_12391 *(page 1882)*

Hopkins D.C.
FSM3_11515 *(page 481)*

Hopkins M.M.
FM18_10983 *(page 1233)*

Horanyi S.
FM19_10931 *(page 1253)*

Horiguchi K.
SM9_11502 *(page 1927)*

Horimoto H.
FSM1_10294 *(page 394)*

Hornowski T.
SM15_12567 *(page 2225)*

Hornych P.
SM18_12634 *(page 2368)*

Horst E.
SM25_12026 *(page 2595)*

Hosseini-Godarzi A.
SM9_10646 *(page 1903)*

Hosseini-Tehrani P.
SM9_10646 *(page 1903)*

Hourlier D.
FM6_12356 *(page 799)*

Howle L.
FM12_12617 *(page 1042)*

Howlin C.P.
FM26_11468 *(page 1532)*

Hoyer K.W.
FM25_12821 *(page 1501)*

Hrenya C.M.
FM17_12073 *(page 1211)*

Hribersek M.
FSM4_10826 *(page 502)*

Hu X.X.
SM19_12224 *(page 2393)*

Hu X.
FM24_11802 *(page 1439)*

Huang H.
FM26_11126 *(page 1515)*
FM4_12894 *(page 734)*

Huang I.-D.
SM1_11193 *(page 1574)*

Huang P.
MS4_11604 *(page 296)*

Huang R.F.
FM11_11043 *(page 986)*

Huang R.
MS3_10699 *(page 247)*

Huang X.
FM4_11165 *(page 714)*

Huang Y.
MS3_12314 *(page 265)*

Huerre P.
FM11_12305 *(page 1004)*
FM13_12425 *(page 1084)*

Hufenbach W.
SM13_12576 *(page 2152)*

Hughes G.
MS6_11499 *(page 352)*

Hughes T.J.R.
SL6_13003 *(page 126)*

Hulbert G.M.
SM11_12772 *(page 2059)*

Hulin J.-P.
FM20_12092 *(page 1304)*

Hulsbaek L.
SM22_12297 *(page 2447)*

Hulsenberg D.
FM19_11906 *(page 1270)*

Hunt G.W.
SM22_12688 *(page 2455)*

Hunter J.K.
FM5_11730 *(page 754)*

Huppert H.E.
FM17_10524 *(page 1195)*
FM21_11320 *(page 1329)*
FM21_11328 *(page 1331)*
FM9_10366 *(page 924)*

Hussein M.I.
SM11_12772 *(page 2059)*

Hutchinson J.W.
MS3_12386 *(page 269)*

Hutter K.
FSM6_12040 *(page 576)*

Huu Nam T.
SM1_12844 *(page 1645)*

Hwang I.G.
FM21_13008 *(page 1355)*

Hwang K.-C.
MS1_12016 *(page 179)*
MS3_12314 *(page 265)*

Hwang P.A.
FM26_11230 *(page 1524)*

Hwang W.-S.
SM24_11858 *(page 2503)*

I

Iafrati A.
FM8_12547 *(page 912)*

Ignaczak J.
SM13_10347 *(page 2091)*

Ilison O.
SM11_12568 *(page 2055)*

Im S.H.
MS3_10699 *(page 247)*

Im S.
SM1_11817 *(page 1599)*

Imai K.
SM15_10790 *(page 2205)*
SM18_11295 *(page 2336)*

Imanishi E.
SM17_12537 *(page 2306)*

Imiełowski S.
SM22_12931 *(page 2457)*

Indinger T.
FM24_12564 *(page 1451)*

Inoue T.
SM14_10434 *(page 2172)*

Insperger T.
FSM2_10252 *(page 437)*

Ionita A.
SM13_11014 *(page 2104)*

Iooss G.
FM26_11290 *(page 1526)*

Ippolito M.
FSM6_12334 *(page 586)*

Irannejad H.R.
SM2_10718 *(page 1663)*

Irgens F.
FM9_12270 *(page 948)*

Irschik H.
MS1_10784 *(page 161)*
SM17_12029 *(page 2294)*

Isermann R.
SM16_12758 *(page 2258)*

Ishihara M.
MS1_11857 *(page 175)*

Ishii K.
FM25_12041 *(page 1483)*

Isoda H.
FM1_12522 *(page 644)*

Isola F. dell'
MS1_12552 *(page 187)*

Itihara M.
SM17_12582 *(page 2312)*

Ivanov A.V.
FM2_10275 *(page 653)*

Ivanov I.B.
FM8_11669 *(page 884)*

Ivanov M.
FM5_10531 *(page 738)*

Ivanov T.P.
SM6_10972 *(page 1806)*

Ivanova E.A.
MS3_11260 *(page 251)*

Iwai K.
FM15_10860 *(page 1134)*

Iwankiewicz R.
FSM2_12972 *(page 469)*

Iwnicki S.D.
SM26_10909 *(page 2634)*

Izawa S.
FM11_12491 *(page 1008)*

J

Jacqmin D.
FM4_10753 *(page 710)*

Jacques N.
SM18_11309 *(page 2338)*

Jacquin L.
FM11_12244 *(page 1000)*

Jaeger A.
SM27_11981 *(page 2658)*

Jakobsen B.
FM23_10247 *(page 1397)*

Jakubiak B.
FM9_12592 *(page 954)*

James C.D.
FM4_10753 *(page 710)*

James R.D.
MS1_10722 *(page 156)*

Jang G.-W.
SM24_10048 *(page 2469)*

Jankowski R.
SM25_12659 *(page 2611)*

Janour Z.
FM9_10467 *(page 926)*

Jansen E.L.
SM19_12346 *(page 2397)*

Jarza A.
FM9_12266 *(page 946)*

Jarzebowski A.
SM20_12848 *(page 2421)*

Jasinska M.
FM22_12415 *(page 1381)*

Jasinski M.
SM1_11389 *(page 1587)*

Jasiuk I.M.
SM6_12189 *(page 1825)*

Jaszczur M.
FM22_12610 *(page 1389)*

Javaitis I.
MS2_11102 *(page 213)*

Jemioło S.
MS2_12100 *(page 231)*

Jenkins A.D.
MS6_12463 *(page 381)*

Jensen H.M.
MS3_11070 *(page 241)*

Jensen J.S.
SM24_12222 *(page 2519)*

Jensen O.E.
FM14_12155 *(page 1124)*

Jeon W.-P.
FM11_11636 *(page 990)*

Jiang H.
SM24_12789 *(page 2533)*

Jiang J.-B.
FM24_11488 *(page 1437)*

Jiang L.J.
FM22_12209 *(page 1375)*

Jie M.
SM4_10961 *(page 1749)*

Jinnouchi Y.
SM7_10691 *(page 1845)*

Joensson P.-A.
SM26_11795 *(page 2640)*

John A.
SM1_12562 *(page 1631)*

Johnson M.E.
FSM1_12497 *(page 417)*

Jolivet L.
SM12_12751 *(page 2085)*

Joly P.
SM2_12382 *(page 1703)*

Jones A.S.
MS1_13011 *(page 195)*
MS1_13010 *(page 157)*

Jones N.
SM5_11107 *(page 1797)*

Jones R.B.
FM18_10565 *(page 1229)*

Jones W.P.
FM3_11914 *(page 696)*

Jop P.
FM17_11775 *(page 1205)*

Jordan P.
FM5_13016 *(page 764)*

Joseph D.D.
FM20_10843 *(page 1296)*

Joseph P.
MS4_12673 *(page 308)*

Josserand C.
FM8_11614 *(page 882)*

Joubert P.
FM7_12220 *(page 848)*

Jullien C.
MS4_12536 *(page 306)*

Jun S.
SM1_11817 *(page 1599)*

Jung I.-H.
SM17_11789 *(page 2292)*

Jung J.-Y.
MS1_10985 *(page 165)*

Jung S.
SL18_10495 *(page 151)*

Juric D.
FM8_11979 *(page 894)*

K

Kabouya N.
FM13_12766 *(page 1098)*

Kachanov Y.S.
FM24_12675 *(page 1455)*
FM2_10275 *(page 653)*

Kacianauskas R.
SM9_11087 *(page 1917)*

Kaczmarek M.
SM15_12566 *(page 2223)*
SM15_12567 *(page 2225)*
SM15_12577 *(page 2227)*

Kaczynski A.
SM9_11980 *(page 1939)*

Kagemoto H.
FSM4_11758 *(page 512)*

Kaiser I.
SM25_12322 *(page 2597)*

Kaliszky S.
SM24_12573 *(page 2527)*

Kalliadasis S.
FM14_10220 *(page 1102)*

Kallivokas L.F.
FSM1_12691 *(page 431)*
FSM1_12717 *(page 433)*

Kaltayev A.
FM3_11031 *(page 692)*

Kam Liu W.
SM1_12167 *(page 1609)*

Kambe T.
FM23_11166 *(page 1403)*

Kameyama T.
FM15_10860 *(page 1134)*

Kan K.
FM14_11739 *(page 1122)*

Kanarska Y.
MS6_12408 *(page 379)*

Kanaun S.K.
SM11_11989 *(page 2043)*

Kaneda M.
FM7_13022 *(page 860)*

Kaneko Y.
FM17_11876 *(page 1207)*

Kang L.-C.
SM1_10270 *(page 1559)*

Kanno Y.
SM2_12646 *(page 1713)*

Kapania R.K.
FSM7_12752 *(page 610)*

Kapitaniak T.
SM2_12246 *(page 1701)*

Kaplanski F.B.
FM25_12032 *(page 1481)*

Kappl K.
SM27_11981 *(page 2658)*

Karagiozova D.
SM5_11107 *(page 1797)*

Karaiwa M.
SM13_11426 *(page 2117)*
SM9_11425 *(page 1923)*

Karajan N.
SM15_11194 *(page 2211)*

Karakasidis T.E.
FSM2_12482 *(page 463)*

Karapetsas G.
FM18_12859 *(page 1245)*

Karas M.S.
SM1_12340 *(page 1617)*

Karcher C.
FM19_12290 *(page 1278)*

Karihaloo B.L.
FSM6_11806 *(page 570)*

Karp B.
SM25_12842 *(page 2623)*

Karpenko E.E.
SM25_10470 *(page 2545)*

Karpov E.G.
SM1_12167 *(page 1609)*

Kashtalyan M.
SM9_10824 *(page 1908)*

Kasperski G.
FM15_12636 *(page 1148)*

Kataoka T.
FM26_11746 *(page 1540)*

Katsuyama T.
FSM2_11535 *(page 455)*

Katz J.
FM24_12757 *(page 1459)*

Kawamoto A.
SM24_12302 *(page 2523)*

Kawazoe H.
FM23_12484 *(page 1411)*

Kazakevitch M.I.
SM25_12632 *(page 2609)*

Kazemzadeh-Parsi M.J.
FM9_10733 *(page 930)*

Kazmierczak B.
FSM2_10823 *(page 441)*
MS2_10838 *(page 209)*

Ke F.
SM7_11764 *(page 1851)*

Keane R.J.
FM22_12545 *(page 1387)*

Keer L.M.
SM2_11215 *(page 1675)*

Kent E.F.
FM18_11915 *(page 1239)*

Keppens R.
FM19_11429 *(page 1259)*

Kere P.
SM13_10667 *(page 2099)*

Kerr R.M.
FM24_12430 *(page 1447)*

Kerschen E.J.
FSM1_12477 *(page 415)*

Keuk J. van
FM5_11229 *(page 750)*

Keunings R.
SL7_10512 *(page 130)*

Khabakhpashev G.A.
FM26_10123 *(page 1505)*

Khabakhpasheva T.I.
FSM4_10911 *(page 504)*

Kharif C.
FM26_11417 *(page 1530)*

Khasanov M.M.
FM12_10548 *(page 1020)*

Kheldij A.
SM4_12749 *(page 1789)*

Kheradvar A.
FM1_12784 *(page 648)*

Khoei A.R.
SM2_10718 *(page 1663)*

Khom'yak T.V.
SM17_10779 *(page 2270)*

Khoo B.C.
FM24_11802 *(page 1439)*

Khoshravan M.R.
SM13_10189 *(page 2087)*

Khotyanovsky D.
FM5_10531 *(page 738)*
FM6_11485 *(page 776)*

Khusid B.
FM16_10361 *(page 1152)*
FM4_10753 *(page 710)*

Khusnutdinova K.R.
SM11_11242 *(page 2021)*

Kiger K.T.
FM1_11900 *(page 626)*

Kim B.-K.
SM27_11827 *(page 2654)*

Kim J.-H.
MS1_10985 *(page 165)*

Kim J.
FM11_11636 *(page 990)*
FM11_12013 *(page 994)*
FM19_11637 *(page 1265)*

Kim K.-S.
MS3_12778 *(page 281)*
SM8_12034 *(page 1876)*

Kim Y.-M.
FM1_12655 *(page 646)*

Kim Y.Y.
FSM7_12752 *(page 610)*
SM24_10048 *(page 2469)*

Kimura Y.
FM23_11660 *(page 1405)*

Kinell M.
FM5_10789 *(page 740)*

King G.P.
FM22_12545 *(page 1387)*

King J.R.
FM14_12155 *(page 1124)*

King M.P.
FM7_10438 *(page 818)*

King R.
FM11_12624 *(page 1012)*

Kireenkov A.A.
SM2_11778 *(page 1689)*

Kishino Y.
SM20_12462 *(page 2417)*

Kit E.
FM26_10245 *(page 1507)*

Kitagawa H.
MS3_11122 *(page 249)*

Kityk A.
FM8_11462 *(page 880)*

Kiyono K.
FSM2_11535 *(page 455)*

Klapp J.
FM6_10857 *(page 768)*

Klarbring A.
MS2_10670 *(page 205)*
SM2_10686 *(page 1661)*

Kleeorin N.
FM10_12070 *(page 973)*
FM7_11053 *(page 824)*

Klepaczko J.R.
SM11_11360 *(page 2025)*
SM14_10046 *(page 2168)*
SM18_10734 *(page 2324)*

Klingbeil D.
SM4_10865 *(page 1745)*

Kloker M.J.
FM13_12381 *(page 1082)*

Kluwick A.
FM2_11083 *(page 659)*
FM2_11084 *(page 661)*
FM5_10789 *(page 740)*

Knap J.
SM1_11154 *(page 1572)*
SM9_12171 *(page 1943)*

Knight D.
FM5_11560 *(page 752)*

Kobayashi S.
FM5_11864 *(page 756)*

Kobiera A.
FM3_12843 *(page 704)*

Kocanda D.
SM8_12914 *(page 1884)*

Kocourek V.
FM19_12290 *(page 1278)*

Koek W. D.
FM10_11088 *(page 965)*

Koenderinck G.H.
MS2_10709 *(page 199)*

Koikari S.
FM23_11660 *(page 1405)*

Kolandavel M.K.
FM1_11851 *(page 624)*

Kolcavova Sirkova B.
FSM3_11247 *(page 477)*

Kolesnikov Y.
FM19_11120 *(page 1255)*
FM19_12090 *(page 1272)*

Kolk K.
SM9_12044 *(page 1941)*

Kolmychkov V.V.
FM15_11893 *(page 1138)*

Kolyshkin A.
FM2_11479 *(page 668)*

Komarova V.Y.
FM2_10275 *(page 653)*

Kondic L.
FM17_12399 *(page 1217)*

Kondo D.
SM15_11941 *(page 2215)*

Kondrachuk A.V.
MS2_12059 *(page 227)*

Konieczny P.
FM11_12602 *(page 1010)*

Kononov Y.N.
SM17_10779 *(page 2270)*

Kopiev V.F.
FM11_12156 *(page 998)*

Koplik J.
FM16_10361 *(page 1152)*

Korczyk P.M.
FM10_12855 *(page 979)*

Korepanov V.V.
SM6_12289 *(page 1827)*

Kornev K.G.
FM4_10140 *(page 708)*

Korvink J.G.
SM24_11316 *(page 2485)*

Koseki T.
SM17_12582 *(page 2312)*

Kosinski W.
SM11_11853 *(page 2041)*

Kositsyn A.
FSM7_11724 *(page 595)*

Kothe D.B.
FM8_12163 *(page 900)*

Kotucha G.
SM24_12074 *(page 2507)*

Koudella C.
MS6_12601 *(page 386)*

Koumoutsakos P.
FM24_11256 *(page 1431)*
FM6_12583 *(page 806)*

Kouznetsova V.
FSM6_11830 *(page 572)*
SM14_11395 *(page 2184)*

Kovacs F.
SM1_11482 *(page 1589)*

Kovaleva A.
SM3_11265 *(page 1733)*

Kovaleva L.
FM12_12528 *(page 1038)*

Kowalczyk P.
FM6_11763 *(page 791)*

Kowalczyk P.
FSM2_11363 *(page 449)*

Kowalczyk P.
SM24_12679 *(page 2531)*

Kowalczyk-Gajewska K.
MS2_11808 *(page 219)*
SM6_10442 *(page 1804)*

Kowalewski T.A.
FM10_12855 *(page 979)*
FM14_11477 *(page 1118)*
FM21_11331 *(page 1333)*
FM4_11184 *(page 716)*
FM7_11160 *(page 826)*
FM7_12173 *(page 846)*
FM8_12873 *(page 920)*
FM9_10576 *(page 928)*

Kowalewski Z.L.
SM27_11957 *(page 2656)*

Kowalski S.J.
SM15_13006 *(page 2240)*

Kozien M.S.
SM25_12511 *(page 2603)*

Kozlov A.A.
FM7_12267 *(page 850)*

Kozlov V.V.
FM2_11339 *(page 664)*

Kołakowski P.
MS1_11810 *(page 173)*

Krasnikovs A.
SM23_10242 *(page 2463)*

Krasnopolskaya T.S.
FM22_12257 *(page 1377)*

Krasovskyy V.L.
SM19_11815 *(page 2388)*

Krauklis A.V.
FM10_12213 *(page 975)*

Krause E.
FM25_12690 *(page 1497)*

Kravtsova M.A.
FM2_11780 *(page 670)*

Krawczyk J.
FM9_12592 *(page 954)*

Kraynik A.M.
FSM5_10597 *(page 532)*

Krein A.
FM10_12070 *(page 973)*

Kreuzer E.J.
FSM4_11912 *(page 518)*
SL8_10544 *(page 132)*

Krieger U.
FM19_11906 *(page 1270)*

Kristiansen O.
FM26_11417 *(page 1530)*

Krivtsov A.M.
MS3_11260 *(page 251)*
SM11_12481 *(page 2051)*

Kroeger M.
SM2_12086 *(page 1697)*

Kruszka L.
SM20_10374 *(page 2405)*

Kruyt N.P.
SM20_10866 *(page 2407)*

Kruzelecki J.
SM24_11634 *(page 2495)*

Kubacki S.
FM6_12076 *(page 795)*

Kubair D.V.
SM10_11177 *(page 1970)*

Kubik J.
SM15_12566 *(page 2223)*
SM15_12577 *(page 2227)*

Kucaba-Pietal A.
MS4_10971 *(page 292)*

Kuczma M.S.
MS1_10136 *(page 159)*

Kudela H.
FM25_12836 *(page 1503)*

Kudryavtsev A.
FM5_10531 *(page 738)*
FM6_11485 *(page 776)*

Kuhl A.
FM3_12745 *(page 702)*

Kuhl E.
SM12_11277 *(page 2071)*
SM1_11211 *(page 1579)*
SM1_12924 *(page 1651)*

Kuhn G.
SM9_12044 *(page 1941)*

Kuilekov M.
FM19_12605 *(page 1286)*

Kuistiala A.
SM4_10960 *(page 1747)*

Kujawski D.
SM9_10334 *(page 1892)*

Kulesh M.A.
SM6_12289 *(page 1827)*

Kullander F.
FSM1_12533 *(page 423)*

Kulvietis G.
SM16_10900 *(page 2248)*

Kumagai T.
FM8_11299 *(page 870)*

Kumar A.
FM4_10753 *(page 710)*

Kuna M.
SM9_11045 *(page 1915)*

Kuna-Ciskał H.
SM4_11796 *(page 1765)*

Kurashige M.
SM15_10790 *(page 2205)*
SM18_11295 *(page 2336)*

Kurkin A.A.
FM9_11433 *(page 940)*

Kurnik W.
SM22_12931 *(page 2457)*
SM22_12934 *(page 2459)*

Kuroda M.
FM11_12491 *(page 1008)*

Kurowski M.
FM25_12275 *(page 1495)*

Kurowski P.
SM7_12799 *(page 1859)*

Kurpa L.V.
SM19_12350 *(page 2399)*

Kursa M.
SM24_11760 *(page 2499)*

Kurzydlowski K.J.
SM7_12666 *(page 1857)*

Kurzyna J.
FSM2_12927 *(page 467)*

Kus W.
SM24_11137 *(page 2483)*

Kwon Y.-I.
FM15_10363 *(page 1132)*

Kyriakides S.
FSM5_11605 *(page 539)*
SM22_11600 *(page 2435)*

L

LLorca J.
SM13_11080 *(page 2107)*

Labiausse V.
FSM5_12578 *(page 551)*

Labuz J.F.
SM20_11845 *(page 2413)*

Lac E.
MS2_11961 *(page 222)*

Lacaze L.
FM13_11396 *(page 1062)*

Lackner R.
SM27_11981 *(page 2658)*

Lacor C.
FM3_11888 *(page 694)*

Ladd A.J.C.
FM16_11418 *(page 1161)*

Ladd T.
FM12_11994 *(page 1034)*

Ladeveze P.J.
SL9_10508 *(page 134)*
SM1_11769 *(page 1595)*
SM25_11246 *(page 2561)*

Lagha M.
FM13_11647 *(page 1066)*

Lamanna G.
FM10_10445 *(page 962)*

Lambros J.
SM10_11177 *(page 1970)*

Lampis M.
MS4_10723 *(page 290)*

Landa M.
MS1_12637 *(page 189)*

Lane-Serff G.F.
FM9_11182 *(page 934)*

Lange C.
SM2_12773 *(page 1715)*

Lange U.
FM8_12388 *(page 908)*

Langevin D.
FSM5_12212 *(page 545)*

Langkamp A.
SM13_12576 *(page 2152)*

Langre E. de
FSM4_11801 *(page 514)*

Lanos C.
SM4_10011 *(page 1741)*

Larecki W.
FSM6_11237 *(page 562)*

Larsson R.
SM15_12518 *(page 2221)*

Larue de Tournemine A.
FM20_12383 *(page 1312)*

Lathrop D.P.
FM19_11681 *(page 1267)*

Lauga E.
FM8_11330 *(page 874)*

Lavinskaya E.I.
FM10_12213 *(page 975)*

Lavrenteva O.M.
FM8_11250 *(page 866)*

Le Bars M.
FM7_12126 *(page 842)*

Le Bris C.
FSM6_12078 *(page 578)*
FSM6_12336 *(page 588)*

Le Dizes S.
FM13_11396 *(page 1062)*
FM13_12509 *(page 1092)*

Le Gal P.
FM13_11396 *(page 1062)*
FM24_10506 *(page 1419)*

Le Grognec P.
SM22_11962 *(page 2443)*

Le Quere P.
FM7_12220 *(page 848)*
FM8_11979 *(page 894)*

Le van A.
SM22_11962 *(page 2443)*

Leal G.L.
FM8_11289 *(page 868)*

Lebedyeva I.V.
SM6_12520 *(page 1835)*

Lebensohn R.A.
SM18_11005 *(page 2330)*

Leblanc S.
FM13_10525 *(page 1054)*

Leblond J.-B.
SM4_12913 *(page 1791)*
SM9_12393 *(page 1951)*

Lecomte-Beckers J.
SM1_11298 *(page 1583)*

Lee C.
FM6_11569 *(page 778)*

Lee D.-H.
SM24_11858 *(page 2503)*

Lee D.
FM11_11636 *(page 990)*

Lee H.T.
FSM5_12851 *(page 553)*

Lee J.-W.
FM6_11569 *(page 778)*

Lee J.
FM16_11418 *(page 1161)*

Lee S.-H.
FM4_11982 *(page 726)*

Lee S.-J.
FM1_12655 *(page 646)*

Lee S.M.
FM9_12738 *(page 958)*

Lee W.-S.
SM27_11827 *(page 2654)*

Lefik M.
SM13_12970 *(page 2164)*

Legarth B.N.
SM13_11794 *(page 2128)*

Legendre D.
FM8_11911 *(page 892)*

Legoll F.
FSM6_12336 *(page 588)*

Legros J.C.
MS5_12427 *(page 327)*

Leine R.I.
FSM2_11183 *(page 443)*

Leiner W.
FM7_12173 *(page 846)*

Lekszycki T.
MS2_12315 *(page 235)*

Lele S.K.
FSM1_11561 *(page 406)*

Lemak M.
SM17_11375 *(page 2282)*

Lenci S.
FSM2_12129 *(page 459)*

Lengyel A.
SM1_12101 *(page 1603)*

Lenormand R.
FM12_10234 *(page 1018)*

Lentzen S.
MS1_11752 *(page 171)*

Leonard A.
FM6_11937 *(page 793)*

Leonardi E.
FM14_11477 *(page 1118)*
FM15_11386 *(page 1136)*

Leong S.S.
FM14_11477 *(page 1118)*

Leorat J.
FM19_11621 *(page 1263)*

Lerbet J.
SM17_11674 *(page 2286)*

Leroy Y.M.
SM12_12751 *(page 2085)*

Lesieur M.
SL10_10731 *(page 136)*

Letser Y.A.
SM2_11933 *(page 1691)*

Leung R.C.K.
FM6_10163 *(page 766)*

Leungvichcharoen S.
SM11_12514 *(page 2053)*

Levin V.M.
SM11_11989 *(page 2043)*

Levitas V.I.
SM14_11325 *(page 2180)*

Levitsky S.P.
FM4_11648 *(page 722)*

Levy Y.
FM3_12199 *(page 698)*
FM3_12348 *(page 700)*

Lewandowska J.
FM12_11059 *(page 1022)*

Lewandowski J.
FSM1_12555 *(page 425)*

Lewinski T.
SM24_10052 *(page 2471)*
SM24_11760 *(page 2499)*

Lewis D.M.
FM1_11908 *(page 628)*

Lewis S.R.
MS6_12494 *(page 384)*

Lexcellent C.
SM14_12225 *(page 2196)*

Li H.
SM9_10676 *(page 1906)*

Li J.
FM2_10103 *(page 651)*
FSM7_12752 *(page 610)*
SM25_10166 *(page 2541)*
SM4_12036 *(page 1773)*

Li K.
SM7_10492 *(page 1843)*

Li Q.
SM9_11934 *(page 1937)*

Li X.M.
FM6_10163 *(page 766)*

Li Y.
MS6_12194 *(page 373)*

Liakopoulos A.B.
FSM2_12482 *(page 463)*

Liang B.
SM26_10909 *(page 2634)*

Liang P. C.
FM1_11187 *(page 620)*

Liao X.
FM7_12168 *(page 844)*
MS6_12169 *(page 371)*

Libersky L.D.
SM1_10829 *(page 1571)*

Liechti K.M.
MS3_12132 *(page 244)*

Lijuan L.
SM24_12287 *(page 2521)*

Lik Chan C.
FM21_11058 *(page 1323)*

Lim C.W.
SM19_12224 *(page 2393)*

Lim J.
FM11_12013 *(page 994)*

Lim K.-M.
SM1_12901 *(page 1649)*

Lim K.-W.
FSM1_11973 *(page 409)*

Lima R.
FM8_11026 *(page 864)*

Lin C.Y.
SM25_11867 *(page 2591)*

Lin J.
SM11_11099 *(page 2019)*

Lin Y.
SM1_10559 *(page 1565)*

Linden P.F.
MS6_10261 *(page 340)*

Lindner M.
SM2_12086 *(page 1697)*

Ling Z.
SM13_12242 *(page 2140)*

Lipniacki T.
FM24_11161 *(page 1429)*

Lipperman F.
FSM5_13033 *(page 557)*

Lipson S.
FM16_11884 *(page 1176)*

Lisitsin Y.V.
SM2_10342 *(page 1655)*

Lisowski W.
SM7_12799 *(page 1859)*

Lister J.
FM8_12388 *(page 908)*

Litewka A.
SM4_11228 *(page 1753)*

Litewka P.
SM2_10415 *(page 1657)*

Liu J.T.C.
FM13_10487 *(page 1050)*

Liu T.
SM24_11532 *(page 2491)*

Liu X.
SM6_11998 *(page 1818)*

Liu Y.-C.
FM3_10367 *(page 686)*

Liu Y.-L.
FM24_11488 *(page 1437)*

Liu Y.
SM18_11005 *(page 2330)*

Lo Jacono D.
FM22_12731 *(page 1393)*
FM3_10918 *(page 690)*

Loboda V.V.
SM9_12249 *(page 1947)*

Lobov N.I.
FM7_12344 *(page 852)*

Loefdahl L.
FM2_11339 *(page 664)*

Loehnert S.
SM1_12534 *(page 1628)*
SM1_12584 *(page 1635)*

Lofdahl L.
FM10_11455 *(page 967)*

Loginov M.S.
FM24_10455 *(page 1417)*

Loglisci N.
MS6_13017 *(page 392)*

Logo J.
SM24_11623 *(page 2493)*
SM24_12573 *(page 2527)*

Logvinova K.
FM12_12376 *(page 1036)*

Lohse D.
FM10_11909 *(page 969)*
FM17_10253 *(page 1191)*
FM1_12400 *(page 638)*

Loimer T.
FM12_11487 *(page 1032)*

Lomunov A.K.
SM20_10374 *(page 2405)*

Long A.C.
SM13_11387 *(page 2115)*

Long S.G.
SM13_12496 *(page 2146)*

Longere P.
SM18_11110 *(page 2332)*

Longhetto A.
MS6_13017 *(page 392)*

Longmao Z.
MS3_12181 *(page 261)*

Lopes S.R.X.
SM22_12420 *(page 2449)*

Lopez-Lopez E.
SM13_11176 *(page 2111)*

Lorenzani S.
MS4_10723 *(page 290)*

Louge M.Y.
MS5_10714 *(page 313)*

Love B.M.
SM10_12594 *(page 1990)*

Lozia Z.
SM26_11832 *(page 2642)*

Lu J.-Z.
FSM4_11668 *(page 508)*

Lu K.
FM4_11165 *(page 714)*

Lu T.J.
FSM1_12527 *(page 421)*
FSM5_12395 *(page 547)*

Lu W.
SM12_11432 *(page 2073)*

Lu X.
SM10_12968 *(page 1996)*

Lube G.
FM17_10524 *(page 1195)*

Lubowiecka I.
SM19_11890 *(page 2390)*

Lucey A.D.
FSM4_11736 *(page 510)*

Luczak M.
SM25_11273 *(page 2565)*

Luding S.
SM17_12133 *(page 2298)*

Lukasiewicz S.A.
SM1_11291 *(page 1581)*

Lukes V.
SM10_11671 *(page 1980)*

Lukomsky V.P.
FM26_11591 *(page 1536)*
MS2_12059 *(page 227)*

Lund E.
SM24_12098 *(page 2513)*
SM24_12916 *(page 2537)*

Lund F.
FSM1_12643 *(page 429)*

Lundberg B.
SM7_12551 *(page 1855)*

Lusseyran F.
FM13_10188 *(page 1046)*

Luznik L.
FM24_12757 *(page 1459)*

Lvov G.I.
SM19_10071 *(page 2376)*

Lyakh V.V.
SM6_12575 *(page 1837)*

Lyly M.
SM13_10667 *(page 2099)*

Lysenko V.V.
SM25_10656 *(page 2547)*

Lyubimov D.V.
FM13_12280 *(page 1076)*
FM7_12344 *(page 852)*
MS5_12402 *(page 325)*

Lyubimova T.P.
FM21_12278 *(page 1343)*
FM7_12344 *(page 852)*
MS5_12402 *(page 325)*

M

Ma J.
SM8_11686 *(page 1865)*

Ma L.
SM10_11551 *(page 1972)*

Maas L.R.M.
FM26_12318 *(page 1550)*

Mac Sithigh G.
SM6_12354 *(page 1831)*

MacKintosh F.C.
MS2_10709 *(page 199)*

MacMartin D.G.
FM11_12387 *(page 1006)*

Maciejewski J.
SM20_12848 *(page 2421)*

Mader M.
FM1_10741 *(page 616)*

Maderich V.S.
FM26_12268 *(page 1548)*

Maderich V.
MS6_12408 *(page 379)*

Maeda T.
SM11_10422 *(page 2009)*
SM25_12593 *(page 2607)*

Magara Y.
SM9_11425 *(page 1923)*

Magariyama Y.
FM1_11441 *(page 622)*

Magatti D.
FM10_10445 *(page 962)*

Magnaudet J.
FM20_12139 *(page 1306)*
FM8_11911 *(page 892)*

Mahadevan L.
MS2_11581 *(page 217)*

Maier G.
SM18_10797 *(page 2326)*

Mailybaev A. A.
SM25_11536 *(page 2573)*

Maj M.
SM18_11185 *(page 2334)*

Majewski J.
FM6_12618 *(page 808)*

Majewski T.
SM25_12984 *(page 2628)*

Majkut M.M.
FM10_11916 *(page 971)*

Majorkowska-Knap K.
SM8_11371 *(page 1863)*

Makhovskaya Y.
SM2_11196 *(page 1673)*

Makin V.K.
FM26_11230 *(page 1524)*

Makinde O.D.
FM3_10747 *(page 688)*

Makipelto J.
SM1_12310 *(page 1615)*

Makowski K.
FM19_12363 *(page 1282)*

Malinowski S.
FM9_12592 *(page 954)*
FM10_12855 *(page 979)*
FM24_12922 *(page 1461)*

Maliwan K.
MS5_10980 *(page 317)*

Malki-Epshtein L.
FM9_10366 *(page 924)*

Maluleke G.H.-S.
SM6_12039 *(page 1820)*

Mamaev I.S.
SM1_12351 *(page 1619)*

Mandal P.
SM19_10233 *(page 2378)*

Mandelis A.
FM10_12719 *(page 977)*

Manela A.
FM7_12850 *(page 856)*

Mang H.A.
SM11_12313 *(page 2047)*
SM19_11021 *(page 2384)*

Manneville P.
FM13_11647 *(page 1066)*

Mansukh M.
MS1_12786 *(page 191)*

Mansur S.S.
FM6_11456 *(page 774)*

Manucharyan G.V.
SM25_12989 *(page 2630)*

Marah D.
MS6_10261 *(page 340)*

Marchioli C.
FM20_13012 *(page 1321)*

Margulies S.S.
MS2_10933 *(page 201)*

Marian J.
SM1_11154 *(page 1572)*

Marie Habraken A.
SM1_11298 *(page 1583)*

Marigo J.J.
SM9_12921 *(page 1957)*

Marinho W.
FM6_11456 *(page 774)*

Marinova D.
SM3_11036 *(page 1725)*

Markert B.
SM15_11194 *(page 2211)*

Markine V.L.
SM24_11015 *(page 2481)*

Marmottant P.
FM1_12400 *(page 638)*

Marquillie M.
FM13_12372 *(page 1080)*

Marsavina L.
SM9_10864 *(page 1910)*

Marsik F.
FM11_12258 *(page 1002)*
FM2_12062 *(page 678)*
MS1_12637 *(page 189)*

Martinand D.
FM13_11186 *(page 1060)*

Martinez J.M.
FM6_12985 *(page 810)*

Martinez-Bazan C.
FM8_11448 *(page 878)*

Martins J.A.C.
SM12_12682 *(page 2083)*
SM2_12646 *(page 1713)*

Martynenko M.A.
SM6_12520 *(page 1835)*

Maruschak P.O.
SM8_11920 *(page 1869)*

Marvalova B.
SM1_12844 *(page 1645)*

Marze S.
FSM5_12212 *(page 545)*

Maslov B.P.
SM27_10018 *(page 2644)*

Mason D.P.
SM6_12039 *(page 1820)*

Masri R.
SM5_12043 *(page 1799)*

Masri S.F.
MS1_13007 *(page 193)*

Massabo R.
SM13_11162 *(page 2109)*
MS10_13048 *(page 981)*

Massart T.J.
SM4_12341 *(page 1787)*

Masuda M.
FSM1_10294 *(page 394)*

Matalon M.
FM3_10918 *(page 690)*

Matar O.K.
FM14_11404 *(page 1114)*

Matas J.P.
FM16_11850 *(page 1174)*

Matioukevitch S.I.
SM9_10897 *(page 1912)*

Matsuda H.
SM19_12224 *(page 2393)*

Matsui R.
MS1_10821 *(page 163)*

Matsumoto Y.
MS2_12192 *(page 233)*

Mattioni A.
FSM6_12334 *(page 586)*

Matveyenko V.P.
SM6_12289 *(page 1827)*

Matvienko A.
FM10_12719 *(page 977)*

Matysiak S.J.
SM9_11980 *(page 1939)*

Matyukhin Y.
SM2_10211 *(page 1653)*

Maugin G.A.
FSM3_11347 *(page 479)*
SM10_11592 *(page 1978)*
SM14_11393 *(page 2182)*
SM6_12434 *(page 1833)*

Maurel A.
FSM1_12643 *(page 429)*
FM24_11303 *(page 1433)*

Maurine P.
SM16_10553 *(page 2244)*

Maurini C.
MS1_12552 *(page 187)*

Mavletov M.
FM12_12528 *(page 1038)*

Maxworthy T.
FM13_11995 *(page 1068)*

Mazdziarz M.
MS2_11808 *(page 219)*
SM20_11584 *(page 2409)*

Mazeika D.
SM16_10900 *(page 2248)*

Mazhorova O.S.
FM15_11893 *(page 1138)*

Mazza E.
MS2_12064 *(page 229)*

Mazzilli C.E.N.
SM25_11494 *(page 2571)*

McElwaine J.N.
FM9_12396 *(page 950)*

McGlashan S.
FSM5_12435 *(page 549)*

McIntyre M.E.
MS6_12157 *(page 370)*
MS6_10977 *(page 346)*

McPhee J.
SM2_12773 *(page 1715)*

McPhie M.G.
FM16_11431 *(page 1163)*

Mebarki A.
SM2_12082 *(page 1695)*

Medeiros M.A.F.
FM13_12381 *(page 1082)*

Medyanik S.N.
SM1_12167 *(page 1609)*

Meer D. van der
FM10_11909 *(page 969)*
FM17_10253 *(page 1191)*

Meftah F.
SM2_12082 *(page 1695)*

Meftah S.
SM14_12747 *(page 2200)*

Megaridis C.M.
FM4_11603 *(page 720)*

Mehandia V.
FM16_10603 *(page 1154)*

Mehshikov Y.L.
SM25_11716 *(page 2581)*

Meiburg E.
FM13_11995 *(page 1068)*
FM13_12425 *(page 1084)*

Meijaard J.P.
SM25_11338 *(page 2567)*

Meinhart C.
FM22_12761 *(page 1395)*

Meironke H.
FM7_11905 *(page 838)*

Mejak G.
SM1_11334 *(page 1585)*

Meleshko V.V.
FM22_12110 *(page 1371)*
FM22_12257 *(page 1377)*
FM22_12633 *(page 1391)*
FM23_12868 *(page 1413)*
FM25_12196 *(page 1493)*

Melnik O.E.
FM9_11703 *(page 942)*

Melnikov D.
MS5_12427 *(page 327)*

Melo J.
FM3_12348 *(page 700)*

Melville W.K.
MS6_12722 *(page 388)*

Men S.
FM19_12605 *(page 1286)*

Mendez C.
FM8_11670 *(page 886)*

Mendonca M.T.
FM13_12381 *(page 1082)*

Mendoza G.
FM6_10857 *(page 768)*

Mendrok K.
SM7_12799 *(page 1859)*

Menetrier L.
MS4_12047 *(page 302)*

Menon N.
FM5_11072 *(page 748)*

Menshykov O.V.
SM9_11195 *(page 1919)*

Menzel A.
FSM3_12392 *(page 496)*

Mercier J.F.
FSM1_12643 *(page 429)*

Mercier S.
SM18_11309 *(page 2338)*

Mergheim J.
SM1_11211 *(page 1579)*

Merodio J.
SM12_11705 *(page 2075)*

Mestel J.A.
FM19_12979 *(page 1290)*

Meunier P.
FM22_10532 *(page 1361)*

Meysman F.J.R.
FM1_12063 *(page 632)*

Mezic I.
FM22_12439 *(page 1383)*
FM22_12761 *(page 1395)*
FSM2_12468 *(page 461)*

Mezyk A.
SM25_12770 *(page 2617)*

Micciche P.
FM10_10445 *(page 962)*

Michael McFarland D.
SM25_10408 *(page 2543)*

Michalowski R.L.
FM17_12790 *(page 1221)*

Michaltsos G.T.
SM22_11172 *(page 2431)*

Michałek T.
FM7_11160 *(page 826)*

Michel U.
FM21_12365 *(page 1347)*

Micunovic M.
SM18_10383 *(page 2316)*

Middelburg J.J.
FM1_12063 *(page 632)*

Miehe C.
FSM6_12112 *(page 580)*
FSM6_12113 *(page 582)*
FSM6_12118 *(page 584)*
SM1_12115 *(page 1605)*
SM4_12116 *(page 1777)*

Miettinen A.
SM2_10459 *(page 1659)*

Mikhalchenko G.
SM26_11589 *(page 2636)*

Mikhayalov D.N.
FM12_11115 *(page 1026)*

Mikkelsen R.
FM17_10253 *(page 1191)*

Millet C.
FM13_12509 *(page 1092)*

Miloh T.
FM20_12342 *(page 1310)*

Min B.-Y.
FM6_11569 *(page 778)*

Minc N.
FM4_11209 *(page 718)*

Minier J.-P.
FM24_10564 *(page 1421)*

Miozzi M.
FM7_11673 *(page 832)*

Miskiewicz M.A.
SM7_12666 *(page 1857)*

Mitsumoji T.
FM13_12291 *(page 1078)*

Miura K.
SM17_12464 *(page 2304)*

Miyamoto H.
FM9_11164 *(page 932)*

Miyazaki T.
FM24_10937 *(page 1423)*
MS6_12194 *(page 373)*

Mizerski K.A.
FM19_12107 *(page 1273)*

Mizuguchi F.
SM25_11066 *(page 2555)*

Mizuno M.
SM18_11350 *(page 2342)*

Moctezuma M.
FM8_11026 *(page 864)*

Modarres-Sadeghi Y.
FSM4_11078 *(page 506)*

Moe A.
FM9_12270 *(page 948)*

Moes N.
SM1_12359 *(page 1621)*

Moffatt K.
FM18_12164 *(page 1243)*
FM19_11458 *(page 1261)*
FSM6_11862 *(page 574)*
FSM7_10016 *(page 592)*

Mohan J.A.
FM5_11072 *(page 748)*

Moisy F.
FM24_11814 *(page 1441)*

Mojtabi A.
MS5_10980 *(page 317)*

Mokos V.G.
SM1_10665 *(page 1567)*

Molenaar D.
FM25_11964 *(page 1479)*

Molinari A.
SM14_11852 *(page 2190)*
SM18_11309 *(page 2338)*

Moller H.T.
SM24_12916 *(page 2537)*

Mondy L.A.
FM18_10983 *(page 1233)*

Monetto I.
SM4_12298 *(page 1781)*

Moniuk W.
FM8_12311 *(page 904)*

Monkewitz P.
FM3_10918 *(page 690)*
FM13_11186 *(page 1060)*
FM24_11454 *(page 1435)*
FM24_12965 *(page 1463)*

Moo Koh H.
SM8_12034 *(page 1876)*

Moore J.S.
MS1_13010 *(page 157)*

Morch K.A.
FM8_11999 *(page 896)*

Moreau J.-J.
SM17_11361 *(page 2280)*

Moreau R.
FM15_10860 *(page 1134)*

Morel A.
MS2_11961 *(page 222)*

Moreno M.J.
FM20_11189 *(page 1298)*

Morgan H.
FM4_12437 *(page 732)*

Morita C.
SM19_12224 *(page 2393)*

Morize C.
FM24_11814 *(page 1441)*

Morland L.W.
FM18_10297 *(page 1227)*

Moroni M.
FM7_11673 *(page 832)*

Morozov N.F.
SM9_10897 *(page 1912)*
MS3_11260 *(page 251)*

Morris J.F.
FM16_11850 *(page 1174)*

Morro A.
SM11_11596 *(page 2031)*

Morzynski M.
FM11_12624 *(page 1012)*
FM11_12736 *(page 1014)*
FM24_11454 *(page 1435)*
SM24_12413 *(page 2525)*

Mouaze D.
FSM4_12557 *(page 526)*

Moulia B.
FSM4_11801 *(page 514)*

Moulin F.
MS6_11829 *(page 360)*

Mounajed G.
SM1_12727 *(page 1641)*

Mousavi S.
SM7_12551 *(page 1855)*

Movchan A.B.
FSM1_11896 *(page 408)*

Movchan N.V.
FSM1_11896 *(page 408)*

Mróz Z.
SM18_10064 *(page 2314)*
SM24_11349 *(page 2487)*
SM2_11074 *(page 1669)*

Muc A.
MS3_12251 *(page 263)*
SM13_11457 *(page 2119)*
SM13_12560 *(page 2150)*

Mueller A.
SM9_11484 *(page 1925)*

Mueller U.
FM19_10931 *(page 1253)*

Mullarney J.
MS6_11499 *(page 352)*

Muller-Slany H.H.
SM1_10423 *(page 1563)*

Murai M.
FSM4_11758 *(page 512)*

Musalimov V.M.
SM2_10342 *(page 1655)*

Muth B.
SM17_12133 *(page 2298)*

Mutschke G.
FM11_12068 *(page 996)*

Myagkov N.N.
SM11_10426 *(page 2011)*

N

Na S.-W.
FSM1_12691 *(page 431)*
FSM1_12717 *(page 433)*

Naegele G.
FM16_11431 *(page 1163)*
FM18_11300 *(page 1235)*

Nagata M.
FM13_12291 *(page 1078)*

Nagib H.
FM24_12965 *(page 1463)*

Nagy P.
MS5_12651 *(page 331)*

Nait Abdelaziz M.
SM18_12339 *(page 2362)*

Nakamura M.
FM1_12522 *(page 644)*

Nakano H.
MS6_11152 *(page 348)*

Nakas A.A.
SM25_11082 *(page 2559)*

Nakata K.
FM1_11441 *(page 622)*

Nakatani A.
MS3_11122 *(page 249)*

Nalepka K.
MS3_11444 *(page 255)*

Nalepka P.
MS3_11444 *(page 255)*

Narayanan S.
MS1_12147 *(page 185)*

Narita F.
SM13_11426 *(page 2117)*
SM13_11610 *(page 2123)*
SM9_11425 *(page 1923)*
SM9_11502 *(page 1927)*

Naumavicius R.
SM16_12546 *(page 2254)*

Naumenko K.
SM27_11368 *(page 2650)*

Nava A.
MS2_12064 *(page 229)*

Navarro C.
SM8_10698 *(page 1861)*

Nayak H.V.
FM16_11991 *(page 1178)*

Nazarenko L.
SM13_10555 *(page 2097)*

Needleman A.
SM1_12737 *(page 1643)*
SM2_11987 *(page 1693)*
SM9_10910 *(page 1913)*

Neel M.-C.
FM12_12376 *(page 1036)*

Neethling S.J.
FSM5_12851 *(page 553)*

Neimark A.V.
FM4_10140 *(page 708)*

Neishtadt A.
FM22_12439 *(page 1383)*
SL11_10551 *(page 138)*

Neitzel G.P.
MS5_12651 *(page 331)*

Nepomnyashchy A.A.
FM14_10543 *(page 1104)*

Nerinckx K.
FM6_11602 *(page 787)*

Nesteruk I.
FM2_11017 *(page 657)*

Netto T.A.
SM22_11600 *(page 2435)*

Neviarouskaya A.V.
SM16_12929 *(page 2260)*

Newsom R.K.
MS6_10513 *(page 342)*

Ngan A.H.W.
FSM5_11663 *(page 541)*

Nguyen A.V.
FM15_11903 *(page 1140)*

Nguyen Q.P.
FSM5_12986 *(page 555)*

Nicolas A.
MS2_12811 *(page 202)*

Nicolas M.
FM16_11749 *(page 1172)*
FM17_11751 *(page 1203)*

Nicolleau F.
FM22_10130 *(page 1357)*

Nigmatulin R.I.
FM8_12190 *(page 902)*

Nihei T.
FM25_12041 *(page 1483)*

Nijmeijer H.
SM25_11783 *(page 2587)*

Nikifirov S.
FM5_10531 *(page 738)*

Nikiforovich E.I.
FM25_12196 *(page 1493)*

Nikitin N.V.
FM15_11929 *(page 1142)*

Nikitin S.A.
FM15_11929 *(page 1142)*
FSM7_11869 *(page 598)*

Nikolaevskiy V.N.
FM12_11109 *(page 1024)*

Nikrityuk P.A.
FM21_12365 *(page 1347)*

Nimmo Smith W.A.M.
FM24_12757 *(page 1459)*

Niordson C.F.
SM18_11790 *(page 2348)*

Nir A.
FM8_11250 *(page 866)*

Nishimura J.
SM3_10879 *(page 1723)*

Nishimura M.
FM1_11441 *(page 622)*

Nishimura T.
SM10_12461 *(page 1986)*
SM17_12464 *(page 2304)*

Niss K.
FM23_10247 *(page 1397)*

Niziol J.
SM25_12511 *(page 2603)*

Noack B.R.
FM11_12624 *(page 1012)*
FM11_12736 *(page 1014)*
FM24_11454 *(page 1435)*

Noda N.
MS1_11857 *(page 175)*

Nogarede B.
FM11_12602 *(page 1010)*

Noguchi H.
SM1_12177 *(page 1611)*
SM22_10692 *(page 2425)***

Nohguchi Y.
FSM7_12488 *(page 604)*

Nore C.
FM13_10640 *(page 1056)*

Norman J.T.
FM16_11991 *(page 1178)*

Norris A.N.
SM25_12404 *(page 2599)*

Noskowicz S.H.
FM17_12308 *(page 1213)*

Nott P.R.
FM16_10603 *(page 1154)*

Nouar C.
FM13_12766 *(page 1098)*

Nouy A.
SM1_11769 *(page 1595)*

Novak V.
MS1_12637 *(page 189)*

Novosiadliy V.A.
FM7_13005 *(page 858)*

Nowacki W.K.
SM14_10046 *(page 2168)*
SM14_11308 *(page 2178)*

Nowak A.J.
FM1_12409 *(page 640)*

Nowak M.
SM24_12413 *(page 2525)*

Nowak Z.
SM19_12328 *(page 2395)*
SM4_12333 *(page 1783)*

Nycander J.
MS6_12210 *(page 375)*

O

Oberste-Brandenburg C.
SM14_12121 *(page 2194)*

Obrecht H.
SM22_12084 *(page 2445)*

Oertel H. Jr.
FM5_11864 *(page 756)*

Ogasawara N.
SM18_10652 *(page 2320)*

Ogden R.W.
FSM3_11227 *(page 475)*
SL12_10143 *(page 140)*
SM12_11705 *(page 2075)*

Ohkitani K.
FM23_10938 *(page 1399)*

Ohl C.-D.
FM8_11999 *(page 896)*

Ohno N.
SM1_12177 *(page 1611)*
SM22_10692 *(page 2425)*

Okada M.
SM17_11700 *(page 2290)*

Okandan M.
FM4_10753 *(page 710)*

Okkels F.
MS4_12047 *(page 302)*
MS4_12130 *(page 304)*
MS4_12536 *(page 306)*

Okulov V.L.
FM13_13019 *(page 1100)*

Okumura D.
SM1_12177 *(page 1611)*
SM22_10692 *(page 2425)*

Olascoaga M.J.
MS6_12776 *(page 390)*

Olhoff N.
SM24_10433 *(page 2473)*

Oliferuk W.
SM18_11185 *(page 2334)*

Olshevsky A.A.
SM2_12559 *(page 1709)*
SM2_12559 *(page 1709)*

Olsson T.
MS2_10670 *(page 205)*

Omang M.
FM19_11809 *(page 1268)*

Onck P.
MS2_10627 *(page 203)*

Ong R.
MS1_11685 *(page 167)*

Ooms T. A.
FM10_11088 *(page 965)*

Ootao Y.
SM10_12465 *(page 1988)*

Orantek P.
SM1_12562 *(page 1631)*

Orlov S.V.
SM2_10342 *(page 1655)*

Oron A.
FM14_10543 *(page 1104)*

Ortiz M.
FSM6_11471 *(page 566)*
SM19_10038 *(page 2374)*
SM1_11154 *(page 1572)*
SM9_12171 *(page 1943)*

Orłowska A.
MS1_11810 *(page 173)*

Osborn T.
FM24_12757 *(page 1459)*

Osipov M.N.
SM7_11556 *(page 1847)*

Osipov V.
FSM1_11508 *(page 404)*

Osiptsov A.A.
FM9_11703 *(page 942)*

Ospennikov N.A.
FM7_12344 *(page 852)*

Ostachowicz W.M.
MS1_10680 *(page 153)*

Ostoja-Starzewski M.
SM11_11682 *(page 2035)*

Ostrowska-Maciejewska J.
SM6_10442 *(page 1804)*

Ostrowski Z.
SM24_11137 *(page 2483)*

Otheguy P.
MS6_12294 *(page 377)*

Ottino J.M.
FM22_11293 *(page 1367)*

Oualli H.
FSM4_13050 *(page 530)*

Ovsyannikov S.V.
SM7_12272 *(page 1853)*

Ozawa H.
MS6_11732 *(page 358)*

Ozmutlu O.
FM10_13048 *(page 981)*

Ozoe H.
FM7_12173 *(page 846)*
FM7_13022 *(page 860)*

P

Padilla E.L.M.
FM13_12250 *(page 1074)*

Pagneux V.
FM24_12740 *(page 1457)*

Paidoussis M.P.
FSM4_11078 *(page 506)*

Pakiela Z.
SM7_12666 *(page 1857)*

Pakleza J.
FM8_12873 *(page 920)*

Pakuła M.
SM15_12566 *(page 2223)*
SM15_12577 *(page 2227)*

Palaniappan D.
FM18_12981 *(page 1247)*

Pamplona D.C.
SM22_12420 *(page 2449)*

Pandolfi A.
SM19_10038 *(page 2374)*
SM9_12171 *(page 1943)*

Pantelyat M.
SM2_10211 *(page 1653)*

Papageorgiou D.
FM26_12715 *(page 1553)*

Papas P.
FM24_11454 *(page 1435)*
FM3_10918 *(page 690)*

Papoulia K.
SM1_12458 *(page 1626)*

Parau E.
FM26_11345 *(page 1528)*

Park J.
FM19_11637 *(page 1265)*

Park N.
FM17_12790 *(page 1221)*

Park S.-J.
SM17_10893 *(page 2272)*

Park T.-W.
SM17_11789 *(page 2292)*

Parland H.
SM2_10459 *(page 1659)*

Parnes R.
MS3_12432 *(page 271)*

Parra M.T.
FM8_11670 *(page 886)*

Parsons A.T.
FM2_12320 *(page 682)*

Pasero E.
FM24_11151 *(page 1427)*

Pasol L.
FM16_10248 *(page 1150)*

Pasqualino I.P.
SM1_12607 *(page 1637)*

Passarel W.
SM24_10594 *(page 2475)*

Pastoor M.
FM11_12624 *(page 1012)*

Patterson M.D.
FM25_12051 *(page 1485)*
FM9_12396 *(page 950)*

Paulino G.
SM10_10135 *(page 1962)*
SM10_12665 *(page 1994)*

Pavlidis M.
FM18_12859 *(page 1245)*

Pavlovskaia E.
SM11_12481 *(page 2051)*
SM25_10470 *(page 2545)*
FSM2_11302 *(page 447)*

Pawłowski P.
MS1_13015 *(page 197)*

Payne D.A.
MS1_11685 *(page 167)*

Peacock T.
FM26_11199 *(page 1522)*

Pecherski R.B.
MS3_11444 *(page 255)*
SM18_10064 *(page 2314)*

Pecquet E.
SM1_11298 *(page 1583)*

Pedersen E.M.
FM1_11851 *(page 624)*

Pedersen N.L.
SM24_10669 *(page 2479)*
SM24_11936 *(page 2505)*

Pedersen P.
SM24_10669 *(page 2479)*

Pedersen S.L.
SM17_12569 *(page 2310)*

Peerlings R.H.J.
SM4_11415 *(page 1759)*
SM4_12341 *(page 1787)*

Pegushin A.G.
SM11_12203 *(page 2045)*

Pellegrino S.
SM22_11097 *(page 2429)*

Peradzynski Z.
FM19_12363 *(page 1282)*
FSM2_12927 *(page 467)*
MS4_10971 *(page 292)*

Perelmuter M.N.
MS3_11599 *(page 259)*

Perez J.A.
FM4_11982 *(page 726)*

Perov V.
MS6_11942 *(page 362)*

Perrin B.
FM17_13029 *(page 1225)*
FM20_12092 *(page 1304)*

Perzyna P.
SM5_12949 *(page 1800)*

Petermann M.
FM22_12610 *(page 1389)*

Petersen R.
FM23_10247 *(page 1397)*

Petit S.
SM13_11180 *(page 2113)*

Petitjeans P.
FM24_11303 *(page 1433)*

Petrova V.E.
SM9_10579 *(page 1901)*

Petryk H.
SM12_10996 *(page 2067)*

Pettermann H.E.
SM13_12321 *(page 2142)*

Pfeiffer F.G.
SM16_10809 *(page 2246)*

Phedina M.E.
SM4_11779 *(page 1763)*

Philippidis T.
SM13_12818 *(page 2162)*

Phillips O.M.
FM9_10366 *(page 924)*

Phillips W.R.C.
FM26_11179 *(page 1521)*

Photiadis D.M.
SM25_12404 *(page 2599)*

Picandet V.
SM4_12749 *(page 1789)*

Picciotto M.
FM20_13012 *(page 1321)*

Pichler B.
SM11_12313 *(page 2047)*

Pichler U.
MS1_10784 *(page 161)*

Piechór K.
MS2_10838 *(page 209)*

Pieczyska E.A.
SM14_11308 *(page 2178)*

Piedboeuf J.-C.
SM2_12773 *(page 1715)*

Piekarski J.
MS2_11808 *(page 219)*

Pienkowska I.T.
FM18_11922 *(page 1241)*

Pierard O.
SM18_13038 *(page 2372)*

Pierre L.
SM4_12277 *(page 1779)*

Pietraszkiewicz W.
SM19_10287 *(page 2380)*

Piiroinen P.
FSM2_11363 *(page 449)*

Pijaudier-Cabot G.
SM4_12749 *(page 1789)*

Pilgun G.V.
SM19_12350 *(page 2399)*

Pinto da Costa A.
SM12_12682 *(page 2083)*
SM2_12646 *(page 1713)*

Piotrowski Z.
FM9_12592 *(page 954)*

Pivovarov M.
SM25_11699 *(page 2577)*

Placidi L.
FSM6_12040 *(page 576)*

Plamenevskii B.A.
SM9_10897 *(page 1912)*

Plotnikov P.
FM26_11290 *(page 1526)*

Plouraboue F.
FM12_11343 *(page 1030)*
FM22_12731 *(page 1393)*

Plunian F.
FM19_12120 *(page 1275)*

Pocheau A.
FM21_12543 *(page 1349)*
FM22_11190 *(page 1365)*

Pocwierz M.
FM6_12565 *(page 804)*

Podgorski T.
FM1_10741 *(page 616)*

Pogorelov D.
SM17_10893 *(page 2272)*
SM17_11640 *(page 2284)*
SM17_11688 *(page 2288)*
SM26_11589 *(page 2636)*

Pohorecki R.
FM8_12311 *(page 904)*

Polach P.
SM17_10647 *(page 2268)*

Polashenski Jr. W.
FM17_10969 *(page 1199)*

Polezhaev V.I.
FM15_11929 *(page 1142)*
FSM7_11869 *(page 598)*

Poloukhina O.E.
FM9_11433 *(page 940)*
Polyakov N.V.
SM25_11716 *(page 2581)*
Polyzos D.
SM1_12845 *(page 1647)*
Pommier S.
SM8_12228 *(page 1880)*
Poncet S.
FM24_10506 *(page 1419)*
Ponta F.
FM25_11676 *(page 1473)*
Ponte Castaneda P.
SM18_11005 *(page 2330)*
Ponter A.R.S.
SM27_11201 *(page 2648)*
Pop O.
SM9_10429 *(page 1899)*
Popov Y.P.
FM15_11893 *(page 1138)*
Popp K.
SM25_12322 *(page 2597)*
SM2_12086 *(page 1697)*
Postek E.
SM13_12141 *(page 2134)*
Pouget J.
MS1_12552 *(page 187)*
SM10_12093 *(page 1982)*
Pouliquen O.
FM16_11749 *(page 1172)*
FM17_11751 *(page 1203)*
FM17_11775 *(page 1205)*
Powers T.R.
MS2_11866 *(page 221)*
Pozorski J.
FM24_10564 *(page 1421)*
Pozorski Z.
SM24_12628 *(page 2529)*
Pozrikidis C.
FM18_10766 *(page 1231)*
Prat M.
FM12_11343 *(page 1030)*
Preumont A.
SL13_10930 *(page 142)*
Price W.G.
FM2_12320 *(page 682)*
FSM4_11833 *(page 516)*
SM25_11834 *(page 2589)*
Princevac M.
FM9_12738 *(page 958)*
Prioris S.
FM5_10984 *(page 744)*
Proczek M.
FM21_11364 *(page 1337)*
Prokunin A.N.
FM18_11460 *(page 1237)*
Prosperetti A.
FM10_11909 *(page 969)*
Prunet-Foch B.
FM4_11954 *(page 724)*
Pukhnachov V.V.
MS5_11757 *(page 321)*
Pumir A.
FM22_12048 *(page 1369)*
Purini R.
MS6_13017 *(page 392)*
Pushkin D.O.
FM24_12436 *(page 1449)*
Putelat T.
SM2_12563 *(page 1711)*
Putin G.F.
FM7_10538 *(page 820)*
FM7_12267 *(page 850)*
Puzzi S.
FSM6_11224 *(page 560)*
Py C.
FSM4_11801 *(page 514)*
Pyryev Y.
SM2_11481 *(page 1681)*
Pyrz R.
SM13_10244 *(page 2089)*
SM13_12489 *(page 2144)*
Páczelt I.
SM2_11074 *(page 1669)*

Q

Qiu X.
FM24_11488 *(page 1437)*
Qiu Z.
FM4_10753 *(page 710)*
Qu J.
SM8_11686 *(page 1865)*
Querin O.M.
SM24_11623 *(page 2493)*
Quey R.
SM14_12421 *(page 2198)*
Quilliet C.
FSM5_11095 *(page 533)*
Quintanilla M.A.S.
FM16_12438 *(page 1185)*
Quintard M.
FM12_10234 *(page 1018)*

R

Rabaud M.
FM17_13029 *(page 1225)*
FM24_11814 *(page 1441)*
Radkowski S.
SM25_12977 *(page 2626)*
Radler K.-H.
FM19_12120 *(page 1275)*
Rafai S.
FM8_13025 *(page 922)*
Raftoyiannis I.G.
SM22_11172 *(page 2431)*
Raghu Prasad B.K.
SM9_10419 *(page 1896)*
RajaSekhar G.P.
FM17_11876 *(page 1207)*
Rajchenbach J.
FM17_10959 *(page 1197)*
Ramachandra L.S.
SM13_12531 *(page 2148)*
Ramaswamy A.
SM3_10098 *(page 1717)*
Rambod E.
FM1_12784 *(page 648)*
Ramm E.
SM19_12606 *(page 2401)*
SM4_11414 *(page 1757)*
Ramos A.
FM4_12437 *(page 732)*
Randles P.W.
SM1_10829 *(page 1571)*
Rani H. P.
FM1_11187 *(page 620)*
Rao R.R.
FM18_10983 *(page 1233)*
Raspo I.
FM6_13051 *(page 814)*
Raszillier H.
FM14_11413 *(page 1116)*
Ravasoo A.
SM11_11620 *(page 2033)*
Ravi-Chandar K.
SM9_12378 *(page 1949)*
Razi Y.P.
MS5_10980 *(page 317)*
Read P.L.
FM22_12545 *(page 1387)*
MS6_12494 *(page 384)*
Reardon P.T.
FM16_11725 *(page 1170)*
Rebow M.
FM21_11364 *(page 1337)*
Redelsperger J.-L.
MS6_10513 *(page 342)*
Rega G.
FSM2_12129 *(page 459)*
Regnier V.
FM15_12591 *(page 1146)*
Regucki P.
FM25_12836 *(page 1503)*
Reinartz B.U.
FM5_11229 *(page 750)*
Reinaud J.N.
MS6_11336 *(page 350)*
Reinelt D.A.
FSM5_10597 *(page 532)*

Reinl A.
FM4_12254 *(page 728)*

Rejniak K.A.
MS2_10689 *(page 207)*

Rekik A.
SM13_11507 *(page 2121)*

Ren M.
FM7_11251 *(page 828)*

Ren W.
SM7_10492 *(page 1843)*

Ren Z.
FSM4_10826 *(page 502)*

Renotte A.
FM11_12602 *(page 1010)*

Resagk C.
FM19_12605 *(page 1286)*

Resseguier T. de
SM18_11110 *(page 2332)*

Rethore J.
SM1_11797 *(page 1597)*

Reusch F.
SM4_10865 *(page 1745)*

Rhines P.B.
SL14_12781 *(page 144)*

Rhodes S.E.
FM4_11982 *(page 726)*

Ribeiro P.
SM25_12759 *(page 2615)*

Ricci S.
SM4_11406 *(page 1755)*

Richard P.
FM17_12883 *(page 1223)*

Richard T.
SM25_12535 *(page 2605)*

Richiardone R.
MS6_13017 *(page 392)*

Richterova J.
FSM3_11247 *(page 477)*

Ricken T.
SM15_10198 *(page 2203)*

Ricoeur A.
SM9_11045 *(page 1915)*

Riedel J.J.
SM20_11845 *(page 2413)*

Rill G.
SM26_11672 *(page 2638)*

Rindt C.C.M.
FM7_11251 *(page 828)*

Ringgaard S.
FM1_11851 *(page 624)*

Rinoshika A.
FM24_12004 *(page 1443)*

Riou H.
SM25_11246 *(page 2561)*

Ris V.V.
FM7_12730 *(page 854)*

Risbet M.
SM8_12228 *(page 1880)*

Risso F.
FM20_12139 *(page 1306)*

Rochinha F.A.
SM10_13018 *(page 2001)*

Rodi W.
FM6_11348 *(page 772)*

Rodriguez M.A.
FM8_11670 *(page 886)*

Rodriguez-Ramos R.
SM13_11176 *(page 2111)*

Rodzewicz M.
SM8_11371 *(page 1863)*

Rogachevskii I.
FM10_12070 *(page 973)*
FM7_11053 *(page 824)*

Rohan E.
SM10_11671 *(page 1980)*

Roig V.
FM20_12383 *(page 1312)*

Rojiani K.B.
FSM7_12752 *(page 610)*

Rosakis A.J.
SM2_11987 *(page 1693)*

Rosenthal B.
SM22_12084 *(page 2445)*

Rossky P.J.
MS3_12132 *(page 244)*

Rothenburg L.
SM20_10866 *(page 2407)*

Rother M.A.
FM8_12329 *(page 906)*

Roumi F.
SM13_10483 *(page 2095)*

Roux S.
SM4_12021 *(page 1771)*

Roy A.
MS3_12718 *(page 279)*
SM18_11820 *(page 2350)*

Roy D.
SM25_10750 *(page 2549)*

Rozhkov A.
FM4_11954 *(page 724)*

Rozvany G.I.N.
SM24_11623 *(page 2493)*

Ruan H.H.
SM5_11051 *(page 1795)*

Ruban A.I.
FM2_11397 *(page 666)*

Rubin M.B.
SM1_12584 *(page 1635)*

Rubinstein A.A.
SM9_11626 *(page 1931)*

Rudi Y.A.
FM25_12032 *(page 1481)*

Rudnyi E.B.
SM24_11316 *(page 2485)*

Rueberg T.
SM15_11119 *(page 2209)*

Ruimy C.
SM6_11901 *(page 1814)*

Ruith M.
FM13_11995 *(page 1068)*
FM13_12425 *(page 1084)*

Rule J.
MS1_13010 *(page 157)*

Ruo A.C.
FM9_11294 *(page 936)*

Ruoff R.S.
MS3_11594 *(page 243)*

Rusinek A.
SM14_10046 *(page 2168)*
SM18_10734 *(page 2324)*

Rymuza Z.
SM2_10999 *(page 1665)*

Ryvkin M.
FSM5_13033 *(page 557)*

Ryzhak E.I.
SM12_10867 *(page 2065)*

S

Saada R.A.
SM2_12082 *(page 1695)*

Saanouni K.
SM4_11885 *(page 1767)*

Sabina F.J.
SM13_11176 *(page 2111)*

Sackmann E.
SL15_11327 *(page 146)*

Sadlej K.
FM16_10993 *(page 1156)*

Sadowski T.
SM13_12141 *(page 2134)*
SM7_11617 *(page 1849)*

Saez A.
SM9_11321 *(page 1921)*

Safarik P.
FM5_12219 *(page 760)*

Safran S.
MS2_12811 *(page 202)*

Sahn D.
FM1_12784 *(page 648)*

Saida S.
FM8_11299 *(page 870)*

Saif T.
MS3_12705 *(page 277)*

Saint-Jalmes A.
FSM5_12212 *(page 545)*

Saintillan D.
FM16_12005 *(page 1180)*

Saito T.
FM5_11049 *(page 746)*

Sakalo V.I.
SM2_12559 *(page 1709)*

Sakiyama T.
SM19_12224 *(page 2393)*

Saksala T.
SM24_10621 *(page 2477)*

Salalha W.
FM4_12319 *(page 730)*

Salem A.
FM13_12766 *(page 1098)*

Salin D.
FM20_12092 *(page 1304)*

Salmon J.-B.
MS4_12047 *(page 302)*

Salupere A.
SM11_11813 *(page 2039)*
SM11_12568 *(page 2055)*

Sam C.-H.
SM1_12458 *(page 1626)*

Sam Han J.
SM24_11316 *(page 2485)*

Samborski S.
SM7_11617 *(page 1849)*

Samsonov A.M.
SM11_10114 *(page 2005)*

Samsonowicz J.
SM25_12977 *(page 2626)*

Sanches C.T.
SM25_11494 *(page 2571)*

Sanchez U.
FM20_11189 *(page 1298)*

Sanchis A.
FSM4_12956 *(page 528)*

Sano O.
FM17_11876 *(page 1207)*
FM17_11883 *(page 1209)*

Sanomura Y.
SM18_11350 *(page 2342)*

Santaoja K.
SM4_10960 *(page 1747)*

Santiago J.G.
MS4_12961 *(page 287)*

Sapountzakis E.J.
SM1_10665 *(page 1567)*

Sarkar S.
FM24_11116 *(page 1425)*

Sarler B.
FM7_11160 *(page 826)*

Sarout J.
SM15_12713 *(page 2231)*

Sartorius D.
FM24_12675 *(page 1455)*

Sato K.
SM15_10790 *(page 2205)*
SM19_10770 *(page 2382)*

Sato M.
SM7_10691 *(page 1845)*

Saussine G.
SM17_11361 *(page 2280)*

Sauzay M.
SM18_12697 *(page 2370)*

Savic L.
FM2_12030 *(page 676)*

Saville D.A.
SL16_10529 *(page 148)*

Savova R.
SM6_10972 *(page 1806)*

Sayir M.B.
SM11_11085 *(page 2017)*

Sburlati R.
SM6_12987 *(page 1841)*

Scarella G.
SM2_12382 *(page 1703)*

Schaeffer N.
FM19_12330 *(page 1280)*

Schanz M.
SM15_11119 *(page 2209)*

Schatzman M.
SM2_12097 *(page 1699)*

Scheichl B.
FM2_11083 *(page 659)*

Scheimberg S.
SM24_10594 *(page 2475)*

Schenkel T.
FM5_11864 *(page 756)*

Schiehlen W.
SM17_11223 *(page 2276)*
SM17_12134 *(page 2300)*

Schjoedt-Thomsen J.
SM13_12489 *(page 2144)*

Schlogl S.M.
SM14_11625 *(page 2186)*

Schmid M.
FM9_12626 *(page 956)*

Schmid P.
FM11_12305 *(page 1004)*

Schmidt C.F.
MS2_10709 *(page 199)*

Schmidt M.J.
SM20_12779 *(page 2419)*

Schmidt R.
MS1_11752 *(page 171)*

Schneider L.C.R.
SM15_12903 *(page 2235)*

Schnerr G.H.
FM5_12066 *(page 758)*

Schoeppner G.
SM10_12664 *(page 1992)*

Schranz C.
SM19_11021 *(page 2384)*

Schrefler B.A.
SM15_12114 *(page 2217)*
SM2_10415 *(page 1657)*

Schreurs P.J.G.
SM1_12131 *(page 1607)*

Schroeder W.
FM25_12690 *(page 1497)*

Schuette H.
SM4_12088 *(page 1775)*

Schulte H.
SM16_12417 *(page 2252)*

Schulze D.
FM19_12290 *(page 1278)*

Schulze T.P.
FM21_12768 *(page 1353)*

Schumacher J.
FM22_10896 *(page 1363)*

Schuster M.
FM6_12337 *(page 797)*

Schwarz U.
MS2_12811 *(page 202)*

Scott R.A.
SM11_12772 *(page 2059)*

Sederman A.J.
FM21_11320 *(page 1329)*

Sedlak P.
MS1_12637 *(page 189)*

Segev R.
SM6_11523 *(page 1810)*

Seguin P.
SM17_12539 *(page 2308)*

Segurado J.
SM13_11080 *(page 2107)*

Seidel C.
SM25_12785 *(page 2619)*

Seiden G.
FM16_11884 *(page 1176)*

Seifried R.
SM17_12134 *(page 2300)*

Sejnoha M.
SM23_12380 *(page 2465)*

Sekiya D.
SM9_11502 *(page 1927)*

Selezov I.
SM11_11401 *(page 2029)*

Self B.P.
FSM7_12642 *(page 608)*

Sellier A.
FM19_10025 *(page 1249)*

Semenov B.
MS3_11260 *(page 251)*

Semenov Y.A.
FM8_10580 *(page 862)*

Semenova I.V.
SM11_10114 *(page 2005)*

Semler C.
FSM4_11078 *(page 506)*

Semma E.
FM15_11386 *(page 1136)*

Seo J.-W.
SM17_11789 *(page 2292)*

Seon T.
FM20_12092 *(page 1304)*

Serebryakov V.
FM5_12066 *(page 758)*

Sergeichev I.V.
SM20_10374 *(page 2405)*

Sergent A.
FM7_12220 *(page 848)*

Serre E.
FM25_12080 *(page 1487)*

Seto T.
SM10_12461 *(page 1986)*

Sevilla A.
FM8_11448 *(page 878)*

Seyranian A.P.
SM22_11939 *(page 2441)*

Shakeri M.
SM13_13009 *(page 2166)*

Shaqfeh E.S.G.
FM16_12005 *(page 1180)*

Shardakov I.N.
SM6_12289 *(page 1827)*

Sharma P.
MS3_11474 *(page 257)*

Sharp R.S.
SM26_10701 *(page 2632)*

Shasholko D.I.
SM2_10999 *(page 1665)*

Shchennikov V.V.
SM7_12272 *(page 1853)*

Shemer L.
FM20_11655 *(page 1300)*
FM26_10245 *(page 1507)*

Shen C.
SM1_11580 *(page 1591)*

Sheng P.
FM4_11165 *(page 714)*

Sherbaum V.
FM3_12199 *(page 698)*

Shergold O.
MS2_10988 *(page 211)*

Sheu T. W. H.
FM1_11187 *(page 620)*

Shevchenko I.V.
FM12_10199 *(page 1016)*

Shevchenko K.V.
SM2_12559 *(page 1709)*

Shevchuk V.
SM2_11697 *(page 1687)*

Shevtsov I.Y.
SM24_11015 *(page 2481)*

Shevtsova V.
MS5_12427 *(page 327)*

Shi D.-L.
MS3_12314 *(page 265)*

Shibutani Y.
SM23_12571 *(page 2467)*

Shillor M.
SM2_11452 *(page 1679)*

Shimizu M.
FM8_11299 *(page 870)*

Shimokawa S.
MS6_11732 *(page 358)*

Shimomura Y.
FSM6_11862 *(page 574)*

Shimoyama K.
FM9_11164 *(page 932)*

Shindo Y.
SM13_11426 *(page 2117)*
SM13_11610 *(page 2123)*
SM9_11425 *(page 1923)*
SM9_11502 *(page 1927)*

Shiono Y.
SM17_12582 *(page 2312)*

Shishkina E.
SM25_11719 *(page 2583)*

Shklyaev S.V.
FM7_12344 *(page 852)*

Shleykel A.L.
FM7_13005 *(page 858)*

Shodja H.M.
SM13_10483 *(page 2095)*

Shrira V.I.
FM13_12233 *(page 1072)*
FM26_12087 *(page 1544)*

Shrivastava S.C.
SM22_11653 *(page 2437)*

Shtern V.
FM19_10235 *(page 1251)*
FM25_10683 *(page 1465)*

Shulzhenko M.
SM2_10211 *(page 1653)*

Shy S.S.
FM22_12209 *(page 1375)*

Shyshkanova G.
SM2_11611 *(page 1683)*

Sichermann W.M.
FSM4_11912 *(page 518)*

Sideman S.
MS2_11148 *(page 215)*

Sidoroff F.
SM14_12747 *(page 2200)*

Sielamowicz I.
FM17_11169 *(page 1201)*

Siemaszko A.
SM1_12579 *(page 1633)*

Sigmund O.
SM24_11744 *(page 2497)*

Silva E.C.N.
SM10_12665 *(page 1994)*

Silveira-Neto A.
FM6_11456 *(page 774)*
FM13_12250 *(page 1074)*

Silvestre N.
SM22_12558 *(page 2451)*

Sim B.-C.
MS5_11483 *(page 319)*

Simoes F.M.F.
SM12_12682 *(page 2083)*

Simons G.
MS3_12384 *(page 267)*

Simpson J.E.
FM25_12051 *(page 1485)*

Sinclair G.B.
FSM3_11704 *(page 487)*

Sinka C.I.
SM15_12903 *(page 2235)*
SM15_12917 *(page 2238)*

Sira E.
FM6_10857 *(page 768)*

Siso-Nadal F.
FM19_11124 *(page 1257)*

Sittner P.
MS1_12637 *(page 189)*

Skali S.
FM13_10185 *(page 1044)*

Skews B.W.
FM5_11072 *(page 748)*

Skotheim J.
MS2_11581 *(page 217)*

Skrzypek J.J.
SM4_11796 *(page 1765)*

Sladek J.
SM10_10836 *(page 1968)*
SM19_11238 *(page 2386)*

Sladek V.
SM10_10836 *(page 1968)*
SM19_11238 *(page 2386)*

Slawianowski J.J.
FSM3_12406 *(page 498)*

Slobozhanin L.A.
MS5_12447 *(page 329)*
MS5_12765 *(page 333)*

Slowicka A.
FM4_12910 *(page 736)*

Smas P.
SM24_11634 *(page 2495)*

Smeulders D.M.J.
SM11_11271 *(page 2023)*

Smirnov E.M.
FM7_12730 *(page 854)*

Smirnov S.
FM3_11888 *(page 694)*

Smirnovskii A.A.
FM7_12730 *(page 854)*

Smith F.T.
FM2_11210 *(page 663)*

Smits A.
SM13_12818 *(page 2162)*

Smyth A.W.
MS1_13007 *(page 193)*

So R.M.C.
FM6_10163 *(page 766)*

Soares M.E.S.
SM25_11494 *(page 2571)*

Sobczyk K.
CL_10697 *(page 113)*

Sobieczky H.
FM5_10945 *(page 742)*

Sofonea M.
SM2_11452 *(page 1679)*

Sokołowska R.
SM25_12984 *(page 2628)*

Sokołowski J.
SM24_10052 *(page 2471)*
SM24_11486 *(page 2489)*

Soldati A.
FM20_13012 *(page 1321)*

Soleymani A.
FM17_10969 *(page 1199)*

Sommeria J.
FM9_12410 *(page 952)*
MS6_11547 *(page 354)*
MS6_12494 *(page 384)*
MS6_12601 *(page 386)*

Soomere T.
FM9_12099 *(page 944)*

Sorensen J.N.
FM13_13019 *(page 1100)*

Sorokin S.
FSM1_11337 *(page 400)*

Sotera M.R.
FSM2_12972 *(page 469)*

Sottos N.R.
MS1_11685 *(page 167)*
MS1_13011 *(page 195)*
MS1_13010 *(page 157)*

Sousa J.M.M.
FM3_12348 *(page 700)*

Souza L.C.G.
SM3_13004 *(page 1739)*

Souza L.F.
FM13_12381 *(page 1082)*

Sparks R.S.
FM17_10524 *(page 1195)*

Spelt P.D.M.
FM8_12106 *(page 898)*

Spencer A.J.M.
SM10_12273 *(page 1984)*

Spiegel E.
SL17_10158 *(page 149)*

Spiegl M.
SM27_11981 *(page 2658)*

Squires T.M.
FM16_12452 *(page 1187)*
MS4_11777 *(page 300)*

Sreenivasan K.R.
FM22_10896 *(page 1363)*

Srigiriraju S.V.
MS2_11866 *(page 221)*

Staalhand J.
MS2_10670 *(page 205)*

Stachurski A.
SM4_12333 *(page 1783)*

Staicu A.D.
FSM5_12373 *(page 546)*

Staquet C.
FM26_12424 *(page 1551)*

Staroszczyk R.
FM18_10297 *(page 1227)*

Stavroulakis G.
SM3_11036 *(page 1725)*

Steblyanko P.A.
SM1_11202 *(page 1577)*

Stechmann S.N.
FM23_12375 *(page 1409)*

Steen M.
FM12_12617 *(page 1042)*

Steenhoven A.A. van
FM7_11251 *(page 828)*

Stefanelli R.
FSM1_12586 *(page 427)*

Stefani F.
FM19_12613 *(page 1288)*

Stefanski A.
SM2_12246 *(page 1701)*

Stegmann J.
SM24_12098 *(page 2513)*

Steigenberger J.
SM25_11699 *(page 2577)*

Steinberg L.
FSM3_11140 *(page 473)*

Steindl A.
SM22_11816 *(page 2439)*

Steinmann P.
FSM3_12392 *(page 496)*
SM12_11277 *(page 2071)*
SM1_11211 *(page 1579)*
SM1_12924 *(page 1651)*

Steinrueck H.
FM2_12030 *(page 676)*

Stepan G.
FSM2_10252 *(page 437)*

Stepanova L.V.
SM4_11779 *(page 1763)*

Stephan P.
FM14_12293 *(page 1126)*

Stevanovic-Hedrih K.
SM17_10624 *(page 2266)*

Stewart D.S.
MS4_12976 *(page 288)*

Stichel S.
SM26_11795 *(page 2640)*

Stieglitz R.
FM19_10931 *(page 1253)*

Stijnman M.
FM10_11909 *(page 969)*

Stiller J.
FM19_12587 *(page 1284)*

Stokes Y.M.
FM8_11855 *(page 890)*

Stolpe M.
SM24_12302 *(page 2523)*

Stone H.A.
FM16_12056 *(page 1182)*
FM1_12423 *(page 642)*
MS4_12966 *(page 310)*

Storakers B.
SM2_11365 *(page 1677)*

Stoychev G.B.
SM18_11953 *(page 2354)*

Stremler M.A.
FM22_12158 *(page 1373)*

Striz B.
FSM3_11247 *(page 477)*

Strozik M.D.
FM10_11916 *(page 971)*

Struzewska J.
FM9_12592 *(page 954)*

Stulov A.
SM1_10728 *(page 1569)*

Stupak E.
SM9_11087 *(page 1917)*

Stupkiewicz S.
SM2_12553 *(page 1707)*

Styczek A.
FM6_12565 *(page 804)*

Su A.
FM3_10367 *(page 686)*

Sudak L.
SM6_12122 *(page 1822)*

Sudhakar V.
SM25_12984 *(page 2628)*

Sugano N.
SM17_12537 *(page 2306)*

Sugii T.
MS2_12192 *(page 233)*

Sugimoto N.
FSM1_10294 *(page 394)*

Sugimoto T.
FM1_10132 *(page 614)*

Sugiura T.
SM11_12418 *(page 2049)*

Sugiura Y.
SM25_12593 *(page 2607)*

Suiker A.S.J.
SM13_12680 *(page 2158)*
SM14_10648 *(page 2174)*

Sukoriansky S.
MS6_11152 *(page 348)*
MS6_11942 *(page 362)*

Sullivan J.M.
FSM5_10597 *(page 532)*

Sun H.
FM10_10445 *(page 962)*

Sun L.
SM10_10135 *(page 1962)*

Sun M.
FM5_11049 *(page 746)*

Sun Q.
SM14_12881 *(page 2202)*

Sun Y.
SM8_11686 *(page 1865)*

Sundaresan S.
FM20_12397 *(page 1315)*
FM20_12671 *(page 1317)*

Sung Lee H.
SM8_12034 *(page 1876)*

Suponitsky V.
FM13_11461 *(page 1064)*

Suzuki T.
FM11_12387 *(page 1006)*
FSM1_11561 *(page 406)*

Svendsen B.
SM4_10865 *(page 1745)*

Swaters G.E.
MS6_10634 *(page 344)*

Swevers J.
SM16_11282 *(page 2250)*

Swiercz A.
MS1_11810 *(page 173)*

Swift F.J.
SM26_10909 *(page 2634)*

Swinney H.L.
SL18_10495 *(page 151)*

Switonski E.
SM25_12770 *(page 2617)*

Symens W.
SM16_11282 *(page 2250)*

Sypeck D.J.
FSM5_12395 *(page 547)*

Szabo R.
FM21_11362 *(page 1335)*

Szalai R.
FSM2_10252 *(page 437)*

Sze K.Y.
SM9_11568 *(page 1929)*

Szekrenyes A.
SM13_11747 *(page 2125)*

Szmyd J.
FM7_12173 *(page 846)*
FM7_13022 *(page 860)*
FM22_12610 *(page 1389)*

Szojda L.
SM4_11228 *(page 1753)*

Szumbarski J.
FM6_12565 *(page 804)*

Szumowski A.
FM11_11918 *(page 992)*

Szwaba R.
FM5_12997 *(page 762)*

Szymczak P.
FM12_11994 *(page 1034)*

Szymczyk J.A.
FM21_11331 *(page 1333)*
FM7_11905 *(page 838)*

Szymkiewicz A.
FM12_11059 *(page 1022)*

Szyszkowski W.
SM3_12756 *(page 1737)*

T

Tabaei A.
FM26_10762 *(page 1511)*
FM26_11199 *(page 1522)*

Tabeling P.
MS4_12047 *(page 302)*
MS4_12130 *(page 304)*
MS4_12536 *(page 306)*
MS4_12673 *(page 308)*
MS4_12960 *(page 283)*

Taberlet N.
FM17_12883 *(page 1223)*

Tadmor G.
FM11_12624 *(page 1012)*
FM24_11454 *(page 1435)*

Tagawa T.
FM7_13022 *(page 860)*

Taillard K.
SM14_12225 *(page 2196)*

Takada T.
MS1_10821 *(page 163)*

Takagi M.
SM14_11308 *(page 2178)*

Takagi S.
MS2_12192 *(page 233)*

Takahashi N.
FM24_10937 *(page 1423)*

Takayama K.
FM5_11049 *(page 746)*

Takeda T.
SM13_11610 *(page 2123)*

Talagrand O.
MS6_10803 *(page 336)*

Taleb L.
SM14_12421 *(page 2198)*
SM14_12747 *(page 2200)*

Tamai K.
FM5_11049 *(page 746)*

Tamuzs V.
FSM7_12259 *(page 600)*

Tan L.H.
FM14_11477 *(page 1118)*

Tan S.H.N.
SM13_10412 *(page 2093)*

Tan V.B.C.
SM13_10412 *(page 2093)*

Tang J.X.
MS2_10709 *(page 199)*

Tang M.
FM24_12652 *(page 1453)*

Tang Y.
SM9_11626 *(page 1931)*

Tanigawa Y.
SM10_12465 *(page 1988)*

Tanizawa K.
SM17_11700 *(page 2290)*
SM3_10879 *(page 1723)*

Tanno H.
FM5_11049 *(page 746)*

Tanskanen V.
FM17_10969 *(page 1199)*

Tardu S.
FM11_11394 *(page 988)*

Tarn J.-Q.
SM10_10364 *(page 1964)*

Tarnai T.
SM1_11482 *(page 1589)*
SM25_11384 *(page 2569)*

Tartar M.
FM13_10640 *(page 1056)*

Tatsumi T.
FM24_12151 *(page 1445)*

Tauchert T.R.
MS1_12018 *(page 181)*

Tay A.A.O.
SM1_12901 *(page 1649)*

Tay T.-E.
SM13_10412 *(page 2093)*

Taya M.
SM10_12978 *(page 1999)*

Tcholakova S.S.
FM8_11669 *(page 884)*

Tejchman J.
SM15_12358 *(page 2219)*

Telega J.J.
FM12_11248 *(page 1028)*
FSM3_11642 *(page 485)*
MS2_12100 *(page 231)*
SM13_11895 *(page 2132)*
SM13_12667 *(page 2156)*
SM13_12732 *(page 2160)*
SM1_12562 *(page 1631)*
SM2_11452 *(page 1679)*

Ten Hagen T.L.M.
FM1_11900 *(page 626)*

Teodorczyk A.
FM3_12911 *(page 706)*

Terletska K.V.
SM11_11377 *(page 2027)*

Tesdall A.M.
FM5_11730 *(page 754)*

Teymur M.
SM11_10891 *(page 2015)*

Thermann K.
SM12_10996 *(page 2067)*

Thess A.
FM19_11120 *(page 1255)*
FM19_11906 *(page 1270)*
FM19_12090 *(page 1272)*

Thiria B.
FM11_12736 *(page 1014)*

Thite S.
SM1_12441 *(page 1622)*

Thivolle-Cazat E.
MS6_11547 *(page 354)*

Thomas P.J.
MS6_10261 *(page 340)*

Thomer O.
FM25_12690 *(page 1497)*

Thompson A.F.
FM21_11328 *(page 1331)*

Thomsen J.J.
SM25_11679 *(page 2575)*
SM25_12694 *(page 2613)*

Tian J.
FSM5_12395 *(page 547)*

Tian Z.
SM9_12174 *(page 1945)*

Tigoiu V.M.
FSM3_11638 *(page 483)*

Tihon J.
FM14_12656 *(page 1128)*

Tilgner A.
FM19_12125 *(page 1277)*

Timchenko V.
FM15_11386 *(page 1136)*

Ting E.C.
SM1_10270 *(page 1559)*

Ting L.
FM25_11683 *(page 1475)*

Tkachev P.V.
SM12_12223 *(page 2079)*

Tobushi H.
MS1_10821 *(page 163)*
SM14_11308 *(page 2178)*

Tokarzewski S.
FSM3_11642 *(page 485)*
SM13_11895 *(page 2132)*
SM13_12667 *(page 2156)*

Toland J.F.
FM26_11290 *(page 1526)*

Toll S.
SM15_12518 *(page 2221)*

Tomita Y.
SM12_11432 *(page 2073)*

Topolnikov A.S.
FM8_12190 *(page 902)*

Toropov V.
SM24_12870 *(page 2535)*

Touhei T.
SM1_10274 *(page 1561)*

Tran-Cong T.
FSM5_12435 *(page 549)*

Travnicek Z.
FM11_12258 *(page 1002)*

Trebicki J.
SM11_11682 *(page 2035)*

Trevelyan P.
FM14_10220 *(page 1102)*

Troger H.
SM22_11816 *(page 2439)*

Trostinetsky E.
FM20_11655 *(page 1300)*

Trotsyuk A.
FM5_10531 *(page 738)*

Trulsen J.
FM19_11809 *(page 1268)*

Trumel H.
SM18_11110 *(page 2332)*

Trzcinski R.
FM8_12873 *(page 920)*

Trzebicki M.
SM13_12560 *(page 2150)*

Tsai J.C.
FM17_12445 *(page 1219)*

Tsai P.-S.
SM16_12712 *(page 2256)*

Tsamopoulos J.
FM14_12858 *(page 1130)*
FM18_12859 *(page 1245)*

Tsekhmister Y.V.
FM26_11591 *(page 1536)*

Tsemakh D.
FM8_11250 *(page 866)*

Tsepoura K.G.
SM1_12845 *(page 1647)*

Tsetserukou D.O.
SM16_12929 *(page 2260)*

Tsubota K.-I.
FM1_12522 *(page 644)*

Tsubota K.
MS2_12453 *(page 237)*

Tsuru T.
SM23_12571 *(page 2467)*

Tsutahara M.
FM26_11746 *(page 1540)*

Tsypkin G.G.
FM21_11926 *(page 1339)*

Tuck E.O.
FM8_11855 *(page 890)*

Tucker P.G.
FM24_12430 *(page 1447)*

Tuckerman L.
FM6_10921 *(page 770)*
FM7_10914 *(page 822)*
FM13_10640 *(page 1056)*
FM13_12431 *(page 1086)*

Tuliszka-Sznitko E.
FM25_12080 *(page 1487)*

Tumin A.
FSM1_12477 *(page 415)*

Tur M.
SM8_10698 *(page 1861)*

Turner M.R.
FM2_12241 *(page 680)*

Turska E.
SM24_12679 *(page 2531)*
SM9_11910 *(page 1935)*

Turteltaub S.
SM14_10648 *(page 2174)*

Tutty O.R.
FM2_12320 *(page 682)*

Tvergaard V.
SM9_10910 *(page 1913)*

Tylikowski A.
SM10_10045 *(page 1959)*

Tyliszczak A.
FM3_11914 *(page 696)*

Tyrkiel E.
FSM2_11416 *(page 451)*

U

Ualiev Z.
FM3_11031 *(page 692)*

Ualiyev G.
SM17_10533 *(page 2264)*

Ualiyev Z.G.
SM17_10533 *(page 2264)*

Ubachs R.L.J.M.
SM1_12131 *(page 1607)*

Udwdia F.E.
SM3_11163 *(page 1727)*

Ugawa A.
FM17_11883 *(page 1209)*

Uhl T.
SM7_12799 *(page 1859)*

Uj J.
SM13_11747 *(page 2125)*

Ulbrich R.
FM20_11745 *(page 1302)*
FM20_12886 *(page 1319)*

Ulrych B.
SM2_10211 *(page 1653)*

Ungarish M.
FM16_11884 *(page 1176)*
MS6_11585 *(page 356)*

Urban D.
SM5_12043 *(page 1799)*

Ursem N.T.C.
FM1_11900 *(page 626)*

Ustohalova V.
SM15_10198 *(page 2203)*

Utsunomiya T.
FSM4_12175 *(page 522)*

V

Vadillo J.L.
FM11_10872 *(page 984)*

Vainchtein D.
FM22_12439 *(page 1383)*

Vaisberg L.A.
SM25_11055 *(page 2553)*

Vakakis A.F.
SM25_10408 *(page 2543)*

Vakhitova N.K.
FM8_12190 *(page 902)*

Vakhrouchev A.V.
SM1_12054 *(page 1601)*

Vakulenko S.
FSM2_10823 *(page 441)*

Valance A.
FM17_12883 *(page 1223)*

Valdek U.
SM7_12551 *(page 1855)*

Valle V.
SM9_10429 *(page 1899)*

Valtorta D.
MS2_12064 *(page 229)*

Valverde J.
FM16_12438 *(page 1185)*
SM17_12071 *(page 2296)*

Van Brussel H.
SM16_11282 *(page 2250)*

Van Hemelrijck D.
SM13_12818 *(page 2162)*

Vanden-Broeck J.-M.
FM26_11345 *(page 1528)*
FM26_12715 *(page 1553)*

Vanneste J.
MS6_12104 *(page 366)*

Varghese S.
FM9_12980 *(page 960)*

Varhsney K.
FM15_12349 *(page 1144)*

Varyanychko M.A.
SM19_11815 *(page 2388)*

Vasiljev P.
SM16_10900 *(page 2248)*

Vasilkov V.B.
SM25_11055 *(page 2553)*

Vasudeva Murthy A.S.
FM9_12980 *(page 960)*

Velasco Fuentes O.U.
FM25_12748 *(page 1499)*

Vennemann P.
FM1_11900 *(page 626)*

Vereecke B.
SM4_10974 *(page 1751)*

Veres I.A.
SM11_11085 *(page 2017)*

Vereshchaka S.M.
SM19_10071 *(page 2376)*

Veron F.
MS6_12722 *(page 388)*

Versluis M.
FM17_10253 *(page 1191)*
FM1_12400 *(page 638)*

Vesenjak M.
FSM4_10826 *(page 502)*

Viallat A.
FM1_12423 *(page 642)*

Viatkina E.M.
SM1_12723 *(page 1639)*

Viba J.
FSM7_12259 *(page 600)*

Vidya Sagar R.
SM9_10419 *(page 1896)*

Vierendeels J.
FM6_11602 *(page 787)*

Vignes-Adler M.
FM4_11954 *(page 724)*

Villa V.
MS2_13049 *(page 239)*

Villafruela J.M.
FM8_11670 *(page 886)*

Villermaux E.
FM22_10532 *(page 1361)*
FM22_12326 *(page 1379)*
FM8_11317 *(page 872)*

Vimmr J.
FM6_11702 *(page 789)*

Vinod N.
FM2_12631 *(page 684)*

Viovy J.-L.
FM4_11209 *(page 718)*

Vit T.
FM11_12258 *(page 1002)*
FM2_12062 *(page 678)*

Vitkova V.
FM1_10741 *(page 616)*

Vlachogiannis M.
FM14_10557 *(page 1106)*

Voigt L.K.
FM23_10247 *(page 1397)*

Volkov K.N.
FM20_10416 *(page 1292)*

Volkova V.E.
SM25_12632 *(page 2609)*

Volles R.
SM1_11298 *(page 1583)*

Vollmann J.
MS3_12384 *(page 267)*

Volodko I.
FM2_11479 *(page 668)*

Vorobev A.M.
MS5_12402 *(page 325)*

Voyiadjis G.Z.
SM18_10393 *(page 2318)*

Vu-Delcarte C.D.
FM15_12636 *(page 1148)*

W

Waarsing J.H.
MS2_11808 *(page 219)*

Wacławczyk M.
FM24_10564 *(page 1421)*

Wada S.
FM1_12522 *(page 644)*
MS2_12453 *(page 237)*

Wadley H.N.G.
FSM5_12395 *(page 547)*

Wagner C.
FM8_11462 *(page 880)*

Wagner S.
FM24_12675 *(page 1455)*

Wahi P.
SM25_12814 *(page 2621)*

Wajnryb E.
FM16_11409 *(page 1159)*
FM18_11300 *(page 1235)*
FM8_11411 *(page 876)*

Wakaba L.
FM20_12332 *(page 1308)*

Walenta Z.A.
FM4_12910 *(page 736)*
FM3_12911 *(page 706)*
MS4_10971 *(page 292)*

Walker P.G.
FM1_11851 *(page 624)*

Wall D.P.
FM13_12291 *(page 1078)*

Wall W.A.
SM19_12606 *(page 2401)*

Walsh A.M.
FM17_12338 *(page 1215)*

Wan F.S.
FM8_12596 *(page 916)*

Wan Y.
MS1_12016 *(page 179)*

Wang C.-Y.
SM1_10270 *(page 1559)*

Wang C.
FM8_12596 *(page 916)*
SM1_11580 *(page 1591)*

Wang D.W.
FM26_11230 *(page 1524)*

Wang H.-T.
SM9_11568 *(page 1929)*

Wang H.
SM1_11720 *(page 1593)*

Wang J.
SM11_11099 *(page 2019)*

Wang L.-S.
SM16_12712 *(page 2256)*

Wang M.
MS3_12132 *(page 244)*

Wang P.
SM1_11720 *(page 1593)*
SM9_12174 *(page 1945)*

Wang R.-Z.
SM1_10270 *(page 1559)*

Wang Z.
SM9_12174 *(page 1945)*

Warner M.R.E.
FM14_11404 *(page 1114)*

Watanabe E.
FSM4_12175 *(page 522)*

Weaire D.
MS5_10598 *(page 312)*

Weber J.E.
FM26_11803 *(page 1542)*

Weber M.
SM16_12758 *(page 2258)*

Wei M.
FSM1_10907 *(page 396)*

Wei Q.
MS6_12194 *(page 373)*

Wei Y.
MS3_11279 *(page 253)*

Weichen S.
SM10_10501 *(page 1966)*

Weichert D.
SM13_12588 *(page 2154)*
SM18_12058 *(page 2360)*

Weidman P.
FM26_11199 *(page 1522)*
FM2_11984 *(page 674)*
FSM4_11986 *(page 520)*

Weier T.
FM11_12068 *(page 996)*

Weigand B.
FM10_10445 *(page 962)*

Weir G.J.
SM2_11008 *(page 1667)*

Weiss D.A.
FM4_12254 *(page 728)*

Weitsman Y.J.
SM13_11014 *(page 2104)*

Weiwen L.
SM24_12287 *(page 2521)*

Welch K.
SM7_12551 *(page 1855)*

Wen W.
FM4_11165 *(page 714)*

Weronko J.
SM22_12934 *(page 2459)*

Wesfreid J.E.
FM11_12736 *(page 1014)*

Westerweel J.
FM1_11900 *(page 626)*
FM10_11088 *(page 965)*

Wheeler L.
MS3_11474 *(page 257)*

White J.M.
MS3_12132 *(page 244)*

White S.R.
MS1_13011 *(page 195)*
MS1_13010 *(page 157)*

Whitesides G.M.
MS4_12966 *(page 310)*

Wiacek D.
MS1_11810 *(page 173)*

Widmann R.
SM15_10198 *(page 2203)*

Wieckowski Z.
SM20_10231 *(page 2403)*

Wiercigroch M.
FSM2_11302 *(page 447)*
SM11_12481 *(page 2051)*
SM25_10470 *(page 2545)*
SM2_12246 *(page 1701)*

Wierschem A.
FM14_10642 *(page 1108)*
FM14_10928 *(page 1110)*

Wieteska R.
FM6_12618 *(page 808)*

Wiggins S.
FM22_11293 *(page 1367)*

Wijeyewickrema A.C.
SM11_12514 *(page 2053)*

Wijngaarden L. van
OL_10498 *(page 112)*

Willers B.
FM21_12365 *(page 1347)*

Williams P.D.
MS6_12494 *(page 384)*

Willis J.R.
SM13_11782 *(page 2127)*
SM2_12563 *(page 1711)*

Wilmanski K.
SM11_10612 *(page 2013)*

Wilson H.J.
FM16_11473 *(page 1165)*

Wilson M.
FM7_10438 *(page 818)*

Wingerde A.M. van
SM13_12818 *(page 2162)*

Winter R.M.
MS3_12132 *(page 244)*

Wisniewski K.
SM19_12328 *(page 2395)*
SM24_12679 *(page 2531)*
SM9_11910 *(page 1935)*

Witkowski A.S.
FM10_11916 *(page 971)*

Witkowski W.
FM3_12911 *(page 706)*
SM19_11890 *(page 2390)*

Wnuk M.P.
SM9_10250 *(page 1886)*

Wojciechowski J.
FM11_11918 *(page 992)*

Wojewoda J.
SM2_12246 *(page 1701)*

Wojnar R.
SM13_12732 *(page 2160)*

Wolanski P.
FM3_12745 *(page 702)*
FM3_12843 *(page 704)*

Wong Y.W.
SM22_11097 *(page 2429)*

Woods A.W.
FM21_11926 *(page 1339)*

Worster M.G.
FM21_11270 *(page 1327)*
FM21_11320 *(page 1329)*
FM21_11328 *(page 1331)*
FM21_12276 *(page 1341)*

Woude D. van der
FM22_12633 *(page 1391)*

Woznica K.
SM18_12339 *(page 2362)*

Wriggers P.
SM1_12534 *(page 1628)*
SM1_12584 *(page 1635)*
SM2_10415 *(page 1657)*

Wroblewski W.
FM6_11578 *(page 785)*

Wu D.
SM9_12492 *(page 1953)*

Wu J.
SM4_12036 *(page 1773)*

Wu L.
FM15_12591 *(page 1146)*
SM10_11551 *(page 1972)*

Wuest A.
FM9_12626 *(page 956)*

Wurz W.
FM24_12675 *(page 1455)*

Wysocki M.
SM15_12518 *(page 2221)*

X

Xia M.
SM7_11764 *(page 1851)*

Xiao Q.Z.
FSM6_11806 *(page 570)*

Xing J.T.
FSM4_11833 *(page 516)*
SM25_11834 *(page 2589)*

Xiong A.-K.
FM11_12491 *(page 1008)*

Xiong Y.
SM25_11834 *(page 2589)*

Xu H.
MS5_10714 *(page 313)*

Xu X.
SM7_11764 *(page 1851)*

Y

Yadav A.
FM3_12348 *(page 700)*

Yakimova K.S.
SM25_11055 *(page 2553)*

Yamaguchi E.
MS4_11607 *(page 298)*

Yamaguchi T.
FM1_12522 *(page 644)*
MS2_12453 *(page 237)*

Yamamoto K.
SM17_11700 *(page 2290)*
SM3_10879 *(page 1723)*

Yamashita K.
FSM1_10294 *(page 394)*

Yamasue K.
FSM2_12014 *(page 457)*

Yamazaki Y.H.
MS6_12494 *(page 384)*

Yang J.
SM1_11580 *(page 1591)*

Yang S.-Y.
SM8_12001 *(page 1874)*

Yang S.
FM4_11165 *(page 714)*
SM8_11737 *(page 1867)*

Yang X.
FM24_10149 *(page 1415)*

Yang Y.
FSM4_12521 *(page 524)*

Yano J.-I.
MS6_12140 *(page 368)*

Yao Z.
SM1_11720 *(page 1593)*

Yaremchuk V.P.
FSM7_11869 *(page 598)*

Yarin A.L.
FM4_10932 *(page 712)*

Yasinskyi A.
SM2_11697 *(page 1687)*

Yasniy P.V.
SM8_11920 *(page 1869)*

Yau J.-D.
SM3_11287 *(page 1735)*

Yazdi S.S.H.
SM25_11904 *(page 2593)*

Yazykov V.
SM26_11589 *(page 2636)*

Ye H.
FSM3_11515 *(page 481)*

Yevdokymov D.V.
MS5_10958 *(page 315)*

Yin H.
SM10_10135 *(page 1962)*

Yokosawa S.
FM1_12522 *(page 644)*

Yokota K.
FM8_11299 *(page 870)*

Yoo W.-S.
SM17_10893 *(page 2272)*

Yoon Y.
FM8_11289 *(page 868)*

Yoshida F.
SM24_12870 *(page 2535)*
SM27_12450 *(page 2660)*

Yoshimura T.
FM24_12151 *(page 1445)*

Yoshinaga T.
FM14_11739 *(page 1122)*

Youn S.-K.
SM24_11826 *(page 2501)*
SM27_11827 *(page 2654)*

Young K.Y.
SM24_12185 *(page 2515)*

Young T.H.
SM25_11867 *(page 2591)*

Yourdkhani A.
SM13_10189 *(page 2087)*

Yu S.
SM9_11934 *(page 1937)*

Yu T.X.
SM5_11051 *(page 1795)*

Yuan T.H.
FM22_12209 *(page 1375)*

Z

Zabielski L.
FM19_12979 *(page 1290)*

Zachara A.
FM8_12873 *(page 920)*

Zadpoor A.A.
FSM2_10070 *(page 435)*

Zaera R.
SM18_10734 *(page 2324)*

Zahn M.
FM4_11982 *(page 726)*

Zairi F.
SM18_12339 *(page 2362)*

Zajac D.
FM20_12886 *(page 1319)*

Zakharov V.E.
FM26_10861 *(page 1513)*

Zaleski S.
FM8_11614 *(page 882)*
FM8_11723 *(page 888)*

Zamankhan P.
FM17_10969 *(page 1199)*

Zametaev V.B.
FM2_11780 *(page 670)*

Zammali C.
SM11_12763 *(page 2057)*

Zampolli M.
FSM1_11373 *(page 402)*

Zangeneh M.S.
SM25_11904 *(page 2593)*

Zaoui A.
SM13_11507 *(page 2121)*
SM13_11805 *(page 2130)*

Zappoli B.
FM6_13051 *(page 814)*

Zardecki D.
SM26_11832 *(page 2642)*

Zarnovskij V.
SM9_11087 *(page 1917)*

Zavala-Garay J.
MS6_12776 *(page 390)*

Zavaliangos A.
SM15_12917 *(page 2238)*

Zboinski G.
SM1_11389 *(page 1587)*

Zebib A.
MS5_11483 *(page 319)*

Zeghmati B.
FM6_12985 *(page 810)*

Zeidis I.
SM25_11699 *(page 2577)*

Zeilstra C.
FM17_10253 *(page 1191)*

Zelinger Z.
FM9_10467 *(page 926)*

Zeman J.
SM23_12380 *(page 2465)*

Zeman V.
SM25_11759 *(page 2585)*

Zeng L.
FM20_12332 *(page 1308)*

Zenit R.
FM8_11026 *(page 864)*

Zenkovskaya S.M.
FM7_13005 *(page 858)*

Zhang C.
SM10_10836 *(page 1968)*

Zhang K.
FM7_12168 *(page 844)*
MS6_12169 *(page 371)*

Zhang N.-H.
FSM2_12674 *(page 465)*

Zhang R.
SM27_10906 *(page 2646)*

Zhang R.
SM8_11686 *(page 1865)*

Zhang W.W.
FM8_12429 *(page 910)*

Zhang X.
FM26_11680 *(page 1538)*

Zhao X.
SM17_11020 *(page 2274)*

Zhao Y.-P.
SM16_10510 *(page 2242)*

Zheltovodov A.A.
FM24_10455 *(page 1417)*

Zheng L.
SM9_12174 *(page 1945)*

Zheng X.J.
MS3_12486 *(page 273)*

Zheng X.
SM6_11998 *(page 1818)*

Zhou C.
SM8_12391 *(page 1882)*

Zhou M.
MS3_10105 *(page 246)*

Zhou W.
SM1_12901 *(page 1649)*

Zhou Y.C.
MS3_12486 *(page 273)*
SM13_12496 *(page 2146)*
SM9_12492 *(page 1953)*

Zhou Y.
FM24_12004 *(page 1443)*
FSM4_12521 *(page 524)*

Zhu H.X.
FSM5_11292 *(page 537)*

Zhu W.
FM24_12757 *(page 1459)*

Zielinski T.G.
MS1_11810 *(page 173)*

Zilitinkevich S.
FM7_11053 *(page 824)*

Zimmermann K.
SM25_11699 *(page 2577)*

Zinchenko A.Z.
FM8_12329 *(page 906)*
FM8_12741 *(page 918)*

Ziolkowski M.
FM19_12605 *(page 1286)*

Ziopaja K.
SM24_12628 *(page 2529)*

Zitha P.L.J.
FSM5_12986 *(page 555)*

Zmitrowicz A.
SM2_11613 *(page 1685)*

Zochowski A.
SM24_11486 *(page 2489)*

Zouhar G.
FM21_12365 *(page 1347)*

Zukowski J.M.
FM10_11916 *(page 971)*

Zussman E.
FM4_10932 *(page 712)*
FM4_12319 *(page 730)*

Zyczkowski M.
SM24_12075 *(page 2509)*

OLI_10498:Mon:1100:000

XXI International Congress of Theoretical and Applied Mechanics
Warsaw, Poland, August 15-21, 2004



Interplay Between Air and Water

Leen van Wijngaarden

University of Twente J.M. Burgers Centre for Fluid Mechanics, Netherlands

In the Introduction I will recall, among others, the period of the Cold war in which thanks to Polish colleagues scientific contacts between East and West were maintained . After that several aspects of the flow of mixtures of air and water will be discussed and illuminated with examples. Finally I will give some comments on the differences and similarities between fundamental and applied science and scientists.

XXI ICTAM, 15-21 August 2004, Warsaw, Poland

Closing (plenary) lecture

STOCHASTIC DYNAMICS OF ENGINEERING SYSTEMS

Kazimierz SOBCZYK

Institute of Fundamental Technological Research,
Polish Academy of Sciences, Warsaw, Poland

Abstract

The objective of the lecture is to expose the main features of stochastic dynamics with a special emphasis on its methodological beauty and applicatory power.

Stochastic dynamics is a relatively new but greatly advanced field of science comprising the models and methods for investigation of real dynamical systems (of diverse physical nature) subjected to parametric and/or external random excitations. It includes, for instance, the analysis of control systems in the presence of random noises, stochastic vehicle dynamics, stochastic structural dynamics studying the response to earthquake, wind, sea waves, etc. In addition, today the methods of stochastic dynamics are widely used in many other fields including population dynamics, groundwater (pollution) transport, meteorological processes as well as economic and financial systems.

The genesis of stochastic dynamics is connected with problems of physics. Although the probabilistic/statistical thinking is present in physics already in the 19-th century (e.g. the Maxwell distribution of velocities of a gas molecules, Boltzmann entropy and his H-theorem), the first years of the 20-th century brought a systematic formulation of statistical mechanics (Gibbs – 1903) and the models of the phenomenon of the Brownian motion (Einstein – Smoluchowski, 1905/06, Langevin, 1909). These results can be regarded to be the roots of contemporary stochastic dynamics of a wide class of real systems. The lecture is inspired by this one-hundred anniversary and, therefore, starts from short comments on these great origins.

The basic content of the lecture is devoted to contemporary stochastic dynamics of physical/engineering systems and consists of six short parts.

In the 1-st part the general mathematical model of stochastic dynamics is shown in the form of a system of stochastic differential equations. The basic theorem concerning this system and relation to the Fokker-Planck Kolmogorov equation is presented. The 2-nd part expounds the models of engineering stochastic vibratory systems and explains how they can be embedded in the general mathematical model of stochastic Itô system. In order to make the model applicable for practical situations, the real random excitations (loads) have to be appropriately described; so, the 3-rd part shows how such excitations as sea wave load and the earthquake action can be characterized. The 4-th part is about characterization of the response by the effective solution methods. The basic existing methods are sketched with some additional emphasis on the method of maximum informational entropy. Hawing characterized the random response of a system the problem of basic engineering importance concerns failures of stochastic dynamical systems and the reliability assessment. In part 5-th of the lecture some light is shed on the characterization of safe performance of stochastic systems.

The last part of the lecture is concerned with the question: are any phenomena or effects generated by random noises/excitations which affect the most internal, “microscopic” dynamics of the systems? There are a number of qualitative effects which are called the “noise-induced transitions”. Such phenomena as: stabilization and destabilization by random noise, noise-induced bifurcations, “regularization” of chaotic dynamics by random noise, the Korteweg de Vrics waves in randomly varying medium are shortly discussed.

The lecture ends with closing remarks on the future of stochastic dynamics and stochastic/probabilistic methods – in general.

MULTIBODY DYNAMICS: BRIDGING FOR MULTIDISCIPLINARY APPLICATIONS

Jorge A.C. Ambrósio
IDMEC Instituto Superior Técnico, Av. Rovisco Pais 1, 1049-001 Lisboa, Portugal

Summary Simple or complex systems characterized by large relative motions between its components find in the multibody dynamics formalisms the most general and efficient computational tools for their analysis. Initially restricted to the treatment of rigid bodies, the multibody methods are now widely used to describe the system components deformations, regardless of their linear or nonlinear nature. The ease of including in the multibody models different descriptions of the contact problems, control paradigms, equations of equilibrium of other disciplines is demonstrated here to show the suitability of these approaches to be used for multidisciplinary applications.

MULTIBODY DYNAMICS METHODS AND INTEGRATION WITH OTHER DISCIPLINES

The design requirements of advanced mechanical and structural systems and the real-time simulation of complex systems exploit the ease of use of the powerful computational resources available today to create virtual prototyping environments. These advanced simulation facilities play a fundamental role in the study of systems that undergo large rigid body motion while their components experience material or geometric nonlinear deformations, such as vehicles, deployable structures, space satellites, machines operating at high speeds or robot manipulators. If in one hand the nonlinear finite element method is the most powerful and versatile procedure to describe the flexibility of the system components on the other hand the multibody dynamic formulations are the basis for the most efficient computational techniques that deal with large overall motion. Therefore, it is no surprise that many of the most recent formulations on flexible multibody dynamics and on finite element methods with large rotations share some common features.

In multibody dynamics methods body fixed coordinate frames are generally adopted to position each one of the system components and to allow for the specification of the kinematic constraints that represent the restrictions on the relative motion between the bodies. Several formalisms are published suggesting the use of different sets of coordinates, such as Cartesian [1], natural [2] and relative coordinates [3]. Depending on the type of applications pursued by the user, on the experience of the developer or on any specific objectives each one of the referred types of coordinates has advantages and disadvantages relative to the others. Due to their ease of computational implementation, their physical meaning and the wide spread knowledge of their features all the formalisms presented in this work are based on the use of Cartesian coordinates. However, it must be noted that the same formulations can also be developed with any other type of coordinates selected to describe the multibody systems.

The equations of motion of the multibody systems are obtained using the Euler-Lagrange equations and the principle of virtual works [1]. To kinematic constraints that restrict the relative motion between the different components of the system are added to the equilibrium equations by using Lagrange multipliers. The set of equations obtained in this manner, together with the acceleration constraint equations, are solved to obtain the system accelerations. The system state variables are then integrated in time, using typically a variable order and variable time step integration algorithm [4] for a pre-defined period of time.

The methodological structure of the equations of motion of the multibody system obtained allows the incorporation of the equilibrium equations of a large number of disciplines and their solution in a combined form. The description of the structural deformations exhibited by the system components by using linear[5] or non-linear finite elements [6] in the framework of multibody dynamics is an example of the integration of the equations of equilibrium of different specialities. Of particular importance in the applications pursued with the methodologies proposed is the treatment of contact and impact which are introduced in the multibody systems equations either by using unilateral constraints [7] or by applying a continuous contact force model [8]. The readily availability of the state variables in the multibody formulation allows for the use of different control paradigms in the framework of vehicle dynamics, biomechanics or robotics and its integration with the multibody equations [9]. The coupling between the fluid and structural dynamics equations allows for the development of applications where the fluid-structure interaction is of importance, especially for cases where the large absolute motion of the system or the large relative rotations between the system components are of importance [10,11].

The research carried at IDMEC and the different collaborative works developed with other research groups provide the examples offered in this presentation. Application cases involving the modelling of realistic mechanisms, passive safety of road and rail vehicles, impact and human locomotion biomechanics, automotive and railway dynamics and the control of multibody systems are used to demonstrate the developments listed in this presentation. In the process of presenting the different applications several possibilities for future developments are discussed.

FLEXIBILITY OF THE SYSTEM COMPONENTS

Multibody models for which the flexibility of the system components play a fundamental role in their behavior efficiently describe a large number of mechanical and structural systems of high importance. Vehicles, space satellites, deployable structures, machines operating at high speeds or robot manipulators are just some of the applications where the systems undergo large rigid body motion while their components experience structural deformations. The correct modeling of these systems requires that the formulations used in their description not only account for the motion and deformation of their components but also describe their inertial coupling. The methodology applied here uses an updated Lagrangean formulation to obtain the continuum mechanics equations of motion of a general flexible body. The finite element method is then used to obtain a representation of the flexible bodies suitable to the description of any general flexible component of the multibody system in a computational environment. The equations obtained at this stage are computationally inefficient due to their high nonlinearity. The use of a lumped mass formulation and a change of nodal coordinates lead to much simpler equations of motion, still accounting for the inertial coupling between large rigid body motion and the body flexibility. In the sequel of proposed methodology it is shown that if the flexible body material behavior is linear and the deformations are small the equations obtained can be greatly simplified by using the component mode synthesis. In order for the flexible bodies to be used in the multibody system model it is required that a set of kinematic joints, describing algebraic constraints between the system coordinates, are defined. The concept of virtual bodies provides a general framework to develop general kinematic joints. The application of the formulation proposed to the study of the comfort and stability of road vehicles allows appraising the treatment of the system deformations. The virtues and shortcomings of the formulation proposed are appraised through applications to vehicle structural impact cases and to highly deformable structures.

CONTACT MODELS FOR MULTIBODY DYNAMICS

The simulation of vehicles and structures under contact and impact conditions requires accurate descriptions of the structural and mechanical characteristics of the colliding bodies and suitable contact models. The models must be computationally efficient, especially if they need to be used in different stages of the design process. A formulation able to handle the large rigid body motion of the system components and their nonlinear deformations is discussed here. A continuous contact force model based on Hertzian contact, including energy dissipation, is shown to be suitable to handle both rigid and flexible body contact. A second model based in the addition and deletion of kinematic constraints between flexible body nodes and contacting surfaces is presented to represent flexible body impact. The friction forces are used with both contact models. The influence of the different contact and structural models in the system response is discussed through a simple application to the impact of a flexible beam. The suitability of the approach proposed for the design of complex multibody systems under impact conditions is further exemplified with an application to vehicle rollover, which involves all the major features of the formulation. Other type of applications where the contact force models play a fundamental role, and that are discussed here, are those concerned with railway dynamics.

BIOMECHANICS MODELING

The biomechanics, being in itself a multidisciplinary area, has its fundamentals in the scientific disciplines that deal with physiology and applied mechanics. The computer-aided modeling of the human body biological phenomena enables the designer to think, understand and decide the different stages of the design or of the analysis. The part of the biomechanics that deals with the motion of the human body allows for the integration of realistic models of the human body and of the phenomena associated to them in computer environments that range from the pure entertainment to the design of complex medical equipment for diagnosis or rehabilitation. The multibody dynamics formulations that support the biomechanical models for the study of human motions are described and presented here. The principles for modeling the human body motion through their large anatomical segments for the study of human gait, vehicle occupants in crashworthiness or athletic performance are reviewed in this work. It is shown through applications how these biomechanical multibody models enable the quantification of the potential for the injury of vehicle occupants during a crash or the internal muscle efforts of a person during different physical activities. In the process of discussing this type of applications, the use of the optimization procedures is presented for the solution of the muscle force sharing problem.

CONTROL OF MULTIBODY SYSTEMS

The use of multibody dynamics formulations to support the development of specific control models is exemplified here through applications to the automatic control of the angular orientation of a multibody system based upon the preservation of its angular momentum and to the development of a virtual driver for a vehicle running in a given track. The control strategy used for the human spatial attitude in a zero gravity environment is hierarchical and decentralized arranging the control stages in levels of attributions and complexity. At a lower level the controllers are responsible for handling each of the multibody degrees-of-freedom forcing them to follow prescribed reference motions through the use of error feedback. Middle level controllers coordinate the lower level controllers so that each of the multibody sub-

systems achieve prescribed reorientation. These reorientations are defined by a higher level controller with the final objective of reorienting the complete multibody system to reach a different attitude. The control laws associated with the controllers are parametrically adjusted for the biomechanical model under analysis. The results obtained are discussed in face of the modeling assumptions made and control laws used. The second application is to devise a multibody based methodology that allows for the design of a vehicle virtual driver, which can be used in the search of optimal vehicle trajectories for given manoeuvres. In order to achieve this objective it is necessary to have detailed vehicle and road models that can simulate with accuracy a driving scenario, to develop a proper control strategy for the vehicle, and to use a set of parameters of the detailed model that represent the interaction between the control model and the vehicle model. A simplified control model for the vehicle, which makes use of extended bicycle model, is implemented. The outcome of the controller based on the bicycle model is used to control a detailed multibody model of the real vehicle, including all suspension elements and tire/road forces, which provide the observed motion. The only variables that the control acts upon are the steering wheel angle and vehicle wheels' torques, which represent the traction and braking.

STRUCTURE-FLUID INTERACTION

The models for the fluid-structure coupling keep getting more and more advanced with the feasibility of complex 3D computations on fluid-structure interaction problems. Based on the work by Moeller et al. [12,13] this problem is solved by using a computer code aimed at simulating complex flexible multibody systems (linear elastic bodies) and another code aimed at the analysis of incompressible viscous flow. The types of problems that can be efficiently simulated in the framework of flexible multibody dynamics are elastic problems with gross overall displacements and rotations but small vibrations. Typical examples of this type of problems are wind turbines, helicopters and pumps. In the context of strongly coupled fluid-structure interaction, the motion of the structure can be the only significant nonlinearity affecting the fluid domain. If a standard finite element model was to be used, due to the possible large overall motion of the structure, it would be necessary to use a geometrically nonlinear finite element analysis for the structure, even though the actual deformation of the solid is within the linear elastic range. Then if the deformations in a moving coordinate system are small it is reasonable to use a small strain formulation for the solid in this reference frame. Besides from getting faster evaluation of element terms, the representation of the solid in this new coordinate system also eliminates the need for solving nonlinear equations for the solid deformations. The overall motion is still described by nonlinear equations that need to be solved at each time step, unless a fully explicit algorithm is used to integrate the equations for the solid. For long time dynamic behavior of structural systems it is often computationally more efficient to integrate a modally decomposed structural system because the frequency spectrum of the solid is reduced and the size of the system is reduced to the number of eigenfrequencies considered reducing in this form the computational cost.

References

[1] P. Nikravesh, *Computer-Aided Analysis of Mechanical Systems*, Prentice-Hall, Englewood Cliffs, New Jersey, 1988.
[2] J. Garcia de Jalon, E. Bayo, *Kinematic and Dynamic Simulation of Mechanical Systems – The Real-Time Challenge,* Springer-Verlag, Berlin, Germany, 1994.
[3] P. Nikravesh and G. Gim, "Systematic Construction of the Equations of Motion for Multibody Systems Containing Closed Kinematic Loops", *Journal of Mechanical Design*, **115**(1), 143-149, 1993.
[4] C.W. Gear, "Numerical Solution of Differential-Algebraic Equations", *IEEE Transactions on Circuit Theory*, Vol. CT-18, 89-95, 1981.
[5] J. Gonçalves and J. Ambrósio, "Complex Flexible Multibody Systems with Application to Vehicle Dynamics", *Multibody System Dynamics*, **6**(2), 163-182, 2001.
[6] J. Ambrósio and P. Nikravesh, "Elastic-Plastic Deformation in Multibody Dynamics", *Nonlinear Dynamics*, **3**, 85-104, 1992.
[7] F. Pfeiffer and C. Glocker, *Multibody Dynamics with Unilateral Contacts*, John Wiley and Sons, New York, New York, 1996
[8] H. Lankarani and P. Nikravesh, "Continuous Contact Force Models For Impact Analysis In Multibody Systems", *Nonlinear Dynamics*, **5**, 193-207, 1994.
[9] M. Valasek, Z. Šika, "Evaluation of Dynamic Capabilities of Machines and Robots", *Multibody System Dynamics*, **5**, 183-202, 2001.
[10] H.Møller and E.Lund, "Shape Sensitivity Analysis of Strongly Coupled Fluid-Structure Interaction Problems". In: *Proc. 8th AIAA/USAF/NASA/ISSMO Symposium on Multidisciplinary Analysis and Optimization, Long Beach, CA*. AIAA Paper No 2000–4823, 2000,
[11] H.Møller, E.Lund, J.Ambrósio and J.Gonçalves, "Simulation of Fluid Loaded Flexible Multiple Bodies", *Multibody Systems Dynamics*, 2004 (to appear).

XXI ICTAM, 15–21 August 2004, Warsaw, Poland

RAPID FORMATION OF STRONG GRADIENTS AND DIFFUSION IN THE TRANSPORT OF SCALAR AND VECTOR FIELDS

Konrad Bajer
Institute of Geophysics, Warsaw University, ul. Pasteura 7, 02-093 Warszawa, Poland

Summary An important issue in the theory of transport by moving fluids is the role of dissipation when the medium is *nearly ideal*. The central problem of this nature is understanding viscous dissipation at very large Reynolds numbers. We will discuss a few problems in the same category but *linear* and therefore more promising although, as it turns out, surprisingly rich and far from being resolved. Their common denominator is the interplay between diffusion and advection. In a typical flow the latter tends to decrease the characteristic length scales of the spatial variations of the transported quantity, thus increasing the rate of diffusion. Depending on a particular configuration either this rapid diffusion prevails and efficiently annihilates all gradients, or a kind of balance is reached and a quasi-steady dissipative structure emerges.

ACCELERATED DIFFUSION INDUCED BY VORTICES

Concentrated vortex has strong influence on the diffusion of passive scalars and vectors, like magnetic fields, in its neighbourhood [1,3-9,12-17]. Placed in a region of the large-scale gradient of an advected quantity, say temperature, it wraps the isotherms into spirals and therefore decreases the radial length-scale. This causes the process known as *accelerated diffusion*. The gradients of, say, temperature are expelled from the vicinity of the vortex which is then surrounded by a nearly isothermal region.

In two-dimensional magnetohydrodynamics this process, called *flux expulsion*, was noticed quite early [17], but initially there was an uncertainty as to the time-scale on which it occured. Much later simple models and arguments were put forward [12,16] proving this process to be quite rapid. It is faster by the factor $Pe^{-2/3}$ than normal diffusion across the vortex. Here $Pe = \Gamma/2\pi\kappa$ is the appropriate dimensionless number based on the total circulation Γ of the vortex and measuring the relative magnitudes of the advective and diffusive terms. In the case of temperature κ is thermal diffusivity and Pe is the Péclet number. Their MHD analogues are magnetic diffusivity and magnetic Reynolds number respectively.

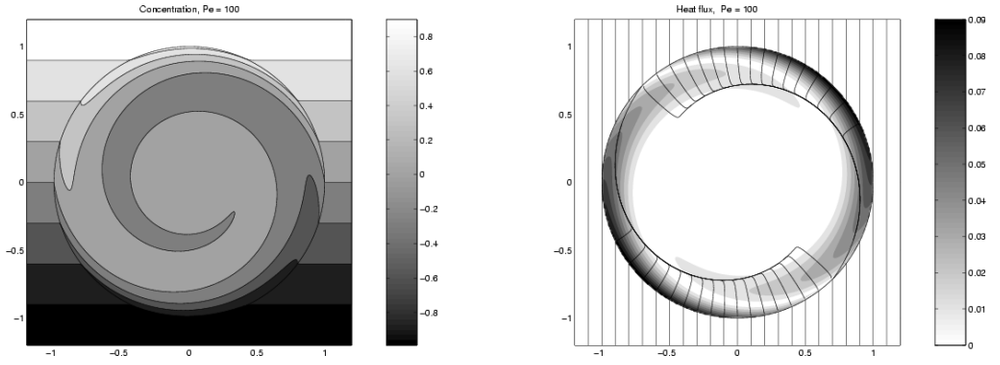


Figure 1. Cylindrical cavity filled with inviscid fluid surrounded by solid with imposed uniform temperature gradient. The steady flow in the cavity is due to a point vortex at the centre. In a fluid with finite thermal diffusivity a non-trivial steady state is reached with uniform temperature around the vortex and spiral isotherms in a thermal boundary layer near the wall (left panel). The right panel shows the integral lines of the heat flux which is completely expelled from the central area. The figure shows an exact analytical solution with $Pe = 100$. From [1].

The evolution equations of the mechanical quantities in fluids, like momentum and its derivatives, also contain advective terms and Fickian diffusion and therefore are also subject to accelerated diffusion. Batchelor [7] demonstrated the tendency of vorticity to become uniform but the mechanism and the time-scale were still unknown.

If a strong streamwise vortex is embedded in a boundary layer, then the streamwise component of *velocity* of the boundary layer flow is governed by the same advection-diffusion equation as for passive scalar [13-15]. The accelerated diffusion of streamwise momentum locally induces a complex velocity profile in the boundary layer. Due to the rapidity of the process it may have signifficant impact even if the streamwise vortex 'lives' only for a few turnover times.

STRONG COHERENT VORTEX INTERACTING WITH WEAK AMBIENT VORTICITY

When a strong concentrated vortex is embedded in the 'sea' of background vorticity aligned with it but *weak*, then this background (possibly a small perturbation of the strong vortex) is governed by an equation similar but not the same as the 'normal' advection-diffusion [4]. However, accelerated diffusion still operates creating spiral structures in the background vorticity. Those structures may in turn affect the vortex which is then displaced from its initial position. To illustrate this,

we show, theoretically and numerically, a self-induced motion of a single vortex in a Poiseuille flow. Modern experiments on turbulence in liquids as well as numerical simulations reveal the presence of elongated vortices whose diameter is somewhere between the Kolmogorov and the Taylor microscale. At small scales vorticity seems to be organised in a web of filaments and weak background. We will discuss the interaction between them.

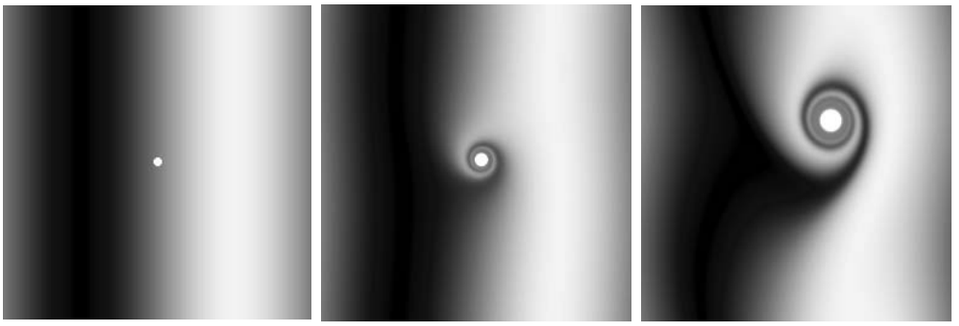


Figure 2. Strong gaussian vortex started in a weak background vorticity. The vortex creates a perturbation by winding non-uniform background into spirals. The flow associated with this perturbation displaces the vortex from its initial position. From [4].

FORMATION OF CURRENT SHEETS IN MAGNETOHYDRODYNAMICS

Vortex filaments are in many ways analogous to the magnetic flux tubes which are coherent structures found in magnetohydrodynamics (MHD), especially prominent in the solar dynamo process. Interacting flux tubes create current sheets and, in the ideal limit, tangential discontinuities - the generic MHD singularities which form in the process of relaxation towards magnetostatic equilibrium [10]. The conditions in the solar photosphere are nearly ideal, so the topological constraints imposed by non-dissipative MHD are important, as are the singularities where these constraints are most easily broken.

Both slender vortices and flux tubes can have topologically complex form (e.g. knotted or linked) and the mathematical apparatus necessary to describe and classify the topology is the same. Their steady states are mathematically equivalent, but there are important differences in their evolution [11]. The influence of the topology on the dynamics provides an important common ground. We will explore different aspects of the formation of strong gradients in vortex dynamics and in magnetohydrodynamics exploiting the analogies between the the governing equations.

Current sheets are believed to play an important dynamical role being a seat of vigorous Ohmic heating. However, the rate of Ohmic heating in a *single* sheet in a quasi-steady state *decreases* with increasing electrical conductivity of the fluid. Therefore, such individual sheets cannot provide efficient source of heat in a highly conducting medium like, for example, plasma in the solar corona. Qualitative models, usually involving dissipation related to turbulence driven by magnetic reconnection in the sheet, are often invoked to explain this apparent heating deficit. We will discuss a possibility of increased heat release in a *set* of simultaneous current sheets that are likely to form in any relaxing magnetic field that has *chaotic field lines* [2].

The relaxation process in a perfectly conducting fluid preserves all topological invariants. This set of constraints imposes strict lower bounds on magnetic energy of the equilibrium state. With reconnection, at least some of the constraints are relaxed, the topology of the field lines may change and lower energy states become accessible. If a multi-scale system of current sheets is present than we may expect less energetic final equilibria and more dissipation in the meantime.

References

[1] Bajer K.: Flux expulsion by a point vortex. *Eur. J. Mech.* B/*Fluids* **17**(4):653–664, 1998.
[2] Bajer K.: Abundant singularities. *Fluid Dyn. Res.* Submitted, 2004.
[3] Bajer K., Bassom, A.P. & Gilbert A.D.: Accelerated diffusion in the centre of a vortex. *J. Fluid Mech.* **437**:395–411, 2001.
[4] Bajer K., Bassom, A.P. & Gilbert A.D.: Vortex motion in a weak background shear flow. *J. Fluid Mech.* **509**:281–304, 2004.
[5] Bajer K., Moffatt H.K.: On the effect of a central vortex on a stretched magnetic flux tube. *J. Fluid Mech.* **339**:121–142, 1997.
[6] Bajer K., Moffatt H.K.: Tubes, Sheets and Singularities in Fluid Dynamics. Kluwer, 2002.
[7] Batchelor G.K.: On steady laminar flow with closed streamlines at large Reynolds number. *J. Fluid Mech.* **1**:177–190, 1956.
[8] Flohr P., Vassilicos J.C.: Accelerated scalar dissipation in a vortex. *J. Fluid Mech.* **348**:295–317, 1997.
[9] Gilbert A.D.: Spiral structures and spectra in two-dimensional turbulence. *J. Fluid Mech.* **193**:475–497, 1988.
[10] Moffatt H.K.: Magnetostatic equilibria and analogous Euler flows with arbitrary complex topology. *J. Fluid Mech.* **159**:359–378, 1985.
[11] Moffatt H.K.: Structure and stability of solutions of the Euler equations: a lagrangian approach. *Phil. Trans. Roy. Soc.* A **333**:321–342, 1990.
[12] Moffatt H.K., Kamkar H.: On the time-scale associated with flux expulsion. In *Stellar and Planetary Magnetism*, 91–97. Gordon & Breach, 1983.
[13] Moore D.W.: The interaction of a diffusing vortex and an aligned shear flow. *Proc. R. Soc. Lond.* A **399**:367–375, 1985.
[14] Pearson C.F., Abernathy F.H.: Evolution of the flow field associated with a streamwise diffusing vortex. *J. Fluid Mech.* **146**:271–283, 1984.
[15] Pullin D.I., Lundgren T.S.: Axial motion and scalar transport in stretched spiral vortices. *Phys. Fluids*, **13** (9):2553–2563, 2001.
[16] Rhines P.B., Young W.R.: How rapidly is a passive scalar mixed within closed streamlines? *J. Fluid Mech.* **133**:133–145, 1983.
[17] Weiss N.O.: The expulsion of magnetic flux by eddies. *Proc. Roy. Soc. Lond.* A **293**:310–328, 1966.

NEAR-CRITICAL POINT HYDRODYNAMICS AND MICROGRAVITY

D. Beysens

CEA, Service des Basses Températures, Grenoble
dbeysens@cea.fr

Postal address: CEA-ESEME, ICMCB, 87, av. Dr. A. Schweitzer, 33608 Pessac Cedex (France)

The critical point of fluids is the termination point of the gas-liquid saturation curve (Fig.1), when gas and liquid phases merge in a unique supercritical "state". This state exhibits very particular properties. Above the critical temperature and pressure, supercritical fluids exhibit a number of specific properties (large density, low viscosity, large diffusivity), which make them intermediate between liquids and gases [1-2]. In addition, their isothermal compressibility and thermal expansion can become very large, especially when they approach the critical point. The highly variable properties of near-critical fluids make them very attractive for studying many phenomena that hold for all fluids because of the critical universality. On the other hand, supercritical fluids are increasingly used by the food and waste management industry [2] for their solubilization properties (e.g. supercritical CO_2), as host of "cold" combustion (e.g. supercritical water), in energetics (supercritical thermal or nuclear plants), and in astronautics (e.g. storage of cryogenic fluids). However, their behavior under terrestrial (1-g) or space (zero-g) conditions is not so well investigated and their use raises fundamental questions concerning fluid dynamics, heat transfer, interfacial and nucleation phenomena, and chemical processes. Experiments in the absence of gravity-induced effects are often necessary to answer these questions and enhance knowledge in this field.

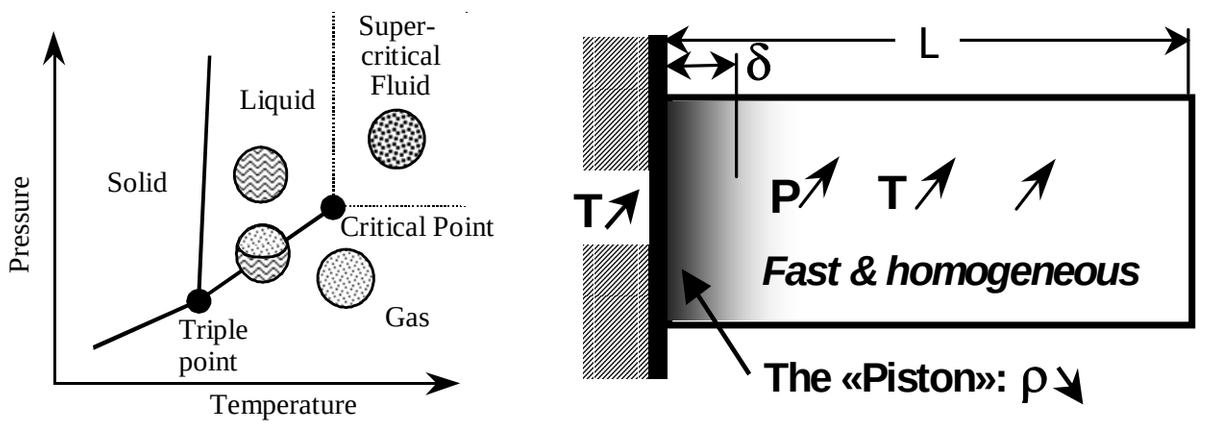


Fig. 1. *(a) Phase diagram of a pure substance. (b) The Piston Effect mechanism [3-4]: a thin hot boundary layer expands and compresses the bulk fluid. The corresponding temperature profile shows a thin zone of strong gradients near the heated boundary (thermal boundary layer δ) and a homogeneous rise in the rest of the fluid, that settles at the speed of sound.*

Scaling. An important aspect of the critical region is that most of the anomalies in the thermodynamic and transport properties can be set in the form of scaled, universal functions (power laws) with respect to the critical temperature or density. A very important consequence follows, that any results obtained with one fluid can be immediately rescaled to describe any member of a whole class of systems, called a "class of universality". This class is only defined by the space dimensionality d (=3 in normal space) and n (=1 for fluids), the 'order parameter' dimension.
By enabling measurements to be performed extremely close to the critical point, zero-g experiments have made possible the precise measurements of important, weak power law divergence, such as that of the specific heat at constant volume C_v. From space experiments, the temperature divergence of the specific heat has been determined with a very high precision. With the reduced temperature $\varepsilon = |T-T_c|/T_c$ (T is temperature, T_c is the critical temperature), the specific heat diverges as $C_v \sim \varepsilon^{-\alpha}$ near the critical point. The "critical" exponent α is universal. The value deduced from the space experiments, $\alpha = 0.1105 + 0.025 \pm 0.027$ [5], indeed appears to be very close to the result of the Renormalization Group theory, $\alpha = 0.110 \pm 0.005$.

Thermalization. The thermal diffusivity of fluids vanishes near the critical point and a simple calculation shows that it would need more than one month to reach thermal equilibration in a sample of 1 cm^3 at $T-T_c=1$ mK . At the beginning of the microgravity experiments, it thus seemed hopeless to the scientists to try to homogenize in temperature and density a sample of fluid close to the critical point in a reasonable experiment time. However, it appeared that, when heating a sample wall, the hot diffuse boundary layer expanded to compress adiabatically the whole fluid. As a result, a spatially uniform heating of the bulk fluid was observed. We coined this adiabatic heating phenomenon the "Piston effect" (PE). This Piston effect is at the origin of very particular behaviours; one is particularly paradoxical, when the vapor is in equilibrium with liquid below the critical point. While heating the cell, the temperature of the vapor becomes *greater* than that of the wall, seemingly contradicting the laws of thermodynamics [6].

Phase transition. It is a very out of equilibrium process. In a typical experiment, the supercritical fluid is thermally quenched from a region of the phase diagram where it is homogeneous (at temperature T_i) to a region where it is thermodynamically stable as two phases (at temperature T_f).
On earth, the denser phase flow down and the lighter up, in a turbulent way that prevents the underlying mechanisms to be clearly identified. Under weightlessness, growth is only limited by the coalescence of bubbles or droplets that nucleate [7]. When the volume fraction ϕ of the nucleated phase is low, the droplets collide by Brownian motion. The average distance L_m between the drops evolves as $L_m = 2\pi(k_BT/6\pi\eta)t^{1/3}$ where t is time, η is the shear viscosity, T is absolute temperature and k_B is the Boltzmann constant.
To a given ϕ corresponds a typical interaction length between domains. When $\phi > 0.3$, the flow generated by a coalescence event is able to move a neighboring drop and thus induces other coalescence events [8]. Such a process therefore creates a chain reaction of coalescence. In the viscous limit, the pattern looks interconnected. Growth is limited by the balance between the capillary pressure gradient σ/R (σ is the gas-liquid surface tension) and the friction due to the shear viscosity, so that $L_m = b(\sigma/\eta)\, t$. Here $b \approx 0.03$ is a universal constant.
The development of domains by coalescence events is very general. The universality of behavior, which is observed in fluids and liquid mixtures, can be extended to others areas of science. In particular, it can be applied to developmental biology [9] where tissues can be considered as very viscous liquids (viscosity $\approx 10^6$ Po), with a weak surface tension arising from the balance of adhesion sites between the tissue cells (effective interfacial tension ≈ 10 dyn. cm^{-1}).

Vibrations. Another situation is concerned with phase transition under an external field that is not gravity. A study of phase separation was performed in H_2 under vibration. Weight was compensated by a volumic magnetic force. It appears that the effect of vibrations is primarily governed by inertial effects that initiate different velocities inside the growing gas and liquid domains. A major result is that the growth is unaffected as long as the domain size is smaller than the viscous boundary layer thickness. When the size is larger, vibrations speeds up phase transition, whatever interconnected or separate bubbles are concerned, and localize the liquid and vapor phases perpendicular to it. The investigations suggest that a periodic excitation can act as a kind of artificial gravity, which speeds up phase transition and localizes the liquid and vapor phases perpendicular to it [10].

REFERENCES

[1] See e.g. Stanley H.E., *" Introduction to phase transitions and critical phenomena"* , Clarendon Press, Oxford, New York, 1971); Beysens D., Straub J., Turner D., in *"Fluid Sciences and Materials Science in Space"*, ed. by H. U. Walter , Springer, Berlin, 1987) pp.221-256.
[2] Cansell F., Beslin P., Berdeu B., *Environmental Progress* 17, 258-263, 1998
[3] Zappoli B., Bailly D., Garrabos Y., Le Neindre B., Guenoun P., Beysens D., *Phys. Rev. A* 41, 2264-2267, 1990.
[4] Onuki A., Hao H., Ferrell R.A., *Phys. Rev.*A 41, 2255-2259, 1990; Onuki A., Ferrell R.A., *Physica* A 164, 245-264, 1990.
[5] Nitsche K., Straub J., Naturwissenschaften 73, 370, 1986; Straub J, Eicher L., Haupt A., Phys. Rev. E 51, 5556-5563, 1995.
[6] Wunenburger R., Garrabos Y., Chabot C., Beysens D. and Hegseth J., *Phys. Rev. Lett.* 84, 4100-4103, 2000; Sincell M., *Science* 288, 789-791, 2000.
[7] Beysens D., Garrabos, Y, Physica A 281, 361-380, 2000 and Refs. therein.
[8] Nikolayev V., Beysens D., Guenoun P., *Phys. Rev. Lett.* 76, 3144-3147, 1996;
[9] Beysens D., Forgacs G., Glazier J.A., P.N.A.S. 97, 9467-71, 2000
[10] Beysens D., Chatain D., Evesque P., Garrabos Y., preprint (2004)

XXI International Congress of Theoretical and Applied Mechanics
Warsaw, Poland, August 15-21, 2004

Suspensions: From Micromechanics to Macroscopic Behavior

John F. Brady
California Institute of Technology

It's morning. You pour cereal in your bowl, shake the orange juice, fill your glass, and pour milk over your cereal. Why did you shake the orange juice and not the milk? Why do you pour cereal? These are just some everyday examples of complex fluids -- materials that often behave like water or air, but just as often display quite different behavior. Many complex fluids are in the form of particles dispersed in a host liquid or gas, and it is the particle-level interactions that give rise to interesting macroscopic phenomena, such as shear thinning and thickening, viscoelasticity and structure formation. This talk will discuss the micromechanics of particulate dispersions and how the interplay of colloidal, Brownian and hydrodynamic forces sets the material's microstructure and determines its macroscopic properties. So why did you shake the orange juice and not the milk?

XXI International Congress of Theoretical and Applied Mechanics
Warsaw, Poland, August 15-21, 2004

NANOSCALE MECHANICS OF BIOLOGICAL MATERIALS

Huajian Gao

Max-Planck Institute for Metals Research, D-70569 Stuttgart

Biological materials, such as shell, bone and tooth are organic-inorganic hybrid composites of protein and mineral with superior strength, hardness and fracture toughness. It is quite a marvel that nature produces such tough materials out of protein constituents as soft as human skin and mineral constituents as brittle as a classroom chalk. Understanding the mechanisms by which nature design strong and tough composites with weak materials can give us a guideline for the synthesis of man made novel materials. Previous researches showed that although they have various hierarchical structures, the biological materials have similar elementary building blocks. X-ray scattering (SAXS), Transmission Electron Microscopy (TEM) and high voltage electron microscopy (HVEM) have shown that many biomaterials share a generic nanostructure consisting of staggered nanoscale mineral crystals with very large aspect ratios embedded in a soft protein matrix. Why is nanoscale so important to nature materials? What are the roles of protein in the strength and toughness of biological materials? Why do the mineral crystals have a large aspect ratio? In this lecture, we will discuss these questions from several aspects, such as mechanics of protein, the fracture strength of mineral crystal at nanoscale, stability of the nanostructure and the interface strength between mineral and protein, etc.

Protein arrests the crack and dissipates fracture energy

Protein plays a crucial role in the strength and toughness of biological materials due to its intrinsic mechanical properties. We have developed a fracture model of biocomposites based on a Virtual-Internal-Bond (VIB) approach. With this model we have simulated the fracture behaviors of biocomposites. The results show that the protein layer is very effective in eliminating stress concentration near crack-like flaws, thereby arresting the crack. We also observed microcrack nucleation at the tensile zone between the mineral platelets, while not destroying the integrity of the structure, can dissipate fracture energy and delocalize damage in the material. In addition, protein has strong viscoelastic properties that can help biomaterials dissipate fracture energy under dynamic loading. A composite model evaluating the viscoelastic properties of biocomposites is developed to describe the effect of protein on the viscoelastic properties of composites. By this composite model, we demonstrate that bone and dentin with larger volume concentration of protein exhibits better viscoelastic properties than sea shells.

Fracture strength of nanometer sized mineral crystals

We find that there exists a critical length scale for the maximum strength of mineral crystals. This critical length scale is estimated as

$$h^* = \alpha^2 \frac{E\gamma}{\sigma_{th}^2}$$

where E and γ are Young's modulus and surface energy, and σ_{th} is the theoretical strength of mineral. The parameter α is approximately equal to $\sqrt{\pi}$ for a thumbnail-crack spreading over half the thickness of a mineral crystal. When the size of the mineral crystal is less than this critical length scale, the fracture strength of the cracked crystal is identical to that of a perfect crystal. This length scale indicates that the nanometer size of mineral platelets in biomaterials may be the result of fracture strength optimization. When the mineral size exceeds this length scale, the fracture strength is sensitive to structural size and the material is sensitive to crack-like flaws and fails by stress concentration at crack tips. As the mineral size drops below this length scale, the strength of a perfect mineral crystal is maintained despite of defects. In order to model failure mechanisms in nanocrystals, we have used the VIB method which incorporates an atomic cohesive force law into the constitutive model of materials. Our simulation shows that the stress field becomes more and more uniform as the thickness of the platelet decreases and eventually reaches the theoretical strength at the critical length scale as the crystal is loaded close to the failure limit.

Stability of nanocrystals

The fact that the mineral nanocrystals in biomaterials exhibit very large aspect ratios raises the issue of structural buckling under compressive loading. We show that the key to this question is the generic nanostructure of biomaterials in which the mineral nanocrystals are stabilized by the surrounding protein matrix. This is especially interesting in view of the three-orders of magnitude difference in elastic modulus between protein and mineral. A unique feature of the biological nanostructure is that, at large aspect ratios of mineral crystals, the buckling strength approaches a constant lower threshold value independent of the crystal geometry. The existence of a buckling strength independent of the detailed geometrical parameters of mineral is critically important from the point of view of structure robustness as the composite behavior of biomaterials or biomimicking materials should not depend sensitively on small variations in crystal size and shape. The large aspect ratios play a key role in the stability of mineral crystals by which relatively weak support from protein layer is accumulated and amplified to be significant. This is analogous to the stability of DNA double helix in which relatively weak hydrogen bonds can make the double helical structure quite stable under the help of its long chain.

Interface strength

The interface between mineral and protein plays a critical role in the viability of biocomposites. The interface properties can be extremely crucial as the force transfer between inclusions and matrix hinges upon a robust interfacial bonding along their interface. For nanocomposites, the interface properties can dominate overall material properties. A simple

fracture model is developed to study the composite fracture strength in the presence of interface failure, where we find that the large aspect ratio again plays an important role in amplifying the interfacial strength. Molecular dynamic simulation is performed to study binding between protein and mineral under various loading conditions.

Biological Attachment Systems

Geckos have evolved elaborate adhesive structures which allow them to move along vertical walls and ceilings against their body weight. There is strong evidence that the adhesion of Gecko is due to van der Waals interaction between a contacting surface and hundreds of thousands of keratinous hairs or setae on Gecko's foot; each seta is 30-130 μm long and contains hundreds of 200-500nm projections or spatula. While contact mechanics suggests that the refinement of structure size results in greater adhesive strength, some important questions remain unsolved: What is the significance of nanometer length scale for adhesion? What is the optimum adhesive strength of a structure? How can a structure optimized for attachment simultaneously allow easy detachment, as reversible adhesion is crucial for animal's movement? We show that the nanometer range of the spatula size of Gecko may have evolved to optimize the adhesive strength and maximum tolerance of imperfect adhesion (for robustness). Our analysis also indicates that the asymmetrical structure of Gecko's seta structure may been designed to simultaneously allow robust attachment and easy detachment.

Reference:

[1] H. Gao, B. Ji, I.L. Jaeger, E. Arzt and P. Fratzl, "Materials Become Insensitive to Flaws at Nanoscale: Lessons from Nature," 2003, *Proceedings of the National Academy of Sciences of USA*, Vol. **100**, pp. 5597–5600.

Multiscale Methods in Turbulence

Thomas J. R. Hughes, Victor M. Calo and Guglielmo Scovazzi

Institute for Computational and Engineering Sciences,
University of Texas at Austin
201 E. 24th Street
ACE 6.412, 1 University Station C0200,
Austin, Texas 78712-0027, U.S.A

Extended Summary

Variational multiscale concepts for Large Eddy Simulation (LES) were introduced in Hughes et al. [7]. The basic idea was to use variational projections in place of the traditional filtered equations and to focus modeling on fine-scale equations rather than coarse-scale equations. Avoidance of filters eliminates many difficulties associated with the traditional approach, namely, inhomogeneous non-commutative filters necessary for wall-bounded flows, use of complex filtered quantities in compressible flows, the closure problem, etc. In addition, modeling confined to the fine-scale equations retains numerical consistency in the coarse-scale equations and thus permits full rate-of-convergence of the underlying numerical method in contrast with the usual approach which limits convergence rate due to artificial viscosity effects in the fully resolved scales ($O(h^{4/3})$ in the case of Smagorinsky-type models). Initial versions of the variational mulsticale method focused on dividing resolved scales into coarse and fine designations, and eddy viscosities, inspired by traditional models, were *only* included in the fine scale equations and acted *only* on the fine scales. This version was studied in [8, 9, 16] and found to work very well on homogeneous isotropic flows and fully-developed equilibrium and non-equilibrium turbulent channel flows. Static eddy viscosity models were employed in these studies but superior results were subsequently obtained through the use of dynamic models, as reported in Holmen et al. [4] and Hughes et al. [11]. Good numerical results were obtained with the static approach by other of investigators, namely, Collis [2], Jeanmart and Winckelmans [14] and Ramakrishnan and Collis [18, 19, 20, 21]. Particular mention should be made of the work of Farhat and Koobus [3], and Koobus and Farhat [15], who have implemented this procedure in an unstructured mesh, finite volume, compressible flow code, and applied it very successfully to a number of complex test cases and industrial flows. We believe that this initial version of the variational multiscale concept has already demonstrated its viability and practical utility and is, at the very least, competitive with traditional LES turbulence modeling approaches.

Nevertheless, there is still significant room for improvement. The use of traditional eddy viscosities to represent fine-scale dissipation is an inefficient mechanism. Employing an eddy viscosity in the resolved fine scales to represent turbulent dissipation introduces a consistency error which results in the resolved fine scales being "sacrificed" to retain full consistency in the coarse scales. (In our opinion, this is still better than the traditional approach in which consistency in *all* resolved scales is sacrificed to represent turbulent dissipation.) This procedure is felt to be "inefficient" because approximately 7/8 of the resolved scales are typically ascribed to the fine scales. Another shortcoming noted for the initial version of the variational multiscale method is too small an energy transfer to unresolved modes when the discretization is very coarse (see, e.g., Hughes et al. [11]). This phenomenon is also noted for some traditional models, such as the dynamic Smagorinsky model [11], but seems to be somewhat more pronounced for the multiscale version of the dynamic model. The objectives of recent multiscale work have been to capture all scales consistently and to avoid use of eddy viscosities altogether. This holds the promise of much more accurate

and efficient LES procedures. In this work, we describe a new variational multiscale formulation which makes considerable progress toward these goals. In what follows, all resolved scales are viewed as coarse scales, which obviates the issue of inefficiency *ab initio*.

We begin by taking the view that the decomposition into coarse and fine scales is exact. For example, in the spectral case, the coarse-scale space consists of all Fourier modes beneath some cut-off wave number and the fine-scale space consists of all remaining Fourier modes. Consequently, the coarse-scale space has finite dimension whereas the fine-scale space is infinite dimensional. The derivation of the coarse- and fine-scale equations proceeds, first, by substituting the split of the exact solution into coarse and fine scales into the Navier-Stokes equations, then, second, by projecting this equation into the coarse- and fine-scale subspaces. The projection into coarse scales is a finite dimensional system for the coarse-scale component of the solution, which depends parametrically on the fine-scale component. In the spectral case, in addition to the usual terms involving the coarse-scale component, only the cross-stress and Reynolds-stress terms involve the fine-scale component. In the case of non-orthogonal bases, even the linear terms give rise to coupling between coarse and fine scales. The coarse-scale component plays an analogous role to the filtered field in the classical approach, but has the advantage of avoiding all problems associated with homogeneity, commutativity, walls, compressibility, etc. The projection into fine scales is an infinite-dimensional system for the fine-scale component of the solution which depends parametrically on the coarse-scale component. We also assume the cut-off wave number is sufficiently large that the philosophy of LES is appropriate. For example, if there is a well-defined inertial sub-range, then we assume the cut-off wave number resides somewhere within it. This assumption enables us to further assume that the energy content in the fine scales is small compared with the coarse scales. This turns out to be *crucial* in our efforts to analytically represent the solution of the fine-scale equations. The strategy is to obtain approximate analytical expressions for the fine scales then substitute them into the coarse-scale equations which are, in turn, solved numerically. If the scale decomposition is performed in space and time, the *only* approximation in the procedure is the representation of the fine-scale solution. To provide a framework for the fine-scale approximation, we assume an infinite perturbation series expansion to treat the fine-scale nonlinear term in the fine-scale equation. By virtue of the smallness of the fine scales, this expansion is expected to converge rapidly under the circumstances described in many cases of practical interest. The remaining part of the fine-scale Navier-Stokes system is the *linearized* operator which is formally inverted through the use of a Green's function. The combination of a perturbation series and Green's function provides an exact formal solution of the fine-scale Navier-Stokes equations. The driving force in these equations is the Navier-Stokes system residual computed from the coarse scales. This expresses the intuitively obvious fact that if the coarse scales constitute a good approximation to the solution of the problem, the coarse-scale residual will be small and the resulting fine-scale solution will be small as well. This is the case we have in mind and it provides a rational basis for assuming the perturbation series converges rapidly. Note that one cannot use such an argument on the original problem because in this case the perturbation series would almost definitely fail to converge. (If we could have used this argument, we would have solved the Navier-Stokes equations analytically! Unfortunately, it does not work.) The formal solution of the fine-scale equations suggests various approximations may be employed in practical problem solving. We are tempted to use the word "modeling" because approximate analytical representations of the fine scales constitute the only approximation and hence may be thought of as the "modeling" component of the present approach but we want to emphasize that it is very different from classical modeling ideas which are dominated by the *addition* of *ad hoc* eddy viscosities. We will present numerical results that demonstrate these eddy-viscosity terms are unnecessary in the present circumstances. There are two aspects to the approximation of the fine scales: 1) Approximation of the Green's function for the linearized Navier-Stokes system; and 2) approximation of the nonlinearities represented by the perturbation series. The first and obvious thought for the latter aspect, nonlinearity, is to simply truncate the perturbation series. This idea is investigated, as well as another promising idea, in conjunction with some simple approximations of the Green's function. It turns out there is considerable experience in local scaling approximations of the Green's function based on the theory of *stabilized methods* [5, 6, 10]. The Green's function is typically approximated by locally defined algebraic operators (i.e., the "τ's" of stabilized methods) multiplied by local values of the coarse-scale residual. With this approximation of the solution of the linearized operator, nonlinearities can be

easily accounted for in perturbation series fashion. Another approach that accounts for nonlinearities in the fine-scale equations is to introduce a nonlinear algebraic scaling of the Navier-Stokes equations. The resulting local nonlinear algebraic system can be analytically solved. It possesses the reasonable analytical property that if the coarse-scale residual is small, it converges to the linearized solution.

These newer variational multiscale ideas, and the older variants, were implemented in a finite volume code that has enjoyed widespread use in turbulence simulations (see Pierce and Moin [17]). Following along the lines of Jacobs and Durbin [12, 13], who performed DNS investigations of bypass transition of a boundary layer, we examine this difficult problem from the point of view of the variational multiscale and classical LES. Our aim was to solve this problem as an LES and demonstrate the efficacy of the new ideas in the process.

In our work we endeavor to show the effectiveness, or deficiencies, of LES approaches by studying them over a range of resolutions, from coarse to fine. In our studies of bypass transition we went as far as DNS in the fine-scale end of the spectrum, and 1/8 DNS resolution in each spatial direction. The coarsest LES mesh then involves about 1/512 the number of equations as the DNS mesh and approximately 1/4,096 of the computational effort. We found, independent of the LES method, that in order to accurately simulate bypass transition, the decay of input homogeneous, isotropic, free-stream turbulence must be the same for all meshes. A procedure was developed in which we were able to simulate consistent energy decay with distance of the free-stream turbulence across the range of meshes considered. We then compared the methods to represent bypass transition. We found that the "1/8 DNS mesh" was incapable of representing either the laminar region of the boundary layer or the free-stream turbulence evolution due to too few points in the wall normal direction. We found that all methods gave essentially the same solution at the DNS level, whereas only the new variational multiscale formulation was able to attain relatively mesh independent solutions without parameter adjustment for the 1/4, 1/2 and full DNS mesh cases. The 1/4 DNS involves 1/64 the number of mesh points as the DNS case and 1/512 the computational effort. Comparison is made with classical LES procedures, such as the dynamic Smagorinsky model, which tends in this instance to exhibit significant sensitivity to the filter-width ratio, and previous versions of the variational multiscale method in which a fine-scale dynamic Smagorinsky model is employed. Comparison is also made with some classical stabilized methods, such as SUPG (see Brooks and Hughes [1]). We conclude that the newest method is superior to all previous methods and offers a promising new path for turbulence research in LES. However, it obviously needs testing on a wider variety of flows and implementation in a variety of numerical frameworks, such as, spectral, finite difference and finite element, before definitive conclusions can be drawn. In our experience, the particular numerical discretization method has an enormous impact on the results, and its influence is often underestimated by practitioners evaluating models.

References

[1] A. N. Brooks and T. J. R. Hughes. Streamline upwind / Petrov-Galerkin formulations for convection dominated flows with particular emphasis on the incompressible Navier-Stokes equations. *Computer Methods in Applied Mechanics and Engineering*, 32:199–259, 1982.

[2] S. S. Collis. Multiscale methods for turbulence simulation and control. Technical Report Version 1.1, Mechanical Engineering and Materials Science, Rice University, 2002. Available at `http://www.mems.rice.edu/~collis/papers/vki2002_notes.pdf`.

[3] C. Farhat and B. Koobus. Finite volume discretization on unstructured meshes of the multiscale formulation of large eddy simulations. In Rammerstorfer F. G. Mang H. A. and Eberhardsteiner J., editors, *Proceedings of the Fifth World Congress on Computational Mechanics (WCCM V)*, Vienna University of Technology, Austria, July 7-12 2002. Fifth World Congress on Computational Mechanics.

[4] J. Holmen, T. J. R. Hughes, A. A. Oberai, and G. N. Wells. Sensitivity of the scale partition for variational multiscale LES of channel flow. *Physics of Fluids*, 16(3):824–827, 2004.

[5] T. J. R. Hughes. Multiscale phenomena: Green's functions, the Dirichlet-to-Neumann formulation, subgrid scale models, bubbles, and the origins of stabilized methods. *Computer Methods in Applied Mechanics and Engineering*, 127:387–401, 1995.

[6] T. J. R. Hughes, G. Feijóo., L. Mazzei, and J. B. Quincy. The variational multiscale method–A paradigm for computational mechanics. *Computer Methods in Applied Mechanics and Engineering*, 166:3–24, 1998.

[7] T. J. R. Hughes, L. Mazzei, and K. E. Jansen. Large eddy simulation and the variational multiscale method. *Computing and Visualization in Science*, 3:47–59, 2000.

[8] T. J. R. Hughes, L. Mazzei, A. A. Oberai, and A. A. Wray. The multiscale formulation of large eddy simulation: Decay of homogeneous isotropic turbulence. *Physics of Fluids*, 13(2):505–512, 2001.

[9] T. J. R. Hughes, A. A. Oberai, and L. Mazzei. Large eddy simulation of turbulent channel flows by the variational multiscale method. *Physics of Fluids*, 13(6):1784–1799, 2001.

[10] T. J. R. Hughes, G. Scovazzi, and L. P. Franca. Multiscale and stabilized methods. In E. Stein, R. de Borst, and T. J. R. Hughes, editors, *Encyclopedia of Computational Mechanics*. John Wiley & Sons, Ltd., 2004.

[11] T. J. R. Hughes, G. N. Wells, and A. A. Wray. Energy transfers and spectral eddy viscosity of homogeneous isotropic turbulence: Comparison of dynamic Smagorinsky and multiscale models over a range of disretizations. Technical Report 04-20, Institute for Computational Engineering and Sciences, University of Texas at Austin, 2004. Available at `http://www.ticam.utexas.edu/reports/2004/0420.pdf`.

[12] R. G. Jacobs and P. A. Durbin. Bypass transition phenomena studied by computer simulation. Technical Report TF-77, Flow Physics and Computation Division, Department of Mechanical Engineering, Stanford University, 2000.

[13] R. G. Jacobs and P. A. Durbin. Simulations of bypass transition. *Journal of Fluid Mechanics*, 428:185–212, 2001.

[14] H. Jeanmart and G. S. Winckelmans. Comparison of recent dynamic subgrid-scale models in the case of the turbulent channel flow. In *Proceedings Summer Program 2002*, pages 105–116, Stanford, CA, 2002. Center for Turbulence Research, Stanford University & NASA Ames.

[15] B. Koobus and C. Farhat. A variational multiscale method for the large eddy simulation of compressible turbulent flows on unstructured meshes–application to vortex shedding. *Computer Methods in Applied Mechanics and Engineering*, 193(15–16):1367–1383, 2004.

[16] A. A. Oberai and T. J. R. Hughes. The variational multiscale formulation of LES: Channel flow at $Re = 590$. In 40^{th} *AIAA Ann. Mtg.*, AIAA 2002-1056, Reno, NV, Jan. 2002.

[17] C. D. Pierce and P. Moin. Progress-variable approach for large eddy simulation of turbulent combustion. Technical Report TF-80, Flow Physics and Computation Division, Department of Mechanical Engineering, Stanford University, 2001.
Available at `http://ctr.stanford.edu/Pierce/thesis.pdf`.

[18] S. Ramakrishnan and S. S. Collis. Variational multiscale modeling for turbulence control. In *AIAA* 1^{st} *Flow Control Conference*, AIAA 2002-3280, St. Louis, MO, June 2002.

[19] S. Ramakrishnan and S. S. Collis. Multiscale modeling for turbulence simulation in complex geometries. In 40^{th} *AIAA Aerospace Sciences Meeting and Exhibit*, AIAA 2004-0241, Reno, NV, Jan. 2004.

[20] S. Ramakrishnan and S. S. Collis. Partition selection in multiscale turbulence modeling. *Preprint*, 2004.

[21] S. Ramakrishnan and S. S. Collis. Turbulence control simulation using the variational multiscale method. *AIAA Journal*, 42(4):745–753, 2004.

Non-Newtonian Fluid Mechanics Using Molecular Theory

Roland Keunings
CESAME, Universite catholique de Louvain, Belgium

Many natural and synthetic fluids are viscoelastic materials, in the sense that the stress endured by a macroscopic fluid element depends upon the history of the deformation experienced by that element. Notable examples include polymer solutions and melts, liquid crystalline polymers, and fibre suspensions. The remarkable rheological properties of viscoelastic liquids cannot be described by the Navier-Stokes equations, but rather are governed by the flow-induced evolution of molecular configurations [1].

Models of kinetic theory provide a coarse-grained description of molecular configurations wherein atomistic processes are ignored altogether [2]. They are meant to display in a more or less accurate fashion the important features that govern the flow-induced evolution of configurations. In recent years, kinetic theory of entangled systems, such as concentrated polymer solutions and polymer melts, has known major developments that go well beyond the classical reptation tube model developed by Edwards, de Gennes, and Doi [3]. In addition to reptation, other physical mechanisms such as convective constraint release, contour length fluctuations, and tube stretch, have been shown to play an important role. The most recent tube models take account of these effects and correct many of the deficiencies of the basic theory (for a review, see [4]).

Kinetic theory models can be very complicated mathematical objects. It is usually not easy to compute their rheological response in rheometrical flows (although these flows have simple, specified kinematics), and their use in numerical simulations of complex flows has long been thought impossible. The traditional approach has been to derive from a particular kinetic theory model a macroscopic constitutive equation that relates the viscoelastic stress to the deformation history. One then solves the constitutive model together with the conservation laws using a suitable numerical method, to predict velocity and stress fields in complex flows. The majority of constitutive equations used in continuum numerical simulations are indeed derived (or at least very much inspired) from kinetic theory. Their use in numerical simulations of complex flows is reviewed in [5-6]. Clearly, the continuum approach remains an essential component of theoretical and computational rheology. There is however a basic issue in the above scheme which motivates the development of the complementary micro-macro approach.

Indeed, derivation of a constitutive equation from a model of kinetic theory usually involves closure approximations of a purely mathematical nature, such as decoupling or pre-averaging. It is now widely accepted that closure approximations can have a significant impact. Thus, micro-macro methods of computational rheology that couple the coarse-grained molecular scale of kinetic theory to the macroscopic scale of continuum mechanics have an important role to play. In a micro-macro simulation, the conservation equations are solved together with a model of kinetic theory. This approach is much more demanding in computer resources than more conventional continuum simulations that integrate a constitutive equation to evaluate the viscoelastic contribution to the stress tensor. On the other hand, micro-macro techniques allow the direct use of kinetic theory models and thus avoid potentially harmful closure approximations. Micro-macro methods have been reviewed recently in [7].

In the present lecture, I survey the field of multiscale simulation of viscoelastic flow using molecular models, and present recent results based on tube theory of linear entangled polymers [8-11]. The talk will be of a general nature so that it is (hopefully) both understandable and useful for colleagues and students working on other topics in theoretical and applied mechanics.

References

1. R.G. Larson, The Structure and Rheology of Complex Fluids, Oxford University Press (1999)
2. R.B. Bird R, C.F. Curtiss, R.C. Armstrong, and O. Hassager, Dynamics of Polymeric Fluids. Vol. 2 Kinetic Theory, 2nd Edition, John Wiley, New York (1987)
3. M. Doi and S.F. Edwards, The Theory of Polymer Dynamics, Oxford University Press (1986)
4. T.C.B. McLeish, Tube Theory of Entangled Polymer Dynamics, Adv. Phys., 51 (2002) 1379-1527.
5. R.G. Owens and T.N. Phillips, Computational Rheology, Imperial College Press, London (2002).
6. R. Keunings, Finite Element Methods For Integral Viscoelastic Fluids, in Rheology Reviews 2003, D.M. Binding and K. Walters (Eds.), British Society of Rheology, 167-195 (2003)
7. R. Keunings, Micro-Macro Methods for the Multiscale Simulation of Viscoelastic Flow using Molecular Models of Kinetic Theory, to appear in Rheology Reviews 2004, D.M. Binding and K. Walters (Eds.), British Society of Rheology, 67-98 (2004)
8. E. van Ruymbeke, R. Keunings, C. Bailly, Determination of the Molecular Weight Distribution of Entangled Linear Polymers from Linear Viscoelasticity Data, J. Non-Newtonian Fluid Mech., Vol. 105, 153-175 (2002)
9. E. van Ruymbeke, R. Keunings, V. Stephenne, A. Hagenaars, and C. Bailly, Evaluation of Reptation Models for Predicting the Linear Viscoelastic Properties of Entangled Linear Polymers, Macromolecules, Vol. 35, 2689-2699 (2002)
10. P. Wapperom and R. Keunings, Impact of Decoupling Approximation Between Stretch and Orientation in Rheometrical and Complex Flow of Entangled Polymers, accepted for publication in J. Non-Newtonian Fluid Mech. (2003), in press
11. P. Wapperom, R. Keunings, and G. Ianniruberto, Prediction of Rheometrical and Complex Flows of Entangled Linear Polymers Using the DCR Model with Chain Stretch, J. Rheology, Vol. 47, 247-265 (2003)

NONLINEAR DYNAMICS IN OCEAN ENGINEERING

Edwin J. Kreuzer
Technical University Hamburg-Harburg, Mechanics and Ocean Engineering, Eissendorfer Strasse 42, D-21073 Hamburg, Germany

The international trade rests to a very large extent on maritime traffic and further growth is predicted. This growth will result in a rapid increase of ship size and the number of ships. The utilization of the oceans will be similar in the long-term. It is expected that the growth in maritime traffic and of offshore installations will cause increasing pollution as well as growing risks for humans and goods at sea. Economical and environmental risks are important, of course, but much more important is the danger to human life. From statistical data we learn that at least one third of total ship losses are due to severe weather conditions. Moreover, serious accidents of oil platforms in recent years have lead to losses of human lives and caused large environmental pollution. We observe, therefore, a growing interest in the improvement of safety measures and criteria in order to keep the risks as small as possible. In the following we will concentrate on floating structures in naval architecture and ocean engineering.

The current regulations and criteria for assuring the stability of a ship and preventing from capsizing (the so-called *prescriptive rules*, see the codes of the International Maritime Organization (IMO) [1]) are empirical and based on the properties of the righting lever of the ship, taking only hydrostatic restoring forces into account. Model tests show, however, that the current stability criteria do not always correlate with the danger of capsizing. The static criteria which neglect the motion of the ship (or only consider the motion in an implicit or very approximate manner) as well as the impact of seaway and wind do obviously not guarantee total stability. Hence, researchers agree that those criteria have to be modified. The IMO is working, therefore, on *performance based rules* which apply to a specific ship.

In order to analyze capsizing due to waves hydrodynamic models of the ship-sea system are necessary, by describing the sea as a (random) field and by analyzing the ship as a rigid body with six degrees of freedom using methods of nonlinear dynamics. Model tests can provide insight into the nature of capsizing, too, but they are quite expensive and do not allow for highly sophisticated analysis, unlike mathematical models.

In the past several computer models have been developed. Because of the complexity of the capsizing problem, they were used to evaluate statistical properties. The probability of the capsizing was estimated and heuristic arguments were used to interpret this probability and to derive stability criteria. More advanced analysis techniques were recently applied to simple single-degree-of-freedom and regular wave excitation models and with few exceptions to more complicated computer models. These techniques are based on nonlinear dynamics theory. Using them, it is possible to locate stability boundaries. The state of the art of (deterministic as well as stochastic) ship models has been recently very well documented in the Theme Issue of the Philosophical Transactions of The Royal Society London (series A) entitled “The nonlinear dynamics of ships”, edited by Spyrou and Thompson [2].

Floating offshore structures are usually held in position by means of mooring systems, which have, depending on the purpose of the structure and the water depth, different levels of complexity. Mooring lines might consist of a combination of chains and cables like spiral strands. Submerged buoyancy tanks might also be used along the mooring lines.

For a realistic motion analysis of floating offshore structures it is inevitable to take all these different properties into account. It is presently common practice to use rather simple models based on a quasi-static approximation for the mooring systems to describe the interaction between the motion of structures and the restoring forces. These simplified models disregard the dynamics of the mooring line including the interaction between the fluid and the line. They also do not consider that the position of a line, which is in contact with the sea bed, varies with respect to time. For lines in deep water, these effects may cause a tremendous increase in the tension force, which cannot be predicted by simplified models.

Under operational conditions an offshore structure and its compliant mooring system is subjected to a variety of environmental nonlinear forces, e.g. current, waves second-order drift forces. Therefore, it is mandatory to determine the dynamics by means of precise mathematical models.

This sectional lecture is intended to discuss some of the latest ideas of nonlinear dynamics of floating marine structures under wave excitation. We start with the discussion of the ship stability assessment based on conventional and modern approaches. In order to determine whether or not a marine vehicle will be capable of maintaining a stable stationary and upright position, it is necessary to examine all forces which act on the vehicle. Therefore, the modeling of freely floating bodies will be presented in detail. Moreover, the modeling of moored systems by means of a multibody systems approach is described such that the prediction of the complicated dynamics is visible. In order to explain the analysis procedure, three important examples from marine technology are considered, the dynamics of ships, a moored platform, and of crane vessels. The nonlinear dynamic responses to waves are investigated theoretically and experimentally. The main subject of interest is the appearance of nonlinear phenomena like bifurcations and the existence of multiple attractors.

References

[1] International Maritime Organization. Code on intact stability for all types of ships covered by IMO instruments. Resolution A.749(18). London: IMO, 1995.

[2] Spyrou, K.J.; Thompson, J.M.T.: The nonlinear dynamics of ship motions: a field overview and some recent developments. Phil. Trans. R. Soc. Lond., Series A (Theme Issue). The Royal Society, 2000.

A BRIDGE BETWEEN THE MICRO- AND MESOMECHANICS OF LAMINATES: FANTASY OR REALITY?

Pierre Ladevèze
LMT-Cachan, ENS Cachan/CNRS/Université Paris 6, 94235 Cachan Cédex, France

Summary The main questions discussed here are how to bridge the micro- and mesomechanics of laminates and how this affects the understanding and prediction of localization and final fracture.

MOTIVATIONS: THE SCIENTIFIC AND INDUSTRIAL CHALLENGES

The last quarter-century has witnessed considerable research efforts in the mechanics of composites in order to understand their behavior and to model or calculate them – the ultimate goal being the design of the materials/structures/manufacturing processes. Even in the case of stratified composites (which are the most studied and, therefore, the best understood), the prediction of damage evolution up to and including final fracture remains a major challenge in the modern mechanics of composite materials and structures. Today, the use of stratified composites in the aerospace industry always involves characterization procedures consisting of huge numbers of tests, which shows the low level of confidence in models. A significant improvement in this situation, i.e. a drastic reduction in the number of industrial tests, could be achieved if one could create a real synergy among the approaches on different scales which, today, are followed quite independently of one another in the case of stratified composites. One could jokingly say that there is, on the one hand, the micromechanics of laminates where one counts cracks and, on the other, the meso- or macromechanics of laminates where one measures stiffnesses – with only few links between the two. How to bridge the micro- and mesomechanics aspects and how this affects the understanding and prediction of localization and final fracture are the two main questions discussed here.

THE DAMAGE MICROMECHANICS OF LAMINATES

Up to now, there have been numerous theoretical and experimental works on the micromechanics of laminates [see (1) – (4)]; the micromechanics approach provides a relatively good understanding of damage mechanisms, such as matrix microcracking. However, these micromechanics models are lacking in some respects: in particular, they are far from being complete for the prediction of localization and final fracture.

THE DAMAGE MESOMECHANICS OF LAMINATES

Alternative, pragmatic computational approaches have also been developed. In our lab, we focus on what we call a « damage mesomodel for laminates » [see (5) – (6)]. In this approach, one assumes that the behavior of any laminated composite for any loading and any stacking sequence can be modeled using two elementary constituents which are continuous media: the ply and the interface. Another important point is that the state of damage is assumed to remain constant throughout the thickness of the single layer (of course, it can vary from one layer of the laminate to the next.)

TOWARD A BRIDGE BETWEEN MICRO- AND MESOMECHANICS

The central question we aim to discuss here is: how can one bridge the micro- and mesomechanics of damage? The belief that such a complete bridge could exist is not shared by all the people working in micromechanics. A first attempt at building such a bridge was made in (7) (8) for plane macrostresses. The mesomodel was found to be fully compatible with the microdamage mechanisms. The micro-meso relations introduce quantities or relations which we call “approximately ply-material”, which are intrinsically related to the cracked ply’s characteristics and, therefore, independent of the characteristics of the other plies. Recently, additional work has extended this approach to out-of-plane stresses (9). This more complex situation involves non-local mesomodels, as there are interactions between the interface’s damage and the microcracking mechanisms of the adjacent plies. The method of investigation is now entering what is called a “virtual testing” stage, in which numerous numerical experiments using the micromodel and involving various possible stacking sequences, thicknesses,… are performed. One can show that the micromechanisms within the plies and interfaces can be homogenized; relations between the micro- and mesoquantities can be obtained through the resolution of several basic problems.

THE MULTISCALE APPROACH AND SOME APPLICATIONS

The second question being discussed here is the impact of such a bridge on the micro- and mesomodels themselves, the objective being to calculate the intensities of the damage mechanisms at any point of a laminated structure subjected to complex loading and at any time until final fracture resulting from strain and damage localization. These improved models require a multiscale approach. A first example is an improved damage mesomodel for laminates allowing the

calculation of the intensities of the damage micromechanisms. A second example is a "computational damage micromodel" which is rather simple, yet semi-discrete and probabilistic; unfortunately, this model leads to prohibitive calculation costs if one uses current industrial codes. The use of a multiscale computational strategy is absolutely essential. Several examples are worked out in order to show the capabilities and the limitations of the different models.

References

[1] Laws N., Dvorak G.J.:Progressive Transverse Cracking In Composite Laminates *J. Comp. Mat.* **22**, 900-916, 1988.
[2] Hashin Z.: Analysis Of Cracked Laminates : A Variational Approach Mech. Mat., **4**, 121-126, 1985.
[3] Nairn J., Hu S.H.: Matrix Microcracking Damage Mechanics of Composites Materials, Taljera R. (Ed), Elsevier, 187-243, 1994.
[4] Berthelot J.M.: Transverse Cracking And Delamination In Cross-Ply Glass Fiber And Carbon-Fiber Reinforced Plastic Laminates : Static And Fatigue Loading Appl. Mech. Rev., **56**, **1**, 1-37, 2003.
[5] Ladeveze P.: On Damage Mechanics Of Composites", C.Bathias And D. Menkès, Comptes-Rendus Des Jnc5, Pluralis 667-683 (In French) 1986.
[6] Ladeveze P., Allix O., Deü J.F., Leveque D.: A Mesomodel For Localization And Damage Computation In Laminates Comput. Methods Appl. Mech. Engrg. **183**, 105-122, 2000.
[7] Ladeveze P., Lubineau G.: On A Damage Mesomodel For Laminates : Micro-Meso Relations, Possibilities And Limits, Comp. Sci. Tech., **61**, 2149-2158, 2000.
[8] Ladeveze P., Lubineau G.: An Enhanced Mesomodel For Laminates Based On Micromechanics Comp. Sci. Tech., **62**, 533-541, 2002.
[9] Ladeveze P., Lubineau G., Marsal D.: Toward A Bridge Between Micro And Mesomechanics Of Delamination Comp. Sci. Tech., (To Appear) 2004

TURBULENCE AND LARGE-EDDY SIMULATIONS

Marcel R. Lesieur
Geophysical and Industrial Flows Lab. (LEGI), BP 53, 38041 Grenoble-Cedex 9. France

Summary After having discussed the limits of turbulence direct-numerical simulations, one presents large-eddy simulations methods, where small scales are filtered out and modelled by appropriate eddy coefficients in the evolution of large scales. We concentrate on models developed originally in Fourier space. One presents coherent-vortex dynamics obtained thanks to these models for incompressible isotropic turbulence and channel flow at low Mach. Then the controlled compressible jet (Reynolds 36000) is studied at Mach 0.7 and 1.4.

THE NEED FOR LES

Direct-numerical simulations (DNS) of turbulence are based on deterministic solutions of Navier-Stokes equation, obtained through a proper discretization on a spatio-temporal grid of partial-differential operators. This implies that the typical grid mesh Δx in space should be inferior to the Kolmogorov scale l_D, under which velocity fluctuations are damped by molecular viscosity. One can thus show that the number of spatial grid points necessary for a well-resolved DNS is $\sim R_\lambda^{9/2}$, where $R_\lambda = u'\lambda/\nu$ is defined thanks to the rms longitudinal velocity and the Taylor microscale. R_λ may be determined experimentally, for instance on a commercial-plane wing where it is equal to 3000 (Jimenez [1]). This yields $\approx 10^{15}$ grid points to handle on the computer, which permits to envisage a DNS of such a flow within 30 to 50 years. For the atmospheric boundary layer it is worst, since we have $R_\lambda = 10000$, and hence 10^{18} grid points. To be able to perform a simulation in such cases, one is thus obliged to reduce drastically the number of degrees of freedom of the system. Large-eddy simulations (LES) are a powerful tool for this purpose. More details concerning the rest of this talk may be found in Lesieur [2] and Lesieur & Métais [3].

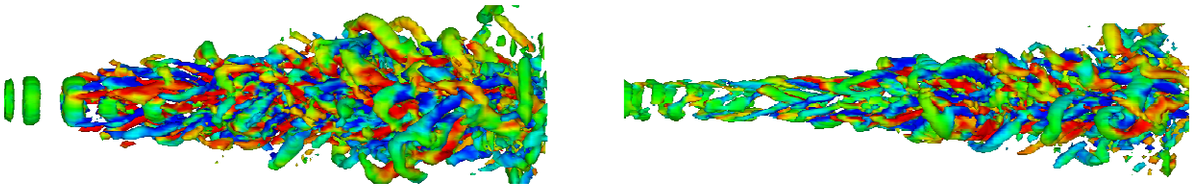
INCOMPRESSIBLE LES

Physical space

Density ρ is uniform. Let Δx be a given spatial grid mesh, and $G_{\Delta x}$ a low-pass filter of width Δx, chosen in order to eliminate subgridscale motions of wavelength $< \Delta x$. One defines for any quantity $\bar{f}(\vec{x},t) = f * G_{\Delta x}$, where $*$ stands for a convolution product. The filter commutes with spatial and temporal derivatives (if Δx is uniform). When it is applied to Navier-Stokes equation, one obtains the same equation for the filtered velocity $\bar{u}_i$, provided a subgridstress tensor $T_{ij} = \bar{u}_i\bar{u}_j - \overline{u_i u_j}$ is added to the filtered viscous stress $2\nu\bar{S}_{ij}$. Here S_{ij} is the deformation tensor, symmetric part of the velocity gradient. An eddy-viscosity assumption $T_{ij} = 2\nu_t(\vec{x},t)\bar{S}_{ij} + (1/3)T_{ll}\delta_{ij}$ allows to form for $\bar{u}_i$ a Navier-Stokes equation where pressure has been replaced by a macro-pressure $\bar{P} = \bar{p} - (1/3)\rho T_{ll}$. The same procedure applied to a scalar $T(\vec{x},t)$ transported by the flow (with a molecular diffusivity κ) yields for $\bar{T}$ a similar equation, with an extra eddy diffusivity κ_t, given from ν_t thanks to a turbulent "Prandtl number" $P_r^{(t)} = \nu_t/\kappa_t$. These eddy coefficients need to be determined. In Smagorinsky's model, the eddy viscosity is based on velocity gradients and taken proportional to to $(\Delta x)^2\sqrt{\bar{S}_{ij}\bar{S}_{ij}}$. There are interesting improvements of this model made by Germano et al. [4] where the constant is calculated dynamically by a double filtering. In fact, the major drawback of an eddy-viscosity assumption in physical space is that it assumes a scale-separation between filtered and subgridscales. This explains the poor correlation between T_{ij} and $\bar{S}_{ij}$ found in a-priori tests based on DNS. This is a serious motivation to work in Fourier space if the geometry of the problem permits it.

Fourier space

Turbulence is first assumed statistically homogeneous. Let $\hat{f}(\vec{k},t)$ be the spatial Fourier transform of any quantity $f(\vec{x},t)$. The filter is a sharp filter, such that $\overline{\hat{f}} = \hat{f}$ for $k = |\vec{k}| < k_C = \pi/\Delta x$; $\overline{\hat{f}} = 0$ for $k > k_C$. If turbulence is statistically isotropic, one can define the kinetic-energy spectrum $E(k,t)$, mean kinetic energy per unit mass at the wavenumber k. In Fourier space, nonlinear interactions go through "resonant" triads of wavevectors such that $\vec{k} = \vec{p} + \vec{q}$. The subgrid modelling consists here in evaluting the momentum transfers due to triads where $k < k_C$ and one at least of wavenumbers p and q is larger than k_C. Since the Fourier transform of Navier-Stokes dissipative term is $-\nu k^2\hat{u}_i(\vec{k},t)$, the subgrid momentum transfer will be modelled as $-\nu_t(k|k_C)k^2\hat{u}_i(\vec{k},t)$, the eddy viscosity in spectral space being calculated at the level of subgrid kinetic-energy transfers through an advanced theory of turbulence, the EDQNM. One gets $\nu_t(k|k_C) = 0.44\, {C_K}^{-3/2}\,[E(k_C)/k_C]^{1/2}\; X\,(k/k_C)$, assuming that k_C lies in a Kolmogorov spectrum $E(k) =$



$C_K\epsilon^{2/3}k^{-5/3}$. Here, $X(k/k_C)$ is a "plateau-peak function" equal to 1 for $k/k_C <\approx 1/3$, and rising above. In the spectral-dynamic model, one accounts for a spectral slope at k_C different from 5/3. We give two applications of this model : for isotropic turbulence at infinite Reynolds number, one presents an animation showing the formation and evolution of the spaghetti-type vortices, seen thanks to the vorticity and the second invariant of the velocity gradient $Q = (1/2)(\Omega_{ij}\Omega_{ij} - S_{ij}S_{ij})$. The spectral-dynamic model has also been applied to a channel at $h^+ = hv_*/\nu = 204$ and 395. It yields very good statistical results compared with Kim's DNS. At $h^+ = 395$, the LES is 70 times faster than the DNS.

Return to physical space : structure-function models

For complicated geometries, numerical methods impose to work in physical space. The spectral eddy viscosity is thus set to a constant calculated assuming the subgrid kinetic-energy dissipation equals ϵ in a Kolmogorov cascade. We have $\nu_t(\vec{x}, \Delta x) = (2/3)C_K^{-3/2}\left[E_{\vec{x}}(k_C)/k_C)\right]^{1/2}$, where $E_{\vec{x}}(k_C)$ is a local kinetic-energy spectrum, determined with the aid of the local second-order velocity structure function. This model improves classical Smagorinsky model for non-sheared turbulence. For sheared turbulence (without or with walls), two excellent versions of the model exist to eliminate the damping effects of large-scale shears : the selective structure-function model, and the filtered structure-function model. They work very well for free-shear flows and boundary layers (in the incompressible and compressible cases), and can be utilized on unstructured grids.

COMPRESSIBLE LES

We work with an ideal gas. The LES formalism is much more complicated in the compressible case. One can simplify it a lot by using Favre filtering $\tilde{f}$, and introducing a "macro-temperature" $\vartheta = \widetilde{T} - \mathcal{T}_{ll}/(2C_v\overline{\rho})$, where $\mathcal{T}_{ll}$ is the trace of the subgridscale tensor $\mathcal{T}_{ij} = \overline{\rho}\tilde{u}_i\tilde{u}_j - \overline{\rho u_i u_j}$. The latter is related to the macro-pressure ϖ by the relation $\varpi = \overline{\rho}R\vartheta + (1/6)(3\gamma - 5)\mathcal{T}_{ll}$. In this relation, the last term is small even at high Mach, so that we neglect it and use the law of ideal gases between $\varpi, \overline{\rho}$ and ϑ. After some other approximations, one obtains a system equivalent to compressible Navier-Stokes equation for $\widetilde{u_i}, \bar{\rho}, \varpi, \vartheta, \widetilde{e}$, most of the molecular-diffusion coefficients being complemented by an eddy counterpart which is the same as in the incompressible case. We work with the filtered structure-function model. We first show an animation of quasi-longitudinal vortices travelling in a channel at low Mach. Then one studies a compressible round jet at Mach 0.7 and 1.4 forced upstream by a close to top-hat velocity to which a random perturbation is superposed. The Reynolds number is 36000. We show on the above figure a picture of the jet (left, Mach 0.7 ; right Mach 1.4) in the case of a white-noise forcing : the supersonic jet is much more focussed in space than the subsonic one, with an increase of the potential core. With other types of forcings, one can generate Reynolds blooming jet.

References

[1] Jimenez J. : Turbulence, in *Perspectives in Fluid Mechanics*, G.K. Batchelor, H.K. Moffatt and M.G. Woster eds, Cambridge University Press, 283-231, 2000.
[2] Lesieur M. : Turbulence in Fluids, 3rd edition, Kluwer, 1997.
[3] Lesieur M. and Métais O. : New trends in large-eddy simulations of turbulence. *Ann. Rev. Fluid Mech.* **28**, 82-45, 1996.
[4] Germano M., Piomelli U., Moin P. and Cabot W. : A dynamic subgrid-scale eddy-viscosity model. *Phys. Fluids A.* **3**, 1765-1760, 1991.

PROBABILITY PHENOMENA IN PERTURBED DYNAMICAL SYSTEMS

Anatoly Neishtadt
Space Research Institute Russian Academy of Sciences, Profsoyuznaya 84/32, Moscow 117997, Russia

Summary We discuss probability phenomena associated with passages through separatices and passages through resonances in perturbed dynamical systems. The theory which describes these phenomena has applications in different problems including problems of capture of satellites into resonances, of acceleration of charged particles, of chaotic advection of impurities.

INTRODUCTION

If in a deterministic dynamical system a small variation of initial data produces a large variation of dynamics, then the behavior of this system can be treated as a random one. This non-rigorous assertion known as a principle "small causes and big effects" is in the basis of the theory of deterministic chaos. Remarkably, such quasi-random behavior exists also in systems that differ by an arbitrarily small perturbations from systems with very simple (periodic, quasi-periodic) dynamics. Different types of the perturbed dynamics have certain probabilities. Analysis of long-term dynamics leads to random walk problems. In the talk we discuss probability phenomena associated with passages through separatices and passages through resonances in perturbed dynamical systems.

PASSAGES THROUGH SEPARATRICES

The problems with passages through separatrices are similar to those of motion of a material point in one dimension in a double-well potential in presence of a small, of order ε, friction (example by V.I.Arnold, 1963). The problem without friction is the unperturbed one. Consider motion of points whose initial energy is higher than energy of the potential hump separating the wells. Under the action of the friction almost everyone of these points after some time (typically, of order $1/\varepsilon$) will be trapped into one of the wells. But the initial data for trapping into different wells are mixed. Small, of order ε, change of initial conditions, can change the result of evolution. So, in the limit as $\varepsilon \to 0$ the deterministic approach to the problem fails. However, it is possible to treat trapping into one or another well as random events and calculate probabilities of these events. Probabilistic approach to problems of such kind was suggested by I.M.Lifshitz, A.A.Slutzkin, V.M.Nabutovskii (1961).

Quite general situation in which similar phenomena arise can be described as follows. The unperturbed system is 1 DOF Hamiltonian system depending on parameters. The phase portrait of this system is divided into several regions ("cells") by separatrices. Small, of order ε, perturbation (small non-conservative forces, slow change of parameters) is imposed on this system. This perturbation produces an evolution. In the course of this evolution a phase point of the perturbed system crosses the separatrix of unperturbed system and passes from one cell into another. The dynamics of perturbed system can be approximately described by a version of the averaging method that takes into account that the trapping into different cells occurs with certain probabilities. In the talk the estimates of accuracy of such averaging method are presented.

The case when the perturbation is just a slow variation of parameters in time or, more generally, the perturbed system is slow-fast Hamiltonian system, is of special interest. In this case the "action" variable of the unperturbed system is the first integral of the averaged system and, therefore, approximate first integral of the perturbed system (i.e. adiabatic invariant) for motion far from separatrices. We discuss asymptotic formulas for jump of adiabatic invariant at separatrix crossings (A.V.Timofeev, 1978, J.Cary, D.Escande, J.Tennison, 1986, A.I.Neishtadt, 1986, 1987). This jump should be treated as a random value. Accumulation of results of these jumps after many passages through separatrices leads to destruction of adiabatic invariance. This phenomenon play important role, in particular, in dynamics of asteroids near the resonance (J.Wisdom, 1985), and of charged particles in the Earth magnetotail (J.Buchner, L. Zelenyi, 1989).

Similar phenomena of jumps of adiabatic invariants at separatrix and destruction of adiabatic invariance take place in volume-preserving systems (K.Bajer, H.K.Moffatt, 1990, D.L.Vainshtein, A.A.Vasiliev, A.I.Neishtadt, 1996).

PASSAGES THROUGH RESONANCES

Consider a system which differs from an integrable multi-frequency system by a small, of order , perturbation. Motion in such a system can be approximately represented as slowly evolving unperturbed one. For description of this evolution the classical averaging method prescribes to average differential equations of a perturbed motion over the phases of unperturbed oscillations. In the course of the evolution the frequencies of motion are changing slowly

and at some time moments they become resonant, i.e. linearly rationally dependent. Due to the influence of resonances the actual motion can be considerably different from the one predicted by the averaging method. The two basic phenomena that are associated with the effect of a single resonance are capture into the resonance and scattering on the resonance.

Capture into a resonance can be described as follows. First the system evolves as it is predicted by the averaging method. At a certain time moment the system approaches a resonance. After that the system evolves in such a way that the resonant relation between frequencies is being kept approximately. As a result, after a time $1/\varepsilon$ the state of the system is completely different from the one predicted by the averaging method. Initial conditions for trajectories with a capture and trajectories without captures are mixed, if ε is small. Thus, it is reasonable to consider the capture as a random event and to calculate a probability of this event. Capture into a resonance was first discussed by P.Goldreich, S.Peale (1966), A.M.Moltchanov (1968) in connection with problems of celestial mechanics.

Scattering on resonances is observed for trajectories which pass through resonaces without being captured. Scattering is a deviation of such trajectory from that predicted by the averaging method. During a passage through a narrow neighborhood of the resonance, position of the system's phase point with respect to the trajectory of the averaged system undergoes a jump small. The amplitude of this jump is very sensitive to the variation of initial conditions, if ε is small. Thus, it is reasonable to consider this jump as random scattering on the resonance. Scattering on a resonance was first discussed by B.V.Chirikov (1959) and V.I.Arnold (1965).

In the talk we discuss calculation of probability of a capture into a resonance, description of motion in a state of a capture into resonance and calculation of a statistical distribution of the amplitude of a scattering on a resonance.

Again, the case when the perturbation is just a slow variation of parameters of the system in time or, more generally, the perturbed system is a slow-fast Hamiltonian system, is of special interest. For this case captures into resonances and scatterings on resonances lead to destruction of adiabatic invariance of "action" variables of unperturbed system. Similar phenomena take place in volume-preserving systems.

XXI ICTAM, 15–21 August 2004, Warsaw, Poland

MECHANICS OF RUBBERLIKE SOLIDS

Ray W. Ogden
Department of Mathematics, University of Glasgow, Glasgow G12 8QW, UK

Summary In this lecture we discuss (i) the large deformation stress-strain response of rubberlike solids based on experimental observations, (ii) the mathematical modelling of this behaviour through its phenomenological treatment using elasticity theory and extensions of the theory to account for inelastic responses such as the Mullins effect and hysteretic stress-strain cycling, (iii) an introduction to the analysis of magnetoelastic effects in magneto-sensitive elastomers.

EXTENDED SUMMARY

Description of experimental results

The lecture begins with an overview of the large deformation stress-strain response of rubberlike solids based on experimental observations, in particular of vulcanized natural rubber. First, experimental results that characterize the elastic behaviour of rubber are described. This is followed by illustrations of how the behaviour departs from the purely elastic. When subjected to cyclic loading many elastomers (and also biological soft tissues) exhibit a *stress softening* phenomenon widely known as the *Mullins effect* (Mullins [1]). The Mullins effect is associated mainly with a significant reduction in the stress at a given level of strain on unloading as compared with the stress on initial loading on the first and successive cycles in stress-strain cyclic tests of fixed amplitude. An example of this behaviour is shown in Figure 1.

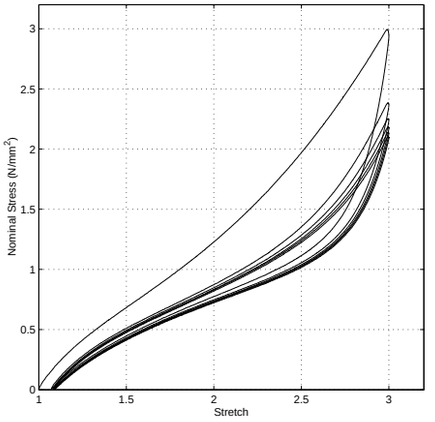


Figure 1. The Mullins effect (first loading-unloading cycle) and subsequent stress-stretch cycles for simple tension of a particle-reinforced specimen of rubber filled with 20 phr of carbon black up to a maximum stretch $\lambda = 3$ (after Dorfmann and Ogden [2]).

This is just one of the various inelastic effects that are evident in materials such as rubbers hardened by the inclusion of fillers. Other inelastic effects include frequency-dependent response and hysteresis. The Mullins effect is closely related to the fatigue of elastomeric parts used in engineering applications. A detailed qualitative and quantitative understanding of the Mullins effect is thus a necessary step towards the scientific evaluation of the *life* of a rubber product.

In this talk we examine stress softening associated with the Mullins effect, and the different degrees of stress softening for different rubbers are highlighted. Other inelastic effects such as hysteretic stress-strain cycling following pre-conditioning of the material (to remove the Mullins effect) are also described.

Theoretical approaches

Many phenomenological theories aimed at modelling the Mullins effect have been proposed in the literature. Some of these are based on the two-phase micro-structural model introduced by Mullins and Tobin [3] and developed more recently by, for example, Johnson and Beatty [4]. Another class of models is based on the introduction of a damage (or stress-softening) variable to describe the internal damage in the bulk material associated with the Mullins effect (see, for example, Gurtin and Francis [5], De Souza Neto et al. [6], Beatty and Krishnaswamy [7] and Zúñiga and Beatty [8] and references cited therein). Ogden and Roxburgh [9, 10] have developed a model based on a theory of *pseudo-elasticity* in which a pseudo-energy function is introduced as in standard nonlinear elasticity theory except that an additional scalar variable (the damage variable) is incorporated. Many of these models share the common feature that the virgin material response is determined by a standard strain-energy function or a stress constitutive function for a perfectly elastic isotropic material. The latter theory is examined in detail to illustrate how the theory can reproduce the main qualitative features of the phenomena in question. A connection between this theory and that of materials with multiple natural configurations due to Rajagopal and Wineman [11] is also noted.

A model of the Mullins effect based on micro-mechanical continuum damage theory was proposed by Govindjee and Simo [12]. The constitutive equation for this model involves the integration of the inverse Langevin function over a history-dependent domain in the phase space of the rubber network. Recently Marckmann et al. [13] have proposed another model using the inverse Langevin function in the description of network alteration associated with the Mullins effect. The non-Gaussian statistics allow one to take into account the limiting stretch of the chains composing the polymeric network. In the Marckmann et al. [13] model the Mullins effect is explained by reference to an alteration of the average chain length driven by the previous maximum stretch in a given deformation. The network alteration idea has been investigated recently by Horgan et al. [14] on the basis of the phenomenological model proposed by Gent [15] for rubberlike elasticity. This is a very simple strain-energy function that accounts for the limiting chain extensibility of rubberlike polymers (for further discussion of the model we refer to Horgan and Saccomandi [16, 17, 18]). The use of the Gent model allows one to bypass the computational problems associated with the inverse Langevin function and to provide a simpler and deeper interpretation of the network alteration phenomenon.

An important feature of the effect of stress softening and any associated residual strains is the change in material symmetry generated. This has received very little attention in the literature thus far, but here we examine some aspects of this briefly following the recent discussion in Horgan et al. [14]. An extensive review of different experimental and theoretical aspects of rubber mechanics and thermomechanics, from the molecular to the phenomenological level, is provided in the volume edited by Saccomandi and Ogden [19], which contains many pointers to the literature.

Magneto-sensitive elastomers

The final part of the talk is motivated by recent renewed interest in the subject of electromagnetic continua generated by the development of so-called 'smart' materials used, for example, in devices for controlling the damping characteristics of vibration absorbers. In particular, we are concerned here with elastomers containing a distribution of ferrous particles embedded within their bulk so that they respond to the application of magnetic fields by changing significantly their stress-strain behaviour. We outline recent theoretical work concerning the coupling of mechanical and magnetic effects in these so-called *magneto-sensitive (MS) elastomers*. Some analysis is contained in the papers by Dorfmann and Ogden [20, 21], but in this talk we touch on a refined version of the theory that enables boundary-value problems to be formulated in a very simple and elegant way [22]. References to the (limited) literature are given in these papers. The theory is applied to some simple prototype boundary-value problems of practical interest, notably the axial or azimuthal shear and the combined extension and torsion of MS material contained within a circular cylindrical tube in the presence of either an axial magnetic field (uniform) or an azimuthal field, the latter generated by an axial steady current within the core of the tube. The influence of the magnetic field strength on the various shear stiffnesses of the material is evaluated.

References

[1] Mullins L.: Effect of stretching on the properties of rubber. *J. Rubber Res.* **16**:275–289, 1947.

[2] Dorfmann A., Ogden R.W.: A constitutive model for the Mullins effect with permanent set in particle-filled rubber. *Int. J. Solids Structures* **41**:1855–1878, 2004.

[3] Mullins L., Tobin N.R.: Theoretical model for the elastic behavior of filler-reinforced vulcanized rubbers. *Rubber Chem. Technol.* **30**:555–571, 1957.

[4] M. A. Johnson M.A., Beatty M.F.: A constitutive equation for the Mullins effect in stress controlled uniaxial extension experiments. *Continuum Mech. Thermodyn.* **5**:301–318, 1993.

[5] Gurtin M.E., Francis E.C.: Simple rate-independent model for damage. *J. Spacecraft Rockets* **18**:285–286, 1981.

[6] De Souza Neto E.A., Perić D., Owen D.R.: A phenomenological three-dimensional rate independent continuum model for highly filled polymers: formulation and computational aspects. *J. Mech. Phys. Solids* **42**:1553–1550, 1994.

[7] Beatty M.F., Krishnaswamy S.: A theory of stress-softening in incompressible isotropic materials. *J. Mech. Phys. Solids* **48**:1931–1965, 2000.

[8] Zúñiga A.E., Beatty M.F.: A new phenomenological model for stress-softening in elastomers. *Z. angew. Math. Phys.* **53**:794–814, 2002.

[9] Ogden R.W., Roxburgh D.G.: A pseudo-elastic model for the Mullins effect in filled rubber. *Proc. R. Soc. Lond. A* **455**:2861–2877, 1999.

[10] Ogden R.W., Roxburgh D.G.: An energy-based model of the Mullins effect, in A. Dorfmann and A. Muhr (eds), *Proceedings of the First European Conference on Constitutive Models for Rubber*, pp. 23–28, Balkema, Rotterdam 1999.

[11] Rajagopal K.R., Wineman A.S.: A constitutive equation for nonlinear solids which undergo deformation induced microstructural changes. *Int. J. Plasticity* **8**:385–395, 1992.

[12] Govindjee S., Simo J.C.: A micro-mechanically based continuum damage model for carbon black-filled rubbers incorporating the Mullins' effect. *J. Mech. Phys. Solids* **39**:87–112, 1991.

[13] Marckmann G., Verron E., Gornet L., Chagnon G., Charrier P., Fort P.: A theory of network alteration for the Mullins effect. *J. Mech. Phys. Solids* **50**:2011–2028, 2002.

[14] Horgan C.O., Ogden R.W., Saccomandi G.: A theory of stress softening of elastomers based on finite chain extensibility. *Proc. R. Soc. Lond. A*, in press, 2004.

[15] Gent A.N.: A new constitutive relation for rubber. *Rubber Chem. Technol.* **69**:59–61, 1996.

[16] Horgan C.O., Saccomandi G.: Constitutive modelling of rubber-like and biological materials with limiting chain extensibility. *Math. Mech. Solids* **7**:353–371, 2002.

[17] Horgan C.O., Saccomandi G.: Finite thermoelasticity with limiting chain extensibility. *J. Mech. Phys. Solids* **51**:1127–1146, 2003.

[18] Horgan C.O., Saccomandi G.: A molecular-statistical basis for the Gent constitutive model of rubber elasticity. *J. Elasticity* **68**:167–176, 2002.

[19] Saccomandi G., Ogden R.W.: Mechanics and Thermomechanics of Rubberlike Solids. CISM Courses and Lectures Series 452, Springer, Wien 2004.

[20] Dorfmann A., Ogden R.W.: Magnetoelastic modelling of elastomers. *European J. Mech A/Solids* **22**:497–507, 2003.

[21] Dorfmann A., Ogden R.W.: Nonlinear magnetoelastic deformations of elastomers. *Acta Mechanica* **167**:13–28, 2004.

Some issues in active vibration control of smart structures

André Preumont

ULB Active Structures Laboratory
Brussels, Belgium
(andre.preumont@ulb.ac.be)

Abstract

The paper is divided into three parts.
The first one is devoted to the active damping of structures with collocated actuator/sensor pairs; the paper first discusses the benefit of the collocated architecture and its consequence on stability and robustness with respect to structural changes. The particular case of a piezoelectric actuator collocated with a force sensor is considered; the attractive properties of the (decentralized) Integral Force Feedback (IFF) are emphasized and simple criteria to assist in performance prediction are presented; the method is illustrated with various examples belonging to space, precision engineering and civil engineering projects; it is shown that the same control strategy can be applied to solve problems with vastly different amplitudes and can be implemented with drastically different technologies, namely piezoelectric actuators for space structures and precision engineering, and hydraulics for civil engineering applications.

The second part is concerned with vibration isolation; two implementations of the celebrated sky-hook single-axis isolator are discussed and compared; the first one is the classical one based on acceleration sensing (acceleration feedback) and the second one is based on the measurement of the total force transmitted by the isolator (force feedback); it is shown that the force feedback implementation benefits from alternating poles and zeros which allows a control law with guaranteed stability, making it very attractive when the payload to be isolated from the disturbance source is very flexible, such as in large space structures. Next, a six-axis isolator based on the architecture of a cubic Stewart platform is discussed in the context of space applications; the control strategy is based on decentralized force feedback. The closed loop behaviour of the ideal isolator is first studied and the deviation from this ideal behaviour due to technological constraints is discussed next; the close relation between performance and technology is emphasized.

The third part is devoted to spatial filtering and the use of spatial filters in structural control. There are two broad ways to achieve spatial filtering: (i) discrete sensor arrays and (ii) distributed sensors. Discrete array sensors are reconfigurable and can be used to construct modal filters as well as to tailor open-loop frequency response functions to achieve desirable properties; however, they are prone to spatial aliasing,

which is responsible for a lack of roll-off at high frequency and has a strong negative impact on the closed-loop performance of control systems. Distributed sensors are not subject to spatial aliasing, but they are not reconfigurable. In this paper, we focuse on piezoelectric (PVDF) films; a porous electrode design is described, which allows the tailoring of the equivalent piezoelectric properties of piezo films to achieve a wide class of distributed filters. The concept is demonstrated by the construction of a volume velocity sensor of a baffled plate.

References:

[1] A.Preumont, *Vibration Control of Active Structures, An Introduction*, Kluwer, second edition, 2002.
[2] A.Preumont (Editor), *Responsive Systems for Active Vibration Control*, Kluwer, NATO Science Series, Vol.85, 2002.
[3] A.Preumont, Active vibration control, *Lecture notes on Structural Control and Health Monitoring* (SMART'01), pp. 13-53, J.Holnicki-Szulc Editor, Warsaw, May 2001.
[4] A.Preumont, J.P.Dufour & C.Malekian, Active Damping by Local Force Feedback with Piezoelectric Actuators, *AIAA Journal of Guidance and Control , Vol.15, No 2, 390-395, 1992.*
[5]A.Preumont, A.François, F.Bossens & A.Abu-Hanieh, Force feedback versus acceleration feedback in active vibration isolation, *Journal of Sound and Vibration,* 257 (4), pp.605-613, 2002.
[6]A.Preumont, A.François, P.De Man & V.Piefort, Spatial filters in structural control, *Journal of Sound an Vibration*, 265, pp.61-79, 2003.

OCEAN CIRCULATION AND ITS ROLE IN GLOBAL CLIMATE

Peter B. Rhines
University of Washington, Seattle, Washington, USA, 98915

Summary Heat- and water transports by the atmosphere- and ocean circulations are principal elements of global climate. Natural variability and human-induced emissions combine to create active patterns of climate change which are not reflected in overall averages like global mean-surface temperature. Some of these patterns are well-known, like el Nino/Southern Oscillation cycles and the North Atlantic Oscillation; others are less familiar and may be abrupt: the 30-year decline in salinity of the northern Atlantic, invasion of the Arctic by warm Atlantic waters, and the rise and subsequent decade-long decline in the subpolar North Atlantic circulation, and the pattern of global heat content and upper ocean salinity increase in the subtropics.

Dynamical elements of Rossby-wave theory, jet dynamics, stratified spin-up, and rotating convection seem to be important. We also describe a new invention, the Seaglider, with which we are patrolling the cold northern oceans to examine the structure of abruptly changing climate.

DYNAMICAL STRUCTURE

Natural fluid dynamics of Earth's oceans, atmosphere and the atmospheres of planets involves classical Navier-Stokes dynamics as a subset of the larger problems in which layered density stratification and planetary rotation are important. Thus one has classic surface gravity waves, buoyant convection, three-dimensional turbulence and the problem of 'stirring and mixing' embedded in motions of larger scale and very different force balances. An organizing principle for this field is energy: the ultimate source in the sun's radiation, its absorption and re-radiation as long-wave infrared radiation, and the two-fluid problem of thermal convection, complicated by phase-change of water and augmented by buoyancy production from dissolved salts in the oceans. The expansion/contraction work cycle takes place in meridional overturning circulations which then drive the principle horizontal winds and currents of the general circulation.

What makes this story so interesting is the ten decades of length-scale spanning the interesting fluid dynamics: from O(1mm) to 10^5 km which could in principal at least ten schools of geophysical fluid dynamics, each attending to a different aspect of flow and waves. The problem is made more tractable by the trapping of energy at fairly large scale by the effect of Earth's rotation. Coriolis effects combined with the strong layering of the stratified fluid prevent massive disintegration of the flows we see on weather maps and ocean charts: paraphrasing Geoffrey Taylor, who first recognized this trapping effect, 'large-scale rotating fluid motions are non-turbulent' in the sense that the bulk of the kinetic- and potential energy is prevented from cascading to fine scales where explicit frictional dissipation can occur. The stiffness imparted to a fluid by rotating it is a surprising effect, and it appears in surprising places (another example being the liquid core of the Earth, where Taylor columns are almost certainly present, sitting adjacent to the solid core, and strongly involved in generating the magnetic field: evidence being that the radial magnetic field has two maxima in northern Canada and Asia rather than at the expected site for a dipole, the rotational pole).

Current research problems in ocean-atmosphere dynamics emphasize particularly the stationary and transient features of the circulation: classically this would be the 'time-mean circulation' and the 'energy-containing eddies or waves' yet we now recognize the vital activity in time-scales ranging beyond seasons, from decades to centuries. Both natural and human-induced variability of climate occurs at these scales. Dynamicists like to believe that potential-vorticity dynamics plays a role in all of these regimes, although augmenting these with study of energy, thermodynamics and radiation of the ocean-atmosphere, is also necessary.

In this lecture the emphasis will be on the observed structure of one or two strong features of the ocean-atmosphere problem, in particular an aspect of the stationary-wave circulation of the atmosphere known as 'storm tracks', their variability known as the 'North Atlantic Oscillation', and the dynamics of the subpolar circulation of the ocean. The first question we address is the oceanic contribution to climate. In the basic heat- and fresh-water transport of the climate system, the strength of sunshine in the tropics and its weakness near the poles requires a poleward heat transport. This has three principal components: atmospheric thermal-energy transport by winds (known as 'sensible heat-transport'), oceanic thermal-energy transport, and a combined ocean-atmosphere mode, transporting freshwater and hence latent thermal energy. The three have comparable amplitudes and their sum peaks at about 5×10^{15} watts; 5 petawatts. While it is a source of continuing

controversy, the most recent observations, properly interpreted, show that the oceanic fraction is indeed substantial, particularly in the Atlantic and contributes to the warming of northern Europe.

One of the expected consequences of global warming is a strengthening of the global water cycle: the evaporation from the oceans, precipitation, freezing, thawing and spatial transport that gives color to the Earth, as seen from outer space. There are now several independent observations suggesting that this is happening. One of these is the decline in oceanic salinity, from top to bottom, in the northern Atlantic Ocean over the past 30 years. The difficult problem facing us is that there are many possible reasons for this decrease in salinity. The 'modes' of variability of the climate system, mentioned above, have been strongly energized during the late 20th Century, and these alone can cause decadal climate shifts, with or without human intervention and the greenhouse effect. We will show 'portraits' of the North Atlantic Oscillation and discuss its dynamical roots.

Fluid dynamics contributes by providing simple idealized models of this variability. Rossby wave dynamics sets the stage, in the presence of global mountain barriers and ocean-land thermal contrast. We will describe the variety of Rossby waves and wake instabilities generated in the westerly winds, and how the storm tracks connecting sub-tropics and Arctic depend on this structure. The 'potential vorticity elasticity' that enables Rossby-wave dynamics works only at large horizontal scales; small-scale yet still geostrophic turbulence readily shreds the potential vorticity field leading to non-classical wavenumber dependence of turbulent mixing. Though dynamical modelling provides an essential tool for progress (complementing the all-encompassing simulations of global numerical models), the major climate shifts of the past few years are not yet resolved.

A good example of the mixture of causes at work is the circulation of the subpolar Atlantic Ocean, which is driven by both wind-stress and cooling in the harsh wintertime. Using the remarkable altimetry measurements from satellites we have found that this cyclonic gyre, which fills the ocean from Labrador to Ireland and Scandavia, has declined in strength steadily over the years since observations began (1992 for the TOPEX/Poseidon satellite). Yet this circulation had accelerated to a high intensity in 1992-1993 by a century-long maximum in driving by the cold, Arctic winds flowing from Canada, so that it may now be returning to 'normal'. Dynamical ideas point to convective forcing as being responsible for this decadal change in circulation, rather than wind-stress. Indeed, the 'beta-plume' solutions of Rossby-wave dynamics are circulations controlled by the basic potential vorticity field (in turn determined by sea-floor topography and Earth's rotation). These show that the short-time response to shifting winds is orthogonal to the basic circulation gyres and hence wintertime cooling rather than wind-stress is likely the driving effect.

A very few key measurements have had great impact on climate studies: examples are Charles Keeling's carbon dioxide measurements at Mauna Loa, Hawaii, and a handful of decades-long weather-ship observations of both ocean and atmosphere. Observations of three-dimensional circulations must be sustained in time long enough to observe the 10- to 100-year timescales. Modern oceanography is maturing, thanks both to basic studies in geophysical fluid dynamics and remarkable new observational methods, which now give us the hope of sustained, yet detailed observation: examples are orbiting satellites measuring sea-surface height variability, surface circulation, surface temperature and ice cover globally and *in situ* observations of chemical tracers and dynamically active temperature, salinity and velocity by autonomous undersea vehicles.

We launched two such vehicles, known as Seagliders, offshore of west Greenland in October 2003. These gliding vehicles move at about 20 km per day across the oceans, diving to 1000m while profiling the ocean with horizontal resolution of about 3 km. At the time of this writing each Seaglider has produced more than 1500 km long sections, while 'phoning home' three times per day (at which time the data is transmitted and course changes can be made). The vehicles, developed by Charles Eriksen at University of Washington, promise to give oceanography the kind of three-dimensional data matched to the oceans' complexity.

The accelerating pace of global change is affecting more 'variables' than temperature, winds and rainfall. In danger of being caught off balance, the science community needs to respond with observational strategies that can overcome the difficulty of the 'baseline': the mean state of past climate means less and less as we climb the exponentials of change, and the implicit linearization of our models and thinking about past baselines daily becomes less and less valid.

Micromechanics and Microviscoelasticity of Cells .

Erich Sackmann
Physik Department Technische Universität München
D-85747 Garching, Germany

Abstract: Magnetic tweezer microrheometry combined with deformation field mapping enables local measurements of viscoelastic moduli of cell envelopes or cytoplasms. Cell envelopes behave as viscoelastic shells composed of slightly crosslinked actin gels while cytoplasms form highly heterogeneous viscoplastic fluids. Creep function analyses enable mapping of viscosites and measurement of local transport forces.

Mechanical forces control life processes on all length scales. On the molecular level forces can act catalytically on chemical reaction and molecular motors serve the directed material transport along macromolecular tracks or drive the replication and transcription of DNA. On the cellular level hydrodynamic shear forces control the blood pressure through force-dependent synthesis of the signal molecule nitroxid (NO) by endothelial cells lining the inner wall of blood vessels which mediate the smooth muscle contraction. Cell adhesion is controlled by interplay of specific (lock-and-key) forces a manifold of interfacial forces and, most importantly, by elastic stresses in the cell membranes. For that reason close relations exist between adhesion strength and elastic properties of cells On the macroscopic scale mechanical forces control the structure and mechanical strength of materials during growth . A particularly beautiful example is the regulation of the mechanical strength of trees by variation of the pitch of helically arranged cellulose fibrilles .For many such tissue growth processes by self assembly of materials, cells play a twofold role by acting as mechanical sensors and as machines for the synthesis of new materials such as collagen, hyaluronic acid and cellulose.

The biological function of forces is mediated by the activation of intracellular signal cascades resulting in the generation or libration of second messengers (such as cyclic AMP) or in the increase of intracellular Ca levels which can stimulate the reorganization of intracellular macromolecular scaffold ,such as the actin cortex , or activate the genetic expression. To gain insight into correlations between mechanical forces and biological functions it is essential to understand the transmission of forces within the composite biological materials .which is determined by the heterogeneous viscoelastic properties.

The main thrust of my lecture is to show that despite of the complex design of cells local viscoelastic moduli can be measured by application of the magnetic tweezer microrheometry and dynamic strain field analysis by colloidal force probes (cf Fig 1). Insight into the correlations between the viscoelastic impedance and structural or dynamic molecular properties of the materials is gained by parallel investigation of natural systems and realistic *in vitro* mechanical models of cells, such as giant vesicles with self-assembled reconstituted actin corteces

In the first part of the lecture we show that creep experiments combined with strain-field analysis [1] enable measurement of absolute Young moduli of the cell envelope. Comparison with viscoelastic impedances data of vitro actin networks show that the deformability of the cell envelope s determined by the membrane associated actin cortex .

The second part describes the application of the technique to evaluate in real time the rapid reorganization of the actin cortex of endothelial cells (embedded in confluent monolayers) by activation with inflammational agents;

such as histamine involved in allergic reactions[2]. We show that the actin cortex is stiffened by a factor of ~100 within ~ 1 sec by formation of stress fibers;a process associated with a sol-gel transition of the actin network which is triggered by activation of myosin and Ca-induced actin polymerization.We provide evidence that the centripetal contraction of cells (leading to the formation of gaps within the endothelium) is driven by the tension generated in the composite shell by the actin reorganization .The important role of integrin receptors as force transducers is discussed .

The viscoelasticity of the cytoplasm is studied by analysing the quasi-random transport of magnetic tweezers internalized by the cells and by local creep experiments. The motion consisists of intermittent transport along microtubuli and local random walks driven by intracellular dynamics; such as flagella-like motions of microtubule. The cytoplasm consists of soft streets separated by forbidden zones and these organized structures prevail for hours

The intracellular transport forces are measured by analysing the change in velocities induced by external force pulses and we show that forces between 8 and 30 pN are found. .Viscoelastic creep experiments demonstrate that the intracellular viscosity varies by orders of magnitude (10 -500 Pasec) .The intracellular space behave as viscoplastic rather than viscoelastic body. Similar to fracture processes in metals , the creep responses are described by force dependent local mobilities and random transitions within a multi-well potential. An important consequence of the viscoplasticity is that weak forces can mediate transport of intracellular compartments through stiff regions by statistical breakage of bonds.

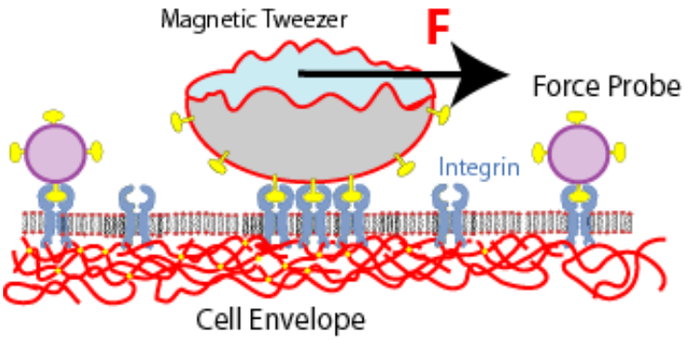


Fig 1. Viscoelastic microscopy with magnetic tweezers combined with strain field analysis based on induced creep of nonmagnetic force probes

[1] E. Sackmann and R. F. Bruinsma , Cell Adhesion as Wetting Transition?
ChemPhysChem 3 , 262-269,2002

[2] A.R. Bausch, U. Hellerer, M. Essler, M. Aepfelbacher and E. Sackmann , Rapid Stiffening of Integrin Receptor-Actin Linkages in Endothelial Cells Stimulated with Thrombin: A magnetic Bead Microrheology Study .Biophys. J. 80, 2649-2657, 2001

Viscoelastic microscopy of cells.

Superparamagnetic beads are biofunctionalized by surface grafting of ligands (such as fibronectin or bacterial proteins) for binding to specific cell surface receptors (such as receptors of the integrin family) or of motor proteins mediating intracellular transport for measurement of intracellular viscoelastic moduli or transport forces

XXI International Congress of Theoretical and Applied Mechanics
Warsaw, Poland, August 15-21, 2004

Electrokinetics and Electrohydrodynamics in Microfluidics

D. A. Saville
Princeton University, USA

Electric fields offer an exquisite means of control over small-scale fluid and particle motion. In some instances *electrokinetics* - the applied field acts on the intrinsic (equilibrium) electric charge arising from covalently bound ionogenic groups bound to an interface. In other cases *electrohydrodynamics* the charge arises from the action of a field on an otherwise electrically neutral system. Despite this similarity, descriptions of electrokinetic and electrohydrodynamic motion developed more or less independently. The theoretical underpinnings of electrokinetics were laid down by Helmholtz and Smoluchowski in the late 19th and early 20th centuries; the theory of electrohydrodynamics was set forth by G.I. Taylor and J. R. Melcher in the 1960's. Nevertheless, both descriptions stem from the same fundamental model: the Navier-Stokes equations augmented with an electrical body force, Gauss's law, and conservation equations for the several ionic species. The development of a unified picture will be described along with its implementation. Special attention will be will be given to microfluidic applications involving the movement of particles and fluids by electrophoresis and electroosmosis and the assembly of colloidal crystals.

XXI ICTAM, 15–21 August 2004, Warsaw, Poland

PROBLEMS IN ASTROPHYSICAL FLUID DYNAMICS

Edward A Spiegel*,
*Astronomy Department, Columbia University, New York NY 10027, USA

Summary The variety of fluid processes observed throughout the universe staggers the imagination, yet the subject has not attracted nearly as much serious interest from professional fluid dynamicists, as have geophysical fluid problems. Yet, in the sixties and seventies of the previous century, several symposia were held that brought astrophysicists and fluid dynamicists together under various titles such as Cosmical Gas Dynamics; we might even follow Lighthill's lead in another subject and speak of Astrofluiddynamics. Those old symposia were well attended and quite stimulating.

To give an idea of the kinds of problems that arise in astrophysics I outline here a (subjective!) selection of fluid dynamical problems faced by astrophysicists. I begin with thermal instability, a characteristic process discussed in astrophysics and this flows naturally into the larger domain of radiative fluid dynamics wherein radiation affects the dynamics both thermally and dynamically and also plays a significant role in the observations. Astrophysicists must also face the problems associated with long mean free paths in plasmas and in their gravitational analogues – gases whose constituent particles are stars or even galaxies. As time permits, I shall also speak of fluid dynamics in accretion disks and rotational processes in the sun.

This selection only scratches the surface of the subject and it is meant to be introductory. My subject is really astrophysically motivated fluid dynamics and the approach to be used in this discourse is largely analytic. However, I would stress that, on the hard core astrophysical side, progress is being made largely in the development of simulations. This is true throughout the subject, and is especially evident in a wide range of compressible flows such are encountered in stellar convection, the dynamics of interstellar gas clouds and in the formation of large-scale structure in the early universe.

THERMAL OVERSTABILITY

A uniform medium that is heated by some mechanical process and cooled radiatively can reach a stationary state given some simple conditions such as hydrostatic equilibrium. In typical situations, a slight increase in temperature leads to an increased cooling that restores the equilibrium temperature. However, in some cases, an increase in temperature may destroy the radiating atoms, and thus lead to a *decrease* in temperature, hence to instability. This situation may arise in the solar corona, in the interstellar medium and in other contexts. As the temperature is further increased, a new radiator takes over and a new equilibrium temperature is achieved. In this way, a mix of equilibria may be found and the result is thought to be the formation of clouds in a multi-temperature medium.

When the linear fluid dynamical theory of such situations also contains oscillatory modes, as it does in stratified media, the instability takes the form of growing, propagating waves. In the weakly nonlinear cases, nonlinear propagating waves are found that may be analyzed by the methods familiar in modern pattern dynamics.

PHOTOFLUIDYNAMICS

Radiative transfer is important in most cosmic bodies and the thermal aspects have been crucial in the study of the structure and internal dynamics of stars and related objects. Radiative fluid dynamics becomes more complicated in hot objects, of which there are many varieties, the simplest of which are stars whose masses are sixty or so times that of the sun and the currently most studied are hot accretion disks and the early universe. When the temperature is high, the pressure of the radiation can be at least as large as that of the material fluid and, in one vision of the situation, we have a two-fluid situation. An interesting situation in hot stars where radiation from below is forces its way through the outer layers to escape. The radiation exerts a levitating force on the medium and, when that force balances the gravitational force, we may expect the dynamics to have some similarities to that of fluidized beds. One may expect photon bubbles to form and this may play a role in explaining the great breadth of spectral lines in hot stars that indicate (what some believe) is supersonic turbulence. Hot stars rotate rapidly and one may wonder whether the this will lead to bubble merger and the formation of vortices. These allow rapid escape of radiation in beams that keep the vortices alive. There are many interesting issues in this subject, not the least of which is the development of adequate approximations that may permit the deepening of our understanding of these rich dynamical processes.

RAREFIED GAS DYNAMICS

As in the problems of radiative transfer, when the mean free paths of the constituent material particles of a fluid become comparable to or larger than the macroscopic scales of motion, the Navier-Stokes equations cease to be accurate. This difficulty must be faced in many problems of astrophysical fluid dynamics from the expected ones in astrophysical plasmas to the gravitational N-body problems in which the bodies may be stars or even galaxies. The issue of whether to improve matters by seeking of improved continuum approximations or directly by working with the kinetic equations is very interesting. Both approaches have their defenders. Perhaps an intermediate approach is appropriate as will be discussed.

VORTICES IN DISKS

Disks commonly form around central objects that are frequently compact. Such structures form in double stars, in galactic center and around newly formed stars with the main radial force balance being between the inward gravitational force and the centrifugal outward force. Many disks are quite thin and a shallow layer approximation may be appropriate for their study in many instances. The linear instabilities that may occur include gyromagnetic instability in which magnetic fields lead to the disorganization the shear flow in the disks and possibly conventional convective instability. The situation with respect to nonlinear instability is controversial. It is however generally agreed that disks are turbulent and this may be the means by which angular momentum in disks is carried outward so that the matter in the disks may be slowly being accreted onto the central object. If disks are like other rotating turbulent fluids, the should form vortices (or perhaps coherent magnetic flux tubes). These play an interesting role in the light variation in hot disks. In the case of cool disks that are thought to become planetary systems, vortices play a remarkable role in sucking in dust particles where they may coalesce to form large objects on the way to planet formation.

SOLAR DIFFERENTIAL ROTATION

As in geophysical fluid dynamics, the interplay of rotation and stratification is important in many cosmic situations. A nearby example is provided by the sun. The outer third of the sun is convective and has relatively low density. The inner two thirds is stably stratified and of higher density. The object as a whole rotates with a period of 28 days. The differential rotation in the convection zone is rather different from that of the interior as determined by helioseismology. The two regions are coupled through a convective boundary layer and a rotational transition layer called the tachocline. The situation is vaguely reminiscent of the terrestrial configuration where the outer layer is the atmosphere, the inner core the ocean and the tachocline is like the oceanographic thermocline. In both cases there seems to be a problem of these layers keep themselves so thin and do not suffer turbulent or diffusive spreading on the times available. Heretofore, as in the older approaches, attention has mainly focused on the influence of the convective layers on the interior, but the time is clearly ripe to look at the coupled system as is being done in studies of the ocean-atmosphere interactions.

PROBABILITY DISTRIBUTION FUNCTIONS FOR A RAPIDLY ROTATING TURBULENT FLOW: EXPERIMENT AND THEORY

H. L. Swinney, C. N. Baroud, and S. Jung
The University of Texas at Austin, Department of Physics
Austin, Texas 78712 USA

We consider a turbulent flow that rotates sufficiently fast so that the Rossby number is small (0.1), that is, the Coriolis force dominates inertial effects. Further, the dissipation, which is due mainly to Ekman friction in the boundary layers, is small. Hence the flow is essentially 2-dimensional (2D), like flows in the atmosphere and oceans on large spatial scales. Such a flow is different from the non-rotating quasi-2D turbulent flows studied in soap films [1] and thin electrolyte layers [2], and different from strictly 2D turbulent flows, which do not exist in nature but have been studied theoretically and numerically. Our study concerns the statistical properties of the low Rossby number flow: the probability distribution function (PDF) measured for the vorticity ω (the component parallel to the rotation axis), and the PDF of increments of a component of the velocity, $\delta v(x) = v(r+x)-v(r)$, where v lies along the line connecting r and $r+x$ [3,4].

Our apparatus is an annular tank with inner diameter 21.6 cm and outer diameter 86.4 cm. The bottom slopes to mimic the earth's beta effect: the depth increases from 17.1 cm at the inner radius to 20.3 cm at the outer radius. Fluid is pumped into the tank through a ring of 120 holes in the tank bottom at a radius of 18.9 cm, and out of the tank through a ring of 120 holes at a radius of 35.1 cm. The result of this radial forcing is a broad azimuthal counter-rotating jet that is turbulent (Reynolds number 20000) [4]. Measurements of the azimuthal component of the velocity are made with hot film probes place midway between the inner and outer radii of the annulus, and these velocity time series measurements are complemented by Particle Image Velocity measurements of the entire 2D velocity field.

The velocity measurements yield a PDF for the velocity increments that is non-Gaussian, but the functional form for $P(\delta v)$ is the same for different distances x, as Fig. 1 illustrates. A consequence of this *self-similar* behavior is that the exponents $\zeta(p)$ for the structure function,

$$S_p(x) = \langle (\delta v)^p \rangle \sim x^{\zeta(p)},$$

should be linear in the order p. We have confirmed this linearity in direct determinations of the scaling of S_p for orders up to $p = 10$ [4].

Equilibrium statistical mechanics has long been used to gain insight into turbulence (e.g., [5-6]). The analyses are usually based on Boltzmann-Gibbs statistical mechanics, which describes weak interactions and does not capture the long range interactions present in low Rossby number flows where there are large coherent jets and vortices. We explore the applicability of a generalization of statistical mechanics proposed by Tsallis, known as nonextensive statistical mechanics [7]. Energy and enstrophy are both approximately conserved in weakly dissipative low Rossby number flows. Assuming that these quantities are conserved in our flow, we derive a form for the PDF of the vorticity by maximizing a nonextensive entropy function. In order to apply the formalism to our experiment, we had to reduce the number of boundary conditions, which was done by pumping fluid through a *single* ring with a semi-circle of 60 holes that were sources, and on the opposite side of this circle was a semi-circle of 60 sinks. The flow configuration is described in [8]. The resultant turbulent flow is turbulent for the pumping rate used [8]. We find that $P(\omega)$ for this flow, computed from our nonextensive analysis, is in good accord with the observations, as Fig. 2 demonstrates.

Acknowledgments: We thank Christian Beck, Brian Storey, E.G.D. Cohen, and Jori Ruppert-Felsot for helpful discussions, and the U.S. Office of Naval Research for grant support.

References:
[1] M. Rivera, P. Vorobieff, and R. Ecke, *Phys. Rev. Lett.* **81**, 1417 (1998).
[2] Paret J., Tabeling P: *Phys. Rev. Lett.* **79**, 4162, 1997.

[3] Jung S, Storey B.D., Aubert J., Swinney H.L.: *Physica D*, to appear, 2004.
[4] Baroud C.N., Plapp B.P., Swinney H.L., She Z.S.: *Phys. Fluids* **15**, 2091, 2003.
[5] Kraichnan R.H.: *Phys. Fluids* 10, 1417, 1967.
[6] Miller J.: *Phys. Rev. Lett* 65, 2137, 1990.
[7] Tsallis, C.: *J. Stat. Phys*. 52, 479, 1988.
[8] J. Aubert J., Jung S., Swinney H. L.: *Geophysical Research Letters* 29, 1876, 2002.

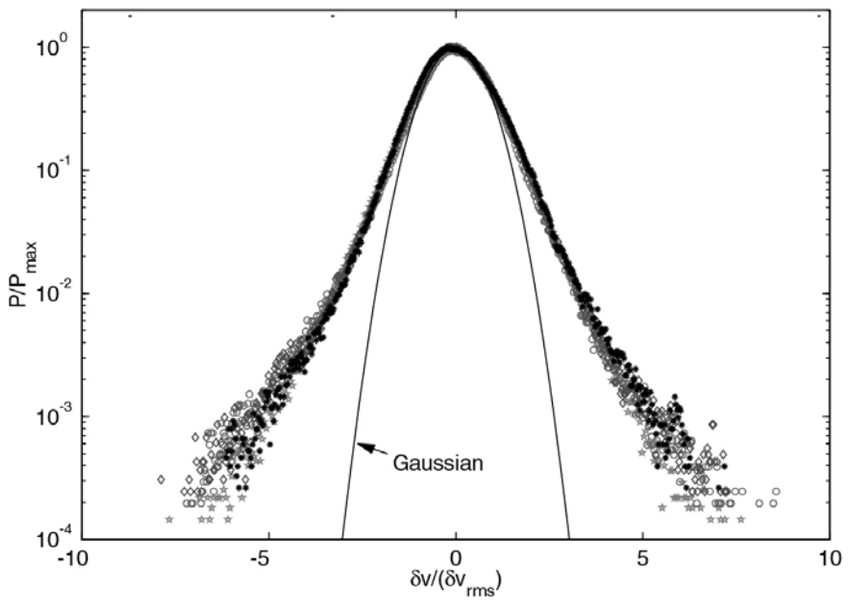


Fig. 1. The velocity increment PDF is *self-similar*, i.e., the functional form of $P(\delta v)$ (normalized by its maximum value) is independent of the distance between measurement points. Data for six distances x ranging from 1.1 to 17.3 cm are shown by different symbols (for comparison, the Kolmogorov dissipation length is 0.07 cm) [4]. The width of the PDF for each distance x is scaled by the corresponding rms value of δv. (from [4]).

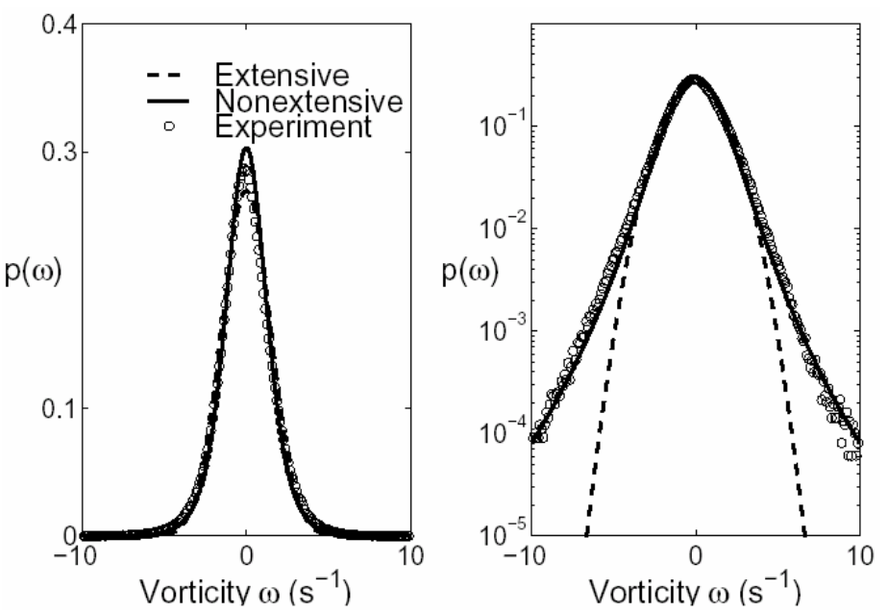


Fig. 2. Vorticity PDF on linear (left) and log (right) scales: comparison of laboratory measurements (o) with predictions obtained from statistical theory. The prediction from nonextensive statistical mechanics agrees well with the observations, while the Gaussian curve given by Boltzmann-Gibbs statistical mechanics is far from the observations. (from [3])

ELASTIC WAVE PROPAGATION DEVELOPMENT FOR STRUCTURAL HEALTH MONITORING

Wiesław M. Ostachowicz*
*Polish Academy of Sciences, IMP PAN, Fiszera 14, PL 80-952 Gdansk, Poland
*Gdynia Maritime University, Faculty of Navigation, Zjednoczenia 3, PL 81-345 Gdynia, Poland

Summary This paper is a personal perspective of structural health monitoring technology and its applications as see from a current literature and projects. The proposed approach deals with the spectral finite element analysis method as a means of solving the wave propagation problems in structures. The change of the wave propagation process due to a damage appearance is examined by comparing the differences between the responses from damaged and undamaged structures. The influence of the damage growth for the wave propagation is also analysed. The differences in the propagating waves allow indicating the damage location and size in a very precise way.

INTRODUCTION

Undetected damage in buildings, bridges, aerospace structures, containers and other large structures will develop if undetected and in some cases result in the collapse of the whole structure. This may have costly disastrous consequences for people and the environment including deaths, injuries, fires, contamination, economic losses, legal costs etc. It has been found that in a lot of cases a small-undetected damage (crack, plastification, delamination) has been the cause for the collapse.
Damage in structures should be detected at an early stage, before it can cause any problems and so that proper decisions for repair and/or part replacement can be taken.
This paper is focused on structural health monitoring technology and its applications in aerospace and civil engineering.
Better understanding of phenomena associated with propagation of elastic waves in structural elements is very important from both the theoretical and the practical point of view. Changes in propagation of elastic waves when observed in structural elements can be used for the purpose of damage detection or identification of material parameters within those elements. In recent years significant progress has been evident in this particular field of applications.
Recently, laminated composites with built-in piezoelectrics have attracted significant attention among researchers because of their potential application to controlling vibrations, suppressing noise, as well as monitoring the health of the structures. The investigated damage detection system is based on the known fact that material discontinuities affect the propagation of elastic waves in solids. The change in material characteristics, such as a local change in stiffness or inertia caused by a crack or material damage, will affect the propagation of elastic waves and will modify the received signals. Wave frequencies that are most sensitive to damage depend on the type of structure, the type of material, and the type of damage. Elastic waves are generated and sensed by an array of transducers either embedded in, or bonded to, the surface of the structure. Wave frequencies associated with the highest detection sensitivity depend, among others, on the type of the structure, the type of material, and the type of the damage.

Structural Health Monitoring Technology

SHM (Structural Health Monitoring) technology works with a built-in sensor network on a structure. These sensors provide information regarding the condition and damage state of the structures as they age. The investigated damage detection system is based on the known fact that material discontinuities affect the propagation of elastic waves in solids. The change in material characteristics, such as a local change in stiffness or inertia caused by a crack or material damage, will affect the propagation of elastic waves and will modify the received signals.

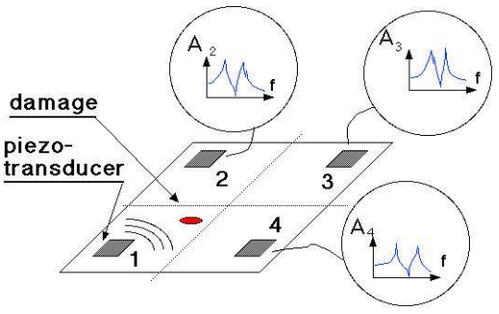


Figure 1 Built in sensor network on a plate

Wave frequencies that are most sensitive to damage depend on the type of structure, the type of material, and the type of damage. Elastic waves are generated and sensed by an array of transducers either embedded in, or bonded to, the surface

of the structure. Wave frequencies associated with the highest detection sensitivity depend, among others, on the type of the structure, the type of material, and the type of the damage. Figure 1 presents a general concept of this technology.

Spectral Finite Element Technique

Among many frequency domain methods, the spectral method is found to be suitable due to its adaptation of displacement based FE technique and therefore enabling one to handle arbitrary skeletal structures. Spectral Element (SE) analysis has been established as a powerful method used for wave propagation. The Spectral Element Method (SEM), high-accuracy numerical method, combines the accuracy of conventional spectral methods and the geometric flexibility of finite element methods. It is the method of Fourier synthesis (or spectral analysis), where the behaviour of the signal is viewed as a superposition of many infinitely long wave trains of different periods (or frequencies). The actual response is synthesised by a judicious combination of these wave trains. Thus the problem of characterising a signal is transformed into one of determining the set of combination coefficients. These coefficients are called the Fourier transform of the signal. The problem being tackled invariably simplifies when it is expressed in terms of the Fourier transform. The last step in the analysis involves performing an inverse transform (reconstructing the signal).

This paper presents a method of wave propagation, which can be further used to detect small delaminations in beam-like and plate structures. The structures are modelled by spectral finite elements.

The approach is similar in style to that of the finite element method but with the very significant difference that the element stiffness matrix is established in the frequency domain. As a consequence, these spectrally formulated elements describe exactly the wave propagation dynamics, and in contrast to the conventional element this means that elements can span all the way from one point to another without losing fidelity.

In a simple form, the solution to a wave propagation problem can be represented as by Doyle [1]:

$$\boldsymbol{w} = \sum_{\boldsymbol{n}} \hat{\boldsymbol{P}}_{\boldsymbol{n}} \left\{ \hat{\boldsymbol{G}}_1(\boldsymbol{k}_{1\boldsymbol{n}}\, \boldsymbol{x}) + \hat{\boldsymbol{G}}_2(\boldsymbol{k}_{2\boldsymbol{n}}\, \boldsymbol{x}) + ... \right\} \exp(\boldsymbol{i}\, \omega_{\boldsymbol{n}} \boldsymbol{t}) = \sum\nolimits_{\boldsymbol{n}} \hat{\boldsymbol{P}}_{\boldsymbol{n}}\, \hat{\boldsymbol{G}}_1(\boldsymbol{k}_{\boldsymbol{m}\,\boldsymbol{n}}\, \boldsymbol{x}) \exp(\boldsymbol{i}\, \omega_{\boldsymbol{n}} \boldsymbol{t}) \tag{1}$$

where: $\hat{\boldsymbol{G}}$ is the analytically derived transfer function of position $\boldsymbol{x}$. $\hat{\boldsymbol{G}}$ has different numerical values at each frequency. $\hat{\boldsymbol{P}}_{\boldsymbol{n}}$ is the amplitude spectrum and is known from input conditions or from measurements. $\hat{\boldsymbol{P}}_{\boldsymbol{n}}\hat{\boldsymbol{G}}$ is recognised as the Fourier transform of the solution.

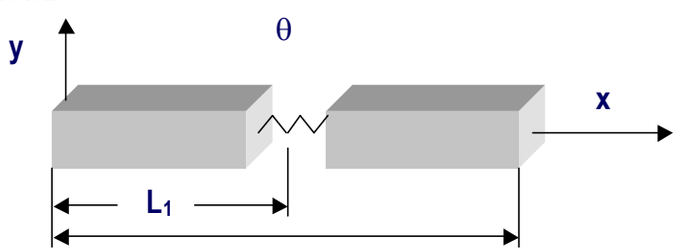


Figure 2 Rod spectral finite element

A simple spectral rod finite element with a transverse open and non-propagating crack is presented in Figure 2. The length of the element is L, and its area of cross-section is A. The crack is substituted by a dimensionless spring, which flexibility θ is calculated by using Castigliano's theorem and laws of the fracture mechanics, Krawczuk and Ostachowicz [2].

Nodal spectral displacements are assumed in the following form for the left and right part of the rod:

$$\begin{aligned} \hat{\boldsymbol{u}}_1(\boldsymbol{x}) &= \boldsymbol{A}_1 \boldsymbol{e}^{-\boldsymbol{i}\boldsymbol{k}_{\boldsymbol{n}}\boldsymbol{x}} + \boldsymbol{B}_1 \boldsymbol{e}^{-\boldsymbol{i}\boldsymbol{k}_{\boldsymbol{n}}(\boldsymbol{L}_1 - \boldsymbol{x})} \qquad \text{for } \boldsymbol{x} \in (0, \boldsymbol{L}_1) \\ \hat{\boldsymbol{u}}_2(\boldsymbol{x}) &= \boldsymbol{A}_2 \boldsymbol{e}^{-\boldsymbol{i}\boldsymbol{k}_{\boldsymbol{n}}(\boldsymbol{x} + \boldsymbol{L}_1)} + \boldsymbol{B}_2 \boldsymbol{e}^{-\boldsymbol{i}\boldsymbol{k}_{\boldsymbol{n}}[\boldsymbol{L} - (\boldsymbol{L}_1 + \boldsymbol{x})]} \quad \text{for } \boldsymbol{x} \in (0, \boldsymbol{L} - \boldsymbol{L}_1) \end{aligned} \tag{2}$$

where: $\boldsymbol{L}_1$ denotes the location of the crack, $\boldsymbol{L}$ is the total length of the rod and $\boldsymbol{k}_{\boldsymbol{n}}$ is the wave number calculated as follows:

$$\boldsymbol{k}_{\boldsymbol{n}} = \omega_{\boldsymbol{n}} \sqrt{\frac{\rho}{\boldsymbol{E}}} \tag{3}$$

where: $\boldsymbol{\rho}$ is the density of the rod material, $\boldsymbol{E}$ denotes Young's modulus and $\boldsymbol{\omega}_{\boldsymbol{n}}$ is a natural frequency.

The coefficients $\boldsymbol{A}_1$, $\boldsymbol{A}_2$, $\boldsymbol{B}_1$ and $\boldsymbol{B}_2$ can be calculated as a function of the nodal spectral displacements using the element boundary conditions (see Krawczuk and Ostachowicz [2]). Using boundary conditions can relate the coefficients A_1, A_2, $\boldsymbol{B}_1$ and $\boldsymbol{B}_2$ to the nodal spectral displacements. The nodal spectral forces can be determined by differentiating the spectral displacements with respect to $\boldsymbol{x}$. Finally, using the relation between nodal forces and nodal displacements the dynamic stiffness matrix of a cracked rod spectral finite element can be evaluated.

This paper presents also other applications of wave propagation, which can be further used to detect small delaminations in beam-like Krawczuk and Ostachowicz [2], Ostachowicz et al. [4], and plate structures Krawczuk et al. [3]. All considered structures are modelled by spectral finite elements.

The SEM approach is based on global approximations of functions, i.e. the analysed functions are at first approximated using basis functions and are then exactly differentiated. As a consequence, relatively small number of elements can be used for modelling without losing accuracy. This is particularly useful for wave propagation modelling.

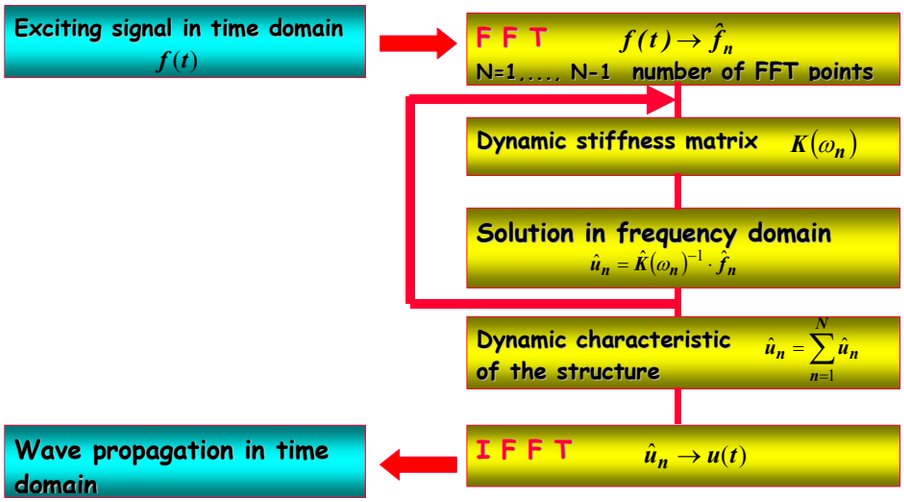


Figure 3 Flow diagram for the wave reconstruction program

The basic steps in the development of SEM can be described as follows. The governing wave equations are first transformed from the time domain to the frequency domain using a discrete Fourier transform (DFT). For computational implementation we use the FFT algorithm built into the FE code. The spatial variation is semi-explicitly obtained by solving the characteristic equation in k-space. This results in a complex shape function matrix representing the linear superposition of all the wave modes. Also, the complex dynamic strain–displacement matrix and the dynamically consistent force vector can both be derived. Following the conventional FE method, the complex dynamic stiffness matrix is then formed, and this is exact. This makes the proposed SEM an efficient model suitable for use within the framework of an automated FE method rather than a trade-off for broadband wave propagation analysis. But the fundamental difference from the conventional FE method is that all the spectral amplitudes that correspond to elemental nodal variables are evaluated at each frequency step (FFT sampling points) instead of pseudo-static variables evaluated at each time step or at each eigenfrequency. The global system is solved for unit spectral amplitude of the applied load history at each FFT sampling frequency. Therefore, computation in this way of the frequency response function (FRF) of the global system is straightforward. The time domain response is obtained using the inverse FFT.
Certainly the solution is different at each position, but once it is evaluated at a particular position then its inverse immediately gives the time history of the solution at that point. Figure 3 shows a flow diagram for the basic algorithm to propagate a wave.

CONCLUSIONS

This paper is a personal perspective of structural health monitoring technology and its applications as see from a current literature and projects. The proposed approach deals with the spectral finite element analysis method as a means of solving the wave propagation problems in structures. The change of the wave propagation process due to a damage appearance is examined by comparing the differences between the responses from damaged and undamaged structures. The influence of the damage growth for the wave propagation is also analysed. The differences in the propagating waves allow indicating the damage location and size in a very precise way.
The proposed model can easily be used for detection of damage in complicated situations, i.e. multiple delaminations located in different places.
The paper is not intended to be a comprehensive survey but merely to present a flavour of recent activity in this important subject.

References

[1] Doyle, J., *Wave Propagation in Structures*, Springer-Verlag, New York, 1997.
[2] Krawczuk M., and Ostachowicz W., *Key Engineering Materials*, Vols. 204-205, 2001, pp. 241-250.
[3] Krawczuk, M., Palacz M., and Ostachowicz W., *Journal of Sound and Vibration*, Vol. 264, 2003, pp. 1139-1153.
[4] Ostachowicz, W., Krawczuk, M., Cartmell, M., and Gilchrist M., *Computers and Structures,* Vol. 82, 2004, pp. 475-483.

A way to search for new smart materials with unprecedented physical properties

Richard D. James
University of Minnesota
james@umn.edu

These thoughts begin with the observation by physicists, probing new phenomena through the use of first principles' studies, that the simultaneous occurrence of ferromagnetism and ferroelectricity is unlikely. While these studies do not consider the possibility of a phase transformation, there is a lot of indirect evidence that, if the lattice parameters are allowed to change a little, then one might have co-existence of "incompatible properties" like ferromagnetism and ferroelectricity. Thus, one could try the following: seek a reversible first order phase transformation, necessarily also involving a distortion, from, say, ferroelectric to ferromagnetic phases. If it were highly reversible, there would be the interesting additional possibility of controlling the volume fraction of phases with fields or stress. The key point is reversibility.

Even big first order phase changes can be highly reversible (liquid water to ice, some shape memory materials), and we argue that it is the nature of the shape change that is critical. We suggest, based on a close examination of measured hysteresis loops in various martensitic systems, that reversibility is governed by the presence of certain special relations among lattice parameters. We give a example of the systematic use of these relations to discover new low hysteresis shape memory materials.

Besides ferroelectricity – ferromagnetism, there are many potential property pairs that exhibit lattice parameter sensitivity and are candidates for the proposed strategy: soluability for H_2, optical nonlinearity, high band gap – low band gap semiconductors, insulator – conductor (electrical or thermal), opaque – transparent (at various wavelengths), high – low index of refraction, luminescent – nonluminescent, and new kinds of thermoelectric and thermomagnetic materials.

AUTONOMIC HEALING OF POLYMERS AND COMPOSITES

S. White[*,§], N. Sottos[§], J. Moore[^], E. Brown[§], A. Jones[§], J. Rule[^]
[§] *Theoretical and Applied Mechanics, University of Illinois Urbana-Champaign, Urbana IL 61801*
[*] *Aerospace Engineering, University of Illinois Urbana-Champaign, Urbana IL 61801*
[^] *Chemistry, University of Illinois Urbana-Champaign, Urbana IL 61801*

Summary Inspired by biological systems in which damage triggers an autonomic healing response, structural polymers and polymer matrix composites have been recently developed that possess the ability to *self-heal.* Self-healing is accomplished by incorporating a microencapsulated healing agent and a catalytic chemical trigger within a polymer matrix. When the material is damaged, the microcapsules rupture and release the healing agent into the damaged region through capillary action. As the healing agent contacts the catalyst, polymerization is initiated and the damage is repaired. One promising healing chemistry based on the ring-opening-metathesis-polymerization (ROMP) of dicyclopentadiene and Grubbs' catalyst has yielded static fracture recovery in excess of 90% and greatly extended fatigue life. New healing chemistries and alternate healing approaches are explored with utility in a variety of structural polymer and polymer composite applications.

SELF-HEALING CONCEPT AND MATERIALS

The self-healing concept is shown in Figure 1. A microencapsulated healing agent is embedded along with a catalyst into a polymer matrix. When damage occurs in the polymer a crack propagates through the matrix rupturing the microcapsules in the crack path. The ruptured microcapsules release the healing agent, which is then drawn into the crack through capillary action. Once the healing agent within the crack plane comes into contact with the embedded catalyst, a chemical reaction is triggered and polymerization of the healing agent occurs. The crack faces are then permanently bonded and the strong singularity at the crack tip is relieved.



Fig. 1. Self-healing polymer. A microencapsulated healing agent (tagged with red dye) is released into the fracture plane behind the propagating crack front that dissects the image from left to right. The capsules in front of the crack (top of image) remain unbroken. (E. Brown, Univ. of Illinois, 2001).

A self-healing epoxy was recently developed at the University of Illinois [1-3] based on the ring-opening-metathesis-polymerization (ROMP) of dicyclopentadiene (DCPD) healing agent with a transition metal (Grubbs') catalyst [4]. DCPD was encapsulated in microcapsules with 0.2-micron thick shell made of urea formaldehyde. A small volume fraction of microcapsules was dispersed in an epoxy resin along with Grubbs' catalyst. The embedded microcapsules were shown to rupture in the presence of a crack and release the DCPD monomer into the crack plane. Contact with the embedded Grubbs' catalyst initiated polymerization of the DCPD and rebonded the crack plane. This self-healing epoxy is able to recover over 90% of its virgin fracture toughness [5].

In addition to providing an efficient mechanism for self-healing, the presence of DCPD-filled UF microcapsules also increases the inherent fracture toughness of the epoxy. Under monotonic loading the average maximum toughness with microcapsules is 127% greater than neat epoxy. Fracture of the neat epoxy is brittle, exhibiting a mirror fracture surface. The addition of microcapsules produces a transition of the fracture plane morphology to hackle markings. The increased toughening associated with fluid-filled microcapsules is attributed to increased hackle marking and subsurface microcracking not observed for solid particle fillers [6]. While fracture toughness is an important property for evaluating self-healing performance, fatigue loading is particularly problematic in brittle polymers. The current investigation seeks to apply recent breakthroughs in self-healing technology to repair fatigue cracks in a polymer autonomically.

STATIC FRACTURE RECOVERY AND HEALING KINETICS

The efficiency of crack healing in static fracture is defined based on the ability of a healed sample to recover fracture toughness (K_{Ic}). Fracture toughness is measured for the virgin sample and then the specimen is allowed to heal. The test is repeated after an appropriate period of time for healing and the healed fracture toughness is obtained. The healing efficiency (η) is expressed simply as a ratio of the healed and virgin fracture toghnesses,

$$\eta = \frac{K_{Ic_{healed}}}{K_{Ic_{virgin}}} \quad . \qquad (1)$$

Fracture test results for self-healing epoxy based on ROMP of DCPD are shown in Fig. 2. For these tests, 2.5 wt% of Grubbs' catalyst was combined with EPON 828 epoxy resin (diglycidyl ether of bisphenol-A) and DETA (diethyl triamine) curing agent. To this matrix was added 5 wt% microcapsules containing DCPD monomer. The dashed horizontal line in Fig. 2 shows the average peak load of epoxy control samples with no self-healing capability (no microcapsules). Comparison of the peak load for the control with that of the self-healing epoxy reveals that the addition of the microcapsules significantly toughens the epoxy. The self-healed samples actually recover more than 100% of the critical load for virgin epoxy with no microcapsules.

The time period over which healing takes place depends on a number of factors including environmental temperature, catalyst concentration, dissolution rate, etc. In Fig. 3 the development of static fracture healing efficiency is plotted versus healing time for self-healing epoxy with 2.5%wt Grubbs' catalyst and 10%wt microcapsules. There is an initial dwell period of about 25 minutes during which no appreciable healing can be measured. Thereafter, the healing efficiency increases rapidly before stabilizing at about 55% for this particular formulation. The initial dwell period is believed to be associated with transport of the healing agent to the fracture plane and gelation of the material in the crack. Once gelled, the healing agent begins to support load across the crack plane and a measurable healing efficiency can be identified. Thereafter, the network structure of the healing agent develops exponentially with time as is reflected in data.

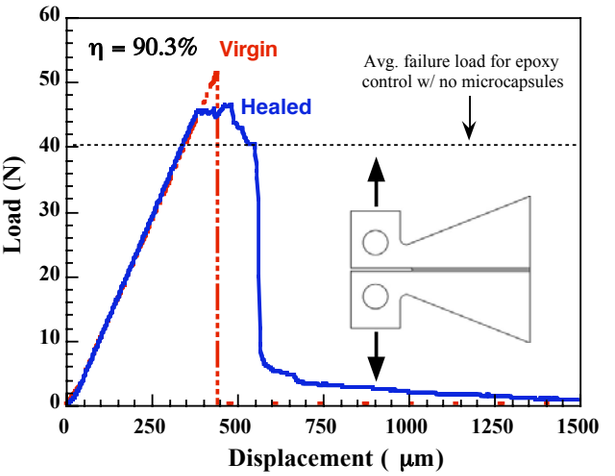


Fig. 2. Load-displacement data for a virgin and healed epoxy fracture toughness specimen [5].

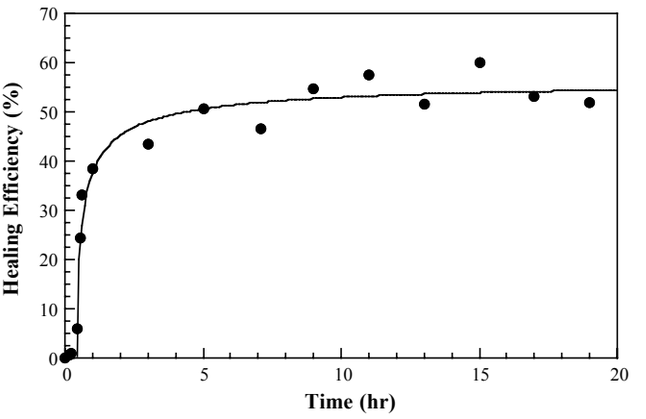


Fig. 3. Development of healing efficiency for a fracture sample with 10 wt % microcapsules and 2.5 wt%. catalyst.

HEALING OF FATIGUE CRACKS

While fracture toughness is an important property for evaluating the performance of self-healing polymers, fatigue loading is the primary cause of structural failures. Preliminary investigations of fatigue crack propagation in self-healing epoxy indicate that significant extension in fatigue life can be obtained. The data in Fig. 4 show the fatigue response for a self-healing epoxy specimen (20%wt microcapsules, 2.5%wt catalyst) in comparison to a control specimen devoid of the catalyst phase. Fatigue crack growth is arrested for about 4 x 105 cycles in the self-healing specimen before it begins to accelerate new the end of the specimen. Overall the fatigue life is extended by a factor of three in this specimen [7].

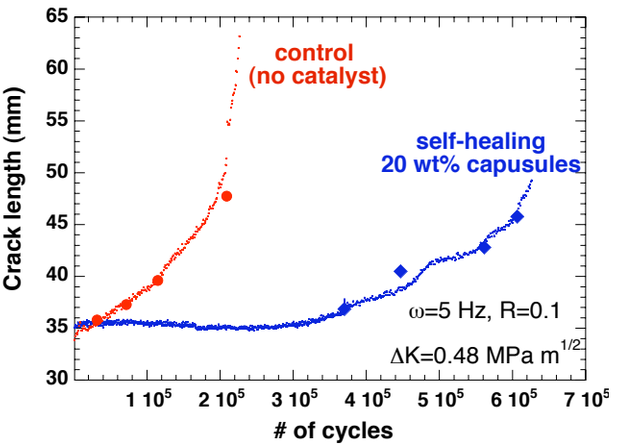


Fig. 4. Crack tip position versus number of cycles to failure for self-healing sample compared to control.

REFERENCES

[1] S.R. White, S.R., N.R. Sottos, P.H. Geubelle, J.S. Moore, M.R. Kessler, S.R. Sriram, E.N. Brown, S. Viswanathan, *Nature*, 409:794-797 (2001).
[2] M.R. Kessler and S.R. White, *Comp Part A: App Sci & Manuf*, 32(5):683-699 (2001).
[3] M.R. Kessler, N.R. Sottos, S.R. White, *Comp Part A: App Sci & Manuf*, 34(8):743-753 (2003).
[4] P. Schwab, R.H. Grubbs, J.W. Ziller, *J Am Chem Soc* 118:100–110 (1996).
[5] E.N. Brown, N.R. Sottos, S.R. White, *Experimental Mechanics*, 42(4):372-379 (2002).
[6] E.N. Brown, N.R. Sottos, N.R., S.R. White, J Mat Sci 39:1703-1710 (2004).
[7] E.N. Brown, N.R. Sottos, S.R. White, *Proc SEM Ann Conf on Exp & App Mech*, Charlotte NC, Society for Experimental Mechanics, CD-ROM, June 2-4 (2003).

XXI ICTAM, 15–21 August 2004, Warsaw, Poland

COMPOSITE PLATES WITH ACTIVE FIBERS

Mieczysław S. Kuczma

Institute of Structural Engineering, University of Zielona Góra, 65-516 Zielona Góra, Poland

Summary The bending problem of composite plates reinforced with active fibers is considered. The fibers are made of a shape memory material which may undergo a martensitic phase transformation. The matrix is treated as an elastic medium. Due to the phase transformation in fibers the deformation process is dissipative and accompanied by hysteresis loops. A macroscopic model of the stress-induced phase transformation under isothermal conditions is applied. The dissipation mechanism is traced by imposing the requirements of the second principle of thermomechanics and making use of a set of internal variables describing distributions of austenite and different variants of martensite. This hysteretic problem is formulated in the form of a variational inequality of evolutional type. The finite dimensional counterpart of it is derived by the finite element method, and is solved incrementally as a sequence of complementarity problems. Results of numerical simulation will be presented.

INTRODUCTION

Novel, the so-called *smart*, *active* or *adaptive* materials allow one to construct new functional types of structures and devices; composite materials can be designed to effectively meet the highly specialized needs of advanced technology [3]. In this presentation we are concerned with the mathematical modeling of composite plates that are symmetrically reinforced with shape memory alloy (SMA) fibers. Perfect bonding between the fibers and the matrix is assumed. Depending on the stress level, the SMA fibers can undergo a martensitic phase transformation. The latter takes place at a micro scale and can be described as cooperative movements of atoms into a new more stable crystal structure. Martensitic transformation is the diffusionless, first-order transformation occurring by nucleation and growth. The parent phase is conventionally called *austenite*, whilst the product of the transformation, which may occur in many variants, is called *martensite*. Although, the martensitic phase transformation is accompanied by energy dissipation, it is crystallographically reversible as the thermoelastic shape memory alloys exhibit a unique ability to recover shape.

We consider a thin plate of total thickness h composed of N_l orthotropic layers, of which N_r are reinforced with SMA fibers. The total domain occupied by the plate is $\Omega_0 \times (-h/2, h/2)$, where Ω_0 stands for the undeformed midplane of the composite plate. Let $\boldsymbol{u} = (u, v, w)$ be the displacement vector with its components u, v, w along the Cartesian coordinate system axes $x\,y\,z$, respectively. Further, let $\boldsymbol{u}_0 = (u_0, v_0, w_0)$ denote the midplane displacements vector, in which $w_0 = w_0(x, y, t)$ is the deflection of the midplane and we set $u_0 = 0 = v_0$ neglecting the extension-bending coupling. In this evolutional nonlinear process t plays a role of a time-like parameter. In the classical Kirchhoff plate theory the nonzero strains written in vector form are $\boldsymbol{\varepsilon} \equiv \mathrm{col}\,(\varepsilon_{xx}, \varepsilon_{yy}, 2\varepsilon_{xy}) = -z\boldsymbol{\gamma}$, where $\boldsymbol{\gamma} = \mathrm{col}\,(\partial^2 w_0/\partial x^2, \partial^2 w_0/\partial y^2, 2\partial^2 w_0/\partial x \partial y)$. The kth layer is located between the points $z = z_k$ and $z = z_{k+1}$ in the thickness axis. We have supposed that the response of the matrix is linearly elastic, whilst that of fiber's material will be governed by the phase transformation rules in the range of isothermal pseudoelasticity.

The linear elastic constitutive equations $\boldsymbol{\sigma} = \boldsymbol{C}\boldsymbol{\varepsilon}$ between components of the stress $\boldsymbol{\sigma}$ and strain $\boldsymbol{\varepsilon}$ tensors can be written for the kth orthotropic layer in its principle material coordinates $x_1\,x_2\,x_3$ in the matrix form

$$\left\{ \begin{array}{c} \sigma_1 \\ \sigma_2 \\ \sigma_6 \end{array} \right\}^{(k)} = \left[\begin{array}{ccc} C_{11} & C_{12} & 0 \\ C_{12} & C_{22} & 0 \\ 0 & 0 & C_{66} \end{array} \right]^{(k)} \left[\begin{array}{c} \varepsilon_1 \\ \varepsilon_2 \\ \varepsilon_6 \end{array} \right]^{(k)}$$

where components C_{ij} of the elasticity matrix $\boldsymbol{C}$ define elastic properties of the layer. In the global coordinate system $x\,y\,z$, relations () become

$$\left\{ \begin{array}{c} \sigma_{xx} \\ \sigma_{yy} \\ \sigma_{xy} \end{array} \right\}^{(k)} = \left[\begin{array}{ccc} \bar{C}_{11} & \bar{C}_{12} & \bar{C}_{16} \\ \bar{C}_{12} & \bar{C}_{22} & \bar{C}_{26} \\ \bar{C}_{16} & \bar{C}_{26} & \bar{C}_{66} \end{array} \right]^{(k)} \left[\begin{array}{c} \varepsilon_{xx} \\ \varepsilon_{yy} \\ \varepsilon_{xy} \end{array} \right]^{(k)} \tag{1}$$

where $\bar{\boldsymbol{C}}^{(k)} = \boldsymbol{T}^{(k)}\boldsymbol{C}^{(k)}\boldsymbol{T}^{(k)^{\mathrm{T}}}$, $\boldsymbol{T}^{(k)}$ – the transformation matrix from $x_1\,x_2\,x_3$ to $x\,y\,z$ for the kth layer, see e.g. [10].

CONSTITUTIVE RELATIONS FOR A SMA LAYER

The shape memory alloy is a multiphase material that may occur in $N+1$ preferred strain states $\boldsymbol{d}_i$ which correspond to austenite and N variants of martensite, whose volume fractions c_i are changing during the martensitic phase transformation process. At fixed volume fractions $\boldsymbol{c}$, the averaged Helmholtz free energy of the austenite-martensite mixture may be

expressed as a locally quadratic multi-well function, cf e.g. [1, 4, 9],

$$W(\boldsymbol{\varepsilon},\boldsymbol{c}) = \frac{1}{2}\left[\boldsymbol{\varepsilon}-\boldsymbol{d}(\boldsymbol{c})\right]\cdot\boldsymbol{C}\left[\boldsymbol{\varepsilon}-\boldsymbol{d}(\boldsymbol{c})\right] + \sum_{i=1}^{N+1} c_i\varpi_i + \frac{1}{2}\sum_{i=1}^{N+1}\sum_{j=1}^{N+1} c_i c_j B_{ij}$$

wherein $\boldsymbol{d}(\boldsymbol{c}) = \sum_{i=1}^{N+1} c_i\boldsymbol{d}_i$ is the effective transformation strain, $\boldsymbol{C}$ the (same) elasticity tensor for each phase, and ϖ_i,B_{ij} material constants. From the 2nd principle of thermomechanics we can obtain an expression for the driving force of phase transformation which must satisfy the positive dissipation constraint [6]

$$\mathcal{D} = -\frac{\partial W}{\partial \boldsymbol{c}}\cdot\dot{\boldsymbol{c}} \equiv \boldsymbol{X}\cdot\dot{\boldsymbol{c}} = \sum_{m=1}^{N} X_m\,\dot{c}_m \geq 0 \tag{2}$$

Accounting for (2) we introduce the threshold functions κ_m for the driving force X_m $(m = 1,\ldots,N)$ and define the phase transformation functions $G_m = G_m(\boldsymbol{\varepsilon},\boldsymbol{c})$ whose positive $()^+$ and negative $()^-$ parts are

$$G_m^+ \equiv \kappa_m^+ - X_m \geq 0, \qquad G_m^- \equiv X_m - \kappa_m^- \geq 0$$

The evolution of volume fractions c_m of martensite variants are governed by the following conditions

$$c_m \geq 0, \quad \sum_{m=1}^{N} c_m \leq 1, \qquad \sum_{m=1}^{N} G_m^{\pm}(\boldsymbol{c})(\xi_m^{\pm} - \dot{c}_m^{\pm}) \geq 0 \quad \text{for all } \xi_m^{\pm} \geq 0 \tag{3}$$

The stresses in the reinforced rth layer are, cf (1),

$$\left\{\begin{array}{c}\sigma_{xx}\\ \sigma_{yy}\\ \sigma_{xy}\end{array}\right\}^{(r)} = \left[\begin{array}{ccc}\bar{C}_{11} & \bar{C}_{12} & \bar{C}_{16}\\ \bar{C}_{12} & \bar{C}_{22} & \bar{C}_{26}\\ \bar{C}_{16} & \bar{C}_{26} & \bar{C}_{66}\end{array}\right]^{(r)} \left[\begin{array}{c}\varepsilon_{xx} - d_{xx}(\boldsymbol{c})\\ \varepsilon_{yy} - d_{yy}(\boldsymbol{c})\\ \varepsilon_{xy} - d_{xy}(\boldsymbol{c})\end{array}\right]^{(r)} \tag{4}$$

CLOSING REMARKS

Using (1) and (4) we arrive at the differential equation for the plate,

$$L\left(\boldsymbol{D}\,\boldsymbol{\gamma}(w_0)\right) + L\left(\boldsymbol{S}\,\bar{\boldsymbol{d}}(\boldsymbol{c})\right) = p(x,y,t) \tag{5}$$

wherein $L(\cdot)$ is the linear partial differential operator of an anisotropic plate, p is loading, and

$$D_{ij} = \frac{1}{3}\sum_{k=1}^{N_l} \bar{C}_{ij}^{(k)}\left(z_{k+1}^3 - z_k^3\right), \qquad S_{ij} = \frac{1}{2}\sum_{r=1}^{N_r} \bar{C}_{ij}^{(r)}\left(z_{r+1}^2 - z_r^2\right)$$

The equlibrium condition (5) and the phase transformation conditions (3) will be written in the form of a variational equation and variational inequalities, respectively, from which we can determine the deflection w_0 and distributions $\boldsymbol{c}^{(r)} = \boldsymbol{c}^{(r)}(x,y,t)$ of different variants of martensite in all reinforced layers of the plate. A computer code for this evolutional boundary value problem has been developed, based on the standard FEM [5]. Results of numerical examples will be presented. As the next step, it would be interesting to apply hierarchical models [7, 8], and to consider the case of magnetic shape memory alloy fibers where an adaptive procedure could be used [2].

References

[1] Ball J., James R.: Fine phase mixtures as minimizers of energy. *Arch. Rational Mech. Anal.*, **100**:13–52, 1987.
[2] Demkowicz L.F.: Fully Automatic hp-Adaptivity for Maxwell's Equation. *TICAM Report* **03-45**, September 2003.
[3] Gandhi M.V., Thompson B.S.: Smart Materials and Structures. Chapman & Hall, London 1992.
[4] Kohn R.: The relaxation of a double-well energy. *Cont. Mech. Thermodyn.*, **3**:193–236, 1991.
[5] Kuczma M.S., Kula K.: Analysis of the elastic composite plates by the finite element method. CURE, Proc. *Effective use of building materials.* 135-138, Sopot, October 8-9, 2003.
[6] Kuczma M.S., Mielke A., Stein E.: Modelling of hysteresis in two phase systems. *Arch. Mech.* **51**:693–715, 1999.
[7] Oden J.T., Cho J.R.: Adaptive hpq-finite element methods of hierarchical models for plate- and shell-like structures. *CMAME* **136**:317–345, 1996.
[8] Oden J.T., Prudhomme S., Hammerand D.C., Kuczma M.S.: Modeling error and adaptivity in nonlinear continuum mechanics. *CMAME* **190**:6663–6684, 2001.
[9] Raniecki B., Lexcellent C., Tanaka K.: Thermodynamic models of pseudoelastic behaviour of shape memory alloys. *Arch. Mech.*, **44**:261–284, 1992.
[10] Reddy J.N.: Mechanics of Laminated Composite Plates. Theory and Analysis. CRC Press, Boca Raton 1997.

TRANSIENT EIGENSTRAINS WITHOUT INCREMENTAL DISPLACEMENTS IN A HYPERELASTIC BODY

Hans Irschik, Uwe Pichler
Institute of Technical Mechanics, Johannes Kepler University of Linz, A – 4040 Linz, Austria

Summary We consider a hyperelastic body in a static intermediate configuration, loaded by an additional distribution of transient eigenstrains, the latter being e.g. due to the electric field in a piezoelastic body, or due to the temperature in a thermoelastic body. We seek for distributions of eigenstrain, such that that the incremental displacements vanish throughout the body. In the present paper, within the framework of the theory of small dynamic deformations superimposed upon a static strain, we derive solutions for eigenstrains that are applied at a sub-region of the body only.

1. INTRODUCTION

Consider a structure that is fixed at some part of its boundary, and that is initially at rest in a pre-deformed intermediate state with a possibly large strain. The constitutive behavior of this body is taken as hyperelastic, and the static intermediate state is assumed to be infinitesimally superstable. The body is loaded by an additional distribution of transient eigenstrains, the actuating effects of which are described by actuation stresses. Eigenstrains e.g. may be due to the electric field in a piezoelastic body, or due to the temperature in a thermoelastic body. We seek for additional actuation stresses, such that that the incremental displacements vanish throughout the body for all times. The body then will remain in the static intermediate configuration, despite its transient actuation by eigenstrains. A static solution for such "nilpotent" distributions was addressed by Irschik and Ziegler [1], and the dynamic extension was given in Irschik and Pichler [2], see Irschik et. al. [3] for beam vibrations. In these solutions, the actuation was required to be distributed all over the body under consideration, and the linear theory of elasticity was employed. In the present paper, we derive solutions for actuation stresses that are applied at a sub-region of the body only, and we work within the framework of the theory of small dynamic deformations superimposed upon a possibly large static strain.

2. A THEOREM ON EIGENSTRAINS WITHOUT DISPLACEMENTS

Consider an elastic body being at rest in some deformed state of equilibrium. This state may represent a large static deformation from an undistorted configuration of the body and is denoted as the intermediate configuration. Due to an additional time-dependent eigenstrain, small incremental displacements u are superimposed upon the intermediate configuration, accompanied by small incremental deformations. In order to describe this small motion, we use the intermediate state as the reference configuration. The incremental first Piola-Kirchhoff stress tensor S then is given as:

$$S = A[H] + S^a \tag{1}$$

with $S = T_R - T$, where T_R is the first Piola-Kirchhoff stress in the actual configuration and T is the static Cauchy stress in the intermediate configuration. The gradient of u with respect to the place in the intermediate configuration is denoted as H. The second order tensor S^a in Eq. (1) represents the incremental stress actuation tensor due to the additional eigenstrain superimposed upon the intermediate state. E.g., in case this eigenstrain is due to an incremental temperature rise θ, the actuation stress can be taken as a linear mapping of θ, since we deal with small incremental displacements, $S^a = A[\theta M]$, the quantity θM representing the tensorial eigenstrain. When the additional eigenstrain is formed by an electric field in a piezoelastic body, S^a can be also written as a linear mapping of the electric field vector. The incremental stress S has to satisfy the local form of the equation of balance of linear momentum,

$$DivS = \rho \ddot{u}, \tag{2}$$

where a superposed dot denotes the time-derivative, and ρ is the mass density. Div stands for the divergence operator with respect to the place in the intermediate configuration. Homogeneous kinematic boundary conditions are assigned at the part ∂B_1 of the boundary, while at the remaining part ∂B_2 the additional surface tractions are taken to vanish. Since we assume the additional motion to start from the intermediate configuration, which is at rest, we deal with homogeneous initial conditions. In the present contribution, we derive the following theorem:
Assume that the intermediate configuration is infinitesimally superstable and that the additional actuation stress S^a acts in some sub-region $\hat{B}$ of the body B, vanishing outside of $\hat{B}$. Consider the class of a non-vanishing divergence-free actuation stress in $\hat{B}$ satisfying homogeneous boundary conditions at $\partial\hat{B}_2$, a so-called statically admissible stress,

$$DivS^a = 0, \qquad \partial\hat{B}_2 : \; S^a \hat{n} = 0. \tag{3}$$

This class produces a displacement that vanishes throughout B, $u = 0 \;\; \forall \;\; t$. Hence, when the actuating stress S^a satisfies Eqs.(3), then the incremental displacements u vanish throughout the body B for all times $t \geq 0$. The body thus will remain in the static intermediate configuration, despite the transient action of S^a.

3. NUMERICAL EXAMPLE

The above result for eigenstrains without displacements should be of technological interest in various fields, due to the widespread applicability of the theory of eigenstrains. The methodology requires that the actuation stress be tailored, which becomes practically visible in view of modern functional and smart materials. In the following, we present a computational example using the Finite Element Code ABAQUS, which allows taking into account a non-homogeneously distributed anisotropic transient actuation stress of thermal origin. Consider the quadratic domain B shown in Fig.1 in a state of plane strain. The region is subdivided into a sufficiently high number of Finite Elements of the type CPE4R. Two adjacent edges, EAC, of B are fixed, forming the part ∂B_1 of the boundary. The remaining edges CDE form the stress-free part ∂B_2 of the boundary. The rectangle $EAFG$ forms the subregion $\hat{B}$. We assume the region B to represent an undistorted, stress-free configuration, with the isotropic tensor of elastic parameters A (Young's modulus $Y = 211.10^6$ in proper units of stress, and Poisson's ratio $\nu = 0.3$).

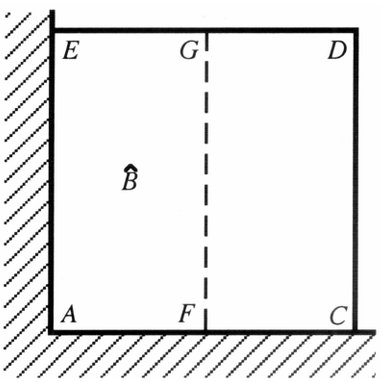


Figure 1: Original problem

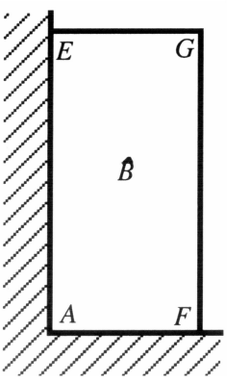


Figure 2: Auxiliary problem

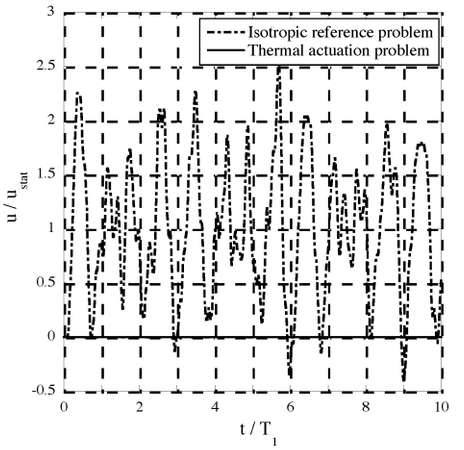


Figure 3: Step response

In order to obtain a non-vanishing reference displacement, we consider the case of a transient isotropic actuation stress of thermal origin, being distributed constantly within the subdomain $\hat{B}$ in Fig. 1, $S_i^a = \hat{S}^a H(t)$, $\hat{S}^a = -\alpha\theta_o A[I]$, and vanishing outside of $\hat{B}$, in the domain $GFCD$. $H(t)$ denotes the Heaviside step function, the unit tensor is denoted as I, and the thermal eigenstrain is chosen as $\alpha\theta_o = 2.10^{-9}$. The corresponding step-response displacements are denoted as isotropic reference problem in Fig.3. We then consider the problem of determining a statically admissible stress, see Eqs.(3), in order to obtain a vanishing displacement. For that sake, we treat the auxiliary problem of Fig.2, where the fixed part $\partial\hat{B}_1$ of the corresponding body with domain $\hat{B}$ is formed by the adjacent edges EAF, and the stress-free part $\partial\hat{B}_2$ is formed by FGE. The static actuation stress $\hat{S}^a$ is applied to the auxiliary body shown in Fig. 2, and the corresponding static stress distribution $\hat{S}$ is computed. Following the above theorem, the transient actuation stress $S^a = \hat{S}\ H(t)$, which is anisotropic and non-homogeneously distributed, then is applied to the subdomain $\hat{B}$ of B in the original problem, since such an S^a satisfies Eqs.(3). The step response of the domain B is again calculated by means of the dynamic Finite Element code. As a typical result, the horizontal displacement of corner D is presented in Fig. 3 (denoted as thermal actuation solution) and compared to the corresponding step response of the isotropic reference problem. It is seen that the dynamic displacement due to S^a (the thermal actuation solution) is not only much smaller than the isotropic reference solution, but that it indeed does vanish, as predicted by our above theorem.

Acknowledgement:

Support of this work by the Austrian government, the government of Upper Austria and the industrial partners of the Kplus Linz Center of Competence in Mechatronics (LCM) is sincerely appreciated.

References

[1] Irschik, H., Ziegler, F.: Eigenstrain without stress and static shape control of structures. *AIAA J.* **39**:1985–1999, 2001.

[2] Irschik, H., Pichler, U.: An extension of Neumann's method for shape control of force-induced elastic vibrations by eigenstrains. *International Journal of Solids and Structures* **41**:871–884, 2004.

[3] Irschik, H., Krommer, M., Belyaev, A., Schlacher, K.: Shaping of Piezoelectric Sensors/Actuators for Vibrations of Slender Beams: Coupled Theory and Inappropriate Shape Functions. *Journal of Intelligent Materials Systems and Structures* **9**:546-554, 1998.

XXI ICTAM, 15-21 August 2004, Warsaw, Poland

SHAPE FIXITY AND SHAPE RECOVERY OF SHAPE MEMORY POLYMER AND THEIR APPLICATIONS

Hisaaki Tobushi*, Ryosuke Matsui*, Tsuyoshi Takada* and Shunichi Hayashi**
** Department of Mechanical Engineering, Aichi Institute of Technology, Toyota, 470-0392, Japan*
*** Advanced Technology Research Center, Mitsubishi Heavy Industries, Yokohama, 236-8515, Japan*

Summary The thermomechanical properties of polyurethane-shape memory polymer (SMP) foams were investigated experimentally. If the foam is compressed at high temperature, the rate of shape fixity is 100 % and that of shape recovery 98 %. Recovery stress is 80 % of the applied stress. The shape deformed at high temperature is maintained for six months under no-load at T_g-60 K without de-pending on maximum strain. If the deformed shape is kept at high temperature, secondary-shape forming appears. Applications of SMP are introduced.

INTRODUCTION

Shape memory polymer (SMP) is one of the high-performance materials which have been developed and used in practical applications. The shape fixity and shape recovery exist due to the glass transition. The shape fixity and shape recovery are used in the fields of technology, medical treatment, aerospace engineering, etc. Since the polyurethane-SMP foams have many superior functions, applications of the SMP foams are expected in the wide fields. In order to design SMP-foam elements rationally, it is important to evaluate the functional properties of the material. In the present paper, in order to study the thermomechanical properties of polyurethane-SMP foams, the shape fixity, shape recovery and recovery stress are investigated. The conditions which affect secondary-shape forming are discussed.

EXPERIMENTAL METHOD

The material used in the experiment was polyurethane SMP foam of the polyether polyol series (Diary MF 5520 : produced by Mitsubishi Heavy Industries, Ltd.). The foam was made by chemical foaming. The expansion ratio was about 14 and the structure was open cell. The foam was produced as slabstock. The specimen was a column with height of 20 mm and diameter 20 mm.

Experimental procedures

In order to investigate the thermomechanical properties, the following four kinds of compression test were carried out.
(1) Thermomechanical test
(2) Recovery-stress test
(3) Aging test held at low temperature
(4) Secondary-shape forming test held at high temperature

RESULTS AND DISCUSSION

Shape fixity and shape recovery

From the stress-strain curves obtained by the thermomechanical test, it can be seen that yielding occurs in the vicinity of a strain of 10 %, stress plateau appears thereafter till a strain of 60 % and the slope of the curve becomes steep above a strain of 60 %. In the region of the stress plateau for strain from 10 % to 60 %, buckling of cells propagates in the axial direction of compression. In the upswing region above a strain of 60 %, the material is compressed uniformly and deformation resistance increases. In the cooling process, stress disappears perfectly below T_g. Therefore maximum strain is maintained, resulting in a rate of shape fixity R_f of 100 %.
From the strain-temperature curves obtained by the thermomechanical test, it can be seen that strain is recovered significantly in the vicinity of T_g in the heating process under no load. Since the micro-Brownian motion of soft segments of SMP is frozen in the glassy region at temperatures below T_g, strain is maintained. Since the micro-Brownian motion becomes active if the material is heated up to temperatures in the vicinity of T_g, strain is recovered. The strain-temperature curves do not change under repetition. Irrecoverable strain remaining after heating is small without depending on the number of cycles, and a rate of shape recovery R_r is 99 %.

Recovery stress

From the stress-temperature curves obtained by the recovery-stress test, it can be seen that stress increases markedly in the vicinity of T_g in the heating process under constant strain. This behaviour occurs due to the fact that, though the micro-Brownian motion of soft segments of SMP is frozen at low temperature and molecular chain can not move, the micro-Brownian motion becomes active by heating up to the vicinity of T_g and recovery stress appears gradually with an increase in temperature.
Recovery stress is proportional to the applied maximum stress. Recovery stress is about 80 % of the applied stress. Since large change in volume can be obtained for SMP foam elements, they can be applied to the easily portable energy sources to use recovery stress.

Aging by holding at low temperature

It can be seen from the aging test held below T_g for maximum compressive strain that a rate of shape fixity R_f is larger than 99 % even if the time has passed for longer than 1000 hours. Although some amounts of shape are not fixed, these values are enough small. Therefore, the deformed shape can be fixed if it is held below T_g-60 K. A rate of shape recovery R_r is larger than 98 % without depending on the holding time. It is ascertained that a rate of shape fixity and a rate of shape recovery by holding the shape below T_g are larger than 98 % without depending the holding time and maximum strain, resulting in good performance.

Secondary-shape forming by holding at high temperature

In the process of the present study, it was found that, if SMP foam was deformed and the deformed shape was held for a long time above T_g, irrecoverable deformation appeared. That is, it was found that the deformed shape was not recovered and fixed. This phenomenon is called secondary-shape forming. From the experimental results obtained by the secondary-shape forming test held at high temperature, it is ascertained that the factors to affect secondary-shape forming are the holding strain, temperature and time. The cause of secondary-shape forming can be considered as follows. In the region of temperature above T_g, thermal motion of molecular chain (micro-Brownian motion) is active and therefore reorientation of molecular chain occurs during holding large strain for a long time.

In order to avoid secondary-shape forming for the deformed SMP foam, it is important to keep the foam under the appropriate condition by considering these conditions. One of the methods to prevent secondary-shape forming is to keep the foam below T_g. In the region of temperature below T_g, secondary-shape forming does not appear and both the rate of shape fixity and that of shape recovery are high. Therefore, holding at low temperature must be effective for applications of SMP foam elements.

APPLICATIONS OF SMP

The shape memory polymers of polyurethane series have many functions as smart materials and have been used for practical applications in many fields. Modulus of elasticity, volume expansion, gas permeability, refractive index and dielectric constant vary depending on variation in temperature. Shape fixity, shape recovery and recovery force appear depending on the thermomechanical properties of SMP. These properties can be applied in the fileds of medical treatment, aerospace engineering, car technology and electrification products.

CONCLUSIONS

Applying various thermomechanical loadings to polyurethane-SMP foams, the thermomechanical properties of the material were investigated. Applications of SMP were introduced. The results obtained by the experiments can be summarized as follows.

(1) The rate of shape fixity and that of shape recovery are 100 % and 99 %, respectively. Both rates do not depend on the number of cycles.
(2) If the SMP foam deformed above T_g followed by cooling is heated while holding the deformed shape, recovery stress appears. The recovery stress is about 80 % of the applied stress.
(3) If the SMP foam is compressed above T_g followed by holding at T_g-60 K, the deformed shape is fixed even if the material is kept under no load for six months. The fixed shape is recovered by heating thereafter. Both the rates of shape fixity and shape recovery are larger than 98 %, which do not depend on the holding time and maximum strain.
(4) If the deformed SMP foam is held above T_g, secondary-shape forming appears. The factors to affect secondary-shape forming are the holding strain, temperature and time.

ACKNOWLEDGEMENTS

The experimental work of this study was carried out with the assistance of the students in Aichi Institute of Technology, to whom the authors wish to express their gratitude. The authors are grateful to Mr. Norio Miwa of Churyo Engineering Co. for his corporation of preparing the material. The authors also wish to extend thanks to the Scientific Research (C) in Grants-in-Aid for Scientific Research by the Japan Society for Promotion of Science for financial support.

REFERENCES

[1] Hayashi, S. *Int. Progr. Urethanes*, 6, 90-115 (1993).
[2] Tobushi, H., Okumura, K., Hayashi, S. and Ito, N. *Mech. Mater.*, **33**, 545-554 (2001).
[3] Tobushi, H., Okumura, K., Endo, M. and Hayashi, S. *J. of Intell. Mater. Syst. & Struct.*, **12**, 283-287 (2001).

VIBRATION CONTROL OF STIFFENED PLATES WITH INTEGRATED PIEZOELECTRICS

Jin-Young Jung, Ji-Hwan Kim

School of Mechanical and Aerospace Engineering, Collage of Engineering, Seoul National University, Seoul 151-742, Korea

Summary Vibration control of stiffened plate with piezoelectric sensors and actuators subjected to normal blast shock wave is studied. The model is a laminated composite plate with stiffeners and PZT piezoceramic layers. Using linear quadratic regulator, vibration characteristics and transient response are studied. The effect of stiffener's location and piezoelectric patch's position on the transient response of the stiffened plate subjected to blast load is investigated.

INTRODUCTION

An application of stiffened laminated composite plate has greatly enhanced structures for aircraft, aerospace and other industries. In the application, the stiffened laminated composite plates are subjected to different loading conditions such as air blast loading. The blast wave makes a sharp pressure to the structure in an instant. Due to the advantages of piezoelectric materials such as fast response, large force output, it is competent to control the vibration of stiffened laminated composite plates under the blast load.

FORMULATION

The stiffened plate element is composed of a plate element and a number of stiffener elements. Both the plate and stiffeners are assumed to be made up of laminated composites. Using the first-order shear deformation theory (FSDT), the plate element has elastic degrees of freedom u_p^o, v_p^o, θ_{xp}, θ_{yp} and w_p^o per node and one electrical degree of freedom ϕ per piezoelectric layer. The electric potential ϕ is assumed to be constant over an element piezoelectric layer and varying linearly through the thickness of the piezoelectric layer. The stiffener element is three-node beam element with three degree of freedom at each node. Using transformation matrix $\mathbf{T}_{xs}$, the nodal displacement of stiffener elements can be written as that of plate elements.

Applying Hamilton's principle, the state-space form of the global dynamic equation can be written as

$\dot{\xi} = \mathbf{A}_{st}\xi + \mathbf{B}_{st}\phi_a + \mathbf{U}_f$. where ϕ_a is the control input.

And actuating voltage of LQR can be expressed as $\phi_a(t) = -\mathbf{G}_c\xi = -\mathbf{R}^{-1}\mathbf{B}_{st}{}^T\mathbf{P}\xi$

NUMERICAL RESULTS

A cantilevered laminated composite plate with two x-stiffeners is analyzed. The plate(T300/976 graphite-epoxy) is bonded at the upper and lower surfaces by piezoelectric ceramics(PZT G1195N). Dimensions of the plate which consists of four composite layers $(15^\circ/-15^\circ/-15^\circ/15^\circ)$ with $(0.4/0.4/0.4/0.4)\,mm$ layers are 0.4m X 0.2m.

The eccentric stiffeners with width 6mm and depth 12mm are made of the same material and consist of four composite layers ($0^\circ/0^\circ/0^\circ/0^\circ$). Each piezoceramic layer is of thickness 0.2mm. The adhesive layers are neglected. In vibration control, the upper piezoelectric layer is assumed as sensor and the lower piezoelectric layer is assumed as actuators. Modal superposition method is used in the analysis, considering first six modes. And the initial damping ratio for each of the modes is assumed to be 0.7%.

The effect of stiffener's location is investigated. The two stiffeners are placed at the same distance (d) from the centerline along the width of the plate. And the stiffener's location can be defined as $\mu = 2d/C$.

where C is the width of the plate. Natural frequencies of the stiffened plate under different stiffener's locations are compared. It can be seen that natural frequencies of the bending mode at $0.4 \le \mu \le 0.6$ are higher than those of the others. And the natural frequencies of the twisting mode at $0.8 \le \mu \le 1$ are higher than those of the others. To investigate the effect of stiffener's location on control performance, typical configurations (μ = 0, 0.5 and 1) of stiffened plate are considered in the present study. From the frequency response and time response of stiffener's location at $\mu = 1$, the piezoelectric sensors and actuators can control the first, second and third bending modes effectively, and the vibration is damped out more quickly for higher control parameter. The other cases can be investigated in a similar way.

The effect of piezoelectric patch's position on the transient response of the stiffened plate subjected to blast load is investigated. Piezoelectric patch model has dimensions of 0.05m X 0.05m. The centers of Model Ⅰ, Ⅱ, Ⅲ and Ⅳ are 0.05m, 0.15m, 0.25m and 0.35m away from the clamped edge, respectively. To compare the control effects, two performance parameters are introduced. One parameter is Settling time which oscillation doesn't exceed limit value of each transient response. The limit values of vertical displacement, transverse bending and lateral twisting are 0.4mm, 0.002 and 0.002, respectively. And the other is maximum response. For $\mu = 1$, Model Ⅰ and Ⅳ have shorter settling time than that of the others in vertical displacement and transverse bending. And Model Ⅲ can control the lateral twisting more effectively.

CONCLUSIONS

When the stiffeners are placed between centerline and free edge, the stiffness of the stiffened plates is increased for bending mode. But the stiffness of twisting mode is increased at free edge. LQR can control bending mode and twisting mode effectively. This is because it changes the system damping including natural frequency. It can be determined the most effective position of piezoelectric patches by comparing with settling time and maximum response. The most effective positions of piezoelectric patches are different for each stiffener location.

References

[1] V. Balamurugan and S. Narayanan, "Shell finite element for smart piezoelectric composite plate/shell structures and its application to the study of active vibration control", Finite Elements in Analysis and Design, Vol. 37, No. 9, 2001, pp. 713-738.

[2] E. A. Sadek and S. A. Tawfik, "A finite element model for the analysis of stiffened laminated plates", Computers and Structures, Vol. 75, No. 4, 2000, pp. 369-383.

[3] A. H. Sheikh and M. Mukhopadhyay, "Linear and nonlinear transient vibration analysis of stiffened plate structures", Finite Elements in Analysis and Design, Vol. 38, No. 6, 2002, pp. 477-502.

RESIDUAL STRESS EFFECTS ON FERROELECTRIC THIN FILM PATTERNING, PROPERTIES AND PERFORMANCE

N.R. Sottos[*], T. Berfield[*], R. Ong[**], and D.A. Payne[**]
[*] *Theoretical and Applied Mechanics, University of Illinois Urbana-Champaign, Urbana IL 61801*
[**] *Materials Science and Engineering, University of Illinois Urbana-Champaign, Urbana IL 61801*

Summary In this paper, we investigate the influence of processing, interfacial adhesion and residual stresses on ferroelectric thin film performance. Residual stress development is characterized for pattered PZT sol-gel films on functionalized substrates and for fully crystallized PZT films of varying thickness. For sol-gel films, residual stress plays a beneficial role in the patterning process, while for fully crystallized PZT films, residual stress is found to decrease electromechanical performance.

PROCESSING AND MEDIATED PATTERNING OF PZT SOL-GEL THIN FILMS

An additive method of patterning was investigated that enables integration of thin film electroceramics on a chip, rather than as a discrete component added into the circuit and system. Patterned oxide thin-film devices are typically formed by uniform film deposition followed by a somewhat complicated post-deposition ion-beam or chemical etching in a controlled environment, i.e., a subtractive method. In recent work, a unique additive approach has been developed that allows for selective deposition of electroceramic thin layers without conventional photolithography and post-deposition etching [1,2]. In this soft lithographic method, substrate surfaces are selectively functionalized with hydrophobic self-assembled monolayers (SAM) to modify the adhesion of subsequently deposited solution-derived electroceramic materials. The selective functionalization is achieved through microcontact printing (μ-CP) of self-assembled monolayers of the chemical octadecyltrichlorosilane (ODS) on a substrate of interest. Subsequent sol-gel deposition of ceramic oxides on the functionalized substrates, followed by lift-off from the monolayer, yields high quality, patterned oxide thin layers on the unfunctionalized regions, exclusively.

The results of a prototypical selective deposition of PZT, before and after oxide lift-off, are shown in Fig. 1. The ODS molecular monolayer or "ink" was applied to a flexible stamp surface molded with the desired pattern from a master (Fig. 1a). The stamp was then placed in contact with a substrate to achieve selective transfer of the ink pattern. Upon removal of the stamp, selective transfer of monolayer was achieved. Mediated deposition of PZT sol-gel layers above the ODS-modified surfaces was accomplished by spin coating deposition of the sol-gel precursor to the patterned substrate. Low temperature (120-140°C) heat treatment was necessary to achieve selective decohesion above the modified regions (Figs. 1b). The resulting patterned film was then dried and heat-treated further to obtain a dense, patterned layer (Fig. 1c). Shrinkage during heat treatment and the resulting residual stress development in the film led to the desired film cracking for lift-off, enabling the mediated patterning process.

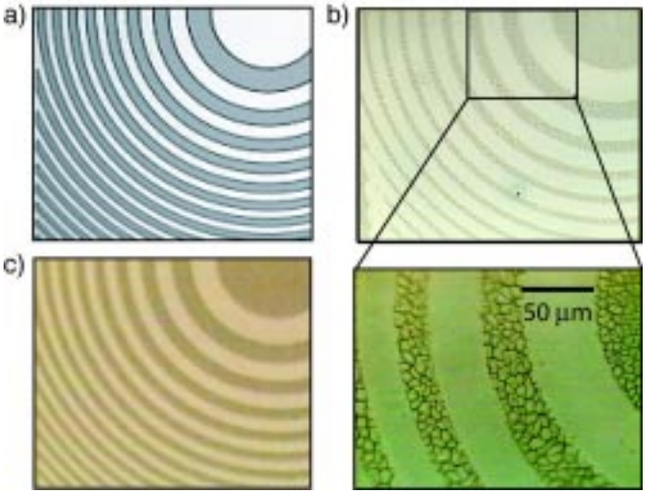


Fig. 1. Mediated deposition of PZT thin film: a) Master mold, b) selective cracking and decohesion over transferred SAM pattern, c) final patterned PZT film, light regions are PZT, dark regions are the Si substrate [1,2].

SHRINKAGE AND RESIDUAL STRESS DEVELOPMENT

Significant residual stresses develop in sol-gel processing of electroceramic thin films during the transformation of the metalorganic gel to the metal oxide (*i.e.*, ceramic) on heat treatment. Intrinsic residual stress is induced by shrinkage and constrained densification during drying and depends on the relative rates of evaporation, viscous deformation and flow of liquid through the pores of the gel. Extrinsic thermal stresses are induced upon cooling due to the mismatch between the developing thermoelastic properties of the film with those of the substrate. Residual stress impacts the mechanical integrity and reliability of the film. The interfacial bond between the film and the substrate must be capable of withstanding the force produced by the integrated stress throughout the film. Stress cracking, buckling and poor adhesion are commonly observed when the stress level exceeds a critical value. The mechanism of monolayer-mediated patterning (Fig. 1) is closely coupled to that of stress release by film decohesion above the functionalized regions of the substrate.

Residual stress development was monitored by in-situ laser reflectance measurements of wafer curvature using a KLA-Tencor FLX-2908 laser reflectance system. This apparatus enables accurate measurement of wafer curvature by carrying out a line scan with up to 100 points fitting the radius of curvature. The stress in the films was calculated from the change in radius of curvature using the Stoney equation [4]. Use of the Stoney equation enabled calculation of stress in the thin film from the substrate elastic properties without the need to know film properties.

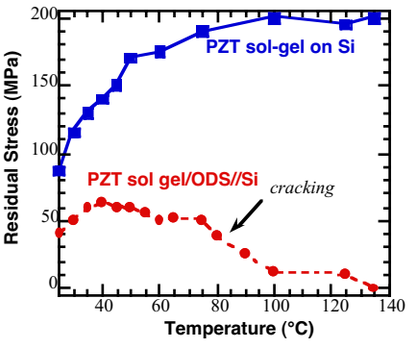


Fig. 2. Residual stress development of PZT sol-gel layers on different ODS-mediated substrates compared with a film on bare Si.

Residual stress development was first investigated during heat treatment and subsequent lift-off of the amorphous sol-gel films. For films deposited on bare substrate (*i.e.,* no ODS layer), constrained shrinkage resulting from adhesion to the supporting substrate led to a coherent (crack-free) film of 50 nm in thickness with biaxial stresses of ~200 MPa (Fig. 2). For ODS-mediated sol-gel films, however, precise *in situ* wafer curvature measurements captured the evolution and release of stresses during de-cohesion of the sol-gel layer. The resultant stresses in the mediated film never exceeded 75 MPa due to the onset of cracking and subsequent decohesion. The relationship between residual stress and interfacial fracture clearly controlled the desired patterning process.

The residual stress of fully crystallized PZT films was then measured after firing in a pre-heated box furnace at 650ºC for 30 minutes. $Pb(Zr_{0.53}Ti_{0.47})O_3$ films ranging in thickness from 190 nm to 500 nm were investigated. Thickness of films was varied by adjusting the number of sol-gel layers (in this case 4, 8, and 12) deposited onto platinized silicon substrates. The measured thickness and residual stress data for each film are listed in Table 1.

Table 1. Measured film properties for different number of sol-gel layer build-ups.

Sample	Thickness (μm)	Residual Stress (MPa)	Dielectric Constant, K'	tan δ
4 Layer	0.19	1500	800	.03
8 Layer	0.35	900	1100	.02
12 Layer	0.50	650	1200	.02

EFFECT OF RESIDUAL STRESS ON ELECTROMECHANICAL PERFORMANCE

Both the dielectric properties and the field-induced strains were measured for the films listed in Table 1. Top electrodes of platinum, 1.2 mm in diameter and 2000Å thick, were sputtered onto the films with no observable change in the measured film stress. The electrodes were jumped using fine copper wire and silver epoxy, and the entire wafer was mounted to a 3"x3" aluminum block. Electrical characterization was carried out on an HP 4284A with an AC signal of 5mV at 1.0 kHz. The dielectric constant (Table 1.) decreased significantly with decreasing film thickness. The field-induced strains of films under varying residual stress states were measured using an interferometric technique developed by Lian and Sottos [3]. Strain-field loops are plotted in Fig. 3 for PZT films of varying thickness and residual state. The strain field response also decreased dramatically with increasing residual stress (decreasing thickness).

Hence, residual stress development during processing of fully crystallized ferroelectric thin films is found to have a significant negative impact on electromechanical properties and performance. The tensile residual stress creates an in plane clamping effect on the domains in the film, hindering polarization switching. While residual stress has a desirable effect on film patterning by inducing selective decohesion, it can have an undesirable impact on the electromechanical performance of the final patterned device.

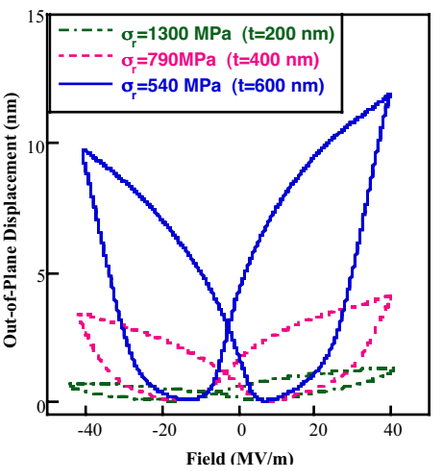


Fig. 3. Effect of residual stress (and film thickness) on field-displacement loops for fully crystallized PZT thin films.

References

[1] Mikalsen, E. and Payne, D.A. Mediated patterning of electroceramic thin films. J. *Electroceramics*, Accepted (2003).

[2] Mikalsen, E. A. Mediated patterning of sol-gel thin layers, shrinkage, de-cohesion, and lift-off. Ph.D. Dissertation, University of Illinois (2003).

[3] L. Lian, and N.R. Sottos, Effects of thickness on the piezoelectric and dielectric properties of lead zirconate titanate thin films. *J. Appl. Phys*. **87**, 3941-3949 (2000).

[4] G. G. Stoney, Proc. R. Soc. London A **82,** 172 (1909).

XXI ICTAM, 15–21 August 2004, Warsaw, Poland

A NOVEL APPROACH TO THE APPLICATION OF FERROELECTRIC THIN FILMS TO MICRO-ACTUATION

Kaushik Bhattacharya
California Institute of Technology, Pasadena CA 91125, USA

Summary A micro-actuator capable of significant force and displacement remains an outstanding challenge in the development of micromachines. Active materials are attractive for their large work per unit volume, and specifically ferroelectrics since they are electrically activated. However, conventional piezoelectric materials display limited strains (0.1%), and conventional configurations like bi-morph cantilevers are too constrained to deliver the necessary performance. This paper describes an alternative strategy that combines a new mode of electrostriction in ferroelectrics that explicitly use domain switching to deliver extremely large strains (1-6%) at moderate forces and electrical fields along with a new approach to microactuators that use partially released thin films. Together this strategy enables micro-actuators with large force and displacement. This paper describes the theoretical analysis of the domain patterns in bulk and thin film ferroelectric perovskites that led to this strategy, detailed computational studies for specific designs and the subsequent experimental validation.

INTRODUCTION

Ferroelectric crystals are widely used in a variety of applications including sensors, actuators, capacitors and non-volatile data storage elements. In particular, poled ceramics of ferroelectric materials are used commonly for their piezoelectric property in actuator applications. However their application as microactuators raises two difficult challenges. First, the strains of ferroelectric ceramics are limited (about 0.1%). Second, these materials have to be adapted to micromachinable configurations and processes. This paper describes a strategy to address these difficulties developed through a theoretical understanding of ferroelectric perovskites. It combines a new mode of electrostriction in ferroelectrics that explicitly use domain switching to deliver extremely large strains (1-6%) at moderate forces and electrical fields along with a new approach to microactuators that use partially released thin films.

DOMAIN SWITCHING AND LARGE ELECTROSTRICTION

Ferroelectric materials are spontaneously electrically polarized and mechanically distorted. A variety of materials display ferroelectricty, but we focus on perovskites like $BaTiO_3$ and $PbTiO_3$. They are nonpolar and cubic at high temperature, but tetragonal and electrically polarized in the $\langle 001\rangle_c$ at room temperature. The transformation from the non-polar cubic to the polarized tetragonal state can proceed along any of the $\langle 001\rangle_c$ directions giving rise to in six symmetry-related variants at room temperature. Switching from one variant to another by the application of electric fields can potentially generate strains equal to the tetragonal distorsion which range from 1-6% depending on the material. However, homogeneous switching has prohibitive barriers, and one has to affect this switching by nucleation and growth. This requires the ability to form large domains of uniform polarization domains and low energy boundaries (domain walls) between them.

Consider a ferroelectric crystal occupying a region Ω in the reference configuration, and undergoing a deformation y and with polarization density $p(y)$ in the current configuration. The total energy of the system at temperature θ is given by [1]

$$\mathcal{E}[y,p;\theta] \quad = \quad \int_\Omega \left\{\alpha|\nabla_x P|^2 + W(\nabla_x y, P, \theta) - (\det \nabla_x y) E_o \cdot P\right\} dx - \int_{\partial_1\Omega} t_0 \cdot y dA_x + \frac{1}{2}\int_{\mathbb{R}^3} |\nabla_y \phi|^2 dy \ , \quad (1)$$

where $P(x) = p(y(x))$ is the pull-back of the polarization density to the reference configuration and the electric potential ϕ is determined by solving Maxwell's equation, $\nabla_y \cdot (-\nabla_y \phi + p) = \rho$ on $\mathbb{R}^3$ subject to appropriate boundary conditions. The first term represents a domain wall energy. The second term is the free energy density W which depends on the deformation gradient, polarization, and temperature. It encodes all information about the crystallography, spontaneous polarization and spontaneous strain. The third term is the potential energy of the applied electric field. The second integral is the potential energy of the applied mechanical load, and the third integral is the electrostatic energy associated with the electric field generated by the spontaneous polarization of the crystal. The equilibrium deformation and polarization can be found by minimizing the total energy over all possible deformations, y, and polarizations, p.

Since there are multiple variants of the ferroelectric state at room temperature, the free energy density W has multiple wells. Therefore, energy minimizers consist of domains of (approximately) uniform polarization and deformation gradient. However, the boundaries between the domains can not be arbitrary; instead, low elastic and electric field energy require that the jump in the spontaneous distortion and polarization be simultaneously compatible across it. This is not satisfied generically, and thus many ferroelectrics are not suited for large electrostriction. However, It turns out that the conditions are simultaneously satisfied in materials which undergo a phase change involving a loss of two-fold symmetry[1]. This is true in materials like $BaTiO_3$ and $PbTiO_3$ and gives rise to gives rise to 180 and 90 degree domain walls. Further, the 90 domain walls provide the low energy pathways for switching with large strain.

However, the electrostatic field energy often forces the formation of very fine domains. Therefore it is important to design

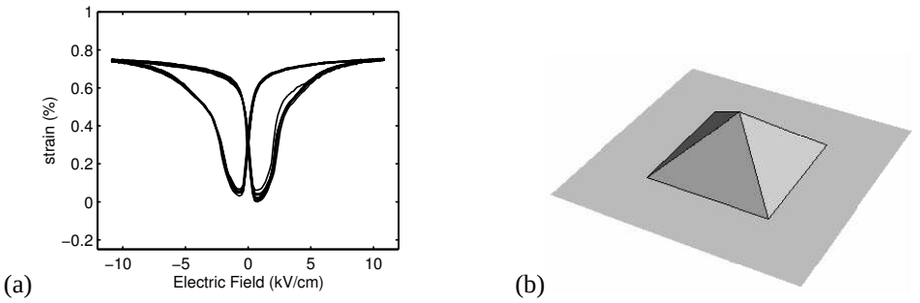


Figure 1. (a) Large electrostriction in $BaTiO_3$. (b) A tent-like actuated shape of a large displacement actuator.

such configuration is the flat plate configuration with electrodes on top and bottom. If the thickness of the plate is small compared to the lateral extent, then the non-local term, the third integral in (1), becomes local[1] and one obtains large domains. Further, if the flat plate is made of a single crystal of $BaTiO_3$ with normal in the $\langle 001 \rangle_c$ direction and subjected to a fixed compressive load and a cyclic electric field across the thickness, then stable (energy minimizing) variant switches between those with in-plane and out-of-plane directions. 90 degree domain walls provide a pathway between these states and one obtains electrostriction of approximately 1% [1]. Figure 1(a) shows the experimentally measured (electrostrictive) strain[2, 3] as a function of applied field verifying the theory. Similar considerations in $PbTiO_3$ predicts strains of about 6.5% and strains of up to 5% have been experimentally obtained.

The considerations above have recently been extended to ceramics or polycrystals[4]. A theory that describes the effective behavior has been derived and has been used to show that cooperative domain switching and consequently large electrostriction is possible if and only if the polycrystal has a $\langle 001 \rangle_c$ fiber texture.

THIN FILMS

An application of ferroelectrics to micromachines calls for the integration of these materials with silicon and in the form of thin films. The traditional method is to make bimaterial cantilevers by depositing ferroelectrics on silicon and micromachinig. Unfortunately, silicon constrains the large strain materials, energy is expended in bending the silicon and it has poor bending scaling (third power of thickness). An alternative is to use partially released films motivated by a theory of thin films of martensitic films [5, 6]. The idea is to deposit a film of active material like ferroelectrics on a substrate, and then back-etch the substrate to release a portion of the substrate. The behavior of the partially released film is described by a rigorously derived membrane-type theory. This theory shows that thin films can indeed form domains. Further, it is possible to form large displacement actuators by carefully matching the geometry of the released region with the crystallography of the material. One such device can be made of a $\langle 001 \rangle_c$ film of $BaTiO_3$ by releasing it along a square region aligned with the pseudocubic direction. Such a device can be made to a cycle between a flat shape and a tent-like shape enclosing a large volume (Figure 1(b)) by domain switching, and thus form the active element of a micropump. Similar strategies can be designed to make linear motors.

CONCLUDING REMARKS

The discussion above was based on a theory of energy minimization. It is possible to derive a time-dependant theory by considering the gradient flow of (1). Finite-difference simulations of the resulting equations validate the discussion above and provide insights into the evolution of domains and the resulting hysteresis[7]. Such simulations also provide insights into the stress and electric field concentrations that can arise were the film not a single crystal or perfectly textured polycrystal. Finally, a program of synthesis of thin films, fabrication of microactuators and experimental evaluation is currently underway at the California Institute of Technology (USA), and the preliminary results are encouraging [8].

References

[1] Shu Y.C., Bhattacharya K.: Domain patterns and macroscopic behavior of ferroelectric materials. *Phil. Mag. B* **81**: 2021-2054, 2001.
[2] Burcsu E. , Ravichandran G., Bhattacharya K.: Large strain electrostrictive actuation in barium titanate. *Appl. Phys. Lett.* **77**: 1698-1700, 2000.
[3] Burcsu E. , Ravichandran G., Bhattacharya K.: Large electrostrictive actuation of barium titanate single crystals. *J. Mech. Phys. Solids* to appear.
[4] Li J., Bhattacharya K.: The effective behavior of ferroelectric ceramics. Forthcoming, 2004.
[5] Bhattacharya K., James R.D.: A theory of thin films of martensitic materials with applications to microactuators. *J. Mech. Phys. Solids* **47**: 531-576, 1999.
[6] Bhattacharya K., Desimone A., Hane K., James R.D., Palmstrøm C.P.: Tents and tunnels on martensitic films. *Mat. Sci. Engng. A* **273-275**:685-689, 1999.
[7] Zhang W. and Bhattacharya K.: Forthcoming.

XXI ICTAM, 15–21 August 2004, Warsaw, Poland

A GEOMETRICALLY NON-LINEAR FINITE SHELL ELEMENT WITH PIEZOELECTRIC LAYERS

Sven Lentzen, Rüdiger Schmidt
IAM, Institute for General Mechanics, Technical University Aachen, D-52062 Aachen, Germany

EXTENDED SUMMARY

In recent years the potential of integrating piezoelectric materials into smart structures has aroused the interest of many researchers. Theoretical models have been developed in order to fully understand the behaviour of smart structures with integrated piezoelectric materials. These models range from relatively simple linear beam theories to complex geometrically as well as physically non-linear models.
Many models are developed in order to investigate the mentioned smart structures. These models are based on either a beam or a plate/shell theory. Piefort [1] has pointed to the fact that the application of a beam theory to model thin smart structures will not produce satisfying results when collocated systems are considered. A plate or shell model is therefore to be preferred.
Considerably less work can be found based in the area of geometrically non-linear shell theories. This is quite surprising considering the fact that many authors refer to a particular benchmark problem also described in [1]. In this benchmark problem a cantilever piezoelectric bimorph beam acting as a sensor is deflected reasonably far away from the geometrically linear regime.
In this work a moderate rotation theory is deployed in the finite element formulation of a composite shell with integrated piezoelectric layers. The strain-displacement relations are valid for small strains but moderate rotations (see Schmidt and Reddy [2]).

A total Langrangian formulation is applied to define the internal virtual work. This requires not only the application of the 2nd Piola-Kirchhof stress and the Green-Lagrange strain tensor, but also the introduction of electrical field quantities defined in material curvilinear coordinates. The covariant elements of the electric field vector ${}_0E_i$ and the contravariant elements of the electric displacement vector ${}_0D^i$ in material curvilinear coordinates can be written as:

$$ {}_0E_i = -\frac{\partial \phi}{\partial \Theta^i} \qquad \text{and} \qquad {}_0D^i = J\, {}_tD^i, \tag{1} $$

where J denotes the determinant of the deformation gradient, Θ^i denotes the surface parameter in direction i, ϕ is the electric potential and the lower left indices 0 and t refer to quantities defined in material respectively spatial coordinates. It can be easily shown that both quantities ${}_0E_i$ and ${}_0D^i$ are energetically conjugated.
These new definitions together with the well-known linear direct and converse piezoelectric effect and the moderate rotation theory is then assembled into a finite shell element. An additional assumption is made in allowing only an electric field in transverse direction which is uniform between the positive and negative pole of an electrode pair.

Considering the benchmark problem discussed in [1] it can be shown that not only considerable differences exist between the analytical beam solution and the finite shell element approximation, but also between the geometrically linear and non-linear finite element results. These differences are even larger than the primarily mentioned ones. In the benchmark problem a cantilever piezoelectric bimorph beam is simulated ($100 \times 5 \times 1$ mm), $E = 2.0$ GPa (Young's modulus), $d_{31} = 2.2 \cdot 10^{-11}$ Cb/N (piezoelectric constant) and $\delta_{33} = 1.062 \cdot 10^{-10}$ F/m (dielectric constant). In order to investigate the actuator and sensor properties of the beam it is either imposed with an electrical voltage or with a transverse tip force. In the latter case the beam is covered with five equal electrode pairs.
To make the differences between the results of beam analysis, the geometrically linear and non-linear finite element approximations more apparent, the boundary conditions have been changed from *clamped-free* to *clamped-hinged* in the actuator case and to *clamped-clamped* in the sensor case. The results are displayed in figure 1.

Actuator

In figure 1a the piezoelectric bimorph beam with the mentioned boundary conditions is imposed with 200 V. The finite element analysis is performed twice. One case is calculated with the normal boundary conditions as mentioned above, and the other case is calculated with adapted boundary conditions to invoke beam-like behaviour. Then both results are compared with the analytical result:

$$ \frac{3 d_{31} \phi}{4 h^2 L} \left(L x^2 - x^3 \right), \tag{2} $$

where h is the total thickness of the beam and L its length. From this comparison one can conclude that the difference between the geometrically non-linear finite shell element approximation and the analytical result is explained by the boundary conditions: Due to the clamping conditions in finite element analysis (MRT shell) high stress concentrations are

induced in these areas. Once these effects are cancelled (MRT beam) the non-linear results agree well with the analytical results. It can then be concluded that the effects of the geometrical non-linearity is not profound in the actuator application.

Sensor

In figure 1b the bimorph beam is used as a sensor. Five equally large electrode pairs are attached to the beam and in the middle a transverse force acts downwards to obtain a mid-point deflection of 2 mm. Comparing the analytical results to the linear finite shell element approximation, the influence of the clamping conditions can be noticed in these areas.
Due to the induced membrane stresses, which are considered in the geometrically non-linear case, the required force to obtain a deflection of 2 mm (1.1843 N), is much greater than in the linear analysis (0.32133 N). For comparison purposes figure 1b additionally displays the results in case the force remains equal (deflection: 1.09 mm). Now one can conclude that the effect of the geometrically non-linearity is more profound than the clamping effect, in the sensor application.
Another phenomenon which appears in this case is the fact that the relative voltage distribution changes when the geometrically non-linear case is considered.

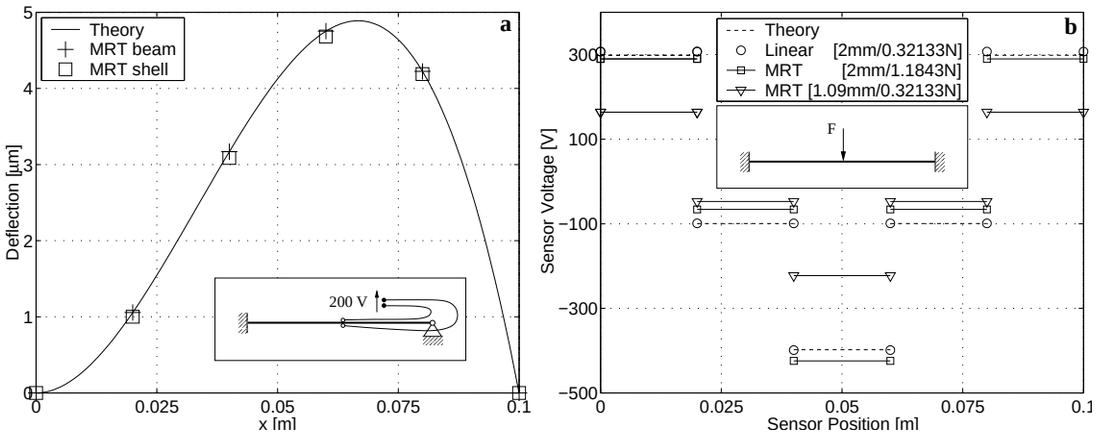


Figure 1. a: bimorph beam acting as an actuator with 200V. **b**: bimorph beam acting as sensor with a mid-point displacement of 2mm.

The effects shown in this benchmark problem, where a beam is clamped on both sides, are representative for many cases in which plates or shells as 2- or 3-dimensional objects are clamped along the sides. Not only the absolute sensor voltage, but also the relative distribution is influenced by the non-linearity. This could influence the effectivity of, for instance, modal damping algorithms used in linear dynamic systems.
Further examples, concerning beams/plates and shells with integrated piezoelectric layers, will be presented to validate the finite shell element formulation and to demonstrate the effect of geometrical non-linearity on actuator and sensor applications.

References

[1] Piefort, V.: Finite Element Modelling of Piezoelectric Active Structures. *PhD Thesis*, Université Libre de Bruxelles, 2001.
[2] Schmidt R., Reddy J.: A Refi ned Small Strain and Moderate Rotation Theory of Elastic Anistropic Shells. *J. Appl Mech* **55**:611-617, 1988.

PIEZODIAGNOSTICS – A NEW SHM METHOD AND ITS POTENTIAL ENGINEERING APPLICATIONS

Jan Holnicki-Szulc, Przemyslaw Kolakowski, Anita Orlowska,
Andrzej Swiercz, Dariusz Wiacek, Tomasz G. Zielinski
Institute of Fundamental Technological Research, SMART-TECH Centre, Warsaw, Poland

Summary This paper presents a novel approach to damage identification based on the phenomenon of elastic waves propagation. The theoretical background is the dynamic Virtual Distortion Method, which is capable of modelling both a reference excitation signal propagated in the intact structure over a time domain and a perturbed signal due to some damage in the structure. The damage is modelled as stiffness loss. A dynamic inverse analysis is carried out in the time domain in order to identify multi-damage cases in terms of their locations and intensities. The main focus is taken on addressing numerical aspects of the presented approach as well as its potential engineering applications. The related methodology is presented including a brief description of experimental verification. Numerical example with successful identification is demonstrated. Advantages of the approach as well as its challenging points are discussed.

INVERSE DYNAMIC PROBLEM

The purpose of this paper is to propose an alternative approach to the inverse dynamic analysis problem. Generalising the so-called VDM (Virtual Distortion Method) approach for dynamic problems, a *dynamic influence matrix D* concept will be introduced. Pre-computing of the time-dependent matrix *D* allows for decomposition of the dynamic structural response into components caused by external excitation in the intact structure (the linear part) and components describing perturbations caused by the internal defects (the non-linear part). As a consequence, analytical formulas for calculation of these perturbations and the corresponding gradients can be derived. The physical meaning of the so-called *virtual distortions* used in this paper are externally induced strains (non-compatible in general, e.g. caused by piezoelectric transducers, similarly to the effect of non-homogeneous heating). The compatible strains and self-equilibrated stresses are structural responses to these distortions.
Assuming possible locations of all potential defects in advance, an optimisation technique with analytically calculated gradients could be applied to solve the problem of the most probable defect location. The considered damage can affect the local stiffness as well as the mass distribution modification. It is possible to identify the position as well as intensity of several, simultaneously generated defects.

DAMAGE IDENTIFICATION SYSTEM

The proposed methodology will be applied to corrosion detection (reduction of material thickness), and identification of its location in steel pipelines, using long-distance transmissions of impulses. The mechanical model can be reduced in this case to the isotropic one, with virtual distortions modelled through thermal-like, deviator-less tensor fields. This problem, similar to thermal shock propagation, can be solved numerically cheaper than the general problem of elastic impulse propagation.
The proposed, time-domain-based methodology of data processing for damage identification (VDM-based *PiezoDiagnostics Software*) fits well to the following technique of measurements (*PiezoDiagnostics Hardware*):

1) wave generator produces a low frequency impulse of flexural wave with long-distance propagation,
2) few well located, distant sensors collect measurements of frontal section of the transferred wave,
3) if the received structural response differs significantly from the reference response (for undamaged structure), the collected measurements are transmitted to a computer centre for further data processing (damage identification).

The main advantage of the proposed approach is large number of measurements (done in consecutive time steps) enabling precise damage identification, including multi-damage cases.

NUMERICAL AND OPTIMISATION ASPECTS

The objective function to be minimised (*PD Software*) describes the distance between the measured response of the damaged structure (red line with squares in Fig. 1) and the computer-simulated response influenced by the composition of all possible defects modelled by *virtual distortions* (green line with circles in Fig. 1). These virtual distortions are parameters to be identified in the efficient, gradient-based optimisation procedure, where gradients are determined analytically. Software vs. experimental verification demonstrated on the above figure has been elaborated making use of small cantilever beam excited with a sinus-shaped impact generated with piezo-actuator, which will be discussed in details in the final presentation.
The VDM-based approach to damage identification consists of the following steps:

1) Assume potential locations of all possible defects
2) Calculate the so-called *influence matrix D* describing global structural dynamic response for unit Dirac-like impulse virtual distortions generated in potential defect locations

3) Formulate the objective functional describing *mean square-distance* between the *measured* structural response to externally generated flexural wave and the numerically composed response (superposition of un-damaged structural response and linear combination of influences from all potential damages)
4) Perform gradient-based identification procedure searching for the intensities of virtual distortions (modelling potential damages) minimizing the objective functional.

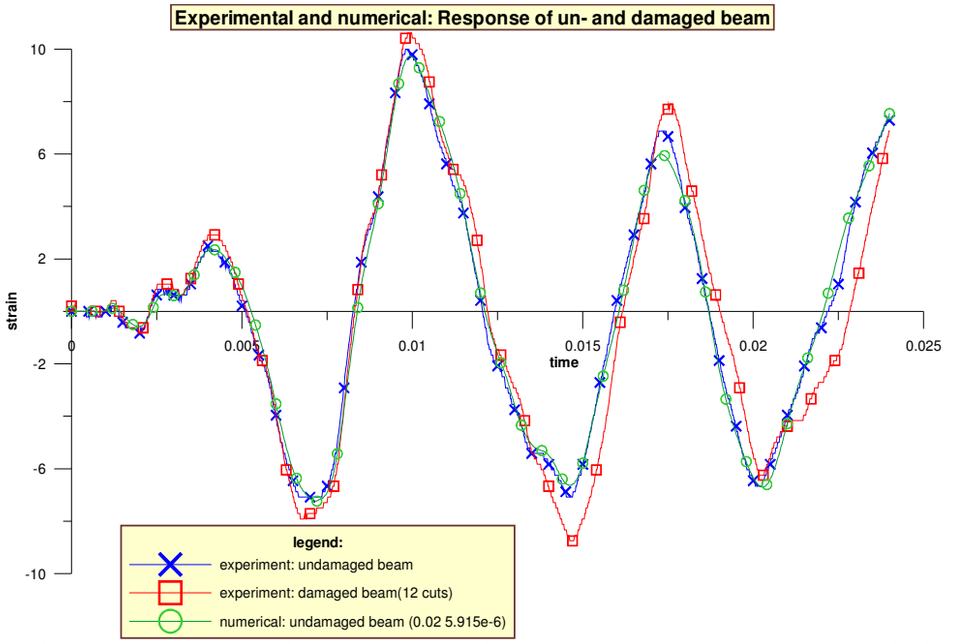


Fig. 1 Numerical simulation for undamaged beam (green line - circles) vs. measured responses for the original (blue line - Xs) and damaged (red line - squares) structure (1000 time steps analysis)

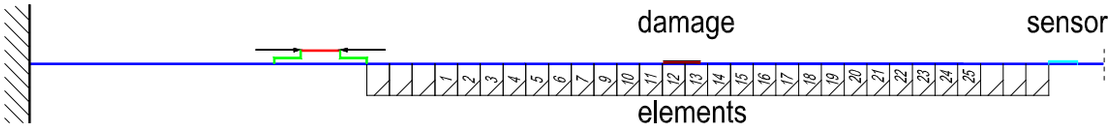


Fig. 2 FE discretization of an aluminium beam specimen subject to damage in the middle section

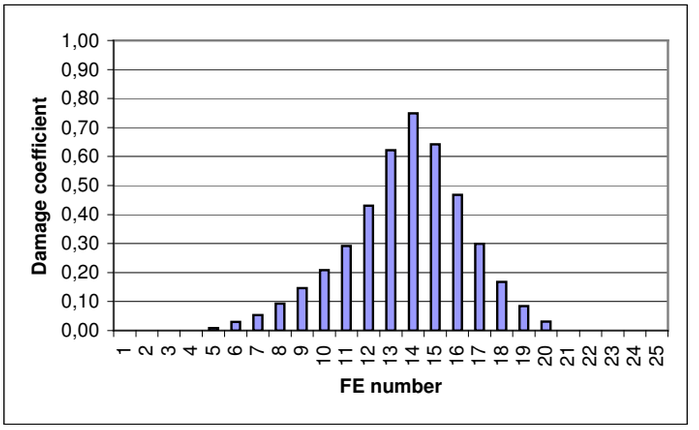


Fig. 3 Results of damage identification for the aluminium beam by the VDM-based PiezoDiagnostics Software

Acknowledgement

Research results presented in this paper have been obtained on the basis of the 5FP Research Project: G1RD-2001-00659 (2002-2005): *Smart Structural Diagnostics using Piezo-Generated Elastic Waves - PIEZODIAGNOSTICS*, supported by the European Commission. Partners: CEGELEC, TWI, WSATKINS, CEDRAT, CIMNE, CDRiA, IFTR, ECL, ALSTOM.

Tuesday , January 06, 2004

THERMAL-INDUCED FRACTURE OF ELECRTODED PIEZOELECTRIC COMPOSITES

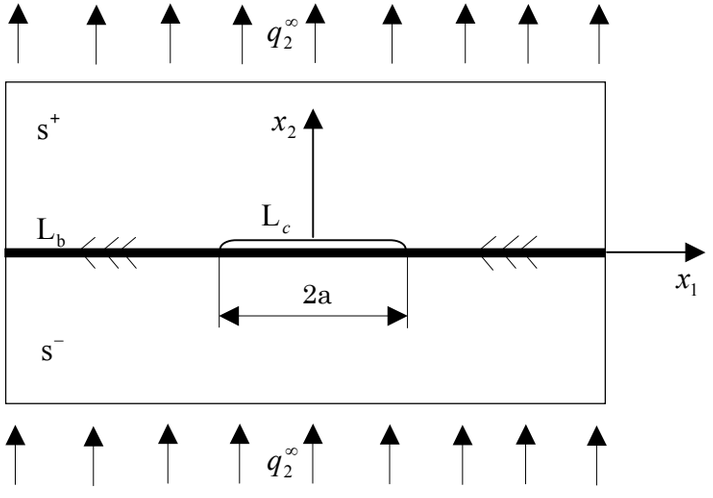
Cun-Fa Gao, Masayuki Ishihara, Naotake Noda

Dept.of Mech. Eng., Shizuoka University, 3-5-1, Johoku, Hamamatsu, Shizuoka 432-8561, JAPAN

Summary A thermally partially- insulated and electrically completely-permeable interface crack is studied based on the Stroh formalism. The crack is located between an internal electrode layer and one of two piezoelectric matrices subject to remote heat flux. It is found that the singular fields near the crack-tip are the same as those in a purely elastic bi-material system with an interface crack.

INTRTODUCTION

The multilayer piezo-ceramic actuators with metal electrodes have widely been used in engineering. Due to material mismatch between electrodes and ceramics, the electrode may partially debond from the matrix when the actuators work in high temperature environment. Some important results have been presented by Dos Santos e Lucato et al. [1] for the case where the electrode is located in a homogeneous material, and also by Deng and Meguid [2] for an electrode embodied between two dissimilar piezoelectric materials. On the fracture problems of electrode-matrix interface cracks, one may referee to the work of Ru [3]. The cited results did not take into account the thermal effort. With the rapidly increasing use of piezoelectric materials in high-temperature environment, it is also of both theoretical and practical importance to study the fracture problems of electrode-matrix interface cracks under thermal loading. This work studies an interface crack in a piezoelectric bi-material system, which consists of a soft internal electrode layer and two dissimilar piezoelectric semi-bodies s^+ and s^-, which are subject to remote heat flux q_2^∞, as shown in the figure. Singular fields near the crack will be analysed and then exact solution for the stress intensity factor will be presented based on the mixed-form Stroh formalism for thermo- piezoelectric materials.



MAIN ASSUNPTIONS

In this work we assume that (i) the traction-free crack is thermally partially-insulated and electrically completely-permeable; (ii) the electrode layer is so thin that its mechanical properties can be neglected, and (iii) the two half-infinite piezoelectric matrices coexist in the state of generalized 2D deformation under the remote heat flux.

Elsevier

Tuesday , January 06, 2004

ESSENTIAL EQUATIONS

Define a generalized stress vector $\hat{\boldsymbol{\phi}}_{,1} = (\sigma_{21}, \sigma_{22}, \sigma_{23}, -E_1)^T$, where σ_{ij} and E_1 are the components of stress and electric field, respectively. Then, we can finally give the expression of $\hat{\boldsymbol{\phi}}_{,1}$ along the x_1 axis as

$$\hat{\boldsymbol{\phi}}_{,1}^{+}(x_1) = \hat{\mathrm{h}}\mathrm{U}^{+}(x_1) + \bar{\hat{\mathrm{h}}}^{-1}\mathrm{U}^{-}(x_1) + \hat{\mathrm{m}}' q_{2\Delta}^{\infty} x_1 + \hat{\mathrm{m}}'' q_{2\Delta}^{\infty}\sqrt{x_1^2 - a^2}\,, \tag{1}$$

where $\hat{\mathrm{h}}$, $\hat{\mathrm{m}}'$ and $\hat{\mathrm{m}}''$ are constant matrix and vectors, respectively, $\mathrm{U}(z)$ is an unknown complex function and $q_{2\Delta}^{\infty} = q_2^{\infty}(\lambda_0 - 1)$, in which $0 \le \lambda_0 \le 1$ is a factor characterizing the heat conductivity of the crack surface.

Taking the fourth row of (1) gives

$$-E_1(x_1) = \sum_{j=1}^{4} \hat{h}_{4j} U_j^{+}(x_1) + \sum_{j=1}^{4} \bar{\hat{h}}_{4j} U_j^{-}(x_1) + \hat{m}_4' q_{2\Delta}^{\infty} x_1 + \hat{m}_4'' q_{2\Delta}^{\infty}\sqrt{x_1^2 - a^2}\,. \tag{2}$$

Using the condition $E_1(x_1) = 0$ along the x_1 axis we can express $U_4(z)$ by using $U_1(z), U_2(z)$ and $U_3(z)$ through use of (2). Then, substituting the obtained $U_4(z)$ into the first three rows of (1) we can get the expression of stress components, which contains only three unknown functions $U_1(z), U_2(z)$ and $U_3(z)$ that is

$$\sigma_2 = \Lambda \mathrm{U}_3^{+} + \bar{\Lambda}\mathrm{U}_3^{-} + \lambda' q_{2\Delta}^{\infty} x_1 + \lambda'' q_{2\Delta}^{\infty}\sqrt{x_1^2 - a^2} \tag{3}$$

where Λ, λ' and λ'' are new constant matrix and vectors, respectively, $\sigma_2 = (\sigma_{21}, \sigma_{22}, \sigma_{23})^T$ and $\mathrm{U}_3 = (U_1, U_2, U_3)^T$. Using the traction-free condition $\sigma_2 = 0$ on the crack faces, together with single-valued conditions of displacements and electric potential, we can give the solution of $\mathrm{U}_3(z)$ from (3). With this solution, all other solutions will finally be determined.

MAIN RESULTS

Main results include the expression of stress intensity factor vector as

$$\mathrm{k}_{\sigma} = \sqrt{\pi a}\,[\Lambda\mathrm{Q}]\,\mathrm{diag}\left((2a)^{-i\varepsilon_\alpha}\right)[\Lambda\mathrm{Q}]^{-1}\,\mathrm{k}_0(\lambda) a q_{2\Delta}^{\infty}\,, \tag{4}$$

with $\mathrm{k}_0(\lambda) = \left\langle\left\langle 1 + 2i\varepsilon_\alpha + \varepsilon_\alpha^2 - 4\varepsilon_\alpha^2/a\right\rangle\right\rangle(\lambda' + \lambda'') - \lambda''/2$, where Q is a known matrix and the positive and real constant ε depends on the material properties and characterizes the oscillatory singularities. For special cases of a homogeneous material we have $\mathrm{k}_{\sigma} = \sqrt{\pi a}\,\lambda' a q_{2\Delta}^{\infty}$.

CONCLUSIONS

Main conclusions are:

(i) The structure of singular fields near the electrode-matrix interfacial crack is the same as that in a purely elastic bi-material system with interface cracks, that is, the crack-tip singularities of electrode-matrix interface cracks can uniquely be characterized by an inverse square root singularity and a pair of oscillatory singularities.

(ii) The intensities of singular fields depend on the heat conductivity of the crack surface.

REFERENCES

[1] Dos Santos e Lucato, S.L., Lupascu, D.C., Kamlah, M., Rödel, J., Lynch, C.S.: Constraint-induced crack initiation at electrode edges in piezoelectric ceramics. Acta Mater. **49**: 2751-2759, 2001.

[2] Deng, D., Meguid, S.A.: Analysis of conducting rigid inclusion at the interface of two dissimilar piezoelectric materials. J. Appl. Mech. **65**: 76-84, 1998.

[3] Ru, C.Q.: Electrode-ceramic interfacial cracks in piezoelectric multilayer materials. J. Appl. Mech.**67**, 255-261, 2000.

Review Copy

THERMAL BUCKLING OF ACTIVE COMPOSITE PLATES WITH SHAPE MEMORY ALLOY FIBERS

Rivka Gilat*, Jacob Aboudi**
* Faculty of Engineering, The College of JAS Ariel, Ariel 44837, Israel
** Faculty of Engineering, Tel Aviv University, Ramat Aviv 69978, Israel

Summary Micromechanically established constitutive equations for unidirectional composites with shape memory alloy fibers embedded in polymeric or metallic matrices are derived. These equations are subsequently employed to analyze the thermal buckling of rectangular composite plates. The shape memory alloy fibers are activated by a mechanical loading and unloading of the composite to an overall traction-free state , prior to the application of the thermal load. The present micro-macro-structural approach enables an accurate modelling that accounts for the interaction of shape memory alloy fibers with its surrounding rather than the commonly adopted simplified analyses.

Introduction

Shape memory alloy (SMA) materials undergo phase transformation which is caused by the application of stress and/or temperature. At high temperatures, the material behavior is nonlinear and hysteretic but yet, yields at the end of a mechanical loading-unloading cycle the original stress-strain-free state (superelastic behavior). At lower temperatures, a mechanical loading-unloading results in a residual deformation which can be recovered by a temperature increase (shape memory effect). The latter effect can be utilized to control the behavior of structures in which SMA materials have been embedded.

Three-dimensional constitutive relations that can model the shape memory behavior have been presented by various investigators, see Boyd and Lagoudas[1], for example. Birman[2] reviewed various constitutive equations and discussed some applications of SMA materials.

One way of incorporating SMA materials in structures is by embedding SMA fibers in polymeric or metallic matrices to generate active composites. The analysis of the such composites should be based on a micromechanical approach in which the detailed interaction between the constituents is accounted for. In the presence of SMA constituents, the micromechanical analysis is necessarily nonlinear and path-dependent. In the presence of metallic materials additional nonlinear effects exist due to their inelastic behavior.

The analysis of composite structures that involve embedded SMA materials should be based on constitutive relations that have been established by a micromechanical approach. Alternatively, several investigators (Tawfik et al.[3], for example) adopted a simplified approach according to which the detailed interaction of the SMA material with its surrounding is neglected and its effect, as deduced from the behavior of the monolithic SMA material, is incorporated.

Analysis

In the present paper, the thermal buckling of plates consisting of active composites is considered. The structural analysis is based on a micromechanical model referred to as the Generalized Method of Cells (GMC) (Aboudi[4]) which establishes constitutive relations of the inelastic composite. Due to the complicated state of stress, strain and temperature resulting from the structural behavior, these constitutive relations are used at every point of the plate. Consequently, such an analysis forms a micro-macro-structural approach.

The modelling of Boyd and Lagoudas[1] is employed to predict the behavior of the SMA phase. This three-dimensional model is capable of producing the superelastic and the shape memory effects. Two kinds of matrices in which the SMA fibers can be embedded are considered in the present paper: (1) a polymeric matrix (such as epoxy) which is assumed to behave as a linearly elastic material and, (2) a metallic matrix (such as aluminum alloy) which is assumed to behave as an elastic-viscoplastic work-hardening material (Bodner [5]).

In order to utilize the shape memory effect, the composite is activated by an isothermal mechanical loading followed by unloading to a state of overall zero stresses associated with non-zero overall strains. Due to the presence of SMA fibers, a subsequent applied thermal loading of traction-free composite plate reduces the overall residual strains. On the other hand, in a pre-loaded composite plate in which the in-plane displacements of the edges are restrained, the heat induced reduction of the residual strains is prevented and recovery tensile

stresses can develop. These tensile stresses, caused by the phase transformation, reduce or even overcome the compressive stresses generated by thermal expansion. Thus the ability to improve the buckling behavior of a structure can be achieved by utilizing the shape memory effect. It is obvious that an activating pre-loading cycle when applied to the active composite, generates internal residual stress and strain fields in the composite constituents. The micromechanical approach enables the incorporation of the effect of these residual micro fields on the structural behavior under the subsequent thermal loading.

Application

Results are presented that exhibit the buckling temperature of SMA/Epoxy and SMA/Aluminum composites, as well as that of the monolithic SMA, the epoxy and the inelastic aluminum constituents. In particular, the effect of the three-dimensional state of stress that exists in the SMA and matrix phases on the overall composite behavior is shown. This effect can, for example, be deduced from Fig. 1 in which the critical temperature increase, ΔT, versus the amplitude of the activating pre-loading, ϵ^0, is displayed for various square simply supported plates.

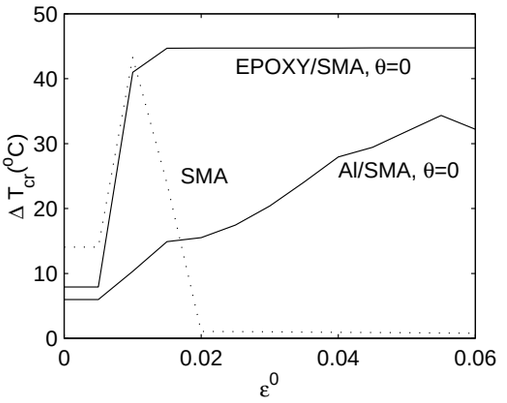


Fig 1: Variation of the buckling temperature with the pre-strain.

References

[1] Boyd, J.G., Lagoudas, D.C.: Thermomechanical response of shape memory composites. J. Intell. Mat. Syst. Struct. 5, 333-346, 1994.

[2] Birman, V.: Review of mechanics of shape memory alloy structures. Appl. Mech. Rev. 50, 629-645, 1997.

[3] Tawfik, M., Ro, J.J. and Mei, C.: Thermal post-buckling and aeroelastic behavior of shape memory alloy reinforced plates. Smart Mater. Struct. 11, 297-307, 2002.

[4] Aboudi, J.: Micromechanical analysis of composites by the method of cells - Update. Applied Mech. Rev. 49, S83-S91, 1996.

[5] Bodner, S.R.: Unified Plasticity for Engineering Applications. Kluwer, New York, 2002.

Study of non-linear magnetomechanical constitutive relations of ferromagnetic materials

Dai-Ning Fang[1], Xue Feng, Yongping Wan and Keh-Chih Hwang
Department of Engineering mechanics
Tsinghua University, Beijing 100084, China

ABSTRACT

Ferromagnetic materials have been widely used in modern science and technology since they become the important functional materials. A robust constitutive relation is desirable in order to guide the processing and development of ferromagnetism and for use in the design of ferromagnetic devices. In this paper, both experimental and theoretical work performed on developing nonlinear magnetomechanical constitutive relations of ferromagnetic materials are presented.

1. A novel magnetomechanical testing setup and the measurement techniques, which were developed for the measurement of the nonlinear magnetomechanical response of both magnetostrictive and soft ferromagnetic materials subjected to coupled magnetomechanical loading, are introduced (see Figure 1). In experiments, there were three kinds of ferromagnetic materials used to investigate the magneto-mechanical coupling behavior, such as the soft-ferromagnetic metal of Ni6 and electrolytic nickel, the giant-magnetostrictive material (Terfenol-D), and Manganese-Zinc ferrite ceramics. The characteristic curves of ferromagnetic materials were measured, including the hysteresis loops, piezomagnetic curves, magnetization curves and the magnetostriction curves under different compressive stress and stress-strain curves under different external magnetic fields.

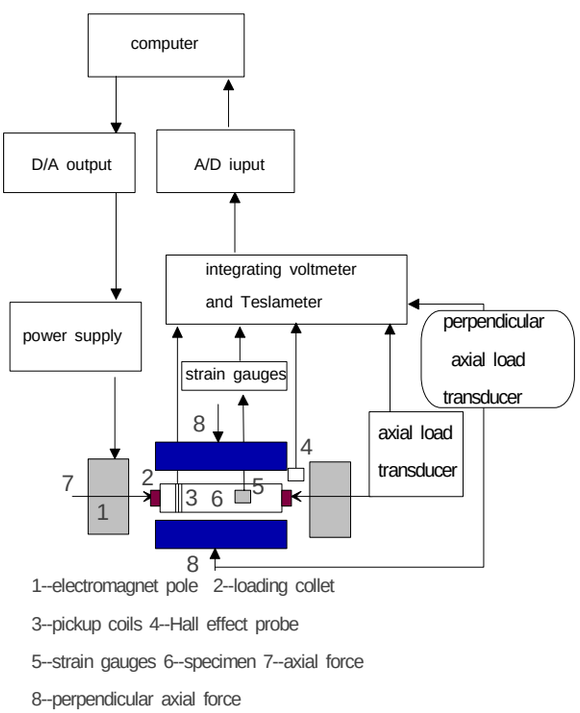


Figure 1: Schematic of the setup. The industrial PC controls the electromagnet supplier and monitors the magnetic H, magnetic induction B and the magnetostriction of specimens by an A/D-D/A interface card.

2. The response of ferromagnetic materials is dependent on the loading history because of energy dissipation, which was similar to the classical plastic theory. According to the Karafillis-Boyce model of the eanisotropic plastic theory, the general constitutive model for ferromagnetic and magnetostrictive materials, based on the internal variable theory, is developed. The remnant magnetization and strain are considered as internal variables, and a three-dimensional constitutive relation can be built in general. Based on the magneto-mechanical yield surface measured by the authors, a non-quadratic magneto-mechanical yield surface is introduced for both isotropic and anisotropic materials (see Fig. 2). The anisotropy includes both magnetic anisotropy and elastic anisotropy, which can be described by introducing a set of irreducible tensorial state variables. The linear transformation from anisotropy to isotropy is presented. Then, the proposed model is generalized for both isotropic materials and anisotropic materials. Furthermore, the magneto-mechanical yield surface of the magnetostrictive material Terfenol-D was measured and the magneto-mechanical hardening moduli can be determined by Helmholtz free energy. The macroscopic features of ferromagnetic materials, such as hysteresis loop, magnetostrictive, magnetostrictive hysterisis, can be predicted. Figure 3 shows that the calculated results are consistent with the experimental data well .

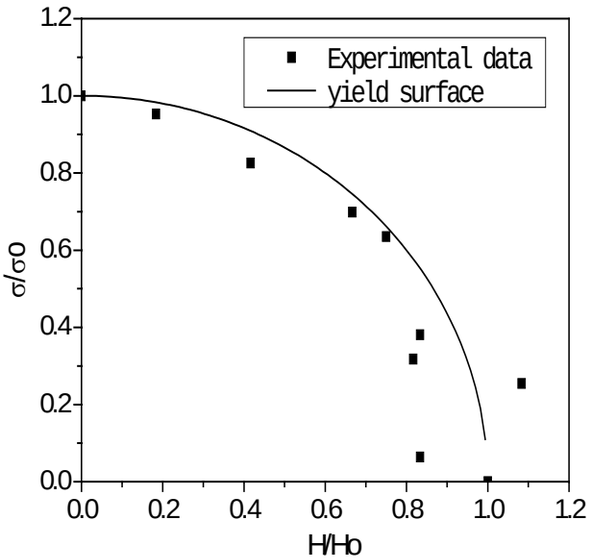


Figure 2. The dimensionless initial yield surface of Terfenol-D

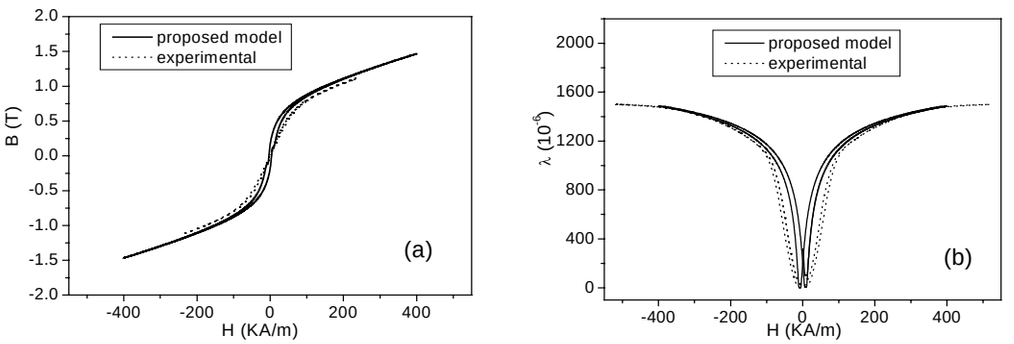


Figure 3. Comparison of the theoretical and measured results under magnetomechanical loading with 3MPa compressive stress: (a) the hysteresis curve; (b) the magnetostrictive curves.

[1] The corresponding author, E-mail: fangdn@mail.tsinghua.edu.cn

OPTIMUM CONTROL OF THERMOELASTIC DEFORMATION IN A SMART COMPOSITE DISK

Fumihiro Ashida[*], Theodore R. Tauchert[**]

[*] *Department of Electronic Control and Systems Engineering, Shimane University, Shimane 690-8504, Japan*

[**] *Department of Mechanical Engineering, University of Kentucky, KY 40506-0503, USA*

Summary This paper deals with a smart composite disk consisting of a structural layer onto which two piezoceramic layers are bonded. An unknown heating temperature distribution acting on the bottom surface is inferred from an electric potential distribution induced in the middle piezoceramic layer. A step-wise electric potential distribution applied to the top piezoceramic layer that controls a thermoelastic displacement distribution on the bottom surface is determined by optimization subject to stress constraints.

INTRODUCTION

By utilizing the direct and converse piezoelectric effects inherent in piezoelectric materials, functions called "self-monitoring" and "self-control", which are essential for smart structures, can be achieved. For smart structures operating in thermal environments, materials must have heat resistance, high strength and high stiffness.

This paper deals with a smart composite circular disk that controls a thermoelastic deformation resulting from an unknown thermal load. The disk consists of a transversely isotropic structural layer and two piezoceramic layers of crystal class 6mm, as shown in Fig. 1. The middle piezoceramic layer serves as a sensor and the top piezoceramic layer serves as an actuator. An unknown heating temperature distribution acting on the bottom surface of the disk is inferred from the induced electric potential distribution assumed to be measured on the upper interface of the sensor layer. Then a step-wise electric potential distribution is applied to electrodes concentrically arranged on the top surface of the actuator layer in order to control the thermoelastic displacement distribution on the bottom surface of the disk. This problem is analyzed by means of the piezothermoelastic potential function approach [1]. The voltage applied to each electrode is determined by optimization using Fletcher-Reeves's conjugate gradient method, so that the difference between the induced and desired displacement distributions is minimized subject to stress constraints.

PROBLEM STATEMENT

Disk characteristics

The layers are numbered 1 to 3 from the bottom. The quantities in the *i*-th layer will be denoted by corresponding symbols with subscript *i*. The layer thicknesses are denoted by c_i. The top and bottom surfaces of the disk are taken to be traction-free, the layers are perfectly bonded at the interfaces, and the cylindrical edge of the disk is constrained against radial deformation and simply supported at the bottom. In this case the elastic boundary conditions are given by

$$\sigma_{1zz}=\sigma_{1rz}=0 \ \text{ on } \ z=0, \quad \sigma_{3zz}=\sigma_{3rz}=0 \ \text{ on } \ z=b_3 \tag{1}$$

$$\left.\begin{aligned} &u_{ir}=u_{(i+1)r}, \quad u_{iz}=u_{(i+1)z}, \\ &\sigma_{izz}=\sigma_{(i+1)zz}, \quad \sigma_{irz}=\sigma_{(i+1)rz} \end{aligned}\right\} \ \text{on} \ \ z=b_i \ \ (i=1,2) \tag{2}$$

$$u_{ir}=0, \sigma_{irz}=0 \ \text{ on } \ r=a \ \ (i=1\sim 3), \quad u_{1z}=0 \ \text{ at } \ r=a, z=0. \tag{3}$$

The lower interfaces of both piezoceramic layers are electrically grounded, while the upper interface of the sensor layer and the cylindrical edge of the disk are free of electric charge. Then the electric boundary conditions are given by

$$\Phi_i=0 \ \text{ on } \ z=b_{i-1} \ \ (i=2,3), \quad D_{2z}=0 \ \text{ on } \ z=b_2 \tag{4}$$

$$D_{ir}=0 \ \text{ on } \ r=a \ \ (i=2,3) \tag{5}$$

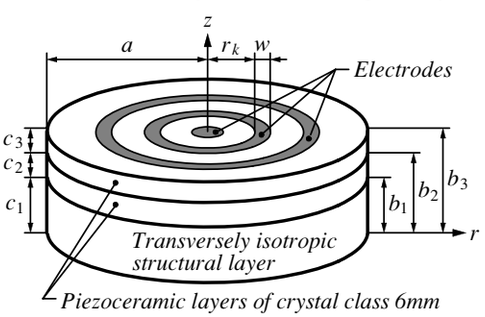


Fig. 1 Geometry of a smart composite disk.

where u_{ik}, σ_{ikl}, Φ_i and D_{ik} denote the elastic displacements, stresses, electric potentials and electric displacements.

Inverse problem

Both layer interfaces provide perfect thermal contact, heat convection occurs over the top surface of the disk, and the cylindrical edge is thermally insulated. In this case the thermal boundary conditions are

$$T_i=T_{i+1}, \ -\lambda_{iz}T_{i,z}=-\lambda_{(i+1)z}T_{(i+1),z} \ \text{ on } \ z=b_i \ \ (i=1,2), \quad T_{3,z}+h_tT_3=0 \ \text{ on } \ z=b_3 \tag{6}$$

$$T_{i,r}=0 \ \text{ on } \ r=a \ \ (i=1\sim 3) \tag{7}$$

where T_i are temperatures, λ_{ik} are coefficients of thermal conductivity and h_k is the boundary conductance.

For the composite disk under the above boundary conditions, it is assumed that an unknown heating temperature distribution $\Theta(r)$ acts on the bottom surface of the disk, the induced electric potential distribution is measured at some points on the upper interface of the sensor layer, the top surface of the disk is free of electric charge, and the measured electric potentials can be approximated by the function $V_0\,v_m(r)$:

$$\Phi_2^T=V_0\,v_m(r) \ \text{ on } \ z=b_2, \quad D_{3z}^T=0 \ \text{ on } \ z=b_3 \tag{8}$$

where V_0 is a constant electric potential and superscript T designates quantities associated with the thermal loading. Instead of invoking the thermal boundary condition on the bottom surface of the disk, the electric boundary condition given in the first of Eqs. (8) is assumed to be available; thus this inverse problem is analyzed and temperatures, elastic displacements, electric potentials, stresses and electric displacements are obtained. The unknown heating temperature is deduced from the temperature in the structural layer by applying the thermal boundary condition on the bottom surface:

$$\Theta(r) = T_1 - T_{1,z}/h_b \quad \text{on} \quad z = 0. \tag{9}$$

Control problem

The control problem entails determination of the step-wise electric potential distribution that must be applied to the top surface of the disk,

$$\Phi_3^E = \sum_{k=1}^{n} V_k \{H(r - r_k) - H(r - r_k - w)\} \quad \text{on} \quad z = b_3 \tag{10}$$

so that the resultant axial elastic displacement on the bottom surface of the disk has a desired distribution $u_0\, g(r)$:

$$u_{1z} = u_{1z}^T + u_{1z}^E = u_0\, g(r) \quad \text{on} \quad z = 0 \tag{11}$$

where $H(r)$ is Heaviside's unit step function, u_0 is a constant elastic displacement, and superscript E designates quantities associated with the electric loading. The voltage V_k applied to each electrode is determined by optimization subject to stress constraints.

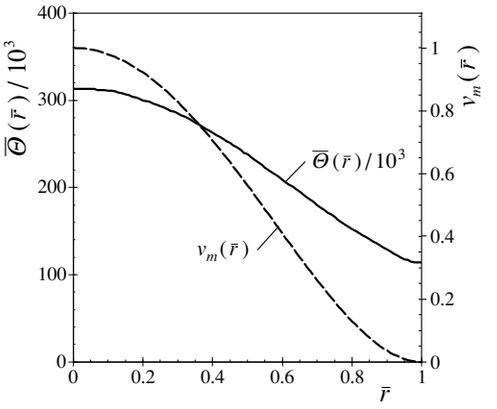


Fig. 2 Obtained heating temperature distribution.

NUMERICAL RESULTS

Numerical results are presented in terms of the following dimensionless quantities:

$$(\bar{r}, \bar{z}) = \frac{(r,z)}{a},\ (\bar{b}_i, \bar{c}_i, \bar{r}_k, \bar{w}) = \frac{(b_i, c_i, r_k, w)}{a},\ B_k = a\, h_k,\ \overline{\Theta} = \frac{a\,\alpha_{1r}\,\Theta}{V_0\,|d_{21}|},\ \overline{V}_k = \frac{V_k}{V_0},\ \overline{u}_{ik} = \frac{u_{ik}}{V_0\,|d_{21}|},\ \overline{\sigma}_{ikl} = \frac{a\,\sigma_{ikl}}{Y_{1r}\,V_0\,|d_{21}|}$$

where Y_{1r} is Young's modulus, α_{1r} is the coefficient of linear thermal expansion and d_{21} is the piezoelectric coefficient. Numerical calculations are carried out for a transversely isotropic graphite/epoxy composite layer and two cadmium selenide layers of crystal class 6mm [1]. The layer thicknesses and Biot's numbers are taken to be $\bar{c}_1 = 0.02$, $\bar{c}_2 = \bar{c}_3 = 0.001$, $B_b = 1$ and $B_t = 0.1$. The measured electric potentials are assumed to be approximated by the function $v_m(\bar{r}) = 1 - 2\bar{r}^2 + \bar{r}^4$. The desired elastic displacement distribution on the bottom surface of the disk is taken to be $g(\bar{r}) = 0$. The electrodes are arranged as $\bar{r}_k = 0.2(k-1)$ and $\bar{w} = 0.1$. For the stress constraints, the allowable compressive, tensile and shear stresses of the cadmium selenide are assumed to be $(\bar{\sigma}_c^A, \bar{\sigma}_t^A, \bar{\sigma}_s^A) = (-150, 10, 10) \times 10^3$. To improve the convergence of response functions, the following function similar to the step function is used for the applied electric potential distribution:

$$\overline{\Phi}_3^E = \sum_{k=1}^{n} \overline{V}_k \,/\, [\{1 + e^{-250\,(\bar{r} - \bar{r}_k)}\}\{1 + e^{250(\,\bar{r} - \bar{r}_k - \bar{w}\,)}\}].$$

The distributions of measured electric potential and obtained heating temperature are illustrated in Fig. 2. Results for the applied voltages $\overline{V}_k$ determined by optimization are shown in Table 1. In this table, n is the number of electrodes, $\bar{\sigma}_c$, $\bar{\sigma}_t$ and $\bar{\sigma}_s$ are the maximum values of the compressive, tensile and shear stresses induced in the cadmium selenide layers, f_{ob} is the value of the objective function defined by $f_{ob} = \sum_{j=0}^{100} [\,\bar{u}_{1z}(0.01j, 0) / \bar{u}_{1z}^T(0.01j, 0)]^2$, and R is the ratio of the maximum value of the controlled elastic displacement to that of uncontrolled elastic displacement on the bottom surface of the disk. It is seen that the maximum value of the controlled elastic displacement is reduced to about one fortieth of that of the uncontrolled elastic displacement in the case of $n = 5$ and the stress constraints are satisfied. For $n = 5$, the distributions of controlled and uncontrolled elastic displacements on the bottom surface as well as the applied electric potential distribution are illustrated in Fig. 3.

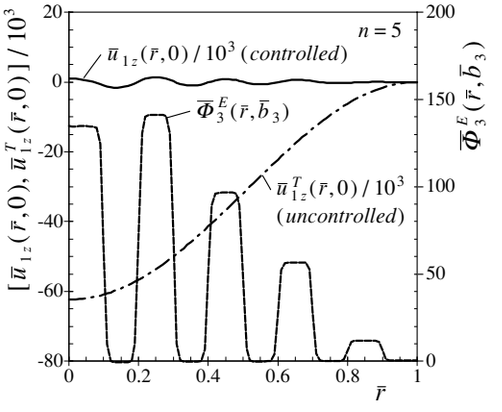


Fig. 3 Distribution of controlled elastic displacement.

Table 1 Determined applied voltages, maximum stresses, and evaluations of optimization.

n	$\overline{V}_1$	$\overline{V}_2$	$\overline{V}_3$	$\overline{V}_4$	$\overline{V}_5$	$\bar{\sigma}_c / 10^3$	$\bar{\sigma}_t / 10^3$	$\bar{\sigma}_s / 10^3$	f_{ob}	R [%]
1	129.81	—	—	—	—	-150.00	0.32	4.10	80.07	77.44
3	33.96	128.37	143.12	—	—	-150.00	0.82	4.58	2.18	11.98
5	135.36	141.69	96.92	56.66	11.50	-139.08	8.91	4.51	0.04	2.59

Reference

[1] Tauchert, T. R., Ashida, F.: Application of the Potential Function Method in Piezothermoelasticity: Solutions for Composite Circular Plates. *J. Thermal Stresses* **22**: 387-420, 1999.

SMA HYBRID COMPOSITES: SELF-HEALING, SELF- STIFFENING, AND SHAPE CONTROL SIMULATIONS

L. Catherine Brinson, Deborah Burton, Xiujie Gao
Northwestern University, Mechanical Engineering Department, Evanston IL 60208, USA

Summary The design and simulation of SMA Reinforced Composites is investigated with particular attention to self-healing, adaptive stiffening and shape control functions. The two types of composites studied use SMA ribbons or wires inside a matrix material to create a self-healing material and a panel/beam with adaptive stiffening or shape control. Finite element analysis is used to simulate the structural response of the composites.

INTRODUCTION

The usage of shape memory materials has extended rapidly to many fields, including medical devices, actuators, composites, structures and MEMS devices. For these various applications, shape memory alloys (SMAs) are available in various forms: bulk, wire, ribbon, thin film, and porous. In this paper, we consider two different types of SMA Reinforced Composites: SMA wires in a low melting point metallic matrix for self-healing materials and SMA ribbons in a polymeric based composite panel/beam for adaptive stiffening or shape control via selective resistance heating. Here we present modelling considerations that are compared to experimental work [1,3,6]. To simulate the structural response of the SMA reinforced composites using finite element analysis, we develop an ABAQUS user element with an SMA constitutive law. Several examples are presented in which the critical design features and possibilities are highlighted. The modelling is introduced next followed by applications and simulations for specific types of composites.

CONSTITUTIVE MODEL AND FINITE ELEMENT IMPLEMENTATION

The Brinson one-dimensional constitutive model for SMA materials is used [4]. It separates the martensite volume fraction into temperature-induced (self-accommodated) and stress-induced (oriented) fractions.

$$\sigma = E(\xi \xi_L \xi_d) + \Omega \Omega T \qquad \xi = \xi_d + \xi_t$$

The martensite transformation is determined by the loading path in a (σ-T) phase diagram (Figure 1a). Since the transformation is history-dependent, the kinetics are determined by using "switching points" ([5], Figure 1b).

$$\xi = F^A\left(Z^A;\sigma_j\right) = \xi_j f^A\left(Z^A(T,\sigma;T_j,\sigma_j)\right)$$

FEA simulations were done with the ABAQUS code. To accomplish this, a user subroutine (UEL) was developed to incorporate the coupled SMA constitutive and kinetics models, including algorithms to handle complex overlapping transformation regions and compressive stress states. The UEL defines a one-dimensional truss which is suitable for SMA wires or ribbons.

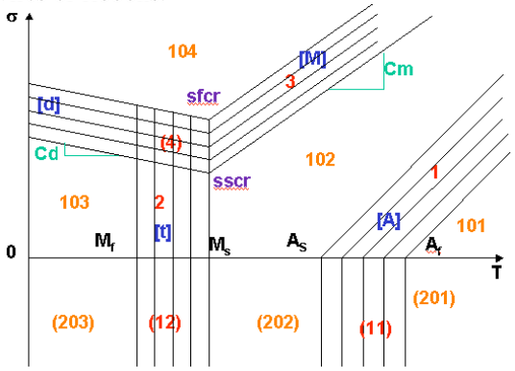


Figure 1a: Transformation phase diagram.

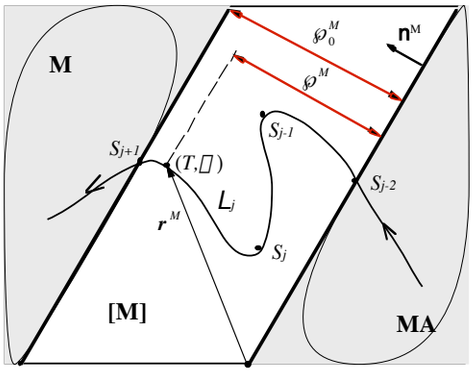


Figure 1b: loading path and switching points in a subregion.

SELF-HEALING MATERIAL

The self-healing metallic composite is composed of SMA wires in a tin-bismuth matrix material. In the situation that is analyzed, a crack develops in the matrix, perpendicular to the reinforcement wires. The SMA wires serve both to increase toughness of the material through "bridging" and also to initiate "healing" of cracks in the composite when heat is applied. "Bridging" can occur because martensite detwinning allows the SMA material to sustain large strains. If the cracked composite is heated above the austenite finish temperature, the SMA wires transform back to the shorter austenite form, pulling the cracked matrix back together. If the wires initially have some detwinned martensite, then transformation from the stress-induced martensite to austenite will cause a negative strain which has the effect of

applying a positive closure force to the crack. The model is able to simulate crack opening, closing, and clamping, and the results can be used to guide the development of high performance NiTi based SMAs for use in composites.

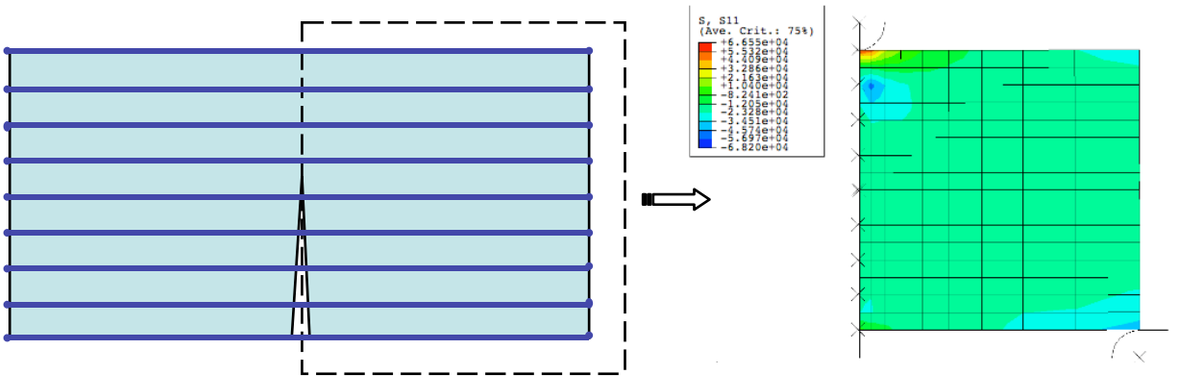


Figure 2: SMA self-healing composite: a) schematic showing wires and existing crack opening after loading; b) half model (symmetry b.c.) with rigid bodies to apply three-point bending; stress contour plot showing closed crack and uniform closure pressure (negative).

ADAPTIVE COMPOSITE

In a polymeric based composite, the pre-strained SMA actuator ribbons are embedded and bonded to the matrix and when actuated via thermal excitation they recover under almost rigid constraints to stiffen the composite or under soft constraints to alter the shape of the composite. Potential applications include suppressing vibration to reduce sonic fatigue and noise transmission and controlling the shape of the leading edge of an airplane. Turner [7] has examined the buckling and dynamic response of a thin beam. Figure 3a shows a prototype beam under investigation of buckling, stiffening, and re-buckling due to combined thermal expansion effects and the reverse transformation of the ribbons. Upon continuous heating, first the beam buckles before the SMA ribbons are actuated; then the deflection is diminished once the ribbons start to recover; and finally at a even higher temperature it re-buckles due to dominant thermal effect. The experimentally observed deflection of the beam is shown in Figure 3b. As shown in Figure 3b, the simulation results for bare matrix and the composite are exactly what one expects. Further simulation on shape control and dynamic problems are ongoing.

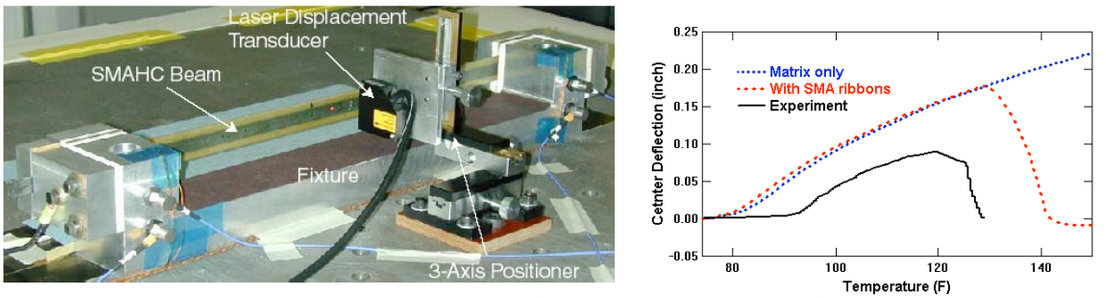


Figure 3: a) Conceptual airplane with airfoil made of shape memory alloy reinforced composite (SMAHC); b) Plate prototype of SMAHC. (Courtesy of Dr. Travis. L. Turner at NASA.)

CONCLUSIONS

The modeling approach and ABAQUS UEL have demonstrated robust performance and very good agreement in predicting self-healing behavior of SMA reinforced metal composite. Adaptive stiffening and shape control behavior of a constrained beam subject to temperature ramping has also been well captured.

References

[1] Files, B. S.: Design of a Biomimetic Self-Healing Superalloy Composite. Ph.D.dissertation, Northwestern University, 1997.

[2] Yamada, Taya: Strengthening of Metal Matrix Composite by Shape Memory Effect. Materials Transactions, 1993.

[3] Krag J., et. al.: Biomimetic Shape-Memory Reinforced Alloy Composite for Mars Rover Self-Healing Axles Project. Report for B.S. Files at NASA, Houston, June 8, 2002.

[4] Brinson, L. C., Huang, M. S: Simplifications and Comparisons of Shape Memory Alloy Constitutive Models. *J. Intell. Matl. Syst. & Struct.* **7**: 108-114, 1996.

[5] Bekker A., Brinson L. C: Phase Diagram Based Description of the Hysteresis Behavior of Shape Memory Alloys. *Acta Mater.* **46**: 3649-3665, 1998.

[6] Turner, T.L.: Structural acoustic response of a shape memory alloy hybrid composite panel (lessons learned). SPIE Vol. 4701, Paper No. 4701-60, San Diego, CA, March 2002.

[7] Turner. T.L.: Experimental validation of a thermomelastic model for SMA hybrid composite. SPIE Vol. **4326**, Paper No. 4326-24, Newport Beach, CA, March 2001.

ACTIVE CONTROL OF FGM PLATES USING DISTRIBUTED PIEZOELECTRIC SENSORS AND ACTUATORS

V. Balamurugan*, S. Narayanan**
*Centre for Engg. Analysis & Design, Combat Vehicles R & D Establishment, Chennai 600 054, India
**Department of Applied Mechanics, Indian Institute of Technology Madras, Chennai 600 036, India

Summary Distributed sensing and active control of FGM plates using piezoelectric sensors/actuators is studied. A nine nodded piezolaminated plate finite element has been developed incorporating the FGM material model and the electromechanical coupling constitutive relations of the piezoelectric sensors/actuators. The FGM plate considered for study is made of the combined aluminum oxide and a titanium alloy, Ti-6Al-4V and its properties are graded through the thickness according to a volume fraction power law distribution. The vibration control performance is explored using the LQR optimal control law. The influence of the constituent volume fraction of Ti-6Al-4V is also studied for the static and controlled dynamic response of FGM plates.

INTRODUCTION AND FORMULATION

"*Functionally graded materials*" (FGMs) are relatively new class of composite materials which are characterized by the smooth and continuous variation of the mechanical properties from one surface to the other. Due to its superior thermo-mechanical properties, FGMs have found extensive applications in aerospace, automobile, biomedical and nuclear industries. A FGM plate made of two materials whose properties are graded through the thickness direction according to volume fraction power law, is considered with thin PZT layers embedded on top and bottom surfaces to act as distributed sensor/actuator. The material properties can be expressed as, $P_{eff}(z) = P_1 V_1(z) + P_2\left(1 - V_1(z)\right)$, where P_{eff} is the effective material property of the FGM, and P_1 and P_2 are the properties of the materials 1 and 2 respectively. V_1 is the volume fraction of the constituent material 1 in the FGM and can be written as, $V_1 = \left(\frac{2z+h}{2h}\right)^n$ where n is the volume fraction exponent $(0 \le n \le \infty)$. A C^o continuous, shear flexible, nine-noded piezolaminated plate finite element derived including electromechanical coupling effects of the piezoelectric sensor/actuator layers [1] has been used for the study. The element has been further developed to include the FGM material model as above. The piezoelectric constitutive equations coupling elastic and electric fields are expressed as, $\{\sigma\} = [c]\ \{\in\} - [e]^T \{E\}$ and $\{D\} = [e]\ \{\in\} + [\varepsilon]\ \{E\}$, where $\{D\}$, $\{E\}$, $\{\in\}$ and $\{\sigma\}$ are electrical displacement, electrical field, strain and stress vectors, while, $[C]$, $[e]$ and $[\varepsilon]$, are elasticity, piezoelectric and dielectric constant matrices. The displacement field, strain definitions, electric field strength definitions and shape functions are as detailed in Ref.[1]. The element has five elastic degrees of freedom, u_o, v_o, w which are displacements and θ_x, θ_y which are rotations of normal in xz & yz planes and one electrical degree-of-freedom, ϕ per piezoelectric layer. Using the variational principles the strain energy functional is given by,

$$U = \frac{1}{2}\int_A [\{\in_p\}^T [A_{ij}] \{\in_p\} + \{\in_p\}^T [B_{ij}] \{\in_b\} + \{\in_b\}^T [B_{ij}] \{\in_p\} + \{\in_b\}^T [D_{ij}] \{\in_b\} + \{\in_s\}^T [E_{kl}] \{\in_s\}]\, dA - \int_{V_p} \left(\{\in_p\}^T + z\{\in_b\}^T\right)[e]^T \{E\}\, dV$$

where, $\{\in_p\}, \{\in_b\}$ and $\{\in_s\}$ are the inplane, bending & shear strains. $[A_{ij}]$, $[B_{ij}]$, $[D_{ij}], (i,j = 1,2,6)$ & $[E_{kl}](k,l = 4,5)$ are extensional, bending-extensional, bending and shear stiffness coefficients of the plate. These are given by,

$$[[A_{ij}],[B_{ij}],[D_{ij}]] = \int_{-h/2}^{h/2} \left(([Q_{ij}^1] - [Q_{ij}^2]) \left(\frac{2z+h}{2h}\right)^n (1, z, z^2) + [Q_{ij}^2](1, z, z^2) \right) dz \quad \& \quad [E_{kl}] = \int_{-h/2}^{h/2} \left(([Q_{kl}^1] - [Q_{kl}^2]) \left(\frac{2z+h}{2h}\right)^n (1, z, z^2) + [Q_{kl}^2](1, z, z^2) \right) dz$$

where $[Q^1]$ & $[Q^2]$ are the elastic properties. The electrical energy is as in [1] while the kinetic energy is given by,

$$T = \frac{1}{2}\int_A \left[P(\dot{u}^{o2} + \dot{v}^{o2} + \dot{w}^{o2}) + I(\dot{\theta}_x^2 + \dot{\theta}_y^2) \right] dA, \quad \text{where,} \quad [P, I] = \sum_{k=1}^{m} \int_{-h_{k-1}}^{h_k} \left((\rho^1 - \rho^2) \left(\frac{2z+h}{2h}\right)^n (1, z^2) + \rho^2 (1, z^2) \right) dz$$

where m is the number of layers. The Langrange's equations of motion, for an element can be written as $[M_{uu}]_e \{\ddot{\delta}\}_e + [K_{uu}]_e \{\delta\}_e + [K_{u\phi}]_e \{\phi\}_e = \{F_s\}_e$ and $[K_{\phi u}]_e \{\delta\}_e + [K_{\phi\phi}]_e \{\phi\}_e = \{F_q\}_e$, where, $[M_{uu}]_e$ is element mass matrix and $[K_{uu}]_e$ is element elastic stiffness matrix obtained from the kinetic and strain energy functionals [1]. $[K_{\phi u}]_e = [K_{u\phi}]_e^T$ are the elastic-electric coupling stiffness matrices and $[K_{\phi\phi}]_e$ is the electric stiffness matrix, $\{F_s\}_e$ is the applied mechanical force and $\{F_q\}_e$ is the applied electrical charge. The sensor voltage is given by, $\{\phi_s\}_e = -[K_{\phi\phi}]_{se}^{-1} [K_{\phi u}]_{se} \{\delta_s\}_e$.

The assembled global equations are converted into state space form and active control performance is studied using LQR optimal control scheme [1]. The FGM plate considered for study is of aluminum oxide and titanium alloy, Ti-6Al-4V and its properties are graded through thickness according to a volume fraction power law. The size of the plate is 400 x 400mm with 5mm thickness and is in the cantilevered configuration with one edge fixed and others free. The PZT sensors/actuators covering the top and bottom surfaces of the FGM plate have a thickness of 0.1mm. The material properties as given in Table 1.

Table 1 : Material properties

Material	E (N/m^2)	N	ρ (kg/m^3)	d_{31}/d_{32} (m/V)	$\in_{33}$ (F/m)
Aluminum oxide	3.2024×10^{11}	0.26	3750	-	-
Ti-6Al-4V	1.057×10^{11}	0.2981	4429	-	-
PZT G1195N	63×10^{9}	0.3	7600	254×10^{-12}	15×10^{-9}

RESULTS AND DISCUSSION

The cantilevered FGM plate is subjected to uniform pressure of $100\ N/m^2$ and the centerline deflection for various values of the constituent volume fraction n is as shown in figure 1. As n increases, the volume fraction of Ti-6Al-4V is decreased and when n tends to ∞, the FGM plate almost totally consists of aluminum oxide. As n increases, the deflection of FGM plate is decreased. To control the plate deflection, active voltages of equal magnitude and opposite sign are applied across the PZT layers, through the thickness. Figure 2 shows the centerline deflection for various values of the power law exponent n under actuator voltage $V = 40\ V$. By adjusting the actuator voltage, one can control shape as well as position of maximum deflection point. These results compare well with ref [2]. Then six natural frequencies of the FGM plate as function of volume fraction power law exponent n are compared with ref [2] as in table 2. The for active vibration control, the top and bottom PZT layers are used as an integrated sensor and actuators. An impact load of $50N$ is applied at the free edge of the plate for a duration of $1\ m\sec$. The LQR optimal control scheme is applied to study the active vibration control with the weighting parameters $Q = 1\times10^{8}$ and $R = 1$. An initial modal damping of 0.2% is assumed and the controller is activated after 0.2 sec of the impact. Figure 3 indicates the controlled dynamic response of the FGM plate for the volume fraction power law exponent n of 0.5 and 1000. The effect of n in this case is similar to that of the static case. i.e., the amplitude decreases with the increase in n.

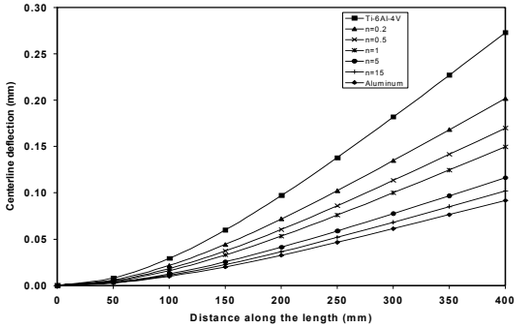


Fig. 1 : Centerline deflection of the FGM plate under uniformly distributed load of 100 N/m^2 and actuator voltage of 0V.

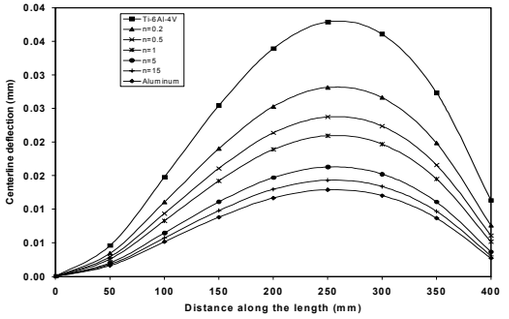


Fig. 2 : Centerline deflection of the FGM plate under uniformly distributed load of 100 N/m^2 and actuator voltage of 40 V.

Mode No.	n=0		n=0.5	n=15	n=1000	
	present	[2]	present	present	present	[2]
1	25.51	25.58	33.224	45.080	47.806	46.55
2	62.49	62.75	82.053	112.13	119.01	116.00
3	156.73	157.20	204.77	278.56	295.49	287.60
4	199.67	200.19	260.31	353.54	374.96	365.00
5	227.93	228.22	298.47	406.91	431.72	419.55
6	396.54	397.58	519.21	707.75	750.91	730.59

Table 2 : Natural frequencies of the cantilevered FGM plate.

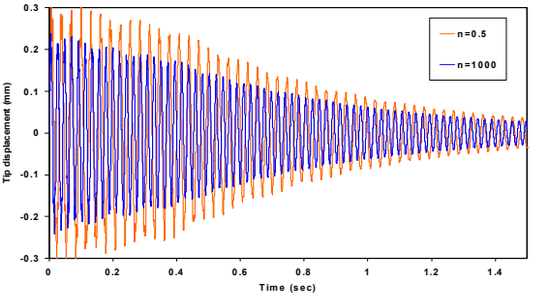


Fig. 3 : Controlled dynamic response of the FGM plate under an edge load of 50 N for 1 msec and LQR control (Q=1e8, R=1)

CONCLUSION

In this work a shear deformable piezolaminated FGM plate finite element has been developed and shape and vibration control performance of an FGM plate is studied using distributed piezoelectric sensors and actuators. The properties of the FGM plate are functionally graded through the thickness direction according to a volume fraction power law distribution. Optimal control theory LQR scheme has been applied for the active control.

References

[1] Balamurugan, V., Narayanan, S.: Shell finite element for smart piezoelectric composite plate/shell structures and its application to study active vibration control, Finite Elem. in Anal and Des., 37, 2001, 713,738.

[2] He, X.Q., Ng, T.Y., Sivashanker, S., Liew, K.M.: Active control of FGM plates with integrated piezoelectric sensors and actuators, Int. Jl. Of Sol. Struct., 38, 2001, 1641-1655.

MODELS OF LAMINATED PIEZOELECTRIC BEAMS INCLUDING EFFECT OF TRANSVERSE INTERACTIONS BETWEEN DIFFERENT LAYERS.

C. Maurini[*], F. dell'Isola[**] and J.Pouget [*]

[*] *Laboratoire d'Etudes Mécanique des Assemblages (FRE 2481), Université de Versailles/Saint-Quentin-en Yvelines, 45, ave. des Etats-Unis, 78035 Versailles cedex, France*

[**] *Dipartimento di Ingegneria Strutturale & Geotecnica, Università di Roma "La Sapienza", via Eudossiana 18, 00184 Roma, Italy*

ICTAM04 ID: 12552.

Summary The present work attempts to present a consistent and efficient approach to piezoelectric laminated beams.. The influence of hypotheses on three-dimensional sectional deformations and stress distributions on the estimate of the beam electromechanical properties is analyzed. By exploiting a mixed variational formulation and Lagrange multipliers method, an Euler-Bernoulli-like beam model which accounts for transverse interactions between different is presented. The fully coupled electromechanical nature of the system is described by including both mechanical and electrical kinematical descriptors and both direct and inverse piezoelectric effects. For a sandwich piezoelectric beam and for a two-layers beam, expressions of the beam constitutive coefficients are provided and the main features of the proposed model are highlighted. Comparisons with experimental data and results from standard modelling approaches are presented. As main peculiarity, the proposed beam model coherently estimates the equivalent piezoelectric capacitance and transverse normal stress distribution also for beam composed by elastic and piezoelectric layers of comparable thickness.

Piezoelectric composites have been widely used for their sensor and actuator functions and research on this area opens many applications in the domain of adaptive structures and structural control [1]. Beam-shaped structures incorporating piezoelectric materials are often used in engineering applications as in robotic arms, airplane wings, helicopter rotor blades, positioning devices, etc. One-dimensional models of such structures provide analytical estimates of their electromechanical properties and useful tools for structural analysis and control system design [2].

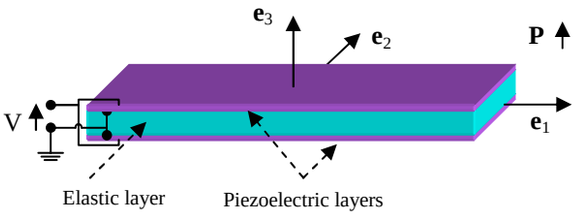


Figure 1. A laminated piezoelectric beam (sandwich configuration).

The aim of the present work is to discuss in details an issue which is often neglected in beam models of piezoelectric laminates: the influence of hypotheses on transverse normal stress (T_{22}) and strain (S_{22}) on the derivation of the constitutive properties of 1D models (mechanical stiffness, coupling coefficient and piezoelectric capacitance) from the 3D geometric and material data.

Beam models presented in literature (see e.g. [3,4]) usually retain classical assumptions for single-layered elastic structure by assuming that either transversal normal stress (T_{22}) or transversal normal strain (S_{22}) are vanishing layer by layer. However, as shown by finite element simulations based on a 3D model, these hypotheses are not verified in piezoelectric laminates with thickness-polarized piezoelectric layers. Indeed, when a potential difference is applied between the electrodes of a piezoelectric layer, it naturally tends to isotropically extend (or shrink) in the plane orthogonal to the polarization axis ($\mathbf{e}_1$-$\mathbf{e}_2$ plane). This behavior is in competition with Poisson effect in elastic layer: when one try to extend an elastic layer in one direction (say $\mathbf{e}_1$), shrinking in the other direction (say $\mathbf{e}_2$) is typically induced. When piezoelectric and elastic layers are bonded together to form a laminated piezoelectric beam, their contrasting behavior is conciliated by the appearance of non-negligible normal stresses both in the axial direction (T_{11} stress) and transverse direction (T_{22} stress). Such problem was discussed also by Beckert and Pfundtner [5], were classical assumptions on transverse stress are improved and complex interactions between different layers in composite piezoelectric laminates are underlined. However, only actuation functions are considered and no attention is paid to the determination of purely electrical properties such as the equivalent piezoelectric capacitance.

In the present paper, an efficient model of laminated piezoelectric beams including transverse interactions between different layers is proposed. It includes both sensory and actuation effects and is based on the following hypotheses:

i) equivalent single-layer Euler-Bernoulli kinematics (only axial extensional strain S_{11} with a linear distribution along the thickness);
ii) layerwise linear distribution of mechanical stress with non-vanishing transverse normal stress (i.e. T_{22});
iii) layerwise linear distribution of electric potential;
iv) layerwise constant distribution of the electric displacement.

The transverse normal stress T_{22} are not determined by corresponding equilibrium equations since transversal deformations are not included in the Euler-Bernoulli kinematics and no energy contribution is associated to them. Their distribution in the different layers is found by imposing the following additional conditions (null force resultant and null moment resultant):

$$N_2 = \int_{Section} T_{22} = 0, \; M_2 = \int_{Section} zT_{22} = 0. \qquad (1)$$

The proposed model which is characterized by assuming null transverse stress resultants (NSR model) is compared to the models assuming either pointwise null transverse stress (T_{22}=0, NS model) or null transverse sectional deformations (S_{22}=0, ND model).

The model above imposes at the same time hypotheses on the distribution of electromechanical kinematical and dynamical state field (strain, electric potential, stress, and electric displacement). Hence, in order to rationally deduce the beam models from the three-dimensional description, a mixed variational formulation based on the Hellinger-Prange-Reissner functional for piezoelectricity is adopted. Moreover, the additional conditions on transverse stresses (1) are introduced into the variational formulation through Lagrange multipliers method.

The influence of the introduced stress field T_{22} and the associated weak conditions on the beam constitutive equations is discussed in details. In particular, it is shown that the different hypotheses (null transverse stress resultants, null transverse stress, null transverse strain) on transversal normal stress (T_{22}) and strain (S_{22}) strongly influence the estimate for the equivalent piezoelectric capacitance. Comparisons to experimental data and finite element simulations are reported (see Table 1) and the peculiar ability of the proposed model of correctly estimating the equivalent piezoelectric capacitance and the transverse normal stress distribution is shown.

	ND model	**NS model**	**NSR model**	**Experimental**
Capacitance per unit line	2.09 nF/mm	3.62 nF/mm	2.81 nF/mm	2.86 nF/mm
Error (%)	+26.7%	-26.6%	-1.75 %	----

Table 1. Comparison between piezoelectric capacitance per unit line predicted by the proposed model (NSR model), standard models (ND and NS models) and the one measured experimentally. The values refer to a sandwich piezoelectric beam (see Figure 1) made of a central aluminium core on which two piezoelectric layers (PZT-5H) are symmetrically bonded (beam width 17.8mm, piezoelectric layers thickness 0.27mm, aluminium layer thickness 2.0 mm).

References

[1] Chopra : Chopra, I., 2002. Review of state of art of smart structures and integrated systems. AIAA Journal 40 (11), 2145-2187.

[2] Saravanos : Saravanos, D.A., Heyliger, P.R., 1999. Mechanics and computational models for laminated piezoelectric beams, plates, and shells. Applied Mechanics Review 52, 305-320.

[3] Crawley : Crawley, E.F., de Luis J., 1987. Use of piezoelectric actuators as elements of intelligent structures. AIAA Journal 25, 1375-1385

[4] Alzahrani, B.A., Alghamdi , A.A.A., 2003. Review of the mechanics of materials models for one-dimensional surface-bonded piezoelectric actuators. Smart Mater. Struct. 12, N1-N4.

[5] Beckert, W., Pfundtner, G., 2002. Analysis of the deformational behaviour of a bimorph configuration with piezoelectric actuation. Smart Materials and Structures 11, 599-609.

[6] Hagood : Hagood, N.W., Von Flotow, A., 1991. Damping of structural vibrations with piezoelectric materials and passive electrical networks. Journal of Sound Vibration 146, 143-168.

Ultrasonic characterization of phase transformation in NiTi wire during thermomechanical loading

Michal Landa[a], Petr Sedlák[ac], František Maršík[a], Petr Šittner[b], Václav Novák[b]

[a]*Institute of Thermomechanics, ASCR, Dolejškova 5, Prague 8, 182 21, Czech Republic*

[b]*Institute of Physics, ASCR, Na Slovance 2, 182 21, Czech Republic*

[c]*Faculty of Nuclear Sciences and Physical Engineering, CTU in Prague, Břehová 7, Prague 1, 110 00, Czech Republic*

Summary Evaluation of thermo-mechanical properties of NiTi wires intended for stent applications is carried out by combination of tensile tests at constant temperature with in-situ ultrasonic measurements (wave speed, attenuation) and electrical resistivity measurements. It is found that the mechanical and electric resistance results are mainly sensitive to R-B19' stress induced martensitic transformation, but the ultrasonic wave speed and attenuation vary most significantly when the R-phase reorientation or distortion take place.

INTRODUCTION

Biocompatibility and high recoverable strain properties of superelastic nickel-titanium alloy make it an interesting material for medical application like vascular support wire-structures (self-expanding stents) [1]. Detailed knowledge of phase transition mechanisms is essential for utilization of the unique properties (shape memory effect and superelasticity) of the NiTi alloys in optimal design of the implants.

The high temperature parent phase of NiTi alloys has B2 type ordered cubic structure that transforms to B19' monoclinic martensite phase by cooling or applied stress. Following suitable termomechanical treatments, the martensitic transformation in NiTi may proceed as two step B2-R-B19' [2]. The intermediate R-phase has rhombohedral structure differing only slightly from the B2 by rhombohedral distortion. The B2-R transformation exhibits very small transformation strain and hysteresis compared to the B2-B19' martensitic transformation. The activity B2-R transformation is rather difficult to recognize in mechanical test on NiTi wires, although it might be responsible for significant part of inelastic strains [3], particularly if loading is limited to small strains (<2%). In this research, an in-situ ultrasonic technique was applied during tensile test on NiTi wire showing R-phase upon cooling slightly below the room temperature. The aim was to check whether the acoustic method can detect activity of the various transformation processes taking place during the tensile tests at various temperatures.

EXPERIMENT

Evaluation of thermo-mechanical properties of commercial NiTi wires (Ni55.75%wt, Fort Wayne Metals Corp. , 0.18mm in diam.) was carried out by strain controlled tensile tests with the ultrasonic pulse-transition in-situ measurement. The temperature of the specimen was kept constant during the load cycle. The wire was heated by electrical current, impedance of the electrical supply was matched to the wire impedance, thus constant heating condition was ensured. The pair of miniature piezoelectric transducers, used as ultrasonic emitter and receiver, were placed at the gripped ends of the wire (Fig.1). At constant time period, the transmitted pulses along the wire were recorded and longitudinal wave velocity c_L and amplitude A were evaluated. The instantaneous Young modulus E is given by

$$E = \rho . c_L^2$$

and wave attenuation α is determined by

$$\alpha = -\frac{1}{H} 20 \log(A / A_{ref}),$$

where ρ is mass density and H is the instantaneous wire length. The attenuation is related to the initial value α_o.

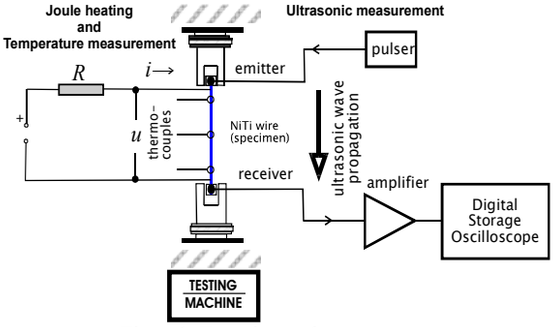


Figure1: Experimental arrangement

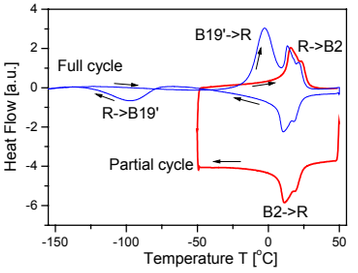


Figure 2: DSC record during full and partial cooling-heating cycles showing temperature ranges where individual transformation events take place.

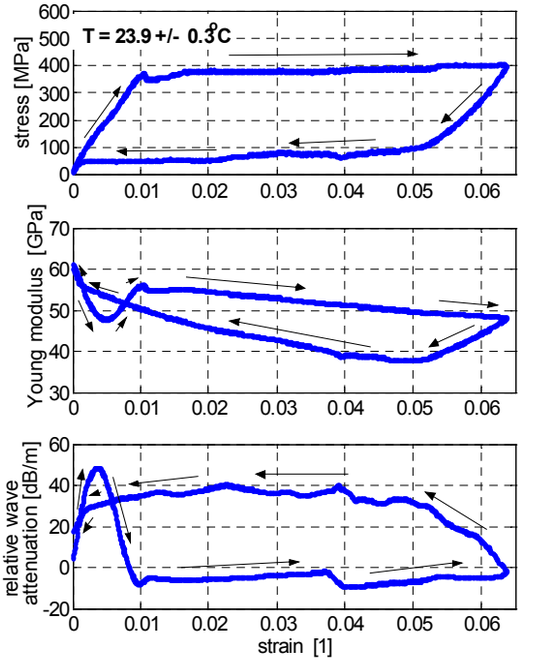


Figure 3: Stress and quantities, determined by ultrasound, during virgin loading of the tested NiTi wire.

RESULTS

Prior the mechanical tests, differential scanning calorimetry measurement was carried out (Fig.2) . It is clear, particularly from the partial cycle scan, that the alloy may exist at room temperature (T=24 ^{o}C) either in R-phase or in the B2 phase state depending on the history. Since the mechanical test (Fig.3) was carried out after cooling to approx. 10 ^{o}C and subsequent heating to room temperature, the specimen was in the R-phase state prior the start of the test. Stress induced transformation to the B19' martensite phase proceeds at approximately constant stress level 400MPa between 1%-6% strain most likely in Luders-like localization mode. It is very interesting to note that significant changes of wave speed and attenuation are not detected during the R-B19' transformation to martensite but in the preceding quasilinear elastic range. In that range, reorientation of R-phase variants takes most likely place at first (strain <0.5%) and later on elastic deformation (or possibly further distortion) of R-phase structure occurs (0.5%< strain <1%) [3]. Clearly, the ultrasonic quantities seem to be much more sensitive to the R-phase phenomena than to the martensitic transformation itself.

CONCLUSION

Combined ultrasonic–mechanical-electrical technique was applied to investigate stress induced martensitic transformation in commercial NiTi wire intended for stent applications. While the mechanical and electric resistance results are mainly sensitive to R-B19' martensitic transformation, the ultrasonic wave speed and attenuation varies significantly when the R-phase reorientation or distortion take place.

Acknowledgement

This work was supported by the Grant Agency of the Czech Republic under the project no. 106/03/1073 and the Institutional project AVOZ2076919.

References

[1] Karel Volenec - ELLA-CS, http://www.ellacs.cz/
[2] K. Otsuka, X Ren, Recent developments in the research of shape memory alloys, *Intermetallics* **7**:511-528, 1999
[3] P.Šittner, M.Landa, P.Lukáš, V.Novák, R-phase transformation phenomena in thermomechanically loaded NiTi polycrystals, in Special issue on SMAs , *Mechanics of Materials*, 2003, in print

UPPER AND LOWER BOUNDS OF ELECTRIC INDUCTION INTENSITY FACTORS FOR MULTIPLE PIEZOELECTRIC CRACKS BY THE BEM

M. Denda*, M. Mansukh*
*Rutgers University, Mechanics & Aerospace Engineering Department, 98 Brett Road, Piscataway, New Jersey 08854-8058, U.S.A.

Summary The upper and lower bounds for the electric induction intensity factors for multiple piezoelectric cracks are obtained by the boundary element method using the impermeable and permeable crack solutions. The numerical Green's function for the crack is developed by the analytical integration of the continuous distribution of the generalized dislocation dipoles. The Green's function has the $1/\sqrt{r}$ generalized stress singularity and no post process for the intensity factor determination is needed.

INTRODUCTION

The coupling of mechanical and electrical behaviors of the piezoelectric materials has find its applications to sensors (e.g., sonars), actuators (e.g., ultrasonic cleaners, ultra-precision positioners, ink jet print heads), signal transmitters (e.g., cellular phone, remote car opener), and surface acoustic wave devices to mention a few. The modern life style cannot be sustained without piezoelectric materials. However, they are plagued with the brittleness of the widely used piezoceramic materials. The lack of understanding and modelling tools of the piezoelectric fracture is limiting the further progress in the piezoelectric material based technology. This paper addresses issues on the crack surface electric boundary conditions and suggests the upper and lower bound approach in the determination of the electric induction intensity factors using the boundary element method.

CRACK SURFACE ELECTRIC BOUNDARY CONDITIONS

While the mechanical boundary condition (BC) on the crack surface is always traction-free, the electric boundary condition comes in different degrees of shielding the electric induction defined by the electric permeability. For a crack along the x_1-axis, the permeable BC

$$D_2^+ = D_2^-; \quad \Phi^+ - \Phi^- = 0, \tag{1}$$

does not shield the electric induction at all, where D_2 and Φ are the electric induction and the electric potential, respectively, with $\pm$ indicating the upper and lower crack surfaces. Meanwhile, the impermeable BC

$$D_2^+ = D_2^- = 0, \tag{2}$$

shields the electric induction completely. The permeable BC is correct if the crack is closed, while the impermeable BC is correct if the permittivity ε_c of the crack medium is zero. Since no medium has zero permittivity (the vacuum has the least permittivity $\varepsilon_0 = 8.854 \times 10^{-12} C/(Vm)$) and we consider open cracks, the both boundary conditions are not correct. Hao and Shen [1] proposed the semi-permeable BC

$$D_2^+ = D_2^-; \quad D_2^+(u_2^+ - u_2^-) = -\varepsilon_c(\Phi^+ - \Phi^-), \tag{3}$$

which is the consistent BC adopted in this proposal. Note that the semi-permeable BC is reduced to the impermeable BC when $\varepsilon_c = 0$ and to the permeable BC when $u_2^+ - u_2^- = 0$ and that the impermeable and permeable BCs set the bounds for the semi-permeable BC. The majority of the earlier works adopted the impermeable BC due to the convenience to obtain the analytical solution. This led to contradiction between the experimental results and the fracture prediction by the (negative) energy release rate. Results predicted by the permeable BC are in much better agreement with the experimental results than those by the impermeable BC. If the crack opening displacement is extremely small, the permeable BC may provide a good approximation despite its inconsistency. The shift toward the consistent semi-permeable BC was made gradually but slowly.

UPPER AND LOWER BOUNDS FOR THE INTENSITY FACTOR

While the solutions of the permeable and the impermeable cracks are linear, that of the semi-permeable crack is non-linear. Since the distribution of the electric induction on the crack surface, which is needed to determine the crack opening displacement and the electric potential jump across the crack, is unknown we need an iteration process to determine all unknowns. This is inherently a nonlinear process even though each step consists of the linear solver. This poses a serious difficulty for the complex multiple crack configurations that appear in the real life applications. Meanwhile, the analytical solution for the single semi-permeable crack suggests the electric induction intensity factor is bounded by those by impermeable and the permeable cracks. So even though we may not get the exact semi-permeable solution, we can still get the upper and lower bound solutions using the impermeable and permeable cracks.

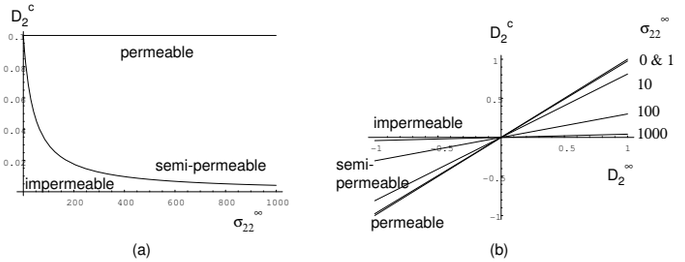


Figure 1. The crack face electric induction D_2^c for BSN with $H_{24} = 0$.

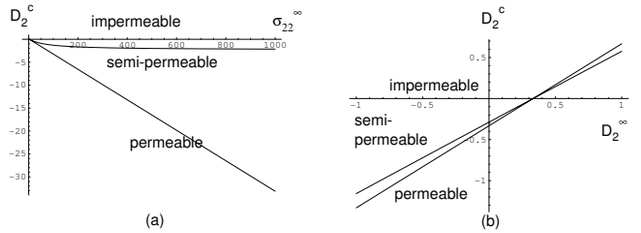


Figure 2. The crack face electric induction D_2^c for BSN with $H_{24} \neq 0$.

NUMERICAL GREEN'S FUNCTION FOR PIEZOELECTRIC CRACKS

While the FEM needs to model the entire domain surrounding a crack, the BEM only needs a single line to model the crack. It makes more sense to use the BEM for crack problems. As the demands for the analysis of more complicated crack configurations, such as multiple and curvilinear cracks, arise the advantage of the BEM over the FEM becomes clearly visible. We propose to use the BEM crack modelling strategy developed by Denda and Mattingly [2] for the general anisotropic solids. It uses the Green's function approach to multiple crack problems. The crack is modeled by the continuous distribution of the generalized dislocation dipoles with the $\sqrt{r}$ crack tip behavior and the resulting integration is evaluated analytically using the complex variable theory. The resulting crack element, called the whole crack singular element, offers a collection of mutually independent crack opening modes each of which has the $1/\sqrt{r}$ crack tip stress singularity. It serves as the numerical Green's function for the crack since the magnitudes of each mode must be determined numerically to satisfy the crack surface boundary condition. The solution strategies for the impermeable and permeable cracks are summarized as follows. (1) For the impermeable crack all the crack surface generalized traction components are set to zero. (2) For the permeable crack set the electric potential jump $\delta_4^{(m)}$ to zero and solve the problem by only applying the traction zero boundary condition on the crack. Since $\delta_4^{(m)} = 0$ we only need three traction free boundary condition on the crack surface to determine three unknown crack opening displacement components. Both (1) and (2) are linear procedures and can be solved by the BEM for multiple crack problems.

NUMERICAL RESULTS AND CONCLUSIONS

Figure 1 shows Variation of D_2^c ($\times 10^{-2} C/m^2$) (a) as the function of σ_{22}^{∞} ($\times 10^7 N/m^2$) for fixed $D_2^{\infty} = 0.1 \times 10^{-2} C/m^2$ and (b) as the function of D_2^{∞} for fixed $\sigma_{22}^{\infty} = (0, 1, 10, 100, 100) \times 10^7 N/m^2$; material is the Barium Sodium Niobate (BSN) with $H_{24} = 0$. Figure 2 shows the corresponding variation for the BSN with $H_{24} \neq 0$. (a) For fixed $D_2^{\infty} = 0.1 \times 10^{-2} C/m^2$ and (b) For fixed $\sigma_{22}^{\infty} = 10 \times 10^7 N/m^2$. Note that H_{24} is the measure of coupling between the crack opening δu_2 and the electric potential jump $\delta\phi$ and depends on the material constants and directions. These figures indicate that the impermeable and the permeable cracks set the bounds for the semi-permeable cracks.

References

[1] Hao T.H., Shen Z.Y. : A New Electric Boundary Condition of Electric Fracture Mechanics and its Applications *Eng. Frac. Mech.* **47**:793-802, 1994.

[2] Denda M., Mattingly, E.: The Whole Crack Singular Element for 2-D Boundary Element Analysis of Multiple Straight Cracks in the General Anisotropic Solids *Electronic J. Boundary Elements* (web site http://tabula.rutgers.edu/EJBE/) **1**:404-417, 2003.

Direct Identification of the State Equation in Complex Nonlinear Systems

by

Sami F. Masri, School of Engineering, University of Southern California, Los Angeles, California, USA
John P. Caffrey, School of Engineering, University of Southern California, Los Angeles, California, USA
Thomas K. Caughey, Division of Engineering, California Instit. Technology, Pasadena, California, USA
Andrew W. Smyth, School of Engineering & Applied Science, Columbia University, New York, NY, USA
Anastasios G. Chassiakos, School of Engineering, California State University, Long Beach, California, USA

SUMMARY

1. INTRODUCTION

A crucial element in the modeling, control and monitoring of adaptive ("smart") systems, is the ability to develop high-fidelity, reduced order and reduced complexity nonlinear (i.e., not-necessarily linear) mathematical models for the physical systems of interest. Recently adaptive estimation approaches have appeared for on-line estimation and identification of hysteretic systems under arbitrary dynamic environments. These adaptive estimation/identification techniques suffer from two drawbacks: (1) they assume that the restoring forces applied to the system's elements are available for measurement and (2) they assume that the differential equation driving these restoring forces can be parameterized as a linear combination of unknown constant parameters and known nonlinear terms.

With the above discussion in mind, the authors have developed an efficient identification algorithm for handling structural systems incorporating severe nonlinearities of the type commonly encountered in the applied mechanics field, spanning the range from large civil structures, to joint-dominated aerospace systems, to micro electromechanical devices (MEMS). The new methodology completely overcomes the above two drawbacks. Specifically, the new approach of this paper solves the problem of estimating/identifying the restoring forces without relying on the need of having the restoring forces directly available for measurement, and without constraining the restoring forces dynamics to have a particular structure.

2. PROBLEM FORMULATION

Building on the basic idea behind the *Restoring Force Method* for the nonparametric identification of nonlinear systems, a general procedure is presented for the direct identification of the state equation of complex nonlinear systems. No information about the system mass is required, and only the applied excitation(s) and resulting acceleration are needed to implement the procedure. Arbitrary nonlinear phenomena spanning the range from polynomial nonlinearities to the noisy Duffing - van der Pol oscillator (involving product-type nonlinearities and multiple excitations) or hysteretic behavior such as the Bouc-Wen model can be handled without difficulty. In the case of polynomial-type nonlinearities, the approach yields virtually exact results. For other types of nonlinearities, the approach yields the optimum (in least-squares sense) representation in nonparametric form of the dominant interaction forces induced by the motion of the system.

To illustrate the basic idea behind the new method, consider a nonlinear single-degree-of-freedom (SDOF) system that is governed by the following differential equation:

$$m\ddot{x} + c_1 x + c_2 \dot{x} + c_3 x^3 + c_4 x_1^2 \dot{x} + c_5 x f_1(t) + r(t) = c_6 f_2(t) \tag{1}$$

where m is the system mass, the c's are specified system parameters, $f_1(t)$ and $f_2(t)$ external forces acting on m, and $r(t)$ is a hysteretic force of arbitrary type. The nonlinear system characteristics inherent in the system of Eq.(1) covers a broad category of problems: (1) the damped Duffing oscillator under the action of an external exciting force $f_2(t)$, (2) the Noisy Duffing- van der Pol oscillator under the action of disturbances $f_1(t)$ and $f_2(t)$, and (3) a nonlinear system with general hysteretic properties which governs a very broad class of hysteretic systems spanning the range from a completely elastic to a completely elasto-plastic hsyteretic oscillator, specified by parameters $\mathbf{p}$, under exciting force $f_2(t)$.

Rewriting the differential equation Eq.(1) in a form convenient for using conventional numerical solution techniques for initial-value problems, leads to

$$\ddot{x} = g(x, \dot{x}, \mathbf{p}, f_1, f_2) \tag{2}$$

where

$$g = -\frac{c_1}{m}x - \frac{c_2}{m}\dot{x} - \frac{c_3}{m}x^3 - \frac{c_4}{m}x_1^2\dot{x} - \frac{c_5}{m}x f_1(t) - \frac{1}{m}r(t) + \frac{1}{m}f_2(t). \tag{3}$$

The central idea behind the present identification approach is to determine an approximating analytical function $\hat{g}$ that approximates the actual (unknown) system state equation g, with the form of $\hat{g}$ including suitable basis functions that are relevant to the problem at hand. Consequently, for the general nonlinear problem under discussion, a suitable choice of basis would be

$$basis = \{f_1, f_1 d, f_1 v, f_2, f_2 d, PS\} \tag{4}$$

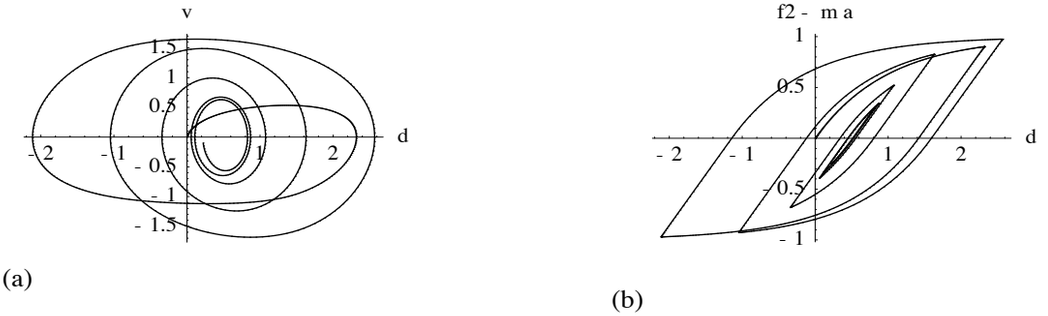
where PS represents the list of basis terms in the power series expansion in the doubly-indexed series

$$PS = \sum_{i=0}^{i_{max}} \sum_{j=0}^{j_{max}} d^i v^j \tag{5}$$

where, for convenience, the symbols d and v are used to represent the system's displacement x and velocity $\dot{x}$, respectively.

3. APPLICATION TO NONLINEAR SYSTEMS

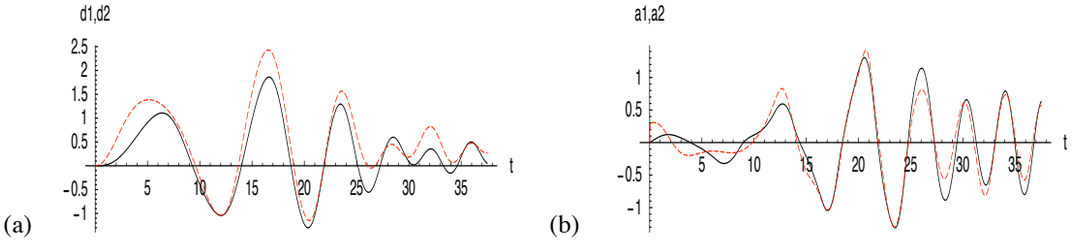
The formulation presented in the paper has been evaluated by calibrating its performance in identifying several types of complex nonlinear systems under deterministic as well as stochastic excitations. The response of an example hysteretic system is shown in Fig.(1). Sample results are shown in Fig.(2), in which a comparison is shown of the simulated hysteretic



(a) (b)

Figure 1: Hysteretic oscillator response data used for identification; (a) Phase diagram of $\dot{x}(t)$ versus $x(t)$; (b) Phase plot of restoring force $f_2(t) - m\ddot{x}(t)$ versus displacement $x(t)$.

system response with a different excitation than what was used for identification, obtained by solving the governing state equation.



(a) (b)

Figure 2: Comparison of simulated hysteretic system response with a different excitation than what was used for identification; (a) Displacement $x(t)$ and $\hat{x}(t)$; (b) Acceleration $\ddot{x}(t)$ and $\hat{\ddot{x}}(t)$.

4. SUMMARY & CONCLUSIONS

A simple yet general approach is presented for the direct identification of the state equation of complex nonlinear systems such as those encountered when dealing with "smart" systems. The procedure is a generalization of the *Restoring Force Method* which develops a low-order, low-complexity, nonparametric representation for a broad class of complex nonlinear systems widely encountered in the applied mechanics field. The utility of the new approach is demonstrated by investigating three different classes of single-degree-of-freedom nonlinear oscillators: the Duffing oscillator, the noisy Duffing - van der Pol oscillator, and the Bouc-Wen hysteretic oscillator. Issues that influence the performance of the method, such as data noise-pollution and the tradeoffs between model fidelity and its complexity, are discussed and guidelines are provided for application to generic cases.

SELF-HEALING POLYMER COMPOSITES FOR EXTENDED FATIGUE LIFE

Eric N. Brown[*,**], Alan S. Jones[*], Scott R. White[***], Nancy R. Sottos[*]
[*]*Department of Theoretical & Applied Mechanics and the Beckman Institute for Advanced Science and Technology, University of Illinois at Urbana-Champaign, Urbana, IL 61820, USA*
[**]*Currently at Los Alamos National Laboratory, Materials Science and Technology Division, MS-E544, Los Alamos, NM 87545, USA*
[***]*Department of Aerospace Engineering and the Beckman Institute for Advanced Science and Technology, University of Illinois at Urbana-Champaign, Urbana, IL 61820, USA*

Summary An extensive experimental investigation is carried out to assess the fatigue response of a self-healing polymer composite. Mode-I fatigue crack propagation is measured for a range of material parameters and loading conditions. Significant fatigue life extension and permanent fatigue crack arrest are achieved at moderate crack growth rates.

A novel approach is explored for improving the fatigue life of thermosetting polymers through the addition of self-healing functionality. Thermosetting polymers are used in a wide variety of applications ranging from composite structures to adhesive joints to microelectronic packaging. Due to their low strain-to-failure these polymers are highly susceptible to damage in the form of cracks. Fatigue loading is particularly problematic, giving rise to the initiation and propagation of small cracks deep within the structure where detection is difficult and repair is virtually impossible. These cracks often lead to catastrophic failure of the material. We utilize a strategy based on recent developments in self-healing technology [1-3] to autonomically repair fatigue cracks and extend the service-life of many polymeric components. The material under investigation is an epoxy matrix composite (EPON 828 cured with 12pph DETA), which utilizes embedded microcapsules [4] to store a healing agent and embedded Grubbs catalyst [5]. A propagating crack exposes particles of catalyst and ruptures the microcapsules, which release healing agent into the crack plane. Polymerization of the healing agent is triggered by contact with the catalyst, reestablishing structural integrity across the crack plane. The fatigue-crack propagation behavior is investigated using the tapered double-cantilever beam (TDCB) specimen with constant range of applied stress intensity factor ΔK. All measurements are made with a loading frequency of 5 Hz and load ratio $R = K_{min}/K_{max}$ of 0.1. Samples are cast in a silicon mold, cured for 24 hrs at room temperature followed by 24 hrs at 30°C, and then precracked with a razor blade.

FATIGUE CRACK GROWTH PRECLUDING SELF-HEALING

Fatigue crack propagation in neat epoxy, epoxy with embedded microcapsules, and epoxy with embedded catalyst is accurately captured by the Paris power law. The effect of embedded microcapsule size and concentration on fatigue crack growth is shown in Fig. 1. The addition of microcapsules significantly reduces the crack growth rate above a transition ΔK_T. Above the transition, the Paris law exponent n is strongly dependent on the content of microcapsules, varying from 9.7 for neat epoxy to approximately 4.5 above 10 wt% microcapsules. Similar retardation behavior has been reported for epoxy with embedded rubber particles [6].

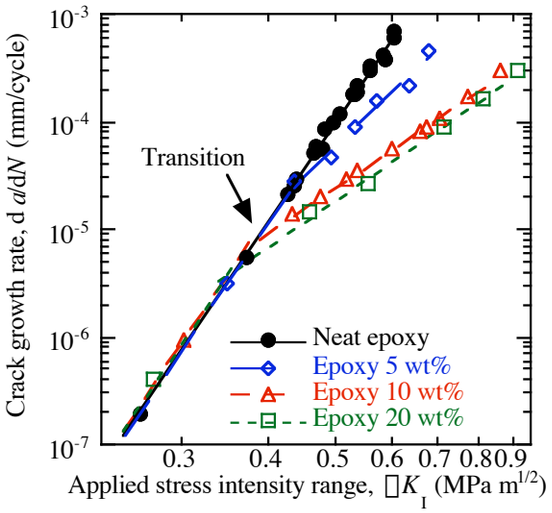


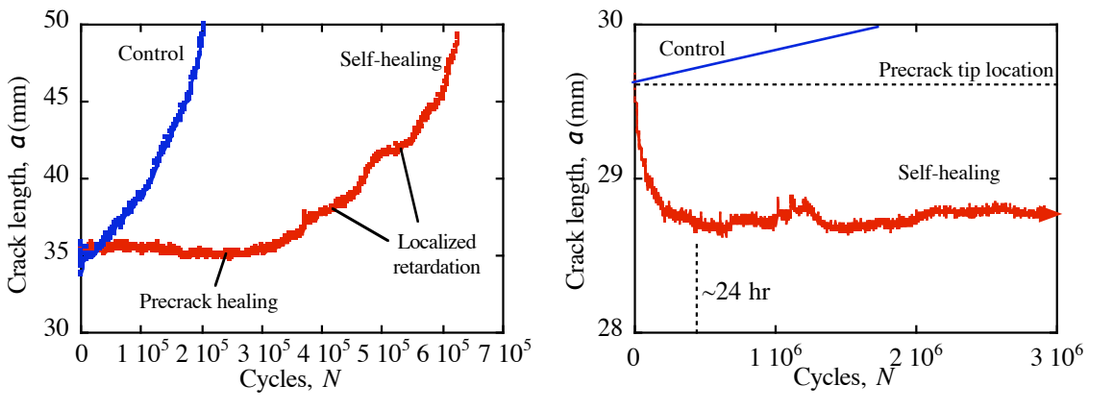
Figure 1. Influence of microcapsule concentration on the fatigue crack growth behavior for 180 μm diameter microcapsules.

IN SITU SELF-HEALING

Fatigue crack retardation and arrest from self-healing functionality result from crack-tip shielding mechanisms. Hydrodynamic pressure generated initially by uncured, liquid healing agent reduces both the loading and unloading of the crack tip. After polymerization, the fully cured healing agent forms a polymer wedge at the crack tip, which inhibits loading of the crack tip through adhesive mechanisms and unloading the crack tip through artificial-crack closure. Healing efficiency of the self-healing epoxy under cyclic loading is characterized with a fatigue-life-extension protocol [7],

$$\eta = \frac{N_{\text{healed}} - N_{\text{control}}}{N_{\text{control}}}, \tag{1}$$

where N_{healed} is the total number of cycles to failure for the self-healing sample and N_{control} number of cycles to failure for a similar sample without healing. Under high-cycle fatigue (moderate ΔK_I), Fig. 2a, and low-cycle fatigue (high ΔK_I) when a rest period was employed, *in-situ* healing extended fatigue life though temporary crack arrest and retardation. *In-situ* self-healing permanently arrested crack growth under low-cycle fatigue conditions at low ΔK_I, Fig. 2b, and at moderate ΔK_I when a rest period was employed.



(a) (b)

Figure 2. Crack length against fatigue cycles of *in-situ* sample tested to failure in (a) the high-cycle fatigue regime, η=213%. ΔK_I=0.338 MPa$\sqrt{m}^{1/2}$ and (b) the threshold regime, η= . ΔK_I=0.270 MPa$\sqrt{m}^{1/2}$.

CONCLUSIONS

A self-healing polymer was developed that improves the reliability of thermosetting polymers by initiating a healing process in response to damage. Fatigue-life extension was achieved by a combination of crack-tip shielding mechanisms induced by self-healing functionality. Viscous flow of the healing agent in the crack plane initially retarded crack growth. Polymermization of the healing agent, resulted in a long-term crack closure effect, which prevented unloading of the crack tip, reduced the crack length and retarded additional crack growth. A material able to autonomically respond to fatigue crack growth represents a milestone in the development of safer, longer-lasting materials.

References

[1] White, S. R., Sottos, N. R., Geubelle, P. H., Moore, J. S., Kessler, M. R., Sriram, S. R., Brown, E. N., Viswanathan, S.: Autonomic Healing of Polymer Composites. *Nature* **409**: 794–797, 2001.

[2] Brown, E. N., Sottos, N. R., White, S. R.: Fracture Testing of a Self-Healing Polymer Composite. *Experimental Mechanics* **42**: 372–379, 2002.

[3] Kessler, M. R., Sottos, N. R., White, S. R.: Self-Healing Structural Composite Materials. *Composites A* **34**: 743–753, 2003.

[4] Brown, E. N., Kessler, M. R., Sottos, N. R., White, S. R.: In Situ Poly(urea-formaldehyde) Microencapsulation of Dicyclopentadiene. *J. Microencapsulation* **20**: 719–730, 2003.

[5] Rule, J. D., Moore, J. S.: ROMP Reactivity of *endo*- and *exo*-Dicyclopentadiene. *Macromol.* **35**: 7878–7882, 2002.

[6] Azimi, H. R., Pearson, R. A., Hertzberg, R. W.: Fatigue of Rubber-Modified Epoxies: Effect of Particle Size and Volume Fraction. *J. Mater. Sci.* **31**: 3777–3789, 1996.

[7] Brown, E. N.: Fracture and Fatigue of a Self-Healing Polymer Composite Material. *PhD Thesis*, UIUC Dept. Theoretical & Applied Mech., 2003.

THE CONCEPT OF MULTIFOLDIG AND ITS EXPERIMENTAL VALIDATION

Jan Holnicki-Szulc*, Piotr Pawłowski*
* *Polish Academy of Sciences, IFTR PAS, Swietokrzyska 21, PL 00-049 Warszawa, Poland*

Summary The problem of energy absorption under impact loading is very important in a wide range of engineering applications. Although typically designed, passive energy absorbing systems provide a sufficient level of energy dissipation, they are unable to optimally decrease the level of acceleration. In contrast to the passive solutions, the proposed approach offers ability of structural adaptation to the conditions of the impact. Due to the presence of controllable micro-fuses, elements of the Multifolding Microstructure can optimally adjust their internal forces and therefore provide better performance in comparison to the passive absorbers. The undertaken experiment aims at the validation of the concept of multifolding and the verification of numerical models and control strategies applied in previous research.

INTRODUCTION

The problem of energy absorption under impact loading is very important in a wide range of engineering applications. (e.g. in the structures exposed to the risk of extreme blast, light, thin wall tanks with high impact protection, vehicles with high crashworthiness, protective barriers, etc).
The three substantial requirements for energy absorbing systems are following:

- to provide full dissipation of the kinetic energy
- to constrain excessive deformation
- to minimise the level of acceleration

The typically designed, passive energy absorbing devices fulfil the first two requirements, but because of the unchangeable characteristics, they are unable to optimally decrease the level of acceleration. Therefore a new generation of systems, which are able to adapt themselves to the conditions of the impact, should be taken into consideration.

MULTIFOLDING MICROSTRUCTURE (MFM)

The concept of the intelligent, energy-absorbing microstructure was first presented in [1] and [2]. The structure is composed of truss-like elements arranged into a special pattern, depicted in Fig.1. The elements are equipped with micro-devices (so-called "micro-fuses") which control the axial force in each element. The stress thresholds, triggering the micro-fuses, are uniformly distributed along horizontal layers but may change in the vertical direction. Therefore, during deformation, layers with the lowest stress values collapse first. The repetitive use of elements (multifolding effect, e.g. element 2 in Fig. 3a.) provides the synergistic effect in the process of energy dissipation.
The initial distribution of the control thresholds plays a crucial role in the adjustment of the stiffness characteristics of the MFM to the impact loading. Different initial distributions of those parameters will result in different folding sequences and therefore will change the capability of energy absorption and the level of acceleration during the impact.

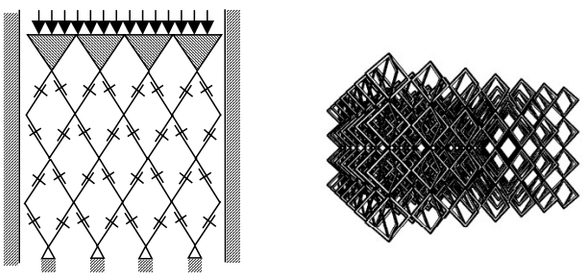


Fig.1. The Multifolding Microstructure layout.

The most basic substructure of the MFM is presented in Fig.2. It consists of six elements with two control parameters (marked 1 and 2). Therefore, only two effective deformation sequences are possible: the folding mode "m1" with the stress threshold 1 lower than 2 and the mode "m2" with an opposite relation of the thresholds. The sequence "m1" provides a low level of acceleration while the folding mode "m2" provides maximal energy absorption.

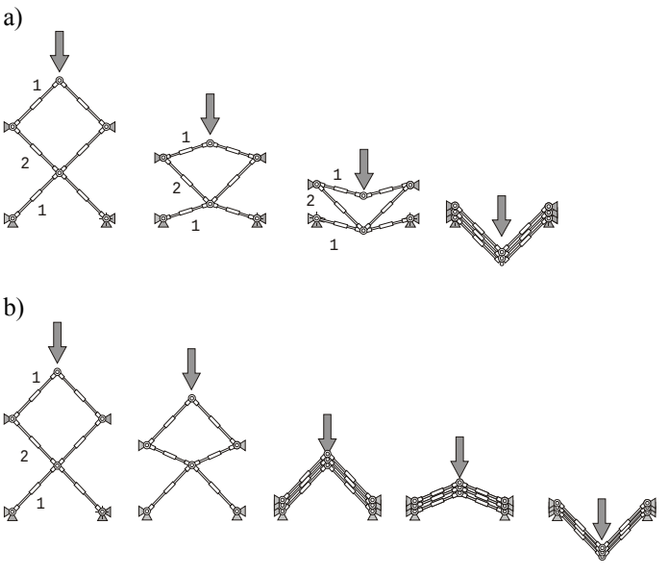


Fig.2. The basic folding modes of the absorber: a) "m1" b) "m2"

EXPERIMENTAL VALIDATION

In order to validate the concept of multifolding and its efficiency, an experimental set-up has been created (Fig. 3). Planned tests aim at verifying the numerical models and control strategies applied in previous research.
The presented device represents the basic MFM substructure, depicted in Fig.2. Six active elements provide control over the behaviour of the structure. Each active element is the RD-1005-3 magnetorheological fluid damper, supplied by LORD-Rheonetic Corporation, with maximum stroke equal to 53mm and maximum tensile force of 4448N. Because the input current (up to 2A) can be applied separately to each damper, apart from the two basic folding sequences, additional, non-symmetric deformation modes are also possible.

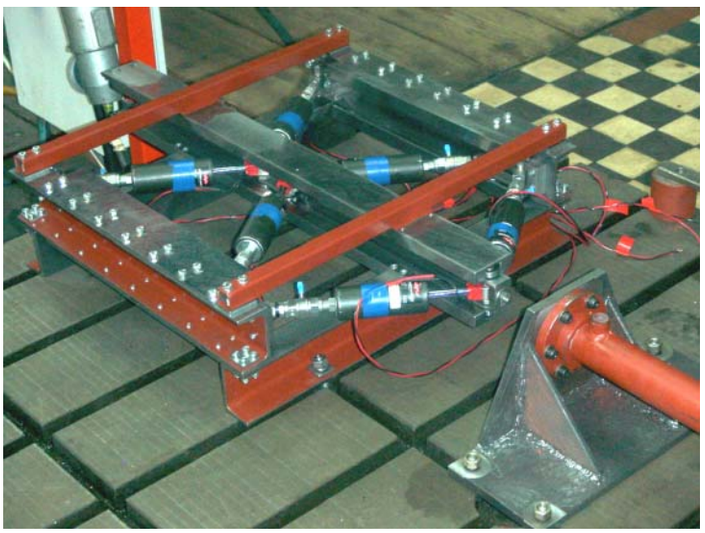


Fig.3. Experimental setup

Force sensors are placed in all six elements and additionally at the loaded node. Nodes of the structure are guided by slide bearings, providing only one direction of movement. Displacements, forced by a hydraulic actuator, are measured at all moving nodes.

References

[1] Holnicki-Szulc J., Pawlowski P., WikloM.: High-performance impact absorbing materials - the concept, design tools and applications, *Smart Materials and Structures*, vol.12, number 3, 2003.

[2] Holnicki-Szulc J., Pawlowski P., Wiklo M.: Optimal Strategies of Adaptive Impact Absorption, Proc. 5th World Congress on Structural and Multidisciplinary Optimisation, Lido di Jesolo, Italy,. May 19-23, 2003.

MOLECULAR MECHANICS OF CYTOSKELETAL COMPONENTS

C.F. Schmidt[1], M. Atakhorrami[1], K. Addas[2], G.H. Koenderinck[1], F.C. MacKintosh[1], J.X. Tang[3]
[1]*Vrije Universiteit Amsterdam, Dept. Phys., Amsterdam, Netherlands*
[2]*Indiana University, Dept. Phys., Bloomington, IN, USA*
[3]*Brown University, Dept. Phys., Providence, RI, USA*

Summary Semiflexible polymers are of great biological importance in determining the mechanical properties of cells. We have used laser interferometry to passively trap and detect the motions of pairs of micron sized silica spheres in solutions of semiflexible polymer. The single- and dual-bead frequency dependent complex shear moduli were extracted from the auto- and cross-correlation response of the beads respectively, with the response being derived from position fluctuation data using dispersion relations from linear response theory.

INTRODUCTION

One of the characteristic lengths that describes a polymer in a solution is the persistence length L_p, which is the length traversed along the filament contour before the tangent vector thermally randomizes its orientation. L_p is proportional to the bending stiffness of the polymer. Flexible polymers are characterized by $L_p << L$, rigid rod polymers by $L_p >> L$. Semiflexible polymers are in the intermediate regime, characterized by $L_p \approx L >>$ filament diameter. The dynamics of polymer systems greatly depends on the degree of flexibility of the individual polymers. Recent theoretical treatment has been made of semiflexible polymer networks [1-4]. Such polymers are found in cells where they form networks that determine the mechanical properties of the cells.
There are clear advantages to the miniaturization of a rheology experiment: only small amounts of material are necessary, spatial inhomogeneities can be studied, and the bandwidth of the measurement can be high. We have developed a microrheology technique using laser interferometric tracking of the Brownian motion of micron sized beads embedded in viscoelastic materials [5]. We have studied the dynamics and compared single- and dual-bead results for wormlike micelle, semiflexible fd virus and actin network solutions. In the semiflexible systems, which are a first approximation to the cytoskeleton of cells, we explore the rich multitude of length and time scales in the dynamic behaviour of these networks, which are usually not accessible to macrorheology.

PRINCIPLE OF THE TECHNIQUE

The microrheology technique used is a passive one in which the thermal fluctuations of pairs of micron sized beads are used to calculate the auto- and cross-correlation response functions of the beads by the fluctuation-dissipation theorem [5, 6]. The complex response function $\alpha_{ij}^{(n,m)}(f)$ relates the Fourier transform $r_i^{(n)}(f)$ of the displacement of the n^{th} bead $r_i^{(n)}(t)$ to the Fourier transform $F_j^{(m)}(f)$ of the force $F_j^{(m)}(t)$ acting on the m^{th} bead (i and j are either 1 or 2 for the parallel and perpendicular directions to the line joining the bead centers, respectively), $r_i^{(n)}(f) = \alpha_{ij}^{(n,m)}(\vec{r}, f) F_j^{(m)}(f)$. The response must first be corrected for the effect of the traps [7]. The fluctuation-dissipation theorem [5] provides the link between the generalized, single sided Power Spectral Density (PSD) [8] $S_{ij}^{(n,m)}(f) = \lim_{t' \to \infty} (2/t)\, r_{t'i}^{(n)}(f) r_{t'j}^{(m)*}(f)$, and the imaginary part of the response function, where $r_{t'i}^{(n)}(f)$ is the Fourier transform of the position $r_i^{(n)}(t)$, defined over a finite time t'. A Kramers-Kronig relation can then be used to calculate the real part of the response function, provided that the imaginary part is known over a large enough frequency range. The connection between the auto correlation response $\alpha_{ii}^{(n,n)}(f)$ of a bead and the corresponding complex shear modulus $G_{ii}^{(n,n)}(f) = G_{ii}'^{(n,n)}(f) + iG_{ii}''^{(n,n)}(f)$ of the viscoelastic medium surrounding the bead is assumed to be provided by the generalized Stokes-Einstein relation (GSER) [5] $G_{ii}^{(n,n)}(f) = 1/[6\pi a\, \alpha_{ii}^{(n,n)}(f)]$, where G' and G'' are the elastic and loss moduli respectively, and a is the radius of the bead. The cross-correlation shear modulus of the solution is derived from the parallel $\alpha_{//} \equiv \alpha_{11}^{(1,2)}$ response by [9] $G_{cross}(f) = 1/[4\pi r\, \alpha_{//}(f)]$, where r is the distance between the centres of the beads.

EXPERIMENTAL SETUP

Pairs of probe particles imbedded in solutions of semiflexible polymer were trapped by two focused laser beams. Position fluctuation data was recorded using laser interferometry and quadrant photodiode detection as described in detail previously [5, 10, 11]. Near-infrared 1064 nm laser illumination was used for one trap and an 830 nm laser for

the second trap. The beams are brought to focus in the sample chamber by a high NA objective. The laser light emerging from the condenser lens, after passing through the sample, is projected onto two quadrant photodiodes in such a way that the back-focal plane of the condenser is imaged [10]. The signals from the four quadrants of each photodiode are combined to obtain the X and Y voltages corresponding to the displacements of each bead in these directions in the plane normal to the propagation direction of the laser. The output voltages are, after analog amplification and pre-processing, recorded using an A/D interface and data acquisition software.

RESULTS

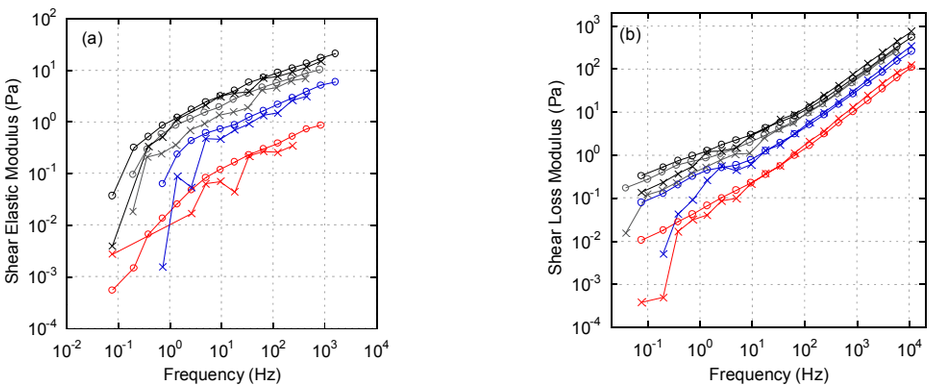


FIG. 1. (a) The concentration dependence of auto and cross correlation elastic modulus data of 1.16 μm diameter beads in 2, 5, 10 and 14 mg/ml fd solutions. (b) The same for the loss modulus. Pairs of auto (circles) and cross (crosses) moduli curves are higher for higher concentrations.

Figure 1a shows the concentration dependence of the frequency dependent single- (circles) and dual- (crosses) bead elastic modulus. The viscous modulus is shown in Fig. 1b. Data are displayed for 2, 5, 10, and 14 mg/ml solutions. The high frequency slope behaviour of the viscous modulus is consistent with single filament dynamics predictions [1, 4]. At such high frequencies, the effect of entanglement of the polymer in its network does not contribute to the modulus. The modulus is proportional to concentration and expected to have a slope of ¾. The elastic modulus is expected to exhibit the same behaviour but due to the cut-off in the Kramers-Kronig integral, the elastic modulus extends to a smaller frequency range below that where high frequency dynamics dominates. The high frequency behaviour is attributed to tension in the filaments due to extension. At lower frequencies, the tension contributes less, and the dominating behaviour is that of bending and orientational contributions to the stress [1, 2]. It has been predicted that single bead measurements will be sensitive to the local properties of the medium surrounding the beads while the dual-bead results would reflect the bulk viscoelastic properties of the solutions probed [9]. Depletion of polymer in the vicinity of the probe particles, or having comparable probe size and network length scales is expected to cause differences in the single- and dual-bead modulus behaviour. We present results for actin networks where a difference between the two techniques is detected, and results from micelle and fd virus solutions (Fig. 1 shows fd virus results) which show agreement between the single- and dual-bead methods.

CONCLUSIONS

We have applied a passive microrheology technique to study the dynamics and compare one- and two-bead complex shear moduli of solutions of various semiflexible polymers. Results were compared to recent theoretical predictions, and one- and two-bead measurements were compared for each polymer system over a large concentration regime.

References

[1] D. C. Morse, Macromolecules **31**, 7030 (1998).
[2] D. C. Morse, Macromolecules **31**, 7044 (1998).
[3] A. C. Maggs, Phys. Rev. E **55**, 7396 (1996).
[4] F. Gittes and F. C. MacKintosh, Phys. Rev. E **58**, 1241 (1998).
[5] B. Schnurr, F. Gittes, F. C. MacKintosh and C. F. Schmidt, Macromolecules **30**, 7781 (1997).
[6] K. Addas, J. X. Tang and C. F. Schmidt (manuscript in preparation)
[7] A. J. Levine and F. Mackintosh (manuscript in preparation)
[8] F. Gittes and C. F. Schmidt, Method. Cell. Biol. **55**, 129 (1998).
[9] A. J. Levine and T. C. Lubensky, Phys. Rev. E **65**, 0115011 (2001).
[10] M. W. Allersma*, et al.*, Biophys. J. **74**, 1074 (1998).
[11] K. Addas, J. X. Tang and C. F. Schmidt (submitted to Phys. Rev. E)

XXI International Congress of Theoretical and Applied Mechanics
Warsaw, Poland, August 15-21, 2004

Tissue Mechanics

Susan S. Margulies
University of Pennsylvania, Philadelphia, USA

The tissue mechanical properties are central to understanding macroscopic and microscopic effects of disease, aging, and altered loading conditions. More recently, the macroscopic mechanical milieu has been shown to affect cellular responses. Furthermore, tissue properties are used in computational models to estimate local and global stresses and strains and predict tissue injury, perfusion, functional responses. As such, determination of accurate tissue mechanical properties is fundamental to the fields of orthopaedics, cardiovascular and pulmonary mechanics, injury mechanics, rehabilitation engineering, and tissue and cellular engineering. Using a broad range of tissues, techniques for in vivo and in vitro measurement of tissue mechanics will be presented, as well as issues related to study design, specimen handling, and validation. Experimental and analytical approaches for nonlinear, anisotropic, and viscoelastic materials will be covered. Influences of developmental age, species, and disease will be introduced with the goal of presenting a format for determining relevant tissue mechanics.

ELASTIC INTERACTIONS OF BIOLOGICAL CELLS

S. A. Safran[*], A. Nicolas[**], U. Schwarz[***]
[*] *Dept. Materials and Interfaces, Weizmann Institute of Science, Rehovot, Israel 76100*
[**] *CRPP, Centre Recherche Paul Pascale, F-33600 Pessac, France*
[***] *Max Planck Institute for Colloids and Interfaces, 14424 Potsdam, Germany*

This talks reviews recent theoretical developments that focus on the the physics of cell adhesion and its implications for cell-cell interactions. Biological cells contain a gel-like cytoskeleton that gives the cell a weak, but measurable elastic response. Modifications of the elasticity of the cytoskeleton of biolgical cells are responsible for dramatic changes in cell shape. Adhering cells exert forces on their environment; experiments on micropatterned elastomer substrates showed that these forces are correlated with the size and orientation of adhesion regions. The adhesions act as mechanosensors that convert the mechanical forces within the cytoskeleton into biochemical signals that cause these adhesions to grow in response to external stress. Averaging the forces due to the adhesions shows that each cell can be modeled as a pair of oppositely directed elastic forces. We predict theoretically that the cells deform the medium (e.g., an elastic substrate or a three-dimensional gel) and this gives rise to an effective interaction among the cells that can be either attractive or repulsive, depending on their orientations and the boundary conditions. These interactions can have important implications for wound healing and tissue formation and engineering. Our theory for the physical origin of the mechanosensor action of focal adhesions, models the adhesion molecules as a grafted layer whose effective elastic modulus determines its response to cytoskeletal forces. The model may explain the observed force dependent anisotropy of the focal adhesions and its kinetics.

[Experimental collaborators: B. Geiger, A. Bershadsky, N. Balaban]

References

1. *Elastic deformations of grafted layers with surface stress*, A. Nicolas and S. A. Safran, Physical Review E, in press and related work in preparation..
2. *Measurement of cellular forces at focal adhesions*, U. Schwarz, N. Balaban, D. Riveline, L. Addadi, B.A. Bershadsky, S.A. Safran, B. Geiger, Mat .Sci. and Engineering **C23**, 387-394 (2003).
3. *Elastic Interactions of Cells*, U. Schwarz and S.A. Safran, Phys. Rev .Letts. **88**, 048102 (2002).
4. *Force applied at single focal adhesions determines their assembly:a study using elastic micro-patterned substrates*, N.Q. Balaban, U.S. Schwarz, D. Riveline, P. Goichberg, G. Tzur, I. Sabanay, D. Mahalu, S.A. Safran, A. Bershadsky, L. Addadi, B. Geiger, Nature Cell Biology **3**, 466-472 (2001).
5. *Calculation of cellular forces at focal adhesions from displacement data of microstructured elastic substrates*, U.S. Schwarz, N.Q. Balaban, D. Riveline, B. Geiger, S.A. Safran, Biophysical Journal 83, 1380 (2002).

This talk was invited for session MS2: Tissue, Cellular, and Molecular Biomechanics

MICROMECHANICS OF CYTOSKELETAL ACTIN NETWORKS

Erik Van der Giessen, Patrick Onck
Dept. of Applied Physics, University of Groningen, 9747 AG Groningen, The Netherlands

INTRODUCTION

The Cytoskeleton

Living cells have the ability to sense mechanical forces and convert them into a biological reponse. Examples are many sensory functions (including touch, hearing and gravity sensation), tissue growth and healing, bone remodeling, but also fundamental processes like cell growth, cell differentiation and cell death involve specialized mechanotransduction mechanisms. At the same time, genetic programs orchestrate complex cellular processes such as mitosis and cell motility, involving the generation of mechanical forces. The key cellular component that is responsible for the sensing, transmission and generation of mechanical forces is the cytoskeleton.

The cytoskeleton consists of three types of polymer fibers (see Fig. 1), made from different proteins and with different diameters: actin microfilaments (7nm), intermediate filaments (8-12nm) and microtubules (24nm). The structural form in which actin microfilaments appear is mediated by cross-links with actin-binding proteins. Near the cell cortex, actin filaments are usually either forming bundles or a three-dimensional network. Intermediate filaments and microtubules are centrally organized and their organization in the cell is often colinear, spanning the distance between nucleus and cell membrane. The three types of polymer fibers do not deform independently, but are usually interpenetrated and form contacts by entanglements or cross-binding proteins.

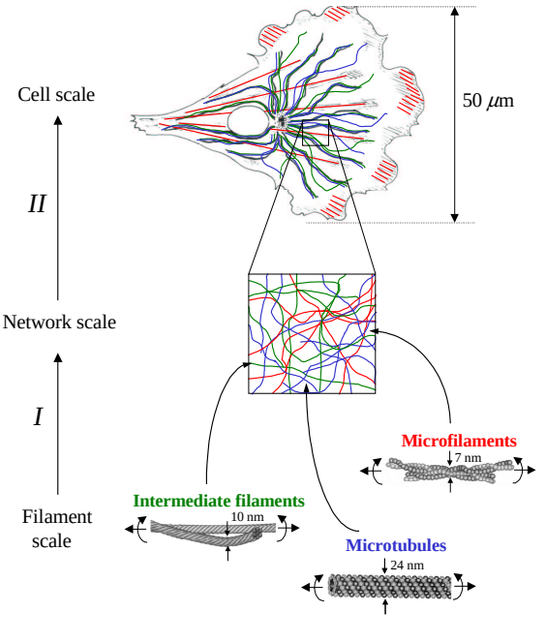


Fig. 1 Multiscale modelling approach to the cytoskeleton in cells.

A Multiscale Approach

We propose to model the cytoskeletal mechanics by using a multiscale modeling methodology (see Fig. 1). Three size scales are identified: (*i*) the scale of individual cytoskeletal filaments, (*ii*) the scale of a network of filaments and (*iii*) the scale of the cell. The goal is to bridge all size scales involved, from the scale of individual filaments all the way up to the cell scale. The focus of the current paper is on the scale transition of the filament scale to the network scale, directing our attention exlusively to the actin filament network.

ACTIN NETWORK MODELING

Single Actin Filament

The starting point in the multiscale approach outlined above is the response of a single F-actin filament. An actin chain is a semiflexible polymer which is often described by the so-called worm-like chain model (see e.g. [1]). This means that the chain is regarded as a very slender beam which is curved due to thermal undulations. The main mode of deformation is bending. Axial extension in the worm-like chain model is caused solely by stretching out the curvature, Fig. 2. Hence, the axial response is governed by the so-called persistance length $\ell = \kappa / k_B T$, where κ is the bending stiffness, T is temperature and k_B is the Boltzmann constant. It will be intruiging for a mechanics person that, even

though this type of chain stretching is akin to buckling but with a different sign, statistical physics treaments (see e.g. [2]) lead to the axial stiffness being proportional to κ^2 instead of κ. This is caused by the fact that the amplitude of the thermal undulations scales with $k_B T = \kappa / \ell$.

Although the worm-like chain model has been commonly accepted as the model for actin [1], this paper addresses some overseen features in order to assess its robustness for application in the multiscale framework. The model assumes that the undulations remain unchanged over the timescale of the applied deformation; what if the two timescales are similar? In particular, this is an issue under compression: how does the stretching-of-thermal-undulations (stiffness κ^2) transform into buckling (stiffness κ)? This requires that the three-dimensionality of the undulations is taken into consideration as well as the coupling between bending, extension and torsion, all of which have been ignored so far.

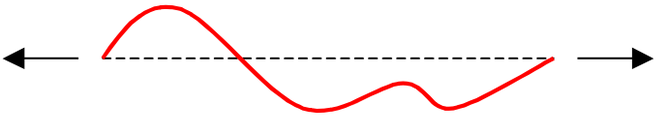


Fig. 2. Axial response of a flexible chain is controlled by the stretching of the thermal undulations.

Actin Network

We use the response of single actin filaments, as discussed in the previous section, to construct initially isotropic three-dimensional networks of actin microfilaments. We use the finite element method to explicitly model the actin network, featuring a tunable density of cross-links (mediated by actin-binding proteins). This enables us to explore the dependence of the overall stress-strain behavior on (*i*) the three-dimensional network architecture, (*ii*) the strength of the network cross-links/entanglements and (*iii*) the actin filament poperties. The effect of different actin-binding proteins (e.g. fascin, filamin, Arp 2/3, alpha-actinin) can be studied through their mechanical behaviour and characteristic cross-binding influence on network morphology (see e.g. [3]). Special emphasis will be put on the structural alterations that occur in the networks during straining. The results will be compared to experimental measurements and observations, and to existing theoretical models based on idealized representations of biopolymer networks, including reptation models, extended for semiflexible polymer networks (e.g. [2,4]), and a cubic unit cell model, representing an orthogonal, cross-linked network [5]. A key difference between the current approach and statistical mechanics approaches is that the three-dimensional network architecture is explicitly accounted for, featuring a direct mechanical coupling between cross-bindings/entanglements to the overall deformation behaviour.

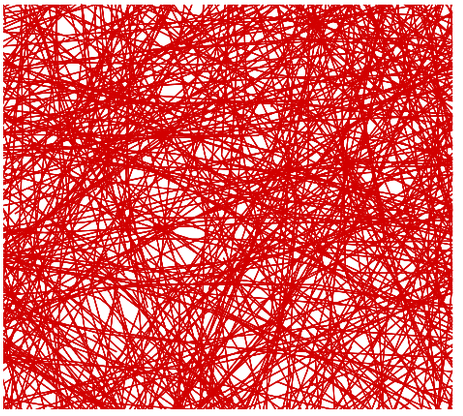


Fig. 3 Actin network model, constructed using the finite element method, enabling large scale simulations.

References

[1] Frey, E. *ChemPhysChem*, 2, 270-275, 2002.
[2] MacKintosh, F.C., Kas, J. and Janmey, P.A. *Phys. Rev. Lett.* 75, 4425-4428, 1995.
[3] Janmey, P.A. *PNAS*, 98, 14745-14747, 2001.
[4] Morse, D. *Phys. Rev. E*, 58, R1237-R1240, 1998.
[5] Satcher, R.L., Jr. and Dewey, C.F, Jr., *Biophys. J.*, 71, 109-118, 1996.

RESIDUAL STRESS FIELDS IN SOFT TISSUES

Anders Klarbring, Tobias Olsson and Jonas Stålhand
Dept. Mech. Eng., Linköpings University, SE-581 83 Linköping, Sweden

Summary: We give a theory based on local stress free reference configurations, for identifying the residual strain in elastic materials. The residual strain is obtained as the solution of a minimization identification problem. As an example, we use this theory on a human aorta and the results agree well with other studies made on such an organ.

GENERAL THEORY

We begin with a description of a general theory for a residually stressed elastic material and end with a stress estimation for the aorta. The main goal is to find the residual strain that gives the residual stress. As a closing example, we use this framework on a human aorta. By optimization we can identify the residual strain and using that information we can calculate the stress and strain in the loaded configuration. In soft tissue mechanics it is important to calculate the residual stress that occurs in a body. This stress is defined as the stress that is left when all external loads are removed. The residual stress is important for the functionality of the tissue. For instance, it reduces stress gradients.

A loaded body configuration $\mathscr{B}$ and a stressed unloaded body configuration $\mathscr{B}_0$ are defined. The tangent map between $\mathscr{B}_0$ and $\mathscr{B}$ is described by a deformation gradient $\boldsymbol{F}$. To obtain a stress free reference configuration we assume that the unloaded configuration can be made stress free by releasing each material point and letting these points deform into a, in general, non compatible, configuration $\overline{\mathscr{B}}$. This stress free configuration can be described by a locally invertible two–point tensor $\boldsymbol{K}^{-1}$. The inverse $\boldsymbol{K}$ can be thought of as a tensor describing the initial strain for each material point and this strain gives a full description of the residual stress if the material is elastic.

The three configurations can be assigned different metric tensors. We define the metric tensors $\boldsymbol{\gamma}$, $\boldsymbol{G}$ and $\boldsymbol{g}$ on $\overline{\mathscr{B}}$, $\mathscr{B}_0$ and $\mathscr{B}$ respectively. We will also define an induced metric on $\mathscr{B}_0$ as

$$\boldsymbol{M} = \boldsymbol{K}^{-T}\boldsymbol{\gamma}\boldsymbol{K}^{-1}.$$

This metric is not necessarily Euclidean. The configuration $\mathscr{B}_0$ with metric $\boldsymbol{M}$ is a Riemannian manifold.

Many types of soft tissues, specially large arteries, can be approximated as incompressible materials. With this assumption the equilibrium equation without body forces becomes invariant with respect to the metric assigned to the configuration. This means that we can solve the equilibrium equation in $\mathscr{B}_0$ with the Euclidean metric $\boldsymbol{G}$ without loss of generality.

APPLICATION ON A HUMAN AORTA

As an example, we have used this theory on a human aorta to try to identify the initial strain tensor $\boldsymbol{K}$. The material behavior of the aorta is assumed to be orthotropic, hyper elastic and incompressible. The aorta is modeled as a thick walled cylinder so we introduce cylindrical coordinates (R, Θ, Z) in $\overline{\mathscr{B}}$ and (r, θ, z) in $\mathscr{B}$. In cylindrical coordinates the components of the metric $\boldsymbol{\gamma}$ and $\boldsymbol{g}$ are

$$\begin{aligned} &\gamma_{11} = 1 \quad \gamma_{22} = R^2 \quad \gamma_{33} = 1 \\ &g_{11} = 1 \quad g_{22} = r^2 \quad g_{33} = 1. \end{aligned}$$

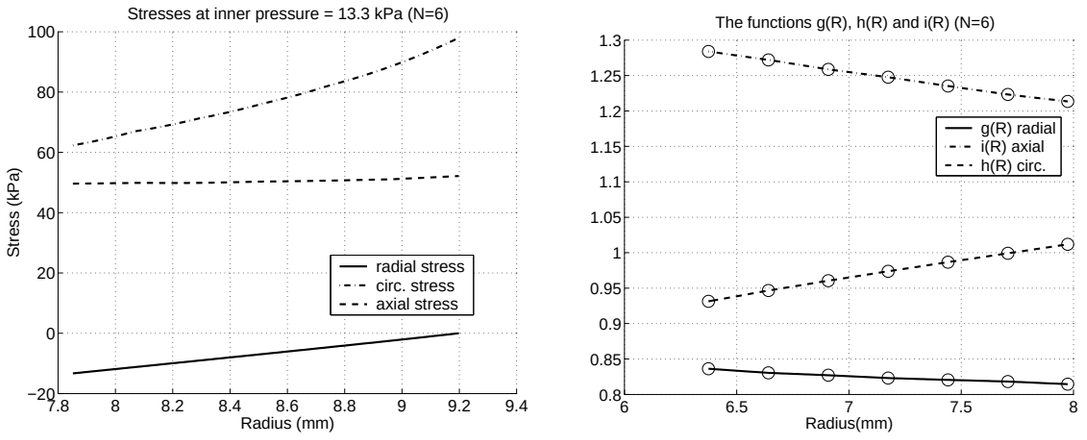
We also assume that the components of the strain tensor $\boldsymbol{K}$ form a diagonal matrix and that they are only dependent on the radial coordinate. Due to the incompressibility condition only two of these components are independent.

The equilibrium equation in $\mathscr{B}$, without external volume forces, and boundary conditions, can be written as

$$\begin{aligned} &\operatorname{div}\boldsymbol{\sigma} = \boldsymbol{0}, \\ &\boldsymbol{\sigma g n} = -P\boldsymbol{n} \quad r = r_0, \\ &\boldsymbol{\sigma g n} = \boldsymbol{0} \qquad r = r_1, \end{aligned}$$

where $\boldsymbol{\sigma}$ is the Cauchy stress tensor, $\boldsymbol{n}$ a unit normal vector and r_0, r_1 is inner and outer radius, respectively, of the pressurized aorta wall. Solving this assuming that the stress is only dependent on the radial coordinate, we obtain a integral equation for the luminal pressure given by

$$P(r_i) = \int_{r_i}^{r_1} \left(r\sigma^{11} - \frac{1}{r}\sigma^{22} \right) \, \mathrm{d}r$$



(a) (b)

Figure 1: (a) Cauchy stresses in $\mathscr{B}$, (b) components of the initial strain tensor $\boldsymbol{K} \sim \mathrm{diag}\,(g(R), h(R), i(R))$ where R is defined in $\overline{\mathscr{B}}$. $N = 6$ is the number of linear functions that comprises $g(R),\ h(R)$ and $i(R)$. The circles in (b) denotes the interpolation points of $\boldsymbol{K}$.

where σ^{11} and σ^{22} are the components of the Cauchy stress tensor. By introducing a constitutive relation for the Cauchy stress that is dependent on the total deformation, we can calculate the inner pressure of the aorta wall. In this example we have chosen the constitutive relation suggested by Holzapfel et. al. [1]. The model parameters included in the constitutive equation can be determined by solving a minimization problem. The components of the initial strain tensor $\boldsymbol{K}$ are also unknown and must be approximated. In this case we have chosen to use continuous C^0 functions with equidistant interpolation nodes, fig. 1(b). This gives a optimization problem were the number of variables is equal to the sum of the number of material parameters and the number of interpolation nodes.

OPTIMIZATION AND RESULTS

Model parameters and residual strains can be obtained as a minimization problem were we try to fit the calculated pressure to measured data points. In this case we treated the minimization as a least square problem, which is formulated as

$$\begin{aligned} &\min_{\boldsymbol{Z},\boldsymbol{K}} ||P(r_i) - \tilde{P}_i||^2 \\ &\text{s.t.} \quad \underline{\boldsymbol{z}} \leq \boldsymbol{Z} \leq \overline{\boldsymbol{z}} \\ &\qquad \underline{\boldsymbol{k}} \leq \boldsymbol{K} \leq \overline{\boldsymbol{k}} \end{aligned}$$

where $\tilde{P}_i$ is the measured pressure at inner radii r_i, $\boldsymbol{Z}$ are the model parameters from the constitutive relation and $\boldsymbol{K}$ are the interpolation values for the initial strain. The over- and underline represent the lower and upper bound on the optimization parameters, respectively. The data was taken from an in–vivo study on the human aorta and consists of pressure and inner radii of the aorta wall. The pressure $\tilde{P}$ was measured invasively using a catheter and the inner radius by ultrasound. The magnitude of the calculated stresses are in agreement with an in–vivo study on the human aorta made by Schulze–Bauer and Holzapfel [2], fig. 1(a). The functional form of the components of the initial strain tensor $\boldsymbol{K}$ are close to linear, see fig. 1 (b). A calculation of the Green–Lagrange strains at 13.3 kPa shows that the circumferential strain is close to constant through the wall. This is in agreement with the generally accepted uniform strain hypothesis.

[1] Holzapfel G.A., Gasser T.C., Ogden R.W., A new constitutive framework for arterial wall mechanics and a comparative study of material models, *J. Elasticity*, 61, 1–48, 2000

[2] Schulze-Bauer C.A.J., Holzapfel G.A., Determination of constitutive equations for human arteries from clinical data, *J. Bio. Mech.*, 36, 165–169, 2003

FROM INDIVIDUAL CELLS TO COMPLEX TISSUES. AN IMMERSED BOUNDARY APPROACH

Katarzyna A. Rejniak
Mathematical Biosciences Institute, Ohio State University, 231 West 18th Ave, Columbus, OH 43210, USA

Summary: We present a computational model of various tissues (such as epithelial sheets or tumor clusters) composed of different types of cells, which nevertheless allows us to focus on biomechanical processes of individual tissue components (such as cell proliferation or chemotactic migration). The discussed model is based on the immersed boundary method and couples the dynamics of separate elastic cells with continuous description of a viscous incompressible cytoplasm.

MODEL DESCRIPTION

Development of complex tissues depends on the behavior of separate cells, that form such a tissue and on communication with cell neighbors or surrounding microenvironment. Therefore, we propose a computational model which treats cells as individual entities, with their own elastic plasma membrane, fluid cytoplasm, point nucleus and partial cytoskeleton. However, this model also enables formation of cell clusters or cell sheets in which all cells act together as one complex tissue. Moreover, this model includes discrete sets of cell receptors which are used to sense signals from the surrounding microenvironment and to send signals to other cells. Based on these signals the cells can undergo different processes, such as cell growth, proliferation, apoptosis or migration toward the chemoattractants. The presented model is based on the immersed boundary method [1] and couples the dynamics of separate elastic cells with continuous description of a viscous incompressible cytoplasm. Applications of this model include several simulations of tumor related phenomena, such as the formation of early ductal carcinomas, an outgrowth of a capillary sprout in the early stage of angiogenesis and the transition of tumor cells from dormant into invasive, which occurs in the early stage of metastasis. Several computer simulation of such phenomena are presented.

Cell structure

The computational model of an individual eukaryotic cell includes the elastic plasma membrane modeled as a collection of boundary points connected by short linear Hooke's springs, the partial cytoskeleton represented by linear spring connections, the cell cytoplasm modeled as a viscous incompressible Newtonian fluid and the cell nucleus represented by a single point located inside the cell. Separate cells are joined together by adhesion links to form a tissue. Figure 1 shows a segment of such a complex tissue from a model of early ductal carcinoma.

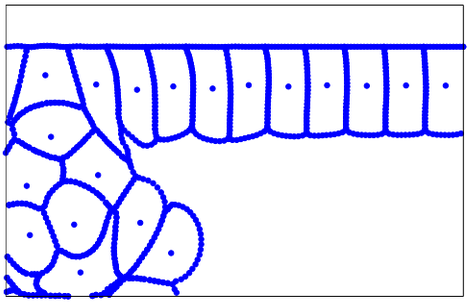


Figure 1: A segment of an early ductal carcinoma model containing different types of cells – a layer of epithelial cells (rectangles) and a cluster of tumor cells (ovals).

Main equations

The immersed boundary method captures interactions between elastic bodies (cell membranes) and a surrounding viscous incompressible fluid (cytoplasm). The fluid flow is influenced by forces generated by the immersed, elastic boundaries, as well as by sinks and sources of fluid distributed in the fluid domain, but at the same time the immersed bodies move at the local fluid velocity. The surrounding fluid, both inside and outside the cells is assumed to be of the same constant viscosity and density. In addition cell growth is modeled by tracking fluid sources located at the cells nuclei. The motion of the fluid is governed by the Navier-Stokes equations [1]:

$$\begin{cases} \rho\left(\frac{\partial \mathbf{u}}{\partial t} + (\mathbf{u}\cdot\nabla)\mathbf{u}\right) &= -\nabla p + \mu\Delta\mathbf{u} + \frac{\mu}{3\rho}\nabla s + \mathbf{f} \\ \rho\nabla\cdot\mathbf{u} &= s \end{cases}$$

Here, ρ is a constant fluid density, μ is a constant fluid viscosity, $\mathbf{u}$ is a fluid velocity field, p pressure, s fluid source distribution and $\mathbf{f}$ an external force density field.

The force density $\mathbf{f}$ captures the forces $\mathbf{F}$ generated by the elastic immersed boundaries of all cells as well as the adhesion or drag motility forces.

$$\mathbf{f}(\mathbf{x},t) = \int_{\Gamma} \mathbf{F}(l,t)\ \ \delta(\mathbf{x} - \mathbf{X}(l,t))dl$$

Here δ is the Dirac delta function and l is an Lagrangian parameter such as arc length. Γ is a finite collection of immersed boundaries of all cells. $\mathbf{X}(l,t)$ represents coordinates of the material points on Γ.

The sources ($S^+ > 0$) of fluid are defined only at the finite collection of cell nuclei Ξ with coordinates $\mathbf{Y}_k(t)$ and sinks ($S^- < 0$) are taken at the boundaries $\mathbf{X}(l,t)$ of growing cells, so that

$$s(\mathbf{x},t) = \sum_{k\in\Xi} S^+(\mathbf{Y}_k,t)\ \ \delta(\mathbf{x} - \mathbf{Y}_k(t)) \quad + \quad \int_{\Gamma} S^-(l,t)\ \ \delta(\mathbf{x} - \mathbf{X}(l,t))dl$$

The material points of immersed boundaries $\mathbf{X}(l,t)$ and cell nuclei $\mathbf{Y}_k(t)$ are moved at the local fluid velocity. Here, R denotes the whole fluid domain.

$$\frac{\partial \mathbf{X}}{\partial t} = \mathbf{u}(\mathbf{X}(l,t),t) = \int_R \mathbf{u}(\mathbf{x},t)\ \ \delta(\mathbf{x} - \mathbf{X}(l,t))\ d\mathbf{x} \qquad \text{and} \qquad \frac{\partial \mathbf{Y}_k}{\partial t} = \int_R \mathbf{u}(\mathbf{x},t)\ \ \delta(\mathbf{x} - \mathbf{Y}_k(t))\ d\mathbf{x}$$

Cell processes

Each cell in this model can sense signals from the surrounding microenvironment and signals sent by its neighboring cells through the receptors located on the cell surface. Based on these signals the cell can undergo different processes, such as growth, proliferation, apoptosis or migration toward the chemoattractants. Here, we give more details only about one of these processes, but mechanisms of all other processes are discussed in our presentation.

A few snapshots of the computer simulation of the multistep process of cell cycle are presented in Figure 2. We include all mechanical phases of cell cycle, but we do not model chromosome replication. We start the process of cell growth and division with introducing two point sources inside the cell, that correspond to two sets of sister chromatids (Figure 2a). The fluid created by both sources causes the cell growth by pushing cell boundaries and by increasing cell volume (Figure 2b). The sources are inactivated when the cell doubles its volume. At this time, the contractile ring is created by attaching the contractile forces on the opposite sites of the cell boundary (Figure 2c). This causes division of the cell into two daughter cells of approximately equal volumes and with their own nuclei (Figure 2d).

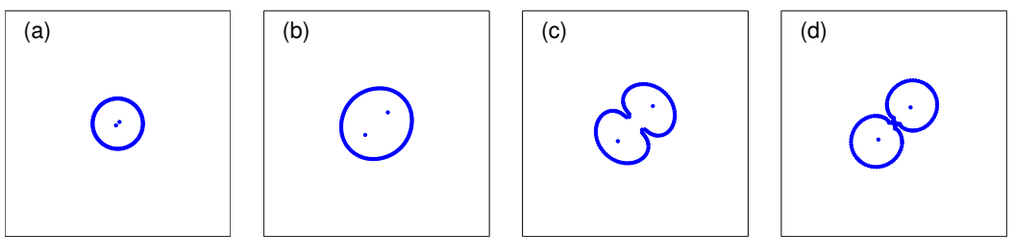


Figure 2: Four main phases of cell growth and division – (a) nucleus division, (b) cell growth, (c) formation of a contractile ring, (d) cellular division which results in formation of two daughter cells.

CONCLUSIONS

The presented technique can be applied in modeling the development of complex tissues composed of various types of cells. It allows us to focus on biomechanical processes of individual cells and on communication between neighboring cells, however it also enables the formation of cell clusters and cell sheets that act together as one tissue. Applications of this model include several computer simulations, such as formation of an early carcinoma or outgrowth of a capillary sprout in the early angiogenesis.

References

[1] Peskin C.S.: The Immersed Boundary Method. *Acta Numerica*, 1-39, 2002.

TRAVELLING WAVES IN A MODEL OF SKIN PATTERN FORMATION

Kazimierz Piechór, Bogdan Kaźmierczak
IPPT PAN, Department of Mechanics & Physics of Fluids, PL 00-049 Warszawa, Poland

Summary. In this paper we study travelling wave solutions to a system of four non-linear partial differential equations, which arise in a tissue interaction model for skin morphogenesis. Under the "strong-body-force" assumption we prove the existence and uniqueness (up to a translation) of solutions with the dermis and epidermis cell densities being positive, which are a perturbation of a uniform epidermal cell density. We discuss the problem of the minimal wave-speed.

Travelling waves are not only a frequent phenomenon in the nature, but also they are of large cognitive value, since they are easy to be generated and measured in experiments. By measuring the profile and the speed of such a wave we can make estimations of the roles of various quantities characterising the medium under consideration.

The aim of this paper is a rigorous mathematical analysis of travelling wave solutions of a model proposed by Cruywagen and Murray [1] to study skin pattern formation.

According to the Cruywagen-Murray model, the skin consists of two layers, epidermis and dermis, separated by a thin basal lamina. The epidermis is modelled as a two-dimensional visco-elasic continuous medium. Under the biologically reasonable assumption that Reynolds number of the motion of the epidermis is low, the inertial terms of the equation of motion are ignored. The body force balances the elastic force, the viscous force, and the cell traction generated within the epidermis by a morphogen produced in the dermis. The force balance equation reads

$$\nabla\cdot\left\{\frac{E}{1+v}\left[\boldsymbol{\varepsilon}-\beta_1\nabla^2\boldsymbol{\varepsilon}+\frac{v}{1-2v}\left(\theta-\beta_2\nabla^2\theta\right)\mathbf{I}\right]+\mu_1\frac{\partial\boldsymbol{\varepsilon}}{\partial t}+\mu_2\frac{\partial\theta}{\partial t}\mathbf{I}+\tau\, s\mathbf{I}\right\}=\rho\mathbf{u}\,, \tag{1}$$

where $\mathbf{u}=\mathbf{u}(\mathbf{x},t)$ is the displacement at time t of a material point in the epidermis which was initially at position $\mathbf{x}$, $s(\mathbf{x},t)$ is the concentration of the signal chemical produced in the dermis, E is the constant Young modulus, v is the constant Poisson ratio, μ_1,μ_2 are the constant shear and bulk viscosities, β_1,β_2 are positive constants, $\mathbf{I}$ is the unit 2×2 matrix, and τ is a positive parameter characterising the strength of the traction τs. The epidermis is attached to the basal lamina and ρ is a positive constant measuring the strength of this attachment. Next, $\boldsymbol{\varepsilon}$ is the strain tensor, and $\theta=\nabla\cdot\mathbf{u}$ is the dilatation.

This equation is supplemented by another two equations expressing the conservation laws of the epidermal cell density $N(\mathbf{x},t)$ and the dermal cell density $n(\mathbf{x},t)$. In the model of Cruywagen and Murray [1], the cells of the epidermis are mutually attached; so the only contribution to the cell density flux is convection. Therefore this equation is of the form

$$\frac{\partial N}{\partial t} = -\nabla \cdot \left(N \frac{\partial \mathbf{u}}{\partial t} \right). \tag{2}$$

The dermal cell density n changes due to random cell migration since the cells in the dermis are loosely packed, due to chemotaxis and due to mitosis, i. e. cell production. To model the random cell migration, the Fick's law of diffusion is used. The conservation equation of the dermal cell density $n(\boldsymbol{x},t)$ reads

$$\frac{\partial n}{\partial t} = \nabla \cdot \left(d(n,N) \nabla n \right) - \alpha \nabla \cdot \left(n \nabla e \right) + m(n), \tag{3}$$

where d is the coefficient of diffusion, which can be a function of the cell densities N and n, α is chemotaxis coefficient, $e(\mathbf{x},t)$ is the concentration of the signal chemical produced in the epidermis, and $m(n)$ describes the mitosis.

The aim of this paper is a rigorous mathematical analysis of travelling wave solutions of the above equations, under a simplifying assumption that the force exerted by the basal lamina is much larger than the other forces acting on the epithelium, i.e. the dominant part of Eq. (1) is the right hand side. Under this assumption, in the lowest order of approximation the displacement $\mathbf{u} = \mathbf{0}$, and the problem reduces to a study of travelling wave solutions to the system (2) and (3). Using the existing results concerning the latter degenerated problem we the existence of travelling waves with positive dermis cell density to the full system (1) – (3). The mathematical apparatus is the Implicit Function Theorem in a suitable Banach space. Also a discussion of the minimal wave-speed problem is carried out..

Reference

1. Cruywagen G. C , Murray J. D. On a tissue interaction model for skin pattern formation. *Journal of Nonlinear Science*. 1992; **2**; 217-240.

MECHANISMS OF DEEP PENETRATION OF SOFT SOLIDS

Norman A. Fleck* and Oliver Shergold
*Cambridge University Engineering Dept. Trumpington St., Cambridge, CB2 1PZ, UK

Summary Micromechanical models are developed for the deep penetration of soft solids by a flat-bottomed and a sharp-tipped cylindrical punch such as a hypodermic needle. The soft solid represents mammalian skin and silicone rubbers, and is modelled by a one term Ogden strain energy function. The flat-bottomed punch penetration model assumes that penetration is by the formation of a mode II ring crack that propagates ahead of the penetrator tip. The sharp-tipped punch penetration model assumes that penetration is by the formation of a planar mode I crack which is wedged open by the advancing punch. The steady-state penetration load is obtained by equating the work done in advancing the punch to the sum of the fracture work and the strain energy stored in the solid. The penetration pressure for a flat-bottomed punch is three times that for a sharp-tipped punch, in agreement with experimental observations.

INTRODUCTION

The deep penetration of soft solids by a punch is of widespread technological importance, with applications ranging from the piercing of mammalian skin by a hypodermic needle (or by a liquid jet) in administering an injection, to the failure of rubber seals or tires by the penetration of a foreign body. Despite the ubiquitous nature of soft solid penetration, the existing literature provides little insight into the underlying mechanisms of penetration.

MICROMECHANICAL MODELS

Micromechanical models are developed for the deep penetration of a soft solid by a flat-bottomed and by a sharp-tipped cylindrical punch, such as a hypodermic needle. The soft solid is taken to represent mammalian skin and silicone rubbers, and is represented by an incompressible, hyper-elastic, isotropic solid described by a one term Ogden strain energy function for an incompressible, isotropic, hyper-elastic solid,

$$\phi = \frac{2\mu}{\alpha^2}\left(\lambda_1^\alpha + \lambda_2^\alpha + \lambda_3^\alpha - 3\right) \qquad (1)$$

where ϕ is the strain energy density per undeformed unit volume, α is a strain hardening exponent and μ is the shear modulus. Table 1 gives measured values of the Ogden constants and toughness J_{IC} for three grades of silicone rubber and human skin used in the deep penetration experiments.

Solid	Grade	μ (MPa)	α	J_{IC} (kJ·m^{-2})
Silicone rubber	Sil8000	2.7	2.5	9.1
Silicone rubber	B452	0.4	3.0	7.9
Human skin		0.11	9.0	2.5

Table 1: Curve fits of the Ogden constitutive law (1), and toughness values of some soft solids

The flat-bottomed punch penetration model assumes that penetration is by the formation of a mode II ring crack that propagates ahead of the penetrator tip, see Fig. 1a. The sharp-tipped punch penetration model assumes that penetration is by the formation of a planar mode I crack which is wedged open by the advancing punch, see Fig.1b. Each mechanism has been observed experimentally for both skin and silicone rubbers.

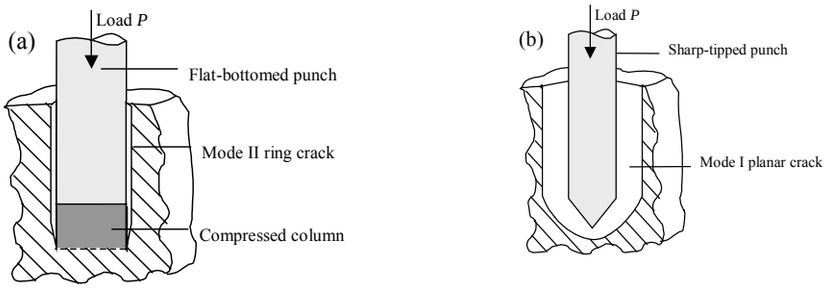


Figure 1: Penetration mechanisms of a soft solid by (a) flat-bottomed and (b) sharp-tipped punch.

Calculation of steady state deep penetration pressure

The steady-state penetration load is obtained by equating the work done in advancing the punch to the sum of the fracture work and the strain energy stored in the solid. For the case of a sharp penetrator, this calculation is performed by considering the opening of a plane strain crack by wedge loading, using a finite element approach. Consider a frictionless, rigid cylindrical punch of radius, R, with a conical tip pushed into a semi-infinite block, as shown in Figure 2a. The solid tears and opens at the tip of the punch. The detailed solution for the punch tip requires a full 3D calculation; however we can consider punch advance by $\delta\ell$ as equivalent to creating a plane strain crack of length 2a

in a slice of thickness $\delta\ell$ and then opening the crack to accommodate the punch. This energy approach is accurate when the strain energy density in each material element is independent of strain path.
Consider the steady state advance of the punch by an axial increment $\delta\ell$ due to a load P_S. The work done by the punch in effecting this advance is $P_S \cdot \delta\ell$. This work increment balances the energy δW_C required to form a crack of length 2*a* in a solid slice of thickness $\delta\ell$, see
Figure 2b, and the strain energy stored in the solid δS_E on opening the crack to accommodate a circular cylindrical inclusion of radius R, see
Figure 2c. Hence,

$$P_S \cdot \delta\ell = \delta W_C + \delta S_E \qquad (2)$$

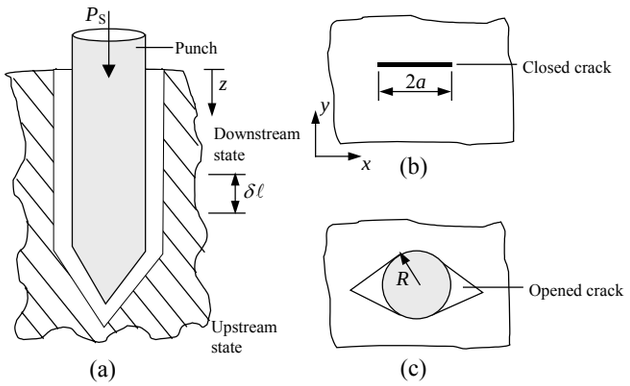


Figure 2: (a) penetration of a soft solid by a sharp-tipped punch, (b) formation of a plane strain crack of length 2*a* in an infinite slice of thickness $\delta\ell$, (c) opening of the crack by an expanding circular cylinder to a final radius *R*.

The work required to create the crack, δW_C, is determined by the mode I toughness of the material, J_{IC} and is given by

$$\delta W_C = 2J_{IC} \cdot a \cdot \delta\ell \qquad (3)$$

In order to calculate the work S_E required to wedge open the crack, we consider the auxiliary finite element problem of expanding a circular wedge of radius R' from $R' = 0$ to a final value of $R' = R$.

Second, consider the case of a flat-bottomed punch. Advance of the punch involves the advance of a mode II ring crack, with compression of a column beneath the punch, as stetched in Fig. 1a. An expression for the stored strain energy in the solid per unit advance of the punch S_E is obtained in closed form, and the punch force is again calculated using relation (2). For both geometries of punch, the crack dimensions are determined by minimising the load on the punch with respect to crack length.

Results

The results for both geometries are shown in Fig. 3. For both geometries of punch tip, the predicted penetration pressure increases with diminishing punch radius, and with increasing toughness and strain hardening capacity of solid. The penetration pressure for a flat-bottomed punch is two to three times greater than that for a sharp-tipped punch (assuming that the mode I and mode II toughnesses are equal), in agreement with experimental observations.

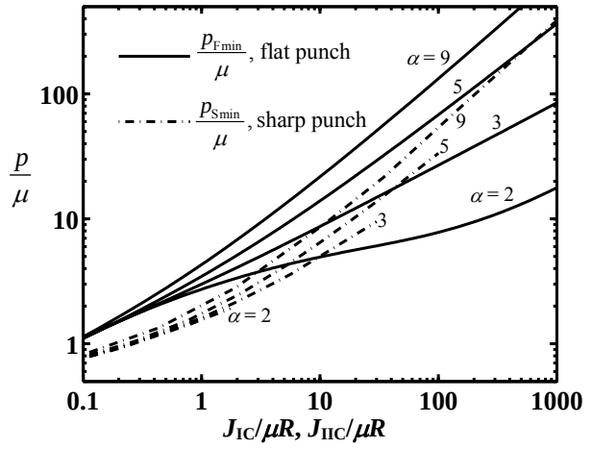


Figure 3: Comparison of p/μ versus $J/\mu R$ for penetration of a solid by a flat-bottomed punch and a sharp-tipped punch.

Mechanics of elastic and viscous magnetic filaments

A.Cebers, I.Javaitis

Insitute of Physics, University of Latvia, Salaspils-1,LV-2169,Latvia

Elastic magnetic filaments have interesting applications in biotechnology [1,2]. They are encountered also in living world, for example in magnetotactic bacteria [3]. Elastic magnetic filaments have interesting static and dynamic properties which are studied by Kirchhoff model of elastic rod taking into account magnetic forces. The total energy of rod is

$$E = \frac{1}{2}C\int\frac{1}{R^2}dl - \frac{2\pi^2a^2\chi^2H_0^2}{\mu+1}\int(\vec{h}\vec{t})^2dl - \int\Lambda dl \tag{1}$$

Here C is the curvature elasticity constant, a is a radius of rod, χ is its magnetic susceptibility, $\mu = 1+4\pi\chi$, R is the radius of curvature of the centerline, $\vec{t}$ is the tangent vector to the centerline, Λ is the tension accounting for inextensibility of the rod. The equations for the rod's tangent angle and tension are obtained if the isotropic Rouse dynamics is assumed $\zeta\vec{v} = \vec{K}$ ($\zeta = \frac{4\pi\eta}{\ln L/a+c}$ is friction coefficient per length unit) and the condition of local inextensibility is imposed. In dimensionless form they read (characteristic length L ($2L$ is the length of the rod), characteristic time $\frac{\zeta L^4}{C}$ and tension $\frac{C}{L^2}$)

$$\theta_t = -(\theta_{lll} + \frac{1}{2}(\theta_l^3)_l) - (\theta_l\Lambda)_l - \Lambda_l\theta_l + Cm(\sin 2\theta)_{ll} - Cm(\theta_l)^2\sin(2\theta) \tag{2}$$

and

$$\theta_l^2\Lambda - \Lambda_{ll} = -\theta_l(\theta_{lll} + \frac{1}{2}\theta_l^3) + Cm\theta_l^2 2\cos 2\theta + Cm(\theta_l\sin(2\theta))_l \tag{3}$$

Here $Cm = \frac{2\pi\chi^2H_0^2\pi a^2L^2}{(\mu+1)C}$ is the magneto elastic number characterizing the ratio of the magnetic and elastic forces. Equations (2),(3) describe the behaviour of the elastic magnetic filaments in different situations. Starting from slightly bent configuration of the rod normal to the magnetic field "U" like turns (hairpins) are formed as metastable configurations (Fig.1a). Stable hairpins exist also with nonequal length of their legs. Introducing the phase lag between the direction of the rotating field and the tangent of the rod $\beta = \omega t - \vartheta$ the equation for the angle β is equivalent to the equation (2) with the forcing term $\omega\tau$ on the right side. In this case there is several regimes of the rod dynamics. For low frequencies of the field the rod rotates synchronously with it and has characteristic bent shapes (Fig.1b). Above the critical frequency which is close to the given by relation $(\omega\tau)_c = 2.37Cm$, which is obtained from simplified model, the periodic regime arises with characteristic bendings and straightenings of the rod (Fig.1c). The simplified model of the rod dynamics the equation for the tangent angle of the rod apart from the regularizing term of curvature elasticity is similar to the equation for the phase lag of the elongated viscous magnetic drop under the action of rotating magnetic field [4].

$$\omega\tau = \frac{\partial\beta}{\partial t} - \frac{\partial^2}{\partial l^2}(\frac{1}{Bm}\beta + \sin 2\beta) + \epsilon\frac{\partial^5\beta}{\partial l^4\partial t} \tag{4}$$

Here $\tau = \frac{(\mu+1)\zeta L^2}{2\pi^2\chi^2H_0^2a^2}$ is characteristic viscous relaxation time, $Bm = \frac{2\pi\chi^2H_0^2a}{(\mu+1)\gamma}$ is the magnetic Bond number characterizing the ratio of magnetic and capillary forces but a small parameter ϵ accounts for the viscous torques arising at the bending of the viscous filament. Since the function $\frac{1}{Bm}\beta + \sin 2\beta$ is nonmonotonous the formation of the shockwave of the tangent occurs at frequencies of the rotating field larger than critical (Fig.1d). From the balance of torques follows that the magnetic torque leads to the normal shearing force $F_n' = -T_0$. Shearing force of such kind arises also in the chains of the magnetic particles in magnetorheological suspensions due to the magnetic dipolar interaction between neighbours. On the other hand the particles are held together due to magnetic interaction forces.

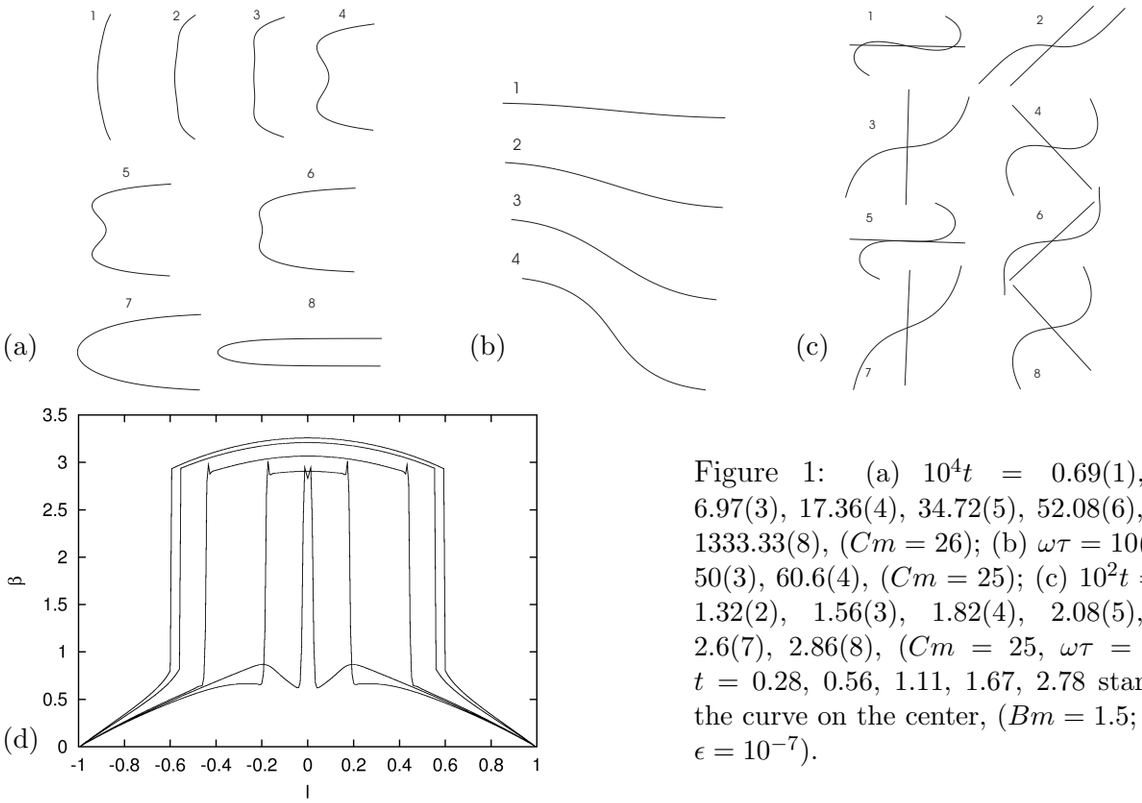


Figure 1: (a) $10^4 t$ = 0.69(1), 3.47(2), 6.97(3), 17.36(4), 34.72(5), 52.08(6), 69.44(7), 1333.33(8), ($Cm = 26$); (b) $\omega\tau = 10(1)$, 30(2), 50(3), 60.6(4), ($Cm = 25$); (c) $10^2 t = 1.04(1)$, 1.32(2), 1.56(3), 1.82(4), 2.08(5), 2.34(6), 2.6(7), 2.86(8), ($Cm = 25$, $\omega\tau = 300$); (d) t = 0.28, 0.56, 1.11, 1.67, 2.78 starting from the curve on the center, ($Bm = 1.5$; $\omega\tau = 5.0$; $\epsilon = 10^{-7}$).

The following relation for the number of particles in the chain N at the critical frequency of the chain breaking due to the transition to nonsynchronous regime holds

$$MaN^2 = 2\pi(\frac{3}{2}\sin 2\beta_c + \beta_c)(\ln\frac{L}{a} + c) \tag{5}$$

where $\beta_c = \frac{\pi}{2} - \frac{1}{2}\arccos 1/3$. Relation (5) shows in agreement with experimental data [5] that the number of particles which may be hold together by the magnetic interaction forces depends on Mason number $Ma = \frac{12\eta\omega}{M^2}$ as $N = \frac{const}{Ma^{1/2}}$. This shows that the model of elastic magnetic rod may play the same role in the understanding of the properties of magnetorheological suspensions which the Kirchhoff model plays for the understanding of biopolymers [6].

The model of elastic magnetic rod allows also to understand some phenomena in the magnetotactic bacteria which contains the chains of magnetic particles. For the chain of magnetic particles the curvature elasticity comes from the magnetic interaction between neighbouring particles. In the case of chain of ferromagnetic particles the curvature elasticity constant turns out to be $C_m = \frac{m^2}{2d^3}d$, where m is the magnetic moment of particle but d is its size. The value of the curvature elasticity constant allows to estimate the critical compression force at which the chain buckles $\Lambda_c = \pi^2 K_c/L^2$ which in the case of the magnetite magnetosomes with ten particles of the size $d = 0.1$ μm [3] in the chain gives $\Lambda_c = 12.3 \quad pN$. This force is in the range of the forces arising in different biological systems - molecular motors, DNA elasticity [6].

References

1. P.S.Doyle et al., Science, 295 2237 (2002)
2. P.Mayer et al.,Mater.Res.Soc.Symp.Proc., 463 57 (1997)
3. V.Scherbakov et al., Eur.Biophys.J., 26 319 (1997)
4. A.Cebers, Phys.Rev.E, 66 061402 (2002)
5. S.Melle et al., Phys.Rev.E 68 041503 (2003)
6. T.R.Strick et al., Rep.Prog.Phys., 66 1 (2003)

INTRACELLULAR CONTROL MECHANISMS OF CARDIAC CONTRACTION & ENERGETICS

Samuel Sideman, DSc, DSc Hon. FAHA & Amir Landesberg, MD, PHD
Dept of Biomedical Engineering, Technion-Israel Institute of Technology, Haifa 32000, Israel

Summary: The regulation of cardiac muscle contraction and efficiency is based on the intracellular control of calcium kinetics and cross-bridge (Xb) cycling.[1-4] Two intracellular feedback mechanisms: cooperativity and mechanical feedback allow successful description of the cardiac fiber dynamic and energetics, i.e., the force-length relationship (FLR),[5] the force-velocity relationship (FVR)[4] the control of relaxation[4] and the linear relationship between energy consumption and the generated mechanical energy.[6]

THE MODEL OF SARCOMERE CONTRACTION

The chemical to mechanical energy transformation in the cells involves: 1) The **mitochondria**, the chemical factory for the main intracellular energetic metabolite, the ATP, by utilizing oxidation phosphorylation 2) The **Sarcoplasmic Reticulum**, (SR), which serves as a dynamic store for calcium ions required for the control of the excitation-contraction coupling. 3) The **sarcomeres**, where the actin-myosin protein filaments mobilize muscular contraction, by the Xbs between the myosin and actin filaments.
The Xb cycling[7-9] between the weak and strong, force generating conformations is regulated by regulatory proteins.[8,9] The troponin regulatory units are defined by their Xb conformation, corresponding to the biochemical kinetics of calcium binding and dissociation from troponin. The ***four state model*** of the troponin regulatory units is given in Fig 1. The physiological stipulations are detailed in Refs 1-4.

The Xb transitions relates to nucleotide binding.[9] Xb turnover from the weak to the strong conformation relates to ATP hydrolysis and phosphate release, while Xb turnover from the strong to the weak conformation, Xb weakening, relates to ADP dissociation and ATP association with the Xb. Energy consumption is proportional to the total amount of Xb turnover from the weak to the strong conformation. Calcium binding to the low affinity troponin sites regulates the rate of phosphate dissociation from the myosin-ADP-P complex.[9] Thus, calcium binding to troponin regulates Xb recruitment and the energy consumption by the sarcomere.

The Sarcomere's control of contraction

Two dominant feedback mechanisms are assumed to regulate the sarcomere function:

A. **The cooperativity mechanism** defines the dependence of the affinity of troponin for calcium on the number of strong Xbs. The rate coefficients k_e and k_{-e} in Fig. 1 represent the rate constants of calcium binding to, and calcium dissociation from, the low affinity sites of troponin. Note that the rate coefficient $\kappa_{-\ell}$ is not constant and depends on states T U and L_s through the cooperativity mechanism. It is the dominant cooperative mechanism in skinned myocytes.[5] The cooperativity mechanism explains the "length dependence calcium sensitivity" , the force-length relationship (FLR), the related Frank-Starling Law of the LV, and it provides the adaptive control of energy consumption to changes in the loading conditions.[10] The cooperativity acts as an adaptive mechanism, assuring that the loading conditions affect the number of strong Xbs and determine calcium affinity. An increase in the load increases the number of strong Xbs, and increase energy consumption by increasing the amount of bond calcium to troponin.

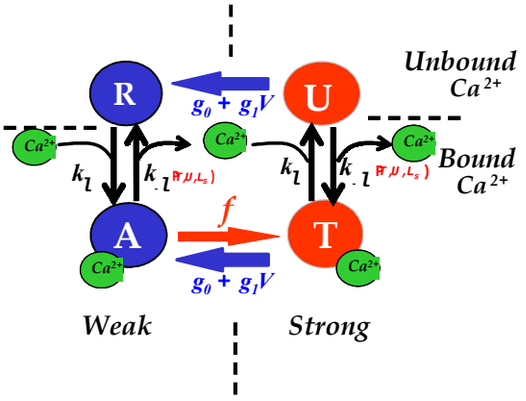


Fig 1. The state variables of the regulatory units

B. **The negative mechanical feedback** is based on biochemical studies of Xb cycling[11] and suggests that the filament Shortening velocity affects the rate of Xb transition from the strong to the weak, conformation a Xb weakening. Thus

$$g = g_0 + g_1 \cdot V \qquad (1)$$

where g_0 is the rate of Xb weakening in the isometric regime and g_1 is the mechanical feedback coefficient, which relates to the sarcomere shortening velocity rate of Xb weakening. (Fig 1) This feedback leads the analytical derivation of the force-velocity relationship (FVR) in the cardiac muscle and the experimentally derived Hill's Equation.[11] It regulates the FVR as well as the generated power and explains the linear relationship between energy consumption and the generated mechanical energy.

CONTROL OF ENERGY CONVERSION

The amount of hydrolyzed, ATP i.e. the energy consumption (E), is proportional to the sum of: the external work (W), the energy dissipation as heat (Q) due to the viscous property of the Xbs[3] and the pseudo potential energy (E_{PE}).[3,4]

$$\rho \; E = W + E_{PE} + Q \qquad (2)$$

The proportionality coefficient ρ represents the **efficiency** of energy conversion. The E_{PE} corresponds to Suga's potential energy, and equals it for isometric contractions. This energy dissipates also as heat.

EFFICIENCY AND ADAPTIVE CONTROL OF ENERGY CONSUMPTION

Whole heart and isolated fiber level studies lead to two fundamental conclusions, which are direct consequences of the two feedback mechanisms.[10]

1) The cardiac muscle efficiency is constant and load independent. The efficiency depends on the basic intrinsic properties of the individual Xb and is constant and independent of the number of activated Xbs or the loading conditions. The efficiency, as defined from Eq. (2) is given by:

$$\rho = \bar{F} \cdot V_u \,/\, \bar{E}\left(g_o + g_1 . V_u\right) \qquad (3)$$

where $\bar{F}$ is the unitary force per single cross-bridge, V_U is the maximal unloaded velocity ($\bar{F} \cdot V_u$ is thus the hypothetical maximal power of the single Xb) and $\bar{E}$ is the free energy liberated from ATP hydrolysis. The efficiency of the whole muscle is identical to the efficiency of the single Xb.

2) There is an adaptive control mechanism whereby changes in the loading conditions modulate the energy consumption. The regulation of energy consumption by the cooperativity mechanism is determined by the number of the activated Xbs. The linear relation between energy consumption and the generated mechanical energy suggests that the energy consumption is determined by the loading conditions. The intracellular adaptive control modulates the consumption to accommodate the load, while maintaining the efficiency, as defined above, constant. The sensors that determine the demands are the Xbs themselves. An increase in the number of strong Xbs increases calcium affinity and thus the energy consumption, and vise versa, when the number of Xbs decreases. The mechanical feedback operates at the single Xb level and relates to the constant efficiency. The cooperativity mechanism operates at the whole sarcomere level and modulates the response of the energy consumption to the changing load.

CONCLUSIONS

The existence of the two control mechanisms imbedded in the model explains a wide spectrum of phenomena of cardiac mechanics and energetics.[3,4] The utility of the suggested cooperativity mechanism has recently been experimentally and analytically established.[14,15] The experimental and simulation studies[14,15] of the force response to large amplitude SL oscillations at a constant calcium concentration confirm the existence of the two intracellular control mechanisms, reveal the force dependency on the history of contraction: the cooperativity dominates at the normal range of low frequencies and allows the muscle to adapt Xb recruitment to slow changes in the loading conditions. The mechanical feedback dominates at higher frequencies where the muscle absorbs rather than generates energy, and controls muscle function by the velocity of contraction. The efficiency (Eq 3) reflects an inherent property of the single Xb and is constant and load independent.

References:

1) Landesberg A, Sideman S., 1994, Coupling calcium binding to Troponin-C and Xb cycling kinetics in skinned cardiac cells. *Am J Physiol*; **266** (*Heart Circ. Physiol.* 35):H1261-H1271; 2) Landesberg A, Sideman S., 1994, Mechanical regulation in the cardiac muscle by coupling calcium binding to troponin-C and Xb cycling. A dynamic model. *Am J Physiol*; **267** (*Heart Circ Physiol* 36):H779-H795; 3) Landesberg A, Sideman S., 1999, Regulation of energy consumption in the cardiac muscle: analysis of isometric contractions. A dynamic model. *Am J Phsyiol*; **276**:H998-H1011; 4) Landesberg A, Sideman S., 2000, Force-velocity relationship and biochemical to mechanical energy conversion by the sarcomere. *Am J Physiol*, **278** (4):H1274-H1284. 5) Landesberg A, Livshitz L, ter Keurs HEDJ., 2000, The effect of sarcomere shortening velocity on force generation, analysis, and verification of models for cross-bridge dynamics In: *Skeletal Muscle Mechanics*, W. Herzog, ed. John Wiley & Sons, UK, Chap.10:155-177; 6) Landesberg A 2003, Efficiency and economy of cardiac muscle contraction based on a kinetic model of the sarcomere. *Ann Biomed. Eng*. Accepted. 7) Huxley AF, Simmons RM, 1971, Proposed mechanism of force generation in striated muscle. *Nature*; **233**:533-538; 8)Eisenberg E, Hill TL., 1985, Muscle contraction and free energy transduction in biological system. *Science*; **227**:999-1006; 9) Otner JD 1995 Theories of muscle contraction, *J Stractural Biol* **115** :119-143; 10) Landesberg A, Levi C Yaniv Y Sideman S, 2003 The adaptive intracellular control of cardiac muscle function, in *Cardiac Engineering, From Genes & Cells to Structure & Function,* Sideman S, Beyar R, Eds. Annals NY Academy of Science Chap 1.6 , in Press; 11) Hill AV., 1938, The heat of shortening and dynamic constants of shortening. *Proc. Royal Soc* London (Biol); **126**:136-195; 12) Suga H., 1990, Ventricular energetics. *Physiol Rev*; **70**: 247-277; 13) Hisano G, Cooper IV. 1987, Correlation of force-length area with oxygen consumption in ferret papillary muscle. *Circ Res*; **61**:318-328; 14) Levy C, Landesberg A, 2003 Hystereses in the force-length relation and the regulation of cross-bridge recruitment in the tetanized rat trabeculae. *Am J Physiol,* in press; 15) Yaniv Y, Landesberg A, Sivan R, 2003, Identification of sarcomere control of cardiac contraction by analysis of force-length and force-calcium hystereses , *Am J Physiol* Accepted.

XXI ICTAM, 15–21 August 2004, Warsaw, Poland

MECHANICS OF VENUS' FLYTRAP CLOSURE

Yoel Forterre*, Jan Skotheim**, Jacques Dumais***, L. Mahadevan**
DAMTP, Cambridge University, Cambridge CB3 OWA, UK
**present address: IUSTI CNRS UMR 6595, 13453 Marseille Cedex 13, France*
***present address: DEAS, Harvard University, Cambridge, MA 02138, USA*
****present address: OEB, Harvard University Herbaria, Cambridge, MA 02138, USA*

Summary We investigate the snapping closure of the carnivorous plant Venus flytrap (*Dionaea muscipula*), which exhibits one of the fastest motion in the vegetable kingdom (typically 100 ms). From experimental measurements using a high-speed camera, we propose that the very fast closure of the trap results from a mechanical instability, based on the change of curvature of the leaves. A simple poroelastic model for the snapping of a spherical cap is written, which allows to explain the main experimental observations.

INTRODUCTION

The quick, snapping closure of the carnivorous plant Venus flytrap (*Dionaea muscipula*) was described by Darwin as 'one of the most wonderful [plant] in the world' [1] and there has been much speculation as to what is the underlying mechanism. Rapid closure ($\sim 1/10$ second) of the trap is initiated by the stimulation (by an insect or any mechanical stimuli-see figure 1) of trigger hairs acting as mechanosensors. Many studies have focused on the response of the trigger hairs to stimuli and shown that upon stimulation an action potential spreads quickly across the leaves. However, the mechanism of the rapid closure itself is still badly understood and is the object of contradictory explanations [2]. Here we aim to reconsider the mechanism of Venus' flytrap closure from a mechanical point of view and ask whether such a rapid motion may results from an elastic instability, by analogy with the buckling of plates and shells.

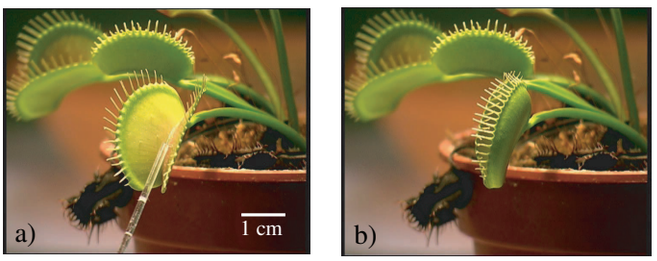


Figure 1. Pictures showing the carnivorous plant 'Venus flytrap' in the open (a) and closed (b) states. In (a) the plant is in the process of being triggered by a tiny glass rod. Note the change of curvature of the lobes before and after closure.

EXPERIMENTS

We have first studied the dynamics of the closure using a high-speed camera (400 frames/s). Small fluorescent dots are painted on the external face of one leaf of the trap (figure 2a) and the closure is filmed simultaneously under two different view angles using a set of mirrors. It is then possible to reconstruct the full 3D shape of the leaf using triangulation. Figure 2a presents a typical sequence of the leaf dynamics during the trap closure. As already noted by Darwin, the leaf is curved outward (convex) in the open state and curved inward (concave) in the final state. The motion itself is characterized by a phase of rapid acceleration ($\leq 1/10$ sec.), which corresponds to the change of sign of the mean curvature, followed by a phase of damping of the system as shown in figure 2b (left). In plate mechanics, changes of curvature are usually associated to differential strains across the thickness. For Venus' flytrap closure, it has been shown that the curvature results from an extension of the outer surface while the inner surface remains unchanged [2]. Using microscopy techniques, we have precisely measured the strain field of the outer surface between the open state and the closed state: the direction of extension (max. 10 %) is observed to occurs mainly in the direction perpendicular to the hinge of the trap (called transverse direction in the following), which corresponds to the main direction of the cells. This suggests that closure is driven by the change of natural curvature of the system only in this direction. We have confirmed this result by cutting in a closed leaf thin strips in different directions. One observes that strips cut in the transverse direction keep their inward curvature whereas strips cut in the longitudinal direction bend spontaneously outward, i.e. the natural curvature is this direction is the same as in the open state.

MODEL

From the experimental results, we propose the following mechanism for the Venus' flytrap closure. Upon stimulation, the closed state becomes the stable state of the system due to the change of the natural curvature in the transverse direction. We

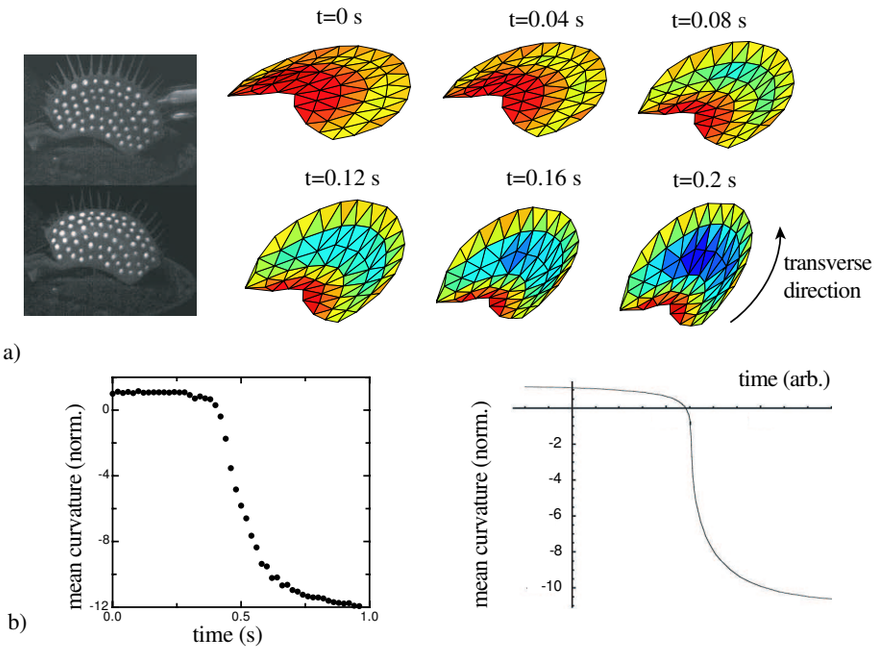


Figure 2. a) Left: pictures of the open and closed states showing the experimental method. Right: 3D reconstruction of the dynamics of the trap closure. The colour gives the local mean curvature (red: convex, blue: concave). b) Mean curvature as a function of time. Left: experiment, right: model.

do not pretend here to explain this natural curvature change, which involved a complex physiological process. However, in order to reach the stable closed state the system has to overcome an energy barrier, which corresponds to the stretching elastic energy needed to change the curvature of the leaf (more precisely the Gaussian curvature). Once this barrier is crossed, the system snaps via a buckling-like instability, which is damped by the diffusion of water inside the leaf. This mechanism is supported by observations of highly curved traps for which the delay between the triggering and the closure may exceed 30 seconds before a violent snap occurs. In order to test the proposed mechanism, we have written a simple mechanical model of the snapping of a poroelastic spherical cap. The elastic energy of the leaf E_{el} involves a bending term and a stretching term, and the control parameter is the natural curvature in the transverse direction. A first result is that there exists a critical geometrical parameter $\alpha = L^4\kappa^2/3t^2 \sim 1$, where L is the size of the leaf, t its thickness and κ its initial curvature, above which the system undergoes an elastic instability and snaps from one state to another. Note that for a typical leaf $\alpha \sim (1\mathrm{cm})^4(0.2\mathrm{cm}^{-1})^2/3(0.1\mathrm{cm})^2 \sim 1$, which roughly corresponds to the smooth/snapping transition. To model the dynamics during the snap, we use the fact that the system is overdamped and balance the variation of energy to the poroelastic dissipation: $dE_{el}/dt = P_d$. The time scale of the snap is then controlled by the poroelastic time $\tau \sim t^2/(EK)$ [3], where E is the Young modulus and K is the water permeability. A typical dynamics predicted by this model is presented in figure 2b (right). For realistic parameters: $E \sim 10$ MPa, $K \sim 10^{-12}$ m^{2}Pa^{-1}s^{-1}, one obtains $\tau \sim 0.1 - 1$ sec., which is consistent with the experimental observations.

CONCLUSION

Our model of Venus' flytrap closure implies that the closure is actually composed of an 'active' part, which builds the stress necessary to overcome the stretching barrier, followed by an elastic 'passive' snapping of the trap. It is interesting to note that this transition occurs in the biological range perhaps implying something about the optimality of the design of the Venus flytrap. On the one hand the plant wants to have a violent and fast snap to catch insects, while on the other hand a violent snap requires more energy to be put before the snap occurs, which may cause a longer period of delay before the snap occurs. In this study, we have only considered the mechanical part of the closure and not the 'active' process by which the natural curvature change. An important future work would be to measure some physiological parameters at the cell scale, such as turgor pressure, in order to better understand this 'active' process and other rapid motions in plants [4].

References

[1] Darwin C.: Insectivorous plants. Murray, London 1875.
[2] Hodick D., Sievers A.: On the mechanism of trap closure of Venus flytrap (*Dionaea muscipula* Ellis). *Planta* **179**:32-42, 1989.
[3] Skotheim J., Mahadevan, L.: Buckling of poroelastic filaments. To be published in *Proc. Roy. Soc. A*, 2004.
[4] Hill B.S., Findlay G.P.: The power of movement in plants: the role of osmotic machines. *Quaterly Reviews of Biophysics* **14**:173-222, 1981.

APPROXIMATIONS OF STIFFNESS TENSOR OF BONE - DETERMINING AND ACCURACY

J. Piekarski*, K. Kowalczyk-Gajewska*, E. Waarsing**, M. Maździarz*
* *Institute of Fundamental Technological Research, PL Świętokrzyska 21, 00-049 Warsaw, Poland*
** *Erasmus Medical Centre , Orthopaedic Research Laboratory, EE 1614, P.O.BOX 1738, 3000 DR Rotterdam, The Netherlands*

Summary Properties of the apparent stiffness tensor of bone are investigated. The computer reconstruction composed of computer microtomograph imaging, finite element reconstruction and numerical tests results in apparent stiffness tensor of bone. Next the stiffness tensor is subjected to spectral and harmonic decompositions. Kelvin moduli and invariants of orthogonal projectors provided by spectral analysis as well as five invariant parts resulting from harmonic decomposition are obtained. These scalar and tensorial invariants enable the analysis of properties of the stiffness tensor such as material symmetry. Finally, the closest isotropic stiffness tensor is derived and the possible orthotropic approximations are proposed and their accuracy is studied.

INTRODUCTION

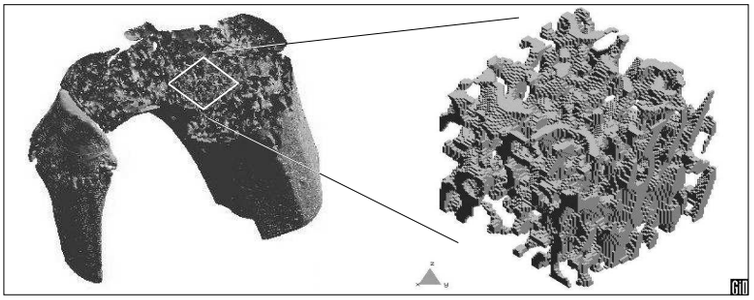
The trabecular structure of bone is spatially oriented. Due to the existence of preferred directions apparent mechanical properties of bone commonly are approximated using orthotropic constitutive models. Cowin in [1] has proposed the second order fabric tensor to describe anisotropy of the bone structure that is capable to deal at most with orthotropic material. Another variant of this approach has been considered by Zysset and Curnier [10]. Numerous attempts have been done in order to identify orthotropic properties of bone, for example [9]. Also homogenization methods [8] has been applied to specify orthotropic constitutive models. Nevertheless, it seems that the accuracy of approximation of bone material with orthotropic model have not been investigated quantitatively so far.

Development of computer microtomography, techniques of reconstruction of bone morphology and assessment of mechanical properties using Finite Element numerical tests provided a significant impact in investigation of constitutive properties of bone tissue. Van Rietbergen, Huiskes at al. [4, 5] showed usefulness of this methodology for quantifying elastic moduli of bone, and Odgaard et al. [3] showed close relation between constitutive tensors evaluated using the computer reconstruction technique and those identified from models based on fabric tensor and mechanical tests.

In this paper we used the computer reconstruction method combined with spectral and harmonic decomposition to investigate properties of the apparent stiffness tensor of bone. Hexahedral samples of trabecular bone was reconstructed from computer microtomograph images, next Finite Element models of samples was build and numerical tests combined with averaging procedure was performed in order to identify the fully anisotropic apparent stiffness tensor. Subsequently, the spectral and harmonic decompositions of the tensor were performed. Six Kelvin moduli and invariants of projectors were evaluated. The closest isotropic tensor and possible orthotropic approximations were specified basing on the harmonic decomposition. Analysis of these quantities allowed to discuss symmetries of apparent stiffness tensor and to measure the deviation of the proposed approximations from the actual stiffness tensor.

COMPUTER RECONSTRUCTION METHOD

The right proximal tibia of rat was scanned using a prototype in-vivo micro-CT scanner (Skyscan 1076, Skyscan, Antwerp, Belgium), resulting in reconstructed data sets with 21.8-micron pixel-size. Data sets were segmented using a local threshold algorithm. Trabecular and cortical bone were separated using EUR in-house software. The example of three-dimensional reconstruction of separated bone structure is presented in Fig.1a. Next, the hexahedral sample was extracted from the reconstructed image, Fig.1b, and the Finite Element (FE) model of the sample was built by replacing each voxel of μCT image with an 8-node brick element. The effective stiffness tensor $\bar{\boldsymbol{C}}$ of the sample was evaluated by applying averaging procedure



a) b)

Fig.1 a) Reconstructed μCT image of bone, b) FE model of hexahedral sample

$$\bar{\boldsymbol{C}}\bar{\boldsymbol{\varepsilon}} = \frac{1}{V}\int_V \boldsymbol{C}\boldsymbol{\varepsilon} dV \qquad (1)$$

where $\boldsymbol{\varepsilon}$ denoted strains induced by applying uniform strain state $\bar{\boldsymbol{\varepsilon}}$ at boundaries, $\boldsymbol{C}$ is the local stiffness tensor and V denoted the volume of the sample. In these numerical tests the trabecular tissue was assumed to be uniform and isotropic. The O'Kelly's nanoindentation tests on the unfixed rat trabecular tissue [11] showed the average value of Young modulus equal $8.9\ GPa$ with a 95% confidence interval of $\langle 7, 9.8\rangle\ GPa$, and this average value has been taken as the material constant of bone matrix.

SPECTRAL AND HARMONIC DECOMPOSITION OF THE STIFFNESS TENSOR

An arbitrary 4^{th} rank stiffness tensor $\boldsymbol{C}$ can be presented in the form [6]

$$\boldsymbol{C} = \lambda_I \boldsymbol{w}^I \otimes \boldsymbol{w}^I + \lambda_{II} \boldsymbol{w}^{II} \otimes \boldsymbol{w}^{II} + \ldots + \lambda_{VI} \boldsymbol{w}^{VI} \otimes \boldsymbol{w}^{VI} \tag{2}$$

where $\{\boldsymbol{w}^I,\ \boldsymbol{w}^{II},\ \boldsymbol{w}^{III},\ \boldsymbol{w}^{IV},\ \boldsymbol{w}^V,\ \boldsymbol{w}^{VI}\}$ constitutes an orthonormal basis in the space of 2^{nd} rank symmetric tensors called elastic eigenstates, and six scalar parameters $\lambda_I,\ \lambda_{II}, \ldots, \lambda_{VI}$ are called Kelvin moduli. The Kelvin moduli and invariants of elastic eigenstates provide 18 independent parameters of the stiffness tensor. By investigating these invariants the structure and properties of the stiffness tensor can be analyzed.

Another tool useful for analysis of the properties of the stiffness tensor $\mathbf{C}$ is the harmonic decomposition [2], [7]. In view of this decomposition the tensor $\boldsymbol{C}$ is uniquely defined by the set of parameters: $\boldsymbol{C} \Longleftrightarrow (\boldsymbol{h_P},\ \boldsymbol{h_D},\ \boldsymbol{\varphi},\ \boldsymbol{\rho},\ \boldsymbol{D})$ among which h_P and h_D are scalars, $\boldsymbol{\varphi}$ and ρ are symmetric second rank deviators and $\boldsymbol{D}$ is totally symmetric and traceless 4^{th} rank tensor called the 4^{th} rank deviator. The particular form and properties of the tensorial parameters give further insight into material symmetry analysis. Moreover, harmonic decomposition enables finding out the closest isotropic approximation of $\boldsymbol{C}$ and provides hints for orthotropic approximation of $\boldsymbol{C}$.

ANALYSIS OF ACTUAL EFFECTIVE STIFFNESS TENSOR OF TRABECULAR BONE

The sample of rat trabecular bone of the edge size 1.75 *mm* has been treated with the procedure described in previous sections. The effective stiffness tensor $\bar{\boldsymbol{C}}$ has been numerically identified. The tensor is characterized by the following Kelvin moduli: $\{252.54,\ 282.81,\ 373.79,\ 421.81,\ 451.34,\ 902.31\}$ [*MPa*] . Nevertheless only one eigenstate related to the third Kelvin modulus is close to a deviator, therefore it is hard to specify significant symmetries of the tensor without additional analysis [2].

Applying the harmonic decomposition one obtains $h_P = 790.33$ *MPa*, $h_D = 378.85$ *MPa* . These values provide the closest isotropic approximation with the Young modulus $E = 458.41$ *MPa* and the Poisson ratio $\nu = 0.210$. The relative difference between the closest isotropic tensor $\bar{\boldsymbol{C}}^{is}$ and the actual tensor $\bar{\boldsymbol{C}}$ measured according to $d = \{[(\bar{\boldsymbol{C}}^{is} - \bar{\boldsymbol{C}}) : (\bar{\boldsymbol{C}}^{is} - \bar{\boldsymbol{C}})]/(\bar{\boldsymbol{C}} : \bar{\boldsymbol{C}})\}^{1/2}$ (see [7]) equals 0.304. Second order deviators $\boldsymbol{\varphi}$ and ρ are almost coaxial suggesting position of approximated orthotropy axes. The orthotropic approximation $\bar{\boldsymbol{C}}^{orth}$, obtained by rotating the tensor to axes specified from harmonic decomposition and neglecting out-of-orthotropy terms in the rotated representation, is characterized by the following Kelvin moduli: $\{262.54,\ 281.58 = G_{12},\ 370.39 = G_{23},\ 427.95,\ 440.48 = G_{13},\ 901.45\}$ [*MPa*] with the Young moduli $E_1 = 435.67$ *MPa*, $E_2 = 282.51$ *MPa*, $E_3 = 705.76$ *MPa*, Poisson ratios $\nu_{12} = 0.252$, $\nu_{13} = 0.161$, $\nu_{23} = 0.131$, and the norm of relative distance to the actual tensor $d = 0.052$.

CONCLUDING REMARKS

The aim of the paper was to discuss the method of determining the isotropic and the orthotropic approximation of actual effective stiffness tensor of trabecular bone and to estimate errors of these approximations. The method is based on both spectral and harmonic decomposition of 4^{th} rank stiffness tensor. The analysis of an actual effective stiffness tensor obtained by means of computer reconstruction method is provided in order to illustrate the proposed procedure. In this particular case the orthotropic approximation appears to be very good in spite of lack of evident symmetries. Nevertheless, general conclusions could be formulated on the basis of more waste set of data. Such work is in progress.

Acknowledgements: This work has been partially supported by European Union grant QLRT-1999-02024 (MIAB).

References

[1] S.C. Cowin. The relationship between the elasticity tensor and the fabric tensor. *Mechanics of Materials*, 4:137–147, 1985.
[2] S. Forte and M. Vianello. Symmetry classes for elasticity tensors. *J. Elasticity*, 43:81–108, 1996.
[3] A. Odgaard, J. Kabel, B. van Rietbergen, M. Dalstra, and R. Huiskes. Fabric and elastic principal directions of cancellous bone are closely related. *Journal of Biomechanics*, 30(5):487–95, 1997.
[4] B. van Rietbergen, A. Odgaard, J. Kabel, and R. Huiskes. Direct mechanics assessment of elastic symmetries and properties of trabecular bone architecture. *Journal of Biomechanics*, 29(12):1653–7, 1996.
[5] B. van Rietbergen, A. Odgaard, J. Kabel, and R. Huiskes. Relationships between bone morphology and bone elastic properties can be accurately quantified using high-resolution computer reconstructions. *Journal of Orthopaedic Research*, 16(1):23–8, 1998.
[6] J. Rychlewski. Unconventional approach to linear elasticity. *Arch. Mech.*, 47(2):149–171, 1995.
[7] J. Rychlewski. A qualitative approach to Hooke's tensors. Part I, II. *Arch. Mech.*, 52(4-5), 53(1):737–759, 45–63, 2000,2001. Supl. 1; 151-160; 2003
[8] J.J. Telega, A. Galka, B. Gambin, S. Tokarzewski. Homogenization methods in biomechanics. *Orthopaedic Biomechanics. AMAS Conf. Proceedings 5.* Ed. J.J. Telega, 227–276, 2003.
[9] C.H. Turner, S.C. Cowin, J.Y. Rho, R.B. Ashman, and J.C. Rice. The fabric dependence of the orthotropic elastic constants of cancellous bone. *Journal of Biomechanics*, 23(6):549–61, 1990.
[10] P.K. Zysset and A. Curnier. An alternative model for anisotropic elasticity based on fabric tensors. *Mechanics of Materials*, 21:243–250, 1995.
[11] Mechanical Integrity and Architecture of Bone Relative to Osteoporosis, Ageing and Drug Treatment (MIAB). *EU Project QLK6-1999-02024, Final Report, November 2003*.

Title:

Theory of Polymorphism in Bacterial Flagella

Authors:

Srikanth V. Srigiriraju,
Thomas R. Powers

Publication of the Extended Summary not permitted by author.

HYDRODYNAMIC INTERACTION BETWEEN TWO BIOARTIFICAL CAPSULES IN SHEAR FLOW

Arnaud Mordel, Etienne Lac, Dominique Barthès-Biesel
UMR CNRS 6600, Université de Technologie de Compiègne, BP20529, 60205 Compiègne, France

Summary The hydrodynamic interaction between two liquid filled identical spherical capsules is studied in simple shear flow. The boundary element method is used with bi-cubic B-splines as basis functions to map the capsule surfaces on two structured mesh. This guarantees continuity of second order geometrical properties with respect to the position of the Lagrangian particles used for tracking the location of the interface at each time step. When crossing, the capsules undergo large deformation that may damage the interface and their trajectories are irreversibly shifted towards larger cross streamline separation.

PROBLEM PRESENTATION

Liquid filled bioartificial capsules enclosed by a thin hyper-elastic membrane are used in many biomedical or industrial applications where encapsulation of living cells or of active agents in a protecting membrane is necessary. The design of such capsules has to take into account the mechanical stress to which the particle will be subjected in order to control burst. There have been a number of numerical and experimental studies of the motion and deformation of a *single* capsule freely suspended in shear flow. However, such particles are often used in suspension and it is then of interest to consider the interaction between several capsules. This is a difficult multi particle problem that has not been studied up to now to our knowledge. In this paper, we present the first numerical study of the hydrodynamic interaction between two identical capsules freely suspended in a simple shear flow.

Two identical initially spherical capsules C_1 and C_2, with radius a, are filled with a Newtonian fluid of viscosity μ and enclosed by a very thin hyperelastic membrane, devoid of bending resistance, and characterised by surface shear and dilation modulus G_s and K. The two capsules are suspended in another Newtonian liquid with same viscosity μ and subjected to a simple shear flow $\mathbf{u}^{\infty}=kx_3\mathbf{e}_1$ with shear rate k in the x_1, x_3 plane. Buoyancy effects are ignored and the fluid motion is governed by the Stokes equations. The centres of mass G_1 and G_2 of the capsules are initially located in the shear plane x_1, x_3 and remain in this plane of symmetry during motion. Since the capsules are identical, their deformed shapes are symmetric with respect to the middle of the segment G_1G_2. The relative position of C_1 and C_2 is given by the difference between the centres of mass position: $\Delta x_i=x_i(G_1)-x_i(G_2)$, with initial value denoted d_i.

The fluid velocity at any point $\mathbf{x_0}$ is given by the boundary integral on the surfaces C_1 and C_2 of the two capsules

$$\mathbf{u}(\mathbf{x}_0)=\mathbf{u}^{\infty}(\mathbf{x}_0)-\frac{1}{8\pi\mu}\int_{C_1\cup C_2}\mathbf{J}(\mathbf{x},\mathbf{x}_0).\Delta\mathbf{f}(\mathbf{x})\,dS(\mathbf{x}) \qquad (1)$$

where $\mathbf{J}$ is the free space Green's function [1]. The jump $\Delta\mathbf{f}$ in viscous traction across the interface is the elastic load on the interface and is thus related to the elastic tensions in the membrane through the shell equilibrium equations [1, 2].

Two membrane constitutive equations are considered [2]: the neo-Hookean (NH) law that corresponds to a very thin sheet of a volume incompressible elastomer or the Skalak et al. [3] two-dimensional law (SK). We consider the case where the two laws are identical for small deformation but lead to different behaviour for large deformation. Since the capsule interface has no bending stiffness, it cannot sustain any compressive stress and will buckle as soon as one of the two principal tensions becomes negative. A simple stability criterion is thus that the two principal tensions should both be positive. Dimensional analysis of the problem shows that an important parameter is the *capillary number* $\varepsilon=\mu k a/G_s$ which measures the ratio between the viscous forces exerted by the fluids and the elastic resistance of the membrane.

NUMERICAL PROCEDURE

The numerical method is based on Lagrangian tracking of the position of the interface material points: starting with the two undeformed capsules at some initial position, we follow their motion and deformation in response to a sudden start of the flow. Following the method developed for an isolated capsule [4], we use a structured mesh for each particle and interpolate the surface with bi-cubic B-spline functions. This guarantees continuity of second derivatives and curvature and allows the direct determination of the elastic load $\Delta\mathbf{f}$ on the interface. The integral in equation (1) is calculated by means of regular Gaussian quadrature. Once the velocity is calculated, the nodes on the surface are convected to their new position over time interval Δt by means of a fourth order Runge-Kutta method. In the present study, the surface of each capsule was mapped with a minimum of 20x40 elements and a maximum of 40x80 elements. Accuracy of the method was checked by using two different mesh and also by monitoring the volume variation of a capsule. For example with a 20x40 mesh, we find a volume change of less than 0.01% at time kt=40 i.e., after 4000 iterations. Another check of the accuracy of the method is to verify that when the two capsules are very far apart, they reach a steady deformed shape that is identical to the one found for an isolated capsule [4].

RESULTS

We discuss in detail the case of two capsules with a membrane obeying SK law ($K=3G_s$) for $\varepsilon=0.6$. Figure 1 shows the successive profiles of the two capsules as they cross. It should be noted that during the whole process, the flow vorticity keeps the membrane rotating around the internal liquid. During the approach phase (kt=4), C_1 and C_2 have approximately the shape they would have if they were alone in the flow and their centre of mass are still separated by the initial distance $\Delta x_3 = 0.5a$. When they get nearer, their deformation increases substantially, and a peak in deformation energy is observed when the interaction is maximum (kt=8.5). High curvature areas appear on the membrane where folding and damage might occur. During the separation phase (kt=9.7) one of the principal tension become very small near the downstream tip and a tendency towards buckling is observed. Finally as the capsules separate fully, they each recover the shape of an isolated capsule, but the distance Δx_3 has increased from $0.5a$ to $1.2a$. Consequently, the hydrodynamic interaction between the two capsules results in an irreversible shift of trajectory and the x_3 separation increases. This phenomenon was also observed for liquid droplets [5].

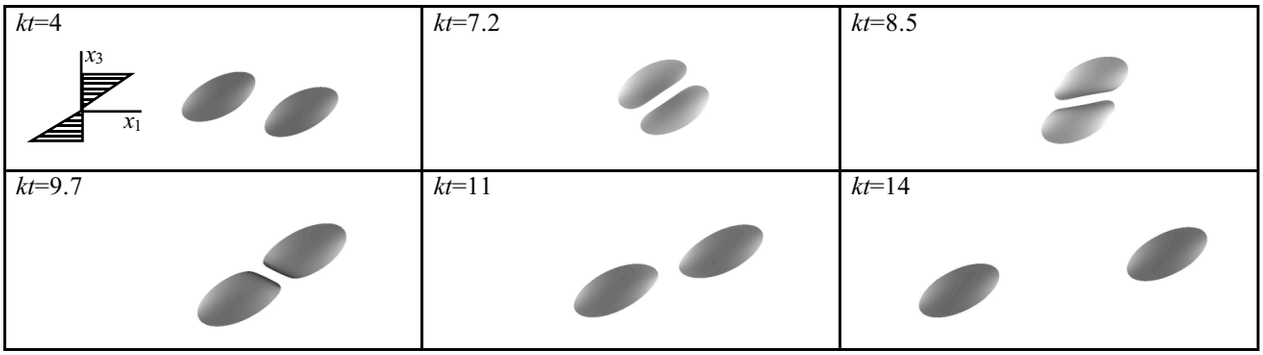


Figure 1. Successive profiles at different time kt, of two capsules for $\varepsilon=0.6$ with a SK membrane. Grey level mapping corresponds to local area dilation. Initial relative position (d_1, d_3)=(-5a, 0.5a).

CONCLUSIONS

There are different interesting features that are specific to capsule interactions. As shown on Figures 1 & 2, when the capsules overpass (Δx_2=0), the centres of mass cross separation Δx_3 is maximum. However, when the capillary number is increased from ε=0.6 to 2.1, the deformation of the capsules is larger, but the final shift in trajectory does not change. The shift seems to depend mainly on initial separation d_3. For the trajectory shift to be negligible, an initial separation $d_3>3a$ is necessary for capsules, whereas $d_3>2a$ is enough for two liquid droplets [5]. The less deformable the capsule, the larger the trajectory shift. Capsules with NH membrane that are strain softening, are easier to deform than capsules with SK membrane, and are thus shifted less. Negative principal tensions appear in the membrane in the wake of separating capsules. Such negative tensions may lead to buckling and burst of the membrane. To avoid this phenomenon, a finite bending resistance of the membrane must be accounted for or the capsule must be pre-stressed by osmotic pressure.

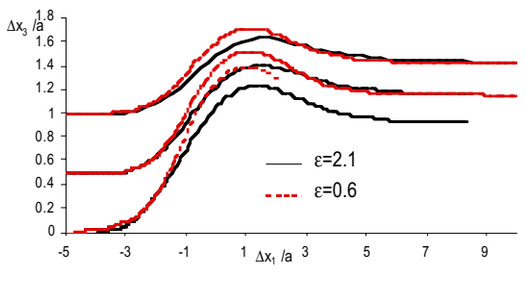


Figure 2. Relative centre of mass trajectories for two capillary numbers

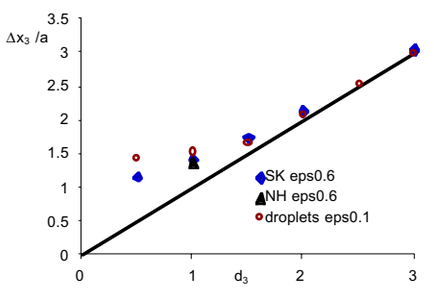


Figure 3 Final shift in trajectory for different membrane laws and initial position

References

[1] Pozrikidis, C. Boundary integral and singularity methods for linearized viscous flow. Cambridge University Press. 1992
[2] Barthès-Biesel, D., Diaz, A. & Dhenin, E. *J. Fluid Mech.* **460**, 211-222, 2002.
[3] Skalak, R., Tozeren, A., Zarda, R.P., Chien, S. *Biophys. J.* **13**, 245-264. 1973
[4] Lac, E., Barthès-Biesel, D., Pelekasis, N. A. & Tsamopoulos, J. *J. Fluid Mech.* Submitted. 2003
[5] Loewenberg, M. & Hinch, E. J. *J. Fluid Mech.* **338**, 299-315, 1997.

STRESS AND STRAIN IN A YEAST CELL UNDER HIGH HYDROSTATIC PRESSURE

Christoph Hartmann*, Antonio Delgado*
*Chair of Fluid Dynamics and Process Control, Technische Universität München, Freising, Germany

Summary The mechanical effects of the compression of a yeast cell (*Saccharomyces cerevisiae*) under high hydrostatic pressure (HHP) are modeled and simulated numerically. Dimensional analysis shows that oscillatory pressure application at frequencies below 700 MHz does not generate mechanical damage. The deformation of the cell under pressure deviates strongly from isotropic volume reduction. In the cell wall, von-Mises stress reaches the critical value upon failure at a pressure load between 415 MPa and 460 MPa.

INTRODUCTION

The treatment of food and biotechnological substances with hydrostatic pressures up to 1000 MPa (i. e. 10000 bars) has manifold effects such as phase transitions, the unfolding of proteins, the inactivation of enzymes, the preservation of aroma compounds and vitamins. High pressure induced inactivation of micro-organisms is investigated intensively on a molecular level, but little is known about the mechanical effects on living cells and the resulting morphological changes [1]. Morphological changes of yeast cells (*Saccharomyces cerevisiae*) under high hydrostatic pressure (HHP) with damage of cell organelles prior to cell wall disruption at pressure levels between 400 MPa and 500 MPa are reported in [2]. The analysis is carried out ex-situ, while in-situ observation of cells exposed to high hydrostatic pressure is still a challenge due to the strong pressure dependency of optical properties. The difficulty of combining a microscopic device with a thick-walled high pressure chamber and the severe requirements on the chamber material are additional handicaps. Moreover, an in-situ observation of cell organelles seems even to be impossible at present. Therefore, the present contribution intends to deliver a mathematical model and a simulation of the mechanical effects during the high hydrostatic pressure treatment of *Saccharomyces cerevisiae* (baker's yeast). This organism is chosen, because it is widely used in food and biotechnology. Furthermore, the organism is of a certain mechanical complexity since it has a cell wall, a membrane and organelles. The paper principally focuses on the distribution of stress and strain within the cell, their correlation to experimental findings and the question, whether transient pressure application protocols can lead to mechanical damage of the cell.

METHODS

Geometry and Structural Elements

In order to describe the mechanical behavior of the cell, the complex structure of the cell is reduced to an axis-symmetric model containing the relevant structural parts of the cell: the cell wall, the cytoplasm (contained in the cell), the nucleus and the vacuole. Other cell organelles are supposed to be of minor importance for the mechanical behavior of the cell. Membranes around the whole cell, the nucleus and the vacuole are taken into account as material surfaces. The geometrical shape of the yeast cell model represents a cross section through an ellipsoid with an imperfection at the bottom representing the bud scar. It contains a spherical nucleus and a spherical vacuole placed along the axis of symmetry at distinct locations. The typical length of the cell is 10μm (Figure 1).

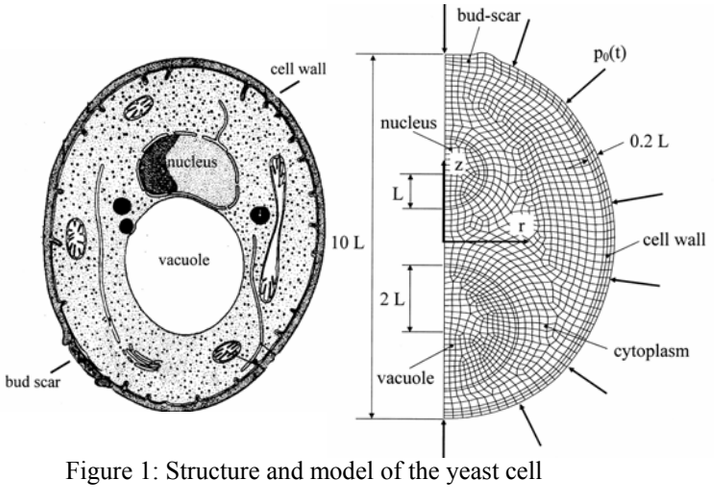


Figure 1: Structure and model of the yeast cell

Governing Equations and Solution Technique

The Cauchy equation of motion for a continuous medium forms the basis of the mathematical model of the present problem. Time dependent pressure load is applied as boundary condition on the outer surface of the cell wall. It is shown by dimensional analysis that the time dependent problem reduces to a stationary one. Since mechanical properties of the individual organelles of the yeast cell are difficult to determine, the current model accounts for simplified material properties of the cytoplasm (a gel filling the voids inside the cell), a fat-containing vacuole and the cell wall. The mechanical properties of the cell wall are taken from [3], where Young's modulus of the cell wall material is determined as E_{cw} = 150 MPa± 15 MPa assuming almost incompressible, linear elastic behavior. Analysis of current model parameters as well as physical properties of cytoplasm suggests that the mechanical properties of cytoplasm exposed to high pressure can be approximated with those of pure water. Therefore, bulk modulus of water is

derived from an equation of state valid under high pressure and is shown to depend linearly on pressure. Analogously, bulk modulus for the lipid contained in the vacuole is determined from published thermodynamic data. The governing equations are solved with finite element methods. We use 1322 axis-symmetric 8-node-solid-elements in the whole computational domain. As shown by dimensional analysis, the problem can be considered to be a static load case. The pressure load is applied incrementally in order to achieve converged solutions at 10 load steps. Successive refinement of the computational mesh did not significantly influence the results.

RESULTS

Our simulation results are compared to experimentally determined volume reduction at pressures up to 250 MPa published in [4]. Generally, it can be stated that the data exhibit a good overall agreement, where the maximum deviation does not exceed 6 %. This is most probably related to the fact that experimental volume measurements are based on the assumption that the cells have a spherical shape.

Application of a pressure load of 400 MPa generates a strong deformation of the initially spherical vacuole and nucleus (Figure 2). The overall shape of the cell approaches a spherical shape. The inner part of the cell remains in a hydrostatic stress state with zero von-Mises stresses. The maximum von-Mises-stress is located in the cell wall around $z = 0$ (coordinated system see fig. 1) and adopts values of up to 64 MPa. The authors of [2] observe ex-situ that the membranes of the organelles are all disrupted after a high pressure treatment at 400 MPa at ambient temperature. The outer shape of the organisms remains unaffected in this case. The present contribution reveals that at any pressure level maximum effective strain values are located in the membranes of the organelles. According to the observations in [3] an estimate of the critical effective strain of $\varepsilon_{VM,f} = 0.8$ upon failure of the organelle membranes can be delivered from the present load case at 400 MPa.

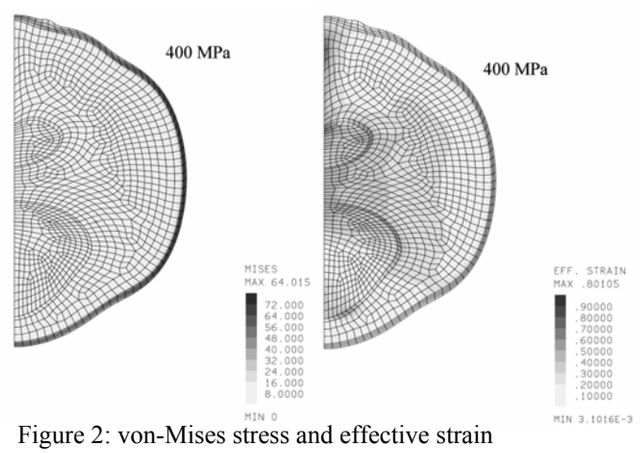


Figure 2: von-Mises stress and effective strain distribution of the 400 MPa load case

Ex-situ investigations of yeast cells treated at pressures of 400 MPa and 500 MPa [2], and critical values of the von-Mises stress upon failure for the cell wall material [3] at ambient non-hydrostatic conditions can be correlated to the results of the present analysis. The authors of [2] observe disruption of the cell wall at pressures above 400 MPa, while a von-Mises stress for failure of the cell wall is given in a range of $\sigma_{VM,f} = 70 \pm 4$ MPa [3]. Figure 2 shows a maximum von-Mises stress of 64 MPa in a 400 MPa load case being slightly below this critical range. Latter is completely covered at a pressure load between 415 and 440 MPa.

In addition to that, it can be concluded from the dimensional analysis of the mechanical problem, that transient pressure application cycles in a high hydrostatic pressure process do not generate any dynamic response of the cell. Structural inactivation of the cells (e. g. damage of the cell wall or membranes) is a result of static load on the cell and can not be enhanced by transient pressure application. The latter has to be expected if the coefficient of the inertia term of the non-dimensional equation of motion takes on values of the order of magnitude of one corresponding to a frequency of approximately 700 MHz. This value is far beyond the range of current application in HHP processing.

CONCLUSION

Referring to the questions formulated in the introduction following conclusions can be drawn: The interior of the cell is exposed to hydrostatic stress conditions as long as the material properties of the organelles do not differ much from those of the cytoplasm. The cell organelle membranes are strongly deformed prior to any damage of the cell wall. Pressure loads between 415 MPa and 460 MPa induce mechanical cell wall damage. Compared to constant pressure application, transient pressure protocols in HHP processing do not enhance the mechanical action on the yeast cells. A dynamic response of the cells can only be expected at pressure oscillation frequencies superior to 700 MHz.

References

[1] Hartmann, C., Delgado A.: Numerical Simulation of the Mechanics of a Yeast Cell under High Hydrostatic Pressure. *J. of Biomechanics*, in press, 2004

[2] Shimada, S., Andou, M., Naito, N., Yamada, N., Osumi, M., Hayashi, R.: Effects of hydrostatic pressure on the ultrastructure and leakage of internal substances in the yeast *Saccharomyces cerevisiae*. *Applied Microbiology and Biotechnology* **40**:123-131, 1993.

[3] Smith, A.E., Moxham, K.E., Middelberg, A.P.J.: Wall material properties of yeast cells. Part II. Analysis. *Chemical Engineering Science* **55**:2043-2053, 2000.

[4] Perrier-Cornet, J. M., Maréchal, P. A., Gervais, P.: A new design intended to relate high pressure treatment to yeast cell mass transfer. *J. of Biotechnology* **41**:49-58, 1995.

MODELS OF HAIR CELL BUNDLE FUNCTIONING

Alexander V. Kondrachuk, Vasyl P. Lukomsky, Ivan S. Gandzha,
Institute of Physics, National Academy of Sciences, Kyiv, Ukraine;
kondr@kondr.kiev.ua / Fax: 38–044–2651589

Summary The model of the mechanoreceptor hair cell bundle (HCB) interaction with the moving viscoelastic gel was considered for two extreme cases:1) the HCBs exactly follow the gel displacement; 2) stiff stereocilia and weak surrounding gel allow the motion of the bundle relative to the gel. The results suggest that the HCB structure is designed to reconstruct the temporal pattern of external acceleration from nonhomogeneous displacement (or its velocity) of the gel in the form of temporal pattern of cell depolarization.

Animals utilize sensory (vestibular, lateral-line, auditory) systems with hair cells to detect a variety of mechanical stimuli from their environment. The forces exerted on the hair cell (cilia) bundle (HCB) due to its interaction with the moving environment result in deformation of the HCB and stretching or shortening of the special fine strands located between stereocilia and called "tip-links". It leads to cell polarization that modulates neural activity of the afferent. The moving medium may be viscoelstic gel or viscous fluid. The HCB interaction with the moving environment is a key problem of sensory organs utilizing the HCBs. Three features of this system are common for all sensory organs with the HCBs: 1) there is a surface bordering the moving medium that results in spatial dependence of displacements (gel) or velocity (fluid) on the distance from the surface; 2) the HCBs protruding from this surface are embedded in this medium, 3) the heights of cilia are monotone varying. The present modeling is focused on the vestibular system, in particular, on an otolith organ that is responsible for perceiving linear accelerations. Transformation of the mechanical input in the chain: acceleration of otolithic membrane (OM)-displacement of the OM gel layer relative to macular surface–deflection of hair cell bundles located on this surface-deformation of the system of tip-links- formation of temporal pattern of polarization was studied using the simplified analytical models of these stages of conversion of mechanical stimulus into the HCB electrical response. The dynamic behavior of an otolithic membrane (OM) was considered using homogeneous viscoelastic (Kelvin-Voight) model of the OM (Fig.1). Let the acceleration vector (A) be parallel to the macular plane (x-axis). The dynamic equation for the displacements $U_x(z)$ of the OM gel may be written as [5]:

$$\rho_{om}\frac{\partial^2 U_x}{\partial t^2}=\frac{E}{2(1+\sigma)}\frac{\partial^2 U_x}{\partial z^2}+\mu\frac{\partial^3 U_x}{\partial t\partial z^2}+\Delta\rho A_x a(t/T);\quad U_x(z=0,t)=0,\ dU_x/dz|_{z=h}=0 \qquad (1)$$

where $\Delta\rho=\rho_{om}-\rho_{endolymph}$, σ is Poisson's ratio, E and μ are the Young's modulus and dynamical viscosity of the OM gel substance. $A(t)=A_0a(t)$, A_0 is the magnitude of the OM acceleration.

Two alternative models of an "HCB-surrounding gel" interaction corresponding to extreme types of functioning of the HCB-gel system were analyzed [3,4]. In the Model 1 the HCBs passively follow gel deformation. This model suggests that: stereocilia are absolutely flexible and non-stretchable structures, the deformations of each stereocilium are independent, an existence of tip-links does not influence the deformation of the HCB, the structure of the HCB in a resting position may be approximated by a set of parallel stereocilia (Figs.1A, 1B); the result of mechanical stimulation of the OM is the change of lengths of the tip-links (l_{ti}) corresponding to neighboring stereocilia. In this case, the time-dependent change of the tip-link lengths due to displacement of the gel will be determined by the trajectories of the points of gel corresponding to the ends of the tip-links between the neighboring stereocilia. Therefore, to find the dynamics of tip-links of stereocilia in the framework of this model, we have to determine the dependence of OM displacements ($U_x(z)$,Eq.1) on the distance from the macular plane, and then, to find the trajectories of the ends of tip-links between i- and (i+1)- stereocilia.

Model 2 suggests that: the HCBs are rather stiff cylinders that can be bent only at the place of their fixation to the surface; their deflection due to the motion of viscous surrounding gel corresponds to the behavior of straight cylinders pivoting around their bases in the moving fluid [1], an existence of tip-links does not influence the deformation of the HCB. Thus due to the stiffness of HCB their deformation is controlled by viscous forces integrated over the length of cylinders and may not follow local deformation of surrounding gel. The deflection of this structure caused by viscous interaction with moving surrounding gel results in deformation of the HCB due to the shift of stereocilia rows relative to each other. Since the heights of the rows are different, their interaction with viscous gel and thus the angles of deflection will be different for these rows. Although the results of application of the model of the action of viscous fluid on straight cylinder (stereocilia) to the HCB-OM gel interaction are mainly qualitative, this simplified model discloses major frequency sensitive features of such interaction. The viscous force exerted on the bundle from surrounding gel is proportional to the velocity of gel displacement relative to the stereocilia. Assuming that the motion of the HCBs does not influence the motion of the OM, we can use the solution of Eq.1 to determine the viscous force deflecting the HCB. Since the velocity of gel is proportional to the time derivative of external acceleration, it implies that depending on mechanical properties of the HCB the system of the HCB-OM gel may record either external acceleration or time variation of this acceleration, if the mechanism of depolarization formation in these two types of the HCBs is the same.

It is assumed [3] that in mechanoelectrical transduction process tip-link tensions produce cell depolarization, which is proportional to the number of open channels. We formulated the following simplified model of cell depolarization kinetics: the elongation of tip-links occurs due to stereocilia deflection; the critical (threshold) elongation triggers the

opening of ion-channel that results in generating cell depolarization (signal) of unit amplitude; the signal remains constant until the elongation exceeds the threshold value a_c; the cell depolarization F(t) is proportional to the sum of signals produced by all ion channels open at the time t. Figs.1C,1D illustrate the result of calculations corresponding to Model 1 in the case of periodic stimulation of the OM. This is simplified imitation of the experiment [2].
The results of modeling show that: 1) depending on its parameters the system "HCB-OM gel" may function as an accelerometer (Model 1-the case of strong gel-HCB interaction) or measures the time derivative of external acceleration (Model 2-the case of weak gel-HCB interaction); 2) the following hypothesis may be proposed: the HCB structure with stereocilia of varying heights is designed to transform the temporal pattern of external acceleration (or its time derivative) to temporal pattern of cell depolarization by measuring spatial distribution of displacements (or velocities) of gel caused by this acceleration near the surface.

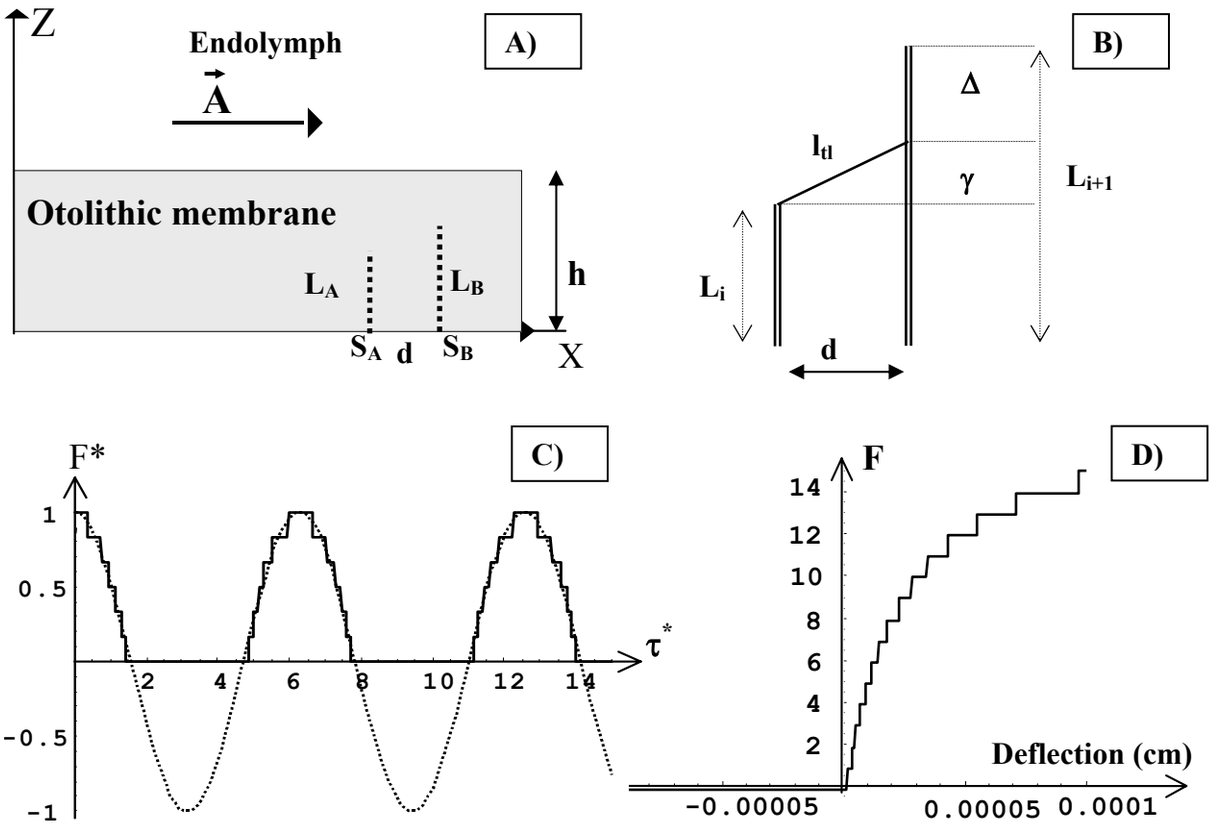


Fig.1. A) Model structure of otolithic membrane: h is the thickness of gel layer (~30μm), d is the distance (~1 μm) between the bases of stereocilia (S_A and S_B), L is stereocilia length (~5-20 μm). B) Simplified structure of the hair cell bundle; l_{tl} is the tip-link length. C) Kinetics of depolarization F^* in Model 1 (F^* denotes F(t) normalized to 1). Dotted lines are for gel displacements $\varphi(\tau^*)=\cos(\tau^*)$,$\tau^*=t/T_2$. Firm lines are for depolarization when the thresholds of tip-links triggering are linear function of stereocilium number i: $a_c=a_0(1+\upsilon i)$) ($a_0=10^{-9}$m, $\upsilon=3$, $L_0/h=0.5$, number of stereocilia k=20). D) The dependence of the number of activated tip-links (F) on the deflection of longest stereocilia if $\varphi(\tau^*)=\cos(\tau^*)$.

References

[1] Henson, B.L., Wilkens L.A., A mathematical model for the motion of mechanoreceptor hairs in fluid environments. *Biophys. J.*, **27**, 277- 286, 1979.

[2] Hudspeth, A.J., Extracellular current flow and the site of transduction by vertebrate hair cells. *J.Neurosci*. **2**,1-10, 1982.

[3] Kondrachuk, A.V., Models of the dynamics of the otolithic membrane and the hair cell bundle mechanics. *J.Vest.Res*., **11**, 29-38, 2001a

[4] Kondrachuk, A.V. Models of otolithic membrane - hair cell bundle interaction. *Hear Res.,* **166**, 96-112, 2002

[5] Landau, L.D., Lifshitz E.M., *Theory of Elasticity,* 3rd Ed., Oxford Pergamon Press, 1986

MEASURING THE MECHANICAL PROPERTIES OF SOFT BIOLOGICAL TISSUES

Edoardo Mazza*, Alessandro Nava*, Davide Valtorta*
ETH Zurich, Department of Mechanical Eng., IMES, 8092 Zurich, Switzerland

INTRODUCTION

The mechanical characterization of soft biological tissues is essential to a number of medical applications, such as surgery planning, surgical training deploying virtual reality based simulators, or diagnosis. Quantitative data sets are available on the in-vivo mechanical properties of soft tissues in animal organs, but very limited data are available on the behavior of soft tissues associated with human organs. This deficiency is primarily due to the severe technical and ethical problems related to the experiments. In this work two new techniques are presented for soft tissue's mechanical testing, that were designed to fulfill the requirements for in-vivo measurements on human organs during open surgery: the aspiration test and the dynamic torsion test.

In the aspiration test relatively large local tissue deformations are imposed and the time dependent behavior of the tissue can be observed. The experiment is characterized by well defined kinematic and static boundary conditions and the time required for each measurement is very short (of the order of 20 seconds). This device has been used already for the in-vivo characterization of the mechanical behavior of human organs during open surgery.

In the dynamic torsion test the soft tissue is made part of a vibrating system. The complex shear modulus of the soft tissue is determined from the transfer function of the system. Measurements are performed at frequencies ranging from 1 to 10 kHz. This non-destructive technique can be applied for in-vivo measurements.

The goal of the quasi-static and dynamic experiments is to derive a constitutive model of the soft tissue. Typically a large number of material constants need to be determined for model formulations that account for viscoelastic or viscoplastic behavior at large deformations. Numerical methods are used for the solution of the inverse problem. From the quasi-static and the dynamic experiments different types of constitutive model are evaluated in their capability of describing the soft tissue response.

EXPERIMENTAL PROCEDURES

Aspiration test

The aspiration test has been designed for in-vivo applications addressing issues associated with: safety, sterilization, space limitation and a short data acquisition cycle time. The device consists of a tube in which the internal pressure can be controlled according to a desired pressure law. The experiment is performed by (i) gently pushing the tube against the tissue to ensure a good initial contact, (ii) creating a (time variable) vacuum inside the tube so that the tissue is sucked in through the aspiration hole (diameter of 10 mm).

Assuming the tissue to be isotropic and homogeneous in the small portion under deformation, a complete description of the deformed tissue can be given by monitoring the side-view profile of the tissue during its deformation. The profile is extracted from the images reflected by a mirror and are captured by a digital camera.

With a pressure control system a predefined pressure law can be obtained inside the tube. Typically the pressure is decreased to a certain vacuum level (in the order of 700 mbar absolute pressure, deemed insufficient to cause tissue damage), is kept constant for a couple of seconds and is than increased back to atmospheric pressure. Each such cycles lasts for about 20 seconds and can be repeated several times, in order to study tissue's preconditioning, [1]. Time histories of measured pressure and deformation profiles are the input data used to evaluate the mechanical properties and to determine the constitutive model.

Dynamic Torsion test

The experimental set-up consists of a cylindrical rod which is excited at its torsional eigenfrequencies (from 1 kHz to 10 kHz) by an electromagnetic transducer (with actuator and sensor function). One extremity of the rod is in contact with the soft tissue. Perfect adherence is ensured by vacuum clamping. The damping characteristics and the resonance frequency of the vibrating system are inferred from the control variables of a phase stabilization loop. Due to the contact with the soft tissue, changes occur in the Q-Factor and in the resonance frequency of the system. These changes are quantified from the differences between a calibration run (without soft tissue contact) and a measurement with soft tissue contact. Based on an analytical model, the mechanical impedance of the material in contact is determined from these data and the complex shear modulus G* is evaluated for each resonance frequency. The dependency of the complex shear modulus on contact force, vibration amplitude, frequency, and number of loading cycles can be studied with this experiment.

CONSTITUTIVE MODELING AND DETERMINATION OF MATERIAL PARAMETERS

Aspiration test

Large deformations occur in the aspiration test, up to stretches in the order of λ=1.3. According to the model proposed by Fung, [1], a common approach to modeling large deformations in soft tissues is by "quasi-linear viscoelsticity". The tissue's hyperelastic response is described in terms of a strain energy function U (we use the so called "reduced polynomial form"); viscoelasticity is taken into account by applying time dependent (relaxation) coefficients to the constants that define the energy function (we express these coefficients in terms of Prony series).

Our quasi-linear viscoelastic model contains 13 parameters, which are determined from the experiments by finite element calculations: (i) the experiment is simulated by a finite element model in which the (time dependent) aspiration pressure is imposed as kinetic boundary condition; (ii) the material constants are determined iteratively from the comparison of calculated and measured soft tissue deformation. With our refined optimization procedure and the current hardware implementation the time required for the definition of the best-fit parameter set is approximately two hours.

Experiments with repeated aspiration cycles were performed to study soft tissue's preconditioning: the internal structure of the material changes due to mechanical loading and eventually reaches a steady state in repeated cycling. The initial response and the changes of the response in early loading cycles is more important for a number of medical applications than the stabilized (preconditioned) mechanical behavior. With the multiple cycle aspiration experiments the history dependence of the mechanical response can be studied. As clearly shown by the tests on animal organs, the evolving cyclic response cannot be described by a quasi-linear viscoelastic model. The elastic-viscoplastic model proposed by Rubin and Bodner [2] is able to describe the relevant physical features of the soft tissue response, including preconditioning, recovery and anisotropy. We have implemented this model in the finite element code and use it for characterizing the soft tissue response in multiple cycle experiments.

Dynamic torsion test

Due to the high sensitivity of the sensor for vibration detection, the vibration amplitude of the dynamic torsion test can be kept very small, so that a linear viscoelastic material model represent a valid approximation for the evaluation of this experiment. In the current implementation, the soft tissue is modeled as a semi-infinite, homogenous, isotropic medium. A kinematic boundary condition is applied for the points in contact with the vibrating rod. The elastodynamic wave equation is solved for the specified torsional excitation. Depending on the soft tissue properties, shear waves (SH waves) propagate mainly in the radial direction or in the vertical direction, toward the tissue interior. From the analytical model, the mechanical impedance of the medium can be expressed as function of the complex shear modulus G* of the tissue. In this way, Q-factor and resonance frequency can be mapped to real and imaginary part of G*.

RESULTS AND CONCLUSIONS

The experimental techniques were applied on animal and human organs. From these experiments the reliability of the measurements has been evaluated. The results obtained from post-mortem aspiration experiments on human liver and kidney, [3], show that the method can describe the differences in the mechanical response of two types of organs and can distinguish between the mechanical behavior of a normal and a diseased liver. These results seem to indicate that the application of this technique can lead to the identification of objective parameters for diagnostic purposes.

A series of tests were performed on adult bovine liver using both aspiration test and dynamic torsion test. From the dynamic torsion test the complex modulus $G^*(\omega)$ is determined in the range of 1 kHz to 10 kHz. There is an appreciable difference in G* values obtained from measurements at the external skin (liver capsula) and in the liver interior. Based on the non-linear constitutive model determined in the aspiration test, a small strain shear relaxation module G(t) is calculated, from which the frequency dependant complex modulus $G^*(\omega)$ is readily derived. In this way the results from the quasi-static and dynamic experiments can be compared in the frequency domain. The constitutive behavior is characterized over a wide frequency range from the combination of the results of the two tests. In contrast with common assumptions, [1], a significant frequency dependency of $|G^*|$ is demonstrated by our measurements, Figure 1.

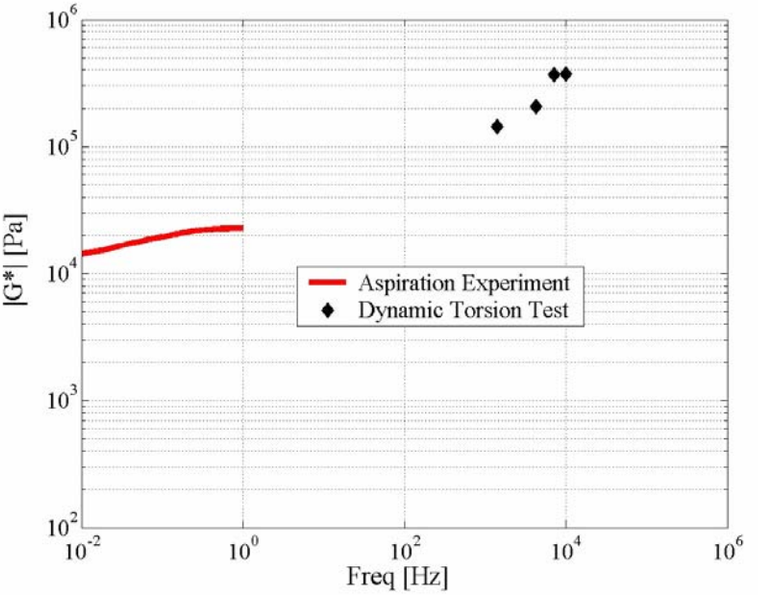


Figure 1: frequency dependence of the complex shear modulus (bovine liver)

References

[1] Y.C. Fung: Biomechanics, Mechanical Properties of Living Tissues, 2nd ed., Springer-Verlag, 1993

[2] Rubin M.B., Bodner S.R.: A three-dimensional nonlinear model for the dissipative response of soft tissue. *Int. J. of Solids and Structures* **39**:5081-5099, 2002.

[3] Nava A., Mazza E., Kleinermann F., Avis N. J., McClure J., Bajka M.: Evaluation of the Mechanical Properties of Human Liver and Kidney through Aspiration Experiments. *Technology and Health Care*, accepted for publication, 2003.

ANISOTROPIC HYPERELASTIC AND PSEUDO-HYPERELASTIC MATERIALS AND APPLICATIONS TO SOFT TISSUE MODELLING

Stanisław Jemioło[*], Józef Joachim Telega[**]
[*]*ISM, Warsaw University of Technology, Aleja Armii Ludowej 16, PL 00-049 Warszawa, Poland*
[**]*Polish Academy of Sciences, IPPT PAN, Swiętokrzyska 21, PL 00-049 Warszawa, Poland*

Summary A consistent mathematical model applicable to pseudo-hyperelastic behaviour of orthotropic soft tissues has been proposed. The model describes loading and unloading processes as well as the dissipation in cyclic process. An appropriate approximation of constitutive relationships in respect to Lagrange strain measure reduces them to the orthotropic model of the Saint-Venant-Kirchhoff. Having in mind available experimental data, our considerations have deliberately been restricted to the plane stress state.

INTRODUCTION

Experimental data clearly show that soft tissues are usually geometrically nonlinear [1]. Those tissues are usually inhomogeneous and anisotropic and only in the case of monotonically loading processes can be described as hyperelastic materials. Indeed, one-dimensional tests show that loading and unloading curve do not coincide, similarly to rubber materials [1,4]. In our earlier papers [3] we underlined that the description of pseudo-elasticity proposed by Fung [1] and employed in many papers is not adequate. In fact Fung's model is not appropriate both from the viewpoint of continuum mechanics and interpretation of experimental data as well as implementation of this model in FEM.

BASIC RELATIONS

We assume the existence of elastic pseudo-potential $P=\overline{P}(\mathbf{C},\mathbf{M},\eta)$, $\overline{P}(\mathbf{C},\mathbf{M},1)=\overline{W}(\mathbf{C},\mathbf{M})$. As usual, by $\mathbf{F}$ we denote the deformation gradient and $\mathbf{C}=\mathbf{F}^T\mathbf{F}$ is the right Cauchy-Green strain tensor, cf. [2]. To describe anisotropy we introduce a parametric tensor $\mathbf{M}$ (or a set of parametric tensors). The function $\overline{W}(\mathbf{C},\mathbf{M})$ is similar to the stored energy function of anisotropic hyperelastic material, cf. [3]. We assume that $J=\det\mathbf{F}>0$, and $\eta\in(0,1]$ as an additional parameter. In loading processes the material exhibits elastic properties with the energy density $\overline{P}(\mathbf{C},\mathbf{M},\eta)$ where $\eta=const$. Potential $P=\overline{P}(\mathbf{C},\mathbf{M},\eta)$ is called the pseudo-hyperelastic potential and satisfies the following conditions

$$\mathbf{T}=\frac{\partial\overline{P}(\mathbf{C},\mathbf{M},\eta)}{\partial\mathbf{C}}+\frac{\partial\overline{P}(\mathbf{C},\mathbf{M},\eta)}{\partial\mathbf{C}^T},\quad 0=\frac{\partial\overline{P}(\mathbf{C},\mathbf{M},\eta)}{\partial\eta}\ , \tag{1}$$

where $\mathbf{T}$ denotes the second, symmetric, Piola-Kirchhoff stress tensor. Conditions (1) ensure the fulfilment of balance of mechanical energy and permit to interpret the unloading process as a behaviour of an elastic material with the elastic energy different from that of the loading process. The parameter η is then an implicit, continuous function of $\mathbf{C}$ and $\mathbf{M}$. We assume that, cf. [4],

$$\overline{P}(\mathbf{C},\mathbf{M},\eta)=\eta\overline{W}(\mathbf{C},\mathbf{M})+\Phi(\eta)\ . \tag{2}$$

According to the assumption of existence of the natural state and using (1) we get $\overline{W}(\mathbf{I},\mathbf{M})=0,\ \Phi(1)=0,\ \overline{\mathbf{T}}(\mathbf{I},\mathbf{M},\eta)=\mathbf{0}$.
Equations (1) and (2) yield

$$\mathbf{T}=\eta\left[\frac{\partial\overline{W}(\mathbf{C},\mathbf{M})}{\partial\mathbf{C}}+\frac{\partial\overline{W}(\mathbf{C},\mathbf{M})}{\partial\mathbf{C}^T}\right],\quad -\frac{\mathrm{d}\Phi(\eta)}{\mathrm{d}\eta}=\overline{W}(\mathbf{C},\mathbf{M})\ . \tag{3}$$

Relation $(3)_2$ defines implicitly the parameter η as a function of $\mathbf{C}$ and $\mathbf{M}$. We assume that the unloading is associated with the decreasing of η, or in other words with the softening of material. The function $\Phi(\eta)$ is assumed to be a concave function; then from Eq. $(3)_2$ we conclude that η is a uniquely defined function dependent on $\overline{W}(\mathbf{C},\mathbf{M})$). In the first, primary, loading cycle we assume that $\eta=1$ whilst the unloading occurs for a certain value $\mathbf{C}_m$. Then Eq. $(3)_2$ gives: $-\frac{\mathrm{d}\Phi(1)}{\mathrm{d}\eta}=\overline{W}(\mathbf{C}_m,\mathbf{M})\equiv W_m$. The last relation means that η depends also on the value of energy W_m. For a complete unloading ($\mathbf{C}=\mathbf{I}$) we assume that η achieves a minimum value η_m. The pseudo-potential assumes then the residual value $\overline{P}(\mathbf{I},\mathbf{M},\eta_m)=\Phi(\eta_m)$. The residual or irreversible value of the energy is interpreted as the energy necessary to provoke the degradation of material. According to the second law of thermodynamics we assume that $\dot{\Phi}(\eta_m)\geq 0$. Here the dot denotes an arbitrary time-like parameter. Equations (3) and (4) imply that it is convenient to postulate a functional dependence for $\Phi(\eta)$ with respect to η, as a function of η and W_m. Let, cf. [4]:

$$-\frac{\mathrm{d}\Phi(\eta)}{\mathrm{d}\eta} = c_1\,\mathrm{Erf}^{-1}\left[c_2(\eta-1)\right] + W_m, \tag{4}$$

where c_1 and c_2 are positive constants, and $\mathrm{Erf}^{-1}(.)$ stands for the inverse of the error function Erf(.).

PSEUDO-HYPERELASTIC ORTHOTROPIC MATERIALS IN THE CASE OF PLANE STRESS STATE

According to the general representation of 2D orthotropic scalar function [3], The stored energy function can be written as follows: $\overline{w}(N_i) = \overline{w}\left(\mathrm{tr}(\mathbf{E}\mathbf{M}_1), \mathrm{tr}(\mathbf{E}\mathbf{M}_2), \mathrm{tr}\mathbf{E}^2\right)$, $\widetilde{W}(J_i) = \widetilde{W}\left(\mathrm{tr}(\mathbf{C}\mathbf{M}_1), \mathrm{tr}(\mathbf{C}\mathbf{M}_2), \det\mathbf{C}\right)$. Here N_i are the so-called orthotropic invariants of the Lagrange strain measure $\mathbf{E} = (\mathbf{C}-\mathbf{I})/2$ whilst J_i denote the invariants of the right Cauchy-Green tensor. The parametric tensors are defined as follows: $\mathbf{M}_1 = \mathbf{m}_1 \otimes \mathbf{m}_1$, $\mathbf{M}_2 = \mathbf{m}_2 \otimes \mathbf{m}_2$. We assume that each of the stored energy function can be, in the range of relatively small strains measured by $\mathbf{E}$, approximated by the stored energy function of the orthotropic SVK (Saint-Venant-Kirchhoff) material

$$\overline{w}(N_i) = w_{SVK}(N_i) + O\left(\|\mathbf{E}\|^3\right), \quad w_{SVK}(N_i) = \frac{1}{2}\left[a_1(N_1)^2 + a_2(N_2)^2 + a_3 N_1 N_2 + a_4 N_3\right]. \tag{5}$$

where a_k $(k = 1,...,4)$ are elastic constants. We propose the following generalization (GSVK) of the stored energy function $(5)_2$:

$$\widetilde{W}(J_i) = \frac{1}{8}\left\{a_1(J_1-1)^2 + a_2(J_2-1)^2 + a_3(J_1-1)(J_2-1) + a_4\left[(J_1+J_2)^2 - 2(J_1+J_2)\right]\right\} + \frac{1}{2}a_5(J_3-1)^2 - \frac{1}{4}a_4\ln(J_3),$$

where a_5 is positive constant. The model GSVK eliminates the fundamental, unrealistic predictions of the model SVK for significant homogeneous deformations in the case of compression. Similarly to Fung's model [1], one can propose the following generalization of $\widetilde{W}(J_i)$ (FGSVK): $\widetilde{W}_F(J_i) = \frac{1}{a}\left(e^{a\widetilde{W}(J_i)} - 1\right)$, where a is a positive constant.

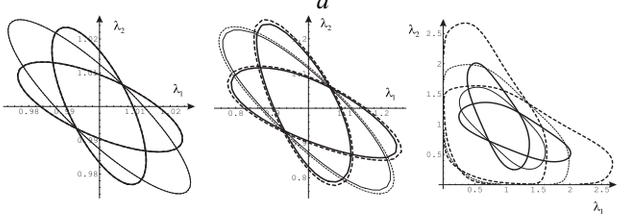


Fig. 1. Comparison of level sets for the stored energy functions of GSVK and FGSVK hyperelastic models. The curves correspond to two-dimensional tests.

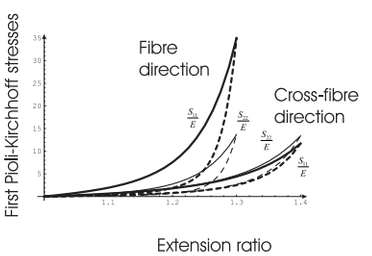


Fig. 2. FGSVK pseudo-hyperelastic model. Comparison of loading and unloading diagrams.

CONCLUSIONS

We have proposed a pseudo-hyperelastic model of soft tissues. The model describes loading and unloading processes as well as the dissipation in cyclic process. An appropriate approximation of constitutive relationships in respect to Lagrange strain measure reduces them to the orthotropic model of the Saint-Venant-Kirchhoff. Then one can correctly interpret the parameters involved in the proposed model and to impose physically motivated restrictions on those parameters.

References

[1] Fung Y.C.: Biomechanics, mechanical properties of living tissues, Springer-Verlag, NY 1993.
[2] Ciarlet P.G.: Mathematical elasticity, North-Holland, Amsterdam 1988.
[3] Jemioło S., Telega J.J.: Modelling elastic behaviour of soft tissues. Part I.; Part II. Transverse isotropy. *Eng. Trans*., **49**, 213-281, 2001.
[4] Ogden R.W., Roxburgh D.G.: A pseudo-elastic model for the Mullins effect in filled rubber. *Proc. R. Soc. Lond. A*., **455**A, 2861-2877, 1999.

MOLECULAR DYNAMICS STUDY OF PERMEATION PROCESS OF SMALL MOLECULES THROUGH A LIPID BILAYER

Taisuke SUGII*, Shu TAKAGI*, and Yoichiro MATSUMOTO*
*Dept. of Mech. Eng., The University of Tokyo, 7-3-1, Hongo, Bunkyo-ku, Tokyo, 113-8656, Japan

Summary In this study, the transport characteristics on the lipid bilayer were analyzed using the molecular dynamics method. We calculated the free energy profiles of several small molecules across the three kinds of lipid bilayers using the cavity insertion Widom method. Furthermore, the three dimensional instantaneous potential field (van del Waals potential field and electrostatic potential field) was also calculated.

INTRODUCTION

The self-assembled amphipathic molecules in water solutions, such as surfactants or lipids, form micelles or bilayers, etc. Especially in a living body, the lipid bilayer forms the basic structure of bio-membranes and supports the various life activities. For example, considering the transport phenomena by simple diffusion, permeation of water molecules or carbon dioxide through a bio-membrane plays an important role. Furthermore, a liposome, that is a vesicle formed from lipid molecules, is useful for an investigation of biological membranes. And many applications are proposed, for instance, the Drug Delivery System and the artificial oxygen carrier. Although the elucidation of the molecular transportation through a lipid bilayer membrane is very important in such biochemical processes, experimental observation has much difficulty and even the mechanism of the molecular penetration is not understood clearly. Hence, in this research, we investigate the transport phenomena through a lipid bilayer. Recently, a cell membrane and a liposome are actively studied in various fields. Marrink et al. calculated the free energy profile of H_2O, NH_3, O_2 and the LJ particles with various radii across the DPPC membrane using the molecular dynamics method [1, 2]. For calculating the free energy, they used several different methods in the different region. More recently, Jedlovszky et al. [3] calculated the profile of the several small molecules using DMPC membrane by the Monte Carlo method. These results indicated that the non-polar molecules exist stably inside the lipid membrane while the interior hydrophobic region works as the energy barrier for the polar molecules. In this research, using the molecular dynamics method, the free energy profiles of small molecules (O_2, CO, NO, H_2O, and several artificial diatomic molecules) across the three kinds of pure lipid membranes (DLPC, DMPC, and DPPC) were calculated. Moreover, we calculated the vdW potential field and the electrostatic potential field of water-membrane system. The potential field is very important for an investigation of transport phenomena because it can represent the local and instantaneous state of the system.

CALCULATION METHODS

We used the three kinds of pure lipid membranes, which consist of DLPC, DMPC, and DPPC molecules, respectively. The difference between the three lipid molecules is the hydrocarbon chain length, that is, DLPC, DMPC, and DPPC molecules have 12, 14, and 16 carbons in each chain, respectively. The each system consists of 64 lipid molecules and 1600 TIP3P water molecules. The potential parameter was taken from Smondyrev et al [4]. The lipid bilayer was constructed using the molecular coordinates of DMPC crystal structure obtained from the x-ray analysis and added two carbons to each hydrocarbon chain for DPPC and reduced two carbons for DLPC. We carried out the calculation in $NP_n\gamma T$ ensemble [5]. We set the reference normal pressure P_{n0}, the reference surface tension γ_0, and the reference temperature T_0 to 1 atm, 0 dyn/cm, and 320 K, respectively. The total calculation time was 2.0 ns.
We calculated the free energy profiles across the membrane using the cavity insertion Widom method [3, 6]. According to this method, the excess chemical potential at position z (z is the normal direction to the membrane.) is calculated as,

$$\mu^{\mathrm{exc}}(z) = -kT \ln \left\langle \exp\left[-\beta v_{N+1}(\mathbf{r}^N) \right] \right\rangle - kT \ln \left\langle P_{\mathrm{cav}}(z) \right\rangle \ . \tag{1}$$

Here, $\mu^{\mathrm{exc}}(z)$ is the excess chemical potential at position z. $v_{N+1}(\mathbf{r}^N)$ is the potentail energy interacting between the test particle inserted in the system and the rest particles. $P_{\mathrm{cav}}(z)$ is the probability of finding the cavity of the radius R_{cav} in the system. We used the results of last 240 ps for calculating the free energy profiles.
The free energy profile mentioned above is an averaged feature over the time and the space. However, when considering the transportation phenomena of the small molecules, the local and instantaneous change of the potential field is also important. Hence, we calculated the vdW potential field (not shown here) and the electrostatic potential field by inserting the test particle into the grid points in the simulation cell. In the calculation of the electrostatic potential field, we used the smoothed particle charges by the Gaussian function [7]. The electrostatic potential becomes,

$$\phi_{\mathrm{elc}}(\mathbf{r}) = \frac{1}{4\pi\varepsilon_0} \sum_i \sum_{\mathbf{n}} q_i \frac{\mathrm{erfc}\left[a_d \left| \mathbf{r}_i + \mathbf{R} - \mathbf{r} \right| \right] - \mathrm{erfc}\left[a \left| \mathbf{r}_i + \mathbf{R} - \mathbf{r} \right| \right]}{\left| \mathbf{r}_i + \mathbf{R} - \mathbf{r} \right|} + \frac{1}{V\varepsilon_0} \sum_i q_i \sum_{\mathbf{G} \neq \underline{0}} \frac{1}{\left| \mathbf{G} \right|^2} \exp\left(-\frac{\left| \mathbf{G} \right|^2}{4a_d^2} \right) \exp\left[i\mathbf{G} \cdot (\mathbf{r} - \mathbf{r}_i) \right] \ . \tag{2}$$

Here, a is a constant number representing the envelope of the Gaussian function. The above expression includes some modifications to the usual Ewald method.

RESULTS AND DISSCUSSION

The snapshot of the simulated DMPC membrane is shown in Fig. 1. Our results show good agreement with the other experiments and simulations, for example, about the order parameter of hydrocarbon chains and the electron density profiles. The calculated free energy profiles are shown in Fig. 2. Here, the mid-plane of the lipid bilayer was set to z = 0. We investigated the transport phenomena in two ways, that is, changing the solute molecules and changing the membrane molecules. Figure 2 (a) shows the free energy profiles of O_2 (non-polar) and the artificial molecules across the DMPC membrane. The artificial diatomic molecules have the dipole moment of 0.5 D, 1.0 D, 1.5 D, and 2.0 D in addition to the vdW potential parameter same as O_2. The results clearly indicate that the non-polar molecule is stable in the center region of the bilayers, and becomes unstable relative to the outside of the membrane (bulk water) with increasing the dipole moment. Accordingly, the stable region (free energy minimum) appears near the lipid/water interface region with an increase of the dipole moment. And in the center region of the membrane, the polarity of the solute molecules has little effect on the profiles. The interface region works as a relatively higher energy barrier in all case. Figure 2 (b) shows the free energy profiles of H_2O across the DLPC, DMPC, and DPPC membrane. The energy barrier at the interface is not found in this case. The width of the energy barrier inside the membrane spreads with increasing the chain length, though the height doesn't almost change. This is probably because the distance from the lipid/water interface is the dominant factor in deciding the free energy of the polar solute.

Figure 3 shows the electrostatic potential field at x = 0 plane of DMPC/water system. The figures correspond to the results for the contribution of (a) the water molecules, (b) the lipid molecules, and (c) all of the molecules, respectively. It is shown that the water molecules make positive potential field inside and negative outside the membrane, and the lipid molecules work oppositely. This result qualitatively agrees with the statistical calculation results of the electrostatic potential by Shinoda et al [8]. Moreover, it is clear that each kind of molecules is counteracting each other, especially around the head groups of the lipid molecules. The total potential due to all molecules is slightly positive inside. Besides, the potential field of the water molecules has small fluctuation spatially while that of the lipid molecules has large fluctuation.

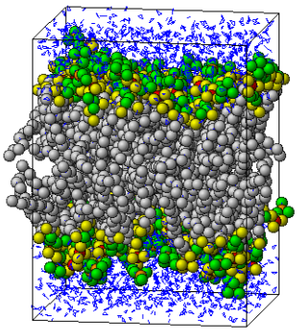


Fig. 1. Snapshot of the simulated membrane. The spheres and the blue line show the lipid molecules and the water molecules, respectively. The coloring scheme is P: Red, N: Orange, C: Green, O: Yellow, and Gray: hydrocarbon chains.

References

[1] Marrink S. J., and Berendsen H. J. C., *J. Phys. Chem.*, **98**, 4155, 1994.
[2] Marrink S. J., and Berendsen H. J. C., *J. Phys. Chem.*, **100**, 16729, 1996.
[3] Jedlovszky P., and Mezei M., *J. Am. Chem. Soc.*, **122**, 5125, 2000.
[4] Smondyrev A. M., and Berkowitz M. L., *J. Comp. Chem.*, **20**, 531, 1999.
[5] Zhang Y., Feller S. E., Brooks B. R., and Pastor R. W., *J. Chem. Phys.*, **103**, 10252, 1995.
[6] Pohorille A., and Wilson M. A., *J. Chem. Phys.*, **104**, 3760, 1996.
[7] Takagi S., Uda T., Kikugawa G., and Matsumoto Y., *Proceedings of 3rd European-Japanese Two-Phase Flow Group Meeting*, *CD-ROM*, 2003.
[8] Shinoda W., Shimizu M., and Okazaki S., *J. Phys. Chem. B*, **102**, 6647, 1998.

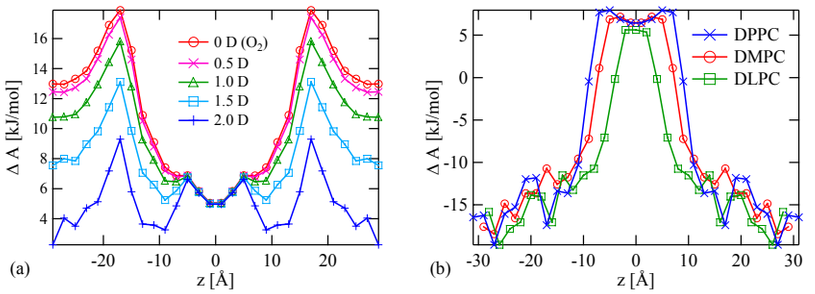


Fig. 2. (a) The free energy profiles of O_2 and the artificial molecules across the DMPC membrane. (b) The free energy profiles of H_2O across the DLPC, DMPC, and DPPC membrane.

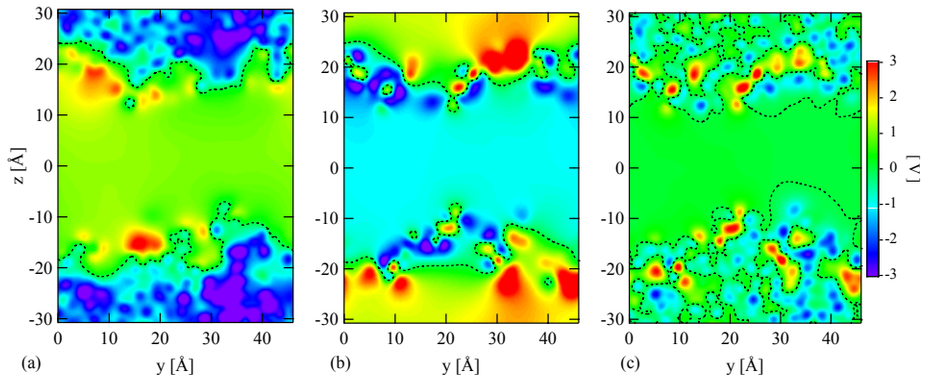


Fig. 3. The electrostatic potential field at x = 0, t = 2.0 ns. The contribution from (a) the water molecules, (b) the lipid molecules, (c) the all molecules, respectively. The black dashed line is 0 electrostatic potential surface.

XXI ICTAM, 15–21 August 2004, Warsaw, Poland

MODELING OF PERIODIC LOAD EFFECTS IN BONE TISSUE ADAPTATION

Tomasz Lekszycki
Institute of Fundamental Technological Research, Polish Academy of Sciences
Swietokrzyska 21, PL 00-049 Warszawa, Poland

Summary Bone functional remodeling is influenced by time characteristics of mechanical loading. Periodic loads usually have more effect on the adaptation and associated evolution of tissue structure than a static one. In the present work, an approach, based on the hypothesis of optimal response of bone, is proposed. It enables derivation for a viscoelastic material a family of adaptation formulas. In this derivation, an assumption is made that the bone is loaded harmonically, and that the frequency of oscillations is so small that the inertia effects are negligible. It follows that the stimulus is frequency dependent and that functional relation between stimulus and load frequency depends on the constitutive material model applied in the formulation. In some cases, the stimulus grows to some maximal value and next drops to zero with steering to infinity frequency of load oscillations. The results of sample computer calculations are included. The proposed approach might offer an attractive tool in investigations of frequency effect on bone remodeling but more research and experimental confirmation are necessary.

INTRODUCTION

It has been observed that bone functional remodeling is influenced by time characteristics of mechanical loading. Variable in time loads usually have more effect on the adaptation and evolution of tissue structure then the static one, see e.g. [1]. However this problem needs more theoretical and experimental investigations, see [2]. There exist proposals for adaptation models based on information concerning micro-damage accumulation, where the number of load cycles is included in the formulation, see [3]. In the present work we propose another approach, based on the hypothesis of optimal response of bone introduced in [4] and [5] and developed till now in context of elastic characteristics of bones. It also enables derivation of a family of adaptation laws for viscoelastic materials under an assumption that bone is loaded harmonically, and that the frequency of oscillations is so small that inertia effects can be neglected. It follows from this derivation that stimulus is frequency-dependent. Thus the rate of changes of tissue micro structure depends not only of the amplitude of loads, but also on their frequencies.

DERIVATION OF ADAPTATION RELATIONS

Assumptions

1) Material has viscoelastic characteristics, slowly evolving in time due to bone adaptation. 2) The mechanical load is varying harmonically in time, but the frequency of oscillations is small and the inertia effects can be neglected. 3) For the sake of simplicity and compactness the problem formulation is made in a space of complex functionals. 4) Two scales of time are introduced denoted by t and τ, the first is associated with load slow oscillations (period counted in seconds) while the second is associated with tissue structure evolution (counted in days).

Basic relations and optimization problem

The constitutive viscoelastic relation:

$$\tilde{\sigma}_{ij}(\mathbf{x},\tau,t) = \int_0^t G_{ijkl}(\mathbf{x},\tau,t-S)\,\frac{d\tilde{\epsilon}_{kl}(\mathbf{x},\tau,S)}{dS}\,dS \tag{1}$$

where G_{ijkl}, $\tilde{\epsilon}_{kl}(\mathbf{x},\tau,t)$ and $\tilde{\sigma}_{ij}(\mathbf{x},\tau,t)$ denote relaxation function, stress and strain fields respectively, t represents time and τ is a real-valued parameter. For the steady-state harmonic oscillations we can assume that

$$\tilde{\epsilon}_{kl}(\mathbf{x},\tau,t) = \epsilon_{kl}\,(\mathbf{x},\tau)\,e^{\imath\omega t}\,, \qquad \tilde{\sigma}_{ij}(\mathbf{x},\tau,t) = \sigma_{ij}\,(\mathbf{x},\tau)\,e^{\imath\omega t}\,. \tag{2}$$

In the above equations $\imath = \sqrt{-1}$, ω is a circular frequency of oscillations while $\epsilon_{kl}(\mathbf{x},\tau)$ and $\sigma_{ij}\,(\mathbf{x},\tau)$ denote complex strain and stress fields. After time elimination we obtain from equation eq.1,

$$\sigma_{ij}(\mathbf{x},\tau) = G^*_{ijkl}(\mathbf{x},\omega)\,\epsilon_{kl}(\mathbf{x},\tau)\,,\;\; G^*_{ijkl}(\mathbf{x},\tau) = k(\mathbf{x},\tau)\,[G'_{ijkl}(\omega) + \imath\, G''_{ijlk}(\omega)]\,, \tag{3}$$

$$\sigma_{ij}(\mathbf{x},\tau) = \sigma^R_{ij}(\mathbf{x},\tau) + \imath\,\sigma^I_{ij}(\mathbf{x},\tau)\,,\;\; \epsilon_{ij}(\mathbf{x},\tau) = \epsilon^R_{ij}(\mathbf{x},\tau) + \imath\,\epsilon^I_{ij}(\mathbf{x},\tau)\,, \tag{4}$$

where $\dot{k} = \frac{dk(\mathbf{x},\tau)}{d\tau}$ represents the control function responsible for bone micro-structure. Complex strain energy is

$$U(\tau,\omega) = \frac{1}{2}\int_V \sigma_{ij}(\mathbf{x},\tau)\epsilon_{ij}(\mathbf{x},\tau) = U^R(\tau,\omega) + \imath\,U^I(\tau,\omega)\,. \tag{5}$$

Comparison functional and associated objective functional can be defined respectively as,

$$C(\tau,\omega,k) = (U^R)^2 + (U^I)^2\,, \qquad G(\tau,\omega,\dot{k}) = \frac{dC(\tau,\omega)}{d\tau}\,. \tag{6}$$

Global and local constraints,

$$\int_V \dot{k}(\mathbf{x},\tau)\, dV = A(\tau)\,, \quad \int_V \dot{k}^2(\mathbf{x},\tau)\, dV = B(\tau)\,, \tag{7}$$

$$k_{min}(\mathbf{x},\tau) \le k(\mathbf{x},\tau) \le k_{max}(\mathbf{x},\tau)\,, \quad \hat{k}_{min}(\mathbf{x},\tau) \le \dot{k}(\mathbf{x},\tau) \le \hat{k}_{max}(\mathbf{x},\tau) \tag{8}$$

Adaptation relations

The global and local constraints can be attached to the objective functional by means of Langrange multipliers. To obtain the functional relation between the unknown control function $\dot{k}$ and actual mechanical state of tissue the hypothesis of optimal response can be used. From the stationary conditions of the objective functional G the set of mathematical relations follow, among them the "adaptation law" controlling the adaptation behavior of bone.

Example

In the previous paper by the author the trabecular adaptive material composed of a large number of elastic beams was discussed, see [4]. In the present example similar, but viscoelastic material is considered. In this case for a simple constitutive viscoelastic relation in the form

$$p_0\tilde{\sigma}_{ij}(\mathbf{x},\tau,t) + p_1\frac{\partial\tilde{\sigma}_{ij}(\mathbf{x},\tau,t)}{\partial t} + p_2\frac{\partial^2\tilde{\sigma}_{ij}(\mathbf{x},\tau,t)}{\partial t^2} = q_0\tilde{\epsilon}_{ij}(\mathbf{x},\tau,t) + q_1\frac{\partial\tilde{\epsilon}_{ij}(\mathbf{x},\tau,t)}{\partial t} + q_2\frac{\partial^2\tilde{\epsilon}_{ij}(\mathbf{x},\tau,t)}{\partial t^2}\,, \tag{9}$$

the stimulus $S(\mathbf{x},\tau)$ for known values of stress amplitude $\sigma_0(\mathbf{x},\tau)$ and variable k can be expressed in the following form,

$$S(\mathbf{x},\tau) = \frac{1}{2}\frac{\sigma_0^4(\mathbf{x},\tau)\; p_0^2 + (p_1^2 - 2p_0\; p_2)\;\omega^2 + p_2^2\omega^4}{k^3(\mathbf{x},\tau)\; q_0^2 + (q_1^2 - 2q_0\; q_2)\;\omega^2 + q_2^2\;\omega^2} \tag{10}$$

The relation between stimulus and circular frequency of periodic load for different sets of parameters is displayed in figure Fig.1 while in Fig.2 the result of computer simulation of bone adaptation is presented. The three pictures respect to the initial homogeneous situation, the result of bone adaptation to indicated external load, and the effect of bone remodeling after prosthesis implantation.

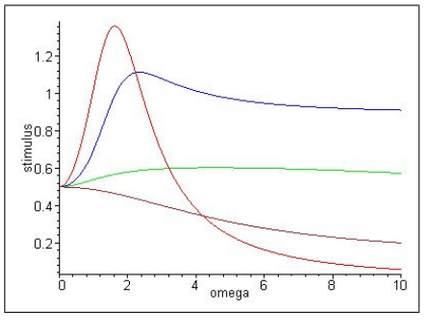


Fig. 1

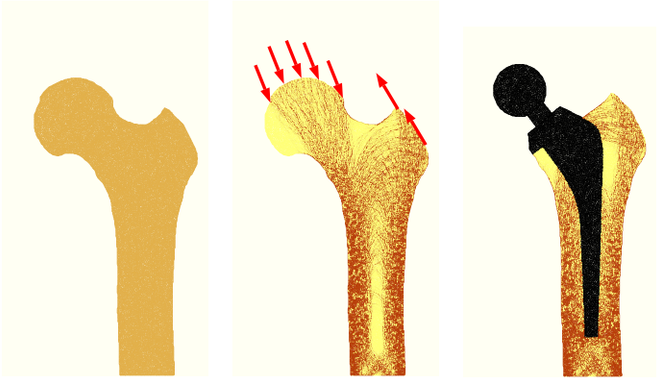


Fig. 2

CONCLUSIONS

The proposed approach enables derivation of different bone adaptation laws with viscoelastic effects included. It results from this derivation that the stimulus is frequency dependent and its functional relation on the frequency depends on the constitutive material model applied. For specific models the stimulus increases to some maximal value and then decreases to zero with growing to infinity frequency of load oscillations. The proposed theoretical approach may offer an attractive tool in investigations of frequency effect on bone remodeling but it needs more theoretical research and an experimental confirmation.

References

[1] Lanyon L.E., Rubin C.T. *J. of Biomechanics* **12**:897–905, 1984.
[2] Taber L.A.: *Appl. Mech. Rev.* **48**, 8:487–545, 1995.
[3] Prendergast P.: *J. of Biomechanics*, **27**:1067–1078, 1983.
[4] Lekszycki T.: *J. of Theoret. and Appl. Mech.*, **3**, 37:607–624, 1999
[5] Lekszycki T.: *Meccanica*, **37**:343–354, 2002

Acknowledgment

The present work was partly supported from the EU Research Project No. QLRT-1999-02014 (MIAB)

A PARTICLE METHOD COMPUTER SIMULATION OF BLOOD FLOW

Ken-ichi Tsubota, Shigeo Wada, Takami Yamaguchi
*Department of Bioengineering and Robotics, Graduate School of Engineering, Tohoku University, 01 Aoba, Aramaki, Aoba, Sendai 980-8579, Japan

Summary A particle method computer simulation of blood flow is proposed to directly evaluate mechanical interactions between red blood cells (RBCs) and plasma. A moving particle semi-implicit method was used for flow analysis of blood plasma. An elastic membrane model was used for RBC deformation. Two-dimensional simulation of blood flow revealed that an RBC moved into downstream direction due to pressure drop of plasma flow and deformed itself in a parachute shape, corresponding to experimental observations.

INTRODUCTION

The blood flow at microscopic level plays an important role in pathological events in the vascular system such as thrombosis and hemolysis. Recent studies show that the particle method is useful in evaluating the mechanical behavior of blood cells under blood flow [1]. Since this method needs only computing nodes and is free from meshes, it is advantageous in directly tracking the blood cell motion by a particle in the Lagrangian coordinates, and in tracking the interface between solid blood cell and liquid blood flow. In this study, a computer simulation method using particle method for blood flow is proposed to directly evaluate mechanical interactions of red blood cells (RBCs) and plasma.

METHODS

Blood Plasma Flow

Navier-Stokes equations were solved for blood plasma flow using a particle method in which continuum body was discretized by moving particles. In this study, moving particle semi-implicit (MPS) method [2] was used as a particle method, where the particle number density was kept to be its reference value in order to express the incompressibility condition. Spatial differentiation such as gradient and Laplacian of physical quantity was expressed by the sum of the interaction between two particles with weighing function of the particle distance.

RBC Deformation

A two-dimensional circular model of RBC membrane was constructed from $N = 60$ line elements, as shown in Fig. 1(a). Elastic energy of the membrane was considered for changes in the length of the element and the angle between the neighbor elements [3]. Based on minimum energy principle, the nodal displacements of the whole membrane were solved using the following equation:

$$m\ddot{\mathbf{r}}_i + \gamma\dot{\mathbf{r}}_i = -\partial W / \partial \mathbf{r}_i , \quad W = E + \Gamma , \qquad (1)$$

where i denotes node, $\mathbf{r}_i$ position vector, m mass, γ coefficient of viscosity, E total elastic energy of the membrane, and Γ penalty function of constant area constraint. As a result, shape change of a swollen RBC was obtained by decreasing the area by $70\,\%$, as shown in Fig. 1(b). The membrane changed its shape from the initial circular to the final biconcave as observed in the actual RBC. In the following sections, the final state of the RBC in this simulation was used for coupled analysis of the RBC deformation and plasma flow.

Particle Model of Blood Flow

A two-dimensional particle model was constructed for the blood flow between parallel rigid plates placed as vessel walls, as shown in Fig. 2. The model consisted of fluid particles for the blood plasma, elastic particles for the RBC membrane, and rigid particles for the vessel wall. The physical property of the plasma was assumed to be the same as that of water. The total number of the particles was 4737, and the mean distance between two particles was $0.5\ \mu$m. The size of the model was $75\ \mu$m in the flow (axial) direction and $12\ \mu$m between the walls. The RBC was placed

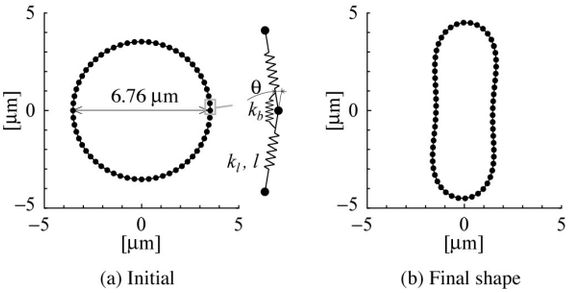


Fig. 1 Two-dimensional simulation of shape change of a swollen red blood cell using elastic membrane model based on minimum energy principle

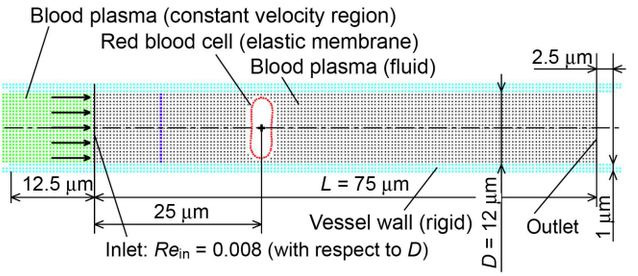


Fig. 2 A particle model of blood flow between parallel plates

between the walls and 25 μm away from the inlet. As a boundary condition, constant and uniform velocity in the axial direction was applied to the virtual fluid particles placed at the inlet, as shown in Fig. 2. Reynolds number to the distance between the plates D was 0.008. Zero pressure was applied at the outlet, and non-slip condition at the inner vessel wall. In the computer simulation, at first, the RBC was fixed and the plasma flow was solved by MPS method. The coupled analysis of the plasma flow and RBC membrane motion and deformation was carried after the plasma flow became steady. In solving the membrane deformation, fluid force was added to the right side of the Eq. (1).

RESULTS

A simulation result revealed change in RBC shape and position in flowing plasma, as shown in Fig. 3. At the initial state, the plasma flow with the fixed RBC was steady as shown in Fig. 3(a). Poiseuille flow of the blood plasma was obtained in the upstream side of the RBC. The plasma flowed between the fixed RBC and the vessel wall, as indicated by the arrows in Fig. 3(a), with decreasing its pressure. The fluid force due to pressure was higher at the upstream side than the downstream. The RBC was subjected to the pressure force near the wall, leading to compression of the RBC in the direction perpendicular to the vessel walls. These forces drove the RBC to move toward the downstream side, and caused deformation of the RBC in parachute-like shape, as shown in Figs. 3(b) and (c).

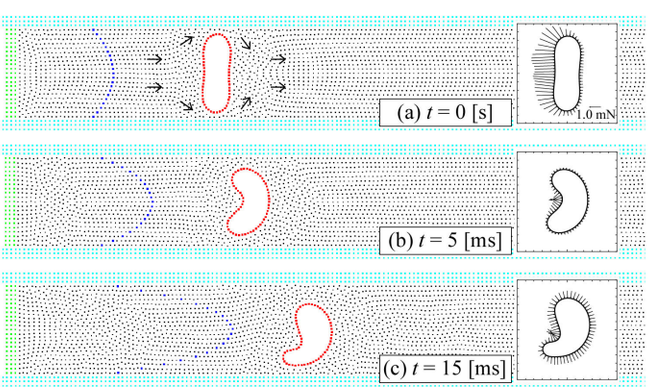


Fig. 3 Motion and deformation of RBC due to fluid pressure under blood plasma flow

DISCUSSION AND CONCLUSIONS

A particle method computer simulation was proposed for the microscopic blood flow by combining a MPS method for blood plasma flow and an elastic membrane model of an RBC. A two-dimensional simulation revealed temporal changes in the RBC movement in the downstream direction due to pressure drop of plasma flow. The RBC was deformed in a parachute shape during the movement, corresponding to experimental observations. The results indicate that the proposed method will give us an insight into the mechanism of the blood flow at from microscopic level of the blood cells and plasma and up to resultant rheological properties.

References

[1] Miyazaki H. and Yamaguchi T.: Formation and Destruction of Primary Thrombi under the Influence of Blood Flow and von Willebrand Factor Analyzed by a Discrete Element Method. *Biorheology* **40**:265-272, 2003.

[2] Koshizuka S. and Oka Y.: Moving-Particle Semi-Implicit Method for Fragmentation of Incompressible Fluid. Nucl Sci Eng **123**:421-434, 1996.

[3] Wada S. and Kobayashi R.: Numerical Simulation of Various Shape Changes of a Swallen Red Blood Cell by Decrease of its Volume. *Trans JSME* **69A**:14-21, 2003.

[4] Gaehtgens P., Duhrssen C. and Albrecht K. H.: Motion, Deformation, and Interaction of Blood Cells and Plasma during Flow through Narrow Capillary Tubes. *Blood Cells* **6**:799-817, 1980.

WRINKLING AND BUCKLING OF ISOTROPIC BIOLOGICAL TISSUES

Luigi Gambarotta, Roberta Massabò and Vittoria Villa
University of Genova, Department of Structural and Geotechnical Engineering, Genova, Italy

Summary The problem of the wrinkling and buckling of membranes characterized by an isotropic Tong-Fung type constitutive behavior has been formulated and solved within the framework of finite strain hyperelasticity. The formulation has been guided by the theories proposed by Wu and Canfield and Pipkin [1,2]. A criterion for the wrinkling based on the *natural width*, which defines the natural contraction of a membrane loaded in uniaxial tension, has been introduced. The out of plane geometric nonlinearities have been treated as constitutive nonlinearities through a modification of the elastic potential. Close form solutions have been found for the natural width and the modified elastic potential. The model has been implemented in a finite element code and applied to simulate procedures of reconstructive surgery where the extrusion of the wound edges may occur after the suture due to the buckling and wrinkling of the skin.

INTRODUCTION

The skin is a complex biological tissue that under short-term loading displays a highly nonlinear and pseudo-elastic mechanical response and finite strains. At low strains the response is mainly controlled by the elastin and at large strains by the collagen fibers, after they have become uncrimped. In addition, in its natural state the skin is stretched and subject to a state of biaxial tension.

The response of the skin under short-term loading is well described by the phenomenological model proposed by Tong and Fung [3]. The model defines the elastic potential $\hat{W}(\mathbf{E})$, or elastic strain energy per unit surface area, as the sum of a quadratic and an exponential function of the Green-Lagrange membrane strain tensor, $\mathbf{E}$, with components $\varepsilon_{\alpha\beta}$ ($\alpha, \beta = 1,2$). Under the assumption of isotropy, which well describes the skin at certain anatomical locations such as the scalp, and assuming the strains to be large enough so that the quadratic part of $\hat{W}$ becomes negligible, the model is:

$$\hat{W}(\mathbf{E})=c\,\exp\left\{B\left[\varepsilon_{11}^2+\varepsilon_{22}^2+2\beta\varepsilon_{11}\varepsilon_{22}+2(1-\beta)(\varepsilon_{12}\varepsilon_{21})\right]\right\}, \qquad (1)$$

where c, B and β are constants to be determined experimentally. The second Piola-Kirchhoff membrane stress tensor, PK2, is derived from (1) and its components are $\sigma_{\alpha\beta}=\partial\hat{W}/\partial\varepsilon_{\alpha\beta}$ ($\alpha, \beta = 1,2$). In [4] the authors calibrated the model (1) using *in vivo* tests on human scalp skin in order to describe the constitutive response of skin flaps within procedures of reconstructive and cosmetic surgery. The investigation also led to the determination of the principal stretch, λ_n, that defines the isotropic and homogeneous stress field of the scalp skin in its natural state. The inferred parameters, c = 1.13 kPa cm, B = 0.89, β = 0.6 and λ_n = 1.1, have been used to analyze the membranes shown in Figs. 1 and 2.

The model (1) does not describe the response of the skin in compression: like all elastic membranes, the skin has a negligible flexural stiffness and it buckles or wrinkles in the presence of strains that would require compressive stresses. Three distinct regions of behaviour may be identified in a stretched membrane (Fig. 1): taut regions, T, where the skin is in biaxial tension and the model (1) is applicable; buckled regions, B, where the skin has buckled and is inactive and wrinkled regions, W, where the skin develops a continuous distribution of infinitesimal wrinkles and is in a state of uniaxial tension in the direction of the wrinkles. Within procedures of reconstructive surgery the phenomena of wrinkling and buckling may lead to the extrusion of the edges of the wound after suture or *dog-ear* formation.

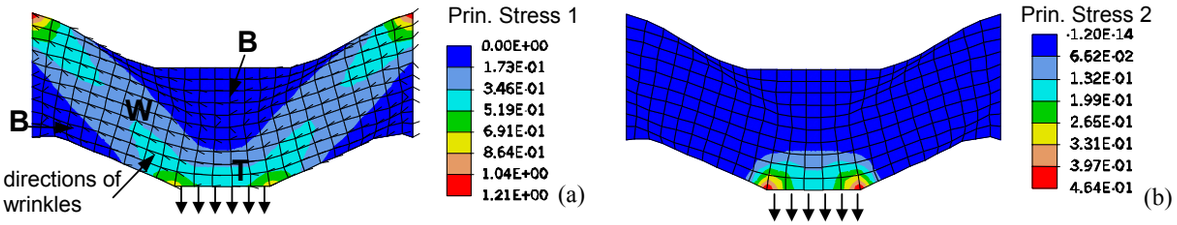


Figure 1: Principal membrane stress fields (PK2, in [kPa cm]) plotted on the actual deformed configuration of a rectangular membrane (reference configuration: 75×25×1mm) laterally clamped and subject to uniform vertical displacements v=10 mm as shown. Analysis performed using model (2) with elastic constants derived in [4]. Buckled regions, B, are inactive (blu in (a) and (b)), wrinkled regions, W, have only one non-zero principal stress (light blu in (a), blu in (b)) and taut regions, T, are in biaxial tension. Direction of the wrinkles defined by the principal stress direction (shown in (a) superposed onto FE mesh). The response is similar to that of polyethylene membrane tested in [5] and subject to same loading configuration (see Fig.1 of [5]).

MODEL, FINITE ELEMENT IMPLEMENTATION, SIMULATION OF RECONSTRUCTIVE SURGERY

In this paper the problem of the wrinkling and buckling of isotropic and hyperelastic membranes characterized by a Tong-Fung constitutive behaviour is formulated within the framework of finite strain elasticity following the approaches of Wu and Canfield and Pipkin [1,2]. It is assumed that the wrinkling occurs in the direction of the principal strains and that the directions of the principal Cauchy stresses do not change because of the wrinkling.

The membrane *natural width*, w, is first defined as the natural transverse contraction of a membrane in uniaxial tension. For a uniaxial tension σ_1 the natural contraction corresponds to the minimum of $\hat{W}$ in Eq. (1) with respect to

ε_{II} and is given by $\varepsilon_{II} = w(\varepsilon_I) = -\beta\varepsilon_I$. The natural width depends on the constant β, which is the parameter that at incipient deformation can be assimilated to a generalized Poisson coefficient, $\beta=(\partial\sigma_{11}/\partial\varepsilon_{22})(\partial\sigma_{11}/\partial\varepsilon_{11})^{-1}$.

A criterion for the wrinkling/buckling of the membrane is set up in terms of w and the principal strain components, ε_I and ε_{II}, and a *relaxed energy density* is introduced through a modification of $\hat{W}$ to describe the actual stress fields:

	Criterion for wrinkling/buckling	Relaxed energy density
Taut regions:	if $\varepsilon_I \geq -\beta\varepsilon_{II}$ and $\varepsilon_{II} \geq -\beta\varepsilon_I$	$\hat{W}_{\text{rel}}(\varepsilon_I,\varepsilon_{II})=\hat{W}(\mathbf{E})=c\,\exp\left\{B\left[\varepsilon_I^2+\varepsilon_{II}^2+2\beta\varepsilon_I\varepsilon_{II}\right]\right\}$
Wrinkled regions:	if $\varepsilon_I \geq 0$ and $\varepsilon_{II} < -\beta\varepsilon_I$	$\hat{W}_{\text{rel}}(\varepsilon_I) = c\,\exp\left\{B\left[\left(1-\beta^2\right)\varepsilon_I^2\right]\right\}$ (2)
	if $\varepsilon_{II} \geq 0$ and $\varepsilon_I < -\beta\varepsilon_{II}$	$\hat{W}_{\text{rel}}(\varepsilon_{II}) = c\,\exp\left\{B\left[\left(1-\beta^2\right)\varepsilon_{II}^2\right]\right\}$
Bukled regions	if $\varepsilon_I < 0$ and $\varepsilon_{II} < 0$	$\hat{W}_{\text{rel}}(\varepsilon_I,\varepsilon_{II})=0$

The expression of the relaxed energy density in the wrinkled regions has been obtained by imposing $\hat{W}_{\text{rel}}(\varepsilon_I)=\hat{W}(\varepsilon_I,\varepsilon_{II}=w(\varepsilon_I))$ for $\varepsilon_I > 0$ [2]. Considering a wrinkled region where $\varepsilon_I > 0$, the stress state is uniaxial and the PK2 principal membrane stresses are $\sigma_I = 2cB\left(1-\beta^2\right)\varepsilon_I\,\exp\left\{B\left[\left(1-\beta^2\right)\varepsilon_I^2\right]\right\}$ and $\sigma_{II}=0$.

The model (2) has been implemented in the finite element code FEAP. The simulation of the stretching of a membrane shown in Fig. 1 highlights the potency of the numerical model to predict the distinct regions of behavior. Figure 2 is the result of a preliminary application of the model (2) to simulate reconstructive surgery. The figure shows membrane stress fields after the suture of a circular excision on a skin flap that has been previously undermined. Solutions obtained assuming that the skin is able to transfer compressive stresses and assuming that the skin wrinkles and buckles in compression are compared to highlight differences in the post-suture response. The extrusion of the edges of the wound takes place in the region ahead of the excision along the line of the incision.

CONCLUSIONS

The problem of the wrinkling and buckling of biological membranes characterized by a isotropic Tong-Fung type constitutive behavior has been solved within the framework of finite strain hyperelasticity. The natural width, which is used in the criterion for the wrinkling and in the definition of the modified elastic potential, is found to depend on only one of the model parameters. The implementation of the model in the finite element code FEAP enables the simulation of procedures of reconstructive surgery where wrinkling and buckling of the skin may occur after the suture of the edges of the wound.

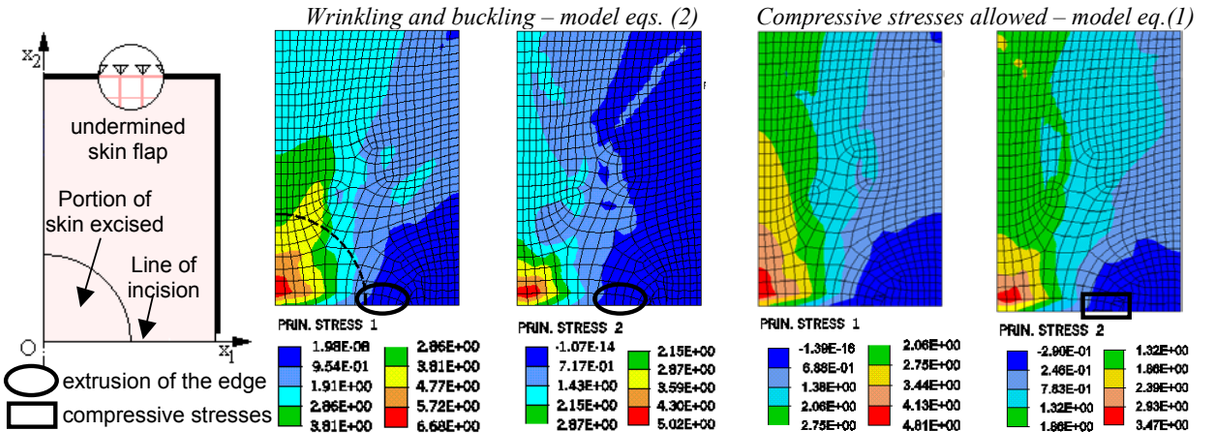


Figure 1: Principal stress fields (PK2, in [kPa cm]) after the excision and the suture of a circular portion of the skin (radius 27 mm) in an undermined skin flap similar to those tested and analyzed in [4] (dimensions of the flap in the natural configuration : 60×90×1 mm).

References

[1] Wu C.H. and Canfield T.R.: Wrinkling in finite plane-stress theory. *Quarterly of Applied Mathematics.* 179-199, 1981.

[2] Pipkin A.C.: The relaxed energy density for isotropic elastic membranes, *IMA J. Applied Mathematics*, 36, 85-99, 1986.

[3] Tong P and Fung Y.C.: The stress-strain relationships for the skin, *Journal of Biomechanics*, **9**, 649-657, 1976.

[4] Gambarotta L., Massabò R, Morbiducci, R., Raposio, E and Santi P.: In vivo experimental testing and model identification of human scalp skin, partially accepted for publication in the *J. of Biomechanics*, 2003.

[5] Barsotti R., Ligaro, S. and Royer-Carfagni, G.F.: The web bridge, *Int. J. Solids and Structures*, 38, 8831-8850, 2001.

MECHANICS OF THIN FILM STRUCTURES

Henrik Myhre Jensen*
*Department of Building Technology and Structural Engineering, Aalborg University, Sohngaardsholmsvej 57, DK-9000 Denmark

Summary With emphasis on interface delamination in thin film structures, a variety of phenomena are discussed. The effects of curvature of the substrate on buckling-driven delamination of thin films in compression are analysed. Details in the morphology of buckling-driven delamination and in particular the causes of the so-called telephone cord blister are discussed. Conditions for delamination at edges and corners are formulated and it is shown that steady-state delamination at a corner is possible at significantly lower stress levels than delaminations at straight-sided edges.

RECENT RESULTS IN THE MODELLING OF INTERFACE DELAMINATION IN THIN FILM STRUCTURES

Curved Substrates

Many applications of thin films involve systems with curved substrates or substrates with corners. The effects of curvature of the substrate and corners in the substrate on buckling-driven delamination of thin films in compression are analysed. In particular an analysis of buckling-driven delamination of a thin film on a spherical substrate has been carried out. The effects of the substrate having a double curvature compared to previous studies of delamination on cylindrical substrates turns out to be non-trivial: In addition to the effect of the shape of the substrate, a new non-dimensional geometrical parameter enters the conditions for steady-state delamination. It is shown that for a certain range of delamination widths, this additional geometrical parameter has only minor influence on the conditions for steady-state delamination. Furthermore, the shape of the substrate has profound influence especially on initiation of delamination growth.

Morphology of buckling-driven delamination

Details in the morphology of buckling-driven delamination and in particular the causes of the so-called telephone cord blister are discussed. Conditions for steady-state growth of buckling-driven delamination in thin film systems can be calculated by a simplified method where details around the growing front are not required. The simplified method relies upon estimates of the phase angle of loading along the propagating front of delamination and the accuracy of these estimates is investigated by comparing with finite element calculations of the fracture mechanics parameters along the growing front. The sensitivity of the parameters to the shape of the front is investigated and it is shown that the simplified approach for estimating the phase angle of loading on the growing front of delamination - based on a re-scaling of the phase angle of loading for a full circular delamination - is reasonably accurate. It has been shown that a semi-circle best approximates the shape of the growing crack front. This, however, is true only at moderate stress levels when a mode II independent interface fracture criterion is assumed. The shape of the front has not been determined at higher stress levels or for other fracture criteria. The simplified approach for estimating the phase angle of loading slightly underestimates the mode I stress intensity factor on the crack front. As a result, the range of stresses where growth along the front is favoured over growth along the sides is larger than predicted with the simple model.
A comparison is made between steady-state delamination growth along circular paths of different curvatures but with identical widths so that the phase angle of loading on the growing front can be assumed to be the same independent of the curvature. The results for the energy release rate show that growth along a straight line is most likely to be observed at low stress levels while growth along curved paths are more likely at higher stresses. The mode of delamination that releases most energy at high stress levels has the centre of the circular path on one of the sides.

Delamination at edges and corners

Conditions for thin film delamination at edges and corners in the absence of film buckling are formulated. A local analysis of the region close to the intersection point between the crack front and the free edge shows that steady-state delamination at corners is possible at stress levels lower than those required to make an edge crack propagate under plane strain conditions due to the stress concentrations at interface corners.

Prediction of crack front shape

A numerical method based on the finite element method coupled to exact solutions near to the crack tip for calculating the shape of the crack front has been applied. The method involves an iterative procedure to adjust the shape of the crack front so that the fracture criterion is satisfied locally along the front. Results based on the numerical scheme shows that the shape of the crack front is sensitive to the interface fracture criterion and the level of residual stresses in the film.

References

[1] Henrik Myhre Jensen and Izhak Sheinman, Straight-Sided, Buckling-Driven Delamination of Thin Films at High Stress Levels. *International Journal of Fracture* **110**, 371-385, 2001.
[2] Henrik Myhre Jensen and Izhak Sheinman, Numerical Analysis of Buckling-Driven Delamination. *International Journal of Solids and Structures* **39**, 3373-3386, 2002.
[3] M.-W. Moon, H.M. Jensen, J.W. Hutchinson, K.H. Oh and A.G. Evans. The Characterization of Telephone Cord Buckling of Compressed Thin Films on Substrates. *Journal of the Mechanics and Physics of Solids* **50**, 2355-2377, 2002.
[4] Henrik Myhre Jensen, Thin Film Delamination at Edges and Corners. *International Symposium on Recent Developments in the Modelling of Rupture in Solids*, (Eds. A. Benallal and S.P.B. Proença), ISBN 2-1-094072-7, 2003.
[5] Ivindra Pane and Henrik Myhre Jensen, Steady-State Delamination at Corners, 2004, in preparation.
[6] K.D. Sørensen and H.M. Jensen, Effects of Substrate Curvature on Thin Film Delamination, 2004, in preparation.

XXI International Congress of Theoretical and Applied Mechanics
Warsaw, Poland, August 15-21, 2004



Mechanics of Nanostructures

Rodney S. Ruoff
Northwestern University, USA

The topics will be (I) Experimental studies by my group of carbon nanotubes and nanocoils, boron nanowires, and carbon nanotubes projecting from the fracture surfaces of CNT composites (a) subjected to tensile loading (b) driven into mechanical resonance by mechanical or electrical excitation. (II) The ideal strength of materials and fracture in nanostructures (a) ab initio calculations of ideal strength (b) experimental work on nanostructure fracture (c) modeling of the fracture strength of nanostructures with 0, 1, 2 adjacent, 3 adjacent, ?, n adjacent defects (d) following this summary of prior work, a new theory (developed with Nicola Pugno, Politecnico di Torino) for fracture of nanoscale structures will be presented. (III). We close with discussion of a new method that my group is developing, for achieving nm-resolution for measurements of the displacement field. I acknowledge grant support from NASA LaRC, NSF, and ONR.

A HYBRID MOLECULAR/CONTINUUM ANALYSIS OF IFM EXPERIMENTS ON A SELF-ASSEMBLED MONOLAYER

Kenneth M. Liechti[*], Mingji Wang[*], John M. White[**], Peter J. Rossky[**] and Robb M. Winter[***]
[*]*Center for Mechanics of Solids, Structures and Materials, University of Texas, Austin, TX 78712*
[**] *Chemistry and Biochemistry, University of Texas, Austin, TX 78712*
[***]*Chemical Engineering, South Dakota School of Mines and Technology, Rapid City, SD 57701*

Summary An interfacial force microscope (IFM) has been used to probe self-assembled monolayers of octadeciletrichlorosilane (OTS) on silicon. Its unique self-balancing force sensor allows the full attractive and repulsive portions of the force-displacement response of the tip/surface interactions to be obtained. The measured force profile is used to validate a molecularly based continuum model of the adhesive contact between the tip and the surface of the OTS monolayer.

EXTENDED SUMMARY

Polymeric self-assembled monolayers on silicon are used in MEMS devices as stiction reducers[1]. They can also be used to control adhesion[2 3 4]. As a result, such monolayers are becoming critical elements in such applications and it is important to understand their mechanical behaviour. Such understanding may come from complementary approaches such as molecular dynamics simulations and experiments with scanning probe microscopes.

The self-assembled monolayer considered in this work is octadecyltrichlorosilane (OTS) on silicon. It is quite commonly used in MEMS applications as it forms covalent bonds with the silicon substrate and has a methyl terminal group which has very weak interactions with other surfaces. The monolayer was probed with an IFM (Fig. 1), which provides complete force profiles in the attractive and compressive regimes due to a unique self-balancing force sensor[5]. This is in contrast to atomic force microscopes (AFM), which encounter an unstable response when the force gradient of the surface interaction exceeds the spring stiffness of their cantilever force sensor. The measured force profiles were compared with continuum level analyses that accounted for surface interactions via traction-separation laws and considered the OTS to be isotropic and (a) linearly elastic and (b) nonlinearly elastic. The latter was motivated by molecular dynamics simulations of simple stress states.

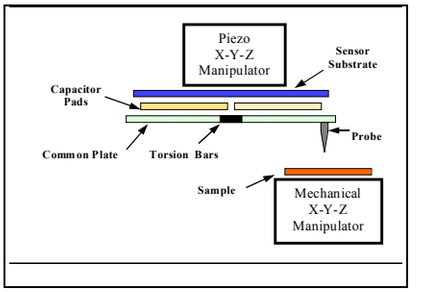


Fig. 1. Schematic of an IFM

The substrate used for the OTS deposition was a polished boron P-type single crystal silicon wafer (100). Its native oxide layer is usually contaminated[6] so it was removed with a dilute hydrofluoric acid solution. A new oxide layer was produced by placing the chips in a piranha solution (96% H_2SO_4 : 30% H_2O_2, 2:1 vol.),which oxidizes and hydrolyzes the silicon surface. An anhydrous, millimolar solution of OTS in dicyclohexyl was prepared in a dry box, the silicon chips were placed in it for 24 hours and then removed and treated with a series of solvents and sonicated to remove any physisorbed layers. Ellipsometry measurements indicated that the oxide and monolayer were 2 and 2.5 nm thick, respectively. Several other contact angle, spectrographic and AFM diagnostics confirmed that a monolayer had indeed been formed.

An electrochemically etched tungsten tip was attached to the sensor of the IFM as an indenter. The geometry of the tungsten tip was measured with a scanning electron microscope (SEM). Tips that had a parabolic shape and radii ranging from 100 nm to 500 nm were recorded and kept for future use. The force profiles (Fig. 2) from bare and coated silicon shows that the IFM is capable of detecting the OTS monolayer.

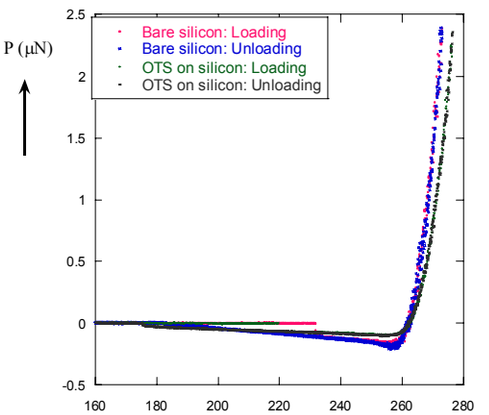


Fig. 2. Comparison of force profiles for bare and coated silicon

The analysis of the IFM experiments was conducted at the continuum level with the finite element package ABAQUS. An axisymmetric analysis was used due to the spherical contact. The tungsten indenter, oxide layer and silicon were all considered to be linearly elastic and isotropic. The OTS was first considered to be the same, but a second series of analyses took it to be a hypoelastic material on the basis of the molecular dynamics analysis described below. Geometrically nonlinear analysis was used in all simulations due to large deformations in the contact region. Quadrilateral linear axisymmetric elements with reduced integration were used for both the indenter and specimen. Infinite elements were used for the far-

field region (>20 times the maximum contact radius) of the half space so that no boundary conditions needed to be enforced on the unbounded domain.

The compressive regime of the nanoindentation was modeled as frictionless contact using standard ABAQUS surface contact interactions. The default contact pressure-clearance relationship in ABAQUS is referred to as the "hard" contact model. It only transmits pressure once the surfaces come into contact. This interaction model is not sufficient for analyzing indentation experiments where the adhesive effect is large. As a result, user-defined elements were incorporated in the abovementioned mesh when adhesive interactions were required. A triangular traction-separation law with three parameters was used[7]: the maximum adhesive traction σ_0, the corresponding displacement δ_0 and the cut-off displacement δ_t. The surface energy was then $\omega = \frac{1}{2}\sigma_0\delta_t$. The adhesive portion of the response was best fitted with $\sigma_0 = 37.5$ MPa, $\delta_t = 7$ nm, $\delta_0 = 5$ nm and $\omega = 131.3$ mJ/m^2. This relatively long-range interaction is probably due to adventitious water on the surface as the experiments were not conducted in vacuum. The results from the linearly elastic analyses indicated that modulus of OTS monolayer was 15±5 GPa when Poisson's ratio was zero, and 5±2.5 GPa when Poisson's ratio was 0.44 (Fig. 3). These values reflect the higher degree of order that is present in self-assembled monolayers.

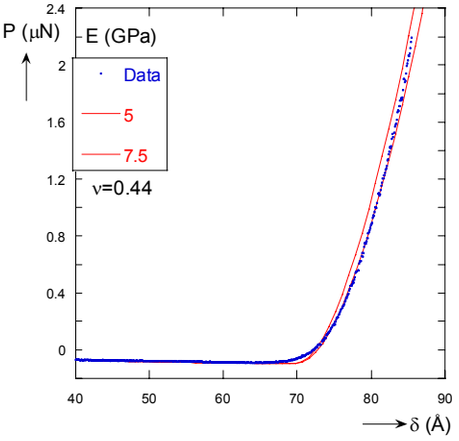


Fig. 3. Comparison of the measured force profile with linear solutions.

The linear elastic solutions were not satisfactory in the low and high force regimes. This suggested that a nonlinear model of the OTS might be preferable. Guidance was sought from molecular dynamics analyses which were used to simulate the self-assembly of an OTS monolayer on an SiO_2 substrate as well as the compression of the monolayer by a tungsten plate. The simulation was performed with the molecular dynamics simulation package DL_POLY 2.0. Room temperature was maintained during the calculation and both the SiO_2 substrate and tungsten plate were modeled as surfaces with one layer of atoms. The SiO_2 was modeled as trydimite[8]. Both SiO_2 and tungsten were treated as rigid because they were expected to be much stiffer than the OTS monolayer. United atoms were used to model the OTS molecular chain, where the CH_3, CH_2, and OH groups were represented as pseudo-atoms. Slab periodic boundary conditions, which are periodic in the plane, were used to represent the infinite extent in the two in-plane directions. The repeating cell had dimensions of 26×27 Å^2 containing 30 OTS molecules. All the OTS molecular chains were initially arranged perpendicular to the SiO_2 surface. A highly nonlinear response resulted, which was then modeled as a hypoelastic material in an ABAQUS analysis of the IFM experiment. The results are compared with the measured force profile (Fig. 4). Better agreement was achieved at low force levels, but a more comprehensive representation of the OTS is required in order to improve the solution at higher load levels. This is currently being pursued in molecular dynamics analyses of simple shear loadings which will then be incorporated in continuum representations such as the Ogden[9] model.

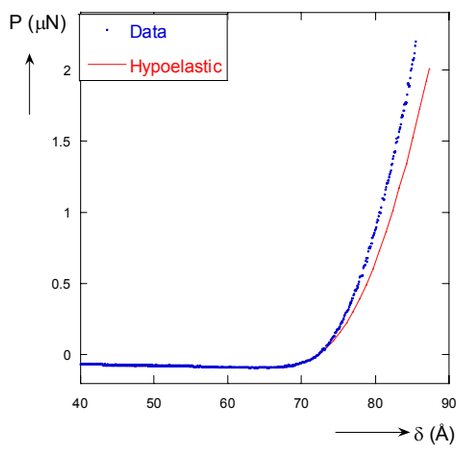


Fig. 4. Comparison of the measured force profile with a nonlinear elastic analysis

References

[1] Bhushan, B., Principles and Applications of Tribology, John Wiley and Sons, Inc, New York, 1999.
[2] Reedy, E. D. Jr., Kent, M. S. and Moody, N. R. *Proceedings of the 26th Annual Meeting of the Adhesion Society*. 502-504, 2003.
[3] Zhuk, A. V., Evans, A. G., Hutchinson, J. W. and Whitesides, G. M. *J. Mat. Res*., **13**, 3555-3564, 1998.
[4] Mello, A. M. and Liechti, K. M. submitted to *J. Appl. Mech*., 2004
[5] Joyce, S.A. and Houston, J.E., *Rev. Sci. Instr*. **62**, 710-715, 1991.
[6] Vajapeyajula, K., MS Thesis, University of Texas at Austin, 2002.
[7] Wang, M., Liechti , K. M., White, J. M. and Winter, R. M. ., submitted to *J. Mech. Phys. & Solids*, 2003.
[8] Stevens, M. J., *Langmuir,* **15**, 2773-2780, 1999.
[9] Ogden R. W. *Proc. Royal Soc. London*, **A326**, 565-582, 1972.

THERMOMECHANICAL CONTINUUM REPRESENTATION OF ATOMISTIC DEFORMATION AT ARBITRARY TIME AND SIZE SCALES

Min Zhou
The George W. Woodruff School of Mechanical Engineering
Georgia Institute of Technology, Atlanta, GA 30332-0405, U.S.A.
Email: min.zhou@me.gatech.edu

A thermomechanical equivalent continuum (TMEC) theory for the deformation of atomistic particle systems at arbitrary size and time scales has recently been developed. The description of coupled thermomechanical continuum behavior is derived directly "from the ground up", using molecular dynamics concepts. This theory is a further advancement from a pure mechanical equivalent continuum (EC) theory developed recently. These new theories provide fully dynamic continuum interpretations of atomistic deformation with different resolutions for atomic particle motion. While the mechanical theory is based on an explicit and full resolution of the atomistic motion, the thermomechanical theory is based on a decomposition of the atomic particle velocity into a relatively slower-varying structural deformation part and a high-frequency thermal oscillation part. Within the meaning of classical mechanics, the TMEC theory establishes the ultimate atomic origin of coupled thermomechanical deformation phenomena at the continuum level. Because the decomposition of atomic velocity into a structural deformation part and a thermal oscillation part is intrinsically dependent on both size- and time-scales and because the theory is explicitly formulated for an arbitrary size scale, the development allows scale-sensitive characterizations of both structural deformation and heat conduction. On one hand, balance of momentum at the structural level yields fields of stress, body force, traction, mass density and deformation as they appear to a macroscopic observer. The full dynamic equivalence between the discrete system and continuum system includes (i) preservation of linear and angular momenta, (ii) conservation of internal, external, and inertial work rates, and (iii) conservation of mass. On the other hand, balance of momentum for the thermal motions as it appears to an observer moving at the structural velocity yields the fields of heat flux and temperature. These quantities can be cast in a manner as to conform to the continuum phenomenological equation for heat conduction and generation, yielding scale-sensitive characterizations of specific heat, thermal conductivity, and thermal relaxation time. The coupling between the structural deformation and the thermal conduction processes results from the fact that the equations for structural deformation and for heat conduction are two different forms of the same balance of momentum equation at the fully time-resolved atomic level. This coupling occurs through an inertial force term in each of the two equations induced by the other process. For the structural deformation equation, the inertial force term induced by thermal oscillations of atoms gives rise to the phenomenological dependence of deformation on temperature. For the heat equation, the inertial force term induced by structural deformation takes the phenomenological form of a heat source.

RATCHETING-INDUCED WRINKLING OF AN ELASTIC FILM ON A METAL LAYER UNDER CYCLIC TEMPERATURES

R. Huang, S.H. Im
Center for Mechanics of Solids, Structures & Materials, The University of Texas, Austin, TX 78712, USA

Summary This paper develops a theoretical model for wrinkling of an elastic film on an elastic-plastic metal layer caused by cyclic temperatures. Both analytical and numerical solutions will be presented. The implications of the results for structural evolution and failure mechanisms in integrated electronic devices and thermal barrier coating systems will be discussed.

INTRODUCTION

Under in-plane compression, a freestanding membrane tends to buckle into an equilibrium state. For a thin film bonded to a substrate, the buckling is constrained. If the substrate is elastic and relatively compliant, the film may still buckle into an equilibrium state. The wavelength of the equilibrium state, however, depends on the compressive stress in the film and the elastic compliance of the substrate, which is shorter than buckling wavelength of a freestanding film and often called wrinkling. If the substrate creeps, wrinkling becomes a kinetic process, as the amplitude grows over time [1-3]. At high temperatures, interfacial diffusion may also facilitate the kinetic process of wrinkling. This paper presents a theoretical study on another mechanism of wrinkling, which is induced by ratcheting plastic deformation under cyclic temperatures.

The deformation in the same direction caused by a cyclic load (e.g., thermal cycling) is known as ratcheting, which has been observed in many engineering structures. Recently, the concept of ratcheting has been used in modeling metal film crawling as well as induced cracking in integrated electronic devices [4-6]. An analogy between ratcheting and creep has been developed to understand the kinetics of ratcheting-induced crack initiation and growth [7]. The same analogy suggests that, under cyclic temperatures, a compressively strained elastic film can form wrinkles on a metal layer. Such ratcheting-induced wrinkling has been observed in thermal barrier coating systems.

THE MODEL

Figure 1 shows the model structure. The elastic film is modeled by the nonlinear von Karman plate theory with both normal and shear tractions at the film/metal interface. The deformation in the metal layer is a superposition of two parts. The thermal expansion mismatch between the metal and the substrate induces a biaxial in-plane stress, which is assumed to be large enough to cause the metal to deform plastically during each cycle. The compressively strained film tends to buckle away from the flat state, which induces normal and shear tractions along the metal/film interface. The interface tractions do not change directions within each cycle and biased the plastic flow at yield, leading to ratcheting deformation of the metal and growth of the wrinkle. Assuming an elastic-perfectly plastic behavior of the metal, we obtain the net displacements of the film per cycle

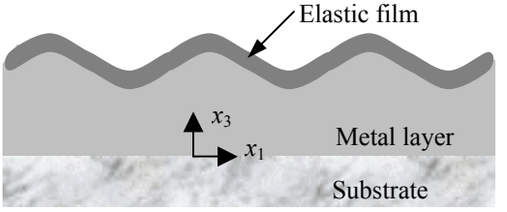


Figure 1: Model structure

$$\frac{\partial w}{\partial N}=\frac{1}{\eta_R}\frac{\partial}{\partial x_\alpha}\left[\frac{H^3}{3}\frac{\partial p}{\partial x_\alpha}-\frac{H^2}{2}\tau_\alpha\right],\qquad \frac{\partial u_\alpha}{\partial N}=\frac{1}{\eta_R}\left(\tau_\alpha H-\frac{H^2}{2}\frac{\partial p}{\partial x_\alpha}\right), \tag{1}$$

where w is the out-of-plane displacement, u_α the in-plane displacement ($\alpha=1,2$), N the number of temperature cycles, H the thickness of the metal layer, p and τ_α the normal and shear tractions at the interface, respectively, and η_R is called ratcheting viscosity [5] as defined below:

$$\eta_R=\frac{E_m}{12(1-\nu_m)}\left[\frac{E_m(\alpha_m-\alpha_s)(T_H-T_L)}{(1-\nu_m)Y_m}-2\right]^{-1}, \tag{2}$$

where α_m and α_s are the thermal expansion coefficients of the metal layer and the substrate, respectively, T_H and T_L define the temperature range of cycles, E_m, ν_m, and Y_m are the modulus, Poisson ratio, and uniaxial yield stress of the metal. The equilibrium of the elastic film relates the tractions at the interface to the current

displacements by the von Karman plate theory. Together we have a set of partial differential equations that evolve the displacement field as the temperature cycles.

The equations in (1) are analogous to those obtained for an elastic film on a viscous layer [2], with the number of cycles N replacing time t and the ratcheting viscosity η_R replacing creep viscosity. The above equations also reduce to those obtained for metal film crawling in [5], where only a constant and uniform shear traction was applied at the surface of a metal layer. The present model suggests that, while a uniform shear traction at the metal surface causes metal to crawl, a non-uniform shear traction and/or pressure cause the metal to crawl and wrinkle simultaneously; on the other hand, a uniform pressure at the surface by itself does not cause any ratcheting deformation in the metal.

RESULTS AND DISCUSSIONS

Assuming a sinusoidal wrinkle of small amplitude, a linear perturbation analysis predicts that the amplitude grows as $A(N) = A_0[1 + s(\lambda)]^N$, where A_0 is the initial amplitude, and the growth rate s depends on the wrinkle wavelength λ. There exists a critical wavelength λ_c, below which the wrinkle decays ($s < 0$) and above which the wrinkle grows ($s > 0$). The value of s reaches a maximum at λ_m, corresponding to the fastest growing mode. Starting from a random perturbation, the fastest growing mode will dominate the initial growth.

For any wavelength $\lambda > \lambda_c$, there exists an equilibrium wrinkling state, in which the tractions at the film/metal interface vanish. Consequently, the metal undergoes cyclic plastic deformation without ratcheting and wrinkle stops growing. The equilibrium amplitude of the fastest growing mode is $A_{eq} = h/\sqrt{6}$, where h is the film thickness.

A finite difference method was employed to numerically simulate the evolution of wrinkles under the plane strain condition. Figure 2 shows the growth of the amplitude of a sinusoidal wrinkle as the temperature cycles. The growth follows the prediction of the linear perturbation analysis for the first 500 cycles, and then saturates to approach the equilibrium amplitude. Next we start from a perturbation described by a Gauss function and assume an elastic constraint layer above the film (e.g., in a thermal barrier coating system). Depending on the stiffness of the elastic constraint, the wrinkle grows differently. Figure 3 shows two limiting cases: without any constraint, the wrinkle grows to a sinusoidal shape corresponding to the fastest growing mode; with a very stiff constraint layer, the upward displacement is completely suppressed, and the wrinkle grows downwards into a deeper and narrower shape.

Ratcheting-induced wrinkling may cause failure in integrated electronic devices and thermal barrier coating systems. Bending of the film induces tensile stress that may cause the film to crack. The normal traction at the film/metal interface oscillates between tension and compression, and a tensile traction may cause debonding of the film.

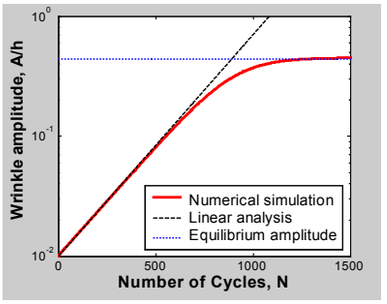


Fig 2: Growth of a sinusoidal wrinkle.

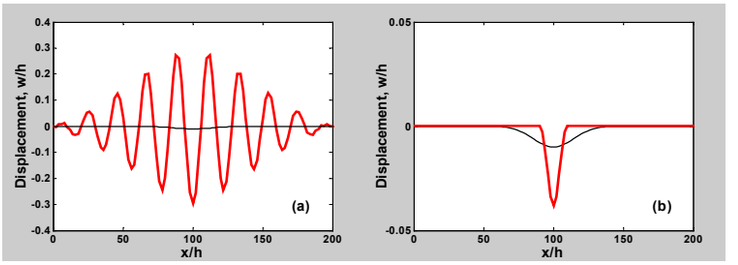


Fig 3: Wrinkling with (a) no constraint and (b) a very stiff constraint.

ACKNOWLEDGMENTS

The authors thank partial support from Microelectronics Research Center of The University of Texas at Austin. Discussions with Z. Suo of Harvard University were both encouraging and helpful.

References

[1] Sridhar N., Srolovitz D.J., Suo Z., Appl Phys Lett 78, 2482–2484, 2001.
[2] Huang R., Suo Z., J. Appl Phys 91, 1135–1142, 2002.
[3] Balint D.S., Hutchinson J.W., Acta Mater. 51, 3965-3983, 2003.
[4] Huang M., Suo Z., Ma Q., Fujimoto H., J. Mater Res **15**, 1239-1242, 2000.
[5] Huang M., Suo Z., Ma Q., Acta Mater. **49**, 3039-3049, 2001.
[6] Huang M., Suo Z., Ma Q., J. Mech Phys Solids **50**, 1079-1098, 2002.
[7] Liang J., Huang R., Prevost J.H., Suo Z., Experimental Mechanics 43, 269-279, 2003.

ATOMISTIC STUDY OF SIZE EFFECT IN TORSION TESTS OF NANOWIRE

Akihiro Nakatani*, Hiroshi Kitagawa*
*Osaka University, Department of Adaptive Machine Systems, 2-1 Yamadaoka, Suita, Osaka 565-0871, Japan

Summary The inelastic deformation of an atomistic model of single crystal and polycrystalline wire under torsion is studied using molecular dynamics. Torsion deformation is incorporated using a twisted periodic boundary condition proposed by the authors. We focus on grain refinement and size effect as they are affected by the combination of two length scales, i.e., radius of specimen and grain size. The result is compared with that from continuum strain-gradient plasticity.

INTRODUCTION

The strength of polycrystalline material is increased with decreasing grain size. This tendency is known as the Hall-Petch relation (HPR). Strengthening through grain refinement of polycrystalline materials is a promising process because it has the advantage of recycling. In particular, a severe plastic deformation (SPD) process using cheap equipment attracts a great deal of attention. On the other hand, there is a trend towards miniaturization. Many small-scale structures are designed. However, the assumption on which conventional continuum theories are based breaks down for them. Many strain gradient theories are proposed to explain the size effect (e.g. [1]). The physical base of the theories is usually backed up by dislocation theory [2, 3]. However, the problem is still unsolved for nanostructured material where the HPR also breaks down, i.e., smaller is softer.

We conduct an atomistic simulation of torsion tests of nanowire. There is some literature on torsion tests (e.g. [4]) but most findings are affected by boundary constraints. In this study, we propose a novel treatment of the boundary condition, a twisted periodic boundary condition (TPBC). Ideally, torsion can give SPD to the specimen without any change of its profile. In particular, the application called high pressure torsion (HPT) is notable for grain refinement. Mechanically, there is interest in the fact that the deformation field in torsion has its gradient along radial coordinates. The specimen size effect is significant in the torsion test, as well as in the bending test [2], and the results are used to verify the validity of strain-gradient theory in the nano-scale region.

FORMULATIONS AND COMPUTATIONAL SETUP

The materials of the nanowire for the torsion problem are single- and polycrystalline iron in which interatomic interaction is introduced by the Finnis-Sinclair type potential [5]. Solid cylindrical wire with a radius R is modeled as shown in Figure 1 and analysis models are listed in Table 1.

A brief summary of TPBC is shown as follows. A coordinate transformation between the natural coordinate's component $(Q^{(\alpha)})^I$ and the twisted coordinate's component $(q^{(\alpha)})^i$ is considered for an atom α. The canonically conjugate moments $(P^{(\alpha)})_I$ and $(p^{(\alpha)})_i$ with coordinates $(Q^{(\alpha)})^I$ and $(q^{(\alpha)})^i$ are introduced as follows:

$$(q^{(\alpha)})^i = h^i{}_J (Q^{(\alpha)})^J, \qquad (p^{(\alpha)})_i = [(\boldsymbol{h}^{-1})^T]^J_i (P^{(\alpha)})_J, \tag{1}$$

When we assume Cartesian coordinates, and $\boldsymbol{Q}^{(\alpha)}$ and a specific twist angle θ along the z axis are taken into account, $\boldsymbol{h}$ is the transformation matrix and the metric $g^I{}_J = (\boldsymbol{h}^T)^I{}_k h^k{}_J$ specifies the macroscopic deformation.

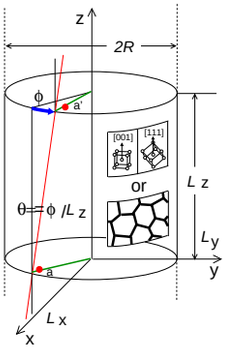


Figure 1. Schematic of test model. TPBC is employed in z direction with dimension L_z of the unit cell. The lateral dimensions L_x and L_y of the unit cell are taken to be sufficiently larger than the diameter $2R$.

Table 1. Material models, specimen geometries, analysis conditions and procedures

Specimen (d: Grain size, R: Radius of specimen)		Height l_z	Number of atoms
Single crystal	in $\langle 001 \rangle$ torsion	20 nm	535 711
	in $\langle 111 \rangle$ torsion	20 nm	544 235
Nanocrystal	$d =$ 5 nm ($R = 10$ nm)	20 nm	511 943
	$d = 10$ nm ($R = 10$ nm)	20 nm	522 607
	$d =$ 5 nm ($R = 20$ nm)	10 nm	994 167
	$d = 10$ nm ($R = 20$ nm)	40 nm	4 026 817

Analysis conditions and Procedures
* The wire is twisted monotonically by the increment of specific twist angle $\Delta\theta = 1.25 \times 10^6$ rad/m, which is added to the specific twist angle θ every 0.5 ps.
* The nominal surface shear strain $\gamma_0 = R\theta$ is used to express the strain level.
* The system temperature is set as 300 K during the calculation.
* Defect atom is defined as the atomic site at which less than 10 bcc-characteristic atoms are found among the 8 first neighbors and the 6 second neighbors by using common neighbor analysis (CNA).

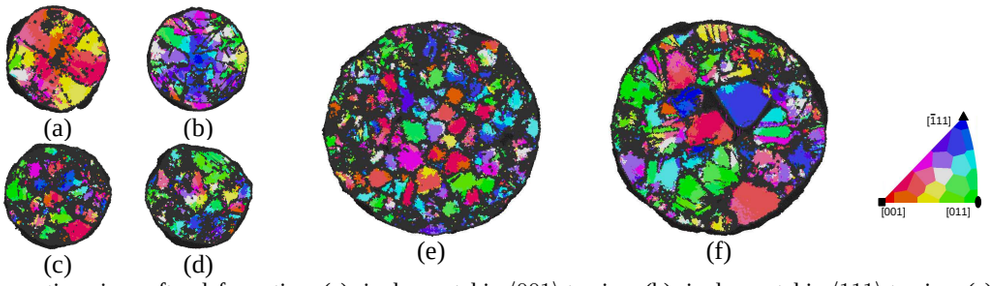


Figure 2. Cross-section views after deformation: (a) single crystal in $\langle 001 \rangle$ torsion. (b) single crystal in $\langle 111 \rangle$ torsion. (c) nanocrystal with $d = 5$ nm ($R = 10$ nm). (d) nanocrystal with $d = 10$ nm ($R = 10$ nm). (e) nanocrystal with $d = 5$ nm ($R = 20$ nm). (f) nanocrystal with $d = 10$ nm ($R = 20$ nm). Defect atoms are colored in black. Colors correspond to the crystallographic orientation of the twist axis in the unit triangle of the reverse stereographic pole figure.

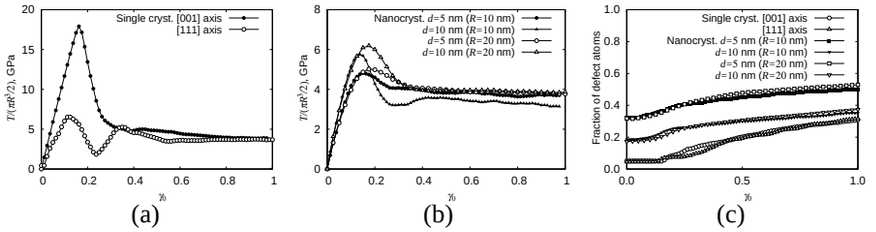


Figure 3. Torque versus twist curves for (a) single crystals and (b) nanocrystals: (c) Fraction of defect atoms as a function of twist. Torque value is converted to a representative value having the dimension of stress with multiplication by a factor of $2/\pi R^3$; twist is expressed by nominal surface strain $\gamma_0 \equiv R\theta$.

RESULTS AND DISCUSSION

Figure 2 shows cross-section views after the deformation. It is observed that a polycrystal structure is developed near the surface in the cases of the twisted single crystals (Figures 2 (a) and (b)). In the polycrystalline case (Figures 2 (c), (d), (e) and (f)), no significant difference between the surface and the interior is recognized in small specimens (Figures 2 (c) and (d); however, grain refinement proceeds more severely near the surface in large specimens (Figures 2 (e) and (f)).

Figures 3 (a) and (b) show the torque versus twist curves for single crystals and for nanocrystals respectively. Anisotropy in the maximum torque is significant in the single crystal cases and the maximum torque in $\langle 001 \rangle$ torsion is two and half times as large as in $\langle 111 \rangle$ torsion. In the polycrystal cases, it is clear that the elastic modulus of nanocrystals with $d = 5$ nm is less than $d = 10$ nm. Comparison between radius $R = 10$ nm models shows that the peak value of torque in the $d = 5$ nm model is about 80 percent of that in the $d = 10$ nm model. Comparison of the peak stress between different radius R models for the same grain size models shows that the peak stress in the $R = 20$ nm model is slightly higher than that in the $R = 10$ nm model. This is a discrepancy with the well known size effect observed by experiment and explained by the strain gradient theory [1]. One reason for the strain rate effect is that the deformation behavior of nanocrystals with small grain size is mainly caused by the deformation on the grain boundary rather than by dislocation behavior; the latter is important in the coarse grain polycrystals [2].

Figure 3(c) denotes the fraction of defect atoms as a function of twist. There is no significant difference between different values of R. The number of defect atoms increases with increase of strain, but the rate gradually becomes low.

CONCLUSIONS

The twisted periodic boundary condition is newly proposed. Its efficiency is confirmed through the analysis of the torsion problem of nanowire. Polycrystallization is observed in single crystal cases. The tendency that smaller is softer is a discrepancy with continuum predictions from dislocation theory. We conclude that the deformation at the grain boundary is significant in nano-scale deformation.

Acknowledgments AN thanks Nobuhiro Tsuji, Tomotsugu Shimokawa, and Ryosuke Matsumoto for fruitful discussions. The authors gratefully appreciate support from NEDO of Japan and support from Handai Frontier Research Center.

References

[1] Fleck N.A., Hutchinson, J.W.: A Reformulation of Strain Gradient Plasticity. *J.Mech Phys Solids* **49**:2245-2271, 2001.
[2] Weertman J.: Anomalous Work Hardening, Non-Redundant Screw Dislocations in a Circular Bar Deformed in Torsion, and Non-Redundant Edge Dislocations in a Bent Foil. *Acta Mater* **50**:673-689, 2002.
[3] Cleveringa,H.H.M., Van der Giessen,E., Needleman,A.: A Discrete Dislocation Analysis of Bending. *Int J.Plast* **15**:837-868, 1999.
[4] Horstemeyer M.F. *et al.*: Torsion/Simple Shear of Single Crystal Copper. *Trans ASME J.Eng Mater Tech* **124**:322-328, 2002.
[5] Finnis M.W., Sinclair J.E.: A simple empirical n-body potential for transition metals. *Phil Mag A***50**:45-55, (1984), **53**:161(1986)

Solid mechanics methods in nano-technologies

Elena A. Ivanova, Anton M. Krivtsov, Nikita F. Morozov, Boris N. Semenov

morozov@NM1016.spb.edu

In recent years, rapid development of nanotechnologies led to the necessity of constructing adequate physical models that make it possible to describe physico-mechanical properties of objects with a nanometersize (nanosize) scale. The majority of existing models of such a kind adopt that basic mechanical characteristics of nanosize objects correspond to those obtained in macroscopic experiments. However, when dealing with structures containing only several atomic layers, the discrepancy arises between the evident discreteness of an object under study and a continual method of its description. The inconsistency of values of elastic moduli, which were obtained in microscale and macroscale experiments, was noted by many researchers. The solution to an equivalent continual problem allows the Poisson's ratio and Young modulus for the coating to be determined from such experiments. However, the values of elastic characteristics measured by this method exhibit a substantial inconsistency by their macroscopic values for the same material. The aim of the presented paper is to investigate theoretically the scale effect for the Poisson's ratio, Young modulus and the bending stiffness of thin nanocrystalline structures. The interest to these problems is connected with the necessity of investigation of the mechanical deformation of nanotube devices, which are used intensively in the recent years in nanotechnology developments. Engineering materials and structures at the nanoscale are expected to play a key role in the production of the next generation of electronic devices such as single electron transistors, terabit memories, quantum computers, and etc.

Poisson's ratio and Young modulus determination. We consider a twodimensional single crystal shown in the Figure 1. The crystal possesses an infinite length along the x direction and $N \geq 2$ atomic layers in the direction. Each atom interacts only with its nearest neighbors, as is shown in the Figure 1. Constant tensile

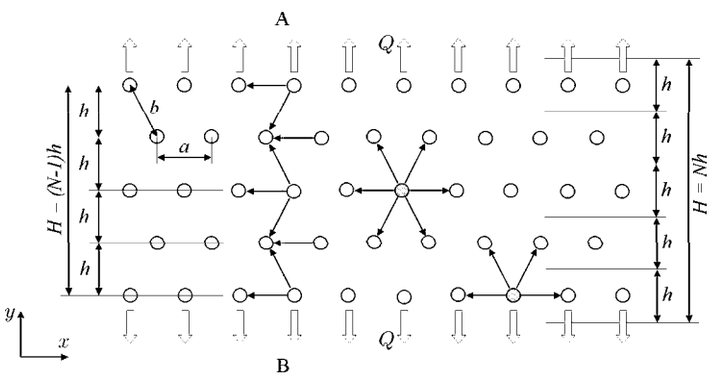


Figure 1:

forces Q are applied to atoms located at crystal ends. The deformed singlecrystal state under consideration is completely determined by the distance a between neighboring atoms in each layer and by the interlayer distance h. Let us note, that the crystal thickness H (its extension along the y direction), in principle, cannot be determined unambiguously. For example, if we assume that the crystal thickness is equal to the distance between atomic layers lying on opposite crystal ends (see Figure 1), then, in this case, $H = (N-1)h$. On the other hand, it is quite reasonable to determine the crystal thickness as a product of the number of layers by the thickness of a single layer, which results in the formula $H = Nh$. Therefore, we denote $H = N_* h$, $N - 1 \leq N_* \leq N$, where N_* is the quantity reflecting an arbitrariness in the determination of H. The crystal under consideration is anisotropic. We recall that the infinite crystal with the HCP crystal lattice is isotropic

and, hence, the anisotropy indicated is a manifestation of the scale factor. Furthermore, we denote

$$\nu_1 = -\left.\frac{\epsilon_2}{\epsilon_1}\right|_{\sigma_2=0} \qquad E_1 = \left.\frac{\sigma_1}{\epsilon_1}\right|_{\sigma_2=0} \qquad \nu_2 = -\left.\frac{\epsilon_1}{\epsilon_2}\right|_{\sigma_1=0} \qquad E_2 = \left.\frac{\sigma_2}{\epsilon_2}\right|_{\sigma_1=0}. \tag{1}$$

Here, ν_1 and E_1 are the Poisson's ratio and Young modulus for tension along the x axis; the quantities ν_2 and E_2 correspond to tension along the y axis. Using relationships (1) and equations of equilibrium of the crystal, we obtain

$$\nu_1 = \nu_\infty \qquad E_1 = \frac{N}{N_*}\,E_\infty \qquad \nu_2 = \frac{N-1}{N-\frac{1}{9}}\,\nu_\infty \qquad E_2 = \frac{N}{N-\frac{1}{9}}\,E_\infty\,, \tag{2}$$

where, ν_∞ and E_∞ are values of the Poisson's ratio and Young modulus, which correspond to the infinite crystal.

Based on the studies performed, we can list the basic properties intrinsic to nanocrystals. 1. For the elastic moduli of a nanocrystal, only a possible interval of values is determined. This is associated with the impossibility of unambiguously determining the size of a nanoobject. 2. Elastic properties of a nanocrystal substantially depend on the number of atomic layers forming it. 3. The shape and size of a nanocrystal introduce an additional anisotropy into its elastic properties.

Bending stiffness determination. Let us consider a two-dimensional single crystal shown in Figure 2. The crystal possesses $N \geq 1$ atomic layers in the y direction and $J \gg N$ layers in the x direction. Forces Q_n

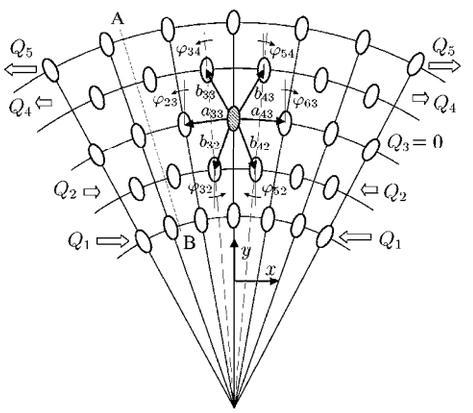


Figure 2:

are applied to atoms located at crystal end-walls, where n is the number of the horizontal layer, containing the specified atom. These forces are changing linearly with coordinate, keeping the zero average value of the overall force acting on the end-wall, so that we can consider the macroscopic boundary conditions as an action of a pure moment (without tensile stress). If the moment interaction of particles is not taken into account, the bending stiffness of the monocrystal has the form

$$D = D_\infty\left(1 - \frac{1}{N^2}\right), \qquad D_\infty = \frac{E_\infty H^3}{12}. \tag{3}$$

Here D_∞ is the value for the bending stiffness from the macroscopic theory of elasticity. According to formula (3), the bending stiffness of the nanocrystal is varying in the limits of $0 \leq D \leq D_\infty$. For the small values of N formula (3) gives the bending stiffness values smaller then D_∞ and finally it vanishes for $N = 1$.

However, it is known that the bending stiffness of single-wall nanotubes does not equal to zero. Taking into account the moment interaction of particles, we obtain the following expression for the bending stiffness

$$D = D_\infty\left(1 - \frac{1}{N^2}\right) + E^*_\infty H\left(1 - \frac{1}{3N}\right), \tag{4}$$

where E^*_∞ is the value of rotational Young modulus from the macroscopic moment theory of elasticity. It is easy to see that the bending stiffness of the nanocrystal given by formula (4) does not vanishe for $N = 1$.

The model of the delamination processes of a preliminary stressed bi-layered plate from rigid foundation is proposed. On the basis of the considered solution of specified dependence of its diameter on the parameters of plate layers is found.

MICROSTRUCTURAL AND ATOMISTIC SIMULATION FOR DEFORMATION OF NANO-GRAINED METALS

Wei Yang
Department of Engineering Mechanics, Tsinghua University, Beijing 100084, CHINA

Summary The deformation of nano-grained metals is explored from three aspects: computation under a recently developed microstructural evolution algorithm; mechanics modelling for the cooperative insertion-rotation process under the 9-grain cluster model; and molecular dynamics simulation for fast isochoric stretching under large deformation.

Recently, experiment of rolling nano-crystalline copper at room temperature to an elongation of 5100% was reported [1]. Nano-grain metals of such small grain sizes deform mainly by neighboring grains sliding pass each other with insignificant distortion in the grain shape. We adopted a structural evolution algorithm to simulate the process. Accommodation mechanisms such as grain boundary diffusion, sliding and grain rotation control the kinetics of the process. Actual deformation minimizes the plastic dissipation and stored strain energy for representative steps of grain neighbor switching. Numerical simulations based on these principles are given for a representing cell composed of 200 non-uniform grains. The deformation process is portrayed in the snapshots shown in the left of Fig. 1, while the straight line in the log-log plot on the right indicates an inverse power dependence (-2.61) of the strain rate on the grain size under a sustained stress.

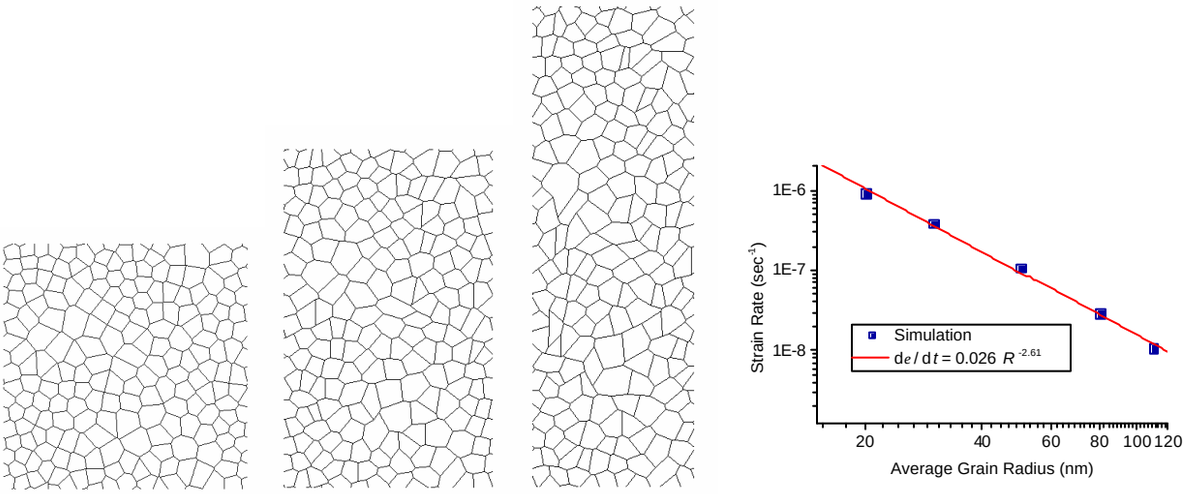
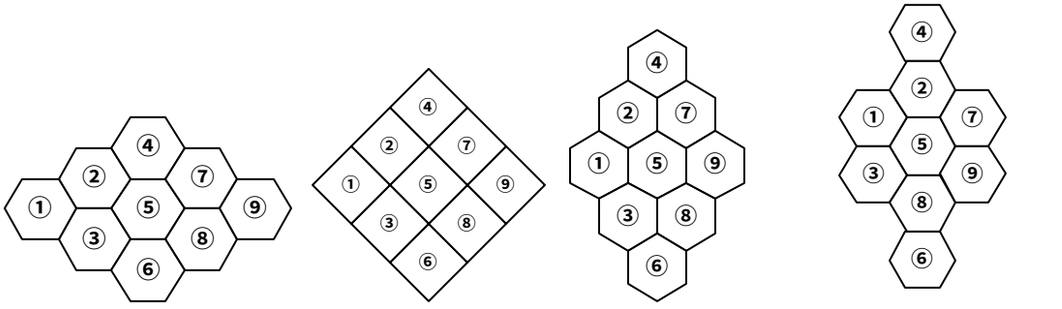


Figure 1 Simulated deformation process and scale dependence.

The 4-grain cluster model of Ashby and Verrall [2], with its concrete calculation and the perception of grains squeezing pass each other, should serve as the starting point for the mechanism model of nano-grained metals. Figure 2 illustrates an attempt to complete the Ashby-Verrall mechanism by adding a rotation of closely contacted grain pairs. The cell contains 9 regular hexagon grains and is termed the 9-grain cluster model.



(a) initial configuration (b) critical configuration (c) completion of insertion (d) rotation of 30 degrees

Figure 2 Model of 9-grain cluster

The constitutive law for fully relaxed creeping behavior is [3]:

$$\dot{e} = C(s - s_{\text{th}}) \tag{1}$$

where the creep rate C is given by

$$C = \frac{\sqrt{3}\Delta e^2}{8D}\left[\frac{m^2 K_B T D}{3\Omega\left\{nD_V + D_B\sum_{i=1}^{n}\frac{d}{l_i}\right\}} + \frac{h_B}{d}s^2\right]^{-1} \tag{2}$$

and the threshold stress is:

$$s_{\text{th}} = \frac{1}{\Delta e}\left[\left(\sqrt{2\sqrt{3}} - \sqrt{3}\right)\frac{4\Gamma}{3D} + \left(1 - \frac{p}{2\sqrt{3}}\right)\Delta g\right] \tag{3}$$

The linear creep law in (1) agrees in form with the experimental data by Cai et al. [4] for nano-grained copper, as indicated in Fig. 3. An extension of the coorperative insertion-rotation mechanism to the plane strain and three-dimensional cases is achieved by Wang and Yang [5].

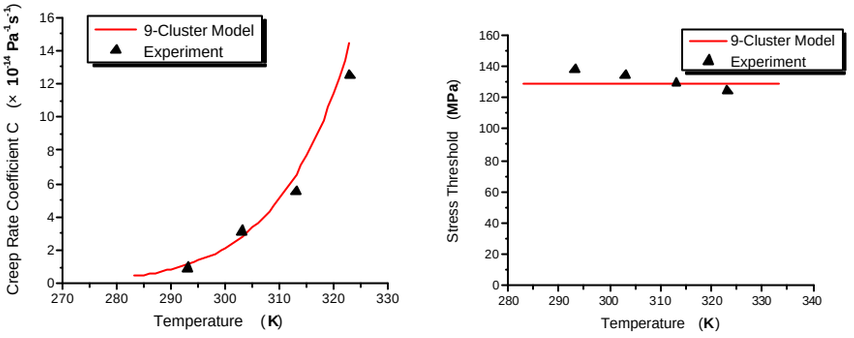


Figure 3 Creep rate (left) and threshold stress (right) for nano-grained copper.

The method of molecular dynamic simulation is only capable of the case of fast stretching. The previous works concerning on this subject were not conducted to the regime of large deformation. Here we only present a simulation for copper of 1,000,000 atoms under EAM potential. The loading is imposed by a quasi-homogeneous manner. The profiles of the local crystalline order are plotted in Figure 3. The sites where local fcc order are colored green, those of hcp order (stacking faults) are colored red, and those of amorphous state are colored blue. As the amount of tension increases, one observes the bursts of defects (in the disordered form of stacking faults) within the grains. Most stacking faults are arrested by the grain boundaries and rotate slightly toward the tensile direction. A different family of stacking faults may be observed during the later stages of tension, and some areas dissolve into sub-grains of smaller size.

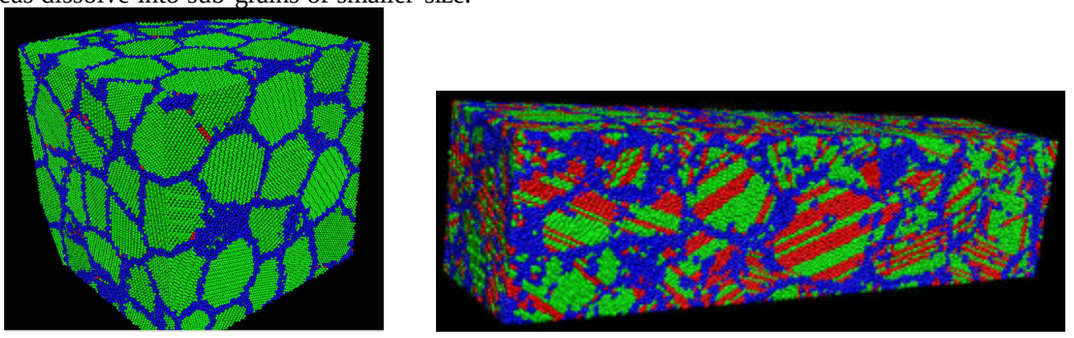


Figure 4 Profiles of local crystalline order for stretching nanocrystalline Cu. Left: initial configuration; right: elongated to a logarithmic strain of 100%.

References

[1] Lu L., Sui M. L. and Lu K., Superplastic extensibility of nanocrystalline copper at room temperature. Science, 287(2000): 1463-1466.

[2] Ashby M.F. and Verrall R.A. Diffusion-accommodated flow and superplasticity. Acta Metallurgica, 21 (1973): 149-163.

[3] Yang W. and Wang H. T., Mechanics modeling for deformation of nano-grained metals, J. Mech. Phys. Solids, 52(2004), In Press.

[4] Cai B., Kong Q.P., Lu L. and Lu K. Interface controlled diffusional creep of nanocrystalline pure copper, Scr. Metall., 41(1999): 755-759.

[5] Wang H. T and Yang W., Constitutive modeling for nanocrystalline metals based on cooperative grain boundary mechanisms, J. Mech. Phys. Solids, 52(2004), In Press.

ENERGY-BASED APPROACH TO LIMIT STATES IN NANOSTRUCTURES. CALCULATION OF THE CRITICAL VALUES OF ENERGY FROM FIRST PRINCIPLES

Kinga Nalepka*, Paweł Nalepka**, Ryszard B. Pęcherski*
*Cracow University of Technology, Chair of the Strength of Materials, Institute of Structural Mechanics, Faculty of Civil Engineering, Warszawska 24, PL 31-155 Kraków, Poland
**Agriculture University of Cracow, Department of Engineering and Machinery for Food Industry/ IPPT PAN, Department of Mechanics of Materials and Biomechanics, Swietokrzyska 21, PL 00-049 Warszawa, Poland

Summary The considered energy-based approach can appear helpful in the field of nanomechanics filling the gap between atomistic calculations and continuum mechanics modelling of the behaviour of different kinds of crystalline nanostructures. We propose to calculate the critical energy of pertinent proper states from quantum mechanical theory of nanostructures. The quantum mechanical model for an ideal single crystal of Cu is studied and the comparison with the results obtained for Al crystal is made.

Energy-based approach to limit states – the Rychlewski criterion

An energy-based approach to limit states in elastic solids of arbitrary anisotropy was developed by Rychlewski [1]. The Rychlewski limit condition is based on the theory of proper elastic states and the concept of energy orthogonal stress states, which make it possible to decompose additively the elastic energy density stored in an anisotropic body into not more than six disjoint parts. According to our opinion, the proposed approach can appear also helpful in the field of nanomechanics filling the gap between atomistic calculations and continuum mechanics modelling of the behaviour of different kinds of crystalline nanostructures [2, 3]. Under the limit state in nanostructures, we can understand the limit of linear elastic behaviour; although the other interpretations of the limit state are also possible. The energy-based criterion is formulated in terms of elastic strain states:

$$\frac{\lambda_1(\boldsymbol{\varepsilon}_1)^2}{\Phi_1^{cr}} + \ldots + \frac{\lambda_p(\boldsymbol{\varepsilon}_p)^2}{\Phi_p^{cr}} \le 1, \quad p \le 6, \tag{1}$$

where $\lambda_1,\ldots,\lambda_p$ are the Kelvin elastic moduli corresponding to the proper elastic states of the elastic stiffness tensor $\mathbf{S}$, $\Phi_1^{cr},\ldots,\Phi_p^{cr}$ are the critical values of energy for each of the proper states, hence each term of the above criterion is the ratio of the accumulated elastic energy of the proper state to the critical one. The crucial point for the applications of the energy-based limit condition is to know the critical values of energy. They can be determined experimentally. However, it is difficult to measure it experimentally in the nano-scale. Therefore, we propose to calculate the critical energy of pertinent proper states from quantum mechanical theory of nanostructures. The analysis is confined to the cubic crystals. In such a case, three elastic proper states exist. They correspond to: a uniform expansion of a cube, equal contraction and elongation, respectively, along two cube edges, and change of the angle between the respective two edges of the cube.

The quantum mechanical model for Cu crystal

The quantum mechanical model for an ideal single crystal of Copper is studied. The assumed Born-Oppenheimer approximation enables the application of Bravais lattice to model the deformation of the crystal. Using the Wigner-Seitz cellular method, Fig.1, we replicate the radial density of the charge distribution calculated with the application of the Hatree method for a single Cu^+ ion, what results in the charge distribution for the crystal shown in Fig.2.

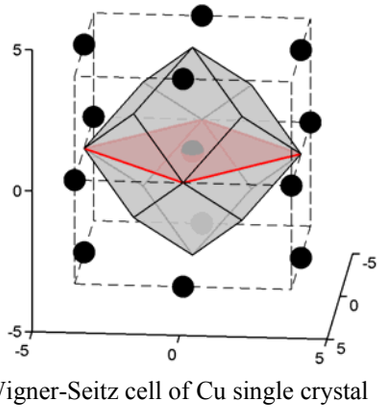


Fig.1. Wigner-Seitz cell of Cu single crystal

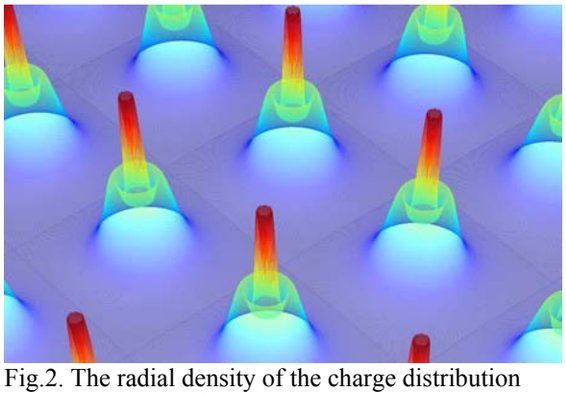


Fig.2. The radial density of the charge distribution in the plane marked in Fig.1

Applying the calculated radial density of the charge distribution and using the Slater method [4], the structure of the *s*, *d, f* and *p* energy bands was calculated, Fig.3. The first qualitative analysis of the band structure was made by Krutter [5], whereas our numerical results make a basis for the calculations of the electron energy in deformed crystal. The energy bands are parameterised by the half distance "p" between the central ion and one of its nearest neighbours, cf. Fig.1. The parameter "p" is the controlling variable of the uniform extension of the crystal. The increase of the variable "p" produces

the gradual transition of the energy bands into the energy level. The particular interpretation has the transition of the energy band *s* into the energy level, which corresponds to the hypothetical disintegration of the crystal into the separate atoms, cf. Fig. 4.

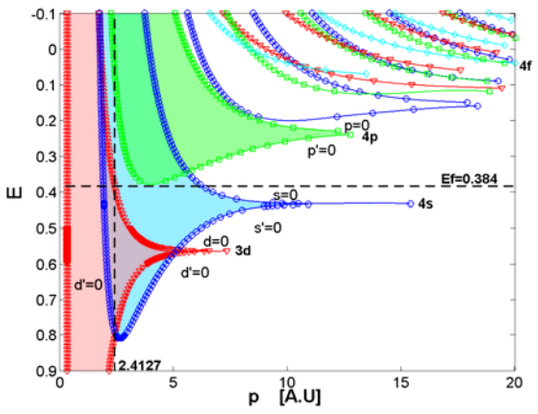


Fig.3. The calculated band structure of Cu crystal, $p_{eq} = 2.4127$ A.U.

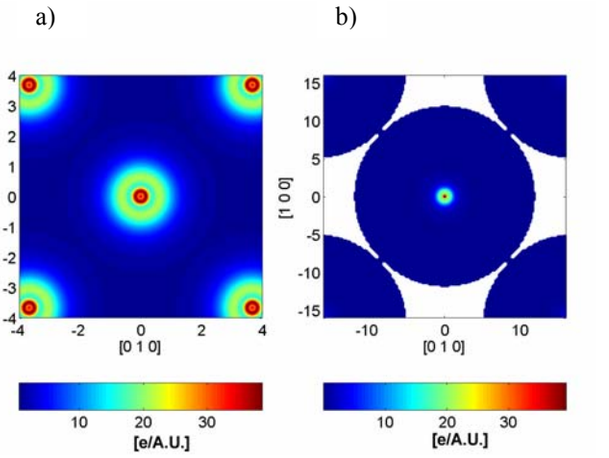


Fig.4. The calculated radial density of the charge distribution: a) in the equilibrium state, b) in the state of hypothetical disintegration of the crystal into the separate atoms.

The internal energy of the crystal volume $\Omega(p)$ confined in the expanding Wigner-Seitz cell was calculated from $(2)_1$, where the internal energy is the sum of the repulsive energy of the Cu^{11+} ions and the energy of the electrons of the energy bands *s* and *d*.

$$U(p) = U_{rep}(p) + \int_{-\infty}^{E_f(p)} E(p)\rho(E(p))dE(p), \qquad \Phi(p) = \frac{1}{\Omega(p)}\left[U(p) - U(p_{eq})\right], \qquad \Phi_1^{cr} = \Phi(p_{cr}). \qquad (2)$$

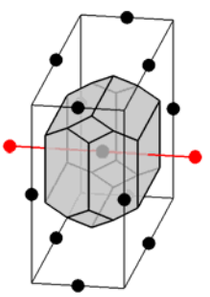


Fig.5. The Wigner-Seitz cell deformed according to the second proper state.

The similar analysis can be made for the deformation of the Wigner-Seitz cell according to the second proper state illustrated in Fig. 5. In such a case, the distance between the central ion and the neighbouring ones, marked in red, diminishes. This requires taking into account in the calculation of energy band structure the ellipsoidal charge distribution. The structure of the equations (2) leading to the calculation of the critical energy Φ_2^{cr} remains the same. For the third proper state, related with the change of the angle between the respective two edges of the cube, the similar algorithm of the calculation of the critical energy Φ_3^{cr} holds.

Conclusions

The similar identification of the energy-based Rychlewski criterion can be made for other crystals. The Al crystal was studied for the comparison. It posses the same symmetry as Cu, but has the different electronic structure, as for Al belongs to *sp*-valent metals. Therefore, the three critical energies are calculated, but by using the approximation of Nearly Free Electrons (cf. e.g. [6]). If we consider the relations between the critical energies, we can observe that it is the electronic structure that plays the crucial role in the strength distribution in the crystal of the same symmetry.

Literature

[1] J. Rychlewski, *Elastic energy decomposition and limit criteria*, Uspekhi Mekh.-Advances in Mech., **7**, 51-80, 1984 (in Russian) and: *Unconventional approach to linear elasticity*, Arch. Mech., **47**, 149-171, 1995.

[2] K. Nalepka, R.B. Pęcherski, *Energy-based criteria of limit states. How to calculate energy limits from first principles*, Rudy Metale, **R48**, 533-536, 2003 – in Polish.

[3] K. Kowalczyk, J. Ostrowska-Maciejewska, R.B. Pecherski, *An energy-based yield criterion for solids of cubic elasticity and orthotropic limit state*, Arch. Mech., **55**, 509-525, 2003.

[4] J.C. Slater, Electronic energy bands in metals, Phys. Rev., **45**, 794-801, 1934.

[5] H.M. Krutter, *Energy bands in Copper*, Phys. Rev., **48**, 664-671, 1935.

[6] D. Pettifor, *Bonding and Structure of Molecules and Solids*, Oxford University Press, Oxford, New York, 1995.

SIZE-DEPENDENT ELASTIC STATE OF EMBEDDED NANO-INCLUSIONS & QUANTUM DOTS

Pradeep Sharma, Lewis Wheeler
University of Houston, Department of Mechanical Engineering, Houston, TX, 77204, U.S.A

Summary The classical formulation of Eshelby for embedded inclusions is revisited and modified to at least partially account for size-effects likely to be prominent at the nanoscale. Unlike the classical results, our modified formulations render the elastic state of an embedded inclusion size-dependent. Among others, applications to quantum dots are presented.

INTRODUCTION

The classical formulation of Eshelby [1] for embedded inclusions is revisited and modified to account for size-effects likely to be prominent at the nanoscale. In this two-pronged work, we firstly incorporate the previously excluded surface/interface stresses, tension and energies. The latter effects come into prominence at inclusion sizes in the nanometer range where surface-to-volume ratios are appreciable. Unlike the classical results, our modified formulations incorporating surface energies render the elastic state of an embedded inclusion size-dependent making possible the extension of Eshelby's original formalism to nano-inclusions.

Presuming that, at least for some material systems, the inherent long-wavelength assumption of elasticity is violated for inclusions in the nanometer range, we also derive a modified Eshelby tensor in the framework of second gradient elasticity with couple stresses. Closed-form expressions of the modified Eshelby's tensor(s) are presented for spherical and cylindrical inclusions.

We also present some simple illustrative examples of the present work i.e. size-dependent stress concentrations and size-dependent effective properties of composites containing nano-inclusions. However, perhaps the most technologically important application of the present work lies in arena of quantum dots and wires. While physicists routinely take into account the impact of strain on band structure and opto-electronic properties, the strain calculations are typically based upon classical elasticity and are thus size-independent [2]. In the present work, a first order calculation clearly shows that large errors in both the band structure and the emitted wavelength can be incurred if the aforementioned size effects are neglected. Limited empirical evidence is also presented to support our results.

SIZE-DEPENDENT ESHELBY'S TENSOR FOR NANOINCLUSIONS INCORPORATING SURFACE ENERGIES

Employing Gurtin et. al's [3] framework for surface/interface elasticity, surface & interface energies are coupled to conventional bulk elasticity formulation for inclusions [1]. New (inclusion) curvature related terms are introduced rendering the elastic state size-dependent. Eshelby's original conjecture that only inclusions of the ellipsoid family admit uniform elastic state under uniform stress-free transformation strains must be modified in the context of coupled surface/interface-bulk elasticity. We reach an interesting conclusion in that only inclusions with a constant curvature admit a uniform elastic state, thus restricting this remarkable property only to spherical and cylindrical inclusions.

SIZE-DEPENDENT ESHELBY'S TENSOR FOR NANOINCLUSIONS INCORPORATING GRADIENT & COUPLE STRESS EFFECTS

Based entirely on simple group theoretic symmetry arguments and some associated continuum postulates, a second gradient elasticity theory with couple stresses can be constructed [4]. Based upon the Green's function for such a theory, the elastic state of inclusions is determined i.e. Eshelby's tensor is formulated and at least for spherical and circular cylindrical shapes explicitly derived. The results are size-dependent however, for the applications that the present authors are interested in (strains in embedded semiconductor quantum dots), these effects were found to be small in comparison to surface energy effects. The formal framework though, will be of immense use in polymeric or biological materials as well as metallic ones with large number of defects.

APPLICATIONS (QUANTUM DOTS, SIZE-DEPENDENT STRESS CONCENTRATIONS & EFFECTIVE PROPERTIES)

For sake of brevity only application to quantum dots is summarized here. As well known [2] strain impacts the band structure and hence optoelectronic properties of quantum dots. In Figures (1-2), we illustrate the error that may be incurred in the estimation of the band structure and emitted wavelength of an InGaN quantum dot embedded in a GaN matrix if the aforementioned size-effects are neglected. These errors far exceed the strict tolerances in optoelectronic applications. Note that this effect is of importance only in the size range of a few nanometers. Some limited empirical evidence appears to support our assertions.

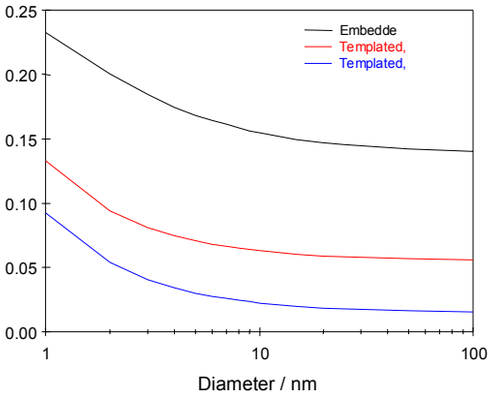


Figure 1:Size-dependent band structure shift due to surface energy effects

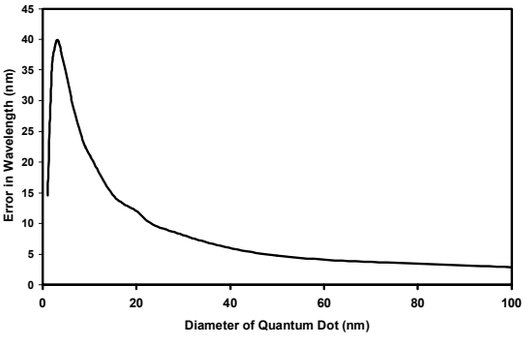


Figure 1:Size-dependent wavelength shift due to surface energy effects

References

[1] Eshelby, J.D, *Proceedings of the Royal Society of London A*, A241, pp. 376-396, 1957
[2] Singh, J., *Physics of Semiconductors & their Heterostructures*, McGraw-Hill Higher Education, 1992
[3] Gurtin, M.E., Weissmuller, J., and Larche, F., *Philosophical Magazine A*, vol 78, 1093, 1998
[4] Kleinert, H., *Gauge Fields In Condensed Matter*, Vol. II, *Stresses And Defects,* World Scientific Singapore, 1989

FRACTURE CRITERIONS FOR BRIDGED CRACK: FROM MACRO TO NANOSCALE

Mikhail N. Perelmuter

Institute for Problems in Mechanics of RAS, pr. Vernadskogo 101-1, Moscow, 119526, Russia

Summary A multi-scale bridged crack model for the evaluation of fracture and strength parameters of interfaces with cracks is proposed. We suppose that distributed nonlinear bonds link the crack surfaces in some zones starting from the crack tips. The sizes of these zones are not assumed to be small as compared to the crack length on every bridging level. The system of singular integral-differential equations is derived for normal and shear bond stresses evaluation. Two fracture criterions of quasistatic crack growth are considered. The first condition in the both criterions is the same: it is the condition of the bond limit stretching or the limit strain at the trailing edge of the bridged zone. Two types of the second condition of fracture is considered: a) the force condition which is the condition for the critical stress intensity factor and b) the proposed energetic condition based on the equality of the values of the strain energy release rate and the energy dissipation by the bonds at the crack limit equilibrium state. The regimes of the bridged zone and the crack tip equilibrium and growth are analyzed for the both types of these criterions.

INTRODUCTION

Let us consider a straight crack of length 2ℓ at an interface of two dissimilar elastic half-planes such that the crack is placed at $|x| \le \ell, y = 0$. Assume that the uniform tensile stresses, σ_o, are applied at infinity normal to the interface. Consider segments of length d (end zones) adjacent to the tips of the crack $(\ell - d) \le |x| \le \ell$. In these zones the surfaces of the crack interact with each other, which suppresses the crack opening. The physical nature of the crack surfaces interaction is generally changed depending on the crack scale and distance from the crack tip. The interatomic and intermolecular forces, bundles of nanotubes are limiting mechanisms of the surfaces interaction for a crack of small size or at the very small distances from the crack tips for large crack, while "macro-mechanical" forces prevail at relatively larger distances. These macro-mechanical forces can be caused, e.g., by reinforcing action of fibers in composites or polymer chains connecting the crack surfaces in polymer-polymer joints or polymer joints with other materials (metals, ceramics and etc). To mathematically describe the interaction between the surfaces of the crack, we assume that there exist bonds between the surfaces of the crack at the end zone. The law of deformation of these bonds, which is generally nonlinear, is given. Under the action of external loads, σ_0, the stresses $Q(x)$ appear in the bonds between the surface of the interface crack at the boundary between different materials. These stresses have the normal $q_y(x)$ and tangential $q_x(x)$ components $Q(x) = q_y(x) - iq_x(x),\ i^2 = -1$. The surfaces of the crack are acted on by the normal and tangential stresses which are numerically equal to these components. The opening of the interface crack, $u(x)$ at $|x| \le \ell, y = 0$, can be written as follows $u(x) = u_y(x) - iu_x(x)$ where $u_y(x) = u_y^+(x) - u_y^-(x)$ and $u_x(x) = u_x^+(x) - u_x^-(x)$ are the projections of the crack opening on the coordinate axes, u_x^+, u_y^+ and u_x^-, u_y^- denote the components of the displacements of the upper and lower crack surfaces. The relation between the crack opening and the bond tractions (the bond deformation law) depends on the physical origin of the bonds and their properties. In the case of spring-like bonds the deformation law can be written as follows [1] $u_i(x) = c_0(x,\sigma)q_i(x)$, $c_0(x,\sigma) = \gamma_0(x,\sigma)\frac{H}{E_B}$, where γ_0 is a dimensionless function, H is a linear scale proportional to the bonding zone thickness, E_B is the effective Young modulus of the bonds and the function c_0 can be considered as the effective bond compliance, $\sigma = \sqrt{q_x^2 + q_y^2}$ is the modulus of the traction vector. For the bond deformation law with the displacements depends on the bonds stresses the crack opening along the crack end zone and the bond stresses can be determined from the solution of the singular integral-differential equations system, the detail can be found in [1].

TWO PARAMETRIC FRACTURE CRITERION

Supposing that the bonds stresses and the crack opening along the crack end zone are known, the total potential energy of a body containing a crack with bridged zone (in the absence of body forces) is

$$\Pi = \int_v w(\varepsilon_{ij})dv - \int_{s_e} t_i u_i ds + \int_{s_i} \Phi(u)ds, \tag{1}$$

where $w(\varepsilon_{ij})$ is the density of the deformation energy in the body volume v, ε_{ij} are the components of the strain tensor; t_i, u_i are the tractions and displacements at the body boundary and (or) crack surfaces s_e; $\Phi(u)$ is the density of the strain energy of the bonds in the crack end zones, u is the crack opening in the end zones of area s_i. The crack limit equilibrium corresponds to the following condition

$$-\frac{\partial \Pi}{\partial \ell} = -\frac{\partial}{\partial \ell}\left[\int_v w(\varepsilon_{ij})dv - \int_{s_e} t_i u_i ds\right] - \frac{\partial}{\partial \ell}\int_{s_i} \Phi(u)ds = 0 \tag{2}$$

The terms in the brackets represent the strain energy release rate at creation of a new crack surface and the last term is the rate of the energy absorption in the crack end zone and is associated with the energy necessary to create a unit of its

new surface. Note, that within the framework of the model the rate of the energy absorption depends on the end zone size and bond characteristics. The equilibrium end zone size is not assumed to be constant. The strain energy release rate in the case of an interface crack under the external loading σ_0 and the stresses $-Q(x)$ applied to the crack surfaces in the bridged zone can be written as follows [3] $G_{tip}(d,\ell) = \left(\frac{k_1+1}{\mu_1} + \frac{k_2+1}{\mu_2}\right)\frac{K_B^2}{16\,\cosh^2(\pi\beta)}$, where $k_{1,2} = 3 - 4\nu_{1,2}$ or $k_{1,2} = (3-\nu_{1,2})/(1+\nu_{1,2})$ for the plane strain or plane stress states, respectively; $\nu_{1,2}$, $\mu_{1,2}$ are the Poisson ratios and shear moduli of the joint materials $1(y > 0)$ and $2(y < 0)$, $\alpha = (\mu_2 k_1 + \mu_1)/(\mu_1 k_2 + \mu_2)$, $\beta = \ln\alpha/2\pi$ and $K_B = \sqrt{K_{\rm I}^2 + K_{\rm II}^2}$ is the modulus of the stress intensity factors due to the external loads and the stresses in the crack end zone. The stress intensity factors $K_{I,II}$ are determined by [1, 2] .

Let us calculate the rate of the energy absorption for the interface crack with bonding. Denote by $U_{bond}(d,\ell)$ the work of the deformation of bonds and by $G_{bond}(d,\ell)$ the rate of the energy absorption per unit thickness of the body. Then

$$U_{bond}(d,\ell) = b\int\limits_{\ell-d}^{\ell}\Phi(u)dx\ , \quad G_{bond}(d,\ell) = \frac{\partial U_{bond}(d,\ell)}{b\,\partial\ell} \tag{3}$$

where b is the body thickness. The density of the strain energy of the bonds is equal to $\Phi(u) = \int\limits_0^{u(x)}\sigma(u)du\ , \quad u(x) = \sqrt{u_x^2(x) + u_y^2(x)}, \quad \sigma = \sqrt{q_x^2 + q_y^2}$. After differentiation in formula (3) with respect to the upper and the bottom limits of the integral we can get

$$\frac{\partial U_{bond}(d,\ell)}{b\partial\ell} = \int\limits_{\ell-d}^{\ell}\left(\frac{\partial\,u(x)}{\partial\,\ell}\sigma(u)\right)dx + G_c - G_b, where, G_c = \int\limits_0^{u(\ell)}\sigma(u)du; \quad G_b = \int\limits_0^{u(\ell-d)}\sigma(u)du \tag{4}$$

If we consider the model of the crack with zero opening at the crack tip $(u(\ell) = 0)$ then $G_c = 0$ and it is necessary to add in the left part of (4) the value of the intrinsic toughness of the matrix material $G_c = 2c_m\gamma_m$, where c_m is the volume fraction of the matrix material and $2\gamma_m$ is the matrix toughness. Finally, we obtain the following expression for the rate of the energy absorption

$$G_{bond}(d,\ell) = \int\limits_{\ell-d}^{\ell}\left(\frac{\partial\,u_y(x)}{\partial\,\ell}q_y(u) + \frac{\partial\,u_x(x)}{\partial\,\ell}q_x(u)\right)dx - \int\limits_0^{u(\ell-d)}\sigma(u)du + G_c \tag{5}$$

where the second term is the density of deformation energy allocated at break of the bond at the trailing edge of the crack end zone.

For a homogeneous material or an adhesion layer connecting different materials the following relations are held $G_c = G_b = \int\limits_0^{u(\ell-d)}\sigma(u)du$. In this case the expression (3) completely coincides with similar expression from [1, 2].

The condition of the crack tip limit equilibrium can be written as follows

$$G_{tip}(d,\ell) = G_{bond}(d,\ell) \tag{6}$$

The condition (6) is necessary but insufficient for searching for a limit equilibrium state of the crack tip and the end zone. To search for the limit state of both the crack tip and end zone one should introduce the condition of the bond limit stretching at the trailing edge of the end zone. Solving jointly these critical equations we can determine the critical external loads, the end zone size d_{cr}, and the adhesion fracture resistance $G_{tip}(d_{cr},\ell)$ at the crack limit equilibrium state for the given crack length and the bond characteristics. In this part of the abstract the energetic fracture criterion is considered in the detail. The description of the force fracture criterion can be found in [2].

CONCLUSIONS

The application of the proposed model and the comparison the criterions for different problems from macro to nanoscale of the interface cracks are presented. It is noted that the most differences between the results from the force and energetic fracture conditions are observed for the cracks of micro and nano sizes.

Work was partly supported by RFBR, the grant number is 02-01-00116.

References

[1] Goldstein, R V and Perelmuter M N (1999) *Modelling of bonding at an interface crack*, International J. of Fracture, **99** (1-2), 53-79.

[2] Perelmuter, M N (2002) *Fracture criterion for cracks with bridged zone* In: Proc. of IUTAM Symposium 'Asymptotics, Singularities and Homogenisation in Problems of Mechanics', pp.261-270, Kluwer Academic Press.

[3] Salganik, R L (1963) *Brittle fracture of glued bodies,* Appl. Math. Mech. (PMM), **27**(5), 957-965.

Investigation of Wave Propagation in Multiwall Carbon Nanotubes

Sha Fenghuan Zhao Longmao Yang Guitong
Institute of Applied Mechanics, Taiyuan University of Technology,
79West Yingze str. Taiyuan. Shanxi, 030024, P. R. of China

Carbon nanotubes (CNTs) possess extraordinary physical properties. The fundamental understanding of nano-structure material properties and their effect on the mechanical behavior are required in order to develop reliable constitutive models for various design purposes. Since controlled experiments at nanoscales is difficult, and molecular-dynamics simulations remain formidable expense especially for large-scale systems, continuum elastic models have been widely and successfully used to study buckling、vibration and wave propagation in CNTs. MWCNTs (Multiwall Carbon Nanotubes) have been modeled as a single elastic beam which ignored non-coaxial intertube radial displacements and the related internal degrees of freedom. Ru[1] *et al* suggested a multiple-elastic-beam mode. This model is only applicable for CNTs with the certain range radius when $R_{NT}/\ a_{NT} \approx 1$(a_{NT} is the width of hexagonal carbon rings ,of about 0.24nm).The diameter of NTs , d_{NT} , may vary from about 0.4 to 100nm.

CNTs are novel cylindrical macromolecules composed of carbon atoms in a periodic hexagonal arrangement. The structural characteristics of CNTs make them similar to beams for CNTs with small radii, and cylindrical shells for CNTs with large radii. When L_{NT} (nanotube length)and R_{NT} (nanotube radius) are substantially larger than its maximum thickness, CNTs have some dimensional characteristics of a macroshell. The CNTs with the certain range ratio of thickness to radii ($h_{NT}/\ R_{NT}$), namely $1/1000<h_{NT}/\ R_{NT}<1/10$, should be considered thin shells[2].

The study of vibration and wave propagation in CNTs is one of interest of researchers. We suggest a multiple-elastic-shell model, in which each of the originally concentric nest nanotubes of MWCNTs is described using an individual elastic shell, and the deflections of all nest tubes are coupled through the van der Waals interaction between any two adjacent tubes. Transverse disturbing wave propagation in a N-wall CNT is described using the following N-couple equations.

$$\begin{aligned} &d_1[w_2-w_1]=2\pi R_1 D_1\frac{\partial^4 w_1}{\partial x^4}+\rho A_1\frac{\partial^2 w_1}{\partial t^2}\\ &d_2[w_3-w_2]-d_1[w_2-w_1]=2\pi R_2 D_2\frac{\partial^4 w_2}{\partial x^4}+\rho A_2\frac{\partial^2 w_1}{\partial t^2} \end{aligned} \qquad (1)$$

$$-d_{N-1}[w_N-w_{N-1}]=2\pi R_N D_N\frac{\partial^4 w_N}{\partial x^4}+\rho A_N\frac{\partial^2 w_N}{\partial t^2},$$

where x is the axial coordinate, t is time,$w_i(x,t)$(i=1,2—N) is the deflection of the i-th nanotube, D_i and A_i are the effective bending stiffness and the area of the cross section of the i-th tube, the subscripts1,2,.....,N are used to denote the quantities of the tube, respectively, and all tubes have the same young's modulus E=1TPa and the mass density $\rho=1.3 g/cm^3$,the interaction coefficients d_i (i=1,2---N-1) can be estimated approximately

$$d_i=\frac{200\times(2R_i)erg/cm}{0.16e^2}, \qquad (2)$$
$$e=0.142nm,\quad i=1,2,\cdots,N-1$$

Consider a doublewall nanotubes (DWNT). The equation for a DWNTs is given by the two of Eq.(1) withd_2=0.Thus, for a sinusoid disturbing wave, substituting $w_1=a_1e^{i(kx-\omega t)}, w_2=a_2e^{i(kx-\omega t)}$ to Eq (1) ,the following equation can be got two wave speeds C_1 and C_2.

$$C_1=\frac{\sqrt[4]{2}\omega}{\sqrt[4]{\xi+\sqrt{\xi^2-4\eta}}}, \qquad (3)$$
$$C_2=\frac{\sqrt[4]{2}\omega}{\sqrt[4]{\xi-\sqrt{\xi^2-4\eta}}},$$

where

$$\xi=\left(\frac{\rho A_1}{2\pi R_1 D_1}+\frac{\rho A_2}{2\pi R_2 D_2}\right)\omega^2-d_1\left(\frac{1}{D_1}+\frac{1}{D_2}\right), \qquad (4)$$
$$\eta=\frac{\rho^2 A_1 A_2}{(2\pi)^2 R_1 R_2 D_1 D_2}\omega^4-\frac{d_1\rho(A_1+A_2)}{(2\pi)^2 R_1 R_2 D_1 D_2}\omega^2$$

$$\frac{a_1}{a_2}=1+\frac{2\pi R_2 D_2 k^4}{d_1}-\frac{\rho A_2\omega^2}{d_1} \qquad (5)$$

Where a_1 and a_2 represent the amplitudes of the inner

and the outer tubes, respectively. k and ω are the wave number and the circular frequency.

For the sake of comparison, the transverse wave speed of a DWNT given by the single-shell model is

$$c_o = \left(\frac{2\pi RD\omega^2}{\rho A} \right) \qquad (6)$$

where D and A are the total moment of and the cross sectional area of DWNT. As $k \to 0$, the cut-off frequencies are:

$$\omega = \sqrt{\frac{(A_1 + A_2)d_1}{\rho A_1 A_2}} \qquad (7)$$

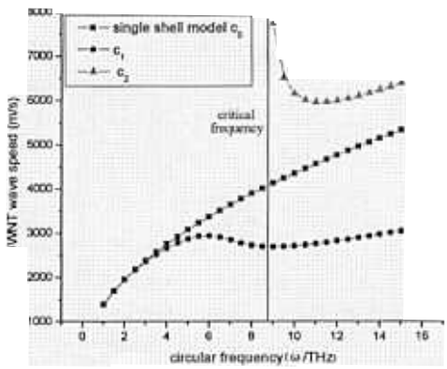


Fig.1. DWNT wave speeds vs frequency

Two wave speeds of double- wall-shell model is given in Fig.1. It is seen from Fig.1 that when the frequency is below the critical frequency , only one wave speed exists, and the associated vibration mode of the DWNT is almost coaxial. However, once the frequency exceeds the critical frequency, a non-coaxial vibration mode emerges. The two wave speeds (Eq.3) predicted by the present model are significantly different from that given by the single-shell model, and their vibration modes are substantially non-coaxial.

Further, a five-wall CNTs with the innermost diameter 3.5nm and the outermost diameter 10.0nm are discussed. In this case, Eq.(1) gives five coupled equation. There exist five critical frequencies for five-wall CNTs. They are $\omega_1 = 6.68THz$ $\omega_2 = 7.42THz$ $\omega_3 = 8.45THz$ $\omega_4 = 8.75THz$ and $\omega_5 = 5.59THz$

Tel.: +86-0351-6018624
Fax: +86-0351-6010820
E-mail : Shafenghuan.sohu.com

respectively. Five wave speeds of five-wall CNTs are given in Fig.2, with comparison to the speed given by the single-shell model. It is seen from Fig.2 that when the frequency is below the critical frequency, only one wave

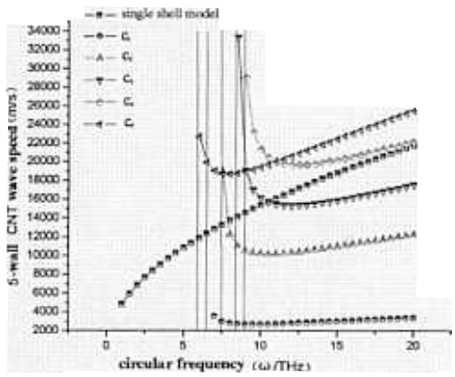


Fig.2. 5-wall CNTs wave speeds vs frequency

speed exists, and the vibration mode of the MWNT is almost coaxial. However, once the frequency exceeds one of critical frequency, a part of vibration modes is coaxial and another is non-coaxial.

These results clearly show that the single-shell model fails to predict the wave speed and vibration mode for MWNTs at ultrahigh frequencies and wave propagation in MWNTs exhibits complex phenomena and is highly non-coaxial. Therefore, wave propagation in MWNTs at ultrahigh frequencies has to be described by the present model which account for the intertube radial displacements and the related internal degrees of freedom.

Reference

1. J.Yoon, C. Q. Ru, A. Mioduchowski, Sound wave propagation in multiwalled carbon nanotubes, [J]. Journal of Applied Physics, 2003, 93,1—6.

2. V. M. Harik, Mechanics of carbon nanotubes: applicability of the continuum beam models, Computational materials science, 24 (2002) 328—342.

HOMOGENISATION MODELS OF CARBON NANOCOMPOSITES MECHANICAL PROPERTIES

Aleksander Muc, Małgorzata Chwał
Institute of Machine Design, Cracow University of Technology, Kraków, Poland

Introduction

It is well known that single walled (SWCN) or multi walled carbon nanotubes (MWCN) offer a significant amount of stiffness (1-4 TPa) or strength comparing with those obtained for classical graphite or carbon fibres. However, those nanomaterials cannot form structures used for engineering purposes. On the other hand, nanocomposites made of SWCN or MWCN can loose a lot of their magnificent mechanical properties when will be joined with the matrix. Of course, the same situation is observed for classical carbon/graphite microcomposites.
The general aim of the present paper is following:

- to present the theoretical homogenisation models for the evaluation of the Young modulus values for nanocomposites reinforced with SWCN and MWCN,
- to propose method of numerical modelling nanocomposites reinforced by SWCN and a polymer matrix,
- to compare the obtained results with classical microcomposites in order to demonstrate advantages and disadvantages of both composite materials.

Modelling of nanocomposites mechanical properties

Two theoretical models have been presented and discussed in details – see also [1]. The first one is based on the physical description by taking into account interatomic interaction and nonotubes geometry. This approach employs the form of the physical potential proposed by the Tersoff-Brenner. The elementary cell definition, here nanotube, with surrounding resin layer is treated as the homogeneous body - the material continuum. Next, the similar model to phenomenological engineering approach has been presented that is created by the junction of the law of mixture with the Cox mechanical model. This model describes the stress distribution along stretched short fibres surrounded by the resin matrix. The similarity between the composite materials reinforced by short fibres and nanotubes has been considered and pointed out. The evaluation of the Young modulus requires the basic information about the materials parameters of the nanotubes and resins. This method can be easily adopted in all engineering computations and possible applications.
The numerical model corresponds directly to the 3-D form of a single carbon nanotube (i.e. a graphene sheet rolled up to a cylinder) surrounded by a polymer resin layer. The interaction between two neighbourhood carbon atoms in the nanotube and between carbon atoms and the resin are expressed with the use of the Tersoff-Brenner potential and van der Waals forces. Numerically the interaction is modelled by a 1-D spring FE having a stiffness derived from the above mentioned relations. It is assumed that the single nanotube surrounded by the resin forms an elementary cell. That subcell is a starting point for the derivation of averaged mechanical properties using standard homogenisation rules – see e.g. [2].

Results and Concluding Remarks

In order to compare the interatomic interaction model with phenomenological model the value of Young modulus has been calculated for two different volume fraction of nanostructures: 10% and 20% - see Fig.1. The experimental investigations proved that the values of modulus are close to the modules, which is obtained from the interatomic interaction model.
The considered carbon nanocomposites have lower Young modulus than that for classical fibre microcomposites. In our opinion, the factors leading to such rather bad properties are following the low volume fraction of the reinforcement in composites, random distribution of the nanotubes and the length of reinforcement which deformation results in many unfavourable effects.
In present phase of evolution composites reinforced by nanotubes do not allow to get better mechanical properties than microcomposites. However, there is a great possibility of using nanotubes

in industrial applications due to higher strength and Young modulus than analogous properties for micro-fibres.
Numerical homogenisation models are complicated due to necessity of taking into account specific nanotube geometry (see [1]), and not only the nanotube diameter. Therefore, the plot demonstrates only one pointed obtained from numerical analysis. However, it should be emphasised that carbon nanotubes have two general average dimensions: the diameter and the length and both of them that can affect significantly the nanocomposite mechanical properties. In our opinion, the length should be also taken into consideration, especially for short nanotubes, and it shows explicitly the advantages of numerical modelling.

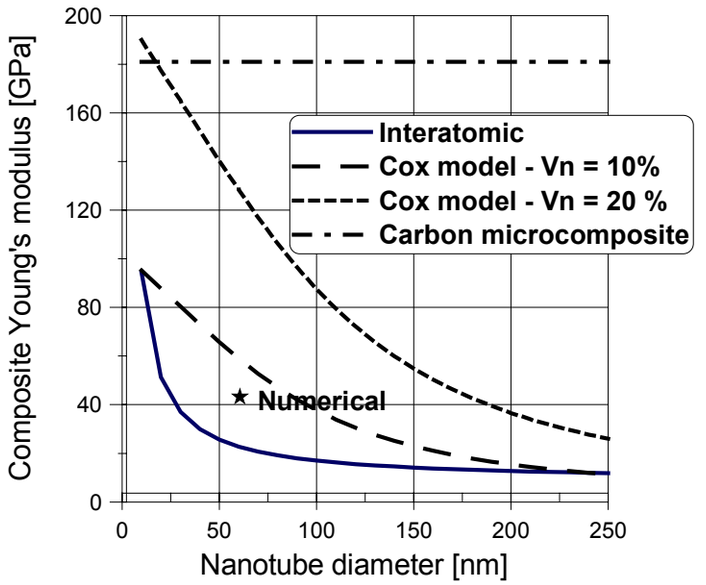


Fig.1 A comparison of mechanical properties for carbon micro- and nano- composites

In present phase of evolution composites reinforced by nanotubes do not allow to get better mechanical properties than microcomposites. However, there is a great possibility of using nanotubes in industrial applications due to higher strength and Young modulus than analogous properties for micro-fibres. Theoretical considerations demonstrate only modest improvement in mechanical properties for nanocomposites. To improve it is necessary to solve various technological problems dealing with: alignment of nanotubes, dispersion of nanotubes in the matrix, functionalization of the nanotubes to enhance matrix bond/load transfer, efficient use of the different types of nanotube reinforcements (SWCN vs. MWCN vs. nanoropes). Now, a number of methods have been used to achieve highly oriented CN – see e.g. [3]. All these methods are limited to microscale and are not suitable for commercial manufacturing process.
Validity of the assumptions relating the applicability of continuum based theories vs. physical models (understood in the sense of both solid state physics and quantum mechanics) is still an open problem. However, the results presented in the paper demonstrate that physical models gives much better description for low values of nanotubes diameters, whereas for high values two approaches leads to the almost same results.

References

[1] Muc A., *Mechanics of fibrous composites*, Księgarnia Akademicka, Kraków 2003, (in Polish).
[2] P. M. Suquet, *Lecture Notes in Physics*, **272**, 1987.
[3] C. Bower, R. Rosen, L. Jin, J. Han, O. Zhou, *Phys. Lett.* , **74**, 1999, pp. 3317-19.

MICRO- AND NANO-MECHANICS OF CARBON NANOTUBES COMPOSITES

XI-QIAO FENG [*], DONG-LI SHI [*], Y. HUANG [**], KEH-CHIH HWANG [*]
[*] *Department of Engineering Mechanics, Tsinghua University, Beijing 100084, P. R. China*
[**] *Department of Mechanical and Industrial Engineering, University of Illinois at Urbana-Champaign Urbana, IL 61801, U.S.A.*

Summary In the present paper, the constitutive relation and failure behaviorsof carbon nanotube-reinforced composites are studied using methods of micromechanics and nanomechanics. First, we examined the factors that influence the overall mechanical property of carbon nanotube composites, including the weak bonding between carbon nanotubes and matrix, the curviness and agglomeration of carbon nanotubes. Second, we established a hybrid continuum/micromechanics/atomistic method to investigate the defect nucleation in a carbon nanotube embedded in a polymer matrix.

INTRODUCTION

Both experimental and theoretical studies have shown that carbon nanotubes (CNTs) have extraordinary mechanical and electrical properties [1, 2]. Such superior properties make CNTs a very promising candidate as the ideal reinforcing fibers for advanced composites with high strength and low density. Though some encouraging results have been reported, there are many other experiments that demonstrate only modest improvement in the strength and stiffness after CNTs are incorporated into polymers. Why there are no consistent improvements in mechanical properties of CNT-reinforced composites? This is investigated in this paper and it is shown that the unsatisfactory improvement in the mechanical properties of CNT-reinforced composites could be attributed to the weak bonding and interaction between CNTs and polymer matrices, as well as the waviness and agglomeration effects of CNTs. In addition, we presented a combined continuum/micromechanics/atomistic method to investigate the defect nucleation and fracture behaviours of CNTs in polymers.

STIFFENING MECHANISMS OF CARBON NANOTUBES

Waviness effect

Because CNTs have very low bending stiffness due to the small tube diameter (~ 1 nm), most CNTs in composites exist in a curved state. However, there is yet no theoretical model to estimate the stiffening effect of curved CNTs. We presented here a micromechanics model to examine the waviness effect of curved CNTs on the elastic properties of CNT-reinforced composites. A unit cell is chosen containing a curved CNT, which is modeled as a helical spring and its waviness is governed by the spiral angle. The RVE is divided into slices of infinitesimal thickness to estimate the stress and strain fields in the unit cell. The Mori-Tanaka method is employed to estimate the stiffening effect of curved CNTs. Some examples are given to show the dependence of the effective elastic modulus of composites as a function of the elastic constants and the volume fraction of CNTs having different wavinesses and orientation distributions. It is observed that the modulus of carbon nanotube composites decreases rapidly as the waviness increases.

Agglomeration effect

Due to their low bending stiffness and high aspect ratio, CNTs are very easy to agglomerate in the polymer matrix. We develop a micromechanics model to study the influence of the agglomeration of CNTs on the effective elastic moduli of CNT-reinforced composites. The spatial distribution of CNTs in the matrix is assumed to be non-uniform such that some local regions have a higher concentration of CNTs than the average volume fraction in the material. These regions with concentrated CNTs are assumed to have spherical shapes, and are considered as "inclusions" with different elastic properties from the surrounding material. Thus, we consider the CNT-reinforced composite as a system consisting of inclusions of sphere shape embedded in a hybrid matrix. Both the matrix and the inclusions contain CNTs. This model have two parameters describing the agglomeration of CNTs. We estimate the effective elastic stiffness of the composite containing either straight or curved CNTs by using the above micromechanics. The changing curves of the effective tensile moduli with the agglomeration parameters are given. It is clearly shown that the agglomeration of CNTs exerts a significant weakening effect to CNT-reinforced composites. In addition, the anisotropic property of CNTs affects to a considerable extent the overall effective elastic moduli, especially the Young's modulus at uniform distribution.

Interface effect

Interfaces often play a significant role in mechanical and physical properties of nanostructured materials. For CNT-reinforced composites, the high surface area of CNTs creates a large interfacial region, which has properties different

from the bulk matrix. We used a three-phase unit cell method to calculate the impact of interface adhesion on the effective elastic moduli of composites. This micromechanics method can easily derive the effective moduli of composites with good accuracy, even for a high volume fraction of inclusions. It is assumed that each CNT is assumed to have very high length-to-radius ratios and considered as fibers of infinite length. For polystyrene composites reinforced with aligned CNTs, the tensile elastic moduli are given as a function of the parameters of interfaces. For a weak interface, the effective elastic moduli are insensitive the interface thickness. Therefore, the unsatisfying improvement of the stiffness of CNT-reinforced composites observed experimentally cannot be explained by the interface effect. These results can be easily understood because the axial elastic modulus of CNTs is much higher than those of the polymer matrix and the interface phase, and so the stiffening effect of CNTs is predominated by the elastic constants, geometric parameters, spatial distribution and microstructures of CNTs in composites.

DEFECT NUCLEATION AND FRACTURE OF NANOTUBES IN COMPOSITES

Hybrid continuum/atomistic method

To investigate the deformation and fracture behaviors of carbon nanotubes, we conducted a hybrid continuum/atomistic study [3, 4] based on the Tersoff-Brenner potential and the Cauchy-Born Rule. Atoms far away from the defect are represented by an atomistic-based continuum theory, which has been shown to agree well with molecular dynamics simulations studies without any parameter fitting. For atoms near the defect, we use molecular mechanics coupled with the atomistic-based continuum theory to determine the atom positions. This hybrid continuum/atomistic study significantly reduces the computation.

Defect nucleation and evolution in carbon nanotubes

The above hybrid continuum/atomistic method is employed to consider the problem of defect nucleation and evolution of CNTs under tension. The tensile stress-strain curves of CNTs are first simulated, without any parameter fitting, as a function of the chiral angle and diameter, and the results agree well with the experimental curves [5]. As the tensile strain reaches a critical value, the so-called Stone-Wales transformation (i.e., 90^o rotation of a C-C bond, resulting in a low energy 5-7-7-5 ring pair) occurs. The critical strain of occurrence of a Stone-Wales depends strongly on the chiral angle, and ranges from 8.2% for armchair CNTs and 15.3% for zigzag CNTs. The Stone-Wales defect will become unstable when a second critical load is reached. The fracture paths and instability modes after defect nucleation are dependent also upon the chiral angle.

Fracture of carbon nanotubes embedded in a polymer matrix

To simulate the fracture process of carbon nanotubes interacting with the surrounding matrix, which is of great interest in field of nanomechanics and nanomaterials, we adopted a combined continuum/micromechanics/atomistic method, as an extension of the above analysis of CNTs without interaction with matrix. The far-field stress in the unit cell around a CNT is determined by the Mori-Tanaka method of micromechanics. Our calculations show that the interaction between CNTs and matrix lowers the critical strain of fracture of CNTs, in comparison with that without interaction effect.

CONCLUSIONS

In the present paper, the stiffening and strengthening physical mechanisms of CNTs in polymer matrix are investigated theoretically by using micromechanics and nanomechanics methods. The effect of waviness, agglomeration and interfaces of CNTs are examined. It is established that the waviness and agglomeration may significantly reduce the stiffening effect of CNTs. A combined continuum/micromechanics/atomistic method is developed to simulation the fracture process of CNTs in a polymer. We have given the critical tensile strains of defect nucleation and final fracture, which show a strong dependence on the chiral angle The present study not only provides the important relationship between the effective properties (both elastic modulus and strength) and the microstructure parameters of CNT-reinforced composites, but also may be useful for improving and tailoring their mechanical properties.

Acknowledgements

The authors acknowledges the support from NSFC (Grant No. 10028204, 10121202 and 10102008).

References

[1] Saito R., Dresselhaus G., Dresselhaus, M. S.: Physical Properties of Carbon Nanotubes, Imperial College Press, London, 1998.
[2] Qian D., Wagner G. J., Liu W. K., Yu M. F., Ruoff, R. S.: *Appl. Mech Reviews*, **55**:495–533, 2002.
[3] Zhang P., Huang Y., Gao H. Hwang K. C.: *J. Appl. Mech.* **69**:454–458, 2002.
[4] Jiang H., Feng X. Q., Huang Y., Hwang K. C., Wu P. D.: *Comput. Meth. Appl. Mech. Eng.* 2004 (in press).
[5] Yu M. F., Lourie O., Dyer M. J., Moloni K., Ruoff R. S.: *Science*, **287**:637–640, 2000.

CHARACTERIZATION OF MEMS MATERIALS

Jurg Dual*, Gerd Simons*, Jacqueline Vollmann*
*Institute of Mechanical Systems, Center of Mechanics, ETH Zurich
8092 Zurich, Switzerland

Summary Mechanical characterization of MEMS materials is increasingly important in view of improving reliability and assessing the life time of new devices. In this paper a number of testing methods are described. These methods include tensile, torsion and fatigue testing of specially designed microstructures, as well as wave propagation methods based on an optical pump probe setup to test thin films. Difficulties arise from manufacturing and handling of small structures and the determination of its geometrical dimensions, which directly affect the accuracy of material parameters extracted from the experiments. In addition the measurement of the mechanical parameters like small forces and torques or strains on small specimens or with ps time resolution pose challenges. This paper focuses on size effects in copper foils of thickness between 10 and 250 microns as determined from tensile testing and probing of inhomogeneities caused e.g. by diffusion at interfaces in thin films.

INTRODUCTION

With increasing use of miniaturized systems a strong need arises for the mechanical characterization of the materials used. In particular for polycrystalline materials it is often not possible to use properties obtained from macroscopic experiments, as the microscopic elements have particular microstructures, which are related to the special manufacturing processes used. Therefore, specimens need to be tested in their "small" configurations in view of measuring the relevant design parameters.
In this paper an overview of a set of measurement techniques is given, which complement the well known nanoindentation technique: Mechanical wave propagation techniques based on laser generated ultrasound for determining elastic properties, and tensile, torsion and fatigue tests with high crack resolution on specially manufactured microscopic specimens. These techniques are applied to probe material property gradients in thin film structures and to investigate size effects in thin rolled copper foils, respectively.

THIN FILM TESTING USING AN OPTICAL PUMP PROBE SETUP

When wave propagation techniques are to be used to determine elastic properties, very high frequencies need to be generated because of the small size of the specimens: The wavelength needs to be small compared to the relevant geometrical parameters. Such high frequency waves can be generated and measured in a contactless manner using a pump probe set-up with an ultra short pulse laser. [1] (Fig. 1) In a project called "Nanosonics" this set-up is used to characterize thin films, their adhesion to the substrate and material property gradients. [2]
A short pulse laser is used to excite mechanical pulses thermoelastically by means of a pump pulse. Echoes of these mechanical pulses reaching the surface are causing a slight change in the optical reflectivity, which is superimposed on the reflectivity change caused by the temperature change. The surface reflectivity is scanned vs. time with a probe pulse by varying the relative time shift between the incidence of pump pulse and probe pulse with a variable delay line. Thus the time of flight of the acoustic pulse is measured. In Fig. 1 a typical record of reflectivity vs. time is shown.

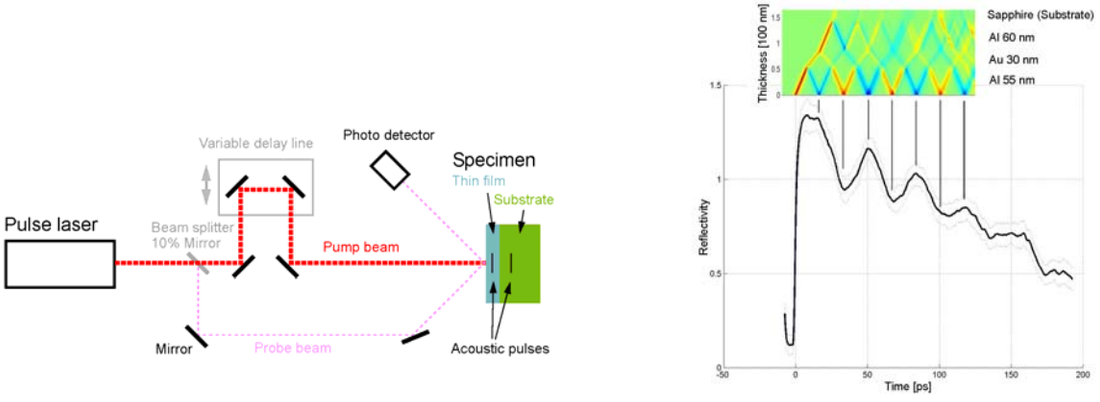


Figure 1. Nanosonics: Pump probe set-up for testing of thin films (left) and typical result of a reflectivity curve vs. time (right) showing an exponentially decaying part due to a temperature change and superimposed echoes of mechanical waves. A Lagrange diagram at the top shows the theoretical arrival times. The system investigated consists of 55nm Al, 30 nm Au, 60 nm Al on a sapphire substrate.

TENSILE TESTING

While elastic properties do not seem to vary with the size of the specimen [3,4], for other quantities large discrepancies might arise. When testing Ni specimens made with the LIGA technology it was found, that the ultimate strength was considerably higher than for macroscopic specimens [5]. An overview of possible size effects is given in [6]. Fleck et al. have explained size effects in copper wires in torsion using a strain gradient plasticity theory [7]. Thin rolled copper foils were tested in tension in order to minimize effects of strain gradients. Nevertheless, a large change was observed in its plastic deformation when decreasing its size. [8] The specimens in [8] consisted of two plates and a small connecting testing region, were made of 99.9% pure copper foils (Goodfellow) and had ratios of thickness to width to gauge length of 1 to 20 to 200, which was kept constant when downscaling. The thickness range considered was 10μm to 250μm. The specimens were manufactured by photolithography and etching and had the longitudinal axis in the rolling direction. They were tested using the setup described in [9]. While foils with a thickness of 34 μm and more show large plastic deformation, foils of 10 μm thickness behave macroscopically rather brittle. (Fig. 2, left) This behavior is also reflected in the SEM pictures of the fracture surface. (Fig. 2, right) The 10 μm foils show quite a flat fracture surface, while the 34 μm foils show voids and dimples. In terms of fracture strain, when going from 100 μm to 10 μm thickness, the fracture strain is reduced dramatically from 15% to 0.2%. The reason for this discrepancy is unclear at the moment. Considerable efforts are currently made to characterize the specimens used in terms of surface roughness (about 0.2 μm), grain shapes, orientations, size, dislocation densities, etc. Because of the small size this turns out to be quite difficult though. The latest characterization results will be reported.

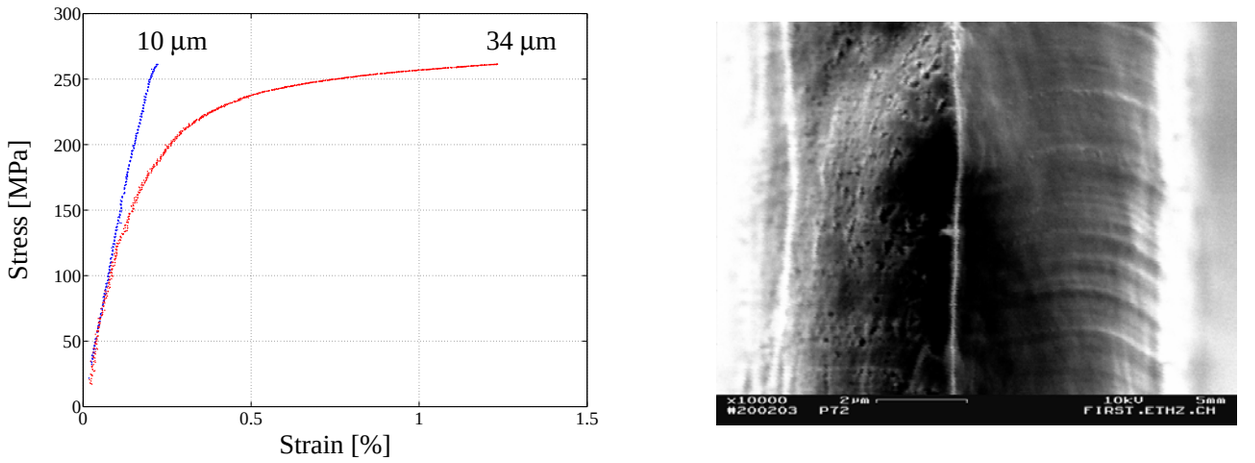


Figure 2. Engineering stress - strain curves for geometrically similar specimens of copper with foil thickness of 10μm and 34μm and SEM picture of fracture surface for the 10 μm thick specimen (right) of copper in tensile testing.

SUMMARY AND OUTLOOK

In addition to the well-known nanoindentation technique a number of other methods for material testing of micromaterials exist, which have received increasing attention. They offer insight into many interesting phenomena like size effects (bending, microtensile and torsion tests) or probing of continuous interfaces (pump probe pulsed laser set-up). Together with elaborate manufacturing possibilities as known from MEMS and IC fabrication, they offer possibilities of probing material behaviour in the nm range. With this it is hoped that an improved understanding of processes important for the life time and reliability of MEMS components will be possible in the near future.

REFERENCES

[1] C. Thomsen, H. T. Grahn, H. J. Maris, and J. Tauc, *Physical Rev. B*, vol. 34, pp. 4129-4138, 1986
[2] J. Vollmann, D. M. Profunser, J. Dual, *Ultrasonics,* vol. 40 (1-8), pp. 757-763, 2002
[3] T. Namazu, Y. Isono, T. Tanaka, *Journal of Microelectromechanical Systems*, vol. 9, pp. 450-459, 2000.
[4] W. N. Sharpe, K. M. Jackson, K. J. Hemker, Z. L. Xie, *Journal of Microelectromechanical Systems*, vol. 10, pp. 317-326, 2001.
[5] E. Mazza, S. Abel, J. Dual, *Microsystem Technologies*, vol. 2 (4), pp. 197-202, 1996
[6] E. Arzt, *Acta Materialia*, vol. 46 (116), pp. 5611-5626, 1998
[7] N.A. Fleck, G. M. Muller, M. F. Ashby, J.W. Hutchinson, *Acta metal. Mater*., vol. 42 (2) , pp. 475-487, 1994
[8] J. Villain, C. Weippert, G. Simons, J. Dual, *Proceedings of Materialsweek* 2002, Munich, Germany
[9] E. Mazza, G. Danuser, J. Dual, *Microsystem Technologies*, vol. 2 No. 2, pp. 83-91, 1996

2/JD

XXI ICTAM, 15–21 August 2004, Warsaw, Poland

AN ANALYTICAL MODEL OF OXIDE RUMPLING AS THE MECHANISM LEADING TO FAILURE IN THERMAL BARRIER COATINGS

Daniel S. Balint*, John W. Hutchinson**
*Cambridge University, Engineering Department, Cambridge CB2 1PZ, U.K.
**Harvard University, Division of Engineering and Applied Sciences, Cambridge, MA 02138, U.S.A.

Summary A model providing an analytical approximation of undulation growth in the oxide layer of a multi-layer thermal barrier coating incorporating most of the important details is presented for a realistic cyclic thermal history; thickening, yield and lateral growth within the oxide layer are included, and creep in the metallic bond-coat and ceramic top-coat is modeled using a power-law description. Common observations are explained and the connection between rumpling and fracture in the top-coat is elucidated.

INTRODUCTION

Ceramic films with low thermal conductivity are used to protect internally cooled machine components from the extreme temperatures of their surroundings by establishing a thermal gradient across the coating that can lower the temperature of the underlying substrate by several hundred degrees. Perhaps the most important application of thermal barrier coatings at present is on the blades in turbine engines used for aircraft and power generation. Internal temperatures can be well in excess of $1000\,^{\circ}\mathrm{C}$. A thermal barrier system consists of four layers. The ceramic top-coat is typically zirconia and 100-200 μm thick. Beneath the top-coat is a metallic bonding layer that is attached to a thick superalloy substrate. The bond-coat is roughly 50 μm thick and is usually PtNiAl or FeCrAl. At elevated temperatures a film of aluminum oxide forms between the bond-coat and the zirconia top-coat that is several μm thick and acts as a barrier that prevents oxidation of the superalloy substrate. The bond-coat and porous ceramic top-coat creep easily at temperatures in excess of $600\ ^{\circ}\mathrm{C}$. Both layers are modeled at elevated temperatures as power-law creeping materials. The oxide is modeled as elastic at temperatures below $1150\,^{\circ}\mathrm{C}$ and elastic/perfectly-plastic at $1150\,^{\circ}\mathrm{C}$ based on recent high-temperature indentation data. In addition, thickening and growth within the oxide layer are incorporated that drive changes in the oxide stress.

It is becoming increasingly clear that development of undulations in the oxide layer, otherwise known as oxide rumpling, and the stresses they induce in the ceramic top-coat and on the oxide/bond-coat interface are perhaps the main factors affecting the lifetime of thermal barrier coatings. At the present time, no comprehensive understanding exists of the mechanics of rumpling, and a model that captures the behavior of both PtNiAl and FeCrAl systems is lacking. A model providing an analytical approximation of undulation growth in the oxide layer of a complete four-layer thermal barrier system, incorporating most of the important details, is presented for a full cyclic thermal history.

RESULTS AND CONCLUSIONS

Details of rumpling as predicted by the model depend on the bond-coat material. In all cases, rumpling driven by a compressed, undulating oxide film relies upon the highly nonlinear power-law creep behavior of the bond-coat. Results suggest that the differences between PtNiAl and FeCrAl that are most relevant to rumpling are that PtNiAl experiences a large mismatch strain when the system is cycled, whereas FeCrAl does not (c.f. Fig. 1). For appreciable undulation growth to occur, the model requires amplitudes of undulations in FeCrAl systems prior to thermal cycling to be approximately an order of magnitude larger than they are in PtNiAl systems. In addition, the yield stress of oxide grown on FeCrAl is roughly 3 times larger than for PtNiAl, which leads to a higher driving force for undulation growth. Both systems are predicted to rumple appreciably upon thermal cycling with FeCrAl also rumpling under isothermal conditions, consistent with observations (c.f. Fig. 2).

The mechanics underlying rumpling differs between the two systems. PtNiAl has a relatively large mismatch with the substrate, i.e. the equi-biaxial stress in the bond-coat is essential (c.f. Fig. 1). The change in volume that accompanies the reversible phase transformation in PtNiAl is critical, as it is the primary cause of large bi-axial stress in the bond-coat. An undulation with an amplitude of 5 nm in a PtNiAl system can grow by nearly 1 μm in 100 cycles. Any perturbation in the surface of a PtNiAl bond-coat is highly unstable. Thus, controlling the bond-coat stress appears to be the most feasible way to suppress rumpling in PtNiAl systems. Modifying the phase transformation by shifting the hysteresis to lower temperatures, which decreases the stress in the bond-coat at elevated temperatures (c.f. Fig. 1), can dramatically reduce rumpling; a shift of $-200\,^{\circ}\mathrm{C}$ reduces total undulation growth by 90%. This is a potentially viable way to modify the design of PtNiAl thermal barrier coatings for longer lifetimes.

FeCrAl systems have little or no mismatch with the substrate. Thus, bond-coat equi-biaxial stress does not play a major role in FeCrAl rumpling. The normal traction at the interface between bond-coat and oxide controls rumpling in FeCrAl systems. Much less rumpling would occur if the initial undulations were comparable in size to those in PtNiAl systems. Decreasing the initial amplitudes, which seems feasible, would be sufficient to effectively suppress growth in FeCrAl systems; this is not true of PtNiAl. The model predicts that the difference between cyclic and isothermal rumpling for FeCrAl systems is not nearly as large as in PtNiAl systems, which is consistent with experimental observations (c.f. Fig. 2).

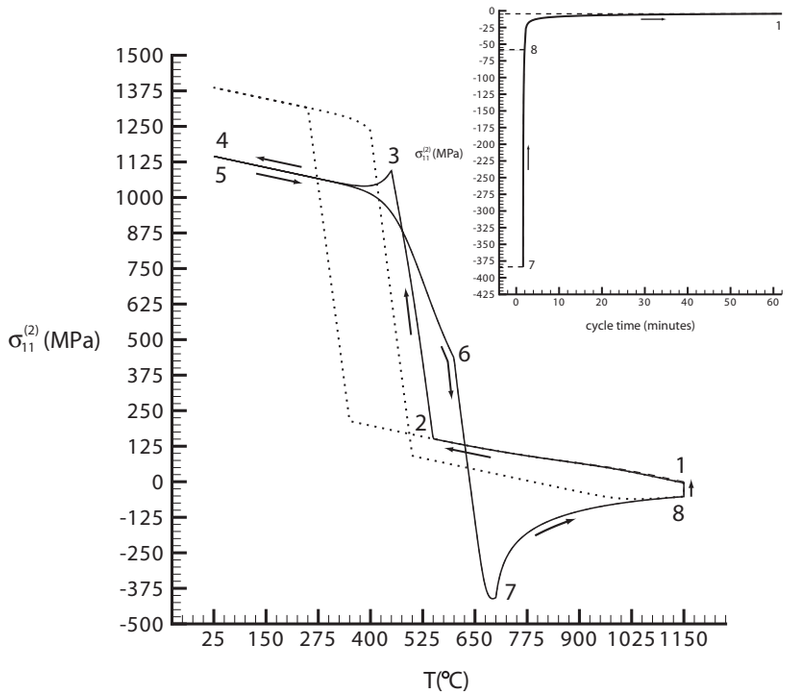


Figure 1. The equi-biaxial stress cycle in a PtNiAl bond-coat when subjected to a typical cyclic thermal history. Most of the total undulation growth per cycle occurs between points 7 and 1, when the creep strength is low and the stress is large (c.f. inset). Although the stress is relatively small at point 8, approximately -60 MPa, the creep strength of the bond-coat is sufficiently small to allow further undulation growth to occur during the 1-hour isothermal period that lasts from point 8 to point 1. The dotted line shows the stress cycle for a modified phase transformation; the hysteresis of the phase transformation is shifted by -200 °C.

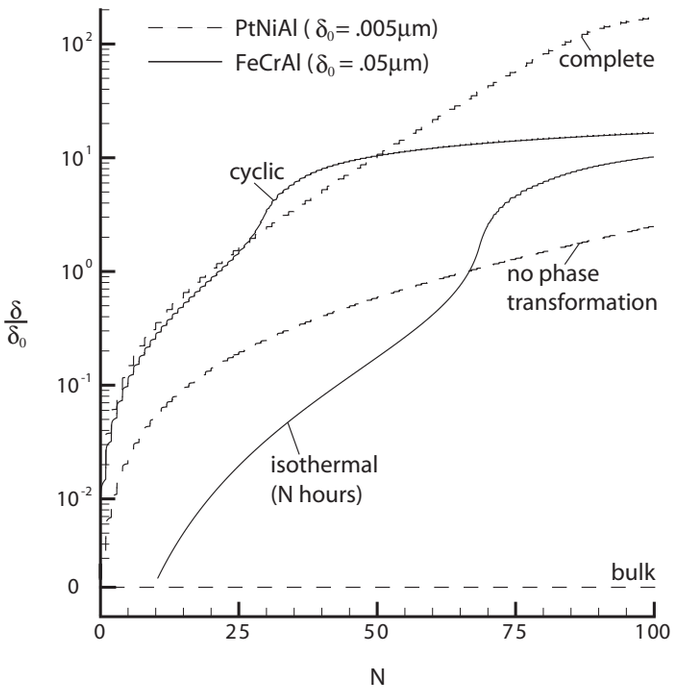


Figure 2. Shown here: 1) no undulation growth occurs on oxidized bulk PtNiAl (i.e. not attached to a thick substrate) 2) the phase transformation leads to much more undulation growth in PtNiAl systems ($\delta_{N=100}$ =.875 μm with the transformation included, $\delta_{N=100}$ =.0125 μm without it) 3) significant undulation growth ($\delta_{N=100}$ =.75 μm) can occur on FeCrAl despite having little or no mismatch with the substrate because the initial undulations are larger than PtNiAl and the oxide yield stress is higher 4) there is little difference between cyclic and isothermal histories for FeCrAl, i.e. significant undulation growth can occur for FeCrAl under isothermal conditions ($\delta_{N=100}$ =.5 μm).

INSTABILITIES OF COMPOSITE MATERIALS REINFORCED BY NANO-FIBRES : A RE-EXAMINATION OF ELASTIC BUCKLING

R. Parnes and A. Chiskis
Dept. of Solid Mechanics, Materials and Systems
Faculty of Engineering, Tel-Aviv University, 69978 Ramat Aviv, Israel

Elastic buckling is studied as a possible failure mechanism of a composite. Although it appears that common polymer matrix composites (e.g. glass/epoxy or carbon-graphite/epoxy) undergo plastic micro-buckling or fail due to other mechanisms (such as fibre crushing, delamination, etc.)[Fleck (1997)], nevertheless, for very dilute composites fabricated in the emerging framework of nanotechnology, elastic buckling may, in fact, be the dominant failure mechanism.

The phenomenon of elastic buckling of composites was first investigated in the 1960's. Since then, it has been generally accepted that elastic buckling of a composite consisting of straight fibres in a matrix can occur in two modes : a shear buckling mode (SBM), where the fibre and matrix exhibit in-phase deformation (i.e. assume the same deformed shape and a transverse buckling mode (TBM) where the fibre and matrix exhibit anti-phase deformation Moreover, it is asserted that transverse buckling occurs for relatively low values of the fibre volume fraction, v_f, while shear buckling takes place for larger values of v_f [Jones (1975)]. These two types of buckling modes were first studied by Rosen (1964) using, in both cases, simple approximations together with an energy approach.

For the case of shear buckling, assuming in-plane buckling, Rosen treated the problem by means of a model consisting of thin layers embedded in a matrix and thus obtained a buckling stress [see Rosen (1964) and Jones (1975)]

$$\sigma = R_0 + R_1 \left(\frac{H_f}{L}\right)^2, \tag{1.1b}$$

where

$$R_0 = \frac{G_m}{v_m}, \qquad R_1 = \frac{\pi^2}{3} E_f \, v_f. \tag{1.1c,d}$$

In the above, G_m denotes the shear modulus of the matrix material, E_f Young's modulus of the fibre, and $v_m = 1 - v_f$, the volume fraction of the matrix; H_f is the fibre (layer) thickness and L is the buckling wavelength (which is not specified in the analysis). Clearly, according to this solution, the lowest buckling mode occurs as the wave length $L \to \infty$ with a corresponding buckling stress,

$$\sigma_R^{(S)} = \frac{G_m}{v_m}.$$

In his investigation of the transverse buckling mode (TBM), Rosen, derived an expression for the critical buckling stress,

$$\sigma_R^{(T)} = 2v_f \left(\frac{E_f E_m R_v}{3}\right)^{1/2}$$

where E_m denotes the Young's modulus of the matrix and $R_v = \frac{v_f}{v_m}$ denotes the ratio of the volume fractions.

The Rosen solutions have, since then, been widely used and have been applied to common composites such as glass/epoxy. For these classes of composites with stiffness ratios E_f/E_m of the order of 20, the Rosen solution in the shear buckling mode leads to buckling stresses with corresponding strains – clearly unrealistic – of the order of 10% and higher. Indeed, Rosen and Dow (1972) pointed out the unreasonableness of such strains. Nevertheless, to the authors' best knowledge, in all existing literature devoted to buckling of composites, the Rosen approximation is adopted.

In the present investigation, assuming initially the existence of the two possible modes of buckling, we consider the problem of elastic buckling of a composite consisting of periodically spaced layers, using as a model, fibres embedded in an elastic matrix for which an exact 2-D stress fields is determined. By investigating the two modes of elastic buckling, we show that the stress required to cause buckling in the TBM is always greater than that for the SBM. For the particular case of dilute composites, corresponding to nano-fibre reinforced composites, the TBM stress is seen to converge (from above) to the SBM stress. Thus we demonstrate that the transverse buckling mode is, in fact, a spurious mode and that buckling of a composite always occurs in the SBM. In addition, we show that while buckling of non-dilute composites in the SBM occurs with infinite wavelengths, for relatively dilute composites, buckling in this mode occurs with *finite* wavelengths and therefore the approximate Rosen solution fails to be valid in these cases.

Since the investigation under consideration is concerned with buckling of composites as an instability phenomenon, a linear analysis is used here. In fact, as opposed to the Rosen solution, in the present investigation, elastic buckling is found to occur with realistic strains within the elastic range of composites having relatively small fibre volume concentrations and high stiffness ratios, E_f/E_m. Such cases may be found, for example, in composites reinforced by carbon nano-fibres of high stiffness.

Indeed, carbon nanotubes, whose estimated values of Young's modulus as reported by Treacy, Ebbensen and Gibson (1996) range up to 4.15 TPa (with an average value of 1.8 TPa), appear to show great promise as fibres in light-weight composites. Based on recent experiments, Wagner et al (1998) give estimates of the maximum tensile stress of such fibres (when embedded in a polymer matrix) of approximately 55 GPa. Moreover, based on experimental investigations of buckling of multi-wall embedded carbon nanotubes of finite length, Lourie, Cox and Wagner (1998) calculated, on the basis of simple shell theory, critical stresses of 135 GPa to 147 GPa. While common epoxy materials (e.g. BP907 and AF126) can undergo strains with linear elastic behavior of the order of 2% simulated experiments of individual isolated nanotubes show that, due to their high strength and morphology, they can exhibit strains greater than 10% in tension and 5% in compression [Yakobson et al. (1996)]. A comprehensive review of nanofibre technology is presented in Yakobson and Smalley (1997).

As a result of these developments, a re-examination of elastic buckling as a realistic failure mechanism in the framework of nanotechnology appears warranted.

References

Fleck, N. A. (1997) Compressive failure of fiber composites. *Advances in Applied Mechanics*, **33**, 43–117.

Jones, R. (1975) *Mechanics of composite materials.* McGraw–Hill, New York.

Lourie, 0., Cox, D.M. and Wagner, H.D. (1998) Buckling and collapse of embedded carbon nanotubes. *Phys. Rev. Letters*, **81** (8), 1638–1641.

Rosen, B. W. (1964) Mechanisms of composite strengthening. *Fiber Composite Materials*, Chapter 3, American Society of Metals, 37–75.

Rosen, B. W. and Dow, N. F. (1972) Mechanics of failure of fibrous composites, in *Fracture, An Advanced Treatise*, ed. by H. Liebowitz, Chapter 8, Academic Press, Vol. **7**, New York, London, 612–672.

Treacy, M.M.J., Ebbesen, T.W. and Gibson, J.M. (1996) Exceptionally high Young's modulus observed for individual carbon nanotubes. *Nature*, **381**, 678–680.

Wagner, H.D., Lourie, O., Feldman, Y. and Tenne, R. (1998) Stress-induced fragmentation of multiwall carbon nanotubes in a polymer matrix. *Appl. Phys. Lett.*, **72** (2), 188–190.

Yakobson, B.I., Brabec, C.J. and Bernholc, J., (1996) Nanomechanics of Carbon Tubes : Instabilities beyond Linear Response, *Phys. Rev. Letter.*, **76**, 2511-2514.

Yakobson, B. I and Smalley, R. E. (1997) Fullerene nanotubes: $C_{1,000,000}$ and beyond. *American Scientist*, **85**, 324–337.

INTERFACIAL ADHENSION OF PZT FERROELECTRIC THIN FILMS DETERMINED BY NANO-INDENTATION METHOD

X. J. Zheng*, Y. C. Zhou**
*Institute of Fundamental Mechanics and Materials Engineering, Xiangtan University, Xiangtan, Hunan, 411105, China
** Faculty of Materials & Optoelectronics Physics, Xiangtan University, Xiangtan, 411105, China

Summary We propose an elastic groundsill beam model with piezoelectric effect considered to assess the interfacial adhesion of ferroelectrics thin films, complemented and validated by nano-indentation fracture test on $Pb(Zr_{0.52}Ti_{0.48})O_3$ (PZT) thin films. It was observed from the load-indentation depth curves and atomic force microscopy (AFM) images that the fracture failure of PZT thin films induced by nano-indentations can be divided into three typical stages: no damage, bulging and spallation. The delamination of thin film systems was modeled as an interfacial crack propagation problem, with the energy release rate determined from the elastic groundsill beam model. For PZT thin films deposited on single Si substrate with thickness of 350nm and 450nm, the energy release rates per unit new crack area are in the range of 3.399~52.432J/m^2 and the phase angles are constant of 13.357^0.

INTRODUCTION

$Pb(Zr_xTi_{1-x})O_3$ (PZT) thin film is an important ferroelectric system with potential applications in MEMS, but the conventional models can not be used to analyse the interfacial adhesion and indentation fracture of ferroelectrics thin films accurately because of the piezoelectric effect. The description of fracture toughness of a poled piezoelectric ceramic is very complicated, involving fracture toughness measured perpendicular and parallel to the poling direction [1,2]. In this paper, we propose an elastic groundsill beam model to evaluate the interfacial adhesion of PZT thin films, characterized by energy release rate per unit crack area in nano-indentation test when the largest indentation depth is close to the film thickness. The piezoelectric effects are fully considered in the model. We conducted nano-indentation fracture test on PZT films deposited on single Si substrate by metal organic decomposition (MOD), using a cube corner indenter and atomic force microscopy (AFM). The spallations of the thin film were observed when indentation depths exceeded 13% of the film thickness and when the diamond indenter penetrated through the thin film into the substrate. Interfacial delamination is approximately consisted of the classical mode I and mode II cracks and the corresponding mode II crack dominates the interfacial crack in the ferroelectrics thin films.

THEORETICAL MODEL

We present a general theory for the axisymmetric indentation of transversely isotropic piezoelectric solids, governed by the following equations

$$\begin{cases}\sigma_{ij}=c_{ijkl}\varepsilon_{kl}-e_{kij}E_k \\ D_i=e_{ikl}\varepsilon_{kl}+\in_{ik}E_k\end{cases}\quad\begin{cases}\sigma_{ij,j}=0 \\ D_{i,i}=0\end{cases}\quad\begin{cases}\varepsilon_{ij}=(u_{i,j}+u_{j,i})/2 \\ E_i=-\phi_{,i}\end{cases}\qquad(1)$$

where, $\sigma_{ij}, D_i, \varepsilon_{ij}, u_i, E_i$ and ϕ are stress, electric displacement, strain, displacement, electric field and electric potential, respectively, and $c_{ijkl}, \varepsilon_{ik}, e_{kij}$ are elastic, dielectric and piezoelectric constants, respectively. The normal indentation of a piezoelectric thin films was considered as shown in Figs.1(a), where h, H, 2α and P_0 are thin film thickness, substrate thickness, apex angle and indentation load, respectively, and 2c is the largest imprint made on the surface of the film by the indenter. Combined with the assumption that the indenter is an insulator and does not reach the substrate, we have the relationship between the indentation load P_0 and the largest imprint 2c derived by Giannakopoulos and Suresh [3]. Because both the film thickness h and indenter contact region size c are in the nanometer scale, the approximations $\frac{\partial u_r}{\partial z}=\frac{\Delta u_r}{h}=\frac{u_r(r,0)}{h}$, $\frac{\partial u_z}{\partial r}=\frac{\Delta u_z}{c}=\frac{u_z(c,0)}{c}$, $E_z=-\frac{\partial\phi}{\partial z}=-\frac{\phi(r,0)}{h}$ are given. Using the above relationships and boundary conditions, the stress σ_{rr} in the indentation region of the thin film can be obtained as,

$$\sigma_{rr}=c_{11}\varepsilon_{rr}+c_{12}\varepsilon_{\theta\theta}+c_{13}\varepsilon_{zz}-e_{31}E_z\qquad(2)$$

We then present an elastic groundsill beam model as shown in Figs.1(b) to describe the indentation fracture characteristics of thin films, where the indentation depth is assumed to be close to the film thickness. When $\eta=\frac{h}{H}\to 0$, the constitutive equations of film and substrate are respectively given as

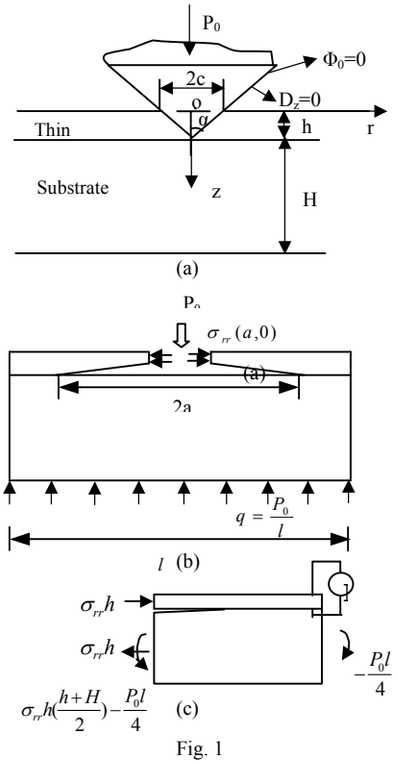


Fig. 1

$$\sigma_{rr}=\left(c_{11}-\frac{c_{13}^2}{c_{33}}+\frac{e_{13}^2}{\in_{33}}-\frac{c_{13}e_{13}e_{33}}{c_{33}\in_{33}}\right)\varepsilon_{rr} \quad 0\le z\le h, \qquad \sigma_{rr}=\frac{8\mu_2}{\kappa_2+1}\varepsilon_{rr} \quad h\le z\le h+H \tag{3}$$

which is derived from the composite beam theory, with $\kappa_2=3-4\nu_2,\nu_2$ and μ_2 being the Poisson扭 ratio and shear modulus of substrate, respectively.

We consider the interface crack problem as shown in Figs.1(c) using the theory of composite beam. The interface intensity factors K_1 and K_2 reduce to the classical mode I and mode II factors K_I and K_{II},

$$K_1=\frac{1}{\sqrt{2}}\left[Ph^{-1/2}\cos\omega+2\sqrt{3}Mh^{-3/2}\sin\omega\right], \quad K_{II}=\frac{1}{\sqrt{2}}\left[Ph^{-1/2}\sin\omega+2\sqrt{3}Mh^{-3/2}\cos\omega\right] \tag{4}$$

where the angle ω is a function related with the Dundurs' parameters α and β [4]. The energy release rate per unit new crack area can be then written in terms of the complex stress intensity factor,

$$G=\frac{c_1+c_2}{16\cosh^2\pi\varepsilon}|\mathbf{K}|^2, \quad \mathbf{K}=K_I+iK_{II}, \quad \varepsilon=\frac{1}{2\pi}\ln\frac{1-\beta}{1+\beta} \tag{5}$$

where, ε is the bimaterial constant.

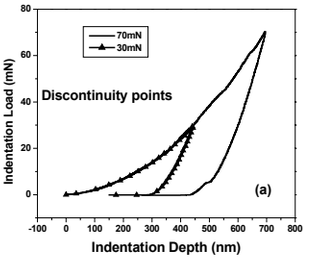


Fig.2

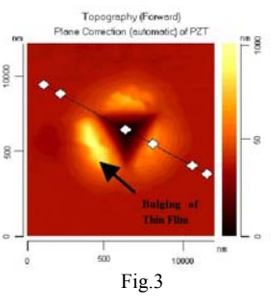


Fig.3

EXPERIMENTAL

The indenter was driven perpendicularly into, then out of, PZT thin films prepared by MOD. In order to understand indentation fracture process of PZT, we used three types of peak indentation loads to induce the fracture of the samples and recorded the corresponding load-indentation depth curves. Each indentation experiment consisted of loading, holding, and unloading completely. After the unloading, associated crack patterns were examined by AFM. The typical load-displacement curves and AFM image of indentations made at indentation loads are given as Fig.2 and Fig.3.

To determine the parameters for the theoretical model, we obtain elastic, piezoelectric and dielectric constants of PZT thin films from the reference [3]. The interfacial crack length 2a, the largest imprint 2c at the peak indentation load P_0, and the residual depth could be obtained from the AFM image. As a result the interfacial adhesion of PZT thin films could be determined from our theoretical model given as equation (5).

EXPERIMENTAL RESULTS AND DISCUSSIONS

From the load-indentation depth curves and AFM images, the different failure process can be observed. Summarizing the experimental observation, one concludes that each discontinuity indicates the point where the nano-indenter was driven from one medium into another, and the propagation of interfacial cracks increases with increasing indentation load.

After determining the radius of the residual indent mark region *c*, the interface intensity factors K_1, K_2, and energy release per unit new crack area G can be calculated by equations (4) and (5). The energy release rate versus the interfacial fracture area is shown in Fig.4, which showed that the energy release rate decreased as the interfacial crack length increased.

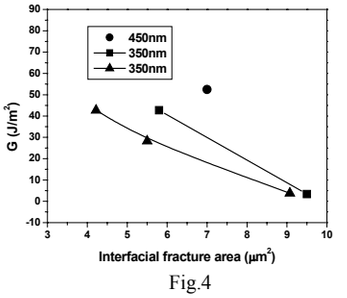


Fig.4

CONCLUDING REMARKS

We proposed a model to measure interfacial adhesion in ferroelectric thin films. An elastic groundsill beam model taking into account the piezoelectric effect is developed to describe the interfacial crack for ferroelectrics thin films when the indentation depth is close to the film thickness. The model was validated by nano-indentation tests made on PZT thin films, where the elastic modulus and hardness of PZT thin films were determined from load-indentation depth curves, and energy release rate and stress intensity factors were calculated.

References

[1] Uchino K.. Piezoelectric Actuators and Ultrasonic Motors. Kluwer Academic Press, Boston, 1997.

[2] Mehta K., Virkar A.. Fracture Mechanisms in Ferroelectric-Ferroelastic Lead Zirconate Titanate (Zr:Ti=0.54:0.46) Ceramics. *J. Am. Ceram. Soc*. **73(3)**: 567-574, 1990.

[3] Giannaropoulos A. E., Suresh S.. Theory of Indentation of Piezoelectric Materials. *Acta mater.* **47(7)**: 2153-2164, 1999.

[4] Suo Z., Hutchinson J. W.. Interface Crack Between Two Elastic Layers. *I. J. Fract*. **43**: 1-18, 1990.

A CELLULAR AUTOMATON FOR MODELLING EVOLUTION OF HETEROEPITAXIAL SYSTEMS

Simon P.A. Gill
Department of Engineering, University of Leicester, Leicester, UK, LE1 7RH

Summary An algorithm is presented for the implementation of surface and bulk diffusion within a cellular automaton. Relaxation of the elastic strain in heteroepitaxial systems via morphological change and interdiffusion is investigated.

INTRODUCTION

The large elastic strain energy present in epitaxial heterogeneous thin film systems due to elastic mismatch acts to destabilize the growth of a flat planar film. This can lead to the development of self-organised clusters of atoms which have many potential microelectronic and optoelectronic applications. The electronic properties of these islands (clusters) is highly dependent on their internal strain state. The mismatch strain originates from the compositional differences within these multi-component systems. During deposition these structures can evolve to reduce the compositional variations by alloying, leading to the development of islands with complex internal compositional distributions (and hence complex internal strain states). A number of experimental studies have observed this strain-driven alloying in the Ge/Si [1] and InAs/GaAs [2,3] semiconductor systems. It is the aim of this work to develop a 2D simulation of the evolution of these islands during growth to gain insight into the processes by which these structures relax. This requires a novel multi-component model for surface and (near-surface) bulk diffusion under the influence of elastic strain. Such a model is outlined below with some initial benchtesting examples.

THE BASIC MODEL

The geometry is described within an hexagonal grid of cells (or lattice of atomic sites). We assign an occupancy probability, $p(i,j)$, to a cell (i,j) and allow it to evolve statistically as a continuous variable. The occupancy probability of each cell is then evolved at a rate given by the flux between the cell and its nearest neighbours. This flux is determined from a simple atomistic hopping model. Assume that each cell (lattice site) can either contain an atom or not. An atom is only allowed to move to an adjacent cell if that cell is unoccupied and has one or more other nearest neighbours, i.e. an atom cannot leave the surface. The activation energy for a jump is equal to $2Kn$ where K is the half-bond energy and n is the number of nearest neighbours (1 to 6). This is an initial state model, i.e. the activation energy does not depend on the final state. This approach is commonly adopted within kinetic Monte Carlo simulations and ensures that the rate and probability of a hopping event is completely determined by only the atoms six nearest neighbours. There are consequently 2^6=64 different atomic configurations local to a cell. The flux between each cell is calculated as the product of the transition rate and probability of a particular configuration summed over all possible configurations. The probability of each local configuration is determined from the occupancy probabilities of the six nearest neighbour cells. Despite the simplicity of these rules, complex behaviour representative of that seen in real physical systems can be produced. Figure 1 illustrates a simple test simulation for surface diffusion is a single-component system.

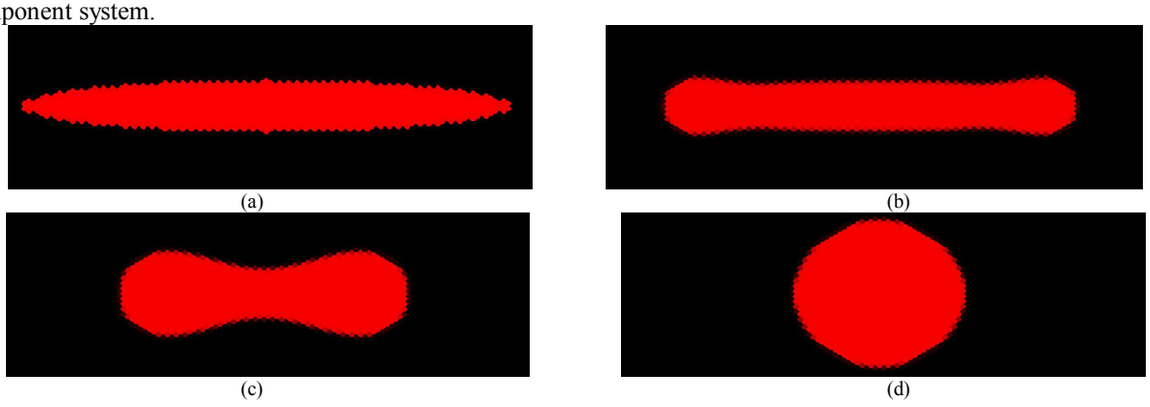


Figure 1. An ellipse evolves into a circle via surface diffusion to reduce its surface energy for K=1. (a) initial shape, (b) the high curvature ends quickly become more rounded, (c) the body gradually becomes more rounded over time, (d) the final stable state.

MULTI-COMPONENT SYSTEMS

The advantage of cellular automata is that they can readily be implement into a numerical simulation and it is easy to add additional physics. Here the previous model is easily extended to include two different components, A and B. There are now two state variables, $p_A(i,j)$ and $p_B(i,j)$, the probabilities that a cell (i,j) is occupied by an atom of A or an atom of B respectively. The transition rates subsequently depend on the different types of bond. K_{AA}, K_{AB} and K_{BB} are taken to be the half-bond energies of the A-A, A-B and B-B bonds respectively. The average mass fluxes between each cell are determined from the sum of the probability weighted transition rates over all possible configurations as before. The introduction of more material parameters leads to a wealth of different phenomena. A simple illustration of one case of two-component diffusion is shown in Figure 2.

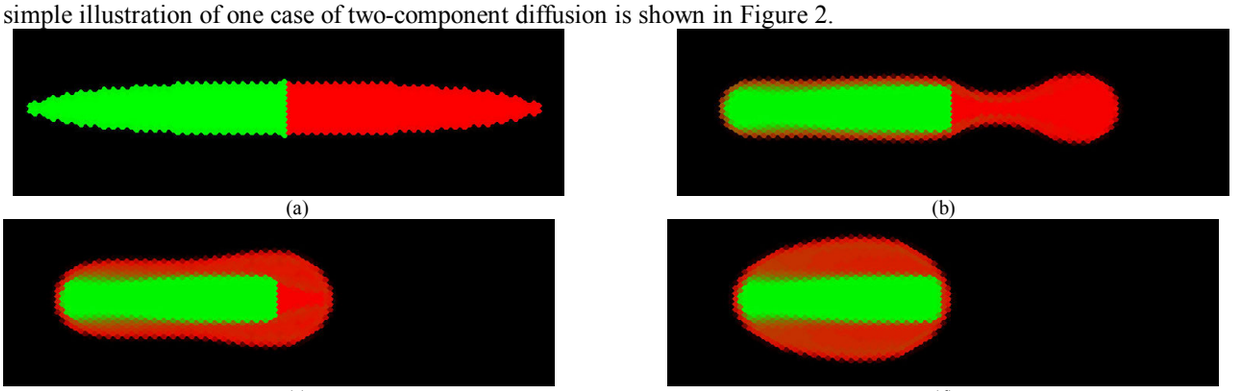


Figure 2. Evolution of a two-component elliptical body with K_{AA}=1.0, K_{AB}=1.2 and K_{BB}=1.4. Component A is red and B is green. (a) initial state, (b) A is more mobile than B, hence the low energy A surface quickly envelops B to remove the high energy B surface. (c) the evolution continues and (d) the body starts to become more circular.

ELASTICALLY STRAINED SYSTEMS

The bond energy is now a function of bond strain, ε. Assuming linear elasticity, the bond energy is modified to $K = K_0(1-\alpha\varepsilon^2)$. The forces between each cell due to the elastic term (weighted by the relevant cell occupancy probabilities) are equilibrated locally every iteration. They are equilibrated globally every 2000 iterations. The cell occupancy probabilities are evolved as before but with the strain dependent activation energy. Consequently, atoms in highly strained regions are more mobile than those in less strained regions. An example is shown in Figure 3.

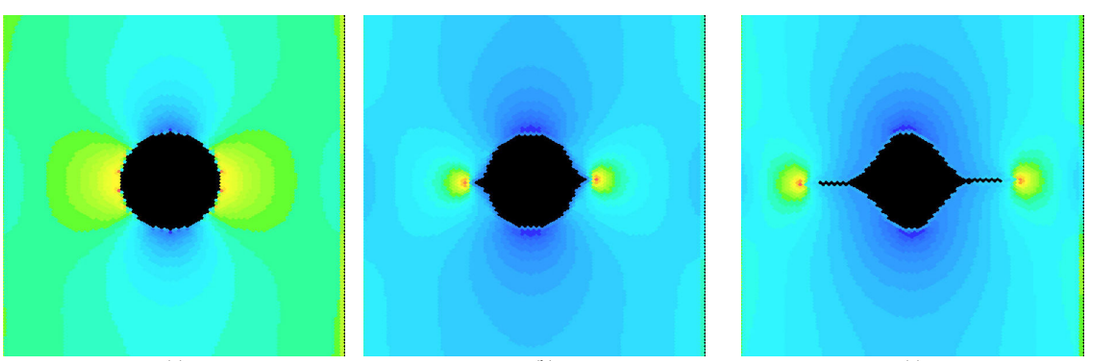


Figure 3.Evolution of a void in an elastically stressed body for K_0=1, α=6000 and an applied strain of 0.3%. (a) The plate is under uniaxial tension in the vertical direction. (b) Material flows over the surface of the void from areas of high elastic energy (red) to areas of low elastic energy (blue) causing small notches to appear on the side of the void, (c) the stress is raised at the notch tips causing them to grow into crack-like features.

CONCLUSION

The necessary mechanisms required to develop a model for coherent heteroepitaxial systems have been demonstrated. These features will be combined into one simulation to investigate the problems discussed in the Introduction.

ACKNOWLEDGEMENTS

Financial support for this work from EPSRC grant no. GR/R24104 is gratefully acknowledged.

References

[1] S.A. Chaparro, J. Drucker, Y. Zhang, D. Chandresekhar, M.R. McCartney and D.J. Smith, *Phys. Rev. Lett.* **83**, 1199 (1999).
[2] N. Lui, J. Tersoff, O. Baklenov, A.L. Holmes & C.K. Shih, *Phys. Rev. Lett.* **84**, 334 (2000).
[3] X.Z. Liao, J. Zou, D.J.H. Cockayne, R. Leon and C. Lobo, *Phys. Rev. Lett.* **82**, 5148 (1999).

MECHANICAL BEHAVIOR OF NANO GRAINED METALS

Aman Haque and Taher Saif
Mechanical and Industrial Engineering, University of Illinois, Urbana, IL 61801, USA

Summary: The paper presents (1) a novel instrumentation for studying mechanical behavior of nano scale free standing thin films in-situ in Scanning or Transmission electron microscope, as well as under optical microscope, (2) results on mechanical behavior of nano grained Al and gold films (3) mechanistic interpretation of the experimental data.

Thin metal films are extensively used in electronics and micro/nano mechanical systems where components are often less than 100nm. These metal structures are typically poly crystalline in nature with abundant grain boundaries. The fundamental role of such boundaries in determining the thermomechanical properties is not well understood, a study that is often challenged by the limitations of the instrumentation that allows testing nano structures.

Experimental procedure: We have developed a micro mechanical experimental method to study the stress-strain response of free standing thin metal films with thickness 20 nm or higher. It allows in-situ observation of the microstructue of the sample in transmission electron microscope (TEM) when the sample's stress-strain behavior is measured. Hence, the fundamental micro structural mechanisms that give rise to the mechanical behavior can be investigated. Figure 1 shows the SEM micrograph of the micro apparatus. It is a tensile test stage made of Single Crystal Silicon (SCS), 10mm long, 3mm wide and 100μm thick. The freestanding sample is made of sputtered Aluminum [1]. One end of the sample is attached to a force sensor beam, A_1A_2, while the other end to the support beams B_1B_2. A piezo motor is employed to stretch the stage along its longitudinal direction which strains the sample. Two markers gaps, A and B, measure the force and stretch of the sample: marker A gives the displacement of the beam A_1A_2, and hence the force on the sample (spring constant of A_1A_2 is calibrated using a nano indenter), and the difference between the gaps A and B gives the stretch of the sample.

Results: We have successfully carried out in-situ uniaxial tensile experiment in TEM on 100nm thick Al film while its stress-strain response is measured. Figure 2 shows the quantitative stress-strain response and the in-situ transmission electron micrograph at regions C and D of the stress-strain curve. To the best our knowledge, this is the first time that such quantitative measurement and qualitative observation of material's microstructure have been performed. Note that the grains are mostly less than 100nm, there are very few dislocations and they do not generate during straining, but grains rotate with increasing strain as is evident from the change of contrast of the same grain under increased loading. Furthermore there is no evidence of voids or intergranular cracks in the film.

We have employed the instrument to test Aluminum films with grain sizes 10-80nm with the corresponding thicknesses of 30-200nm. The results are shown in Table 1. We note that as grain size decreases, (1) elastic modulus decreases, (2) yield stress increases and reaches a maximum value when the grain size is 50nm. With further decrease of the grain size, yield stress decreases. We also find that metal shows non-linear elastic behavior with small plastic deformation when grain size is small. Experiments on gold films show similar behavior.

Interpretations: As grain size decreases, grain boundary to volume ratio increases. Atomic arrangements near the boundary region is distorted compared to the granular counterpart to accommodate the misfit between the two adjacent grains. The distorsion is induced by various planar defects such as dislocations, steps and lattice dilations which result in a region with lower elastic modulus. Thus, as the metal is strained, due to higher elastic compliance, the boundary region takes more strain that the granular counterpart. With increasing strain, the boundary region becomes more distorted, and its compliance increases. Thus, the overall metal response becomes increasingly softer. Upon unloading, the metal returns to the unloaded configuration with small permanent deformation. Figure 3 shows a mechanistic model that considers the metal as composed of grains with size *d* and grain boundaries with thickness δ. If the modulus of the boundary is half that of the grains, and δ=1.1nm, then the effective modulus of the metal as a function of grain size agrees well with experiments (Table 1).

With decreasing grain size, there is thus a change of deformation mechanism. The dislocation slip ceases simply due to lack of dislocations, and grain boundary mechanisms begin to play a major role in taking deformation. Yield stress increases. If the grain size is such that there are not many dislocations for plasticity, but the size is not small enough that the abundance of dislocation is yet sufficient for the boundary mechanisms to facilitate the deformation, then the metal may show highest strength. For Al, 50nm appears to be this transition size.

[1] A. Haque and M. T. A. Saif, *Scripta Materialia*, 47, pp 863-867, 2002.

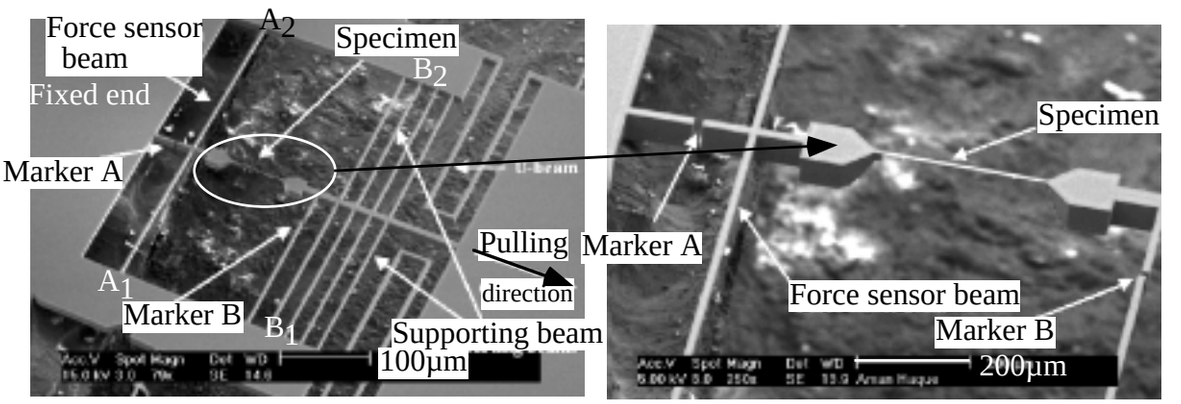


Figure 1. Scanning electron micrograph of the micro stage and the smaple. The stage is 100µm deep, 10mm long and 3mm wide.

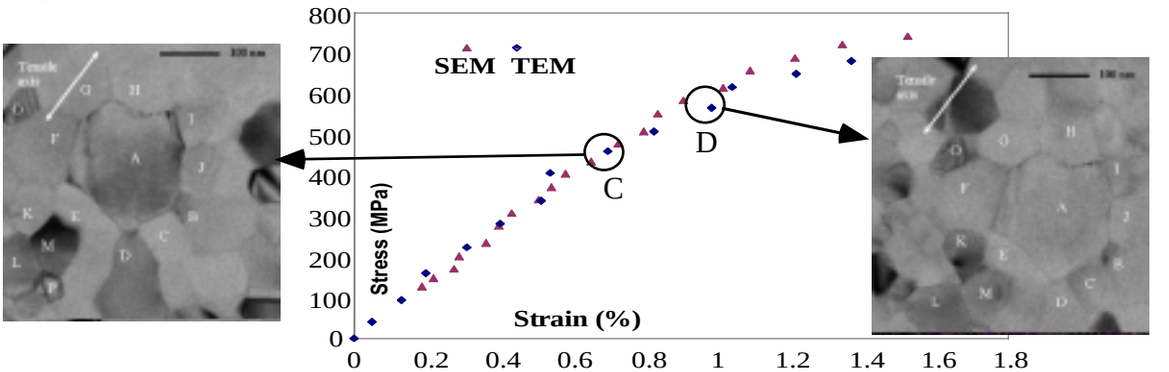


Figure 2. Stress-strain behavior of 100nm thick aluminum film studied in Scanning and Transmission electron microscopes.

Film thickness t (nm)	Grain size d (nm)	E (GPa)	Yield stress (GPa)	Ultimate stress (MPa)	Ultimate strain ε_u (%)
200	80	70	327	531	1.995
100	50	68	710	726	1.525
50	20	63	328	497	1.099
30	10	60	249	318	0.638

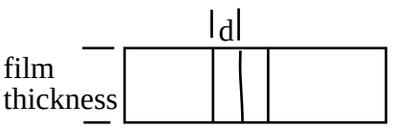


Table 1. Mechanical properties of Al films with varying thickness and grain sizes

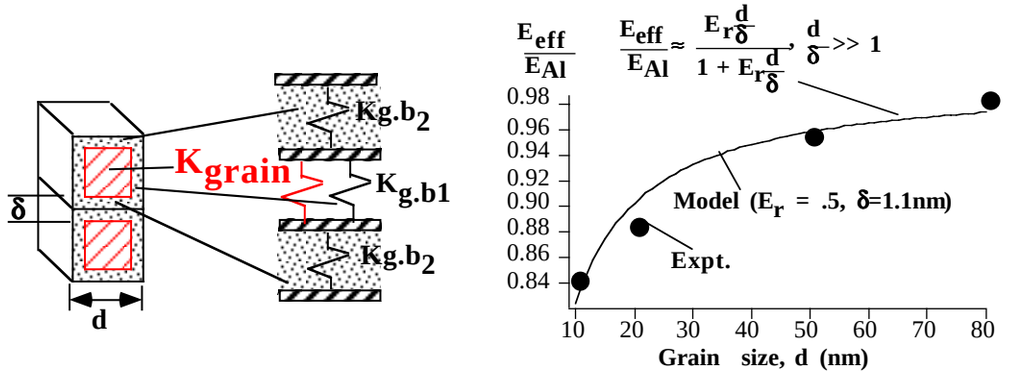


Figure 3. An elastic model of a polycrystalline metal with grains and grain boundaries. If $E_r=E_{gb}/E_g$ = .5, and the grain boundary thickness is 1.1nm, then the model prediction matches well with the experimental data.

Effective thermoelastic properties of nanocomposites with prescribed random orientation of nanofibers

A. Roy*, V. A. Buryachenko**
*Air Force Research Laboratory, AFRL/WPAFB, OH 45433-7750, USA
**University of Dayton Research Institute (UDRI), Dayton, OH 45469-0168, USA

Summary. Nanocomposites (NC) are modeled as a linearly elastic composite medium, which consists of a homogeneous matrix containing a statistically homogeneous random field of spheroid nanofibers with prescribed random orientation. Estimation of symmetric effective thermoelastic properties of NC was performed by the effective field method taking into account the random orientation of nanofibers as well as justified selection of spatial correlations of fiber location.

Experimental research and molecular dynamic simulation indicated that nanofibers can be effectively considered in the framework of continuum mechanics as the homogeneous prolate spheroidal anisotropic homogeneous inclusions (see [1]) with a large aspect ratio ($\alpha\approx1000$). In this paper, a nanocomposite is modeled as a linearly elastic composite medium, which consists of a homogeneous matrix containing a statistically homogeneous random field of nanofibers v_i with prescribed random orientation described by the orientation distribution function (ODF). Estimation of effective elastic moduli of nanocomposites was performed by means of the effective field method (MEF, see for references and details [2]) based on effective field hypothesis: each fiber is embedded in the homogeneous effective field that is dependant on prescribed random orientation of this fiber [contrary to the Mori-Tanaka method (MTM) where the effective field coincides with the average stresses in the matrix]. It may be noted the certain drawbacks of the extension of Mori-Tanaka method to multiphase composites: Mori-Tanaka moduli may violate the Hashin-Shtrikman bounds and are nonsymmetric for the general diphase composites. In the authors' knowledge, no models exist that satisfy all of theoretical criteria mentioned above for arbitrary phase anisotropy and fiber-orientation distributions, and a micromechanical approximation devoid of the mentioned contradictions is highly desirable.

MEF was used in the framework of quasicrystalline approximation when the spatial correlations of inclusion location called "correlation hole" take particular ellipsoidal forms. This "correlation hole" v_i^0, enclosing the representative fiber v_i, does not occupy the centers of surrounding fibers (since they cannot overlap) and are compatible with mutual orientations of fibers. The independent justified choice of shapes of inclusions and correlation holes provides the formulae of effective moduli which are completely explicit and easy to use. If the shapes of fibers v_i and the correlation holes v_i^0 coincide, then the estimations of the effective moduli $\boldsymbol{L}^*$ are symmetric and coincide for both the MEF and MTM for both the arbitrary random field of isotropic fibers and aligned anisotropic fibers. However, the main advantage of the proposed approach is that it is free from some drawbacks of other approximations such as the Mori-Tanaka scheme, which can generate tensors of effective moduli which fails to satisfy a necessary symmetry requirement. Most significantly, the MEF's estimations are found to be in disagreement with corresponding estimations by the MTM in the case of the randomly oriented anisotropic inclusions in the composites. The current approach takes into account both the anisotropic moduli of fibers and specific shape of the correlation holes v_i^0 reflecting the anisotropy of ODF that was not considered in the past (see, e.g., [3]). In the parametric analysis we considered both isotropic (see [4]) and anisotropic fibers (see [1]) in the Epon 862 matrix (see [5]). Three random orientations of fibers were considered: aligned fibers parallel to the axis Ox_1 (1-D uniform random orientation), uniform plane random orientation of fiber parallel to the plane Ox_1x_2 (2-D uniform random orientation), and 3-D uniform random orientation. The effective elastic Young's moduli E^* and UDRI's experimental data [6] vs. the fiber volume concentrations c of the isotropic and anisotropic fibers with 3-D uniform random orientation are presented in Fig. 1. In the case of 3D uniform random orientation of nanofibers, the tensors of the effective elastic moduli $\boldsymbol{L}^*$ obtained by the MTM and MEF are symmetric and coincide in cases with the same domain shapes v_i and v_i^0 for both the isotropic and anisotropic fibers. It can be seen that Young's modulus E^* estimated for anisotropic fibers is 1.5 times stiffer than E^* for the isotropic fibers, although the transversal Young modulus E_3 of anisotropic fibers is 30 times softer than E_3 for the isotropic fibers. However, for 2D uniform random orientation of fibers, the MTM generates the tensors of effective moduli which fail to satisfy a necessary symmetry requirement (see Fig. 2). To avoid the deficiency in the case of 2D uniform random orientation of nanofibers, the MEF was applied with the reasonable shape of "correlation hole" v_i^0 in the form of oblate spheroid (with aspect ratio $1/\alpha$) with big semiaxes parallel to the plane Ox_1x_2. In comparison, the estimations of the effective elastic moduli by the MEF and by MTM are different for any nonzero components of the tensor L^*_{ijkl}. The matrix of effective moduli estimated by the MEF is symmetric ($L^*_{ijkl}= L^*_{klij}$) in all the range of a fiber concentration c stadied, and their elastic moduli. The diagonal elements of the matrices L^*_{ijkl} estimated by the MEF and by the MTM agree well at $c<0.5$ (for example, the Young's moduli E^*_1 and E^*_3 estimated by both the MEF and MTM are agree well, see Fig. 3, however,

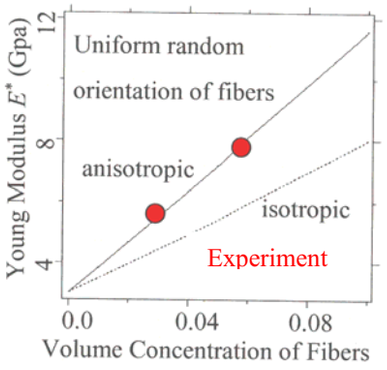


Fig. 1. Modulus E^* (GPa) vs c

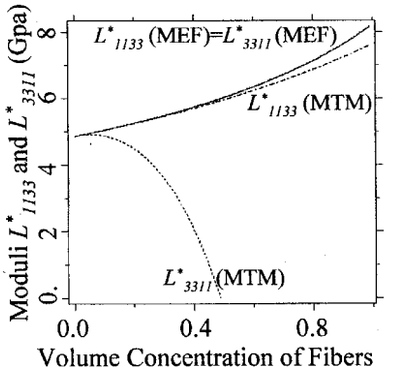


Fig. 2. L^*_{1133} and L^*_{3311} (GPa) vs c

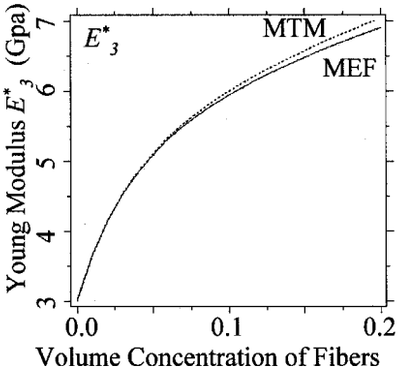


Fig. 3. E^*_3 (GPa) vs c

the nondiagonal elements can differ to a great extent for c>0.2. Thus, the matrix L^*_{ijkl} estimated by the MTM is not symmetric ($L^*_{ijkl} \neq L^*_{klij}$, see Fig. 2).

The same approach was used for the estimation of effective coefficient of thermal expansion (CTE). As expected, CTEs estimated by both MTM and by MEF coincide for both 1-D and 3-D uniform random orientation for both the anisotropic and isotropic fibers. However, for 2-D uniform random orientation, the estimations carried by the MTM and by MEF are differ from one another. Further, the prediction of the behavior of composite materials by the use of mechanical properties of the constituents and their microstructure ultimately lead to the estimation of statistical averages of stress fields in the constituents and at the interface fiber-matrix. These stress concentrators depend on the orientation of the fiber being considered as well as on the justified choice of the shape of correlation holes, concentration and ODF of nanofibers. Additional significant impact of CNT on the effective properties of nanocomposites is based on the fact that CNTs provide very high interfacial area if embedded in the matrix. The interface fiber-matrix was modeled as a thick coating with cylindrically anisotropic varying thermoelastic properties distinguishing from the properties of the fiber and matrix. The MEF prescribed above for homogeneous spheroidal fibers was generalized in the light of the model [7] for the coated fibers based on the notion of fictitious homogeneous spheroidal fibers. The parametric analyses indicate essential dependence of effective properties on the parameters of interface coating.

In conclusion, the results of the parametric analyses can be summarized as following (see [8]):

1) Effective stiffness of NC is defined by the axial stiffness of fibers rather than their transversal stiffness.

2) The variation of fiber orientation is critical and can lead to the variation of the effective stiffness of nanocomposites as much as 6 times for the fiber volume concentration c<0.1.

3) The estimation method of the effective stiffness of nanocomposites is critical. For the plane uniform orientation of anisotropic fibers, the use of the MTM is inappropriate as revealed by the MEF prediction.

Acknowledgments: The work is supported by Materials and Manufacturing Directorate, AFRL/MLBC, USA

References

[1] Odegard, G. M., Gates, T. S., Wise, K. E., Park, C. and Siochi, E. J. (2003) Constitutive modeling of nanotube-reinforced polymer composites. *Composites Science and Technology,* **63**, 1671–1687.

[2] Buryachenko, V.A. (2001) Multiparticle effective field and related methods in micromechanics of composite materials. *Appl. Mech. Review* **54**(1), 1-47.

[3] Ponte Castaneda, P. and Willis, J. R. (1995) The effect of spatial distribution on the effective behavior of composite materials and cracked media. *J. Mech. Phys. Solids.* **43**, 1919-1951.

[4] Tibbetts, G. G. and McHugh, J. J. (1999) Mechanical properties of vapor-grown carbon fiber composites with thermoplastic matrices. *J. Mater Res.* **14**, 2871-2880.

[5] Tandon, G. P., Kim, R. Y. and Rice, B. P. (2002) Influence of vapor-grown carbon nanocomposites on thermomechanical properties of graphite-epoxy composites. *Proc. American Society for Composites 17th Technical Conference,* Purdue University, West Lafayette, Indiana, Paper 2039.

[6] Lafdi, K. and Matzek, M. (2003) Carbon nanofibers as a nano-reinforcement for polymeric nanocomposites. *The 35th International SAMPE Technical Conference,* Dayton, Ohio.

[7] Buryachenko, V. A., Rammerstorfer, F. G. On the thermostatics of composites with coated randomly distributed inclusions. *Int. J. Solids Struct*. 2000, **37**, 3177-3200.

[8] Buryachenko, V. A. and Roy. A. (2003) Effective elastic moduli of nanocomposites. (Submitted).

NANO-SCALE PLANAR FIELD PROJECTION OF ATOMIC DECOHESION

S. T. Choi and K. –S. Kim
Division of Engineering, Brown University, Providence, RI 02912, USA

ABSTRACT An atomistic cohesive zone of a crack tip is characterized by a nano-scale planar field projection of the elastic field of a crack tip, analyzing the near-tip deformation field with a molecular statics simulation of gold. A general form of planar elastic field projection is derived to identify cohesive-zone constitutive relations from the elastic field of a cohesive crack tip sitting on an interface between two anisotropic solids. The cohesive traction, the interface separation and the surface-stress caused by gradual variation of surface formation within the cohesive zone can be obtained by the nano-scale planar field projection.

INTRODUCTION

When atomistic simulations or atomic resolution experiments are carried out to analyze deformation energetics of atomic lattices near a crack tip, the results of the atomic positions and the total energy of the system have not been systematically converted to field quantities such as stresses or tractions near the crack tip. In this paper, we introduce a mathematically consistent way of defining and measuring the cohesive tractions, separations and surface stresses in an atomic decohesion process zone using the atomic displacement data at some distance away from the crack tip. The method is called "nano-scale planar field projection method." This is a generalization of the method developed for isotropic homogeneous solids by Hong and Kim (2003). The formulation introduced here is applicable to interface cracks between anisotropic solids as well as to cracks in homogeneous solids whether they are anisotropic or isotropic. The field projection method is then applied to a crack tip field in gold, simulated atomistically. The atomistic simulation is made with an embedded atom method (EAM) potential for a crystal decohesion along $[\bar{1}\,\bar{1}2]$ direction in a (111) plane. Then, the details of energy partition in various modes of nano-scale separation processes are analyzed with the field projection method.

PLANAR FIELD PROJECTION METHOD FORMULATION

The field projection method uses interaction J integral (Chen and Shield, 1977) between the atomistic field of interest and a configurational-work-conjugate eigenfunction field of an interface cohesive crack tip. Therefore, a complete set of the eigenfunction fields is constructed with the Stroh formalism (Stroh, 1959) for which the displacement field $\boldsymbol{u}$ of a two dimensional elastic deformation in anisotropic bimaterials is represented in terms of a complex column matrix function $\mathbf{f}(z)$ as $\{\boldsymbol{u}\} = 2\,\mathrm{Re}\left[\mathbf{A}\mathbf{f}(z)\right]$. Here $\mathbf{A}$ is the Stroh eigenvector matrix and z a reduced representation of complex variables $z_j = x_1 + p_j x_2$ with the Stroh eigenvalue p_j for $j = 1,2,3$. Then, the cohesive crack tip field can be expressed in terms of an eigenfunction expansion as

$$\mathbf{f}'_{<\mu>}(z) = \frac{1}{2}\mathbf{B}^{-1}_{<\mu>}\left[\mathbf{I} - (-1)^{\mu} i\boldsymbol{\beta}\right]\left\{\mathbf{Y}\left[(z+c)^{-i\varepsilon}\right]\sqrt{z+c}\,\mathbf{g}(z) - \mathbf{Y}\left[(z-c)^{-i\varepsilon}\right]\sqrt{z-c}\,\mathbf{h}(z)\right\}$$
$$+\frac{i}{2}\mathbf{B}^{-1}_{<\mu>}\left[\mathbf{I} - (-1)^{\mu}\boldsymbol{\alpha}\right]\left[\sqrt{z^2-c^2}\,\mathbf{q}(z) + \mathbf{r}(z)\right],$$

for $\mu = 1$ or 2 referring to the materials 1 or 2 respectively, where $\mathbf{B}$ is another Stroh matrix, and $\mathbf{g}(z)$, $\mathbf{h}(z)$, $\mathbf{q}(z)$ and $\mathbf{r}(z)$ are analytic real matrix functions. The symbols $\boldsymbol{\alpha}$ and $\boldsymbol{\beta}$ represent the generalized Dundurs-parameter real matrices, ε the bi-material oscillatory index, and $\mathbf{Y}\left[\eta(z)\right]$ for an arbitrary function $\eta(z)$ is the bi-material real function matrix for anisotropic bi-materials (Choi and Kim, 2004). In this expression, terms of $\{\mathbf{g}(z),\ \mathbf{h}(z)\}$ and $\{\mathbf{q}(z),\ \mathbf{r}(z)\}$ are interaction J-integral work conjugate pairs respectively, and the power series of the analytic functions can be arranged to construct J-orthogonal sets for the two function pairs. Interaction J integral between an eigenfunction field and the atomistic field of interest provides the magnitude of the conjugate term included in the atomistic field.

Since interaction J integral is path independent, the integral can be carried out at far field, and the magnitudes of the conjugate fields obtained in this way determine the cohesive zone characteristics.

RESULTS ON MOLECULAR STATICS SIMULATION

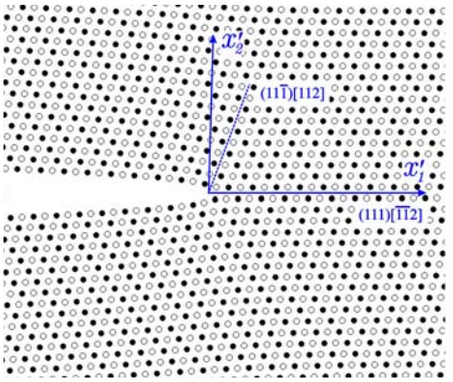


Fig. 1. Atom positions in a crack tip field in gold, simulated with an EAM potential

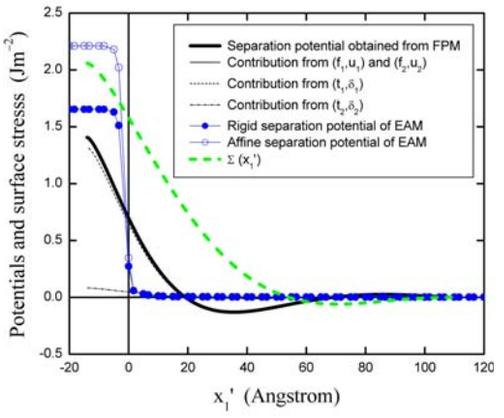


Fig. 2. Cohesive zone potentials measured by the field projection method

Figure 1 shows an equilibrium position of gold atoms relaxed from linear elastic K field positions, holding the linear elastic positions of two atomic layers at the outer boundary with $K_I = 0.38\, MPa\sqrt{m}$ and $K_{II} = -0.10\, MPa\sqrt{m}$. EAM potentials of Foiles et. al. (1986) were employed for this simulation. Then, the atomic positions are used to extract the cohesive zone characteristics applying the field projection method. Figure 2 shows various cohesive zone potentials. The open circle indicates the affine-deformation separation potential of the (111) inter-atomic plane ahead of the crack tip, while the solid dot denotes rigid separation potential. The solid and dashed lines represent the separation potential and the surface stress determined by the field projection method respectively. Here two times of the surface energy, 2γ, of gold (111) is measured $1.41\, J/m^2$ and that of the surface stress $2.06\, J/m^2$.

CONCLUSION

A general formulation of a planar elastic field projection is derived for identifying cohesive zone constitutive relations from the elastic field of a cohesive crack tip sitting on an interface between two anisotropic solids. The formulation is also applicable to the elastic field of a cohesive crack tip in a single isotropic or anisotropic solid. The field projection using the interaction J integrals provides the cohesive traction, the interface separation as well as the surface energy and surface-stress gradients caused by gradual variation of surface formation within the cohesive zone. Therefore, the cohesive traction, the surface-energy and the surface stress could be measured as functions of the interface separation. Molecular statics simulation is performed for crystal decohesion along $[\bar{1}\bar{1}2]$ direction in gold (111) plane with an embedded atom method (EAM) potential, and the field projection method was successfully used to measure the nano-scale cohesive zone characteristics.

REFERNCES

Chen, F. H. K., and Shield, R. T., 1977, *ZAMP J. Appl. Math. Phys.*, **28**, 1.
Choi, S. T. and Kim, K. –S., 2004, manuscript to be submitted to *Phil. Mag.*
Foiles, S. M., Baskes, M. I., and Daw, M. S., 1986, *Phys. Rev. B*, **33**, 7983.
Hong, S., and Kim, K. -S., 2003, *J. Mech. Phys. Solids*, **51**, 1267.
Stroh, A. N., 1958, *Phil. Mag.*, **3**, 625.

This work was supported by the MRSEC Program of U.S. National Science Foundation under Award Number DMR-0079964 and the Post-doctoral Fellowship Program of Korea Science & Engineering Foundation (KOSEF).

Slip, patterns and other small things in microfluidic systems

P.Tabeling[(1)], A. Dodge[(1)], P. Joseph[(1)], C. Jullien[(2)], L. Menetrier[(1)], H. Willaime[(2)]
[(1)]Microfluidics lab, MMN, ESPCI, 10 rue Vauquelin, 75231 Paris (France)
[(2)]BIOMIS, Campus Ker-Lahn, Rennes (France)

Microfluidics is about flow of liquids and gases, through microdevices fabricated by MEMS (i.e. Micro ElectroMechanical Systems) technology, using hard (silicon or glass) or soft (polymers) materials. The domain is fostered by exciting applications, representing important industrial challenges. It also embraces a number of fundamental issues interesting in their own right. The introductory talk will concentrate on some of them, through a presentation of a number of experiments we have been carrying out at ESPCI, over the last three years.

Let us start with the controversial topics of slip between liquid and solid. In classical textbooks, it is considered that liquids do not slip on solid surfaces ; the so called "no-slip" boundary condition on the tangential velocity u, for ordinary liquids, has the form :

$$u=0$$

on fixed solid surfaces. This provides a fundamental condition in fluid mechanics, allowing for detailed calculations of velocity profiles and flow structures. In contrast with this picture, we now have experimental evidence that simple liquids significantly slip on atomically smooth solid surfaces and, consequently, the no-slip condition is better replaced by the more general relation:

$$u = L_S\left(\frac{\partial u}{\partial n}\right)$$

in which L_s is the extrapolation or slip length, n is the normal (inwards to the fluid). This equation – justified only with perfect gases - is called the Navier condition. The estimate of the slip length *Ls* is controversial at the moment. By using PIV, and working with coated non wetting smooth surfaces, Tretheway and Meinhart[(1)] measured slip lengths on the order of 1 μm. We performed similar experiments, using glass and a variety of coatings, working with wetting and non wetting surfaces, with different roughnesses[(2)]. We obtained slip lengths below 100 nm in all cases; Fig 1 shows an example where the measured slip length that we found is below 100nm, for the case of a non wetting smooth glass surface, coated with OTS, (contact angle 95°, roughness 0.31 nm). We don't know the origin of the discrepancy between these results ant those of Ref 1. In order to account for large slip lengths, one usually speculate on the existence of a thin gas layer confined between the liquid and the solid. This perhaps may reconcile the two sets of experimental observations.

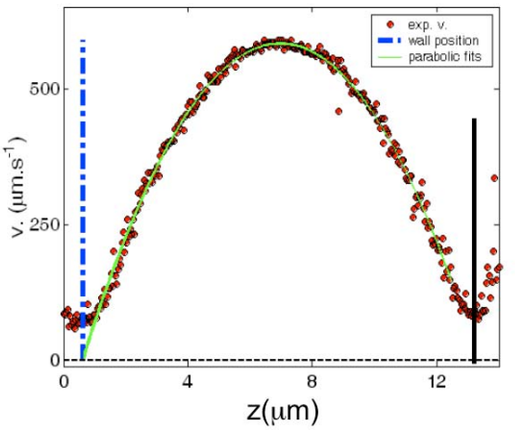


Figure 1 : Example of a velocity profile, obtained by using PIV, in a 12 μm deep microchannel (red disks). The green line is a best fit, providing a slip length equal to –35±100nm . The "foots" of the profile, within the first 400 nm close to the walls, are due to experimental errors. The data located within 400 nm is discarded in the best fit procedure.

Mixing is difficult in microsystems, and this has been a source of motivation for studying chaotic micro-mixers. We present here an experimental study of chaotic micromixing, which led to observe a novel resonance phenomenon. In this geometry, a pair of fluids flows side by side, in a channel, then pass through an intersection. At the intersection, a time-dependent flow coming from the sides is superimposed with the main stream. This additional flow perturbs the shape of the interface between the two fluids to different extents depending on the amplitude and frequency of the side-flow[3]. Typically, when the perturbation amplitude is small, or its frequency large, weak oscillations are generated at the interface between the pair of fluids forming the mean stream. When the amplitude is large, and the frequency moderate, stretching and folding of the interface is produced, leading to chaotic regimes. "Resonance" conditions also exist, for which the interface is strongly distorted in the active region, but returns to a flat shape afterwards. An example is shown in Fig. 2. This effect is a novel dynamical phenomenon, involving a particular interaction between space and time[4]. From a dynamical system viewpoint, resonant regimes are linked to the existence of KAM trajectories[5]. This regime can be exploited to realize an efficient micromixer/microextractor.

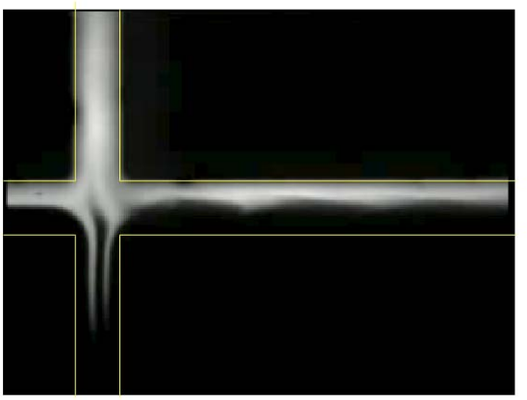


Figure 2 : In this particular case, the interface is strongly perturbed in the active zone, but returns straight as it leaves it. This is the "resonance" state. This state may be used produce efficient extraction of particles of

different sizes, forming initially an homogeneous mixture. On the picture, the width of the main channel is 200 μm, and its depth is 25 μm. A series of integrated valves produces the oscillatory flow, perturbing the main stream. The whole system is made in PDMS

The last topics deals with two-phase flows in microsystems. We consider here a miniaturized version of the tangential filter. The system is composed of a main channel, which drives most of the flow, and a side channel, through which a small fraction of the main stream is sucked. In our case we work with a two phase flows, initially composed of water drops dispersed in hexadecane[6]. Depending on the flow-rate conditions, drops may simply move with the main stream, or break up into two parts, each part being entrained in a different channel. In the break-up process, a filament first forms at the derivation. This filament breaks-up when it becomes too elongated (in a sense which can be made more precise by analysing in detail its geometry); an example of such a filament is given in Fig.3. The break-up conditions turned out to be well accounted for by using a theory based on Rayleigh Plateau instability.

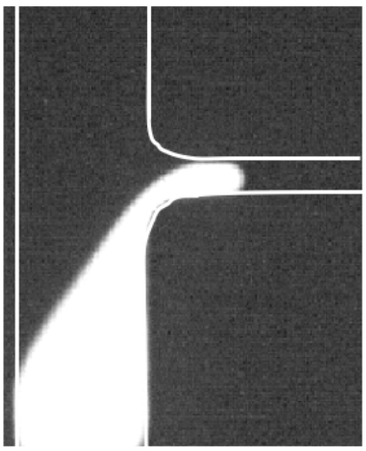


Figure 3 : Formation of a filament prior to drop break-up. The water drop (labeled with fluorescein, thus appearing as white on the picture) which is moving downwards will further split into two parts, one in the derivation channel, and the other in the main channel.

The second experiment one may mention here emphasizes on the role of the walls - a direct consequence of miniaturization - : In Ref 7, it is shown that wetting characteristics are exceedingly important in miniaturized liquid-liquid flows : depending on the wetting characteristics, one obtains well defined structures or featureless patterns, under the same flow conditions.

In conclusion, it appears through a few examples that microfluidics offers a context for the development of unfamiliar, sometimes surprising behaviors of fluid systems. Moreover, it is a often a source of inspiration for novel (micro)engineering concepts. These two aspects are discussed in more detail in Ref 8

References

1. Tretheway D., Meinhart C.: Apparent fluid slip at hydrophobic microchannel walls. *Physics of Fluids*, Vol 14, No. 3, 2002, pp. L9-L12 .

2.The experiment will be presented by P. Joseph at the conference.

3.Y.K.Lee, J Deval, P. Tabeling, C.M.Ho, *Proc MEMS2001*, 483, Interlaken (2001).

4.F. Okkels, P. Tabeling, Phys. Rev. Lett., **92**, 38301 (2004)

5. X. Niu, Y.K.Lee, *.l of Microechanics and Microengineering*, **13**, 452 (2003).

6.The experiment is carried out by Laure Menetrier (unpublished).

7. R Dreyfus, H Willaime, P Tabeling, Phys. Rev. Lett., **90** (14), 144505 (2003)

8. "*Introduction à la microfluidique"*, P. Tabeling, Coll. Echelles, Eds BELIN, 207 pages (2003)

Electrokinetic Flow Instabilities in Microfluidic Systems

Professor Juan G. Santiago
Stanford Microfluidics Lab
Department of Mechanical Engineering
Stanford University

Microfabrication technology has enabled the application of electrokinetics as a method of performing chemical analyses and achieving liquid pumping in electronically-controlled microchip systems with no moving parts. This talk reviews progress at Stanford including novel methods for sample stacking and fundamental studies of electrokinetic flow instabilities. Field amplified sample stacking (FASS) leverages conductivity gradients as a robust method of increasing sample concentration prior to capillary electrophoresis separation. We have developed novel chip systems that can achieve signal increases of more than 1000 fold using FASS. Electrokinetic instabilities (EKI) present a major challenge to optimizing FASS devices, as well as an opportunity to achieve rapid on-chip mixing. We have developed generalized models for heterogenous electrokinetic systems for both FASS and EKI, and validated these models with experiments. This work shows that electric body forces associated with the accumulation of charge in the bulk liquid are the cause of EKI. Suppression and/or control of electrokinetic flow instabilities is directly applicable to sample stacking as conductivity-gradient-induced instabilities dramatically increase dispersion rates and thereby limit stacking efficiency.

MINIATURIZATION OF EXPLOSIVE TECHNOLOGY AND MICRODETONICS

D. Scott Stewart*
Department of Theoretical and Applied Mechanics, University of Illinois, USA ,dss@uiuc.edu

Summary Condensed phase explosives used in conventional explosive systems have a charge size on the order of a meter or a sizable fraction of a meter. We discuss a range of issues, theoretical, computational and experimental required to scale the size of explosive systems downwards by a factor of one hundred to one thousand, and applications and prospects for a ubiquitous new technology.

BACKGROUND

A detonation is a chemical reaction driven shock wave in molecularly premixed material called an explosive. The chemical energy released in the reaction zone behind the lead shock is converted into kinetic energy and pressure/volume work done by the reactants. Explosives can be gases, liquids and solids. Detonation pressures in organically based condensed phase explosives (typically made from nitrated hydrocarbons) are in the range of 300-400 Kbar (30-40 GPa), and can potentially induce hundreds of Kbars of pressure in inert materials for fractions of microseconds. Detonation shock speeds are on the order of 3-10 kilometers/sec. The thermodynamic cycle and high pressure, high compression states that can be induced in donor materials are unlike those that can be obtained with other thermo-mechanical systems, including lasers. Hence detonative processes offer unique methods of altering the state of material surfaces and can serve as a high energy density source for micro-devices. Properly engineered, stable explosive detonation fronts work in combination by a principle of synchronicity (i.e. the detonation is a phase-controlled explosion front) and detonations can generate precise motion-controlled flows that can be used for materials processing and other applications mentioned.

Applications

While condensed phase explosives are used in military, mining and demolition applications, other less commonly known applications of explosives include their use for materials processing, precision cutting and pulsed power application. Specifically, detonation of explosive films can be used in surface treatment and hardening of materials. Other material processing applications include cladding and explosive welding, sintering, shock consolidation of powders and shock-induced chemical synthesis. Pulsed power applications include magnetic flux compression, pulsed detonation engines, explosive lasing and the generation of extremely high intensity light pulses. There are biomedical applications for detonation of micro-sized explosive charges that include lithotripsy and localized destruction of pathological tissue [1]. Explosive and pyrotechnic elements pervade satellite and aerospace systems and hence there is interest in the miniaturization of explosive systems for micro-aerospace and satellite platforms. Suitably controlled detonation fronts represent a basic technology with unique aspects. By establishing the basic parameters of micro-scale explosive systems it should be possible to design micro-scale devices for welding, cladding, pulsed power, surface treatment and so on (as mentioned above) in novel, ubiquitous and unforeseen ways. Micro-explosive systems hold the promise of being a basic enabling technology with wide-spread application.

Figure 1. shows a sketch of a typical experimental configuration being studied at the University of Illinois. The initiator consists of a capacitance discharge unit (CDU) that fires a 10-micron thick wire (typically gold) or metallic film embedded in the detonable film. The electrical current dump causes the metal to expand from a nominally cylindrical or flat source as plasma and drive a shock wave into the film to start the chemical reaction in the film. The detonation supported shock sweeps across the sample and the detonation shock drives an inert shock into the donor material to do the localized processing of near surface material. Other initiation configurations include laser driven micro-flyers that induce shocks to start reaction.

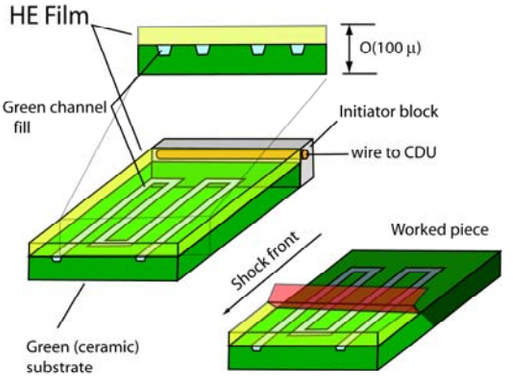


Figure 1. Micro-explosive system for material processing

EXPLOSIVE SYSTEM SCALING ARGUMENTS AND REQUIREMENTS

An explosive system includes the main charge (the secondary explosive), the initiation system (which includes the initiation train and booster (made of primary explosives or electrical or optical laser initiators) and the inerts, upon which the explosive products act. Conventional macro-scale explosive system design paradigms exist for explosive systems that have dimensions on the order of a meter or sizable fraction of a meter. Scaling arguments, [2] show that extreme miniaturization by a scale reduction of current large-scale explosive systems by a factor of 100 to 1000 is possible.

Short reaction-zone explosive materials (with small critical diameters) must be used for main charges in order to use the well-known design paradigms for large-scale devices. This means that one must select the main charge explosives from the list of primary explosives (used in large-scale initiator trains or detonators). Also one might consider using very short reaction zone explosives that in the past that have never been considered for use because of safety considerations. Reliable and safe initiation systems for miniaturized systems can be built using existing exploding wire and exploding foil initiation systems with existing, well-understood electrical designs.

Subcritical charge dimensions (used with main charge explosives that have longer reaction zones might be used successfully, but one expects to experience significant transients that do not fall in the existing quasi-steady design paradigms. Notably, one might expect to see the dynamic consequence of galloping instability or low velocity detonation.

NEW SCIENCE NEEDED TO ENABLE THE TECHNOLOGY

In order to define the properties of the new explosive materials there is a need for a comprehensive linear and nonlinear stability theory for non-ideal detonation that can incorporate non-ideal equation of state and realistic reaction rate laws for condensed explosives. Recent efforts are underway to develop novel nano-engineering composite energetic materials and explosives that can be candidates for the miniaturized secondary charge. An entirely new linear stability theory for steady detonation has been developed by us at Illinois to guide design of miniaturized explosive systems in a rational way that incorporates descriptions of nonideal equation of state and reaction rate kinetics.

In order to define detonation propagation in small dimensions one must understand the critical conditions required for ignition and propagation of detonation for both ideal and nonideal explosives [3]. We will briefly describe new work based on asymptotic theory of fast and sensitive chemical kinetics. It is important to understand aspects of detonation and shock diffraction and how that phenomena affects successful detonation propagation.

Design of integrated systems requires modern high resolution, multi-dimensional and multi-material, time-dependent simulation. High fidelity simulation is an essential tool that is required to specify the geometry and select materials for miniaturized explosive system. We describe some of the high-resolution solvers that we use that are combined with level-set methods for interfaces and the Ghost Fluid Method to enable multi-material simulation required for microdetonic devices.

We will give an overview of the subject and discuss some of the basic configurations and operating conditions of micro-explosive systems and integrated theory simulation and experiments by our extended research group of colleagues at Illinois and the US National Laboratories.

Acknowldegements This work is supported by the US Department of Energy, DOE/LANL, and the US Air Force Research Laboratory, AFOSR-Mathematics and Eglin AFB, Florida

References

[1] Takayama, K. and Saito, T.,.Shock Wave/Geophysical and Medical Appliecations, *Annual Review of Fluid Mechanics* . ***36,*** :347-379, 2004.

[2] Stewart D.S, Toward Miniaturization of Explosive Technology, *Shock Waves*, .Shock Waves (2002) 11: 467–473

[3] Kasimov, A. and Stewart, D. S., Asymptotic theory of ignition and failure of self-sustained detonations, TAM Report No. 1042 UILU-ENG-2004-6003, ISSN 0073-5264, submitted to *Journal of Fluid Mechanics*

PLANE POISEUILLE FLOW IN A RAREFIED GAS WITH GENERAL BOUNDARY CONDITIONS

C. Cercignani, M. Lampis, S. Lorenzani

Dipartimento di Matematica, Politecnico di Milano,
Milano, Italia

Abstract

Rarefied gas flows in ultra-thin film slider bearings are studied in a wide range of Knudsen numbers. Since in ultra-thin films (when gas rarefaction effects dominate) the molecular interactions with the surfaces affect strongly the velocity profile and the gas flow rate, we solve the generalized Reynolds equation in the most general case of two surfaces with different accommodation coefficients.

EXTENDED ABSTRACT

Rarefied gas flows occur in many micro-electro-mechanical systems (MEMS) [1], [2], therefore a correct prediction of these flows is important to design and develop MEMS. Nanoscale design occurs for computer components as well.

In most computers today, magnetic disk storage devices use a flying head slider suspended nanometers above the rotating recording surface to support the read/write head. A thin gas-lubricated film formed between the slider and the rotating disk is used to maintain the spacing between them. The air between the read/write head and the surface of the spinning platter forms a so-called slider air bearing. The basic geometry of the two-dimensional gas film is outlined in Fig. 1. In order to achieve higher storage densities, the head is required to levitate progressively closer to the spinning platter. For ultra-high density recording systems, a 5-10 nm clearance between the head and the floating media is required. Considering that the mean free path for air is about 65 nm at standard conditions, the current hard drives already operate in the transition flow regime, while the next generation drives will push this limit towards the free-molecular flow regime. Therefore, development of lubrication models valid in a wide range of Knudsen regimes is necessary.

Traditionally, the classical Reynolds lubrication equation has been used to model slider bearings. The Reynolds equation is an approximation of the full Navier-Stokes equation with the continuum no-slip boundary conditions. However, rarefaction effects are significant for gas flows in close spacings and appropriate corrections to this equation were first introduced by Fukui and Kaneko [3], [4]. We have extended the generalized Reynolds equation derived by Fukui and Kaneko, by allowing for bounding surfaces with different physical structures, as an issue of relevance for applications. The Maxwell scattering kernel has been used to describe the gas-wall interactions in the most general case of two surfaces with different accommodation coefficients. The generalized Reynolds equation is a flow rate based model, therefore its solution requires that the fundamental flows in

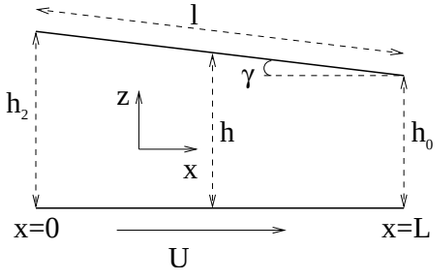


Figure 1: Geometry of a slider bearing.

the lubrication film, Poiseuille and Couette flow rates, have to be accurately calculated in advance. The Poiseuille and Couette flow rate coefficients have been evaluated by means of a numerical integration of the Boltzmann equation [5] using a finite difference technique first introduced by Cercignani and Daneri [6]. Moreover, the Poiseuille flow rate has been evaluated by means of a variational technique which applies to the integrodifferential form of the Boltzmann equation [7] based on the BGK model [8].

References

[1] K. L. Deckert, "Computer-aided design of slider bearings in magnetic disk files," IBM. J. Res. Devel. **35**, 660 (1990).

[2] N. Tagawa, "State of the art for flying head slider mechanisms in magnetic recording disk storage," Wear **168**, 43 (1993).

[3] S. Fukui and R. Kaneko, "Analysis of ultra-thin gas film lubrication based on linearized Boltzmann equation: first report-Derivation of a generalized lubrication equation including thermal creep flow," J. Tribology **110**, 253 (1988).

[4] S. Fukui and R. Kaneko, "Analysis of ultra-thin gas film lubrication based on the linearized Boltzmann equation (influence of accommodation coefficient)," JSME International Journal **30**, 1660 (1987).

[5] C. Cercignani, M. Lampis, and S. Lorenzani, "Flow of a rarefied gas between parallel and almost parallel plates," Presented at 24^{rd} Int. Symp. on Rarefied Gas Dynamics, Bari, Italy (2004).

[6] C. Cercignani and A. Daneri, "Flow of a Rarefied Gas between Two Parallel Plates," J. Appl. Phys. **34**, 3509 (1963).

[7] C. Cercignani, M. Lampis, and S. Lorenzani, "Variational approach to gas flows in microchannels," Physics of Fluids **16**, 3426 (2004).

[8] P. L. Bhatnagar, E. P. Gross, and M. Krook, "A model for collision processes in gases. I. Small amplitude processes in charged and neutral one-component systems," Phys. Rev. **94**, 511 (1954).

WATER FLOWS IN COPPER AND QUARTZ NANOCHANNELS

Anna Kucaba-Pietal*, Zbigniew Walenta**, Zbigniew Peradzynski***, **

**RUT, Department of Fluid Mechanics & Aerodynamics, Powstańców Warszawy 8, 35-959 Rzeszów, Poland*
***IPPT PAN, Polish Academy of Sciences, Department of Mechanics and Physics of Fluids, Swietokrzyska 21, 00-049 Warszawa, Poland*
****Institute of Applied Mathematics and Mechanics, Warsaw University, Banacha 2, 02-097, Warszawa, Poland*

Summary: The molecular dynamics simulations of water flows in rectangular channels, induced by gravitational force field, have been compared with theoretical predictions for micropolar fluid flows. The similarities and differences, particularly in velocity fields and microrotation have been discussed. Two different channel widths and two kinds of wall material have been taken into account. .

INTRODUCTION

Numerous experimental results indicate, that the microscale flows are essentially different from flows in large scale [1], [2]. The continuum Navier-Stokes approach, suitable for large sale flows, is not applicable to small scales. At the same time, however, there exists an extension of the Navier – Stokes approach, also based on the assumption of a continuous medium – the micropolar fluid model – which agrees quite well with some experiments in microscale. The micropolar fluid model – proposed by Eringen in 1966 [3] - takes into account microrotation of the molecules, different from the local vorticity of the flow.
The experiments and theoretical estimations indicate, that for real flows through narrow channels the importance of the micropolar effects grows when the channel width decreases down to the values comparable with the dimensions of the particles of the fluid. However, under such conditions, the assumption of continuous medium, essential for the theory of micropolar fluids, does not seem to be justified. The problem of validity of the micropolar fluid model for the flows through narrow channels is yet to be solved.
Some information on the validity of the micropolar model to description of the flows of Cl_2 or P_5 in narrow channels are given in [4], [5] however these results concern fluids which very rarely flow in microdevices. Moreover, the used molecular model of the channel wall is so simplified, that it cannot simulate any real physical material.
Since water is the fluid, most often flowing through microchannels and the channel walls are most often made of silicon, quartz or copper, we concern ourselves to water flows in copper and quartz channels. We compare the theoretical predictions for flow velocity and microrotation with results of molecular dynamics simulations of flows under gravity field down rectangular channels.

MOLECULAR DYNAMICS SIMULATION

As mentioned before, we calculated the flow of water through narrow slits (plane Poiseuille flow) with walls made of cooper or quartz. Two channel widths, equal to 5 and 10 diameters of the water molecule were considered.
The Lennard-Jones 6–12 potential was assumed for interactions between water molecules and also between water molecules and wall atoms. For water the four site molecular model of Jorgrnsen [6] was employed. The molecular parameters of quartz and copper were taken from [7] and [8].
To minimize the influence of the boundaries of the calculation domain the periodic boundary conditions were used. The number of wall atoms taken for calculation ranged from 236 for copper wall to 250 quartz molecules otherwise. The number of water molecules - from 280 for the flow between quartz walls to 720 for the broader channel between copper walls. Simulations were carried out (in reduced units) with the number density 0.989 for water at T= 3.6. To drive the flow, a constant force F was applied to the centre of mass.of each water molecule. Several values of F, ranging from 0.5 to 5 were used.:The calculation were performed with the MOLDY program [9]. They were carried out over 200000 time steps, equal to t=0.005.

RESULTS

The obtained results show that for channel widths equal to 10 diameters of the molecule the results of the micropolar theory are in a reasonable qualitative agreement with molecular dynamics simulation. In particular, the microrotation velocity (missing in the classical Navier-Stokes theory) and the translational streaming velocity profiles agree well with those from MD simulation.

In all cases under consideration some slip velocity and non-zero microrotation at the walls could be observed. The slip effects are stronger for smaller channel widths and for walls made of copper. They seem to be influenced by interaction of water molecules – which have electric dipole moment - with the charges of the walls. Quartz does have some electric charge, copper does not. For water molecules the quartz wall behaves as an attractive one, whereas the cooper wall (without charge) as a repulsive one.
The obtained results are consistent with earlier research. The effect of attractive and repulsive walls on the slip velocity was observed in Poisseuille flow simulations of dense gas flows in narrow channels [10] [11]. The present results, however, are the first obtained for flows of fluid whose molecules possess electric dipole moment.
The problem of interaction between fluid and solid surfaces has received increased attention over the past ten years as engineering applications reached the micrometer and nanometer scale. For the past century the non-slip boundary condition was considered to be appropriate for macroscopic flows. However, with the decrease of the length scale the non-zero slip velocity should be taken into account. Our results, as well as experimental and simulation results of other authors show that the slip velocity in micro and nanoflow exists and strongly depends on wall – fluid interaction.

CONCLUSIONS

The predictions of the micropolar fluid theory and the results of molecular dynamics simulation of water flows through narrow slits with copper and quartz walls agree reasonably well for channels widths equal to 10 diameters of the water molecule.for more narrow channels the agreement is poor. It can be concluded then, that the micropolar theory may be applied to modelling the fluid flows in channels of width not smaller than 10 fluid molecular diameters. This conclusion is also supported by earlier results of other investigators.
The simulation results show that the velocity slip in micro and nanoflows exists and strongly depends on wall – fluid interaction, particularly on whether the forces between the wall and fluid are attractive or repulsive.

References

1. Sharp, K.V., Adrian R. J., Santiago J.G., Molho J.I.: TAM Report No961, UIUC, 2000
2. Gad el Hak.: The MEMS Handbook, CRC Press, NY 2001
3. Eringen A.C.: J.Math.Mech., **116**, 1, 1-16, 1996
4. Delhommelle J., Evans D. J.Molecular Physics, **100**, 17, 2857-65, 2002
5. Rapaport D.C. Europhysics Letters, **26**, 6, 401-406, 1994
6. Jorgensen W.L.: J.Chem. Phys. **77**, 4156-63, 1982
7. Adler J.: https//reu. Magnet.fsu.edu/program/2003/paper/adler
8. Van Beest B.W., Kramer G. and Van Santen R.A.; Physical Rev. Letters **64,** 16, 1955-1975, 1990
9. Refson K.: MOLDY, ftp://ftp.earth.ox.ac.uk/pub
10. Cieplak M., Koplik J., Banavar J.R.: Physica A, **274**, 281-293, 1999
11. Cieplak M., Koplik J., Banavar J.R.: Physica A, **287**, 153-160, 2000

A second-order slip model for early-transition-regime flows

Small scale gaseous flows have been the subject of significant interest in connection with micro- and nanoscale science and technology. The failure of the Navier-Stokes description as the characteristic system scale (H) approaches the mean free path (ℓ) makes these problems both challenging and interesting from a scientific point of view.

The deviation from Navier-Stokes is quantified by the Knudsen number typically defined as $\mathrm{Kn} = \ell / H$. It is well known that in the regime $0 < \mathrm{Kn} < 0.1$, known as slip flow, the Navier-Stokes description may still be used, albeit supplemented by slip boundary conditions rather than the usual no-slip boundary conditions. In the transition regime $(0.1 < \mathrm{Kn} < 10)$, the slip-flow approximation is no longer accurate, and gaseous hydrodynamics can only be described by more fundamental approaches such as Boltzmann equation solutions or molecular simulations. Due to the considerable complexity and computational cost associated with these alternative approaches, models which extend the applicability of the Navier-Stokes description beyond $\mathrm{Kn} = 0.1$ are highly desirable.

In this paper we present a second-order slip model [1] based on the hard-sphere approximation which extends the applicability of Navier-Stokes description well beyond the slip flow regime. This model is based on rigorous solutions of the Boltzmann equation [2,3], and has no adjustable parameters. We show that the key to obtaining a reliable second-order slip model is accounting for the non-equilibrium layer close to the walls, known as the Knudsen layer. In this paper we discuss how the latter:

1. Impacts the accuracy of the solution
2. Has led previous attempts to incorrect results
3. Is taken into account by the current model.

In particular, we show that the slip model provides a baseline Navier-Stokes solution which does not capture the effects of the Knudsen layer. In fact, as the Knudsen number increases beyond $\mathrm{Kn} = 0.1$, the Knudsen layer whose thickness is of the order of one mean free path, covers an increasingly larger fraction of the physical domain. It is for this reason that previous attempts attempting to fit the velocity profile throughout the physical domain were not successful.

However, despite the increasing importance of the Knudsen layers, the second-order slip model remains accurate and useful well into the transition regime. The effect of the Knudsen layer can be fully accounted for [2] in calculating the average (over the physical domain) flow velocity. Of course the stress field is also accurately captured with no extra adjustable parameters.

We verify our results by comparing with numerical solutions of the Boltzmann equation. In particular, we show that the proposed model is in excellent agreement with direct Monte Carlo solutions of the Boltzmann equation. Three different flows are considered:

steady pressure-driven flow, an oscillatory shear driven flow and an unsteady impulsive start problem. In all cases, excellent agreement is found up to $Kn = 0.4$. The slip model remains in qualitative agreement with Boltzmann equation solutions beyond this Knudsen number.

References

[1] N.G. Hadjiconstantinou, "Comment on Cercignani's Second-Order Slip Coefficient," Physics of Fluids, **15**, 2352, 2003.
[2] C. Cercignani, "Higher order slip according to the linearized Boltzmann equation," Institute of Engineering Research Report AS-64-19, University of California, Berkeley, 1964.
[3] T. Ohwada, Y. Sone, and K. Aoki, "Numerical analysis of the shear and thermal creep flows of a rarefied gas over a plane wall on the basis of the linearized Boltzmann equation for hard-sphere molecules," Physics of Fluids A, **1**, 1588, 1989.

XXI ICTAM, 15-21 August 2004, Warsaw, Poland

DIRECT MEASUREMENT AND SIMULATION OF APPARENT SLIP VELOCITIES IN SUB-MICRON-SCALE FLOWS

Peter Huang and Kenneth S. Breuer
Division of Engineering, Brown University, Providence, Rhode Island 02912, USA

Summary The possible existence of slip of liquids in close proximity to a smooth surface is studied experimentally and numerically via the dynamics of small particles suspened in a shear flow. Sub-micron fluorescent particles suspended in water and imaged using Total Internal Reflection Fluorescence Microscopy (TIRFM) and a PTV algorithm. The measurements are in excellent agreement with Monte Carlo simulations of particle dynamics, and show that the observed "apparent slip velocity" is a direct consequence of the small, but finite, measurement volume, and that slip, if present, is minimal at the low shear rates tested (< 2500 s^{-1}). Issues associated with the experimental and simulation techniques and the interpretation of results are also discussed.

The validation of the no-slip boundary condition on both hydrophilic and hydrophobic surfaces has been a subject of intense recent interest [1-3] with results predicting "apparent slip" lengths ranging from nanometers to microns. In related research, the motion of submicron particles and macromolecules as they approach the solid surface is also a matter of both scientific and technological interest in microfluidic systems [4]. In this paper, we report on complementary experiments and simulations of particles flowing in a microchannel as they move within 200 nm of a smooth surface that has been treated to be either hydrophilic or hydropobic.

The experiments use Total Internal Reflection Fluorescence Microscopy (TIRFM) and Particle Tracking Velocimetry (PTV). A pair of 532-nm, 5-nsec laser pulses are directed through a high numerical aperture microscope objective at an angle that creates total internal reflection at the glass-water interface (figure 1), thus illuminating the near-wall region with the evanescent light field. Test channels were fabricated using PDMS molding techniques and bounded onto a glass wafer, (RMS surface roughness less than 4 nm). Image pairs of particles were captured using an intensified CCD camera and analyzed using custom PTV algorithms [5].

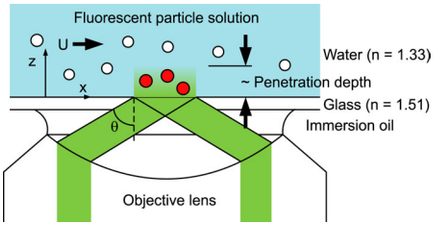


Figure 1. Schematic of objective-based TIRFM setup.

The experimental results were compared with a Monte Carlo simulation of particle Brownian motion in a shear flow. 10,000 particles were uniformly distributed in a shear layer within the evanescent wave penetration depth. At each time step, Δt, the particle was moved at the local velocity (using an assumed velocity profile) and subjected to Brownian motion, sampled from a normal distribution with a zero mean and a standard deviation of $(2D\Delta t)^{1/2}$, where D is the diffusion constant. The diffusion constant was modified to account for the presence of the wall using corrections based on analytical solutions to the problem of confined diffusion both normal and parallel to the surface [6,7]. To prevent particles from moving through the wall, a specular reflection boundary condition was imposed when particles come into contact with the wall (this is not strictly accurate and will be improved in future simulations, however the solution is not very sensitive to this feature of the technique). After many thousand timesteps, particles that remained in an "observation depth" (defined in conjunction with the experiment and based on minimum image intensity threshold) were counted and particle displacements from their initial positions were calculated to obtain displacement, and consequently apparent velocity distributions, similar to those obtained from the physical experiments. It is important to realize that the distributions are sensitive to both the choice of the observation depth and the character of the slip/no-slip boundary condition at the solid surface.

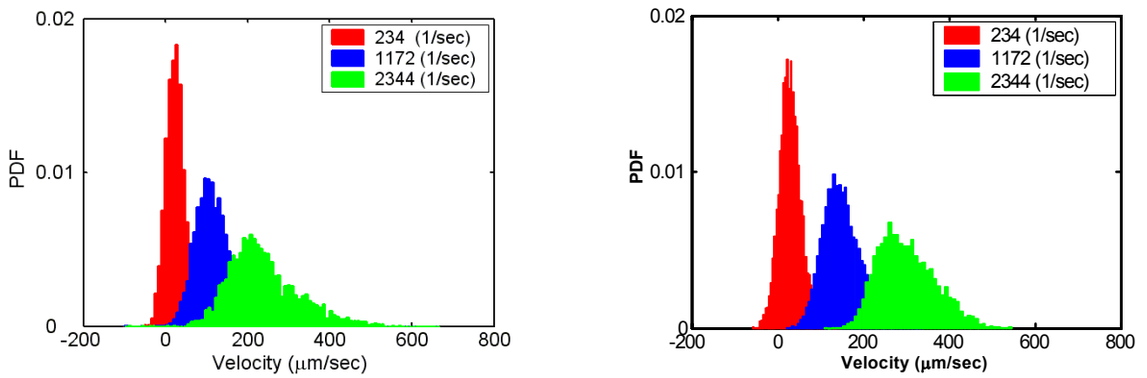


Figure 2. Distributions of velocity at three shear rates. The left frame shows the experimental results while the right frame shows the corresponding result from the Monte Carlo simulation (using an assumed observation depth of 175 nm).

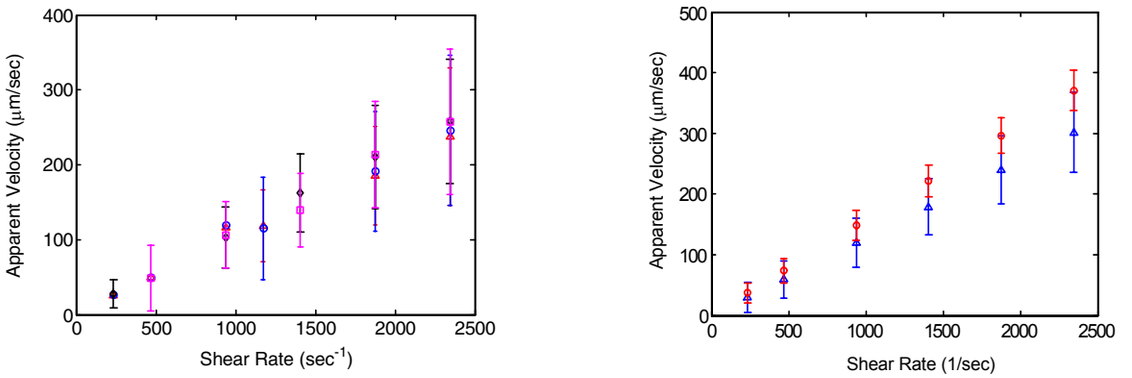


Figure 3. Apparent velocity vs. shear rate. The left frame shows the experimental results (hydrophilic: 200-nm particles – red; 300-nm particles – black / hydrophobic: 200-nm particles – blue; 300-nm particles – pink) while the right frame shows the Monte Carlo simulation (200-nm particles – blue; 300-nm particles – red) at observation depth = 175 nm.

Figure 2 shows an example of the distribution of streamwise apparent velocities obtained from (a) physical experiment and (b) simulation. We observe that the peak of the distribution increases with increasing shear rate, as do both the distribution width (standard deviation) and its skewness. Such observation merely reflects the fact that tracking particles with a finite interrogation volume samples particles traveling at several local velocities all of which contribute to the apparent velocity. This also explains the increasing width and skewness of the distributions as the shear rate increases, although the high skewness is primarily due to the sharp reduction in the diffusion coefficient when the particle is very close to the wall. Figure 3 shows the variation of the mean velocities and their standard deviations (denoted as error bars) as a function of shear rate. The velocities appear to fall on a straight line through the origin and that there is no clear difference between hydrophilic and hydrophobic surfaces at these (low) shear rates. The slope of the line suggests that the slip length, if it exists, has a magnitude of less than 20 nm – consistent with some of the recent measurements [1], but in contrast to others [2,3]. One puzzling observation is that there appears little difference between the streamwise velocities obtained using 200- and 300-nm particles, while numerical simulation suggests that a difference should exist if a uniform observation depth is used. The shape of the distributions from both the numerical simulation and experimental measurements are quite sensitive to the selected observation depth (figure 4). Consequently, the similarity between the 200- and 300-nm particle experimental data is likely due to the differences in selected observation depths, and their overlap is merely coincidental. Experiments are currently underway to obtain calibrated particle intensity profiles at different observation depths, which will enable direct measurement of the three-dimensional motion of the particle and the observation depth and thus resolve this issue.

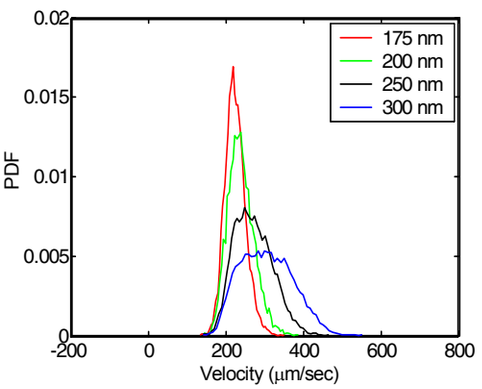


Figure 4. Simulated velocity distributions of 300-nm particles at a shear rate of 1400 sec^{-1} with four different observation depths.

The current results shed light on the dynamics of small particles in microfluidic systems and reinforce measurements that suggest that slip, if present, is small at low shear rates. Furthermore, we conclude that at the microscale, estimations of fluid velocity from observed particle motions near a solid surface should be treated with care. Experiments at higher shear rates and using more accurate (three-dimensional) measurements, are currently underway as well as more extensive and refined simulations,. These will be reported upon at the ICTAM meeting.

References

[1] Choi C. H., Westin K. J. A., Breuer K. S.: Apparent Slip Flows in Hydrophilic and Hydrophobic Microchannels. Physics of Fluids, **15**(10), 2897-2902, 2003

[2] Zhu Y., Granick S.: Viscosity of Interfacial Water. Physical Review Letters, **87**, 096104, 2001.

[3] Tretheway D. C., Meinhart C. D.: Apparent Fluid Slip at Hydrophobic Microchannel Walls. Physics of Fluids, **14** (3), L9-L12, 2002.

[4] Lin B., Yu J., Rice S. A.: Direct Measurement of Constrained Brownian Motion of an Isolated Sphere between Two Walls. Physical Review E, **62**(3), 3909-3919, 2000.

[5] Jin S., Huang P., Park J., Yoo J. Y., Breuer K. S.: Near-Surface Velocimetry Using Evanescent Wave Illumination. Experiments in Fluids (in review), 2004

[6] Goldman A. J., Cox R. G., Brenner H.: Slow Viscous Motion of a Sphere Parallel to a Plane Wall - I Motion through a Quiescent Fluid. Chemical Engineering Science, **22**, 637-651, 1967.

[7] Brenner H.: The Slow Motion of a Sphere through a Viscous Fluid towards a Plane Surface. Chemical Engineering Science, **22**, 637-651, 1961.

Theoretical and Experimental Study of Microchannel Blockage Phenomena

Eiichiro Yamaguchi, Ronald J. Adrian
University of Illinois at Urbana-Champaign, TAM, 104 S. Wright St., Urbana, IL 61801-2983, USA

Summary Microchannel blockage by hard, spherical particles have been investigated. The experiments on taking statistical data, and the visualization of the particles dynamics in the channel, were performed over a particle-to-channel diameter ratio of $0.14<R<0.65$. The experimentally obtained critical particle concentrations of the blockage (ϕ_c) are surprisingly low. The modified flocculation theory failed to explain the strong relation between ϕ_c and share rate (G), although it predicted the dependency of ϕ_c and R well.

Recent developments in fabrication techniques for micro-fluidic systems and in methods for the study of micro-fluid dynamics allow engineers to design integrated, complicated micro-fluidic devices, such as lab-on-chip total analysis systems and implant-type medical monitoring systems. The device usually consists of series of closed microchannels having cross-sectional dimension less than 1 *mm* and greater than 1 μm to transport materials with or without having chemical or biological reactions. In real applications, micro-fluidic devices are often used to transport a variety of particle-laden liquids at various flow speeds. Blockage of micro-channel by the particles may limit the life expectancy or usage of the micro-fluidic devices. Although, great number of potential applications for bioengineering and chemical analysis devices could be found, few experimental and theoretical studies about a mechanics of particle-laden liquids at large Peclet number (Pe) have been done. It is crucial to know when, or how often, blockages occur in each channel of a particle bearing micro-fluidic system. Also, operations to remove a blockage or replace a channel in a micro scale device involve numerous technical complexities.

Sharp (2001)[1] and Sharp and Adrian (2001)[2] have proposed shear induced arching (also called hydrokinetic arching) as the main mechanism causing a blockage based on observation of final blockage geometrical configurations. The explanation is based on the likelihood of particles colliding when placed in a non-uniform laminar flow velocity profile, followed by the formation of "arches", much like the arching phenomena in dry granular flows. It indicates that sufficient large number of particle must be in close distance prior to the arch formation. Assuming that the particles are uniformly dispersed at the inlet of channel, some mechanisms must bring the particles together in the channel. Study of flocculation of particles in the microchannels could gives us some insight of the mechanism about how the particle come together to form the arches.

The original work on orthokinetic flocculation theory (particle aggregation cause by fluid motion, $Pe>>1$) was that of Smoluchowski (1917), who described the collision rate of spherical particles, travelling along parallel streamlines. Gregory (1981)[4] simplified it for the case of mono dispersed suspension of uniform radius spheres,

$$-\frac{dn}{dt}=\frac{4\alpha\phi Gn}{\pi}$$

where n is number of aggregates in unit volume, ϕ is the volumetric concentration of particles, G is the local shear rate and α is a dimensionless collision efficiency factor which indicates number percentage of collision of particles could result aggregate over total number of collision. The theory is based on the assumption that form of aggregate is spherical. For example, colliding two particles merge into one sphere having double volume. The possibility that shear force or the effect of repulsion force can separate the doublet is neglected. Brownian diffusion has also been neglected. Further simplification was done by applying the cylindrical straight channel with laminar flow. Then it was integrated to give;

$$J=\frac{n_0}{n_{tot}}=\exp(\frac{128}{9\pi}\beta R^3 N)$$

where J is mean number of particles per aggregate, N is number of individual particles in the volume of the tube, R is diameter ratio of particle and tube, β is modified collision efficiency factor for a large aggregate. The equation nicely predicts the particle collision rate in early stage of flocculation process (doublet forming rate). It should be noted that the equation over estimates the growth rate of larger aggregate.

It can be inferred that the tube should be blocked when the mean aggregate diameter becomes larger than the tube diameter (D). Therefore to avoid the blockage in the tube, $N_B(R)>J$ must be satisfied, where $N_B(R)$ is the number of particles in the aggregate of diameter D. The number of particles in the aggregate having diameter equal to D is determined only by R. The solution of $N_B(R)$ can be generalised as the problem of finding a number of small spheres that can be packed inside of a lager sphere, the so-called spheres in a sphere problem. The general, exact solution for the dense packing is still unknown. Simple numerical cord has been written to approximate the solution. The obtained results have agreed very well with the results calculated by the algorithm from Boll and Donovan (1998)[5,6].

Now, at critical particle number $N=N_c$, J can be replaced by $N_B(R)$. Then the equation can be solved for N_c to obtain following final form.

$$N_c=\frac{9\pi}{128\beta}\ln(N_B(R))\frac{1}{R^3}$$

Experiments were performed in the micro-fluidic apparatus described in Figure 1. Due to technical limitations, the experiments can be repeated limited number of times with limited experimental time length. The following conditions have been set to determine the experimental N_c from the limited number of data. (i) Each experiment is stopped after *10 minutes* (*0.5 ml* of injection) or when the monitoring system detects a blockage. (ii) The 'critical' point N_c was decided after four consecutive experiments that were finished without the blockage, including at least one experiment at slightly lower concentration.

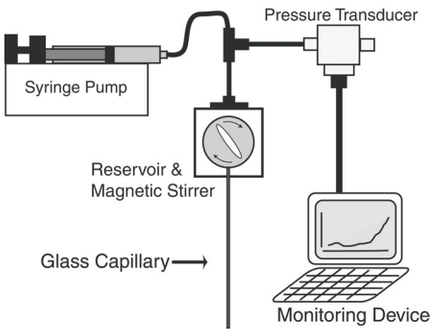


Figure 1: Setup for the blockage experiment

Figure 2 shows the experimental results (dots) and theoretical predictions (lines). The equation predicts relationship between R and N_c well, however the experimental results are classified by average share rate ($\overline{G}$). β = 0.1 is determined to match the experimental data at average share rate $\overline{G} = 5440.8 s^{-1}$ (D = 100 μm). Values of β for the other $\overline{G}$ are also determined to fit the experimental results. Figure 3 shows how $\overline{G}$ affects on the blockage data. In the figure, $\overline{G}$ is only variable changed throughout the experiment. It clearly indicates that shear (averaged shear) rate increases the blockage probability at all stages. It shifts the probability distribution curve. This could not be predicted by the theory.

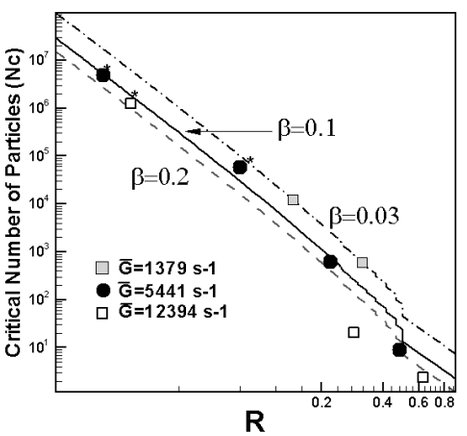


Figure 2: Theoretical predictions (lines) and experimental data (dots). Data with * were based on the blockage data taken by Sharp (2001). Their critical values were decided by the author.

As it is stated above, the modified flocculation theory is an extension of the collision frequency between the particles. It does not provide sufficient information to predict the blockage at large *Pe* for two possible reasons. First of all, it ignores the possibility that the large aggregate having size to occupy the channel could slip though the channel without interrupting the flow. Another theoretical possibility is that the arch can be formed with enough number of single particles if they are located at collect geometry simultaneously. It does not require single large aggregation to fill the channel. In fact, Figure 3 is indicating that forming of the large aggregation may not be necessary for the blockage.

The effect of flocculation must be distinguished from the effect of following arching formation to evaluate the effect of share on the blockage formation. Visual information regarding formation of arches and the following blockage forming process could provide hints to understand the mechanisms of the above possibilities, however due to the complexity of the analysis, the experiment setting and device is still under development. Also, the current experimental setting is insufficient to evaluate whether or not the blockage depends on some other parameters or initial configurations. Further discussion for this probability distribution requires further data collection with much more accurate experiment setting.

The work is in progress. The presentation will discuss comparison of theoretical prediction based on the flocculation theory and experimental results in a limited range of $0.14<R<0.65$. It will show how the preceding step to the arching will form and whether or not understanding of the complex arching mechanism is required to establish a reliable prediction of the blockage.

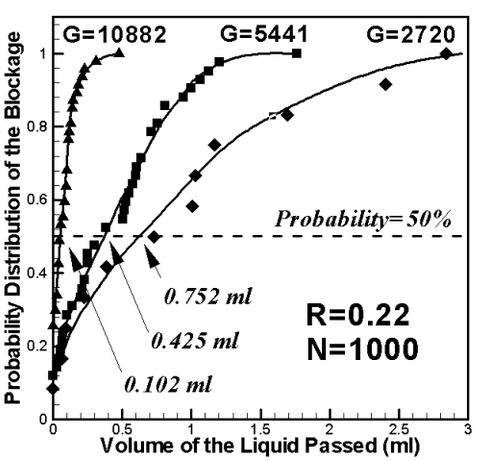


Figure 3: Probability distribution at various G. The probability of the blockage increases with average shear rate.

References

[1] Sharp, K.V.: Experimental investigation of liquid and particle-laden flows in microtubes. *PhD thesis*, University of Illinois at Urbana-Champaign, Urbana, IL, 2001.

[2] Sharp, K.V., Adrian, R.J.: Shear-induced arching of particle-laden flows in microtubes. *In 2001 ASME International Mechanical Engineering Congress and Exposition*, Vol.2, New York, NY, Nov. 2001.

[3] Russel, W.B., Saville, D.A., Schowalter, W.R.: *Colloidal Dispersions*, Cambridge University Press, Cambridge, UK, 1989.

[4] Gregory, J.: Flocculation in Laminar Tube Flow. *Chemical Engineering Science*, 16(11): 1789-1794, 1981.

[5] Boll, D.: Packing results, *web site*, http://www.frii.com/dboll/packing.html.

[6] Donovan, J.: Packing circles in square and circles, *web site*, http://www.home.att.net/donovanhse/Packing.

XXI ICTAM, 15–21 August 2004, Warsaw, Poland

INDUCED CHARGE ELECTRO-OSMOSIS: THEORY AND MICROFLUIDIC APPLICATIONS

Todd M. Squires*,Martin Z. Bazant**
*Depts. of Applied and Computational Mathematics and Physics, Caltech, Pasadena, CA 91125
**Dept. of Mathematics and Institute for Soldier Nanotechnologies, MIT, Cambridge, MA 02139

Summary Induced-charge electro-osmosis (ICEO) involves the nonlinear electro-osmotic slip flow caused by an applied field acting on ionic charge *induced* around a conducting body or surface, wherein a rectification allows steady microfluidic flows to be driven using AC fields. Breaking the symmetry of the surface or field allows steady flows to be driven parallel or perpendicular to the applied AC field, suggesting a number of devices and strategies for microfluidic mixing, pumping, and manipulation.

INTRODUCTION

Electrokinetic techniques are one of the most popular of non-mechanical fluid manipulation strategies for microfluidic flows (*e.g.* [1]). This popularity stems in part from the fact that many microfluidic applications naturally integrate electronic circuits for electrophoretic separations. Electro-osmotic flows are further favored in that they allow dispersionless plug flows (as opposed to parabolic pressure-driven flow) and because the large surface/volume ratios of microchannels suggest surface-driven flows. However, electro-osmosis has drawbacks: they depend sensitively on solution pH, salt concentration, and surface charge densities, and electrochemical (Faradaic) reactions are required to maintain a constant electric field, which introduces bubbles, metallic ions, and concentration gradients. Furthermore, high voltages are required to apply appreciable fields over significant distances.

In traditional electro-osmosis, an applied field acts upon the diffuse cloud of counter-ions surrounding a charged surface. The resulting body force drives the fluid into motion, resulting in Smoluchowski's 'slip velocity'

$$u_{\mathrm{EOF}} = \frac{\epsilon_w \zeta E}{\mu}, \tag{1}$$

where ϵ_w and μ are the permittivity and viscosity of water, E is the applied field, and ζ is the potential drop across the double-layer (proportional to surface charge density for small ζ). Clearly, a periodic applied field $E(t)$ gives no time-averaged electo-osmotic flow.

Recently, AC electrokinetic techniques have been introduced which overcome many of the drawbacks inherent in traditional electro-osmotic flow. In AC electro-osmosis, a time-varying applied field acts upon the transient charge cloud it *induces*. Since the applied field and the induced charge cloud both exhibit the same time-dependence, the resulting nonlinear electro-osmotic slip velocity has a non-zero, rectified component. Such phenomena have been exploited in colloidal self-assembly near electrodes [2, 3], driving counter-rotating fluid rolls above planar electrodes [4], and (by breaking spatial symmetry) to create microfluidic pumps [5, 6].

Such techniques involve transient charge clouds induced around the working electrodes, and thus work in a limited frequency range: they do not work at extremely high frequencies (where charge clouds do not have time to form), nor do they work at low frequencies (where the charge cloud completely screens the electrode, leaving no applied field). They do, however, avoid electrochemical reactions and are relatively insensitive to solution properties.

INDUCED-CHARGE ELECTRO-OSMOSIS

Nonlinear electrokinetic phenomena, however, have a wider range of validity than AC electro-osmosis implies. Because the key physical ingredients involve electro-osmotic flows due to charge clouds *induced* by the applied field, we prefer the more general term 'induced-charge electro-osmosis' (ICEO) for their description. Fig. 1 presents the most basic picture of ICEO, which represents perhaps the simplest and cleanest example of a nonlinear electrokinetic phenomenon. In what follows, we discuss the scaling and relevant time scales for of ICEO flows (under DC or AC fields), as well as microfluidic devices which employ them.

The basic phenomenon of ICEO is illustrated in Fig. 1, where a conducting cylinder is immersed in an electrolytic fluid. Immediately after an external field is applied, an electric field is set up that intersects the conductor at right angles (Fig. 1a). If the conductor were in vacuum, this would represent the steady-state field configuration. Mobile ions in solution, however, move in response to the applied field, and a current $\mathbf{J} = \sigma\mathbf{E}$ drives positive ions into a charge cloud on one side of the conductor, and negative ions to the other. An equal but opposite charge is induced on the conducting surface to maintain the equipotential surface. A dipolar charge cloud grows until no field lines penetrate the double-layer in steady state (Fig. 1b). In steady state, the tangential field

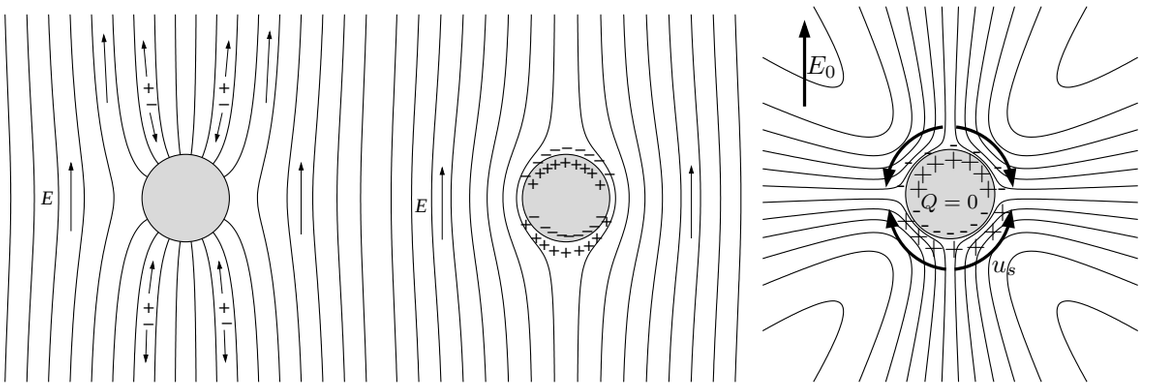


Figure 1. Induced-charge electro-osmosis. (a) Just after a DC field is applied, field lines intersect an ideally polarizable metal cylinder at right angles. Bulk currents charge a dipolar charge cloud over a charging time $\tau_c = \lambda_D a/D$, reaching steady state (b) when no field penetrates the double layer. The resulting zeta potential, however, is nonuniform, giving a quadrupolar ICEO flow (c).

from the 'poles' of the particle towards the 'equator' (Fig. 1c). Note that an AC applied field gives the same flow, since an oppositely-directed field induces an oppositely-charged screening cloud, and the net flow (which dependends on the product of the field and the charge) is unchanged.

Simple pictures give the scaling of ICEO flows: locally, the electrokinetic slip velocity obeys (1), except that the local ζ is now given by the difference between the potential of the conductor and the potential 'outside' the double-layer. For a cylinder of radius a, the induced ζ has magnitude Ea, and the ICEO slip velocity has magnitude $U_{\mathrm{ICEO}} \sim \epsilon_w E^2 a/\mu$. The time scale on which induced double layers form is given $\tau_c = \lambda_D a/D$, where D is the ionic diffusivity. This time scale, in an equivalent form, was also found in the context of AC electro-osmosis, where τ_c^{-1} is roughly the frequency for optimal response [7]. The ICEO flow shown in Fig. 1c, however, can be driven by any field with sufficiently small frequency $\omega < \tau_c^{-1}$, even DC fields.

The analogous colloidal picture was originally explored in the Russian literature (see [8] and references therein.) We are interested in ICEO from a microfluidic standpoint, where additional degrees of freedom arise that are unavailable in colloidal systems. For example, in microfluidic devices, the potential of the 'working conductor' can be actively controlled, *e.g.* by grounding it to one of the driving electrodes. In this case of 'fixed-potential' ICEO, an additional rectification arises that causes a net, *directed* fluid flow.

The above examples have been highly symmetric. Breaking spatial symmetries often results in additionally rich physical phenomena, as shown by Ajdari [5]. Breaking the symmetry of the conducting cylinder in any of a number of ways causes a *directed* flow along the axis of broken symmetry, so that a steady flow can be driven either parallel or perpendicular to an AC applied field. Microfluidic pumps based on this effect are promising for several reasons: stronger flows can be driven using arrays of asymmetric posts distributed along a channel. Furthermore, strong flows can be driven with a small AC potential applied *across* the channel, using asymmetric posts to drive flows *along* the channel. Finally, asymmetric conducting colloids experience a directed electrophoretic motion under AC fields, and, *e.g.*, objects can be designed that rotate under AC fields.

CONCLUSION

In summary, induced-charge electro-osmosis is a potentially useful new technique for driving microfluidic flows. Low applied voltages are required, and a strong flow results that is insensitive to solution chemistry. We have presented a simple but general physical picture and touched upon the rich variety of ICEO phenomena, and thus we suggest ICEO as a promising new tool for the microfluidic toolbox.

References

[1] G. J. M. Bruin, Electrophoresis **21**, 3931 (2000).
[2] M. Trau, D. A. Saville, and I. A. Aksay, Langmuir **13**, 6375 (1997).
[3] S. R. Yeh, M. Seul, and B. I. Shraiman, Nature **386**, 57 (1997).
[4] A. Ramos, H. Morgan, N. G. Green, and A. Castellanos, J. Colloid Interface Sci. **217**, 420 (1999).
[5] A. Ajdari, Phys. Rev. E **61**, R45 (2000).
[6] A. B. D. Brown, C. G. Smith, and A. R. Rennie, Phys. Rev. E **6302**, art. no. 016305 (2001).
[7] A. Gonzalez, A. Ramos, N. G. Green, A. Castellanos, and H. Morgan, Phys. Rev. E **61**, 4019 (2000).

USING MICROFLUIDICS TO INVESTIGATE REACTION-DIFFUSION PHENOMENA IN SIMPLE FLOWS

Laure Ménétrier*, Fridolin Okkels*, Charles N. Baroud**, Jean-Baptiste Salmon*, and Patrick Tabeling*
* *Microfluidique, MEMS et Nanostructures – ESPCI, 10 rue Vauquelin, 75005 Paris, France*
** *LADHYX, Ecole Polytechnique, Palaiseau, France*

Summary We report new experimental and theoretical results on the problem of reaction-diffusion in a microfluidic chip. The chemical reactor under study is a T-shaped microchannel (about 200 μm wide and 10–20 μm deep) in which the two analytes are bring into contact at a constant flow rate. In the interdiffusion zone, the local concentration of the reaction product is measured using optical epi-fluorescence. To extract useful informations about the reaction kinetics, one needs to model the reaction-diffusion zone and compare the simulations with the experiments. We show that such a microfluidic device is a well-suited method to access fast chemical kinetic rates.

INTRODUCTION

In the macroworld, chemical reactors usually operate in three dimensional turbulent regimes. Investigating such systems requires measuring, locally, the concentration field of the reactants, along with the velocity fluctuations, which is an extremely difficult task. More generally, the coupling between flow and chemical reactions lacks of experimental input at the moment, and this is unfortunate, owing to the considerable importance that such an interaction has, in industrial and natural contexts.

We show here that microfluidics allows to improve the situation, by offering the possibility to analyze, on an experimental basis, fundamental chemical diffusion phenomena, under an unprecedented control level. The physical reason is that, by miniaturizing, the laminar nature of the flow is fully guaranteed, whatever the liquid of interest we may use in the experiment. The paper focuses on the particular case of the spread of a reaction zone along a channel flow.

REACTION-DIFFUSION DYNAMICS IN A MICROCHANNEL: COMPARISON BETWEEN THEORY AND EXPERIMENTS

The microchannel we use here is in form of a T, similar to the one proposed in Refs. [1, 2] (see Fig. 1). The channels are

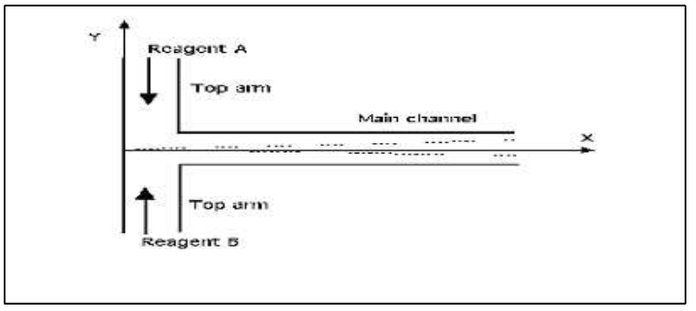


Figure 1. Sketch of the experimental system used, in form of a T-sensor, to measure fast chemical kinetics.

etched in glass, and covered by a silicon wafer, anodically bonded to the glass [3]. Reactants are driven along the T arms and are further collected in the main channel, forming a diffusion reaction front, which grows downstream. In this work, we use thin channels, 10 μm deep, so as to put three-dimensionnal effects under control. Figure 2 shows the reaction zone, formed by a Ca^{2+}/ CaGreen reaction, in such a system. We show here that the system is amenable to full theoretical understanding, provided we assume the chemical reaction to be of second order. To show this result, we compared the observed fluorescent field with the numerical solutions of the two-dimensional reaction diffusion equations, which govern the system evolution. In this comparison, the diffusion constants are measured independantly, or are known from existing tables. Only one parameter is left free – the kinetic factor k – and we adjust this parameter so as to optimize agreement between the numerics and the experiment (this in turn may provides a method of determination of k). Figure 3 indicates that agreement obtained under these conditions is good.

The method was used for a set of different flow rates and concentrations. At the largest concentrations we considered, the kinetic factor k we used was $k = 10^6$ L.(mol s)$^{-1}$, corresponding to a half-time reaction of 1 ms. This illustrates the idea that microfluidics may improve the measurements of the kinetics of fast chemical reactions, compared to the traditional stopped-flow techniques. In conclusion, we have investigated a fundamental situation of chemical diffusion (the spread of a reaction zone in a channel flow), and we have shown that the system is fully amenable to theoretical understanding.

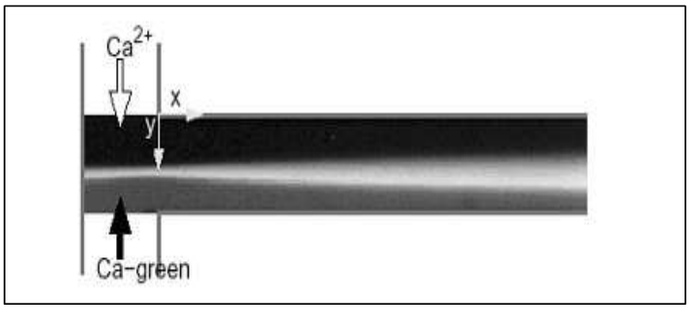


Figure 2. Experimental micrograph of the diffusion reaction zone for a Ca^{2+}/ CaGreen reaction, for 40 nL.min^{-1}

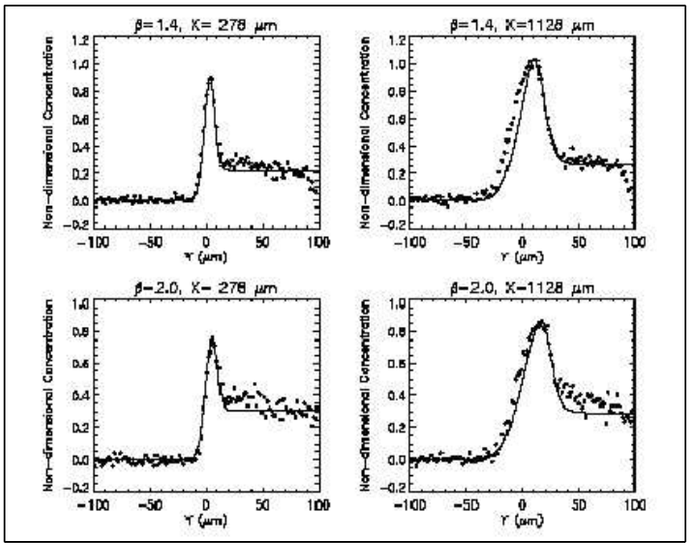


Figure 3. Comparison between the numerical concentration profiles of the product obtained by solving the two-dimensional reaction diffusion equations (full lines) and the experimental measurements (points), at various locations, for two values of the reactant concentration ratio; X and Y are the same as in Fig. 2.

Microfluidics systems may indeed allow to investigate other situations, under well controlled situation, and we hope this will be done, so as to elaborate an experimental basis for the important problem of handling reaction-diffusion phenomena in hydrodynamic systems.

References

[1] S. Pabit and S. Hagen: A laminar-flow fluid mixer for fast fluorescence kinetics studies. *Biophys. Journal* **83**:2872, 2002.

[2] A. E. Kamholz, B. H. Weigl, B. A. Finlayson and P. Yager: Quantitative analysis of molecular interaction in a microfluidic channel: the T-Sensor. *Annal. Chem.* **71**:5340, 1999.

[3] C. N. Baroud, F. Okkels, L. Ménétrier and P. Tabeling: Reaction-diffusion dynamics: Confrontation between theory and experiment in a microfluidic reactor. *Phys. Rev. E* **67**:060104, 2003.

MAGNETIC PARTICLES AGGREGATION IN THE PRESENCE OF A HYDRODYNAMIC SHEAR

Guillaume Degré, Edouard Brunet, Fridolin Okkels, Patrick Tabeling
MMN, Ecole Supérieure de Physique et Chimie Industrielle de Paris
10, rue Vauquelin Paris, France

Summary We present an experimental study of the aggregation of paramagnetic particles, carried out in the presence of a controlled laminar shear. Particles advected by the flow and suddenly immersed in a magnetic field are found to spontaneously form chains. Their lengths have proven to increase linearly with time, with a growth rate increasing as a power function of the shear. Observations agree well with a theoretical model based on a Smoluchowsky approach.

INTRODUCTION

Most of the patterns produced in natural or industrial situations – fingers, dendrites, fractals – result from aggregation processes. The importance and ubiquity of these phenomena has motivated, over the last ten years, the implementation of well controlled experiments carried out in laboratories, using dielectric and magnetic particles. This effort led to confirm the relevance of the Smoluchowsky theory for these systems, a conclusion obtained for fluids at rest, i.e for diffusive situations. In natural systems however, the fluid in which aggregation takes place is most often moving, and it is known that, by bringing particles close to each other more rapidly than brownian motion, shear flows may considerably speed up clustering phenomena. The issue is thus raised as to know to which extent the piece of knowledge obtained in purely diffusive situations may be used when aggregation develops in the presence of a flow. The goal of the present work is to make a step forward in this direction, by performing controlled experiments in microfluidic systems.

DESCRIPTION OF THE EXPERIMENT

We use microchannels moulded in PDMS, or etched in glass and covered with a silicon wafer. Channel dimensions are 20 μm deep, 200 μm wide and 20 mm long. We investigate flowrates ranging between 5 and 50 nL/min. The superparamagnetic particles are 0.83 μm in diameter, encapsulating Fe_3O_4 microdomains (Bang Laboratories). The bead concentration used throughout the experiments varies between 4 and 10 μg/ml.
A magnetic field is created with a pair of Samarium Cobalt magnets, 0.3 T of maximum intensity, as presented in Fig.1. Magnetic fied lines are parallel to the flow. The experimental protocol consists first in imposing the flow without the magnetic field, and then, at time t=0, rapidly bring the magnets close to the channel. We further follow the temporal evolution of the system. In the experiment, the particles are vizualized by using dark field microscopy, using a LEICA inverted microscope, with an X10 objective. The image is further processed, using software NIH-IMAGE with private macros. The program allows to determine the mean chain length L(t), along with the corresponding number N(t) of isolated particles carried by the flow.

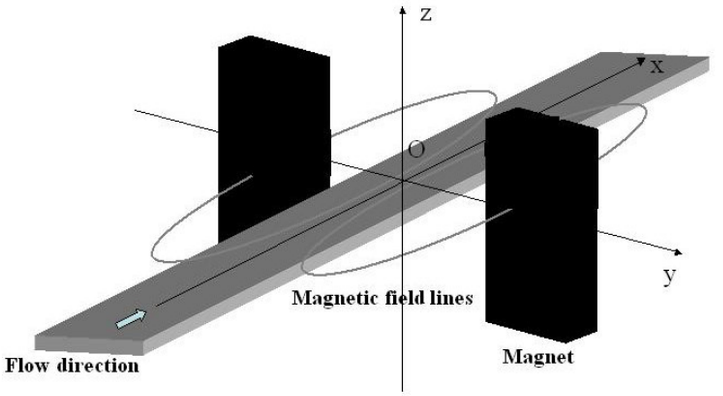


Figure 1: Schematic view of the experimental setup, represeting the pair of magnets, the micro-channel and a sketch of the magnetic field lines.

QUALITATIVE ASPECTS OF THE AGGREGATION PROCESS

We observe that the mechanism involved in chain formation most frequently involves particle-chain interaction : one chain and one particle located on two nearby streamlines, and therefore moving at different velocities, unavoidably approach each other and thus have the opportunity to aggregate, as illustrated in Fig2.

This process essentially takes place in the bulk, within fluid layers located close to the walls, where the shear is close to its maximum.

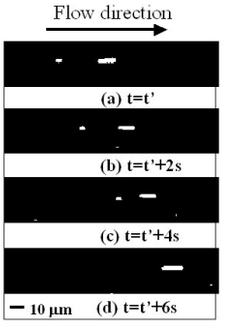


Figure 2 : Sequence of images showing the capture process. The flow goes from left to right at 40 nl/min. The magnetic field is longitudinal, with respect to the flow. The first images shows one particle appoaching a chain; some time later both have agregated.

RESULTS AND DISCUSSION

Fig 3a. represents the evolution of the average chain length L(t), for two different flow-rates, in a range of time comprised between 0 and 200 s. One sees that L(t) increases linearly with time, with slopes β depending on the flow-rate. Fig 3b. shows the evolution of the growth rate β with the shear rate S, estimated near the walls – where most of the chains lie.

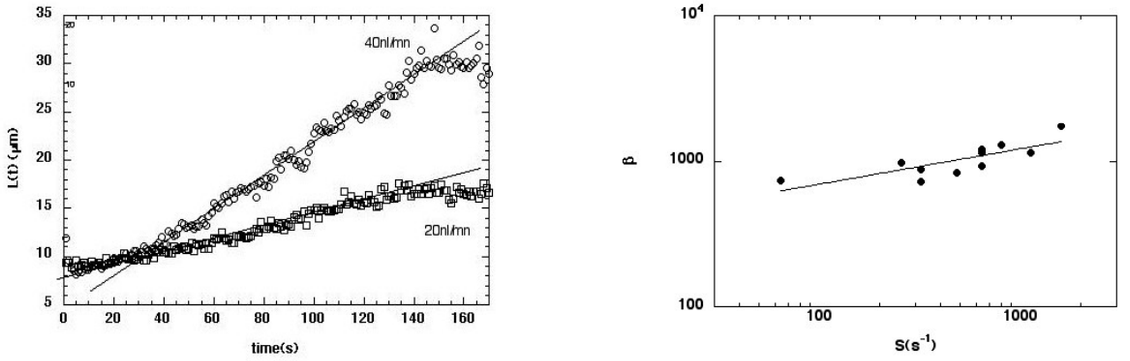


Figure 3 : a) Temporal evolution of the mean chain length for two different flow rates, 20 nl/min (squares) and 40 nl/min (circles) b) Evolution of the growth rate β with the shear in a log-log plot. One obtains the following power law as fitting the data : $\beta = 220.S^{0.25\pm0.1}$.

We further propose a theoretical model based on the analysis of the competition between the viscous forces and magnetic forces acting on a system particle-chain. We determine a radius of capture, within which particles coming from infnity aggregate onto a preexisting chain while the others escape. In this approach, one can show that the mean chain length increases linearly with time, with a slope proportional to the local shear raised to the power 1/4. The experimental observations made here are in good agreement with these expectations.

CONCLUSIONS

In conclusion, this work analyzes the aggregation process leading to the formation of chains, in the presence of shear flow, in micro-channels . We described the chain formation process, both theoretically and experimentally. The main observation is that the presence of the shear, coupled to the fact that the system is open, favors particle-chain interaction rather than chain-chain interactions, as in "ordinary" aggregation processes. As a result, the growth is linear in time. We found that, as a whole, theory explains the experiment quite satisfactorily. In these systems, miniaturization allows to produce substantial shears, while keeping the flows laminar.

ACKNOWLEDGEMENTS

The authors acknowledge J.Bibette, A.Ajdari, C.Baroud for valuable discussions. We thank CNRS, Universités Paris VI and VII, the Ministery of Research, Ecole Supérieure de Physique et Chimie Industrielle and Ecole Normale Supérieure for their support.

CHAOTIC MIXING AND RESONANCES IN A MICROFLUIDIC SYSTEM

Arash DODGE[(a)], Marie Caroline JULLIEN[(b)], Fridolin OKKELS[(a)], Patrick TABELING[(a)]
(a)MMN-ESPCI, 10 rue Vauquelin, 75231 Paris, France
(b) SATIE, ENS-Cachan, campus de Ker Lann, 35170 Bruz, France

Microfluidic systems are too small to shelter turbulence ; thus, unlike ordinary size systems, mixing cannot bear on hydrodynamic fluctuations in microsystems. Mixing cannot rely on molecular diffusion either, because microsystems are, in many cases, too large for diffusive mixing to act as a fast process. To summarize the situation, one may say that microsystems are often inhospitable to mixing. In a standard lab on a chip device, if nothing is done, it would take hundreds of seconds to develop sequences of reactions, and this is barely compatible with the general prospective that lab-on-a chips provide fast responses to analytical concerns.

These issues were raised in the early nineties. Since then, more than twenty micromixers have been reported in the literature. [1]. The present paper is dedicated to the presentation of a particular mixer - the cross-channel micromixer (here called X-mixer) ; owing to its simplicity, this mixer may probably be viewed as representative of a broad class of active chaotic micromixers. It happens that this particular system is the host of a novel phenomenon - a spatio-temporal resonance effect - which, to the best of our knowledge, has not been noticed before. The objective of the present work is to perform an experimental study of this phenomenon.

The device was microfabricated in PDMS using two-level soft lithography technology [3]. The layout of the device, along with its operation mode, is illustrated in Figure 1. It consists of a main channel where two streams of glycerol flow side by side, one flow being marked with fluorescein and the other not. The main flow is perturbed by a transverse, oscillating periodic flow created at the cross-channel intersection. This induces chaotic-like regimes as described in Ref [2]. The oscillating flow is produced by two integrated PDMS valves fabricated as described in Ref [3]. The valves consist of a membrane compressing the transverse flow channels actuated by nitrogen arriving in actuation channels. The compression thus creates displacement of fluid in the transverse channels with an amplitude proportional to the surface of the actuation membrane. With this method, control of the perturbation has been found excellent for both amplitude and frequency, a feature unattainable in previous systems.

Theoretical and numerical study of the system yielded different regimes of mixing, depending on the amplitude and the frequency of the transverse perturbation. Figure 2 shows a phase diagram of the different regimes obtained for a fixed flow rate, and various amplitudes and frequencies of the oscillating flow. Solid contour-lines represent regimes with the same interface contact length. One finds chaotic and non-chaotic regimes, separated by oak leave patterned lines. The peculiar structure of this diagram can be explained by a resonance effect which, as mentioned above, has been discovered in this research [5]. In the chaotic regions, material lines coming out of the intersection are elongated and folded thus producing chaotic mixing. Under resonance conditions, the material lines are elongated and folded in the intersection region, but they return to their original shape as they leave the intersection.

Figure 3 shows a snapshot of two fluids at the cross-channel intersection observed experimentally, and one produced numerically, in similar conditions, in the chaotic regime, where tendrils and whorls are produced. One sees good qualitative agreement between simulation and experiment. A similar agreement is obtained in the resonant regimes, which have been observed, in conditions consistent with the theoretical expectations.

REFERENCES

[1] D. Reyes, D. Iossifidis, P-A. Auroux, A. Manz, *Anal.Chem.*, **74**, 2623 (2002)
[2] Y.K. Lee, J. Deval, P. Tabeling, C.M. Ho, *Proc MEMS2001*, 483, Interlaken (2001)

[3] M. Unger, H. Chou, T. Thorsen, A. Sherer, S. Quake, *Science*, **288**, 113 (2000)
[4] J.M. Ottino, The kinematics of mixing, Cambridge University Press, (1989)
[5] F. Okkels, P. Tabeling, to appear in *Phys. Rev Lett.* (2004)

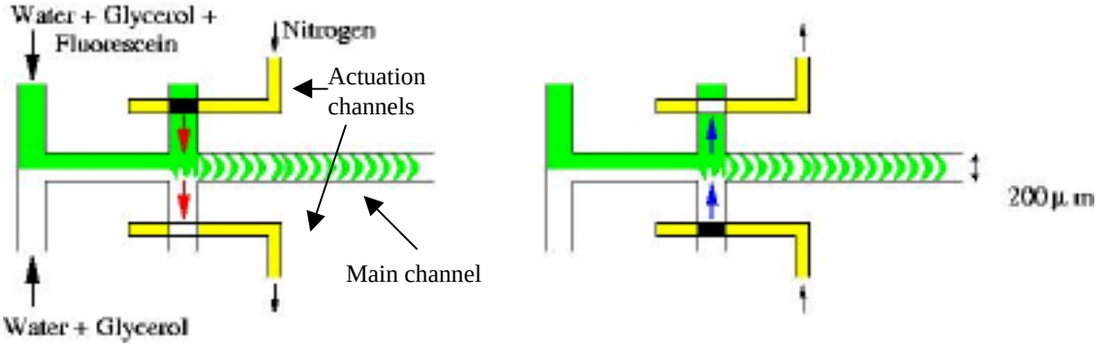


Figure 1: Layout of the device with operation mode. 46% glycerol 54% water solutions were used. Fluorescent solution incorporated 1 mM fluorescein. Membrane actuation was performed using nitrogen at 0.5 bar.

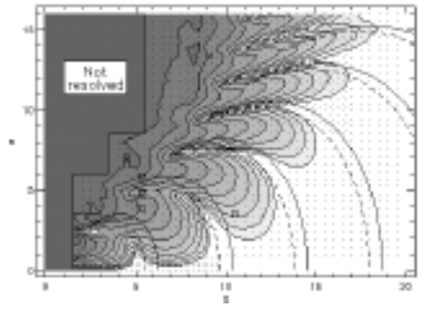
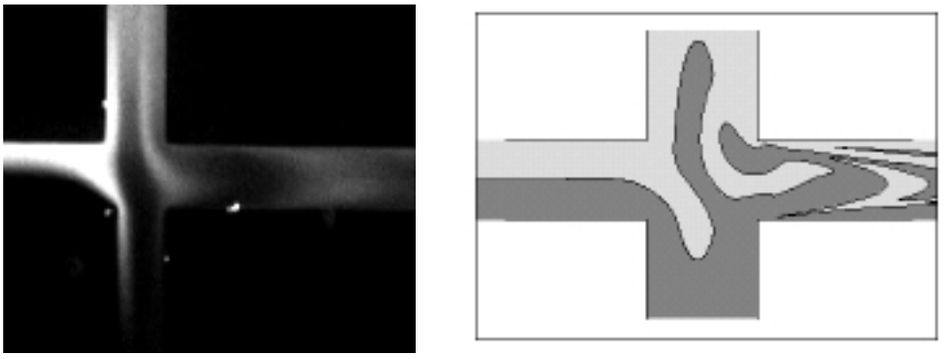


Figure 2: Contour-plot showing the amount of mixing as a function of the non-dimensional amplitude _ and frequency _, where darker gray means better mixing and visa versa. The resonances are the light spikes entering the darker region, and their theoretical predictions are the solid thick curves.



(a) (b)

Figure 3: Shape of the interface at the cross-channel intersection a) experimental b) numerical simulation. Experiment agrees with numerical simulations.

AN ACCURATE VELOCITY PROFILE MEASUREMENT SYSTEM FOR MICROFLUIDICS : A DIRECT MEASUREMENT OF THE SLIP LENGTH.

Pierre Joseph, Patrick Tabeling
MMN, Ecole Supérieure de Physique et Chimie Industrielle de Paris, CNRS
10 rue Vauquelin, 75231 Paris, France

Summary We describe an accurate method to measure velocity profiles inside microchannels, using particle image velocimetry combined with a nano-positioning system. The experimental setup is used to measure the slip length for water flowing along an hydrophilic surface, pyrex glass, and an hydrophobic one, a monolayer of octadecyltrichlorosilane (OTS) over an atomically flat silicon substrate. In the pyrex case, we achieve an unprecedented accuracy (±100nm) for a direct measurement of the slip length; this length is found to be essentially zero. For silicon surfaces functionalized with OTS, the accuracy is lower. One obtains 200±300nm for the slip length in this particular case.

INTRODUCTION

In classical textbooks, it is considered that liquids do not slip on solid surfaces. This provides a fundamental condition in fluid mechanics, allowing for detailed calculations of velocity profiles and flow structures. The physical justification bears on the assumption that attractive Van der Waals forces tend to link fluid atomic layers to the solid, preventing slip to occur. More generally speaking, this condition has been confirmed by an overwhelming abundance of experimental measurements, performed in ordinary fluid systems. In contrast with this picture, recent experiments have shown that simple liquids significantly slip on atomically smooth solid surfaces and, consequently, the no-slip condition should be replaced by a more general relation. On usually adopts the following form :

$$v = b\left(\frac{\partial v}{\partial z}\right)$$

in which b is the extrapolation or slip length, z is the normal (inwards to the fluid). Measurements of b have been performed in various situations, for a variety of solid surfaces, and several fluids (Ref [1], [2], [3]). Results indicate the slip length is on the order of micrometers, or fractions of micrometers, i.e much larger than typical intermolecular scales. There is no clear understanding, at the moment, for this set of observations. A possibility suggested by Ref [4], is that a gaseous layer nucleates at the interface between the fluid and the solid, favouring slippage. This proposal remains to be investigated experimentally.
The objective of this paper is to make progress on the measurement of slip lengths, by developing a direct method of determination of the velocity (using PIV), in thin microchannels. The technique we present here allows, with unprecedented accuracy (±100 nm), to measure the slip length of water flowing over glass; the same technique is applied for atomically smooth silicon substrates, functionalized with OTS.

EXPERIMENTAL SETUP AND MEASUREMENT METHOD

A general scheme of the experiment is shown on figure 1 :

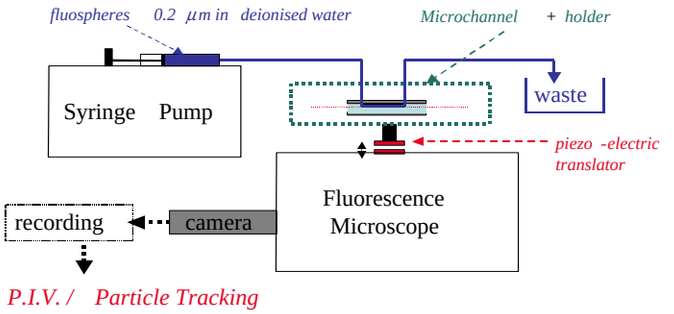


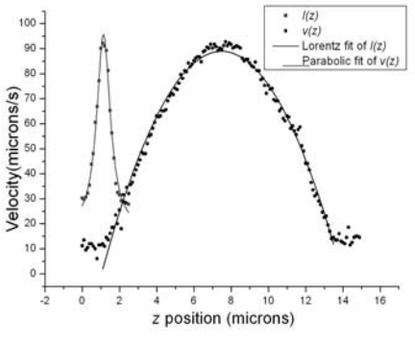
Figure 1 : Schematic view of the experimental setup.

Rectangular microchannels used in this experiment are 15µm thick, 200µm wide, and 2cm long. The stationary flow-rate (25nL per minute) is controlled by a syringe pump, the corresponding shear rate, at the wall, being $50s^{-1}$. The working solution is deionized water seeded with a 200nm-diameter fluorescent polystyrene beads. The lower surface of the channel is made of glass or atomically flat silicon, chemically modified by self-assembled-monolayer deposition of

a 2.3nm thick octadecyl-trichlorosilane (OTS). In the first case, water wets the surface, while in the second case, one gets a hydrophobic surface, showing a contact angle 95°, with an hysteresis of 10°.
Observation is made with an epifluorescent microscope (emission filter λ=515nm), a 100x oil immersion objective (index of refraction n=1.515), with a numerical aperture NA=1.3. The depth of field is then 460nm. In such conditions, one may image a thin layer of fluid, within the channel. In order to have a few beads in this volume, the volumetric fraction of the suspension is fixed to 2.10^{-5}.
The objective is mounted on a piezo-electric nano-positioner (20nm precision), which allows an accurate control of the fluid layer being imaged. A typical experiment consists of recording images with a video camera while scanning different z-positions inside the channel, in order to determine the entire velocity profile. Velocity is determined by PIV technique. For a reduction of random noise induced by brownian motion, measurements are typically obtained after averaging over 25 images.
In order to obtain an accurate determination of the wall position (with respect to the fluid), we measure the intensity emitted by stuck particles, for various positions of the objective (Figure 4b.). The experimental curve is then fitted with a Lorentzian, and the maximum is eventually determined, with an accuracy on the order of ±50nm.

RESULTS

A typical velocity profile obtained with a glass surface, in a 13µm thick microchannel, is shown on figure 4.



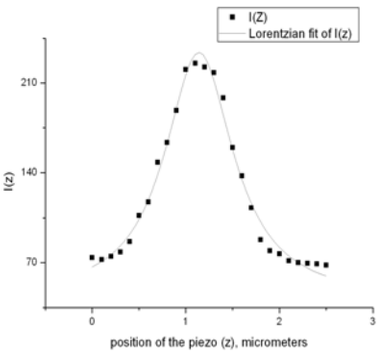


Figure 4 : a) velocity profile for glass b) Lorentzian fit of the intensity of a sticked bead on the glass surface. (arbitrary unit for *I(z)*)

The velocity profile corresponding to a Poiseuille flow is fitted with a parabola. The slip length is then inferred from the position of the zero of this curve compared to the actual position of the wall.
The slip length for glass (wetting case) is found equal to 0±100nm, while, for OTS functionalized silicon substrates, one gets (non-wetting case) 200±300nm.

DISCUSSION AND CONCLUSIONS

The experimental method we present here allows us to measure velocity profiles in thin microchannels, with a few percent precision on the velocity, ±50nm-accuracy on the determination of the wall position, with respect to the fluid, and ±30nm accuracy for the position of the fluid layer where the measurement is performed. These characteristics allow to determine, with unprecedented accuracy (±100nm), slip lengths for water flows over glass ; this represents a substantial improvement (a factor of 6 or so) compared to previous work using a direct method (see Ref [1]). When applied to pyrex glass surfaces, one gets slip lengths equal to 0±100nm. For silicon surfaces, functionalized with octadecyltrichlorosilane, the accuracy is lower. One obtains 200±300nm for the slip length in this particular case.

ACKNOWLEDGEMENTS

The authors acknowledge E. Brunet, J.B. Salmon, G. Degré for discussions. We thank CNRS and Ecole Supérieure de Physique et Chimie Industrielle for their support.

References

[1] Tretheway D., Meinhart C.: Apparent fluid slip at hydrophobic microchannel walls. *Physics of Fluids,* Vol 14, No. 3, 2002, pp. L9-L12 .
[2] Pit R., Hervet H., Leger L.: Direct experimental evidence of slip in hexadecane: solid interfaces. *Physical Review Letters,* Vol 85,No. 5, pp. 980-983, 2000
[3] Cottin-Bizonne C. *et al.*: An experimental study of slipping *length.* Eur. Phys. J. E.**9**, 47-53, 2002.
[4] De Gennes P.G.: On fluid/wall slippage. *Langmuir* **18,** 3413-3414, 2002.

TUNABLE MICROFLUIDIC BUBBLE GENERATOR

Piotr Garstecki[1], Howard A. Stone[2], George M. Whitesides[1]
[1] Department of Chemistry and Chemical Biology, Harvard University 12 Oxford St., Cambridge, MA, U.S.A.
[2] Division of Engineering and Applied Sciences, Harvard University 29 Oxford St., Cambridge, MA, U.S.A.

Abstract

We describe a microfluidic flow-focusing device, and report: i) stable formation of monodisperse, micron scale bubbles, with an independent control over their size and volume fraction in the continuous phase, ii) dynamic behavior exhibiting period doubling and transition to chaos, and iii) dynamic formation of ordered arrays of bubbles. We present a quantitative analysis of breakup and explain the mechanism underlying the narrow size distribution of bubbles or droplets formed in a flow-focusing geometry.

Background

Several techniques for formation of micron scale droplets have been proposed within the last decade – from a shear rupturing technique [1], breakup in a co-flowing stream [2], to microfluidic systems [3-5]. Our study falls into a particularly important focus of work during recent years – the idea of a lab-on-a-chip and exercising precise control of microscale multiphase flows with an emphasis on formation of discrete fluid segments, with size, shape, and concentration independently manipulated.

Experimental

The microfluidic device used in our study is presented in Figure 1a. It was fabricated in PDMS using standard photolithography techniques[6]. We use nitrogen as the gas phase and aqueous solutions of glycerol with the addition of Tween20 surfactant as the liquid. At the end of the middle channel, upstream of the orifice, the liquid and gas phases form an interface. The pressure drop forces the tip of the gas ligament into the orifice where it assumes an unstable, cylindrical, morphology and periodically breaks to release bubbles into the outlet channel. In order to determine the mechanism of break-up we varied viscosity of the liquid μ, surface tension γ, geometry of the device and pressures applied to the system.

Results

We find that i) the volume V_b of the bubbles scales with the flow-rate q and the viscosity μ of the liquid, and the pressure p of the gas stream as $V_b \propto p/q\mu$ (Fig. 1c), ii) the rate at which the diameter of the gaseous thread decays in time during a single breakup event is linearly proportional to the rate of flow of the continuous liquid and is independent of the viscosity and surface tension (Fig. 1d). The first observation leads to the ability to control the size of the bubbles ($\propto$p/q) independently of the volume fraction of the dispersed phase ($\propto$pq). The second observation forms the basis of a controlled capillary instability mechanism, in which the rate of collapse of the unstable thread is greatly slowed down by the effect of confinement of the orifice and relaxation of the surface energy proceeds at the rate of supply of the continuous fluid.

As the bubbles are released at the orifice they are carried away by the liquid flowing in the outlet channel. The bubbles interact both directly by elastic shape-restoring forces when colliding with each other and indirectly by affecting the liquid flow field. The extent of order in the outlet channel is determined by the gas volume fraction ϕ. As ϕ approaches the value of surface coverage for a two-dimensional closed-packed lattice the bubbles self-assemble into ordered, flowing lattices. The repeat unit and geometry of the lattice depends on the ratio of the bubble radius to the outlet channel width. The characteristics of the ordered bubble structures can be tuned adjusting the pressures applied to the inlet channels. Few examples of flowing lattices formed in our devices are shown in Figure 1e.

Conclusions

The bubbles produced in the flow focusing devices are almost ideally uniform in size. A single orifice device produces up to several thousand bubbles per second. The volume fraction of the dispersed phase can be tuned and can approach almost unity (foams). Adjustable lattices of micron size bubbles or droplets can be integrated with other microfluidic or MEMS devices. As such, the tunable, flowing, lattices could become a new element of the lab-on-a-chip toolbox.

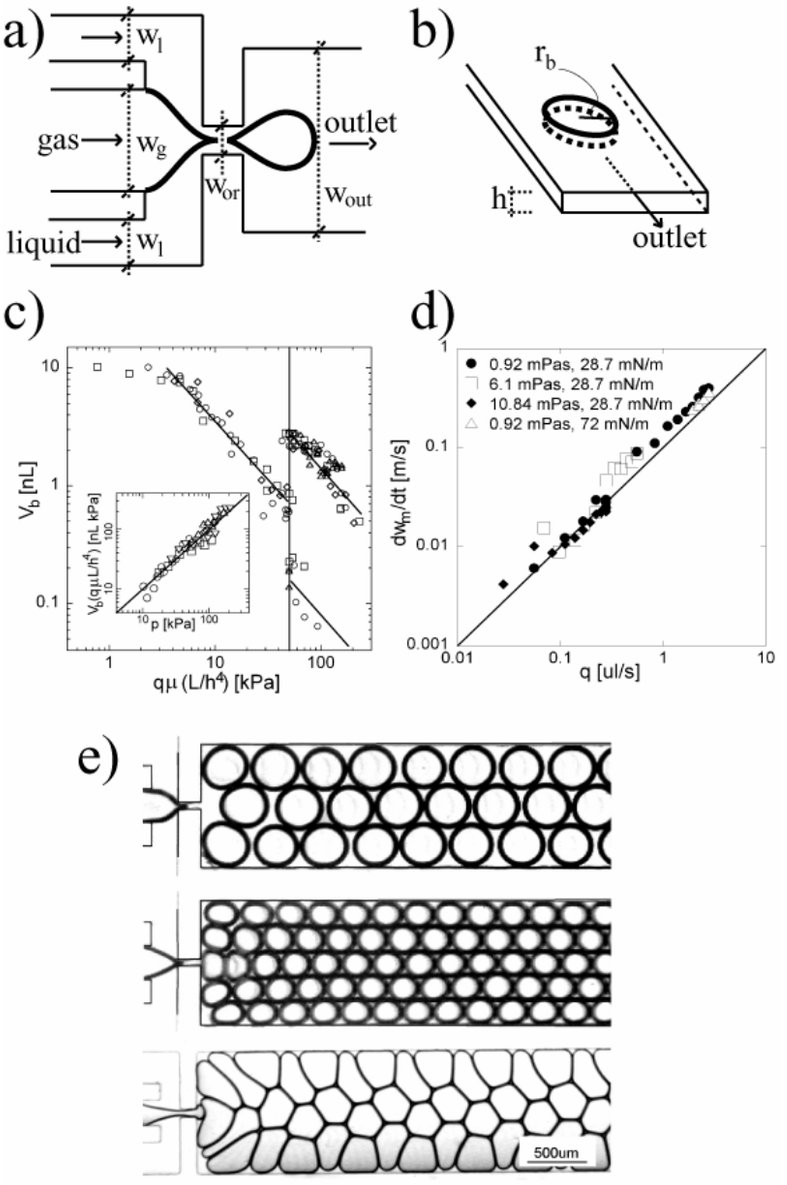


Figure 1. a) Schematic illustration of the microfluidic flow-focusing device (top view). The channels are uniform in depth. b) A schematic illustration of a bubble in the outlet channel. c) Scaling of the volume of the bubbles with the pressure applied to the gas stream, and rate of flow and viscosity of the continuous fluid. d) the rate of collapse (dw/dt), where w is the width of the collapsing thread, as a function of the rate of flow of the continuous fluid. e) Micrographs of dynamically assembled ordered lattices. The structure of the array depends on the ration of the size of the bubble to the channel width and on the volume fraction of the dispersed phase.

References

[1] Mason TG, Bibette J, Langmuir 13, 4600 (1997)
[2] Umbanhowar PB, Prasad V, Weitz DA, Langmuir 16, 347 (2000)
[3] Thorsen T, Roberts RW, Arnold FH, Quake SR, Physical Review Letters 86, 4163 (2001)
[4] Sugiura S, Nakajima M, Iwamoto S, Seki M, Langmuir 17, 5562 (2001)
[5] Anna SL, Bontoux N, Stone HA, Applied Physics Letters 82, 364 (2003)
[6] Whitesides GM, Xia YN, Angewandte Chemie International Edition, 37, 551 (1998)

FOAMS, FILMS AND SURFACES IN MICROGRAVITY

Denis Weaire, Simon Cox
Department of Physics, Trinity College, Dublin 2, Ireland

Summary Beginning with a broad view of the role of surface tension and gravity in free liquid surfaces, thin films and foams, we identify the motivation for the microgravity research conducted in these systems over the last quarter century. In the case of foams, experiments have been quite limited in scope, and the intention to study *wet* foams has yet to be fully realized, except perhaps in the case of two-dimensional samples. New experiments are planned for MAXUS rockets and possibly the International Space Station (ISS).

Foams, films and liquid surfaces present three inter-related fields of research in which the force of surface tension may play a primary role. Unless the length scale (bubble size for example) is much smaller than the capillary length, gravity is also important. Hence there has been from the outset (the book of Plateau in 1873 [1]) a desire to somehow suppress gravity and study surface tension effects alone. In particular, this would enable us to study wet foams. There are several ways of doing this, but the microgravity environment of space offers the most straightforward and general method.

In addition, there are obvious practical reasons to be concerned about the behaviour of liquids in containers in space.

Such motivations have stimulated a variety of experiments over many years, ranging from drop-tower observations to sounding rocket experiments, and there are plans for future ISS facilities. An entertaining example is the observation of non-coalescence of droplets in the experiments of Monti *et al.* [2].

Despite many years of foam experiments, there has remained some uncertainty about reliable methods of foam production to generate samples, since gravity often plays a role in familiar terrestrial methods. There is also a difficulty in observing wet foams since light is diffusely scattered by them. Hence three-dimensional experiments have been quite rudimentary up to this point (despite complex technical elaboration). Experiments on two-dimensional samples by Noever [3] and recently by Caps *et al.* [4] have offered more readily interpreted data.

In tandem with this experimental work, theoretical advances have been made, often with the aid of simulations. One such simulation tool is Brakke's Surface Evolver [5], which models surfaces governed by the forces of surface tension and gravity, among others, subject to given constraints. In our own work we have used it to successfully predict the occurrence of surface-tension dominated instabilities in foams [6]. Such work proceeds alongside models of, for example, liquid flow through foams under a range of micro- and zero-gravity conditions [7].

Foams (and analogous emulsions) are ubiquitous in occurrence and in application in the terrestrial environment, and should be so in the man-made space environment as well, where they will behave quite differently. The next generation of experiments should indicate where the important differences will lie. The planned experiments involve both the familiar aqueous foams of the bathroom and kitchen but also the production of metallic foam materials that are of current industrial interest – see figure 1.

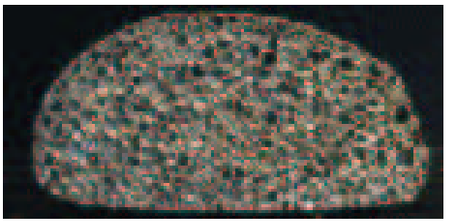


Figure 1. An example of a metallic foam. These materials have excellent properties, such as high strength-to-weight ratio, making them ideal for many industrial applications. In this case the foamed metal is zinc. Image courtesy of J. Banhart, HMI Berlin.

ACKNOWLEDGEMENTS

We gratefully acknowledge support from the Prodex and ELIPS programmes of ESA.

References

[1] Plateau, J.A.F.: Statique Expérimentale et Théorique des Liquides Soumis aux Seules Forces Moléculaires. Gauthier-Villars, Paris, 1873.
[2] Dell'Aversana, P., Monti, R. and Gaeta, F.S.: Marangoni Flows and Coalescence Phenomena in Microgravity *Adv. Space. Res.*, **16**:(7)95–(7)98, 1995.
[3] Noever, D.A. and Cronise, R.J.: Weightless bubble lattices: A case of froth wicking. *Phys. Fluids* **6**:2493–2500, 1994.
[4] Caps, H., Decauwer, H., Chevalier, M.-L., Soyez, G., Ausloos, M., and Vandewalle, N: Foam imbibition in microgravity. *Euro. Phys. J. B*, **33**:115–119, 2003.
[5] Brakke, K.: The Surface Evolver.*Exp. Math.* **1**:141–165, 1992.
[6] Cox, S.J., Weaire, D. and Vaz, M.F.: The transition from two-dimensional to three-dimensional foam structures. *Euro. Phys. J. E* **7**:311–315, 2002.
[7] Cox, S.J. and Verbist, G.: Liquid flow in foams under microgravity. *Microg. Sci. and Technol.* **XIV/4**:45–53, 2003.

Collisional Granular Flows with and without Gas Interactions in Microgravity

Mini-Symposium on "Microgravity Flow Phenomena"

21^{st} International Congress of Theoretical and Applied Mechanics

August 15-21, Warsaw, Poland

Michel Y. Louge and Haitao Xu
Sibley School of Mechanical and Aerospace Engineering,
Cornell University, Ithaca, NY
Michel.Louge@cornell.edu
http://www.mae.cornell.edu/microgravity/
(Dated: January 6, 2004)

We illustrate the convenience of a long-lasting microgravity environment for studying flows of granular materials with and without gas interaction. We consider collisional granular flows of nearly elastic spheres featuring a single constituent or binary mixtures in various bounded geometries. We review governing equations for these flows, illustrate their solutions and compare them with numerical simulations and data from microgravity experiments.

PACS numbers: 45.70.M, 64.75, 47.55.K, 83.10.L

I. EXTENDED ABSTRACT

The talk illustrates the convenience of a long-lasting microgravity environment for studying flows of granular materials with and without gas interaction.

We begin by considering collisional flows of nearly elastic grains featuring a single constituent of identical spheres or mixtures of two kinds of spheres that differ by mass or size at Stokes numbers large enough for the gas to play a negligible role.

At such high Stokes numbers, we carry out experiments and numerical simulations in two shear cells with a rectangular cross-section bounded by two flat walls and moving boundaries on which cylindrical bumps are affixed. One of the cells is shaped as a race track. The other is axisymmetric.

We outline the equations of the kinetic theory for the conservation of mass, momentum, fluctuation energy and species concentration in the granular phase [1] [2] [3]. We illustrate their solutions for shear flows in rectilinear or axisymmetric rectangular channels with or without a body force. We show that proper boundary conditions yield numerical solutions in good agreement with molecular dynamical simulations and with data from experiments carried out on NASA's KC-135 microgravity aircraft. [4]

Next, we describe future microgravity experiments with bounded shear flows of agitated, homogeneous, inelastic solid spheres colliding in a gas in the axisymmetric shear cell at finite particle Reynolds numbers, volume fractions between 0.05 and 0.4, and Stokes numbers large enough for collisions to determine the velocity distribution of the spheres. We briefly outline a continuum theory in which constitutive relations and boundary conditions for the granular phase are derived from the kinetic theory, and in which the gas contributes a mean drag force to the momentum of the grains and a viscous dissipation term to their fluctuation energy [5]. The theory underscores the role played by the walls in the balances of momenta and fluctuation energy, and predicts variations of volume fraction, mean and fluctuation velocities between the walls. We employ it to determine a set of experimental conditions suitable for recording the mean drag force and the viscous dissipation. Finally, we compare predictions of the theory to the recent Lattice-Boltzmann simulations of Verberg and Koch [6].

Acknowledgments

This work was supported by NASA grants NCC3-468 and NAG3-2112. It is the product of a long-standing collaboration with James T. Jenkins and Anthony Reeves. The authors are grateful to Rolf Verberg and Donald Koch for access to their Lattice-Boltzmann simulations and for fruitful discussions on the subject. The authors also acknowledge Stephen Keast and the NASA engineering and science team led by Enrique Ramé and John Caruso in helping set up and conduct the microgravity experiments described in the talk. .

[1] J. Jenkins and M. Richman, Arch. Rat. Mech. Anal. **87**, 355 (1985).
[2] J. Jenkins and F. Mancini, Phys. Fluids A **1**, 2050 (1989).
[3] B. Arnarson and J. Willits, Phys. Fluids **10**, 1324 (1998).
[4] H. Xu, M. Y. Louge, and A. Reeves, Continuum Mech. Thermodyn. **15**, 321 (2003).
[5] A. S. Sangani, G. Mo, H. Tsao, and D. L. Koch, J. Fluid Mech. **313**, 309 (1996).
[6] R. Verberg and D. L. Koch, in preparation (2004).

XXI International Congress of Theoretical and Applied Mechanics
Warsaw, Poland, August 15-21, 2004

Microgravity and Microscale Fluid Mechanics

George M. Homsy
Mechanical Engineering, UCSB, USA

This Introductory Lecture will cover aspects of Microgravity Fluid Mechanics by first describing the characteristics of the microgravity environment and establishing the manner in which the body force of gravity appears in the basic scalings and diimensionless parameters. The following themes are then developed: (i) the Space environment is characterized by transient accelerations, which implies that both the magnitude and direction of g are time-dependent, and; (ii) the magnitude of g is important only in combination with other intrinsic scales, with the consequence that microgravity and microscale fluid mechanics have much in common. The lecture will then focus on two classes of problems. The first is a class of so-called g-jitter phenomena driven by the time dependence of g, and the second is a class of interfacial fluid mechanics problems in which the essential driving force is applied tangential stresses due to Marangoni effects. If time allows, the inclusion of non-hydrodynamic forces will be mentioned, particularly in reference to the invited talk SL16, Electrokinetics and electrohydrodynamics in microfluids, by D.A. Saville.

HYDRODYNAMIC EFFECT OF SLOW PHASE TRANSITIONS IN MICROGRAVITY

Eleonora K. Bevza[*], Olexander O. Kochubey[*], Dmytro V. Yevdokymov[*]

[*]*Dniepropetrovsk National University, Mechanics and Mathematics Faculty, Nauchna str. 13, Dniepropetrovsk, 49050, Ukraine*

Summary The hydrodynamic effect of slow phase transitions is investigated using small parameter method. The mentioned effect is caused by density difference in phase transformation. Analytical and numerical calculation methods are developed for the proposed mathematical model. Estimations of correspondent convective flux influence on phase transition process are obtained.

STATEMENT OF PROBLEM

In general case origin and created phases have sufficiently different densities (case of equal densities is extremely seldom), what leads to fluid flows in liquid phases. Especially large this difference in evaporation (boiling) and condensation processes. Consider, as an example, an evaporation process. Created gaseous phase initially occupies the same volume, what was occupied by the transformed liquid phase, but it means that the created gaseous phase is strongly compressed and, as a result, the pressure in the created volume of new phase is more than in the rest of gas. This pressure difference induces gas flow which tends to equate the pressure in the whole gas phase and therefore the density too. On the other hand, the liquid phase can move too due to the same high pressure action, however, since the liquid density is much more, the gas density under the same conditions, the velocity of the liquid phase is smaller than gaseous one. Similar effects take place for other kind of phase transitions.

There are a lot of specific features in heat and mass transfer during phase transformation in microgravity condition. The main difference between heat and mass transfer in microgravity condition and in terrestrial condition is, of course, absence of natural convection. In the present work an absence of the forced convection is assumed, because forced convection is rather seldom phenomena in microgravity. By these reasons the process is mainly determined by heat conduction or diffusion phenomena, but influence of several other effects can be sufficient too. The main aim of the present work is restricted by slow phase transformations, that is, by the case of quite small gradients of parameters, which determined the phase transition. Such situation is enough widespread onboard of space vehicles and in some other cases of microgravity.

Consider a general mathematical model of phase transition:

$$\frac{\partial T_1}{\partial t} + V_1 \mathrm{grad} T_1 = a_1 \Delta T_1, \tag{1}$$

$$\frac{\partial T_2}{\partial t} + V_2 \mathrm{grad} T_2 = a_2 \Delta T_2, \tag{2}$$

Where V_1, V_2 are fields of velocities in the first and second phases, T_1, T_2 are fields of temperatures in the first and second phases. For the sake of simplicity let prescribe first kind boundary conditions on the outer boundary of phases

$$T_1\big|_{\Gamma_1} = T_{1s}, T_2\big|_{\Gamma_2} = T_{2s}, \tag{3}$$

and the initial conditions

$$T_1(t=0) = T_{10}, \; T_2(t=0) = T_{20} \tag{4}$$

The following conditions take place on phase transformation boundary:

$$T_1\big|_{\Gamma_{p.t.}} = T_{p.t.}, \; T_2\big|_{\Gamma_{p.t.}} = T_{p.t.}, \tag{5}$$

and the Stefan condition

$$\lambda_1 \frac{\partial T_1}{\partial n}\bigg|_{\Gamma_{p.t.}} - \lambda_2 \frac{\partial T_2}{\partial n}\bigg|_{\Gamma_{p.t.}} = \sigma\rho \frac{\partial n}{\partial t}, \tag{6}$$

where ρ is density of one phase (usually incompressible). Note that the right hand part of relation (6) is not full velocity of interphase boundary propagation, but it is only its component corresponding to phase transformation. The full velocity of interphase boundary is described by following relation

$$V_{p.t.} = \frac{\partial n}{\partial t}\bigg|_{\Gamma_{p.t.}} + V_h, \tag{7}$$

where V_h is hydrodynamic velocity of interphase boundary. As a result, the interphase boundary motion is described by equation

$$\frac{\partial \eta}{\partial t} = V_{p.t.}, \tag{8}$$

here η is generalized coordinate of interphase boundary referred along a normal to it, $V_{p.t.}$ is determined from (7). The equation (8) should be supplemented by the initial condition reflecting initial position of the interphase boundary:

$$\eta(t=0)=\eta_0 . \tag{9}$$

However, above formulated boundary-value problem is non-completed, as it doesn't contain an algorithm of velocity field determination. It is specific hydrodynamic problem. Traditionally as a model of hydrodynamics in heat and mass transfer processes Navier-Stokes or Reynolds equations are used. However, there isn't a tangent velocity component on the interphase boundary in the considering problem, that is, if there is not any other flow in the liquid domain, the flow caused by phase transition can be modeled by potential ideal fluid flow, what is much easier. On the other hand, if there is any other flow, viscous liquid model must be applied. Other specific feature of the considered problem is low speeds of flow, that is, the fluids in both phases can be considered as incompressible $\operatorname{div} V_1 = 0$, $\operatorname{div} V_2 = 0$.

Let the problem is described by Navier-Stokes equations or Euler equations formulated by traditional way. Let prescribe boundary conditions for the problem (restrict the consideration by interphase boundary, because traditional conditions are prescribed on other parts of boundaries). Equality of tangential velocity is assumed there (for Navier-Stokes equations)

$$V_{1\tau}\big|_{\Gamma_{p.t.}} = V_{2\tau}\big|_{\Gamma_{p.t.}}, \tag{10}$$

(or $V_{1\tau}\big|_{\Gamma_{p.t.}} = V_{2\tau}\big|_{\Gamma_{p.t.}} = 0$ for Euler equations). The normal velocity components are coupled by relation

$$|V_1|+|V_2| = \left(\frac{\rho_2}{\rho_1}-1\right)\left|\frac{\partial n}{\partial t}\right|. \tag{11}$$

Pressure equality condition must be added

$$P_1\big|_{\Gamma_{p.t.}} = P_2\big|_{\Gamma_{p.t.}} . \tag{12}$$

The problem can be can be simplified, if it is neglected by motion of one phase. Consider, for example, one-dimensional case of one moving phase, described by equation

$$\frac{\partial T}{\partial t} + V\frac{\partial T}{\partial x} = a\frac{\partial^2 T}{\partial x^2}, \tag{13}$$

with correspondent boundary and initial conditions. The following relations are important among boundary conditions

$$\lambda\left.\frac{\partial T}{\partial n}\right|_{x=y} = \sigma\rho_2\frac{dy}{dt}, \tag{14}$$

$$V = -\left(\frac{\rho_2}{\rho_1}-1\right)\frac{\partial y}{\partial t}, \tag{15}$$

where y is coordinate of phase transition, ρ_1 is density of pair, ρ_2 is density of liquid. Thus

$$\frac{\partial T}{\partial t} - \left(\frac{\rho_2}{\rho_1}-1\right)\frac{dy}{dt}\frac{\partial T}{\partial x} = a\frac{\partial^2 T}{\partial x^2}. \tag{16}$$

Correspondent dimensionless form of the problem is

$$\frac{\partial \theta}{\partial t}_{st}\,St + W\frac{\partial \theta}{\partial x} = a\frac{\partial^2 \theta}{\partial x^2}, \tag{17}$$

where $St = \dfrac{cp(T_n - T_{p.t.})\rho_1}{\sigma\rho_2}$ is Stefan number, W is dimensionless velocity. It is easy to show that equation (17) is transformed to

$$St\left(\frac{\partial \theta}{\partial \tau_{St}} - \left(\frac{\rho_2}{\rho_1}-1\right)\frac{d\eta}{d\tau_{St}}\frac{\partial \theta}{\partial x}\right) = \frac{\partial^2 \theta}{\partial x^2}. \tag{18}$$

Application of small parameter method (Stefan number is the small parameter) to equation (18) with dimensionless boundary and initial conditions gives an opportunity to solve the problem analytically. Note that convective term doesn't influence on zero approximation.

The proposed approach is easy generalized to two- and three-dimensional cases, the correspondent boundary-value problems are solved by boundary element method.

Heat transfer due to high frequency vibration: a new approach for achieving thermally optimum geometry under microgravity conditions

M.C. Charrier Mojtabi[1], Y. P. Razi[2], K. Maliwan[2] and A. Mojtabi[2]

1 : *Laboratoire d'Energétique (LESETH), EA 810, UFR PCA, Université Paul Sabatier, 118 route de Narbonne , 31062 Toulouse Cedex, France.*
2 : *IMFT, UMR CNRS/INP/UPS N°5502, UFR MIG, Université Paul Sabatier, 118 route de Narbonne, 31062, Toulouse Cedex, France.*

During recent years considerable effort has been directed towards the study of complex body forces whereby convective heat transfer rates might be increased. In natural convection, the interaction of non-homogeneities of density field with body force produces convective motion. Space related technologies have demanded a profound knowledge of these kinds of body forces; for example vibration, magnetic, etc which under earth condition are of second order importance.

The study of thermo-vibrational problems was originally inspired by its applications in cryogenic propellants in rocket system, Fashbaugh and Streeter [1]. This type of convection differs from natural convection induced by gravity in that it may be produced even under microgravity or space station conditions. The systematic study of this type of convection began in the early sixties, Schoenhals and Clark [2], and was later essentially focused on the mathematical aspect of body force modulation, for example see the review paper of Davis [3]. There, he emphasizes the importance of the relevant scales of the problem, and how it is possible to control the hydrodynamic stability of convective motion by proper tuning of modulation parameters.

The idea of using mechanical vibration as a mean for enhancing the heat transfer rate has also received equal attention from the early beginning. Forbes et al. [4] present an experimental study of the influence of vibration on heat transfer and fluid dynamic behavior of a differentially heated vertical slot. The direction of vibration is perpendicular to the temperature gradient. They find that there is a possibility of resonance, which leads to the heat transfer augmentation. This idea has been exploited in numerous papers [5-7] in which the geometry is a rectangular cavity. However, it should be pointed out that this idea is limited to the cases in which the thermal system possesses a natural frequency. This means that the external acceleration field should be thought as the superposition of a constant acceleration and a periodic acceleration with zero mean where the constant acceleration produces the natural motion in enclosure. Therefore, logically, for the system under the effect of periodic acceleration with zero mean there is no possibility of resonance.

The important issues related to the enhancement of heat transfer concern the type of thermal boundary conditions, relative orientation of vibration vector with the temperature gradient (non-parallelism) and the considered geometry. Here, we only review the papers under microgravity conditions in which the boundaries of enclosure are maintained at different but uniform temperatures and the direction of vibration is perpendicular to the temperature gradient. For other types of boundary conditions and vibrational direction, see Christov and Homsy [8] , Savino et al. [9] and Gershuni and Lyubimov [10].

Kamotani et al. [11] examine the influence of vibration with zero mean on the heat transfer behavior of the thermal system. Their results show that, in this case, vibration has no significant effect on the heat transfer rate. This finding may be explained by considering the range of frequency and amplitude used in that study; the amplitude and frequency were both very small.

The fundamental question that we address here is how to select the frequency and amplitude of vibration under microgravity in order to obtain optimal geometry for which heat transfer is maximized.

Of numerous possible combinations between amplitude and frequency of vibration, high frequency and small amplitude possesses particular characteristics, which make it attractive for heat transfer studies [10]. The most important of these characteristics is that it provides us with a closed system of equations governing mean field, which does not contain periodic coefficients.

Khallouf et al. [12] consider the influence of vibration on heat transfer and fluid flow behavior of the thermal system in the range of high frequency and small amplitude. Their study is limited to the case of a Prandtl number Pr = 1 and a vibrational Rayleigh number $Ra_v=10^5$ with the objective of studying the fluid flow structures. They propose the possibility of the heat transfer augmentation with respect to aspect ratios, A.

Our objective in this paper is to extend the result of [12] in the context of geometric optimization method, Bejan [13]. The governing equations under Boussinesq approximation, in a reference frame linked to the rectangular cavity, are written by adopting the time-averaged formulation [10]. The governing equations of the mean fields depend on three dimensionless parameters, namely Ra_v, Pr and the aspect ratio A. The relevant parameters considered are in the range of: $10^3 < Ra_v < 10^5$, $0.5 < Pr < 10$ and $1 < A < 5$. The typical fluid motion structures under microgravity conditions are obtained, as for example symmetrical four vortex-cell and a diagonal extended roll with strong intensity and two counter-rotative cells with weaker intensity.

By performing numerical experiments with a finite volume method, we have obtained power law correlation for Nusselt number, Nu, for each aspect ratio A. Some of the results are presented in table 1:

$$Nu = C\, Ra_v^{m}\, Pr^{n}$$

A	*C*	*m*	*n*
1	*0.07*	*0.3*	*0.01*
2	*0.001*	*0.5*	*0.02*
3	*0.001*	*0.7*	*0.02*
4	*0.0002*	*0.9*	*0.02*

Table 1

It should be noted that, we have also studied the evolution of the Nusselt number as a function of the Prandtl number. Our results show that for Pr >3, there is no significant influence on the Nusselt number.

In addition, we have presented a correlation, which provides optimum configuration maximizing heat transfer:

$$A_{opt} = 0.04 \frac{Ra_v^{0.4}}{Pr^{0.005}}$$

References:

[1] R. H. Fashbaugh, V.L. Streeter, Resonance in liquid rocket engine systems, J. Basic Eng. Trans. ASME, 87 (1965) 1011-1017.
[2] R.J. Schoenals, J.A. Clark, Laminar free convection boundary layer perturbations due to transverse wall vibration, J. Heat transfer.ASME, 84 (1962) 225-234.
[3] S.H. Davis,The stability of time-periodic flows, Ann. Rev. Fluid Mech., 8 (1976) 57-74.
[4] R.E. Forbes, C.T. Carley and C.J. Bell, Vibration effects on convective heat transfer in enclosure, J. Heat transfer.ASME, 92 (1970) 429-438.
[5] K.H. Kim, J.M. Hyun and H.S. Kwak, Buoyant convection in a side-heated cavity under gravity and oscillations, Int. Heat Mass Trans., 44 (2001) 857-861.
[6] W. Y. Chen, C. F. Chen, Effect of gravity modulation on the stability of convection in a vertical slot, J. Fluid Mechanics, 395 (1999) 327-344.
[7] S.K. Kim, S.Y. Kim and Y.D. Choi, Resonance of natural convection in a side heated enclosure with mechanically oscillating bottom wall, Int. Heat Mass Trans , 45(2002)3155-3162.
[8] C. I. Christov, G. Homsy, Nonlinear dynamics of two-dimensional convection in a vertically stratified slot with and without gravity modulation, J. Fluid Mechanics, 430 (2001) 335-360.
[9] R. Savino, R. Monti and M. Piccirillo, Thermo-vibrational convection in a fluid cell, Comp. & Fluids, 27 (1998) 923-939.
[10] G.Z. Gershuni and D.U. Lyubimov, Thermo-vibrational convection, Wiley, 1998.
[11] Y. Kamotani, A. Parasad and S. Ostrach, Thermal convection in an enclosure due to vibration aboard spacecraft, AIAA J, 19 (1981) 511-516.
[12] H. Khallouf, G. Z. Gershuni and A. Mojtabi, Numerical study of two-dimensional thermo-vibrational convection in rectangular cavities, Num. Heat Trans. A, 27 (1995) 297-305.
[13] A. Bejan, Shape and structure from engineering to nature, Cambridge, 2000.

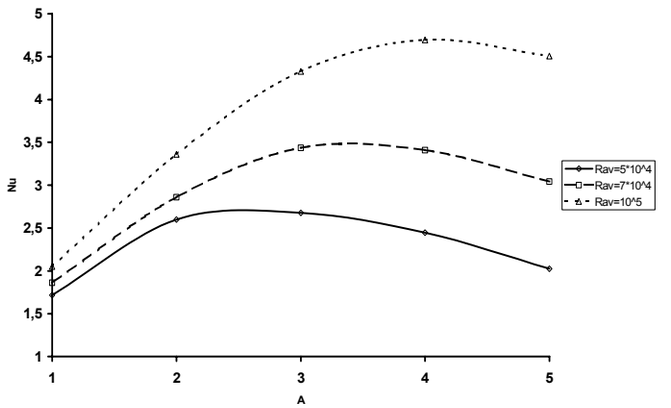


Figure 1. *Variation of de Nusselt number as a function of aspect ratio A for Pr =1 and different values of* Ra_v

THERMOCAPILLARY CONVECTION IN CYLINDRICAL GEOMETRY

Bok-Cheol Sim*, Abdelfattah Zebib**
*Crystal Growth Research Team, Wafer R & D Center, LG Siltron, Gumi, Gyeongbuk 730-724, Korea
**Department of Mechanical & Aerospace Eng., Rutgers University, Piscataway, NJ 08854, USA

Summary Thermocapillary convection in two types of cylindrical geometry is investigated in two- and three-dimensional numerical simulations: a liquid bridge heated from the upper wall and an open annulus heated from the outside wall. For the parameter ranges considered, it is found that dynamic free-surface deformations are negligible and do not induce transitions to oscillatory convection in axisymmetric models. Moreover, only steady convection is possible at any Reynolds number (Re) in strictly axisymmetric computations. In our three-dimensional models, the nondeformable free surfaces are either flat or curved as determined by the fluid volume (V) and the Young-Laplace equation. Convection is steady and axisymmetric at sufficiently low values of Re with either nondeformable or deformable surfaces. Transition to oscillatory three-dimensional motions occurs as Re increases beyond a critical value dependent on the aspect ratio, the Prandtl number and V. Good agreement with available experiments is achieved in all cases.

INTRODUCTION

The most popular methods for growing crystals are the Czochralski and floating zone techniques. In the present paper, we consider thermocapillary convection in a pair of relevant cylindrical geometry: a liquid bridge in a half-zone model of the float-zone crystal-growth process as shown in Fig. 1(a), and an open cylindrical annulus heated from the outside wall as shown in Fig. 1(b) constituting a model for the Czochralski crystal growth system. Thermocapillary convection with undeformable flat or curved surfaces is investigated in two- and three-dimensional numerical simulations, and critical conditions for transition to oscillatory states are established. Dynamic free-surface deformations are discussed only in the axisymmetric numerical simulations.

MATHEMATICAL AND NUMERICAL MODELS

Surface tension is assumed a linear function of temperature $\sigma = \sigma_0 - \gamma(T - T_0)$ where $\gamma = -\partial\sigma / \partial T$, and subscript 0 represents a reference state. Neglecting body forces, the non-dimensional governing equations are as follows:

$$\nabla \cdot \mathbf{v} = 0 \tag{1}$$

$$\mathrm{Re}\left(\frac{\partial \mathbf{v}}{\partial t} + \nabla \cdot (\mathbf{vv})\right) = -\nabla P + \nabla^2 \mathbf{v} \tag{2}$$

$$Ma\left(\frac{\partial T}{\partial t} + \nabla \cdot (\mathbf{v}T)\right) = \nabla^2 T \tag{3}$$

where **v**, P and T are respectively the non-dimensional velocity vector, pressure and temperature. Re is the Reynolds number, Pr is the Prandtl number, and Ma is the Marangoni number.

In order to numerically solve the problem with either undeformable or deformable surfaces, the governing equations and boundary conditions are transformed from the physical domain into a rectangular computational domain. The transformed equations and boundary conditions are solved by a finite volume method employing a SIMPLER algorithm.

RESULTS AND DISCUSSION

Thermocapillary convection in liquid bridges

We have investigated thermocapillary convection up to Re=5000 with Pr=1, Ar (aspect ratio) =1, V=1, Bi (Biot number) =0 and capillary numbers (Ca < 0.1), and have found no oscillatory axisymmetric states in liquid bridges with either nondeformable or deformable free surfaces. Assuming non-deformable flat interfaces with Pr=1 and Ar=1, the critical Re, Re_c, for transition to oscillatory states is about 2500 from linear theory and three-dimensional numerical simulations. Since Ca is in the range $O(10^{-2})$-$O(10^{-3})$ in most experiments, we conclude that dynamic free-surface deformations do not induce transition to oscillatory, axisymmetric convection. Thus only azimuthal waves can generate oscillations in a liquid bridge with either nondeformable or deformable free surfaces. Fig. 2 shows two-dimensional free surfaces with Pr=1, Ar=1, Bi=0, Ca=0.05 and various Re. The free surfaces are convex near the lower cold wall, and change from concave to convex near the hot wall with increasing Re because of stronger return-flow in the interior. At sufficiently low Re, the free surface is almost asymmetric about its mid point. It has two peaks and is elevated near the cold stagnation point where surface pressure achieves its maximum value. As Re increases at fixed Ca, the free surface develops three peeks. The extremely small magnitude of the deformations should be noted.

In three-dimensional models with Ar=0.714, Pr=27, Re_c for onset of oscillations with V=1.138 (convex), 1 (flat) and 0.755 (concave) are about 210, 210 and 220, respectively. The temperature fluctuations with V=1 consist of a hot and a cold spot rotating clockwise, i.e m (wavenumber) =1. This rotating pattern with m=1 remains unchanged with increasing Re. Two pairs of hot and cold spots, i.e. a wavenumber of 2, are rotating clockwise with V < 1.

Thermocapillary convection in open annuli

Thermocapillary convection up to Re=5000 with Pr=30, Ar=1, Bi=0 and Ca=0.1 was computed and no axisymmetric oscillatory states with either nondeformable or deformable surfaces were found. In three-dimensional numerical simulations with Pr=30, Ar=1, Bi=0 and Ca=0 (nondeformable flat surface), Re_c was about 2200. Thus dynamic free-surface deformations do not induce transition to unsteady, oscillatory axisymmetric convection. Fig. 3 shows free surfaces with Ca=0.05 and various Re in axisymmetric annuli heated from the inside wall. The surface is convex near the cold wall where surface pressure has a maximum positive value at the stagnation point, and concave near the hot wall. Two peaks appear at the free surface at sufficiently low Re. As Re increases, additional ripples occur at the free surface which can be convex close to the hot corner. Surface elevations and depressions decrease with increasing Re due to this change in topology, volume conservation and curvature. Again, we observe extremely small surface deflections.

Re_c for onset of oscillations in three-dimensional annuli with Bi=0, Pr=6.84 and Ar=1, 2.5, 3.33 and 8 are about 740, 490, 490 and 560, respectively. With Ar=1, 2.5 and 3.33, we observe 5, 9 and 12 azimuthal wavetrains, respectively, rotating clockwise at the free surface near the critical Re. Twenty pulsating azimuthal wavetrains with Ar=8 are found on the free surface. The inside wall looks like the source of the waves: the waves are generated at the inside cold wall and travel to the outside hot wall. We thus have travelling r-waves and pulsating θ-waves in cylindrical-shallow liquid layers. The critical wavelength λ=2.5 (Pr = 6.84) from linear theory implies a wave number of 20 at the inside wall, which is in good agreement with our numerical result.

CONCLUSIONS

Thermocapillary convection in liquid bridges and open cylindrical annuli is investigated in two- and three-dimensional numerical models. For the parameter ranges considered, dynamic free-surface deformations are negligible and do not induce transitions to oscillatory convection in axisymmetric models. Thus only steady convection is possible at any Re in strictly axisymmetric computations. In the three-dimensional models, the nondeformable free surfaces are either flat or curved as determined by the fluid volume, and the Young-Laplace equation. Convection is steady and axisymmetric at sufficiently low values of Re with either nondeformable or deformable surfaces. Transition to oscillatory three-dimensional motions occurs as Re increases beyond a critical value dependent on the aspect ratio, the Prandtl number and V. Good agreement with available experiments is achieved in all cases.

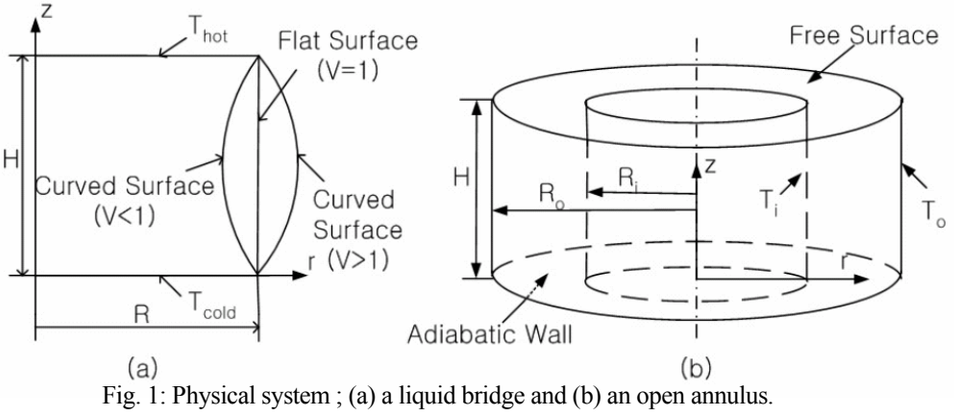


Fig. 1: Physical system ; (a) a liquid bridge and (b) an open annulus.

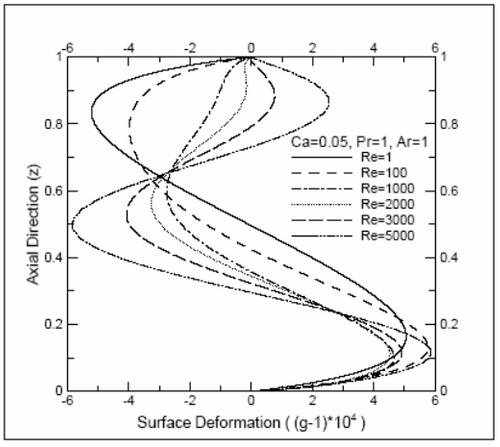


Fig. 2: Free surface deformations in liquid bridges.

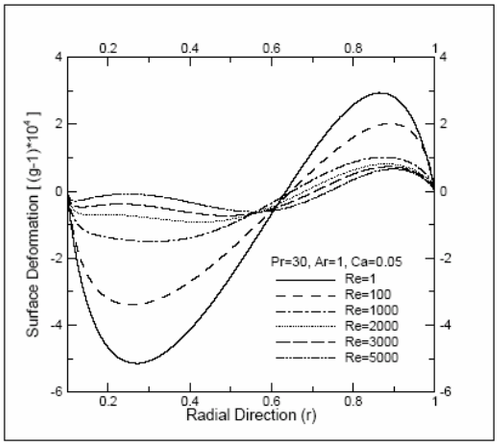


Fig. 3: Free surface deformations in open annuli.

XXI ICTAM, 15–21 August 2004, Warsaw, Poland

MATHEMATICAL MODELS OF MICROCONVECTION FOR ISOTHERMALLY INCOMPRESSIBLE AND WEAKLY COMPRESIBLE LIQUIDS

Vladislav V. Pukhnachov*, Olga N. Goncharova**

*Lavrentyev Institute of Hydrodynamics, Siberian Division of the Russian Academy of Sciences, Novosibirsk, Russia

**Lavrentyev Institute of Hydrodynamics, Siberian Division of the Russian Academy of Sciences, Novosibirsk, and Altai State University, Barnaul, Russia

Summary The term "microconvection" was originally introduced to characterize non-solenoidal flows driven by density (depending on temperature only) changes. These phenomena were analyzed for thermal buoyancy-driven convection (Pukhnachov, 1991) and for diffusive-induced flows (Perera and Sekerka, 1997). The effect on non-solenoidality is equally important for the description of non-stationary convection in microgravity conditions and in microscales. Recently this approach was extended up to convective motions of a weakly compressible liquid (Pukhnachov, 2002). On the basis of the microconvection model, there are studied a number of problems describing the convection in a vertical layer with the thermal fluxes oscillating in a phase and in an anti-phase, flows in a circular ring and in a prolate rectangular, mixed thermocapillary/gravitational convection in a semicircle with a free flat boundary.

We consider the mathematical models for the thermal gravitational convection assuming smallness of the microconvection parameter, which is equal to ratio of the velocity orders produced by liquid expansion and buoyancy factor. They are the model of microconvection for isothermally incompressible liquid known since 1991 (see full presentation in [1], Chapter VI) and the model for weakly compressible liquid [2]. Characteristic property of both models is the non-solenoidal velocity field. The parameter of microconvection is an additional similarity criterion regarding to Grashoff and Prandtl numbers. It is equal to gravity acceleration multiplied by cube of the characteristic linear scale and divided by the product of the kinematic viscosity and the thermodiffusion coefficient. Thus, we study the convective fluid flows under low gravity, in small scales and at fast changes of the boundary thermal regimes.

At first, the model of microconvection was proposed and used for the analytical and numerical research of the convection in a closed cavity under low gravity. This model is based on the assumption that the liquid density depends on its temperature only. It is demanding that the total heat flux through the boundary of a closed cavity should be equal to zero at each moment of time. The model of weakly compressible liquid is free of this deficiency. The liquid is considered now as a thermodynamic medium with two state parameters: temperature and pressure.

The model of weakly compressible liquid includes systems of exterior and interior expansions in time. Since the equations of the exterior expansion are not evolutional with respect to pressure, we should construct an interior expansion to compensate the discrepancy in the initial condition for pressure. This problem is solved in a linear approximation.

We develop the ideas from [1, 2], explain the definitions of the isothermally incompressible and weakly compressible liquids, give an analysis of the criteria of similarity and of the characteristic values for the convective flows and present the analytical and numerical results for some mathematical problems.

Taking into account the non-solenoidality for the stationary problems of microconvection in the closed domains leads to the corrections of the orders of Boussinesq number (V.V. Pukhnachov, 1996; O.N. Goncharova, 1997).

The qualitative differences in flow characteristics for the stationary problems with free boundary in a semicircular region are observed, when boundary thermal regimes have local singularity (O.N. Goncharova, 2001).

The most bright qualitative and quantitative differences from the classical results or so-called non-Boussinesq flow effects are obtained by the simulations for the non-stationary problems of microconvection: convection in an annular domain at time dependent microgravity forces (O.N. Goncharova, 1995, 1997); convection in a vertical layer (V.V. Pukhnachov, 1994; O.N. Goncharova, 2000); convection in a long rectangle at the periodic boundary thermal regimes(O.N. Goncharova, 2000); convection in a vertical layer with the thermal fluxes, which oscillate in a phase and in an anti-phase (O.N. Goncharova, 2004).

Our mathematical modeling of the convection can be called alternative approach in the convection theory. In fact, we are starting from the exact conservation laws of mass, momentum and energy and are building an hierarchy of the models in the convection theory: the Navier-Stokes equations for compressible fluid ă the model for weakly compressible fluid ă the model of microconvection ă the Oberbeck-Boussinesq model.

From the mathematical point of view, the alternative theories of the convection of fluids were developed by J.M. Mihaljan (1962), V.I. Yudovich (1983, 1999), K.A. Nadolin (1989, 1995). The stability of the solutions in the microconvection model was studied by V.K. Andreev (since 1996). P.S. Perera and R.F. Sekerka (1997) proposed the non-solenoidal model for the concentration convection analogous to the microconvection model. The investigation of mathematical problems in the non-solenoidal model of convection was done by V.B. Moseenkov (1998).

References

[1] Andreev V.K., Kaptsov O.V., Pukhnachov V.V., Rodionov A.A.: Applications of Group-Theoretical Methods in Hydrodinamics. Kluwer Academic Publ., Dordrecht/Boston/London, 1998.

[2] Pukhnachov V.V., Hierarchy of the models in the convection theory. *Notices of Petersburg Division of Steklov Mathematical Institute* **288**: 152–177, 2002.

ONSET OF OSCILLATIONS IN HIGH-PRANDTL THERMOCAPILLARY LIQUID BRIDGES: LINEAR-STABILITY ANALYSIS VS. EXPERIMENT

Michael K. Ermakov
Institute for Problems in Mechanics RAS, prosp. Vernadskogo 101, block 1, 119526 Moscow, Russia
Institute of Mechanics, MSU, Michurinsky prosp. 1, 119192 Moscow, Russia

Summary The float-zone crystal-growth process is studied in the framework of the half-zone model. The linear-stability analysis is used to compare the onset of oscillations in liquid bridge thermocapillary convection upon liquid bridge volume with experimental data for high-Prandtl fluid. Well-known structure of neutral stability curve for high-Prandtl fluid, consisting of two branches separated by an "overstability" gap, has been clearly reproduced. Moreover, for low-volume branch there is a good quantitative correspondence between experimental data and linear stability analysis. Travelling hydrothermal waves with unit azimuthal wave number correspond to critical perturbations for both branches. An influence of the temperature-dependent viscosity, the heat loss through the free surface and the gravity level on the stability limits is determined.

Introduction

Numerous experiments on transparent high-Prandtl liquids show essentially non-monotonic behaviour of stability limit versus liquid-bridge relative volume: the stability diagram consists of two branches with an “overstability” gap. In different experiments the “overstability” gap corresponds to relative volume V $0.8 \le V \le 1.0$. The studies of high Pr flows suffer from practically the lack of direct comparisons of experimental data, linear-stability analysis and direct numerical simulation results. The reasons are severe numerical difficulties, preventing from the reliable modelling, and too many factors, affecting convection in real liquid bridge experiments. The lack of cross-checkings could excite reasonable doubts in reliability of the models applied and the results performed by linear stability analysis and direct numerical simulation. The goal of this paper is to apply linear-stability analysis to determine the stability limits for liquid bridge with highly deformed free surface versus liquid- bridge volume and to compare them with experimental data [1].

Formulation of the problem

The geometry considered consists of an axisymmetric liquid bridge, which is suspended between two horizontal co-axial rigid disks of equal radius r_0 in a distance d (Fig. 1). The lower and upper disks are kept at constant temperatures T_0-$\Delta T/2$ and T_0+$\Delta T/2$, respectively, where T_0 is the mean (reference) temperature. The lateral side of the liquid $r=h(z)$ is a free surface and it's shape is governed by the mutual action of the gravity and the surface tension. The governing equations are the Boussinesq equations for a Newtonian fluid with viscosity ν and surface tension σ assumed to be a linear function of temperature. At the rigid disks the boundary conditions are no-slip and no-penetration and the temperature is fixed. For the free surface the mixed thermal boundary condition is assumed and the velocity-boundary conditions are derived from the free-surface stress balance. The kinematic boundary condition at the free surface interface requires the normal velocity to be zero. Appropriate symmetry boundary conditions at r=0 complete the problem. Non-dimensional geometrical parameters are the aspect ratio Γ and the relative volume V. Other non-dimensional governing parameters are the Prandtl Pr, the Reynolds Re, the viscosity group R_ν, the Bond Bo, the Grashof Gr, the Biot Bi numbers and the non-dimensional external temperature. The details of the problem statement, and methods of the linear stability problem solution could be found in [2].

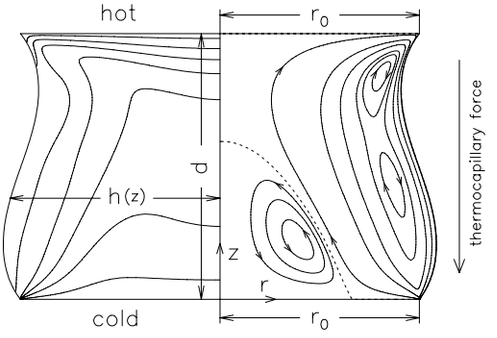


Fig. 1. The liquid bridge, the coordinate system (r,z), the fluid flow structure: the isotherms (left side)

Results and discussion

Detailed calculations have been carried out for the liquid-bridge experimental stability study [1]. The liquid-bridge had the fixed aspect ratio Γ=1.5, where as the relative volume V was varied from 0.5 to 1.4 and the temperature difference was varied up to 70 ºC. The 5 cS silicone oil used in experiment has a linear temperature dependence of the surface tension and an exponential temperature dependence of the kinematic viscosity. For numerics, the exponential behaviour is approximated by a linear dependence. The Fig. 2 shows the comparison of the experiment and linear stability analysis for temperature-dependent viscosity and constant viscosity cases for zero Biot number. Following the

experimental data [1], the linear stability analysis reproduces two branches structure of the stability diagram with the "overstability" gap, in contrary to the energy-stability analysis has been additionally employed in [1]. Both temperature-dependent viscosity limits and constant viscosity limits differ insignificantly except the range of relative volumes V $0.7 \le V \le 1$, where there is the most slope of neutral curve. For the low-volume branch there is a good quantitative correspondence between the experiment and the numerical analysis for the temperature dependent viscosity case. However, for the high-volume branch there is only a good qualitative correspondence between experiment and numerical analysis. Travelling hydrothermal waves with unit azimuthal wave number correspond to critical perturbations for both branches. To improve the high-volume branch, the non-zero heat flux through the free surface is proposed. The Fig. 3 shows linear stability results for Biot number $Bi=0.2$ and external temperature equals the temperature of the cold bottom disk. The linear-stability results fit the experiment better now, however for relative volumes V $0.85 \le V \le 1.05$ the flow becomes to be much more stable. Note, that the heat flux through the free surface decreases the critical Marangoni number for high-volume branch. The reason is that a very flat temperature distribution on the free surface increases the slope due to the heat loss. This leads to flow enhancement and a loss of stability. Calculations for zero gravity level show small difference in the critical temperature difference less then 4 °C because of enough small Bond and Grashof numbers.

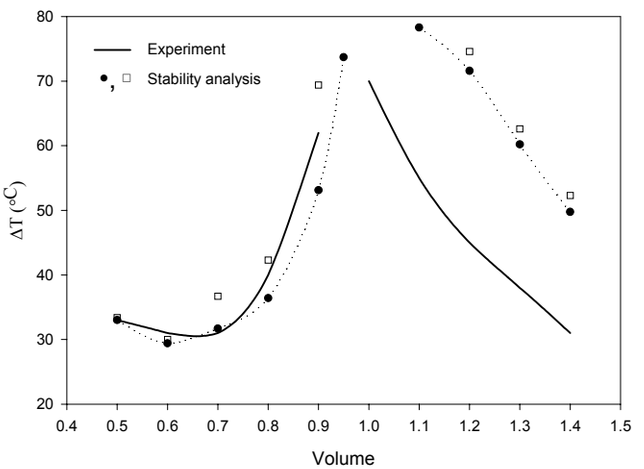


Fig. 2. Stability diagram: the critical temperature difference versus the liquid bridge relative volume. The solid lines correspond to the experiment [1], the dotted lines and filled circles correspond to the linear stability analysis to the temperature-dependent viscosity case, hollow squares - to the constant viscosity case for $Bi=0$.

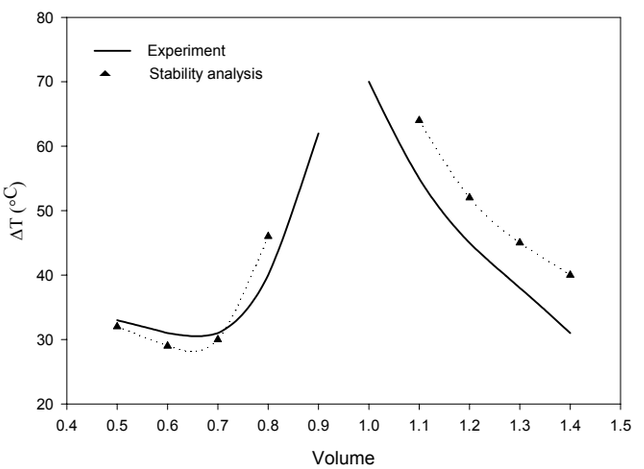


Fig. 3. Stability diagram: the critical temperature difference versus the liquid bridge relative volume. The solid lines correspond to the experiment [1], the dotted lines and filled triangles correspond to the linear stability analysis to the temperature-dependent viscosity case and Biot number $Bi=0.2$.

References

[1] Sumner L.B.S., Neitzel G.P., Fontaine J.-P., et al. *Phys. Fluids* 13 (2001) 107.

[2] Ermakov M.K., Ermakova M.S. *J. Crystal Growth* 266 (2004) 160.

SPHERICAL TWO-PHASE INTERFACE IN A NEAR-CRITICAL FLUID. GRADIENT APPROACH

Anatoliy M. Vorobev[*], Dmitriy V. Lyubimov[**], Tatyana P. Lyubimova[*]
[*]*Institute of Continuous Media Mechanics UrB RAN, Perm, Russia*
[**]*Perm State University, Perm, Russia*

Summary On macro-scales the liquid-gas interface is classically modelled by a surface of discontinuity. However, on micro-scales, there is a transition region, where the properties are changed continuously. This makes reasonable to describe the two-phase system, including the interface, within a hydrodynamic approach. In this approach, the new term proportional to density gradient is added to free energy. Near the critical point, where there is no strong difference between a liquid and its vapour, the gradient approach is quite reasonable. Based on this approach we considered the formation of nucleus in a closed cavity and studied its stability. The results are found to be in a good agreement with the classical Laplace approach, while considering the states far from the critical point. In near-critical region, the results are proved surprising. It is shown that within the framework of one-dimensional problem the system remains single-phase and uniform even for negative values of mechanical compressibility.

STATEMENT OF THE PROBLEM

We applied the gradient theory [1] for consideration of nucleus formation in a closed cavity, considering a spherical inclusion in a spherical container. The free energy of fluid in this approach is supposed to be a function of density gradient,

$$f = f^0(r) + l\frac{(\nabla r)^2}{2}$$

where f is volumetric free energy, f^0 is classical part, and l is capillary coefficient.

The free energy of a spherical nucleus is then as follows

$$F = 4p\int_0^{a_0}\left[f_0 + \frac{l}{2}(r')^2 + k\,r\right]r^2\,\mathrm{d}r\,,$$

where k is Lagrangian multiplier responsible for condition that system is closed.

In equilibrium the functional of free energy should be minimal. Minimum of free energy is determined using the gradient method. The following equation is postulated:

$$\frac{\partial r}{\partial t} = -\frac{dF}{dr}$$

Here t is not real physical time, but just an auxiliary variable. However, the steady solutions of this equation correspond to the extremum of functional F.

This results in the following problem for density profile:

$$\frac{\partial r}{\partial t} = \frac{1}{a_0^2}\left(r'' + \frac{2}{r}r'\right) - r^3 + r - q - 3\int_0^1 r^3x^2\,\mathrm{d}x,$$
$$r'\big|_0 = r'\big|_1 = 0$$

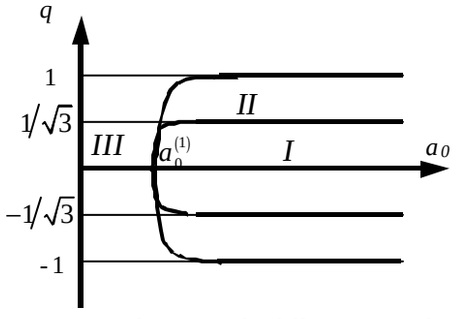


Fig. 1. Regions of existence for different types of solutions

We use here the following units of length and density: $L = \bar{a}_0$ (container radius), $[r] = (a/b)^{-1/2}$; $a = -T\left(\partial a_T^2/\partial T\right) > 0$, $b = 1/6\left(\partial^2 a_T^2/\partial r^2\right) > 0$. Two non-dimensional parameters appeared, $a_0 = \bar{a}_0\sqrt{l\,r_c/a}$ is dimensionless radius of a container, and $q = m/\left([r]L^3\right)$ is average density of a system.

Uniform solution of the problem is trivial $r = q$. In region I (fig. 1) ($|q| < \sqrt{3^{-1}\left(1-\left(a_0^{(1)}/a_0\right)^2\right)}$, where $a_0^{(1)} = 4.49$), these solutions are unstable with respect to small disturbances, and develop to non-uniform (nucleus-type) solutions. Out of this region (in region *II*), uniform solutions are stable with respect to small disturbances, however, they unstable in respect to finite perturbations. As a result, non-uniform solutions can also realise in this region.

Isothermal compressibility determined by expression $\left(\partial p/\partial r\right)_T = -1 + 3q^2$ is negative inside region *III* and a physical system cannot exist here in a uniform state [2]. Introduction of capillary term into free energy results in surprising effect, in a sufficiently

small container the system can be uniform even if $(\partial p/\partial r)_T < 0$. This critical radius is very small far from the critical point and cannot be considered within a hydrodynamic approach. Near the critical point this radius can be not small since $\bar{a}_0^{(1)} \sim 1/\sqrt{(-T)}$, i.e., diverge if $T \to 0$.

NUMERICAL RESULTS

The typical density profiles obtained by finite-difference method are given in fig. 2. The thickness of a transitional layer, the so-called capillary length, equals $d_l = 1/a_0 = 1/\bar{a}_0 \cdot (l r_c/a)^{1/2}$.

Radius of nucleus and coefficient of surface tension were calculated with the help of the following effective formulas:

$$a_1^3 = 3\int_0^1 \frac{r - r(1)}{r(0) - r(1)} r^2 dr \ , \ s = \frac{1}{a_0 a_1^2}\int_0^1 \left(\frac{\partial r}{\partial r}\right)^2 r^2 dr \ .$$

Dependences of nucleus radius on average density are given in fig. 3.

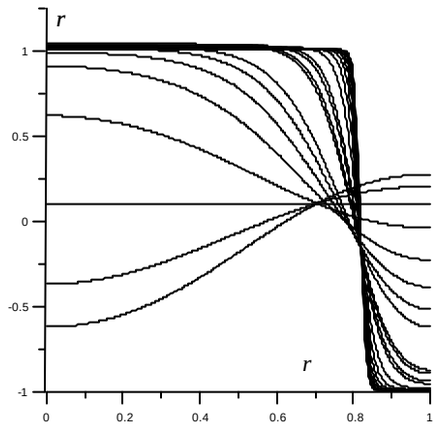


Fig. 2. Typical density profiles. $q = 0.1$, a_0 changes from 4 (uniform solution) to 100 (stepwise solution)

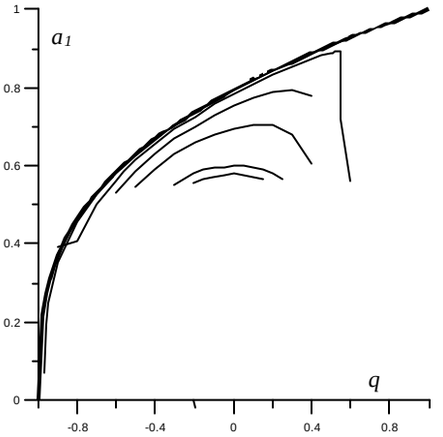


Fig. 3. Dependence of nucleus radius on average density. Thick line, $a_1 = \sqrt[3]{(1+q)/2}$; the curves are plotted for $a_0 = 20, 10, 7, 5, 4.7$ (from top to bottom)

CONCLUSION

The gradient approach is convenient to study the fluid behaviour, since the same system of equations is sufficient to find the flows throughout the two-phase region; the phase transitions, shape and evolution of phase interface are solutions of this system [3]. This description is particularly worth near the critical point where the gradient approach is more reasonable than the classical Laplace theory.

The problem considered was just a preliminary stage of the investigation with the objective in studying the hydrodynamics of near critical two-phase media.

The results obtained are in a good agreement with the classical approach for the states far from the critical point, and for large containers and nuclei. In near critical region the results are intriguing; system can be uniform even for negative values of the derivative $(\partial p/\partial r)_T$, which is absolutely impossible within the classical approach.

The work was carried out under financial support of the US Civilian R&D Foundation (grant PE-009-0).

References

[1] Gouin H. Utilization of the second gradient theory in continuum mechanics to study the motion and thermodynamics of liquid-vapor interfaces // From Physiochemical Hydrodynamics, Interfacial phenomena, p.p. 667-682, Plenum Publishing Corporation, 1987.

[2] Landau L.D., Liftshiz Å.Ì . Theoretical Physics. vol. V. Statistical Physics. - M.: Nauka, 1964.

[3] Jamet D. et al. The second gradient method for the direct numerical simulation of liquid-vapor flows with phase change // J. of Computational Physics 169, 624-651, 2001.

TRANSITION TO CHAOTIC MARANGONI CONVECTION IN LIQUID BRIDGE

Valentina Shevtsova , Denis Melnikov and Jean Claude Legros
MRC, CP-165/62, Université Libre de Bruxelles, 50, av. F.D. Roosevelt, B-1050, Brussels, Belgium

Summary Marangoni convection is investigated in cylindrical column using a liquid with Pr=4. The present results are targeting on the study of the non-linear characteristics of the flow under zero-gravity conditions. The transitions to periodic, quasi-periodic and chaotic flows are investigated numerically. The 3-D oscillatory flow is a result of a supercritical Hopf bifurcation and the periodic orbit represents the unique stable solution near the onset of the instability. The non-linear system admits regime of bi-stability. A traveling wave with azimuthal wave number m=2 bifurcates from the basic branch of axisymmetric steady state; this branch remains stable in the considered range of parameters. A second stable branch with azimuthal wave number m=3 appears for higher Marangoni numbers and reveals other periodic, quasi-periodic and chaotic properties. The transitions between the two stable orbits with m = 2 and m = 3 have never been observed.

INTRODUCTION

An increasing number of experimental studies in a half-zone model, which corresponds to floating zone (FZ) techniques of crystal growth, indicates that convection in melt should be turbulent, e.g. see Hurle[1]. Nevertheless, because of great complexity of the turbulent flows, all numerical simulations of transport processes were performed assuming laminar flow in the liquid phase. Apart of that, from the more physical side, the hydrodynamics effects in the half-zone model is of basic interest for the dynamics occurring in the system, as it is an excellent example of a dissipative dynamical system. Therefore, the present study is aimed at the investigation of time-dependent convective flows in the strongly supercritical regimes.

FORMULATION OF THE PROBLEM

A liquid bridge consists of a fluid volume, which is held between two differentially heated horizontal flat concentric disks of radii R, separated by a distance d. The temperatures T_h and T_c ($T_h > T_c$) are prescribed at the upper and lower solid-liquid interfaces respectively, yielding a temperature difference $\Delta T = T_h - T_c$. The surface tension and kinematic viscosity are taken as linear functions of temperature. Throughout this parametric study the Prandtl number and the aspect ratio $\Gamma = d/R$ are kept constant; Pr=4, Gr=0 and $\Gamma = 1$. Then the only one parameter, the Marangoni number, which is proportional to the temperature difference between the rods, controls the flow.

The governing Navier-Stokes, energy and continuity equations are written in non-dimensional primitive-variable formulation in cylindrical co-ordinate system, see details in Shevtsova et al[2]. The three-dimensional, fully non-linear governing equations were solved in a primitive-variable form on a staggered stretched mesh. These equations were integrated over non-overlapping finite volumes. The computation of the velocity field at each time step was carried out with the projection method. A combination of fast Fourier transform in the azimuthal direction and of an implicit ADI method in the others was applied for calculating the Poisson equation for pressure.

RESULTS AND DISCUSSION

The different spatiotemporal patterns of the thermocapillary flow are numerically analyzed, beginning from the onset of instability up to appearance of non-periodic flow and further on. The calculations were performed up to $\varepsilon = (\Delta T - \Delta T_{cr})/\Delta T_{cr} \approx 8.5$. For the small temperature difference between supporting disks the thermocapillary flow is two-dimensional (i.e. invariant in the azimuthal direction), steady and has a toroidal-like structure. The 3-D oscillatory flow is a result of a supercritical Hopf bifurcation and the periodic orbit (traveling wave with azimuthal wave number m = 2) represents the unique stable solution near the onset of the instability, Ma_{cr} =2520. This periodic branch remains stable in the considered range of parameters. A second branch of solution with azimuthal wave number m=3 appears for higher Marangoni numbers, $Ma_{cr}^{(2)}$=3240, and reveals other periodic, quasi-periodic and chaotic properties.

Beyond this second bifurcation point, Ma >3240, the system admits the coexistence of two stable oscillatory solutions with two different wave numbers, m = 2 and m = 3. The transitions between the two stable orbits with m = 2 and m = 3 have never been observed. Notice, that these two solutions do not represent the different modes of the linear problem; on the contrary, they are both the results of the solution of the full non-linear problem. The final solution depends on the initially chosen wave number guess.

The symmetry of the final solution keeps the memory of the initial state of the system for Ma> $Ma_{cr}^{(2)}$=3240. Namely, taking an initial guess with m = 1, 2, 4, 6 etc. symmetries, after some transient time the system will arrive to m = 2 traveling wave (TW) solution. Otherwise, all the odd basic symmetries m = 3, 5, 7 (except m = 1) give m = 3 traveling wave as final state of the system.

For the m = 2 solution, the critical mode at the first bifurcation, the flow remains strictly time-periodic for $\varepsilon < 8.5$.

The m=3 flow pattern undergoes a transition from the periodic to a weakly chaotic flow via quasi-periodic and period-doubling states. This study is extension of recently published results, see ref.3, where all above-mentioned temporal transitions have been analysed. Here the special attention is paid to the investigation of the *spatial* structure of the flow with increasing of Marangoni number. The results of spatial and temporal Fourier analysis are shown in Fig.1 and Fig.2 for Ma= 18000, while temporal chaos is progressing.

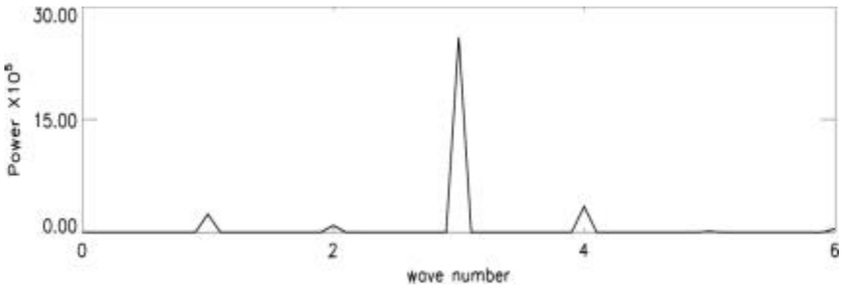


Fig.1. Spatial Fourier spectrum, Pr=4, Ma=18000.

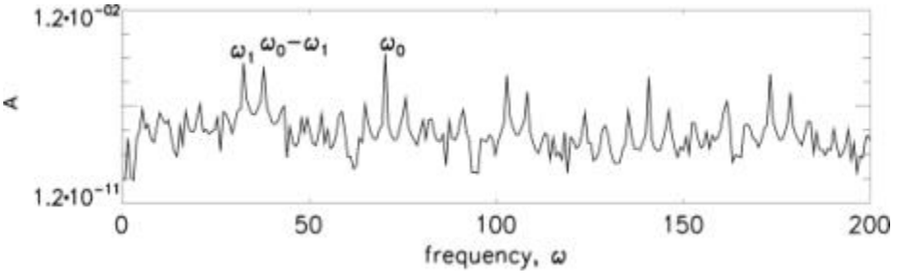


Fig.2. Temporal Fourier spectrum, Pr=4, Ma=18000.

To distinguish numerically the chaotic and non-chaotic (aperiodic) behaviour is a delicate problem. There are several ways to recognize chaotic behaviour features in oscillatory systems, such as analysing their Poincare (return) maps, phase space trajectories and power spectra. One of the fundamental characteristics of a chaotic state is its sensitivity to the initial state. If the same system starts from two different but close initial conditions (initial guesses in our numerics) their dynamical trajectories would diverge on the attractor very quickly. The distance between two close trajectories has to grow exponentially with time.

Of course, the simulation of the linear equations obtained by linearization of the Navier-Stokes equations around the non-linear solution would give the exponential law more directly. Nevertheless, very small disturbances should evolve in the exponential way even if one simulates the original Navier-Stokes equations. For the present system, the difference between original and different disturbed solutions were carefully analyzed to demonstrate that temporal aperiodic flow is chaotic.

CONCLUSIONS

The development of Marangoni convection in liquid bridge has been studied in 3D numerical model. To the best of our knowledge, the bifurcation of thermocapillary flow in a liquid bridge in the strongly supercritical regime has not yet been mapped out. Tracing the route to temporal chaos, two attractors corresponding to traveling waves with different wave numbers have been found. One of the attractors exhibits temporal chaotic behaviour, while the other one is strictly periodic. The spatial structure of the flow does not reveal chaotic features.

References

[1] Handbook of Crystal Growth 2. Bulk crystal Growth. Part B: Growth Mechanism and Dynamics. Edited by D.T.J.Hurle. North--Holland, (1994).

[2] Shevtsova V.M., Melnikov D.E., Legros J.C.: Three-dimensional simulations of hydrodynamical instability in liquid bridges. Influence of temperature-dependent viscosity. *Phys. Fluids* , **13**, 2851, 2001.

[3] Shevtsova V.M., Melnikov D.E., Legros J.C.: Multistability of the oscillatory thermocapillary convection in liquid bridge. *Physical Rev. E*, **68**, 066311, 2003.

CAPILLARY PRESSURE OF A LIQUID BETWEEN UNIFORM SPHERES ARRANGED IN A SQUARE-PACKED LAYER

J. Iwan D. Alexander*, Lev A. Slobozhanin* and Steven H. Collicott**

* *Department of Mechanical and Aerospace Engineering and National Center for Microgravity Research on Fluids and Combustion, Case Western Reserve University, Cleveland, Ohio 44106, USA*

** *School of Aeronautics and Astronautics, Purdue University, West Lafayette, Indiana 47907, USA*

Summary The capillary pressure in the pores defined by equidimensional close-packed spheres is analyzed numerically. In the absence of gravity the menisci shapes are constructed using Surface Evolver code. This permits calculation the free surface mean curvature and hence the capillary pressure. The dependences of capillary pressure on the liquid volume constructed here for a set of contact angles allow one to determine the evolution of basic capillary characteristics under quasi-static infiltration and drainage. The maximum pressure difference between liquid and gas required for a meniscus passing through a pore is calculated and compared with that for hexagonal packing and with an approximate solution given by Mason and Morrow [1]. The lower and upper critical liquid volumes that determine the stability limits for the equilibrium capillary liquid in contact with square packed array of spheres are tabulated for a set of contact angles.

EXTENDED SUMMARY

The capillary pressure in the pores defined by equidimensional close-packed spheres is analyzed numerically. In the absence of gravity the menisci shapes are constructed using Surface Evolver code. This permits calculation the free surface mean curvature and hence the capillary pressure. The dependences of capillary pressure on the liquid volume constructed here for a set of contact angles allow one to determine the evolution of basic capillary characteristics under quasi-static infiltration and drainage. The maximum pressure difference between liquid and gas required for a meniscus passing through a pore is calculated and compared with that for hexagonal packing and with approximate solution given by Mason and Morrow [1]. The lower and upper critical liquid volumes that determine the stability limits for the equilibrium capillary liquid in contact with square packed array of spheres are tabulated for a set of contact angles.

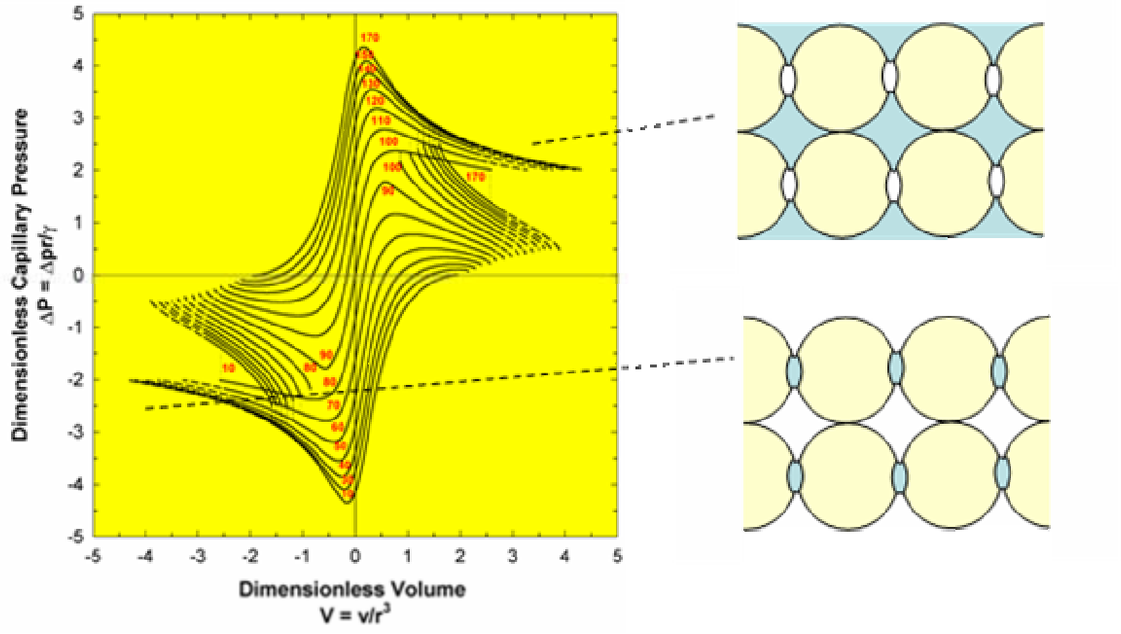


Fig. 1. Dependence of dimensionless capillary pressure, ΔP, on dimensionless liquid volume, V, (liquid on bottom) for pores formed by square close-packed spheres Numbers on curves denote the value of the contact angle θ (in degrees). For $\theta \neq 90°$, the dependence consists of two branches. The vertical dotted lines represent transitions between two branches of capillary surfaces. The segments shown by dash lines are valid only for a single-layer packing.

Our calculations show that the limiting cases of hexagonal and square packing diverged considerably. The maximum capillary pressures for $90° \le \theta \le 180°$ (the minimum capillary pressures for $0 \le \theta \le 90°$) differ by $1.75 \div 2.5$ times. There are also qualitative distinctions. In the case of hexagonal packing and $90° < \theta \le 180°$, the existence of two branches of equilibrium configurations has been illustrated in [2] only for $\theta = 100°$ and $110°$, and there is no evidence that the same holds for $120° \le \theta \le 180°$. For the case of $\theta = 110°$ that was analyzed in [2], the value of the dimensionless volume V at the extreme right point of the long branch (LB) is less than that at extreme right point of the short branch (SB), i.e. $V_p^* < V_r^*$.

For square packing, two branches exist for any $90° < \theta \le 180°$. Here $V_p^* < V_r^*$ if $90° < \theta \le 109°$, and $V_p^* > V_r^*$ if $110° \le \theta \le 180°$. This causes different ways of infiltration and drainage in a wide interval of θ. Under infiltration, a layer of a square packed arrangement becomes completely coated by liquid as a result of loss of meniscus stability if $90° < \theta \le 109°$, and as a result of a pendular gas ring formation if $110° \le \theta \le 180°$. Similar conclusions are valid for detachment of liquid from the spheres during drainage: loss of the capillary surface stability for the case of square packing and $71° \le \theta < 90°$, and formation of a pendular liquid ring in the case of $0 \le \theta \le 70°$.

In contrast to analysis of hexagonal packing [2], for square packing the stability boundaries for an equilibrium capillary liquid in contact with spherical array have been determined here with a reasonable accuracy and will be presented as tabulated data. It is notable that according to numerical results the modulus of mean curvature for a free surface with self-tangency is practically independent of θ.

For both hexagonal and square packing there is a hysteresis behavior in quasi-static infiltration and drainage processes. The hysteresis is due to irreversible transitions between configurations that belong to different branches, and between a horizontal free surface and a capillary surface in contact with spheres.

All descriptions are valid for mono-layer packing. It is significant that for any contact angle the menisci corresponding to maximum and minimum capillary pressures never cross spheres from the next layers of three-dimensional packing. We have verified this for both square and hexagonal packing. This suggests that for multilayer packing the extreme capillary pressures are the same as for mono-layer packing. Thus, our results allow for an estimation of the lower limit of penetration pressure for mixed types of packing.

References

[1] G. Mason, N. R. Morrow, J. Colloid Interface Sci. 168 (1994) 130-141.

[2] J. L. Hilden, K. P. Trumble, J. Colloid Interface Sci. 267 (2003) 463-474.

RECENT RESULTS ON NONCOALESCING AND NONWETTING SYSTEMS

G. Paul Neitzel*, Maria-Isabel Carnasciali*, Peter Nagy*, Pasquale Dell'Aversana
*G. W. Woodruff School of Mechanical Engineering, Georgia Institute of Technology, Atlanta, GA 30332-0405, USA
**Microgravity Advanced Research and Support Center, 80146 Naples, Italy

Summary Recent results from laboratory and numerical experiments on noncoalescing and nonwetting systems will be presented. Of specific interest are aspects of nonwetting systems of importance to their ultimate use as "frictionless" bearings in low-load applications.

INTRODUCTION

Permanent noncoalescence and nonwetting are driven through the imposition of relative, tangential surface motion between the liquid-liquid or liquid-solid surfaces of interest. This is accomplished either through the forced motion of one of the surfaces or through the use of thermocapillarity to drive the motion. The relative motion serves to drag surrounding air into the gap between the surfaces to form a lubrication layer. We have found through experimentation and theoretical computation that such lubricating films are able to sustain reasonably large loads. Consequently, we have proposed the use of such systems for use as virtually frictionless bearings in low-load applications.

Current efforts are focused on two fronts: 1) quantifying the degree to which nonwetting systems are indeed "frictionless"; and 2) identifying the conditions under which the application of a load causes the lubricating film, and hence the "bearing" to fail. Both of these issues are important to the eventual development of applications for noncoalescing and nonwetting systems.

Measurement of sliding friction of isothermal nonwetting droplets

An apparatus has been built to create an isothermal nonwetting situation and measure the friction in the lubricating film between a drop and the moving solid surface adjacent to it. The surface consists of a rotating disk coated with a transparent metallic coating to permit the surface to be grounded electrically (to prevent static-charge-induced wetting as discussed below). A droplet is suspended from a cantilever and pressed against the rotating disk without wetting it. The deflection of the calibrated cantilever, measured using Michelson interferometry, is used to determine the total load applied to the cantilever/droplet configuration. Figure 1 shows a schematic of the idea.

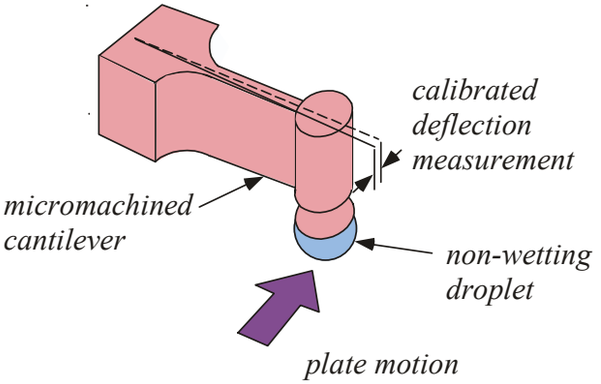


Figure 1. Schematic for non-wetting friction measurement.

One of the difficulties in making this measurement is distinguishing between the frictional force in the lubricating film between the droplet and disk and the aerodynamic drag force exerted upon the droplet/support structure due to the flow dragged by the rotating disk. To minimize this force, the use of shrouds of various shapes is being examined computationally to determine the optimum configuration and positioning to permit the friction measurement. The results of these computation and preliminary results from the experiments will both be discussed during the presentation.

Failure modes for nonwetting droplets

For a nonwetting droplet to function as a bearing, the system must designed in such a manner that the range of operating conditions will avoid conditions known to lead to failure of the lubricating gas film or the contact line holding the droplet to its underlying surface. With respect to film failure, we have observed two types in our experiments with thermocapillary-nonwetting droplets. The first type, with the solid surface electrically grounded, appears to be due to a shape instability of the film that occurs as the droplet is squeezed more firmly against the surface. Failure is initiated at one point on the droplet periphery, where the film is thinnest, and proceeds across the droplet. The second type of failure is seen when the nonwetted surface is electrically charged. In this case, the droplet failure is initiated in the droplet center, where the film is thickest, and proceeds axisymmetrically outward. Both these cases are shown in Figure 2.

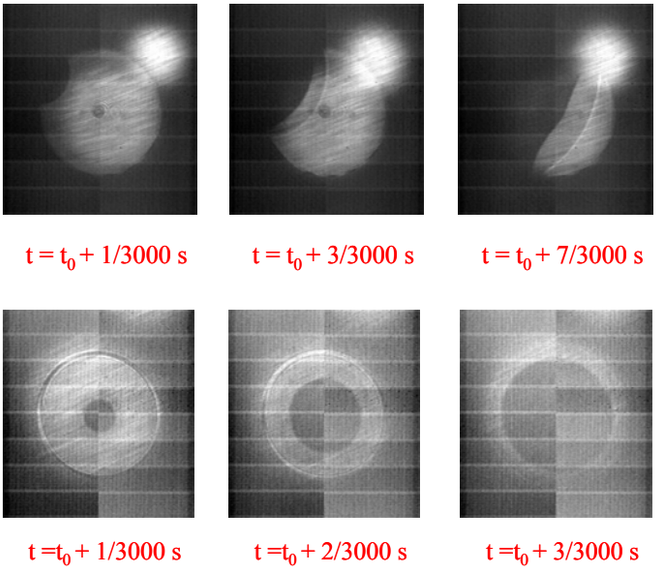


Figure 2. Time sequences of film rupture of thermocapillary nonwetting droplets in the cases of (top) grounded and (bottom) charged surfaces.

The droplets used in our experiments are attached to sharp-edged supports and pinned to this edge by the contact line. Another mode of failure for a nonwetting droplet occurs when this contact line is non longer capable of holding the droplet to its support. Experiments that demonstrate this failure will also be discussed.

Acknowledgment

This work is supported by the Office of Biological and Physical Research, NASA and by the Italian Space Agency.

XXI ICTAM, 15–21 August 2004, Warsaw, Poland

WAVE–VORTEX INTERACTIONS IN THE ATMOSPHERE AND OCEANS; WITH APPLICATIONS TO CLIMATE

Onno Bokhove
Department of Applied Mathematics
7500 AE, P.O. Box 217, Enschede
University of Twente, The Netherlands
o.bokhove@math.utwente.nl

Summary Our aim is to address the following question: can we construct an accurate atmospheric climate model with a balanced model representing its fluid mechanics or dynamical core, and with dissipative as well as non-dissipative parameterization schemes for the gravity-wave activity? To do so, we therefore review the concepts of potential vorticity, balanced flow, linear waves and wave-vortex interactions.

INTRODUCTION

In the atmosphere, there is often a large separation in time scales between the slow large-scale motion of air and the rapid small-scale three-dimensional turbulence, the air motion around particles such as water droplets, and the kinetics of chemical trace gases. Knowledge of the chemical constitution of the atmosphere is required to understand the radiative damping and solar forcing of the atmosphere (Andrews *et al*., 1987). Also in the oceans, the time scale separation between the large-scale dynamics of water and the small-scale dynamics of turbulence and particle motions is vast. Numerical weather and climate prediction models of the atmosphere and oceans are therefore usually formulated as primitive equations for the motion air and water, respectively, for which the influence of (large quantities of) small-scale particles and chemicals is parameterized.

Even though we approximate the atmospheric and oceanic systems separately as single-phase systems, the small-scale quasi two-dimensional and three-dimensional wave and turbulent motion cannot be captured adequately by the numerical models. Consequently, also the feedback of the unresolved wave and turbulent motion on the large-scale dynamics requires parameterization. Only the large-scale dynamics is thus captured approximately in weather and climate prediction.

In addition, the dynamics of the atmosphere and oceans occurs on different time scales. Nevertheless, their large-scale dynamics share important characteristics and include similar asymptotic regimes in particular in terms of small Rossby- or Froude numbers. Hence, atmospheric and oceanic dynamics can be described to some extent in a unified way.

Of central importance in atmospheric and oceanic fluid dynamics is the (linear) dynamics of gravity-waves and vortical modes, the concept of potential vorticity, and the approximate or balanced description of the slow, large-scale dynamics in terms of the rotational or vortical motion. The advantage of these three items lies in their conceptual and mathematical clarity. The disadvantage is that the actual dynamics is more complicated, nonlinear and turbulent, and that the vortical motion is only approximately balanced. We introduce the above items for the simplified rotating Navier-Stokes equations by ignoring viscosity, invoking hydrostatic balance and using a layer-wise stratification.

LINEAR WAVES AND POTENTIAL VORTICITY

Consider the equations of motion for a one-and-half layer tropospheric-stratospheric model on the f-plane (Bokhove and Verkley, 2003)

$$\frac{\partial \sigma_\alpha}{\partial t} + \boldsymbol{\nabla}\cdot(\sigma_\alpha\, \mathbf{v}_\alpha) = 0 \qquad \text{and} \qquad \frac{\partial \mathbf{v}_\alpha}{\partial t} + (\mathbf{v}_\alpha\cdot\boldsymbol{\nabla})\mathbf{v}_\alpha + f\,\hat{\mathbf{z}}\times\mathbf{v}_\alpha = -\boldsymbol{\nabla} M_\alpha \tag{1}$$

with $\alpha = 2$ in the active lower tropospheric layer, horizontal coordinates x and y, horizontal gradient $\boldsymbol{\nabla}$, time t, $\hat{\mathbf{z}}$ the unit vector in the vertical, the pseudo-density $\sigma_2 = (p_2 - p_1)/g$ in the lower layer, the horizontal velocity $\mathbf{v}_2 = \mathbf{v}_2(x, y, t)$ in that layer, p_2 the pressure above the topography and p_1 the pressure at the stratosphere-troposphere interface, gravitational acceleration g, Coriolis parameter f, and Montgomery potential $M_2 = M_2(p_2)$. The lower tropospheric layer is asymptotically decoupled from the upper stratospheric layer since its thickness is much smaller than that of the deep overlying layer. This Montgomery potential M_2 is

$$M_2 = c_p\,\theta_2\,(p_2/p_r)^\kappa + g\,z_2, \tag{2}$$

where $\kappa = R/c_p$, the gas constant $R = c_p - c_v$, and $c_{p,v}$ is the specific heat at constant pressure and volume, respectively, p_r is a reference pressure, $z_2 = z_2(x, y)$ the vertical position of the topography, and θ_2 is the constant potential temperature related to the constant entropy in the lower layer. The model is closed by showing that $M_2 = M_2(\sigma_2)$, which follows from constraining the Montgomery potential in the decoupled stratospheric upper layer to be constant $M_1 = M_1(p_1, p_2) = cst$ (Bokhove and Verkley, 2003). After linearizing (1) around a resting basic state, in particular for constant f, the linear waves emerging consist of a pair of dispersive gravity waves with a frequency $\omega \geq f$, and a vortical mode with $\omega = 0$. The isentropic model (1) conserves energy and mass, and potential vorticity $q_2 = (f + \hat{\mathbf{z}}\cdot\boldsymbol{\nabla}\times\mathbf{v}_2)/\sigma_2$ is materially conserved such that $\partial_t q_2 + \mathbf{v}_2\cdot\boldsymbol{\nabla} q_2 = 0$. The one-and-half layer tropospheric-stratospheric model (1) can be extended to a model with $(N + 1/2)$ isentropic layers, also on the sphere.

BALANCED MODELS

When the stratification and the background rotation due to the Coriolis effect are relatively strong, the Froude and Rossby numbers are small, respectively, and balanced models can predict the large-scale vortical dynamics in an accurate and sometimes surprisingly accurate way (McIntyre and Norton, 2000). Within the phase space of the primitive equations of motion, *e.g.* (1), balanced vortical dynamics occur on a slow manifold devoid of acoustic and gravity waves.
In addition, we emphasize the nonlinearity in the dynamics in the inviscid limit by using Hamiltonian techniques. The preservation of conservation laws or even the Hamiltonian structure of balanced models in this limit is favored on heuristic grounds because of the assumed importance of conservation laws as constraints on the long-time (climatological) dynamics. Extending Vanneste and Bokhove (2002), Hamiltonian balanced models can be derived for equations (1) and its counterparts on the sphere (Buitendijk 2003). Since the Rossby and Froude numbers are not always small, and since the dynamics on the slow manifold is only approximate even for small Rossby and Froude numbers, the gravity-wave and vortical dynamics are interacting, often only weakly, but intermittently and locally also strongly.

WAVE–VORTEX INTERACTIONS

Although current weather and climate prediction models do resolve some of the (large-scale) gravity wave motion, the necessity to parameterize most of the gravity wave activity (also in the foreseeable future) suggests that we could instead use a global balanced model in which the gravity waves are fully parameterized or simplified. Olaguer (2002) built a global balanced climate model, including transport and chemistry, and tested it against other climate models. This comparison was reasonably good. Olaguer (2002) used the (stratified) vertical vorticity equation and the temperature equation as dynamical core using hydrostatic balance and global quasi-geostrophic balance.
In most current parameterizations (McFarlane, 1987; and such as used in Olaguer, 2002), gravity waves are for simplifying reasons only considered as forcing to the large-scale motion by dissipative means at locations where gravity-wave breaking occurs. These gravity waves are forced by orographic wave-mean fbw interactions, and shear or convective instabilities.
The approximate nature of balanced vortical dynamics, or more precisely the lack of an exact slow (vortical) manifold, is exemplified by the generation of gravity waves by the vortical dynamics (Ford *et al*, 2000; Vanneste, 2004). In contrast to the orographic generation of gravity waves and the subsequent dissipative forcing of the large-scale fbw, these gravity waves emerge from and leave an impact on the large-scale motion in a non-dissipative way. A key question is how we can parameterize these non-dissipative means of gravity-wave emission and absorption, and how important they are in forcing the mean, nearly balanced fbw. The various mechanisms to generate and absorb gravity waves have received a lot of attention lately (Bühler, 2000; Bühler and McIntyre, 2003), and we will review some of these mechanisms with an eye on extending current parameterization schemes of (computationally unresolved) gravity waves.

PRELIMINARY CONCLUSIONS

We have started to address the following question: can we construct an accurate atmospheric climate model with a (Hamiltonian) balanced model as dynamical core and with dissipative as well as non-dissipative parameterization schemes for the gravity-wave activity? Olaguer (2002) uses an energy-preserving balanced model as dynamical core for climate predictions. Our preliminary conclusion is that this dynamical core can be replaced by a more accurate balanced model. Imposing an more accurate global balanced constraint, an Hamiltonian balanced model can be used as dynamical core extending existing results to the sphere (Buitendijk, 2003) and to stratified models. Alternatively, a stratified, mass conserving higher order balanced model could be used (*e.g.*, following McIntyre and Norton, 2000). One outstanding question is how the novel insights on the emission and absorption of gravity waves by the vortical motion can be incorporated efficiently in climate models. Another open question is how accurate and how much faster a climate model with a more advanced balanced model as dynamical core will be compared to existing climate models based on the hydrostatic primitive equations. The tests done by Olaguer (2002) with balanced vorticity and temperature equations as dynamical core and using hydrostatic and quasi-geostrophic balance appear, however, to be encouraging.

References

[1] Andrews, D.G., Holton, J.R., & Leovy, C.B.: *Middle Atmosphere Dynamics*. Academic Press, 489 pp, 1987.
[2] Bokhove, O. & Verkley, W.T.M.: Constrained Isentropic models of tropospheric dynamics. With an appendix "Slaved Hamiltonian dynamics" by O. Bokhove & T.G. Shepherd, *Math. Comm.* 1685, University of Twente, www.math.utwente.nl/publications/ , 19 pp, 2003.
[3] Bühler, O.: 'On vorticity transport due to dissipating or breaking waves in shallow-water fbw'. *J. Fluid Mech.* **407**: 235–263, 2000.
[4] Bühler, O. & McIntyre, M.E.: 'Remote recoil: a new wave-mean interaction effect'. *J. Fluid Mech.* **492**: 207–230, 2003.
[5] Buitendijk, C.: *Hamiltonian balanced shallow-water equations on a sphere*. M.Sc. Thesis University of Utrecht, 2003.
[6] McFarlane, N.A.: The effect of orographically excited gravity wave drag on the general circulation of the lower stratosphere and troposphere. *J. Atmos. Sci.* **44**: 1775–1800, 1987.
[7] McIntyre, M.E. & Norton, W.A.: Potential vorticity inversion on a hemisphere. *J. Atmos. Sci.* **57**: 1214–1235, 2000.
[8] Olaguer, E.P.: An effi cient 3-D model for global circulation, transport and chemistry. *IMA Vol. Math. Appl.* **130**: 205–276, 2002.
[9] Vanneste, J. & Bokhove, O.: Dirac-bracket approach to nearly-geostrophic Hamiltonian balanced models. *Physica D* **164**: 152–167, 2002.
[10] Vanneste, J.: Inertia-gravity-wave generation by balanced motion: revisiting the Lorenz-Krishnamurthy model. *J. Atmos. Sci.* **61**, 224-234, 2004.

ASSIMILATION OF OBSERVATIONS INTO NUMERICAL MODELS

Olivier Talagrand
Laboratoire de M t orologie Dynamique, IPSL, ENS, Paris, France

Summary *Assimilation* of meteorological or oceanographic observations is the process by which observations are combined together with a numerical dynamical model of the flow in order to produce as accurate as possible a description of the state of the atmosphere or the ocean.. The basic problems raised by the development and implementation of assimilation, as well as the methods and numerical algorithms that are used in practice, are presented and discussed.

Numerical modeling has now become a major component of the study of the dynamics of the atmosphere and the oceans. A large variety of numerical models, which compute the temporal evolution of the atmospheric or oceanic flow for given initial and lateral boundary conditions, have been developed, and cover a very broad range of physical processes, as well as of spatial and temporal scales. Some models are intended at studying specific fundamental dynamical phenomena, such as convection or baroclinic instability. At the other extreme, models have been developed for simulating, as accurately as allowed by the present state of knowledge and the available computing resources, the whole range of complex interactions which determine and govern the climate˚: mechanical and thermal exchanges between the atmosphere and the oceans, atmospheric water cycle and oceanic salinity cycle, biogeochemical cycles, atmospheric and oceanic chemistry, etc. Other models have been developed for a very specific, directly utilitarian purpose, such as for instance weather prediction.

It is numerical weather prediction that is at the origin of the development of *assimilation of observations*. In order to perform a numerical weather forecast, it is necessary to have at one's disposal, not only an appropriate numerical model, but also as accurate as possible a description of the corresponding initial conditions. The available observations do not provide however the temporally synchronous and spatially homogeneous description of the atmosphere that is required by a numerical model. In addition, many observations, such as satellite observations, which have now become the major source of information on the state of the atmosphere, are "indirect" in that they bear, not on the physical quantities in terms of which the state of the flow is normally described (temperature, pressure, wind components, ...), but on more or less complicated functions (often, one-dimensional space integrals) of those quantities. Assimilation of observations is the process by which observations are combined together with a numerical model of the flow in order to produce as accurate as possible a spatially homogeneous description of the state of the flow.

Any information will always be affected with some uncertainty. Uncertainty is most easily described by probability distributions, and this leads to consider assimilation as a problem in *bayesian estimation*, *i. e.*, to look for the conditional probability distribution of the state of the flow, given the available information and the probability distribution of the associated uncertainty. In that respect, assimilation of observations is one of many *inverse problems* that are encountered in many fields of science of technology. In spite of the variety of applications, most (if not all) inverse problems are solved using the same basic mathematical methods. Difficulties that are specific to meteorological and oceanographical applications are the large numerical dimensions of the problems to be solved (the number of individual scalar meteorological observations is now in the range 10^6-10^7 per 24-hour period**,** with a similar value for the state vector dimension of the assimilating models), and the nonlinearity of the underlying dynamics. In the case of numerical weather prediction, one must add to those two basic difficulties the need for timely, reliable and robust production of the forecast.

Because of various reasons, and particularly of the large numerical dimensions involved, bayesian estimation cannot be implemented in practice, in its full generality, in meteorological and oceanographical applications. One must restrict one's ambitions to much more modest goals. Two basic approaches have been used so far.

Statistical linear estimation [1], which looks for the estimated state as the linear combination of the data (observations and model equations) that minimizes the statistical variance of the corresponding estimation error. Linear estimation can be useful for what is basically a nonlinear problem to the extent the so-called *tangent linear approximation* is valid. This means that a prior estimate, or *background*, is available for the state of the flow, which is close enough to the real state so that the estimation problem can be linearized in terms of deviations from that prior estimate. Statistical linear estimation produces the so-called *Best Linear Unbiased Estimate* (*BLUE*) of the state of the flow, and requires the *a priori* knowledge of only the expectation and covariance matrix of the data errors. In addition to an estimate of the state of the flow, statistical linear estimation also provides in theory an estimate of the covariance matrix of the corresponding estimation error. Moreover, if the data errors are gaussian, the *BLUE* achieves bayesian estimation in the sense that if entirely defines the conditional probability distribution of the state of the flow, given the data.

Ensemble assimilation [2], which produces an ensemble of possible states of the flow, whose distribution is meant to describe the desired conditional probability distribution. Ensemble assimilation is of particular interest in circumstances where a tangent linear approximation is not valid.

Most assimilation methods have so far been based on statistical linear estimation, with innumerable variants as to the specification of the expectation and covariance matrix of the data error, and as to the algorithmic implementation. When the temporal dynamics of the flow is explicitly taken into account, two classes of algorithms are possible. *Sequential assimilation* constantly updates the most recent estimate of the state of the flow with new observations. The exact *BLUE* form of sequential assimilation is *Kalman filtering* [3] which, because of the need for explicitly computing the temporal evolution of the covariance matrix of the estimation error, goes however well beyond available numerical

resources. *Variational assimilation* globally adjusts the assimilating model to observations distributed over a period of time. It becomes numerically feasible through the use of the *adjoint* of the assimilating model. One advantage of variational assimilation is that it provides a very efficient way to carry information both forward and backward in time. In addition, and contrary to Kalman filter, whose optimality requires that the errors affecting the data must be uncorrelated in time, it can relatively easily cope with time-correlated errors. On the other hand, and contrary to Kalman filter, it does not provide an explicit estimate of the estimation error.

Ensemble assimilation, which, as said, is particularly appropriate for situations when a local linear approximation is not valid, is most often sequential in nature. The ensemble of possible states is evolved in time, and constantly updated as new observations become available. It is a natural extension of Kalman filtering to nonlinear dynamics.

All assimilation algorithms require an *a priori* estimate of, at least, part of the probability distribution of the errors affecting the data. That information cannot be obtained from the data themselves, even through appropriate statistical processing. It entirely depends on independent hypotheses that cannot be objectively validated from the data themselves. This introduces an additional difficulty in the development of assimilation algorithms.

As said, assimilation of observations originated from the needs of numerical weather prediction. Together with improvements in numerical models and (to a lesser extent) improvements in the observing system, improvements in assimilation techniques have led to the steady progress, over the last three decades, of the quality of meteorological forecasts. Assimilation has also extended to many various applications. It first extended to observations of the oceanic circulation, then to reassimilation of past observations, and to other domains, such as atmospheric and oceanic chemistry and biochemistry. Assimilation has also led to the development of powerful numerical tools (for instance, adjoint models, or algorithms for computing the dominant unstable modes of the flow) which have in turn been applied to a large variety of diverse uses. One can mention in particular sensitivity studies, and the definition and optimization of observing systems. One specific example is *observation targeting*, intended at identifying, for a particular meteorological situation, critical areas in which observations can be expected to be particularly useful. Assimilation has also played a basic role in the development of ensemble and probabilistic prediction, intended at determining, not one possible future state of the flow, but a whole probability distribution, reflecting the various sources of uncertainty on the future evolution of the atmosphere or the ocean.

References

[1] Talagrand, O.: Assimilation of Observations, an Introduction. *J. Meteor. Soc. Japan* **75**:191-209, 1997.

[2] Evensen, G.: The Ensemble Kalman Filter: Theoretical Formulation and Practical Implementation. *Ocean Dynamics* **53**:343-367, 2003.

[3] Ghil, M.: Advances in Sequential Estimation for Atmospheric and Oceanic Flows. *J. Meteor. Soc. Japan* **75**:289-304, 1997.

TRANSPORT AND MIXING IN THE ATMOSPHERE

Peter Haynes
Department of Applied Mathematics and Theoretical Physics, University of Cambridge

Summary Transport and mixing processes in the atmosphere operate on scales from millimeters to thousands of kilometers. In certain parts of the atmosphere the large-scale 'layerwise two-dimensional' flow appears to play the dominant role in transport and in the stirring process that leads ultimately to true (molecular) mixing at very small scales. There is therefore much in common with fluid dynamical topics such as 'chaotic advection' or 'Batchelor-regime turbulence'. My talk will describe how, with appropriate modification, some of the theoretical tools developed in these contexts can be used, in conjunction with observational data on large-scale velocity fields or on chemical species, to quantify different aspects of transport and mixing in the atmosphere.

MOTIVATION

On sufficiently large scales in the atmosphere, e.g. larger than a few tens of kilometers, rotation and buoyancy stratification both tend to inhibit strong three-dimensionality of the flow. The flow is quasi-horizontal, with air parcel trajectories along weakly sloping surfaces, so that horizontal displacement are generally much larger than vertical displacements. These flows have a dual character, with some aspects of their behaviour appearing organised and wave-like and other aspects exhibiting considerable nonlinearity and randomness. In the latter respect these flows might therefore be regarded as a kind of turbulence, analogous to the two-dimensional turbulence studied in idealised numerical simulations and laboratory experiments. However, the strong difference of these flows from three-dimensional turbulence is that strong vortex stretching is inhibited and therefore the cascade of energy to small scales is inhibited. The velocity field has a finite spatial scale and hence there is no strong increase of velocity gradients as scale shrinks.

It is now realised that flows with a relatively simple structure in space and time may be highly effective at stirring and mixing through the phenomenon now widely known as 'chaotic advection'. Velocity fields with a very simple structure in space and time may lead to complex and irregular, i.e. chaotic, particle trajectories, with, for example, the distance between initially nearby particles, increasing exponentially in time. This separation of nearby particles implies that the fields of advected quantities, such as chemical species, rapidly become complex, with variations on scales much smaller than that of the advecting flow. Chaotic advection has often been studied in the context of time-periodic flows. But what essentially distinguishes chaotic advection from, say transport and mixing in three-dimensional turbulence, is that in the latter the small-scale velocity field plays an active role in stirring. Thus the term chaotic advection may be usefully applied to any flow with a finite spatial scale that naturally leads to spatial structure in advected chemical species on a much smaller scale. In this sense the atmospheric flow is a chaotic advection flow.

USE OF OBSERVATIONAL VELOCITY FIELDS IN TRANSPORT STUDIES

Global datasets of atmospheric dynamical quantities including velocity fields are now routinely produced as part of the weather forecasting process. These datasets are typically at a horizontal resolution of 100km or so. The datasets include a subtle blend of information direct from observations and information from the numerical models used to generate forecasts. The velocity datasets are now widely used as input to transport models. These might be Lagrangian models, which advect large numbers of particles (or sometimes finite parcels containing reacting chemical species), or Eulerian models, which represent global fields of different chemical species. Such models have been used with great success for many different scientific purposes, e.g to interpret high-resolution one-dimensional sections of chemical species measured in observational campaigns or to predict chemical ozone destruction in the stratosphere (e.g. Waugh et al., 1994, Methven et al., 2003). Of course, this whole approach depends on the chaotic advection idea that the large-scale flow dominates, otherwise the fact that information from spatial scales below the resolution of the datasets is not included would be a serious limitation.

TRANSPORT AND STIRRING

Simple chaotic advection models and analagous dynamical systems show that transport and stirring is often highly inhomogeneous, with regions of strong stirring (i.e. strong stretching) separated by barrier regions in which stirring is weak and across which there is no, or relatively little, transport. In time periodic and quasiperiodic flows the barriers are usually perfect (they are composed of invariant tori) for some ranges of values of the parameters defining the flow.

In the real atmosphere observations and models show similarly inhomogeneous transport and stirring. In the stratosphere, for example, the edge of the winter polar vortex seems to form a transport barrier which is not perfect, but across which transport is very weak. Outside the vortex, in mid-latitudes, and to a lesser extent inside the vortex, there are regions of strong stirring. Lower in the atmosphere the subtropical jet seems to form a similar, if less effective, barrier to quasi-horizontal transport which separates the upper troposphere and the lowest part of the stratosphere. Once again, poleward and equatorward of the subtropical jet there are regions of strong stirring. This sort of spatial structure, with transport barriers and stirring regions, is found in a wide class of geophysical flows and depends on the strong relation, provided by

the potential vorticity field, between transport and stirring on the one hand and dynamics on the other.

The relation between the dynamical transport barriers in the geophysical flows and the invariant tori of the simple time-periodic flows is not very clear at all. Nonetheless the various mathematical tools originating in dynamical systems theory that have been applied to simple chaotic advection flows are potentially of interest in considering realistic atmospheric flows and several have been carefully studied in this context (e.g. Koh and Plumb 2000, Joseph and Legras 2002). Other tools such as 'effective diffusivity' calculated from an advected test tracer look promising (e.g. Haynes and Shuckburgh 2000). Such tools are needed to compare effectively the transport and stirring structure of velocity fields in different observational datasets or generated by different numerical models.

STIRRING AND MIXING

The reduction in spatial scale of fields of advected chemical species by stirring ultimately terminates in true mixing by molecular diffusion. This could be achieved in laminar flow, but in practice in the real atmosphere the effects of molecular diffusion are likely to be enhanced through intermittent encounters of air parcels with three-dimensional turbulence. This enhancement might be substantial in the troposphere, where convection is relatively common, is likely to be much weaker in the lower stratosphere and then to increase again in the upper stratosphere and mesosphere, where three-dimensional turbulence associated with the breaking of gravity waves is more widespread. To some approximation the mixing effects of encounters with turbulence may be represented as an enhanced molecular diffusion and the stirring and mixing process is therefore one in which the stirring (i.e. stretching) effects of the large-scale flow interact with diffusion.

This is a classical problem in fluid dynamics, often studied in the context of the 'Batchelor regime' of turbulence, where the diffusivity of the advected quantity is assumed to be much less than the momentum diffusivity, so that there is a sort of chaotic advection at scales smaller than the Kolmogorov scale. A promising theoretical approach to this problem has been to consider the interaction between stretching and diffusion in a flow that is a random function of time and a linear function of space. This theory has undergone significant developments recently (e.g. Balkovsky and Fouxon 1999, Falkovich et al 2001). Whilst it has apparent limitations in the initial-value problem (i.e. free decay from a specified initial field for the chemical concentration) these limitations do not seem to extended to the forced problem (where the chemical concentration is maintained by some source/sink distribution) and potentially it offers a quantitative theory for the chemical concentration field that arises from a specified combination of large-scale flow and small-scale mixing processes. The standard theories need some extension to be applied to the atmosphere. Firstly the atmospheric flow is layerwise two-dimensional and therefore strongly isotropic. This extension is relatively straightforward (Haynes and Anglade 1997). Secondly the spatial and temporal organisation of atmospheric flows (the persistent stratospheric polar vortex, for example) mean that the standard randomness assumptions do not apply. This extension is not straightforward at all.

References

[1] Methven, J. et al.: Estimating photochemically produced ozone throughout a domain using flight data and a Lagrangian model. *J. Geophys. Res.* **108**: art. no. 4271, 2003.

[2] Waugh, D. W. et al.: Transport of material out of the stratospheric Arctic vortex by Rossby wave breaking. *J. Geophys. Res.* **99**: 1071–1088, 1994.

[3] Koh, T. -Y., Plumb, R. A.: Lobe dynamics applied to barotropic Rossby-wave breaking. *Phys. Fluids* **12**, 1518-1528, 2000.

[4] Joseph, B., Legras, B.: Relation between kinematic boundaries, stirring and barriers for the Antarctic polar vortex. *J. Atmos. Sci.* **59**, 1198-1212, 2002.

[5] Haynes, P. H., Shuckburgh, E. F.: Effective diffusivity as a diagnostic of atmospheric transport. Part I: stratosphere. *J. Geophys. Res.* **105**, 22777-22794, 2000.

[6] Balkovsky, E., Fouxon, A.: Universal long-time properties of Lagrangian statistics in the Batchelor regime and their application to the passive scalar problem. *Phys. Rev. E* **60**: 4164–4174, 1999.

[7] Falkovich, G., Gawedzki, K., Vergassola, M.: Particles and fields in fluid turbulence. *Revs. Mod. Phys.* **73**: 913–975, 2001.

[8] Haynes, P. H., Anglade, J.: The vertical-scale cascade of atmospheric tracers due to large-scale differential advection. *J. Atmos. Sci.* **54**, 1121-1136, 1997.

MODELLING OCEANOGRAPHIC COASTAL CURRENTS IN SMALL-SCALE AND LARGE-SCALE LABORATORY EXPERIMENTS

Peter J. Thomas[*], Paul F. Linden[**], David Marah[*]

[*]*Fluid Dynamics Research Centre, University of Warwick, Coventry CV4 7AL, United Kingdom*

[**]*Department of Mechanical and Aerospace Engineering, University of California, San Diego, La Jolla, Ca 92093-0411, USA*

Summary Laboratory experiments simulating gravity-driven oceanographic coastal surface currents are discussed. Results from two complementing studies on substantially different spatial scales and in different parameter regimes are compared. A geostrophic model is developed in terms of a set of non-dimensional parameters obtained from dimensional analysis. Very good agreement with experiments is found.

INTRODUCTION

When estuarine river water discharges into the coastal zone a gravity-driven surface flow is established. The flow develops as a consequence of the density difference between the discharged, buoyant fresh water and the denser, salty ocean water. The flow can be affected by the Coriolis force arising from the rotation of the earth. This confines it to the coastal zone where it forms a current flowing along the coast [1-3]. To date there exists no complete model which can predict the current width, its height and its propagation speed on the basis of a simple geostrophic approximation. The purpose of this study was to develop such a model and test it against comprehensive experimental laboratory data.

THEORETICAL ANALYSIS OF THE FLOW

Dimensional analysis

Five quantities are involved; dimensional analysis yields three non-dimensional parameters to summarise the data:

$$I = q_0^{1/5}\,\Omega\, g'^{-3/5}, \qquad T = g'^{3/5}\, t\, q_0^{-1/5}, \qquad \Pi(X) = X\; g'^{1/5}\, q_0^{-2/5} \tag{1a-c}$$

(q_0 : volumetric discharge rate at source, Ω : rotation rate, g' : reduced gravitational acceleration $g' = (\rho_2 - \rho_1)\, g/\rho_1$ with ρ_1 and ρ_2 representing densities of fresh and ocean water respectively and g is the gravitational acceleration, t : time). Eq. (1a) summarises the independent experimental parameters and characterises experiments in parameter space. Eq. (1b) represents a non-dimensional time. Eq. (1c) is a non-dimensional length; where X represents, alternatively, the current length $l(t)$, its width w_0 or its height h_0 (see Fig. 1). We write $\Pi(l) = L$, $\Pi(w_0) = W_0$ and $\Pi(h_0) = H_0$.

Theoretical model for the current

Our model assumes that the flow velocities normal to the wall and in the vertical direction (see Fig. 1) are negligible in comparison to the along-wall flow velocity. We allow for motion along the *x*-axis but neglect all variations $\partial/\partial x$.

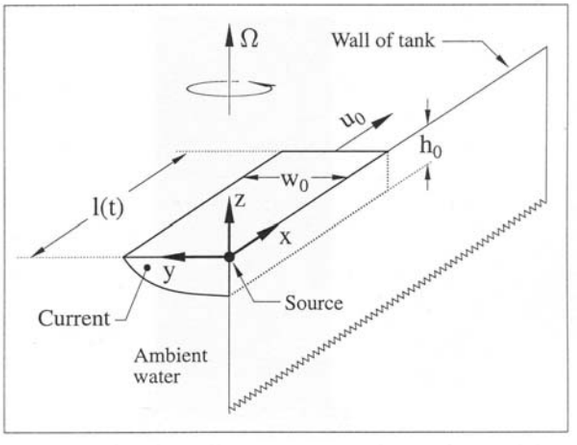


Fig. 1 : Sketch to illustrate nomenclature for model.

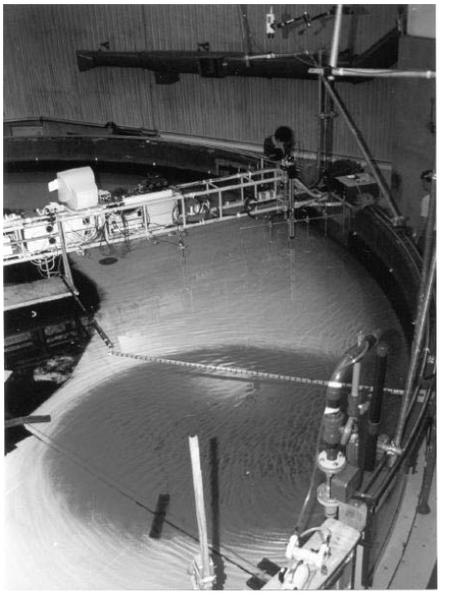


Fig. 2 : A current in the large-scale facility.

We use the geostrophic approximation, assume that the potential vorticity is zero and conserved and we employ mass conservation. The theoretical analysis then reveals that the most appropriate time scale is $T_0 = I^{1/4} T$ and that

$$H_0 = 2I^{1/2}, \qquad W_0 = I^{-3/4}, \qquad L = \frac{3}{4} T_0, \qquad U_0 = \frac{L}{T_0} = \frac{3}{4}. \tag{2a-d}$$

Equations (2a,b) yield $h_0/w_0 = 2I^{5/4}$. One can define a Rossby number Ro and a Froude number Fr and finds

$$Ro = \frac{u_0}{\Omega\, w_0} = \frac{3}{4}, \qquad Fr = \frac{u_0}{\sqrt{g'\, h_0}} = \frac{3}{2^{5/2}} = 0.5303 \tag{3a,b}$$

The results expressed by Eqs. (2a-d) and (3a,b) have not appeared in the literature previously. The expressions can be tested against experimental data.

THE EXPERIMENTS

Two complementing experimental studies were carried out. One study was conducted in a small rotating tank with diameter 1 m. The second was on much larger spatial scale; it employed the world's largest rotating turntable at the Coriolis Facility (Grenoble) with its 13-metre diameter tank [4]. For the experiments the tank was filled with dense salt water. This was brought into solid-body rotation and represented the ocean. Fresh water, simulating river discharges, was released continuously from a source mounted at the wall of the tank. The source was adjusted to be level with the surface of the salt water. The fresh water was dyed with food coloring to enable distinguishing the current from the ambient clear water. Defining a Reynolds number $\mathrm{Re} = w_0\, u_0/\nu$, ($\nu$: kinematic viscosity) conditions were such that $116 \le \mathrm{Re} \le 5223$ and $5007 \le \mathrm{Re} \le 185542$ for the small- and large-scale experiments respectively.

EXPERIMENTAL RESULTS

Qualitative observations

Figure 2 shows part of a large-scale current. The current fluid is dyed red. The source from which the fluid ejects is located at the wall of the tank near the lower right-hand corner of the photo. The currents in the small-scale facility look qualitatively very similar. A total of 34 large-scale and 66 small-scale experiments were conducted and analyzed. Depending on the experimental conditions currents can be stable or unstable. Figure 2 shows a stable current. Unstable currents are characterized by the development of baroclinic instabilities establishing eddies on the currents.

Quantitative results

Figure 3 serves as one example illustrating the accuracy with which our geostrophic model describes the current dynamics. The figure summarises the data for the development of the non-dimensional current length L as a function of the non-dimensional time T_0 for the 34 large-scale experiments. The solid line superposed on the data represents the theoretical prediction of Eq. (2c). It can be seen that the model describes the experimental data very well. The currents are initially slightly faster than predicted because their height decreases along the current from the source to the current head. The corresponding figure for the 66 small-scale experiments looks essentially identical to Fig. 3. All figures for the current height H_0 and the current width W_0 as a function of the parameter I display a similarly good agreement with theory when experimental conditions are geostrophic. The data show how agreement becomes less favourable as ageostrophic experimental conditions are approached.

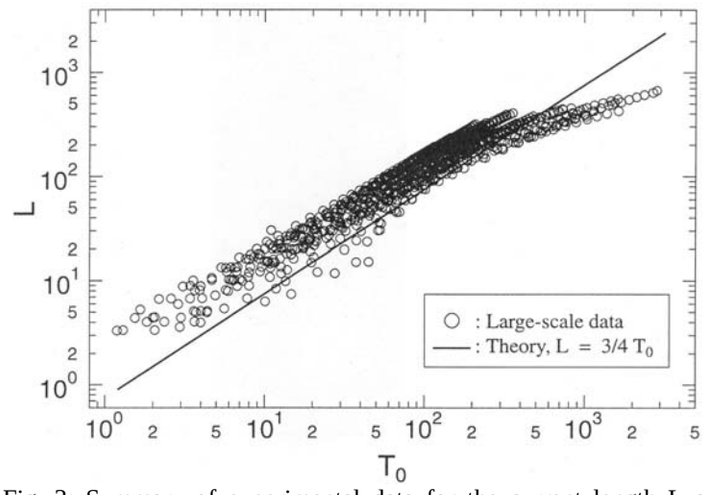


Fig. 3: Summary of experimental data for the current length L as a function of time T_0 for the 34 large-scale experiments.

SUMMARY AND CONCLUSION

A geostrophic model describing gravity-driven buoyant surface currents in a rotating system was developed. Comparisons with data from small-scale and large-scale experiments show good agreement in the geostrophic parameter regime. Discrepancies between model and experiment are associated with the surface Ekman layer which is not governed by geostrophy. The agreement between measured and predicted current height scales with an Ekman number $Ek(h_0)$ defined on the basis of the current height h_0. Agreement between model and experiments deteriorates with increasing Ekman number as $Ek^{0.12}$. The current width appears to scale with a the ratio of $Ek(h_0)$ and the Reynolds number $\mathrm{Re}(w_0, u_0)$ defined on the basis of the current width w_0 and the current speed u_0.

References

[1] Griffiths, R.W.: Gravity Currents in Rotating Systems. *Ann. Rev. Fluid Mech.* **18**:59-89, 1986.
[2] Simpson, J.E.: Gravity Currents in the Environment and the Laboratory (2nd Edition). Camb. Univ. Press, 1997.
[3] Lentz, S.J., Helfrich, K.R.: Buoyant Gravity Currents Along a Sloping Bottom in a Rotating Fluid. *J. Fluid Mech.* **464**:251-278, 2002.
[4] Coriolis Facility, web site http://www.coriolis-legi.org

XXI ICTAM, 15–21 August 2004, Warsaw, Poland

NEAR SURFACE TURBULENCE IN A NEUTRAL PLANETARY BOUNDARY LAYER: COMPARISON OF LES WITH THE CASES'99 EXPERIMENT OBSERVATIONS

Pierre Carlotti[(1)], Philippe Drobinski[(2)], Jean-Luc Redelsperger[(3)],
Rob K. Newsom[(4,5)], and Robert M. Banta[(4)]
[(1)] *CETU, Bron, France;* [(2)] *IPSL/SA, Paris, France;* [(3)] *CNRM/Météo-France, Toulouse, France;*
[(4)] *ETL/NOAA, Boulder, Colorado, USA;* [(5)] *CIRA, Ft. Collins, Colorado, USA.*

Summary
This work compares the results of the field experiment CASES'99 (in a neutral atmosphere) with an idealized LES simulation performed with Méso-NH. Energy profiles and flow patterns of the real case and the LES are compared, showing a good agreement. In particular, the LES shows the formation of near-surface streaks spaced of approximately 390 m, in agreement with high resolution Doppler lidar radial velocity recorded in CASES'99, which shows evidence of an approximate spacing of the streaks of 315 m.

INTRODUCTION

The turbulence structure and its spectral characteristics in the neutral surface layer (SL) has been the subject of considerable research effort for the last decades, since turbulence is one major process controlling energy and matter exchanges between the surface and the planetary boundary layer (PBL).

At present, most of the effort is focused on (i) understanding the dynamical processes that contribute to the turbulent surface fluxes, and particularly the role of turbulent eddies; (ii) deriving reliable and accurate parametrizations of atmospheric surface turbulence, from large-eddy simulations (LES) to general circulation models (GCM). Indeed, in atmospheric modelling, most of the turbulent processes occur at sub-grid scale and are thus not explicitly resolved by numerical models. The resolved scales are assumed to contain most of the energy of turbulent motion whilst on subgrid scales, motions are the less energetic. This approach works well far from regions of large gradients, whereas subgrid contribution may become larger than the resolved part near the surface. Consequently, model results become more sensitive to the subgrid scheme in this region.

The issue of this paper is to evaluate how a LES performs in retrieving the near-surface turbulence properties in terms of organized eddies and their related energetics. To do so, simulated fields of highly resolved LES of a neutrally stratified surface layer are compared with the near-surface data collected during the CASES'99 experiment.

DATA SETS

The CASES'99 experiment

The CASES'99 experiment was designed to be a nighttime experiment to study the stable boundary layer and to study physical processes associated with the morning and evening transition periods (Poulos et al. 2002). The experimental period was from 1 to 31 October 1999 near Leon 50 km east of Wichita, Kansas.

The current study uses data collected on the 13 October 1999 near-neutral case from six 10-m and one 60-m meteorological towers, radiosonde releases and the High-Resolution Doppler Lidar (HRDL) developed by NOAA/ETL in cooperation with the NCAR/ATD and ARO (Grund et al., 2001).

LES model and simulation

The large-eddy simulations presented have been made using Méso-NH (Lafore et al., 1998). In this paper, it is used exclusively in its LES mode.

A neutrally-stratified, midlatitude, barotropic, dry atmosphere PBL flow was simulated with forcing similar to the near-neutral surface layer case documented in the framework of the CASES'99 experiment (Drobinski et al., 2003). The simulations were made on a domain 3 km long, 1 km wide and 750 m high with 6.25 m grid resolution (Carlotti, 2002). The computing grid is cubic to avoid any influence of anisotropy of the grid with periodic boundary conditions on the lateral sides and a rigid lid at the top.

The initial condition was a laminar geostrophic flow $U_g = 10$ m.s^{-1} aligned along the x-axis with small random temperature perturbations to generate turbulence. The surface buoyancy flux is zero and the surface friction velocity is constant ($u_* = 0.42$ m.s^{-1}). Table 1 compares the mean and turbulence variables used to force the LES dynamics and the corresponding values obtained from the CASES'99 measurements (radiosounding and sonic anemometer).

A relatively deep logarithmic surface wind profile formed with no veering up to 40 m. The surface roughness length is about 0.04 m.

COMPARAISON OF LES WITH OBSERVATIONS

The LES results show a good agreement with the observations collected between the surface and about 100 m. The variables that we compared with the observations are the vertical profile of wind velocity, of the variances of the three

components of the wind, of the turbulent kinetic energy flux and of the momentum fluxes. For example, Figure 1 shows the comparison of the vertical profiles of the longitudinal and transverse velocity fluctuation variances retrieved from Méso-NH (dashed line) and from the radial velocities obtained with HRDL (solid line). The overall profile is satisfactorily simulated with nearly constant variances up to about 30 m and decreasing variances above. In the upper levels, Méso-NH slightly underestimates the variances.

In addition to the vertical profiles, LES flow visualization shows a characteristic near-surface streak spacing of approximately 390 m oriented at 8^o from the geostrophic wind and aligned with the surface wind, in good agreement with HRDL radial velocity horizontal field which shows evidence of 315 m horizontally spaced streaks (Figure 2). The simulated and observed finescale streaks extend up to 50 m above the ground.

References

[1] Carlotti, P. Bound.-Layer Meteor., 104, 381-410 (2002).
[2] Drobinski P., Carlotti P., Newsom R.K., Banta R.M., Foster R.C., Redelsperger J.L. J. Atmos. Sci., in press (2003)
[3] Grund, C.J., Banta R.M., George J.L., Howell J.N., Post M.J., Richter R.A., Weickmann A.M. J. Atmos. Ocean Technol., 18, 376-393 (2001).
[4] Lafore J.P. and co-authors. J. Ann. Geophys., 16, 90-109 (1998).
[5] Poulos, G.S. and co-authors. Bull. Amer. Meteor. Soc., 83, 555-581 (2002).

Table 1: Mean and turbulence variable retrieved from Méso-NH and the observations

Variable	LES	CASES'99
u_* (m/s)	0.42	0.4
U_g (m/s)	10	8-10
z_0 (m)	0.04	0.04
z_i (m)	750	700-750

Figure 1 : Vertical profiles of the streamwise (a) and spanwise (b) wind component fluctuation variances from the Méso-NH simulations (dashed line) and the Doppler lidar (solid line).

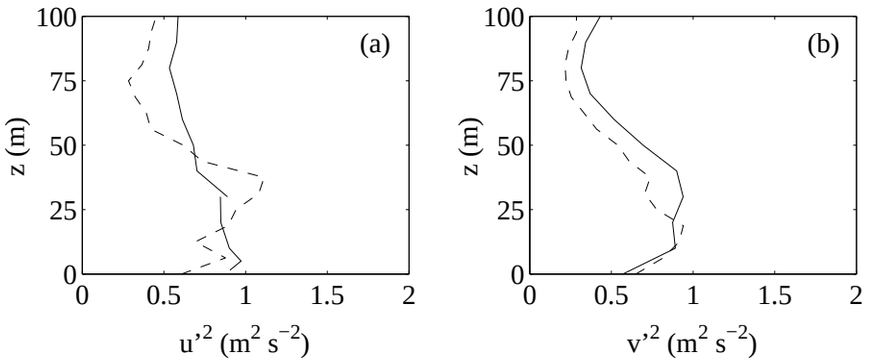
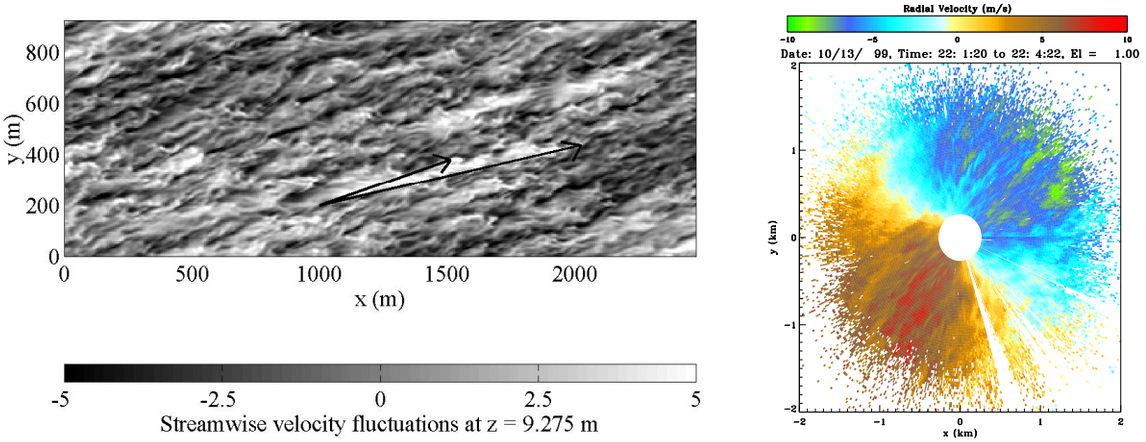


Figure 2 : (a) Snapshot of the streamwise velocity fluctuations found in the LES; (b) HRDL radial velocity field.



MERIDIONAL FLOW OF GROUNDED SOURCE DRIVEN ABYSSAL CURENTS IN A WIND DRIVEN BASIN WITH TOPOGRAPHY

Gordon E. Swaters
Applied Mathematics Institute, Department of Mathematical & Statistical Sciences
and, Institute for Geophysical Research, University of Alberta, Edmonton, Canada

Summary A hybrid 3-layer quasi-geostrophic/planetary geostrophic (QG/PG) model is introduced to examine the baroclinic evolution and meridional flow of abyssal currents in a wind-driven, stratified and differentially rotating basin with variable bottom topography. The model resolves mesoscale processes and allows for the formation of a wind driven surface intensified ocean circulation, with a pole ward western boundary current, and a source driven equatorward flowing deep western boundary undercurrent. Baroclinic and barotropic instability within the surface intensified western boundary current, and baroclinic instability between the abyssal current and the overlying wind driven circulation, is resolved. The model allows for finite amplitude variations in the height field of the abyssal current so that groundings in the thickness or isopycnal field associated with the undercurrent are resolved. A southern boundary upwelling scheme is introduced, within the context of a closed basin with no-slip boundary conditions, to balance the northern source of abyssal water thereby allowing the meridional transport of abyssal water to evolve toward a steady state.

INTRODUCTION

Stommel and Arons [1] showed that the Sverdrup vorticity balance predicts the equatorward flow of a source driven abyssal water mass. Thus, in the immediate vicinity of the region of deep-water production in high latitudes, there is an intrinsic tendency for preferential equatorward abyssal flow. Away from the source region, much of the abyssal circulation is strongly characterized by the isopycnal field being grounded against sloping topography (e.g., the deep western boundary undercurrent in the North Atlantic, Richardson [2]) and the flow being in geostrophic balance. Indeed, as shown by Nof [3], a fully grounded (i.e., compactly supported) abyssal water mass, in the fully nonlinear but reduced gravity dynamical limit, moves nondispersively and steadily in the along slope direction (in a right (left) handed sense in the northern (southern) hemisphere), regardless of the height or vorticity field within the abyssal water mass.

These two results provide a compelling scenario for the initiation and maintenance of grounded abyssal flow. That is, in high latitude source regions where deep water is produced (often over sloping topography), the Sverdrup vorticity balance initiates equatorward flow. One produced, this abyssal flow can become grounded and geostrophic adjusted, maintaining a Nof balance which permits sustained basin scale meridional quasi-steady and coherent propagation regardless of the spatial structure of the water mass. Of course, this picture leaves out many important dynamical processes such as diabatic effects, baroclinicity, instability and mixing. In addition, such a scenario cannot explain cross-equatorial abyssal currents where the underlying assumptions of geostrophically balanced grounded flow must necessarily breakdown.

The principal purpose of the present contribution is to briefly describe some results from a model for the sub-inertial evolution and meridional flow of source driven grounded abyssal currents over sloping topography and their baroclinic interaction with the overlying wind driven circulation.

MODEL EQUATIONS

Succinctly summarized, the model is an amalgamation, with the inclusion of variable topography and mass conserving up and downwelling, of the two layer QG model used by Holland [4] to investigate the baroclinic evolution of the wind driven circulation and the QG/PG abyssal current model of Swaters [5] used to investigate the baroclinic instability of grounded geostrophic flow. A continuously stratified version of the present model is described by Poulin and Swaters [6] and Reszka *et al.* [7].

Assuming a Boussinesq, rigid-lid approximation with wind stress, horizontal and bottom friction, topography, and mass conserving up or downwelling, the nondimensional model can be written in the form

$$\left[\partial_t + J(\phi_1, \cdot)\right]\left[\Delta\phi_1 - F_1(\phi_1 - \phi_2) + \beta y\right] = \Upsilon\, \nabla\times\boldsymbol{\tau} + \frac{F_1}{F_1 + F_2} Q + \frac{1}{R_e}\Delta^2\phi_1,$$

$$\left[\partial_t + J(\phi_2, \cdot)\right]\left[\Delta\phi_2 - F_2(\phi_2 - \phi_1) + h + h_B + \beta y\right] = -r_2\Delta\phi_2 + \frac{F_1}{F_1 + F_2}Q + \frac{1}{R_e}\Delta^2\phi_2,$$

$$h_t + \frac{1}{1+s\beta y}J(\phi_2 + h_B, h) - \frac{s\beta h}{(1+s\beta y)^2}(\phi_2 + h_B + h)_x = Q + r_3\Delta(\phi_2 + h_B + h),$$

where the notation is standard.

The wind stress is explicitly distributed only over the upper layer and the upper layer does not have surface Ekman friction. The upper two layers have horizontal friction, but this has been neglected in the abyssal layer. The abyssal layer does, however, include bottom friction. It can be shown that, in the unforced, inviscid limit, the horizontal divergence of the barotropic mass flux is zero. That is, whatever mass is accumulated into or lost from, say, the abyssal layer, is assumed to have been instantaneously gained from or lost into the upper two layers (where the distribution over the upper two layers is in proportion to the individual upper layer volume fractions). The net barotropic QG mass transport is forced only by wind stress and bottom friction. The unforced, inviscid dynamics of the model is, therefore, purely baroclinic. Though in geostrophic balance, the leading order abyssal layer equations are not geostrophically degenerate and allow for finite amplitude dynamic deflections in the abyssal layer height. The model can be formally derived in a small Rossby number limit of the 3-layer shallow water equations (Swaters [5], Poulin and Swaters [6] and Reszka *et al.* [7]).

There are a number of sub-dynamical, or distinguished, limits in the model which are well known such as the *Nof balance* describing grounded abyssal flow (Nof [3]), the *Stommel-Arons Sverdrup vorticity balance* describing the equatorward flow of a source driven abyssal water mass (Stommel and Arons [1]), the *planetary shock wave balance* (Anderson and Killworth [8] and Dewer [9]) describing the amplitude-beta induced isopycnal steepening associated with the frontal geostrophic dynamical regime (Karsten and Swaters [10]) and, finally, the coupling between the abyssal layer and the overlying ocean which can lead to baroclinic instability and mixing (Swaters [5,11], Poulin and Swaters [6], Reszka *et al.* [7] and Mooney and Swaters [12]).

References

[1] Stommel, H. & Arons, A. B., On the abyssal circulation of the world ocean - I. Stationary flow patterns on a sphere. *Deep-Sea Res.*, **6**, pp. 140-154, 1960.

[2] Richardson, P. L., On the crossover between the Gulf Stream and the Western Boundary Undercurrent. *Deep-Sea Res.*, **24**, pp. 139-159, 1977.

[3] Nof, D., The translation of isolated cold eddies on a sloping bottom. *Deep-Sea Res.*, **30**, pp. 171-182, 1983.

[4] Holland, W. R., The role of mesoscale eddies in the general circulation of the ocean - Numerical experiments using a wind-driven quasi-geostrophic model. *J. Phys. Oceanogr.*, **8**, pp. 363-392, 1978.

[5] Swaters, G. E., On the baroclinic instability of cold-core coupled density fronts on sloping continental shelf. *J. Fluid Mech.*, **224**, pp. 361-382, 1991.

[6] Poulin, F. J. & Swaters, G. E., Sub-inertial dynamics of density-driven flows in a continuously stratified fluid on a sloping bottom. I. Model derivation and stability conditions. *Proc. R. Soc. Lond. A*, **455**, pp. 2281-2304, 1999.

[7] Reszka, M. K., Swaters G. E. & Sutherland, B. R., Instability of abyssal currents in a continuously stratified ocean with bottom topography. *J. Phys. Oceanogr.*, **32**, pp. 3528-3550, 2002.

[8] Anderson, D. & Killworth, P. D., Non-linear propagation of long Rossby waves. *Deep-Sea Res.*, **26**, pp. 1033-1050, 1979.

[9] Dewer, W. K., Planetary shock waves. *J. Phys. Oceanogr.*, **17**, pp. 470-482, 1987.

[10] Karsten, R. H. & Swaters, G. E., A unified asymptotic derivation of two-layer, frontal geostrophic models including planetary sphericity and variable topography. *Phys. Fluids*, **11**, pp. 2583-2597, 1999.

[11] Swaters, G. E., Numerical simulations of the baroclinic dynamics of density-driven coupled fronts and eddies on a sloping bottom. *J. Geophys. Res.*, **103**, pp. 2945-2961, 1998.

[12] Mooney, C. J. & Swaters, G. E., Finite amplitude baroclinic instability of a mesoscale gravity current in a channel. *Geophys. Astrophys. Fluid Dyn.*, **82**, pp. 173-205, 1996.

XXI ICTAM, 15–21 August 2004, Warsaw, Poland

REMOTE RECOIL AND WAVE CAPTURE: WAVE–VORTEX INTERACTIONS IN ATMOSPHERE–OCEAN MODELS

Oliver Bühler*, Michael McIntyre**
* *Atmosphere Ocean Science & Mathematics, Courant Institute of Mathematical Sciences, New York University, 251 Mercer St, New York, NY 10012, U. S. A.*
obuhler@cims.nyu.edu
** *Centre for Atmospheric Science at the Department of Applied Mathematics and Theoretical Physics, Wilberforce Rd, Cambridge CB3 0WA, United Kingdom*
mem@damtp.cam.ac.uk

Summary In a recent paper [1] we described a fundamentally new wave-mean or wave-vortex interaction effect able to force persistent, cumulative change in mean flows in the absence of wave breaking or other kinds of wave dissipation. It is associated with the refraction of nondissipating waves by inhomogeneous mean (vortical) flows. The simplest relevant case is that of a narrow beam of sound waves, or shallow-water gravity waves, weakly refracted by a single vortex in two dimensions. An effective recoil force arises. This accords with expectation from a naive photon analogy or "pseudomomentum rule" *except* that the force acts not where the waves refract, but at the vortex core, even if the core is spatially separated from the refracting beam of waves. Strong refraction brings further phenomena including catastrophic "wave capture", a nontrivial variant of classical critical-layer absorption; see the more detailed presentation on this by Bühler in this Minisymposium. One implication is that there are missing forces not yet accounted for in atmospheric climate and weather-prediction models. Connections with the "pseudomomentum rule" and the "wave momentum myth" are discussed.

INTRODUCTION

Wave-induced eastward or westward mean forces and the consequent "gyroscopic pumping" drive persistent, global-scale, greenhouse-gas-transporting meridional circulations in the Earth's middle atmosphere, between about 15 and 100 km altitude. In the middle latitudes of the summer hemisphere, for instance, persistent eastward forces mediated by internal gravity waves pump air equatorwards, through the Coriolis effect, at mesospheric altitudes around 90 km; for a recent review see [2]. The resulting polar upwelling supplies water vapour from below and acts as a gigantic natural refrigerator. Despite intense solar radiation, maximal at the pole because of the Earth's tilt, temperatures as low as 105 K have been observed in the summer polar cap. These are by far the lowest of naturally-occurring terrestrial temperatures: to that extent, the sunniest place on Earth is also the coldest place on Earth.

The wave-induced forces responsible for this remarkable refrigeration phenomenon — and other equally remarkable phenomena such as the "quasi-biennial oscillation" of the east–west winds in the tropical lower stratosphere — cannot all be directly represented in global numerical models of the atmosphere. The reason is the small spatial scale of the waves, many of which are not resolvable by the global-model numerics. Therefore standard practice today is to represent the waves through so-called "parametrization schemes" based on ray theory and wave–mean interaction theory. However, the version of the wave–mean theory on which all such schemes are based is the classical version that neglects horizontal refraction, in which the only persistent wave-induced forces are those associated with wave breaking and other wave-dissipation processes. Lifting this restriction reveals a new set of interesting wave–mean interaction phenomena.

EFFECTS OF HORIZONTAL REFRACTION

There are two main points. First, a generalized wave–mean theory that includes horizontal refraction implies the existence of persistent wave-induced forces of a fundamentally different kind from those considered in classical wave–mean theory. These "missing forces" are unrelated to wave dissipation, yet have a cumulative impact. They may furthermore involve interesting "remote recoil" effects, one of which is that the effective wave-induced force, for wave parametrization purposes, may act at a location removed from the locations where the waves refract. The simplest relevant model problem is the refraction of a narrow beam of acoustic or gravity waves by a single vortex, in a two-dimensional gas-dynamic or shallow-water system. There, the effective force is felt at the vortex core, regardless of its spatial separation from the waves. The reality and precise mechanism of this remote recoil effect is clearly demonstrated, in detail, by the analysis given in ref. [1]. That such remote recoil effects are, moreover, generic is clear from the results in [1] taken together with classical studies of internal gravity waves, notably that of Bretherton [3].

Second, horizontal refraction, a seemingly slow process on naïve order-of-magnitude grounds, for internal gravity waves in typical background wind fields in the atmosphere, can nevertheless accelerate catastrophically in a significant proportion of cases through a process that may be called "wave capture". This is a nontrivial variant of classical critical-layer absorption, in which the magnitude $|\mathbf{k}|$ of the wavenumber vector $\mathbf{k}$ increases not linearly with time, as in the classical case, but exponentially. The reason for the exponential behaviour is the diminution to zero of phase and group velocities as $|\mathbf{k}| \to \infty$, so that the wavecrests behave asymptotically like passive tracers in a horizontal deformation field. Note that in this situation $|\mathbf{k}| \to \infty$ because the *horizontal components* of $|\mathbf{k}|$ tend to infinity. The wave-capture phenomenon provides some striking variations on the theme of missing forces and remote-recoil effects.

[**STOP PRESS:** after submission of this Abstract, we discovered that the linear theory of wave capture (though not the missing-force and remote-recoil aspects) has already been discussed in a paper by Badulin and Shrira [10] under the heading "wave trapping". There is further discussion in a paper by Staquet and Edwards to this Minisymposium.]

WAVE CAPTURE AND THE WAVE MOMENTUM MYTH

Wave capture provides what at first sight appears to be a further counterexample to "wave momentum myth", the conflation of momentum with pseudomomentum with its long history in which, as the physicist E. I. Blount once wrote, "the list of disputants is very distinguished" [4],[5]. The conflation, moreover, tends to be perpetuated in the sound-wave and water-wave literatures because of the special and peculiar properties of irrotational wave motion [6],[7]. The myth can often be seen enshrined in statements like "the waves gave *their momentum* [sic] to the mean flow."

The pseudomomentum **p** of a wave packet is the wave property that often behaves *as if* it were momentum; for this reason, it is also called the quasimomentum. More precisely, wave–mean interaction theory implies that in many cases of interest the following "pseudomomentum rule" holds, here stated in the form used as the basis for atmospheric gravity-wave parametrizations. The rule states that persistent mean forces arise only where the waves break or otherwise dissipate, and that these wave-induced mean forces are the same *as if* [5]

1. the fluid were absent, and
2. a wave packet had horizontal momentum equal to the horizontal component of **p**.

The circumstances in which, and sense in which, the rule is justified, have been clarified in ref. [7], and are further clarified in the present work. Within the standard ray-theoretic approximations, we have the well known formula

$$\mathbf{p} \approx E\mathbf{k}/\hat{\omega}$$

where $\mathbf{k}$ is the wavenumber vector and $\hat{\omega}$ the intrinsic frequency, or frequency seen in a co-moving reference frame, i.e. a frame moving locally with the background flow; E is the (positive definite) energy of the wave packet, seen in the same co-moving reference frame, i.e., the intrinsic wave-energy in the Bretherton–Garrett sense [9], the wave-energy derivable from the linearized equations, as distinct from the pseudoenergy, the (sometimes negative) energy used in plasma physics. This leads to an apparent paradox when wave capture is involved, because of the fact, already mentioned, that $|\mathbf{k}| \to \infty$ with the horizontal components tending to infinity. (In classical critical-level absorption, by contrast, only the vertical component tends to infinity.)

So a wave packet undergoing wave capture in, for instance, a pure-strain horizontal deformation field, would have unbounded $|\mathbf{p}|$, suggesting arbitrarily large forces, far larger than those involved in generating the wave packet. The resolution of the paradox involves further remote-recoil effects and is most simply discussed using the concept of Kelvin impulse, following [3]. This too is discussed in more detail by Bühler in this Minisymposium, in terms of the implied "wave–vortex duality": a captured wave packet becomes a vortex dipole, and the wave–mean interaction problem becomes a nontrivial extension of the standard vortex-interaction problem. Full details are presented in ref. [11].

A point to emphasize, therefore, is that the effective forces related to the pseudomomentum **p** act only on the rotational part of the flow derived from a Helmholtz decomposition of the horizontal part of the velocity field. The pseudomomentum rule never has relevance to the irrotational part. This is most clearly seen from the relation between **p** and Kelvin's circulation theorem, adumbrated in Rayleigh's *Theory of Sound* and evident from the "generalized Lagrangian-mean" form of wave–mean theory via its exact definition of **p** [6]–[8]. In the case of large-scale atmosphere–ocean dynamics the effective forces associated with **p** are therefore related to the distribution of Rossby–Ertel potential vorticity [2]. In particular, it is is the apparent contribution of **p** to the circulation and potential vorticity that behaves in the simplest way during wave capture, resolving the apparently paradoxical behaviour associated with $|\mathbf{p}| \to \infty$ and bringing in the Kelvin impulse concept. Work toward turning this insight into a practical wave parametrization scheme is being undertaken.

References

[1] Bühler O. McIntyre, M.E.: Remote recoil: a new wave–mean interaction effect. *J. Fluid Mech.* **492**:207–230, 2003.

[2] McIntyre M.E.: On global-scale atmospheric circulations. *In:* Perspectives in Fluid Dynamics: A Collective Introduction to Current Research, ed. G.K. Batchelor, H.K. Moffatt, M.G. Worster. Cambridge, University Press: 557–624 (First paperback edition, with corrections), 2003.

[3] Bretherton F.P.: On the mean motion induced by internal gravity waves. *J. Fluid Mech.* **36**:785–803, 1969.

[4] McIntyre M.E.: On the "wave momentum" myth. *J. Fluid Mech.* **106**:331–347, 1981.

[5] McIntyre M.E.: On the role of wave propagation and wave breaking in atmosphere–ocean dynamics (Sectional Lecture). *In:* Theoretical and Applied Mechanics 1992, Proc. XVIII Int. Congr. Theor. Appl. Mech., Haifa, ed. S.R. Bodner, J. Singer, A. Solan, Z. Hashin. Elsevier, New York, 281–304, 1993.

[6] Andrews D.G., McIntyre M.E.: An exact theory of nonlinear waves on a Lagrangian-mean flow. *J. Fluid Mech.* **89**:609–646, 1978.

[7] Bühler O.: On the vorticity transport due to dissipating or breaking waves in shallow-water flow. *J. Fluid Mech.* **407**:235–263, 2000.

[8] Gjaja, I., Holm, D. D.: Self-consistent Hamiltonian dynamics of wave mean-flow interaction for a rotating stratified incompressible fluid. *Physica D* **98**:343–378, 1996.

[9] Bretherton F.P., Garrett C.J.R.: Wavetrains in inhomogeneous moving media. *Proc. Roy. Soc. Lond.* **A302**:529–554, 1968.

[10] Badulin, S. I., Shrira V. I.: On the irreversibility of internal-wave dynamics due to wave trapping by mean flow inhomogeneities. Part I: Local analysis. *J. Fluid Mech.* **251**:21–53, 1993.

[11] Bühler O. McIntyre, M.E.: Wave capture and wave–vortex duality. *J. Fluid Mech.*, submitted 2004.

XXI ICTAM, 15–21 August 2004, Warsaw, Poland

ANISOTROPIC LARGE-SCALE TURBULENCE ON GIANT PLANETS AND IN THE OCEAN

Boris Galperin*, Semion Sukoriansky**, Hideyuki Nakano+
*College of Marine Science, University of South Florida, St. Petersburg, FL 33701, USA
**Department of Mechanical Engineering, Ben-Gurion University of the Negev, Beer-Sheva 84105, Israel
+Oceanographic Research Department, Meteorological Research Institute, 1-1 Nagamine, Tsukuba, Ibaraki, 305-0052, Japan

Summary Barotropic two-dimensional turbulence with Rossby waves is distinguished by strong anisotropy and energetic zonal jets in alternating directions. Flows on the β-plane and in thin shells on the surface of a rotating sphere develop strongly anisotropic spectrum with steep, n^{-5}, slope for the zonal flows and Kolmogorov-Kraichnan, $n^{-5/3}$, slope for the residuals. The n^{-5} zonal spectrum was found on all four giant planets of our solar system, both with regard to its slope and the amplitude. This spectrum can be used to analyze some basic characteristics of large-scale circulations on giant planets and for interplanetary comparisons. Recently, it was found that the mid-depth ocean currents in the North Pacific ocean also develop a system of alternating zonal jets and build up the same n^{-5} and $n^{-5/3}$ zonal and residual spectral distributions. The main characteristic of the planetary and oceanic flows under consideration is the smallness of their Burger number, $Bu = (L_d/R)^2$, where L_d is the first baroclinic Rossby radius of deformation and R is the planetary radius. Exploring the planetary-ocean analogy, we conclude that the fine-scale oceanic zonal jets are driven by strongly nonlinear, anisotropic dynamics of quasi-2D turbulence with Rossby waves and argue that the latitudinal scaling of these jets is determined by the large-scale friction processes.

ANISOTROPIC TURBULENCE ON GIANT PLANETS

Our previous simulations of barotropic two-dimensional (2D) turbulence on β-plane [1] and on the surface of a rotating sphere [2] have indicated that such flows give rise to strongly anisotropic spectra. In spherical geometry, with R being the radius of the sphere, Ω being its angular velocity, and n and m being the total and the meridional wave numbers, respectively, the following zonal ($E_Z(n)$) and residual ($E_R(n)$ spectral distributions are established:

$$E_Z(n) = C_Z(\Omega/R)^2 n^{-5}, \quad m = 0, \ n/n_\beta < 1, \tag{1}$$

$$E_R(n) = C_K \epsilon^{2/3} n^{-5/3}, \quad \forall m \neq 0, \tag{2}$$

where $C_K \approx 6$ is the Kolmogorov-Kraichnan constant, $C_Z \simeq 0.5$, ϵ is the rate of the small-scale energy input, and $n_\beta = [(\Omega/R)^3/\epsilon]^{1/5}$ is the transitional wave number associated with the crossover between the spectra (1) and (2). The same spectral distributions were observed in steady-state simulations with a linear large-scale drag [3]. The latter paper also provides a detailed analysis of various interrelationships between the zonal and residual spectra.

The development of the flow regime with the spectra (1) and (2) is stipulated by fulfilling the requirement $n_{fr}/n_\beta \ll 1$, where n_{fr} is the wave number associated with the large-scale friction. This requirement is difficult to satisfy in the laboratory conditions and in the Earth atmosphere where friction with the underlying surface is high. However, the atmospheres of the giant planets may provide natural laboratories that can sustain such flows. Since the gas giants don't have solid boundaries, their friction and, therefore, n_{fr} are low. The requirement of the quasi-two-dimensionality is naturally fulfilled for the giant planets' atmospheres as the vertical thickness of the weather layers is much smaller than their horizontal extent. Another crucial requirement pertains to the value of the Burger number, $Bu = (L_d/R)^2$, where L_d is the first baroclinic Rossby deformation radius. It is well known that flows with $Bu \ll 1$ exhibit tendency to barotropization [4] and are, thus, likely to develop the spectral regime (1) and (2) if the criterion $n_{fr}/n_\beta \ll 1$ is also fulfilled. The existing data indicate that indeed, $Bu \ll 1$ for all four solar giant planets [5].

Using zonal velocity profiles obtained from the space stations Voyager 1 and 2 as well as from the Hubble Space Telescope, we have calculated the zonal spectra for all four solar giant planets in spherical representation; they are shown in Fig. 1. One can see a good agreement between the theoretical, Eq. (1), and observed zonal spectra for all four giant planets both with respect to the spectral slope and the amplitude (note that the data for Uranus is insufficient to establish the spectral slope but can be used to test the agreement in the amplitude).

One can observe that the slope -5 extends to some wave number which can be associated with n_{fr} and remains approximately level for $n < n_{fr}$. This zonal spectrum distribution allows one to analyze some large-scale characteristics of the atmospheric circulation on giant planets. By integrating Eq. (1) from 0 to ∞, obtain the total kinetic energy of the circulation,

$$E_{\rm tot} = (5C_Z/4)(\Omega/R)^2 n_{fr}^{-4}. \tag{3}$$

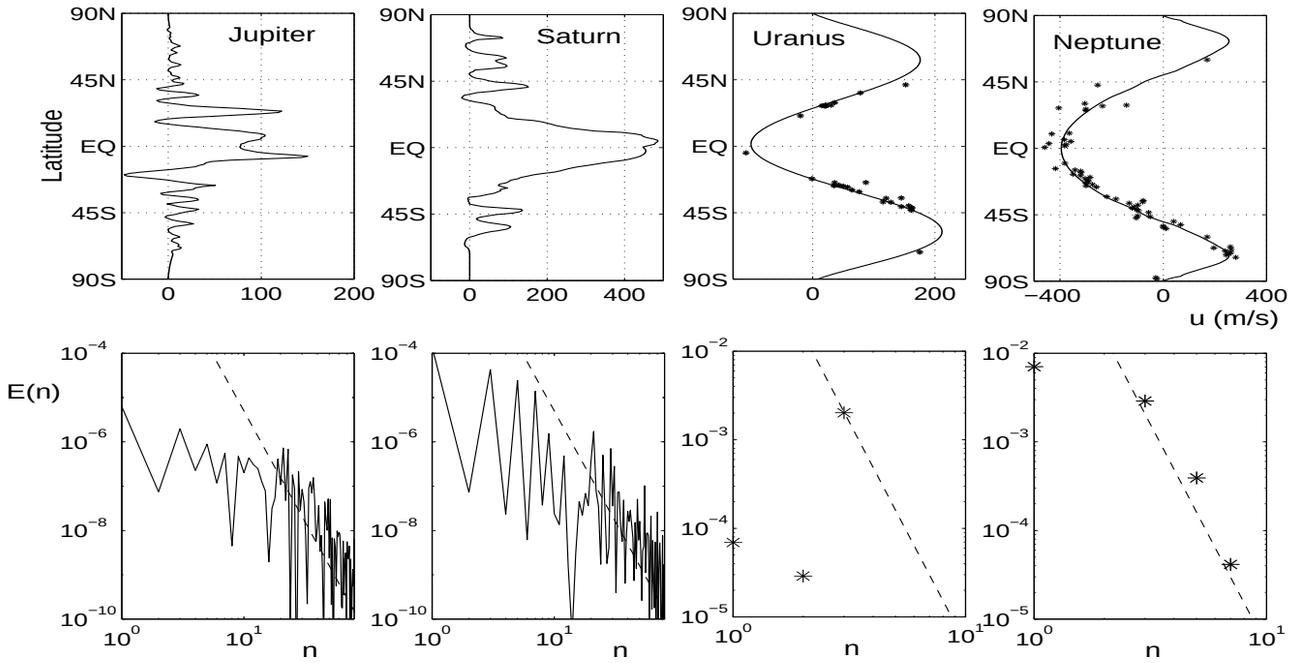


Figure 1. Top row: observed zonal profiles deduced from the motion of the cloud layers [6, 7, 8, 9]; bottom row: observed zonal spectra (solid lines and asterisks) and theoretical zonal spectra Eq. (1) (dashed lines) on the giant planets [all spectra are normalized with their respective values of $(\Omega/R)^2$].

Equation (3) indicates that $E_{\rm tot}$ depends on R, Ω and n_{fr} only and does not depend on the rate of the energy injection ϵ. Being the only flow-dependent parameter in (3), the frictional wave number n_{fr} plays a paramount role in the global energetics.

ANISOTROPIC TURBULENCE IN THE OCEAN

In recent simulations with high resolution, eddy-permitting ocean general circulation model it was found that the mid-depth ocean currents in the north Pacific ocean also develop a system of alternating zonal jets and obey the zonal and residual spectral distributions (1) and (2). Since the Burger number in the ocean is small, one can infer that the planetary and sub-surface terrestrial ocean jets are generated and maintained by the same mechanism pertaining to quasi-2D turbulence with anisotropic inverse energy cascade. The connection between the planetary and terrestrial circulations sheds some new light on the basic properties of stability and variability of the large-scale flows in both systems.

References

[1] Chekhlov A., Orszag, S.A., Sukoriansky, S., Galperin, B. and Staroselsky, I.: The effect of small-scale forcing on large-scale structures in two-dimensional flows. *Physica D* **98**: 321–334, 1996.

[2] Huang, H.-P., Galperin, B. and Sukoriansky, S.: Anisotropic spectra in two-dimensional turbulence on the surface of a rotating sphere. *Phys. Fluids* **13**: 225–240, 2001.

[3] Sukoriansky, S., Galperin, B. and Dikovskaya, N.: Universal spectrum of two-dimensional turbulence on a rotating sphere and some basic features of atmospheric circulation on giant planets. *Phys. Rev. Lett.* **89**: 124,501–4, 2002.

[4] Salmon, S.: Lectures on Geophysical Fluid Dynamics. Oxford University Press, NY Oxford 1998.

[5] Menou, K., Cho, J. Y-K., Seager, S. and Hansen, B.M.S.: "Weather" variability of close-in extrasolar giant planets. *Astrophys. J.* **587**: L113–L116, 2003.

[6] Garcýa-Melendo, E. and Sanchez-Lavega, A.: A study of the stability of Jovian zonal winds from HST images: 1995–2000. *Icarus* **152**: 316–330, 2001.

[7] Sanchez-Lavega, A., Rojas, J.F. and Sada, P.V.: Saturn's zonal winds at cloud level. *Icarus* **147**: 405–420, 2000.

[8] Hammel, H.B., Rages, K., Lockwood, G.W., Karkoschka, E. and de Pater, I.: New measurements of the winds of Uranus. *Icarus* **153**: 229–235, 2001.

[9] Sromovsky, L.A., Fry, P.M., Dowling, T.E., Baines, K.H. and Limaye, S.S.: Coordinated 1996 HST and IRTF imaging of Neptune and Triton III. Neptune's atmospheric circulation and cloud structure. *Icarus* **149**: 459-488, 2001.

STRONG VORTEX INTERACTIONS IN QUASI-GEOSTROPHIC FLOWS

Jean N. Reinaud, David G. Dritschel, Ross R. Bambrey

Mathematical Institute, University of St Andrews, St Andrews KY16 9 SS, UK.

Summary We examine the strong interaction two quasi-geostrophic vortices. The interaction depends on 6 parameters: the volume ratio, the potential vorticity ratio, the height-to-width aspect ratios, and the vertical and horizontal offsets. The parameter space is huge and highly efficient methods are needed to cope with the size of the problem. We primarily use a novel solution method, the Ellipsoidal Model (ELM), which models vortices as ellipsoids and filters higher-order deformations. It proves to be highly accurate and allows us to determine steadily rotating equilibria for both like-signed and opposite-signed vortices. We next determine the margin of linear stability of these states which we associate with the critical distance for strong vortex interactions. We complete the description of the interactions by illustrating the nonlinear evolution of delected unstable interactions here using the full dynamical equations (including non-ellipsoidal deformations).

INTRODUCTION

Vortical structures are frequently observed in the Earth's atmosphere and oceans. Vortices or coherent volumes of anomalous potential vorticity (hereinafter referred to as PV) play an important dynamical role in these environments since the dominant 'balanced' flow can be recovered from the knowledge of the PV distribution alone, cf Hoskins, McIntyre & Robertson (1985). In the adiabatic and inviscid fluid studied here, the PV is materially conserved and gives rise to a layerwise two-dimensional motion (there is negligible vertical advection due to the stable density stratification and the background rotation of the Earth). Coherent regions of PV are naturally associated with vortices. It is important to determine how nonlinear these structures interact since they are a key feature of atmospheric and oceanic dynamics. *Two-dimensional* vortex interactions have been extensively studied in the literature both for co-rotating and counter-rotating vortices, see Dritschel (1995) and references therein. However, in the context of *three-dimensional* quasi-geostrophic flows, which are more relevant to the atmosphere and oceans, little is known about strong vortex interactions despite previous research. The main reason for this lack of knowledge is arguably the size of the parameter space of the problem. Previous studies had to restrict attention to small parts of the full parameter space, normally considering situations in which numerous symmetries were imposed in the initial conditions, see *e.g.* von Hardenberg *et al.* (2000), Dritschel (2002) and Reinaud & Dritschel (2002). *We still do not know how vortices interact in general.*
To tackle this formidable problem, we first introduce a novel solution method: The Ellipsoidal Model (ELM) described in Dritschel, Reinaud & McKiver (2003) which gives the equations for the evolution of interacting uniform PV ellipsoids. The ELM is a finite Hamiltonian system given by

$$\frac{\mathrm{d}\boldsymbol{X}_i}{\mathrm{d}t} = -\frac{1}{\kappa_i}\mathcal{L}\frac{\partial H}{\partial \boldsymbol{X}_i}, \tag{1}$$

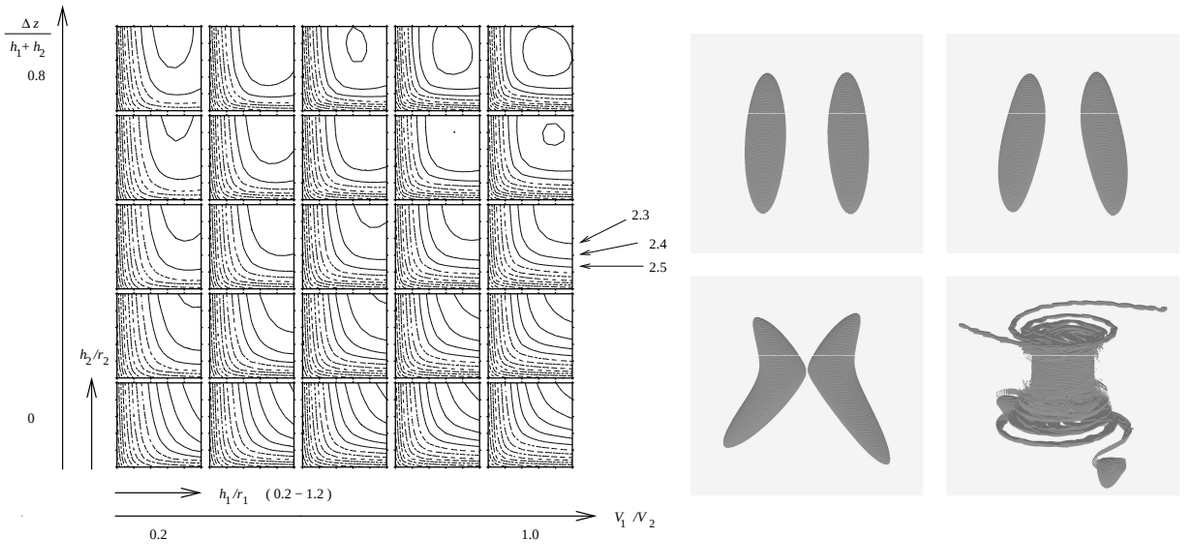
$$\frac{\mathrm{d}\mathcal{B}_i}{\mathrm{d}t} = \mathcal{S}_i\mathcal{B}_i + \mathcal{B}_i\mathcal{S}_i^T, \quad \text{and} \quad \mathcal{S}_i = -\frac{10}{\kappa_i}\mathcal{L}\frac{\partial H}{\partial \mathcal{B}_i}, \tag{2}$$

where $\boldsymbol{X}_i = (X_i, Y_i, Z_i)$ is the centroid of the i^{th} ellipsoid, and $\mathcal{B}_i$ denotes the 3×3 symmetric matrix in terms of which the boundary of the ellipsoid is expressed by $(\boldsymbol{x} - \boldsymbol{X}_i)^T\mathcal{B}_i^{-1}(\boldsymbol{x} - \boldsymbol{X}_i) = 1$. Also, κ_i is the 'strength', i.e. the volume integral of PV divided by 4π, and H is the Hamiltonian of the system, namely the total energy of the system divided by 4π. Finally, $\mathcal{S}_i$ is the 'flow matrix' depending on all ellipsoids. From these equations, we have derived a linearized system to compute equilibrium states by an iterative method. The states are then subjected to a linear stability analysis derived from the ELM equations. The low computational load required by the ELM enables us to study vortex interactions over wide ranges of the 6 parameters. Here, we primarily focus on like-signed (*equal-PV*) and opposite-signed (*opposite-PV*) interactions. We determine the margin of stability for vortices having aspect ratios consistent with what is actually observed in turbulence, namely $0.2 < h/r < 1.6$, see Reinaud, Dritschel & Koudella (2003). We perform the study considering 5 different values for both the vertical offset and the volume ratio.

Moreover we investigate the temporal evolution, *solving the full equations*, of characteristic interactions. We wish to determine the outcome of such vortex interactions and to study the way that both the energy and the enstrophy cascade during interactions and how this relates to what is observed in quasi-geostrophic turbulence.

RESULTS

We present here a sample of the results which have been obtained. The total volume of PV is set to $4\pi/3$. Contour plots of the critical distance between the vortex centroids are given in figure (1a) in a large parameter space. Results indicate for example that vortices moderately offset in the vertical (by about 1 mean radius) are likely to strongly interact for larger separation distances. Another important discovery is that prolate vortices are affected by a newly discovered instability: the *tilt* instability which has been overlooked by previous studies.



This instability appears first at distances for which vortices were thought to be stable in previous studies. It consists of the collapse of the vortices toward one another. Such an instability is illustrated in figure (1b) by a Contour Dynamics simulation of two vertically aligned vortices with $h/r = 4$.

As for the opposite-signed vortex interactions, a rather surprising result has been found. Only a few interactions are unstable according to the ELM. I.e., most of the cases investigated over a large parameter space are stable. For example, oblate vortices of equal volume and aligned in the vertical are stable even when they are touching. It is however not clear at the moment if such situations are genuinely stable or only stable to ellipsoidal perturbations. The equilibria might still be unstable to non-ellipsoidal perturbations – modes disregarded by the ELM. On the other hand, weak ellipsoidal instabilities may be observed for prolate vortices. Considering different examples of opposite-signed interactions none of them have been found to be particularly destructive. After a small amount of debris is cast off, the vortices return to a near equilibrium. An interesting result is found for vortices which are offset in the vertical by more than about $\frac{1}{2}(h_1+h_2)$. For these interactions, oblate vortices are likely to be unstable to ellipsoidal modes whereas prolate vortices are seen to be stable – the opposite situation to the one obtained for vortices aligned in the vertical or only slightly offset.

CONCLUSION

A combination of accurate and efficient numerical methods enable us to provide the first comprehensive study of vortex interactions in quasi-geostrophic flows. We use a promising new numerical model developed in Dritschel *et al.* (2003) that models vortices by ellipsoids of uniform potential vorticity. This model allows us to determine the margin of stability for equilibrium states that coincides with the critical distance for strong interactions. More than this, using the well-established CASL algorithm, we can study the outcome of these interactions and study how energy and enstrophy are redistributed spectrally as a result of the interactions.

References

[1] Hoskins, B. J., McIntyre, M. E. & Robertson, A. W. 1985 On the use and significance of isentropic potential-vorticity maps. *Q. J. Roy. Meteorol. Soc.* **111**, 877–946.

[2] Dritschel, D. G. 1995 A general theory for two-dimensional vortex interactions. *J. Fluid Mech.* **293**, 269–303.

[3] von Hardenberg, J., McWilliams, J. C., Provenzale, A., Shchpetkin, A. & Weiss, J. B. 2000 Vortex merging in quasi-geostrophic flows. *J. Fluid Mech.* **412**, 331–353.

[4] Dritschel, D. G. 2002 Vortex merger in rotating stratified flows. *J. Fluid Mech.* **455**, 83–101.

[5] Reinaud, J. N. & Dritschel, D. G. 2002 The merger of vertically offset quasi-geostrophic vortices. *J. Fluid Mech.* **469**, 287–315.

[6] Dritschel, D. G., Reinaud, J. N. & McKiver, W. J. 2003 The quasi-geostrophic ellipsoidal model. *J. Fluid Mech.* **in press**.

[7] Reinaud, J. N., Dritschel, D. G. & Koudella, C. R. 2003 The shape of the vortices in quasi-geostrophic turbulence. *J. Fluid Mech.* **474**, 175–192.

Turbulent Horizontal Convection and the Global Thermohaline Circulation of the Oceans

R. W. Griffiths, G. O. Hughes and J. C. Mullarney

Research School of Earth Sciences, The Australian National University,
Canberra, ACT 0200, Australia

A very simple conceptual model for the meridional overturning component of the ocean circulation is the convective flow driven by a horizontal surface temperature gradient. The meridional overturning circulation (also referred to as the global thermohaline circulation) carries warm subtropical surface waters to high latitudes, where it cools and sinks. In the present pattern of circulation the dense cold (and sufficiently saline) water sinks in confined regions at high latitudes to form `Deep' and `Bottom' waters. There must be a slow, possibly basin-wide, upwelling to the surface to match the poleward mass flux, with the loop closed by an inferred zonal average return flow toward the equator at depths below the thermocline. The density structure and heat transport must depend on the rate of vertical diffusion of heat. In the oceans the diffusion is attributed internal, turbulent mixing processes, which act to increase the potential energy of the water column. The resulting heat flux carried by the overturning circulation has a significant role in the climate system, and changes in this circulation have been implicated as a cause of climate variability on decadal to millennial timescales. However, there is uncertainty in the source of the energy for internal mixing, and a discrepancy between predicted and measured rates of mixing. There is also controversy as to whether the meridional heat flux (*i.e.* buoyancy) is a significant forcing for the oceans. Some have concluded that the heat flux is simply incidental to a flow forced by surface wind stress and in which the density structure is maintained by mixing energised by winds and tides. We address these issues by examining circulation forced purely by thermal buoyancy.

Our laboratory and numerical experiments show that convective circulation driven by differential heating at a horizontal boundary can be vigorous and turbulent. The circulation in a long box forced at the base (by heating one half and cooling the other half, with all other boundaries insulated) includes a stable boundary layer against the forcing boundary. Water in this layer (the thermocline) flows from the region of stabilising buoyancy flux towards the region of destabilising flux, and feeds into a vertical plume at the end of the box. The plume `sinks' to the opposite boundary. We have achieved large Rayleigh numbers with a small basin aspect ratio, such that the plume and its outflow are turbulent. The destabilising boundary flux also produces small-scale three-dimensional convection in a mixed layer within the stably stratified thermocline, and this mixed layer deepens toward the end of the box. The mixing penetrates through the depth of the thermocline only at the end of the box. Hence the deepest mixing and the bulk `sinking' are coincident.

In the non-rotating case, the mean flow in the plume supplies a turbulent return flow that fills 1/3 of the depth of the box. Thus we conclude that a temperature difference imposed along a horizontal surface (such as the ocean surface) can drive a vigorous and turbulent flow throughout the basin. In the rotating case, the small-scale convection in the turbulent mixed layer is unaffected by rotation, but the `sinking' occurs in localized, unsteady chimney structures. The geostrophic return flow is approximately independent of depth above the thermocline and tends to take the form of eddies that carry water, heat and tracer across high-gradient frontal zones between large gyres that fill the width of the basin.

We correctly predict the measured mass transport and density structure in the experiments from a simple model in which vertical advection and diffusion of density in the interior are balanced to give a steady state. In this model we impose a zero net buoyancy flux at the forcing boundary and allow for a depth-dependence of the interior vertical velocity (owing to entrainment of water into the `sinking' region). The vertical velocity is therefore larger further from the forcing boundary. For simplicity, and in line with previous ocean models, we also assume a uniform vertical diffusion coefficient. The model is related to the "filling-box" model for a container that is filled with density stratification by a turbulent plume. Applying the same model to the meridional overturning circulation of the global ocean, we find that the volume flux of Antarctic Bottom Water and the measured globally-averaged density profile through the ocean depth can both be maintained by the estimated surface heat fluxes, if we assume the vertical diffusivity equal to that measured in the open oceans (order 10^{-5} m^2/s). We conclude that the much larger diffusivity inferred by Munk (1966) and the larger external energy input to interior mixing predicted by Munk & Wunsch (1998) are not required if downwelling regions and sloping bottom currents entrain surrounding waters. The overturning circulation can, in principle, be driven by the surface heat fluxes alone, and we suggest that energy arguments purporting to imply that the heat flux is passive and coincidental are may not be correct. However, additional energy inputs to internal mixing from tides and winds will enhance the uptake of buoyancy at the surface and may increase the overturning mass flux.

INSTABILITY OF GRAVITY DRIVEN COASTAL CURRENT IN A TURNTABLE EXPERIMENT

Thivolle-Cazat E. and Sommeria J.*,
*LEGI-CORIOLIS (CNRS), 21 Rue des Martyrs 38000 Grenoble, France

Summary The instability of a current driven by gravity and maintained along a vertical lateral wall by the Coriolis force is investigated in laboratory experiments, performed in the large Coriolis turntable (Grenoble). The current floats over a homogeneous denser layer. It represents for instance the Algerian current, made of the light Atlantic water entering the Mediterranean Sea. This current is unstable, generating meanders and vortices. This is classically attributed to baroclinic instability, but in our case this is forbidden by the absence of potential vorticity gradient in the lower layer. However we find that the instability of the viscous boundary layer initiates the process: the wall vorticity rolls up into vortices, which then interact with the main current potential vorticity as propagating dipoles, mimicking the usual process of baroclinic instability.

INTRODUCTION

Coastal currents are commonly produced by gravity, and maintained along the coast by the Coriolis force. For instance the Atlantic water entering the Mediterranean Sea forms the Algerian current, remaining at the surface by its low density (salinity). Such boundary currents generally become unstable, producing meanders and detachment of vortices away from the coast (see figure 1). Eventually, these instabilities control the horizontal mixing of the current. They play therefore a major role in the distribution of the biogeochemical components and their transfer between different basins.

Boundary currents have been reproduced in various laboratory experiments. They can be obtained by the geostrophic adjustment of a constant volume of light fluid floating on a heavier homogeneous layer. Griffith and Linden ([1]) initially contained a light water ring between two concentric cylinders. The current was rotating around the inner cylinder after the outer cylinder was lifted. In other experiments, the flow is produced by a constant flux of light fluid from a confined source near the free surface. The heavier homogeneous layer is initially at rest in the rotating frame of reference. Obaton et al. ([2]) have studied similar process at higher Reynolds numbers, using the large “Coriolis” rotating platform in Grenoble.

We here reproduce some of these experiments, providing a detailed measurement of velocity fields by Particle Imaging Velocimetry (PIV) at different vertical levels. The potential vorticity profiles can be derived from these measurements, leading to a better analysis of the instability process.

The simpliest theoretical interpretation of boundary current instability is provided by the classical quasi-geostrophic model of Phillips (1954), considering two layers with uniform velocity. In this model of baroclinic instability, the potential vorticity has a uniform transverse gradient, with opposite sign in each layer. More generally, a necessary condition for instability in quasi-geostrophic models is that the transverse gradient of potential vorticity changes sign somewhere in the flow (Charney & Stern, 1962). This is appropriate for the constant volume case, as potential vorticity anomalies of opposite sign is set in each layer by the initial interface displacement.

However in the constant flux experiments, the lower layer is initially at rest with undisturbed interface, so its potential vorticity is uniform, at least in an initial stage, before the influence of viscous effects. Therefore the usual baroclinic instability is forbidden. This is confirmed by two-layer models beyond the quasi-geostrophic approximation [3] Indeed Obaton et al. ([2]) noticed that the instability first appears in the thin shear layer along the wall, and the baroclinic instability only develop at a later stage, which can be much delayed in time. Our velocity measurements in both layers confirm and clarify such a two-stage process.

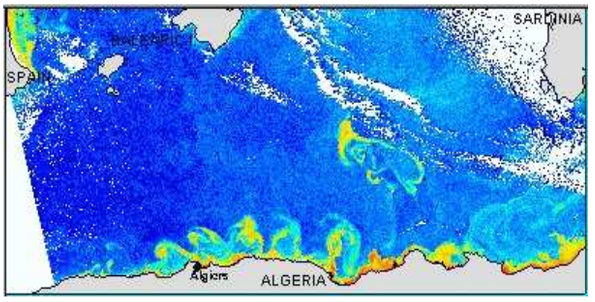


Figure 1. The Algerian current visualized by sea surface temperature: the formation of meanders and vortices is clearly seen along the algerian coast

EXPERIMENTAL SYSTEM

The experiments have been performed in the“Coriolis” rotating tank (LEGI, France), 13 m in diameter. The boundary current is produced along a straight wall on a diameter of the tank.

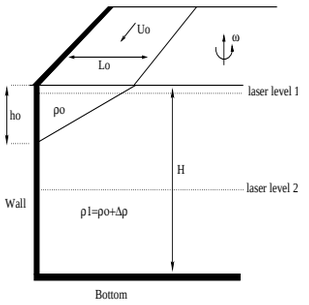


Figure 2. Sketch of the boundary current in the experiments

Initially, an homogeneous water layer, with thickness H=60 cm is at rest in the tank. The rotation period is set to T=50s. A steady flow rate Q_0 is imposed, starting at an initial time t=0. The density ρ_1 and ρ_0, respectively in the lower and upper layers, are controlled by salinity. We define $g' = g\frac{\rho_1-\rho_0}{\rho_1}$ the reduced gravity. The flow is introduced by an injector with a triangular cross section. The height and width of this triangle are adjusted to initiate a geostrophically balanced current. Measurements of horizontal velocity fields have been realized by PIV (Particle Imaging Velocimetry), using a laser sheet illumination at two different levels (1cm and 21 cm from the surface) in a 2.5m x 2.5m domain. The first level provides the velocity field in the upper layer, while the second one remains always inside the lower layer. Density profiles are obtained using translating conductivity probes.

RESULTS

In a first stage, a quasi-parallel boundary current is produced, behind a current head with sharp interface. A weak counter-current is also produced in the lower layer, due to the compression of the material lines, vertically displaced under the upper current. We have checked that this counter-current has a uniform potential vorticity, except in a viscous boundary layer near the vertical wall, 1 cm thick.

As the first stage of the instability process, this thin vorticity layer rolls up forming a chain of small vortices near the wall in the lower layer. In a second stage, these vortices induce transverse displacements in the main current, resulting in vorticity anomalies. Thus vortex pairs are formed, coupling a cyclonic vortex in the lower layer with an anticyclonic vortex with components in both layers. Such vortex pairs (heton) tend to propagate outward, resulting in the development of a jet meander. Experimental vorticity fields showing this process are shown in figure 3.

CONCLUSIONS

In conclusion the jet instability is initiated in the viscous boundary layer: the wall vorticity concentrates into vortices, which then interact with the main current potential vorticity as propagating dipoles. This nonlinear stage mimicks the usual process of baroclinic instability, forbidden here by the uniform potential vorticity in the lower layer. For oceanic modelling, a proper representation of this meander initiation therefore requires a good resolution of the viscous boundary layer. Further studies should analyse the complex meandering jet developing after the initial instability.

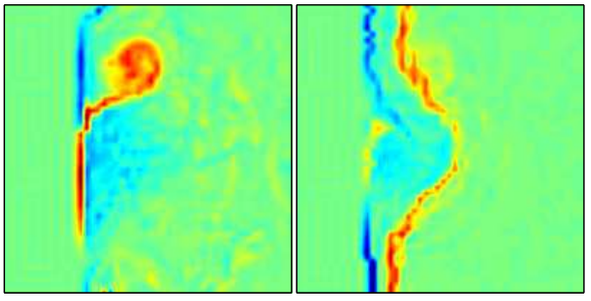


Figure 3. vorticity field at t=27 tank periods;(a)in the lower layer (b) in the upper layer (cyclonic vorticity is in red, anticyclonic in blue)

References

[1] Griffi th R.W., Linden : *Dyn. Atmos. Ocean* **5**:281-306, 1981.
[2] Obaton D., Millot C., Chabert d'Hières G., Taupier-Letage, I.: *Deep Sea Res.* **I 47**:2159-2190.
[3] Killworth P.D., Paldor N., Stern M.E.: *J. Marine Res.* **42**:761-785.

INTRUSIVE GRAVITY CURRENTS IN A STRATIFIED AMBIENT - NOVEL THEORETICAL RESULTS AND INSIGHTS

Marius Ungarish
Department of Computer Science, Technion, Haifa 32000, Israel

Summary The intrusion of a fixed volume of "mixed" fluid which is released from a lock (of rectangular or cylindrical shape) and then propagates horizontally at the neutral buoyancy level in a stratified ambient fluid is considered. The investigation, based on a closed one-layer shallow-water model supported by comparisons with experiments and Navier-Stokes numerical results, provides new and accurate insights for the initial motion.

We consider the mainly horizontal motion which develops when a fixed volume of fluid of constant density, ρ_c, is released from a lock of length x_0 and height h_0 into a vertically stratified ambient at the level of neutral buoyancy, see Fig. 1. We assume that the density of the ambient fluid, $\rho_a(z)$, varies linearly over a layer of finite thickness, l, or over the full depth of the container, H, and that the Reynolds number is large. The problem is relevant to natural "mixed region collapse" in oceans and atmosphere, hydraulic reservoirs management, spread of pollutants and sewage, etc. The previous investigations were concerned with both experimental observation (mainly with salt-water systems) and theoretical interpretations ([1]-[8], [10]). However, important gaps remained open in the theoretical understanding and formulation, including some confusion about the scaling of the variables and the effect of the shape of the lock. Wu [10] suggested a curve-fit description for the position of the nose x_N as a function of time t, based on a very restricted set of data acquired in a configuration with a cylindrical lock. Kao [3] and Manins [4] developed box-model approximations for $x_N(t)$ under the assumption that intruding fluid has a fixed shape (an ellipse or a rectangle); both models used adjustable parameters based on some ad-hoc matchings. Actually, no predictive model based on governing balance equations for the initial stages of the lock-release and related problems has been presented, and the "state-of-the-art" was accurately summarized by Faust and Plate [2]: "intrusions into a linearly stratified environment behave very differently from theoretical calculations". The need to close this gap provided the motivation of the work reported here.

The present work introduces a new analysis, based on the inviscid Boussinesq-fluid shallow-water (SW) equations of motion and backed by numerical solutions of the Navier-Stokes (NS) problem. This SW formulation provides a hyperbolic system for the (z-averaged) velocity u and (half-) thickness h of the intruding fluid as functions of t and x, subject to realistic initial and boundary conditions, and uses no adjustable constants. From this model many essential features of the motion are derived: the constant velocity in the initial slumping stage (for rectangular lock configuration), the propagation with $t^{1/2}$ at large times, the dependency of the velocity on the thickness of the density transition layer l, the differences between the flows generated by rectangular and cylindrical locks, the "sub-critical" property of the velocity of propagation (as compared with the mode 2 linear waves). The analytical results were corroborated by comparisons with experiments and finite-difference simulations based on the NS equations.

The analytical model is an extension of the one-layer shallow-water formulation developed by Ungarish and Huppert [9] for the investigation of gravity currents which propagate at the bottom of a linearly-stratified ambient. A major simplification is the assumption that the ambient can be considered quiescent for some significant initial period of time. We show that the neglect of the internal gravity waves in the SW formulation is justified for some initial period of propagation, and we estimate the position where the nose-waves interaction becomes important. We show that for a deep-ambient configuration the SW formulation admits a similarity solution with $x_N(t) = Kt^{1/2}$, where K is a constant that reflects the volume of the mixed fluid (note the difference from the $t^{2/3}$ propagation of the classical gravity current in a homogeneous ambient). We also show that the previous analytical models of Kao and Manins are sub-sets of the present formulation.

The theory predicts that an intrusion released from a rectangular lock will propagate during the initial slumping stage with constant velocity, u_N, like a classical gravity current. In contrast, the propagation after release from a cylindrical lock displays a clear acceleration-deceleration pattern; the maximum velocity is, remarkably, equal to the slumping u_N of a counterpart rectangular lock configuration.

Comparisons with experimental data ([1], [2], [7], [10]) were performed, and consistency with theory was obtained. The discrepancy between the experimental and analytical velocities of propagation is typically about $2-10\%$. The differences are not systematic and can be attributed to experimental errors and deviations from the idealizations of the models. Overall, we think that the agreement is very good, actually as good as can be expected from the SW theory (in the classical homogeneous circumstances similar errors were obtained).

Typical results of propagation, x_N as a function of t, are shown in Fig. 2. Again, agreement between the SW solution and the experiment is very good (the discrepancies can be attributed to viscous and mixing effects). We emphasize that the theory has been developed from first principles without the use of any adjustable parameters or other information taken from the experiment. For the rectangular lock configuration in Fig. 2 at $t \approx 6$ a strong deceleration of the intrusion is indicated by both experiment and NS simulation. This is attributed to the interaction between the nose and the internal gravity waves, an effect not resolved by the SW formulation. An estimate for the position where this interaction occurs has been derived, in good agreement with observations; afterwards, the SW formulation needs modifications. Directions of further research will be discussed.

References

[1] R. Amen and T. Maxworthy. The gravitational collapse of a mixed region into a linearly stratified fluid. *J. Fluid Mech.*, 96:65–80, 1984.

[2] K. M. Faust and E. J. Plate. Experimental investigation of intrusive gravity currents entering stably stratified fluids. *J. Hydraulic Res.*, 22:315–325, 1984.

[3] T. W. Kao. Principal stage of wake collapse in a stratified fluid: Two-dimensional theory. *Phys. Fluids*, 19:1071–1074, 1976.

[4] P. C. Manins. Mixed region collapse in a stratified fluid. *J. Fluid Mech.*, 77:177–183, 1976.

[5] T. Maxworthy. On the formation of nonlinear internal waves from the gravitational collapse of mixed regions in two and three dmensions. *J. Fluid Mech.*, 96:47–64, 1980.

[6] T. Maxworthy. Experiments on solitary internal Kelvin waves. *J. Fluid Mech.*, 128:365–383, 1983.

[7] F. de Rooij. *Sedimenting particle-laden flows in confined geometries.* PhD thesis, DAMTP, University of Cambridge, 1999.

[8] A. H. Schooley and B. A. Hughes. An experimental and theoretical study of internal waves generated by the collapse of a two-dimensional mixed region in a density gradient. *J. Fluid Mech.*, 51:159–175, 1972.

[9] M. Ungarish and H. E. Huppert. On gravity currents propagating at the base of a stratified ambient. *J. Fluid Mech.*, 458:283–307, 2002.

[10] J. Wu. Mixed region collapse with internal wave generation in a density-stratified medium. *J. Fluid Mech.*, 35:531–544, 1969.

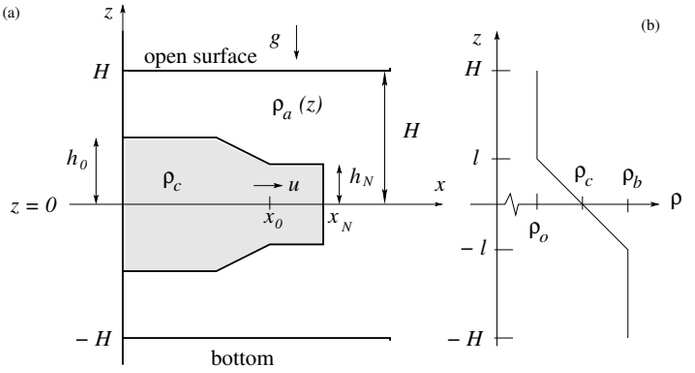


Figure 1: Schematic description of the system: (a) geometry after release from a rectangular lock; (b) density profile in the ambient (note $\rho_c = 0.5(\rho_b + \rho_o)$). In dimensionless form, vertical and horizontal lengths are scaled with x_0 and h_0, respectively. Velocity and time are scaled with $U = (g' h_0)^{1/2}$ and x_0/U, where $g' = (\rho_c/\rho_o - 1)g$. The subscripts denote: N - nose (or front); a - ambient; b - bottom; c - current (intrusion); o - open surface.

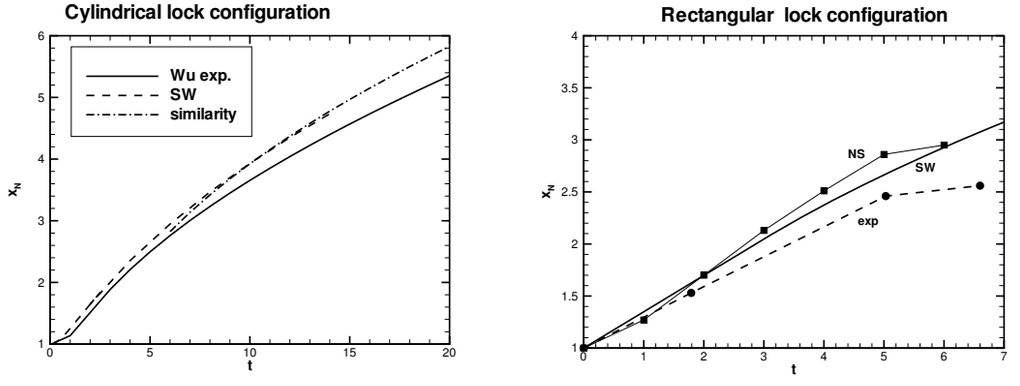


Figure 2: Propagation results x_N as a function of time, in full-depth linearly stratified ambient ($l = H$), dimensionless. The cylindrical lock configuration corresponds to the experiments of Wu [10], and comparison is with the present SW results and similarity solution. The rectangular lock configuration is for experiment run 117 of Amen and Maxworthy [1], and comparison is with the present SW and Navier-Stokes results.

Irreversible transition to a state with higher entropy production in oceanic general circulation

Shinya Shimokawa * and Hisashi Ozawa **
* National Research Institute for Earth Science and Disaster Prevention, Tsukuba 305-0006, Japan
** Frontier Research System for Global Change, Yokohama 236-0001, Japan

Summary The mechanism of transitions among multiple steady states of thermohaline circulation is investigated from a thermodynamic viewpoint by using an oceanic general circulation model. All the results of the simulations tend to support the hypothesis that a nonlinear system, when perturbed, is likely to move to a state with maximum entropy production.

1. Introduction

It is well known that thermohaline circulation has multiple steady states under the same set of boundary conditions (Stommel, 1961). However, the mechanism which regulates the selection of a realistic solution from multiple steady states and the transitions among them is not yet fully understood. It has been suggested that the rate of entropy production associated with an open dissipative system is related to the stability of the system. Sawada (1981) stated that the entropy of thermal reservoirs connected via a nonlinear system will increase along an evolutionary path, favoring the maximum entropy production among manifold possible paths (the principle of maximum entropy production). However, there is no study that tests the principle of maximum entropy production for the ocean system. The objective of this study is to examine the principle for the transitions among the multiple steady states of thermohaline circulation by using an oceanic general circulation model.

2. Model description and Experimental method

The numerical model used in this study is the Geophysical Fluid Dynamics Modular Ocean Model (GFDL MOM) version 2. The model domain is a rectangular basin with a cyclic path, representing an idealized Atlantic Ocean. The horizontal grid spacing is 4 degrees. The depth of the ocean is 4500 m with twelve vertical levels. Our experiments (Shimokawa and Ozawa, 2002) consist of three phases: (1) spin-up under restoring boundary conditions for 5000 years, (2) integration under mixed boundary conditions with a high-latitude salinity perturbation for 500 years, and (3) integration under mixed boundary conditions without perturbation for 1000 years. As a result of phase (1), the system reaches a statistically steady state with northern sinking circulation (N_{RBC}, Fig. 1a). In phase (2), the system moves to a state which is determined by the perturbation applied. In phase (3), the system is adjusted satisfactorily to the boundary condition without perturbation. Then, in some cases, the system returns to the initial state, while in other cases, it does not, instead remaining in the state of being determined by the perturbation or moving to a different steady state which is independent of the perturbation. If a new steady state is obtained, procedures (2) and (3) are repeated using the new steady state as the initial state. If a new steady state is not obtained, these procedures are repeated using a different salinity perturbation. As a result, a series of multiple steady states of thermohaline circulation under the same set of wind forcing and mixed boundary conditions are obtained (Fig. 1). The standard salinity perturbation used in this study (Δ in Fig. 2) is 2×10^{-7} kg m^{-2} s^{-1} (= -0.1 m year^{-1} fresh water flux), which is usually applied to the north of 46N and occasionally to the south of 46S.

3. Calculation method of entropy production

The rate of entropy production is calculated during the time integration for all experiments such as

$$dS/dt = \int \rho c/T\, \partial T/\partial t\, dV + \int F_h/T\, dA - \alpha k \int \partial C/\partial t\, \ln C\, dV - \alpha k \int F_s \ln C\, dA \qquad (1)$$

where ρ is the density, c is the specific heat at constant volume, T is the temperature, α=2 is van't Hoff's factor representing the dissociation effect of salt into separate ions (Na^+ and Cl^-), k is the Boltzmann constant, C is the number concentration of salt per unit volume of sea water, F_h and F_s are the heat and salt fluxes per unit surface area, defined as positive outward, respectively; dV is the small volume element, the volume integration is taken over the whole ocean volume, dA is the small surface element, and the surface integrations are taken over the whole ocean surface. The first term on the right hand side represents the rate of entropy increase in the ocean system due to heat transport, and the second term represents that in the surrounding system. The third term represents the rate of entropy increase in the ocean system due to salt transport, and the fourth term represents that in the surrounding system. Overall, Equation (1) represents the rate of entropy increase of the whole system. This equation is applicable to a large-scale model whose scale of resolution is coarser than the dissipation scale because it

dose not include a microscopic representation of the dissipation process (Shimokawa and Ozawa, 2001).

4. Results

The results of our experiments are summarized in Fig. 2. Starting from S1 (Fig. 1e), the system moves to S2 (Fig. 1f) regardless of the sign of the perturbation (r04 and r05); whereas starting from S2, the system does not return to S1, but remains in the initial state (S2) regardless of the sign of the perturbation (r08 and r09). In addition, starting from S3 (Fig. 1g), the system moves to S4 (Fig. 1h) regardless of the sign of the perturbation (r14 and r15); whereas starting from S4, the system does not return to S3, but remains in the initial state (S4) regardless of the sign of the perturbation (r18 and r19). When these transitions occur (r04, r05, r14 and r15), the rates of entropy production in the final states are always higher than those in the initial states (see Fig. 2). These results show that the transition from a state with lower entropy production to a state with higher entropy production tends to occur, but the transition in the inverse direction does not occur, i.e. the transition is *irreversible* or *directional* in the direction of the increase of the rate of entropy production. On the other hand, starting from N1 (Fig. 1b) with negative perturbation (r12), the system moves to S1. Starting from S1 with double positive perturbation (r06), the system moves to N1. Starting from N2 (Fig. 1c) with the negative perturbation (r13), the system moves to S3. Starting from S3 with double positive perturbation (r16), the system moves to N3 (Fig. 1d). These results show that the transitions in mutual directions between southern sinking and northern sinking are possible depending on the direction of the perturbation. In these cases, the rates of entropy production for the northern sinkings are higher than those for the southern sinkings. These results may appear to contradict the principle of maximum entropy production. However, we can show that the decrease is only caused by the negative perturbation applied to the sinking region which destroys the initial circulation altogether (Shimokawa and Ozawa, 2002). After this destruction, the entropy production is found to increase as a new circulation develops. All these results tend to support the hypothesis that a nonlinear system, when perturbed, is likely to move to a state with maximum entropy production.

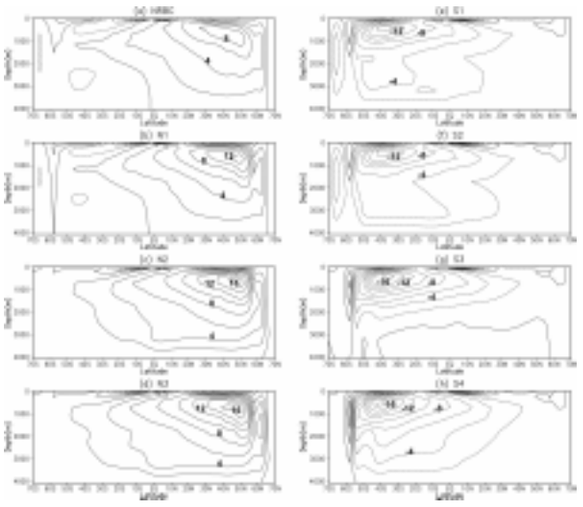


Fig. 1 All steady states obtained from this study. (a) N_{RBC}, (b) N1, (c) N2, (d) N3 (e) S1, (f) S2, (g) S3, (h) S4. Fields shown are zonally integrated meridional stream function at year 5000 for (a) spin-up and at year 1500 for (b) r06, (c) r02, (d) r16, (e) r01, (f) r04, (g) r13 and (h) r14. The contour line interval is 2 SV (10^6 m^3 s^{-1}). The capital letters "N" and "S" refer to northern sinking and southern sinking, respectively. N_{RBC} is a unique solution under restoring boundary conditions.

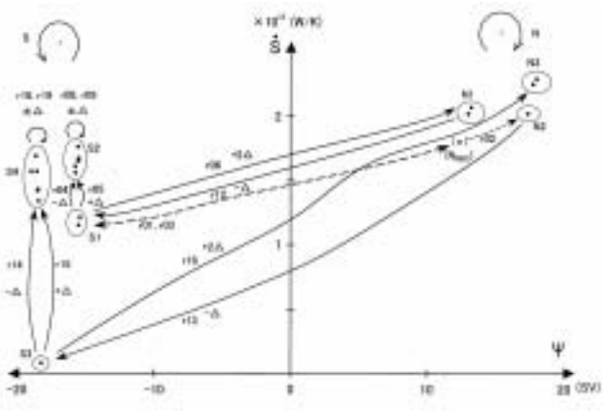


Fig. 2 The relationship between transitions among multiple steady states and rates of entropy production. The vertical axis ($\dot{S}$) indicates the rate of entropy production, and the horizontal axis (Ψ) shows the maximum value of the zonally integrated meridional stream function for the main circulation. The dots are corresponding to the steady states (initial and final states) of each experiment. The circles surrounding the dots show the circulation pattern (e.g. N1). The arrows show the direction of the transitions. The symbols besides the arrows show the experiment number and the perturbation used in the experiment (e.g. r04 and -Δ).

REFFERENCES: Sawada, Y. (1981) Prog. Theor. Phys., **66**, 68-76., Stommel, H. (1961) Tellus, **13**, 224-230., Shimokawa, S. and H. Ozawa (2001) Tellus, **A53**, 266-277., Shimokawa, S. and H. Ozawa (2002) Q. J. Roy. Meteorol. Soc., **128**, 2115-2128.

INTERACTIONS OF PLANAR WAVES WITH A BAROCLINIC VORTEX IN A ROTATING STRATIFIED FLUID

Frédéric Moulin, Jan-Bert Flór
LEGI, INPG-CNRS-UJF BP 53, 38041 Grenoble Cedex 09 FRANCE

Summary We investigate the interaction of inertia-gravity waves with a baroclinic vortex in a rotating stratified fluid using WKB theory in combination with experimental observations. We show that wave breaking occurs mainly in the periphery of tall vortices, leading to a deposit of momentum, which modifies the vortex velocity profile.

INTRODUCTION

In large-scale geophysical flows, the dominant presence of background rotation and stratification not only prompt the inverse energy-cascade towards large scales, but also support waves e.g. generated during geostrophic adjustment. Here we consider interactions of inertia-gravity waves with a baroclinic vortex in a rotating linearly-stratified fluid, using WKB approach and experimental results. In contrast to most studies on interactions of waves with a unidirectional shear (see e.g. [1]), we consider the interaction of waves with the curved shear of a lenticular vortex.

WKB-APPROACH

To model the wave-vortex interaction with the WKB approach, we consider an isolated lenticular vortex, characterized by a core of constant cyclonic vorticity of radius R embedded in a ring of constant anticyclonic vorticity such that the circulation vanishes at radius L, whereas in the vertical direction a Gaussian vorticity distribution is assumed. Because of stability arguments (see [2]) we take $L = 2R$; the vertical length scale is H, and the amplitude is given by the maximum azimuthal velocity U_{max}. The vortex is in cyclo-geostrophic balance thus setting the density field in accordance with the velocity field. The propagation of inertia-gravity waves can then be described in the framework of the WKB theory by introducing the expressions for density and velocity into the set of ray and refraction equations [3].

The non-dimensional dispersion relationship for the intrinsic frequency ω_0 is a function of the components of the wave vector and the buoyancy frequency field, and reads

$$\omega_o^2 = \frac{N^{*2}(k_r^2 + k_\theta^2) + (f/N_o)^2 k_z^2}{k^2}, \tag{1}$$

where N^* is the buoyancy frequency corrected for the velocity induced density field, and the intrinsic frequency ω_o is a function of the components of the wave vector and the buoyancy frequency field. The non-dimensional form of the Doppler-shift relationship reads

$$\omega_{abs} = \omega_o + \mathrm{Fr}\, k_\theta r \left(\frac{U}{r}\right) \tag{2}$$

with $Fr = U_{max}/(N_0 R)$ the Froude number. In view of this Doppler shift, we distinguish waves propagating in the direction of the azimuthal velocity field of the vortex (briefly $k_\theta > 0$) which experience an increase in intrinsic frequency, and waves propagating against this velocity field (briefly $k_\theta < 0$) which experience a decrease in frequency.

When Fr_w=k Fr $<< 1$, the intrinsic frequency ω_o, and implicitly the orientation of the rays are weakly modified. With increasing Fr_w rays reflect and interact with the vortex. Some rays remain inside the vortex, exhibiting a strong decrease in wave-length associated with the trapping in a critical layer. We use this decrease in wavelength as a criterion to distinguish trapped rays from untrapped waves, and define waves as trapped when the wavelength has decreased to one-tenth of its initial value.

To investigate the effect of the vortex characteristics on the trapping of an ensemble of waves, simulations were carried out for three different aspect ratio H/L, 0.1, 1 and 5 with Fr_w in the range between 0.1 to 1000.0, and ω_{abs} in the range $[f/N_o, 1]$ (and fixed values of the rotation to buoyancy frequency $f/N_o = 0.1$, and $L/R = 2$). To compare the results, we defined a vortex area, σ_{vortex}, seen by incident rays of frequency ω_{abs}. The values $\mathrm{Fr}_w = U_{max}/(N_o\lambda)$, with λ the wavelength, correspond to the same strength in Doppler shift. For a vertically gaussian-shaped vortex of aspect ratio H/R, the non-dimensional form of this expression yields

$$\sigma_{vortex}\left(\omega_{abs}, \frac{H}{R}, \frac{L}{R}\right) = \frac{L}{R}\left(4.0\frac{H}{R}\sqrt{\frac{1-\omega_{abs}^2}{1-(f/N_o)^2}} + \pi\frac{L}{R}\sqrt{\frac{\omega_{abs}^2-(f/N_o)^2}{N^2-(f/N_o)^2}}\right).$$

The trapping area σ is defined as the area of trapped rays divided by the vortex area σ_{vortex} defined above. Generally, rays with low values of Fr_w are not trapped, whereas for higher values of Fr_w trapping area depends on the aspect ratio H/R of the vortex.

For flat vortices, rays propagating with the flow are trapped in the core and periphery by the strong vertical shear, while rays propagating against the flow escape, except very short waves for which the flow curvature in the vortex is negligible.

These rays are trapped near the edge of the vortex, $z = 0$, $r = L$, close to the reflection layer $\omega_o = N$ where the horizontal shear is dominant.
For tall vortices, rays propagating with the flow reflect and escape, whereas waves propagating against the flow are trapped along almost vertical critical layers that are located near the reflection layer $\omega_o = N$. In contrast to flat vortices, all waves with $k_\theta > 0$ escape after reflection in the outer core region (for details see [3]). For increasing Fr_w, the trapping region gets gradually closer to the vortex periphery and increases in energy density. Conservation of wave action flux then leads to an energy amplification, which in real flows leads to breaking or viscous damping by diffusive effects.

EXPERIMENTAL RESULTS

Experimentally, a flat vortex is generated with a thin disk rotating about the vertical axes at mid-depth in the fluid; the vortex is characterized by a core with approximately constant vorticity enclosed by a ring of negative vorticity (for details see [4,6]). A tall vortex is generated by siphoning a given quantity of fluid via a vertical tube over a relatively large depth. After removal of the tube a tall vortex with a velocity profile close to that of a Lamb-Oseen vortex remains. Respectively, quantitative and qualitative information is obtained from PIV measurements and dye or shadow-graph pictures. Comparing the initial and perturbed vortex state for an ensemble of cross-sectional velocity profiles revealed the impact on the velocity profile.
Planar waves propagating against the flow wrap around the vortex while their energy accumulates until their amplitude is high enough to trigger overturning and breaking (see figure 1). For the tall vortex, this wave breaking leads to a deposit of negative momentum in the vortex periphery, and modifies the velocity profile of the vortex from a Lamb-Oseen vortex to an isolated vortex [5,6].

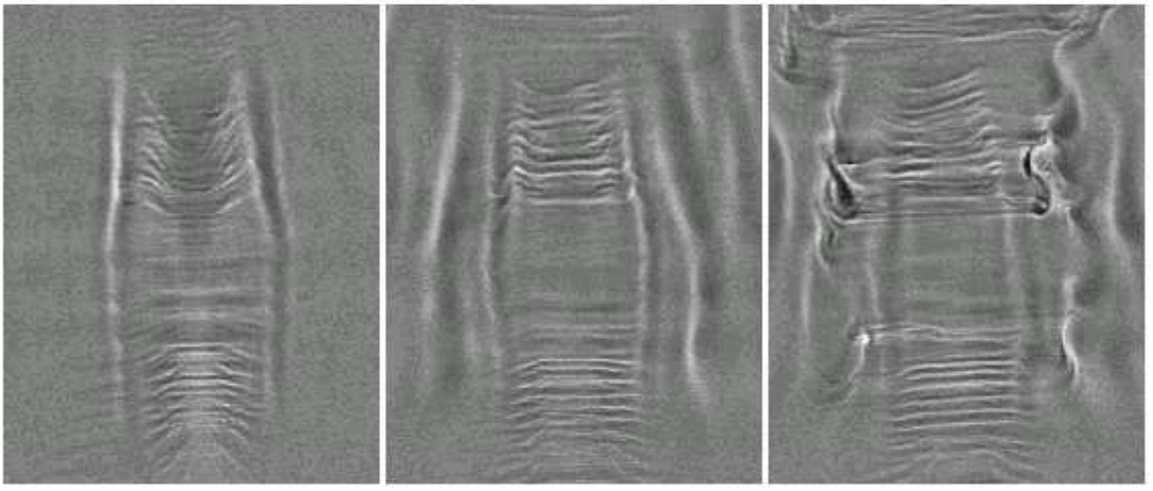


Figure 1. Shadowgraph pictures of inertia gravity waves, emitted by an oscillating cylinder at the right side of the vortex near the bottom, breaking in the shear flow of a tall vortex. The cylinder diameter is $D = 5.0$ cm, while oscillation frequency and amplitude are $0.88s^{-1}$ and $1.0\ cm$ respectively, and $N_0/f = 1.5$. Times of observation are: 79, 123 and 137 s after forcing.

References

[1] Olbers, 1980, "The propagation of Internal Waves in a geostrophic current". *J. Physical Oceanography* **11**, 1224–1233.
[2] Flierl G.R., 1988, "On the instability of geostrophic vortices". *J. Fluid Mech.* **197**, 349–388.
[3] Moulin, F.Y. & Flór, J.B., 2004, "Vortex wave interaction in a rotating stratified fluid: WKB theory". *J. Fluid Mech.(in preparation).*
[4] Moulin, F.Y. & Flór, J.B., 2004, "On the spin-up by a rotating disk in a rotating stratified fluid". *J. Fluid Mechanics* (accepted).
[5] Moulin, F.Y. & Flór, J.B., 2004, "Experimental study on the wave-breaking and mixing properties of an elongated vortex".*Dyn of Atm. Oceans* (Submitted).
[6] Moulin, F.Y., 2002, PhD-theses. Université Joseph Fourier.

XXI ICTAM, 15–21 August 2004, Warsaw, Poland

,

A NEW SPECTRAL CLOSURE MODEL OF TURBULENT FLOWS WITH STABLE STRATIFICATION AND ITS APPLICATION TO ATMOSPHERIC SBLS

Semion Sukoriansky*, Boris Galperin**, Veniamin Perov+
*Department of Mechanical Engineering, Ben-Gurion University of the Negev, Beer-Sheva 84105, Israel
**College of Marine Science, University of South Florida, St. Petersburg, FL 33701, USA
+Department of Research and Development, Swedish Meteorological and Hydrological Institute, SE-601 76 Norrköping, Sweden

Summary A new model for turbulent flows with stable stratification is presented. This model belongs in the class of the quasi-Gaussian closures; its parameters are calculated based upon a self-consistent recursive procedure of small-scale modes elimination starting at the Kolmogorov scale k_d. The model includes both vertical and horizontal eddy viscosities and diffusivities thus explicitly recognizing the anisotropy induced by stable stratification. There are significant differences in the behavior of these turbulent exchange coefficients with increasing stratification. Generally, the vertical coefficients are suppressed while their horizontal counterparts are enhanced. The model accounts for the combined effect of turbulence and internal waves on the exchange coefficients. A dispersion relation for internal waves in the presence of turbulence is derived. A threshold criterion for the wave generation in the presence of turbulent scrambling is obtained. The new model can be used to derive subgrid-scale parameterizations for LES and eddy viscosities and diffusivities for RANS models. The latter approach is used to develop a new $K-\epsilon$ model which is tested in simulations of the atmospheric stable boundary layer (SBL) over sea ice. The new model performs well in both moderately and strongly stratified SBLs.

THE SPECTRAL MODEL

The spectral closure theory is developed for a fully three-dimensional, incompressible, turbulent flow field with imposed homogeneous, vertical, stable temperature gradient; the flow is governed by the momentum, temperature and continuity equations in Boussinesq approximation,

$$\frac{\partial \mathbf{u}}{\partial t} + (\mathbf{u}\nabla)\mathbf{u} + \alpha g\theta\hat{e}_3 = \nu_0\nabla^2\mathbf{u} - \frac{1}{\rho}\nabla P + \mathbf{f^0}, \quad (1)$$

$$\frac{\partial \theta}{\partial t} + (\mathbf{u}\nabla)\theta + \frac{d\Theta}{dz}u_3 = \kappa_0\nabla^2\theta, \quad (2)$$

$$\nabla\mathbf{u} = 0, \quad (3)$$

where $\mathbf{u}$ and θ are the fluctuating velocity and the fluctuating potential temperature, respectively; P is the pressure, ρ is the constant reference density, ν_0 and κ_0 are the molecular viscosity and diffusivity, respectively, α is the thermal expansion coefficient, g is the acceleration due to gravity directed downwards, $\frac{d\Theta}{dz}$ is the mean potential temperature gradient, and $\mathbf{f}^0$ represents a large-scale external energy source customarily used in spectral theories of turbulence; it maintains turbulence in statistically steady state and may originate from large-scale shear instabilities. According to Kolmogorov theory of turbulence, the details of this forcing are immaterial in statistical description; its net effect is communicated to the fluid via a single integral parameter, the rate of the energy injection at large scales. Due to strong nonlinear interactions, the external forcing excites all Fourier modes down to the dissipative scale k_d. The modes exert indiscriminant, random agitation upon each other which manifests as a stochastic *modal* forcing $\mathbf{f}$. This forcing is used to replace the non-linear equations (1), (2) by modal stochastic equations

$$u_i(\mathbf{k},\omega) = G_{ij}(\mathbf{k},\omega)f_j(\mathbf{k},\omega), \quad (4)$$

$$\theta(\mathbf{k},\omega) = -\frac{d\Theta}{dz}u_3(\mathbf{k},\omega)G_\theta(\mathbf{k},\omega), \quad (5)$$

also known as the Langevin equations. Here, $G_{ij}(\mathbf{k},\omega)$ and $G_\theta(\mathbf{k},\omega)$ are the velocity and the temperature Green functions, respectively. They include terms accounting for the damping of a given mode by all other modes due to nonlinear interactions. Eventually, these terms are associated with k-dependent viscosities and diffusivities [1, 2]. The Langevin equations can be viewed as a device that facilitates the replacement of the original nonlinear Navier-Stokes and temperature equations by a system of linear, forced, stochastic equations in which the energy budget is systematically adjusted for every Fourier mode. In more rigorous interpretation, the replacement of the fully nonlinear Navier-Stokes equations by the Langevin equations represents a *mapping* of the original flow field onto a quasi-Gaussian field $\mathbf{f}(\mathbf{k},\omega)$ under the constraints of incompressibility and conservation of the modal energy flux. In the case of neutral stratification, this approach recovers some basic features of isotropic homogeneous turbulence including the Kolmogorov spectrum [1].

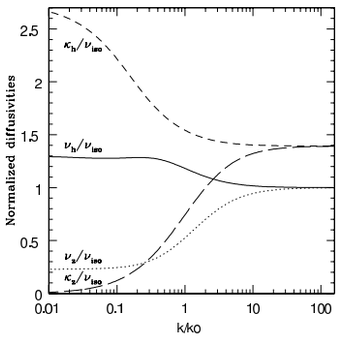


Figure 1. Normalized horizontal and vertical eddy viscosities and diffusivities as functions of k/k_O.

The parameters of the eddy damping are calculated using a systematic algorithm of successive averaging over small shells of velocity and temperature modes. The algorithm consists of computation of small increments to the vertical and the horizontal viscosities and diffusivities generated by the averaging over small shells of the velocity and the temperature modes using the Langevin equations (4) and (5). It results in a system of four coupled ODEs for turbulent viscosities and diffusivities,

$$\frac{d}{dk}(\nu_h, \nu_z, \kappa_h, \kappa_z) = -\frac{\epsilon}{k^5} R_{1,2,3,4}(\nu_h, \nu_z, \kappa_h, \kappa_z), \tag{6}$$

where ϵ is the rate of the viscous dissipation; ν_h and ν_z are the horizontal and the vertical eddy viscosities, respectively; κ_h and κ_z are the horizontal and the vertical eddy diffusivities, respectively, and R_1 through R_4 are algebraic expressions. The procedure takes account of the combined effect of turbulence and internal waves. The computation starts at the Kolmogorov scale k_d where the initial values of the vertical and the horizontal viscosities and diffusivities are equal to their respective molecular values ν_o and κ_0 and is continued to an arbitrary wave number $k < k_d$. The system (6) can only be solved numerically. Solutions obtained for the non-dimensional variables $\nu_h/\nu_{\rm iso}$, $\nu_z/\nu_{\rm iso}$, $\kappa_h/\nu_{\rm iso}$ and $\kappa_z/\nu_{\rm iso}$ are presented in Fig. 1 as functions of the ratio k/k_O, where $k_O = (N^3/\epsilon)^{1/2}$ is the Ozmidov wave number and $\nu_{\rm iso}$ is the eddy viscosity for neutral stratification ($N = 0$) obtained with the same ϵ.

IMPLEMENTATION OF THE SPECTRAL RESULTS IN $K - \epsilon$ MODELING

The process of small scales elimination can be extended to the largest scales of the system, i.e., the integral length scale, k_L^{-1}. This approach is analogous to the Reynolds averaging and the resulting equations represent a sort of a RANS model. We have used ν_z and κ_z to develop a $K - \epsilon$ model based upon the spectral theory rather than the Reynolds stress closure. In simulations of SBLs, it was found necessary to generalize the formulation of the ϵ-equation given in [3] to include the effect of stratification in addition to the rotation,

$$C_1 = C_1^0 + C_f Ro_*^{-1} - C_N Fr_*^{-1}, \tag{7}$$

where $Ro_* = u_*/|f|L$, $Fr_* = u_*/NL$, u_* is the friction velocity, f is the Coriolis parameter, C_1^0 is the standard coefficient equal to 1.44, $L = 0.16K^{3/2}/\epsilon$ is the turbulence macroscale used in the $K - \epsilon$ modeling, $C_f = 111$ and $C_N = 0.58$ are empirical constants. The new $K - \epsilon$ model has been tested in simulations of ABL over sea ice and compared with the data from Beaufort Arctic Storms Experiment (BASE) and LES [4]. The results of the simulations with the new $K-\epsilon$ model are in good agreement with the LES for both cases of the moderate and strong stable stratification and provide significant improvement over the standard $K - \epsilon$ model.

References

[1] Sukoriansky, S., Galperin, B. and Staroselsky, I.: Cross-term and ϵ-expansion in RNG theory of turbulence. *Fluid Dyn. Res.* **33**: 319–331, 2003.

[2] Sukoriansky, S. and Galperin, B.: A spectral closure model for turbulent flows with stable stratification. In: *Marine Turbulence - Theories, Observations and Models*, H. Baumert, J. Simpson, J. Sundermann, eds., Cambridge University Press, in press.

[3] Detering, H. and Etling, D.: Application of the $E - \epsilon$ model to the atmospheric boundary layer. *Boundary-Layer Meteorol.* **33**: 113–133, 1985.

[4] Kosovic, B. and Curry, J.A.: A large eddy simulation study of a quasi-steady, stably stratified atmospheric boundary layer. *J. Atmos. Sci.* **57**: 1052–1068, 2000.

XXI ICTAM, 15-21 August 2004, Warsaw, Poland

ROLL VORTICES IN THE ATMOSPHERIC BOUNDARY LAYER

Dieter Etling, Micha Gryschka
Institute of Meteorology and Climatology, University Hannover,
Herrenhauser Str. 2, 30419 Hannover, Germany, etling@muk.uni-hannover.de

Summary Numerical simulations on the formation of organized structures (roll-vortices) in the atmospheric boundary layer are presented and compared to field observations and related features in laboratory Ekman layers.

Despite being quite turbulent, the atmospheric boundary layer shows forms of organized vortices with horizontal axis orientated in the mean flow direction. The secondary circulations (lateral and vertical) can be identified by clouds organizing themselves as parallel lines in the updraft regions between pairs of counter-rotating roll vortices, as shown e.g. in Figure 1. From the Lagrangian point of view, air parcels exhibit a swirling motion along the mean wind direction due to the combined effect of axial, radial and tangential velocity components of the vortices. Those kind of horizontal roll vortices are well known from laminar boundary layers over rotating disks or Ekman layers in rotating fluids [1].

In the atmospheric boundary layer, the origin of roll vortices is attributed to classical Ekman layer instability for unstratified flow and to buoyancy – induced instability in unstably stratified cases [2]. Both mechanisms are known for laminar flows from linear theory and laboratory experiments. But as the atmospheric boundary layer is always turbulent, one might wonder, how large scale structures can still form. To investigate this problem, we have conducted numerical simulations with a parallelized large-eddy simulation (LES) model. The model is described [3] and has been applied e.g. to small scale vortex structures [4]. Here we present a case of the unstably stratified boundary layer, which resembles the spatial development of the air flow of an cold-air-outbreak over warm ocean water.

The three-dimensional model domain covered an area of about 200 x 6 x 4 km with a grid size of about 50m in all directions. Results of the simulations are displayed for a horizontal (x, y) slice of the vertical velocity at about mid-boundary layer and as vertical cross-section (x, z) at some downstream-distance (Figure 2). One can recognize quasi lineal structures in upward and downward motion which are attributed to quasi two-dimensional roll vortices. The cross section in Figure 2 gives some impression of these roll vortices, which exhibit a cross-wind wavelength of about 2km equivalent two times of the boundary layer depth. Further downstream this roll organization is somewhat broken up (not shown here), but some vortex features are still be seen. Concerning the physical mechanism of roll formation we suggest a combination of thermal convection and boundary layer wind shear.

Vertical transport of momentum by these vortices leads to the formation of stripes of enhanced and reduced surface wind stress oriented in the direction of the roll axis. These features can be compared to observations of the sea surface by Synthetic Aperture Radar (SAR) from satellites, where similar structures have been identified on numerous occasions [5].

References

[1] Lingwood, R.J. : Absolute instability of the Ekman layer and related rotating flows. *J. Fluid Mech.* **333**, 405-428, 1997.

[2] Etling, D., Brown, R.A.: Roll vortices in the planetary boundary layer: A review. *Boundary Layer Meteorol.* **65**, 215-248, 1993.

[3] Raasch, S., Schröter, M.: PALM – A Large-Eddy Simulation Model Performing on Massively Parallel-Computers, *Meteorol. Z.*. **10** 363-372, 2000.

[4] Weinbrecht, S, Raasch, S: High Resolution Simulations of theTurbulent Flow in the Vicinity of an Arctic Lead. *J. Geophys. Res*. **106**, 27035-27046, 2001.

[5] Mourad, P.: Inferring multiscale structure in atmospheric turbulence using satellite-based synthetic aperture radar signature.. *J. Geophys. Res* **101,** 18433-18449, 1996.

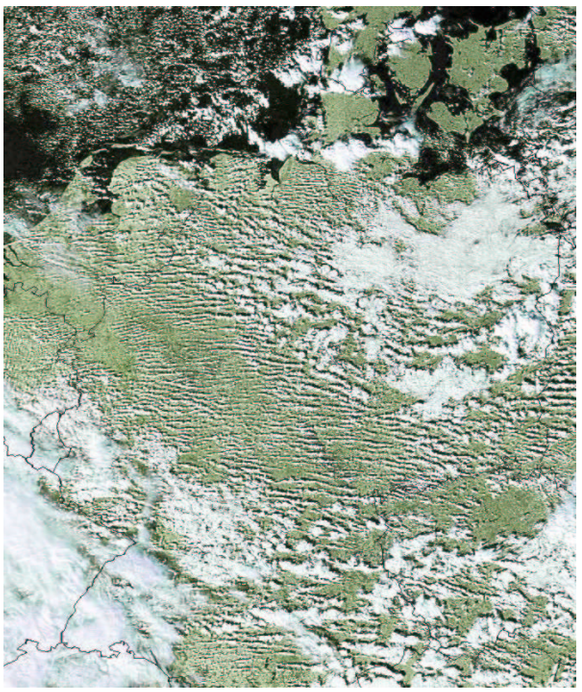


Figure 1: Clouds organized into rows due to roll-vortices in the atmospheric boundary layer.

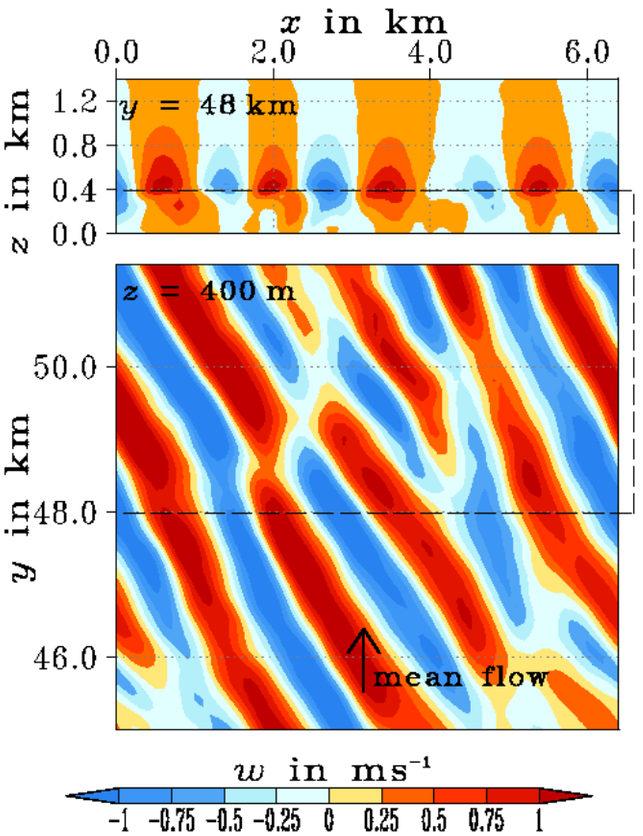


Figure 2: Model simulations of vertical velocity in the atmospheric boundary layer.
Bottom: horizontal cross section; top: vertical cross section. Red = upward motion, blue = downward motion.

SPONTANEOUS GENERATION OF INERTIA-GRAVITY WAVES BY BALANCED MOTION

Jacques Vanneste
School of Mathematics, University of Edinburgh, Edinburgh EH9 3JZ, UK

Summary The spontaneous generation of inertia-gravity waves by balanced motion leads to fundamental limitations in the accuracy of balanced models. In the standard quasi-geostrophic regime (with small Rossby number and order-one Burger number) the amplitude of the inertia-gravity waves can be expected to be exponentially small in the Rossby number. We demonstrate this explicitly by deriving asymptotic estimates for this amplitude in two models described by ordinary differential equations: the five-component model of Lorenz and Krishnamurthy; and a model describing the evolution of sheared disturbances in a three-dimensional Boussinesq fluid. In both cases the asymptotic estimates are confirmed by numerical experiments. The concepts and techniques used in the analysis (optimal truncation of asymptotic series, Borel–Laplace transform, complex-time dynamics) help clarify a number of issues in balanced dynamics and initialization. Their relevance to more realistic models of the atmosphere and oceans is discussed.

INTRODUCTION

The rapid rotation and strong stratification of the atmosphere and oceans at mid-latitudes lead to a clear separation between the advective time scales and the inertia-gravity-wave (IGW) time scales. This time-scale separation, characterized by a small parameter $\epsilon \ll 1$ (essentially the Rossby number), implies that the flow can remain close to a balanced state, free of IGWs. Such a state is best thought of as a manifold of reduced dimensionality in the state space of the system — a slow manifold. Balanced models (e.g. the quasi-geostrophic model) then result from the projection of the primitive equations onto such a manifold, and initialization procedures amount to the projection of initial data.

Using power-series expansions in ϵ, one can in principle obtain a hierarchy of slow manifolds, $\mathcal{M}_n$ say, by truncation at some power ϵ^n. Trajectories of the primitive equations then remain (for a finite time) within an $O(\epsilon^n)$ distance of $\mathcal{M}_n$. Were this procedure to converge, one could define *the* slow manifold $\mathcal{M}_\infty$, an exactly invariant manifold on which the motion is entirely devoid of IGWs. However, it has become clear that such an exactly invariant slow manifold does not exist in general, and that balanced motion, however well initialized, spontaneously generates IGWs. This is consistent with the definition of the (approximately invariant) $\mathcal{M}_n$ for arbitrary n because the expansion procedures are divergent, and because the amplitude of the IGWs that are generated is smaller than any order ϵ^n. Typically, one expects wave amplitudes to be exponentially small, scaling like $\exp(-\alpha/\epsilon)$ for some $\alpha > 0$.

The conclusions just outlined have been drawn using a combination of numerical and analytical results, mostly for low-order models (e.g. [1, 2] and references therein). The analytic results are mainly upper bounds on IGW amplitudes. What appears to be lacking, however, are explicit estimates of these amplitude in the regime most relevant to geophysical fluids, namely the quasi-geostrophic regime, with small Rossby and Froude numbers, both of a similar order of magnitude. This paper reports on the asymptotic derivation of such estimates in two simple models [4, 5]. To capture the amplitude of IGWs spontaneously generated by balanced motion, the techniques of exponential asymptotics, or asymptotics beyond all orders, must be used. By associating the generation of IGW to a Stokes phenomenon, these reveal the importance of considering complex values of the time variable t and, specifically, of identifying the complex values of t for which the balanced motion becomes singular.

LORENZ'S FIVE-COMPONENT MODEL

The system of ordinary differential equations

$$\dot{u} = -vw + \epsilon bvy, \quad \dot{v} = uw - \epsilon buy, \quad \dot{w} = -uv, \quad \epsilon\dot{x} = -y, \quad \epsilon\dot{y} = x + buv, \tag{1}$$

was derived by Lorenz by truncation of the shallow-water equations (see [3]). In the quasi-geostrophic regime, with $\epsilon \ll 1$ and $b = O(1)$, it is easy to derive equations for the slow manifolds $\mathcal{M}_n$; these are given by the (asymptotic but divergent) series

$$x = -buv + \epsilon^2 b(uv^3 - u^3v - 4uvw^2) + \cdots, \quad y = \epsilon b(u^2 - v^2)w + \cdots.$$

Truncating these expansions optimally, one can define the balanced contribution $(x_{\mathsf{bal}}, y_{\mathsf{bal}})$ to (x, y) and, by subtraction, the IGW contribution, expected to be of the form

$$(x_{\mathsf{igw}}, y_{\mathsf{igw}}) \approx C(\cos(t/\epsilon + \phi), \sin(t/\epsilon + \phi))$$

for some C and ϕ.

Now, the evolution of a balanced initial condition, with $C = 0$, leads to the generation of IGWs and thus to an exponentially small $C > 0$. The change in C occurs abruptly, in an $\epsilon^{1/2}$ neighbourhood of the intersection of the real t-axis with a Stokes line joining complex conjugates poles of (u, v, w) in the complex t-plane. Using exponential asymptotics, we show in [4] that the amplitude of the waves generated is

$$C \sim \epsilon^{-2} f(b) \exp(-\alpha/\epsilon),$$

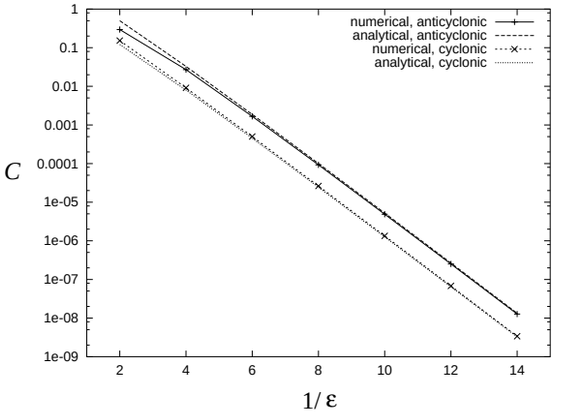


Figure 1. IGW amplitude C as a function of $1/\epsilon$ for sheared disturbances.

where α is the distance of the poles of (u, v, w) to the real t-axis, and the nonlinear function $f(b)$ is determined by a convergent recurrence. Numerical experiments confirm this result.

SHEARED DISTURBANCES

In joint work with I. Yavneh [5], we consider the spontaneous generation of IGWs in exact (nonlinear) solutions of the 3-D Boussinesq equations. Specifically, we examine the evolution of sheared disturbances superimposed to a horizontal Couette flow $\mathbf{u} = (\Sigma y, 0, 0)$. The vertical vorticity of these disturbances has the form

$$\xi(t) \exp[\mathrm{i}(kx + ly + mz)] + \text{c.c.},$$

with $l = -\Sigma k t$ as a result of the shear. The complex amplitude $\xi(t)$ satisfies a linear second-order inhomogeneous equation.

As in Lorenz's model, a balanced contribution to $\xi(t)$ can be defined using an optimally truncated asymptotic series with $\epsilon = |\Sigma|/f$ as small parameter; the remainder takes the form of waves, with

$$\xi_{\mathsf{igw}}(t) \sim C \exp\left(\mathrm{i} \int \omega \, \mathrm{d}t/\epsilon + \phi\right),$$

where ω/ϵ is the IGW frequency. Exponential asymptotics indicates that a (balanced) solution with $C = 0$ for $t < 0$ results in

$$C \sim \epsilon^{-1/2} \beta \exp(-\alpha/\epsilon) > 0$$

for $t > 0$. Here, α and β are given explicitly in terms of elliptic functions of m/k and f/N. A comparison between this estimate and the results of numerical experiments in shown in Figure 1. Interestingly, the wave generation is stronger (by an $O(1)$ factor) for anticyclonic shear than for cyclonic shear.

DISCUSSION

The models studied demonstrate that the spontaneous generation of IGWs by balanced motion is inevitable, although extremely weak in the quasi-geostrophic regime. This confirms the non-existence of an exactly invariant slow manifold and sets a fundamental limit to the accuracy of balanced models. Our more recent work on the subject seeks to extend the results to more realistic models and, ultimately, to the full primitive equations. Also of interest is the definition of a (unique) optimal slow manifold, and the derivation of the corresponding balanced models. Progress on these issues will be reported on.

References

[1] Bokhove, O. & Shepherd, T. G.: On Hamiltonian balanced dynamics and the slowest invariant manifold, *J. Atmos. Sci.* **53**, 276–297, 1996.
[2] Camassa, R. & Tin, S.-K.: The global geometry of the slow manifold in the Lorenz–Krishnamurthy model, *J. Atmos. Sci.* **53**, 3251–3264, 1996.
[3] Lorenz, E. N. & Krishnamurthy, V.: On the nonexistence of a slow manifold, *J. Atmos. Sci.* **44**, 2940–2950, 1987.
[4] Vanneste, J.: Inertia-gravity-wave generation by balanced motion: revisiting the Lorenz–Krishnamurthy model, *J. Atmos. Sci.* **61**, 224–234, 2004.
[5] Vanneste, J. & Yavneh, I.: Exponentially small inertia-gravity waves and the breakdown of quasi-geostrophic balance, submitted to *J. Atmos. Sci.* **61**, 211–223, 2004.

THE ENERGY CYCLE OF THE TROPICAL MADDEN-JULIAN OSCILLATIONS SEEN THROUGH WAVELETS

Jun-Ichi Yano
LMD, Boite 99, UPMC, 4, place Jussieu 75252 Paris cedex 05 France

Summary
The Madden–Julian Oscillations (MJO) are probably the most notable planetary-scale convective equatorial waves in the tropical atmosphere, which propagates around the globe eastwards with 30–60 day period. The MJO constitute a good example among the complex phenomena associated with geophysical flows. Their understanding and simulations remain a challenging fluid mechanics problem with complex interactions between planetary–scale flows and small-scale moist deep convection. Even their basic mechanism is hard to identify by conventional Fourier–based analyses due to strong nonlinearities in cloud physics associated with moist deep convection. Here, the wavelet is proposed as a general methodology for analyzing complex geophysical flows, and this method is used in order to identify the maintenance mechanism of MJO under an energy cycle. The analyses of the simulation results from global models show that this system is not necessarily maintained by moist deep convection in a simple manner as expected from the current dominant view.

INTRODUCTION

The geophysical phenomena are often complex with many physical processes associated together. Thus, lucid applied mathematical approaches must be called for in order to clearly identify their mechanism by untangling these many processes. The Madden–Julian Oscillation (MJO) is such a major example.

Phenomenologically, MJO is initiated in the Indian Ocean as a convective anomaly associated with a low–level convergence, an upper–level divergence and a pressure anomaly. The whole structure, which scales 5000–10000 km, corresponding to the longitudinal wavenumbers 1–3 in the wavenumber space, propagates eastwards as it enhances. Its activity reaches its peak over the Western Pacific, and its convective component almost dissipates out as it crosses the Dateline, although the dry dynamical component is observed to circulate around the globe. The whole cycle takes 30–60 days.

The numerical simulation of this phenomenon remains challenging due to its complex and intrinsic coupling with moist–convective processes of 10–100 km in horizontal scales. With limited horizontal scales of the current standard global models, the latter process must be somehow "parameterized", along with many other physical processes. These parameterizations not only remain overall *ad hoc*, but their existence make the identification of the basic physical mechanism in global climate–model simulations far more difficult, although these models often generate MJO–like features. In other words, no theory is easy tested by these global models due to the complexity of the latter.

Identification of the mechanism is further hindered by the current dominant thinking assuming these phenomena as oscillatory waves. The actual MJO is dominated by an isolated pulse–like structure both in convective precipitation fields and winds. By emphasizing this aspect, the wavelet is employed in order to extract MJO more efficiently as a pulse-like feature, and the energy cycle of MJO is analyzed by identifying it by its most dominant wavelet mode in a coordinate moving with MJO.

THE ANALYSIS METHOD

The adopted energy cycle (Fig. 1) is identical to the so–called Lorenz's four boxes, but both the kinetic (K) and the potential (P) energies are decomposed into a MJO mode (a single wavelet mode, designated by the subscript MJO)) and all the remaining wavelet modes (non–MJO mode, designated by the subscript $\overline{MJO}$), instead of zonal mean and eddies.

The current dominant view for MJO assumes that it is driven by moist–convective heating. Thus, energetically, its potential energy (P_{MJO}) is generated by diabatic heating associated with moist convection (G); the generated potential energy is converted into the kinetic energy (K_{MJO}) by the buoyancy forcing (C); then the kinetic energy is dissipative by frictional processes (D). The energy components for the non–MJO mode are expected to be not playing a major role in this domiant view.

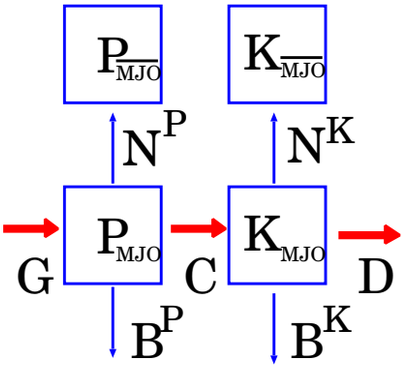


Figure 1: Schematics of the energy cycle used in the analysis, also indicating the prediction from standard theories by thick arrows.

RESULTS

This analysis method is applied to the MJO–like features simulated by two global climate models, designated by abbreviations LMDZ and ECMWF in the followings. MJO–like features in both models propagate eastwards with the phase speeds of 1.5 m/s and 7 m/s, and the dominant wavelet mode has the wavenumber band 8 and 4, respectively. The MJO–like features simulated by the LMDZ model are too slow in phase speed, and too small in scale, whereas those in the ECMWF model is reasonable.

However, MJO–like features of both models are maintained by qualitatively very different mechanism than that of the dominant view.

In the case of LMDZ (Fig. 2), diabatic heating effect (G) is not efficient enough for generating the potential energy (P) for the MJO mode. Instead, the potential energy for this mode is generated by nonlinear transfers (N^P) of potential energy from different scales ($P_{\overline{MJO}}$). Our preliminary analysis implies that the distortions of the zonal–mean temperature field by meridional advections generate the potential energy for the MJO mode. Nevertheless, the generated potential energy is used for maintaining the kinetic energy for MJO, as the standard theories predict.

The energy cycle identified from an ECMWF simulation (Fig. 3) is again, qualitatively different from the standard theories, and also in different manners than LMDZ. In the case of the ECMWF simulation, the potential energy is mostly generated by diabatic heating, but the generated potential energy is not much converted into the kinetic energy. It is simply transfered into the different scales. More surprisingly, the kinetic energy for MJO is mostly supplied by the subgrid–scale "dissipation" ($i.e.$, negative dissipation). If this is literally correct (emphasizing a preliminary nature of the analysis), MJO in ECMWF model is dynamically generated by inverse cascade of energy from the subgrid scales.

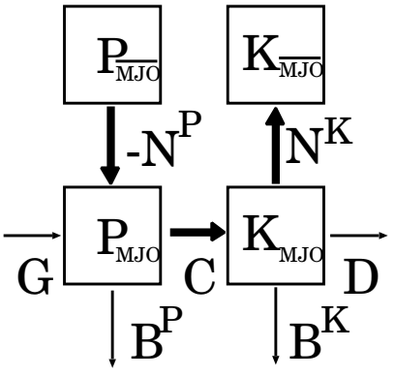


Figure 2: The schematics of the energy cycle identified for MJO in the LMDZ simulation.

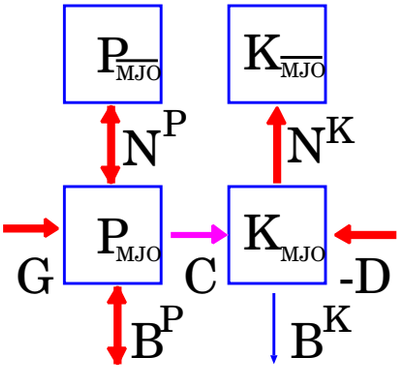


Figure 3: The schematics of the energy cycle identified for MJO in the

CONCLUSIONS

The present work demonstrates how the wavelet can be used in order to efficiently capture coherent structures in complex geophysical fbws and identify their basic maintenance mechanism. Our analysis shows that MJO–like features simulated in two global climate models are not maintained by moist deep convection, but suggest importance of various nonlinearities.

XXI ICTAM, 15–21 August 2004, Warsaw, Poland

WAVE CAPTURE AND WAVE–VORTEX DUALITY

Oliver Bühler*, Michael E. McIntyre**
* *Courant Institute of Mathematical Sciences, New York University, New York City, USA*
** *Department of Applied Mathematics and Theoretical Physics, University of Cambridge, Cambridge, UK*

Summary
New and unexpected results are presented regarding the nonlinear interactions between a small-scale wavepacket and a large-scale mean flow, with an eye towards internal wave dynamics in the atmosphere. These are to do with an unusual wave breaking scenario termed 'wave capture', which differs significantly from the standard wave breaking scenarios due to critical layers or mean density decay. We focus on the very peculiar wave-mean interaction scenario that accompanies wave capture.
We present examples of these interactions in 2d shallow water and in the 3d Boussinesq system. Specifically, we point out an analogy between slow wavepackets and vortex dipoles that shows a peculiar and apparently so-far unrecognized 'wave-vortex duality', which throws a new light on the relation between wave dissipation and mean-flow forcing.

Wave capture and wave–mean interaction

This is on-going work in wave–mean interaction theory based on [2]; the new results are reported in full in [3]. The basic idea [1] is to exploit the partial analogy between the evolution of the wavenumber vector $\boldsymbol{k}$ in ray theory with a non-uniform mean flow $\boldsymbol{U}$ and the evolution of the gradient of a passive tracer advected by the same flow:

$$\left(\frac{\partial}{\partial t} + ([\boldsymbol{U} + \hat{\boldsymbol{u}}_g] \cdot \boldsymbol{\nabla})\right) \boldsymbol{k} = -\boldsymbol{\nabla}\boldsymbol{U} \cdot \boldsymbol{k} \quad \text{and} \tag{1}$$

$$\left(\frac{\partial}{\partial t} + (\boldsymbol{U} \cdot \boldsymbol{\nabla})\right) \phi = 0 \;\Rightarrow\; \left(\frac{\partial}{\partial t} + (\boldsymbol{U} \cdot \boldsymbol{\nabla})\right) (\boldsymbol{\nabla}\phi) = -\boldsymbol{\nabla}\boldsymbol{U} \cdot (\boldsymbol{\nabla}\phi). \tag{2}$$

The only difference is the intrinsic group velocity $\hat{\boldsymbol{u}}_g$. Therefore, for slow wavepackets such that $\hat{\boldsymbol{u}}_g \ll \boldsymbol{U}$ the analogy is very good. This implies the readily verified potential for exponentially fast growth in $\boldsymbol{k}$ and concomitant growth in wave amplitude, which must lead to rapid wave breaking [1]. We call this basic effect "wave capture" here, to emphasize that the wavepacket gets captured by (and subsequently travels with) the mean flow. We stress that capture can occur without the need for any critical layer in the classical sense, and without any density decay with altitude.
This capture has profound implications for pseudomomentum budget and wave–mean interaction, and these will be discussed. A detailed example is illustrated in figure 1, which is taken from [3].

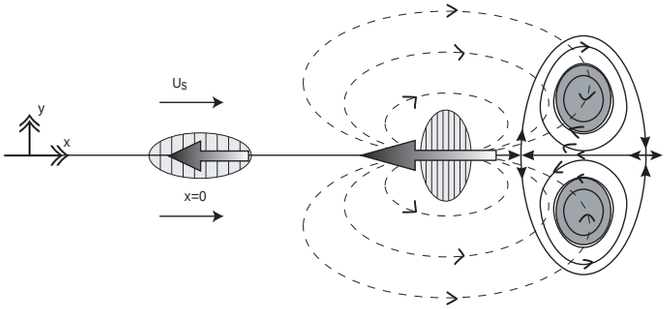


Figure 1. Horizontal isentropic view of a mountain wavepacket that was generated below by a surface wind U_s over topography and which is now undergoing capture due to the blocking dipole on the right. The wavepacket drifts towards the dipole stagnation point whilst being strained by the mean flow such that there is exponential growth in $\boldsymbol{k}$ and pseudomomentum $\mathbf{p}$, which are indicated by the large arrows. At the same time, the mean-flow response return flow at second order in wave amplitude (illustrated by the stippled stream lines) acts to squeeze the dipole and thereby reduces its impulse. It can be shown that vortex impulse change and wave pseudomomentum changes balance each other.

References

[1] Badulin, S. I., Shrira, V. I.: On the irreversibility of internal-wave dynamics due to wave trapping by mean flow inhomogeneities. Part 1. Local analysis. *J. Fluid Mechanics*, **251**: 21–53, 1993.
[2] Bühler, O., McIntyre, M. E.: Remote recoil: a new wave–mean interaction effect. *J. Fluid Mechanics*, **492**: 207–230, 2003.
[3] Bühler, O., McIntyre, M. E.: Wave capture and wave–vortex duality. *J. Fluid Mechanics*, **submitted 2004**.

XXI ICTAM, 15–21 August 2004, Warsaw, Poland

A NEW THEORY FOR CONVECTION IN RAPIDLY ROTATING SPHERICAL SYSTEMS

Keke Zhang*, Xinhao Liao**
*School of Mathematical Sciences, University of Exeter EX4 4QJ, UK
**Shanghai Astronomical Observatory, Chinese Academy of Sciences, Shanghai 200030, China

Summary Thermal convection in rapidly rotating, self-gravitating Boussinesq fluid spherical systems is a classical problem and has important applications for many geophysical and astrophysical problems. The convection problem is characterized by the three physical parameters, the Rayleigh number R, the Prandtl number P_r and the Ekman number E. This paper reports a new convection theory in rapidly rotating spherical systems valid for $E \ll 1$ and $0 \leq P_r < \infty$. The new theory units the two previously disjointed subjects in rotating fluids: inertial waves and thermal convection. Both linear and nonlinear properties of the problem will be discussed.

INTRODUCTION

Thermal convection in rapidly rotating, self-gravitating Boussinesq fluid spherical systems driven by a uniform distribution of heat sources has been extensively studied. There are two major reasons why much attention has been attracted to this problem: it has important applications for many geophysical and astrophysical problems and it provides a fundamental understanding of general dynamics of rotating fluids.

The classical convection problem is characterized by the three physical parameters, the Rayleigh number R, the Prandtl number P_r and the Ekman number E. In their seminar papers, Roberts (1968) and Busse (1970) established a local asymptotic theory for the onset of convection in the limits $E \to 0$ and $P_r/E \to \infty$. The Roberts-Roberts local theory assumed the following asymptotic laws

$$\frac{\partial}{\partial s} \sim \frac{1}{s}\frac{\partial}{\partial \phi} = O(E^{-1/3}),\ \frac{\partial}{\partial z} = O(1),\ R_c = O(E^{-1/3}) \ \text{ as } \ E \to 0 \ \text{ and } \ P_r/E \to \infty, \tag{1}$$

where (s, ϕ, z) are cylindrical polar coordinates with the rotation axis in the z-axis. Progress on the asymptotic theory in the limits $E \to 0$ and $P_r/E \to \infty$ for the onset of convection was made by Jones et al. (2000) (see also Soward, 1977), who found the asymptotic solution that produces a correct critical Rayleigh number. The central issue in their analysis is to extend the local solution onto the complex s-plan in which the phase mixing vanishes.

A different asymptotic theory for the onset of convection in a rapidly rotating sphere was developed by Zhang (1994) for the limits $E \to 0$ and $Pr/E \to 0$. It was shown that convective motions are at leading order represented by single inertial wave that has the simplest structure along the axis of rotation. Buoyancy forces appear at next order to drive the inertial wave against the weak effects of viscous damping. It was recognized that the localized convective motion spreads out with decreasing P_r, obeying the following asymptotic laws

$$\frac{\partial}{\partial s} \sim \frac{1}{s}\frac{\partial}{\partial \phi} = O(1), \qquad \frac{\partial}{\partial z} = O(1),\ R_c = O(E) \qquad \text{as} \qquad E \to 0 \text{ and } P_r/E \to 0. \tag{2}$$

In this limit, an analytical expression for the complete convection solution in closed form was obtained (Zhang, 1994). Our new theory attempts to study the solutions of convection for $0 \leq P_r < \infty$ at $E \ll 1$.

A NEW CONVECTION THEORY

Weakly nonlinear solutions of convection can be expressed as

$$\mathbf{u} \quad = \quad \epsilon(\mathbf{u}_0 + \mathbf{u}_0^*) + \frac{\epsilon^2}{E} U(s)\hat{\phi} + ... \tag{3}$$

where ϵ is the amplitude of convection, $\mathbf{u}$ is the flow velocity, $U(s)$ is the nonlinear mean flow, and F^* denotes the complex conjugate of F. The velocity boundary conditions assumed in this paper are stress-free and impenetrable, which give

$$\frac{\partial(\hat{\phi} \cdot \mathbf{u}_0/r)}{\partial r} = \frac{\partial(\hat{\theta} \cdot \mathbf{u}_0/r)}{\partial r} = \hat{\mathbf{r}} \cdot \mathbf{u} = 0 \tag{4}$$

at the outer bounding spherical surfaces. Our new theory for the convection problem is based on the following three hypotheses.

The first hypothesis: For an arbitrary small but fixed Ekman number $E \ll 1$, the localized convection spreads out quickly in both the $s-$ and $\phi-$directions with decreasing P_r. We thus assume that for $0 \leq P_r < \infty$ at an arbitrary small but fixed Ekman number $E \ll 1$,

$$O(1) < \frac{\partial}{\partial s} < O(E^{-1/3}) \qquad O(1) < \frac{1}{s}\frac{\partial}{\partial \phi} < O(E^{-1/3}) \qquad \frac{\partial}{\partial z} \sim O(1) \tag{5}$$

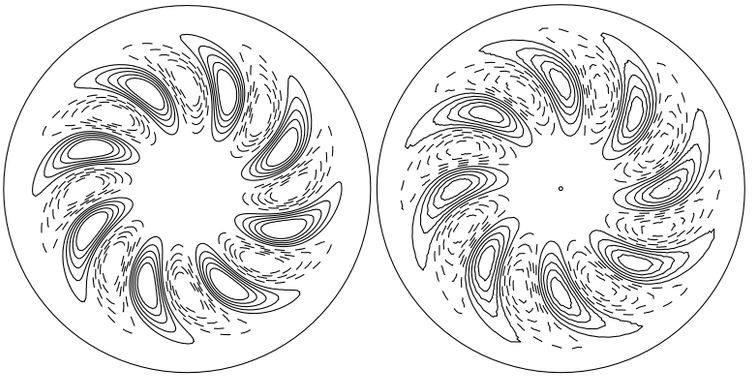


Figure 1. Contours of the radial flow in the equatorial plane. Left panel is the solution derived from the new theory and the solution on right panel is obtained from the fully three dimensional numerical simulations.

A significant consequence is that we must solve partial differential equations. Note that the local theory is concerned with a second-order ordinary differential equation in z.

The second hypothesis: For $0 \leq P_r < \infty$ at an arbitrary small but fixed Ekman number E, we assume that there exists a flow, $\tilde{\mathbf{u}}_0$, that is non-zero only in the Ekman boundary layer on the bounding spherical surface such that

$$\mathbf{r} \cdot \nabla \left[\frac{\mathbf{r}}{r^2} \times (\mathbf{u_0} + \tilde{\mathbf{u}}_0) \right] = 0. \tag{6}$$

The third hypothesis: For an arbitrary small but fixed Ekman number E, we assume that the leading-order velocity of convection can be expressed in the form

$$\mathbf{u}_0 = \sum_N \left[\mathcal{U}_N (\mathbf{U}_N + \tilde{\mathbf{U}}_N) \right] e^{i2\sigma t} \tag{7}$$

where σ is the half-frequency of thermal convection, $\tilde{\mathbf{U}}_N)$ is the boundary layer flow in the Ekman layer, $\mathbf{U}_N$ are nearly geostrophic inertial wave (NGIW) modes for which explicit analytical expressions are now available (Zhang et al., 2001, see also Zhang et al., 2004).

Our analysis demonstrated that agreement between the results obtained from the new theory and fully numerical simulations is excellent. For example, we obtain the critical Rayleigh number $R = 263.5$ from the new theory while the fully numerical simulation gives rise to $R = 264.56$ for $E = 5 \times 10^{-5}$. Based on the linear solution of the problem, we are able to derive an analytic expression for the differential rotation generated by nonlinear interactions of the waves.

CONCLUSION

We show that leading-order convection in a rapidly rotating sphere is either single NGIW mode or a number of coupled NGIW modes modified by viscosity and sustained by thermal buoyancy. The new convection theory unites two previously disjointed subjects in rotating fluids: inertial wave theory and convection theory. This unification furthers our understanding of rotating fluids and opens an exciting line of the future research.

References

[1] Busse, F. H. (1970) Thermal instabilities in rapidly rotating systems. *J. Fluid Mech.* **44**, 441-460.

[2] Chandrasekhar, S. (1961) *Hydrodynamic and hydromagnetic stability.* Clarendon Press, Oxford.

[3] Jones, C. A., Soward, A. M. & Mussa, A. I. (2000) The onset of thermal convection in a rapidly rotating sphere *J. Fluid Mech.* **405**, 157-179.

[4] Roberts, P. H. (1968). On the thermal instability of a self-gravitating fluid sphere containing heat sources. *Phil. Trans. R. Soc. Lond.* **A263** , 93-117.

[5] Zhang, K. (1994) On coupling between the Poincaré equation and the heat equation. *J. Fluid Mech.* **268**, 211-229.

[6] Zhang, K., Earnshaw, P., Liao X. and Busse F. H. (2001) On inertial waves in a rotating fluid sphere. *J. Fluid Mech.* **437**,103-119.

[7] Zhang, K., X. Liao and P. Earnshaw (2004) On inertial waves and oscillations in a rapidly rotating fluid spheroid. *J. Fluid Mech.* **504**:1-40.

VORTEX-BASED MODELS OF QUASIGEOSTROPHIC TURBULENCE

Takeshi Miyazaki, Qin Wei, Yingtai Li
Department of Mechanical Engineering and Intelligent Systems, University of Electro-Communications, 1-5-1 Chofugaoka, Chofu-shi, Tokyo 182-8585, Japan

Summary A vortex-based model of the quasigeostrophic turbulence is developed, based on the fact that the interactions between vortex structures dominate the dynamics of the turbulence. Each coherent vortex is modeled by an ellipsoid of uniform potential vorticity embedded in a 'locally uniform shear field' induced by other vortices. The equations of motion are derived following the procedure of Hamiltonian moment reduction. The degree of freedom of N interacting vortices is $3N$, and even a two-body system shows chaotic behavior. The validity of the ellipsoidal moment model is assessed by performing direct numerical simulations based on the CASL-algorithm. It is shown that the model captures the merger of co-rotating vortices well but that it fails to predict the robustness of a counter-rotating vortex pair.

N INTERACTING ELLIPSOIDAL VORTICES - ELLIPSOIDAL MOMENT MODEL -

We consider the motion of N interacting ellipsoidal vortices of uniform potential vorticity $q_i : i = 1, 2, \cdots, N$, whose center of vorticity is located at (X_i, Y_i, Z_i). Here, the z-axis denotes the vertical axis. The potential vorticity q_i is uniform inside the i-th ellipsoid, whose principal axes lengths are $\alpha_i, \beta_i, \gamma_i$, respectively. Their orientations are specified by the Euler angles ϕ_i, θ_i, ψ_i. The state (location, shape, and orientation) of each ellipsoid is also specified by the values of 10 moments up to the second order. [1] The equations of motion are expressed, using a Poisson bracket of the cosymplectic matrix of the Lie-Poisson form. The Hamiltonian of the system is expressed as a summation of the self-energy of each vortex and the mutual interaction energy. We introduce an approximation in order to express the mutual interaction, by using only the moments up to the second order. The obtained equations of motion are similar to those of Meacham *et al.*,[2] in which we have summed up the background vorticity, the strain field, and the vertical shear induced at the center of the $i-$th ellipsoidal vortex by the '$j-$th virtual point vortex'.

This Hamiltonian dynamical system has several invariants, of which three are Casimirs; i.e., the total vorticity (vortex volume) of the ith ellipsoid $\hat{\Gamma}_i$, the $z-$coordinate of the center of the ith ellipsoid Z_i, and the vortex-height of the ith ellipsoid. The degree of freedom of each ellipsoid is reduced to three (six independent variables). There are other conserved quantities; i.e., the total energy H, the vorticity center of the whole system P and Q, and the angular momentum L. Here, $H, P^2 + Q^2, L$ are Poisson-commutable invariants. Even a two-ellipsoids system is not integrable, because it has 'six degrees of freedom'.

MERGER OF CO-ROTATING VORTICES

Miyazaki *et al.*[1] investigated the interaction of two co-rotating spheroidal vortices of the same shape, by adjusting the initial distance between the vortices. When two vortices were placed close enough initially, the motion became chaotic, the horizontal distance $D(t) = \sqrt{(X_2 - X_1)^2 + (Y_2 - Y_1)^2}$ between two vortices oscillated irregularly with a large amplitude, and a 'merger' of vortices occurred. By defining the 'merger' to be a phenomenon in which the following two conditions were satisfied (i.e., the vertical overlap ($|Z_2 - Z_1| < zh_1 + zh_2$) and the horizontal overlap ($D(t) < V_1^{1/3} + V_2^{1/3}$) with $V_{1,2}^{1/3}$ denoting the 'average radii'), the threshold of the initial distance leading to the merger was determined. The threshold of the merger was almost the same as that of the chaotic motions. Figure 1 shows the region of the initial position of the second vortex ($a = X_2(0) - X_1(0), h = Z_2 - Z_1$), relative to the first vortex, for the case of $\alpha_{1,2} = \beta_{1,2} = 0.3162, \gamma_{1,2} = 1$. The shadowed region represents the 'defined' merger region. Starting from the region inside the broken curve (model-threshold), a merger according to the above definition occurs over the course of time.

We performed numerical simulations (CASL) in order to assess the validity of predictions based on the model. The open squares in Fig.1 indicate the cases in which the vortices do not merge. The open circles denote the cases in which the merger is observed. The open triangles indicate the cases of intermediate behavior. The vortices merge once, then separate again into two vortices. This occurs because the transiently created vortex is unstable. The boundaries between three zones are represented by two solid lines. The ellipsoidal vortex model works well for the region $h > 0.5$ (large vertical off-set). The model, however, over-estimates the critical distance in the region $h < 0.5$; i.e., when the vortices are placed on nearly the same horizontal plane.

COUNTER-ROTATING VORTEX PAIR

Next, we investigate the motion of a counter-rotating pair of two vortices of the same shape, a so-called 'dipole'.[3] Here a 'dipole' means a counter-rotating pair of ellipsoids with vanishing total vorticity. They are vertically off-set. We consider prolate spheroids with $\alpha_{1,2} = \beta_{1,2} = 0.3162, \gamma_{1,2} = 1$. Both spheroids are vertically standing at the initial time. The initial vortices are placed on the $x - z$ plane and off-set vertically. The model predicts three patterns, depicted in Fig.2, as

follows: (1) stable translation in the positive y direction, (2) translation in the negative y direction with large precessions, and (3) singular behavior (tilting down) of both vortices. In region (1), the motion is doubly time-periodic with a main period of 46.2 and the secondary period of 6.18. The translation velocity in the region (1) is positive. In region (2), both the inclination and orientation change non-periodically. In region (3), the most striking thing occurs; i.e., both vortices are stretched infinitely. The gradient h/a of the boundary-line between the regions (2) and (3) is about 1.41. The tilting pair translates along the y axis in the negative direction. Because of this singular behavior, the numerical computation of the ellipsoidal moment model stops in region (3), which is a serious drawback of the ellipsoidal moment model. It is noteworthy that no singular behavior is observed in the symmetric interactions between fatter vortices, such as $\alpha/\gamma >$ about $2/3$.

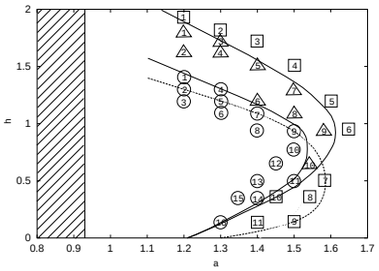


Fig. 1 FigMerger threshold of the co-rotating vortices with $\alpha_{1,2}/\gamma_{1,2} = 0.3162$.

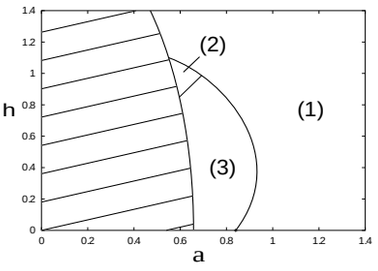


Fig. 2 Three patterns found for a counter-rotating vortex pair with $\alpha_{1,2}/\gamma_{1,2} = 0.3162$.

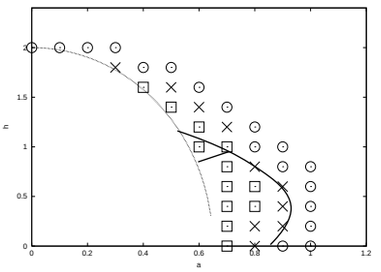


Fig. 3 Pattern map of nonlinear development of counter-rotating vortices.

We performed numerical computations (CASL) corresponding to the above three categories. In case (1), both vortices precess slightly, retaining the ellipsoidal forms, and the energy and enstrophy are conserved. In cases (2) and (3), the vortices tilt largely in the early stage of computation. Later, the vortices emit filaments from the top and bottom and the inclination angles decrease after filamentation (dancing). The singular behavior predicted by the ellipsoidal moment model is not observed; it appears to be circumvented via the dissipative filamentation.

In Fig.3, the nonlinear behavior is summarized as a pattern map in the (a, h) plane. Open circles show the cases of stable translation without dissipation, and crosses represent the cases of vortex-dancing with considerable filamentation. Squares represent the cases in which many satellites remain after filamentation. The solid lines are thresholds predicted by the ellipsoidal moment model. We can see that practically, the model works if the vortices are not off-setted vertically ($h < 1$), for it captures the dissipative processes by giving alarms; i.e., by showing infinite stretching or large precession of one or both of the contour-rotating vortices. When the vortices are largely off-setted ($h > 1$), non-ellipsoidal deformation becomes important, even if the ellipsoidal moment model predicts no singular behavior.

REFINEMENT OF THE ELLIPSOIDAL MOMENT MODEL

Recently, Dritschel and his group proposed an accurate model, [4] in which an ellipsoid is represented by seven point vortices in computing the induced flow field, not by a single point vortex as it is in the ellipsoidal moment model. We have refined the Wire-model (slender limit of the ellipsoidal moment model) following their idea; i.e., by representing a wire-vortex by several point vortices in the integration of the mutual energy. The wire-vortex becomes robuster as the number of point vortices increases. A reasonable choise is 'three', considering both the accuracy and the computaional time. According to the refined model, the critical merger-distance between co-rotating vortices is also modified in favor of the numerical results.

CONCLUSIONS

A vortex-based model of quasigeostrophic turbulence is developed. The validity (or limitation) of the model is assessed by performing direct numerical simulations based on the CASL-algorithm. The model captures the merger of co-rotating vortices well, but it fails to predict the robustness of a counter-rotating vortex pair. A possible way to refine the model is suggested. We have extracted a workable reset-rule after dissipative events, which enables us to perform 'quasi-turbulence simulations' based on the refined ellipsoidal moment model.

References

[1] Miyazaki, T., Furuichi, Y. and Takahashi, N.: *J. Phys. Soc. Jpn.* **70**:1942-1953, 2001.
[2] Meacham, S.P., Morrison, P.J. and Flierl, G.R.: *Phys. Fluids* **9** 2310-2328, 1997.
[3] Miyazaki, Yamamoto, M. and Fujishima, S.: *J. Phys. Soc. Jpn.* **72**:1948-1962, 2003.
[4] McKiver W. and Dritschel, D.G.: *J. Fluid Mech.* submitted, 2003.

GENERATION OF INTERNAL WAVES IN THE DEEP OCEAN BY BAROTROPIC TIDES

Jonas Nycander
Department of Meteorology, Stockholm University, 106 91 Stockholm, Sweden

INTRODUCTION

By itself, the heating and cooling of the ocean surface would only be be capable of driving a significant flow in a thin surface layer ("Sandström's theorem"). The flow below this layer must be mechanically driven, and the two possible sources of mechanical energy are the winds and the tides [1]. In the main thermocline, the winds play a dominating role, mainly via Ekman pumping, but in the abyss below, the tides are probably more important.

When tidal currents encounter rough topography on the bottom of the ocean, internal waves are created, and when these waves steepen and break through nonlinear interactions, they cause vertical mixing. This mixing is what drives the deep circulation. It is therefore of great interest to calculate the energy flux from the tides to the internal wave field.

THEORY

A general expression for the total energy flux C to the internal waves has been derived by Bell [2] and Llewellyn Smith and Young [3]:

$$C = C_+ + C_-, \tag{1}$$

where

$$C_+ = \frac{\rho_0 N U_+^2}{8\pi^2}\sqrt{1-\frac{f^2}{\omega^2}}\iint \frac{k_x^2}{k}|\tilde{h}(\mathbf{k})|^2 d\mathbf{k} \tag{2}$$

and C_- is given by a similar expression with U_+ replaced by U_- and k_x by k_y. Here ρ_0 denotes the mean density of sea water, N the buoyancy frequency, f the Coriolis parameter, ω the angular frequency of the tide, and $\mathbf{k} = \hat{x}k_x + \hat{y}k_y$ and $k = |\mathbf{k}|$. The velocities U_+ and U_- are the major and minor axes of the tidal ellipse, respectively, and the x-axis has been chosen to lie along the major axis. $\tilde{h}(\mathbf{k})$ denotes the Fourier transform of the bottom topography:

$$\tilde{h}(\mathbf{k}) = \iint e^{-i\mathbf{k}\cdot\mathbf{r}} h(\mathbf{r})\, d\mathbf{r},$$

where $\mathbf{r} = \hat{x}x + \hat{y}y$.

In eq. (2) the total energy flux has been written as an integral over spectral space. Equivalently, it may be written as an integral over real space. The product of the two functions k^{-1} and $\tilde{h}$ in spectral space then translates to a convolution integral between the two corresponding inverse transforms, $(2\pi r)^{-1}$ and h, respectively. We obtain

$$C_+ = \iint P_+\, d\mathbf{r}, \tag{3}$$

where the energy flux density is given by

$$P_+(\mathbf{r}) = \frac{\rho_0 N U_+^2}{4\pi}\sqrt{1-\frac{f^2}{\omega^2}}\frac{\partial h}{\partial x}\iint \frac{1}{|\mathbf{r}-\mathbf{r}'|}\frac{\partial h(\mathbf{r}')}{\partial x'}\, d\mathbf{r}'. \tag{4}$$

A number of simplifying assumptions were made in the derivation of eq. (2). The flow was assumed to be hydrostatic, the buoyancy frequency uniform, the tidal excursion much smaller than the horizontal scale of the topography, and the bottom slope subcritical (which is necessary for the linear wave theory to be valid). Finally, the ocean was assumed to be infinitely deep. The assumptions of vertically uniform N and infinite depth were removed in a recent study by Llwellyn Smith and Young [3]. In an ocean of finite depth, the internal waves can be expressed as a discrete series of vertical modes. The most essential effect of this is that the wave generation by topographic scales longer than the horizontal wavelength of the first mode is suppressed. The criterion for this to occur can be written $L > ND/(\omega^2 - f^2)^{1/2}$, where L is the topographic scale and D the ocean depth. For verticallly nonuniform N, WKB-analysis shows that N in this expression should be replaced by its vertical average $\bar{N}$, i.e. we replace ND by $\int_0^D N(z)dz$.

In numerical calculations, it is impractical to use the exact expression, involving an infinite series. We therefore take the finite depth into account in an approximate way, by multiplying the integrand in eq. (2) by a spectral high-pass filter $\alpha(ak)$, with the properties $\alpha(\kappa) \approx 1$ for $\kappa \gg 1$ and $\alpha(\kappa) \approx 0$ for $\kappa \ll 1$. The cutoff length a is proportional to the wavelength of the first mode. Both a rational filter $\alpha(\kappa) = \kappa^2/(1+\kappa^2)$ and a Gaussian filter $\alpha(\kappa) = 1 - exp(-\kappa^2)$ have been tried, with very little difference in the results.

After inverse Fourier transformation, the effect of the high-pass filter is that the function $1/r$ in the integrand of eq. (4) is replaced by the convolution of $1/r$ and the inverse Fourier transform of the filter function α. Denoting the result of this

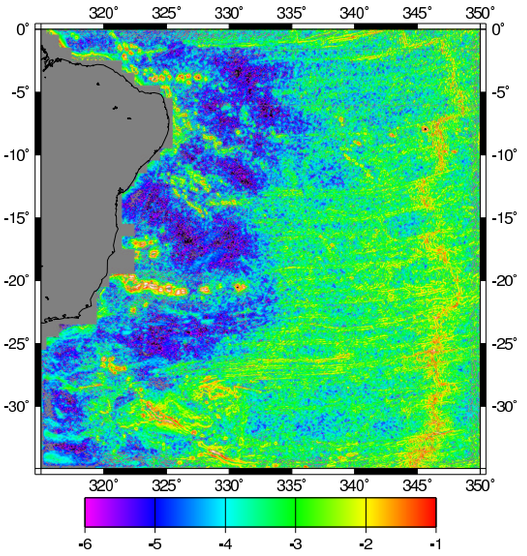


Figure 1. Logarithm of the energy flux density in W/m^2 from the M2 tide to internal waves in the Brazil Basin (e.g. -3 means 10^{-3}W/m^2).

convolution $g_a(r)$, the resulting final expression for the flux density is

$$P_+(\mathbf{r}) = \frac{\rho_0 N_B U_+^2}{4\pi}\sqrt{1-\frac{f^2}{\omega^2}}\frac{\partial h}{\partial x}\iint g_a(|\mathbf{r}-\mathbf{r}'|)\frac{\partial h(\mathbf{r}')}{\partial x'}\,d\mathbf{r}', \tag{5}$$

where N_B is the buoyancy frequency at the bottom. The function $g_a(r)$ is approximately equal to $1/r$ for $r \ll a$, while $g_a(r) \sim r^{-3}$ for $r \gg a$. For the rational and Gaussian filter functions used here, g_a can be expressed analytically in terms of integrals of Bessel functions. The cutoff length a is defined by

$$a = \frac{\beta \bar{N} D}{\pi\sqrt{\omega^2 - f^2}},$$

where β is a numerical coefficient of order unity that is determined by by comparison with an analytically solvable test problem with a simple ridge topography. The contribution P_- from the minor tidal component is given by a similar expression as eq. (5), with U_+, x and x' replaced by U_-, y and y', respectively.

RESULTS

The energy flux density $P = P_+ + P_-$ is calculated numerically from eq. (5) and the corresponding equation for P_-. In order to evaluate P in one point, one must integrate over a region around this point. Since $g_a(r)$ decreases rapidly beyond the cutoff length a, the integral was truncated at a distance $5a$ from the evaluation point. For the real ocean, a is typically a few tens of kilometers or less. Over this length scale, N, $U_\pm$ and f can be considered horizontally uniform, as assumed in the derivation of eq. (2). (This issue would be more problematic if a calculation in spectral space were attempted.)

The input data used in the calculations were the Smith and Sandwell bottom topography with a nominal resolution of 1/30 degrees, the Egbert tidal velocities, and the buoyancy frequency obtained from the SAC hydrographic database. Calculations for the global ocean are underway, but have not yet been completed. Results for the Brazil Basin are shown in Fig. 1. The calculated total energy flux for the M2 tide over the area shown is approximately 26 GW. The main uncertainty is due to unresolved topography. It can been seen from other calculations with an additional low-pass filter that most of the energy flux is generated by topographic scales below 10 km, and it therefore seems very likely that a larger energy flux would be obtained with a higher topographic resolution. Another uncertainty is the effect of supercritical slope. For the area shown in the figure, the total energy flux from points where the slope is supercritical (and the theory therefore unvalid) is approximately 12 GW.

References

[1] Munk W.H., Wunsch C.I.: Abyssal recipes. II: Energetics of tidal and wind mixing. *Deep-Sea Res.* **45**: 1977-2010, 1998.
[2] Bell T.H.: Lee waves in stratified flows with simple harmonic time dependence. *J. Fluid Mech.* **67**:705–722, 1975.
[3] Lewellyn Smith S.G., Young W.R.: Conversion of the barotropic tide. *J. Phys. Oceanogr.* **32**:1554–1566, 2002.

INSTABILITY OF COROTATING VERTICAL VORTICES IN A STRATIFIED FLUID : WHY STRONGLY STRATIFIED TURBULENCE IS NOT SIMILAR TO 2D TURBULENCE

Pantxika Otheguy, Paul Billant and Jean-Marc Chomaz
LadHyX, CNRS-École Polytechnique, 91128 Palaiseau Cedex, France

Summary We present numerical, theoretical and experimental studies of a new instability of two corotating vertical vortices in a vertically stratified fluid. This instability induces the formation of thin horizontal layers with a thickness inversely proportional to the Brünt-Väisälä frequency. This three-dimensional instability is believed to make stratified turbulence depart from two-dimensional turbulence since it alters the pairing of vortices.

INTRODUCTION

The atmosphere, the stratosphere and the ocean are characterized by a stable stratification that limits vertical motions of fluid. As a result, the velocity field is mainly horizontal and Riley et *al* [8] have shown that if both the horizontal and the vertical scales of the flow are large enough, the leading order dynamics are two dimensional. Lilly [4] has proposed that the kinetic energy spectra observed in the atmosphere at mesoscale are manifestation of the two dimensional dynamics with a transfer of energy from small (100 m) to large (100 km) scales. Recently, Lindborg [5] invalidated this interpretation using high order statistical moments and showing that the energy cascade was in the opposite direction : from large to small scales. Billant & Chomaz [2] and Lindborg [6] proposed that the dynamics were not two dimensional because the selected vertical scale at each step of the cascade was the local buoyancy length scale U/N (where U is the velocity of the vortices at the scale considered and N the Brünt-Väisälä frequency) which is small, invalidating the hypothesis of Riley [8]. Billant & Chomaz [1] also proposed that the vertical scale selection was due to an instability, named zigzag instability, able to decorrelate the flow on the vertical. They demonstrated this instability on the specific case of a counter-rotating vortex pair that is seldom encountered in turbulent flows. On the contrary, pairing of same sign vortices is believed to be the dominant process of two dimensional turbulence and to account for both the upscale energy transfer and the downscale enstrophy cascade. In the present paper, we extend the work of Billant & Chomaz and study the stability of a pair of corotating vortices in a stratified fluid. We show that the zigzag instability also affects the pairing of vortices and decorrelates the flow on the buoyancy length scale.

NUMERICAL STABILITY ANALYSIS

A numerical stability analysis is performed using a pseudo-spectral solver of the Navier-Stokes equations linearized around a vertically uniform basic state made of two corotating Lamb-Oseen vortices (figure 1a). A Krylov method is implemented to extract the leading eigenmodes. For weak stratification, we found two unstable modes with distinct symetries that are due to the elliptic instability as described in the unstratified case by Le Dizès and Laporte [4]. An excellent agreement has been obtained with the latter study. For strong enough stratification, the elliptic modes are inhibited and a new mode takes over. As shown on the vertical vorticity field of the eigenmode (figure 1b), the perturbation corresponds to a symmetric displacement of the two vortices at an angle with respect to the x-axis. This mode is similar to the zigzag type since it translates the vortices without almost no deformation bringing them closer or further, alternatively along the vertical.

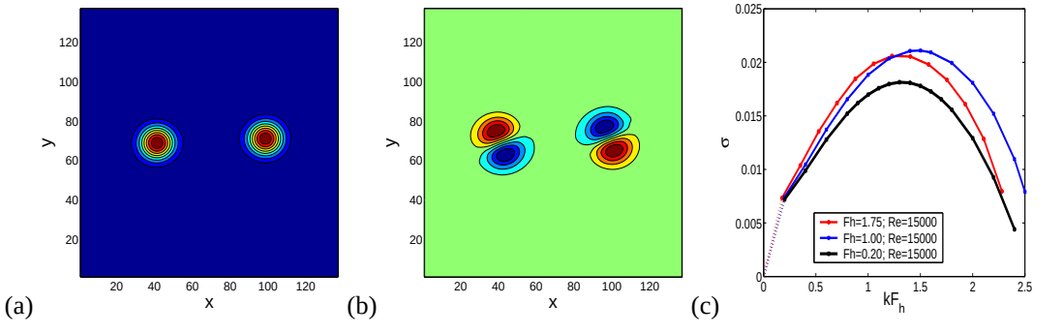


Figure 1. (*a*) Vertical vorticity of the basic state, (*b*) Vertical vorticity of the most unstable mode in a stratified fluid, (*c*) Growth rate against wave number times the horizontal Froude number for different Froude numbers.

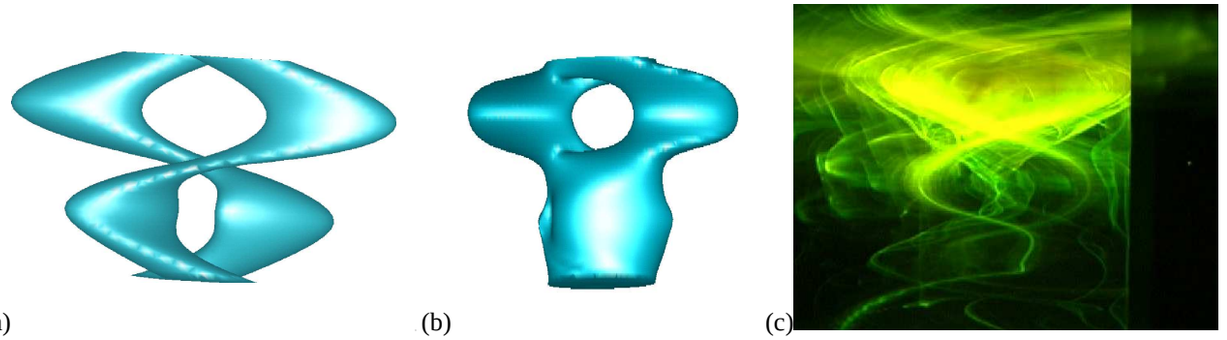
Furthermore, the instability respects the scaling law found for zigzag instability, ie the most unstable wave number increases linearly with stratification (figure 1c).

PHYSICAL EXPLANATION

This instability can be explained physically by the coupling between neutral waves on a single vortex in a stratified fluid and the strain field due to the companion vortex. If the corotating vortex pair is twisted along the vertical with respect to the rotation center, the motion induced by mass and potential vorticity conservation tends to bring the two vortices closer at the maximum of the twist. Thus, they rotate faster and the initial twist increases in an unstable way. A direct numerical simulation shows that the instability does not saturate due to non-linear effects so that vortex merging is speed up in some layers and inhibited in others resulting in a strong vertical decorrelation of the flow (figure 2a,b).

EXPERIMENTAL OBSERVATION

The existence of this new instability has been confirmed experimentally with an apparatus consisting of two corotating flaps in a large stratified tank similar to the set up used by Meunier [7]. We can see on figure 2c that as in the DNS (figure 2a,b) the pairing is delayed in the top layer and accelerated in the bottom one.



(a) (b) (c)

Figure 2. (*a*) DNS of the instability : 3D side view of a vertical vorticity contour. In the bottom layer, the vortices are getting closer whereas they are getting farther in the top layer. (*b*) The same as (*a*) later. The pairing has occurred in the bottom layer. (*c*) Experimental observation of the zig-zag instability. The green color is obtained by UV lighting and fluorescein initially painted on the edge of the flaps. When the flaps are closed, the fluorescein rolls up in the vortex cores. The eight shape visible on the picture is similar to the DNS result (figure 2a). It is the result of the zigzag instability that twists the vortex pair, promoting the pairing in the bottom layer and delaying it in the top layer.

CONCLUSION

A new zigzag instability has been studied in the case of corotating vertical vortices in a stably stratified flow. The numerical stability analysis has shown that the instability consists in displacement of the vortices and selects a vertical wave length proportional to the buoyancy length (L_B=U/N). The coupling between the displacement mode of a vortex with the strain field generated by its companion is identified to be the physical mechanism of the instability. Experimental observation and DNS show that the instability does not saturate and leads to the vertical decorrelation of the flow on a scale proportional to L_B. As vortex merging plays a crucial role in two-dimensional turbulence, this new instability is believed to alter the energy transfer and therefore make three-dimensional stratified turbulence depart from two-dimensional turbulence.

References

[1] Billant P., Chomaz J.M.: Experimental evidence for a new instability of a vertical columnar vortex pair in a strongly stratified fluid. *J. Fluid Mech* **418**:167–188, 2000.
[2] Billant P., Chomaz J.M.: Self-similarity of strongly stratified inviscid flows. *Physics of fluids* **13**:1645–1651, 2001.
[3] Le Dizès S., Laporte F.: Theoretical predictions for the elliptical instability in a two-vortex flow. *J. Fluid Mech* **471**:169–201, 2002.
[4] Lilly D.K.: Stratified turbulence and the mesoscale variability of the atmosphere. *Journal of Atmospheric Sciences* **40**:749–761, 1983.
[5] Lindborg E.: Can the atmospheric kinetic energy spectrum be explained by two-dimensional turbulence ? *J. Fluid Mech* **388**:259–288, 1999.
[6] Lindborg E.: Strongly stratified turbulence: A special type of motion *Proceedings of the Ninth European Turbulence Conference*, 2002.
[7] Meunier P.: Étude expérimentale de deux tourbillons corotatifs. *PhD Thesis*, Université de Provence Aix-Marseille I, France, 2001.
[8] Riley J.J., Metcalfe R.W., Weissman M.A.: Direct numerical simulations of homogeneous turbulence in density stratified fluids. *Proc. AIP Conf. Nonlinear properties of internal waves, ed. B.J. West* : 79–112, 1981.

LABORATORY AND NUMERICAL MODELING OF WATER EXCHANGE IN LONG STRAITS

Yuliya Kanarska*, Vladimir Maderich*
*Ukrainian Academy of Sciences, IMMSP, 42 Glushkov av., 03187 Kiev, Ukraine

Summary In this paper the hydrodynamics of exchange flows is investigated with focusing on the role of non-hydrostatic effects, friction and entrainment in the long straits. The simulation of the exchange flows in a laboratory long and narrow straits were performed with three-dimensional, non-hydrostatic, numerical model of free surface stratified flows. The calculations show importance of entrainment and friction in such flows. As a result the composite Froude number is significantly lower in comparison to predictions of two-layer hydraulic theory.

INTRODUCTION

The internal hydraulics of short and wide straits is the most studied. A concept of maximum exchange was developed for these flows. Recently additional effects such as time dependence, non-hydrostatic effects, mixing and interfacial instabilities which modify two-layer hydraulic theory were studied. The hydrodynamics of water exchange in long straits are less studied. The objective of this study is validation of concept of maximal exchange for long straits.

METHODOLOGY AND RESULTS

The results of laboratory experiment [1] exchange flow through long and narrow strait connecting two deep and wide basins filled with water of different density and the same strait with sill in the middle of the strait [2] are considered and compared with numerical simulations. A buoyancy flux between the two basins was maintained by heating the left basin and cooling the right. The numerical tool for investigations is a three-dimensional, non-hydrostatic, numerical model of free surface stratified flows [3]. The model is a non-hydrostatic extension of the free-surface primitive equation POM model. A mode splitting technique, decomposition of pressure and velocity fields into hydrostatic and non-hydrostatic components are the base of numerical algorithm of the model. A buoyancy flux between the two basins was simulated by including Newtonian relaxation terms in the heat transport equation.
The flow is laminar but experiment data and calculations (Fig. 1 a,b) indicate the presence of a broad thermocline which is evidence of entrainment between the fluid layers. The experiment and computations show (Fig. 2) that composite Froude number G is lower than expected from predictions of two-layer hydraulic theory according to the concept of maximal exchange. The entrainment between layers suggests more complicated structure of flow than two-layer approximation. The computed velocity and density profiles at Fig. 3 show that the flow could be described by the three layer structure with two bounding layers separated by an interfacial layer of finite thickness and variable properties. From Fig. 4 we see that the zero isotach is not centered in the interfacial layer. Fig. 5 shows the role of each layer in carrying the mass. These results demonstrated that the entrainment and friction in this configuration of the long strait is crucial for hydrodynamics and hydraulics of exchange flow in the strait.
The presence of the sill in the middle of the long strait (experiment 701 in [2]) changes the character of the circulation in the strait (Fig. 6, Fig. 8a). The detailed pattern of the velocity field is shown in Fig. 8b. It indicates the presence of a complicated flow structure at the sill zone. The flow slows down at the left side of the sill and then creating a countercurrent. The dense water lifts along the left side of the sill and turns finally to the left, forming a broad interface layer. The broad thermocline is evidence of entrainment between the fluid layers. As well as in the previous experiment the entrainment and friction cause reduction the maximum values of G^2 (Fig. 7). The comparison of non-hydrostatic and hydrostatic calculations was carried out with the same spatial resolution. Fig.8c indicates essential difference between non-hydrostatic and hydrostatic velocity fields. It is about 22% at the slope and the foot of the sill.

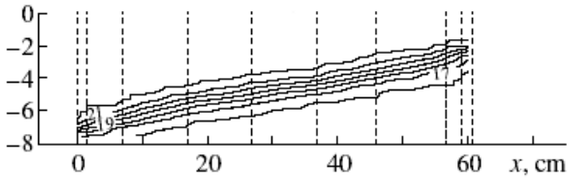
CONCLUSIONS

The question about hydraulic control in real long straits like the Bosphorus and Dardanelles is still open. The investigation of the hydrodynamics of the water exchange in the laboratory long straits using 3D non-hydrostatic numerical model demonstrated that the entrainment

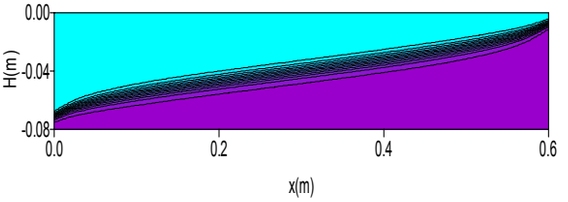
Acknowledgments
This study was partially supported by INTAS Fellowship for Young Scientists № YSF 2002-127 (Yuliya Kanarska).

References

[1] Maderich V. S.: Laboratory modeling of water exchange through sea straits. *Oceanology* 38 No 5: 602-608, 1998.
[2] Maderich V. S.: Two-layer exchange flows through long straits with sill. *Oceanic Fronts and Related Phenomena. Konstantin Fedorov Int. Memorial Symp., IOC Workshop Rep. Series*, N 159, UNESCO'2000, 326-331, 2000.
[3] Kanarska Y., Maderich V.: A non-hydrostatic numerical model for calculating free-surface stratified flows. *Ocean Dynamics* 53 No3: 176-185, 2003.



(a)



(b)

Figure 1. Temperature along the strait. (a) measured data, (b) computed results

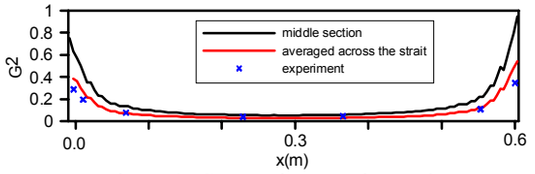


Figure 2. Composite Froude number

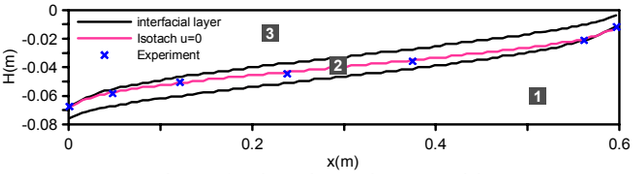


Figure 4. Three layer decomposition

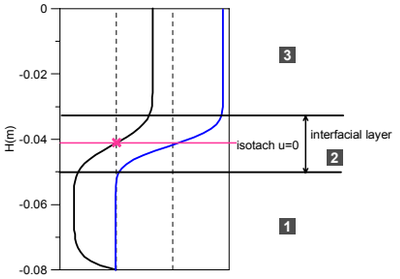


Figure 3. Velocity and density profiles

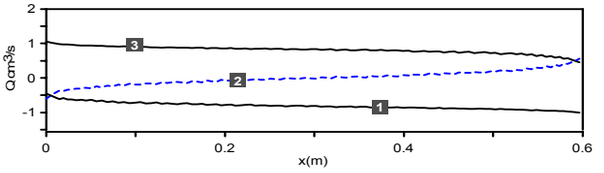


Figure 5. Discharges in each of three layers

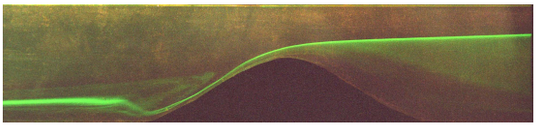


Figure 6. Photo of experiment 701.

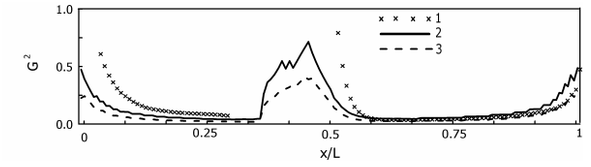


Figure 7. Composite Froude number along the strait calculated from the experiment 701 (1) vs. the computed one in the middle longitudinal section of the strait (2) and computed one using average flow parameters across the strait (3)

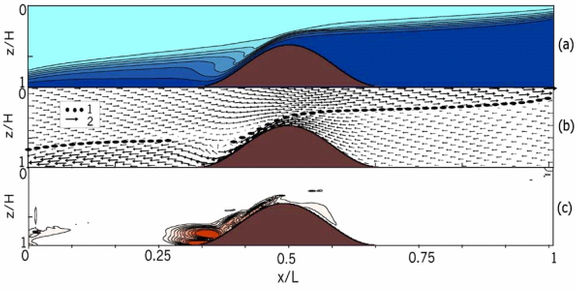


Figure 8. Computed density and velocity fields. (a) Contour plot of computed density from experiment 701. (b) Interface position in experiment 701 (1) and non-hydrostatic velocity field (2). (c) Absolute value of difference between hydrostatic and non-hydrostatic velocity fields.

XXI ICTAM, 15–21 August 2004, Warsaw, Poland

WAVE—MEAN FLOW INTERACTION IN COUPLED ATMOSPHERE–ICE–OCEAN SYSTEMS

Alastair D. Jenkins*
*Bjerknes Centre for Climate Research, Bergen, Norway

Summary A dynamically consistent framework for modelling atmosphere–ocean interaction must take account of surface waves, either implicitly or explicitly. We may account for the waves explicitly by employing a numerical spectral wave model, and applying a suitable theory of wave—mean flow interaction. Below the water surface the generalized Lagrangian mean (GLM) formulation is suitable, and a closed system of equations may be obtained to second order in wave slope by applying wave action conservation equations in the propagation of the spectral wave components. The coupled model system will also take account of the Earth's rotation, the momentum balance during wave generation and dissipation, the effect of depth-varying currents on wave propagation, the presence of surface films and sea ice, the effect of waves on the mean water level, and the generation of Langmuir circulations.

INTRODUCTION

Surface waves comprise an important aspect of the interaction of the atmosphere and the ocean. Any dynamically consistent framework for the modelling of atmosphere–ocean interaction must take them into account, either implicitly, via a Charnock-type dependence of aerodynamic surface roughness on the air–sea momentum flux or wind speed, or explicitly, using, for example, a spectral wave prediction model. In the latter case, the momentum flux from the airflow to the waves may be computed by analytical or numerical models for wave generation, or by related quasilinear theory [1, 2, 3]. The flux of momentum from the waves to the ocean current may be a result of wave energy dissipation, by breaking [4], or by turbulent stresses within the water column [5, 6] or at the sea bottom [7]. A third method of representation of the dynamical effect of waves is by inertial coupling theory [8, 9], in which the wave field acts to transport momentum vertically, from the critical level in the atmospheric boundary layer, where the dominant wave phase speed is equal to the wind speed, to a level below the wave troughs where the current approximates the wave-induced Stokes drift.

COORDINATE SYSTEMS

In a spectral wave model, such as, for example, WAM [10], we compute the distribution of the variance of the surface displacement amongst components of different wavenumber, and so may couple such a model with an ocean current model by means of an $O(\epsilon^2)$ interaction theory where ϵ is a representative wave slope. Although we may formulate the problem in fixed Cartesian (Eulerian) coordinates, there are advantages to using curvilinear coordinate systems which follow the water surface during the course of a wave cycle. We may resolve vertical variations in the near-surface mean flow and other variables, at small distances from the surface, which can be essential for applications such as heat and gas exchange through the water surface, and ice formation.

Although it is possible to employ a curvilinear coordinate system in which the coordinate displacements are purely vertical [11], it may be more satisfactory to allow the coordinate surfaces also to move horizontally. A particularly useful coordinate system is employed in the generalized Lagrangian mean (GLM) formulation of Andrews and McIntyre [12], in which the mean velocity $\overline{\mathbf{u}}^L$ and the coordinate displacement ξ are related by $\partial\xi/\partial t + \overline{\mathbf{u}}^L \cdot \nabla\xi = \mathbf{u}^\xi - \overline{\mathbf{u}}^L$, where $\mathbf{u}^\xi$ is the instantaneous velocity in the curvilinear coordinate frame. The coordinate system is close to a Lagrangian coordinate system for small values of $\overline{\mathbf{u}}^L$, so we may use results from Lagrangian perturbation expansions.

The effect of the GLM mean flow on wave propagation can also be formulated in terms of finite-amplitude conservation laws for wave action [13], so that to $O(\epsilon^2)$, a closed system of equations for the coupled wave—mean flow system may be obtained. A systematic treatment of wave–current interaction in two dimensions (horizontal and vertical) was given by Groeneweg and Klopman [14]. The GLM formulation cannot be used in the vicinity of critical layers, so more general curvilinear coordinates are required for airflow over waves, cf. Jenkins [3].

OUTLINE OF A COUPLED SYSTEM

For a coupled wave–mean flow model system in a region possibly covered by sea ice, we require the following factors to be included:

1. *The Earth's rotation* is included in the GLM equations [12]. We may, neglect terms of higher order than $O(f/\sigma)$, where f is the Coriolis parameter and σ is the wave intrinsic angular frequency. The effect of Coriolis force and vorticity in the mean current on the Stokes drift also comes naturally from the GLM equations.

2. Momentum balance in wave generation. This comes from the surface oscillatory boundary conditions for pressure and shear stress, see [3, 5, 6].

3. *Momentum balance in wave dissipation*. Wave pseudomomentum which is lost through dissipation will reappear as a forcing of the mean current.

- *Wave breaking* may be nevertheless often regarded as 'weak in the mean' [16], and we may simulate it empirically as dissipation by other means (e.g. turbulence, viscosity).
- *Within the water column*. Dissipation of waves by turbulence (or by breaking, see above) may be simulated by an eddy viscosity which, however, in practice must be less than that used to diffuse momentum within the mean flow field [5, 6, 17]. If the eddy viscosity varies with the vertical coordinate, there is a source of mean momentum within the water column [5, 6].
- *Surface and bottom boundary layers*. Analytical solutions are most straightforward if we assume the eddy viscosity ν_E to be constant within the boundary layers. The surface boundary layer modifies the boundary conditions for the fluid in the interior. The no-slip bottom boundary condition results in a relatively strong mean flow [7].
- *Sea ice and surface films* alter the boundary conditions radically, increase the wave damping substantially, induce a strong near-surface mean flow from the dissipation of wave pseudomomentum, and may lead to convergence and downwelling at the ice edge [18, 19, 21].

4. *Effect of the mean flow on wave propagation*. Waves on a vertically-sheared current obey the Orr–Sommerfeld (or Rayleigh) equation. If the shear in the current is weak, the wave phase speed is changed by the weighted integral of the current, where the weighting factor is e^{2kz} in deep water, k being the wavenumber and z the (upward) vertical coordinate [22].

5. *Changes in sea-surface elevation*. One disadvantage of the GLM equations is that the Jacobian determinant of the coordinate transformation is not constant, which makes the continuity equation more complex than its counterpart in Eulerian coordinates. If this effect is properly taken into account, the 'set down' of the mean sea surface is reproduced, as waves propagate without breaking into shallow water, as well as the wave setup which occurs as they dissipate [23, 24].

6. *Langmuir circulations*. The Craik–Leibovich equations [25] are straightforward to derive from the GLM equations [26]. The helical roll circulations which are solutions to these equations, either via an instability mechanism, or as a result of forcing by crossing wave trains [27], may either be simulated directly by the coupled model equations, or averaged out if a grid scale coarser than the circulation scale is used.

The Coriolis and dissipative effects mentioned above can be regarded as 'small' perturbations, so may be added together in the equations for the mean flow.

References

[1] Miles J.W.: On the generation of surface waves by shear flows. *J. Fluid Mech* **3**:185–204, 1957.
[2] Janssen P.A.E.M.: Wave-induced stress and the drag of air flow over sea waves. *J. Phys. Oceanogr* **19**:745–754, 1989.
[3] Jenkins A.D.: A quasi-linear eddy-viscosity model for the flux of energy and momentum to wind waves, using conservation-law equations in a curvilinear coordinate system. *J. Phys. Oceanogr* **22**:843–858, 1992.
[4] Weber J.E.: Virtual wave stress and mean drift in spatially damped surface waves. *J. Geophys. Res* **106**:11653–11657, 2001.
[5] Jenkins A.D.: Wind and wave induced currents in a rotating sea with depth-varying eddy viscosity. *J. Phys. Oceanogr* **17**:938–951, 1987.
[6] Jenkins A.D.: The use of a wave prediction model for driving a near-surface current model. *Dt. Hydrogr. Z* **42**:133–149, 1989.
[7] Longuet-Higgins M.S.: The mechanics of the boundary-layer near the bottom in a progressive wave. — Appendix to R. C. H. Russell and J. D. C. Osorio, 'An experimental investigation of drift profiles in a closed channel'. In *Proc. 6th Conf. on Coastal Engng*, pages 171–193. Council on Wave Research, Univ. of California, Berkeley, 1958.
[8] Bye J.A.T.: The coupling of wave drift and wind velocity profiles. *J. Mar. Res* **46**:457–472, 1988.
[9] Bye J.A.T., Wolff J.O.: Momentum transfer at the ocean–atmosphere interface: the wave basis for the inertial coupling approach. *Ocean Dyn* **52**:51–57, 2001.
[10] Komen G.J., Cavaleri L., Donelan M.A., Hasselmann K., Hasselmann S., Janssen P.A.E.M.: *Dynamics and Modelling of Ocean Waves*. Cambridge University Press, 1994.
[11] Mellor G.: The three-dimensional current and surface wave equations. *J. Phys. Oceanogr* **33**:1978–1999, 2003.
[12] Andrews D.G., McIntyre M.E.: An exact theory of nonlinear waves on a Lagrangian-mean flow. *J. Fluid Mech* **89**:609–646, 1978.
[13] Andrews D.G., McIntyre M.E.: On wave-action and its relatives. *J. Fluid Mech* **89**:647–664, 1978.
[14] Groeneweg J., Klopman, G.: Changes of the mean velocity profiles in the combined wave–current motion described in a GLM formulation. *J. Fluid Mech* **370**:271–296, 1998.
[15] Jenkins A.D.: A theory for steady and variable wind and wave induced currents. *J. Phys. Oceanogr* **16**:1370–1377, 1986.
[16] Hasselmann K.: On the spectral dissipation of ocean waves due to white capping. *Bound.-Layer Meteorol* **6**:107–127, 1974.
[17] Belcher S.E., Harris J.A., Street R.L.: Linear dynamics of wind waves in coupled turbulent air–water flow. Part 1. Theory. *J. Fluid Mech* **271**:119–151, 1994.
[18] Alpers W., Hühnerfuss H.: The damping of ocean waves by surface films: A new look at an old problem. *J. Geophys. Res* **94**:6251–6265, 1989.
[19] Weber J.E. Wave attenuation and wave drift in the marginal ice zone. *J. Phys. Oceanogr* **17**:2351–2361, 1987.
[20] Weber J.E. Sætra Ø.: Effects of film elasticity on the drift velocity of capillary–gravity waves. *Phys. Fluids* **7**:307–314, 1995.
[21] Jenkins A.D., Jacobs S.J.: Wave damping by a thin layer of viscous fluid. *Phys. Fluids* **9**:1256–1264, 1997.
[22] Teague C.C. Multifrequency HF radar observations of currents and current shears. *IEEE J. Oceanic Engng* **OE-11**:258–269, 1986.
[23] Longuet-Higgins M.S., Stewart R.W.: Radiation stress and mass transport in gravity waves with application to 'surf beats'. *J. Fluid Mech* **13**:481–504, 1962.
[24] Ardhuin F., Chapron B., Elfouhaily, T.: Waves and the air–sea momentum budget, implications for ocean circulation modelling. Submitted to *J. Phys. Oceanogr*, 2002.

[25] Craik A.D.D., Leibovich S.: A rational model for Langmuir circulations. *J. Fluid Mech* **73**:401–426, 1976.
[26] Leibovich S.: On wave–current interaction theories of Langmuir circulations. *J. Fluid Mech* **99**:715–724, 1980.
[27] Weber J.E.: Friction-induced roll motion in short-crested surface gravity waves. *J. Phys. Oceanogr* **15**:936–942, 1985.

XXI ICTAM, 15–21 August 2004, Warsaw, Poland

MULTIPLE JET FORMATION IN A CONVECTIVELY DRIVEN FLOW ON A BETA-PLANE

Peter L. Read*, Yasuhiro H. Yamazaki*, Stephen R. Lewis*, Paul D. Williams*, Kuniko Miki-Yamazaki*, Joël Sommeria**, Henri Didelle**, Adam Fincham**

*Department of Physics, University of Oxford, Clarendon Laboratory, Parks Road, OXFORD, OX1 3PU, UK
**LEGI Coriolis, 21 rue des Martyrs, 38000 Grenoble, France

Summary We present results from laboratory experiments carried out on the Coriolis rotating platform in Grenoble, France, to investigate the influence of a topographic beta-plane (obtained via a sloping bottom) on convectively-driven geostrophic turbulence. Dense, salty water is sprayed continuously onto the surface of the tank, which leads to the formation of a field of convective vortices. In the presence of a sloping bottom, the vortices interact nonlinearly, leading to the formation of a series of quasi-steady, parallel azimuthal jets on a scale comparable with the so-called Rhines scale $L_R = \pi\sqrt{2U/\beta}$. Such jets are not found with a flat bottom. Implications will be discussed in the context of various geophysical problems, including the atmospheres of the outer planets and the Earth's oceans.

Introduction

The banded pattern of ammonia clouds is one of the most striking features of the atmospheres of Jupiter and Saturn. These bands are associated with multiple zonal jets of over 100 m s^{-1} with alternating sign against latitude[1]. A similar pattern of zonation also occurs in the Earth's oceans. The dynamical origin of this banded structure remains poorly understood, but most approaches towards understanding the zonation have suggested that the pattern may originate from the anisotropy in a shallow turbulent layer of fluid due to the β effect, i.e., due to the latitudinal variation of the effective planetary vorticity[2]. Until recently, quantitative understanding of this process has been based principally on numerical simulations of two-dimensional or geostrophic turbulence in stirred rotating fluids[3], but such models are highly idealised and take little account of the vertical structure. Laboratory experiments provide an alternative means for studying these processes, though previous investigations[4] have been unable to access regimes at sufficiently high Reynolds number to convincingly demonstrate nonlinear zonation effects. Here we report the results of new experiments, conducted on the world's largest rotating platform, which confirm that multiple zonal jets may indeed be generated and maintained by this mechanism.

Methods

Our experiments were performed on the 14 m diameter "Coriolis" turntable in Grenoble, France. The schematic layout of our configuration is illustrated in Fig. 1. A circular cylindrical container was set on the turntable, and convective forcing was applied by gently spraying dense water from above the main fluid layer. An equivalent topographic β-effect was obtained by imposing a conical slope at the bottom of the circular container. The slope was implemented with a plastic-coated stretched fabric sheet, which could be removed for additional experiments with a flat bottom in order to compare the flow structure both with and without a topographic β-effect (apart from a weak centrifugal deformation of the free upper surface). The rotation period for most experiments was set to 40 seconds for the results to be presented herein.

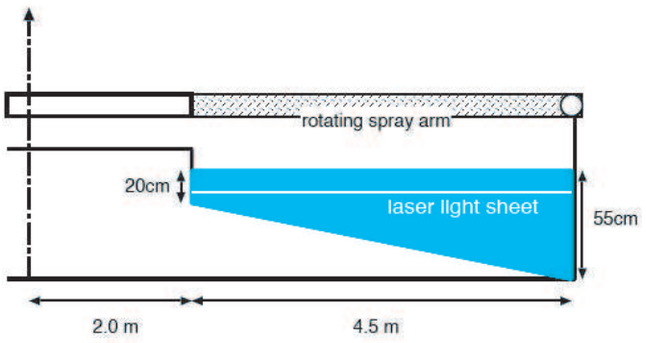


Figure 1: Schematic cross-section of the circular container, showing the rotating spray arm used to provide continuous convective forcing. The entire apparatus is set on a circular turntable.

Results

The horizontal velocity fields were obtained from plan view CCD images by a Correlation Imaging Velocimetry method. In order to diagnose the anisotropy of the evolving flow, the velocity fields were decomposed into radial and zonal (*i.e.,* azimuthal) components and mapped into (r, $r\theta$) coordinates, where r is the radius and θ the azimuthal angle. The well-developed horizontal flow is dominated by eddies of various sizes, but there is also a clear indication of banded structure along the zonal direction. The temporal fluctuation of the radial profile of mean zonal flow is shown in Fig. 2a, well after the initial growth of the kinetic energy has saturated. The formation of sustained alternating jets is now evident

when the topographic β effect is imposed, although there is substantial meandering of these jets during this period and occasional splitting and mergers. Fig. 2b shows the evolution of the zonal mean flow observed in a corresponding flat bottom experiment. The domain-filling single-cell circulation, which is most evident in this case, is presumably due at least in part to differential wind stress effects. The characteristic scale-widths of the jets are closer to the Rhines scale L_R (on the order $L_R = \pi\sqrt{2U/\beta}$, where U is a typical horizontal velocity scale) of 0.63 to 1.4 m, rather than to the external radius of deformation ($L_D \sim \sqrt{gD}/f$, where f is the Coriolis parameter and D the fluid depth), which ranged from $L_D \sim 4.5$ m (along the inner wall) to 7.4 m (near the outer wall).

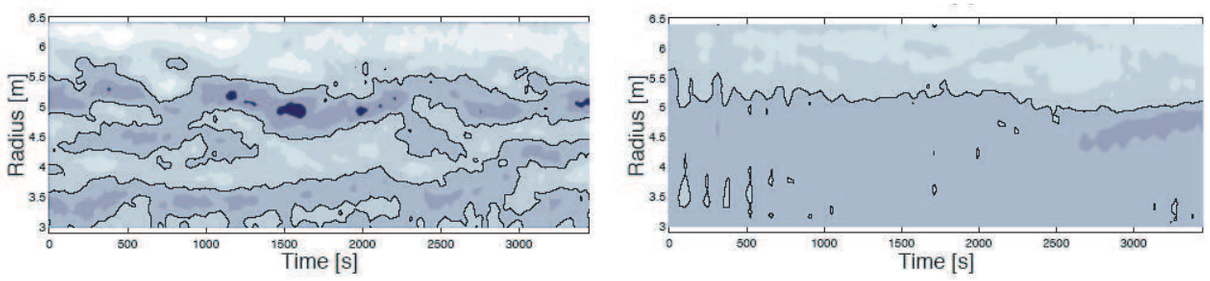


Figure 2: Horizontal velocity field. a, structure and fluctuation of the mean zonal velocity of the mature flow. The contour interval is 0.2 cm s^{-1} and the solid line denotes the contour of null velocity. b, initial development of the zonal mean flow in the flat bottom experiment.

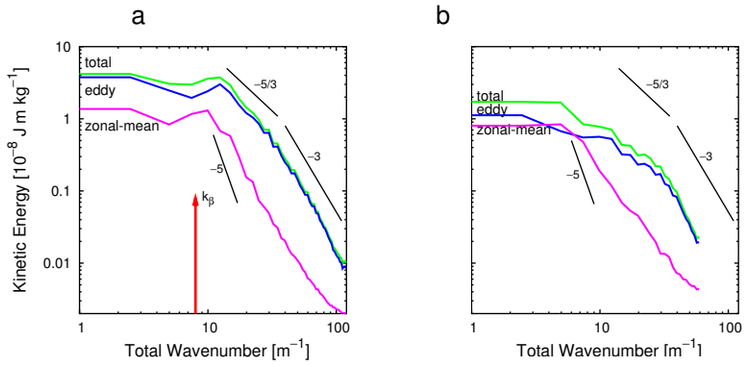


Figure 3: Spectra of total, zonal-mean and eddy components of kinetic energy versus total wavenumber (2π / wavelength) for (a) the sloping bottom experiment and (b) the flat bottom case. The straight lines are references for the $-5/3$, -3 and -5 slopes. The arrow in a indicates the wavenumber k_β associated with the Rhines scale.

Spectra

Fig. 3 shows spatial kinetic energy spectra for the two configurations. The spectra of the zonal-mean and eddy components of kinetic energy were calculated from velocity fields obtained by a high resolution camera as a function of the total wavenumber. In the sloping bottom case, there is a peak near the Rhines scale (indicated as k_β) for both the zonal and eddy components, with the peak wavenumber of the eddy energy being slightly higher than that of the zonal mean. The spectrum matches well with a $-5/3$ slope at large scales and -3 at small scales, which is predicted by the theory of geostrophic and two-dimensional turbulence[2]. Interestingly, the spectrum of the zonal mean kinetic energy at wavenumbers between 10 and 30 m^{-1} shows a significantly steeper decay with k, though does not quite reach the k^{-5} variation anticipated from the work of Huang et al.[3]. The apparent near-equilibration of the jets at a scale comparable to L_R would seem to indicate that we are in a regime for which bottom drag is relatively insignificant in the selection of jet scale.

References

[1] Limaye, S. S., Jupiter: New estimates of the mean zonal flow at the cloud level. *Icarus*, **65**, 335–352 (1985); Sanchez-Lavega, A., J. F. Rojas and P. V. Sada, Saturn's zonal winds at cloud level, *Icarus*, **147**, 405 (2000).

[2] Rhines, P. B., Waves and turbulence on a beta-plane. *J. Fluid. Mech.* **69**, 417–443 (1975); Rhines, P. B., Geostrophic turbulence. *Ann. Rev. Fluid Mech.* **11**, 401–441 (1979).

[3] Williams, G.P., Planetary circulations: 1. Barotropic representation of Jovian and Terrestrial turbulence. *J. Atmos. Sci.*, **35**, 1399 (1978); Huang, H. P., B. Galperin and S. Sukoriansky, Anisotropic spectra in two-dimensional turbulence on the surface of a rotating sphere. *Phys. Fluids* **13** (1), 225–240, (2001).

[4] Condie, S. A. and P. B. Rhines, A convective model for the zonal jets in the atmospheres of Jupiter and Saturn. *Nature*, **367**, 711–713 (1994); Bastin, M. E. and P. L. Read, Experiments on the structure of baroclinic waves and zonal jets in an internally heated, rotating, cylinder of fluid. *Phys. Fluids* **10**(2), 374–389 (1998).

INTERMITTENCY IN STRATIFIED TURBULENCE PRODUCED BY BREAKING INTERNAL GRAVITY WAVES

Pascale Bouruet-Aubertot*, Joël Sommeria**, C.R. Koudella***
*LODYC/IPSL, Paris, France
**LEGI/Université Joseph Fourier, Grenoble, France
***DAMTP/University of Cambridge, Cambridge, England

Summary Internal gravity waves nonlinear interactions lead to intermittent breaking events with density overturning and vertical turbulent mixing. We analyze the statistics of density and velocity fluctuations in this process, using direct numerical simulations.
We characterize the density and velocity gradients at different scales along the vertical direction. The velocity gradients behave in a very similar way to usual turbulence, while the density gradients are very intermittent. This can be attributed to the formation of sheets with strong stable density gradients. Unstable density gradients are rare and form intermittent patches of different scale for which we have analyzed the statistics. We discuss the link with mixing properties of the internal wave field and compare with observations in the ocean and the atmosphere.

INTRODUCTION

Internal wavebreaking is an important source of turbulence in stably stratified fluids. Because wavebreaking occurs intermittently in space and time it is important regarding the interpretation of microstructure measurements (for instance the estimate of mixing) to have a "good" knowledge of the statistical properties at small scales. To this aim process-oriented studies performed with the use of numerical simulations constitute an efficient approach. We start with a simple initial condition (a large scale internal gravity wave), so that turbulence is produced by an intrinsic sequence of instabilities, without external noise, and our calculations can be exactly reproduced and checked. We performed two-dimensional direct numerical simulations which allow better resolution. It is representative of three dimensional cases, as shown by different comparisons Bouruet-Aubertot *et al* (2001), Carnevale *et al* (2001). We analyze as well three-dimensional numerical simulations (but with a lower resolution). The purpose of this paper is to analyze statistical properties of the turbulence induced by the breaking of a large scale primary wave, characterize rare events responsible for the intermittency and discuss the link with mixing processes.

RESULTS

Moments and exponents

We computed the moments of the horizontal and vertical velocity, u and v, and of the density fluctuations, ρ' versus the separation δz. We obtained power laws versus δz over one decade approximately. We then looked at the behavior of the exponents ζ_n of the moments of u, v and ρ'. Both velocity components and density are intermittent. Interestingly scaling exponents for u and v are very closed suggesting that physical events responsible for the intermittency of the flow occur at very small scales where the anisotropy introduced by the stratification does not come into play. In contrast density fluctuations are more intermittent than velocity components. This point is very similar to ordinary turbulence in which the passive scalar has a more intermittent behavior than velocity. We then compared the scaling exponents for the density fluctuations with those obtained in ordinary three-dimensional turbulence. Density fluctuations are found more intermittent than passive scalar in three-dimensional turbulence. This suggests that the dynamical coupling between buoyancy and inertial forces is a crucial process for the intermittency of density fluctuations.

Pdfs of vertical density gradients at small vertical scales

We next characterized the density and velocity gradients at different scales along the vertical and horizontal directions. The velocity gradients behave in a very similar way to usual turbulence, while the density gradients at small scales are very intermittent. More precisely probability density functions (pdfs) of the density gradients at small scales are highly skewed. The pdf decreases more strongly toward unstable density gradients while the decrease is less steep toward stable stratification until the pdfs reaches almost a plateau for the highest values (Fig.1). We identified the physical events responsible for this density structure. These strongly stratified regions are correlated with breaking events. Indeed density overturnings can lead in some cases to a convergence of fluid which results in a local increase of the vertical density gradient. The resulting density structure is made of a succession of sheets with strong stable density gradients and turbulent regions of greater vertical extent.

Two processes may be responsible for the increased skewness of the pdf of density gradients at small vertical scale, either the reversible straining produced by internal gravity waves or irreversible mixing events. These two alternatives were addressed in theoretical models. We focus here on the gamma pdf model, proposed by Hayes *et al.* (1975), which describes a staircase density profile with randomly distributed steps separating mixed layers with uniform density. This model provides a reasonable fit to our numerical data at scales smaller than $30\delta_0$ (where δ_0 is the Ozmidov length scale defined by $\delta_0 = \sqrt{\frac{\varepsilon}{N^3}}$, ε is the energy dissipation and N the buoyancy frequency). The probability density of

the density difference $\Delta\rho$ at separation Δz is given by Eq.9 of Hayes *et al* (1975) and it is determined by a single parameter μ which denotes the mean number of steps per unit of height. The formation of sheets and layers is clearly associated with energy dissipation and vertical mixing. We therefore expect a link between the Ozmidov scale, related to energy dissipation, and the mean vertical distance between sheets, μ^{-1}. Figure 2 shows indeed that these two quantities are proportional : $\mu^{-1} \approx 5.3\lambda_0$.

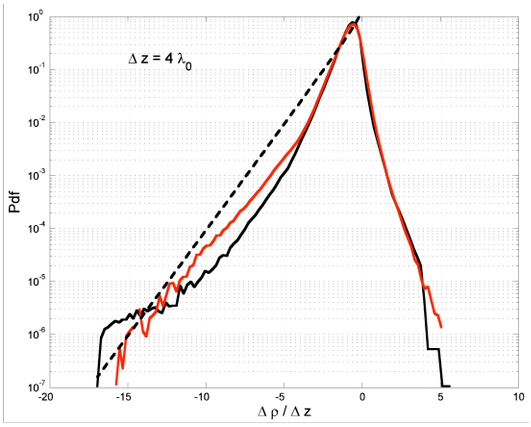


Figure 1: Pdfs of density gradient at vertical scale $\Delta z = 4\lambda_O$ for a wave of amplitude $A = 0.256$, 3d results are represented in red and 2d results in black, theoretical prediction of the Hayes *et al* model with a dashed line.

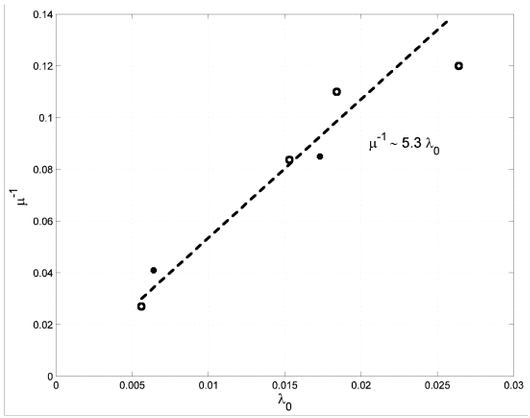


Figure 2: Mean distance between steps μ^{-1} as a function of the Ozmidov length scale λ_O, 2d results are represented with empty circles and 3d results with filled circles.

CONCLUSION

We analyzed some statistical properties of the turbulence induced by the breaking of internal gravity waves. This dynamics corresponds to the so-called buoyancy subrange and it is characterized by kinetic and available potential energy spectra that follow a k_z^{-3} power law. In the ocean such behavior is obtained in the finescale domain, in between weakly nonlinear waves and three dimensional turbulence, corresponding to vertical scales typically within the range $[1m, 10m]$. We focused on the vertical structure of the density field with the main purpose of providing a link between density intermittency, energy dissipation and mixing processes.

Density gradients are strongly intermittent at small scales. The main feature is the strong skewness of the histograms toward stable stratification that becomes evident as soon as overturning events occur. We have characterized these rare and intense events. These take the form of strongly stratified sheets of thin vertical thickness close to the Ozmidov scale and horizontal scale related to that of the large scale breaking wave. These structures are generated through strong convergent motions induced by surrounding overturning events. Indications of these structures were obtained in the atmosphere from vertical profiles of temperature as well as in the ocean in the seasonal thermocline of the Sargasso Sea.

We then checked the ability of the sheet and layer model or gamma pdf model to reproduce the shape of the histograms of vertical density gradient at small vertical scales (typically within $[4\lambda_0, 30\lambda_0]$). This model, which assumes that the step-like structure is the result of mixing processes, depends on one parameter, the mean number of sheets (or steps) per unit length.
The main result of this paper is that the sheet spacing varies linearly with the Ozmidov length scale defined with the total energy dissipation rate. This thus provides a link between density statistics at finescale and energy dissipation. As a consequence, the mean eddy diffusivity that characterizes breaking events varies linearly with a dimensionless parameter defined with μ^{-1} : $\frac{\mu^{-2} N}{\varepsilon}$ which provides a link with mixing processes. In future work we plan to further check this indirect estimate of mixing based on density statistics at finescale on a large set of in situ oceanic data and compare this estimate with direct measurements of mixing as inferred from microstructure measurements.

References

[1] Bouruet-Aubertot, P., Koudella, C.R., Staquet, C., Winters, K.B. 2001 , *Dyn. Atmos Oceans,* **33**, 95-134.
[2] Carnevale, G.F., Briscolini, M. and Orlandi, P. 2001, *J. Fluid Mech.*, **427**, 205-239.
[3] Hayes, S.P., Joyce, T.M., Millard, J.R., 1975, *J. Geophys. Res.*, **80**, no.3, 314-319.

Measurements of the influence of ocean surface kinematics on air-sea heat fluxes

Fabrice Veron[*], W. Kendall Melville[**]
[*]*University of Delaware, College of Marine Studies, Newark DE, USA.*
[**]*University of California, San Diego, Scripps Institution of Oceanography, La Jolla CA, USA.*

Summary: We present results of several field experiments on the kinematics of small-scale surface turbulence, the influence on the surface skin layer, and the resulting transfers of heat across the diffusive layer at the surface of the ocean. A variety of optical and electro-mechanical instruments are used to measure the evolution of the surface and sub-surface velocity, and temperature fields. These include visible and infrared imaging of the surface, thermal/IR surface velocimetry, and fast-response thermometry. We show that at low wind speed, it is the small-scale turbulence at the surface of the ocean, rather than breaking waves that most influence and disrupt the surface skin layer. We find that the enstrophy of the surface turbulence correlates with the surface heat flux, and that the surface wave field modulates a component of the total air-sea heat flux.

INTRODUCTON

The top few meters of the oceanic boundary layer play a key role in the transfer of momentum, gas, heat and mass between the atmosphere and the ocean. The magnitude of these fluxes is strongly influenced by the dynamics of the surface layer. For the ocean-atmosphere heat flux, the sea surface temperature (SST) is a key variable [1, 2]; however, accurate measurements of SST are quite difficult. Directly beneath the surface is a thin diffusive sublayer where the exchange of momentum is principally governed by molecular processes. With the difference between kinematic viscosity and thermal diffusivity being almost an order of magnitude, there is also a thermal sublayer within the viscous sublayer. The thermal sublayer is typically a few mm thick, and with much of the net heat flux from the ocean to the atmosphere being positive upward, the surface temperature, or "skin temperature", is often a few tenths of a degree colder than the bulk sea temperature. This temperature difference has long been a problem for remote SST measurements and is commonly referred to as the cool skin bias. To date, a robust parameterization of the skin temperature is still elusive.

With the globally averaged wind speed (traditionally U_{10}, the wind speed at 10m) in the range of 6-8 m/s, much of the time the air-sea interface is in a low-wind regime with the surface boundary layer in a transitional regime. From previous work [3], both in the laboratory and the field, it is the Langmuir circulations and small-scale turbulence, and not wave breaking, that first destroy the cool surface skin. However, if the winds are sustained, micro scale breaking may quickly follow [4]. Nevertheless, we expect that small-scale surface turbulence is a controlling factor of the temperature of the cool skin at low wind speeds.

EXPERIMENTS & RESULTS

Experiments were performed from the research platform FLIP during the spring of 2002 and summer of 2003. An infrared and video system was fabricated and consisted of an Infrared (IR) camera, a video camera, a CO_2 laser, a marking head assembly and a motion sensing package. The infrared camera captured images at a 60Hz frame rate. An active IR measurement is taken when the CO_2 laser is fired and the beam is redirected by the marking head to lay down a thermal pattern on the surface. (The penetration depth of the infrared radiation at the laser wavelength (10.6μm) is just a few microns.) In our experiments, we laid down a series of points in a sparse array such that the thermal marks could be followed within the IR images. The translation, rotation and deformation of the pattern give direct measures of the velocity, vorticity, rate of strain, and divergence at the surface. In addition, the decay rate of the heat spots leads to an estimate of the surface heat flux.

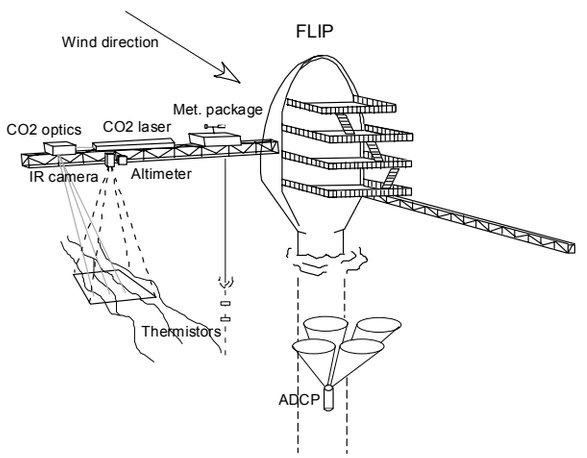


Figure 1. Experimental setup on the R/P FLIP

Figure 2a) and b) show examples of infrared images of the ocean surface for a wind speed of 3.7m/s. The images are 2.5m x 2.5m and show a full temperature contrast of about 0.4°C. Thermal patterns consisting of three dots are clearly visible in the images. Also visible is the variance of the skin temperature due to the turbulence that disrupts the surface layer with warmer water from below. One can identify linear, semi-coherent structures on the images that resemble small-scale Langmuir circulations. The thermal pattern moves with the surface currents (including Stokes drift) and clearly deforms, indicating that the surface is sheared. Figure 2c) show the result of tracking the markers in the thermal images. In this example, the x-component of displacement exhibits wave activity, while the y-component is dominated by advecting surface currents. The temperature

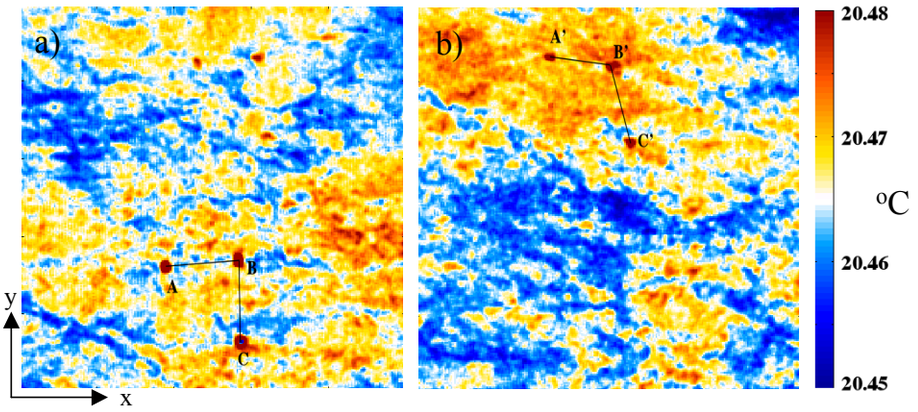


Figure 2 a) and b) Infrared images of the ocean surface taken 2s apart. Image size is 2.5m x 2.5m. The 3 warm dots labeled A, B, and C are the thermal marker laid down by the CO2 laser.

of the spot decays exponentially, with the e-folding time being a direct measure of the air-sea heat flux through the thermal boundary layer.

The Eulerian surface velocity field is measured by cross-correlating successive IR images. It was found that the divergence of the Eulerian velocity correlates with the surface temperature. Where the divergence is positive (upwelling), the surface temperature is consistently warmer than the average image temperature. This is consistent with turbulent surface renewal events disrupting the cool surface skin

In this context, the control flux technique (CFT) developed by Jahne [5] gives an estimate of the surface heat flux based on the decay rate of the heat markers. Applying this technique to the active infrared data such as that shown in figure 2. leads to an estimate of the heat flux in various conditions. We found that the heat air-sea heat flux estimated with the CFT method correlates with the surface turbulence parameters (e.g. rms surface vorticity) better than it does with bulk parameters like wind speed. This indicates that, as expected, the small-scale turbulence is, at low speed, a controlling factor in determining the heat transfer.

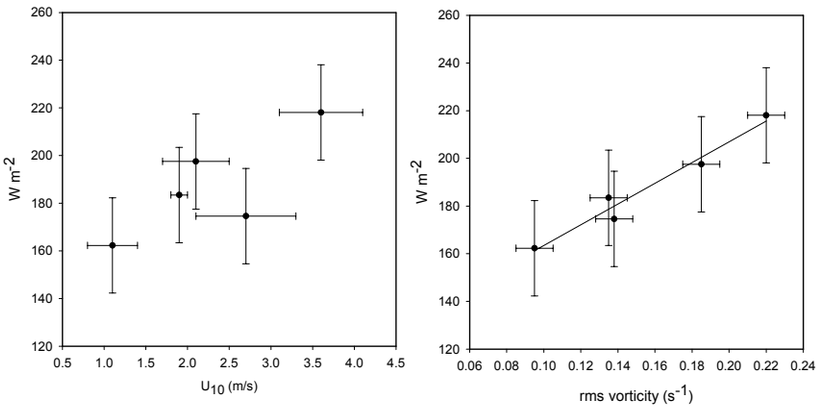


Figure 3. a) Surface heat flux as a function of wind speed and b) as a function of surface rms vorticity.

CONCLUSIONS

We have performed high-resolution measurements of the sea-surface temperature and kinematics using both active and passive infrared imaging techniques. We found that passive and active IR imaging techniques are well suited for the measure of both Langragian (tracking) and Eulerian (cross correlation) surface kinematics. It consequently appears that air-sea heat flux correlates well with the small-scale surface turbulence parameters.

References

[1] Soloviev, A. V., and P. Schluessel. Parameterization of the cool skin of the ocean and of the ai-ocean gas transfer on the basis of modeling surface renewal. *J. Phys. Oceoangr.*, **245**, 1139-1346. 1994.

[2] Fairall, C. W., E. F. Bradley, D. P. Rogers, J. B. Edson, and G. S. Young. Bulk parameterization of air-sea fluxes for tropical Ocean-global atmosphere coupled-ocean atmosphere response experiment. *J. Geophys. Res*., **101**, 3747-3764. 1996.

[3] Veron, F. and W. K. Melville, 2000: Experiments on the stability and transition of wind-driven water surfaces. *J. Fluid. Mech*., **446**, 25-65, 2000

[4] Jessup, A. T., C. J. Zappa, and H. Yeh. Defining and quantifying microscale breaking with infrared imagery. *J. Geophys. Res*., **102**, 23145-23153. 1997

[5] Jahne, B, P. Libner, R. Fisher, T. Billen, and E.J. Plate. Investigating the transfer processes across the free aqueous viscous boundary layer by the controlled flux method. *Tellus*, **41B**, 177-195. 1989

LINEAR WAVES AND BAROCLINIC INSTABILITY IN AN INHOMOGENEOUS-DENSITY LAYERED PRIMITIVE-EQUATION OCEAN MODEL

F. J. Beron-Vera[1], M. J. Olascoaga and J. Zavala-Garay
RSMAS, University of Miami, Miami, FL 33149, USA

Summary We consider a multilayer generalization of Ripa's inhomogeneous-density single-layer primitive-equation model. In addition to vary arbitrarily in horizontal position and time, the horizontal velocity and buoyancy fields are allowed to vary linearly with depth within each layer of the model. Preliminary results on linear waves and baroclinic instability suggest that a configuration involving a few layers may set the basis for a quite accurate and numerically efficient ocean model.

INTRODUCTION

Because of the physical and practical relevance of layered models, methods to accommodate thermodynamic processes into these models have been developed. The simplest method consists of allowing the buoyancy field to vary in horizontal position and time, but keeping all dynamical fields as depth independent. This is formally achieved by replacing the horizontal pressure gradient by its vertical average [4]. The resulting inhomogeneous-density layered models, usually referred to as "slab" models, have been extensively used in ocean modeling.

Despite their widespread use, slab models are known to have several limitations and deficiencies [6]. For instance, a slab single-layer model cannot represent explicitly the thermal-wind balance which dominates at low frequency. This balance is fundamental in processes like cyclogenesis, which has been shown [3] to be incorrectly described with a slab single-layer model.

To cure the slab models limitations and deficiencies, Ripa [5] proposed an improved closure to partially incorporate thermodynamic processes in a one-layer model. In addition to allowing arbitrary velocity and buoyancy variations in horizontal position and time, in Ripa's model the horizontal velocity and buoyancy fields are allowed to vary linearly with depth. The model, which has been generalized to an arbitrary number of layers by Beron-Vera [1], enjoys a number of properties which make it very promising for applications.

As a base test for the validity of the generalized Ripa's model we consider linear waves, focusing particularly on vertical normal-mode phase speeds, and classical baroclinic instability.

THE GENERALIZED MODEL

The starting point to generalize Ripa's single-layer model is to consider a stack of n active fluid layers of thickness $h_i(\mathbf{x},t)$. These layers can be limited from below by an irregular, rigid surface and from above by a soft surface or vice versa. We call the former possibility a rigid bottom setting and the latter a rigid lid setting. Above (resp., below) the active fluid there is an inert, infinitely thick layer of lighter (resp., denser) fluid in the rigid bottom (resp., lid) case. For the ith-layer horizontal velocity and buoyancy relative to the inert layer, respectively, one must then write

$$\mathbf{u}_i(\mathbf{x},\sigma,t)=\bar{\mathbf{u}}_i(\mathbf{x},t)+\sigma\mathbf{u}_i^\sigma(\mathbf{x},t),\quad \vartheta_i(\mathbf{x},\sigma,t)=\bar{\vartheta}_i(\mathbf{x},t)+\sigma\vartheta_i^\sigma(\mathbf{x},t). \tag{1}$$

Here, the overbar stands for vertical average within the ith layer, and σ is a scaled vertical coordinate which varies linearly from ±1 at the base of the ith layer to ∓1 at the top of the ith layer. [The upper (resp., lower) sign corresponds to the rigid bottom (resp., lid) configuration.] The generalized model equations, which follow upon replacing (1) in the continuously and arbitrarily stratified (i.e. exact) primitive equations, namely rotating incompressible hydrostatic Euler–Boussinesq equations, then take the form

$$\partial_t h_i+\boldsymbol{\nabla}\cdot h_i\bar{\mathbf{u}}_i=0, \tag{2a}$$

$$\overline{\mathrm{D}_i\vartheta_i}=0,\quad (\mathrm{D}_i\vartheta_i)^\sigma=0, \tag{2b,c}$$

$$\overline{\mathrm{D}_i\mathbf{u}_i}+f\hat{\mathbf{z}}\times\bar{\mathbf{u}}_i+\overline{\boldsymbol{\nabla}p_i}=\mathbf{0},\quad (\mathrm{D}_i\mathbf{u}_i)^\sigma+f\hat{\mathbf{z}}\times\mathbf{u}_i^\sigma+(\boldsymbol{\nabla}p_i)^\sigma=\mathbf{0}. \tag{2d,e}$$

Here, f is the Coriolis parameter (twice the local angular rotation frequency); $\hat{\mathbf{z}}$ is the vertical unit vector; $\boldsymbol{\nabla}$ is the horizontal gradient; $\overline{\mathrm{D}_i\bullet}$ and $(\mathrm{D}_i\bullet)^\sigma$ are, respectively, the vertical average and σ components of the ith-layer material derivative; and $\overline{\boldsymbol{\nabla}p_i}$ and $(\boldsymbol{\nabla}p_i)^\sigma$ are, respectively, the vertical average and σ components of the ith-layer pressure gradient force. [For details cf. Refs. 5,1.]

Some of the attractive properties of this model are the following. First, the model can represent explicitly within each layer the thermal-wind balance which dominates at low frequency. Second, volume, mass, buoyancy variance, energy, and momentum are preserved by the dynamics. Third, because of the possibility of vertical stratification within each layer, thermodynamic processes (e.g. heat and freshwater inputs across the ocean surface, vertical mixing, etc.) can be incorporated more realistically than in slab models.

[1]Electronic mail: fberon@rsmas.miami.edu.

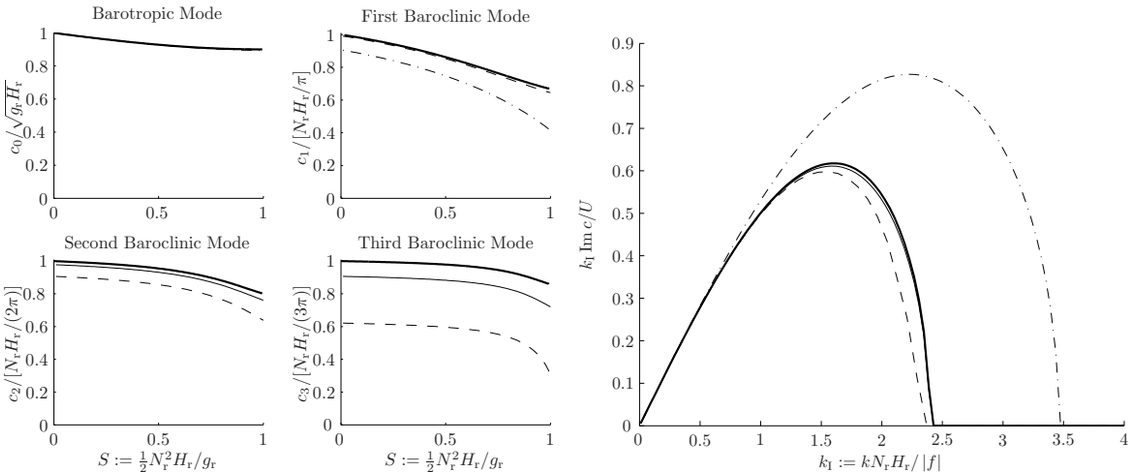


Figure 1. (a) Phase speed of long gravity waves as a function of the stratification in a reference state with no currents. (b) Growth rate of the most unstable Eady wave as a function of wavenumber. In both panels the exact result is indicated by a heavy-solid line, and the layered model predictions with dot-dashed (one layer), dashed (two layers), and light-solid (three layers) lines.

LINEAR WAVES AND BAROCLINIC INSTABILITY

System (2), linearized with respect to a *reference state* with no currents, can be shown to sustain the usual midlatitude and equatorial gravity and vortical waves in several vertical normal modes. In this work we concentrate on how well these modes are represented by considering the phase speed of long gravity waves in a reference state characterized by the stratification parameter $S := \frac{1}{2}N_r^2 H_r/g_r$. Here, N_r is the Brunt–Väisälä frequency, H_r is the total thickness of the active fluid layer, and g_r denotes the vertically averaged buoyancy. All these three quantities are held constant. The reference buoyancy then varies linearly from $g_r(1 \mp S)$ at the top of the active layer to $g_r(1 \pm S)$ at the base of the active layer. Physically acceptable values of S must be such that $0 < S < 1$ [5, 2]. Figure 1a compares, as a function of S, the phase speed of long gravity waves assuming exact dynamics and (2) with $n = 1$, 2, and 3. The comparison is perfect for the barotropic mode phase speed even including only one layer. The use of two layers amounts to an excellent representation of the first baroclinic mode phase speed, and a very good representation of the second baroclinic mode phase speed. To reasonably represent also the third baroclinic mode phase speed, no more than three layers are needed.

We now turn our attention to classical baroclinic instability. We thus consider a *basic state* with a parallel current in an infinite channel on the f plane, which has a uniform vertical shear and that is in thermal-wind balance with the across-channel buoyancy gradient. We further set the basic velocity to vary (linearly) from $2U$ at the top of the active layer to 0 at the base of the active layer. Accordingly, the basic buoyancy field varies from $g_r(1 - 2fUy/H_r \mp S)$ at the top of the active layer to $g_r(1 - 2fUy/H_r \pm S)$ at the base of the active layer (y denotes the accross-channel coordinate). Figure 1b compares in the classical Eady limit, as a function of the along-channel wavenumber the growth rate) of the most unstable normal-mode perturbation assuming exact dynamics and (2) with $n = 1$, 2, and 3. The comparison is almost perfect when three layers are included and very good when two layers are included. When only one layer is considered, the comparison is not as good but a high wavenumber cutoff of baroclinic instability is present. This important dynamical feature cannot be represented with a slab single-layer model.

PRELIMINARY CONCLUSIONS

We have tested the performance of a novel inhomogeneous-density primitive-equation layered model, which features vertical shear and stratification within each layer, in two important aspects of ocean dynamics, namely linear waves and baroclinic instability. Preliminary results suggest that a model with a small number of layers may be used as a basis for a quite accurate and numerically economic ocean model. To make stronger statements on the model's accuracy and efficiency, fully nonlinear, forced–dissipative problems must of course be considered. This work is currently underway.

References

[1] Beron-Vera, F. J.: Multilayer primitive-equation ocean model with variable vertical shear and stratification within each layer. *J. Fluid Mech.*, to be resubmitted, 2004 (e-Print arXiv:physics/0312083).

[2] Beron-Vera, F. J. and P. Ripa: Free boundary effects on baroclinic instability. *J. Fluid Mech.* **352**:245–264, 1997.

[3] Eldevik, T.: On frontal dynamics in two model oceans. *J. Phys. Oceanogr.* **32**:2,915–2,925, 2002.

[4] Ripa, P.: Conservation laws for primitive equations models with inhomogeneous layers. *Geophys. Astrophys. Fluid Dyn.* **70**:85–111, 1993.

[5] Ripa, P.: On improving a one-layer ocean model with thermodynamics. *J. Fluid Mech.* **303**:169–201, 1995.

[6] Ripa, P.: On the validity of layered models of ocean dynamics and thermodynamics with reduced vertical resolution. *Dyn. Atmos. Oceans* **29**:1–40, 1999.

SIMULATION OF SEA SURFACE TEMPERATURE TRENDS UNDER SEVERE WIND FORCING WITH A FULL ATMOSPHERE-OCEAN COUPLED MODEL

Arnaldo Longhetto*, Roberto Purini**, Claudio Cassardo*, Nicola Loglisci***, Silvia Ferrarese*, Renzo Richiardone*

*Department of General Physics, University of Turin, Torino, Italy
**CNR-ISAC, Rome, Italy
***ARPA, regional Meteorological Service, Torino, Italy

Summary The main object of this paper concerns the numerical simulation of air-sea interactions in situations of high frequency variability connected to abrupt severe atmospheric forcing over the sea. A particular attention has been turned to singling out the most relevant mechanical and thermal coupling schemes between the two media and their proper parametrization in terms of mechanical, radiative, and thermal energy fluxes through the air-sea interface. It was demonstrated the importance of a two way forcing mechanism between air and sea in order to explain the experimental observations

Air-sea interaction context

The atmosphere and the ocean represent a stratified two-layer fluid system whose dynamic and thermodynamic state evolution in space and time complies with different forcing conditions. However, they also interact with each other, through exchanges of mechanical and thermal energy. It is a widespread opinion that atmospheric forcing on the ocean (mainly wind stress and partly radiation and sensible and latent heat flux) is far more efficient than the opposite ocean forcing on the atmosphere, when the interaction episodes are characterised by conditions of shallow water and high frequency variability with respect to the situation of deep water and longer interaction periods.

This study aims at going into the above belief, through a comparison of the results of numerical simulations with field observation of mechanical and thermal interaction of strong and intermittent wind with shallow water ocean.

Numerical simulation

The main perturbations induced by wind forcing over the sea concern its circulation, level and pattern of Sea Surface Temperature (SST). In order to better understand the specific role played by each interaction mechanism and its forcing direction (from air to water and vice-versa), we decided to investigate high frequency variability processes connected to abrupt severe atmospheric forcing over the sea. For this reason, cold and intense Bora wind outbreaks over the northern and central Adriatic sea were elected as the investigation subject due not only to their high variability but also to their potential capability to perturb the equilibrium winter regimes of air-sea interaction in the Adriatic Basin (like vertical mixing and dense water production)

Another peculiar aspect of Bora is its short duration and limited spatial extent, which cannot be resolved by the wind fields provided by ECMWF or similar organizations. In order to capture the main features relevant to air-sea interaction in the Adriatic basin through Bora wind episodes, a regional two-way Atmosphere/Ocean Coupled Model (TWAOCM) developed by our group has been used with the purpose to appraise the possible benefit of a two-way coupling with respect to the simpler one-way coupling even in short term variability conditions. The numerical simulations of the above mentioned mechanical and thermal perturbations between air and sea have been performed in the spatial domain corresponding to the northernmost region of the Adriatic Sea basin. Fig. 1 shows the bathymetry of the whole Adriatic basin just in order to show the topographical complexity of the selected domain. The northern Adriatic Sea is shallow and has a fairly even slope gradually deepening to 100 m. The intermediate part has its main feature in a bathymetric depression about 200 m deep. The southernmost part is deeper than the other two parts, and reaches a maximum depth of almost 1200 m(South Adriatic Pit).

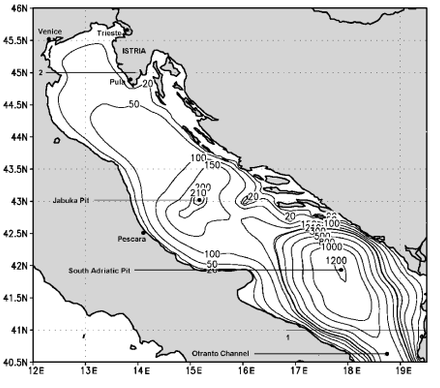


Figure 1

All these features bring about steady and unsteady vortices whose influence is felt as far as the northern regions. Due to the strong cold advection in the planetary boundary layer during Bora episodes, SST becomes an easy-to-monitor "tracer" of the dynamic and thermal response of the water to the wind forcing, which allow a fast quantitative comparison between observed data and model simulations. The SST evolution has been chosen as a validation parameter because it is closely connected to dynamics and thermodynamics of the whole depth of the sea, and also owing to its easy availability.

The peculiar aspect of Bora mentioned before, i.e. its short duration and limited spatial extent, cannot be resolved by the wind fields provided by ECMWF or similar organizations. In order to capture the main features relevant to air-sea interaction in the Adriatic basin through Bora wind episodes, a regional two-way Atmosphere/Ocean Coupled Model (TWAOCM), developed by our group and incorporating two circulation models [RAMS for the atmosphere and DieCAST for the ocean] driven by the global host model of ECMWF, has been used with the purpose to appraise the possible benefit of a two-way coupling (fig.2) with respect to the simpler one-way coupling even in short term variability conditions.

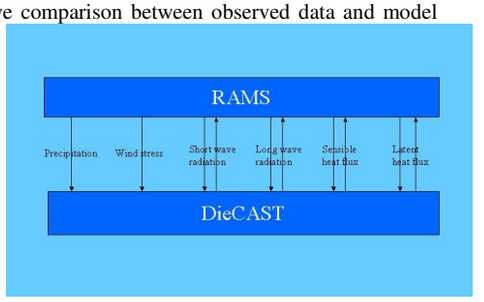


Figure 2

The ECMWF model (T213/L31) is a global semilagrangian model that calculates the meteorological fields on a three-dimensional grid with 31 vertical levels (thereby L31). The input are satellite data, data taken on the ground, on the oceans and in the free atmosphere. The output for the horizontal plane are compressed in a series of spherical harmonics with triangular truncation and a maximum resolution of 213 wavelengths on a great circle (thereby T213).
The RAMS model (Pielke at al., 1992) is a highly versatile numerical code for simulating meteorological phenomena based on the full set of primitive dynamical equations which govern atmospheric motions with The supplements of these equations include optional parameterisations for subgrid phenomema.. The RAMS model proved to be particularly able to downscale the meteorological fields from synoptic to regional scale (Qian and Giraud, 2000)
The DieCAST model (Dietrich et al., 1987; R.L. Walko et al., 1995) was derived from the modified Arakawa C grid SOMS (Sandia Ocean Modeling System) model (Dietrich and Ko, 1994). It is a three-dimensional model in a rotating frame, z-level, hydrostatic, Boussinesq, incompressible, rigid-lid model.
Both models (RAMS and DieCAST) use a vertical stretching that allows a better resolution near their separation interface .They have been set up with the same horizontal geometry in a area which includes almost the whole Adriatic Sea as far as the Otranto Strait.
The boundary conditions at the interface of the two-way TWAOCM coupled model used for the simulation of the Bora event are the analyses of the ECMWF model referring to the horizontal rectangular area of the integration domains of the two models, nested inside the larger one of ECMWF. The initial conditions for the SST of the TWAOCM coupled model is the output of a 3 -month "stand-alone" run of the DieCAST initialized and forced by its own MODB-MED4 seasonal climatology. "Stand alone" means that there was no coupling of the DieCAST and the atmosphere model. Initialization obtained in this way is expected to approach the actual initial conditions of the case study rather well, although not always exactly equaling it. In fact, under some circumstances, the use of climatological data might affect the performance of a numerical model due to the actual thermal structures of the upper ocean which do not follow the climatological trend. For this reason, we used also an alternative initialisation of hybrid type, by running DieCAST in "stand alone" mode with the seasonal climatological database but converging toward satellite observation of the SST during the winter season, i.e. the season in which strong Bora winds are more frequent. These satellite observation of SST were retrieved in the file collecting satellite-base AVHRR measurements derived by the Pathfinder Project, after a space-time interpolation using the objective analysis of Mariano and Brown (University of Miami). Once the simulation of the Bora with the coupled model was started ,the ocean model DieCAST no longer used the climatological or satellite data anymore, but was forced completely by the real time atmospheric fields provided by the RAMS, hence constituting the boundary conditions during the model run.
In a previous study, we started the coupling of our regional atmosphere-ocean model with a one-way interaction scheme. With this scheme, the model ocean received surface forcing (such as wind stress, radiation, sensible and latent heat fluxes) every ten minutes from the model atmosphere, without giving feedback to the same. Model results of the one-way coupled approach with climatological initialisation gave very low simulated SSTs after the Bora episode, in fact SST on the Gulf of Trieste side of the Adriatic Sea was shown to drop by 4 °C within five days of the Bora, whilst observations showed a drop of only 1 °C. In addition, the overestimate did not keep constant, but was accentuated with the passing of time.
In the present study, the two-way coupling procedure, in which the model ocean gives its calculated SST values back to the model atmosphere, has bee adopted in order to allow it to compute heat fluxes in a more realistic way and receive surface forcing at each time step of integration (every 30 seconds). The simulations performed with this full coupling used both the above mentioned climatological initialisation and the hybrid initialisation described above.

Results

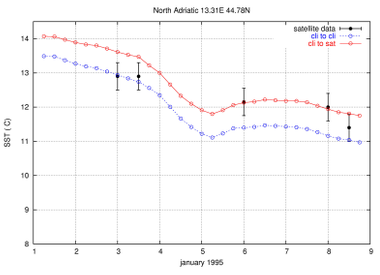


Figure 3

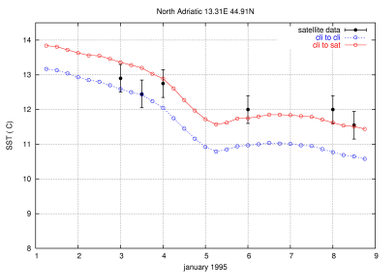


figure 4

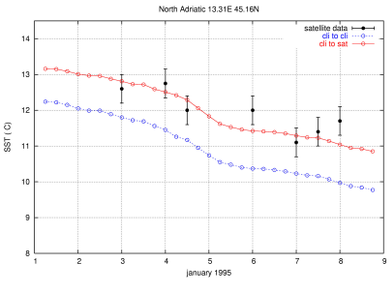


figure 5

This third simulation provided even better agreement with satellite observation made with satellite made in many points of the integration domain, made by satellite (Figs 3,4,5). These figures show the simulated SST trends during the Bora episode respectively at 3 different positions of the Adriatic Sea. Blue dotted lines represent simulation with initial conditions purely climatological; red dotted lines represent simulations with initial conditions of the Hybrid type; black dots, at last, show the satellite observations with their errors. It is evident the improvement of the use of satellite observation in preparing the initial conditions. This new comparison with satellite field observation has confirmed the importance of the two-way coupling for a correct representation of the interaction between the two layers of a sheared and stratified two-layer fluid system
With particular reference to the fluid system represented by wind forcing the sea, this result also shows the importance of satellite observations in preparing the initial conditions.

References

[1] Dietrich D. et al., *A semi-collocated ocean model based on the SOMS approach*, Int. J. Num. Meth.in Fluids, **19**, 1103-1113, 1994
[2] Dietrich D., *Application of a modified Arakawa 'a' grid ocean model having reduced dispersion to the Gulf of Mexico circulation*, Dyn. Atmos. And Oceans, **27**, 201-217, 1997
[3] Pielke R.A.et al.: *A comprehensive meteorological modeling system – RAMS, Meteor.Atmos.Phys.,* **49**, 69-91,1992
[4] Qian M.W. et al.:., *A Preliminary Numerical Simulation of Bora Wind with a Limited Area Model of Atmospheric Circulation*, Il Nuovo Cimento, **23C**, **5**, 515-523, 2000
[5] Walko, R.L. et al.:*The Regional Atmospheric Modeling System User's Guide", Fort Collins Aster Division*, pp 121., 1995

XXI ICTAM, 15–21 August 2004, Warsaw, Poland

DISSIPATIVE EFFECTS ON PROPAGATION OF THE ACOUSTIC SOLITARY WAVES

N. Sugimoto, M. Masuda, K. Yamashita, H. Horimoto
Department of Mechanical Science, Graduate School of Engineering Science,
University of Osaka, Toyonaka, Osaka 560-8531, Japan

Summary This paper examines dissipative effects on the acoustic solitary waves propagating in an air-filled tube with an array of Helmholtz resonators. The dissipation is brought about by wall friction through boundary layers and by jet loss in resonators' throat. For pressure profiles measured experimentally, numerical simulations are carried out to identify the respective effects. Discussions are included on how the dissipative effects are reduced to realize a pulse as closely as possible to the solitary wave in lossless limit.

INTRODUCTION

The acoustic solitary wave can be propagated in an air-filled tube if a periodic array of Helmholtz resonators is connected to the tube axially [1-4]. The solitary wave is a localized pulse consisting of compression phase only and propagating steadily at a subsonic speed [2]. It is made possible without forming a shock by the action of dispersion that the array yields. Experiments have been performed to verify the existence of the solitary waves [3,4].

In reality, however, dissipative effects are unavoidable more or less so that the solitary waves in lossless limit would be masked. The dissipation is brought about by friction through boundary layers developing on the tube wall and by jet loss when air flows through narrow throat of the resonator. Effects due to the diffusivity of sound are negligible because the acoustic Reynolds number is extremely high. For pressure profiles measured experimentally, numerical simulations are carried out by solving an initial-value problem to evolution equations derived previously [1] to identify the respective effects. To realize a pulse close to the solitary wave, discussions are given on how the dissipative effects are reduced.

EXPERIMENTAL PRESSURE PROFILES

Experiments have been carried out by using an air-filled tube of inner diameter $2R$ ($= 80$ mm) and of length l_t ($= 10.6$ m). The resonators of volume V ($= 49.8\ \mathrm{cm}^3$) with throat of inner diameter $2r$ ($= 7.11$ mm) and of length L ($= 35.6$ mm) are connected to the tube in array with axial spacing d ($= 50$ mm). The total number of the resonators connected is 212. The natural angular frequency of the resonator ω_0 is given by $\sqrt{a_0^2 B/L_e V}$ where a_0, B and L_e denote, respectively, the sound speed, the cross-sectional area of the throat and the effective length of the throat $L + 2 \times 0.82r$ with end corrections. It takes 242 Hz at temperature $24.8\ ^\circ$C where the experiments have been made.

An initial pulse is generated by driving impulsively a plane piston mounted at one end of the tube. The other end of the tube is closed by a flat plate. The form of the initial pulse is far away from the solitary wave. Figure 1 shows the temporal profile of the initial pulse measured at a position distant about 0.4 m from the piston where p_0 and p' denote, respectively, the equilibrium (atmospheric) pressure (= 0.1010 MPa) and the excess pressure over p_0. The pulse is propagated down the tube and reflected by the flat plat to return to the piston. Then reflected by the piston, it continues to propagate back and forth in the tube, decaying out eventually by dissipation. In this process, it is observed that the initial pulse evolves into a pulse similar in form to the solitary wave.

Figure 2 shows the profile measured at a position distant about 5.2 m from the piston after reflected three times by the flat plate and twice by the piston. The thick line and thin line indicate, respectively, the profiles measured and given by the solitary-wave-solution with the peaks coincided with each other. It is seen that the profile except for a hump and a tail on the right-hand side of the peak agrees with the solution very well. This agreement motivates us to identify whether another solitary wave might emerge from the hump by the dispersion or dissipative effects would be accumulated.

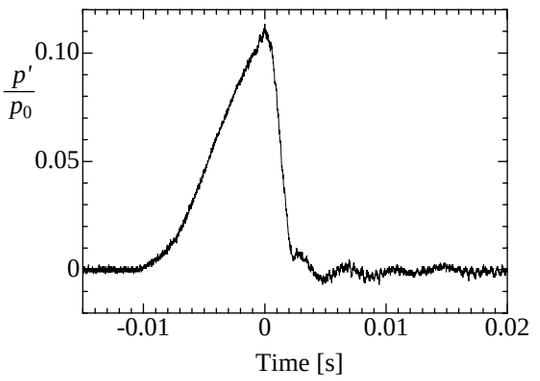


Figure 1. *Temporal pressure profile of the initial pulse measured at a position distant about 0.4 m from the piston.*

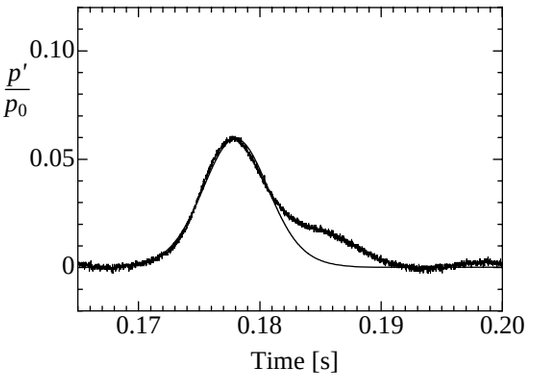


Figure 2. *Temporal pressure profiles at a position distant about 5.2 m from the piston where the thick and thin lines indicate the profile measured and the one of the solitary wave, respectively.*

NUMERICAL SIMULATIONS

In order to answer this, numerical simulations are performed by solving the following evolution equations:

$$\frac{\partial f}{\partial X} - f\frac{\partial f}{\partial \theta} = -\delta_R \frac{\partial^{\frac{1}{2}} f}{\partial \theta^{\frac{1}{2}}} - \frac{\partial g}{\partial \theta}, \tag{1}$$

and

$$\frac{\partial^2 g}{\partial \theta^2} + \delta_r \frac{\partial^{\frac{3}{2}} g}{\partial \theta^{\frac{3}{2}}} + g = f + \tfrac{1}{2}\kappa N, \tag{2}$$

where f and g denote, respectively, the excess pressure in the tube and in the cavity, while X and θ denote, respectively, the axial coordinate and the retarded time in a frame moving with the sound speed, all quantities being appropriately normalized; the hereditary effects due to the boundary layers on the tube wall and throat wall are expressed in terms of the fractional derivatives of 1/2- and 3/2-order, respectively, δ_R and δ_r being positive constants much smaller than unity; the jet loss is represented by the second term in N given by

$$N = \left(\frac{\gamma-1}{\gamma+1}\right)\frac{\partial^2 g^2}{\partial \theta^2} - \frac{2V}{(\gamma+1)BL_e}\left|\frac{\partial g}{\partial \theta}\right|\frac{\partial g}{\partial \theta}, \tag{3}$$

γ being the ratio of specific heats and κ the size parameter of the array defined as $V/Ad\,(\ll 1)$ with $A = \pi R^2$.
An initial-value problem is solved by imposing an initial value of f at $X = 0$, which is taken by fitting the initial profile in figure 1 with an appropriate function. The axial coordinate X measures distance along which the pulse has travelled in the tube. Although (1) and (2) are derived originally for uni-directional propagation in a tube of infinite length, it is revealed that they still can be used to interpret the real propagation of the pulse in the bounded tube. Only difference lies in slight phase shifts where the profiles simulated are lagged behind the ones measured. The phase shifts result from reflection at both ends since it may be regarded as head-on collision of two identical solitary waves in a tube of infinite length.
The simulations are carried out for three cases. Firstly the lossless case is solved, for reference, by ignoring both the boundary-layer effects and the jet loss. Of course, the solitary wave is the steady-progressive-wave solutions in this case. Secondly only the boundary-layer effects are taken into account, and finally the full equations are solved. In the lossless case, it is found that the initial pulse evolves into a pulse like the solitary wave and no hump appears. When the boundary-layer effects come into play, the peak pressure becomes smaller and a tail tends to develop. But no hump is seen. When the jet loss comes in, the peak pressure is further reduced and a hump emerges. Thus the hump observed is identified to be brought about by the jet loss.

DISCUSSIONS

Now that the evolution equations can simulate the real evolution quantitatively well, it implies that the dissipative effects can be controlled to achieve a pulse as closely as possible to the solitary wave. To reduce the boundary-layer effects, it is preferable to use a wider tube and throat. In addition, the kinematic viscosity should be reduced by raising equilibrium pressure p_0. On the other hand, the jet loss appears in (2) through the parameter $\kappa V/(\gamma+1)BL_e$, which is determined by geometry of the resonator only. Therefore the value of κ should be reduced by taking longer axial spacing, while the resonators with smaller value of V/BL_e should be used. In the present experiment, κ takes 0.198. But $\kappa V/(\gamma+1)BL_e$ takes a large value 2.50 in spite of that the term of jet loss is regarded as being small in (2).
In view of these, new simulations are made by assuming the throat diameter and its length to be double in size, and the value of κ to be half. Then the parameter of the jet loss takes 0.304. Furthermore p_0 is set to be 10 MPa. Taking the same initial pulse as the one in figure 1, it is found that the initial pulse evolves into a single pulse much closer to the solitary wave. Since the boundary-layer effects are now suppressed, the tail in this case may be brought about by the dispersion and a new solitary wave might emerge from it if a further long-time behaviour would be pursued.

CONCLUSIONS

Making the numerical simulations, the respective dissipative effects due to the boundary layers and the jet loss can now be identified. Although they decay the pulse in common, the former gives rise to the tail, while the latter yields the hump. But their effects are limited to trailing behaviour of the pulse and the leading behaviour is well described locally by the solitary waves in lossless limit.

References

[1] Sugimoto N.: Propagation of Nonlinear Acoustic Waves in a Tunnel with an Array of Helmholtz Resonators. *J. Fluid Mech.* **244**:55–78, 1992.
[2] Sugimoto N.: Acoustic Solitary Waves in a Tunnel with an Array of Helmholtz Resonators. *J. Acoust. Soc. Am.* **99**:1971-1976, 1996.
[3] Sugimoto N., Masuda, M., Ohno, J., Motoi, D.: Experimental Demonstration of Generation and Propagation of Acoustic Solitary Waves in an Air-filled Tube. *Phys. Rev. Lett.* **83**:4053–4056, 1999.
[4] Sugimoto N., Masuda, M., Yamashita, K., Horimoto, H.: Verification of the Acoustic Solitary Waves. accepted for publication in *J. Fluid Mech.*

XXI ICTAM, 15–21 August 2004, Warsaw, Poland

AN EMPIRICAL 'LOWER BOUND' ON FREE-SHEAR-FLOW NOISE

Jonathan B. Freund, Mingjun Wei
University of Illinois at Urbana-Champaign, Department of Theoretical and Applied Mechanics, Urbana, IL 61801, USA

Summary The adjoint of the linearized compressible flow equations is formulated in such a way that it can be used to optimize local control actuation to reduce the noise radiated by a free shear flow. Both the flow and the adjoint are solved numerically and without modeling approximations. Jet noise is the technological application of interest, and a two-dimensional mixing layer is studied as a model of the near-nozzle region of a jet. It is found that the correct small perturbations near the inflow can dramatically reduce the radiated noise. This approach allows us to establish an empirical lower bound on the noise radiation by a this flow subject to our constraints. More importantly, it gives us an opportunity to study its mechanisms by providing noisy and quieted versions of the same flow. Superficially, the unsteady flow dynamics are remarkably unchanged despite a 10dB reduction in the noise.

BACKGROUND

Since the beginning of the jet age, the most significant noise reductions derive from lower nozzle velocities U and Lighthill's famous acoustic power $\mathcal{P} \propto U^8$ scaling,[1] but at fixed flow conditions it is also now being found that certain nozzle modifications can reduce noise with acceptable thrust losses. Unfortunately, there is no firm theory to guide their design and no known upper limit on their effectiveness. The greater flexibility afforded by active actuation at the nozzle holds even greater promise, but the complexity of the flow and the subtleness of the noise mechanisms have hampered modeling efforts seeking to guide its use. Turbulence models simply lack the fidelity necessary to provided the detailed theoretical noise sources derived in aeroacoustic theories. Our direct numerical simulation effort[2] has shown that despite accuracy concerns deriving from the large energy mismatch between the flow and its noise, the sound field of a turbulent jet flow can indeed be computed accurately, but these simulation are both expensive and have not yet yielded a simplifying principle that can be used to improve models. Large-eddy simulation holds long term promise for prediction, but its direct use in design optimization of complex geometries or of actuation is not imminent. It remains unclear how quite a jet can be made at fixed nominal jet exit conditions or if there is even any use in pursuing active control.

APPROACH AND OBJECTIVES

In view of this we have developed an automatic procedure to optimize near-nozzle control actuation in a model jet to reduce its noise. It will be seen that the procedure is an iterative prediction-based optimization that employs a direct numerical simulation of the flow including its radiated sound coupled with a direct solution of the adjoint of the linearized flow equations. However, these requirements do not limit the usefulness of the approach for our objectives. We will use it to discover how quiet the unsteady structures in a free shear flow can be made, which is important from the perspective of assessing whether or not active control should be pursued at all. It will also provide us a unique opportunity to compare a loud and a slightly perturbed but significantly quieter flow. Ideally, it will eventually guide the development of general control laws.

The model jet flow we consider is the two-dimensional mixing layer shown schematically in figure 1. The unsteadiness in the mixing layer is randomly excited in an absorbing boundary zone extending upstream of the computational domain, through the subsequent control, of course, has no direct knowledge of this excitation. This two-dimensional model flow has several of the salient features of the near-nozzle flow of a jet yet can be simulated cheaply enough to allow us explore different parameters and types of controls. Still, tens of thousands of processor hours on parallel systems are necessary for the current study of various controls.

The flow equations are linearized about the time dependent flow solution and their adjoint is then formulated in such a way that the adjoint solution provides the sensitivity of the noise, defined in terms of acoustic pressure p' by

$$\mathcal{J} = \int_0^T \int_\Omega p'p' \, dx dt,$$

to changes in the control in $\mathcal{C}$. Ω and $\mathcal{C}$ are labeled in figure 1. The flow and adjoint solutions are both attained numerically by direct numerical solution. The mesh is fine enough to preclude the need for any artificial dissipation or other modeling approximations.

The sensitivity information provided by the adjoint solution is used in a conjugate-gradient minimization algorithm to find control $\phi(\mathbf{x}, t)$ such that $\mathcal{J}(\phi)$ is minimized. In this fundamental study, we consider the most general control possible. It appears as source terms in the compressible flow equations having compact support in $\mathcal{C}$. Each space-time point of the discrete representation of $\phi(\mathbf{x}, t)$ is treated as an independent control parameter.

RESULTS

After 10 to 20 line minimizations within the conjugate gradient search algorithm, the values of $\mathcal{J}$ can be reduced by over a factor of 10 with minimal physical control effort. For example, when the control term is added to the y-momentum equation, which would crudely model the action of an actuator blowing normal to the shear layer, the peak instantaneous mechanical power is only 0.019% of the time averaged x-direction turbulence kinetic energy flux at $\mathcal{C}$. The details of the control identified are complex and are under further investigation. It is clear, however, that the action of ϕ is convective, tracking flow structures as they pass.

The most notable result, perhaps, concerns how little the unsteady characteristics of the vortex roll-ups and pairings have changed. The net fluctuation kinetic energy at any particular downstream x-location is always within 14% of the uncontrolled case. Figure 2 visualizes the large structures in the mixing layer with vorticity before and after the control has been applied. There is clearly little difference. Subtracting controlled and uncontrolled fields suggest that the most significant change may be in the relative spacing of the eddies. Pairings and other such structural interactions are qualitatively unchanged by the control. The small difference may suggest that it is a simple noise cancellation (anti-sound) rather than a mechanistic change in the flow dynamics that reduces the radiated noise. However, a test simulation with the control region $\mathcal{C}$ moved off the mixing layer only was able to reduce $\mathcal{J}$ by less than a factor of 2, suggesting that it is indeed subtle changes in the flow dynamics that reduces the noise so significantly. Fourier transforming near-field flow quantities in the x-direction (giving wavenumbers k) and time t (giving frequencies ω), shows that modes with radiation capable phase velocities ($|\omega/k| > a_\infty$) experience a large (factor of 3 in cases) reduction after the control is optimized.

CONCLUSIONS

We have designed an automatic control optimization algorithm that substantially reduces the acoustic radiation of a two-dimensional mixing layer with minimal control effort, encouraging further pursuit of active control of free-shear-flow noise. The observable features of the flow are little changed by the control, suggesting that efforts to directly observe the noise making mechanics of jets are misguided. The only significant changes observed in our simulations thus far occur in the near-field and are in modes with radiation capable supersonic phase velocity. Physically, these are associated with the evolution of the unsteady flow structures as they advect downstream. (Funding from AFOSR is greatly appreciated.)

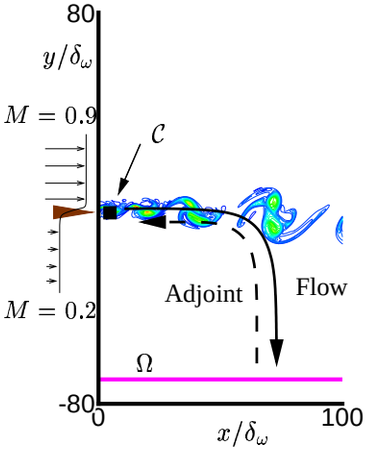


Figure 1. Schematic showing the target line for control Ω and the region of support of the control $\mathcal{C}$. The arrows indicate the general direction of information transport: the numerical flow solution carries perturbations form the nozzle lip to the sound field and the adjoint solution carries the sensitivity of the noise from Ω back to the region of control $\mathcal{C}$.

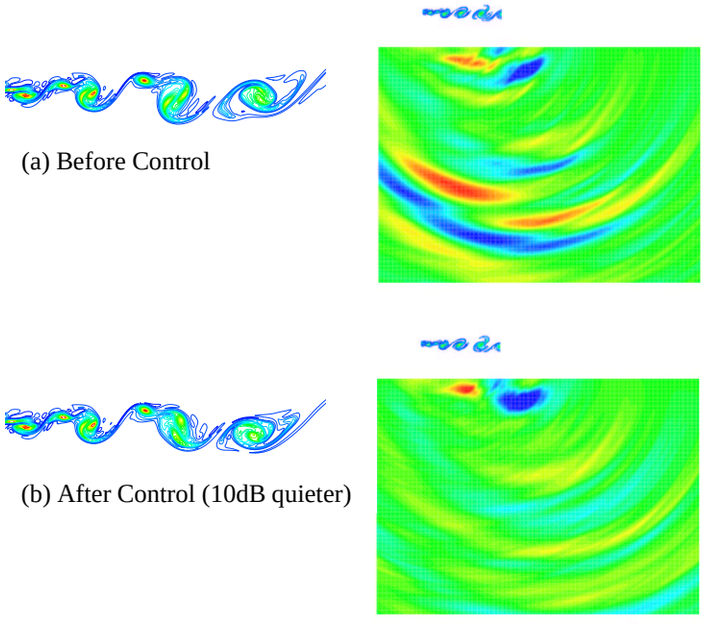


Figure 2. Vorticity magnitude visualization (contours) and pressure visualization (colors): (a) before adjoint-based optimization; (b) after adjoint-based optimization.

References

[1] M. J. Lighthill, "On sound generated aerodynamically: I. General theory," Proc. Royal Soc. Lond. A **211**, 564 (1952).
[2] J. B. Freund, "Noise sources in a low-Reynolds-number turbulent jet at Mach 0.9," J. Fluid Mech. **438**, 277 (2001).

SPECIAL SHORT WAVE FINITE ELEMENTS FOR FLOW ACOUSTICS

Jeremy Astley, Pablo Gamallo
Institute of Sound and Vibration Research, Univ. of Southampton, Highfield, SO17 1BJ, Southampton, UK

Summary A numerical scheme based on the Partition of Unity Finite Element Method is proposed for solving shortwave problems in flow acoustics. The goal of this approach is to obtain accurate solutions with fewer degrees of freedom than are required for conventional grid or node based schemes. Preliminary numerical results obtained for 2-D and axisymmetric models indicate that this approach may offer significant performance improvements.

INTRODUCTION

Situations in which wavelike disturbances propagate with wavelengths which are small compare to the dimensions of the solution domain are common in many branches of engineering and physics. The work reported here focusses on a particular problem of this type, that of sound propagation in the ducted regions of turbofan aircraft engines, where the diameter of the engine is generally an order of magnitude larger than the characteristic wavelength of the sound field. The (subsonic) Mach number within such ducts also varies giving rise to significant inhomogeneous propagation effects. Although the current analysis is directed specifically at this problem, the general approach that is proposed can be applied to a wider class of problems which involve convective wave propagation (surface gravity waves on nonuniform currents for example).

When traditional Finite Element (FE) models are applied to short wave problems, approximability considerations alone dictate a minimum resolution of 8 - 10 nodes per wavelength, a requirement which is exacerbated by 'pollution' error [2] when many wavelength variations are present in the computational domain. Moreover, when flow is present, wave-shortening due to the mean flow may further increase mesh requirements.

Aero-engine short wave FE computations can currently be performed at acceptable computational cost only by using axisymmetric models [3, 1]. These generally contain of the order of 10^5 degrees of freedom. The same approach becomes prohibitively expensive for fully 3-D problems, even when parallel codes are used [6].

In this article a novel method is proposed for the solution of such problems. It is based on the Partition of Unity Finite Element Method (PUFEM) [5] and uses very sparse 'meshes' (< 1 node per wavelength). The method is an extension to flow acoustics of the PUFEM approach which has been applied to the standard Helmholtz equation [4] and shown to be relatively free of pollution error. The method is based on a discrete set of local plane wave solutions which are used to 'enrich' a conventional finite element trial space. The method is implemented in the frequency domain using a weak variational formulation.

FORMULATION OF THE PROBLEM

We consider an inviscid, isentropic, compressible fluid in which a small time-harmonic acoustic disturbance propagates upon a steady irrotational mean flow. The acoustic field is represented by an acoustic velocity potential $\phi(\mathbf{x})e^{i\omega t}$ consistent with an assumption of an irrotational mean flow. The linearised mass and momentum equations yield the following convected acoustic wave equation

$$\omega^2 \frac{\rho_0}{c_0^2}\,\phi - i\omega\left(\frac{\rho_0\mathbf{u_0}}{c_0^2}\cdot\nabla\phi + \nabla\cdot\left(\frac{\rho_0\mathbf{u_0}}{c_0^2}\,\phi\right)\right) - \nabla\cdot\left(\left(\frac{\rho_0\mathbf{u_0}}{c_0^2}\cdot\nabla\phi\right)\mathbf{u_0}\right) + \nabla\cdot(\rho_0\nabla\phi) = 0, \tag{1}$$

where ρ_0, p_0, c_0, and $\mathbf{u_0} = \nabla\phi_0$ are the density, pressure, sound speed and flow velocity of the mean flow. A weak formulation of the above equation forms the basis for both conventional FE and PUFEM analyses.

THE PARTITION OF UNITY FINITE ELEMENT METHOD (PUFEM)

The Partition of Unity method - first proposed by Melenk and Babuška [5] - allows information about the local physical solution to be included in an approximation subspace. In the case of equation (1), a finite set of plane wave solutions defined at nodal points is used to build a discrete trial space. By setting the mean flow Mach number to a constant (axial) value M, equation (1) becomes

$$\frac{\partial^2\phi}{\partial y^2} + (1-M^2)\frac{\partial^2\phi}{\partial x^2} - 2ikM\frac{\partial\phi}{\partial x} + k^2\phi = 0, \tag{2}$$

and a family of exact local solutions is defined by

$$\phi(x,y) = A\,e^{-i(k_x\,x + k_y\,y)} = A\,e^{-ik\frac{(x\cos\theta + y\sin\theta)}{1+M\cos\theta}}, \tag{3}$$

where $k = \omega/c_0$, $A \in \mathbb{C}$ and $\theta \in [0, 2\pi)$ is the angle between the flow velocity and the wave direction. The convective effect of the mean flow gives a different wave speed for each direction and hence a wavenumber which varies with θ. In the case of non-uniform mean flow, the local solutions are orientated in the direction of the

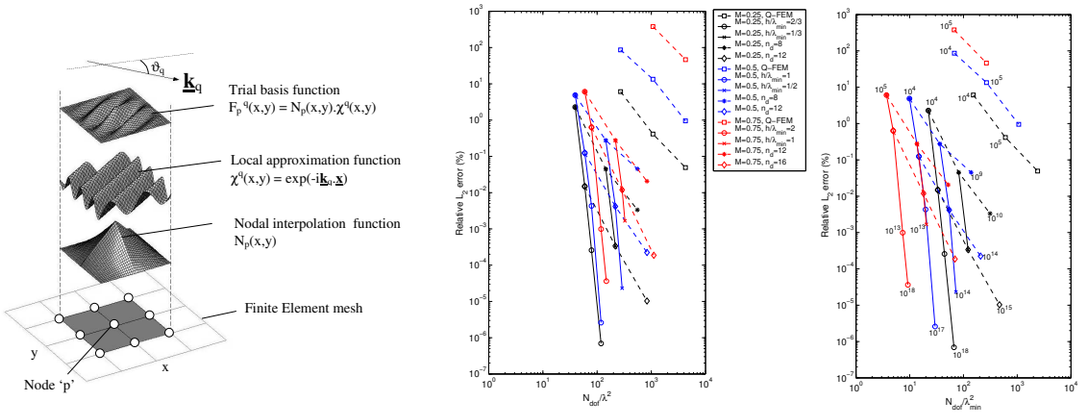


Figure 1: Construction of the PUFEM trial basis (left). Results for a lined 2-D uniform duct (right).

mean flow. The PUFEM discrete trial space is then constructed by selecting a *finite* number of wave directions, $n_d(l)$ say, at each node l of a conventional FE mesh. A generic element ϕ_h of the PUFEM finite element space is written

$$\phi_h(x,y) = \sum_{l=1}^{N_{nodes}} N_l(x,y) \sum_{j=1}^{n_d(l)} A_l^j \, e^{-ik\frac{(x\cos\theta_j + y\sin\theta_j)}{1+M\cos\theta_j}}, \quad \text{with} \sum_{l=1}^{N_{nodes}} N_l(x,y) = 1 \;\; \text{(partition of unity)}$$

where N_{nodes} is the number of nodes in the mesh, $N_l(x,y)$ $(l = 1, \cdots, N_{nodes})$ are the conventional nodal shape functions and A_l^j $(l = 1, \cdots, N_{nodes}$ and $j = 1, \cdots, nd(l))$ are the unknown nodal amplitudes. These form the d.o.f. for the model. i.e. A typical PUFEM trial basis function is the product of a shape function and a wave function as illustrated in the left hand picture in Figure 1. A weak variational formulation is used to obtain a set of discrete algebraic equations for the unknown variables A_l^j.

Results are presented in Figure 1 for a 2-D test case in which prescribed modes propagate in a uniform lined duct. The L_2 error in the computed solution is plotted against a resolution parameter N_{dof}/λ^2. Results are shown for a reduced frequency $ka = 20$ (a is the duct width) with $M = 0.25, 0.5, 0.75$. Two definitions of the wavelength λ are considered in the parameter N_{dof}/λ^2; the mean value in the left hand graph, and the minimum (i.e upstream) value in the right hand graph. The condition number of the coefficient matrix is noted beside selected data points. The accuracy of the solution can be improved either by refining the mesh (h refinement, indicated by the dashed lines) or by increasing the number of wave directions at each node (a sort of 'p' refinement, indicated by solid lines). Clearly the improvement due to 'p' refinement is more rapid but also increases the condition number. Also shown are data for a series of conventional quadratic FE solutions (Q-FEM). *All* of the PUFEM models offer a significant improvement in accuracy over the conventional FE model for a given problem size. Results (not shown) indicate that the same conclusions hold for nonuniform ducts.

CONCLUSIONS

The PUFEM approach has given promising results for 2-D test problems. These incorporate many aspects of propagation in 'real' inlet and bypass ducts (non-uniform geometry, flow gradients and liners) but further studies are needed to determine whether PUFEM can deliver the execution times which are needed for practical three dimensional problems.

References

[1] R. J. Astley, J. A. Hamilton, N. Baker, and E. Kitchen. Modelling tone propagation from turbofan inlets - the effect of extended lip liners. *AIAA paper 2002-2449*, 2002.

[2] A. Deraemaeker, I. Babuska, and P. Bouillard. Dispersion and pollution of the FEM solution for the Helmholtz equation in one, two and three dimensions. 46:471–499, 1999.

[3] W. Eversman. Mapped infinite wave envelope elements for acoustic radiation in a uniformly moving medium. *J. Sound Vib.*, 224:665–687, 1999.

[4] O. Laghrouche, P. Bettess, and R. J. Astley. Modelling of short wave diffraction problems using approximating systems of plane waves. *Int. J. Numer. Meth. Engng.*, 54:1501–1533, 2002.

[5] J.M. Melenk and I. Babuška. The partition of unity finite element method: Basic theory and applications. *Comput. Methods Appl. Mech. Engrg.*, 139:289–314, 1996.

[6] D. Stanescu, M. Y. Hussaini, and F. Farassat. Aircraft engine noise scattering - a discontinuous spectral element approach. *AIAA paper 2002-0800*, 2002.

WAVE PROPAGATION IN AND SOUND EMISSION FROM A SANDWICH PLATE UNDER HEAVY FLUID LOADING

Sergey V. Sorokin
Institute of Mechanical Engineering, Aalborg University, Pontoppidanstraede 101, DK 9220 Denmark

Summary The talk addresses wave motion in an unbounded fluid-loaded elastic sandwich plate composed by two identical isotropic skin plies and an isotropic core ply in a general three-dimensional problem formulation. Several alternative theories for stationary dynamics of such a plate are suggested, including a formulation in the framework of a theory of elasticity applied for the core ply. In the first instance, a fluid loading at the both sides of a plate is considered and 'in-phase' and 'anti-phase' wave motions (with respect to transverse deflections of skins) are analysed independently upon each other. Dispersion curves are compared and it is shown that the simplified models are capable to give a complete and accurate description of all propagating waves in not too high frequency range, which is sufficient in practical engineering. The role of sound emission into the acoustic medium in wave propagation phenomena is studied. Furthermore the analysis is extended to take into account for the 'symmetry-breaking' effects, e.g., a static pre-stress of one of skin plies and a fluid loading at one side of the sandwich plate. The standard perturbation technique is applied to analyse an interaction between dispersion curves in these cases.

INTRODUCTION. THE PROBLEM FORMULATION

Sandwich plates are widely used in many technical applications because this composition of a thin-walled structure conveniently combines the properties of a high strength and a low weight. The issues of strength and reliability of such structures have been thoroughly studied in many publications. The stability and dynamics of sandwich beams and plates have also been explored quite extensively. However, the effects of heavy fluid loading (which are particularly relevant to various naval applications) have not yet been studied in details. There are two possibilities to describe dynamics of sandwich plates. Equations of motions of a core ply may be formulated in the framework of a theory of elasticity, whereas in-plane and out-of-plane dynamics of each skin is governed by reduced equations of elasto-dynamics and by a conventional plate theory, respectively. This system of equations of the 'refined' theory is supplemented by continuity conditions at the interfaces between plies. Alternatively, some hypotheses may be adopted concerning the deformation of an arbitrary cross-section of the whole package of plies and reduced low-order equations are then derived in a 'simplified' theory. Inasmuch a heavy fluid loading is included, additional continuity conditions are formulated at fluid-structure interfaces and the wave equation is introduced for an acoustic medium in both the 'refined' and the 'simplified' theories. Naturally, the 'simplified' formulation does not permit to capture short-wave high-frequency motions in sandwich plates, but the essential (from the practical viewpoint) features of wave propagation in these structures are related to the audio frequency range. In this range, the length of a propagating wave exceeds a thickness of the whole package of plies at least in 3-4 times. Thus, for low and intermediate frequencies, it is expedient to estimate the actual validity of the 'simplified' theories in describing wave motions in a sandwich plate under heavy fluid loading. Three small non-dimensional parameters are introduced to characterise the internal structure of a sandwich plate: the geometry parameter ε as a ratio of the thickness of a skin to the thickness of a core, the density parameter δ as a ratio of the density of a core to the density of a skin and the stiffness parameter γ as a ratio of the Young's module of a core to the Young's module of a skin. Each of these parameters is small and it facilitates an asymptotic analysis of dispersion equations of the 'refined' theories, which proves that the 'simplified' theories in effect deliver the same dispersion equations up to the leading order terms. Stationary wave propagation is considered and the frequency parameter is defined as $\Omega = \dfrac{\omega h_{skin}}{c_{skin}}$ (c_{skin} is a sound speed in the material of skin plies).

THE SYMMETRIC CASE

In the absence of static pre-stress of skins, two uncoupled classes of waves exist in a plate of symmetric composition, which is fluid-loaded at both sides. They may conveniently be characterised by a phase shift between the lateral displacements of skin plies. The 'in-phase' waves are specified as those which preserve the thickness of a sandwich plate (they characterise 'global' flexural motions of the whole package of plies), whereas the 'anti-phase' waves are developed if the lateral displacements of skins are in opposite direction to each other at any instant of time.

'In-phase' waves

A dominantly flexural propagating wave, which exists in a fluid-loaded sandwich plate at an arbitrary low frequency, is adequately captured by the 'simplified' theory. Besides, two propagating waves of dominantly shear deformation

emerge in the 'low-frequency range' ($\Omega < 0.5$). Their cut-on frequencies are controlled by the parameters ε, γ of the sandwich plate composition and by the compressibility parameter defined as a ratio of the sound speed in an acoustic medium to the sound speed in the material of skins. The magnitudes of these cut-on frequencies and location of dispersion curves are also adequately predicted by the 'simplified' theory when $\gamma < 0.005$, which is a typical situation for the sandwich plates used in technical applications.

'Anti-phase' waves

In this case, the methodology to derive the 'refined' theory is not altered as compared with the previous case, whereas three 'simplified' theories are derived independently upon each other to describe the dominantly dilatational, the dominantly shear and the dominantly flexural wave. The dependence of their cut-on frequencies upon the parameters of sandwich plate composition and on the compressibility parameter is studied. A good agreement between the results obtained by a use of the 'refined' and the simplified' theories is observed in the whole 'low-frequency range' ($\Omega < 0.5$) except for relatively narrow frequency bands, where the dispersion curves predicted by 'simplified' theories cross each other. In these zones, more complicated behaviour of dispersion curves (including generation of the waves with phase and group velocities in opposite directions) detected by a use of the 'refined' theory, explains the failure of the 'simplified' ones.

TWO 'SYMMETRY-BREAKING' CASES

The results reported in the previous section show that several elementary theories, each of which is derived from *a-priori* hypotheses of kinematics of plate's deformation are capable to provide a complete and accurate description of all propagating waves in not too high frequency range, which is sufficient in practical naval and aerospace engineering. In practice, it is often the case that only one skin is pre-stressed or, (e.g., for a ship's hull) a compressible fluid is located only at one side of a sandwich plate. Then the 'in-phase' and 'anti-phase' wave are not decoupled from each other, but it is possible to apply standard perturbation technique to study an interaction between different branches of the dispersion curves. An attention is focused at the analysis of the modes in the intersection cases (when the individually taken 'in-phase' and 'anti-phase' dispersion curves cross each other). It is shown that it does not present serious difficulties to predict location of all dispersion curves in the low-frequency range for the both considered cases by a use of perturbation methods.

THE ROLE OF EMISSION OF ACOUSTIC WAVES

The comparison of dispersion curves obtained for various values of the sound speed ratio sheds a light on the role of emission of acoustic waves. As is found out this phenomenon influences propagation of the dominantly in-plane waves (both 'in-phase' and 'anti-phase' ones) stronger than the propagation of the dominantly flexural waves. In particular, the threshold sound speed ratio is found, which (at the fixed excitation frequency) separates the regime of propagation of a trapped wave and the regime of its decay. In the case of an incompressible fluid, there is no energy flow from a plate to infinity in the direction perpendicular to the surface of a vibrating plate. As soon as the fluid becomes sufficiently compressible, the energy transmission ('leakage') from the plate into surrounding acoustic medium is developed. Respectively, the structural energy flow disappears and the free propagating wave cannot be supported in plate under such a fluid loading.

CONCLUSIONS

The set of 'simplified' theories is suggested to describe wave propagation phenomena in sandwich plates under heavy fluid loading. Comparison of dispersion curves obtained by solving characteristic equations derived from these theories with dispersion curves obtained in the 'refined' problem formulation shows that these theories predict adequately wave motions in a sandwich plate in the whole frequency range of practical interest. It is shown that dominantly in-plane waves may either be propagating or decaying depending on the magnitude of the compressibility parameter (the ratio of a sound speed in a fluid to a sound speed in skin's material) and a simple explanation of this transition is given.

References

[1] Sorokin S. V.: A Note on the Effect of Compressibility on the Propagation of Free Waves in Sandwich Plates with Heavy Fluid Loading *J. Sound and Vibration*: corrected proof available on-line.
[2] Sorokin S. V.: Analysis of Wave Propagation in Sandwich Plates with and without Fluid Loading. *J. Sound and Vibration*: corrected proof available on-line.

3-D STRUCTURAL ACOUSTICS MODELING WITH HP-ADAPTIVE FINITE ELEMENTS

David S. Burnett, Mario Zampolli
NATO Undersea Research Centre, Viale S. Bartolomeo 400, 19138 La Spezia, Italy

Summary The Centre has developed a 3-D *hp*-adaptive finite-element structural acoustics code for modeling acoustic scattering from underwater elastic structures. 3-D continuum mechanics is used throughout the computational domain; thin structural components, such as plates and shells, are modeled with 3-D physics rather than plate or shell theories. The paper describes an unusual approach to code development, explains the underlying physics and mathematics, and presents several scattering and propagation models.

INTRODUCTION

Man-made undersea structures are typically enclosed thin shells (e.g., submarines, mines) with interior reinforcements (e.g., rib-stiffeners, partitions). For over thirty years the structural acoustics community has been developing finite-element codes to model the radiation and scattering of sound from such structures. Despite all this effort, there are still large discrepancies in the acoustic fields computed by different codes, for even the simplest structures at low frequencies, e.g., differences of 5 to 10 dB or more (well over 100%) for a simple closed shell with minimal interior structure at $ka \cong 2$. It has been the hypothesis of the first author for several years that these very large differences are probably due to the underlying physics, i.e., the use of plate and shell theories, which are 2-D physics inside a 3-D geometry. Near structural discontinuities, such as shell intersections, the elastic field is strongly 3-D, with complicated evanescent elastic waves in the vicinity of the discontinuities. Errors in these localized fields will produce errors in the propagating elastic waves, which in turn will produce errors in the acoustic waves "launched" into the exterior fluid. In short, the scattered or radiated acoustic field may depend strongly on the localized 3-D elastic fields in the shell.
Motivated by this hypothesis, the Centre initiated a research effort five years ago to develop a high-fidelity 3-D finite-element structural acoustics code for modeling acoustic scattering from underwater elastic structures, primarily undersea mines located in or near the seabed in shallow water. Thin structural components, such as plates and shells, are modeled with 3-D physics rather than plate or shell theories. The code is therefore fully 3-D, i.e., in both physics and geometry. The first version of a steady-state (time-harmonic) code, named FESTA, for Finite Element Structural Acoustics, was released in 2003.

CODE DEVELOPMENT APPROACH

The Centre is using the commercial software package ProPHLEX [1] developed by the R&D Division of Altair Engineering (formerly COMCO). This package is a suite of software tools for *developing* customized FE codes. It contains a library of several thousand routines [O(10^6) lines] that perform all the detailed tasks of a FE analysis. To develop an application code, the researcher derives the Galerkin residual equations from the governing PDEs and then links self-written code [O(10^3) lines] with the vendor-written library, which creates an application code with a commercial-quality GUI, e.g., FESTA. A central feature of ProPHLEX is its *hp*-adaptivity – an automated procedure for achieving near-optimal FE meshes, based on the use of high-order "hierarchic" basis functions and element-by-element error estimators.
ProPHLEX is applicable to any system or process that can be mathematically formulated as a system of coupled 2nd-order PDEs, in the following tensor form:

$$\left(a_{\alpha i\beta m} q_{\beta,m}\right)_{,i} + b_{\alpha\beta m} q_{\beta,m} + c_{\alpha\beta} q_{\beta} = -f_{\alpha} \tag{1}$$

where $(\ )_{,i} = \partial(\ )/\partial x_i$ and x_i are the independent variables. For physically oriented systems, x_i are usually spatial coordinates. The components of the vector q_β may be any meaningful quantities, but q_β need not be sensible as a vector. For example, the components can include displacements in an elastic solid and pressures in an acoustic fluid. The coefficients $a_{\alpha i\beta m}$, $b_{\alpha\beta m}$ and $c_{\alpha\beta}$ may be a function of q_β (for nonlinear processes) and/or a function of the independent variables x_i (for spatial inhomogeneities) and/or a function of time (for transient processes). All variables must be real-valued; hence, any PDEs with complex variables must be decomplexified. Equation (1) can describe a very broad range of phenomena, including the coupling of different types of phenomena.
ProPHLEX uses eq. (1) in each and every finite element in the computational domain. Therefore, to develop a structural acoustics code, the analyst must cast the governing PDEs for both the vibrating solid and acoustic fluid into a single system of PDEs in the form of eq. (1). This, in effect, treats the entire fluid-structure domain as a single continuum, which is modeled using only one type of finite element: a fluid-solid element.

A UNIFIED CONTINUUM MECHANICS DERIVATION OF A FLUID-SOLID ELEMENT

Both the solid and the fluid are elastic media, experiencing small, steady-state vibrations about a quiescent state. The solid may be viscoelastic, anisotropic and inhomogeneous. The fluid is inviscid but may include volume dissipation, and is isotropic and inhomogeneous. Under these conditions, *the continuum mechanics for the fluid are a special case of those for the solid*. Hence, to derive the acoustic wave equation for the fluid, one may begin with the governing PDEs

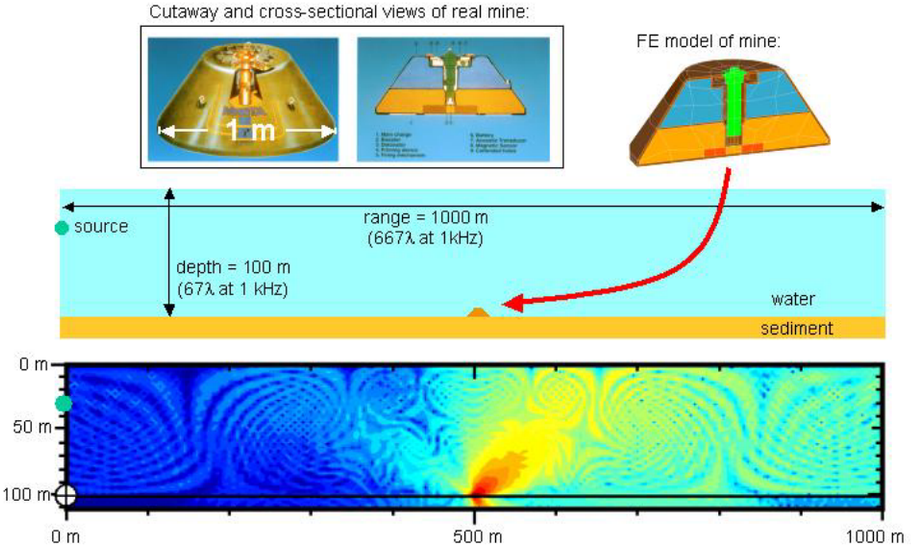
for wave propagation in an elastic solid and apply the appropriate limiting conditions. The wave equations in both media can then be combined into a single tensor wave equation in the form of eq. (1), where

$$q_\beta = \begin{Bmatrix} u_x^R \\ u_y^R \\ u_z^R \\ u_x^I \\ u_y^I \\ u_z^I \\ p^R \\ p^I \end{Bmatrix} \begin{matrix} \\ \\ \\ \\ \\ \\ \\ \\ \end{matrix} \begin{matrix} \text{displacement} \\ \text{in solid} \\ \\ \\ \\ \\ \text{acoustic pressure} \\ \text{in fluid} \end{matrix}, \quad a_{\alpha l \beta m} = \begin{array}{c|cc|cc|cc|cc} & \beta=1 & 2 & 3 & 4 & 5 & 6 & 7 & 8 \\ \alpha=1 & & & & & & & & \\ 2 & & c^R_{\alpha l \beta m} & & -c^I_{\alpha l (\beta-3) m} & & & 0 & \\ 3 & & & & & & & & \\ 4 & & & & & & & & \\ 5 & & c^I_{(\alpha-3) l \beta m} & & c^R_{(\alpha-3) l (\beta-3) m} & & & 0 & \\ 6 & & & & & & & & \\ 7 & & & & & & & & \\ 8 & & 0 & & 0 & & & \frac{1}{\omega^2 \rho^f} \delta_{\alpha\beta} \delta_{lm} & \end{array}, \quad c_{\alpha\beta} = \begin{array}{c|cc|cc|cc|cc} & \beta=1 & 2 & 3 & 4 & 5 & 6 & 7 & 8 \\ \alpha=1 & & & & & & & & \\ 2 & & \omega^2 \rho^s \delta_{\alpha\beta} & & & 0 & & 0 & \\ 3 & & & & & & & & \\ 4 & & & & & & & & \\ 5 & & 0 & & & \omega^2 \rho^s \delta_{\alpha\beta} & & 0 & \\ 6 & & & & & & & & \\ 7 & & & & & & & & \\ 8 & & 0 & & & 0 & & K_{\alpha\beta} & \end{array} \tag{2}$$

The superscripts R and I indicate real and imaginary parts, respectively. Equation (2) shows the α,β-"plane" of the 4th-order tensor $a_{\alpha l \beta m}$; each of the 64 positions is a 3×3 tensor in l,m, where l,m = 1,2,3 for the 3 spatial coordinates. The 4th-order tensors $c^R{}_{\alpha l \beta m}$ and $c^I{}_{\alpha l \beta m}$ are the real and imaginary parts, respectively, of the complex elastic moduli. The fluid and solid densities are ρ^f and ρ^s, respectively, and $K_{\alpha\beta}$ is the decomplexified fluid compressibility.

EXAMPLE PROBLEM

The oral presentation will show several models of acoustic propagation and target scattering, including verification vis-à-vis analytic solutions and other numerical codes. One of the most challenging of these problems is shown here: scattering from a realistic mine sitting on a sedimentary seabed in shallow water (see figure below). The ocean surface and water/sediment interface are flat. The sediment is modeled as a heavy, dissipative fluid. A 1 kHz monopole source is located at a range of 500m from the mine and a depth of 30m. Although FESTA can model scattering in complex waveguides (as will be shown in the oral presentation), this computational domain is too large in terms of wavelengths, λ, for available computer resources. Since λ = 1.5m, the source/mine separation is 333λ and the depth is 67λ. A high-accuracy 3-D scattering model would require several tens of millions of DOF. Therefore a more efficient *hybrid* approach is employed: FESTA computes the local scattered field in the vicinity of the mine and a non-FE propagation code computes the large-scale propagation of the incident and scattered fields in the waveguide. The propagation code used in this problem is OASES [2], which is based on wavenumber integration. A 3-step method couples the inputs and outputs of the two codes. The final scattered field throughout the waveguide is shown by the contour plot.



CONCLUSIONS

Using *hp*-adaptive finite-element technology, a 3-D structural acoustics code has been developed for modeling acoustic scattering from underwater elastic structures. 3-D continuum mechanics is used in both the fluid and solid media, making the code 3-D in both physics and geometry. The code continues to be verified against a variety of test problems.

References

[1] Liszka, T.J., et. al.: ProPHLEX – An *hp*-adaptive finite element kernel for solving coupled systems of partial differential equations in computational mechanics. *Comput. Methods Appl. Mech. Engrg*. **150**: 251-271, 1997.

[2] Schmidt, H.: OASES, Version 3.1, User Guide and Reference Manual. Dept. of Ocean Engrg., M.I.T., (2003). Available at http://acoustics.mit.edu/faculty/henrik/oases.html

XXI ICTAM, 15–21 August 2004, Warsaw, Poland

THE LOW-TEMPERATURE ACOUSTICAL AND THERMAL PROPERTIES OF MATERIALS DUE TO THE DYNAMICS OF LINEAR TOPOLOGICAL DEFECTS

Dmitry V. Churochkin*, Vladimir Osipov*
*Bogoliubov Laboratory of Theoretical Physics, Joint Institute for Nuclear Research, 141980 Dubna, Moscow region, Russia

Summary The specific heat and frequency-dependent loss due to twist disclinations are investigated. The low-temperature internal friction and thermal conductivity due to dipoles of edge dislocations are explored.

TWIST DISCLINATION

In general, the equation of motion of twist disclination has the form [1]

$$m\frac{\partial^2\epsilon(z,t)}{\partial t^2} = \frac{\partial}{\partial z}\left(T\frac{\partial\epsilon(z,t)}{\partial z}\right) - B\frac{\partial\epsilon(z,t)}{\partial t} + F_i, \tag{1}$$

where $\epsilon(z,t)$ is the position of the disclination line in the glide plane, F_i is the external force, m is the mass of twist disclination, T is the line tension, and B is the damping parameter. All these parameters are determined per unit length of the disclination line and they are z-dependent [1,2] The equation (1) means that twist disclination can be represented as a string with the understanding that this is *heterogeneous* string. We calculate the specific heat C and internal friction Q^{-1}, resolving the equation of motion (1). As a result, it was obtained that $C \sim \Lambda T$ [2] and under the low frequency acoustical influence $Q^{-1} \sim \Lambda L^4$ [1], where Λ is the twist disclination density, T is the temperature, L is the length of twist disclination. An important conclusion can be drawn: that the individual(local) properties of linear defects get lost whithin the string model. That is the main physical characteristics(heat capasity, internal friction) are found to be determined only by some general parameters of linear defects (the length of defect line, the density of defects) and elastic body (the density of the solid, sound velocities, the shear modulus).

DISLOCATION DIPOLE

We suggest that a dipole can be modeled by means of two damped interacting vibrating strings. Supposing that all the parameters of the string model are common for both dislocations one can formulate the general equations of damped glide motion for the edge dislocation dipole.

$$\begin{aligned} m\frac{\partial^2\epsilon(z,t)}{\partial t^2} + B\frac{\partial\epsilon(z,t)}{\partial t} - T\frac{\partial^2\epsilon(z,t)}{\partial z^2} &= F_1^{ext+} \\ m\frac{\partial^2\psi(z,t)}{\partial t^2} + B\frac{\partial\psi(z,t)}{\partial t} - T\frac{\partial^2\psi(z,t)}{\partial z^2} &= F_1^{ext-}, \end{aligned} \tag{2}$$

where $\epsilon(z,t)$ and $\psi(z,t)$ are the position of positive and negative dislocations in the glide plane, m is the effective mass, T is the line tension and B is the damping parameter, F_1^{ext+},F_1^{ext-} are the total external forces which exert on the positive and negative dislocations correspondingly, in their glide planes. In our case, the total external force

$$F_1^{ext\pm} = f_1^{\pm} + F_1^{\pm} \tag{3}$$

where $f_1^{\pm}$ is interaction force between the dislocation into dipole and the force $F_1^{\pm}$ due to phonon stress field σ_{ik}. Hereafter, the sign plus (minus) correspond to a positive (negative) dislocation, and the summation over repeated indices is assumed. In the particular case of the linear long-wave approximation, the explicit form of (3) was presented in [3]. Notice that, in general, the force (3) is essentially nonlinear.

Internal friction due to the motion of dislocation dipole

In [4], the amplitude-independent dislocation absorption (internal friction) was investigated under the joint action of constant and random external forces on the dislocation. The action of random forces of different types were considered with due regard for the inertial properties of the dislocation and the effect of the internal (parabolic) potential relief of the crystal. The dependence of the internal friction from the degree of correlation of random forces and the parameters of the dislocation and the medium were obtained. It was revealed that the regularities of the energy loss by excitation of the dislocation structure under random external actions essentially differ from those observed under harmonic actions. Unlike the Granato-Lucke classical case of periodic actions on a dislocation, the internal friction in the low-frequency range for the random actions nonlinearly depends on the frequency. The decrement in this frequency range is considerably larger than that under periodic

actions. The dependence of the damping decrement from the dislocation segment length L is governed by the parameters of the dislocation, the medium, and the random force and can exhibit different behavior in contrast with the corresponding dependence observed under periodic actions. We suppose that a similar mechanism of the dissipation due to the random external force is responsible for the explanation of an unexpected high value of low-temperature internal friction in high-purity plastically deformed aluminium experimentally observed in [5]. Actually, we apply the scheme developed in [4] to the dynamics of dislocation dipole and obtain the reasonable value of the decrement Q^{-1} in Al. The theory gives a good agreement with experiment under the appropriate density of dislocation dipoles.

Thermal conductivity

As is well-known, metals in the superconducting state conduct the heat via phonons. At the lowest temperature the thermal conductivity is due to scattering of phonons by the surface of the sample(boundary scattering) and by lattice defects. We suppose that the most part of lattice defects are the dislocation dipoles. In order to obtain the contribution to the thermal conductivity we use the relaxation-time description. In this case, within the framework the Debye approximation and if normal-process scattering is neglected, the lattice thermal conductivity is given by

$$k = (k_B^3/2\pi^2\overline{v}\hbar^3)T^3 \int_0^{\theta/T} x^2\tau(x)C(x)dx \tag{4}$$

where θ the Debye temperature, $\overline{v}$ is the averaged sound velocity, τ is the total phonon relaxation time and C is the specific heat. We will assume that all phonon modes are scattered almost equally by the dislocation dipoles. The total relaxation rate τ^{-1} is

$$\tau^{-1} = \tau_c^{-1} + \tau_d^{-1} \tag{5}$$

where τ_c^{-1} is the relaxation rate of the boundary scattering which is obtained from the data of an undeformed specimen and τ_d^{-1} is the relaxation rate due to the dynamic phonon-dipole interaction.
The calculations shows that in Al below 0.15 K, in Ta below 0.6 K and in Nb below 1.5 K when the influence of the electronic contribution to the thermal conductivity is neglected, our model demonstrates a rather good agreement with experiments.

References

[1] Churochkin D.V., Osipov V.A.: On the disclination-induced internal friction. *Phys. Lett. A* **277**:277–273, 2001.
[2] Churochkin D.V., Osipov V.A.: Contribution of mobile twist disclinations to the specific heat of crystals. *Phys. Lett. A* **96**:96–92, 2001.
[3] Kneezel G.A., Granato A.V.: Effect of independent and coupled vibrations of dislocations on low-temperature thermal conductivity in alkali halides. *Phys.Rev. B* **2866**:2866–2851, 1982.
[4] Kamaeva O.V., Chernov V.M.: Amplitude-Independent Dislocation Internal Friction under Random External Actions. *Physics of the Solid State,* **1608**:1601–1608, 2002.
[5] Liu X., Thompson E., White B.E., Jr., Pohl R.O. : Low-temperature internal friction in metal films and in plastically deformed bulk aluminum. *Phys.Rev. B* **11776**:11776-11767, 1999.

SHOCK LEAKAGE THROUGH A VORTEX-LADEN MIXING LAYER CAUSING JET SCREECH

Takao Suzuki*, Sanjiva K. Lele**
*California Institute of Technology, Engineering and Applied Science, Pasadena, CA 91125, USA
**Stanford University, Aeronautics and Astronautics, Stanford, CA 94305-4035, USA

Summary The interaction between shock-cells and vortices in a mixing layer of a jet generates intense shock noise causing jet screech. This paper studies this shock noise phenomenon using a geometrical theory for weak shock motion. The unsteady ray-tracing equation shows that the local vorticity in the mixing layer behaves as a barrier and the standing shock leaks near the saddle points between vortices. Direct numerical simulation demonstrates this by showing good agreement of the shock front with the geometrical theory.

INTRODUCTION

When a supersonic jet is under-expanded, a shock-cell structure generated due to pressure mismatch interacts with the vortices convected in a mixing layer of the jet. As a result, some acoustic energy associated with the shock leaks through the mixing layer and, in turn, radiates as intense noise in the far field. When the radiated sound propagating upstream excites another instability wave from the nozzle lip, the whole system creates a feedback loop, known as "jet screech." The frequency of the screech tone has been successfully predicted in past [1], but the mechanisms of intense sound generation remain somewhat elusive.

Although several previous studies have modeled the shock noise as non-linear interaction between the shock-cell structure and shear layer instability waves, those models was not able to explain the intense noise generation nor provide quantitative prediction. A recent work [2] introduced geometrical acoustics and computationally investigated the sound radiation pattern of shock noise with the linearized Euler equations. However, the validity of the high frequency limit for standing shock waves was uncertain, and the shock noise amplitude was still unpredictable.

The objective of this study is to identify the mechanism of intense shock noise generation and to predict the amplitude as well as the wave-front evolution. The key idea here is to demonstrate that the governing equations for weak shock motion are identical to the equations derived from geometrical acoustics. We validate the model based on the geometrical theory by performing direct numerical simulation (DNS) in two-dimensions (refer to [3] for details).

MODEL OF SHOCK LEAKAGE THROUGH A VORTEX-LADEN MIXING LAYER

When the angle of waves (defined based on the wave-front normal) issued from the potential core is higher than $\theta^{cr} \equiv \cos^{-1}[-a_{\rm jet}/(a_\infty + u_{\rm jet})]$, total internal reflection occurs in a supersonic jet. Since the Mach angle, $\theta^M \equiv \cos^{-1}(-1/M_{\rm jet})$, is always higher than this angle, the shock-cell structure should be confined in the potential core. However, as instability waves change the vortical structure of the mixing layer, a portion of shock can "leak" across the mixing layer.

To describe the shock motion, we introduce a geometrical theory, which is analogous to the high frequency limit of acoustics. We solve the evolution of a pressure jump expressed by a geometrical form (i.e. $p(t,\mathbf{x}) = P(t,\mathbf{x})h[\phi(t,\mathbf{x})/\epsilon]$, ϵ being the width of the shock and $h[\phi/\epsilon]$ a ramp function). Substituting it into the Euler equations, the leading order terms of $\epsilon \to 0$ become the eikonal equation (the ray-tracing equation) for unsteady flows:

$$(\phi_{,t} + u_j\phi_{,j})^2 - a^2\phi_{,j}^2 = 0\ . \tag{1}$$

In turn, the equation for constant ϕ solves a line of discontinuity corresponding to the shock-front. Subsequently, the second highest order terms yield the first order transport equation, in which the quantity

$$\frac{P^2 S}{p(\phi_{,t} + u_k\phi_{,k})}\sqrt{a_\infty^2 + |\frac{d\mathbf{x}}{dt}|^2} \tag{2}$$

is conserved along ray tubes in space-time coordinates (where S denotes the area of the tube in a four-dimensional sense). This quantity corresponds to the "Blokhintzev invariant" [4] in four dimensions, which provides the intensity of the shock. Thus, we can solve the unsteady shock motion as well as its intensity by the method of characteristics.

By solving the equation of the wave-front normal, we find that the local vorticity rotates the shock-front: If the vorticity distributed along the shock trajectory is high, the trajectory creates a loop and total reflection occurs. In contrast, rays can leak near the saddle points of vortices where the local vorticity is thinner. As the vortices are convected, the reflection site of the shock-cell structure is pinched off periodically and this portion is radiated as intense tonal noise.

NUMERICAL METHODS

We demonstrate the geometrical theory by performing DNS of an iso-thermal supersonic mixing layer ($M_{\rm jet} = 1.2$) in two-dimensions. In one case we directly solve the shock motion by imposing a standing shock in DNS, while in the other case we calculate the unsteady ray tracing equation and apply the ray tube theory (i.e. the Blokhintzev invariant) with the DNS background flow data. These two cases are compared in terms of the shock-front evolution and shock amplitude.

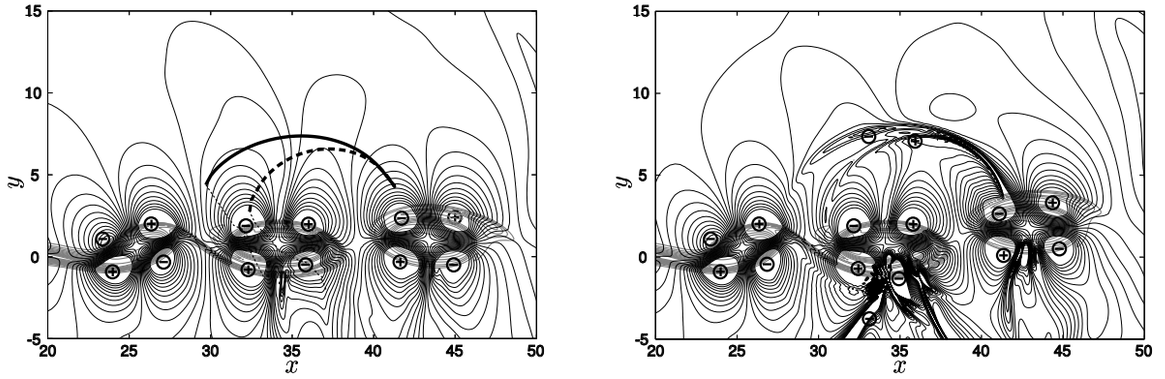


Figure 1. Comparison of the shock noise from a mixing layer. Shock-fronts calculated with the eikonal equation on the left, and that from DNS on the right. Vorticity contours are superposed on dilatation field: (+), expansion; (−), compression.

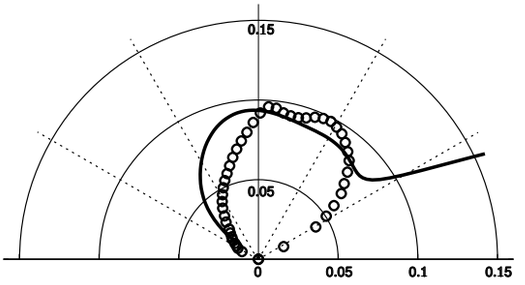


Figure 2. Comparison of shock wave amplitude. Pressure jump of the shock at distance $R \approx 14\delta_V$ centered at $(35.0, 0)$ was measured, and the pressure ratio defined as $(\Delta p_{R=14})/(\Delta p_{y_{\text{initial}}})$ is plotted: ——, geometrical theory; ∘, DNS. $\Delta p_{y_{\text{initial}}} \approx 0.1 p_\infty$

RESULTS OF SIMULATION

Figure 1 compares the shock-fronts obtained from the eikonal equation and from DNS and shows good agreement in which the standing shock wave starts to leak near the saddle point and forms a compression branch followed by an expansion branch. This circular wave propagates in the far field with nearly the speed of sound. Since the geometrical theory assumes linearity, the wave-fronts obtained from the eikonal equation tends to delay compared with those calculated with DNS.

The comparison of shock amplitude in figure 2 shows that the overall sound pressure level of DNS is comparable to that of the geometrical theory, although the detailed directivity pattern has slight discrepancy. Since a portion of the shock itself changes into sound wave, its intensity becomes much higher than that generated by the non-linear flow interaction. We can also observe that appreciable amplitude of shock noise propagates upstream, which potentially causes the feedback mechanism of jet screech.

CONCLUSIONS

This study has theoretically and computationally demonstrated that standing shock waves in a potential core can most easily leak near the saddle points of vortices in a supersonic mixing layer. Previous experimental studies have indicated that the shock noise is most intensive somewhere between the second and fourth shock-cell locations. We can interpret this trend from the current study: Shock waves can leak through the mixing layer only after the unsteady vortices have sufficiently developed. However, when smaller scale eddies develop further downstream, the organized vortical structure is disrupted so that distinctive saddle points are no longer formed, and the shock noise intensity is reduced again. Instead, broadband shock noise is generated due to scattering by turbulence.

As mentioned, the difference between the Mach angle and the critical angle of total reflection is given by a function of the jet Mach number and the temperature ratio of the mixing layer. This relation indicates that the threshold for shock leakage becomes lower as the jet temperature increases, which is consistent with the previous observation that screech noise becomes intensive downstream for heated jets.

References

[1] Powell A.: On the mechanism of choked jet noise. *Proc. Phys. Soc. Lond.* B **66**:1039–1056, 1953.
[2] Manning T.A., Lele S.K.: A numerical investigation of sound generation in supersonic jet screech. *AIAA paper*: AIAA-2000-2081, 2000.
[3] Suzuki T., Lele S.K.: Shock leakage through an unsteady vortex-laden mixing layer: application to jet screech. *J. Fluid Mech* **490**:139–167, 2003.
[4] Blokhintzev B. I.: The propagation of sound in an inhomogeneous and moving medium. *J. Acoust. Soc. Am.* **18**:322–328, 1946.

TRANSMISSION OF ELASTIC WAVES AND LOCALISED MODES IN COMPOSITE STRUCTURES

Natasha V. Movchan, Alexander B. Movchan
Department of Mathematical Sciences, University of Liverpool, Liverpool L69 3BX, U.K.

Summary This work addresses the spectral analysis of elasticity problems in doubly periodic composite structures represented either by arrays of inclusions embedded into an elastic matrix or discrete lattice structures. Particular attention is paid to filtering properties, i.e. the presence of stop bands within the spectrum, and localised modes for composite structures containing defects.

First, we consider a problem of propagation of elastic waves through an elastic medium containing an infinite doubly periodic array of circular cylindrical inclusions. Each inclusion consists of a core of radius r_1 surrounded by a coating of width r_2. The materials of the core, the coating and the surrounding matrix are all isotropic and have different elastic properties and densities. Displacements and tractions remain continuous across each interface. We assume here that the cylinders are infinitely long and all aligned perpendicular to the plane of propagation. In this case the problem is decoupled into two, in-plane and out-of-plane, problems. We analyse a Bloch-Floquet problem posed in an elementary cell of an infinite doubly periodic array. In particular, we show that the parameters of the coating can be tuned in such a way that, in the long-wave approximation, the elastic system responds as a homogeneous medium without inclusions; in this case the inclusions are classified as 'neutral', and their presence does not affect the value of the effective refractive index. However, for higher frequencies such structures exhibit stop bands and possible localisation of eigen-modes within either the coating or the inclusion core. The mathematical model used for analysis of this class of problems is based on the concept of multipole approximations as well as the transfer matrix approach discussed in detail in [1], [2].
Further, we note that it is efficient to model localised eigen-modes using approximations involving discrete lattice structures. As outlined in [3], the presence of 'defects' within a macro-cell of an infinite periodic lattice may generate a highly localised eigen-mode and low frequency stop bands for Bloch-Floquet elastic waves. This concept is developed in the present work, together with explicit asymptotic estimates for the eigen-frequencies of localised modes that exist in the densely-packed composite structures containing thin ligaments.
Since the modelling of discrete dynamic lattice structures is more straightforward compared to the analysis of continuum composites, it is important to be able to approximate the high-contrast densely packed composite structures by discrete lattices. This issue is also addressed in the present work.

References

[1] Platts S.B., Movchan N.V., McPhedran R.C., Movchan A.B.: Two-dimensional phononic crystals and scattering of elastic waves by an array of voids. *Proc. Roy. Soc. London* A**458**: 2327-2347, 2002.
[2] Movchan A.B., Movchan N.V., Poulton C.G.: Asymptotic Models of Fields in Dilute and Densely Packed Composites. Imperial College Press 2002.
[3] Martinsson P.G., Movchan A.B.: Vibrations of lattice structures and phononic band gaps. *Quart. J. Mech. Appl. Math.* **56**: 45-64, 2003.

ARBITRARILY WIDE-ANGLE WAVE EQUATIONS AND THEIR APPLICATIONS TO UNBOUNDED DOMAIN MODELING AND SUBSURFACE IMAGING

Murthy N. Guddati, A. Homayoun Heidari, and Keng-Wit Lim
Department of Civil Engineering, North Carolina State University, Raleigh, NC 27695-7908, USA

INTRODUCTION

Standard (full) wave equations are used to model the propagation of disturbances in acoustic and elastic media. These disturbances tend to propagate in all directions, i.e. 360° range of angles. In contrast to full wave equations, one-way wave equations (OWWEs), as their name implies, represent waves propagating in 180° range of angles. Due to this special property, OWWEs have found applicability in the areas of unbounded domain modeling, underwater acoustics and subsurface imaging. In order to make OWWEs computationally tractable, they are approximated. While there are many good approximations of OWWE are available, most of them have limitations with respect to their applicability, especially for more complex problems involving wave propagation in anisotropic elastic and poro-elastic media. Most of the approaches to date are based on rational approximation of the factorized wave equation. The fundamental difficulty with the existing approximations of OWWE for complex anisotropic media is that there do not appear to be a plausible way of factorizing the wave equation.

With the goal of developing OWWE for complex media, Guddati [1] has recently developed a systematic framework for deriving OWWEs that are of arbitrarily high accuracy. Named Arbitrarily Wide Angle Wave Equations (AWWE), they do not require explicit factorization and, depending on the order of the approximation, tend to accurately propagate waves in a range of angles as high as 180°. This presentation includes a brief overview of the procedure, followed by the application of AWWE to subsurface imaging and modeling acoustic waves in unbounded domains.

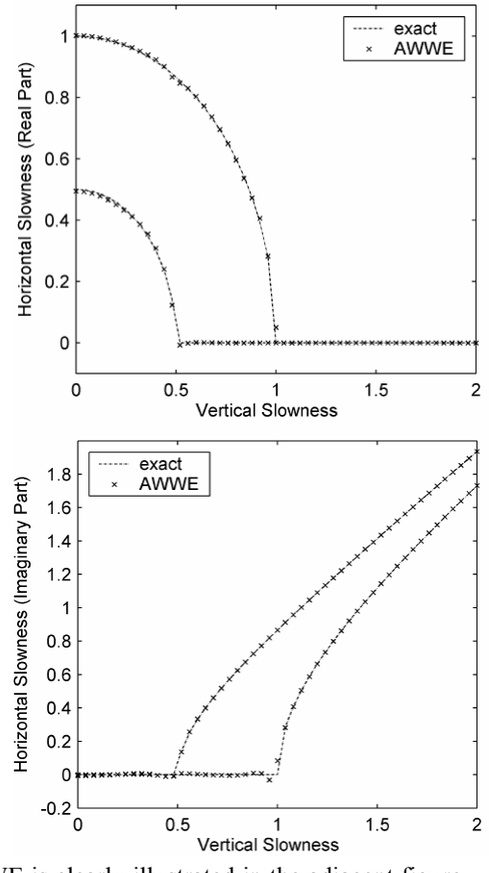
ARBITRARILY WIDE ANGLE WAVE EQUATIONS

AWWEs are derived using a five-step procedure. The first step uses the idea of representing one-way wave equations in terms of half-space stiffness, subsequently reducing the problem into approximating the half-space stiffness. The half-space is discretized using finite element mesh (step 2), and the resulting discretization error in half-space stiffness is completely eliminated with the help of special integration rules (step 3). Fourth step involves truncating the number of elements to make it computationally tractable, while the final step requires the use of imaginary finite-element lengths to represent traveling waves, or complex lengths to represent both traveling and evanescent waves. The resulting AWWE would take the form, for example for elastic waves,

$$\begin{Bmatrix} \mathbf{G}_{xx}\dfrac{\partial^2 \mathbf{u}}{\partial x^2} \\ \mathbf{0} \\ \vdots \\ \mathbf{0} \end{Bmatrix} + \left(\boldsymbol{\Lambda}_1 + \boldsymbol{\Lambda}_2\right)\frac{\partial^2}{\partial t^2}\begin{Bmatrix} \mathbf{u} \\ \mathbf{u}_1 \\ \vdots \\ \mathbf{u}_{n-1} \end{Bmatrix} + \boldsymbol{\Lambda}_3\frac{\partial^2}{\partial z \partial t}\begin{Bmatrix} \mathbf{u} \\ \mathbf{u}_1 \\ \vdots \\ \mathbf{u}_{n-1} \end{Bmatrix}$$

$$+\frac{\partial}{\partial z}\left(\boldsymbol{\Lambda}_3^T\frac{\partial}{\partial t}\begin{Bmatrix} \mathbf{u} \\ \mathbf{u}_1 \\ \vdots \\ \mathbf{u}_{n-1} \end{Bmatrix}\right) - \frac{\partial}{\partial z}\left(\boldsymbol{\Lambda}_4\frac{\partial}{\partial z}\begin{Bmatrix} \mathbf{u} \\ \mathbf{u}_1 \\ \vdots \\ \mathbf{u}_{n-1} \end{Bmatrix}\right) = \mathbf{0}.$$

In the above, $\mathbf{u}$ is the displacement vector, while $\mathbf{u}_1, \cdots, \mathbf{u}_{n-1}$ are auxiliary variables defined implicitly by the equation. $\mathbf{G}_{xx}, \boldsymbol{\Lambda}_1, \boldsymbol{\Lambda}_2, \boldsymbol{\Lambda}_3, \boldsymbol{\Lambda}_4$ are positive definite or positive semi-definite coefficient matrices. The accuracy of AWWE depends on the number of auxiliary variables as well as AWWE parameters (reference phase velocities) that determine the coefficient matrices. The accuracy of AWWE is clearly illustrated in the adjacent figure, which contains the slowness diagram for the elastic AWWE (using six auxiliary variables) with pressure wave velocity $\alpha = 2$ and shear wave velocity $\beta = 1$. The exact slowness is also shown in the same figure. It is clear from the figure that AWWE was able to approximate the slowness in a highly accurate manner. Similar observations were made for anisotropic acoustic and elastic media.



Salient Features of AWWE

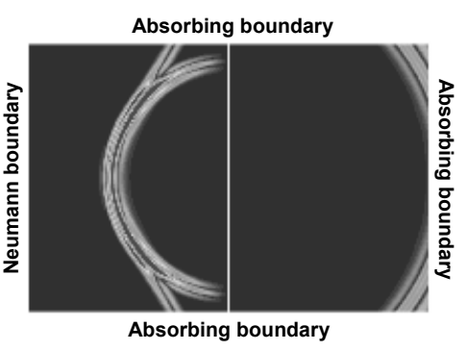
AWWEs have several desirable properties: (a) AWWEs represent forward propagating waves associated with the general wave equations, even in anisotropic and poro-elastic media. The only restriction of the procedure is that the governing differential equation (full wave equation) must be second order. (b) AWWEs are exact for waves propagating with phase velocities coinciding with the reference phase velocities. Thus, knowledge of the approximate propagation characteristics could be used to easily design an effective AWWE. (c) AWWEs can not only represent propagating waves, but also evanescent waves. This is done by simply choosing imaginary or complex-valued reference phase velocities. (d) Increasing the number of auxiliary variables will make the AWWE accurate for wider angles of propagation. (e) The choice of complex reference phase velocities are expected to aid in developing stable approximations in cases where one-way approximations could be unstable (e.g. elastic wave propagation).

APPLICATION TO ACOUSTIC IMAGING



This section contains a representative result from an AWWE-based imaging procedure [2] applicable for acoustics waves. The problem involves detecting a hidden crack by sending ultrasonic waves into the structure and measuring the reflected waves at the surface. In order to test the imaging algorithm, the surface trace is generated synthetically using a computational experiment with the help of forward finite-difference wave propagation model. The resulting surface response is processed using a downward continuation procedure based on acoustic AWWE to predict the location of the crack. Adjacent figure contains the actual crack (bold white line), as well as the predicted crack location. As explained in reference [2], the accuracy of this prediction is significantly better than using more conventional 15° and 45° wave equations that are popular in seismic migration literature.

APPLICATION TO UNBOUNDED DOMAIN MODELING



Unbounded domain modeling using AWWE can be shown to be equivalent to the continued fraction absorbing boundary conditions (CFABC) previously developed in [3]. AWWE formalism, however, helps in extending CFABC to elastic media, media with corners and heterogeneous media. The adjacent figure is a representative result from reference [4], which shows the wave front snapshot for an explosion. The domain consists of a vertical acoustic layer attached to a half space extending to the right. The explosion is at the middle of the interface. It can be clearly seen that all the waves are being absorbed by the absorbing boundaries in a very effective manner.

CONCLUSIONS

Arbitrarily wide-angle wave equations (AWWEs) are highly accurate approximations of OWWE. Since they do not need explicit factorization, they are applicable for simulating one-way propagating complex heterogeneous and anisotropic, elastic and poro-elastic media. Preliminary applications of AWWE to acoustic imaging and unbounded domain modeling show excellent promise of AWWE. Ongoing research focuses on the application of AWWE to wider array of problems including elastic imaging and modeling unbounded elastic and poro-elastic domains.

Acknowledgement

This material is based upon work supported by the National Science Foundation under Grant No. CMS-0100188. Any opinions, findings, and conclusions or recommendations expressed in this material are those of the authors and do not necessarily reflect the views of the National Science Foundation.

References

[1] Guddati M.N.: Arbitrarily Wide Angle Wave Equations for Complex Media, to be submitted.
[2] Guddati M.N., Heidari A.H: Acoustic Migration with Arbitrarily Wide Angle Wave Equations, *Geophysics*, in review.
[3] Guddati M.N., Tassoulas J.L.: Continued Fraction Absorbing Boundary Conditions for the Wave Equation, Journal of Computational Acoustics, **8**: 139-156, 2000.
[3] Guddati M.N., Lim K.W.: Continued-Fraction Absorbing Boundary Conditions for Corner Regions, to be submitted.

ULTRASONIC TRAVEL-TIME TECHNIQUE FOR DIAGNOSTIC OF GRID-GENERATEDTURBULENCE

Tatiana A. Andreeva, William W. Durgin
Mechanical Engineering Department, Worcester Polytechnic Institute,
Worcester, MA, 01609.

Summary The study utilizes an ultrasonic travel-time technique to diagnose grid-generated turbulence produced in a wind tunnel. The statistics of the travel-time variations of ultrasonic wave propagation along a path are used to determine some metrics of the turbulence.

EXPERIMENTAL SET-UP

In this section we shortly discuss experimental technique and equipment. Detail description of the experimental apparatus can be found in Andreeva and Durgin [2003][1].In the experimental part of the study we utilize ultrasonic pulses traveling in straight paths as shown in Fig. 1. The sound propagates across a grid-generated turbulence from a transmitter to a receiver separated by a distance s. The flowmeter equation may be used to derive an expression for a travel time t of a wave traveling from the speaker to microphone.

$$t = \int_s \frac{dy}{c-u} \approx t_0 + \frac{1}{c^2}\int_s u'dy; u = U\sin\beta + u' \qquad (1)$$

where t_0 is a travel time in the undisturbed media, U is a mean velocity, c is a sound speed, u' are fluctuations of the mean flow velocity.

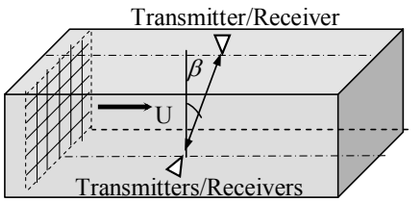


Figure 1. Sketch of wind-tunnel test section with ultrasonic flowmeter.

In the experiment the only parameter that is measured is a travel time of ultrasound pulses. The experiments were carried out in the $1.75'' \times 11.62'' \times 45.25''$ test section of low turbulence, low speed open circuit type wind tunnel. The velocity and temperature fluctuations were generated simultaneously using a heated grid. Nine cases of different distances S for two different temperatures $T = 59^{\circ}F$ and $T = 159^{\circ}F$, are studied.

EXPERIMENTAL RESULTS

Non-heated Grid Experiments

In Fig. 2 we compare our experimental data for travel time variance firstly with theoretical results obtained by Iooss et al.[2] In their work authors were investigating travel time using geometrical optics approach, which neglects all diffraction phenomena. Secondly, we compare our results with solution of the parabolic equation for the travel time variance of a plane wave in a moving random media, derived by means of the Rytov method and Markov approximation for the Gaussian spectrum of medium inhomogeneities.[3] Comparison reveals that some of the results of geometric acoustics are acceptable even beyond the area of the validity of the approach, which was shown analytically by Rytov.

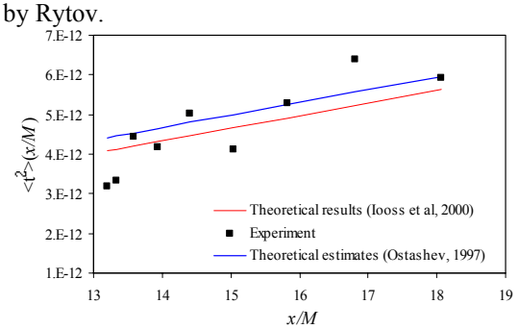


Figure 2 Experimental data for the travel time variance versus normalized travel distance x/M. Rytov solution and theoretical model by Iooss et al., are plotted for qualitative comparison. $U = 3.5m/s$.

However, nonlinear effects at a certain propagation distance were observed in numerical experiments by Karweit et al.[4] In Fig. 3 we compare the travel-time variance with Chernov[Error! Reference source not found.] estimates and with theoretical estimations of second-order travel time variance by Iooss et al.[Error! Reference source not found.] The experiment performed for large distances. The departure from the linear Chernov prediction increases with travel distance. Probability densities for the occurrence of caustics were calculated theoretically. For our experimental data we estimate the probability density of occurrence of caustics using theory developed by Klyatskin[5] and explored by Iooss[2].

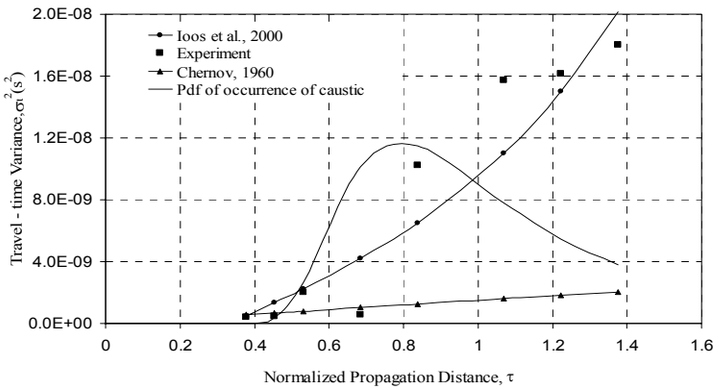


Figure 3 Probability density function of occurrence of caustic along with nonlinear dynamics of the travel time variance. $U = 18m/s$, $M = 6 \cdot 10^{-3} m$.

Heated grid Experiments

We have developed a methodology for determination of correlation functions of turbulent velocity and sound speed fluctuations. In order to do that the ultrasonic flowmeter equation (1) is reconsidered, where the effects of turbulent velocity and sound speed fluctuations are included. The result is the integral equation in terms of correlation functions for travel time, turbulent velocity and sound speed fluctuations. Experimentally measured travel time statistic data with and without grid heating are approximated by Gaussian function and used to solve integral equation analytically in terms of the turbulent velocity and sound speed correlations functions. Figs. 4 and 5 demonstrates correlation functions of turbulent velocity and sound speed fluctuations obtained using developed semi-analytical methodology.

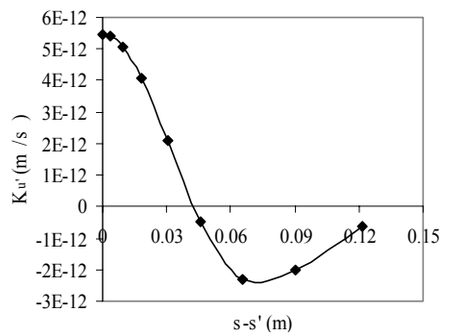


Figure 4 Experimentally obtained correlation function of turbulent velocity. $U = 3.5m/s$, $T = 59^\circ F$.

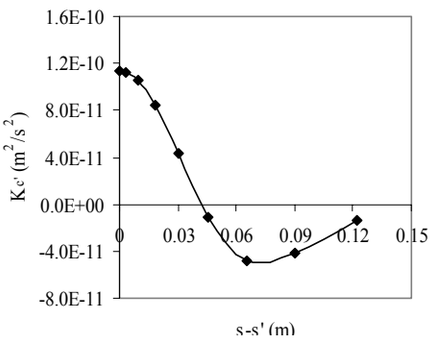


Figure 5 Correlation function of sound speed fluctuations. $U = 3.5m/s$, $T = 159^\circ F$.

Fourier Transform allows determination of spectrum of the turbulent velocity and sound speed fluctuations shown in Fig. 6.

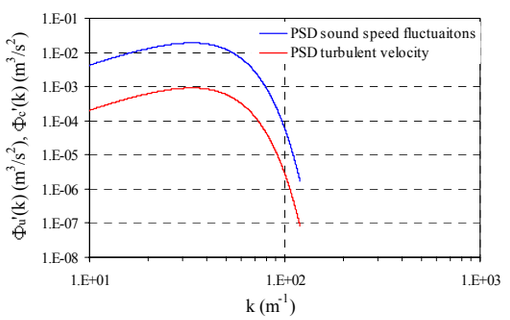


Figure 6 1-D energy spectra of turbulent velocity and sound speed fluctuations $U = 3.5m/s$.

REFERENCES

1. Andreeva T.A. and Durgin, W.W., "Ultrasound Technique for Prediction of Statistical Characteristics of Grid-Generated Turbulence," *AIAA Journal*, Vol. 41(8), 2003, pp.1438-1443.
2. Iooss, B., Blanc-Benon, Ph. and Lhuillier, C., "Statistical moments of travel times at second order in isotropic and anisotropic *random* media," *Waves in Random Media* Vol. 10, 2000, pp. 381-394.
3. Rytov, S.M., Kravcov, Yu.A., Tatarskii, V.I., Elements of Random Process Theory: Principles of Statistical Radiophysics, Springer-Verlag, Berlin, 1987, Vol. 4.
4. Karweit, M., Blanc-Benon, Ph., Juvé, D. and Comte-Bellot, G., Simulation of the Propagation of an Acoustic Wave through a Turbulent Velocity Field: a Study of Phase Variance," *The Journal of the Acoustical Society of America,* Vol. 89(1), 1991, pp. 52-62.
5. Klyatskin, V.I., "Caustics in Random Media," *Waves in Random Media*, Vol. 3, 1993, pp. 93-100.

The acoustics of two-dimensional leapfrogging vortex interactions

Jeff D. Eldredge
Mechanical and Aerospace Engineering Department
University of California, Los Angeles, USA, eldredge@seas.ucla.edu

The acoustics of low-speed cold shear flows are dominated by the sound produced by vortex interactions. In a two-dimensional jet, these interactions often take the form of coupling between adjacent pairs of counter-rotating vortices. In such a coupling, the spacing of the aft pair tends to narrow, causing it to accelerate, while the forward pair widens and decelerates. The result is a leapfrogging process that continues to repeat indefinitely, or until the pairs merge. In this work, we investigate the acoustics produced by two-dimensional leapfrogging vortex interactions.

Figure 1 illustrates the initial positions and parameters of two vortex pairs. We will present results from simulations for a range of values of the relative vortex strengths, $(\Gamma_2 - \Gamma_1)/(\Gamma_2 + \Gamma_1)$, relative spacing, δ_{y0}/δ_{x0}, and core sizes, r_{10}/δ_{x0} and r_{20}/δ_{x0}. In addition, we will explore the effects of the Mach number of the mean forward propagation velocity, $M_0 = U_0/a_\infty$ and the Reynolds number, $\mathrm{Re} = (\Gamma_1 + \Gamma_2)/2\nu$.

The direct numerical simulation of the compressible near field is performed with the dilating vortex particle method, developed in previous work [1]. Via a Helmholtz decomposition of the velocity field, this method extends the vortex particle method to compressible flows. The computational elements are mass-preserving particles that convect with the local velocity, and carry vorticity, dilatation, enthalpy and entropy strengths that vary in accordance with the Navier-Stokes equations. Derivatives are treated by the method of particle strength exchange, with an eighth-order-accurate kernel in order to faithfully capture acoustic waves of small magntitude. The particle coverage is surrounded by a circular zone of buffer particles that enforce a radiation-type condition to absorb incident acoustic waves. For each case, the initial enthalpy field is established by solution of a Poisson equation, and the initial dilatation and entropy are set to zero.

The acoustic field is derived by a Kirchhoff method, wherein the data on a control surface in the acoustic region of the near-field simulation domain are used to extrapolate the external acoustic field through the integral form of the wave equation. The vortex method simulations are performed in a region that is sufficiently large to include the innermost portion of the acoustic field. The fluctuating stagnation enthalpy and its normal derivative are evaluated on the control surface from the simulation results, and supplied to the Kirchhoff integrals.

As an example of the results we will show, consider the case of two identical pairs initially arranged equidistant from each other ($\Gamma_1 = \Gamma_2$ and $\delta_{y0}/\delta_{x0} = 1$). The initial vorticity of each vortex is Gaussian-distributed, with $r_{10}/\delta_{x0} = r_{20}/\delta_{x0} = 0.15$. The Reynolds number is 10^4, and the Mach number of the mean forward motion is 0.108. The panels of Figure 2 depict the vorticity and resultant acoustic field of a single leapfrogging event, observed in a reference frame that moves with the system. As the aft vortex pair is threaded through the forward pair, a large four-lobed pressure pulse is generated, immediately followed by a second one of opposite sign. Each of these subsequently radiates outward. The outer portion of the pressure field in each panel contains the acoustic pulse produced by the previous event. Note that the region between pulses is relatively silent. Also, the forward-propagating pulses encompass a larger sector than the rearward-propagating ones, due to a slight fore-to-aft convection induced by the dipolar vortex system.

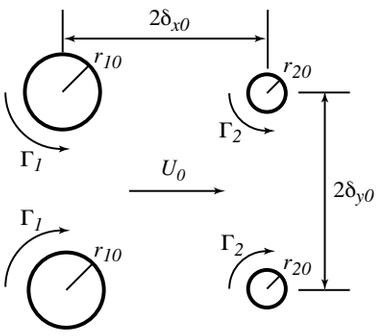


Figure 1. Schematic of initial vortex positions

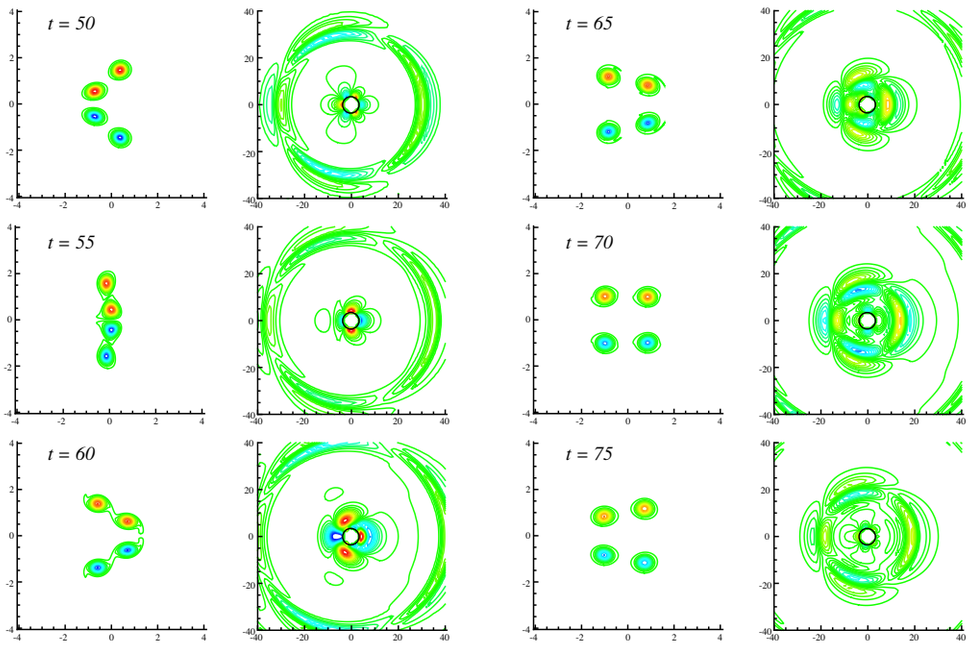


Figure 2. Vorticity (left) and pressure (right) at six instants. Kirchhoff surface shown as black circle at center. Time is scaled by a_∞ and δ_{x0}.

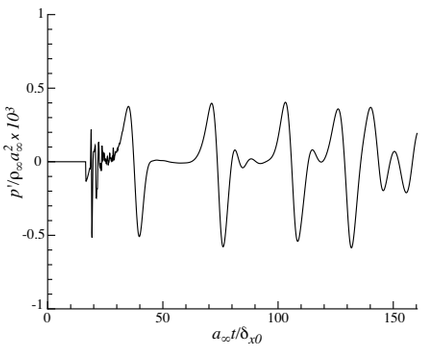


Figure 3. Pressure history at $(x/\delta_{x0}, y/\delta_{x0}) = (0, 20)$.

The pressure history from this process, observed at a single point at $(x/\delta_{x0}, y/\delta_{x0}) = (0, 20)$, is shown in Figure 3. After the initial time lag, the usual nonphysical transient—a consequence of the near-field dilatation adjusting to the correct level—persists for approximately 15 time units. This is followed by a narrow pulse of positive and negative pressure, resulting from the first leapfrogging event; the second event produces a pulse observed at $a_\infty t/\delta_{x0} = 70$. Also apparent are some small, higher frequency oscillations at $a_\infty t/\delta_{x0} = 80$, due to the nutation of the non-circular vortex cores. As time progresses, the quiet interval between the pulses becomes shorter. As the vortex pairs begin to couple, they move closer together and their leapfrogging accelerates. At $a_\infty t/\delta_{x0} = 140$, the cycle is broken by a large positive pressure followed by smaller oscillations, as the vortex pairs begin to merge. The resulting single counter-rotating pair is a much less efficient emitter.

We will present results such as these from simulations for a wide range of the parameters. Particular attention will be devoted to the kinematics of the merging process, and the acoustics generated by it. We will show that the acoustics of this process are similar to those produced by a pair of counter-rotating elliptical vortices with shrinking core aspect ratio.

References

[1] J. D. Eldredge, T. Colonius, and A. Leonard. A vortex particle method for two-dimensional compressible flow. *J. Comput. Phys.*, 179:371–399, 2002.

XXI ICTAM, 15–21 August 2004, Warsaw, Poland

A THEORETICAL MODEL FOR RESONANCES IN FLOW PAST A CAVITY

E. J. Kerschen, J. O. Alvarez, A. Tumin
University of Arizona, Tucson, Arizona, USA

Summary Cavity resonances involve a coupling between instability waves on the shear layer across the face of the cavity and acoustic waves that propagate between the cavity ends. The instability and acoustic waves are coupled by the scattering processes at the cavity ends. We utilize the Wiener–Hopf technique to analyze these scattering processes. Combining the scattering solutions with propagation solutions for the central region of the cavity, we obtain a global model whose predictions are in good agreement with experimental data.

INTRODUCTION

Acoustic resonances leading to high unsteady pressure levels may occur in flow past cavities. These are of concern in a variety of applications, including military aircraft weapons bays. The resonance involves a coupling between the downstream-propagating instability wave on the shear layer spanning the open face of the cavity, and acoustic waves propagating within and external to the cavity. These elements of the disturbance field are coupled by scattering processes at the upstream and downstream ends of the cavity.

A seminal contribution to the understanding and prediction of cavity resonances was made by Rossiter [1], who performed an extensive experimental study of cavity resonances for free-stream Mach numbers in the range $0.5 \leq M \leq 1.2$, and also proposed a semi-empirical formula for the resonant frequencies that remains widely used even today. Rossiter's formula is based upon an $n2\pi$ phase shift around a simple resonant loop consisting of a downstream-propagating instability wave and an upstream-propagating acoustic wave. Rossiter introduced an empirical constant to account for the phase shifts associated with the scattering processes at the two ends of the cavity, which couple the instability and acoustic waves. Heller & Bliss [2] presented experimental results over an extended Mach number range $0.3 \leq M \leq 3.0$, and proposed a modified Rossiter formula in which the static temperature in the cavity is assumed to be the stagnation temperature of the stream. The importance of this effect increases with Mach number.

Tam & Block [3] carried out an extensive experimental investigation at low Mach numbers. They also developed a theoretical model which involved excitation of the shear layer instability wave by the acoustic field generated at the downstream end of the cavity. The scattering process at the downstream end was represented in a simplified fashion, by introducing a concentrated acoustic monopole source at the downstream corner of the cavity. The phase of the source relative to the local instability wave motion was chosen heuristically, in a manner similar to the empirical constant of Rossiter's formula. The excitation of the shear layer instability wave was then calculated through a 'distributed receptivity' model, which ignored details of the interaction at the upstream end of the cavity. The amplitude of the monopole source was not determined. Therefore, the theory produced an expression for the resonance frequencies (with some empirical input), but did not determine whether a particular resonant mode corresponded to a globally stable or unstable disturbance.

Cavity resonances have received increased attention recently. This recent research has involved primarily numerical simulations and experiments, with a significant focus on active control. Many recent contributions can be found in the acoustics and fluid mechanics journals.

Thus, previous theoretical models for cavity resonances have generally provided only incomplete representations of the phenomenon. In particular, the scattering processes at the cavity ends have generally not been analyzed, or have been treated heuristically. The phases of the scattering coefficients at the two ends of the cavity are required for a first-principles prediction of the resonant frequency, while the amplitudes of the scattering coefficients are required in order to determine the temporal growth (or decay) rate of the mode, and the instability boundaries of the mode in parameter space.

ANALYSIS

In this paper, we present a model for cavity resonances that incorporates theoretical predictions for the scattering coefficients at the two ends of the cavity. The scattering coefficients are determined by local solutions which treat the square-corner geometry exactly. The scattering coefficients are then combined with theoretical predictions for the propagation of the shear-layer instability wave and the acoustic waves along the length of the cavity. The combined system takes a form similar to a matrix eigenvalue problem, where the eigenvalue is the complex frequency. The real part of the frequency determines the temporal oscillation of the unsteady field, while the imaginary part of the frequency determines the temporal growth (or decay) rate of the mode.

Consider a two-dimensional rectangular cavity of length L and depth d under a stream of speed U, as illustrated in figure 1. The external stream is separated from the quiescent fluid in the cavity by a shear layer. The total field is the sum of a mean field and a time-harmonic perturbation field with complex frequency ω. For the case of a supersonic stream, the time-harmonic perturbation field consists of a shear-layer instability wave of (complex) amplitude $\mathcal{S}$, upstream- and downstream-propagating cavity acoustic modes of amplitudes $\mathcal{U}$ and $\mathcal{D}$, and 'fast' and 'slow' wave fields in the supersonic stream of amplitudes $\mathcal{E}_f$ and $\mathcal{E}_s$. Note that $\mathcal{S}$, $\mathcal{D}$, $\mathcal{E}_f$ and $\mathcal{E}_s$ are all downstream-propagating components. For a supersonic stream, the only upstream-propagating component is $\mathcal{U}$. The elements of the unsteady field for a supersonic

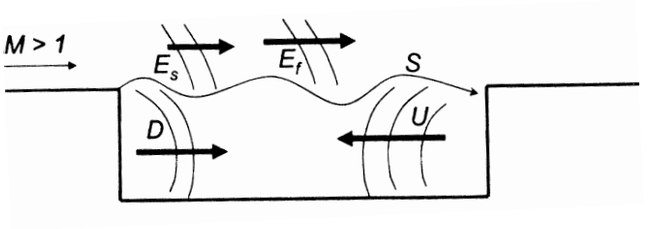


Figure 1. Illustration of the global model for a cavity acoustic resonance in supersonic flow.

gle) downstream-propagating wave field $\mathcal{E}_d$ and an upstream-propagating wave field $\mathcal{E}_u$. We have developed theoretical prediction methods for both supersonic and subsonic streams. However, for the sake of brevity, in describing the analysis we shall focus on the case of a supersonic stream.

For the scattering process at the upstream end, the incident field is the upstream-propagating cavity mode $\mathcal{U}$, while the scattered field contains $\mathcal{S}$, $\mathcal{D}$, $\mathcal{E}_s$ and $\mathcal{E}_d$. At the downstream end, there are four separate incident fields ($\mathcal{S}$, $\mathcal{D}$, $\mathcal{E}_s$ and $\mathcal{E}_d$) and a single scattered field ($\mathcal{U}$).

The scattering process at each end is analyzed separately. The analysis involves the following steps. First, the end wall of the cavity is removed and the case of a semi-infinite overhanging lip is considered. The geometry is then amenable to application of the Wiener–Hopf technique [4]. The scattered field produced by impingement of the incident field consists of an infinite set of acoustic cavity modes that propagate back into the cavity, an infinite set of acoustic duct modes that propagate into the 'duct' formed by the cavity bottom and the semi-infinite overhanging lip, and an external acoustic field in the stream. For the scattering process at the upstream end, a shear-layer instability wave is also generated.

A second scattering problem for the case of a semi-infinite overhanging lip is then solved, in which the incident field is an acoustic duct mode propagating toward the cavity. This also generates a scattered field containing the same components as described in the preceding paragraph.

The solution for a finite-length overhanging lip geometry, including the presence of the end wall, is then obtained by noting that the complete field under the overhanging lip is composed of an infinite set of upstream- and downstream-propagating duct modes. Applying the no-penetration condition on the cavity end wall, an infinite-dimensional matrix equation for the duct mode coefficients is obtained. However, for a fixed frequency, only a finite number of the duct modes are cut-on. The rest decay exponentially away from their point of origin, so that only a finite number of modes are important at the location of the end wall. The infinite-dimensional matrix equation can then be truncated at finite order and solved numerically. The rapid convergence of the solutions with increasing matrix order is remarkable. In fact, the procedure works well even in the limit of a rectangular cavity (when the overhang length b is set to zero), and the exponential decay of the higher-order terms is replaced by algebraic decay.

The evolution of each component of the unsteady field in propagating from one end of the cavity to the other is then calculated using the method of multiple scales to account for the streamwise variation of the shear layer. The scattering and propagation transfer functions are then combined in the form of a homogeneous matrix equation $AX = 0$, where $X = [\mathcal{U}, \mathcal{S}, \mathcal{D}, \mathcal{E}_f, \mathcal{E}_d]^T$. The complex frequencies of eigenfrequencies are determined by the condition $\det(A) = 0$. Since the eigenfrequencies are complex, the analysis determines both the temporal frequency and the growth (or decay) rate of each mode.

Theoretical predictions have been carried out for both supersonic and subsonic flows. Comparisons with experimental results for both supersonic and subsonic flows are very encouraging. Our predictions for the temporal frequency are generally in good agreement with experimental data; in some cases the agreement with experimental data is better than that obtained with Rossiter's semi-empirical formula. We believe this is a significant accomplishment, considering the fact that our theory contains no empirical constants. Our theory also determines whether each mode is unstable or stable; this important aspect of the physics was not addressed by Rossiter's semi-empirical formula or previous theoretical models.

This work was sponsored by the Air Force Office of Scientific Research under AFOSR Grant # F4962001-1-04.

References

[1] Rossiter J.E.: Wind Tunnel Experiments on the Flow Over Rectangular Cavities at Subsonic and Transonic Speeds. Royal Aircraft Establishment, TR No. 64307, October 1964.

[2] Heller H.H., Bliss D.B.: The Physical Mechanism of Flow Induced Pressure Fluctuations in Cavities and Concepts for Suppression. AIAA Paper 75-491, March 1975.

[3] Tam C.K.W., Block P.J.: On the Tones and Pressure Oscillations Induced by Flow over Rectangular Cavities. *J. Fluid Mech* **89**:373–399, 1978.

[4] Noble B.: Methods Based on the Wiener-Hopf Technique. Chelsea 1988.

XXI ICTAM, 15–21 August 2004, Warsaw, Poland

STRUCTURE OF SONIC BOOMS IN A MEDIUM WITH MULTIPLE RELAXATION MODES

P.W. Hammerton, M.E. Johnson
School of Mathematics, University of East Anglia, Norwich, NR4 7TJ, UK

Summary The inner shock structure of a sonic boom propagating through the atmosphere is controlled by dispersion and dissipation associated with the relaxation modes of oxygen and nitrogen. Using asymptotic and numeric methods, the shock structure is analysed and the change in shock thickness along the ray path is determined.

Accurate predictions of shock overpressure and shock rise-time are important in determining the subjective annoyance of sonic booms produced by supersonic aircraft. To assess the problems associated with sonic booms at ground level, the propagation of disturbances over long ranges must be investigated for a realistic atmosphere. In particular the effect of atmospheric parameters on the shock amplitude and shock thickness/rise-time must be predicted accurately.

For a supersonic body, a disturbance is generated in the form of a Mach cone. Close to the body, the exact form of the disturbance depends on the detailed geometry of the body, but over a number of wavelengths, the effect of the quadratic nonlinearity is to form a N-wave. Predictions of shock overpressure and shock rise-time are important in determining the subjective annoyance of sonic booms at the ground. Hence, the propagation of disturbances over long ranges must be investigated for a realistic atmosphere. In particular the effect of atmospheric parameters on the shock amplitude and shock thickness/rise-time must be predicted accurately. The evolution of the disturbance along ray paths normal to the shock front is governed by the combined effects of geometrical spreading, finite-amplitude effects, stratification and diffusion/dispersion due to molecular processes. For acoustic propagation through the atmosphere, thermoviscous diffusion does not fully describe the complex molecular processes present and relaxation due to internal vibration energies of polyatomic molecules must be included. Each relaxation mode is characterised by a relaxation time τ and the difference Δ between low- and high-frequency linear sound speeds.

Ignoring the effect of stratification, the governing equation for the perturbation pressure, suitably non-dimensionalised, is

$$\frac{\partial p}{\partial T} - p\frac{\partial p}{\partial X} + j\frac{p}{2T} = \delta\frac{\partial^2 p}{\partial X^2} + \sum_{\nu}\Delta_\nu e^{-X/\tau_\nu}\int^X e^{Y/\tau_\nu} p_{YY}(Y,T)\,dY, \qquad j = \begin{cases} 0 & \text{Plane Wave,} \\ 1 & \text{Cylindrical Wave.} \end{cases}$$

where δ is the coefficient of thermoviscous diffusivity and the summation is over the number of relaxation modes present. For a single relaxation mode, ignoring viscosity, it is well known that the shock structure can be classified as either partly- or fully-dispersed depending on the shock amplitude and the relaxation parameters [1, 2]. For fully-dispersed shocks, the relaxation mode determines the entire shock structure, while in the case of partly-dispersed shocks relaxation alone is insufficient to support the whole shock and a viscous sub-shock arises. Thus transition from a full-dispersed to a partly-dispersed shock corresponds to a sharp decrease in shock thickness.

For the case of a single relaxation mode, taking into account the effect of stratification, it has been shown that the shock rise-time is very sensitive to the relaxation parameters [3]. Indeed, along certain ray paths the shock structure can change from partly-dispersed, to fully-dispersed, then finally becoming partly-dispersed again, with a resulting change in shock thickness. However, for air, relaxation modes associated with oxygen and nitrogen are both significant. Thus in the present paper we consider the shock structure for two relaxation modes using both asymptotic and numeric methods.

For parameter values typical of sonic booms in the atmosphere, we find $\tau_1 \gg \tau_2 \gg \delta$, where τ_1 is the non-dimensional relaxation time associated with N_2 molecules and τ_2 the relaxation time for O_2 molecules. Thus an asymptotic analysis is possible. First travelling wave solutions are obtained. The structure of the solution is found to depend on the relative

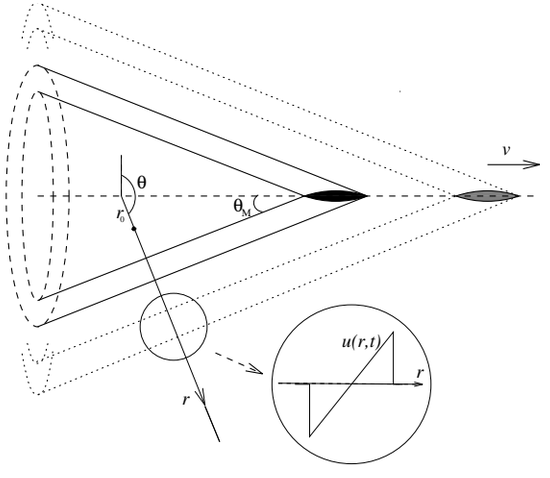


Figure 1. Generation of sonic booms by a supersonic body.

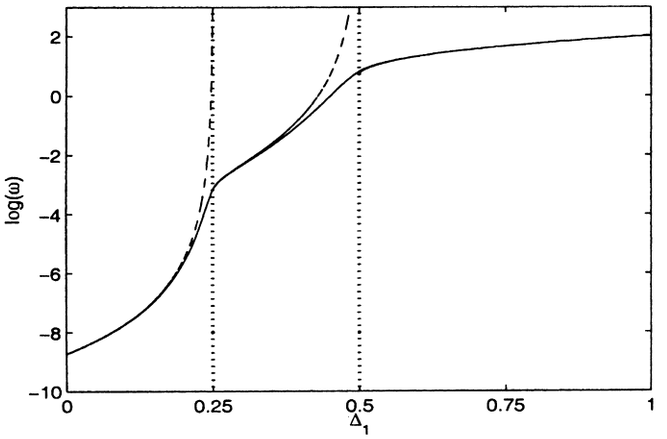


Figure 2. Plot of shock width as a function of Δ_1 for travelling wave solution with $\Delta_2 = 0.25$, $\tau_1 = 1$, $\tau = 0.01$ and $\delta = 5 \times 10^{-6}$.

sizes of Δ_1 and Δ_2. Considering first a plane wave, for $\Delta_1 > 1/2$, the shock is described entirely by the fully-dispersed solution associated with the N_2 relaxation mode. For $\Delta_1 < 1/2$ and $\Delta_1 + \Delta_2 > 1/2$, the outer shock is a partly-dispersed N_2 solution with an embedded sub-shock consisting of a fully-dispersed O_2 solution. Finally for $\Delta_1 < 1/2$ and $\Delta_1 + \Delta_2 < 1/2$, the shock structure is particularly intricate with an outer partly-dispersed N_2 solution, which contains a narrower sub-shock controlled by the O_2 relaxation mode and embedded in this is a Taylor-like viscous shock. This behaviour is illustrated in figure 2, where the shock width (defined as the minimum value of $\frac{\partial p}{\partial X}$) is plotted against Δ_1 for fixed Δ_2. The solid line shows the numerical result obtained by shooting.

Including geometric effects and solving the PDE from an initial N-wave signal, asymptotic solutions are determined, with the shock structure depending now on shock amplitude (which is dependent on the history of propagation) as well as on the local parameters Δ_1 and Δ_2. Numeric results were obtained using finite-difference schemes. However, for the small values of τ_1, τ_2 and δ considered, computation was extremely time consuming due to the fine length scales within the shock. Hence a variable mesh scheme was used, utilising knowledge of the shock position from the aymptotic results. Figure 3 shows the change in shock width with propagation distance. The solid line is the numerical result. Asymptotic theory predicts that for $T < 2.78$ the shock structure consists of a narrow O_2 sub-shock within a partly-dispersed N_2 shock, but that for $T > 2.78$ the N_2 shock becomes fully-dispersed and hence the shock loses its finer scale.

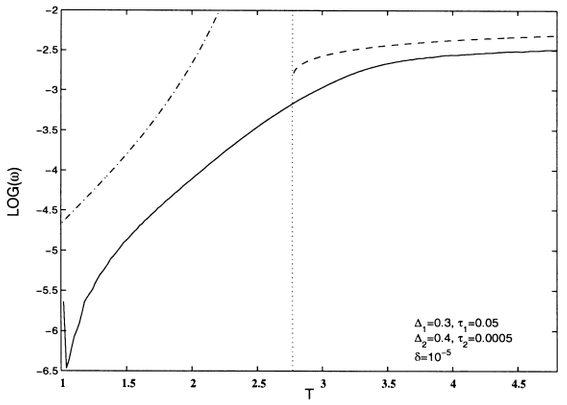


Figure 3. Plot of shock width as a function of T for $\Delta_1 = 0.3$, $\Delta_2 = 0.4$, $\tau_1 = 5 \times 10^{-2}$, $\tau_2 = 5 \times 10^{-4}$ and $\delta = 10^{-5}$.

Further results presented show that for certain parameter ranges, a combination of asymptotic and numeric methods is the only practical approach for accurate prediction of shock rise-time. Numerics alone prove impractical due to the need to resolve three different lengthscales within the shock, while in some cases the asymptotic analysis must be supplemented by numeric solutions of the disturbance outside the shock region.

References

[1] H. Ockendon and D.A. Spence, "Nonlinear wave propagation in a relaxing gas", *J. Fluid Mech.* **39** (1969) 329–345.

[2] P.W. Hammerton and D.G. Crighton, "Overturning of nonlinear acoustic waves. Part 2: Relaxing gas dynamics". *J. Fluid Mech.* **252** (1993) 601–615.

[3] P.W. Hammerton, "Effect of molecular relaxation on the propagation of sonic booms through a stratified atmosphere", *Wave Motion* **33** (2001) 359–377.

GAS OSCILLATIONS IN A CLOSED TUBE AT RESONANCE

Alexander Alexeev*, Chaim Gutfinger
Faculty of Mechanical Engineering, Technion - Israel Institute of Technology, Haifa 32000, Israel

Summary Periodic gas oscillations in a closed tube are investigated experimentally and numerically. At resonance, these oscillations are accompanied by shock waves traveling back and forth along the tube. Gas temperature and pressure measurements are reported. It is found that the gas temperature changes substantially along the tube. A two-dimensional numerical model of turbulent gas oscillations is formulated and verified by comparison with experiments. It is found that the experimental data of temperature and pressure inside the resonance tube are well correlated by this model. Using the numerical model, turbulence and acoustic streaming at resonance are investigated. It is shown that the normalized pressure amplitude, as well as other flow characteristics, are functions of a single parameter, which is a combination of the acoustic Reynolds number and dimensionless tube length.

INTRODUCTION

When a gas in a closed tube is excited by an oscillating piston driven at the fundamental resonance frequency, periodic shock waves arise within the tube.[1] The shock waves travel back and forth along the tube with a frequency equal to that of the oscillating piston and velocity close to that of sound. As a result of the shock waves, the heat and mass transfer processes within the resonance tube are enhanced significantly compared to those outside the resonance band. Other interesting phenomena taking place in a resonance tube are temperature and pressure gradients along the tube, as well as particle drift and agglomeration, which could be used for new commercial applications.

An analytical model for resonant oscillations in a closed tube[2] predicts that within a narrow resonance band the disturbances in the thermodynamic variables are of the order of $O(\varepsilon)$, and the axial gas velocity of $O(\varepsilon C_0)$; while for non-resonant frequencies, the disturbances are of order $O(\varepsilon^2)$, and the gas velocity of $O(\varepsilon^2 C_0)$, where $\varepsilon = \sqrt{\pi l / L}$ is a small parameter and C_0 is the speed of sound. Here, l and L are the piston amplitude and tube length, respectively.

Ilgamov et al.[3] reviewed many recent theoretical and experimental studies on resonance oscillations, and found that the discrepancy between theory and experiments increases with ε. They concluded that all existing theories are unsatisfactory when $\varepsilon \geq 0.1$, indicating the necessity to account for viscous and thermal effects, which can notably modify gas oscillations.[4] Moreover, experiments have shown that for relatively large ε, oscillatory flow in closed tubes at resonance is turbulent.[5] Since there is no reliable analytical model for unsteady turbulent flow accompanied by shock waves, we are forced to analyze numerically such flows.

In the present study, we investigate numerically and experimentally gas flow in closed resonance tubes. We perform temperature and pressure measurements in several tubes filled with air and simulate numerically resonance gas oscillations. We solve by a finite-difference algorithm the two-dimensional Navier-Stokes equations supplemented by a two-equation turbulence model. We verify the applicability of this numerical model by comparison with experimental data. The developed model is used to study resonant gas oscillations, including turbulence and acoustic streaming. We also perform a parametric numerical investigation of gas oscillations in closed tubes at resonance.

NUMERICAL MODEL

Two-dimensional axisymmetric flow of a perfect gas is governed by the equations of continuity, momentum and energy, written for mean variables of turbulent flow. These equations have to be supplemented by a turbulence model. We use a two-equation k-ω turbulence model of Wilcox.[6] Thus, a closed set consisting of six differential equations describing turbulent gas motion can be formulated. To solve these equations, we employ a non-iterative finite-difference implicit scheme developed by Beam and Warming.[7] We use a rectangular grid, which is clustered in the physical domain near the tube wall within the boundary layer. The grid spacing in the axial direction is time dependent and chosen to fit the distance between the plug and the moving piston. The simulations are started with the uniform initial conditions and continued up to the moment when a time periodic solution is obtained.

EXPERIMENTAL SETUP

The experiments are performed with air inside a vertical tube fitted with a vibrating piston at one end and closed by a plug at the other. We perform the experiments with several tubes of different lengths, L, and internal diameters, D, and measure the gas temperature and pressure inside the resonance tube.[8] An Endevco 85306-15 pressure sensor is mounted on the tube plug. Three chromel-alumel thermocouple sensors, with 0.1 mm junction diameters, are used for temperature measurements. The first sensor is used for measuring the gas temperature and can be moved to different positions along the tube. The second thermocouple sensor measures the inner tube surface temperature and the last sensor, installed at a fixed point at the tube wall, is used as a reference thermocouple.

* Present address: Darmstadt University of Technology, Chair of Technical Thermodynamics, Petersenstr. 30, 64287 Darmstadt, Germany.

RESULTS

It is found that the proposed numerical model provides a plausible description of the flow inside the resonance tube, as verified by experimental data. In particular, this model predicts accurately the temperature distribution inside the tube and pressure variations on the plug. Our experiments show that the average gas temperature has a minimum at the tube middle and increases toward the tube ends. This temperature distribution is due to the non-linearity of flow with periodic shocks and to turbulence intensity along the tube.

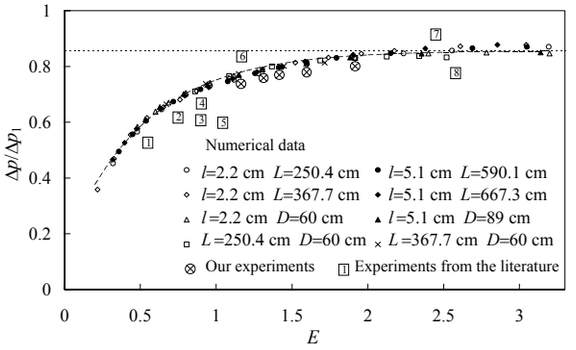


Fig. 1 Normalized pressure amplitude at resonance versus dimensionless parameter $E = \mathrm{Re}_a^{1/3}/\Lambda$. The horizontal dotted line presents the maximal pressure amplitude $\Delta p/\Delta p_1 = 6/7$, while the dashed line is an approximation. The dots present our numerical results, while the circles with crosses indicate our experimental data. The squares with numbers indicates experimental data from the literature by: 1 – Lettau;[9] 2 – Merkli and Thomann;[10] 3 – Lehmann;[11] 4 – Temkin;[12] 5 – Cruikshank;[13] 6 – Saenger and Hudson;[1] 7 – Sturtevant;[14] 8 – Galiev et al.[15]

We show that the flow in a resonance tube is governed by the following dimensionless parameters: tube parameter $\varepsilon = \sqrt{\pi l/L}$, acoustic Reynolds number $\mathrm{Re}_a = C_0 l/\nu$, dimensionless tube length $\Lambda = L/D$, and dimensionless frequency $\phi = (f - f_{res})/f\varepsilon$. Here, ν is the kinematic viscosity, f the piston frequency and $f_{res} = C_0/2L$. It is found that at resonance the normalized pressure amplitude $\Delta p/\Delta p_1$, is a function of a single parameter $E = \mathrm{Re}_a^{1/3}/\Lambda$, where Δp_1 is the pressure amplitude at resonance according to the isentropic model.[2] This is shown in Fig. 1, where we have drawn data from our experiments and calculations, as well as from the literature. Experiments from different sources, although scattered, seem to follow the general shape of the curve. The parameter E is found to be the governing parameter for other flow characteristics as well.[8]

It is found that the numerical model predicts in a plausible manner flow transition to turbulence. As demonstrated by our simulations, the turbulent energy sharply increases behind the shock wave, although, the flow remains practically laminar near the tube ends. These results agree qualitatively with experimental observations.[5]

Simulations show that strong acoustic streaming arises within the tube at resonance. Our calculations predict two large flow patterns, in which the fluid near the wall moves toward the tube middle cross-section, while the flow at the tube centerline is directed toward the tube ends. Notably, the flow in these streaming patterns is in the reverse direction to that occurring at non-resonant frequencies. At frequencies about the resonance band, the number of streaming patterns increases, which is in agreement with experimental observations.[5] We show that within the resonance band, the streaming velocity is of the order of $O(\varepsilon^2 C_0)$, while outside this band, where flow is continuous, it is of the order of $O(\varepsilon^4 C_0)$. This implies that all processes of heat and mass transfer related to acoustic streaming are enhanced dramatically, when the flow is at the resonance band and is accompanied by periodic shock waves.

CONCLUSIONS

We investigated experimentally and numerically gas flow in a closed tube at resonance, accompanied by periodic shock waves traveling back and forth along the tube. Good agreement was found between the proposed numerical model and experimental results. The numerical model was used to investigate resonance gas oscillations including turbulence and acoustic streaming, showing that only one parameter $E = \mathrm{Re}_a^{1/3}/\Lambda$ governs averaged flow characteristics.

References

[1] Saenger R.A. and Hudson G.E.: Periodic shock waves in resonating gas columns. *J. Acoustic Soc. Am.* **32**:961, 1960.
[2] Chester W.: Resonant oscillations in closed tube. *J. Fluid Mech.* **18**:44, 1964.
[3] Ilgamov M.A., Zaripov R.G., Galiullin R.G. and Repin V.B.: Nonlinear oscillations of a gas in a tube. *Appl. Mech. Rev.* **49**:137, 1996.
[4] Alexeev A., Goldshtein A. and Gutfinger C.: Heat interaction in a resonance tube. *Phys. Fluids* **14**:1812, 2002.
[5] Merkli P. and Thomann H.: Transition to turbulence in oscillating pipe flow. *J. Fluid Mech.* **68**:567, 1975.
[6] Wilcox D. C.: Turbulence modeling for CFD. La Canada, 1993.
[7] Beam R.M. and Warming R.F.: An implicit factored scheme for the compressible Navier-Stokes equations. *AIAA J.* **16**:393, 1978.
[8] Alexeev A. and Gutfinger C.: Resonance gas oscillations in closed tubes − numerical study and experiments. *Phys. Fluids* **15**:3397, 2003.
[9] Lettau E.: Messungen an schwingungen von gassaulen mit stellen fronten in rohrleitungen. *Deutsche Kraftfahrtforschung* **39**:1, 1939.
[10] Merkli P. and Thomann H.: Thermoacoustic effects in a resonance tube. *J. Fluid Mech.* **70**:161, 1975.
[11] Lehmann K.D.: Die dampfungsverluste bei starken schallschwingungen in rohren. *Ann. Phys.* **21**:101, 1934.
[12] Temkin S.: Nonlinear gas oscillations in a resonance tube. *Phys. Fluids* **11**:960, 1968.
[13] Cruikshank D.B.: Experimental investigation of finite-amplitude acoustic oscillations in closed tubes. *J. Acoustic Soc. Am.* **52**:1024, 1972.
[14] Sturtevant B.B.: Non-linear gas oscillations in pipes. Part 2: experiment. *J. Fluid Mech.* **63**:97, 1974.
[15] Galiev S.U., Ilgamov M.A. and Sadykov A.V.: Periodic shock waves in gas. *Izv. Akad. Nauk SSSR Mekh. Zhidk. Gaza* **2**:57, 1970.

XXI ICTAM, 15–21 August 2004, Warsaw, Poland

THE EFFECT OF VISCOSITY ON THE PROPAGATION OF ACOUSTIC WAVES THROUGH FINE CYLINDRICAL MESHES

Iain D.J. Dupère*, Ann P. Dowling* and T.J. Lu*
Cambridge University Engineering Department, Trumpington Street, Cambridge, CB2 1PZ , United Kingdon

Summary In this paper we discuss the effect that viscosity has on the propagation of acoustic waves through meshes consisting of small diameter cylindrical elements. The acoustic Reynolds number in such cases is extremely small except at very high amplitudes. Propagation which is parallel or perpendicular to the cylinder axis are both consider together with propagation through a mesh.

INTRODUCTION

Sound absorbing materials often involve fine scale structures in which the spacing between elements is so fine that the drag forces due to viscous effects are significant. In many cases the structures consist of nearly cylindrical elements arranged in a variety of different ways. In such cases the effect of the drag is twofold. First it reduces the propagation speed of the acoustic waves. Secondly it introduces an acoustic damping in which energy in the acoustic waves is converted into heat. The former can also help at low frequencies where smaller dimensions are required than is generally the case. In this paper we discuss the effect of the viscosity on the propagation characteristics of acoustic waves travelling through cylindrical meshes of arbitrary geometry. The paper is split into three parts: the effect of viscosity on the propagation of acoustic waves travelling parallel to the axes of an array of rigid cylinders; the effect of viscosity on the propagation of acoustic waves travelling perpendicular to the axes of a rigid cylinder; and the effect of propagation through a mesh consisting of rigid cylinders.

THE EFFECT OF VISCOSITY ON THE PROPAGATION OF ACOUSTIC WAVES TRAVELLING PARALLEL TO THE AXES OF AN ARRAY OF RIGID CYLINDERS

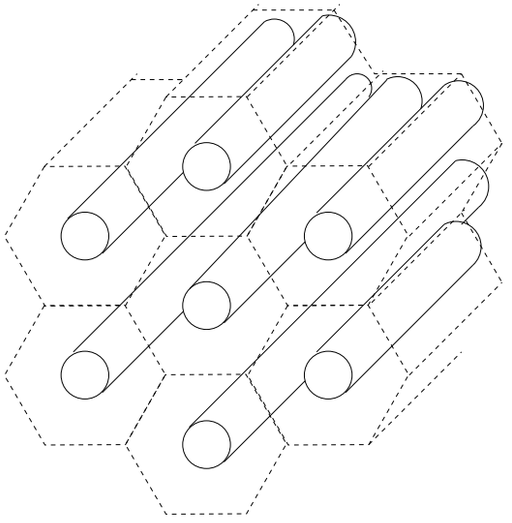


Figure 1. Propagation along an array of cylinders.

In the first part of the paper we consider the situation illustrated in figure 1. The spacing between the cylinders is sufficiently small that the acoustic boundary layer on each cylinder is significant and the amplitude of the acoustic waves combined with the cylinder size are such that the acoustic Reynolds number is low. We account for the attenuation of the sound field by viscous effects by solving the viscous Navier Stokes equation following Rayleigh [5] and others, notably Lighthill[4]. Here, however, the inner no slip boundary is a cylinder, rather than a plane surface and the outer boundary consists of set of periodic boundaries, representing the interaction of adjacent cylinders, and forms a regular polygon, as illustrated by the dashed lines in figure 1. The number of sides of the polygon is arbitrary in the analysis and depends upon the geometry. The momentum equation [2] results in a solution of the form:

$$u_z(r,\theta) = \sum_{\alpha=-\infty}^{\infty} \left(A_\alpha K e_\alpha \left(\sqrt{\frac{\omega}{\nu}} r \right) + B_\alpha B e_\alpha \left(\sqrt{\frac{\omega}{\nu}} r \right) \right) \left(C_\alpha e^{i\alpha\theta} + D_\alpha e^{-i\alpha\theta} \right) - \left(\frac{1}{\rho i \omega} \right) \frac{\partial p}{\partial z} \qquad (1)$$

where u_z is the axial acoustic velocity, ω is the angular frequency, ν is the kinematic viscosity, r is the radius, p is the pressure, ρ is the density and θ is the angle. $A_\alpha, B_\alpha, C_\alpha$, D_α and α are unknown constants, and the functions Ke_α and Be_α are defined as:

$$Ke_\alpha(x) = ker_\alpha(x) + ikei_\alpha(x); \qquad Be_\alpha(x) = ber_\alpha(x) + ibei_\alpha(x) \tag{2}$$

where ber, bei, ker and kei are the Kelvin (or Thomson) functions [1, 3].
The unknown coefficients, A_α and B_α are found by applying the boundary conditions and using colocation. The effects of cylinder spacing, number of periodic boundaries, frequency and cylinder diameter are all discussed in terms of three non-dimensional parameters, $\sqrt{\frac{\omega}{\nu}}r_1$, $\frac{x_2}{r_1}$ and N (the number of sides). Here x_2 is the perpendicular distance to the periodic boundary.

THE EFFECT OF VISCOSITY ON THE PROPAGATION OF ACOUSTIC WAVES TRAVELLING PERPENDICULAR TO THE AXES OF A RIGID CYLINDER

In the second part of the paper the we consider the situation illustrated in figure 2. As before the acoustic Reynolds number is assumed low. The spacing is also considered to be sufficiently large for the cylinders to be independent of each other. The solution is obtained following the procedure used by Stokes [6] to calculate the steady drag on a sphere but including the unsteady term. It is worth noting that whilst a solution does not formally exist in Stokes' limit for a cylinder, one does exist for the unsteady problem described in the paper.

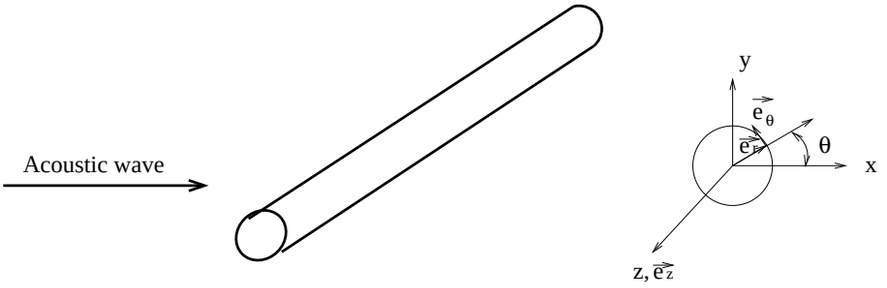


Figure 2. Propagation across an isolated cylinder.

PROPAGATION THROUGH A MESH CONSISTING OF RIGID CYLINDRICAL ELEMENTS

Finally, we combine the two analyses to obtain a model of the propagation through a mesh noting that both models are linear and so can be linearly summed.

CONCLUSIONS

The effect of viscosity on propagation of acoustic waves through fine cylindrical meshes is considered in detail. Two major effects are noted in the study. First the propagation speed of the acoustic waves is reduced by an order of magnitude, a helpful feature at low frequencies. Secondly considerable attenuation of the acoustic energy is observed. We also note that, although a secondary effect, the effect of polygonal periodic boundaries is noticeable. The number of boundaries, however, has little effect on the propagtion characteristics.

References

[1] M. Abramowitz and I.A. Stegun. *Handbook of Mathematical Functions.* Dover publications, 1965.
[2] G.K. Batchelor. *An Introduction to Fluid Dynamics.* Cambridge University Press, 1967.
[3] I.S. Gradshteyn and I.M. Ryzhik. *Table of Integrals, Series and Products.* Academic Press, 5 edition, 1965.
[4] M.J. Lighthill. *Waves in Fluids*. Cambridge University Press, 1978.
[5] Lord Rayleigh. *The Theory of Sound*. Dover Publications, 1945.
[6] G. Stokes. On the effect of the internal friction of fluids on the motion of pendulums. *Transactions of the Cambridge Philosophical Society*, 9:106–108, 1851.

XXI ICTAM, 15–21 August 2004, Warsaw, Poland

MODELLING OF HYDROPHONE BASED ON A DFB FIBER LASER

Lars Voxen Hansen*, Fredrik Kullander**
* *Technical University of Denmark, Department of Mechanical Engineering, Lyngby, Denmark*
** *FOI, Swedish Defence Research Agency, Department of Laser Systems, Linköping, Sweden*

Summary This paper deals with modeling of a DFB fiber laser based hydrophone. Both an analytical and a finite element model are developed to describe the acoustic response of the hydrophone. Particularly, the calculated hydrophone sensitivity using the finite element model is compared to the analytical result.

INTRODUCTION

Hydrophones based on distributed feedback (DFB) fiber lasers [1] are examined using both an analytical and a finite element model. The small dimensions (length 3-6 cm) and low frequency noise of DFB fiber lasers make them useful as hydrophones. Even extremely small changes in fiber laser cavity length yield measurable laser frequency signals. Generally, an acoustic pressure field will result in a deformation of the DFB fiber laser and a change of its length. The effect is small when a bare fiber laser is placed directly in water (sensitivity $\epsilon/p = 3.2 \cdot 10^{-12}\ 1/Pa$). If desired the ambient pressure sensitivity can be modified by using a mechanical mounting. Typically for underwater surveillance applications an amplification of the sensitivity of about 400 times is required to approach the noise level in the sea.
The hydrophone design shown in fig.1 changes the loading of the fiber laser from hydrostatic to axial. The outer cylinder is rigid. In each end of the cylinder an end-plate is placed which can move in the axial direction thus straining the laser. The surface area of the end-plates can be increased to obtain the necessary sensitivity. To avoid buckling the fiber laser is strained before being glued to the end-plates. The soft-material in the center maintain this pre-stain.

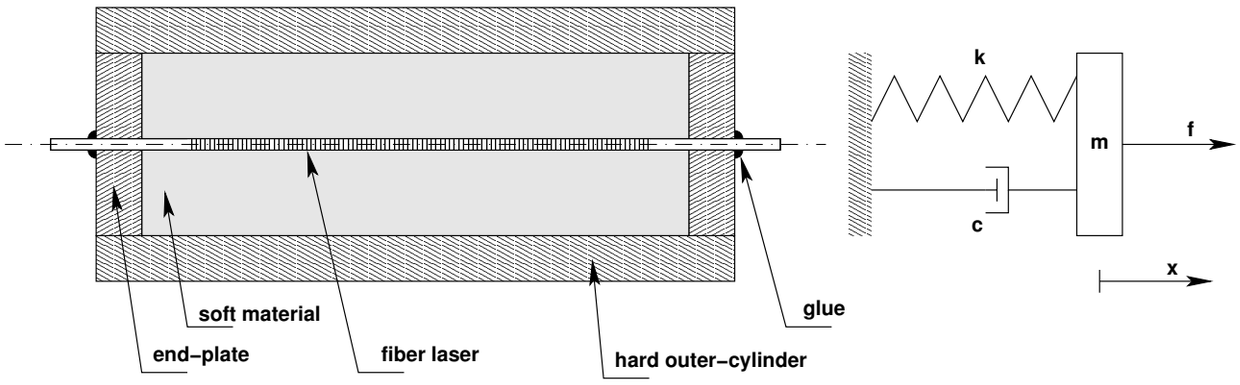


Figure 1. Left: Sketch of hydrophone based on a DFB fiber laser. Right: Damped force oscillator used to model hydrophone with symmetric loading.

HARMONIC RESPONSE ANALYSIS

The hydrophone is assumed to be small compared to the wavelength of the incoming acoustic wave. Moreover, the pressure is assumed to be the same at the two end-plates such that symmetry can be used to model only half of the hydrophone. Under certain conditions a damped forced oscillator, see fig. 1, will sufficiently well describe the mechanical properties of the hydrophone. The harmonic response is described by

$$-m\omega^2 x + ic\omega x + kx = f, \tag{1}$$

where ω is the frequency and x is the complex displacement amplitude of the end-plate of mass m. The acoustic force f acting on the end-plate is found using equation

$$f = Sp - Z_{rad} i\omega x, \tag{2}$$

given in [3] for acoustic receivers. Here S is the surface area of the end-plate, Z_{rad} is the radiation impedance and p is the acoustic pressure in the absence of the hydrophone. The acoustic radiation of the end-plate is modeled as a circular piston [3]

$$Z_{rad} = (\frac{(\hat{k}r)^2}{2} + i\frac{8\hat{k}r}{3\pi})\rho_w c_w S, \tag{3}$$

where the real and imaginary part correspond to frequency dependent damping and added mass respectively. Here $\hat{k}$ is the acoustic wavenumber, r is the end-plate radius, ρ_w and c_w are the density and sound speed of water. The sensitivity of

the hydrophone is found from (1), (2), (3) and by using that the axial strain in the fiber laser is given by, $\epsilon = 2x/l$, where l is the fiber laser length. Thus

$$\frac{\epsilon}{p} = \frac{2}{l}\frac{S}{k - \omega^2\tilde{m} + i\tilde{c}}, \tag{4}$$

where $\tilde{m}$ and $\tilde{c}$ express the total mass and damping including the added terms in (3). For $\omega = 0$ the static sensitivity is obtained as, $\epsilon/p = 2S/lk$. The resonance frequency determining the nominal bandwidth of the hydrophone is $\omega = \sqrt{k/\tilde{m}}$.

FINITE ELEMENT MODELING OF ACOUSTIC FIELD

A Finite Element Model (FEM) of the acoustic field surrounding a fiber laser hydrophone is implemented using FEMLAB. To test the analytical expression derived in (4) The acoustic pressure field p is governed by the three-dimensional Helmholtz equation

$$\nabla^2 p - \hat{k}^2 p = 0. \tag{5}$$

The presence of the hydrophone is taken into account by applying boundary conditions to the acoustic field at the outer surface of the hydrophone. At the domain boundaries we introduce the boundary conditions

$$\mathbf{n}\cdot\nabla p = 0 \qquad \mathbf{n}\cdot\nabla p = -i\omega^2\rho x \qquad \mathbf{n}\cdot\nabla p = -i\hat{k}p, \tag{6,7,8}$$

where $\mathbf{n}$ is an outward pointing unit vector at the domain boundaries. The B. C. (6) specifies a rigid boundary and is applied to the outer cylinder of the hydrophone. B. C. (7) specifies a moving rigid boundary and is applied at each of the hydrophones end-plates. Finally, B. C. (8) specifies a radiative boundary condition which is applied to all exterior boundaries. The displacement amplitude x depends on the pressure at the end-plate surface and on the mechanical system. If the symmetric assumption is used, as in the previous section, x can be obtained from (1) using that the acoustic force is $f = \int_S p\, dS$.

NUMERICAL EXAMPLE

A hydrophone with aluminum end-plates having a radius of $r = 2mm$ and a thickness of $t = 2mm$ is used as an example. The DFB fiber laser has a length of $l = 6cm$ and is made from a fiber, similar to standard single mode optical fiber, with a radius of $65\mu m$ and a Young modulus of $72GPa$, giving a fiber stiffness of $k = 31.8kN/m$. A stiffness of $4kN/m$ for the soft center material is added to this. The end-plate mass is $m = 0.08g$ and the fiber mass is neglected. The computed sensitivities are shown in fig. 2. Apparently a lower resonance frequency is obtained using the FEM model. This indicates a larger added acoustic mass than the one obtained from (3), giving the hydrophone a lower bandwidth. The sensitivity below resonance is $1.17 \cdot 10^{-8}\ 1/Pa$, almost a factor of 10 higher than required for typical underwater surveillance applications, and therefore the hydrophone is potentially usable.

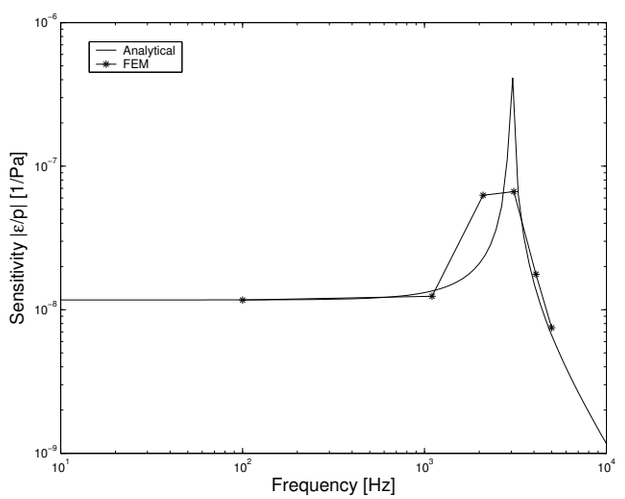


Figure 2. Hydrophone sensitivity.

References

[1] H. Storøy, B. Sahlgren, R. Stubbe, "Single polarization fibre DFB laser", *Elec. Lett*, vol. 33, pp. 56-58, 1997.
[2] J. A. Bucaro, H. D. Dardy, E. Carome, "Fiber optic hydrophone", *J. Acoust. Soc. Amer.*, vol. 62, pp. 1302-1304, 1977.
[3] L. E. Kinsler, A. R. Frey, A. B Coppens and J. V. Sanders, "Fundamentals of Acoustics", 4th ed. John Wiley & Sons Inc., 2000.

NUMERICAL ANALYSIS OF THE TEXTURE AND ACOUSTOELASTIC PROPERTIES OF A PRESTRESSED POLYCRYSTALLINE AGGREGATE

Józef Lewandowski
IPPT PAN, Department of Theory of Continuous Media, PL 00-049 Warszawa, Poland

Summary. The propagation of ultrasonic waves in a polycrystalline aggregate is considered for a bulk sample made of cubic crystals (e.g., Fe) and subjected to stress, the principal directions of the stress being coincident with the axes of the orthorhombic symmetry of the macroscopic acoustoelastic properties of the sample. The dependence of the acoustoelastic properties and texture of the bulk sample on the stress are analysed numerically.

EXTENDED SUMMARY

Some forming processes (e. g., rolling, drawing, forging) of polycrystalline aggregates (e.g., steel) are accompanied by plastic deformation which induces residual stresses in the materials and leaves their crystallites (grains) in certain preferred orientations called the texture. In turn, the texture cause the symmetry of the macroscopic acoustoelastic properties of polycrystals. In the present paper, we are interesting in the situation where the forming processes caused the orthorhombic symmetry of the macroscopic acoustoelastic properties of a polycrystal and induced in that residual stresses, which have been removed after finishing the forming process. Next the stress-free bulk sample of the textured polycrystal is subjected to small applied stresses $\Delta\sigma^0_{ij} = 1\,MPa$, $i\,j = 1, 2, 3$. After approaching the equilibrium deformed configuration [1], the values of the applied stresses are increased again by the same constant and small steps $\Delta\sigma^0_{ij}$ and the material points of the bulk sample approache a new equilibrium deformed configuration. Increasing the applied stresses σ^0_{ij} by the steps $\Delta\sigma^0_{ij}$ and approaching the new equilibrium deformed configuration are repeated as many times ($N = 750$) as the applied stresses $\sigma^0_{ij} = n \cdot \Delta\sigma^0_{ij}$, $n = 1, 2, \ldots, N$ reache the desired limiting values $N \cdot \Delta\sigma^0_{ij}$. The purpose of the work is to propose a method (algorithm) of computing numerically the changes in the texture and acoustoelastic properties as functions of σ^0_{ij} varying in the way described above. The method is based on the observations and theoretical predictions confirming that the speeds at which elastic waves propagate through a textured and prestressed body depend on the directions of the wave propagation and polarization as well as on the texture of the body and stress to which the body is subjected. For the sake of brevity, we confine ourselves to present here only the preliminaries of the method applied to the case of σ^0_{ij} being plane stresses. The problem will be presented in detail and in more general form in [2].

To describe briefly the algorithm, an Euler orthogonal reference system $0x_1x_2x_3$ with the axes $0x_1$, $0x_2$ and $0x_3$ is suitably chosen for the present equilibrium configuration of the material points of the sample, the axes $0x_1$, $0x_2$ and $0x_3$ being coincident with the axes of the orthorhombic symmetry. The other orthogonal reference system $0X_1X_2X_3$ is supposed to be chosen for a single cubic crystallite, the axes being chosen in the crystallographic directions [100], [010] and [001], respectively. The unit vectors along the directions of the axes $0x_1$, $0x_2$ and $0x_3$ as well as along the directions of the axes $0X_1$, $0X_2$ and $0X_3$ are denoted by $\mathbf{e}_1$, $\mathbf{e}_2$, and $\mathbf{e}_3$ as well as by $\mathbf{E}_1$, $\mathbf{E}_2$, and $\mathbf{E}_3$, respectively. Henceforth, all equations, relations and formulae are written with locating the vector and tensor quantities as well as the orientations and coordinates to the $0x_1x_2x_3$ reference system. Then the position vector $\mathbf{x}$ can be writen as $\mathbf{x} = (x_1, x_2, x_3)$ where $x_i = \mathbf{x} \cdot \mathbf{e}_i$, $i = 1, 2, 3$. In the subsequent considerations, the orientation of a single crystallite within the polycrystalline sample is defined by giving the values of three Eulerian angles, θ, φ, and ϕ, of the axes $0X_1$, $0X_2$ and $0X_3$ relative to the sample axes, $0x_1$, $0x_2$ and $0x_3$. The notations θ ($\theta = cos^{-1}(\mathbf{E}_3 \cdot \mathbf{e}_3) \doteq cos^{-1}\xi$), φ, and ϕ stand for the angle of nutation, precession and proper rotation, respectively, where $0 \leq \theta \leq \pi$, $0 \leq \varphi \leq 2\,\pi$, $0 \leq \phi \leq 2\pi$. The texture of a subdomain may be characterized by the probability density function of the crystallite orientation, $p\,(\theta, \varphi, \phi)$. Then $p\,(\theta, \varphi, \phi)\,d\theta\,d\varphi\,d\phi$ expresses the probability that a crystallite in the subdomain of the sample has an orientation described by the Euler angles θ, φ, and ϕ, lying in the intervals $<\theta, \theta + d\theta)>$, $<\varphi, \varphi + d\varphi>$ and $<\phi, \phi + d\phi>$, respectively.

Since it is not possible to measure the phase velocity of an acoustic wave at a point $\mathbf{x}$, such terms as the *local* texture and *local* acoustoelastic properties of the sample material revealed by or deduced from the *local* measurements of ultrasosonic phase velocity do not mean the texture and properties at a point $\mathbf{x}$ in the sample under study but mean the texture and properties at every point of the sample material filling a subdomain (mesodomain) Ω centered at the point $\mathbf{x}$. Such a subdomain corresponds to the intermediary scale and has at least the *smallest size* at which performing the ultrasosonic measurements is still possible. On the other hand, the subdomain Ω is assumed to be enough large to contain a statistical ensemble of crystallites. The analysis of the acoustoelastic response of the material to a dynamic loading, which is presented below, concerns also the subdomain Ω, however the texture $p\,(\theta, \varphi, \phi)$, effective elastic stiffness moduli C^{eff}_{ijkl} and the phase velocities of ultrasonic waves are treated within the subdomain as independent of $\mathbf{x}$.

The subsequent considerations are confined to a statistical ensemble of identical bulk samples made of the examined polycrystalline aggregate, the samples being subjected to the plane stress, $\sigma^0(\mathbf{x})_{ij}$ $(i, j = 1, 2, 3)$. The

principal directions of the plane stress, $\sigma^0(\mathbf{x})_{11}$, $\sigma^0(\mathbf{x})_{22}=\gamma\cdot\sigma^0(\mathbf{x})_{11}$, $\gamma=constant$, $\sigma^0(\mathbf{x})_{11}\leq 750MPa$, coincide with the symmetry axes $0x_1$ and $0x_2$. It is considered the case when each sample is acted on by an ultrasonic transducer oscillating with the ultrasonic angular frequency ω in such a way that the assembly averaged displacement response, $\langle\mathbf{u}(\mathbf{x},t)\rangle$, of the polycrystalline aggregate to this dynamic loading is of the form of one of the nine different plane displacement ultrasonic waves, $\langle\mathbf{u}(\mathbf{x},t)\rangle=\mathbf{p}\,u_0\,exp\,[ik_{np}(\mathbf{n}\cdot\mathbf{x}-V_{np}t)]=\mathbf{p}\,u_0\,exp\,[i(k_{np}\mathbf{n}\cdot\mathbf{x}-\omega t)]$ with phase velocities V_{np}, n, $p=1,\,2,\,3$. The bracket angles $\langle ...\rangle$ denote assembly averaging. The subscripts n and p denote the directions of the propagation $\mathbf{n}$ ($|\mathbf{n}|=1$, $\mathbf{n}=\mathbf{e}_1,\,\mathbf{e}_2,\,\mathbf{e}_3$) and polarization $\mathbf{p}$ ($|\mathbf{n}|=1$, $\mathbf{p}=\mathbf{e}_1,\,\mathbf{e}_2,\,\mathbf{e}_3$) of each mode being coincident with one of the axes $0x_1$, $0x_2$ and $0x_3$. u_0 denotes the amplitude of the wave $\langle\mathbf{u}(\mathbf{x},t)\rangle$, k_{np} stands for the wave number and $k_{np}=\omega/V_{np}$. In every heterogeneous elastic body, the ultrasonic velocities depend on the effective density and the tensor of the so-called effective dynamic moduli of stiffness as well as on the frequency. In the limit, as the wavelength increases to infinity (or $\omega\to 0$), the dynamic effective moduli in these relations are replaced from now by the static effective moduli C^{eff}_{ijkl}. For the reason explained in [3,p.385], we employ the Voigt [4] averaging procedure as a suitable one for evaluating $C^{eff}_{ijkl}=\langle C(\mathbf{x}_s)_{ijkl}\rangle$ for a subdomain Ω_s centered at $\mathbf{x}_s$ and in this way arrive at the following equations for evaluating C^{eff}_{ijkl}:

$$C^{eff}_{ijkl}=\langle C(\mathbf{x}_s)_{ijkl}\rangle,\quad \langle C(\mathbf{x}_s)_{ijkl}\rangle\doteq\int_{-1}^{1}d\xi\int_0^{2\pi}d\varphi\int_0^{2\pi}d\phi\,C(\mathbf{x}_s)_{ijkl}\,p\,(\xi,\varphi,\phi),\quad i,j,k,l,m,n,p,q=1,\ 2,\ 3,$$

$$C(\mathbf{x}_s)_{ijkl}=t(\xi,\varphi,\phi)_{mi}\,t(\xi,\varphi,\phi)_{nj}\,t(\xi,\varphi,\phi)_{pk}\,t(\xi,\varphi,\phi)_{ql}\,c_{mnpq},\quad X_i=t(\xi,\varphi,\phi)_{ij}\,x_j\ \text{ where }\ \xi\doteq cos\theta.$$

c_{mnpq} denote the elastic stiffness moduli of a single crystallite (for example, c_{11}, c_{12} and c_{44} in the case of cubic crystallite) and $t(\xi,\varphi,\phi)_{im}$ stands for the components of the transformation matrix $\mathbf{t}(\xi,\varphi,\phi)$ relating x_i to X_i. Now we substitute the plane wave solution $\langle\mathbf{u}(\mathbf{x},t)\rangle$ successively in the form of each of the nine modes with phase velocities $V_{ij}, i,\,j=1,\,2,\,3$, into the following equations of the considered wave motion, which is superimposed on an equilibrium deformed configuration of the material points of the body:

$$(\tilde{C}_{ijkl}+\tilde{\sigma}^0_{jl}\delta_{ik})\frac{\partial^2\langle u(\mathbf{x},t)_k\rangle}{\partial x_j\partial x_l}=\frac{\partial^2\langle u(\mathbf{x},t)_i\rangle}{\partial t^2};\ \rho(\mathbf{x})^{eff}=\langle\rho(\mathbf{x})\rangle,\ \tilde{c}=\frac{c_{ij}}{\rho^{eff}},\ \tilde{C}_{ij}=\frac{C^{eff}_{ij}}{\rho^{eff}},\ \tilde{\sigma}^0_{ij}=\frac{\sigma^0_{ij}}{\rho^{eff}},\ i,j,k,l=1,\ 2,\ 3.$$

In this way we obtain the following equations, after a little analysis and utilizing some results of [1, 5],

$$\tilde{C}_{11}=\tilde{c}_{11}-2(\tilde{c}_{11}-\tilde{c}_{12}-2\tilde{c}_{44})\langle r_1(\xi,\,\varphi,\,\phi)\rangle=V_{11}^2-\tilde{\sigma}^0_{11},\quad \tilde{C}_{22}=\tilde{c}_{11}-2(\tilde{c}_{11}-\tilde{c}_{12}-2\tilde{c}_{44})\langle r_2(\xi,\,\varphi,\,\phi)\rangle=V_{22}^2-\tilde{\sigma}^0_{22},\ (1)$$

$$\tilde{C}_{33}=\tilde{c}_{11}-2(\tilde{c}_{11}-\tilde{c}_{12}-2\tilde{c}_{44})\langle r_3(\xi,\,\varphi,\,\phi)\rangle=V_{33}^2,\quad \tilde{C}_{44}=\tilde{c}_{44}+(\tilde{c}_{11}-\tilde{c}_{12}-2\tilde{c}_{44})\langle r_4(\xi,\,\varphi,\,\phi)\rangle=V_{23}^2-\tilde{\sigma}^0_{22},\ (2)$$

$$\tilde{C}_{55}=\tilde{c}_{44}+(\tilde{c}_{11}-\tilde{c}_{12}-2\tilde{c}_{44})\langle r_5(\xi,\,\varphi,\,\phi)\rangle=V_{13}^2-\tilde{\sigma}^0_{11},\quad \tilde{C}_{66}=\tilde{c}_{44}+(\tilde{c}_{11}-\tilde{c}_{12}-2\tilde{c}_{44})\langle r_6(\xi,\,\varphi,\,\phi)\rangle=V_{12}^2-\tilde{\sigma}^0_{11}\ (3)$$

$$\tilde{\sigma}^0_{11}=V_{13}^2-V_{31}^2,\ \tilde{\sigma}^0_{22}=V_{23}^2-V_{32}^2,\ \tilde{\sigma}^0_{11}-\tilde{\sigma}^0_{22}=V_{12}^2-V_{21}^2,\ \langle r_m(\xi,\,\varphi,\,\phi)\rangle=\int_{-1}^{1}d\xi\int_0^{2\pi}d\varphi\int_0^{2\pi}d\phi\,r_m(\xi,\,\varphi,\,\phi)\,p(\xi,\varphi,\phi)\quad (4)$$

where $m=1,\,2,\,...,\,6$ and $r_m(\xi,\,\varphi,\,\phi)$ are defined by Sayers [5]. Accepting Jaynes' [6] principle of maximum Shannon entropy I (see Eqs. (5)) as a reliable basis for the evaluation of $p(\xi,\,\varphi,\,\phi)$, we seek $p(\xi,\varphi,\phi)$ in the form (6).

$$\langle 1\rangle\doteq\int_{-1}^{1}d\xi\int_0^{2\pi}d\varphi\int_0^{2\pi}d\phi\,p(\xi,\varphi,\phi)=1,\quad I\propto-\int_{-1}^{1}d\xi\int_0^{2\pi}d\varphi\int_0^{2\pi}d\phi\,p(\xi,\varphi,\phi)\,ln\,p(\xi,\varphi,\phi),\qquad (5)$$

$$p(\xi,\varphi,\phi)=(1\ Z)\,exp\,[-L_1\,r_1(\xi,\varphi,\phi)-L_3\,r_3(\xi,\varphi,\phi)-L_5\,r_5(\xi,\varphi,\phi)].\qquad (6)$$

In estimating $p(\xi,\,\varphi,\,\phi)$, we employ the normalization condition $\langle 1\rangle=1$ (Eqs. 5) and only three equations from the set of Eqs. (1)-(3) since only three of the six expectation values $\langle r_t(\xi,\,\varphi,\,\phi)\rangle$, $t=1,\,2,\,...,\,6$, are linearly independent on each other and, henceforth, may be involved in the problem of determining $p(\xi,\,\varphi,\,\phi)$ by maximizing conditionally entropy I. $1-ln\,Z$, L_1, L_3, and L_5 are the Lagrangian multipliers corresponding to the mentioned conditions. $1-ln\,Z$ corresponds to normalization condition. Eqs. (1)-(6) and three linear relations between some of $\langle r_t(\xi,\,\varphi,\,\phi)\rangle$, $t=1,\,2,\,...,\,6$, are the basis of the numerical analysis of the problem being of interest for us.

References

[1] Yih-Hsing Pao, Sachse W., Hidekazu Fukuoka: Acoustoelasticity and Ultrasonic Measurements of Residual Stresses, *PHYSICAL ACOUSTICS Principles an Methods*, Vol. XVII, 61-142, 1984.

[2] Lewandowski J.: Dependence of the acoustoelastic properties and texture of an orthorhombic polycrystalline aggregate on stress, *Acta Mechanica*, to be published.

[3] Lewandowski J.: Maximum-entropy estimate of the othorhombic texture from ultrasonic measurements. *Ultrasonics*, 229-238, 1995.

[4] Voigt W.: Lehrbuch der Krystall Physik, Teubner, Leipzig 1928.

[5] Sayers C. M.: Ultrasonic Velocities in Anisotropic Polycrystalline Aggregates. *J. Phys. D.* **15**, 2157-2167, 1982.

[6] Jaynes E. T.: Information theory and statistical mechanics. *Phys. Rev.* **106**, 620-630, 1957.

MEASUREMENTS AND CALCULATIONS RELATED TO CURVE SQUEALING IN THE RAILWAY SYSTEM

Rossano Stefanelli, Jürg Dual, Eric Cataldi-Spinola, Mathias Götsch
Swiss Federal Institute of Technology, IMES - Center of Mechanics, Tannenstrasse 3, CH-8092 Zurich, Switzerland

Summary: Within a collaboration between the Federal Institute of Technology (ETH) and the Swiss Federal Railwys (SBB), the phenomenon of curve squealing is studied. The aim is to understand the phenomenon causing this noise. Therefore various measurements and studies have been done. These include long-term-measurements on regular railway traffic, test runs with a test train, lab tests and simulations. Results are discussed.

INTRODUCTION

Curve squealing in railway systems is an annoying phenomenon that railway operators and nearby residents have to deal with, when railway lines have curves with small radii. In particular urban locations are problematic, as the acoustic impact affects a large number of people. Therefore mainly urban railway and tramway operators go to huge efforts to get curve squealing under control. A resent newspaper article [1] shows the importance and the activities in this field.
Trial and error is the most common way to deal with curve squealing. Thus different kind of friction modifiers, including water or lubricants, or different wheel or rail dampers are used. Sometimes acoustic barriers are built, influencing the townscape. This aims more to combat the effects of the noise than to understand the phenomenon.
The focus in the research project between the Swiss Federal Institute of Technology (ETH) and the Swiss Federal Railways (SBB) is to understand the mechanism of curve squealing. This would probably give the possibility to eliminate the source of the phenomenon.

LONG-TERM-MEASUREMENTS

Studies of literatures and discussions with operators, showed that often only a distinction between wet, moist, smeared and dry conditions were made. Differentiations between different trains, wheels and speeds were not discussed.
Long-term-observations showed an important influence of these factors. The database consists of more then a thousand train passages of accelerating or passing by trains. Trains slowing down were not considered, as break noise could falsify the results. For this purpose specific measurement equipment was designed [2].
The equipment recorded: meteorological data (air temperature, rail temperature, air humidity), acoustic noise, rail vibrations, train speed, running direction and recording time. More over the composition of the single train was collected.
Rail traffic was quite homogeneous, consisting of mainly four types of suburban trains and a few freight trains crossed the automatic measurement plant.
Because suburban trains of one particular type were the loudest and at the same time the most frequently passing trains, four representative trains of this type were selected for further signal investigation, corresponding to 524 train passages.
The intuitive expectation has been to obtain a clear dependence of squealing on humidity and rainfall, but the recorded data didn't validate these expectations. Moreover some trains squealed during a period while others didn't. This meant that different trains, although consisting of the same type of vehicles, differed in a relevant way from each other.
By use of the Doppler effect, it could be established whether a wheel set squealed at the measurement location or not. The analysis showed that only a few wheels were subjected to squeal.
The analyses of the acoustic signals show that the considered trains commonly squealed at a frequency in the range from 4000 to 4700 Hz.

MEASUREMENT OF STRIKING ANGLE AND DISPLACEMENT VERSUS MOISTURE OF RAIL

The circumstance that only a few wheels of a large number of the same type of wheel fitted on the same type of vehicle generate curve squealing, encouraged the authors to do measurements of the relative position and the striking angle of each wheel during the passing by the measurement location [3].
A new set of measurements was performed to investigate how moisture on the rail influences the running behavior of trains in curves. Therefore a series of measurements with one suburban train was performed. Water was used to alter the friction coefficient, which strongly influences the train running behavior. The train ran back and forth on the rails which were periodically artificially moistened, in order to simulate drying of the rail surface after rain. To avoid a too rapid dry up, about 200 m of rail were moistened. Two high definitions lasers measured the distance of the wheel rim to a virtual plane perpendicular to the flange of rail (figure 1).
As a result it could be measured that train speed and moisture on rails have an important influence on the running behavior of railway trains. The lower the train speed, the higher the lateral displacement of the rear wheel towards the center of the curve. Moisture is able to influence the lateral displacement by up to 10 mm for a rear wheel set. The

lower the moisture, the lower is the lateral displacement. In addition, it influences considerably the occurrence of squealing.
The analysis of the data shows that, after a certain number of passages, lateral displacement becomes stable. The achieved values correspond to the values for dry rail. This phenomenon could be observed for each wheel set in all measurement series.
Curve squealing occurred only at a particular lateral displacement. This was related to a specific moisture on rail, train speed and running direction.
The test will be repeated to verify the reproducibility.

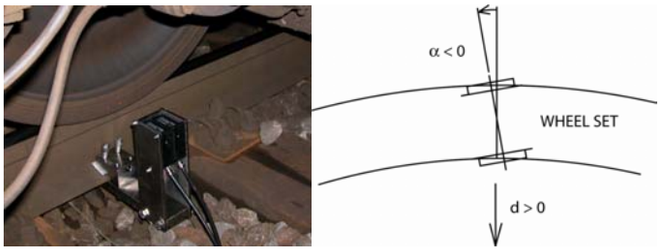


Figure 1: Setup for the measurement of striking angle (a) and lateral displacement (d). The setup consists of two high definition lasers attached directly on the flange of rail.

CHARACTERIZATION OF WHEEL PROPERTIES DEPENDING FROM WEAR PROGRESS

The eigenmodes of wheels and rails relating to the squealing frequencies, were analyzed. To this end a common FE-Analysis has been used. The data have been verified by full scale measurements on assembled and on disassembled wheels.
As the radius may have an important influence on the squealing phenomenon, the influence of the wheel diameter on the eigenfrequencies and eigenmode was studied [4]. The results showed an important shift in the eigenfrequencies of the eigenmodes during wheel lifetime (Figure 2 right).

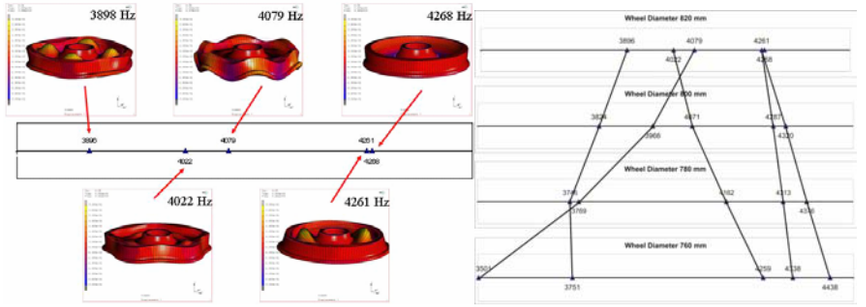


Figure 2: Left: Eigenforms of new wheels in the area of 4000 Hz. Right: Eigenfrequencies versus wheel radius for different eigenforms.

CONCLUSIONS

The occurrence of curve squealing is strongly associated to a particular wheel going around a curve. Train speed, moisture on the rail, running direction, wheel and rail profile influence the way the wheel goes around the curve and these factors are expected to play a fundamental role in the occurrence of squealing influencing the contact point and probably the mechanism of excitation. More over the wheel diameter influences the vibration characteristic of the wheel and its response, therefore it has also to be taken in account.
Only a model including all these factors can reproduce this phenomenon.

References

[1] J. Rohrer, Mit Hightech gegen das Quietschen, Tagesanzeiger 7-1-2004, Zurich
[2] R. Stefanelli, J. Dual, Preliminary Measurements for Characterization and Location of Curve Squealing, in Proceedings of Forum Acusticum Sevilla 2002, Sevilla, 2002, paper NOI-03-011.
[3] R. Stefanelli, J. Dual, E. Cataldi-Spinola, M. Götsch, Investigation of the Influence of Angle of Attack, Lateral Displacement and Moisture on Rails on the Occurrence of Curve Squealing, Proceedings of the 5th European Conference on Noise Control, Naples 2003
[4] E. Cataldi-Spinola, Ch. Glocker, R. Stefanelli, M. Götsch, Influence of the Wheel Diameter on the Curve Squealing of Railway Vehicles, Proceedings of the 5th European Conference on Noise Control, Naples 2003

ACOUSTIC WAVE PROPAGATION THROUGH A RANDOM ARRAY OF DISLOCATIONS

Agnes Maurel[1], Jean François Mercier[2] and Fernando Lund[3]
[1]Laboratoire Ondes et Acoustique, UMR CNRS 7587, ESPCI, Paris, France
[2]Laboratoire de Simulation et de Modélisation des Phénomènes de Propagation, URA 853, ENSTA, Paris, France
[3] Departamento de Física and CIMAT, Universidad de Chile, Santiago, Chile.

The dynamics of dislocations in interaction with acoustic waves is a problem at the root of a number of outstanding issues in the mechanics of materials. Mechanically excited phonons in interaction with dislocations appear in acoustics experiments, and the vibrating string model of dislocation damping [1] has been quite succesful in explaining a wealth of data, such as measurements of damping, internal friction and modulus change of solids. Nevertheles, there are many unexplained results, especially those obtained through thermal conductivity measurements at low temperatures and the review of Anderson [2] has highlighted the need for an improved theoretical understanding of the interaction between acoustic and elastic waves on the one hand, and dislocations on the other. Two important aspects that the vibrating string model does not take into account are the vector nature of wave and dislocation, and the collective effects arising from the presence of many obstacles along the way of wave propagation.

There are further outstanding problems in the mechanics of materials, such as the brittle to ductile transition and fatigue [3] where acoustic, or ultrasonic, measurements could lead to an improvement in their understanding. However, for this to be feasible, an improved theoretical understanding of the sound-dislocation interaction is needed. Recently it has become possible to visualize, through X-ray imaging, surface acoustic waves in interaction with dislocations[4].

With the above considerations as motivation, the purpose of the present paper is to offer results towards filling the gap concerning the understanding of the elastic wave-dislocation interaction: we consider first anti plane (resp. in plane) waves in interaction with screw (resp. edge) single dislocations, and obtain formulae for the scattering cross section in which their vector nature is considered in full. Next, these results are used in a multiple scattering perturbative treatment of the coherent behaviour of an acoustic wave that travels through a random array of dislocations, and we obtain formulae for the effective speed of wave propagation, and for the attenuation length.

Scattering of an acoustic wave by a single dislocation[5] We consider acoustic waves of wavelengths large compared to dislocation core size, so that nonlinear effects near the core can be neglected. The scattering mechanism is thus as follows: The wave hits the dislocation, and as a consequence the latter oscillates. This oscillation then generates outgoing waves in directions other than the incident direction. The challenge is to compute the scattering amplitude for an edge dislocation in interaction with an in plane wave, and to fully take into accout mode conversion between the two modes present in two dimensions: longitudinal (acoustic) and transverse (shear). The response of the dislocation to an incoming wave is described by the equations found in [6], and the re-radiated waves are computed using the formaluation of Mura [7]. The main result is a formula for the scattering amplitude in two dimensions. It is a two-by two matrix, to take into account the possible ingoing and outgoing polarizations. For example, for an incoming acoustic wave and outgoing shear wave it is

$$f_{\alpha\beta}(\theta) = \frac{\mu b^2}{2M} \frac{e^{i\pi/4}}{\sqrt{2\pi\Omega\alpha^3}} \cos 2\theta_0 \ \sin(2\theta - 2\theta_0)$$

Where α (resp β) are the speeds of acoustic (resp. shear) wave propagation, θ_0 is the angle of incidence with respect to the Burgers vector b, θ is the scattering angle, μ is the shear modulus, Ω

is the wave frequency and M is the dislocation mass.

Coherent propagation through a random array of dislocations[5] In this section we determine the coherent wave number of an acoustic wave that is multiply scattered by a random array of dislocations in two dimensions. The real part of the coherent wave number gives the effective wave velocity and the imaginary part gives the attenuation length, or mean free path. A low density of dislocations is assumed and the formalism is based on a wave equation with a right hand side term whose structure is tailored to take into account the interaction described in the previous paragraph. In the simple case of a shear wave propagating through a random array of screw dislocations with density n, the effective wave number K_β is obtained at first order in perturbation theory: $K_\beta = k_\beta(1 - (\mu n b^2)/(2M\Omega^2))$, where k_β is the unperturbed wavenumber. This provides the effective wave velocity. A computation to second order gives the attenuation length, and an generalization provides the formulae for an in-plane wave propagating through a random array of edge dislocations.

Coherent propagation in three dimensions through a random array of dislocation loops[5] Dislocation loops introduce an additional length scale—the loop size—into the problem, and the main result here is a change in the scaling of the scattering cross section: rather than increasing with wavelength, it decreases.

References

[1] A. V. Granato and K. Lücke, in "Physical Acoustics", Vol 4A, edited by W. P. Mason (Academic, 1966); Phys. Rev. **B24**, 7007 (1981); K. Lücke and A. V. Granato, *Phys. Rev.* **B24**, 6991 (1981).

[2] A. C. Anderson, in "Dislocations in Solids", edited by F. R. N. Nabarro, Ch. 29 (North Holland, 1983).The introduction of radiation damping due to kink oscillations has improved qualitative agreement with measurements, but quantitative agreement remains elusive. See A. Seeger, in "Dislocations 1984", edited by P. Veyssière, L. Kubin and J. Castaing, Editions du CNRS (Paris, 1984), p. 141; A. Hikata and C. Elbaum, *Phys. Rev.* **B9**, 4529 (1974). See also G. A. Kneezel and Granato, *Phys. Rev.* **B25**, 2851 (1982); T. Ninomiya, *J. Phys. Soc. Japan* **25**, 830 (1968).

[3] S.G. Roberts, in "Multiscale Phenomena in Plasticity", edited by J. Lepinoux et al. (Kluwer, 2000); S. Kenderian, T. P. Berndt, R.E. Green Jr and B.B. Djordjevic, Mat. Sci. & Eng. A**348**, 90 (2003); J. Test. Eval. **31**, 98 (2003).

[4] E. Zolotoyabko, D. Shilo and E. Lakin, Mats. Science and Eng. **A309-310**, 23 (2001); D. Shilo and E. Zolotoyabko, Ultrasonics **40**, 921 (2002).

[5] A. Maurel, J.-F. Mercier and F. Lund, "Scattering of an elastic wave by a single dislocation", submitted to *JASA*; "Elastic wave propagation through a random array of dislocations", submitted to *Phys. Rev. B*; D. Boyer, F. Lund, A. Maurel, J.-F. Mercier and V. Pagneux, unpublished.

[6] F. Lund, *J. Mat. Res.* **3**, 280 (1988).

[7] T. Mura, *Phil. Mag.* **8**, 843 (1963).

XXI ICTAM, 15–21 August 2004, Warsaw, Poland

DISTRIBUTED PARAMETER CONTROL OF A 2D ACOUSTIC HELMHOLTZ PROBLEM ON A HALFSPACE

George Biros*, Loukas F. Kallivokas**, Seong-Won Na**
* *Department of Mechanical Engineering & Applied Mechanics, Department of Computer & Information Science, University of Pennsylvania, Philadelphia PA 19104, USA*
** *Department of Civil Engineering, The University of Texas at Austin, Austin TX 78712, USA*

Summary In this work we present the formulation and numerical solution of a distributed parameter control problem for the acoustic equation in a halfspace with potential applications to the seismic insulation of surficial structures. We consider the case of SH-waves in a two-dimensional materially inhomogeneous halfspace. The goal is to invert for the necessary material injections in a pre-selected region near the free surface so that, for a range of excitation frequencies of an incoming disturbance, the displacement response on the free surface is constrained below a threshold value. We use an infinite-dimensional constrained optimization formulation, in which the constraints are given by a set of (uncoupled) Helmholtz problems corresponding to a range of excitation frequencies. The Helmholtz problems are discretized using a finite element formulation on a half disk with absorbing boundary conditions prescribed over the truncation boundary. We use a Lagrange-Newton-Krylov-Schur algorithm (LNKS) to solve the system of nonlinear PDEs that correspond to the first-order necessary optimality conditions. We present the formulation and numerical results.

INTRODUCTION

The desire to control the frequency content and the amplitude of the response to arbitrary excitations is commonly shared amongst various engineering applications. For example, highway noise-barriers aim at reducing the acoustic pressure signatures to predefined acceptable levels in residential areas by, essentially, altering the material profile that sound encounters in its path. Of interest here is a similar problem, also governed by the Helmholtz equation, that arises in the propagation of SH waves in soft soil deposits. We consider the case of a halfspace exposed to either traveling waves (antiplane case), or underground blasts. We explore the feasibility of limiting the response of a pre-selected near-surface region embedded within a valley of soft deposits, by artificially altering the deposits (material injections) within a narrow region lying between the origin of the excitation and the region of interest (Fig. 1).

Motivated by the physical application, we formulate a distributed control problem for the inhomogeneous Helmholtz problem. The objective is to minimize the amplitude of the response (displacement profile) on and near the surface (target zone Ω_t in Fig. 1). The control parameters are provided by the material properties (shear modulus μ) within a control zone Ω_c. We choose a constrained optimization approach in which we are minimizing the amplitude of the response across a narrow band of the frequency spectrum reflecting the expected excitation frequency content. From an optimization perspective, the control problem is a formidable one, for the number of unknowns one needs to solve for at each frequency is at least equal to twice the nodal points of the spatial discretization (for a scalar unknown). Until recently such problems were computationally intractable. Recent algorithmic approaches that combine Newton-Krylov methods with appropriate preconditioners that take advantage of the structure of the underlying PDEs, allow the efficient solution of the nonlinear equations corresponding to the first order optimality conditions.

There is a considerable amount of work on inverse problems for inhomogeneous media. Most problems however are related to the recovery of the material properties, or obstacle detection by observing the far-field response (e.g. [5], [6]). There is also work in noise reduction for acoustics, but the work is concentrated more on shape optimization (e.g. [7]). Moreover there is little work on the algorithmic scalability of the numerical methods.

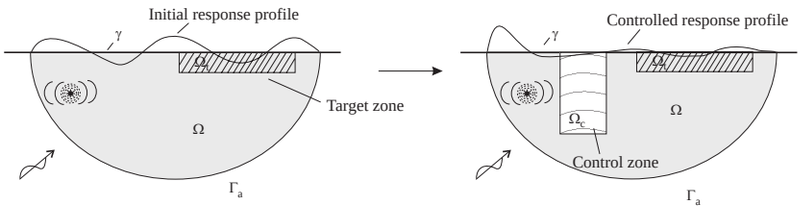


Figure 1. Schematic of a two-dimensional distributed control problem for SH waves (Helmholtz).

In short: We use a LNKS algorithm for the Helmholtz equation, we numerically investigate the feasibility of insulating surficial structures by soil injections, we incorporate multiple frequencies, we use second-order absorbing boundary conditions for the forward and adjoint operators, and we investigate the effect of different regularization functionals.

FORMULATION

We consider the halfspace Helmholtz problem for an inhomogeneous medium in the absence of damping. For simplicity, we assume constant density ρ throughout the domain, but variable shear modulus (μ_0). In the following u denotes the displacement and u_ν its (outward) normal derivative along Γ_a and γ. We use $\mu(\mathbf{x})$ ($\mathbf{x} \in \Omega$) to denote a perturbation from

the background material $\mu_0(\mathbf{x})$. We assume a smaller region, Ω_c, in which μ can be controlled, i.e. Ω_c is the support of $\mu(\mathbf{x})$. We are interested in the behavior of the system in m excitation frequencies ω_j. We introduce the following notation: $a_j(\mu,u,\tilde{u}) := -\int_\Omega(\mu_0+\mu)\nabla u\cdot\nabla\tilde{u}\,d\Omega+\int_\Omega \rho\omega_j^2\,u\,\tilde{u}\,d\Omega$, $g(v,\tilde{u}) := \int_{\Gamma_a}\mu_0\,v\,\tilde{u}\,d\Gamma_a$, $(v,\tilde{u})_D := \int_D v\,\tilde{u}\,dD$, where D denotes a generic integration domain. We define H^1 to be the space of functions with square-integrable first derivatives in Ω, and L^2 the space of functions that are square-integrable in Ω. Then, given an excitation $b_j(\mathbf{x})$ in L^2 at frequency ω_j a weak-form statement of the acoustic problem is to find $u_j\in H^1$ such that $a_j(\mu,u_j,\tilde{u})+g(u_{j_\nu},\tilde{u})=(b_j,\tilde{u})_\Omega$, $\forall\tilde{u}\in H^1$, were u_j is the solution that corresponds to the frequency ω_j. We use a FEM-based approximation scheme, and thus a truncated domain is necessary. On its boundary Γ_a an absorbing boundary condition has to be prescribed. The simplest one is given by $\mu_0 u_{j_\nu}-i\omega u_j=0$. In our implementation we prescribe second-order boundary conditions; details can be found in [2].

Control problem: Using the above relations we seek to minimize a measure of the response u for several different frequencies. The objective functional is based on the observation of the displacement on the target domain Ω_t. We use the (square of the) $L^2(\Omega_t)$ norm to measure the amplitude of the response. We choose m frequencies in which we want to test our control. In that sense we want to choose μ as the minimizer of $\frac{1}{2}\sum_j(u_j,u_j)_{\Omega_t}+\frac{1}{2}(\nabla\mu,\nabla\mu)_{\Omega_c}$. The last term is a regularization term that controls the smoothness of the perturbation. Depending on Ω_c this term might be necessary for well-posedness. (Different regularization functionals, like total variation or L^2, are also possible.) For simplicity we explain our approach when $m=1$. We introduce the adjoint λ, also in H^1, and we look for stationary points of the Lagrangian defined by:

$$\mathcal{L}(u,\lambda,\mu) := \frac{1}{2}(u,u)_{\Omega_t}+\frac{1}{2}(\nabla\mu,\nabla\mu)_{\Omega_c}+a(\mu,u,\lambda)+g(u_\nu,\lambda)-(b,\lambda)_\Omega. \tag{1}$$

Let $K:=\{\mu\in H^1(\Omega_c):\mu(\overline{\Omega_c}\backslash\gamma)=0\}$. Taking variations with respect to u,λ and μ we obtain the so-called Karush-Kuhn-Tucker (KKT) first-order optimality conditions in which we seek u,λ in H^1 and μ in K such that:

$$\begin{aligned}
a(\mu,u,\tilde{u})+g(u_\nu,\tilde{u})-(b,\tilde{u})_\Omega=0, \quad \forall\tilde{u}\in H^1 && \text{forward problem,}\\
a(\mu,\lambda,\tilde{\lambda})+g(\tilde{\lambda}_\nu,\lambda)+(u,\tilde{\lambda})_{\Omega_t}=0, \quad \forall\tilde{\lambda}\in H^1 && \text{adjoint problem,}\\
(\nabla\mu,\nabla\tilde{\mu})_{\Omega_c}+(\mu_0+\tilde{\mu},\,\nabla u\cdot\nabla\lambda)_{\Omega_c}=0, \quad \forall\tilde{\mu}\in K && \text{control problem.}
\end{aligned} \tag{2}$$

It is easy to show that the boundary condition for the adjoint variables is the same with the one of the forward problem. Finally, an additional constraint of the form $\mu\geq-\alpha\mu_0$ is required; $0<\alpha<1$ is a parameter chosen to keep $\mu_0+\mu$ positive and thus ensure strong ellipticity. This constraint is treated with a penalty term in the objective function.

NUMERICAL SOLUTION

One way to solve (2) is to use a nonlinear Gauss-Seidel iteration: given some initial μ_0 we solve the forward problem for the displacement field, then we use this field as a forcing term for the adjoint equation and finally we solve the control equation for an update μ. This is a popular approach since it is relatively easy to implement, especially for self-adjoint problems. However this approach is expensive, since at each optimization step we solve $m\times 2$ Helmholtz problems (for the forward and adjoint problem) plus one Laplacian in Ω_c for the control equations. A similar approach is to first linearize (2) and then apply the Gauss-Seidel sweep. In the optimization community this method is also known as reduced space sequential quadratic programming (RSQP). Instead, here we use a Newton-Krylov method applied directly to the KKT conditions. The key component for the success of the method is the application of a preconditioner which is based on an approximate version of the RSQP step. The method is termed *Lagrange-Newton-Krylov-Schur* and it first appeared in the context of boundary flow control [3, 4]. Variants of this method have been applied in inverse wave propagation, in which the acoustic propagation is written in the time domain [1]. (For inverse problems phase information is important and time-domain formulations are preferable.) The forward, adjoint, and control equations are discretized using Galerkin FEM with quadratic elements. Results will be presented on the well-posedness of the optimization problem, with a discussion on the numerical and scalability results for different mesh sizes, loading scenarios, and regularization functionals.

References

[1] V. Akcelik, G. Biros, and O. Ghattas. Parallel multiscale gauss-newton-krylov methods for inverse wave propagation. In *Proceedings of SC2002*, The SCxy Conference series, Baltimore, Maryland, November 2002. ACM/IEEE.

[2] J. Bielak, L. F. Kallivokas, J. Xu, and R. Monopoli. Finite element absorbing boundary for the wave equation in a half-plane with an application to engineering seismology. In *Proceedings Third International Conference on Mathematical and Numerical Aspects of Wave Propagation (INRIA-SIAM)*, pages 489–498, Juan-les-Pins, France, April 1995. INRIA-SIAM.

[3] G. Biros and O. Ghattas. Parallel Lagrange-Newton-Krylov-Schur methods for PDE-constrained optimization. Part I: The Krylov-Schur solver. *SIAM Journal on Scientific Computing*. to appear.

[4] G. Biros and O. Ghattas. Parallel Lagrange-Newton-Krylov-Schur methods for PDE-constrained optimization. Part II: The Lagrange Newton solver, and its application to optimal control of steady viscous flows. *SIAM Journal on Scientific Computing*. to appear.

[5] D. Colton and R. Kress. *Inverse Acoustic and Electromagnetic Scattering Theory*. Springer, 1997.

[6] G. R. Feijóo, A. A. Oberai, and P. M. Pinsky. An application of shape optimization in the solution of inverse acoustic scattering problems. *Inverse Problems*, 20:199–229, 2004.

[7] A. Habbal. Nonsmooth shape optimization applied to linear acoustics. *SIAM Journal on Optimization*, 8(4):989–1006, 1998.

XXI ICTAM, 15–21 August 2004, Warsaw, Poland

FREQUENCY- AND DIRECTIONALITY-CONTINUATION SCHEMES FOR SCATTERER SHAPE DETECTION IN ACOUSTICS

Seong-Won Na* and Loukas F. Kallivokas*
*Department of Civil Engineering, The University of Texas at Austin, Austin, TX 78712, USA

Summary In this paper we discuss continuation schemes for detecting the location and shape of rigid scatterers embedded in a host acoustic medium when considering scant measurements of the scattered acoustic pressure in the region exterior to the scatterer (near- or far-field). Underlying the inversion process are frequency- and directionality-continuation iterative schemes that allow robust determination of the unknown shape using a small number of frequencies and directions of the probing insonifying waves. The methodology is based on boundary integral equation for the solution of the forward problem. The scattered pressure is measured only in the backscatter region and at receiver locations that do not circumscribe the sought scatterer. Several numerical results are presented, both for parametrically defined shapes (e.g. circle, ellipse, etc), as well as for penny-shaped scatterers and completely arbitrary geometries. For the latter cases, conditions for non-self-intersecting shapes complement the numerical implementation to allow for the recovery of the nodal coordinates of the meshed scatterer boundary.

INTRODUCTION

Inverse scattering problems are of considerable practical interest in various areas of science and engineering due, in part, to the ever broadening spectrum of important applications that range from medical, to geophysical, to target identification investigations. In particular, inverse problems arising in acoustics are of relevance in, amongst others, ultrasound imaging (for medical or other non-destructive assessments), seismic imaging, underwater surveillance and target acquisition, and in the detection of objects in the ocean, either fully submerged or partially buried in the seafloor. Various approaches to resolve the unknown scatterer from the scant measurements are investigated among many researchers [1, 2, 3] and one may roughly classify them into methods that rely on optimization-based schemes [2] and methods that do not explicitly seek to minimize a misfit functional [3]. The advantage of the latter category is that the shape reconstruction can be carried out without a-priori information, whereas, when optimization methods are used, the feasibility space may be considerably narrow. In this work we favor optimization methods for the generality they offer and report on a dual frequency- and (optionally) directionality-continuation algorithm that has, thus far, provided promising results.

THE FORWARD PROBLEM

We consider sound-hard scatterers in 2D full-space (Ω) insonified by traveling plane waves. The forward problem is described by the Helmholtz equation for the scattered pressure u^s, subject to a Neumann condition on the scatterer's surface (Γ), and the Sommerfeld radiation condition at infinity. We use a standard integral equation formulation to arrive at a solution of the forward problem at each iteration of the inverse problem. Using customary notation for denoting the single-layers ($\mathfrak{S}$ and S), the double-layers ($\mathfrak{D}$ and D), and the normal derivative (u^s_ν), the scattered pressure is given as:

$$u^s = \mathfrak{S}[u^s_\nu] - \mathfrak{D}[u^s], \text{ in } \Omega, \quad \text{and} \quad \frac{1}{2}u^s - S[u^s_\nu] + D[u^s] = 0, \text{ on } \Gamma. \tag{1}$$

THE INVERSE PROBLEM

In order to resolve the unknown location and shape of the interrogated scatterer, we seek to minimize, subject to the governing Helmholtz equation, the misfit functional defined either by:

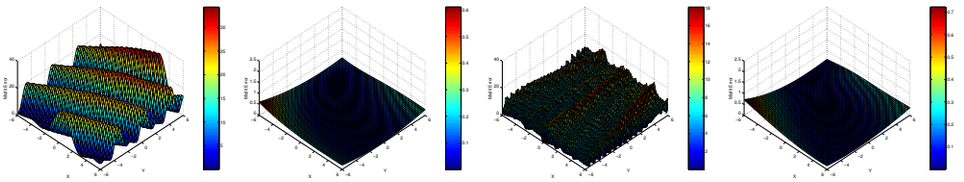
$$\mathcal{L}_1(\Gamma) = \frac{1}{2}\sum_{m=1}^{M} \frac{|u^s(\mathbf{x}_m) - u^s_m(\mathbf{x}_m)|^2}{|u^s_m(\mathbf{x}_m)|^2} \text{ or } \mathcal{L}_2(\Gamma) = \frac{1}{2}\sum_{m=1}^{M} \frac{||u^s(\mathbf{x}_m)| - |u^s_m(\mathbf{x}_m)||^2}{|u^s_m(\mathbf{x}_m)|^2} \tag{2}$$

In (2), $\mathbf{x}_m$ denotes the location of the stations, u^s_m denotes the measured scattered field at the same points, and u^s denotes the forward solution (computed), also at the M locations. Numerically, we experimented with both functionals (2) and opted to carry out the location and shape detection using $\mathcal{L}_2$ to avoid the highly oscillatory nature of $\mathcal{L}_1$ at high frequencies that is responsible for very narrow valleys of attraction and multiple minima (Fig. 1).

NUMERICS

Implementation

To seek a minimum to the functionals (2) we used a conjugate-gradient method (Polak-Ribiere variant); for the computation of the gradient functionals we used a finite difference scheme. For each update of the design parameters (location and shape parameters) the forward problem needs to be solved; we implemented the integral equations (1) using quadratic isoparametric boundary elements. Throughout all numerical experiments we chose 3 to 5 station locations along a fixed



(a) $ka = 1.0, \mathcal{L}_1$ (b) $ka = 1.0, \mathcal{L}_2$ (c) $ka = 5.0, \mathcal{L}_1$ (d) $ka = 5.0, \mathcal{L}_2$

Figure 1. Distribution of misfit functionals $\mathcal{L}_1$ and $\mathcal{L}_2$ (k: wave number; a: radius of the scatterer)

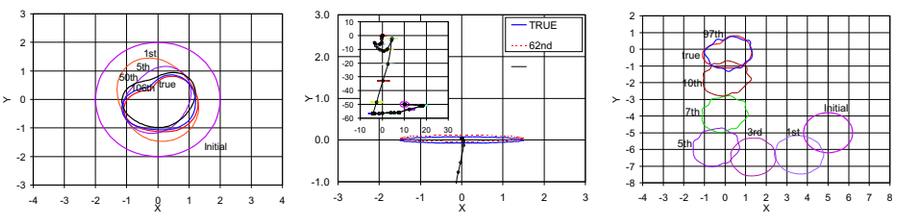
y-coordinate; the motivation stems from practical considerations, for it is rare that sensor distributions circumscribe a scatterer.

Frequency- and directionality-continuation scheme

Given a frequency and a set of initial guesses for the unknown shape and location parameters, our scheme for a single frequency is encapsulated in a standard algorithm. However, even if convergence is achieved, there is no guarantee that the converged parameters are the true ones. To improve, we iterate on the frequency (or wavenumber) space and use the converged parameters of the last frequency as initial guesses for the next frequency. Once the highest frequency of the frequency continuation scheme has resulted in converged parameters, we revisit the misfit for each one of the frequencies we considered earlier and re-compute the misfit for the final parameter values. If the computed values of the new misfits are less than the ones we obtained at the end of the previous convergence cycle, we consider the scheme to have converged. Optionally, the same scheme can be used for iterating over user-chosen directions of the interrogating waves, either as a stand-alone scheme, or in conjunction with the frequency continuation.

Numerical Results

We used the continuation schemes to resolve the location and shape of various scatterers and report here a subset of our results. In all cases of using $\mathcal{L}_2$, convergence to the true parameters was attained using a small number of frequencies. Though we have observed sensitivity of the number of iterations to the initial guess, we have not been able to construct a problem for which the continuation scheme would fail. Figure 2 depicts the detection scheme for various scatterers including a parametrically defined arbitrarily-shaped scatterer (Figure 2 (a)), a parametrically defined penny-shaped scatterer (Figure 2 (b)) and completely arbitrary geometries (Figure 2 (c)). For completely arbitrary geometries based on scatterer boundary discretizations, a non-self-intersecting shape algorithm was implemented to eliminate odd shape solutions.



(a) Arbitrarily-shaped scatterer (6 parameters) (b) Penny-shaped scatterer (4 parameters) (c) Arbitrarily-shaped scatterer (42 nodal coordinate parameters)

Figure 2. Numerical experiments for various scatterer shapes

CONCLUSIONS

We investigated numerically and reported on the algorithmic stability of frequency- and directionality-continuation schemes for detecting the location and shape of insonified scatterers using a small number of measurement stations. The results demonstrate that the schemes allow robust determination of the unknown shape using a small number of frequencies and directions of the probing insonifying waves.

References

[1] Colton D., Coyle J., Monk P.: Recent Developments in inverse scattering theory. *SIAM Review* **42**:369–414, 2000.
[2] Angell T.S., Jiang X., Kleinman R.E.: A Distributed Source Method for Inverse Acoustic Scattering. *Inverse Problems* **13**:531–545, 1997.
[3] Potthast R.: A Point-Source Method for Inverse Acoustic and Electromagnetic Obstacle Scattering Problems. *IMA Journal of Applied Mathematics* **61**:119–140, 1998.

NONLINEAR DYNAMICS OF PARAMETRICAL EXCITED TWO-DEGREES-OF-FREEDOM FREEDOM FLEXIBLE PENDULUM

Amir Abbas Zadpoor*

Department of Mechanical Engineering, Iran University of Science and Technology, Narmak, Tehran 16844, Iran

Summary This paper explores dynamical behaviour of a parametrical excited two-degree-of-freedom pendulum. It has been shown that as excitation period increases, existing period orbit could bifurcates into more-complex invariant manifolds. Complex behaviour of the system is studied by the means of phase portraits, Poincare sections, and Lyapunov exponents and it has concluded that system could become chaotic for some range of involving parameters.

INTRODUCTION

Bayly and Virgin discussed the stability of forced radial oscillations of a flexible pendulum [1]. Zaki *et al* discussed the effect of stiffness nonlinearity on dynamics of the tangential forced flexible pendulum [2] and shown that alternation of system's dynamic is explored when amplitude of the harmonic force is varied. It has been shown that transition of the periodic motion to chaotic one begins with a Hopf bifurcation and follows by a torus doubling. Bifurcation ends by a torus breaking. The present study considers a flexible pendulum with a vertically moving pivot. The vertical motion is assumed to be harmonic. Due to vertical displacement, the system becomes parametrically excited. Stiffness of the spring is assumed linear and dynamics of the system is studied when amplitude of the pivot's vertical motion is varied. Then the linear spring is replaced with weakly nonlinear and strongly nonlinear ones. Dynamical behavior in two latter cases is compared with each other and with the linear stiffened case. Routes to chaos are studied through construction of the phase portraits and Poincare maps and computation of Lyapunov exponents. A schematic of the problem is given in Figure 1.

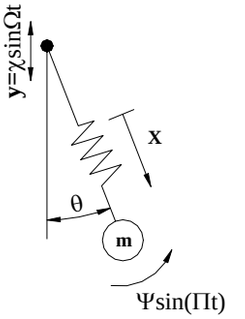


Figure 1 Schematics of the Problem

PROBLEM FORMULATION

Two generalized coordinates, say X and θ, are chosen to derive the governing system of nonlinear ordinary differential equations. The spring, in the general case, assumed cubic. Therefore, the spring force can be represented as

$$F = -kx - \varepsilon x^3$$

Calculating the terms of kinetic and potential energy as well as non-conservative generalized forces and putting them into Lagrange equation leads to the governing system of two nonlinear differential equations. Introducing some new variables and doing some algebra, the non-dimensional form of the governing equation could be written as

$$\ddot{x} + x + \lambda x^3 - [\alpha \sin \Sigma\tau + \beta]\cos\theta - (1+x)\dot{\theta}^2 = 0$$

$$\ddot{\theta}(1+x)^2 + \zeta\dot{\theta} + [\alpha \sin \Sigma\tau + \beta](1+x)\sin\theta + 2(1+x)\dot{x}\dot{\theta} = \psi \sin \Lambda\tau$$

where

$$X = xl \qquad t = \tau\omega \qquad \omega = \sqrt{\frac{k}{m}} \qquad ' = \frac{d}{dt} = \omega\frac{d}{d\tau}$$

$$\tau\Sigma = t\Omega \qquad \lambda = \frac{\varepsilon l^2}{k} \qquad \alpha = \frac{\Omega^2\chi}{l\omega^2} \qquad \beta = \frac{g}{l\omega^2} \qquad \zeta = \frac{c}{m\omega l^2} \qquad \tau\Lambda = t\Pi \qquad \psi = \frac{\Psi}{l^2\omega^2}$$

DYNAMICAL EXPLORATION

An analogy is constructed between rotational and longitudinal motions in one side and ship's rolling angle and ship's pitch on the other side. Current study improves the model to a parametrical excited one, which approximates the reality much closer. Bifurcation study of the system begins from a periodic orbit. Amplitude of the parametric excitation is used as control parameter and alternation of system's dynamics is explored when the control parameter varies. Non-dimensional form of governing equations is digitally simulated using a Runge-Kutta algorithm. Phase portrait in conjunction with Poincare section are used for dynamical study of the system. Poincare sections are constructed in a manner to give a stroboscopic picture of the system's trajectory. Therefore the point in which trajectory cross the Poincare section is recorded for a fixed phase angle of harmonic pivot's excitation. When the system seems to be chaotic, it becomes necessary to use chaos identification methods to realize if it is a true chaotic motion. Lyapunov exponents who are a measure of divergence of nearby trajectories are used for quantification of the system's dependence on initial conditions.

Figure 1 depicts phase portrait of the periodic orbit. The parameters used for integration of the system are given in the Table 1. As excitation amplitude increases, dynamical behavior of the system changes. Figure 3, 4 and 5 show the chaotic behavior of the system. Lyapunov exponents are used for identifying the chaos. The computed values are also listed in Table 1.

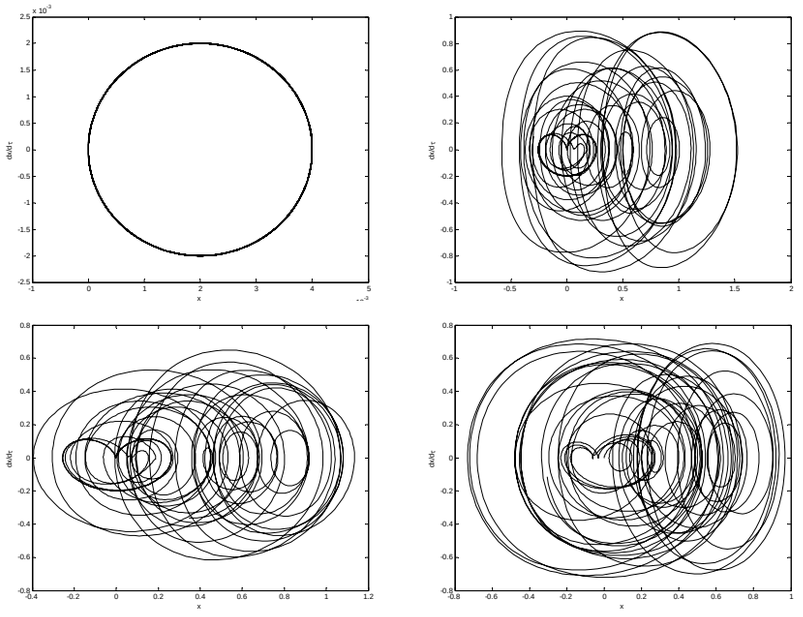


Figure 2. Above Left **Figure 3. Above Right** **Figure 4. Below Left** **Figure 5. Below Right**

	α	β	λ	Σ	ζ	ψ	Λ	Lyapunov Exponent
Figure 2	1e-6	0.002	0	0.5	0.005	0.0001	0.3	-2.43657e-9
Figure 3	0.15	0.002	0	0.5	0.005	0.0001	0.3	0.0596394
Figure 4	0.15	0.002	0.05	0.5	0.005	0.0001	0.3	0.0199838
Figure 5	0.15	0.002	0.9	0.5	0.005	0.0001	0.3	0.0666035

Table 1

CONCLUSIONS

It has been shown that the system becomes chaotic for some range of involving parameters. Computed Lyapunov exponents and phase portraits are used to demonstrate complexity of the involving system. Due to space constraints, Poincare sections and phase portraits, which are used for bifurcation study of the system, are omitted in this extended summary.

References

[1] Bayly, P. V., and Virgin L. N.: On the Forced Radial Oscillations of an Experimental Spring Pendulum, *Proceedings of the 14th Biennial ASME conference on Mechanical Vibrations and Noise*, 1993, pp. 229-236

[2] Zaki, K., Rajagopal, K. R., and Srinivasa, A. R.: Effect of Nonlinear Stiffness on the Motion of a Flexible Pendulum, *Nonlinear Dynamics*, **27**:1-18, 2002

NONLINEAR DYNAMICS OF HIGH-SPEED MILLING

Gabor Stepan, Tamas Insperger, Robert Szalai
Department of Applied Mechanics, Budapest University of Technology and Economics
Budapest, H-1111, Hungary

Summary In case of highly interrupted machining, the ratio of time spent cutting to not cutting is considered as a small parameter, and the classical regenerative vibration model breaks down to a simplified discrete mathematical model. The linear analysis of this discrete model leads to the recognition of the doubling of instability lobes in the stability charts of machining parameters. This kind of lobe doubling is related to the appearance of period doubling bifurcations occurring primarily in low-immersion high-speed milling along with the classical self-excited vibrations (or secondary Hopf bifurcations). The present work investigates the nonlinear vibrations in case of period doubling and compares this to the well-known subcritical nature of the Hopf bifurcations in turning processes. Our experimental results draw the attention to the limitations on the highly interrupted cutting condition. The analysis of the general milling model requires the use of the stability chart of the delayed Mathieu equation, which is also constructed.

INTRODUCTION AND MODELLING

High-speed milling is one of the most preferred and efficient cutting processes nowadays. It is a challenging task for researchers to explore its special dynamical properties, including the stability conditions of the cutting process and the nonlinear vibrations that may occur near to the stability boundaries. These dynamical properties are mainly related to the underlying regenerative effect in the same way as it is in case of the classical turning process. Still, some new phenomena appear for low-immersion milling as predicted in [2,3]. These phenomena were also reported in [4,5] in case of milling, independently from the immersion or speed characteristics of the milling processes.

High-speed milling often means also low immersion (very small chip thickness) with relatively small number (z = 2 to 4) of cutting edges on the tool (see Figure 1). There is either no contact between the tool and the work-piece, or there is only one edge in contact for a (relatively short) time. In these cases, highly interrupted machining can well approximate the whole machining process. In the simplest models of highly interrupted machining, the ratio of time spent cutting to not cutting is a small parameter. This leads to a mechanical model where the free vibration of the tool is perturbed periodically by an impact to the work-piece. This impact results a sudden change in the tool oscillation velocity and it depends on the actual chip thickness, that is, on the difference of the present and the previous tool position. In this respect, the model includes the classical regenerative effect described for turning in [1]. There is one major difference, though: the periods of no-contact are regulated by the cutting speed parameter. Accordingly, high-speed milling is a kind of parametrically interrupted cutting as opposed to the self-interrupted cutting arising in unstable turning processes.

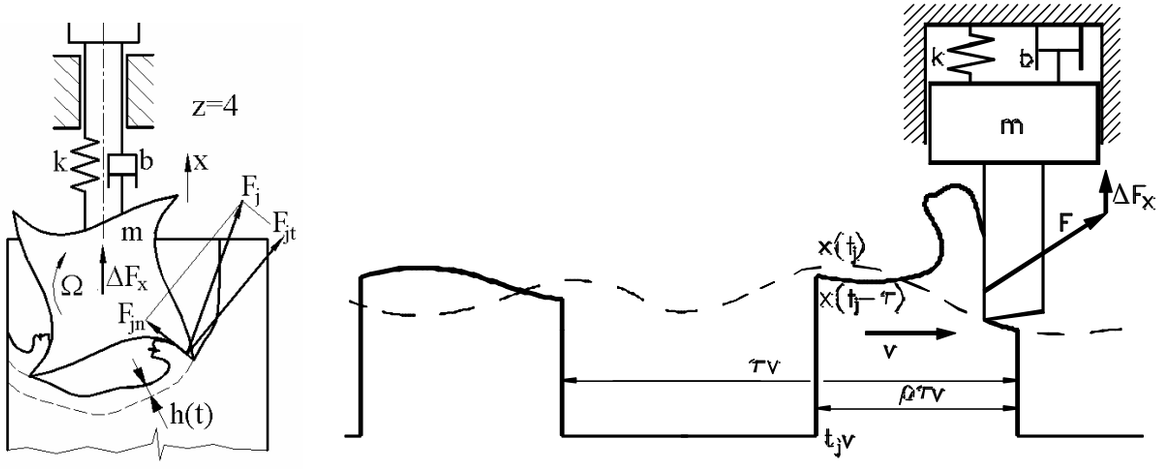


Fig. 1. Mechanical models of high-speed milling for normal and highly interrupted cutting cases

STABILITY AND NONLINEAR VIBRATIONS OF HIGHLY INTERRUPTED CUTTING

The simplest possible, but still nonlinear highly interrupted cutting model leads to a two-dimensional discrete mathematical model. Bifurcation analysis can be carried out along the stability limits related to period doubling bifurcations and (secondary) Hopf bifurcations. These require centre manifold reduction and normal form transformation. The tedious algebraic work can be carried out in closed form and leads to nonlinear phenomena similar to the one experienced in the case of the Hopf bifurcation in the turning process. The resulting subcritical bifurcations are presented in analytical form in the subsequent Sections. The existence of stable period two vibrations is also shown 'outside' the unstable period two vibrations. The stable ones can, however, quickly bifurcate to chaotic

oscillations with increasing chip width. This is also shown by numerical investigation, and some analytical explanation is also given.

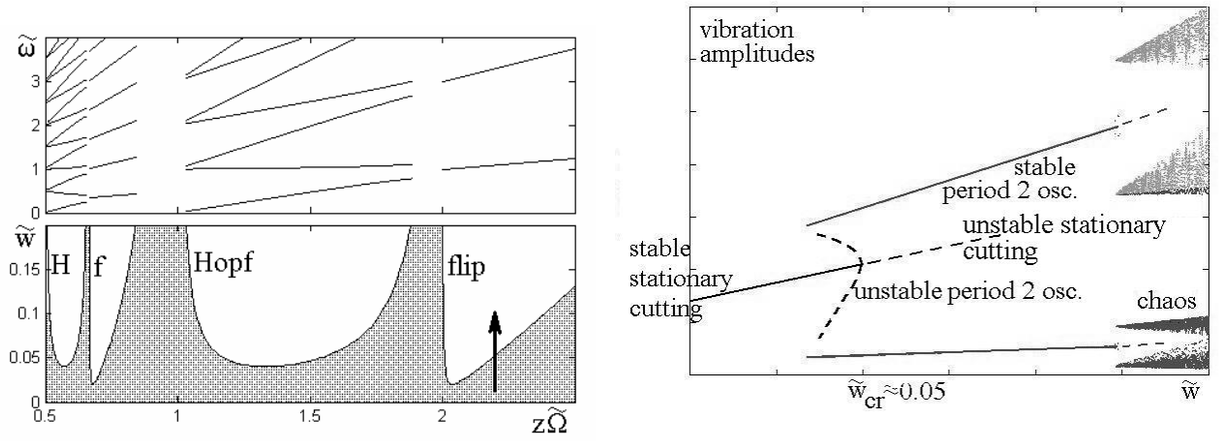


Fig. 2. Stability chart and bifurcation diagram for highly interrupted cutting

The stability chart of Fig. 2 is presented in the plane of the dimensionless cutting speed and chip width parameters, and it also presents the dimensionless vibration frequencies along the stability limits above the stability chart. This chart and the corresponding spectra are all confirmed experimentally, too. Figure 2 also presents the bifurcation diagram at the black arrow crossing the stability boundary at a flip (period doubling) bifurcation in the stability chart.

STABILITY OF MILLING

Experiments drew the attention to the weakness of the small parameter condition on the ratio of time spent cutting to not cutting. If this condition is not applicable, like in the case of full-immersion milling, the mathematical model cannot be simplified to a discrete one, and its structure remains similar to the delayed Mathieu equation:

$$\ddot{x}(t)+(d+e\cos t)x(t)=b\,x(t-2p)\,,$$

where the time-periodicity and the time delay are equal (here, the dimensionless $2p$) and they are both related to the tooth-pass period (as shown in Fig. 1). In Figure 3, the corresponding stability chart in the space of the three parameters inherits the structure of the Incze-Strutt and the Hsu-Bhatt charts, too [6].

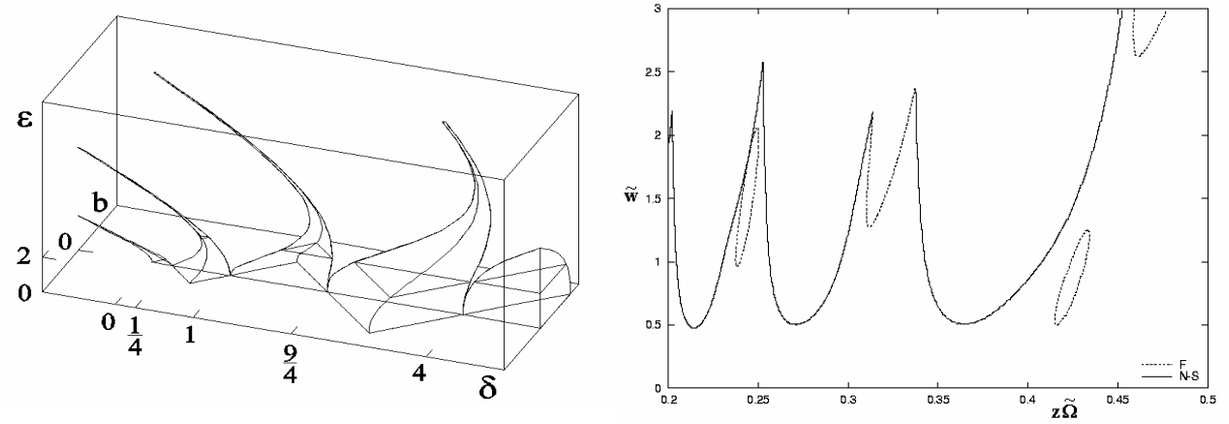


Fig. 3. The stability charts of the delayed Mathieu equation and the corresponding milling process

The construction of the corresponding stability charts in the plane of the same milling parameters as before shows, that the instability lobes related to Hopf bifurcations are actually extended by instability lenses related to the flip or period doubling bifurcations.

References

[1] G. Stépán, Philosophical Transactions of the Royal Society 359, 739-757 (2001).
[2] M.A. Davies, J.R. Pratt, B. Dutterer, T.J. Burns, Journal of Manufacturing Science and Engineering 124(2), 217-225 (2002).
[3] Bayly, P. V., Halley, J. E., Mann, B. P., Davies, M. A., *Journal of Manufacturing Science and Engineering*, 125, 220-225 (2003).
[4] Insperger, T., Stépán, G., *Journal of Manufacturing Science and Engineering*, in press (2004).
[5] B. Balachandran, Philosophical Transactions of the Royal Society 359, 793-820 (2001).
[6] Insperger, T., Stépán, G., *Proceedings of The Royal Society, Mathematical, Physical and Engineering Sciences*, 458, 1989-1998 (2002).

The effect of smoothing on bifurcation and chaos computations in non-smooth mechanics

S.J. Hogan
University of Bristol

January 9, 2004

In rigid body mechanics involving impacts, backlash or friction, mathematical models of these phenomena involve functions that are discontinuous. These non-smooth mechanical systems have been the subject of considerable interest of late. The review [1] is an excellent introduction to this field. See also [2].

These systems can be described by a set of equations of the form

$$\dot{x} = f(x, t, \mu) \tag{1}$$

where t is time, $x \in \mathbb{R}^n$ is a state vector, $f : \mathbb{R}^{n+1} \to \mathbb{R}^n$ is a non-smooth function and $\mu \in \mathbb{R}^p$ is a vector of parameters. Systems can be autonomous or non-autonomous. The function f is smooth in countably many (finite or infinite) regions of phase space, but can have a different functional form in each region.

Not only are these systems of significant importance to engineers but also they present difficult challenges to mathematicians. *Border-collision* or C-bifurcations occur when the system steady state (or Ω limit set) intersects a region boundary under parameter variation. See [3] for a further details.

When numerical computations of the governing equations are carried out, especially when detection of bifurcation or chaos is important, a smoothed version of the dynamics is often used.

For example the step function $S(x)$ defined by

$$S(x) = \begin{cases} 1 & \text{when } x > 0, \\ 0 & \text{when } x = 0, \\ -1 & \text{when } x < 0. \end{cases} \tag{2}$$

occurs frequently in this context and can be approximated by $S(x) = \tanh Kx$. The error in this approximation decreases as $K \to \infty$. The dynamics that persist in this limit are taken (numerically at least) to be those that are present when (2) is the chosen form for $S(x)$.

In this paper we show how smoothing always introduces spurious solutions into some part of parameter space. We also show how the location of the

bifurcation point itself varies according the way in which the smoothing is carried out. In particular we show how to correct for this variation.

We take the simple generic example treated in [3]

$$x^{n+1} = \begin{cases} \alpha x^n - \mu, & x^n > 0 \\ \beta x^n - \mu, & x^n < 0 \end{cases} \tag{3}$$

where for definiteness we take $\alpha > 0$ and $\beta < 0$.

We replace (3) with

$$x^{n+1} = \frac{1}{2} x^n [(\alpha + \beta) + (\alpha - \beta) \tanh K x^n] - \mu \tag{4}$$

which tends to (3) as $K \to \infty$.

Fixed points x^* of (4) now satisfy

$$\frac{\mu}{x^*} = [\frac{1}{2}(\alpha + \beta) - 1] + \frac{1}{2}(\alpha - \beta) \tanh K x^* \tag{5}$$

Graphical means are then used to show that (5) always has two extra roots in some part of parameter space when K is finite. These spurious solutions are not part of the original dynamics of the non-smooth system.

The tanh function in (4) is then expanded as a Taylor series and the bifurcation points determined analytically for small K. These are given by

$$x^* = (\beta - \alpha - 2)/2K(\alpha + \beta) \tag{6}$$

These differ from zero for all finite K. This error can be corrected for by replacing (4) by

$$x^{n+1} = \frac{1}{2} x^n [(\alpha + \beta) + (\alpha - \beta) \tanh K(x^n - x_0)] - \mu \tag{7}$$

for a suitable choice of x_0.

Finally we conclude by showing how different border-collision or C-bifurcations are different limits of smooth bifurcations. This is done by computing the bifurcation diagrams for (7) for different (fixed) values of α, β and varying K. The particular type of bifurcation found at these values of α, β is then shown to be the limit of a smooth bifurcation sequence for finite K.

References

[1] Popp, K. *Non-smooth mechanical systems* J. Appl. Math. Mech., **64**, 2000, 765–772.

[2] Babitsky, V.I. and Krupenin, V.L. *Vibrations of Strongly Nonlinear Systems* Springer Verlag, Berlin, 2001.

[3] Di Bernardo, M., Feigin, M., Hogan, S.J. and Homer, M.E. *Local analysis of C-bifurcations in n-dimensional piecewise smooth dynamical systems* Chaos, Solitons and Fractals **10**, 1999, 1881–1908.

ATTRACTOR AND PATTERN CONTROL IN NONLINEAR MEDIA BY LOCALIZED DEFECTS

S. Vakulenko*, B. Kazmierczak**
*Institute for Mechanical Engineering Problems, Academy of Sciences, Saint-Petersburg, Russia
**Institute of Fundamental Technological Research, Polish Academy of Sciences, Warsaw, Poland

Summary We consider pattern and attractor control in nonlinear dissipative systems. We develop an analytic approach to attractor control for neural, genetic networks systems of coupled oscillators and spatially extended systems. In particular, we apply this method for some systems of Ginzburg-Landau's type and others.

1. Introduction. In the last decade, a great attention has been given to chaos existence [1,18], pattern formation and control. Complicated patterns and large time behaviour can be observed in mechanics, chemistry, biology, physics (liquid crystals, magnetic thin films, Langmuir monolayers, polymers [2, 3]).

We propose new methods for pattern control in continuous and discrete nonlinear dissipative media. We first describe an analytic theory of the attractor and pattern control for the Hopfield neural networks. Basing on it, we then obtain algorithms of pattern and attractor control for many mechanical, physical and biological systems. In particular, we consider systems of Ginzburg-Landau's type, genetic networks, and some hydrodynamical models.

2. Attractor control for neural networks

Consider the Hopfield system (a basic model for so-called attractor neural networks)

$$\frac{dq_i}{dt} = \sigma(\sum_{j=1}^{m} K_{ij}q_j - \eta_i) - cq_i, \tag{2.1}$$

where m is the number of neurons, the matrix K_{ij} defines the interaction between neurons, $c > 0$ is a constant, and η_i are thresholds. The functions $q_i(t)$ define neuron states. The main result is given by the following theorem [4,5]:

Theorem . *Suppose a system of n ordinary differential equations has a structurally stable invariant set $\mathcal{A}$. Then, for any n, parameters m, K, η, c can be adjusted in such a way that system (2.1) will have an invariant set $\mathcal{A}'$ topologically equivalent to $\mathcal{A}$. Dynamics of (2.1) restricted to $\mathcal{A}'$ is orbitally topologically equivalent to the given dynamics on $\mathcal{A}$. If $\mathcal{A}$ is an attractor, then $\mathcal{A}'$ also is an attractor for (2.1).*

This yields that any hyperbolic chaos (studied by works of S. Smale, D. Ruelle and R. Takens, D. V. Anosov et al., see [1,18]) can appear in the Hopfield dynamics. In particular, there are possible a complicated time behaviour connected with transverse homoclinic orbits. Structural stability means that, topologically, dymamics on invariant set persists under small C^1 perturbations (hyperbolic sets possess this property).

Moreover, the neurons form complicated coherent patterns. There are $n << m$ "leading" neurons (for instance, $q_1, ..., q_n$). The dynamics of the remaining ones is completely captured by these leading neurons. Namely, $q_i = \sum_{j=1}^{n} B_{ij}q_j$, where $i > n$ and $\mathbf{B}$ is some matrix. Similar results hold for networks with discrete time [6].

The proof is constructive and gives a method for the attractor control. It is based on multilayered and wavelet approximations. Notice that if $\mathcal{A}$ is the global attractor of a prescribed system of n differential equations, the paramaters in (2.1) can be found in such a way that $\mathcal{A}'$ will the global attractor of (2.1) as well. In a sense, we can "prescribe" dynamics (2.1) (locally, or globally).

If we remove the condition of structural stability, we can control families of trajectories of eq. (2.1) on large (but bounded) time intervals $[0, T]$, where T can be chosen arbitrarily. In this case the parameters in (2.1) depend on T and $m \to \infty$ as $T\infty$.

3. Attractor and pattern control for spatially extended systems.

These results are also useful in finding of other coupled oscillator and spatially extended systems with complicated large time behaviour.

We show that Theorem can be extended to a large class of coupled oscillator systems. We demonstrate that eq. (2.1) can serve as a normal form describing small oscillations at fixed points for many such systems.

It allows us to find an analytical approach on dynamics control for a number of important systems (however, it is necessary to note, that in contrast to (2.1), in general we cannot control the global attractor completely, i.e., we can control only small oscillations at some equilibrium states).

Consider now systems of partial differential equations describing nonlinear dissipative continuous media. Basic ideas are as follows. For such systems a complex behaviour is often generated by interface motion (for reaction-diffusion models) or vortex movement (for hydrodynamical models). We apply the following approach: motion of localized modes (interfaces, vortices etc.) can be effectively controlled by well localized inhomogeneities. The localized modes approach the space defects (pinning effect) and interact with other modes through these defects. This interaction is nonlocal (similarly to (2.1)) and can be described by coupled oscillator systems admitting chaotic behaviour. In this approach, the important mathematical tool is so-called method of realization of vector fields [17].

We have found many important systems, where complicated patterns or chaotic attractors exist and where these attractors and patterns are controllable by system parameters.

The first important example is given by genetic networks. These systems are intensively studied [12-16]. We have considered the model proposed by [16] since this model is similar to the Hopfield equations (2.1).

It can be shown analytically that this model are capable to generate any spatio-temporal patterns [9, 10]. Moreover, there is an numerically effective algorithm allowing us to adjust a gene interaction producing a given pattern. So, genes are capable to produce any time sequences of any space structures.

Another example is two dimensional system of Ginzburg-Landau's type [5,7,8]:

$$u_t = \epsilon^2 u - u^3 + a(x,y)u + b(x,y)v, \tag{3.1}$$

$$v_t = \Delta v - c^2 v + g(x,y)u. \tag{3.2}$$

We consider this system in a two-dimensional rectangle under zero Neumann conditions. Here control parameters are small inhomogeneities a, b and g and ϵ. For this problem our approach essentially uses ideas of [2,3]. The coefficients a, b and g can be found as sums of well localized peaks. The pattern is formed by a number of interfaces (kinks) parallel to y with coordinates $q_i(t), i = 1, ..., m$ depending on time. This solution describes multilayered patterns (which is well studied for the case $a, b, g = const$ [2,3]).

For interface coordinates one obtains a system of differential equations, which is a small perturbation of (2.1) for small ϵ and appropriate functions a, b and g. The matrix K and coefficients η_i depend on a, b and g. Changing these inhomogeneities we can obtain any parameters K, η. It allows us to show that there is possible a complicated large time behaviour [5] (but, for each time moment, the spatial structure is simple: it is always a multilayered pattern).

We have considered three component generalizations of system (3.1), (3.2) [8]. Numerical and asymptotical calculations show existence of more complicated space patterns.

Recently we have extended this method to vortex motion in two-dimensional hydrodynamical systems. We have found a linear feedback boundary control for two-dimensional vortex motion. These boundary control uses a permeable wall following ideas [11].

References

1. S. Smale, Mathematics of Time , Springer, New-York. 1980.

2. D. M. Petrich and R. E. Goldstein, Phys. Rev. Lett. **72**, (1994) 1120-1123

3.T. Ohta and D. Jasnov, Phys. Rev. E **56**, (1997) 5648.

4. S. Vakoulenko, *Complexité dynamique de reseaux de Hopfield*, C. R. Acad. Sci. Paris Sér. I Math., **335**, (2002) 639-642

5. S. A. Vakulenko, *Dissipative systems generating any structurally stable chaos*, Adv. Differential Equations, **5**, (2000), 1139-1177.

6. P. V. Gordon and S. A. Vakulenko, *Neural networks with prescribed large time behaviour*, J. Phys. A: Math and Gen, **31** (1998), 9555-9570.

7. S. A. Vakulenko, *Reaction-diffusion systems with prescribed large time behaviour*, Ann. Inst. H. Poincaré **66** (1997), 373-410.

8. B. Kazmierczak, S. Genieys, and S. A. Vakulenko, *Pattern formation capacity of spatially extended systems*, Phys. Review E, in print.

9. D. Grigoriev and S. A. Vakulenko, *Complexity of patterns generated by genetic circuits and Pfaffian functions* , Prepint of IHES, 2003.

10. S. Vakulenko and D. Grigoriev, *Complexity of gene circuits, Pfaffian functions and morphogenesis problem*, C. R. Acad. Sci. Paris Sér. I, **337** (2003), 721-724

11. R. Temam and X. Wang, *Remarks on the Prandtl equation for a permeable wall. Special issue on the occasion of the 125 th anniversary of the birth of Ludwig Prandtl* ZAMM Z. Angew. Math. Mech. **80**, (2000), no. 11-12, 835-843.

12. L. Glass and S. Kauffman, The logical analysis of continuous, nonlinear biochemical control networks, J. Theor. Biology, **34**, (1973), 103-129.

13. D. Thieffry and R. Thomas, Dynamical behaviour of biological regulatory networks, II.Immunity control in bacteriophage lambda, Bull. Math. Biology, **57**, (1995) 277-295.

14. R. Edwards, T.H. Siegelmann, K.Aziza and L. Glass, Symbolic dynamics and computation in model gene networks, Chaos, **11** , (2001) 160-169.

15. P. Smolen, D. Baxter, J. H. Byrne, Mathematical modelling of gene networks, Review in Neuron, **25**, (2000) 247-292.

16. E. Mjolness,D. H. Sharp and J. Reinitz, A connectionist Model of Development, J. Theor. Biol. **152**, (1991) 429-453.

17. P.Polácik, High-dimensional ω-limit sets and chaos in scalar parabolic equations, J. Diff. Equations, **119** (1), (1995), 24-53.

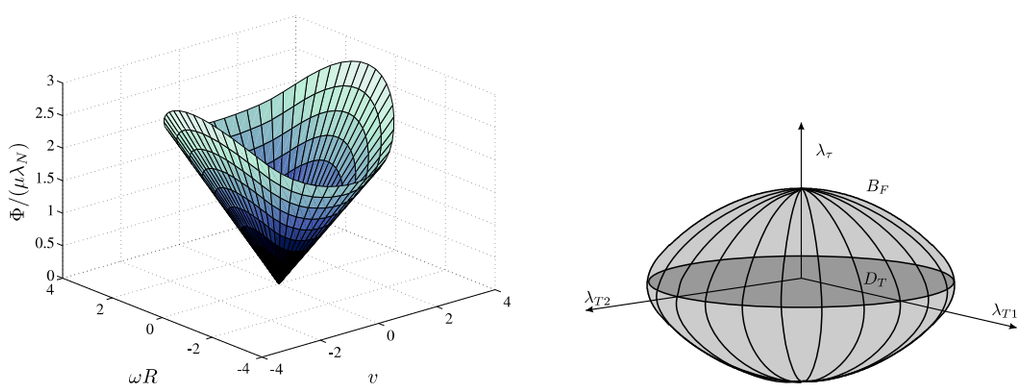
18. S. Wiggins, Global Bifurcations and Chaos, Spinger, New-York (1988).

A SET-VALUED FORCE LAW FOR SPATIAL COULOMB-CONTENSOU FRICTION

Remco I. Leine Christoph Glocker

Institute of Mechanical Systems,
Center of Mechanics, ETH Zentrum,
CH-8092 Zürich, Switzerland,
remco.leine@imes.mavt.ethz.ch
christoph.glocker@imes.mavt.ethz.ch

The aim of this paper is to develop a contact law for combined spatial Coulomb friction and normal friction torque (drilling friction) as a function of sliding velocity and spin. We will call this extended contact law the Coulomb-Contensou friction law. The Contensou phenomenon occurs for instance in an electric polishing machine with turning brushes used to clean floors. The machine is hard to move when the brushes are non-rotating (Coulomb friction) but the machine can easily be pushed over the floor with rotating brushes (Contensou phenomenon).



(a) Cone of the velocity potential.

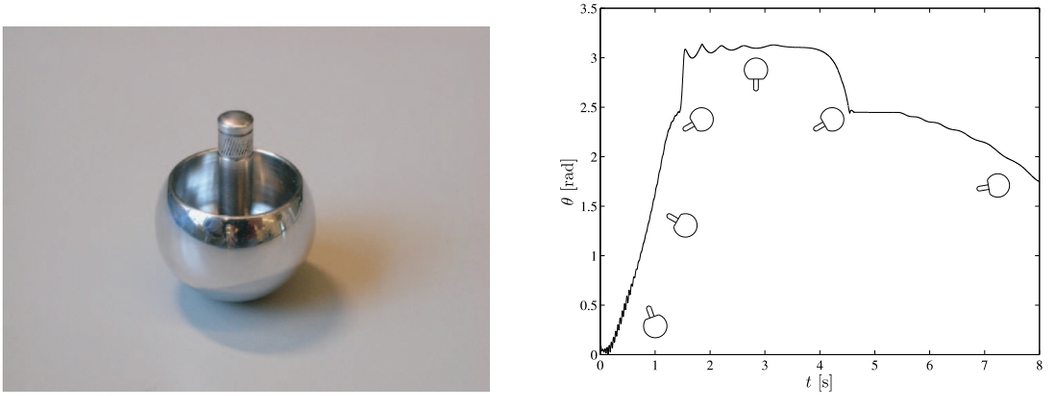
(b) Friction ball B_F.

Figure 1: The velocity potential Φ and set of admissible contact forces and torque B_F.

The Coulomb-Contensou friction law shows a continuous behaviour for non-zero sliding velocity and spin and a set-valued behaviour for zero sliding velocity and spin (stick). Coulomb's friction law is generally formulated as a set-valued force law within a framework of convex analysis [1, 3]. The formulation of frictional contact problems of mechanical rigid multi-body systems with set-valued contact laws leads to a nonlinear algebraic inclusion, which is complicated to solve. The first (and often worst) method is to regularize the set-valued force laws and obtain a stiff problem with an inexact solution. Instead, one simply has to accept the set-valued nature of the problem and deal with the nonlinear algebraic inclusion. The present study formulates the contact problem for spatial Coulomb-Contensou friction in the framework of potential theory and convex analysis [2]. The velocity potential Φ for Coulomb-Contensou friction has been derived as function of the sliding

speed v and the angular rotation speed ω and is shown in Figure 1a. The set-valued force law can be derived from the non-smooth velocity potential Φ. The set of admissible friction forces and normal friction torque is depicted in Figure 1b.

The theory and numerical methods are applied to the Tippe-Top, a toy top which inverts its orientation when spun fastly (see Figure 2). The gyroscopical moment which inverts the orientation of the top is friction induced. The analysis and numerical results on the Tippe-Top illustrate the importance of Coulomb-Contensou friction for the dynamics of systems with friction.



(a) The top in steel.

(b) Inclination

Figure 2: The Tippe-Top

References

[1] Ch. Glocker. *Set-Valued Force Laws, Dynamics of Non-Smooth Systems*, volume 1 of *Lecture Notes in Applied Mechanics*. Springer-Verlag, Berlin, 2001.

[2] R. I. Leine and Ch. Glocker. A set-valued force law for spatial Coulomb–Contensou friction. *European Journal of Mechanics – A/Solids*, 22:193–216, 2003.

[3] R. I. Leine, Ch. Glocker, and D. H. Van Campen. Nonlinear dynamics of the woodpecker toy. *Proceedings of DETC 2001 ASME Symposium on Nonlinear Dynamics and Control In Engineering Systems*, September 9-12 2001. Pittsburgh, CD-ROM, DETC2001/VIB-21608.

CHAOTIC ATTRACTORS WITH LONG REGULAR SEQUENCES

Ugo Galvanetto*
* *Department of Aeronautics, Imperial College London, South Kensington Campus*
London SW7 2AZ – UK

Summary This paper presents examples of chaotic motions in non-smooth mechanical systems affected by dry friction. The chaotic attractors are composed of zones characterized by very different rates of divergence of nearby orbits. The mechanical system generates one-dimensional maps the orbits of which seem to exhibit sensitive dependence on initial conditions only in an extremely small set of their field of definition. The Lyapunov exponent of the map is computed to characterise the steady state motions.

INTRODUCTION

Chaotic motions are characterised by sensitive dependence on initial conditions, that means that nearby orbits belonging to a chaotic attractor (and corresponding to nearly identical states) will soon behave differently [1]. Rates of divergence or convergence of nearby orbits are different in different zones of an attractor. Lyapunov exponents are a quantitative measure of the *average* exponential rates; they give information on the whole attractor and therefore do not provide any clear information on the zones where divergence rates are higher or lower. This paper aims at presenting an example of chaotic attractor in which it is possible to clearly identify distinct zones with different divergence properties. The idea of distinguishing zones in chaotic attractors with different divergence properties is not commonly pursued in the scientific literature and represents an element of novelty of the present paper.
The dynamical system under investigation is a mechanical system subjected to elastic and dry friction forces which exhibits many features typical of non-smooth dynamical systems as chaotic motions, non-smooth transitions and non-smooth bifurcations [2, 3].

THE MECHANICAL SYSTEM AND ITS MAP

The mechanical system

The mechanical system investigated in this paper is shown in figure 1. It is composed of two blocks supported by a belt which moves with constant velocity V_{dr}. Elastic springs couple the blocks and connect them to a fixed support. Dry friction forces act between the blocks and the belt and they can be static, when the blocks ride on the belt, or kinetic, when the blocks slip with respect to the belt. The kinetic friction characteristic F_k is assumed to be a continuous, single-valued decreasing function of the velocity of the block relative to the belt [3]:

$$F_k(\dot{X}-V_{dr}) = \begin{cases} \dfrac{F_s}{1-\gamma(\dot{X}-V_{dr})} & \text{if } V_{dr} > \dot{X} \\ -\dfrac{F_s}{1+\gamma(\dot{X}-V_{dr})} & \text{if } V_{dr} < \dot{X} \end{cases}$$

Where F_s, the maximum static friction force, is unity for block 1 and 0.9 for block 2. The blocks have the same mass but the system is not symmetric because of the difference in the maximum static friction forces. The following parameters completely define the mechanical system: m=1, k=1, k_{12}=1.2, γ=3.0, $V_{dr}=10^{-7}$.

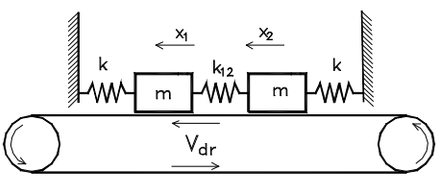


Figure 1

One-dimensional map

The 2-block stick-slip system of figure 1 can generate a one-dimensional map [3]. When both blocks are riding on the belt (such a phase of motion will be called global stick phase, g.s.p.) the relative displacement between the two blocks is fixed; therefore the g.s.p.'s of the system may be characterised by the constant value of a variable d:

$$d=X_2-X_1$$

The g.s.p. will finish where one of the two blocks starts slipping. Then the motion of the slipping block may trigger a new slipping phase also for the other block but eventually, if V_{dr} is sufficiently small, both blocks will reach a configuration in which they ride simultaneously on the belt. The new g.s.p., in general, will be characterised by a value of the relative displacement d different from the one assumed during the previous g.s.p. In this way a motion of the system generates an infinite sequence of values of the variable $d=d_1, d_2, d_3, \ldots$, which can be interpreted as a map expressing d_{k+1} as a function of d_k:

$$d_{k+1}=f(d_k)$$

The 1-dimensional map is single valued because a given value of the variable d univocally determines the initial conditions at which one of the blocks will start slipping. The one-dimensional map will be used to describe in a compact way the dynamics of the two-block model; in particular it will be used to compute the main Lyapunov exponent of the system according to [4].

RESULTS

Figure 2 shows a portion of the 1-d map generated by the system of figure 1 and two enlarged views. Note that the scales of the figures are different so that the main properties of the maps can be appreciated. A considerable portion of the map seems to be parallel to the line $d_{k+1}=d_k$ and very close to it. When the orbit of the map is captured within that region, figure 2 – enlarged view 'a', a large number of 'regular' iterations of the map takes place. This sequence of regular iterations is interrupted when the orbit of the map reaches the zone where the slope of the map changes suddenly and in a discontinuous way ('chaotic' zone), figure 2 – enlarged view 'b'. Then in a very small number of iterations the orbit is pushed back in the 'regular' zone. The attractor is therefore composed of two qualitatively different zones: a 'regular zone', the branch 'parallel' to the line $d_{k+1}=d_k$, where neighbouring orbits do not separate with high rate, and a 'chaotic zone', the branch with steep slopes, which separates nearby orbits and send them back in different positions of the 'regular zone'. Note that, in the enlarged view 'b', the horizontal scale is magnified by 100 and the almost horizontal branch to the right is the most left part of the 'regular zone'.
The dynamics of the map, and therefore of the underlying mechanical system, can be characterised by the Lyapunov exponent of the 1-d map [4]:

$$\lambda = \lim_{k\to\infty} \frac{1}{k} \Sigma \log \left| f'(d_k) \right|$$

where $f'(d_k)$ is the derivative of the map, that can be approximately computed with suitable finite difference techniques. The limit in the above expression can be evaluated by integrating the dynamics of the map for a very large number of iterations [4]. Figure 3 shows how the numerical computation of the Lyapunov exponent 'converges' to a value bigger than zero. The enlarged view of figure 3 shows that the diagram of the value of the exponent versus the number of iterations has a saw-tooth shape due to the alternate occurrence of 'regular' and 'chaotic' zones. Therefore the computation of the Lyapunov exponent confirms the idea that of an attractor composed of zones characterised by clearly different dynamic behaviours. Several algorithmic parameters affect the computed value of the Lyapunov exponent which, in the range between 400000 and 1 million iterations, fluctuates between 0.0022 and 0.0028.

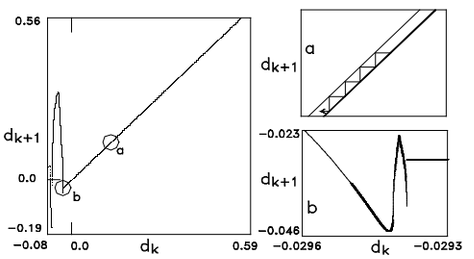


Figure 2

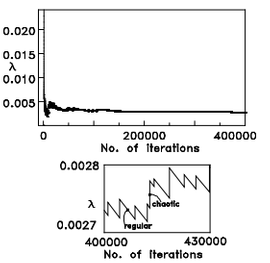


Figure 3

CONCLUSIONS

This paper describes a chaotic attractor in which the zone of high divergence rate of nearby orbits (chaotic zone) is clearly distinct from another zone in which the divergence rate is much lower (regular zone). In the regular zone the dynamics of the system is composed of long sequences of similar iterations whereas an orbit can only stay in the chaotic zone for a small number of iterations. The numerical calculation of the Lyapunov exponent confirms that the motion is composed of long regular phases interrupted by short chaotic phases. Some caution has to be used when examining the numerical results.

References

[1] Wolf A., Swift J.B., Swinney H.L., Vastano J.A.: Determining Lyapunov exponents from a time series. *PhysicaD*, **16**: 285-317, 1985.
[2] di Bernardo M., Kowalczyk P., Nordmark A.: Classification of sliding bifurcations in dry-friction oscillators. To be published *J. Bif. Chaos.*
[3] Galvanetto U.: Sliding bifurcations in the dynamics of mechanical systems with dry friction. To be published *J. Sound Vib.*
[4] Galvanetto U.: Numerical computation of Lyapunov exponents in discontinuous maps implicitly defined. *Comp. Phys. Comm.*, **131**: 1-9, 2000.

REDUCTION OF MULTIDIMENSIONAL FLOW TO LOW DIMENSIONAL MAP FOR PIECEWISE SMOOTH SYSTEM EXPERIENCING CHAOS

Ekaterina E. Pavlovskaia and Marian Wiercigroch
Centre for Applied Dynamics Research School of Engineering and Physical Sciences, University of Aberdeen King's College, Aberdeen AB24 3UE, UK

Summary We consider dynamics of the piecewise smooth nonlinear systems for which general methodology of reducing multidimensional flows to low dimensional maps is proposed. This includes creation of the global map by stitching together local maps, which are constructed in the smooth sub-regions of phase space. Full details are given for a case study of drifting impact oscillator where five-dimensional flow is reduced to one dimensional (1D) approximate map. An appropriate co-ordinate transformation allowed the drift to be de-coupled from the bounded system oscillations. For these oscillations an exact two-dimensional map has been formulated and analysed. A further reduction to 1D approximate map is possible and will be discussed in the lecture. A standard nonlinear dynamic analysis reveals a complex behaviour ranging from periodic oscillations to chaos, and co-existence of multiple attractors. Accuracy of the constructed maps by comparing the dynamics responses with the exact solutions for a wide range of system parameters will be examined.

MULTIDIMENSIONAL FLOWS

Dynamics of vast majority of physical systems can be defined as multi-dimensional flows. If these flows are described by linear differential equations there are well developed mathematical theories, which can provide analytical solutions. However, a good deal of multi-dimensional flows is governed by nonlinear differential equations and, in particular, piecewise smooth differential equations, which naturally brings complications in providing effective solutions. For example the engineering systems with online control require simple robust models. One way of obtaining them is reduction of differential flows to iterative maps obviously if such transformation is feasible. In the published literature there is practically no systematic examples how such maps are built, therefore, in this article a sketch of such process is provided for an impact oscillator with drift.

We consider a drifting oscillator [1], where a mass is driven by an external force containing static and dynamic components. The weightless slider has a linear visco-elastic pair. As reported in [1, 2] the slider drifts in stick-slip phases where the relative oscillations between the mass and the slider are bounded and range from periodic to chaotic. The progressive motion of the mass occurs when the force acting on the slider exceeds the threshold of the dry friction force. $x,\ z,\ v$ represent the absolute displacements of the mass, slider top and slider bottom, respectively. It is assumed that the model operates horizontally, or the gravitational force is appropriately compensated. At the initial moment $\tau = 0$ there is a distance between the mass and the slider top called gap, e.

The considered system operates at the time in one of the following modes: *No contact*, *Contact without progression*, and *Contact with progression*. A detailed consideration of these modes and the dimensional form of equations of motion can be found in [1, 3]. As it was reported in [2] by introducing a new system of co-ordinates (p, q, v) instead of (x, z, v):

$$p = x - v, \quad q = z - v, \tag{1}$$

it is possible to separate the oscillatory motion from the drift. In fact, in the new co-ordinates system p and q are displacements of the mass and the slider top relative to the current position of the slider bottom v. The phase space of the bounded system is shown in Figure 1(a). During *No contact* mode trajectory of the system lies in vicinity of the horizontal plane and during *Contact without progression* and *Contact with progression* modes it belongs to the inclined plane. The borders of the different modes are represented by lines $\Sigma_1 - \Sigma_4$. Equations of motion for this system are given below:

$$\begin{aligned} p' &= y(1-\mathcal{H}_3) - \frac{1}{2\xi}(q-1)\mathcal{H}_1\mathcal{H}_3\mathcal{H}_4 \\ y' &= a\cos(\omega\tau+\varphi) + b - (2\xi y+q)\mathcal{H}_1\mathcal{H}_2(1-\mathcal{H}_3) - \mathcal{H}_1\mathcal{H}_3\mathcal{H}_4 \\ q' &= y\mathcal{H}_1\mathcal{H}_2(1-\mathcal{H}_3) - \frac{1}{2\xi}(q-1)\mathcal{H}_1\mathcal{H}_3\mathcal{H}_4 - \frac{1}{2\xi}q(1-\mathcal{H}_1) \\ \text{where} \quad & \mathcal{H}_1 = H(p-q-e), \quad \mathcal{H}_2 = H(2\xi y+q), \quad \mathcal{H}_3 = H(2\xi+q-1), \quad \mathcal{H}_4 = H(y). \end{aligned} \tag{2}$$

Here $H(\cdot)$ is Heaviside step function, y is the velocity of the mass, 2ξ is a damping ratio of the slider, $a\cos(\omega\tau+\varphi)$ is the dynamic and b is the static components of the external force. During *No contact* and *Contact without progression* phases the slider bottom remains stationary, $v' = 0$, and during *Contact with progression* phase it moves with velocity $v' = y + \frac{1}{2\xi}(q-1)$.

The equations of motion are linear for each phase, therefore the global solution can be constructed by joining the local solutions at the points of discontinuities. The set of initial values $(\tau_0; p_0, y_0, q_0)$ defines in which phase the system will operate. If $p_0 < q_0 + e$, it will be *No contact* phase. For $p_0 = q_0 + e$, it will be *Contact without progression* phase if $0 < 2\xi y_0 + q_0 < 1$ or *Contact with progression* phase if $2\xi y_0 + q_0 \geq 1$. When the conditions corresponding to the

current phase fail, the next phase begins, and the final displacements and velocities for the preceding phase define the initial conditions for the next one. All details of the semi-analytical method allowing to calculate the responses of the system using this method are given in [2].

LOW DIMENSIONAL MAPS

The four dimensional flow $(\tau; p, y, q)$ can be locally three dimensional (during contact phases $p = q + e$). The cross-sections of the flow with the phase borders allows to formulate two dimensional discrete map. The borders of the different modes of the system shown in Figure 1(a) are given as:

$$\begin{aligned}
\Sigma_1 &= \{(\tau_i; p_i, y_i, q_i) |\ p_i = e,\ y_i > 0,\ q_i = 0\} \\
\Sigma_2 &= \{(\tau_i; p_i, y_i, q_i) |\ p_i = 1 + e - 2\xi y_i,\ y_i > 0,\ q_i = 1 - 2\xi y_i\} \\
\Sigma_3 &= \{(\tau_i; p_i, y_i, q_i) |\ p_i = 1 + e - 2\xi y_i,\ y_i < 0,\ q_i = 1 - 2\xi y_i\} \\
\Sigma_4 &= \{(\tau_i; p_i, y_i, q_i) |\ p_i = e - 2\xi y_i,\ y_i < 0,\ q_i = -2\xi y_i\}
\end{aligned} \tag{3}$$

Based on the four subspaces (3), six local maps shown in Figure 1(a) can be defined as follows:

$$\mathbf{P}_1 :\ \Sigma_1 \to \Sigma_2, \quad \mathbf{P}_2 :\ \Sigma_2 \to \Sigma_3, \quad \mathbf{P}_3 :\ \Sigma_3 \to \Sigma_4, \quad \mathbf{P}_4 :\ \Sigma_4 \to \Sigma_1, \quad \mathbf{P}_5 :\ \Sigma_1 \to \Sigma_4, \quad \mathbf{P}_6 :\ \Sigma_3 \to \Sigma_2.$$

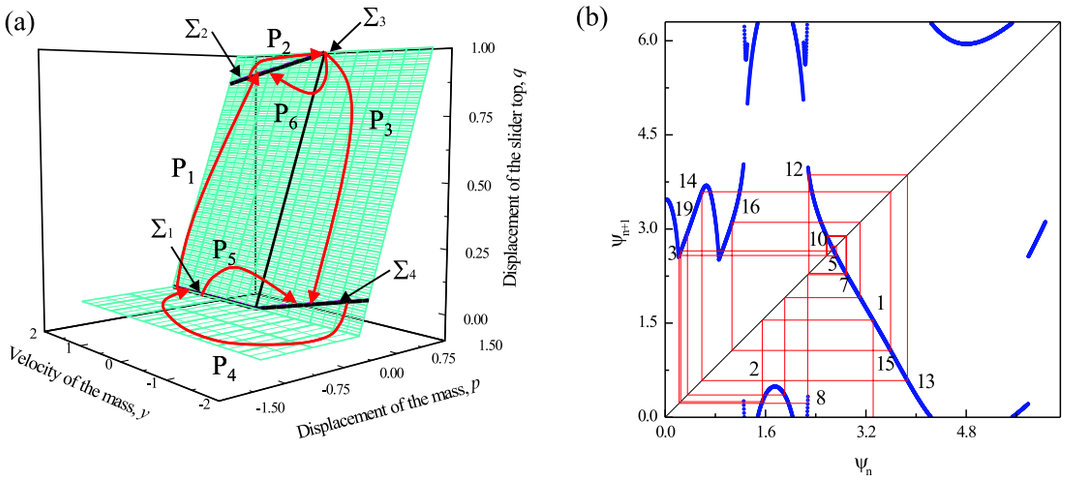


Figure 1. (a) Local mappings in three dimensional phase space; (b) iteration of the approximate one dimensional map experiencing chaos for $a = 0.3,\ b = 0.08,\ \xi = 0.01,\ \omega = 0.1,\ \varphi = 0,\ e = 0.02$.

At the beginning of the *Contact with progression* phase four dimensional flow crosses the line Σ_2 and system dynamics can be monitored using global two dimensional map $\mathbf{P} :\ \Sigma_2 \to \Sigma_2$ which maps velocity and angular displacement ($\psi = \omega\tau + \varphi$) at the beginning of the *Contact with progression* phase to themselves, $(y_{n+1}, \psi_{n+1}) = \mathbf{P}(y_n, \psi_n)$ [4]. Map $\mathbf{P}$ is unknown composition of the local maps, e.g it can be equal to $\mathbf{P} = \mathbf{P}_1 \circ \mathbf{P}_4 \circ \mathbf{P}_3 \circ \mathbf{P}_2$ or $\mathbf{P} = \mathbf{P}_6$ or $\mathbf{P} = \mathbf{P}_1 \circ \mathbf{P}_4 \circ \mathbf{P}_5 \circ \mathbf{P}_4 \circ \mathbf{P}_3 \circ \mathbf{P}_2$. For the periodic external force the introduced two dimensional map is defined in the bounded region $\psi_n \in (0, 2\pi),\ \ y_n \in (0, y^{max})$ and it can be calculated numerically [4].

The detailed analysis of the considered system reveals that a further reduction to 1D approximate map is possible. It has been found that the actual positions of the system at the end of the *Contact with progression* phase (points belonging to the subspace Σ_3) are very close to the points $\tilde{\Sigma}_3 = \{(\tau_i; p_i, y_i, q_i) |\ p_i = 1 + e,\ y_i = 0,\ q_i = 1\}$. In this case the approximate one dimensional map $\mathcal{F} :\ \tilde{\Sigma}_3 \to \tilde{\Sigma}_3$ can be introduced. The iteration of the proposed 1D approximate map for chaotic regime is shown in Figure 1(b).

References

[1] E. Pavlovskaia, M. Wiercigroch, and C. Grebogi: Modeling of an impact system with a drift, *Phys. Rev. E* **64**: 056224, 2001.

[2] E. Pavlovskaia and M. Wiercigroch: Analytical drift reconstruction for impact oscillator with drift, *Chaos, Solitons and Fractals* **19**: 151-161, 2004.

[3] E.E. Pavlovskaia and M. Wiercigroch, "Periodic solutions finder for vibro-impact oscillator with a drift", Journal of Sound and Vibration **267**, 893-911 (2003).

[4] E. Pavlovskaia and M. Wiercigroch: Two dimensional map for impact oscillator with drift, submitted in 2003.

NUMERICAL DETECTION AND CONTINUATION OF SLIDING BIFURCATIONS IN A DRY-FRICTION OSCILLATOR

M. di Bernardo, P. Kowalczyk, P. Piiroinen
Department of Engineering Mathematics, University of Bristol, Bristol BS8 1TR, U.K.

Summary We will discuss a novel numerical method for the detection and continuation of codimension-1 sliding bifurcations of limit cycles in piecewise-smooth dynamical systems. A dry-friction oscillator is used as a representative example of relevance in applications.

INTRODUCTION

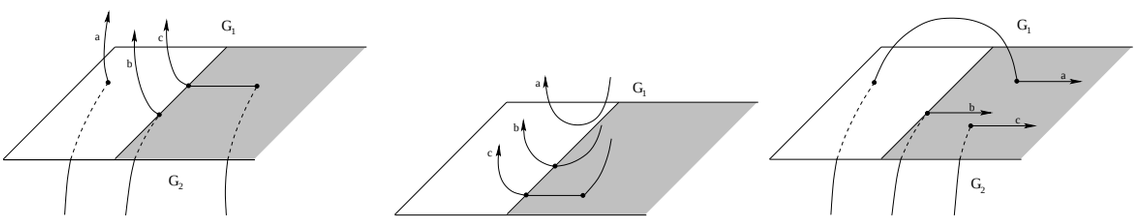
In this paper we focus our attention on numerical investigations of *sliding bifurcations* which are non-standard bifurcations intrinsic to systems modelled by a set of ordinary differential equations with discontinuous right hand side, which we can write as $\dot{x} = F_1(x, \mu)$ for $H(x) > 0$ and $\dot{x} = F_2(x, \mu)$ for $H(x) < 0$, where F_1, F_2 are sufficiently smooth vector functions and $H(x)$ is some scalar function depending on the system states. Such systems are known as *Filippov systems* [4, 7] and often model dry-friction oscillators. Discontinuous friction characteristics gives rise to a vector field which is discontinuous across some region in the phase space.

DRY-FRICTION OSCILLATOR

We focus our attention on a representative model of dry friction oscillator, which in the non-dimensionalised form can be written as

$$\ddot{x} + x = \sin(\omega t) - F\mathrm{sgn}(\dot{x}), \tag{1}$$

where x is the position, $\dot{x}$ the velocity, and t the time while ω and F respectively represent the frequency and the amplitude of the forcing term. The discontinuity set where the vector field switches between F_1 and F_2 in (1) is defined as $\Sigma := \{(x, \dot{x}, t) \in \mathbb{R}^3 : H(x, \dot{x}, t) = \dot{x} = 0\}$. An intriguing feature of Filippov systems is the possibility of exhibiting solutions evolving within Σ, termed as *sliding motion*. Sliding corresponds to a stick phase in the dry-friction oscillator dynamics of interest [6]. We can define a vector field, say F_s governing the stick phase of the system dynamics (sliding motion) using Utkin's equivalent control method [7]. This method also allows to determine a sliding subset, say $\hat{\Sigma}$ where the system dynamics is governed by the vector field F_s. Existence of the sliding subset $\hat{\Sigma}$ may qualitatively influence the system dynamics through the occurrence of sliding bifurcations. Sliding bifurcations are events due to the interaction of a system trajectory with the boundary of the sliding region. As shown in [3], there are four distinct codimension-1 sliding bifurcation scenarios of limit cycles namely: *crossing sliding* (Fig. 1(a)), *grazing sliding* (Fig. 1(b)), *switching sliding* (Fig. 1(c)) and *adding sliding* (not depicted). Sliding bifurcations can organise complex dynamics. For example in [1] it was shown that the grazing-sliding bifurcations scenario was responsible for the onset of chaotic stick-slip mode of motion in the dry-friction oscillator. Therefore, it is important to be able to detect and continue branches of sliding bifurcations. The theory allowing analysis of codimension-1 sliding bifurcations of limit cycles as well as of the so-called degenerate codimension-2 sliding bifurcation which are organising centres for branches of codimension-1 sliding bifurcations was developed recently in [2, 5]. However, there are no available numerical tools for general systems allowing for the detection and continuation of sliding bifurcations. In what follows, taking as an example the dry friction oscillator (1), we will present a novel numerical technique to allow the



(a) Crossing sliding (b) Grazing sliding (c) Switching sliding

Figure 1: Bifurcation scenarios depicting the interaction of a trajectory with the boundary of the sliding region when (a) bifurcating limit cycle switches between F_1 and F_2 vector fields at the bifurcation point, (b) one of the vector fields (F_1 or F_2) has a point of tangency with Σ at the boundary of $\hat{\Sigma}$ and (c) the vector field switches between F_1 or F_2 to F_s at the bifurcation point.

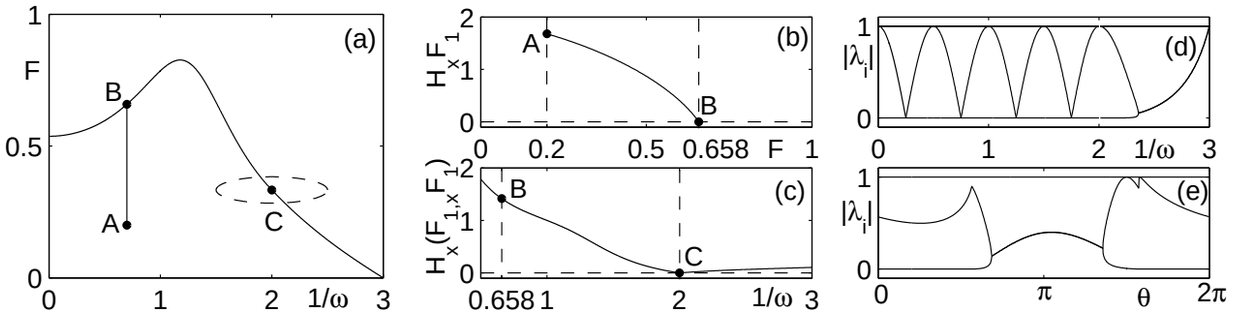


Figure 2: (a) A two-parameter bifurcation diagram. (b),(c) Analytical conditions for the detection of codimension-1 (b) and codimension-2 (c) sliding bifurcations under F and ω variations, respectively. (d),(e) The magnitude of the floquet multipliers λ_i along the codimension-1 branch (d) and along the ellipse (e) in Fig. 1(a).

detection and continuation of periodic orbits in systems with sliding, to follow branches of codimension-1 sliding bifurcations and to detect codimension-2 degenerate sliding bifurcations.

Briefly, the technique is based on the use of Newton's method to locate periodic orbits, for which the first variational equations are solved. Moreover, to account for the presence of switchings between different flows, local discontinuity mapping methods are used [8]. A pseudo-arclength strategy is used for the continuation of limit cycles in one or two parameters, which allows for continuation around fold points. Bifurcation detection is achieved through the set of analytical conditions for the occurrence of sliding bifurcations presented in [2, 5].

Fig. 2 shows some representative numerical results. Here, a periodic orbit located at the point 'A' in Fig. 2(a), characterised by crossing Σ twice per period outside of the sliding region, is continued in two-parameter space. By using the technique described above, a crossing-sliding bifurcation was successfully detected at $F = 0.658$ (see 'B' in Fig. 2(a)) when the analytical condition for its detection is found to be zero (see Fig. 2(b)).

The crossing-sliding bifurcation branch was then followed in two parameters (F and ω) while monitoring the analytical conditions for degenerate codimension-2 sliding bifurcations to occur. A codimension-2 bifurcation was then found numerically for the first time at the point 'C' in Fig. 2(a). (Fig. 2(c) shows the zero-crossing of the analyical condition characterising such bifurcation).

As expected from the analysis presented in [5] we were able to locate two additional codimension-1 bifurcations curves branching out from 'C' of which we continued the grazing-sliding bifurcation curve (see Fig. 2(a)). It was found that the numerics matches the analytical expectations as the bifurcationg limit cycle preserves its stability and period while crossing the codimension-1 bifurcation curves locally to the codimension-2 node. This was confirmed by computing Floquet multipliers of the periodic orbit along the elipse given by $(\frac{1}{\omega}, F) = (2 + 0.5\cos(\theta), \frac{1}{3} + 0.05\sin(\theta))$ around 'C' (see Fig. 2(a), (e)). Finally, we also present Floquet multipliers (see Fig. 2(d)) calculated along the codimension-1 curve in Fig. 2(a).

CONCLUSIONS

Novel numerical techniques were developed for the detection and continuation of codimension-1 sliding bifurcations of limit cycles and applied to investigate the dynamics of a representative dry-friction oscillator model. Branches of codimension-1 sliding bifurctaions were found and continued. Furthermore, a codimension-2 bifurcation node was found. The numerical results are found to match the analytical expectations.

References

[1] M. di Bernardo, P. Kowalczyk, and A. Nordmark. Explaining the onset of complex behaviour in dry-friction oscillators. *International Journal of Bifurcations and Chaos*, 13(10), 2003.

[2] M. di Bernardo, P.Kowalczyk, and A.Nordmark. Bifurcations of dynamical systems with sliding: derivation of normal form mappings. *Physica D*, 170:175–205, 2002.

[3] M. I. Feigin. *Forced Oscillations in systems with discontinuous nonlinearities.* Nauka, Moscow, 1994. In Russian.

[4] A. F. Filippov. *Differential equations with discontinuous right hand sides.* Kluwer, 3300 Dordrecht, The Netherlands, 1988.

[5] P. Kowalczyk and M. di Bernardo. Two–parameter sliding bifurcations of limit cycles in filippov systems. Submitted for publication to Physica D, June 2003.

[6] S. W. Shaw. On the dynamic response of a system with dry friction. *Journal of Sound and Vibration*, 108(2):305–325, 1986.

[7] V. I. Utkin. *Sliding Modes in Control Optimization.* Springer-Verlag, Berlin, 1992.

[8] H. Dankowicz and P. T. Piiroinen. Exploiting discontinuities for stabilization of recurrent motions. *Dynamical Systems*, 17:317–342, 2002.

ON GENERATING CHAOTIC DYNAMICS IN NOLINEAR VIBRATING SYSTEMS

Elżbieta Tyrkiel
IPPT PAN, Department of Dynamics of Complex Systems, PL 00-049 Warszawa, Poland

Summary The paper is aimed at demonstrating the mechanism triggering chaotic phenomena in nonlinear dynamical systems, i.e. the formation of nonattracting invariant chaotic sets (chaotic saddles), which originates from the global bifurcations. Characteristic examples of the resulting chaotic system behaviors, such as chaotic transient motions, fractal basin boundaries and an unpredictability of the final outcome, are shown and discussed. Numerical study is carried out for two low dimensional but representative models of nonlinear dissipative oscillators driven externally by periodic force.

INTRODUCTION

A central problem in nonlinear dynamics is that of discovering how the qualitative dynamical properties of regular solutions change and evolve as the dynamical system is continuously changed. It is known that nonlinear systems typically possess more than one solution at given values of control parameters, and that two or more solutions may be locally stable. In periodically forced oscillators, typical nonlinear resonance responses reveal various types of sudden changes (bifurcations) of coexisting stable periodic orbits, resulting in a qualitatively new state when forcing parameters are varied. However, there are the existing unstable solutions, which, although physically unrealizable, play decisive roles in the organization of the phase space of a dynamical system, and lead to sudden changes in system behavior that are not caused by local bifurcations. These changes belong to the category of global bifurcations and are typically triggered by tangencies, and further transversal intersections of the invariant manifolds associated with the unstable orbits [4,5]. With the sweep of the forcing parameter, it results in creating an uncountable nonattracting invariant set, called a chaotic saddle [1,2]. Mathematically, chaotic saddle is a closed, bounded invariant set having a dense orbit (i.e. including a Cantor set). It means that it possesses a chaotic trajectory that never leaves the phase-space region containing the set, while almost every trajectory leaves the region after some transient time, possibly reaching a remote attractor. In other words, all initial conditions except for a set of Lebesque measure zero leave the region. This type of dynamics is referred to as a horseshoe-type one, as it is similar to the "stretching and contracting" action of the prototypical two-dimensional horseshoe map possessing a hyperbolic invariant set [6,7]. Existence of a chaotic saddle is the source of complexity of the system dynamics (even in simple one-dimensional systems), as it generates sensitivity to initial conditions, and this implies chaotic responses.
Theoretically, the chaotic trajectory initialized exactly at the point belonging to a chaotic saddle will stay on this set for ever, wandering to and fro, but this situation is neither physically nor numerically realizable, due to round-off and the exponential growth in errors. In practice, the orbit can spend a possibly long time in the vicinity of the chaotic saddle before it leaves, thus producing chaotic transient motion. In a large class of oscillators with at least one maximum of potential energy, in certain regions of control space chaotic transient may be characterized by multiple crossings of the potential barrier [4,5]. This makes the question of necessary conditions for the chaotic transient to occur to be an important point in the analysis of dynamical responses of engineering systems.

MODELS OF OSCILLATORS AND NUMERICAL TECHNIQUES

In the paper, characteristic examples of the chaotic system dynamics due to expanding chaotic saddles as a result of the sequence of global (homoclinic and heteroclinic) bifurcations, with the increase of the forcing parameter, are presented and discussed, making use of the two low-dimensional mathematical models of nonlinear, strictly dissipative oscillators driven externally by periodic force.
The first model is the twin-well potential system (Duffing's oscillator):

$$\ddot{x}+h\dot{x}-\tfrac{1}{2}x+\tfrac{1}{2}x^3=F\sin\omega t, \qquad T=2\pi/\omega, \tag{1}$$

with the potential energy having two minima (stable equilibrium positions) at $x=\pm 1$, and one maximum (unstable equilibrium position, potential barrier) at $x=0$.
The second model is the plane pendulum system

$$\ddot{x}+h\dot{x}+\sin x=F\sin\omega t, \qquad T=2\pi/\omega, \tag{2}$$

with the potential energy having minima at $x=2n\pi$ and maxima at $x=(2n-1)\pi$, ($n=\pm 0, 1, 2, 3....$). If the system is viewed in cylindrical space, it can be treated as a single-well potential system, with single stable (hanging) and single unstable (inverted, potential barrier) equilibrium positions.
For the sake of convenience, both equations are sought in a nondimensional form, with the time rescaled by linear eigenfrequencies of the undamped systems. With the fixed damping coefficient h (h = 0.1), the control parameters are the amplitude F and the frequency ω of the driving force.
The oscillators belong to archetypal representative models for the analysis of inherently nonlinear phenomena and are often used in engineering dynamics because they model a wide class of multidimensional systems whose dynamics can be captured by a single active mode (e.g. buckled beams, offshore structures, buildings in earthquake etc.). In both cases, we confine attention to the region of the principal resonance with respect to driving force ($\omega\approx 1$), i.e. the region

where the nonlinear resonance hysteresis occurs.
In the study we use ideas and numerical techniques of the nonlinear dynamics and chaos, which lead to clear interpretation of the system regular and chaotic properties in particular regions of the forcing parameters. The most valuable in studying the related phenomena is the concept of the *Poincaré return map* which consists in discrete time sampling of the periodic motion $x(t) = x(t+T),\ \dot{x}(t) = \dot{x}(t+T)$ in the phase space (with the sampling time equal to the known excitation period $T = 2\pi/\omega$), thus allowing to study the 3D flow governed by the ordinary differential equation by considering the associated 2D map. The idea of Poincaré map is successfully applied for the visualization of the *basins of attraction* of the stable solutions (attractors), i.e. the domains of all initial conditions in the Poincaré section plane whose sampled trajectories approach asymptotically the particular attractors. The geometrical representation of the stable and unstable invariant manifolds in the Poincaré section, in connection with the related basin-phase structure and the detected existence of a chaotic saddle, allows us to establish the appropriate critical thresholds of global bifurcations, which define the sequential build-up of chaotic system responses.
We detect and visualize the existing chaotic saddle by plotting numerically a chaotic trajectory that never leaves the saddle. Such numerically obtained trajectory is referred to as a *saddle straddle trajectory*, and the method capable of finding it is known as the PIM (Proper Interior Maximum) triple method [2].
The figures have been created using the *Dynamics* software [3].

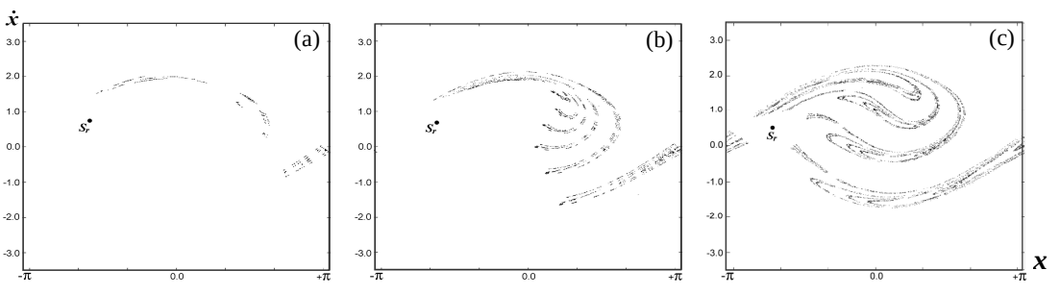


Fig. 1. Expansion of a chaotic saddle due to the Melnikov homoclinic bifurcation in a pendulum system (2), in the region of existence of a single attractor S_r (ω = 0.84); (a) F = 0.30; (b) F = 0.37; (c) F = 0.57.

CONCLUDING REMARKS

The phenomenon of formation of the nonattracting invariant chaotic sets (chaotic saddles) that occurs in nonlinear dissipative oscillators as the forcing parameter changes, and its crucial role in generating chaotic dynamics (sensitivity to initial conditions), is highlighted. It is shown that the phenomenon is strictly related to a sequence of the global (homoclinic and heteroclinic) bifurcations, i.e. transversal intersections of stable and unstable invariant manifolds of the particular existing unstable orbits. The lowest critical threshold of formation of a chaotic saddle is defined by the homoclinic bifurcation of the unstable orbit that corresponds to the potential barrier, and can be derived analytically (Melnikov criterion [7]). It is demonstrated that creation of a chaotic saddle manifests itself by the appearance of chaotic transient motions of an unpredictable, possibly long time duration. as well as that transient chaos typically appears at the level of control parameter values much lower than the one giving rise to a steady-state chaos (chaotic attractor). If two or more attractors with their basins of attraction coexist, chaotic saddle (embedded in a basin boundary) destroys its regular one-dimensional structure and generates fractal structure of the boundary, thus causing a loss of predictability of the final attractor reached. However, numerical evidence has been presented that, due to an existing chaotic saddle, chaotic transient motions are also generated in the case of a single attractor (Fig. 1).
The study allows establishing critical values of forcing parameters which are important in safe engineering, i.e. which define the domains of the safe (regular and predictable), relatively safe (possible chaotic, but confined to the inside of the potential well) and unsafe (chaotic with crossing the potential barrier and so dangerous for the structure) transient system motion.

References

[1] Lai, Y.C., Życzkowski, K., Grebogi, C.: Universal Behavior in the Parametric Evolution of Chaotic Saddles. *Physical Review E* **59**(3):5261-5265, 1999.
[2] Nusse, H.E., Yorke, J.A.: A Procedure for Finding Numerical Trajectories on Chaotic Saddles, *Physica **D*** **36**:137-156, 1989.
[3] Nusse, H.E., Yorke, J.A.: Dynamics: Numerical Explorations. Springer-Verlag NY 1998.
[4] Szemplińska-Stupnicka, W., Tyrkiel E.: Sequences of Global Bifurcations and the Related Outcomes after Crisis of the Resonant Attractor in a Nonlinear Oscillator. *Int. J. Bifurcation and Chaos* **11**(7):2437-2457, 1997.
[5] Szemplińska-Stupnicka W., Tyrkiel E.: The Global Bifurcations That Lead to Transient Tumbling Chaos in a Parametrically Driven Pendulum. *Int. J. Bifurcation and Chaos* **10**(9):2161-2175, 2000.
[6] Ott, E.: Chaos in Dynamical Systems. Cambridge University Press, Cambridge NY 1993.
[7] Wiggins, S.: Introduction to Applied Nonlinear Dynamical Systems and Chaos. Springer-Verlag NY 1990.

CHAOS IN WAVE FRONT PROPAGATION IN HETEROGENEOUS MEDIA

Anatoly V. Chigarev[**], Yuri V. Chigarev[*], Aleksander Brostovich[*], Larysa N. Bialiatskaya[**],
[*] *Academy of Agricultural, Basic of Technics, P. Papicża VI, N 1, 71-459 Szczecin, Poland*
[**] *BNTU, Dept. of Theoretical Mechanics, Skorina Ave. 65, 220027 Minsk, Belarus*

Summary The appearing of the determined chaos at propagation of nonstationary volume and surface waves in heterogeneous media is investigation. The waves represent fronts, on which stresses have a discontinuity. The conditions which satisfy distributions of the determined heterogeneity and appear stochastic states in behaviour of rays are obtained. A changes of intensity of discontinuity and geometrical parameters of wave fronts take place along trajectories of rays. Two different type of going to the determined chaos in dynamic of rays.

OBTANING OF THE EQUATIONS FOR INTENSITIES, PARAMETERS OF INTERIOR GEOMETRY OF FRONTS AND RAYS

The propagation of nonstationary waves in an isotropic heterogeneous elastic medium is describing by the equations

$$\nabla_j \sigma_{ij} - \rho(x)\ddot{u}_i = 0, \quad i,j = 1, 2, 3 \tag{1}$$

$$\sigma_{ij} = \lambda \nabla_k u^k G_{ij} + \mu(\nabla_i u_j + \nabla_j u_i) \tag{2}$$

where G_{ij} - metric tensor of space for volume waves and free surface for surface waves, λ, μ are elastic modulus.

Conditions on a free surface S

$$\sigma_{ij} n_j = 0, \; x^n \in S. \tag{3}$$

The investigation of the determined chaos for system of equations (1) in partial derivatives is possible to do going to the ordinary differential equations with the help of dynamic, kinematic, geometrical conditions of compability at the front waves and Fermat's principle.

The obtained closed systems of the nonlinear differential equations for volume waves have the form

$$\frac{d\omega}{ds} - (\Omega - \frac{1}{2} \cdot \frac{d \ln c}{ds})\omega = 0, \; c = \sqrt{\frac{\Lambda_\alpha}{\rho}}, \; \Lambda_l = \lambda + 2\mu, \quad \Lambda_t = \mu \;, \quad \alpha = l, t. \tag{4}$$

$$\frac{d\Omega}{ds} = 2\Omega^2 - \mathrm{K} - \frac{c_{,\alpha\beta}\, g^{\alpha\beta}}{2c}, \; \frac{dK}{ds} = 2\Omega\mathrm{K} + \frac{2\Omega c_{\alpha,\beta} g^{\alpha\beta}}{c} - \frac{c_{,\alpha\beta}\, b^{\alpha\beta}}{c}. \tag{5}$$

$$\frac{d\bar{r}}{ds} = \bar{\nu}, \quad \frac{d\bar{\nu}}{ds} = -g^{\alpha\beta}\bar{\tau}_\beta (\ln c)_{,\alpha} \tag{6}$$

where ω is the intensity of the stress jump, Ω, K are the mean and Gaussian curvatures, respectively, $\bar{\nu}$ is the normal to the front, $\bar{\tau}$ is the vector of the tangent to the front. For $g^{\alpha\beta}$, $g_{\alpha\beta}$, $b^{\alpha\beta}$, $b_{\alpha\beta}$, $c^{\alpha\beta}$, $c_{\alpha\beta}$ the equations are also obtained.

For surface waves the system of equations have the form

$$\frac{d\mathrm{X}}{ds} + \frac{1}{4}\frac{d \ln g_{22}^{(s)}}{ds}\mathrm{X} + \frac{1}{2}\frac{d \ln R}{ds}\mathrm{X} = 0, \tag{7}$$

$$\frac{d \ln g_{22}^{(s)}}{ds} = -4\Omega, \quad \frac{d\Omega}{ds} = 2\Omega^2 + \frac{g^{22} c_{,22}}{c}, \tag{8}$$

$$\frac{d\bar{r}}{ds} = \bar{\nu}, \quad \frac{d\nu_i}{ds} = -g^{22} x_{i,2} (\ln c)_{,2} \tag{9}$$

where X is the intensity level of surface waves, g_{22} is the component of a metric tensor.

CONDITIONS OF APPEARING OF THE DETERMINED CHAOS

Investigation of a possibility of appearing of the determined chaos in propagation of waves in heterogeneous media on the basis of the equations (4) - (6) and (7) - (9) to realize practically it is very complicated.

In case of bivariate distribution of a heterogeneity it is possible to split systems of equations (4) - (6) and (7) - (9). Then the equations for rays volume and surface waves manage to be considered separately from other equations. Stochastization of

rays causes appearing of chaos in behaviour of dynamic and geometrical parameters at propagation of fronts volume and surface waves in heterogeneous media.

The fluctuations y for rays volume longitudinal and transverse waves about an axis of a waveguide (axis x) are described by the equation

$$\frac{d^2y}{dx^2}+\frac{dy}{dx}\left[1+\left(\frac{dy}{dx}\right)^2\right]f_1(x,y)+\left[1+\left(\frac{dy}{dx}\right)^2\right]f_2(x,y)=0\,, \tag{10}$$

$$f_1=-c^{-1}\frac{dc}{dx},\quad f_2=-c^{-1}\frac{dc}{dy},\quad c=c_\alpha(x,y),\quad \alpha=l,t$$

where $c(x,y)$ is the wave velocity for longitudinal $\alpha=l$ and for transverse $\alpha=t$ waves.

Expanding functions $f_1(x,y)$, $f_2(x,y)$ in a neighbourhood of an axis of a waveguide at $\left|\frac{dy}{dx}\right|<<1$ we reduce the equation (10) to form

$$\frac{d^2y}{dx^2}+\frac{dy}{dx}f_1-y\frac{\partial f_2(x,0)}{\partial y}-y^2\frac{\partial^2 f_2(x,0)}{\partial y^2}-y^3\frac{\partial^3 f_2(x,0)}{\partial y^3}=\varepsilon F(x,y),\quad \varepsilon<<1\,. \tag{11}$$

Let's consider some particular cases of distribution of a heterogeneity along an axis of a waveguide. In a case, when along an axis of a waveguide a medium is stratified with piecewise constant properties we obtain the equation

$$\frac{d^2y}{dx^2}+\omega^2(1+\alpha y^2)y=\varepsilon\omega\sum_{k=-\infty}^{\infty}(x-k\mathrm{X})\ \text{ where }\ \frac{\partial f_2(x,0)}{\partial y}=-\omega^2,\ \frac{\partial^2 f_2(x,0)}{\partial y^2}\equiv 0,\ \frac{\partial^3 f_2(x,0)}{\partial y^3}=-\alpha\omega^2\,. \tag{12}$$

The going to chaos investigated by behaviour of correlation function $R(r)$ of a phase of a ray. For $R(r)\xrightarrow[r\to\infty]{}0$ happens stochastization of a ray since some x_{st}. The going to stochastic behaviour is stipulated by overlapping of resonances.

Other type of going to chaos is realized for medium in which the heterogeneity along an axis of a waveguide varies periodically. Then the equation is obtained

$$\frac{d^2y}{dx^2}-y+y^3+\varepsilon\delta\frac{dy}{dx}=\varepsilon\gamma\frac{dy}{dx}\cos\omega x\ \text{ where }\ \frac{\partial f_2(x,0)}{\partial y}=-1,\ \frac{\partial^2 f_2(x,0)}{\partial y^2}=0,\ \frac{\partial^3 f_2(x,0)}{\partial y^3}=3\,. \tag{13}$$

At the expense of presence in the equation (13) derivative $\frac{dy}{dx}$ the going to a chaotization state is realized through a stochastic attractor.

Analogously the equation for rays in case of surface waves are obtained and investigation. The respective equations are analogous to the equations (12) and (13).

CONCLUSIONS

1. In under waveguide propagation of a ray along an axis of a waveguide an distribution of a heterogeneity is absent the ray oscillates about an axis. At the count of a heterogeneity on this driving in a neighbourhood of a resonant frequency the modulation of a ray on x is superimposed and the amplitude and localization of a ray for a stratified piecewise constant medium is defined.
2. In the second case the existence of stochastic attractors, coherent with a cascade of bifurcations is possible. The trajectory wanders in a neighbourhood of a separatrix until hit yet on an attractor.

Reference

[1] Rossikhin Y. A., Shitikova M. V.: Ray Method for Solving Dynamic Problems Connected with Propagation of Wave Surfaces of Strong and Weak Discontinuities. *Appl. Mech. Rev.* Vol. 48, №1,1995.
[2] Sobczyk K.: Stochastic Wave Propagation, Warsaw, Elsevier, 1985.
[3] Likhtenberg A., Liberman M.: Regular and Stochastic dynamics. Moscow 1984.
[4] Awrejcewicz J., Krysko V., Krysko A.: Spatial-Temporal Chaos Solutions Exhibited by von Karman Model. *Int. J. Bifurcation and Chaos (IJBC) in Appl. Sci. Eng.* Vol. 12, № 7, 2002.
[5] Bialiatskaya L.: Appearing of Determined Chaos at Propagation of Vibrations and Waves in the Mechanical Systems. *Mathematical modeling of deformable solid: Proc. of Inst. of Tech. Cybernetics*, Minsk, 1999.

LOW-DIMENSIONAL CHAOTIC DYNAMICS IN DRIPPING FAUCETS

Ken Kiyono[*], Tomoo Katsuyama[**]
[*]*Graduate School of Education, University of Tokyo, 7-3-1 Hongo, Bunkyo, Tokyo 113-0033, Japan*
[**]*Division of Liberal Arts, Numazu College of Technology, 3600 Ooka Numazu 410-8501,Japan*

Summary Chaotic dynamics of the dripping faucet was investigated both experimentally and theoretically. In our experiment using a high-speed camera, we measured continuous change in the position and velocity of the center of mass of the pendant drop prior to its detachment. Continuous trajectories of a low-dimensional chaotic attractor were reconstructed from these data, which was not previously obtained but predicted in our fluid dynamic simulation. From the numerical analysis, we further obtained an approximate potential function with only two variables, the mass of the pendant drop and the position of the center of mass, which corresponds to a set of solutions of Young-Laplace equation. On the basis of the potential landscape we discuss the mechanism of the chaotic dripping faucet.

The rhythm of a dripping water faucet is not always regular and sometimes exhibits irregular behavior, which sensitively depends on the flow rate. It is nowadays well-known that the irregularity of this system arises from deterministic chaos. Most previous studies of the chaotic dripping faucet have involved measuring the time interval T_n between successive drips, because the dripping time is easily measured using a drop-counter apparatus [1]. The time intervals are then plotted in pairs (T_n, T_{n+1}) for each n to give a return map. Because the return maps typically appear low dimensional, the behavior is often described by a simple dynamical model composed of a variable mass and a spring. In this mass-spring model, a mass point, whose mass increases linearly with time at a given flow rate Q, oscillates with a fixed value of the spring constant k; and a part Δm of the total mass m is removed when the spring extension exceeds a threshold, which describes the detachment of a falling drop. Although the model exhibits chaotic return maps similar to those obtained experimentally, its empirical nature means that it does not provide a unified explanation for the complex behavior of the real dripping faucets. Thus, the direct link between the low-dimensional dynamical system and a presumably infinite-dimensional fluid dynamical system remains elusive.



Fig. 1. Simulation results for a dripping water faucet (7 mm diameter).

The aim of this paper is to understand how the dripping faucet dynamics can exhibit low-dimensional chaos. To this end, we tracked the drop formation in continuous time using fluid dynamic simulations based on a new algorithm involving Lagrangian description [2]. Using the simulation, we can reproduce not only the time-dependent shapes of the pendant drops (Fig. 1), but also various characteristics of chaotic dynamical systems [3]. Together with the numerical simulation, we conducted experiments using a high-speed camera. In our experiments, the mass m and the position z_G of the center of mass of the pendant drop under the nozzle was estimated from the shape of the pendant drop using the digitized image recorded by the high-speed video camera every 1/500 s.

Measurement of the continuous-time variables $\{z_G(t), m(t)\}$ made it possible to visualize the reconstructed chaotic attractor in a continuous state space for the first time. The projection of the attractor in the plane (z_G , $\dot{z}_G$) corresponding to a chaotic motion is shown in Fig. 2, including the return map of T_n (Fig. 2 (d)(e)). The top panel of Fig. 2 is the experimentally observed strange attractor, and the bottom panel is numerical simulations. The qualitative agreement between the experiment and the simulation is excellent. On average, $z_G(t)$ oscillated six times during each time interval T_n, which corresponds to the spiral structure of the attractor in Fig. 2. The transition from the oscillating process to the 'necking' process occurs in the region S in which trajectories starting with slightly different remnant masses

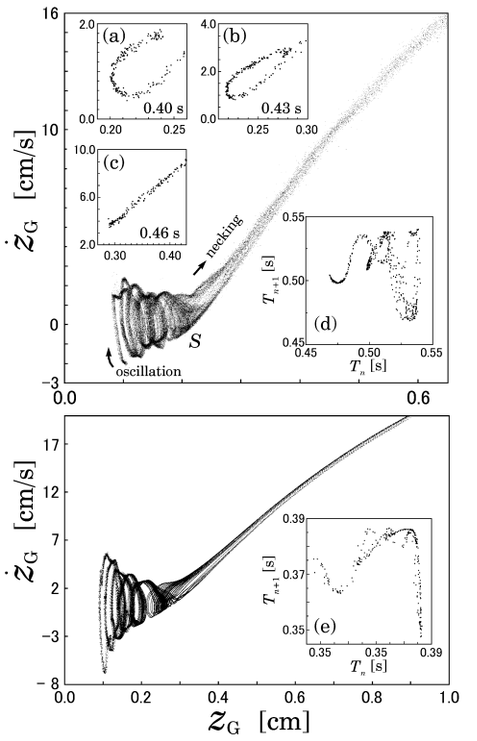


Fig. 2. The top panel is the experimentally observed strange attractor, where the position z_G and the velocity $\dot{z}_G$ of the pendant drop under the nozzle are plotted at every 1/500 s. (a)-(c) Poincaré cross sections of the attractor (plotting of $\dot{z}_G$ vs. z_G at time t measured from each breakup moment. (d) Return map of dripping time intervals T_n. The bottom panel is numerical simulations, where a dripping water faucet (7 mm diameter) is simulated at the flow rate Q = 0.32 g/s. (e) Return map of dripping time intervals T_n.

separate exponentially from each other (Fig. 2 (top)). The cross sections (Fig. 2 (a)-(c)) show the existence of the stretching and folding mechanism, which plays an essential role in chaotic dynamics. The cross sections of the attractor in Fig. 2 (a)-(c) look nearly one-dimensional and explicitly show that the motion of the pendant drop is well characterized by a few state variables. In a wide range of relatively small flow rate (for the nozzle diameter ~ 5 mm, Q < 0.4 g/s), approximately one-dimensional structure of cross sections was observed in both our experiments and numerical simulations.

The motion of the pendant drop is subjected to gravitational force and surface tension. Since the surface energy depends on the shape of the pendant drop, the total potential energy U (i.e., gravitational plus surface) should be a function of the many degrees of freedom of the liquid. Our simulations show, however, that approximating U as a function of two variables, m and z_G, yields a conceptually clear picture for the basic low-dimensional structure of the system. Cross sections of U/m, the potential energy per unit mass, at several fixed values of m for the chaotic attractor shown in Fig. 2 (bottom) are presented in Fig. 3 (a). Although the cross sections in Fig. 3 (a) look two-folded, if they are approximated as single-valued functions, then a sheet of the potential surface $U(m, z_G\})/m$ is obtained as shown in Fig. 3 (b). It can be shown that without solving the fluid dynamical equations the potential function U is obtained from Young-Laplace equation which describes the static equilibrium shape of drops. In 1973, Padday and Pitt proposed a hypothesis that perturbations from one solution of Young-Laplace equation to another are perturbations of the lowest energy [4]. On the basis of this hypothesis, they obtained energy profiles of pendant drops like Fig. 3 (c) from the Young-Laplace equation and discussed stability of the static equilibrium shape. We will demonstrate that the above mentioned potential function U is equivalent to that computed using the Young-Laplace equation. The potential surface is characterized by a U-shaped valley and a ridge which converge as m increases and have totally merged when $m = m_{crit}$, the maximum mass of the static stable shape.

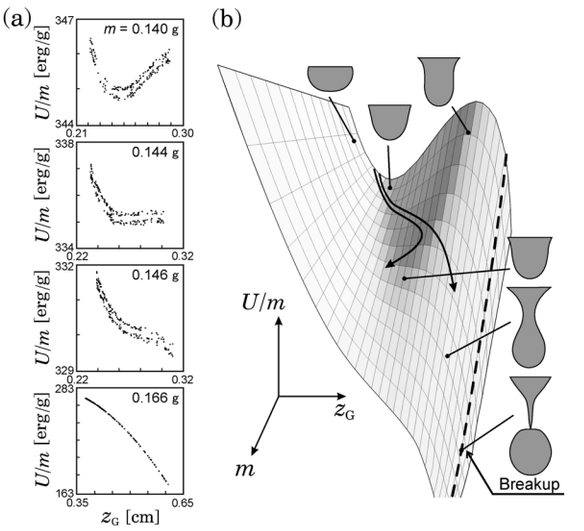


Fig. 3. (a) Fluid dynamic simulation (7 mm diameter, the flow rate $Q = 0.32$ g/s). Cross section of U/m for the attractor is plotted vs. z_G on a constant mass surface, where U/m is the total potential (= surface tension plus gravitation) energy per unit mass as a function of m (pendant drop mass in units of gram in each panel) and z_G (position of the center of mass). (c) Schematic view of a typical potential surface. The pendant drop shapes in various state points (z_G, m) on the potential surface are indicated. The breakup occurs on the dashed line.

Our result leads to the motion of the dripping faucet being described in terms of the approximate potential function U. If the flow rate Q is small enough so that the initial oscillation after the breakup is damped, the state point of the pendant drop goes along the bottom of the valley as m increases. At $m = m_{crit}$, where the valley merges into the ridge, the pendant drop loses its stability (start of the necking process) and rapidly approaches the breakup point (on the broken line in Fig. 3 (b)). Since the instability always begins at the same point $m = m_{crit}$ in this case, the size of each falling drop is uniform (i.e., Tate's law). If, on the other hand, the oscillation of the pendant drop affects the start of necking, the dripping motion exhibits a variety of flow rate-dependent periodic and chaotic patterns. Note that the state point of a pendant drop generally gets over the ridge before m reaches m_{crit} when it is oscillating. At a flow rate resulting in a chaotic motion, two trajectories starting with slightly different m values (different remnant masses) are initially close to each other. As m increases, however, one trajectory may get over the ridge at a certain m value, while the other remains in the valley owing to a small difference in z_G (two lines with arrow in Fig. 3 (b)). The potential landscape illustrates how the trajectories experience stretching and folding as shown in Fig. 2 (a)-(c).

In conclusion, we showed experimentally and numerically the low-dimensionality of the reconstructed chaotic attractor in a continuous state space. Moreover, we demonstrated that the dripping faucet dynamics can be basically described using a potential function with only two variables, the mass of the pendant drop and the position of the center of mass. The potential landscape is the key to understanding how the dripping faucet dynamics can exhibit low-dimensional chaos.

References

[1] Martien P., Pope S. C., Scott P. L., Shaw R. S.: The chaotic behaviour of the leaky faucet. *Phys. Lett. A* **110**: 399-404, 1985.

[2] Fuchikami N., Ishioka S., Kiyono K.: Simulation of dripping faucet. *J. Phys. Soc. Jpn.* **68**: 1185-1196, 1999.

[3] Kiyono K., Katsuyama T., Masunaga T., Fuchikami N.: Picture of the low-dimensional structure in chaotic dripping faucets. *Phys. Lett. A* **320**:47-52, 2003.

[4] Kiyono K., Fuchikami N.: Dripping faucet dynamics by an improved mass-spring model. *J. Phys. Soc. Jpn.* **68**: 3259-3270, 1999.

[5] Padday J. F., Pitt A. R.: The stability of axisymmetric menisci. *Phil. Trans. R. Soc. Lond. A* **275**: 489-527, 1973.

XXI ICTAM, 15–21 August 2004, Warsaw, Poland

INFLUENCE OF REMAINING CHAOS ON CONVERGENCE OF SOLUTIONS IN TIME DELAYED FEEDBACK CONTROLLED DUFFING SYSTEM

Kohei YAMASUE*, Takashi HIKIHARA*
*Department of Electrical Engineering, Kyoto University, Katsura, Nishikyo, Kyoto 615-8510, Japan

Summary Time delayed feedback control is well-known as a practical method for stabilizing unstable periodic orbits embedded in chaotic attractors. However, its control performance has not been clarified with relation to global dynamics of controlled systems. In this paper, we numerically discuss the influence of a remaining chaotic invariant set under control for chaos of Two-well Duffing system. We reveal that it causes highly complicated domain of attraction for target orbits and long chaotic transient before the convergence.

Since the pioneer work by Ott, Grebogi and Yorke [1], methods for stabilizing unstable periodic orbits embedded in chaotic attractors have been extensively studied in the field of nonlinear dynamics [2]. Among several advanced methods, the time delayed feedback control method has an ability to stabilize target unstable periodic orbits by using the difference between present output signals and past ones of controlled objects [3]. The control method is easily implemented without the exact model of the controlled object nor complicated computer processing for reconstruction of the underlying dynamics. For these practical advantages, the control method has been successfully applied to experimental chaotic systems in various fields of research including electronic circuits [4], laser systems [5], mechanical oscillators [6] and chemical systems [7] and so on. In addition, its theory has developed based on local stability analysis around the target unstable periodic orbits. One of the important results is the derivation of odd number condition. The odd number condition gives a class of unstable periodic orbits which can not be stabilized by the control method [8, 9, 10]. Against this negative condition, Pyragas has recently improved the control method [11].

On the other hand, there still remain open problems for clarification of control performance [13]. In particular, the following two problems are here focused on with relation to the convergence of states to target orbits. One is the domain of attraction for target orbits under control [13]. Its tract and structure are closely related to practical problems such as deciding onset timing of control and estimating effects of noise. It also gives information necessary for targeting scheme when multiple orbits coexist in the controlled system. Another is transient behavior after onset time of control. It is expected that the controlled system quickly converges toward the target orbit without irregular behavior before convergence. While these problems are quite important for engineering use of the control method, there was no detailed discussion about them. The problems are directly connected to global dynamics of the controlled system with time delay. Therefore it is essential to consider the structure of the phase space in function space, which has infinite dimension.

In this paper, we numerically discuss the global structure of the time delayed feedback controlled Two-well Duffing system. The discussion is based on the existence of the one dimensional global unstable manifold originating from a directly unstable fixed point, which corresponds to an unstable periodic orbit which can not be stabilized due to the odd number condition. The homoclinic intersection of its unstable manifold and stable manifold generates a chaotic invariant set in the uncontrolled system [14, 15]. In the following, the presence of the chaotic invariant set in the controlled system and its influence on the domain of attraction and transient behavior are discussed.

The Two-well Duffing system is a model of the first-mode vibration in magnet-elastic beam system with sinusoidal forcing [14]. This paper deals with a Two-well Duffing system controlled with use of velocity component for delayed feedback. The system is described by the following delay differential equation : $\ddot{x}(t) + \delta\dot{x}(t) + x(t)^3 - x(t) = A\cos\omega t + u(t)$, where $x(t)$ and $\dot{x}(t)$ denote the displacement and velocity of the Two-well Duffing system, respectively. The $u(t)$ indicates control signal simply given as $u(t) = K[\dot{x}(t-\tau) - \dot{x}(t)]\,;\, t \geq t_0$, where K is feedback gain and t_0 onset time of control. The τ is time delay, which is adjusted to the period of target unstable periodic orbits embedded in chaotic attractors. The $u(t)$ obviously keeps null before onset time of control. Once control turns on, the control signal converges to null according to the stabilization of the system to one of the target orbits. As a result of the convergence, the controlled system degenerates from the infinite dimensional system with time delay to the original two dimensional system. Since the domain of attraction and transient behavior are characterized by the infinite dimensional system under remarkable control input, their treatment is obviously beyond the scope of local stability analysis of target orbits. In the following, the parameter is fixed at $(\delta,\, A,\, \omega) = (0.16,\, 0.27, 1.0)$, where the uncontrolled system generates the chaotic attractor [15]. δ here denotes damping coefficient. A represents forcing amplitude and ω the frequency. The dynamics under $\omega = 1.0$ was summarized in [15]. τ is adjusted to 2π for stabilizing two symmetric inversely unstable periodic orbits with period-2π. Note that the number and location of orbits with period-2π keeps under control [16]. The controlled system has three unstable periodic orbits with period-2π [15], as shown in Fig. 1. Two of them are the target orbits (denoted by $^1\mathsf{I}$ and $^1\mathsf{I}'$) mentioned above. They are easily stabilized by the control. The other is a directly unstable periodic orbit (denoted by $^1\mathsf{D}$) which can not be stabilized due to the odd number condition. The $^1\mathsf{D}$ has one dimensional global unstable manifold in the controlled system, because it possesses only one real characteristic multiplier greater than unity. In the following, the global structure of the controlled system is discussed with relation to this unstable manifold.

Figure 2 shows the unstable manifold of $^1\mathsf{D}$ in the controlled system. When $K = 0$, the unstable manifold is obviously identical to that in the uncontrolled system, as shown in Fig. 2(a). The closure of the unstable manifold coincides with the only one chaotic attractor shown by stroboscopic points. Since the unstable manifold of $^1\mathsf{D}$ transversely intersects the stable manifold of $^1\mathsf{D}$ [14, 15], the controlled system has a chaotic invariant set. Then the regions of phase space are stretched and folded along the unstable manifold with evolution of time. Figure 2(b) shows the unstable manifold

at $K = 0.75$. At this feedback gain, the two target orbits are stable. They are denoted by $^1\mathsf{S}$ and $^1\mathsf{S}'$ in Fig. 2(b). The unstable manifold appears to intersect itself, because the unstable manifold on stroboscopic map is the projection from the function space. The two branches of the unstable manifold start from $^1\mathsf{D}$ in the opposite direction from each other. However they are folded and then come close to $^1\mathsf{D}$ again parallel to the branches itself. The branches further grows in the opposite direction from each other. The regions of phase space is stretched near $^1\mathsf{D}$ and then folded around left and right hand sides in Fig. 2(b) with evolution of time. It implies that the phase space at $K = 0.75$ inherits the characteristic of the chaotic dynamics obtained at $K = 0$, although there is a difference that the phase space is here defined in function space under control signal. With the same approach, we also confirmed that further increase of feedback gain brings some global bifurcations which completely break the homoclinic intersection obtained in the uncontrolled system. After this bifurcation, the unstable manifold becomes quite simple compared with that in Fig. 2(b). Therefore, the unstable manifold in Fig. 2(b) shows the remain of chaotic invariant set in the controlled system, while it is not an attractor because of the presence of stabilized target orbits. The trajectory after onset time of control wanders between $^1\mathsf{S}$ and $^1\mathsf{S}'$ along the unstable manifold, as shown by the stroboscopic points in Fig. 2(b). Its change in time is shown in a window of Fig. 2(b). It shows that the controlled trajectory irregularly goes back and force between $^1\mathsf{S}$ and $^1\mathsf{S}'$ many times, before final convergence to $^1\mathsf{S}$. Then, the steady state obtained by the control is not predictable because of this long and irregular transient behavior. Figure 3 shows the classification of stroboscopic points with steady states. Each point here corresponds to different onset timings of control which is taken every period-2π. Before each onset time, the system generates the chaotic attractor, which coincides with the closure of the unstable manifold at $K = 0$ (See Fig. 2(a)). The points are classified with green and red color, which imply convergence to $^1\mathsf{S}$ and $^1\mathsf{S}'$, respectively. The green and red points are finely mixed one another all over the chaotic attractor. It implies that the steady states almost randomly alternate between $^1\mathsf{S}$ and $^1\mathsf{S}'$ with onset timing of control and influence of external disturbance. In addition, since the two types of points are mixed even in the neighborhood of the target orbits, the controlled system possibly converges to the target orbit in the opposite side from the other target, near which control started. Therefore, it is inevitable that the targeting scheme based on linearisation has no possibility of effective convergence. These characteristics are obviously disadvantage for engineering use of the control method. However, no detail discussion for the characteristics has been obtained.

In summary, the original chaotic invariant set possibly remains in the controlled Two-well Duffing system, even when the feedback gain is enough large to stabilize the target orbits. The remain of the chaotic invariant set causes highly complicated domain of attraction of two symmetric target orbits and long chaotic transient before convergence to them. It shows that the further extension of the control method including targeting scheme and design of feedback gain should be established in the light of the global structure in function space.

References

[1] Ott E., Grebogi C. and Yorke J.A.: Controlling chaos. *Phys. Rev. Lett.* **64**:1196–1199, 1990.
[2] Schuster H.G., ed.:Handbook of Chaos Control. Wiley-VCh, 1999.
[3] Pyragas K.: Continuous control of chaos by self-controlling feedback. *Phys. Lett. A* **170**:421–428, 1992.
[4] Pyragas K. and Tamaševičius: Experimental control of chaos by delayed self-controlling feedback. *Phys. Lett. A* **180**:99–102, 1993.
[5] Bielawski S., Derozier D. and Glorieux P.: Controlling unstable periodic orbits by a delayed continuous feedback.*Phys. Rev. E* **49**:R971–R974, 1994.
[6] Hikihara T. and Kawagoshi T.: An experimental study on stabilization of unstable periodic motion in magnet-elastic chaos. *Phys. Lett. A* **211**:29–36, 1996.
[7] Parmananda P., Madrigal R., Rivera M., Nyikos L., Kiss I. Z. and Gáspár V.: Stabilization of unstable steady states and periodic orbits in an electrochemical system using delayed-feedback control.*Phys. Rev. E* **59**:5266–5271, 1999.
[8] Ushio T.: Limitation of delayed feedback control in non-linear discrete-time dynamical systems. *IEEE Trans. CAS-I* **43**:815–816, 1996.
[9] Just W., Bernard T., Ostheimer M., Reibold E. and Benner H.: Mechanism of time-delayed feedback control. *Phys. Rev. Lett.* **78**:203–206, 1997.
[10] Nakajima H. and Ueda Y.: Limitation of generalized delayed feedback control. *Physica D* **111**:143–150, 1998.
[11] Pyragas K.: Control of chaos via an unstable delayed feedback controller. *Phys. Rev. Lett.* **86**:2265–2268, 2001.
[12] Hikihara T. and Ueda Y.: An expansion of system with time delayed feedback control into spatio-temporal state space. *Chaos* **9**:887–892, 1999.
[13] Just W., Reibold E., Kacperski K., Fronczak P., Holyst J.A. and Benner H.: Influence of stable Floquet exponents on time-delayed feedback control. *Phys. Rev. E* **61**:5045–5056, 2000.
[14] Moon F.C. and Holmes P.J.: A magnetoelastic strange attractor. *J. Sound Vib.* **65**:275–296, 1979.
[15] Ueda Y., Nakajima H., Hikihara T. and Stewart H.B.:Forced two-well potential Duffing's oscillator, in Dynamical Systems Approaches to Nonlinear Problems in Systems and Circuits (Eds. by Tzafestas S.G. and Borne P.):173–180, SIAM, 1988.
[16] Nakajima H.: On analytical property of delayed feedback control of chaos. *Phys. Lett. A* **232**:207–210, 1997.

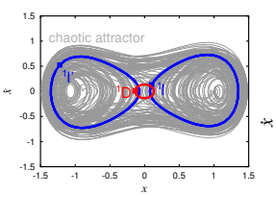
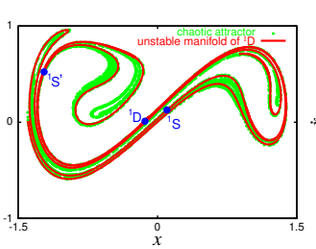
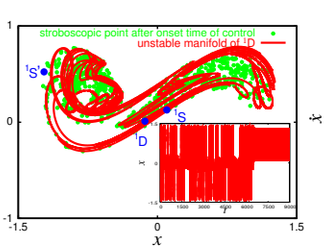


Figure 1. Target unstable periodic orbits (denoted by $^1\mathsf{I}$ and $^1\mathsf{I}'$) embedded in chaotic attractor



(a) $K = 0$



(b) $K = 0.75$

Figure 2. Unstable manifold of $^1\mathsf{D}$ projected on stroboscopic map

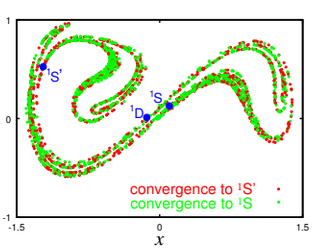


Figure 3. Classification of stroboscopic points with stabilized states.

A DYNAMICAL SYSTEMS ANALYSIS OF THE OVERTURNING OF RIGID BLOCKS

Stefano Lenci [*], Giuseppe Rega [**]

[*] *ISTC, Polytechnic University of Marche, via Brecce Bianche, I-60131 Ancona, Italy*

[**] *DISG, University of Rome "La Sapienza", via A. Gramsci n. 53, I-00197 Rome, Italy*

Summary This work deals with the overturning of a rocking rigid block on an oscillating base, an old fascinating topic which is reconsidered by modern techniques of dynamical systems theory. The paper is divided in two parts: The first is theoretical and concerns the amplitude threshold for contact between stable manifolds and rest position, while the second is numerical and leads to the definition of the "true" safe basin of attraction. These points are somehow correlated, and they go thoroughly into previous authors' insights [2, 3].

INTRODUCTION

The overturning behaviour of rocking rigid blocks has been attracting interest of researchers for a long time, starting with its interest for the estimation of ancient earthquake magnitudes from observations of monuments ruins [4]. Many other practical problems have also been seen to involve this paradigmatic model (see [2, 3] for a brief account), which has a very complex dynamical behaviour in spite of its apparent simplicity. The well-known Housner model [1]:

$$\ddot{\varphi}+\delta\dot{\varphi}-\varphi+\alpha+\gamma\cos(\omega t+\psi)=0,\ \varphi>0, \qquad \ddot{\varphi}+\delta\dot{\varphi}-\varphi-\alpha+\gamma\cos(\omega t+\psi)=0,\ \varphi<0, \qquad \dot{\varphi}(t^{+})=r\,\dot{\varphi}(t^{-}),\ \varphi=0, \tag{1}$$

is used (δ=damping=0.02, α=block diagonal angle=0.2, γ, ω, ψ=amplitude, frequency and phase of the horizontal excitation). It is based on the assumption that the block can only rock without sliding and uplifting, and undergoes instantaneous impacts (r=restitution coefficient=0.95). It is a quite accurate model for investigating the overturning, which is the practically more interesting outcome. This question has been recently reconsidered by the authors, who studied in detail the heteroclinic bifurcation of the hilltop saddles [2], as well as the question of its optimal control.

Heteroclinic bifurcation is a lower bound for the actual overturning threshold, because below the penetration of the tongues of the overturned attractor into the safe in-well basin is prevented. This is shown in Fig. 1 [3]. Extensive numerical simulations have shown that (Fig. 1): (1) for small γ the block does not overturn (grey) at all; (2) for large γ it directly topples (white) without oscillations. The third intermediate region, where overturning may or may not occur, possibly with a bounded transient, exhibits fractal features.

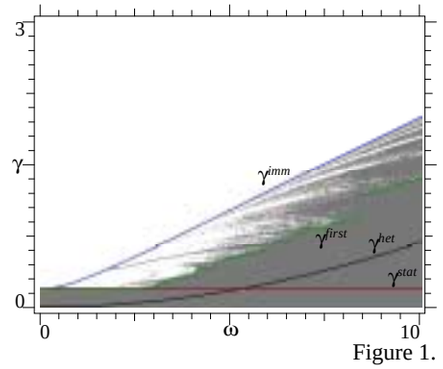


Figure 1.

The boundary between high and intermediate regions is the *immediate* overturning threshold γ^{imm}, and corresponds to the minimum γ above which there is overturning without oscillations in the potential well. The boundary between low and intermediate regions is the *first* overturning threshold γ^{first}, and corresponds to the minimum γ above which the rest position topples irrespective of the transient length in the potential well. γ^{imm} has been determined also analytically, while γ^{first} has been analytically approximated from *below* by γ^{het} (heteroclinic bifurcation threshold) and γ^{stat} (static overturning criterion), as shown in Fig. 1. γ^{imm} is also an *upper* bound for γ^{first} (Fig. 1).

The paper [3] has emphasized two important aspects: i) the role of the excitation phase, which is strictly related to the fact that one deals with a single initial condition (the rest position $(\varphi,\dot{\varphi})=(0,0)$) instead of the whole dynamics, and (ii) the role of the invariant manifolds in the immediate overturning. In particular, it has been shown that γ^{imm} corresponds to the first *direct* touching of the stable manifolds W^{s} with the rest position (i.e., when A touches O for an arbitrary phase, Fig. 2).

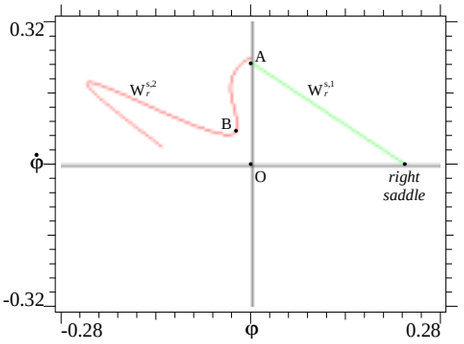


Figure 2. γ=0.7, ω=5 , ψ=0.

THEORETICAL ANALYSIS

Actually, practical interest is rather in determining analytical conditions for *first* overturning, to be possibly pursued through an invariant manifold interpretation of the dynamics occurring for values of $\gamma<\gamma^{imm}$ and finally ending (for a certain phase) with block toppling. It is accomplished in this work by looking for the analytical condition corresponding to touching of point B with the rest position O (Fig. 2). This will allow us to identify a lower upper bound of γ^{first}.

The generic point $(\varphi,\dot{\varphi})$ of the second, left, branch of the perturbed stable manifold $W_r^{s,2}$ of the right saddle (Fig. 2) can be written in the form

$$\varphi=E_1\alpha+\gamma[E_2\cos(\psi)+E_3\sin(\psi)], \qquad \dot{\varphi}=E_4\alpha+\gamma[E_5\cos(\psi)+E_6\sin(\psi)], \tag{2}$$

where the coefficients E_i depends on δ, r, ω and on the time β necessary to this initial condition to impact before

asymptotically approaching the right saddle. When the excitation phase ψ varies, the point (2) describes an ellipse in the plane $(\varphi, \dot{\varphi})$ (pseudo phase space), and the point having the maximum value of $\varphi(\psi)$ is given by

$$\varphi_{max}=E_1\alpha+\gamma\sqrt{(E_2^2+E_3^2)}, \qquad \dot{\varphi}_{max}=E_4\alpha+\gamma[E_5E_2+E_6E_3]/\sqrt{(E_2^2+E_3^2)}, \qquad \psi=\text{atan}(E_3/E_2). \tag{3}$$

The critical condition corresponding to the touching of B with O is mathematically given by $\varphi_{max}=0$ and $\dot{\varphi}_{max}=0$. When α, δ, r, ω are fixed, this is a system of two equations in the two unknowns γ and β. The solutions γ° give the amplitude threshold for this critical event. For example, for δ=0.02, r=0.95, α=0.2, ω=5 the lowest solution is γ°=0.8492 and ψ°=0.6476, and the corresponding manifold-phase-portrait is reported in Fig. 3. Note that γ° is below γ^{imm}=1.0297 (Fig. 4).

The solutions $\gamma^\circ=\gamma^\circ(\omega)$ of the previous system are depicted in Fig. 4. They are constituted by several branches, which are reported with different colors. As expected, the red line represents a better analytical upper bound of γ^{first}.

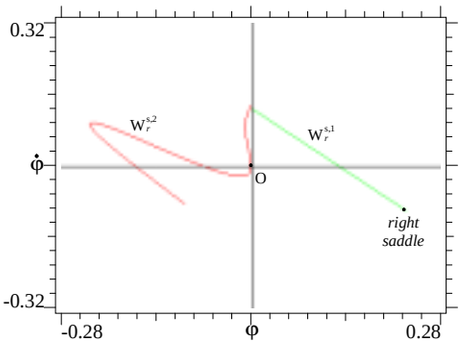


Figure 3. ω=5 γ°=0.8492, ψ°=0.6476.

NUMERICAL INVESTIGATION

In the problem of overturning the initial condition is fixed and the excitation phase is unknown. Thus, safe basins of the attraction in the classical sense (the union of the basins of all in-well attractors), related to a fixed ψ (Fig. 6), do not provide adequate informations. It can, and actually does, occur that for a given phase the block does not overturn, while it topples for a different ψ.

Then, one must look for phase-independent arguments, and the idea is that of defining the "true" safe basin of attraction as the intersection of all classical safe basins when ψ ranges over the period: this is the smallest phase-indendent set of initial conditions which do not entail overturning, and it is therefore reliable from a practical point of view.

To practically determine the "true" safe basin we project the 2D stable manifolds (in the 3D phase space $(\varphi, \dot{\varphi}, t)$) onto the plane $(\varphi, \dot{\varphi})$: the out of projection area surrounding the rest position (0,0) is the "true" safe basin (Fig. 5).

The comparison between Figs. 5 and 6 permits to appreciate the differences between the "true" and the classical safe basins. In particular it is seen how by classical arguments the safety from overturning, here interpreted as the farness from the closest initial condition leading to toppling, is strongly overestimated.

The erosion of the "true" safe basin when the excitation grows is the triggering phenomenon for toppling.

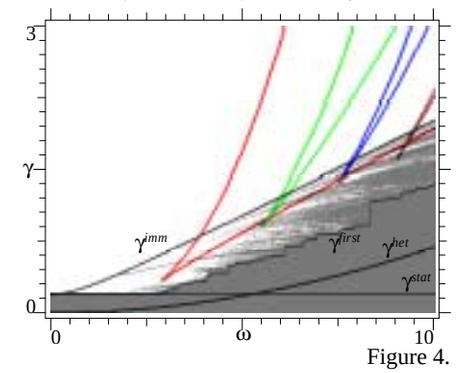


Figure 4.

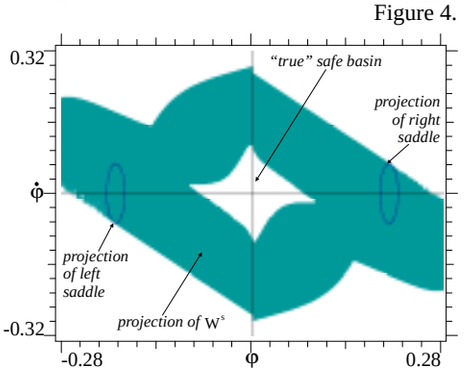


Figure 5. ω=5 γ=0.35.

CONCLUSIONS

To the authors knowledge, this work is one of the first attempts to make *explicit* the role played by the invariant manifolds on the overturning of rigid blocks, thus providing a theoretical interpretative framework of this important practical phenomenon.

The obtained γ° threshold corresponds to touching of the stable manifold with the rest position. The investigation of the possible occurrence of homo/heteroclinic connections between the hilltop and secondary saddles, likely responsible for erosion of the safe basin below γ^{first} and for touching with $\gamma^{first}<\gamma<\gamma^\circ$, is left for future work.

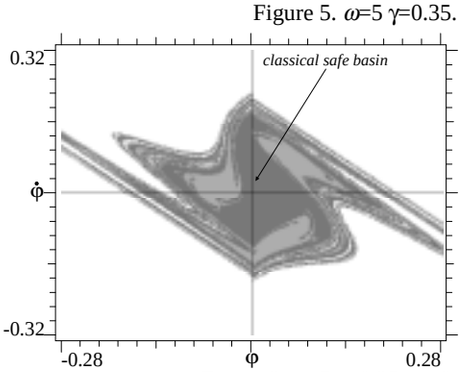


Figure 6. ω=5 γ=0.35, ψ=0.

References

[1] Housner, G.W.: The Behaviour of Inverted Pendulum Structures During Earthquakes, *Bull. Seism. Soc. Am.* **53**: 403-417, 1963.

[2] Lenci S., Rega G.: Heteroclinic Bifurcations and Optimal Control in the Nonlinear Rocking Dynamics of Generic and Slender Rigid Blocks. In press on *Int. J. Bif. Chaos*, 2004.

[3] Lenci S., Rega G.: Overturning Thresholds of a Rocking Block Subjected to Harmonic Excitation: Computer Simulations and Analytical Treatment. *Proc. of "2003 ASME International Mechanical Engineering Congress & Exposition (IMECE'03)"*, Washington, D.C., U.S.A., 16-21 November 2003 (CD-rom). Paper n. IMECE2003-44600.

[4] Milne, J.: Experiments in Observational Seismology, *Trans. Seism. Soc. Japan* **3**: 12-24, 1881.

XXI ICTAM, 15–21 August 2004, Warsaw, Poland

ON THE NONLINEAR DYNAMICS OF MULTICOMPONENT DYNAMICAL SYSTEMS

Igor Mezić*,
*Department of Mechanical and Environmental Engineering, University of California, Santa Barbara, CA 93106, USA

Summary We propose a framework for analysis of dynamical systems with a large number of heterogeneous coupled components. This framework is used to propose a graph-theoretic decomposition that exhibits a chain of vertically unidirectionaly coupled levels and horizontally decoupled components within each vertical level. The decomposition is used to prove a number of results on asymptotic dynamics of coupled dynamical systems.

INTRODUCTION

A number of applications of current interest, such as large-scale engineered systems and genetic regulatory networks involve a large number of heterogeneous, connected components, whose dynamics is affected by possibly an equally large number of parameters. The classical dynamical systems approach attempts to analyze such systems via studying their trajectories in their high-dimensional phase space. However, dynamical systems techniques are mostly developed for low-dimensional systems. We introduce here a framework for studying such multicomponent systems and a graph-theoretic decomposition that for a particular class of networks allows for efficient application of methods of low-dimensional dynamical systems. We also present examples of such decomposition for some high-dimensional systems.

HORIZONTAL-VERTICAL DECOMPOSITION

The following result on decomposition of systems of ordinary differential equations can be proven using a graph-theoretic approach:

Theorem 1 *(Horizontal-vertical decomposition) Any system of ordinary differential equations can be decomposed into k vertical levels, such that each higher level is driven by the dynamics of levels below. Every horizontal level $i \subset \{1, ..., k\}$ can be decomposed into m_i sets, which have dynamics independent of each other.*

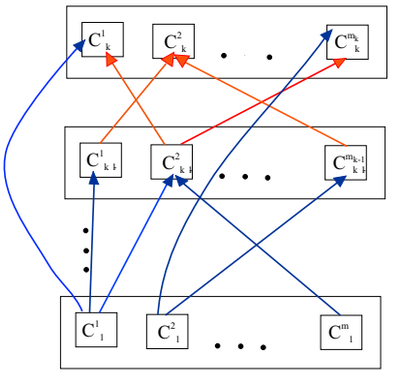


Figure 1. Decomposition described in the theorem

The states at the lowest level in some sense "control" the behavior of all the others. This representation of the system allows for analysis using low-dimensional dynamical systems methods, as we describe next.

APPLICATIONS

The decomposition above is quite useful for analyzing asymptotic dynamics of a variety of coupled systems. The simplest

Proposition 2 *Assume every C_i^j contains only one state and the dynamics of each is bounded. Then the system asymptotes to a fixed point that is not at infinity.*

Proof. If each of the systems at the first level is a one-dimensional system asymptotically converging to a fixed point, its "input" into the second and higher levels is asymptotically constant in time. But, since each of the subsystems C_i^j has bounded, one-dimensional dynamics, this means that each C_i^j will converge to a fixed point. ■

A fuel cell model

Here we show an application of the above decomposition to the 10-state fuel-cell dynamics model discussed in [1]. The system has 10 components, states of which are defined on $\mathbb{R}$, that we label by the index set $\mathcal{N} = \{1, ...10\}$. We obtain decomposition shown in figure 2. Every variable affects itself, but self-loops are not shown in the figure for clarity. Level

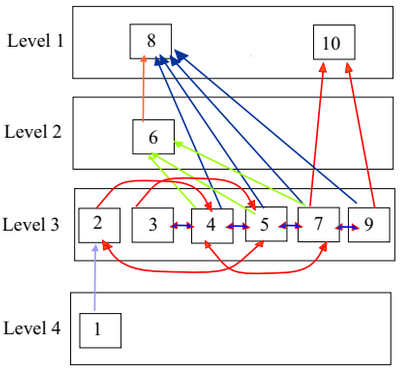


Figure 2. Decomposition for the fuel cell problem.

4 of the decomposition contains only state 1. The dynamics of this state thus tends to a fixed point and asymptotically can be taken just as a parameter input into level 3, where it enters through dynamics of state 2. Note that Level 3 of the decomposition contains six states that have various feedback loops. Level 3 in turn affects states 6, 8, 9, but each of these is a one dimensional state at either level 2 or level one so it is easy to prove that

Proposition 3 *If the subsystem $\{2, 3, 4, 5, 7, 9\}$ tends to a fixed point, then the system tends to a fixed point. If the subsystem $\{2, 3, 4, 5, 7, 9\}$ tends to a limit cycle, then the system tends to a limit cycle.*

Proof. All of the systems at levels higher than 2 are 1-dimensional. If input to these is asymptotically constant, these subsystems will tend to a fixed point. If the input is time-periodic with a fixed period T, these will oscillate in time with the same period as the input. ■

CONCLUSIONS

Graph-theoretic methods lead to a decomposition fo a system of ordinary differential equations into vertical levels. At each vertical level there are subcomponents that do not interact with each other. Each vertical level only affects levels above it, and is affected by states at the same level and below. The method of decomposition is useful for showing that large classes of possibly very high dimensional networked systems can possess low dimensional (periodic, quasi-periodic, low-dimensional chaotic) dynamics. We presented an application to a 10-state model of fuel cell dynamics.

References

[1] Pukrushpan, J., Stefanopolou, A., Varigonda, S., Eborn, J. and Haughtetter, C.: Control-Oriented Model of Fuel Processor for Hydrogen Generation in Fuel Cell Applications,*Submitted*,2003.

SHORT-TIME DYNAMICAL BEHAVIOR OF FLUIDS AT THE ATOMIC SCALE

Theodoros E. Karakasidis*, Antonios B. Liakopoulos*
*Hydromechanics Laboratory, Department of Civil Engineering,
School of Engineering, University of Thessaly, Pedion Areos, 38334 Volos, Greece

Summary In this paper we discuss fundamental aspects of the dynamical behaviour of fluids at the atomic scale using Molecular Dynamics simulation. We present time-series analyses of instantaneous temperature and pressure using linear and non-linear methods. Within the framework of the linear analysis methods, power spectra show evidence of a two-regime power-law ($1/f^a$) behaviour with a large exponent at the high frequency region and a smaller exponent at low frequencies. The dependence of exponent *a* on system density and temperature is discussed. All time-series exhibit essentially the same characteristics for short times (high frequencies). In contrast, at low frequencies, pressure shows a faster loss of memory. Extracted characteristic times are consistent with results obtained from mean square displacements calculations. Rescaled range analysis reveals also a two-regime behavior. In the framework of nonlinear time series analysis, mutual information is employed for the determination of the optimal embedding delay leading to phase space reconstruction.

INTRODUCTION

Molecular dynamics (MD) is a widely used materials simulation method at the atomic level. The equations of motion are solved and successive states of the system in phase space are generated. Using statistical mechanics relations physical quantities such as temperature, pressure, etc., can be obtained as functions of time [1]. Studies of the instantaneous temperature and pressure generated during constant energy MD simulation of a grain boundary of nickel oxide exhibit $1/f^a$ behaviour [2]. 1/f noise is also found in other physical systems [3]. In general, the occurrence of $1/f^a$ noise is considered as an indication of system complexity, a=1 being the most commonly encountered case in the literature [4]. We report on analyses of instantaneous temperature and pressure generated by constant energy molecular dynamics simulation as the system (average) temperature and density are varied.

MODELLING AND COMPUTATIONAL ASPECTS

The Lennard-Jones (12-6) potential $\varphi(r_{ij}) = 4\varepsilon[(\sigma / r_{ij})^{12} - (\sigma / r_{ij})^{6}]$ where r_{ij} denotes the distance between atoms i and j is used throughout this work. The cut-off distance for the interactions was set to 2.5σ. For argon the values of the parameters are σ=3.408A and ε/k_B=119.8 K, k_B being the Boltzmann constant. The simulated system contains N=256 atoms. At t=0, atoms are located on an fcc lattice in a cube with edges parallel to the directions x:[100], y:[010] and z:[001]. The dimensions of the computational cell are such that we match the reduced density of the simulated system. Periodic boundary conditions are applied in all directions. Simulations were performed in the microcanonical ensemble and the equations of motion were integrated using Verlet's algorithm. We focus our attention on the analysis of two time-series: Temperature, defined by $T = \frac{1}{3Nk_B}\sum_{i=1}^{N} m_i \vec{\upsilon}_i^2$ and pressure $P = \frac{N}{V}k_B T - \frac{1}{3V}\sum_{i=1}^{N}\sum_{j>i}^{N} r_{ij}\frac{\partial \phi(r_{ij})}{\partial r_{ij}}$, where r_{ij} stands for the distance between two particles i and j, and υ_i denotes the velocity of particle i. Further details can be found in [5]. We report here on MD simulations at various reduced densities ρ^* and temperatures T^*. Equilibration runs of 3×10^4 steps were performed before starting production runs. Each production run was 10^{-10} s long and all relevant quantities were saved every 10^{-14} s.

RESULTS

Linear methods: Spectral and Rescaled Range Analysis

Spectral analysis reveals that T and P exhibit a two-regime $1/f^a$ power-law behavior with small exponent *a* for low frequencies and larger values for high frequencies (see figure 1a). For temperature we have a high frequency regime with a large exponent indicating strong memory effects and a low-frequency regime where the power-law exponent is smaller indicating rapid loss of memory. Pressure behaves similarly at high frequencies, but at low frequencies it is characterized by exponents close to zero indicating faster loss of memory. The high frequency exponents for both T and P are insensitive to the system density variation while the low-frequency exponents become smaller as density increases. As the system temperature increases the values of *a* are in general smaller indicating weakening memory effects.

Rescaled range analysis (Hurst test) confirms the presence of a two-regime behaviour with strong memory effects at small times (high frequencies) and weaker memory effects at large times (see figure 1b). Pressure loses memory faster than temperature at long time intervals.

The two-regime behaviour reflects the two types of motion that atoms perform: vibrations around a given location and diffusive motion among such sites. Typical atomic trajectories are shown in figure 1c. For short times, Mean Square

Displacement (MSD) calculations show a parabolic dependence on time practically the same for all fluid densities. It is interesting to note that the maximum time that this behaviour is observed is around $2x10^{-13}$ s which corresponds to a frequency about $5x10^{12}$ Hz which, in turn, is the lower limit of the high-frequency zone in the power spectra.

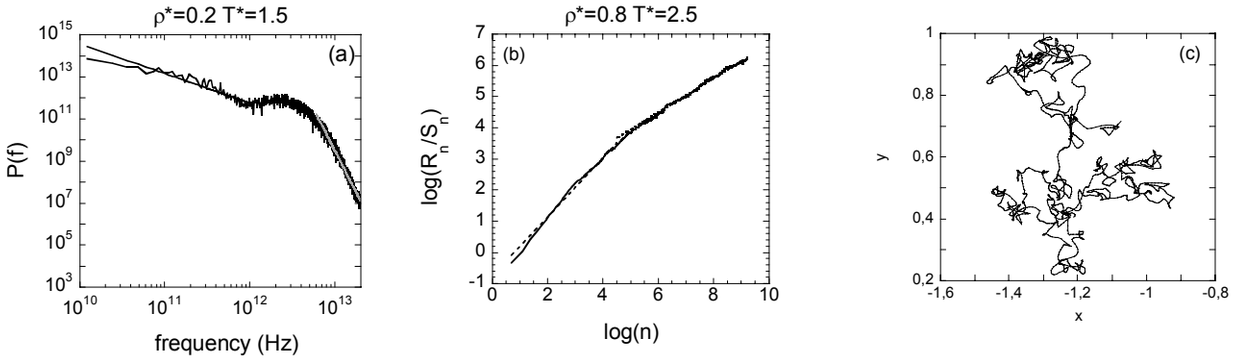


Figure 1. a) power spectrum of temperature time series at ρ*=0.2, T*=1.5 b) rescaled range analysis results of pressure time series at ρ*=0.8, T*=2.5 c) Typical atomic trajectory at T*=1.5 ρ*=0.8 (projection on the x-y plane).

Non-Linear tools: Average Mutual Information

The average mutual information, I, is defined as $I = -\sum_{ij} p_{ij}(\tau) \ln\left(p_{ij}(\tau) / p_i p_j\right)$ where for some partition on the real numbers, p_i is the probability to find a value in the i-th interval, and $p_{ij}(\tau)$ is the joint probability that an observation falls into the i-th interval and time τ later falls into the j-th. Mutual information takes into account nonlinear correlations between successive measurements of a given quantity. If I(τ) has a marked minimum at $\tau=\tau_d$, then it is argued that τ_d is a reasonable choice of time delay for embedding in phase space reconstruction [6]. Note in figure 2 that the minimum is observed in the vicinity of $\tau=1.5\text{-}2x10^{-13}$ s which is close to the characteristic time deduced from MSD. As we can see in figure 2 for the temperature time series at a given density, as system temperature increases I(τ) falls faster, which means that correlation, i.e., memory is lost faster. A similar behaviour is observed for pressure but we do not observe a clear minimum of I(τ). For a given system temperature correlations are lost faster as system density increases. These observations are not only in agreement with the results of power spectrum and rescaled range analysis but they provide the appropriate input for phase space reconstruction of both T and P time series.

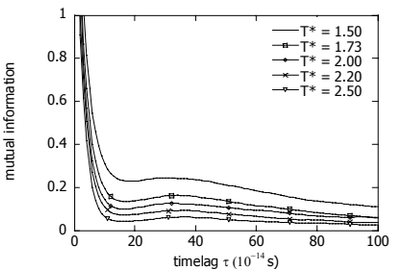


Figure 2. Mutual information of temperature time series at ρ*=0.2

CONCLUSIONS

Spectral and rescaled range analyses of T and P time series indicate two-regime power-law behaviour. For temperature, we have a high frequency regime with a large exponent indicating strong memory effects and a low-frequency regime where the power-law exponent is smaller indicating rapid loss of memory. For high frequencies, pressure behaves similarly. In contrast, at low frequencies, pressure is characterized by exponents close to zero indicating even faster loss of memory. The high frequency exponents are insensitive to density variation while the low-frequency exponents become smaller as density increases. As the system temperature increases the values of the power spectrum exponents are in general smaller indicating that increasing temperature weakens memory effects. Characteristic times based on MSD calculations are found to be in agreement with characteristic times extracted from the time series analysis. Nonlinear correlation measures based on mutual information have been proved very useful in determining delay times for embedding in phase space reconstruction of P and T time series.

Acknowledgements

This research has been partially supported by the program «PYTHAGORAS-EPEAEK II» jointly funded by the European Community and the Greek Ministry of Education.

References

[1] M.P. Allen, T.J. Tildesley, Computer Simulation of Liquids. Oxford, Clarendon Press, 1987.
[2] Karakasidis T.E. and Andreadis I. A homogenous random fractal model for time series produced by constant energy molecular dynamics simulations, *Chaos, Solitons & Fractals*, **15**:87-98, 2003.
[3] Weissman M.B.: What is as spin-glass – a glimpse via mesoscopic noise, *Rev. Mod. Phys*. **65**: 829-839, 1993.
[4] B.J. West, M.F. Shlesinger, *Int. J. Mod. Phys. B* **3**: 795, 1989.
[5] Karakasidis T.E. and Liakopoulos A.B.: Two-regime dynamical behaviour in Lennard-Jones systems: Spectral and rescaled range analysis, *Physica A* **333**: 225-240 (2004)
[6] Fraser A. M. and Swinney H. L.: Independent coordinates for strange attractors from mutual information, *Phys. Rev. A* **33**:1134-1140,1986.

NONLINEAR DYNAMICS OF AXIALLY MOVING VISCOELASTIC STRINGS BASED ON TRANSLATING EIGENFUNCTIONS

Li-Qun Chen , Neng-Hui Zhang

Department of Mechanics, Shanghai University, Shanghai 200436, China

Summary Nonlinear dynamics is investigated for transverse vibration of axially moving strings. The Kelvin viscoelastic model is chosen to describe the viscoelastic property of the string material. The tension is characterized as a small periodic perturbation on a constant mean value. The translating string eigenfunctions are employed to discretize the governing equation, a nonlinear partial differential equation. By use of the Poincaré maps, the dynamical behaviors are identified based on the numerical solutions of the ordinary differential equations that define respectively the 1, 2, 3 and 4-term truncated systems. The bifurcation diagrams are calculated in the case the dynamic viscosity is varied while other parameters are fixed. The bifurcation diagrams of 1, 2, 3 and 4-term truncated systems are qualitatively same. The numerical results indicate that chaos occurs for the small dynamic viscosity, and regular and chaotic motions alternately appear for the increasing dynamic viscosity.

INTRODUCTION

Many engineering devices involve the vibrations of axially moving strings. Traditionally, the investigations on axially moving strings were focused on equilibriums and periodic motions [1]. Recently, there are some researches on chaos and bifurcation of axially moving strings[2-4]. However, all these researches discretized the governing equation based on the stationary string eigenfunctions. The present work applies the translating eigenfunctions [5], which has the good convergence properties, to discretize the governing equation.

DISCRETIZATION BASED ON THE TRANSLATING EIGENFUNCTIONS

The dimensionless form of the governing equation for transverse vibration of an axially moving viscoelastic string is[2]

$$\frac{\partial^2 v}{\partial \tau^2}+2\gamma\frac{\partial v}{\partial \tau\partial \xi}+\left(\gamma^2-1-\alpha\cos\omega\tau\right)\frac{\partial^2 v}{\partial \xi^2}-\frac{3E_{\mathrm{e}}}{2}\left(\frac{\partial v}{\partial \xi}\right)^2\frac{\partial^2 v}{\partial \xi^2}-\frac{E_{\mathrm{v}}}{2}\frac{\partial}{\partial \tau}\left(\frac{\partial v}{\partial \xi}\right)^2\frac{\partial^2 v}{\partial \xi^2}+E_{\mathrm{v}}\frac{\partial v}{\partial \xi}\frac{\partial}{\partial \tau}\left(\frac{\partial v}{\partial \xi}\frac{\partial^2 v}{\partial \xi^2}\right)=0 \qquad (1)$$

where $v(\xi,\tau)$ is the transverse displacement at time τ and axial coordinate ξ, γ is the axially moving speed, α and ω are respectively the amplitude and frequency of the periodic tension perturbation, and E_{e} and E_{v} are respectively the stiffness constant and the dynamic viscosity in the Kelvin model of the viscoelastic string, all in the dimensionless form.

Equation (1) can be cast into the state variable form

$$\boldsymbol{A}\frac{\partial \boldsymbol{w}}{\partial \tau}+\boldsymbol{B}\boldsymbol{w}-\boldsymbol{N}\boldsymbol{w}=0 \qquad (2)$$

where

$$\boldsymbol{w}=\begin{Bmatrix}u\\ v\end{Bmatrix}=\begin{Bmatrix}\dfrac{\partial v}{\partial \tau}\\ v\end{Bmatrix},\ \boldsymbol{A}=\begin{bmatrix}1 & 0\\ 0 & \left(\gamma^2-1\right)\dfrac{\partial^2}{\partial \xi^2}\end{bmatrix},\ \boldsymbol{B}=\begin{bmatrix}2\gamma\dfrac{\partial}{\partial \xi} & \left(\gamma^2-1\right)\dfrac{\partial^2}{\partial \xi^2}\\ \left(\gamma^2-1\right)\dfrac{\partial^2}{\partial \xi^2} & 0\end{bmatrix}$$

$$\boldsymbol{N}=\begin{Bmatrix}E_v\left(\dfrac{\partial v}{\partial \xi}\right)^2\dfrac{\partial^2}{\partial \xi^2} & \left[\alpha\cos\left(\omega\tau\right)+\dfrac{3}{2}E_e\left(\dfrac{\partial v}{\partial \xi}\right)^2+2E_v\dfrac{\partial v}{\partial \xi}\dfrac{\partial u}{\partial \xi}\right]\dfrac{\partial^2}{\partial \xi^2}\\ 0 & 0\end{Bmatrix} \qquad (3)$$

Under the homogeneous boundary condition, the solution of Equation (2) can be assume as the expansion

$$\boldsymbol{w}=\begin{Bmatrix}u\\ v\end{Bmatrix}=\begin{Bmatrix}\displaystyle\sum_{n=1}^{\infty}\omega_n\left[-q_n^{\mathrm{R}}(\tau)\psi_n^{\mathrm{I}}(\xi)+q_n^{\mathrm{I}}(\tau)\psi_n^{\mathrm{R}}(\xi)\right]\\ \displaystyle\sum_{n=1}^{\infty}\left[q_n^{\mathrm{R}}(\tau)\psi_n^{\mathrm{R}}(\xi)+q_n^{\mathrm{I}}(\tau)\psi_n^{\mathrm{I}}(\xi)\right]\end{Bmatrix} \qquad (4)$$

where and q_n^{R} are q_n^{I} components of the generalized coordinates, and the translating eigenfunctions, which are orthogonal with respect to both operator matrix $\boldsymbol{A}$ and $\boldsymbol{B}$, are [5]

$$\psi_n^{\mathrm{R}}(\xi)=\frac{1}{n\pi}\sqrt{\frac{2}{1-\gamma^2}}\sin(n\pi\xi)\cos(\gamma n\pi\xi),\ \psi_n^{\mathrm{I}}(\xi)=\frac{1}{n\pi}\sqrt{\frac{2}{1-\gamma^2}}\sin(n\pi\xi)\sin(\gamma n\pi\xi) \qquad (5)$$

Substituting Equation (4) into Equation (2), taking the inner product of both hands of the resulting equation, using the orthonormality of the eigenfunctions, and retaining only the first *m* terms in the resulting equation yield the *m*-term truncated system

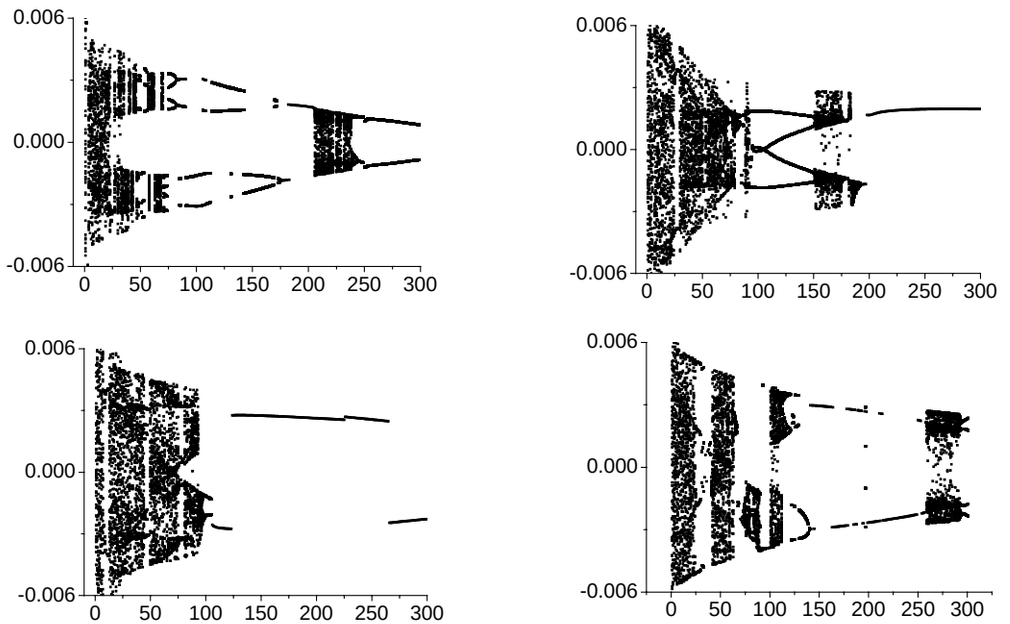
$$\dot{q}_i^{\mathrm{R}}(\tau)=\omega_i q_i^{\mathrm{I}}(\tau)+\sum_{n=1}^{m}\left[q_n^{\mathrm{R}}(\tau)c_{ni}^{\mathrm{RR}}(\tau)+q_n^{\mathrm{I}}(\tau)c_{ni}^{\mathrm{IR}}(\tau)\right],\ \dot{q}_i^{\mathrm{I}}(\tau)=-\omega_i q_i^{\mathrm{R}}(\tau)+\sum_{n=1}^{m}\left[q_n^{\mathrm{R}}(\tau)c_{ni}^{\mathrm{RI}}(\tau)+q_n^{\mathrm{I}}(\tau)c_{ni}^{\mathrm{II}}(\tau)\right] \tag{6}$$

where (a and b stand for R and I)

$$c_{ni}^{\mathrm{ab}}(\tau)=\left\langle N\boldsymbol{\phi}_n^{\mathrm{a}}(\xi),\boldsymbol{\phi}_i^{\mathrm{b}}(\xi)\right\rangle,\ \boldsymbol{\phi}_n^{\mathrm{R}}(\xi)=\begin{Bmatrix}-\omega_n\psi_n^{\mathrm{I}}(\xi)\\ \psi_n^{\mathrm{R}}(\xi)\end{Bmatrix},\ \boldsymbol{\phi}_n^{\mathrm{I}}(\xi)=\begin{Bmatrix}\omega_n\psi_n^{\mathrm{R}}(\xi)\\ \psi_n^{\mathrm{I}}(\xi)\end{Bmatrix} \tag{7}$$

NEMERCAL RESULTS

The Poincaré map is a convenient tool to identify the dynamical behavior, especially chaos. To view globally over a range of parameter values, the bifurcation diagrams are computed. The Poincaré maps of the dimensionless displacement of the center of the moving string, which is obtained by numerical integration of Equation (6) for m=1,2,3,4 respectively. The bifurcation diagrams of the dimensionless center displacement of the string against the dimensionless dynamic viscosity E_{V} are shown in the following fingers.



CONCLUSIONS

This paper treats nonlinear dynamical behaviors of transverse vibration of an axially moving strings constituted by the Kelvin viscoelastic. The string is subject to the pulsating tension. The governing equation is discretized based on the translating string eigenfunctions For the 1, 2, 3 and 4-term truncated systems. The bifurcation diagrams of the Poincaré maps are calculated for varying the dynamic viscosity. The bifurcation diagrams of 1, 2, 3 and 4-term truncated systems are qualitatively same. The numerical results indicate that chaos occurs for the small dynamic viscosity, and regular and chaotic motions alternately appear for the increasing dynamic viscosity.

Acknowledgments

The work was supported by the National Natural Science Foundation of China (Project No. 10172056).

References

[1] Chen L.-Q.: Analysis and control of transverse vibrations of axially moving strings. *Appl. Mech. Rev.*, in press

[2] Chen L.-Q., Zhang N.-H., Zu J. W.: The regular and chaotic vibrations of an axially moving viscoelastic string based on 4-order Galerkin truncation. *J. Sound & Vib.*, **261**: 764-773, 2003.

[3] Chen L.-Q., Wu J., Zu J. W.: Asymptotic nonlinear behaviors in transverse vibration of an axially accelerating viscoelastic string. *Nonlinear Dyn.*, **35**: 347-360, 2004.

[4] Chen L.-Q., Wu J., Zu J. W.: The chaotic response of the viscoelastic traveling string: an integral constitutive law. *Chaos, Solitons & Fractals*, 21: 349-357, 2004.

[5] Wickert J. A., Mote C. D. Jr.: Classical vibration analysis of axially moving continua. *J. Appl. Mech.*, **57**: 738-744, 1990

NONLINEAR OSCILLATORS WITH TIME DELAYS

Z.Peradzyński[1,2] and J. Kurzyna[2]

[1]*Warsaw University, Department of Mathematics, Banacha 2, 00-097 Warsaw, Poland*
[2]*Polish Academy of Sciences, IPPT PAN, Świętokrzyska 21, 00-049 Warsaw, Poland*

Summary: A nonlinear damped oscillator, with a small part of the restoring force retarded in time is considered. It appears that the dynamics of such a system becomes quite complex. Depending on the retardation time τ a number of Hopf bifurcations as well as a number of various chaotic regimes exist. The equation considered here was invented as the simplest model of keyhole instabilities observed during the laser welding.

A delay differential equation is proposed to model the dynamics of a capillary crated in the molten metal by the laser beam in the process of laser welding. The capillary, called also keyhole, is filled with ionized metallic vapours. The pressure of these vapours acts against the forces of surface tension and prevents the capillary from the collapse [1,2,3,5]. In experiments, the deterministic chaos has been detected in the laser welding process [6,7].
By introducing the oscillation frequency ω of the linearized equation in the vicinity of the stable equilibrium point r_0, taking into account only radial oscillations, one can write after some simplifications the equation describing the radial motion of the keyhole capillary walls in the following form:

$$\ddot{r} + \gamma\,\dot{r} = -\omega^2\,\frac{(r-r_1)(r-r_0)}{r^3}, \qquad 0 < r_1 < r_0, \tag{1}$$

where γ represents dampening, proportional to the viscosity of the liquid. and r_1 , r_0 are depending on the laser power. Obviously Eq. (1) does not produce self-excited oscillations and moreover self-sustained chaotic oscillations, which are observed in the experiment. However the ionised vapour expanding from the channel forms a plasma plume above the welded surface. This plasma plume absorbs part of laser beam energy and radiates it away. Additionally, the refraction of the laser radiation in the plasma plume results in defocusing of the laser beam causing further decrease of the power reaching the capillary. One of the reasons for the appearance of chaotic fluctuations seems to be the time delay between the variations of the pressure in the keyhole capillary and changes of the size and density of the plasma plume, resulting in the variations of the energy transfer from laser beam to the material. The size of the plasma plume is a function of the channel radius history, which may be represented here by a certain delay time τ. We can assume that the laser power reaching the keyhole is given in the first approximation by the linear expression $P = P_0 + \alpha\, r(t-\tau) + \ldots$ where α is some small parameter. Consequently up to higher order terms in the expansion into power series one can postulate $r_0 = a + \alpha\, r(t-\tau) + \ldots$. Taking the period of the linearized oscillations as a time unit ($T = 2\pi\,\omega^{-1}$ for $\alpha = 0$) and introducing the normalised channel radius $x(t) = r(t)/a$, and finally, neglecting radius r_1 as a small value in Eq. (1) one arrives at the following delay differential equation

$$\ddot{x} + \gamma\,\dot{x} + \frac{1}{x^2}\left\{(x-1) + \alpha\left(x_r - 1\right)\right\} = 0, \qquad \text{where} \qquad x_r = x(t-\tau). \tag{2}$$

Linearizing our equation around equilibrium state $x \equiv 1$ we obtain a simple linear damped oscillator perturbed by a linear force terms retarded in time. The characteristic quasi-polynomial obtained by inserting $y = e^{\lambda t}$ for the solution of this equation is

$$\lambda^2 + \gamma\lambda + 1 + \alpha e^{-\lambda\tau} = 0. \tag{3}$$

For further analysis let us decompose $\lambda = p + iq$. We are interested in possible Hopf bifurcations, i.e. in the purely imaginary solutions of Eq. (3). When $p = 0$, the equation (3) can be written in the following form

$$\cos^2 q\tau + \frac{\gamma^2}{\alpha}\cos q\tau + \left(\frac{\gamma^2}{\alpha^2} - 1\right) = 0, \qquad q = \frac{\alpha}{\gamma}\sin q\tau, \tag{4}$$

In particular, for small γ/α and small $\alpha < 1$ the approximate solutions of Eqs (4) can be given and finally we have the following values of τ for which Hopf bifurcation takes place:

$$\tau_k^+ = \frac{\gamma}{\alpha} + \frac{2\pi k}{\sqrt{1+\alpha}} + \ldots \qquad \tau_k^- = \pi - \frac{\gamma}{\alpha} + \frac{2\pi k}{\sqrt{1-\alpha}} + \ldots, \qquad k = 0,\ 1,\ 2,\ldots \tag{5}$$

Let us notice that the points $\tau_k^{\pm}$ are the values of τ at which the curve $p=p(\tau)$ satisfying equations (3) crosses the axis of τ. Since for τ close to zero the stationary solution is stable, therefore, up to the first point of bifurcation $\tau_0^+ = \gamma/\alpha$, the value of $p(\tau)$ is negative and it changes sign for $\tau > \gamma/\alpha$. Then again after passing the next point τ_0^-, $p(\tau)$ becomes negative, which implies the stability of the stationary solution $x \equiv 1$. In this way we deduce that the stationary solution is stable for $\tau \in (\tau_{k-1}^-, \tau_k^+)$ and unstable for $\tau \in (\tau_k^+, \tau_k^-)$, where $k = 0,1,2,3,...$ and $\tau_{-1}^- = 0$. In the first approximation the corresponding frequency is not dependent on k and is equal to $q_{\pm} = \sqrt{1 \pm \alpha}$, respectively.

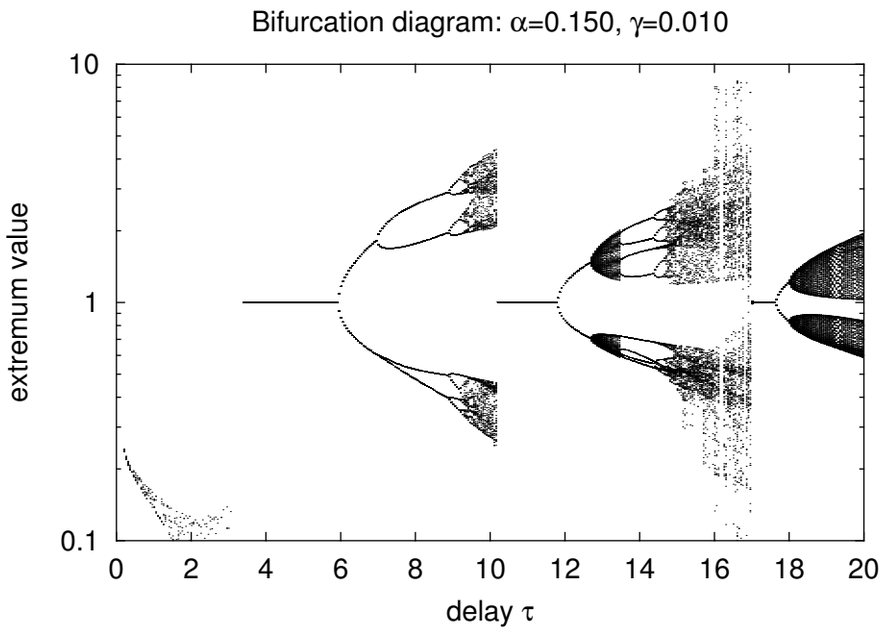


Fig. 1. Bifurcation diagram as a function of time delay τ, for γ=0.01 and α=0.15, resulting from the numerical integration of Eq. (2). One can notice the transitions to chaos by cascades of period doubling as well as through the torus breakdown (for larger values of τ). Please note a good agreement of bifurcation points with theoretical predictions.

Conclusions. Although the numerical simulation presented here were performed for quite specific equation (Eq. (2)) , our experience shows that qualitatively other nonlinearities lead to similar behavior. Clearly, our analytical bifurcation analysis is in fact not dependent on the nonlinearity as long as there exists an equilibrium state for every $\tau \geq 0$ which is asymptotically stable for $\tau = 0$. Some part of results presented here can also be given for systems of delay differential equations. Thus possible area of applications can be much wider then the presented here example. Finally, as it follows from our analytical considerations and also from the numerical simulations, the Hamiltonian systems or Hamiltonian systems with weak dissipative terms can exhibit drastically different dynamics when slightly polluted with the time delay terms.

References

[1] T. Klein, M. Vicanek, J. Kross I. Decker and G. Simon, *J.Phys. D: Appl. Phys.*, **27**, 2023, 1994.
[2] J. Kurzyna, Z. Szymański and Z. Peradzyński, *J.Tech. Phys.*, **36**, 131, 1995
[3] T. Klein, M. Vicanek and G. Simon, *J.Phys. D: Appl. Phys.*, **29**, 322, 1996.
[4] Z. Szymański, J. Kurzyna and W. Kalita, *J.Phys. D: Appl. Phys.*, **31**, 3153, 1997
[5] Z. Peradzyński and J. Kurzyna *Phys., J.Tech. Phys.*, Special Issue **40,** No 2, 113-119, 1999
[6] J. Kurzyna, *J.Phys. D: Appl. Phys.*, **31**, 680, 1998.
[7] Z. Szymański, J. Hoffman and J. Kurzyna, *J.Phys. D: Appl. Phys.*, **34**, 189-199, 2001.

NON-LINEAR OSCILLATOR UNDER RANDOM RENEWAL-DRIVEN TRAINS OF IMPULSES

Radosław Iwankiewicz, Matilde Rundo Sotera
University of the Witwatersrand, Johannesburg, Private Bag 3, WITS 2050, South Africa

Summary A non-linear, non-hysteretic oscillator under a random train of impulses driven by a class of renewal processes is considered. The original state vector of the oscillator is augmented by a number of auxiliary state variables. The augmented state vector is governed by two independent Poisson processes, hence the original non-Markov problem is converted into a Markov one. Response mean value and variance are obtained from the equations for moments and are verified against Monte Carlo simulations.

INTRODUCTION

Random pulse trains are valid models of actual excitations processes such as e.g. irregular trains of shocks and impacts. If the dynamic system is acted upon by a non-Poisson distributed train of impulses and/or the pulses have general shapes, the state vector is not a Markov process. Various techniques have been developed to convert original non-Markov pulse problems into Markov ones, for example for trains of impulses driven by Erlang renewal processes [1], or for sine half-wave Poisson-driven pulses [2]. A random train of impulses with interarrival time being a sum of two independent, negative exponential distributed random variables with different parameters (generalized Erlang renewal process) was dealt with in [3]. The excitation process was exactly expressed in terms of an auxiliary variable, governed by a stochastic equation driven by two independent Poisson processes with different parameters.

In the present paper a non-linear, non-hysteretic oscillator under a random train of impulses driven by a renewal process is considered. The class of renewal impulse processes considered is obtained by multiplying the impulse magnitudes of an Erlang renewal impulse process by the values of an intermittent, zero-one auxiliary stochastic variable. This variable is governed by a stochastic differential equation driven by two independent Erlang renewal processes, each of which is exactly expressed, with the aid of a set of auxiliary variables, in terms of a Poisson process. Thus the augmented state vector, consisting of the original state vector and of auxiliary variables, is driven by two independent Poisson process, and becomes a Markov process. The Ito's differential rule is used to derive the differential equations governing the response statistical moments. The usual and special cumulant-neglect closure techniques are used to truncate the hierarchy of moments equations. The mean value and variance of the response are obtained by numerical integration of a suitably truncated set of moment equations and verified against Monte Carlo simulations.

STATEMENT OF THE PROBLEM

Consider a non-linear, non-hysteretic oscillator governed by the equation

$$\ddot{X}(t) + f\big(X(t), \dot{X}(t)\big) = \sum_{i,R=1}^{R(t)} P_{i,R}\delta(t - t_{i,R}), \tag{1}$$

where $f\big(X(t), \dot{X}(t)\big)$ is the function of the instantaneous values of $X(t)$ and $\dot{X}(t)$ and the stochastic excitation is the random train of impulses whose arrival times $t_{i,R}$ are driven by the renewal process $R(t)$. Sample functions of counting processes are assumed herein to be left-continuous with right limit. The impulses magnitudes $P_{i,R}$ are given by independent random variables with common probability density function.

The renewal driven train of impulses in (1) may be represented as follows

$$\sum_{i,R=1}^{R(t)} P_{i,R}\delta(t - t_{i,R}) = \sum_{i=1}^{R_\nu(t)} Z(t_i)P_i\delta(t - t_i), \tag{2}$$

where the arrival times t_i are driven by an Erlang renewal process $R_\nu(t)$ with parameters ν and k and $Z(t_i)$ is a value at t_{i-} of an intermittent, zero-one stochastic variable $Z(t)$ governed by the stochastic equation

$$dZ(t) = (1 - Z)dR_\mu(t) - ZdR_\nu(t), \tag{3}$$

where $R_\mu(t)$ is an Erlang renewal process with parameters μ and l. The Erlang process $R_\nu(t)$ and $R_\mu(t)$ are assumed to be independent. The variable $Z(t)$ equals zero except in the time interval between the first $R_\mu(t)$ driven event occurring after an $R_\nu(t)$ driven event and the first subsequent $R_\nu(t)$ driven event. In other words, $Z(t_i)$ is zero at all instants t_i driven by $R_\nu(t)$, except the first ones occurring after $R_\mu(t)$ driven events. The equation (3) is a generalisation of an equation driven by two independent Poisson processes given in [4].

The increment of the underlying renewal process $R(t)$ equals, with probability 1, $dR(t) = Z(t)dR_\nu(t)$, which follows from the fact that both counting processes are regular (the increments only take values 0 or 1).

An Erlang renewal process $R_\alpha(t)$ ($\alpha = \mu, \nu$) may be expressed in terms of the Poisson process $N_\alpha(t)$ ($\alpha = \mu, \nu$) at the expense of introducing auxiliary variables, for any integer parameter k or l [5]. For any α the following replacement is valid

$$dR_\alpha(t) = \rho_\alpha(t) dN_\alpha(t), \quad \alpha = \mu, \nu \tag{4}$$

where the $\rho_\alpha(t)$ is a variable which only takes values 0 or 1 and is expressed in terms of a number of further, discrete-valued, auxiliary variables which are governed by stochastic differential equations driven by the Poisson process.

SOLUTION TECHNIQUE

The augmented state vector $\mathbf{X}(t)$ consisting of $X(t)$, $\dot{X}(t)$, $Z(t)$ and other auxiliary variables is governed by the stochastic equation

$$d\mathbf{X}(t) = \mathbf{c}\Big(\mathbf{X}(t)\Big)dt + \mathbf{b}\Big(P(t), \mathbf{X}(t)\Big)d\mathbf{N}(t), \quad d\mathbf{N}(t) = \begin{bmatrix} dN_\nu(t) \\ dN_\mu(t) \end{bmatrix}, \tag{5}$$

hence $\mathbf{X}(t)$ is a non-diffusive Markov process.

Differential equations governing the response moments (statistical moments of the state variables $\mathbf{X}(t)$) are obtained from the generalized Itô's differential rule [5], [6]. For the non-linear oscillators with terms $f\left(X(t), \dot{X}(t)\right)$ which are polynomials in $X(t)$ and $\dot{X}(t)$, the right-hand sides of the equations for moments involve the unknown expectations of the non-linear transformations of state variables . The equations for moments form an infinite hierarchy and cannot be directly solved. These unknown expectations, or moments, can only be evaluated approximately, using suitable closure approximations. In the present paper two closure techniques are used. The first one is the ordinary cumulant-neglect closure. The second one is a special closure technique developed for the present problem. The latter closure technique is obtained from the tentative joint probability density of the state vector, assumed in form of the sum of a discrete and a continuous part. The discrete part accounts for the fact that is the system is at rest at the initial time instant, it is still at rest before the first impulse occurs. The continuous part is constructed from two kinds of conditional probability densities, conditioned on the states 0 and 1 of the variable $Z(t)$. Then the ordinary cumulant-neglect closure approximations are applied to conditional moments only, yielding the modified closure approximations for the unconditional moments of the present problem.

The mean value and variance of the response are obtained by numerical integration of a suitably truncated set of moment equations and verified against direct Monte Carlo simulations.

CONCLUSIONS

For a non-linear, non-hysteretic oscillator under a renewal impulse process stochastic excitation a technique is devised to convert the original non-Markov problem into a Markov one. This is done at the expense of introducing auxiliary, discrete-valued state variables. A special cumulant-neglect closure techniques is devised to truncate the hierarchy of moments equations. This closure technique as well as the ordinary one are used in order to evaluate the mean value and variance of the response. The approximate analytical results are verified against direct Monte Carlo simulations.

References

[1] Iwankiewicz R., Nielsen S.R.K.: Dynamic response of non-linear systems to renewal impulses by path integration. *J. Sound Vib Mech* **195**:175–193, 1996.

[2] Ricciardi G.: Random vibration of a beam under moving load. *J. Engrg Mech* **120**, 1994.

[3] Iwankiewicz R.: Dynamic systems under random impulses driven by a generalized Erlang renewal process. In: Proceedings of the 10th IFIP WIG 7.5 Working Conference on Reliability and Optimization of Structural Systems, 25-27 March 2002, Kansai University, Osaka, Japan. Eds. H.Furuta, M.Dogaki and M.Sakano, Balkema 2003,103-110.

[4] Iwankiewicz R.: Dynamic response of non-linear systems to random trains of non-overlapping pulses. *Meccanica*, **37**:167–178, 2002.

[5] Iwankiewicz R., Nielsen, S.R.K.: Vibration Theory, Vol. 4, Advanced methods in stochastic dynamics of non-linear systems, Aalborg University Press, Denmark, 1999.

[6] Snyder, D.L.: Random point processes, John Wiley, New York, 1975.

PSEUDO-RIGID BODIES VIEWED AS GLOBALLY CONSTRAINED CONTINUA

James Casey
Department of Mechanical Engineering,
University of California, Berkeley, CA94720, USA

Summary Pseudo-rigid continua can maintain homogeneous deformations in the presence of arbitrary applied loads. Their ability to do so can be explained by treating them as globally constrained continua. A system of indeterminate reactive stresses, analogous to those in a rigid body, are called into play to maintain the homogeneity of the deformation. The governing equations are deduced and a set of Lagrange's equations are also established.

Bodies assumed to be capable of keeping their deformation fields homogeneous have been studied extensively. Initiated by Slawianowski [1, 2], this field was elaborated by Cohen [3] and by Cohen & Muncaster [4, 5]. The theory of elastic pseudo-rigid bodies has enjoyed considerable success (see e.g., [6, 7]). Rubin [8] introduced the concept of a Cosserat point, which is a particle to which are attached deformable directors satisfying appropriate balance laws. The Cosserat point has been investigated in several studies, e.g., [9, 10]. A Cosserat point with three directors is isomorphic to a pseudo-rigid body.

In the present treatment, pseudo-rigid bodies are treated as 3-dimensional continua that can undergo only homogeneous deformations, no matter what loads are applied to them. Adopting the viewpoint of Antman & Marlow [11] and Marlow [12], we say that a pseudo-rigid body is *globally constrained*. As in the case of ordinary internal constraints, some system of indeterminate reaction stresses must exist to maintain the global constraint. Global material constraints arise in the theories of plates, shells, and rods whenever the 3-dimensional deformation field is assumed to have a restricted form. Podio-Guidugli [13] recognized the essential role that reaction stresses play in the theory of linearly elastic plates. The pseudo-rigid continuum may be viewed as an idealized reinforced body in which the Cauchy stress tensor $\mathbf{T}$ at each material point is the sum of an "active stress" $\mathbf{T}^{(A)}$, which is specified by a constitutive equation, and a "reactive stress" $\mathbf{T}^{(R)}$, which takes on whatever values are necessary to maintain homogeneity of the deformation field [14]. Remarkably, the active stresses in a pseudo-rigid body form an equilibrated system, while the reactive stresses play exactly the same role as in rigid body dynamics. It is shown that the governing equations of the pseudo-rigid continuum $\mathcal{B}$ can be written in the form

$$\mathbf{f} = m\ddot{\bar{\mathbf{x}}} \ , \quad \mathbf{M}^{(A)} = V\bar{\mathbf{T}} \ , \quad \widetilde{\mathbf{M}} = \mathbf{AE} \ ,$$

where

$m =$ mass of $\mathcal{B}$, $\rho =$ density of $\mathcal{B}$ at time t , $V =$ volume of $\mathcal{B}$, $S =$ boundary of $\mathcal{B}$,
$\bar{\mathbf{x}} =$ position vector of mass center of $\mathcal{B}$, $\mathbf{f} =$ resultant external force acting on $\mathcal{B}$,
$\bar{\mathbf{T}} =$ mean Cauchy stress in $\mathcal{B}$, $\mathbf{E} =$ Euler tensor of $\mathcal{B}$ with respect to the mass center ,
$\mathbf{F} =$ deformation gradient , $\boldsymbol{\pi} =$ position vector relative to the mass center ,
$\mathbf{L} =$ velocity gradient $= \dot{\mathbf{F}}\mathbf{F}^{-1}$, $\mathbf{A} =$ acceleration gradient tensor $= \ddot{\mathbf{F}}\mathbf{F}^{-1}$,
$\mathbf{M}^{(A)} = \int_S \mathbf{t}^{(A)} \otimes \boldsymbol{\pi} \, da =$ Möbius (or "astatic") tensor of active traction field $\mathbf{t}^{(A)}$,
$\widetilde{\mathbf{M}} =$ Möbius tensor of reactive traction field and body force field.

The kinetic energy of $\mathcal{B}$ is the sum of two terms, namely

$$\bar{T} = \frac{1}{2} m \dot{\bar{\mathbf{x}}} \cdot \dot{\bar{\mathbf{x}}} \ , \quad T^\star = \frac{1}{2} \operatorname{tr}(\mathbf{L}\mathbf{E}\mathbf{L}\mathbf{E}^T) \ .$$

Then,

$$\widetilde{\mathbf{M}} \cdot \mathbf{L} = \dot{T}^\star \ .$$

Following a geometrical procedure utilized by Casey [15] for rigid bodies, it is demonstrated how a pseudo-rigid body can be represented by an abstract particle moving in a 12-dimensional Euclidean space, with points $(\bar{\mathbf{x}}(\eta^1, \eta^2, \eta^3), \mathbf{F}(\xi^1, \ldots, \xi^9))$, and whose metric is determined by the radius of gyration of the body. A set of Lagrange's equations for the pseudo-rigid body are derived (without any appeal to virtual work or variational principles):

$$\frac{d}{dt}\left(\frac{\partial \bar{T}}{\partial \dot{\eta}^\gamma}\right) - \frac{\partial \bar{T}}{\partial \eta^\gamma} = \mathbf{f} \cdot \frac{\partial \dot{\bar{\mathbf{x}}}}{\partial \dot{\eta}^\gamma} \ , \quad \frac{d}{dt}\left(\frac{\partial T^\star}{\partial \dot{\xi}^\gamma}\right) - \frac{\partial T^\star}{\partial \xi^\gamma} = \widetilde{\mathbf{M}} \cdot \frac{\partial \mathbf{L}}{\partial \dot{\xi}^\gamma} \ .$$

References

[1] Slawianowski, J.J.: Analytical Mechanics of Finite Homogeneous Strains. *Arch. Mech.* **26**:569–587, 1974.

[2] Slawianowski, J.J.: Newtonian Mechanics of Homogeneous Strains. *Arch. Mech.* **27**:93–102, 1975.

[3] Cohen, H.: Pseudo-Rigid Bodies. *Utilitas Math.* **20**:221–247, 1981

[4] Cohen, H., Muncaster, R.G.: The Dynamics of Pseudo-Rigid Bodies: General Structure and Exact Solutions. *J. Elasticity* **14**:127–154, 1984.

[5] Cohen, H., Muncaster, R.G.: The Theory of Pseudo-Rigid Bodies. Springer-Verlag, 1988.

[6] Cohen, H., MacSithigh, G.P.: Plane Motions of Elastic Pseudo-Rigid Bodies. *J. Elasticity* **21**:193–226, 1989

[7] Kanso, E., Papadopoulos, P.: Dynamics of Pseudo-Rigid Ball Impact on Rigid Foundation. *Int. J. Non-Lin. Mech.* **39**:299–309, 2004.

[8] Rubin, M.B.: On the Theory of a Cosserat Point and its Application to the Numerical Solution of Continuum Problems. *J. Appl. Mech.* **52**:368–372, 1985.

[9] Rubin, M.B.: On the Numerical Solution of One-Dimensional Continuum Problems using the Theory of a Cosserat Point. *J. Appl. Mech.* **52**:373–378, 1985.

[10] Rubin, M.B.: Numerical Solution of Two- and Three-Dimensional Thermomechanical Problems using the Theory of a Cosserat Point. *Z. angew. Math. Phys.* **46**:S308–S334, 1995.

[11] Antman, S.S., Marlow, R.S.: Material Constraints, Lagrange Multipliers, and Compatibility. *Arch. Rational Mech. Anal.* **116**:257–299, 1991.

[12] Marlow, R.S.: Global Material Constraints and their Associated Reactive Stresses. *J. Elasticity* **33**:203–212, 1993.

[13] Podio-Guidugli, P.: An Exact Derivation of the Thin Plate Equation. *J. Elasticity* **22**:121-133, 1989.

[14] Casey, J.: Pseudo-Rigid Continua: Basic Theory and a Geometrical Derivation of Lagrange's Equations. *Proc. Roy. Soc. Lond.* **A**, in press.

[15] Casey, J.: On the Advantages of a Geometrical Viewpoint in the Derivation of Lagrange's Equations for a Rigid Continuum. *Z. angew. Math. Phys.* **46**:S805–S847, 1995.

CONSTITUTIVE EQUATIONS OF MESOELASTIC DEFORMATION

Lev Steinberg
Department of Mathematics, University of Puerto Rico, Mayaguez, PR 00680-9018, USA

Summary

We study deformations of mesoelastic materials that display different types of imperfections with a typical size of 1μm. Stress-strain relationships of these materials depend on the processing history and exhibit common behaviour, including non-linearity, hysteresis, etc. We focus our study on the continuous distribution of singularities in the deformation field, which are described in terms of dislocation densities and fluxes. We define the mass mesodensity tensor and deduce the constitutive relationship between the dislocation current and the linear mesomomentum. Based on the modification of Peach-Koehler formula we propose the constitutive relationship between the line mesostress tensor and the dislocation density. These constitutive relationships allow us to model stresses in mesoelastic materials.

INTRODUCTION

Deformation stress in elastic materials may appear not only by the actions of external forces on them but also because of singularities of internal structure. This paper represents our study of the role of dislocations as a source of stress fields. Experimental studies of deformations of elastic materials with imperfections of a typical size of 1μm indicate that their stress-strain relationships depend on the processing history and show a common behaviour, exhibiting non-linearity, hysteresis, etc [1]. We assume that these imperfections play a significant role in the development of singularities of deformation gradient $\boldsymbol{\beta}$.

The continuum of dislocations is described in term of the dislocation density tensor $\boldsymbol{\alpha} = \nabla \times \boldsymbol{\beta}$. The balance equation of the Burgers vector in defect dynamics $\nabla \times \mathbf{J} + \partial_t \boldsymbol{\alpha} = \mathbf{0}$ relates the dislocation current (the flux density) **J** and the dislocation density $\boldsymbol{\alpha}$ [2].

Peach and Koehler's study of the action of an elastic stress field on a dislocation led to the discovery that the force acting on a unit length of a dislocation line has the following form: $f^i = \varepsilon^{ikl}\tau_k S_{lm} b_m$, where ε^{ikl} is antisymmetric in the k and l indices, τ_k is the tangent vector to the dislocation loop, **S** is the elastic stress, and **b** is the Burgers vector [3].

DYNAMICS

The main point of our consideration is to reveal a stress response to the continuum of dislocations. We associate this response with, as we call it, mesostress, which arises in an elastic body in addition to the elastic stress.

Dislocation Mass and Linear Momentum of Dislocation

We evaluate the mass density vector of a dislocation as the following:

$$\rho^i = \oint_L \rho_{ref} \beta^{ij} dX_j,$$

where ρ_{ref} is the material mass density in the reference configuration.

Also, we use the Kosevich formula [1] for the dislocation current

$$\mathrm{J_{ik}} = \varepsilon_{ilm} \tau^l \mathrm{b_k} \mathrm{V^m} \delta(\xi), \tag{1}$$

where **V** is the velocity at a given point on the dislocation line, $\delta(\xi)$ is a two-dimensional delta function, and ξ is a two-dimensional position vector from a given point on the dislocation axis in a plane perpendicular to the tangent vector τ.

In order to account for the relations between inertia of the dislocation movement and the dislocation mass, we define

$$\gamma^{\mathrm{mn}} = \rho^{\mathrm{n}} \mathrm{V^m} \delta(\xi)$$

Then the Kosevich formula (1) takes the following form:

$$\mathrm{J_{ik}} = \varepsilon_{\mathrm{ilm}} \frac{\alpha^{\mathrm{l}}{}_k}{\rho_n} \gamma^{\mathrm{mn}} = L_{ikmn} \gamma^{\mathrm{mn}} \tag{2}$$

Continuous distribution of dislocations

In accordance with our point of view, mesoelastic material incorporates a continuously distributed network of dislocations. For this material we propose the following generalization of (1):

$$\boldsymbol{\gamma} = \boldsymbol{\rho} \cdot \mathbf{J}$$

Here we call the tensor γ the surface linear mesomomentum and $\rho = \mathbf{L}^{-1}$ as the dislocation mass mesodensity tensor in the continuum.

The mesomomentum of inertia **P** for any region U on a body B can be written as flux over closed surface ∂ R bounding this volume

$$\mathbf{P}=\iint_{\partial U}\gamma\cdot d\mathbf{A}=\iiint_{U}\mathbf{p}\,dV$$

Here vector p we call linear mesomomentum. The balance of mesomomentum for smooth functions and for any portion U of a body B provides conditions for the formula $\mathbf{p}=\nabla\cdot\gamma$.

Line Mesostress

We consider a line with a unit normal cross section area. We call a force **P** acting along the line a mesoforce and define the line mesotraction to be **f =dP/dl**. For the mesocontinuum of these lines we postulate the existence of the line mesostress tensor **I= I(X,t)** with the following property: $\mathbf{f}=\mathbf{I}\cdot\boldsymbol{\tau}$ and define surface mesostress tensor $\mathbf{C}=\nabla\times\mathbf{I}$ [4]. In the following consideration we regard these lines as dislocation lines in elastic body.

Line Mesostress for Continuum of Dislocations

We choose the following generalization of Peach Koehler formula for the continuum of dislocations: $\mathbf{I}=\mathbf{K}(\mathbf{S})\cdot\boldsymbol{\alpha}$

MESOELASTIC MODEL

Here we assume that the mesostresses play the main role in the response to the material deformation. For this case we combine the following mesoelasticity system:

$$\nabla\times\mathbf{I}+\partial_t\gamma=\mathbf{C},\quad \nabla\cdot\gamma=\mathbf{p}$$
$$\nabla\times\mathbf{J}+\partial_t\alpha=\mathbf{0},\quad \nabla\cdot\alpha=\mathbf{0}$$

with the constitutive expressions:

$$\mathbf{I}=\mathbf{K}(\mathbf{S})\cdot\alpha \text{ and } \gamma=\rho(\alpha)\cdot\mathbf{J}$$

Statics

We consider the statics of an irregular structure as a steady state. Thus, we assume that **H=0, p=0** and **γ=0**. Then the system of equations is reduced to the following form:

$$\nabla\times(\mathbf{K}(\mathbf{S})\cdot\alpha)=\mathbf{C}\qquad \nabla\cdot\alpha=0$$

Taking into account that $\alpha=\nabla\times ß$ we transform the system above, in the case of constant **K(S)** and $\nabla\cdot ß=0$, to the integral equation:

$$ß(y)=\frac{1}{4\pi}\mathbf{K}^{-1}(\mathbf{S})\int_{B}\mathbf{G}(x,y)\mathbf{C}\,dV$$

If we assume that an unloading of the stressed mesoelastic body B is pure elastic then the mesoelastic stress C is responsible for the existence of the residual stress in that body.

CONCLUSIONS

The presented constitutive theory for material deformations describes the constitutive relationship between the dislocation current and the linear mesomomentum. This relationship is based on the generalization of the Kosewich formula. Based on the generalization of the Peach-Koehler formula, we propose the constitutive relation between the line mesostress tensor and the strain singularities density. These constitutive relationships have allowed us to model the stress of the mesoelastic materials.

References

[1] Guyer R. and Johnson P. A.: Nonlinear mesoscopic elasticity: evidence for a new class of materials, *Physics Today*, pp. 30-36, April 1999

[2] Landau, L. D., Lifshitz, E. M. and Kosevich, A. M.: Chapter IV: Dislocations in Theory of Elasticity, L.D. Landau and Lifshitz E. M., third (revised) ed., Pergamon Press, NY, 1986

[3] Peach, M. and Koehler, J. S.: The forces exerted on dislocations and the stress fields produced by them, *Physical Review*, 80, 436—439, 1950

[4] Steinberg, L.: Mesoelastic Deformation with Strain Singularities, *Mathematics and Mechanics of Solids*, accepted for publication, 2004

NONLINEAR RESPONSE OF MAGNETOELASTIC SOLIDS

A. Dorfmann*, R. W. Ogden **

*Institute of Structural Engineering, Peter Jordan Strasse 82, 1190 Vienna, Austria

**Department of Mathematics, University of Glasgow, Glasgow G12 8QW, UK

Summary Recently, growing interest in magnetoelastic solids has motivated a renewed interest in electromagnetic continua with particular reference to large magnetoelastic deformations. We derive governing equations of equilibrium and constitutive laws expressed in either Lagrangian and Eulerian form. The equations are then applied to the solution of a prototype boundary-value problem.

MOTIVATION AND BASIC EQUATIONS

Recently, growing interest in the mechanical and the electromagnetic properties of composites consisting of an elastomeric matrix and a distribution of ferrous micron-sized particles embedded within their bulk has been observed. This interest is motivated by newly developed engineering applications, which involve, for example, sensors, vibration absorbers, and controllable membranes for use in civil and automotive engineering. See, for example, Ginder et al. [1] and Carlson and Jolly [2]. These materials have mechanical properties that can be altered rapidly by a change in the magnitude or direction of an applied magnetic field. The magnetic response is optimized by distributing within the bulk matrix particles with a high magnetic saturation, such as an alloy of iron, and volume fractions between 0.1 and 0.5. The choice of the matrix material is based on its thermomechanical properties and, for example, silicone and other elastomers are found to be suitable materials.

In this talk we first summarize the basic equations governing the magnetic field and its interaction with a deforming continuum. To derive the constitutive properties of the magnetoelastic composite we assume the existence of a free energy function, which depends on a deformation or strain measure in addition to a magnetic field variable. Following the description of nonlinear magnetoelastic deformations of elastomers given in recent papers by the present authors [3, 4, 5], we select the magnetic induction vector $\mathbf{B}$ and the deformation gradient tensor $\mathbf{F}$ as the basic variables and write the free energy $\Psi = \Psi(\mathbf{F}, \mathbf{B})$. Applying the Clausius-Duhem inequality, expressions for the Cauchy stress tensor $\boldsymbol{\sigma}$ (in general non-symmetric) and for the magnetization vector field $\mathbf{M}$ are derived. Secondly, we provide a Lagrangian counterpart of the free energy formulation such that $\Psi(\mathbf{F}, \mathbf{B}) = \Phi(\mathbf{F}, \mathbf{B}_0)$, where $\mathbf{B}_0$ is the Lagrangian vector field corresponding to $\mathbf{B}$. The free energy Φ is used to derive expressions for the symmetric total stress tensor $\boldsymbol{\tau}$ for both compressible and incompressible materials, with the appropriate specialization for isotropic material response. The total stress tensor $\boldsymbol{\tau}$ includes, in addition to the Cauchy stress $\boldsymbol{\sigma}$, the so-called Maxwell stress. The specialization of these equations to the situation where there is no deformation but only an applied magnetic field is considered and it is pointed out that the magnetic induction $\mathbf{B}_0$ generates a residual stress in the material.

Then, we introduce an augmented free energy formulation, denoted $\Omega = \Omega(\mathbf{F}, \mathbf{B}_0)$ and defined, for incompressible materials, by

$$\Omega = \rho_0 \Phi + \frac{1}{2}\mu_0^{-1}\mathbf{B}_0 \cdot (\mathbf{c}\mathbf{B}_0),$$

where ρ_0 is the mass density in the reference configuration, the constant μ_0 is the magnetic permeability in free space and $\mathbf{c} = \mathbf{F}^T\mathbf{F}$ is the right Cauchy-Green deformation tensor. This allows the magnetoelastic equilibrium equations to be written in a very compact form.
For incompressible materials, the total stress $\boldsymbol{\tau}$ can be written in the simple form

$$\boldsymbol{\tau} = \mathbf{F}\frac{\partial \Omega}{\partial \mathbf{F}} - p\mathbf{I},$$

where p is a Lagrange multiplier associated with the constraint $\det \mathbf{F} \equiv 1$. The other relevant Eulerian quantities are given by

$$\mathbf{H} = \mathbf{F}^{-T}\frac{\partial \Omega}{\partial \mathbf{B}_0}, \quad \mathbf{M} = \mu_0^{-1}\mathbf{B} - \mathbf{H}, \quad \mathbf{B} = \mathbf{F}\mathbf{B}_0.$$

where $\mathbf{H}$ is the magnetic field.

The corresponding Lagrangian equations are the nominal stress $\mathbf{T} = \mathbf{F}^{-1}\boldsymbol{\tau}$ given by

$$\mathbf{T} = \frac{\partial \Omega}{\partial \mathbf{F}} - p\mathbf{F}^{-1}$$

and the magnetic field

$$\mathbf{H}_0 = \frac{\partial \Omega}{\partial \mathbf{B}_0}.$$

Finally, the theory is applied to the solution of a prototype boundary-value problem. We consider the problem of inflation and extension of a circular cylindrical tube under internal pressure and axial load. A closed-form solution for this problem is obtained for a particular choice of energy function.

References

[1] Ginder J. M., Nichols M. E., Elie L. D., Tardiff J. L.: Magnetorheological elastomers: properties and applications, in: M. Wuttig (Ed.), Smart Structures and Materials 1999: Smart Materials Technologies, Proceedings of SPIE 3675, 131–138, 1999.

[2] Carlson J. D., Jolly M. R.: MR fluid, foam and elastomer devices, *Mechatronics* **10**: 555–569, 2000.

[3] A. Dorfmann A., Ogden R. W.: Magnetoelastic Modelling of Elastomers, *European Journal of Mechanics - A/Solids*, **22**, 497–507, 2003.

[4] A. Dorfmann A., Ogden R. W.: Nonlinear magnetoelastic deformations of elastomers, *Acta Mechanica*, **167**: 13–28, 2004.

[5] A. Dorfmann A., Ogden R. W.: Nonlinear magnetoelastic deformations, *Q. J. Mech. Appl. Math.*, submitted, 2004.

APPLICATION OF THE CONTINUUM MECHANICS IN THE TEXTILE FABRICS

Bohuslav Stříž*, Brigita Kolčavová Sirková*, Jaroslava Richterová**
*Technical University of Liberec, Faculty of Textile Engineering, 461 17 Liberec, Czech Republic
** Technical University of Liberec, Research Center "TEXTILE", 461 17 Liberec, Czech Republic

Summary Textile fabrics represent complicated structures. The mechanical properties of these formations are possible to describe on the basis of theirs specific idealization. One of the methods of problem solving of the mechanics textiles is substitute of the textile formation by continuous environment – continuum. The substitute continuum has identical mechanical properties like testing textile fabric.

The substitution of the loaded textile fabric with specific structure by the continuum with identical mechanical properties enables to use the equations of the continuum mechanics. Then on the basis of these equations we can define the basic mechanical fabric properties. Dependencies between Euler and Lagrange coordinates of the points is possible to determine on the basis of the measured shifts of the monitoring points of the textile fabric, see Fig. 1:

$x_i^p = x_i^{\circ p} + u_i^p$, i = 1,2; p… is the number of point. (1)

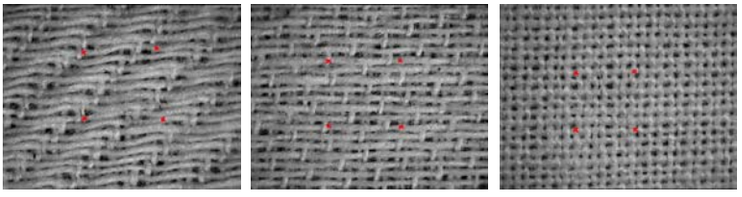


Fig. 1 Depiction of the monitoring points of the textile fabric with different thread's interlacing

For description of mechanical properties in this case we needn't thing the fictive thickness of the textile fabric if we use the definition of the relative force [Nm^{-1}] influences in area of the textile fabric. Therefore for description of the mechanical properties of the fabric we will use not tensors in the space (three-dimensional) but the tensors on the surface (two-dimensional). The tensors are:

- the material deformation gradient $F = \left(x_{i;j}\right)$, (2)
- Cauchy tensor of relative forces $\sum = \begin{pmatrix} \sigma_{11} & \sigma_{12} \\ \sigma_{12} & \sigma_{22} \end{pmatrix}$, (3)
- this tensor comes from Cauchy equation $S_i = \sigma_{ij} n_j$ at the element of textile;
- the tensor of extension $U = \left(F^T F\right)^{1/2}$; (4)
- the tensor of deformation $E = \frac{1}{m}\left(U^m - I\right)$ for $m = -2, -1, 0, 1, 2$; (5)
- the tensor of the relative forces $S = \begin{pmatrix} c_{11} & c_{12} \\ c_{12} & c_{22} \end{pmatrix}$, (6)
- the tensors satisfy the condition of the conjugation with tensors of deformation E;
- tensor of rotation R is given from the tensor F by the polar decomposition.

The measures of the deformation as well as tension are different. For calculation of the modulus of elasticity is necessary to choose suitable combination of the couple of the deformation tensor and tension tensor. For description of the textile fabric, from under mentioned conjugated couple are most used the couple with number III and IV:

I. $m = 2; \quad E = \frac{1}{2}\left(F^T F - I\right) \Leftrightarrow JF^{-1} \sum \left(F^{-1}\right)^T = S,$ (7)

II. $m = -2; \quad E = \frac{1}{2}\left(I - \left(F^T F\right)^{-1}\right) \Leftrightarrow JF^T \sum F = S,$ (8)

III. $m = 0; \quad E = \ln U \Leftrightarrow JR^T \sum R = S,$ (9)

IV. $m = 1; \quad E = U - I \Leftrightarrow \frac{J}{2}\left[F^{-1} \sum R + R^T \sum \left(F^{-1}\right)^T\right] = S,$ (10)

V. $m = -1; \quad E = I - U^{-1} \Leftrightarrow \frac{J}{2}\left[F^T \sum R + R^T \sum F\right] = S.$ (11)

The loaded textile fabrics have anisotropic character. In dependence at the manner of the loading (the loading in the principal axes of the textile structure or the loading in the general angle in view of principal axes of the textile structure) the textile fabrics can have the character of:

1) monoclinic anisotropy with six modulus of elasticity $\overline{E}_{ij}$ in the surface of the textile fabric,
2) rhombic anisotropy with four modulus of elasticity in the surface of the textile fabric.

If the tensors satisfy the specific conditions [1] for Poisson number $\overline{\nu}_{12}$, then the textile fabrics have the character of:

3) hexagonal anisotropy with two modulus of elasticity at the loading in the principal axes of the textile structure,
4) tetragonal anisotropy with four modulus of elasticity at the loading in the general direction.

The lane above the quantities $\overline{E}_{ij}$, $\overline{\nu}_{12}$ represent the parameters of the plane state of stress. For description of the modulus of elasticity $\overline{E}_{ij}$ is necessary to resolve the non-linear problem of the continuum mechanics using the constitutive equations:

$$Jc_{ij} = 2\frac{\partial\Phi}{\partial\Psi_k}\frac{\partial\Psi_k}{\partial\varepsilon_{ij}} \quad i,j = 1,2;\ k = 1,2,...,n, \tag{12}$$

where:

c_{ij}, ε_{ij} are the components of the tensors of the selected conjugated couple,

2Φ is the elastic potential given by the conjugated couple and Ψ_k its invariant.

According to type of anisotropy above-mentioned equations is necessary to connect with under mentioned dependencies:

$$tg2\omega = \frac{2\left(\overline{E}_{14} + \overline{E}_{24}\right)}{\overline{E}_{11} - \overline{E}_{22}}, \tag{13}$$

$$\overline{E}_4 = \frac{\tau_i}{\gamma_i}, \tag{14}$$

$$\overline{E}_{11}\overline{E}_{22} - \overline{E}_{12}^2 - \overline{E}_4\left(\overline{E}_{11} + \overline{E} + _{22} + 2\overline{E}_{12}\right) = 0, \tag{15}$$

$$2\overline{E}_4 - \overline{E}_{11} + \overline{E}_{12} = 0. \tag{15a}$$

where:

ω is the angle between the principal axis of anisotropy and the direction of the textile loading,

τ_i, γ_i are the intensity of relative shearing forces and shear strain, the equation (15a) describes the transversal isotropy of the textile.

Discussion

Firstly –Description of the textile mechanics

Identification of the mechanical textile fabric properties stressed by uniaxial or biaxial state of stress is possible to pursue only for specific concrete state of stress and strain. The changes of the state of stress lead to the change of the mechanical parameters.

Secondly –Description of the textile structure

Each of textile fabric has different structure; it is not homogeneous [2]. From the textile parameters viewpoint is necessary to describe the structure of the textile as well as the kind of textile fabric (woven fabric, non-woven fabric or knitting fabric). The input parameters of these fabrics and their parameters in the longitudinal as well as transverse section influence the final mechanical properties [3].

References

[1] Stříž, B.: Mechanics of Textiles I, II. Technical University of Liberec, 2001, 2003
[2] Nosek, S.: Structure and Geometry of Woven Fabrics, Liberec 1996
[3] Sirková, B., Richterová, J.: The Influence of Thread's Interlacing as well as Yarn's Parameters on the Mechanical Properties of the Woven Fabrics, 5th EUROMECH, Thessaloniki, 2003

GENERALIZED CONTINUUM MECHANICS : THREE PATHS

Gérard A. Maugin,
Laboratoire de Modélisation en Mécanique, UMR CNRS 7607
Université Pierre et Marie Curie, Paris, France
e-mail : gam@ccr.jussieu.fr

Summary The material framework is considered to place in evidence three essential ways of generalizing standard continuum mechanics, the latter being the theory of one-component simple materials (after W.Noll) with symmetric Cauchy stress. The three possible paths to generalization are (i) the loss of the Euclidean nature of the background material manifold, (ii) the loss of validity of Cauchy's construct of the notion of stress and (iii) the loss of symmetry of the latter. Special attention is paid to the consequences of these different losses on the canonical balance of momentum and its moment, whose ontological status is the same as the balance of energy, i.e., they concern the whole physical system under consideration (in particular, all degrees of freedom simultaneoulsy). Because of (i), these considerations of necessity are in that material framework which is the realm of configurational forces and forces driving structural defects.

BACKGROUND

With the advent of homogenization techniques, the inclusion of metallurgical -and other - microstructures, the production of artificial materials with a controlled microstucture, and a growing interest in continuum mechanics at a smaller scale, the question of what is a generalized continuum comes up naturally. Here we would like to ponder the general notion of " generalized continuum " in the light of our thirty five years involvment in the field and the more recent developments in the so-called " material " mechanics of materials where the Eshelby stress is the main force-like ingredient (a longer paper in French is Ref.[1]).

What is to be understood by " generalized continuum mechanics " ? It obviously is dangerous, and somewhat preposterous to define the degree of generalization of a theory. For instance, many mathematicians and engineers called " generalized Hooke law " the constitutive equation for a linear , homogeneous but *anisotropic* elastic material. we shall all admit that this is a very weak generalization. The same holds true of the Hooke-Duhamel stress constitutive equation in *linear* thermoelasticity. The situation still is of the same type is the now again fashionable (because of the consideration of so-called smart materials) linear theory of *piezoelectricity* since not only the required anistropy can be dealt with easily but many problems can be reformulated using a four-dimensional " displacement " (being the classical one to which is adjoined the electrostatic potential). This is true because of the smallness of the electric fields involved. The situation is totally different when one deals with heterogeneous elasticity where a characteristic length introduces itself in the formulation, rendering dynamical wave-like problems *dispersive*. In all these cases, though, the Cauchy stress tensor remains *symmetric*.

THE THREE PATHS

The first temptation to call a continuum theory really *generalized* comes with the consideration of a *non-symmetric* Cauchy stress tensor , e.g., when the ponderomotive couple due to electromagnetic fields in finitely electrically polarizable or magnetizable bodies is no longer neglegible. This is documented in detail in Ref.[2] as well as the much more complicated case when electric and magnetic degrees of freedom are associated with a corresponding microstructure (due to electric or magnetic dipoles, such as in ferroelectrics and ferromagnets of different types, etc). Note only is the Cauchy stress tensor no longer symmetric but then the basic Euler-Cauchy equation of motion (balance of physical linear momentum) is coupled to additional local balance equations related to these microstructures. This introduces the notion of additional degrees of freedom, albeit of a nonmechanical nature. Clearly, the introduction of additional degrees of freedom of a mechanical nature a each material point will produce the same type of generalization. This occurs when one recognizes that the kinematic-deformation modelling of a material point $\mathbf{X}$ by the usual degree of translation (the " displacement " giving rise by spatial differentiation to the notions of deformation and classical rotation) is not sufficient to describe the clearly present microstructure of many materials. The relevant concepts go back to Duhem and the Cosserat brothers, but they were revisited in the 1960s by many authors (Aero and Kuvshinskii, Palmov, Grioli, Eringen and Suhubi, Toupin, Green and Rivlin, Mindlin and Tiersten, W.Nowacki, etc). Two types of approaches are to be put forward, one attributing a set of *directors* , rigidly or nonrigidly attached to one another, to each material point (the Duhem-Toupin-Ericksen way) and another one introducing at each material point $\mathbf{X}$ a micro-deformation of a purely rotating type (the Cosserat or micropolar model) or of a

general deformation type (so-called micromorphic model of Eringen *et al* [3]). All these models are conveniently introduced without ambiguity by using the principle of virtual power as the essential tool of formulation [4]-[5].

Two other steps of going further toward generalization consist in considering first a *weak*, and then a *strong* nonlocality in the *internal force* effects of which stress is an example. The first of these consists in introducing successive gradients of a field as a priori independent field variables at the same point **X** (the idea of a Cauchy expansion of a field). This in principle is applicable to all fields but the displacement is that field considered in the purely mechanical case. Noll's notion of a *simple material* is lost as well as the traditional Cauchy construct for the introduction of the stress notion [6]-[7]. The situation is worst for a strongly nonlocal theory in which the mechanical response at a material point **X** theoretically depends on what occurs kinematically at all points in the body [8]. The argument is strictly valid only for an infinite body, so that in truth the notion of Cauchy stress itself is lost. Finally, in all previous examples we assumed that the material manifold is a classical Euclidean one. This hypothesis may be given up by choice or necessity in the presence of continuous distributions of defects which hinder the continuity of the displacement field. This is the Bilby-Kroener-Noll-Wang-Epstein-Maugin-Rakotomanana (and others) way.

From the above, putting now the arguments in the logical order, we can propose a definition of " generalized continuum mechanics " : We say that we have such a mechanics whenever one of the following three basic tenets of classical continuum mechanics is no longer true : (i) the background material manifold is Euclidean, (ii) Cauchy's construct of the notion of stress holds true, (ii) Cauchy's stress is symmetric. Because of point (i) above the present contribution examines consequences of the loss of anyone of the hypotheses directly on the *material manifold*, where the appropriate stress measure is Eshelby's material stress tensor and this is the realm of all kinds of true or pseudo material inhomogeneities, as emphasized in many recent works [9]-[11]. Special attention is paid to the local *canonical* balance of momentum and its moment that accompany the balance of energy. All considerations are developed in comparison with the somewhat standard purely elastic, although nonlinear anisotropic, inhomogeneous case. Not only does this capture all the fields introduced but, as is known, it also permits constructive considerations in the theory of field singularities.

References

[1] G.A.Maugin, Inaugural lecture " Introduction à la mécanique des milieux continus généralisés ", *National MECAMAT Colloquium*, eds. J.-F. Ganghoffer *et al*, Aussois, January 2004, Published by Association Mécamat.-France [CD-Rom]
[2] G.A.Maugin, *Continuum Mechanics of Electromagnetic Solids*, North Holland -Elsevier, Amsterdam (1988).
[3] A.C.Eringen , *Microcontinuum Field Theories-I-Foundations*, Springer-Vrelag, New York (2000).
[4] G.A.Maugin, The Method of Virtual Power in Continuum Mechanics : Application to coupled fields. *Acta Mechanica*, **35**, 1-70 (1980).
[5] P.Germain, La méthode des puissances virtuelles en mécanique des milieux continus-I-:Théorie du second Gradient, *J.Mécanique*, **12**, 235-274 (1973).
[6]W.Noll and E.Virga, On Edge Interactions and Surface Tension, *Arch.Rat.Mech.Anal.*, **111**, 1-31 (1990).
[7] F.dell'Isola and P.Seppecher, The Relationship Between Edge Contact Forces and Intersticial Working allowed by the Principle of Virtual Power, *C.R.Acad.Sci.Paris*, **321-IIb**, 303-308 (1995).
[8] A.C.Eringen, *Nonlocal Continuum Field Theories*, Springer-Verlag, New York (2002).
[9] GA.Maugin, *Material Inhomogeneities in Elasticity*, Chapman and Hall, London (1993)
[10] G.A.Maugin, Thermomechanics of Inhomogeneous-heterogeneous Systems : Application to the Irreversible Progress of two and Three-dimensional Defects, *ARI*, **50**, 41-56 (1997).
[11] G.A.Maugin, Pseudo-plasticity and Pseudo-inhomogeneity effects in Materials Mechanics, C.A.Truesdell Memorial Issue, eds. C.S.Man and R.Fosdick, *J.Elasticity*, **71**, 81-103 (2003).

DEFORMATION OF SOLDER JOINTS UNDER CURRENT STRESSING: EXPERIMENTAL MEASUREMENT AND NUMERICAL SIMULATION

Hua Ye[*], Cemal Basaran[*], Douglas C. Hopkins[*], Darrel Frear[**]
[*]*Electronic Packaging Lab, SUNY at Buffalo, Buffalo, New York, USA 14260*
[**]*Interconnect System Laboratory, Motorola, Tempe, Arizona, USA 85284*

Summary The in-situ displacements evolutions of lead-free solder joints under electric current stressing are measured with Moiré Interferometry technique. Large deformations due to electromigration were observed in solder joint under high density current stressing. An electromigration constitutive model is applied to simulate deformations of the lead-free solder joints under current stressing. The simulations predict reasonably close displacement results to Moiré Interferometry experimental results in both spatial distributions and time history evolutions.

INTRODUCTION

Electromigration in solder joints under high direct current density is known as a reliability concern for the future high density microelectronic packaging and power electronic packaging. The trend in flip-chip and Ball Grid Array (BGA) packaging to increase I/O count drives the interconnecting solder joints to be smaller in size and, thus, carry higher current density. A physical limit to increasing current density in both microelectronics and power electronics is electromigration in solder joints. In this paper, the deformation of lead-free solder joint under high density current stressing is measured with Moiré Interferometry technique. The lead-free solder alloy used in the Moiré Interferometry experiment is Sn95.5/Ag4/Cu0.5. With improved thermal management in the experiments, high current density ($10^4 A/cm^2$) was applied to the solder joint without much heat generation. An electromigration constitutive model is presented and applied to simulate the deformation evolution in lead-free solder joints under electromigration. The simulation results are compared with the experimental results.

EXPERIMENTAL

Figure 1 shows the scheme of the test BGA module and the test fixture. The fabrication of BGA module follows the same procedure described in a previous paper [1]. Copper plates are used to clamp the test module in order to provide electrical contacts. The set-up of the stressing circuitry and a description of Moiré Interferometry technique used in the experiment can be found in our previous paper [1]. The height of the solder joint is 1.5*mm* and the width is reduced to 1*mm*. The thickness of the solder joint is polished down to about 0.25mm. When 30 *Amps* of current is applied, a current density above 10^4 A/cm^2 can be achieved in the solder joint. The temperature on the sample was measured (with thermal couples) to be uniformly distributed in the test module and was kept almost constant (around 30ºC) during the entire period of current stressing (up to 1000 hours).

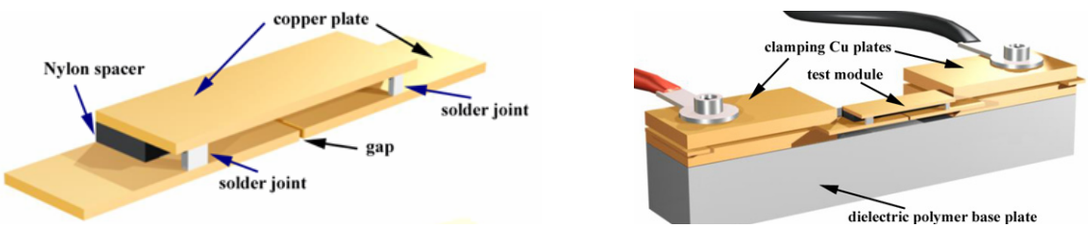


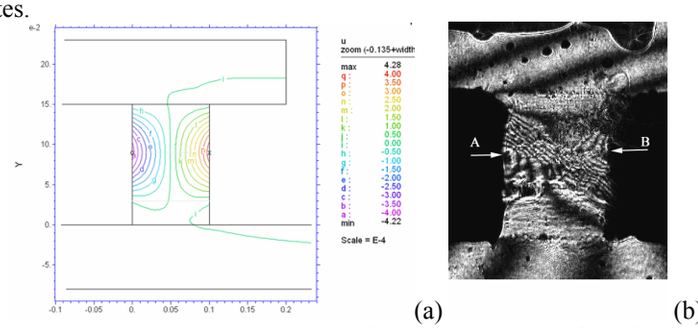
Figure 1 Scheme of the test module and the test fixture

Both U and V fields developed a lot of Moiré fringes during the course of current stressing (Figure 2b and Figure 3b). The U field fringes were predominantly in the vertical direction and the V field fringes were predominantly in the horizontal direction, indicating that normal deformations were predominant during stressing. The evolutions of Moiré fringes in both fields were observed to become steady after 1000 hours of current stressing, indicating that the deformation of solder joint under electric current stressing reaches steady state after 1000 hours of stressing. The measured deformations are mostly due to current stressing in that: first, thermal deformation in the solder joint would be mainly shear deformation in such test structure. However, the measured deformations were mainly normal deformations. Second, the temperature increase due to joule heating was only several degrees. Therefore, thermal deformation should be negligible. Third, temperature was kept almost constant during stressing. Thermal deformation should become steady within a short period of time. However, the observed deformation took hundreds of hours to reach steady state. Fourth, a supportive experiment indicates that no deformation would be measured if no current is applied to the test vehicle.

NUMERICAL SIMULATION OF DEFORMATIONS OF SOLDER JOINTS UNDER CURRENT STRESSING

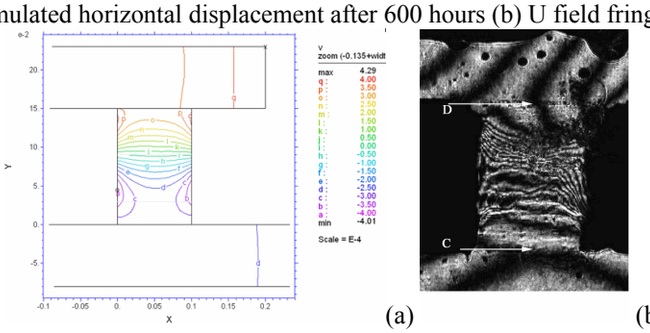
The electromigration in solder joints is viewed as a coupled diffusion-mechanical process in the modeling. The electron flow assisted vacancy diffusion process gives rise to volumetric strain in the conducting solder alloy. This volumetric strain is superimposed into the strain due to mechanical loading (analogous to thermal strain) as proposed by Sarychev

[2].Under the mechanical boundary constrains, the volumetric strain due to diffusion results in stress build-up within the structure. If the hydrostatic stress state within the conducting solder is changed or there is hydrostatic stress gradient created, the stress state will in turn affect the vacancy flux or vacancy generation rate in the diffusion process. The deformations within the solder joints can be determined by solving the coupled diffusion and mechanical equilibrium partial differential equations. The detailed formulation of the electromigration model is reported in a previous paper [3]. In this paper, we extend this constitutive model to simulate the electromigration of lead-free solder alloy. We performed 2-D FEM simulations, in which the plane stress assumption is applied to solder joints and plane strain assumption is applied to cupper substrates.



(a) (b)

Figure 2 (a) Simulated horizontal displacement after 600 hours (b) U field fringe after 605 hours



(a) (b)

Figure 3 (a) Simulated vertical displacement after 600 hours (b) V field fringe after 605 hours

Figures 2-3 show the comparisons between the numerical simulation and Moiré Interferometry results. The simulated distributions of both horizontal and vertical displacements resemble the distributions measured by experiment: there are large normal deformation developed in the horizontal direction but the horizontal normal deformations are not uniform along the both edges of the solder joint; there are also large normal deformation developed in the vertical direction. The simulation results are not exactly the same as the experiment measurements. But considering all the assumptions that were taken and many simplifications of the simulation model, the simulation results are quit reasonable. Comparisons of time history evolutions of displacements between the simulation and the experimental results also show close agreements. This indicates that this electromigration model is reasonably good at predicting the mechanical behavior of lead-free solder alloy under electric current stressing. In the experiments, the thicknesses of the solder joints were not uniform. In the simulation, this non-uniformity is taken into account by means of applying non-uniformly distributed current density. Solder joints with different current density level were tested and numerically simulated. Both the experimental results and simulations suggest that, in addition to the current density level, current density distribution within the solder joint has a great effect on the displacement development in the solder joint under current stressing. Specifically, greater non-uniformity in current density leads to greater normal deformations within the solder joint.

CONCLUSIONS

In this paper, the in-situ displacements evolutions of lead-free solder joints under electric current stressing are measured with Moiré Interferometry technique. Large deformation was observed in solder joint under high density current stressing. The deformations are due to electromigration in the solder joints. An electromigration constitutive model is applied to simulate deformations of the lead-free solder joints under current stressing. The simulations predict reasonably close displacement results to Moiré Interferometry experimental results in both spatial distributions and time history evolutions. This indicates that this electromigration model is reasonably good at predicting the mechanical behavior of lead-free solder alloy under electric current stressing. Both the experimental observations and finite element simulation results indicate that, in addition to the current density level, the current density distribution within the solder joint has a great effect on the displacement development in the solder joint under current stressing.

References

[1] Ye, H., Hopkins, D. C., and Basaran, C., *Microelectronics Reliability*, 43, pp. 2021-2029, 2003.
[2] Sarychev, M. E. and Zhinikov, Yu. V., *Journal of Applied Physics*, vol. 86, no. 6, pp. 3068-3075, 1999.
[3] Ye, H., Basaran, C., and Hopkins, D., *IEEE Transactions on Components and Packaging Technologies*, vol. 26, no. 3, pp. 673-681, 2003

XXI ICTAM, 15–21 August 2004, Warsaw, Poland

VISCOELASTIC FLUID FLOWS IN A FALLING CYLINDER VISCOMETER AND THE EVALUATION OF SHEAR VISCOSITY

Victor M. Tigoiu*,
*University of Bucharest, Faculty of Mathematics and Informatics, 14 Academiei, 012014 Bucharest, Romania

Summary In this paper we consider the problem of the flow of some non-newtonian fluids (second grade, third grade and second order fluids) in a falling cylinder viscometer. If the problem for a second grade fluid is similar to the corresponding problem for linear viscous fluids, largely discussed in Cristescu and all (2002), the other two problems are essentially different. The differences (appearing in the velocity field and shear stress component) are put into evidence. More, the formula of the shear viscosity for a third grade fluid can be interpreted (for instance) as a relation for the determination of the sum $\beta_2+\beta_3$ of constitutive moduli (and leads, in the case of the law obtained by Fosdick and Rajagopal (1980), to the complete determination of constitutive moduli).

POSITION OF THE PROBLEM

The problem of the falling cylinder viscometer filled with a linear incompressible viscous fluid was recently analyzed in Cristescu and all [1]. Here it was presented the theory of this apparatus, some experiments and obtained an analytical solution, for the flow problem and a formula for the shear viscosity (which, in this case, coincides with the kinematic viscosity). An extensive bibliography is also presented and discussed in this paper and we refer to this one. However many biological fluids have a significant non-newtonian behaviour and for this reason we consider here the problem for some classes of non-newtonian fluids like: second grade, third grade and second order fluids. We rely on the description of the apparatus made in [1]. We emphasize here that the radius of the falling cylinder R_1 is of the order of 10^{-4} m, while the radius of the outer (fixed) cylinder, R_2 is: $R_1 < R_2 < 10^{-3}$ m. The velocity of the falling cylinder is of the order of $10^{-4} - 10^{-3}$ m/s, l « h, where l is the length of the falling (inner) cylinder and h is the length of the outer cylinder. We also remind that, in viscoelastic fluids, the shear viscosity is more significant than in a linear viscous fluid (and generally depends on shear rate). We remark on the one hand that, for second grade fluids, the problem is similar to those described in [1] for a linear viscous fluid and, on the other hand that, for third grade fluids, as well as for second order fluids, the problems are completely different. The existence and uniqueness of the solutions are proved and numerical calculations are performed in order to (graphically) compare the velocity fields and the shear stress components. A new formula (after our knowledge) which connect the shear viscosity, the plateau viscosity and the constitutive moduli β_2, β_3 is obtained, for a third grade fluid (which is useful in order to evaluate the sum $\beta_2+\beta_3$). We underline (see also [1]) that the measurements must be made into the "central" part (in respect to the length of the outer cylinder) of the flow such as to provide for V_1 a constant value during the experiment (see [1] Fig.2). The admissible velocity field considered here is (in cylindrical coordinates)

$$v_r = 0, \quad v_\theta = 0, \quad v_z = V_1 f(r),\ r \in [R_1, R_2]. \tag{1}$$

and the boundary conditions are

$$v_z(R_1) = V_1, \quad v_z(R_2) = 0. \tag{2}$$

From this point we suppose that (due to the fact that h » l, the discussions from [1] and the introduction to [2]) the pipe (outer fixed cylinder) has of infinite length and we choose the reference (cylindrical) system with the z-axis oriented in the same sense as the acceleration of gravity. As the considered motion is viscometric Cauchy's stress tensor will be given by $\mathbf{T} \equiv -p\mathbf{I} + \overline{\mathbf{T}}(\mathbf{A_1}, \mathbf{A_2})$ and we consider the following formulae for second grade (see Dunn and Fosdick [3]), third grade (see Tigoiu [4], with the mention that $\mathbf{A_3} = \mathbf{0}$, or Fosdick and Rajagopal [5] for a different formula) and second order fluids ([3])

$$\begin{aligned}
\overline{\mathbf{T}}(\mathbf{A_1}, \mathbf{A_2}) = &\quad \mu\mathbf{A_1} + \alpha_1(\mathbf{A_2} - \mathbf{A_1}^2), \quad \mu,\ \alpha_1 \in \mathbf{R},\ \mu \geq 0;\\
\overline{\mathbf{T}}(\mathbf{A}_1, \mathbf{A}_2) = &\quad \mu\mathbf{A}_1 + \alpha_1(\mathbf{A}_2 - \mathbf{A}_1^2) + \beta_1\mathbf{A}_3 + \beta_2(\mathbf{A}_1\mathbf{A}_2 + \mathbf{A}_2\mathbf{A}_1) + \beta_3(tr\mathbf{A}_1^2)\mathbf{A}_1,\\
&\quad \mu \geq 0,\ \beta_1 < 0,\ \beta_1 + 2(\beta_2+\beta_3) \geq 0;\\
\overline{\mathbf{T}}(\mathbf{A_1}, \mathbf{A_2}) = &\quad \mu(tr\mathbf{A_1^2})\mathbf{A_1} + \alpha_1(\mathbf{A_2} - \mathbf{A_1}^2), \quad \alpha_1 \in \mathbf{R},\\
&\quad \mu(tr\mathbf{A_1^2}) = \eta_0 exp\left\{-Aln10\Big[\frac{1}{2}log\big(\frac{R_1^2}{V_1^2}tr\mathbf{A_1^2}\big) + 3\Big]^2\right\}.
\end{aligned} \tag{3}$$

Here, for the formula for a second order fluid, we have employed (for the choice of shear viscosity expression (3)$_3$) the graphs from Coleman, Markowitz and Noll [6], for a polyisobutylene in decaline solution (13%) in

SOLUTIONS FOR THE BOUNDARY VALUE PROBLEM AND EVALUATION OF SHEAR VISCOSITY

Introducing the admissible velocity field (1) into (3) and the resulting formulae into the balance of linear momentum equations we obtain (adding also the boundary conditions (2)) the corresponding flow problems. For the second grade fluid, the solution of the boundary value problem is analytically obtained and for the dimensional velocity field and for the shear stress component we have

$$\begin{aligned}
&\mu v_z(r) = \frac{1}{4}(\frac{\partial p}{\partial z} - \rho_l g)r^2 + \mu V_1 C_1 ln(r/R_1) + \mu V_1 C_2;\\
&T_{rz}(r) = \frac{1}{2}(\frac{\partial p}{\partial z} - \rho_l g)r + \mu V_1 C_1 \frac{1}{r};\\
&C_1 = -\big[\frac{1}{4}Re\sigma_z \frac{R_2^2 - R_1^2}{R_1^2} + 1\big]\frac{1}{ln(R_2/R_1)};\ \ C_2 = 1 - \frac{1}{4}Re\sigma_z;\\
&Re \equiv \frac{\rho_l g R_1^2}{\mu V_1},\quad \sigma_z \equiv \frac{\partial p}{\partial z} - \rho_l g,
\end{aligned} \tag{4}$$

where ρ_l is the mass density of the fluid. It is simply to remark that in this case the shear viscosity $\eta = (\mu) = const.$ (unfortunately) and the solution is slightly different from the relation (3.15) in [1].
For a third grade fluid $(3)_2$, a first integral for the flow problem leads to the determination of the nondimensional shear stress by

$$f' + \beta f'^3 = (T_{rz}) = \frac{1}{2}Re\sigma_z r + C_1 \frac{1}{r} \tag{5}$$

and the unique solution of equation (5) has the form

$$f'(r) = \frac{1}{(2\beta)^{\frac{1}{3}}}\Big\{\sqrt[3]{C + \sqrt{C^2 + \frac{4}{27\beta}}} + \sqrt[3]{C - \sqrt{C^2 + \frac{4}{27\beta}}}\Big\}, \tag{6}$$

where we have denoted $C \equiv C(r) \equiv ar + \frac{C_1}{r}$, $a \equiv \frac{1}{2}Re\sigma_z$ and $\beta \equiv \frac{2(\beta_2 + \beta_3)V_1^2}{\mu R_1^2}$. The solution of (6) was obtained by numerical integration and graphically compared with the corresponding solution for a second grade fluid (or a linear viscous fluid). From the formula for the shear viscosity, computed for $r = R_1$, for instance, we obtain the relation

$$\eta = \mu(1 + \beta f'^2(1;\beta)), \tag{7}$$

for the determination of β, once the plateau viscosity, η_0, is known (here $\eta_0 = \mu$).
For a second order fluid $(3)_{3,4}$, the first integral (giving the shear stress component) is

$$\mu(f'^2)f' = (T_{rz}) = \tfrac{1}{2}\mathrm{R}e\sigma_z r + C_1\tfrac{1}{r}. \tag{8}$$

This equation can be written in first approximation as

$$f'(r) = (\tfrac{1}{2}\mathrm{R}e\sigma_z r + C_1\tfrac{1}{r})\Big\{1 + \mathrm{A}ln10\Big[\tfrac{1}{2}\mathrm{log}f'^2 + 3\Big]^2\Big\}. \tag{9}$$

On a part this last equation (by combining with a shooting method) can be numerically solved (and the solution is graphically compared with those for a third grade and second grade fluid). On an other part, restricting ourself to the first approximation of (9), we obtain a forth order equation with an unique negative solution (f'<0), which finally is again numerically computed.

References

[1] Cristescu N.D., Conrad B.P., Tran-Son-Tay R.: A closed form solution for falling cylinder viscometers, Int.J.Engn.Sci, 40:605-620, 2002.
[2] Tigoiu V., Cipu C.: Flow of some viscoelastic fluids in a falling cylinder viscometer and the evaluation of shear viscosity, New trends in continuum mechanics, Proc. of the International EURROMMAT Seminar, Constanta, sept.2003 (to appear).
[3] Dunn J.E., Fosdick R.L.: Thermodynamics, stability and boundedness of fluids of complexity 2 and fluids of second grade, Arch.Rat.Mech.Anal., 56: 191-252, 1971.
[4] Tigoiu V.: Wave propagation and thermodynamics for third grade fluids, St.Cerc.Mat., 39, 4: 279-347, 1987.
[5] Fosdick R.L., Rajagopal K. R.: Thermodynamic and stability of fluids of third grade, Proc. Roy. Soc. London A, 339: 351-377, 1980.

FUNDAMENTAL INEQUALITIES FOR THE BOUNDS ON THE EFFECTIVE TRANSPORT COEFFICIENTS OF TWO–PHASE MEDIA

S. Tokarzewski[1], J.J. Telega[1], J. Gilewicz[2]
[1] *Polish Academy of Sciences IPPT PAN, Swiętokrzyska 21, 00–049 Warsaw, Poland*
[2] *Centre de Physique Théorique, CNRS, Luminy Case 907, 13288 Marseille Cedex 09, France*

Summary By starting from the truncated power expansions given at a number of discrete real points we establish the general inequalities for the effective transport coefficients Q of macroscopically isotropic two phase media.The inequalities obtained provide the new upper and lower bounds on Q the best with respect to the available power series coefficients. For specific cases these new bounds reduce to the classical ones due to Wienner and Hashin-Shtrikman. They are also coincide with the estimations of Bergman [1] and Milton [3] derived for the fitting problem. Many illustrative examples show the usefullness of the results obtained..

FORMULATION OF THE PROBLEM

It is well-known that the effective transport coefficient of a two-phase medium with macroscopic isotropic symmetry has a Stieltjes integral representation:

$$f_1(x)=\frac{Q(x)-1}{x}=\int_0^1\frac{d\gamma_1(u)}{1+xu},\ d\gamma_1(u)>0,\ x=\frac{q_2}{q_1}-1,\ Q(x)=\frac{q_{ef}(x)}{q_1};\ f_1(-1)\le 1. \tag{1}$$

Here q_{ef} denotes the effective modulus of the composite material, while q_1, q_2 describe the physical properties of its constituents. Assume that the truncated power expansions of $f_1(x)$ at $x_1,\ x_2, ...,\ x_N, -1$ be given, where $-1<x_j,\ j=1,2,...,N,$

$$f_1(x)=f_1(-1)+O(x+1);\ f_1(-1)\le 1;\ f_1(x)=\sum_{i=0}^{p_j-1}c_{ij}(x-x_j)^i+O((x-x_j)^{p_j}),\ j=1,2,...,N\ . \tag{2}$$

The following abbreviated notation for the truncated power series (2) will also be used:

$$f_1(x)=f_1|_{\boldsymbol{x}}^{\boldsymbol{p}}(x-\boldsymbol{x})+O(x-\boldsymbol{x})^{\boldsymbol{p}},\ \boldsymbol{x}=[x_1,x_2,...,x_N,-1]\,,\ \boldsymbol{p}=[p_1,p_2,...,p_N,1]\,,\ f_1(-1)\le 1 \tag{3}$$

The aim of this contribution is to establish, starting from the power expansions (3), the general inequalities for the Stieltjes function $f_1(x)$, and next via (1) the best upper and lower bounds on the effective coefficient $Q(x)$.

THE METHOD OF SOLUTION

In the first step the inequality $f_1(-1)\le 1$ is replaced formally by the equality $f_1(-1)=1$, cf. (3). The input data (3) transform to

$$f_1(x)=f_1|_{\boldsymbol{x}}^{\boldsymbol{p}}(x-\boldsymbol{x})+O(z-\boldsymbol{x})^{\boldsymbol{p}},\ \boldsymbol{x}=[x_1,x_2,...,x_N,-1]\,,\ \boldsymbol{p}=[p_1,p_2,...,p_N,1]\,,\ f_1(-1)=1. \tag{4}$$

Next by introducing $P_0=0,\ P_j=\sum_{i=1}^j p_i,\ j=1,2,...,N;\ \ P=P_N+1$ we expand the original Stieltjes function $f_1(x)$ given by (1) to the new Stieltjes one $f_{_P}(x)$

$$\begin{gathered}
f_{P_0+1}(x)=\frac{f_{P_0+1}(x_1)}{1+(x-x_1)f_{P_0+2}(x)},\ f_{P_0+2}(x)=\frac{f_{P_0+2}(x_1)}{1+(x-x_1)f_{P_0+3}(x)},\ ...,\ f_{P_1}(x)=\frac{f_{P_1}(x_1)}{1+(x-x_1)f_{P_1+1}(x)},\\
f_{P_1+1}(x)=\frac{f_{P_1+1}(x_2)}{1+(x-x_2)f_{P_1+2}(x)},\ f_{P_1+2}(x)=\frac{f_{P_1+2}(x_2)}{1+(x-x_2)f_{P_1+3}(x)},\ ...,\ f_{P_2}(x)=\frac{f_{P_2}(x_2)}{1+(x-x_2)f_{P_2+1}(x)},\\
\cdots\cdots\cdots

The functions $F_P(x,0)$ and $F_P(x,-1)$ are the multipoint Padé approximant $[m_P/n_P](x)$ and $[m_{P-1}/n_{P-1}](x)$ to $f_1(x)$, where $[m_P/n_P] = \frac{a_0+a_1x^1+\cdots+a_{m_P}x^{m_P}}{1+b_1x^1+\cdots+b_{n_P}x^{n_P}}$, $m_P = P-1-n_P$, $n_P = E(P/2)$, $P = \sum_{j=1}^{N} p_j + 1$. Relations (9) provide the fundamental inequalities for the multipoint Padé approximants to the Stieltjes function $f_1(x)$ representing via (1) the effective transport coefficient $Q\,(x)$.

FUNDAMENTAL INEQUALITIES

Let $L_R(x) = \sum_{j=1}^{N} p_j H(x-x_j)$ determining the total number $p_1 + p_2 + ...p_s$ of the coefficients of the power expansions of $f_1(x)$ available at points $x_1,\ x_2,\ ...,x_s \le x$ be given, see (4). By introducing the piecewise continnous function $M_R(x) = (L_R(x)$ if $-\infty < x < 0$ or $L_R(x)+1$ if $-\infty < x < 0)$, the relations (9) can be easily transformed to the following inequalities for the multipoint Padé approximants $x[m_R/n_R]$ and $x[m_{R+1}/n_{R+1}]$ to the effective transport coefficient $Q(x)-1$, cf. (1),

$$(-1)^{M_R(x)} x[m_{R+1}/n_{R+1}](x) \le (-1)^{M_R(x)}\,(Q(x)-1) \le (-1)^{M_R(x)} x[m_R/n_R](x),\ x \in [-1,\infty). \qquad (10)$$

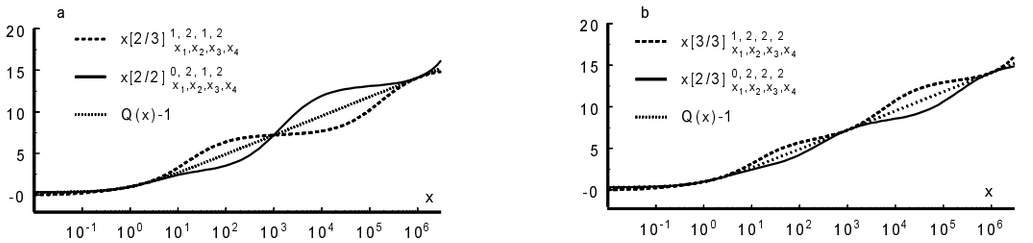


Fig. 1: Three- and four-point Padé approximants to the function $Q(x)-1 = xf_1(x),\ f_1(x) = \frac{\ln(0.5(2+x))}{x}$. representing the bounds on $Q(x)-1$ predicted by the fundamental inequality (10). Here $x_1 = -1,\ x_2 = 0,\ x_3 = 999,\ x_4 = 999999$.

Inequalities (10) provides the best upper and lower bounds on $Q(x)-1$ as a function of $L_R(x)$ depending on the given numbers of coeffcients of power series (4). The multipoint Padé approximant bounds given by (10) generalize all previous bounds reported in the literature, cf. [1,2,3,4]. From that point of view the general bounds (10) are new.

PARTICULAR CASES

From $Q(x) = 1 + O(x),\ Q(x) = Q(-1) + O(x+1),\ Q(-1) \le 1$the elementary bounds follow.

$$(-1)^{H(x)}(1+x) \le (-1)^{H(x)}Q(x) \le (-1)^{H(x)},\ x \in [-1,\infty), \qquad (11)$$

For $Q(x) = 1 + \varphi_2 x + O(x^2),\ Q(x) = Q(-1) + O(x+1),\ Q(-1) \le 1$ the Wienner bounds result.

$$(-1)^{2H(x)}\left(1 + \frac{\varphi_2 x}{1+\varphi_1 x}\right) \le (-1)^{2H(x)}Q(x) \le (-1)^{2H(x)}\,(1+\varphi_2 x)\,,\ x \in [-1,\infty). \qquad (12)$$

For $Q(x) = 1 + \varphi_2 x + 0.5\varphi_2\varphi_1 x^2 + O(x^3),\ Q(x) = Q(-1) + O(x+1),\ Q(-1) \le 1$ the H–S bounds are obtaine

$$(-1)^{3H(x)}\left(1 + \frac{\varphi_2 x + 0.5\varphi_2 x^2}{1+0.5(1+\varphi_1)x}\right) \le (-1)^{3H(x)}Q(x) \le (-1)^{3H(x)}\left(1 + \frac{\varphi_2 x}{1+0.5\varphi_1 x}\right),\ x \in [-1,\infty). \qquad (13)$$

Here φ_1 and φ_2 denote the volume fractions of the first and second component of the two-phase composite.

CONCLUSIONS

By using special multipoint continued fraction technique, from several truncated power series we have derived the general inequalities for the multipoint Padé approximants to the effective transport coefficients (dielectric or diffusion constants, magnetic permeabilities, thermal or electrical conductivities) of two-phase media. Those inequalities are new and provide the best upper and lower bounds on $Q(x)$ over the entire class of rational functions. Note that they are obtained in a unified and coherent form as a function of $M_R(x)$ depending on given numbers of coeffcients of the power expansions of $Q(x)$ only. Moreover, they generalize all previously known relevant bounds, cf. [1,2,3,4].

Acknowledgment The first two authors were also supported by the State Committee for Scientific Research (KBN, Poland) through the Grants No 8 T07A 052 21 and No 3 P04D 007 25

References

[1] D.J. Bergman, Hierarchies of Stieltjes functions and their application to the calculation of bounds for the dielectric constant of a two-components composite medium, SIAM J. Appl. Math., 53:915–930, 1993.

[2] J. Gilewicz, M. Pindor, J.J. Telega, and S. Tokarzewski, N-point Padé approximants and two sided estimates of errors on the real axis for Stieltjes functions J. Comp. Appl. Math., 2004, in press.

[3] G.W. Milton, Bounds on the the transport and optical properties of a two- component composite material, J. Appl. Phys., 52:5294–5304, 1981.

[4] S. Tokarzewski, J.J. Telega, M. Pindor, and J.Gilewicz, Basic inequalities for multipoint Padé approximants to Stieltjes functions, Arch. Mech., 56:141–153, 2002.

ON THE SOURCE OF SINGULARITIES IN MECHANICS

G. B. Sinclair
Department of Mechanical Engineering, LSU, Baton Rouge, LA 70803, U.S.A.

Summary Stress singularities occur in both fluid and solid mechanics. Such singularities may be viewed as breakdowns in the modeling which produces them. To begin to improve this modeling, the source of these singularities needs to be identified. Here this is demonstrated to be infinite stiffnesses in underlying intermolecular laws. When finite stiffnesses are introduced instead, finite stresses result for a diverse variety of erstwhile singular configurations.

INTRODUCTION

In fluid and solid mechanics, stress or pressure singularities appear at sharp corners, step modifications to boundary conditions, and abrupt changes in continuum properties. Such discontinuity singularities abound in solid mechanics (e.g., [1]). Though perhaps not as widely recognized, they also occur quite frequently in fluid mechanics (e.g., [2,3]).

The stresses attending discontinuity singularities qualitatively reflect physical stress concentrations, but are quantitatively physically inapplicable. While there has been some success in interpreting these physically wayward fields, in general they remain a serious impediment to meaningful physical inferences. Consequently it is of interest to try and improve the modeling that occasions discontinuity singularities, and thereby eliminate them.

One longstanding suggestion to this end (Kelvin circa 1860) is to remove the discontinuity associated with the singularity by, say, rounding corners. For the example of a cracked solid, certainly there are no singular stresses with any root radius that is greater than zero. However, for a radius that is zero we get the physical absurdity of infinite stresses. This raises the question of just how physically relevant are the finite but extremely large stresses that result from extremely small radii. Moreover, crack tips can have such radii, so the question is not moot. And similar concerns apply to rounding other sharp corners.

Other suggestions entail modifications to the governing field equations. In general such modifications do not really remove singularities. This is shown in the literature for solid mechanics (for plasticity, viscoelasticity, large strains and displacements, couple stresses, and inertial effects), and to some extent for fluid mechanics (for viscosity, compressibility, and inertial effects).

What needs to be changed to remove discontinuity singularities in both field theories is the boundary conditions. Specifically, infinite stiffnesses in underlying intermolecular laws need to be removed. We demonstrate this next.

SAMPLE SINGULAR/NONSINGULAR CONFIGURATIONS

We begin with a simple one-dimensional example from particle dynamics. This concerns a sphere of mass m and velocity V normally impacting a relatively rigid wall. Then the maximum contact force F when the sphere comes to rest given by

$$F = V(km)^{1/2},\ 8\left(V^6k^2m^3\right)^{1/5}/7. \tag{1}$$

The first expression for F stems from taking a linear force-displacement relation with stiffness k. The second stems from taking a nonlinear relation corresponding to Hertzian contact of a rubber (incompressible) ball with $k=5E\sqrt{R}$. What (1) shows is that, in either case, we have finite contact forces and stresses if k is finite. We draw on this appreciation in our next example.

For our second example, we consider the steady flow without separation of an ideal incompressible fluid of density ρ over an impervious step. The fluid has an upstream velocity of V. In terms of r, θ coordinates, locally it flows through a region bounded by $r>0, |\theta|<3\pi/4$. Traditional boundary conditions take the velocity normal to the step to be zero, and lead to singularities in both velocity v and stress σ fields, viz.,

$$v_\theta = 0\ @\ \theta = \pm 3\pi/4 \Rightarrow v = \mathrm{ord}\left(V(l/r)^{1/3}\right) + O\left(r^{1/3}\right),\ \sigma = \mathrm{ord}\left(\rho V^2(l/r)^{2/3}\right) + O(1), \tag{2}$$

as $r\to 0$, where l is a characterizing length. Similar singular fields participate for other proud step corners.

Now instead treat the molecules comprising the fluid as spheres impacting a wall as in our original example. That is, allow for the deformation of these molecules as they impact. One simple means of doing this is to replace the traditional boundary conditions in (2) with a linear relationship between the normal stress and velocity, then nonsingular v and σ result, viz.,

$$\sigma_\theta = \mp kv_\theta\ @\ \theta = \pm 3\pi/4 \Rightarrow v = \mathrm{ord}\left(\rho^{-1}k\left(\left(1+2\rho^2V^2k^{-2}\right)^{1/2}+1\right)\right) + o(1),\ \sigma = \mathrm{ord}(kv) + o(1), \tag{3}$$

as $r\to 0$. Thus we have no singularity for k finite. Similar results can be obtained for other proud corners. Results of like character can also be obtained if the first of (3) is replaced with a relation reflecting something akin to Hertzian contact.

If we revisit our step flow example with viscosity included, then either for Stokes flow or for the full Navier Stokes equations, the analogues of the boundary conditions in (2),(3) lead to

$$\sigma = O\left(r^{-0.46}\right), O\left(r^{-0.09}\right),\ \sigma = \mathrm{ord}(k) + O(1), \tag{4}$$

as $r\to 0$, respectively, with bounded v for both. That is, once deformation is admitted with finite k, singularities are removed.

Further examples in fluid mechanics of configurations that can be rendered nonsingular with a like approach to the foregoing are: Taylor's scraping problem for an incompressible viscous fluid (singularity given in [2]), and Reynolds equation for a compressible air bearing when contact occurs (singular and nonsingular fields indicated in [3]).

Turning to solid mechanics, we first consider a stress-free reentrant corner under torsion. The elastic material comprising the corner locally occupies the same region as the fluid earlier ($r>0, |\theta|<3\pi/4$). For antisymmetric response, the out-of-plane displacement is traditionally set to zero on the bisector. This together with zero shear on a face lead to antiplane shear stresses τ that are singular, viz.,

$$w=0\,@\,\theta=0,\ \tau_{\theta z}=0\,@\,\theta=3\pi/4 \Rightarrow \tau=\mathrm{ord}\left(G\bar{W}\left(l/r\right)^{1/3}\right)+O\left(r\right), \tag{5}$$

as $r\to 0$, where G is the shear modulus, $\bar{W}$ a dimensionless representative displacement. Similar singular stresses participate for other reentrant corners.

Now for a sharp corner, consistency requires that cohesive laws must act between the flanks as the corner is approached to within molecular distances because these are the laws giving rise to the constitutive relations within the bulk of the continuum. With this appreciation it becomes apparent that, when separating the corner into two halves as in (5), we need to formulate problems for the molecules comprising the boundaries of the two halves. These molecular boundaries can be displaced with respect to one another along the bisector, so that the first of (5) only holds for their average displacement. Instead, therefore, we replace the first of (5) with a cohesive stress-separation law, then nonsingular shear components result, viz.,

$$\tau_{\theta z}=2kw\,@\,\theta=0^{+} \Rightarrow \begin{Bmatrix}\tau_{rz}\\ \tau_{\theta z}\end{Bmatrix}=kW\left[\sin\theta\begin{Bmatrix}-\\ +\end{Bmatrix}\cos\theta-2\frac{kr}{G}\begin{Bmatrix}\sin 2\theta\\ \cos 2\theta\end{Bmatrix}\right]+O\left(r^{1/3}\right), \tag{6}$$

as $r\to 0$. Thus no singularity for finite k. Similar results can be obtained for other reentrant corners.

As a second example, we consider a composite wedge under torsion. The wedge is comprised of an elastic sector occupying $0<\theta<3\pi/4$ and a rigid sector occupying $3\pi/4<\theta<5\pi/4$, and has stress-free exterior faces. With traditional perfect matching assumed on the interface, the boundary conditions for the elastic sector are as in (5) but with θ values reversed, and lead to singular shears also as in (5). With an adhesive law instead on the interface, the first of (5) is replaced with the boundary condition in (6) but on $\theta=3\pi/4$ with $2k\to -k$, and nonsingular shears as in (6) result with $\theta\to 3\pi/4-\theta$. Thus no singularity for finite k. Similar results can be obtained for other bimaterial wedges.

If we revisit our reentrant corner example within the context of plane elasticity, singularities as in (4) result with traditional symmetry, antisymmetry conditions (stress-free conditions in plane elasticity are analogous to zero-velocity conditions in Stokes flow). If instead we introduce cohesive laws with finite k, nonsingular stresses as in (4) result. And such removal of singularities holds in general throughout plane elasticity (requisite asymptotic analysis follows [4]). That is, with the appropriate introduction of cohesive/adhesive laws with finite k, all the singularities in [1] can be removed.

There is one caution of note in effecting this removal of singularities throughout two-dimensional elasticity. This is for cracks when stiffnesses on crack flanks are reduced from those ahead of crack tips to model stress concentrations at tips. If shear stresses are involved, such reductions need to be continuous, otherwise log singularities can be shown to be induced. With this caveat, however, even the interface crack can be rendered completely free of stress singularities.

As a final example we consider the now classical three-dimensional (3D) problem of a crack intersecting the surface of a half-space. Traditional symmetry and antisymmetry conditions ahead of the crack set one out-of-crack-plane displacement and two in-crack-plane displacements to zero, respectively. Thus, in effect, symmetry conditions imply one infinite stiffness in a cohesive law while antisymmetry imply two. Hence symmetry conditions lead to one singularity, antisymmetry to two for the 3D crack problem (see [5]). Replacing these traditional conditions with cohesive laws can be shown (via the alternating method) to remove all three singularities.

For some of the preceding two-dimensional examples with traditional boundary conditions, asymptotic expansions can be shown to be complete only when the singular eigenfunctions are included. This all but guarantees the participation of these singular fields in corresponding global problems. Irrespective of completeness, participation of such singularities has been confirmed for a number of global problems with diverging numerical analyses (space limitations prevent summarizing results here). For some of the two-dimensional examples with intermolecular laws in boundary conditions, asymptotic expansions can be shown to be complete without any singular eigenfunctions. Irrespective of completeness, the nonparticipation of singularities has been confirmed for a number of global problems with converging numerical analyses.

Last we observe that, in all the local configurations with intermolecular laws in their boundary conditions, taking $k\to\infty$ makes these conditions revert to traditional ones with their singularities. This is therefore consistent with the identification of infinite stiffnesses as sources of discontinuity singularities in mechanics.

CONCLUSIONS

There are a wide variety of stress singularities at discontinuities in fluid and solid mechanics. Traditional boundary conditions for these singularities effectively contain infinite stiffnesses in underlying intermolecular laws. When finite continuous stiffnesses are used instead, finite stresses result, even with the original discontinuity still present. Thus it is infinite stiffnesses

that are the source of singularities rather than their associated discontinuities themselves. This recognition offers the potential for replacing singular stresses with physically meaningful stresses throughout mechanics.

Acknowledgement The support of this research by the National Science Foundation is gratefully acknowledged.

References

[1] Seweryn A., Mokski K.: Elastic Stress Singularities and Corresponding Generalized Stress Intensity Factors for Angular Corners Under Various Boundary Conditions. *Engng Fracture Mech* **55**: 529-556, 1996.

[2] Moffatt H.K.: Viscous and Resistive Eddies Near a Sharp Corner. *J. Fluid Mech.* **18**: 1-18, 1964.

[3] Anaya-Dufresne M., Sinclair G.B.: Towards a Reynolds Equation for Gas Lubricated Bearings When Contact Occurs. *J. Tribology* **124**: 226-273, 2002.

[4] Sinclair G.B.: On the Influence of Cohesive Stress-Separation Laws on Elastic Stress Singularities. *J. Elasticity* **44**: 203-221, 1996.

[5] Benthem J.P.: State of Stress at the Vertex of a Quarter-Infinite Crack in a Half-Space. *Int. J. Solids Struct.* **13**: 479-492, 1977.

XXI ICTAM, 15–21 August 2004, Warsaw, Poland

EXTENDED POLAR DECOMPOSITIONS FOR FINITE PLANE STRAIN

Michael Hayes*, Philippe Boulanger**
*University College Dublin, Department of Mechanical Engineering, Belfield, Dublin 4, Ireland
**Université Libre de Bruxelles, Dpt. de Mathématique, Campus Plaine CP218/1, 1050 Bruxelles, Belgium

Summary The concept of unsheared triads of material line elements in a body was introduced by Boulanger & Hayes who showed that there is a link between these triads and new decompositions of the deformation gradient, called "extended polar decompositions", generalizing the classical polar decomposition. In the present paper attention is confined to finite plane strain so that the deformation gradient is essentially two-dimensional. The whole range of corresponding extended polar decompositions is presented.

BASIC EQUATIONS

Let a body of material be subjected to the deformation

$$\mathbf{x} = \mathbf{x}(\mathbf{X}) \ , \quad x_i = x_i(X_A) \ , \qquad (i, A = 1, 2, 3), \tag{1}$$

in which the particle initially at $\mathbf{X}$ is displaced to $\mathbf{x}$. All quantities are referred to a fixed rectangular Cartesian coordinate system. A material line element $d\mathbf{X}$ at $\mathbf{X}$ is deformed into the element $d\mathbf{x} = \mathbf{F}d\mathbf{X}$, where $\mathbf{F}$, the deformation gradient at $\mathbf{X}$ is given by $F_{iA} = \partial x_i/\partial X_A$. The right Cauchy-Green strain tensor $\mathbf{C}$, and the left $\mathbf{B}$, are given by

$$\mathbf{C} = \mathbf{F}^T\mathbf{F} \ , \quad C_{AB} = \frac{\partial x_i}{\partial X_A}\frac{\partial x_i}{\partial X_B} \ , \qquad \mathbf{B} = \mathbf{F}\mathbf{F}^T \ , \quad B_{ij} = \frac{\partial x_i}{\partial X_A}\frac{\partial x_j}{\partial X_A} \ . \tag{2}$$

If $\mathbf{N}$ is a unit vector along a material line element of infinitesimal length L before deformation, at $\mathbf{X}$, then, after the deformation the length of the element at $\mathbf{x}$ is $\lambda(\mathbf{N})L$, where $\lambda(\mathbf{N})$, called the "stretch along $\mathbf{N}$", is given by

$$\lambda_{(\mathbf{N})} = |\mathbf{F}\mathbf{N}| = (\mathbf{N}\cdot\mathbf{C}\mathbf{N})^{1/2} = (C_{AB}N_AN_B)^{1/2} \ . \tag{3}$$

Similarly, if $\hat{\mathbf{n}}$ is a unit vector along a material line element of infinitesimal length l after deformation, at $\mathbf{x}$, then, before the deformation the length of the element at $\mathbf{X}$ is $\lambda(\mathbf{n})l$, where

$$\lambda_{(\mathbf{n})} = (\hat{\mathbf{n}}\cdot\mathbf{B}^{-1}\hat{\mathbf{n}})^{1/2} = (B^{-1}_{ij}\hat{n}_i\hat{n}_j)^{1/2} \ . \tag{4}$$

If $\mathbf{n} = \mathbf{F}\mathbf{N}$, so that $\mathbf{n}$, along $\hat{\mathbf{n}}$, is the element into which $\mathbf{N}$ is deformed, then $\lambda_{(\mathbf{n})} = 1/\lambda_{(\mathbf{N})}$.

UNSHEARED TRIADS

Unsheared triads consist of the three material line elements at $\mathbf{X}$ along the unit vectors $\mathbf{M}, \mathbf{N}, \mathbf{P}$, such that the three pairs of material line elements along $(\mathbf{M}, \mathbf{N}), (\mathbf{N}, \mathbf{P})$ and $(\mathbf{P}, \mathbf{M})$ are unsheared, i.e. suffer no change in angle. Recently, it has been shown[2] that, in any deformation, there is an infinity of unsheared triads at $\mathbf{X}$.
The conditions for $\mathbf{M}$, $\mathbf{N}$ and $\mathbf{P}$ to form an unsheared triad are (e. g. Truesdell & Toupin[3])

$$\mathbf{M}\cdot\mathbf{C}\mathbf{N} = \lambda_{(\mathbf{N})}\lambda_{(\mathbf{M})}\mathbf{M}\cdot\mathbf{N} \ , \ \ \mathbf{N}\cdot\mathbf{C}\mathbf{P} = \lambda_{(\mathbf{N})}\lambda_{(\mathbf{P})}\mathbf{N}\cdot\mathbf{P} \ , \ \ \mathbf{P}\cdot\mathbf{C}\mathbf{M} = \lambda_{(\mathbf{P})}\lambda_{(\mathbf{M})}\mathbf{P}\cdot\mathbf{M} \ . \tag{5}$$

Assuming that an unsheared pair $(\mathbf{M}, \mathbf{N})$ is known, and considering only non coplanar triads, a formula for $\mathbf{P}$ forming with $\mathbf{M}$ and $\mathbf{N}$ an unsheared triad is[2]

$$p\mathbf{P} = \{\mathbf{C}\mathbf{M} - \lambda^{-1}_{(\mathbf{N})}(\det\mathbf{C})^{1/2}\mathbf{M}\} \times \{\mathbf{C}\mathbf{N} - \lambda^{-1}_{(\mathbf{M})}(\det\mathbf{C})^{1/2}\mathbf{N}\} \ , \tag{6}$$

where p is a scalar factor such that $\mathbf{P}\cdot\mathbf{P} = 1$.
Thus, in general, for any chosen unsheared pair $(\mathbf{M}, \mathbf{N})$, there is a unique unit vector $\mathbf{P}$ (by "unique", we here mean unique up to a $\pm$ sign) such that $(\mathbf{M}, \mathbf{N}, \mathbf{P})$ is an unsheared triad. In other words, if an unsheared pair of material line elements is given at a point $\mathbf{X}$, then, in general, a unique third material line element at $\mathbf{X}$ may be found such that the three material line elements form an unsheared triad.
However, special cases may occur because for special choices of the unsheared pair $(\mathbf{M}, \mathbf{N})$, (6) yields $p\mathbf{P} = \mathbf{0}$, or $p\mathbf{P}$ along $\mathbf{M}$ or $\mathbf{N}$ (see [2] for details).

EXTENDED POLAR DECOMPOSITIONS

Let $\mathbf{M}$, $\mathbf{N}$, $\mathbf{P}$ be unit vectors along the edges of a (non coplanar) unsheared triad of material line elements, and let $\mathbf{m} = \mathbf{F}\mathbf{M}$, $\mathbf{n} = \mathbf{F}\mathbf{N}$, $\mathbf{p} = \mathbf{F}\mathbf{P}$. It has been shown [2] that $\mathbf{F}$, the deformation gradient, may be written

$$\mathbf{F} = \mathbf{Q}\mathbf{G} = \mathbf{H}\mathbf{Q} \ , \tag{7}$$

where $\mathbf{Q}$ is a proper orthogonal tensor($\mathbf{Q}\mathbf{Q}^T = \mathbf{1},\ \det \mathbf{Q} = 1$), and $\mathbf{G}$, $\mathbf{H}$ are given by

$$\mathbf{G} = \lambda_{(\mathbf{M})}\mathbf{M}\otimes\mathbf{M}^* + \lambda_{(\mathbf{N})}\mathbf{N}\otimes\mathbf{N}^* + \lambda_{(\mathbf{P})}\mathbf{P}\otimes\mathbf{P}^* \ , \tag{8}$$

$$\mathbf{H} = \lambda^{-1}_{(\mathbf{m})}\mathbf{m}\otimes\mathbf{m}^* + \lambda^{-1}_{(\mathbf{n})}\mathbf{n}\otimes\mathbf{n}^* + \lambda^{-1}_{(\mathbf{p})}\mathbf{p}\otimes\mathbf{p}^* \ . \tag{9}$$

Here, $(\mathbf{M}^*, \mathbf{N}^*, \mathbf{P}^*)$ is the triad reciprocal to $(\mathbf{M}, \mathbf{N}, \mathbf{P})$, and $(\mathbf{m}^*, \mathbf{n}^*, \mathbf{p}^*)$ is the triad reciprocal to $(\mathbf{m}, \mathbf{n}, \mathbf{p})$. The decompositions (7) have echoes of the classical polar decomposition $\mathbf{F} = \mathbf{R}\mathbf{U} = \mathbf{V}\mathbf{R}$, in which $\mathbf{R}$ is proper orthogonal and $\mathbf{U}$, $\mathbf{V}$ are positive definite symmetric. They are called "extended polar decompositions"[2]. Because there is an infinity of unsheared triads, there is an infinity of such "extended polar decompositions". Also we note that $\mathbf{C} = \mathbf{G}^T\mathbf{G}$ and $\mathbf{B} = \mathbf{H}\mathbf{H}^T$.

PLANE STRAIN

Here we consider plane deformations

$$x_\alpha = x_\alpha(X_\Lambda) \ , \quad x_3 = X_3 \ , \qquad (\alpha, \Lambda = 1, 2) \ . \tag{10}$$

Let $\mathbf{F}'$ denote the two by two deformation gradient $F'_{\alpha\Lambda} = \partial x_\alpha/\partial X_\Lambda$, and $\mathbf{C}'$, $\mathbf{B}'$ be the corresponding two by two right and left Cauchy-Green strain tensors.

We now restrict our attention to unsheared triads $\mathbf{M}$, $\mathbf{N}$, $\mathbf{P}$ consisting of material line elements along two vectors $\mathbf{M}$, $\mathbf{N}$ in the X_1X_2–plane, and the vector $\mathbf{P} = \mathbf{K} = (0, 0, 1)$ along the X_3–axis. Thus, $(\mathbf{M}, \mathbf{N})$ may be any unsheared pair in the X_1X_2–plane. There is an infinity of such pairs : if $\mathbf{N}$ is given in the plane, there is, in general, a unique companion $\mathbf{M}$ forming with $\mathbf{N}$ an unsheared pair[1]. Here, we may obtain the companion $\mathbf{M}$ of a given $\mathbf{N}$ by using (6), because $\mathbf{M}$ is the third edge af an unsheared triad whose first two edges are $\mathbf{N}$ and $\mathbf{P} = \mathbf{K}$. If Ψ denotes the arbitrary angle that $\mathbf{N}$ makes with the X_1–axis, it follows that (omitting a scalar factor in $\mathbf{M}$)

$$\mathbf{N} = (\cos\Psi, \sin\Psi, 0) \ , \ \mathbf{M} = ([\det \mathbf{C}^{1/2} - C_{22}]\sin\Psi - C_{12}\cos\Psi,\ C_{12}\sin\Psi - [\det \mathbf{C}^{1/2} - C_{11}]\sin\Psi,\ 0) \ . \tag{11}$$

Then, using (8) with $\mathbf{P} = \mathbf{K} = \mathbf{P}^*$, and retaining only the components in the X_1X_2–plane, we have

$$\mathbf{G}' = \lambda_{(\mathbf{M})}\mathbf{M}\otimes\mathbf{M}^* + \lambda_{(\mathbf{N})}\mathbf{N}\otimes\mathbf{N}^* \ . \tag{12}$$

We give explicit details in terms of the angle Ψ.

Similarly, using the angle ϕ that $\mathbf{n} = \mathbf{F}\mathbf{N}$ makes with the x_1–axis, and the components of $\mathbf{B}^{-1}$, an expression may be obtained for $\mathbf{H}'$:

$$\mathbf{H}' = \lambda^{-1}_{(\mathbf{m})}\mathbf{m}\otimes\mathbf{m}^* + \lambda^{-1}_{(\mathbf{n})}\mathbf{n}\otimes\mathbf{n}^* \ . \tag{13}$$

For each given Ψ (or ϕ), we have the corresponding two by two decomposition

$$\mathbf{F}' = \mathbf{Q}'\mathbf{G}' = \mathbf{H}'\mathbf{Q}' \ , \tag{14}$$

where $\mathbf{Q}'$ is a two by two proper orthogonal tensor. It is a two by two "extended polar decomposition". The results are illustrated in the case of simple shear.

References

[1] Boulanger Ph. & Hayes M.: On finite shear. *Arch. Rational Mech. Anal.* **151**:125–185, 2000.

[2] Boulanger Ph. & Hayes M.: Unsheared Triads and Extended Polar Decompositions of the Deformation Gradient. *Int. J. Nonlinear Mech.* **36**:399–420, 2001.

[3] Truesdell C. & Toupin R.:The Classical Field Theories, Handbuch der Physik III/1. Springer Verlag, Berlin 1960.

XXI ICTAM, 15–21 August 2004, Warsaw, Poland

NONLINEAR WAVES IN ELASTIC SOLIDS

Wlodzimierz Domanski
Polish Academy of Sciences, IPPT PAN, Swietokrzyska 21, PL 00-049 Warszawa, Poland

Summary We derive evolution equations for the amplitudes of weakly nonlinear elastic waves. Some of these equations are new in the context of elastodynamics, like e.g. the complex Burgers equation describing the propagation of amplitudes of quasi-shear waves along the diagonal of a cube in a cubic crystal. New formulas are obtained for the wave interaction coefficients and then are used in the formulation of the condition which guarantees global existence of a classical solution to the initial-value problem of nonlinear elastodynamics equations.

INTRODUCTION

One of the open problems in continuum mechanics is to understand nonlinear dynamics of a deformable medium. Mathematical equations which describe macroscopic dynamics of a continuum are systems of balance laws, like e.g. balance of mass, momentum, energy etc. If we disregard dissipative and dispersive effects, these balance laws become, under natural assumptions, hyperbolic systems of conservation laws. Understanding the propagation and interaction of nonlinear waves, that is solutions of these nonlinear hyperbolic partial differential equations, is extremely important and challenging. Nonlinear waves, unlike linear, do not superimpose additively but instead may interact resonantly producing new waves which have frequencies and wave numbers being linear combinations of the frequencies and wave numbers of interacting waves. Besides, nonlinearity may cause formation of shock waves. Both of these nonlinear effects: *resonances* and *shocks* formation imply instability and create difficulties in analyzing the initial and initial-boundary value problems in continuum mechanics. In this paper we present some new results devoted to nonlinear waves in solids.

PROBLEM FORMULATION

Assumptions

We restrict ourselves to the *hyperelastic* continuum. Both *geometric* and *material* nonlinearities are taken into account. We assume that the system of elastodynamics equations is *hyperbolic*. It is convenient to write our equations as a first order system of partial differential equations:

$$\begin{aligned} \rho_0 \frac{\partial \boldsymbol{v}}{\partial t} &= \boldsymbol{Div}\, \boldsymbol{T}(\boldsymbol{F}), \\ \frac{\partial \boldsymbol{F}}{\partial t} &= \boldsymbol{Grad}\, \boldsymbol{v}, \end{aligned} \tag{1}$$

here ρ_0 is a constant density, $\boldsymbol{v}$ is a velocity, $\boldsymbol{T}$ is the first Piola-Kirchhoff stress, $\boldsymbol{F}$ is a deformation gradient tensor, and $\boldsymbol{Div}, \boldsymbol{Grad}$ denote the divergence and gradient operators in the reference configuration. The body forces are disregarded. We study the initial-value problem for the system (1) with different data and for different media. Both isotropic and some examples of anisotropic elastic solids are investigated.

Plane waves

It turns out that in many cases it is enough to look at plane wave solutions of (1). This allows to reduce the technical difficulties connected with the analysis of a 12×12 system (1) in three space dimension, to a 6×6 system (2) in one space dimension x (see e.g. [1] or [4]):

$$\frac{\partial \boldsymbol{w}}{\partial t} + \boldsymbol{A}(\boldsymbol{w}, \boldsymbol{k}) \frac{\partial \boldsymbol{w}}{\partial x} = \boldsymbol{0}, \tag{2}$$

where

$$\boldsymbol{w} = \begin{bmatrix} \boldsymbol{v}(x,t) \\ \boldsymbol{m}(x,t) \end{bmatrix} \quad \text{and} \quad \boldsymbol{A}(\boldsymbol{w}, \boldsymbol{k}) = - \begin{bmatrix} \boldsymbol{0} & \boldsymbol{B}(\boldsymbol{m}, \boldsymbol{k}) \\ \boldsymbol{I} & \boldsymbol{0}, \end{bmatrix} \tag{3}$$

$\boldsymbol{B}$ is a symmetric 3×3 matrix composed of second derivatives of the strain energy with respect to the components of the 1-D strain vector $\boldsymbol{m}$, and $\boldsymbol{k}$ is the direction of the wave propagation, $\boldsymbol{I}$ is a 3×3 identity matrix.
Due to the special block structure of the matrix $\boldsymbol{A}$ we may further reduce computational problems of finding the eigensystem of a 6×6 matrix $\boldsymbol{A}$ to the eigensystem of the reduced 3×3 matrix $\boldsymbol{B}$.

METHODS

Asymptotic expansion

We use the method of weakly nonlinear asymptotics to the initial-value problem for (2), around the constant state $\boldsymbol{w}_0$, in the form:

$$\boldsymbol{w}^\epsilon(x,t) = \boldsymbol{w}_0 + \epsilon \boldsymbol{w}_1(x,t,\eta) + \epsilon^2 \boldsymbol{w}_2(x,t,\eta) + \mathcal{O}(\epsilon^3) \tag{4}$$

with $\eta \equiv \epsilon^{-s}(x - \lambda t)$ being the phase variable, and the constant s determining appropriate scaling.
This is a multiple scales perturbation method which allows to derive nonlinear evolution equations for the waves amplitudes. We are particularly interested in nonclassical cases when *loss of strict hyperbolicity* and\or *loss of genuine nonlinearity* occur which happens in nonlinear elastodynamics. We analyze the evolution equations and we make conclusions about the behavior of the original elastodynamics system.

RESULTS

Evolution equations

We derive evolution equations which are new in the context of nonlinear elastodynamics. This is the case e.g. for a cubic crystal where the *complex Burgers equation* is a canonical equation for two pairs of quasi-shear waves propagating along the diagonal of a cube in a cubic crystal (see [1] or [5]). It can be written as a coupled system of two nonlinear equations with quadratic nonlinearity.

Interaction coefficients

The crucial role in the analysis of interaction of waves is played by the wave *interaction coefficients* Γ^j_{pq} (see [2] or [4]) which appear in the evolution equations. These coefficients describe which waves interact and also give information how strong the interaction is. The interaction coefficients are defined in terms of the left $\boldsymbol{l}_j$ and right $\boldsymbol{r}_j$ eigenvectors of matrix $\boldsymbol{A}$:

$$\Gamma^j_{pq} = \boldsymbol{l}_j \, \nabla_{\boldsymbol{w}} \boldsymbol{A}(\boldsymbol{w}) \, \boldsymbol{r}_p \, \boldsymbol{r}_q . \tag{5}$$

In our joint paper [4] with Robin Young we have derived new formulas for the coefficients (5) and expressed them entirely in terms of the derivatives of the strain energy. These new formulas allow us to calculate all the interaction coefficients for arbitrary elastic media. It turns out that the interaction coefficients may give information about stability or instability, as well as blow up or global existence of the original system of nonlinear elastodynamics.

Null condition

In another joint paper [3] with Ray Ogden we have investigated the so called *null condition* which implies global existence of a classical solution to the initial- value problem for the nonlinear elastodynamics equations. We were able to express this condition in terms of interaction coefficients and to analyze it for different types of elastic materials.

CONCLUSIONS

We have presented several new results which deal with solutions of nonlinear elastodynamics equations and help in understanding the problem of propagation and interaction of nonlinear elastic waves.

References

[1] Domanski W.: Weakly Nonlinear Elastic Plane Waves in a Cubic Crystal. *Contemp. Math.* **255**:45-61, 2000.
[2] Domanski W., Jablonski T.: On Resonances of Nonlinear Elastic Waves in a Cubic Crystal. *Arch. Mech.* **53**:91-104, 2001.
[3] Domanski W., Ogden R. W.: Null Condition for Nonlinear Elastic Materials. *to appear*.
[4] Domanski W., Young R.: Interaction of Plane Waves in Nonlinear Elasticity. *to appear*.
[5] Domanski W.: Asymptotic Equations for Weakly Nonlinear Elastic Shear Waves in a Cubic Crystal. *to appear*.

XXI ICTAM, 15–21 August 2004, Warsaw, Poland

EXPLICIT SECULAR EQUATIONS FOR SURFACE AND INTERFACE WAVES IN ANISOTROPIC SOLIDS

Michel Destrade
Laboratoire de Modélisation en Mécanique, CNRS, Université Pierre et Marie Curie (UMR 7607), 4 place Jussieu, case 162, 75252 Paris Cedex 05, France.

Summary The derivation of secular equations in closed form for acoustic waves propagating at the interface of semi-infinite elastic bodies is made possible, using a simple method.

INTRODUCTION

Consider an inhomogeneous plane wave propagating in a semi-infinite anisotropic elastic solid with speed v and wave number k in the direction x_1 (say), and with attenuation in the direction x_2 (say), orthogonal to x_1. Its mechanical displacement is modeled as

$$\mathbf{u} = \mathbf{U}(kx_2)\mathrm{e}^{\mathrm{i}k(x_1-vt)}, \quad \mathbf{U}(\infty) = \mathbf{0}.$$

Anisotropic stress-strain relations, $\sigma_{ij} = c_{ijkl}u_{l,k}$ where $\mathbf{c}$ is a constant fourth-order elasticity tensor, imply that the stress components are of the form,

$$\sigma_{ij} = \mathrm{i}kt_{ij}(kx_2)\mathrm{e}^{\mathrm{i}k(x_1-vt)}, \quad t_{ij}(\infty) = 0.$$

The equations of motion can be written as a first-order differential system for the components of the displacement-traction vector $\boldsymbol{\xi}$,

$$\boldsymbol{\xi}' = i\mathbf{N}\boldsymbol{\xi}, \quad \text{where} \quad \boldsymbol{\xi}(kx_2) := [U_1, U_2, U_3, t_{12}, t_{22}, t_{32}]^{\mathrm{T}}. \tag{1}$$

Here $\mathbf{N}$ is a real 6×6 matrix, whose components depend on the elastic constants and mass density characteristic of the material, and on the speed v. Finally, some boundary conditions are imposed at the interface $x_2 = 0$ for some (or all) components of $\boldsymbol{\xi}(0)$,

$$f(U_i(0), t_{i2}(0)) = 0, \tag{2}$$

such as for instance the vanishing of the tractions for a solid/vacuum interface (Rayleigh waves) or the continuity of the displacements and of the tractions for a solid/solid interface (Stoneley waves).

The usual method of resolution of (1)-(2) consists in the following steps. First take the solution to (1) in exponential form, $\boldsymbol{\xi}(kx_2) = \boldsymbol{\xi}^{\mathbf{0}}\mathrm{e}^{\mathrm{i}kpx_2}$. Then find the attenuation factors p_j as roots of: $\det(\mathbf{N} - p\mathbf{I}) = 0$, $\Im(p) > 0$, and the partial waves $\boldsymbol{\xi}^{\boldsymbol{j}}$ as eigenvectors of: $\mathbf{N}\boldsymbol{\xi}^{\boldsymbol{j}} = p_j\boldsymbol{\xi}^{\boldsymbol{j}}$. Finally use the general solution $\boldsymbol{\xi}(kx_2) = \sum \gamma_j\boldsymbol{\xi}^{\boldsymbol{j}}\mathrm{e}^{\mathrm{i}kp_jx_2}$, to write (2): then a homogeneous system of equations with unknowns γ_j arises, and the corresponding determinantal equation is the secular equation, with v as the sole unknown. This approach was introduced by Stroh [1] and later used by Barnett & Lothe and others to address and answer many outstanding theoretical questions about the existence and uniqueness of a solution, bounds on the wave speed, etc. Moreover, Barnett & Lothe [2] also developped an "integral formalism" which yields efficient numerical schemes for the determination of the wave speed without having to compute the p_j. However this method is not appropriate in general to derive a secular equation explicitly. Indeed, only when the wave is polarized in the sagittal plane and certain elastic constants vanish can the p_j (and thus the secular equation) be found explicitly, as the roots of a biquadratic (Royer & Dieulesaint [3] identified the corresponding 16 configurations for solids with rhombic, tetragonal, cubic, and hexagonal symmetries.) Otherwise, the equation $\det(\mathbf{N} - p\mathbf{I}) = 0$ is a bicubic, a quartic, or even a sextic for p, leading to an involved analysis in the first and second cases, or to an unsolvable problem in the latter case.

Hence a different procedure must be adopted. This search was initiated by Currie [4] and completed by Taziev [5] for Rayleigh waves, using some results of the Stroh formalism. Here a generalization is proposed for this and other types of interface waves (Stoneley waves, Scholte waves), without relying on the Stroh formalism.

FUNDAMENTAL EQUATIONS

The properties of the matrix $\mathbf{N}$ in (1) are well established. In particular, it can be checked that $\widehat{\mathbf{I}}\mathbf{N}^n$, where $\widehat{\mathbf{I}}$ is defined below and n is an integer, is a *symmetric* matrix with the following block structure,

$$\widehat{\mathbf{I}}\mathbf{N}^n = \begin{bmatrix} \mathbf{K}^{(\mathbf{n})} & \mathbf{N_1}^{(\mathbf{n})\mathrm{T}} \\ \mathbf{N_1}^{(\mathbf{n})} & \mathbf{N_2}^{(\mathbf{n})} \end{bmatrix} = (\widehat{\mathbf{I}}\mathbf{N}^n)^{\mathrm{T}}, \quad \widehat{\mathbf{I}} := \begin{bmatrix} 0 & \mathbf{I} \\ \mathbf{I} & 0 \end{bmatrix}.$$

Here, $\mathbf{K}^{(\mathbf{n})}$ and $\mathbf{N_2}^{(\mathbf{n})}$ are symmetric 3×3 matrices, and $\mathbf{I}$ is the 3×3 identity matrix. Thus, multiplying both sides of (1) by $\widehat{\mathbf{I}}\mathbf{N}^n\overline{\boldsymbol{\xi}}$ and adding the complex conjugate yields $\overline{\boldsymbol{\xi}}\cdot\widehat{\mathbf{I}}\mathbf{N}^n\boldsymbol{\xi}' + \overline{\boldsymbol{\xi}}'\cdot\widehat{\mathbf{I}}\mathbf{N}^n\boldsymbol{\xi} = 0$, and so by integration, $\overline{\boldsymbol{\xi}}\cdot\widehat{\mathbf{I}}\mathbf{N}^n\boldsymbol{\xi} = \text{const.} = 0$, its value at infinity. In particular,

$$\overline{\boldsymbol{\xi}}(0)\cdot\widehat{\mathbf{I}}\mathbf{N}^n\boldsymbol{\xi}(0) = 0. \tag{3}$$

These *fundamental equations*, valid for any positive or negative values of the integer n, are sufficient to solve many problems of interface waves. Because of the Cayley-Hamilton theorem, if $\mathbf{N}$ is a 6×6 matrix then there are 5 independent fundamental equations, and if $\mathbf{N}$ is a 4×4 matrix (decoupling of in-plane from anti-plane strain and stress) then there are 3 independent equations. Examples solved so far are now briefly presented.

EXAMPLES

Rayleigh waves

For a solid/vacuum interface, the boundary conditions at $x_2=0$ are: $\boldsymbol{\xi}(0)=[\mathbf{U}(0),\mathbf{0}]^{\mathrm{T}}$, and (3) reduce to [4,5],

$$\overline{\mathbf{U}}(0)\cdot\mathbf{K}^{(\mathbf{n})}\mathbf{U}(0)=0. \tag{4}$$

Then the secular equation is found explicitly for a completely arbitrary direction of propagation. Moreover, when the wave travels along a crystallographic axis of a rhombic crystal or along a principal direction of a pre-stressed hyperelastic material, then the body can be put into uniform rotation (gyroscopes, tires, ...) along one of the crystallographic/principal axes and the secular equation can also be found [6] (see Fig. 1(a)) ; in that case $\mathbf{K}^{(\mathbf{n})}$ is Hermitian and (4) still applies.

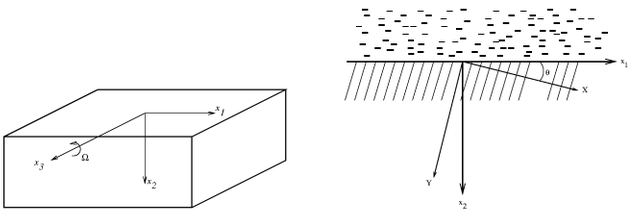


Figure 1. (a) Rayleigh wave in a rotating body; (b) Scholte wave polarized in a plane of symmetry.

Scholte waves

For a solid/fluid interface, the boundary conditions at $x_2=0$ are: $\boldsymbol{\xi}(0^+)=[U_1(0^+),U_2(0^+),U_3(0^+),0,t_{22}(0^+),0]^{\mathrm{T}}$ in the solid and: $t_{22}(0^-)=-\mathrm{i}ZU_2(0^-)$ in the fluid, where Z is the (real) normal impedance of the inviscid fluid. The continuity of U_2 and t_{22} accross the interface, combined with (3), yield the secular equation for waves either polarized in a symmetry plane [7] (see Fig. 1(b)) or propagating in a symmetry plane.

Stoneley waves

For a solid/solid interface, the boundary conditions at $x_2=0$ are: $\boldsymbol{\xi}(0^+)=\boldsymbol{\xi}(0^-)$. The fundamental equations (3) yield the secular equation when the semi-infinite bodies are made of same crystal [8] (see Fig. 2) , or of the same hyperelastic material subject to the same pre-stress [9], but with misaligned crystallographic/principal axes.

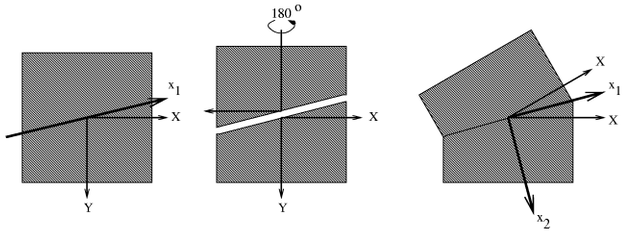


Figure 2. Cutting, rotating, and bonding of a rhombic crystal; a Stoneley wave exists at $x_2=0$.

References

[1] Stroh A.N.: Dislocations and Cracks in Anisotropic Elasticity. *Phil. Mag.* **3**: 625–646, 1958.
[2] Barnett D.M., Lothe J.: Synthesis of Sextic and Integral Formalism for Dislocations and Line Forces in Anisotropic Media. *Phys. Norv.* **7**: 13–18, 1973.
[3] Royer D., Dieulesaint E.: Rayleigh Wave Velocity and Displacement in Orthorhombic, Tetragonal, and Cubic Crystals. *J. Acoust. Soc. Am.* **76**: 1438–1444, 1984.
[4] Currie P.K.: The Secular Equation for Rayleigh Waves on Elastic Crystals. *Quart. J. Mechs. Appl. Math.* **32**: 163–173, 1979.
[5] Taziev R.M. : Dispersion Relation for Acoustic Waves in an Anisotropic Elastic Half-Space. *Sov. Phys. Acoust.* **35**: 535–538, 1989.
[6] Destrade M.: Surface Waves in Rotating Rhombic Crystals. *Proc. Roy. Soc. Lond. A* (to appear).
[7] Destrade M.: Explicit Secular Equation for Scholte Waves Over a Monoclinic Crystal. *J. Sound Vibr.* (to appear).
[8] Destrade M.: Elastic Interface Acoustic Waves in Twinned Crystals. *Int. J. Solids Struct.* **40**: 7375–7383, 2003.
[9] Destrade M.: On Interface Waves in Misoriented Pre-stressed Incompressible Elastic Solids. *IMA J. Appl. Math.* (to appear).

XXI ICTAM, 15–21 August 2004, Warsaw, Poland

VIEWS ON MATERIAL FORCES IN MULTIPLICATIVE ELASTOPLASTICITY

A. Menzel, P. Steinmann
Chair of Applied Mechanics, Faculty of Mechanical and Process Engineering
University of Kaiserslautern, P.O. Box 3049, D–67653 Kaiserslautern, Germany
email: amenzel@rhrk.uni–kl.de & ps@rhrk.uni-kl.de, url: http://mechanik.mv.uni–kl.de

Summary The main goal of this contribution is the examination of a general framework for finite hyper–elastoplasticity that reflects the nature of material forces. In particular, we thereby address representations of Eshelbian stress tensors and Eshelbian volume forces with respect to different configurations, namely the spatial, the material and – what we call – the intermediate setting which allows alternative interpretation as being referred to a local rearrangement. Deriving these relations, one naturally incorporates connections which are determined by either the irreversible or the reversible portion of the deformation gradient. The physical interpretation of these contributions consists in the fact that their skew part can be related to the, say, dislocation density. With these Eshelbian stress tensors and volume forces at hand, we finally come up with different representations of balances of linear momentum which are carried out with respect to the spatial or material setting, referring either to the spatial or to the material motion problem. The developed framework serves as the fundamental outset for the application of the material force method.

ESSENTIAL KINEMATICS

Let the deformation gradient of the (sufficiently smooth) spatial motion problem, $\boldsymbol{x} = \boldsymbol{\varphi}(\boldsymbol{X}, t)$ in $\mathcal{B}_t$, be decomposed via $\mathrm{D}_{\boldsymbol{X}}\boldsymbol{\varphi} = \boldsymbol{F} \doteq \boldsymbol{F}_{\mathrm{e}} \cdot \boldsymbol{F}_{\mathrm{p}}$. The corresponding tangent map of the material motion problem, $\boldsymbol{X} = \boldsymbol{\Phi}(\boldsymbol{x}, t)$ in $\mathcal{B}_0$, consequently reads $\mathrm{d}_{\boldsymbol{x}}\boldsymbol{\Phi} = \boldsymbol{f} \doteq \boldsymbol{f}_{\mathrm{p}} \cdot \boldsymbol{f}_{\mathrm{e}}$ whereby $\boldsymbol{f} \doteq \boldsymbol{F}^{-1}$, $\boldsymbol{f}_{\mathrm{e}} \doteq \boldsymbol{F}_{\mathrm{e}}^{-1}$ and $\boldsymbol{f}_{\mathrm{p}} \doteq \boldsymbol{F}_{\mathrm{p}}^{-1}$. For completeness, let appropriate velocity fields be denoted by $\boldsymbol{v} = \mathrm{D}_{\mathrm{t}}\boldsymbol{\varphi}$ with $\boldsymbol{l} = \mathrm{d}_{\boldsymbol{x}}\boldsymbol{v} = \mathrm{D}_t\boldsymbol{F} \cdot \boldsymbol{f}$ and $\boldsymbol{V} = \mathrm{d}_{\mathrm{t}}\boldsymbol{\Phi}$ with $\boldsymbol{L} = \mathrm{D}_{\boldsymbol{X}}\boldsymbol{V} = \mathrm{d}_t\boldsymbol{f} \cdot \boldsymbol{F}$ as well as $\boldsymbol{v} = -\boldsymbol{F} \cdot \boldsymbol{V}$.

BALANCES OF LINEAR MOMENTUM

The classical format of balance of linear momentum is usually outlined in terms of, e.g., the spatial motion first Piola–Kirchhoff stress tensor, $\boldsymbol{\Pi}^{\mathrm{t}}$. When referring to both, the spatial as well as to the material motion problem (here for the static case) we end up with different representations which are related via Piola transformations, to be specific

$$\begin{aligned} &\nabla_{\boldsymbol{X}} \cdot \boldsymbol{\Pi}^{\mathrm{t}} + \boldsymbol{b}_0 = \boldsymbol{0}\,, \quad \nabla_{\boldsymbol{x}} \cdot \boldsymbol{\sigma}^{\mathrm{t}} + \boldsymbol{b}_t = \boldsymbol{0} \quad \text{with} \quad \boldsymbol{\sigma}^{\mathrm{t}} = \det(\boldsymbol{f})\, \boldsymbol{\Pi}^{\mathrm{t}} \cdot \boldsymbol{F}^{\mathrm{t}} \quad \text{and} \quad \boldsymbol{b}_t = \det(\boldsymbol{f})\, \boldsymbol{b}_0 \quad (\text{in } T\mathcal{B}_t) \\ &\nabla_{\boldsymbol{X}} \cdot \boldsymbol{\Sigma}^{\mathrm{t}} + \boldsymbol{B}_0 = \boldsymbol{0}\,, \quad \nabla_{\boldsymbol{x}} \cdot \boldsymbol{\pi}^{\mathrm{t}} + \boldsymbol{B}_t = \boldsymbol{0} \quad \text{with} \quad \boldsymbol{\pi}^{\mathrm{t}} = \det(\boldsymbol{f})\, \boldsymbol{\Sigma}^{\mathrm{t}} \cdot \boldsymbol{F}^{\mathrm{t}} \quad \text{and} \quad \boldsymbol{B}_t = \det(\boldsymbol{f})\, \boldsymbol{B}_0 \quad (\text{in } T\mathcal{B}_0) \end{aligned} \tag{1}$$

DISSIPATION INEQUALITY

Let the free Helmholtz energy take the format

$$\psi_0 = \psi_0(\boldsymbol{F}, \boldsymbol{F}_{\mathrm{p}}; \boldsymbol{X}) = \det(\boldsymbol{F}_{\mathrm{p}})\, \psi_{\mathrm{p}}(\boldsymbol{F} \cdot \boldsymbol{f}_{\mathrm{p}}; \boldsymbol{X}) \tag{2}$$

such that the (isothermal) Dissipation inequality of the spatial motion problem, $\mathsf{D}_0^{\mathrm{loc}} = \boldsymbol{\Pi}^{\mathrm{t}} : \mathrm{D}_t\boldsymbol{F} - \mathrm{D}_t\psi_0 \geq 0$, reads

$$\mathsf{D}_0^{\mathrm{loc}} = [\, \boldsymbol{\Pi}^{\mathrm{t}} - \mathrm{D}_{\boldsymbol{F}}\psi_0 \,] : \mathrm{D}_t\boldsymbol{F} - \mathrm{D}_{\boldsymbol{F}_{\mathrm{p}}}\psi_0 : \mathrm{D}_t\boldsymbol{F}_{\mathrm{p}} \doteq -\, \boldsymbol{\Pi}_{\mathrm{p}}^{\mathrm{t}} : \mathrm{D}_t\boldsymbol{F}_{\mathrm{p}} = -\, \boldsymbol{\Pi}_{\mathrm{p}}^{\mathrm{t}} : [\, \mathrm{d}_t\boldsymbol{F}_{\mathrm{p}} - \nabla_{\boldsymbol{X}}\boldsymbol{F}_{\mathrm{p}} \cdot \boldsymbol{V} \,] \geq 0 \tag{3}$$

When placing emphasis on the definition of the force driving $\mathrm{D}_t\boldsymbol{F}_{\mathrm{p}}$ one observes that $\boldsymbol{\Pi}_{\mathrm{p}}^{\mathrm{t}}$ takes an almost Eshelbian format, namely

$$\boldsymbol{\Pi}_{\mathrm{p}}^{\mathrm{t}} = \mathrm{D}_{\boldsymbol{F}_{\mathrm{p}}}\psi_0 = \psi_{\mathrm{p}}\, \mathrm{D}_{\boldsymbol{F}_{\mathrm{p}}}\det(\boldsymbol{F}_{\mathrm{p}}) + \det(\boldsymbol{F}_{\mathrm{p}})\, \mathrm{D}_{\boldsymbol{F}_{\mathrm{e}}}\psi_{\mathrm{p}} : \mathrm{D}_{\boldsymbol{F}_{\mathrm{p}}}\boldsymbol{F}_{\mathrm{e}} = \psi_0\, \boldsymbol{f}_{\mathrm{p}}^{\mathrm{t}} - \det(\boldsymbol{F}_{\mathrm{p}})\, \boldsymbol{F}_{\mathrm{e}}^{\mathrm{t}} \cdot \mathrm{D}_{\boldsymbol{F}_{\mathrm{e}}}\psi_{\mathrm{p}} \cdot \boldsymbol{f}_{\mathrm{p}}^{\mathrm{t}} \tag{4}$$

with $\mathrm{D}_{\boldsymbol{F}_{\mathrm{e}}}\psi_{\mathrm{p}} = \mathrm{D}_{\boldsymbol{F}}\psi_{\mathrm{p}} : \mathrm{D}_{\boldsymbol{F}_{\mathrm{e}}}\boldsymbol{F} = \mathrm{D}_{\boldsymbol{F}}\psi_{\mathrm{p}} \cdot \boldsymbol{F}_{\mathrm{p}}^{\mathrm{t}}$ and $\det(\boldsymbol{F}_{\mathrm{p}})\, \mathrm{D}_{\boldsymbol{F}}\psi_{\mathrm{p}} = \mathrm{D}_{\boldsymbol{F}}\psi_0 = \boldsymbol{\Pi}^{\mathrm{t}}$ which results in

$$\boldsymbol{\Pi}_{\mathrm{p}}^{\mathrm{t}} = \psi_0\, \boldsymbol{f}_{\mathrm{p}}^{\mathrm{t}} - \det(\boldsymbol{F}_{\mathrm{p}})\, \boldsymbol{F}_{\mathrm{e}}^{\mathrm{t}} \cdot \mathrm{D}_{\boldsymbol{F}}\psi_{\mathrm{p}} = \psi_0\, \boldsymbol{f}_{\mathrm{p}}^{\mathrm{t}} - \boldsymbol{F}_{\mathrm{e}}^{\mathrm{t}} \cdot \boldsymbol{\Pi}^{\mathrm{t}} = [\, \psi_0\, \boldsymbol{I}_{\mathrm{p}} - \boldsymbol{F}_{\mathrm{e}}^{\mathrm{t}} \cdot \boldsymbol{\Pi}^{\mathrm{t}} \cdot \boldsymbol{F}_{\mathrm{p}}^{\mathrm{t}} \,] \cdot \boldsymbol{f}_{\mathrm{p}}^{\mathrm{t}} = \boldsymbol{\Sigma}_{\mathrm{p}}^{\mathrm{t}} \cdot \boldsymbol{f}_{\mathrm{p}}^{\mathrm{t}} \tag{5}$$

whereby $\boldsymbol{F}_{\mathrm{e}}^{\mathrm{t}} \cdot \boldsymbol{\Pi}^{\mathrm{t}} \cdot \boldsymbol{F}_{\mathrm{p}}^{\mathrm{t}} = \boldsymbol{M}_{\mathrm{p}}^{\mathrm{t}}$ characterizes a Mandel stress tensor of the spatial motion problem. With this relation in hand, it is now straightforward to show that the Eshelbian stress field $\boldsymbol{\Sigma}_{\mathrm{p}}^{\mathrm{t}}$ is the driving force of the plastic velocity gradient $\boldsymbol{L}_{\mathrm{p}} = \mathrm{D}_t\boldsymbol{F}_{\mathrm{p}} \cdot \boldsymbol{f}_{\mathrm{p}} = -\, \boldsymbol{F}_{\mathrm{p}} \cdot \mathrm{D}_t\boldsymbol{f}_{\mathrm{p}}$, i.e.

$$\mathsf{D}_0^{\mathrm{loc}} = -\, [\, \boldsymbol{\Pi}_{\mathrm{p}}^{\mathrm{t}} \cdot \boldsymbol{F}_{\mathrm{p}}^{\mathrm{t}} \,] : [\, \mathrm{D}_t\boldsymbol{F}_{\mathrm{p}} \cdot \boldsymbol{f}_{\mathrm{p}} \,] = -\, \boldsymbol{\Sigma}_{\mathrm{p}}^{\mathrm{t}} : \boldsymbol{L}_{\mathrm{p}} \geq 0 \tag{6}$$

In view of the material motion problem, we first define the free Helmholtz energy as

$$\psi_t = \psi_t(\boldsymbol{F}, \boldsymbol{F}_{\mathrm{p}}; \boldsymbol{X}) = \det(\boldsymbol{F}_{\mathrm{p}} \cdot \boldsymbol{f})\, \psi_{\mathrm{p}}(\boldsymbol{F} \cdot \boldsymbol{f}_{\mathrm{p}}; \boldsymbol{X}) \tag{7}$$

and second exploit the (isothermal) dissipation inequality of the material motion problem, $\mathsf{D}_t^{\rm loc} = \det(\boldsymbol{f})\,\mathsf{D}_0^{\rm loc}$, in detail

$$\mathsf{D}_t^{\rm loc} = \boldsymbol{\pi}^{\rm t} : {\rm d}_t \boldsymbol{f} - \boldsymbol{B}_t^{\rm int} \cdot \boldsymbol{V} - {\rm d}_t \psi_t = [\,\boldsymbol{\pi}^{\rm t} - {\rm d}_{\boldsymbol{f}} \psi_t\,] : {\rm d}_t \boldsymbol{f} - [\,\boldsymbol{B}_t^{\rm int} + \partial_{\boldsymbol{X}} \psi_t\,] \cdot \boldsymbol{V} - {\rm d}_{\boldsymbol{F}_{\rm p}} \psi_t : {\rm d}_t \boldsymbol{F}_{\rm p} \geq 0 \tag{8}$$

whereby $\boldsymbol{\pi}^{\rm t} = {\rm d}_{\boldsymbol{f}} \psi_t$ denotes the material motion first Piola–Kirchhoff stress. Comparing eqs.(3) and (8) ends up with the remarkable result

$$-\,[\,\boldsymbol{B}_t^{\rm int} + \partial_{\boldsymbol{X}} \psi_t\,] \cdot \boldsymbol{V} - {\rm d}_{\boldsymbol{F}_{\rm p}} \psi_t : {\rm d}_t \boldsymbol{F}_{\rm p} = -\,\det(\boldsymbol{f})\,\boldsymbol{\Pi}_{\rm p}^{\rm t} : [\,{\rm d}_t \boldsymbol{F}_{\rm p} - \nabla_{\boldsymbol{X}} \boldsymbol{F}_{\rm p} \cdot \boldsymbol{V}\,] \tag{9}$$

which we restate via

$$\det(\boldsymbol{F})\,{\rm d}_{\boldsymbol{F}_{\rm p}} \psi_t : {\rm d}_t \boldsymbol{F}_{\rm p} = \boldsymbol{\Pi}_{\rm p}^{\rm t} : {\rm d}_t \boldsymbol{F}_{\rm p} \quad \text{and} \quad \det(\boldsymbol{F})\,\boldsymbol{B}_t^{\rm int} = \boldsymbol{B}_0^{\rm int} = -\,\boldsymbol{\Pi}_{\rm p}^{\rm t} : \nabla_{\boldsymbol{X}} \boldsymbol{F}_{\rm p} - \partial_{\boldsymbol{X}} \psi_0 \tag{10}$$

With these relations in hand, one observes that the material motion first Piola–Kirchhoff stress takes the format

$$\boldsymbol{\pi}^{\rm t} = {\rm d}_{\boldsymbol{f}} \psi_t = {\rm d}_{\boldsymbol{F}_{\rm p}} \psi_t : {\rm d}_{\boldsymbol{f}} \boldsymbol{F}_{\rm p} = \det(\boldsymbol{f})\,\boldsymbol{\Pi}_{\rm p}^{\rm t} : {\rm d}_{\boldsymbol{f}} \boldsymbol{F}_{\rm p} = \det(\boldsymbol{f})\,\boldsymbol{F}_{\rm p}^{\rm t} \cdot \boldsymbol{\Pi}_{\rm p}^{\rm t} \cdot \boldsymbol{F}^{\rm t} = \det(\boldsymbol{f})\,\boldsymbol{\Sigma}^{\rm t} \cdot \boldsymbol{F}^{\rm t} \tag{11}$$

For completeness, we finally highlight the material motion Cauchy or rather Eshelby stress $\boldsymbol{\Sigma}^{\rm t}$, which enters one of the balances of linear momentum in eq.(1), as well as the correlated source term

$$\boldsymbol{\Sigma}^{\rm t} = \det(\boldsymbol{F}_{\rm p})\,\boldsymbol{F}_{\rm p}^{\rm t} \cdot {\rm d}_{\boldsymbol{F}_{\rm p}} \psi_t = \boldsymbol{F}_{\rm p}^{\rm t} \cdot \boldsymbol{\Pi}_{\rm p}^{\rm t} \quad \text{and} \quad \boldsymbol{B}_0 = -\,\boldsymbol{F}^{\rm t} \cdot \boldsymbol{b}_0 - \boldsymbol{\Pi}_{\rm p}^{\rm t} : \nabla_{\boldsymbol{X}} \boldsymbol{F}_{\rm p} - \partial_{\boldsymbol{X}} \psi_0 \tag{12}$$

Remark 1 Please note that the self forces in eq.(3) due to $\partial_{\boldsymbol{x}} \psi_t$ are neglected since the free Helmholtz energy does not depend (explicitely) on $\boldsymbol{x}$. In fact, this is a consequence of invariance under superposed (spatial, orientation preserving) Euclidian transformations, i.e. $\psi_{\rm p}(\boldsymbol{\varphi}, {\rm D}_{\boldsymbol{X}} \boldsymbol{\varphi}, \ldots) = \psi_{\rm p}(\boldsymbol{\varphi}', {\rm D}_{\boldsymbol{X}} \boldsymbol{\varphi}', \ldots)$ with $\boldsymbol{\varphi}' = \boldsymbol{x}' = \boldsymbol{Q} \cdot \boldsymbol{x} + \boldsymbol{c}$ and $\boldsymbol{Q}^{\rm t} = \boldsymbol{Q}^{-1}$.

Remark 2 An alternative derivation of eq.(12) is based on the classical representation of linear momentum, $\nabla_{\boldsymbol{X}} \cdot \boldsymbol{\Pi}^{\rm t} + \boldsymbol{b}_0 = \boldsymbol{0}$, and the relations $-\,\boldsymbol{F}^{\rm t} \cdot [\,\nabla_{\boldsymbol{X}} \cdot \boldsymbol{\Pi}^{\rm t}\,] = \boldsymbol{\Pi}^{\rm t} : \nabla_{\boldsymbol{X}} \boldsymbol{F} - \nabla_{\boldsymbol{X}} \cdot (\,\boldsymbol{F}^{\rm t} \cdot \boldsymbol{\Pi}^{\rm t}\,)$, with $\nabla_{\boldsymbol{X}} \boldsymbol{F}^{\rm t} : \boldsymbol{\Pi}^{\rm t} = \boldsymbol{\Pi}^{\rm t} : \nabla_{\boldsymbol{X}} \boldsymbol{F}$, and $\nabla_{\boldsymbol{X}} \cdot (\,\psi_0\,\boldsymbol{I}\,) = \boldsymbol{\Pi}^{\rm t} : \nabla_{\boldsymbol{X}} \boldsymbol{F} + \boldsymbol{\Pi}_{\rm p}^{\rm t} : \nabla_{\boldsymbol{X}} \boldsymbol{F}_{\rm p} + \partial_{\boldsymbol{X}} \psi_0$, respectively.

Remark 3 The contribution to the internal material force stemming from either the irreversible or reversible part of the total deformation gradient allow representation in terms of, e.g., the material motion Cauchy or rather Eshelby stress, i.e $\boldsymbol{\Pi}_{\rm p}^{\rm t} : \nabla_{\boldsymbol{X}} \boldsymbol{F}_{\rm p} = [\,\boldsymbol{f}_{\rm p}^{\rm t} \cdot \boldsymbol{\Sigma}^{\rm t}\,] : \nabla_{\boldsymbol{X}} \boldsymbol{F}_{\rm p} = \boldsymbol{\Sigma}^{\rm t} : [\,\boldsymbol{f}_{\rm p} \cdot \nabla_{\boldsymbol{X}} \boldsymbol{F}_{\rm p}\,] = \boldsymbol{\Sigma}^{\rm t} : \boldsymbol{\Gamma}_{\rm p}$. Apparently, the skew part of $\nabla_{\boldsymbol{X}} \boldsymbol{F}_{\rm p}$ or $\boldsymbol{\Gamma}_{\rm p}$, respectively, characterize the dislocation density.

References

[1] S. Cleja-Ţigoiu and G.A. Maugin. Eshelby's stress tensors in finite elastoplasticity. *Acta Mech.*, 139:231–249, 2000.

[2] M. Epstein and G.A. Maugin. The energy–momentum tensor and material uniformity in finite elasticity. *Acta Mech.*, 83:127–133, 1990.

[3] M. Epstein and G.A. Maugin. On the geometrical material structure of anelasticity. *Acta Mech.*, 115:119–131, 1996.

[4] D. Gross, S. Kolling, R. Müller, and I. Schmidt. Configurational forces and their application in solid mechanics. *Euro. J. Mech. A/Solids*, 22:669–692, 2003.

[5] M.E. Gurtin. *Configurational Forces as Basic Concept in Continuum Physics*, volume 137 of *Applied Mathematical Sciences*. Springer, 2000.

[6] R. Kienzler and G. Hermann. *Mechanics in Material Space – with Application to Defect and Fracture Mechanics*. Springer, 2000.

[7] K.C. Le and H. Stumpf. Strain measures, integrability condition and frame indifference in the theory of oriented media. *Int. J. Solids Struct.*, 35(9):783–798, 1998.

[8] J. Mandel. Thermodynamics and plasticity. In J.J. Delgado Domingos, M.N.R. Nina, and J.H. Whitelaw, editors, *Foundations of Continuum Thermodynamics*, pages 283–304. MacMillan, 1974.

[9] G.A. Maugin. *Material Inhomogeneities in Elasticity*, volume 3 of *Applied Mathematics and Mathematical Computation*. Chapman & Hall, 1993.

[10] G.A. Maugin. Pseudo–plasticity and pseudo–inhomogeneity effects in materials mechanics. *J. Elasticity*, 71:81–103, 2003.

[11] G.A. Maugin and M. Epstein. Geometrical material structure of elastoplasticity. *Int. J. Plasticity*, 14(1–3):109–115, 1998.

[12] A. Menzel. *Modelling and Computation of Geometrically Nonlinear Anisotropic Inelasticity*. PhD thesis, Chair of Applied Mechanics, University of Kaiserslautern, 2002. http://kluedo.ub.uni-kl.de/volltexte/2002/1389/.

[13] A. Menzel, R. Denzer, and P. Steinmann. On the comparison of two approaches to compute material forces for inelastic materials. Application to single–slip crystal–plasticity. *Comput. Methods Appl. Mech. Engrg.*, 2004. accepted for publication.

[14] A. Menzel and P. Steinmann. On the continuum formulation of higher gradient plasticity for single and polycrystals. *J. Mech. Phys. Solids*, 48(8):1777–1796, 2000. Erratum 49(5):1179–1180, 2001.

[15] P. Steinmann. Views on multiplicative elastoplasticity and the continuum theory of dislocations. *Int. J. Engng. Sci.*, 34(15):1717–1735, 1996.

[16] P. Steinmann. On spatial and material settings of hyperelastostatic crystal defects. *J. Mech. Phys. Solids*, 50(8):1743–1766, 2002.

[17] P. Steinmann. On spatial and material settings of thermo–hyperelastodynamics. *J. Elasticity*, 66:109–157, 2002.

[18] B. Svendsen. On the modeling of anisotropic elastic and inelastic material behaviour at large deformation. *Int. J. Solids Struct.*, 38(52):9579–9599, 2001.

[19] C. Truesdell and W. Noll. *The Non–Linear Field Theories of Mechanics*. Springer, 2nd edition, 1992.

AFFINE SYMMETRY IN MECHANICS OF DISCRETE AND CONTINUOUS SYSTEMS

Jan J.Slawianowski
IPPT PAN, Department of the Theory of Continuous Media
Laboratory of Analytical Mechanics and Field Theory

Summary Discussed is the status of kinematical and dynamical affine symmetry in mechanics of discrete multiparticle systems and in continuum mechanics.In particular,we develop affinely-invariant geodetic models of mechanical systems with affine degrees of freedom.Discussed is the model of nonlinear elastic vibrations with the dynamics encoded entirely in the kinetic energy form,without any use of potentials or generalized forces.Certain mechanical and microphysical applications ale briefly discussed.

INTRODUCTION

The impact of geometry on the structure of physical laws is a well-known fact.It is commonly known that kinematics and dynamics of discrete multiparticle systems and continuous media have a very important purely geometrical component following from the Euclidean structure of the physical space or pseudo-Euclidean structure of Minkowskian space-time.Surprisingly enough,geometry of the Galilean space-time is much more complicated than the relativistic one,not yet completely understood and full of surprizes.There is an important sector of macroscopic mechanics and fundamental physics which may be simply deduced from the structure of isometry and rotation groups,or,in certain problems – from the structure of Galilei and Poincare groups.It is sufficient to mention various invariance and objectivity principles in continuum mechanics and its constitutive laws [4],general statements concerning the shape of internal forces in isolated systems,and,in fundamental physics,classification of elementary particles and corresponding fields,based on irreducible representations of the rotation and Lorentz groups (homogeneous and inhomogeneous).In macroscopic mechanics of solids this is reflected by the particular role of rigid body mechanics among all constrained mechanical systems [1].In mechanics of microstructured bodies this impact of geometry on mechanics is very striking and convincing in the theory of micropolar Cosserat continua [7],[8],[10].And rigid body is the simplest nontrivial example,just the particular master pattern of a dynamical systems on Lie-group-spaces [1],[2].

AFFINE BACKGROUND OF MECHANICS

But in elementary geometry there exists also a more fundamental sector,namely,the theory of affine and projective invariants.This is everything which has to do with Tales theorem,collinearity,congruence of segments on the same straight-line ,parallelism,the very straight-line concept,etc,but does not use the notions like the length of segments and angular measure.At least from the purely academic point of view of rational mechanics and geometry it is natural to formulate a programme of affine mechanics and physics.Incidentally,the very fundamentals of Newton theory do not assume metrical geometry and are based on puely affine concepts.Euclidean geometry with its measure of lengths and angles ,i.e.scalar product of vectors,becomes essential on the constitutive level,when constructing realistic expressions for interparticle forces or potentials,although even in this respect one can formulate some academic models based on purely affine relationships.It is worth to mention that also in the very fundamental physics there were some attempts of formulating purely affine theory,based on affine invariants and classifying fundamental particles and fields in terms of irreducible representations of the linear and affine groups.On the level of mechanics of extended bodies such an approach suggests us to replace the metrical rigid body concept by that of affinely rigid one,with degrees of freedom fully described by affine group.When using traditional metrical terms we would say that such an object undergoes translations in space,rotations and homogeneous deformations.Systems with purely affine, GL(3,**R**) – based models of
collective and internal degrees of freedom were considered in various problems of microstructured solids.It seems that A.C.Eringen [4] and his followers were pioneers here when formulating the theory of micromorphic continua.The model was also used in macroscopic elasticity,astrophysics and molecular and nuclear dynamics [3],[7],[8],[11] .Obviously,the two latter applications are based on the quantized version of the theory;the nuclear applications have to do with the droplet model of atomic nuclei.Applications in dynamics of molecular crystals are also possible;by the way,the mechanics of micromorphic continua appears as a long-wave limit of molecular crystals dynamics.However,in all such attempts it was only kinematics that was ruled by affine group ,whereas the all existing in literature models violated affine symmetry on the level of dynamics.The novelty of our models is that the dynamics and the structure of kinetic energy is invariant under spatial or material (or both) affine transformations.Therefore,our models may be interpreted in terms of Arnold-Hermann-Marsden analytical mechanics on Lie groups and their homogeneous spaces,with invariant kinetic energy forms.It is very interesting that bounded motions,e.g.,nonlinear elastic vibrations

may be dynamically encoded in the very form of the appropriately chosen kinetic energy ,i.e.,metric tensor on the configuration space,even without any use of potentials or generalized forces.This enables one to obtain some rigorous analytical solutions exactly due to the dynamical invariance under affine group. Such models may be interpreted as a discretization of the Arnold,Marsden,Binz,and others description of ideal fluids as right-invariant dynamical systems with the configuration space given by the infinite-dimensional manifold of all volume-preserving diffeomorphisms [2].This is obviously the very drastic discretization,reducing the non-denumerable continuous number of degrees of freedom to a finite one,equal the dimension of the affine,or linear group.The full invariance of our geodetic models on the affine group enables one to obtain ,at least in certain cases,the general solution in an explicit analytical form.More generally,one can obtain some qualitative information about the phase portrait of the system and some family of special solutions,distinguished by the symmetry group of the problem .These solutions,so-called relative equilibria,or relative closed orbits [1],[9],[12] enable one to understand qualitatively the general solution even if we are unable to find it explicitly in terms of elementary functions or well-known special functions.Having in view some microscopic applications we develop also the quantum version of the theory.It may be applied in mechanics of solids,nanostructures and in dynamics of certain essentially microscopic objects which simultaneously may be interpreted in terms of deformable bodies theory.Applications in relativistic microstructured continua are also possible and certain primary results in this field will be presented.In a sense,they develop certain ideas of Eringen,Bressan and others.

ADDITIONAL REMARKS AND CONCLUSIONS

Models of this type are very interesting from the point of view of pure mathematics and rational mechanics,but apparently,they might seem rather academic toy models.We show that it seems to exist a field of non-standard applications in dynamics of such objects like gas bubbles in fluids,fluid droplet inclusions in fluids,defects in solids,and also in certain versions of the droplet model of atomic nuclei.Applications in nanomechanics are not excluded.Some of results we present are also relevant for the theory of one-dimensional chains (one-dimensional multi-body problems) related to various versions of completely integrable lattices (Calogero-Moser,Sutherland and others) [6].We mention also about generalizations based on Hamiltonian systems on other Lie groups like the projective,conformal,and unitary ones.Some affine generalizations of objectivity principles may be also developed.Certain results in micromorphic relativistic continuum theory were obtained.

References

[1] Abraham R.,Marsden.J.E.: Foundations of Mechanics. The Benjamin/Cummings Publishing Company, London,Amsterdam, 1978.

[2] Arnold V.I.:Mathematical Methods of Classical Mechanics. Springer Graduate Texts in Math.No **60**.Springer,New York, 1978

[3] Bogojavlenskij O.I.: Methods of Qualitative Theory of Dynamical Systems in Astrophysics and Gas Dynamics. Springer-Verlag, Berlin-Heidelberg-New York, 1985.

[4] Eringen A.C.:Nonlinear Theory of Continuous Media. McGraw Hill,NY 1962.

[5] Eringen A.C.:Mechanics of Micromorphic Continua, Proc.IUTAM Symposium Freudenstadt and Stuttgart 1967, Ed.:E.Kroener. 1968.

[6] Moser J.: The Integrable Hamiltonian Systems Connected with Isospectral Dformations. Adv.Math **16,** 1, 1975.

[7] O'Reilly O.M., Varadi P.C.: Unified Treatment of Constraints in the Theory of a Cosserat Point. Zeitschrift fuer Angewandte Mathematik und Physik **49**, 205-223, 1998.

[8] Papadopoulos P.: On a Class of Higher-Order Pseudo-Rigid Bodies. Mathematics and Mechanics of Solids **6** ,631-640,2001.

[9] Roberts M.,Wulff C.,Lamb J.: Hamiltonian Systems Near Relative Periodic Orbits.SIAM J.Dyn.Syst. **1**, 1-43, 2002.

[10] Rubin M.B.: Cosserat Theories,Shells,Rods and Points,Solid Mechanics and its Applications.Vol.**79**.Kluwer,the Netherlands, 2000.

[11] Slawianowski J.J.: The Mechanics of the Homogeneously-Deformable Body.Dynamical Models with High Symmetries. Zeitschrift fuer Angewandte Mathematik und Mechanik **62** , 229-240, 1982.

[12] Wulff C.,Roberts M.: Hamiltonian Systems Near Relative.Equilibria. J.Differential Equations **179**, 562-604, 2002.

COUPLED FREQUENCIES OF A FLUID-STRUCTURE INTERACTION CYLINDRICAL SYSTEM

Elena Gavrilova
Department of Mathematics, St. Ivan Rilski University of Mining & Geology, Sofia 1700, Bulgaria

Summary An upright fixed circular cylindrical tank with rigid bottom and side wall, where as a part of the side wall is an axial-symmetrical vibrating thin shell with clamped edges, is partly filled with an incompressible and inviscid fluid. Using the Bubnov-Galerkin method, the analytical solution of the problem about the determination of the free coupled vibrations of the obtained fluid-structure interaction system is found and some numerical examples are discussed.

INTRODUCTION

The study of the dynamic behavior of a tank and internal fluid is becoming of increasing importance in many fields such as the earthquake-proof design and the reliability assessment of fluid storage tanks. The problem about the determination of the coupled vibrations of systems fluid-tank with some elastic elements is under consideration by many authors. Bauer and co-authors [1] investigate the coupled oscillations of a cylindrical container with elastic walls and rigid bottom partially filled with liquid using the bending theory for the analysis of the container. The general problem of hydroelastic sloshing of fluid in a partially filled circular cylindrical container with rigid bottom and elastic walls is investigated in [2]. In [3] the liquid-filled flexible cylindrical container is considered as the velocity potential of a compressible fluid is found by the Galerkin method.

FORMULATION OF THE PROBLEM

An upright fixed circular cylindrical tank of diameter $2R$ and height L is partially filled with a homogeneous, incompressible and inviscid fluid to the depth H $(H < L)$.

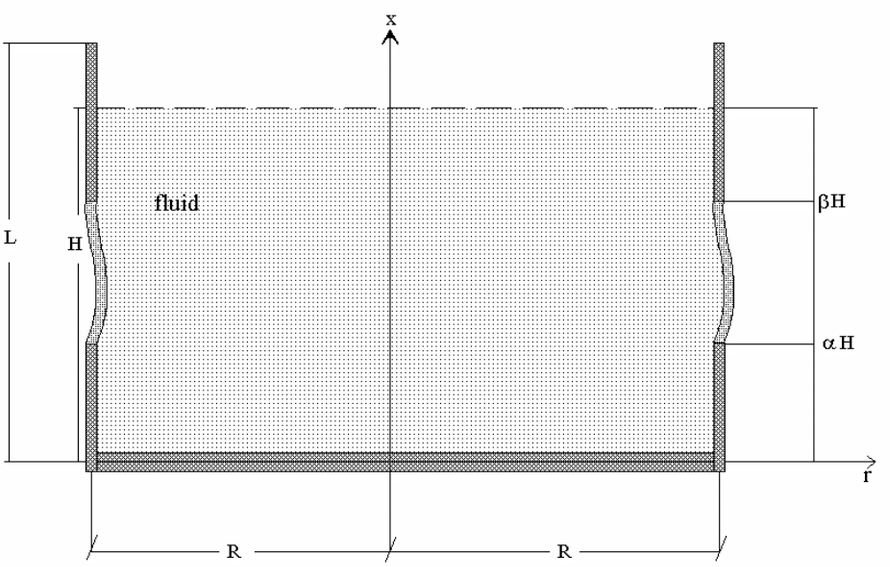


Figure 1. The geometry and co-ordinate system

The tank bottom at $x = 0$ (x is the vertical co-ordinate) and its side wall at $r = R$ are rigid as a part of the last one - $\alpha H \le x \le \beta H$ $(0 \le \alpha < \beta < 1)$ - is an axial-symmetrical vibrating thin shell with clamped edges, completely under the fluid. Its radial displacement along the outward normal is described with the function $w(x;t)$, where t is time. Such a system constitutes a fluid-structure interaction system. The fluid motion in the tank is supposed to be axisymmetrical and potential. Its velocity potential function $\varphi(r, x; t)$ is a solution of the partial differential equation

$$\frac{\partial^2 \varphi}{\partial r^2} + \frac{1}{r}\frac{\partial \varphi}{\partial r} + \frac{\partial^2 \varphi}{\partial x^2} = 0 \qquad 0 \le x \le H,\ 0 \le r \le R \tag{1}$$

with the boundary conditions:

$$\frac{\partial\varphi}{\partial x}=0 \quad \text{at the tank bottom } x=0,\ 0\le r\le R; \qquad \frac{\partial^2\varphi}{\partial t^2}+g\frac{\partial\varphi}{\partial x}=0 \quad \text{at the free surface } x=H,\ 0\le r\le R, \tag{2}$$

where g is the gravitational acceleration. The function $w(x;t)$ satisfies the partial differential equation

$$\frac{\partial^4 w}{\partial x^4}+\frac{Eh}{DR^2}w+\frac{\rho h}{D}\frac{\partial^2 w}{\partial t^2}=-\frac{\rho_0}{D}\frac{\partial\varphi}{\partial t}\Big|_{r=R} \qquad \alpha H\le x\le\beta H \tag{3}$$

$$w\Big|_{x=\alpha H}=w\Big|_{x=\beta H}=\frac{\partial w}{\partial x}\Big|_{x=\alpha H}=\frac{\partial w}{\partial x}\Big|_{x=\beta H}=0, \tag{4}$$

which express that the elastic shell is clamped along its edges. Here ρ_0 is the fluid density, h - the shell thickness, E - Young's modulus of elasticity of the shell material, ρ - the density of the shell material and D - its flexural rigidity. Equation (3) is derived based on the assumption that the longitudinal inertia of the elastic shell has negligible effect on its motion. Both functions $\varphi(r,x;t)$ and $w(x;t)$ must satisfy the compatibility condition

$$\frac{\partial\varphi}{\partial r}\Big|_{r=R}=\begin{cases}\dfrac{\partial w}{\partial t} & \alpha H\le x\le\beta H,\\ 0 & 0\le x\le\alpha H,\quad \beta H<x\le H.\end{cases} \tag{5}$$

ANALYTICAL SOLUTION

It is assumed that

$$\varphi(r,x;t)=i\omega\Phi(r,x)e^{i\omega t},\ w(x;t)=W(x)e^{i\omega t}, \tag{6}$$

where ω is the undetermined coupled natural frequency of the fluid-tank vibrations and $i^2=-1$. Using the equations (1)-(4), the following expressions can be written:

$$\Phi(x,r)=\sum_{n=1}^{\infty}A_n\cos(k_n x)I_0(k_n r),$$

$$W(x)=\frac{\rho_0\omega^2}{D}\sum_{n=1}^{\infty}\sum_{m=1}^{\infty}A_n\frac{I_0(k_nR)}{k_n^4+4\Omega^4}\sin\frac{m\pi(x-\alpha H)}{H(\beta-\alpha)}(a_{nm}+F_{1n}b_m+F_{2n}c_m+F_{3n}d_m+F_{4n}e_m), \tag{7}$$

where

$$tg(k_nH)+\frac{\omega^2}{gk_n}=0,\quad \Omega^4=\frac{1}{4D}\left(\frac{Eh}{R^2}-\rho h\omega^2\right), \tag{8}$$

and the constants a_{nm}, F_{in} $(n,m=1,2,3,...;i=1,2,3,4)$ have completely determined values. After satisfying the compatibility condition (5) some infinite system of homogeneous algebraic equations about the unknown coefficients A_n is obtained. It will have a nontrivial solution, if the determinant of the coefficient matrix is equal to zero - thus the frequency equation is obtained.

The made numerical calculations show that the elastic part of the tank side wall lowers the natural frequency in comparison with the case of the rigid tank as the coupled frequency increases with the increase of the shell thickness and decreases with the increase of the fluid depth.

CONCLUSIONS

In this paper an upright fixed circular cylindrical tank with rigid bottom and side wall, where as a part of the side wall is an axial-symmetrical vibrating thin shell with clamped edges, is partly filled with an incompressible and inviscid fluid. The fluid motion in the tank is supposed to be axisymmetrical and potential.

Using the Bubnov-Galerkin method, the analytical solution of the problem about the determination of the free coupling vibrations of the obtained fluid-structure interaction system is found. Numerical examples show that the presence of some elastic shell in the tank side wall lowers the frequencies appearing.

The case with more elastic inclusions in the side wall of the tank can be considered in a similar way.

References

[1] Bauer H. F., Hsu T. -M., Wang J. T. -S.: Interaction of a Sloshing Liquid with Elastic Containers. *Trans ASME, J. Basic Eng.* **90**, Ser. D, No. 3: 373-377, 1968.

[2] Bauer H. F., Siekmann J.: Note on Linear Hydroelastic Sloshing. *ZAMM* **49**, Heft 10: 577-589, 1969.

[3] Fischer D.: Dynamic Fluid Effects in Liquid-Filled Flexible Cylindrical Tanks. *Earthq Eng. Str Dyn* **7**: 587-601, 1978.

FLUID STRUCTURE INTERACTION IN MULTIPHASE MIXING VESSEL

Matej Vesenjak, Zoran Ren, Matjaž Hriberšek
University of Maribor, Faculty of Mechanical Engineering,
Smetanova 17, SI-2000 Maribor, Slovenia

Summary In this paper a problem of fluid-structure interaction in a mixing vessel is solved with weakly coupled fluid-structure interaction computational analysis. The computational fluid dynamics code CFX, based on the finite volume method, is used for determination of the multiphase flow field (water and air) in the mixing vessel. The results in form of pressure distribution are then applied to the blade model, which is then analysed with the finite element structural analysis system MSC.visualNastran for Windows. The resulting deformations and stresses are evaluated. The proposed procedure can be effectively used for optimization of structures with significant fluid flow influences.

INTRODUCTION

Two or more physical systems frequently interact with each other, where the independent solution of one system is impossible without a simultaneous solution of the others. Such systems are known as coupled, where coupling may be weak or strong, depending on the degree of interaction. In case of weakly coupled systems, where one physical system has only a small influence on other systems, only one-way information stream is sufficient. Strongly coupled systems necessitate a full exchange of information between two or several interacting physical systems. An obvious coupled system is that of a dynamic fluid-structure interaction. [8]
In this paper a computational analysis of the fluid-structure interaction in a mixing vessel is presented. In mixing vessels the fluid can have a significant influence on the deformation of blades during mixing, depending on speed of mixing blades and fluid viscosity. For this purpose a computational weakly coupled analysis has been performed to determine the multiphase fluid influences on the mixing vessel structure. The multiphase fluid field in the mixing vessel was first analyzed with the computational fluid dynamics (CFD) code CFX. The results in the form of pressure were then applied to the blade model, which was the analysed with the structural code MSC.visualNastran for Windows, which is based on the finite element method (FEM).

CFD ANALYSIS OF THE VESSEL

In this paper the mixing of two fluids (water and air) in a mixing vessel is considered. To perform the CFD analysis of the posed physical problem, the mixing tank vessel containing four baffles is discretised with finite volumes. In the interior four rotating impeller blades are connected to a shaft which runs vertically through the vessel (Figure 1). Air is injected into the vessel through an inlet pipe located bellow the impeller blade at a speed of 5 m/s. The angular velocity of the shaft is 3 s^{-1}. The double symmetry of the vessel allows for only ¼ of the vessel to be modelled. The model was analyzed with the finite volumes CFD code CFX and the results in the form of pressure filed on the blade are shown in Figure 2. In spite of the fact that the most important values are those on a boundary between the fluid and the structure, the results of the analysis can be evaluated in every single point of the fluid. The most important results are the loads of the fluid applied to the vessel structure. It was determined that the highest pressure is located at the upper corner of the blade, where the blade is fixed to the shaft. It must be taken into consideration that the results are always conservative because the CFX code treats the fluid boundaries (in our case vessel and blades) as rigid. The computed forces (pressure) were then being used as the boundary conditions in the structural analysis of the vessel blade.

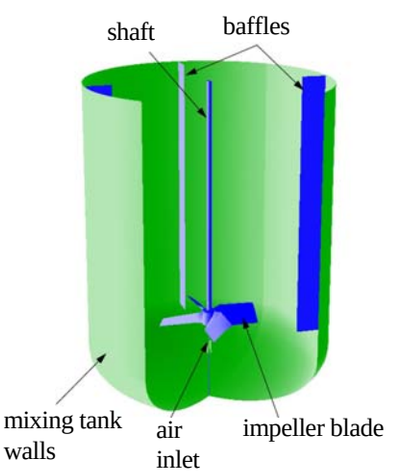


Figure 1: Mixing Vessel

TRANSFORMATION OF CFD DATA TO NASTRAN

The first condition that must be fulfilled is to establish an equilibrium state between the fluid and the structure. The fluid pressure (force) which acts on the structural surface must be equal to the force in the structure, which acts in the opposite direction

$$\mathbf{p} = p \cdot \mathbf{n}_{structure} = p \cdot \mathbf{n}_{fluid}\,, \tag{1}$$

where $\mathbf{n}_{structure} = -\mathbf{n}_{fluid}$ are the external interface normals between the fluid and the structure. To transfer pressure loads from the CFD mesh to the FEM mesh, it is most convenient if the nodes on interfaces are coincident, since the data transfer is the

trivial. In case where those nodes are not coincident, the loads must be properly interpolated (the load field must not change during data transfer) in order to achieve reasonable results. In case of a weakly coupled analysis the constraints are defined with regard to the physical constraints since they are not a result of the computational fluid dynamics. They are defined in the displacement vector of a finite element.
The CFX has the ability to export results in the ASCII format. In case of the presented coupled analysis the most important exported data were: nodes positions (used for establishing a new finite element mesh of the blade model) as well as water and air pressures acting on the blade. The results from the CFX and the finite element mesh data were then written in a proper MSC.visualNastran for Windows form.
The first step was the definition of node positions for the structural analysis. The same node positions as used in the CFD analysis were transferred, although only triangular elements were used. After defining the nodes, loads from both fluids (water and air) were summarized and redefined. Because the CFX is not able to export the topology of elements, the finite element mesh was modelled manually according to the transferred nodes.

FEM ANALYSIS OF THE BLADE

The finite element method was used for determination of the deformation and stress fields of the blade under the influence of computed fluid forces shown on Figure 2.
For the structural analysis of the blade the transformed data, described in the previous chapter, were imported into the MSC.visualNastran for Windows system. Then the material properties of the blade were defined as follows: elasticity modulus 210000 MPa and Poisson ration 0,3. The blade has a constant thickness of 35 mm and was meshed with 3-node shell elements. It was fixed at the edge were it is welded to the shaft (right edge of the discretised model shown on Figure 3). A linear elastic quasi-static computational analysis resulted in blade deformations and stresses as shown in Figure 3. The largest computed deformation of the blade was 0.076 mm at the leftmost free corner, while the stresses were the highest at the point of attachment to the shaft in the upper right corner and equal to 32.23 MPa.

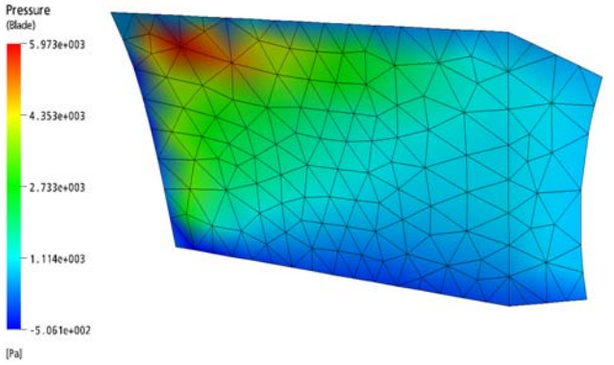


Figure 2: Load field of the blade in CFX

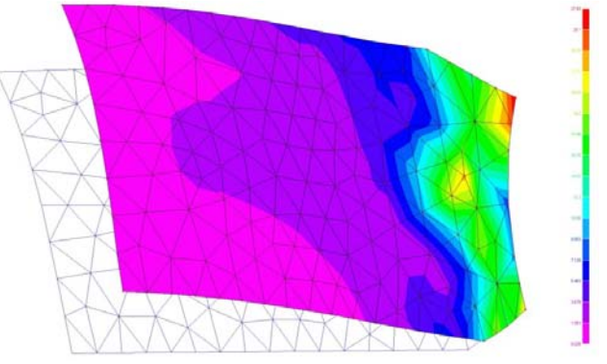


Figure 3. Deformations of the blade

CONCLUSION

The deformations of the blade in a multiphase mixing vessel were determined by means of a weakly coupled computational analysis. The fluid field was analysed with the computational fluid dynamics code CFX. The results in the form of the pressure (forces) were then used for structural analysis of the blade with the finite element system MSC.visualNastran for Windows.
Described procedure can be applied to any problem concerning a weakly coupled fluid-structure interaction. However, a significant research effort is directed to develop robust and accurate fully coupled fluid-structure interaction analysis methods, also considering material and geometrical nonlinearities.

References

[1] CFX Manual, Tutorial
[2] Kuzmin, D.: Introduction to Computational Fluid Dynamics. University of Dortmund, Dortmund.
[3] Kilroy K.: MSC/Nastran – Quick Reference Guide. The MacNeal-Schwendler Corporation, 1998.
[4] NAFEMS: A Finite Element Primer. NAFEMS. Glasgow, 1992.
[5] Schäfer M., Teschauer I., Kadinski L., Selder, M.: A numerical approach for the solution of coupled fluid – solid and thermal stress problems in crystal growth processes. Elsevier, Darmstadt, 2002.
[6] Stein K. R.: Simulation and Modeling Techniques for Parachute Fluid – Structure Interaction. Doctor Thesis, University of Minnesota, Minnesota, 1999.
[7] The fluid equations. [Online] http://astron.barkeley.edu/~jrg/ay202/node152.html [8. September. 2003].
[8] Zienkiewicz O. C., Taylor R.L.: The Finite Element Method – Volume 1 – The Basis. McGraw-Hill Ltd., London, 2000.

XXI ICTAM, 15–21 August 2004, Warsaw, Poland

PISTON IMPACT ONTO THE BOUNDARY OF TWO–LAYER FLUID

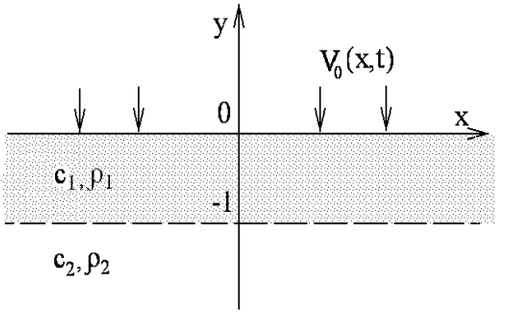
Tatiana I. Khabakhpasheva
Lavrentiev Institute of Hydrodynamic, SB RAS, Novosibirsk, 630090, Russia

Summary The plane unsteady problem of fluid flow caused by impact onto its boundary is considered. Initially fluid is at rest and occupies a lower half-plane. The fluid consists of two horizontal layers with different densities and sound velocities. The fluid flow is described within the acoustic approximation. For the special case, when impact velocity is a step function, both the velocity potential and the distribution of the pressure along the upper boundary of the fluid are obtained in the forms of series at any time instant.

General statement of the problem

The plane unsteady problem of fluid flow caused by an impact on its boundary is considered. Initially ($t = 0$) the fluid is at rest and occupies a lower half-plane ($y < 0$). The fluid consists of two horizontal layers. We take the thickness of the upper layer ℓ as the lengthscale and the maximal value of the boundary velocity V_0 as the velocity scale of fluid flow. In dimensionless variables the line $y = -1$ corresponds to the interface between the layers and the line $y = 0$ to the rigid boundary of the flow region. The density of the resting fluid and its sound velocity are ρ_1, c_1 in the upper layer, $-1 < y < 0$, and ρ_2, c_2 in the lower layer, $y < -1$, respectively. Unsteady flow of the compressible fluid is caused by displacement of its rigid and initially flat boundary. At each time instant $t > 0$ the boundary position is given by the equation $y = -(V_0/c_1)f_b(x,t)$. The function $f_b(x,t)$ and its first derivatives are assumed to be bounded with $f_b(x,0) = 0$. The ratio ℓ/c_1 is taken as the timescale and the product $\rho_1 c_1 V_0$ as the scale of the hydrodynamic pressure.

We shall determine the hydrodynamic pressure along the moving rigid boundary under the following assumptions: (i) the fluid is ideal and compressible; (ii) the Mach number $V_0/c_1 \ll 1$; (iii) $c_1/c_2 \le 1$; (iv) external mass forces are absent.



The fluid flow is described within the framework of the acoustic approximation provided that $V_0/c_1 \ll 1$ and $V_0/c_2 \ll 1$. This approximation is valid for impact speeds well below the medium's acoustic velocity and for times in which the displacements of the rigid boundary are small compared to the thickness of the upper layer.

During the initial stage considered here displacements of the fluid particles are small compared to the lengthscale, which allows us, as a first approximation, to impose boundary conditions on the initial positions of the rigid surface ($y = 0$) and the interface ($y = -1$), and to linearize them and the equations of motion near the initial rest state (see [1] for details).

The linearization leads to the well–known acoustic approximation, where the liquid motion is irrotational and is descried by the velocity potentials $\phi_1(x,y,t)$ in the upper layer ($-1 < y < 0$) and $\phi_2(x,y,t)$ in the lower layer ($y < -1$). The potentials $\phi_j(x,y,t)$, $j = 1, 2$ are identically zero and when $t > 0$ satisfy the wave equations

$$\frac{\partial^2\phi_1}{\partial t^2} = \frac{\partial^2\phi_1}{\partial x^2} + \frac{\partial^2\phi_1}{\partial y^2} \qquad (-1 < y < 0), \qquad \frac{\partial^2\phi_2}{\partial t^2} = m^2\left(\frac{\partial^5\phi_2}{\partial x^2} + \frac{\partial^2\phi_2}{\partial y^2}\right) \qquad (y < -1),$$

where $m = c_2/c_1$, $m \ge 1$, the linearized boundary condition on the rigid surface

$$\frac{\partial\phi_1}{\partial y} = f(x,t) \qquad (y = 0),$$

where $f(x,t) = -(\partial f_b/\partial t)(x,t)$, the linearized dynamic and kinematic boundary conditions on the interface ($k = \rho_1/\rho_2$)

$$\phi_2 = k\phi_1, \qquad \frac{\partial\phi_2}{\partial y} = \frac{\partial\phi_1}{\partial y} \qquad (y = -1).$$

The distribution of hydrodynamic pressure along the rigid boundary, $y = 0$, is given in the non-dimensional variables as $p_1(x,0,t) = -(\partial\phi_1/\partial t)(x,0,t)$ within the acoustic approximation. Below we determine the potential $\phi_1(x,0,t)$ along the rigid boundary and differentiate it with respect to time thereafter to derive the final formula for the hydrodynamic pressure distribution.

Method of solution

We use the Fourier transform with respect to the horizontal coordinate x and the Laplace transform with respect to time t. It allow us to presented solution of the problem in the form

$$\phi_1(x,0,t) = \phi_1^{(0)}(x,0,t) + 2\sum_{n=1}^{\infty} q_\infty^n \phi_1^{(n)}(x,0,t) + 2\sum_{n=1}^{\infty} \phi_{1n}(x,0,t).$$

Each element in these series are obtain separately. We consider below important particular case, when impact velocity is a step function. Then $f_x(x)H(t) = \sum_{N=1}^{P_*} S_N \delta(x - x_N)H(t), \quad S_N = f(x_N + 0) - f(x_N - 0)$, where $H(t) = 1$ if $t \geq 0$ and $H(t) = 0$ if $t < 0$. It was obtain (see [1] for details)

$$\frac{\partial \phi_1^{(0)}}{\partial t}(x,0,t) = f_0(x)H(t) - \frac{1}{2}\sum_{N=1}^{N_*} S_N \frac{x - x_N}{|x - x_N|} H(t - |x - x_N|) + \frac{1}{\pi}\sum_{N=1}^{N_*} S_N \arcsin(\frac{x - x_N}{t})H(t - |x - x_N|).$$

$$\frac{\partial \phi_1^{(n)}}{\partial t}(x,0,t) = \frac{\partial \phi_2^{(0)}}{\partial t}(x,0,\sqrt{t^2 - 4n^2})H(t^2 - 4n^2) \quad (n \geq 1),$$

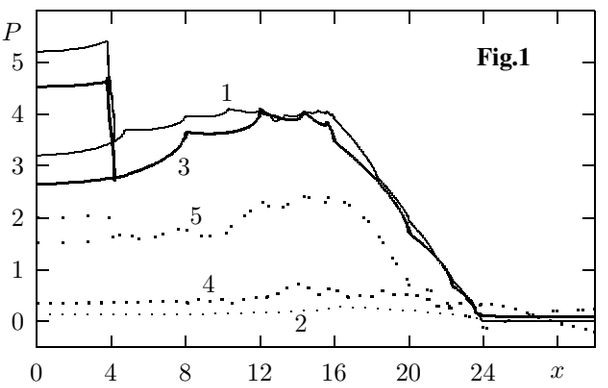
$$\frac{\partial \phi_{1n}^{(2)}}{\partial t}(x,t) = \frac{1}{\pi}\sum_{N=1}^{N_*} S_N H(x_N - x - \sqrt{t^2 - 4n^2})H(x - x_N + a_n(t,m)) \int\limits_{\lambda_1(x_N - x,t)}^{m} \frac{\sin[2n\varphi(\lambda)]}{\sqrt{\lambda^2 - 1}}\, d\lambda H(t - \frac{2nm}{\sqrt{m^2 - 1}}) -$$

$$-\frac{1}{\pi}\sum_{N=1}^{N_*} S_N H(x - x_N - \sqrt{t^2 - 4n^2})H(x_N - x + a_n(t,m)) \int\limits_{\lambda_1(x - x_N,t)}^{m} \frac{\sin[2n\varphi(\lambda)]}{\sqrt{\lambda^2 - 1}}\, d\lambda H(t - \frac{2nm}{\sqrt{m^2 - 1}}),$$

where $\lambda(z) = \sqrt{1 + (m^2 - 1)z^2}$.

Numerical results

Calculations were performed for the case, with $f(x) = 0, \ x \in (-\infty, -4) \cup (4, \infty)$ and $f(x) = 1, \ x \in [-4, 4]$. This corresponds to the problem of piston entering two-layer liquid through its unconformable boundary. We consider following cases: (1) impact on compressible liquid of finite depth, $k \ll 1$ (in calculation $k = 0.001, \ m = 1$) (curve 1); (2) impact on compressible liquid of infinite depth, $k = 1, \ m = 1$ (curve 2); (3) incompressible fluid in the lower layer, $m \gg 1$ ($m = 300, \ k = 1$) (curve 3); (4) both fluid are compressible but different $m = 3, \ k = 0.9$ (curve 4); (5) both fluid are compressible $m = 10, \ k = 0.7$ (curve 5).



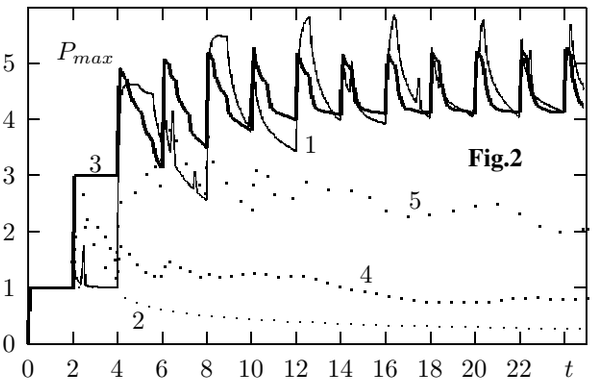


Figure 1 presents distributions of the pressure along the boundary at the moment $t = 20.01$ for $x > 0$. One can see that the pressure expands along the boundary and reaches maximum value outside of impact region for cases (2),(4),(5). For cases (1) and (3) and times $t = 2n + \Delta$ (times, when reflected waves come to the upper boundary) maximums occur inside the impact region. Figure 2 depicts the pressure maximums depending on time. One can see that the maximum of the pressure decreases for cases (2),(4),(5). For case (2) the pressure peak moves along the boundary at sound speed. For cases (4),(5) this velocity a little bit lower. Maxima of the pressure keep the values long time, if c_1 and c_2 or ρ_1 and ρ_2 very different (cases (1) and (3)).

Conclusions

Model of the impact onto the boundary of two–layer fluid in acoustic approximation is presented. For the case, when impact velocity is a step function, both the velocity potential and the distribution of hydrodynamic pressure along the upper boundary of the fluid are obtained in the forms of series at any time instant. With the help of this model the problem of the piston impact is analyzed. The problem is to illustrate the scopes of the presented method. The analysis can be extended to the such important case as impact of fluid with the bubbly fore-part.

Acknowledgement This work was supported by the grant of President of Russian Federation for the Leading Scientific Schools (NS-902.2003.1) and Int. project 3-13-1.

References

[1] Korobkin A.A.: Impact onto the boundary of two–layer fluid. 2003, *under preparation*.

NONLINEAR DYNAMICS OF PINNED-PINNED CYLINDERS IN AXIAL FLOW

Michael P. Païdoussis[*], Yahya Modarres-Sadeghi[*], Christian Semler[*]
[*]*Department of Mechanical Engineering, McGill University, Montreal, Quebec, Canada H3A 2K6*

Summary It is known that cylinders with supported ends subjected to high enough axial flow develop divergence and at higher flow coupled-mode flutter, as shown experimentally and confirmed by linear theory. Also, the same dynamics is predicted by linear theory for the closely related problem of a pipe conveying fluid, but post-divergence flutter in this case has never been observed. Its non-existence was confirmed by nonlinear theory. The problem of the cylinder in flow is re-examined in this paper by means of weakly nonlinear theory. It is shown that post-divergence flutter does exist, but not as an instability of the trivial equilibrium, but as a Hopf bifurcation emanating from the divergence solution. For high enough flow, interesting dynamics follow, including quasiperiodicity and chaos. Reasons for the different dynamics with internal and external flow are explored.

BACKGROUND

It has been shown, in the 1960s, that cylinders with supported ends immersed in sufficiently high axial flow are subject to divergence (buckling), and at higher flow to coupled-mode flutter – by means of linear theory, confirmed by experiment [1,2]. Linear theory predicts the same dynamical behaviour for the closely related system of a pipe conveying fluid with supported ends (i.e. a cylinder with internal flow): divergence followed by flutter. In this case, however, flutter was never observed. This was confirmed and elucidated by nonlinear theory [3,4]. The question is "why does the same not hold true for external flow?"
To answer this question, the problem of a cylinder with simply supported ends ("pinned-pinned") immersed in axial flow is re-examined by nonlinear theory, as outlined in what follows.

A WEAKLY NONLINEAR MODEL

Assuming the lateral deflection of the cylinder to be $v \sim O(\varepsilon)$, and consequently the axial extension to be $u \sim O(\varepsilon^2)$, and presuming that the cylinder centreline is extensible, the equations of motion for a pinned-pinned cylinder in confined axial flow have been derived, correct to $O(\varepsilon^3)$. These equations are based on the potential flow derivation of the lift on a flexible slender body derived by Lighthill [5], modified by including semi-empirical expressions for the viscous forces and, to deal with vertically mounted systems, buoyancy, gravity and pressure-loss related forces as well [6,7]; see also Ref. [8] for cantilevered cylinders. These equations may be expressed as

$$L_i\left(u\left(x,t\right),v\left(x,t\right)\right)=0, \qquad i=1,2,$$

where the L_i are nonlinear differential operators, with $i=1,2$ corresponding, respectively, to the predominantly axial and transverse motion PDEs.
The equations are discretized by Galerkin's method, leading to a set of coupled ODEs, the solution of which is complicated by the presence of inertial nonlinearities. Solutions are obtained by Houbolt's finite-difference method and, to a limited extent, using AUTO.

TYPICAL RESULTS

A typical bifurcation diagram is shown in Fig. 1(a). It is seen that this particular system loses stability by divergence at a nondimensional flow velocity $U \simeq \pi$, in conformity with linear theory. Coupled-mode flutter, however, associated with another loss of stability of the trivial equilibrium, as predicted by linear theory, does not arise: the bifurcation leads to an unstable solution. Instead, at approximately the same U as predicted by linear theory, the non-trivial static solution becomes unstable by a Hopf bifurcation, leading to flutter.
Hence, post-divergence flutter does exist, as seen in experiments – unlike the situation with internal flow. The difference has been found to be related to the frictional terms. The dynamics of the pipe problem (internal flow) has been shown to be independent of frictional forces, since they are exactly counterbalanced by the pressure-loss forces along the pipe; as a result, both pressure-loss and frictional forces vanish from the equation of motion [4]. This is not true for external flow, in which the mean pressure is largely unaffected by frictional effects on the cylinder. Some of the frictional terms give rise to terms in the equation of motion of a different derivative form *vis-à-vis* the inviscid-force terms and hence the internal flow case. These are the terms responsible for eliminating post-divergence restabilization, even in the absence of dissipative terms. It is also shown by energy considerations that, for flutter to arise from the trivial equilibrium, even in terms of linear theory, the frictional force coefficients in the longitudinal and lateral directions must be unequal [7]; although this is generally true, the restriction seems to be peculiar. In fact, the flutter obtained by nonlinear theory can arise also when these frictional coefficients are equal, and indeed this is the case in the results shown in Fig. 1(a). Hence, although viscous frictional forces are small and by no means dominant, their effect on the post-divergence behaviour of the system is profound.

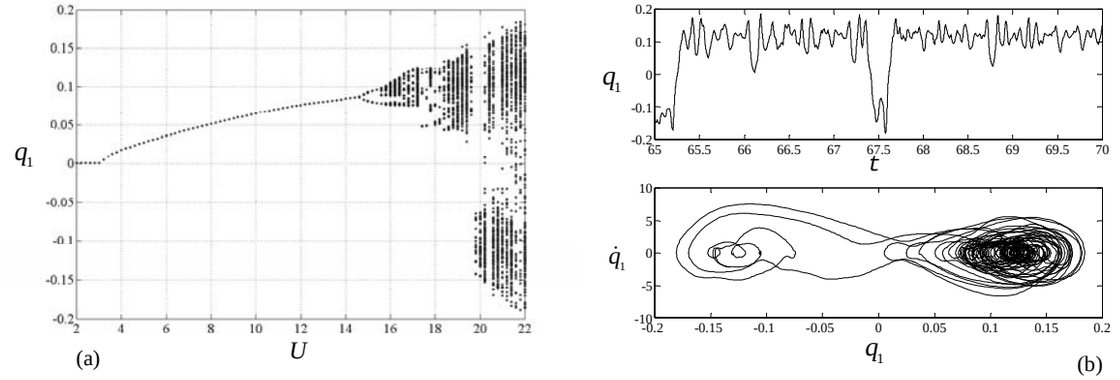


Figure 1. (a) A typical bifurcation diagram; (b) time trace and phase-plane plot for U=21.8

The post-flutter dynamics can be quite interesting, as seen in Fig. 1(a,b). Depending on parameters, the system may develop quasiperiodic and sometimes chaotic behaviour. For the results in Fig. 1(a), the system develops flutter via a Hopf bifurcation at $U \simeq 14.6$. The resulting limit cycle then becomes unstable via a torus bifurcation at $U \simeq 15.7$, indicating that quasiperiodic solutions are possible thereafter. For example at U=17, a time history, and phase-plane and power spectral density plots (none shown here) all indicate a quasiperiodic oscillation.

At higher flow velocities, AUTO reveals the emergence of a number of unstable solutions as the flow is increased; their existence makes chaotic motion more likely. Indeed, in the bifurcation diagram of Fig. 1(a), obtained by the finite difference method (FDM), it is found that chaotic motions are possible over the range $U \simeq 20$ to 22. The time trace and phase-plane plots of Fig. 1(b) show chaotic motions for U=21.8. Similar behaviour has been confirmed to exist over the whole range of $U \simeq 20$ to 22.

CONCLUSIONS

The nonlinear dynamics of a slender cylinder with simply supported ends immersed in axial flow has been explored by means of newly derived weakly nonlinear equations of motion for the case where inextensibility of the centreline is not invoked. It is found that the system loses stability by a pitchfork bifurcation leading to divergence, and the new equilibrium at higher flow becomes unstable by a Hopf bifurcation, leading to flutter. With further increases in the flow velocity, the dynamics becomes more complex, and quasiperiodic and chaotic solutions have been obtained. The different post-divergence dynamics for internal and external flow is discussed and the source of the differences identified.

ACKNOWLEDGEMENT

Support of this research by NSERC of Canada and FCAR of Québec is gratefully acknowledged.

References

[1] Païdoussis, M. P. 1966 Dynamics of flexible slender cylinders in axial flow. Part 1: theory; Part 2:experiments. *Journal of Fluid Mechanics* **26**, 717-736 and 737-751.

[2] Païdoussis, M. P. 1973 Dynamics of cylindrical structures subjected to axial flow. *Journal of Sound and Vibration* **29**, 365-385.

[3] Holmes, P. J. 1976 Pipes supported at both ends cannot flutter. *Journal of Applied Mechanics* **49**, 619-622.

[4] Païdoussis, M. P. 1998 *Fluid-Structure Interactions: Slender Structures and Axial Flow*, Vol. 1. London: Academic Press.

[5] Lighthill, M. J. 1960 Note on the swimming of slender fish. *Journal of Fluid Mechanics* **9**, 305-317.

[6] Modarres-Sadeghi, Y., Païdoussis, M. P., Semler C. & Picot, P. 2003 Nonlinear dynamics of slender cylinders supported at both ends and subjected to axial flow. *IUTAM Symposium on Fluid-Structure Interaction*, Rutgers University, USA.

[7] Païdoussis, M. P. 2003 *Fluid-Structure Interactions: Slender Structures and Axial Flow*, Vol. 2. Oxford: Elsevier.

[8] Lopes, J. -L., Païdoussis, M. P. & Semler, C. 2002 Linear and nonlinear dynamics of cantilevered cylinders in axial flow, Part 2: the equations of motion. *Journal of Fluids and Structures* **16**, 715-737.

INTERACTION OF OSCILLATING FLOW WITH A PAIR OF SIDE-BY-SIDE SQUARE CYLINDERS

Ming-Jyh Chern, Ji-Zen Lu
Department of Mechanical Engineering, National Taiwan University of Science and Technology, Taipei 106, Taiwan

Summary The behaviour of vortices induced by a pair of square cylinders in an oscillating flow was investigated. The flow pattern in the vicinity of the square cylinders was visualized using the experimental approach and the numerical model. Strong interaction among vortices was found. Force coefficients of cylinders become chaotic as the gap ratio decreases and Keulegan-Carpenter number increases.

INTRODUCTION

Oscillating fluid flows are very common in ocean engineering problems. It may be induced by traveling waves or tides. Hence, offshore structures may experience oscillating flows. It is well known that vortices are generated by solid structures in flows. In the past, oscillating flows interacting with a single obstacle was investigated by several researchers. For example, Bearman and Obasaju [1] conducted experiments to investigate the force variation exerted on a square cylinder in oscillating flows. However, there may be more than one structure in practice. Vortices induced by multi-obstacles may interact with others. Subsequently, forces exerted on those obstacles may be different from the case with a single obstacle. Williamson [2] performed the flow visualization and force measurement for a pair of circular cylinders in oscillating flows. He found the various patterns due to the interaction of vortices due to the pair of circular cylinders. The purpose of this study is to investigate oscillating flows interacting with a pair of side-by-side square cylinders. The vortices are affected by Reynolds number, Keulegan-Carpenter (KC) number and the gap between them. Especially when the gap is very small, the interaction among vortices is very strong. Numerical and experimental approaches were utilized to observed the flow variation. The flow structure were visualized. The forces exerted on two cylinders were determined using the numerical model.

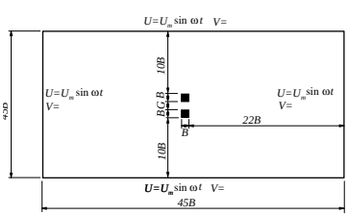


Figure 1: Configuration of the study problem

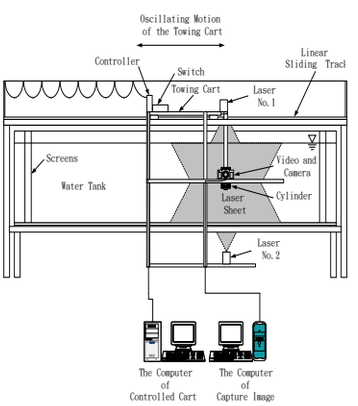


Figure 2: Configuration of the experimental facility for flow visualization

MATHEMATICAL MODEL & NUMERICAL APPROACHES

Figure 1 shows the configuration of the problem. Fluids considered are incompressible. The 2-D continuity equation and Navier-Stokes equations were utilized as the governing equations. The oscillating flow condition was imposed on the far-field boundaries and given by

$$\mathbf{U} = \mathbf{U_m} \sin(\omega t) \quad , \tag{1}$$

where ω and $\mathbf{U_m}$ refer to the angular frequency and the amplitude of the velocity variation. Moreover, the non-slip boundary condition was imposed on the solid boundaries of two square cylinders. The initial-boundary-value

problem (IBVP) was solved by the proposed numerical model based on the finite volume method. Cartesian cells constituted the whole computational domain. The numerical simulations were performed in a PC cluster which includes 16 AMD 2.5G CPUs.

PARTICLE TRACKING FLOW VISUALIZATION TECHNIQUE

The flow visualization technique based on the particle tracking technique was also used to observe the flow patterns. The results were used to validate the numerical solutions. Figure 2 reveals the schematic configuration for the experiments. A water tank with a towing cart was used to perform the oscillating motion for those two square cylinders. PS particles of diameters 50-70 μm were employed to traced the flow motions. When particles experienced the laser sheet, light was scattered by particles. Subsequently, the flow patterns can be captured by a CCD camera. Due to the page limit, the flow pattern can be shown in the final manuscript.

PRIMARY RESULTS AND DISCUSSION

Figure 3 demonstrates one of numerical solutions at $KC = 5$ and $Re = 400$ in a period. Flows were visualized in terms of the vorticity distribution. The gap, G, between two cylinders was equal to their length, B. It reveals that vortices shedded successively from the two sides of cylinders. The strong flow in the gap affects the vortices in the vicinity of the gap. This phenomenon is different from the case with a single cylinder. Furthermore, Figure 4 shows the time histories of lift coefficients of those two cylinders. The lift coefficient for a single cylinder is very small compared with the studied case. The main reason is that the symmetry of the vortical system is broken due to the gap flow. The variation of peak in the time histories were found in Figure 4. When the flow is at large gap ratios and low KC numbers, the wave forms of time histories are the same at each periods. As the interaction becomes strong due to small gap ratios and high KC numbers, nonlinearity in the flow can be observed and the wave forms are distorted.

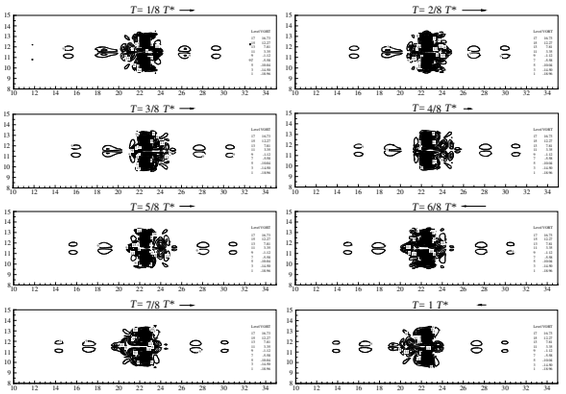


Figure 3: Flow patterns in a period in terms of vorticity distribution

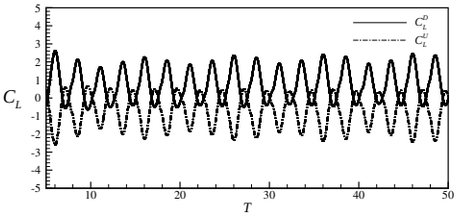


Figure 4: Time histories of lift force exerted on two square cylinders

CONCLUSIONS

The force variation and flow patterns for an oscillating flow interacting with a pair of side-by-side square cylinders were obtained. Vortices induced by square cylinders were strongly affected by each other. Nonlinearity in the vortical system was induced in small gap ratios and high Keulegan-Carpenter numbers.

References

[1] Bearman, P.W. and Obasaju, E.D.: An experimental study of pressure fluctuations on fixed and oscillating square-section cylinders. *J. of Fluid Mech* **119**:297-321, 1982.

[2] Williamson, C.H.K.: Sinusoidal flow relative to circular cylinders. *J. of Fluid Mech*: **155**:141-174, 1985.

Extended Summary for: *December 2003*

21st INTERNATIONAL CONGRESS ON THEORETICAL AND APPLIED MECHANICS

Warsaw, Poland; 15-21 August 2004

The hydroelastic destabilisation of finite compliant panels

by: Anthony D. Lucey

Department of Mechanical Engineering, Curtin University of Technology, GPO Box U1987, Perth, WA 6845, Australia.

1. Introduction

The interactive dynamics of a flexible panel and an external fluid flow underpins a great variety of technological applications. When the panel comprises the skin of an aircraft or ship, instability of the panel, fed by the transfer of fluid kinetic energy to the structure, is highly undesirable; for example see [1,2]. However, the motion of a flexible boundary can also yield beneficial effects such as skin-friction drag reduction through the postponement of boundary-layer transition; for example see [3]. This paper focuses on the evolution of linear instability of a flexible panel in the presence of a uniform flow. The assumption of uniform flow renders the study applicable to the fluid-loading effects of turbulent boundary-layer flows wherein flow shear is principally confined to a very thin layer adjacent to the wall. However, it also approximates laminar boundary-layer flows when the boundary-layer thickness is small in comparison to the wavelength of the panel deformation. Seminal studies of this fundamental problem, for example [1,2,4], took a boundary-value approach, mapping out the instability boundaries associated with divergence and flutter. Attention later turned to the question of how the hitherto assumed system disturbances might come into being. Thus, in [5,6] line-excitation was introduced to initiate disturbances and the resulting system studied as a proper initial-value, boundary-value, problem. This approach revealed the very subtle complexities of the wave-bearing system identifying a vast range of waves each distinguished by their combination of phase speed, group velocity, energy flux and activation energy, being positive/negative-energy or Kelvin-Helmholtz type waves. These studies considered an unsupported, thin, elastic plate of infinite extent. Governed by a single control parameter, the non-dimensional flow speed, a critical velocity for absolute instability, associated with a triple point in the complex wavenumber plane, was identified. At flow speeds lower than critical a single downstream-propagating convective instability was predicted. The absolute and convective instability boundaries for a range of related flow-structure systems have been mapped in [7] and recently it has been shown [8] that a further low-flow-speed absolute instability can exist when structural damping is incorporated.

All of the theoretical analyses described immediately above considered flexible panels of infinite extent. In doing so, the importance of convective instability is understated because it ultimately 'washes out' of a localised spatial region in the long-time limit. For a finite panel different wave-dynamics and instability evolutions occur. Our numerical experiments, [9], that incorporated fixed panel leading and trailing edges uncovered a further convective instability and showed that the destabilisation of a finite panel is dominated not by absolute instability, but by a combination of upstream- and downstream-propagating convective instabilities at flow speeds below the absolute-instability threshold. This paper considers a more general class of flexible-wall structure and demonstrates that that hydroelastic destabilsation by convective instabilities prevails for finite systems.

2. Computational Methods and Investigation

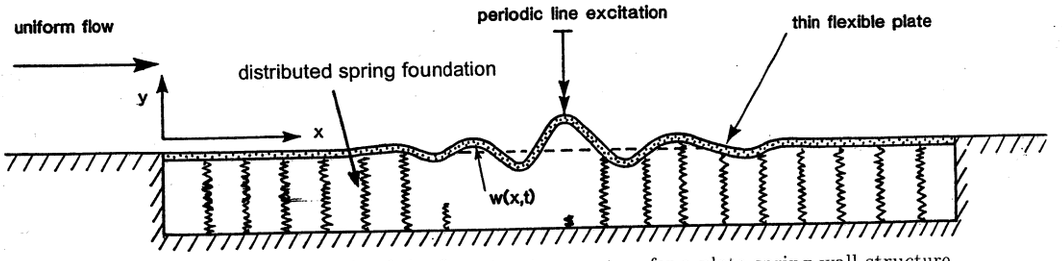


Figure 1. Schematic of the flow-structure system for a plate-spring wall structure.

Figure 1 is a schematic of the general system that we study. The key difference from previous theoretical studies with a source of excitation is the inclusion of the spring foundation. This leads to a system with two control parameters, the non-dimensional flow speed, U, as for the unsupported plate, and the non-dimensional spring-stiffness coefficient, K. In contrast to the unsupported plate, a dispersion-relation analysis predicts distinct non-zero divergence-onset and modal-coalescence flutter critical flow speeds; these were respectively derived in [10] as $U_D = (2)(3^{-\frac{3}{8}})K^{\frac{3}{8}}$ and $U_F \approx \sqrt{2}K^{\frac{1}{4}}(K^{\frac{1}{4}}+1)^{\frac{1}{2}}$. Our investigation concerns the instability regime $U > U_D$. We also note, see [11], that the structure of the dispersion relation for a plate-spring wall is identical to that of a thin elastic shell with K replaced by the shell's radius of curvature. Thus, the destabilsaton mechanism identified in §3 below will, most probably, apply to fluid-loaded finite elastic shells with fixed ends.

Our computational methods for the fully coupled system combine a boundary-element method to solve the Laplace equation subject to the wall-generated interfacial kinematic boundary condition with a finite-difference method to solve

for the wall motion driven by the fluid pressure and the applied line-excitation. In contrast to a theoretical boundary-value approach, there is no prescription of wall deformation, nor is the frequency of interfacial waves restricted to that of the line-excitation.

We also model a flexible wall comprising a homogeneous viscoelastic continuum; for this wall the two control parameters are the the non-dimensional flow speed and wall thickness. The wall dynamics are modelled using a specially developed finite-element method capable of accommodating a near incompressibility of a rubber-type material. Again, our investigation focuses upon the destabilisation of the wall at flow speeds above that of divergence-onset for this type of wall.

3. Illustrative results and brief discussion

Figure 2a shows a typical result for a spring-backed flexible plate for a flow speed $U_D < U < U_F$ with oscillatory line-excitation applied at its mid-point. The salient feature to note is the ultimate emergence of a pair of distinct unstable waves from the leading and trailing edges. Both have downstream-directed phase velocity but their wall energy-density propagations are in opposite directions. The higher wavenumber wave seen near the trailing edge propagates upstream whilst the lower wavenumber wave propagates downstream. Subsequently, each time that a wave reaches the spatial extent of its propagation, permitted by the finite length of the panel, it launches its counterpart. Thus wholescale instability of the panel occurs through this combination of convective instabilities. We also note that this panel-destabilsation mechanism also occurs in the flow-speed regime $U > U_F$, whereas a dispersion-relation analysis predicts modal-coalescence flutter. Figure 2b shows a typical result for a viscoelastic continuum. The initial excitation was a point impulse applied the panel's mid-point. Like the result of Fig. 2a, it is found that wall instability is ultimately dominated by the pair of convective instabilities seen to emerge from the leading and trailing edges of the panel. In both Figs. 2a and 2b the wave types that ultimately dominate can also be seen emanating from the initial source of excitation at earlier times; thereafter the panel ends effectively serve as wave-excitation sources.

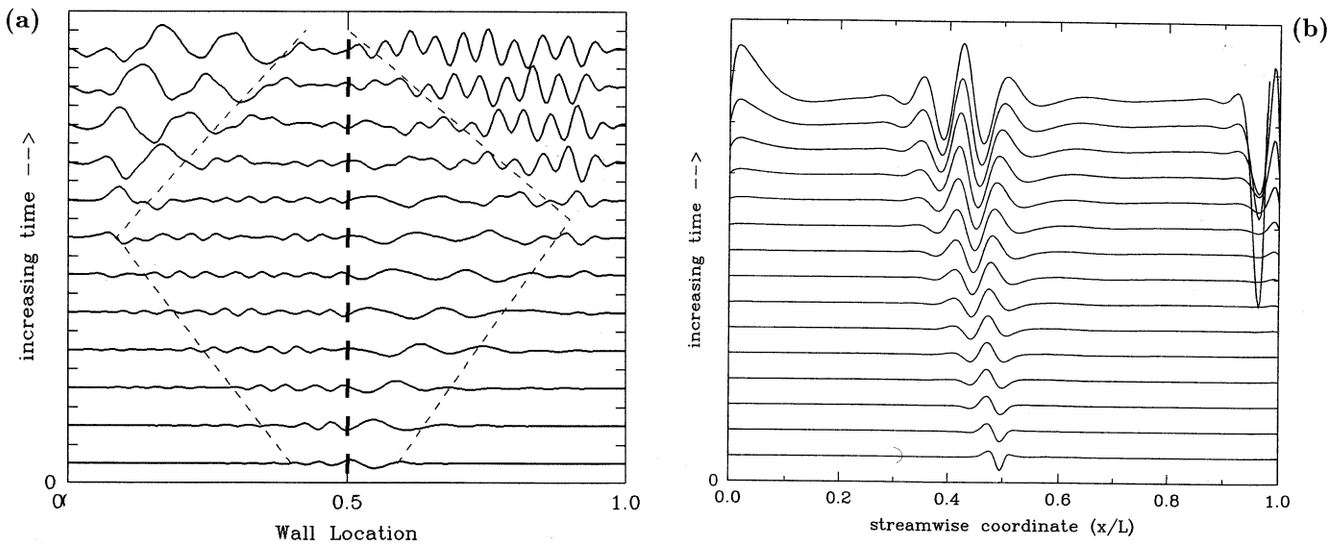


Figure 2. Space-time plots of wall-surface deformation showing the destabilsaton of: (a) a spring-backed flexible plate with oscillatory excitation at its mid point and, (b) a viscoelastic continuum initially excited by a point impulse. (The fluid flow is from left to right.)

In summary, we demonstrate that convectively unstable waves are of crucial importance in the ultimate hydroelastic destabilisation of finite flexible panels. Moreover, the characteristics of these waves are independent of the applied excitation, instead, being governed solely by the flow-structure properties. From the results of our numerical experiments, we are able to devise a frequency-wavenumber chart that offers an improved description of system instability than predictions based upon the dispersion relation for the corresponding infinite system.

References

1 Dugundji, J., Dowell, E. & Perkin, B. 1963 *AIAA J.* **1**, 1146-1154.

2 Weaver, D.S. & Unny T.S. 1971 *Trans. ASME* E**37**, 823-827.

3 Carpenter, P.W., Lucey, A.D. & Davies, C. 2001 *AIAA: Journal of Aircraft* **38**(3), pp. 504-512.

4 Carpenter, P.W. & Garrad, A.D. 1986 *J. Fluid Mech.* **170**, 199-232.

5 Brazier-Smith, P.R. & Scott, J.F. 1984 *Wave Motion* **6**, 547-560.

6 Crighton, D.G. & Oswell, J.E. 1991 *Phil. Trans. R. Soc. Lond. A* **335**, 557-592.

7 de Langre, E. 2002 *J. Sound Vib.*, **256**, 299-317.

8 Abrahams, I.D. & Wickham, G.R. 2001 *Wave Motion* **33**, 7-24.

9 Lucey, A.D. 1998 *Phil. Trans. R. Soc. Lond. (Series A)* **356**, 2999-3039.

10 Lucey, A.D. & Peake, N. 2003 In *IUTAM: Flow through collapsible tubes and past other highly compliant boundaries* (eds. P.W. Carpenter & T.J. Pedley), Kluver Academic Pubs., 118-145.

11 Peake, N. 1997 *J. Fluid Mech.*, **338**, 387-410.

WATER-SURFACE DYNAMICS AMONG A PERIODIC ARRAY OF FLOATING BODIES SUBJECT TO REGULAR INCIDENT WAVES

Hiroshi Kagemoto*, Motohiko Murai**
*Dept. of Environmental Studies, The University of Tokyo, Japan
**Faculty of Environment and Information Sciences, Yokohama National Univ., Japan

Summary Theoretical and experimental study on the water-surface dynamics among a periodic array of floating bodies placed in an incident regular wave train are conducted. The focus is placed on the possible wave trapping among the array and non-linear double-frequency oscillations of the water-surface.

WAVE TRAPPING

When a body is placed at the very center of a narrow wave tank of width B in a regular wave train, which is hydrodynamically equivalent to a regular-wave incidence to an array of an infinite number of identical bodies placed with center-to-center distance B apart along the line perpendicular to the direction of the incident waves, it is indicated theoretically that waves could be trapped between the body and the tank walls and thus the energy of the incident waves are accumulated in the trapped waves as time goes by, which eventually may result in an extremely large water-surface movement. Recently it has been shown that, even when a long periodic array of identical bodies is placed in head waves, wave trapping could occur (Maniar & Newman).

Since, if this is really the case, it is obvious that it has very serious implications for the design of such structures as a column-supported semi-submersible oil rig or a very large floating airport supported on a periodic array of a large number of legs (possibly several thousands) now projected in Japan, experiments were conducted to see if wave trapping really occurs. In the experiment, an array of 50 identical truncated vertical cylinders intersecting the free surface was fixed in regular head waves with equal distance in one line and the water-surface movements among the array were measured at 14 locations. Figure 1 shows the typical results on the spatial distributions of the water-surface elevations along the array obtained in the experiment. In the figure, the corresponding calculation results based on the linear potential theory are also shown for comparison. As the wave period was changed by as small as 1/100 second from 0.68sec. to 0.69sec., the theoretical calculation results suddenly blew up while the experimental results remained as if nothing happened.

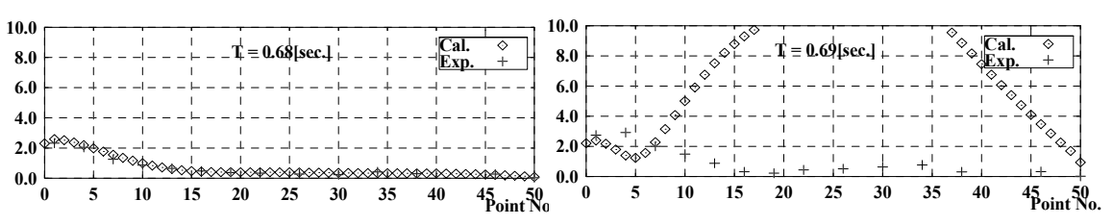


Figure 1 The spatial distributions of the water-surface elevation amplitude along the array of 50 vertical truncated cylinders in head waves (The vertical axis represents the ratio of the water-surface elevation amplitude and the incident-wave amplitude.)

As it turned out that the wave period 0.69sec. coincides with the onset of the wave trapping, it is apparent that the theoretically predicted extreme water-surface movement due to trapped waves does not take place in reality. It will be shown that if damping forces due to viscosity are properly accounted for in the theory, the experimental results obtained in trapped waves can be well reproduced in the calculation.

NON-LINEAR DOUBLE FREQUENCY OSCILLATIONS OF THE WATER SURFACE

Besides the experiment using a 1x50 array of truncated cylinders shown above, another experiment was carried out in which an array of 2x9 cylinders was placed in regular head waves. An interesting fact observed in this experiment is that noticeable movements of the water surface oscillating with the frequency 2ω were induced in incident waves of frequency ω between the two rows as shown in Figure 2.

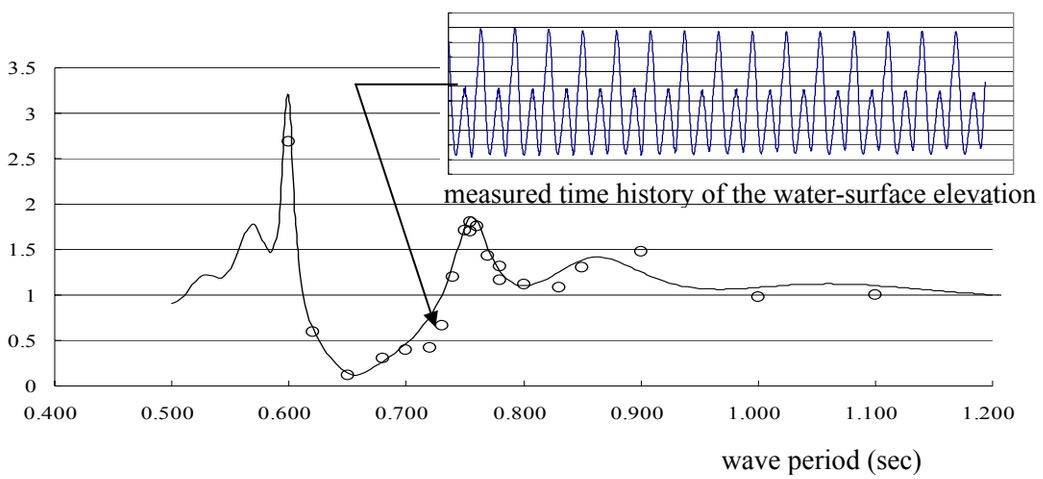


Figure 2 The frequency response characteristics of the water-surface elevations between the two rows of the array of 2x9 cylinders in head waves (solid line: linear-theory calculation, circles: experimental results)

APPLICATION OF A PERIODIC ARRAY OF BODIES TO A BREAK-WATER

Since, when incident waves are trapped in a periodic array of bodies, little energy is transmitted to the other side of the array, an attempt was made to apply the array to a break-water. The unique feature of this type of break-water is that, at least theoretically, the wave transmission can be controlled by tuning the center-to-center distance of the bodies to the incident-wave length and thus the transmission of long waves could be suppressed without geometrically enlarging the bodies themselves.

References

[1] H.D. Maniar and J.N. Newman: Wave diffraction by a long array of cylinders, *J. Fluid Mech.* **339**; 309-330, 1997.

THE MIXING LAYER INSTABILITY OF WIND OVER A FLEXIBLE CROP CANOPY

Charlotte PY*, Emmanuel de Langre*, Bruno Moulia**
*Laboratoire d'Hydrodynamique (LadHyX), CNRS, École Polytechnique, 91128 Palaiseau Cedex, France
**Unité d'Ecophysiologie des Plantes Fourragères, INRA, 86600 Lusignan, France

Summary A coupled fluid-stucture model is proposed to study the dynamics of a flexible crop canopy exposed to wind. The canopy is represented by an elastic continuous medium and coupled to the wind mixing layer through a drag load. The mixing layer instability is shown to remain the principle instability mechanism but its characteristics are modified when taking into account the flexible canopy. The size of the coherent structures is decreased as well as the instability growth rate.

INTRODUCTION

Lodging of crops and thigmomorphogenesis, which is the effect of wind on plants growth, have brought a large interest on the study of wind-induced plant motions [1, 2, 3]. Wind flow over a vegetal canopy is turbulent and leads to oscillatory plant motions. The mean wind velocity profile is known to be inflected at the top of the canopy, as a result of the momentum absorption by drag on the leaves [2]. The induced shear is at the origin of an instability mechanism similar to that of a mixing layer. This yields the formation of large scale coherent flow structures propagating over the canopy [1, 2]. Previous studies of wind-induced plant motions have represented the canopy as a set of mechanical oscillators [3, 4], with elastic interactions [5], and have considered simple wind load models. We propose a fully coupled fluid-structure model to study the dynamics of a flexible canopy exposed to wind. A mixing layer configuration with a broken line flow profile represents the wind flow over and inside the canopy. The flexible canopy is modeled by a wave equation following Doaré *et al* [5]. The fluid-structure coupling is realized through a drag load. We identify the main instability mechanism of the coupled problem, and study the effect of the mechanical characteristics of the canopy on the instability properties in the particular case of an alfalfa field.

THE MODEL

The vegetal canopy is composed of an infinite row of identical plants with elastic contacts, Figure 1. Following Doaré *et al* [5], it is modeled as an equivalent continuous medium, with mass m, flexion stiffness r and contact stiffness a . The position of any point of the canopy is described by the horizontal displacement $\underline{X}(x,y,t) = \chi(y)\ Q(x,t)\ \underline{e_x}$, χ being a mode shape, and Q the corresponding generalized displacement. The canopy movement results from a local drag force, acting on the equivalent surface of each plant and dependent on the difference between the local wind velocity and the horizontal plant velocity. This drag force is then projected on the modal shape χ. The dynamics of the canopy is thus governed by the following wave equation:

$$m\ \partial_{tt}Q\ +\ r\ Q\ -a\ \partial_{xx}Q\ =\ \int_0^h \frac{1}{2}\rho C D\left[\left(\underline{U}-\underline{\dot{X}}\right).\underline{e_x}\right]^2 \chi\ dy \tag{1}$$

where C is a drag coefficient and D an effective diameter of a plant.
The wind velocity $\underline{U}$ is governed by the Euler equations within and above the canopy. A source term corresponding to the drag effect is added to the momentum equation. We neglect here the effect of fluid viscosity since the mixing layer instability mechanism is known to be inviscid [6].
In order to investigate the stability of a given basic velocity profile U_b and canopy displacement Q_b, we consider the small perturbations u, v, p and q. We use here a broken line profile U_b defined by a vorticity thickness δ and a shear parameter $R = (U_1 - U_2)/2U$ with the mean velocity $U = (U_1 + U_2)/2$ (see Figure 1). The momentum and mass balance for the flow and the wave equation for the canopy may be developed at the first order in terms of the perturbations which yields the set of coupled equations:

$$\rho\left(\partial_t u\ +\ U_b\,\partial_x u\ +\ u\,\partial_y U_b\right) = -\partial_x p - \rho C U_2 D\ /l^2\ (u - \chi\,\partial_t q) \tag{2}$$

$$\rho\left(\partial_t v\ +\ U_b\,\partial_x v\right) = -\partial_y p \tag{3}$$

$$\nabla.\underline{u} = 0 \tag{4}$$

$$m\,\partial_{tt}q\ +\ r\ q\ -a\,\partial_{xx}q = \int_0^h \rho C U_2 D\,(u - \chi\,\partial_t q)\,\chi\ dy \tag{5}$$

The drag coefficient C in (2) is set to zero outside the canopy ($y > h$). We use here a linear mode shape $\chi(y) = y/h$. A traveling wave solution is sought in the form: $(u, v, p, q) = (\hat{u}, \hat{v}, \hat{p}, \hat{q})\ e^{i(kx-\omega t)}$. Assuming the flow to be irrotational, the analytical dispersion relation is obtained.

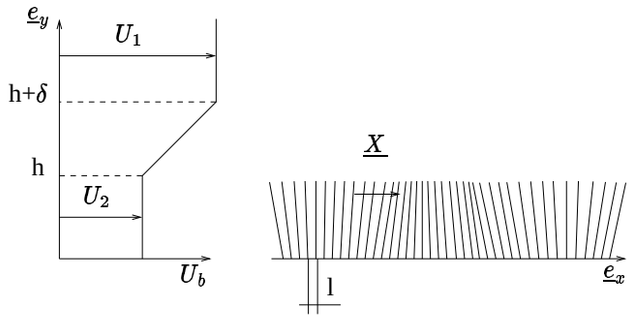


Figure 1. Basic flow U_b and model of the crop canopy.

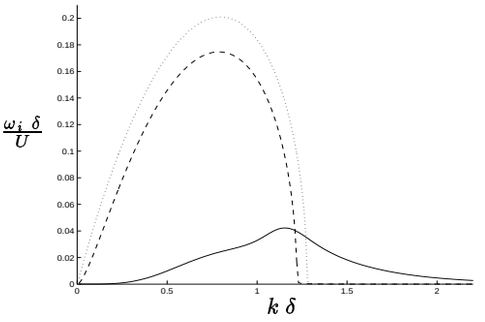


Figure 2. Dimensionless temporal branch. (—) model with experimental values of the parameters, (- -) $C = 0$: Kelvin-Helmholtz branch in a bounded medium, ($\cdot\ \cdot\ \cdot$) Kelvin-Helmholtz branch in an infinite medium.

ANALYSIS AND RESULTS

We analyze the temporal stability of propagating waves by calculating numerically the growth rate $\omega_i = Im(\omega)$ associated with a given real wavenumber k [6] through the dispersion relation. Only the most unstable branch $\omega_i = f(k)$ is considered. The temporal analysis is performed using experimental values for the parameters of the model. These are taken from experiments on alfalfa [5] and wind characteristics over a crop canopy [1]. We use here : $m/(\rho\delta^3) = 0.007$, $r/(\rho\delta U^2) = 0.009$, $a/(\rho\delta^3 U^2) = 1.5\ 10^{-5}$, $h/\delta = 1$, $l/\delta = 0.1$, $D/\delta = 0.02$, $C = 1$, $R = 0.5$. Figure 2 shows the temporal branch derived from the dispersion relation.

The growth rate may be compared with that arising from uncoupled fluid and solid dynamics by setting the drag coefficient C to zero. In that case, the unstable branch is that of the Kelvin-Helmholtz instability in a bounded domain, Figure 2. Then, by setting h/δ equal to infinity, the Kelvin-Helmholtz temporal branch for a broken-line profile in an infinite medium is recovered, with the most amplified wavenumber at $k\ \delta = 0.8$ [6]. We may therefore assert that taking into consideration the flexible canopy through the drag term modifies the shape of the Kelvin-Helmholtz temporal branch, but this latter is still the most amplified. The mixing layer instability therefore remains the main mechanism of vortex formation over canopies, even when considering the drag on the flexible plants. The first effect of the coupling by a drag force is to decrease the maximum growth rate of the instability : dissipative effects in mixing layers are indeed known to be stabilizing, see for instance [7].

The effect of the mechanical characteristics of the plants on the instability mechanism may be investigated by comparing the most amplified temporal branch between a flexible canopy and a rigid one. This results in an evolution of the most amplified wavenumber as a function of the dimensionless flexural compliance $s^* = \rho U^2 \delta / r$. The crop compliance has a non regular but significant effect on the size of the coherent stuctures arising from the instability. For the particular case of an alfalfa canopy using a $3\ m/s$ mean wind ($s^* \simeq 100$), the wavelength is approximatively 25 % smaller than it would be for an equivalent rigid canopy.

The mixing layer instability is known to be responsible for the existence of strong coherent motions of canopies exposed to wind [2]. We have solved here the interaction problem where the mixing layer dynamics is fully coupled with the motion of the canopy. The main conclusion is that for realistic values of the crop flexibility the mixing layer instability persists but its characteristics are significantly modified. The most amplified wavelength is reduced, as well as the corresponding growth rate of the instability. This may explain some discrepancies between the original mixing layer model and measurements of the size of coherent structures observed in wind over various canopies such as corn or forest as reported in [1].

References

[1] Finnigan J.J.: Turbulence in plant canopies. *Annual Review of Fluid Mechanics* **32**:519-571, 2000.
[2] Raupach M.R., Finnigan J.J., Brunet Y.: Coherent eddies and turbulence in vegetation canopies: the mixing layer analogy. *Boundary-Layer Meteorology* **78**:351-382, 1996.
[3] Farquhar T., Eggleton C.D.: Pulsatile flow heightens vertical exchanges in a wheat canopy, in: Spatz H.C. and Speck T. (Eds): Proceedings of the 3rd Plant Biomechanics Conference, Freiburg, 2000.
[4] Farquhar T., Zhou J., Haslach H.: A possible mechanism for sensing crop canopy ventilation, in: Barth F., Humprey J., Secomb T. (Eds): Sensors and sensing in biology and engineering, Springer Press, Wien/New-York, 2003.
[5] Doaré O., Moulia B., de Langre E.: Effect of plant interaction on wind-induced crop motion. Transactions of the ASME, *Journal of Biomechanical Engineering*. To appear, 2004.
[6] Huerre P. & Rossi M.: Hydrodynamic instabilities in open flows, in: Godrèche C. & Manneville P. (Eds): Hydrodynamics and Nonlinear Instabilities, Cambridge University Press, Cambridge, 1998.
[7] Panton R.L.: Introduction to Stability and Transition, in: Incompressible Flow, 2nd edition, Wiley-Interscience publication, New-York, 1996.

AN UPDATED ARBITRARY-LAGRANGIAN-EULERIAN DESCRIPTION IN CONTINUUM MECHANICS AND ITS APPLICATION TO NONLINEAR FLUID-STRUCTURE INTERACTION DYNAMICS

Jing Tang Xing, W. G. Price
School of Engineering Sciences, Ship Science, University of Southampton, Southampton SO17 1BJ, UK,

Introduction

The applications of finite element methods (FEM) in structural analysis [1-2] and computational fluid dynamics (CFD) [3-4] have achieved increased sophistication and success in recent years. However, when these methods are used to solve problems in nonlinear fluid-solid interaction dynamics (NFSID), problems arise. For example, in a Lagrangian description of solids, variables describing structural motion are functions of the material coordinates fixed to each particle of the solid whereas in an Eulerian description of fluids, variables describing the fluid flow are functions of the coordinates fixed in space. When the structure moves, the material coordinate points also move from their original positions to new positions in space but, in the surrounding fluid, the Eulerian coordinates remain unchanged. On fluid-structure interaction interfaces, this difference of description produces a separation of the mesh points defining the solid from those of the fluid, which coincided before the system was disturbed. To retain the validity of compatibility conditions on the coupling interfaces in (NFSID), an Arbitrary-Lagrangian-Eulerian (ALE) system [5] has been adopted to describe the fluid motions [6-10]. The mathematical models reported include the FEM model for both fluids and solids and combination models adopting a FEM in solids and a finite volume (FV) or finite difference (FD) approaches in fluids. To solve NFSID problems, FD/FV techniques of CFD and FEM techniques for solids are used and the developed numerical method is referred as a *partitioned* or *iterative* solution procedure.

In these ALE descriptions, the reference coordinates remain unchanged during fluid motion and therefore form a curvilinear system of which the base vectors of the system are functions of time and space. The consequence of this is that all mathematical operations and formulations involving derivatives, volume and area transformations, etc are very complex functions and not readily adaptable to a numerical analysis [11]. In nonlinear FEA analysis of solids, an Updated Lagrangian (UL) system has been developed and successfully used to deal with large motions of the solid [1-2]. For an UL system, the current position coordinates (CPC) of each material point are chosen as its Lagrangian coordinates to describe the motions. With the marching of time, the material point moves to a new position and its Lagrangian coordinates are updated to its new CPC. Following this idea, this paper proposes and develops an updated ALE (UALE) system in which the CPC of the reference point in CESS are chosen as the reference coordinates to describe the motions of the fluids. As time advances, the reference point moves to its new position and its reference coordinates are updated to its new CPC. To fully understand the proposed concept, geometrical and physical explanations for this UALE system are described. In development of the theoretical model, derivations and formulations are included of mathematical operation rules for time and spatial derivatives, differential and integral conservation laws in continuum mechanics and variational formulations in the UALE system. A variational approximate solution is presented and a mixed FEM-FV method to NFSID problems developed to demonstrate the applications of this UALE system.

UALE system

In a Cartesian Eulerian spatial system (CESS) $o - x_1 x_2 x_3$ with base vectors $\mathbf{a}_i$, a mesh point *p,* located at a position $\mathbf{r}^0 = x_i^0 \mathbf{a}_i$ at time $t = 0$, moves to a new point p' with position vector $\mathbf{r} = x_i \mathbf{a}_i$ at time $t = t_1$. In a total ALE system, the original position coordinates of the mesh point *p* are chosen as the reference coordinates, i.e. $\xi^i = x_i^0$. During the process of motion, the reference coordinates ξ^i remain unchanged, although a mesh line undergoes deformation. The base vectors at the mesh point ξ^i of the mesh system at time $t = 0$ and $t = t_1$ are $\mathbf{g}_i^0 = \partial \mathbf{r}^0 / \partial \xi^i = \mathbf{a}_i$ and $\mathbf{g}_i^t = \partial \mathbf{r} / \partial \xi^i = \mathbf{a}_j \partial x_j / \partial \xi^i$, respectively. However, an UALE system chooses the current position coordinates x_i to denote a mesh point. At time $t = 0$, the mesh coordinates are $z_i = x_i^0$ and the base vectors at the point *p* are $\mathbf{g}_i^0 = \mathrm{a}_i$. At time $t = t_1$, the mesh point *p* moves to a new position P', which now has an *updated* mesh coordinate

$z_i = x_i$. The base vectors at p' of the updated system at time $t = t_1$ are given by $\mathbf{g}_i^t = \partial \mathrm{r} / \partial z_i = \partial x_j / \partial x_i \mathrm{a}_j = \mathrm{a}_i$. Therefore, the UALE system has the same base vectors as the CESS during all motions. The *updated velocity of the reference coordinates* is shown to be the moving velocity of the mesh in the ALE system. The UL system can be considered as a special case of an UALE system in which the reference point is replaced by a material point.

Conservation laws, mathematical operations and variational principles for NFSID

The differential and integral forms of the generalized conservation laws in an UALE system are derived and the mathematical operation rules applicable to derivatives, integral and variations are presented. The transformation relations between ALE and UALE systems are provided. A *Eulerian virtual displacement* of a material point in a spatial description and its *relative virtual displacement* (i.e., *convective* and *local virtual displacements*) of the material point in the ALE reference description are defined. For a field function, the material, Eulerian local and ALE reference local variations as well as their transformation relations are formulated. For a functional $H[\phi]$ defined over the region $\Omega(x_i, t)$, the material, Eulerian local and ALE reference local variations of this functional are given. In the UALE system, special variational relations are derived. From these relations, variational principles for NFSID in an UALE system are obtained and compared with the forms appertaining to spatial coordinate systems [12]. An example of a variational approximate solution to a NFSID problem is presented. These variational principles provide a basis to construct numerical schemes of study in the UALE system.

A mixed FEM-FV approach

Both UALE and UL systems choose the same CPC in CESS as the updated reference or updated material coordinates and have the same base vectors and updated velocity. This provides benefits when dealing with mesh matching difficulties in the numerical analysis of NFSID problems and allows development of a mixed FEM-FV. That is, an UL incremental formulation [1-2] for solids and a FV method for fluids are used. The integral forms of the conservation laws of the fluid developed in UALE system are easily related to the computational grid, where the volume integrals are taken over a current finite volume. A coupling iteration is used to solve the coupling equations using FEA and FV software. On the assumption that the solution of the fluid, solid and all variables in the fluid-solid interaction problem at time *t* have been derived in the previous cycle, the configuration of the system at time $t + \Delta t$ needs to be calculated. The developed coupling iteration solution process starts by solving the solid equation using prescribed load intensities at time $t + \Delta t$, the fluid stress on the wetted interface and an integration over the volume and area last calculated to predict load vectors and to derive an approximate displacement. The FV calculation for the fluid is now completed by evaluating an approximation of the fluid configuration and field variables, which are in turn used in the solid analysis to check convergence and to determine if the iteration process may proceed.

References

[1] Bathe, K. J.: Finite element procedures in engineering analysis. Prentice-Hall, 1982.

[2] Zienkiewicz, O. C., Taylor, R. L.: The finite element method, Vol.1, 2. McGraw-Hill, 1989, 1991.

[3] Anderson, J. D.: Computational fluid dynamics, the basics with applications. McGraw-Hill, 1995.

[4] Hirsch, C.: Numerical computation of internal and external flows, Vol. 1,2, Wiley & Sons, 1989,1990.

[5] Hirt, C. W., Amsden, A. A., Cook, J. L.: An arbitrary Lagrangian-Eulerian computing method for all flow speeds. *Journal of Computational Physics***,** 14, 227-253, 1974.

[6] Hughes, T. J. R., Liu, W. K., Zimmermann, T. K.: Lagrangian-Eulerian finite element formulation for incompressible viscous flows. *Com. Meth. Appl. Mech. Eng.,* 29, 329-349, 1981.

[7] Donea, J., Giuliani, S., Halleux, J. P.: An arbitrary Lagrangian-Eulerian finite element methods for transient dynamic fluid-structure interactions. *Com. Meth. Appl. Mech. Eng.,* 33, 689-723, 1982.

[8] Belytschko, T., Flanagan, D. P. & Kennedy, J. M.: Finite element methods with user-controlled meshes for fluid-structure interaction. *Com. Meth. Appl. Mech. Eng.*, 33, 669-688, 1982.

[9] Bathe, K. J.: Computational fluid and solid mechanics. Elsevier Science, 2001.

[10] Xing, J. T., Price, W. G., Chen, Y.: A mixed finite element-finite difference method for nonlinear fluid-solid interaction dynamics. I. Fluid-rigid structure interaction. *Proc. R. Soc. Lond.* **A** 459, 2399-2430, 2003.

[11] Thompson, J. F., Soni, B. K., Weatherill, N. P.: Handbook of grid generation, CRC Press, 1999.

[12] Xing, J. T. & Price, W. G.: Variational principles of nonlinear dynamical fluid-solid interaction systems. *Phil. Trans. R. Soc. Lond.* A355, 1063-1095, 1997.

XXI ICTAM, 15–21 August 2004, Warsaw, Poland

SLENDER BODY THEORY APPROACH TO NONLINEAR SHIP MOTIONS

Edwin J. Kreuzer*, Wolfgang M. Sichermann*
*Technical University Hamburg-Harburg, Mechanics and Ocean Engineering, 21071 Hamburg, Germany

Summary A solution method for the time-domain investigation of nonlinear heave and pitch motions of ships in head waves is presented. By virtue of the slender body assumption, the three-dimensional flow problem is decomposed into a series of two-dimensional problems. The major nonlinearities are induced by motions with large amplitude and by the physical nature of the free water surface.

INTRODUCTION

The accurate prediction of large amplitude ship motions in severe seas poses still a delicate problem in the field of fluid-structure interaction. While three-dimensional panel methods have reached the state of maturity in linear seakeeping analysis, the original problem, governed by strongly nonlinear boundary conditions, is far from being solved efficiently. The principal nonlinearities are associated with the variable wetted surface of the ship hull and with the nonlinear hydrodynamic conditions on the free surface.

Over a period of years, the problem of solving an instantaneous nonlinear boundary value problem has been circumvented by integrating the pressure of the undisturbed incoming waves over the actual wetted surface (to obtain the so-called nonlinear Froude-Krylov force) while treating a linear radiation/diffraction problem. The negligence of nonlinear hydrodynamic effects was justified by the different magnitudes of the linear Froude-Krylov and the radiation/diffraction forces. However, it has been proved in an exemplary study [2], that the nonlinear hydrodynamic effects can attain the same order of magnitude as the contributions from the nonlinear Froude-Krylov force. In consequence, a consistent investigation of nonlinear ship motions must consider both, geometric and hydrodynamic nonlinearities.

A promising approach, with regard to efficiency, is provided by the so-called $2D+t$ theory [1] which has been successfully applied to the prediction of high-speed craft wave resistance and ship bow waves. Following the lines of slender body theory, the three-dimensional flow problem may be decomposed into a series of consecutive two-dimensional problems. Until present, only the forced motion problem has been investigated with $2D + t$ theory. This paper generalizes the approach to free body motions.

STATEMENT OF PROBLEM

Slenderness and Scaling

The rigid body motion of the ship and the wave flow will be described with respect to an inertial reference frame. The (x, y) plane defines the free water surface at rest and the z-axis is pointing vertically upward out of the fluid domain. We consider a ship advancing in head waves with forward velocity U in direction of the x-axis. The ship is free to heave and pitch. All other modes of motion are constrained.

The characteristic hull dimensions are length l, draft d, and maximum beam b of the ship. We assume that the ship is slender, i.e., $b \simeq d \ll l$. Then, the components of the outward surface normal vectors are $n_X = \mathcal{O}(b/l) = \mathcal{O}(\epsilon)$, $n_Y = \mathcal{O}(1)$ and $n_Z = \mathcal{O}(b/d) = \mathcal{O}(1)$. For many ships, like container ships, frigates or cruise vessels, $d/l = \epsilon = \mathcal{O}(10^{-1})$. The parameter ϵ is referred to as the slenderness parameter. The boundary value problem describing the ship flow will be linearized with respect to the slenderness parameter in order to reduce the physical dimension of the problem. However, the nonlinear character of the boundary conditions will be retained.

Boundary Value Problem

We imply, that the wave patterns around the ship are described sufficiently by an inviscid, incompressible and irrotational flow. Then, the flow may be determined by a potential ϕ which has to satisfy Laplace equation

$$\frac{\partial^2\phi}{\partial x^2} + \frac{\partial^2\phi}{\partial y^2} + \frac{\partial^2\phi}{\partial z^2} = 0. \tag{1}$$

Order of magnitude analysis reveals that the first term in (1) is of $\mathcal{O}(\epsilon^2)$ in comparison to the latter. It is therefore neglected in the sense of slender body theory. The total flow potential is given by the potential of the unperturbed wave ϕ_w and the ship induced disturbance potential ϕ. The unknown disturbance potential must satisfy the zero-flux condition on the body surface S_0

$$\frac{\partial\phi}{\partial n} = \nabla\phi\cdot\vec{n} = -Un_X - \Big[U\theta + \dot{z}_G - \dot{\theta}(x - x_G) - \dot{\eta}_w\Big]\, n_Z, \tag{2}$$

where $\vec{n}$ is the normal vector in the (y, z) cross plane, pointing out of the fluid domain. The heave velocity is denoted by $\dot{z}_G$, the pitch angle and velocity by θ and $\dot{\theta}$, respectively. The vertical velocity of the incoming wave is given by $\dot{\eta}_w$.

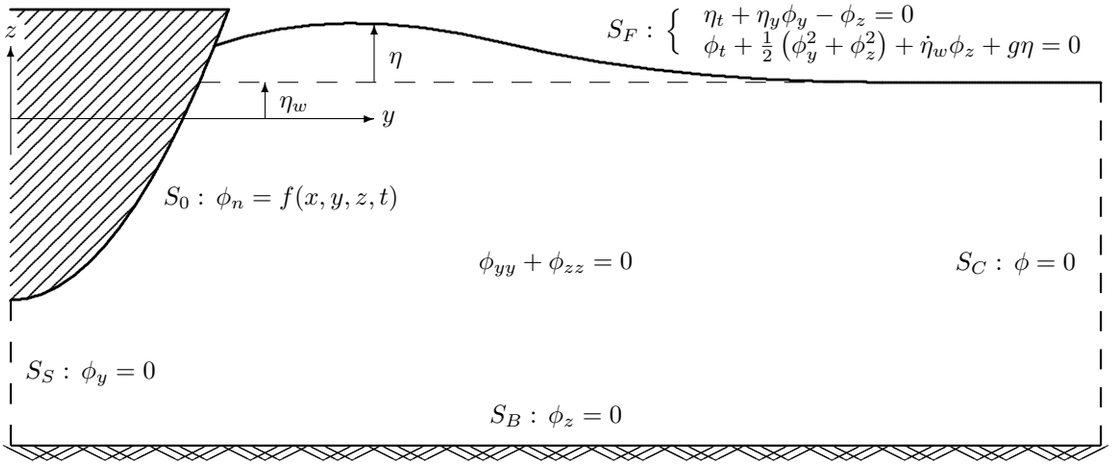


Figure 1. Boundary conditions for axis symmetric problems.

The kinematic and dynamic conditions on the free surface $z = \eta + \eta_w$ yield

$$\eta_t + \eta_y\phi_y - \phi_z = 0, \tag{3}$$

$$\phi_t + \tfrac{1}{2}\left(\phi_y^2 + \phi_z^2\right) + \dot{\eta}_w\phi_z + g\eta = 0. \tag{4}$$

In order to obtain a finite and bounded computational domain, additional boundary conditions are enforced at the symmetry plane S_S, at the bottom plane S_B, and at a vertical control plane S_C far away from the body, Figure 1.

The instantaneous boundary value problem is further decomposed into an initial value problem for the temporal evolution of the free surface quantities (ϕ, η) and a boundary value problem for (ϕ on S_0, ϕ_n on S_F) fixed in time, which is solved by a standard Boundary Element Method. Equation (2) is used to provide the flux on the body boundary S_0. The free surface quantities are updated from (3) and (4) by the Mixed Eulerian-Lagrangian Method [3].

Integration of Body Motions

In order to resolve the three-dimensional flow, two-dimensional boundary value problems have to be solved at 20 to 30 sections along the ship hull. The hydrodynamic forces and moments are computed from the pressure distribution over the ship hull, where the pressure is obtained from the total flow potential by Bernoulli's equation.

Instability may arise in the numerical integration scheme due to the particular nature of the hydrodynamic force. From linear seakeeping theory it is well known that the total hydrodynamic force contains terms proportional to the position, velocity and acceleration of the ship. General numerical stability of ordinary differential equations, however, requires that all terms proportional to the highest derivative, i.e. the acceleration, have to be isolated.

RESULTS AND CONCLUSIONS

Stable numerical solutions of heave and pitch motions are obtained at a reasonable time step size when the ship induced flow potential is further decomposed into the contributions depending on acceleration, velocity, and displacement like in linear theory. Due to nonlinearity, the decomposition is no longer unique and the coefficients for added mass, radiation damping and hydrostatic restoring have to be updated in every time step. The results of the nonlinear analysis show asymptotic behavior to the linear solution when the height of the incoming waves is decreased.

The application of $2D + t$ theory to ship motions allows to treat the nonlinear problem eluding the complexity of three-dimensional computations. The present analysis of heave and pitch motions may be extended consistently to ship roll motions at moderate cost. This will enable the investigation of parametric rolling in head and quartering seas which represents a significant risk to modern day ships.

References

[1] Fontaine E., Tulin M.P.: On the prediction of nonlinear free-surface flows past slender hulls using 2D+t theory. *Ship Tech. Res.* **48**:56–67, 2001.
[2] Huang Y., Sclavounos P.D.: Nonlinear ship motions. *J. Ship Res.* **42**:120–130, 1998.
[3] Longuet-Higgins M.S., Cokelet E.D.: The deformation of steep surface waves on water (I) – A numerical method of computation. *Proc. R. Soc. Lond.* A **350**:1-26, 1976.

INVERSE MAGNUS FORCE IN FREE MOLECULAR FLOW

Andrzej Herczynski*, Patrick Weidman**
*Department of Physics, Boston College, Chestnut Hill, MA, 02467 USA
**Department of Mechanical Engineering, University of Colorado, Boulder, CO, 80309, USA

Summary We present a particle dynamics method for calculating the transverse force on a spinning solid translating in a rarefied gas and show that it is in the opposite direction to the classical Magnus effect in continuum flow. For a surprisingly large class of shapes, this inverse Magnus force is steady and given by a universal expression.

EXTENDED SUMMARY

The earliest known description and explanation of the transverse deflection of a spinning projectile is contained in Newton's first scientific publication, "New theory about light and colors" [1]. Newton "had often seen a Tennis ball, struck with an oblique Racket, describe such a curved line" and wondered if particles of light are similarly deflected. This effect for spinning solids is now usually named after Gustav Magnus who investigated spinning cylinders. An analysis based on the Navier-Stokes equations for a rotating and translating sphere at low Reynolds numbers is due to Rubinov and Keller [2] who showed that the force is proportional to, and directed as the cross product of, the angular rotation rate $\boldsymbol{\omega}$ and translational velocity $\mathbf{v}$, $\boldsymbol{\omega} \times \mathbf{v}$. However, under some conditions the Magnus force is known to be in the opposite direction to that usually observed [3], [4]. This reverse Magnus effect is thus far only qualitatively understood.

Interest in the Magnus effect in free molecular flows, that is flows with high Knudsen number, has been sparked by a recent article by Borg, et al [5]. Using Maxwellian distribution functions, the paper presents a calculation of the transverse force on a spinning sphere translating in a rarefied gas. The direction of this force is shown to be opposite to that calculated in [2] for continuum flow. We will refer to this phenomenon as the inverse Magnus force. The calculation by Borg and his collaborators also includes the effect of heat transferred to the rotating sphere from the impinging particles. Experimental verification of the inverse Magnus force has not yet been reported. An intriguing possible application is to vortex dynamics in superfluids and superconductors, which is currently a subject of the debate in the solid state physics community (see, *e.g.* [6]).

A simpler and physically more transparent approach for understanding the high Knudsen number Magnus effect, presented here, is based on a particle dynamics model similar to, but crucially different from, that introduced by Newton (propositions 34 and 35, Book II of *Principia*) to calculate fluid resistance. Our alternative approach [7], is applicable not for a medium in which molecule-molecule interaction is the dominant effect, but to a rarefied gas where molecular interactions with boundaries are dominant. This model reproduces the result obtained by Borg et. al. [5] for the isothermal case (infinite conductivity of the rotating sphere). Further, it can be readily used to obtain both the total drag and lift forces on a spinning object of arbitrary shape translating through a rarefied gas.

Newton's model for fluid resistance "consists of equal particles freely disposed at equal distances from each other" impinging on a body such that their normal components of momenta are transferred to the body while their tangential components are preserved. This leads to the famous sine-squared law for the pressure coefficient over the surface of a body. (While this result is found not to be applicable to subsonic flow, it is fortuitously useful at hypersonic speeds.) Our model, different from Newton's, assumes: (i) mass of a gas particle is orders of magnitude smaller than the projectile mass, (ii) particle collisions with the body are perfectly elastic, and (iii) during collisions, gas particles acquire the fraction of the tangential velocity at the surface of the spinning body measured by α_τ, the Maxwellian accommodation coefficient.

We consider in turn a sphere, a cylinder, and right parallelepipeds of various sections, each in uniform translation and spinning about the primary axis of symmetry normal to the line of flight. Rather than dealing with the unsteady motion of a body moving through a cloud of particles, we take in each case a body fixed in space, but rotating about an axis of symmetry and exposed to an oncoming stream of uniformly dispersed molecules. For the sphere, cylinder, and right parallelepipeds of regular polygon sections with even number of faces, we show that the Magnus force is steady, opposite in direction to the usual force in continuum flow, and has the magnitude proportional to one-half the mass M of gas displaced by the body and the vector product of its angular and translational speeds:

$$\mathbf{F} = -\frac{1}{2} M \alpha_\tau \, \boldsymbol{\omega} \times \mathbf{v}.$$

For the sphere and the cylinder, the drag is steady and the lift (understood here as the sidewise force that does not disappear in the limit of vanishing accommodation coefficient, $\alpha_\tau \to 0$) is zero. As expected, the lift and drag are both unsteady for all parallelepipeds of regular polygon section. For parallelepipeds whose sections are polygons with odd-number of faces, the Magnus force is unsteady as well. Figure 1 shows the magnitude of the inverse Magnus force as a function of the rotation angle for the "worst case," namely that of a parallelepiped of triangular (equilateral) section.

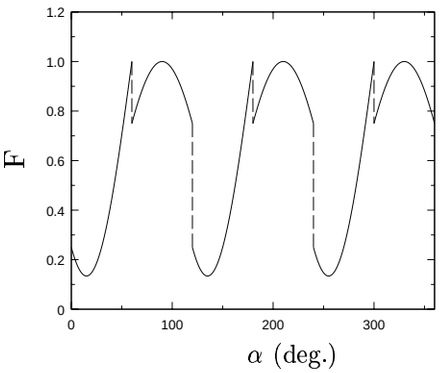


Figure 1: The normalized magnitude of the inverse Magnus force F as a function of rotation angle α for a parallelepiped of triangular, equilateral section. The force is unsteady, both wobbly and jerky.

Our results lead to the following general hypothesis. The inverse Magnus force for any planar object of convex section possessing two perpendicular axes of reflectional symmetry will be steady and given by the above expression. We consider also the case of spinning solids embedded in shear flow and discuss under what conditions the inverse Magnus force remains steady.

References

[1] Newton, I.: New theory about light and colors. *Philos. Trans. Roy. Soc.* **80:**3078, 1671-72.
[2] Rubinov, S. I., Keller, J. B.: The transverse force on a spinning sphere moving in a viscous fluid. *J. Fluid Mech.* **11:**447, 1961.
[3] Davies, J. M.: The aerodynamics of golf balls. *J. Appl. Physics* **20:**821, 1949.
[4] Tritton, D. J.: Physical Fluid Dynamics. Van Nostrand Reinhold, 1977, 124-126.
[5] Borg, K. I., Söderholm, L. H., Essén, H.: Force on a spinning sphere moving in a rarefied gas. **15:**736, 2003.
[6] Wexler, C.: Magnus and Iordanskii forces in superfluids. *Phys. Rev. Letters* **79:**1321, 1997.
[7] Weidman, P. D., Herczynski, A.: On the inverse Magnus effect in free molecular flow. *Phys. Fluids*, in press.

FAST MULTIPOLE ALGORITHM FOR WAVE RESPONSE ANALYSIS OF FLOATING STRUCTURES

Tomoaki Utsunomiya [*], Eiichi Watanabe [*]
[*] *Department of Civil & Earth Resources Engineering, Kyoto University, Kyoto, Japan*

Summary The conventional Boundary Element Method (BEM) employing free-surface Green's function is practically impossible to be applied for large-scale analysis such as wave diffraction/radiation analysis for Very Large Floating Structures (VLFS) in general sea-bed topography. This is mainly due to $O(N^2)$ requirement for storage and $O(N^3)$ characteristics for CPU time, where N is the number of unknowns for the BEM. The Fast Multipole Algorithm (FMA) has thus been applied to the BEM utilizing the Green's function by the present authors. The method has O(N) characteristics both for storage requirement and CPU time. The method has been applied to large-scale analysis such as wave response analysis of pontoon type VLFS in general sea-bed topography, and hybrid-type VLFS having complicated shape, where N is the order of 10^4 - 10^5.

INTRODUCTION

For analyzing wave response of floating structures, wave diffraction and radiation forces have to be evaluated. The Boundary Element Method (BEM) employing free surface Green's function is one of the most promising methods which can handle general and complicated shape of floating structures as well as general sea-bed topography.
However, when the methods are applied for the analysis of Very Large Floating Structures (VLFS), the number of unknowns (=N) reaches the order of 10^4-10^5 and thus large storage requirement ($O(N^2)$) and the excessive computation time of $O(N^3)$ (for factorization solvers) make the application of conventional BEM impractical. The precorrected-FFT method [1] has been successfully applied to such a large scale analysis, but not yet for a VLFS in shallow water. We hereby present an alternative approach using Fast Multipole Algorithm (FMA) [2], which has been more commonly used in many fields that would require excessive computation resources.
We have implemented the FMA to our higher-order boundary element program, and examined its efficiency by benchmark calculations. The benchmark calculations include VLFS wave response analysis in variable water depth environment of a real sea [3], and the analysis for a hybrid-type VLFS, which is composed of pontoon part and semi-submersible part [4].

FORMULATIONS

Consider a general shape VLFS (Very Large Floating Structure) floating in the open sea of variable depth (with constant depth h at infinity). The wetted-surface of VLFS is defined by the symbol S_H. The variable depth sea-bottom surface (S_B) is defined such that the boundary line (Γ_B) touches on the flat bottom base-surface of z=-h and the S_B must locate higher than the base surface (z=-h). The coordinate system is defined such that the xy plane locates on the undisturbed free surface and the z-axis points upward.
Consider the long-crested harmonic wave with small amplitude. Assuming the water to be perfect fluid with no viscosity and incompressible, and the fluid motion to be irrotational, then the fluid motion can be represented by a velocity potential Φ. Also, we consider the steady-state harmonic motions of the fluid and the structure, with the circular frequency ω. Then, all of the time-dependent quantities can be represented similarly as follows:

$$\Phi(x,y,z;t) = \mathrm{Re}[\phi(x,y,z)e^{i\omega t}] \tag{1}$$

where i is the imaginary unit (i^2=-1) and t is the time.
In this study, we employ the following integral equation as a fundamental equation, which is applicable to floating bodies with variable-depth sea bottoms and/or breakwaters:

$$(4\pi + \int_{S_I} \frac{\partial G_2}{\partial z} dS)\phi(\vec{x}) + \int_{S_H \cup S_B} \{\phi(\vec{\xi}) \frac{\partial G}{\partial n} - \phi(\vec{x}) \frac{\partial G_2}{\partial n}\} dS - \int_{S_H \cup S_B} G \frac{\partial \phi(\vec{\xi})}{\partial n} dS = 4\pi\phi_I(\vec{x}) \tag{2}$$

Here, $\vec{x} = (x, y, z)$ and $\vec{\xi} = (\xi, \eta, \zeta)$. The symbol S_I designates the inner plane of $z = -h$ inside the boundary Γ_B. The function $G \equiv G(\vec{x}; \vec{\xi})$ represents the Green function representing water waves, and satisfying the boundary conditions on the free surface, on the flat sea bottom ($z = -h$), and the radiation condition at infinity. The series form can be represented as follows:

$$G(\vec{x}; \vec{\xi}) = \sum_{m=0}^{\infty} \frac{2K_0(k_m R)}{N_m} \cos k_m(z+h) \cos k_m(\zeta + h) \tag{3}$$

$$N_m = \frac{h}{2}(1 + \frac{\sin 2k_m h}{2k_m h}), \quad k_m \tan k_m h = -K \tag{4}$$

where k_m ($m \geq 1$) is a positive real number, and $k_0 = ik$. The symbol R represents horizontal distance between $\vec{x}$ and $\vec{\xi}$. As an alternative expression of the Graf's addition theorem for the Bessel function, the next equation can be obtained.

$$K_0(k_m R) = \sum_{n=-\infty}^{\infty} K_n(k_m r) e^{in\theta} I_n(k_m \rho) e^{-in\Phi} \tag{5}$$

Here, $\vec{x}=(r,\theta,z)$ and $\vec{\xi}=(\rho,\Phi,\zeta)$ are the points measured from newly defined cylindrical coordinate systems, of which origin O may be referred to as the multipole expansion point. The multipole expansion point O can be located arbitrarily on the undisturbed free surface (thus on the xy plane of the global rectangular coordinate system) under the restriction of $\rho<r$. Substituting Eq. (5) into Eq. (3), we have

$$G(\vec{x},\vec{\xi})=\sum_{m=0}^{\infty}\sum_{n=-\infty}^{\infty}M_{mn}K_n(k_m r)e^{in\theta}\cos k_m(z+h) \tag{6}$$

$$M_{mn}=\frac{2}{N_m}I_n(k_m\rho)e^{-in\Phi}\cos k_m(\zeta+h) \tag{7}$$

Thus, we have obtained the expression of the Green function represented in the form of the multipole expansions. Combining the above formula with the acceleration technique using hierarchical algorithm, the acceleration of the HOBEM program has been made. In this study, we have employed the quadrant-tree to define the tree structure of cells and the hierarchical computation algorithm [2].

NUMERICAL EXAMPLES

The wave response analysis of a box-like VLFS has been made by using the fast multipole method developed in this study and by the program using direct LU factorization solver. The specifications of the VLFS are: the length L=1,500m, the beam B=150m, the draft d=1m, the rigidity as an elastic plate D=3.88x10^7 kNm, and the Poisson's ratio ν=0.3. Number of modal functions employed is 160 (20 in longitudinal and 8 in beam). The water depth is 8m (constant). The wave period is 18 seconds (the corresponding incident wave length is λ=156.8m), and the angle of wave incidence is $\beta=\pi/4$. **Table 1** shows the performance of the benchmark calculations, where in the developed program, GMRES solver is used with the residual tolerance $\varepsilon=10^{-4}$. We note that the fast multipole method (FMM) is efficient both in CPU time and memory allocation compared to the direct method using either LU factorization solver or GMRES solver. Next, the wave response analysis of the same VLFS model located in the variable depth sea representing natural reef has been made. The variable depth surface (S_B) is discretized into 20,278 elements of the size of 12.5mx12.5m, and the number of nodes is 61,721. For meshing the VLFS model, the model B (number of nodes is 5,377) in **Table 1** is used; thus the total node number of the analyzed model becomes 67,098. The computation time was 38.4 hour using 5 CPUs for the wave period of 18 seconds, the wave direction of $\beta=\pi/4$, and the residual tolerance $\varepsilon=10^{-2}$. **Fig. 1** shows the deflection amplitudes in the variable depth sea. **Fig. 2** shows a snapshot of the surface elevation around the floating body, where the diffraction and the radiation waves are both included. Results for a hybrid-type VLFS will be presented in the Congress.

Table 1 Benchmark calculations by FMA and direct method.

Model	Typical panel size	Number of nodes	Fast multipole method		Direct method		
			CPU time	Memory allocation	CPU time		Memory allocation
					LU factorization	GMRES solver	
A	25.0m	1,609	1.8 min	27 MB	1.55 min	3.28 min	54 MB
B	12.5m	5,377	10.4 min	89 MB	28.5 min	36.4 min	489 MB
C	6.25m	19,393	77.4 min	315 MB	(907 min)	(474 min)	(6 GB)
D	3.125m	73,345	775 min	1.15 GB	(708 hr)	(113 hr)	(85 GB)
E	1.5625m	284,929	1689 min	1.75 GB	(1658 days)	(71 days)	(1.2 TB)

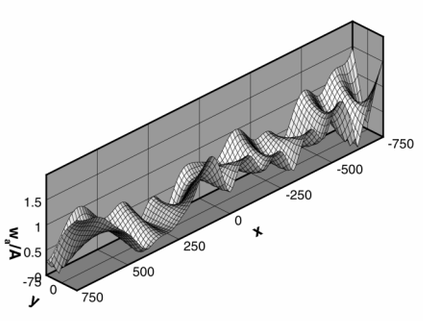


Fig. 1 Deflection amplitude for Model B in variable depth sea (in the reef sea).

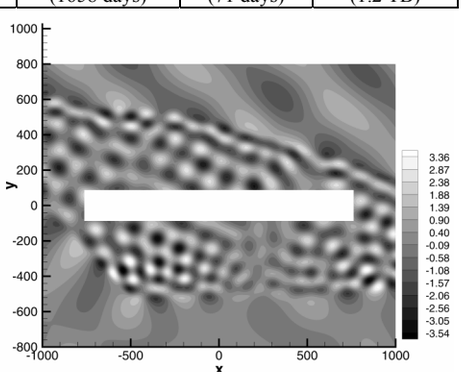


Fig. 2 Snapshot of the surface elevation around the VLFS in the reef sea.

References

[1] Korsmeyer T., Phillips J., White J.: A Precorrected-FFT Algorithm for Accelerating Surface Wave Problems, *Proc. 11th Int. Workshop on Water Waves & Floating Bodies*, 1996.

[2] Greengard L.: The Rapid Evaluation of Potential Fields in Particle Systems, MIT Press, 1988.

[3] Utsunomiya T., Watanabe E., Nishimura N.: Fast Multipole Method for Hydrodynamic Analysis of Very Large Floating Structures, *Proc. 16th Int. Workshop on Water Waves & Floating Bodies*, 161-164, 2001.

[4] Utsunomiya T., Watanabe E.: Wave Response Analysis of Hybrid-type VLFS by Accelerated BEM, *Hydroelasticity in Marine Technology* 297-303, 2003.

EFFECT OF AN OSCILLATING CYLINDER ON A NEIGHBOURING CYLINDER WAKE

Y. Yang [1], Y. Zhou [2] and Z. Guo [3]
[1] *Graduate School (Shenzhen Campus), Harbin Institute of Technology, Shenzhen 518055, China*
[2] *Department of Mechanical Engineering, The Hong Kong Polytechnic University, Hung Hom, Kowloon, Hong Kong*
[3] *National Laboratory of Coal Combustion, Huazhong University of Science and Technology, Wuhan 430074, China*

Summary Vortex shedding from a neighbouring stationary cylinder in the presence of a neighbouring oscillating cylinder is numerically investigated using a newly developed Lattice Boltzmann technique. Other than reconfirming previous experimental finding that the oscillation of one cylinder can lock in vortex shedding from the stationary cylinder as well as from the oscillating one, the calculation documents the dependence on *T/d*, *A/d* and f_e/f_o of the lock-in phenomenon, typical flow structure and forces on the cylinders.

EXTENDED SUMMARY

Flow-induced vibration on a bluff body in crossflow has been extensively reported in the literature because of its practical significance. Nevertheless, our understanding of this problem is far from complete. For instance, how would an oscillating fluid-cylinder system influence a neighbouring cylinder wake? This question is relevant in engineering, where an oscillating fluid-structure system is frequently associated with the presence of a neighbouring structure such as heat exchanger tubes, a cluster of high-rise buildings, bundled transmission lines and piles of offshore structures. Lai et al. [1] investigated experimentally flow interference between one oscillating and one stationary cylinder and found that the frequency (f_s) of vortex shedding from the stationary cylinder could be modified by the oscillation of the other cylinder, resulting in the lock-in of f_s with the oscillation frequency (f_e). However, due to the limitation of experiments, many issues on this problem remain to be resolved. For example, the drag and lift forces on cylinders were not measured. There is insufficient information on how this type of lock-in depends on the cylinder centre-to-centre spacing, *T/d*, the cylinder oscillating amplitude, *A/d*, and the frequency ratio, f_e/f_o, where *d* is the cylinder diameter and f_o is the vortex shedding frequency when the oscillation is absent. The present work aims to investigate numerically how an oscillating fluid-structure system affects vortex shedding from a neighbouring stationary cylinder, thus complementing the experimental investigation.

The numerical technique employed is a recently developed lattice Boltzmann method (LBM), as introduced by Chen and Doolen [2]. LBM is characterized by a clear picture of the physics of fluids, the natural parallelism, and ease to handle interactions between fluids and structures. The reliability and efficiency of LBM have been well demonstrated by a number of studies in various fields. Numerical simulations were carried out for a two-dimensional flow around two side-by-side circular cylinders, one oscillating laterally at $A/d = 0 \sim 1$ and $f_e/f_o = 0.4 \sim 1.6$. Three *T/d* values, i.e. 1.8, 2.2 and 3.5, were examined, which cover the asymmetrical and coupled street flow regimes when both cylinders are stationary (e.g. Zhou et al. [3]). The Reynolds number (*Re*) is 150. The computational domain is given by a rectangular area of 40d x 20d with a uniform grid of 640 x 320. Numerical results at $T/d = 2.2$ and 3.5 (not presented) show essentially the same flow structures as those observed experimentally at the same f_e/f_s and *A/d* by Lai et al [1]., thus providing a validation for the numerical technique presently used.

The numerical data reconfirm the experimental finding that the oscillation of one cylinder can lock in vortex shedding from the stationary cylinder as well as from the oscillating one. The hatched area in Figure 1 represents the region where vortex shedding from the lower stationary cylinder is locked in with the oscillation of the upper cylinder. The lock-in region for a single cylinder case is included in Fig. 1 for the purpose of comparison. The inserts in the figure show the iso-contours of spanwise vorticity, which display typical flow structures in the lock-in and non-lock-in regions. A number of interesting observations can be made based on the figure. Firstly, as *A/d* increases, the f_e/f_o range over which the locked-in response is observed grows, similarly to the single cylinder case. Secondly, for a larger *T/d*, the lock-in f_e/f_o range shrinks at a fixed *A/d*. This is expected since the oscillating influence impairs as the two cylinders are farther separated. Thirdly, at $T/d = 1.8$, the present lock-in region completely embraces that of a single cylinder, implying that the interference between the cylinders enhances the occurrence of lock-in. However, at $T/d = 2.2$, the oscillating influence on the stationary cylinder weakens and subsequently the lock-in f_e/f_o range at $A/d < 0.5$ retreats significantly for $f_e/f_o < 1$, even smaller than a single cylinder case. This retreat is substantially more evident at $T/d = 3.5$. For $f_e/f_o > 1$, the lock-in f_e/f_o range is always larger than a single cylinder case. Apparently, the oscillating effect is more persistent at a higher frequency ratio. Finally, it is worth commenting on the typical flow structures. In the absence of lock-in, the near-wake structure for $f_e/f_o < 1$ appears in-phased at $T/d = 1.8$ and 2.2 but anti-phased at $T/d = 3.5$. The flow structure is apparently different between $f_e/f_o < 1$ and $f_e/f_o > 1$ even at the same *A/d*. When the lock-in response is observed, vortex shedding from the two cylinders can be either in-phased or anti-phased and the flow structure further depends on *T/d*.

The time-averaged and root mean squared (rms) values of the drag and lift forces on the stationary cylinder are also tabled (not shown). Preliminary analysis indicates that the lock-in response does not affect to a great extent the time-averaged lift, drag and the rms drag but leads to an increase by 8 ~ 15% in the rms lift on the stationary cylinder. The result conforms to the increased vortex strength as lock-in occurs (not shown). The investigation indicates that LBM can be used reliably to calculate the flow field around two side-by-side cylinders, one vibrating. Further analysis

will be focused on the classification of typical flow structures based on A/d and f_e/f_o at different T/d. The effect of the presence of the stationary cylinder on vortex shedding from the oscillating cylinder will also be examined.

References

[1] Lai W. C., Zhou Y., So R.M.C. & Wang T.: Interference between stationary and vibrating cylinder wakes. *Phys. Fluids*, **15**; 1687-1695, 2003.
[2] Chen S. & Doolen G.: Lattice Boltzmann method for fluid flows. *Ann. Rev. Fluid. Mech*, **30**: 329, 1998.
[3] Zhou, Y., Wang, Z. J., So, R. M. C., Xu, S.J. and Jin, W.: Free vibrations of two side-by-side cylinders in a cross flow. *Journal of Fluid Mechanics*, **443**: 197-229, 2001.
[4] Mahir N. & Rockwell D.; Vortex formation from a forced system of two cylinders, *Fluids and Structures*, **10**: 473-500, 1996.

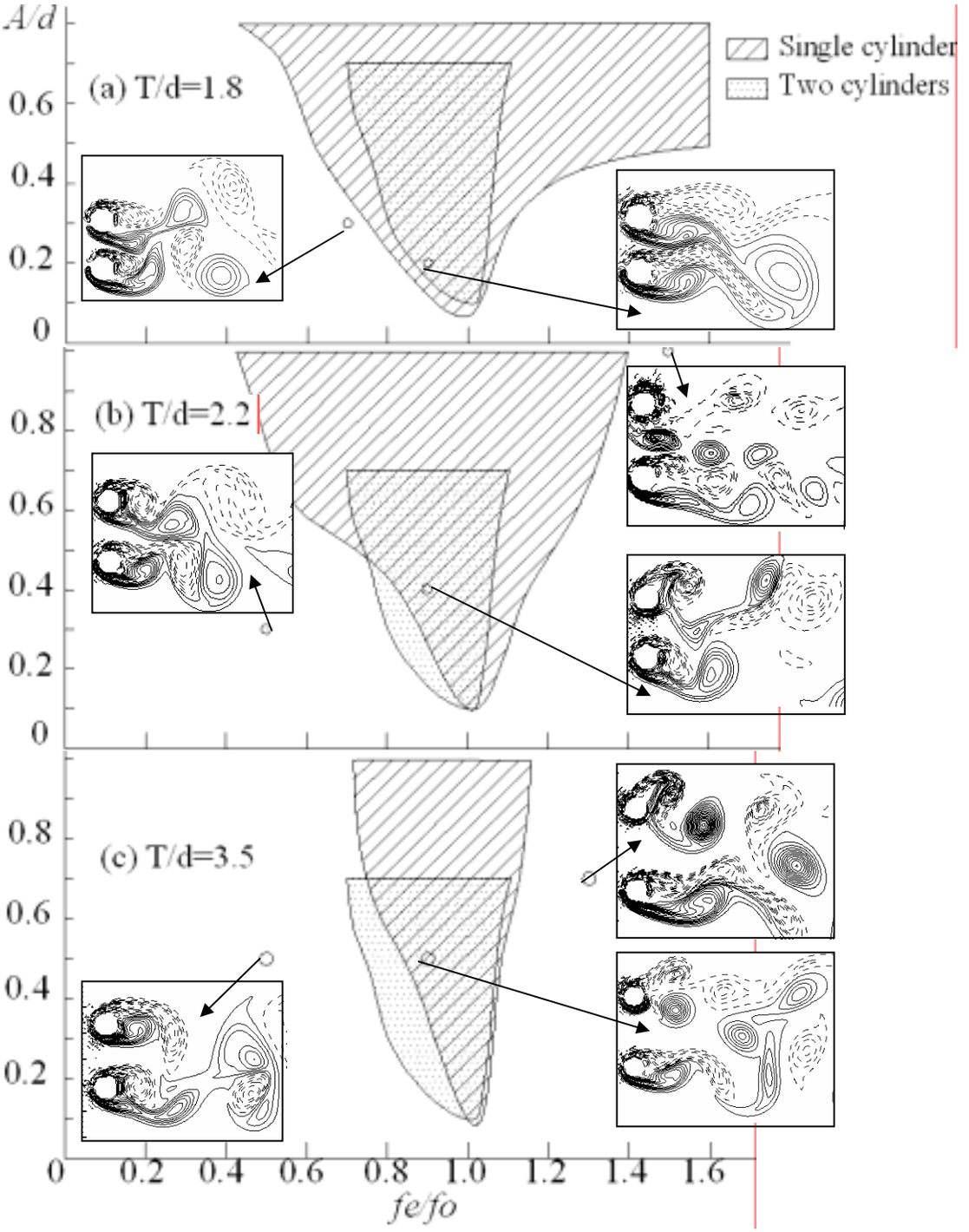


Figure 1 Region where vortex shedding from the lower stationary cylinder is locked in with the upper oscillating cylinder.

DISTURBED-LAMINAR FLOW OVER AN OSCILLATING CYLINDER

John R Chaplin, Dominique Mouazé
School of Civil Engineering and the Environment,
University of Southampton, Highfield, Southampton SO17 1BJ

Summary The flow around a cylinder oscillating at small amplitude in fluid otherwise at rest is subject to instabilities that, at a certain amplitude, trigger a regime of three-dimensional disturbed-laminar flow. This paper discusses apparent conflicts that are evident in recent observations, and describes new measurements of hydrodynamic damping and flow visualisations. Attention is directed at the range $1{,}000 < \beta < 20{,}000$ where β is the Stokes parameter based on the cylinder's diameter.

The flow around a circular cylinder oscillating in a direction normal to its axis with a small amplitude-to-diameter ratio in a fluid otherwise at rest is relevant in several practical applications and represents a fundamental problem of longstanding interest to fluid dynamicists. A reasonable starting point is to assume that the flow is laminar and two-dimensional, and for this case Stokes (1851) obtained a celebrated solution which was later extended by Wang (1968). A key result is that the fluid is predicted to resist the motion of the cylinder with a force

$$W = 2\pi\mu U\left[(\pi\beta)^{\frac{1}{2}} + 1 - \frac{1}{4}(\pi\beta)^{-\frac{1}{2}} + \ldots\right], \tag{1}$$

per unit length, where $\mu = \nu\rho$ is the viscosity, U is the cylinder's velocity, and β is the Stokes parameter $d^2 f/\nu$; d is the diameter of the cylinder and $f = \omega/2\pi$ its frequency. There is also a viscous force that is in phase with the acceleration, but this is dominated by the inertia force and is generally of less practical importance.

In connection with the problem of predicting the hydrodynamic damping of compliant offshore structures, recent efforts have concentrated on measuring the force on a cylinder oscillating at high β and small Keulegan Carpenter number, $K = 2\pi a/d$ where a is its amplitude. The results of these measurements have helped to identify the range of validity of equation (1). In 1981 Honji discovered a now well-known instability which marks a boundary between 'laminar' and 'disturbed-laminar' regimes, and one upper limit for the validity of the Stokes-Wang solution. In disturbed-laminar flow the fluid motion remains well-organised but has three-dimensional features not present in the laminar regime. An example from our measurements is shown in figure 1.



Figure 1. 'Mushroom' vortices along the widest part of the cylinder generated by oscillatory motion in the direction normal to the page.

A stability analysis by Hall (1984), valid for $\beta \to \infty$, indicated that the two-dimensional flow would first become unstable to these Taylor-Görtler vortices when the Keulegan Carpenter number of the motion exceeded

$$K_{\mathrm{H}} = \frac{5.78}{\beta^{1/4}}\left(1 + \frac{0.21}{\beta^{1/4}} + \ldots\right). \tag{2}$$

This agrees with observations of the conditions in which three-dimensional flow first occurred, as can be seen in figure 2, which includes Honji's results and other data from of Sarpkaya (1986). Both these and Honji's results seem to confirm K_{H} as the threshold for the onset of the disturbed-laminar regime. Turbulence and separation first appeared at amplitudes that were greater than this by about another 50%.

However, more recent measurements of forces at higher values of β suggest that in other conditions equation (2) does not represent the limit of validity of the Stokes-Wang theory. Vertical lines in figure 2 identify the ranges over which forces have been measured, in experiments using a smooth cylinder oscillating at small amplitudes in still water – or in the kinematically identical case of a stationary cylinder in an oscillating flow. Each one is labelled with the observed amplitude of the damping force, in terms of the Stokes-Wang result W, defined in equation (1). These experiments become more and more difficult as β is increased, but techniques have evolved considerably over the last 10 years and there is now widespread agreement (supported also by further measurements of Sarpkaya at $\beta \approx 10^6$ (2001)) on a rather surprising result. For values of β from some threshold to the highest values yet reached, and for Keulegan Carpenter

numbers that extend as much as *two orders of magnitude below* K_H, the damping is very close to $2W$. This suggests that the flow is subject to some other instability that has not yet been identified, since it seems very unlikely that small disturbances described by Sarpkaya (2002) can alone be responsible for a doubling of the viscous force. Recent measurements by Johanning (2003) indicate that at constant K the jump from W to $2W$ takes place at around $\beta = 4{,}500$.

The aims of the work described in this paper are to review the current position and attempt an answer to the question: why does the damping force on an oscillating cylinder in fluid otherwise at rest not appear to agree with the Stokes-Wang theory, when $K < K_H$ and β is greater than some threshold of order 10^3? The paper presents new measurements and visualisations of the flow in the region where the changes take place and in the light of this, discusses the apparent conflicts in earlier measurements of hydrodynamic damping.

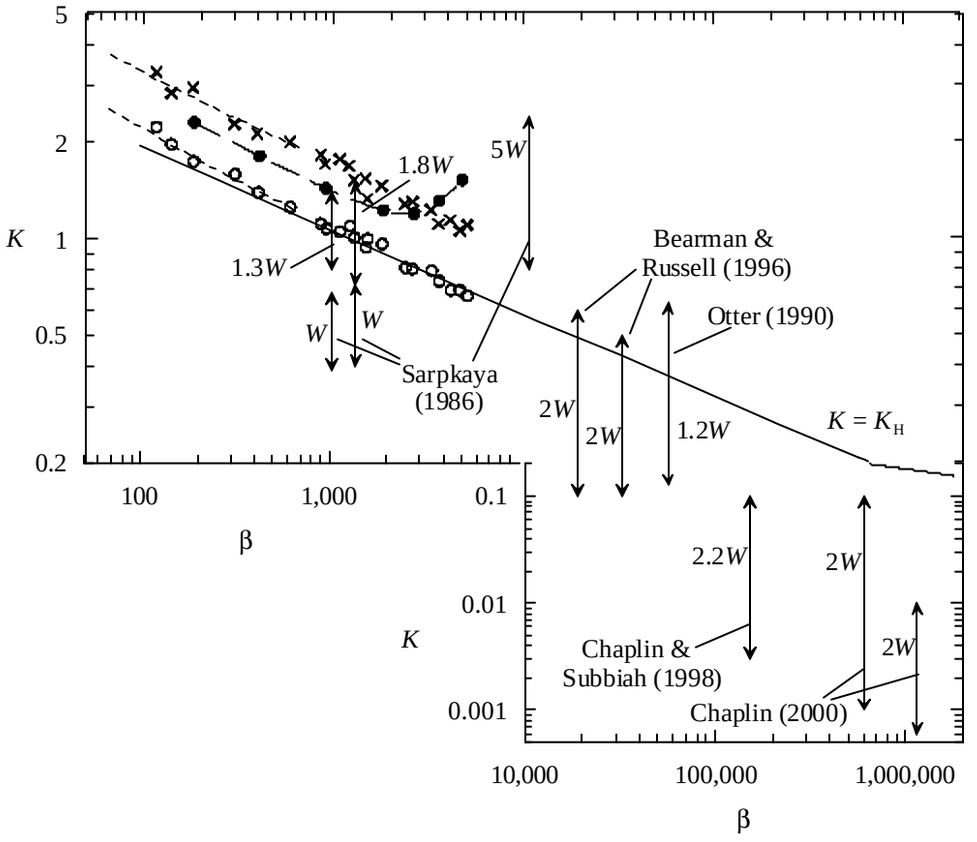


Figure 2. Measurements of flow and forces on a cylinder oscillating at small amplitudes in water otherwise at rest. Apart from the broken lines (which pass through Honji's (1981) data) all the results for $\beta < 12{,}000$ are from Sarpkaya (1986) and indicate observations of the onset of the Honji instability (○); separation (●); turbulence (×). Vertical arrows represent the ranges over which force measurements have been made, with an adjacent indication of the force magnitude, in terms of the Stokes-Wang result W. Hall's stability criterion (2) is shown as a continuous line.

References

Bearman P W & Russell M P, *Proc 21st Symp. Naval Hydrodyn.*, Trondheim, 1996.
Chaplin J R & Subbiah K. *Appl. Ocean Res.* **20**, 251-259, 1998.
Chaplin J R *J. Fluids Struct.*, **14**, 1101–1117, 2000.
Hall P. *J. Fluid Mech.* **146**, 337-367, 1984.
Honji H. *J. Fluid Mech.* **107**, 507-520, 1981.
Johanning L. PhD thesis, Imperial College London, 2003
Otter, A. *Appl. Ocean Res.* **12**, 153-155, 1990.
Sarpkaya T. *J. Fluid Mech.* **165**, 61-71, 1986.
Sarpkaya T. *J. Fluids Structs.* **15**, 909-928, 2001.
Sarpkaya T. *J. Fluid Mech.* **457**, 157-180, 2002.
Stokes G G. *Trans. Camb. Phil. Soc.* **9**, 8-106, 1851.
Wang, C-Y. *J. Fluid Mech.* **32**, 55-68, 1968.

(Subm. as contributing paper for the Fluids and Structures Session, ICTAM2004, Warzaw, 16-20 August 2004)

PIV experiments on vortex induced vibrating cylinders at high Reynolds numbers

by John Grue, Odin Gramstad, Arnaud Sanchis
Mechanics Division, Department of Mathematics, University of Oslo, Norway

Problem focus. The recent paper by Sarpkaya (2003) gives state-of-the-art description of the intrinsic nature of vortex induced vibrations (VIV) and lists a number of conclusions and recommendations for further studies of the phenomenon. The difficulties in numerical simulations of VIV at high Reynolds numbers are mentioned as particular challenges for future studies. The difficulties arise because of the turbulent character of the fluid motion close to the cylinder boundary and within the shear layers behind the cylinder. Sarpkaya noted that the numerical simulations are to be guided by flow-visualization experiments on high Reynolds number using non-intrusive techniques like PIV (Particle Image Velocimetry). Desired PIV measurements include: effect of the ambient turbulence on separation excursions and VIV, the evolution of the instability of unsteady shear layers emanating from the cylinder, effects in the body proximity, effects of the ambient turbulence on shear layer instability.

Predictions of the loads and motion of long pipelines and cables in the ocean, and motions of risers that connect floating production units on the ocean surface to wells on the sea floor, represent a continuous practical challenge for industries operating offshore. The needs within practice request better theoretical and experimental understanding of VIV and motivates for continuous efforts in developing improved simulation tools. These should be capable for use and accurate predictions of vortex induced vibrations and loads at high Reynolds numbers.

With this motivation we carry out PIV measurements for Reynolds numbers primarily in the range around 100.000. Smaller values of Re down to about 4000 are also investigated. A rigid (horizontal) cylinder of diameter 0.08 m, mounted to springs, is moved with constant speed in a water tank of dimensions (25 m, 0.5 m, 1 m) (length, width, depth). The cylinder is allowed to vibrate in the cross-flow and in-line directions. During each experiment, we record vertical and horizontal forces using gauges at the ends of the cylinder, as well as recording the flow field in sections parallel to the side walls of the tank. The field of views (FOV) in use are typically of size 2d x 2d and d x d, where d denotes the diameter of the cylinder. While the big FOV gives the more global fluid motion behind the cylinder, the close up d x d FOV is useful to extract details in the flow. The local turbulence distribution, the eddy dissipation rate, the Reynolds stresses, and thus the various terms contributing to the turbulent kinetic energy budget (TKEB), are extracted from the PIV measurements. The PIV measurements enable a detailed study of the flow separation occurring at the shoulders of the cylinder. The movement of the separation point is extracted.

The Digital PIV system consists of dual pulsed lasers, a high speed camera with resolution 1k x 1k, storing to computer a sequence of 100 double images per second in the examples below, with subsequent data analysis by the MatPIV program developed in our laboratory.

Results. An ensemble-average of the velocity field, of size 2d x 2d, is performed at constant phases during one cycle of the transverse lift force, thus separating the phase-locked motion from the random turbulent motion. In these tests the cylinder has constant forward motion with speed U, is restrained from vibrations, and Re=24.000. A control box moving with the cylinder has 28 by 41 velocity arrows (horizontal by vertical). This field is decomposed into an (ensemble) averaged part plus a fluctuation, i.e. $(u, v) = (< u >, < v >) + (u', v')$. (Velocities (u, v, w) and coordinates (x, y, z) denote components along the far-field stream, across and along the cylinder contour, respectively.) In figure 1, 75% of the forward speed U is subtracted from

the mean velocity field, such as to exhibit the classical flow topology in the near-wake, consisting of a newly formed vortex center at (-0.7,0.2) and saddle point at (-1,-0.6). The position of the separation areas on both shoulders is clearly asymmetric. The two-dimensional normal Reynolds stresses $< u' >^2$ and $< v' >^2$ show peak values of about 10% of U at x=-1,y=0. For $< u' >^2$ a corresponding peak value occurs in the lower shear layer emanating from the separation at the cylinder boundary. On the contrary, the shearing Reynolds stress $< u'v' >$ concentrates away from the centerline, with a maximum close to the saddle point defined above. The sign indicates a flux of x-momentum from the free-stream into the near wake.

Production. The turbulence production is estimated from $\mathcal{P} = - < u_i' u_j' > S_{ij}$ where $S_{ij} = \frac{1}{2}(\frac{\partial < u_i >}{\partial x_j} + \frac{\partial < u_j >}{\partial x_i})$. In the present examples it suffices to approximate the production by $\mathcal{P} = - < u'u' > \frac{\partial < u >}{\partial x} - < u'v' > \frac{\partial < u >}{\partial y}$, since $< v > << < u >$ and $\frac{\partial}{\partial x} << \frac{\partial}{\partial y}$. The turbulence production is remarkably concentrated at the saddle point, which highlights the crucial role of these singularities in the physics of such flows: turbulence levels close to the cylinder are the same as found by Cantwell and Coles (1983) in the far field.

Motion of the separation point. A detailed analysis of the normal and tangential velocity components along the cylinder contour shows that flow separation occurs at about 15 degrees from the shoulder of the cylinder, on its lee side. The flow separation is moved about 10 degrees towards the lower (upper) shoulder when the downward (upward) lift is at maximum.

Forces are recorded, fitting with published results by Norberg (2003).

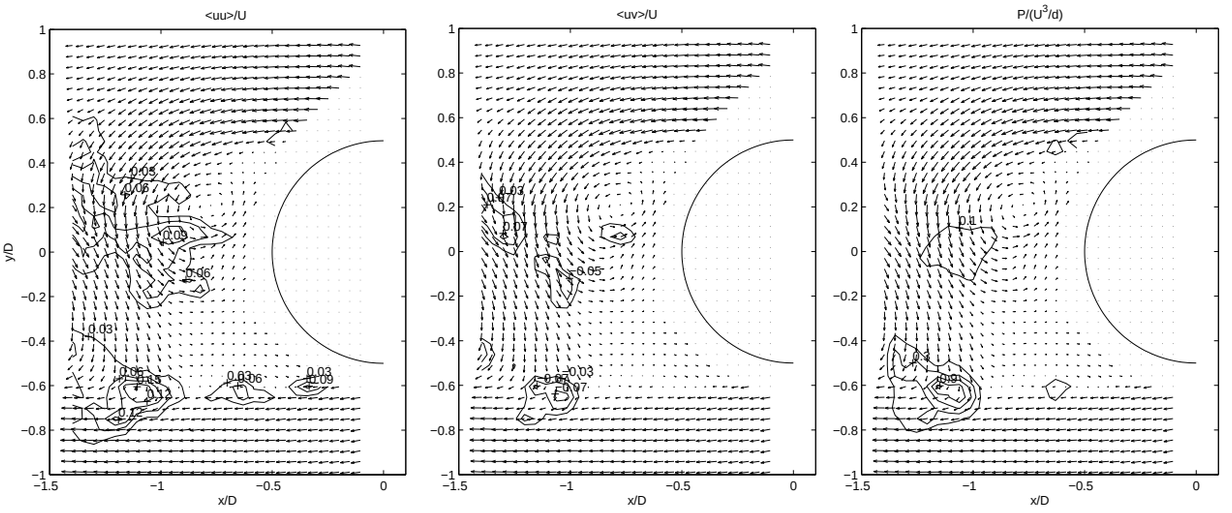


Figure 1: Mean velocity fields at constant phase (75% of U subtracted). Superimposed are the $< u'u' >$ normal Re stress (left), the shearing Reynolds stress (center) and the turbulent production (right).

References

T. Sarpkaya. A critical review of the intrinsic nature of vortex induced vibrations. NPS-ME–03-002. Naval Postgraduate School, Monterey, California, 2003, 111 pp.

B. Cantwell & D. Coles. An experimental study of entrainment and transport in the turbulent near wake of a circular cylinder. J. Fluid Mech. 136, 1983.

C. Norberg. Fluctuating lift on a circular cylinder: review and new measurements. J. Fluid and Structures 17, 2003.

INFLUENCE OF THE CIRCULAR CYLINDER CROSS-SECTION VARIATION ON THE NEAR WAKE BEHAVIOUR

Oualli Hamid*, Hanchi Samir**, Bouabdallah Ahcene*, Askovic Radomir***
** LTSE,Physics Institute,University of Sciences & Technology (USTHB), 16111 Algiers, Algeria*
***MDF,Department of Mechanics EMP, Bordj El Bahri, 16111 Algiers, Algeria*
**** LME, UVHC, 59313 Valenciennes Cedex 9, France*

Summary The present study is both numerical and experimental. Numerically, Navier-Stocks equations in vorticity formulation are solved using finite differences method and taking into account the superimposed vibrating motion. Experimentally, a setup is conceived and realised. Investigations are carried out around a deformable cylinder using flow visualisations, PIV and anemometry techniques. Important results on the drag coefficient Cd, primary and secondary vortices interplay, heat transfer around the cylinder and the shedding mechanism are obtained and discussed.

This study is concerned with the understanding of the flow phenomena which occur in the wake of a circular cylinder superimposed to radial oscillation. The Reynolds numbers investigated herein extend along the range of the onset of the transition in the shear layers. The work is both experimental and numerical. Experiments are carried out in an aerodynamic subsonic wind tunnel which led to interesting conclusions completed with some numerical results. The influence of a radial pulsative motion of a circular cylinder, fig1 and 2, on the primary and secondary vortices of the wake is investigated by means of smoke visualisations, PIV and hot wire techniques. Important results on the bluff body drag coefficient Cd are obtained. In fact, the Cd rate of fluctuation increases considerably while the corresponding mean value $C\bar{d}$ decreases correspondingly, to reach negative values making the cylinder to be propelled in the streamwise direction, fig3. A spectral analysis showed that the flow tends to reorganisation in response to the applied actuation. The fundamental harmonic of the spectrum for the actuated cylinder case reduces to half of the value of the non controlled configuration, fig4 and 5. A calculation code using finite differences method for the viscous vortex street behind a circular cylinder is developed and has applications for the simulation of the vorticity field in the near wake, the shedding mechanism and drag coefficient. The near wake response to the imposed perturbation and an understanding of the various induced modifications is subsequently achieved.

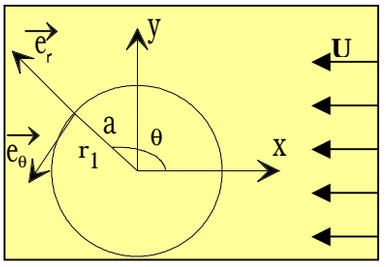


Fig1. System of coordinates

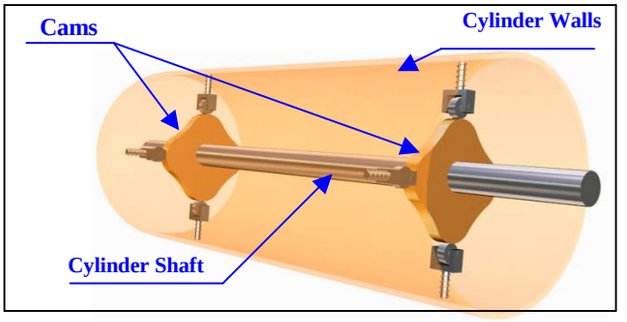


Fig2. Deforming cylinder

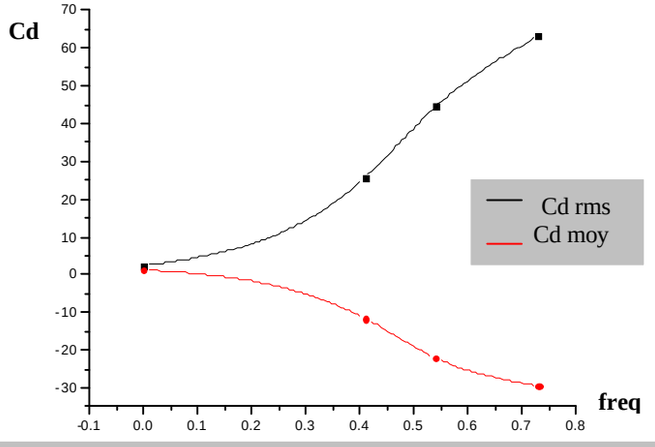


Fig3. Drag coefficient variation for an actuated circular cylinder for Re = 9500

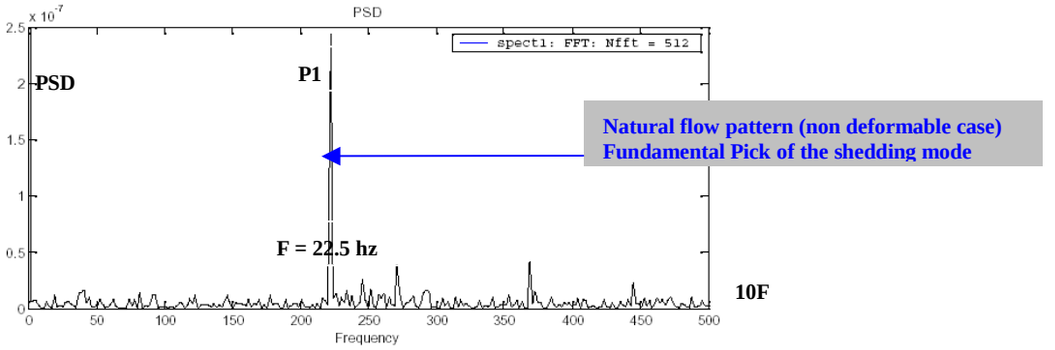


Fig4. Power Spectral Density for a flow around a cylinder at rest, f = 0hz et St = 0.176

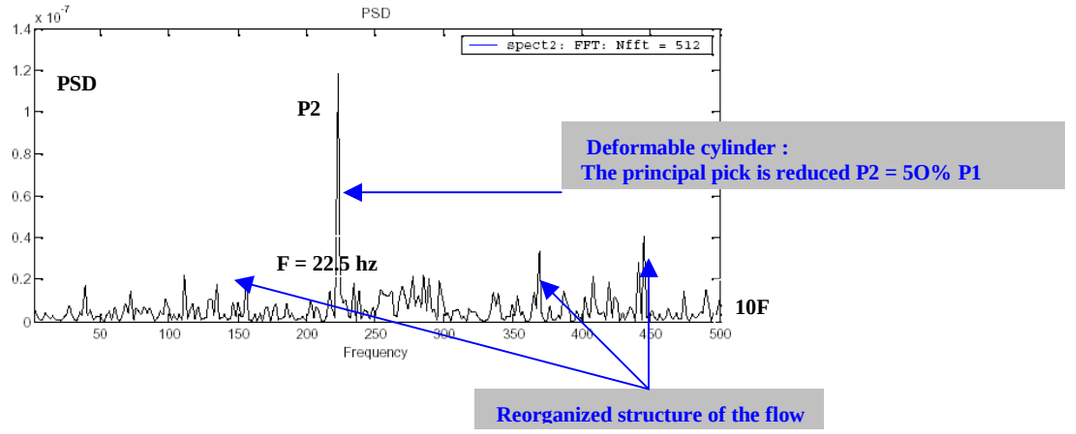


Fig5. Power Spectral Density for a flow around a deformable cylinder, f = 0.66hz et St = 0.176

CONCLUSION

The proposed actuating method allows to enhance or retard turbulence according to superimposed conditions by means of frequency and amplitude of deformation. Convection is considerably increased with the continuously renewed fluid in the cylinder vicinity. Moreover, alteration of the shedding mechanism makes the lock-in phenomenon, for instance, around bridges and thick electrical wires can be avoid as well as cavitation effects in hydrodynamic fluids. When the superimposed frequency is increased the mean value of the drag coefficient decreases drastically and becomes even negative propelling thus the cylinder.

References

[1] Frequency of a Radially Deforming Circular Cylinder impulsively Started on Cylinder Wake, Int. J. Num. Meth. Fluids. 41 (2003) 905-930.

[2] Shiels D., Leonard.A: Investigation of a drag reduction on a circular cylinder in rotary oscillation, J. Fluid Mech 100 (2001) 431, 297-322.

[3] Zdravkovich M.M.: Flow Around Circular Cylinders, Oxford Sc. Publications, Vol 1, (1997).

[4] Koumotsakos P., Leonard A.: High-Resolution Simulations of the Flow Around an Impulsively Started Cylinder Using Vortex Method, J. Fluid Mech. 196 (1995) 1-38.

[5] Coutanceau M., Defay, J. R.: Circular Cylinder Wake Configuration, App. Mech. Rev., Vol. 44, No.6, pp 255-305, (1991).

[6] Ta Phuoc Loc, Bouard R.: Numerical solution of the early stage of the unsteady viscous flow around a circular cylinder: A comparison with experimental visualisation and measurements, J. Fluid Mech 160(1985) 93-117.

Bubble shapes in foams: The importance of being isotropic

Sascha Hilgenfeldt[1], Andrew M. Kraynik[2], Douglas A. Reinelt[3], John M. Sullivan[4]

[1]*Department of Applied Physics, University of Twente, The Netherlands;*

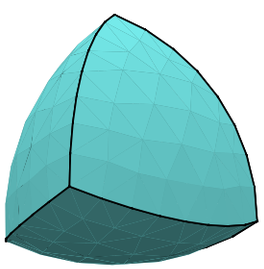
[2]*Department 9144 MS0834, Sandia Natinal Laboratories, Albuquerque, NM;*

[3]*Department of Mathematics, Southern Methodist University, Dallas, TX;*

[4]*Department of Mathematics, TU Berlin, Germany*

A three-dimensional random foam exemplifies a large class of cellular materials undergoing processes known as coarsening or aging. This evolution proves intimately connected with the geometry of the cells (bubbles), particularly in generic cases where the cells are space-filling polyhedra. In a mean field-like approach, we define classes of isotropic bubbles (called *Isotropic Plateau Polyhedra*) [1], whose geometrical properties such as specific surface area or edge length are (i) close to the average found in random foam, and (ii) can be analyzed without resorting to approximations. These bubbles serve as "yardsticks" for cell geometry as well as "pacemakers" for foam coarsening.

Individual isotropic bubbles can also be found in experiment, and put to good use: While thin films can be measured interferometrically when they are prepared in isolation, such a measurement becomes very difficult for films on foam bubbles in their "natural environment". We measure the shape and degree of isotropy of tetrahedral bubbles using a stereoscopic setup, and observe their rate of diffusive coarsening. With this information, the thickness of the films is determined with a few nm accuracy. Black film thicknesses of several 10 nm are measured, demonstrating a slow rate of film drainage [3].



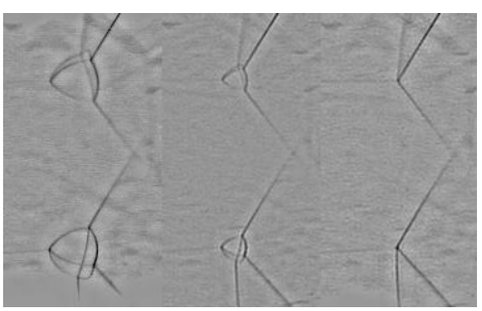


FIG. 1. Left: Theoretical shape of an isotropic tetrahedral foam bubble (Reuleaux tetrahedron). Right: Time series of a shrinking tetrahedral bubble in a foam in stereoscopic view.

[1] S. Hilgenfeldt, A. M. Kraynik, D. A. Reinelt, and J. M. Sullivan, *The structure and properties of random foam: Isotropic Plateau polyhedra*, submitted to Europhys. Lett. (2003).

[2] S. Hilgenfeldt, A. M. Kraynik, S. A. Koehler, and H. A. Stone, Phys. Rev. Lett. **86**, 2685 (2001).

[3] A. van Doornum and S. Hilgenfeldt, *Foam tetrahedra: Isotropic bubbles as a tool for* in situ *film thickness measurements*, submitted to Phys. Rev. Lett.

XXI ICTAM, 15–21 August 2004, Warsaw, Poland

MECHANICS OF BIDIMENSIONAL LIQUID FOAMS

Benjamin Dollet*, François Graner*, Catherine Quilliet*, Miguel Aubouy**, Florence Elias***
*Laboratoire de Spectrométrie Physique, UMR 5588 CNRS, Université Joseph Fourier, BP 87, 38402 Saint-Martin-d'Hères Cedex, France
**SI3M, DRFMC, CEA, 38054 Grenoble Cedex 9, France
***Laboratoire des Milieux Désordonnés et Hétérogènes, Université Paris 6, Tour 13, Case 78, 4 place Jussieu, 75251 Paris Cedex 05, France

Summary An experimental study of foam flow is presented. A 2D foam is confined between a soap solution and a glass plate. It flows through a channel around an obstacle. This device enables to perform simultaneously external sollicitation, measurement of the response force and image analysis. We perform a systematic study of the drag exerted by the foam on the obstacle, *versus* the experimental control parameters: flow rate, bubble size and fluid fraction. Simultaneously, local velocity and stress fields are measured; we also measure a statistical strain field. The comparison of both types of measurements enables to study the link between local events and the global mechanical behaviour of the foam.

MOTIVATIONS

Liquid foams, made of two fluids, sometimes behave as solids. Actually, they can exhibit elastic, plastic or fluid response depending on external sollicitations. In bidimensional foams, one can easily obtain from images of the deformed structure the pressure, capillary stress and velocity fields. Liquid foams are thus complex fluids which are convenient to study.

EXPERIMENTAL GOALS AND DEVICES

When shearing a foam, one does not know *a priori* how stress and strain vary within it. Hence, a local analysis is needed to find an accurate description of the local mechanical behaviour of the foam. This description can then be used to predict the global behaviour of the foam, and must be validated by a global measurement. The local analysis is provided by acquisition and processing of the images of the deformed foam, and the global measurement is either a force or a torque exerted between the foam and an external sensor. We present different experimental set up (2D Stokes experiments) built in order to do both image analysis and mechanical measurement simultaneously: a Langmuir foam sheared by an optical fiber [1], a soap foam in a Hele-Shaw cell [2], and a current experiment combining the advantages of both [4].

BUBBLE DEFORMATION – LOCAL DESCRIPTION

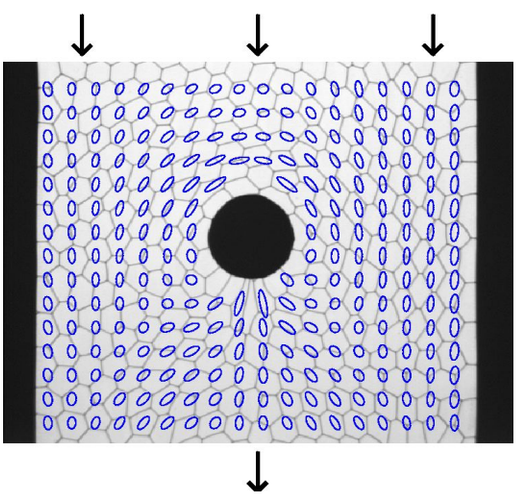


Figure 1. Analysed image from the experiment. The foam flows from top to bottom at a velocity of order 1 cm/s. The width of the channel if 10 cm and the typical size of bubbles is 5 mm. The ellipses represent bubble deformation, averaged over time at each point. With this representation one can visualise the deformation experienced by bubbles at the vicinity of the obstacle, compression uphill and stretching downhill [2] (picture M. Asipauskas).

In 2D foams, one has a geometrical intuition of the bubble deformation from an image (fig. 1). We quantify this intuition by the texture tensor $\bar{\bar{M}} = \langle \vec{\ell} \otimes \vec{\ell} \rangle$, where $\vec{\ell}$ represents a bubble edge and the spatial and/or tempoal average is taken at a mesoscopic scale to have sufficient statistics. We define a statistical strain as $\bar{\bar{U}} = (\log \bar{\bar{M}} - \log \overline{\overline{M_0}})/2$, where $\overline{\overline{M_0}}$

corresponds to a reference state [3]. This tensor coincides with the classical strain $\bar{\bar{u}}$ as long as no bubble rearrangement (neighbour swapping) occurs, and is always defined. The comparison between measured stress and statistical strain yields a linear relation, hence enables to measure the shear modulus of the foam, which agrees with an independent mechanical measurement [1].

FORCE MEASUREMENTS AND RESULTS

By blowing nitrogen in a soap solution, we prepare one layer of bubbles confined between the top glass plate of the channel and the soap solution. An obstacle stands in the channel and modifies the foam flow. Depending on the flow rate, this flow is quasistatic or not. We measure the drag exerted by the foam on this obstacle, as well as the stress, statistical strain and velocity fields induced within the foam by the presence of the obstacle. The control parameters of this experiment are numerous and easily tunable: flow rate, bubble size, fluid fraction, obstacle size and shape, viscosity and surface tension. We present a systematic study of the variation of the drag determining the elastic and viscous contributions. Furthermore, we emphasize the main features of the stress, strain and velocity fields. The effect of bubble rearrangements is studied to take into account the specific mechanical behaviour of the foam. We also compare these two kinds of measurements, drag versus local data, to study the effect of local events at the global foam scale.

References

[1] Courty S., Dollet B., Elias F., Heinig P., Graner F., *Europhys. Lett.* **64** (5): 709–715, 2003.
[2] Asipauskas M., Aubouy M., Glazier J. A., Graner F., Jiang Y., *Granular Matter* **5**: 71–74, 2003.
[3] Aubouy M., Jiang Y., Glazier J. A., Graner F., *Granular Matter* **5**: 67–70, 2003.
[4] Dollet B., Graner F., Quilliet C., Aubouy M., Elias F., work in progress.

XXI ICTAM, 15–21 August 2004, Warsaw, Poland

AVERAGE $\mathcal{N}$-HEDRA AS DESCRIPTORS OF 3-D NETWORK CELLS

Martin E. Glicksman,
Materials Science & Engineering Dept., Rensselaer Polytechnic Institute, Troy, NY, USA 12180-3590

Summary Network cells represent physical entities, such as grains in polycrystals, bubbles in foam, or cells in biological tissues. We represent network cells with $\mathcal{N}$ neighbors by "proxies" called average $\mathcal{N}$-hedra, satisfying space filling and network topological averages. Analysis of the set of $\mathcal{N}$-hedra yields estimates of the metric and energetic properties of irregular cells in isotropic foams and polycrystals as functions of the number of neighbors, $\mathcal{N}$.

INTRODUCTION

The energetics and growth kinetics of space-filling networks, such as polycrystals and foams, remain important topics within the general subject of microstructure evolution. The foundation for grain and bubble growth in two dimensions was established a half-century ago by C.S. Smith [1] and J. von Neumann [2], and by W.W. Mullins [3]. This paper reports on an analysis of idealized "average $\mathcal{N}$-hedra" (ANH's) that may be used as "proxies" to determine the excess free energy and growth kinetics of an isotropic network structure in $\mathbb{R}^3$. ANH's have $\mathcal{N}$ identical curved faces, each enclosed by $p = 6 - \frac{12}{\mathcal{N}}$ edges; $2(\mathcal{N}-2)$ identical vertices equidistant from its centroid; and $3(\mathcal{N}-2)$ identical curved edges. ANH's form a complete set for $3 \leq \mathcal{N} \leq \infty$, although only four members ($\mathcal{N} = 3, 4, 6,$ and 12) are actually constructible, i.e., where p is an integer. All other ANH's are abstract geometric forms. Nonetheless, each ANH provides a descriptor of the average geometric, energetic, and kinetic properties of all irregular network cells within the same class, $\mathcal{N}$. Figure 1 compares an ANH with an irregular member of its class, $\mathcal{N} = 12$. Note that the ANH shown on the left has 12, identical, slightly bulging, pentagonal faces, whereas the irregular 12-hedron on the right contains a mixture of quadrilateral, pentagonal, and hexagonal faces. The p-value, vertex count, etc., according to Euler's theorem, are nonetheless identical.

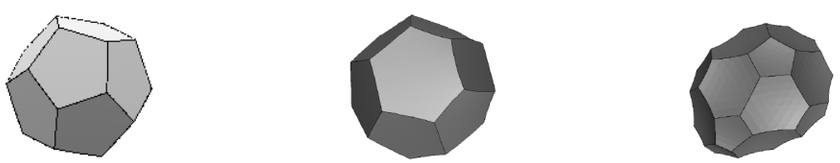


Figure 1. ***Left****: Average 12-hedron, consisting of identical pentagonal faces. Its 20 identical vertices are positioned equidistant from the volume centroid.* ***Middle****: Irregular 12-hedron exhibiting of a mixture of quadrilateral, pentagonal, and hexagonal faces. The average properties of any 12-hedron in an isotropic network (number of edges, vertices, p-value, vertex image, average dihedral angle, etc.) are identical to those of its ANH proxy.* ***Right****: Irregular 24-hedron, for which a constructible ANH does not exist. Note its concave faces. Renderings provided through the courtesy of Dr. S.J. Cox, Trinity College, Dublin, Ireland [4].*

NETWORKS IN 3-D

Geometry of ANH's

The area, $\mathbb{A}(\mathcal{N})$, and volume, $\mathbb{V}(\mathcal{N})$ of any ANH, are expressible as fractions of the corresponding areas and volumes of a sphere with the same radius of curvature as that of the faces of the ANH. These are, respectively,

$$\mathbb{A}(\mathcal{N}) = \mathcal{G} \cdot A_{sph}, \quad \text{and} \quad \mathbb{V}(\mathcal{N}) = \mathcal{F} \cdot V_{sph}, \tag{1}$$

where the fractions $\mathcal{G} = \frac{1}{4\pi} \iint_{faces} K dA$ is the ratio of the total spherical image of the ANH to that of a sphere (4π), and $\mathcal{F} = \frac{\mathcal{N}}{2} + \frac{\mathcal{N}-2}{16\pi}\left[2^{\frac{3}{2}} - 57 \arccos\frac{1}{3} + 33 \arcsin\left(\frac{2}{\sqrt{3}}\cos\frac{\pi}{p}\right) - \tan\arcsin\left(\frac{2}{\sqrt{3}}\cos\frac{\pi}{p}\right)\right]$. The integral of the Gaussian curvature, K, appearing in the area fraction, $\mathcal{G}$, can also be found exactly for any ANH using the Gauss-Bonnet theorem,

$$\iint_{faces} K dA = 4\pi - 3(\mathcal{N}-2)\Omega^{edge} - 2(\mathcal{N}-2)\bar{\Omega}, \tag{2}$$

where the constant $\bar{\Omega} = 0.551287\ldots$ is the spherical image of each trihedral vertex as demanded by topology. The function Ω^{edge} is the spherical image contributed by each curved edge and varies with $\mathcal{N}$ according to the formula

$$\Omega^{edge} = \pi + 2\arctan\left(\sin\frac{\alpha(\mathcal{N})}{2}\tan\frac{\pi}{p}\right) - 2\arccos\left(-\frac{1}{3}\right), \tag{3}$$

where $\alpha(\mathcal{N})$ is the angle between poles located on an ANH at the geometric centers of adjacent faces, namely

$$\alpha(\mathcal{N}) = 4\arctan\sqrt{1 - 2\sec\left(\frac{\pi}{2\,(\mathcal{N}-2)}\right)\cos\left(\frac{\pi\,(2\mathcal{N}-3)}{6\,(\mathcal{N}-2)}\right)}. \tag{4}$$

Network energetics

The excess free energy of a 3-d network, ΔF, such as a foam or polycrystal, is given by its interfacial area sum

$$\Delta F = \frac{\gamma}{2} \sum_i A_i = \frac{\gamma}{2} \sum_i e(\mathcal{N}_i) \left[V(\mathcal{N}_i)\right]^{\frac{2}{3}}, \tag{5}$$

where γ is the specific interfacial free energy of the faces of the polyhedra. Cox and Fortes [5] showed that the free energy, may be expressed as a sum over the volumes of polyhedral network cells as shown in the second equality displayed in Eq.(5), where the dimensionless ratio, $e(\mathcal{N})$, is defined as

$$e(\mathcal{N}) \equiv \frac{\mathbb{A}(\mathcal{N})}{\left[\mathbb{V}(\mathcal{N})\right]^{\frac{2}{3}}}. \tag{6}$$

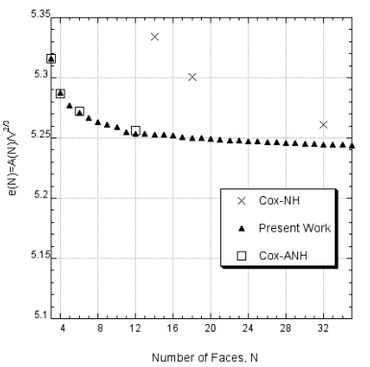


Figure 2. *Plot of $e(\mathcal{N})$ versus $\mathcal{N}$. Shown are the analytical values derived here for ANH's (solid symbols), and recent simulation data reported by Cox and Fortes for constructible ANH's (open squares) and irregular network $\mathcal{N}$-hedra (crosses) [5].*

Equation (6), which is scale independent, is easily evaluated with the analytical expressions for the areas, $\mathbb{A}(\mathcal{N})$, and the volumes, $\mathbb{V}(\mathcal{N})$, shown in Eqs.(1). Cox and Fortes [5] extended results derived originally by Vaz et al. for 2-d networks [6], and confirmed that in 3-d the ratio $e(\mathcal{N})$ also varies extremely weakly with $\mathcal{N}$. Figure 2 provides a comparison of the present analytic results, as expressed through Eq.(6), with the numerically computed values reported by Cox and Fortes for several $\mathcal{N}$-hedra using Brakke's surface evolver [7] to evaluate the areas and volume. The analytical values for $e(\mathcal{N})$ agree well with the values computed by Cox and Fortes, especially in the four cases where the simulated $\mathcal{N}$-hedra correspond to constructible ANH's ($\mathcal{N} = 3, 4, 6,$ and 12). For the three cases reported in [5] where the polyhedra are not ANH's, the simulations yield slightly higher values (0.5% to 2%).

Coxeter [8], and more recently, DeHoff [9] showed that the average number of faces per polyhedron in a large isotropic 3-d network is $\langle \mathcal{N} \rangle \approx 13.397$, corresponding to the "ideal" flat-faced cell that satisfies local equilibrium. The average value $\bar{e} \approx 5.254$, so after substitution into Eq.(5) the total excess free energy arising from its interfaces of an isotropic 3-d network consisting of i polyhedral cells is

$$\Delta F \approx 2.63\, \gamma \sum_i \left[\mathbb{V}(\mathcal{N}_i)\right]^{\frac{2}{3}}. \tag{7}$$

CONCLUSION

Highly symmetric average $\mathcal{N}$-hedra (ANH's) may be used as topological "proxies," or descriptors for polyhedral network cells. Although ANH's are constructible only in a few cases ($\mathcal{N} = 3, 4, 6, 12$), their general analysis yields important geometric and energetic properties of *all* irregular (constructible) network cells. The kinetic properties of ANH's and the evolution of 3-d network structures will be discussed elsewhere [10] due to space limitations.

References

[1] C.S. Smith, "Grain Shapes and other Metallurgical Applications of Topology," Chapter in *Metal Interfaces*, American Society for Metals, Cleveland, OH, 1952, p. 65.
[2] J. von Neumann, in *Metal Interfaces*, written discussion, American Society for Metals, Cleveland, OH, 1952, p. 108.
[3] W. W. Mullins, *J. Appl. Phys.* **27**, 1956, p. 900. *Phys. Rev. E.*, **63**, 2001, p. 402.
[4] S.J. Cox, *Private Communication*, Trinity College, Dublin, Ireland, 2003.
[5] S.J. Cox and M.A. Fortes, *Phil. Mag. Lettr.*, **83**, 2003, p. 28.
[6] M.F. Vaz, M.A. Fortes, F. Graner, *Phil. Mag. Lett.*, **82**, 2002, p. 575.
[7] K. Brakke, 1992, *Exper. Math.*, 1, 141.
[8] H.S.M. Coxeter, M.S. Longuet-Higgins, and J.C.P. Miller, *Phil. Trans. Roy. Soc. London, Series A*, **236**, 1954, p.401.
[9] R.T. DeHoff, *Acta Metall. Mater.*, **42**, no. 8, 1994, p. 2633.
[10] M.E. Glicksman, "Analysis of 3-D Network Structures," *Phil. Mag.*, submitted, 2003.

Modelling the round-off and the tensile/compressive failure behaviour of plant and vegetable tissues

H. X. Zhu

School of Engineering, Cardiff University, Queen's Buildings, Cardiff, UK

Generally, the constitutive relations of cell walls, the cell turgor pressure, cell geometry, and the cell-to-cell mechanical interactions all have a bearing on the macroscopic stress strain properties of the whole tissue [1-3]. The challenge is, therefore, to develop rheological theories specially for the cellular structure, so that the applied external stress or strain can be related to the internal stress or strain that arise in the cell walls of the individual cells. Experimental results show that the stiffness of plant and vegetable tissues increases strongly with the cell turgor pressure [1, 3]. Assuming that the cell wall material is homogeneous, isotropic and linear elastic, Nilson et al [1] analysed the small deformations of a lattice of identical sphere cells; Pitt [4] and McLaughlin and Pitt [5] qualitatively modelled the cellular structure as a two-dimensional array of hexagons or cylinders; Pitt and Davis [6] modelled the cell wall as a spherical shell by finite element analysis. Using idealised cell structures and experimentally measured cell wall constitutive laws [3, 7,8,9], Pitt et al modelled the compression of plant and vegetable tissues. In reality, the cell walls of plant and vegetable tissues are polymeric composite materials [10], consisting of relative amorphous matrix and a highly structured network of microfibrils embedded in the cell wall matrix [11, 12]. Consequently, the cell wall properties are different in different directions [11, 13]. Taking a lattice of identical and fluid-filled three-dimensional hexagonal cells as the structural model, and using large elasticity theory, Zhu and Melrose [14, 15] introduced three microfibrils stiffening factors in the three principle directions of the cell walls and derived the effective compressive stress-strain relations for the tissue. However, according to our knowledge, all the existing models are mainly focused on modelling the effective properties of the tissues, and none of them can well demonstrate all the main failure mechanisms for a plant or vegetable tissue when it is under an increasing turgor pressure, or under an external compressive/tensile stress.

In this work, plant and vegetable tissues are treated as a lattice of identical 3D hexagonal cells, which are turgored and glued by a layer of the middle lamella pectin, as shown in Fig. 1a. The primary cell walls are treated as an anisotropic rubber-like material and the layer of the middle lamella pectin is treated as a set of one-dimensional springs made of a rubber-like material, as shown in Fig. 1b. Based upon the above mechanical model (Fig. 1b), the following works have been done: a) The cell round-off behaviour is modelled by looking at the deformed cell structure upon the continuously increasing turgor pressure (Fig. 2a), the possible resulting consequence of the cell round-off is cell separation (debonding) or cell wall fracture; b) For a given initial turgor pressure p_{ci}, the mechanical response of the cells to the applied tensile/compressive stress has been simulated (as shown in Fig. 2b). During the tensile/compressive deformation process of the tissue, the turgor pressure in the cells increases while the cell volume remains the same (we assume that the time scale is small and no fluid diffusion takes place during the deformation); c) All the possible failure mechanisms have been analysed, and the effects of the initial turgor pressure on the results a) and b) are discussed.

References

[1] Nilsson, S B, Hertz, C H and Falk, S: **Physiol. Plant. 11**: 818-837, 1958.

[2] Murase, H, Merva, G E and Segerlind, L J: **Trans. ASAE, 23**: 794-796, 1980.

[3] Lin, T T and Pitt, R E : **J. Texture Study. 17**: 291-313, 1986.

[4] Pitt, R E : **Trans. ASAE 25**: 1776-1784, 1982.

[5] McLaughlin, N and Pitt, R E: **Trans. ASAE 27**: 311-320, 1984.

[6] Pitt, R E and Davis, D C: **Trans. ASAE 27**: 1976-1983, 1984.

[7] Gates, R S, Pitt, R E, Ruina, A and Cooke, J R: **Biorheology 23**: 453-466, 1986.

[8] Gao, Q, Pitt, R E and Bartsch, J A: **J. Rheol. 33**: 233-256, 1989.

[9] Gao, Q and Pitt R E: **Trans. ASAE 34**: 232-238, 1991.

[10] Cleland, R: **Ann. Rev. Plant Phys., 22**: 197-222, 1971.

[11] Hettiaratchi, D R P and O'Callaghan, J R: **J. Theor. Biol. 74**: 235-257, 1978.

[12] Wu, H, Spence, R D, Sharpe, J H and Goeschl, J D: **Plant Cell Environ. 8**: 563-570, 1985.

[13] Khan, A A and Vincent, J F V: **J. Texture Stud. 24**: 423-435, 1993.

[14] Zhu, H X and Melrose, J R: **J. Theor. Biol. 221**: 89-101, 2003.

[15] Zhu, H X and Melrose, J R: ***J. Mater. Sci.***, **38**: 2489-2498, 2003.

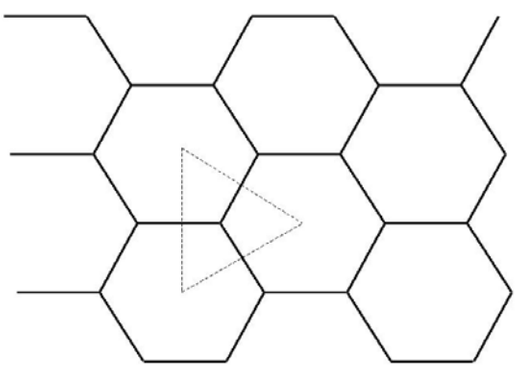


Fig. 1a Plant and vegetable tissue consists of a lattice of identical 3D hexagonal cells.

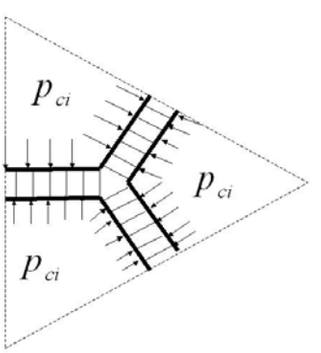


Fig. 1b The lattice of the initially turgored cells are glued by a layer of middle lamella pectin which are treated as a set of one-dimensional springs.

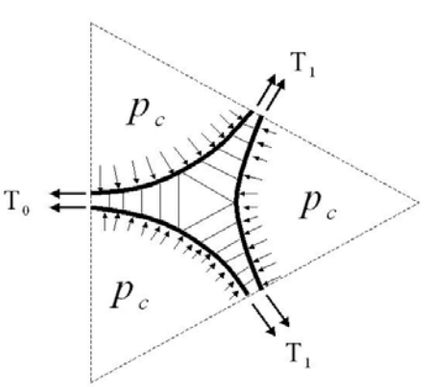


Fig. 2a The cells become round-off under an increasing turgor pressure, with possible resulting consequences: cell separation and cell wall fracture [14, 15].

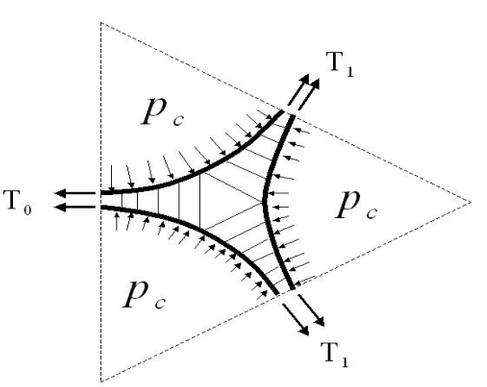


Fig. 2b For a given initial turgor pressure p_{ci}, the cells are deformed under an external tensile/compressive stress, with possible resulting consequences: 1) cell wall fracture and 2) cell deconding initially by separation then by shear [14, 15].

ON THE CRUSHING RESPONSE OF OPEN CELL FOAMS

Lixin Gong and Stelios Kyriakides
Center for Mechanics of Solids, Structures & Materials, The University of Texas at Austin, WRW
Austin, TX 78712, USA

Summary The paper deals with the compressive response of polymeric, open cell solid foams which exhibit excellent energy absorption. Through a combination of experiment and analysis it has been confirmed that elastic buckling involving interaction of global modes and modes at the cell level are responsible for the stress plateau governing the foam's energy absorption capacity.

Solid foams is a class of light-weight cellular materials with exceptional energy absorption characteristics. They are widely used in shock mitigation, in packaging and in cushioning but also as cores in sandwich structures. Common to most foams is a compressive stress-displacement response with the characteristic three regime shape shown in Fig. 1. Initially the response is stiff and essentially linearly elastic (E). This terminates into a limit load (σ_I) followed by an extensive load plateau (mean stress level $\bar{\sigma}_P$ and extent $\Delta\bar{\varepsilon}_P$) responsible for their excellent energy absorption characteristics. The plateau usually ends into a second branch of stiff response. Design of foams requires that the deformation history of the microstructure be related to the main variables of this response $\{E,\ \sigma_I, \bar{\sigma}_P,\ \Delta\bar{\varepsilon}_P\}$.

Experiments on polyester urethane open cell foams have confirmed that the limit load corresponds to the onset of unstable behavior. During the stress plateau, localized deformation bands involving buckled cells initiate and spread throughout the material. The stress plateau terminates when most of the microstructure has collapsed. This paper will present the results of a study combining experiments coupled with several levels of modeling aimed to understand and model the underlying mechanisms of this type of response. The experiments involved characterization of the cell and ligament morphology; measurement of the mechanical properties of the polymer using ligaments extracted from the foam; and crushing of blocks of foams between rigid parallel plates at various constant displacement rates. The major findings are summarized below.

The microstructure consists of interconnected polyhedra each with an average of 13.7 faces, each face having an average of nearly 5 sides. To first order, the microstructure scales with the cell size. In these foams the size of the cells does not vary significantly but the cells are elongated in the rise direction ($\lambda \equiv$ ratio of diameters in rise-to-lateral directions). The ligaments have a three-cusp *Plateau borders* cross section and the cross sectional area varies along their length. The base material is an elastomer and, as a result, it is viscoelastic. In a first modeling attempt the material is assumed to be rate independent and linearly elastic.

Because of the anisotropy of the microstructure, the compressive responses in the rise and transverse directions of the foams are different (see Fig. 1). The rise direction response exhibits the characteristic three regime behavior described above. It was observed that the blocks tested buckled in an overall manner irrespective of the specimen size. As the stress plateau was traversed, localized bands of deformation developed. Their numbers gradually multiplied, while others broadened and coalesced. The response in the transverse direction has a smaller elastic modulus and is essentially a monotone. Overall buckling of the test specimen was not observed in this direction.

A sequence of models for predicting all mechanical foam properties of interest has been developed. The foam is idealized to be periodic using the space filling Kelvin cell assigned several of the geometric characteristics of the actual foams. The cells are elongated in the rise direction (Fig. 2); the ligaments are assumed to be straight, to have Plateau border cross sections and nonuniform cross sectional area distribution. Using this microstructure, closed form expressions have been developed for the elastic constants of the anisotropic foam. The initial response, the onset of instability and the initial post buckling response have been established through characteristic cell type-models discretized with FEs. Figure 3 shows that in the rise direction the prevalent instability exhibits a long wavelength mode while in the transverse direction involves buckling at the cell level. In the rise direction the long wavelength mode leads to a limit load indicating a tendency of localization. By contrast, in the transverse direction, the response of the local cell buckling is monotonic (Fig. 4). The localization of deformation, its spreading and the associated stress plateau are reproduced using large scale finite size type models involving a large number of cells.

References

[1] Gong, L., Kyriakides, S., Jang, W.-Y.: Compressive response of open-cell foams. Part I: Morphology and elastic properties. *J. Mech. Phys. Solids* (submitted) 2003
[2] Gong, L. and Kyriakides, S. (2003). Compressive response of open-cell foams. Part II: Initiation and spreading of crushing. *J. Mech. Phys. Solids* (submitted) 2003

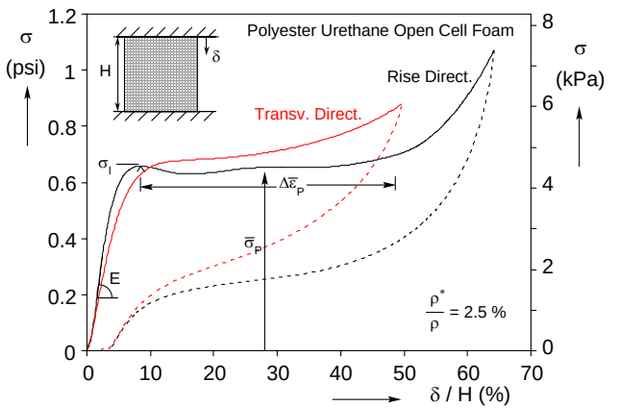


Fig. 1 Compressive stress-displacement responses in rise and transverse directions of polymeric open cell foam.

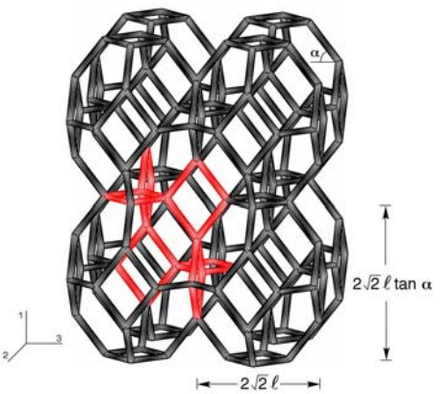
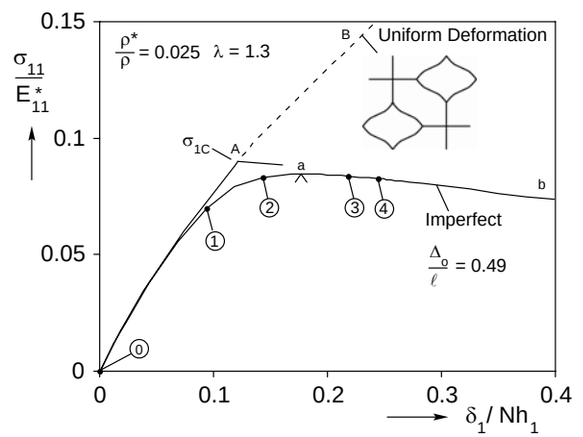
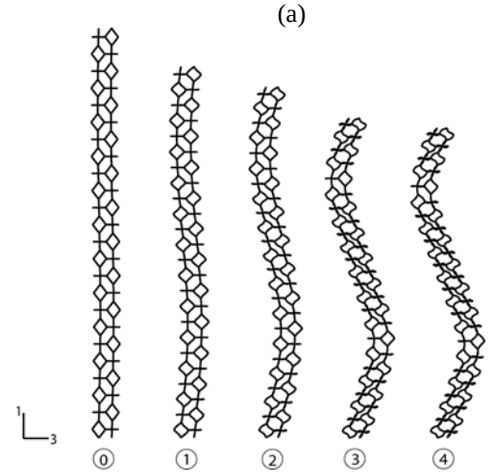


Fig. 2 Anisotropic Kelvin cell. Characteristic cell drawn in red.

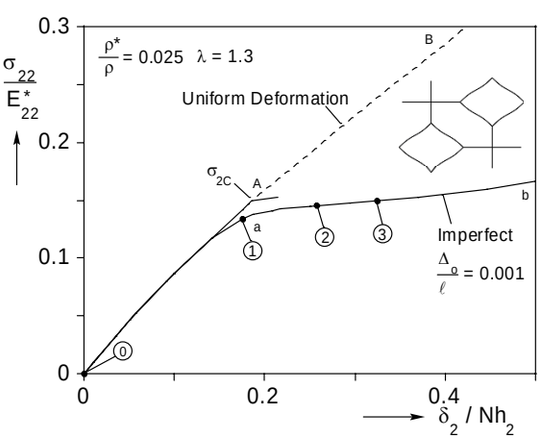


(a)

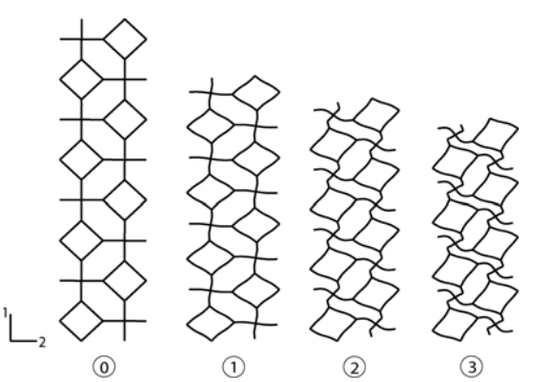


(b)

Fig. 3 (a) Calculated prebuckling and postbuckling responses corresponding to long wavelength mode of rise direction. (b) Deformed configurations of a characteristic column of cells



(a)



(b)

Fig. 4 (a) Calculated prebuckling and postbuckling responses corresponding to local mode of transverse direction shown in (b).

A STATISTICAL MECHANICS THEORY OF RANDOM HONEYCOMB AND OPEN-CELL FOAM STRUCTURES

Alfonso H.W. Ngan
Department of Mechanical Engineering, The University of Hong Kong, Pokfulam Road, Hong Kong, P.R. China

Either by design or otherwise, many engineering materials are randomly structured. Examples include atomistically disordered or partially disordered materials such as bulk metallic glasses or polymers, and macroscopically disordered materials such as foam materials or random grain piles. Because of structural randomness, the internal force distribution in these materials due to external loadings would not be uniform, yet a thorough understanding of the force distribution is of paramount importance in the development of, for example, yield criteria for these materials. In this work, finite element simulations are used to investigate the force distribution in stressed random honeycomb and open-cell foam structures. A statistical-mechanics-based theory is also presented to describe the force distribution.

FINITE ELEMENT SIMULATIONS

2-D honeycombs and 3-D open-cell foam structures were simulated in this work using the FEAP finite element package developed by R.L. Taylor. Fig. 1(a,b) shows a simulated perturbed square grid (2-D) and a cubic grid (3-D). A series of increasingly irregular structures were built from a regular square or cubic grid by randomly displacing each node in the grid within a range which is a certain fraction r_d (< 0.5) of the mean grid spacing. The fraction r_d then becomes a parameter characterising the randomness of the structure. The linear elastic behaviour of the structures under different load states was calculated using the Euler-Beam Element in the FEAP package.

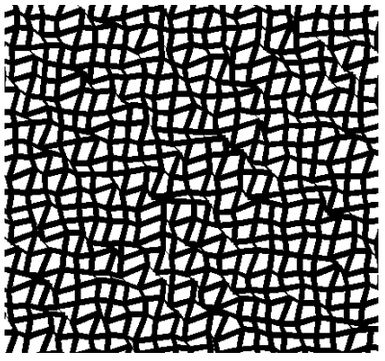


Fig. 1(a) 2-D perturbed square grid (r_d = 0.4).

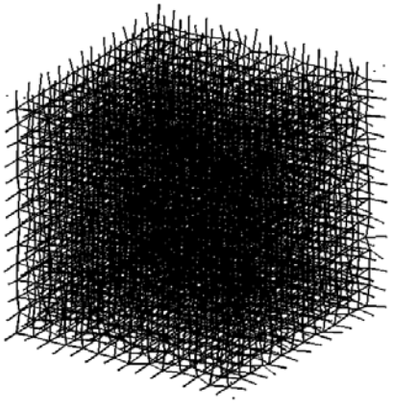


Fig. 1(b) 3-D perturbed cubic grid (r_d = 0.4).

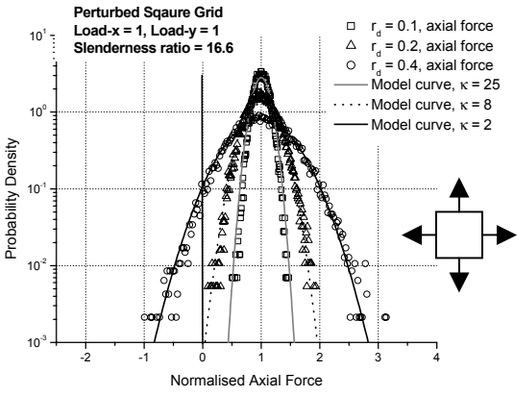


Fig. 2(a) Axial force distributions of 2-D perturbed square grid under hydrostatic loading.

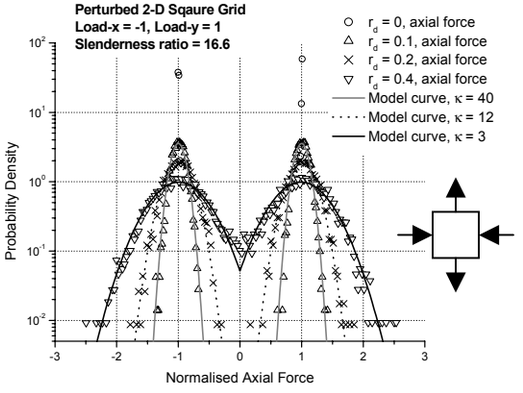


Fig. 2(b) Axial force distributions of 2-D perturbed square grid under biaxial pure shear loading.

Fig. 2(a) shows the simulated axial force distribution in 2-D grids with different values of r_d under hydrostatic loading. It can be seen that the sharpness of the axial force distribution decreases as r_d, or the structural randomness, increases. Fig. 2(b) shows the axial force distributions under biaxial pure shear. At $r_d = 0$, the distribution comprises two delta functions positioned at two (bifurcated) values of the mean force. This is to be expected because in the regular square grid configuration ($r_d = 0$), all struts which are aligned parallel to the tensile axis will be subject to the same tensile force, and all those parallel to the compression axis will be subject to the same compressive force. As r_d increases from zero, the structure becomes increasingly perturbed and the force distribution becomes more spread as shown in fig. 2(b). Results in 3-D show similar features.

THEORY

A theory based on statistical mechanics concepts will be presented to predict the general form of the force distributions shown typically in fig. 2. The key concept in this theory is the introduction of an entropy constraint in the search for the ground state configuration of the structure. Thus, instead of minimising the strain energy U alone as the condition for static equilibrium, we minimise a free energy functional defined as

$$F = U - \theta S \tag{1}$$

where S is an entropy functional and θ is an analog of temperature, but it is not the real temperature since the problem is athermal. θ also has the meaning of a Lagrange multiplier for the constraint imposed on S during minimization of U.

If the problem is single-component, as would be the case if the struts in the foam structure are all hinged together so that there is only axial force f but no bending moment or shear force in each strut, then the functional U and S can be expressed in terms of the axial force f and the probability density function $P(f)$ of f. If shear forces (s) and bending moments (m) are present, an elementary analysis shows that U and S can still be expressed as functionals of f, s and m, and their corresponding probability density functions. The variational problem in (1) can therefore be solved analytically to obtain the probability density functions of f, s and m. It can be shown that for the simple hydrostatic and pure shear stress states, these probability density functions are Gaussian if the struts are linear elastic. The model curves in fig. 2(a,b) are such Gaussian curves and the parameter κ shown there is an inverse measure of the temperature analog θ.

For load mixities other than the hydrostatic or pure shear states, the force distributions can be obtained by superposition of the hydrostatic and pure shear states. The result is that the force distributions under general load mixities are given as convolution integrals of Gaussian functions. Fig. 3 shows the predicted axial force distribution (the solid curve) in a 2-D grid under uniaxial loading, which is the convolution of two Gaussian functions centred at 0.5 and 1.5 of the abscissa. There is no fitting parameter involved in the predicted force distribution here and the agreement with the finite element results (the discrete points), especially the capturing of the m-shaped bifurcation behaviour, is excellent. With the force distributions at different load mixities worked out this way, the failure criteria for the structure can be constructed using a survival probability concept. Fig. 4 shows the predicted first-yield and buckling loci (the triangles and squares respectively), in comparison with a plastic collapse mean-field theory[¶] available in the literature (the circles).

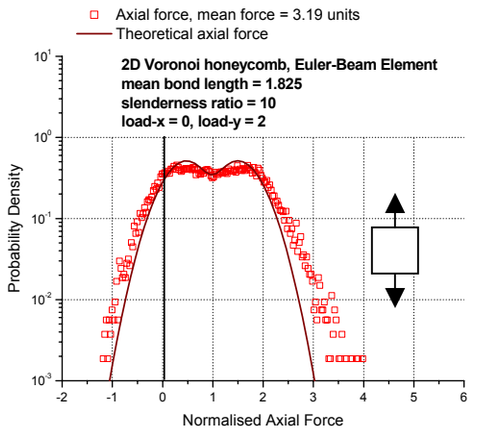


Fig. 3 Axial force distributions of 2-D perturbed square grid under unaxial loading.

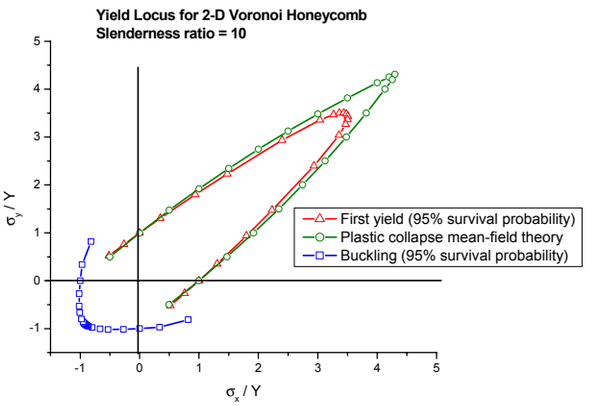


Fig. 4 Predicted yield locus of 2-D perturbed square grid. Y is material yield strength.

[¶] Gibson, L.J. and Ashby, M.F., 1988, *Cellular Solids – Structure and Properties*, Pergamon Press (Oxford, UK), p. 103.

XXI ICTAM, 15–21 August 2004, Warsaw, Poland

DISSIPATION IN 2D FOAM FLOW

Isabelle Cantat*, Renaud Delannay*
*GMCM, UMR 6626, Université Rennes 1, FRANCE

Summary We study the dynamical behavior of large bubbles embedded in the plug flow of a 2D foam made of smallest bubbles. At a critical velocity the foam structure becomes instable and the largest bubbles migrate through the foam faster than the mean flow. This size segregation is due to viscous effects and happens only for flow velocities larger than a given threshold. We compare our theoretical predictions (*Cantat, Delannay, Phys. Rev. E. 2003*) to experimental and numerical recent results and thus we give a extended description of this original instability involving the full visco-elastic properties of the foam. We show that the phenomenon can induce flow destabilization with dramatic effects on foam transport, like avalanches of film ruptures and flow intermittency.

INTRODUCTION

A monodisperse foam subject to a pressure gradient in a Hele Shaw cell with smooth lateral boundaries gives rise to a simple plug flow. In contrast, in case of a polydisperse foam, the plug flow undergoes a sharp dynamical transition at a critical velocity threshold v_t, depending on the aspect ratio. Larger bubbles insinuate themselves trough the foam faster than the mean flow. This phenomenon cannot be explained with a quasi-static point of view. In fact, unlike shear flows, no external constraint enforces bubble reorganization, and changes in the foam structure are intrinsically related to dissipative processes. A large bubble gives rise to a smaller local film density and, consequently, to a low effective viscosity averaged on a mesoscopic scale. Like for the Saffman Taylor instability, the large bubbles migration is driven by viscosity contrast. However, the coupling with the elasto-plastic response of the film network leads to subtle specific behaviors.

Viscous dissipation

A crucial parameter in this problem is the viscous force exerted by the wall. Even at relatively small velocity, this force is important in foam rheology in a quasi two-dimensional geometry (see e.g. [1]), or in a classical rheometer for which sliding effects on the plates may be crucial. In the "2D" experiments a foam is confined between two parallel glass plates, which are separated by a distance smaller than the bubble radius (typically by a few millimeters). When the whole foam is pushed ahead between the plates, complex flows take place in the network of the Plateau borders as they slide on the plates. Most of the injected energy is dissipated in this process, which involves nonlinearities arising from the deformability of the films delimiting the Plateau borders. A scaling relation for the pressure drop in relation to the flow velocity V of the bubbles $P \sim V^{2/3}$ has been found in the regime of small capillary numbers ($Ca = \eta V/\gamma \ll 1$, where η is the viscosity of the liquid phase and γ the surface tension at the interface) [2]. Our experimental results are in good agreement with the previous law. The dissipation seems to be dominated by the normal motion of the films leading thus to the following force expression [3]

$$F = \lambda\, L_{proj}\, \gamma\, Ca^{2/3}\ , \tag{1}$$

with L_{proj} the length of contact between foam and glass, projected in the direction of motion and λ a numerical prefactor. This result is used in the numerical simulation detailed below.

Analytical and numerical predictions

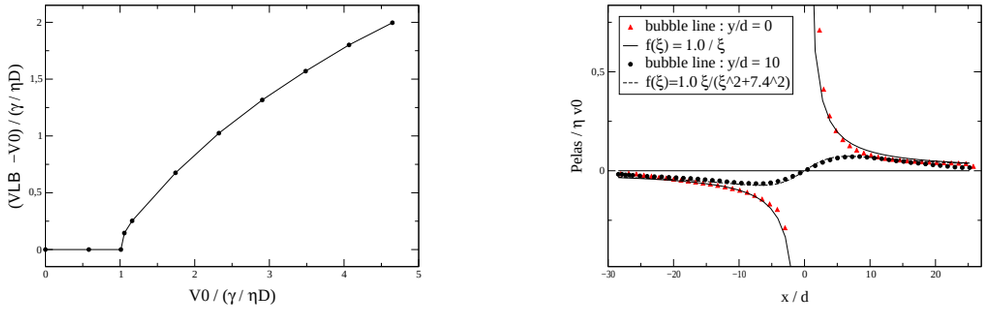


Figure 1. *(a) Relative velocity of one large bubble embedded in a monodisperse foam flowing at velocity v_0. (b) Pressure for two representative bubbles columns oriented along the flow, once P_{eq} and the average pressure gradient have been subtracted. Symbols are numerical predictions at the positions shown and lines are mathematical functions indicated on the legend. The theory predicts a function of similar shape $f(\xi) = 1.9\xi/(\xi^2 + (y/d)^2)$.*

The presence of a large bubble locally decreases the dissipation and thus the driving force needed to produce the flow. The elastic network distortion adjusts to compensate for this force discrepancy at low velocity, and the plug flow is maintained. Past a critical threshold, the plastic limit is reached and the compensation is driven instead by viscous forces, thus making the films around the large bubble move faster than the mean flow. The analytical predictions are based on a mesoscopic description of the foam involving a pure elastic response at low stress and a plastic threshold γ/d, with d the typical bubble size. We get a velocity threshold $v_t \sim \gamma/(\eta D)$ (with D the large bubble diameter) and the pressure fields given in picture 2(b) [4]. The numerical simulation is based on the vertex model [5] and is performed in a periodic array. The initial condition is an ordered monodisperse foam of bubbles with uniform size and a single large bubble LB. At each time step, a bubble line far from LB is pushed at constant velocity $v_0\mathbf{u}_x$, and other vertices are displaced with velocities ensuring the balance between viscous forces, tension and pressure. A neighbor swapping event (T_1 process) is performed when two vertices become closer than a given value ϵ. After a transient depending on the initial large bubble shape, a stationary regime is reached in which the large bubble exhibits a regular almond shape oriented along the flow. Plug flows are observed at low velocity. However, as Fig.1(a) illustrates, the large bubble reaches a velocity $v_{LB} > v_0$ for velocities faster than v_t.

Experimental results

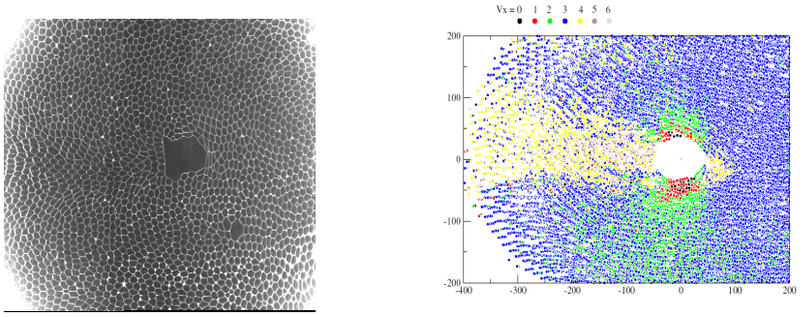


Figure 2. *(a) 2D foam image, flowing to the right. (b) Velocity field around the large bubble, the color indicates the velocity component in the mean flow direction.*

Our channel is made with two horizontal glass plates ($1.5m \times 0.6m$) connected to a vertical cell where the foam is produced and drained. Foaming solution is SDS 3g/l, dodecanol 0.01 g/l, glycerol 10% and water. The foam is continuously produced by nitrogen blowing at a controlled rate and the large bubble is obtained with pulsed infra red YAG laser. Images are recorded and analyzed with the software Visilog (see a raw image Fig. 2(a)). We get the full velocity field as shown picture 2(b). We determine the threshold instability and the dynamical behavior after this threshold.

Conclusion

This study naturally leads to new questions on the dynamic interactions between several large bubbles in a bidisperse or polydisperse foam. In particular, we have experimentally observed the formation of long streamwise chains of large bubbles percolating through the Hele Shaw cell. This phenomenon has profound effects on the flow. These chains transport the major part of the volume flux, at high speed. The soap films involved are submitted to high stresses and avalanches of film breakage occur frequently, thus destroying suddenly the whole column and short circuiting the overall pressure drop until new foam fulfill again the free passage. This process related to the large bubbles interactions and organization is highly undesirable in industrial flow and further studies of this phenomenon are thus of practical interest.

References

[1] N. Kern, D. Weaire, A. Martin, S. Hutzler, and S. J. Cox, preprint (2004).
[2] F. P. Bretherton, J. Fluid Mech. **10**, 166 (1961).
[3] N. Kern, I. Cantat, and R. Delannay, to appear in Europhys. Lett. (2002).
[4] I. Cantat and R. Delannay, Phys. Rev. E **67**, 031501 (2003).
[5] T. Okuzono and K. Kawasaki, Phys. Rev. E **51**, 1246 (1995).

SURFACTANT AND PROTEIN FOAMS : DIFFERENCES IN DRAINAGE AND RHEOLOGY

Arnaud Saint-Jalmes, S. Marze, D. Langevin
Laboratoire de Physique des Solides, Universite Paris-Sud, 91405 Orsay, France

Summary We report results on the drainage and rheology of foams made with different surface active compounds : small surfactant molecules, large proteins, and their mixture. Our experimental multi-scale approach provides us information at different length scales in the foam, and allow us to understand the origin of the macroscopic differences. It turns out that surface mobility in the foam channels is important for drainage, whereas the thin film structure is more crucial for rheology.

Aqueous foams are dispersion of gas in a liquid, containing surface active agents stabilizing the dispersion. As often in these dispersed systems, there are many typical length scales, and the global macroscopic behavior results from balances and coupling between effects at different scales. In order to elucidate these coupling, we have started a multi-scale experimental approach where we study how to change the foam macroscopic properties, and then track down within the foam sub-structures what are the microscopic origins of these changes.
Changing the surfactant compounds is one way to change the foam properties, though all the foams look the same by eyes. We have used (1) classical small surfactant (like Sodium Dodecyl Sulfate), (2) large protein molecules (casein) and (3) the mixture of these 2 chemicals. These chemicals provide different mechanical conditions at the surfaces of the bubbles, as well as different thin film structures. Beside the chemical composition affecting the surfaces and the films, we have also change -the gas used (effect on the rate of coarsening) - the initial liquid fraction (effect on the compactness of the bubbles) -the sizes of the bubbles, -and the bulk rheological properties of the liquid itself.

We have focused on drainage and rheology issues, searching for differences in macroscopic properties. We used classical bulk rheology, measuring storage and loss moduli, shear rate-dependent viscosity, and normal forces. Air-liquid interfacial studies were performed to get information on the surface dilatational and shear rheology, as well as adsorption dynamics. Thin film textures, fluidity and thickness were evaluated by video-microscopy on single films on frames. Light scattering techniques (in the multiple scattering regime) were also used, in a static mode, to follow the front displacement in the forced-drainage experiments.

The forced-drainage experiments showed that two well-defined drainage regimes can be found, while varying either bubble size and surface properties. It turns out that a rather simple description of these regimes can be done by including the concept of surface mobility, describing the coupling between flow within the surface and in the bulk of the foam channels (and incorporating the surface shear viscosity).
At low mobility, obtained for the protein foams having a very high surface viscosity, the results show that the main hydrodynamic resistance comes from the foam channels, which surfaces are rigid, and in which the flow is Poiseuille-like. These results are in good quantitative agreement with the foam models. As the mobility is increased, there is a smooth crossover from one drainage regime to another. As this crossover is approached, the hydrodynamics resistance of the channels slowly decreases (corresponding to an increase of the dimensionless permeability). From these data, we can estimate surface shear viscosities of the different solutions and found good agreement with other measurements. Around and above the crossover, the biggest hydrodynamic resistance is no longer the one inside the channels but becomes the one inside the foam nodes (where channels get together by four). This node contribution eventually becomes the predominant one, leading to the second drainage regime. We found that in this regime the dimensionless permeability depends slightly on the surface mobility, and remains quantitatively very closed to the one of the other limit (low mobility). The role of the thin films, in terms of controlling the boundary conditions of the foam channels will be discussed, as well as anomalous results obtained for very small bubbles (smaller in diameter than 0.5mm).

The rheology results also show some differences while changing the surface compounds. It seems that the complex structure of the protein thin films (thick and gelified) have to be taken into account, and that properties at this foam sub-structure are important. These thick gelified protein films provide complementary storage and loss contributions, resulting in more elastic though brittle foams.
We also investigated the homogeneity of shear and the possible occurrence of shear localizations (shear banding). We found some evidences of such shear banding, occurring at low shear rates and being more marked for dry foams.

The case of the mixture of small surfactants and proteins is also very rich, as the resulting foams differ from those made of the two pure compounds. We discuss the results in regard of specific interfacial adsorption competition between small and large molecules. It also seems that the result of such adsorption competition is different within the films and at the channel surfaces (there are relatively less proteins within the films, due to a more stringent local confinement).

Determining stress during finger propagation in 2D foams

Adrian D. Staicu, Bas van Gelder, and Sascha Hilgenfeldt

Applied Physics, University of Twente, P.O. Box 217, 7500 AE Enschede, The Netherlands

We investigate the formation of fingering patterns in a radial Hele-Shaw cell filled with quasi-two-dimensional polydisperse foam of very small liquid content. Air is used as the low-viscosity driving fluid, in both radial and parallel-channel geometries. Using high speed imaging (up to 2000fps), we directly observe the topological rearrangements on the size scale of single bubbles at the air-foam interface. We find that the growth process of the finger can be discretized as successive elementary T1-type edge exchanges between neighboring bubbles at the interface of the advancing finger. Compared to the prominence of the T1, film rupture events are rare.

Unlike other viscoelastic materials, foams give away direct information about their rheology through deformations of the bubbles that constitute the foam. Analyzing the statistical distributions of bubble properties yields insight in the behavior of the foam as a whole. Using a coordinate system moving with the finger, we obtain good spatial resolution for quantities such as the rate of T1 events, measures of local bubble anisotropy (e.g. the texture tensor), and connectivity. The deviatoric stress tensor in the material can be deduced from these data. The results are compared to continuum theory in the viscous liquid and elastic solid limits, shedding light on the continuum behavior of foam as a viscoelastic material, by virtue of exploiting bubble geometry.

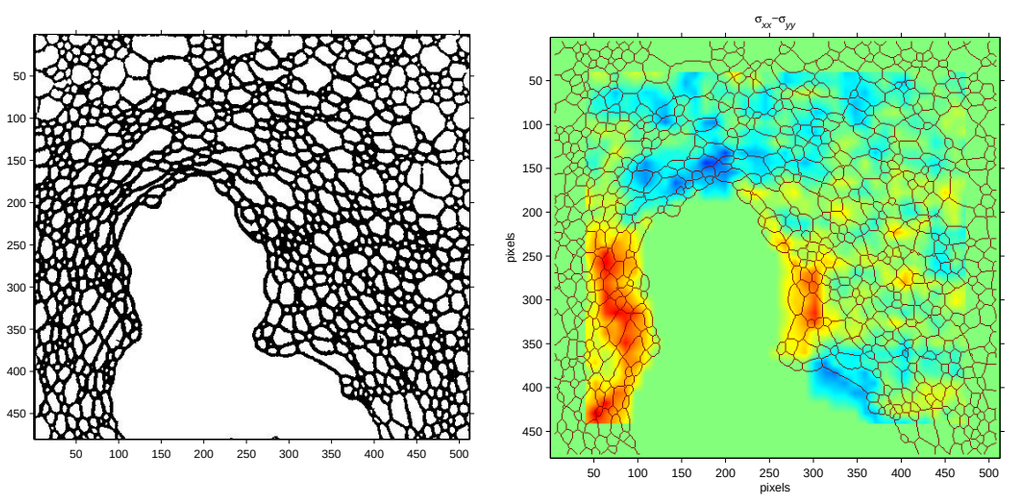


FIG. 1. Left: Snapshot of advancing finger in a 2-D Hele-Shaw cell filled with foam. Right: The bubble shapes have been analyzed to yield the $\sigma_{xx} - \sigma_{yy}$ component of the deviatoric stress tensor, whose magnitude is color-coded in the figure.

XXI ICTAM, 15-21 August 2004, Warsaw, Poland

THERMAL FLOW THROUGH BRAZED WOVEN SCREENS

J. Tian*, T. J. Lu*, H. P. Hodson*, D. T. Queheillalt**, & H. N. G. Wadley**
*Cambridge University Engineering Department, Trumpington Street, Cambridge, CB2 1PZ, UK
**Materials Science Department, University of Virginia, Charlottesville, VA 22903, USA

Summary This paper presents experimental measurements and analytical predictions of pressure loss and heat transfer through brazed woven textiles under forced air convection. The main characteristics considered include porosity, solid thermal conductivity, and surface area density. The heat transfer performance of woven textiles is compared with other heat exchanger media including metal foams.

INTRODUCTION

High porosity, ultra-lightweight, cellular metal structures with open cell topologies have emerged in the past decade as attractive heat exchange media for a wide range of applications where dissipation of high intensity heat over relatively small spaces is demanded [1]. These cellular metal structures can be classified into two broad classes, one with a stochastic topology (e.g., metal foams) and the other with a periodic structure (e.g., brazed woven textiles, see figure 1). While stochastic cellular structures can be good compact heat exchangers, they are not as structurally efficient as their periodic counterparts. This arises because their deformation under mechanical loading is dominated by cell wall bending as opposed to cell wall stretching [2]. In this study, sandwich panels with woven textile cores are fabricated by using a transient liquid phase (TLP) bonding method to create robust nodes at wire crossovers and between the laminae. The overall pressure loss and heat transfer of the panels under forced air convection are measured and compared with those predicted using analytical models. Comparison with other heat exchange media is also made.

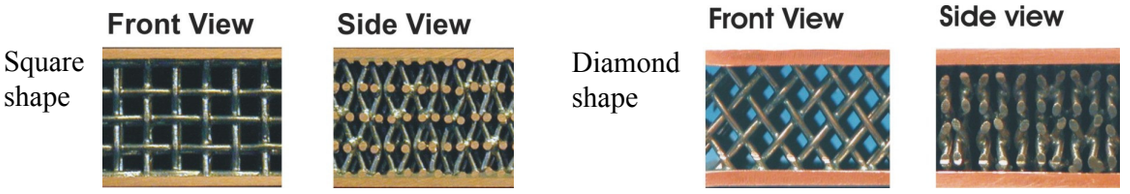


Figure 1. Two prototype textile laminate heat exchangers.

PRESSURE LOSS

Two pressure tappings placed separately in front of and after the test samples are used to obtain the pressure drop through woven screen structures. Samples with two different cellular configurations are measured: square shape and diamond shape (figure 1). The experimental results show that, at high Reynolds numbers, the pressure loss through woven screens is mainly caused by the pressure drag behind the wire ligaments. Friction factor based on channel height is independent of Reynolds number, indicating form-dominant flow in the range of Reynolds number considered. Different cellular configurations and different solid materials (copper and stainless steel are used in this study) are found to have negligible effect on pressure loss due to similar flow patterns. The main characteristic is porosity.

According to the analysis of pressure drag behind a wire ligament, the pressure loss through the structure is a function of open area ratio. Since the porosity and open area ratio are both functions of the ratio of wire diameter to aperture (d/w), the pressure loss depends mainly on porosity (or open area ratio). The analytical predictions agree closely with experimental measurements. The relationship between friction factor and open area ration is obtained as:

$$f = \frac{\Delta P}{1/2\rho V^2}\cdot\frac{H}{t} \sim \left(\frac{1-R_{open}}{R_{open}}\right)^2\cdot\frac{H}{t}$$, where H is the channel height and t is the thickness of one layer ($t=2d$)

HEAT TRANSFER

Textile laminate heat exchangers with different porosities and different solid materials are studied. The overall heat transfer performance of these samples depends on the conduction through wire ligament, convection from the structure, and convection from the facesheets.

Experiment

The heat transfer performance of woven screens under steady-state forced air convection is obtained by measuring the inlet and outlet air temperatures and bottom wall temperatures. Nusselt numbers based on channel height are used. The

results show that the heat dissipation capability of diamond shape samples are about 20%-30% higher than that of square shape samples having identical wire diameter and aperture. Copper samples have better heat transfer performance than stainless steel ones due to the higher solid thermal conductivity.

Analytical model

A fin analogy model is used to analyze the heat transfer performance of wire screens. Overall, the predictions compare favourably with those measured.

Discussion

Experimental and analytical results both reveal that the heat transfer performance of diamond shape samples is superior to square shape ones. Because of similar internal flow patterns, the main cause of this difference is due to conduction through wire ligaments. Even though the thermal conductivity of copper is about 20 times larger than that of stainless steel, the Nusselt number of copper textiles is only 3 times higher. At high porosity levels, the contribution of conduction through wire ligaments is less important than that contributed by convection from the cellular structures. At the same surface area density, it is found that a peak value of porosity exists for heat transfer. High porosity implies less solid material, and hence the contribution of conduction will be lower while the void volume will be bigger for convection. The different effects of porosity on conduction and convection lead to an optimum porosity (~ 0.8) for maximum heat transfer.

COMPARISON WITH OTHER HEAT EXCHANGE MEDIA

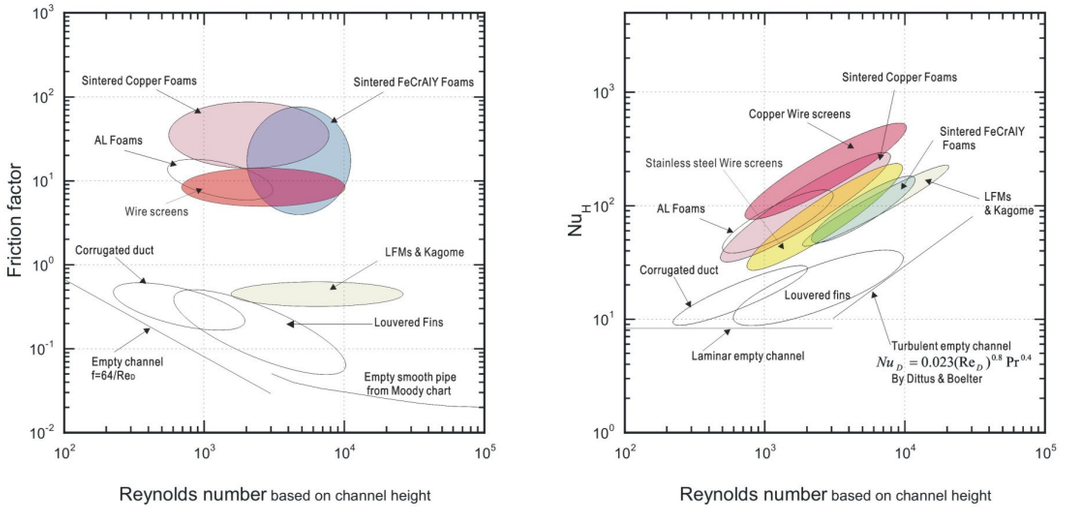


Figure 2. Thermal performance comparison of different heat exchange media.

Figure 2 compares the pressure loss and heat transfer performance of brazed wire screens with other heat exchange media including metal foams, LFMs (lattice frame materials) with tetrahedral unit cells [1], Kagome truss structures [2] and louvered fins. Notice that although the periodic woven structures typically have lower porosities than the stochastic metal foams, their friction factor is much smaller than those of metal foams. The fluid flow mechanisms of these two structures are different, which cause the difference in pressure loss. The heat transfer capability of copper wire screens appears to be superior to other media considered.

CONCLUSIONS

The overall heat transfer across woven textiles includes conduction and forced convection. Porosity and surface area density are two important characteristics at a given Reynolds number. Conduction and convection change in different ways with varying porosity. With increasing porosity, conduction decreases while convection increases. An optimal porosity for maximum heat transfer exists for a given surface area density. At a given porosity, the overall heat transfer increases as the surface area density is increased. Significant opportunities exist to maximize the heat transfer performance of periodic cellular metals by varying the pore fraction, anisotropy of the pores and metallic alloy used. Such manipulation can be accomplished by selection of the appropriate wire mesh.

References

[1] T. Kim, H.P. Hodson and T.J. Lu. Fluid flow and endwall heat-transfer characteristics of lattice-frame materials. *Int. J. Heat and Mass Transfer*, 47:1129-1140, 2004.

[2] A. G. Evans, J. W. Hutchinson, N. A. Fleck, M. F. Ashby and H. N. G. Wadley. The topological design of multifunctional cellular metals. *Progress in Materials Science*, 46:309-327, 2001.

DRAINAGE OF EMULSION AND FOAM FILMS IN SCHELUDKO-EXEROWA CELLS

J. Coons[*], P. Halley [**], S. McGlashan[**], and T. Tran-Cong[***]
[*]*Los Alamos National Laboratory, P.O. Box1663, MS C930 Los Alamos, NM 87545, USA*
[**]*Department of Chemical Engineering, University of Queensland, St. Lucia, QLD 4072, Australia*
[***]*Faculty of Engineering and Surveying, University of Southern Queensland, Toowoomba, QLD 4350, Australia*

Summary Here the Manev-Tsekov-Radoev (MTR) drainage theory in the form of a semi-empirical equation is shown to be the most consistent with existing drainage time data from emulsion and foam films.

INTRODUCTION

Thin liquid films (TLFs) are fundamental components in a variety of industrial processes including foam manufacturing, oil exploration, and the growth of bio-organisms. Improved understanding of the drainage is essential for accurate predictions of the stability and lifetime of a film. Numerous fundamental studies of thin films have been conducted in specially designed capillary cells, referred to as Scheludko-Exerowa cells, in which a biconcave foam or emulsion film is created by suspension of a thin film across the capillary. A foam film is surrounded by a gas and an emulsion film is surrounded by an immiscible liquid. The capillary tube is permeable to permit the drainage and thinning of the film. Coupled with optical probes, the film thickness can be measured with high precision. In this paper, predictions of drainage times from the lubrication theory of Reynolds [1] and the theory of Manev et al [2], referred to as the Manev-Tsekov-Radoev (MTR) theory, are compared to experimental measurements obtained from numerous investigators. The objective of the comparison is to determine the extent to which drainage theory is consistent with the body of thin film measurements. MTR theory is represented with the original equation derived by Manev et al and a semi-empirical equation recently described by Coons et al [3]. It is shown that the semi-empirical MTR equation is most consistent with available data, and the Reynolds equation and theoretical MTR equation provide effective upper and lower bounds of drainage times, respectively.

THEORY

Reynolds [1] simplified the Navier-Stokes equations to describe the flow of a viscous liquid being squeezed between two rigid surfaces. In a geometry analogous to a TLF, each surface is circular and the film has the shape of a cylinder. The film thickness decreases with time as a consequence of a force acting between the film surfaces. Application of lubrication theory where the surfaces are nearly plane parallel and no slip occurs at the interfaces leads to the Reynolds equation for the film thinning velocity.

$$V_{\mathrm{Re}} = -dh/dt = 2h^3 \Delta P / 3\mu R^2$$

h is the average film thickness, ΔP is the average radial pressure drop across the film, R is the film radius, and μ is the bulk viscosity of the film. In a Scheludko-Exerowa cell, a cylindrical film forms in the center of the biconcave film spanning the capillary tube. The liquid pressure at the perimeter of the film is reduced due to the interfacial curvature. The reduced pressure causes the film to drain and the film thickness decreases. As the thickness approaches a few hundred nanometers, long range van der Waals forces become significant. These forces are attractive in nature and act to increase the intrafilm pressure. Under the conditions described, the average pressure drop in a TLF is given by the following expression.

$$\Delta P = 2\sigma\left(\frac{R_c}{R_c^2 - R^2}\right) + \frac{A}{6\pi h^3}$$

A is the Hamaker constant, R_c is the radius of the capillary tube, and σ is the interfacial tension. In a free standing TLF, the interfaces are not rigid and the non-uniform film pressure causes the interface to deform. Hence, the interfaces bounding TLFs become corrugated and nonparallel as thinning proceeds. Radoev et al [4] was the first to report the size and behavior of the hydrodynamic corrugations. They found that the amplitude is proportional to the radius of the film and independent of the film thickness. The drainage theory of Manev et al [2] assumes that the local film thickness is a homogeneous function of the average film thickness and the pressure drop across a corrugated film is directly proportional to the driving pressure divided by the square root of the eigenvalue of the dominant waveform. These assumptions lead to the following expression for the thinning velocity.

$$V = V_{\mathrm{Re}} l^{3/2}$$

MTR theory provides the following theoretical expression for l, the number of domains or extrema in the film.

$$l = \left[\frac{\Delta P}{h\sigma}\left(\frac{R}{4}\right)^2\right]^{2/5}$$

Use of the above expression for the number of domains in the MTR thinning velocity equation is referred to as the theoretical MTR equation. As is shown in Figure 1, a comparison has been reported [3] between the theoretical domains and the thinning velocity ratio at the critical point of rupture using the data of Radoev et al [4]. The data suggest a different proportionality, which is adequately represented by the following semi-empirical equation.

$$l = \frac{1}{2}\left\{\left[\frac{\Delta P}{h\sigma}\left(\frac{R}{4}\right)^2\right]^{2/5} + \frac{4}{3}\right\}$$

This semi-empirical form of the MTR equation provides significantly different thinning velocities in comparison to the theoretical MTR equation. Both equations predict that thick films drain in accordance to Reynolds equation. However, the thickness at which the thinning velocity deviates from the Reynolds equation differs. The semi-empirical MTR equation predicts this deviation will occur slightly prior to the theoretical MTR equation, i.e. at larger film thicknesses. However, shortly after this Reynolds thickness is traversed, the theoretical MTR equation predicts faster thinning velocities in comparison to the semi-empirical form. It has also been shown [3] that the theoretical MTR expression for the number of domains goes to 2/3 when ΔP is dominated by the van der Waals term, which leads to sub-Reynolds thinning velocities. Under the same conditions, the semi-empirical MTR equation goes to unity suggesting that the film drains in accordance with the Reynolds equation. The condition of the driving pressure being dominated by the van der Waals component leads to the lowest possible Reynolds thickness for a given film. A major conclusion of the MTR theory is that no TLF is able to drain to the point of rupture and maintain a thinning velocity consistent with Reynolds equation [3].

Figure 1

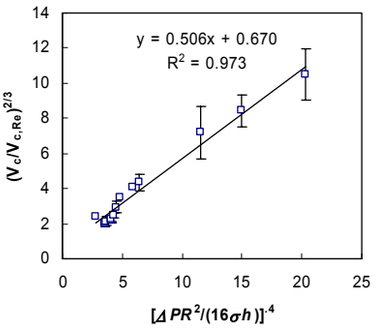
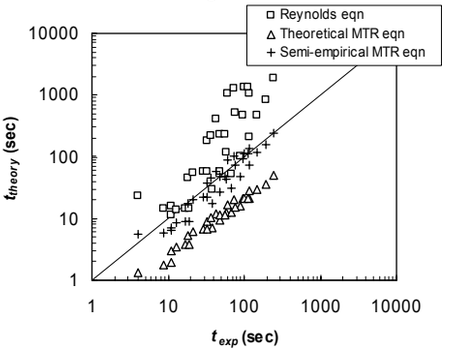


Figure 2



RESULTS

The purpose of this paper is to compare predictions of the Reynolds, theoretical MTR, and semi-empirical MTR equations to experimental measurements on thin films from the literature. All films were studied under conditions in which the interfaces were tangentially immobile. Drainage time between two thicknesses was calculated by integration of the following equation.

$$t_d = \int_{h_{\min}}^{h_{\max}} \frac{dh}{V}$$

Further details including the physicochemical properties are provided elsewhere [5]. Results are shown in Figure 2.

CONCLUSIONS

The semi-empirical form of the MTR equation was found to be more accurate in predicting the drainage times of a variety of emulsion and foam films. This reinforces the validity of the drainage theory proposed by Manev et al [2].

References

[1] Reynolds, O.: On the Theory of Lubrication and Its Application to Mr. Beachamp Tower's Experiments, including an Experimental Determination of the Viscosity of Olive Oil, *Philos. Trans. R. Soc. London,* **177**, 157-234, 1886.

[2] Manev, E., R. Tsekov and B. Radoev: Effect of Thickness Non-Homogeneity on the Kinetic Behaviour of Microscopic Foam Films, *J. Dispersion Sci. Technol.,* **18**, 769-788, 1997.

[3] Coons, J.E., P.J. Halley, S.A. McGlashan and T. Tran-Cong: Review of Drainage and Spontaneous Rupture in Free Standing Thin Films with Tangentially Immobile Interfaces, *Adv. Colloid Interface Sci.,* **105**, 3-62, 2003.

[4] Radoev, B.P., A.D. Scheludko and E.D. Manev: Critical Thickness of Thin Liquid Films: Theory and Experiment, *J. Colloid Interface Sci.,* **95**, 254-265, 1983.

[5] Coons, J.E., P.J. Halley, S.A. McGlashan and T. Tran-Cong: A Bounding Analysis of Spontaneous Rupture in Thin Films. I. Film Drainage, *in preparation.*

SHEAR-INDUCED NORMAL STRESS DIFFERENCES IN AQUEOUS FOAMS

Vincent Labiausse, Reinhard Höhler, Sylvie Cohen-Addad
LPMDI/UMR 8103, Université de Marne-la-Vallée, 5 Bd Descartes, Champs-sur-Marne, 77454 Marne-la-Vallée cedex 2, France

Summary We have studied experimentally the shear induced normal stress response of aqueous foams, using a new experimental approach. The data are compared to predictions derived from a general theorem of nonlinear elasticity as well as to an elasto-plastic behaviour, suggested by recent numerical simulations.

Introduction - Aqueous foams are concentrated dispersions of gas bubbles in water, stabilized by small amounts of surfactants. Even though they are constituted only of fluids, these materials show solid-like viscoelastic behaviour when they are subjected to very small stresses. If the stress is progressively increased, the structure yields and plastic flow sets in. This rheological behaviour as well as the low specific weight of foams give rise to a great variety of applications, ranging from oil production to fire fighting, the floatation of minerals, pharmaceutical products, and many forms of food [1]. Yielding typically occurs at strains of the order of 0.1-1, sufficiently large so that nonlinear elastic behaviour may be expected before the onset of significant plastic flow. For an elastic homogeneous isotropic solid, a finite shear strain γ in a direction 1, with a displacement gradient in a perpendicular direction 2, is well known to induce not only a shear stress σ_{12}, but also normal stress differences $N_1 = \sigma_{11} - \sigma_{22}$ and $N_2 = \sigma_{22} - \sigma_{33}$. Comparing measured normal stresses *as well as* shear stresses to predicted values constitutes a severe test, allowing to validate theoretical rheological constitutive laws. Concerning the first normal stress difference on which the present paper is focussed, it has been shown using very general theoretical arguments that in any elastic isotropic body with an isotropic reference state the relation $N_1 = \sigma_{12}\,\gamma$ describing the Poynting effect must hold [2]. In the elastic regime where $\sigma_{12} = G\,\gamma$ where G is the shear modulus (which may weakly depend on γ), one expects $N_1 = G\,\gamma^2$. This result is in excellent agreement with quasistatic numerical simulation of disordered dry 3D foams [3] as well as with analytical models based on a statistical description of the foams structure [4,5,6]. However, these approaches ignore the fact that real foams are by no means perfectly elastic: there is significant dissipation due to the bulk viscosity in the liquid films, the interfacial viscoelasticity of the surfactants and the intermittent local structural rearrangements induced by the Laplace pressure driven diffusion of gas between neighbouring bubbles ("coarsening process") [1]. As a consequence, it is a priori unclear to what extent the relation $N_1 = \sigma_{12}\,\gamma$ holds for real foams. Moreover, foams and yield stress fluids in general conserve a "memory" of their flow history. Pre-shearing procedures may create to some extent a well defined initial state of the system, but it is not possible to eliminate uncontrolled trapped internal stresses completely. Therefore, the existence of a well defined stress free isotropic reference state in real foams is questionable. This fundamental difficulty which we have resolved using a new experimental approach may explain the absence (to our knowledge) of any previous published experimental normal stress data for foams and many other yield stress fluids in the solid-like regime.

Methods and Materials - The foams were generated by injecting nitrogen gas containing perfluorohexane vapour and a foaming liquid into a column filled by a close packing of glass beads, as described elsewhere [7]. The liquid was an aqueous solution of α-olefin sulfonate (AOK, Witco Chemicals), Polyethylene-oxide (Aldrich) and dodecanol (Aldrich). Foam gas volume fractions of 0.92 and 0.97 were produced. For the rheological measurements, we used a Bohlin CVOR rheometer (cylindrical Couette geometry) as well as a special purpose cone plate rheometer, allowing to measure N_1 with a very high sensitivity. Measuring the response to oscillating shear is the key for a successful study of normal stresses in solid-like yield stress fluids. For an elastic sample where $N_1 = G\,\gamma^2$, with $\gamma = \gamma_o\,\mathrm{Cos}(\omega t)$, one expects a first normal stress oscillation Fourier component of frequency 2ω and amplitude (denoted $N_{1,\,2\omega}$ in the following) equal to G/2. If some uncontrolled trapped shear strain which may even slowly evolves with time is superposed to γ, this will not alter the second harmonic stress oscillations but create a superposed normal stress oscillation of frequency ω which can easily be discarded experimentally using the lock-in detection technique. Of course, this simple argument needs to be refined, since trapped strains can be of any orientation and tensorial nature. We have studied this question by rigorous calculations for sample materials described by the Mooney-Rivlin class of constitutive equations, confirming the very efficient suppression of artefacts related to trapped stresses in measurements using oscillating strains. Let us note that we have recently shown theoretically that aqueous foams may be expected to behave indeed following a Mooney-Rivlin law in the solid like regime [6]. Besides the normal stress measurements, we have also studied the shear stress response to an imposed oscillatory shear strain. For small strain amplitudes, such data can be described by the usual complex shear modulus. At large strain amplitudes, the stress response contains a spectrum of harmonics, but they remain much smaller than the fundamental stress oscillation, even up to the yield strain. We

therefore discuss the results in terms of a generalized complex shear modulus, calculated from only the fundamental harmonic component of the stress oscillation. A discussion of the harmonics will be presented in future work. All rheological experiments were carried out at a frequency of 1 Hz, so that an approximately quasistatic response can be expected. To check for strain localization effects, the free edge of the sample was observed during the experiment.

Results and Discussion - Fig. 1A shows an example of the results obtained in the present study, for a gas volume fraction of 0.92. The rapid continuous drop of the real part G' of the generalized complex shear modulus and the maximum of the imaginary part G" indicate the onset of plastic flow and finally of yielding. The continuous line is the behavior theoretically expected for an ideal elastoplastic material, subjected to an imposed oscillating shear strain. The yield stress is the only free parameter of this fit of G' as well as G". The data suggest that dry aqueous foams behave at least approximately as elastoplastic materials under quasistatic conditions.

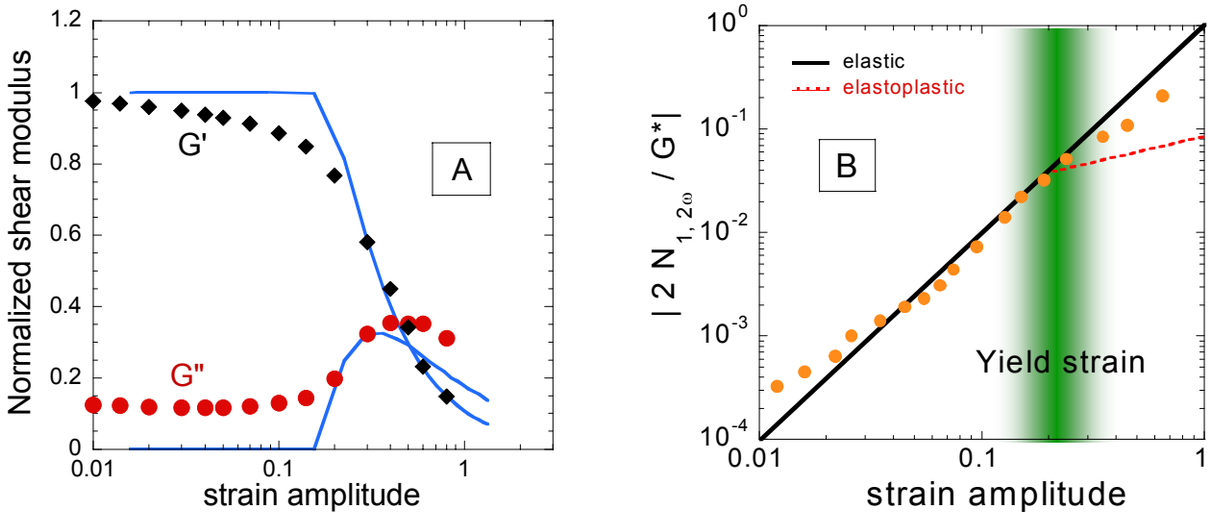


Figure 1 *Fig 1A shows the generalized complex shear modulus defined in the text, normalized by its real part obtained in the limit of small strains. The two continuous lines represent a fit to the ideal elastoplastic law described in the text, using a single free parameter. Fig 1B shows, as a function of strain amplitude, the amplitude of second harmonic normal stress oscillations, normalized by half the absolute value of the complex shear modulus. The continuous line shows the behaviour expected for an elastic body. Beyond the onset of plastic flow, represented by the thick vertical line, the dashed line corresponds to the behaviour theoretically expected for elastoplastic behaviour.*

Figure 1B shows the normalized second harmonic normal stress oscillation amplitude, in response to the same oscillating shear as in Fig 1A. The quadratic scaling with strain amplitude expected for elastic materials is clearly observed, over a decade in strain amplitude. Indeed, we have obtained theoretical arguments strongly suggesting that the influence of viscoelastic dissipation on the normal stress response is negligible in foams at low frequencies, as long as G' >> G". Close to the yield strain, plastic flow is expected to play an important role. In this regime, the signature of elastoplastic behaviour would be a cross-over to a scaling with an exponent ½, smaller than the one found experimentally. Our next objective is to develop a more physical constitutive model, taking also into account the dissipation effects mentioned in the introduction. A key feature of a more quantitative model may be the mesoscopic fluctuation of mechanical properties in foams, as described by the recent SGR class of models [8, 9].

References

[1] Weaire D., Hutzler S.: The Physics of Foams Oxford University Press, New York 1999.
[2] Mal A., Singh S.: Deformation of Elastic Solids, Prentice Hall, London 1991.
[3] Kraynik, A.M., Reinelt, D.A and van Swol, F.: Proceedings of the 3rd Euro Conference on Foams, Emulsions and Applications, Zitha,P., Banhart, J., Verbist, G. Editors, MIT Publishing Bremen, 191-198 (2000).
[4] Doi M., Otha T., J. Chem. Phys. **95**, 1242-1248 (1991).
[5] Larson, R.G., J. Rheol. **41**, 365-372 (1997).
[6] Höhler R., Cohen-Addad S., Labiausse, V.: Submitted to Journal of Rheology (2003).
[7] Rouyer F., Cohen-Addad S., Vignes-Adler M., Hohler R., Phys. Rev. E, **67**, 021405 (2003).
[8] Sollich P., F., Hebraud P. Cates M., Phys. Rev. Letters, **78,** 2020-2024 (1997).
[9] Cates M., Sollich P., cond-mat/0307098 (2003).

The Dispersion of Particles within Foams

Neethling, S.J., Lee, H.T. and Cilliers, J.J.
Froth and Foam Research Group, Department of Chemical Engineering, UMIST
P.O. Box 88, Manchester, UK
Email: Stephen.Neethling@umist.ac.uk

The motion of particles within foams has important industrial relevance. Froth flotation is an important separation technology in the minerals industry, as well as in paper de-inking and water treatment. The motion of the particles within the foam has a major impact on the performance of the equipment. Within these flotation froths there are particles that are attached to the air/water interfaces, as well particles that are not attached to the interfaces. The attached particles are thus predominantly associated with the films within the foam, while the unattached particles are predominantly found within the Plateau borders.

This study focuses on the unattached particles, as their motion is the most complex to model. Unattached particles predominantly follow the net motion of the liquid, but are able to move relative to the liquid by means of both settling and dispersion. Two types of dispersion have been identified; Geometric dispersion and Plateau border dispersion. The Geometric dispersion is brought about by the layout of the Plateau borders within the foam. These Plateau border form for an interconnected branching network throughout the foam and any particles must thus follow a meandering course through the foam. This results in dispersion in a direction perpendicular to the net liquid motion (Neethling and Cilliers, 2002).

Plateau border dispersion is a result of the velocity profile of the liquid in Plateau borders. The liquid/gas interfaces of Plateau borders are not necessarily fully mobile, but are able to support a certain amount of shear, either by surface viscosity or Marangoni stresses. Seeing that the interfaces of the Plateau borders are not fully mobile and, in many circumstances, can actually be considered immobile (Verbist *et al.*, 1996), the liquid velocity at the interface will be substantially different to that near the centre of the Plateau border. The liquid velocity profile across the Plateau border results in dispersion of the suspended particles in a direction parallel to the direction of net liquid motion. It is this Plateau border dispersion that is the focus of the work described here.

Optical detectors were placed on a column of foam in order to measure the concentration of particles within the Plateau borders. The foam was undergoing continuous forced drainage so that the liquid content was constant over virtually all the height of the foam. The optical sensors are sensitive to changes in both solids concentration and the liquid content. It was thus important to add the particles in such a way that the total volumetric flow rate into the foam was not affected by the solid addition. This was achieved by means of a switch that very rapidly substituted a portion of the water feed with an equal volume of solid suspension.

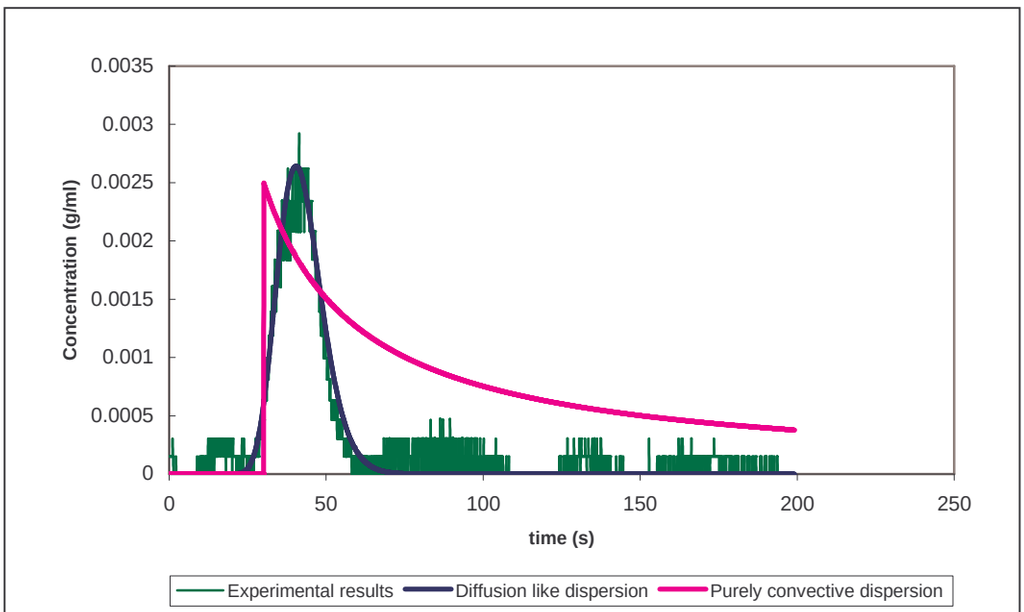


Figure 1: Experimental and Theoretical concentration vs time profiles showing that the Plateau border (axial) dispersion is diffusion like in its behaviour

The first aim of this work was discover if radial mixing within individual Plateau borders or the vertices was a significant factor in the dispersion of the particles. If radial mixing was not a major factor in the dispersion, then the

concentration profile would exhibit the sharp initial peak that is characteristic of purely convective dispersion. With some radial mixing in the Plateau borders or vertices, the concentration profile would exhibit a near normal distribution that is similar to what would be obtained from diffusion. Figure 1 demonstrates that the profile obtained is very similar to the diffusion like profile and that there is therefore some radial mixing in either the Plateau borders or vertices. This is despite the fact that the flow is very laminar. Some of the potential sources of this mixing are the changing of the relative position in the Plateau borders of particles as the go through vertices, Brownian motion (as the particles are very fine), lift effects and particle-particle interactions.

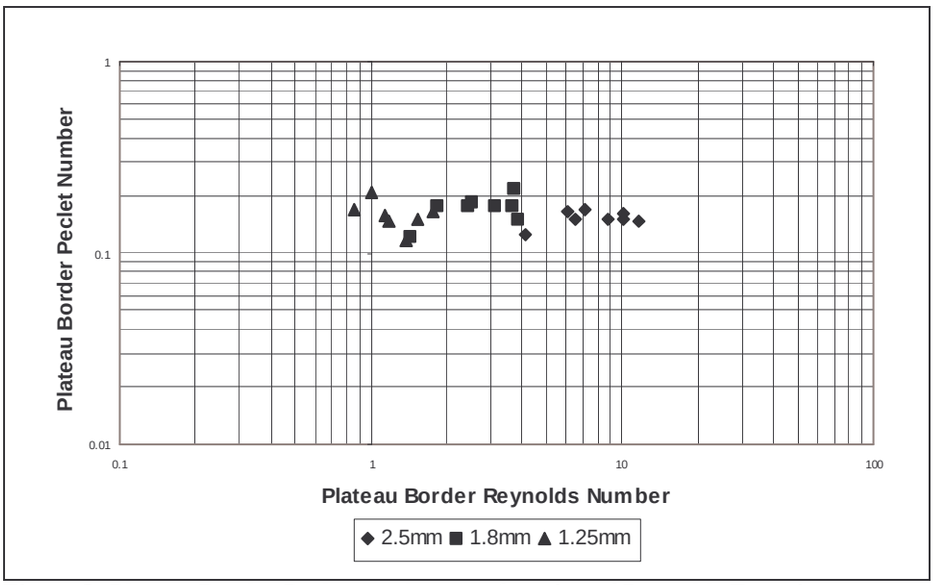


Figure 2: Plateau Border Peclet number as a function of Reynolds Experiments performed at different liquid contents and bubble sizes.

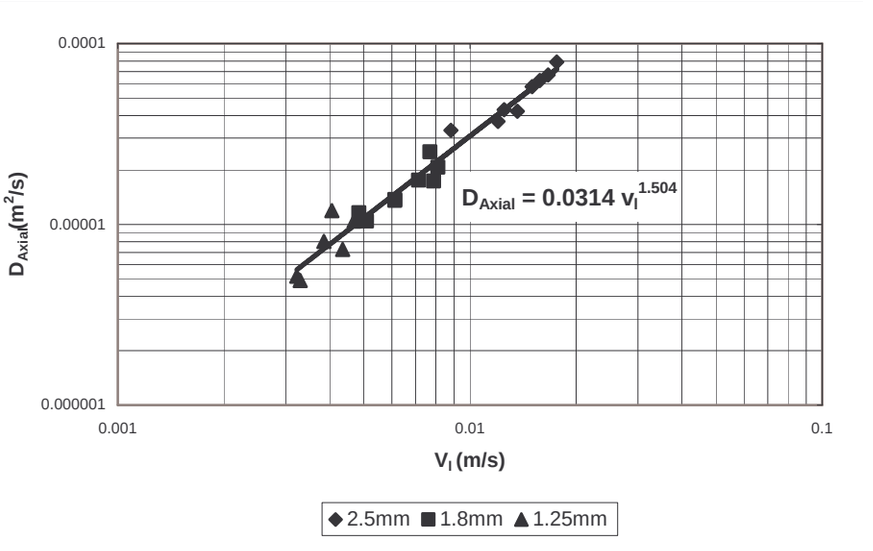


Figure 3: The relationship between the axial dispersion coefficient and the liquid velocity for fine particles (legend indicates bubble diameter).

The aim of the second portion of this work was to examine the dependence of the Peclet number on system conditions. The characteristic length scale chosen for use in the Peclet number was the radius of curvature of the Plateau border. Unlike in Packed beds, the channel (Plateau border) diameter can be varied independently of the particle (bubble) size. Figure 2 shows that the Peclet number is virtually independent of both bubble diameter and Plateau border Reynolds number over quite a wide range of conditions.

By using the foam drainage equation (Verbist *et al.*, 1996) and assuming that the Peclet number is constant, it is predicted that the Axial Dispersion coefficient would be proportional to the liquid content raised to the power 1.5. Figure 3 shows that this is indeed the case.

References

Neethling, S.J. and Cilliers, 2002, J.J. Solid Motion in Foams. *Chemical Engineering Science*., **57**, 607-615

Verbist, G., Weaire, D., and Kraynik, A.M. , 1996, The foam drainage equation, *J. Phys.: Condens. Matter*, **8**, 3715-3731

XXI ICTAM, 15-21 August 2004, Warsaw, Poland

INVESTIGATION OF FOAM DEVELOPMENT IN POROUS MEDIA USING X-RAY COMPUTED TOMOGRAPHY.

Quoc P. Nguyen, Peter K. Currie and Pacelli L. J. Zitha,
Delft University of Technology, Faculty of Applied Earth Sciences,
Mijnbouwstraat 120, 2624 RX Delft, The Netherlands
E-mail: p.l.j.zitha@citg.tudelft.nl

Keywords: foam, porous media, bubble generation, experiments, X-ray, tomography.

Summary: In this paper, we investigate foam development in granular porous media, where fluid fractions variations are visualized and quantified using X-ray computed tomography. We provided direct evidence that foam flows in a front like manner leading to a residual liquid fraction of 0.18 ± 0.01, far from the inlet surface of the porous sample. Ideas about the physics of foam flow in porous media are revised in the light of our findings.

When gas is forced through granular porous media containing a surfactant solution, the mobility of the fluids decreases considerably due to foam development [1-3]. This effect can be understood in terms of the increase gas fraction in the porous medium and concurrent decrease in liquid fraction. It is widely accepted that gas resident in the porous medium can be split into a (rather small) mobile fraction and a (rather large) stationary fraction. The apparent viscosity associated with the motion of foam films contributes significantly to the reduction of gas mobility. This experimental work has been undertaken to examine in the dynamic fluid partitioning induced by foam development in porous media which has remained speculative thus far.

X-ray computed tomography (CT) enables the visualization of process within opaque objects by reconstructing the X-ray attenuation coefficients from multidirectional X-ray transmission data. In this study, this technique has been combined with a specially designed experimental set-up for studying porous media flow, enabling thus a real time visualization and quantification of fluid distributions during foam flow through porous media. This approach was used previously (see for instance Kovscek et al. [1] and references therein) but the higher spatial and temporal resolution of more recent CT scanners offers the possibility to probe more accurately the fluid distributions.

Nitrogen gas (N_2) and the surfactant solution were co-injected into the saturated core at fixed rates of 5.0 ± 0.1 standard cm^3/min and 0.5 ± 0.05 cm^3/min, respectively (fraction of gas to total flow rate 91.0 ± 0.5%). After reaching steady state, a mixture of nitrogen (N_2) and Xenon (Xe) and a surfactant solution is co-injected to visualize foam local foam spead. Foam displacement process is visualized by constructing a series of 5 parallel images slicing the core along its axis. The central image is on the plane of the core axis (axis plane) while the other ones are place two by two, symmetrically with respect to the axis plane. The spacing between two adjacent images (i.e., the couch feeding) was 8 mm. Each image series is scanned in sequence from a couch position CP, with CP = 0 for the central image.

The CT images in Fig. 1 reveal that foam displaces the surfactant solution in a characteristic front-like manner (blue is foam and red is the surfactant solution). Three regions can be distinguished along the flow direction. (a) An upstream region, where foam is roughly uniformly distributed and the liquid fraction is low (the relatively high liquid fraction at the inlet is imposed by the injection system and is physically not very significant), (b) A downstream region, where the liquid fraction is unity and finally (c) a frontal region characterized by a mixing of the flowing foam and liquid and by a fine fingering. The scale of the fingering appears to be of the order of the inhomogeneity of the porous medium (in the order of tenths or hundreds of micrometers)

As foam advances in the porous medium the liquid fraction continues to diminish within the foam region. The continuing drop in liquid fraction appears more clearly after the foam front reaches the outlet of the porous medium, however, as indicated by the darkening of the blue region. This secondary liquid desaturation initiates in the central portion of the core and propagates towards the inlet and the outlet and ceases only when a steady state flow regime is reached, which happens at dimensionless times larger than 25.6. Note that the dimensionless time is obtained by diving the current time by characteristic time needed to inject one pore volume of liquid. The relatively high liquid fraction at the inlet mentioned above and the capillary liquid entrapment at the outlet (capillary end effect) are suppressed by the desaturation wave, the former partially and the latter completely within the accuracy of the experiments.

The liquid fractions, averaged over thin slice areas, are shown in Fig. 2 for several dimensionless times. In the early stages of foam injection the liquid fraction profile is an upward-concave function of the position as illustrated by the curve obtained at t = 0.11. The remaining curves before foam breakthrough exhibit roughly the same trend: (a) a low (less than 55%) upstream liquid fraction, (b) a high (100%) downstream liquid fraction, and finally (c) a transition zone where the liquid fraction increases smooth and rapidly towards the downstream. In the upstream region the liquid fraction gradually declines from the inlet towards the frontal region instead of being constant. For example, at t = 0.61 the liquid fraction decreases by almost 10% from the inlet to the position 7.5 cm. This proves that the secondary desaturation starts soon after the beginning of foam flow.

Nevertheless, the desaturation effect manifests itself more clearly after foam breakthrough. First of all, as discussed above just after breakthrough liquid fraction is still significant near the in- and outlet of the core. Then considering a fixed position, for example at 12.0 cm, the liquid fraction decreases over time, from about 38% to less than 18%. Even at the position 2.0 cm, where

the steady state profile indicates that much liquid still remains in the core, the liquid fraction decreases from 55% to 48%. It is not completely clear why so much liquid is retained near the core inlet. Perhaps the injected liquid somehow undergoes a filtration in that region.

The secondary liquid desaturation appears to be driven by gas expansion and to be controlled by the competition between viscous and capillary forces. When foam flows for the first time in the porous medium it penetrates primarily the largest pores as dictated by dominant capillary forces. Gas expansion sets in immediately as the foam travels down the pressure gradients but foam does not easily penetrate the smallest pores because of these have a large entry capillary pressure. As foam development proceeds, its apparent viscosity increases and thus the gas can progressively invade smaller pores containing liquid. The expanding gas and partial remobilization of trapped bubbles is likely to trigger further lamella generation mostly by snap-off and leave behind mechanisms [1,2], leading to a the refinement of the foam texture. It is not easy to quantify separately the contribution of snap-off and lamella division as the pressure gradient for lamella mobilization is exceeded. The process of foam generation associated with liquid desaturation is self-amplifying as the former requires the local pressure gradient to be sufficiently high while, on the other hand, further foam generation leads to high pressure gradient. Bubble generation is expected to cease, however, when foam approaches the limiting capillary pressure.

In conclusion, the idea of foam partitioning in mobile and immobile fractions the situation is not supported by our experiments. In the light of the visual data obtained in this study, it appears that the role of trapped gas during transient foam flow is not as important as it might have been believed previously. Apparently the transient foam displacement appears to be under the influence of a much subtler interplay between capillary and viscous forces. A further elaboration will be discussed in the future.

References

[1] A. R. Kovscek, and C. J. Radke, Fundamentals of Foam Transport in Porous Media, in *Foams: Fundamentals and Applications in the Petroleum Industry*, ACS Advances in Chemistry Series, N. 242, American Chemical Society, Washington D.C. (1994).

[2] W.R. Rossen, Foams in Enhanced Oil Recovery, Chapter 12 in *Foams: Theory, Measurements and Applications*, Prud'homme, R.K. and Khan, S. (Eds.), Marcel Dekker, New York (1996).

[3] Vinegar, H.J. and Wellington, S.L., Tomographic Imaging of three-phase flow experiments, *Rev. Sci. Instrum.*, 58(1), 96-107 (1986)

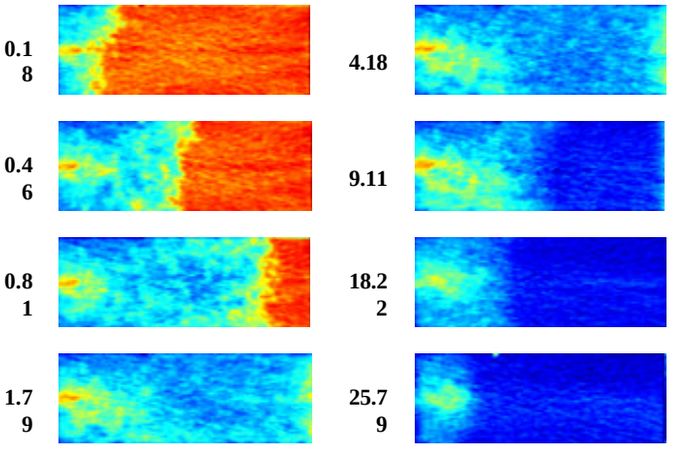


FIG. 1: CT images (CP = 0) of foam displacement (green/blue) in a porous medium initially saturated with surfactant solution (red/yellow). Nitrogen and surfactant solution are co-injected at 5 (standard) cm^3/min and 0.5 cm^3/min, respectively. The sharp foam front traverses the core and breaks through after at t = 1.79. A secondary liquid deliquid fraction arises in the foam bank and spreads towards the in- and outlet of the porous medium. Steady state is reached at t = 25.

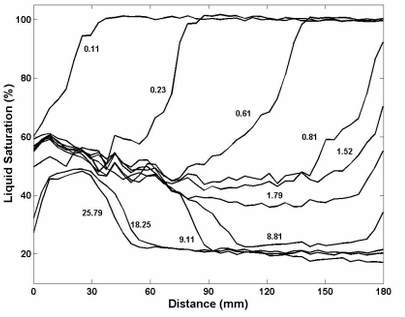


FIG. 2 Liquid liquid fraction profiles (liquid fractions versus distance from the inlet) corresponding to foam motion in a porous medium initially saturated with surfactant solution (see images in Fig. 1). The liquid fraction profiles exhibit a characteristic diffuse front-like pattern from t = 0.11 up to the breakthrough at t = 1.79. The secondary liquid deliquid fraction is visible from t = 061. This secondary liquid deliquid fraction becomes dominant from t = 1.79 up to t = 25.79.

XXI ICTAM, 15–21 August 2004, Warsaw, Poland

NUCLEATION OF CRACKS IN TWO-DIMENSIONAL PERIODIC CELLULAR MATERIAL

Michael Ryvkin, Moshe Fuchs and Fabian Lipperman
Tel Aviv University, School of Mechanical Engineering, Ramat Aviv 69978, Israel

Summary The brittle fracture behavior of cellular material modeled as 2D regular beam lattice is examined. The flaw development from a single failure of a beam to a macrocrack produced by multiple beam breaks is observed. The representative cell analysis method enabled to consider infinite lattices of different topologies without any simplifying assumptions. Fracture toughness evaluated for both in plane fracture modes helps to explain the obtained propagation paths.

FRACTURE SCENARIO

Consider an infinite plane beam lattice possessing 2D translational symmetry. The elastic response of the lattice is defined by the bending and the axial stiffnesses of the beams rigidly connected at the lattice nodes. The lattice is subjected to remote tensile loading generating a periodic stress state. Increasing the remote loading leads to rods failures. If the damage is distributed single breaks one has a problem of determining the decrease in material strength [2]. Another limiting situation is when a sufficiently large number of broken rods produce a crack on a macrolevel. In this case the fracture properties of cellular material can be investigated by the use of semi-infinite crack model [1,3,6]. The goal of the present work is to study the complete process of crack nucleation from a single break.

In order to examine the nucleation phenomenon we have to accept some failure criterion. It is assumed that when the maximum tensile stress in a beam approaches some critical value brittle fracture of the beam takes place. This value is approximately equal to the modulus of rupture σ_{fc} for the bulk material [3]. After the first rod failure the stresses around the flaw redistribute. The analysis of the stress state shows which of the neighboring rods will fail next, then the lattice with two rods missing is examined. Continuation of this procedure produces a flaw pattern. For all the considered layouts with triangular, square and heagonal cells this flaw becomes stable after a sufficiently large number of broken rods and is composed of one or two macrocracks.

ANALYSIS METHOD

In the literature there are two main approaches to the analysis of infinite beam lattice failure[3]. The first one is to consider a sufficiently large finite domain and to employ the finite element method. The second approach relates the infinite lattice to an elastic continuum using some simplifying assumptions. Herein we use another way and carry out the exact analysis of infinite lattice structure. This is done by means of the reprecentative cell method based on the discrete Fourier transform [4,5]. This method enables to reduce the analysis of arbitrary loaded structure possessing translational symmetry to the analysis of a single representative periodicity cell. For the triangular and hexagonal layouts this cell consists of three beams and for the square layout of two beams. The boundary problem for the cell is formulated with respect to the complex valued displacement transforms. Their values at the opposite cell boundaries are related by Born - Von Karman type boundary conditions.

The absence of the translational symmetry in the lattice structures with several broken beams is overcomed by introducing fictitious forces applied at the ends of these beams. The amplitudes of the forces are obtained at each step from a linear algebraic system of $3N$ equations where N is the number of broken elements.

RESULTS

The results of numerical experiments carried out in accordance with the described fracture scenario for three different layouts are presented. Note that the triangular and hexagonal lattices on a macrolevel possess isotropic elastic effective properties. The remote loading is uniaxial tension as shown in Fig. 1. For the triangular layout there is nothing surprising: a straightlinear crack perpendicular to the loading direction is produced. In the case of honeycomb lattice the result is different: after several initial breaks a crack propagating in the direction inclined at 30 degrees with the loading direction is observed (Fig. 1b) Note, that this crack propagation path differs from the one found in a similar problem [6]. The square layout provides somewhat unexpected result. cracks propagating parallel to the applied loading direction (Fig. 1c).

In order to explain the observed propagation paths the fracture toughnesses K_{Ic} and K_{IIc} have been determined. To this end a long straightlinear crack undergoing corresponding deformation modes was considered. The accuracy of the results was verified by the comparison of the energy release rates evaluated from the lattice analysis and from the problem of a crack in a homogenized elastic continuum possessing effective elastic properties.

The obtained results reveal a significant influence of the material microstructure on the crack propagation direction and show that in cellular materials, in contrast to homogeneous ones, the condition $K_{II} = 0$ (zero Mode II stress intensity factor) can not be employed for predicting the crack propagation path.

References

[1] Chen, J.Y., Huang, Y. and Ortiz, M.: Fracture analysis of cellular materials: a strain gradient model. *Journal of Mechanics and Physics of Solids*, **46**:789–828, 1998.

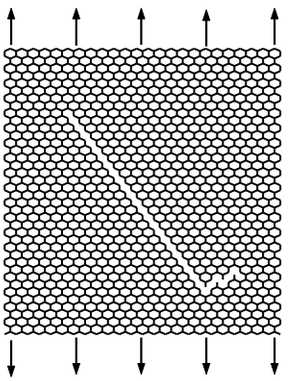
[2] Chen, C., Lu, T.J. and Fleck, N.A.: Effect of imperfections on the yielding of two-dimentional foams. *Journal of Mechanics and Physics of Solids*, **47**:2235–2272, 1999.

[3] Gibson, .J. and Ashby, M.F.: Cellular solids. Structure and Properties. Cambridge University Press, 2001.

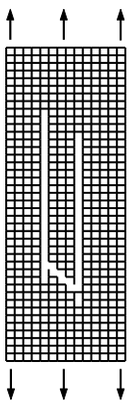
[4] Nuller, B. and Ryvkin, M.: On boundary-value problems for elastic domains of a periodical structure deformed by arbitrary loads, *Izvestia VNIIG, Sbornik nauchnych trudov*, **136**: 49–55, 1980.

[5] Ryvkin, M., Fuchs, M.B. and Nuller, B.: Optimal design of infinite repetitive structures. *Structural and Multidisciplinary Optimization*, **18**:202–209.

[6] Schmidt, L. and Fleck, N. A. Ductile fracture of two-dimentional cellular structures, *International Journal of Fracture*, **111**, 327-342.(2001)



(b)



(c)

Figure 1 Cracks produced in hexagonal(b) and square cell (c) infinite lattices under uniaxial tensile remote loading.

Simulations of micro- and nano -channel flows by a Dissipative Particle Dynamics Method

Justyna Czerwinska, Nikolaus A. Adams
email: Justyna.Czerwinska@ism.mw.tu-dresden.de, Nikolaus.Adams@ism.mw.tu-dresden.de
Institute of Fluid Mechanics, Department of Mechanical Engineering, Technical University, Dresden, Germany

The numerical modeling of micro- and nano- flows is very important for understanding micro-fluidics phenomena in industrial applications. However the methods, which are widely used, have various limitations. The continuum models cannot provide correct description of near wall behavior of fluids (no–slip boundary conditions is enforced). Molecular Dynamics approach is very expensive computationally. Therefore the industrial application is limited.

In this paper we propose to model nano- and micro-flows by Dissipative Particle Dynamics. The method is particle based simulation techniques. The method can be derived from Molecular Dynamics by means of coarse graining. Dissipative Particle consists of many molecular particles. Therefore the simulations by DPD are much less computationally expensive than MD and easier to apply for industrial flows modeling.

The dissipative particle can be defined in two ways. Soft fluid particle model assumes that particles are spherical and interparticle interaction is restricted to specified region. The Voronoi particle model [5,6,7,8] describe particles as Voronoi cells and interacting with adjusted neighbors. The Voronoi approach helped to solve many problems such as treatment of boundary conditions, fluctuation in the volume and inaccuracies in equilibrium fluid properties. Here, we will present results of 2-D computations of some flow configurations (micro-channel) applying Voronoi approach of Dissipative Particle Dynamics. This is a new and promising approach to compute micro and nano- fluidics phenomena.

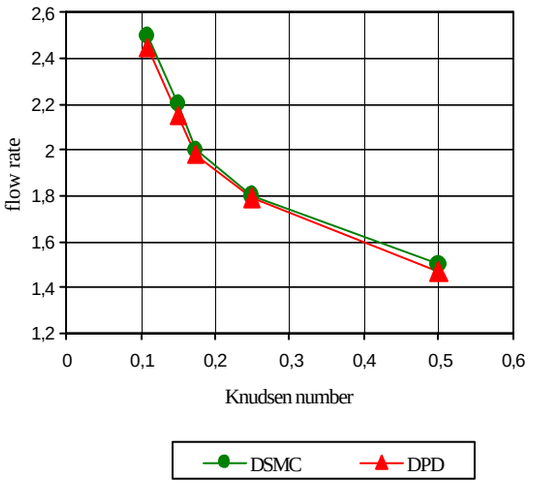


Figure 1.: Flow in the micro-channel simulated by Dissipative Particle Dynamics (DPD) and Direct Simulation Monte Carlo (DSMC). Figure presents the flow rate – Knudsen number relation.

References

[1] E.G. Flekkøy, P.V. Coveney, G. de Fabrittis, *Foundation of Dissipative Particle Dynamics*, Phys. Rev E., vol. 62, 2000
[2] M. Serrano and P. Español, *Thermodynamically Consistent Mesoscopic Fluid Particle Model*, Phys. Rev. E, 64, 2001
[3] M. Serrano,G. de Fabritiis, P. Español, E.G. Flekkøy, P.V. Coveney, *Mesoscopic Dynamics of Voronoi Fluid Particles*, J. Phys. A: Math. Gen. vol. 35, 2002
[4] G. de Fabritiis, P.V. Coveney and E.G. Flekkøy, *Multiscale Dissipative Particle Dynamics*, Phil. Trans.R.Soc.Lond.A, 360:317-331, 2002
[5] J. Czerwinska, N. A. Adams, *Numerical Modeling of Micro-channel Flows by a DPD Method*, Proceedings of ASME FEDSM'03, 2003
[6] J. Czerwinska, N. A. Adams, *Dissipative Particle Dynamics for Modeling Complex Fluids*, Summer School in Multi-Scale Modeling and Simulation, Lugano Switzerland, 2003 (in print)

MULTI-SCALING APPROACH IN THE MECHANICS OF DISORDERED MATERIALS

Alberto Carpinteri, Simone Puzzi
Department of Structural Engineering and Geotechnics, Polytechnic of Turin, Italy

Summary The present paper reports the major results of the fractal approach to scaling of mechanical properties in solid mechanics. Among them, it will be put forward the size-independent *fractal cohesive crack model* and the definition of fractal quantities (hence with non-integer dimensions) which are the true material size-independent properties. Particular attention is paid to the fractal strain, defined by means of fractional calculus, and to the Principle of Virtual Work for fractal media.

One of the most important topics in solid mechanics is the study of the so-called *size effects*, whose importance has been widely recognised during the last decades. The first to address this topic was Leonardo da Vinci, in the 15th century, in his considerations about the strength of ropes of different length. Size-scale effects on the strength of materials were evidenced also by Galileo Galilei, about two centuries later, and by Mariotte. Despite of these enlightened, pioneering contributions, well ahead of their time, it took more or less five hundred years, before the importance of scaling, which cannot be predicted by classical continuum mechanics, clearly emerged. Probably, the most important step forward in the history of scaling of strength was given by Griffith in 1921, as he posed the basis of the linear elastic fracture mechanics (LEFM). And it took about fifty years more before the size-scale effects were recognised not only on strength, but also on the fracture energy, when arose the problem of designing large concrete structures, for which the gap between the scale of the structure and that of laboratory specimens is very large. Since the 1970's, the interest to scaling inside the scientific community has continuously grown and many valuable contributions have been given to the development of this nowadays fast growing, broad branch of solid mechanics. In the present century, the new challenge is at the opposite side: down-scaling, i.e. the size-scale effects when the structural scale is reduced and approaches the micro- (or even the nano-) scale. This strong interest is clearly emerging for various high-tech materials and applications. Several of these novel materials can be successfully represented and modelled as heterogeneous and disordered. For this reason we are convinced that the fractal approach, originally developed for this kind of materials, and the only one capable to encompass in a unified framework, through the definition of the Principle of Virtual Work for fractal media, the scaling on strength, fracture energy and critical strain, will succeed in capturing the essentials also of down-scaling.

The size-independent fractal cohesive crack model

The cohesive crack model is able to simulate tests where high stress gradients are present, e.g. tests on pre-notched specimens. Particularly, the model captures the ductile-brittle transition occurring by increasing the size of the structure. On the other hand, uniaxial tensile tests on dog-bone shaped specimens [3] have shown that the three material parameters defining the cohesive law are not size independent: particularly, increasing the specimen size, the tensile strength σ_u tends to decrease, whilst the fracture energy G_F and the critical displacement w_c tend to increase. These *size effects* can not be predicted by the cohesive model. In other words, the parameters of the cohesive crack model introduced by Barenblatt and Hillerborg [1] depend on the structural size. In order to overcome the original cohesive crack model drawbacks, a *scale-independent* (fractal) *cohesive crack model* has been proposed recently by the first Author. This model is based on the assumption of a fractal-like damage localisation in a *fractal band* at the mesostructural level. The fractal nature of the damage process allows us to explain the size effects on σ_u, G_F and w_c as well as the rising of the cohesive law tail observed in [5].

As fundamental hypothesis, bore out by experimental evidence, we define fractal geometries for both the resistant cross section at maximum load (fig. 1b) and the dissipation domain (fig. 2b) [4]. Hence we can compute the maximum load F, the critical displacement w_c and the total dissipated energy W as:

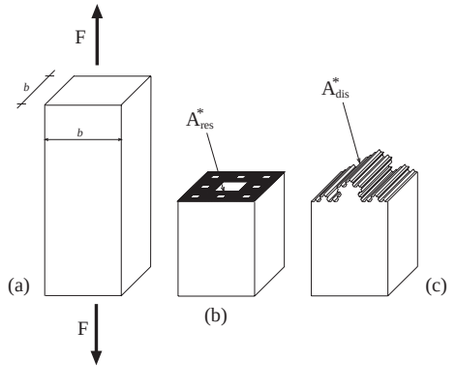


Figure 1: Tension specimen (a). Fractal localization of the stress upon the resistant cross section (b) and of the energy dissipation upon crack surface (c).

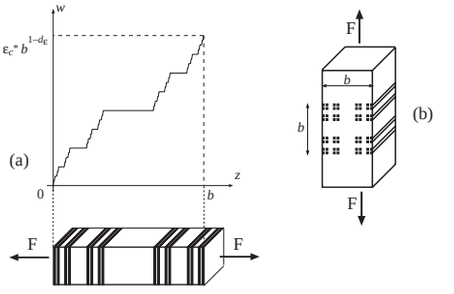


Figure 2: Fractal localization of the strain (a) and of the energy dissipation inside the damaged band (b).

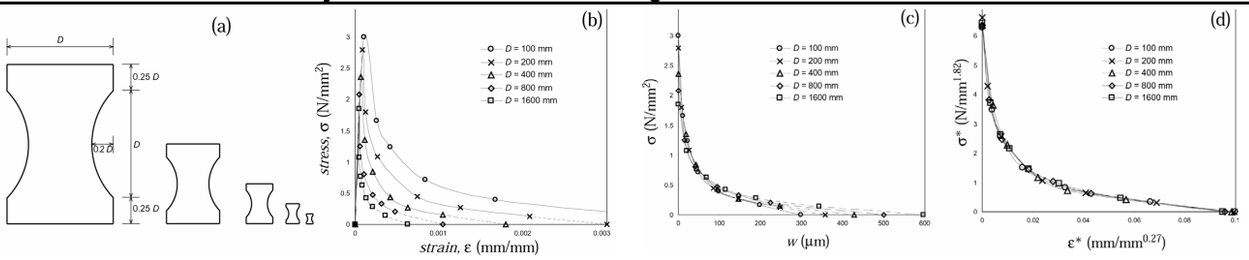


Figure 3: Tensile tests on dog-bone shaped specimens (a) by van Vliet [3]: stress-strain diagrams (b), cohesive law diagrams (c), fractal cohesive law diagrams (d). The dashed lines refer to extrapolated values.

$$F = \sigma_u A_0 = \sigma_u^* A_{\text{res}}^* , \qquad w_c = \varepsilon_c b = \varepsilon_c^* b^{1-d_\varepsilon} , \qquad W = G_F A_0 = G_F^* A_{\text{dis}}^* . \tag{1}$$

These quantities are size-dependent. The true scale-independent quantities are the right hand side ones, i.e. the *fractal strength* σ_u^*, the *fractal critical strain* ε_c^* and the *fractal fracture energy* G_F^*. They show non-integer physical dimensions: $[F][L]^{-(2-d_\sigma)}$ for σ_u^*, $[L]^{d_\varepsilon}$ for w_c^*, and $[FL][L]^{-(2+d_G)}$ for G_F^*. Because of the measure of the resistant cross section A_{res}^* and the dissipation domain A_{dis}^*, from (1) the scaling laws for strength, critical displacement and fracture energy can be obtained:

$$\sigma_u = \sigma_u^* \, b^{-d_\sigma} , \qquad w_c = \varepsilon_c^* \, b^{1-d_\varepsilon} , \qquad G_F = G_F^* b^{+d_G} . \tag{2}$$

Eqns (2) provide size effects in perfect agreement with the trends arising from experiments. The third scaling law can be derived also from the assumption, experimentally verified, of invasive fractal crack surface (fig. 1c). Moreover, we know that the sum of the three scaling exponents is always equal to one : $d_\sigma + d_\varepsilon + d_G = 1$ [4]. According to these definitions, we call the σ^*-ε^* diagram the *fractal or scale-independent cohesive law*. Contrarily to the classical cohesive law, which is experimentally sensitive to the structural size, this curve is an exclusive property of the material since it is able to capture the fractal nature of the damage process. The area below the softening fractal stress-strain diagram represents now the fractal fracture energy G_F^*.

The model has been applied to some data obtained by van Mier & van Vliet [3] from direct tensile tests under rotating boundary conditions and in a scale range 1:32 (fig. 3a). Interpreting the size effect on the ultimate stress and on the fracture energy by means of fractals and fitting the experimental results, the values $d_\sigma = 0.18$ and $d_G = 0.09$ are calculated. Some of the σ–ε and the σ-*w* (the cohesive law) diagrams are reported respectively in fig. 3b and 3c, where *w* is the displacement localized in the damage band, obtained by subtracting, from the total one, the displacement due to elastic and inelastic pre-peak deformation. Note how the tail of the cohesive law rises while its peak decreases increasing the size. The fundamental relationship between the scaling exponents yields to find for d_ε a value equal to 0.73, so that the fractal cohesive laws can be plotted in fig. 3d. As expected, all the curves related to different sizes tend to merge in a unique, scale-independent cohesive law.

Local fractional calculus and the Principle of Virtual Work for fractal media

The most recent work [5,6] is devoted to the possible application of the fractional calculus (i.e. integrals and derivatives of non-integer order) to the study of fractal phenomena, which cannot be handled by classical calculus. Kolwankar [2] introduced the *local fractional derivative* (LFD) and proved that, in the singular points, the LFD is either zero or infinite; it assumes a finite value only if the order of derivation is equal to the Hölder exponent. For the devil's staircase graph of fig. 2a, for instance, the LFD of order equal to the dimension of the Cantor set is zero everywhere except in the singular points where it is finite. This leads to the definition of the fractal strain as the LFD of order $(1- d_\varepsilon)$ of the displacement. As inverse of the LFD, Kolwankar introduced the *fractal integral*. With this tool it is possible describing the mechanics of fractal media, calculating the size effects on tensile and flexural strength, and writing the equation of Principle of Virtual Work, which, in contrast with its continuum counterpart, has an intrinsic multi-scale structure.

References

[1] Hillerborg A., Modeer M., Petersson P.E.: Analysis of crack formation and crack growth in concrete by means of fracture mechanics and finite elements. *Cem. Concr. Res.* **6**:773-782, 1976.
[2] Kolwankar K.M., Gangal A.D., Local fractional Fokker-Plank equation, *Phys. Rev. Lett.*, **80**, pp. 214-217, 1998.
[3] Van Vliet M.R.A. Size effect in tensile fracture of concrete and rock. *PhD Thesis*, Technical University of Delft, 2000.
[4] Carpinteri A., Chiaia B., Cornetti P.: A scale-invariant cohesive crack model for quasi-brittle materials. *Eng. Frac. Mech.*, **69**:207-217, 2002.
[5] Carpinteri A., Cornetti P.: A fractional calculus approach to the description of stress and strain localization in fractal media, *Chaos, Solitons and Fractals,* **13**:85-94, 2002.
[6] Carpinteri A., Chiaia B., Cornetti P.: On the mechanics of quasi-brittle materials with a fractal microstructure. *Eng. Frac. Mech.*, **70**:2321-2349, 2003.

GRAD-TYPE EXPANSION ABOUT NONEQUILIBRIUM STATES FOR THE RELAXATION-TIME APPROXIMATION OF THE BOLTZMANN-PEIERLS EQUATION

Zbigniew Banach, Wiesław Larecki
Polish Academy of Sciences IPPT PAN, Świętokrzyska 21, PL 00-049 Warszawa, Poland

Summary A new type of heat transport equations for transient processes under high thermal loads is derived from the microscopic, kinetic-theory description of a phonon gas. The modified Grad expansion method is applied to the relaxation time approximation of the Boltzmann-Peierls kinetic equation. The proposed new type of the expansion about nonequilibrium states conforms to the time scales of the phonon gas relaxation processes and admits arbitrarily large heat fluxes.

In many modern technological applications, high transient thermal loads are applied to dielectric and semiconducting materials. It is well recognized that, in those cases, neither the classical Fourier law nor the Maxwell-Cattaneo-Vernotte heat wave equation accurately predict the thermal response of the material. Since the heat transport by phonons (quanta of a crystal vibrational energy) predominates in dielectrics and semiconductors, the suitable heat transport equations should be derived in some way from the microscopic, kinetic-theory description of a phonon gas. Hence, we consider the Boltzmann-Peierls kinetic equation governing the phonon distribution function (i.e., the phase density or the number density of phonons) with the commonly used Callaway's relaxation time approximation of the collision term. It involves the relaxation time τ_R of resistive processes (i.e., scattering processes which do not conserve quasi-momentum and which tend to return the phonon gas to an equilibrium Planck distribution function) and the relaxation time τ_N of normal processes which conserve quasi-momentum and which lead to a nonequilibrium anisotropic Planck distribution function, also called a drifting distribution. These two relaxation times determine natural time scales for the flow of a phonon gas and, in general, three regimes of the phonon gas flow can be distinguished, namely, the ballistic, hyperbolic, and diffusive regimes.

Our objective is to obtain the approximate description of the phonon gas flow in the time scale of the order of τ_N, in the hyperbolic regime. Moreover, we aim at the theory admitting virtually arbitrarily large values of the heat flux vector components. Thus, the use of the expansion of the phonon distribution function about a nonequilibrium anisotropic Planck distribution function and the enlargement of the set of independent gas-state variables through the introduction of higher-order moments of the distribution function suggest themselves.

In order to derive the evolution equations for the gas-state variables, we propose to generalize the classical method of Grad in the sense that, instead of the local equilibrium distribution function, we take the known specific no equilibrium distribution function as a base for the expansion. Hence, we aim at modifying the classical Grad-type expansion for the phonon gas about the local equilibrium Planck distribution function, derived in [1,2], by employing the nonequilibrium anisotropic Planck distribution given in [3] in terms of the energy density and the heat flux vector. For the classical gas, a similar idea of expanding the distribution function about the (nonequilibrium) anisotropic Gaussian was employed in [4] but not in the form of a systematic Grad-type expansion and without any justification in the relaxation processes.

For simplicity, no distinction is made between longitudinal and transverse phonons. Also, linear isotropic dispersion relation $\Omega = c\,|\mathbf{k}|$ is assumed (c is the constant Debay speed) and the components of the wave vector $\mathbf{k}$ are assumed to range from $-\infty$ to $+\infty$. Since emphasis is placed on the flow time scale of the order of τ_N, we assume that τ_N depends on $\mathbf{k}$ while τ_R remains independent of $\mathbf{k}$.
Our reasoning is the following. First, we set up a weighted Hilbert space for the expansion with the aid of the formula for the kinetic entropy of a phonon gas. Subsequently, we define an orthogonal basis in this Hilbert space. The expansion coefficients are determined and the relations between those coefficients and the moments of the distribution function are established. Substitution of the truncated expansion into the corresponding system of moment equations results in a closed system of the evolution equations for the moments. In this way, a hierarchy of closed systems can be obtained, such that each system involves two relaxation times τ_N and τ_R, is nonlinear in energy density and heat flux, and depends linearly on the higher-order moments of the distribution function. These higher-order moments are fast variables that decay to their values corresponding to the nonequilibrium drifting distribution after a short relaxation time τ_N , so that our approach seems to be particularly useful if $\tau_N \ll \tau_R$.
The first system in this hierarchy is the nine-moment system which involves the deviatoric part of the flux of the heat flux as the only fast variable. For this system, explicit closed-form expressions for the moment fluxes and productions are obtained. It is expected that this nine-moment system can describe more adequately transient processes under high thermal loads than the previous theories which treat the heat flux in a perturbative manner.

Acknowledgment

This work was supported by the State Committee for Scientific Research (KBN) through the grant No 5 T07A 046 24.

References

[1] Banach Z., Piekarski S.: Irreducible tensor description. II. A quasiparticle gas. *J. Math. Phys* **30**:1816-1825, 1989

[2] Banach Z., Piekarski S.: Irreducible tensor description. III. Thermodynamics of a low-temperature phonon gas. *J. Math. Phys* **30**:1826-1836, 1989

[3] Larecki W.: Symmetric Conservative Form of Low-Temperature Phonon Gas Hydrodynamics. II. – Equations of Heat Transport and Thermal Waves in the Case of Linear Isotropic Approximation of Phonon Frequency spectrum. *Nuovo Cimento* **14D:**141-176, 1992.

[4] Groth C.P.T., Gombosi T. I., Roe P.L., Brown S.L.: Gaussian-based moment-method closures for the solution of the Boltzmann equation, in: Fifth International Conference on Hyperbolic Problems, Stony Brook, NY, June 13-17, 1994

A two-scale model for epitaxial surfaces

Heike Emmerich*, Christof Eck**
*LS TH, FB BCI, Dortmund University, 44227 Dortmund, Germany
**IAM, University Erlangen-Nuernberg, 91058 Erlangen, Germany

1 Summary

Spiral surface growth is well understood in the limit where motion of the spiral ridge is controlled by the local supersaturation of adatoms in its surrounding. In liquid epitaxial growth, however, spirals can form governed by both, transport of heat as well as solute. We propose for the first time a two-scale model of epitaxial growth which takes into account all of these transport processes assuming a separation of time scales for the transport of heat compared to that of the solutal field.

2 Introduction

The spiral morphology is known to be one of the most widespread growth morphologies for crystals with atomically flat surfaces. Growth of such crystals is due to the incorporation of new atoms at monoatomic steps in the surface. If a step is pinned at a screw dislocation (see Fig. 1), they wind around this dislocation. As a consequence a spiral forms at the surface (see Fig. 2). The dynamics of the monoatomic steps as well as the final steady-state spacing l between successive steps[1] is determined by the interplay of surface diffusion, attachment kinetics of atoms at the steps, and line tension of the steps. Recently, the observations of spiral ridges in sputtered high-temperature superconducting thin films [1] and in certain semiconductor materials grown by molecular beam epitaxy (MBE) [2] has stimulated renewed interest in spiral surface growth.

Classically this growth problem is modeled by the Burton-Cabrera-Frank (BCF) approach to surface growth [3]. According to that approach atoms are first adsorbed to the crystalline surface, where they involve in a diffusion process along the surface. During this stage these atoms are called *adatoms*. Such adatoms can either desorb from the surface with a probability $1/\tau$ per unit time, or they are incorporated into the crystal at a step and thereby contribute to its growth process. Therefore, two different growth regimes can be distinguished, which depend on the ratio of l and the diffusion length $x_s = \sqrt{D\tau}$. Here D denotes the surface diffusion constant. Regime one refers to surface growth for which desorption is fast ($x_s \ll l$). As a consequence only adatoms which are deposited near a step can be incorporated, and thus step dynamics is *local*, i.e. the step velocity is completely determined by local supersaturation and by step curvature. This regime is well understood and fully accounted for by the classical BCF theory of spiral growth [3, 4].

The second regime refers to step-flow growth at temperatures where desorption is negligible. In this regime all deposited atoms reach a step. As a consequence successive turns of the spiral are strongly coupled via adatom diffusion and step dynamics turns out to be a highly non-local free boundary problem. The steady-state growth of this regime has been investigated by approximate theories [5, 6] and by the boundary integral method [7]. Succeedingly these results have been validated by full dynamical simulations of the model equations proposed by Burton, Cabrera and Frank originally based on a phase field model [8]. Moreover, the latter dynamical simulations allowed to investigate the crossover from the local to the desorption-free limit with respect to two characteristic aspects. The first of these two aspects concerns the scaling of l, the second the approach to steady-state

[1] Equivalently one could focus on the surface slope a/l, where a is the lattice parameter.

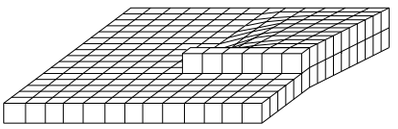


Figure 1: Dislocation at a flat surface. This dislocation might trigger spiral growth (see Fig. 2).

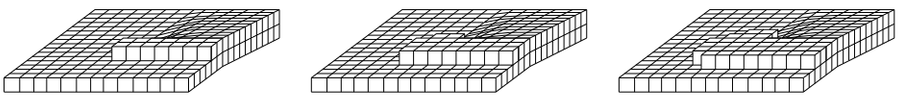


Figure 2: Step formation due to the pinning at a screw dislocation.

growth: In the local limit, spirals find their final step spacing after a single rotation. Without desorption, however, a slower relaxation to steady-state growth due to the global redistribution of adatoms is encountered. The numerical simulations in [8] reveal, that this relaxation time depends on the third power of the system size. This result refers to a surface with a single dislocation. However, it is well known that relaxation may depend on the density of screw dislocations as well.

The main goal of this contribution is to investigate spiral dynamics for a characteristic domain of a macroscopic surface containing an array of screw dislocations. I.e., we will extend the results of [8] to include the dependence on the density of screw dislocations at a surface. Doing so we will focus on the scaling of l and the relaxation to steady-state growth, as well. Our results are based on a two-scale model for surface growth, which derivation we will discuss briefly. We will then report on numerical investigations of our model resulting in our new scaling relations for dislocation growth of competing spirals. Finally we will conclude with an outlook on further applications to understand the mechanisms and consequences of spiral interaction at epitaxial surfaces in more detail.

References

[1] M. Hawley, I. D. Raistrick, J. G. Beery, and R. J.Houlton, Science **251**, 1587 (1991); C. Gerber, D. Anselmatti, J. G. Bednorz, J. Mannhart, and D. G. Schlom, Nature **350**, 279 (1991).

[2] G. Springholz, A. Y. Ueta, N. Frank, and G. Bauer, Appl. Phys. Lett. **69**, 2822 (1996).

[3] W. K. Burton, N. Cabrera, and F. C. Frank, Philos. Trans. R. Soc. London, Ser. A**243**, 299 (1951).

[4] N. Cabrera and M. M. Levine, Phil. Mag. **1**, 450 (1956).

[5] N. Cabrera and R. V. Coleman, in: *The Art and Science of Growing Crystals*, ed. by J. J. Gilman, John Wiley, New York (1963).

[6] T. Surek, J. P. Hirth, and G. M. Pound, J. Cryst. Growth **18**, 20 (1973).

[7] J. P. van der Eerden, J. Cryst. Growth **53**, 305, 315 (1981); see also J. P. van der Eerden, in *Handbook of Crystal Growth, Vol. 1a*, ed. by D. T. J. Hurle, Elsevier (1993).

[8] A. Karma, and M. Plapp, Phys. Rev. Lett. **81**, 4444 (1998).

A GEOMETRICAL THEORY OF DISCRETE DISLOCATIONS IN LATTICES, WITH APPLICATIONS TO DISLOCATION DYNAMICS AND CRYSTAL PLASTICITY

M. P. Ariza and M. Ortiz
Division of Engineering and Applied Science
California Institute of Technology
Pasadena, CA 91125

Abstract

The mechanics of crystal lattices containing dislocations can be expressed in terms of fields that are supported on the lattice itself, e. g., the displacement field and the energy density; and fields that are defined on certain ancillary lattices, e. g., the eigendeformation fields which describe the dislocations. In the harmonic approximation, the energy is a quadratic form in the displacement field and the eigendeformations. At fixed dislocation density, the displacement field of the crystal lattice follows by energy minimization. We show that the structure of the resulting mechanics of defective lattices can be streamlined and given a compelling interpretation in terms of a discrete version of homology and differential calculus. The resulting differential operators generalize the conventional differential operators of exterior calculus in a manner which reflects and takes full account of the structure of the crystal lattice. Based on this mathematical framework, we generalize to lattices classical constructs and relations from the geometrical theory of continuously distributed dislocations, such as the notion of Burgers circuit and slip system; and Frank's and Kröner's formulae. We also show how the forest-hardening model can be phrased in terms of certain topological invariants. We illustrate the versatility of the theory by means of a number of selected applications, including: core energies of bcc dislocations; the dislocation field of an expanding nanovoid; and the dislocation structures selected by the forest mechanisms and the attendant hardening rates.

EXTENDED SUMMARY

The classical geometrical theory of continuously distributed dislocations relies on the notion of Burgers circuit to characterize the distribution of dislocations in an otherwise linear elastic continuum (cf, e. g., [3]). Thus, if $\beta^e : \mathbb{R}^3 \to gl(\mathbb{R}^3, \mathbb{R}^3)$ is the elastic deformation field, the formula

$$\mathbf{b}(C) = \oint_C \beta^e \mathbf{dx} \tag{1}$$

gives the total Burgers vector of all the dislocations encircled by the closed loop C, or Burgers circuit. In particular, two circuits C_1 and C_2 are equivalent if one can be mapped homotopically to the other without changing the total Burgers vector $\mathbf{b}(C)$ along the way. In particular, this requires that $\mathbf{b}(C_1) = \mathbf{b}(C_2)$. This introduces an equivalence relation among loops in $\mathbb{R}^3$, each of which represents a dislocation bundle. The equivalence classes consisting of loops having a common point have a group structure in which the group operation between two loops consists of traversing the loops consecutively. The resulting *fundamental group* provides an intrinsic characterization of the topology of the dislocation ensemble. Alternatively, the geometry of the dislocation ensemble is described by Nye's dislocation density tensor

$$\alpha = \beta^e \times \nabla \tag{2}$$

since, by Stoke's theorem

$$\mathbf{b}(C) = \oint_C \beta^e \mathbf{dx} = \int_S (\beta^e \times \nabla) \boldsymbol{n} dS \tag{3}$$

where S is any surface having C as boundary and $\boldsymbol{n}$ is the (consistently oriented) unit normal to S. In crystals, the dislocation motion is confined to crystallographically determined slip planes, which requires that the displacement gradient be of the form

$$\nabla \boldsymbol{u} = \beta^e + \beta^p \tag{4}$$

with β^e absolutely continuous and the plastic deformation β^p defining a measure supported on discrete crystallographic planes. The energy of the crystal is then variously given by

$$E = \int \frac{1}{2} c_{ijkl} \beta^e_{ij} \beta^e_{kl} dx = \int \frac{1}{2} c_{ijkl} (u_{i,j} - \beta^p_{ij})(u_{k,l} - \beta^p_{kl}) dx \tag{5}$$

At fixed β^p, the displacement field follows by energy minimization. It is also of interest to determine the energy minimizing dislocation structures that arise under suitable constraints and loading conditions, and the energy stored in the dislocation structures.

This classical picture suffers from a number of fundamental shortcomings, all of which can be traced to the idealization of the crystal as a continuum and the corresponding jettisoning of its lattice structure. Thus, perfect or Volterra dislocations have infinite energy per unit length. This type of divergence can be eliminated by the introduction of a core cut-off radius, but this fix is ad-hoc and not rooted in fundamental theory. Other maladies that afflict the continuum theory are the absence of any natural minimum separation between slip planes, and the extraneous nature of the Burgers vectors.

A satisfactory resolution of these deficiencies *a fortiriori* requires an acknowledgement from the outset of the discrete nature of crystals and the formulation of a mechanics of defective crystal lattices. In this framework, the familiar notion of continuum is replaced by that of a Bravais lattice of points. This substitution immediately begs a number of fundamental questions, namely:

i) What is the discrete analog of a Burgers circuit?

ii) What is the discrete analog of the *grad*, *curl* and *div* operators?

iii) What is the discrete analog of line integrals, surface integrals, unit normals and Stokes theorem?

iv) What is the discrete analog of a slip system?

among others. In the present work we address these issues systematically with the aid of basic tools from algebraic topology, such as CW complexes and homology; from differential calculus, such as differential complexes and integration; and from analysis, such as the Fourier transform and Γ-convergence. The picture that emerges gives rigorous mathematically expression to: the notion of a perfect or defect-free lattice, in which, in particular, every loop is the boundary of an area and can be shrunk to a point, and every close surface is the boundary of a volume and can be likewise shrunk to a point; the notion of discrete differential operators and integrals, including Stoke's theorem; the notion of a crystallographic slip system, with well-defined Burgers vectors and a minimum spacing between slip planes; and the notion of dislocation densities, dislocation entanglements such as junctions, and the topological transitions attendant to the formation and dissolution of junctions. These tools provide a powerful framework for the formulation of a discrete dislocation dynamics in crystal lattices. The theory supplies a full three-dimensional generalization of some existing theories of crystallographic slip on a single plane [2, 1]. We illustrate the versatility of the theory by means of a number of selected applications, including: core energies of bcc dislocations; the dislocation field of an expanding nanovoid; and the dislocation structures selected by the forest mechanisms and the attendant hardening rates.

References

[1] A. Garroni and S. Mueller. Gamma-limit of a phase-field model of dislocations. (92), 2003. Preprint, Max-Planck-Institut fur Mathematik in den Naturwissenschaften, Leipzig, Germany.

[2] M. Koslowski, A. M. Cuitiño, and M. Ortiz. A phase-field theory of dislocation dynamics, strain hardening and hysteresis in ductile single crystals. *Journal of the Mechanics and Physics of Solids*, 50:2597–2635, 2002.

[3] T. Mura. *Micromechanics of Defects in Solids*. Kluwer Academic Publishers, Boston, 1987.

XXI ICTAM, 15–21 August 2004, Warsaw, Poland

STRESS-DEFECT INTERACTIONS AT MOLECULAR/CONTINUUM SCALES

Mathieu Bouville*, Krishna Garikipati**, Michael L. Falk*
*Department of Materials Science & Engineering, University of Michigan, Ann Arbor, USA
**Department of Mechanical Engineering, University of Michigan, Ann Arbor, USA

Summary External stress on a crystal affects the Gibbs free energy of formation and migration of point defects, thereby lowering/raising defect concentrations and mobilities. This effect is determined by the volume change of the crystal—for defect creation it is the formation volume, V_f. Lattice distortion *at the defect itself* can only be predicted by atomistic simulations, not by continuum elasticity. However, this distortion, represented as a dipole tensor of forces in continuum elasticity, determines the far-field deformation, and hence V_f. For the vacancy in silicon, we have quantified V_f by such studies, using the Stillinger-Weber empirical potential at atomic scales and elasticity at continuum scales. We also have treated issues related to bridging these scales, obtained consistent interpretations of parameters, identified the limitations of continuum, molecular and *ab initio* calculations, and found overall agreement with relevant results by Eshelby.

BACKGROUND

Point defect (vacancy/interstitial) concentrations are determined by their Gibbs free energies of formation, G_f. The influence of an *external stress*, $\boldsymbol{\sigma}$, is to raise or lower G_f. For mobile defects, this modulation is apparent also on the migration energy. Consequently, the concentration and mobility of point defects are strongly influenced by $\boldsymbol{\sigma}$. Solid state diffusion of dopant atoms in silicon and germanium requires pairing of these atoms with mobile point defects. Therefore, it is presently of great technological importance to understand the interaction mechanism between external stress and defects. A formation volume, V_f, quantifies the interaction and is entirely determined by deformation of the crystal around the point defect (following section). Continuum elasticity cannot predict the distortion at the defect itself; this field must be extracted from atomistic calculations. For vacancies/interstitials the distortion at this scale is strongly influenced by changes in bonding between first- and second-nearest neighbor atoms. The accuracy of *ab initio* calculations [1] notwithstanding, this class of methods may not be ideal for determining the overall crystal deformation, and hence V_f: While values of V_f converge only for systems much larger than 500 atoms, *ab initio* calculations are currently limited to about 500 atoms, placing larger systems beyond the present reach of these methods.

Molecular simulations allow system sizes that, at millions of atoms, are larger by many orders of magnitude. Realistic crystal sizes are still not attained, but the systems are large enough that displacement and stress fields escape the effect of lattice discreteness at the point defect. Most importantly, they converge to the elastic fields which, when appropriately scaled, are invariant of crystal size. We have carried out such atomistic calculations of the mono-vacancy in silicon using the Stillinger-Weber interatomic potential. If the deformation at the defect is represented as a dipole tensor, continuum elasticity solutions of the displacement and internal stress fields can be obtained using the Green's function for anisotropic elasticity. These fields are indispensable for checking the far-field solutions from atomistic calculations. In turn, far-field solutions determine V_f.

ELASTICITY AND MOLECULAR STUDIES OF VACANCY-INDUCED DEFORMATION

The dipole tensor (preceding section), $\boldsymbol{D}$, used as the continuum elasticity analogue of a vacancy, is called a center of contraction. The displacement and internal stress fields around a vacancy can be obtained by using the Green's function for anisotropic elasticity [3]. The body force in the Green's function method is specified by $\boldsymbol{D}$. Being a continuum representation of the forces on nearest-neighbor atoms of the vacancy, $\boldsymbol{D}$ must be extracted from molecular calculations. An accurate quantification of $\boldsymbol{D}$ thus determines the deformation field and hence V_f. Any method to obtain $\boldsymbol{D}$ essentially imposes consistency between the fine scale atomistic calculations and "coarse scale" continuum elasticity for this problem.

Employing the Stillinger-Weber interatomic potential for silicon, the dipole tensor, $\boldsymbol{D}$, was obtained by a least squares' minimization of difference between interatomic forces from the molecular calculations, and the elasticity solution for force at the same point due to the vacancy as center of contraction. For ease of writing we describe this functional using the isotropic elasticity solution in an infinite medium:

$$\mathcal{F} = \sum_i^{n_\mathrm{atom}} \left| \boldsymbol{f}_i - \frac{\mu\, \boldsymbol{D}\boldsymbol{r}_i}{\pi(\lambda+2\mu)|\boldsymbol{r}_i|^4} \mathrm{d}A_i \right|^2 . \tag{1}$$

Here, n_atom is the total number of atoms, $\boldsymbol{f}_i$ is the force on the i^th atom, $\boldsymbol{r}_i$ is the position vector of the atom relative to the vacancy, λ and μ are the Lamé parameters of the isotropic medium, and $\mathrm{d}A_i$ is the radial projection of the atom's cross-sectional area. The necessary condition for minimization of $\mathcal{F}$ with respect to $\boldsymbol{D}$ gives a closed-form result for the dipole tensor. Assuming a dipole tensor of the form $\boldsymbol{D} = D\mathbf{1}$, where $\mathbf{1}$ is the second-order isotropic tensor, the extracted value of D is found to vary as explained in Figure 1.

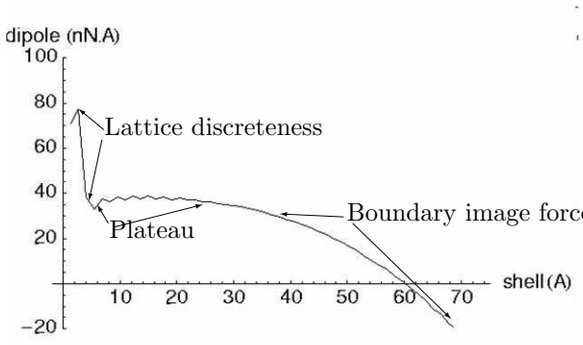


Figure 1. Atomistic calculations for variation in D with radial position of shell of atoms used to extract it. (i) Discreteness effect: Continuum elasticity does not hold close to the vacancy; the discreteness of the lattice dominates the results here. (ii) Plateau: In a range sufficiently far from the vacancy, continuum elasticity holds, and as it predicts, D is essentially constant. (iii) Boundary image force: For a finite computational cell of atoms, image forces from the periodic boundaries exert their influence. Therefore, D fitted to the exact elasticity result for an infinite crystal deviates from the expected constant value.

Our detailed calculations use the anisotropic elasticity solution for a *finite crystal*, in which case D is more nearly constant as the free boundary is approached. The important result, that $D \approx 38\,\mathrm{nN}\cdot\mathrm{\AA}$ holds.
As a check for consistency the extracted dipole value was used in continuum elasticity calculations on an anisotropic silicon crystal, of finite extent, and cubic in shape. The relaxation volume measured at the crystal free surface is independent of the crystal size, as can be understood by considering the case of the isotropic, spherically-shaped crystal of radius R:

$$V(r) = \frac{D}{\lambda + 2\mu}\left(1 + \frac{4\mu}{3\lambda + 2\mu}\left(\frac{r}{R}\right)^3\right). \tag{2}$$

For a crystal of any radius, $V(R) = \frac{D}{\lambda+2\mu}(1 + \frac{4\mu}{3\lambda+2\mu})$ is independent of R. For anisotropic finite crystals of cubic shape, finite element calculations resulted in a relaxation volume $\approx 30\,\mathrm{\AA}^3$. This is in reasonably good agreement with the relaxation volume of $\approx 34\,\mathrm{\AA}^3$ obtained directly from the molecular calculations (Figure 2).

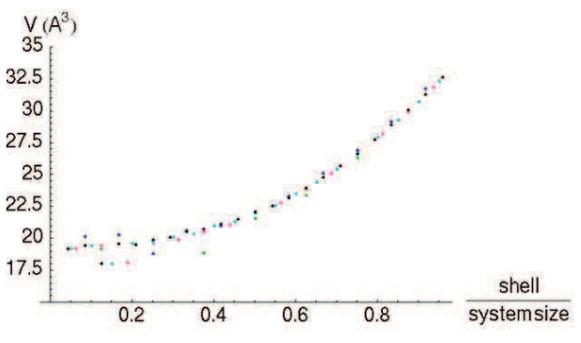


Figure 2. Variation of relaxation volume with r/L from molecular calculations on cubic computational cells of side $2L$.

A final question that arises is whether the internal volume, $V(0)$ in (2), or the external volume, $V(R)$ is the thermodynamically-appropriate formation volume that is conjugate to an external stress. In other words, under a uniform external stress, $\boldsymbol{\sigma} = p\mathbf{1}$, when the stress-free Gibbs free energy G_f^0 is modified to $G_\mathrm{f} = G_\mathrm{f}^0 - pV_\mathrm{f}$, is $V_\mathrm{f} = V(0)$ or $V(R)$? Eshelby [2] shows that for a continuum body, when a sub-domain undergoes a *stress-free* reduction in volume ΔV, the work done by p is $p\Delta V$. It is not immediately obvious how this result can be applied to the present case, since here the sub-domain is the defect, which is discrete, and does not admit the continuum arguments used by Eshelby. Also, it is unclear what the stress-free reduction in volume is at the defect, and how it is related to $V(0)$ and $V(R)$. We have devised a construction in the spirit of Eshelby's "cutting and welding" operations which shows conclusively that $V_\mathrm{f} = V(R)$ is conjugate to $\boldsymbol{\sigma}$. Thus $G_\mathrm{f} = G_\mathrm{f}^0 - pV(R)$ is the correct Gibbs free energy of formation under external stress.

CONCLUSION

We have consistently combined continuum elastic and atomistic calculations to answer fundamental questions on the thermodynamics of point defect formation under stress. By our calculations we have arrived upon a deformation field that is consistent between atomistic and continuum methods, and yields the vacancy formation volume. Notably, the result is in agreement with the stress-defect interaction result of Eshelby [2]. Our methods will be used to study the thermodynamics of vacancy migration, and the formation/migration of the interstitial and dopant-defect pairs.

References

[1] A. Antonelli, E. Kaxiras, and D.J. Chadi. Vacancy in silicon revisited: Structure and pressure effects. *Phys. Rev. Lett.*, 81:2088–2091, 1998.
[2] J.D. Eshelby. Elastic inclusions and inhomogeneities. In J. Sneddon and R. Hill, editors, *Progress in Solid Mechanics*, volume II, page 89. North Holland Publishing Co., 1961.
[3] D.M. Barnett. The precise evaluation of derivatives of anisotropic elastic Green's functions. *Phys. Stat. Sol.*, 59:541, 1972.

DETERMINISTIC SIZE EFFECT IN THE STRENGTH OF CRACKED QUASI-BRITTLE STRUCTURES

B. L. Karihaloo, H. M. Abdalla, Q. Z. Xiao

School of Engineering, Cardiff University, Queen's Buildings, P O Box 925, Cardiff, CF24 0YF, UK

There are two fundamental causes of size effect in the strength of structures made from quasi-brittle materials, such as concrete, namely the material heterogeneity and the occurrence of discontinuities in the flow of stress, such as at cracks and notches. The former leads to the statistical size effect and the latter to the so-called deterministic size effect. In these materials, any crack or notch tips are blunted by the formation of a fracture process zone (FPZ) so that the deterministic strength size effect is less severe than that predicted by the Griffith theory for brittle materials. In the FPZ the stresses are redistributed and energy is dissipated which is thus not available for crack propagation. The size of FPZ can be commensurate with that of most structural elements. Only in very large structures can this size be regarded as small in comparison with their characteristic dimensions.

The redistribution of stresses and dissipation of energy in the FPZ were considered by Baž ant who derived a size effect formula by performing a Taylor's expansion of the size of FPZ from its small asymptotic limit for large structures. This formula is claimed to be applicable to structures in the size range 1:32 but the determination of accurate coefficients appearing in it from tests on laboratory size specimens is questionable and has led to controversy in the literature.

Another approach to capturing the FPZ within a nonlinear theory of fracture for quasi-brittle materials is the so-called ficticious crack model (FCM) which has its origin in the Barenblatt-Dugdale cohesive zone concept. In this model, the FPZ ahead of a real crack is replaced with a fictitious crack in which the material exhibits softening with a residual stress transfer capability across the crack faces dependent on the crack opening displacement, $\sigma(w)$. The faces of the fictitious crack are assumed to close smoothly, so that the stress is finite at its tip and the stress intensity factor (SIF) due to external loading is cancelled by the closure pressure $\sigma(w)$ in the FPZ. The real crack grows only when $w = w_c$. The area under the $\sigma(w)$ diagram from $0 \le w \le w_c$ is the true specific fracture energy G_F of the material. This approach was taken by Karihaloo who however made several approximations which rendered the predictions of his size effect formula suspect for small structures. In the derivation of this formula, it was recognized that quasi-brittle materials develop a diffuse FPZ before the formation of a traction-free crack whose size can be commensurate with that of a small test specimen. Within the FPZ the stresses are redistributed so that it is necessary to consider not only the singular term in the asymptotic crack tip field but also higher order non-singular terms. In the derivation however approximations were used for these higher order terms. Moreover, weight functions for a semi-infinite crack in an infinite plane were used instead of the correct weight functions for a finite crack in a finite specimen.

In this talk, we shall present results in which all these approximations have been eliminated and a new size effect formula derived. This formula is found to be in excellent agreement with test data and to cover a very large size range of 1:80. Its predictions are confirmed by experimental observations, namely that the deterministic strength size effect becomes stronger as the size of structure increases but weakens as the size of the crack relative to the structural size reduces.

The mathematical formulation is based on the decomposition of a traction-free crack of size a in a structure of characteristic size W with a FPZ of length ℓ_p at its tip into (i) a traction-free crack with the following stress field at its tip

$$\sigma_y(r) = \frac{a_1}{\sqrt{r}} + 3a_3\sqrt{r} + 5a_5 r^{\frac{3}{2}} + \cdots \qquad (1)$$

and (ii) a FPZ with the net stress $[\sigma(s) - \sigma_0(\ell p\text{-}s)]$ and the displacement $w(s)$ across its faces. The coefficients a_1, a_3, a_5, … depend on a, W, applied load σ and shape of the body. The authors have obtained these coefficients for several commonly used specimen geometries. Note that a_1 =

$K_I/\sqrt{(2\pi)}$ where K_I is the applied mode I SIF. The opening displacement of the fictitious crack faces $w(t)$ (representing the FPZ) are given by

$$\int_0^{l_p} g(s,t;a)\left[\sigma(s)-\sigma_0\left(l_p-s\right)\right]ds=-w(t) \tag{2}$$

and the smooth closure condition for the fictitious crack tip is

$$\int_0^{l_p} k(s;a)\left[\sigma(s)-\sigma_0\left(l_p-s\right)\right]ds=0 \tag{3}$$

The weight functions $g(s, t; a)$ and $k(s; a)$ are the respective crack face opening displacement at the location t and the SIF at the finite crack tip in a specimen of finite size due to a pair of unit normal forces at s. These have been derived by the authors for several commonly used test specimen geometries. The singular integral equations (2) and (3) have been solved incrementally for the unknown cohesive stress $\sigma(s)$ and ℓ_p for given applied stress σ or K_I and materials properties G_F and $\sigma(w)$ until the ultimate stress σ_u at failure has been reached. σ_u has been found to vary with the size of the structure W and the crack size a ($\alpha = a/W$) as follows

$$\frac{\sigma_u}{f_t}=D_1(\alpha)\left(1+\frac{W/l_{ch}}{D_2(\alpha)}\right)^{-\frac{1}{2}}+\frac{D_1(\alpha)}{2D_2(\alpha)}\frac{W}{l_{ch}}\left(1+\frac{W/l_{ch}}{D_4(\alpha)}\right)^{-1} \tag{4}$$

where f_t and $l_{ch}=EG_F/f_t^2$ are the material properties which must be independently determined. The coefficients $D_1(\alpha)$, $D_2(\alpha)$ and $D_4(\alpha)$ are obtained by nonlinear regression of the test results on geometrically similar specimens of varying sizes. The formula (4) is found to be in excellent agreement with test data and to cover a very large size range of 1:80. In complete agreement with experimental observations, it predicts a weakening of the size effect as α reduces and a strengthening when W increases at constant α. The strength size effect is however never stronger than that predicted by the Griffith theory.

MULTI-SCALE SECOND-ORDER COMPUTATIONAL HOMOGENIZATION OF HETEROGENEOUS MATERIALS

V. Kouznetsova[*,**], M.G.D. Geers[**], W.A.M. Brekelmans[**]
[*] *Netherlands Institute for Metals Research, Rotterdamseweg 137, 2628 AL Delft, The Netherlands*
[**] *Eindhoven University of Technology, P.O. Box 513, 5600 MB Eindhoven, The Netherlands*

Summary A novel second-order computational homogenization scheme suitable for a multi-scale modelling of macroscopic localization and size effects is proposed. The second-order scheme is an extension of the classical first-order computational homogenization framework and is based on a proper incorporation of the gradient of the macroscopic deformation gradient tensor and the associated higher-order stress measure into the macro-micro scale transition. The applicability of the approach is illustrated by several examples.

INTRODUCTION

Most of the materials produced and utilized in industry are heterogeneous on one or another spatial scale. Typical examples include metal alloy systems, porous media, polycrystalline materials and composites. The different phases present in such materials constitute a material microstructure. The (possibly evolving) size, shape, physical properties and spatial distribution of the microstructural constituents largely determine the macroscopic, overall behaviour of these multi-phase materials.

COMPUTATIONAL HOMOGENIZATION

To predict the macroscopic behaviour of heterogeneous materials various homogenization techniques are typically used. However, most of the existing homogenization methods are not suitable for large deformations and complex loading paths and cannot account for an evolving microstructure. To overcome these problems a computational homogenization approach has been developed, which is essentially based on the solution of two (nested) boundary value problems, one for the macroscopic and one for the microscopic scale. Techniques of this type (i) do not require any constitutive assumption with respect to the overall behaviour; (ii) enable the incorporation of large deformations and rotations on both the micro and macrolevel; (iii) are suitable for arbitrary material behaviour, including physically non-linear and time dependent behaviour; (iv) provide the possibility to introduce detailed microstructural information, including a physical and/or geometrical evolution of the microstructure, in the macroscopic analysis and (v) allow the use of any modelling technique at the microlevel. Existing *first-order computational homogenization* schemes [1, 2] fit entirely into a standard local continuum mechanics framework. The macroscopic deformation (gradient) tensor is calculated for every material point of the macrostructure and is next used to formulate kinematic boundary conditions for the associated microstructural representative volume element. After the solution of the microstructural boundary value problem, the macroscopic stress tensor is obtained by averaging the resulting microstructural stress field over the volume of the microstructural cell. As a result, the (numerical) stress-strain relationship at every macroscopic point is readily available. The first-order computational homogenization technique proves to be a valuable tool in retrieving the macroscopic mechanical response of non-linear multi-phase materials.

However, there are a few severe restrictions limiting the applicability of the first-order computational homogenization scheme (as well as conventional homogenization methods). Firstly, although the technique can account for the volume fraction, distribution and morphology of the constituents, it is insensitive to the absolute size of the microstructure. As a consequence, effects related to variations of this size cannot be predicted. Secondly, the approach is not applicable in critical regions of intense deformation, where the characteristic wave length of the macroscopic deformation field is in the order of the size of the microstructure. Moreover, if softening occurs at a macroscopic material point, the solution obtained from first-order computational homogenization leads to a mesh dependent macroscopic response due to ill-posedness of the macroscopic boundary value problem.

In order to overcome these limitations, a novel, *second-order computational homogenization* procedure is proposed [3, 4]. The second-order scheme is based on a proper incorporation of the gradient of the macroscopic deformation tensor into the kinematical micro-macro framework. The macroscopic stress tensor and a higher-order stress tensor are retrieved in a natural way based on an extended version of the Hill-Mandel energy balance. A full second-gradient continuum theory appears at the macroscale, which requires solving a higher-order equilibrium problem by a special finite element implementation.

RESULTS

Several microstructural analyses show that the second-order computational homogenization framework captures changes of the macroscopic response due to variations of the microstructural size as well as variations of macroscopic gradients of the deformation. If the microstructural size becomes negligible with respect to the length scale of the macroscopic deformation field, the results obtained by the second-order modelling coincide with those of the first-order approach. This important observation demonstrates that the second-order computational homogenization scheme is a natural extension of the first-order framework.

The most important feature of the second-order computational homogenization method is in fact that the relevant length

scale of the microstructure is directly incorporated into the description on the macrolevel via the size of the representative cell. This size should reflect the scale at which the relevant microstructural deformation mechanisms occur. The concept of a representative volume element (RVE) has to be reconsidered in the second-order computational homogenization. Contrary to the classical definition of the RVE, it may not be taken arbitrarily large, since the RVE size sets the length scale of the macroscopic higher-order homogenized continuum. Therefore, the RVE size for a second-order computational homogenization analysis should generally be determined from physical and/or numerical experiments. On the other hand, introduction of the macroscopic length scale directly related to the size of the microstructure allows to describe certain phenomena that cannot be addressed by the first-order scheme, such as macroscopic localization and size effects, as will be illustrated in the following.

Tension of a voided plate (as a heterogeneous configuration), Figure 1a, with a material imperfection, which triggers the development of a localization band, is analyzed using the first-order and the second-order computational homogenization scheme. The first-order computational homogenization analysis results in a mesh dependent strain distribution, Figure 1b,c. The second-order scheme leads to a localization band, which is independent of the mesh size, Figure 1d,e.

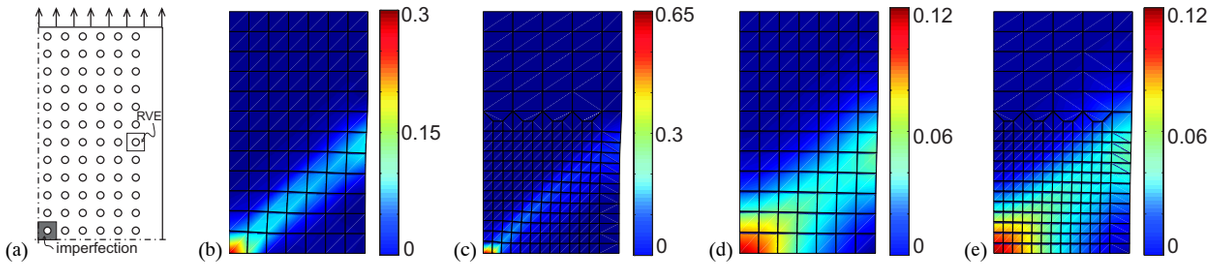


Figure 1. Homogenization analysis of a macroscopic localization problem. Geometry (a) and the strain distribution obtained by the first-order (b), (c) and second-order (d), (e) computational homogenization analysis using two finite element discretizations.

Furthermore, the second-order framework allows the modelling of surface layer effects via the incorporation of higher-order boundary conditions. Simple shear of a thin heterogeneous strip with several ratios of the strip thickness H to the microstructural length scale d is considered, Figure 2a. The constraints on the top and bottom surfaces are modelled using higher-order boundary conditions. Boundary layers with a vanishing shear are clearly observed, Figure 2b, giving rise to a size effect, Figure 2c. Figure 2d shows microstructural deformation patterns in three RVEs corresponding to different locations in the macrostructure.

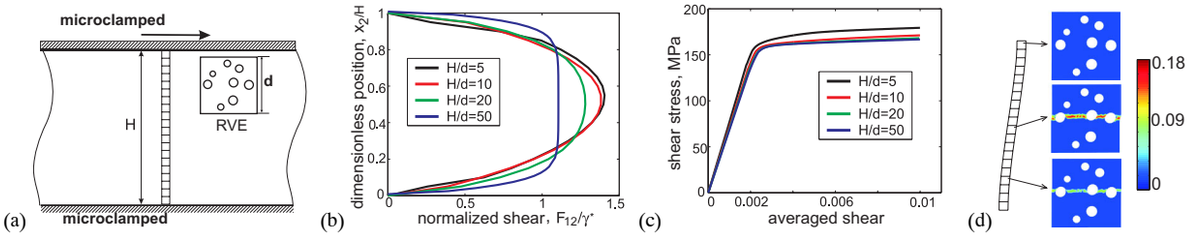


Figure 2. Homogenization analysis of the macroscopic boundary shear layer problem. Geometry (a), distribution of shear across the height of the macroscopic strip (b), shear stress-strain response (c) and microstructural deformation patterns in the sheared macroscopic layer for $H/d = 5$ (displacements are 10 times magnified).

CONCLUSIONS

Computational homogenization provides a versatile strategy to establish micro-macro structure-property relations based on the collective behaviour of the evolving, multi-phase microstructure. The novel second-order computational homogenization scheme allows to describe certain phenomena that cannot be addressed by the classical first-order scheme, such as (geometrical) size effects, macroscopic localization and surface layer effects.

References

[1] Miehe C., Schröder J., Schotte J.: Computational homogenization analysis in finite plasticity. Simulation of texture development in polycrystalline materials. *Comput. Methods Appl. Mech. Engrg.* **171**:387–418, 1999.

[2] Kouznetsova V., Brekelmans W.A.M., Baaijens F.P.T.: An approach to micro-macro modeling of heterogeneous materials. *Comput. Mech.* **27**:37-48, 2001.

[3] Kouznetsova V., Geers M.G.D., Brekelmans W.A.M.: Multi-scale constitutive modelling of heterogeneous materials with a gradient-enhanced computational homogenization scheme. *Int. J. Numer. Meth. Engrg.* **54**:1235–1260, 2002.

[4] Kouznetsova V., Geers M.G.D., Brekelmans W.A.M.: Multi-scale second-order computational homogenization of multi-phase materials: a nested finite element solution strategy. *Comput. Meth. Appl. Mech. Engrg.*, 2004, in press.

XXI ICTAM, 15–21 August 2004, Warsaw, Poland

JUMPING OF A SPINNING SPHEROID

Yutaka Shimomura*, Michal Branicki**, Keith Moffatt**
*Department of Physics, Hiyoshi Campus, Keio University, Yokohama 223-8521, Japan
**Department of Applied Mathematics and Theoretical Physics, Cambridge CB3 0WA, UK

Summary As is well known, a hard-boiled egg will rise from the horizontal to the vertical if it is spun sufficiently rapidly on a table with its axis of symmetry initially horizontal. We consider here the problem of a spinning spheroid, and show that in certain circumstances the spheroid may lose contact with the table in the course of this rising motion. Allowing for slip and weak friction at the point of contact, the dynamical equations for a uniform spheroid, are treated by the multiple-scale perturbation method to resolve the two time-scales intrinsic to the dynamics. An approximate solution for the high frequency component of the motion shows a growing oscillation of the normal reaction, and predicts the circumstances in which this can fall to zero (leading to jumping of the body). The exact solution for the free motion after jumping and until contact with the table is reestablished. The analytical results agree well with numerical simulations of the exact equations.

BACKGROUND AND OBJECTIVE

Moffatt & Shimomura [1] discussed the familiar phenomenon of the rise to the vertical of a hard-boiled egg set in rapid spinning motion on a table. In that paper, the governing equations were simplified on the assumption that the friction is weak and the spin is large (so that the Coriolis force is dominant). Under this 'gyroscopic' assumption, a first-order differential equation for the inclination of the axis of symmetry was obtained, which, for the case of a prolate spheroid, did indeed describe the rise of the axis to the vertical. This rise was associated with the effect of the weak friction at the point of contact, and occurred on a 'slow' time-scale $O(\mu^{-1})$, irrespective of the nature of the frictional force ('dry' Coulomb friction, or 'wet' viscous friction). However this rising motion is accompanied by fluctuations occurring on a 'fast' $O(1)$ time-scale. In fact, a carbon trace of the moving point of contact, which is initially a continuous curve, can turn into a broken and then a dotted one in an intermediate stage of the rising motion (See Figure 1). This at least means a rapidly oscillating fluctuation of the normal reaction R acting on the point of contact. Furthermore, a linear stability analysis by Moffatt, Shimomura & Branicki [2] showed the existence of modes oscillating on 'fast' time-scale. These 'slow' and 'fast' time-scales embedded in the dynamics are expected to be clearly separated when the friction is weak. In the papers [1] and [2], the computations presented were restricted to circumstances in which R remains positive and the spheroid does therefore remain in contact with the table throughout the motion. However, in some regions of parameter space, the growth of the fluctuations allows R to decrease to zero. The purpose of the present paper is to analyse these fluctuating motions, which depend on the two time-scales, and to find their effect on the dynamics.

METHODS

The motion of a spinning spheroid occuring on slow and fast time-scales is analytically studied for small Coulomb friction parameter μ, using the multiple-scale perturbation method. First, two time-scales are introduced and the mean part of the motion is defined by filtering out the fast motion. (In reference [1], the solutions for this mean part was found under the 'gyroscopic' assumption.) The fluctuating parts to order μ are approximately solved by the WKB method to derive the time-dependence of the normal reaction R. Numerical simulation of the problem is also carried out by using the Runge-Kutta method to solve the exact governing sixth-order nonlinear dynamical system.

RESULTS

The following results are found analytically and confirmed numerically. The normal reaction R for a spinning spheroid oscillates with a growing amplitude. Depending on the aspect ratio and the initial condition, the oscillatory modes can grow to such an extent that R can fall to zero (see Figure 2). This leads to a 'jumping' phenomenon, in which obviously the spheroid passes into a free motion under gravity without friction. The exact solution for this free motion describes the distance of the gap between the spinning spheroid and the table, which increases in proportion to t^3 in the initial stage of jumping. The time of free motion before contact is determined.

CONCLUSION

If a spinning spheroid is spun sufficiently rapidly on a table with its axis of symmetry horizontal, then it will lose contact with the table at some stage during the rising motion [3]. In these circumstances, its subsequent behaviour consists of rapidly alternating periods of motion with and without frictional contact with the table.

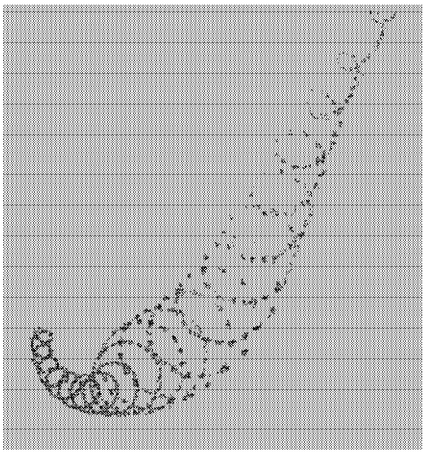


Figure 1. Carbon trace of the point of contact for a spinning prolate spheroid of aspect ratio 3/2.

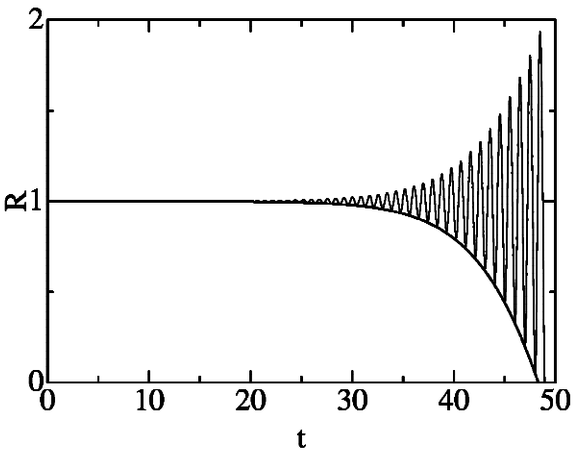


Figure 2. Normal reaction force R versus time t for a spinning prolate spheroid in the case of "Coulomb" friction. The thin line shows the numerical simulation, and the bold one plots the theoretical result.

References

[1] Moffatt, H. K. & Shimomura, Y.: Spinning Eggs – a Paradox Resolved. Nature 417:385–386, 2002.
[2] Moffatt H. K., Shimomura, Y. & Branicki, M.: Dynamics of an Axisymmetric Body Spinning on a Horizontal Surface. Part I: Stability and the Gyroscopic Approximation. to appear in Proc. Roy. Soc. A, 2004.
[3] Shimomura, Y., Branicki, M. & Moffatt H. K.: Dynamics of an Axisymmetric Body Spinning on a Horizontal Surface. Part II: Self-Induced Jumping. in preparation.

Characteristics of orientation and grain-size distributions

Luca Placidi, Kolumban Hutter

Department of Mechanics, Darmstadt University of Technology Hochschulstr. 1, 64289 Darmstadt, Germany

Summary Crystal Size Distribution (CSD) provides a mean grain-size that depends upon the sensitivity of the microscope. The Orientation Distribution Function (ODF) does not guarantee that the random distribution predicts, as would be natural, isotropic behavior. In this regard, we analyze shortcomings of CSD and ODF that can be eliminated when the Theory of Mixtures with Continuous Diversity is employed and orientation-and-grain-size mass density is used.

EXTENDED SUMMARY

The Physical background of CSD and ODF

The mechanics of polycrystalline material depends upon the mechanical response of crystallites from which it is made and upon their interactions. Such analysis, which is called microscopic, is very accurate, and can be done via computer simulations. If the polycrystal is huge, the computational time increases rapidly. This implies the need of a macroscopic point of view. However, the microscopic characteristics affect the macroscopic behavior. Therefore, the behavior at the microscopic level must still be accounted for. Among the large number of microscopic parameters, grain-size and crystal-orientation are very important physical characteristics. The first provides a rough measure of the boundary and the second represents the interior structure of the crystallite. The grain-size, $\bar{D}$, is a scalar quantity that gives the characteristic length of the crystallite. Since D_M is the largeness of the sample, one can use the non-dimensional grain-size $D = \bar{D}/D_M$. In the simple case of transverse isotropic microstructure, the orientation, denoted by $\mathbf{n}$, is a non-dimensional unit vector describing the direction of the crystallite with respect to a fixed frame of reference. Generally, such characteristics are described by two distinct functions: Crystal Size Distribution $N^{\blacktriangleright}(D)$ and Orientation Distribution Function $f^*(\mathbf{n})$. The implicit continuum approximation of these functions is as follows. A large number of crystallites, say N_{tot}, is supposed to be present at all time and in each spatial point. $N^{\blacktriangleright}(D)$ and $f^*(\mathbf{n})$ represent the fractions of number of crystallites that have non-dimesional grain-sizes between D and $D + dD$, where dD is the element of length, and orientation directed towards $\mathbf{n}$ within the solid angle $d^2\mathbf{n}$, respectively. Thus, integration of CSD over the whole range of non-dimesional grain-size, $\mathcal{I} = [0, 1)$, and of ODF over the unit sphere, $\mathcal{S}^2$, give unity, i.e.,

$$\int_{\mathcal{I}} N^{\blacktriangleright}(D)\, dD = 1, \qquad \int_{\mathcal{S}^2} f^*(\mathbf{n})\, d^2\mathbf{n} = 1. \tag{1}$$

The importance of CSD and ODF in the derivation of the constitutive law of a polycrystalline material is determined by the respective influence of outer and interior boundaries in the mechanisms of deformation. As an example, we consider the case of ice, which has a transverse isotropic microstructure and the orientation $\mathbf{n}$ is parallel to the c-axis. In this case the main mechanism of deformation is believed to be glide on the basal plane (the plane orthogonal to the c-axis), that introduces a very strong anisotropic mechanical response of the single crystal. The macroscopic behavior of polycrystals is determined by the distribution of c-axes orientations, i.e. by $f^*(\mathbf{n})$. A recent investigation of samples composed of very fine ice grains, revealed a super-plastic (grain-size dependent) flow law [2], that the authors try to justify through the deformation mechanism of Grain Boundary Sliding. In this case the flow law depends upon the mean grain-size, that can be evaluated, e.g., by the CSD. However, the mean grain-size is a rough approximation and one is compelled to deal directly with the whole distribution.

Mixture with Continuous Diversity and definition of orientation-and-grain-size mass density

The investigation of microstructures using mixture theory is not new; the theory of Porous Media is a remarkable example. The introduction of the Theory of Mixtures with Continuous Diversity [1] can provide new directions for this field. The fundamental idea of its application to the mechanics of polycrystalline materials is based on the continuum approximation of CSD and ODF: a large number of crystallites is located at the same time in the same point. However, the definition of the distribution of grain-size and orientation is different. Here, the orientation-and-grain-size mass density is defined by $\varrho^{\triangleright}(\mathbf{n}, D)$, which, integrated over $\mathcal{I}$, gives the orientation mass density $\varrho^*(\mathbf{n})$, and over $\mathcal{S}^2$ the grain-size mass density $\varrho^{\blacktriangleright}(D)$, respectively, i.e.,

$$\varrho^*(\mathbf{n}) = \int_{\mathcal{I}} \varrho^{\triangleright}(\mathbf{n}, D)\, dD, \quad \varrho^{\blacktriangleright}(D) = \int_{\mathcal{S}^2} \varrho^{\triangleright}(\mathbf{n}, D)\, d^2\mathbf{n}. \tag{2}$$

In the same way the macroscopic mass density ϱ of the mixture is given by the chain of identities

$$\varrho = \int_{\mathcal{S}^2}\int_{\mathcal{I}} \varrho^{\triangleright}(\mathbf{n}, D)\, dD d^2\mathbf{n} = \int_{\mathcal{I}} \varrho^{\blacktriangleright}(D)\, dD = \int_{\mathcal{S}^2} \varrho^{*}(\mathbf{n})\, d^2\mathbf{n}. \tag{3}$$

The definitions of the grain-size mass density $\varrho^{\blacktriangleright}$ and the orientation mass density ϱ^* in (2) and (3) have very important meanings: the quantity $\varrho^{\blacktriangleright}\, dD$ is the part of the mass density due to crystallites with non-dimesional grain-sizes between D and $D + dD$ and the quantity $\varrho^* d^2\mathbf{n}$ is the part of the mass density due to crystallites with orientations directed towards $\mathbf{n}$ within the solid angle $d^2\mathbf{n}$. The analogy between $\varrho^{\blacktriangleright}$ and CSD and between ϱ^* and ODF is straightforward and is analyzed in the next two sections. Now, it is important to remark that the evolution equation of such distributions is given by the balance of mass and it is not necessary, as in the case of ODF and CSD, to define in an *ad hoc* way.

Comparison between CSD and grain-size-dependent mass density

We prove a relation between CSD and grain-size mass density in terms of the so-called true mass density, $\gamma^{\blacktriangleright}$, and for incompressible polycrystalline materials, i.e.,

$$\varrho^{\blacktriangleright} = N^{\blacktriangleright} N_{tot} \alpha^{\blacktriangleright} D^3 \gamma^{\blacktriangleright}, \tag{4}$$

where $\alpha^{\blacktriangleright} = \alpha^{\blacktriangleright}(D)$ is the quantity that is defined as the shape factor of crystallites with non-dimesional grain-size equal to D. In principle, the choice of one of the two distributions ($N^{\blacktriangleright}$ or $\varrho^{\blacktriangleright}$) is arbitrary. However the mean grain-size computed with these two functions are different. We will call $\langle D \rangle_{_N}$ the mean grain-size computed with respect to $N^{\blacktriangleright}$ and $\langle D \rangle_{_\varrho}$ the mean grain-size computed with respect to $\varrho^{\blacktriangleright}$, i.e.,

$$\langle D \rangle_{_N} = \int_{\mathcal{I}} D N^{\blacktriangleright}\, dD, \qquad \langle D \rangle_{_\varrho} = \int_{\mathcal{I}} D \varrho^{\blacktriangleright}\, dD. \tag{5}$$

Our main aim here is to make it clear that the evaluation of the mean grain-size $\langle D \rangle_{_N}$ has a very important weak point, it strongly depends upon the sensitivity of the measuring instruments. We demonstrate it with a very simple example. The presence of tiny grains, not detectable by the microscope, has a great influence on the value of $\langle D \rangle_{_N}$. On the other hand, $\langle D \rangle_{_\varrho}$ is almost independent of it. In fact, $\langle D \rangle_{_\varrho}$ is a weighted average and the weight is the mass of the grains. Now, if the grains are very small, their contribution to $\langle D \rangle_{_\varrho}$ is negligible. Moreover, the definition of grain-size mass density implies a very important condition as D tends to zero, i.e.,

$$\varrho^{\blacktriangleright}(0) = 0, \tag{6}$$

that can not be obtained a priori for CSD.

Comparison between ODF and orientation-dependent mass density

It was possible to derive relation (4), because the grain-size of incompressible crystallites has an implicit connection with its mass. A similar relation can not be derived between ODF and orientation mass density due to the fact that the orientation of a crystallite is not related with its mass. The ODF and the orientation mass density are independent quantities unless the mass of each crystallite is known. Therefore the choice of one of the two distributions is arbitrary and it is necessary to look at one single problem. Here we want to analyze the connection between ODF and orientation mass density. It will thus become clear that the ODF has a weak point that can be overcome by using the orientation mass density. Generally, the mechanical response of polycrystalline ice is related to the distribution of the c-axes of their crystallites. A random distribution must give isotropic behavior. This characteristic is not satisfied by the ODF. We will demonstrate the failure by a simple example. The main point is that the ODF can not include the largeness of each crystallite in its form. Since the crystallites oriented towards a given orientation are larger than the others, a random distribution in terms of the ODF does not correspond to isotropic behavior. On the other hand, the orientation mass density contains the required information one is looking for. This eliminates the failure of ODF.

References

[1] Faria, S. H.: Mixtures with continuous diversity: general theory and application to polymer solutions. *Continuum Mech. Thermodyn.* **13**: 91 - 120 (2001)

[2] Goldsby, D.L.; Kohlstedt, D.L.: Grain boundary sliding in fine-grained ice I. *Scripta Mater.* **37**: 1399 - 1406 (1997)

XXI ICTAM, 15–21 August 2004, Warsaw, Poland

NUMERICAL HOMOGENIZATION OF A LOCALLY HYPERELASTIC CONSTITUTIVE LAW

Antoine Gloria, Claude Le Bris
CERMICS, Ecole Nationale des Ponts et Chaussées, 77455 Champs-sur-Marne, France

Summary We briefly recall the results in periodic homogenization of nonlinear constitutive laws and address in an empirical way the question of the number of periodic cells one has to consider in a particular non convex case of practical interest. We suggest a numerical approach, for which definite conclusions are yet to be obtained, to simulate an inhomogeneous hyperelastic material. Numerical tests are currently under progress.

THEORETICAL BACKGROUND

Let us consider a material whose mechanical energy is of the form $W_\epsilon = W(\frac{x}{\epsilon}, \xi)$ where W is 1-periodic with respect to its first argument, ϵ is a small positive parameter describing the size of the microstructure, x denotes the position in $\mathbb{R}^3$ and ξ is the deformation tensor in $\mathcal{M}_3(\mathbb{R})$. The functional W is nonlinear and for almost all $x \in \Omega$ (a finite domain in $\mathbb{R}^3$) has some convexity properties with respect to ξ. An approximation of this energy functional for small values of ϵ is the "limit" in an appropriate sense when $\epsilon \to 0$. The sense one has to give to this limit depends on the convexity properties of $W(x, \cdot)$.

Strictly convex case

In the case when $W(\cdot, \xi)$ is uniformly continous, coercive, and when for almost all $x \in \Omega$, $W(x, \cdot)$ is strictly convex, one can prove that for any boundary value problem the displacement u_ϵ associated to the energy functional W_ϵ converges strongly in $H^1(\Omega)$ towards a displacement u^* associated to a homogenized energy functional W^* defined as follows :

$$W^*(\xi) = \inf_{u \in E(\xi)} \int_\omega W(x, \nabla u(x)) dx \tag{1}$$

where $\omega = [0,1]^3$ and $E(\xi) = \{u \in H^1(\omega)^3 | u(x) = \xi \cdot x + v(x)$ with v a ω-periodic function$\}$. Correspondingly one can define a stress tensor $\pi^*(x) = \dfrac{\partial W^*}{\partial \xi}(\nabla u^*(x))$ as the weak limit of π_ϵ when $\epsilon \to 0$ in $L^2(\Omega)^9$.

We emphasize that in this strictly convex case the homogenized energy functional (1) is obtained with a problem set on a single cell $\omega = [0,1]^3$.

Quasiconvex case

Consider now an energy functional $W(x, \cdot)$ quasiconvex for almost all $x \in \Omega$. One can also define a homogenized energy functional W^*, a displacement limit u^* and an associated stress tensor π^* satisfying $u^* = \lim_{\epsilon \to 0} u_\epsilon$ in $L^2(\Omega)^3$ and $\pi^* = \lim_{\epsilon \to 0} \pi_\epsilon$ as a Young measure. However W^* is not given by (1) as shown by Müller in [2]. One has to consider many periodic cells, and in fact infinitely many, as:

$$W^*(\xi) = \lim_{n \to \infty} \frac{1}{8n^3} \inf_{u \in E(\xi)} \int_{\omega_n} W(x, \nabla u(x)) dx \tag{2}$$

where $\omega_n = [-n, n]^3$.

This formula gives a convergence result that we propose to numerically investigate for a rubber-like constitutive law.

NUMERICAL STRATEGY SUGGESTED

We consider the problem $\operatorname{div} \pi_\epsilon = 0$ posed in a finite domain Ω of $\mathbb{R}^3$ with appropriate boundary conditions, where $\pi_\epsilon = \dfrac{\partial W_\epsilon}{\partial \nabla u_\epsilon}$. We solve a coupled problem consisting in a macro problem and a micro problem providing a numerical constitutive law (ie a stress/strain relation) .

Extended FE^2

Our approach aims at treating high nonlinearities and large deformations, and thus uses a Newton type resolution of the macro problem. The micro problem provides the macro problem with two informations: the homogenized stress tensor and a homogenized stiffness matrix. The Newton method for the macro problem reads at step $n+1$

$$\operatorname{div} \pi_M^n + \operatorname{div} \left(\frac{\partial \pi_M^n}{\partial \nabla u_M^n} : (\nabla u_M^{n+1} - \nabla u_M^n) \right) = 0 \ \text{ in } \Omega \tag{3}$$

with the same boundary conditions as the original problem (to fix the ideas) and where π_M^n and $\dfrac{\partial \pi_M^n}{\partial \nabla u_M^n}$ are respectively given at each Gauss point X by the resolution of the following two micro problems.

Stress tensor

At step n, given a macroscopic deformation ∇u_M^n at a Gauss point X and given a micro cell $\omega(X)$, the micro problem provides a microscopic stress tensor π_μ^n solution of

$$\text{div } \pi_\mu^n(x) = 0 \text{ in } \omega(X) \tag{4}$$

$$u_\mu^n(x) = \nabla u_M^n(X).x \text{ on } \partial\omega(X) \tag{5}$$

This problem is posed on a domain whose size is of order ϵ. We recall that this problem is nonlinear and its resolution itself requires an iterative Newton type method, for which one can use the analytical constitutive law $\pi_\mu = \dfrac{\partial W_\epsilon(x, \nabla u_\mu)}{\partial \nabla u_\mu}$.

We then define the macroscopic stress tensor $\pi_M(X)$ as the mean value of the solution π_μ^n of (4)-(5).

$$\pi_M(X) = \frac{1}{|\omega(X)|} \int_{\omega(X)} \pi_\mu^n(y) dy \tag{6}$$

If the microstructure does not depend on the macroscopic point considered (that is exactly what we assumed in the first section), the micro cell does not depend either on the Gauss point X. That definition of the macroscopic tensor is not new (cf. [3]) and is consistant with the theoretical homogenization results we recalled above.

Stiffness matrix

Differentiating (6), we have

$$\frac{\partial \pi_M^n}{\partial \nabla u_M^n}(X) = \frac{1}{|\omega(X)|} \int_{\omega(X)} \frac{\partial \pi_\mu^n(y)}{\partial \nabla u_M^n(X)} dy$$

where $\dfrac{\partial \pi_\mu^n(y)}{\partial \nabla u_M^n(X)}$ is the solution of the PDE (4) once differentiated with respect to its boundary condition (5). The new problem we obtain is then a set of 9 linear PDEs with the same linear operator and nine different second members. In addition we can approximate this linear operator by the stiffness matrix used to solve the problem (4)-(5).

NUMERICAL TESTS PROPOSED

The strategy described above is being implemented. The main issue of practical interest is the number of cells one should consider for the averaging. Quantifying this for classical rubber-like material examples is the aim of the first tests under progress.

Contrary to the case of linear elasticity where an analytical formula for the homogenization of a chessboard composite is available, no such formula is known in nonlinear elasticity. The goal of our second series of tests is to explore the situation for a composite made of two nonlinear materials.

The talk will give the conclusions concerning these tests.

References

[1] Braides A., Defranceschi A.: Homogenization of Multiple Integrals. Oxford University Press, 1999.

[2] Müller S.: Homogenization of nonconvex integral functionals and cellular elastic materials. *Arch. Rat. Anal. Mech.* **99**:189–212, 1987.

[3] Féyel F.: Multiscale FE^2 elastoviscoplastic analysis of composite structures. *Comp. Mat. Sci.* **16**:344–354, 1999.

XXI ICTAM, 15–21 August 2004, Warsaw, Poland

MULTISCALE ANALYSES OF GRANULAR MEDIA AT FINITE STRAINS BASED ON MICRO–MACRO TRANSITIONS WITH DIFFERENT BOUNDARY CONSTRAINTS

Joachim Dettmar, Christian Miehe
University of Stuttgart, Institute of Applied Mechanics (Civil Engineering), 70550 Stuttgart, Germany

Summary Considered is a homogenized macro–continuum with locally attached microstructures of discrete character. For example, these microstructures may represent granular assemblies of particles used in analyses in soil mechanics or aggregates of atoms for analyses in nanoscale mechanics of metals. Specific micro–macro transitions are derived by a consistent transfer of the discrete micro–variables to macroscopic field variables on a continuous (smeared) macrostructure. On the microscopic side, the classical boundary conditions of homogenization theory of continuous structures are consistently transferred to their discrete counterparts including the effect of particle rotations. It is shown that those for linear displacements and uniform tractions on the surface yield upper and lower bound characteristics, respectively, for the periodic boundary constraints with regard to the stiffness of the aggregate. Therein, special attention is paid to the definition of the periodic unit cell of granular particles which leads to specific constraints for both displacements and rotations of the granules on the well–defined boundary frame of the microstructure. On the macroscopic side, the homogeneous problem is solved by a finite element method where the material model is implemented by means of directly evaluated micro–macro transitions based on the above mentioned discrete microstructures for the case of periodic boundary constraints. Thus, the two–scale simulations are linked by solving coupled boundary–value problems on both the micro– and macroscales. Finally, some representative numerical examples are investigated and discussed which underline and clarify the proposed method.

Introduction

Within the classical setting of large–strain continuum mechanics, phenomenological macroscopic material models are developed where the material parameters are fitted according to experimental observations. In recent years, attention has been shifted to multiscale analyses of materials where the real microscopic structures of such materials are accounted for. Many materials show discrete microstructures such as granular media like soils and sand or even metals with a discrete, particulate–like atomistic structure on the nanoscale. So far, in the modeling of discrete granular structures, attention has mostly been paid to the simulation of the evolution of microstructures, not its embedding into large–scale macroscopic simulations. With the advent of powerful computers, coupled micro–macro analyses of those problems are only the next logical step. Figure 1 shows a homogenized macro–continuum where a microstructure is attached locally

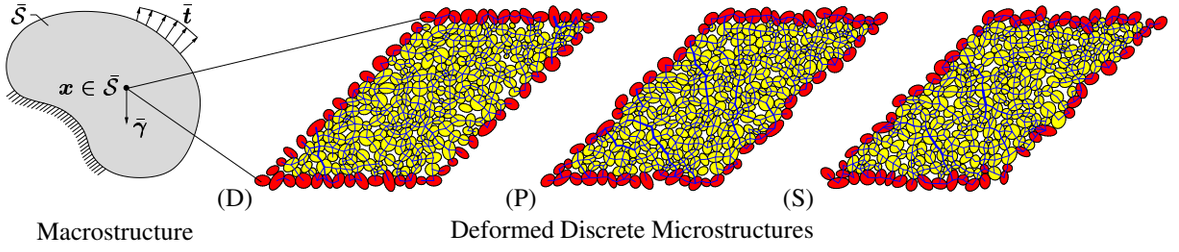


Figure 1. Deformed continuous macrostructure with a granular microstructure locally attached at a point $\bar{\boldsymbol{x}} \in \bar{\mathcal{S}}$ under (D) linear deformations, (P) periodic displacements and (S) uniform traction constraints on the surface of the representative volume element.

at a point $\bar{\boldsymbol{X}} \in \mathcal{S}$ of the macrostructure and deformed in a compression–shear mode. A micro–macro transition of such a discrete aggregate is concerned with the definition of homogenized overall properties such as strains, stresses and powers. A central difference to other works on granular microstructures is a distinct definition of the aggregate volume and its boundary conditions which govern the representation of the macro–stresses. A well–defined periodic cell allows a consistent transfer of overall definitions for continuous microstructures of heterogeneous materials to discrete particle microstructures. Recall from classical homogenization theory that periodicity conditions reflect exact results with regard to the aggregate stiffness for periodic structures, while linear deformation and uniform traction constraints yield upper and lower bound characteristics, respectively. It will be shown that these statements also hold true for granular materials. Consequently, the proposed periodicity conditions are considered to be an optimal choice for particle aggregate and will thus be used for the proposed *two–scale micro–macro simulations* where we link boundary–value problems on both the micro– and macroscales.

Micromechanical modeling

For analyses of granular materials, the discrete element method has become a popular tool. Microscopic constitutive equations for the discrete particle interactions are introduced which govern the macroscopic response by computational exploitation of micro–macro averaging theorems. In each incremental step the current branch meshes are computed and the equation of motion is solved for all particles until quasistatic equilibrium states are reached. An optimized technique that accelerates the dynamic relaxation procedure is introduced. The Cauchy macro–stresses are the volume average of the Cauchy micro–stresses and appear in the form $\bar{\boldsymbol{\sigma}} = \frac{1}{2|v|} \sum_q (\boldsymbol{f}_q \otimes \boldsymbol{x}_q + \boldsymbol{x}_q \otimes \boldsymbol{f}_q)$ where we sum over only the M

particles on the defined boundary frame the actual particle positions $\boldsymbol{x}_q$ and externally applied support forces $\boldsymbol{f}_q$. Note that due to our distinct definition of the boundary frame only the particle–centroid forces enter the stress formulation. For periodic boundary conditions, all couples drop out due to the antiperiodicity condition and thus do not influence the stress calculation. The three classical boundary constraints for continuous structures, see [2], are consistently transferred to their discrete counterparts. In order to implement these into a deformation–driven scenario, for the particle–centroid interaction forces of all particles in the aggregate we assume potentials which need to be minimized. Therein, special assumptions are made for the particle rotations in the cases of linear displacement and uniform traction constraints. The boundary constraints are then incorporated by a penalty method in the form of quadratic terms such that for the three boundary constraints we end up with the fictitious potentials

$$\begin{array}{lrcl} \text{(D)} & \Pi_p^D(\boldsymbol{x}_q, \boldsymbol{Q}_q) & = & \Pi(\boldsymbol{x}_q) + \frac{\epsilon_f}{2} \sum_{q=1}^{M} ||\boldsymbol{x}_q - \bar{\boldsymbol{F}} \boldsymbol{X}_q||^2 + \frac{\epsilon_c}{4} \sum_{q=1}^{M} ||\boldsymbol{Q}_q - \boldsymbol{1}||^2 \\ \text{(P)} & \Pi_p^P(\boldsymbol{x}_q, \boldsymbol{Q}_q) & = & \Pi(\boldsymbol{x}_q) + \frac{\epsilon_f}{2} \sum_{q=1}^{M^+} ||\,[\![\boldsymbol{x}_q]\!] - \bar{\boldsymbol{F}}\,[\![\boldsymbol{X}_q]\!]\,||^2 + \frac{\epsilon_c}{4} \sum_{q=1}^{M^+} ||\,[\![\boldsymbol{Q}_q]\!]\,||^2 \\ \text{(S)} & \Pi_p^S(\boldsymbol{x}_q) & = & \Pi(\boldsymbol{x}_q) + \frac{\epsilon_f}{2} || \sum_{q=1}^{M} (\boldsymbol{x}_q \otimes \boldsymbol{A}_q) - |\mathcal{V}| \bar{\boldsymbol{F}} ||^2 \end{array} \tag{1}$$

Derivations of these particle interaction force–potentials with respect to the actual positions $\boldsymbol{x}_q$ and rotations ϑ_q then give the support forces $\boldsymbol{f}_q$ and couples m_q needed to attain the boundary constraint considered:

$$\begin{array}{lrclrcl} \text{(D)} & \boldsymbol{f}_q & = & \epsilon_f (\boldsymbol{x}_q - \bar{\boldsymbol{F}} \boldsymbol{X}_q)\,, & m_q & = & \epsilon_c (\vartheta_q - \Theta_q) \\ \text{(P)} & \boldsymbol{f}_q^+ & = & \epsilon_f ([\![\boldsymbol{x}_q]\!] - \bar{\boldsymbol{F}} [\![\boldsymbol{X}_q]\!]) = -\boldsymbol{f}_q\,, & m_q^+ & = & \epsilon_c [\![\vartheta_q]\!] = -m_q^- \\ \text{(S)} & \boldsymbol{f}_q & = & \epsilon_f [\sum_p (\boldsymbol{A}_p \cdot \boldsymbol{A}_q) \boldsymbol{x}_p - |\mathcal{V}| \bar{\boldsymbol{F}} \cdot \boldsymbol{A}_q]\,, & m_q & = & 0 \end{array} \tag{2}$$

where ϵ_f and ϵ_c are penalty factors, $\boldsymbol{Q}$ is a proper orthogonal rotation tensor and $\boldsymbol{A}_q$ an outward area normal vector on the undeformed surface of the microstructure. ϑ_q and Θ_q are the actual and referential rotations of a particle q. Figure 2 shows homogenized normal and shear stresses versus a macroscopic simple shear deformation mode for a typical microstructure made of 256 elliptical particles as shown in Figure 1. The bound character of the linear displacement and uniform traction constraints with respect to the periodic conditions is clearly obvious.

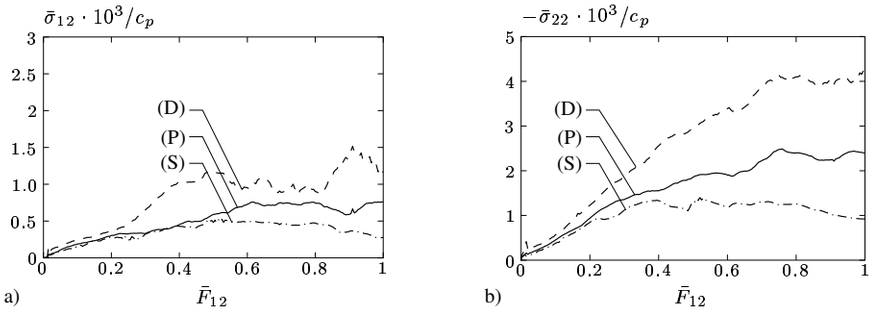


Figure 2. Homogenized a) shear stresses $\bar{\sigma}_{12}$ and b) compressive stresses $-\bar{\sigma}_{22}$ versus macroscopic shear deformation $\bar{F}_{12}$ for the three types of boundary conditions (D) linear displacements, (P) periodic deformations and (S) uniform tractions on the surface. The simulation was carried out with a granular plane microstructure of 256 elliptically–shaped particles.

Macroscopic Finite Element Modeling

The point of departure for the finite element method is the strong form of quasistatic equilibrium. A Galerkin procedure and some algebraic manipulations yield the weak counterpart, further discretization finally the well–known form $\int_{\bar{\mathcal{B}}} \boldsymbol{B}^T \cdot \bar{\boldsymbol{P}}(\boldsymbol{d})\, dV = \int_{\bar{\mathcal{B}}} \boldsymbol{N}^T \cdot \bar{\gamma}\, dV + \int_{\partial \bar{\mathcal{B}}} \boldsymbol{N}^T \cdot \bar{\boldsymbol{t}}\, dA$. The left hand side of the equation are the internal forces that depend on the actual nodal displacements $\boldsymbol{d}$ and thus on the deformed particulate microstructure. The first Piola–Kirchhoff stresses $\bar{\boldsymbol{P}}$ are determined by direct evaluation of micro–macro transitions on the microscale. This is done at each sampling point of the finite element by passing the increment of the actual deformation gradient in each step onto the microstructure, where then the microscopic simulation is carried out, the macroscopic stress determined and passed back to the macroscale. This step marks the link between the simulations on both scales. We apply an explicit solution strategy in context with an accelerated dynamic relaxation procedure. After each load step the system is iteratively solved until the quasistatic equilibrium configuration is reached.

References

[1] Miehe C., Dettmar, J.: A framework for micro–macro transitions in periodic particle aggregates of granular materials, *Computer Methods in Applied Mechanics and Engineering*, **193**: 225-256, 2004.

[2] Miehe C.: Computational micro–to–macro transitions for dicretized micro–structures of heterogeneous materials at finite strains based on the minimization of averaged incremental energy, *Computer Methods in Applied Mechanics and Engineering*, **192**:559–591, 2003.

[3] Miehe C., Dettmar, J.: A new class of boundary conditions for micro–macro transitions in particle aggregates of granular materials, *International Journal of Solids and Structures*, submitted.

XXI ICTAM, 15–21 August 2004, Warsaw, Poland

EXPLOITATION OF INCREMENTAL ENERGY MINIMIZATION PRINCIPLES IN COMPUTATIONAL MULTISCALE ANALYSES OF INELASTIC SOLIDS

Christian Miehe
University of Stuttgart, Institute of Applied Mechanics (Civil Engineering), 70550 Stuttgart, Germany

Summary The lecture provides an overview about recent developments in the formulation and numerical implementation of incremental minimization principles for inelastic solids and their exploitation with regard to multiscale analyses of deformation microstructures. The incremental energy minimization is applied to conceptual model problems which treat multiscale microstructure evolutions in stable / instable and a priori heterogeneous / homogeneous elastic–plastic solids.

Introduction

The lecture overviews recent developments in the formulation and numerical implementation of incremental minimization principles for inelastic solids and their exploitation with regard to multiscale analyses of deformation microstructures. Key aspect is the outline of *minimization principles for standard dissipative materials* that govern the microstructure development of a priori heterogeneous materials as well as deformation phase decompositions in initially homogeneous materials. These principles allow to recast incremental initial boundary–value problems for inelastic solids into minimization problems. The minimization structure provides a *canonical approach to inelastic solid mechanics under quasistatic conditions*, with important consequences to almost all subsequent aspects of the modelling and the numerical implementation: • The existence of solutions of the incremental IBVPs depends on weak convexity properties of a stress potential. • Stress update algorithms in plasticity, viscoplasticity and damage mechanics appear in a natural format in the form of energy minimizers. • Micro–to–macro transitions for the modelling of the overall response of a priori given heterogeneous microstructures can be defined in terms of a principle of minimum averaged incremental energy. • The material stability of incremental plastic deformations can be defined in terms of the quasi–convexity of incremental stress potentials in analogy to elasticity, which provides a more general criterion than the classical Hadamard condition. • Deformation micro–structure developments in non–stable solids can be interpreted as phase decompositions and be resolved by energy minimization principles of quasi– and rank–one convexifications of the incremental stress potential.

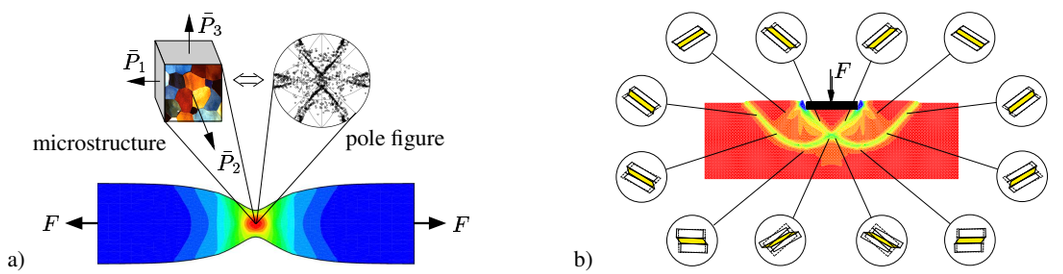


Figure 1. Examples of multiscale microstructural analyses in finite plasticity. a) Homogenization analysis predicts texture development in heterogeneous polycrystals. b) Relaxation analysis of instable solids governs the evolution of postcritcal deformation phases.

Incremental Constitutive Minimization Problem (C)

The point of departure is a general internal variable formulation for the constitutive response of standard dissipative materials in terms of an energy storage and a dissipation function. Nonlinear standard materials cover a broad spectrum of constitutive models in finite elasticity, viscoelasticity, plasticity or damage mechanics. Consistent with this type of finite inelasticity we outline a distinct *incremental variational formulation of the local constitutive response* as proposed in [2] and [5], where a quasi–hyperelastic stress potential is obtained from a local minimization problem with respect to the internal variables. It is shown that this local minimization problem determines the internal state of the material for finite increments of time. The approach is conceptually in line with works on incremental variational formulations and variational updates in plasticity by [7] and [1].

Incremental Minimization Problem of Relaxation (R)

The existence of this variational formulation allows the definition of the *material stability of an inelastic solid based on weak convexity conditions* of the incremental stress potential in analogy to classical treatments of finite elasticity. Furthermore, material instability phenomena may be interpreted as deformation microstructure developments associated with non–convex incremental stress potentials in analogy to elastic phase decomposition problems. These micro–structures can be resolved by the relaxation of non–convex energy functionals based on a convexification of the stress potential. The relaxed problem provides a well–posed formulation for a mesh–objective analysis as close as possible to the non–convex original problem. Following the recent work [4], we give a conceptual outline of a relaxation analysis for non–convex standard dissipative solids and specify a procedure to a one–level rank–one convexification procedure.

- **Constitutive Model (M).** $\boldsymbol{F} \in GL_{+(3)}$ at $\boldsymbol{X} \in \mathcal{B}$ is the local deformation of the material and $\boldsymbol{\mathcal{I}} \in \mathcal{G}$ a generalized vector of internal variables. A normal–dissipative set of local material equations has the structure

  stresses $\quad \boldsymbol{P} = \partial_{\boldsymbol{F}} \psi(\boldsymbol{F}, \boldsymbol{\mathcal{I}}; \boldsymbol{X})$

  evolution equation $\quad \partial_{\boldsymbol{\mathcal{I}}} \psi(\boldsymbol{F}, \boldsymbol{\mathcal{I}}; \boldsymbol{X}) + \partial_{\dot{\boldsymbol{\mathcal{I}}}} \phi(\dot{\boldsymbol{\mathcal{I}}}, \boldsymbol{\mathcal{I}}; \boldsymbol{X}) = 0 \quad , \boldsymbol{\mathcal{I}}(0) = \boldsymbol{\mathcal{I}}_0$

  defined in terms of an energy storage function ψ and a dissipation function ϕ.

- **Incremental Variational Formulation of Constitutive Model (C).** In a finite time increment $[t_n, t_{n+1}]$, the *minimization problem of the constitutive response*

  stresses $\quad \boldsymbol{P}_{n+1} = \partial_{\boldsymbol{F}} W(\boldsymbol{F}_{n+1}; \boldsymbol{X})$

  stress potential $\quad W(\boldsymbol{F}_{n+1}; \boldsymbol{X}) = \inf_{\boldsymbol{\mathcal{I}}} \int_{t_n}^{t_{n+1}} [\dot{\psi} + \phi] \, dt \quad , \boldsymbol{\mathcal{I}}(t_n) = \boldsymbol{\mathcal{I}}_n$

  determines the current internal state $\boldsymbol{\mathcal{I}}_{n+1} \in \mathcal{G}$ and provides a potential for the stresses at time t_{n+1}. Approximation by variational update algorithm.

- **Stability of Incremental Constitutive Response (S).** In $[t_n, t_{n+1}]$ the *material is locally stable if the incremental stress potential W is quasi–convex*

  stable response $\quad \frac{1}{|D|} \int_D W(\boldsymbol{F}_{n+1} + \nabla \boldsymbol{w}(\boldsymbol{y})) \, dV \geq W(\boldsymbol{F}_{n+1})$

  for all possible fluctuations $\boldsymbol{w}(\boldsymbol{y})$ on the domain D.

- **Microstructure Development in Homogeneous Materials (R).** For an instable non–convex response, the *incremental minimization problem of convexification*

  macro–stresses $\quad \boldsymbol{P}_{Qn+1} = \partial_{\boldsymbol{F}} W_Q(\boldsymbol{F}_{n+1})$

  relaxation $\quad W_Q(\boldsymbol{F}_{n+1}) = \inf_{\boldsymbol{w}} \frac{1}{|\mathcal{V}|} \int_{\mathcal{B}} W(\boldsymbol{F}_{n+1} + \nabla \boldsymbol{w}(\boldsymbol{y})) dV$

  provides a relaxed convex hull W_Q of W and determines the current microstructure fluctuation field $\boldsymbol{w}(\boldsymbol{y})$. Possible approximation by first–order rank–one relaxation.

- **Microstructure Development in Heterogeneous Materials (H).** $\bar{\boldsymbol{F}}_{n+1} \in GL_+(3)$ is the macro–deformation of a heterogeneous microstructure $\mathcal{B}$ at time t_{n+1}. The *incremental minimization problem of homogenization*

  macro–stresses $\quad \bar{\boldsymbol{P}}_{n+1} = \partial_{\bar{\boldsymbol{F}}} \bar{W}(\bar{\boldsymbol{F}}_{n+1})$

  homogenization $\quad \bar{W}(\bar{\boldsymbol{F}}_{n+1}) = \inf_{\boldsymbol{w}} \frac{1}{|\mathcal{V}|} \int_{\mathcal{B}} W(\bar{\boldsymbol{F}}_{n+1} + \nabla \boldsymbol{w}(\boldsymbol{X}); \boldsymbol{X}) dV$

  determines the homogenized potential $\bar{W}$ and the fluctuation field $\boldsymbol{w}(\boldsymbol{X})$ on the heterogeneous microstructure. Possible approximation by a finite element discretization.

Figure 2. Incremental energy minimization principles of dissipative solids for multiscale homogenization and relaxation analyses.

Incremental Minimization Problem of Homogenization (H)

The existence of the quasi–hyperelastic incremental stress potentials for standard dissipative materials also allows the extension of homogenization approaches of finite elasticity to the incremental setting of inelasticity. Following the works [5] and [3], we outline an *incremental variational formulation of the homogenization problem* for standard dissipative materials at finite strains, where a quasi–hyperelastic macro–stress potential is obtained from a global minimization problem with respect to the fine–scale displacement fluctuation field. It is shown that this global minimization problem determines the state of the heterogeneous micro–structure for finite increments of time.

In the lecture successivly treats theoretical and algorithmic formulations of the above mentioned minimization problems (C), (R) and (H), where Figure 2 provides a guide. The performance of the formulations is demonstrated for conceptual model problems of multiscale microstructure developments in stable and instable materials as indicated in Figure 1.

References

[1] Carstensen C., Hackl K., Mielke A.: Nonconvex potentials and microstructures in finite-strain plasticity. *Proceedings of the Royal Society London A*, **458**:299–317, 2002.

[2] Miehe C.: Strain-driven homogenization of inelastic microstructures and composites based on an incremental variational formulation. *International Journal for Numerical Methods in Engineering*, **55**:1285–1322, 2002.

[3] Miehe C.: Computational micro-to-macro transitions for discretized micro-structures of heterogeneous materials at finite strains based on the minimization of averaged incremental energy. *Computer Methods in Applied Mechanics and Engineering*, **192**:559–591, 2003.

[4] Miehe C., Lambrecht M.: A two-scale finite element relaxation analysis of shear bands in non-convex inelastic solids: Small-strain theory for standard dissipative materials. *Computer Methods in Applied Mechanics and Engineering*, **192**:473–508, 2003.

[5] Miehe C., Schotte J., Lambrecht M.: Homogenization of inelastic solid materials at finite strains based on incremental minimization principles. Application to the texture analysis of polycrystals. *Journal of the Mechanics and Physics of Solids*, **50**:2123–2167, 2002.

[6] Miehe C., Schröder J., Becker M.: Computational homogenization analysis in finite elasticity. Material and structural instabilities on the micro- and macro-scales of periodic composites and their interaction. *Computer Methods in Applied Mechanics and Engineering*, **191**:4971–5005, 2002.

[7] Ortiz M., Repetto E.A.: Nonconvex energy minimization and dislocation structures in ductile single crystals. *Journal of the Mechanics and Physics of Solids*, **47**:397–462, 1999.

XXI ICTAM, 15–21 August 2004, Warsaw, Poland

NON-CONVEX HOMOGENIZATION OF INELASTIC COMPOSITES WITH INTERACTION OF MATERIAL AND STRUCTURAL INSTABILITIES ON DIFFERENT SCALES

Martin Becker, Christian Miehe
University of Stuttgart, Institute of Applied Mechanics (Civil Engineering), 70550 Stuttgart, Germany

Summary In the case of structural instabilities on the micro-scale classical homogenization approaches for composites hit their limitations. Based on an incremental setting of finite inelasticity, a postcritical non-convex homogenization approach is considered for micro-heterogeneous inelastic materials. For these materials stability criteria for structural and material instabilities on the micro- and macro-scale and their connection are presented as well as the size effect of the representative volume element in the nonconvex regime.

Incremental constitutive response of the microstructure and micro-to-macro transition

Micro-instabilities significantly alter the macroscopic material behavior. For example micro-buckling of stiff fibers leads to a considerable softening in the macro-response accompanied by localized discontinuities on the macro-scale. Goal of the presentation is to point out stability criteria on the micro- and macro-scale, as well as their interaction. We discuss their influence on the homogenization procedure and show how instabilities can be incorporated into the micro-to-macro transition. We focus on periodic composites with constituents of standard dissipative materials. For this type of material response we consider an *incremental variational formulation* developed in [3,5,7] where the current stresses at time t_{n+1} are governed by an *incremental stress potential* W which can be constructed by the constitutive minimization problem

$$W(\boldsymbol{F};\boldsymbol{X}) = \inf_{\boldsymbol{\mathcal{I}}\in\mathcal{G}} \int_{t_n}^{t_{n+1}} [\dot{\psi}+\phi]dt \quad \text{with} \quad \boldsymbol{\mathcal{I}}(t_n) = \boldsymbol{\mathcal{I}}_n \tag{1}$$

with respect to a generic vector of internal (history) variables $\boldsymbol{\mathcal{I}} \in \mathcal{G}$, constraint to some manifold $\mathcal{G}$. Here, $\psi(\boldsymbol{F},\boldsymbol{\mathcal{I}};\boldsymbol{X})$ is a *constitutive free energy storage function* and $\phi(\dot{\boldsymbol{\mathcal{I}}},\boldsymbol{\mathcal{I}};\boldsymbol{X})$ a *dissipation function* of the material of the microstructure. With the constitutive functional W at hand we apply a deformation driven homogenization procedure where for given macro-deformation $\bar{\boldsymbol{F}}$ the micro-deformation field $\boldsymbol{\varphi}$ is specified by the *incremental minimization problem of homogenization*

$$\bar{W}(\bar{\boldsymbol{F}}) = \inf_{\boldsymbol{\varphi}\in V_\#} \bar{W}(\boldsymbol{\varphi}) \quad \text{with} \quad \bar{W}(\boldsymbol{\varphi}) = \frac{1}{|\mathcal{V}|}\int_{\mathcal{B}} W(\boldsymbol{F};\boldsymbol{X})\, dV, \tag{2}$$

which defines the homogenized quasi-hyperelastic potential $\bar{W}$ as the minimum volume average of the microscopic potential W with respect to the micro-deformation field $\boldsymbol{\varphi}$. Here $|\mathcal{V}|\bar{W}(\boldsymbol{\varphi})$ is the total incremental energy of the microstructure, the set $V_\#$ restricts the micro-deformation to periodic boundary conditions on the on the surface $\partial\mathcal{B}$ of the microstructure.

Material instabilities on the macro-scale

The existence of a minimizing solution of the homogenization principle $(2)_1$ is guaranteed if the variational functional $(2)_2$ is *sequentially weakly lower semicontinuous* (s.w.l.s.). This generalizes statements of finite elasticity as outlined in [1,8] to the finite incremental response of generalized standard materials. A loss of *macroscopic rank-1-convexity* implies a lack of *quasiconvexity* and hence a violation of the s.w.l.semincontinuity condition for the homogenized potential. Consequently the existence of minimizing solutions for $(2)_1$ is no longer ensured. An algorithmic control of infinitesimal rank-1-convexity bases on an analysis of the *acoustic tensor* $\{\bar{Q}\}_{ac} = \{\partial^2_{\bar{\boldsymbol{F}}\bar{\boldsymbol{F}}}\bar{W}(\bar{\boldsymbol{F}})\}_a{}^B{}_c{}^D \bar{N}_B\bar{N}_D$ as follows

$$\min_{||\bar{\boldsymbol{N}}||=1} \{\det[\bar{\boldsymbol{Q}}]\} \begin{cases} > 0 & \text{for strictly infinitesimal rank-1-convex } \bar{W}(\bar{\boldsymbol{F}}) \\ \leq 0 & \text{for not strictly infinitesimal rank-1-convex } \bar{W}(\bar{\boldsymbol{F}}). \end{cases} \tag{3}$$

For materials being initially homogeneous over all scales a loss of macroscopic rank-1-convexity indicates the development of fine-scale microstructures. In the case of a priori micro-heterogeneous materials a loss of rank-1-convexity on the superior homogeneous scale is due to the development of structural instabilities on the micro-scale.

Structural instabilities on the micro-scale and interaction between micro- and macro-instabilities

We define a criterion for the analysis of structural instabilities within the incremental setting of finite inelasticity. Structural instabilities like the buckling of stiff fibers may occur on the microscale if the *infinitesimal structural stability condition*

$$\bar{W}(\bar{\boldsymbol{F}},\boldsymbol{\varphi}) - \bar{W}(\bar{\boldsymbol{F}},\boldsymbol{\varphi}+\delta\boldsymbol{\varphi}) = \frac{1}{2|\mathcal{V}|}\int_{\mathcal{B}} \nabla\delta\boldsymbol{\varphi} : \partial^2_{\boldsymbol{FF}} W(\bar{\boldsymbol{F}},\boldsymbol{\varphi}) : \nabla\delta\boldsymbol{\varphi}\, dV > 0 \tag{4}$$

is violated. Thus any infinitesimal perturbation $\delta\boldsymbol{\varphi}$ induces an increase of the averaged infinitesimal energy if the micro-deformation $\boldsymbol{\varphi}$ describes an equilibrium state of the microstructure. Condition (4) is satisfied for *positive definite tangent moduli* $\partial^2_{\boldsymbol{FF}}W$ in the whole domain of the microstructure. A macroscopic structural stability criterion can be defined in a similar way. The interaction between micro- and macro-instabilities for nonlinearly elastic materials has been analyzed in [1], a generalization to inelastic materials can be obtained in the incremental setting. Comparison of the infinitesimal structural stability criteria on the micro- and macro-scales shows that a long-wavelength form $\delta\boldsymbol{F} = \bar{\boldsymbol{p}}\otimes\bar{\boldsymbol{N}} + \nabla\delta\boldsymbol{w}$ of the micro-deformation induces a Maxwell form $\delta\bar{\boldsymbol{F}} = \bar{\boldsymbol{p}}\otimes\bar{\boldsymbol{N}}$ of the macro-deformation. Thus a structural instability on the micro-scale can be detected by an analysis for loss of macroscopic rank-1-convexity (for detailed discussions see [4,6]).

Homogenization of nonconvex incremental stress potentials

Structural instabilities on the micro-scale lead to the problem of the necessary homogenization of a non-convex incremental stress potential. We extend results on Γ-convergence obtained by [2] for the elastic regime to the incremental setting of inelasticity based on the potential W. Thus in order to account for structural instabilities within the homogenization procedure the ensemble averaged potential has additionally to be minimized with respect to the size n_c (n_c being the number of characteristic cells) of the microstructure when computing the homogenized incremental stress potential $\bar{W}$

$$\bar{W}(\bar{\boldsymbol{F}}) = \inf_{n_c} \left\{ \inf_{\boldsymbol{\varphi}} \frac{1}{|\mathcal{V}(n_c)|} \int_{\mathcal{B}(n_c)} W(\bar{\boldsymbol{F}}, \boldsymbol{\varphi}) dV \right\} . \tag{5}$$

Hence for example for a cellular microstructure the number of characteristic cells (i.e. the smallest unit capable of representing the periodic structure of the micro-scale) has to be varied. The relevant representative volume element is then characterized by the number of cells n_c which minimizes the incremental energy at the micro-bifurcation point.

Stability analysis of an inelastic fiber-reinforced microstructure

Figure 1 a) shows a schematic picture of a microscopically fiber-reinforced compression member. In order to determine n_c (in this problem n_c is fully determined by the length l of the microstructure), l is varied and the respective bifurcation points at which the structural instabilities occur on the micro-scale are determined from the macroscopic stress-strain relation (Fig. 1b)). Next the values of the total potential $\bar{W}^{tot}$ (sum of the incremental potentials up to the present time step) at the bifurcation points are determined (Fig. 1c)). Corresponding to eq. (5) the relevant microstructure is the one giving the minimum potential at the bifurcation point (Figure 2b), i.e. the microstructure has to be of a length of $l \geq 10$. Comparing Figures 1 b) and 2 c) reveals that for the relevant microstructure the structural instability on the micro-scale (Fig.1b)) occurs at the same compression parameter of $\lambda^{10}_{crit} = 0.016$ as the macroscopic material instability (Fig.2c)).

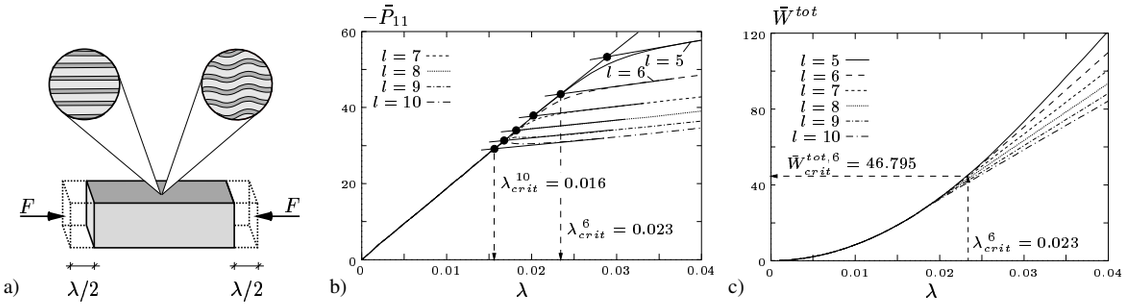


Figure 1. a) Schematic picture of a microscopically fiber-reinforced compression member, subjected to a compressive force F. b) Determination of the bifurcation points; macroscopic 1^{st} Piola-Kirchhoff stress-components $\bar{P}_{11}$ versus compression parameter λ and c) total stress potentials $\bar{W}^{tot}$ versus compression parameter λ for different lengths l of the microstructure.

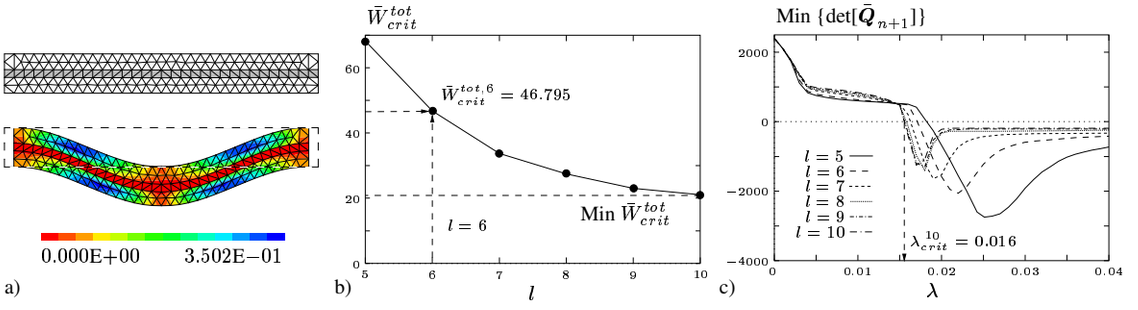


Figure 2. a) Postcritical buckling mode and distribution of equivalent plastic strains at a horizontal compression of 6% for a microstructure of length $l = 8$. b) Determination of relevant size of microstructure; $\bar{W}^{tot}$ at respective bifurcation points versus length l. c) Macroscopic material instability; minimum value of determinant of acoustic tensor versus compression parameter λ.

References

[1] Dacorogna, B.: Direct Methods in the Calculus of Variations. Springer-Verlag, Berlin 1989.

[2] Geymonat, G.; Müller, S.; Triantafyllidis N.: Homogenization of Nonlinearly Elastic Materials, Microscopic Bifurcation and Macroscopic Loss of Rank-One Convexity. *Archive of Rational Mechanics and Analysis* **122**: 231–290, 1993.

[3] Miehe, C.: Strain-Driven Homogenization of Inelastic Microstructures and Composites Based on an Incremental Variational Formulation. *International Journal for Numerical Methods in Engineering* **55**: 1285–1322, 2002.

[4] Miehe, C.; Becker, M.: Homogenization Analysis in Finite Plasticity Based on Incremental Minimization Principles. Material and Structural Instabilities on the Micro- and Macro-Scales and their Interaction. Submitted to *CMAME*, 2003.

[5] Miehe, C.; Schotte, J.; Lambrecht, M.: Homogenization of Inelastic Materials at Finite Strains Based on Incremental Minimization Principles. Application to the Texture Analysis of Polycrystals. *JMPS* **50**: 2123–2167, 2002.

[6] Miehe, C.; Schröder, J.; Becker M.: Computational Homogenization Analysis in Finite Elasticity: Material and Structural Instabilities on the Micro- and Macro-Scales of Periodic Composites and their Interaction. *CMAME* **191**: 4971–5005, 2002.

[7] Ortiz, M.; Stainier, L.: The Variational formulation of viscoplastic constitutive updates. *CMAME* **171**: 419–444, 1999.

[8] Silhavy, M.: The Mechanics and Thermodynamics of Continuous Media. Springer-Verlag, Berlin 1997.

PHYSICAL MODELING OF FRACTURE MECHANICS IN COMPLEX MATERIALS

Fabrizio Cleri*, Luciano Colombo**, Pier Giuseppe Gabrielli*, Mariella Ippolito**, Alessandro Mattoni**

*ENEA, UTS Nuovi Materiali, C.R. Casaccia, Roma, Italy

**INFM-DEMOCRITOS and Department of Physics, University of Cagliari, Cagliari, Italy

Summary. The mechanical behaviour of brittle materials is very sensitive to microstructure defects, like point or extended lattice imperfections, elastic inclusions, voids. Since the local stress conditions (i.e. the conditions nearby a defect) of such complex materials may largely differ from their average values, the prediction of the overall mechanical response to external loads results to be a though theoretical problem. This is, for instance, the case of the stress threshold at which a microcrack starts propagating, or the interaction features bewteen the defect and the incoming crack. In this work, we investigate at the proper nanoscale the interaction between a crack tip and elastic inclusions by combining a hierarchy of different computational tools, namely atomistic simulations (carried out at the molecular dynamics level) and statistical mechanics models (based on replica-symmetry breaking). The investigated material is silicon carbide, i.e. the prototypical example of brittle material with directional and covalent bonding.

INTRODUCTION and MOTIVATIONS FOR PHYSICAL MODELING

The design of new materials for advanced applications requires a better fundamental understanding of the correlation between microstructure, elastic/plastic properties, and mechanical response. This is, in particular, the case of covalently-bonded materials where several technological applications (namely, in aerospace and nuclear industry) are affected by their fragility under external mechanical and/or thermal stresses. In fact, such materials (in this context we will mainly refer to SiC) are extremely brittle, undergoing fast fracture at low temperatures.

The complex interplay of microscopic (indeed, atomic-scale) events hidden behind the apparently simple phenomenology of brittle fracture has led in the past years to an ever increasing number of theoretical and computer-based simulation studies. Among the mechanical properties, the problems of the nucleation and the evolution (growth) of brittle cracks – which are a key issue in the design of engineering stuctures – have generated a considerable body of theoretical work. Nevertheless, there are several fundamental issues still unsolved in the modern theory of brittle fracture, both in the quasi-static and dynamic domain.

Whitin the above scenario the computer-based investigations firmly rooted in the atomistic description of the material – hereafter referred to as *physical* (or *atomistic*) *modeling* [1] – are playing an increasingly important role. For example, in modern atomic-scale studies of crack propagation all of possible behavior show, from a strictly discontinuous dynamics ("lattice trapping") characterized by a complex emission of sound waves accompanying the discontinuos crack tip velocity, to a continuous behavior with a smooth opening of the running crack.

In this work we present a typical application of such an atomistic modeling to fracture mechanics with a twofold aim: (i) we like to present and discuss both conceptual and numerical problems underlying physical modeling, and (ii) we want to investigate the specific case of the interaction between a crack tip propagating into SiC towards/against elastic inclusion(s).

Since atomistic simulations are severly limited by their huge computational workload, they cannot in fact represent the only tool for the theoretical physicist interested in fracture mechanics. As a matter of fact, they need to be hierarchically combined to higher-order models (spanning the meso-/macro-scale) like, relevant to the present case, statistical mechanics ones. We therefore develop in the second part of this work a statistical approach to connect the theoretical strenght, the aging effects on mechanical properties and the local fracture toughness randomness (and/or fluctuations). In particular, we will study the macroscopic dynamics of crack fronts in disordered media by means of a statistical mechanics approach based on the replica-symmetry breaking

ATOMISTIC SIMULATIONS

The atomistic modeling relies on the description of the investigated system as an assembly of interacting particles. The goal is to derive the mechanical properties of interest directly from the collective response of atoms to suitable external loads. According to this definition, atomistic modeling represents for fracture mechanics a fundamental theory, not requiring the definition of *ad hoc* constitutive equations and/or phenomenological parameters.

The most natural way to carry out atomistic modeling is by means of molecular dynamics (MD) simulations: the atomic trajectories of a set of interacting particles – representing the mechanical system – are generated by computer in arbitrary conditions of temperature, load, state of aggregation. As for the present investigation, MD naturally drives to the optimal atomic-scale description of those relevant phenomena occurring at the tip of a mobile crack. In fact MD can effectively model the complex bond-breaking, bond switching, and rebond events observed at the very end of a crack propagating into a covalenty-bonded material. They represent, in turn, the "elementary" events ruling fracture.

We developed an efficient MD code suitable to simulating the propagation of a fracture into an atom-resolved β-SiC lattice. The propagation of the crack has been simulated by the application of an external driving force (load),

according to the modern theory of the representation of mechanical loads within a MD simulation scheme [2]. This technique will allow for the simulation of the relevant phenomena in arbitrary conditions of temperature and/or stress.
Our results provide a thorough analysis of the interaction feature between a crack tip and an elastic inclusion, either harder (diamond-like) or softer (silicon-like or void) than the host matix. The analysis is carried out in terms of both strain and stress fields.

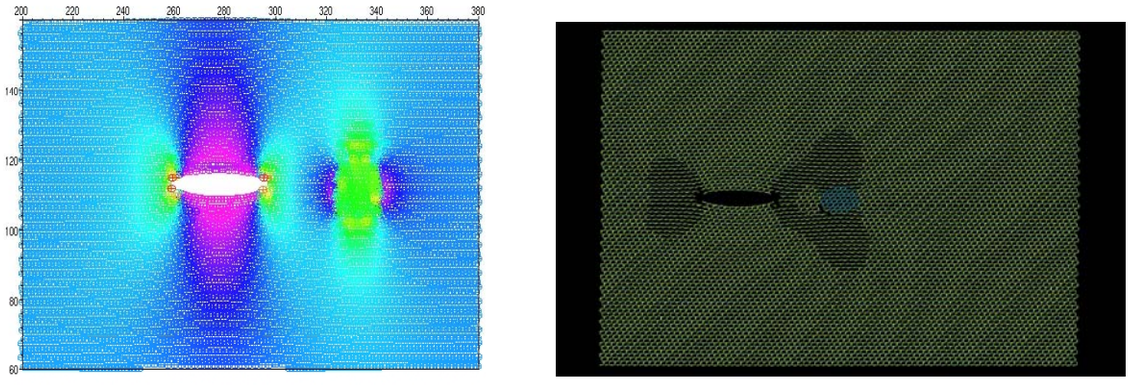


Fig.1 – *Side view for the interaction between a crack and a diamond-like inclusion in cubic SiC. A tensile load is applied normally to the pricipal crack axis. Left: total stress field (green: tensile; purple: compressive; light blue: stress conditions corresponding to the applied load). Right: similar situation now shown in terms of atomic positions and (distorted) chemical bonds. The dimensions of the computational sample are 1nm×47nm×36nm, corresponding to 155520 particles in the simulation cell*.

STATISTICAL MECHANICS MODELS

When considering more complex situations like, for instance, the roughening of a crack front during a fracture event, a straightforward atomistic simulation is simply impossible because of computer limitations. In this case we need to implement mesoscopic models based on statistical mechanics which, however, must still maintain some basic information about the underlaying lattice nature of the material.
We discuss a specific model developed to address the problem of a crack front propaganting in elastically disordered media. In this case, the crack front is faced to a pinning force due, in turn, to local (i.e. randomly distributed on lattice sites) fracture toughness. The elastic restoring force is therefore a result of the line tension of the crack front due to local bulk elasticity of the medium (in brittle materials). Under strong pinning conditions, it is well known that, when subjected to an external driving load, the crack front displays local instabilities that force it to advance quasistatically. This property makes it difficult to handle the problem in the continuum approximation and makes the present statistical approach worthy.
We effectively described the above problem by an extremal model: only the fracture site (which is mappend onto the lattice) closest to its instability threshold advances. After a jump, the instability thresholds of all the sites are modifed by the (elastic) couplings between sites. The proposed model belongs in fact to a wide class of extremal models which have already been studied extensively. The common feature consists in the attempt to explain driven motion under strong pinning by means of a discrete, deterministic dynamics. Only one site is active at every instant of time. Further the extremal condition can be thought of as a way to retain the information of the spatially quenched heterogeneities that determine the evolution of the front. All the information in this dynamics is clearly contained in a space-time "cracking plot", i.e. the geometriucal locus where the front is active: most of the relevant physical information will be discussed in terms of the probability density function of such a plot.

ACKNOWLEDGEMENT

This work has been funded by MIUR under project PRIN-2002.

REFERENCES

[1] D. Frenkel and B. Smit, "*Understanding molecular simulations*" (Academic Press, San Diego, 1996).
[2] F. Cleri, Phys. Rev. B **65**, 014107 (2001).

XXI ICTAM, 15–21 August 2004, Warsaw, Poland

ANALYSIS OF A VARIATIONAL METHOD COUPLING DISCRETE AND CONTINUUM MECHANICS

Xavier Blanc*, Claude Le Bris**, Frederic Legoll**,
*Laboratoire J.L.-Lions, Université Paris 6, F-75252 Paris, France
** CERMICS, Ecole Nationale des Ponts et Chaussées, F-77455 Marne la Vallee, France

Summary The description and computation of fine scale localized phenomena arising in a material (during nanoindentation, for instance) is a challenging problem that has given birth to some multiscale methods. In this work, we propose an analysis of a simple one dimensional method that couples two scales, the atomistic one and the continuum mechanics one. The method includes an adaptative criterion in order to split the computational domain into two subdomains, that are described at different scales.

INTRODUCTION

The traditional framework in mechanics is the continuum description. However, when nanoscale localized phenomena arise, the atomistic nature of material cannot be ignored: for instance, to understand how dislocations appear under a nanoindenter, one has to describe the deformed atomistic lattice. The situation is the same when one wants to have a detailed understanding of the behaviour of grain boudaries in a polycristal. In all these examples, an appropriate model to describe the localized phenomena is the atomistic model, in which the solid is considered as a set of discrete particles interacting through given interatomic potentials.

However, the size of materials that can be simulated by only using the atomistic model is very small in comparison to the size of the materials one is interested in. Fortunately, in the situations we considered above, the deformation is smooth in the main part of the solid. So, a natural idea is to try to take advantage of both models, the continuum mechanics one and the atomistic one, and to couple them. In this work, we analyse a method initially proposed in [1] that couples these two models into a single one. Other coupling methods have been proposed in [2], [3]. Another possibility is to use continuum mechanics models in which the elastic energy depends not only on the strain, but also on higher derivatives of the displacement [4], or to add a surface energy [5]. Time-dependent methods based on mixed hamiltonians have also been proposed in [6].

The atomistic and continuum mechanics models

Let us consider a one dimensional material occupying in the reference configuration the domain $\Omega = (0, L)$, submitted to body forces f and fixed displacement boundary conditions on $\partial\Omega$. In the atomistic model, the solid is considered as a set of $N+1$ atoms, whose current positions are $(u^i)_{i=0}^N$. The energy of the system is given by

$$E_\mu(u^0, \ldots, u^N) = h \sum_{i=0}^{N-1} W\left(\frac{u^{i+1} - u^i}{h}\right) - h \sum_{i=0}^{N} f(i\,h)\, u^i, \tag{1}$$

where W is an interacting potential between atoms, and h is the atomic lattice parameter, which is linked to the number of atoms and the size of the solid by $L = Nh$. We have assumed only nearest neighbour interaction. The potential W is such that its minimum is attained at 1, so, at equilibrium without body forces and boundary conditions, the interatomic distance is h. The microscopic equilibrium configuration is a solution of the variational problem

$$\inf\left\{E_\mu(u^0, \ldots, u^N),\ u^0 = 0,\ u^N = a\right\}. \tag{2}$$

In the continuum mechanics model, the solid deformation is described by the map $u : \Omega \to R$, and the elastic energy associated with the deformation u reads

$$E_M(u) = \int_\Omega W(u'(x))\, dx - \int_\Omega f(x)\, u(x)\, dx. \tag{3}$$

The equilibrium of the solid is defined by the minimization problem

$$\inf\left\{E_M(u),\ u(0) = 0,\ u(L) = a\right\}. \tag{4}$$

In principle, the equilibrium configuration of the solid is given by (1)-(2), but the huge number of particles to be considered makes the problem impossible to solve in practice. For a given smooth deformation u, it can be shown [7] that the microscopic energy $E_\mu(u(0), u(h), \ldots, u(Nh))$ converges to $E_M(u)$ when the atomic lattice parameter h goes to 0 and the number of atoms goes to infinity such that Nh remains constant, $Nh = L$. Thus, solving (3)-(4) gives a good approximation of the solution of the atomistic problem, when the equilibrium deformation is smooth.

A coupled model

When non regular deformations are expected to play a role, following [1], we approximate the solution of the atomistic problem with the solution of a coupled model. A partition $\Omega = \Omega_M \cup \Omega_\mu$ of the domain being given, a natural expression

for a coupled energy reads

$$E_c(u) = \int_{\Omega_M} W(u'(x)) - f(x)u(x)\,dx + h \sum_{i;\, ih, ih+h \in \Omega_\mu} W\left(\frac{u^{i+1}-u^i}{h}\right) - h \sum_{i; ih \in \Omega_\mu} f(ih)u^i. \tag{5}$$

The equilibrium of the solid is given by the minimization problem

$$\inf \left\{ \begin{array}{c} E_c(u),\ u_{|\Omega_M} \text{ is a map on } \Omega_M,\ u_{|\Omega_\mu} \text{ is a discrete set of variables } (u^i)_{ih\in\Omega_\mu}, \\ \\ u \text{ is continuous at the interface } \partial\Omega_M \cap \partial\Omega_\mu,\ u(0)=0,\ u(L)=a \end{array} \right\} \tag{6}$$

The questions we address here are:

- is the previous definition (5) of the coupled energy always the most appropriate?
- how to (adaptively) define the partition $\Omega = \Omega_M \cup \Omega_\mu$ such that the solution of the coupled problem (5)-(6) is a good approximation of the solution of the atomistic problem (1)-(2)?
- Can error bounds be derived?

RESULTS

We study both the general case of a convex energy density W, and a specific example of non convex energy, the Lennard-Jones case.

The convex case

In this case, we propose an *a priori* definition for the partition which is only based on properties of the body forces f. Essentially, the subdomain Ω_M (in which the continuum mechanics model will be used) is the part of the domain where the body force f and its derivative f' are small.
With this definition, we show that the solution of the coupled problem (5)-(6) is a good approximation of the solution of the atomistic problem (1)-(2): when the atomic lattice parameter h goes to 0, the displacement u_c and the strain given by the coupled model converge to the displacement u_μ and the strain given by the atomistic model.

A non convex case: the Lennard-Jones case

In this case, we show that expression (5) for the coupled energy might be inappropriate, and we thus propose a modified expression.
If the material is submitted to an extensional loading (i.e., if $u(L) = a > L$ in the case of no body forces), the macroscopic model and the atomistic model solutions exhibit a fracture. With the natural coupled model (5)-(6), the equilibrium also exhibits a fracture, but this fracture is always located in the macroscopic subdomain Ω_M. However, we would rather like the atomistic subdomain Ω_μ to contain the fracture. To solve this issue, we propose to work with the coupled energy

$$E_c^h(u) = \int_{\Omega_M} W_h(u'(x)) - f(x)u(x)\,dx + h \sum_{i;\, ih, ih+h \in \Omega_\mu} W\left(\frac{u^{i+1}-u^i}{h}\right) - h \sum_{i; ih \in \Omega_\mu} f(ih)u^i,$$

with $W_h(t) = W(t) + \rho_h(t-t_0)_+$, where t_0 is some threshold and ρ_h goes to 0 when h goes to 0. Several choices are possible for ρ_h. Finally, the algorithm we propose consists in two steps:

- compute a solution u_M of the macroscopic problem (3)-(4), and from the properties of u_M, define a partition $\Omega = \Omega_M \cup \Omega_\mu$.
- with this partition, minimize the coupled energy $E_c^h(u)$ to find u_c.

We will show that the resulting solution u_c is a good approximation of the atomistic solution. In particular, if the solid is submitted to extensional loadings, the atomistic subdomain Ω_μ contains the fracture.

References

[1] Tadmor E.B., Ortiz M., Phillips R.: QuasiContinuum analysis of defects in solids, *Phil. Mag. A* **73**(6):1529-1563, 1996.
[2] Zhang P., Klein P.A., Huang Y., Gao H., Wu P.D.: Numerical simulation of cohesive fracture by the virtual-internal-bond model, *Computer Modeling in Engineering and Sciences*, **3**(2):263-289, 2002.
[3] Van Vliet K.J., Li J., Zhu T., Yip S., Suresh S.: Quantifying the early stages of plasticity through nanoscale experiments and simulations, *Phys. Rev. B* **67**:104105, 2003.
[4] Triantafyllidis N., Bardenhagen S.: On higher order gradient continuum theories in 1-D nonlinear elasticity. Derivation from and comparison to the corresponding discrete models, *J. of Elasticity* **33**:259-293, 1993.
[5] Del Piero G., Truskinovsky L., Macro- and micro-cracking in one-dimensional elasticity, *Int. J. of Solids and Structures* **38**:1135-1148, 2001.
[6] Abraham F.F., Broughton J.Q., Bernstein N., Kaxiras E.: Spanning the length scales in dynamic simulation, *Comput. Phys.* **12**:538, 1998.
[7] Blanc X., Le Bris C., Lions P.-L.: From molecular models to continuum mechanics, *Arch. Rat. Mech. Anal.* **164**(4):341-381, 2002.

Toys and Games in Mechanics Education

Hassan Aref
College of Engineering, Virginia Polytechnic Institute and State University
Blacksburg, VA 24061, USA

Extended summary

Toys and games have considerable educational potential. In some fields of mathematics, such as combinatorics, probability and statistics, the use of examples involving playing cards and dice is well established and these examples reflect portions of the early history of development of those subjects. The field of game theory is, intrinsically, all about strategies for winning games. In mechanics certain toys and games that particularly lend themselves to analysis have been afforded comprehensive scholarly treatment. The monumental treatise on the motion of the top by Sommerfeld and Klein, and the monograph on billiards by Coriolis may be cited as two key examples. It follows already from these examples that a comprehensive analysis of a simple toy or game is often not at all simple and may challenge even advanced students and scholars.

In this paper a number of toys and games that rest on and illustrate basic mechanical principles are described. Some of the smaller toys will be brought to the presentation. The author's (admittedly limited) experience in using toys and games for project work with undergraduates is recounted, and some ideas on how to expand the use of toys and games in an educational setting are presented.



Fig.1: Pauli and Bohr fascinated by the Tippe Top



Fig.2: Commercially available rattlebacks

There are several good reasons for exploring mechanical toys. First, they are fun. Students of all ages find them intriguing and engaging. Who can forget the picture of Wolfgang Pauli and Niels Bohr enthralled by the counter-intuitive, angular-momentum-reversing behavior of the Tippe Top (Fig.1)? Second, they are (typically) quite cheap. The rattlebacks shown in Fig.2, for example, are available for pennies. Third, toys are often surprisingly complicated. It follows that they hold fascination for even seasoned researchers, an important consideration when taking on the supervision of an independent project by a student. It follows, fourth, that many illustrious mechanicians have studied them to the point of publishing articles or monographs (besides Coriolis, Klein and Sommerfeld, we may mention Bondi, Synge and Stewartson; see the references given below). They continue to do so, *cf*. recent papers by Hinch & Saint-Jean on "Newton's cradle", the study by Berry on the "Levitron™" and the work by Moffatt on the "Euler disk" (vividly demonstrated during his closing lecture at ICTAM2000). Toys and games have great motivational value at all levels, from school children to mature researchers. Finally, they are part of our cultural heritage, a fact illustrated, for example, by the inclusion of the "Slinky" in a series of US postage stamps entitled "Celebrate the Century" (Fig.3). The introduction of this flexible spring in 1945 created a fad that has lasted to this day.



Fig.3 US postage stamp featuring "Slinky"



Fig.4: Shoot the Moon game/toy

Examples of mechanical toys and games with relatively simple mechanical principles underlying them include the "Sand Wand", the "Ooze Tube", and "Shoot the Moon" game/toy (Fig.4). More complicated dynamics is displayed in toys such as "Newton's cradle", "Slinky", the "Euler disk", the "Tippe Top", and the rattleback (celt or wobblestone). Numerous articles exist on the "Tippe Top" and the rattleback. Three-dimensional dynamics of rigid bodies in contact with a rough surface continues to hold many challenges!

I will describe two independent study projects done with the "Ooze Tube" and "Shoot the Moon". In the former case it was possible to touch on the topic of fluid flow instability with which a US undergraduate student will typically have little familiarity. (This included studying the paper by G. I. Taylor presented at the 12th ICTAM in 1968.). The project with "Shoot the Moon" involved relatively intricate, albeit two-dimensional dynamics of a rigid body, and simple ideas about control of a dynamical system.

Apart from analytical mechanics projects the world of mechanical toys opens up a number of "softer" questions that may be used to attract students into the field of mechanics. One can, for example, pursue issues of materials selection, assembly of bibliographic material, or construction of websites on toys. It is cheap and relatively simple to construct prototypes of novel toys (often variations on existing toys). Diagnostic experiments are relatively cheap since the length and time scales involved are typically macroscopic. Finally, demonstrations involving toys tend to be great "crowd pleasers" (particularly for crowds including children) at various outreach events.

References

Berry, M. V. 1996"The Levitron™: an adiabatic trap for spins." *Proceedings of the Royal Society, London* A **452**, 1207.

Bondi, H. 1986 "The Rigid Body Dynamics of Unidirectional Spin." *Proceedings of the Royal Society of London* A **405**, 265.

Coriolis, G-G. 1835 *Théorie mathématique des effets du jeu de billiard* (1835).

Hinch, E. J. & S. Saint-Jean, S. 1999 "The fragmentation of a line of balls by an impact," *Proceedings of the Royal Society, London* A **455**, 3201.

Klein, F. & Sommerfeld, A. 1897-1910 *Über die Theorie des Kreisels,* (4 vols.) Leipzig.

Moffatt, H. K. 2000 "Euler's disk and its finite time singularity," *Nature* **404**, 833.

Stewartson, K. 1959 "On the stability of a spinning top containing liquid." *Journal of Fluid Mechanics* **5**, 577.

Synge, J. L. 1952 "On a case of instability produced by rotation," *Philosophical Magazine* (Series 7) **43**, 724.

Taylor, G. I. 1968 "Instability of jets, threads, and sheets of viscous fluids". Proceedings of the 12th International Congress of Applied Mechanics (Stanford, 1968). Springer-Verlag (1969) pp.382-388.

XXI ICTAM, 15–21 August 2004, Warsaw, Poland

AFRICAN INSTITUTE IN MATHEMATICAL SCIENCES: A CAPACITY-BUILDING INITIATIVE IN WHICH IUTAM HAS AN ACTIVE INVOLVEMENT

H.K.Moffatt
Department of Applied Mathematics and Theoretical Physics, Cambridge, UK

Summary The African Institute for Mathematical Sciences (AIMS) is a new educational centre recently established in Cape Town, South Africa, with the goal of strengthening scientific and technological capacity across the African continent. This lecture will summarize the background to this initiative, and the first year of its activity.

In February 2003, IUTAM [with the support of IUGG, IMU, IUPAP, IUPAC, IAU, TWAS, and four National Scientific Members of ICSU (South Africa, UK, Netherlands and Brazil)] submitted an application to ICSU under the ICSU 2004 Grants programme for support for an important new initiative in capacity building in science education. This initiative was designed to provide an Africa-based solution to African problems, facilitated by the international scientific community; it was to be realised in South Africa and would have a primary impact there, but its influence and benefit would extend throughout the African continent. The initiative, which had already received the support of the South African National Research Foundation, and the endorsement of the Nelson Mandela Foundation, was to establish an African Institute for Mathematical Sciences (AIMS) in Muizenberg, a suburb of Cape Town, where an outstandingly well-adapted building had been donated for this purpose. Here, 'Mathematical Sciences' was to be understood as mathematics together with its applications in such diverse fields as mechanics, physics, chemistry, geophysics, astrophysics, engineering, information technology, biology and medecine. AIMS is an initiative stemming from an international collaboration between three South African Universities (the Universities of Cape Town, Stellenbosch and the Western Cape) and the University of Cambridge Faculty of Mathematics, UK. Association with the University of Paris XI (Orsay) is in progress, and further institutions may be involved as the project develops.

The goals of AIMS were two-fold: first to offer a one-year diploma course specially designed for mathematics and science graduates of African Universities, which would be taught by a team of internationally renowned lecturers in close collaboration with South African academic staff; the course would give the students the mathematical and computing research skills needed to address important modern areas of application of mathematics, and would inspire a new generation of African students to undertake scientific research of great practical importance. AIMS would serve to elevate the general level of education in the mathematical sciences in Southern Africa, and would provide a beacon that would attract school students to careers in science and mathematics.

The second goal of AIMS was to provide the base for a Schools Enrichment Centre (AIMS-SEC), whose objectives were (i) to support African educationists, teachers and students, especially those from the formerly disadvantaged communities, in raising the standards of teaching, learning and attainment in mathematics in African schools; and (ii) to raise aspirations and enable all students, especially mathematically talented students, to achieve their full potential. AIMS-SEC would provide opportunities and assistance to both teachers and students of mathematics, working to achieve the highest possible standards in the subject. Strong links would be forged in particular with the 102 schools in South Africa that the government has identified for specialisation in the teaching of mathematics and science. [It is relevant here to note that the South African Government has an agreement with IBM for the provision of computers for schools, and that it has recently established a partnership with Microsoft for the provision of software to every school in the country; the SA Government is committed to have every school online by 2010. The AIMS-SEC initiative is therefore extremely timely.]

IUTAM's application to ICSU was successful, the full grant requested (US$100k) being awarded. IUTAM generously agreed to supplement this grant with a further $20k from its own resources. The total annual budget of AIMS is approximately $750k, substantial funds having been secured from a wide range of other sources. AIMS was inaugurated at a launch meeting in September 2003, and its first diploma course, involving some 30 graduate students from all over Africa is currently in progress. This course includes a strong element of application of mathematics to the physical and biological sciences, in which of course mechanics, both solid and fluid, plays a fundamental role. The IUTAM grant is being applied during 2004 (i) to support a Workshop at AIMS on Capacity Building in the Mathematical Sciences, to be held during April 2004; (ii) to support AIMS-SEC; and (iii) to contribute to the support of the students enrolled for the 2003/4 and 2004/5 sessions.

This lecture will report on the operation of AIMS (and AIMS-SEC) during its first complete year of activity (September 2003 – August 2004), and on the outcomes of the above Workshop, which will involve representatives from many African States and representatives of IUTAM and other supporting International Scientific Unions and related ICSU bodies.

Two tributes to AIMS:

"We have been informed of the African Institute for Mathematical Sciences (AIMS) and find it one of the most interesting projects presented to us. Mr Mandela has repeatedly declared his concern about the advancement of science teaching and research in South Africa. This initiative is an outstanding instance of concrete collaboration between leading scientists in the advanced countries and our own scientists. This Foundation enthusiastically supports AIMS in the name of the former President Mandela."
[John Samuel, Chief Executive, The Nelson Mandela Foundation]

"Our country and continent badly need a broad, concerted effort to improve the quality, participation and performance of South Africa and African researchers and learners in the mathematical sciences. The African Institute for Mathematical Sciences is destined to become a flagship institution, giving concrete expression to this need and ensuring that Africa's contribution to the mathematical sciences receives the recognition that it deserves. The in-service training of mathematics teachers is indeed a top priority of the Government's educational transformation plan, TIRISANO – hence my unequivocal support for the establishment of this Institute."
[Mosibudi Mangena, Deputy Minister of Education, South Africa.]

AIMS website: <http://www.aimsforafrica.org>

ON MECHANICS/ENGINEERING SCIENCE EDUCATION

Carl T. Herakovich
University of Virginia, Charlottesville, VA, 22904-4742, USA

EXTENDED SUMMARY

It seems that just about everything under the sun has been re-engineered in the past quarter-century except that which may need it the most – engineering education. In fact, it's hard to say that engineering education has ever been re-engineered. In the management field, re-engineering is defined as " the fundamental rethinking and radical redesign of … processes to achieve dramatic improvements in critical, contemporary measures of performance…". It is further stated that "re-engineering seeks to change a broader span of the process, it questions fundamental assumptions", and "re-engineering tends to be riskier".

At a time when the world is going through dramatic changes with intense engineering activity in such diverse fields as biology, medicine, environmental science, computer science, information technology, space exploration, development and efficient use of energy, and materials science, to name some fields, it is imperative that engineers be equipped not only to actively contribute to these fields, but to assume leadership roles. Many share the view that engineering education needs an overhaul. Professor Sheila Widnall of MIT (and former Secretary of the U. S. Air Force) has said "I believe that a revolution in undergraduate engineering education is required not just for women but to improve the effectiveness of engineering in this country. Unless we develop more of a holistic approach to problem solving, we will become a niche profession." And Dr. William Wulf, President of the U. S. National Academy of Engineering has spoken of "The Urgency of Engineering Education Reform".

As the knowledge base has exploded, engineering education has actually retrenched. Whereas fifty years ago, essentially all undergraduate engineering students took a wide variety of courses in diverse fields including statics, dynamics, fluid mechanics, solid mechanics, materials science, chemistry, electricity and electronics, heat transfer and thermodynamics, today's curricula are very narrow with the great majority of all engineering courses in the field of the student's major department. Breadth and diversity have been further restricted by the addition of new majors such as bioengineering, computer engineering and materials engineering, again with most engineering courses limited to the departmental major. As a result of this narrowing of the curricula, engineering graduates have a very limited specialty with little appreciation for the broader picture of how their discipline integrates with other engineering fields and society at large. In Widnall's words, we are becoming a niche profession. Indeed, engineers with only an undergraduate degree border on being limited to activities typically associated with a technician.

One answer to this problem is a complete re-engineering of undergraduate engineering education. To use the management approach, "a fundamental rethinking and radical redesign of the process". A single undergraduate curriculum in Engineering Science would go a long way toward producing an engineer who is better equipped to actively contribute and lead in the 21st Century. By concentrating on the fundamental science of engineering, the curriculum can be subjected to a radical redesign with the potential to achieve dramatic improvements in the ability of engineers to lead in the solution of societal problems. To be sure, engineers actively engaged in the practice of engineering will require further study in a specialty. However, all engineering undergraduates would be prepared to actively participate in the societal decision making processes that are so dependent on engineering knowledge.

Mechanicians can, and should, play an important, critical, leadership role in the redesign to a broadly based engineering science curriculum. By efficiently integrating mechanics with engineering science, the curriculum can be streamlined to provide sufficient coverage of the engineering sciences as well as the important fields of biology, computing, human interactions and societal problems.

The presentation will more fully explore these ideas.

«MECHANICS» – A NEW INTERNET TUTOR

Dr. Aleksandr Kositsyn
Odessa State Academy of Civil Engineering and architecture, Department of Theoretical Mechanics, Odessa, Ukraine

Summary Website "Mechanics" (URL: www.emomi.com) – is an attempt to create a capacious ducational resource for the Internet on theoretical mechanics with the purpose of helping those interested in learning mechanics, and making it by far more attractive tostudents. The Site is intended for both students end educators.

In teaching theoretical mechanics there is quite often a gap between learning theoretical models by a student and the comprehension of the possibility of their practical use. To help in learning Mechanics, to show how abstract models work in engineering tasks and to make Mechanics more attractive for students are the basic ideas which were incorporated in the concept of the website "Mechanics" (URL: http://www.emomi.com).
The history of engineering knows many cases when mistakes have resulted in serious consequences. The analysis of such incidents from the point of view of mechanics happens rather instructively. The site pages <Situations> and <Practice-theory> are devoted to such analysis. In sections <Training>, <Crossword and Tests> a trainee can get the opportunity to experience on-line control of skills on Mechanics. In <Download> it is possible to find educational and methodical literature on Mechanics. Good help to the student in studying this discipline, and to the educator in organizing classes can be rendered with applets-demonstrations of various mechanical processes. One can expand the outlook, having visited pages <History of engineering> and <News of engineering>.
The architecture of the site allows for participation in its development. Each visitor can offer qualified materials or references to Internet-resources on the page <Our references>, which do not break the concept of the site. Professors, experts and students can take part in the discussion of problems of Mechanics and Education on the page <Forum>.
The site is already rather extensive and is replenished regularly. In <News> it is easy to keep up with the occurrence of new materials and to receive access to them. To navigate around the site one can use the detailed <Site map>.
The realization of <Contests> on Mechanics for students of all rates is being planned in the future. Professors can find for their work examples of the tasks of a number of contests on Theoretical Mechanics. Not only students, but also young educators will find useful materials for their work. Each visitor can leave record in the <Guest book>, and in case of the necessity to contact the authors there is the page <Contacts>.
The biographies of great scientists and inventors, crosswords, literature, bibliography, abstracts, demonstration programs on Mechanics and others can be found on the site «Mechanics». The project gives new opportunities for distant learners to increase the level of their knowledge on Engineering Mechanics. An opportunity of opening a new heading <Improvement of professional skills for engineers> is being considered.
The site «Mechanics» has been available to visitors since July 2003, and is continuing to be developed. Each month we record thousands of visitors from many countries in the world. There are Russian and the initial English versions of the Site now. We believe, that the English version of a site will render help in studying Mechanics for tens of thousands of students annually, allowing distant learning to raise the qualification of future engineers and beginner educators from many countries of the world. Experts could share their experiences in teaching Theoretical/Engineering Mechanics.

TEACHING MECHANICS AS AN ENGINEERING SCIENCE IN CHINA

Yilong Bai
State Key Laboratory of Non-linear Mechanics, Institute of Mechanics, Chinese Academy of Sciences, Beijing 100080, PR. China

Since Prof Tsien HS came back to China from CalTech in fifties last century, the education in mechanics has been treated as an engineering science. And the students, especially postgraduates, are trained to be between engineer and scientist, to be able to explore new fields in engineering. The main points are as follows.

1. It is an independent discipline to bridge natural science and engineering. It is not only engineering, but a guide to new trades in industry, with new concepts, theories and methods.
2. It is aimed at engineering. So, it is not so accurate and general as natural sciences. Since the objects are usually complex systems in practice, it is a necessity for the graduates to grasp the main governing mechanisms, to develop proper models and to get approximate conclusions in agreement with observations.
3. It is not aimed to a specific engineering trade, but concerns common issues in engineering. So, it must be an expanding discipline with the progress in engineering.
4. The ability building should include mathematics as a tool, natural sciences as basis, being familiar with problems and methods in engineering and being able to extract the implications from practical problems to form natural laws.

The graduate training in the Institute of mechanics, Chinese Academy of Sciences (CAS); the research classes of engineering mechanics in Qinghua University; the department of modern mechanics, University of Science and Technology of China are all the examples of such education in mechanics in China.

Take the department of modern mechanics, University of Science and Technology of China as an example. Even in fifties, the department consists of several new specializations, which are hypersonic gas dynamics, high-temperature solid mechanics, chemical hydrodynamics, explosion dynamics as well as physical mechanics. Recently, the specialization on material design was started there. These new directions make mechanics become attractive for the students.

Therefore, the students should master extensive knowledge of mathematics, physics, chemistry, namely top level courses of mathematics, physics and chemistry. The students should have a good command of applied mathematics and computations. The students should be familiar with engineering design and practice. In these aspects, a number of technical courses, like electronics, computing, engineering graphics and design, experimental mechanics, manufacturing, etc., are needed. In addition, the students should also be involved in some scientific projects outside classes.

If there are not proper textbooks on the subjects, the lecture notes were prepared by professors. “Lecture on Physical Mechanics”(1962) and “Introduction to Space Voyage” (1961) written by Tsien HS are two examples of such teaching notes of mechanics in China.

Certainly, in this way students should also learn more than traditional courses of mechanics. For instance, material physics and mechanics, statistical physics etc should be included in the list of courses.

Of course, these extensive and intensive requirements may need longer terms and may make students extremely busy. However, the graduated can become stronger and more flexible when facing new challenges in engineering.

References

[1] Tsien HS, Engineering and engineering sciences, J Chinese Institute of Engineers, 1948, 1-14.

[2] Zhuang FG and Zheng ZM, Tsien’s thoughts on Engineering Sciences and Mechanics, 2001, Defense Industry Press, (in Chinese)

ABSTRACT

Promoted by Prof Tsien HS, the education in mechanics in China is made as an engineering science. And the graduates are trained to be between engineer and scientist. The main points are as follows.

It is an independent discipline to bridge natural science and engineering. It is not only engineering, but concerns common issues in engineering. And it is a guide to new trades in industry, with new concepts, theories and methods.

It is aimed at engineering. Since the objects are usually complex systems in practice, it is a necessity for the graduates to grasp the main governing mechanisms, to develop proper models and to get approximate conclusions in agreement with observations.

The ability building should include mathematics as a tool, natural sciences as basis, being familiar with problems and methods in engineering and being able to extract the implications from practical problems to form natural laws.

EDUCATION AND TUTORIAL ON FLUID MECHANICS ON THE BASIS OF COMPUTER LABORATORY

Vasily P.Yaremchuk, Mikhail K. Ermakov, Sergei A. Nikitin and Vadim I. Polezhaev
Institute for Problems in Mechanics, Laboratory of Mathematical and Physical Modelling in Fluid Mechanics, 119526, Vernadsky ave. 101 b.1, Moscow, Russia

Summary Experience in the education and tutorial in modeling of the elementary flows, heat and mass transfer during crystal growth in ground-based and microgravity environment using computer system COMGA is presented. The system supports free and forced convection problems on the basis of the Navier - Stokes equations. The computer laboratory as intellectual shell of this system includes basic double-diffusion gravity-driven and Marangoni problems in enclosures, Bridgman model, and Czochralski model for microgravity and ground-based applications.

INTRODUCTION

Elementary flows and heat/mass transfer processes in real technological range of parameters are nonlinear, unsteady and multiscale. They have a number of important peculiarities in ground-based and in microgravity conditions (see, for instance, [1]). The development of technology needs more detailed analysis as well as modeling systems, access to the education process and modern knowledge for new generation of researchers.
The paper presents experience in the education and tutorial in modeling of the elementary flows, heat and mass transfer in ground-based and microgravity environments using the computer system COMGA (COnvection in MicroGravity and Applications). This system provides modeling free and forced convection on the basis of the Navier - Stokes equations (the Boussinesq approach). It was developed and systematically used in the Laboratory of Mathematical and Physical Modeling in Fluid Dynamics IPM RAS since early of the 90^{th}. The computer laboratory as intellectual shell of this system was realized on the next stage of the development [2] and includes now microgravity and ground-based applications with the use of high performance personal computers. A focus of the paper is the basic aspects of fluid dynamics and heat/mass transfer such as hydrostatic equilibrium stability and stability of steady flow.

BASIC VERSION & INITIAL STAGE OF EDUCATION

A basic version of the system and computer laboratory includes most of classical problem of convective heat and mass transfer with different types of the boundary conditions, external forces, and fluid (gas) properties. Initial stage of education starts from the definition of the physical properties of the typical liquids and gases in crystal growth applications and hydrostatic equilibrium. Convection is induced by the buoyancy and gradient of the surface tension (Marangoni convection). A general mechanism of the onset of convection and convective instability is included. Elements of the modeling theory and the basic knowledge of fluid dynamics and numerical methods should be also studied for understanding the options of the finite difference schemes.
Classical problems of the gravity-driven convection with side heating, Rayleigh-Bernard convection with rigid and free surfaces, and similar types of the Marangoni convection should be firstly studied. A fragment of the solution of the problem on thermocapillary convection in horizontal layer during bottom heating (Marangoni instability) presented in Fig. 1. The onset of Marangoni convection after the loss of hydrostatic equilibrium stability and formation of the steady-state regime is shown for the classical Pearson problem with zero body force [3]. The field of stream function (roll structure) is on the top and isotherms of thermocapillary convection are below. On the right side the temporal evolution of the maximum of stream function is shown. A fragment of Menu of the computer system COMGA_W is shown on the left side. One can see here a title of the problem and items inside the "Problem category", which characterizes only a given problem: parameters Ma, Pr, region L/H, body force (g=0 in this case), and type of initial conditions.
Study all aspects of the problem with output the information in real time make it possible to use this system (together with interface of the input information, library of the problems, physical properties, references of the related papers etc.) as a computer laboratory. The students can study most of the elementary convection problems in real-time calculation during the tutorial process. Research works related to unsolved classical problems may be carried out in the end of this part of education. As an example of the bachelor degree work the result of analysis of temporal bound of the onset of gravity-driven convection in a horizontal layer with bottom heating is shown in [4].

EDUCATION & TUTORIAL IN MICROGRAVITY FLUID DYNAMICS

Following [1] a special version of this system for the applications in microgravity environment was developed. The Navier - Stokes equations for two-dimensional Cartesian coordinates in the Boussinesq approach is used with account of body forces in microgravity environment. The definitions of quasi-steady and vibratory forces are presented in [5].

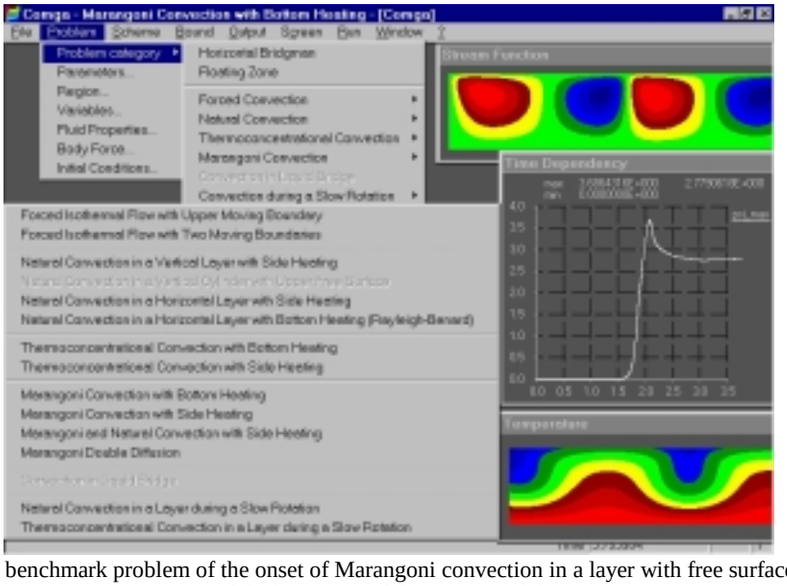


Fig. 1. Example of the benchmark problem of the onset of Marangoni convection in a layer with free surface and bottom heating. Menu of the basic part of the computer laboratory.

EDUCATION IN FLUID DYNAMICS & HEAT TRANSFER IN CZOCHRALSKI MODEL

Last part of the paper illustrates the process of studying of the hydrodynamical (idealized) Czochralski model, which presents a nonlinear multi-parametrical hydrodynamic system with wide range values of governing parameters (Rayleigh, Marangoni, Prandtl, Reynolds numbers, aspect ratio, initial and boundary conditions). The COMGA_W is a full Windows application with friendly interface, which makes it possible to change all of them. General characteristics of the flow and temperature fields and heat/mass transfer as well as local and average Nu numbers, temperature profiles are possible to visualize. For the first tutorial, the simplest benchmark configuration [6] is used. URL Appendix http://www.ipmnet.ru/~yarem/paper3 contains three elementary examples of the unsteady temperature fields behavior for the thermal diffusion processes with different initial conditions and boundary conditions on the melt surface for a given geometry and two elementary examples of the buoyancy-driven convection with low and high Pr numbers, which show the role of the boundary conditions and melt properties in the change of mechanism of convective instability and temperature oscillation in the melt.

CONCLUSIONS

A plan of education and tutorials for basic convective heat/mass transfer processes and applications on the basis of the Navier-Stokes equation (the Boussinesq approach) is presented. They were used during 1998-2001 for the preparing bachelor and master works in Moscow Institute of Physics and Technology. The education process and tutorial include:

- thermal diffusion processes and equilibrim of the hydrostatic stability,
- classical problems of the natural, forced convection,
- convection problem in microgravity, including realistic microgravity environment,
- ground-based melt flow in Bridgman and Czochralki models.

One can find free version of COMGA_W system on URL http://www.ipmnet.ru/~ermakov/comga/download_e.php.

Acknowledgements

This work is supported partly by the Russian Foundation for Basic Research (RFBR) (grant 03-01-00682), by the Ministry of Education of Russian Federation (project ”Integratziya” by the guidance of Rostov State University No. 74). The authors express their gratitude to Prof. V.V. Sazonov for the quasi-steady data in space flight and Prof. V.I. Yudovich and his colleagues (Rostov State Univ.) for the encouraging discussions.

References

[1] V.I. Polezhaev, M.S. Bello., N.A.Veresub et al. Convective processes in microgravity, (Nauka, Moscow, Russia, Moscow), 240 p. (in Russian).
[2] M.K. Ermakov, S.A. Nikitin and V.I. Polezhaev, Fluid Dynamics 32, 3, (1997), 338.
[3] J.K.A. Pearson J. Fluid Mech., 4 (1958), 489.
[4] V.I. Polezhaev , V.P. Yaremchuk, Fluid Dynamics, Vol. 36, No. 4 (2001), 556.
[5] V.V. Sazonov, M.M. Komarov, V.I., Polezhaev et al, Cosmic Research, 40, 1 (1999), 86.
[6] N.V. Nikitin , V.I. Polezhaev, J. Crystal Growth, 230 (2001), 30.

EDUCATION IN MECHANICS IN LATVIA HIGHER SCHOOLS

Vitauts Tamuzs*, Janis Viba**
*University of Latvia, Institute of Polymer Mechanics, Riga, Latvia
** Riga Technical University, Institute of Mechanics, Riga, Latvia

Summary. The historical review of mechanics development in Latvia from 18. Century till to the present day is given. Variations and birth of mechanical direction courses after Second World War are more considered. Is shown that the main learning subjects in the area of mechanics are included in study programmes for large Latvia higher schools. The main scientifically and textbooks of Mechanics that are made and published by Latvian scientists and professors are given. The main study programs and courses in Latvian higher schools are mentioned.

HISTORY

The first works of mechanics in Latvia where connected with city Jelgava, with Academy of Peters ["Academy Petrina" - which was established by Courland duke Peter's Birons 1775. - academically gymnasium. The educational and scientifically institution of Courland. The regulation and education plans was work out by academician J. G. Zulcer from Berlin Academy of Science]. Here professor V. Beitlers (1745. - 1811.) (Mathematician) published proceedings about aerostatics of air-balloon, then E. Bidemanis (1785. year) designed and lifts of in air several air-balloons. When in 1862. In Latvia was established Riga Polytechnics the next investigations in the field of Mechanics (till First World War) was connected with that higher school. Here may be mentioned Swiss Vilhelms Ritters (1847. - 1906.) with works in graphical static, works of Pirs Bols (1825. - 1925.) in sky body mechanics and others. After First World War professor of Latvia University Alfred Vitols (1875. - 1945.) made investigations in theory of hydraulics and expanded activities in the international scientifically work, but professor N. Rozenauers (1890. - 1970.) made great investigations in kinematics of machines and mechanisms and others. Must be mentioned engineer and inventor Fridrihs Canders (1887. - 1933.) which was born in Riga and graduate the Riga Politechnically institute (1914.). Today one time in two years period Latvian Academy of Science awarded prise of Fridrihs Canders in the field of physics and technical sciences. The first remarkable authors of mechanics textbooks in Latvian language must be mentioned N. Rozenauers: - in the 30-ty years he published in Latvia University several books mainly about kinematics questions. The next period is observed below.

HISTORY OF BOOKS

According to the contents and quantity the courses of Mechanics are different in University of Latvia (LU), Riga Technical University (RTU), Latvia Agriculture University (LLU), Latvia Sea Academy (LJA) and others higher schools in Latvia, but they main goal is the same - to give the students faithful explanation and enough deep understanding about world wide mechanical interactions and motions of objects with they dynamics analysis. It may be shown that courses of mechanics forms fundamental base for higher education and engineering sciences, it helps to students successful adopt further subjects of mechanical cycle according to higher school profile and specialisation.

All books published in Latvian language customary may be separated into three groups.

The first group includes books published in Latvia from 1920. till 1940. Years, the manly all publications are from Latvia University. Here enter many books of N. Rozenauers as well as works of A. Vitols, J. Inveiss, E. Leimanis, J. Muiznieks, E. Veiss, E. Veidemanis and others.

The second group may include books that are translated from Russian language after Second World War.

The third group includes books of Latvian professors, published after Second World War period. In these group professors of LU, RTU and LLU made the large work.

As results they are published many conspectus of lectures, practical and scientifically works. From they considerable are the next books:

1. Course of Strength of Materials. J. Panovko, A. Leppiks, A. Strekis. Latvia State Press. 1955. Riga. - 432. p. (In Latvian).
2. Course of Theoretical Mechanics. O. Ozols, A. Strekis, J. Vasermanis, A. Muiznieks. Riga. 1961. -565. p. (In Latvian).
3. Course of Theoretical Mechanics. O. Ozols, A. Strekis, J. Vasermanis, A. Muiznieks. Publishing office " Zvaigzne". Riga. 1966. - 616. p. (In Latvian).
4. Strength of Materials in Tasks. J. Auzukalns, E. Ceplitis, I. Kalnins, I. Liepins. Publishing office " Zvaigzne". Riga. 1973. - 742. p. (In Latvian).

5. Theory of mechanisms and machines. O. Ozols. Publishing office " Zvaigzne". Riga. 1974. - 418. p. (In Latvian).
6. Theoretical Mechanics in Exercises. Editor O. Kepe (authors: V. Akmentins, O. Kepe, E. Krumins. J. Lauva, J. Mikelsons, A. Muiznieks, J. Svetins, J. Viba). Publishing office " Zvaigzne". Riga. 1976. - 647. p. (In Latvian).
7. V.Kuksenko, V.Tamuzs. Fracture Micromechanics of Polymer Materials. *Riga: Zinatne*, 1975 (in Russian; (English translation by Martinus Nijhoff Publ. 1981), - 310 p.
8. Theoretical Mechanics. O. Kepe, J. Viba. Publishing office " Zvaigzne". Riga. 1982. - 577. p. (In Latvian).
9. Strength of Materials. E. Lavendelis. Publishing office " Zvaigzne". Riga. 1986. - 341. p. (In Latvian).
10. Short Tasks in Theoretical Mechanics. Editor O. Kepe. Moscow. "Vissaja skola". 1989. - 368. p. (In Russian).
11. N.Romalis, V.Tamuzs. Fracture of Nonhomogenous Solids. Riga: Zinatne, 1989, 224pp. (in Russian).
12. Theoretical Mechanics. Dynamics. Editors O. Kepe, J. Viba. Riga. RTU. Part I. 1994. - 259. p. (In Latvian), Part II. 1996. - 174. p. (In Latvian)., Part III. 1999. - 183. p. (In Latvian).
13. H. Altenbach, J. Altenbach, R. Rikards. Introduction in Mechanics of Laminated and Sandwich Structures, Deutscher Verlag fuer Grundstoffindustrie, Stuttgart, 1996, 410 p, (in German). Deutscher Verlag fuer Grundstoffindustrie, Stuttgart, 1996, - 410 p, (in German).
14. Dictionary of Mechanics terminology in 4 Th languages (Latvian, English, German, Russian). Editor V. Tamuzs. Publishing office "Latvian National Committee of Mechanics. Riga. 1997. - 253. p.
15. V.Tamuzs, N.Romalis, V.Petrova. Fracture of Solids with Microdefects. New York: Nova Science Publ., 2000, -238 p.

EDUCATION DEPARTMENTS AND COURSES OF MECHANICS IN A LATVIA TODAY

Latvian National Committee for Mechanics (LNCM), (Chairman Prof. Vitauts Tamuzs) and LNCM Seminary (Chief Prof. Janis Viba) has next information about education departments and courses of mechanics in Latvia. The first is an Institute of Polymers Mechanics (director Dr.habil.sc.eng., Juris Jansons) at University of Latvia (LU), Faculty of physics and mathematics. In University of Latvia main study programs and sciences problems in Mechanics are connected with students and professors of physics and mathematics specialisation. The main education courses in Mechanics (Bachelors, Masters and Doctoral study programs) are connected with: - Theoretical mechanics; - Applied mechanics; - Mechanics of Solids; - Fracture Mechanics; - Fatigue; - Mechanics of continuous medium; - Investigation in the field of electrodynamics; - Theoretically and Experimental investigations of materials mechanical properties; - Mechanics of composite materials constructions; - Development of mathematically modelling methods for analysis electromechanical processes and others. http://www.pmi.lza.lv/.

At the Riga Technical university (RTU), faculty of Transport and Mechanical Engineering in the Institute of Mechanics (director Dr.habil.sc.eng., prof. Janis Viba) main works in Mechanics are connected with study programs (Bachelors Sc., Eng., Masters Sc., Eng. and Doctoral studies): - Engineering Technology, Mechanics and Mechanical Engineering; - Production Technology; - Railway transport; - Auto transport; - Aviation Transport. The elements of mechanics are used in courses: - Theoretical mechanics; - Technical mechanics; - Strength of materials; - Dynamics and lasting of machines; - Vibration and stability of technical systems; - Numerical analysis in engineering mechanics; - Investigation of impact systems; - Analytical mechanics - EM analysis of constructions; - Non-linear dynamics and chaos; - Biomechanics of muscle systems; - Investigations of composite materials; - Investigation of traffic accidents and others.

At the Latvian Agriculture University (LLU), Technical faculty in the Institute of Mechanics (director Dr.habil.sc.eng., prof. Guntars Uzklingis) main works in Mechanics are connected (Bachelors, Masters and Doctoral studies) with specialisation in the fields of: - design of agriculture techniques; - production and maintenance of agriculture techniques; - forest manufacture; - wood-working and others. The elements of mechanics are used in courses: - Theoretical mechanics; - Technical mechanics; - Applied mechanics; - Strength of materials; - Dynamics of machines and others. http://www.cs.llu.lv/. At the Latvian Sea Academy in the Institute of Ships Mechanics (director Dr.habil.sc.eng., prof. Juris Cimanskis) main works in Mechanics are connected (Bachelors, Masters and Doctoral studies) with specialisation in the fields of analysis of ships motion stability and dynamics of rotors. In study program " Ships Mechanics " the main elements of mechanics are used in courses: - Theoretical mechanics; - Strength of materials; - Analytical mechanics; - Theory of mechanical vibrations; - Methods of optimisations; - Dynamics and stability of ships motion. http://www.aic,lv/ENIC/lat.

The professors and students of higher schools of Latvia have very close contacts with students and scientists inside Baltic region in the field of mechanics, for example: International DAAAM conferences - Tallinn, Vibroengineering conference - Kaunas, Non-linear dynamics, catastrophes and chaos - Riga. The professors of higher schools of Latvia take wide part in the international projects in the field of mechanics (Prof. V. Tamuzs - fracture of composite materials; Prof. R. Rikards - calculation of laminated composite structures, Prof. I. Knets - problems of biomechanics, Prof. J. Viba - vibrations and collisions in connected bodies systems).

MULTIIMEDIA FLUID MECHANICS: A FLEXIBLE EDUCATIONAL TOOL FOR TEACHING AND LEARNING FLUID MECHANICS

G. M. Homsy[*], K. S. Breuer[**]
[*]*Mechanical Engineering, UCSB, Santa Barbara CA, USA*
[**]*Division of Engineering, Brown University, Providence RI, USA*

Summary This paper describes *Multimedia Fluid Mechanics* (Homsy, et al., Cambridge Univ. Press, 2001), a new, versatile multimedia tool for education in fluid mechanics. We discuss the pedagogical principles on which it is based, together with a description of many of its features. The presentation of this paper will include a demonstration of these features, with an emphasis on broad educational approaches that apply to all fields of Applied Mechanics.

INTRODUCTION AND EDUCATIONAL CHALLENGES

"Multi-Media Fluid Mechanics" [1] (MMFM) is a CD-Rom, compatible with a wide range of platforms, processors, and operating systems, containing multimedia materials for teaching undergraduate fluid mechanics. It is marketed by Cambridge University Press and priced at a cost ($20/copy) that ensures its widest possible dissemination. This paper outlines some educational challenges and shows how we have dealt with them.

Fluid mechanics remains a core subject within many disciplines of engineering and applied science. The fundamental basis of the subject is reasonably easy to state, since it is firmly rooted in the principles of conservation of mass and Newton's Second Law of Motion. The mathematical statement and the consequences of these principles for continuously deforming media are, however, often confusing and daunting to the student. The subject is mathematically sophisticated, involving (i) time dependent, 3D partial differential equations, (ii) the essential use of vectors, tensors, and vector analysis, (iii) an often bewildering array of dimensionless groups, (iv) the dependence of fluid phenomena on various parameters over a wide range of those parameters, and (v) the surprising behavior of fluids that often runs counter to a naive set of intuitive concepts.

The teaching of fluid mechanics has been aided by the existence of visual aids, the most notable of which are the series of films produced in the 1960's by the National Committee on Fluid Mechanics Films, and the Album of Fluid Motion [2]. MMFM seeks to improve on these resources by addressing the following challenges to be met by the next generation of educational materials in fluid mechanics.

Connect concrete physical phenomena with mathematical / analytical abstraction. Many of the important concepts in fluid mechanics, e.g. vorticity, velocity, and pressure fields, and vector analysis are not particularly tangible to beginning students. A major challenge is to teach how physical concepts are expressed in mathematical terms, and to develop the ability to move freely between mathematical context and physical reality.

Incorporate modern computer simulation into the curriculum. Learning is enhanced by the ability to simulate and visualize flows which cannot be expressed by analytical theory. The use of computation is invaluable in providing the ability to systematically vary parameters and study the evolution of flow structures and flow physics. However, the time involved in writing and validating of robust software for flow simulations often puts the use of computer simulation outside the range of student projects on the one hand, and the time and expertise of the instructor on the other. Delivery of such robust software through interactive media results in enhanced capabilities that can be widely disseminated.

Expose students to state-of-the-art experiments in fluid mechanics. Experiments and the qualitative and quantitative knowledge they express are invaluable in reinforcing concepts from the mathematical theory of fluid flow. Modern flow visualization using high-speed cameras, along with tracers such as small particles, bubbles, and laser induced fluorescent dyes, has greatly extended the range of flow visualization techniques and the insight gained from them. Such images are indispensable in building physical intuition. However, construction of state of the art apparatus is expensive, difficult to maintain, and often beyond the financial resources of many colleges and universities.

Increase student learning by generating curiosity and exploiting the medium. Instruction in fluid mechanics in the traditional lecture format sometimes suffers from the false perception that the subject is "mature", and that nothing new has happened in it for a long time. Interactive computer exercises, visualizations, and demonstrations can have considerable impact in generating interest and excitement in this vital subject among the best and brightest students.

MULTIMEDIA FLUID MECHANICS

MMFM contains four modules covering the subjects of Dynamics, Kinematics, Boundary Layers, and History. Each has a number of topics, and each of these topics is developed in a number of pages. These visual materials are in 1/4 screen video format, and are viewed using standard QuickTime software, as shown in the Figure. The interactive material includes simulations, virtual labs, and well over 250 video visualizations, animations, and demonstrations of fluid phenomena material that are intended to complement any of the standard fluid mechanics textbooks.

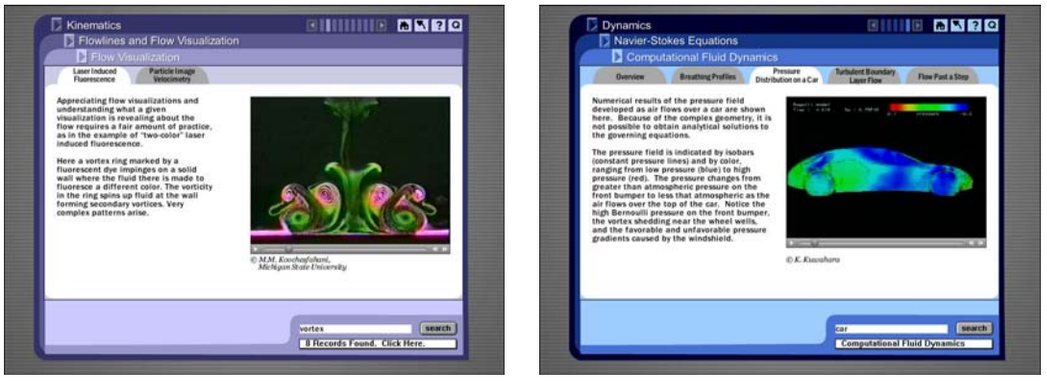


Figure: Examples of pages. (a) Flow visualization. (b) Computational Fluid Dynamics

The videos can be accessed through a separate Video Library, thus enhancing its use by instructors in the classroom. Navigation between and within the modules is clear and easy, and is facilitated through the use of hyperlinks. The structure is flexible, allowing its use in a wide variety of contexts ranging from community college physics courses to first year graduate level courses at universities. The primary features are:

Simulators: Students use computer simulations to vary parameters and/or illustrate a principle. MMFM has three such simulators: Molecular Dynamics, Integration of the Laminar Boundary Layer Equations, and the Potential Flow Builder.

Virtual Labs: Students take quantitative data from videos and/or use a simulator to compare theory and experiment, including (i) matching potential flow theory with Hele-Shaw experiments; (ii) verifying dynamic similarity in vortex shedding; (iii) measurement of laminar boundary layer growth in the Blasius boundary layer; and (iv)verification of self-similarity in the impulsive start of a plate.

Charts and Demonstrations: Extensive series of over 50 charts and demonstrations includes side-by-side comparison of flows at different Reynolds numbers and for different shapes; comparison of potential flow theory with bluff and streamlined shapes; flow structure around sports balls; origin of drag forces as a function of Reynolds number and body shape; techniques and methods of flow visualization; and many others.

The Flow Gallery: In this gallery, the student may view any of a large number of videos of fluid phenomena, including flight, vortices, mixing, swimming, thermal plumes, airplanes, natural and environmental flows, etc. These are arranged pairwise according to the Reynolds number, and include a description of the principles involved.

MMFM AS A MODEL

Conquering abstract concepts in fluid mechanics has positive consequences for students in other contexts. Fluid mechanics is a field theory, and as such provides the student his or her first exposure to a continuum description of mass, momentum, energy, force, and other quantities in a familiar, mechanical context. These concepts will emerge often in later studies, where they may be set in considerably more abstract contexts, e.g., in electromagnetic field theory and solid mechanics. Modern interactive multimedia modules that emphasize experiments and computations (as distinct from simple animations) can be extremely effective in other fields of mechanics. The use of multimedia brings material to the student in an attractive, understandable, visual and stimulating way, piquing curiosity, and drawing the student deeper into the subject. It creates an environment in which students can manipulate experimental and computational knowledge to increase their learning and retention of the subject by engaging them with the material through a series of simulations and virtual laboratories.

MMFM has enjoyed broad support among the community and a second volume is in the production stage. But it has found its greatest use thus far in the USA. Our purpose in submitting this paper is to broaden the exposure to the international community, interact with others involved in Education in Mechanics, and generate ideas for further improvement of educational materials.

Acknowledgement

"Multi-Media Fluid Mechancs" was sponsored by the US National Science Foundation through grant NSF/DUE 9752199.

References

[1] "Multi-Media Fluid Mechanics", G. M. Homsy, H. Aref, K. S. Breuer, S. Hochgreb, J. R. Koseff, B. R. Munson, K. G. Powell, C. R. Robertson, S. T. Thoroddesen, Cambridge Univ. Press (2001) ISBN 0-521-78748-3.

[2] "An Album of Fluid Mottion" Milton Van Dyke, Parobolic Press (1982).

SIMULATOR, NOHGUCHI BOTTLE, OF SOIL LIQUIFACTION FOR EDUCATION

Yasuaki Nohguchi*
*National Research Institute for Earth Science & Disaster Prevention, Tsukuba, 305-0006, Japan

Summary For the purpose of science education a method of the demonstration of soil liquefaction by earthquake was considered. As a result, experiments of various phenomena caused by liquefaction become possible in a closed bottle in small size by adjusting the densities of materials in the bottle under a similarity law.

INTRODUCTION

The phenomenon of soil liquefaction generated by seismic vibration of earthquake in nature is one of the most interesting demonstrations for science education because it illustrates the strange behaviors that go beyond the realm of common sense. The conventional methods for the educational demonstration are not necessarily easy. Hutter[1] introduced a simple experiment for soil liquefaction by the Nohguchi bottle which was a closed plastic bottle filled with water, push-pins and sand developed by Nohguchi[2]. The bottle named *Licky* can easily simulate this phenomenon any time, anywhere and on many occasions. The simulator comprises a closed bottle, fluid, granular material and some push-pins with plastic ball. This simulation is always set up by shaking or turning the bottle upside down to mix the fluid and granular material and by settling the granular material. The liquefaction is generated by giving the bottle a light mechanical shock, and as a result under certain conditions the push-pins completely buried in the granular material partly rise up to the surface of the sediment of the granular material and under other conditions the push-pins standing on the surface of the sediment sink into it. In this paper we introduce the fundamental theory of the law of similarity and the mechanism for setting up this apparatus.

MECHANISM FOR SETTING UP

The mixing and settling for setting up have two meanings. One is to make the saturated sand loosely settled because such loose sediment is necessary for the occurrence of liquefaction. Another is to reset the push-pins at the same position with initial state. This depends on the density of the mixing multiphase fluid formed only during the mixing and settling of granular material. There are three kinds of densities: the fluid, the sediment and the mixing multiphase fluid.

Sinking phenomenon caused by liquefaction

When the density of push-pin is lower than that of the mixing multiphase fluid, the pins rise up to the settling surface of the mixing multiphase fluid during the settling, so that the pins stand on the surface of the sediment after the settling. Then, if a mechanical shock is given to the bottle, the pins partly sink into the sediment by liquefaction.

Rising phenomena caused by liquefaction

When the density of push-pin is higher than that of the mixing multiphase fluid, the pins sink into the mixing multiphase fluid during the mixing and settling and are buried in the sediment. Then, if the density of pin is lower than that of the sediment, the pins rise up to the surface of the sediment by liquefaction caused by a mechanical shock to the bottle.

SIMILARITY

The similarity of this demonstration is governed by the Froude number determined by the thickness of sediment as a characteristic length, the terminal velocity of an isolated particle of the granular material in the fluid as a characteristic velocity. Under this similarity it is easy to do the experiment even in the 3ml bottle as well as the 500ml bottle. This is very advantageous for the demonstration for the purpose of education.

CONCLUSIONS

In this method, by adjusting the density of mixing multiphase fluid, it becomes possible to set up the demonstration of various phenomena caused by liquefaction in a closed bottle. As a result, anyone can repeat the experiment several times within a minute. Moreover, also experiments in a very small size become possible under the similarity, so the bottle can easily simulate the liquefaction phenomena anytime, anywhere and in a low cost.

References

[1] Hutter K.: Kinetic and Continuum Theories of Granular and Porous Media. SpringerWienNewYork, 20-23, 2000.

[2] Nohguchi Y.: Liquefaction Simulator “Licky” for Science Education. Report of the National Research Institute for Earth Science and Disaster Prevention, ***61***, 2001.

MECHANICS EDUCATION IN SWEDEN

Anders Boström
Department of Applied Mechanics, Chalmers University of Technology,
SE 412 96 Göteborg, Sweden

Summary The role of mechanics in the swedish university system is described on the batchelor, master, and PhD levels. On the master and PhD levels the quantity and quality of the students are more or less satisfactory. On the batchelor level there are problems with many students performing too poorly. Recent and on-going changes in the system are briefly described.

INTRODUCTION

The education in mechanics in Sweden is of course very dependent on the engineering education in general. There has been and will continue to be great changes in this education, partly due to the Bologna process (the trend towards a more harmonized education system within Europe to promote mobility and transparency). The intention is here to describe how mechanics enters the engineering education at various levels and to try to give the strengths and weaknesses of the mechanics education.

Traditionally, the engineering education in Sweden leads to only two degrees, the Master and PhD degrees. The master programs have been 4 years, but switched to 4.5 years about 15 years ago. The PhD programs have been 4 years nominally for many years, but due to teaching and other assignments the real time has been around 6 years. The last couple of years the teaching load has decreased and the time is now around 5 years.

About 10 years ago, shorter engineering programs leading to a Batchelor degree were introduced. These programs are offered at many smaller colleges and now attract about the same number of students as the traditional master programs. The batchelor programs are more 'operational' and contain less basic science and more applied subjects. It is possible to enter a master program after 3 years with an appropriate Batchelor degree, but usually it is necessary to complement with courses in mathematics and mechanics. Rather few actually use this way to obtain a Master degree.

During the last 10 years international master programs have gradually increased in numbers. These offer specialized educations, e.g. in turbulence, structural engineering, and automotive engineering, and are for 1.5 or 2 years. These programs mostly attract foreign students but can also be chosen by the regular master students for their specialization.

BATCHELOR PROGRAMS

The shorter engineering programs contain relatively little basic science and therefore only the programs in mechanical and civil engineering have courses in mechanics, typically introductory courses in statics and dynamics, strength of materials, and maybe fluid dynamics. Typically, the total amount of mechanics in these programs is 10-15 c.u. (credit units; in Sweden one academic year contains 40 c.u., each c.u. should correspond to one full week of work for the student). Optionally, one or two more courses may be taken in these subjects or in FEM.

There have been great problems with the quality of the programs, initially only about 20% of the students got their degree in reasonable time. This situation is somewhat better now, but at least partly this has occured due to easier exams or other types of examination as home assignments (where many students cooperate and the accomplishments of the weaker students are very uncertain).

The first three years of the master programs also have introductory courses in mechanics. Typically all, or almost all, programs, also in chemical and computer engineering, have a course in statics and dynamics. In mechanical engineering the introductory courses amount to around 20 c.u. In addition, the quality of the courses and the demands on the students are generally high. The problem is instead that many students fail, typically only 50–80% of the students pass the courses the first time. Even after the two reexaminations that are offered during the year many students have still not passed a course. This leads to a situation where many students have courses left behind, which means that they may not get their degree until 5 or more years (compared to the nominal 4.5). One or two more courses in mechanics may be taken optionally, in particular many students take a course in FEM.

MASTER PROGRAMS

During the last two years the master programs contain a specialization and the students have a large variety of courses and programs to choose from. Those wishing to specialize in mechanics can take courses in advanced dynamics, continuum mechanics, advanced FEM, structural dynamics, material mechanics, fatigue, advanced fluid dynamics, CFD, turbulence, etc, and also more applied courses e.g. in machine elements, turbo machinery, automotive engineering, and acoustics. At this level the students usually perform well with almost all students passing their exams. Of the students in mechanical engineering around 25% take a specialization in mechanics, meaning that they take 30–40 c.u. of courses in mechanics. But also other students take courses in mechanics, some of the courses attract students from civil engineering, engineering physics, and automation engineering.

PHD PROGRAMS

Depending on the programs some 10–20% of the master students continue towards a PhD exam (in Sweden there is also an intermediate licentiate exam, after which some students quit). Only about 10–20% of the students come from abroad, this is partly due to the swedish system with using the PhD students also as teaching assistants which is mostly expected to be done in swedish. The PhD students are emplyoed by the university for 5 years and the teaching load is usually 20%. In this way the students almost become as staff members. In general it is not difficult to attract good master students to become PhD students and the quality of the PhD students is thus satisfactory in most cases.

Unlike in many other countries the PhD program also contains a course part, typically 40–50 c.u. (about one year). These may be master courses, but the departments also offer in-depth PhD courses, often with direct coupling to the research. Due to funding reasons almost all PhD projects today are externally funded, and this is the limiting factor for the number of PhD students. The projects are thus often of a more applied nature, and this seems to be preferred by most students.

THE FUTURE

Presently, there is on-going work to further separate the batchelor and master levels. Still, it will be possible to be admitted to a program leading all the way to a Master degree, but an intermediate Batchelor degree will also be offered. It will also become more natural to enter at the master level with an appropriate batchelor exam. Although it is possible to complement the batchelor, this may still lead to problems for master programs in mechanics with students entering with a weaker background in mechanics than earlier.

Most master programs are presently 1.5 year, but there are advanced plans to make them all 2 years, both to conform better to other countries and to prepare better for the PhD progam. Simultaneously there are more tentative discussions to reduce the PhD programs, the swedish program being very demanding in an international comparison.

As mentioned above there are problems with the mechanics education at the batchelor level with students performing too poorly. There are many discussions on how to tackle this. One change that is under way in some places is to concentrate the courses more and only have two courses running in parallel (presently the norm is three courses in parallel). Other suggestions include an increased use of computer-based learning methods and alternative examination forms such as project work and home assignments (with the problems of securing the quality of each individual student).

CONCLUSIONS

In summary it can be stated that the position of mechanics is relatively strong in the swedish university system. At the master and PhD level the trend seems to be positive with a good number of students of sufficient quality entering and performing well. At the batchelor level the situation is more problematic. Of the large number of students taking introductory mechanics courses at this level too many seem to be poorly motivated and to perform unsatisfactory. There is a large challenge in changing this.

Rigid Body Dynamics: Student Misconceptions and Their Diagnosis[1]

D. L. Evans[2], Gary L. Gray[3], Francesco Costanzo[4], Phillip Cornwell[5], Brian Self[6]

Introduction: As pointed out by a rich body of research literature, including the three video case studies, *Lessons from Thin Air, Private Universe*, and, particularly, *Can We Believe Our Eyes?*, students subjected to traditional instruction in math, science and engineering often do not adequately resolve the misconceptions that they either bring to a subject or develop while studying a subject. These misconceptions, sometimes referred to as alternative views or student views of basic concepts because they make sense to the student, block the establishment of connections between basic concepts, connections which are necessary for understanding the macroconceptions that build on the basics. That is, the misconceptions of basic phenomena hinder the learning of further material that relies on understanding these concepts.

The literature on misconceptions includes the field of *particle mechanics*, but does not include rigid body mechanics. For example, it has been established[7] "that … commonsense beliefs about motion and force are incompatible with Newtonian concepts in most respects…" It is also known that replacing these "commonsense beliefs" with concepts aligned with modern thinking on science is extremely difficult to accomplish[8]. But a proper approach to accomplishing this replacement must begin with understanding what the misconceptions are, progress to being able to diagnose them, and eventually, reach the point whereby instructional approaches are developed for addressing them.

In high school, college and university physics, research has led to the development of an assessment instrument called the Force Concept Inventory[9] (FCI) that is now available for measuring the success of instruction in breaking these student misconceptions. This work, and the data collected and published on its use[8], have created a very active physics education research community that is pursuing reform in teaching pedagogies and classroom management techniques in that subject.

The Current Work: This paper presents results of research on important, but troublesome-to-students, concepts in *rigid body mechanics*. Its purpose is to better inform instructors in undergraduate dynamics courses so that they better understand the nuances and intricacies of student learning of this subject. Although much of a first course in dynamics covers Newtonian particle mechanics where the learning of the concepts could be assessed by the FCI, an important element to common dynamics courses is the introduction of rigid bodies of finite extent (i.e., non-point particles). For this topic there is little research on student misconceptions and no equivalent FCI that can be used to diagnose them. This means that it is hard to evaluate the success of any experimentation with instructional techniques.

---

[1] Work partially supported by the US National Science Foundation grant #EEC-9802942 to the Foundation Coalition.

[2] Mechanical and Aerospace Engineering Department, Arizona State University (devans@asu.edu).
[3] Engineering Science and Mechanics Department, Pennsylvania State University (gray@engr.psu.edu).
[4] Engineering Science and Mechanics Department, Pennsylvania State University (costanzo@engr.psu.edu).
[5] Mechanical Engineering Department, Rose-Hulman Institute of Technology (cornwell@rose-hulman.edu).
[6] Engineering Mechanics Department, United States Air Force Academy (Brian.Self@usafa.af.mil).

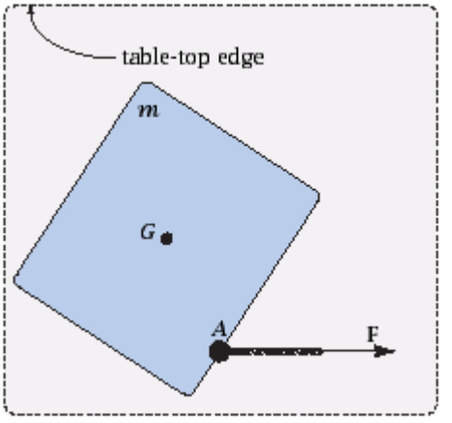
[7] Halloun, I., and D. Hestenes, "Common-sense concepts about motion," *Am. J. Phys*. **53**, 1056 (1985).
[8] Hake, R., ***Am. J. Phys*. 66**, 64-74 (1998), or see *hitchcock.dlt.asu.edu/media2/cresmet/hake/.*
[9] Hestenes, Wells and Swackhamer, *The Physics Teacher* **30**, 141 (1992) Revised edition available at *http://modeling.la.asu.edu/R&E/Research.html.*

This current work began by using a Delphi process to reach near-consensus agreement among a large number of dynamics instructors on the major concepts of the topic. This same group and process was used to reach near-agreement on which of the concepts students typically did poorly. This led to the definition of 11 concepts which were important but for which most students had severe difficulty.[10]

For these 11 concepts, questions were designed that might showcase misconceptions. The unique feature of the FCI is that the multiple choice possible answers, in addition to the one correct answer, had commonly held misconceptions as other possible answers. The task in the current research was to research the misconceptions on each of the concepts defined in the Delphi study.

Student focus groups conducted at three different universities were used in this research, followed up by wider-scale testing of students at additional universities. Early focus groups were asked to write out their responses to posed questions and to dialog with the focus group leaders about the questions. These responses produced material with which to refine the questions and to construct answers that expressed the students' misconceptions. These were then tested on more focus groups and further refined. After stability was reached, the questions were given at six universities to students who were just completing a dynamics course.

An Example Misconception: An original question posed to check students' understanding of the motion of rigid bodies was: You are currently driving down the highway in an automobile and you have to apply the brakes. When you do this, the front end of the auto tends to "nose-dive" or move closer to the road and the rear of the vehicle goes up. Why does this always happen? None of about 20 students in two separate focus groups gave anywhere near the correct answer. After a couple of iterations, the question was simplified to (see figure below): The box of mass *m* is initially at rest on smooth, frictionless, horizontal table. The box is pulled by a string that exerts a constant force **F** applied at the hinge at A. The orientation of the line of action of **F** is constant and the center of mass of the box is at G. Concerning the path of the mass center, G, of the box and how the orientation of the box will change, which of the following statements applies? a) Mass *m* will begin to rotate and point G will begin to move up and to the rights; b) Mass *m* will begin to rotate and point G will begin to move down and to the right; c) Mass *m* will begin to rotate and point G will begin to move to the right; d) Mass *m* will begin to rotate but G will not move; e) Mass *m* should not begin to rotate. In the large scale tests, only 25% of the students picked the correct answer (c), showing that, although they might have been able to write down the equations of motion and solve the problem, they had not yet connected the equations to the interpretation of a physical situation. They still preferred their pre-dynamics (mis)conceptions about the type of motion that would occur. More examples will covered in the paper.



The Development of an Assessment Instrument: The results are being used in the development of an easy-to-administer, easy-to-score assessment instrument that can reveal whether these common misconceptions have been affected by instruction. The instrument, called the Dynamics Concept Inventory (DCI) is patterned after the FCI. The current presentation, while showing Version 1.0 of the DCI, will highlight more the research findings on student misconceptions.

[10] Gray, G. L., D. Evans, P. Cornwell, F. Costanzo, and B. Self, "Toward a nationwide dynamics concept inventory," ASEE Annual Conference, Nashville, TN (2003).

WEB-BASED INSTRUCTIONAL UNITS FOR TEACHING MECHANICS

Kamal B. Rojiani[*], Rakesh K. Kapania[**], Yong Y. Kim[**], and Jing Li[**]
[*]*Department. of Civil and Environmental Engineering, Virginia Tech, Blacksburg, VA 24061, USA*
[**]*Department of Aerospace and Ocean Engineering, Virginia Tech, Blacksburg, VA 24061, USA*

Summary A series of novel web-based instructional units that facilitate the teaching of basic concepts in mechanics have been developed. The instructional units are delivered over the Web as HTML documents containing embedded Java applets. The advantage of providing these instructional units in the form of web documents is that they can be accessed from anywhere. Examples of instructional units developed include Mohr's circle for two- and three-dimensional stress, shear center for open and closed section thin walled tubes, section properties of built-up sections, and shear, moment and deflection analysis of beams. The advantages of using Java applets and the web for teaching are also discussed.

INTRODUCTION

The World Wide Web is a popular vehicle for publicizing information in text or graphical form. In recent years it has also become a valuable resource for educators. A significant weakness of web pages is that they offer only static access to information. With the advances in technology in the form of the Java programming language the web now offers real opportunities for delivering interactive, dynamic content essential for active learning. Java is an object-oriented programming language with capabilities similar to advanced programming languages. Java is unique in that Java applications can be embedded in web pages (where they are called applets) and can be executed from within the web browser. Java is also platform independent. Thus, web pages containing Java applets can be accessed by anyone with an Internet connection and a Java capable web browser.

FORMAT OF INSTRUCTIONAL UNITS

Each instructional unit consists of a series of HTML documents which present fundamental concepts and theoretical background, instructions for running the Java applet, example problems, exercises, and a feedback form. Each instructional unit is independent and addresses a single topic. This makes it easy for educators to incorporate the instructional units into existing courses. Instructional units are organized in a format that makes it easy for students to access the applet, learn how to use it, study the theory behind the applet and provide feedback. The first page gives students the option to start the applet, view instructions, or study the theory. The instruction page describes the user interface. The theory page presents the fundamental concepts behind the applet. An examples page provides several example problems for students to solve and compare their answers with those given by the applet. Lastly, there is a survey page which gives students an opportunity to provide feedback for improving the applet and instructional units.

BRIEF DESCRIPTION OF APPLETS

In this section brief descriptions of some of the applets developed are presented. The reader is encouraged to visit the web site http://*www.engapplets.vt.edu* to access the instructional units and to view detailed descriptions of the applets.

Mohr's Circle Applet for 2D and 3D Stress: The Mohr's circle applets for 2D and 3D state of stress assists in the understanding of two of the most important concepts in mechanics - stress and strain. The Mohr's circle applet shown in Figure 1 draws the Mohr's circle for 2D stress analysis. Upon entering the three stress components, σ_x, σ_y, and τ_{xy}, the applet computes the principal stresses, σ_1 and σ_2, the maximum shear stress, σ_{max} and the angle of inclination of the principal planes. The average stress and the radius of the circle are also displayed. This applet is a useful tool in understanding the construction of Mohr's circle and the concepts associated with the use of Mohr's circle since it graphically illustrates the relationships between the various stress components. The Mohr's Circle 3D applet draws Mohr's circles for 3D stress analysis. Input to the applet consists of the six stress components, σ_x, σ_y, σ_Z, τ_{xy}, τ_{xz}, τ_{yz}. The applet computes the three principal stresses, σ_1, σ_2, and σ_3 and the three maximum stresses, τ_{max1}, τ_{max2}, τ_{max3}. The computation procedure involves performing an eigenvalue analysis and solving for the roots of the characteristic polynomial equations. These roots represent the three principal stresses, σ_1, σ_2 and σ_3.

Section Properties Applet: An important topic in undergraduate mechanics courses is the computation of section properties of planar areas. These section properties appear frequently in design formulas used in fluid mechanics, solid mechanics and structural design. With the section properties applet (see Figure 2) students can build a section consisting of a combination of various shapes such as polygons, rectangles, ellipses and quarter-ellipses. The applet computes section properties of the built-up section. The properties computed include area, centriod, moments of inertia, and the product of inertia. Principal moments of inertia and the orientation of the principal axes are also computed. A useful feature of the applet is that it lets students experiment with different types of sections and to study the effect of changes in section geometry on the properties of the section.

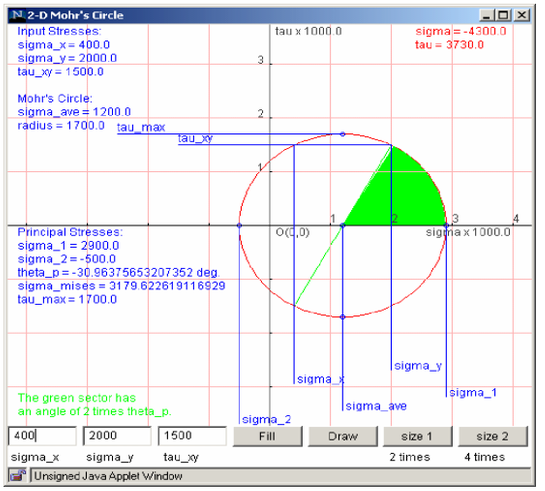


Figure 1. Mohr's Circle Applet for 2D State of Stress.

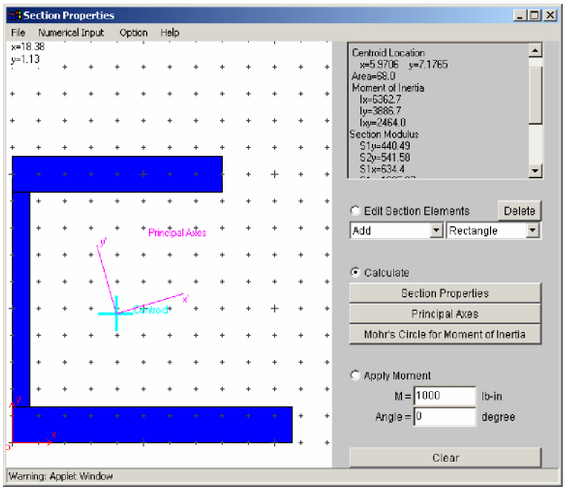


Figure 2. Section Properties Applet.

Shear Center Applet: The shear centre applet shown in Figure 3 determines the shear centre of open and closed thin-walled sections having one-axis of symmetry. When entering the geometry of the section in the applet it is only necessary to draw the top half of the symmetric cross-section. The section geometry can also be specified by providing numerical values instead of entering points with the mouse. This applet lets applet students try different cross-sections and obtain a better understanding of the concepts associated in the determination of the shear centre.

Beam Analysis Applet: This applet computes the shear, moment and deflection at a number of points along a beam. It also draws the shear, moment and deflection diagrams. The applet is shown in Figure 4. The types of beams that can be analysed include cantilever beams, simply supported beams, propped cantilever beams and beams with both ends fixed. A variety of loads can be applied including uniformly distributed loads, concentrated loads, linearly varying loads, and moments applied at the ends or at intermediate points along the beam. These loads can be applied in any combination. The beam analysis applet allows students to study how the distribution of shear, moment and deflection changes under each load. It also demonstrates graphically the effect of different support conditions and of adding different types of load and thus serves as a very useful tool for studying these concepts without having to perform lengthy and tedious computations by hand.

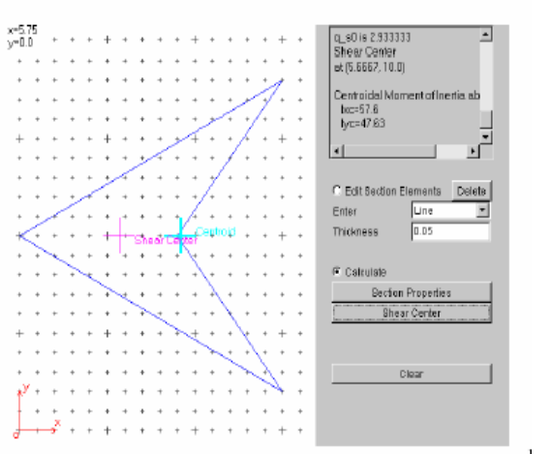


Figure 3. Shear Center Applet.

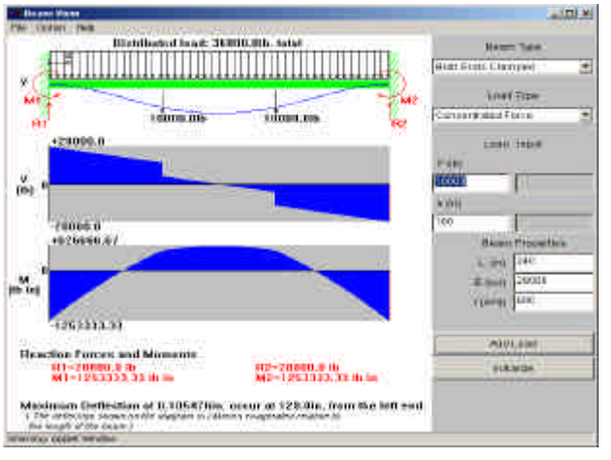


Figure 4. Beam Analysis Applet.

CONCLUSIONS

Web-based instructional units containing embedded Java applets can provide students with a dynamic interactive learning environment and can significantly increase students' understanding of the subject matter. They also provide many benefits for instructors. Java class files are compact and can be easily distributed over the internet to remote users thereby eliminating many of the difficulties associated with delivering and updating software via other media such as CD-ROM. The latest version of the applet is always available since the files are stored on the server instead of the client machine. Java applets are universally available since they are platform independent. The approach presented in this paper is well suited for educational use especially for topics requiring a dynamic graphical interactive presentation and instant and broad access. It is believed that interactive teaching units delivered via the Web will have a significant impact on enhancing the quality of mechanics education.

CD-ROM Proceedings

W. Gutkowski and
T. A. Kowalewski (Eds.)

MECHANICS OF 21st CENTURY



PART 2

International Union of
Theoretical and Applied Mechanics

Springer Academic Publishers

MECHANICS OF THE BOUNDING FLIGHT REVISITED

Takeshi Sugimoto
Faculty of Engineering, Kanagawa University, Yokohama 221-8686, Japan

Summary Bounding flight, the technique used by many small birds, is studied by control theory and rigorous argument in terms of time averages. Two major conclusions are obtained: the bounding flight is considered as the optimal bang-bang control for the unstable back-side flight; the bounding flight saves more energy than the continuous powered-flight in wide speed ranges, in particular at low speeds, and hence that the formerly known speed bound is found to be insufficient to account for the phenomenon.

INTRODUCTION

Many birds fly with a technique by mixing wing-flapping and wing-folding phases. Such a flight trajectory undulates up and down. This is the bounding flight. The former studies showed the lower bound of flight velocity suited for the bounding flight [1-3]. Most researchers in biomechanics reached the same conclusion. But biologists did not admit the theory, because birds fly intermittently in almost all the speed ranges. Even now there are two hypotheses proposed: the fixed-gear hypothesis and the body-lift hypothesis. The present study affords a strong support to the former hypothesis from a mechanical viewpoint. In the extended summary we use nomenclatures without notice if those are conventional.

THEORY

Basic equations

We take x- and z-axes parallel and perpendicular to the horizon, respectively. We assume a bird with its mass m flying at the speed u toward the positive x direction. Let us define the fraction of the flapping duration t_p to the total flight-cycle time T by $f = t_p/T$. To be aloft, it is necessary $mg = f\rho\langle u^2\rangle SC_L/2$ for t in $[0, t_p]$, where $\langle\ \rangle$ denotes a time-averaged value over one cycle. But the analysis becomes concise if we adopt the following sufficient condition: $mg = f\rho u^2 SC_L/2$ for t in $[0, t_p]$. Then the equation of vertical motion assumes the form:

$$\ddot{z} = \begin{cases} \left(f^{-1}-1\right)g & \text{for } t \in [0, t_p] \\ -g & \text{for } t \in [t_p, T] \end{cases}, \quad \text{while } \dot{u} = \begin{cases} \tau - (A_{w0}+A_b)u^2 - A_{w1}u^{-2} & \text{for } t \in [0, t_p] \\ -A_b u^2 & \text{for } t \in [t_p, T] \end{cases}$$ corresponds to the equation of horizontal motion. In the equations shown above, τ and A-something respectively denote the acceleration due to the thrust and aerodynamic coefficients, while the subscripts w and b designate wing and body, respectively. Fig.1 shows the typical phase portrait of the bounding flight for a cycle. We used Tennekes's data of a White Wagtail [4]. A bird starts flapping at $t = 0$ and $u = u_{min}$ till $t = t_p$ and $u = u_{max}$, then it switches off till $t = T$ and $u = u_{min}$. This is one cycle.

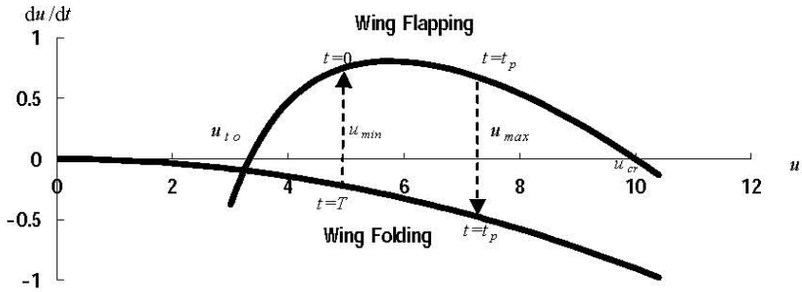


Fig.1. Phase portrait of the bounding flight

RESULTS AND DISCUSSION

Implication of the bounding flight as optimum control

Flapping flight with the minimal constant thrust is attained at $u = u_{opt} \equiv [A_{w1}/(A_{w0}+A_b)]^{1/4}$ as $\tau = \tau_{opt} \equiv 2[(A_{w0}+A_b)A_{w1}]^{1/2}$. The stationary solution becomes unstable with the constant thrust if the target cruising speed u^* is less then u_{opt}. This situation is called back side. Then it becomes necessary to control flight conditions. We shall consider the thrust as a control variable and formulate the problem as the optimum regulator:

$$\underset{\tau}{\text{Minimize}} \int_0^T (u-u^*)^2 dt,$$

subject to the equality constraint, *i.e.*, the equation of horizontal motion, and the inequality constraint on the thrust: $0 \le \tau \le \tau_{max}$. Since this regulator is linear in terms of τ, the solution is given by the well-known bang-bang control:

$$\tau = \begin{cases} \tau_{max} & \text{if } \partial J / \partial u > 0, \\ 0 & \text{otherwise,} \end{cases}$$

where J denotes the objective functional above. This corresponds exactly to the bounding flight.

Derivation of the exact time-averaged values and annotation of the results

The former studies relied solely on the analysis of instantaneous powers, for this formalism needs simple algebra only. This simplification, however, misled us to the insufficient conclusion declined by biologists.

Let us consider the bounding flight with the speed range u in $[u_{min},u_{max}]$. The time-averaged flight velocity $\langle u \rangle$ can be calculated by integrating the equation of horizontal motion:

$$\langle u \rangle = \frac{u_{cr}^{\,2} \ln\left|\frac{u_{cr}^{\,2}-u_{min}^{\,2}}{u_{cr}^{\,2}-u_{max}^{\,2}}\right| + u_{to}^{\,2} \ln\left|\frac{u_{max}^{\,2}-u_{to}^{\,2}}{u_{min}^{\,2}-u_{to}^{\,2}}\right| + \frac{2\sqrt{\tau^2-4(A_{w0}+A_b)A_{w1}f^{-2}}}{A_b} \ln\left|\frac{u_{max}}{u_{min}}\right|}{u_{cr} \ln\left|\frac{u_{cr}+u_{max}}{u_{cr}-u_{max}}\right|\left|\frac{u_{cr}-u_{min}}{u_{cr}+u_{min}}\right| + u_{to} \ln\left|\frac{u_{max}-u_{to}}{u_{max}+u_{to}}\right|\left|\frac{u_{min}+u_{to}}{u_{min}-u_{to}}\right| + \frac{2\sqrt{\tau^2-4(A_{w0}+A_b)A_{w1}f^{-2}}}{A_b}\left(\frac{1}{u_{min}}-\frac{1}{u_{max}}\right)},$$

where u_{cr} and u_{to} denote the high- and low-speed stationary solutions, respectively. Using $\langle u \rangle$, we obtain the required specific-power for the bounding flight $P_b = \tau_{max}\langle u \rangle$. On the other hand in the continuous powered-flight both the thrust and the flight velocity are constant. To fly at $u = \langle u \rangle$ the thrust has to be adjusted such that $\tau = (A_{w0}+A_b)\langle u \rangle^2 + A_{w1}\langle u \rangle^{-2}$. Hence we have the required specific-power for the continuous powered-flight $P_c = [(A_{w0}+A_b)\langle u \rangle^3 + A_{w1}\langle u \rangle^{-1}]T$.

The scheme to solve the entire problem starts from giving u_{min} and u_{max}, and then we shall calculate the corresponding fraction f and finally $\langle u \rangle$. Fig.2 shows $\langle u \rangle$-contours in $[u_{min},u_{max}]$ plane. Fig.3 shows f-contour in $[u_{min},u_{max}]$ plane. The darker the gradation becomes, the higher those calculated values become. Roughly speaking, the mean velocity $\langle u \rangle$ is close to the arithmetic mean between u_{min} and u_{max}. The fraction f has the minimum value, which assures the physically meaningful solution and depends on A_{w0}, A_{w1}, A_b, τ_{max}, u_{min} and u_{max}. In the present case the minimum ranges from around 0.6. Fig.4 summarizes the essence of our findings: P_b–P_c contour in $[u_{min},u_{max}]$ plane; red and blue denote negative and positive, respectively. The diagonal part, in other words $u_{min} \approx u_{max}$, is the most likely flight region, where the bounding flight saves more energy than the continuous powered-flight in wide speed ranges, in particular at low speeds. Fig.5 is the White Wagtail's typical flight path reconstructed by solving the equations of motion: T = 1.4 s, f = 0.62, $\langle u \rangle$ = 6.5 m/s with u_{min} = 6.4 m/s and u_{max} = 6.6 m/s. The variation in altitude is around 1 m during the bird flies horizontally 8.5 m ahead.

CONCLUSIONS

The mathematically rigorous analysis leads us to the conclusions: the bounding flight is the optimal bang-bang control; this technique saves more energy than the continuous powered-flight in wide speed ranges, in particular at low speeds.

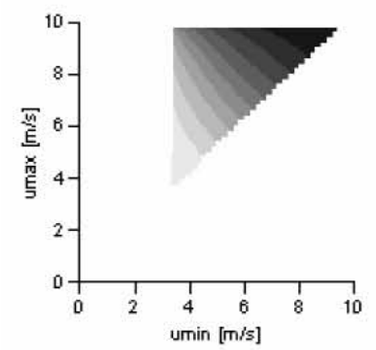


Fig.2. $\langle u \rangle$-contour in $[u_{min},u_{max}]$ plane.

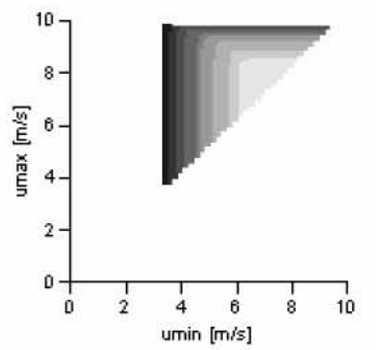


Fig.3. f-contour in $[u_{min},u_{max}]$ plane.

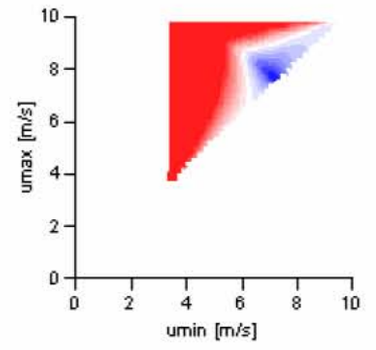


Fig.4. P_b–P_c contour in $[u_{min},u_{max}]$ plane.

References

[1] Lighthill, J.: Introduction to the Scaling of Aerial Locomotion, in Pedley, T.J. (Ed.), *Scale Effects in Animal Locomotion*. Academic Press, New York 1977, 365-404.

[2] Rayner, J.M.V.: The Intermittent Flight of Birds, in Pedley, T.J. (Ed.), *Scale Effects in Animal Locomotion*. Academic Press, New York 1977, 437-443.

[3] Rayner, J.M.V.: Bounding and Undulating Flight in Birds. *J. Theor. Biol.* **117**: 47-77, 1985.

[4] Tennekes, H.: The Simple Science of Flight: From Insects to Jumbo Jets, MIT Press, Massachusetts 1997.

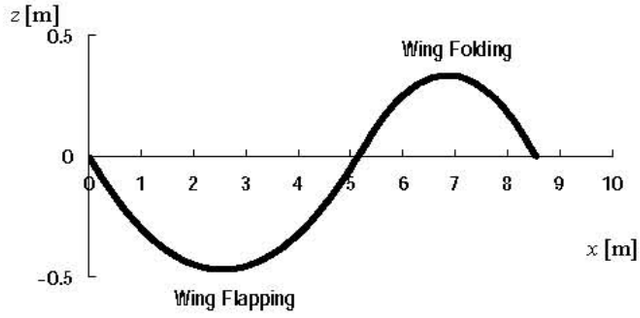


Fig.5. Reconstructed flight path of a White Wagtail.

DEFORMATION OF VESICLES FLOWING THROUGH A CAPILLARY

Victoria Vitkova, Maud Mader and Thomas Podgorski

[*]Laboratoire de Spectrométrie Physique, CNRS-UJF, 140 rue de la Physique – BP 87, 38402 St Martin d'Hères CEDEX, France

Summary Giant vesicles are closed, deformable membranes which can be a useful model when trying to understand the fluid mechanics and rheology of cell suspensions, such as blood. The flow of giant vesicles through cylindrical capillaries is experimentally investigated. Vesicles (20 to 50 microns in diameter) are deflated with reduced volumes between 0.8 and 1. Both interior and exterior fluids are sugar solutions with viscosities close to 1 cP. Vesicles are aspirated into a capillary tube with a diameter close to the vesicle size and a constant flow rate is imposed. Significant deformation of the membrane occurs, with vesicle shapes such as ellipsoids, bullet shapes or parachute shapes. We quantitatively investigate the deformation as a function of velocity, reduced volume and confinement. The mobility of vesicles (ratio of their velocity to the average velocity of the carrier fluid) is also studied and consequences on flow resistance are discussed.

INTRODUCTION

The motion of deformable particles in a flow has led to a considerable amount of work in various contexts. From a mathematical viewpoint, it is a challenging problem because of the non-locality of the problem and the existence of moving boundaries. Deformable objects govern the rheology of various fluids and mixtures, such as emulsions, suspensions of droplets or bubbles, or blood. In addition, the mechanical response of cells to hydrodynamical stresses is potentially important in many biological processes.

Giant Unilamellar Vesicles (GUV) are closed membranes made of a phospholipid bilayer enclosing a fluid. They can be considered a rough model of biological cells, especially red blood cells which do not have a nucleus.

Many studies have been devoted to microchannel flows of objects such as drops or bubbles [1], capsules [2,3], and in-vitro measurements have been made on blood [4]. As opposed to capsules, whose membranes are elastic solids, the vesicle membrane is an almost incompressible bidimensional fluid, with a bending energy that governs its equilibrium shape [6]. Those properties also significantly differ from simple interfaces characterized by a surface tension. We report here an experimental study of vesicles flowing through narrow capillaries.

EXPERIMENT

Giant unilamellar vesicles were prepared by the electroformation method [5] with *L* - α phosphatidylcholine (DOPC) in a 280 mM sucrose solution (interior fluid). We obtained vesicles with diameters between 10 and 70 μm. The vesicle suspension was then diluted in a 320 mM glucose solution (exterior fluid) which has a slightly higher osmolarity than the interior solution. After a while, vesicles are slightly deflated with reduced volumes between 0.9 and 1 (reduced volume v is defined as the ratio of the final volume of a vesicle to the volume of a sphere with the same surface area). Both interior and exterior fluids have viscosities close to 1 cP and densities close to 1 g/cm^3.

The suspension of deflated vesicles was placed in a chamber made of two parallel glass slides separated by teflon spacers (1.5 mm thick). One side of the chamber was kept partly open to allow the introduction and micromanipulation of a glass micropipette (diameter: 40-50 μm) connected to a microsyringe attached to a syringe pump. The experimental chamber was placed on an Olympus IX71 inverted microscope equipped for phase contrast microscopy with a 40x objective lens. A COHU video camera was used to capture images which were analyzed with Scion Image software.

Vesicles were individually sucked up into the pipette and a constant flow rate was set via the pump, leading to a stationary flow of vesicles in the pipette, at speeds up to 300 μm/s.

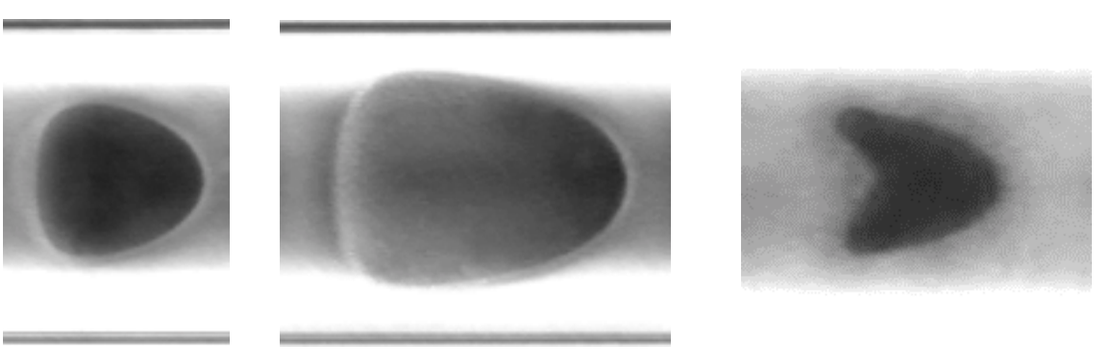


Fig. 1: Vesicles flowing through a capillary (from left to right). Pipette walls are visible on the first two pictures.

OBSERVATIONS

Since their density is close to that of the surrounding fluid, and because they experience a lift force that pushes them away from the wall, vesicles stay along the centerline of the pipette and an axisymmetric situation is obtained. Depending on various parameters such as reduced volume ν, velocity U or ratio λ of vesicle radius to pipette radius, a variety of axisymmetric shapes is obtained as shown on Fig. 1.
At rest, vesicles with reduced volumes in the range 0.9 – 1 have an approximately prolate ellipsoidal shape dominated by Helfrich bending energy [6]. As soon as a flow is imposed, significant deformations of the membranes occur and the fore-aft symmetry is lost, with a decreasing curvature at the trailing end, possibly leading to concave shapes.
We characterize deformations by measuring the displacement of the vesicle's center of mass relative to its middle point on the symmetry axis. The ratio of this displacement to the vesicle's half-length defines an eccentricity a.

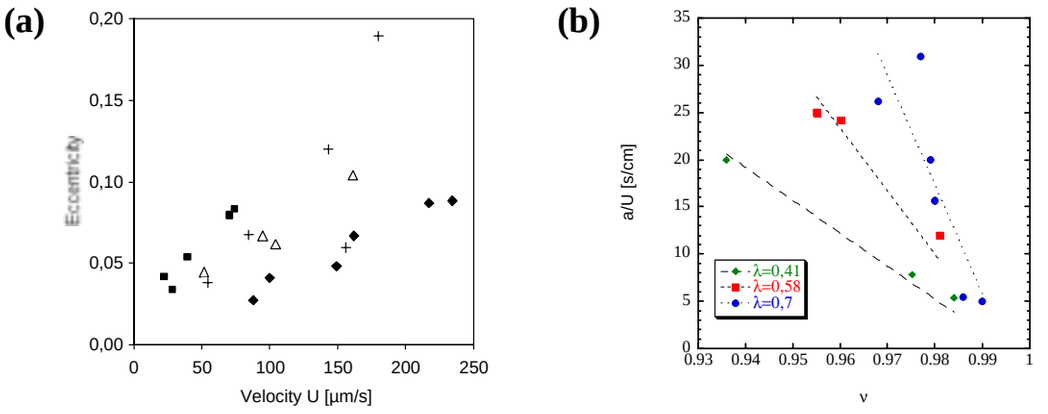


Fig. 2: (a) Eccentricity a vs. Velocity U for various vesicles. (◆): ν=0.975, λ=0.397; . (△): ν=0.980, λ=0.684; . (+): ν=0.971, λ=0.666; . (■): ν=0.982, λ=0.604; (b)a/U vs. ν for various values of confinement λ.

The influence of velocity U on deformation is directly illustrated on Fig. 2(a). Eccentricity a is a roughly linear increasing function of velocity. Eccentricity is also a decreasing function of ν and an increasing function of the confinement λ as shown on Fig. 2(b): vesicles that are more confined and more deflated are significantly more sensitive to shear stresses. If the reduced volume is sufficiently small (around 0.9), vesicles can exhibit a semi-concave shape under flow which is reminiscent of shapes of red blood cells in capillaries.
We also measured the ratio of the vesicle velocity U and average fluid velocity V (as imposed by the pump). As for other systems of particles flowing through tubes, such as drops or capsules [1,2,3], the vesicle velocity is higher than the average velocity V (but lower than the maximum velocity on the axis for a Poiseuille-like pipe flow). We find that the vesicle mobility U/V follows closely an asymptotic result obtained for small, rigid particles [1]:

$$\frac{U}{V} \approx 2 - \frac{4\lambda^2}{3}$$

Because of the axial symmetry of the problem, there cannot be any membrane flow, and thus the vesicle behaves like a solid particle once it has reached its stationary shape. An analysis of relevant dimensionless numbers shows that the membrane bending modulus is very small compared to viscous forces, while the stretching modulus is so large that the surface area of the vesicle must remain constant during the deformation, unlike capsules [2,3] which have a relatively lower elastic modulus. Vesicles appear to be unique objects with a constant volume, constant surface area and very flexible boundary, whose properties cannot be rescaled to be described by a macroscopic system in the same range of dimensionless numbers (Re, Ca…).
The presence of an object in pipe flow is responsible for an additional pressure drop. As a consequence of vesicle deformability, stronger deformations occur upon increasing velocity, which lead to a decrease of the additional pressure drop. A shear-thinning behavior of vesicle suspensions in microchannel flow follows. These phenomena, currently under investigation, are relevant to the rheology of blood in microcirculation.

References

[1] W. L. Olbricht, *Ann. Rev. Fluid Mech* **28**, 187-213, 1996.
[2] C. Quéguiner and D. Barthès-Biesel, *J. Fluid Mech* **348**, 349-376, 1997.
[3] F. Colle-Paillot, F. Rissot and M. Zagzoule, ICMF 2001, New Orleans, LA, USA (2001)
[4] T. W. Secomb et al., *J. Fluid Mech.* **163**, 405-423, 1986.
[5] M. I. Angelova et al., *Prog. Colloid Polym. Sci.* **89**, 127-131 (1992)
[6] W. Helfrich, *Naturforsch. C* **26**, 12 (1973)

XXI ICTAM, 15–21 August 2004, Warsaw, Poland

HOW TO BREATHE IN A LIQUID-FILLED LUNG: SYMMETRY OF AIRWAY REOPENING.

Charles N. Baroud*, Matthias Heil**
*Laboratoire d'Hydrodynamique (LadHyX), CNRS-Ecole Polytechnique, F-91128 Palaiseau, France.
**Department of Mathematics, University of Manchester, Manchester M13 9PL, UK.

Summary Many respiratory diseases cause the occlusion of pulmonary airways with viscous fluid. The subsequent airway reopening is assumed to occur by the propagation of an air finger into the liquid-filled airways. We investigate the behavior of the air finger as it reaches a single bifurcation and determine under what conditions the finger branches symmetrically. If the fluid pressure in both channels ahead of the branching finger are equal, the finger will preferentially reopen a single path through the branching network. If the ends of the channels are capped with compliant chambers, representing the lung elasticity, the pressure required to drive the air finger can be dominated either by viscous losses or by elastic forces. Below a critical velocity, elastic forces dominate and symmetric branching is predicted to occur. We augment our theoretical model with an experimental study in which the problem is investigated using microfluidic channels.

MOTIVATION: THE LUNG AND THE MODEL

Many respiratory diseases, such as the Respiratory Distress Syndrome, may cause the occlusion of the pulmonary airways with viscous fluid. Occluded airways are believed to be reopened by a propagating air finger [1]. Previous models of pulmonary airway reopening (e.g. [2]) have only considered the propagation of air fingers in individual airway branches. Since the airways of the lung branch frequently, the question arises if the propagating air finger will reopen the whole lung tree or simply follow a single path, keeping most of the lung occluded.

We address this question at the level of a single bifurcation by modeling the flow of an air finger as it reaches a branching point, as shown in Fig. 1. An inviscid air finger propagates along a parent tube[1] of cross sectional area $\mathcal{A}$. The finger is driven by the injection of air at a constant flow rate, Q, and it displaces viscous fluid of viscosity, μ. The interfacial tension is σ. Downstream of the bifurcation, the lung's elasticity is represented by two compliant chambers whose volumetric elastic modulus is given by k.

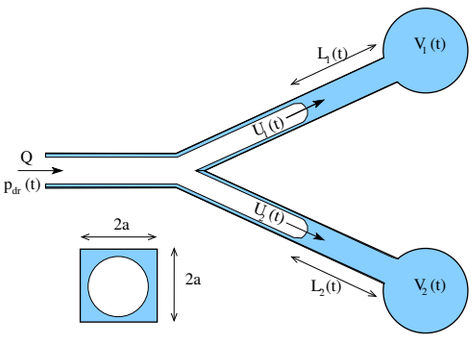


Figure 1. Model of a propagating finger through a single bifurcation.

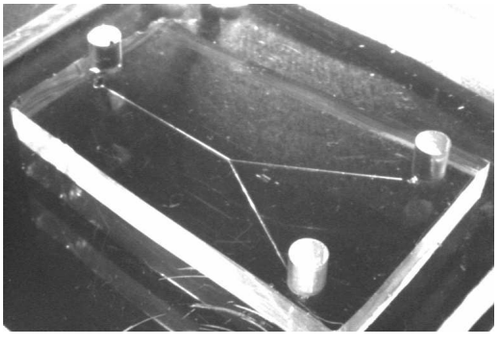


Figure 2. Experimental bifurcating channel, built using standard microfluidic technology.

MATHEMATICAL FORMULATION AND LINEAR STABILITY ANALYSIS

The flow rates in the two daughter tubes are given by $Q_i = U_i\, A_i$, where A_i is the cross-sectional area occupied by the air finger in daughter tube i. The sum of the flow rates in the daughter tubes must equal the incoming flux Q. The velocity of the finger tips is given by $U_i = -dL_i/dt$ where L_i is the length of the occluded section in daughter tube i. In the absence of inertial and gravitational effects, A_i is given by $A_i = \mathcal{A}\,\alpha(\mathrm{Ca}_i)$, where $\alpha(\mathrm{Ca}_i)$ is a function of the capillary number $\mathrm{Ca}_i = \mu U_i/\sigma$ and was computed in reference [3].

In each of the daughter branches, the pressure drop across the occluded section has three components:

- The viscous pressure drop through the liquid-filled section, $\Delta p_{\mathtt{visc}} = \mathcal{R} L_i(t) Q_i(t)$, where $\mathcal{R} \propto \mu/a^4$ depends on the geometry and the viscosity of the fluid.
- The capillary pressure drop across the curved tip of the air finger, $\Delta p_{\mathtt{cap}} = \mathtt{C}(\mathrm{Ca}_i)$. Numerical results for $\Delta p_{\mathtt{cap}}$ are available from reference [3].
- The pressure $p_{\mathtt{elast}}$ in the elastic end-chambers. We assume that $p_{\mathtt{elast}}$ depends only on the injected volume such that $p_{\mathtt{elast}} = \mathcal{P}(V_{0i} + \int_0^t Q_i(\tau)d\tau)$ and we assume that $k = d\mathcal{P}(V)/dV = const.$

[1] To facilitate comparisons with the experiment, we consider the parent and daughter tubes to be rigid with square cross-section and constant cross-sectional area $\mathcal{A} = 4a^2$; the analysis is easily extended to other geometries.

Since the air fingers in both daughter branches are subject to the same driving pressure $p_{dr}(t)$, we have

$$p_{dr}(t) = \mathtt{C}(U_i) + \mathcal{R}L_i(t)Q_i(t) + \mathcal{P}(V_{0i} + \int_0^t Q_i(\tau)d\tau) \quad \text{for} \quad i = 1, 2. \tag{1}$$

We differentiate Eq. 1 with respect to t, and use $U_i = -dL_i/dt$ and $Q_1 + Q_2 = Q$, to obtain a set of five ordinary differential equations with five unknowns: p_{dr}, U_1, U_2, L_1 and L_2. These equations admit a symmetric solution of the form $U_i = \mathcal{U}$; the stability of this solution to small perturbations determines if the finger branches symmetrically or propagates along a single path.

A stability criterion for the symmetric solution is obtained using standard linear perturbation theory. Asymmetric perturbations are predicted to grow for positive values of the function

$$F(\mathrm{Ca}) = \alpha(\mathrm{Ca})\left(2 - \frac{K}{\mathrm{Ca}}\right) + \mathrm{Ca}\frac{d\alpha(\mathrm{Ca})}{d\mathrm{Ca}}\left(1 - \frac{K}{\mathrm{Ca}}\right), \tag{2}$$

where $\mathrm{Ca} = \mu\mathcal{U}/\sigma$ is the capillary number based on the propagation velocity of the symmetrically branching fingers; the dimensionless parameter $K = k\mu/\mathcal{R}\sigma$ indicates the importance of the elastic forces relative to viscous losses.

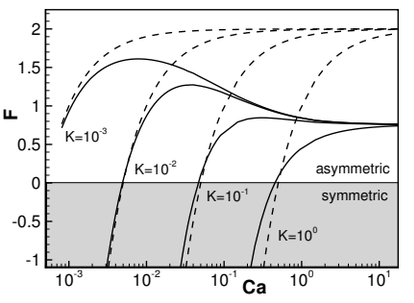


Figure 3. Variation of the function F with capillary number Ca: $F < 0$ corresponds to stable symmetric branchings, while $F > 0$ corresponds to asymmetric solutions. The dashed lines ignore capillary effects.

Figure 3 shows plots of $F(\mathrm{Ca})$ for a range of values of the parameter K. For every value of K, there exists a critical value of Ca above which $F > 0$, and therefore symmetric solutions are unstable. Two special cases are noteworthy:

1. If we set $\alpha(\mathrm{Ca}) = 1$ and $\mathtt{C}(\mathrm{Ca}) = 0$ and thus ignore the capillary effects, the predictions for $F(\mathrm{Ca})$ are given by the dashed lines in Fig. 3. In this case it is possible to derive an explicit prediction for the critical velocity, $U_c = k/2\mathcal{R}$, such that for $\mathcal{U} > U_c$ the propagation is asymmetric, while $\mathcal{U} < U_c$ yields symmetric propagation. Figure 3 shows that U_c is an excellent approximation for the critical velocity predicted by the full analysis.

2. If we further ignore the compliance terms by setting $k = 0$, we find that $F > 0$ and the branching is *always* asymmetric.

EXPERIMENTAL METHODS AND PRELIMINARY RESULTS

The above mathematical model describes an actual experimental system, built using standard microfluidic soft lithography methods and shown in Fig. 2. The channel has a square cross-section with side $2a = 100$ μm and total length 4 cm. It is initially filled with 100 cSt Silicone Oil, into which a water-fluorescein mixture is injected using a computer-controlled micropump. The injection rate varies in the range $0.3-3$ μL/min. The elasticity of the end chambers is achieved through the use of thin membranes with variable thickness and diameter, so as to yield different values of K. The fluorescent finger is followed as it advances through the bifurcation for different flow rates, in order to determine the symmetry of the branching.

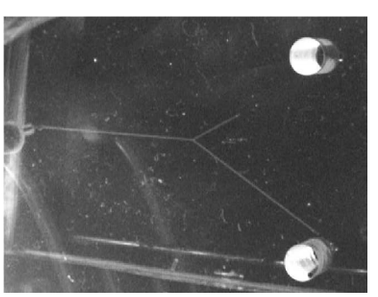


Figure 4. Asymmetric branching in open-ended microchannel

A preliminary experimental image is shown in Fig. 4. Here, the end-chambers have no compliance but are open to the atmosphere, corresponding to special case 2 above. We obtain experimentally that the branching is always asymmetric, as expected from the analysis. Further experiments are currently being conducted with the elastic chambers to verify the theoretical predictions above.

CONCLUSIONS

Our model predicts two distinct régimes for air fingers penetrating liquid-filled networks. The behavior that is chosen depends on the relative dominance of the viscous vs. the elastic forces. In the case when viscous effects are dominant, an air finger will follow a linear path in the network, leaving the other branches occluded. Future work aims to investigate the application of similar models to real lungs in order to understand the reopening of fluid-filled airways in living organisms.

References

[1] D.P. Gaver, R.W. Samsel, and J. Solway. Effects of surface tension and viscosity on airway reopening. *J. Appl. Physiol.*, 369:74–85, 1990.

[2] A.L. Hazel and M. Heil. Three-dimensional airway reopening: The steady propagation of a semi-infinite bubble into a buckled elastic tube. *J. Fluid Mech.*, 478:47–70, 2003.

[3] A.L. Hazel and M. Heil. The steady propagation of a semi-infinite bubble into a tube of elliptical or rectangular cross-section. *J. Fluid Mech.*, 470:91–114, 2002.

COMPUTATIONAL EXPLORATION OF LIVER ACINUS MICROSTRUCTURE

H.P. Rani[1]*, Tony W.H. Sheu[2]*, P.C. Liang[3]

[1] Post Doctorate ;[2] Professor and Chair
*Scientific Computing and Cardiovascular Simulation Laboratory, Department of Engineering Science and Ocean Engineering, National Taiwan University, Taipei, Taiwan.
[3]National Taiwan University Hospital, Taiwan.

Summery For the treatment of microcirculation disorders, the three-dimensional representation of the hepatic circulation is crucial for the physian. Such a representation is provided in this paper for an exploration of the blood flow, blood volume and exchange between sinusoids and hepatocytes in the hepatic acinus model.

INTRODUCTION

In this paper, we analyse the 3-D mixing mechanism of blood from hepatic arteriole and portal venule in the hepatic vascular bed [1]. Also, emphasis given to the flow patterns from the space of sinusoid upto the hepatic venule drainage. In the subsequent paragraphs, focus is given to the hepatic circulation especially on hepatic arterioles and hepatic / portal venules. Selle et al., [1] presented the analysis and visualization of hepatic vasculature and provided the shading techniques emphasizing the curvature of vessles. In the case of liver failure, one promising alternative is the development of an extracorporeal bioartificial liver (BAL). This is essentially a bioreactor containing cultured hepatocytes that function as an extracorporeal liver on a temporary basis [2] as liver cells has the capacity to regenerate itself [3]. Hence for a quantitative diagnosis, surgical planning and post operative treatments, a precise knowledge of microcirculation is important. A detailed hepatic acinus structure along with their zones is shown in Figure1.

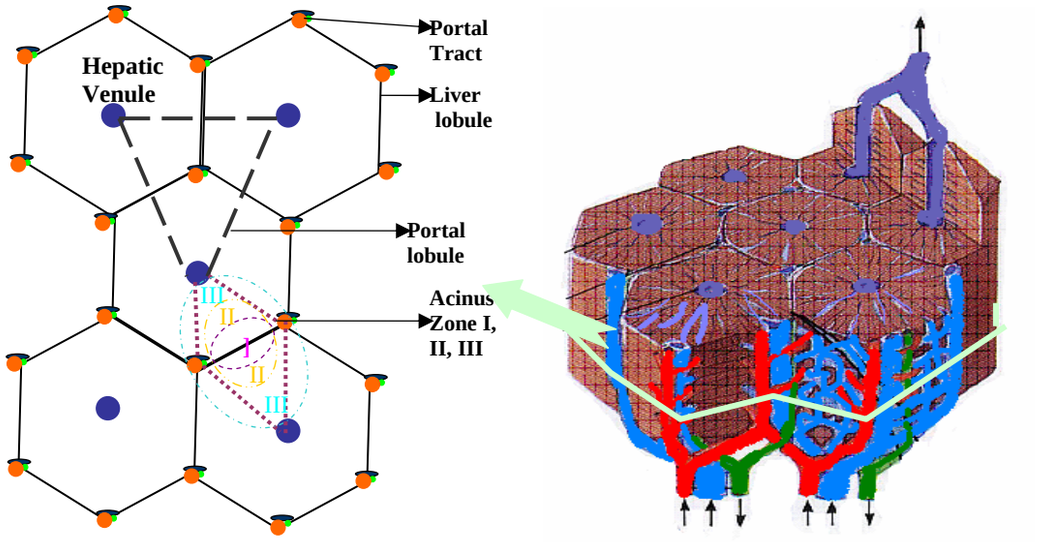


Figure 1. Simple liver Acinus

MODELLING

The parallelization of the liver into lobules, together with the complex hepatic vascular tree, provides the microscopic picture about the flow distribution. At the most gross level, there is an unusual presence of two vascular inputs, the portal and arterial flows, rather than the single arterial input. At the microscopic level, the acinar arrangement of the vascular system creates a unique series of microenvionments, which are acknowledged to be of paramount importance in controlling the functional characteristics of the parenchymal cells. In the current study we considered a simple liver acinus, which represents a small parenchymal mass consisting of pre/terminal hepatic arteriole, pre/terminal portal venule along with

fenestrated endothelial cells and hepatic venule. The present study focuses on the acinus structure of the liver. Usually, the acinus mass is divided into three zones. The representation of Acinus structure is show in Figure 2

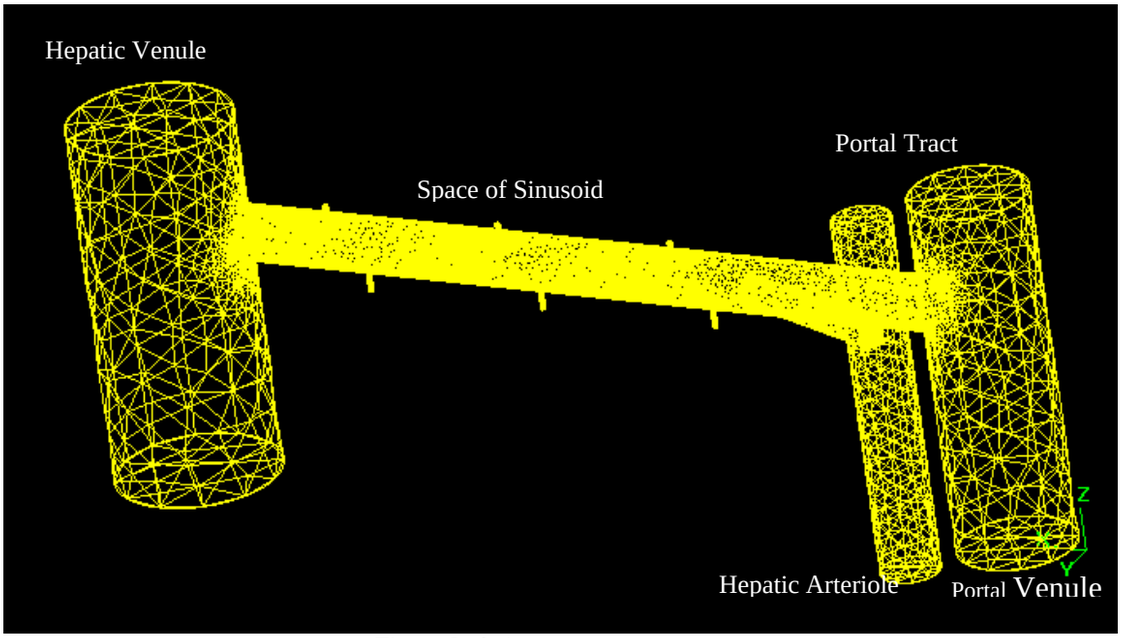


Figure 2. Acinus structure

METHODS

We developed a three-dimensional computational fluid dynamics model of an acinus structure using commercially available software, CFD-ACE (CFD Research Corp., Huntsville, AL). The model solves the full Navier-Stokes equations for unsteady flow of a Newtonian fluid using a finite volume approach. The idealized geometry consists of rigid micrometer cylinders simulating a portal tract, space of sinusoid and hepatic venule. No slip conditions are imposed on the walls of the cylinder. Fully developed flow distribution is assumed for the hepatic arteriole and portal venule.

RESULTS AND DISCUSSION

The hepatic arteriole flow has eight times greater than the flow rate of portal venule interms of mass flow, velocity and pressure. But the transmittent activity is initiated by the hepatic arteriole due to the sphincter mechanism present at the end of each arteriole especially in liver. This mechanism is analysed in detail for the unsteady case. Also when this sphincter is closed there is normal portal venule flow. The functional working difference of zone 1, 2 and 3 are analysed interms of mass flow rate, velocity and pressure distribution.

References

[1] Selle D., Preim, B., Schenk A., Peitgen, H. O.: Analysis of vasculature for liver surgical planning, *IEEE Transactions on Medical Imaging* 21(11): 2002.
[2] Ledezma G. A., Folch A., Bhatia S. N., Balis U. J., Yarmush M. L., Toner M: Numerical Model of Fluid Flow and Oxygen Transport in a Radial-Flow Microchannel Containing Hepatocytes. *Journal of Biomechanical Engineering* 121: 58-64 , 1999.
[3] Michalopoulos G.K., DeFrances M.C.: Liver regeneration. Science, 276: 60, 1997.

Acknowledgement

The authors acknowledge support under NSC Grant NSC 92-2811-E-002-004.

BACTERIUM SWIMMING MOTION CLOSE TO A WALL

Tomonobu Goto[*], Kousou Nakata[*], Yukio Magariyama[**] and Masaharu Nishimura[*]
[*]*Tottori University, Department of Mechanical Engineering, Koyama, Tottori, 680-8552 Japan*
[**]*National Food Research Institute, Food Engineering Division, Tukuba, 305-8642, Japan*

Summary The mechanism of some characteristics about swimming motion of the marine bacterium, *Vibrio alginolyticus*, close to a boundary was investigated. The motion of the microorganism that possesses single polar-flagellum propelling the cell body was dealt with as an outer flow problem from a bio-fluid dynamics viewpoint. Numerical analyses based on the boundary element method in addition to the resistive force theory were applied to elucidate the effects of the boundary on the swimming motion.
The boundary reduces the swimming speed when a bacterium moves along it. Forward swimming is stable in pitching motion and backward swimming is unstable. The swimming speed varies depending on the posture of the bacterium. When the flagellum is closer to the boundary, the trajectory of the bacterium draws a curve. These results qualitatively agree with the observed motions and have potential to explain the mechanism of the phenomena.

INTRODUCTION

Bacteria can swim by use of rotating flagella, each of which is driven by a rotary motor embedded in the cell bodies. The flagellum is like a helix and its rotation produces a force that pushes the cell body forward as a screw propels a ship. The bacteria can also change the swimming direction or swim backward by rotating the flagella in the opposite direction. Monotrichous bacteria each of which possesses only one flagellum swim forward and backward by changing the direction of motor rotation. The swimming direction changes slightly in every turn because of thermal fluctuation or bending of the flagellum.
Recently, Magariyama *et al*. found on the swimming of cells of *Vibrio alginolyticus*, YM4, that the forward swimming speed is slower than the backward swimming speed [1]. Ramia *et al*. calculated the motion of an imaginary microorganism, and the trajectory near a wall became a circular curve and the speed of the microorganism close to the wall was higher than the speed at a distance from the wall [2]. Berg & Turner observed that smooth swimming mutant of *E. coli* swam along the surface of a chamber in circles [3].
According to our recent observation, these interesting phenomena occur only when a bacterium swims in the vicinity of a boundary. When the swimming motion of bacteria is observed through a microscope, the suspension containing bacteria is usually sealed between a glass-cover-slip and a glass-slide. Some of the bacteria swim so close to either glasses that their swimming speeds and tracks are noticeably changed by the presence of those of rigid boundaries. The tracks tend to draw curved lines rather than straight lines as observed when a bacterium swims at a long distance from a boundary.
In this study, the effect of the boundaries on the swimming motion of bacteria was investigated. The resistive force theory and the boundary element method were applied to elucidate the difference between forward and backward motions of bacteria swimming near a wall. We found that the distance from a wall and the posture of the bacterium are influential in the swimming motion.

SUMMARY OF OBSERVATION

In this paper, mainly analytical results will be presented. However, as background information to them, some of observational results related to the analyses are summarized below.
The suspension including the bacteria, YM4, was sealed in a chamber of almost 150μm depth. When the microscope was focused near a wall, bacteria swimming in the range of about 10μm from the wall were observed. And when the microscope was focused in the middle of the chamber, observed bacteria swam at least 50μm apart from the walls. Unfortunately, by the phase-contrast microscopy we could not see the flagella, which means we could not judge whether the bacterium swam forward or it swam backward. Nevertheless, we treated two speeds as a set, one of which was just before a turn and the other was after the turn, and compared the speeds in several dozens of sets. The observation revealed the following:
(a) When bacteria swim in the middle of the chamber, there is no significant difference in the speed before a turn and the speed after the turn. On the other hand, when bacteria swim near a boundary, the difference is obvious.
(b) The tracks are also different. When a bacterium swims at a long distance from a boundary, it moves straight, switching the direction back and forth. On the contrary, near a wall, the track becomes a combination of curves whose radii of curvature are in the order of 10mm and straight lines. The direction of the curve is counter-clockwise when it is seen from above.
These facts reveal that the swimming motion of bacteria is considerably influenced by the presence of boundaries.

RESULTS AND DISCUSSIONS

Analysis

The present analysis by use of the boundary element method and the resistive force theory is based on the fact that the size of a bacterium is very small. The typical size of bacteria is approximately 1μm and their swimming speed is 10-100μm/s. Because of the smallness, the viscous force surpasses the inertial force, that is, the Reynolds number is very small. Therefore, at any instant, the net force and the net torque exerted on a bacterium by the surrounding fluid flow should be zero. We can calculate the swimming speed from this condition.
Calculations were carried out for two bacterium models, the size of one was determined according to an averaged cell body size and an averaged flagellum size observed for dozens of cells of YM4 [4], [5] (average cell). The other had a small cell body and had the same flagellum (small cell).

Swimming motion parallel to the wall
According to our calculations by use of the boundary element method, the swimming speed of the average cell decreases when the cell swims closer to the wall. On the other hand, the speed of the small cell increases. Ramia *et al*. [2] carried out boundary element analyses on the swimming motion of an imaginary microorganism similar to a bacterium and reported that when the microorganism of bacterium type swims close to a wall, the swimming speed increases by about 10%. Their microorganism has a relatively small cell body and corresponds to the small cell in the present study.
We investigated the reason of the difference between the averaged cell and the small cell by use of the resistive force theory dividing the wall effects into terms; translational and rotational drag increases of the cell body, translational and rotational drag increases of the flagellum, and propulsive force increase of the flagellum.
As for the average cell, the drag of the cell increases more than the propulsive force when the cell swims near a wall and consequently the speed decreases. As for the small cell, on the contrary, the additional resistance of the flagellum causes additional propulsive force and drag of the flagellum. The former exceeds the latter in the case of the small cell.
The small cell is an imaginary one introduced to indicate the difference from the average cell. According to the results on the average cell of YM4, the cells move slower when they swim in the presence of a boundary than they move in a free space. This has a connection with a reason of the difference in swimming speeds between forward and backward motions that has been confirmed by observations.

Swimming motion at a pitch angle to the wall
Next, we dealt with the posture of a bacterium relative to a wall. If the bacterium swims towards or apart from the wall, the swimming speed may change because the degree of the interaction varies.
Our numerical results were qualitatively consistent with the observed data. According to the results, we have been able to build up an image explaining the swimming speed difference and the circular track that have been observed:
(a) A bacterium swims slower when it swims closely along a wall than when it swims in free space.
(b) When the bacterium swims forward, it tends to move stably parallel to the boundary keeping a certain distance from the wall.
(c) When the bacterium swims backward, its motion is unstable. It continuously leaves from the wall or gets close to the wall.
(d) The backward swimming bacterium swims faster than the forward swimming bacterium because the bacterium swims at a distance from the wall or the flagellum is close to the wall.
(e) Since the pitch angle of the bacterium swimming backward is greater than that of the bacterium swimming forward, the backward swimming bacterium interacts more with the boundary. Consequently, the yaw direction change of the former is greater than that of the latter. Therefore, the track of the swimming backward bacterium is observed as to be bent in a counter-clockwise manner rather than to be straight.

CONCLUSIONS

The cause of the swimming speed difference between forward and backward motion and the cause of the circular trajectory of bacteria were investigated. Since the phenomena were observed in the presence of boundaries, analyses based on the boundary element method and on the resistive force theory were carried out taking a plane wall into account. Numerical results being qualitatively consistent with the observation were obtained. These results showed that considering the distance from the wall and the posture of the bacterium was crucial to explain the phenomena.

References

[1] Y. Magariyama *et al*., "Difference between forward and Backward Swimming Speeds of the Single Polar-Flagellated Bacterium, *Vibrio Alginolyticus*," *FEMS Microbiology Letters*, 205, pp. 343-347, 2001.
[2] M. Ramia, D. L. Tullock and N. Phan-Thien, "The Role of Hydrodynamic Interaction in the Locomotion of Microorganisms," *Biophysical J*., 65, pp. 755-778, 1993.
[3] H. C. Berg and L. Turner, "Chemotaxis of Bacteria in Glass Capillary Arrays," *Biophys. J*., 58, pp. 919-930, 1990.
[4] T. Goto *et al.*, "Comparison between Observation and Boundary Element Analysis of Bacterium Swimming Motion," *JSME~International J.* (C), 44, 4, pp. 958-963, 2001.
[5] Y. Magariyama, *et al.*, "Simultaneous Measurement of Bacterial Flagellar Rotation Rate and Swimming Speed," *Biophys. J*., 69, pp. 2154-2162, 1995.

A CFD STUDY OF THE EFFECTS OF PHYSIOLOGICAL VESSEL WALL MOTION ON OXYGEN TRANSPORT IN CORONARY ARTERIES

Maheshwaran K. Kolandavel[*], Ernst-Torben Fruend[**], Erik M. Pedersen[**], Steffen Ringgaard[**], Peter G. Walker[*]

[*]*Centre for Biomechanics and Medical Engineering, School of Mechanical Engineering, University of Leeds, Leeds LS2 9JT UK*

[**]*MR-Centre, Institute of Experimental Clinical Research, Aarhus University Hospital, Skejby Sygehus, Aarhus N, DK-8200 Denmark*

Summary This paper studies the effects of physiological motion on oxygen transport in a computer aided design model of a coronary artery segment by using Computational Fluid Dynamics (CFD). The pulsatile blood flow and wall motion are based on physiological velocity and vessel motion waveforms derived from previously published works. The results demonstrate that the oxygen transport in coronary arteries is altered by wall motion and indicate that the degree of influence depends on the individual motion patterns.

INTRODUCTION

Hypoxia or low oxygen tension in the arterial wall has long been considered to be a factor responsible for atherogenesis[1]. It induces endothelial cell apoptosis, causes breakdown of endothelial barrier and forms interendothelial gaps which may cause lipid infiltration into the arterial wall. Recent evidences suggest that hypoxia may also increase vascular permeability to macromolecules by upregulating vascular endothelial growth factor (VEGF) release by vascular cells[2]. Therefore, the transport of blood-borne oxygen is essential for the maintenance of normal arterial wall metabolism and any alterations to the normal transport patterns may be expected to promote atherogenesis. In humans an important site for atherosclerotic plaque development is the coronary vasculature. Haemodynamic studies indicate that the physiological motion of coronary arteries may be responsible for their local susceptibility to atherosclerosis[3]. Since local haemodynamics and vessel geometry have been implicated to alter oxygen transport patterns in coronary arteries[4], it is possible that their physiological motion might also contribute to atherogenesis. Therefore, this study was initiated to investigate oxygen transport in a moving Left Anterior Descending (LAD) coronary artery segment by using the commercial finite volume CFD solver, FLUENT (v6.1.18, Fluent Inc, Lebanon, NH). To study the effects of wall motion on oxygen transport, we have run our simulations with (dynamic case) and without (static case) wall motion.

METHODS

The simulations were based on the characteristic LAD geometry, with diameter=0.36cm, length (l)=4.68cm, curvature=0.25cm^{-1}, mean Re=105, and a Womersley parameter of 2.78, which corresponds to a cardiac cycle duration (t) of 0.8s. The LAD inlet velocity profile was assumed to be parabolic. A physiological pulsatile velocity profile[5] and time varying planar vessel wall motion waveforms (Figure 1) obtained from literature were imposed as velocity and wall motion boundary conditions[6,7]. Blood was considered to be an incompressible, homogeneous, Newtonian fluid with a viscosity of 0.0035Pa.s and a density of 1050kg/m^3. The reaction of blood-borne oxygen with the vessel wall was modeled as a first order reaction (reaction rate = 2x10^{-05}m/s) with an oxygen diffusivity of 1x10^{-9}m^2/s[8]. FLUENT uses a finite volume technique to solve the 3D unsteady equations of momentum and mass conservation. The 3D finite volume mesh was created using the CFD pre-processor, Gambit (v2.0.4, Fluent Inc). A body fitted, structured grid composed of hexahedral elements was generated using the Cooper-meshing scheme. In particular a boundary layer was attached to the vessel wall. The fluid and mass transfer boundary conditions controlling the model included no slip at the tube walls, a velocity inlet condition, a traction free condition at the outlet, a uniform inlet mass fraction (=0.005) and a zero gradient in concentration at the outlet. Several trial simulations were carried out to achieve mesh and time step independence of the computational solutions. A mesh containing 186,321 nodes with a time step size of 0.025s was found to be the optimum case. The momentum discretization and pressure-velocity coupling were achieved with QUICK and PISO schemes respectively. The simulations were run for multiple cardiac cycles to obtain periodic solutions. Part of the post-processing work was carried out with the help of MATLAB version 6.5 (The MathWorks Inc., Natick, MA).

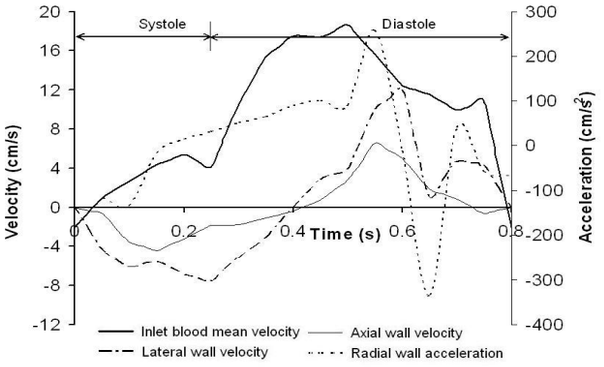


Figure 1: The LAD inlet mean velocity, 2-D wall motion and radial vessel wall acceleration

RESULTS AND DISCUSSION

Figure 2 shows the time-averaged surface deposition rate (SDR) (rate of oxygen consumption by the arterial wall) for the static and dynamic cases. It is evident from these contour plots that the wall motion has led to alterations in the SDR of oxygen. In the static model the hypoxic regions (low SDR) are mainly located along the inner wall; whereas in the dynamic model the SDR of oxygen is not only higher than that of the static case but it is almost similar along both the outer and inner walls. Upon inspection, it is evident that this is caused by secondary flows as shown in Figure 3 for an axial plane along the bend. In the static model the overall patterns of the secondary velocity vectors are typical of a curved tube flow situation in which two symmetric counter rotating vortices (Dean type) form in the cross sectional plane having a tendency to move towards the outer wall. In the dynamic model the vessel wall acceleration led to stronger Dean type vortices when compared to the static case. It seems apparent that the stronger vortices promote

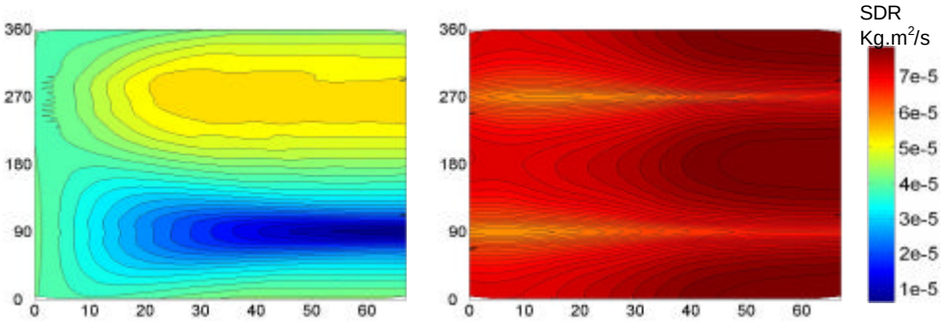


Figure 2: Time-averaged oxygen SDR in static (left) and dynamic (right) models. The vertical axis gives the circumferential location (90^0 = inner wall & 270^0 = outer wall). The horizontal axis indicates the position along the length of the tube in degrees.

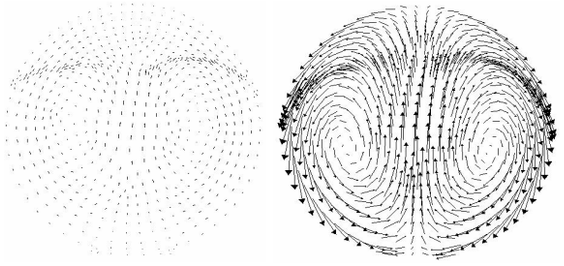


Figure 3: In-plane velocity vector plots in static (left) and dynamic (right) models at t=0.225s at l=2.34cm.

cross mixing and as a result the oxygen rich blood is carried to the arterial wall more effectively. That is why the dynamic case demonstrates little regional differences in the SDR while the static case predicts a low SDR along the inner wall. This is interesting as it is often thought that mass transport in a curved artery is affected along the inner wall due to the influence of local haemodynamics. In contrast our results suggest that the inner wall may not be as vulnerable to atherosclerotic plaque formation as one would have thought it to be. In the cases presented here the SDR was greater in the dynamic model although this will of course depend upon the motion patterns used in this study.

CONCLUSIONS

Taken together, these results suggest that the vessel wall motion may play an important role as far as oxygen transport in coronary arteries is concerned. However, it should be noted that its degree of influence would almost certainly be dependent on the individual motion patterns and reaction mechanisms. This warrants future studies on more physiologic models over a wide range of population to gain a fundamental understanding on wall / blood interactions, hypoxia and consequently on conditions such as atherosclerosis.

References

[1] Crawford D.W., Blankenhorn D.H.: Arterial Wall Oxygenation, Oxyradicals, and Atherosclerosis . *Atherosclerosis* **89**:97-108, 1991.

[2] Tarbell J.M.: Mass Transport in Arteries and the Localization of Atherosclerosis. *Annu. Rev. Biomed. Eng.* **5**:79-118, 2003.

[3] Kolandavel M.K., Fruend E.T., Pedersen E.M., et al.: Three Dimensional Numerical Simulations of Wall Shear Stress Patterns in the Coronary Arteries: A Preliminary Study of the Effects of Wall Motion. *IPEM Conference on Physical, Mathematical and Numerical Modelling of Blood Flow in Cardiovascular Diseases*, York, UK, 2003.

[4] Kaazempur-Mofrad M.R., Ethier C.R.: Mass Transport in an Anatomically Realistic Human Right Coronary Artery. *Ann. Biomed. Eng.* **29**:121-127, 2001.

[5] Marcus J.T, Smeenk H.G, Kuijer J.P.A., et al.: Flow Profiles in the Left Anterior Descending and the Right Coronary Artery Assessed by MR Velocity Quantification: Effects of Through-Plane and In-Plane Motion of the Heart. *J. Comp Asst Tomography* **23**:567-576; 1999.

[6] Mackay S.A., Potel M.J., Rubin J.M.: Graphics Method for Tracking Three-Dimensional Heart Wall Motion. *Comp. Biomed. Res.* **15**:455-473, 1982.

[7] Kozerke S., Scheidegger M.B., Pederson E.M., Boesiger P.: Heart Motion Adapted Cine Phase-Contrast Flow Measurements Through the Aortic Valve. *MRM* **42**:970-978, 1999.

[8] Stangeby D.K., Ethier C.R.: Computational Analysis of Coupled Blood-Wall Arterial LDL Transport. *J. Biomech. Eng.* **124**:1-8, 2002.

IN VIVO PIV MEASUREMENTS IN THE EMBRYONIC CHICKEN HEART

Peter Vennemann[1], Kenneth T. Kiger[2], Beerend P. Hierck[3], Nicolette T. C. Ursem[4], Timo L. M. ten Hagen[5], Jerry Westerweel[1]

[1]*Laboratory for Aero- and Hydrodynamics, Delft Technical University, The Netherlands*
[2]*Department of Mechanical Engineering, University of Maryland, United States of America*
[3]*Department of Anatomy and Embryology, Leiden University Medical Center, The Netherlands*
[4]*Department of Obstetrics and Gynaecology, Erasmus Medical Center, The Netherlands*
[5]*Department of Surgical Oncology, Erasmus Medical Center, The Netherlands*

Summary A Particle Image Velocimetry (PIV) system is developed that enables *in vivo* PIV measurements in the heart of a chicken embryo. Fluorescent lipid micro-spheres serve as tracer particles. Velocity distributions within the ventricle and the atrium can be resolved.

INTRODUCTION

Placental blood flow is expected to play a significant role in normal and abnormal human heart development [1]. For studying this relationship experimentally, an embryonic chicken model with manipulable extraembryonic blood flow can be used [1]. Figure 1 displays a chicken embryo after approximately 60 hours of incubation. On the right and left side of the image one can clearly see vitelline veins leading to and vitelline arteries coming from the embryo. They serve the same function as the placenta in a mammalian embryo. It has been shown that obstructing venous flow by closing one of the vitelline veins with a clip results in severe cardiovascular malformations [1]. Although the exact mechanism responsible for this is not known, it is speculated that the development is strongly linked to specific details of the wall shear stress patterns within the forming heart.

The whole vasculature including the heart is covered by a thin layer of cells, the vascular endothelium. From *in vitro* flow studies on these cells, it is known that flow induced shear stress modulates gene expression [3]. *In vivo* analysis of the intracardiac flow of a zebra fish reveals shear forces beeing a key factor in the embryonic cardiogenesis [2], though a direct relation between abnormal placental blood flow and cardiovascular malformations is missing [1]. By combining the fluorescent visualization of gene expression with a quantitative measurement of the instantaneous flow field *in vivo* using PIV, a relationship might be found.

METHOD

Due to the small dimensions of the embryonic chicken heart (about 200 μm inner diameter) a μPIV system is utilized. In comparison to a conventional PIV system, the measurement plane is defined by the limited depth of focus of the microscope objective, rather than by forming a light sheet. Fluorescence based imaging is used to distiguish between background light that is scattered by blood cells and tissue, and the signal coming from the tracer particles. Rhodamine tagged, polyethylene glycol coated lipid-microspheres, so called “Stealth liposomes”, are suitable as long circulating tracer particles and are used in the reported experiments. Stealth liposomes are coated to prevent wall adhesion and capillary blockage [4]. The nominal diameter is 500 nm, but in practice much larger agglomerates are observed.

Figure 2 shows a schematic overview of the experimental set-up. A double pulse Nd:YAG laser is illuminating the whole flow field through the objective of a Leica fluorescence microscope. The beam is widened by a diffuser plate and then reflected into the optical axis of the objective at a dichroic mirror. Background light, reflected by blood cells and tissue, is guided into the direction of illumination by the same dichroic mirror. Light with longer wavelengths, emitted by the rhodamine, passes the mirror and is imaged by the camera. The rest of background light is stopped at a low-pass filter. An image intensified, double frame CCD-camera with a resolution of 1376 x 1040 pixel was used to capture the PIV-images.

The PIV system is phase-locked to the cardiac cycle of the chicken embryo through the use of an ultrasound Doppler velocimeter. A PC calculates the measured velocity from the Doppler shifted signal in real time and triggers the timing unit of the PIV system with an adjustable delay. In this manner, it is possible to perform ensemble averaged PIV measurements at identical flow conditions to enhance the quality of the obtained velocity vector maps.

RESULTS AND DISCUSSION

Figure 3 shows the average of fifty phase-locked vector fields in the fully expanded ventricle (left) and atrium (right). The images were acquired using a 10x magnification objective for the ventricle and 5x for the atrium. Vectors outside the flow field that represent the contractile motion of the ventricular wall can be recognized.

Although the measurements resolve the flow fields at different points of the cardiac cycle well, further improvement, especially in the near wall region, is required for accurately calculating the wall shear stress from the flow profiles. The large diameter of particle agglomerates and the consequential low seeding density is accompanied by relatively extended interrogation areas of 64 by 64 pixel with the corresponding bias. Improvement is expected from the development of

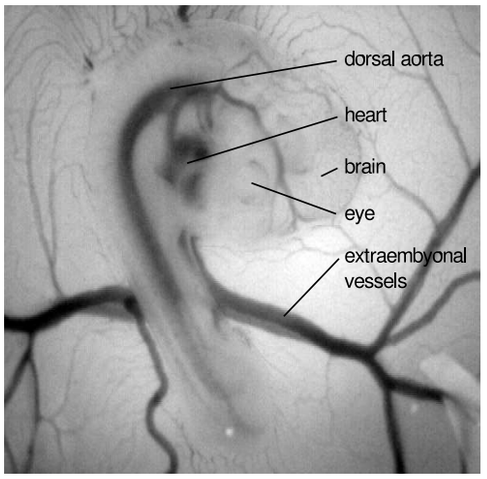


Figure 1. Chicken embryo after approximately sixty hours of incubation.

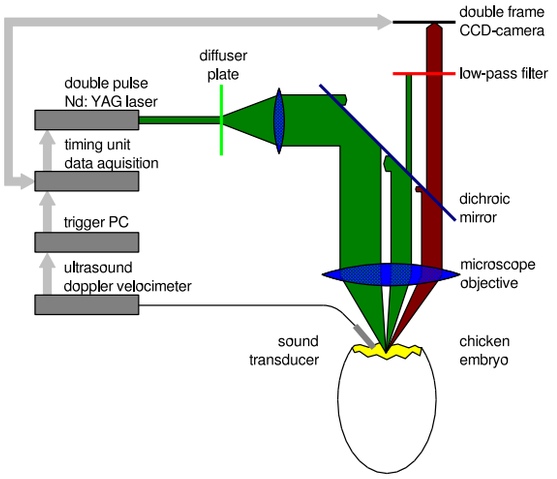


Figure 2. The μPIV set-up, using a fluorescence microscope.

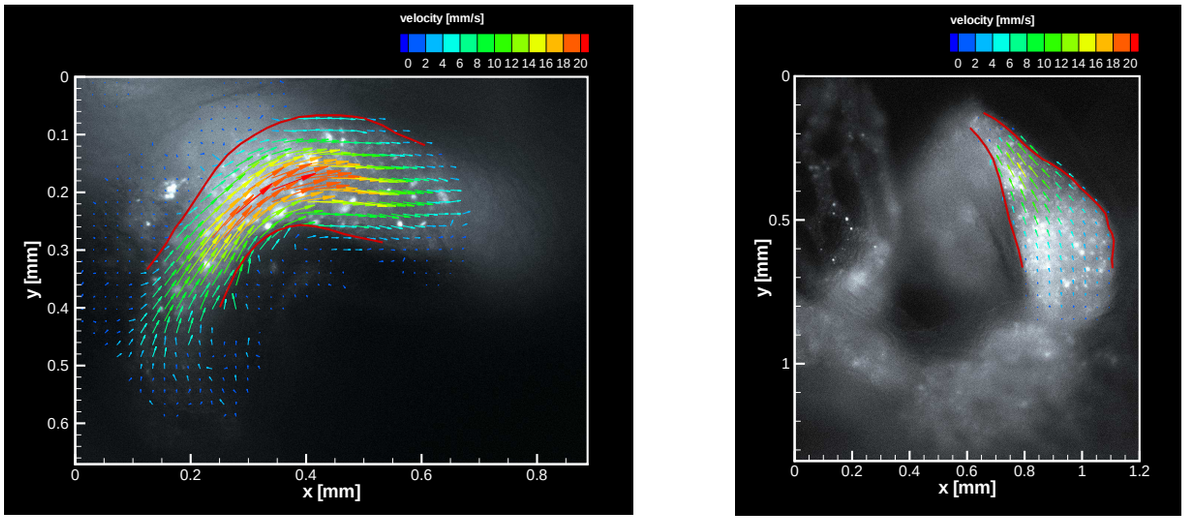


Figure 3. PIV measurement in the ventricle (left) and in the atrium (right) of a chicken embryo.

non-agglomerating particles and by excluding out of focus particles from the evaluation. The spatial resolution might be enhanced dramatically by applying a two-point ensemble correlation method [5]. In addition, a way must be found to detect the vessel wall position accurately. A value for the effective near wall fluid viscosity needs to be determined.

ACKNOWLEDGEMENTS

The authors would like to thank Patrick van Wieringen from Leica who generously provided the microscope. We would like to further mention Rob E. Poelmann[3], Sandra Stekelenburg-de Vos[4], Ralph Lindken[1] and Bianca C. W. Groenendijk[3] who all contributed to this experiments but couldn't be mentioned as co-authors because of the conference restriction to a maximum of six authors.

References

[1] Hogers, B.; DeRuiter M. C.; Gittenberger-de Groot A. C.; Poelmann R. E.: *Extraembryonic venous obstructions lead to cardiovascular malformations and can be embryolethal*, Cardiavascular Research 41, 87-99, 1999
[2] Hove, J. R.; Köster, R. W.; Forouhar, A. S.; Acevedo-Bolton, G.; Fraser, S. E.; Gharib, M.: *Intracardiac fluid forces are an essential epigenetic-factor for embryonic cardiogenesis*, Nature 421, 172-177, 2003
[3] Topper, J. N.; Gimbrone Jr, M. A.: *Blood flow and vascular gene expression: fluid shear stress as a modulator of endothelial phenotype*, Molecular Medicine Today, 1357-4310, 1999
[4] Lasic, D.: *Liposomes*, American Scientist 80, 20-31, 1992
[5] Westerweel, J.; Poelma, C.; Lindken, R.: *Two-point ensemble correlation method for μPIV applications*, Proceedings of the 11th International Symposium Applications of Laser Techniques to Fluid Mechanics, paper 12.3, Lisbon, Portugal, 2002

A MODEL OF PLANKTON DYNAMICS COUPLED WITH A LES OF THE SURFACE MIXED LAYER

Dr D. M. Lewis
Department of Applied Mathematics
University of Liverpool
Peach St
Liverpool L69 7ZL, U.K.
Tel: 0151 794 4014 (U.K.) E-mail: D.M.Lewis@liverpool.ac.uk

The dynamics of phytoplankton populations are not only determined by biological processes such as growth/mortality rates, nutrient levels and predator-prey interactions, but by the distributions of the micro-organisms, which are governed by the physical structures and motions of the ocean (Denman & Gargett 1995). These biological-physical interactions take place over a wide range of different scales, e.g. upwelling gyres over many kilometres are often nutrient rich and associated with high phytoplankton concentrations, whilst individual predator-prey encounters are governed by turbulent motion on the scale of millimetres. In this presentation the influence of physical processes on an intermediate scale (tens of metres), namely those associated with the large-eddy structures of turbulence in the surface mixed layer, on a simple ecosystem will be examined. The objective of the work will be to see what characteristics of the water motion, e.g. horizontal and vertical mixing, vortical structures, are associated with high levels of phytoplankton activity, and how these are correlated with local nutrient and predatory zooplankton concentrations.

The basis of the mixed layer model (assuming uniform density) is formed by a LES code (over a domain 120×120m horizontally and 50m deep), which integrates a spatially filtered form of the Navier-Stokes equations. The mesh size is $40\times40\times100$, implying a horizontal resolution scale of 3m and a vertical resolution scale of 0.5m. The sub-grid scales are parameterised using a standard Smagorinsky LES closure scheme. The applied boundary conditions are horizontal periodicity, whilst at the bottom zero stress and no-normal flow constraints are imposed. At the surface the no-normal flow is retained, but a specified wind stress is imposed in the positive x direction. The code has been validated by comparing the output with some published LES results of McWilliams *et al* 1997 (some examples will be shown). One unusual feature is the incorporation of a 'vortex force' term, brought about by a coupling of the Stokes-drift velocity associated with surface waves with the local vorticity. This 'vortex force' is thought to be the mechanism underlying the formation of Langmuir circulations (Craik & Leibovich 1976), a series of near surface counter rotating roll cells (called Langmuir cells), aligned roughly in the wind direction. Associated with these cells are upwelling and downwelling zones in which levels of vertical mixing are greatly increased. It has been speculated (Bees *et al* 1998) that such enhanced mixing rates, characteristic of 'Langmuir turbulence' will play a significant role in stimulating planktonic activity. The presentation will examine results derived from simulations with and without Langmuir circulations.

The biological model is formed from three coupled advection-diffusion equations for nitrate N, phytoplankton P and zooplankton Z (the sizes of the micro-organisms are assumed to be sufficiently small, <0.1 millimetres, to justify a continuum hypothesis and the treatment of their concentrations as scalar fields) of the form:

$$\frac{\partial N}{\partial t}+\boldsymbol{U}.\nabla N = D_N\nabla^2 N - \text{uptake by phytoplankton + recycled from phytoplankton growth inefficiency}$$

$$\frac{\partial P}{\partial t}+\boldsymbol{U}.\nabla P = D_P\nabla^2 P + \text{growth (based on light and } N \text{ levels) – grazing loss (based on Z concentration)}$$

$$\frac{\partial Z}{\partial t}+\boldsymbol{U}.\nabla Z = D_Z\nabla^2 Z + \text{grazing uptake (based on } P \text{ concentration) – mortality rate}$$

where $\boldsymbol{U}$ is the instantaneous (LES) turbulent velocity field. This model represents a somewhat simplified version of the ideas presented in Baird & Emsley (1999), in which full details of the various source/sink terms are appearing on the right hand side are discussed. Basically they represent parameterisations of processes that take place on the sub-grid scales. For instance the uptake term depends upon the nitrate storage capacity of the phytoplankton species of interest and the efficiency of

the mass transfer of nitrate to the cells estimated by means of a turbulent Sherwood number. This is calculated by means of the horizontally averaged level of the kinetic energy dissipation rate ε at different depths. The growth rate term depends on the local light intensity as well as levels of nitrate concentration. Similarly the grazing rate terms are also calculated from estimates of the local turbulence characteristics parameterised by ε. Grazing levels are calculated from theoretical ideas discussed in Lewis & Pedley 2001 concerning predator-prey encounter rates and capture probabilities for isotropic turbulence. The diffusion coefficients are estimated from the local eddy viscosity assuming low (<1) values for various turbulent Schmidt numbers, suitable for this relatively course grid scale resolution. The model equations above are integrated subject to various boundary conditions (horizontally periodic, zero fluxes at the surface, whilst at the bottom a prescribed inward flux of nitrate, representing nitrate replenishment from the thermocline, and prescribed outward fluxes of *P* and *Z*), over a fixed period of time. Computational constraints limit this to about 10 hours, although longer runs are planned.

Vertical profiles of mean, variance, vertical flux and correlations between the various scalar fields, averaged over time and horizontally, will be presented. Also the nature of the instantaneous evolution of the planktonic concentrations will be examined. Particular attention will be paid to the characteristics of those flow features that correlate to high levels of phytoplankton growth and patch formation. The sensitivity to phytoplankton growth to both biological and physical parameters will also be discussed. Initial conditions play a crucial role. Results will be presented where the initial distributions of both *P* and *Z* are uniform in three dimensions. Later simulations will restrict the *Z* field to lie in certain regions where grazing potential is high. It may also be possible to look at what happens when the zooplankton are allowed to actively hunt their prey by swimming, and/or interspersing their time spent foraging with rest periods.

References

Baird M. E. & Emsley S. E.: Towards a mechanistic model of plankton population dynamics. *J. Plankton Res.* **21**: 85-126, 1999.

Bees M. A., Mezic I. & McGlade J.: Planktonic interactions and chaotic advection in Langmuir circulation. *Mathematics and Computers in Simulation* **44**: 527-544, 1998.

Craik A. D. D. & Leibovitch S.: A rational model for Langmuir circulations. *J. Fluid Mech.* **73**: 401-426, 1976

Denman K. L. & Gargett A. E.: Biological-Physical Interactions in the Upper Ocean. *Ann. Rev. Fluid Mech.* **27**: 225-255, 1995.

Lewis D. M. & Pedley T. J.: The Influence of Turbulence on Plankton Predation Strategies. *J. Theor. Biol*. **210**: 347-365, 2001.

McWilliams J. C., Sullivan P. P. & Moeng, C. H.: Langmuir turbulence in the ocean. *J. Fluid Mech.* **334**: 1-30, 1997.

XXI ICTAM, 15–21 August 2004, Warsaw, Poland

SELF-PROPULSION OF AN OSCILLATORY WING

Adrian S. Carabineanu*
*University of Bucharest, Faculty of Mathematics & Computer Sciences, RO 70109 Bucharest, Romania

Summary In this paper we show that the oscillatory motion of an airfoil (wing) in an incompressible inviscid fluid can determine the apparition of a propulsive force. To this aim we discretize the lifting surface equation and calculate the pressure coefficients. Integrating, we calculate the average drag coefficient which for a range of values of the frequency may happen to be negative. The oscillatory motion of a wing can model the motion of fishes and birds. It is also of great importance in aeroelasticity.

THE INTEGRAL EQUATION

We consider a system of coordinates $Ox^{(1)}y^{(1)}z^{(1)}$ related to the wing and we introduce the dimensionless space coordinates $(x,z)=\left(\frac{x^{(1)}}{a},\frac{z^{(1)}}{a}\right)$, taking the wing length a as reference length along the vertical direction ($Oz^{(1)}$-axis direction) and along the direction of the unperturbed uniform flow ($Ox^{(1)}$-axis direction). We introduce also the dimensionless space coordinate $y=\frac{y^{(1)}}{b}$, taking the wing half-span b as reference length along the $Oy^{(1)}$-axis direction. We denote by $D^{(1)}$ the wing projection on the $Ox^{(1)}y^{(1)}$ -plane. Let

$$0=F(x^{(1)},y^{(1)},z^{(1)})=z^{(1)}-h^{(1)}(x^{(1)},y^{(1)})\exp(i\omega t)\ ;\ (x^{(1)},y^{(1)})\in D^{(1)}, \tag{1}$$

$$\left|h^{(1)}\right|<<1,\ \left|\frac{\partial h^{(1)}}{\partial x^{(1)}}\right|<<1,$$

be the equation of the oscillating wing (we neglect the thickness of the wing).
In the sequel $\rho_0 Re(f\exp(i\omega t))$ is the jump of the pressure over the oscillating wing (ρ_0 is the density of the fluid at rest), ω is the frequency of the oscillation, V_0 is the translation velocity of the unperturbed flow with respect to the $Ox^{(1)}y^{(1)}z^{(1)}$ frame of refference, $\varpi=\frac{b}{a}$ is the aspect ratio.
We introduce the dimensionless functions and variables

$$h(x,y)=\frac{h^{(1)}(x^{(1)},y^{(1)})}{a},\ \tilde{\omega}=\frac{\omega a}{V_0},\ \tilde{f}(x,y)=\frac{f(ax,by)}{V_0^2},\ x_0=x-\xi,\ \ y_0=y-\eta,$$

In the framework of the linearized theory the lifting surface equation for oscillatory airfoils is [1]:

$$\frac{\varpi}{4\pi}\int\int_D^{*}\tilde{f}(\xi,\eta)\exp(-i\tilde{\omega}x_0)\left(\int_{-\infty}^{x_0}\frac{\exp(i\tilde{\omega}u)}{(u^2+\varpi^2y_0^2)^{3/2}}du\right)d\xi d\eta=$$

$$=-\left(\frac{\partial h(x,y)}{\partial x}+i\tilde{\omega}h(x,y)\right),\ D=\{(x,y);(ax,by)\in D^{(1)}\}. \tag{2}$$

In the sequel we are going to put into evidence the singularities of the kernel. We have

$$\int_{-\infty}^{x_0}\frac{\exp(i\tilde{\omega}u)}{(u^2+\varpi^2y_0^2)^{3/2}}du=K^{(1)}(x,y;\xi,\eta)+K^{(2)}(x,y;\xi,\eta)+K^{(3)}(x,y;\xi,\eta),$$

where the kernel

$$K^{(1)}(x,y;\xi,\eta)=\frac{1}{\varpi^2y_0^2}\left(1+\frac{x_0}{\sqrt{x_0^2+\varpi^2y_0^2}}\right),$$

has a strong singularity, the kernel

$$K^{(2)}(x,y;\xi,\eta)=-\frac{i\widetilde{\omega}}{\sqrt{x_0^2+\varpi^2y_0^2}}+\frac{\widetilde{\omega}^2}{2}\ln\left(-x_0+\sqrt{x_0^2+\varpi^2y_0^2}\right),$$

has weak singularities and the kernel

$$K^{(3)}(x,y;\xi,\eta)=\frac{\widetilde{\omega}}{\varpi\,|y_0|}\left(K_1\left(\widetilde{\omega}\varpi\,|y_0|\right)-\frac{1}{\varpi^2y_0^2}-\frac{\widetilde{\omega}^2}{2}\ln\frac{\widetilde{\omega}\varpi\,|y_0|}{2}\right)+$$
$$+i\frac{\pi}{2}\frac{\widetilde{\omega}}{\varpi\,|y_0|}\left(I_1\left(\widetilde{\omega}\varpi\,|y_0|\right)-L_{-1}\left(\widetilde{\omega}\varpi\,|y_0|\right)+\frac{2}{\pi}\right)+\frac{\widetilde{\omega}^2x_0}{2\sqrt{x_0^2+\varpi^2y_0^2}}+\frac{\widetilde{\omega}^2}{2}\ln\frac{\varpi}{2}+$$
$$+\int_0^{x_0}\frac{\exp(i\widetilde{\omega}u)-1-i\widetilde{\omega}u+\frac{1}{2}\widetilde{\omega}^2u^2}{(u^2+\varpi^2y_0^2)^{3/2}}du,$$

has no singularity. (I_1 and K_1 are Bessel functions and L_{-1} is a Strouve function.)

THE PROPULSIVE FORCE FOR A DELTA WING

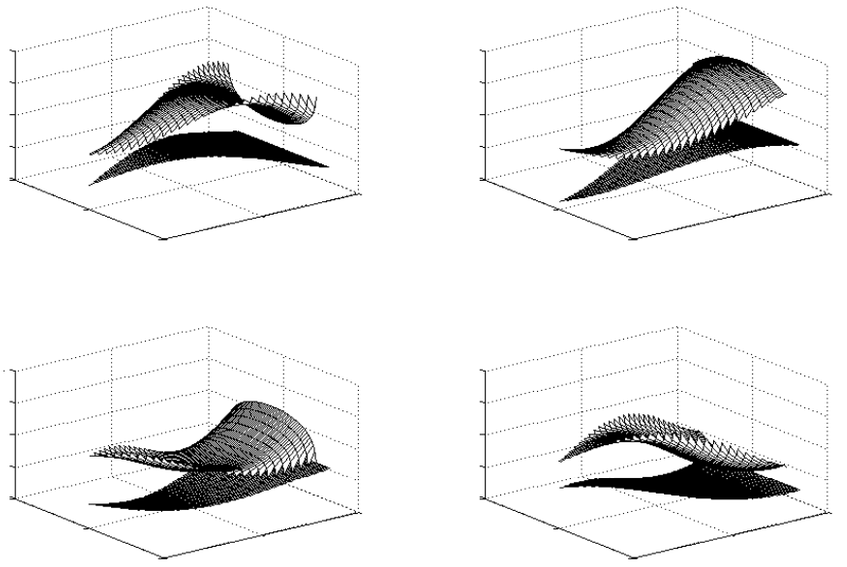
Employing for each type of kernel adequate quadrature formulas, we discretize (2) obtaining the values of $\tilde{f}$ in the nodes of the grid. With the the formulas

$$C_p(x^{(1)},y^{(1)},t)=Re[\tilde{f}(x,y)\exp(i\omega t)],\ C_D(t)=-2\int\int_D n_xC_p(ax,by,t)dxdy,\widetilde{C}_D=\frac{1}{T}\int_0^T C_D(t)\,dt$$

where T is the period of the oscillation, we calculate the pressure coefficient field, the drag coefficient and the average drag coefficient. Considering the oscillating delta wing whose equation is

$$h(x,y)=\alpha\exp(i\widetilde{\omega}_1x),\qquad (x,y)\in D=\{(x,y);0<y<|x|,0<x<1\},$$

we calculate the average drag coefficient and we notice that if $\tilde{\omega}$ surpasses a certain critical value, the average drag coefficient becomes negative i.e. there appears a *propulsive force*. In the following figure we present the oscillating wing (below) and the pressure coefficient fields (above) for the values of the nondimensional time $\frac{V_0}{a}t\in\{1,1,2,4\}$ and for the nondimensional frequencies $\tilde{\omega}=\pi/2,\ \widetilde{\omega}_1=6\pi/5$. We considered $\varpi=1/8$.



References

[1] D. Homentcovschi, Theory of the lifting surface in unsteady motion in an inviscid fluid, *Acta Mechanica* **27**, 205-216, 1977.

BIOIRRIGATION IN MARINE SEDIMENTS: ECOLOGICAL CONCLUSIONS FROM NUMERICAL MODELLING

Oleksiy S. Galaktionov, Filip J. R. Meysman, Jack J. Middelburg
Netherlands Institute of Ecology, NIOO-KNAW, Centre for Estuarine and Marine Ecology, Korringaweg 7, 4401 NT Yerseke, The Netherlands

Summary The porewater flow in marine sediments due to pumping activity of the lugworm *Arenicola marina* is simulated in order to investigate its oxygen requirements. 3D flowline patterns were obtained using a finite element approach. The hydromechanical insulation of the burrow walls turns essential for ensuring the oxygen supply. This possibly explains the allocation of resources by the lugworm to the mucus-lining of its burrows and a semi-permanent nature of the lugworm burrows.

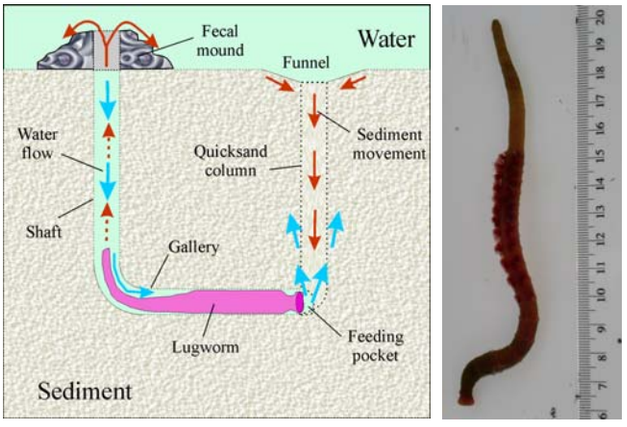


Fig. 1 Schematic drawing of the *Arenicola marina* burrow (left) and the actual photo of the captured adult lugworm (right).

INTRODUCTION: BIOIRRIGATION

The exchange of dissolved substances between the water column and permeable marine sediments plays an important role in the biogeochemistry of the oceans. Molecular diffusion and bio-irrigation (transport of porewater induced by the activity of organisms that inhabit the sediment) comprises the dominant mechanisms of such an exchange. Molecular diffusion restricts oxygen transport merely to the upper millimetres of the sediment. Conversely, the pumping activity of burrowing animals brings oxygen-rich water to far deeper sediment layers, which would otherwise remain anoxic. This allows other bottom-dwelling organisms to proliferate.

NUMERICAL SIMULATIONS OF BIOIRRIGATION BY *ARENICOLA MARINA*

The lugworm *Arenicola marina* was selected as a model organism since it is highly abundant on intertidal sand flats of Europe [1] and displays vigorous bio-irrigation activity. The worm dwells in L-shaped burrows that reach a depth of 20-30 cm. It ingests sediment from the feeding pocket at the closed end of the burrow, causing the downward motion in the upper sediments layers (see Fig.1). This downward transport of sediment leads to the formation of a so-called “quick-sand column”, i.e. a cylinder of loosened sediment that is visible on the sediment surface as a funnel. The lugworm ventilates its burrow by pumping oxygenated water via peristaltic motions. It is able to absorb 32 to 40 % of dissolved oxygen; the rest is released into the surrounding sediment layers. The irrigational flow of water is opposite to the direction of the sediment transport (Fig. 1). Water is pumped via the shaft to the feeding pocket, resulting in an upward, advective transport of pore water to the sediment surface. The common assumption is that the water predominantly rises through the quicksand column. We performed numerical simulations of porewater flow to evaluate the role of the burrow insulation and the significance of the quicksand column.

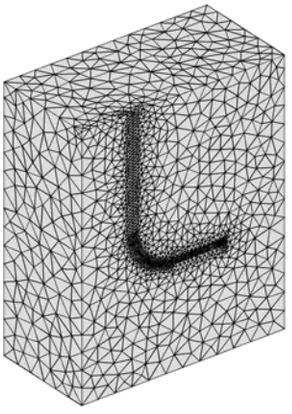


Fig. 2 Finite element mesh used to model the sediment around the lugworm burrow.

A single worm tube is placed in the middle plain of the brick-shaped domain, whose dimensions correspond to a typical density of 25 lugworms per m^2 [1]. Assuming symmetry, only half of that domain needs to be explicitly described (Fig.2 shows the finite element mesh covering the sediment domain). The walls of horizontal gallery are completely impenetrable (lined with thick mucus layer in actual burrows), while for the descending part of the worm tube two cases are considered: permeable for advective flux and completely insulated walls. The worm itself is modelled as a standard mechanical pump, with known flux vs. pressure performance [2]. The flow in the sediment is described by Darcy’s law: $\mathbf{v}_d = -(k/\eta)\nabla p$, which combined with the continuity equation $\nabla \cdot \mathbf{v}_d = 0$ (porosity is assumed to be constant) leads to

$$\nabla \cdot \left(\frac{k}{\eta} \nabla p \right) = 0 .$$

Here $\mathbf{v}_d$ denotes the volume-averaged porewater velocity, p the pressure, k the sediment permeability and η the

water viscosity. The latter equation is solved numerically using the finite element technique implemented in the Chemical Engineering Module of FEMLAB [3].

To evaluate the importance of the quicksand channel (typical diameter is approx. 5mm) additional simulations were performed. The flow inside an axisymmetric (which allows to use finer grids) cylindrical domain with insulated bottom and side walls and open top is generated by a small source located at the axis of symmetry. The quicksand column, where the permeability linearly increases, reaching 10 times higher value in the center, is running from the source to the top of the cylinder. Fig.3 shows the results of passive tracer advection simulation with and without permeability variation in the quicksand. The tracer concentration profiles differ only slightly: although quicksand channel leads to formation of a "finger" along it, the spreading of tracer in other directions is barely affected. This justifies the use of the assumption of uniform sediment properties for computations in the domain depicted in Fig.2.

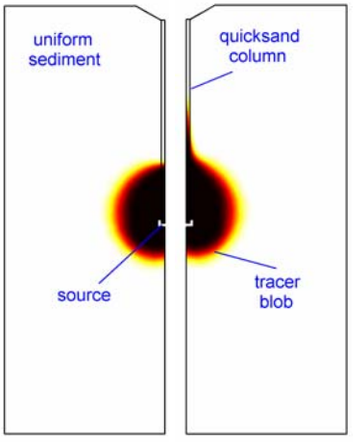


Fig. 3 Passive tracer profile in the uniform sediment and in the presence of quicksand.

In the case of the completely insulated burrow walls the water injected into the sediment rises to the surface over a whole domain mildly affected by the presence of insulated worm tube. However, when the shaft walls are permeable, a significant amount of water pumped by the worm (close to 40 % in the burrow configuration depicted in Fig.2) re-enters the burrow through these permeable walls. The porewater, re-entering the burrow will be already anoxic, all the remaining oxygen already consumed by the benthic bacterial community. Since the sole reason for the pumping activity of the lugworm is to insure the oxygen supply for own respiration, such flow shortcuts should have a strong adverse effect.

The losses of the average lugworm's peristaltic pump performance due to flow short-circuits are illustrated in Fig.4. The lower curve corresponds to the amount of oxygen (oxygenated water from the overlying water column) actually delivered in the case of completely permeable shaft walls as compared to the total pumped flux. The sediment permeability limits the maximum achievable pumping rate and determines the "working point" of the lugworm's pump at the performance diagram (Fig.4). To ensure the animal survival the minimum oxygen demands should be met. Thus, insulating the burrow walls helps to extend the habitat range of the lugworms towards less permeable muddy sediments. Wall insulation may be created not only actively by lining with mucus layer but also indirectly due to accumulation of iron oxides around the burrow as a result of oxygen diffusion through the walls. The burrow shafts are typically surrounded by brownish halo of iron oxides additionally reducing the permeability of the walls. We may speculate that the additional benefit of these slowly developing type of insulation constitute another reason (in additional to avoiding predators) of semi-permanent nature of the tubes and long-time usage of the same shafts.

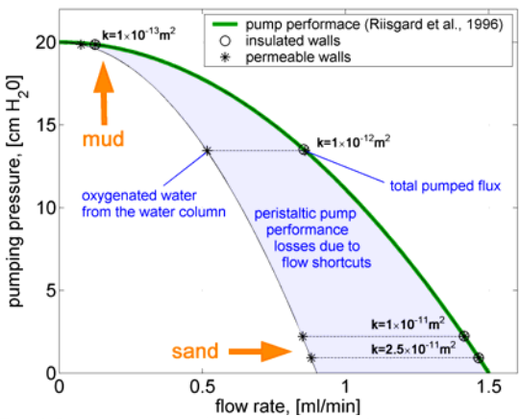


Fig. 4 Lugworm pump efficiency (in delivering oxygen) with and without burrow wall insulation in different sediments.

CONCLUDING REMARKS

Numerical simulations enable a better understanding of bio-irrigation processes caused by the pumping activity of bottom-dwelling marine animals. In particular a significance of the insulation of burrow walls by different mechanisms is evaluated. Limited influence of quicksand column implies that the oxygenated water is reaching below the burrow depth. Another interesting application of such 3D simulations is the development of simplified 1D models (not covered in this summary) to account for the sea bottom in the large-scale models of reactive transport in the ocean.

References

[1] Beukema, J. J. & de Vlas, J.: Population parameters of the lugworm, Arenicola marina, living on tidal flats in the Dutch Wadden Sea. *Neth. J. Sea Res.* **13**:331-353, 1979.

[2] Riisgard, H. U., Bernsten, I. & Tarp, B.: The lugworm (Arenicola marina) pump: characteristics, modelling and energy cost. *Mar. Ecol. Prog. Ser.* **138**:149-156, 1996.

[3] COMSOL AB: FEMLAB Chemical Engineering Module. COMSOL AB, Tegnérgatan 23, SE-111 40 Stockholm, Sweden, 2002.

DIRECT NUMERICAL SIMULATION OF RED BLOOD CELL FLOW AND AGGREGATION

Cyrus K. Aidun and E-Jiang Ding
George W. Woodruff School of Mechanical Engineering; Georgia Institute of Technology,
Atlanta GA. 30332-0620 U.S.A. -- cyrus.aidun@me.gatech.edu

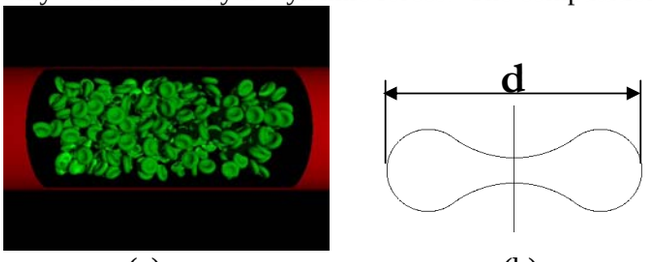
Summary The rheology of blood and its transport have physiological significance in blood circulation. The aggregation of red blood cells (RBC) plays a significant role in the rheology and flow characteristics of blood. Furthermore, RBC aggregation has clinical significance as it is used diagnostically to evaluate blood plasma concentration of certain macromolecules such as immunoglobulin and fibrogen (Reich, 1978 and Fung, 1997).

The aggregation of RBC is being studied using direct numerical simulation based on the lattice-Boltzmann (LB) computational approach (Aidun et al., 1998, Ding and Aidun 2003). The goal of our study is two fold. We aim to develop tools based on direct numerical simulation for analysis of blood flow including the RBC and other cells/particulate with all of the significant factors influencing the cell interaction and aggregation. We are also working on developing 'universal' scales and relations that can be used as predictive tools. Because of the high concentration of the RBC and the deformability of the membrane, a number of modifications are made to the LB method. Most significant is the capability to impose cell-cell and cell-wall interaction forces at the link-to-link level. The deformation of the cell membrane and the effects of surface charge and other surface properties can be added to the current method.

In the present simulations, the deformation of the membrane is neglected and the cell is treated as a solid object. Based on this approach, the dependency of the aggregate size on the shear rate and the RBC volume ratio is determined.

Aggregation of RBC has been considered by many investigators [5-13]. The aggregates may remain cylindrical or they may branch, forming network-like structures. For example, experiments on human erythrocytes show that not only rouleaux but also 3D aggregates develop. On the other hand, experiments on rat blood sample show that erythrocytes only form rouleaux in their own plasma without the development of 3D aggregates (Shiga et al, 1983). Other studies show significant differences in erythrocyte aggregate tendency between various animals and human (for example see Baskurt et al., 1997). The determinant factors for erythrocyte aggregation are complex and not well established. These include cell volume concentration, hydrodynamic effects, plasma proteins, surface charge and other surface phenomena.

When the size of the vessel is much larger than the size of the RBC, the membrane deformation may not be important. In these preliminary simulations, we neglect membrane deformation and only consider the hydrodynamic forces. The computational domain, as shown in Fig. 1, is a 3-D

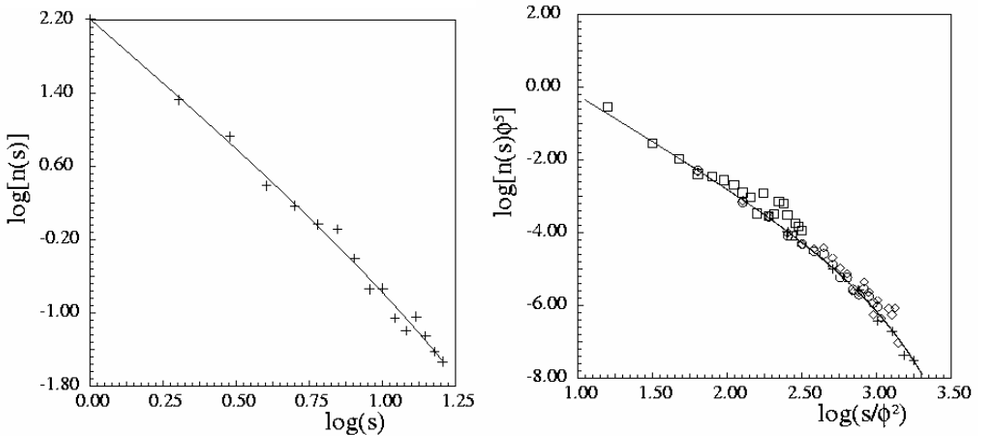


(a) (b)

Fig.1. (a) Computational domain is a cylinder of radius D and length L. (b) The actual size and geometry of the RBC is used in the simulations.

cylinder with the total number of RBCs, N=265. Results of aggregate size distribution are show in Figure 2a. The distribution can be fitted by the power scaling relation given by

$n(s) \propto \phi^{-\tau} \exp(-s/\Omega)$ with exponent τ=2.5 and Ω=9.23.



(a) (b)

Fig.2. (a) Simulation results for ϕ=0.126, Re<<1 can be fitted by a scaling relation, as shown by the solid curve. (b) Simulation results for different volume concentration and slightly different Reynolds numbers (□: ϕ=0.252 & Re<<1, +: ϕ=0.126 & Re<<1, O: ϕ=0.126 & Re=1.84 and ◇: ϕ=0.063 & Re<<1) and the finite-size-scaling relation (solid curve). See the text for details.

Results from direct simulations for different particle volume concentrations and slightly different Reynolds number are used to develop appropriate scaling relations for the aggregate size distribution. Cases with concentration ranging from ϕ=0.252 to .063 and Re=1.84 and Re<<1 show that the exponential τ in the scaling relation does not change while the values of Ω changes in proportion to ϕ^2. Then assuming

$n(s) = \phi^{-\beta} f(s/\phi^{\alpha})$, we obtain $n(s)\phi^5 = f(s/\phi^2)$, and $f(x) = x^{-5/2}\exp(\mathrm{a} - \mathrm{b}x)$

where a=5.20 and b=0.0022. The simulation results and the finite-size-scaling relation are shown in Figure 2b.

The duration for size distribution to approach to the final scaling relation in the lattice-Boltzmann simulation is very short; only about 0.1 seconds. In fact, in the first 4000 time steps the size distribution is already quite close to the equilibrium distribution. The results suggest that the hydrodynamic effects are more responsible for the first stage of the aggregation formation where other interactions we have not included in the simulation, such as the bridging by plasma proteins, and the influence of glycocalyx on RBC motion, might be more important in a longer time scale.

The main result in this simulation is the universal scaling relation for the aggregate size distribution. This scaling relation can be completed by adding the other important factors such as membrane deformation, protein links, and surface charge and other phenomena that have not been considered in this study.

THREE-DIMENSIONAL AIRWAY REOPENING — FINITE-REYNOLDS-NUMBER EFFECTS

Andrew L. Hazel, Matthias Heil
Department of Mathematics, University of Manchester, Oxford Road, Manchester, M13 9PL, United Kingdom

Summary Motivated by the physiological problem of airway reopening, we study the steady propagation of an air finger into a fluid-filled, buckled elastic tube. The resulting three-dimensional, fluid-structure-interaction problem is solved numerically by a fully-coupled, finite-element method. A characteristic two-branch behaviour in the propagation velocity-pressure curve is similar to earlier two-dimensional models [1, 3], and we find that fluid inertia has a significant effect, even at low values of the Reynolds number.

INTRODUCTION

The pulmonary airways are elastic vessels lined with a thin liquid film. Such vessels are susceptible to a fluid-elastic instability that can lead to their collapse and occlusion when the liquid in the film redistributes to form a liquid bridge [4]. The reopening of collapsed airways is believed to occur via the propagation of an air finger into the lungs [1]. The aim of any treatment is to ensure that the propagating air finger clears the liquid blockage and reopens the airways as quickly as possible, but without damaging the lungs. Consequently, the major aim of the theoretical and experimental studies is to determine the propagation speed of the air finger, U, as a function of the applied bubble pressure, p_b^*.

THE MODEL

We model airway reopening by the steady propagation of an inviscid air finger into a buckled, elastic tube containing an incompressible, Newtonian liquid of viscosity μ, density ρ and a constant surface tension, σ^*, at the air-liquid interface. The internal pressure of the air finger is p_b^* and its propagation speed is U. The tube has an undeformed radius R, wall thickness h, Young's modulus E, Poisson's ratio, ν and the cross-sectional area of the tube far ahead of the air finger is A_∞^*. There are four dimensionless parameters governing the system:

$$Ca = \frac{\mu U}{\sigma^*}, \quad Re = \frac{\rho U R}{\mu}, \quad \sigma = \frac{\sigma^*}{RK} \text{ and } A_\infty = \frac{A_\infty^*}{4R^2}, \tag{1}$$

where $K = E(h/R)^3/12(1-\nu^2)$ is the bending modulus of the tube. Ca, the capillary number, is the ratio of viscous to surface-tension forces; Re, the Reynolds number, is the ratio of inertial to viscous forces; σ is the dimensionless surface tension, which represents the ratio of surface-tension forces to the tube's bending stiffness; and A_∞ is the dimensionless cross-sectional area and is a measure of the initial degree of collapse of the tube.

In a moving frame of reference, where the finger tip is fixed at the origin, the fluid motion is governed by the dimensionless, steady Navier–Stokes equations:

$$Re\, \boldsymbol{u}\cdot\boldsymbol{\nabla}\boldsymbol{u} = -\boldsymbol{\nabla}p + \nabla^2\boldsymbol{u} \quad \text{and} \quad \boldsymbol{\nabla}\cdot\boldsymbol{u} = 0, \tag{2}$$

where $\boldsymbol{u}$, the fluid velocity, is non-dimensionalised on U; R is the reference length-scale; and the fluid pressure, p, is non-dimensionalised on the viscous scale.

The behaviour of the elastic tube is described by geometrically non-linear Kirchhoff–Love shell theory, in which the deformation of the tube is described only by the deformation of its midplane. The theory include effects due to both stetching and bending of the tube wall, but assumes that the strains remain small. The governing equation follows from the principle of virtual displacements:

$$\iint E^{\alpha\beta\gamma\delta}\left(\gamma_{\alpha\beta}\delta\gamma_{\gamma\delta} + \frac{1}{12}\left(\frac{h}{R}\right)^2\kappa_{\alpha\beta}\delta\kappa_{\gamma\delta}\right)\,\mathrm{d}S_0 = \frac{1}{12}\left(\frac{h}{R}\right)^3\frac{1}{1-\nu^2}\iint\left(\frac{R}{h}\right)\boldsymbol{f}\cdot\delta\boldsymbol{R}\,\mathrm{d}S, \tag{3}$$

where the Einstein summation convention is used, and $\delta\boldsymbol{R}$ denotes the variations of the position vector to the deformed midplane, $\boldsymbol{R}$; $E^{\alpha\beta\gamma\delta}$ is the plane stress stiffness tensor, non-dimensionalised by Young's modulus; $\gamma_{\alpha\beta}$ and $\kappa_{\alpha\beta}$ are tensors that quantify the stretching and bending, respectively, of the midplane, and $\delta\gamma_{\gamma\delta}$ and $\delta\kappa_{\gamma\delta}$ are their variations; S_0 is the surface of the undeformed midplane; finally, $\boldsymbol{f} = \boldsymbol{f}^*/K$ is the traction per unit area of the deformed midplane, S.

The interaction between the fluid and the elastic shell is imposed via two equations. Firstly, the no-slip boundary condition implies that the fluid velocity on the tube wall must be the same as the local wall velocity. Secondly, the fluid exerts a traction on the shell, and the load terms in the solid equations (3) are given by

$$f_i = P^{(\mathrm{ext})}N_i - \sigma Ca\left(pN_i - \left(\frac{\partial u_i}{\partial x_j} + \frac{\partial u_j}{\partial x_i}\right)N_j\right), \tag{4}$$

where $\boldsymbol{N}$ is the (inward) normal to the deformed shell midplane and $P^{(\mathrm{ext})}$ is the external pressure, non-dimensionalised with respect to the bending stiffness, K.

NUMERICAL RESULTS

The coupled system described above was discretised by finite elements and a direct, monolithic solver, based on Newton's method, was used to solve the resulting sets of non-linear algebraic equations.

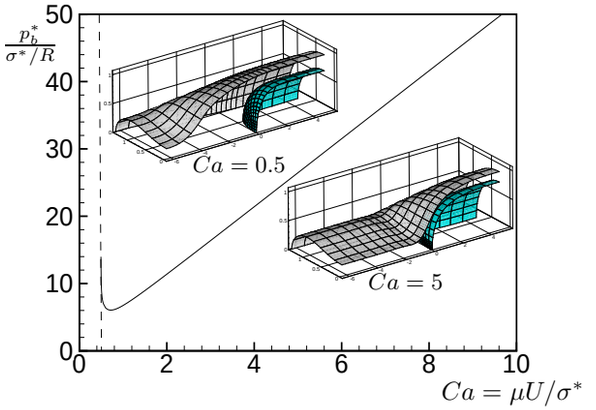


Figure 1. Bubble pressure vs. capillary number in the absence of fluid inertia (zero Reynolds number) for generic system parameters ($\nu = 0.49$, $h/R = 1/20$, $\sigma = 1$, $A_\infty = 0.373$). The dashed line is an asymptotic approximation for the behaviour on the 'pushing' branch. Inset figures illustrate tube and interface shapes on the two branches (adapted from Hazel & Heil 2002).

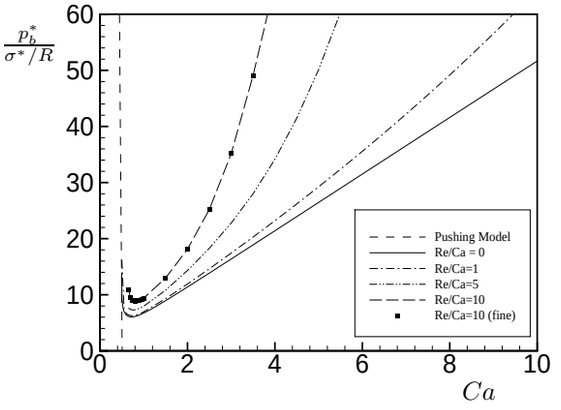


Figure 2. Bubble pressure vs. capillary number for the same parameters as Figure 1, but $Re/Ca = 0$, 1, 5, 10. The markers show the results for $Re/Ca = 10$ on a refined mesh (83,000 dofs), which differ by less than 0.5% from the results at the standard resolution (43,000 dofs).

The behaviour of the system in the absence of fluid inertia, $Re = 0$, was investigated by Hazel & Heil [2], and a typical p_b^*–U curve for the 3D model is shown in figure 1 and is similar to the behaviour observed in previous two-dimensional models [1, 3]. At high speeds, the physically expected behaviour is observed and an increase in bubble pressure causes an increase in propagation speed. In this regime, termed the 'peeling' branch, the tip of the bubble is close to the tube walls and appears to 'peel' them apart, see inset in figure 1. At low speeds, the behaviour changes and a decrease in bubble pressure is required to increase the propagation speed of the air finger. In this regime, termed the 'pushing' branch, a large volume of fluid is 'pushed' ahead of the bubble tip, now located far from the tube walls, see second inset in figure 1.

In any experimental setup, consisting of a given working fluid and a given elastic tube, σ will be constant, as will the ratio $Re/Ca = \rho R\sigma^*/\mu^2$, which depends only upon material parameters and not on the bubble speed, U. We shall therefore assess the effects of fluid inertia on the system by examining curves of bubble pressure versus propagation speed for fixed values of the ratio Re/Ca, rather than for fixed values of Re. Figure 2 shows such curves for $Re/Ca = 0$, 1, 5 and 10, and as in Heil's [3] two-dimensional model, even relatively weak fluid inertia has a very strong effect on the system's behaviour. In particular, compared to the case of zero Reynolds number, much larger bubble pressures are required to drive the air finger at a given capillary number. Inertial effects become more pronounced as Ca increases, owing to the corresponding increase in $Re = \text{const} \times Ca$. Conversely, at small values of Ca, and hence Re, inertial effects become negligible and Hazel & Heil's [2] 'pushing' model provides a good approximation for the system's behaviour for all values of Re/Ca.

References

[1] Gaver, D. P. III, Halpern, D., Jensen, O. E., Grotberg, J. B.: The steady motion of a semi-infinite bubble through a flexible walled channel. *J. Fluid Mech* **319**:25–56, 1996.

[2] Hazel, A. L., Heil, M.: Three-dimensional airway reopening: The steady propagation of a semi-infinite bubble into a buckled elastic tube. *J. Fluid Mech* **478**:47–70, 2003.

[3] Heil, M.: Finite Reynolds number effects in the propagation of an air finger into a liquid-filled flexible-walled tube. *J. Fluid Mech* **424**:21–44, 2000.

[4] Pride, N. B., Macklem, P. T.: Lung mechanics in disease, in *Handbook of Physiology. Section 3: The Respiratory System* **Vol III, Part 2**:659–692, American Physiological Society, 1986.

XXI ICTAM, 15–21 August 2004, Warsaw, Poland

CELL PERMEABILISATION AND TRANSPORT FOCUSED AROUND OSCILLATING MICROBUBBLES

Philippe Marmottant*, Sascha Hilgenfeldt*, Michel Versluis*, Han Gardeniers**, Albert van den Berg** and Detlef Lohse*

*Department of Applied Physics, University of Twente, PoBox 217, 7500AE Enschede, The Netherlands
**MESA+ Research Institute, University of Twente, PoBox 217, 7500AE Enschede, The Netherlands,

Summary The ultrasound-driven oscillation of a microbubble drives a steady streaming focused around the bubble. The study of individual bubbles attached to a wall shows vivid recirculations. When cells are in the vicinity of these bubbles, also used in medecine as contrast agent for ultrasound echography, they experience considerable shear rates. We introduce in the flow giant unilamelar lipid vesicles, acting as artificial cells. Rupture of the lipidic membrane with the opening of pores is revealed by high-speed camera recordings. A reversible permeation of the membrane wall can also be obtained, demonstrating at the micron scale the efficiency of microbubbles to deliver drugs in cells. The streaming flow of bubble on a surface can be further controlled, with the adjunction of a solid obstacle nearby: the flow turns to be directed. We will present a microfluidic device using the principle of bubble/obstacle doublets to locally transport small objets such as cells.

INTRODUCTION

Under an acoustic pressure a bubble can undergo large amplitude oscillations of its volume. This property is exploited in ultrasound echography to enhance the constrast: small micron size bubbles are injected in the blood flow and scatter back the sound. The small scale oscillation of the liquid around the bubble exerts forces on its surrounding. We will be interested in two effects of the microbubble oscillations on neighbouring small, cell-like, objects: shear stress forces and directed transport.

We will describe in a first part the intense acoustic streaming circulations around a single microbubble siting on a wall, and the effect on soft vesicles, mimicking cells. The observations help to understand a recent therapeutic application: the increased permeability of cell walls for drug delivery, in the presence of microbubble [1].

The focusing power of bubbles can be incorporated in small microfluidic applications. We will show in a second part how the streaming can be oriented, which gives the principles for a micron scale analysis device designed to transport cells without the specific use of channels.

DEFORMATION AND PERMEABILISATION OF BIOMIMETIC VESICLES

To study the interaction of a bubble with a single cell, we designed a set-up allowing direct microscopic observation. We consider air bubbles (10 to 100 microns radius) fixed by capillarity to a wall, and excited by an ultrasound standing wave (20 to 200 kHz).

We observe fast liquid recirculations around the bubble, even for low amplitudes of vibration. The origin of the motion is a steady acoustic streaming, a non-linear effect driven by the oscillation of the bubble [2]. The steady flow pattern near a wall can be derived analytically [3]. The streaming presents strong velocity gradient, which exerts shear stress on objects

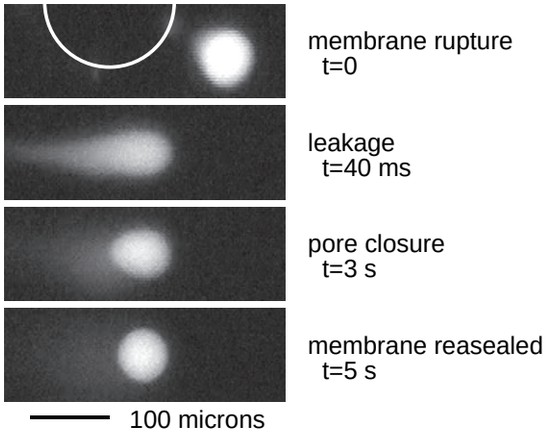


Figure 1. Deformation and rupture of a unilamellar lipid vesicle, near an oscillating microbubble (white circle) for a short instant of time. Leakage of the fluorescent inside liquid, and resealing of the membrane.

embedded in the neighbouring liquid. To study the effect of shear stress on cell membranes, we introduced biomimetic lipid vesicles in the flow: the vesicles are vividly deformed, which can lead to membrane rupture and the opening of pores

(see figure 1). Reversible poration is observed when the stress is applied for a small time, a process that can be used in the context of drug delivery.
Direct imaging of the bubble oscillation is achieved with the ultra-high frequency camera Brandaris 128 [4], that can record sequences of 128 images at frequencies up to 25 million frames per second.

DIRECTED STREAMING: MICROFLUIDIC TRANSPORT OF SMALL OBJECTS

The presence of a solid particle nearby the bubble breaks the axisymmetry of the streaming flow (a particle like the bump of figure 2a). The particle, placed in the oscillating flow of the bubble, exerts an acoustic streaming as well, directed away from the bubble [5]. The far-field velocity of the solid particle is the one generated by a point force (Stokeslet) parallel to the wall. The flow field of the ensemble of bubbles/particle doublets is easily computed in the low Reynolds number approximation (figure 2b), showing streamline going from bubble to bubble.

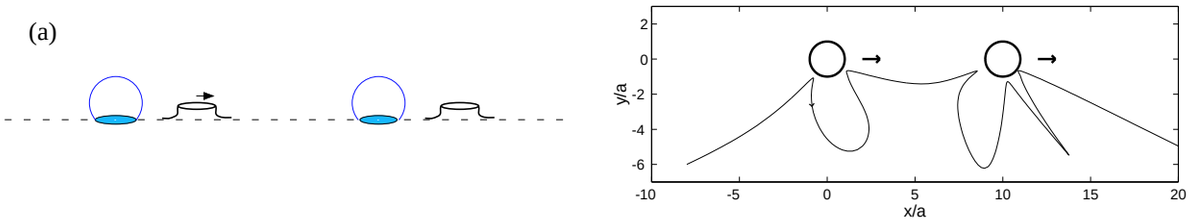


Figure 2. (a) Schematic structural elements for a microfluidic device: solid bumps are placed near the bubbles to direct the flow. (b) Predicted streaming.

Through a collaboration with the MESA+ Institute, we could prepare substrates, aligning pairs of holes and bumps on a PDMS substrate. From the gas pockets enclosed in the holes, bubbles are grown by warming up slightly the liquid, thus reducing the solubility of dissolved air. Upon ultrasound emission the acoustic streaming does not show a symmetric pattern around the bubbles any more. Tracer particles introduced in the fluid show the transport to be directed by the bubble/particle doublet (see figure 3), as predicted.

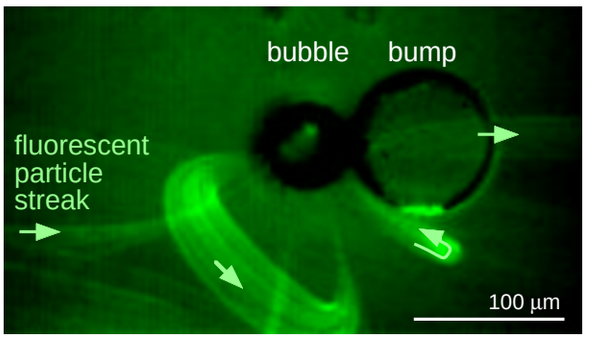


Figure 3. Transport of fluorescent tracer particle (2 micron bead) by a bubble/bump element.

CONCLUSIONS

The oscillation of a microbubble generates fast local streaming motions, concentrated on micron scale. The shear stress induced deforms and ruptures lipid vesicles, whose membrane is identical to the one of a cell. The permeabilisation is reversible when the shear is vanishing after the rupture.
An other application of bubble is found in the microfluidic field. A directed motion of the fluid can be impressed when an obstacle is nearby. The acoustic streaming of the obstacle allows to realise a focused small scale transport.

References

[1] Miller, D. L., Quddus, J.: Sonoporation of monolayer cells by diagnostic ultrasound activation of contrast-agent gas bodies. *Ultrasound Med. Biol.* **26**:661–667, 2000.
[2] Longuet-Higgins, M. S.: Viscous streaming from an oscillating spherical bubble. *Proc. R. Soc. Lond. A* **454**:725-Ð742, 1998.
[3] Marmottant, P., Hilgenfeldt, S.: Controlled vesicle deformation and lysis by single oscillating bubbles. *Nature* **423**:153–156, 2003.
[4] Chin, C.T., Lancée, C., Borsboom, J., Mastik, F., Frijlink, M., de Jong, N., Versluis, M., Lohse, D.: Brandaris 128: A digital 25 million frames per second camera with 128 highly sensitive frames. *Rev. Sci. Instrum.* **74**:5026–5034, 2003.
[5] Amin, N., Riley, N.: Streaming from a sphere due to a pulsating source. *J. Fluid Mech.* **210**:459–473, 1990.

XXI ICTAM, 15–21 August 2004, Warsaw, Poland

COMPUTATIONAL MODEL OF SELECTED TRANSPORT PROCESSES IN AN INFANT INCUBATOR

Maciej K. Ginalski*, Andrzej J. Nowak *
*Institute of Thermal Technology, Silesian University of Technology, Konarskiego 22, 44-100 Gliwice, Poland

Summary The major objective of this study was, using the modern numerical techniques, to investigate transport processes of heat and mass transfer within an infant incubator, were the premature newborn baby is nursed. This investigation consists of calculations of the air flow inside the incubator, including coupled heat transfer due to heat conduction, convection, thermal radiation and evaporation. Obtained results of calculations were numerically verified as well as compared with results published in the subject literature.

INTRODUCTION

Infant incubators are widely used in hospitals to save newborns lives and to provide them with appropriate environmental conditions which are essential for their proper grow in the very early stage of life. In the presented paper results of the applications of the numerical techniques used to describe thermal and flow environmental conditions occurring in the modern neonatal units are discussed. Understanding of these phenomena is absolutely essential for the correct design of comfortable, save and what is the most important, effective medical equipment. Because of the very complex nature of those physical phenomena the whole available information regarding that subject was up-to-now obtained through experimental techniques tested only on neonates animals [2] and adults [1]. Some of these tests were carried out even 40-50 years ago [3]. All that information must be treated as general guidelines and used with certain factor of mistrust. Because of that but also bearing in mind a rapidly growing number of premature births, seems to be essential to develop relevant numerical algorithms capable of examining, with appropriate accuracy, the heat and fluid flow processes and their results in an incubator environment. In this study a commercial CFD (Computational Fluid Dynamics) package called Fluent is applied to build a computational model and calculate results. Computational Fluid Dynamics is the technique which solves problems involving fluid flow, heat transfer and associated phenomena such as chemical reactions by means of computer-based simulation. The technique spans also a wide range of industrial and non-industrial application areas.

Objectives

The main objective of this study was to developed computational model of selected transport processes, including heat transfer due to conduction, convection and radiation as well as heat and mass transfer due to evaporation of moisture from the surface of the newborn skin. In the following projects a sensitivity analysis will be performed in order to find optimal environment conditions for the analyzed newborn baby nursed inside of the modelled incubator. Finally, for a possibility of analyzing different type of medical cases (*i.e.* different shape and weight of patients) parameterization of the geometric model is aimed to be implemented.

METHODOLOGY

In the first stage of this work a parametric three-dimensional geometrical model of the newborn infant, placed inside incubator, was designed. For this purpose a CAD-type software (called Catia [4]), capable of designing even very complex geometrical objects, was applied. Geometry transferred from Catia to CFD package preprocessor is much more flexible and accurate then that created with preprocessor itself.

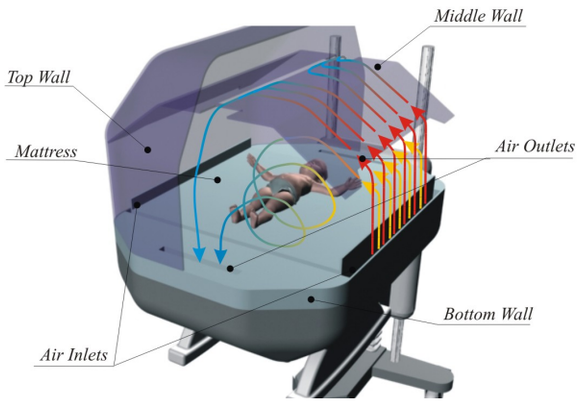


Figure 1. Modelled newborn infant placed within an infant incubator.

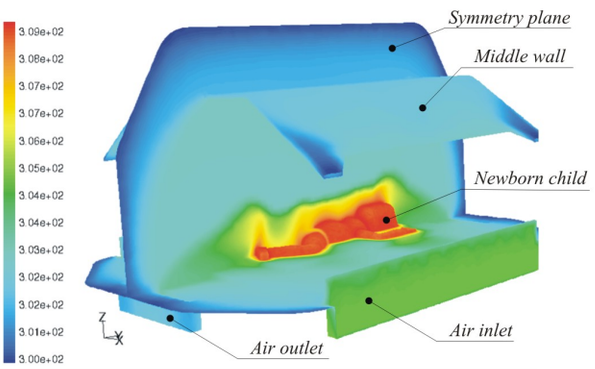


Figure 2. Perspective view of the temperature field.

For all flows, Fluent solves the the energy equation [5]

$$\nabla(k\nabla T) = \varrho\, c\, \frac{\mathrm{D}T}{\mathrm{D}t} \tag{1}$$

where T is the temperature (K), k stands for thermal conductivity (W/mK), ϱ represents the density, c is the specific heat (J/kgK) and t is time (s). The derivative on the right-hand side is the substantial derivative:

$$\frac{\mathrm{D}T}{\mathrm{D}t} = \frac{\partial T}{\partial t} + w_x\frac{\partial T}{\partial x} + w_y\frac{\partial T}{\partial y} + w_z\frac{\partial T}{\partial z} = \frac{\partial T}{\partial t} + \boldsymbol{\nabla} T\cdot \boldsymbol{w} \tag{2}$$

where w_x, w_y, w_z are the velocity components of vector $\boldsymbol{w}$ in the x-, y- and z-direction, respectively (m/s) while x, y and z represent the Cartesian coordinates.
The above equations have to be complemented by the continuity and the momentum equations [5]

$$\boldsymbol{\nabla}\cdot\boldsymbol{w} \;=\; 0 \tag{3}$$

$$\varrho\frac{\mathrm{D}\boldsymbol{w}}{\mathrm{D}t} = \boldsymbol{F} - \boldsymbol{\nabla}p + \mu\nabla^2\boldsymbol{w} \tag{4}$$

where p is the pressure (N/m^2), $\boldsymbol{F}$ represents the body force term which in the present case has only a vertical component $F_z = \varrho g$ in the z-direction (N/m^3), g is gravity acceleration (m/s^2) and μ is the dynamic viscosity (Ns/m^2).
The Boussinesq approximation was adopted for the buoyancy term in the equation (4). Thus, density takes the usual form

$$\varrho = \varrho_0\left[1 - \beta(T - T_0)\right] \tag{5}$$

where β is the thermal expansion coefficient (1/K), T_0 and ϱ_0 represent the so-called operating parameters.
For flows involving radiative heat transfer or a discrete phase change, additional equations are solved.

CONCLUSIONS

Computational model of selected transport processes presented in this study, provides much more effective and flexible tool compared with previous techniques used in the neonatal intensive care. It can be easily employed for verification of the new technologies, materials and ideas being run with many different input data sets. Proposed procedure can also be useful in testing new medical treatments.
Numerical analysis can provide important and what is the most important, very accurate results without exposing patients at unnecessary risk which is always involved in the medical research. It can also save time and money during the process of developing new medical equipment. This is mainly due to reduction of the number of experimentally tested prototypes.
Sensitivity analysis proved that results obtained from this model are in good agreement to those received from medical literature. Also parameterization of the geometrical inputs proved to be very useful for analyzing individual cases, where one can easily change the weight and shape examined premature newborns.

References

[1] Yunus A. Cengel. *Heat transfer a practical approach.* McGraw-Hill 2001
[2] Albert Okken, Joahim Koch. *Thermoregulation of Sick and Low Birth Weight Neonantes.* Springer/Berlin 2000
[3] Joachim Wasner. *Heat Balance of Premature Infants.* Dragwerk AG, Lubeck, Germany, 1994.
[4] CATIA v5 Solutions. Version 5, Release 9. *English Online Documantation.* Generative Shape Design.
[5] J.D. Anderson, Jr.: *Computational Fluid Dynamics. The Basics with Applications*, McGraw-Hill, USA, 1995.
[6] FLUENT, User's guide, Release 4.4, August 1996, Fluent Inc.
[7] Maciej K. Ginalski, Andrzej J. Nowak, Luiz C. Wrobel: *Analysis of combined heat and fluid flow procesess in an infant incubator*, CMM-2003 - Computer Methods in Mechanics. Wisla 2003.

Red blood cell dynamics, deformation and rheology via microfluidic experiments

Manouk Abkarian[*], Magalie Faivre[*], Annie Viallat[**] and Howard A. Stone[*]

[*] *Division of Engineering and Applied Sciences, Harvard University, Cambridge, MA, 02138*

[**] *Laboratoire de Spectrométrie Physique, UMR 5588, Université J. Fourier, BP 87, 38402 Saint Martin d'Hères cedex, France*

Summary Blood is principally made of a calibrated suspension of red blood cells (RBC). Depending on the flow, RBCs move alone or in aggregates (rouleaux), often in capillaries of smaller sizes than their own radius. Blood is an "intelligent" fluid, as its rheological properties adapt according to the different situations of the flow. This capacity, which is not fully understood, comes partly from the significant deformability of RBCs. The understanding of the flow behavior of a single confined RBC is a first step to understand the basic rheological properties of the blood in arteries. To achieve this goal, we used microfluidic technology as a tool to explore hydrodynamics of a single cell and the hydrodynamic interactions among cells. We are also using such measurements to infer the individual mechanical properties of their membrane.

The aim of this paper is to present preliminary experiments of the motion of red blood cells in microfluidic channels mimicking the circulation in microvessels. We want to explore the role of the deformability of red blood cells on their motion in confined geometries such as capillary vessels. For example, we are interested to know how deformability can affect, or even assist, the formation of rouleaux of red blood cells (stacks of several red blood cells), which are believed to reduce the apparent viscosity in small capillaries [1,2]. Indeed, accounting for basic molecular forces (e.g. adhesion between proteins, depletion forces, etc.) the formation of rouleaux has been extensively studied in quiescent blood; such forces cause or prevent aggregation and can explain the elastic properties of coagulated blood [3,4,5,6]. Nevertheless, the formation of rouleaux is a dynamical process, as it occurs during the flow of blood in arteries. It is difficult to understand how molecular or depletion forces could play a role on the first stage of the aggregation of red blood cells and therefore, we study experimentally the effect of deformability and hydrodynamic interactions with the walls and among cells to explain the first steps of the rouleaux formation. To the best of our knowledge, these are some of the first, if not the first, detailed measurements focusing on the interplay between cell deformability, confinement, and hydrodynamic interactions. Finally, we are exploring the mechanical properties of red blood cells by using microfluidics as a measurement tool.

The technique that we use to produce the microchannels is the well-known technique of soft lithography [7,8]. The method consists of producing a negative relief of the channels in poly(dimethylsiloxane) (PDMS), curing the prepolymer (Sylgard 184, Dow-Corning) on a Si-wafer master having the positive relief of the microchannels, which themselves are formed with a photoresist (SU 8-2 to SU 8-50, Microchem). This PDMS membrane is peeled off the SI wafer and applied against a glass microscope slide previously oxidized (with the PDMS membrane) in a plasma chamber. High-speed video is used to follow the motion and deformation of the cells.

HYDRODYNAMICS INTERACTIONS BETWEEN DEFORMABLE RED BLOOD CELLS

Interaction of red blood cells in 1D channels

To analyse the interactions among red blood cells, we made very small and square channels (5μm x 5μm in cross-section), which are smaller than the red blood cell size. During flow, the red blood cells flow in a single file and are forced to deform into a parachute-like shape, which is commonly already referenced in the literature [9,10]. We refer to this configuration as "1D". Our interests are in the hydrodynamic interactions between the cells, which to the best of our

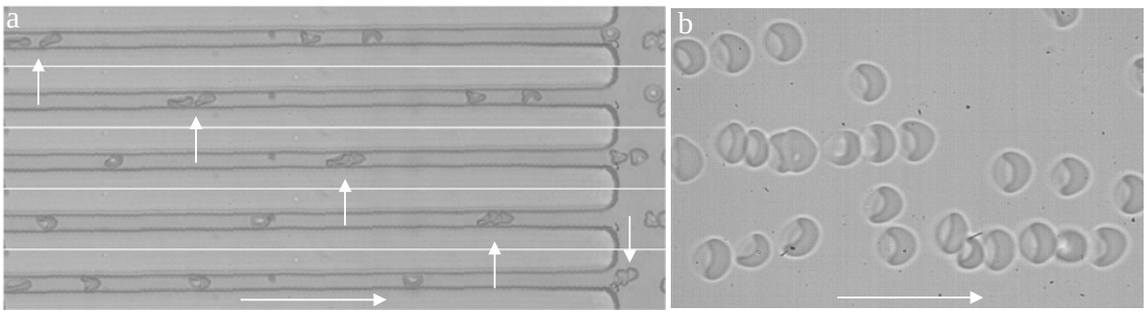


Figure 1. (a) Sequence of the motion and the deformation of two red blood cells (indicated with small white arrows) in a microchannel. The cross section of the channel is 5μm x 5μm in cross-section. The time between two frames is 100ms and the large white arrow represents the direction of the flow. (b) Red blood cells flow in a Hele-Shaw type channel (100 μm wide and 5μm high). We can observe on the figure the formation of files of red blood cells aligned in the direction of the flow.

knowledge have not been experimentally measured. In Figure 1a we show the results of several preliminary experiments highlighting the hydrodynamic interactions, which lead to eventual aggregation, that occur as the cells flow along the

channel. Basic results of low-Reynolds-number hydrodynamic argue that cell deformability is necessary to account for the kinds of interactions shown in the Figure 1a; some part of this effect may be due to changes of mobility of the cell owing to deformation during flow. Detailed measurements are in progress to completely characterize this hydrodynamic interaction and will be compared with theoretical calculations.

Interaction of red blood cells in 2D channels

In a second set of experiments we relaxed the constraint of the walls in one direction. The flow is produced in plane channel (100μm x 5μm section), or Hele-Shaw cell, where the same average flow is maintained across the channel. We refer to this flow configuration as "2D" and it is shown in Figure 1b. We observe that an initially uniform suspension of red blood cells arrange themselves into files, which is clearly a precursor of rouleaux formation. Obviously, hydrodynamic interactions are responsible for this pattern formation. Detailed measurements are in progress to understand the dynamical progression of the rouleaux formation.

ENTRANCE AND EXIT OF RED BLOOD CELLS IN MICRO-CHANNELS

In a third set of experiments, shown in Figure 2, we are focusing on the time-dependent shape changes that occur when a red blood cell enters or exits a small channel. The deformation is related to mechanical properties of the membrane. For example, the "entrance length" over which the cell adopts a steady shape has been numerically calculated [11,12] and a comparison of our experiments with the results of simulations should allow the extraction of mechanical properties of the membrane.

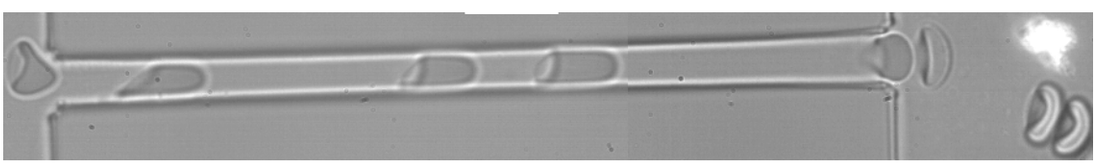


Figure 2. Entry and exit of red blood cells from a 1D micro-channel: We can see on the figure the different steps of the deformation: first the entry where the red blood cell deforms until it reaches a stationary shape in the channel. Then, the exit process that is different from the entry and presents totally different deformation features.

CONCLUSIONS

In conclusion we have indicated three sets of on-going experiments, which probe dynamical response and mechanical properties of deformable red blood cells. To the best of our knowledge, these are some of the first, if not the first, detailed measurements focusing on the interplay between cell deformability, confinement, and hydrodynamic interactions. By using microfluidic techniques, we are also using these ideas in reverse by making microfluidic devices for biomedical applications that allow us to check the mechanical properties between healthy and sick red blood cells.

References

[1] Skalak R., Chen P.H., Chien S. : Effect of hematocrit and rouleaux on apparent viscosity in capillaries *Biorheology* **9**:67-82, 1972.

[2] Sugihara-Seki M., Skalak R.: Numerical study on a multi-file flow of red blood cells in capillaries. *Microcirculation-an update vol. 1*. Elsevier Science, 1987

[3] Goldsmith H.L.: The microrheology of human erythrocyte suspensions. *Theoretical and applied mechanics Proc 13th IUTAM Congress*. Springer, N.Y. 1972

[4] Chien S., Jan K-M.: Ultrastructural Basis of the mechanism of rouleaux formation. *Microvas. Res.*, **5**:155-166,1973

[5] Skalak R., Zarda P.R., Jan K-M, Chien S.: Theory of rouleau formation , *Cardiovascular and Pulmonary dynamics*, **71**:299-308, 1977

[6] Skalak R., Zarda P.R., Jan K-M, Chien S.: Mechanics of rouleau formation. *Biophys. J.*, **35**:771-781, 1981

[7] Whitesides G.M., Ostuni E., Takayama S., Jiang X., Ingber D.E.: Soft lithography in biology and biochemistry. *Annu. Rev. Biomed. Eng.* **3**:335-373, 2001

[8] Whitesides G.M., Love J.C.: The art of building small. *Sci. Am.* **285(3)**:38-47, 2001

[9] Bagge U., Branemark P-I., Karlsson R., Skalak R.: Three dimensional observations of red blood cell deformation in capillaries. *Blood Cells*. **6**:231-237, 1980

[10] Gaehtgens P., Duhrssen C., Albrecht K.H.: Motion, deformation and interaction of blood cells and plasma during flow through narrow capillary tubes. *Blood Cell*. **6:**799-812, 1980

[11] Queguiner C., Barthes-Biesel D.: Axisymmetric motion of capsules through cylindrical channels. *J. Fluid. Mech.* **348**:349-376, 1997

[12] Diaz A., Barthes-Biesel D.: Entrance of a bioartificial capsule in a pore. *CMES* **3(3)**:321-337, 2002

FLOW IN AN INTEGRATED MODEL OF HEART AND AORTA

Masanori Nakamura*, Shigeo Wada*, Suguru Yokosawa*,
Haruo Isoda**, Ken-ichi Tsubota*, Takami Yamaguchi*
*Graduate School of Engineering, Tohoku University, Aoba 01, Aoba-ku, Sendai 980-8579, Japan
**Hamamatsu University School of Medicine, 1-20-1 Handayama, Hamamatsu 431-3192, Japan

Summary CFD of blood flow was carried out in an integrated model of the left ventricle and the aorta. It was shown that the formation of recirculating flow beneath the aortic valve (AV) during diastole effectively redirected inflow to the outflow tract, accommodating systolic ejection. The results also demonstrated that blood flow through AV had markedly skewed velocity profiles with swirling flows, provoking helical flow in the aorta. These findings addressed the importance of inclusion of the ventricular flow in the analysis of the aortic flow.

INTRODUCTION

Many computational fluid dynamics (CFD) studies of aortic flow have been carried out to clarify the pathophysiological significance of hemodynamics on localization of vascular diseases [1 and references therein]. However, despite the fact that blood flowing into the aorta is pumped by the left ventricle (LV), in most studies, the aortic section is analyzed isolatedly and an inlet flow is ideally conditioned. Liu [2] stated that the swirl inflow condition could affect the flows downstream of the aorta significantly. Hence, for the analysis of the aortic flow, flow dynamics stemmed from LV has to be taken into account. In this study, we carried out CFD of blood flow in LV and the aorta in an integrated manner to investigate the effects of the intraventricular flow on the aortic flow. Simulated results of cross-sectional velocity profiles at AV were compared to the ones obtained with magnetic resonance (MR) phase-contrast mapping.

METHODS

A computational model was built by combining an aorta model [1] and a left ventricle (LV) model [3]. Briefly, the model of aorta was constructed on the basis of clinical data, but three main aortic branches as well as other small branches were neglected. The total length of the aorta was 25 cm. As viewed from the top of the aortic arch, the angle between the ascending aortic arch and the descending aortic arch was 144°. The cross-section perpendicular to the centerline of the aorta was assumed to be a circle with its radius of 1.3 cm uniformly from the inlet to the outlet. The LV model was also modeled based on clinical data. LV was assumed to be symmetric with respect to a long-axis plane. The mitral valve (MV) and the aortic valve (AV) were both circular with radius of 1.3 cm. The deformation of LV was calculated by prescribing weighting functions of ventricular wall movement and the amount of volume change at every time step. It was assumed that the ventricular surface moved inwards or outwards in a normal direction independently of internal blood pressure. A time variation of the volume of LV was set based on MRI-derived data [4]. The length of systole and diastole were 0.413 s and 0.337 s. A stroke volume over a cardiac cycle was 70 ml.
It was assumed that flow was laminar, and blood was an incompressible Newtonian fluid. The flow simulations were performed under the moving boundary condition using a finite element method, as implemented in ANSYS-FLOTRAN ver. 7.0 (distributed by Cybernet System Ltd., Tokyo). The simulation was commenced from diastole, at the onset of which a quiescent flow state was assumed. In a diastolic flow simulation, the MV model [5] was used, and only intraventricular flow was calculated. During systole, flow in LV and aorta was calculated in an integrated manner.

RESULTS

Figure 1 shows streamlines of blood flow in mid diastole (t = 0.250 s), early (t = 0.426 s), mid (t = 0.573 s) and end systole (t = 0.749 s). The images are viewed from the left of the body with the septum (anterior) side towards the left. Once LV started to expand, blood flowed through the open MV into the ventricular cavity. In mid diastole, blood inflow gave rise to recirculating flow beneath AV, redirecting blood inflow preferentially towards the outflow tract (Fig. 1a). Later, this recirculating flow extended circumferentially to the posterior side, developing into an annular vortex that encircled blood inflow along the LV long axis. When LV started to contract, intraventricular blood flow was ejected to the aorta (Fig. 1b). It was accommodated by the recirculating flow under the aortic valve. Until mid systole, blood in the aorta was axially directed to the outlet along the curve of the aortic arch (Fig. 1c). However, with progress of systole, a helical flow developed. It firstly appeared in an ascending aorta, and extended to a descending aorta. By the end of systole, secondary helical flows dominated the whole part of the aorta as seen in Fig. 1d.
In Fig. 2, vector plots of secondary flow at the inlet section of the aorta at the same moments as Fig. 1b, 1c and 1d are illustrated, on which contour plots of the magnitude of flow velocity normal to this plane are superimposed. The image was viewed from the distal side, with the ventricular septum towards the up and with MV towards the bottom. In the beginning of systole, velocity profile was fairly flat (Fig. 2a). As LV contraction progressed, velocity profile was skewed to the MV side and a pair of swirls developed across the symmetric plane of LV (Fig. 2b). With the swirls, high

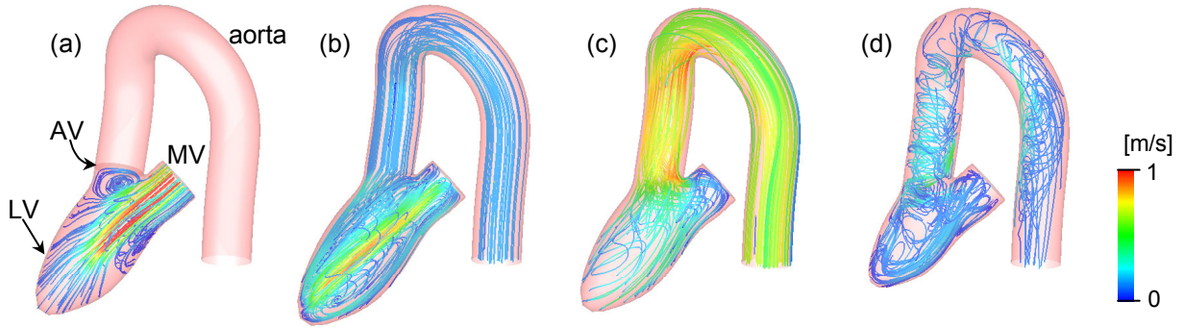


Fig. 1 Streamlines of blood flow in (a) mid diastole, (b) early, (c) mid, (d), end systole. Images are viewed from the left of the body with its septum (anterior) side towards the left. LV: left ventricle, AV: aortic valve. MV: mitral valve.

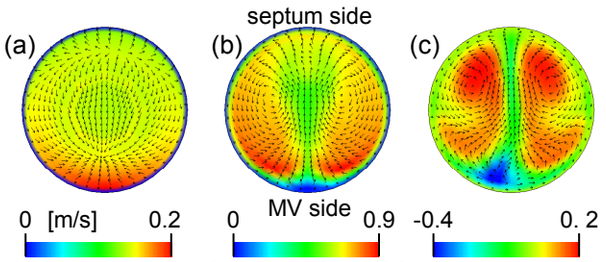


Fig. 2 Vector and counter plots of the flow at the plane at the aortic valve constructed from the simulation results. (a) early, (b) mid, (c), end systole.

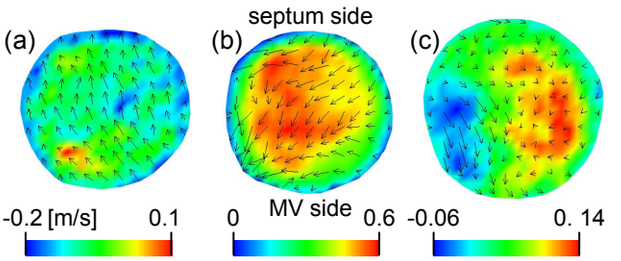


Fig. 3 Vector and counter plots of the flow at the plane 1.3 cm above from the aortic valve constructed from MR data. (a) early, (b) mid, (c), end systole.

velocity portion of the flow moved to the septum side, and flow through AV became faster close to the ventricular septum than beside MV (Fig. 2c).

DISCUSSION AND CONCLUSIONS

Flow patterns, especially generations of recirculating flows in LV and the helical flow in the aorta, simulated here were overall similar to *in vivo* results measured by Kilner et al [6][7]. It was found that the formation of recirculating flows beneath AV in the LV during diastole accommodated ventricular blood ejection to the aorta during systole.

It was observed that swirl secondary flows developed and the velocity profile at AV changed dynamically during systole. For comparison, a velocity profile at the cross-section about 1.3 cm above AV was measured with magnetic resonance phase-contrast mapping. Figure 3 shows examples of measurement results in early, mid and end systole plotted in the same manner as Fig. 2. They demonstrate that the skewness of the velocity profile started during mid systole and persisted to the end while a region of high velocity moved from the MV side to the septum side, as being consistent with our results. However, different subjects showed different patterns. Therefore, it was not possible to evaluate our results solely from these data. A large variation of the velocity profile at AV suggested that various factors such as a joint angle between LV and the aorta, LV motion and configuration of the aorta, could affect it.

At this moment, the fluidic mechanism that promotes the secondary flows at AV was unclear. However, it is at least likely that they affect the aortic hemodynamics including wall shear stress, particularly in the ascending aorta. If so, it would be possible that a change in a LV function is related to the occurrence of vascular diseases in the aorta. Thus, it is important to take into account intraventricular flow dynamics when analyzing pathophysiological significance with respect to pathogenesis of the vascular diseases.

References

[1] Mori, D., Yamaguchi, T.: Computational fluid dynamics analysis of the blood flow in the thoracic aorta on the development of aneurysm. *J. Jpn. Coll. Angiol.,* **43**:94-97, 2003.

[2] Liu, H.: A computational fluid dynamic study of the helical flow in aorta. Conference Proceedings of ICTAM 2000.

[3] Nakamura, M., Wada, S., Mikami, T., Kitabatake, A., Karino, T.: Computational study on the evolution of an intraventricular vortical flow during early diastole for the interpretation of color M-mode Doppler echocardiograms. *Biomech. Model. Mechanobiol.*, **2**:59-72, 2003.

[4] Saber, N.R., Wood, N.B., Gosman, A.D., Merrifield, R.D., Yang, G.Z., Charrier, C.L., Gatehouse, P.D., Firmin, D.N.: Progress towards patient-specific computational flow modeling of the left heart via combination of magnetic resonance imaging with computational fluid dynamics. *Ann. Biomed. Eng.,* **31**:42-52, 2003.

[5] Nakamura, M., Wada, S., Mikami, T., Kitabatake, A., Karino, T.: A computational fluid mechanical study on the effects of opening and closing of the mitral orifice on a transmitral flow velocity profile and an early diastolic intraventricular flow. *JSME Int. J. Ser. C*, **45**:913-922, 2002.

[6] Kilner, P.J., Yang, G.Z., Mohiaddin, R.H., Firmin, D.N., Longmore, D.B.: Helical and retrograde secondary flow patterns in the aortic arch studied by three-directional magnetic resonance velocity mapping. *Circulation*, **88:**2235-2247, 1993.

[7] Kilner, P.J., Yang, G.Z., Wilkes, A.J., Mohiaddin, R.H., Firmin, D.N., Yacoub M.H.: Asymmetric redirection of flow through the heart. *Nature*, **404**:759-761, 2000.

In Vivo Visualization of the Water Refilling Process in Xylem Vessels Using Synchrotron X-ray Micro-imaging

Yang-Min Kim [*], Sang-Joon Lee[*]
[*]*Department of Mechanical Engineering, POSTECH, Pohang, 790-784, Korea*

Synchrotron X-ray micro-imaging was employed to non-invasively monitor the refilling process of water inside the xylem vessels in bamboo leaves. The consecutive phase-contrast X-ray images clearly showed both plant anatomy and the transport of water within the xylem vessels. Traces of water-rise, vapor bubbles and variations in contact angle between the water front and the xylem wall were all measured in real time. During the drying out process, while some xylem vessels were cavitated, cavitation did not propagate to the upper vessels of upright plant due to the hydraulic valve features of vessel end. During refilling process, similar flow pattern repeats in each xylem vessel. Water front stops at a vessel end for a while, thereafter it restarts rising in the next vessel with a higher velocity than the normal refilling speed. Vapor bubbles are removed when water front stops at the vessel end and xylem lumens are pressurized. These observations demonstrate that intervessel pits act as a valve to pressurize the xylem vessel for gas removal. The bordered pits seem to be architected to manage embolism occurred frequently in conducting vessels under tension and to control water supply into a vascular plant. Repeated cavitation was found to lessen the refilling ability in xylem vessels. In the absence of light, the water refilling process in xylem vessels was facilitated more effectively than in bright illuminated conditions. Finally, X-ray micro-imaging was deemed to be a powerful, high resolution, real time imaging tool to investigate the water refilling process in xylem vessels.

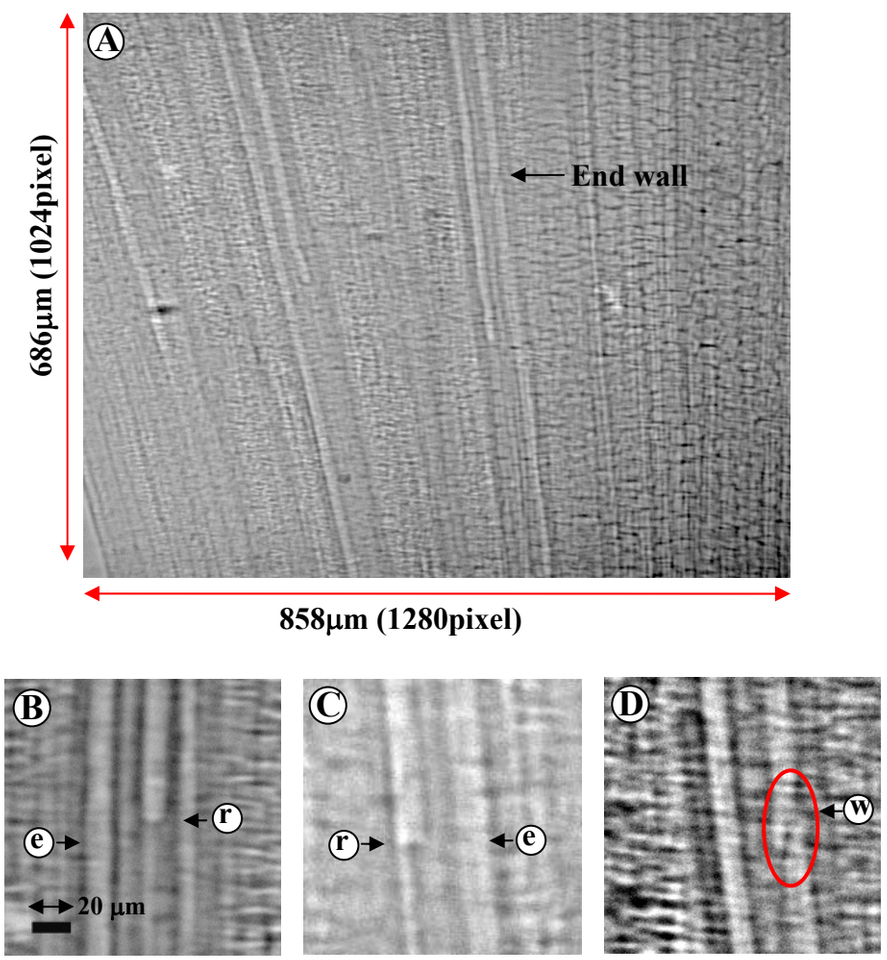
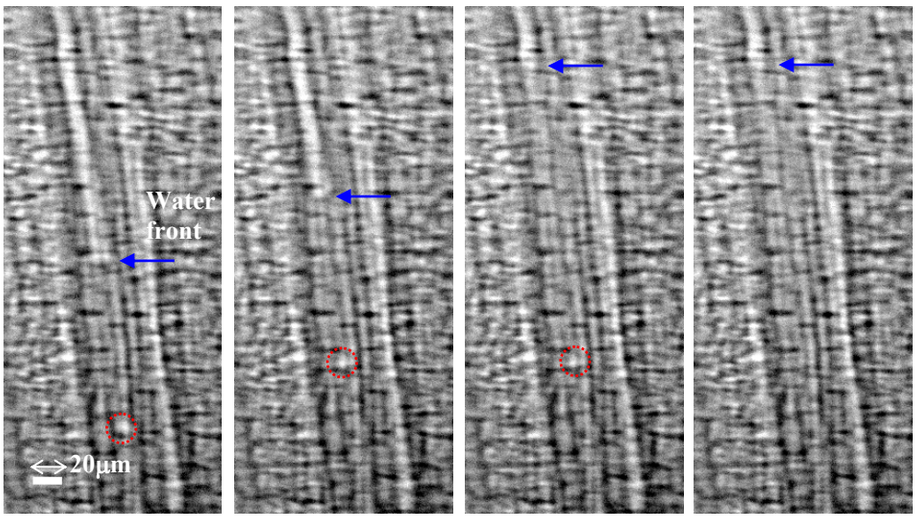


Figure 1. A typical X-ray image of bamboo leaf showing xylem vessels



(a) t = 0 s (b) t = 3 s (c) t = 9 s (d) t = 20 s

Figure 2. Removal process of vapor bubble in a xylem vessel

References

[1] Holbrook N. M., Ahrens E. T., Burns M. J., Zwieniecki M. A.: In Vivo Observation of Cavitation and Embolism Repair Using Magnetic Resonance Imaging. *Plant Physiol.* **126**: 27-31, 2001.

[2] Hwu Y, Hsieh H. H., Lu M. J., Tsai W. L., Lin H. M., Goh W. C., Lai B., Je J. H., Kim C. K., Noh D. Y., Youn H. S., Tromba G., Margaritondo G.: Coherence-enhanced Synchrotron Radiology: Refraction versus Diffraction Mechanisms. *J. Appl. Phys.* **86**: 4613-4618, 1999.

[3] Kockenberger W., Pope J. M., Xia Y., Jeffrey K. R., Komor E., Callaghan P. T.: A Non-invasive Measurement of Phloem and Xylem Water Flow in Castor Bean Seedlings by Nuclear Magnetic Resonance Microimaging. *Planta* **201**: 53-63, 1997.

[4] Lee S. J., Kim G. B.: X-ray particle image velocimetry for measuring quantitative flow information inside opaque objects. *J. Appl. Phys.* **94**: 3620-3623, 2003.

[5] Wagner H. J., Schneider H., Mimietz S., Wistuba N., Rokkita M., Krohne G., Haase A., Zimmermann U.: Xylem Conduits of a Resurrection Plant Contain a Unique Lipid Lining and Refill Following a Distinct Pattern after Desiccation. *New Phytol.* **148**: 239-255, 2000.

[6] Westneat M. W., Betz O., Blob R. W., Fezzaa K., Cooper W. J., Lee W. K.: Tracheal Respiration in Insects Visualized with Synchrotron X-ray Imaging. *Science* **299**: 558-560, 2003.

On The Issue of Optimal Trans-mitral Flow

*M. GHARIB, E. RAMBOD, A. Kheradvar,D. SAHN**

California Institute of Technology, Pasadena, California
**Oregon Health Science University, Portland, Oregon*

One of the primary challenges remaining in cardiac hemodynamics is the issue of optimal diastolic filling. The Left Ventricle .(LV) fills during the diastolic phase in two separate stages. The first stage starts at the onset mitral valve opening while the second stage begins with the arterial systole. During the first stage, known as E-wave, the trans-mitral flow responds to the rapid pressure drop in LV by accelerating through the valve followed by a decelerating phase due to the weakening of the pressure gradient across the mitral valve. A short pulse of arterial systole generates another pressure gradient and a second flow wave, known as A-wave, in the late diastole. The major filling of the LV (more than %85 of the ejection fraction) occurs during E-wave period.

From various ultrasound and MRI studies, it is now known that the trans-mitral flow during E-wave period results in a rapid roll-up of the flowing blood into vortical structures within the left ventricular body. This vortex formation occurs during the diastolic period. Lee and Talbot [1], tried to apply the concept of the Strouhal number $St=fd/u$, where f is the heart rate, d is the mitral valve diameter, and u is the maximum velocity during diastole, in order to characterize the dynamics of the filling process of the left ventricle. They concluded that the Strouhal number did not indicate any useful trend in characterizing the mitral flow. However, the concept of the Strouhal number has been used successfully by Crow and Champagne [2] to characterize the maximum efficiency of pulsed jets and by Triantafyllou, et al., [3] to characterize the maximum efficiency of swimming fish. In our opinion, to apply a Strouhal frequency approach to the flow in the left ventricle is not appropriate because, in reality, cardiac pulsating filling flow more closely resembles a single transient vortex puff than a continuous jet. This is due to the more than 100% variation in the velocity amplitude during the left ventricle filling process. Therefore, a more appropriate parameter that can demonstrate the dynamics of this vortex roll-up process is a non-dimensional time scale based on the E-wave period. In this report, we refer to this parameter as Formation number which we define as:

$$F = \frac{T\overline{U}}{D}$$

where T is the filling period (E-wave), U is the average velocity for the filling period and D is the mitral valve annulus. This number is different in its nature from the "Strouhal number" where the time scale is the frequency of occurrence rather than the period of the event.

To test whether the Formation number could characterize the flow process in the .left ventricle, we conducted a series of in vivo tests on 73 normal, healthy subjects ranging in age from 5 years to 84 years. In addition, 8 patients with dilated cardiomyopathy were selected to be examined by the echocardiography described below.

Echocardiography

Two-dimensional, pulsed Doppler echocardiography was performed using commercially available ultrasound machines (Toshiba 140A and Hitachi EUB-165 with 2.5, 3.75, or 5 MHz transducers). We recorded transmittal flows with the ultrasound transducer paced at the cardiac apex and guided by two-dimensional echocardiographic imaging in a four chamber view. A pulsed Doppler sample volume was placed in the center of the atrio-ventricular junction at the level of the mitral annulus. Once adequate transmittal blood flow velocities had been recorded, velocity time integrals for early diastolic transmittal flow (VTI cm) were measured using the track ball systems on the echo systems. The mitral annular diameter (D cm) was also measured at end-diastole using the calibrated track ball measurements from the frozen images. Doppler measurements were averaged over three cardiac beats. Then, the Formation number was calculated as the ratio of DNTI (non- dimensional number).

A power law curve presents the general behavior of the Formation number with age. This curve shows a steady decrease of the Formation number in the early stages until it reaches a base line value of 4.5 for ages over 30. The mean Formation number for the whole data set is about 4.795.A marked decrease in the formation number can be seen for all of the DCM patients ranging from 2.88 to .27 (mean 1.89:±7).

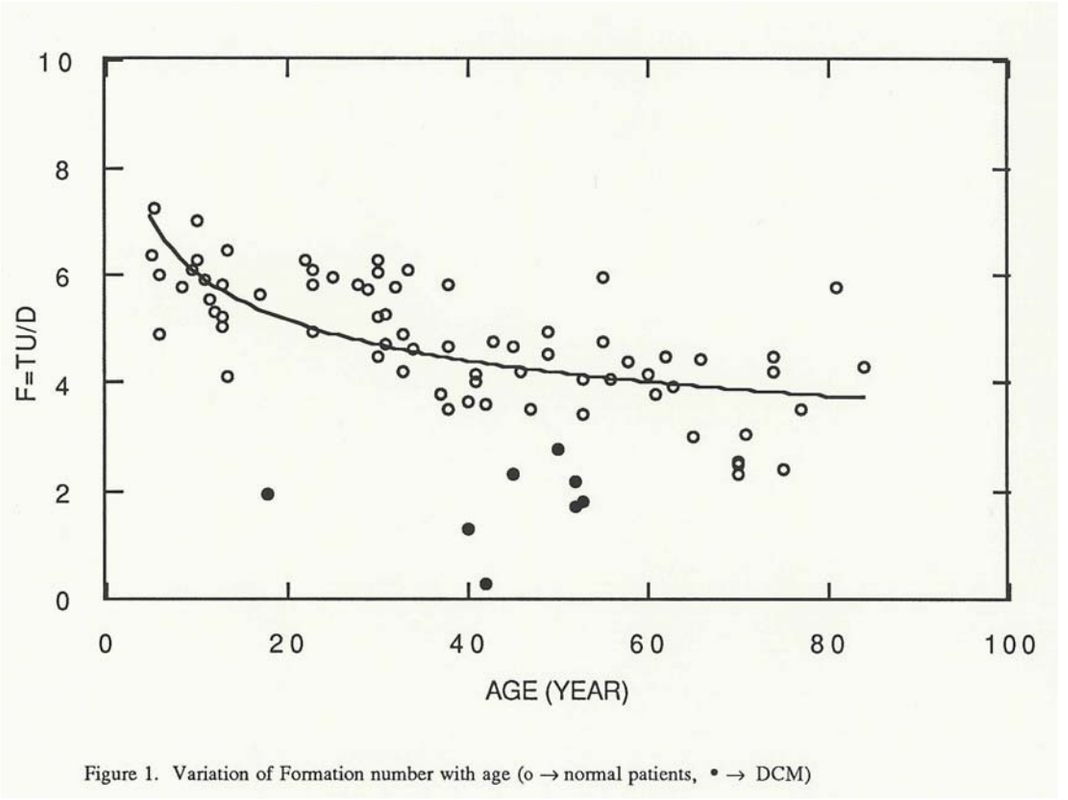


Figure 1. Variation of Formation number with age (o → normal patients, • → DCM)

The mean value of 4 for the formation number appears to indicate the existence of a universal time scale that may describe the optimum range for trans-mitral flow during diastole. The statistical significance and importance of the narrow range of the formation number becomes obvious when one considers the broad spectrum of the ages and backgrounds of the test subjects. A low formation number might indicate poor volume efficiency due to low average velocity or a short diastolic period. A typical example can be found for the cases with dilated cardiomyopathy when decreased systolic function and increased cardiac chamber size is accompanied by reduced left ventricular wall motion, increased filling pressures and abnormal relaxation of heart muscle. A high value of Formation numbers can be indicative of a high heart rate which results in excessive mean velocities through the mitral valve.

The results presented in Figure 1 indicate that the normal heart as a responsive system operates around a Formation number of approximately 4. Whether this base line has a significant fluid mechanical value is an important issue that needed to be addressed through an understanding of the vortex formation process. Gharib et al (1998) showed that the formation number of 4 is directly related to the circulation saturation of forming vortex rings. Kruger and Gharib(2000) extended these studies to show that this range of formation number is associated with the optimal (maximum) impulse that can be produced by a forming vortex ring. These studies all indicate that perhaps the formation number of 4 is an effective parameter for defining

an optimal range of trans-mitral flow dynamics. It is important to mention that other trans-mitral flow parameters such as peak E-wave to A-wave velocity ratio are not as robust as Formation number. In this report, we will discuss these parameters and other important aspects of Formation number in defining the optimal transmitral flow.

References

Lee, C. S. F, and L. Talbot, *JFM* (1979), vol. 91
Crow, S. C., and F.H. Champagne, *JFM* (1971), vol. 48.
Triantafyllou, G. S. et al., *JFS* (1993), vol. 7.\
Gharib, M., Rambod, E., and Shariff, K. *JFM* (1998) vol. 360, pp. 121-140.
Krueger, P., Gharib, M., Physics of Fluids (2003) vol 15, 5, 1271-1281

THE DEVELOPMENT (AND SUPPRESSION) OF VERY SHORT-SCALE INSTABILITIES IN BUOYANT BOUNDARY LAYERS

James P. Denier*, Peter W. Duck** & Jian Li*
*School of Mathematical Sciences, The University of Adelaide, Australia
**Department of Mathematics, The University of Manchester, United Kingdom

Summary The flow over a heated (or cooled) flat plate is shown to develop very short-scale instabilities independent of Reynolds number. These are in the form of non-modal, algebraically, disturbances. Their existence presents a number of challenges for the numerical simulation of such boundary-layer flows.

The equations governing the boundary-layer flow over a heated (or cooled) surface are

$$\begin{aligned} \frac{\partial u}{\partial x}+\frac{\partial v}{\partial y}=0, \qquad \frac{\partial p}{\partial y}=G_0 T, \\ u\frac{\partial u}{\partial x}+v\frac{\partial u}{\partial y}=-\frac{\partial p}{\partial x}+\frac{\partial^2 u}{\partial y^2}, \\ u\frac{\partial T}{\partial x}+v\frac{\partial T}{\partial y}=\frac{1}{\sigma}\frac{\partial^2 T}{\partial y^2}, \end{aligned} \tag{1}$$

with boundary conditions

$$u=v=T-T_w(x)=0 \quad \text{at} \quad y=0, \qquad u-1=T=p=0 \quad \text{as} \quad y\to\infty. \tag{2}$$

Here (u,v,T,p) represents the basic velocity, temperature and pressure fields within the boundary layer, σ is the Prandtl number and $G_0=GrRe^{-1/2}$ is a buoyancy parameter, $y=Re^{-1/2}y^*$ is the boundary-layer variable with Re the Reynolds number and Gr the Grashof number of the flow (see [2] for full details). In this study the buoyancy parameter G_0 is taken to be order unity, and thus the flows under consideration can be classified as mixed forced-free convection boundary layers.

Recently Denier *et al.* [1] demonstrated that self-similar solutions of the boundary-layer equations (1) can support algebraically growing instabilities whose growth rates are independent of Reynolds number. In this case the boundary-layer field variables can be written in the form

$$(u,T,p)=(u_0(\eta),g_0(\eta),q_0(\eta))+x^{\lambda}(u_1(\eta),p_1(\eta),q_1(\eta))+O(x^{2\lambda}), \tag{3}$$

where $\eta=y/\sqrt{2x}$ is the similarity variable. The numerical solution of the eigenvalue problem for the growth rate yields positive values for λ for $G_0<0$. An asymptotic analysis of the limit $G_0\to 0^-$ demonstrates that $\lambda\to\infty$ in this limit (full details can be found in [1]).

Although these results for self-similar flows are intriguing they assume particular algebraic forms for the surface temperature which provide little insight into the flow over a heated surface that may be experimentally realisable. However for non-self similar flows, non-modal instabilities still arise and they give rise to some serious difficulties with regards the numerical solution of the boundary-layer equations (1). Figure 1 presents a plot of the spatial development of the wall-shear stress for the flow over a flat plate with prescribed wall temperature given by $T_w(x)=e^{-x}+\gamma(1-e^{-x})$, where γ is treated as a parameter. The results in figure 1 are for different values of the streamwise step-size Δx; we see that, irrespective of the size of Δx, the results suffer a spontaneous breakdown which is characterised by the appearance of sudden oscillations (closer inspection shows that these oscillations are of a streamwise point-to-point nature). This behaviour is not dependent upon the plate far-downstream being cooled (as is the case when $\gamma=-0.1$) as evidenced by figure 1(b). Furthermore no such breakdown is found for larger values of γ, as can be seen in figure 1(c), where the solution proceeds downstream with a far-downstream form being asymptotically approached.

To investigate the breakdown encountered in the cases $\gamma=0.1$ and -0.1 we adopt a procedure which is closely analogous to that described above for the similarity states. We seek local solutions of the form

$$(f,g,q)=(f_0(\eta;x),g_0(\eta;x),q_0(\eta;x))+\epsilon(f_1(\eta;x),g_1(\eta;x),q_1(\eta;x))\exp\Theta(x)+O(\epsilon^2), \tag{4}$$

where the amplitude ϵ is assumed small. Writing $\lambda=x\Theta_x$, assuming that the basic flow (f_0,g_0,q_0) and the disturbance amplitudes (f_1,g_1,q_1) are slowly varying in x, the boundary-layer equations give, at $O(\epsilon)$, an eigenvalue problem identical to that which arises for the similarity forms. The results for this eigenvalue problem are presented in figure 2.

It is immediately apparent that in both cases, a large (infinite) eigenvalue forms at a finite downstream location, which therefore suggests that infinitely short wavelength disturbances are responsible for the numerical marching

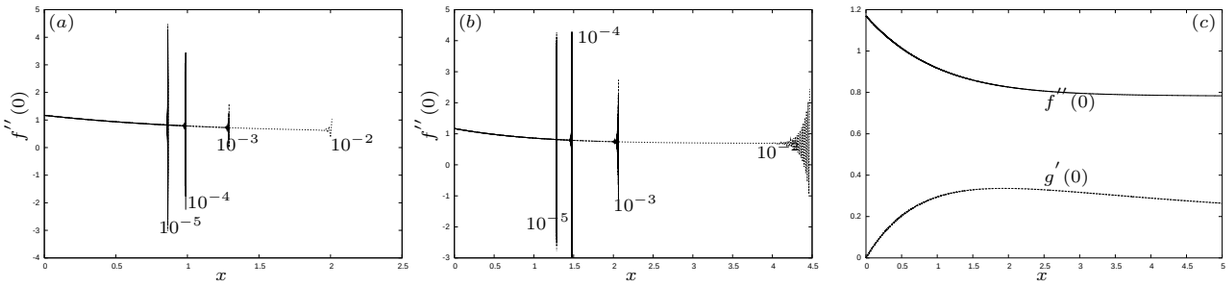


Figure 1: Spatial development of wall-shear stress for the case $G_0 = 0.5$, Δx as shown. Cases (a) $\gamma = -0.1$, (b) $\gamma = 0.1$ and (c) $\gamma = 0.25$ (wall temperature gradient also shown).

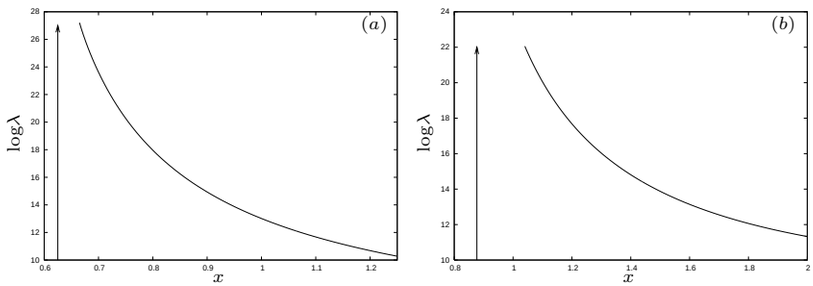


Figure 2: Downstream variation of local eigenvalues for the case $G_0 = 0.5$, (a) $\gamma = -.1$ (b) $\gamma = .1$

difficulties experienced with $\gamma = -0.1$ and $\gamma = 0.1$. A similar eigenvalue searching procedure was adopted for the case $\gamma = 0.25$, but this failed to detect any positive values of λ, an observation entirely consistent with the lack of difficulties encountered with the marching scheme in this case. Therefore in cases where these infinitesimal wavelength unstable disturbances exist, marching schemes will (inevitably) fail. Indeed, the results shown in figure 2 clearly indicate that downstream the wavelength of the disturbances increases, and it is therefore entirely reasonable to conclude that these will only be detected by numerical marching schemes when the numerical grid is of sufficient resolution to detect these disturbances.

The difficulties associated with the failure of marching schemes are a serious restriction on the usefulness of the procedure. However these instabilities can be suppressed by treating the (parabolic) boundary-layer equations (1) in a semi-elliptic manner by imposing (physically reasonable) downstream as well as upstream boundary conditions. This type of procedure, in the context of parabolic systems, can be justified, insofar as it 'selects' the appropriate eigen-form to give the desired behaviour to the problem downstream. The results of just such a calculation, employing Neumann boundary conditions at a finite x location downstream, are shown in figure 3. The complete suppression of the small-scale instabilities is clearly observed.

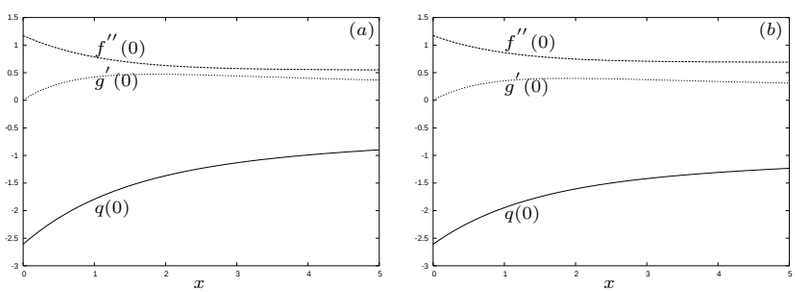


Figure 3: Spatial development of wall-quantities for the case $G_0 = 0.5$, (a) $\gamma = -.1$, (b) $\gamma = .1$

References

[1] Denier, J.P., Duck, P.W. & Li, J., 2004 On the growth (and suppression) of very short-scale disturbances in mixed forced-free convection boundary layers. *J. Fluid Mech.* (submitted).

[2] Denier, J.P. and Mureithi, E., 1996 Weakly nonlinear wave motions in a thermally stratified boundary layer, *J. Fluid Mech.* **315**, 293–316.

3D DISTRIBUTED BOUNDARY-LAYER RECEPTIVITY TO NON-STATIONARY FREE-STREAM VORTICES IN PRESENCE OF SURFACE ROUGHNESS

V.I. Borodulin, A.A. Fedenkova, A.V. Ivanov, Y.S. Kachanov, V.Y. Komarova
Institute of Theoretical and Applied Mechanics of Siberian Branch of Russian Academy of Sciences, 630090 Novosibirsk, Russia

Summary The paper is devoted to investigations of the three-dimensional (in general) problem of the Blasius boundary-layer receptivity to non-stationary free-stream vortices with spanwise and wall-normal orientations of the vorticity vector due to their scattering on distributed surface non-uniformities. The vortices under consideration are harmonic in time and the surface roughness (the waviness) is two-dimensional and periodic in the streamwise direction. The vortex and the roughness amplitudes are small enough to provide the linearity of the problem. The main goal of the study is to develop a method of experimental determination of the distributed receptivity coefficients for the problems specified and to obtain the experimental values of amplitudes and phases of the receptivity coefficients.

ANALYSIS AND EXPERIMENTAL METHOD

Prior to perform the experiments a theoretical analysis of the problem of the three-dimensional distributed vortex receptivity has been performed. The purpose of the analysis was *not* to obtain the distributed receptivity coefficients theoretically but rather to give their proper definitions for the problems under investigation and to develop a method of their experimental obtaining. The governing equation for complex amplitudes of the boundary-layer perturbations, excited by free-stream vortices in a distributed way in presence of surface roughness was obtained, and analytical solutions for resonant and non-resonant receptivity mechanisms were written out. The solutions contained functions and quantities which can be measured in experiment, as well as the unknown complex distributed receptivity coefficients. One of these coefficients is responsible for the distributed vortex receptivity on smooth surface, while another one - for the roughness-vortex distributed receptivity. A method of experimental determination of these coefficients was developed and applied in the experiments. This method is based on approximation of experimental streamwise distributions of spectral amplitudes and phases of the excited boundary-layer disturbances by means of the derived analytical solutions. The least square fit approximation at variation of the receptivity amplitudes and phases gave the possibility to find the unknown receptivity coefficients. An example of such approximation of experimental data by an analytical solution is presented in Fig. 1.

EXPERIMENTAL PROCEDURE

The measurements were performed at controlled disturbance conditions in a low-turbulence wind-tunnel of the Institute of Theoretical and Applied Mechanics in Novosibirsk at the free-stream velocity 9.18 m/s. The boundary layer under investigation was produced on a flat plate mounted in the wind-tunnel test section under the zero angle of attack. The periodical surface non-uniformities (with amplitudes of around 0.1 mm) were manufactured and pasted onto the plate. Their shapes were carefully measured and decomposed to the streamwise-wavenumber spectrum. The streamwise wavelengths of the roughness were varied and adjusted to provide the satisfaction of the resonant condition for the distributed vortex receptivity problem for excitation of either 2D or 3D Tollmien-Schlichting (TS) waves inclined at desirable angles to the flow direction. The non-stationary vortices were excited in the free stream in front of the leading edge by means of a thing oscillating wire. It was shown that the oscillating wire produces in the free-stream a vortex street similar to the von Karman street but with a very low amplitude of velocity fluctuations (below 0.4% of the free-stream velocity). In one set of experiments the wire was parallel to the plate surface and the vortex street was two-dimensional. In another experimental setup the wire produced a vortex street, which had a wall-normal orientation and was localized in the spanwise direction (i.e. it was three-dimensional relative to the boundary layer under investigation). In addition, some complementary linear-stability measurements were performed with the help of a “point source” when the free-stream vortices were switched off.

MAIN RESULTS

Primary results and data processing

The properties of all involved perturbations were investigated experimentally in detail (with the help of the hot-wire technique) both in the free-stream and inside the boundary layer. It was found that for the two studied orientations of the free-stream vorticity vector the vortices excite in the boundary layer TS-waves. In the case of wall-normal vorticity the perturbations represented wave-trains (harmonic in time but localized in the spanwise direction), while for the spanwise vorticity orientation a single 2D TS-wave was excited. The TS-wave amplitudes and phases depended significantly on the surface roughness parameters. In the 3D case the wave-trains were subjected to the spanwise Fourier transform and the streamwise distributions of the spectral amplitudes and phases were obtained in both experiments (for every fixed frequency and spanwise wavenumber). The application of the developed method gave the possibility to obtain the

complex values of the distributed vortex receptivity coefficients for the two cases of vorticity-vector orientation. In case of wall-normal orientation the dependence of the distributed receptivity coefficients on the spanwise wavenumber (and the TS-wave propagation angle) is investigated.

Coefficients of distributed vortex receptivity

The receptivity coefficients are obtained both for the distributed vortex receptivity on smooth surface and for the roughness-vortex distributed receptivity (Fig. 2). A qualitative agreement for the receptivity-amplitude dependence on the TS-wave propagation angle with that obtained in previous experiments [1] have been observed in the former case. In contrast to almost all previously studied receptivity mechanisms, the two types of the distributed vortex-receptivity mechanisms, investigated in the wall-normal vorticity case, are the strongest for free-stream vortices having large spanwise scales, i.e. in a quasi-2D case (Fig. 2). The receptivity amplitudes drop very quickly with increasing the TS-wave propagation angle.

Important role of streamwise-wavenumber resonances

It is found that the most efficient excitation of the boundary-layer instability waves by a free-stream vortex takes place in the resonant receptivity case, which can be realised in the presence of surface roughness. In particular, in the case of wall-normal vorticity the strongest TS-wave excitation was observed at spanwise wavenumbers close to the resonant ones. The width of the resonance turned out to be rather large in the spanwise wavenumber spectrum. In the resonant ranges the efficiency of the excitation is enhanced very much due to the resonant phase synchronization of perturbations, even if the corresponding distributed receptivity coefficients have relatively small amplitudes. It is important to note, that the downstream TS-wave development observed in the resonant receptivity case can not be described by approaches based on the linear stability theory only, without consideration of the distributed receptivity mechanism. In particular, application of the well-known e^N-method of transition prediction is restricted for the resonantly excited modes.

CONCLUSION

The obtained quantitative results can be used for verification of theories of the distributed vortex receptivity, as well as for estimations of the influence of free-stream vortices on the boundary-layer laminar-turbulent transition.

ACKNOWLEDGEMENTS

This work is supported by the Russian Foundation for Basic Research (Grant N 03-01-00299).

References

[1] Wuerz W., Herr S., Wagner S., Kachanov Y.S.: A first experimental approach to the distributed 3D-vortex receptivity of a boundary layer on an airfoil. *In: XI International Conference on Methods of Aerophysical Research. Proceedings. Part II.* - Novosibirsk: Inst. Theor. & Appl. Mech., 2002, pp. 173-178.

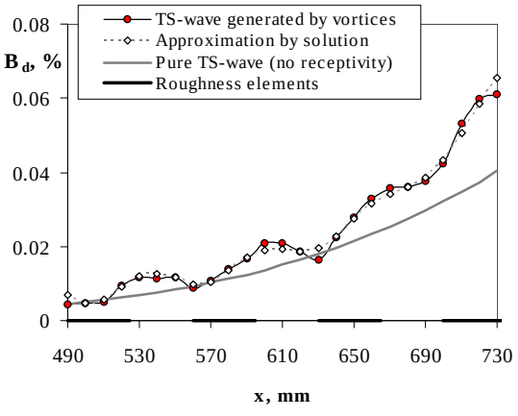


Fig.1. Downstream evolution of amplitudes of distributedly excited TS-wave and their approximation by an analytical solution in comparison with the case of absence of excitation (pure TS-wave) obtained for the spanwise orientation of vorticity vector.

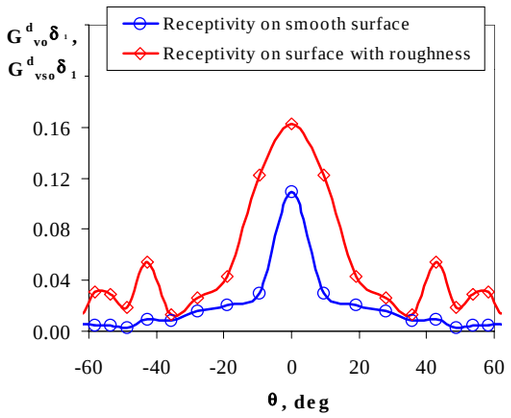


Fig. 2. Amplitudes of distributed receptivity coefficients vs. wave propagation angle for TS-wave excited by free-stream vortices (with wall-normal vorticity) for the smooth-surface vortex receptivity and the vortex roughness receptivity.

EXTENDING THE GENERALIZED LOGARITHMIC LAW TO THE WALL

Matthias H. Buschmann[*], Mohamed Gad-el-Hak[**]
[*] *Technische Universität Dresden, D-0160 Dresden, Germany*
[**] *Virginia Commonwealth University, P. O. Box 843015, Richmond, VA 23284-3015, USA*

Summary Physical arguments for the Reynolds number dependence of the mean velocity profile of canonical turbulent boundary layer with zero pressure gradient are discussed. Based on these ideas the classical two-layer approach is extended and a generalized log law is derived. This new law consists of a logarithmic and exponential term. While the first term covers part of the usual overlap region, the second term describes the inner part of the wake zone. All parameters appearing in the new law are Reynolds number dependent. The new law is extended toward the wall employing a mixing length approach that shows the correct y^{+3}-dependence of the Reynolds stress close to the wall.

PHYSICAL ARGUMENTS

For several years a new debate concerning the mean velocity profile of canonical turbulent boundary layers with zero pressure gradient (ZGTBL) has taken place. Under this type of flow, a fully developed turbulent boundary layer which is free of any effects from roughness, wall curvature and outer turbulence is understood. Mostly experiments are interpreted to confirm or reject one or another theory. Therefore, we will start here with a short physical argument on why a Reynolds number dependence of the mean profile of a ZGTBL exists and persists until Re reaches infinity.

First Argument: Horse shoe vortices which are connected with the wall reach far into the outer region of the boundary layer and fluid structures from the outer region dive deep into the boundary layer [1]. If viscous structures reside in the so-called inertial sublayer of the ZGTBL, then such layer does not exist in reality.

Second Argument: The quantity that appears in the momentum equation is the Reynolds shear stress gradient and not the Reynolds shear stress itself. The momentum balance for channel and pipe flow is:

$$-\frac{1}{\rho}\frac{dp}{dx} + \frac{d\tau}{dy} + \nu\frac{\partial^2 U}{\partial y^2} = 0 \qquad \text{with } \tau = -\overline{uv} \tag{1}$$

At the position where the shear stress has its maximum, the second term $d\tau / dy$ of eq. (1) becomes zero. In the vicinity of this point, pressure force is only balanced by viscous force. The conclusion is that at least in channel and pipe flow viscous forces are of importance in a region that has been thought to be inertial [2].

Third Argument: Instead of a definition, mostly a syndrome is used to characterize a flow as turbulent. This turbulence syndrome consists of several symptoms among them the energy cascade describing the energy transport from turbulence production to dissipation [3]. This process can be observed in all y-regions of a ZGTBL meaning that throughout the entire boundary layer friction is of importance to maintain this energy cascade.

All three arguments together crumble the arguments for a simple log law with constant parameters. A more sophisticated mean velocity profile can be either derived based on first-principles employing Lie-group theory [4], or by extending the classical two-layer approach to higher-Reynolds-number dependent terms [5].

THE GENERALIZED LOG LAW

Traditionally the ZGTBL is split into an inner and an outer layer. While in the inner zone friction dominates, in the outer layer inertia is more important. It is assumed that each can be described with an asymptotic expansion.

$$\text{inner layer:} \quad u^+ \sim \sum_{i=0}^{n} \gamma_i(\delta^+)\, u_i^+(y^+) \qquad \text{outer layer:} \quad U \sim \sum_{i=0}^{n} \Gamma_i(\delta^+)\, U_i(\eta) \tag{2}$$

Here u^+ and y^+ denote the non-dimensional velocity u/u_τ and coordinate $y\,u_\tau/\nu$ of the inner layer, U is the non-dimensional velocity $(u-u_\delta)/u_\tau$, and η the non-dimensional coordinate of the outer layer, $\gamma_i(\delta^+)$ and $\Gamma_i(\delta^+)$ are gauge functions depending on the Kármán number $\delta^+ = \delta\, u_\tau/\nu$. We generalize an idea of Afzal [6] and obtain after a considerable amount of algebra the generalized log law for the inner layer follows:

$$u^+ = \sum_{i=0}^{n} \frac{1}{\delta^{+i}} \left(\frac{1}{\kappa_i} \ln\left(y^+ + D_i\right) + G_{1,i} \exp\left(-G_{2,i}\,\eta\right) \right) \tag{3}$$

For $\delta^+ \Rightarrow \infty$ and $\eta \Rightarrow 0$ the simple log law with an additional constant inside the logarithm is obtained. Due to this constant the generalized log law does not show a straight line in the semi-logarithmic plot. For simplicity we assume that in the vicinity of the wall the exponential term in eq. (3) is close to 1 and $D_i = D_1$ and after rearranging eq. (4) follows.

This relation signifies that the parameters of the generalized log law κ and B are Reynolds number dependent (for details see [5]). Note that the Kármán number is strongly related with the momentum thickness Reynolds number Re_Θ.

$$u^+ = \sum_{i=0}^{n} \frac{1}{\delta^{+i}} \frac{1}{\kappa_i} \ln\left(y^+ + D_1\right) + \sum_{i=0}^{n} \frac{1}{\delta^{+i}} G_{1,i} = \frac{1}{\kappa\left(\delta^+\right)} \ln\left(y^+ + D_1\right) + G_1\left(\delta^+\right) \qquad (4)$$

MIXING LENGTH APPROACH FOR THE GENERALIZED LOG LAW

To extend eq. (4) to the wall, we employ a mixing-length approach originally introduced by Chapman & Kuhn [8] for the simple log law. This mixing-length approach was reformulated (5a) to ensure that eq. (4) is satisfied. Taylor series expansion (5b) at $y^+ = 0$ shows that the new approach has the correct y^{+3} - dependency in the vicinity of the wall.

$$l^+ = \kappa\left(\delta^+\right)\left(y^+ - D_1\right)\left(1 - \exp\left(-\frac{y^+}{\lambda^+\left(\delta^+\right)}\right)\right)^{\frac{3}{2}} \qquad (5a)$$

$$-\overline{uv} = \frac{D_1^2 \kappa\left(\delta^+\right)^2 y^{+3}}{\lambda^+\left(\delta^+\right)^3} + O\left[y^{+4}\right] = A\left(\delta^+\right) y^{+3} + O\left[y^{+4}\right] \qquad (5b)$$

Analysing ZGTBL data from Österlund [7] the parameters for the mixing-length approach were derived. It is found that while κ (fig. 1), G_1 and the damping factor λ^+ depend on the Kármán number the factor A (fig. 2) is nearly constant and has a value of $6 * 10^{-4}$ which is close to $4 - 8 * 10^{-4}$ given in [3].

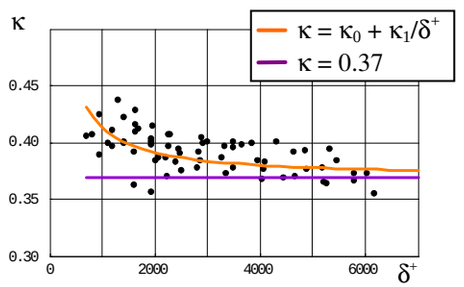


Fig. 1: Kármán "constant" for generalized log law

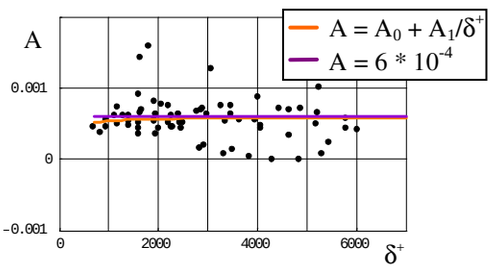


Fig. 2: Parameter A from eq. 6

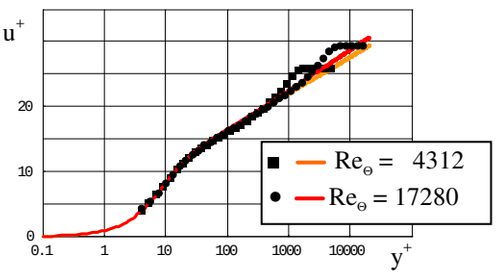


Fig. 3: Mean velocity profile (full line: calculation, symbols: experiments from Österlund [7])

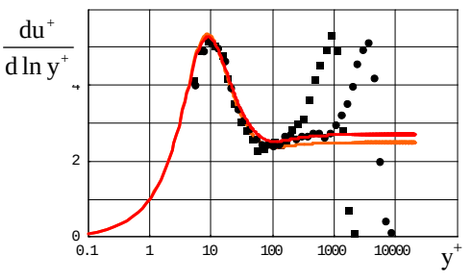


Fig. 4: Normalized gradient of mean velocity profile (curves and symbols as fig. 3)

CONCLUSIONS

Physical arguments which explain the Reynolds number dependence of the mean velocity profile of a turbulent boundary layer are discussed. Based on these ideas the two-layer approach is extended and a generalized log law is derived. A mixing-length approach originally introduced for the simple log law is reformulated to extend the new log law to the wall. Taylor series expansion shows that the new mixing-length approach has the correct y^{+3}-dependence close to the wall.

References

[1] Head, M.R., Bandyopahyay, P.: New aspects of turbulent boundary-layer structure. *J. Fluid Mech* **107**:297-338, 1981.
[2] Sreenivasan, K.R., Sahay, A.: The persistence of viscous effects in the overlap region, and the mean velocity in turbulent pipe and channel flows. *arXiv:physics/9708016v1* 1997
[3] Gersten, K., Herwig, H.: Strömungsmechanik. *Vieweg*, 1992
[4] Oberlack M.: A unified approach for symmetries in plane parallel shear flows. *J. Fluid Mech* **427**:299-328, 2001.
[5] Buschmann, M.H., Gad-el-Hak, M.: Generalized logarithmic law and its consequences. *AIAA J.* **41**:40-48, 2003.
[6] Afzal, N.: Millikan's argument at moderat Reynolds number. *Phys Fluids* **19**:600-602
[7] Österlund, J.M.: Experimental studies of zero pressure-gradient turbulent boundary layer. *Thesis* Stockholm, 1999
[8] Chapman, D.R., Kuhn, G.D.: The limiting behaviour of turbulence near a wall. *J. Fluid Mech* **170**:265-292, 1986

SUB- AND SUPERSONIC SHAPES WITHOUT SEPARATION AND CAVITATION

Ihor Nesteruk
Institute of Hydromechanics, NASU, Zheliabova 8/4, 03680 Kyiv, Ukraine

Summary The slender body theory was applied to calculate axisymmetric bodies with negative pressure gradients at the surface to ensure an unseparated flow pattern and to improve cavitation inception characteristics. A method of calculating of axisymmetric and plane shapes in ideal compressible fluid, based on the potentials of sources and doublets located in the axis of symmetry is proposed. Experimental investigations of axisymmetric shapes with specific pressure distribution are reviewed. Some of such forms ensure unseparated flow pattern at relative small Reynolds numbers. Since the origin of cavitation on a smooth shape is connected with separation, presented bodies could ensure the flow of liquid without cavitation.

AXISYMMETRIC SHAPES WITH NEGATIVE PRESSURE GRADIENTS IN INCOMPRESSIBLE FLUID

There are two ways of obtaining the unseparated forms. The simplest one is to use very slender bodies or very thin profiles, which probably ensure no separation independent of the pressure distribution over the surface. The slender 2D and axisymmetric shapes are investigated in [1] with the use of the Kochin-Loitsiansky method of local similarity (see [2]). A parabolic symmetric profile with the coordinate of the upper surface $Y(x) = 4\varepsilon(1-x)x$ and a body of revolution with the same parabolic generatrix were chosen in [1] to estimate the value of the thickness parameter ε sufficient for the unseparated flow pattern. The calculations show that the separation occurs for very small values of the thickness parameter ε. For example, even for ε=0.01 the coordinates of the separation point are 0.906 (in the 2D case) and 0.912 (in axisymmetric flow). Thus, the simplest way of avoiding the separation is of limited practical interest.

The second way of preventing separation is to use some special forms with appropriate pressure distributions. For example, negative pressure gradients at the body surface are necessary to avoid the separation (see [2,3]). The majority of the researchers consider the minimum of the static pressure coincident with the maximum of the body radius (or with the maximum of the thickness in the 2D case). Moreover, they assume that the pressure gradient is positive after the maximum thickness point. This paradigm was realized in so-called laminarized forms ([3]) obtained by shifting the maximum thickness point as far downstream as possible. It would be interesting to investigate if it is possible to have negative pressure gradients after the maximum thickness point too?

The first approximation of the slender body theory [4] yields the following equation relating the axisymmetric body radius $R(x)$ and the pressure coefficient $Cp(x)$ at its surface (see [1,5]):

$$\frac{d^2R^2}{dx^2} = -\frac{Cp(x)}{\ln\varepsilon}. \tag{1}$$

To make the trailing edge sharp, discontinuities of dR^2/dx or d^2R^2/dx^2 at some point x_*, $0<x_*<1$ are required (see [6]). According to the first approximation equation (1), the discontinuity of the second derivative d^2R^2/dx^2 provides the discontinuity of the pressure. An example of such a solution obtained in [7] has the following form:

$$Cp(x) = \begin{cases} -ax - 2c, & 0 \le x < x_* \\ -a_1(x-1), & x_* \le x \le 1 \end{cases}; \qquad R^2(x) = \begin{cases} Ex^2(ax+6c), & 0 \le x \le x_* \\ Ea_1(x-1)^3, & x_* \le x \le 1 \end{cases}, \quad E = \frac{1}{6\ln\varepsilon} \tag{2}$$

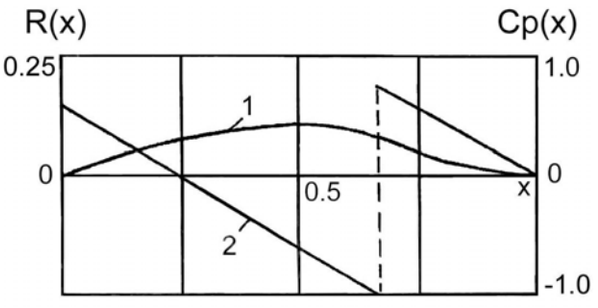


Fig.1 Shape with a negative pressure gradient. First approximation.

.

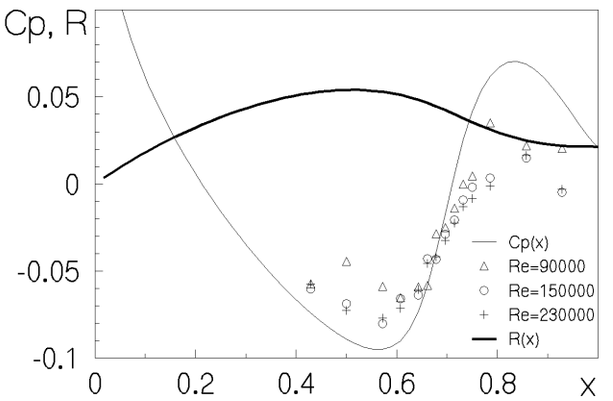


Fig.2. Exact solution. Body radius, theoretical and experimental pressure distributions.

An example of the corresponding axisymmetric shape (curve 1) and the pressure distribution (curve 2) are shown in Fig. 1. To improve the accuracy (eq. (1), (2) are not valid near the point $x = x_*$), some exact solutions of the Euler

equations have been calculated, which can be applied to non-slender bodies as well (see [1, 6, 8]). For this purpose, sources and sinks were placed in the axis of symmetry. The first approximation for their intensity $q(x)$ can be obtained from equation (2) and the relationship $q(x) = \pi dR^2 / dx$ (see [2]):

$$q(x) = \begin{cases} 3\pi Ex(ax + 4c), & 0 \le x < x_* \\ 3\pi Ea_1 (x-1)^2, & x_* \le x \le 1 \end{cases} \qquad (3)$$

The appropriate analytical formula for the stream function $\Psi(x,r)$ is presented in [9]. An example of calculations and the experimental pressure distributions for different Reynolds numbers are shown in Fig. 2. The shapes presented in Figs. 1,2 show that the pressure growth downstream of the maximum thickness point is not obligatory. No separation occurred at the body shown in Fig.2 for 90000<Re<300000. Similar 2D profiles with a negative pressure gradient near to the trailing edge are calculated in [1, 9].

AXISYMMETRIC AND 2D SHAPES WITHOUT SEPARATION IN COMPRESSIBLE FLOW

The results presented above can be easily generalized for the compressible flow. Using the stream function of the sources located in the axis of symmetry the following eqs. can be written in sub- and supersonic cases respectively:

$$\Psi(x,r) = 0.5r^2 - \frac{1}{4\pi}\int_0^1 \frac{(x-\xi)q(\xi)d\xi}{\sqrt{(x-\xi)^2 + (1-M^2)r^2}}; \quad \Psi(x,r) = 0.5r^2 - \frac{1}{2\pi}\int_0^{x-\omega r} \frac{(x-\xi)q(\xi)d\xi}{\sqrt{(x-\xi)^2 + (1-M^2)r^2}}, \ \omega = \sqrt{M^2-1} \qquad (4)$$

Here M is the Mach number at infinity. It was mentioned in [9] that the first approximation eq. (1) is valid both for a subsonic and for a supersonic flow, therefore substituting relationship (3) into eq. (4) analytic formulae for the stream function can be obtained. The body radius and the pressure distributions at different values of M are calculated.
It was shown in [10] that intensity of sources (3) can be used in 2D case to calculate the form of symmetric profile with negative pressure gradient both upstream and downstream the maximum thickness point, which can ensure unseparated flow pattern as well (unfortunately no wind tunnel tests were performed with such shapes). With the use of the stream function of the 2D sources located in the axis of symmetry similar eqs. can be written in sub- and supersonic cases. The coordinate of the upper surface of the profile and the pressure distributions at different values of M are calculated.

CONCLUSIONS

As the experiments show, the shapes with negative pressure gradients (similar to one shown in Fig.2 and to U-1, [1]) provide the unseparated flow pattern. The presented axisymmetrical and 2D forms are of considerable practical interest because they diminish the total drag (due to the small value of pressure drag and the delay of the laminar-turbulent transition). Using such shapes in water should improve the cavitation characteristics, too, since separation is the main reason of cavitation inception (see theoretical considerations in [1, 11] and experimental arguments in [11]). The water tunnel tests are necessary to investigate the cavity inception characteristics of the presented shapes. Unfortunately, the required equipment is not available in Ukraine. Further experimental investigations of the presented bodies and the profiles at higher Reynolds and Mach numbers are also necessary.

References

[1] Nesteruk I.: Can Shapes with Negative Pressure Gradients Prevent Cavitation. 4th ASME/JSME Joint Fluids Engineering Conference, Honolulu, USA, July 2003: FEDSM2003-45323, 2003.
[2] Loitsiansky L.G.: Mechanics of liquid and gas. Moscow, Nauka, 1978 (In Russian).
[3] Schlichting H.: Entstehung der Turbulenz, Handbuch der Physik, v. VII/1. : 341-450, 1959.
[4] Cole J.D.: Perturbation Methods in Applied Mathematics. Blaisdell, Waltham, Toronto, London, 1968.
[5] Nesteruk I.: Investigation of Slender Axisymmetric Cavity Form in Ponderable Fluid. Izv. AN SSSR, MZhG **6**: 133-136, 1979 (In Russian).
[6] Buraga O.A., Nesteruk I., and Shepetyuk B.D.: Subsonic Axisymmetric Forms with a Pressure Jump on the Surface. Naukovi visti, NTUU "Kyiv Polytech. Inst." 1(15): 90-99, 2001 (In Ukrainian).
[7] Nesteruk I.: Some Problems of Slender Axisymmetric Cavitator Dynamics. Transactions of Boundary Problems Seminar in Kazan University, 24: 187-197, 1990 (In Russian).
[8] Nesteruk I.: Experimental Investigation of Axisymmetric Bodies with Negative Pressure Gradients. Aeronautical Journ. **104**: 439-443, 2000.
[9] Nesteruk I.: Body forms of minimal drag. Dopovidi AN Ukr.SSR, ser. A, 4: 57-60, 1989 (in Ukrainian).
[10] Nesteruk I.: Plane Subsonic Forms with Negative Pressure Gradients on Surface. Dopovidi NANU **9**: 63-68, 2001.
[11] Takahashi S., Washio S., Uemura K., Okazaki A.: Experimental study on cavitation starting at and flow characteristics close to the point of separation. Fifth Symposium on Cavitation (Cav2003): No. Cav03-OS-3-003, 2003.

XXI ICTAM, 15–21 August 2004, Warsaw, Poland

NON-UNIQUE QUASI-EQUILIBRIUM TURBULENT BOUNDARY LAYERS

Bernhard Scheichl, Alfred Kluwick
Institute of Fluid Mechanics and Heat Transfer, Vienna University of Technology,
Resselgasse 3/E322, A-1040 Vienna, Austria

Summary An asymptotic investigation of turbulent boundary layers having a moderately large velocity defect is presented. It extends the classical small-defect theory insofar as the defect is measured by a second perturbation parameter besides the sufficiently large global Reynolds number. Most remarkably, the theory is capable of describing non-uniqueness of quasi-equilibrium flows, a property which has been discussed intensively in the literature.

MOTIVATION AND PROBLEM FORMULATION

Near-equilibrium turbulent boundary layers play an important role in internal flow situations. In particular, here diffuser flows serve as a typical engineering application. In such a flow configuration the boundary layer has to sustain a preferably large pressure rise, exerted by the external irrotational bulk flow, whereas the flow shall remain strictly attached. In order to prevent separation it is advisable to control the pressure gradient such that the boundary layer globally admits a self-preserving state, or, equivalently, remains close to equilibrium. As a well-established condition necessary for self-similarity, the streamwise velocity component at the boundary layer edge must vary as a power m of the streamwise coordinate. Moreover, it has been commonly argued on a partially empirical basis that $m > -1/3$, cf. [4].
On the other hand, it is known from experiments that $m \approx -0.22$ characterises a boundary layer exhibiting identically vanishing wall shear ([3]). As a consequence, this suggests that (at least) double-valued solutions are possible as the associated exponent m measuring the strength of the pressure gradient may fall below that critical value but is greater than $-1/3$. Indeed, in the past several studies indicated the non-uniqueness of turbulent near-equilibrium boundary layers ([3], [4]). An early hint is given by Clauser in his pioneering experimental work [1]. Most notably, an explicit clue is found in [5]: In that study the impact on diffuser design of boundary layer flow that withstands a pressure increase much larger than one provoking separation was investigated numerically using an integral method.
However, this striking feature of near-equilibrium flow has not been investigated so far by a strict rational approach based on first principles. It is, among others, the primary objective of our presentation to elucidate this particular flow structure by means of an asymptotic analysis of the Reynolds-averaged Navier–Stokes equations in the limit of a large global Reynolds number *Re*. To this end, first the few basic assumptions underlying the 'classical' theory of self-preserving boundary layers for $Re \to \infty$ have to be summarised briefly.

ASYMPTOTIC THEORY OF SELF-SIMILAR BOUNDARY LAYERS

The 'classical' limit

A rational asymptotic description of high Reynolds number wall-bounded turbulent shear flows has been formulated first in the early 1970ies, see e.g. the seminal paper of Mellor [2]. It can be shown that this self-consistent theory effectively exploits well-known dimensional arguments which determine the scaling of the viscous sublayer adjacent to the wall and is based on a two-layer structure. Inside the viscous wall layer the streamwise velocity component is of $O(1/\ln Re)$. Matching with the results holding in the fully turbulent main layer yields the celebrated universal logarithmic law of the wall. Moreover, it requires that the velocity defect with respect to the imposed external streamwise velocity U_e as well as the boundary layer thickness δ, non-dimensional with a global length scale, are asymptotically small and also of that magnitude. As a result, the theory does not cover separating flows which apparently exhibit a velocity defect of $O(1)$.
It is demonstrated in [3] on basis of this classical approach that equilibrium flows are characterised by a Rotta–Clauser parameter which varies only slowly in streamwise direction x. Let y denote the distance normal to the wall, it is given by

$$\beta(x) = -\frac{\delta^* U_e \,\mathrm{d}U_e/\mathrm{d}x}{\tau_w} = O(1), \quad \text{with} \quad \delta^* = \int_0^\delta (1 - u/U_e)\,\mathrm{d}y. \tag{1}$$

Furthermore, one infers from the leading-order integral momentum balance that $\beta \sim -m/(1+3m)$. Consequently, the classical theory ceases to be valid as $m \to -1/3_+$ since it predicts an unbounded growth of both the velocity defect and the boundary layer thickness. In present literature this failure is commonly attributed to incipient separation ([3]). In contrast to this suggestion it is shown here that this failure can be avoided by a generalized small-defect theory which is based on a three- rather than a two-layer structure. While the velocity defect is still small, it is, however, asymptotically large compared to the one assumed in the classical case.

Distinguished limit $\beta^{3/2}/\ln Re = O(1)$

In the new theory the double limit $\beta \to \infty$, $Re \to \infty$ considered is found to implicate a wake-type flow in the outermost layer which in fact closely resembles a separating flow. Here the defect is measured by a second small parameter besides $1/\ln Re$ which, among others, characterises the slenderness of the boundary layer. In contrast to the classical analysis,

the new one accounts for weakly nonlinear effects due the inertia terms in the equations of motion. Introduction of the coupling parameter $\Gamma \propto \beta^{3/2}/\ln Re = O(1)$ leads to a new distinguished limit where the still finite wall shear enters the flow description in second order. There the solution is shown to satisfy a solvability condition derived from the integral momentum balance. Assuming strict equilibrium up to second order, the resulting algebraic relationship can – without adopting any turbulence closure – be cast into canonical form,

$$9\hat{D}^2\hat{\mu} = 1 + \hat{D}^3, \quad \text{with} \quad \hat{D} \propto \Gamma^{1/3}, \tag{2}$$

which clearly reveals a double-valued flow structure, see the dashed curve in figure 1 (a). Here $\hat{D}$, and $\hat{\mu}$ measure the velocity defect and the small deviation of the exponent m, characteristic of the external flow, from $-1/3$, respectively. From (2) the fundamental conclusion can be drawn that for high but finite values of *Re* the effects caused by nonlinearities indeed imply a restriction $m > -1/3$, where $m + 1/3 \propto \hat{\mu}/(\ln Re)^{2/3}$.

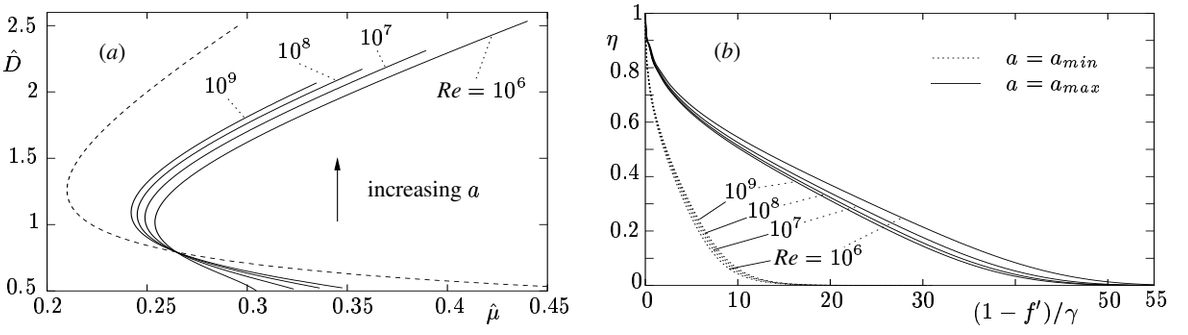


Figure 1. (a) Defect measure $\hat{D}$ (canonical scaling), (b) defect profiles (classical scaling) for different values of *Re*, $a_{min} \le a \le a_{max}$.

Comparison with numerical results for finite values of *Re*

In order to support the asymptotic results a numerical study was performed by solving the nonlinear boundary layer equations assuming strict equilibrium in the fully turbulent flow regime. By introduction of a suitably defined stream function $f(\eta)$ and by applying an appropriate similarity transformation, they become

$$\begin{gathered} m(f'^2 - 1) - (1+m) f f'' = \tau'/a, \quad \eta = y/\delta, \;\; a = \mathrm{d}\delta/\mathrm{d}x = const; \\ \eta \to 0: \;\; f' \sim (\gamma/\kappa)\ln(\eta\, a\gamma Re), \;\; \tau \sim \gamma^2, \;\; f \sim \eta f', \quad \eta = 1: \;\; f' = 1, \;\; \tau = 0. \end{gathered} \tag{3}$$

Here $\kappa \approx 0.42$ denotes the v. Kármán constant. The boundary conditions for $\eta \to 0$ reflect the behaviour of the flow in the overlap regime between the outer region and the viscous wall layer. To solve the resulting problem (3), it is supplemented with an (asymptotically correct) algebraic closure for the Reynolds shear stress τ. Prescribing a (sufficiently large) Reynolds number, a properly chosen (sufficiently small) linear increase of δ denoted by a as well as a minimum value of η, the exponent m is regarded as an eigenvalue and is thus part of the solution. This procedure allows to calculate the expected double-valued velocity distributions, plotted in figure 1 (b), for a given pressure gradient.

From a rigorous rational point of view (3) represents an *ad hoc* approximation of the full set of Reynolds equations. The Reynolds number enters the solution solely via the logarithmic near-wall portion of the flow. As a consequence, the asymptotic error is inherently of $O(\gamma)$. Therefore, extending the domain of the calculations to the boundary $\eta = 0$ by adopting a wall layer model would not improve the quality of the numerical solution in the limit $Re \to \infty$.

By integration of (3) from $\eta = 0$ to $\eta = 1$ one recovers the well-known v. Kármán's integral momentum balance, specified for equilibrium boundary layers. Introducing a canonical equilibrium shape factor $\hat{G} = O(1)$, it is written as

$$\beta(1+3m) = -m + (1+2m)\hat{D}^3, \quad \text{with} \quad \hat{D}^3 = \gamma\beta^{3/2}\hat{G}, \tag{4}$$

where the Rotta-Clauser parameter defined by (1) has to be calculated numerically. The solid curves in figure 1 (a) represent the associated solutions for $\hat{D}$ which show qualitatively good agreement with the predictions of the asymptotic analysis. There the Reynolds number enters in the form $1/\ln Re$, hence the collapse of the numerical results for finite values of *Re* onto the dashed line holding in the limit $Re \to \infty$ is rather slow. Finally, we note that the lower branches in figure 1 (a) reveal the classical results for $\hat{\mu} \to \infty$. In contrast, the upper branches indicate the existence of a fully nonlinear theory predicting a velocity defect of $O(1)$ and, in turn, even separated flows. This issue is a topic of current research.

References

[1] Clauser F.H.: Turbulent Boundary Layers in Adverse Pressure Gradients. *J. Aeron. Sci.* **21**:91–108, 1954.
[2] Mellor G.L.: The large Reynolds number, asymptotic theory of turbulent boundary layers. *Int. J. Engng Sci.* **10**:851–873, 1972.
[3] Schlichting H., Gersten K.: Boundary-layer theory. Springer, Berlin Heidelberg NY 2000.
[4] Schofield W.H.: Equilibrium boundary layers in moderate to strong adverse pressure gradients. *J. Fluid Mech.* **113**:91–122, 1981.
[5] Winter K.G., East L.F.: The Design of Optimum Diffusers for Incompressible Flow. In *Recent Contributions to Fluid Mechanics* (ed. W. Haase), 312–320, Springer, Berlin Heidelberg NY 1982.

NEAR CRITICAL UNSTEADY TREE-DIMENSIONAL TRIPLE DECK FLOWS

S. Braun and A. Kluwick
Institute of Fluid Mechanics and Heat Transfer, Vienna University of Technology, Resselgasse 3/E322, A-1040 Vienna, Austria

Summary Near critical, i.e. transitional laminar separation bubbles are studied using triple deck theory. The investigation is based on a local bifurcation analysis associated with the occurrence of non-unique solutions in the corresponding planar steady flow calculations. This leads to a substantial simplification of the primary problem formulation allowing a largely analytic description of the evolution of unsteady three-dimensional perturbations.

MOTIVATION

Earlier investigations of steady two-dimensional marginally separated laminar boundary layers [1], [2] in the limit of high Reynolds-numbers *Re* have shown that the non-dimensional wall shear (or equivalently the negative non-dimensional perturbation displacement thickness) is governed by a nonlinear integro-differential equation. This equation contains a single *controlling parameter* Γ characterizing, for example, the angle of attack of a slender airfoil and has the important property that (real) solutions exist up to a *critical value* Γ_c of Γ only. Recent investigations [3] of three-dimensional unsteady perturbations of such a steady two-dimensional marginally separated laminar boundary layer with special emphasis on the flow behaviour near Γ_c have shown that the integro-differential equation which governs these disturbances if $\Gamma_c - \Gamma = O(1)$ reduces to a nonlinear partial differential equation - known as (forced) *Fisher equation* - as Γ approaches the critical value Γ_c. The bifurcation analysis of this problem associated with the *non-uniqueness* of the steady planar flow thus leads to a significant simplification of the problem allowing, among others, a systematic study of the application of devices used in boundary layer control and an analytical analysis of the conditions leading to the formation of *finite time singularities* which have been observed in earlier numerical studies of unsteady two-dimensional and three-dimensional flows. Also it was found possible to construct exact solutions which describe waves of constant form travelling in the spanwise direction. These waves may contain singularities which can be interpreted as vortex sheets. The existence of these solutions strongly suggests that solutions of the Fisher equation which lead to finite time blow-up can be extended *beyond* the blow-up time thereby generating *moving singularities* which can be interpreted as vortical structures qualitatively similar to those emerging in direct numerical simulations of transitional laminar separation bubbles. This was further supported by asymptotic analysis. Additionally, it could be shown that finite time singularities describing the phenomenon of bubble bursting may occur in below-critical as well as above-critical situations. However, while this phenomenon requires a certain finite perturbation level if $\Gamma < \Gamma_c$ it is triggered by even infinitesimally small disturbances if $\Gamma > \Gamma_c$ where also *self-sustained oscillations* with periodically repeated bubble bursts ('vortex shedding') are possible. Multiplicity of solutions and critical values of the controlling parameter beyond which steady state solutions do not exist are a characteristic feature of marginally separated flows. However, similar phenomena do occur also in situations where triple-deck theory applies, i.e. in situations where a fully attached boundary layer is forced to separate due to the presence of a large adverse pressure gradient. Examples displaying such a branching behaviour include supersonic flows past flared cylinders, [4], subsonic flows past compression ramps and subsonic trailing edge flows, [5]. Furthermore, in a recent publication [6] it was argued that bursting processes in transitional boundary layer flows share common properties which do not depend on the specific problem under consideration. This suggests that an analysis similar to the one carried out for marginally separated boundary layers should be possible also in the context of classical triple deck theory which is the aim of the present paper.

SHORT OUTLINE

Specifically, we consider the example of the unsteady extension of subsonic planar ramp flow. Boundary layer separation and non-uniqueness of the steady problem was found for negative ramp angles (convex corners), see e.g. [5]. Let t, x, y and u, v denote suitably scaled quantities: time, coordinates in streamwise, wall normal direction and the corresponding velocity components. The governing equations for the flow field in the lower deck of the interaction region located at the corner supplemented with the interaction law then take the form

$$\frac{\partial u}{\partial t} + u\frac{\partial u}{\partial x} + v\frac{\partial u}{\partial y} = -\frac{\partial p}{\partial x} + \frac{\partial^2 u}{\partial y^2}\,, \quad \frac{\partial u}{\partial x} + \frac{\partial v}{\partial y} = 0\,, \quad p = -\frac{1}{\pi}\int_{-\infty}^{\infty} \frac{\partial (A-f)/\partial \xi}{\xi - x}\,\mathrm{d}x \tag{1}$$

with the boundary conditions $y = 0$: $u = v = 0$, $y \to \infty$: $u \sim y + A$, $x \to -\infty$: $u \sim y$. Here p is the pressure, A the displacement function and f the local shape of the (smooth) corner. Near the critical value $\alpha_c < 0$ of the ramp angle α the observed branching behaviour suggests a parabolic approximation of the corresponding field quantities:

$$\begin{aligned} &(u,v) \sim (u_c, v_c)(x,y) + \varepsilon^2 (u_1, v_1)(x,y,\bar{t}) + \varepsilon^4 (u_2, v_2)(x,y,\bar{t}) + \cdots\,, \\ &(p,A) \sim (p_c, A_c)(x) + \varepsilon^2 (p_1, A_1)(x,\bar{t}) + \varepsilon^4 (p_2, A_2)(x,\bar{t}) + \cdots\,, \quad f = f_c(x) + \varepsilon^4 f_2(x,\bar{t}) \end{aligned} \tag{2}$$

where we have introduced the perturbation parameter $\varepsilon^4 := \alpha - \alpha_c \to 0$ and the appropriate scaling $\bar{t} = \varepsilon^2 t$.
The leading order problem $O(\varepsilon^0)$ is simply given by the steady version of (1) at the branching point $\alpha = \alpha_c$. Higher order contributions $O(\varepsilon^{2i})$, $i = 1, 2$ can be written in the form $M\vec{r}_i = \vec{b}_i$, where M denotes a singular linear operator matrix, $\vec{r}_i = (u_i, v_i, p_i, A_i)$ the flow field perturbations and $\vec{b}_1 = \vec{0}$, $\vec{b}_2(\vec{r}_1, f_2)$ the right hand sides. Since M affects the x and y dependency of the field quantities only, one deduces $\vec{r}_1(x, y, \bar{t}) = c(\bar{t})\,\vec{r}(x, y)$. Furthermore, the right eigenfunction $\vec{r}$ of M can be expressed in terms of a single function, the 'perturbation' stream function ψ:

$$\vec{r} = \left(\psi_y, -\psi_x, -\lim_{y\to\infty}\frac{1}{\pi}\int_{-\infty}^{\infty}\frac{\psi_{y\xi}}{\xi - x}\,\mathrm{d}\xi,\ \lim_{y\to\infty}\psi_y\right) . \tag{3}$$

The evolution equation for the shape function $c(\bar{t})$ is obtained from the solvability condition (Fredholm alternative) at $O(\varepsilon^4)$, which finally yields

$$\frac{\mathrm{d}c}{\mathrm{d}\bar{t}} + \mu c^2 = \pm\bar{g}(\bar{t}) , \quad \alpha \gtrless \alpha_c . \tag{4}$$

Here $\mu > 0$ and $\bar{g}$ denote a constant and a forcing term associated with the evaluation of scalar products of left eigenfunctions of M and the right hand side $\vec{b}_2$. The special case of unforced flow characterized by $f_2(x, \bar{t}) = f_2(x)$, $\bar{g}(\bar{t}) = \delta = const > 0$ and subjected to the initial condition $c(\bar{t}_0) = c_0$ allows for an analytical solution of (4)

$$\frac{c}{c_s} = \frac{c_0 + c_s\tanh[\sqrt{\mu\delta}\,(\bar{t} - \bar{t}_0)]}{c_s + c_0\tanh[\sqrt{\mu\delta}\,(\bar{t} - \bar{t}_0)]} , \quad \alpha > \alpha_c , \qquad \frac{c}{c_s} = \frac{c_0 - c_s\tan[\sqrt{\mu\delta}\,(\bar{t} - \bar{t}_0)]}{c_s + c_0\tan[\sqrt{\mu\delta}\,(\bar{t} - \bar{t}_0)]} , \quad \alpha < \alpha_c . \tag{5}$$

The stationary points $\pm c_s$, $c_s = \sqrt{\delta/\mu}$ of (4) correspond to steady lower and upper branch solutions in the below-critical case $\alpha > \alpha_c$, Fig. 1(a), whereas *no* steady state exists for the above-critical regime $\alpha < \alpha_c$, Fig. 1(b). Finite time singularities are seen to develop if $c_0/c_s < -1$ under below-critical, but are found to be inevitable under above-critical flow conditions. Most interestingly, in both cases the corresponding solution can be continued *beyond* the blow-up time. In this context the important question arises, how these singularities can be *resolved* where the present theory breaks down locally by taking into account effects which have been neglected so far. The time period of self-sustained vortex shedding associated with above-critical flow conditions conveniently can be written in terms of the Strouhal-number

$$Str \propto Re^{1/4}(\alpha_c - \alpha)^{1/2} , \quad Re \to \infty , \ (\alpha_c - \alpha) \to 0^+ . \tag{6}$$

As can be shown, incorporation of three-dimensional effects indeed lead to nonlinear evolution equations of Fisher's type as in the case of marginally separated boundary layer flows. The properties of their solutions will be discussed in detail.

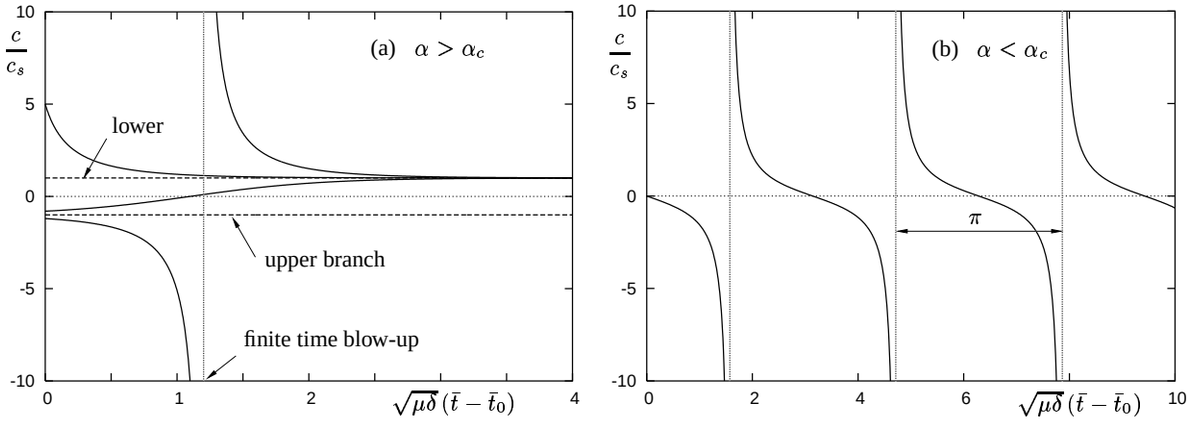


Figure 1: (a) Perturbations of *stable* lower and *unstable* upper branch solutions. (b) Self-sustained bubble bursting.

References

[1] Ruban A.I.: Asymptotic theory of short separation regions on the leading edge of a slender airfoil. *Izv. Akad. Nauk SSSR, Mekh. Zhidk. Gaza* **1** (Engl. transl. *Fluid Dyn.* **17**:33–41), 1981.

[2] Stewartson K., Smith F.T., Kaups K.: Marginal separation. *Stud. in Appl. Math.* **67**:45–61, 1982.

[3] Braun S., Kluwick A.: Unsteady three-dimensional marginal separation caused by surface mounted obstacles and local suction. *J. Fluid Mech.* (submitted), 2003.

[4] Gittler Ph., Kluwick A.: Triple-deck solutions for supersonic flows past flared cylinders. *J. Fluid Mech.* **179**:469–487, 1987.

[5] Korolev G.L.: Interaction theory and non-uniqueness of separated flows around solid bodies. In: Separated Flows and Jets (ed. V.V. Kozlov & A.V. Dovgal), 139–142. Springer, 1990.

[6] Borodulin V.I., Gaponenko V.R., Kachanov Y.S., Meyer D.G.W., Rist U., Lian Q.X., Lee C.B.: Late-stage transitional boundary-layer structures. Direct numerical simulation and experiment. *Theoret. Comput. Fluid Dynamics* **15**:317–337, 2002.

Long layers exhibiting local jumps, in industrial and biomedical applications

Frank T Smith
Mathematics Department
University College London
UK

Various interesting flow configurations, with applications in industry and biomedicine, are found to involve long-scale layers interacting with local property-jumping behaviours. At least three examples of these will be described, relating to ground effects, to multiple blades with wakes and to branching networks. The very latest developments will provide the focus of the presentation and these all concern computation hand in hand with theory / analysis.

Regarding somewhat more detail, as the submitted abstract essentially stated, in various interesting flow configurations, the long-scale thin layer problem interacts with the local property-jumping problem. A first example is that of modelling ground effect for cars. In two or three dimensions the boundary layer system over the scale of the car body and wake cannot be solved without the short-scale leading edge quasi-jump, and vice-versa. The second setting concerns modelling of multi-blade-and-wake behaviour for rotor performance. The short-scale response is again centred on the leading edge, while the long-scale response has interactive boundary layer form but (unusually) over the entire blade and wake. Third is branching flows, with special application to cardiovascular, respiratory, cranial branchings and networks. Short-long analysis agrees with direct simulations. Recent developments, which involve papers that have recently appeared or are shortly to appear with Bowles, Dennis, Jones, Ovenden, Purvis, Tadjfar, in J Engineering Mathematics , J Fluid Mechanics, 2001-2003, will be described throughout.

XXI ICTAM, 15–21 August 2004, Warsaw, Poland

SECONDARY INSTABILITY OF STATIONARY VORTEX PACKETS IN A SWEPT WING BOUNDARY LAYER

Valery G. Chernoray*, Alexander V. Dovgal**, Victor V. Kozlov**, Lennart Löfdahl*
*Thermo and Fluid Dynamics, Chalmers University of Technology, SE-412 96 Göteborg, Sweden
**Institute of Theoretical and Applied Mechanics, 630090 Novosibirsk, Russia

Summary The fact is that stationary vortex packets are most likely to be generated under natural flight conditions on the wing and these disturbances lead to breakdown the fastest. A detailed experimental study on the formation of crossflow vortex mode packets and their secondary instability in a swept wing boundary layer was carried out.

INTRODUCTION

There is a number of indications that three-dimensional velocity perturbations such as streamwise vortices and streaks are involved in transition to turbulence in wall bounded shear layers. Creating local flow distortions, they induce velocity gradients in spanwise and wall-normal directions, which in turn lead to the growth of secondary high-frequency disturbances with further laminar flow breakdown. This transitional phenomenon seems to be general for different flow configurations. The three-dimensional boundary layer of a swept wing is focused on in the current paper.

There are just a few experiments on the secondary instability of swept wing boundary layers. To our knowledge, there are as yet no experimental investigations available which reveal the spatial structure of the secondary instability modes and details of disturbance evolution across the transition region, even though such experiments are of great necessity. Under natural conditions of wing flow, transition packets of stationary crossflow vortex modes, rather than single-mode vortices, develop in the boundary layer. It emerged recently that secondary instabilities develop in a different way on the vortex packets than on the single-mode vortices. Both calculations [3] and experiments [1] show higher instability of packets of stationary crossflow modes as compared to single crossflow vortex modes, hence, a lower limit for secondary instability can be obtained through a consideration of the stability of such packets. Moreover, there are some indications that for crossflow vortices it is not absolutely required to reach a saturation state for a secondary instability to start to grow and this is additionally investigated.

The present experiments were designed with an idea of modelling the phenomenon under fully controlled conditions. In this work, which is mostly based on findings of work [1] utilizing very similar experimental set-up, secondary instability of various packets of stationary crossflow vortex modes is investigated. In our case, to resolve the secondary disturbances as much as possible, a method of point-by-point hot-wire visualization is employed.

PROCEDURE OF THE INVESTIGATION AND SELECTED RESULTS

The study is performed at Thermo and Fluid Dynamics, Chalmers University of Technology. All the experimental runs discussed in what follows were performed at the oncoming flow velocity of 8.2 $\mathrm{m\,s^{-1}}$, making the chord-based Reynolds number about 390000. All data were acquired from hot-wire measurements. The wing model has a C-16 aerofoil profile and was positioned at the sweep angle, Λ, of 45°, see figure 1. Different roughness elements or localized continuous suction were applied at 0.3 of the wing chord to generate stationary crossflow vortices in the boundary layer. High-frequency travelling disturbances evolving along the streaks were excited naturally or in a controlled manner using periodic blowing-suction.

A unique hot-wire traversing mechanism was developed, which is computer controlled and can be completely automated for long experimental runs through definition of a geometrical mesh of measurement points. The software used to control the sampling and saving of data files is linked into a program for automated, triggered flow measurements using the traverse system and a pre-defined mesh of sampling points. Using this high-precision equipment and fully automated experimental procedure it was possible to obtain detailed experimental data.

At first, secondary instabilities which occur naturally were studied and then, to allow phase-locked measurements, these disturbances were modelled and introduced artificially.

In figure 2 the oscillations developing behind the surface roughness element are shown. Two different modes of secondary disturbances are developing on the sides of the roughness element because of the specific symmetry properties of the flow. Different stationary vortex packets (of various symmetry and of different rotation) are to be triggered under 'natural' conditions as well.

In brief, it was observed that the secondary disturbances are located either inside the area of the streamwise velocity deceleration or near the position of highest spanwise gradient of this velocity component. The conditions which favour one or the other instability mode were investigated. As our analysis revealed, the preferred secondary instability modes of the vortex packets are dependant upon their direction of rotation, since different velocity gradients are induced. The presence of a strong positive $\partial U/\partial z$ gradient (of the same sign as the base crossflow) favours so-called 'z' mode of secondary instability. As this gradient is weak and the low-speed streak is wide, different instability mode (of 'y' type) is established within the low-speed streak, which among other properties has a significantly different amplification rate.

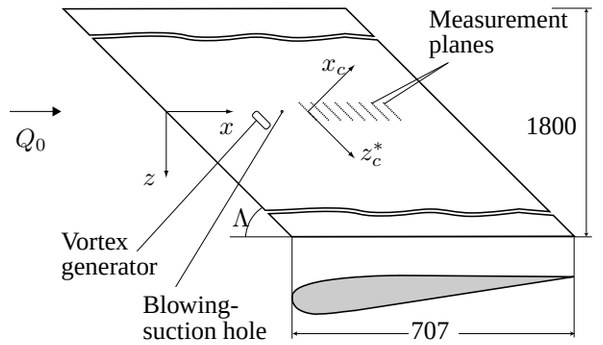


Figure 1. The swept wing model. Dimensions are in mm.

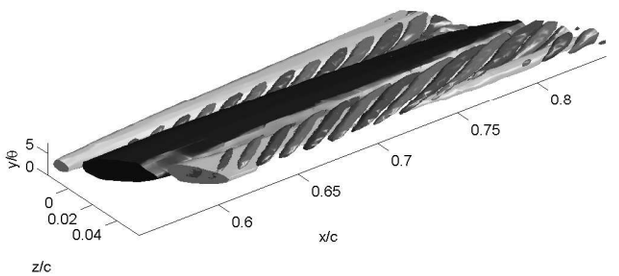


Figure 2. Forced periodical disturbances together with the stationary vortices are shown.

Beyond this, the width-to-height ratio of the primary vortex is also a parameter defining the secondary instability. The vortex packets are found to be more unstable as compared to single-mode disturbances.

CONCLUSIONS

As a result of the current study, experimental data on secondary instability in a swept wing boundary layer including characteristics of the base flow, primary streamwise vortices and secondary perturbations were obtained. Detailed measurements were performed with both stationary vortices and secondary instabilities excited in a controlled manner. The characteristics of secondary instability obtained include phase information, growth rates and the development of nonlinear harmonics.

References

[1] Boiko, A. V., Kozlov, V. V., Sova, V. A. & Scherbakov, V. A.: Generation of streamwise structures in a boundary layer of a swept wing and their secondary instability. *Thermophysics and Aeromechanics* **7** (1): 25–35, 2000.

[2] Kozlov, V., Sova, V. & Shcherbakov, V.: Experimental investigation of the development of secondary perturbations on a swept wing. *Fluid Dynamics* **36** (6): 909–914, 2001.

[3] Wassermann, P. & Kloker, M.: Mechanisms and passive control of crossflow-vortex-induced transition in a three-dimensional boundary layer. *J. Fluid Mech.* **456**: 49–84, 2002.

[4] Chernoray V.G., Dovgal A.V., Kozlov V.V., Löfdahl L.: Experiments on secondary instability of streamwise vortices in a swept wing boundary layer. Under consideration for publication in *J. Fluid Mech.*, 2004.

XXI ICTAM, 15–21 August 2004, Warsaw, Poland

DISCONTINUOUS SOLUTIONS OF THE BOUNDARY-LAYER EQUATIONS

Anatoly I. Ruban

Department of Mathematics, University of Manchester, Oxford Road, Manchester M13 9PL, UK

Summary In this presentation two examples of discontinuous solutions of the boundary-layer equations will be discussed. The first one represents an unsteady analogue of the well known two-dimensional laminar jet. We shall assume that the jet emerges from a narrow slit which was initially closed. The second example concerns the hypersonic boundary-layer flow on a delta wing in the regime of strong viscous-inviscid interaction.

It is already one hundred years since the time when Prandtl (1904) formulated the boundary-layer equations. Starting with his work it was always assumed that, due to the viscous nature of the boundary layers, the solution of the Prandtl equations should be sought in the class of continuous functions. Meanwhile, it can be easily seen that there are clear mathematical reasons for discontinuous solutions to exist. Moreover, discontinuous solutions not only form naturally in unsteady and/or three-dimensional flows, but under certain conditions represent the only possible solutions of the boundary-layer equations. In this paper we will give two examples of such flows.

The first one represents an unsteady analogue of the laminar jet studied by Schlichting as early as in 1933. In Schlichting's steady flow formulation the jet emerges from a narrow slit, as shown in Figure 1, and mixes with otherwise stagnant fluid to the right of the barrier OO'. As a result of the action of viscous stresses the fluid in the jet gradually loses its speed. Still the jet proves to be able to penetrate through the surrounding fluid over an infinite distance, with the velocity in the jet decaying gradually as $x \to \infty$. If the slit width is small, then the solution of the boundary-layer equations may be expressed in a simple analytical form

$$u = x^{-1/3} f'(\eta), \quad v = x^{-2/3}\Big(\frac{2}{3}\eta f' - \frac{1}{3} f\Big), \quad f(\eta) = \sqrt{6C}\,\frac{1 - \exp\Big(-\sqrt{\frac{2}{3}C}\,\eta\Big)}{1 - \exp\Big(\sqrt{\frac{2}{3}C}\,\eta\Big)}. \tag{1}$$

Here constant C characterises the strength of the jet; (x, y) are Cartesian coordinates with x measured along the jet axis and y in the normal direction; u, v are the velocity components in these coordinates and $\eta = y/x^{2/3}$ the similarity variable.

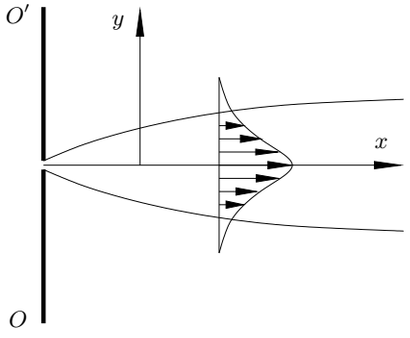


Figure 1. Problem layout

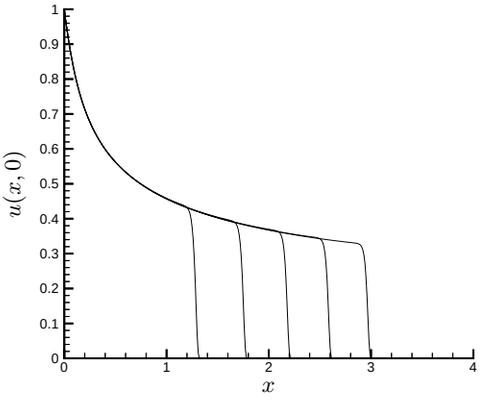


Figure 2. Velocity along the jet axis at $t = 4,\ 6,\ 8,\ 10$ and 12.

In our calculations we use unsteady boundary-layer equations. With t denoting time, the momentum and continuity equations are written as

$$\frac{\partial u}{\partial t} + u\frac{\partial u}{\partial x} + v\frac{\partial u}{\partial y} = -\frac{\partial p}{\partial x} + \frac{\partial^2 u}{\partial y^2}, \qquad \frac{\partial u}{\partial x} + \frac{\partial v}{\partial y} = 0. \tag{2}$$

The momentum equation is parabolic. It, apparently, does not allow for discontinuities in the y-direction to exist. However, the first two terms on the left hand side,

$$\frac{\partial u}{\partial t} + u\frac{\partial u}{\partial x},$$

represent a quasi-linear hyperbolic operator and, by analogy with one-dimensional gas dynamics, one can expect "shock waves" to form in the (t, x)-plane. For these to be captured a conservative scheme has to be used to calculate equations (2).

The calculations were performed assuming that initially the fluid to the right of OO' was kept at rest. At $t = 0$ the slit opens, and a jet starts to form. To illustrate the results of the calculations we show in Figure 2 the distribution of the fluid velocity along the jet axis. The five curves correspond to increasing time $t = 4,\ 6,\ 8,\ 10$ and 12. It is easily seen that the

jet has a well established front which propagates with finite speed in the x direction. Before the front the fluid remains at rest. Across the front the fluid velocity jumps to the value given by the first of formulae (1).

The thickness of the shocks in gas flows is known to be comparable with the molecular mean free path λ, which may be estimated as $\lambda = O(Re^{-1})$, where Re is the Reynolds number. The continuum description of fluid motion is not possible under these conditions. The "shocks" in boundary layers are significantly thicker. They extend in the longitudinal x-direction over a distance Δx comparable with the boundary-layer thickness $y = O(Re^{-1/2})$. Therefore the continuum description is well suited for analysing their internal structure, which is why we call them *pseudo-shocks*. Asymptotic analysis of the Navier-Stokes equations shows that the flow within a pseudo-shock may be treated as inviscid and quasi-steady provided that it is considered in the coordinate frame moving with the shock front. The governing equations may be written as

$$u\frac{\partial \omega}{\partial x} + v\frac{\partial \omega}{\partial y} = 0, \qquad \nabla^2 \psi = -\omega, \tag{3}$$

where ψ is the stream function and ω the vorticity.

The results of a numerical solution of equations (3) with appropriate boundary conditions are presented in Figure 3 in the form of the streamline pattern. It is displayed in the coordinate frame moving with the shock front. One can observe that there is a stagnation point in the flow field. Applying the Bernoulli equation to the two streamlines that lie along the x-axis upstream and downstream of the stagnation point respectively, it may be found that the speed of propagation of the shock front $V_{\rm shock} = \frac{1}{2}u_{\max}$. Here $u_{\max}$ is the maximum value of the longitudinal velocity in the jet immediately behind the shock. Figure 4 reproduces a photograph of a thermal jet made by Shlien & Boxman (1981). When comparing this photograph with the calculated streamline pattern it should be taken into account that the photograph was taken in the laboratory frame.

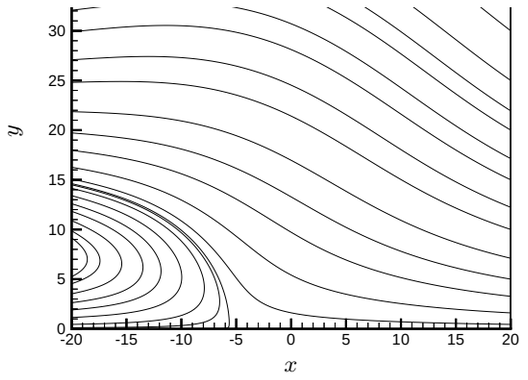


Figure 3. The streamline pattern.

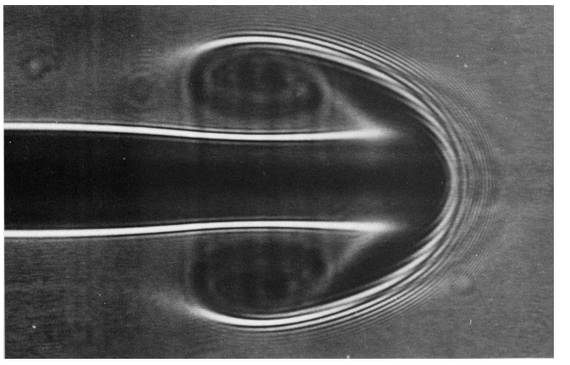


Figure 4. Visualisation of the jet head by Shlien & Boxman (1981).

In order to demonstrate that the pseudo-shocks are not uniquely attributed to unsteady two-dimensional boundary layers, we will also present the results of numerical analysis of the hypersonic flow past a delta wing. The calculations of this flow were performed under an assumption that the hypersonic viscous interaction parameter $\chi \gg 1$. In this case the boundary layer on the entire surface of the wing appears to be in strong interaction with the inviscid part of the flow. In these conditions the flow is governed by steady three-dimensional boundary-layer equations with self-induced pressure. We found that two pseudo-shocks are forming in the flow when the sweep angle of the wing is approaching a critical value. Contrary to earlier expectations (see, for example, Kozlova & Mikhailov, 1970) the shocks were found to lie off the plane of symmetry of the wing.

References

KOZLOVA, I. G. & MIKHAILOV, V. V. 1970 On strong interaction on delta and swept wings. *Izv. Akad. Nauk SSSR, Mech. Zhidk. & Gaza* (6), 94–99.

PRANDTL, L. 1904 Über flüssigkeitsbewegung bei sehr kleiner Reibung. In *Verh. III. Intern. Math. Kongr., Heidelberg*, pp. 484–491. Teubner, Leipzig, 1905.

SCHLICHTING, H. 1933 Laminare strahlausbreitung. *ZAMM* **13**, 260.

BOUNDARY LAYER DEVELOPMENT IN UNSTEADY FLOWS

Andrei Camyshev*, Andrei Kolyshkin*, Inta Volodko*
*Riga Technical University, Department of Engineering Mathematics, LV1048 Riga, Latvia

Summary The development of a boundary layer in unsteady viscous flows is analyzed in the present paper. Methods of linear and weakly nonlinear stability theory are used to investigate the stability characteristics of the flow.

INTRODUCTION

Rapidly changing unsteady flows are important in a wide range of applications. Examples include the design and analysis of water supply systems, flows in natural gas pipelines and flow of blood in arteries. Pump shutdowns or rapid changes in valve settings are known to generate unsteady flows in hydraulic devices or water supply systems. The pressure in unsteady flow can cause cavitation, pitting and corrosion [1]. An atherosclerosis plaque development in regions where shear stress changes direction can be triggered by blood flow unsteadiness [2]. In all these examples the flow characteristics (velocity and pressure) change considerably during short time intervals as a result of rapid deceleration or acceleration of the flow. In order to avoid possible problems associated with short time transients one needs to know the velocity, pressure and shear stress distribution in a channel or pipe.
In the present paper a mathematical model for the solution of rapidly changing unsteady flows is presented. The model is used to analyze the short time behaviour of viscous incompressible fluid subject to rapid deceleration. The paper is organized as follows. First, asymptotic solutions for unsteady laminar fluid flows in cylindrical channels of constant cross-section are derived. Three types of channels are considered: a plane channel, a pipe and an annulus. Flow region can be divided into two parts: a core region (where velocity distribution changes slowly) and boundary layer(s) near the wall where rapid changes are taking place. The method of matched asymptotic expansions is used to derive the solution and analyze the development of the boundary layer(s). Second, the velocity profiles of rapidly decelerating flows have inflection points and therefore are potentially highly unstable. Methods of linear stability theory are used to calculate stability characteristics of the flow under the quasi-steady assumption [3-6]. Hall and Parker [6] showed that the quasi-steady approach is justifiable if a perturbation grows faster than significant changes of the base flow can be observed. The quasi-steady assumption represents the first term of the asymptotic expansion of the WKB-type. It is shown that the critical Reynolds numbers decrease considerably as a result of rapid deceleration of the flow. The influence of the deceleration rate of the stability of the flow is investigated. Third, weakly nonlinear theory is applied in order to describe the evolution of the most unstable mode above the threshold. It is shown that the amplitude of the most unstable mode is governed by the complex Ginzburg-Landau equation.

MAIN RESULTS

The following model is proposed for the analysis of rapidly changing unsteady laminar flows. Consider an infinitely long horizontal cylinder of constant cross-section filled with a viscous incompressible fluid. The flow prior to acceleration or deceleration can be either steady or unsteady (but unidirectional). Starting from time $t = 0$ the flow is rapidly decelerated to zero (different types of channels and different transient scenarios are considered). Assume that the fluid flux through the cross-section of the channel has suddenly changed as a result of rapid deceleration. The change in velocity due to sudden change in pressure does not satisfy the no-slip condition at the wall of the channel (the process is initially inviscid). The sudden pressure change generates additional vorticity near the wall which starts to diffuse towards the core region of the channel. A boundary layer starts to develop near the wall as a result of diffusion. Thus, it is natural to divide the flow region into the (inviscid) core region (where the velocity distribution changes slowly) and the boundary layer(s) where rapid changes of the flow characteristics are taking place.
The method of matched asymptotic expansions is used to construct the solution. In particular, the core region is represented by the outer part of the expansion and the boundary layer is described by the inner part of the expansion. Excellent agreement between exact and asymptotic solutions for the case of a sudden blockage of a pipe is found for short time intervals. Calculations show that the velocity profiles of rapidly decelerating flows have regions of reverse flow with inflection points. Thus, these profiles are potentially highly unstable. Linear stability analysis is used to obtain the stability characteristics of the flow. The stability analysis is performed under the quasi-steady assumption. In other words, it is assumed that the rate of change of the base flow with respect to time is smaller than the growth rate of perturbations. The validity of the quasi-steady assumption for the analysis of rapidly changing unsteady flows in circular pipes is assessed in [3,4].
The linear stability problem is solved by a pseudospectral collocation method based on Chebyshev polynomials. Calculations show that the quasi-steady assumption gives reasonable results for rapidly decelerating laminar and turbulent flows in a pipe. Linear stability analysis for all three types of channels considered in the paper shows that the development of instability depends on the relative importance of two factors: the movement of the inflection point

towards the centre of the channel and the reduction of the difference between the largest and smallest values of the velocity as time increases. The critical Reynolds numbers decrease considerably during short time interval after deceleration. Both symmetric and asymmetric modes are studied for channels with cylindrical symmetry (circular pipe or annulus). It is shown that depending on the deceleration scenario either symmetric or asymmetric modes are the most unstable modes.

The results of linear stability calculations are compared with experimental data [5]. The results are found to be in qualitative agreement with experimental data in [5] (in terms of the pattern of the most unstable mode). The experimentally observed wavelengths of the most unstable mode are close to the values obtained by means of linear stability analysis.

Linear stability theory can be used to determine when does a particular flow become unstable. Methods of linear theory can be used to describe the structure of the critical motion above the threshold. However, linear theory cannot predict the evolution of the most unstable mode. Weakly nonlinear theories [7] are used to derive an evolution equation for the most unstable mode. The Ginzburg-Landau equation is one of the popular equations which is used to study nonlinear dynamics of the flow. Note that the Ginzburg_Landau equation is used in the literature in two ways: first, as a phenomenological equation and second, as an equation which appears in many hydrodynamic stability problems when weakly nonlinear analysis is applied. In the present paper weakly nonlinear theory is used to analyze the effect of nonlinearities analytically. It is shown in the paper that the amplitude of the most unstable mode above the threshold is governed by the complex Ginzburg-Landau equation. That is, the paper shows that the Ginzburg-Landau equation does not have to be assumed; it can be derived from the Navier-Stokes equations. The coefficients of the equation are evaluated numerically for several particular cases, namely, for the case of rapidly decelerating flow in a pipe and plane channel.

The Ginzburg-Landau model is compared with experimental data found in [5]. Some of the experiments in [5] indicate the presence of secondary vortices after the base flow loses stability. We calculated the coefficients of the Ginzburg-Landau equation for these cases. It is found that for all the cases where secondary motions were observed in experiments, the Landau constant was positive. Thus, the existence of a finite equilibrium state is also confirmed by the Ginzburg-Landau equation.

CONCLUSIONS

The paper analyzes the development of a boundary layer in rapidly decelerating viscous flows in channels of constant cross-section. The initial development of the boundary layer is described by the method of matched asymptotic expansions. The velocity profiles are found to contain inflection points. Linear stability theory is used to analyze the behaviour of the flow for short time intervals. It is found that the critical Reynolds numbers of the flow decrease as a result of rapid deceleration. The values of the critical Reynolds numbers depend on the deceleration rate. The shorter is the deceleration time, the greater is the decrease of the critical Reynolds numbers. Methods of weakly nonlinear theory are used to analyze the development of instability above the threshold. It is found that the amplitude of the most unstable mode is governed by the complex Ginzburg-Landau equation. The results are compared with available experimental data in the literature. Reasonable agreement between the experimental and theoretical data is found.

References

[1] Brunone, B., Karney, B., Mecarelli, M., Ferrante, M.: Velocity Profiles and Unsteady Pipe Friction in Transient Flow. *J. Wtater Res. Planning Managemen.t* **126**:236-244, 2000.

[2] Waters, S.L., Pedley, T.J.: Oscillatory Flow in a Tube of Time-Dependent Curvature. Part 1. Perturbation to Flow in a Stationary Curved Tube. *J. Fluid Mech.* **383**:327-352, 1999.

[3] Ghidaoui, M.S., Kolyshkin A.A.: A Quasi-Steady Approach to the Instability of Time-Dependent Flows in Pipes. *J. Fluid Mech.* **465**:301-330, 2002.

[4] Ghidaoui, M.S.,Kolyshkin, A.A. : Stability Analysis of Velocity Profiles in Water-Hammer Flows. *J. Hydr. Engng.* **127**:499-512, 2001.

[5] Das, D., Arakeri, J.H..: Transition of Unsteady Velocity Profiles with Reverse Flow. *J. Fluid Mech.* **374**:251-283, 1998.

[6] Hall, P., Parker, K. H.: The Stability of the Decaying Flow in a Suddenly Blocked Channel. *J. Fluid Mech.* **75**:305-314, 1976.

[7] Stewartson, K., Stuart, J.T..: A Non-Linear Instability Theory for a Wave System in Plane Poiseuille Flow. *J. Fluid Mech.* **48**:529-545, 1971.

NEW NUMERICAL METHOD FOR COMPLEX INTERACTING FLOWS

Vladimir B. Zametaev, Marina A. Kravtsova
Central Aerohydrodynamics Institute (TsAGI), Zhukovsky, Moscow reg., 140180, Russia

Summary New numerical method of second order accuracy for solving the boundary layer equation with interaction is suggested. Flow past a weak corner of a body contour was computed first. Second solved problem with using of proposed method is a mixing of boundary layers flowing from the edge of a wing.

New numerical method of second order accuracy for solving the boundary layer equation with interaction is suggested. It is well known that given displacement thickness defines solution of 2D boundary layer equation by the only way. Owing to this fact iterative methods were constructed to solve interactive problems. Taken first displacement thickness one can solve BL equation and find corresponding pressure gradient. Using computed pressure gradient new displacement thickness may be calculated through interaction law. Repeat of such steps gives a procedure to find the solution of the posted interacting problem. But convergence of such methods is not too high and depends essentially on the complexity of studied flow. Next important step in development of numerical methods was a so-called direct one, see Sychev *et al*. (1998) and references therein. That is equations at all points of grid are considered as algebraic equations which define corresponding unknown variables of flow field. Then this nonlinear algebraic system of equations is solved using Newton method. Advantage of this method is explicit form of Jacobian matrix which is computed at each iteration and gives high convergence. Shortcoming is too great amount of variables and as a result too big linear system to be solved at each iteration. Usually exact treating of such big linear system is possible using special measures. In spite of this shortcoming direct method is the most effective one at the time at least for 2D flows.

Proposed in this paper method is addressed to combine advantages of ones mentioned above. Displacement thickness function is considered as the only unknown grid function in the problem. As a result amount of unknowns equals to number of nodes along X-axis of grid. The main problem now is to create a set of equations which define this displacement thickness function. Such set of equations may be formulated as follows.
Interaction law taken from outer inviscid region of flow usually means linear relationship between displacement thickness function $A_i(x_i)$ and induced pressure gradient $\left.\frac{\partial p}{\partial x}\right|_{inv}$. From other side function $A_i(x_i)$ defines solution of BL equation and as a result gives $\left.\frac{\partial p}{\partial x}\right|_{v}$ unknown in advance. It is clear that difference between above pressure gradients must be zero if $A(x)$ is a solution of posted problem. As a result we can formulate set of implicit equations:

$$F_i = \left.\frac{\partial p}{\partial x}\right|_{inv} - \left.\frac{\partial p}{\partial x}\right|_{v} = 0 \qquad i = 1,..., NX .$$

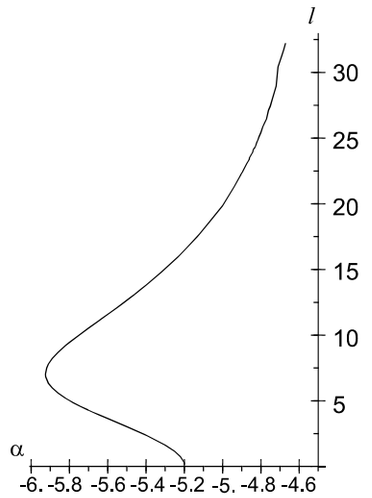
High convergence is based on Newton method of solving the implicit nonlinear system of equations. Unlike the direct method, Jacobian matrix in this case must be computed numerically with aid of a special procedure. Initial system of BL equation was linearized at each iteration on basis of current solution. Solving of linear system for unity perturbations of grid function $A_i(x_i)$ at each node i gives perturbations of pressure gradient and as a result Jacobian matrix. Interesting advantage is found that computation of Jacobian matrix may be made by parallel processors simultaneously. It is important to say that given method may be very effective for 3D flows in comparison with direct one in which number of algebraic equations becomes enormous.

Flow past a weak corner of a body contour was computed as a test. This problem was posted by Stewartson (1970). The results are displayed in figure (a) the growing of length of separation region l against α values and (b) streamlines of the solution for $\alpha = -4.67$ for large separation zone. Method allowed to derive two branches of the solution (a).

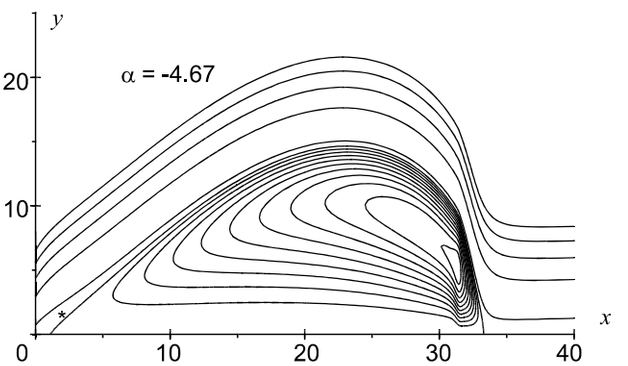
Method was used for complex flow calculation namely for mixing of two boundary layers with interaction which flow past lateral or trailing edge of a wing. The wing was replaced by a flat plate. The interaction problem is similar to symmetrical one near a trailing edge of a flat plate which was formulated by Stewartson (1969) and Messiter (1970). In the considered case the flow is not symmetrical one and contains two parameters $\frac{\lambda_+}{\lambda_-}$ and $\left(\frac{u_+}{u_-}\right)^2$ which mean skin friction and velocity relations in the unperturbed free stream on the upper and lower side of the plate. Additional condition for this flow is equality of pressures in the wake computed from upper and bottom potential flows. To calculate such flow upper and bottom displacement functions were taken as independent variables. Upper pressure is found as a function of upper displacement thickness. Solution of a mixed problem of seeking of analytical function in

lower half plane gives a pressure distribution on the lower side of plate. As a result pressure distribution on the surface is a linear function of both displacement thicknesses and implicit set of equations introduced earlier are applicable for the problem.

The research was supported in part by the Russian Foundation for Basic Research under grant No. 03-01-00918.



(a)



(b)

References

[1] Sychev V.V., Ruban A.I., Sychev Vic.V., Korolev G.L.: *Asymptotic Theory of Separated Flows*, Cambridge University Press, 1998.
[2] Stewartson K.: On the flow near the trailing edge of a flat plate. *Mathematika* **16**, 106-121, 1969.
[3] Messiter A.F.: Boundary-layer flow near the trailing edge of a flat plate. *SIAM J. Appl. Math*. **18**, 241-257,1970.
[4] Stewartson K.: On laminar boundary layers near corners. *Q. J. Mech. Appl. Math*. **23**, 137-152, 1970.

WHY DO DOLPHINS HAVE CUTANEOUS RIDGES?

Peter W. Carpenter, Reza Ali
School of Engineering, University of Warwick, Coventry, CV4 7AL, U.K.

Summary We present a simplified DNS study of 3D disturbances created in a laminar boundary layer with zero external pressure gradient by a line body force, located at the boundary-layer edge, and that varies harmonically with time and sinsusoidally in the spanwise direction. We study walls, that are both rigid and compliant, whose undisturbed surfaces take the form of a small-amplitude static wave with crests normal to the freestream direction. This is analogous to the dolphin's cutaneous ridges.

INTRODUCTION

The existence of small-scale static undulations on the outer surface of dolphin skin has been known for some time[1,2]. These features are known as cutaneous ridges or microscales. They appear as rings around the body, with wave crests aligned approximately normal to the freestream direction, and have wave-lengths of the order of 250 μm, about 5 to 8 times the wave (or 'roughness') height. No function, hydrodynamic or otherwise, has hitherto been suggested for the cutaneous ridges. Here we report on a simplified DNS study that was originally developed to study the effects of manufacturing imperfections in compliant walls used for drag reduction in marine applications. It will be shown that for rigid walls the static wall waves have a similar effect to conventional roughness, namely the boundary-layer disturbances (Tollmien-Schlichting waves) are destabilized and transition advanced. In contrast, for compliant walls, there is a range of 'roughness' wave-lengths for which the 3D TS waves grow less rapidly than over smooth walls.

COMPUTATIONAL METHODS

The velocity-vorticity method of Davies and Carpenter[3] is used for our study. All variables are assumed to be non-dimensional with the freestream speed, U_∞, and boundary-layer displacement thickness, δ^*, used as reference. Only three primary variables are used, namely ω_x, ω_y, w that are respectively two components of the perturbation vorticity and the wall-normal perturbation velocity. These satisfy three governing equations of the form:

$$\frac{\partial \omega_x}{\partial t}+\frac{\partial N_z}{\partial y}-\frac{\partial N_y}{\partial z}=\frac{1}{R}\nabla^2\omega_x-\frac{\partial F_y}{\partial z}, \qquad \frac{\partial \omega_y}{\partial t}+\frac{\partial N_x}{\partial z}-\frac{\partial N_z}{\partial x}=\frac{1}{R}\nabla^2\omega_y+\frac{\partial F_y}{\partial x}, \qquad (1a,b)$$

$$\nabla^2 w=\frac{\partial \omega_x}{\partial y}-\frac{\partial \omega_y}{\partial x}, \qquad (1c)$$

where x, y, z are respectively the streamwise, spanwise and wall-normal co-ordinates, $R=U_\infty\delta^*/\nu$, F_y is the only non-zero component of the body force, and

$$\vec{\mathbf{N}}=\vec{\Omega}\times\vec{u}+\vec{\omega}\times\vec{U}+\vec{\omega}\times\vec{u} \qquad (2)$$

where $\vec{U}$, $\vec{\Omega}$ are the base-state velocity and vorticity, and $\vec{u}$, $\vec{\omega}$ the perturbation velocity and vorticity. In [3] it is shown that subject to rather general conditions as $z\to\infty$ eqs. (1a,b,c) are fully equivalent to the Navier-Stokes equations in primitive variables; it is also shown how the remaining perturbation components and pressure can be determined entirely in terms of the three primary variables. The method can be used to carry out full direct numerical simulations, but here we omit the last term on the right-hand side of eq. (2), thereby effectively linearizing the equations of motion.

One of the advantages of the method is that we can use a base state that is not, strictly, an exact solution of the Navier-Stokes equations. To obtain the base state in the present case we start with a constant-thickness boundary layer with a Blasius velocity profile. A steady-state perturbation to this base state corresponding to a wall in the form of a static wave:

$$z=\eta_w(x)=k\sin(2\pi x/\lambda_w), \qquad (3)$$

If $k << 1$ the wall boundary conditions can be linearized, applied at $z = 0$ and written as

$$w = w_w = \dot{\eta}, \qquad u = u_w = -U'(0)\eta, \qquad v = v_w = 0, \tag{4a,b,c}$$

where η is the total vertical wall displacement (i.e., η_w plus any elastic displacement). Eq (4a) can be applied directly. The no-slip conditions, Eq. (4b,c) are applied through rigorously derived integral conditions[3]:

$$\int_0^\infty \omega_y dz = -u_w - \int_0^\infty \frac{\partial w}{\partial x} dz, \qquad \int_0^\infty \omega_x dz = v_w + \int_0^\infty \frac{\partial w}{\partial y} dz. \tag{5a,b}$$

Computationally this new base state is obtained by starting with the Blasius profile and gradually 'ramping up' the static wall wave until a steady well-behaved solution is obtained. We have also obtained an asymptotic, high-Reynolds-number solution which takes the form of an inner layer at the wall of thickness $O(\varepsilon^{1/3})$ where $\varepsilon = 1/R$. The streamwise velocity perturbation in this inner layer takes the form of an integral of an Airy function.

For the case of a compliant wall it is necessary to solve the equations of motion for the compliant wall interactively with eqs (1a,b,c) subject to conditions of continuity of velocity and tractive force at the interface. Here we use the plate-spring model for the compliant wall introduced by Carpenter & Garrad[4]. This has the advantage of only introducing a single equation for the vertical wall displacement, η.

Once the base state corresponding to the static wave has been established. It is driven by a body force of the form:

$$F_y = \int G e^{i(\beta t + \gamma y)} \exp\{-a(x - x_f)^2 - b(z - z_f)^2\} dz. \tag{7}$$

This corresponds to an approximation of a line vorticity source $\partial F_y / \partial z$ that is oscillating at frequency β and varies sinusoidally in the spanwise direction with wave-number, γ. The exponential term is a numerical approximation to a delta function located at (x_f, z_f). This form of vorticity source can be regarded as a rough approximation to components of freestream turbulence.

RESULTS AND CONCLUSIONS

For rigid walls the disturbances take the form of wave-trains of quasi-plane TS waves. The spanwise extent of individual wave-trains corresponds to the wave-number, γ, of the body force. In this case the presence of static waves always leads to a rise in growth rate and an increase in the unstable zone in (R, β) space. Qualitatively, the results are in accord with previous studies of the effects of roughness on transition and boundary-layer instability. In particular there is fairly close agreement with the experimental data of Reshotko[5]. For compliant walls it is known[6] that oblique waves grow more strongly than plane ones. Accordingly, the wave-trains take the form of oblique TS waves with the sign of the spanwise wave-number alternating in the spanwise direction. In this case for each combination of wall parameters (k, λ_w) there is an optimum value of the driver's spanwise wave-number, β, that corresponds to the most unstable case. It is found that for fixed static-wave amplitude, k, and Reynolds number, there is a range of values of λ_w for which the growth rate of the TS waves is substantially reduced as compared with the smooth wall. This would result in a delay in the onset of transition for the wavy wall. This phenomenon exhibiting a favourable effect of 'roughness' for compliant walls appears to be a new discovery. The favourable effect is greatest for a wave length, $\lambda_w \cong 5k$. This value is close to that found for the dolphin's cutaneous ridges. So they may very well help the dolphin to maintain laminar flow. This provides for the first time an explanation of the possible favourable hydrodynamic effect of the dolphin's cutaneous ridges.

References

[1] Babenko, V.V., Gnitetskii, N.A., Kozlov, L.F.: Preliminary outcomes of research on the elastic properties of the skin of live dolphins (in Russian). *Bionika* **3**, 12-19, 1969.

[2] Ridgway, S.H., Carder, D.A.: Features of dolphin skin with potential hydrodynamic importance. *IEEE Eng. Med. Biol.* **12**, 83-88, 1993.

[3] Davies, C., Carpenter, P.W. : A novel velocity-vorticity formulation of the Navier-Stokes equations with applications to boundary layer disturbance evolution. *J. Comp. Physics* **172**, 119-165, 2001.

[4] Carpenter, P.W., Garrad, A.D.: The hydrodynamic stability of flows over Kramer-type compliant surfaces. Part 1. Tollmien-Schlichting instabilities. *J. Fluid Mech.* **155**, 465-510, 1985

[5] Reshotko, E.: Disturbances in a laminar boundary layer due to distributed surface roughness. *Proc. IUTAM Symp. on Turbulence & Chaotic Phenomena* (Ed. T. Tatsumi), pp. 39-46, Elsevier, 1984.

[6] Joslin, R.D., Morris, P.J., Carpenter, P.W.: The role of three-dimensional instabilities in compliant-wall boundary-layer transition. *AIAA J.* **29**, 1603-1610, 1991.

TWO-FLUID JETS AND WAKES

Patrick Weidman*, Andrzej Herczynski**, Georgy Burde***
*University of Colorado, Boulder, Colorado, 80309, USA
**Boston College, Chestnut Hill, Massachusetts, 02467 USA
***Ben Gurion University, Sede-Boker Campus, 84990 Israel

Summary Analytical solutions for laminar, horizontal, two-fluid jets and wakes are found in the boundary-layer approximation, using a nonstandard similarity solution *ansatz* to account for interface deflection in the presence of gravity. Planar and axisymmetric fan jets as well as classical and momentumless planar wakes are considered. All interfaces deflect from horizontal except the fan jet, and velocity profiles can be strongly asymmetrical.

The streamfunction formulation of the boundary layer equations for planar ($j = 0$) and radial ($j = 1$) laminar motion of fluid ($i = 1$) residing above fluid ($i = 2$) given by

$$(\psi_i)_y(\psi_i)_{xy} - (\psi_i)_x(\psi_i)_{yy} - jx^{-1}(\psi_i)_y^2 = \nu_i\, x^j\, (\psi_i)_{yyy} \tag{1}$$

form the basis for analyzing two-fluid jets and wakes along with (i) far-field conditions of quiescent or uniform flow, (ii) interfacial kinematic, normal and tangential stress conditions, and (iii) an appropriate integral constraint. The fluid densities and viscosities are ρ_i and ν_i and $\mu_i = \rho_i\nu_i$. Example applications are the two-fluid planar and axisymmetric jets formed by spreading water over the free surface of a slightly stratified liquid reservoir exposed to quiescent air; see the experiments of Didden and Maxworthy [1]. In each problem, the position of the interface is determined from the normal stress condition at the interface by assuming a non-standard similarity solution of the form

$$\psi_i = Ax^\alpha f_i(\eta_i), \qquad \eta_i = \frac{(y - \phi(x))}{B}\frac{1}{x^\beta} \tag{2}$$

for appropriate constants A and B with exponents α and β to be determined for each problem considered below.

PLANAR AND RADIAL FAN JETS

Planar and radial two-fluid jets must satisfy the integral constraint

$$J = x^j\left(\int_{-\infty}^{\phi(x)} \rho_2 u_2^2 dy + \int_{\phi(x)}^{\infty} \rho_1 u_1^2 dy\right) \tag{3}$$

where J is the total momentum flux in the two-flud system, $y = \phi(x)$ is the position of the two-fluid interface, and $u_i = x^{-j}(\psi_i)_y$. Solution of the jet problems yield streamwise sech^2-velocity profiles, asymmetric about the interface, and governed by the parameter $\chi = \rho_1\mu_1/\rho_2\mu_2$, isthe same as that found by Lock [2] for spatially-driven free shear flow. The normal stress condition reveals that the interface is flat for the fan jet ($j = 1$), but for the planar jet it is deflected according to

$$\phi(x) \approx J^{3/2}\frac{(\mu - 1)}{g(1 - \rho)}\left(\frac{1}{\chi(1 + \chi^{1/2})}\right)^{2/3}\frac{1}{x^{4/3}} \tag{4}$$

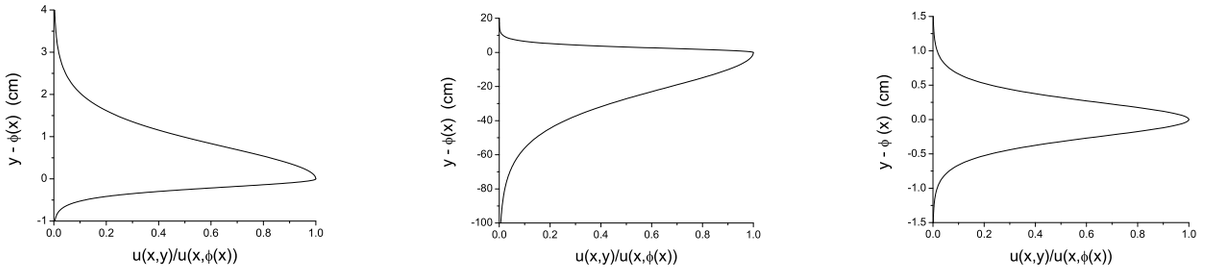
where $\rho = \rho_1/\rho_2$ and $\mu = \mu_1/\mu_2$. Thus the interface deflects either upward for $\mu > 1$ or downward for $\mu < 1$. The velocity profiles are symmetrically disposed about the interface only when $\chi = 1$. This shows that symmetric jets are possible for different fluids that possess a special relation among densities and viscosities. Sample velocity profiles for a planar jet are given in Figure 1.

The momentum flux in each fluid layer is partitioned according to $J_1 = \chi^{1/2}J/(1+\chi^{1/2})$ and $J_2 = J/(1+\chi^{1/2})$, yielding the momentum flux ratio $J_1/J_2 = \chi^{1/2}$. The jets penetrate differently into each fluid layer and their thickness grows according to $\delta_i(x) \sim x^{(2+j)/3}$.

CLASSICAL AND MOMENTUMLESS PLANAR WAKES

The same similarity *ansatz* (2) can be applied to the linearized formulation for the planar far-wake following Goldstein [3] for the classical wake formed by two-fluid flow over a stationary plate at the interface, and following Birkhoff and Zarantonello [4] for a momentumless wake over a self-propelled plate moving along the interface. The integral constraints for the classical and momentumless wakes are

$$D = U\left(\int_{-\infty}^{\phi(x)} \rho_2 w_2\, dy + \int_{\phi(x)}^{\infty} \rho_1 w_1\, dy\right); \qquad K = U\left(\int_{-\infty}^{\phi(x)} y^2\rho_2 w_2 dy + \int_{\phi(x)}^{\infty} y^2\rho_1 w_1 dy\right). \tag{5}$$



(a) (b) (c)

Figure 1: Normalized planar jet velocity profiles for (a) air-over-water, (b) air-over-oil and (c) water-over-water computed for jet momentum $J = 1000$ g/sec^2 at downstream position $x = 100$ cm.

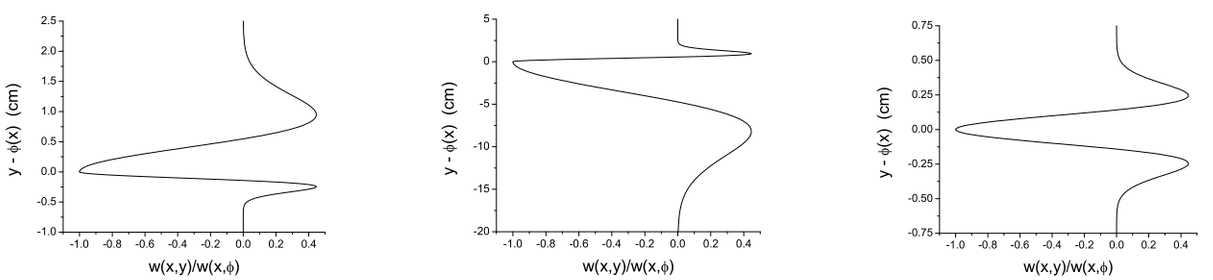
In both cases U is the uniform speed of the two-fluid flow and $w_i(x,y) = U - u_i(x,y)$ is the deficit wake velocity. For the classical wake D is the total plate friction drag, and for the momentumless wake K is the second moment of wake deficit momentum. The respective interface deflections are

$$\phi(x) \approx \frac{D}{gU^{1/2}} \left(\frac{\chi^{1/2}}{1+\chi^{1/2}} \right) \frac{1}{x^{3/2}}; \qquad \phi(x) \approx U^{1/2} K \, \frac{(\mu-1)}{g(1-\rho)} \left(\frac{1}{1+\Omega^{1/2}} \right) \frac{1}{x^{5/2}} \tag{6}$$

where χ is as defined for the two-fluid jets, and the new parameter governing the momentumless wake flow is $\Omega = \rho_1 \mu_2^3 / \rho_2 \mu_1^3$. Note that the interface is always deflected upwards for the classical wake; for the momentumless wake the interface deflection is upward for $\mu > 1$ and downward for $\mu < 1$, just as for the two-fluid jet.

For the classical wake, the momentum deficit fluxes are partitioned according to $J_1 = \chi^{1/2} D/(1+\chi^{1/2})$ and $J_2 = D/(1+\chi^{1/2})$. Thus the deficit momentum flux ratio $J_1/J_2 = \chi^{1/2}$ is identical to that for two-fluid jets. The classical and momentumless wakes penetrate differently into their respective fluid layers, and in both cases their thicknesses grow according to $\delta(x) \sim x^{1/2}$.

Sample normalized momentumless wake velocity deficit profiles are given in Figure 2 below.



(a) (b) (c)

Figure 2: Normalized momentumless wake velocity deficit profiles for (a) air-over-water, (b) air-over-oil and (c) water-over-water computed for jet momentum $U = 100$ cm/sec^2 at downstream position $x = 100$ cm.

References

[1] Didden, N., Maxworthy, T.: The viscous spreading of plane and axisymmetric gravity currents. *J. Fluid Mech.* **121:**27-42, 1982.

[2] Lock, R. C.: The velocity distribution in the laminar boundary layer between parallel streams. *Quart. J. Mech. Appl. Math.* **4:**42-57, 1951.

[3] Goldstein, S.: On the two-dimensional steady flow of a viscous fluid behind a solid body, Part I. *Proc. Roy. Soc.* **A142:**545-562, 1933.

[4] Birkhoff, G., Zarantonello, E. H.: Jets, Wakes and Cavities. Academic Press, New York, 1957.

XXI ICTAM, 15–21 August 2004, Warsaw, Poland

THE TRAILING EDGE PROBLEM FOR MIXED CONVECTION FLOW PAST A HORIZONTAL PLATE

Herbert Steinrück, Ljubomir Savic
*Institute of Fluid Dynamics and Heat Transfer, Vienna University of Technology, Resselgasse 3, A-1040 Vienna, Austria

Summary
The influence of buoyancy onto the boundary-layer flow past a horizontal plate aligned parallel to a uniform free stream is characterized by the buoyancy parameter $K = \mathrm{Gr}/\mathrm{Re}^{5/2}$ where Gr and Re are the Grashof number and the Reynolds number, respectively.
An asymptotic analysis of the complete flow field including potential flow, boundary layer, wake and interaction region near the trailing edge will be given for small buoyancy parameters and large Reynolds numbers in the distinguished limit $K\mathrm{Re}^{1/4} = \mathrm{O}(1)$.

INTRODUCTION

Laminar two-dimensional mixed convection flow along a horizontal heated plate (plate temperature θ_w) aligned parallel to a uniform free stream (velocity u_∞, temperature θ_∞) will be investigated for large Reynolds Re and large Grashof numbers Gr in a distinguished limit. In previous papers [1], [3] the boundary layer flow for $K = \mathrm{Gr}/\mathrm{Re}^{5/2} = O(1)$ has been investigated. Since the buoyancy force is orthogonal to the main flow direction the boundary layer flow is affected only indirectly by the buoyancy force. The buoyancy force is compensated by a hydro-static pressure distribution. Since the boundary-layer thickness is not uniform this hydro-static pressure distribution is not uniform either resulting in a horizontal pressure gradient accelerating or decelerating the boundary layer flow. Thus we speak of a favorable or an adverse buoyancy. We note that for a fluid with a positive isobaric expansion coefficient buoyancy affects the boundary layer flow on the upper side favorably and on the lower side adversely for a heated plate.
In case of adverse buoyancy the boundary-layer equations have the remarkable properties:

(i) They have a one parametric family of solutions.

(ii) Perturbations can propagate upstream in the boundary layer flow without interaction with the outer potential flow.

Both properties indicate that the boundary-layer flow has to be analyzed in context with the global flow field. A special role will play the trailing edge region where we will apply triple deck methods. Thus the buoyancy parameter K has to be chosen appropriately: $K = \kappa\mathrm{Re}^{-1/4}$ with the reduced buoyancy parameter $\kappa = O(1)$.

ASYMPTOTIC ANALYSIS

For the analysis the coordinates x and y parallel and normal to the plate, respectively, are made dimensionless with the plate length. Velocities are referred to the velocity of the free stream and temperature difference are referred to $\theta_w - \theta_\infty$. According to triple deck theory. We have to decompose the flow field into the different regions using the scalings listed in table 1 and sketched in figure 1.

outer flow field (potential flow)	x	y
boundary layer	x	$\bar{y} = y\mathrm{Re}^{1/2}$
trailing edge upper deck	$X = x\mathrm{Re}^{3/8}$	$Y = y\mathrm{Re}^{3/8}$
trailing edge main deck	$X = x\mathrm{Re}^{3/8}$	$\bar{y} = y\mathrm{Re}^{4/8}$
trailing edge lower deck	$X = x\mathrm{Re}^{3/8}$	$\hat{y} = y\mathrm{Re}^{5/8}$
wake	x	$\bar{y} = y\mathrm{Re}^{1/2}$

Table 1: Scalings of the different flow regions

Boundary-layer

The expansion of the flow and temperature field in the boundary-layer is given by

$$u(x,\eta) \sim \bar{u}_0(\eta) + K\bar{u}_1(x,\bar{y}) + ..., \quad \theta(x,\eta) \sim \bar{\theta}_0(\eta) + K\bar{\theta}_1(x,\bar{y}) + ... \quad \text{with} \quad \eta = \bar{y}/\sqrt{x+1}, \tag{1}$$

where $\bar{u}_0$ is the Blasius velocity profile. Note that the leading order terms $\bar{u}_0$, $\bar{\theta}_0$ are independent of buoyancy. The first order terms $\bar{u}_1$ and $\bar{\theta}_1$ are affected by buoyancy in two ways: Firstly by the hydro-static pressure distribution in the boundary layer and secondly by the first order correction of the potential flow.

Wake

In the wake the solution has a similar expansion as in the boundary layer. We note that across the wake there is a hydro-static pressures difference :

$$\Delta p_h(x) = K(p_1(x,0+) - p_1(x,0-)) = K\int_{-\infty}^{\infty} \bar{\theta}_0(x,\bar{y})\,\mathrm{d}\bar{y} \tag{2}$$

Moreover a curvature of the centerline of the wake has to be considered.

Potential flow

In contrast to usual boundary-layer flow problems the first order correction of the potential flow is not induced by the displacement of the boundary but by the hydrostatic pressure difference across the wake which is of order $K = \kappa \mathrm{Re}^{-1/4}$. Thus the stream function ψ of the outer flow field has the expansion $\psi(x,y) = y + K\psi_1(x,y) + ...$ where ψ_1 satisfies the boundary conditions:

$$\psi_{1,x}(x,0) = 0 \quad \text{for} \quad -1 < x < 0, \qquad \psi_{1,y}(x,0) = -\int_{-\infty}^{\infty} \bar{\theta}_0(x,\bar{y})\,\mathrm{d}\bar{y} \quad \text{for} \quad 0 < x. \tag{3}$$

In [2] the potential flow problem for $\psi_y(x,0) = const$ for $x > 0$ has been solved. It turned out that this potential flow problem for the first order correction has no solution if considered in the entire plane. The singularity of the potential flow can be removed if one considers the flow between two distant walls [2].

Trailing Edge

Near the trailing edge the usual triple deck scaling applies [5]. We expand all flow quantities with respect to Re and K with $\mathrm{KRe}^{1/4} = \mathrm{O}(1)$. Thus to leading order we recover the well known trailing edge problem for a plate in a parallel uniform free stream [4]. Buoyancy influences only the second order terms, which can be decomposed into terms that are affected by buoyancy and terms which are independent of K:

$$u = 1 + \mathrm{Re}^{-1/4}u_s + \mathrm{Re}^{-3/8}(u_2 + K\mathrm{Re}^{1/4}\Delta u_2) + ... \tag{4}$$

Note that subscript s denotes the solution of the well-known trailing edge problem [4]. For the buoyancy correction terms we obtain the linearized triple deck problem:

$$u_s\Delta u_{2,X} + \Delta u_2 u_{s,X} + v_s\Delta u_{2,Y} + u_{2,Y}\Delta v_2 = -\Delta p_{2,X} + \Delta u_{2,YY}, \quad \Delta u_{2,X} + \Delta v_{2,Y} = 0 \tag{5}$$

with the interaction law

$$\Delta p_2 = A_s(X) - (1 + h(-X))a_s|X|^{1/3} + \frac{1}{\pi}\int_{-\infty}^{\infty} \frac{\Delta A_2'(\xi) + \sqrt{3}a_s\xi^{1/3}h(\xi)}{X - \xi}\,\mathrm{d}\xi. \tag{6}$$

Here $X = x\mathrm{Re}^{3/8}$ and $Y = y\mathrm{Re}^{5/8}$ denote the lower deck variables, respectively. The leading order term of the displacement thickness A_s has the expansion $A_s \sim a_s X^{1/3}$ for $X \to \infty$. At the plate $X < 0, Y = 0$ the no slip boundary conditions hold and since Δu_2 and Δp_2 are antisymmetric with respect to $Y = 0$ we obtain the boundary conditions $\Delta u_2(X,0) = 0, \Delta p_2(X,0) = 0$ in the wake ($X > 0$). The matching condition to the main deck is $\Delta u_2(X,\infty) = \Delta A_2(X)$ where $\Delta A_2(X)$ is the correction of the displacement thickness due to buoyancy.

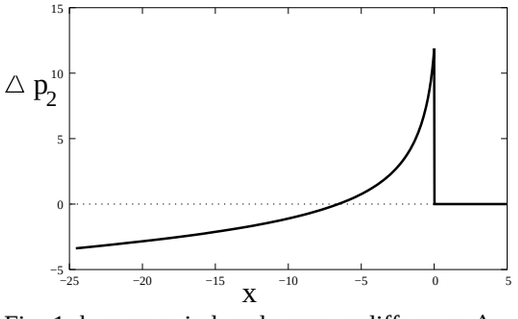


Fig. 1: buoyancy induced pressure difference Δp_2

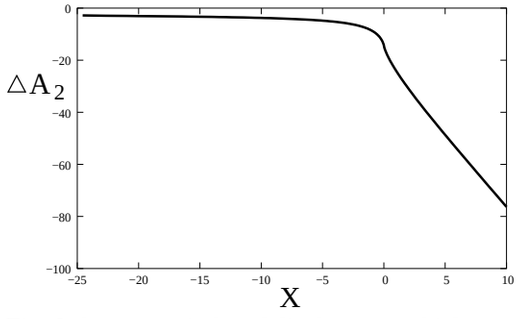


Fig. 2: buoyancy induced displacement thickness ΔA_2

Using Veldman's method [5] the triple deck problem and the buoyancy correction problem (4)-(6) is solved numerically. In figures 1 and 2 the pressure correction and the displacement correction are shown, respectively. The pressure has a discontinuity at the trailing edge. This is reflected in the vertical tangent of the displacement thickness ΔA_2 at $X = 0$. Thus there is a flow around the trailing edge.

References

[1] Schneider W.; A similarity solution for combined forced and free convection flow over a horizontal plate, Int. J. Heat and Mass Transfer **22**, 1979, 1401-1406.
[2] Schneider W.: Lift and thrust by the buoyant wake behind a horizontal plate, submitted to JFM, 2003.
[3] Steinrück H.: A review of the mixed convection boundary-layer flow over a horizontal cooled plate, GAMM-Mitteilungen.**24**, 2001, 127-158.
[4] Stewartson K.: On the flow near the trailing edge of a flat plate II, Mathematika, **16**, 1969, 106-121.
[5] Sychev V. V., Ruban A. I., Sychev Vic. V., Korolev G. L: Asymptotic Theory of separated flows, Cambridge University Press, 1998.

EXPERIMENTAL AND THEORETICAL STUDY OF HEATED COANDA JET

Tomáš Vít*, František Maršík**
*TU Liberec, Department of Power engineering, Liberec, Czech. Rep.
**Academy of Sciences of the Czech Republic, Institute of Thermomechanics, Praha, Czech. Rep.

Summary The results of the experimental and analytical study of the effect of temperature on circumfluenced wall and temperature gradient on the stability of the boundary layer along the curved wall (Coanda jet) are presented. Heating of the circumfluenced wall results in stabilizing the boundary layer which leads to a shift of the transition to turbulence. In the case of the Coanda jet this phenomenon is manifested by the shift of reattachment to higher values of the Reynolds number.

INTRODUCTION

The Coanda jet is defined as the wall jet along the curved wall. The flow of fluid along the curved wall is accompanied with the decrease of the pressure on the wall. The pressure on the wall drops below the surrounding pressure resulting in the attachment of the fluid flow to the wall. This phenomenon is best observed in two-dimensional or nearly two-dimensional flow. The laminar curved wall jet has the tendency to follow the circumfluenced wall only for small angles. The rapid increase of pressure along the wall occurs due to the influence of the curvature of the wall and the adverse pressure gradient in the direction of flow. It leads to flow separation for small values of the angle ϕ. On the other hand the turbulent flow has a strong tendency to remain attached to the circumfluenced wall up to $\phi=270^{o}$ as found in [2]. The magnitude of the angle of separation depends on the geometric configuration (especially, on the ratio of the radius of the wall to the width of the nozzle *R/b*) and on the magnitude of the Reynolds number $\mathrm{Re} = \frac{1}{\sqrt{2}} \frac{\mathrm{v}\sqrt{Rb}}{\nu}$; v is the velocity in the nozzle and ν is the kinematic viscosity corresponding to the temperature of the air flow in the nozzle.
There is no continuous increase of the angle of separation associated with the increase of velocity of the flow in the nozzle from the laminar flow up to the values corresponding to the fully developed turbulent flow. The flow is laminar for the low values of Re and the increase of the angle of separation with the increasing Re is very small. As the meas-

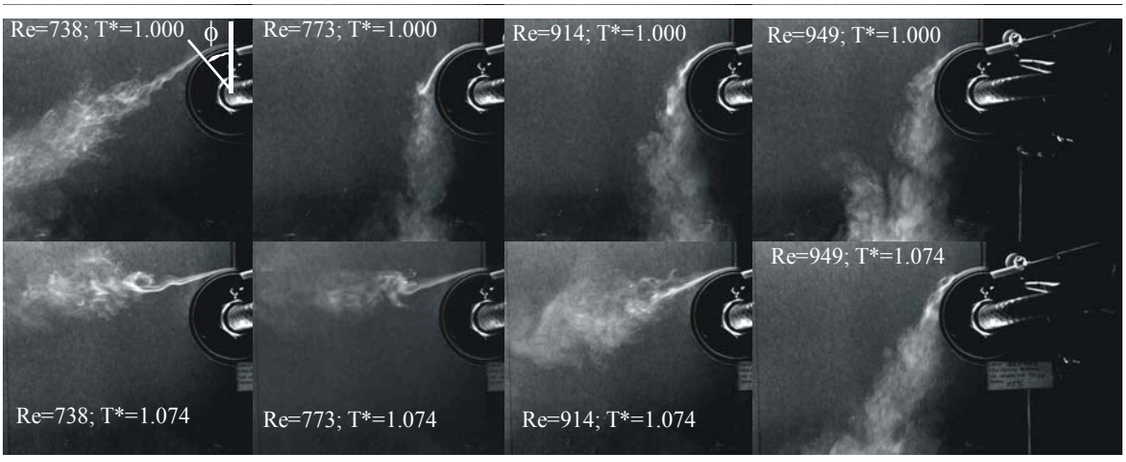


Fig. 1. Variation of the flow character with temperature. The upper pictures show the flow character at T*=1. The lower pictures show the flow character at T*=1.074. (R/b=8.16)

urement of the turbulence intensity carried out by the HWA method shows that this change is associated with the transition of flow to turbulent regime. The further increase of the flow velocity leads to the gradual increase of the angle of separation. The angle of separation is not dependent on the magnitude of Re only for high values of Re [2].
Most publications dealing with the Coanda jet are focused on the isothermal turbulent flow. There are only several publications investigating the problems of the flow along the heated/cooled wall [3]. The problems of the laminar flow along of the curved wall and the problems of the transition to turbulence are usually marginalized in the literature. The only exception known to the authors is the work by V. Tesař [4] where the effect of the temperature gradient on the character of the curved wall jet was observed.
The temperature change of the circumfluenced wall has a fundamental effect on the character of the flow and the transition to turbulence. This contribution brings new experimental results of the heated Coanda jet obtained using the smoke wire visualization method and the hot-wire anemometry (HWA). The analysis of the results based on the theory of the boundary layer stability has also been carried out.

RESULTS

The following conclusions can be formulated based on the smoke-wire visualization:

- At a certain value of the Reynolds number (Re_c) the reattachment of the separated flow occurs. For the isothermal case, the magnitude of Re_c depends on the slot width b and on the radius of curvature of the cylindrical surface R.
- The heating of the circumfluenced surface causes the increase of Re_c with increasing ratio $T^*=T_w/T_\infty$ (T_w is the temperature of the wall; T_∞ is the temperature of air flow that is not affected). This phenomenon is significant even for small values of T^* (see Fig. 2). The increase of Re_c with T^* is not linear – the rate of increase is reduced with increasing T^*.

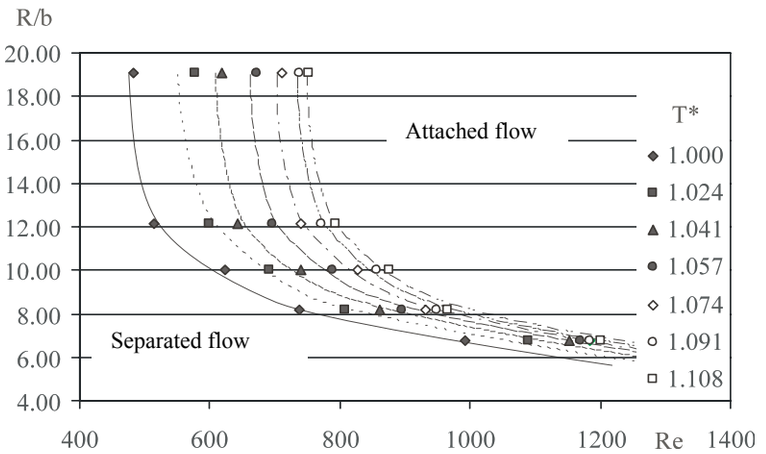


Fig. 2.The dependence of critical Reynolds numer $\mathrm{Re}_c = \frac{\mathrm{v}\sqrt{Rb}}{\nu}$ on R/b ratio and on temperature ratio $T^* = T_w / T_\infty$

On the basis of the velocity and temperature profiles and the profiles of the turbulence intensity obtained from the HWA experiments it is possible to show that the separated flow is laminar until the separation point. The measured values of the turbulence intensity in the boundary layer do not exceed 5%. A significant increase of the turbulence intensity occurs near the separation point. For Re_c the attached flow has the character of the transitional turbulent flow. It was not possible to consider the turbulent flow as being completely developed with regard (due?) to the observed velocity range. The measured course of the intensity of velocity fluctuations in the streamwise direction shows a gradual increase of the turbulence intensity. Neither significant changes of the velocity profile, nor any significant profile changes of the turbulence intensity with the temperature gradient for the investigated ranges of the temperature gradient and the Reynolds numbers were observed.

Our theoretical analysis based on the similarity solution and the numerical simulation of the heated curved wall jet yields the following stability conditions:

1. The thermodynamic criterion [1] requires the following inequality to be fulfilled: : $\frac{\lambda}{T}\left(\frac{\partial T}{\partial y}\right)^2 + \mu\left(\frac{\partial v_x}{\partial y}\right)^2 + \mu v_x\left[\frac{d\ln\mu}{dT}\frac{\partial T}{\partial y}\frac{\partial v_x}{\partial y} + \frac{\partial^2 v_x}{\partial y^2}\right] \geq 0$. This criterion is responsible for the significant stabilization of the velocity profile for the heated curved wall jet. The convexity of the velocity profile $\partial^2 v_x / \partial y^2 < 0$ is compensated by the temperature gradient $\partial T / \partial y$. The stabilization effect increases with increasing T^* and decreases with increasing velocity.
2. The Rayleigh criterion requires that $\partial^2 v_x / \partial y^2 \neq 0$ is fulfilled in the boundary layer, i.e. the laminar velocity profile both for the non-heated and the heated cases of the curved wall jet is unstable.

CONCLUSION

The problem of the Coanda jet with the temperature gradient requires further theoretical, extensive experimental and numerical research. The principal advantage of the configuration with the temperature gradient is the distinguished position of the separation point of the boundary layer which coincides with the flow transition into turbulence. Both flow separation and flow transition into turbulence are phenomena which have not been satisfactorily described so far by any of the available complex theories.

References

[1] Vit T.: Experimental and theoretical study of heated Coanda jet, PhD Thesis, 2004 (submitted to defence)

[2] Newman B. G.: The deflection of Plane Jets by Adjacent Boundaries, Coanda Effect, 232-264 *in Boundary Layer and Flow Control, G. V. Lachman (ed)*, Pergamon Press, 1961

[3] Dakos T.,Verrioulos C.A.,Gibson M.M.: Turbulent flow with heat transfer in plane and curved wall jets, *Jour. Fluid Mech.*, **145**, 339-360, 1984

[4] Tesař V.: Control of flow separation by temperature gradient, in *Euromech Colloquium 377*, ISBN 80-85918-43-9, IT CAS, Praha, 54-55, 1998

A combined numerical and asymptotic approach to boundary layer receptivity problems

M. R. TURNER and P. W. HAMMERTON

School of Mathematics, University of East Anglia, Norwich, NR4 7TJ, England, UK

SUMMARY: With the aim of predicting the transition point on a general body given the free-stream conditions, we devised a method using asymptotic receptivity analysis as an upstream boundary condition for numerical stability analysis.

For small free-stream disturbances, the problem of predicting transition can be split into two parts, the receptivity part and the stability part. Receptivity is concerned with how the free-stream disturbances give rise to disturbances in the boundary layer and typically arises when the boundary layer changes over short streamwise scales, such as near the leading edge of a body.

For large Reynolds number, Re, the neutral stability point is $O(\epsilon^{-2})$ downstream of the leading edge, where $\epsilon = Re^{-\frac{1}{6}}$, and its position is independent of the exact form of the free-stream disturbance in the receptivity region. The amplitude of the boundary layer mode which eventually becomes unstable is determined by a receptivity region. Downstream of the neutral stability point, disturbances grow, leading eventually to nonlinear breakdown and transition to turbulence. Thus the amplitude of the unstable mode at the neutral stability point is crucial in determining the position of transition.

Three approaches to understanding the transition process are available.

(i) **Experiments**: Experimentalists, e.g. Saric *et al.* (1995), typically measure the transition point and the amplitude of the Tollmien-Schlichting (T-S) wave downstream of the neutral stability point.

(ii) **Numerics**: Numerical Navier-Stokes (N-S) solvers have been used to solve the receptivity/stability problem simultaneously (Wanderley and Corke, 2001). However these solvers only work for moderately large Reynolds numbers, obtaining solutions is very time consuming, and identifying the amplitude of the unsteady modes which eventually become unstable is difficult.

(iii) **Asymptotics**: At large Reynolds numbers, the receptivity process close to the leading edge is analysed separately and then matched to a triple-deck asymptotic analysis of the Orr-Sommerfeld region (Goldstein, 1983). The asymptotic structure is summarised in figure 1. The advantage of such an approach is that scaling on Reynolds number and dependence on the exact form of the free-stream disturbance is directly determined. However, even for a semi-infinite flat plate, the asymptotic analysis of the Orr-Sommerfeld region is so intricate that comparing wave amplitudes at the neutral stability point with experiments is impractical.

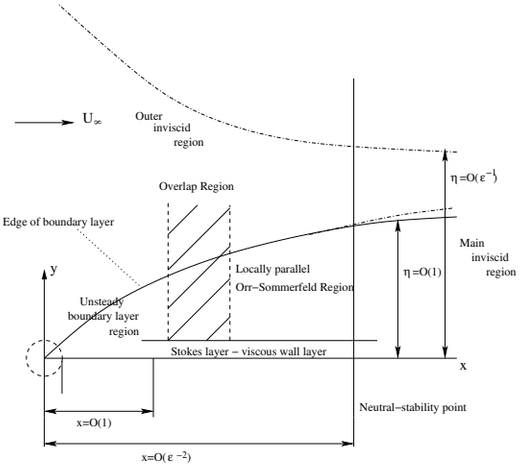


Figure 1: Figure showing the regions on a flat plate

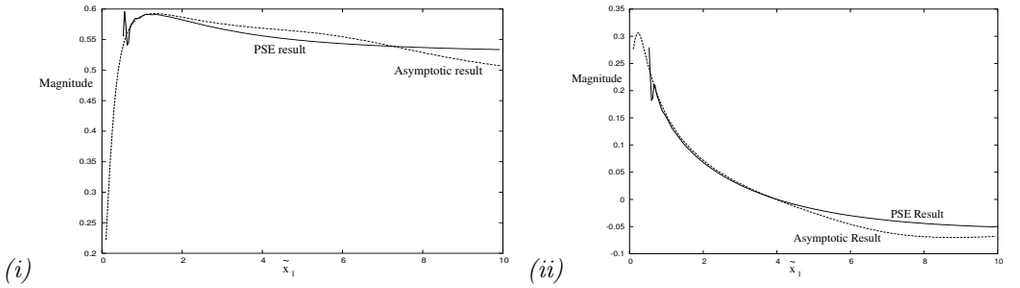


Figure 2: Comparison of numerical solution of PSE and asymptotic results of *(i)* the real and *(ii)* imaginary parts of the wavenumber , κ, as a function of downstream distance for $\epsilon = 0.1$

In this paper we consider an asymptotic analysis of the receptivity region and then use the far-downstream limiting form as an initial condition for a numerical solution marching downstream using the Parabolized Stability Equation (PSE) (Bertolotti *et al.*, 1992). The PSE method reduces computation time greatly compared to full N-S solvers. The advantage of the combined approach compared to the fully asymptotic treatment is that bodies with curved surfaces can easily be considered. However, before we can extend this method to more general bodies, we first present comparisons with the semi-infinite flat plate analysis.

Figure 2 shows the comparison between the numerical solution to the PSE and Goldstein's asymptotic solution for the wavenumber, κ, as a function of distance downstream, for $\epsilon = 0.1$. We use as our initial condition a composite solution constructed from the three decks of the eigensolution determined by the receptivity analysis. Downstream of the starting point of the PSE calculations there is good agreement between numerical results and the asymptotic predictions, at least as far as the neutral stability point, located at $\tilde{x}_1 \approx 3.65$. Further downstream agreement is not as good, probably due to non-uniformity in the small-ϵ expansion of κ. However, this is not significant since it is the wave amplitude at the neutral stability point which is of prime importance in the current work. Reducing ϵ improves the agreement, although it has not been possible to demonstrate that all orders in the asymptotic expansion of κ are correctly determined. The rapid variation in κ in the early stages of the PSE calculation are due to the adjustment in the mode shape from the composite solution based on the small asymptotic theory. In the example shown, PSE calculations were started at $\tilde{x}_1 = 0.5$. Calculations were repeated starting from other values of $\tilde{x}_1$ and the behaviour further downstream showed similar agreement with asymptotic results.

We also compared the wave shape from the PSE analysis with the triple deck asymptotic form from Goldstein's Orr-Sommerfeld analysis. The results were very encouraging, although no results are printed here.

CONCLUSIONS

The results shown confirm the PSE formulation has been implemented correctly in the numerical codes and the upstream boundary conditions imposed are consistent. Results will be presented for bodies with non-zero mean pressure gradients and comparisons made with N-S results and experimental data.

References

Bertolotti, F. P., Herbert, T., and Spalart, P. R. (1992). Linear and nonlinear stability of the Blasius boundary layer. *J. Fluid Mech*, **242**, 441–474.

Goldstein, M. E. (1983). The evolution of Tollmien-Schlichting waves near a leading edge. *J. Fluid Mech.*, **127**, 59–81.

Saric, W. S., Wei, W., and Rasmussen, B. K. (1995). Effect of leading-edge on sound receptivity. *Laminar-Turbulent Transition, (IUTAM Sendai, 1994, ed. R. Kobayashi), Springer*, pages 413–420.

Wanderley, J. B. V. and Corke, T. C. (2001). Boundary layer receptivity to free-stream sound on elliptic edges of flat plates. *J. Fluid Mech.*, **429**, 1–21.

FLOW ALONG A LONG THIN CYLINDER

O. R. Tutty*, A. T. Parsons**, W. G. Price*
*School of Engineering Sciences, University of Southampton, Southampton SO17 1BJ, United Kingdom
**QinetiQ, Winfrith Technology Centre, Dorset DT2 8XJ, United Kingdom

Summary Calculations have been performed for the flow along long thin cylinders using a variety of methods, from a boundary layer code with a turbulence model to a full, time accurate, Navier-Stokes solver. The results have been validated by comparison with those from experiments. It has been found that there are major differences between the flow on a cylinder and the equivalent flow on a flat plate, with the wall shear stress tending to a constant mean value far downstream. Calculations of the power spectral density of the surface pressure fluctuations show that the noise generated by the turbulence initially increases as the radius of the cylinder is decreased, but eventually decreases as the radius is decreased further.

INTRODUCTION

The external flow along a long thin cylinder has been the subject of relatively few studies compared with that on a flat plate or in channels and pipes. The results that do exist show significant differences in the flow as compared with that for a flat plate. For both laminar and turbulent flows the velocity profile is fuller and the wall shear stress is higher than in the equivalent flow on a flat plate. All available experimental results show turbulent flow, even for Reynolds numbers of $O(10^2)$. Also, perhaps surprisingly, for long cylinders, in practice the drag per unit length appears to be constant, indicating a constant mean surface shear stress. Experimental results for higher Reynolds numbers ($O(10^5 - 10^6)$) show that the noise from the turbulent pressure fluctuations at the surface of the cylinder increases as the Reynolds number decreases. In practice, this implies that the noise increases as the cylinder radius decreases. Clearly this trend cannot continue to the limit of zero Reynolds number. Our interest is in investigating the behaviour for the flow along long cylinders, typical of the towed sonar arrays used for underwater sensing. This may have aspect ratios of up to $O(10^5)$, with a length of the order of a kilometre and a radius in the order of centimetres. Clearly it is impractical to perform a full Navier-Stokes calculation for a bodies of this size. Hence a series of problems, as outlined below, was studied, with validation using the results of the different model problems and comparison with experimental results.

SIMULATIONS USING A TURBULENCE MODEL

A series of calculations were performed for a cylinder aligned with the flow governed by the boundary layer equations with a variable viscosity given by the Spalart-Allmaras turbulence model. Very long cylinders with Reynolds numbers, Re, of $O(1)$ to $O(10^6)$ were considered, where $Re = U_\infty a/\nu$, a is the radius of the cylinder, and U_∞ the freestream velocity. Turbulent flow was predicted in all cases. A detailed comparison was made of the numerical results with the experimental measurements of Willmarth *et al* [1] and Lueptow *et al* [2], for flows with Reynolds numbers from 482 to 92310. Values for the displacement thickness, momentum thickness and friction velocity, and for the Reynolds stress across the boundary layer, showed excellent agreement, i.e. within the expected experimental error. There was also excellent agreement between the predicted and experimental velocity profiles, as can be seen in Figure 1. Note that the difference in the curves for the lowest Reynolds number in the far field comes from the difference in the numerical and experimental values for the friction velocity used to scale the velocity, when the radius of the cylinder is smallest, and the largest experimental errors might be expected. In all these calculations, standard values were used for the parameters

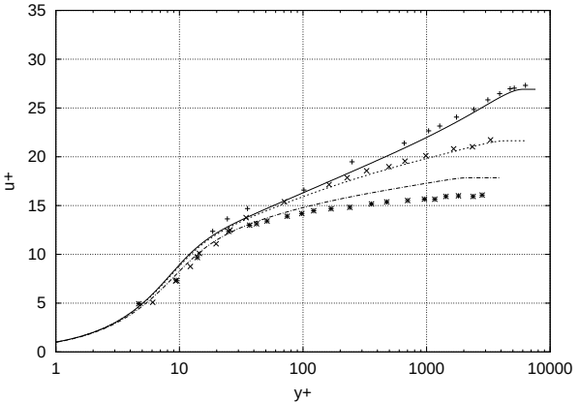


Figure 1. Velocity profiles in wall coordinates. Lines are numerical and symbols experimental from Willmarth *et al*: lower $Re = 736$, middle $Re = 4330$, top $Re = 74260$.

in the turbulence model, i.e. no tuning of the model was performed. In agreement with experimental observations, the

calculations predicted that the far downstream value of the shear stress was essentially constant. Also, the values predicted for the drag per unit length are consistent with those obtained from towed arrays when deployed.

DNS AND LES SIMULATIONS

Although the enormous computational requirement rules out a full unsteady Navier-Stokes calculation, a model problem can be formulated for the far downstream region when the mean wall shear stress is predicted to be constant. This consists a finite region of the cylinder in which the flow is assumed to be periodic in the streamwise direction, with the boundary layer growing in thickness in time. A series of calculations was performed for Reynolds numbers from 500 to 10^5. For the lower Reynolds numbers (2000 or less) a Direct Navier-Stokes (DNS) calculation was performed, with no approximations. For higher Reynolds numbers, a Large Eddy Simulation (LES) approach was employed. A standard subgrid model was used for the LES, i.e. again, no tuning was performed. A basic prediction is that the mean wall shear stress obtained from this problem should tend toward the value predicted by the turbulence model, and by implication, the experimental values. That this occured can be seen from Figure 2 which shows the spatially averaged shear stress for $Re \leq 2000$. A similar level of agreement was found for the higher Reynolds numbers. The convection (phase) speed of the turbulence

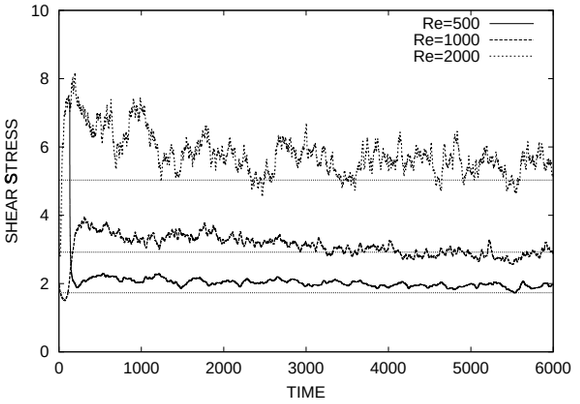


Figure 2. Spatially averaged wall shear stress against time for $Re = 500$ (bottom), $Re = 1000$ (middle), and $Re = 2000$ (top). Also shown are the far downstream values obtained using the Spalart-Allmaras turbulence model.

was estimated from the cross spectrum of the pressure fluctuation at two different points. This was approximately 70% of the free stream velocity, consistent with experimental values. Power spectral densities for the surface pressure fluctuations were calculated. These predicted that while for the noise from the turbulence at the surface would increase as Reynolds number (radius of the cylinder) decreased for the higher Reynolds number, as would be expected, eventually the noise would decrease with Reynolds number (radius).

CONCLUSIONS

Calculations have been performed for the zero mean pressure gradient turbulent boundary layer on a long thin cylinder over a wide range of Reynolds numbers. The Spalart-Allmaras turbulence model has been validated for this problem for the Reynolds numbers for which detailed experimental results are available. Both experimental and numerical results show that the boundary layer on a cylinder is thinner and has higher shear stress than for the equivalent flow on a flat plate. For all practical purposes the mean shear stress on the surface of the cylinder tends to a constant downstream. When this occurs the flow near the surface is independent of the downstream coordinate, while the outer part of the boundary layer continues to evolve, with the boundary layer growing in thickness as the square root of the distance.

Calculations have also been performed for flow on a finite section of the cylinder using a Navier-Stokes solver, including where necessary a subgrid model. There is good agreement with the results obtained using the Spalart-Allmaras turbulence model. Also, the predictions of the convection speed are consistent with those obtained in experiments.

Calculations of the power spectral density of the pressure at the surface show that for the higher Reynolds numbers, the noise from the turbulence increases as the radius of the cylinder decreases, consistent with experimental results. However, when the radius is reduced sufficiently, the noise peaks, then decreases, at least for the lower frequencies.

References

[1] Willmarth W.W., Winkel R.E., Sharma, L.K., Bogar T.J.: Axially symmetric turbulent boundary layers on cylinders: mean velocity profiles and wall pressure fluctuations. *J. Fluid Mech.* **76**:35–64, 1976.

[2] Lueptow R.M., Leehey P., Stellinger T.: The thick, turbulent boundary layer on a cylinder: mean and fluctuating velocities. *Phys Fluids* **28**:3495–3505, 1985.

XXI ICTAM, 15–21 August 2004, Warsaw, Poland

ASPECTS OF THE LAMINAR-TURBULENT TRANSITION IN AXISYMMETRIC BOUNDARY LAYERS

N. Vinod, Rama Govindarajan*
Engineering Mechanics Unit, Jawaharlal Nehru Centre for Advanced Scientific Research
Bangalore -560 064, INDIA *e-mail:rama@jncasr.ac.in*

Summary
The boundary layers over axisymmetric bodies have been studied far less than those over two-dimensional surfaces. Our main obective is to understand how the laminar-turbulent transition process in a boundary layer over an axisymmetric body is different from that over a two-dimensional surface. We study the primary (linear) instability, the secondary instability, and the transition zone, and find that all these are qualitatively different from 2D boundary layers. It is shown that transverse curvarture has a significant stabilizing effect on the primary stability. Consistent with the recent findings of Tutty *et al* [1], we see that three-dimensional modes can go unstable first, whereas over a 2D surface 2D modes are most unstable (Squire's theorem[2]), Interestingly, an opposing effect of curvature is seen on secondary instability behaviour: competing primary modes produce a rich variety in secondary disturbance growth, indicating early entry into the nonlinear domain. Early stages of the transition zone, where turbulent spots grow as they convect, are similar to 2D flow, while due to the spots wrapping around the body, transition proceeds slower in the later stages.

INTRODUCTION

The laminar to turbulent transition in a two-dimensional boundary layer has been a subject of great interest for several decades, but the boundary layer created by axial flow past an axisymmetric body, such as in underwater applications, has received far less attention. We find the laminar instability and transition process in axisymmetric boundary layers to be qualitatively different from its two-dimensional counterpart at every stage, and there are aspects of mathematical interst. We study secondary and algebraic disturbance growth to determine whether, and which of, these mechanisms are dominant in axisymmetric boundary layers.

SUMMARY OF MAIN RESULTS

A summary of our findings is presented schematically in figure 1. Transverse curvature has the effect of stabilizing the primary (linear) mode, so the first critical Reynolds number is higher. A totally new route to transition is however possible due to the geometry since Squire's theorem [2], stating that 2D modes are the most unstable primary (linear) modes, may now be violated. (Due to the transverse curvature, the resulting stability equations cannot be transformed in the manner proposed by Squire.) Our linear stability studies find that, at various levels of curvature, three dimensional modes of azimuthal wavenumber $n = 1$ or 2 are indeed the least stable (figure 2a). These results are consistent with the findings of Tutty *et al* [1].
A secondary instability analysis is carried out in the standard manner following Herbert[3]. Secondary disturbance growth is much more complex than in 2D. Since several primary modes are nearly as stable as each other, a variety of secondary modes are triggered at a given Reynolds number. Nonlinear interactions among these modes are therefore likely to bring the transition Reynolds number forward, as depicted in figure 1. The growth of secondary disturbances for a few example modes is shown in figure 2b, a detailed analysis and comparison with 2D will be presented at the conference. As in the flat plate boundary layer the sub-harmonic modes are found to be more dominant than the harmonic.

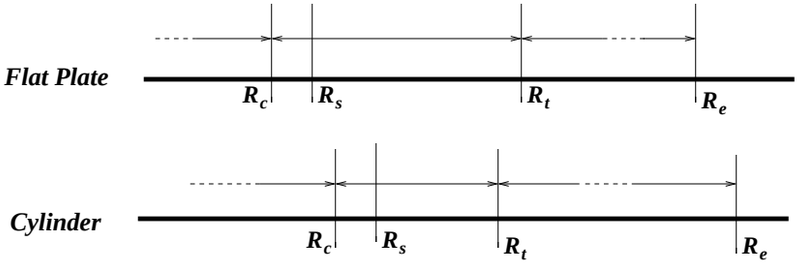


Figure 1. Schematic representation of the differences in onset of different stages of the transition process in 2D and axisymmetric boundary layers. R_c is the Reynolds number of linear instability, R_s is the onset of secondary disturbance growth, R_t is the onset of transition to turbulence, and R_e shows the end of the transition zone, where the flow is fully turbulent.

We have carried out stochastic simulations inspired by a cellular automaton approach of the birth and downstream propagation and growth of turbulent spots in the transition zone of an axisymmetric boundary layer, details will be presented

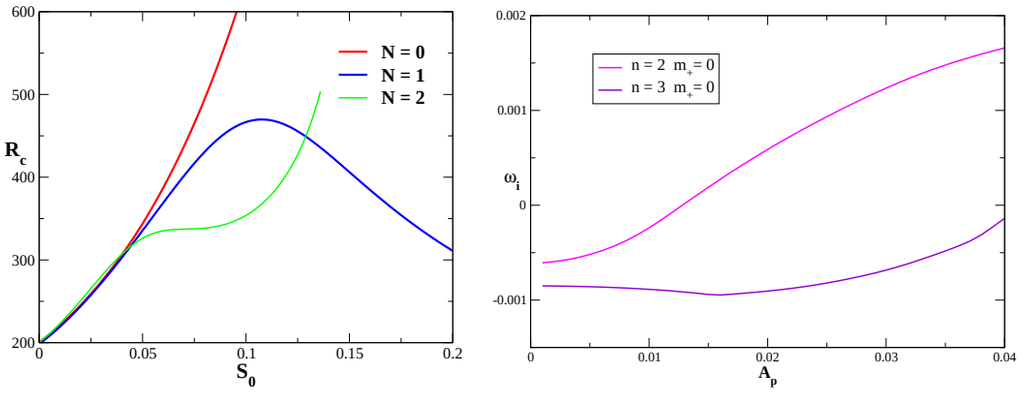


Figure 2. (a) Variation of critical Reynolds number with curvature, S for different modes,[4]. Growth of secondary waves with different A_p at Reynolds number 300, primary wavenumber $(\alpha) = 0.10$, $S_0 = 0.05$ and n and m are the number of primary and secondary waves encircling the body respectively. A_p is the amplitude of the primary disturbance.

is shown in figure 3 a. The quantity c is the circumference of the body. In the initial region, transition proceeds exactly as it would in 2D flow. This is because the spots are too small to "see" the body. When spots wrap themselves around the cylinder, however, there is no further room for lateral growth, and transition proceeds much more slowly after this. The burst rate B shown in figure 3 b is another indication of the differences in the transition process. Here, B is a measure of the rate at which the flow switches from laminar to turbulent.

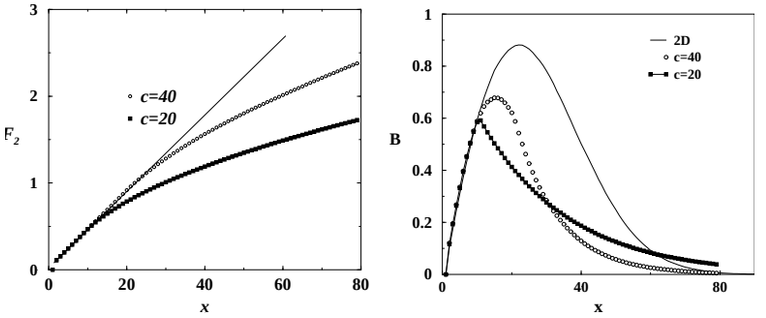


Figure 3. a. The intermitteny factor $F_2 \equiv \sqrt{-(log(1-\gamma(x))}$ Vs. x, for different c. The straight line is the 2D result. b. The burst rate in the transition zone.

Acknowledgement

We thank Aeronautical Research and Development Board, INDIA for prooviding the financial support yo carry out this project.

References

[1] O.R. Tutty, W.G. Price, & A.T. Parsons, Boundary layer flow on a long thin cylinder, *Phusics of Fluids*, Vol. 14, No. 2, pp. 628–637, 2002.
[2] H. Squire, On the stability of three dimensional disturbances of viscous fluid between parallel walls *Proc. Roy. Soc. London Ser. A.* , 142, 1933, pp. 621–628
[3] T. Herbert, Secondary instability of boundary layers, *Annu. Rev. Fluid Mech.* Vol.20, pp. 487–526 1988.
[4] N. Vinod, H. Balakrishnan & R. Govindarajan, Stability analysis of an axisymmetric boundary layer, *Proc. Ninth Asian Cong. Fluid Mech.*, Isfahan, 2002.

Enhancement of the Impinging Diffusion Flame by Splash Plate

Ay Su*, Ying-Chieh Liu**

*Department of Mechanical Engineering, Yuan Ze University,Taiwan

**Chung-Shan Institute of Science and Technology, Taiwan

Summary The flame stretch mechanism of the impinging flame is investigated by splash plate. Two types of the splash plate with flat plate and 60 degrees in sharp edge are conducted in this experiment. Slip condition occurs at the jet-to-jet impingement and no-slip condition takes place at the jet flow on the splash plate. A portion of the fluid energy will transfer to the radial direction by the no-slip condition. Therefore, it tends to overcome the flame stretch and spreads the impinging flame out. Because the direction of the splash plate with shape-edge, the fuel and the air entrain mutually. The higher temperature region spreads toward the air side. The enhancement of combustion efficiency by splash plate is evident.

BACKGROUND

It is clear that the potential core of the jet flow increases with the jet velocity. Similarity, the flame length of the jet flame also increases with jet velocity. Two opposing jets impinge together at an inclined angle, and form a mixing flow field illustrated in Fig.1. During the impinging process, the jet flow velocities may decrease and attain a minimum at the impinging point. The momentum energy transfers to increase the flow intensities and mixing rate. Therefore, the combustion rates are accelerated as compared with a single jet flame [Su & Liu, 1999].

In order to investigate the entrainment and mixing effect, one of the impinging jet was replaced by nitrogen gas [Su & Liu, 2002]. Compared with the pure impinging diffusion flame, it becomes transparent and stable. The flame stretch is destroyed by the nitrogen molecules and increases the mixing rate with the surrounding air. The flame length is also shortened.

In the present research, the flame stretch effect is investigated by splash plate mechanism illustrated in Fig.2. Two types of the splash plate with flat plate and 60 degrees in sharp edge are conducted in this experiment. The boundary conditions of the impinging point in Fig.1 and Fig.2 are different. Slip condition occurs at the jet-to-jet impingement and no-slip condition takes place at the jet flow on the splash plate. A portion of the fluid energy will transfer to the radial direction by the no-slip condition. Therefore, it tends to overcome the flame stretch and spreads the impinging flame out.

The methane fuel and air jets are supplied from high-pressure tanks with high sensitive pressure regulators. Half of the intersection angle between the two jets, θ, is adjusted to 72^{o} in this investigation. The distance between these two jets is 4 times that of its inside-diameter. The geometric coordinates of the impinging flame, the co-plane of the jet-to-jet are set to the X-Y plane. The Y-Z plane is then perpendicular to the co-plane. The origin of the coordinates is at the center of the impinging points. According to the temperature range in these tests, a K-type thermocouple is selected and located on the three-dimensional transverse.

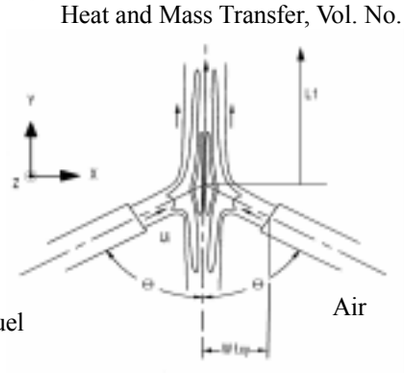
The fuel and air jets locate at opposite side, the result of the main reaction zone will concentrates at the fuel side as illustrated in Fig.3. The higher temperature region above 1000 degrees Celsius are distributed from X= 4 mm to 7 mm and Y= 9 mm to 17 mm. Figure 4 illustrates the temperature results of the impinging flame on the splash plate of flat-plate type. The higher temperature region above 1000 degrees Celsius are distributed from X= 2 mm to 10 mm and Y= 4 mm to 22 mm. Its combustion efficiency is higher than the result in Fig.3. Figure 5 illustrates the temperature results of the impinging flame on the splash plate of shape-edge type. The higher temperature region above 1000 degrees Celsius are distributed from X= 0 mm to 7 mm and Y= 5 mm to 21 mm. Because the direction of the splash plate with shape-edge,

the fuel and the air entrain mutually. The higher temperature region spreads toward the air side. The enhancement of combustion efficiency by splash plate is evident.

References

[1] Su, A. and Liu, Y. C., 1999, "Pulsation of Impinging-Diffusion Flame on the Flat Plate," Proceeding of PSFVIP-2.

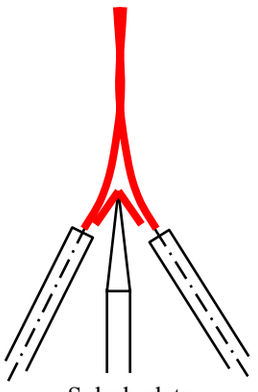
[2] Su, A. and Liu, Y. C., 2002, "Investigation of Impinging Diffusion Flames with Inert Gas," International Journal of Heat and Mass Transfer, Vol. No. 45/15, pp. 3251-3257.





Y-Z plane

Figure 1: Configuration of the impinging flame.





Y-Z plane

Figure 2: Configuration of the mechanism of the splash plate between these two jets.

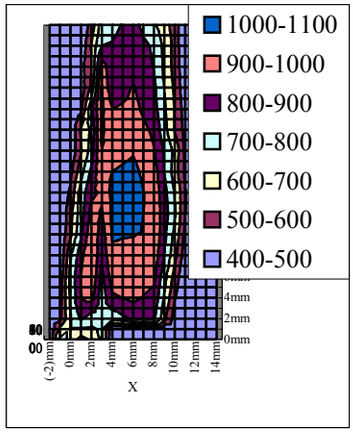


Figure 3: Temperature profile at X-Y plane of Z=0 under air at Re=185 and CH4 at Re=225

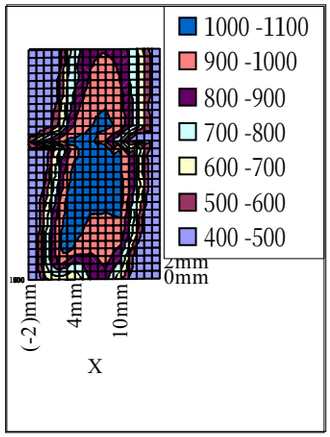


Figure 4: Temperature profile at X-Y plane of Z=0 with flat-plate type of splash plate under air at Re=185 and CH4 at Re=225.

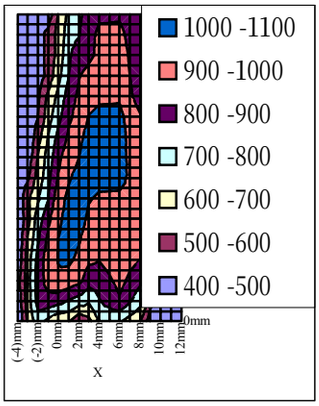


Figure 5: Temperature profile at X-Y plane of Z=0 with shape-edge type of splash plate under air at Re=185 and CH4 at Re=225.

EXOTHERMIC EXPLOSIONS IN A SLAB: A CASE STUDY OF SERIES SUMMATION TECHNIQUE

O. D. MAKINDE
Applied Mathematics Department, University of the North,
Private Bag X1106, Sovenga 0727, South Africa.

ABSTRACT

This paper examine the steady-state solutions for the strongly exothermic decomposition of a combustible material uniformly distributed between symmetrically heated parallel plates under Bimolecular, Arrhenius and Sensitised reaction rates, neglecting the consumption of the material. Analytical solutions are constructed for the governing nonlinear boundary-value problem using perturbation technique together with a special type of Hermite-Padé approximants and important properties of the temperature field including bifurcations and thermal criticality are discussed.

Keywords: Multivariate algebraic approximation, Thermal explosions, Bifurcation.

1. INTRODUCTION: The problem of evaluation of critical regimes thought of as regimes separating the regions of explosive and non-explosive ways of chemical reactions is the main mathematical problem of the thermal explosion theory ([1], [2]). The classical formulation of this problem is first introduced by Frank-Kamenetskii ([2]). Neglecting the reactant consumption, the equation for the heat balance in the original variables together with the boundary conditions can be written as

$$k\frac{d^2T}{d\bar{y}^2}+QC_0A\left(\frac{KT}{\upsilon h}\right)^m e^{-\frac{E}{RT}}=0,\ \frac{dT}{d\bar{y}}(0)=0,\ T(a)=T_0 \tag{1}$$

where T is the absolute temperature, T_0 the wall temperature, k the thermal conductivity of the material, Q the heat of reaction, A the rate constant, E the activation energy, R the universal gas constant, C_0 the initial concentration of the reactant species, h the Planck's number, K the Boltzmann's constant, υ vibration frequency, a the slab half width, $\bar{y}$ is distance measured in the normal direction to the plane and m is the numerical exponent such that m={-2, 0, ½} represent numerical exponent for Sensitised, Arrhenius and Bimolecular kinetics respectively ([1],[2]). Following [2], we introduce the following dimensionless variables in equation (1):

$$\theta=\frac{E(T-T_0)}{RT_0^2},\ \varepsilon=\frac{RT_0}{E},\ y=\frac{\bar{y}}{a},\ \lambda=\frac{QEAa^2C_0K^mT_0^{m-2}e^{-\frac{E}{RT_0}}}{\upsilon^m h^m Rk}\ , \tag{2}$$

and obtain the dimensionless governing equation together with the corresponding boundary conditions as

$$\frac{d^2\theta}{dy^2}+\lambda(1+\varepsilon\theta)^m e^{\left(\frac{\theta}{1+\varepsilon\theta}\right)}=0,\ \ \frac{d\theta}{dy}(0)=0,\ \theta(1)=0\,, \tag{3}$$

where λ ,ε represent the Frank-Kamenetskii and activation energy parameters respectively. In the following sections, equation (3) is solved using both perturbation and multivariate series summation techniques ([3],[4],[5]).

2. PERTURBATION TECHNIQUE: To solve equations (3), it is convenient to take a power series expansion in the Frank-Kamenetskii parameter λ, i.e., $\theta=\sum_{i=0}^{\infty}\theta_i\lambda^i$. Substitute the solution series into equation (3) and collecting the coefficients of like powers of λ, we obtained and solved the equations governing the coefficients of solution series. The solution for the temperature field for Sensitized, Arrhenius and Bimolecular reaction rates are given as

$$\theta(y;\lambda,\varepsilon,m=-2)=-\frac{\lambda}{2}(y^2-1)-\frac{\lambda^2}{24}(y^2-1)(y^2-5)(2\varepsilon-1)+\frac{\lambda^3}{360}(y^2-1)(-11y^4\varepsilon \tag{4a}$$
$$+2y^4+11y^4\varepsilon^2+64y^2\varepsilon-13y^2-64y^2\varepsilon^2+221\varepsilon^2-221\varepsilon+47)+O(\lambda^4)$$

$$\theta(y;\lambda,\varepsilon,m=0)=-\frac{\lambda}{2}(y^2-1)+\frac{\lambda^2}{24}(y^2-1)(y^2-5)+\frac{\lambda^3}{360}(y^2-1)(-2y^4 \tag{4b}$$
$$+3y^4\varepsilon-12y^2\varepsilon+13y^2+33\varepsilon-47)+O(\lambda^4)$$

$$\theta(y;\lambda,\varepsilon,m=1/2)=-\frac{\lambda}{2}(y^2-1)-\frac{\lambda^2}{48}(y^2-1)(y^2-5)(2+\varepsilon)+\frac{\lambda^3}{1440}(y^2-1)(4y^4\varepsilon \tag{4c}$$
$$-8y^4+y^4\varepsilon^2+4y^2\varepsilon+52y^2+y^2\varepsilon^2-14\varepsilon^2-56\varepsilon-188)+O(\lambda^4)$$

-- Converted from Word to PDF for free by Fast PDF -- www.fastpdf.com --

Using computer symbolic algebra package (MAPLE), we obtained the first 21 terms of the above solution series (4) as well as the series for maximum fluid temperature $\theta_{max} = \theta(y=0;\lambda,\varepsilon,m)$.

3. BIFURCATION STUDY: The main tool of this paper is a simple technique of series summation based on a special type of Hermite-Padé approximation technique and may be described as follows. Let us suppose that the partial sum

$$U_{N-1}(\lambda)=\sum_{i=0}^{N-1} a_i \lambda^i = U(\lambda)+O(\lambda^N) \quad \text{as } \lambda \to 0, \tag{5}$$

is given, we construct a multivariate series expression of the form

$$F_d(\lambda, U_{N-1}) = A_{0N}(\lambda) + A_{1N}^d(\lambda)U^{(1)} + A_{2N}^d(\lambda)U^{(2)} + A_{3N}^d(\lambda)U^{(3)}, \tag{6}$$

whereby, we substitute in equation (6) $U^{(1)} = U$, $U^{(2)} = U^2$, $U^{(3)} = U^3$ for cubic algebraic approximant and $U^{(1)} = U$, $U^{(2)} = DU$, $U^{(3)} = D^2U$, $D=d/d\lambda$ for second order differential approximant, such that

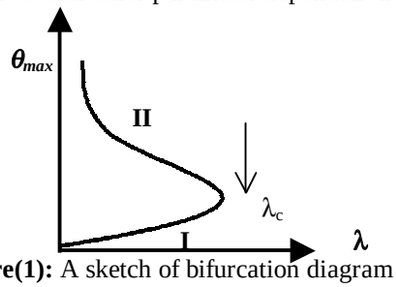
$$A_{0N}(\lambda) = 1, \; A_{iN}(\lambda) = \sum_{j=1}^{d+i} b_{ij}\lambda^{j-1}, \text{ and } F_d(\lambda, U) = O(\lambda^{N+1}) \text{ as } \lambda \to 0, \tag{7}$$

and $d \geq 1$, i =1, 2, 3. The condition (7) nomalises the F_d , reduces the problem to a system of N linear equations for the unknown coefficients of F_d and ensures that the order of series A_{iN} increases as i and d increase in value. We shall take $N=3(2+d)$, so that the number of equations equals the number of unknowns. The algebraic approximant enables us to obtain the solution branches while the dominant singularity or criticality in the problem is obtained easily using the differential approximant. For details on the above procedure, interested readers can see ([3], [4], [5]). Using the above procedure on the solution series in section (2), we obtained the results as shown in table (1) below:

Table (1): Computation showing criticality for Sensitised, Arrhenius and Bimolecular reaction (N=21)

m	ε	θ_{max}	λ_c
-2.0, 0.0, 0.5	0.0	1.186842168	0.8784576797
-2.0	0.1	2.222393808	1.3138875302
0.0	0.1	1.524355912	0.9882078037
0.5	0.1	1.420243862	0.9322160716

4. RESULTS AND CONCLUSIONS: From table (1) above, we observe that at very large activation energy, thermal explosions criticality is independent of the type of reaction. However, for moderately large value of activation energy, the criticality varies from one reaction to another. Explosion in Bimolecular reaction seems to occur faster than in Arrhenius and Sensitised reactions. Two solution branches (type I and II) are identified with a bifurcation point at λ_c as shown in a sketch of bifurcation diagram in figure (1) below. Finally, the above series summation procedure can be used as an effective tool to investigation several other parameter dependent nonlinear boundary-value problems.



Figure(1): A sketch of bifurcation diagram

References

[1] Bebernes J., Eberly D.: Mathematical problems from combustion theory. Springer-Verlag, New York, 1989.
[2] Frank Kamenetskii D. A.: Diffusion and Heat Transfer in chemical kinetics. Plenum Press, New York, 1969.
[3] Makinde O. D.: Heat and mass transfer in a pipe with moving surface-effect of viscosity variation and energy dissipation. Quaestiones Mathematicae 24, 93-104, 2001.
[4] Sergeyev A. V., Goodson D. Z.: Summation of asymptotic expansions of multiple valued functions using algebraic approximations-application to anharmonic oscillators. J. Phys. A31, 4301-4317, 1998.
[5] Tourigny Y., Drazin P. G.: The asymptotic behaviour of algebraic approximants. Proc. Roy. Soc. London A456, 1117-1137, 2000.

-- Converted from Word to PDF for free by Fast PDF -- www.fastpdf.com --

XXI ICTAM, 15–21 August 2004, Warsaw, Poland

A NEARLY 1-D NON-PREMIXED FLAME NEAR EXTINCTION. CELL FORMATION AND THE EFFECT OF THE DIRECTION OF BULK FLOW.

David Lo Jacono[1], Paul Papas[1], Moshe Matalon[2], Peter A. Monkewitz[1]
[1] *Fluid Mechanics Laboratory, Swiss Federal Institute of Technology Lausanne, Switzerland*
[2] *McCormick School of Engineering and Applied Sciences, Northwestern University,Evanston, U.S.A.*

EXPERIMENTAL REALIZATION OF A NEW 1-D FLAME FACILITY

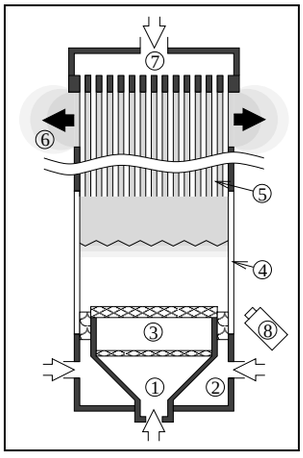


Figure 1. Schematic of the burner. (1) bottom reactant flow, (2) inert co-flow, (3) porous plates, (4) fused silica windows, (5) tube array for reactant supply from top, (6) hot product exhaust, (7) top reactant flow, (8) movie camera.

The *unstrained* one-dimensional diffusion flame has often served as an idealized construct for theoretical modelling [1, 2, 3]. The idealized burner in these studies is supplied with one reactant from the bottom through a "semi-permeable plate" (impermeable in the downward direction). The other reactant diffuses from the top of the chamber to the flame, against the upward flow of products. The supply of both reactants is assumed to be uniform over the burner cross section such that the velocity, which is upwards everywhere, and all other physical quantities depend only on the (vertical) coordinate normal to the planar flame. Since the uniform supply of the reactant diffusing against the bulk flow is a major experimental problem, laboratory investigations of non-premixed flames have until now been limited to burners with non-uniform conditions over the flame surface.

In order to more directly compare the theoretical results for the 1-D ideal flame with experiments, a new improved experimental realization of the ideal burner has been constructed. It is shown schematically in Fig. 1 on which the various components are identified. The combustion chamber with a square cross section of 46×46 mm has a solid back wall with igniter and three fused silica windows. The bottom reactant is introduced into the combustion chamber through a 34 mm square porous plate surrounded by a slot allowing the introduction of an inert co-flow (not used here). In order to obtain a uniform distribution of the top reactant over the cross section, while also allowing the products to escape uniformly, the top reactant is supplied through a cartesian array of 25×25 stainless steel tubes (1 mm O.D., 0.8 mm I.D.) between which the products can escape upwards. Just below the ends of the tubes (located 20 mm above the bottom porous plate), the flow is clearly 3-D on the scale of the tube spacing. Some simple estimates suggest however that the thickness of this 3-D layer is of the order of one tube diameter, and that below this injection region the oxidizer is transported towards the flame by 1-D diffusion against the product flow, as in the ideal burner.

INVESTIGATION OF EXTINCTION LIMITS AND CELL FORMATION IN THE NEW BURNER

Previous experimental investigations on cell formation in non-premixed flames include the work of Chen et al. [4] who clearly demonstrated that low Lewis and Damköhler numbers are required for cells formation. More recently, the influence of the initial mixture strength on cell formation in an axisymmetric jet flame has been documented at EPFL [5, 6]. While these studies qualitatively confirm the influence of the different parameters predicted theoretically for an ideal 1-D flame, the new burner described above should permit quantitative comparisons. In the following, preliminary results with the new burner are reported for CO_2-diluted H_2-O_2 *nearly unstrained*, non-premixed flames near extinction. Two configurations are considered: One with the fuel supplied from the bottom (FB) and the oxidizer counterdiffusing from the top, and the configuration with inverted supplies, i.e. the fuel counterdiffusing from the top (FT). Note that the FB configuration is analogous to the steady axisymmetric jet flame, where the radial bulk flow through the flame is directed outwards from the fuel to the oxidizer side. The same situation is also found in a "lean" flamelet. Finally, for opposed jet flames with highly diluted fuel (e.g. N_2-diluted CH_4 burning with pure O_2 [7]), the flame sits on the fuel side of the stagnation plane and O_2 reaches the flame by counterdiffusion, again as in the FB configuration.

First, the extinction limit for the FB and FT configurations were determined as a function of the initial O_2 and H_2 concentrations. For this, the top reactant composition was held constant, while the bottom reactant concentration was gradually decreased in small steps until the flame could barely be maintained (a further 0.1% reduction of the bottom reactant concentration below this “near-extinction” limit always resulted in complete extinction). As shown in Fig. 2, these extinction curves have asymptotes corresponding to limiting H_2 and O_2 concentrations, below which a diffusion flame cannot be established, irrespective of how “rich” the other reactant is. The influence of the direction of bulk flow on the limiting O_2 concentration is evident: when O_2 is supplied convectively by the bulk flow (FT configuration), a flame with excess fuel supply can be sustained at about 5% less O_2 concentration than in the FB configuration, where O_2 has to diffuse against the bulk flow. The comparison of the limiting H_2 concentrations, on the other hand, has not yet been carried out. Furthermore, it is noted that all the limiting concentrations in Fig. 2 are significantly lower than in the axisymmetric jet flame [5], which is believed to be at least partly due to the negligible flow strain rate in the present

burner. Other effects, such as heat loss, remain to be investigated: for any given reactant composition, the flowrate of the bottom reactant had to be limited keep the flame away from the upper injection manifold. The limit where heat loss to this manifold affects the extinction limits, however, remains to be determined.

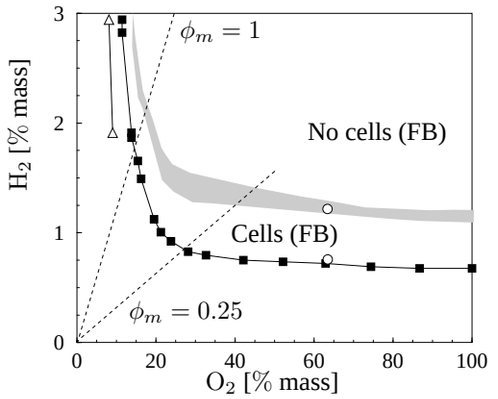


Figure 2. Near-extinction limits and region of cellular instability in nearly unstrained planar non-premixed CO_2-diluted H_2-O_2 flames; Shaded region: transition from non-cellular to cellular flames for the FB configuration; —■—: FB near-extinction limit; —Δ—: FT near-extinction limit; ○: conditions for Fig. 3.

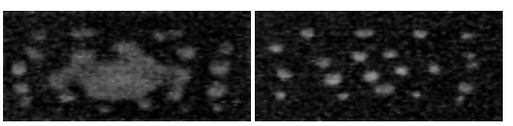


Figure 3. Digital images of the cells observed at the two points (○) in Fig. 2 for the FB configuration. Left: transition from no cells to the fully cellular regime; Right: near the extinction limit.

Next, the parameter space in which cellular flames are observed was determined for the *FB configuration only* . For the limited conditions examined to date in the FT configuration, no cells have been found yet. The transition region from a steady "featureless" flame to a flame with cells over its entire surface is identified in Fig. 2 by shading. Since the reactant Lewis numbers, based on the overall reactant mixture at 300 K, are relatively constant over the entire experimental range (0.97–1.33 for O_2 and 0.22–0.29 for H_2), Fig. 2 shows mainly the influence of Damköhler number (decreasing towards extinction) and initial mixture strength ϕ_m on cell formation in the FB configuration (the experiments cover the range 0.05–3.55 and two lines of constant ϕ_m are added in the figure for reference). Note that ϕ_m is defined here as the ratio of the H_2 and O_2 mass fractions supplied in the fuel and oxidizer streams, respectively, normalized by the stoichiometric ratio. As in previous work [5], the distance in Fig. 2 between the appearance of cells and the extinction boundary increases with decreasing ϕ_m.

To illustrate the transition process to a fully cellular flame, Fig. 3 shows digital images taken for two conditions corresponding to the open circles in Fig. 2. They were taken with a movie camera at an oblique angle of about 45 degrees with respect to the vertical (cf. Fig. 1). About half way through the transition (left image of Fig. 3), cells have already formed on the periphery of the flame, while the center is still non-cellular. One possible explanation for this observation is the relatively larger heat loss of the flame edges to the chamber walls as compared to the flame center, i.e. a decrease of effective Damköhler number towards the flame edges. In the right image of Fig. 3 taken close to extinction, on the other hand, the entire flame consists of cells, which appear to be generated near the flame center and travel outwards before vanishing. The cell size at this point is smaller than at the transition, but still about 2 times the tube spacing. Therefore, the cell size over the entire cellular regime appears to be unrelated to the spacing of the oxidizer supply tubes. Further towards extinction, the number of cells decreases progressively until the last cell "goes out".

OUTLOOK

Theoretical studies [1, 2, 8] have shown that the reactant convected to the flame zone has a significant influence on the conditions for thermo-diffusive instabilities in non-premixed flames. When O_2 diffuses against the bulk flow (our FB configuration), the current study and others (cf. [5]) have shown that cellular instabilities are more prevalent at low initial mixture strength and Lewis numbers, in agreement with theoretical predictions. In the opposite FT configuration, theory predicts that *high* initial mixture strength promotes cell formation. In addition, as opposed to the FB configuration, a low O_2 Lewis number would be more important for cell formation than a low H_2 Lewis number. The new burner, which has been shown to produce an essentially 1-D planar non-premixed flame with virtually no strain, appears to be well suited to test these theories. As mentioned above, no cells have so far been observed near the FT extinction limit in Fig. 2, despite the high ϕ_m. The next step will therefore consist in lowering the oxidizer Lewis number and minimizing the effects of heat loss.

References

[1] S. Kukuck, M. Matalon, *Combust. Theory Modeling* 5 (2001) 217–240.
[2] S. Cheatham, M. Matalon *J. Fluid Mech.* 414 (2000) 105–144.
[3] J.S. Kim, *Combust. Theory Modelling* 1 (1997) 13–40.
[4] R.-H. Chen, G.B. Mitchell, P.D. Ronney, *Proc. Combust. Inst.* 24 (1992) 213–221.
[5] D. Lo Jacono, P. Papas, P.A. Monkewitz, *Combust. Theory Modelling* 7 (2003) 634–644.
[6] M. Füri, Non-Premixed Jet Flame Instabilities, Ph.D. Thesis no. 2468, Swiss Federal Institute of Technology Lausanne (EPFL), (2001).
[7] J. Du, R.L. Axelbaum, *Proc. Combust. Inst.* 26 (1996) 1137–1142.
[8] V.N. Kurdyumov, M. Matalon, *Proc. Combust. Inst.* 29 (2002) 45–52.

SIMULATION OF FLAME PROPAGATION IN A TUBE WITH OBSTACLES

Aidarkhan Kaltayev, Zhomart Ualiev
al-Farabi Kazak National University, Department of Mechanics, Almaty, Kazakstan

Summary A fictitious domain method is extended and implemented for time dependent combustion problems in non-regular closed domains. The propagation of 2D laminar methane-air flame in a tube with obstacles are simulated and studied.

BACKGROUND

A fictitious domain method (FDM) for partial differential equations has recently shown a most interesting potential for solving complicated problems from Science and Engineering [1-3]. The main reason for popularity of FDM is that they allow using of fairly structured meshes on a simple shape fictitious domain (typically rectangle in 2D) containing the actual domain, therefore allowing to use of fast solvers. Another important point is that the stability condition of the resulting scheme is the same as the one of the finite difference scheme [1]. Up to now a FDM was used for solving the problems of physics with Dirichlet boundary conditions. But many problems of science are Neumann problems (for example, like the combustion problems) and application of FDM to them has essential peculiarities.

PROBLEM FORMULATION AND NUMERICAL TECHNIQUE

A fictitious domain method is extended and implemented for combustion problems in non-regular domains. The most prominent example of those problems is the propagation of flame in a tube with obstacles. It is known that the combustion process of premixed gases in tubes or vessels is strongly affected by obstacles. For freely propagating flames grids or obstacles can cause violent flame acceleration and enhanced transition to detonation.
It is considered the cases when 2D flame propagates in a closed rectangular tube with obstacles and we focus our attention on its numerical solution by FDM approach to study the hydrodynamic structure of the flame. The combustible gas is a stoichiometric methane-air mixture. The study is based on the assumption of a low Mach number flow and uses a one-step global chemistry model of the methane-air laminar flame. The problem is simulated using unsteady conservation equations of energy, species, mass, momentum and equation of state. The transport coefficients, thermodynamic data, kinetic coefficients and numerical algorithm are given elsewhere [4-5]. The fictitious transport coefficients are

$$\lambda^{\varepsilon}(\bar{x}) = \begin{cases} \lambda, & if\ \bar{x}\in\Omega \\ \varepsilon, & if\ \bar{x}\in\Omega_f \end{cases}, \qquad D^{\varepsilon}(\bar{x}) = \begin{cases} D, & if\ \bar{x}\in\Omega \\ \varepsilon, & if\ \bar{x}\in\Omega_f \end{cases}, \qquad \xi^{\varepsilon}(\bar{x}) = \begin{cases} 0, & if\ \bar{x}\in\Omega \\ \varepsilon^{-1}, & if\ \bar{x}\in\Omega_f \end{cases},$$

where λ is the heat conductivity, D is the diffusion coefficient, Ω is the actual flow domain, Ω_f is the fictitious domain (obstacle domain), ε is the small positive parameter. Boundary conditions are non-slip and heat- and mass isolated at the solid boundaries and symmetric at the symmetry line. At initial time the gas mixture is at rest at a temperature of 300 K and pressure of $P_t(0)=P_0=10^5\ Pa$, $p_d=0$, $\varepsilon=10^{-6}$.

RESULTS

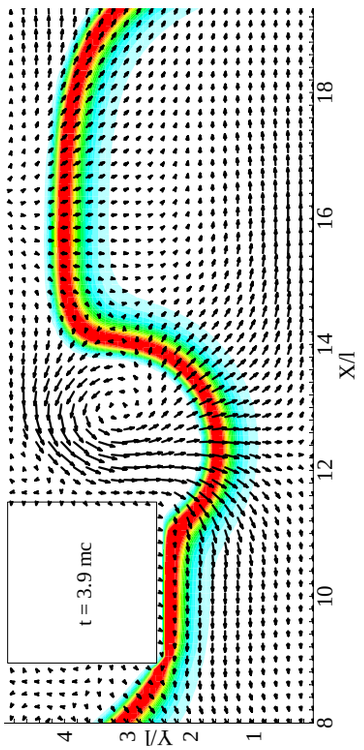
Figures 1,2 displays the samples of the temporal evolution of velocity fields and methane consumption rate contours in the upper part of the symmetric rectangular vessel with length $L=30\ l$ and cross section $5l$x$5l$ in presence of rectangular obstacles, where $l=0.5mm$. The flame is ignited at the centre of left vessel side. The Reynolds number $\mathrm{Re} = u_n l\rho_0 / \mu_0 = 12.3$, $u_n = 40\ cm/sec$ is the flame speed, the Prandtl number is 0.73, the Lewis number is 1.

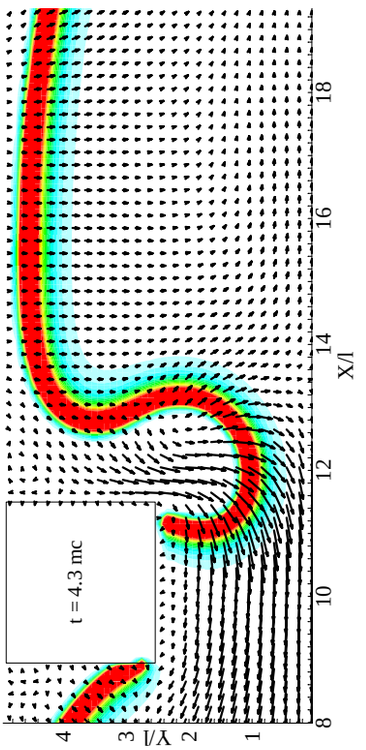
CONCLUSIONS

A fictitious domain method is extended for combustion problems. A detailed simulation of flame propagation in the tube at various locations of obstacles is implemented and the results are analaized. It is found that the computational cost is almost the same as in the case of tube without obstacles.

References

[1] Smagulov Sh., Orunkhanov M.: Method of Solution of Hydrodynamic Equations in Multiconnected domains. *Dokl. AN USSR* **260**:1078-1082, 1981.
[2] Glowinski R., Pan T. W., and Periaux J.: A fictitious domain method for external incompressible viscous flow modeled by Navier-Stokes equations. *Comp. Meth. Appl. Mech. Eng* **112**:133-148, 1994.
[3] Collino F., Milot F.: Fictitious domain method for unsteady problems: application to Electro-Magnetic scattering. *J. of Comp. Physics* **138**:907-938, 1997.
[4] Kaltayev A., Riedel U., and Warnatz J.: The Hydrodynamic Structure of a Methane-Air Tulip Flame. *Comb. Sci. and Tech* **158**: 53-69, 2001.
[5] Kaltayev A., Ualiev Zh.: A Fictitious Domain Method for Combustion Problems. 19th ICDERS 2003, web site http://19thICDERS.matsuo.mech.keio.ac.jp





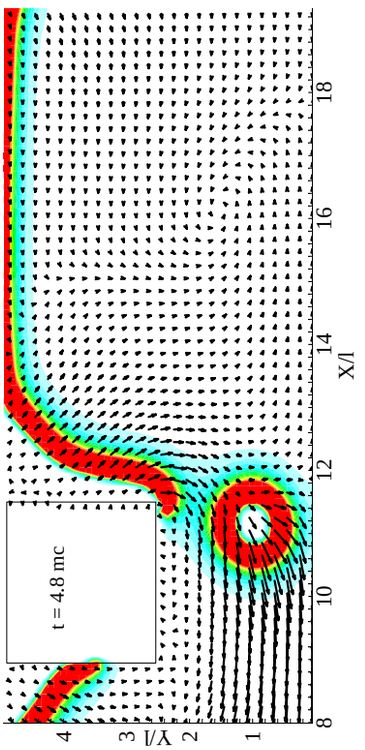
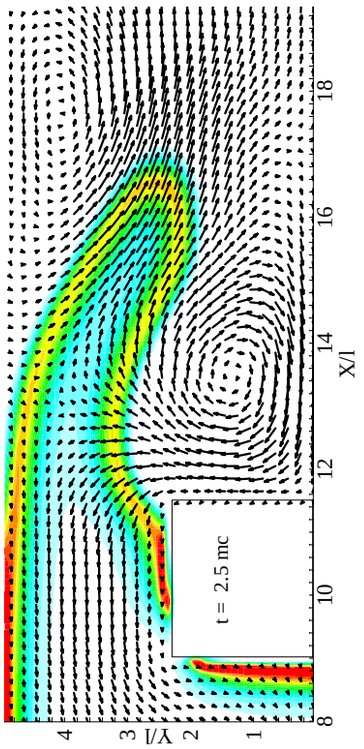
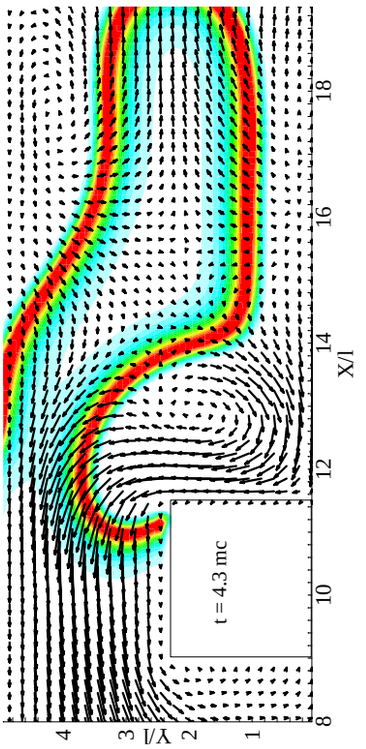


Figure 2





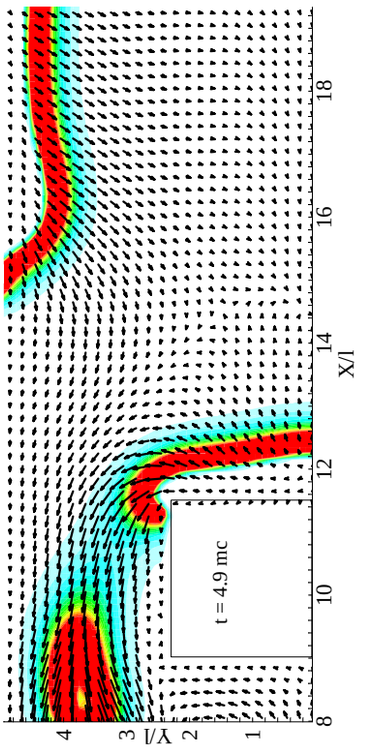


Figure 1

LARGE EDDY SIMULATION OF PILOTED AND BLUFF-BODY DIFFUSION FLAME

Tim Broeckhoven*, Sergey Smirnov*, Chris Lacor*, Eduardo Brizuela**
* *Deptartment of Fluid Mechanics, Vrije Universiteit Brussel, Brussels, Belgium*
** *Facultad de Ingenieria, Universidad Nacional de La Plata, Buenos Aires, Argentina*

Summary Large Eddy Simulation (LES) appears to be a very promising tool for the prediction of turbulent combustion processes. In this paper a basic mixed-is-burnt combustion model combined with a presumed pdf approach is used for simulations on two non-premixed combustion test cases. Results obtained with RANS-simulations using different turbulence models are compared with LES results.

INTRODUCTION

A variety of reasons makes it desirable to fully predict flow fields in gas combustors: cost reduction in the testing phase, increase in performance and durability of gas turbines and a reduction of pollutants. The key aspect in modeling turbulent reactive flows is the realistic representation of the turbulence-chemistry interaction. The combustion process in a turbulent diffusion flame may be viewed as a competition between mixing and chemical reaction. In [1] several advantages of using LES in combustion are put forward. LES provides a better description of turbulence-combustion interactions because the large structures are explicitly computed and instantaneous fresh and burnt gas zones, where turbulence characteristics are quite different, are clearly identified. Combustion instabilities come with large scale coherent structures which are better predicted with LES [2]. In [3] the usefulness of an assumed pdf approach in non-premixed combustion combined with LES is confirmed, whereas the use with RANS is questionable.

GOVERNING EQUATIONS AND COMBUSTION MODEL

As in any flow the laws of conservation of mass, momentum, energy and species mass fraction are valid. One of the key problems in modeling turbulent diffusion combustion is the closure of the averaged chemical source terms that appear in the species equations. A way to circumvent this, is the introduction of a 'conserved scalar', i.e. a scalar not affected by the chemical reactions. The mass fraction of the different species can then be related to this scalar through a chemistry model. The used conserved scalar is the mixture fraction Z which expresses at a certain location the mass coming from the fuel stream. This variable obeys the following conservation law:

$$\frac{\partial \rho Z}{\partial t} + \frac{\partial \rho u_j Z}{\partial x_j} = \frac{\partial}{\partial x_j}\left(\mu_{eff}\frac{\partial Z}{\partial x_j}\right) \tag{1}$$

The combustion model implemented is the mixed-is-burnt model assuming infinitely fast chemistry. The entire state of the gas is determined by piecewise linear relations $Y_i = Y_i(Z)$, $\rho = \rho(Z)$, $T = T(Z)$. Species mass fraction, mixture density and temperature are related to the mixture fraction but in turbulent flows where the governing equations are solved for the averaged variables, the simple use of averaged values in the chemical model, yield inaccurate results due to the high non-linearity of the relations. To describe the influence of turbulent fluctuations on the mean thermochemical quantities more accurately, a more sophisticated averaging procedure must be applied. In this paper a presumed pdf approach is used with a β-shaped probability density function determined by the mean mixture fraction $\tilde{Z}$ and its variance $\widetilde{Z"^2}$. For the RANS simulations, a $k-\epsilon$ type turbulence model is used and the variance of mixture fraction is determined by solving the conservation equation (2).

$$\frac{\partial \rho Z"^2}{\partial t} + \frac{\partial \rho u_j Z"^2}{\partial x_j} = \frac{\partial}{\partial x_j}\left(\mu_{eff}\frac{\partial Z"^2}{\partial x_j}\right) + S_{Z"^2} \tag{2}$$

For the LES simulations a scale-similarity model is used for this variance where $\tilde{}$ denotes the LES filter and $\hat{}$ denotes a test filter:

$$\widetilde{Z"^2} \approx C_v \widetilde{\hat{Z}'^2} = C_v\left(\widehat{\tilde{Z}^2} - (\hat{\tilde{Z}})^2\right) \tag{3}$$

TEST CASES

In this paper results of two LES-simulations on combustion test cases are presented and compared to the RANS-solution with several turbulence models and with experimental results [4, 5]. The first test case is a piloted CH_4/air diffusion flame (Sandia D) which has been studied experimentally by Barlow et al. [6] and measurements have been done at Darmstadt University of Technology. The geometry is given in figure 1.

The central fuel jet with a mean velocity of $49.6m/s$ consists of 75% air and 25% methane by volume and is surrounded by a co-flow of air with a free stream velocity of $0.9m/s$. To stabilize the flame a high temperature region near the burner is created by a pilot flame. The Reynolds number of the central fuel jet, based on the fuel nozzle diameter and mean velocity is $Re = U_m D_n/\nu = 22400$.

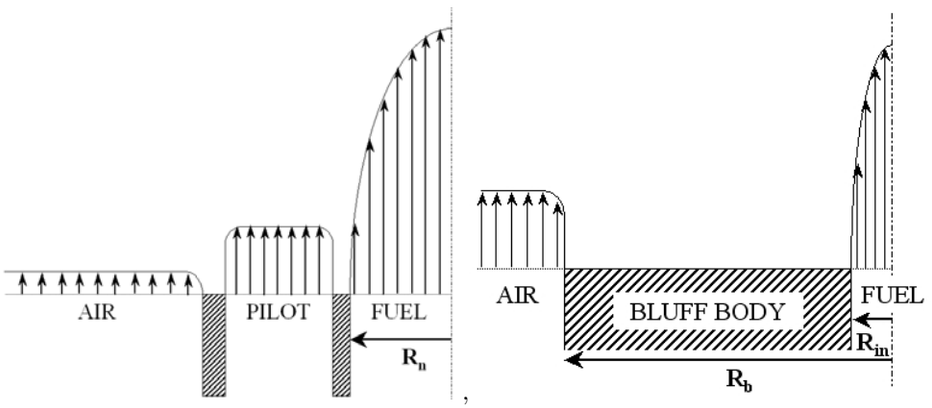


Figure 1: Geometry of the considered test cases (left: Sandia D, right : Bluff Body)

The second case is a bluff-body burner with a central fuel jet of $50\%H_2/50\%CH_4$ by volume which mixes with the co-flow of air [7]. The geometry is characteristic for a modern type industrial burner and is shown in figure 1. This unconfined flame remains attached because there is a recirculation zone behind the bluff body where fuel and air are intensely mixed. The chemical reaction creates a high temperature region which stabilizes the flame. This test case is more demanding of the chemistry model because local extinction may occur. The Reynolds number of the central fuel jet, based on the fuel nozzle diameter ($R_{in} = 3.6mm$) and mean velocity ($U_m = 118m/s$) is $Re = U_m D_n/\nu = 15900$.

CONCLUSIONS AND FURTHER WORK

A basic mixed-is-burnt combustion model has been tested on two well known test cases combined with both RANS and LES simulations. The influence of turbulence modeling has been investigated and discrepancies between experimental and numerical results have been identified. In future research more advanced combustion models will be used to investigate the influence of the chemistry modeling on the flow field prediction in non-premixed combustion test cases.

References

[1] O. Colin, F. Ducros, D. Veynante, and T. Poinsot. A thickened flame model for les of turbulent premixed combustion. *Physics of Fluids*, 12:1843–1863, 2000.

[2] B. Lessani, J. Ramboer, and C. Lacor. Efficient large-eddy simulation of low mach number flows using preconditioning and multigrid. *To be published : International Journal of Computational Fluid Dynamics*, 2004.

[3] C.D. Pierce and P. Moin. A dynamic model for SGS variance and dissipation rate of a conserved scalar. *Physics of Fluids*, 10:3041–3044, 1998.

[4] H. Pitsch and H. Steiner. Large-eddy simulation of a turbulent piloted methane/air diffusion flame (sandia flame d. *Physics of Fluids*, 12(10):2541–2554, 2000.

[5] B. Merci, E. Dick, J. Vierendeels, D.Roekaerts, and T.W.J. Peeters. Application of a new cubic turbulence model to piloted and bluff-body diffusion flames. *Combustion and Flame*, 126:1533–1556, 2001.

[6] Barlow R.S. and Frank J.H. Proceedings of the 27^{th} international symposium on combustion. page 1087, Pittsburgh, 1998. The Combustion Institute. See also: http://www.ca.sandia.gov/tnf/Workshop.html.

[7] Dally B.B., Masri A.R., Barlow R.S., and Fiechtner G.J. Instantaneous and mean compositional structure of bluff-body stabilized nonpremixed flames. *Combustion and Flame*, 114(1/2):119–148, 1998.

XXI ICTAM, 15–21 August 2004, Warsaw, Poland

INFLUENCE OF THE SUBGRID MODELS ON COMBUSTION MODELING

Artur Tyliszczak*, William P. Jones**, Andrzej Boguslawski*, Stanislaw Drobniak*
*Institute of Thermal Machinery, Czestochowa University of Technology, 42-200 Czestochowa, Poland
**Department of Mechanical Engineering, Imperial College London, SW7 2AZ London, United Kingdom

Summary Turbulent flow with combustion is modelled numerically using LES (Large Eddy Simulation) method together with the flamelet approach. The governing equations applied in this work are based on the low Mach number approximation. High order compact differences/pseudospectral discretization method is applied to guarantee accurate results. The computations are performed for Sandia D flame configuration.

Introduction

Turbulent flows with combustion are among the most difficult problems occurring in nature and in industrial applications. A common appearance and importance of such flows require their correct prediction allowing for their optimization and control. The unsteady character of the turbulence implies the use of LES method which in turn allows to obtain time dependent solutions. This work concerns the analysis of the influence of subgrid models (subgrid viscosity) used within a framework of the LES method of turbulence/combustion modelling. To be able to perform such research it is necessary to exclude the effect of the numerical dissipation and its possible influence on the subgrid viscosity. The high order compact differences/pseudospectral numerical discretization method applied in computations allows for such analysis and also guarantees very accurate results. In this short summary all quantities (if not mentioned separately) appearing in the equations have standard meaning e.g. ρ - density, u_i - velocity, etc.

Combustion modeling

In the most general case modelling of the combustion processes is very expensive computationally since together with the solution of the flow field, based on the Navier-Stokes equations, it requires solution of additional transport equations for particular N species (e.g. CO, CO2, H2O, H2, etc.) produced in chemical reactions. Furthermore, the chemical kinetics which accounts for various reactions for which it is difficult to assess their importance a priori, should also be considered as a part of the solution. From the point of view of capability of available computers, approach of this type is still impossible since the numerical code would require implementation of the equations for tens species and tens (or even several hundred) chemical reactions. An approach used in this work is based on a flamelet concept [1] which states that flame can be seen as an ensemble of laminar flamelets. The equation for the conserved scalar is used, which is refereed to as the mixture fraction and denoted wherein after as z, in the form of the simple convection-diffusion equation:

$$\frac{\partial \rho z}{\partial t} + \frac{\partial \rho u_i z}{\partial x_i} = \frac{\partial}{\partial x_i}\left(\rho \mathcal{D} \frac{\partial z}{\partial x_i}\right) \tag{1}$$

The mixture fraction is a normalized quantity ($z \in [0,1]$) and represents a local fuel to oxidizer ratio ($z = 0$ - pure oxidizer; $z = 1$ - pure fuel). The assumption that one conserved scalar is sufficient to describe thermochemical state of the flow decouples the modeling of reactive phenomena from that of flow modelling. Assuming that particular species concentration, Y_k, and temperature, T, are the functions of the mixture fraction ($Y_k(\vec{x},t) = Y_k(z(\vec{x},t),t)$, $T(\vec{x},t) = T(z(\vec{x},t),t)$) the equations for these quantities may be transformed into the mixture fraction space resulting in the equations of the form:

$$\rho \frac{\partial Y_k}{\partial t} = \dot{\omega}_k + \rho \mathcal{D}\left(\frac{\partial z}{\partial x_i}\frac{\partial z}{\partial x_i}\right)\frac{\partial^2 Y_k}{\partial z^2} = \dot{\omega}_k + \frac{1}{2}\rho\chi\frac{\partial^2 Y_k}{\partial z^2} \tag{2}$$

where $\mathcal{D}$ is the diffusion coefficient assumed the same for each species and $\dot{\omega}$ is the reaction rate depending on the chemical kinetics. The above equation together with the equation for the temperature constitute the unsteady flamelet approach in which the dependence of the temperature and species on time is retained. However, knowing that characteristic time of the chemical processes is much smaller than time of the turbulent phenomena one can assume the structure of the flamelet to be steady even though the mixture fraction itself depends on time. With this assumption, at every instantaneous time of the solution, the values of $Y_k(\vec{x})$ and $T(\vec{x})$ may be computed based on the mixture fraction. The functional dependences $Y_k(\vec{x}) = Y_k(z(\vec{x}))$ and $T(\vec{x}) = T(z(\vec{x}))$ are provided from the solution of the laminar flamelet calculations of the steady flamelet equations. Knowing the species concentration corresponding to a given value of the mixture fraction the density may be computed based on the equation of state and then also expressed as the functional dependence of z. In the context of LES method of turbulence modeling, where every quantities are represented as the superposition of their filtered and subgrid parts, the mixture fraction equation has the form:

$$\frac{\partial \bar{\rho}\tilde{z}}{\partial t} + \frac{\partial \bar{\rho}\tilde{u}_i\tilde{z}}{\partial x_i} = \frac{\partial}{\partial x_i}\left(\left(\rho\mathcal{D} + \frac{\mu_t}{Pr_t}\right)\frac{\partial \tilde{z}}{\partial x_i}\right) \tag{3}$$

where $\bar{(\cdot)}$ and $\tilde{(\cdot)}$ represents the LES-filtered and Favre-filtered variables, Pr_t stands for the turbulent Prandtl number and μ_t is the turbulent viscosity obtained from the subgrid model.

Flow field modeling

For the strongly variable density/temperature low speed (low Mach) flows it is necessary to take into account their spatially and temporally unsteady character. In this research we applied the so-called low Mach number approximation of the governing equations, where the flow variables are expressed as power series of $\epsilon = \gamma M^2$ (γ - ratio of the specific heats, M - Mach number) in the form: $f = f^{(0)} + \epsilon f^{(1)} + \epsilon^2 f^{(2)} + \mathcal{O}(\epsilon^3)$. The LES-filtered continuity and the Navier-Stokes equations at the zero order quantities (except for the pressure) are given as:

$$\frac{\partial \overline{\rho^{(0)}}}{\partial t} + \frac{\partial \overline{\rho^{(0)}} \widetilde{u^{(0)}}_j}{\partial x_j} = 0 \tag{4}$$

$$\frac{\partial \overline{\rho^{(0)}} \widetilde{u^{(0)}}_i}{\partial t} + \frac{\partial \overline{\rho^{(0)}} \widetilde{u^{(0)}}_i \widetilde{u^{(0)}}_j}{\partial x_j} = -\frac{\partial \overline{p^{(1)}}}{\partial x_i} + \frac{\partial}{\partial x_j}\left((\mu + \mu_t)\left(\frac{\partial \widetilde{u^{(0)}}_i}{\partial x_j} + \frac{\partial \widetilde{u^{(0)}}_j}{\partial x_i} - \frac{2}{3}\delta_{ij}\frac{\partial \widetilde{u^{(0)}}_k}{\partial x_k}\right)\right) \tag{5}$$

We note that in the framework of low Mach number approximation the equation for the mixture fraction should also be seen as an equation for zero order quantities ($\overline{\rho^{(0)}}$, $\widetilde{z^{(0)}}$). In the present work the turbulent viscosity is modelled using Smagorinsky subgrid model together with its dynamic counterpart and filtered structure function model [2].

Solution procedure and sample results

The solution procedure for the set of equations (4), (5) and (3) is based on the projection method which allows to determine the pressure field $p^{(1)}$ from the Poisson equations. The time advancement is performed by low storage III^{th} order Runge-Kutta method, all space derivatives are discretized using VI^{th} order compact differences method or Fourier pseudospectral method in the directions for which periodic boundary conditions are assumed. The preliminary results showing the contours of the mixture fraction for Sandia D flame are presented in Fig.1, they are in reasonably good agreement with experimental data. The periodic boundary conditions are applied on the boundaries parallel to the jet axis, at the outflow we applied convective type boundary conditions while at the inlet the velocity and mixture fraction profiles correspond to experimental data. These computations were performed with the filtered structure function model for the subgrid scale.

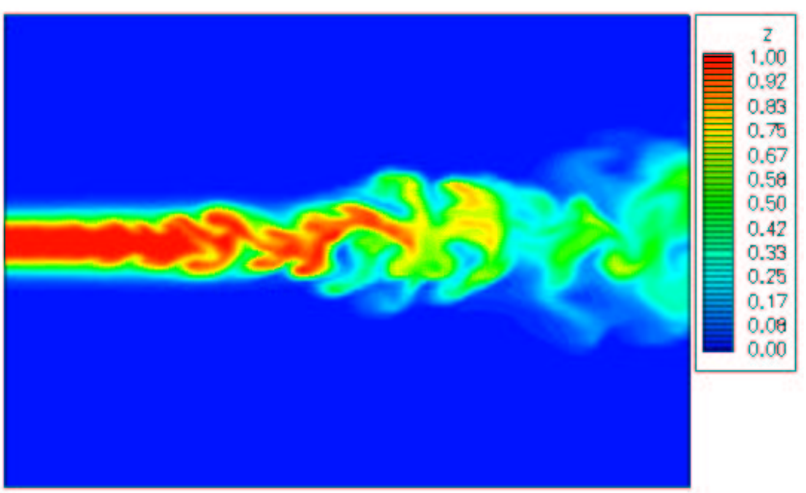


Figure 1. Mixture fraction contours in Sandia D flame.

CONCLUSIONS

This summary presents the main idea and the solution strategy for modeling turbulent flow with combustion. The obtained results are very promising, the research concerning comparison of the accuracy of various subgrid models is currently in progress.

This research was performed partly within the EU MOLECULES project, contract N^o G4RD-CT2000-00402, and grant of Polish Committee for Scientific Research, contract N^o KBN 8T10B 009 19.

References

[1] Peters N.: Turbulent combustion. *Cambridge University Press*, 2000.
[2] Metais O., Lesieur M., Comte P.: Transition, turbulence and combustion modeling, pp. 349-420, KLUWER Academic Publisher, 1999.
[3] Lele S.K.: Compact finite difference with spectral-like resolution. *JCP*, vol. 103, pp. 16-42, 1992.

CHEMICAL ASPECTS OF THE FLAMELESS OXIDATION APPLIED FOR GAS TURBINE COMBUSTOR

Yeshayahou Levy, Valery Sherbaum, Vladimir Erenburg
Faculty of Aerospace Engineering, Technion, Haifa, Israel

Low pollutant emissions became the basic issues in new combustion technologies concept. One of the ways to achieve this goal is flameless oxidation process (named also "mild combustion"). It was found by Wunning [1], that under special conditions a stable form of combustion is possible for high recirculation rates of exhaust gases. Wunning points that only exhaust gas recirculating into combustor before the reaction flame front must be taken into consideration. The recirculation of hot products into the flame to improve flame stabilization is not considered as the recirculating gas.
All benefits of such combustion, i.e. low-NOx emissions, low noise levels and uniform temperatures at the combustor exit motivated further research in this field. Flameless oxidation principle for flame in furnaces with high temperature inlet air was used by Wunning and Wunning [2] Katsuki and Hasegawa [3], Milani and Saponaro [4].
To obtain low NO_x emissions, a critical requirement is to avoid direct combustion before the dilution of air with burnt gases. Intense mixing of air with a significant amount of the burnt gases before combustion is essential and mixing must be enhanced in the preparation process prior to combustion. Internal circulation is initiated by the dynamic action of the flue gases within the furnace. When the fuel is discharged into the air, the shear-generated aerodynamic strain rate is usually high enough to quench both premixed and diffusion flames. Further downstream the strain rate relaxes and consequent burning ensues. Study of such combustion regime is very active during last few years.
The present work is aimed to find the performance characteristics of a gas turbine combustor operating in the flameless oxidation regime. It considers the specific operating conditions of gas turbine combustors with recirculating flue gases. In contrast to industrial furnaces where oxygen content in flue gases is 1-3 % [1], in gas turbine can be more than 10-15%. Its value depends on temperature before combustor (through compressor pressure ratio and efficiency) and combustion temperature (Fig.1). For stirring gas the oxygen content this value can be as high as 17 %.

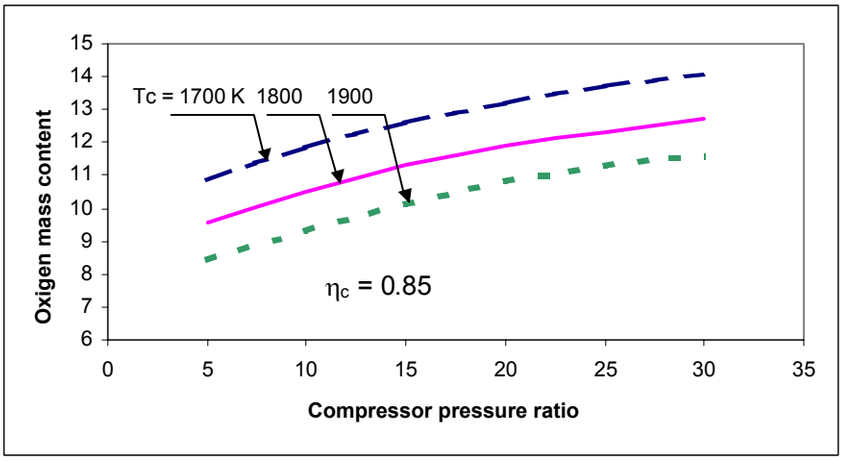


Fig.1.Variation of oxygen mass content (%) after combustion with compressor pressure ratio and efficiency.

Due to the high temperature after compressor, the ignition temperature can achieve, through the recirculation, of much lower gas quantities (hence recirculation ratios) than in industrial furnaces. Residence time in gas turbine is in the range of about 3-20 ms, i.e. in two orders of magnitudes less than in industrial furnaces. Calculation scheme of the present study included a mixing reactor, where air is mixed with combustion products in pre-set proportion (according to recirculation ratio), plug reactor for chemical process simulation, plug reactor for dilution process simulation. Residence time equaled 5 and 10 ms as the actual values for gas turbine combustors. CHEMKIN 3.7 code with application "AURORA" for "PSR" and "PLUG" for chemical reaction calculations were applied. For calculation of chemical reactions used GRI-MECH Version 3.0 package with 350 reactions.
The following main results were obtained:

1. NO_x formation is governed mainly by combustion temperature (Fig. 2), almost does not depend on recirculation ratio (when combustion temperature lower 1850 K) and depends on combustion pressure.

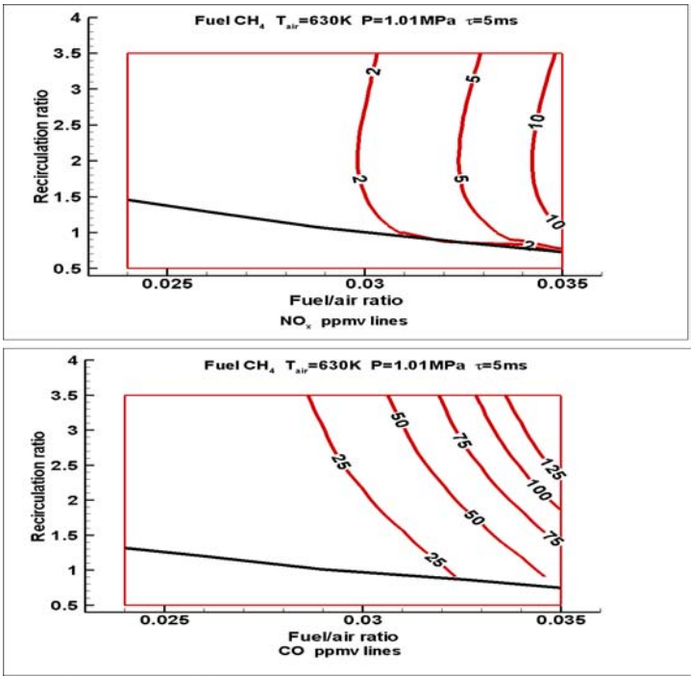


Fig. 2. Dependence NO_x and CO on fuel-air and recirculaion ratios (residence time is equal to 5 ms).

2. Minimal combustion temperature (for a given residence time) depends on combustion pressure. For a given pressure it depends slightly on flue gas content.
3. Combustion delay time decreases with the recirculation ratio as stirring temperature increases (for a given fuel/air ratio *q*).
4. Variation of NO_x and CO with time for combustion pressure indicates that NO_x production increases slowly with time after combustion has completed (temperature achieved 99.9% of its final value).
5. Although this analysis considered only chemical reactions, it enables to estimate the required recirculation ratios for gas turbine combustor and the NO_x and CO emission levels.

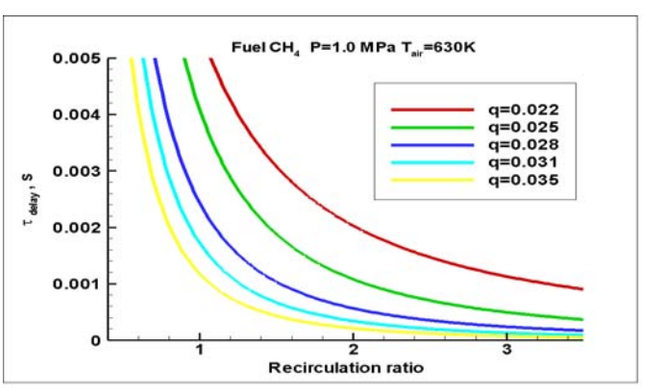


Fig. 3. Effect of the recirculation ratio on combustion delay time for various fuel/air ratios q. Combustion pressure is equal to 1.0 MPa.

References

[1] Wunning J. A.: Flamelelose Oxidation von Brenstoff (German). *Thesis*, Aachen, 1991.

[2] Wunning J. A., Wunning J.G.: Flameless Oxidation to Reduce Thermal NO – Formation. *Progress in Energy and Combustion Sciences* 23: 81-94, 1997.

[3] Katsuki M., Hasegawa T.: The Science and Technology of Combustion in Highly Preheated Air. *27th Symposium (International) on Combustion,* The Combustion Institute Pittsburgh, 3135-3146, 1998.

[4] Mulani A., Saponaro A.:Deluted Combustion Technologies*, IFRF Combustion Journal,* Article #200101, February 2001.

EXPERIMENTAL AND NUMERICAL INVESTIGATION OF A FLAMELESS OXIDATION COMBUSTOR

J. Melo*, A. Yadav*, J. M. M. Sousa*, M. Costa*, P. J. Coelho* and Y. Levy**
*Instituto Superior Técnico, Mechanical Engineering Department, 1049-001 Lisboa, Portugal
**Technion – Israel Institute of Technology,Technion City, Haifa 32000, Israel

Summary The flow characteristics of a combustor model under non-reacting conditions have been experimentally and numerically investigated using LDA and the Fluent code, respectively. Data is reported for mean and turbulent velocities as a function of the air mass flow rate. The isothermal flow characterization was followed by combustion measurements at the exit of the combustor model. Measurements and predictions of gas species concentration are reported as a function of the equivalence ratio and thermal input.

INTRODUCTION

Flameless oxidation is a combustion regime identified about one decade ago and characterized by strong internal gas recirculation, relatively low temperature in the reaction zone, which occupies a large volume rather than exhibiting a flame front, no visible flame, and very low NO_x emissions and noise. This work describes an experimental and numerical investigation of a new combustor designed to operate in this combustion regime.

EXPERIMENTAL FACILITIES

Figure 1 shows a schematic of the combustor model. Prior to the combustion experiments, the isothermal flow in the combustor model was characterized by the application of Laser-Doppler Anemometry (LDA). Under reacting conditions, the gases for the measurement of the flue-gas data (O_2, CO, CO_2, hydrocarbons (HC), and NO_x concentrations) were extracted using a water-cooled stainless steel probe. The analytical instrumentation included a magnetic pressure analyzer for O_2 measurements, non dispersive infrared gas analyzers for CO_2 and CO measurements, a flame ionization detector for HC measurements, and a chemiluminescent analyzer for NO_x measurements.

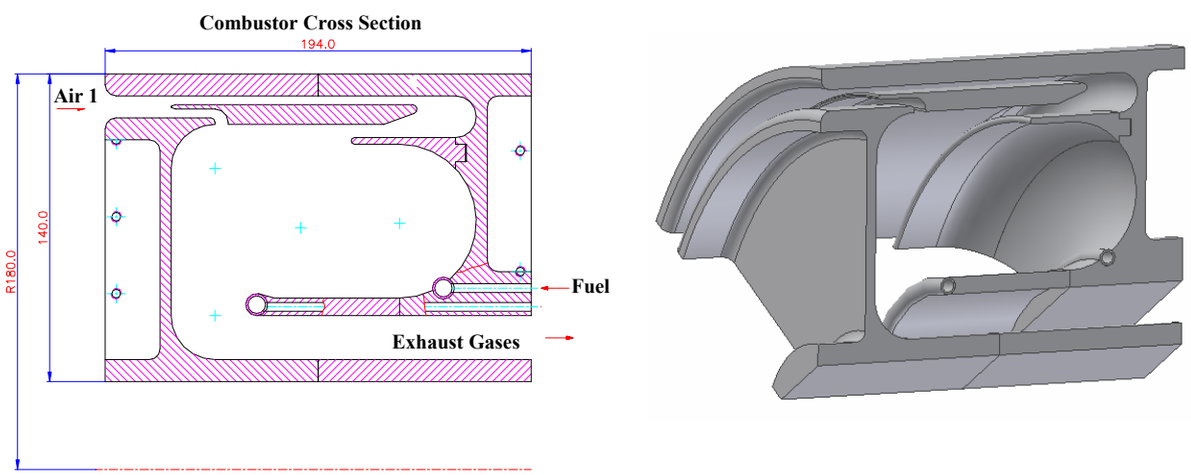


Figure 1. Schematic of the Combustor Model

MODELLING

The flow field was numerically simulated using the Fluent commercial code. Turbulence was simulated using either the k-ε model or the Reynolds stress model. In the case of a reactive flow, the laminar flamelet model along with an assumed probability density function was employed for combustion modelling. The NO emissions were predicted using a post-processor module based on the solution of a transport equation for the mass fraction of NO with the source term accounting for the thermal and prompt mechanisms of NO formation and for the turbulent fluctuations.

RESULTS AND DISCUSSION

Experiments under non-reacting conditions

Figure 2 shows the effect of the flow rate of Air 1 (see Fig. 1) on the mean flow structure and reveals that a common feature to all test conditions is the establishment of a large recirculation zone and that the mean velocities increase within the recirculation zone as the Air 1 mass flow rate increases.

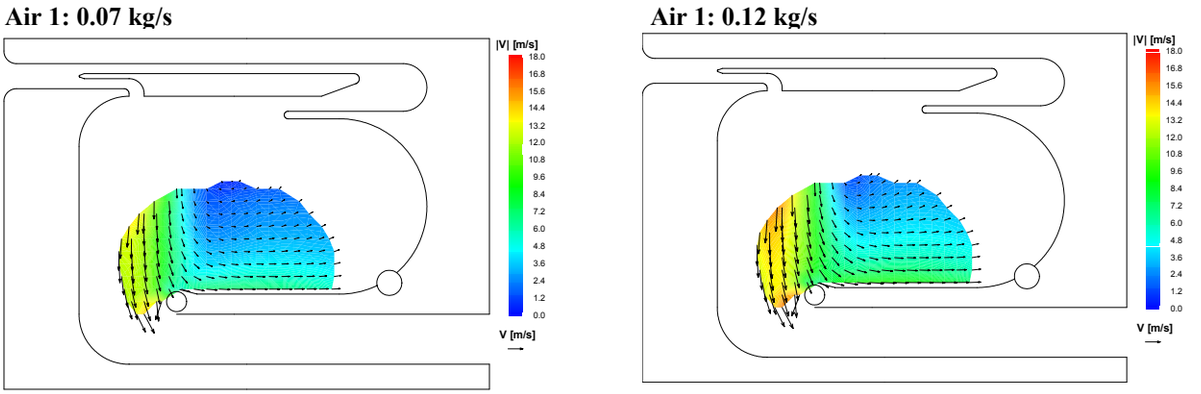


Figure 2. Effect of the Air 1 Flow Rate on the Mean Flow Structure

Experiments under reacting conditions

Figure 3 shows the measured flue-gas data for the combustor as a function of the equivalence ratio and of the thermal input. The figure reveals that combustion efficiency is highest (about 90%) for both low values of thermal input as well as of equivalence ratio. It is interesting to note that NO_x emissions are very low over a large range of the combustor operating conditions.

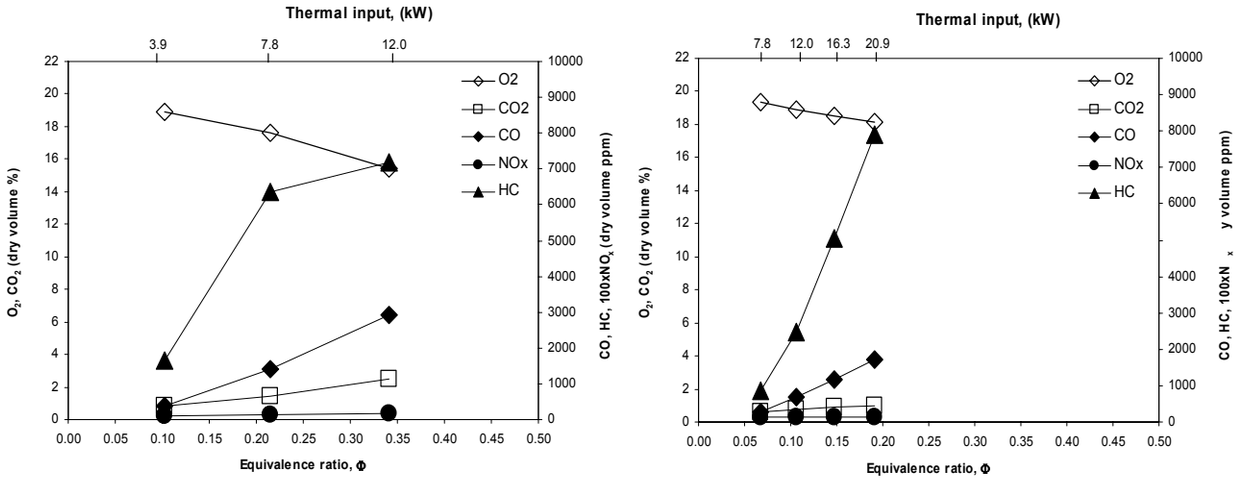


Figure 3. Measured volumetric fractions of species at the combustor exit.

CONCLUSIONS

The flow characteristics of a combustor model under non reacting conditions were investigated using Laser-Doppler Anemometry. Data is reported for mean and turbulent velocities as a function of the air mass flow rate. The main conclusions are as follows: i) a common feature to all test conditions is the establishment of a large recirculation zone and ii) mean and turbulent velocities increase within the recirculation zone as the air mass flow rate increases. The computational simulation correctly predicts these trends. The isothermal flow characterization was followed by combustion measurements at the exit of the combustor model. Measurements of mean gas species concentration (O_2, CO_2, CO, HC and NO_x) are reported as a function of the equivalence ratio and thermal input. The main conclusions are as follows: i) combustion efficiency is highest (about 90%) for both low values of thermal input and equivalence ratio, ii) NO_x emissions are very low over a large range of operating conditions and iii) the predicted concentrations of O_2, CO_2 and CO are in agreement with the experiments, but only qualitative agreement was found for the emissions of HC and NO_x.

ACKNOWLEDGMENTS

Financial support for this work was provided by the European Commission under the contract Nº ENK5 – CT 2000 – 0014 and is acknowledged with gratitude. The first author (J. Melo) is pleased to acknowledge the Fundação para a Ciência e Tecnologia for the provision of a scholarship (SFRH/BD/6345/2001).

DETONATIONS OF HEXANE VAPOR/DROPLETS-AIR MIXTURES

Stanisław Cudziło[1] , Allen L. Kulh[2], Piotr Wolański[3]

[1]*Military University of Technology, 00-908 Warsaw, Poland*
[2]*Lawrence Livermore National Laboratory, L30, Livermore, California, 94550-9234 USA*
[3]*Warsaw University of Technology, PL 00-665 Warsaw, Poland*

Summary Detonation characteristics of hexane droplets/vapor-air mixtures were determined on the basis of experiments in a vertical 13-m long detonation tube. Hexane droplets were injected at the top of the test section with generators containing different numbers of needles of 0.5-, 0.8- and 1.2-mm in internal diameter. The droplets moved down and – when first of them reached the bottom of the test section – a initiating shock wave (generated by detonation of oxygen-hydrogen-helium mixture) entered the tube.

INTRODUCTION

For a better understanding of the nature of fuel-air explosions and detonations it is important to evaluate basic explosive and detonation parameters of such mixtures. There are a lot of data available on gaseous detonations but spray detonations have not been explored so thoroughly, especially when it comes to sprays with big droplets (> 1 mm).
The purpose of the present research is to obtain fundamental hexane droplets/vapor–air detonation characteristics in a vertical 13-m long detonation tube (0.13 m in internal diameter). The main objectives of the initial part of the experiments included design of the droplet generator and determination of time-space characteristics of droplet motion in air. At the beginning we carried out a theoretical analysis of breakup of a liquid jet and free motion of a droplet in air. Results of the analysis were applied to design the first model of the droplet generator. Next the theoretical predictions were verified experimentally and the average hexane droplet and suspension parameters (diameters, concentrations) were determined. During the second stage of the detonation tube experiments we performed following tasks:

- characterization of the droplets produced by droplet generator with needles of 0.5, 0.8, and 1.2 mm in internal diameter,
- determination of the of the shock velocity and pressure of the initiating pulse in air (i.e. without hexane injection) and in suspension of water droplets,
- determination of shock wave and flame velocities for different droplet diameters and hexane concentrations,
- determination of pressure histories for different droplet diameters and hexane concentrations and at different distance from the initiation section,
- determination of the detonation characteristics of the hexane droplets/vapor – air mixtures produced with generators containing 0.5-, 0.8-, and 1.2-mm needles,
- estimation of the detonation limits of hexane droplets/vapor – air mixtures at three average droplet sizes and one intensity of the initiating shock wave.

EXPERIMENTAL

A scheme of the test stand is shown in Fig. 1. The detonation tube was equipped with twelve membrane pressure switches (M0÷M11) for shock wave velocity measurement, six photodiodes (D1÷D6) for monitoring flame propagation and three piezoquartz transducers (P1÷P3) for pressure measurement.
Pressure profiles in the detonation tube at three different distances from the booster were recorded by means of a 4-channel oscilloscope. The oscilloscope was connected with quartz pressure transducers through a 4-channel signal conditioner with selectable gain. To record signals generated by six photodiodes and twelve pressure switches (Fig. 1), a 24-channel tape recorder was applied.
To generate the initiating pulse, the 1.3- m long initiation section (booster was filled with a mixture containing 2 moles of oxygen, 4 moles of hydrogen and 9 moles of helium. Thin plastic foil separated the booster from the test section. The detonation of the mixture was ignited with electric spark. The detonation parameters were changed by changing the initial pressure in the booster within a range of 0.1÷0.5 MPa, with a step of 0.1 MPa.

RESULTS

Pressure profiles and shock velocities obtained when hexane was injected through 12, 25 and 70 needles of 0.8 mm in internal diameter showed that the shock wave parameters are nearly the same and they decrease along the test section. This means that in each case hexane concentration was too low to affect the shock front propagation and below the lower explosibility limit. Therefore in consecutive experiments we used generators with 85, 100 and 110 needles. Results of the pressure and velocity measurements are given in Fig 2.

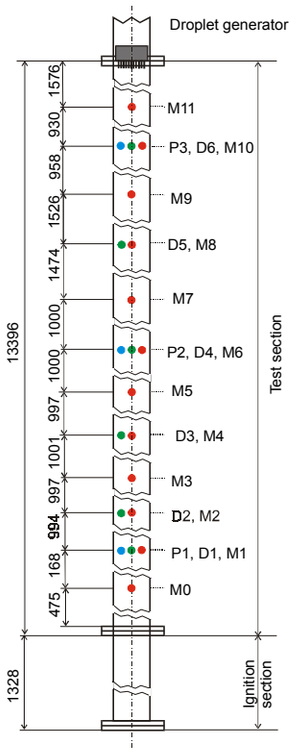


Fig. 1. Experimental setup

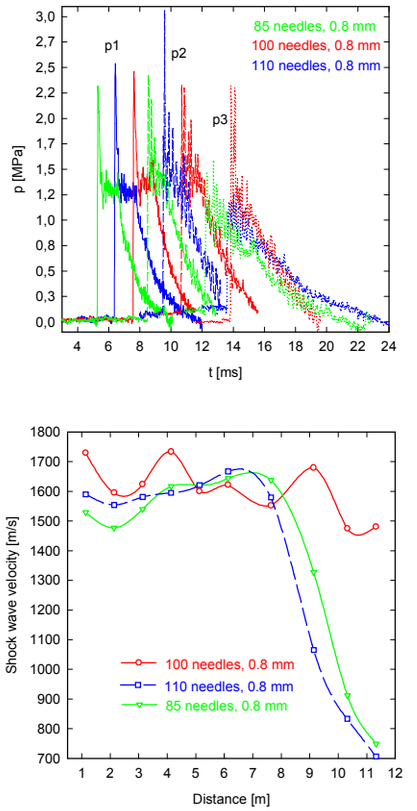


Fig. 2. Pressure profiles and shock wave velocities in hexane spray – air mixtures produced with 85-, 100- and 110-needle generators, pressure in the booster – 0.4 MPa

Identical tests were carried out with generators containing different number of 0.5- and 1.2-mm needles. Their results can be summarized as follows:

1. The droplet generators equipped with 1.2- 0.8- and 0.5-mm needles and working at an inside overpressure of 0.02 MPa produce hexane droplets of ca. 3.2, 1.9 and 1.3 mm in an average diameter, respectively. By changing the number of needles, it is possible to obtain hexane droplets/vapor – air mixtures in the detonation tube within the needed concentration range – up to 1.6 g of hexane per 1 g of air.
2. An initiation of hexane droplets/vapor – air mixtures by a strong shock wave generated by the hydrogen-oxygen-helium mixture at an initial pressure of 0.4 MPa can result in detonation. For the tested droplets the detonation velocity equals to 1600±100 m/s with corresponding peak pressure rise of 2.5÷2.7 MPa. The maximum parameters do not depend on the droplet diameter.
3. The detonative regime is achieved for hexane suspensions produced with the generators containing 28 needles of 1.2 mm in internal diameter for which the estimated concentration of hexane in the detonation tube equals to ca. 0.7 g of hexane per 1 g of air. The optimal hexane concentration equals to ca. 0.9 g_{hexane}/g_{air} (35 needles in the generator). The detonation does not occur when the generator contains 70 needles. Under this conditions the estimated concentration of hexane 3.2-mm droplets/vapor in the tube is ca. 1.6 g of hexane per 1 g of air.
4. For generators containing 0.8-mm needles, the detonative regime was observed for hexane suspension produced with the 85-needle generator. Then the estimated concentration of hexane in the detonation tube equals to ca. 0.9 g of hexane per 1 g of air. The detonation decays when the number of needles in a generator is higher than 120. Under this conditions the estimated concentration of hexane droplet/vapor in the tube is ca. 1.2 g of hexane per 1 g of air. The best conditions for initiation and propagation of detonation were observed when hexane was injected with the 100-needle generator providing hexane droplets/vapor – air mixtures with concentration of ca. 1 g of hexane per 1 g of air
5. In the case of generators with 0.5-mm needles, detonation processes occur when hexane was injected with 150-needle generator. Then the hexane concentration is ca. 0.6 g of hexane per 1 g of air. The hexane droplet/vapor – air mixtures produced with 170-needle generator is not able to detonate under the test conditions. This means that the rich detonation limit for the droplets of 1.3 mm in diameter equals to ca. 0.7 g of hexane per 1 g of air.
6. The upper detonation limit increases with increasing hexane droplet diameters – it equals to: 0.7 $g_{hexane}/1g_{air}$ for 1.3-mm droplets (0.5 mm needles), 1.2 $g_{hexane}/1g_{air}$ for 1.9-mm droplets (0.8 mm needles) and 1.6 $g_{hexane}/1g_{air}$ for 3.2-mm droplets (1.2 mm needles).

SIMULATION OF RAM ACCELERATOR WITH PETN LAYER

Arkadiusz Kobiera[*], Piotr Wolański[**]
[*]*Warsaw University of Technology, Institute of Heat Engineering, PL 00-665 Warszawa, Poland*
[**] *Warsaw University of Technology, Institute of Heat Engineering, PL 00-665 Warszawa, Poland*

Summary The paper presents a new idea of ram accelerators with high explosive layer. The layer is an additional source of chemical energy which enhances trust generated by the device. In the paper there is described model of flow and two-phase combustion in ram accelerator. Results of numerical simulation show that it is possible to increase the trust about several percent.

INTRODUCTION

Ram accelerators are a new type of hypersonic propulsion known since 1980's [4]. Basic idea of the ram accelerator base on utilizing chemical energy released during combustion of gaseous mixture caused by high velocity projectile. In the conventional ram accelerator high velocity projectile generates shock waves which ignite combustible gaseous mixture. Combustion of gas leads to increase of pressure in rare part of projectile and generates trust (Fig. 1 a). Proposed modification depends on addition of high explosive layer. Combustion of gas causes ignition of the layer and releases of additional heat. It should give a rise of trust (Fig. 1 b).

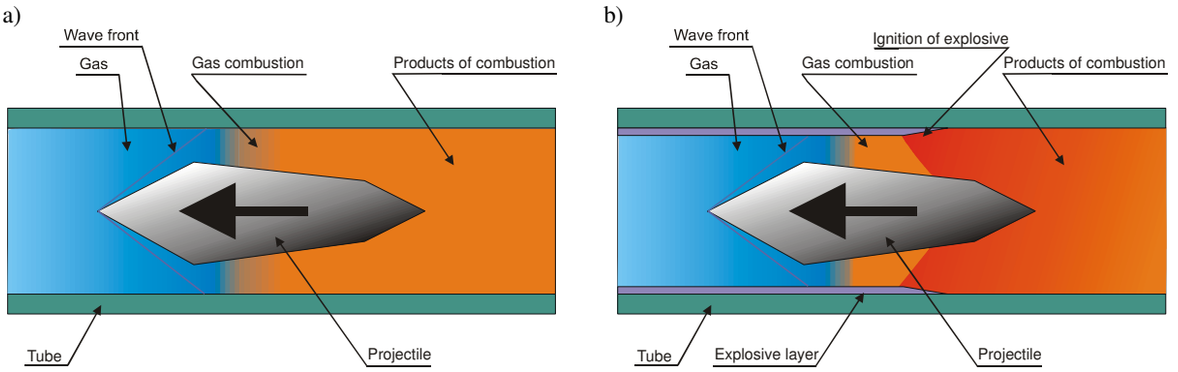


Fig. 1. a) Convetional ram accelerator, b) ram accelerator with high explosive layer.

Possibilities of enhancing of performances is studied in this work. A numerical simulation of the device is used in order to get information about increase of trust.

THEORETICAL MODEL

A two- dimensional model of the ram accelerator with PETN layer consist of two parts:

- flow and chemical reaction model of gas,
- heat conduction and chemical reaction model of high explosive.

First model is based on Euler equation of reactive gas with global reaction chemistry. Such model was successfully used in simulation of gaseous detonation and conventional ram accelerators.
Model of combustion of high explosive is based on equation of heat conduction with source term. Decomposition of high explosive is described by Arrhenius' law. Parameters of kinetics of high explosive decomposition were take from experimental data for PETN [1],[5]. Interconnection between gas flow model and model of PETN layer was realised by boundary condition. There is used Sichel's theory of heat exchange behind detonation front [2],[3]. This theory was chosen because physics of combustion in ram accelerators is very similar to detonation. The model was used in simulation of ignition of PETN layer by gaseous detonation and gave good qualitative agreement with experiments.

RESULTS

Described model was used in simulation of ram accelerator working with H_2-O_2 mixtures. The mixture composition was 40% H_2 and 60% O_2. Calculations were carried out in superdetonative mode for velocity ranging from 2300 to 4000 m/s. They proved that it is possible enhance performance of the device. Layer ignite enough quickly. Combustion of the PETN layer causes increase of thrust from 11% for V=2300m/s to ~0 for V=3250 m/s for lower initial pressure and from 6% for V=2400 m/s to 1.5% for V=4000 m/s for higher pressure (Fig. 2). Comparison of pressure field around projectile shows that additional thrust is generated mostly in rare part of projectile (Fig. 3). Next observation is that only very thin part of layer was burnt in neighbourhood of projectile.

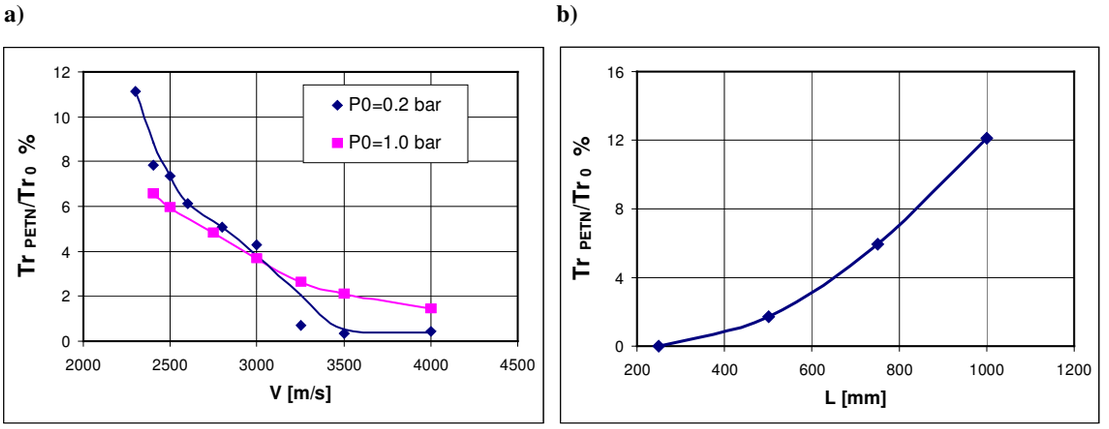


Fig. 2. a) Increase of thrust caused by combustion of the layer as a function of velocity for varius initial pressures (mixture: 40% H2, h=1mm). b) Relation between thrust enhancement and length of projectile (mixture: 40% H2, h=1 mm, V=2400m/s).

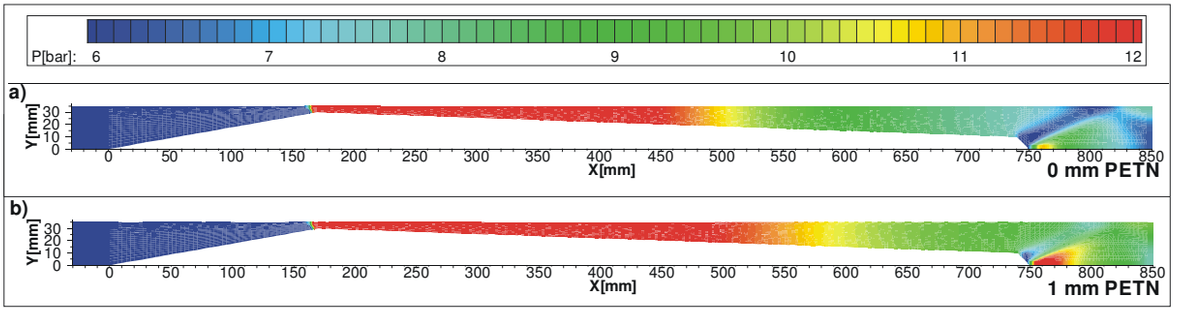


Fig. 3. Pressure field in: a) the convetional ram accelerator, b) the ram accelerator with the layer of high explosive, V = 2400 m/s, gaseous mixture: 40% H2 + 60 % O2, p_0 = 1 bar, h_{layer} = 1 mm.

CONCLUSIONS

Simulation of modified ram accelerator shows that combustion of PETN layer is a good way to improve its performance. Applied numerical model is sufficient and allows analysis of influence of different parameters of ram accelerators on trust e.g. geometry of projectile, kind of high explosive. Carried out calculations allow formulating following conclusions:

1. The combustion of the PETN layer causes increase of thrust of several percent.
2. Only very thin part of the layer contributes to the thrust increase.
3. The influence of the PETN decomposition decreases at higher velocities.
4. There is a strong dependence between the projectile length and increase of the thrust.
5. The thrust increase does not depend on the layer thickness if it is thicker than 0.2 mm.
6. There exists an optimal composition of gaseous mixture which ensures the best utilisation of the layer.

Results of analysis also point out the ways of further improvements. Especially important may be increasing of rate of PETN burning e.g. by developing of layer surface.

References

[1] Kobiera A., Wolanski P., Ignition of liquid and dust fuel layers by gaseous detonation. *Shock Waves*, Vol. 12, No 5, 2002

[2] Sichel M., David T.S.: Transfer behind Detonations in H_2-O_2 Mixtures. AIAA Journal Vol 4, No. 6, 1966

[3] Sichel M., Rao C.S. ,Nicholls J.A.: A simple theory of film detonation*: Thirteenth Symposium on Combustion*. The Combustion Institute, Pittsburgh, Pennsylvania pp 1141-1149, 1971

[4] Takayama K., Sasoh A. (Eds.): Ram Accelerators, *Procedings of Third International Workshop on Ram Accelerators Held in Sendai, Japan 1997*, Springer-Verlag, Berlin Heidelberg New York, 1998

[5] Wolanski P., Kobiera A.: Experimental and numerical research on interaction between gaseous detonation and solid explosive. *19th International Colloquium on the Dynamics of Explosions and Reactive Systems*, Hakone, 2003

SIMPLE MODEL OF A DETONATING GAS FOR USE WITH THE DIRECT MONTE – CARLO SIMULATION TECHNIQUE

Zbigniew A. Walenta*, Andrzej Teodorczyk**, Waldemar Witkowski***

** Institute of Fundamental Technological Research,*
Polish Academy of Sciences
Swietokrzyska 21, 00-049 Warszawa, Poland

*** Institute of Heat Engineering*
Warsaw University of Technology
Nowowiejska 25, 00-665 Warszawa, Poland

**** Institute of Industrial Organic Chemistry*
Annopol 6, 03-236 Warszawa, Poland

Summary: The research on gaseous detonation has recently become a very important issue because of increasing importance of gaseous fuels. We propose to use the Direct Monte – Carlo Simulation technique, which is a very powerful tool for solving complex flow problems. We propose a very simple model of a molecular collision, which makes it possible to increase the thermal energy of a gas, which is similar to the processes in the flame. We show then, that this model can produce the wave, which has all the features, characteristic for a detonation wave.

INTRODUCTION

The research on gaseous detonation has recently become a very important issue, in connection with increasing importance of gaseous fuels.
The Direct Monte – Carlo Simulation (DMCS) technique [1] has proven to be a very powerful tool for solving complex flow problems. It offers also a possibility of taking into account the relaxation phenomena and chemical reactions [1, 2], as well as influence of solid walls (friction and heat exchange). However the relaxation phenomena and chemical reactions increase substantially complexity of the computer programs and the necessary computing times. Fortunately, in the case of simulating gaseous detonation, considerable simplifications can be made thanks to the fact, that in a detonation wave the state of the medium is far from equilibrium, therefore combustion proceeds very fast and all relaxation processes at the molecular level may be disregarded. The only important factor, that remains, is the produced thermal energy.

MODEL OF A COMBUSTIBLE GAS

As always in the Monte – Carlo simulations we treat the gas as an ensemble of molecules, which collide with each other and with walls, and move along straight lines with constant speed between collisions. We assume for simplicity, that all molecules are identical hard spheres. We assume, finally, that some of the molecules, uniformly distributed in space, carry certain amount of "internal" energy (of unspecified character), the same for each of them. This may be transformed into kinetic energy during collision with another molecule (carrying no energy), provided that the two colliding molecules approach each other with sufficient velocity (Fig.1a). If this is the case, the relative velocity of the molecules after collision is increased suitably (Fig.1b).

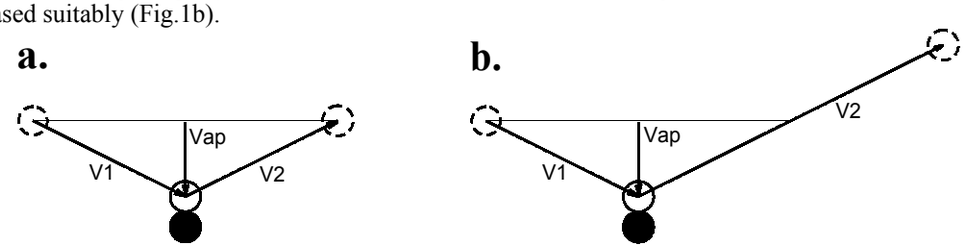


Fig. 1. Collision of two molecules in reference frame connected with one of them:
a. – elastic, b. – with energy release.
V1– relative velocity of the molecules before collision, V2 – after collision,
Vap – "velocity of approach" of the molecules.

RESULTS

To prove, that the proposed model can actually simulate the detonation wave, calculations for various geometries were performed.
Fig. 2 presents the simplest case – a plane, perpendicular wave, moving along x – axis in a positive half-space. The wave was initiated by removal of a diaphragm, placed at x = 100 units of length (mean free paths) from the origin of coordinates. The gas in front of the diaphragm contained 10 per cent of the molecules carrying the "internal" energy. The energy released in a single collision was such, that the relative velocity of the colliding molecules was increased by the value equal to 10 times the most probable molecular velocity. The temperature of the driver gas was 10 times higher than that of the driven gas. The pressure was such, that after the diaphragm removal the shock wave with Mach number Ms = 2 was produced.
The presented figure shows the diagrams of the gas temperature in terms of distance along the x – axis for the initial situation and for 15 subsequent instants, equally spaced in time. Formation of the primary shock wave after the diaphragm removal is clearly visible. Later, the shock gradually speeds up, transforming into a detonation wave, which then moves with constant speed and constant intensity, as expected.

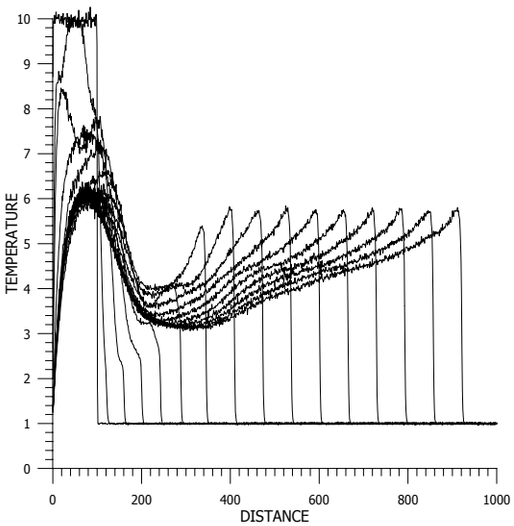


Fig. 2. Formation of a plane detonation wave without influence of walls.

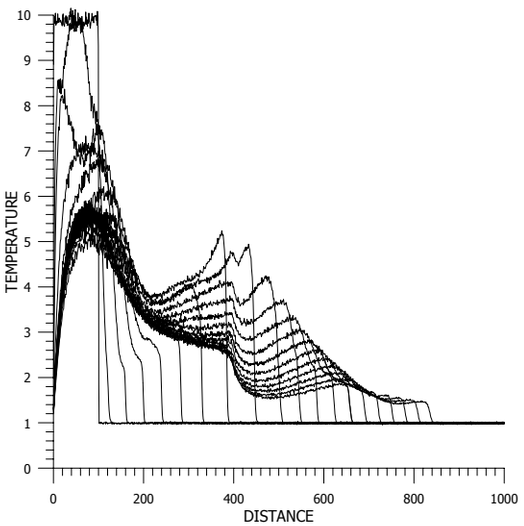


Fig. 3. Formation and decay of a detonation wave in a narrow pipe.

Fig. 3 shows similar picture for the wave, moving in a cylindrical pipe, in the same gas. The diameter of the pipe was equal to 100 mean free paths of the gas molecules. For $x < 400$ the molecules reflected from the pipe walls specularly, i.e. without exchange of tangential momentum and energy. For $x > 400$ the molecules reflected diffusely, i.e. their average kinetic energy after reflection corresponded to the temperature of the wall and the average tangential momentum was equal to zero.
The left part of the picture, up to x = 400, looks similarly to that in Fig. 2 – formation of shock and detonation waves is evident. For $x > 400$ however the walls cool the gas down, below the ignition point, and the shock moves ahead, unsupported by the flame front, getting weaker and weaker.

Acknowledgements

This research work was supported by the State Committee for Scientific Research (KBN, Poland) under grant No 4T09C 015 22; this support is gratefully acknowledged.

References

[1] G.A. Bird: Molecular gas dynamics and the direct simulation of gas flows, Clarendon Press, Oxford, 1994.

[2] P.S. Larsen, C. Borgnakke, in *Rarefied Gas Dynamics* (ed. M. Becker and M. Fiebig), **1,** Paper A7, DFVLR Press, Porz-Wahn, Germany, 1974.

CAPILLARY MICROFLUIDICS FOR VISCOELASTIC FLUIDS

Konstantin G.Kornev Gerardo Callegari, and Alexander V.Neimark
TRI/Princeton, P.O. Box 625, Princeton, New Jersey 08542, U.S.A.

Summary We discuss the effects of fluid viscoelasticity, inertia and capillarity during fast and slow absorption of droplets by fibrous porous conduits and micro-devices. The major attention is paid to applications of rheological viscoelastic effects to the development of new methods for handling and fraction separation of biopolymer solutions.

INTRODUCTION

In conventional microfluidic devices, fluids are pumped by applying either pressure drop or temperature or voltage differences. In biomedical technologies dealing with fluids of a complex rheology, the forced fluid transportation is sometimes hardly applicable. We present a new principle of controlled fluid transport at micro- and nanoscale. This approach is based on the phenomenon of spontaneous absorption of wetting fluids by porous materials. That is, capillarity drives the droplet self-propulsion without the need for any additional external mean. We study viscoelastic fluids and develop some theoretical and experimental approaches to tackle this problem. Aqueous solutions of polyacrylamide (PAM), polyethyleneoxide (PEO) and lambda-DNA are taken as model polymeric fluids.

WEISSENBERG EFFECT AND CAPILLARITY DRIVEN FLOW OF VISCOELASTIC FLUIDS THROUGH MICROCHANNELS.

First, we discuss the droplet absorption by capillaries (Fig.1). Absorption of droplets by capillaries of a few hundred microns in diameter is characterized by surprisingly high Reynolds numbers, which may exceed 100! At these conditions, the viscous forces seem to be negligible compared to the inertial, elastic, and capillary forces. Fluid elasticity caused by stretching of polymer molecules by velocity gradients is manifested by the appearance of a force, which is directed opposite to the direction of the meniscus motion. Essentially, the stretching of polymers in the channel gives rise to an extra stress additional to the pressure. This flow-induced stressing of viscoelastic fluids, known as the Weissenberg effect, causes a reduction of the capillary pressure at the meniscus. Effectively, the Weissenberg effect leads to a weakening of the driving force. A quantitative estimate of the Weissenberg effect can be done by considering the momentum balance for the moving liquid column. Neglecting Poiseuillean friction and flow in the droplet, and assuming that the velocity and pressure at the capillary entrance are zeroth, one finds $0 = A[p + \rho U^2] - (\sigma_d - \sigma_w)L$, where ρ is fluid density, U is meniscus velocity, $(\sigma_d - \sigma_w)$ is the difference of surface energy densities of the dry and wet capillary, and p is the Weissenberg extra pressure. A is the cross sectional area of the capillary and L is its circumference. Calculation of the Weissenberg extra pressure within the Upper Convected Maxwell Model gives: $Ap+ =16\ \lambda\eta U^2$, where λ is relaxation time and η is fluid viscosity. Collecting all terms, we obtain the relation between the initial velocity of droplet penetration and the parameters of the capillary and liquid as $U^2=2(\sigma_d - \sigma_w)/[1+16\ \lambda\eta/\rho R^2]$, here R is the radius of capillary. Remarkably, the velocity U attains the maximum at the radius $R=4\ (\lambda\eta/\rho)^{1/2}$, which is independent of the wetting properties of liquids, but depends only on the rheological properties.

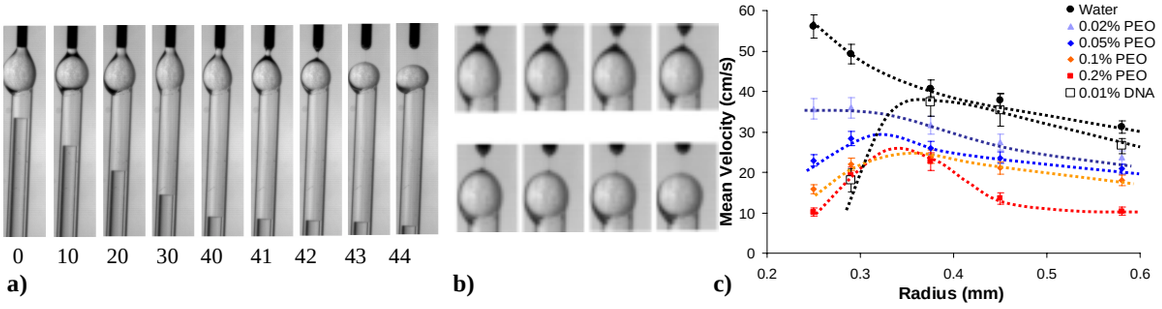


Figure 1. Penetration of 0.01% TE Buffer solution (8 pH) of lambda-DNA ($M=61x10^6$ Da) into a glass capillary, ID=0.58 mm. Feeding needle on the top of a) and b) has ID= 0.51. The time under each picture is given in milliseconds. b) Dynaics of filament thinning. Enlarged pictures of a) taken between 41.25 and 43 ms, each picture is taken at 1/4000 frames per second.c) Mean velocity of meniscus as a function of radius of receiving capillary.

A systematic experimental analysis of the droplet absorption was done with a special optical electronic measuring system [1]. CMOS camera was used to film the meniscus propagation and the filament rupturing. A typical series of frames is presented in Figures 1a) and b). As seen, meniscus travels the path of about ten radii in a few milliseconds. During its motion, meniscus remains almost flat thus indicating that the velocity is approximately constant across the capillary. It is still a long way to go to reach the equilibrium shape. These findings contradict to a conventional believe that the meniscus shape equilibrates almost immediately. We pay a particular attention to the

analysis of flow patterns at the meniscus using special tracers. An asymptotic theory of flow with inertial and elastic forces as dominants supports the experimental observations.

The phenomenon of filament formation in polymer solutions and the mechanism of filament rupturing deserve a special consideration. The dynamics of filament thinning is recorded with a millisecond resolution. Real images and diffraction fringes are used to monitor the kinetics of filament thinning. Typical real images of bridge thinning and rupturing are shown in Figure 1b). The analysis of images shows that the filament changes its radius not only because of mechanical stretching, but also because of squeezing solvent out of the filament. We suggest a model to explain the kinetics of filament thinning and to relate the rheological parameters of the model to the experimental data.

While the hydrodynamic details of meniscus motion and associated flows are quite complicated and much different from what was expected, a qualitative description of the process can be captured by a simple one-dimensional model. In Figure 1c), we show the experimental data confirming the existence of a maximum velocity of absorption of viscoelastic droplets. Also, the one-dimensional approximation predicts that the meniscus travels about five capillary radii keeping the velocity constant. This is in agreement with experimental observations.

ABSORPTION OF VISCOELASTIC FLUIDS BY NANOFIBROUS SUBSTRATES.

Using the same experimental approaches, we study the process of droplet absorption by nanofibrous materials produced by spinning of carbon nanotubes and polymeric nanofibers. It is shown that the rate of absorption of viscous and viscoelastic fluids are significantly different. For nanoporous fibers made of SWNT (Fig 2a) we observe slow kinetics of absorption (Fig 2b). Namely, viscous fluids follow the Lucas-Washburn kinetics, but absorption of viscoelastic fluids is different. In the nanowebs produced by electrospinning, the rate of droplet absorption is extremely high. It takes a few milliseconds to absorb a millimeter sized droplet. It is remarkable, that while nanofibers are dissolvable in water, because of fast evaporation, there is no time to destroy the web. SEM micrographs of dried nanowebs reveal striking features of polymer/fiber interactions. Polymers in dilute solutions penetrate through the pores completely from one side of the sample to the other. No separation occurs in the regime of fast absorption. As a result, the sample after evaporation takes on a new morphology, namely, it becomes foamy. Polymers from solutions form lamellas with the thickness much less than the nanofiber diameter. These films span the pores, and the nanofibers serve as frames to hold the films (Fig. 2c). A theoretical analysis of slow and fast kinetics is based on the Maxwell model. We develop a model accounting for the flow in the droplet and in the porous substrate. As shown in experiments, flow through porous fibers and thin nanofibrous membranes is typically frontal. That is a droplet absorbing by nanoporous fibers sends fingers ahead of the visible contact lines. These fingers occupy the fiber cross-section completely. In this sense, the absorption is frontal. Same thing occurs for planar nanowebs. We have a ring of fluid that runs ahead of the visible contact line. Associated free boundary problems are featured by the presence of two fronts: the first is the contact line and the second is the front propagating ahead of the contact line. In the case of slow absorption by porous fibers, the problem is mathematically similar to the Stefan problem with a nonlinear undercooling kinetics that is solved analytically. The problem of droplet absorption by nanowebs reveals unusual features caused by an effective slip at the saturated web. We discuss in detail a role of high extension rates in the formation of foamy structures.

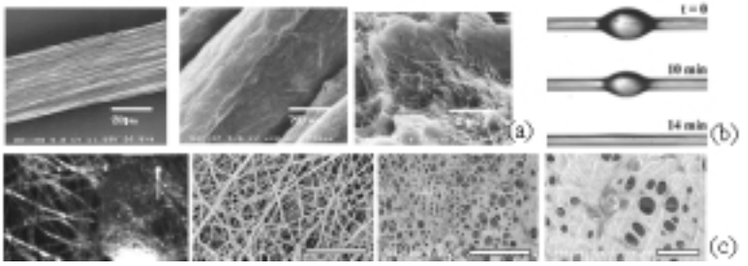


Fig. 2. SWNT fiber as nanofluidic conduit. a) Hierarchical pore structure of SWNT fiber; b) Dynamics of microdroplet spreading and absorption; c) change of nanoweb morphology after absorption of droplets of 0.05% of PAM. From left to right: microdroplet spreading over the nanoweb; dry nanoweb, bar corresponds to 15 microns; same after absorption; foamy structure, bar corresponds 6 microns.

We acknowledge the support of NIH through Grant R21 EB002889-01.

References

[1] Bazilevsky, A.V., Kornev, K.G., Rozhkov, A.N., Neimark, A.V.: Spontaneous absorption of viscous and viscoelastic fluids by capillaries and porous substrates. J.Colloid Interface Sciences, **262,** 16-24, 2003.

FIELD-INDUCED DIELECTROPHORESIS AND PHASE SEPARATION IN SUSPENSIONS

Dawn J. Bennett[*], Boris Khusid[*], Conrad D. James[**], Paul C. Galambos[**], Murat Okandan[**], David Jacqmin***, Anil Kumar****, Zhiyong Qiu****, Andreas Acrivos****

[*]*New Jersey Institute of Technology, University Heights, Newark, NJ 07102, USA*
[**]*Sandia National Laboratories, POB 5800, Albuquerque, NM 87185, USA*
[***]*NASA Glenn Research Center, Cleveland, OH 44135, USA*
[****]*City College of New York, 140th St., New York, NY 10031, USA*

Summary We report observations of a new electric field- and shear-induced many-body phenomenon in the behavior of suspensions whose origin is dielectrophoresis accompanied by the field-induced phase separation. As a result, a suspension undergoes a field-driven phase separation leading to the formation of a distinct boundary between regions enriched with and depleted of particles. The theoretical predictions are consistent with experimental data even though the model contains no fitting parameters. It is demonstrated that the field-induced dielectrophoresis accompanied by the phase separation provides a new method for concentrating particles in focused regions and for separating biological and non-biological materials, a critical step in the development of miniaturizing biological assays.

Compared to other available methods, ac dielectrophoresis is particularly well-suited for the manipulation of minute particles in microfluidics [1]. The concepts currently favored for the design and operation of dielectrophoretic micro-devices consider the trend of the field-induced particle motions by computing the spatial distribution of the field strength over a channel as if it were filled only with a liquid and then evaluating the direction of the dielectrophoretic force, exerted on a single particle placed in the liquid. However, the exposure of suspended particles to a field generates not only the dielectrophoretic force acting on each of these particles, but also the dipolar interactions of the particles due to their polarization. Furthermore, the field-driven motion of the particles is accompanied by their hydrodynamic interactions. These long-range electrical and hydrodynamic interparticle interactions are entirely neglected in analyzing the performance of currently used micro-fluidic devices. In [2-4], we demonstrated that a single-particle model which only takes into account the dielectrophoretic force, the Stokes drag force, and the gravity force acting on a particle predicts fairly well the rate of the field-driven particle redistribution for dilute suspensions containing ~ 0.1% (v/v) but does not predict the aggregation pattern formed by these particles. Furthermore, the presence of the interparticle dipole-dipole interactions was found to imposes a lower bound on the scale of microelectrode arrays for the precise positioning of positively polarized particles in selected locations of a dielectrophoretic micro-channel even for ~0.1% (v/v) suspensions [4]. Now we report observations of ac dielectrophoresis accompanied by a field-induced phase separation whose origin is the interparticle electric interactions.

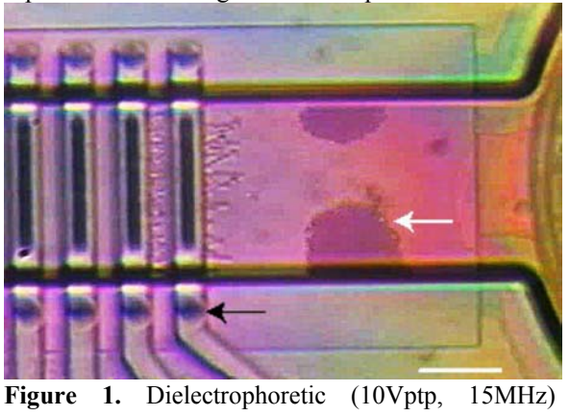


Figure 1. Dielectrophoretic (10Vptp, 15MHz) separation of bacterial cells and beads. The cells adhere to the energized electrode (black arrow) while the beads experience negative dielectrophoresis accompanied by a phase separation (white arrow). The flow is from right to left. Scale bar = 20 μm [6].

Microfluidic devices for experiments were fabricated in Sandia National Laboratories Microelectronics Development LAB using Sandia's SwIFTTM (Surface micromachining with Integrated microFluidics Technology) process [5] for producing highly-integrated monolithic multilayer structures. The fluidic channels [6], fabricated using single 6 inch Si wafers, are 40 μm wide, 6 μm high, and 570μm long and contain 6 μm wide p-doped polysilicon traces, with each trace being split into two electrically-connected electrodes located on the ceiling and the floor of the fluidic channel and arranged perpendicular to the flow (Fig. 1). The suspension was delivered into the channel at a flow rate ranging from 0.24 pL/s to 9.6 pL/s. The electrodes were energized with a sinusoidal wave, 10 V peak-to-peak (ptp) and 15-30 MHz while the silicon substrate was grounded. These electrodes act like "dielectrophoretic gates," that control the motion of polarized particles flowing through the channel. The photo presented in Fig. 1 illustrates the ac dielectrophoretic separation of a heterogeneous mixture of negatively polarized 1μm polystyrene spherical beads (1.05 g/cm3, Duke Scientific Co.) and positively polarized heat-killed bacterial cells (Staphylococcus aureus; Molecular Probes) dispersed in DI water. The beads, experiencing negative dielectrophoresis, are repelled from the dielectrophoretic gate and accumulate in a region near the electrodes (Fig. 1). On account of compressive electric and shear stresses, the layer of these beads forms two boluses with a distinct front between the regions enriched with and depleted of particles. The average particle concentration in the boluses was estimated to run as high as 40-50% (v/v).

An electro-hydrodynamic model [6] proposed for simulating the bolus formation generalizes a thermodynamic theory [7] for a suspension subject to a spatially non-uniform ac field. This model encompasses the quasi-steady electrodynamic equations together with the momentum and continuity balance equations of the "mixture" model for a

suspension, which are averaged over the field oscillations. The suspension is viewed as an effective Newtonian fluid the viscosity which varies with the particle concentration according to the Leighton-Acrivos expression. The bulk electric force exerted on a suspension, and the particle velocity relative to the suspending fluid are expressed in terms of the chemical potential of the particles [7]. The theoretical predictions for the bolus growth, for the particle concentration in the bolus, and the fact that particles travel around the circumference of the bolus and are then drawn into the bolus side closest to the electrode, are consistent with the observations.

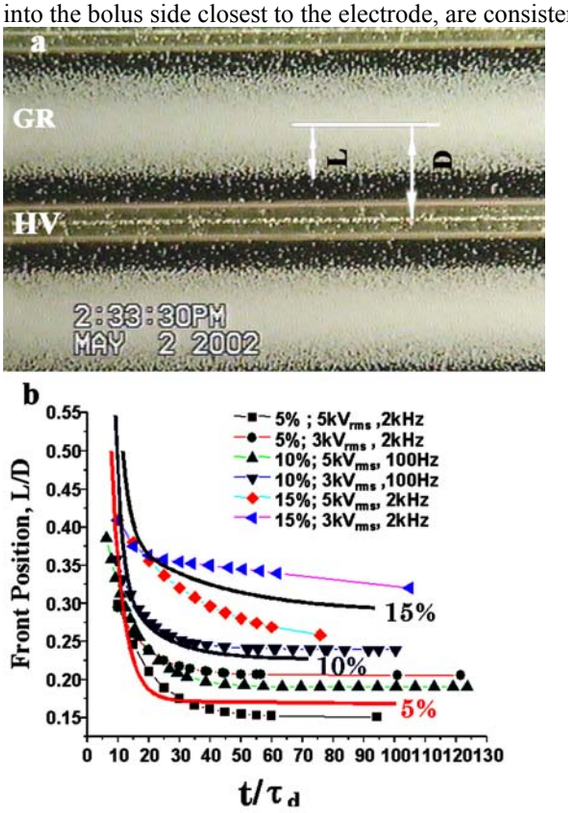


Figure 2. (a) The photo illustrates how the front location was measured; HV and GR refer to the high-voltage and grounded electrode respectively. (b) The experimental data (symbols) and computational results (solid lines) for the front propagation in 5, 10, and 15% (v/v) suspensions [8].

To test theoretical predictions quantitatively, experiments were conducted [8] on 5%–15 %(v/v) suspensions of neutrally buoyant spherical (average diameter of 87 μm) polyalphaolefin particles (AVEKA, Woodbury, MN) suspended in corn oil ($0.92 g/cm^3$, 59.7 cp at 23^0C) which exhibit negative dielectrophoresis [8]. The experiments were performed in a horizontal parallel-plate chamber (6 cm wide, 12 cm long, and 3 mm high). The bottom of the chamber was equipped with electrodes (1.6 mm wide) which were embedded into groves at 2 mm intervals and were alternately connected to the high voltage and to the ground (Fig. 2a). The top of the chamber, consisting of a transparent glass coated with a conducting layer of indium tin oxide, was grounded. Under these conditions, the field configuration consists of two high-strength regions near the electrode edges and a wide low-strength region above the center of the grounded electrode near the channel midplane [8]. We found that, due to interparticle electrical interactions, such suspensions undergo a phase separation when subjected to a high-gradient ac field (~ kV/mm), and form a propagating distinct front between the regions enriched with and depleted of particles (seen as white spots in Fig. 2a). As time progressed, the front slowly moved away from the high field regions and the particles became progressively confined to a thin column above the grounded electrode. Note that the same configuration of an electric field does not lead to the front formation in dilute suspensions, ~0.01%-0.2% (v/v) [2]. The theory predicts that the use of the characteristic time for dielectrophoresis, τ_d [2, 3], makes it possible to combine the data on the time dependence of the front position for different voltages and frequencies (Fig. 2b) into one band. As can be seen from Fig. 2b, the simulation results are in a reasonable agreement with the experimental data for $t/\tau_d \le 20$ even though the model contains no fitting parameters.

In conclusion, we demonstrated that ac dielectrophoresis accompanied by a field-induced phase transition provides a powerful method for strongly concentrating particles and for separating biological and non-biological particles. In particular, the use of dielectrophoretic gates enables one to remove any substance less polarizable than water (nearly all inorganic materials) from aqueous solutions.

The work was supported, in part, by grants from the NASA, NAG3-2698 (B.K., Z.Q., and A.A), and from the DARPA through the Bioflips/Simbiosys Program, Mission Research Corporation/DARPA Contract # DAAH01-02-C-R083 (B.K.). D.B. thanks Sandia's MESA Institute and the NSF MAGNET/SEM program for support. The properties of polystyrene beads were measured by Len Duda (Sandia). The properties of polyalphaolefin particles were measured at the NJIT W.M. Keck Foundation Laboratory. Sandia is a multiprogram laboratory operated by Sandia Corporation, a Lockheed Martin Company, for the U.S. DOE under contract DE-ACO4-94-AL85000.

References

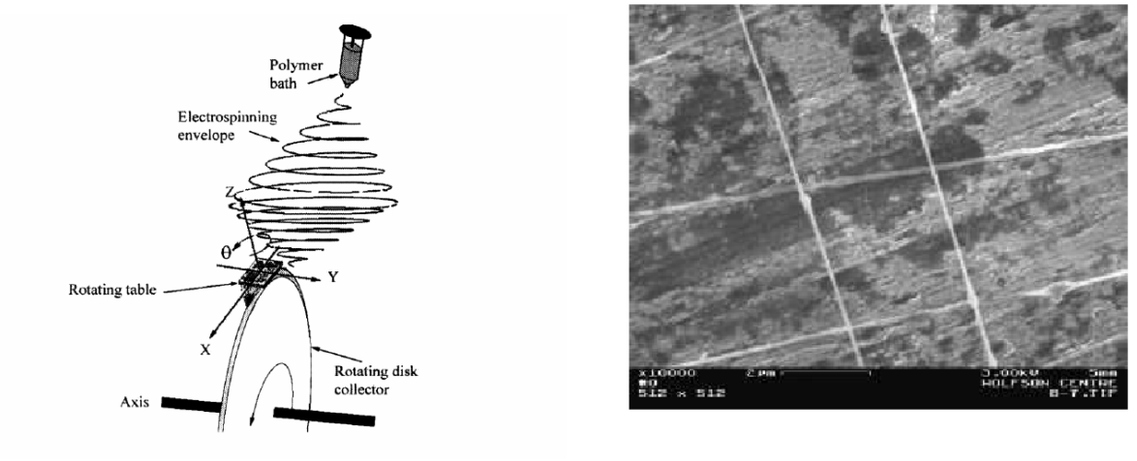
[1] P.R.C. Gascoyne and J. Vykoukal, *Electrophoresis,* 23, 1973, 2002.
[2] A. Dussaud, B. Khusid, and A. Acrivos, *J. Appl. Phys*., 88, 5463, 2000.
[3] Z. Qiu, N. Markarian, B. Khusid, and A. Acrivos, *J. Appl. Phys.,* 92, 2829, 2002;
[4] N. Markarian, M. Yeksel, B. Khusid, K. Farmer, and A. Acrivos, *Appl. Phys. Lett*., 82, 4839, 2003; *J. Appl. Phys*., 94, 4160, 2003.
[5] M. Okandan, P. Galambos, S. Mani, and J. Jakubczak, *Proceedings of SPIE*, 4560, 133, 2001; *Micro Total Analysis Systems* 2001, 305-306.
[6] D.J. Bennett, B. Khusid, C.D. James, P.C. Galambos, M. Okandan, D. Jacqmin, and A. Acrivos, A*ppl. Phys. Lett*., 83, 4866, 2003.
[7] B. Khusid and A. Acrivos, *Phys. Rev. E*, 52, 1669, 1995; 54, 5428, 1996; 60, 3015, 1999.
[8] A. Kumar, Z. Qiu, A. Acrivos, B. Khusid, and D. Jacqmin, *Phys. Rev. E* 69, accepted, 2004

ELECTROSPINNING OF NANOFIBERS FROM POLYMER SOLUTIONS

A.L.Yarin , E.Zussman
Department of Mechanical Engineering, Technion-Israel Institute of Technology, Haifa 32000, Israel

Summary A straightforward, cheap and unique method to produce novel fibers with diameter in the range of 100 nm and even less, is related to electrospinning. For this goal polymer solutions, liquid crystals, suspensions of solid particles and emulsions are electrospun by a field of about 1 kV/cm. The electric force results in an electrically charged jet of polymer solution outflowing from a droplet tip. After the jet flows away from the droplet in a nearly straight line, it bends into a complex path and other changes in shape occur, during which electrical forces stretch and thin it by very large ratios. After the solvent evaporates, solidified nanofibers are left. The present work deals with the mechanism and electrohydrodynamic modeling, experimental realization and a number of applications. In particular, we developed a unique electrostatic field-assisted assembly technique with the aim to position and align individual conducting and light-emitting nanofibers in arrays, crossbars and ropes. These structures are of potential interest in development of novel polymer-based light-emitting diodes, diodes, transistors, photonic crystals and flexible photocells. We also discuss our experiments on electrospinning of nanofibers reinforced by carbon nanotubes, and on coelectrospinning, which yields core-shell nanofibers and nanotubes.

The reasons for the observed bending instability are explained and the process modelled. Several novel approaches in the electrospinning technique are introduced. In particular, to overcome technological challenges in fabrication of microdevices, techniques for in situ alignment of as-spun nanofibers/nanotubes using electrostatic repulsion forces are demonstrated as a route for alignment of nanofibers/nanotubes. A sketch of the experimental apparatus is shown in Fig. 1a.



(a) (b)

Fig. 1 (a) Schematic drawing of the electrospinning process, showing the double-cone envelope of the jet. The collector disk is equipped with a table that assists to collect the nanofibers. The table can be rotated about the Z-axis when the disk rotation is temporarily stopped to enable layer-by-layer collection at a desired angle between the nanofiber array layers, (b) Typical SEM image of the crossed arrays of PEO-based nanofibers collected on an aluminum table.

The jet flows downward from the surface of a pendant drop of polymer solution toward a rotating disk with a tapered edge in order to create a stronger converging electrostatic field (an electrostatic lens). During the electrospinning process, the disk was rotated at a constant speed to collect the developing nanofibers onto its sharp edge,or onto a small plate positioned at the edge. Two- and three-dimensional (crossbars) nanofiber arrays were produced by this method, Fig. 1b. Nanoropes of nanofibers are also easily doable. Arrays similar to those shown in Fig. 1b represent themselves as key elements of light-emitting diodes (LEDs), polymer lasers, and photonic crystals - a composite of a periodic array of dielectric scatterers in a homogeneous dielectric matrix. These devices affect the properties of a photon similar to a semiconductor effect on the properties of an electron. As a result, photons can have band structures, localized defect modes and surface modes. A foreseen ability to mold and guide light can enable a variety of novel applications of nanofibers/nanotubes in such fields as microelectronics, telecommunications and solar energy conversion.

The electrospinning process was also used successfully to fabricate nanofibers of poly(ethylene oxide) [PEO] in which multiwalled carbon nanotubes (MWCNT) are embedded. Initial dispersion of MWCNTs in water was achieved using amphiphiles, either as small molecules (sodium dodecyl sulfate - SDS) or as a high molecular weight, highly branched polymer (Gum Arabic). These dispersions provided separation of the MWCNTs and their individual incorporation into the PEO nanofibers by subsequent electrospinning. The focus of this work is on the development of axial orientations in these multi-component nanofibers. Continuous nanofibers of controlled diameter were thus obtained either as an unoriented mat on a flat collector or as an oriented rope by deposition on a rotating wheel.

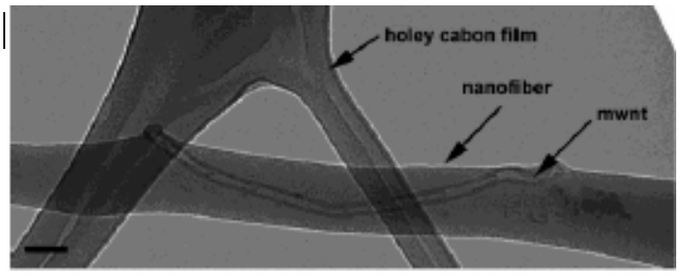


Fig 2: Oriented MWCNT in MWCNTs/PEO/SDS nanofiber. Bar=50 nm.

TEM images of nanofibers containing MWCNTs/PEO/SDS are shown in Fig. 2. It is evident that individual MWCNTs were successfully embedded in the dispersing polymer/surfactant matrix. This indicates that the original dispersion contained individual nanotubes rather than aggregates or bundles. In many regions of the electrospun nanofibers the embedded nanotubes appeared to be well-oriented along the fiber axis. Polymer nanofibers reinforced by an embedded oriented system of carbon nanotubes will allow development of advanced materials possessing ultimate tensile strength and significant electric conductivity.

A core-shell nano/meso fibers were produced by coelectrospinning of two materials. In the present approach both liquids outflowing from the core- and the surrounding concentric annular nozzles are polymer solutions or a combination of polymer solution and a non-polymeric liquid or even a powder. A compound droplet sustained at the edge of such compound nozzles should undergo transformation into a compound Taylor cone with a compound jet co-electrospun from its tip. Then, as in the ordinary electrospinning process, the jet will be pulled by the electric field, and stretched by the bending instability far enough from the droplet. Solvent will evaporate and the compound jet will solidify, resulting in compound core/shell nanofibers. Compound nanofibers electrospun from PEO/PSU solutions had an outer diameter of the order of 60 nm, and a core diameter of about 40nm as apparent from Fig. 3.

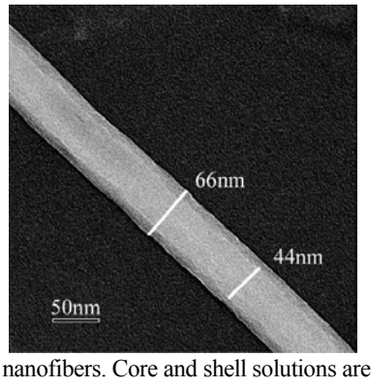


Fig. 3: TEM of a compound nanofibers. Core and shell solutions are PSU and PEO, respectively.

Thicker fibers (of the order of 800 nm) were also obtained, however TEM studies did not succeed in revealing their inner structure. The compound nanofiber shown in Fig. 3 demonstrates a relatively smooth core/shell interface. The method of co-electrospinning should be very versatile for the processing of a wide variety of systems and will certainly foster new materials design. It can also result in a novel two-stage method of fabrication of hollow nanofibers (nanotubes) instead of the previously used three-stage one. Co-electrospinning should be followed by a selective removal of the core material in the compound fiber via selective solvents or heat treatment. The preparation of organic, inorganic materials, of semiconductor systems which are functionalized via a structuring process taking place on the submicrometer scale is the main goal of the coelectrospinning process described here. The manufacturing of structured yet compact polymer fibers with diameters in the sub-micrometer range down to ten nanometers meets with considerable interest for various applications. Examples in case are nanofibers for various filter applications and protective clothing, composite-fiber reinforced materials, biomedical applications (tissue engineering, drug release systems), fibers loaded with catalysts, core/shell fibers for optical applications (waveguides), or nanocables for microelectronics applications. The reduction of the diameter into the nm-range gives rise to a set of favorable properties including the increase of the surface to volume ratio, variations in the wetting behavior, modifications of the release rate or a strong decrease in the concentration of structural defects on the fiber surface which will enhance the strength of the fibers.

THE GIANT ELECTRORHEOLOGICAL EFFECT IN SUSPENSIONS OF NANOPARTICLES

Weijia Wen[1], Xianxiang Huang[1], Shihe Yang[2], Kunquan Lu[3], Ping Sheng[1]

[1]*Department of Physics and Institute of Nano Science and Technology, The Hong Kong University of Science and Technology, Clear Water Bay, Kowloon, Hong Kong, China*
[2]*Department of Chemistry and Institute of Nano Science and Technology, The Hong Kong University of Science and Technology, Clear Water Bay, Kowloon, Hong Kong, China*
[3]*Institute of Physics, Chinese Academy of Sciences, Beijing 100080, China*

Summary We have prepared suspensions of coated nanoparticles which exhibit electrically controllable, reversible liquid-solid transitions on a time scale of 1 to 10 msec. The solid state exhibits maximum yield stress on the order of 130 kPa, breaking the theoretical upper bound derived on the general assumption of linear electrical response of the component materials. Predictions based on the model of surface saturation polarization in the contact region of neighboring particles are in excellent agreement with the experiments.

A transmission electron microscope (TEM) image of the GER particles is shown in Fig. 1 (A). They have an average size of 50-70 nm, each with a surface coating of ~3-10 nm. Under an applied electric field, induced polarization in the particles causes their aggregation into columns aligned along the field direction (Fig. 1(B)). These columns are responsible for the solid yield stress when sheared along the transverse direction. A closer look at one of the columns is shown by the TEM image in Fig. 1(C), where it is seen that the particles' contact areas are somewhat flattened, indicating a degree of softness in the coatings.

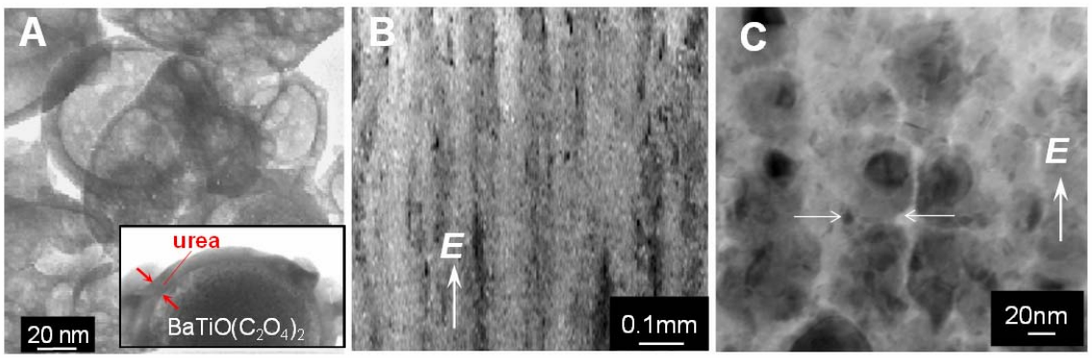


Figure 1 Images of nanoparticles in GER suspensions. (A) TEM image of coated nanoparticles. Urea coatings are clearly seen. (B) Optical microscope image of a sample prepared in epoxy, solidified under an applied field of 2000 V/mm. Aligned columns along the field direction are visible. (C) TEM image of a section of the column shown in (B). The arrows indicate one of the flattened interfaces [1].

The static yield stress curves for two volume fractions, measured under DC electric fields, are shown in Fig. 2. The corresponding current densities are shown in the inset. The current density J is below 4 μ A/cm^2 for E<2 kV/mm for the 30% sample. The yield stress varies as a function of temperature from 10 to 120 ^{o}C to within 30%. A similar temperature variation in current density was observed. At 1000 V/mm and 30% volume concentration, our GER has a measured Young's modulus $Y \approx 6$ Mpa under pulling. At concentrations <15%, both the onset and decay times of the yield stress are on the order of 10 ms. However, at high concentrations the initial fast decay of the yield stress is usually accompanied by a long time tail (extending to ~ 1 sec) that is small in magnitude, implying a degree of metastability.

The magnitude of GER's static yield stress, reaching 130 kPa at 5 kV/mm, sets it apart from the conventional ER fluids because it exceeds the theoretical upper bound, $(138\sqrt{R})(\varepsilon_\ell E^2/8\pi)$ (with R in units of microns), derived on the general assumption of linear dielectric and electrical conductive response of the component materials. With ε_ℓ =2 for the silicone oil dielectric constant, R=0.04 (micron) and E=5000 V/mm, the upper bound is 6.1 kPa, ~20 times smaller than the observed value. Another characteristic of GER is its near-linear field dependence of the yield stress. In general, the static yield stress is proportional to the energy density

$-\vec{P}\cdot\vec{E}$, where $\vec{P}$ is the polarization density. A linear dependence of $\vec{P}$ on $\vec{E}$, i.e., $\vec{P}=\chi\vec{E}$, implies a quadratic field dependence of the yield stress. The observed near-linear field dependence suggests the GER mechanism to involve a constant $\vec{P}_o$, i.e., a saturation polarization.

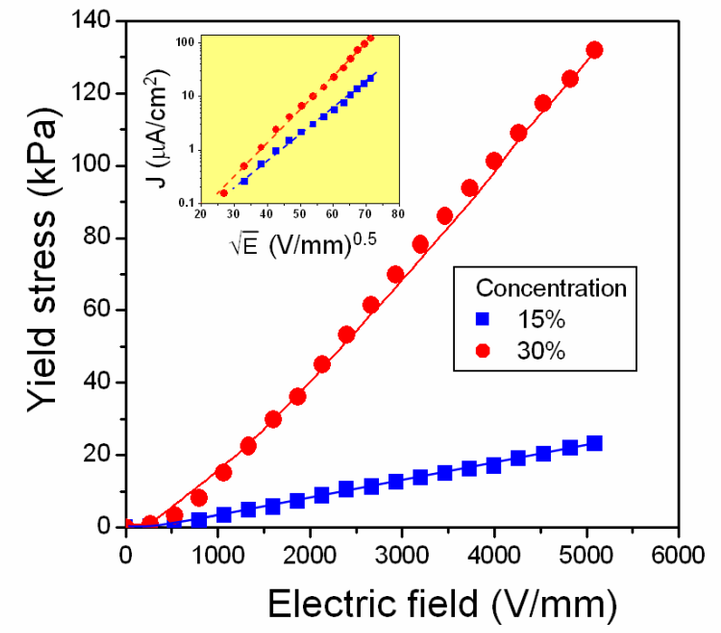


Figure 2 Static yield stress variation plotted as a function of applied electric field for two solid concentrations. Symbols denote experiment; solid lines are theory. Inset: logarithm of the current density *J* plotted as a function of $\sqrt{E}$. The dashed straight lines serve to delineate the $\ell nJ \propto \sqrt{E}$ relationship, indicating the mechanism of activation over the Coulomb barrier [1].

We propose the mechanism of saturation surface polarization, in the contact region of the neighboring spheres, to be responsible for the GER effect. The contact region is modeled by a 2Å gap separating the two surfaces, with an area determined by the Hertzian solution of two elastic spheres pulled together by a force F[21]: $\pi F^{2/3}[\kappa R/2]^{2/3}$, where R denotes the coated sphere radius and κ^{-1}, the deformation modulus of the coating, is the only adjustable parameter of our model. In the contact region the surface dipoles form two aligned layers, in contrast to other areas where such a configuration represents a higher energy state. The aligned configuration is possible due to (1) the high dielectric constant of the coating, which reduces the repulsive interaction between the aligned dipoles, (2) the favorable attractive interaction across the gap that considerably lowers the overall energy, and (3) the magnitude of the favorable interaction energy, which is sufficient to overcome the entropy effect. To buttress our argument, we have used finite element approach to calculate the interaction energy for two (nearest neighbor) pairs of dipoles. The result shows that the interaction energy at the gap separation of 2 Å is ~ -7 *kT*, sufficient to overcome the entropy effect and to induce a localized collective transition to the aligned state.

The predicted yield stress as a function of *E* is shown in Fig. 2 as the solid lines. Excellent agreement between theory and experiment is seen. In particular, the discernable deviation from linearity is well-captured by the elastic component of the model. However, for the 15% concentration, our model (by using a larger average volume per particle) obtains agreement only by using a solid concentration of 5%. This is plausible because the theory concentration is that of the network backbone responsible for the overall rigidity; at lower concentrations the probability increases that a solid particle in the actual (random) system does not belong to the backbone. With no adjustable parameter, the Young's modulus was calculated to be 5 MPa at 1000 V/mm for a concentration of 30%, in good agreement with the experiment (6 Mpa).

Reference

[1] W. Wen, X. Huang, S. Yang, K. Lu, Ping Sheng, *Nature Materials* **2**, 727-730 (2003).

Electrospinning of liquid jets

S. Blonski[*], A. Blasinska[**], T.A. Kowalewski[*]

[*]*Polish Academy of Sciences IPPT PAN, Swietokrzyska 21, PL 00-049 Warszawa, Poland*
[**]*Technical University of Lodz, The Faculty of Textile Engineering and Marketing, Zeromskiego 116, PL 90-543 Lodz, Poland*

Summary: A very thin liquid jets can be obtained using electric fields. The electrically-driven bending instability of the jet enormously increases the jet elongation path and effectively leads to its tinning by very large ratios and can be used to produce nanofibres. The mechanism of electro-thinning of liquid jets, discovered almost one century ago, is yet not fully understood. In the following study detailed experimental data are collected for electrospinning of different liquids in the purpose to correlate these data with the existing models describing basic mechanisms responsible for the electrospinning.

INTRODUCTION

Slender axially symmetric liquid jets emerging from an orifice into passive gaseous environment play an important role in fluid mechanics as well as in many practical applications. The phenomena is characterized by an intrinsic capillary instability which under action of surface tension forces leads to disintegration of the jet into drops. It was found that high viscosity of the liquid as well as extensional stress reduce growth rate of the capillary instability. Further stabilization of the jet is possible for viscoelastic liquids [1], and led to maybe the most revolutionary application - liquid jet spinning used to produce long and stable textile fibres. Mechanical spinning of fibres has its practical limits however, and only recently it appeared that further elongation of the liquid jet is possible by applying electrical field to enforce its controlled winding. This process is called electrospinning. It allowed for enormous increase of the spinning path, decreasing diameter of the created fibre several orders of magnitude, arriving to dimensions of hundreds or tens of nanometers. Unique mechanical properties of nanofibres activated wide interest in many fields of mechanics, physics, chemistry and material science.

Unfortunately, the control of electrospinning process relies mostly on empirical data up to now. Semi-analytical models present up to know are difficult to apply in practice as usually they are based on very limiting assumption concerning physics of the process [2]. Our experimental study is primary devoted to elucidate role of such basic parameters like liquid viscosity, surface tension, electric conductivity, reological properties as well as strength of the electric field on the electrospinning process. The aim of the present study is to obtain detailed experimental data on the process itself and to correlate these data with the existing models describing basic mechanisms responsible for the electrospinning.

The experimental setup consists of a pipette sustaining a pendant droplet, a high voltage DC source, a conducting mat for the nanofibres collection, and optical system for image acquisition. A bright field illumination using Fresnel lens is used in most cases. Three camera systems are used to collect transient parameters of the jet and measure details of the collected nanofibres: standard 25fps video camera (768x564 pixels), high-resolution PIV camera (1280x1024 pixels) and high speed (40500fps) Fastcam imaging system (256x256 pixels). As a working fluids mainly water-glycerol solutions and water-alcohol solution of poly(ethylene oxide) - (PEO) are used. By adding surfactant and sodium chloride surface tension and conductivity of the fluid is modified. In addition applicability of electrospinning to two commonly used polymer solution polyacrylonitrile (PAN) and chitin derivatives is tested. Several electrospinning jets emerging from parallel orifices are investigated to estimate possibility of creating boundless nanofibres. The high speed imaging system, as well as a double pulse laser with the PIV camera are used to evaluate local velocity of the jet during its tinning process. Details of geometry of the looping cone are recorded by the standard video camera. Structure of the product is analysed using microscopic system and the high-resolution camera. To estimate magnitude of the jet stretching forces, controlled air flow is used and its effect on the deformation of a segment of the jet analysed.

RESULTS

Typical form of the electrically charged jet of polymer solution is shown in Fig. 1a. The path of jet formed at the tip of a pendant droplet is characterised by three distinct segments. The first one, is a classical straight or slightly curved cylinder with typical length of several millimetres. Its length varies nearly linear with the electrical potential applied and depends on liquid properties (viscosity, surface tension). The second segment starts by sudden bending of the straight cylinder leading to development of a conical spiral. Its height and diameter at the bottom may reach size of several centimetres. The growth rate of the spiral diameter (envelope of the cone) depends on the electrical potential and fluid properties. Due to the electrical forces and stretching the fluid is accelerated reaching velocity of several m/s. After following several loops the conical shape becomes distracted, several difficult to characterise instabilities, small local looping or irregular large loops characterize last jet segments, which are finally collected on the metal electrode. The collected web is usually irregular in form, however by proper adjustment of the collector and the jet loop

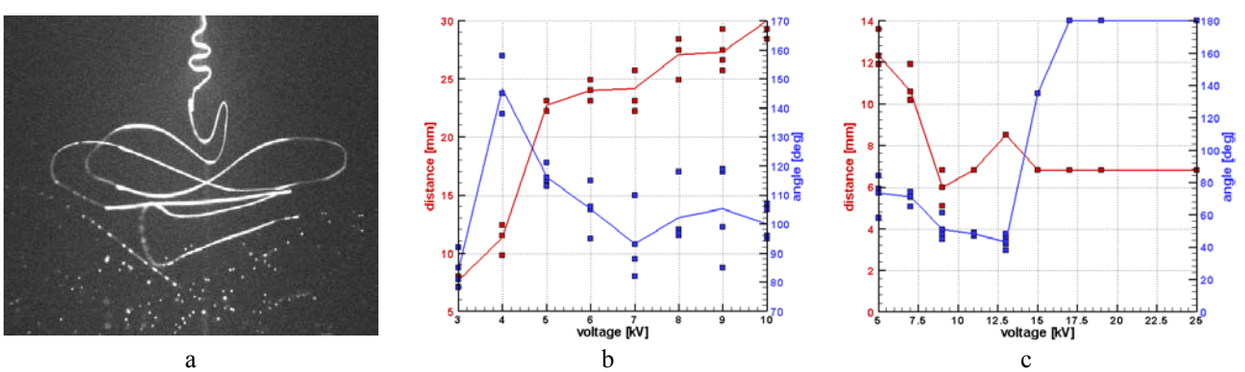
inclination relatively regular, nearly parallel mesh of thin filaments was obtained. Diameter of the remaining segments of the jet can be as small as 50 – 100nm, giving starching factor of more then thousand (Fig. 1b,c).



a b c

Figure 1. Electrospinning of polymer solution of poly(ethylene oxide): frame from high speed movie showing development of the bending instability (a); collected nanofibres web under optical microscope (b) and electron microscope (c).

To elucidate main mechanisms responsible for development of electro-bending instability electrified jets of glycerol solutions were used. It was found that despite of lack of viscoelasticity electrospinning of glycerol water solution (88%) is possible (Fig2a). The jet forms relatively long and well controllable spiral before it disintegrated into tiny droplets due to the capillary instability. However, the stretching factor is much smaller and amounts only about ten. By decreasing contents of water in glycerol electrospinning disappears, the relatively straight jet of highly viscous breaks up to many small droplets after passing path of several centimetres. It indicates importance of viscosity but also of an electrical conductivity for the development of the bending instability.
Mathematical description of the bending process given by Reneker et al [2] offers simple model describing relation between forces due to electrical charges, liquid viscoelasticity, surface tension and shearing. According to the model length of the rectilinear segment of the jet increases linearly with voltage, whereas angle of the spiralling cone decreases. The model appeared to work well for poly(ethylene-oxide) solution (Fig. 2b). Experiments performed for several other tested solutions could not confirmed validity of the model, giving even reversal relations (Fig. 2c). The model developed for small perturbations seems to overestimate role of viscoelastic forces compared with surface tension and viscous stresses.



a b c

Figure 2. Electrospinning of 88% glycerol solution (a); variation of the straight segment and angle of the spiral cone with electrical potential for poly(ethylene oxide) solution (b) and polyacrylonitrile (c).

CONCLUSIONS

Experimental investigation performed for several polymeric solutions and for glycerol solutions demonstrated possibility to stretch liquid jets in the electrical field into fractions of their initial diameter. Variety of jet paths are observed depending on material and electrical potential applied. It appears difficult to match observed characteristics with theoretical relations available in literature. Experiments demonstrated possibility to created boundless electrospinning jets, however long range electrostatic interaction was observed to hinder their alignment onto the collector grid.

References

[1] Yarin A.L., Free liquid jets and filds: hydrodynamics and reology, Longman, Harlow and Wiley, new York 1993
[2] Reneker D.H., Yarin A.L., Fong H., Koombhongse S.: J. Appl. Physics **87**, 4531 (2000)
[3] Yarin A.L., Koombhongse S., Reneker D.H.: J. Appl. Physics **89,** 3018 (2001)

MODELING DNA SEPARATIONS IN SELF-ASSEMBLED MAGNETIC ARRAYS: COMPARISON OF THEORY AND EXPERIMENT

Kevin D. Dorfman, Nicolas Minc, Claus Fütterer and Jean-Louis Viovy
Laboratoire Physicochimie-Curie, CNRS/UMR 168, Institut Curie,
26 Rue d'Ulm, F-75248 Paris Cedex 5, France

Summary We present a theoretical model of macroscopic DNA transport in a self-assembled array of magnetic posts. The model parameters are determined either experimentally or from a microscale model. Experiments confirm our scaling results, and we achieve reasonable quantitative agreement with an experimental measurement of the average trapping time.

INTRODUCTION

Microfluidic arrays of posts proffer great potential for rapid, reproducible electrophoretic separations of long DNA. Moreover, such arrays provide an ideal platform for testing fundamental theories of polymer dynamics in confined media, since the arrays are strongly organized, tunable, and highly reproducible between experiments. We focus here upon predicting the macroscale motion and separation properties for arrays formed by the self-assembly of nanosize magnetic beads [1] under the influence of an external magnetic field.

EXPERIMENTAL METHOD

Microchannels with widths of 150 μm and depths of either 10 or 12μm were fabricated in PDMS using rapid prototyping technology. The magnetic matrix is formed reversibly by injecting an emulsion of monodisperse superparamagnetic beads (size 570 nm, dispersion 5%, kind gift of Ademtech SA, Pessac, France) into the channel and applying a magnetic field of approximately 10mT, as in Fig. 1a. The size-dependent interaction of the DNA with the post (Fig. 1b) gives rise to the separation. We compute the average column diameter d and center-to-center spacing a from the autocorrelation function of an image of the array. Mixtures containing λ (48.5 kbp), 2λ (97 kbp) and/or T4 DNA (168.9 kbp), stained with Yoyo-1, were injected using a double-T and detected by epifluorescence at the entrance (to measure the initial plug half-width l_0) and at a distance $L = 7.5$mm downstream, the latter depicted in Fig. 1c. Further details of the experimental setup are available in Ref. [2].

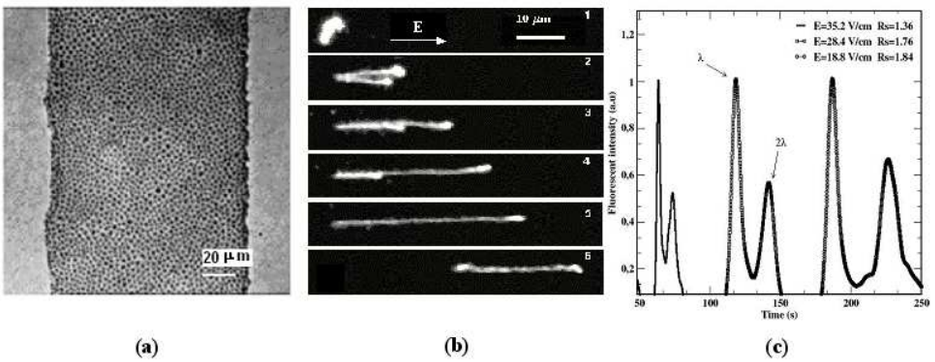


Figure 1: (a) Image of a typical matrix. (b) Mechanism of separation. Long DNA become hooked on the posts and extend in the field direction. The retention time on the post depends upon the the size of the DNA. (c) An electrophoregram of a separation between λ and 2λ DNA.

THEORETICAL MODEL

We used a coarse-grained, exactly solvable lattice Monte Carlo model [3] to compute the mean velocity and dispersivity of the DNA as it moves through a quasi-regular staggered array of columns. Interactions with the posts, quantified by the average trapping time τ and collision probability Π_c, are determined by a microscale model. The exact solution of our lattice model furnishes the mean velocity $\bar{U}^*$ and dispersivity $\bar{D}^*$

$$\bar{U}^* = \frac{U}{1+\Pi_c(\alpha-1)}, \quad \bar{D}^* = Ua\frac{\Pi_c(\alpha-1)\left[1+(2-\Pi_c)(\alpha-1)\right]}{2\left[1+\Pi_c(\alpha-1)\right]^3}, \tag{1}$$

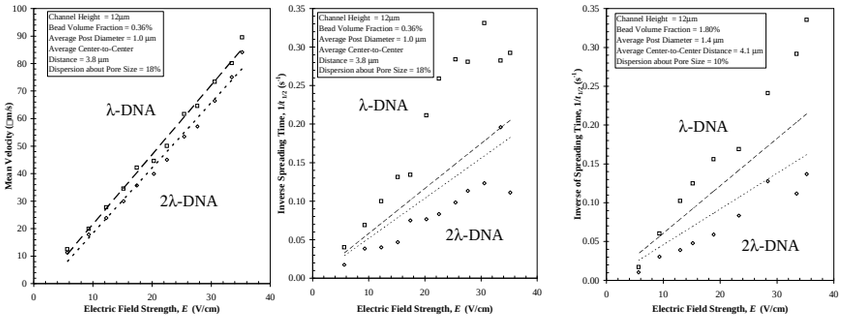
where U is the free solution velocity obtained in a matrix-free channel. The dimensionless trapping time $\alpha = \tau U/a > 1$ measures the retardation caused by the posts. For experimentally relevant values of τ and Π_c, $\bar{D}^*$ increases with increasing Π_c for $\tau < 4/3$ and decreases otherwise. The dispersion caused by the posts is 60-300 times greater than molecular diffusion.

COMPARISON BETWEEN THEORY AND EXPERIMENT

To make a comparison between theory and experiment [2], we assumed that the trapping time is inversely proportional to the field, which is valid for strong fields, and that the collision probability only depends upon the density of posts, $\Pi_c = d/a$. Using these assumptions in eq. (1) and its associated Gaussian macrotransport equation [2], we arrive at the scalings

$$\bar{U}^* \sim E, \quad \bar{D}^* \sim E, \quad t_{1/2} \sim E^{-1}, \quad R_s \sim E^0. \tag{2}$$

where $t_{1/2}$ is the time for the half peak to pass the detector and R_s is the separation resolution. The scaling for $t_{1/2}$ and R_s follows from that for $\bar{U}^*$ and $\bar{D}^*$; thus, we can confirm our scaling results with only two experimental measurements, $\bar{U}^*$ and $t_{1/2}$.



(a) (b) (c)

Figure 2: Comparison of theory and experiment for the mean velocity (a) and band broadening (b,c) for the matrix geometries indicated in the insets. Short dashed lines (theory) and □ (experiment) refer to λ DNA; long dashed lines (theory) and ◇ (experiment) refer to 2λ DNA.

As evidenced by Fig. 2, both $\bar{U}^*$ and $t_{1/2}^{-1}$ scale linearly with the field. Although not shown here, the resolution also passes through a plateau over 15-30 V/cm [2], further confirming our scaling results. We made the numerical estimates in Figs. 2b,c by computing the proportionality coefficient for τ from the slope of $\bar{U}^*$ and then computing the difference between the roots $C(t) - 1/2 = 0$ of the concentration profile at the detector,

$$C(t) = \sqrt{\frac{L/\bar{U}^* + T}{t+T}} \exp\left[-\frac{\left(L - \bar{U}^* t\right)^2}{4\bar{D}^*\left(t+T\right)}\right], \quad T = \frac{l_0^2}{16\ln(2)\bar{D}^*}. \tag{3}$$

We achieved reasonable quantitative agreement between theory and experiment using this simple model, with much of the error attributable to the initial condition estimate. Similar values of $t_{1/2}$ in Figs. 2b,c confirm the theoretical prediction of a decrease in $\bar{D}^*$ with Π_c.

Acknowledgments
Ademtech SA, Human Science Frontiers Program and Institut Curie Postdoctoral Fellowships (KDD), Marie Curie Fellowship from the European Union (CF), funding from *Ministère de la Recherche* and *Association pour la Recherche sur le Cancer*, A. Bancaud, C. Gosse, C. Goubault, P.S. Doyle (MIT). This work was performed in part in the UMR 168 microfabrication clean room.

References

[1] P.S. Doyle et al.: Magnetic Matrices for DNA Separation Chips. *Science* **295**:2237, 2002.
[2] N. Minc et al.: Rapid and Quantitative Microfluidic Separation of DNA in Self-Assembled Magnetic Matrices. (submitted).
[3] K.D. Dorfman and J.-L. Viovy: A Semiphenomenological Model for the Dispersion of DNA During Electrophoresis in a Microfluidic Array of Posts. *Phys. Rev. E* (in press).

XXI ICTAM, 15-21 August 2004, Warsaw, Poland

CONTACT ANGLE DYANMICS OF DROPLETS IMPACTING ON FLAT SUBSTRATES

Ilker S. Bayer, Constantine M. Megaridis
Department of Mechanical and Industrial Engineering, University of Illinois at Chicago, Chicago USA

Summary An experimental study is presented on contact angle dynamics of water droplets impacting on smooth surfaces with widely disparate wetting characteristics (wetting to non-wetting). Fundamental information relating to the relation between apparent (macroscopic) contact angle θ and contact line speed V_{CL} is presented. The impact conditions correspond to $Re = O(100) - O(1000)$, $We = O(1) - O(10)$, $Ca = O(0.001) - O(0.01)$, $Oh = O(0.001)$ and $Bo = O(0.1)$. For wetting configurations, the classical θ vs. V_{CL} trend is observed, while for partially wetting configurations, advancing contact angles are found to be insensitive to contact line speed. Impact on non-wetting surfaces is followed by rebound, and reveals that both advancing and receding contact angles do not change with contact line speed. The combined molecular-hydrodynamic theory predicted θ -V_{CL} trend data satisfactorily yielding physically reasonable molecular constants.

INTRODUCTION

Droplet impingement phenomena [1] are relevant to a host of emerging technologies. In free form manufacturing [2] for example, droplets of materials can be repeatedly dispensed in their molten form and subsequently solidify upon impact, producing a desired shape or structure. Sophisticated numerical models have been developed to investigate the cumulative effect of the multitude of droplet impingement parameters [3]. The evolution of the contact angle during droplet spreading contains largely unresolved physics. Intermolecular forces govern the microscopic dynamics of contact angle at the molecular level [4]. Furthermore, comparison of hydrodynamic theories and experiment for systems where the liquid does not completely wet the target surface gives physically unreasonable parameters such as subatomic slip lengths (λ). The θ -V_{CL} trend is not well established in forced droplet spreading. There exists a few studies on the combination of hydrodynamic and molecular theories and these models proved satisfactory in predicting θ vs. V_{CL} data in some forced spreading systems [6]. In view of the need for data on contact angle variation with contact line speed for various surfaces, no dynamic contact angle data has been reported to date for impact on super-hydrophobic surfaces. Recent droplet impact studies on such surfaces have considered the effect of impact inertia and droplet size on the residence time of droplets on the substrates. The aim of the present study to experimentally investigate dependence of contact angle θ on contact line speed V_{CL} for impact spreading droplets on surfaces with different degrees of wetting and to test the applicability of the combined molecular-hydrodynamic model.

EXPERIMENTAL

Using an infusion pump, single, distilled water drops of controlled size (D_0=*1.38 ± 0.03 mm*) and velocity (V_0 = *0.45 and 0.77 m/s*) were injected onto three different horizontal dry surfaces corresponding to wetting, partially wetting and non-wetting configurations. High-speed digital motion pictures of single droplet impact and spreading were recorded at 3000-5000 frames/s with a *1280×168* pixel resolution using a *Redlake* Motion Pro image analyzer at 54 μs exposure rate. Measurements of droplet spread diameter and contact angle were made by a commercial image processing software. The resolution of the droplet diameter measurements was *± 0.02 mm*. Macroscopic (apparent) contact angle measurements were made from the captured images with a resolution estimated to be $\pm 5^o$.

RESULTS AND DISCUSSION

Figure 1a represents a typical droplet impact sequence recorded during an experiment. The backlit droplets appear dark against a bright background. The "mirroring" of the droplet on the polished substrate below can be seen in all images. The severe free surface deformation seen in the early impact stages in Fig. 1 is accompanied by the formation of horizontal ripples on the liquid/gas interface. Gradual flattening of the droplet occurs next, with subsequent recoil and eventually droplet rebound at 8.4 ms on the non-wetting surface. It is emphasized that rebound did not occur during impact on any of the wetting and partially wetting substrates. As can be seen, apart from the early impact dynamics, droplet spreading and contact angle dynamics are totally different on the three surfaces studied. It was observed that due to high inertial energy of the impacting droplet, forced spreading dynamics with □ $>90^o$ is independent of surface-fluid wetting interactions. In all spreading curves, dimensionless contact diameter increased with approximately $t^{0.5}$ until it reached to the maximum value. It was also found that under the given impact conditions, as the degree of target surface wetting decreases droplet diameter at maximum spreading (D_{max}/D_o) decreases. The capillarity force arising from the difference between equilibrium droplet shape and extensively deformed droplet shape drives recoiling flow. In our study, the primary spreading of water droplets belongs to the inviscid, impact-driven flow regime since $We>1$ and $Oh<We^{1/2}$. However, during final stages of spreading contact line motion slows down and viscous effects become significant. Therefore, droplet dynamics is governed by the capillary-driven regime. In this regime, it is Oh that

determines whether the resistance to flow is dominantly viscosity (high *Oh*) or inertia (low *Oh*). For the impact conditions studied herein, *Oh=0.0032* (*We<50*), both the inertia and the viscous forces play significant roles in resisting the flow. Thus, recoiling is vigorous. In the non-wetting case, the recoiling rate is very similar to the spreading rate, thus indicating minimal interaction between the liquid and the substrate. Four different graphs given in Figure 1b detail the dependence of the contact line speed on the dynamic contact angle on all surfaces. Since on the partially wetting surface droplet recoils more than once, its first and second cycles were separately plotted. For the case of *wetting* and high impact inertia (V_0 = 0.77 m/s) the advancing contact angle increases with contact line speed. Although the trend is similar to that of spontaneous spreading, the data could not be fitted with the classical parameters of the Hoffman hydrodynamic theory. The analytical study of Hoffman suggested that flow inertia could influence contact line velocity dependence of dynamic contact angle for We > *0.015* [5]. The analyses of hydrodynamic theories focused on the slow viscous flow regime, neglecting flow inertia in the Navier-Stokes equations. As will be shown, however, the combined molecular-hydrodynamic theory predicts θ vs. V_{CL} trend on wetting and partially wetting surfaces.

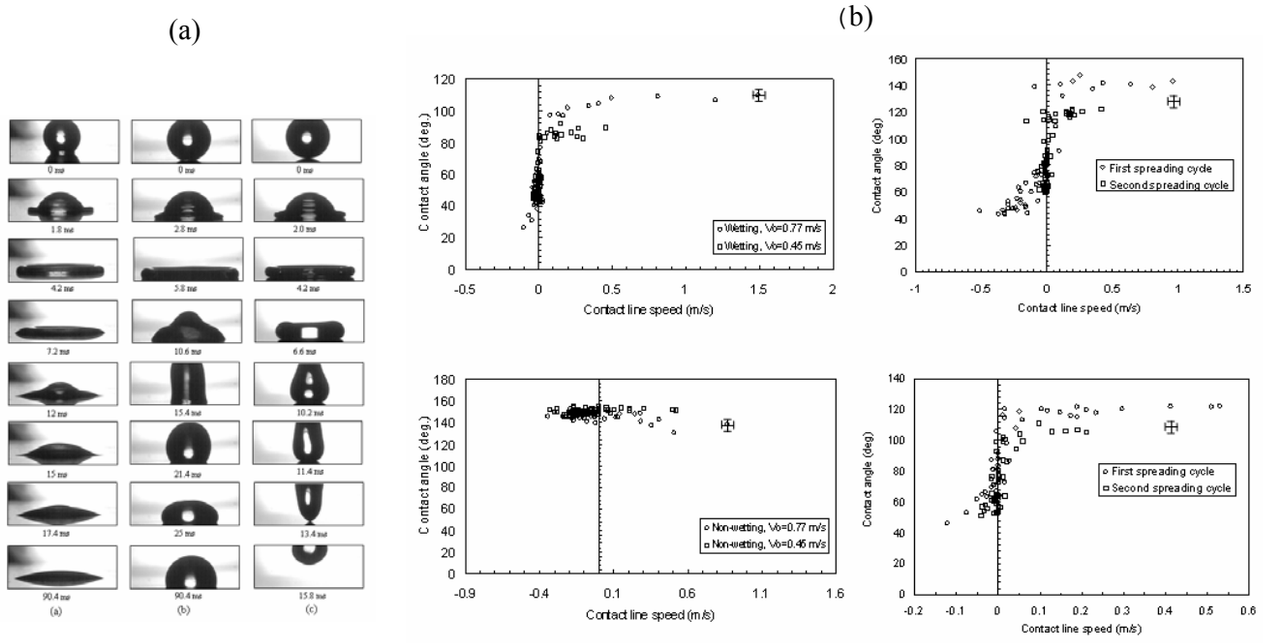


Figure 1. Sequence of time evolution of droplet impact on three different surfaces (a) and contact line speed dependence of the contact angle for all the surfaces studied (b).

CONCLUSIONS

By correlating the temporal behaviors of apparent contact angle θ and contact-line location, the angle vs. speed relationship was established. For wetting configurations, the classical θ vs. V_{CL} trend was observed both for advancing and receding conditions. For partially wetting configurations, advancing contact angles were found to be insensitive to contact line speed, while receding contact angles followed the classical trend. Impact on non-wetting surfaces was followed by rebound, and showed that both advancing and receding contact angle values did not change much with contact line speed. It will be shown that the combined molecular-hydrodynamic theory can be used in the modeling of θ -V_{CL} trend on wetting and partially wetting surfaces.

References

[1] Rein, M.: Phenomena of liquid drop impact on solid and liquid surfaces. *Fluid Dyn. Res.* **12**: 61-93, 1993.

[2] Orme, M.E., C.Z. Huang, and J. Courter: Precision droplet-based manufacturing and material synthesis: Fluid dynamics and thermal control issues. *Atomization and Sprays* **6**: 305-329, 1996.

[3] Bussmann, M., J. Mostaghimi, and S. Chandra: On a three-dimensional volume tracking model of droplet impact. *Physics of Fluids* **11**(6):1406-1417, 1999.

[4] Kistler, S.F.: Hydrodynamics of wetting, in *Wettability*, J.C. Berg, Editor. Marcel Dekker, NY 1993.

[5] Hoffman, R.L.: A study of the advancing interface I. Interface shape in liquid-gas systems. *J. Colloid Interface Sci*.,. **50**:228-235, 1975.

[6] Petrov J. G. and Petrov P. G.: Forced advancement and retraction of polar liquids on a low energy surface. *Colloids and Surfaces,* **64**: 143-149, 1992.

DISSIPATION FEATURES AT NONLINEAR PULSATIONS OF BUBBLES IN VISCOELASTIC FLUIDS

Semyon P. Levitsky, Jehuda Haddad
Negev Academic College of Engineering, Department of Mathematics, 71 Bazel St., POB 45, Beer-Sheva, 84100 Israel

Summary Nonlinear interaction of heat-conducting gas bubble with viscoelastic liquid in a sound field of small but final amplitude is described. The liquid phase is treated as non-Newtonian fluid following Oldroyd type rheological equation. Solution of the problem is received within the volume approach in quadratic approximation with respect to the incident wave amplitude. Resulting relation for the scattered wave intensity is studied numerically with the emphasis on the dissipation features. The study is motivated by the problem of acoustic control of microbubbles trapping in flows of smart fluids with memory.

INTRODUCTION

Microbubbles can change drastically dynamic properties of the liquid and therefore their appearance in smart fluids flows must be controlled carefully. One of perspective tools for microbubbles diagnostics is the acoustic method based on high scattering ability of small inclusions of free gas in a liquid. Among different modifications of acoustic method, the nonlinear ones attract special attention because allow to detect bubbles already at low bubble concentrations and sufficiently small amplitudes of the fundamental wave [1]. It is explained by the fact that nonlinearity of gas within compressible bubble is responsible for the major input in nonlinear properties of the gas-liquid mixture [2]. Small gas bubble in a sound field of final amplitude can be treated as nonlinear oscillator generating the scattered signal at multiple frequencies along with the basic one. The theory of second harmonics generation by small bubbles has been developed in [2] and it was shown that the amplitude of this harmonic is sufficiently large to be registered [3]. The goal of the present study is to generalize this theory for the case of viscoelastic liquid. The volume approach [2] is used here, but, as distinct to the previous studies [2-4], the liquid nonlinearity is taken into account, the losses are not supposed to be additive and are calculated consecutively within the general perturbation scheme.

FORMULATION OF THE MODEL

Hydrodynamic problem

It is supposed that rheological properties of the liquid can be described by Oldroyd type rheological equation:

$$\tau = \tau^{(1)} + \tau^{(2)}, \qquad \tau^{(1)} + \lambda[D\tau^{(1)}/Dt - \alpha(\tau^{(1)}\cdot e + e\cdot\tau^{(1)})] = 2\eta\beta e, \qquad \tau^{(2)} = 2\eta(1-\beta)e \tag{1}$$

Here τ, ω and e are deviator of the stress tensor, vorticity and rate deformation tensors, respectively; λ - relaxation time; η - Newtonian viscosity of the liquid; β - parameter, characterizing input of the Maxwell element in the effective viscosity of the liquid ($0 \le \beta \le 1$); α - parameter of the liquid nonlinearity; D/Dt - Jaumann derivative. The generalized Raleigh equation for small spherical bubble, oscillating in a sound field, is formulated in suggestions that the bubble can be considered as a monopole scatterer (the sound wavelength is much larger than the equilibrium bubble radius R_0), the liquid is incompressible and its rheology, the same as in the case of a purely viscous liquid, is manifested only in the close vicinity of the interface. The resulting integro-differential equation for the bubble radius $R = R(t)$ can be reduced to two coupled differential equations:

$$\rho(R\ddot{R} + \tfrac{3}{2}\dot{R}^2) = \Delta p_g - p_a + \frac{2\sigma}{R_0}\left(1-\frac{R_0}{R}\right) - 4\eta(1-\beta)\frac{\dot{R}}{R} + \tau_R, \quad \tau_R\left(1 + 4\alpha\lambda\frac{\dot{R}}{R}\right) + \lambda\frac{\partial\tau_R}{\partial t} = -4\eta\beta\frac{\dot{R}}{R} \tag{2}$$

Here ρ, σ are density and surface tension coefficient of the liquid; $\Delta p_g = p_g - p_{g0}$, $p_{g0} = p_0 + 2\sigma R_0^{-1}$, where p_0, p_g are equilibrium pressure in the liquid and current pressure in the gas phase; p_a - pressure disturbance in the incident wave with frequency ω. The far-field component of the pressure in the scattered wave has the form (rheology of the liquid influences the scattered signal through the bubble dynamics equation only):

$$p_S(r,t) = \rho\left(R^2(t_r)\ddot{R}(t_r) + 2R(t_r)\dot{R}^2(t_r)\right)r^{-1}, \qquad t_r = t - r/c_0, \tag{3}$$

where c_0 is the sound speed in the liquid, r is the radial coordinate and t_r - the retarded time [3].

Gas dynamic problem and boundary conditions

The pressure within pulsating gas bubble in a wide range of conditions doesn't depend from the radial coordinate and therefore the internal problem can be written in the following form:

$$\rho_{g0}c_{pg}\left(\frac{\partial T_g}{\partial t}+v_g\frac{\partial T_g}{\partial r}\right)=k_g\frac{1}{r^2}\frac{\partial}{\partial r}\left(r^2\frac{\partial T_g}{\partial r}\right)+\frac{dp_g}{dt},\qquad \frac{dp_g}{dt}=-\frac{3(\gamma_g-1)}{R}q_R-\frac{3\gamma_g}{R}p_g\frac{dR}{dt} \tag{4}$$

$$q_R=-k_g\left(\frac{\partial T_g}{\partial r}\right)_{r=R(t)},\qquad \frac{\partial \rho_g}{\partial t}+\frac{1}{r^2}\frac{\partial}{\partial r}(\rho_g r^2 v_g)=0,\qquad p_g=\rho_g T_g c_{vg}(\gamma_g-1),\quad \gamma_g=c_{pg}/c_{vg}$$

Here T_g, ρ_g, v_g are gas temperature, density and the radial velocity in gas; k_g, c_{pg}, c_{vg} - heat conductivity and specific heat capacities of gas. The boundary conditions at $r=R(t)$ mean: $T_g=T_0$, $v=\dot{R}(t)$. At the bubble centre $\partial T_g/\partial r=0$, $v_g=0$.

NONLINEAR SCATTERING OF THE INCIDENT WAVE

Following the volume displacement approach [2, 3], the disturbance of the bubble volume ΔV is introduced in (2)-(4) instead of the radius R ($\Delta V=(4\pi/3)(R^3-R_0^3)$). The result is written in dimensionless form, keeping all the terms up to ΔV^2. Solution of the problem is searched in the form:

$$\{\delta\widetilde{V},\ \delta\widetilde{p}_s,\ \delta\widetilde{u},\ \delta\widetilde{p}_g,\ \delta\widetilde{\rho}_g,\ \delta\widetilde{v}_g,\ \delta\widetilde{T}_g\}=\{\delta\widetilde{V}_1,\ \delta\widetilde{p}_{s1},\ \delta\widetilde{u}_1,\ \delta\widetilde{p}_{g1},\ \delta\widetilde{\rho}_{g1},\ \delta\widetilde{v}_{g1},\ \delta\widetilde{T}_{g1}\}+ \tag{5}$$

$$+\{\delta\widetilde{V}_2,\ \delta\widetilde{p}_{s2},\ \delta\widetilde{u}_2,\ \delta\widetilde{p}_{g2},\ \delta\widetilde{\rho}_{g2},\ \delta\widetilde{v}_{g2},\ \delta\widetilde{T}_{g2}\},\qquad \widetilde{p}_a=\frac{1}{2}\widetilde{P}_a e^{i\widetilde{\omega}\widetilde{t}}+c.c.,$$

where $\delta\widetilde{V}$, $\delta\widetilde{p}_s$, $\delta\widetilde{u}$, $\delta\widetilde{p}_g$, $\delta\widetilde{\rho}_g$, $\delta\widetilde{v}_g$, $\delta\widetilde{T}_g$ are dimensionless disturbances of the bubble volume, pressure in the scattered wave, radial component of the stress tensor deviator in liquid at the interface, gas pressure and density, velocity and temperature in the gas phase, respectively. Vector components with the subscript 1 have the order of $\widetilde{P}_a$ and are proportional to $e^{i\widetilde{\omega}\widetilde{t}}$ while that with the subscript 2 have the order of $\widetilde{P}_a^2$ and are proportional to $e^{2i\widetilde{\omega}\widetilde{t}}$. The scaling is done with the use of equilibrium parameters R_0, p_0, ρ, T_0. A tilde is used to distinguish dimensional variables from their nondimensionalized equivalents. The equations governing the pressure in the linear scattered wave and the amplitude of the second harmonics are obtained and solved consecutively. The resulting relations are analyzed and the basic features of nonlinear wave scattering by small gas bubble in viscoelastic liquid are established.

CONCLUSIONS

The thermal and rheological losses in viscoelastic liquid at linear wave scattering can be treated as additive factors the same as in a pure viscous liquid [5]. This result isn't hold for the signal scattered at the second harmonics frequency, that is explained by the losses coupling. The influence of rheological nonlinearity on the amplitude of the second harmonics grows with the amplitude of the incident wave. Nevertheless, in a wide frequency region the gas nonlinearity is the dominant factor; the features of liquid nonlinearity are manifested mainly in the vicinity of the linear resonance ($\omega\sim\omega_0$). Scattering cross section of the bubble lowers with growth of the liquid viscosity η both for basic and second harmonics as a result of increase in rheological losses. Relative amplitude of the second harmonics (with respect to the basic one) for viscoelastic liquid is always greater than for similar pure viscous liquid because of frequency-dependent behavior of dynamic viscosity. The results of simulations indicate that even for sufficiently viscous smart viscoelastic liquids the amplitude of nonlinear scattered wave at the resonance is large enough to be detected by the same acoustic equipment that is used for bubbles diagnostics in water. It opens possibilities for acoustic control of bubbles trapping in flows of viscoelastic smart liquids with high viscosity in the same manner as for low viscous Newtonian fluids.

References

[1] Naugolnykh K., Ostrovsky L.: Nonlinear Wave Processes in Acoustics. Cambridge University Press, 1998.
[2] Zabolotskaya, E.A., Soluyan, S.I.: Emission of Harmonic and Combination Frequency Waves by Air Bubbles. Sov. Phys. Acoust. **18**: 396-398, 1972.
[3] Sutin, A.M., Yoon, S.W., Kim, E.J., Didenkulov, I.N.: Nonlinear Acoustic Method for Bubble Density Measurements in Water. J. Acoust. Soc. Am., **103** (5): 2377-2384, 1998.
[4] Levitsky S. On Nonlinear Scattering of Sound by Small Bubble in Polymeric Liquid. Proc. IUTAM-16: Nonlinear Acoustics at the Beginning of the 21st Century. Eds. Rudenko O., Sapozhnikov O. Moscow, MSU, 2002. **2**: 927-930.
[5] Prosperetti A. The Thermal Behaviour of Oscillating Gas bubbles. J. Fluid Mech. **222:** 587-615, 1991.

BREAKUP OF POLYMER SOLUTION DROP IMPACTING A SMALL TARGET

Aleksey Rozhkov*, Bernard Prunet-Foch and Michele Vignes-Adler
Laboratoire de Physique des Matériaux Divisés et des Interfaces, UMR8108 du CNRS, Université de Marne-la-Vallée, Bât. Lavoisier - 5, bd. Descartes, F-77454 Marne-la-Vallée Cedex 2, France
**Present address: Institute for Problems in Mechanics RAS, 101(1) Prospect Vernadskogo, Moscow 119526, Russia*

Summary The effects of high molecular additives on the splashing of liquid drops impacting a small target were studied experimentally. A splashing threshold criterion has been constructed.

MOTIVATION

The collision of a liquid drop with a small target is a model for the collision of a drop with a hydrophobic plane surface when there is no viscous friction between the liquid and the surface. The hydrodynamic features of the collision, which are usually hidden by the viscous effects, can be observed in "a pure view" [1]. Such type of experiment is particularly convenient to study the effects of polymeric additives on the impacting drop splashing in great details.

EXPERIMENTAL PROCEDURE AND RESULTS

The collisions of drops of dilute polymer solutions with a small disk-like target were investigated experimentally. Aqueous solutions of polyethylene oxide of molecular mass 4 millions at weight concentration 1, 10, 100 p.p.m. (PEO-1, PEO-10, PEO-100) were used. The velocities of the impacting drops were 3.8 m/s, and their diameters before impact were 2.7 mm. The target was a stainless steel disk of diameter 4 mm. The collision was visualized by high-speed videorecording. As in the case of pure water [1], a lamella in the shape of a circular film with a relatively thick rim was formed upon impact. At first it increased in diameter, and then, it retracted with formation of radially directed secondary jets (Figure 1). The lamella dynamics results from the competition between the inertial, surface and probably elastic forces (in the case of polymeric liquid) that control the rim motion. No essential difference in the maximum lamella diameters and their retraction rates was observed between the water and the polymeric fluids [2]. But the polymeric additives essentially changed the features of the lamella retraction. Secondary jets, which broke up into separate secondary droplets with water, were transformed into thinning filaments, connecting the lamella to the secondary droplets with polymeric fluids (Figure 1). Depending on the polymer concentration two situations were realized: either the filaments broke up, and the secondary droplets were ejected – *i.e.* splashing happened (PEO-1); or the filaments did not release the secondary droplets, until the latter coalesced back with the main drop – splashing did not happen (PEO-100).

SPLASHING THRESHOLD

A transition criterion for drop impact with or without splashing [2] was constructed. The analysis is based on the comparison between the time at which the filament breaks and the time that is necessary for both the retraction of the filament with attached droplet and the coalescence of the droplet with the main drop. If the first time is smaller than the second one then the filament breaks and the droplet is ejected. In the opposite case the droplet coalesces with the main drop before the filament rupture. It was found that the influential factors are the dynamic conditions of impact and the elasticity of the liquid. The splashing threshold is written as:

$$(\rho\, d_i^3/(\gamma\theta^2))\cdot We_i^{\chi}=K\,, \qquad (1)$$

where ρ is the liquid density, d_i is the diameter of a drop before impact, γ is the liquid surface tension, θ is the fluid relaxation time [3], $We_i=\rho\, v_i^2 d_i/\gamma$ is the impact Weber number, v_i is the velocity of impact; $\chi = 3/8$, $K = 1140$ at the splashing threshold. Relation (1) predicts, that if its left-hand part is larger than 1140, the drop breaks up into separate droplets, and it does not occur in the opposite case. For the particular cases of collisions of drops of PEO-1, PEO-10 and PEO-100 solutions displayed in Figure 1, the left-hand part of relation (1) receives the values 20637, 872 and 44, accordingly. The drop of PEO-1 breaks up into separate droplets. The case of PEO-10 is the closest one to the critical situation (among the three values, 872 is closest to the critical parameter K=1140). Although few droplets are separated, the main part of the liquid saved its continuity. With PEO-100 drops, no liquid losses are observed. Relation (1) can therefore be proposed as an empirical expression of splashing threshold for impact on plane surface: the parameters χ and K can be determined experimentally.

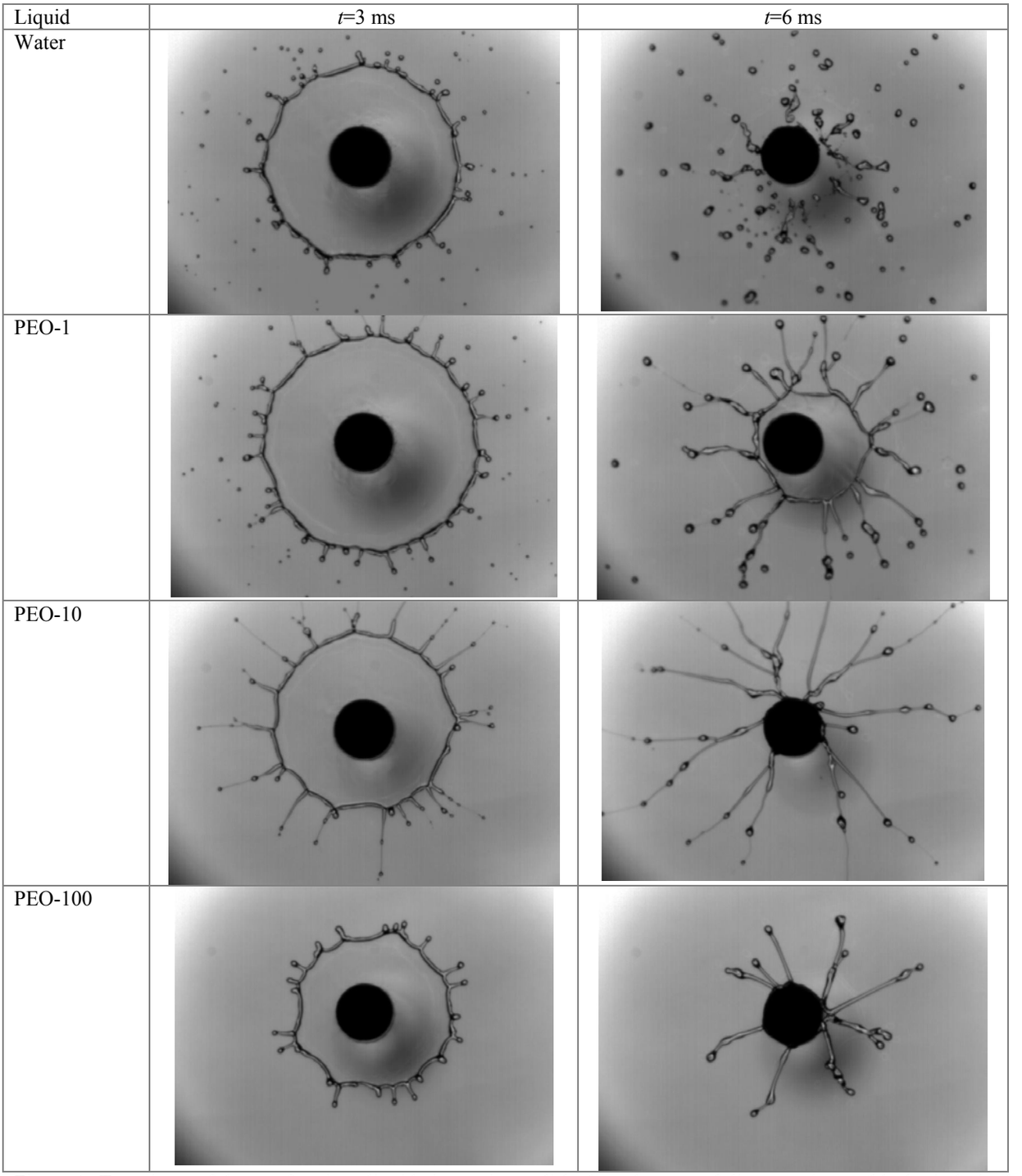


Figure 1. Top views of drops of various liquids impacting a disk-shaped target of diameter 4 mm (black circle in the centre of each frame). Drop diameter before impact is 2.7 mm; the impact velocity is 3.87 m/s. The motion of the drops before impact is directed from the reader to the figure plane. Time increases from left to right from 3 up to 6 ms.

Acknowledgements

A.R. took part in this work during his stay at the Laboratoire de Physique des Matériaux Divisés et des Interfaces, Université de Marne-la-Vallée. He thanks CNRS for the support of the visit.

References

[1] Rozhkov A., Prunet-Foch B., Vignes-Adler M.: Impact of water drops on small targets. *Physics of Fluids* **14**, 3458-3504, .2002.

[2] Rozhkov A., Prunet-Foch B., Vignes-Adler M.: Impact of drops of polymer solutions on small targets. *Physics of Fluids* **15**, 2006-2019, 2003.

[3] Bazilevskii A.V., Entov V.M., Rozhkov A.N.: Breakup of an Oldroyd liquid bridge as a method for testing the rheological properties of polymer solutions. *Polymer Science* **A43**, 716-726, 2001.

FERROHYDRODYNAMIC HELE-SHAW CELL FLOWS AND INSTABILITIES WITH SIMULTANEOUS DC AXIAL AND IN-PLANE ROTATING MAGNETIC FIELDS

Scott E. Rhodes*, Juan A. Perez*, Shihab M. Elborai*, Se-Hee Lee*,**, and Markus Zahn*
*Massachusetts Institute of Technology, Department of Electrical Engineering and Computer Science, Laboratory for Electromagnetic and Electronic Systems, Cambridge, MA, USA
**MIT Visiting Scientist from Sungkyunkwan University, School of Information and Communication Engineering, Institute of Information and Communications Technology, Suwon, South Korea.

EXPERIMENTS

New flows and instabilities are presented for a ferrofluid drop contained in glass Hele-Shaw cells of 0.9 - 1.4 mm gap with simultaneously applied in-plane rotating and DC axial uniform magnetic fields. The rotating uniform magnetic field is formed using a stator winding from a 2 pole induction motor which is excited by balanced three phase currents. The fluoro-carbon based ferrofluid has saturation magnetization ≈400 Gauss and low field magnetic susceptibility of $\chi \approx 3$. The ferrofluid is surrounded by a 50/50 mixture of isopropyl alcohol and deionized water which prevents ferrofluid wetting of the glass plates. The rotational field strength is up to 100 Gauss rms at frequencies 20-40 Hz while a DC axial field is varied from 0 to ~250 Gauss [1].

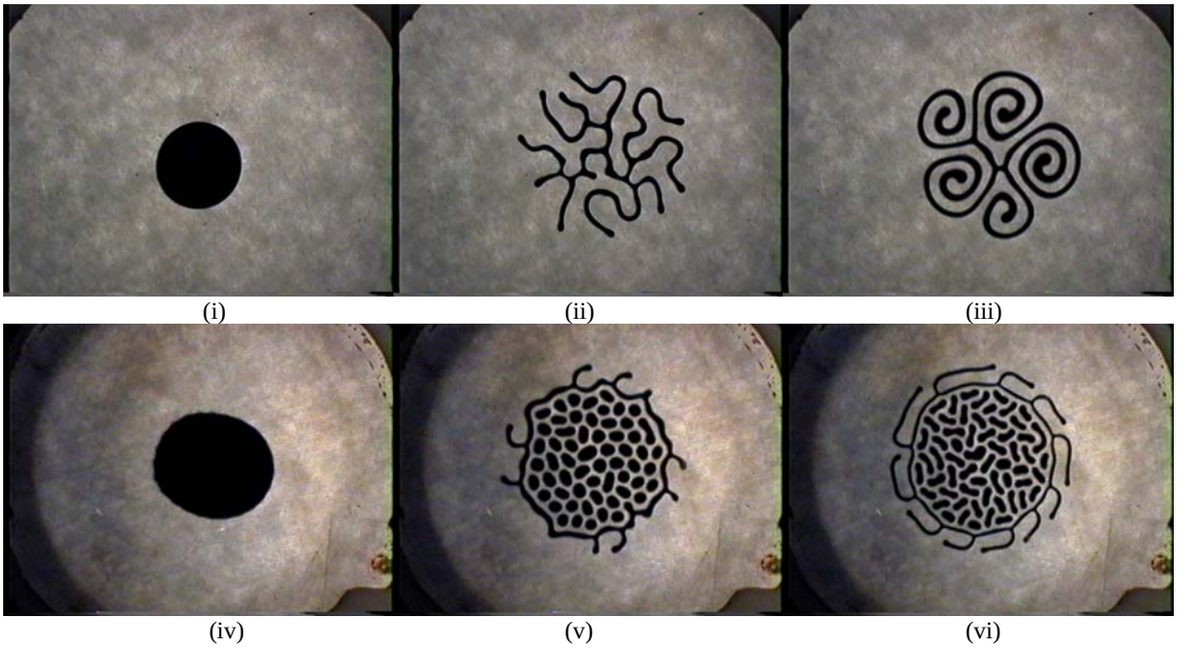


Figure 1 – Spiral pattern formed when a 100 microliter ferrofluid droplet in a 1.1 mm gap Hele-Shaw cell (i) is stressed by a 155 Gauss uniform DC axial magnetic field to form the labyrinth in (ii) and then an in-plane uniform clockwise rotating magnetic field of 47.5 Gauss rms at 20 Hz is applied to create a spiral flow (iii). A larger 200 microliter drop (iv) stressed by a 40 Gauss rms, 25 Hz uniform rotating field, is held together without a labyrinth until the uniform DC axial magnetic field is about 186 Gauss, subsequently forming the discrete droplet structure in (v). As the DC field is further increased to 228 Gauss the drops and "surface hair" further deform.

The representative images in Figure 1 describe two experiments with a 1.1 mm Hele-Shaw cell gap. The first experiment, images (i)-(iii), uses 100 microliters of ferrofluid and the DC axial field is first increased to 155 Gauss and then the clockwise rotating field at 47.5 Gauss rms, 20 Hz is turned on. Figure (i) shows the circular ferrofluid drop before the magnetic field is applied, while figure (ii) shows the labyrinth pattern formed by the ferrofluid after only the DC axial field has been applied. Then the clockwise rotating field is applied and the spikes begin to curl in on themselves, eventually forming the smooth spiral pattern shown in figure (iii). The smooth spirals form from viscous shear as the clockwise rotating magnetic field causes clockwise flow on the outside ferrofluid surfaces which return on the inside surfaces.

The second experiment, with 200 micro-liters of ferrofluid, is seen in figures (iv)-(vi). The test cell is first placed in the clockwise rotating field which causes a clockwise flow that holds the fluid drop together without spikes. Then a DC axial field is gradually applied. This results in the ferrofluid drop appearing to expand before the phase-like transition to figure (v) at a critical DC magnetic field strength around 186 Gauss. Careful observations show that the pattern of

figure (v) forms at ~170 Gauss DC field under a thin ferrofluid coating on the top glass plate, which then abruptly peels away at slightly increased DC axial magnetic field. In figure (vi) the magnetic field is increased to 228 Gauss.

PRELIMINARY MODEL

A minimum free-energy analysis, like that used in modeling ferrofluid labyrinth phenomena [2], is performed to model the phase transformation from a single large drop to many discrete small drops. The model assumes that the initial large cylindrical drop has a radius *R* and height *t*, equal to the Hele-Shaw gap thickness, which at a critical DC axial magnetic field strength spontaneously form *N* smaller droplets of radius *r* and height *t*, where to conserve mass, $R = \sqrt{N}r$. The uniform applied DC axial field $\bar{H}_0$ magnetizes the ferrofluid drop and droplets to magnetization $\bar{M}$ generating a demagnetizing field $\bar{H}_d = -\bar{M}D$ where

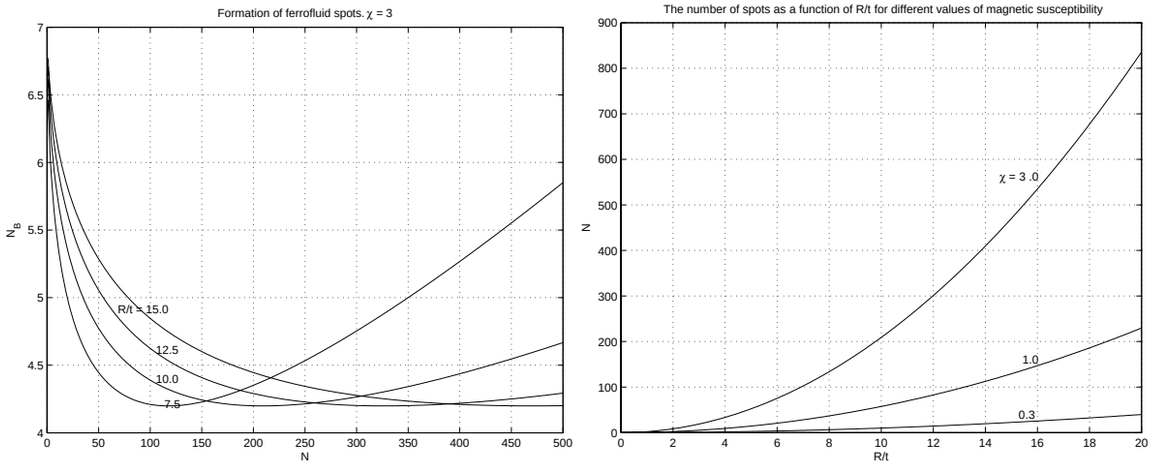
$$D \approx 1 - \frac{1}{\sqrt{\left(\frac{2r}{t}\right)^2 + 1}} = 1 - \frac{1}{\sqrt{\frac{1}{N}\left(\frac{2R}{t}\right)^2 + 1}} \tag{1}$$

is the approximate demagnetization coefficient for each droplet of radius *r*. The magnetization for linearly magnetizable ferrofluid with magnetic susceptibility χ is then

$$\bar{M} = \chi\bar{H} = \chi\bar{H}_0/(1+\chi D)\,. \tag{2}$$

The energy in the *N* droplets, each with surface tension γ, is assumed to be due to interfacial surface energy, $U_S = N2\pi rt\gamma = 2\pi Rt\gamma\sqrt{N}$ and to magnetization energy [3]

$$U_M = -\frac{\mu_0}{2}\int \bar{M}\bullet\bar{H}_0 dV = -\frac{\mu_0}{2}\frac{N\pi r^2 t\chi H_0^2}{1+\chi D} = -\frac{\mu_0}{2}\frac{\pi R^2 t\chi H_0^2}{1+\chi D}\,. \tag{3}$$



(a) (b)

Figure 2 – Calculated minimum energy condition of (a) magnetic Bond number $N_B = \mu_0 H_0^2 t/(2\gamma)$ versus number of phase transformation droplets *N* for various values of *R/t* with magnetic susceptibility $\chi = 3$; (b) The number of droplets *N* at minimum N_B as a function of *R/t* for various values of χ. For our experiments with a 200 microliter drop, shown in Fig. 1 (iv)-(vi), *R/t*≈7.

Acknowledgment: This research is supported by National Science Foundation Grant# CTS-0084070. We gratefully thank Ferrofluidics Corp., now FerroTec Corp., for contributing the ferrofluid used in these experiments.

References

[1] Lorenz C., Zahn M.: Hele-Shaw Ferrohydrodynamics for Rotating and dc Axial Magnetic Fields, Phys. Fluids 2003 Gallery of Fluid Motion, 15 (9), S4, 2003; www.aps.org/units/dfd/index.html
[2] Rosensweig R.E., Zahn M., Shumovich, R.: Labyrinthine Instability in Magnetic and Dielectric Fluids. *J. Magnetism and Magnetic Mtl*. **39**: 127-132, 1983.
[3] Paris D.T., Hurd F.K.: Basic Electromagnetic Theory. McGraw Hill, NY 1969, p.286.

SPRAY IMPACT ON SOLID WALLS OF NON-NEWTONIAN FLUIDS, INCLUDING YIELD STRESS AND THIXOTROPIC BEHAVIOR

Daniel A. Weiss[*], Annett Reinl[*], David M. Binding[**]
[*]*DaimlerChrysler, Research and Technology, P.O. Box 23 60, D-89013 Ulm, Germany*
[**]*Dept of Mathematics, University of Wales Aberystwyth, Ceredigion SY23 3BZ, UK*

Summary In a variety of applications the interactions of sprays with solid walls play an important role. The fluid may be pseudoplastic, possessing a non-vanishing yield stress, and thixotropic, with a viscosity showing a time-dependency, in addition to the shear-rate-dependency. Spray impact of thixotropic fluids with yield stress onto a dry smooth solid wall is investigated numerically. The rheological behavior of the fluids is modelled by a stationary flow curve, completed by a Quaak model for the time-dependent change of the viscosity. A commercially available code, based on the volume-of-fluid method is used. The code has been verified for fluids with yield stress and thixotropy, respectively, in viscosimetric flows and in impact processes of single drops. Calculations are performed for thixotropic fluids with yield stress of practical relevance. The results are compared with cases without thixotropy. They provide initial conditions for the subsequent evolution of the coherent fluid film.

INTRODUCTION

In a variety of applications the interactions of liquid drops and sprays with solid walls play an important role. Some of the applied fluids possess a non-zero yield stress; this behavior, characteristic for a pseudoplastic fluid, may be crucial for the impact and deposition process. In some cases the fluid viscosity shows a time-dependency in addition to the shear-rate-dependency, in such a case the fluid manifests thixotropic behavior.
The question of whether thixotropic effects have to be taken into account or not depends essentially on the ratio between the physical time scale considered, and the time scale needed by the fluid for viscosity changes to occur. If this ratio is small, thixotropic effects will not be of importance; if the ratio is large, they are expected to have a significant influence. [1] In the context of spray-wall-interactions for practically relevant fluids, this ratio is frequently small for the spray-impact itself, but becomes large for the subsequent evolution of the coherent fluid film. Thus, in view of studies of the latter, thixotropic effects have to be taken into account already for the former, since this will provide initial conditions for the subsequent evolution of the coherent fluid film. In this paper we present numerical results on the impact of sprays onto dry smooth solid walls, where the fluid concerned shows pseudoplastic and thixotropic effects.

MODELING

The fluid is modelled in its flow behavior by the flow curve for stationary shear states, which is completed by a model to account for thixotropy.
The flow curve is described by a sum of two parts; one containing the yield-stress effect and the other represented by a Cross type model with a finite dynamic viscosity η_0 at low shear rates ($\eta_0 > \eta_\infty$ or even $\eta_0 >> \eta_\infty$):

$$\tau = \tau_0 + \dot{\gamma}\eta(\dot{\gamma}), \qquad \eta(\dot{\gamma}) = \eta_\infty + \frac{\eta_0 - \eta_\infty}{1 + k\,\dot{\gamma}^{1-n}} \tag{1}$$

Thixotropic effects are described here by a Quaak model, i. e. by a transport equation which describes the evolution of the apparent (total) viscosity $\eta_{ap} = \tau/\dot{\gamma}$:

$$\frac{d\,\eta_{ap}}{dt} = \frac{1}{t_R}\left(\eta_{dyn_{equ}} - \eta_{ap}\right) \text{ for } \eta_{dyn_{equ}} \geq \eta_{ap} \tag{2}$$

where t is time, t_R denotes a relaxation time, $\eta_{dyn_{equ}}$ is the equilibrium viscosity to the instantaneous shear rate $\dot{\gamma}$, according to the stationary flow curve. A similar equation as (2) holds for $\eta_{dyn_{equ}} \leq \eta_{ap}$, but with a retardation time t_r instead of t_R; $t_r << t_R$ for the fluid considered here.
Wetting effects of the solid wall are expressed in terms of the static contact angle θ_{stat}.

NUMERICAL METHOD AND VERIFICATION OF THE NUMERICAL IMPLEMENTATION

To perform the simulations a commercially available code, Flow3D®, based on the volume-of-fluid method, has been used. The yield-stress and the shear-thinning behavior are implemented in terms of the flow curve, by expressing $\tau/\dot{\gamma}$ as a function of $\dot{\gamma}$. The flow curve is fitted to data from viscosimetry and extrapolated to very high as well as very low shear rates $\dot{\gamma}$. The time dependant thixotropic effects are implemented by equation (2) and its corresponding equation for retardation processes. Moreover a vanishing strain rate $\dot{\gamma}$ has to be avoided in numerical calculations; this is done

by prescribing a minimal value $\dot{\gamma}_c$ for the strain rate, which has to be small as compared to typical strain rates related to the spray impact process.
Capillary and wetting effects are taken into account by the static contact angle. Periodic boundary conditions are assumed in directions parallel to the wall.
The main verification of the numerical code has been carried out elsewhere [1]. To verify the yield-stress model, single drop impact has been studied for a pseudoplastic fluid without thixotropy, with a reasonable agreement between experiments and numerical calculations [2]. The verification of thixotropy effects occurs by studying rheometric flows.
The implementation of the spray data has been made by including subroutines, that were developed earlier, into the commercial code [1]. These subroutines make use of spray data obtained from experiments.

SPRAY IMPACT OF THIXOTROPIC FLUIDS EXHIBITING A YIELD-STRESS

A typical result of a spray impact calculation is shown in figure 1. The fluid is characterized by a yield stress $\tau_0 = 8.0$ Pa. Its relaxation and retardation times are 8.5 s and 0.1 ms, respectively. Impinging drops are assumed to have an initial viscosity of 0.12 Pa s, which corresponds, in the stationary case, to a shear rate of 1000 s^{-1}. Their velocities and diameters are taken from spectra determined experimentally.
It is found that impinging drops spread along the solid wall, finally they form a connected fluid volume covering the wall. This configuration provides the initial condition for the subsequent film evolution.
On impact the drops are sheared and thus liquefied, this decrease in viscosity can clearly be recognized in figure 1. Liquefaction occurs on time scale t_r and down to a viscosity $\eta_{liq} \geq \eta_\infty$ at the most. As long as the strain rates within the individual drop impact processes are sufficient to achieve liquefaction down to essentially η_∞, the arising connected volume has roughly homogeneous viscosity, it basically relaxes as a whole on the time scale t_R. Otherwise, significant local differences in viscosity may remain, and the connected volume relaxes in a more complicated way.
In practice, thermodynamic processes like phase transitions or chemical reactions may occur on these time scales and interfere with the relaxation process.

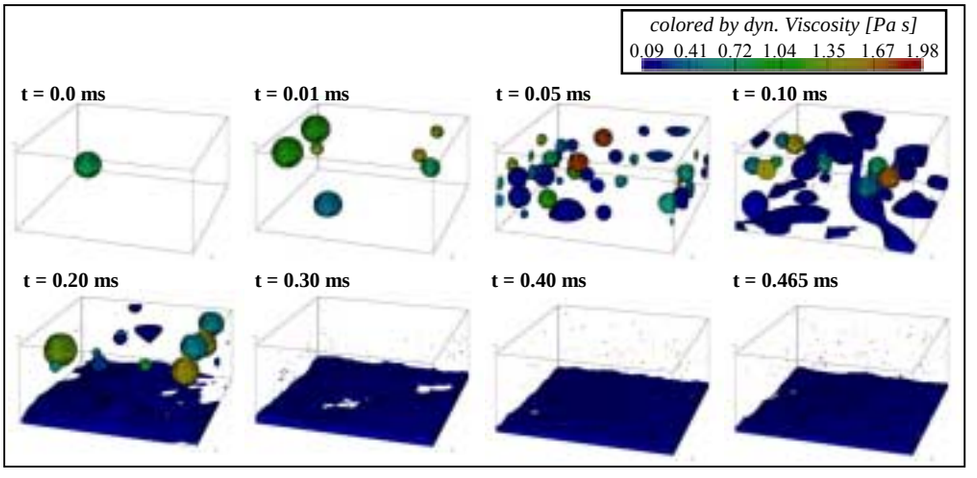


Figure 1. Spray impact and subsequent film evolution in the case of a pre-sheared thixotropic spray with a yield-stress

CONCLUSION

Spray impact for fluids with yield stress and thixotropy has been calculated numerically. It has been found that the impinging drops spread on the wall under strong shear and form a connected volume. The volume has significant local differences in viscosity or relaxes towards a more viscous state, according to whether the strain rates in the individual drop impact processes are sufficient to achieve η_∞ or not. It is therefore concluded that in practice it is crucial to know accurately the flow behavior at very high strain rates.

References

[1] Böhm C A, PhD Dissertation, Technical University of Darmstadt (D), 2002.
[2] Böhm C, Reinl A, Weiss D A, Nigen S & Binding D M, *Eurheo - 6th ECR,* Erlangen (Germany), 2002.

XXI ICTAM, 15-21 August 2004, Warsaw, Poland

NANOWIRES ASSEMBLY USING MICROFLUIDIC: AN EXPERIMENTAL INVESTIGATION

Wael Salalha, Eyal Zussman
Department of Mechanical Engineering, Technion-Israel Institute of Technology, Haifa 32000, Israel

Summary Nanowires are common building blocks for the bottom-up assembly of electronic and photonic devices. A significant challenge is to introduce the individual building block in an oriented assembly in order to express its unique anisotropic properties or to create a nano-device. In this work we focus on fluidic alignment of nanowires suspended in an incompressible liquid. The approach is based on manipulation of a micro droplet with suspended nanowires in a confined shape, such as a micro-channel. These nanowires are eventually deposited on patterned surfaces forming parallel arrays. We report on alignment results of nanowires using Poiseuille flow and also report on the motion of the nanowires, in the vicinity of the dynamic contact lines, which follow non-closed spirally shaped streamlines and in certain case, the streamlines of sink- or source-like flows.

Nanowires (NWs) and carbon nanotubes are common building blocks for the bottom-up assembly of electronic and photonic devices. A significant challenge is to introduce the individual building block in an oriented assembly in order to express its unique anisotropic properties or to create a nano-device. Electric[1] and magnetic[2] fields have been used to manipulate dielectric nanowires that are suspended in liquid media. These methods require extensive lithography to fabricate the micro-electrodes. Fluidics-based methods[3] for aligning NWs have also been reported but mainly for assembly of individual or small numbers of devices.

Here we report on an experimental investigation of a fluidic-based approach. The approach is based on a manipulation of a micro droplet with suspended NWs in a confined shape, such as a micro-channel. Controlling the capillary flow inside the micro-channel results in well oriented NWs. These NWs are eventually deposited on patterned surfaces forming parallel arrays of controllable dimension that facilitate mass assembly of nanostructures.

Our assembly approach uses the flow inside micro-channel that is induced by thermocapillary motion. Since the surface tension of a liquid usually decreases with the rise of its temperature, a liquid index (droplet) can flow away from the heated end of a capillary channel. The motion of the droplet results in transferring, extension and compression flow leading to oriented NWs. In the system investigated, the micro-channel cross-section is w x h $(w>>h)$ (see Fig. 1a). A thermocapillary motion is achieved by creating a temperature gradient T1-T2, which results in pressure difference P1-P2. The wetting liquid was Hexadecane:Octadecane 1:1 solution with 1% of Mercaptoethanol thiol to avoid aggregation of the NWs. The NWs used were made of gold and were produced through an electrodeposition process using templates with a typical diameter of 200 nm and a length of 5um. The NWs (0.2% wt.) were dispersed in the above solution forming a dilute suspension. The micro-channel was made of glass and has a typical rectangular cross-section dimensions of $w \times h = 400 \times 40 \mu m$. The droplet was heated using *5W* thermal head. The motion of the NWs was observed using optical microscope (X1000) and a video camera (50fps).

In Fig. 2 (a) we see aligned NWs by means of a steady Poiseuille flow created at the droplet far from the menisci. Aligned NWs that were deposited after the movement of the droplet can be seen in Fig. 2 (b). In Fig. 3 we can see NWs behind the moving contact line (air-liquid-solid) of the front meniscus. The NWs are moving along non-closed spirally shaped streamlines. Most likely, we observed combination of the rotation generated by the corner eddies[4] and the corner flow (see Fig. 1a). Apparently, this complicated behavior is caused by the three-dimensional nature of the flow; however the type of imaging used provides us only with two dimensional pictures. It is also possible that the inertia of the nanowires, which in some cases may aggregate, is not neglected; hence the observed spiral motion is a result of bouncing between the corner-like flow streamlines. In Fig. 4 we can see a case where a pre-wetting condition exists formed by a capillary flow in the rectangular shaped channel. This situation especially occurs at the corner of the micro channel (see Fig. 1b). We can see that the NWs are moving along sink-like streamlines. However, this depends on the corner location; namely in the front or the rear meniscus we can observe sink- or source-like flow respectively.

In summary, we observed that the majority of the NWs were aligned with the flow direction using a Poiseuille flow. However, due to the complicated shape of the streamlines in the vicinity of the dynamic contact line, the alignment of numerous NWs is affected. Therefore, it is of great importance to analyze and control these types of flow close to the moving contact line.

References

[1] Smith P.A., Nordquist C.D., Jackson T.N., Mayer T.S., Martin B.R., Mbindyo J., Mallouk T.E..: Electric-Field Assisted Assembly and Alignment of Metallic Nanowires, *Appl. Phys. Lett.*, **77**:1399-1401, 2000.

[2] Tanase M., Bauer L. A., Hultgren A., Silevitch D.M., Sun L., Reich D.H., Searson P.C., and Meyer G.J.: Magnetic Alignment of Florescent Nanowires, *Nano Letters*, **1**:155-158, 2001.

[3] Huang Y., Duan X., Wei Q., and Lieber C.M.: Directed Assembly of One-Dimensional Nanostructures into Functional Networks, *Science*, **291**: 630-633, 2001.

[4] Moffatt H. K.: Viscous and Resistive Eddies Near a Sharp Corner, *J. Fluid Mech.*, **18**:1-18, 1964.

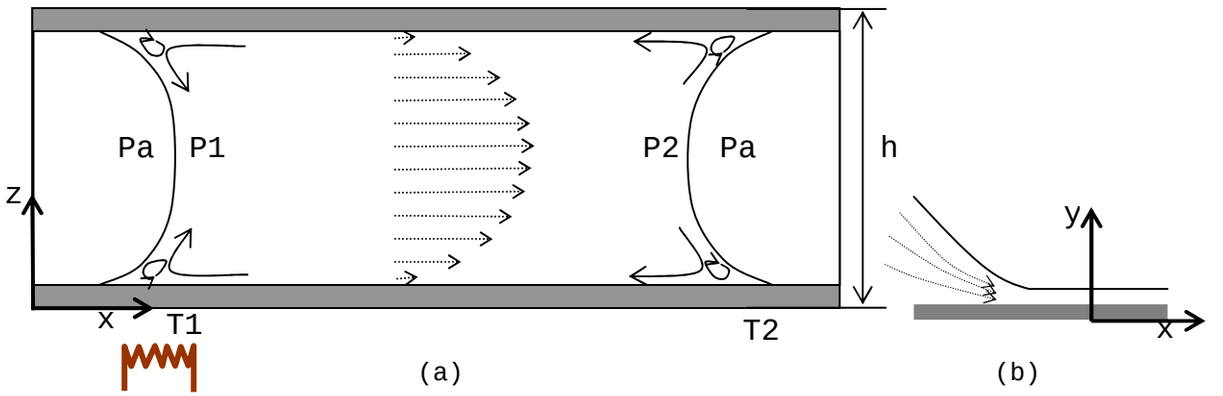


Figure 1: (a) A Schematic illustration of the studied system of a liquid drop moving in micro-channel with a rectangular cross section. The flow inside the micro-channel is induced by thermocapillary motion. (b) A sink-like flow illustration at the corner of the micro-channel as a result of a pre-wetting condition.

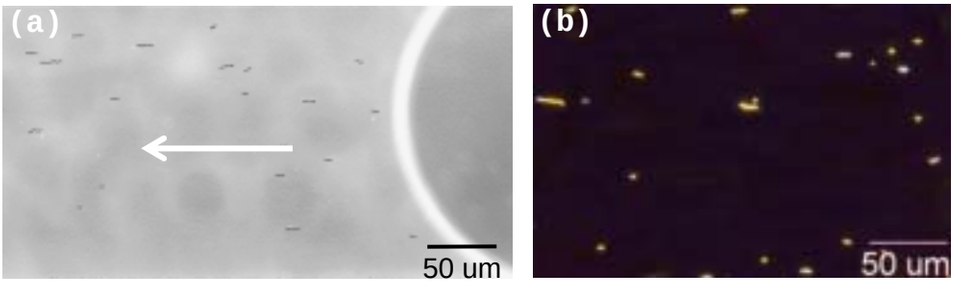


Figure 2: (a) Optical picture of nanowires aligned in a droplet. (b) Deposited NWs after the movement of the droplet.

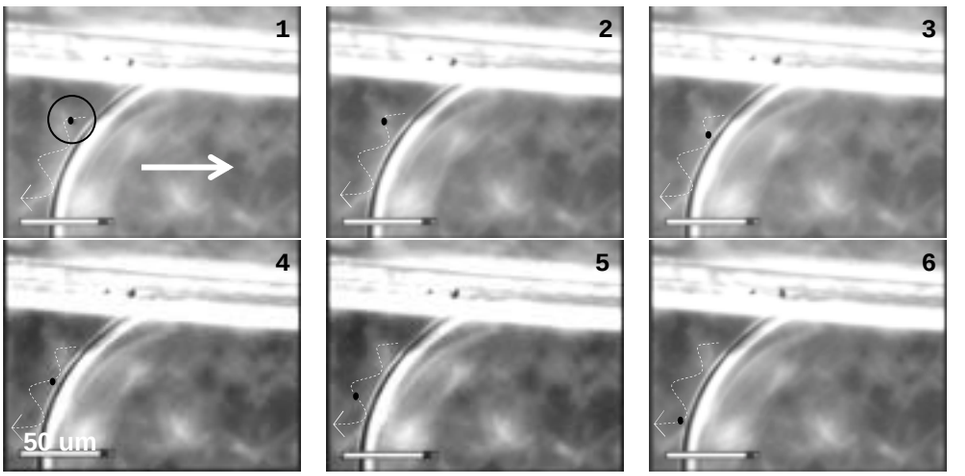


Figure 3: A series of pictures taken in the vicinity of the dynamic contact line during the droplet movement. The center of gravity of a nanowire (marked with a black dot) is moving along a non-closed spirally shaped streamline.

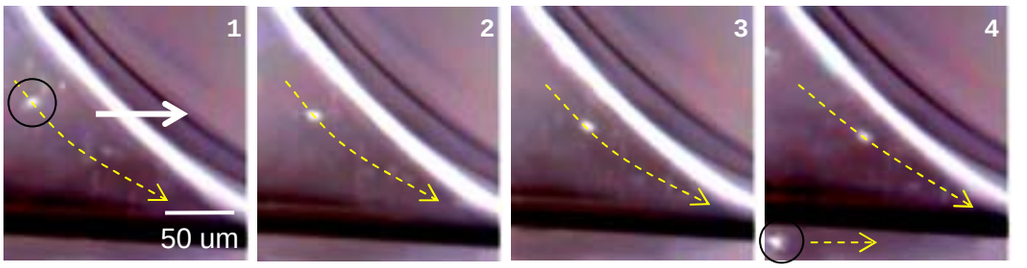


Figure 4: A series of pictures taken in the vicinity of the dynamic contact line during the droplet movement where a pre-wetting condition of the channel exists. The centers of gravity of the nanowires (marked with a white dot) are moving along sink-like flow streamlines.

PARTICLE MANIPULATION IN MICROFLUIDICS: THE ROLE OF DIELECTROPHORESIS, ELECTROHYDRODYNAMICS AND AC ELECTROKINETICS

Antonio Castellanos*, Antonio Ramos*, Antonio González*,**, Nicolas G. Green***, Hywel Morgan***

**Dpto. Electrónica y Electromagnetismo, Facultad de Física, Universidad de Sevilla, Reina Mercedes s/n, 41012 Sevilla, Spain.*

***Dpto. de Física Aplicada III, E.S.I. Universidad de Sevilla, Camino de los Descubrimientos s/n 41092 Sevilla, Spain*

****3 Bioelectronics Research Centre, Dept. Electronics and Electrical Engineering, University of Glasgow, Oakfield Avenue, Glasgow G12 8LT, UK.*

INTRODUCTION

The application of a.c. electric fields to control and manipulate isolated particles in suspension using microelectrode structures is a well-established technique. In particular, the dielectrophoretic manipulation of sub-micron bioparticles such as viruses, cells and DNA is now possible. As the size of the particle is reduced, so the effects of Brownian motion become greater. Therefore, to enable the dielectrophoretic manipulation of sub-micron particles using realistic voltages, the characteristic dimensions of the system must be reduced, to increase the electric field. However, a high strength electric field also produces a force on the suspending electrolyte, setting it into motion. Indeed, this motion may be a far greater limiting factor than Brownian motion.

Owing to the intensity of the electric fields required to move sub-micrometre particles, Joule heating can be a problem, often giving rise to electrical forces induced by the variation in the conductivity and permittivity of the suspending medium (electrothermal forces) [1]–[3]. In certain circumstances Joule heating may be great enough to cause buoyancy forces. In addition to Joule heating, the geometry of the electrodes used to generate dielectrophoretic forces produces a non-zero tangential electric field at the electrode-electrolyte double layer. This induces steady motion of the liquid, a flow termed ac electroosmosis, because of its similarity to electroosmosis in a dc field [5]-[7]. It should be emphasised that the ac electroosmotic flow observed over microelectrodes differs from ac electroosmosis observed in capillaries. In the later case the electric field is time-varying, but the diffuse double layer charge is fixed and the fluid motion is oscillatory, whereas in the former case both the electric field and double layer charge are time-varying and give rise to a steady fluid motion.

Based on these mechanisms, the magnitude and direction of the surface and volume forces acting on the liquid can be predicted analytically, or alternatively using numerical simulations. This means that it should be possible to design and develop microelectrode structures that can translate experimental and theoretical understanding into a given specification. However, the precise design of a complicated microelectrode structure would require extensive numerical calculations. This requires to develop a general framework which outlines the basic constraints of a system, thus reducing the need for intensive computation. A first step in this process is prior knowledge of how the forces on the particle scale with the size of the system, the shape of the electrodes, the particle diameter, the magnitude and frequency of the applied ac electric field, and the conductivity of the suspending solution [8].

The aim of this presentation is to highlight these scaling laws for the control of particles. First, we present an analysis of the motion of particles caused by gravity, dielectrophoresis (DEP) and Brownian motion only. Second, the mechanical, electrical and thermal equations that govern liquid motion in these microelectrodes structures are formulated. Thirdly, the volume and surface forces acting on the system are given, emphasizing how these forces scale with system parameters. Finally, the relative importance of the drag force, (which comes from electrohydrodynamic flow) is discussed and compared with Brownian motion, DEP and gravitational forces.

RESULTS

The measurement and analysis of flow has been performed using a simple electrode design consisting of two coplanar rectangular electrodes fabricated on a glass substrate. The electrodes are 2mm long and 500 μm wide, with parallel edges separated by a 25 μm gap. Because the gap is small compared to the length and width of the electrodes the system can be considered to be two-dimensional so that the analysis is restricted to the 2D cross-section.

For the following results we use typical physical quantities for aqueous saline solutions at ambient laboratory temperature (25 K). For particles we use sizes ranging from 0.1 μm up to 10 μm. Typical examples are viruses (0.01-0.1 μm), bacteria (0.5-5 μm), or cells (5-15 μm). These bioparticles are usually suspended in an aqueous saline solution with a conductivity that ranges between 10^{-4} and 1 S/m. Typical system lengths of the microelectrodes (interelectrode gaps) used in the dielectrophoretic manipulation of bioparticles vary from 1 to 500 μm. The signals applied to these electrodes can be up to 20 Volts giving rise to electric fields that can be as high as 2×10^7 V/m. The applied signals have frequencies in the range 10^2 to 10^9 Hz.

Figures 1 and 2 show the different domains of influence of the flows for the case of a particle of radius $a = 0.25\mu$m

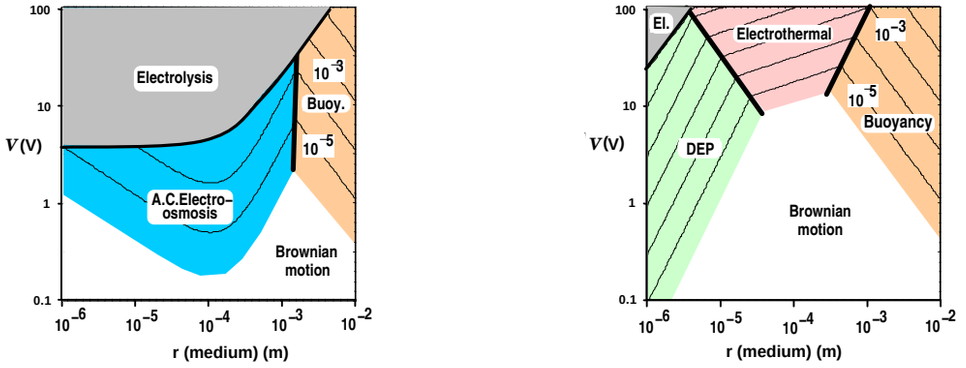


Figure 1. Particle velocity maps in the plane V versus r for a particle with radius $a = 0.25\mu$m in medium with $\sigma = 10^{-3}$S/m: (left) $f = 10^2$ Hz; (right) $f = 10^5$ Hz.

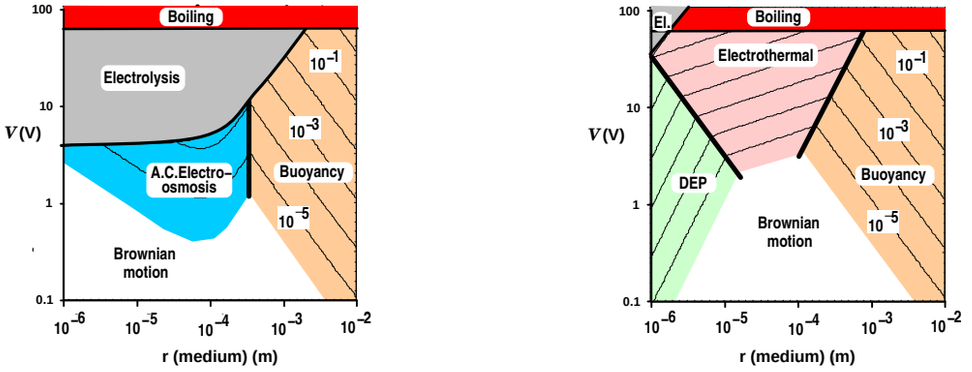


Figure 2. Particle velocity maps in the plane V versus r for a particle with radius $a = 0.25\mu$m in medium with $\sigma = 10^{-1}$S/m: (left) $f = 10^4$ Hz; (right) $f = 10^7$ Hz.

and density $\rho_p = 2 \times 10^3$ Kg/m^3. We assume that 2 volts drop across the double layer is enough to produce electrolysis. Another limit on permissible voltages is given by boiling. The level curves represent the magnitude of the particle velocity (velocities below 0.01 μm/s are considered as dominated by Brownian motion and are represented by a white region in the diagrams). The results indicate that ac electroosmosis dominates fluid motion at low frequencies and small system sizes, electrothermal flow dominates at high frequencies and voltages, and buoyancy at typical system sizes of the order or greater than 1 mm. DEP governs the motion of sub-micrometre particles for small systems and at high frequencies, otherwise, the particle motion is due to fluid drag.

Extending the general results obtained for the 2-D planar electrode to other geometries must be done with care, since in general several different length scales act at the same time. This extension will be illustrated for two cases of practical importance: the hyperbolic polynomial electrode and the castellated electrode.

References

[1] T. Muller, A. Gerardino, T. Schnelle, S. G. Shirley, F. Bordoni, G. DeGasperis, R. Leoni, and G. Fuhr, Trapping of micrometre and sub-micrometre particles by high-frequency electric fields and hydrodynamic forces, J. Phys. D: Appl. Phys., 29, 340-349, 1996.

[2] A. Ramos, H. Morgan, N. G. Green, and A. Castellanos. AC Electrokinetics: a review of forces in microelectrode structures. J. Phys. D: Appl. Phys. 31, 2338-2353, 1998.

[3] G. Fuhr, R. Hagedorn, T. Müller, W. Benecke and B. Wagner, Microfabricated electrohydrodynamic (EHD) pumps for liquids of higher conductivity. J. Microelectro-mech. Systems, 1, 141-146, 1992.

[4] A. Ramos, H. Morgan, N.G. Green and A. Castellanos, AC Electric-field induced fluid flow in microelectrodes J. Colloid and Interface Science, 217 420-422, 1999.

[5] N.G. Green, A. Ramos, A. Gonzalez, H. Morgan and A. Castellanos, Fluid flow induced by non-uniform AC electric fields in electrolytes on microelectrodes I: experimental measurements, Phys. Rev. E, 61, 4011-4018, 2000.

[6] A. González, A. Ramos, NG. Green, A. Castellanos and H. Morgan, Fluid flow induced by non-uniform ac electric fields in electrolytes on microelectrodes II: A linear double-layer analysis, Phys. Rev. E, 61, 4019-4028, 2000.

[7] N.G. Green, A. Ramos, A. González, H. Morgan and A. Castellanos, Fluid flow induced by non-uniform ac electric fields in electrolytes on microelectrodes III: Observation of streamlines and numerical simulation, Phys. Rev. E, 66, 026305, 2002.

[8] A. Castellanos, A. Ramos, A. González, N.G. Green, and H. Morgan. Electrohydrodynamics and dielectrophoresis in microsytems: Scaling laws, J. Phys. D: Appl. Phys. 36, 2584–2597, 2003

Non-Newtonian effects of ink-jet printed droplets

P.C. Duineveld[*], J.F. Dijksman[*], H. Huang[**]

[*]*Philps Research, Eindhoven, The Netherlands,*
[**]*York University, Toronto, Canada*

Summary The influence of non-Newtonian effects on the droplet formation in an ink-jet printer has been investigated both experimentally and theoretically. For the experiments, Newtonian liquids and solutions of flexible and stiff polymers were used. The non-Newtonian effects were modelled by only using the elongational viscosity and not the stress history effect. It is shown that this in itself is not sufficient; the stress history effects can not be neglected.

The viscosity of an ink is an important parameter for the droplet formation in an ink-jet head. Standard in the ink-jet printing world is to measure the shear viscosity of the liquid. Most common inks in graphical applications are Newtonian liquids and therefore the shear viscosity is a suitable characterization technique.

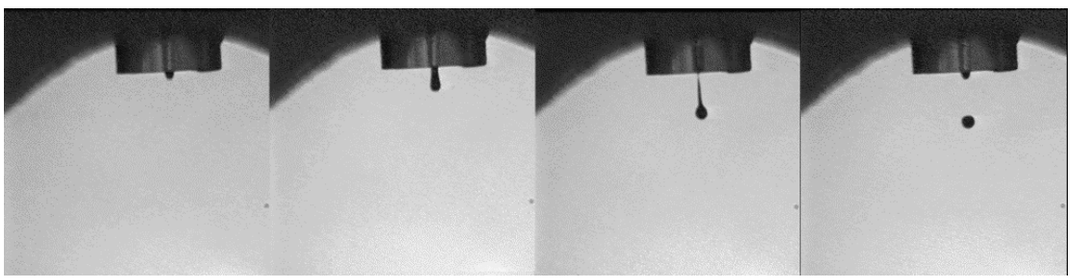
Recently, several applications are appearing where small concentrations of high molecular weight, functional, polymers in a suitable solvent are deposited by means of an ink-jet printer. Examples are light-emitting polymers for display applications, polymers for transistors and biological applications. The drop formation of these solutions is considerably different from a pure Newtonian liquid. There is more energy needed to eject the droplet from the nozzle and droplets are formed with a filament connecting the nozzle and the main droplet. When this filament is too long it can break up in satellite droplets and also the directional accuracy of the main droplet can decrease, which is problematic in applications. An example of the different stages of droplet formation of a Newtonian liquid and a non-Newtonian liquid are shown in figure 1.

When these solutions are measured in a shear rheometer the viscosity is constant as a function of the shear rate, and in the proper regime for ink-jet printing, i.e. 3 to 20 cP. The droplet formation, however, shows the strong filament formation, which is due to non-Newtonian effects. There are two effects that may contribute to this non-Newtonian behaviour: stress history effects and an increase of the elongational viscosity. There are no suitable rheometers that can measure in the regime of ink-jet printing, which has a very large elongational rate of order 10^5 s^{-1}. Therefore we have studied if it is possible to use the droplet formation in an ink-jet printer as a simple method to obtain information on the non-Newtonian effects of the solution.

The functional polymers often are quite polydisperse, therefore experiments were performed with Newtonian liquids and model polymer solutions, with both very flexible polymers (PEO, polyethylene oxide) and stiff polymers (Xanthan Gum). The molecular weight of the PEO was 10^5 and 3.10^5 gr/mol. The length and the radius of the filament was measured during the droplet formation for initial droplet velocities varying between 5 and 20 m/s.

We have set-up a very simple model for the non-Newtonian effects. Only the elongational viscosity was taken into account and stress history effects were neglected. With this simple approach we have investigated whether the increase in elongational viscosity is sufficient for the long filament formation. The elongational viscosity of the flexible PEO was modelled with a FENE-P model, while for the rigid polymers the rigid rod theory of Batchelor was used. The contribution of the elongational viscosity is incorporated in a model, together with surface tension effects, that describes the filament formation and droplet motion.

From our calculations and experiments we can conclude that the elongational viscosity is not sufficient to describe the long filament formation. Especially in the later stages of thinning of the filament it can be shown that the contribution of the elongational viscosity is negligible compared to the surface tension. Yet the filament does not break-up which we attribute to the neglected stress history effects.



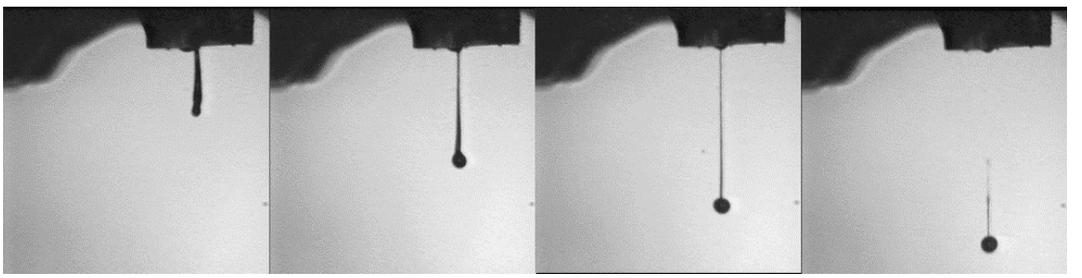


Figure 1: Stroboscopic images of droplets, produced by ink-jet printing. The upper picture series shows a Newtonian fluid. The lower picture series shows the effect of an addition of a small amount of a high molecular weight polymer. Note the formation of a filament connecting drop and nozzle. The diameter in the lower right image is 70 μm. Typical time scale for the events is less than 100 μs.

CONDITIONS FOR CREATING THIN LIQUID LAYERS AT THE CONTACT SURFACE OF TWO OTHER LIQUIDS

Agnieszka Słowicka*, Zbigniew A. Walenta*

** Institute of Fundamental Technological Research,*
Polish Academy of Sciences,
Świętokrzyska 21, 00-049 Warszawa, Poland.

Summary: The design of new technologies, for manufacturing the nano – structured materials is one of the important tasks of the contemporary materials science. The use of emulsion droplets as templates for producing nanostructures out of solid particles, suspended in the liquid phase is already under development. In the present work we investigate the possibility of using a liquid film instead of solid particles. To simulate the behaviour of the liquids we apply the Molecular Dynamics simulation technique. Since the behaviour of the liquids depends mainly on the interaction potentials of the molecules, we look for combination of the interaction potentials, which might produce the required liquid film at the surfaces of the emulsion droplets.

INTRODUCTION

The design of new technologies, making it possible to manufacture the nano – structured materials is one of the most important tasks of the contemporary materials science. The technologies, utilizing the emulsion droplets as templates for producing nanostructures out of solid particles, suspended in the liquid phase, seem very promising; work on developing such technologies is progressing fast [1]. It seems however conceivable, that even smaller structures could be obtained, if instead of solid particles a liquid film was utilized.
In the present research we investigate the conditions necessary for producing a liquid film at the interface of two nonmixing liquids.

SIMULATION DETAILS

To simulate the behaviour of the three liquids we apply the Molecular Dynamics simulation technique. For the detailed calculations we use the program "MOLDY" [2].
Since, at the molecular level, the behaviour of the liquids depends, in the first place, on the interaction potentials between the molecules [3], we look for the combination of the interaction potentials, which might produce the required liquid film at the surfaces of the emulsion droplets. We perform a number of simulation runs, assuming different interaction potentials. The liquids used for simulations are actually model liquids with desired properties, not the real ones. Still, the information, relevant for the technology, is obtained in this way. Having the information on the required interaction potentials one can look for the real liquids, fulfilling these requirements.

PRELIMINARY RESULTS

The aim of the preliminary calculations was to simulate formation of the liquid droplet in a vacuum and in another, nonmixing liquid. We placed a number of liquid molecules in a recangular lattice and allowed them to move freely with velocities, corresponding to a prescribed temperature.
At the beginning we tried, for simplicity, to use the Simplified Water Model (SWM) – a liquid of spherically symmetric molecules, interacting with each other only through the Lennard – Jones potential, the same as that for water. Such molecules, placed in a vacuum, spread uniformly in the whole simulation domain. To form a well – defined droplet it was necessary to use more realistic model of the water molecule (TIPS2, [4]), taking into account the electrostatic dipole interactions. Such interactions, on top of the Lennard – Jones potential, are the most important factor influencing the behaviour of water.
The initial configuration of the water molecules, taken for simulation, was actually very far from spherical. This produced oscillations of the shape of the droplet, visible for certain amount of time. The frequency of these oscillations was comparable to the mean molecular speed divided by the diameter of the droplet.
To simulate the formation of a liquid droplet, immersed in another, nonmixing liquid, we first tried the SWM molecules, however without electrostatic dipole interactions certain amount of mixing was always present. To produce a liquid droplet successfully we had to immerse the SWM liquid, (which now could represent oil) in water described by the TIPS2 model.
The following pictures present some of the obtained results.

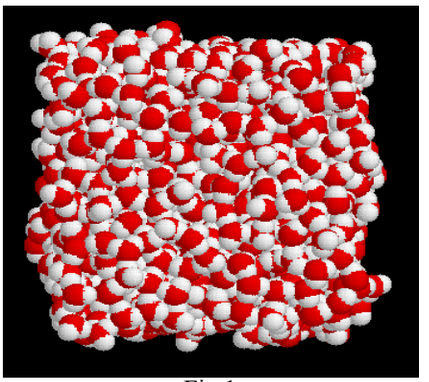


Fig.1.

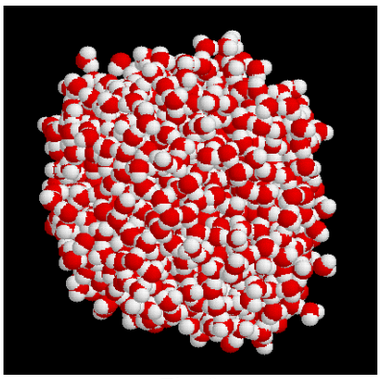


Fig. 2.

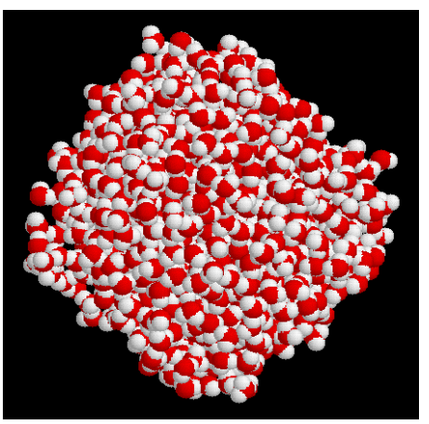


Fig. 3.

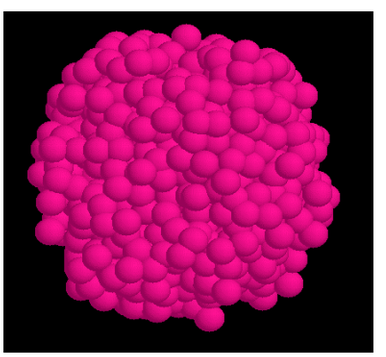


Fig. 4.

Fig. 1. Water droplet in vacuum short after start of simulation.
Fig. 2. The same after ¼ of the oscillation period.
Fig. 3. The same after ½ of the oscillation period.
Fig. 4. Oil droplet immersed in water after equilibration.

Acknowledgements

The authors would like to express their most sincere gratitude to Dr Keith Refson for the possibility of using the program Moldy [2].
This research work is being supported by the CONEX Project: "Emulsions with nanoparticles for new materials". This support is gratefully acknowledged.

References

[1] S. Tcholakova, N. D. Denkov, D. Sidzhakova, I. B. Ivanov, B. Campbell: Interrelation between Drop Size and Protein Adsorption at Various Emulsification Conditions. Langmuir, vol. 19, No. 14, 2003, 5640 – 5649.

[2] K. Refson: Moldy: a portable molecular dynamics simulation program for serial and parallel computers, Comput. Phys. Commun. 126, 3, 2000, 309 – 328.

[3] M. P. Allen, D. J. Tildesley: Computer simulation of liquids, Clarendon Press, Oxford, 1987.

[4] W.L. Jorgensen, Revised TIPS model for simulations of liquid water and aqueous solutions. J. Chem. Phys. 77, 1982, 4156 – 63.

HYSTERESIS-RELATED PHENOMENA IN SHOCK WAVE REFLECTION

Mikhail Ivanov, Dmitry Khotyanovsky, Alexey Kudryavtsev,Stanislav Nikiforov, Anatoly V. Trotsyuk
Institute of Theoretical and Applied Mechanics, Russian Academy of Sciences,
Siberian Division, 4/1 Insitutskaya St., 630090 Novosibirsk, Russia

Summary The results of our recent numerical and experimental investigations of hysteresis-related phenomena in the shock wave reflection transition are presented. It is demonstrated that the existence of more than one stable configuration and the hysteresis seem to be a universal feature of the interaction of flow discontinuities. A wide range of problems is considered, including various aspects of shock wave reflection in supersonic gas flows, shock and detonation wave interaction in chemically reacting flows, and reflection of steady bore waves (hydraulic jumps) in supercritical shallow water flows.

INTRODUCTION

In 1979 H.Hornung et al. put forward a hypothesis that the transition between steady regular and Mach configurations of shock waves should be accompanied by a hysteresis [1]. Though the first experiments did not confirm this conjecture, in 1995 the hysteresis was observed in both numerical simulations [2] and wind-tunnel experiments [3]. Numerous investigations of this phenomenon undertaken during the last eight years allow one to understand that, within the so-called *dual solution domain*, the supersonic flow with interacting shock waves can indeed be considered as a bi-stable system. For identical flow parameters, either a regular or a Mach steady shock wave configuration can be obtained, depending on the initial conditions. It was demonstrated especially unambiguously by numerical simulations owing to the absence of flow disturbances, which are unavoidable in any experimental facility. Though both regular reflection (RR) and Mach reflection (MR) are stable to infinitesimal flow disturbances, finite-amplitude perturbations can induce the transition between them. It is most likely that the free-stream disturbances are responsible for an earlier (as compared to theoretical criteria and results of numerical simulations) transition to MR, which was observed in several wind-tunnel experiments.

The goal of the present paper is to describe the most recent results of investigations of the shock reflection hysteresis and related phenomena, including simulations of chemically reacting flows and shallow water flows. We would like to particularly demonstrate the universal nature of non-uniqueness of steady configurations and hysteresis behaviour upon the interaction of flow discontinuities in different physical systems.

SHOCK WAVE REFLECTION TRANSITION AND HYSTERESIS

Experiments in low-noise wind tunnel

Experimental observation of the shock wave reflection hysteresis is hampered by the influence of flow disturbances inherent in experimental facilities. To reduce their effects to minimum, we have performed experiments in a low-noise wind tunnel, which was usually used to investigate the laminar-turbulent transition. The free-stream Mach number is M = 4. As a result, for the first time, the hysteresis phenomenon has been observed, which is very close to that predicted theoretically and obtained in numerical simulations. Thus, the transition to MR occurs at the shock wave angle of incidence α = 38.2º while the theoretical *detachment angle* is α_d = 39.2º. The back transition to RR is observed at α = 34.0º while the theoretical *von Neumann angle* is α_N = 33.4º. These results confirm very clearly that the transition between RR and MR under ideal conditions where flow disturbances are absent (maybe, in a flight experiment with a low-turbulent atmosphere) should occurs exactly as was earlier predicted theoretically and observed in numerical simulations.

Numerical simulations of transition controlled by laser energy deposition

It was previously established [4] that, in numerical simulations, flow disturbances of some special type could induce the transition between regular and Mach configurations. It opens the possibility of active control of such bi-stable configurations. The most available tool for flow control can be the generation of flow disturbances with laser energy deposition. A laser pulse focused upstream of the steady shock wave configuration causes formation of a hot-spot region and a blast wave, which interacts in a complex way with the steady configuration. This interaction can induce the transition to another configuration. Preliminary experiments on the influence on laser energy deposition on steady shock wave patterns were performed at Rutgers University [5]. In the present paper, the results of 3D numerical simulations of the blast wave/steady shock configuration interaction are described. Figure 1 shows the sequence of events during the interaction with MR. As a result, the steady Mach configuration is completely destroyed and the transition to RR is forced.

Numerical simulations of asymmetric reflection with reflected shock wave of strong family

A number of interesting features can be observed in asymmetric interaction of two shock waves. In addition to the hysteresis phenomenon and the so-called *inverse Mach reflection*, a unique situation is possible in this case where regular reflection with a reflected shock of a strong family is formed. It can be obtained with no special downstream boundary conditions because the subsonic zone behind the reflected shock is closed and the flow is rapidly accelerated again up to supersonic velocities by the expansion fan emanating from the trailing edge of the wedge.

CHEMICALLY REACTING FLOWS

A shock wave propagating in a combustible mixture causes an abrupt increase in temperature and, consequently, can induce ignition and lead to formation of a detonation wave (DW), a united complex of a shock wave and a reaction zone moving through the ambient media with an extremely high velocity (normally, 2-3 km/s). Theoretically, standing detonation waves can also exist, provided the incoming flow velocity exceeds the so-called *Chapman-Jouguet velocity* D_{CJ}. A theoretical analysis of the properties of oblique standing detonation waves was performed several decades ago. For many years, this subject has aroused a great interest because of possible applications of standing detonation waves for design of a new type of engines exploiting detonation instead of slow combustion. However, experimental evidence of their existence is scarce and ambiguous owing to difficulties in performing such experiments. We have performed a theoretical analysis of MR with a detonation wave as a Mach stem and numerical simulation of the transition to such a configuration from nonreacting RR. The computations are performed for hydrogen/oxygen and hydrogen/air gas mixtures. The existence of MR with a detonation wave is shown within a wide range of incoming flow Mach numbers, and a hysteresis is observed during the transition.

SHALLOW WATER FLOWS

It is well known that there is an analogy between the compressible Euler equations and those governing shallow water motion. The Froude number $Fr = u/\sqrt{gh}$, where u is the flow velocity, g is the acceleration of gravity, and h is the water depth, plays the same role as the Mach number, and supercritical flows with $Fr > 1$ resemble, in many aspects, supersonic flows. In particular, there are jumps in the water depths and bore waves, which are counterparts of shock waves. The interaction of steady oblique bore waves (hydraulic jumps) can lead to either regular or Mach reflection, depending on the Froude number and the angle of incidence α. Our theoretical analysis shows that the dual solution domain where both types of reflection are possible exists at $Fr > Fr_* = 2.95$. Numerical simulations confirm that, if α first increases and then decreases, the transition to Mach reflection and the back transition to regular reflection occur at different values of α, so that the hysteresis phenomenon is observed.

It can be assumed that experiments on the bore wave reflection transition would enable us to elucidate important features concerning the role of flow disturbances in inducing the transition, because it should be much easier to detect and measure disturbances in a supercritical hydraulic flume flow than in a supersonic wind tunnel flow.

References

[1] Hornung H., Oertel H., Sandeman R.: Transition to Mach reflection of shock waves in steady and pseudosteady flow with and without relaxation. *J. Fluid Mech* **90**:541-560, 1979.

[2] Ivanov M., Gimelshein S., Beylich A.: Hysteresis effect in stationary reflection of shock waves. *Phys. Fluids* **7**(4): 685-687, 1995.

[3] Chpoun A., Passerel D., Li H., Ben-Dor G.: Reconsideration of oblique shock wave reflections in steady flows. Part 1. Experimental investigation. *J. Fluid Mech* **301**:19-35, 1995.

[4] Kudryavtsev A., Khotyanovsky D., Ivanov M., Hadjadj A., Vandromme D.: Numerical investigation of transition between regular and Mach reflections caused by free-stream disturbances. *Shock Waves* **12**(2): 157-165, 2002.

[5] Yan, H., Adelgren, R., Elliott, G., Knight, D., Beutner, T.: Effect of energy addition on MR→RR transition. *Shock Waves*, **13**(2): 113-121, 2003.

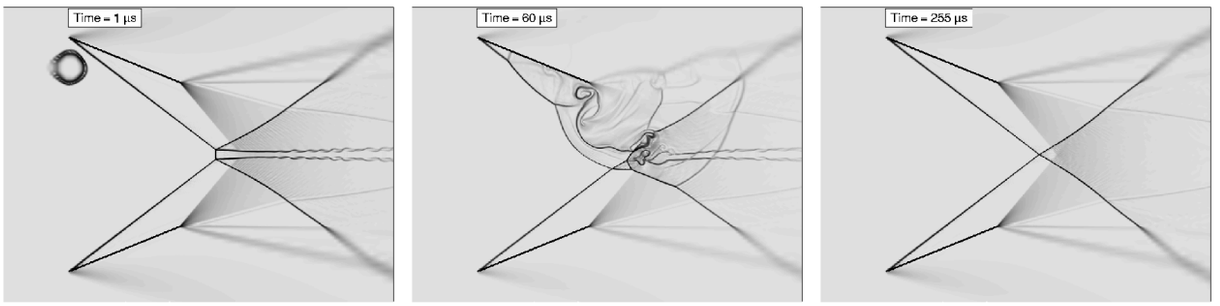


Fig.1. Interaction of a laser pulse of 0.215 J with a steady Mach configuration in a supersonic flow at M=3.45.

NONCLASSICAL DYNAMICS OF LAMINAR DENSE GAS BOUNDARY LAYERS

M. Kinell and A. Kluwick
Institute of Fluid Mechanics and Heat Transfer, Vienna University of Technology, Resselgasse 3/E322, A-1040 Vienna, Austria

Summary While inviscid flows of dense gases have been studied intensively in the past, viscous effects have received much less attention so far. It is the aim of the present study to show that the observed unconventional gasdynamic behaviour of such gases may strongly influence the behaviour of laminar boundary layers. Specifically it is found that boundary layer separation may be delayed in decelerating flows while acceleration of the external flow may cause a substantial reduction of the wall shear.

GASDYNAMIC PROPERTIES OF DENSE GASES

In the last 15 years the flow properties of dense gases, i.e. gases in the general neighbourhood of the thermodynamic critical point, have received increasing interest. Studies in which thermo-viscous effects where neglected have shown that such flows may lead to a number of new and unexpected phenomena provided that the molecular complexity of the medium under consideration is sufficiently high, see for example [1]. These effects can be inferred from the behaviour of a single thermodynamic quantity, the so-called fundamental derivative

$$\Gamma = \frac{\tilde{v}^3}{2\tilde{c}^2}\left(\frac{\partial^2 \tilde{p}}{\partial \tilde{v}^2}\right)_{\tilde{s}} . \tag{1}$$

Here $\tilde{c}, \tilde{p}, \tilde{v} = 1/\tilde{\rho}$ and $\tilde{s}$ denote, respectively, the speed of sound, the pressure, the specific volume and the entropy. According to equation (1) Γ characterises the curvature of isentropes in the $\tilde{p}, \tilde{v}-$diagram. In the case of perfect gases $\Gamma \geq 1$. However, Γ may assume values less than one or even negative values in fluids having large isochoric heat capacity $\tilde{c}_v$ relative to the gasconstant $\tilde{R}$. Fluids with this property are now commonly termed BZT-fluids in recognition of the pioneering work of Bethe, Zel'dovich and Thompson and exhibit a number of unconventional gasdynamic properties. For example, differentiation of the local Mach number M with respect to $\tilde{v}$ at constant $\tilde{s}$ yields the result

$$\frac{1}{M}\frac{dM}{d\tilde{v}}\bigg|_{\tilde{s}} = \frac{1}{\tilde{v}}\left[\frac{1}{M^2} + \Gamma - 1\right] . \tag{2}$$

If $\Gamma \geq 1$ the expression on the right hand side is a strictly positive quantity and, consequently, M increases monotonically with increasing values of $\tilde{v}$. In contrast, regions of $\Gamma < 1$ in the $\tilde{p}, \tilde{v}-$diagram may lead to a non monotonous Mach number dependency on $\tilde{v}$. Here we are interested if and how this nonclassical gasdynamic effect influences the behaviour of laminar boundary layers.

LAMINAR BOUNDARY LAYER FLOWS

Specifically we consider flows past an adiabatic flat plate and assume that the streamwise velocity component $\tilde{u}_e$ varies linearly with increasing distance $\tilde{x}$ from the leading edge. Using suitable defined non-dimensional quantities this can be expressed in the form

$$u_e = 1 + \alpha x, \quad \alpha \pm 1. \tag{3}$$

Linearly retarded flows of dense gases, $\alpha = -1$, have been considered first in [2]. Similar to incompressible flows and

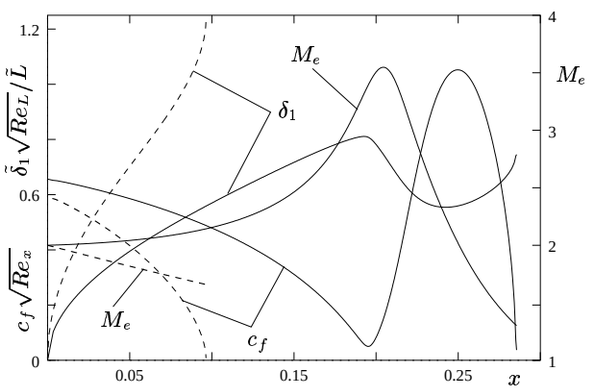


Fig. 1: Distributions of c_f, M_e and δ_1 for $\tilde{\rho}_\infty = 0.2\tilde{\rho}_c$, $\tilde{T}_\infty = 1.001\tilde{T}_c$, $M_\infty = 2$ and $\alpha = -1$.
--- N_2 —— FC-71

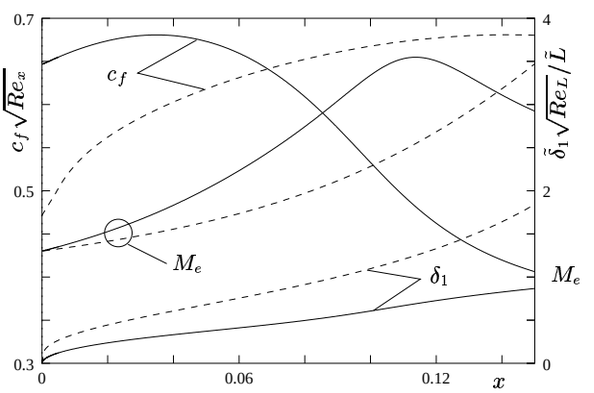


Fig. 2: Distributions of c_f, M_e and δ_1 for $\tilde{\rho}_\infty = 1.4\tilde{\rho}_c$, $\tilde{T}_\infty = 1.03\tilde{T}_c$ and $M_\infty = 1.3$ and $\alpha = 1$.
--- N_2 —— FC-71

compressible flows of ideal gases, e.g. [4], the boundary layer development in dense gases with small or moderately large heat capacities is found to terminate in a separation singularity. An example is provided by Nitrogen N_2 with freestream conditions $\tilde{\rho}_\infty = 0.2\tilde{\rho}_c, \tilde{T}_\infty = 1.001\tilde{T}_c, M_\infty = 2$ at $x = 0$. Here $\tilde{\rho}_c$ and $\tilde{T}_c$ denote the values of the density and the temperature at the thermodynamical critical point. Calculations based on the Martin-Hou equation of state which is able to capture dense gas effects, e.g. [1], then yield $\Gamma_\infty = 2.2$ and $\Gamma > 1$ in the whole computational domain. As a consequence, decreasing values of u_e are associated with decreasing values of the Mach number M_e in the external inviscid flow region. The resulting pressure rise causes the local friction coefficient c_f to decrease also and the wall shear stress distribution eventually tends to zero in an irregular manner while the displacement thickness $\delta_1 = \tilde{\delta}_1/\tilde{L}$ grows without bound, Fig. 1. Here Re_x and Re_L denote Reynolds numbers formed with the distance $\tilde{x}$ from the leading edge and the reference length $\tilde{L}$, respectively.

Also included in Fig. 1 are results for the BZT-fluid FC-71 having the same freestream conditions as N_2. In contrast to Nitrogen, however, $\Gamma_\infty = 0.71 < 1$ and M_e, therefore, increases rather than decreases with growing distance x initially. How this affects the boundary layer development can be inferred most easily from the gasdynamic equation holding in the outer inviscid flow region. It predicts that decelerating supersonic flows of the form (3) generate negative normal velocity components which increase in magnitude as the distance from the plate becomes larger. This counteracts the effect resulting from the boundary layer displacement and may cause a reduction of the associated momentum outflux leading in turn to a delay of separation as observed in Fig. 1. Moreover, since the phenomenon of "negative displacement"intensifies with increasing values of M_e one expects that the displacement body felt by the external inviscid flow may shrink rather than expand in the flow direction if M_e is sufficiently large. This is confirmed by the numerical solution for FC-71. The associated momentum flux towards the wall then is able to overcome the onset of separation and c_f rises sharply. Eventually, however, Γ leaves the range of values necessary for a Mach number increase. M_e then starts to drop which in turn quenches this effect. As a consequence, c_f drops also and the formation of a separation singularity is inevitable. Nevertheless, the results plotted in Fig. 1 clearly show that dense gas effects may be utilised to delay boundary layer separation in BZT-fluids.

A NEW FORM OF MARGINAL SEPARATION

If the freestream density is slightly reduced while the temperature and the Mach number are kept fixed the minimum in the wall shear stress distribution is found to decrease and one finally obtains the limiting case $\tilde{\rho}_\infty = \tilde{\rho}^*$ where the wall shear vanishes in a single point but immediately recovers. At the point of vanishing wall shear the displacement body is found to exhibits a sharp corner. As a consequence, classical boundary layer theory fails locally but this failure can be overcome by applying an interaction strategy which then also allows to account for the occurrence of short separated flow regions. To this end the full Navier-Stokes equations are analysed in the double limit $Re_L \to \infty$, $\tilde{c}_v/\tilde{R} \to \infty$ using asymptotic methods. This results in a three layer structure of the local interaction region and an integro-differential equation for the scaled wall shear known from the theory of marginally separating incompressible flows, e.g. [3]. However, the controlling parameter a entering the equation now has a completely different meaning

$$a \propto Re_L^{2/5} \frac{\tilde{\rho}_c \left(\tilde{\rho}^* - \tilde{\rho}_\infty\right)}{\tilde{\rho}^* \tilde{\rho}_\infty}. \tag{4}$$

Also it should be noted that the physical mechanism causing the boundary layer to overcome the onset of separation is new. Marginal separation here occurs in a strictly decelerated flow which is possible only due to the non-monotonic Mach number variation.

CONCLUSIONS

Applications of the considerations concerning the external flow field associated with (3) to cases of favourable pressure gradient, $\alpha = 1$, suggest that the phenomenon of non monotonous Mach number variation may have a negative effect on the boundary layer evolution by reducing the wall shear stress. Again this is confirmed by numerical calculations as shown in Fig. 2 where, similarly to the case of linearly retarded flows depicted in Fig. 1, results for the regular fluid N_2 and the BZT fluid FC-71 are compared. In summary one therefore concludes that dense gas effects can effectively be exploited to delay or even avoid separation under the action of adverse pressure gradients but may drive the flow towards separation if a favourable pressure gradient is imposed. This is certainly of basic scientific interest but of importance also in engineering applications.

References

[1] Cramer, M.S.: Nonclassical dynamics of classical gases. *Nonlinear waves in real fluids* (ed. A. Kluwick). Springer, Wien, 1991.

[2] Kluwick, A.: Marginally separated flows in dilute and dense gases. *Phil. Trans. Roy. Soc. Lond., special issue dedicated to Sir James Lighthill* **358**:3169-3192, 2000.

[3] Ruban A.I.: Asymptotic theory of short separation regions on the leading edge of a slender airfoil. *Izv. Akad. Nauk SSSR, Mekh. Zhidk. Gaza* **1**:42-52, 1981.

[4] Schlichting H. and Gersten K.: *Boundary layer theory*. Springer, 1996.

ANALYTICAL MODELS FOR SHOCKS IN TRANSONIC FLOW

Helmut Sobieczky

DLR German Aerospace Center, Bunsenstr. 10, Göttingen, 37073 Germany

Summary Objective is trying to maintain the value of analytic modelling for deeper insight, education and development of new design concepts. Analytical flow models are used to confirm wellknown and find new solutions: Logarithmic structure of surface pressure distribution occurs with occurence of different shock waves interacting with contour geometry.

MAPPING THE FLOW PROBLEMS TO THE HODOGRAPH

A recent IUTAM symposium [1] on transonic flow has shown that analytic treatment of complex flows still draws interest as an efficient tool to shed light into complex flow details where numerical results give no clear answers. Complexity of flow problems may stem from special boundary conditions as well as from dynamics within the flow field. In transonic flow, the latter source of complexity, for instance, occurs due to shock waves within the flow field. This holds already for steady, inviscid 2D flow. Aerodynamic applications, of course, require the simulation of steady and unsteady viscous and 3D flows, but with recent developments in flow control technology, as seen in [1], prescribing target pressure distributions to control viscous interaction becomes important. We are therefore interested to preserve some of the findings from inviscdid, 2D flows models, guiding us to suitably parameterize design parameters.

Here we use the idealized 2D near sonic flow equations (1) for velocity components U, V desribing perturbed sonic velocity parallel flow (U = 0, V = 0). These equations model potential flow for vorticity $\omega = 0$ and also represent a small perturbation approximation of the Euler equations. For $\omega = 0$ the hodograph transformation to velocity variables ν,θ (Prandtl-Meyer angle, $\nu \sim \pm|U|^{3/2}$, and flow angle θ) results in the Beltrami mapping equations (2). We note that this system is linear and weakly singular at $\nu = 0$, it is the basis for near sonic flow phenomena modelling. Investigation of flow phenomena, which do not include the sonic condition $\nu = 0$, but focus around perturbing a special value of ν, lead to simple Cauchy-Riemann (C-R) or wave equations (3) in the hodograph plane. This is equivalent to suitably linearizing (1) around a given value of $U \neq 0$ and this way also obtaining C-R or wave equations in the (X,Y) physical plane.

$$U \cdot U_X - V_Y = 0 \qquad U_Y - V_X = \omega \tag{1}$$

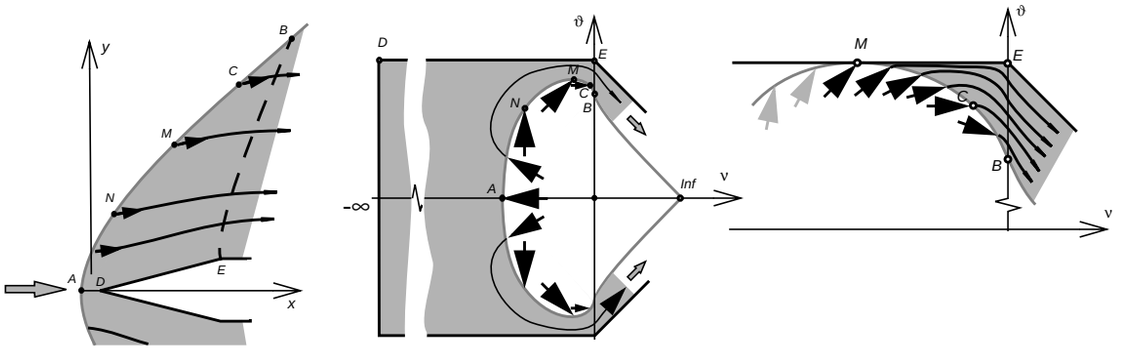
$$X_\nu = \nu^{1/3} \cdot Y_\vartheta \qquad X_\vartheta = \pm\nu^{1/3} \cdot Y_\nu \tag{2}$$

$$X_\nu = \pm Y_\vartheta \qquad X_\vartheta = Y_\nu \tag{3}$$

A wellknown example: Normal shock on the curved wall

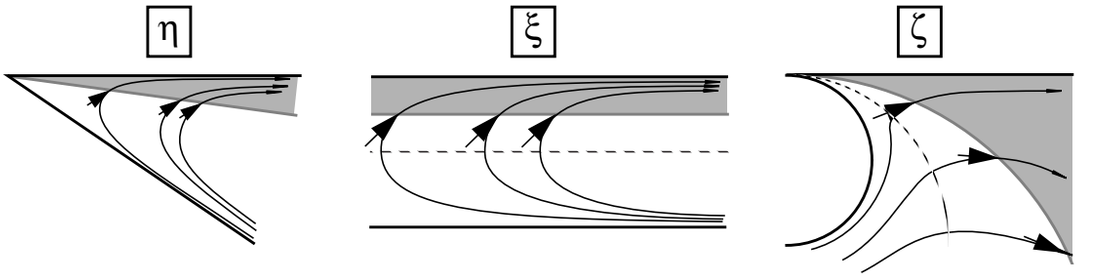
A series of publications has dealt with the problem of a normal shock on a curved wall. A study of the relevant milestones which confirmed the analytical structure of a logarithmic solution for the pressure distribution along the wall, cp ~ a+bXlog(X)+..., should start with the work of v.Koppenfels [2] about incompressible flow past walls with curvature jumps. Emmons [3] numerically solved the compressible flow Euler equations and mentions qualitative relations of his results to flows as investigated by v.Koppenfels. Gadd [4] clearly points out this earlier work to arrive at a logarithmic model, Oswatitsch and Zierep [5] confirm the logarithmic solution by studying the above equation (1), linearized around the value of U behind a normal shock and without vorticity. Final doubts about validity of such local potential solution, based on the occurrence of shock-curvature-induced vorticity, are removed by Fung [6] concluding that the vorticity terms are of a higher order than those governing the logarithmic character of the solution.

Finally, our own work in transonic airfoil design fits to this model, if a shock is being designed using the Fictitious Gas technique: Sobieczky and Niederdrenk [7] use subsonic initial boundary conditions with a curvature jump to solve an elliptic (“fictitious”) boundary value problem, before in a second step a supersonic flow pattern terminated by a shock wave and the smoothly curved contour wetted by supersonic flow is constructed by the method of characteristics and the shock relations. Such academic examples led us to develop novel wing design strategies, to be applied subsequently to 3D, viscous and even unsteady aerodynamics. Examples are shown in [1].



a b c

Fig. 1: Shock attachment to a wedge in low supersonic Mach number flow (a), analog to growing shock polar with flow emanating under given directions in hodograph plane (b) until touching fixed contour DE, (c).



$$Z = X - iY = \eta^n \qquad \eta = e^{\xi} \qquad \zeta = (\nu - \nu_M) + i(\vartheta - \vartheta_M) = 1/\xi$$

Fig. 2: Conformal mappings to find solution ζ = Fct(Z), resulting in wedge surface pressure $c_p(\nu)$ = fct$(X)_{Y=0}$

Another logarithmic flow singularity: shock attaching to a wedge airfoil leading edge

Here another problem is presented involving the shock relations near a singular location on the boundary: Shock attachment to a wedge leading edge (Fig. 1a) requires a transition from a detached normal shock to an oblique shock. This problem is treated easier in the hodograph plane (Fig. 1b) using the Beltrami mapping system (2), the shock polar and investigating the vicinity of the shock polar maximum deflection point M (Fig 1c). This allows for linearization around the subsonic ν_M using C-R system (3). With systems (2) and (3) representing analog flow in the hodograph plane (ν,θ), we have to describe a potential flow model in the sharp angle left of M, with a straight solid boundary above and a curved transpirating boundary with flow emanating under 45^o from it. For solution of this boundary value problem a series of simple conformal mappings is used and illustrated in Fig. 2. From these the pressure coefficient along the wedge contour near the tip results to $c_p \sim a+b/\log(X)+.....$, obviously a hitherto not yet described detail of shock attachment to a wedge.

CONCLUSION

Analytical flow models are still seen as precise tools to: (1) understand complicated flow patterns generated by special boundary conditions, (2) subsequently explain and educate about flow phenomena and (3), finally use their suitably parameterized mathematics for aerospace design and optimization.

References

1 Sobieczky, H. (Ed.): Proc. IUTAM Symposium Transsonicum IV. Kluwer Acad. Publ., Dordrecht 2003
2 v.Koppenfels, W.: Luftfahrtforschung Bd. 17, Lfg. 7, (1940), translated in NACA TM 996, 1941
3 Emmons, H. W.: Flow of a Compressible Fluid past a Symmetrical Airfoil. NACA TN 1746, 1948
4 Gadd, G. E.: The Possibility of Normal Shock Waves on a Body with Convex Surfaces in Inviscid Transonic Flow. *ZAMP* **11**, 1960
5 Oswatitsch, K., Zierep, J.: Das Problem des Senkrechten Stosses an einer Gekrümmten Wand. *ZAMM* **40**, 1960
6 Fung, K.-Y.: Vorticity at the Shock Foot in Inviscid Flow. *AIAA Journal* **21**, No. 6, 1983
7 Sobieczky, H., Niederdrenk, P.: Entwurf einer Transsonischen Strömung mit Verdichtungsstoss *ZAMM* **65**, 1985.

LDA INVESTIGATION OF A TRANSONIC BUMP FLOW

H. Babinsky, S. Prioris
Cambridge University Engineering Department Trumpington Street, Cambridge, CB2 1PZ, UK

Summary The transonic flow over a circular arc bump has been investigated in a blow-down wind-tunnel. A variety of shock strengths between M=1.2 and M=1.48, depending on the experimental configuration, were studied. Laser Doppler Anemometry has been used to gather detailed information on turbulent flow properties. The results highlight the effects of favourable and adverse pressure gradients on turbulence properties, in particular the influence of shock waves and separation / reattachment.

BACKGROUND AND MOTIVATION

In many transonic and supersonic flows of practical importance the interaction of a shock wave with a boundary layer plays a critical role. Shock wave / boundary layer interactions (SWBLIs) not only significantly influence local features, but they can also strongly affect the global flow by causing separation or by changing boundary layer characteristics for a large distance downstream. In terms of simulation, the computation of SWBLI is arduous for two main reasons. The first one is the complex nature of the flow physics due to the high level of interdependence between the shock wave and the boundary layer. For instance, the disturbance/recovery process in the boundary layer is generally not predicted correctly when extensive separation occurs. The second difficulty is the high Reynolds numbers encountered when trying to simulate full-scale flows. Typically for in-flight conditions, the Reynolds number based on the displacement thickness varies between 10,000 and 30,000 whereas Direct Numerical Simulation (DNS) can currently only provide results for Reynolds numbers in the 1000s. One alternative solution is to use Reynolds Averaged Numerical Simulation (RANS) methods. However, the accuracy of such codes relies on the ability of the turbulence model to reproduce the fundamental mechanisms of turbulence production and dissipation through the interaction. This requires the model to be calibrated and tested against experimental data, which is not widely available.

In this experiment, the case of a normal shock interacting with a boundary layer developing over a circular arc bump (as shown schematically in Fig.1) is studied because it makes it possible to investigate a wide range of SWBLI configurations on the same geometry. By varying the back-pressure in the wind tunnel the location and strength of the shock wave can be adjusted to achieve a number of configurations ranging from a weak shock without separation to a strong shock with extensive separation. The experiment was designed to provide a detailed SWBLI database including turbulent properties measured using Laser Doppler Anemometry (LDA) for comparison with RANS and DNS calculations. Furthermore, it is intended to provide further insight into the fundamental physical mechanisms driving SWBLI at realistic Reynolds numbers.

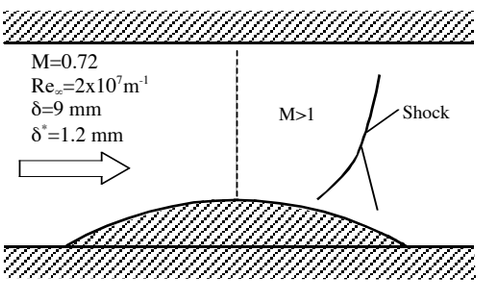


Fig. 1 Schematic diagram of experimental set-up

EXPERIMENTAL SET-UP

The experiments were performed in a transonic blow-down wind tunnel. Total conditions in the settling chamber (T_t = 290 K, P_t = 184 kPa) were maintained constant to within 2% while the pressure downstream of the test section (and therefore the flow configuration) was controlled using an adjustable second throat. A circular bump is fitted on the floor of the test section as shown in Fig. 1. The incoming boundary layer upstream of the bump is fully turbulent with a displacement thickness of 0.75 mm yielding a Reynolds number Re_{δ^*} = 24,000.

A two-dimensional LDA system was used to obtain measurements of normal and streamwise instantaneous velocity. The measuring volume is an ellipsoid of 75mm in diameter in the measuring plane and 1.88 mm in the transverse direction (effective integration width). The dynamic ranges of the LDA processors are respectively for each component [-160; +610] m/s and [-150; +580] m/s. The receiving optics were offset relatively to the axis of the emitting optics in order to prevent optical noise due to the light scattering from the test section floor or windows. A physical beam-stop was employed so that the maximum lens aperture could be used on the receiving optics to improve detection. This allowed measurements as close as 0.1 mm from the wall (y^+_{min}<80-100) except around the trailing edge where optical access difficulties and a reduced signal-to-noise ratio was experienced. Boundary layer traverses typically explored twenty points – the number of measurement locations being limited by the running time of the wind tunnel. In order to allow for reliable statistical post-processing, at least 1000 coincident and validated velocity samples were recorded at each traverse location, although most data presented here were obtained with significantly higher numbers of samples (several 1000s). In the calculation of turbulent kinetic energy, the contribution of the unknown transverse velocity fluctuation <w'> was taken equal to an average contribution between both streamwise and normal velocity fluctuations. Although oil flow patterns revealed three-dimensional effects in the vicinity of the side-walls, the flow kept displaying a two-dimensional behaviour around the centreline for all cases. The measuring volume was always well within this region.

The flow was seeded using olive oil droplets with an average size of around 250 nm. This ensured a negligible level of lag in regions of high velocity gradients. In order to remove any velocity-induced bias on average quantities, the velocity measurements were weighted using the transit time, i.e. the residency time of each particle within the measuring volume. Indeed, arithmetic weighting is only appropriate if all velocity samples are independent; otherwise, it can introduce a bias towards higher velocities. In these experiments, transit times as short as 50 ns were recorded and used for all statistical analysis.

RESULTS AND DISCUSSION

In total four configurations were investigated in detail. These ranged from a very weak shock (below incipient separation) as seen in Fig.2 (top) to a strong shock located at the trailing edge of the bump as shown in Fig.2 (bottom). In both cases separation was present at the trailing edge, in the former case caused by the abrupt change of curvature at the trailing edge alone, and in the latter case due to the combined effects of geometry and the shock induced pressure gradient. The two configurations not shown here displayed flowfields in between these two extremes. Detailed LDA information has been obtained for all four configurations allowing the presentation of u, v, u', v', turbulent shear stress and turbulent kinetic energy throughout the flowfield. As an example, Fig.3 shows the Reynolds shear stress <u'v'> for the configurations seen in Fig.2. Note that only the area starting at the crest of the bump is seen in these figures. The results clearly show the significant increase in Reynolds shear stress near the shock wave and at separation. In configuration 1 it is possible to distinguish between the effects of the shock and the separation occurring at the trailing edge. In configuration 4, the compactness of the separated region and the closeness of the shock wave and the trailing edge causes the effects of the shock, separation and re-attachment to all merge together.

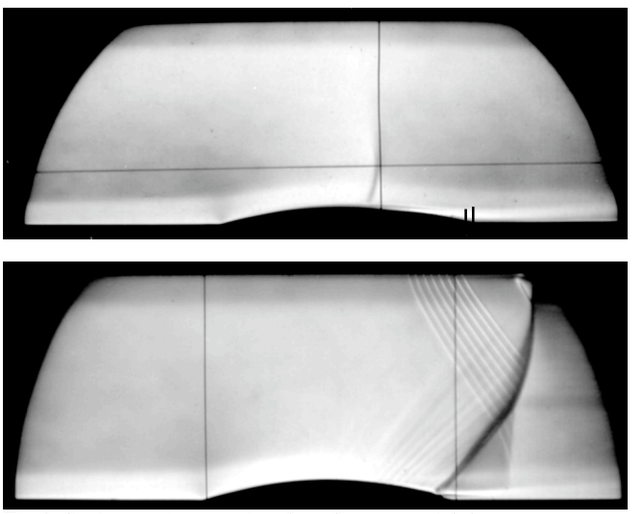


Fig.2 Schlieren photographs of configurations 1&4

The full paper will give more detail, concentrating in particular on:
- The flow development due to the presence of a strong favourable pressure gradient by comparing boundary layer properties upstream and on the crest of the bump.
- The flow properties in the interaction and separation regions
- The recovery of the boundary layer downstream of the bump – after re-attachment.

By further analysis of the LDA data it has also been possible to obtain an estimate of the transverse pressure gradient in the boundary layer up to the interaction. This has revealed that the wall normal pressure gradients (often assumed to be negligible) are of the same order as the streamwise pressure gradients in most of the flow. This is caused by the considerable curvature of the flow and has implications for the numerical modelling of similar flows such as over aerofoils and turbine blades.

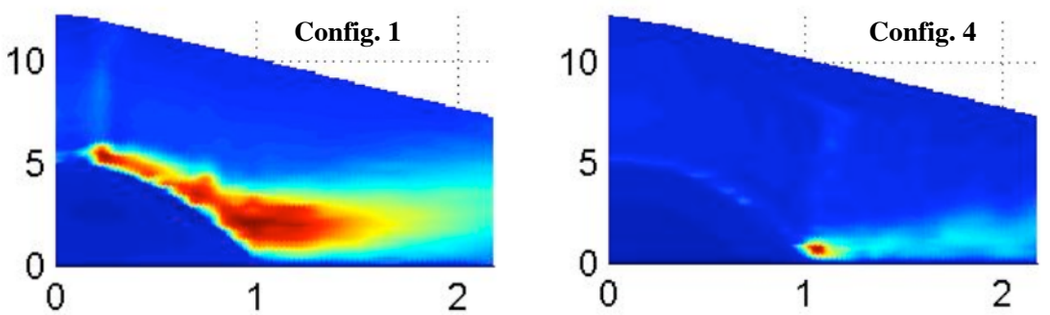


Fig.3 Map of Reynolds shear stress <u'v'> for configurations 1&4

UNSTEADY DRAG FORCE MEASUREMENTS OF SHOCK LOADED BODIES SUSPENDED IN A VERTICAL SHOCK TUBE

Kazuyoshi Takayama*, Tsutomu Saito*, Min Gyu Sun*, Koji Tamai**, Hiroyuki Tanno***, Joseph Falcovitz****
*ISWRL, Inst Fluid Science, Tohoku Univ., Sendai Japan
**Central Glass Co. Ltd., Matsuzaka, Japan
***Kakuda Space Propulsion Research Center, JAXA, Kakuda, Japan
****Inst Mathematics, Hebrew Univ. of Jerusalem, Israel

Summary Unsteady drag forces acting on bodies suspended in a 300mm×300mm vertical shock tube were measured for shock loading with Ms = 1.22 shocks in air and Re = 7.6×10^6/m. The test models in which an accelerometer was installed were a sphere, an ellipsoid, rough and smooth cones, a cylinder, a combination of two cones. Unsteady drag forces due to the blast wave generated by detonating a 0.1 g PETN charge in air were also measured. The experimental results were compared with numerical simulations.

Experiments

Shock tube

We used a vertical shock tube of Interdisciplinary Shock Wave Research Center of the Institute of Fluid Science, Tohoku University which consists of four segments as follows. A 2.5 m long and 420 mm/480 mm inner/outer diameter steel tube high-pressure chamber; a 300 mm×300 mm, 5 m long low-pressure channel made of stainless steel; a 1.0 m long test section with a 300 mm×500 mm view field; a 700 mm inner diameter and 1.5 m long dump tank at the end of the shock tube. The driver gas was nitrogen at 240 kPa, producing a shock Mach number of 1.22 in air at 101 kPa and room temperature, with a corresponding Reynolds number of 7.6 x 10^6/m. The shock tube cross-section is large enough to minimize the blockage effect of test models of 60 to 80 mm in diameter and the reflected shock wave from the side walls arrived at the model surface after 0.6 ms.

Test model

Test models weighing from 450 g to 700 g were made of aluminum and had various configurations: a 80 mm diameter sphere; cones of 40 degree apex angle and 60 mm base diameter with both smooth surface and grooved surfaces; a 60 mm diameter and 120 mm long cylinder; a 60 mm diameter and 90 mm long ellipsoid; and a double cone consisting of two 45 mm long and 60 mm base diameter connected at their base surface. Each model was suspended vertically from just below the diaphragm section with a 3.5 m long and 1.2 mm diameter steel wire, positioning it at the test section. A compact Endevco piezo-electric accelerometer 2250A-10, sensitivity of 1.02 V/m/s^2 and resonance frequency of 80 kHz was installed in each model for detecting the vertical component of acceleration during shock loading. Output signals from the accelerometer were taken out via co-axial cable from the rear stagnation point and stored in a high-speed digital memory. In the case of the sphere of about 700g in weight, a shock wave of Ms = 1.22 produced a maximum force of about 400 N at 0.1 ms after the arrival of incident shock at the frontal stagnation. The tensile stress wave propagating in the suspension wire took about 0.7 ms to reach the support point and reflected back to the sphere model. Hence the effect of the suspension would first be felt after about 1.4 ms, so that the wire stress was negligibly small, never affecting the measured acceleration (Tanno et al 2003).

Blast wave loading

In addition to the planar shock loading, we tested these models exposed to blast waves produced by the detonation of 0.1 g PETN ignited with a laser-initiated 10 mg silver azide pellet. The stand-off distance between models' frontal stagnation point and the PETN pellet was 200 mm and the PETN had a volume of 50 mm^3, small enough to be regarded as point source. The shock Mach number of the blast wave at this stand-off distance was about 1.2.

Flow visualization

In both shock tube and blast wave tests, the interaction of waves with individual models was sequentially observed by double exposure holographic interferometry and also with a high-speed video camera of 1.0 x 10^6frame/s at exposure time of 250 ns. Visualization results explained clearly the sequence of dynamic interaction between the moving shock wave and the model surface, producing the measured resulting drag force.

Numerical Simulation

Numerical simulations were performed with a finite-difference scheme solving the axi-symmetric Navier-Stokes equation using turbulent flow modeling (Tanno et al 2003). At first we tested with the sphere model by applying adaptive meshes very densely distributed over the sphere surface. The sensitivity of mesh sizes on the solution convergence was examined. A good agreement between the measured result and the numerical one was obtained for sphere case.

We also solved the Euler equations under the same conditions. The difference between the viscous and the inviscid results was surprisingly small. This therefore implies that at the earlier stage of shock/body interaction, drag forces are generated mostly by the process of wave interaction and the contribution of wall friction and of shear layer effects is very marginal. Hence for other test models we used only Euler computations. The integration of the Euler equations was performed by the finite-difference conservation laws scheme GRP (Ben-Artzi and Falcovitz, 2003). In that scheme the fluxes are evaluated from (analytical) solutions to a Generalized Riemann Problem set up at each cell-interface. The MBT (Moving Boundary Tracking) version with a stationary boundary line was used to implement the surface contour of each model (the Cartesian grid consisted of square cells).

Results and Discussion

Data reduction of force measurement

To evaluate the output signals of the accelerometer, the force measuring system was calibrated by so-called hammering test. The models were impacted with a hammer at their rear stagnation area, whose frequency response was already known. The calibration is based on the concept that from the known time variation of hammer impact force and from the recorded time variation of the acceleration by the model-installed accelerometer, one can deduce the frequency response function of the system. Applying this function to the data recorded in the experiment, we can readily determine the time variation of measured drag forces.

Comparison of measured and numerical results

Excellent agreement between the measured result and numerical one was obtained for the sphere model (Tanno et al 2003) and good agreements were obtained for other models on shock and blast wave loadings (Tamai 2004). In the case of a 80 mm diameter sphere and a 60 mm and 90 mm long ellipsoid at Ms = 1.22, drag forces peak at about 0.1 ms after shock impingement and subsequently decrease to a slightly negative value, then gradually approach the steady (positive) drag value. The negative drag force is generated when the diffracted Mach stem of the transmitting shock wave along the model's rear surfaces implodes at the rear stagnation area. This trend agrees well with the wave motions sequentially visualized. The appearance of negative drag force is for the first time confirmed by direct force measurement in a vertical shock tube. The trend of drag forces so far measured differs from that on two-dimensional bodies. In the case of cones and a cylinder, drag forces increase to a maximum value and then decrease monotonically to the corresponding steady drag value, without a negative phase.

Significance of the results

It is interesting to comment on these results in light of the classical d'Alembert paradox, namely the vanishing of drag force in the case of steady potential flow. On one hand we know that in a steady "real" flow the separation in the rear part of the body is responsible for the bulk of the drag force (at high Reynolds numbers). On the other hand, when a flow can be idealized as an unsteady potential flow, the drag is non-vanishing and is explained by the "added mass" effect related to the acceleration of the surrounding fluid. In the case of unsteady compressible flow considered here the transient drag is due to wave interactions. This drag-producing mechanism is decidedly different from all the others, as indicated by the large ratio of about 20:1 between the peak unsteady drag coefficient (about 8 for a sphere) and the corresponding steady value (about 0.4 for a sphere).

References

Ben-Artzi M, Falcovitz J (2003) Generalized Riemann problems in computational fluid dynamics. Cambridge University Press, London, 2003.

Tanno H, Itoh K, Saito T, Abe A, Takayama K (2003) Interaction of a shock with a sphere suspended in a vertical shock tube, Shock Waves, 13: 191-200

Tamai K, Unsteady interaction of bodies with various configuration loaded by shock and blast waves. Dr. Thesis Graduate School of Tohoku University 2004

SHOCK WAVE REFLECTION IN A NON-CIRCULAR INLET.

Beric W. Skews, Jithin A. Mohan, Nandkishore Menon
School of Mechanical, Industrial, and Aeronautical Engineering, University of the Witwatersrand, PO WITS, 2050, South Africa

Summary The flow between two finite wedges placed symmetrically in a supersonic flow with one or both sides capped with a semi-cone is studied. Imaging with laser vapour screen and shadowgraph techniques give images that can be difficult to interpret and result in flows which appear aphysical. Further experimentation and CFD techniques are used to resolve the confusion.

INTRODUCTION

It has been established that the shock wave reflection pattern on a plane surface below a supersonic body can comprise of regular reflection immediately below the body, which then transits to Mach reflection in the lateral direction [1]. The initial interest in the current work was to examine the nature of the three-dimensional flow in the vicinity of the point of transition from the one type of reflection to the other. This arose from the examination of three-dimensional effects in studies of wave reflection between two finite width wedges placed symmetrically in a supersonic wind tunnel [2]. The study used shadowgraph visualisation but with the light beam passing through the test section yawed so that the 3d wave profiles could be established. Figure 1a is a conventional shadowgraph showing regular reflection, which could be interpreted as a two dimensional flow. The exact same flow but with 45^o optical yaw is shown in Fig 1b. Here the reflection is clearly of Mach type as the optical beam is now grazing the peripheral Mach surface. This surface then wraps forward until it transitions to regular reflection. This is imaged as a dark protuberance immediately behind the visible Mach stem changing to a white line that is the line of regular reflection. Towards the right of the image this again splits into the Mach reflection on the near-side of the wedge. It is these transition points that are of interest. The third image of Fig. 1 is a more detailed view taken at 55^o optical yaw, which shows slight fluctuations in stem height before it settles to regular reflection raising concern about its suitability for transition studies. Against the background of previous studies which show significant sensitivity to upstream perturbations it was decided to explore a different geometry for this work. This is the subject of this paper.

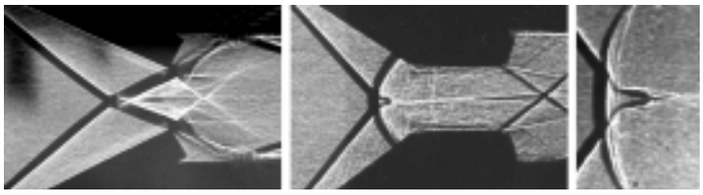


Fig. 1. Shock reflection pattern off finite width wedges [2]

GEOMETRY INVESTIGATED AND EXPERIMENTAL ARRANGEMENT

Since it is known that an internal conical shock wave cannot reflect regularly from the axis of symmetry even for small wall angles that will result in regular reflection for a double wedge, a geometry consisting of a double wedge with the open ends closed off with two semi-cones should result in a transition from Mach to regular reflection. A schematic of this arrangement with one semi-cone cut away is shown in Fig. 2. The line of reflection should change from that around a Mach disk to a line as indicated in the schematic. A number of wind tunnel models were built, a so-called cut-model of the shape shown in Fig. 2 with a 15^o wall angle and a full model with both semi-cones. The cut-model was made to facilitate the starting shock in the tunnel to be swallowed and to enable visualisation using laser vapour screen techniques (LVS) since the interactions of interest occur within the length of the model and are thus not visible using conventional shadowgraph techniques. The full model was made with a 10^o wall angle resulting in the reflection occurring downstream of the trailing edge, enabling conventional shadowgraphy to be employed. All tests were conducted at a nominal Mach number of 3.



Fig. 2. Cut-model geometry.

RESULTS AND DISCUSSION

The initial experimental work showed the flow to be complex and, in particular, three features of particular interest are identified for discussion. Understanding them necessitated subsequent CFD evaluation. Fig. 3 shows three LVS images with the sheet normal to the free-stream direction, taken at successive positions in the downstream direction. The first image, approximately halfway down the model shows an expected incident wave pattern consisting of a semi-circular wave on the right arising from the semi-cone, through plane in the centre, arising from the wedge, to curved on the left as the wave diffracts around the edge of the model. Note, however, a slight unevenness developing in the conical wave profile. The second image shows a slice of the flow just 4 mm further downstream. A Mach stem of significant size,

reflected shocks, and slipstreams have appeared. The transition is apparently very rapid. The third image, beyond the trailing edge, shows that the Mach stem has reduced in size and transition to regular reflection has occurred. The dark patch behind the reflection point is the area encompassed by the shear layers arising from the Mach stem surface.

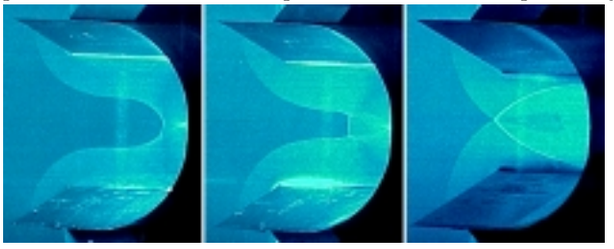


Fig. 3. LVS images of shock wave profiles

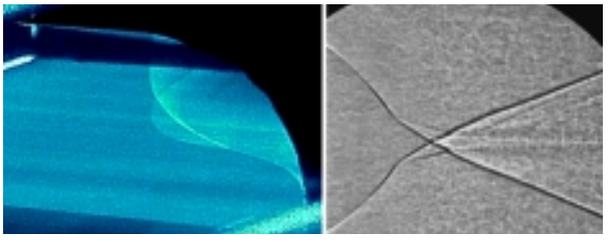


Fig.4. Views in and through the symmetry plane

Figure 4 shows an LVS image taken with the laser sheet near the plane of symmetry of the cut-model (flow from lower left to upper right), and a shadowgraph behind the full model (flow from left to right) and taken perpendicular to the wedge leading edge. Both of these show very interesting features. In the LVS image the incident shock starts at the cone leading edge (lower right) curves significantly into the flow as it increases in strength due to convergence on the cone axis, and then appears to bifurcate. Two waves then propagate in this symmetry plane and appear to cross giving an overall impression that is problematical when viewed in a two-dimensional sense. An equally inexplicable flow appears in the shadowgraph. The two incident conical waves curve inwards towards the model axis, suddenly develop a kink, which sheds a slipstream, and then reflect regularly with each other. It should be noted that the shadowgraph records all features within the full depth of the flow field, and in this case does not show any other features resulting from the three-dimensional flow.

These flows can be elucidated with the help of CFD (Fluent©). The full complexity of the flow requires considerable explanation but the selected images below allow the main features to be identified.

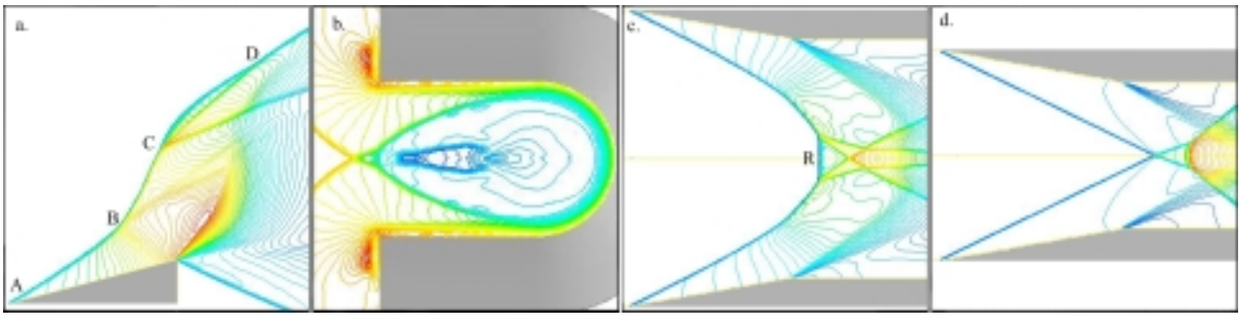


Fig. 5 Flow contours. a,b) Cut model, c,d) Full model

Figure 5a is a symmetry plane density contour plot for the cut model. The conical shock starts at the lip A, curves inwards and then rapidly transitions to a Mach reflection of significant size over a short distance at B. A contact surface and weak reflected wave emanate from this region. The height of the Mach disk then steadily decreases until it transitions to regular reflection at C. A strong contact surface is shed and the shock appears to bifurcate and then rejoin at D. The reason for this is evident from the transverse contours in a plane just downstream of the bifurcation, Fig. 5b. The green egg shape is the reflected wave coming off the Mach disk. The waves diffracting around the model edges now reflect in a regular fashion, which outstrips this contour, and thus two waves are evident in Fig. 1a. At later times the diffracting wave weakens and is overtaken again by the Mach disk reflected wave. A weak shear layer results from this merging, and although not clear in the contour plot appears in the LVS image. Similar phenomena occur for the full model: Fig. 5 b&c are for the mutually perpendicular symmetry planes. Bifurcation still occurs but the shock arising from the regular reflection is now perpendicular to the oncoming flow. What is interesting is that this shock marked R is not visible in the shadowgraph, presumably because the light beam simply passes through the two oblique waves and the line of intersection is too narrow to resolve, coupled with refraction effects.

CONCLUSION

It is shown that complex shock interactions occur in internal 3d flows. The study graphically demonstrates the possibility of mis-interpreting three-dimensional flow results, from both experiment and simulation, in terms of familiar two-dimensional patterns. Three interesting features are identified and clarified, and are the subject of further investigation.

References

[1] Marconi, F. *AIAA J.* **21:**707-713, 1983
[2] Skews, B.W. *J. Fluid Mech.* **407**:85-104, 2000

Turbulent Effects in Type4 Shock Interactions

J. Ballmann*, F. D. Bramkamp, B. U. Reinartz, J. van Keuk
Lehr- und Forschungsgebiet für Mechanik, RWTH Aachen, Templergraben 64, 52056 Aachen, Germany

Type4 shock interactions in hypervelocity flows are investigated numerically using two different codes: The well-known DLR FLOWer-code as well as the QUADFLOW-code developed at the RWTH Aachen. Main focus of the paper is the correct prediction of the high heat loads for the contour caused by these interactions.

The Navier–Stokes equations represent the appropriate model for the simulations. The two–dimensional Navier–Stokes equations for flows in chemical nonequilibrium in a simply connected domain V with boundary ∂V can be written as

$$\int_V \frac{\partial \mathbf{U}}{\partial t} dV + \oint_{\partial V} \left\{ (\mathbf{F} - \mathbf{F}_v)\, e_{n_x} + (\mathbf{G} - \mathbf{G}_v)\, e_{n_y} \right\} dA = \int_V \mathbf{Q} dV \quad (1)$$

where

$$\mathbf{U} = (\rho, \rho u, \rho v, \rho e, \rho X_1, ..., \rho X_{N-1})^T \quad (2)$$

is the vector of conserved quantities with the total density ρ, the cartesian components of velocity u, v, the total energy e and the mass fractions X_i of the corresponding ith species of altogether N species being considered.

$$\mathbf{Q} = (0, 0, 0, 0, \dot{\omega}_1, ..., \dot{\omega}_{N-1}) \quad (3)$$

is the source term as a consequence of the non–equilibrium chemistry, where $\dot{\omega}_i$ are the mass production rates, respectively. Finally $\mathbf{F}$ and $\mathbf{G}$ are the physical flux functions of the convective part of Eq.(1) in the x and y direction, respectively, whereas $\mathbf{F}_v$ and $\mathbf{G}_v$ are the physical flux functions of the diffusive part.

The first numerical algorithm used to calculate approximate solutions of the two–dimensional Navier–Stokes equations is based on the DLR FLOWer–Code (Version 116.x (DLR 2001)). This code was originally developed for the simulation of subsonic and transonic flows and has been extended to supersonic and hypersonic flow computations (van Keuk, Ballmann 1998, Reinartz et al. 2002). In this context several flux–vector– and flux–difference–splitting techniques like AUSM (Liou et al. 1993), AUSMDV (Wada et al. 1994), LDS (Edwards 1997) or the well known scheme of Roe (Roe 1981) have been implemented. Second order in space accuracy is reached by means of MUSCL–Extrapolation where different limiter functions are used to guarantee the TVD property of the schemes. For the discretization of the diffusive part of Eq.(1) central discretization is used. Time integration is performed by an explicit 5–stage Runge–Kutta scheme and for steady state solutions several techniques for convergence acceleration like multigrid, local time stepping and implicit residual smoothing are used. In the framework of a postdoctoral fellowship from the Deutsche Forschungsgemeinschaft the FLOWer–Code is extended to real gas flow simulations with both chemical reactions in local equilibrium and chemical nonequilibrium (van Keuk et al. (2003)). Further modifications concern the calculation of the mixture transport properties. The species viscosities are calculated using Blottner's curve fits (Blottner et al. 1971) whereas Gupta's curve fits are applied for thermal conductivity (Gupta et al. 1990). The mixture properties are calculated following Wilke's mixing rule (Wilke 1950). In the case of chemical nonequilibrium the forward and backward reaction rates in the source term of Eq.(1) are calculated as discussed by Gupta et al. (Gupta et al. 1990).

The QUADFLOW program system is an integrated framework for solving the Euler- and Reynolds-averaged Navier-Stokes equations for compressible fluid flow. Its central objective is to realize adaptively generated discretizations. Preference is given to curvilinear meshes, which are embedded into a multiblock concept. A key idea is to represent such meshes by a parametric mapping from the computational domain into the physical domain by means of B-spline techniques. The mesh is locally adapted to the solution according to the concept of h-adaptation. Adaptation criteria are based on multiresolution techniques. The spatial discretization is based on a finite volume scheme for two- and three-dimensional flow problems. Thereby, the grid is considered as a fully unstructured mesh, composed of simply connected elements with otherwise arbitrary topology. The method is of second order accuracy in space and time. The convective fluxes are discretized with upwind schemes, while diffusive fluxes are handled in a quasi-central fashion. Time integration is based on a fully implicit Newton-Krylov type approach.

At the Graduate Aeronautical Laboratories (California Institute of Technology) hypervelocity flows around blunt bodies with and without impinging oblique shock have been investigated in detail both theoretically and experimentally (e.g. Wen, Hornung 1995, Sanderson 1995). The freestream conditions are for example $\rho_\infty = 0.0155 kg/m^3$, $T_\infty = 1190.60K$, $M_\infty = 6.29$, $Re_\infty/m = 1.63 \cdot 10^6$ and $X_{N_2} = 0.99$. Depending on the impinging point of the oblique shock with the detached bow shock different complex shock interactions arise, that - particularly in the case of the so-called Type4 interaction - lead to very strong thermal loads for the contour. Numerical computations for such flows are carried out with the modified FLOWer–Code. Fig. 1-2 show exemplary measured and calculated results for the density distribution and the wall

*e-mail: ballmann@lufmech.rwth-aachen.de

heat flux. The density distribution is qualitatively well captured, but the numerically predicted heat flux is lower than experimentally observed. So in this paper the influence of turbulent effects on the heat flux is investigated. Furthermore, the improvements using the adaptive flow solver on the one hand and considering the non-equilibrium chemistry on the other hand of the quality of the results is assessed.

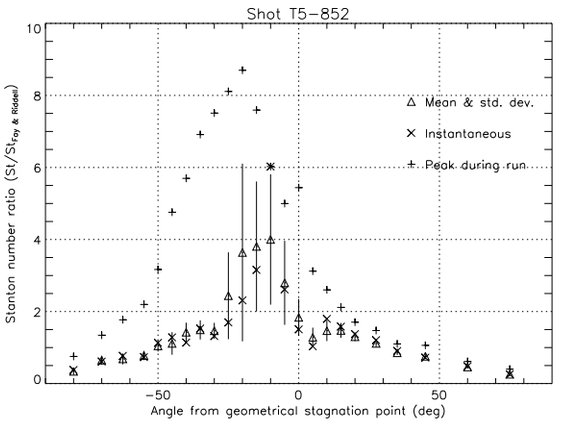


Figure 1. Measured Wall Heat Flux for Type4 Shock-Interaction at $Ma_\infty = 6.29$ (Sanderson 1995).

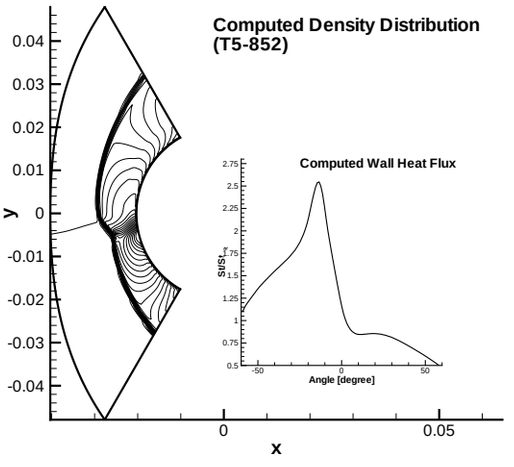


Figure 2. Calculated Density Distribution and Wall Heat Flux for Type4 Shock Interaction at $Ma_\infty = 6.29$ (van Keuk et al. (2003)).

References

Blottner FG, Johnson M, Ellis M (1971) Chemically Reacting Viscous Flow Program for Multi–Component Gas Mixtures. Report No. SC–RR 70-754, Sandia Laboratories, Albuquerque, New Mexico

Bramkamp FD, Gottschlich-Müller B, Hesse M, Lamby P., Müller S, Ballmann J, Brakhage KH, Dahmen W (2003) *H*-Adaptive Multiscale Schemes for the Compressible Navier-Stokes Equations - Polyhedral Discretization, Data Compression and Mesh Generation. Notes Num. Fluid Mech. **84**, pp. 125-204

Deutsches Zentrum für Luft- und Raumfahrt e. V. (2001) FLOWer Version 116.4, Installation and User Handbook. Projekt MEGAFLOW

Edwards JR (1997) A Low–Diffusion Flux–Splitting Scheme for Navier–Stokes Calculations. Computers & Fluids **26**, No. 6 pp. 635-659

Gupta RG, Yos JM, Thompson RA, Lee K (1990) A Review of Reaction Rates and Thermodynamic and Transport Properties for an 11–Species Air Model for Chemical and Thermal Nonequilibrium Calculations to 30000 K. NASA RP–1232

Liou MS, Steffen CJ (1993) A New Flux Splitting Scheme. J. Comp. Phys. **107**, pp. 23-39

Reinartz BU, Herrmann CD, Ballmann J, Koschel WW (2002) Analysis of Hypersonic Inlet Flows with Internal Compression. AIAA Paper 2002-0506

Roe PL (1981) Approximate Riemann Solvers, Parameter Vectors and Difference Schemes. J. Comp. Phys. **43**, pp. 357-372

Sanderson SR (1995) Shock Wave Interaction in Hypervelocity Flow. PhD Thesis, GALCIT, California Institute of Technology

van Keuk J, Ballmann J (1998) Numerical Simulation of Symmetric Corner Flows in the Hypersonic Regime. Notes Num. Fluid Mech. **72**, pp. 250-257

van Keuk J, Ballmann J, Sanderson SR, Hornung HG (2003) Numerical Simulation of Experiments on Shock Wave Interactions in Hypervelocity Flows with Chemical Reactions. AIAA Paper 2003-0960

Wada Y, Liou MS (1994) A Flux Splitting Scheme with High–Resolution and Robustness for Discontinuities. AIAA Paper 94-0083

Wen CY, Hornung HG (1995) Non-Equilibrium Dissociating Flow over Spheres. J. Fluid Mech. **299**, pp. 389-405

Wilke CR (1950) A Viscosity Equation for Gas Mixtures. J. Chem. Phys. **18**, pp. 517-519

Numerical Optimization of 2D Scramjet Inlets

Susumu Hasegawa*#, Doyle Knight*

* Department of Mechanical and Aerospace Engineering
Rutgers University - The State University of New Jersey
98 Brett Road, Piscataway, NJ, 08854-8058
Space Propulsion Research Center
Institute of Space Technology and Aeronautics
Japan Aerospace Exploration Agency
Kimigaya, Kakuda, Miyagi 981-1525, JAPAN

Introduction

A scramjet engine is viewed as a promising propulsion system for a spaceplane, and significant research is in progress worldwide on scramjet engine design and performance. Japan Aerospace Exploration Agency (JAXA) has been conducting scramjet engine research at the flight conditions of Mach 4, 6 and 8 by using the RamJet engine Test Facility (RJTF). A free-piston high-enthalpy shock tunnel (HIEST), the largest in the world, was completed in November 1997. Scramjet Engine Testing in the range of Mach 8 to 15 has been conducted.

The design of an efficient compression system for an airframe-integrated scramjet engine is essential for acceptable performance of a scramjet airbreathing vehicle. The goal in the design of a scramjet inlet is to define a minimum weight geometry that provides an efficient compression process, and provides these characteristics over a wide range of flight and engine operating conditions. The design of a scramjet inlet is complicated by the many constraints, both aerodynamic and mechanical, that are imposed on the inlet. Examples of aerodynamic constraints include starting limits, boundary layer separation limits, and constraints on combustor entrance flow profiles. Examples of mechanical constraints include variable geometry flexibility and cooling system limits. The design of scramjet inlets is influenced greatly by vehicle and flight constraints.

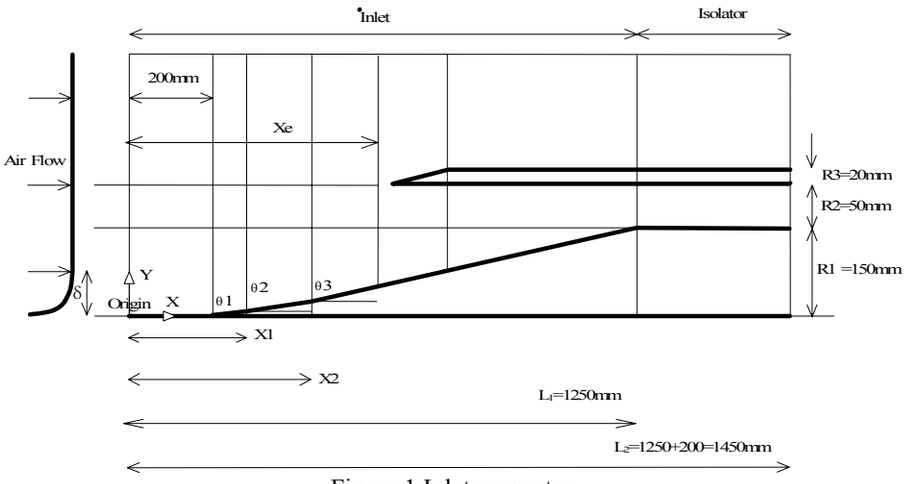


Figure 1 Inlet geometry

This paper focuses on the development and application of an efficient and powerful tool to optimize the aerodynamic performance of a 2D scramjet inlet. The 2D scramjet inlet configuration is presented in Fig.1. The scramjet inlet has three ramps. The computation of the flowfield inside the inlet is performed using the General Aerodynamic Simulation Program (GASPex). In our computations, the inviscid flux scheme is Roe's Method with third-order spatial accuracy restruction using the Min Mod limiter. Turbulence model is represented by the Wilcox k-omega model. A steady state solution is obtained by applying Gauss-Seidel relaxation scheme.

The flowfield inside the inlet is calculated numerically including all relevant flow features such as the interactions between shock waves and expansion waves. The calculated Mach number distribution is

shown in Fig.2.

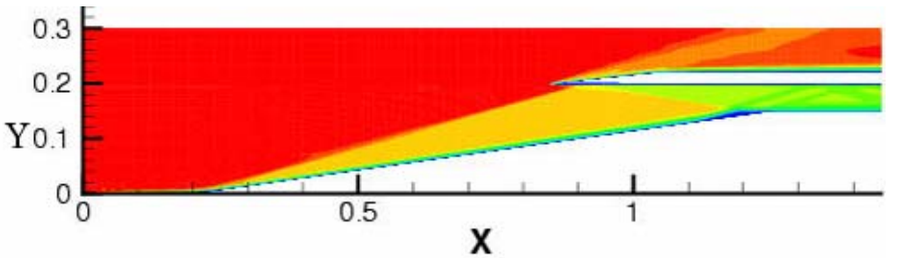


Figure 2 Calculated Mach number distribution

Optimization Algorithm

We consider the general nonlinear problem

$$\text{minimize } F(x) \text{ (or maximize } F(x) \text{)} \quad \text{subject to } G(x) \leq 0$$

where $x = (x_1, x_2, \ldots, x_n)$ is the vector of design variables, F(x)is a scalar function and G（x） is a vector-valued set of nonlinear constraints. F(x) is the fitness function characterizing how much the shape suits the optimization problem. G(x) represents all the constraints of the problem. The design variables x_i are typically geometric parameters defining the inlet shape （*e.g.*, lengths and angles).

There are two families of optimization algorithms. One family is local algorithms such as gradient methods. Another family is constituted by global algorithms such as genetic algorithm (GA), and simulated annealing (SA). In our research, the optimization of the 2D scramjet inlet began to be performed by the gradient-based algorithms. From a basic shape, the gradient-based algorithms are able to quickly find an optimum. However, they have some drawbacks that make their use difficult for complex industrial problems. They can easily be trapped by local minima. The method used is C code for feasible sequential quadratic programming (CFSQP). CFSQP is a set of C functions for the minimization of the maximum of a set of smooth objective functions (possibly a single one) subject to nonlinear equality and inequality constraints, linear equality and inequality constraints, and simple bounds on the variables.

In this optimization program, the objective function is the total pressure recovery η. To maximize the total pressure recovery is as same as to maximize the kinetic energy efficiency. The geometrical constraints are linear inequality constraints, and a nonlinear equality constraint, which are shown in the following.

$$0 \leq \theta_1 \leq \theta_2 \leq \theta_3 \text{ (radians)}, \; 0.2 \leq X_1 \leq X_2 \leq 1.25 \text{ (m)}, \; 0.2 \leq Xe \leq 1.25 \text{ (m)}$$

$$(X_1 - 0.2)\tan(\theta_1) + (X_2 - X_1)\tan(\theta_2) + (1.25 - X_2)\tan(\theta_3) = 0.15 \quad \text{(m)}$$

Scramjet Inlet Optimization

To perform the scramjet inlet optimization, our first step was to optimize the inlet assuming uniform inflow condition. The initial total pressure recovery coefficient η is obtained as 0.545. Depending on the runs, from 5 to 13 line searches were performed during these optimizations. The maximum value obtained by these computations is η_{max} =0.599. The maximum value is higher than the initial value by 9.9%. Then, the optimization was performed in case that the inflow boundary layer δ is 61.7mm. The initial total pressure recovery η is 0.575, and the maximum value obtained by these computations is η_{max} =0.626. The maximum value is higher than the initial value by 8.9%. Further optimized results and discussion will be presented in the conference.

XXI ICTAM, 15–21 August 2004, Warsaw, Poland

THE MACH REFLECTION OF WEAK SHOCKS

John K. Hunter*, Allen M. Tesdall**
*Department of Mathematics, University of California at Davis, CA, USA
**Department of Mathematics, University of California at Davis, CA, USA

Summary We present numerical solutions of weak shock Mach reflections that contain a remarkably complex sequence of supersonic patches, triple points, and expansion fans immediately behind the leading triple point. This structure resolves the von Neumann triple point paradox of weak shock Mach reflection.

During the second world war, von Neumann carried out an extensive study of shock reflection [5]. He suggested a number of criteria for the transition from regular to Mach reflection, and compared his theoretical results with observations. There was generally excellent agreement for strong shocks, but for weak shocks serious discrepancies were found. In particular, a pattern closely resembling simple Mach reflection is observed for weak shocks, but no standard triple point configuration is compatible with the jump relations across shocks and contact discontinuities. This discrepancy was called the 'von Neumann triple point paradox' by Birkhoff [1]. Many different resolutions of this paradox have been suggested over the years [3].

In this paper, we present numerical solutions of initial and boundary value problems for the unsteady and steady transonic small disturbance equations that provide an asymptotic description of weak shock Mach reflection. These solutions contain a sequence of supersonic patches, shocks, expansion fans, and triple points in a tiny region behind the leading triple point. We conjecture that this sequence is infinite for an inviscid weak shock Mach reflection. At each triple point, there is an additional expansion fan, thus resolving the apparent conflict with von Neumann's theoretical arguments. Furthermore, an infinite sequence of shrinking supersonic patches resolves theoretical difficulties connected with the transition from supersonic to subsonic flow at the rear of the supersonic region.

The existence of a supersonic patch and an expansion fan at the triple point of a weak shock Mach reflection was proposed by Guderley [2], although he did not give evidence that this is what actually occurs, nor did he suggest that there is, in fact, a sequence of supersonic patches and triple points. Previous numerical solutions of weak shock Mach reflections with supersonic patches behind the triple point were obtained in [4, 7, 8], but none of these solutions were sufficiently resolved to show the true structure of the solution.

An asymptotic shock reflection problem for the unsteady transonic small disturbance equations, which have the normalized form

$$u_t + \left(\frac{1}{2}u^2\right)_x + v_y = 0, \qquad u_y - v_x = 0, \tag{1}$$

together with appropriate initial and boundary conditions, may be derived from the compressible Euler equations by the method of matched asymptotic expansions [4]. A numerical solution of this problem, from [6], using a highly refined grid near the triple point is shown in Figure 1. There is a sequence of supersonic patches, shocks, expansion fans, and triple points in a tiny region immediately behind the leading triple point. The change from supersonic to subsonic flow at the rear of the region by means of a subsonic triple point appears to be impossible because no expansion fan can then occur, and a continuous change across a sonic line is unlikely because it would result in an apparently overdetermined boundary value problem for a partial differential equation of mixed-type (the hyperbolic region would be enclosed by a sonic line that lacks a 'gap'). This argument, together with the numerical results, suggests that the sequence of supersonic patches is infinite.

This phenomenon of repeating supersonic patches is likely to be widespread, and we will also show recent numerical results of similar steady Mach reflections that occur in transonic flows.

References

[1] G. Birkhoff, *Hydrodynamics*, Princeton University Press, Princeton, 1950.
[2] K. G. Guderley, *The Theory of Transonic Flow*, Pergamon Press, Oxford, 1962.
[3] L. F. Henderson, Regions and boundaries for diffracting shock wave systems, *Z. Angew. Math. Mech.*, **67** (1987), 73–86.
[4] J. K. Hunter, and M. Brio, Weak shock reflection, *J. Fluid Mech.*, **410** (2000), 235–261.
[5] J. von Neumann, Oblique reflection of shocks, U.S. Dept. Comm. Off. Tech. Serv. No. PB37079 (1943), reprinted in *John von Neumann, Collected Works*, Vol. VI, Pergamon Press, New York, 1963.
[6] A. M. Tesdall, and J. K. Hunter, Self-similar solutions for weak shock reflection, *SIAM J. Appl. Math.*, **63** (2002), 42–61
[7] E. I. Vasilev, and A. N. Kraiko, Numerical simulation of weak shock diffraction over a wedge under the von Neumann paradox conditions, *Computational Mathematics and Mathematical Physics*, **39** (1999), 1393–1404.
[8] A. R. Zakharian, M. Brio, J. K. Hunter, and G. Webb, The von Neumann paradox in weak shock reflection, *J. Fluid Mech.*, **422** (2000), 193–205.

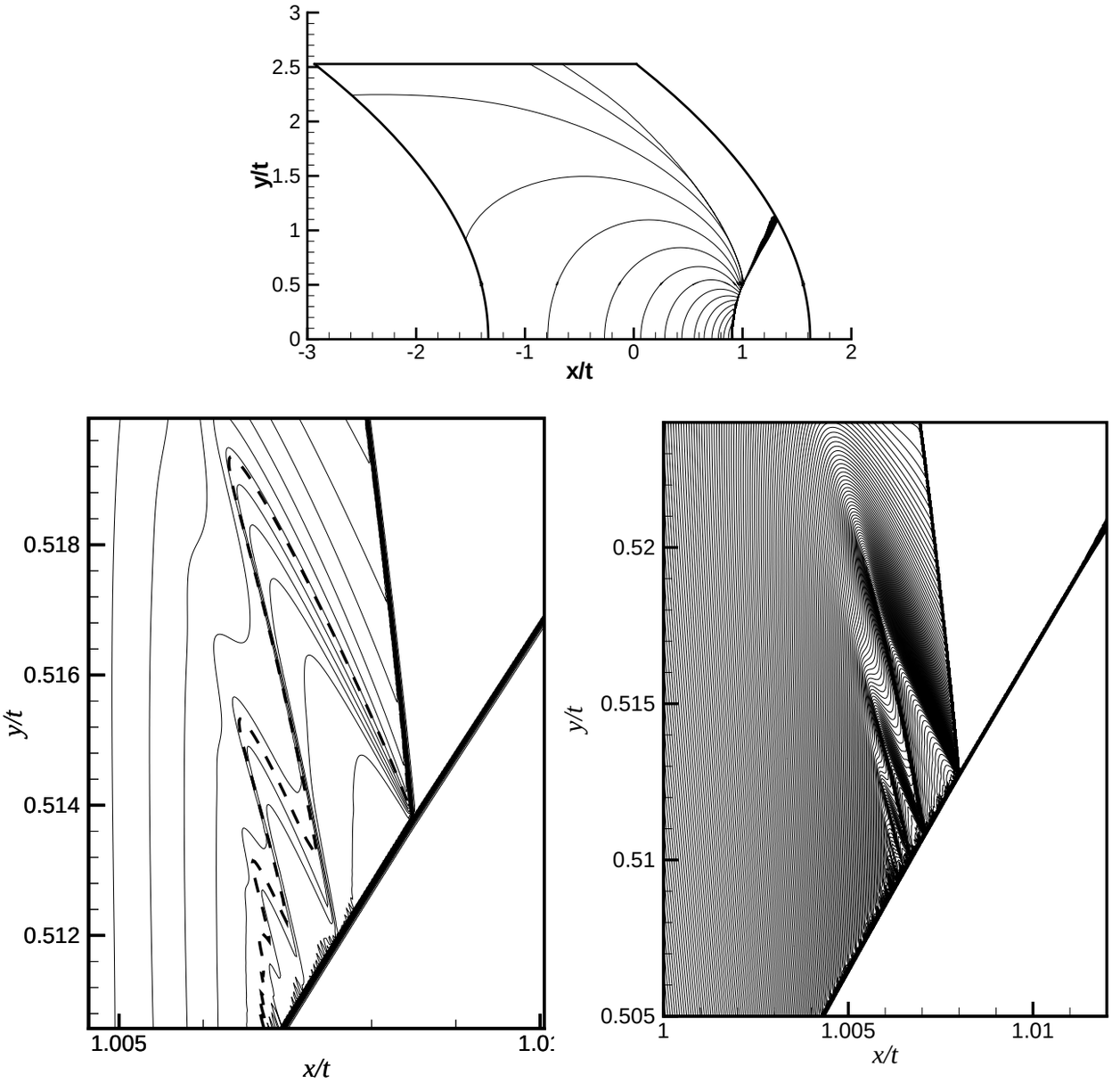


Figure 1. Plots of u-contours in a self-similar Mach reflection solution of the unsteady transonic small disturbance equation (1). The top picture shows the global solution as a function of self-similar coordinates $(x/t, y/t)$. The lower picture shows the local structure of the solution in a tiny region near the triple point, with a sequence of shocks, fans, triple points, and supersonic patches immediately behind the leading triple point. The dashed line in the lower left picture is the numerically computed location of the sonic line where the self-similar equations change type.

EFFECT OF SURFACE ROUGHNESS ON MACH REFLECTION

Susumu Kobayashi*, Takashi Adachi*, Klaus Debatin**, Torsten Schenkel**, Herbert Oertel, Jr.**
* Department of Mechanical Engineering, Saitama Institute of Technology, 369-0293 Saitama, Japan
** Institut für Strömungslehre, Universität Karlsruhe, 76128 Karlsruhe, Germany

Summary The effects of surface roughness and transport properties have been compared experimentally to investigate non-self-similar Mach reflection phenomena. The surface roughness was given by pasting a piece of sand paper on the model surface. The results were compared with those for smooth surfaces. The effect of surface roughness turned out to be small compared with viscosity effect so that the effect of transport properties is proved to be dominant.

INTRODUCTION

It was first reported by Walenta [1] some twenty years ago that, under rarefied-gas conditions, the transition from regular to Mach reflection takes place during the incident shock propagation over a wedge. This non-self-similar phenomenon was first considered to be a phenomenon characteristic of extremely low-pressure, low-density atmosphere, because such dynamic transition phenomena have never been observed in ordinary atmospheric conditions. However, the authors observed a same kind of phenomenon even in atmospheric pressure for the first time [2], proving that such non-self-similar phenomenon is not restricted to low-pressure conditions.
The disruption of self-similarity suggests that a length scale has been introduced into the system. There are two candidate causes: viscosity and surface roughness. According to Henderson et al.'s numerical experiment [3], the condition on the solid boundary plays a key role in the phenomenon. The authors' experiment in Karlsruhe found different wave angles from those obtained in Saitama [4]. In the Karlsruhe experiment, the initial pressure p_1 of the driven section was below atmospheric pressure and ranges from 280 mmHg to 610 mmHg depending on shock Mach number M_i. In addition, the model surface roughness was estimated from 6 to 12 μm. In contrast, in the Saitama experiment, p_1 was atmospheric pressure and the surface roughness ranged from 1 to 2 μm. When the pressure is low, the effect of viscosity is enhanced, as seen by the definition of kinematic viscosity. Therefore, the results for both experiments are subject to mixed effects of viscosity and surface roughness. In this paper, we investigated the effect of surface roughness on the behavior of Mach reflection.

EXPERIMENT

Experimental Apparatus

We performed the experiments using a conventional shock tube in our institute. The working gas was air, and the driven section was set at room temperature and atmospheric pressure at each experiment run. The models were ordinary smooth wedges of 20º and 30º, over which a sheet of sandpaper was firmly pasted to keep it flat. We could select from two surface roughnesses by changing sandpaper (#60 and #240). This means the surface is not hydraulically smooth according to Ben-Dor et al [5]. In contrast, the surface roughness in past experiments [4] was 12 μm maximum, and the wedge surface was hydraulically smooth. The incident shock Mach number M_i was 1.10, 1.20, 1.30 and 1.40. However, only partial results are presented here due to page restrictions.

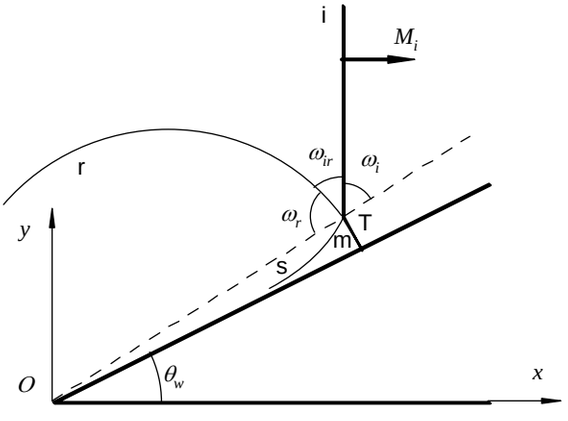


Fig. 1 Definition of geometric variables

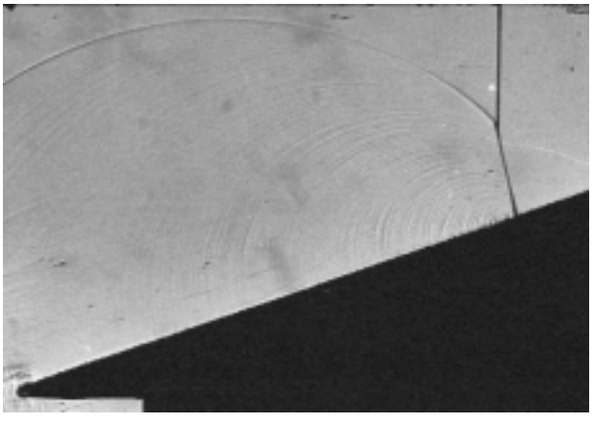


Fig. 2 Visualized reflection configuration

Measurement

The triple-point coordinate (x, y) and the angle ω_{ir} made by the incident and reflected shocks at the triple point were measured (see Fig. 1) directly from photographic negatives enlarged by a factor of about 50 using a profile projector (V-12, Nikon, Inc.). In measuring the triple-point location, the model corner ahead of the incident shock was taken as a

reference point to avoid the influence of optical distortion behind the shock waves. The triple-point location was easily converted in the coordinate system with the leading edge taken as the origin *O*, and the incident shock propagation direction as the *x*-axis. The *y*-axis was defined upward normal to the *x*-axis. The maximum error involved in measuring the angle ω_{ir} is ±2.0º at an early stage of reflection (10 mm < x < 30 mm) where the radius of curvature of the reflected shock is small. However, the error is reduced within ±1.0º as the incident shock proceeds (x > 40 mm). The error was very large (around ±5º) for x < 5 mm.

RESULTS

Reflected wave configuration

Figure 2 shows a representative image of shock reflection over the wedge with surface roughness (M_i = 1.40, θ_w = 20º, #60, x = 64.19mm). A group of compression wavelets issues cylindrically from the wedge surface (see behind the foot of the Mach stem). The wavelets are more clearly observed when the surface roughness is larger, and their pattern is quite similar to the shock reflection over a multi-guttered wedge or a step-like wedge [6]. Although the data are omitted here, the triple-point trajectory proved to be almost independent of the surface roughness.

Variation of the angle between incident and reflected shocks

Figure 3 illustrates the variation of the angle ω_{ir} made by the incident and reflected shock waves at the triple point as the incident shock proceeds (M_i = 1.40). Angle ω_{ir} is large near the wedge tip but decreases and approaches an asymptotic value with the progress of the incident shock wave. The behavior of ω_{ir} shows that the Mach reflection is not self-similar. On the whole, angle ω_{ir} is smallest for smooth wedges. However, the difference is not clear for large x. Therefore, the effect of surface roughness on the wave angles is not strong.

The effect of viscosity can be taken into account by defining the dimensionless variable, $\zeta = \dfrac{\rho_1 u_r}{\mu_1} x$, where ρ_1 and μ_1 are the density and viscosity behind the incident shock, and u_r is the flow velocity there. With this transformation of space variable x, the difference of ω_{ir} obtained in Saitama and Karlsruhe diminishes as in Fig. 4 (M_i = 1.30). The difference is still large for M_i = 1.20 and 1.40. Possibly the error in angle measurement was larger than expected.

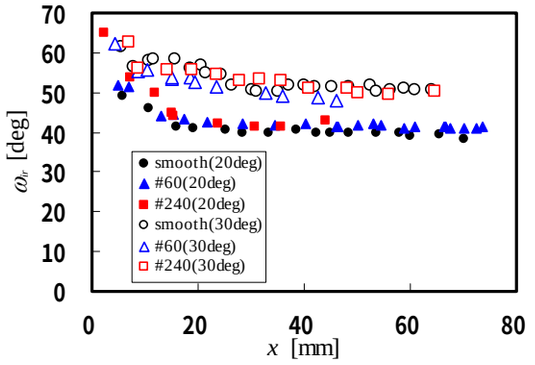


Fig. 3 The angle ω_{ir} between incident and reflected shocks

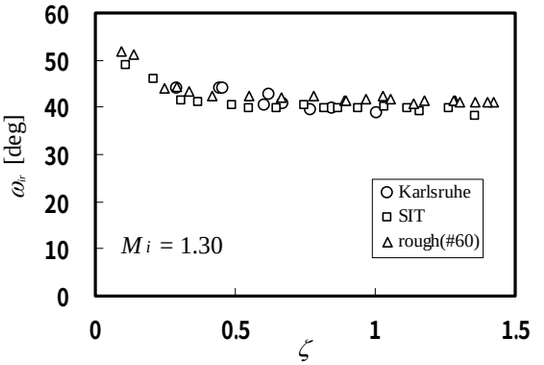


Fig. 4 The angle ω_{ir} in the dimensionless coordinate

CONCLUSIONS

The results show that the effect of surface roughness is not distinct with smooth (less than the surface roughness of about 10μm) wedges. This negative result leads to the conclusion that the effect of viscosity is dominant in non-self-similar phenomena of Mach reflection. Consequently, the difference in the two kinds of experiments [4] should be ascribed solely to viscosity.

References

[1] Walenta Z.: Formation of Mach-type reflection of shock waves, Arch. Mech. 35: 187-196, 1983.
[2] Kobayashi S., Adachi T., Suzuki T.: On the unsteady transition phenomenon of weak shock waves, Theoret. Appl. Mech.: 49: 271-278, 2000.
[3] Henderson L. F., Crutchfield, W. Y., Virgona R. J.: The effects of thermal conductivity and viscosity of argon on shock waves diffracting over rigid ramps, J. Fluid Mech. 331: 1-36 , 1997.
[4] Kobayashi S., Debatin K., Oertel Jr. H., Adachi T.: Non-selfsimilar nature of Mach reflection over a flat smooth slope, Proc. 23rd Int. Symp. Shock Waves: 1262-1267, 2002.
[5] Ben-Dor G., Mazor G., Takayama K., Igra O.: Influence of surface roughness on the transition from regular to Mach reflection in pseudo-steady flows, J. Fluid Mech. 176: 333-356, 1987.
[6] Suzuki T., Adachi T., Kobayashi S.: Nonstationary shock reflection over nonstraight surfaces, Shock Waves 7: 55-62 , 1997.

ON THE THEORY FOR SUBSONIC, TRANSONIC AND SUPERSONIC FLOWS IN WATER WITH SUPERCAVITATION

Vladimir Serebryakov [**], Guenter H. Schnerr [*]

[**] *Ukrainian Academy of Sciences, Institute of Hydromechanics, 8/4 Sheliabov Str., 03057Kiev, Ukraine*

[*] *Technical University of Munich, Dept. of Gasdynamics, Boltzmanstraße 15, D-85748 Garching, Germany*

Summary Theoretical consideration are performed to improve further understanding of compressibility effects as a whole in the new field of hydrodynamics at super high speeds in the range of the speed of sound of water which is order of c~1500m/s.

For very high speed in water the body motion is realized in a vapor filled cavity, created by a small blunt nose part of the body, the so called cavitator. Under these conditions most part of the body is separated from the liquid fluid, which implies the possibility to avoid considerable viscous losses and achieve a very low total drag, comparable to that of high speed motion in air. Up to now classical supercavitation modelling is based mainly on the incompressibility assumption and can be found in number of well known books, e.g. of G Birchoff and E. Zarantonello [1], M. Gurevich [2]. Axisymmetric flow can be illustrated by a simple heuristic model which follows from the Slender Body Theory (SBT). Moving through a fluid at rest, the cavitator pushes fluid aside and its momentum is converted into energy of a practically radial flow in every lateral section of the cavity. Further, a practically independent expansion and compression of lateral cavity sections occur in interaction with the surrounding pressure p_∞ and pressure in the cavity $p_c \sim 0$. Minimum drag coefficients are achieved by establishing the maximal slenderness of the cavity. One of the most effective technique for prediction of minimum drag is the application of simple heuristic models, together with integral conservation laws and combined with the perturbation theory. In the past, this approach gave the possibility yet for 40-50 years to estimate shape and main scaling of cavities, e.g. by H. Reichardt, A. May , G. Logvinovich , P. Garabedian and others. Considerable advances have been achieved by M. Tulin and his 2-D linear theory for supercavitation, which stimulated the development of a linearized axisymmetric theory using the SBT and the Matched Asymptotic Expansion Method (MAEM) [3-4]. Important results here were obtained by C.C. Grigorian, Yu. L. Yakimov, A.G. Petrov too. The base of the linearized theory is the integro-differential equations (IDE) for slender axisymmetric cavities and it's solution with help of asymptotic expansions with the slenderness parameter δ. The most important configuration is the singular case for small cavitators including a disc. The solution is separated into the 3 zones: The inner near cavitator solution (nonlinear for disc), the intermediate solution on the base of known Gurevich - Levinson asymptotic development at infinity and the solution for the outer field as ellipsoidal cavity perturbation problem. With the help of matching and by using the M. Van Dyke additive rule suitable solutions are found. The (IDE) for $M = 0$ has the same form as that for $M < 1$ and for $M > 1$ it has the same structure, which gives the possibility to apply this approach for the theory for $M < 1$ and $M > 1$ too. Despite of essential achievements the situation in the field of super high speeds in water a as whole is far from ideal. Note, here one of the first experiments for $M > 1$ [5] at speeds of motion till $1000\,m/s$ has been performed by Yu. Yakimov, speeds till $1200 - 1300\ m/s$ - in [6], not high $M > 1$ have been investigated in [7]. Small scale experiments have been performed by: Yu. Bivin - Yu Gluchov - Yu. Permiakov, C. Voidneck, M. Schaffar too. All experiments are for the natural pressure of $1\,bar$ only. Nonlinear numerical calculations in case of cone and disc for $M < 1$, $M > 1$ are obtained in [8], a numerical-analytical approach for $M < 1$ is developed in [9]. Results of linearized approaches for $M < 1$, $M > 1$: linear 2-D theory in [10], axisymmetric linearized theory in [11,12], 2-D plane theory in [14]. Numerical calculations have been presented by A. Terentiev - A. Chechnev, generalization of the model for top high speed - by R. Saurel, J.P Cocchi, P.B. Butler, and an attempt to predict finite cavities in the regime of not large $M > 1$ - by A. Vasin. The existing theoretical models have been developed for total pressures till $25000 - 30000\ bar$, by applying Tait's equation of state for water in adiabatic form, together with the compressible Bernoulli equation and the know dependence for the speed of sound:

$$\text{a)}\ \frac{P+\mathbf{B}}{\rho^n} = \frac{P_\infty+\mathbf{B}}{\rho_\infty^n}, \qquad \text{b)}\ c^2 = \frac{dP}{d\rho} = \frac{n(P+\mathbf{B})}{\rho}, \qquad \text{c)}\ \frac{n}{n-1}\frac{P+\mathbf{B}}{\rho} + \frac{(U_\infty+u)^2+v^2}{2} = \frac{n}{n-1}\frac{P_\infty+\mathbf{B}}{\rho_\infty} + \frac{U_\infty^2}{2}, \qquad (1)$$

$\mathbf{B} = 3045\,\mathbf{kg}/\mathrm{cm}^2$, $n = 7{,}15$, p, p_∞; ρ, ρ_∞ pressure, density in the flow and at infinity, respectively, u, v components of perturbation speed, U_∞ speed at infinity. (IDEs) for the slender axisymmetric cavities $r = R(x)$ on the base of SBT are:

$$M<1: \quad \frac{1}{2R^2}\left(\frac{dR^2}{dx}\right)^2 + \frac{d^2R^2}{dx^2}\ln\frac{m^2R^2}{4x(L-x)} - \int_0^{x_o}\frac{\frac{d^2r_1^2}{dx^2}|_{x=x_1} - \frac{d^2R^2}{dx^2}}{|x_1-x|}dx_1 - \int_{x_o}^{L}\frac{\frac{d^2R^2}{dx^2}|_{x=x_1} - \frac{d^2R^2}{dx^2}}{|x_1-x|}dx_1 - \frac{\frac{dr_1^2}{dx}|_{x=0}}{x} + \frac{\frac{dR^2}{dx}|_{x=L}}{L-x} = 2\sigma_\infty$$

$$M>1: \quad \frac{1}{2R^2}\left(\frac{dR^2}{dx}\right)^2 + \frac{d^2R^2}{dx^2}\ln\frac{m^2R^2}{4x^2} - 2\int_0^{x_o}\frac{\frac{d^2r_1^2}{dx^2}|_{x=x_1} - \frac{d^2R^2}{dx^2}}{|x_1-x|}dx_1 - 2\int_{x_o}^{x}\frac{\frac{d^2R^2}{dx^2}|_{x=x_1} - \frac{d^2R^2}{dx^2}}{|x_1-x|}dx_1 - 2\frac{\frac{dr_1^2}{dx}|_{x=0}}{x} = 2\sigma_\infty \qquad (2)$$

$x = x_o$ -separation section, $\sigma_\infty = 2(p_\infty - p_c)/\rho_\infty U_\infty^2$ - cavitation number, $m = \sqrt{|M_\infty^2 - 1|}$, $r = r_1(x)$ - a slender cavitator form. Interstitial (ODE) are extracted from (IDE) and its intermediate asymptotics Eqs.3, and from asymptotic solutions for $\sigma = 0$ in the particular in case of a disc for $M < 1$ Eq. 4a , and for a slender cone for $M > 1$ Eq. 4b are obtained:

$$M<1:\quad R^2 = \frac{2\sqrt{c_{do}}\,x}{\left[\ln\left(x^2/R^2\right)\right]^{0.5}}\left[1-\frac{1}{2}\frac{\ln\left(4/em^2\right)}{\ln\left(x^2/R^2\right)}+...\right] \sim \frac{x}{(\ln x)^{0.5}}; \qquad M>1:\quad R^2 = \frac{K_s}{(\ln x^2/R^2)^{3/2}}\left[1+\frac{3}{2}\frac{\ln m^2/4}{\ln x^2/R^2}\right] \sim \frac{x}{(\ln x)^{3/2}} \qquad (3)$$

a) $$R^2 = 1+\frac{2\sqrt{(c_{do})}\,x}{\sqrt{\ln\left\{\dfrac{4(\Delta+x/\sqrt{e})^2/m^2}{[1+2\sqrt{(c_{do}}\,x/\sqrt{\ln(4\Delta^2+x)}]}\right\}}}, \quad R_n = 1, \quad \Delta = 0.5\left[\sqrt{c_{do}} + 1/\sqrt{c_{do}}\right];$$ b) $$R^2 = \varepsilon^2\left[2x\left(\frac{\ln 1/\varepsilon^2}{\ln x/\varepsilon^2}\right)^{3/2} - 1\right]_{x\to\infty} \sim \frac{x}{(\ln x)^{3/2}} \qquad (4)$$

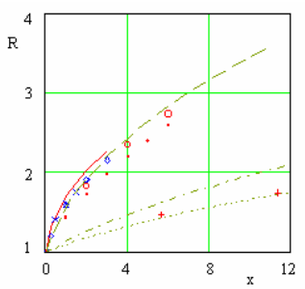


Fig. 1 Front part of cavities, $\sigma = 0$
— — — disc $M = 0$ solution Eq.4,
——— numerical calculation L. Guzevsky ,
◇◇◇◇, × × × × experiment G. Logvinivich
— - — cone $\gamma = 10^o$ solution for $M = 0$
o o o o , • • • • disc $M = 1$, $M = 2$ nonlinear numerical calculation [7]
------ cone $\gamma = 10^o$, $M > 1$ solution Eq. 4
+ + + cone $\gamma = 10^o$, $M = 2$ [7]

Here $R_n = 1$ is the disc radius, $\varepsilon = \tan\gamma$, γ - cone semi-angle, c_{do} - cavitator drag coefficient for $\sigma = 0$, K_s - asymptotic constant for $M > 1$. The linearized second order theory [11-12] predicts not large compressibility influence at $M < 1$, experiments [6] confirm Eqs. 3, 4 until $M \sim 0.6\text{-}0.8$. In case of cavities behind slender cavitators for $M > 1$ the compressibility influence is not large, but if the cavity become essentially large as compared to the cavitator this influence can become very important. For $M < 1$ the solutions of the Eqs. 3, 4 express the energy conservation law, for $M > 1$ - a considerable wave loss appears depended on the cavitator form. For $M > 1$ the asymptotic behavior of Eq. 3 is confirmed by experiments [7], even for very not high $M > 1$, solutions of the type of Eq. 4 for a cone are confirmed by numerical calculations [8]. As result the shape of the front part of cavities at $M > 1$ can be considerable more narrow as compared with $M < 1$. The results of the prediction of the front part of the cavities are demonstrated by Fig. 1. The compressibility influence on the aspect ratio of finite cavities is not large and is estimated by the known dependence $\lambda = \sqrt{(\ln 1.5m^2/\sigma)/\sigma}$. At the same time the coefficient $k \sim 1$ in the known formula for the maximal radius $R_k = R_n\sqrt{c_d/k\sigma}$ at $M < 1$ - in case of $M > 1$ can be essentially more than 1 and accordingly the size of the finite cavities can be considerable more small as compared with the $M < 1$ case. Thanks to the very high adiabatic coefficient $n = 7{,}15$ a very vide transonic Mach number regime in water with mixed flow of $M < 1$ and $M > 1$ is discovered, here transonic equation is applied:

$$\frac{\partial^2\varphi}{\partial r^2} + \frac{1}{r}\frac{\partial\varphi}{\partial r} + \left[\left(1-M_\infty^2\right) - \frac{(n+1)M_\infty^2}{U_\infty}\frac{\partial\varphi}{\partial x}\right]\frac{\partial^2\varphi}{\partial x^2} = 0,$$

what gives the possibility to estimate the aspect ratio of transonic cavities and the drag coefficient of slender cavitators [12]. At present the most important topic is the investigation of the transonic supercavitating flows and making additional special experiments for verifications of the theory.

References

[1] Birkhoff G., Zarantonello E.: Jets, Wakes and Cavities. New York, Academic Press,1957.
[2] Gurevich M. I.: Theory of Jets of Ideal Fluid. Moscow, Nauka. 1978.
[3] Serebryakov V.V.:Asymptotic Solution of the Problem on Slender Axisymmetric Cavity", *J. DAN of Ukranian SSR, ser. A* , 12, 1973.
[4] Logvinovich G. , Serebryakov V.: On Methods of Calculation of Slender Axisymmetric Cavities Shape. *J. Hydromechanics* 32, 1975.
[5] Howard Mc-Millen J., Newton Harwey E.: A Spark Shadow Graphic Study of Body Waves in Water". J. Applied Physics, 17, 7, 1946.
[6] Savchenko Yu. N., Semenenko V. N.., Serebryakov V. V.: The Experimental Investigations of Supercavitation in Subsonic Flow. *J. DAN of Ukraine* 2 , 1993.
[7] Kirschner I. N.: Supercavitating Projectile Experiments at Supersonic Speeds. Agard-R-827, 1998.
[8] Aleve G. A.: Separating Flow of Circle Cone by Transonic flow of Water. *J. Trans. of AS USSR, MFG* :1, 1983.
[9] Zigangareva L. M. , Kiselev O. M.: Subsonic Flow of Compressible Fluid for Small Cavitation Numbers. *Trans RAN, MFG* 4, 1998.
[10] Nishiyama T. and Khan O.: Compressibility effects upon cavitation in High-Speed Liquid Flow (Transonic and Supersonic Liquid Flows). *Bulletin of the Japanese Society of Mechanical Engineers* 24, 190, 1981.
[11] Serebryakov V.V.: Asymptotic Solutions of Axisymmetric Problem for Sub- and Supersonic Separate Flows in Water under Zero Cavitation Number. *J. DAN of Ukraine* 9, 1992.
[12] Serebryakov V.V., Schnerr: G.H.: Some Problems of Hydrodynamics for Sub-, Trans- Supersonic Motion in Water with Supercavitation. *Proc. of 4-th Intern. Symposium on Cavitation, Osaka, Japan*, 2003, web site **http://flow.me.es.osaka-u.ac.jp/cav2003**.
[13] Mayboroda A. N.: Planing for Sub- and Supersonic Speeds. Intern. Sci. School "High Speed Hydrodynamics", Chebocsary, Russia, 2002.

INTERACTION OF SUPERSONIC FLOWS IN AN EJECTOR

Václav Dvořák [*], Pavel Šafařík [**]
[*]*Technical University of Liberec, Department of Power engineering, 461 17 Liberec, Czech Republic.*
[**]*Czech Academy of Sciences, Institute of Thermomechanics, 182 00 Praha, Czech Republic.*

Summary The article deals with experimental, theoretical and numerical study of the interaction of supersonic flows on the trailing edge of a primary flow nozzle of an ejector. The mechanism of mutual deflection of supersonic flows is explained. The influences of back pressure ratio and stagnation pressure ratio of both flows on the interaction are presented. Recommendations for design and for operation of supersonic ejectors are formulated.

INTRODUCTION

The geometry of the trailing edge of the primary flow nozzle of a supersonic ejector is visible on Figure 1a. If the back pressure ratio is sufficiently low, both flows are supersonic and the interaction of supersonic flows on the trailing edge occurs. We studied this interaction by means of experimental, theoretical and numerical methods [1]. We used schlieren and interferometric methods to visualise two-dimensional flow field. We used Fluent 6.0 program for numerical computation and we get theoretical results with help of relations of shock waves theory. We observed that there can be two different solution for given stagnation pressure ratio and that the process of mutual deflection of supersonic flows is more complicated. The aim of this study is to understand the interaction and how it influences the mixing processes in the ejector. It allows us to optimise the design and operation of supersonic ejectors.

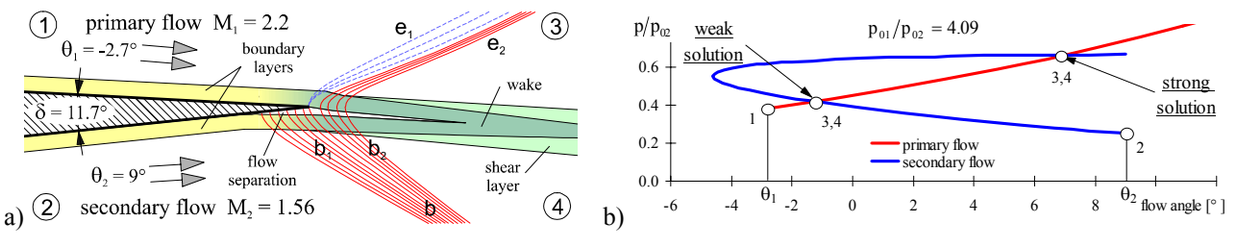


Figure 1: The interaction of supersonic flows on the trailing edge of the primary flow nozzle; a - scheme, b - theoretical solution for the regime of $p_{01}/p_{02} = 4.09$.

RESULTS

The influence of the back pressure ratio p_p/p_{02} was investigated for stagnation pressure ratio $p_{01}/p_{02} = 4.09$. The possibility of two different solutions of the interaction of supersonic flows on the trailing edge of the primary flow nozzle can by explained with help of theoretical results on Figure 1b. The two pressure-deflection shock polars representing both flows in diagram static pressure ratio - flow angle have two common points representing two solutions. The sum of deflection of both flows is given by the angle of the trailing edge δ .When the back pressure ratio is $p_p/p_{02} =< 1.1$ a weak solution occurs. There are weak shock waves in either flow and both flows remain supersonic. When the back pressure ratio is $p_p/p_{02} = 1.12$ a strong solution appears [2]. There is a weak shock wave in the primary flow and a strong shock wave in the secondary flow. The primary flow remains supersonic while the secondary flow becomes subsonic. The schlieren and the interferometric pictures of the weak solution are on Figure 2a and pictures of strong solutions are on Figure 2b. Let us focus on the weak solution. We can see from pictures, that the process of interaction of supersonic flows is more complicated due to the effects of viscosity.

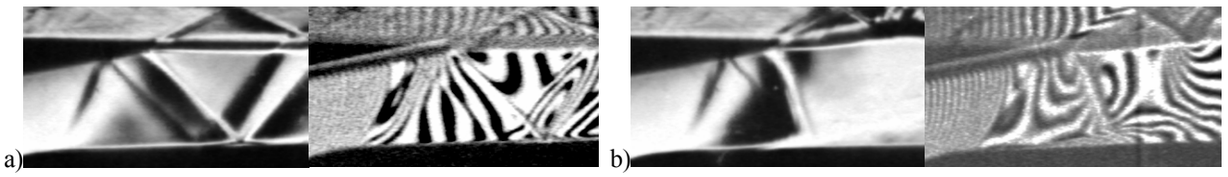


Figure 2: Schlieren and interferometric pictures of the interaction for $p_{01}/p_{02} = 4.09$, a - weak solution, b - strong solution.

The effects of viscosity can be explained with help of numerical solutions in Figure 3 and with help of scheme in Figure 1a. The whole process of mutual deflection of supersonic flows begins just ahead of the trailing edge by pressure levelling. The static presser is different on both sides of the trailing edge and its equalising ahead the trailing edge is allowed by subsonic part of boundary layers on both sides of the trailing edge. It caused a pressure rise in the

secondary flow and the secondary flow separates. This flow separation yields compression wave signed (b1) - see Figure 1a. There is a pressure drop in the primary flow ahead of the edge and it gives a Prandtl-Meyer expansion signed (e1). As we can see on static pressure contours on Figure 3, the static pressures of both flows are equal just on the trailing edge. The flow angles downstream of the edge are matching and the pressure rises. It gives compression wave (b2) in the secondary flow and compression wave (e2) in primary flow.

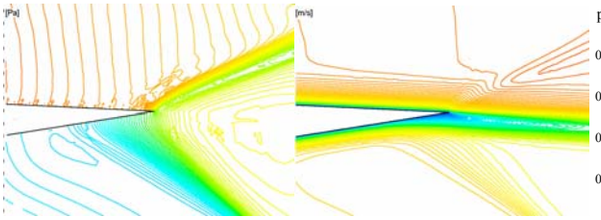


Figure 3: Numerical solutions - contours of static pressure and contours of velocity for $p_{01}/p_{02} = 4.09$.

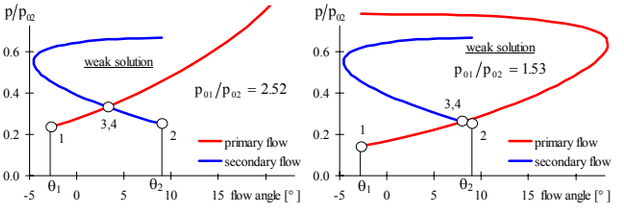


Figure 4: Theoretical solutions of interaction for regimes of $p_{01}/p_{02} = 2.52$ and $p_{01}/p_{02} = 1.53$.

The shear layers begin on the trailing edges and they propagate downstream. The shear layer is seen as a light area, the dark area is a wake which is formed by boundary layers streaming off both sides of the trailing edge and at the secondary flow separation. The wake is very relevant for mixing processes, because it separates both flows and so the mixing processes are delayed.

The influence of stagnation pressure ratio on the interaction of supersonic flows can be shown on regimes of the ejector on Figure 5. There is a regime of $p_{01}/p_{02} = 2.52$ on Figure 5a and a regime of $p_{01}/p_{02} = 1.53$ on Figure 5b. Theoretical solutions of these regimes are on Figure 4. The lower stagnation pressure ratio p_{01}/p_{02} causes: Less intensive shock wave (b) in the secondary flow, which changes into the expansion wave for $p_{01}/p_{02} = 1.53$. The expansion wave (e1) disappears and the compression wave (e2) becomes more intensive. The wake is shorter and thinner for low p_{01}/p_{02} , because static pressures of both flows are less different before interaction and secondary flow separation is negligible.

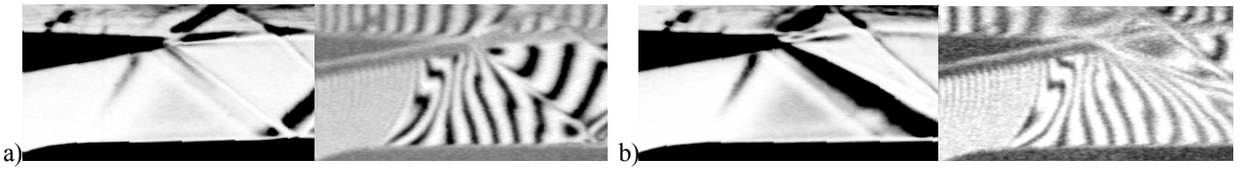


Figure 5: Schlieren and interferometric pictures of regimes of $p_{01}/p_{02} = 2.52$ and $p_{01}/p_{02} = 1.53$.

From results we can formulate recommendations for designing and operating of supersonic ejectors. To reduce losses due to shock waves from interaction of supersonic flows is necessary to design the trailing edge of the primary flow nozzle with very low angle. Of course, we can not make edge with zero angles and with zero thickness. To stifle the existence of the wake is needed to insure, that pressures of flows in front of the trailing edge are equal. We can do it in two ways. First we can design both nozzles with respect to the operating stagnation pressure ratio or change stagnation pressure ratio according to design of nozzles of an existing ejector.

CONCLUSION

The interaction of supersonic flows on the trailing edge of the primary flow nozzle of an ejector was studied by experimental, numerical and theoretical methods. The influences of back pressure ratio and stagnation pressure ratio on the interaction were presented. Recommendations for design of the entrance part of the supersonic ejectors and recommendations for operation of the supersonic ejectors were formulated. The optimisation problems of design and of operation of supersonic ejectors are very complex and these problems must be solved with respect of subsequent mixing processes in the mixing chamber.

References

[1] Dvořák V, Šafařík P.: Supersonic Flow Structure in the Entrance Part of a Mixing Chamber of 2D Model Ejector, Journal of Thermal Science, Vol.12, No.4, November 2003, pp.344-349.

[2] Dvořák V.: Flow Processes in an Ejector, Ph.D. Thesis, Technical University of Liberec, 2003, CR.

[3] Dvořák V, Šafařík P.: The Influence of Back Pressure on the Flow Structure in the Mixing Chamber in an Ejector, Colloquium Fluid Dynamics 2003, IT CAS, 22. - 24.10., 2003, pp. 17 - 20, Praha, CR.

SHOCK WAVE – BOUNDARY LAYER INTERACTION CONTROL BY STREAMWISE VORTICES

Piotr Doerffer, Ryszard Szwaba

IMP PAN, Department of Transonic Flows and Numerical Methods, PL 80-952 Gdansk, Poland

Summary Control of shock wave and boundary layer interaction finds still a lot of attention. Methods of this interaction control have been especially investigated in a recent decade. This research was mostly concerned with flows without separation. However, in many applications shock waves induce separation which often leads to strong unsteady effects. In this context it is proposed to use streamwise vortices for the interaction control and the results of experiments are presented here.

Normal shock wave – boundary layer interaction (SWBLI) is still an important problem in compressible aerodynamics. It demands further investigation of the flow structure in the interaction area, but already large effort has been invested in the interaction control. It was usually considered for low Mach numbers below the range of incipient separation induced by a shock wave.

During the last decade many methods of the SWBLI control have been investigated. These concerned a local wall modification in a form of a bump and many applications of the transpiration flow through walls. Passive control, active control and mixed hybrid type of flow control by suction and blowing have been extensively studied in many research centres. These methods although not very effective, showed that new technologies are seriously considered and that application of perforated walls, slots and holes for suction or blowing is not a technological problem nowadays.

SWBLI leads to separation at Mach numbers above M = 1.3. The process of separation usually becomes unsteady and causes buffeting at airfoils and shock oscillations in the internal flows. In such cases it is important to use control methods which are able to suppress or reduce separation and to diminish the unsteady effects. Reduction of shock movement is a very important aspect, which results in dumping of the vibrations induced by unsteady forces.

It has been proposed to investigate the potential of the stream-wise vortices for the control of SWBLI. Already in 70-s it has been proven that streamwise vortices have a significant effect on the shock wave – boundary layer interaction, but so far, research has been primarily focused on the fixed vortex generators (vain type) and they predominate in the airplane technology applied today. However, it was shown that air-jet vortex generators (AJVG) are also very effective in the production of streamwise vortices. This type of vortex generators was somehow forgotten. But in the 90-s vortex generation by air jets was looked into again, especially in the aspect of the intensity of a generated vortex, at subsonic speeds.

The most useful method of the stream-wise vortex generation is by air jets because it allows a simple method of switching it on and off. The jets have to be given appropriate angle of injection in relation to the main stream. This inclination affects the intensity of the generated vortices and should be analysed for its optimisation.

This paper presents our first results of the application of this new SWBLI control technique which allows displaying very clearly the advantages of the AJVG's in the shock wave boundary layer control.

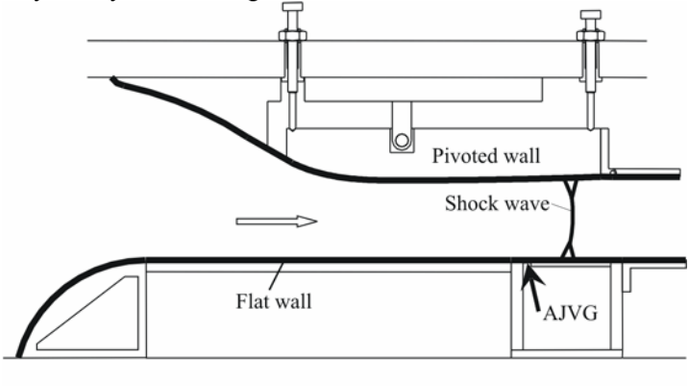


Fig.1. Test section lay-out

An experimental program has been carried out in the transonic wind tunnel of IMP PAN. In Fig.1. the test section sketch is presented. A normal shock wave was located in an appropriate place in a divergent part of the nozzle and an example is presented in Fig.2. One wall of the nozzle is flat and the interaction is studied at this wall. An opposite wall has a slight convex shape and its inclination may be varied. Thanks to this, shock waves of different intensity may be located at the same place in the nozzle. This is an important feature making measurements easier and allows maintaining the same distance of the interaction place from the AJVGs for different Mach number cases. Chosen Mach numbers are M = 1.25, 1.35, 1.45 and 1.55 which cover the range from unseparated to strongly separated flows.

One important feature of AJVG is that the intensity of generated vortices is only weakly dependent on the jet momentum. This is because the vortex is formed in the lower part of the boundary layer in the area of large gradient of velocity. High jet momentum, penetrating into the main stream, does not intensify the vortex but only increases the disturbance. For this reason we decided that the stagnation pressure of air jets is in our investigations equal to the stagnation pressure of the main stream. With this assumption our results will be applicable for all cases without any driving system for jets. Air for jets may be supplied from any leading edge or other stagnation air drainage in all studied cases. This approach enhances the applicability of our AJVG considerably.

AJVG in the test section are located in one row across the whole width of the test section. The jets are located in a distance of 9 × δ (boundary layer thicknesses) upstream of the interaction location beginning (minimum of the static pressure at the wall). The measurements consist of:



Fig.2. Shock wave and AJVG in operation, M=1.45

- static pressure distribution along the centre line of the test wall,
- boundary layer velocity profile 5 × δ upstream of the interaction area
- boundary layer velocity profile in two locations 6 × δ and 10 × δ downstream of the interaction area
- schlieren visualization of the shock wave structure, position and oscillation
- oil flow visualization at the test wall to display separation size and structure
- measurement of the hot-film sensor indications, placed in the shock vicinity to display shock's oscillations
- high speed movie visualization of the shock oscillation by a line CCD camera.

In Fig.2 flow is from the left to the right side. The oblique wave system originating at the wall is caused by the operating air jets. Further to the right side a shock system forming a λ-foot is present. Boundary layer is visible as a light zone adjacent to the wall. Shock wave causes significant increase of the boundary layer thickness.

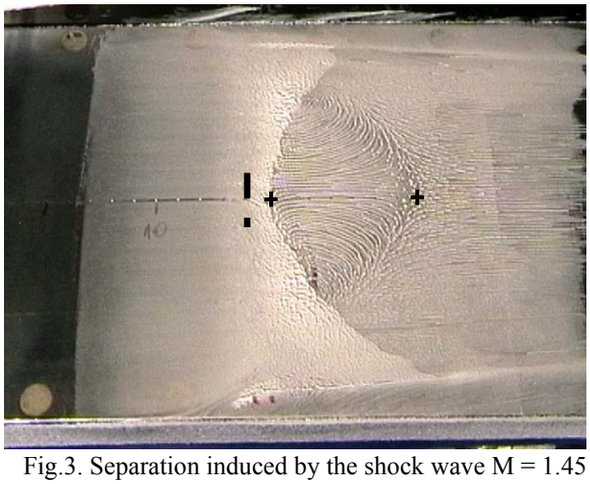


Fig.3. Separation induced by the shock wave M = 1.45

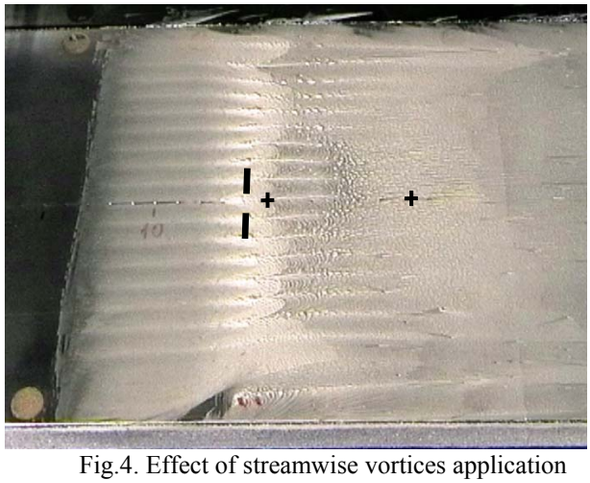


Fig.4. Effect of streamwise vortices application

The effect of streamwise vortices application is presented by Fig.3 and 4. They show surface oil flow visualisation on a flat wall in the area of SWBLI. The flow is from left to right. In Fig.3 undisturbed interaction is taking place. In the middle of the flat wall a well defined separation area is displayed by the oil streaks indicating a reverse flow area. The beginning and the end of separation are marked by small crosses. Shock location, upstream of the separation area is marked by two short lines drawn transverse to the flow direction. This is indicated by the oil accumulation. In Fig.4 the case with AJVG is presented at the same Mach number case. In the shock upstream part the traces of vortices are visible. Streamwise accumulation of oil indicates separatrices located between neighboring vortices. Two lines and two crosses are copied from Fig.3. Along the mentioned separatrices the disturbance reach far more upstream than in Fig.3. It means that it should have some effect on the shock structure causing an earlier compression. This should reduce shock losses. Another feature is that the separation line becomes a repeating span-wise 3-D structure with pitch corresponding to AJVG spacing. Simultaneously the separation looks more straight in span-wise sense.
Stream-wise vortices penetrate the separation area but are terminated at the reattachment line in the middle of the test wall. Reattachment takes place much earlier thanks to proposed flow control method.
Appearance of separation is usually connected to the induction of unsteady behavior of the interaction area. First of all this concerns instability of the separation zone caused by the vortex shedding and other 3-D vortex structure variation. Coupled with this is unsteady behavior of the shock wave. Oscillations of the shock wave are significantly reduced by the application of the AJVG. Its effect on interaction unsteadiness was measured in three locations. One is the oblique shock formation in the boundary layer which showed that the separation point fluctuations are not large but are reduced by our control method. Another location is the rear shock close to the separated zone. In this location the unsteadiness reduction is the strongest. And the last one is the unsteadiness of the main shock wave above the triple point. In this location the oscillations bear characteristics of the channel flow and are very weakly affected by our flow control means.

XXI ICTAM, 15–21 August 2004, Warsaw, Poland

CORRELATION OF NEARFIELD PRESSURE WITH MIXING LAYER VELOCITY IN A SUPERSONIC JET

François Coiffet, Carine Fourment, Patrick Braud, Joël Delville, Peter Jordan
Laboratoire d'Études Aérodynamiques, UMR-CNRS 6609, CEAT, 86036 Poitiers, France

INTRODUCTION

The pressure fluctuations generated by a rocket exhaust at lift-off can induce structural vibration capable of damaging the payload. Reduction of these effects requires that the nearfield phenomena be better understood. The said field comprises a complex superposition of hydrodynamic and acoustic fluctuations and the part played by each in terms of the upstream field is poorly understood. To this end experimental measurements have been performed on an isothermal jet with a Mach number of 1.4 and a nozzle diameter of 50mm. The objectives of these experiments are:

- generation of a database to facilitate physical analyses,
- reconstruction of the velocity field using a limited number of nearfield pressure measurements by means of Linear Stochastic Estimation (LSE, Adrian [1]),
- separation of acoustic and hydrodynamic fields with a view to developing phenomenological models capable of predicting the nearfield, farfield and upstream dynamic,
- identification of acoustic-hydrodynamic interactions in the nearfield.

Extensive nearfield pressure measurements have thus been performed, synchronously with two-component LDV measurements, and cartographies of pressure-pressure and pressure-velocity correlations obtained.

EXPERIMENTS

The near pressure field was sampled using a linear array of 39 pressure transducers, and the velocity field investigated using a two-component LDV system. Velocity measurements comprised radial profiles at 8 axial stations, from 1D to 8D, with 30 measurement points per profile. The simultaneous nearfield measurements were performed using a microphone array inclined at 9 deg to the jet axis (in order to follow the expansion of the flow) the upstream microphone being located 0.8D from the jet axis and 1 diameter downstream of the jet exit plane. Additional nearfield pressure measurements were also performed for 8 radial positions of the array (from 0.8D to 4D).

RESULTS AND DISCUSSION

A sample of some preliminary results are shown in figure 1 and 2. Figure 2-a shows the pressure-pressure correlation coefficient for a reference microphone at 5D, where the convection velocity is clearly identified by the slope of the maxima. It is interesting to note that even at this location there is evidence of propagative phenomena, manifest in a weak pattern comprising lines with slope of opposite sign (corresponding to propagation in the uptream direction). Figure 1 shows similar measurements for a radial array location of 1.5 diameter. The pressure field here contains a more significant contribution from the acoustic field, this being manifest in the more marked presence of the upstream propagation pattern. Figures 2-b show the velocity-pressure correlation coefficient for a velocity measurement 3 diameters downstream of the exit plane and 0.3 diameters from the jet axis - this corresponds to the high speed side of the mixing layer. Here again it appears that the convection of large structures is identified by the slope, however there is a slight change of slope implying an increase in convection velocity as we move downstream. This would appear to be related to the increased influence of propagative phenomena as we move in the downstream direction. In effect the microphones at the downstream end of the array are downstream of the main noise generating region of the jet (the end of the potential core). In addition, the criteria of $kr' = 2$ (where k is the wave number and r' is the radiale distance to the center line of the mixing layer) which defines the demarcation between zones where hydrodynamic and acoustic phenomena dominate (see Arndt et al. [2]), gives for these locations cut-off frequencies between 2.5 and 1.5 kHz, which means that the downstream microphones are in a region where the principal acoustic and hydrodynamic energies are of similar order. Thus the downstream microphones are increasingly subject to the acoustic field, hence the change in slope implying higher convection velocities - the slope manifest on the downstream microphones being in effect due to both convective and propagative phenomena.

CONCLUSION

The results presented here represent just a preliminary sample of the results obtained. The next step in the work will involve using the velocity-pressure correlations to generate instantaneous velocity fields using LSE, from which source terms can be generated, whence using an acoustic analogy the farfield noise can be predicted (see Picard and Delville [3], Ricaud [4]). In addition the capacity of a Proper Orthogonal Decomposition (Lumley [5]) to separate contributions from acoustic and hydrodynamic fields will be discussed. Finally these tools will be used to study and better understand the acoustic-hydrodynamic interactions manifest in the near field of the jet.

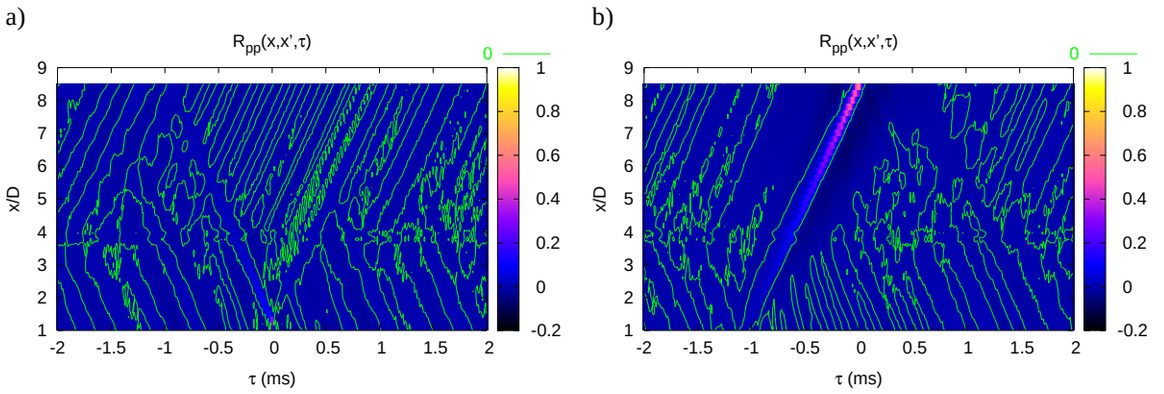


Figure 1. Pressure-Pressure correlation coefficient on a microphone array following the jet expansion, located at the radial position $r/D \in [2, 3.2]$ for a reference microphone at $x/D = 1$ (a), or $x/D = 8.5$ (b). The green lines correspond to a value of zero.

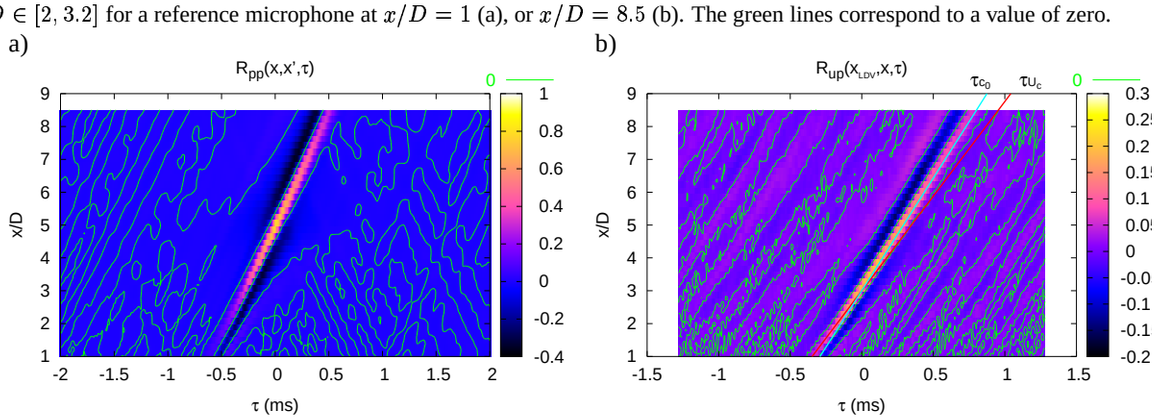


Figure 2. a)Pressure-Pressure correlation coefficient on a microphone array located at the radial position $r/D \in [0.8, 2]$ for a reference microphone at $x/D = 5$. b) Velocity-pressure correlation coefficient for a ldv measurement point located at the position $x/D = 3$ on the high speed side of the mixing layer. The green lines correspond to a value of zero, the cyan and red lines representing propagative and convection velocities respectively.

References

[1] Adrian, R.J.: On the Role of Conditionnal Averages in Turbulence Theory, in *Proceeding of the 4th Biennal Symposium on Turbulence in Liquids*, eds Patteson, G. and Zakin, J.:322–332, Science Press, Princeton, 1977.

[2] Arndt R.E.A., Long D.F. and Glauser M.N.: The proper orthogonal decomposition of pressure fluctuations surrounding a turbulent jet. *J. Fluid Mech* **340**:1–33, 1997.

[3] Picard C., Delville D.: Pressure velocity coupling in a subsonic round jet. *Heat and Fluid Flow* **21**:359–364, 2000.

[4] Ricaud F.: Étude de l'identification des sources acoustiques à partir du couplage de la pression en champ proche et de l'organisation instantanée de la zone de mélange de jet. *PhD Thesis*, Université de Poitiers, France, 2003.

[5] Lumley J.L.: The structure of inhomogeneous turbulent flows. in *Proceeding of the International Colloquium on th Fine Scale Structure of the Atmosphere and its Influence on Radio Wave Propagation*, eds Yaglom A.M. and Tatarsky V.I.:166–178, Doklady Akademii Nauk SSSR, Moscou, Nauka, 1967.

21st International Congress of Theoretical and Applied Mechanics 2004

Non-Reflecting Boundary Condition for Direct Aeroacoustic Computation

X. M. Li, R. C. K. Leung and R. M. C. So

Department of Mechanical Engineering, The Hong Kong Polytechnic University
Hung Hom, Kowloon, Hong Kong

Short Summary

A new non-reflecting boundary condition (NSPML), based on perfectly matched layer concept applied to compressible Navier-Stokes equations, is proposed for direct aeroacoustic computation. The boundary condition is designed to absorb acoustic waves incident at all angles. The NSPML is validated with aeroacoustic flows of increasing complexity, and found that it provides higher non-reflectivity than existing boundary conditions but at a much lower computational cost.

Extended Summary

Non-reflecting boundary condition is an important issue in computational aeroacoustic studies. In direct aeroacoustic computations, high-order schemes are required to resolve the small amplitudes of the acoustic waves in order to distinguish them from the large amplitude fluid dynamic fluctuations due to the unsteady flows. High-order schemes provide low numerical dissipation to resolve the acoustic wave propagation, but require precise boundary conditions to avoid spurious numerical errors generated at the computational boundaries. A numerical non-reflecting condition at all the computational boundaries is necessary; otherwise the spurious erroneous waves reflecting from the boundaries would contaminate the solution in the computational domain, decrease the computational accuracy, and may even drive the solutions towards a wrong time-stationary state.

Because of its simplicity, the classical one-dimensional non-reflecting characteristics-based boundary condition (NRCBC) is very popular [1]. However, when the physical waves are two-dimensional and incident at any angle towards the boundaries, only the normal components are adequately absorbed and significant numerical error waves are reflected. Recently, two approaches of numerical boundary conditions, namely perfectly matched layer (PML) method [2] and the Freund's buffer zone technique [3], have been proposed in the search for truly non-reflecting boundary conditions for two-dimensional aeroacoustics problems. Hu [2] derived a stable PML formulation for the linearized Euler equations in unsplit physical variables, which essentially forces the amplitudes of two-dimensional acoustic waves to zero in a PML region beyond the physical domain. Freund [3] rewrote the Navier-Stokes equations with additional damping terms, which act to suppress all the flow unsteadiness and force the flow towards a prescribed uniform flow in a buffer zone beyond the physical domain.

In this paper, a PML-based boundary condition for Navier-Stokes equations (NSPML) is proposed and its performance in aeroacoustic computation is accessed. Benchmark aeroacoustic flows of increasing complexity are computed to validate the NSPML. From the computation of a Gaussian pulse propagating radially outwards in a square domain, the two-dimensional non-reflectivity of the NSPML has been proven excellent (Figure 1). In general, propagating vortices play a critical role in sound generation, absorption and diffraction in unsteady flows. Therefore, the boundary conditions should, while providing non-reflectivity for the acoustic propagation, enable the vortices passing through them without any error waves generated at the boundaries. This capability has been tested by solving a canonical problem of convection vortex interacting with a Gaussian pulse on a uniform grid. The non-reflectivity of NSPML and the associated computational cost are compared with Freund's technique, NSCBC and a reference solution, which is computed with the domain size double. The NSPML zone is 10-grid wide. Figure 2 shows the time history of the error at the outlet boundary. Obviously the NSPML gives the least error, less than NSCBS and Freund's technique by two and one orders of magnitude respectively. In fact the performance of the NSPML is optimal in computational cost. The same NSPML accuracy can be obtained with a 40-grid wide Freund's buffer zone but the computational time has to be doubled. Direct aeroacoustic computations of a laminar boundary layer flow over an open cavity are carried out (Figure 3). It is found that the NSPML allows boundary layers passing through the computational boundaries without creating significant error waves. Furthermore, for the same number of grid points, the accuracy of NSPML is much better than Freund's buffer zone technique.

Acknowledgements

Support from the Research Grants Council of the HKSAR Government given under Grant Nos. PolyU 5174/02E, PolyU 1/02C, and from The Hong Kong Polytechnic University given under Central Research Grant G-T686 is gratefully acknowledged.

References

[1] Poinsot T. J., Lele S.K: Boundary Conditions for Direct Simulations of Compressible Viscous Flows. *J. Comp. Phys.* **104**: 104-129, 1992.

[2] Hu F. Q.: A Stable, Perfectly Matched Layer for Linearized Euler Equations in Unsplit Physical Variables. *J. Comp. Phys.* **173**: 455-480, 2001.

[3] Freund J. B.: Proposed Inflow/Outflow Boundary Condition for Direct Computation of Aerodynamic Sound, *AIAA J.* **35**: 740-742, 1997.

(a) (b)

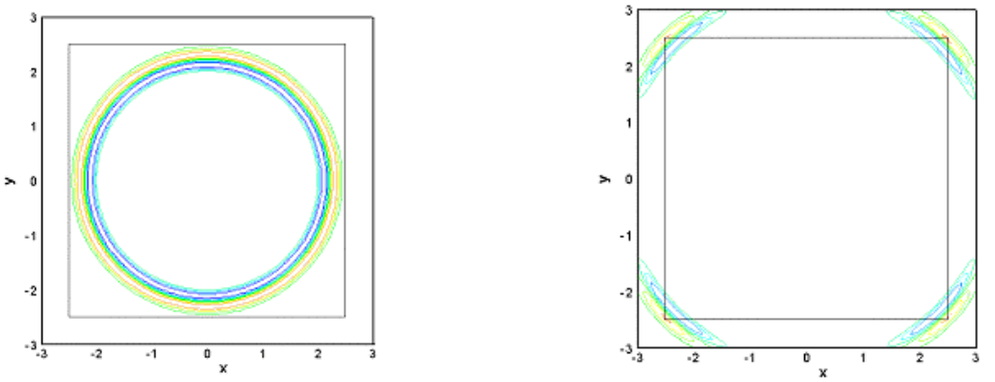


Figure 1. Computation of propagating Gaussian pulse with NSPML. (a) T' = 0.12; (b) T' = 0.18

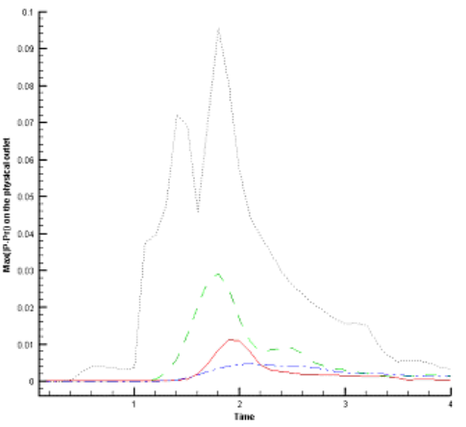


Figure 2. Time history of the maximum error in pressure fluctuations at outlet. ——, NSPML (10 grids); – – – Freund's buffer zone (10 grids); – · – · –, Freund's buffer zone (40 grids); ·····, NSCBC.

(a) (b)

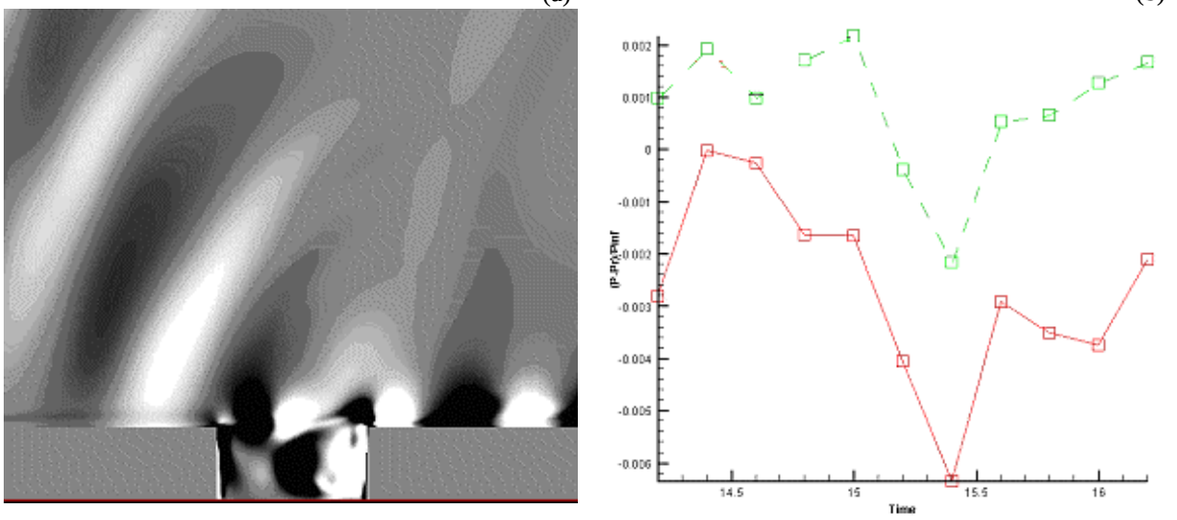


Figure 3. Computation of open cavity flow with NSPML. (a) Pressure wave; (b) time history of pressure error at the mid-point of domain outlet; —□—□—, NSPML; – □ – □ –, Freund's buffer zone.

TREESPH SIMULATIONS OF CHOKED FLOW SYSTEMS USING SMOOTHED PARTICLE HYDRODYNAMICS

Jaime Klapp[*], Leonardo Di G. Sigalotti[*], Eloy Sira[**], Gonzalo Mendoza[*]
[*]*Departamento de Física, ININ, A. P. 10-1027, México 11801 D. F.*
[**]*Centro de Física, IVIC, Apartado 21827, Caracas 1020A, Venezuela*

Summary We present exploratory two-dimensional calculations of the flow of a viscous, single-phase fluid through a wellhead choke of real dimensions using the method of Smoothed Particle Hydrodynamics coupled with a simple isothermal equation of state for description of the flow.

The flow of gas-liquid mixtures through restrictors, like flow control valves and chokes, in pipeline systems is of great practical interest in many applied branches of engineering. In the oil industry, wellhead chokes are installed to control flow rates and protect the surface equipment from unusual pressure fluctuations. Due to its practical significance, single-phase and two-phase flows through chokes have been the subject of numerous investigations in the past 40 years. However, the complexity of the problem has limited the investigation mostly to the development of empirical correlations based on experimental measurements and theoretical studies based on simplified treatments. In general, when a flowing mixture crosses a choke its velocity increases and its pressure drops. The empirical correlations aimed at predicting the dependence of the pressure drop on velocity through the choke are usually valid over the range where experimental data are available but may fail when extrapolated to new conditions. With the exception of a very few instances, such simulations are practically inexistent in the literature even for the case of single phase flows.

In this paper, we search for a way of solving the Navier-Stokes equations in order to simulate the flow of a single-phase, viscous fluid through a wellhead choke using a modified version of the TREESPH method originally introduced by Hernquist & Katz [1]. In particular, a Smoothed Particle Hydrodynamics (SPH) formulation is used which has been shown to produce accurate results for both compressible flows at high and moderate Reynolds numbers and incompressible flows at low Reynolds numbers without the need of special modifications. Unlike other SPH-based schemes for treating viscous flows, the present method strictly relies on symmetrized SPH representations for the equations of motion and energy coupled with the usual kernel smoothing for the density. This results in a variationally consistent SPH scheme in which momentum preservation can be addressed properly.

In problems involving flow through pipes and chokes where solid walls are present, the accuracy of the calculations is sensitive to the treatment of the interaction between the fluid and the solid surface. For simulations of a viscous fluid flow in presence of solid walls, it is necessary to impose no-slip boundary conditions to mimic the sticking of the fluid to the wall. We model such boundary conditions using image particle methods, which in turn are useful in removing the severe crippling density deficiency that arises when the usual SPH continuity equation is applied to particles near a boundary. Image particles are created by reflecting fluid particles across the boundary. This operation results in a collection of imaginary particles which are external to the fluid domain. Such particles are treated as actual SPH particles and so they contribute to the density and pressure gradients. In practice, accurate results for the kernel smoothing of the density are obtained by reflecting no more than four fluid particles aligned in the normal direction to the surface. Unlike actual fluid particles, imaginary particles are not allowed to move relative to the solid surface. Although a velocity is necessarily assigned to each of them, they are always constrained to remain anchored to the solid wall in the course of the calculation. That way, each imaginary particle is given a density equal to the value of its closest image within the fluid domain.

We have performed exploratory two-dimensional model calculations of single-phase flow through a wellhead choke of dimensions like those installed in real production tubing using the Smoothed Particle Hydrodynamics (SPH) method. As a first approximation, we have assumed that negligible heat transfer occurs between different parts of the fluid and so the models were carried out using an isothermal equation of state. The choice of the geometry and parameters are such that the models are well suited to describe the flow of gas through a pipe with a choke throat in the middle as shown in Fig. 1. Three different models were considered which differed either in the form of the outlet boundary condition or the value of the constant coefficient of kinematic viscosity. In model A, the pipe is designed by placing a lid with a small orifice at its end in order to inhibit the outlet flow, while models B and C, differing only in the value of the kinematic viscosity, allow for an infinitely long tube downstream. In all cases, the inlet conditions correspond to Poiseuille flow with a constant density. The results for these model calculations indicate that the flow achieves an approximate steady state in a very short timescale. The stationary solution is always characterized by a well-pronounced drop in the density and pressure through the choke throat. In Fig. 2 we shown the evolution of the density and velocity for model B that corresponds to a calculation with a constant coefficient of kinematic viscosity equal to $\nu = 5.0x10^{-4} cm^2 s^{-1}$.

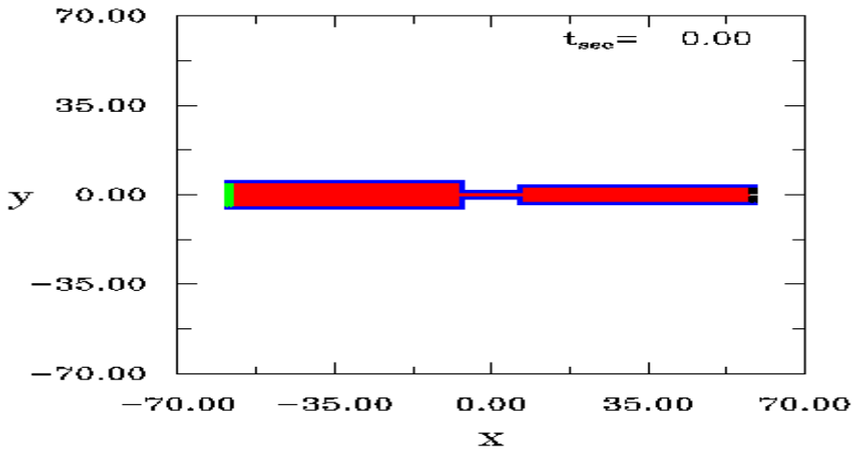


FIG. 1: Geometry of the wellhead choke model used in the calculations. The flow within the choke system is along the x-axis in the direction of increasing x. The numbers on the box sides are given in centimeters

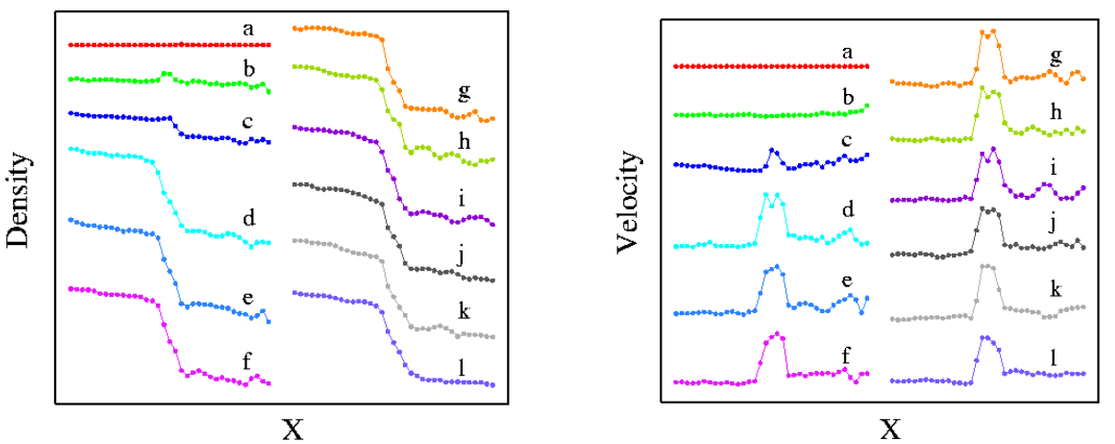


FIG. 2: Mean density (left panel) and velocity (right panel) profiles across the full length of the tube for model B. The curve labels correspond to the following times: 0.0 s (a), 0.0025 s (b), 0.010 s (c), 0.0275 s (d), 0.070 s (e), 0.0875 s (f), 0.1175 s (g), 0.1925 s (h), 0.2025 s (i), 0.230 s (j), 0.270 s (k), and 0.2975 s (l). An approximate steady-state solution is achieved in (d).

At the entrance of the choke the flow velocity increases steeply, reaching typical values which are on average factors of 5 to 6 times higher than those for the upstream flow. The flow velocity also decreases steeply at the choke exit, dropping to downstream values that are slightly higher compared to those for flow in the upstream section of the tube. The flow across the choke throat remains always subsonic with typical velocities of about 0.1c, where c denotes the sound speed. In particular, when the flow is inhibited downstream, the density drop is of about 20% and decreases to 13% or less when the entire outlet cross-section of the tube is free of any restrictions. Because of the isothermal equation of state, the density drop across the choke is equivalent to a pressure drop. Experimental available measurements and correlations for natural gas flowing across wellhead chokes indicate that for speeds of 0.1c, the ratios of the pressure before to that after the choke may be as high as 0.97 - 0.99, implying a much lower pressure drop than predicted by the present calculations. A direct comparison of the results with the available experimental data will certainly be possible for more realistic equations of state.

The present two-dimensional calculations represent a step ahead in consistently simulating choked flow systems. In addition to improving the equation of state, future extensions of this work will include full three-dimensional simulations of flow through wellhead chokes of circular cross-section for both pure gas and gas-liquid mixtures.

References

[1] Hernquist L., Katz N.: TREESPH -- A unification of SPH with the hierarchical tree method. *Astrophys. J.* **70**, 419, 1989.

XXI ICTAM, 15–21 August 2004, Warsaw, Poland

POLOIDAL-TOROIDAL DECOMPOSITION IN CYLINDRICAL VON KÁRMÁN FLOW

Piotr Boronski, Laurette Tuckerman
LIMSI (CNRS-UPR 3251), Department of Mechanics, BP 133 91403 Orsay, France

Summary The goal of the VKS experiment is to observe a laboratory-scale *dynamo effect* in the cylindrical von Kármán flow. Because there exists at present no complete numerical treatment of this configuration, we have developed an efficient three-dimensional pseudo-spectral code capable of solving the Navier-Stokes equations in a finite cylindrical geometry, to be coupled with the Maxwell equations. A *poloidal-toroidal* decomposition insures that fields are divergence-free by construction which is very important for applications to the magnetohydrodynamic case. The cylindrical domain is treated by using in the radial direction a polynomial basis which is regular at the domain axis. The satisfaction of high-order and/or coupled boundary conditions is guaranteed by the *influence matrix* method.

MOTIVATION

The *dynamo effect* is thought to be responsable for planetary and solar magnetic field. The VKS (von Kármán Sodium) experiment [1] aims to reproduce this effect at laboratory scales. Our goal is to develop a fully three-dimensional magnetohydrodynamic code capable of numerically simulating this experiment. Two features make this a particularly challenging task: a cylindrical geometry is used in conformity with the experiment, and the velocity and magnetic fields are constructed so as to be exactly divergence-free. Although three-dimensional coupled magnetohydrodynamic codes have been written in spherical geometries, to our knowledge, there exist no such codes in a cylindrical geometry of finite height.
A secondary motivation is to study the advantages and drawbacks of a pseudo-spectral method based on potentials of the velocity and magnetic fields, as well as to understand the importance of the regularity condition at the axis in a cylindrical geometry.

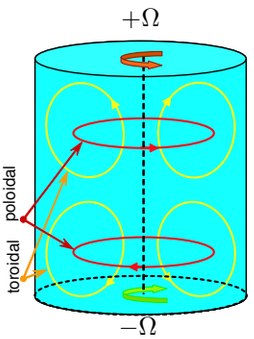


Figure 1. The simulated configuration. The counter-rotating discs generate two main flow structures - *toroidal* and *poloidal*.

MAIN ASSUMPTIONS

The configuration simulated consists of a conducting fluid enclosed in a cylinder of radius R and height h whose upper and bottom bases rotate in opposite directions with angular velocity Ω (fig. 1), generating the von Kármán swirling flow. This flow is considered to be a good candidate for a self-sustained dynamo [1]. The system is described by the Navier-Stokes and Maxwell equations coupled by induction and the magnetic tension and pressure.

$$\partial_t \mathbf{u} + (\mathbf{u}\cdot\boldsymbol{\nabla})\,\mathbf{u} + \tfrac{1}{\rho\mu}(\mathbf{B}\cdot\boldsymbol{\nabla})\,\mathbf{B} = -\tfrac{1}{\rho}\boldsymbol{\nabla}\left(p + \tfrac{1}{2\mu}B^2\right) + \nu\nabla^2\mathbf{u} \quad (1a)$$

$$\partial_t \mathbf{B} = \boldsymbol{\nabla}\times(\mathbf{u}\times\mathbf{B}) + \tfrac{1}{\rho\mu}\nabla^2\mathbf{B} \quad (1b)$$

$$\boldsymbol{\nabla}\cdot\mathbf{u} = \boldsymbol{\nabla}\cdot\mathbf{B} = 0 \quad (1c)$$

where $\mathbf{u}$ and $\mathbf{B}$ are the velocity and magnetic fields. No-slip boundary conditions are imposed on $\mathbf{u}$ while continuity with a surrounding insulating region is to be imosed on $\mathbf{B}$. Both the velocity $\mathbf{u}$ and the magnetic field $\mathbf{B}$ are required to be solenoidal; for $\mathbf{B}$ this is especially crucial [2]. For this reason, we represent $\mathbf{u}$ and $\mathbf{B}$ by the *poloidal-toroidal* decomposition given by:

$$\mathbf{u}(r,\theta,z) = \boldsymbol{\nabla}\times(\psi\hat{\mathbf{e}}_\mathbf{z}) + \boldsymbol{\nabla}\times\boldsymbol{\nabla}\times(\varphi\hat{\mathbf{e}}_\mathbf{z}) \quad (2)$$

where ψ and φ are scalar potentials. To simplify the description, we consider only the hydrodynamic equations (1a); the numerical scheme is applied in an analogous way to the magnetic part (1b). Substituting (2) for the velocity field $\mathbf{u}$ in (1a), we derive equations for ψ and φ by taking the $\hat{\mathbf{e}}_\mathbf{z}$ component of the curl and double curl of (1a), resulting in:

$$(\partial_t - \nu\Delta)\,\Delta_h\psi = \hat{\mathbf{e}}_\mathbf{z}\cdot(\boldsymbol{\nabla}\times\mathbf{b}) \quad (3a)$$

$$(\partial_t - \nu\Delta)\,\Delta\Delta_h\varphi = \hat{\mathbf{e}}_\mathbf{z}\cdot(\boldsymbol{\nabla}\times\boldsymbol{\nabla}\times\mathbf{b}) \quad (3b)$$

where $\mathbf{b}$ contains all nonlinear terms resulting from (1a). As for boundary conditions, the potentials ψ and φ cannot be completely decoupled and in the no-slip case give:

$$u_r:\ \tfrac{1}{r}\partial_\theta\psi + \partial^2_{rz}\varphi = 0 \qquad \begin{cases} r=R \\ z=\pm h \end{cases} \quad (4a)$$

$$u_\theta:\ \partial_r\psi - \tfrac{1}{r}\partial^2_{\theta z}\varphi = \begin{cases} 0 & r=R \\ \pm r\Omega(r) & z=\pm h \end{cases} \quad (4b)$$

$$u_z:\ \Delta_h\varphi = 0 \qquad r=R \quad (4c)$$

Additional conditions must be imposed on the sixth-order PDE system (3). Some of these are gauge conditions, whose purpose is to select among the potentials ψ and φ which yield the same $\mathbf{u}$. Others are due to the necessity to make the

differentiation leading to (3) reversible; these generalized integration constants insure that (3) leads to the same solution as (1a). The general form of these conditions was given in [3] and in our case gives

$$\varphi = 0 \qquad z=\pm h \tag{5a}$$

$$r\partial_{rz}\Delta_h\psi - \partial_\theta\Delta\Delta_h\varphi = 0 \qquad r=R \tag{5b}$$

NUMERICAL APPROACH

Axis condition

In a cylindrical geometry, the *axis condition* expresses the requirement that functions be continuous and infinitely differentiable at the axis. If a Fourier representation is used in the angular direction, this condition links the Fourier mode number with the degree and parity of the polynomial used in the radial direction (6) (as in the case of cylindrical Bessel functions):

$$f(r,\theta,z) = \sum_{\substack{k=0\ldots K \\ m=-M\ldots M \\ n=|m|\ldots N\,(m+n\ even)}} f^*_{m,n,k}\, e^{im\theta} r^n z^k \tag{6}$$

We choose a orthogonal basis of radial polynomials [4] satisfying the regularity condition at the cylinder axis. The polynomials are solutions of a Sturm-Liouville equation and are related to the shifted Jacobi polynomials. Taking into account the symmetry and degree relation significantly reduces the numerical cost of the algorithm, and more importantly, enforces the correct balance between the representable radial and azimuthal variation of the flow near the axis. This uniform scaling is achieved because, for each Fourier mode number, the associated radial polynomials decay sufficiently fast at the origin (fig. 2). The difference between a regularized and a non-regularized treatment is schematically demonstrated on figure 3.

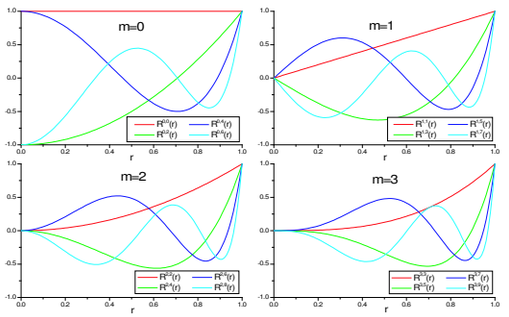


Figure 2. The radial polynomials [4]. The first four polynomials for the different Fourier modes $m = 0 \ldots 3$ have been plotted. The polynomials associated with Fourier wave number m contain powers $m, m+2, \ldots, N$ of r.

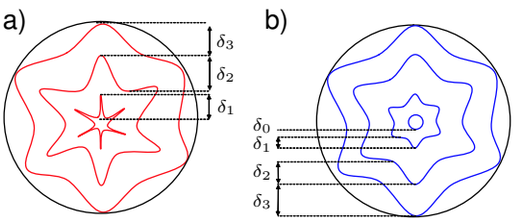


Figure 3. The visual interpretation of a pole singularity. The wavy lines represents schematically the profile of $e^{im\theta}P(r)$. a) A singular case: $P(r) \approx O(1)$; $\delta_1 \approx \delta_2 \approx \delta_3$. The peaks near to the origin are much steeper than those near the boundary. b) A regularized case: $P(r) = O(r^m)$ (here $m \geq 6$) ; $\delta_0 < \delta_1 < \delta_2 < \delta_3$. The peaks near the origin are of similar steepness to those near to the boundary.

Imposing the boundary condition

In order to satisfy the more complicated or coupled boundary conditions, we use the influence matrix technique. The main idea is to decompose the solution into particular and homogenous contributions. Simple decoupled boundary conditions are substituted for the actual conditions (4, 5) at each of these steps. The influence matrix measures the "influence" of each of the simplified boundary conditions on the quantities (4, 5) which are required to be zero for the final solution. Once the particular solution is calculated, the influence matrix is inverted to determine the coefficients of the Greens functions whose superposition is the required homogeneous contribution.

References

[1] Bourgoin M., Marié L., Pétrélis F., Gasquet C., Guigon A., Luciani J.B., Moulin M., Namer F., Burguete J., Chiffaudel A., Dauvid F., Fauve S., Odier P., Pinton J.F., MHD measurements in the von Kármán sodium experment, *Phys. Fluids*, **14**, 9 2002

[2] Brackbill J.U., Barnes D.C., The Effect of Nonzero $\nabla\cdot\mathbf{B}$ on the Numerical Solution of the Magnetohydrodynamic Equations, *J. Comput. Phys.* **35** 1980

[3] Marqués F., On boundary conditions for velocity potentials in confined flows: Application to Couette flow *Phys. Fluids A*, **2** 1990.

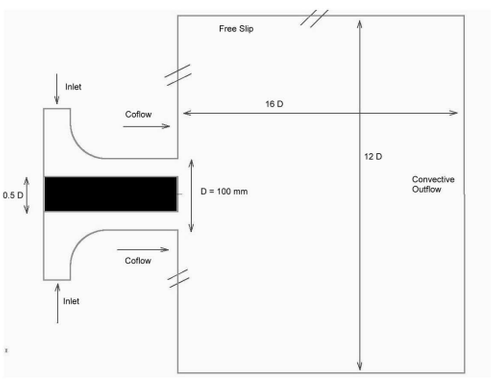
[4] Matsushima T. & Marcus P.S., A Spectral Method for Polar Coordinates, *J. Comput. Phys.* **120**, 365 (1995)

ON INFLOW BOUNDARY CONDITIONS FOR LARGE EDDY SIMULATION OF TURBULENT SWIRLING JETS

M. García-Villalba, J. Fröhlich and W. Rodi
SFB 606, University of Karlsruhe, Kaiserstr. 12, 76128 Karlsruhe, Germany

Summary For a swirling jet, three LES have been performed with different inflow boundary conditions. It is shown that good agreement of mean and rms velocities is not, in general, sufficient for a realistic representation of the experimental conditions. The unsteady large scale structures of the flow must also be taken into account. Also, for swirling jets, the simulation of the flow in the actual swirl generator is not always needed. A less expensive strategy is proposed.

Large Eddy Simulations (LES) of spatially inhomogeneous flows require unsteady inflow boundary conditions with a proper representation of the turbulent fluctuations. The results are often highly sensitive to these boundary conditions. In the validation of the different approaches to the problem,[1, 2], it is usual to compare first and second order moments of the velocity field with the corresponding experimental data. We will show that this is not sufficient in flows containing highly unsteady large scale coherent structures. A good representation of the turbulence statistics does not necessarily guarantee a good representation of these features.
In this paper, three-dimensional incompressible LES of an unconfined annular swirling jet are presented. The geometry of the reference case, which is based on experiments performed at the University of Karlsruhe [3], is shown in Fig. 1. It includes a crude representation of the inlet duct upstream of the jet exit. The Reynolds number of the flow based on the bulk velocity u_b and the jet diameter D is $Re = 163000$. The Swirl number defined in Fig. 1 is $S = 0.9$. With this level of swirl, a central recirculation zone is formed. The simulations are performed with the code LESOCC2, using a second order accurate finite volume method. In the reference case (Sim 1), top-hat profiles are imposed at the radial inflow and the inlet swirl is designed so that the swirl at the jet exit matches the swirl in the experiment. In a second simulation (Sim 2), the inflow plane is placed directly at the jet exit $x = 0$ and the inflow conditions are obtained by performing a separate, periodic LES of swirling flow in an annular pipe using body forces as described in [4]. A third simulation (Sim 3) was performed using the same procedure but the inflow plane is now located at $x = -D$. Therefore, the geometry shown in Fig 1 corresponds to the computational domain of Sim 1. The computational domain of Sim 2 starts at the jet exit $x = 0$ and the domain of Sim 3 starts upstream of the jet exit at $x = -D$. In all three simulations, the block structured mesh consists of about 2.5 million cells. No-slip boundary conditions are applied at the walls. The entrainment is simulated using a mild coflow and free-slip conditions are applied at the open side boundary which is placed far away from the region of interest. A convective outflow condition is used at the exit boundary. The Smagorinsky and the dynamic subgrid-scale models have been employed, the latter with smoothing by temporal relaxation.



$$S = \frac{\int_0^R \rho u w r^2 \, dr}{R \int_0^R \rho u^2 r \, dr}$$

u axial velocity
w tangential velocity

FIG. 1: Geometry of the flow and definition of the swirl number .

In Sim 1, large scale precessing vortex cores are observed, typical for this kind of flow [5]. A characteristic picture is shown in Fig. 3d. Fig. 3a shows a typical frequency spectrum exhibiting a pronounced peak at twice the precessing frequency due to the presence of two structures.
In Sim 2, the inlet plane is placed at the jet nozzle ($x = 0$) and the experimental mean axial and tangential velocity profiles measured very close to the jet exit are enforced as described above. Figs. 2a and 2b show a comparison between measurements and calculations at an axial location half a diameter downstream of the jet exit. The agreement is excellent for the mean velocities and very good for the fluctuations. The results from Sim 1 and 3 (not shown here) are virtually the same for these quantities. The frequency spectrum of Sim 2, however, does not show any peak, Fig. 3b, and no large scale organized motion can be seen in iso-surface plots, Fig. 3e. Hence good agreement with mean and rms experimental velocities is not always enough for the realistic representation of inflow conditions in an unsteady calculation.

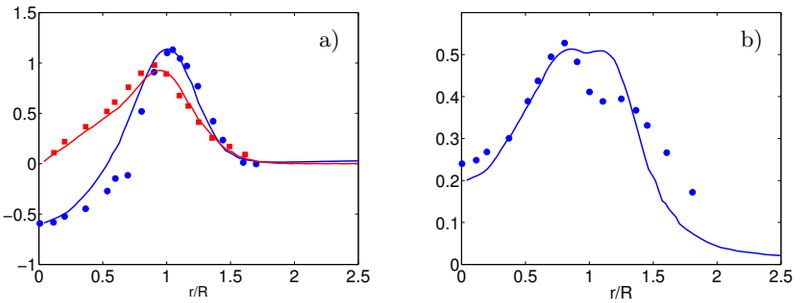


FIG. 2: Results from Sim 2 at an axial position of $x = R$. Symbols, experiment. Lines, present simulation. a) Mean axial velocity (blue) and tangential velocity (red). b) Rms fluctuations of axial velocity.

In a recent numerical investigation of a similar configuration [6], using a very complex grid to simulate the flow in the actual swirl generator, a precessing vortex core was also detected.
In Sim 3 the inlet plane is placed upstream of the jet nozzle ($x = -D$) and the inflow velocity profiles are taken from Sim 1 at that position (they might also be taken from experiments if measurements are available at that position) The precessing frequency of the structures is well obtained (Fig. 3c) and iso-surfaces show similar large-scale structures as for Sim 1. This demonstrates that an elaborate treatment of the flow in the actual swirl-generating mechanism is not necessarily needed and less expensive strategies can be employed.

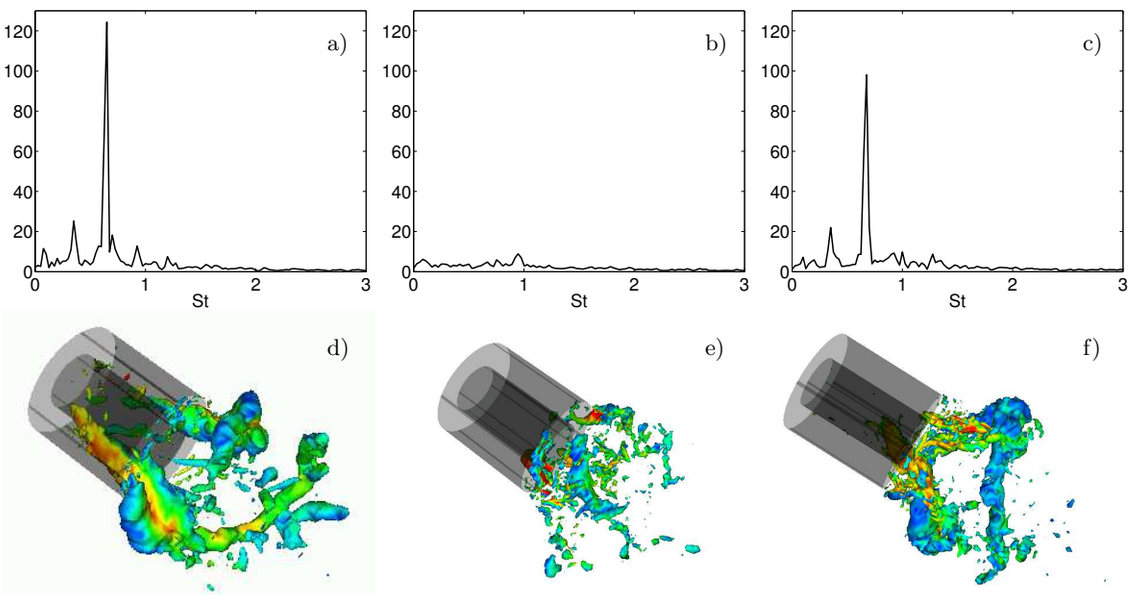


FIG. 3: a), b), c) Frequency spectrum of tangential velocity fluctuations as a function of the Strouhal number $St = fD/u_b$ at $x = 0.2D$, $r = 0.4D$. d), e), f) Isosurface of pressure fluctuation, $p- < p >= -0.4$. Color represents the modulus of the velocity vector. a), d) Sim 1. b), e) Sim 2. c), f) Sim 3.

[1] J.U. Schlüter. Consistent boundary conditions for integrated RANS-LES simulations: LES inflow conditions. AIAA paper no. 2003-3971, 2003.

[2] M. Klein, A. Sadiki, and J. Janicka. A digital filter based generation of inflow data for spatially developing direct numerical or large eddy simulations. *J. Comp. Physics*, 186:652–665, 2003.

[3] R. Hillemanns. *Das Strömungs und Reaktionsfeld sowie Stabilisierungeigenschaften von Drallflamen unter dem Einfluss der inneren Rezirkulationszone.* PhD thesis, University of Karlsruhe, 1988.

[4] C.D. Pierce. *Progress-variable approach for large-eddy simulation of turbulent combustion.* PhD thesis, Stanford University, 2001.

[5] O. Lucca-Negro and T. O'Doherty. Vortex breakdown: a review. *Prog. Energy and Comb. Sci.*, 27:431–481, 2001.

[6] B. Wegner, A. Maltsev, C. Schneider, A. Sadiki, A. Dreizler, and J. Janicka. Evaluation of U-Rans performance in predicting an unconfined swirling flow with precessing vortex core based on LES and experiments. In *Proceedings of Turbulence and Shear Flow Phenomena 3. Sendai (Japan)*, pages 51–56, 2003.

NUMERICAL SIMULATION OF THE FLOW OVER A BACKWARD-FACING STEP IN A BEOWULF-CLASS CLUSTER

Rubens Campregher[*], Aristeu da Silveira Neto[*], Wellington Marinho[*], Sérgio S. Mansur[**]
[*]*Federal Univ. of Uberlandia, School of Mech. Engineering, 38400-902 Uberlandia - MG, Brazil*
[**]*Sao Paulo State University, Dept. of Mech. Engineering, 15385-000 Ilha Solteira - SP, Brazil*

Summary This work proposal is to present a three-dimensional numerical simulation of the classical flow over a backward-facing step in a very fine mesh. The in-house parallel numerical code was written in Fortran 90 and has solved the Navier-Stokes Equations discretised by the FVM and has run in a Beowulf-class cluster of PCs. The flow Reynolds number was 38000, a LES turbulence modelling technique was employed with Smagorinsky's subgrid model. The results were compared against the literature.

INTRODUCTION

The parallel computing techniques have gaining importance since the 90's as the modern parallelization libraries has evolved and, as long as can be foreseen, they'll be in a continuing growth [3]. It is worth noting that the processing capabilities increasing rates of mainframes and supercomputers have been far from beat the PC's rates. In addition, the new network hardware and software resources have pushed up the parallelization approaches that employ ordinary PCs. Among the several parallel techniques using clusters of PCs, the probably most renowned one is the Beowulf–class cluster, developed at NASA in 1994 [3] and employed in this present work. Some of the main features, presented in a cluster of computers that follow the Beowulf "philosophy" must have are: the independence of software and hardware suppliers, scalable peripherals, and free open source codes with minimum changes. All of these requirements meet the needs of most universities, more remarkably in those from developing countries, which very often face funding restrictions.

The cluster is composed by five 2.8GHz clock and 1GByte DDR RAM machines connected by a Gigabit network. The message-passing system employed was the MPI, more specifically the MPICH implementation. The numerical code has been written in Fortran 90.

In the field of the Computational Fluids Dynamics (CFD), powerful computer capabilities are frequently requested, because as the flow regime increases, its structures become smaller, requiring also smaller grid sizes in order to reproduce them properly. Consequently, greater computational resources are needed to store and perform the operations on the flow parameters. In this context, the parallel computing in cluster of PCs is suitable.

The flow over a backward-facing step, despite of its simple geometry, produces very rich structures involving a great number of physical mechanisms representative of the separated internal flows [2]. So, this kind of configuration is probably the best numerically documented, and experimentally as well [1]. This work aims to present the successful employment of an in-house cluster of ordinary PCs running an in-house parallel numerical code for evaluating the flow over a backward-facing step, comparing it against the data in the literature [1,2].

NUMERICAL PROBLEM

The flow dynamics can be very well determined, in most of the engineering applications, by the solution of the system generated by the momentum and continuity equations, known as Navier-Stokes Equations:

$$\frac{\partial(\rho u_i)}{\partial t} + \frac{\partial(\rho u_i u_j)}{\partial x_j} = -\frac{\partial p}{\partial x_i} + \frac{\partial}{\partial x_j}\mu_{eff}\left(\frac{\partial u_i}{\partial x_j} + \frac{\partial u_j}{\partial x_i}\right) \tag{1}$$

$$\frac{\partial(\rho u_i)}{\partial x_i} = 0 \tag{2}$$

The temperature is evaluated by solving the Energy Equation:

$$\frac{\partial(\rho T)}{\partial t} + \frac{\partial(u_j T)}{\partial x_j} = \frac{\partial}{\partial x_j}\left(\alpha \frac{\partial T}{\partial x_j}\right) \tag{3}$$

And the effective viscosity is evaluated by the Smagorinsky's subgrid model [4]:

$$\mu_{eff} = \rho \upsilon_{eff} = \rho(C_s \Delta)^2 \sqrt{2 S_{ij} S_{ij}} \tag{4}$$

Where C_s is the Smagorinsky's constant, Δ is the mesh size, and S_{ij} is the strain rate of the filtered velocity field [5].

The numerical domain was built as depicted in the Figure 1, and follows the experiments described in [2]. The Reynolds number was due the height H (Re_H), the step span width was three times the W dimension and maximum step length X was 30H.

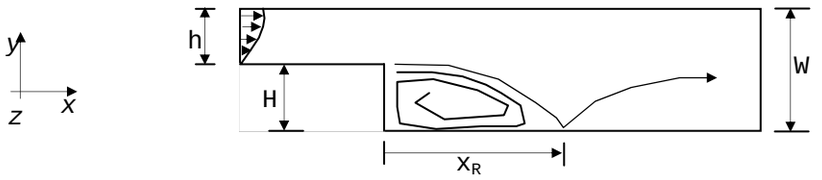


Figure 1 – The numerical domain.

Although the numerical code generates only structured cartesian grid, it is possible to construct a non-uniform mesh in order to concentrate grids in areas where the gradients are stronger, i.e., behind the step and closer to the channel bottom wall. This configuration was done in this work, which allowed saving computer memory. The grid size employed was 740x62x182, i.e., approximately 8.35 millions of cells.
Several flow properties were analyzed, that is, the reattachment length x_R, the velocity profiles (Fig. 2 a,b), the stream and spanwise vorticities (Fig. 3), the Strouhal number (Fig. 2 c) in several points downstream the domain, as well as the energy decay (Fig. 2d).

RESULTS

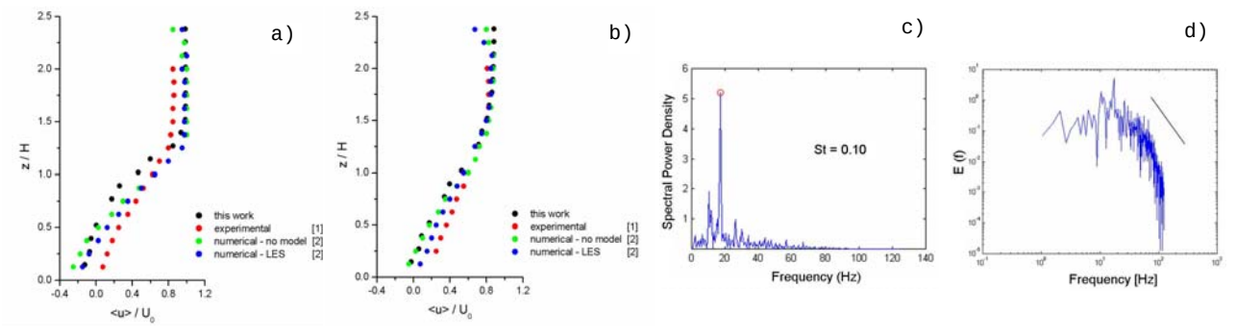


Figure 2 – Velocity profile at x/H = 8 (a), and at x/H = 10 (b), the frequency signal (c), and energy decay (d).

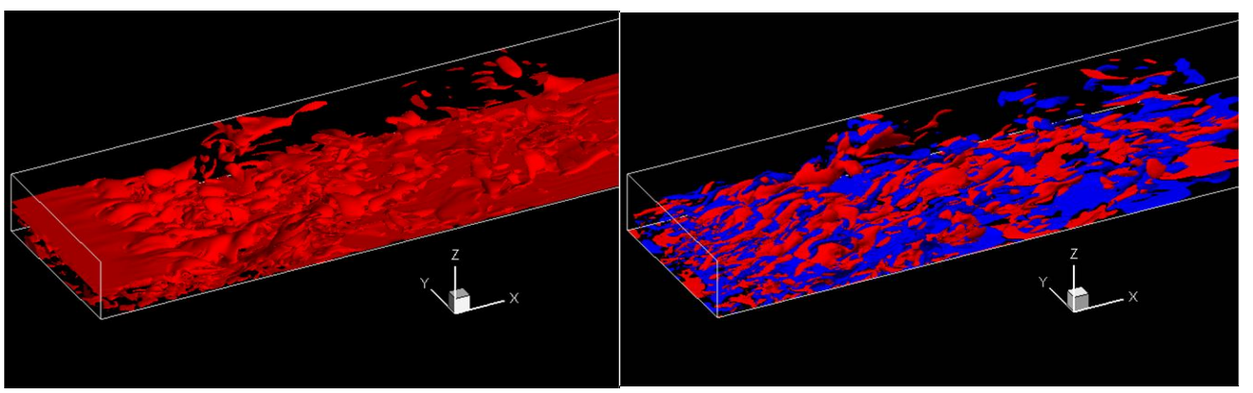


Figure 3 – Isovalues of spanwise vorticity ($\omega_y = 1.8U_\infty/H$) (left) and streamwise vorticity ($\omega_x = 1.5U_\infty/H$).

References

[1] Eaton, J. K. & Johnston, J. P.: "Turbulent flow reattachment: an experimental study of the flow and structure behind a backward-facing step", Stanford University, Rep. MD-39, 1980.

[2] Silveira Neto A., Grand D., Metais O., Lesieur M.: A Numerical Investigation of the Coherent Vortices in Turbulence behind a Backward- Facing Step. *J. Fluid Mechanics*, **256**:1-25, 1993.

[3] Baker, L., Smith, B.J.: Parallel Programming. McGraw-Hill., 1996

[4] Lesieur, M.: Turbulence in Fluids, 3rd Ed., *Kluwer Academic Publishers*, 1997.

[5] Sagaut, P.: Large Eddy Simulation for Incompressible Flows, 2nd Ed., Springer, 2002.

DEVELOPMENT AND PRACTICAL APPLICATION OF WENO SCHEMES FOR COMPRESSIBLE FLUID FLOW COMPUTATIONS

Alexey N. Kudryavtsev, Dmitry V. Khotyanovsky
Institute of Theoretical and Applied Mechanics, 630090 Novosibirsk, Russia

Summary Application of high-order shock-capturing schemes to numerical simulation of problems in supersonic aerodynamics is considered. Euler and Navier-Stokes solvers based on employing modern essentially non-oscillatory (ENO) and weighted essentially non-oscillatory (WENO) schemes are described. Examples of numerical simulations of 2D and 3D shock-dominated flows with high-order schemes are given. For a number of problems, high-quality numerical schlieren visualizations and interferograms are compared with experimental patterns. It is demonstrated that WENO schemes can be considered as a very promising candidate for Direct Numerical Simulation (DNS) and Large Eddy Simulation (LES) of high-speed compressible fluid flows.

MOTIVATION

The spectral and high-order finite-difference methods are succesfully used now for simulation of incompressible and subsonic compressible flows. They are inappropriate, however, for flows with shocks and other flow disconinuites due to the absence of shock-capturing properties. On the other side, the standard, second order, shock-capturing total variation diminishing (TVD) schemes are optimally suited for simulations of supersonic flows with a small number of isolated shock waves. However, at local extrema of the solution, they are reduced to first-order schemes and pollute the solution by excessive numerical diffusion. Therefore, problems containing both shocks and a large number of complex structures in the region of smoothness require more precise numerical tools. This need is especially evident for such applications as Direct Numerical Simulation (DNS) and Large Eddy Simulation (LES) of compressible transitional and turbulent flows, simulation of separated and jet flows, computational aeroacoustics, simulation of supersonic combustion and detonation, and many others.

The present paper is aimed at development of algorithms and codes that can robustly capture shocks and, simultaneously, accurately simulate the smooth part of flows, which contain complicated shock/shock, shock/vortex, shock/instability wave interactions. The modern ENO and WENO schemes [1] are natural candidates for the role of a basic numerical tool in these algorithms and codes. We describe Euler and Navier-Stokes solvers based on WENO schemes and give examples of their application to numerical simulation of complicated, 2D and 3D, shock-dominated flows.

DEVELOPMENT OF ALGORITHMS AND SOLVERS

Though high-order ENO and WENO schemes are proved to be both high-accurate and efficient in numerical sumulations of simple test problems, there are some difficulties in their application to more complicated flows of practical importance. In particular, finite-volume (FV) high-order schemes are very expensive for multidimensional problems while finite-difference (FD) ENO/WENO schemes suffer from violation of the so-called geometrical conservation law and do not conserve exactly a uniform flow. It hinders simulation of problems with complex geometry. In fact, FV WENO schemes are expensive because their numerical fluxes are not pointwise ones and should be calculated by integration along a cell face. Also, a correct, high-order, treatment of curvilinear grids with FD WENO schemes is difficult since their numerical fluxes approximate the exact pointwise fluxes only with the 2nd order. A new FD WENO scheme using only pointwise values of the conservative variables and fluxes, which are high-order approximations of exact quantities, is constructed. For curvilinear grids, it has the property of exact conservation of the uniform flow.

Further, a 4th-order approximation of the viscous terms on a compact 5-point (in each direction) stencil is introduced, which is coupled in a natural way with the new WENO scheme when solving the Navier-Stokes equations.

EXAMPLES OF NUMERICAL SIMULATIONS

A number of numerical simulations of 2D and 3D compressible flows containing complex configurations of shock waves and other flow discontinuities have been performed with high-order WENO schemes. They include shock wave propagation and diffraction, shock/shock and shock/boundary layer interaction, shock-wave structure of imperfectly expanded supersonic jets, development of hydrodynamic instability and transition to turbulence in high-speed free shear flows, etc. Below two examples of computations are given.

Figure 1 shows the shock wave diffraction on a triangular body at the shock wave Mach number $\mathrm{M}_s = 1.3$. A comparison of numerical and experimental pictures (the latter is taken from [2]) reveals that numerical simulation reproduces very accurately all features of the flow structure including such delicate details as the tiny secondary Mach stem, the chain of vortices near the trailing edges, the double slip lines linking the triple points with the main vortices, etc.

The second example is LES of a plane underexpanded jet at the jet Mach number $\mathrm{M}_j = 1.5$ and the jet/ambient pressure ratio $p_j/p_a = 2$. Flow turbulence with a prescribed spectrum is used as inflow forcing. Instanteneous vorticity isosurfaces are shown in Fig. 2. For these flow conditions, approximately two barrel-like jet cells develop in the computational domain. Accelerations and decelerations of the jet flow owing to the system of expansion and compression waves have

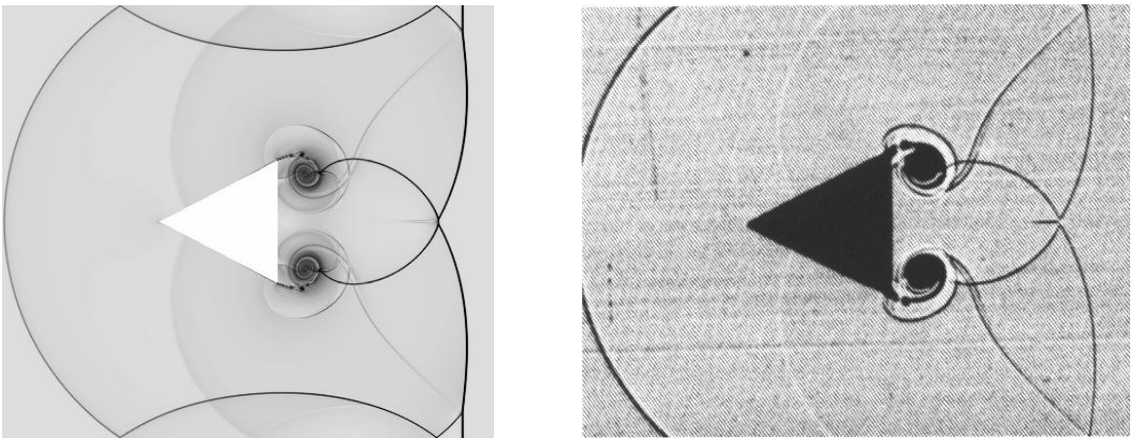


Figure 1. Numerical schlieren picture (left) and experimental shadowgraph (right) of shock wave diffraction on a finite wedge.

a great effect on turbulence characteristics. The expansion waves cause decreases in the turbulence level, whereas the compression results in a sharp increase in the turbulent fluctuations. This is illustrated by Fig. 3, where the time averaged r.m.s. streamwise velocity fluctuations in the central plane are given versus the downstream distance. The sharp peaks in the distribution correspond to the locations where the shock wave reflects from the central plane.

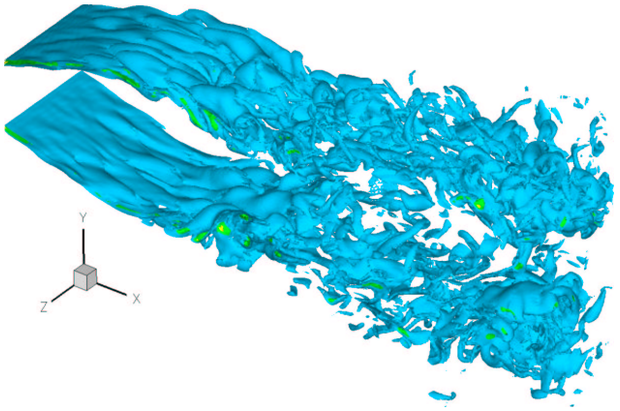


Figure 2. Instanteneous vorticity isosurfaces of LES of a plane underexpanded jet.

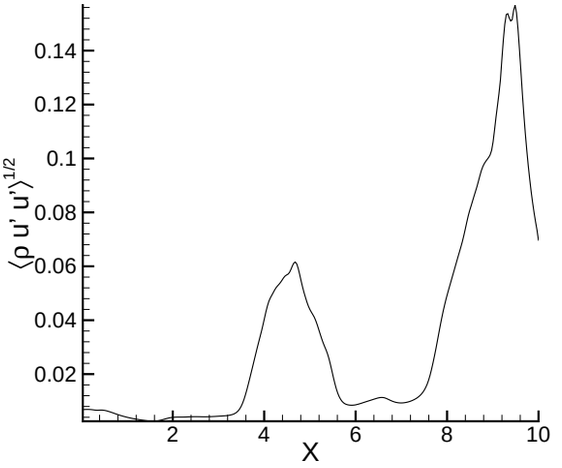


Figure 3. Distribution of r.m.s. velocity fluctuations along the jet centerline.

CONCLUSIONS

Computations performed for a number of different problems confirm that high-order WENO schemes are powerful tools for simulation of compressible fluid flows. They can be considered as very promising candidates for DNS and LES of turbulent supersonic flows.

References

[1] Shu C.-W.: High Order ENO and WENO Schemes for Computational Fluid Dynamics. In *High-Order Methods for Computational Physics*, Ed. by T.J. Barth and H. Deconinck, Lecture Notes in Computational Science and Engineering, **9**, Springer, 1999, 439–582.
[2] Van Dyke M.: An Album of Fluid Motion. Parabolic Press, Stanford, CA, 1982.

Numerical Analysis and Design Optimization of Lateral Jet Controlled Missile

Jae-Woo Lee, Byung-Young Min, Yung-Hwan Byun, and Changjin Lee
Department of Aerospace Engineering, Konkuk University
1 Hwayang, Gwangjin, Seoul,143-701, Korea

Summary Numerical parametric study of the lateral jet controlled missile has been performed. The behavior of the normal force and the pitching moment characteristics have been investigated through the numerical analyses for the different jet flow conditions, angle of attacks, circumferential jet nozzle locations and spouting jet angles. Based on the results of the aerodynamic analyses of the supersonic flow around lateral jet controlled missile for various jet and flow conditions, pitching moment and normal force are selected as the objective and constraint functions, and the flight Mach number, the angle of attack and the spouting lateral jet angle are selected as the design variables. By implementing the genetic algorithm for the global optimum, and the response surface method, the design optimization of the lateral jet controlled missile is performed to find out the most effective flight conditions for the missile control.

Introduction

Existing fin controlled missiles have delayed response time and limitations on maneuvering at low velocity or high altitude because they are controlled by the moments produced at the control surfaces that need high dynamic pressure. On the other hand, the lateral jet controlled missiles have short response time and high maneuverability even at low velocity and low-density area. Therefore, the lateral jet attitude control has been a preferred concept as a new missile defense system [1].

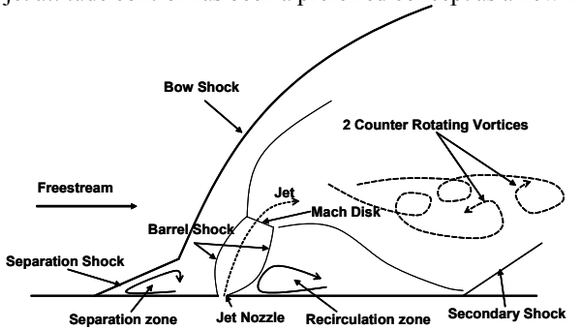


Fig. 1 Complicated flow structure around jet nozzle

As shown at Fig. 1, the aerodynamic characteristics of a lateral jet are complicated because of the local shock-shock interaction [2]. By the separation shock and bow shock interaction, a high-pressure region is formed in front of the lateral jet nozzle, and a low-pressure region is generated behind the jet nozzle because of the suction effect by lateral jet. Therefore, normal force loss and pitch down moment is generated at the jet nozzle, which locates at the center of gravity of the missile. These phenomena are affected by the jet nozzle arrangement, the jet configuration parameters and the jet flow characteristics such as jet spouting angle, jet thrust, jet nozzle location, and jet nozzle shape [1,3]. Therefore, for the effective lateral jet controlled missile design, the influence of those parameters must be studied thoroughly.
In this study, three dimensional Navier-Stokes computer code (AADL3D) was developed and validated for the analysis of the complex lateral jet flow characteristics. The paper will investigate the effect of several jet flow conditions, angle of attacks, circumferential jet nozzle location and spouting jet angle by comparing the normal force coefficient and the moment coefficient. Also, based on the results of the aerodynamic analyses of the supersonic flow around lateral jet controlled missile for various jet and flow conditions, a numerical design optimization study for the effective flight condition is performed.

Aerodynamic Analysis Method

For the analysis of complex flow phenomena around the lateral jet controlled missile, a three-dimensional Navier-Stokes computer code, AADL3D, is developed for the unsteady, compressible flow. Roe's FDS(flux difference splitting) scheme is implemented for the spatial discretization with the MUSCL for higher order extension. The minmod limiter is used to remove solution oscillations. Central difference scheme is used for the calculation of viscous flux term and fully implicit LU-SGS scheme is employed for time integration. Spalart-Allmaras one equation turbulence model is implemented on the AADL3D code for relatively rapid computational time.

Validation of the numerical approach

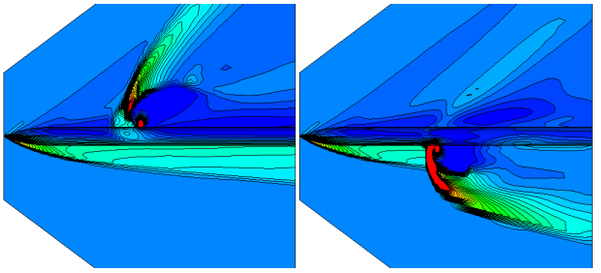
To validate the accuracy of the code for the three-dimensional missile shape with both angle of attack and lateral jet, the analyses results of AADL3D code are compared with the existing calculation results and the wind tunnel experimental

data of B. Srivastava[3]. Free stream Mach number and the Reynolds number are 2.97 and 8.2×10^5, respectively. Comparison is performed for five test cases. The experimental conditions of each case are summarized at Table 1.

Table 1 Experimental condition[3]

Test Case	C_T	Angle of Attack	Jet Location
1	1.0	20°	leeward jet
2	1.0	20°	windward jet
3	4.0	20°	leeward jet
4	4.0	20°	windward jet
5	jet off	20°	-

Figure 2 shows C_p contour at the symmetry plane of Cases 3 and 4. It shows distinctly different barrel shock and bow shock shapes and different flow phenomena around the jet nozzle. In the case of jet located at the windward side, the flow separation region in front of the jet nozzle is reduced and the vortices bent by freestream are wrapping around the missile body. Moreover, the propagated vortices to the down stream hit the missile body, hence, another high-pressure region is generated. AADL3D results are compared with the Raytheon calculation and experimental results at Table 2. AADL3D has better normal force prediction than ref. 3.



(a) Case 3 (b) Case 4

Fig. 2 C_P contour at the symmetry plane

Table 2 Normal force coefficient comparison

Test case	C_N (Raytheon Exp.)	C_N (Raytheon Calc.)	C_N (AADL3D)
1	3.37	2.77	3.20
2	4.64	4.56	4.52
3	0.21	-0.19	0.25
4	7.33	7.27	7.35
5	4.36	3.73	4.15

Grid system selection

The missile configuration for the case studies is simple tangent ogive-cylinder body without fin, as shown at Fig. 3. To increase the computational efficiency, a grid system, which is coarse but can guarantee solution accuracy, is selected by investigating the convergence rate and the converged solutions of several grid systems.

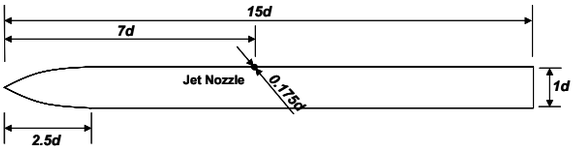


Fig. 3 Missile configuration for the case studies

The freestream Mach number was 2.6 and jet Mach number was 2.04. $P_{ratio}(P_{jet}/P_{freestream})$was 45.7 and the Reynolds number was 6.63×106. From the result of Fig. 4, the 95×34×33 grid system has been selected, and the grid system is shown at Fig. 5.

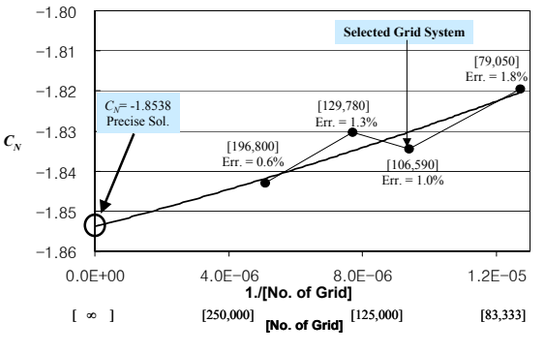


Fig. 4 The result of grid density test

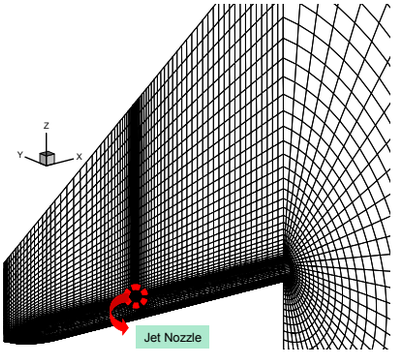


Fig. 5 Selected grid system (95×34×33)

Case Studies of Lateral Jet Controlled Missile

Analysis conditions and nomenclature definition

For all calculations, the analysis condition of freestream flow is same as the grid system selection case and the atmospheric condition is that of the 10km altitude. To find out the effect of the jet flow characteristics on the missile attitude control, the different pressure ratios and the jet Mach number variations cases are selected and Table 3 summarizes the jet flow conditions of each case and angles of attack of those cases were set to zero. Furthermore, to find out the freestream-jet angle effect, case studies have been performed for the different angles of attack, the circumferential jet locations and the spouting jet angle. Table 4 represents each analysis condition.

Table 3 Jet flow conditions for case 1 ~ case 6

	Case 1	Case 2	Case 3	Case 4	Case 5	Case 6
P_{ratio}	**150**	**300**	**450**	150	150	**850**
M_{jet}	**1**	1	1	**2**	**3**	**1**
$\dot{m}_{jet}$ [kg/s]	14.04	28.08	42.12	28.08	42.12	79.56
C_T	2.323	4.653	6.983	6.401	13.196	13.196

Table 4 Analysis conditions for each case

a) Angle of attack effect / b) Jet location effect

	Case 7	Case 8	Case 9	Case 10	Case 11	Case 12	Case 13	Case 14	Case 15	Case 16
P_{ratio}	45.7	45.7	45.7	45.7	45.7	45.7	45.7	45.7	45.7	45.7
M_{jet}	2.04	2.04	2.04	2.04	2.04	2.04	2.04	2.04	2.04	2.04
M_∞	2.6	2.6	2.6	2.6	2.6	2.6	2.6	2.6	2.6	2.6
α	**-20°**	**-10°**	**0°**	**10°**	**20°**	10°	10°	10°	10°	10°
ψ	90°	90°	90°	90°	90°	90°	90°	90°	90°	90°
θ_{jet}	180°	180°	180°	180°	180°	**0°**	**45°**	**90°**	**135°**	**180°**

c) Spouting jet angle effect

	Case 17	Case 18	Case 19	Case 20	Case 21	Case 22	Case 23	Case 24
P_{ratio}	45.7	45.7	45.7	45.7	45.7	45.7	45.7	45.7
M_{jet}	2.04	2.04	2.04	2.04	2.04	2.04	2.04	2.04
M_∞	2.6	2.6	2.6	2.6	2.6	2.6	2.6	2.6
α	0°	0°	0°	0°	0°	0°	0°	0°
ψ	**30°**	**45°**	**60°**	**75°**	**90°**	**105°**	**120°**	**135°**
θ_{jet}	180°	180°	180°	180°	180°	180°	180°	180°

The missile configuration is nondimensionalized by the missile diameter, *d*. Force, moment and other nomenclatures are defined at Fig. 6. Missile surface is divided into four regions with respect to the center of gravity, and the normal force and moment distribution at each region were compared.

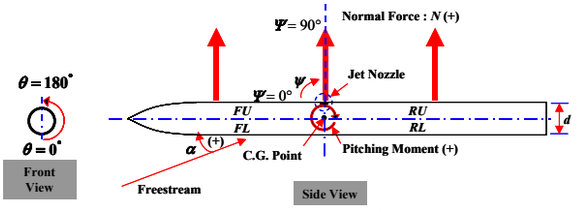
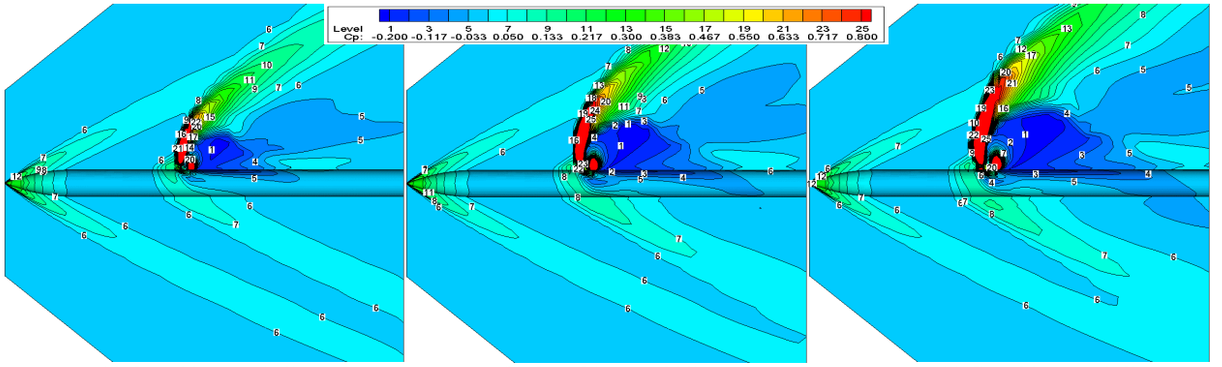


Fig. 6 Nomenclature definition

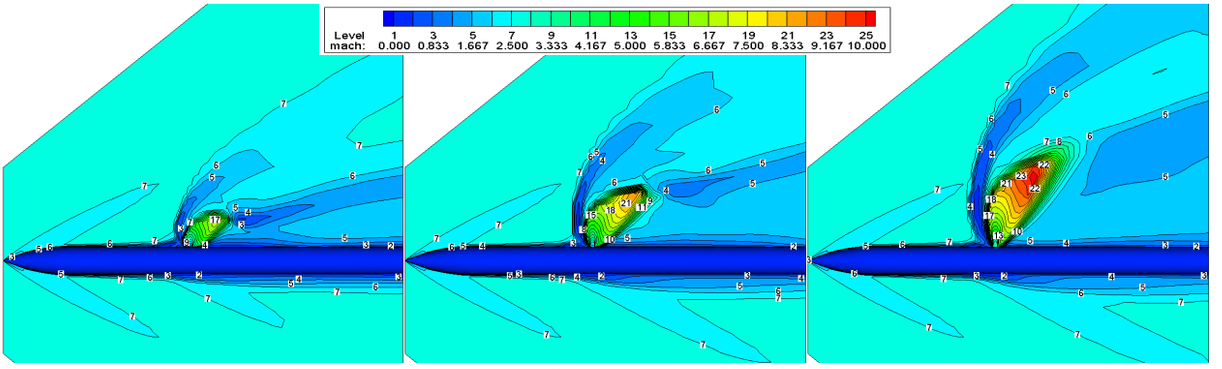
Jet flow condition effect

For the different pressure ratios and the jet Mach number variations, the normal force and the moment coefficients of a missile body are compared to find out the effect of the jet flow characteristics on the missile attitude control. Fig. 7 compares the pressure contours of Case 1, 2 and 3 and Fig. 8 compares the Mach number contours of Case 1, 4 and 5. From these two figures, different shape changes of barrel shock can be observed; bigger barrel shock for higher pressure ratio and steeper barrel shock for higher jet Mach number. Table 5 and Fig. 9 show the normal force and pitching moment results.



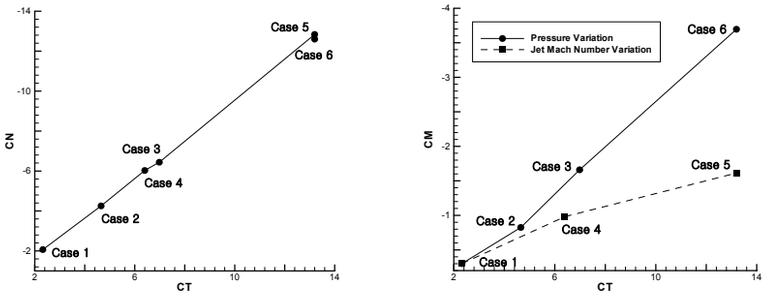
(a) Case 1(P_{ratio} = 150) (b) Case 2(P_{ratio} = 300) (c) Case 3(P_{ratio} = 450)

Fig. 7 C_P Contour at the symmetric plane



(a) Case 1(M_{jet} = 1) (b) Case 4(M_{jet} = 2) (c) Case 5(M_{jet} = 3)

Fig. 8 Mach number Contour at the symmetric plane



(a) C_N *vs.* C_T (b) C_M *vs.* C_T

Fig. 9 C_N, C_M *vs.* C_T plots

Table 5 The results of calculations (jet pressure variation effect)

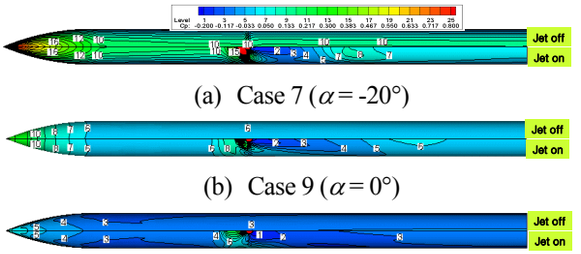
	C_T	C_N	$C_{N_{FU}}$	$C_{N_{FL}}$	$C_{N_{RU}}$	$C_{N_{RL}}$	C_M	$C_{M_{FU}}$	$C_{M_{FL}}$	$C_{M_{RU}}$	$C_{M_{RL}}$
Case 1	2.323	**-2.067**	-0.236	0.099	**0.426**	-0.034	**-0.302**	-0.162	0.053	**-0.701**	0.508
Case 2	4.653	**-4.254**	-0.376	0.144	**0.689**	-0.058	**-0.825**	-0.224	0.084	**-1.511**	0.827
Case 3	6.983	**-6.440**	-0.470	0.205	**0.903**	-0.095	**-1.660**	-0.330	0.156	**-2.533**	1.046
Case 4	6.401	**-6.028**	-0.373	0.118	**0.661**	-0.032	**-0.981**	-0.187	0.059	**-1.686**	0.833
Case 5	13.196	**12.837**	-0.436	0.122	**0.641**	0.032	**-1.613**	-0.197	0.059	**-2.077**	0.602

The results show that the normal force is almost proportional to the jet thrust but the behavior of the moment is different between jet pressure increased case and the jet Mach number increased case. The increased jet thrust by increasing jet Mach number produces less pitch down moment than the same thrust with increased jet pressure. Therefore, increasing jet Mach number is more advantageous than increasing jet pressure ratio in order to obtain higher jet thrust while maintaining minimum pitch down moment. Furthermore, Table 5 shows that most of the normal force loss and the pitching moment generation are taken place at the low-pressure region behind the jet nozzle.

Angle of attack effect

Figure 10 compares surface pressure contours with jet-off case. At α = -20°, the generated vortex is bent by the freestream, and it sweeps the missile surface, as a result, vortex prevents the downward freestream hits the missile surface. Therefore, strong bow shock effect caused by downward freestream velocity component is vanished above

upper rear body surface, and more large low-pressure region is formed compared to jet-off case. Figure 11 shows angle of attack effect results. A negative angle of attack (windward jet) causes a relatively big normal force loss and pitch down moment compared with the positive angle of attack case (leeward jet).

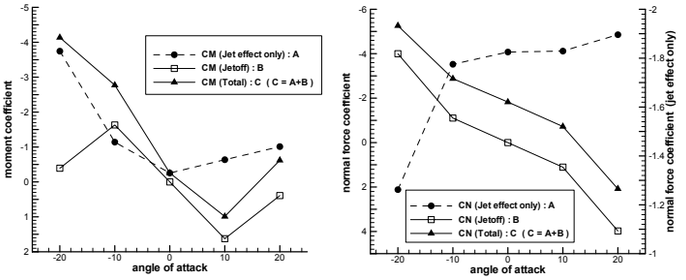


(a) Case 7 (α = -20°)

(b) Case 9 (α = 0°)

(c) Case 11 (α = 20°)

Fig. 10 C_P contour on the surface



(a) C_N *vs.* angle of attack (b) C_M *vs.* angle of attack

Fig. 11 C_N, C_M *vs.* angle of attack plots

Circumferential jet location effect

Figure 12 shows surface pressure comparison and Fig. 13 shows the results. Greater normal force loss and pitching down moment were generated when jet nozzle is located at θ=0° than θ=180°. However, maximum normal force and minimum pitching down moment were generated when jet nozzle is located at θ=90° because of the largest high pressure region on the rear body upper surface behind the nozzle, which contributes to the increase of the normal force and to decrease of the pitching down moment, due to the strong bow shock by freestream (Fig. 12), and another low pressure region at the opposite side of the nozzle due to the bent jet by freestream. Hence, the lateral jet should be operated with concerning these varying aerodynamic characteristics.

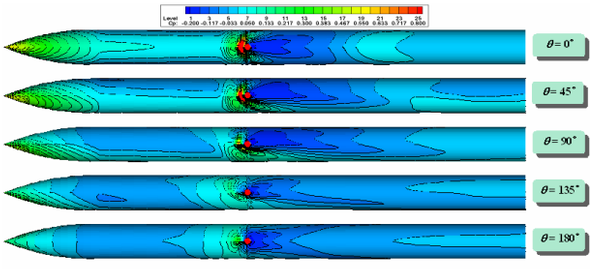
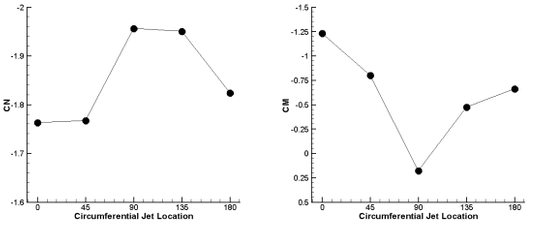


Fig. 12 C_P contour on the surface

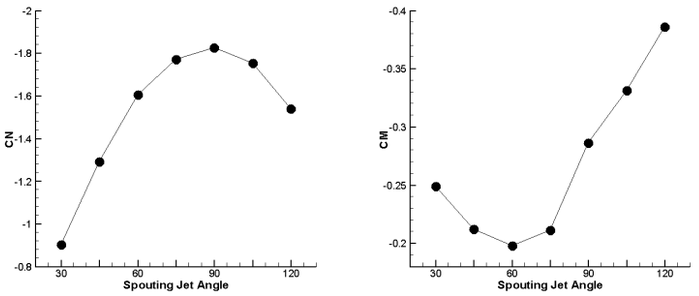


(a) C_N *vs.* θ (b) C_M *vs.* θ

Fig. 13 C_N, C_M *vs.* circumferential jet location

Spouting jet angle effect

Figure 14 summarizes the results of the spouting jet angle effect. Pitching down moment is decreased as the spouting jet angle is inclined forward. However, when the spouting jet angle is inclined forward excessively(below 60° in this study), pitching down moment is increased again. Normal force becomes maximum when ψ=90° and is decreased as spouting jet angle is inclined forward or backward because the jet thrust is decreased by cosine law. Therefore, the pitching moment can be minimized by selecting proper spouting jet angle while satisfying required normal force for attitude control.

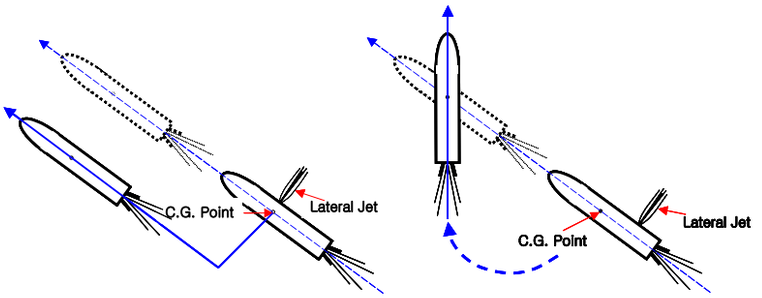


(a) C_N *vs.* ψ (b) C_M *vs.* ψ

Fig. 14 C_N, C_M *vs.* spouting jet angle

Optimal Design of the Lateral Jet Controlled Missile

There are two kinds of missile attitude control types using lateral jet(Fig. 15). First, by locating the jet at the center of gravity of the missile, a transition movement of missile can be obtained without any pitching moment generation. The other type is to control the missile attitude using the pitching moment generated by the jet located at a certain distance from the missile center of gravity. In this study, the first type, a lateral jet locates at the center of gravity, is considered. Therefore, generation of the pitching moment is negative effect to the missile control and should be diminished.



(a) Using normal force (b) Using moment

Fig. 15 Missile attitude control using lateral jet

Based on the results of the parametric study, a numerical design optimization study for the effective flight condition is performed. First of all, the design problems are formulated by defining the design variables and the design constraints. By incorporating the proven optimization and approximation techniques, the design optimization at the altitude of 10km is performed. Pitching moment and normal force are selected as the objective and constraint functions, and the flight Mach number, the angle of attack and the spouting jet angle are selected as the design variables. GENOCOP III[4], a genetic algorithm is used to obtain the global optimum, and the response surface method[5] is employed.
The optimization formulation is as follows;

Minimize

$$\boldsymbol{F}(\vec{\boldsymbol{X}}) = \left|\boldsymbol{C}_{M_{total}}\right|$$

Subject to

$$\boldsymbol{g}(\vec{\boldsymbol{X}}) = \boldsymbol{C}_{N_{10G}} - \boldsymbol{C}_{N} \le 0$$

Where

$$\vec{\boldsymbol{X}} = \left\{\boldsymbol{\alpha},\quad \boldsymbol{\psi},\quad \boldsymbol{M}_{freestream}\right\}$$

$$-20 \le \boldsymbol{\alpha} \le 20$$

$$30 \le \boldsymbol{\psi} \le 90$$

$$2 \le \boldsymbol{M}_{freestream} \le 4$$

The $\boldsymbol{C}_{N_{10G}}$ represents normal force coefficient required to obtain initial 10G acceleration for the missile transition without respect to drag. The assumed missile weight is 500kg, jet Mach number is 2.0 and P_{ratio} is 150. The missile shape is the same as the shape for the case study.
The optimization strategy using response surface is shown at Fig. 16.

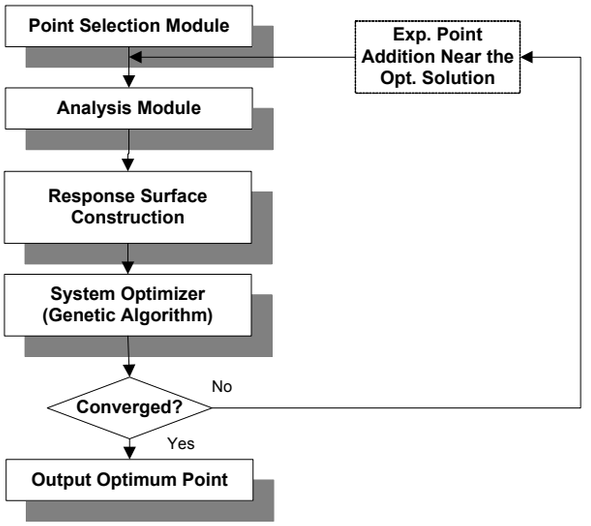


Fig. 16 Optimization strategy

Conclusions

The normal force was almost proportional to the jet thrust and there has been thrust loss because of shock interactions. However, the moment was not only a function of jet thrust, but also of the jet pressure and the jet Mach number.
The nonlinearity of the normal force and pitch down moment according to the angle of attacks has been confirmed. Especially, negative angle of attack (windward jet) case shows greater normal force loss and the pitch down moment. θ = 90°). Also, existence of least pitching moment point was identified through the case study of the spouting jet angle effect. The low-pressure region behind the jet nozzle contributes more greatly to normal force loss and pitch down moment generation than the high-pressure region. Therefore, for the efficient lateral jet attitude control system design, it is identified that the study on reducing the low-pressure region is required. Based on the results of case studies, the design optimization of the lateral jet controlled missile is performed to minimize the pitching moment while satisfying the normal force constraint using genetic algorithm and response surface method.

Acknowledgement

This work was supported by grant number R01-2000-000-00319-0 from the Basic Research Program of the Korea Science and Engineering Foundation.

References

[1] R. G. Lacau and M. Robert, "The use of Lateral Jet Control at Aerospatiale", Nielsen Engineering & Research, 1988.
[2] F. S. Billig, R. C. Orth, and M. Lasky, "A Unified Analysis of Gaseous Jet Penetration", *AIAA Journal*, Vol. 9, No. 6, June 1971, pp.1048-1058.
[3] B. Srivastava, "Computational Analysis and Validation for Lateral Jet Controlled Missiles", *Journal of Spacecraft and Rockets*, Vol. 34, No. 5, Sep-Oct 1997, pp. 584-592.
[4] Michalewicz, Z., *Genetic Algorithms + Data Structures = Evolution Programs*, Springer-Verlag, 1996.
[5] Myers, R. H. and Montgomery, D. C., *Response Surface Methodology*, John Wiley & Sons Inc., 1995.

NUMERICAL PREDICTION OF ENERGY DISSIPATION IN CONDENSING STEAM FLOW

Tadeusz Chmielniak, Włodzimierz Wróblewski, Sławomir Dykas
Silesian University of Technology, Institute of Power Engineering and Turbomachinery, 44-100 Gliwice, Poland

Summary In the presented work the analysis of energy dissipation in steam expansion flows is carried out. The adiabatic flow, with homogeneous and with heterogeneous condensation is considered. The influence of the condensation phenomenon and steam impurity on the losses is analyzed. For modelling of the steam properties the IAPWS-IF'97 formulation is implemented. The numerical computations are performed using an in-house multi-block code and commercial code TascFlow.

INTODUCTION

From the technical point of view in the fluid-flow machinery analysis and improvement is very important to localize the energy dissipation sources in the flow and reduce them. In the steam turbine an improvement in last stage efficiency can significantly impact the output of the total unit, considering the fact that the last stages produces a significant part of the total unit output. In the last stages of the steam turbine flow occurs condensation process and the flow is two-phase.

The aim of this research is to estimate the energy dissipation in the condensing steam flow. In the blade cascade flows exist the two types of losses, are aerodynamic losses (profile, secondary flow) and thermodynamic (caused by condensation phenomenon). Because the steam in power cycle includes always some impurities, the question connected with influence of steam impurities on the losses is considered. The comparison between the flow with homogeneous and heterogeneous condensation with respect to the losses is intended. The condensation produces thermodynamic losses in the flow and changes the flow parameters, which influences the aerodynamic losses. To date the estimations of the losses in the turbine flow are in the centre of interest for many researchers. However, the research on the influence of the condensation phenomenon on the losses is not often published. There are well known the works of Schnerr [1], Stastny [2] or White [3] dealing with the investigations of the 2-D cascade flow with condensation. This paper includes the complete analysis of the adiabatic steam flow and the steam flow with homogeneous and heterogeneous condensation with respect to the losses in the Laval nozzle and through the 3-D blade-to-blade channel. The numerical investigations presented in this paper are performed on a geometry of the low pressure part of the large steam turbine.

PHYSICAL AND NUMERICAL MODEL

The numerical simulation is based on the time dependent 3-D Reynolds averaged Navier-Stokes equations, which are coupled with a two-equation turbulence model (k-ω SST model) and additional mass conservation equations for the liquid phase (two for homogeneous and one for heterogeneous condensation). The set of governing equations is closed by means of a real gas equation of state [4]. The 'local' form of the real gas equation of state is used.

The condensation phenomena are modeled based on the classical nucleation theory of Volmer, Frenkel and Zeldovich, which is well suited for modeling technical flows [1,2,3]. The droplet growth equation of Gyarmathy is used. The system of governing equations is discretized on a multi-block structured grid using the finite-volume method and integrated in time using an explicit Runge-Kutta method. An upwind scheme proposed by Godunov, is used as the Riemann solver. The MUSCL technique is implemented to approach the TVD scheme with the van Albada flux limiter to avoid oscillations [5].

The commercial code TascFlow is a widely used code for the turbomachinery applications. TascFlow is based on the averaged Navier-Stokes equations employing the finite volume method (FVM) with an implicit, multi-block algorithm. The solution strategy is based on the Algebraic Multi-grid method. The steam properties are modelled using the virial equation of state with three virial coefficients. The flow is considered as an equilibrium dry/wet steam model without nucleation process.

RESULTS

The numerical calculations are carried out for the Laval nozzle and for the last and penultimate stages of the low-pressure part of steam turbine. The nozzle flow is the simplest test case for comparison with experiments and validation of the numerical codes. For nozzle flows different expansion processes are considered: adiabatic, diabatic with homogeneous and heterogeneous condensation. Expansion lines obtained for this cases are shown in h-s chart (Fig.1).

For the turbine stages different operating conditions are considered. The distributions of the flow parameters, distributions of the losses (Fig. 2), efficiency and power generated through the stage are investigated. Computational domain was discretized using the structural multi-block grid, in which the O-type grid near the blade is embedded within

a C-type grid and in the inlet and outlet domain the H-type grid is used. The energy dissipation is described using loss coefficient.

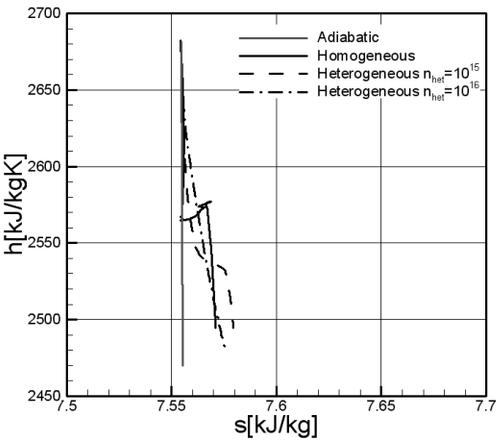


Fig.1.Expansion line in the Laval nozzle

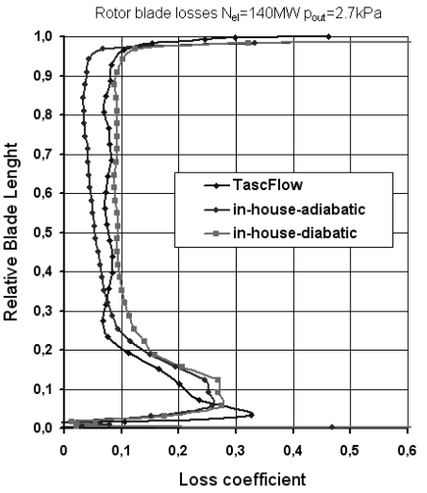


Fig.2. Loss coefficient distributions along the blade length

CONCLUSIONS

The analyses of the losses in the flow without condensation, with homogeneous and heterogeneous condensation are carried out. The influence of the impurities concentration on the losses is also investigated. The presented numerical results for the flow without condensation are performed on an in-house numerical code as well as commercial code CFX TascFlow. In the case of condensing flow the in-house code is used. The comparison of the results obtained by means of the in-house code and TascFlow code shows:

- very good agreement regarding the flow field parameters and energy dissipation distributions,
- very good agreement in the modelling of the steam (real gas) properties (The simplest equation of state used in the in-house code gives identical results like the virial equation of state with three virial coefficients applied in TascFlow).

For the 3-D flow through the LP steam turbine geometry the following conclusions can be drawn:

- for the flow with heterogeneous condensation the wetness is the highest,
- the worst with respect to efficiency and losses is the flow with homogeneous/ heterogeneous condensation,
- the condensation phenomenon can decrease or increase the power generated in the turbine stage, depends on the operating conditions,
- influence of the impurities (heterogeneous condensation) on the losses is not as significant, compared to the condensation itself,
- quality of the code and numerical grid influences the accurate solutions of aerodynamic as well thermodynamic losses.

References

[1] Schnerr, G.H., Heiler, M., 1998, "*Two-Phase Flow Instabilities in Channels and Turbine Cascade*", CFD Review –1998, Vol. II, World Scientific, pp. 668-690

[2] Stastny M., Sejna M., "*Numerical analysis of hetero-homogeneous condensation of the steam flowing in turbine cascade"*, ImechE, Conference Transactions, Turbomachinery Vol.B, 2-5 March, Royal National Hotel, London, 1999

[3] White A.J., Young J.B., Walters P.T., 1996, *"Experimental Validation of Condensing Flow Theory for a Stationary Cascade of Steam Turbine Blades",* Phil. Trans. R. Soc. London A, Vol.354, pp.59-88

[4] Dykas, S., 2001, *„Numerical calculation of the steam condensing flow"*, Task Quarterly, Scientific Bulletin of Academic Computer Center in Gdansk, Vol. 5, No 4, pp.519-537, Gdansk, Poland

[5] Wróblewski, W., 2000, *„Numeryczna symulacja zjawisk przepływowych w turbinach cieplnych"*, Energetyka Vol.132, Zeszyty Naukowe Politechniki Śląskiej., Gliwice, Poland

[6] Chmielniak, T., Łukowicz, H., 1992, *„Numerical Calculation of Turbine Stage forOff-Design Condition"*, Zeszyty Naukowe Politechniki Łódzkiej, Cieplne Maszyny Przeplywowe, Vol.103, pp.143-165, Łódz, Poland

XXI ICTAM, 15–21 August 2004, Warsaw, Poland

A PRESSURE-CORRECTION METHOD FOR ALL MACH NUMBERS

Krista Nerinckx*, Jan Vierendeels*, Erik Dick*
*Ghent University, Department of Flow, Heat and Combustion Mechanics,
Sint-Pietersnieuwstraat 41, B-9000 Ghent, Belgium

Summary We present a collocated finite-volume-based pressure-correction method, for all speed flows of a general fluid. Over the whole Mach number range, the algorithm shows an excellent efficiency and accuracy. Mach-uniform accuracy is obtained by applying the Advection Upstream Splitting Method (AUSM+) for the flux definitions. Mach-uniform efficiency is obtained by treating the convective phenomena and the acoustic/thermodynamic phenomena separately: a velocity predictor from the momentum equations, and a coupled solution of the continuity and energy equation for pressure and temperature corrections.

INTRODUCTION

We present a collocated finite-volume-based pressure-correction method, for all speed flows of a general fluid. Over the whole Mach number range, the algorithm shows an excellent efficiency and accuracy.

MACH-UNIFORM ACCURACY

Mach-uniform accuracy is obtained by applying the Advection Upstream Splitting Method (AUSM+) [1] for the flux definitions. We do not take over the Rhie-Chow interpolation from the incompressible pressure-correction method since it causes an extreme smearing of shocks in high Mach number flows [2]. A pressure dissipation term is added to prevent pressure-velocity decoupling at low Mach numbers. Furthermore, a preconditioned speed of sound is introduced to scale the fluxes properly when the Mach number diminishes [3].

MACH-UNIFORM EFFICIENCY

To obtain Mach-uniform efficiency, the stifness problem has to be remedied. A breakdown of convergence at low Mach numbers occurs if the stability of the scheme imposes an acoustic CFL-limit. This limit is removed if the terms which hold the acoustic information are treated implicitly. Analyzing the Euler equations reveals that the acoustic information is found in specific terms of the momentum and energy equation. The algorithm first determines a predictor value for velocity from the momentum equations. Then corrections are introduced into the implicit terms, which are the acoustic terms in the momentum and energy equations. For the momentum equations this results in a relation between velocity and pressure corrections. In the energy equation, the internal energy ρe, (ρ density, e specific internal energy) is expanded as a function of pressure and temperature, according to the equation of state for a general fluid. Thus, the energy equation contains both pressure and temperature corrections. A second equation containing these two kind of corrections is derived from the continuity equation. The two equations containing both pressure as well as temperature corrections, are solved in a coupled way.
Valid for a general fluid, it is instructive to see how the algorithm behaves in some special cases:

- If density is constant, the continuity equation becomes a pure pressure-correction equation. The energy equation becomes a convection-diffusion equation for temperature corrections. The algorithm therefore reduces to the classical incompressible pressure-correction method [4].

- If an ideal gas is considered, ρe depends only on pressure. In absence of heat transfer, the energy equation then contains only pressure corrections. Thus, a coupled solution with the continuity equation is no longer neccessary: a pressure-correction equation based on the energy equation can be used to update pressure. This is consistent with the low Mach number perturbation analysis for an ideal gas [5]. Figure 1 shows the convergence plots for computations of a one dimensional nozzle flow at a throat Mach number of 0.001. There is no acoustic CFL-limit and the Mach-uniform algorithm shows an excellent convergence rate. Figure 1 also shows the convergence plots for a compressible pressure-correction algorithm that uses the continuity equation to construct the pressure-correction equation. The computations could only be made stable under a severe underrelaxation, and the convergence rate at this low Mach number is very bad. It clearly suffers from the stiffness problem and therefore doesn't reach Mach-uniform efficiency. However, several examples of pressure correction methods based on the continuity equation are found in the literature.
  If heat transfer is present, temperature appears into the conductive terms of the energy equation. To escape a diffusive Neumann limit, these terms have to be treated implicitly. This implies that temperature corrections are introduced there. Therefore, a coupled solution with the continuity equation is needed once again.

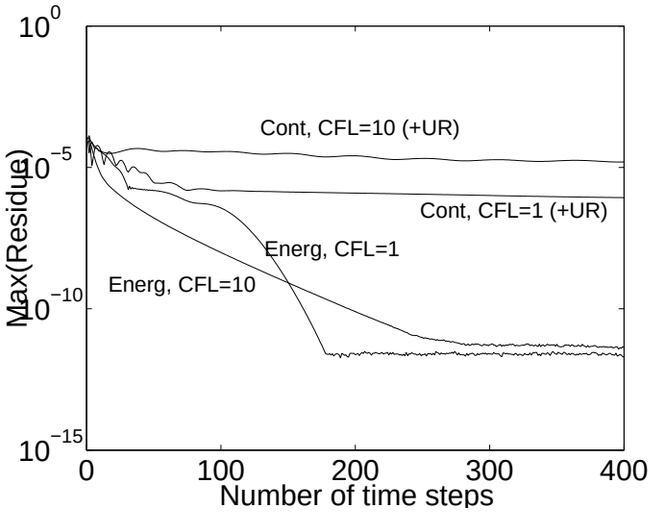


Figure 1. Subsonic nozzle flow, $M_{throat} = 0.001$. Convergence plot for computations at convective CFL numbers of 1 and 10. *Energ*: Mach-uniform algorithm. *Cont*: equivalent algorithm based on the continuity equation (computation with underrelaxation (UR))

CONCLUSION

The described algorithm, with a predictor step from the momentum equation, and a coupled solution of the energy and continuity equation, is the most general form. The essential idea is that convective phenomena and acoustic/thermodynamic phenomena are treated seperately. Doing so, only the appropriate terms are treated implicitly, contrary to fully implicit coupled methods. The described algorithm finds its place in between a fully segregated and a fully coupled approach. It allows an efficient and accurate flow computation of any kind of fluid, at any speed.

References

[1] M.-S. Liou. Mass flux schemes and connection to shock instability. *Journal of Computational Physics*, 160:623–648, 2000.
[2] K. Nerinckx, J. Vierendeels, and E. Dick. A mach-uniform pressure correction algorithm using ausm flux definitions. *Advances in Fluid Mechanics V*, 40:33–43, 2004.
[3] J.R. Edwards and M.-S. Liou. Low-diffusion flux-splitting methods for flows at all speeds. *AIAA Journal*, 36:1610–1617, 1998.
[4] S.V. Patankar and D.B. Spalding. A calculation procedure for heat, mass and momentum transfer in three-dimensional parabolic flows. *International Journal of Heat ans Mass Transfer*, 15:1787–1806, 1972.
[5] B. Müller. Low mach number asymptotics of the navier-stokes equations and numerical implications. *VKI Lecture Series*, 1999-03, 1999.

XXI ICTAM, 15–21 August 2004, Warsaw, Poland

NUMERICAL COMPUTATION OF COMPRESSIBLE VISCOUS FLOW THROUGH A MALE ROTOR-HOUSING GAP OF SCREW COMPRESSORS

Jan Vimmr*

*University of West Bohemia in Pilsen, Faculty of Applied Sciences, Department of Mechanics, Univerzitní 22, CZ-306 14 Plzeň, Czech Republic

Summary This contribution deals with the numerical computation of a compressible viscous fluid flow through a two-dimensional model of the male rotor-housing gap in the screw compressor. Numerical solution of the nonlinear conservative system of the compressible Navier-Stokes equations is obtained by means of the cell-centred finite volume formulation of the explicit two-step TVD MacCormack scheme proposed by Causon on a structured quadrilateral grid using the own numerical code.

INTRODUCTION

Gas leakage is a phenomenon that has a lot of different features, many of significant importance. Compressor engineers are mostly interested in estimation for the mass flow rate. It has a great influence on the compressor performance, especially with regard to its internal efficiency. Therefore it is necessary to make reasonable estimates for mass flow rates or to investigate the details of the leakage flow. The aim of this contribution is to show the numerical computation of a compressible viscous fluid flow through the male rotor-housing gap (the gap between the stator and the head of the male rotor tooth), Fig. 1, in the screw compressor for the pressure ratio $p_{01}/p_2 = 2$. It is assumed that the leakage flow is laminar in most cases and that the male rotor-housing gap can be simulated by a two-dimensional bounded domain $\Omega \subset \mathbb{R}^2$, occupied by the perfect gas, with the boundary $\partial\Omega = \partial\Omega_I \cup \partial\Omega_O \cup \partial\Omega_W$, where $\partial\Omega_I$ is the inlet and $\partial\Omega_O$ the outlet section of the computational domain Ω, $\partial\Omega_W = \partial\Omega_{WR} \cup \partial\Omega_{WS}$ are impermeable walls of the computational domain corresponding to the stator $\partial\Omega_{WS}$ and the head of the male rotor tooth $\partial\Omega_{WR}$.

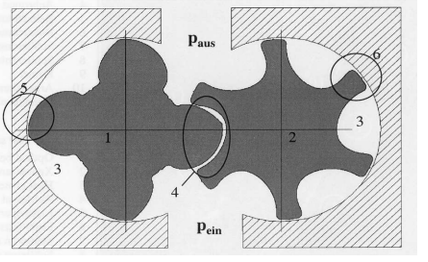


Fig. 1. Frontal section of rotors, 5 – male rotor-housing gap

MATHEMATICAL MODEL OF LAMINAR COMPRESSIBLE FLOW

Let $(0, \mathcal{T})$ be a time interval. The mathematical model of a laminar compressible flow is described by the nonlinear conservative system of the Navier-Stokes (NS) equations. For 2-D problems it can be written in nondimensional form as

$$\frac{\partial \boldsymbol{w}}{\partial t} + \frac{\partial \boldsymbol{f}(\boldsymbol{w})}{\partial x} + \frac{\partial \boldsymbol{g}(\boldsymbol{w})}{\partial y} = \frac{1}{Re_\infty}\left[\frac{\partial \boldsymbol{f}_V(\boldsymbol{w})}{\partial x} + \frac{\partial \boldsymbol{g}_V(\boldsymbol{w})}{\partial y}\right] \qquad \text{in } \Omega \times (0, \mathcal{T})\,. \tag{1}$$

The vector $\boldsymbol{w}$ of conservative variables and the inviscid $\boldsymbol{f}(\boldsymbol{w}), \boldsymbol{g}(\boldsymbol{w})$ and viscous fluxes $\boldsymbol{f}_V(\boldsymbol{w}), \boldsymbol{g}_V(\boldsymbol{w})$ are defined as

$$\boldsymbol{w} = \left(\varrho,\, \varrho u,\, \varrho v,\, E\right)^T, \quad \boldsymbol{f}(\boldsymbol{w}) = \left(\varrho u,\, \varrho u^2 + p,\, \varrho uv,\, (E+p)\,u\right)^T, \quad \boldsymbol{g}(\boldsymbol{w}) = \left(\varrho v,\, \varrho uv,\, \varrho v^2 + p,\, (E+p)\,v\right)^T, \tag{2}$$

$$\boldsymbol{f}_V(\boldsymbol{w}) = \left(0,\, \tau_{xx},\, \tau_{xy},\, u\tau_{xx} + v\tau_{xy} - q_x\right)^T, \quad \boldsymbol{g}_V(\boldsymbol{w}) = \left(0,\, \tau_{yx},\, \tau_{yy},\, u\tau_{yx} + v\tau_{yy} - q_y\right)^T, \tag{3}$$

where t is time, ϱ density, p static pressure, E total energy per unit volume, u, v are Cartesian components of velocity vector $\boldsymbol{v}$ and $\tau_{xx}, \tau_{xy}, \tau_{yx}, \tau_{yy}$ are laminar shear stresses given for a Newtonian fluid. The external volume forces are neglected.

To close the system of the compressible NS equations (1) it is necessary to specify the equation of state for the perfect gas $p = \varrho\, r\, T = (\kappa - 1)\, \varrho\, c_v\, T$ and the relation for total energy per unit volume $E = \frac{p}{\kappa - 1} + \frac{1}{2}\varrho|\boldsymbol{v}|^2$, where T is thermodynamic temperature, $r = c_p - c_v$ the gas constant per unit mass, c_p and c_v are the specific heats at constant pressure and volume, respectively and $\kappa = 1.4$ is so-called Poisson's constant. Heat flux terms q_x, q_y can be written as

$$q_x = -k\frac{\partial T}{\partial x} \equiv -\frac{\kappa}{\kappa - 1}\,\frac{\eta}{Pr}\,\frac{\partial}{\partial x}\left(\frac{p}{\varrho}\right), \qquad q_y = -k\frac{\partial T}{\partial y} \equiv -\frac{\kappa}{\kappa - 1}\,\frac{\eta}{Pr}\,\frac{\partial}{\partial y}\left(\frac{p}{\varrho}\right), \tag{4}$$

where η is molecular viscosity, k thermal conductivity and $Pr = c_p\eta/k$ is the laminar Prandtl number which is taken to be 0.72 for the calorically perfect gas. All quantities are considered as nondimensional. The reference Reynolds number is defined as $Re_\infty = \varrho_{ref} u_{ref} l_{ref}/\eta_{ref}$.

Boundary conditions

We consider the flow with $Re_\infty = 3900$. At the inlet $\partial\Omega_I$, the stagnation pressure $p_{01} = 1$, the stagnation temperature $T_{01} = 1$, the inlet angle α_1, $\frac{\partial T}{\partial n} = 0$ and $\tau^{ij} n_j = 0$, $i = 1, 2$ are prescribed. At the outlet $\partial\Omega_O$, the static pressure $p_2 = 0.5$, $\frac{\partial T}{\partial n} = 0$ and $\tau^{ij} n_j = 0$, $i = 1, 2$ are kept. On the walls $\partial\Omega_{WS}$ and $\partial\Omega_{WR}$, the boundary conditions $u = 0$, $v = 0$ and $\frac{\partial T}{\partial n} = 0$ are satisfied. It is assumed that the male rotor does not move. These nondimensional boundary conditions give the inlet Mach number $M_1 = 0.05$ and the outlet Mach number $M_2 = 0.63$, see Fig. 2 and Fig. 3.

NUMERICAL METHOD

For the discretization of the nonlinear conservative system of the compressible NS equations in nondimensional form (1) the cell-centred finite volume (FV) method on a structured quadrilateral grid is used. Time integration of the inviscid part of the system (1) is performed by using the FV formulation of the explicit two-step Causon's simplified TVD MacCormack scheme, cf. [1, 2] for its derivation. The approximations of the viscous part of the system (1) are added to the predictor and corrector steps of the MacCormack scheme

$$\boldsymbol{w}_{ij}^{n+\frac{1}{2}} = \boldsymbol{w}_{ij}^{n} - \frac{\Delta t}{|\Omega_{ij}|}\sum_{m=1}^{4}\left(\boldsymbol{f}_m^n\, S_m^x + \boldsymbol{g}_m^n\, S_m^y\right) + \frac{\Delta t}{|\Omega_{ij}|}\, Visc(\boldsymbol{w}_{ij}^{n})\,, \tag{5}$$

$$\overline{\boldsymbol{w}_{ij}^{n+1}} = \frac{1}{2}\left\{\boldsymbol{w}_{ij}^{n} + \boldsymbol{w}_{ij}^{n+\frac{1}{2}} - \frac{\Delta t}{|\Omega_{ij}|}\sum_{m=1}^{4}\left(\boldsymbol{f}_m^{n+\frac{1}{2}} S_m^x + \boldsymbol{g}_m^{n+\frac{1}{2}} S_m^y\right)\right\} + \frac{1}{2}\,\frac{\Delta t}{|\Omega_{ij}|}\, Visc(\boldsymbol{w}_{ij}^{n+\frac{1}{2}})\,, \tag{6}$$

$${}^{(TVD)}\boldsymbol{w}_{ij}^{n+1} = \overline{\boldsymbol{w}_{ij}^{n+1}} + d\boldsymbol{w}_{ij}^{1n} + d\boldsymbol{w}_{ij}^{2n}\,, \tag{7}$$

where ${}^{(TVD)}\boldsymbol{w}_{ij}^{n+1}$ is the corrected numerical solution at time t_{n+1}, $|\Omega_{ij}|$ denotes the face area of the finite volume Ω_{ij}, the inviscid numerical fluxes $\boldsymbol{f}_m^n$ through the edges Γ_{ij}^m, $m = 1, \ldots, 4$, of the cell Ω_{ij} at time t_n are evaluated as $\boldsymbol{f}_1^n = \boldsymbol{f}_{i+1j}^n$, $\boldsymbol{f}_2^n = \boldsymbol{f}_{ij+1}^n$, $\boldsymbol{f}_3^n \equiv \boldsymbol{f}_4^n = \boldsymbol{f}_{ij}^n$ and at time $t_{n+\frac{1}{2}}$ as $\boldsymbol{f}_1^{n+\frac{1}{2}} \equiv \boldsymbol{f}_2^{n+\frac{1}{2}} = \boldsymbol{f}_{ij}^{n+\frac{1}{2}}$, $\boldsymbol{f}_3^{n+\frac{1}{2}} = \boldsymbol{f}_{i-1j}^{n+\frac{1}{2}}$, $\boldsymbol{f}_4^{n+\frac{1}{2}} = \boldsymbol{f}_{ij-1}^{n+\frac{1}{2}}$. The numerical fluxes $\boldsymbol{g}_m^n$ are computed in the same way. $\boldsymbol{S}_m = \left(S_m^x\,,\, S_m^y\right)^T$ are cell side normal vectors to the edges Γ_{ij}^m, where $\boldsymbol{S}_1 = \boldsymbol{S}_{i+\frac{1}{2}j}$, $\boldsymbol{S}_2 = \boldsymbol{S}_{ij+\frac{1}{2}}$, $\boldsymbol{S}_3 = \boldsymbol{S}_{i-\frac{1}{2}j}$ and $\boldsymbol{S}_4 = \boldsymbol{S}_{ij-\frac{1}{2}}$.

The viscous terms $Visc(\boldsymbol{w}_{ij})$ in (5) and (6) are approximated by using a FV version with central differences, cf. [3] for details. The added one-dimensional TVD-type viscosity terms $d\boldsymbol{w}_{ij}^{1n}$ and $d\boldsymbol{w}_{ij}^{2n}$ in the direction of change of index i and j respectively, are proposed by Causon, cf. [1].

NUMERICAL RESULTS

For the laminar flow computation through a two-dimensional model of the male rotor-housing gap in the screw compressor, Fig. 2, the relatively fine computational grid with 250×76 quadrilateral cells is used. In order to resolve the boundary layer with sufficient accuracy, the computational grid is refined in the direction normal to the walls. Fig. 2 displays the Mach number distribution in the male rotor-housing gap after 267000 iterations. See Fig. 3 for detail.

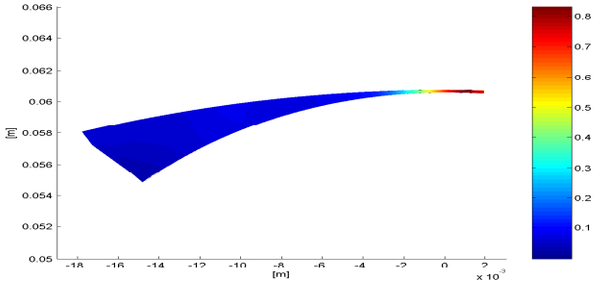


Fig. 2. Mach number distribution

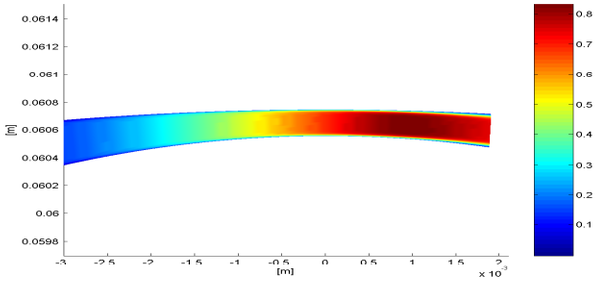


Fig. 3. Detail of the male rotor-housing gap

CONCLUSIONS

The numerical computation of the compressible laminar fluid flow through the male rotor-housing gap of screw compressors is discussed and the obtained results in the form of the Mach number distribution are shown. In the contribution is assumed that the male rotor does not move. At the time of the Congress the numerical results gained for the case of rotary motion of the male rotor with angular velocity $\omega_3 = 523\, rad/s$ will be presented too. In the near future I would like to include the effect of turbulence in a flow field and perform the turbulent computations in the male rotor-housing gap using the algebraic Baldwin-Lomax turbulence model, cf. [4], which can be simply implemented into the own numerical code.

The contribution was supported by the grant GA ČR 101/03/P090 of the Grant Agency of the Czech Republic to which I express my grateful thanks.

References

[1] Causon, D. M.: High Resolution Finite Volume Schemes and Computational Aerodynamics. *In Nonlinear Hyperbolic Equations - Theory, Computation Methods and Applications, Vol. 24 of Notes on Numerical Fluid Mechanics*, pp. 63–74, Vieweg, Braunschweig, 1989.

[2] Hirsch, Ch.: Numerical Computation of Internal and External Flows. Vol. 1, 2. John Wiley & Sons, Chichester, 1990.

[3] Vimmr, J.: A treatise on numerical computation of non-stationary laminar compressible flow. *Proceedings of the 19th Conference Computational Mechanics 2003*, pp. 483–494, Nečtiny, Czech Republic, 2003.

[4] Vimmr, J.: Introduction to the mathematical modelling of turbulent compressible fluid flow. *Zeszyty naukowe katedry mechaniki stosowanej*, zeszyt no. 21, pp. 207–212, Gliwice, Poland, 2003.

FAST NUMERICAL METHOD FOR THE BOLTZMANN EQUATION ON NONUNIFORM GRIDS

Alexei Heintz*, Piotr Kowalczyk**
*Department of Mathematics, Chalmers University of Technology and Göteborg University, SE-412 96 Göteborg, Sweden
**Department of Mathematics, Informatics and Mechanics, Warsaw University, Banacha 2, 02-097 Warszawa, Poland

Summary A new numerical method for the solution of the homogeneous Boltzmann equation on nonuniform grids is developed. The collision operator is written using the Fourier transform. This formulation and a special new discretization of the gain part allow for the fast numerical computations on nonuniform grids in velocity space. The results of a numerical test are presented.

We consider the classical Boltzmann equation in a homogeneous case

$$\frac{\partial f}{\partial t} = Q^+(f,f)(\mathbf{v}) - fq^-(f)(\mathbf{v}),$$

where $f := f(t,\mathbf{v})$ and $f : \mathbb{R}_+ \times \mathbb{R}^3 \to \mathbb{R}_+$. The collision operator, which decomposes into the gain $Q^+(f,f)(\mathbf{v})$ and the loss $fq^-(f)(\mathbf{v})$ parts, is reformulated using the Fourier transform as follows

$$Q^+(f,f)(\mathbf{v}) = F_l^{-1}(\mathbf{v})F_m^{-1}(\mathbf{v})\left[\hat{f}_l\hat{f}_m\hat{B}_R(\mathbf{l},\mathbf{m})\right], \qquad q^-(f)(\mathbf{v}) = F_m^{-1}(\mathbf{v})\left[\hat{f}_m\hat{B}_R(\mathbf{m},\mathbf{m})\right],$$

where $\hat{f}_m$ is the Fourier transform of the function f, the inverse Fourier transform to the velocity variable $\mathbf{v}$ is denoted by $F_m^{-1}(\mathbf{v})$ and $\hat{B}_R(\mathbf{l},\mathbf{m}) = \int_{\mathcal{B}(0,R)}\int_{S^2} B(|\mathbf{u}|,\theta)e^{2\pi\imath(\frac{\mathbf{l}+\mathbf{m}}{2},\mathbf{u})}e^{2\pi\imath|\mathbf{u}|(\frac{\mathbf{m}-\mathbf{l}}{2},\omega)}\,d\omega d\mathbf{u}$ denotes the regularized transform of the collision kernel $B(|\mathbf{u}|,\theta)$. Here we assume an arbitrary model of collision interaction. The distribution function f is usually negligibly small outside some ball. Thus for the numerical treatment of the Boltzmann equation we assume that $\mathbf{v} \in \Omega$, where Ω is the bounded velocity domain.

One of the main problems with efficient computations of the Boltzmann equation is that the deterministic methods use the fixed discretization in the velocity domain. Hence a huge number of discretization points is required to get the desired accuracy. We overcome this problem introducing a nonuniform grid $\Omega_v \subset \Omega$. The discrete points of the grid are chosen in such a way that the jump of the function value between the neighbouring points is lower than some prescribed threshold. In order to treat the discountinuous functions we impose additional condition that the neighbouring points should not be closer than some given number. Thus we have much more discrete points in the grid where the function changes rapidly than in the regions where the function is almost constant. Moreover this nonuniform grid is changed adaptively at each time step to follow the changes of the distribution function f.

Figure 1 shows a sample discontinuous initial condition function used in the numerical tests. Points on the graphs denote the nodes of the nonuniform grid. One can observe the irregular distribution of the grid points – more points are chosen in the regions where the gradient of the function is larger.

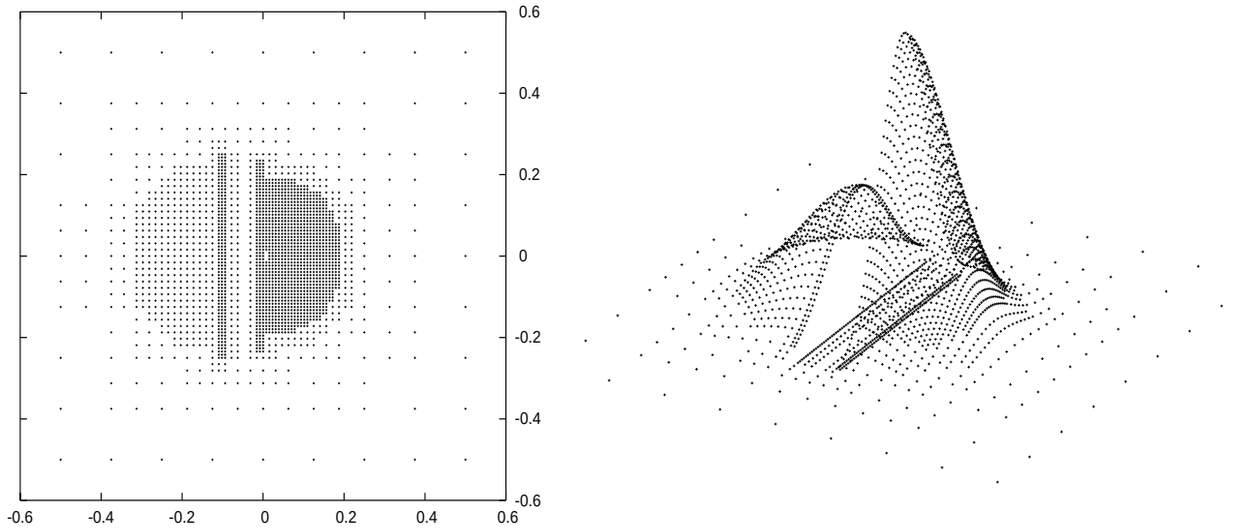


Figure 1. Initial condition function on nonuniform grid: 2D view from the top (left) and the side view (right).

To evaluate numerically the Fourier transform $\hat{f}_m = \int_\Omega f(\mathbf{v})e^{2\pi\imath(\mathbf{v},\mathbf{m})}\,d\mathbf{v}$ we approximate the function f on the grid Ω_v by a piecewise constant function $\bar{f}_K$ with K being the cell of the grid. This gives the formula $\hat{f}_m = C_m \sum_j \bar{f}_j\, e^{2\pi\imath(\mathbf{v}_j,\mathbf{m})}$,

where $\bar{f}_j$ is a value of the function $\bar{f}_K$ in a discrete point $\mathbf{v}_j \in \Omega_v$ and C_m is a constant. To compute this trigonometric sum we use the Unequally Spaced Fast Fourier Transform (USFFT) algorithm developed by Beylkin [1]. It is a variant of the standard Fast Fourier Transform especially suitable for nonuniform grids. The computational cost of this algorithm is $\mathrm{O}(N_v) + \mathrm{O}(M^3 \log M)$, where N_v is the number of discrete velocity points and M denotes the number of modes in the Fourier domain in one direction.

The collision operator is splitted into two parts, thus we discretize independetly the gain and the loss parts to get

$$Q^+(f,f)(\mathbf{v}) = \sum_{\mathbf{l},\mathbf{m}=-M}^{M-1} \hat{f}_l \hat{f}_m \hat{B}(\mathbf{l},\mathbf{m}) e^{-2\pi\imath(\mathbf{l}+\mathbf{m},\mathbf{v})}, \quad q^-(f)(\mathbf{v}) = \sum_{\mathbf{m}=-M}^{M-1} \hat{f_m} \hat{B}(\mathbf{m},\mathbf{m}) e^{-2\pi\imath(\mathbf{m},\mathbf{v})}.$$

To compute the loss part we apply straightforwardly the USFFT algorithm. To efficiently evaluate the gain part we separate variables $\mathbf{l}$ and $\mathbf{m}$ in the kernel $\hat{B}(\mathbf{l},\mathbf{m})$ using the eigenvalue decomposition. Then we approximate the kernel using only the significant eigenvalues. This greatly reduces the computational effort – due to the special properties of the kernel the number of significant eigenvalues is relatively small. Hence we get the following approximation to the gain term

$$Q^+(f,f)(\mathbf{v}) = \sum_{p=1}^{\sigma} d_r \left[\sum_{\mathbf{m}=-M}^{M-1} \hat{f}_m U_r(\mathbf{m}) e^{-2\pi\imath(\mathbf{m},\mathbf{v})} \right]^2,$$

which can be easily evaluated using USFFT algorithm. Here σ is the number of significant eigenvalues of the kernel matrix, which is typically $\frac{1}{8}$ to $\frac{1}{4}$ of the total number for the Maxwellian gas and hard spheres models, and U_r is the eigenvector corresponding to the eigenvalue d_r.

The total computational cost of the numerical approximation of the collision operator is $\mathrm{O}(N_v) + \mathrm{O}(\sigma M^6 \log M)$.

To justify the method we perform a number of numerical computations. Below we present the result of a sample test – the relaxation problem. We take the sum of two "half"-Maxwellians as the initial function (see Figure 1). Figure 2 shows the 1D cut of the initial function (dashed line) and the relaxed numerical solution (continuous line).

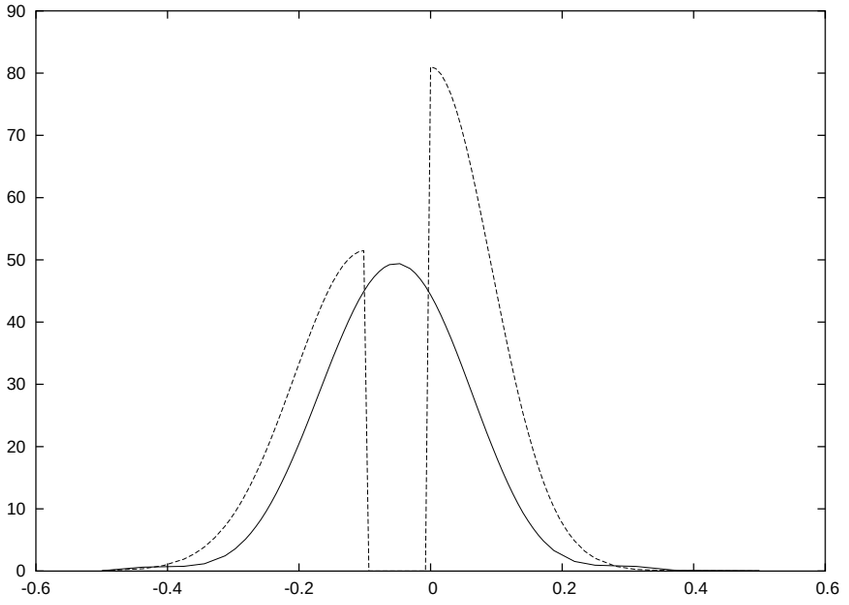


Figure 2. Relaxation problem; 1D cut at $v_y = 0$, $v_z = 0$.

References

[1] Beylkin G.: On the Fast Fourier Transform of Functions with Singularities, *Appl. Comp. Harm. Anal.*, **2**:363–381, 1995.

COMPUTATION OF VISCOUS VORTICES WITH FULLY MESHLESS METHOD

L. A. Barba*, A. Leonard**
*Department of Aerospace Engineering, University of Bristol, Bristol BS8 1TR UK
**Graduate Aeronautical Labs, California Institute of Technology, Pasadena CA 91125 USA

Summary Viscous vortex interaction is hard to compute due to numerical diffusion of traditional CFD methods. To tackle this problem, a Lagrangian vortex particle method that is fully meshless has been developed. Spatial adaption of the particles is provided using radial basis function (RBF) interpolation. The calculation of a quasi-steady vortex tripole has been used as proof of concept. The method has been implemented in parallel using the PETSc library, and the RBF system has been solved using pre-conditioned GMRES.

INTRODUCTION

The computation of viscous vortex flows at high Reynolds numbers using traditional numerical methods, such as finite elements or finite volume formulations, can be severely hindered by numerical diffusion. In certain applications, such as the interaction of vortices with structures, the useful prediction of loads on the structures depends on being able to resolve the concentrated areas of vorticity with accuracy, and with minimal numerical diffusion. Mesh-based methods, however, can never be devoid of numerical diffusion, and vortices are simply diffused too fast.

An alternative to traditional mesh-based methods for solving the Navier-Stokes equations is the Lagrangian vortex method. In the vortex method, elements of vorticity move with the local fluid velocity and thus satisfy the convective part of the vorticity transport equation without numerical diffusion. In other words, the nonlinear term of the Navier-Stokes equation is accounted for by integrating the ordinary differential equations for the particle trajectories, such that the truncation error is non-diffusive. The velocity field, in turn, is obtained from the vorticity via the Biot-Savart law, and the viscous effects can be provided by a variety of methods. This is an essentially mesh-free method; in practice, however, many workers rely on mesh-based additions to the method to provide for long-term accuracy. For example, one of the prevalent viscous schemes for vortex methods, called particle strength exchange or PSE, is derived from an integral operator that approximates the Laplacian in the viscous term. In this formulation, quadratures used to discretize the integral operator are very sensitive to the location of the vortex particles. Hence, workers apply a "remeshing" scheme, in which the vortex particles are periodically re-located onto a Cartesian mesh, and their circulation strength is interpolated to these locations using high-order kernels in tensor product formulations. See, for example, [1].

Recent numerical experiments have demonstrated, however, that standard remeshing schemes, although allowing long-time calculations, do introduce noticeable interpolation errors [2]. In fact, these schemes bring back the mesh to an otherwise meshless method, and with it, numerical diffusion.

A less ubiquitous viscous scheme than PSE, the core spreading method, does not suffer from quadrature errors. On the other hand, some means of controlling particle core sizes is necessary to keep convection error small thereby ensuring convergence, tackling the concerns of [3]. Application of vortex splitting has been proposed for this effect, and proved to be convergent [4]. However, vortex splitting, like remeshing, introduces numerical diffusion.

In this work, a mesh-free method for processing the locations of vortices in the Lagrangian formulation, as well as controlling core sizes when core spreading is used to provide viscous effects, is formulated and demonstrated. This method is based on radial basis function (RBF) interpolation ideas. Proof-of-concept has been carried out by computing the tripole attractor of a quadrupole-perturbed monopole. Work in progress includes implementation of the method in parallel using the PETSc library [5], and the computation in parallel of the interaction of viscous vortices.

NEED FOR SPATIAL ADAPTION AND MESHLESS FORMULATION

Regardless of whether the vortex method is implemented with an integral operator-based viscous scheme, or any other (*e.g.*, core spreading, diffusion velocity, taking the Laplacian of the basis function), there is a need for providing some form of spatial adaption. This is due to the fact that the cores of the vortex particles, or 'blobs', must have some overlap to be able to represent accurately the smooth vorticity field. Thus, gaps in the particle distribution produced by the flow strain in a time-marching calculation will degrade the accuracy. Recent numerical experiments demonstrate how the accuracy of the blob discretization deteriorates over several orders of magnitude when the overlap ratio, defined as the inter-particle spacing divided by the core size (h/σ), increases passing through the value of one [2]. Using a new parallel implementation of the vortex blob discretization, the cited experiments have been replicated, and the results are presented in Figure 1. The test case is the classic Lamb-Oseen vortex, which was discretized using Gaussian vortex blobs on a square lattice; the blob circulation strengths were obtained by solving the RBF-like linear system, where the right-hand-side vector corresponds to the vorticity values at

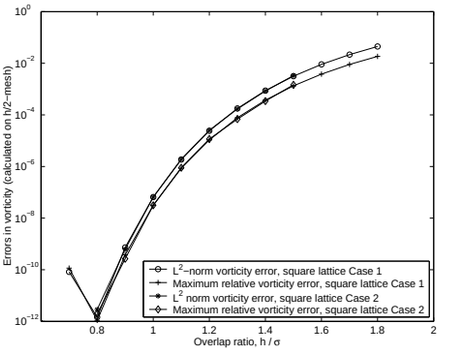


Figure 1. Blob discretization errors.

particle centres. That is, one solves for the γ_j's in $A_{ij}\gamma_j = \omega_i$ (indicial summation implied), with $\omega_i = \omega(x_i)$ and $A_{ij} = \frac{1}{2\pi\sigma^2}\exp\left\{-(x_i - x_j)^2/2\sigma^2\right\}$. This linear system was solved using preconditioned GMRES, a solution approach that was demonstrated for other radial basis functions (not Gaussian) in [6], using a specially designed pre-conditioner. Here, in contrast, the built-in pre-conditioners of the PETSc library were used, which can be specified as run-time options (four or six processors were used). In the figure, Case 1 corresponds to a set of discretizations using a fixed value $h = 0.01$ (about 10^4 particles) and variable core size σ; Case 2 corresponds to fixed $\sigma = 0.01$ and variable h, resulting in variable number of particles between 4500 and 15000. The vorticity error increases again at the lowest h/σ due probably to exceeding ill-conditioning of the linear system; indeed, at $h/\sigma = 0.8$ convergence of the GMRES at the desired tolerance was achieved with 59 iterations, whereas 1590 iterations were needed at $h/\sigma = 0.7$.

The "super-exponential" dependence on the overlap ratio of the vortex blob discretization demonstrated in Figure 1 justifies the need for spatial adaption in a Lagrangian method. Without it, as the particles are allowed to move with the flow, overlap may be lost in areas of the flow and accuracy would be degraded. To provide spatial adaption for the vortex method without resorting to a mesh-based approach, radial basis function (RBF) interpolation [7] is applied.

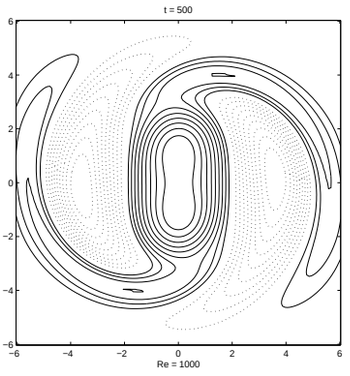


Figure 2. $Re = 10^3$.

Time-marching numerical experiments with the Lamb-Oseen vortex test case (using core spreading) have demonstrated that this approach can provide higher accuracy than standard remeshing [2]. In addition, the RBF spatial adaption allows one to correctly use core spreading for providing viscous effects, by controlling core size in the meshless adaption process. That is, core sizes are reset to their original smaller values during the RBF interpolation process. This offers an alternative to the vortex splitting method [4], which as already mentioned can generate considerable numerical diffusion.

Proof of concept calculations have been performed using a Gaussian monopole with a quadrupole perturbation, which results in a quasi-steady state in the form of a tripole. The results of these calculations show noticeable improvement in comparison with similar calculations using core spreading with splitting [8], where numerical diffusion erodes the tripole attractor for the lower Reynolds number case (see Figure 2, which can be compared to Figure 8 –left– of [8]). For the higher Reynolds number (Figure 3), the present calculations reproduce the rotation angle and shape of contours of the tripole in the calculations of [8], but produce much smoother vorticity contours. Also, the decay of the quasi-steady tripole attractor in the Re timescale is accurately obtained with the present method.

CONCLUSION

The computation of viscous vortex interaction with traditional CFD methods is hindered by numerical diffusion. To deal with this problem, a fully meshless method has been developed that is characterized by non-diffusive truncation errors. It consists of a new formulation of the vortex particle method, using core spreading for diffusion, and radial basis function interpolation to provide for spatial adaption of the particles and core size control. Numerical experiments indicate that this meshless formulation can provide higher accuracy in comparison with the standard remeshing that is used with the particle strength exchange viscous scheme, as well as the vortex splitting idea of [4]. Presently, we continue in the development of the parallel implementation using message passing with MPI and the PETSc library. An application is now being developed to study the viscous interaction of two co-rotating vortices, which develop an elliptical deformation of the cores in the weak regions of vorticity, which is very challenging to reproduce numerically. This problem was studied in [9] using spectral methods, but we estimate that the same accuracy can be obtained using the meshless vortex method with a considerably reduced problem size.

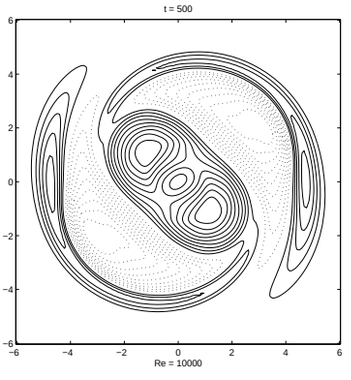


Figure 3. $Re = 10^4$.

References

[1] Koumoutsakos P.: Inviscid axisymmetrization of an elliptical vortex. *J. Comp. Phys.* **138**:821–857, 1997.
[2] Barba L. A., Leonard A., Allen C. B.: Numerical investigations on the accuracy of the vortex method with and without remeshing. AIAA paper #2003–3426, June 2003.
[3] Greengard C.: The core spreading vortex method approximates the wrong equation. *J. Comp. Phys.* **61**:345–348, 1985.
[4] Rossi L. F.: Resurrecting core spreading vortex methods: A new scheme that is both deterministic and convergent. *SIAM J. Sci. Comput.* **17**:370–397, 1996.
[5] Satish B., Buschelman K., Gropp W. D., Kaushik D., Knepley M., Curfman-McInnes L., Smith B. F., Zhang H.: PETSc User's manual. Technical Report ANL-95/11 - Revision 2.1.5, Argonne National Laboratory, 2002.
[6] Beatson R. K., Cherrie J. B., Mouat C. T.: Fast fitting of radial basis functions: Methods based on preconditioned GMRES iteration. *Adv. Comp. Math.* **11**:253–270, 1999.
[7] Buhmann M. D.: Radial basis functions. *Acta Numerica*, pp. 1–38, 2000.
[8] Rossi L. F., Lingevitch J. F., Bernoff A. J.: Quasi-steady monopole and tripole attractors for relaxing vortices. *Phys. Fluids* **9**:2329–2338, 1997.
[9] Le Dizès S., Verga A.: Viscous interactions of two co-rotating vortices before merging. *J. Fluid Mech.* **467**:389–410, 2002.

XXI ICTAM, 15–21 August 2004, Warsaw, Poland

DIRICHLET/DIRICHLET AND NEUMANN/NEUMANN PARALLEL NON-OVERLAPPING DOMAIN DECOMPOSITION METHOD

Slawomir Kubacki, Andrzej Boguslawski
Institute of Thermal Machinery, Czestochowa University of Technology,
Al. Armii Krajowej 21, 42-200 Czestochowa, Poland

Summary Solution of two-dimensional Helmholtz equation using spectral non-overlapping domain decomposition method on parallel computer is presented. The Chebyshev tau method is used for discretization of the subdomian problems, and diagonalization technique is used for solution of the local system of equations.

The paper presents the tests of the algorithms for parallel solution of two-dimensional Helmholtz equation using non-overlapping spectral domain decomposition method. The 2-D Helmholtz equation is shown below with Dirichlet boundary conditions at the bounds $\partial\Omega$ of computational domain Ω

$$\nabla^2 u - \sigma u = f(x,y) \quad \text{in} \quad \Omega, \qquad\qquad u = g \quad \text{on} \quad \partial\Omega \tag{1}$$

where σ is the constant value, $f(x,y)$ is given function of the space coordinates and Ω is a square $(-1,1)\times(-1,1)$.
The computational domain Ω was split following one direction into the N_{el} number of subdomains. For all of the tests presented here the number of processors was equal to the number of subdomains. The Helmholtz equation (1) was transformed into the local coordinate systems and continuity of the solution at the interfaces was enforced specifying the suitable patching conditions. As it was proposed by Orszag [1] for solution of the second-order differential equation the suitable patching conditions at the interfaces are continuity of the function and continuity of its first-order derivative.
Solution of two-dimensional Helmholtz equation with Dirichlet as well as Neumann boundary conditions is presented using the iterative method proposed by Zanolli [5] and its modification proposed by Louchart and Randriamampianina [3]. The novel feature presented in the paper consists of the solution of the Helmholtz equation using the original iterative method proposed in [6]. The parallel performance of this method was already compared in [6] with the efficiency obtained using the other iterative methods for the solution of one-dimensional Helmholtz equation. The present paper summarizes the tests performed for solution of two-dimensional problem using the iterative schemes presented above. The spectral Chebyshev tau method was used for discretization of subdomain problems. The local system of equations (at each of processors) was solved using the matrix diagonalization method proposed by Haidvogel and Zang [7]. In the present paper the diagonalization technique proposed by Haldenwang et al. [8] for the tau method was used. Diagonalization method allows for transformation of two-dimensional system of equations into the sequence of one-dimensional ones, reducing substantially the time needed for its solution. The computation of eigenvalues, eigenvectors and inversion of the coefficient matrix was performed once at the preprocessing step. Thus, at each iteration step the solution of the subdomain problem was obtained by matrix product. The results obtained using Zanolli, Louchart and Randriamampianina algorithms as well as the proposed method for solution of linear 2-D Helmholtz equation can easily be compared with the exact solution.
The research presented is aimed at development of new, effective solutions methods for Navier-Stokes (N-S) equations, however one should remember that solution of N-S equations using projection method proposed e.g. by Hugues and Randriamampianina [4] consists of solution of the Helmholtz problems. If one uses the projection scheme presented above (for two dimensional problem), then two Helmholtz equations for determination of velocity components and two Poisson equations ($\sigma = 0$ in Helmholtz equation) for computations of pressure predictor and corrector are needed to be solved. The constant σ in the Helmholtz equation is inversely proportional to the time step if solution of unsteady Navier-Stokes equations is considered. As the next stage, solution of the Navier-Stokes equations using the Hugues and Randriamampianina scheme is considered, with explicit treating of the non-linear terms.
The first of the iterative algorithms (Zanolli scheme) consists of solution of two subdomain problems. In order to fulfil the patching conditions at the interface the data transmission between subdomains is needed. The iterative step (i) consists of two stages. At the first stage the problem with Dirichlet boundary condition at the interface Γ is solved:

$$\begin{aligned} L u_{[1]}^{(i+1)} &= f_{[1]}(x,y) \quad \text{in} \quad \Omega_1 \\ u_{[1]}^{(i+1)}(a) &= g_- \\ u_{[1]}^{(i+1)}(\Gamma) &= B^{(i+1)} \end{aligned} \tag{2}$$

next the value of the first derivative at the interface is computed. The value of the first derivative is sent to the other subdomain and at the second stage of iterative step the problem with Neumann boundary condition at the interface is solved at the second subdomain:

$$\begin{aligned} Lu_{[2]}^{(i+1)} &= f_{[2]}(x,y) \quad \text{in} \quad \Omega_2 \\ u_{[2]}^{(i+1)}(c) &= g_+ \\ \frac{\partial u_{[2]}^{(i+1)}}{\partial n}(\Gamma) &= \frac{\partial u_{[1]}^{(i+1)}}{\partial n}(\Gamma) \end{aligned} \tag{3}$$

where the n is the unit vector normal to Γ. The value of the function B^{i+1} at the interface Γ between subdomains at each of iterative steps is computed using the following relation

$$B^{(i+1)} = \theta u_{[2]}^{(i)}(\Gamma) + (1-\theta)B^{(i)}, \quad i \geq 1 \tag{4}$$

where $u_{[2]}$ is the function value computed at the boundary of the adjacent subdomain, $B^{(i)}$ is the value of the function from the previous iterative step and θ is the relaxation parameter. Funaro, Quarteroni and Zanolli [2] showed that this algorithm converge in two iterations if computational domain is split into two subdomains for one- as well as two-dimensional problems. As it was mentioned above, the efficiency of Louchart and Randriamampianina algorithm was also considered. Using the Louchart and Randriamampianina scheme one may avoid synchronisation problem encountered in the original Zanolli method, where one of the processors must wait for the other at each stage of iterative step (Eqs. 2-3). In the modified Zanolli scheme, the Dirichlet/Dirichlet and Neumann/Neumann boundary conditions are set at the interfaces in the successive stages of iterative step, allowing more efficient parallel computing.

As it was shown in [3] solution of differential equation using iterative domain decomposition algorithms with Dirichlet/Dirichlet and Neumann/Neumann boundary conditions specified at the interfaces is effective if the number of the subdomains is small enough. However, when increasing the number of subdomains, substantial increase of the number of iterations needed to obtain converged solution was observed. As an alternative, a new iterative algorithm for parallelization of numerical code using Chebyshev tau method was proposed [6]. In the algorithm proposed the Dirichlet boundary conditions are specified at the interfaces. At the beginning of iterative process the values of the functions at the interfaces are set to arbitrary values. Next, the correction of the previous solution is computed at one of the processors by solution of the common problem taking into account the patching conditions at all of the interfaces considered. The patching conditions are: continuity of the function and its first-order derivative. Correction of the solution is scattered to all processors (subdomains) and the values of the functions at the internal boundaries are modified. The iterative process is continued until converged solution is obtained.

For all of the iterative methods considered, influence of the choice of the number of subdomains, relaxation parameter θ and constant σ in Helmholtz equation as well as influence of the type of boundary condition (Dirichlet or Neumann) at the boundaries $\partial\Omega$ of domain Ω on the convergence of iterative process was tested. The parallel performance of the iterative methods was measured by means of speed-up $S = t_1/t_p$, which is defined as the ratio of time needed to execute the program on one processor to the time needed by p processors.

References

[1] Orszag S.A.: Spectral methods for problems in complex geometries. *J. Comput. Physics* **37**:70–92, 1980.

[2] Funaro D., Quarteroni A., Zanolli P.: An iterative procedure with interface relaxation for domain decomposition methods. *SIAM J. Numer. Anal.* **25**(6):1213–1236, 1988.

[3] Louchart O., Randriamampianina A.: A spectral iterative domain decomposition technique for the incompressible Navier-Stokes equations. *Appl. Numer. Math.* **33**:233–240, 2000.

[4] Hugues S., Randriamampianina A.: An improved projection scheme applied to pseudospectral method for the incompressible Navier-Stokes equations. *Int. J. Numer. Meth. in Fluids* **28**:501-521, 1998.

[5] Zanolli P.: Domain decomposition algorithms for spectral methods. *Calcolo* **24**:202–240, 1987.

[6] Boguslawski A., Kubacki S., Tyliszczak A.: Dirichlet/Dirichlet domain decomposition parallel spectral method for computing of Navier-Stokes equations. Budapest, Hungary, 2003.

[7] Haidvogel D.B., Zang T.A.: The accurate solution of Poisson's equation by expansion in Chebyshev polynomials. *J. Comput. Physics* **30**:167–180, 1979.

[8] Haldenwang P., Labrosse G., Abboudi S.: Chebyshev 3-D spectral and 2-D pseudospectral solvers for the Helmholtz equation. *J. Comput. Physics* **55**:115–128, 1984.

CFD METHODS IN INDUSTRIAL APPLICATIONS – VEHICLE EXTERNAL AERODYNAMICS AND AERODYNAMIC INTERACTION OF MOVING VEHICLES

Milan Schuster*
*SKODA RESEARCH, Department of Fluids Mechanics, CZ 316 00 Pilsen, Czech Republic

Summary The paper deals with the properties of 3-D flow around a moving vehicle during the aerodynamic interaction with its environs. The models of rail vehicles intended for the public mass transport (fast trains, sub-urban trains units, underground and municipal railways trains) are simulated. Driving speeds of those vehicles are supposed in the range of 80 – 220 km/h. The computer simulations contribute to understanding and summarising the complex description of aerodynamic load of rail vehicles during various running regimes and situations, important aerodynamic effects occur during the passing of vehicles and/or under side wind. Simulations are carried out by means of commercial CFD code. Aerodynamic load is modelled as a special boundary condition in form of aerodynamic effect models. Those models describe (and to calculate) aerodynamic and interaction effects onto vehicles during passing and under side-wind and include time-dependent and space-dependent values of load. The studies allow to increase efficiency and accuracy of computer simulations.

EXTERNAL AERODYNAMICS OF TRAINS

Development of public transport is of a great priority in nowadays Europe. A great effort is done in the field of developing effective and rapid surface which should ensure ability to compete and meet requirements for comfort and safety of passengers with adequate driving time, availability and roads´ network density. When considering environmental demands those services can be ensured by railway transport with driving speed in the range of 150 - 250 km/h. When projecting both rail lines and trains under those driving conditions aerodynamic effects of running rail vehicles and interaction vehicles-environs is considered to be useful to investigate deeper. The situation is similar at long distance bus traffic, only a greater role is played by the influence of side-wind on the course stability of the vehicle on the road. Aerodynamic influence of interaction comes to light in the form of supplementary loading of vehicles and environments and buildings. Aerodynamic forces influence the output of driving units, vehicle stability, added loading, generation of aerodynamic noise etc.
The computer simulation is aimed at the research into external aerodynamics and interaction between running rail vehicles of public transport and environs, which is surrounding mass of air, other means of transport and various buildings in the vicinity of the line of running (tunnels, terrain corridors, wind barriers etc.). Aerodynamic interaction is mediated or caused by flowing air, important aerodynamic effects on vehicles occur during the passing of vehicles, under side wind and during the propagation of pressure waves and pulses in tunnels.

COMPUTER SIMULATION

Computer simulation is aimed at 3-D flow in the vicinity of moving vehicle during the aerodynamic interaction with its environs. The main aim is:
- simulation of drive regimes using the commercial CFD program,
- preparation of the methodology for the evaluation of the way of loading and the magnitude of values of added aerodynamic loading of the vehicles surface during the typical regimes of the drive and ranges of flow rate,
- creation of user models of aerodynamic effects as a special boundary condition setup.

Systematic steps of simulation are:
- modelling of physical properties of flow around vehicles,
- modelling of motion of vehicles in computational domain.

Vehicle motion is modelled in two ways:
- relative motion – relative velocity between train surface and surrounding air is presented as velocity in inlet plane to computational domain, the train geometry is non-moved, (see Fig. 1 and 2),
- real motion – geometries of passing trains are moving, in this case we can use interface, sliding mesh or deforming grids tools of CFD codes (see Fig. 3 – there is 2D-train models' passing).

The subject of simulations is to analyse the physical relations between moving vehicle and environs, to classify important parameters and to include these parameters into the computational CFD programs for the purposes of technical simulations. The task is to prepare the model of aerodynamic effects and the interaction (passing, side-wind). These models are expected as:
- special function as a similar polynom will be include into CFD code (UDF – user-defined function),
- complicated mathematical terms and polynoms as external codes will be implemented into CFD code (data file),
- external code, which will compute the most complicated load parameters.

The goals and tasks of computer simulation in this period:

- creation of aerodynamic effect models as an in-house code or UDF-functions (various structure of codes corresponding with load conditions),
- implementation and test of models in commercial CFD code as special boundary conditions,
- verification calculation and simulation of typical running regimes of vehicles,
- test of capabilities and cooperation between CFD (computational fluid dynamics) code and MBS (multibody simulation) code to solve vehicle dynamic response and course stability during aerodynamic load regimes.

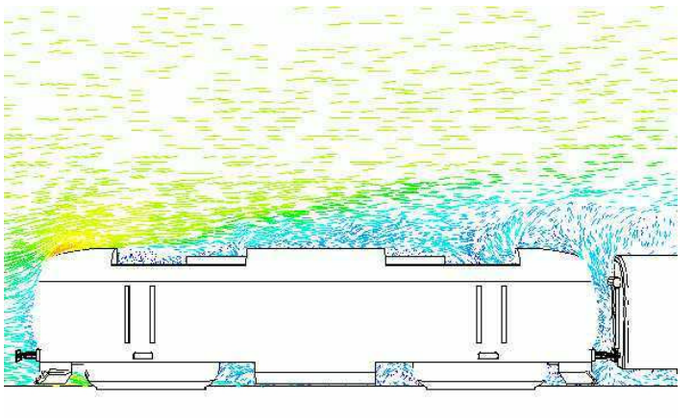


Fig. **1**

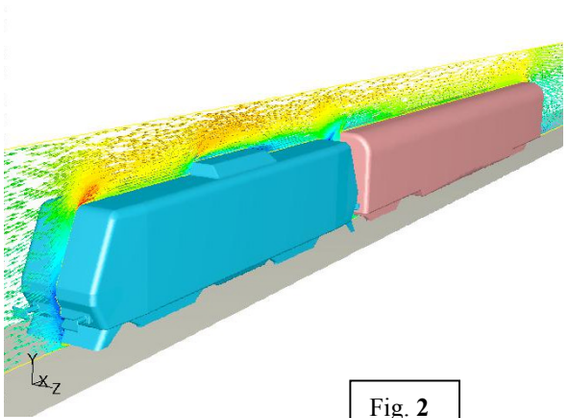


Fig. **2**

Simulation of non-moving train and velocity vectors in symmetry plane, Fig. **1** is train in the open air going at speed 200km/h, Fig. **2** is train in tunnel (train relative motion speed is 100km/h).

Fig. **3** - simulation of passing 2D- train models, there is pressure map of one time step of unsteady calculation only.

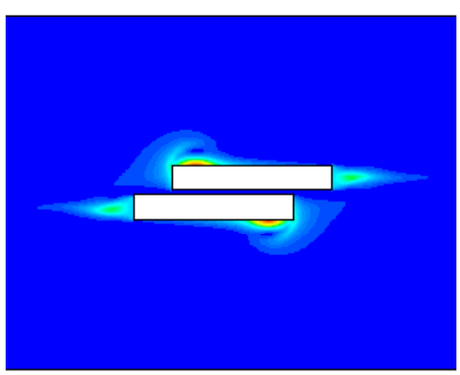


Fig. **3**.

GRID COMPUTING PROJECT

The external aerodynamics and interaction flow simulation tasks need big capacity of computing resources. The EU-funded project IST-2001-38433 “Flow simulations on-demand using grid computing” (acronym FlowGrid) creates a virtual organisation of Europe CFD centres to develop and validate software and knowledge for grid-based CFD computations. Developing and sharing CFD software and computing resources will enable this. FlowGrid system will control and manage computer grid and computing resources making to possible to increase power of CFD analyses. Several tasks from vehicle external aerodynamics are used for FlowGrid testing.

CONCLUSIONS

Computer simulations of rail vehicle external aerodynamics are described in the paper. Possibilities of CFD analyses by commercial CFD code are discussed. CFD grid computing is briefly meant.

A computational model for the Si/C/N nanopowder synthesis by laser pyrolysis

M. Amara, M. El Ganaoui, D. Hourlier

SPCTS, UMR 6638. Université de Limoges Faculté des Sciences et Techniques, 123 rue Albert Thomas. 87 060 Limoges.

Summary A numerical model was developed for the ceramic powder synthesis by the laser pyrolysis, in order to study the experiment feasibility and to optimise the synthesis process. This model takes into account heat and mass transfers during the experiment.

INTRODUCTION

For manufacturing nanocomposite ceramics, the synthesis of powder with nanometeric scale, is a promising candidate for structural applications allowing higher temperature values than those for metallic super-alloys.
This synthesis was performed by CVD, arc-plasma-heated or laser pyrolysis processes [1, 2]. The last process involves the interaction between an infrared laser beam and a gas precursor or a liquid in aerosol form. The principle is based on the resonance phenomena between the emitted laser frequency (continuous CO_2, λ=10.59 μm) with at least one of the reactant band absorption. The powder obtained by this method shows very interesting characteristics, the small reaction volume and the ability to maintain steep temperature gradients allows an accurate control of the nucleation rate, that leads to the formation of fine particles.
The control of these powders during their synthesis requires the understanding of coupled physical and chemical phenomena. Indeed, the nucleation and the growth of the particles depend directly on the resulting temperature field, dynamic field and particles concentration. These parameters are related to the operating conditions including conductive, convective and radiative heat transfers. The goal of the present work is to develop a three dimensional model of the reactor and to investigate the influence of the various thermal parameters involved during the process. The validation and the qualification at this stage are essential for any extension of the particles growth.

MODEL

Except Akmandor work at the beginning of the eighties [3], the main part of the published researches are focused on the development of the experimental part of the process. The author built a simplified model, incorporating the gas dynamics and the chemical reactions. The simulations were limited in the fact that, the thermal heat transfer did not take into account the mixture between the carrying and the reactive gas. This later becomes very important in the cooling processes of the reactive gas. The simulations were limited to a 2D-axisymmetrical geometry on a domain located around the jet, whereas the real experiment is three-dimensional and the powder synthesis may be influenced by supposed minor phenomena taking place in the full reactor in the Akmondor calculations.
In order to understand the solid particles formation mechanism and the relations which exist between experimental parameters (laser power, pressure, etc) and resulting powders characteristics, three-dimensional simulations are conducted.
Nowadays, powerful calculation means are developed in such a way that complex geometries are taken into account, incorporating the deep analysis of the physical phenomena. An industrial Computational Fluid Dynamic (CFD) package is used [4]; this software allows the modelling of various fluid flows in complex geometries area and particularly including reactive flow and permitting the incorporation of specific developed routines.

A model was developed to represent the laser pyrolysis synthesis. Steady state solution of fluid flow is commonly considered as a required condition to have a good reproducibility of the synthesis process and especially for the powder characteristics.
As a first step, the energy loss of the system by the particles thermal radiation is not taken into account. Moreover, the system incorporating the chemical species and the solid particles is under development.

The model consists of introducing the coupled conservation laws involving Navier-Stokes, energy and chemical species equations. The coupled system of Partial Differential Equations is formulated on primitive variables and solved under a finite volumes approximation on an unstructured grid.
The investigated geometry is close to the experimental configuration developed in our laboratory (figures 1, 2). It consists of the interaction between silane (SiH_4) jets surrounded by an annular argon flow (carrier gas) with an infrared laser radiation. The laser has a fixed diameter permitting the use of focused or unfocused rays.

RESULTS AND DISCUSSION

Two simulations were made to investigate the effect of the dilution of the reactant gas stream with argon that affects the heating rate. Indeed, the overall absorption coefficient is decreased, because argon does not absorb IR radiation at 10.6 μm. As seen in figure 3, the heating rate decreases and the reaction is more confined with increasing flow rate of argon.
An increase of the total pressure cell, results in an increase peak of temperature (figure 4). This indicates that, a slower velocity (velocity is inversely proportional to the density) promotes a longer residence time within the laser beam. Consequently, this leads to a higher peak the temperature.

CONCLUSIONS

A computational model for laser synthesis is developed. The temperature, dynamic, and chemical species fields are computed. These calculations are carried out in three dimensions, and take into account all thermal transfers. These results correspond to an extension of those of Akmandor's limited to a two-dimensional axisymmetric geometry and are in agreement with experimental data. Finallly, it is important to couple the local models of particles growth, with the global models of the flow to study simultaneousey the growth of the powders and their advection in the collector.

References

[1] Suhas V. Patankar, and Spalding, D. B., 1970, Heat and Mass Transfer in Boundary Layers, 2nd Edition, Intertext Books, London.
[2] W. R. Cannon SCD, J. S. Haggerty, R. A. Marra. Sinterible Ceramic Powders from Laser-Driven Reactions: I, Powder Characteristics and Process Variables. Journal of the American Ceramics Society. 65 (7):324 (1982).
[3] Akmandor I. S. Theoritical and Computational Models of Reacting Silane Gas Flows: laser Driven Pyrolysis of Subsonic and Supersonic Jets [PhD]. Cambridge, MIT (1985).
[4] CFX5, developed by AEA technology. http://www.software.aeat.com/



Figure 1 : Experimental setup of the nanopowder reactor

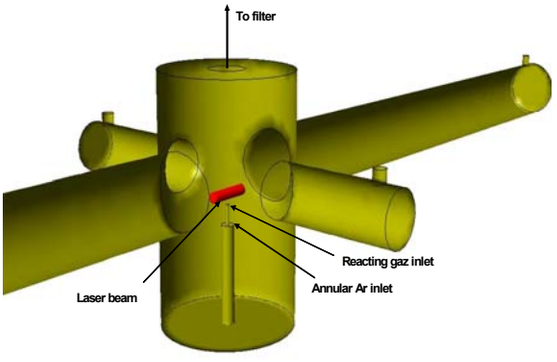


Figure 2 : Model of the reactor

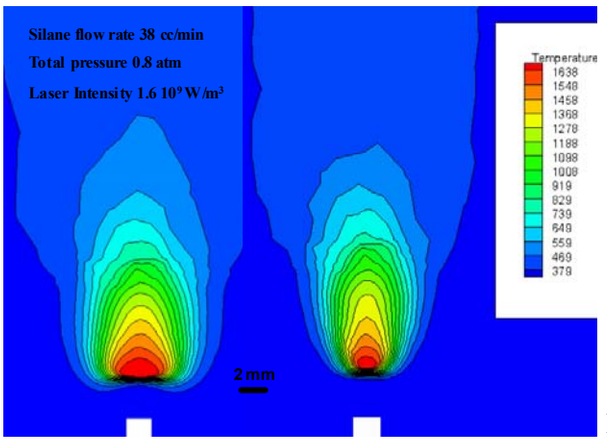


Figure 3: Temperature field for two flow rates of dilute gas STP. : 500 cm^3/min (left); 1000 cm^3/min (right).

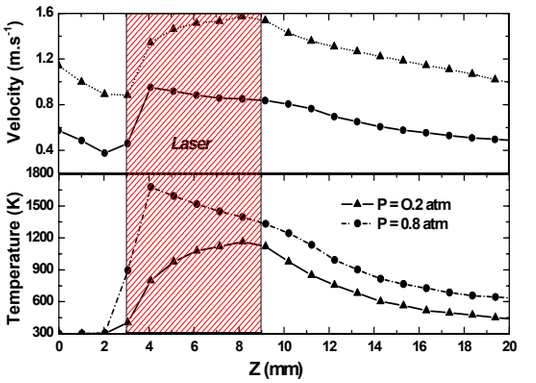


Figure 4: Maximum temperature variation and velocity, as functions of the distance above the inlet nozzle (silane flow rate 38 cm^3/min, $I_0=1.6\times10^9$ W/m^3).

XXI ICTAM, 15–21 August 2004, Warsaw, Poland

NUMERICAL ERROR EVALUATION FOR TIP CLEARANCE FLOW CALCULATIONS IN A CENTRIFUGAL COMPRESSOR

G. Dufour*, X. Carbonneau*, P. Arbez **, J.-B. Cazalbou* and P. Chassaing*
*ENSICA, Department of Fluid Mechanics, 1 pl. Emile Blouin, 31056 Toulouse Cedex 5, France
**Liebherr-Aerospace Toulouse S.A., 408 av. des États Unis, BP 2010, 31016 Toulouse Cedex 2, France

Summary Since globally mesh independent solution are still beyond available computer resources for industrial cases, a method to quantify locally the numerical error is proposed. The design of experiments method helps selecting mesh parameters that influence the tip clearance solution, so that additional meshes are computed to evaluate the numerical error on the shroud friction coefficient.

In the field of CFD applied to turbomachinery, this study results from a partnership between ENSICA, Liebherr-Aerospace Toulouse and Numeca International. This paper focuses on numerical error evaluation for RANS simulations, applied to centrifugal compressor flow field calculations. CFD is now commonly used for centrifugal compressor design optimization, but, as Hutton and Casey develop in [1], there is an urging demand for improved quality and trust in industrial CFD. Indeed, this stresses the need for comprehensive and thorough numerical error evaluation, namely the process of *verification*, as defined for example by Oberkampf and Trucano in [2]. Unfortunately, 3D turbulent calculations for turbomachinery components are still very demanding in computational resources and, to the knowledge of the author, there is no published result concerning comprehensive verification of the entire flow field in centrifugal compressors. As a first step on the way to achieve that, this paper presents a method aiming at the obtention of a numerical solution that can be regarded as *locally* mesh-independent. In other words, the objective is to compute the flow field on a grid such that the solution obtained has a specific region where the numerical error is negligible.

It has long been recognized that the tip clearance of a centrifugal compressor is of paramount importance for aerodynamic performances, which means that accurately predicting the flow field in this region is crucial for accurate prediction of performances by means of CFD codes. Numerous studies have been published that compare numerical and experimental results in the tip region. However, in these studies, numerical error still remains an issue; for instance Basson and Lakshminarayana [3] show excellent comparisons with experiments, but they attribute the remaining discrepancies to insufficient grid resolution. Indeed, accurate predictions of global effects, such as efficiency, require a fine description of flow details. Therefore, friction at the shroud endwall is the concern of the study, since it is a very sensitive indicator of the quality of the velocity profile's prediction at the wall.

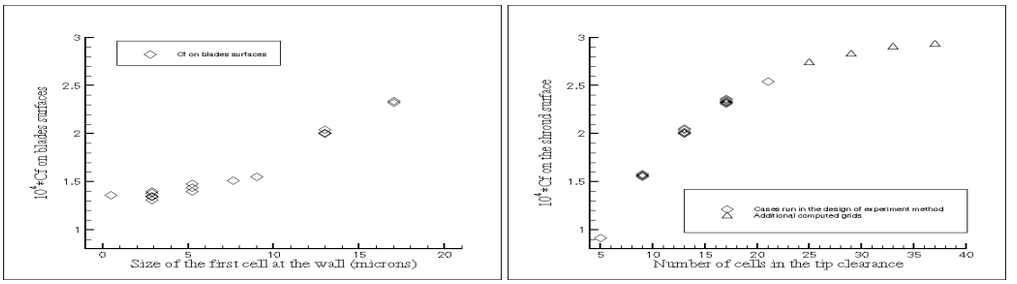
INFLUENCE OF GLOBAL MESH PARAMETERS ON FLOW QUANTITIES IN THE TIP CLEARANCE

Any numerical result is marred with two sources of errors: numerical error, and error due to models. Validation is the process of evaluating the former, and verification assesses the later. The scope of this paper is numerical error.

Although other sources of numerical error can be pointed out, the effects of grid size are dominant in most industrial cases. Therefore, the challenge is to be able to assess the global influence of the mesh on the solution, and in particular on the clearance flow field prediction. The basic idea is to first select relevant parameters that characterize the mesh, and then to evaluate their influence on specific calculated quantities, through the use of the design of experiments method.

The selection of basic parameters and its justification is thoroughly presented in a paper submitted to the ASME Fluid Engineering Summer Conference 2004 (HT-FED2004-56314). It will be sufficient here to recall the 6 selected mesh parameters : (i) the number of points in the spanwise direction (regardless of the cells in the gap); (ii) a multiplicative factor to obtain the number of points in the 2 other directions ; (iii) a parameter quantifying the discretization in the center of the channel; (iv) the size of the first cell on the hub and the blades; (v) a parameter quantifying the discretization of the leading- and trailing-edges; (vi) and the number of cells in the tip clearance.

The design of experiment method used for this study is second order accurate, that is to say it evaluates each parameter influence and 2 by 2 correlations. Therefore, 28 meshes (with total numbers of points ranking from 300.000 to 2.000.000 points) had to be generated and computed on the same test-case. The test case is a 2.7:1 pressure ratio centrifugal impeller, running at 38000 RPM with a mass-flow rate of 0.632 kg/s. Figure 1 presents friction coefficients obtained for the 28 grids. Figure 1(a) is an attempt to correlate the friction coefficient integrated on blade surfaces with the size of the first cell at the wall. The scatter of the data for each cell size demonstrates that this mesh parameter is not the only one influencing the friction value predicted. On the other hand, figure 1(b) demonstrates that the value of the friction coefficient (after scalar integration on the shroud surface) is entirely fixed by the number of cells in the gap. It means that the numerical error due to the influence of other parameters is negligible. This result is confirmed by the analysis of the design of experiment, which allows influence coefficient to be derived that characterize the influence of each mesh parameters on the solution. It shows that 99% of the value of the solution is fixed by the number of cells in the gap. Thus, the results of design of experiment method suggest that, by increasing the number of cells in the gap only and keeping all other parameters to reasonable values, it should possible to derive a mesh such that the numerical error on the shroud friction coefficient tends to a negligible value.



(a) (b)

Figure 1. Friction coefficients. (a) On blades surfaces. (b) On the shroud

DERIVATION OF A "LOCAL BENCHMARK" SOLUTION

Refinement is performed only in the tip region of the grid, and the other parameters are kept to reasonable values (that is, the values centered in the initial range of parameters). This allows rather cheap meshes to be used, so that grid points (*i.e.* computational resources) can be dedicated to the tip gap discretization. Four more meshes are generated and computed, with up to 37 points in the tip clearance.

As shown on figure 1(b), a qualitative convergence of the friction coefficient value is observed. An interesting property of numerical convergence (when the asymptotic range is reached) is that each new refinement should entail a relative change of the solution inferior to the change due to the previous refinement. This is the case here.

NUMERICAL ERROR ESTIMATION FOR THE FRICTION AT THE SHROUD

In the frame of verification procedure, Richardson Extrapolation is commonly used to help evaluating the numerical error with a given set of computed grids. Oberkampf and Trucano [2] use the Taylor development of the numerical solution to derive an *a posteriori* error estimate. Several assumptions need to be made to obtain this estimate: (i) the output considered must be a smooth solution (in the sense of the existence of sufficient derivatives to justify the Taylor Serie expansion); (ii) the formal convergence order of the scheme is known; (iii) the mesh spacing must be small enough for the asymptotic range to be reached.

Assuming all three hypotheses, the use of three grids (Coarse Medium and Fine) yields the following error estimate : $\delta_F = \left(\frac{S_M - S_F}{h_M^p - h_F^p}\right) h_F^p$, where δ_F is the error on the Fine grid, S the computed solution and h a measure of the grid size. The terms neglected in this estimate are of the order $\mathcal{O}(h_F^{p+1}) + \mathcal{O}(h_M^{p+1})$, hence negligible.

Applying this error estimate to the three last computed grids, *i.e.* with 29, 33 and 37 points in the gap, the error on the 37 point case is 4.9% (relative to the estimated exact solution).

To check *a posteriori* for the asymptotic range assumption, Oberkampf and Trucano propose to compare the error on the coarse case (29 points) with the theoretical error. The error in the 29 point case is obtained using the just-computed exact value (using the error estimate and the 37 point case). The theoretical error is deduced from the knowledge of the error in the finest case and the ratio of refinement between the coarse and the fine case, that is to say: $\delta_{C-theoretical} = (37/29)^2$ because it is a second order scheme. The results compare very well: 8.3% for the theoretical error compared to 8% for the computed error. According to Oberkampf, this demonstrates *a posteriori* that all three grids lie in the asymptotic range.

The reliable estimate of the exact solution provided by this method allows for the error to be evaluated on any grid. For instance, if a calculation is run with 21 points in the gap, the error can be estimated to be 17% of the exact solution, and for the 9 point case the error approaches 50%.

To sum up, considering that memory requirements prevent globally mesh independent solutions for industrial cases, this study aimed at generating a locally mesh independent solution. The proposed method enabled the derivation of a grid for accurate tip clearance description, and the numerical error on the friction coefficient was estimated to be less than 5%.

The benefit of the proposed method is to offer a way to assess locally numerical error accurately. This can be regarded as an affordable way to identify local requirements that will still have to be fulfilled when global independence is the concern.

References

[1] A.G. Hutton and M.V. Casey: Quality and Trust in Industrial CFD- A European Initiative. *AIAA Journal* 2001-0656, 2001.

[2] W.L. Oberkampf and T.G. Trucano: Verification and Validation in Computational Fluid Dynamics. SANDIA National Laboratory SAND2002-0529, 2002.

[3] A. Basson and B. Lakshminarayana: Numerical Simulation of Tip Clearance Effects in Turbomachinery. *Trans. ASME* 93-GT-316, 1993.

XXI ICTAM, 15–21 August 2004, Warsaw, Poland

SIMULATION OF A VISCOUS FLOW PAST A THREE DIMENSIONAL OBSTACLE USING VORTEX PARTICLES

Piotr Duszyński, Marta Poćwierz, Andrzej Styczek and Jacek Szumbarski
Department of Aerodynamics, Warsaw University of Technology
24 Nowowiejska Str, 00-665 Warsaw, POLAND

Summary The new formulation of the stochastic vortex particle method has been presented. Main elements of the algorithms: the construction of the particles, governing equations, stretching modeling and boundary condition enforcement are described. The test case is the unsteady flow past a spherical body. Sample results concerning patterns in velocity and vorticity fields, streamlines, pressure and aerodynamic forces are presented.

Governing equations

The problem of determination of the a viscous incompressible flow can be formulated in terms of velocity and vorticity fields. The equation of the vorticity transport (the Helmholtz equation) contains the advection and diffusion terms, and also the source term describing the vorticity stretching. One can split this equation (using the Lee-Trotter theorem) into the advection/diffusion equation without a source term and the equation describing vorticity dynamics due to pure stretching. The first one can be interpreted as a Fokker-Planck-Kolmogorow (FPK) equation. Thus, the advection/diffusion part of the vorticity evolution can be simulated by means of stochastic tools. The vorticity field is discretized by a large ensemble of (artificial) vortex particles. Motion of these particles is governed by Ito stochastic differential equations corresponding to FPK equation, i.e., they move with a local fluid velocity and perform a random motion modeling viscous diffusion of the vorticity.

Vortex particles

The construction of a vortex particle is an important element of the method. The velocity field induces by a particle is determined by the rotation operator applied to the product of vector time-dependent quantity (the ”vorticity charge” of the particle) and spherically symmetric scalar function. The vorticity charges change in time accordingly to the stretching equation. It should be emphasized that both velocity and vorticity fields induced by such particles are strictly divergence-free.

Boundary conditions

The no-slip boundary condition is imposed on the surface of an immersed body. To enforce this condition, the surface vorticity layer should be continuously generated. Such layer can be approximated by a number of newly created vortex particles covering tightly the surface of the obstacle. An instantaneous velocity field can be decomposed into the several parts: the one induced by the vortex particles created in the past time steps, the other induced by the new vortex particles added to the vorticity layer and the potential components (gradients of harmonic potentials), which are necessary to cancel out the normal component of the velocity at the material boundary. The velocity field described above is divergence-free and satisfies a far-field boundary condition and impermeability condition on the obstacle’s surface. The cancellation of the tangent velocity on this surface is achieved by an appropriate selection of the vectors vorticity charges of the new particles. It turns out that these vectors can be assumed parallel to the body’s surface. Once the new vortex particles are fully determined, they become the ”old” particles and begin to move in the flow domain as described earlier.

Global vorticity constrains

The analysis of the Helmholtz equation reveals an important constrain imposed on the vorticity field: the total vorticity charge of the vortex particles has to be steady in time. If the flow starts from rest the total charge remains zero. In principle, the proposed method of the vortex particles obeys this restriction automatically. However, in practical computations it is not necessarily the case because of inevitable numerical errors. In order to avoid a possible instability, an artificial vortex particle located outside the flow domain (in the interior of the obstacle) is introduced, which compensates error in the vorticity balance.

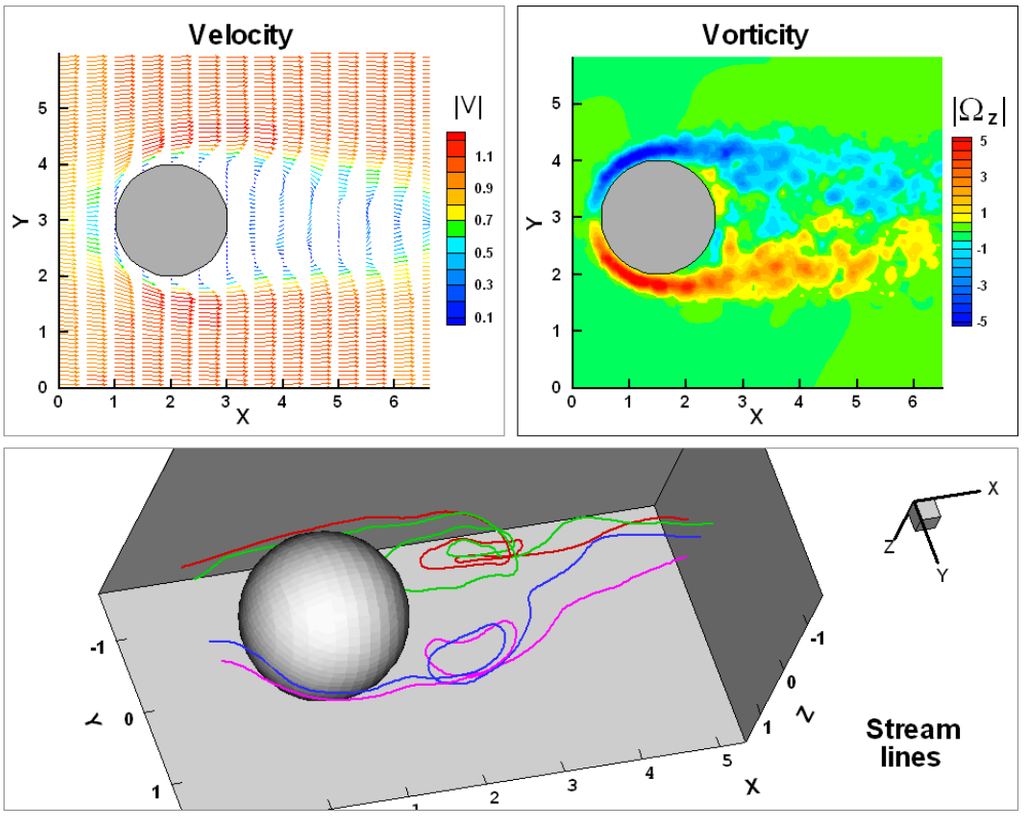
Pressure field

The pressure field is determined afterwards on the basis of previously calculated velocity and vorticity fields. In contrast to 2D flows (where the flow domain is not simply connected), the pressure problem is well-defined and posses the unique physically meaningful solution without any additional restriction.

Numerical computations

The numerical computations have been carried out for the spherical body. The results have been obtained for several Reynolds numbers. Instantaneous patterns in the velocity and vorticity fields have been obtained. The complexity and shape sensitivity of the instantaneous streamlines originating from closely located points has been demonstrated (see Figure below), which gives idea about the mixing intensity in the wake region. The numerically calculated aerodynamic

reactions do not differ much from the experimental measurements.
The key problem of the practical calculation is the numerical cost of the induced velocity evaluation. For 3D problem, fast summation methods (e.g. Greengard-Rokhlin algorithm) do not work as efficiently as in 2D case. Other tricks like using indirect velocity evaluation (the far-field induced velocity is calculated in the nodes of an auxiliary grid(s) and then interpolated) might help, but various artifacts can be expected. This is why the current implementation of the method relies on direct ”each-to-each” computations of the induced velocity. Future improvement of this part of the algorithm will significantly increase its practical value.



XXI ICTAM, 15–21 August 2004, Warsaw, Poland

MULTISCALE SIMULATIONS USING PARTICLES

J. H. Walther, T. Werder and P. Koumoutsakos
Institute of Computational Science, ETH Zürich Hirschengraben 84, 8092 Zürich, Switzerland

Summary We outline a multiscale algorithm for the simulation of dense fluids that couples molecular dynamics and continuum fluid dynamics. The coupling between the two models is realized by a common overlap domain and by the alternating Schwarz method. We prefer this method to those based on direct flux exchange, since the accurate estimation of the fluxes requires much more statistics. The boundary conditions on the atomistic region are imposed using stochastic walls to thermalize and confine the molecular dynamics system, and the USHER algorithm to insert new atoms. The forcing of the continuum is achieved using appropriate source terms in the momentum equations. To test the algorithm, we study the flow of liquid argon past a carbon nanotube.

INTRODUCTION

The study of fluid mechanics at the nanoscale level [1] has received wide attention due to its importance for the understanding and development of biosensors. From the computational side, classical molecular dynamics (MD) have so far been the most useful tool to characterize phenomena such as wetting, hydrophobicity and boundary conditions. One system of particular interest with regard to biosensors is carbon nanotubes in water, which has recently been studied in some detail [2, 3]. Despite the success of molecular dynamics, its limitations in terms of accessible length and time scales are currently of the order of $10\,\mathrm{nm}^3$ and $10\,\mathrm{ns}$. In order to allow the computational analysis of nanoscale systems integrated in microfluidic environments, a multiscale approach is indispensable Here, we present an algorithm to impose arbitrary, non-periodic boundary conditions on MD simulations of dense fluids. We show how this algorithm couples standard molecular dynamics codes with commercial computational fluid dynamics packages. As a first application we consider a flow of liquid argon around a carbon nanotube (CNT), where only the CNT and its interaction with the nearby argon are modeled using MD, cf. Fig. 2, and where the continuum part is described by the isothermal, incompressible, Navier-Stokes (NS) equations.

THE COMPUTATIONAL METHOD

The central part of any hybrid scheme is the coupling of the atomistic and continuum regions. One can distinguish between two fundamental types of coupling, the former aim at matching the fluxes of mass, momentum, and energy at the interface [4, 5] and, the others are based on overlapping cells where the mass density ρ, the mean velocity $\boldsymbol{u}$, and the temperature T are imposed. The latter schemes have two main advantages over flux based schemes, namely that they decouple time scales [6] and that densities are substantially easier to sample than fluxes.

The Schwarz algorithm

The algorithm is based on the Schwarz iteration scheme [6], i.e., the computational domain consists of continuum cells C, particle cells A, and overlap cells X, where both descriptions are valid, cf. Fig. 1 The following iteration is run until

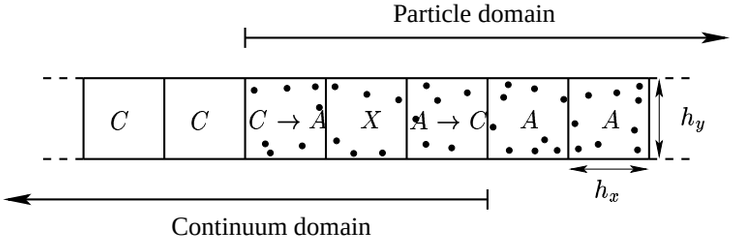


Figure 1. One dimensional sketch of a computational domain. There are pure continuum (C) and particle cells (A), as well as overlap cells $C \to A$, X, and $A \to C$, where both descriptions are valid. The Schwarz iteration by turns imposes the values measured in the $C \to A$ cells on the atomistic region and the values measured in the $A \to C$ cells on the continuum region until the solution converges in X.

the solution is converged in the overlap region.

Step 1) Run an MD simulation until a steady state is reached, with $(\rho, \boldsymbol{u}, T)$ imposed in the $C \to A$ cells.

Step 2) Solve the continuum equations with the steady state solution of the MD in the $A \to C$ cells as boundary conditions.

The atomistic part

The main difficulties in imposing the continuum field values on the atomistic system in the $C \to A$ domain are the

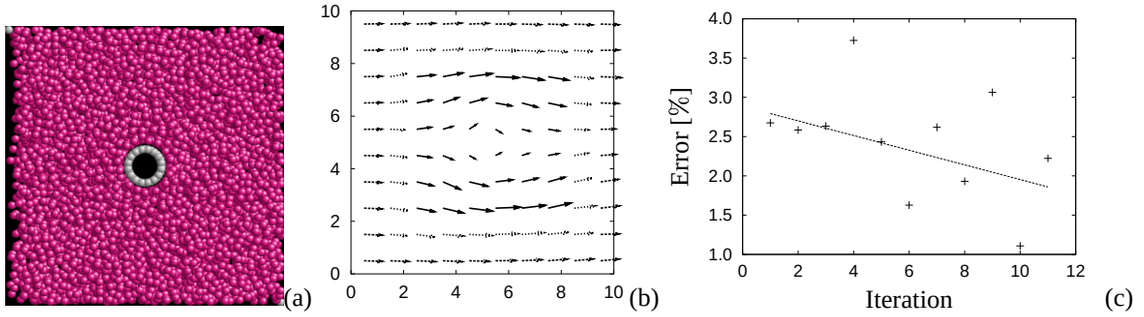


Figure 2. Flow of argon around a carbon nanotube. (a): A snapshot of the atomistic system. (b): The converged velocity field in the atomistic domain. (c): Convergence of the velocity field imposed on the edge of the atomistic domain. The error measure is defined in Eqn. (**??**). The solid line is a linear fit to the data.

"missing particles" exteriour to the atomistic domain. For a monatomic Lennard-Jones fluid, the first problem is solved using the USHER algorithm [7]. For the second problem, we use the notion of stochastic boundary condition introduced to simulate the contact of an MD system with a thermal reservoir [8].

The continuum part

The continuum system is described by a finite volume discretization of the isothermal, incompressible, Navier-Stokes (NS) equations in the entire computational domain including the atomistic region. By the complete overlay, we avoid explicit internal interfaces in the continuum system and instead utilize body forces to impose the average molecular velocity field. We note that the external boundary conditions of the continuum system are not limited to cyclic conditions, but can take any for the flow solver admissible form.

RESULTS

To test the proposed algorithm, we have interfaced a commercial Navier-Stokes solver (StarCD [9]), with an in-house molecular dynamics code (FASTTUBE [10]). In the study the carbon nanotube is modeled as a rigid structure which interacts with the argon through a Lennard-Jones potential. The size of the finite-volume cells are chosen to match the size and location of the bins used in the molecular system for the averaging and for the imposition of the boundary conditions. In the present study we use cells of size $1.0 \times 1.0 \times 4.26\,\mathrm{nm}$ to secure a sufficient averaging and forcing of the molecular system. The continuum mesh consists of $30 \times 30 \times 1$ mesh points. The boundary conditions of the continuum system are chosen to be periodic in y and z. A flow is imposed along the x-direction with an inlet velocity of $u_x = 100\,\mathrm{ms}^{-1}$ at the left boundary and an outlet boundary condition at the right boundary. The atomistic domain extends over $10 \times 10 \times 4.26\,\mathrm{nm}$ (including the $C \rightarrow A$ cells) and contains 5600 argon atoms. A snapshot of the atomistic domain is given in Fig. 2a. In every iteration of the atomistic domain, we let the system adapt to the new boundary conditions for $20\,\mathrm{ps}$, and we subsequently sample the system during $80\,\mathrm{ps}$. We quantify the convergence by measuring the change (E) in the velocity field between each main iteration. In Fig. 2c, we show this measure as a function of the iteration number. The statistical error in sampling the velocity in the atomistic region is estimated to be $\approx 2.5\%$. Therefore we conclude that the solution has nearly converged after the first iteration, cf. Fig. 2c.

CONCLUSION

We have presented a hybrid multiscale algorithm for the coupling of atomistic and continuum systems. It is based on the Schwarz domain decomposition technique, the Usher algorithm for particle insertions, and stochastic walls.

References

[1] P. Koumoutsakos, U. Zimmerli, T. Werder, and J. H. Walther, ASME/SPIE handbook of Nanotechnology in press (2003).
[2] T. Werder *et al.*, J. Phys. Chem. B **107**, 1345 (2003).
[3] J. H. Walther, T. Werder, R. L. Jaffe, and P. Koumoutsakos, Phys. Rev. E accepted (2003).
[4] E. G. Flekkøy, G. Wagner, and J. Feder, Europhys. Lett. **52**, 271 (2000).
[5] R. Delgado-Buscalioni and P. V. Coveney, Phys. Rev. E **67**, 046704 (2003).
[6] N. G. Hadjiconstantinou, J. Comput. Phys. **154**, 245 (1999).
[7] R. Delgado-Buscalioni and P. V. Coveney, J. Chem. Phys. **119**, 978 (2003).
[8] G. Ciccotti and A. Tenenbaum, J. Stat. Phys. **23**, 767 (1980).
[9] STAR-CD Version 3.1A. Manual, 1999.
[10] J. H. Walther, R. Jaffe, T. Halicioglu, and P. Koumoutsakos, J. Phys. Chem. B **105**, 9980 (2001).

XXI ICTAM, 15–21 August 2004, Warsaw, Poland

INVESTIGATION OF WENO SCHEMES FOR 3D UNSTRUCTURED GRIDS.

Jerzy Majewski*, Robert Wieteska*
*Warsaw University Of Technology, Institute of Aeronautics and Applied Mechanics, Nowowiejska 24, 00-665 Warsaw, Poland

Summary The paper presents a comparison of WENO (Weighted Essentially Non Oscillatory) reconstruction applied within two common approaches to Finite Volume Method (FVM), i.e. Cell Centered (CC) and Vertex Centered (VC) method, which are used for simulation of compressible inviscid flows. The CC and VC methods were subject to comparison in order to assess their quality with regards to accuracy of the scheme and to the computational cost. The CC method was found producing more accurate results than VC method but it was obtained at higher computational cost. The detailed analysis will be presented for 3D supersonic flow in a channel and for the Onera M6 wing.

METHOD OVERVIEW

The paper presents an algorithm used for simulation of 3D inviscid compressible flows on unstructured grids with Finite Volume Method (FVM).
Flow field obtained with Finite Volume Method is represented by averaged values assigned to each control volume. The fluxes are computed at control volume boundaries and then it is necessary to provide a mechanism for reconstruction of the flow function inside a control volume. The accuracy of the algorithm determines the overall order of the method.
Our approach is using Weighted Essentially Non Oscillatory (WENO) scheme for reconstruction. Main advantage of this scheme lies in possibility to keep high order also in the vicinity of strong discontinuities (shock waves) without introducing oscillations. It is also possible to use this approach for different kind of grids, e.g., structured, unstructured and also grids consisting of mixed type elements. The only information required is an information about neighborhood of a given cell.
The disadvantage of the method is a fact that stencils needed for reconstruction can create quite complicate patterns.

In general the algorithm can be presented in the following way:

- Define for a control volume Ω_h m stencils $S_1, S_2, \cdots, S_m$ consisting of the neighboring control volumes.
- Create a function P_i which approximates solution inside Ω_h for each stencil S_i.
- Calculate oscillation indicator o_i for each function P_i.
- Calculate weights for each P_i using oscillation indicator.
- Find global reconstruction function for a control volume Ω_h as a weighted average of P_i.

CELL CENTERED AND VERTEX CENTERED APPROACHES

Two codes using FVM with WENO reconstruction were developed. The difference between them lies in treatment of control volume. The first code with Cell Centered approach is treating each grid cell as a control volume. The second one with Vertex Centered approach (known also as Cell Vertex) is using a dual mesh and then the control volumes are built around vertices. Since number of cells in typical 3D unstructured tetrahedral grid is around 6 times greater than number of vertices, the Cell Centered approach has to store 6 times more variables (which are defined per control volume) than VC approach. It is clear that for the same grid the Cell Centered method will consume much more memory than Vertex Centered one but we expect at the same time more accurate results since there are more control volumes.
Both codes were using first order reconstruction which should lead to second order accuracy in space. In future development the higher order (second, third) reconstruction is planned.

RESULTS

The detailed analysis of the performance of two discretization approaches will be presented for two 3D cases:

- supersonic flow inside the wedge channel (see Fig. 1).
- transonic flow past Onera M6 wing (see Fig. 2).

CONCLUSIONS

WENO reconstruction gives high quality results for both approaches. As expected Cell Centered method gives more accurate results at higher cost than Vertex Centered one.

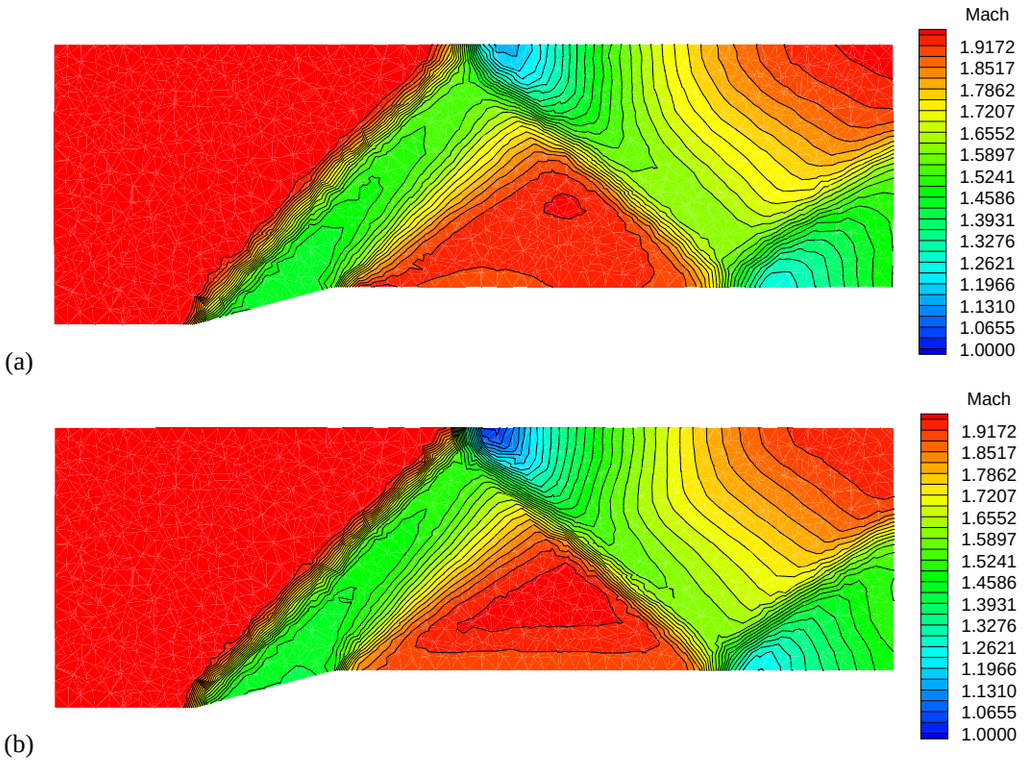


Figure 1. Supersonic flow inside a wedge channel ($Ma_{inlet} = 2.0$).
a) Mach number field calculated with Vertex Centered method (middle cut).
b) Mach number field calculated with Cell Centered method (middle cut).

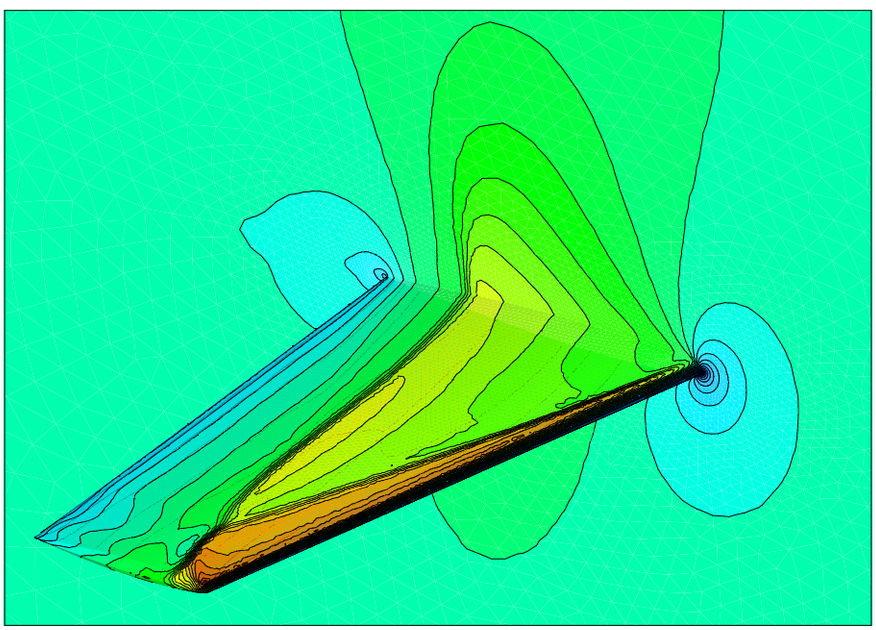


Figure 2. Transonic flow past a M6 Onera wing ($Ma_{\inf} = 0.8$).

References

[1] Abgrall R., Sonar T., Friedrich O., Billet G., High Order Approximations for Compressible Fluid Dynamics on Unstructured and Cartesian Meshes, in High-Order Methods for Computational Physics, Eds. Barth T.J., Deconinck H., Springer-Verlag, Berlin Heidelberg, 1999.
[2] Chi-Wang Shu, High Order ENO and WENO Schemes for Computational Fluid Dynamics, in High-Order Methods for Computational Physics, Eds. Barth T.J., Deconinck H., Springer-Verlag, Berlin Heidelberg, 1999.
[3] Shu C.-W., Osher S., Efficient Implementation of Essentially Non-oscillatorey Shock-Capturing Schemes, in Upwind High-Resolution Schemes, Eds. Hussaini, M.Y., van Leer B., Van Rosendale J., Springer-Verlag, Berlin Heidelberg, 1997.

XXI ICTAM, 15–21 August 2004, Warsaw, Poland

NUMERICAL STUDY OF THE DYNAMIC COALESCENCE OF TWO AIR BUBBLES IN QUIESCENT COLUMN WATER

Jean-Michel Martinez*, Xavier Chesneau*, Belkacem Zeghmati*
* *Laboratoire de mathématiques et de physiques des systèmes - Groupe de mécanique et Energétique MEPS-GME,*
Université de Perpignan, 52 avenue Paul Alduy, 66860 Perpignan cedex

Summary We present a new numerical method to calculate curvature and surface tension force in PLIC-VOF with the Continuum Surface Force (CSF). Based on staggered grid, this method is more accurate in determining surface tension contribution and therefore reduce moreover "spurious currents". We applied our method in the study of dynamics coalescence between two air bubbles. The results are presented as reconstructed interface with velocity field images.

Studies of two-phase flow are interesting for numerous applications ranging from environmental sciences to engineering. The presence of moving interface in two-phase flow is commonly approached with different numerical methods. The one, we used has been developed by Hirt and Nichols [1].The VOF (Volume Of Fluid) method allows the knowledge of the liquid-vapor interface evolution by the use of a colour function commonly noted C or F which points out the volumic fraction of liquid ranging from 0 and 1. This method needs to solve a non diffusive transport equation, given by:

$$\frac{\partial F}{\partial t} + \vec{\nabla}\left(\vec{V}F\right) = 0 \tag{1}$$

in which F represents the colour function and $\vec{V}$ the velocity field. The resolution of this equation is based on geometrical hypothesis which ensures the interface's integrity . The PLIC-VOF (Piecewise Linear Interface Construction - Volume of Fluid) method reconstructs the interface by a segment of straight line contained within each computational cell. This method is more accurate, less diffusive and allows a more important mass conservation. In order to include surface tension force in the Navier-Stokes's equations, several models have been developped, amongst which Brackbill et al.'s is the most commonly used [2]. This model transforms surface force into volumic force by using Dirac peak centered on the interface. The force thus being described (Continuum surface force-CSF) is expressed by the following relation:

$$\vec{F}_{sv} = \sigma\kappa\delta_s\vec{n} \tag{2}$$

in which σ represents supercifial tension, δ_s Dirac peak centered on the interface, $\vec{n}$ the interface normal vectors and κ the curvature giving:

$$\kappa = -\vec{\nabla}_s.\vec{n} \tag{3}$$

in which $\vec{\nabla}_s.\vec{n}$ represents the surface divergence of the normals for an interface surface element. The normal vectors is determined by the normalised gradient of the colour function F. A smoothed colour function by convolution with a $\beta - spline$ kernel is commonly used to increase the numerical accuracy of the normal and of the curvature.
In order to optimise numerical calculation on the evaluation of surface tension's contribution without using a smoothed colour function by CSF, we have developped a new technique calculation for curvature and superficial tension force. This method leads to reduce drastically the presence of "spurious current" which developping at the interface and allows to use the surface tension contribution with more accuracy.
The method we worked out uses the direct definition of two dimensionnal surface divergence and does not need smoothed colour function to improve accuracy.

$$k = \left|\frac{\partial \vec{n}}{\partial S}\right| \tag{4}$$

in which S is the length along the curves which represent the interface.
The normal vector is calculated on each face and at the corners of a MAC cell. The positionning of the segment within the cell leads the choice of the normal vector which are the nearest from the intersection point between the cell and the segment. The length ∂S is approximated by an average of all the segments presented in the main cell since each stagerred cell produce its own segment. The calculus is then renewed for each cell on the entire domain with the same assumptions. Once calculated the curvature, the superficial tension force is deduced from equation 2, which is included in the Navier Stokes equations as an external forces field. The latters are discretised on MAC grid, which is defined as a control volume and the projection algorithm is used for solving the Navier-Stokes equations. Therefore the superficial tension force have to be included on face of each computationnal cell. This contribution is numerically defined on a staggered cell. Obviously, our method allows to calculate curvature on center of each cell. Consequently colour function values F are determined on staggered cell with geometrical assumptions, which allow to define the curvature on the face of the main cell and this technique is applied on each face of the volume control. The validation tests show that our method is more

accurate than those previously implemented [3, 4] and leads to less "spurious currents".

This method were applied on two air bubble coalescence in quiescent column water, with temperature ranging from $20°$ to $80°$, different radius size and different Bond and Reynolds number. Results presented concern the reconstructed interface with velocity field for four different time step iteration ranging from 1 to 300 at $20°$ temperature with radius $R_0 = 1$ mm and initial time step $\Delta t = 0.05$ ms.

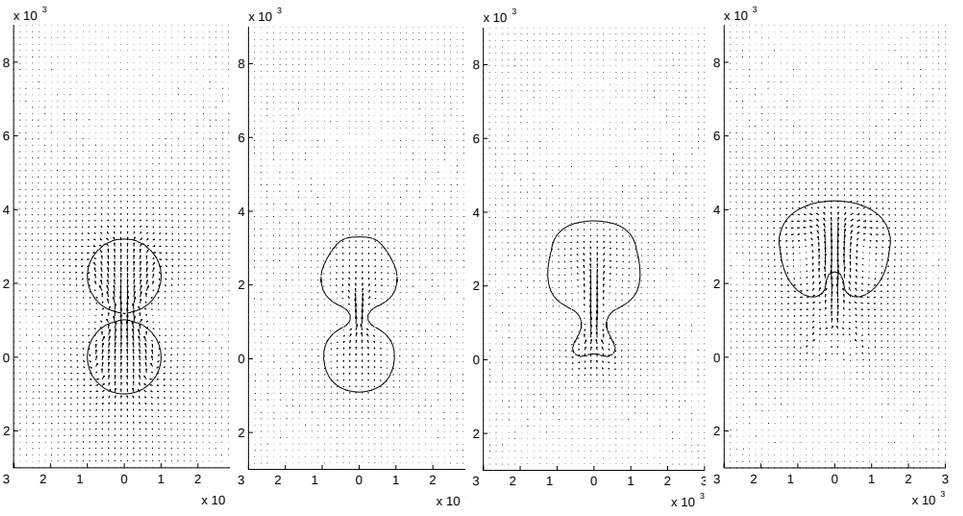


Figure 1. Coalescence between two bubbles

The sequence reported on figure 1 proves the potentiality of our method. The modelisation thus deduce on coalescence reveals several important parameters as the distance between each bubble, the radius and the time step Δt. Further results show a real dependance from surface tension with Bond number, and also temperature. This parameters leads to different deformations and sometimes breakup of bubbles before the coalescence.

CONCLUSION

We developed a new method based on staggered grid for calculating curvature and surface tension force of which the results present better agreement with reality. The surface tension force is included in the Navier-Stokes equations which are solved numerically with projection method. We applied this resolution on the coalescence between two air bubble in quiescent water at constant temperature and we caracterised different parameter, which induce the deformation or the breakup of bubbles before coalescence. We implemented different case of coalescence which lead to find correlation between size, surface tension, and the distance which separate each bubble.

References

[1] Hirt C.W., Nichols B.D., Volume of fluid (VOF) Method for the dynamics of free boundaries, Los Alamos Scientific Laboratory, Los Alamos, New Mexico, (1979).

[2] Brackbill J.U., Kothe D., Zemach C., A continuum method for modeling surface tension, Theoritical division, Los Alamos National Laboratory, Los Alamos, New Mexico, (1991).

[3] Meier M., Yadigaroglu G., Smith B.L., A novel technique for including surface tension in PLIC-VOF methods, Eur.J.Mech.B/Fluids **21**, pp 61-73, (2002).

[4] Zaleski S., Computation of multiphase flow by volume of fluid and high-order front tracking methods, Rapport d'activité de modélisation en mécanique, Université Pierre et Marie Curie, Paris VI.

Commutator-errors in large-eddy simulation of turbulent flow

Bernard J. Geurts [1,2], *Fedderik van der Bos* [1] *and Darryl D. Holm* [3,4]

1: Mathematical Sciences, University of Twente, P.O. Box 217, 7500 AE Enschede, The Netherlands
2: Faculty of Applied Physics, Technical University of Eindhoven, P.O. Box 513, 5600 MB Eindhoven
3: Center for Nonlinear Studies, Los Alamos National Laboratory, MS B284, Los Alamos, USA
4: Mathematics Department, Imperial College, London, SW7 2AZ, UK

Abstract

Commutator-errors in large-eddy simulation of incompressible turbulent flow arise from the application of non-uniform filters to the continuity – and Navier-Stokes equations. As a consequence, the filtered velocity field is no longer solenoidal. For non-uniform, high-order filters the order of magnitude of the commutator-errors is shown to be the same as that of the turbulent stress fluxes. Consequently, one can not reduce the size of the commutator-errors independently of the turbulent stress terms by some judicious construction of the filter operator. Independent control over the commutator-errors compared to the turbulent stress fluxes can only be obtained by appropriately restricting the spatial variations of the filter-width and filter-skewness. For situations in which the dynamical consequences of the commutator-errors are significant, e.g., near solid boundaries, explicit similarity modeling for the commutator-errors is proposed, including the application of Leray regularization. The performance of this commutator-error parameterization is illustrated for the one-dimensional Burgers equation. The Leray approach captures the filtered flow with higher accuracy than conventional similarity modeling, which is particularly relevant for large filter-width variations.

In large-eddy simulation (LES) of turbulence one aims to predict the primary features of an unsteady flow without explicitly resolving all dynamically relevant length-scales. The modeling of turbulent flow in large-eddy simulation starts from the introduction of a spatial, low-pass filter with externally specified filter-width Δ. This allows to locally distinguish flow-features with a length-scale larger than Δ from flow-features with length-scale smaller than Δ. In the LES context, the former are referred to as 'resolved' while the latter class of flow-structures is identified as 'subgrid' or 'sub-filter'. During a simulation, the time-dependent resolved scales are explicitly calculated while the dynamic effects of the subgrid scales on the evolution of the resolved scales is represented through the introduction of an explicit 'subgrid' model. In the filtering approach to large-eddy simulation the spatial filter is traditionally assumed to be characterized by a single, spatially uniform operator, in particular, with a single value for Δ throughout the flow domain.

The desire to extend large-eddy simulation to flows in complex domains generally implies that one is confronted with strongly varying turbulence intensities within the flow-domain. In the filtering approach this can be accommodated using a filter operator with non-uniform filter-width. The use of such filters, however, complicates the subgrid closure problem through the appearance of additional commutator-errors. These terms arise from the fact that non-uniform filters do not commutate with differentiation, e.g., $\overline{\partial_x u} \neq \partial_x \overline{u}$ where ∂_x denotes differentiation of the solution u with respect to x and the overline indicates the filter operation. In our contribution we will *(i)* derive the complete, non-uniformly filtered equations and establish the magnitude of the additional commutator-error closure-terms relative to the fluxes arising from the turbulent stress tensor, *(ii)* identify under what conditions for the filter, the commutator-errors are likely to be dynamically relevant and *(iii)* for such situations, propose and illustrate explicit similarity modeling based on Leray regularization. These findings support the extension of the large-eddy approach to turbulence under realistic flow conditions and in complex flow domains. Some applications in three spatial dimensions will be included in the final contribution.

There have been considerable developments related to the application of such non-uniform filters in recent literature. These developments are primarily associated with the construction of specific high-order filters. For such general 'N-th order' filters the magnitude of commutator-errors can be controlled to some degree. Specifically, in literature it is emphasized that the size of the commutator-errors can be sufficiently reduced for these terms to become negligible, simply by appropriately increasing the order of the adopted filter. This impression is, however, somewhat over-simplifying matters since it is not fully complete. In the present paper we take a different approach to commutator-errors. In fact, it is shown that non-uniform filtering leads to commutator-errors which are of the same formal order of magnitude as the turbulent stress fluxes in the filtered Navier-Stokes equations. This holds for any higher-order filter and emphasizes the point that the magnitude of the commutator-errors can not be reduced *independently* of the turbulent stress fluxes by high-order filtering only; commutator-errors can not simply

be 'filtered away' independently. Consequently, the question under which conditions commutator-errors are dynamically relevant, is still open.

Rather than controlling the size of the commutator-errors by increasing the order of the filter, the magnitude of these contributions can also be influenced by controlling the spatial variations in the filter properties. We sketch under what conditions the commutator-errors can be expected to be negligible relative to the turbulent stress fluxes, i.e., identify situations such that the commutator-errors do not require explicit closure. Conversely, if these conditions can not be satisfied, the introduction of an additional, explicit subgrid model for the commutator-errors is warranted. For this purpose, we present an alternative formulation for LES based on Leray regularization which allows to systematically develop a subgrid model for the commutator-errors. The explicit Leray modeling is compared to extended traditional similarity subgrid modeling.

To provide a modest illustration of explicit dynamical consequences of commutator-errors and their similarity models, the evolution of running 'ramp-cliff' waves in the viscous Burgers equation is studied. It is shown that the 'Leray-regularized' formulation provides a better representation of the non-uniformly filtered velocity field than the usual similarity model. In particular, the Leray approach provides a simultaneous capturing of turbulent stress fluxes as well as commutator-errors without increasing computational costs compared to the traditional case of uniform filters. The extension toward non-uniformly filtered turbulent flow in three dimensions is subject of ongoing research.

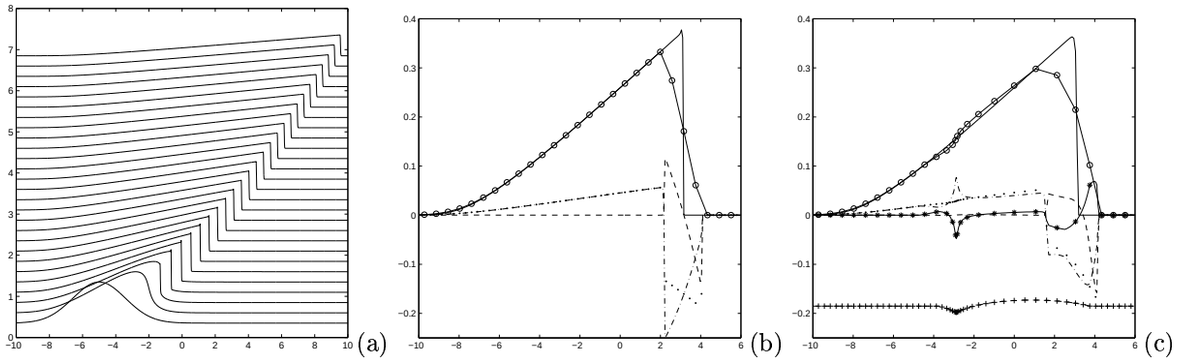


Figure 1: (a): Solution to the Burgers equation initiated with a Gaussian profile, developing into a ramp-cliff structure at $Re = 500$. The solution is shown at times $t = 0, 1, 2, \ldots$. Snapshot of the solution (multiplied by $1/2$) (solid) and filtered solution (solid; markers o). Convective flux: total (dots), mean (dash-dotted), turbulent stress (dashed), commutator-error (solid with $*$). In (b) we use $\Delta = \ell/16$ and in (c) a non-uniform case is shown. Underneath in (b), the grid-spacing (minus 0.2) as a function of x is presented.

The Burgers equation provides a model-system which has the same basic structure under filtering. All relevant commutators appear in the filtered Burgers equation. The initial solution is a Gaussian profile which rapidly develops into the well-known 'ramp-cliff' structure. The initial profile has a width equal to 1. We use $Re = 500$ to obtain a sharply localized cliff region. In figure 1(a) we show an example solution. To analyze the LES-fluxes, we collected the contributions to the total convective flux for a representative uniform and non-uniform case. We write

$$\overline{\partial_x(u^2)} = \partial_x(\overline{u}^2) + \partial_x(\overline{u^2} - \overline{u}^2) + \{\overline{\partial_x(u^2)} - \partial_x(\overline{u^2})\}$$

identifying on the right hand side the 'mean', 'SGS' and 'commutator' flux respectively. In figure 1 the solution and the filtered solution are included displaying the 'ramp-cliff' structure. The total flux in figure 1(a) is piecewise linear and the SGS flux is localized in the cliff-region. In figure 1(b) the filtered solution is significantly distorted due to the filter-width non-uniformity. On the 'ramp side', the non-uniform filter-width near $x = -3$ strongly influences the mean flux. The commutator-error compensates for this such that the total flux remains nearly linear in x. The commutator-flux and the SGS-flux have comparable magnitude.

Three-dimensional Rayleigh-Bénard instability in a supercritical fluid by direct numerical simulation

Gilbert Accary[1], Isabelle Raspo[1], Patrick Bontoux[1], and Bernard Zappoli[2]

[1]*MSNM-GP UMR 6181 CNRS, 38 rue Frédéric Joliot Curie, 13451 Marseille, France*
[2]*CNES, 18 avenue Edouard Belin, 31401 Toulouse, FRANCE*

An experimental observation by Nitsche & Straub in *1987* initially showed a fast thermal equilibrium in the absence of convection in supercritical fluids (SCF). This phenomenon termed as the 'piston effect' (PE), was predicted theoretically in *1990* by Boukari *et al.*, Onuki *et al.*, and Zappoli *et al.* In the past ten years, most of the attention was devoted to the interaction between the PE and natural convection. Experimental investigations in the Rayleigh-Bénard configuration revealed the development of a convective instability near critical conditions. Direct numerical simulations (DNS) of 2D Navier-Stokes equations contributed to the understanding of the hydrodynamic behaviour of such complex flows. The continuation of previous works led us to extend DNS to fully three-dimensionalcases [1].

A SCF is enclosed in a cubic shape box, heated from below, and subjected to the earth vertical gravitational field g (Fig. *1*). Initially, the fluid is in thermodynamic equilibrium at constant temperature T_i slightly above its critical temperature Tc such that: $T_i = (1+\varepsilon)T_c$ where $\varepsilon << 1$. The fluid is stratified in pressure and density, with a mean density equal to its critical value ρ_c. Numerical simulation starts with the application of a progressive weak heating ($\Delta T \sim$ few mK) to the bottom box wall, while maintaining the upper one at its initial temperature T_i. The mathematical model for a SCF flow is described by the Navier-Stokes and energy equations written for a van der Waals fluid. We consider the CO_2 critical coordinates ($T_c=304.13K$, $\rho_c=467.8Kg.m^{-3}$) and transport properties, and the simulations were carried out for $T_i-T_c=1K$. The governing equations are solved using a finite-volume method, second order accurate in space and third order in time.

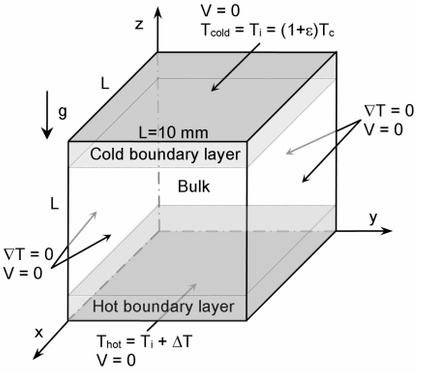


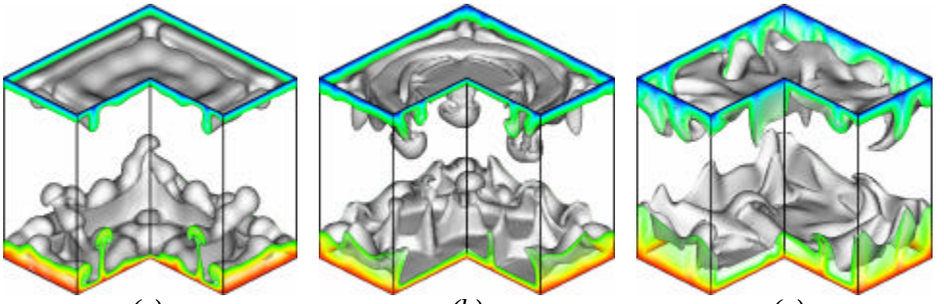
Figure 1. SCF in the Rayleigh-Bénard configuration, with no-slip walls and insulated vertical ones.

Bottom heating induces a wall temperature gradient and the development of a thin thermal boundary layer along the hot wall. This boundary layer expands upward, compressing adiabatically the rest of the fluid, and leading to a fast and homogeneous heating of the cavity bulk by thermoacoustic effects (PE). Since the top wall temperature is maintained at its initial value, a cold boundary layer settles near the top wall. In this PE-dominated phase, the flow is divided into three distinct zones: two thermal boundary layers along the horizontal walls and the cavity bulk.

As long as the flow in the boundary layers is dominated by the diffusion, the thermal boundary layers grow in time at heat diffusion speed. This thermal expansion is hindered by the density stratification of the fluid, leading to a well-known situation ending with a convective instability when the local Rayleigh number exceeds a critical value. Owing to the divergence of the isothermal compressibility of the SCF, the classical Rayleigh criterion includes a stabilizing contribution, the Schwarzschild criterion

usually encountered in atmospheric sciences for large air columns. We recently showed that this stabilizing effect can lead to a reverse transition towards a stable state [2].

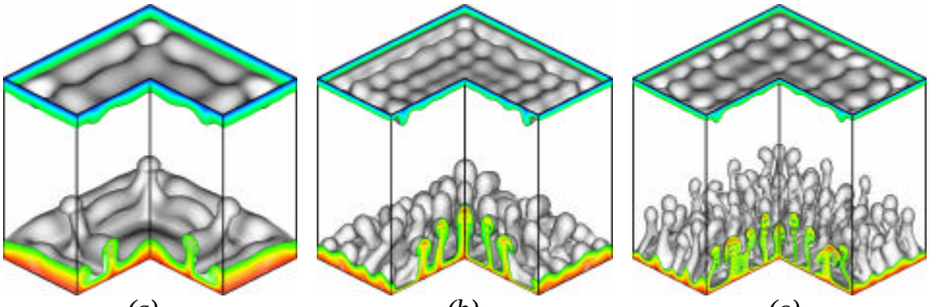
Figure *2-a* illustrates the convection onset: convective plumes rise from both thermal boundary layers; the space distribution of these structures in *(x,y)* plan seems to match the squared geometric shape. In figure *2-b*, temperature field is subjected to radical changes: on the top wall, a circular distribution of the thermal plumes is observed, while on the bottom wall, some convective structures take vertical fin shapes. In figure *2-c*, these new shapes are more localized on the bottom wall and spread on the insulated walls leaving flat zones where convective plumes rise, are pinched off, and release thermal balls floating upwards, leaving horn-like shafts. The convective improvement of the heat transfer between the isothermal walls and the cavity bulk leads to the faster temperature equilibrium in the whole cavity.



(a) *(b)* *(c)*

Figure 2. Instantaneous temperature fields for *DT=1mK*, exhibiting the three-dimensionality of the flow. From *(a)* to *(c)*, *t = 22.6s, 36.9s, 63.1s*, and the shaded isotherms of $(T-T_i)$ in *mK* are respectively: *(0.4,0.6), (0.44,0.6), (0.37,0.65)*

Figure *3* shows a comparison of the temperature patterns obtained for three values of heating *DT=0.5mK*, *2.5mK*, and *5.0mK*. A stronger heating increases the number of the convective plumes while reducing their space scales. As the heating increases, the convective instability is released earlier, starting always with an organized space distribution in the horizontal plan that matches the squared geometric shape.



(a) *(b)* *(c)*

Figure 3. Heating effects on the instantaneous temperature field. From left to right, *DT=0.5mK, 2.5mK, 5.0mK*; *t=45.3s, 16.7s, 11.4s*; and the shaded isotherms of $(T-T_i)$ in *mK* are respectively: *(0.2,0.3), (1.0,1.5), (2.2,3.2)*.

[1] *G. Accary, I. Raspo, P. Bontoux, and B. Zappoli*, Three-dimensional Rayleigh-Bénard instability in a supercritical fluid. *C. R. Méc*. **332**, 209-216 (2004).

[2] *G. Accary, I. Raspo, P. Bontoux, and B. Zappoli*, Reverse transition to hydrodynamic stability through the Schwarzschild line in a supercritical fluid layer. *In preparation*.

XXI ICTAM, 15–21 August 2004, Warsaw, Poland

CELLULAR COMPRESSIBLE MAGNETOCONVECTION: A MECHANISM FOR MAGNETIC-FIELD AMPLIFICATION AND STRUCTURING

Alexander V. Getling*, Wolfgang Dobler**
*Institute of Nuclear Physics, Lomonosov Moscow State University, 119992 Moscow, Russia
**Kiepenheuer-Institut für Sonnenphysik, Schöneckstrasse 6, 79104 Freiburg, Germany

Summary The amplification and structuring of magnetic field by cellular compressible magnetoconvection is studied using numerical simulations. The cases of both horizontal and inclined initial magnetic fields are considered. Magnetic structures with a substantial bipolar component (typical of solar magnetic regions) are produced, and their development seems to be inherent in the very topology of the cellular convective flow. If the initial field is inclined, a compact unipolar concentration of magnetic flux is also present. These new effects are complemented with the well-studied sweep of the vertical magnetic field to the cell boundaries and with a strong concentration of the horizontal magnetic field near the bottom boundary of the layer (so-called topological pumping).

INTRODUCTION

Numerical simulations of magnetoconvection are largely motivated by problems of solar physics. Most investigators (M.R.E. Proctor, N.O. Weiss, Å. Nordlund, R. Stein, F. Cattaneo, and others) have concentrated on such issues as the spatial separation of the flow and magnetic flux, oscillations and waves associated with magnetoconvection in a compressible fluid, or a "realistic" description of the evolution of magnetic flux tubes in a turbulent medium under conditions similar to solar ones (which is only possible for very small computational domains). In contrast, little attention has been given to the role of cellular magnetoconvection in amplifying and structuring magnetic fields, although the possibility of such effects was demonstrated by Tverskoy (based on a simple kinematic model) as long ago as in 1966 [1]. Meanwhile, the properties of a convection cell as the producer of specific, "solar" configurations of the amplified magnetic field are of paramount importance in the context of comprehending the origin of local magnetic fields on the Sun — an important ingredient of solar activity.

We present here the first results of our study of magnetoconvection in a compressible fluid and demonstrate the formation of localized structures of the strongly amplified magnetic field to be an inherent property of the cellular flow topology; some results concerning the effects under discussion were previously obtained in a Boussinesq approximation using spectral simulations [2, 3].

THE PROBLEM AND SIMULATION TECHNIQUE

We consider a plane horizontal fluid layer $0 < z < h$ heated from below. The dynamics of the flow and magnetic field is described by the standard system of equations, which includes the equation of motion, the continuity equation, the energy-transfer equation written in terms of entropy, and the induction equation. We assume that the bottom and top boundaries of the layer have infinite thermal and electric conductivities, so that the temperature is fixed, normal velocity and normal magnetic field are zero at these boundaries, while the tangential stresses and the tangential electric current vanish there. As initial state, we choose a superposition of a polytropic stratification and a weak thermal perturbation in the form of a spatially periodic pattern of hexagonal, Bénard-type convection cells. The horizontal wavenumber of this perturbation is equal to the critical value for the onset of convection in a Boussinesq fluid, $k_\mathrm{c} = \pi/\sqrt{2}h = 2.22/h$.

For our simulations, we use the Pencil Code developed by Brandenburg and Dobler [5]. This is a cache-efficient, high-order finite-difference code (sixth order in space and third order in time) that solves the compressible magnetohydrodynamic equations. The computations are restricted to a rectangular box $3.27 \times 5.66 \times 1$ with periodic boundary conditions at the side boundaries, and the grid typically contains $138 \times 240 \times 41$ points.

The layer depth h, the gravitational acceleration g, and the quantity $\sqrt{h/g}$ are used as the units of length, acceleration, and time, respectively. The mean gas density $\overline{\rho}$ is set to unity, which specifies the unit of mass. The unit magnetic field corresponds to a nondimensional Alfvén speed of unity. For any run, we specify the kinematic viscosity ν, the mean thermal diffusivity $\chi = \lambda/\overline{\rho}c_p$ (where λ is the thermal conductivity and c_p is the specific heat at constant pressure), the magnetic viscosity ν_m, the initial magnetic field B_0, and the ratio $\Delta T/\overline{T}$ (where ΔT is the temperature difference between the bottom and top boundaries and $\overline{T}$ is the mean temperature).

The initial magnetic field $\mathbf{B}_0$ is uniform and either directed along the x axis or inclined to it by 45°. The input quantities map to the usual nondimensional parameters of the problem,

$$R = \frac{g\,h^3(\Delta T - g/c_p)}{\nu\chi\overline{T}}, \quad Q = \frac{B_0^2 h^2}{\mu_0\overline{\rho}\nu\nu_\mathrm{m}}, \quad P_1 = \frac{\nu}{\chi}, \quad P_2 = \frac{\nu}{\nu_\mathrm{m}}$$

(where μ_0 is the vacuum permeability), called the Rayleigh number, the Chandrasekhar number, the hydrodynamic Prandtl number, and the magnetic Prandtl number.

RESULTS

We kept $P_1 = 1$ and varied R from 2000 to 20 000, P_2 from 1.5 to 30, and Q from 0.1 to 10. In addition, we varied the compressibility of the fluid. Throughout this region of parameter space, the magnetic structures produced by convection were largely similar. This is evidence for the decisive role of the flow topology in the formation of these structures.

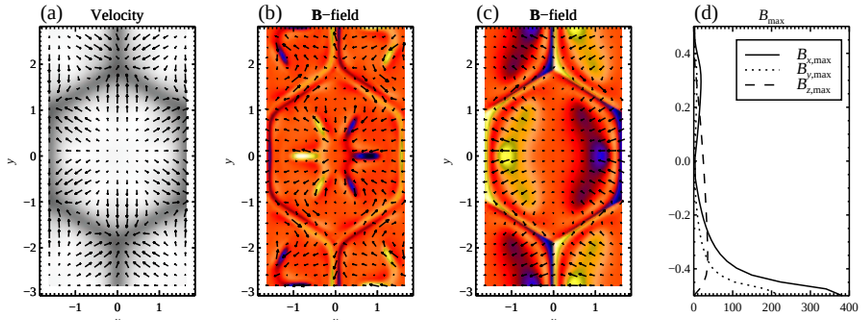


Figure 1. Simulation results for the case of a horizontal initial magnetic field, $R = 5 \times 10^3$, $P_1 = 1$, $P_2 = 30$, $Q = 1$, $\Delta T/\overline{T} = 0.83$, and time $t = 40$: (a) velocity field in the plane $z/h = 0.487$; (b, c) magnetic field in the planes $z/h = 0.066$ and 0.487, respectively (light for positive and dark for negative values of the vertical component, arrows for the horizontal components); and (d) the vertical distribution of the maximum values of all three magnetic-field components (expressed in units of the initial field B_0).

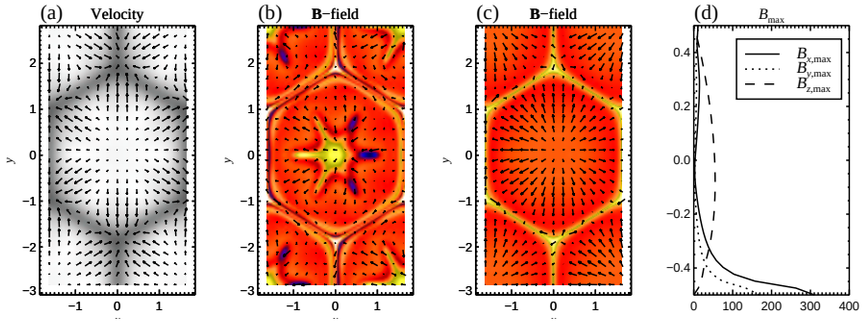


Figure 2. Same as in Fig. 1 but for an initial magnetic field inclined by 45° to the horizontal direction.

At an early stage of the process, decaying acoustic oscillations accompany a steady growth in the amplitudes of the velocity and magnetic field (which grows mainly kinematically). After this linear stage, the flow settles down to a nearly steady state, and the strongly amplified magnetic field also varies little during some time interval. It has now a mainly bipolar structure superposed with finer details. Figure 1 illustrates a well-developed magnetic structure of this type obtained in a run started from a horizontal initial magnetic field. (Except these new features, sweeping of the magnetic flux toward the cell boundaries is observed. Another remarkable effect is the "topological pumping" of the horizontal magnetic field [5]: as Fig. 1d indicates, an intense horizontal magnetic flux is accumulated near the bottom of the layer.)

Subsequently, a transition from the hexagonal cells to a roll flow occurs, which ultimately results in the decay of the amplified component of the magnetic field. However, at high magnetic Prandtl numbers ($P_2 = 30$), the magnetic-field strength reaches its absolute maximum only during the breakdown of the cellular flow. This occurs since the relatively disordered remnants of the previously regular, amplified field experience local compressions by the flow.

If the initial magnetic field is inclined (Fig. 2), the evolution of the flow and magnetic field is similar, but an intense unipolar concentration of magnetic flux is present in the pattern of the amplified field. Near the midheight in the layer, this is manifest in a substantial asymmetry of polarities.

CONCLUSION

We have shown that cellular magnetoconvection in a horizontal layer of compressible fluid can act as an efficient mechanism of magnetic-field amplification and structuring. It exhibits the fairly stable property of producing specific patterns of strongly amplified magnetic field, and they do not change their qualitative features over a fairly wide region in parameter space. Such a magnetic structure is generally a superposition of a bipolar and a unipolar configuration mixed in a proportion that depends on the inclination of the initial magnetic field to the horizontal plane. Magnetic patterns of this type closely resemble solar magnetic regions. The mechanism described here is an alternative to the rising-tube model widely known in solar physics and seems very promising in terms of better compatibility with observations.

References

[1] Tverskoy B.A.: A Contribution to the Theory of Hydrodynamic Self-Excitation of Regular Magnetic Fields. *Geomagn. Aeron.* **6**:11–18, 1966.
[2] Getling A.V.: Convective Mechanism for the Formation of Photospheric Magnetic Fields. *Astron. Zh.* **45**:661,2001 (Engl. transl.: *Astron. Rep.* **45**:569, 2001).
[3] Getling A.V., Ovchinnikov I.L.: Solar Convection as the Producer of Magnetic Bipoles. *Proc. 10th European Solar Physics Meeting, "Solar Variability: From Core to Outer Frontiers," Prague, Czech Republic, 9–14 September 2002 (ESA SP-506, December 2002)*, pp. 819–822.
[4] Brandenburg A., Dobler W.: http://www.nordita.dk/data/brandenb/pencil-code
[5] Drobyshevski E.M., Yuferev V.S.: Topological Pumping of Magnetic Flux by Three-Dimensional Convection. *J. Fluid. Mech.* **65**:33–44, 1974.

SCALING LAWS FOR THERMAL CONVECTIONS

Martin P. King*, M. Wilson**
*The Abdus Salam ICTP, Strada Costiera 11, Trieste 34014, Italy.
**Department of Mechanical Engineering, University of Bath, Bath BA2 7AY, U.K.

Summary Recently, there has been much progress in deriving comprehensively the scaling laws for Rayleigh-Bénard convections. We show here that the relatively intuitive and simple model of Castaing et al, with minor modifications, can give many of these 'new' scaling laws as well. We also apply this method to convections in an unsealed enclosure (i.e. one with an inlet and an outlet) to obtain the scaling laws for different convective regimes.

THE CASTAING ET AL MODEL REVISITED

For Rayleigh-Bénard convections obeying the Boussinesq approximation, both the Reynolds number Re (for the large scale velocity) and the Nusselt number Nu are functions of Rayleigh number Ra and Prandtl number Pr. Specifically, there is strong evidence from various theories and experiments to suggest that the scaling laws $Nu \sim Ra^{\gamma}$ and $Re \sim Ra^{\beta}$ exist. The models presented here mainly concern calculating the values of the real number exponents γ and β.
Castaing et al [1] devised a model to explain their experimentally measured $\gamma = 0.282 \pm 0.006$. (N.B. Here, we have simplified the derivations as we are less concerned with other scalings. We have also adapted it to account for the effect of Prandtl number).
Three flow regions are identified: fluid breaks from the boundary layer and accelerates in the mixing zone to speed that allows the fluid to merge into the well-mixed central region with a large-scale stirring velocity and temperature fluctuations (much like a lava lamp, see FIG. 1).

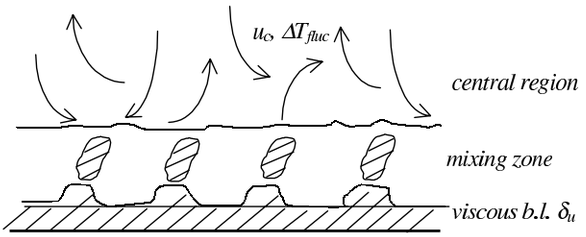


FIG. 1 For $Pr \gtrsim 1$. A stable thermal boundary layer cannot exist outside the viscous boundary layer. Detaching thermal filaments have a length-scale of δ_u.

The method uses mostly well-known relationships involving the large scale velocity, heat flux, both the thermal and kinetic boundary layer thicknesses, the dimensionless numbers, and the balancing of the buoyancy force and the viscous force where the filaments have accelerated to sufficiently high velocity to join the central region. The result from combining these relationships are $Nu_{(Pr \gtrsim 1)} \sim Ra^{2/7}$ and $Re_{(Pr \gtrsim 1)} \sim Ra^{3/7}Pr^{-2/3}$. We then apply the technique for the $Pr \lesssim 1$ case and derive $Nu_{Pr \lesssim 1} \sim Ra^{2/7}Pr^{2/7}$ and $Re_{(Pr \lesssim 1)} \sim Ra^{4/7}Pr^{-3/7}$. Results from more sophiticated theories and recent experiments (e.g. [2,3]) are used for comparisons.
As Grossmann & Lohse [2] have shown theoretically, and Niemela & Sreenivasan [4] with experiments, this is not the end of the story. We show that the Castaing et al model with slight modifications can produce a range of other scalings (and suggesting what processes or assumptions are involved) including $Nu_{(Pr \gtrsim 1)} \sim Ra^{1/4}Pr^{-1/12}$, $Re_{(Pr \gtrsim 1)} \sim Ra^{1/2}Pr^{-5/6}$, $Nu_{(Pr \lesssim 1)} \sim Ra^{1/5}Pr^{1/5}$, $Re_{(Pr \lesssim 1)} \sim Ra^{2/5}$, and even the classical so-called ultimate regime $Nu_{(Pr \lesssim 1)} \sim Ra^{1/2}Pr^{1/2}$. The last scaling, incidentally, agrees with Grossmann & Lohse's suggestion that the ultimate regime may exist only in small enough Prandtl and large enough Rayleigh number.

HEAT TRANSFER IN ENCLOSURE WITH THROUGHFLOW

In this section, we are interested in how forced convections affect the scaling laws. An enclosure similar to that in Rayleigh-Bénard convections, but with inlet and outlet throughflow, is being considered (FIG. 2). We use techniques similar to those described above, the main adaption being that in the forced convections, the inertial force balances the viscous force instead of the balance of buoyancy and viscous forces as in free convections.

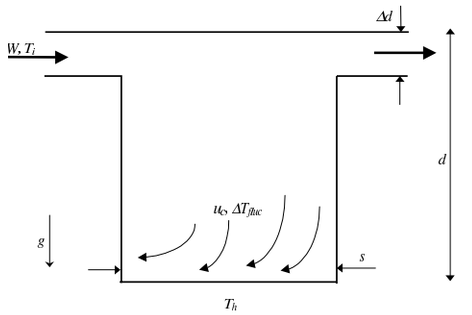
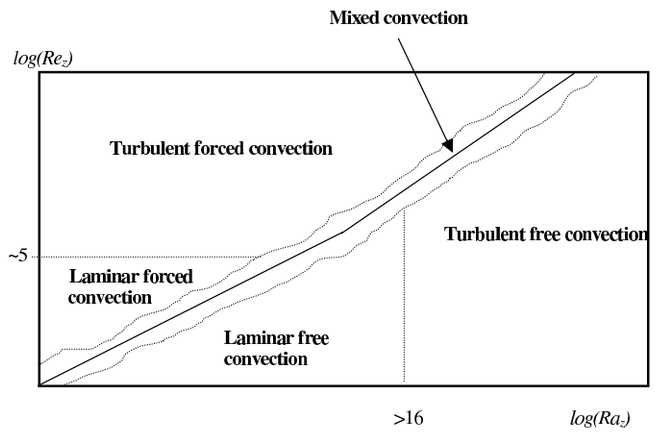


FIG. 2 A stationary cavity with heating from below and throughflow of cooling air with speed W and temperature T_i.

Scaling laws for the regimes of forced convections and turbulent (or laminar) boundary layer, free convections and turbulent (or laminar) boundary layer, and mixed convections are derived. The boundaries delineating the different regimes are obtained too. FIG. 3 summarises the results in a Reynolds number vs. Rayleigh number phase diagram.



Correlations for the different regimes:

Turbulent forced convection: $Nu_z \sim Re_z^{3/4}$
$Nu_z \sim Ra_z^{1/3} Pr^{-2/3}$

Laminar forced convection: $Nu_z \sim Re_z^{1/2}$
$Nu_z \sim Ra_z^{1/5}$

Turbulent free convection: $Nu_z \sim Ra_z^{1/2} Pr^{1/2}$
$Nu_z \sim Re_z^{1/2} Pr^{1/3}$

Laminar free convection: $Nu_z \sim Ra_z^{1/4} Pr^{-1/12}$
$Nu_z \sim Re_z^{1/2} Pr^{1/3}$

FIG. 3 Convections regime diagram for enclosure with throughflow. That for the horizontal or vertical flat plate has similar delineations.

Not too surprisingly, the scalings and regimes are similar to those obtained by other methods for flows over a flat plate. The diagram indicates that many laboratory and computational studies are conducted in the laminar free convections and laminar forced convections regimes. The results thus obtained are combinations of $\gamma = 1/4$ and $\gamma = 1/5$ scalings.

References

[1] Castaing, B., Gunaratne, G., Heslot, F., Kadanoff, L., Libchaber, A., Thomae, S., Wu, X–Z., Zaleski, S. & Zanetti, G., Scaling of hard thermal turbulence in Rayleig–Bénard convection, *J. Fluid Mech.*, **204**:1–30, 1989.
[2] Grossmann, S. & Lohse, D., Scaling in thermal convection: a unifying theory, *J. Fluid Mech.*, **407**:27–56, 2000.
[3] Cioni, S., Ciliberto, S. & Sommeria, J., Strongly turbulent Rayleigh-Bénard convection in mercury: comparison with results at moderate Prandtl number, *J. Fluid Mech.*, **335**:111–140, 1997.
[4] Niemela, J.J. & Sreenivasan, K.R., Confined turbulent convection, *J. Fluid Mech.*, **481**:355–384, 2003.

ON FEATURES OF MAGNETIC CONVECTION IN FERROFLUID

A.A. Bozhko, E. N. Beresneva, G.F. Putin
Department of General Physics, Perm State University, 15 Bukirev St., 614990, Perm, Russia

Summary Experiments were performed to examine the influence of external homogeneous magnetic field on ferrofluid convection. The results indicate that with the help of a magnetic field it is possible to control the stability and the form of convection motions. A number of non-linear regimes of convection, e.g. spiral-defect chaos, blinking and localized states were observed.

Magnetically driven convection in insulating media is actively investigated last years due to uses in the field of materials processing, e.g. crystal growth from protein solution and paramagnetic melts. The magnetic body force in magneto-polarized liquids is not the pondermotive force of magnetohydrodynamics, which requires a conducting fluid, but arises simply from the force of a nonuniform magnetic field on the molecular dipoles. This force is independent of gravity and its greatest utility will surely be in microgravity environments. However, for diamagnetic and paramagnetic materials, the pondermotive force exerted by a typical magnet is insignificant compared to gravity-induced buoyancy one. Therefore, a ferrofluids (colloidal suspension of monodomain particles), which has the susceptibility thousand times higher then natural fluids, are very convenient medium for ground-based modeling of magnetic convection.
The experiment was performed to examine the influence of external homogeneous magnetic fields on convective instability, heat transfer and flow patterns in ferrofluid layer heated from one wide side and cooled from another in a range of inclination angles from $\alpha = 0^0$ (heating from below) to 180^0 (heating from above). Visualization of flow structures is provided by a temperature-sensitive liquid crystal. The heat transport was measured by integral or local temperature sensor.
The influence of an externally applied magnetic field upon a buoyant convection within a magnetic fluid is characterized by two main factors. The first one is the driving force connected with a spatial variation in magnetization and it is realized in transversal field. The second factor is comparatively weak suppressive force arising due to interaction between applied field and distortions of magnetization induced by a convection motion. The demagnetizing effect is primarily researched as related to horizontal fluid layer subjected to a longitudinal field.
The experiment also shown that the sedimentation effects due to the settling of magnetic particles and their aggregates in gravity field can play the material role in magnetic fluid convection. The competitive action of thermal and concentration density gradients results in oscillatory and traveling wave, mostly spatiotemporally chaotic, convection in the entire region of control parameters [1]. Besides, under definite conditions the gradients of concentration nature may influence on convection instability. For example, in the absence of magnetic field in contrast to a single component fluid, the thermal convection in ferrofluid appears “hard” and with hystersis, and the patterns consist of disordered convection rolls and cells, which prominently feature the persistent spontaneous appearance and disappearance of spirals irregularly in time and in space (fig. 1(a)).
At laboratory tests to intensify the magnetic body forces in comparison with gravity buoyancy ones it is necessary to create the conditions when magnetic Rayleigh number $Ra_M = \mu_0(\beta_m M\Delta Th)^2/\rho\nu a(1+\chi)$ exceeds or compares with gravitational parameter $Ra = g\beta\Delta Th^3/\nu a$. Here β_m, M, ν, χ, a are relative pyromagnetic coefficient, magnetization, kinematic viscosity, differential susceptibility, thermal conductivity of magnetic fluid, μ_o -permeability of free space, ΔT - temperature difference across the layer, h – layer thickness, g and β - acceleration due to gravity and thermal expansion coefficient. The ratio $Ra_M/Ra \sim M^2\Delta T/h$ shows that it is need to use the layers with small thickness, the great temperature drops and liquids with high magnetization.

Ferrofluid convection in the presence of transversal magnetic field

The experiments on convection instability of horizontal ferrofluid layer in the presence of transversal magnetic field revealed that the behaviour of system strongly depends on value of magnetic Rayleigh number. To control Ra_M the colloids with different values of magnetic saturation M_S, i.e. with the different concentrations of magnetic phase, are taken in our experiments. Under concept overview [2], in concentrated ferrofluid with $M_S = 48$ kA/m and $Ra_M \sim 3\cdot10^3$ the driving forces prevail over suppress ones. In this case the magnetic forces facilitate the onset of convection and increase its intensity of motion. At moderate magnetic fields critical temperature difference of convection onset decreases twice and heat transport across fluid layer is intensified three times even under layer heating from above. Under inclination of ferrofluid layer from $\alpha = 0^0$ to 180^0 the magnetic field also renders destabilising effect on the development of Rayleigh roll motion.
In weak concentration colloid ($M_S = 18$ kA/m), when $Ra_M \sim 50$, the concentration drops of density overwhelm thermomagnetic and buoyancy stirring and begin to render essential stabilizing influence on the convective instability. In the presence of magnetic field the convection starts via subcritical bifurcation and with hysteresis; critical temperature differences and depth of hysteresis increase with the rise of magnetic field strength. The rate of fluid movement and the heat transfer at the heating from below are distinctly decreased.
One should note that unicellular buoyancy driven shear flow in a vertical layer subjected to transversal magnetic field breaks down due to excitation of the thermomagnetic rolls, aligned with the direction of the basic motion. Thus, in this situation the magnetic field influences on the instability, heat transfer but also on structure of secondary flow.

Ferrofluid convection in the presence of longitudinal magnetic field

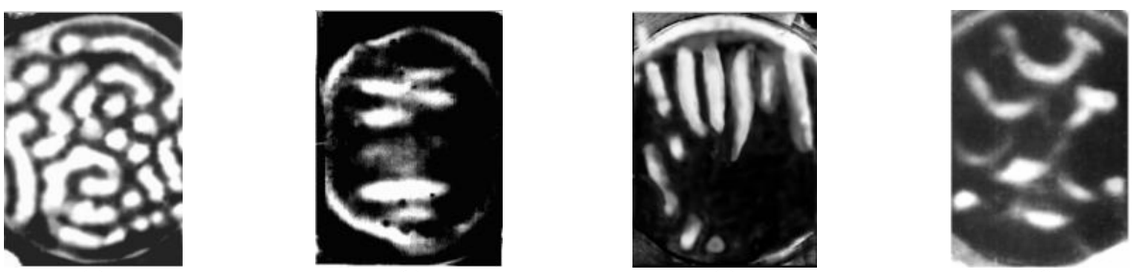
In accordance with the theory [3], the convection threshold in horizontal ferrofluid layer heated from below and subjected to longitudinal magnetic field does not depend upon magnetic field strength and the convection rolls in magnetic field align themselves so that their axes tend to be parallel to the imposed field. However, in contrast to linear theory in the entire region of control parameters only oscillatory traveling wave convection is observed. The confined states when the regions with conductivity and convection heat transfer are irregular changed in different parts of container occur not far from the onset of convection (fig. 1(b)). At highest values of control parameters the traveling rolls known as "blinking state" [4] arise.

Ferrofluid convection in an inclined layer

A similar orientation effect as in the case of a longitudinal magnetic field occurs in a liquid stream in the presence of Rayleigh instability. The thermally driven shear flow in an inclined layer draws up convection rolls in the direction of inclination. In the absence of magnetic field the multiplicity of nonlinear wave regimes as in the case of longitudinal magnetic field are observed (fig. 1(c)). The repeated transients involving roll convection and pure shear flow are also revealed.

Interaction of gravitational and magnetic mechanisms of convection in an inclined layer

In contrast to the horizontal layer, the action of longitudinal magnetic field orientated perpendicular to flux velocity of base shear motion can lead to completely stabilization of Rayleigh roll convection in the case of inclined layer. Near the stability boundaries of basic thermally driven shear flow the complicated patterns and different types of chaotic localized states (or pulses) take place (fig. 1(d)) because of hydrodynamic and magnetic interplay.



(a) (b) (c) (d)

Figure 1. Liquid crystal surface photographs for Rayleigh convection in ferrofluid layer at: (a) $\alpha = 0°$, $H = 0$, $\Delta T/\Delta T_C = 1.5$; (b) $\alpha = 0°$, $H = 17$ kA/m, $\Delta T/\Delta T_C = 1.3$; (c) $\alpha = 15^0$, $H = 0$, $\Delta T/\Delta T_C = 1.8$; (d) $\alpha = 25°$, $H = 1$ kA/m, $\Delta T/\Delta T_C = 2$; $\Delta T_C = 5.1$ K – critical temperature difference of the onset of Rayleigh convection in the absence of magnetic field. Temperature drop from cool (black) to warm (white) liquid is approximately 3 K. Each light (dark) strip in photographs corresponds to the same handedness of two neighboring rolls. Magnetic field is directed aflat to the plane of photographs from the left to the right.

CONCLUSION

Thus, the ferrofluid may be used as modeling fluid to study thermomagnetic convection mechanism that can act in all diamagnetic and paramagnetic media. On the other hand, it offers a new magnetic field controllable system for the study of so-called spatio-temporal chaos near the convection threshold [5], which previously have been studied experimentally in gases, binary mixtures, nematic liquid crystals and so on.

The research described in this publication was made possible in part by Russian Foundation for Basic Research under grant 04-01-00586 and Award No PE-009-0 of the U.S. Civilian Research & Development Foundation for the Independent States of the Former Soviet Union (CRDF).

References

[1] Bozhko A.A., Putin G.F.: Heat transfer and flow patterns in ferrofluid convection. *Magnetohydrodynamics*, **39**: 147 – 169, 2003.

[2] Finlayson B.A.: Convective instability of ferromagnetic fluids. *J. Fluid Mechanics*, **40**: 753 – 767, 1970.

[3] Bashtovoi V.G., Pavlinov M.I.: Convective instability of a horizontal ferrofluid layer in longitudinal magnetic field. *Research on convective and wave processes in ferrofluids*, Minsk, USSR: 74 – 79, 1975.

[4] Bestehorn M., Friedrich R., Haken H. Pattern formation in convective instabilities. *Int. J. Modern Phys. B*, **4**: 345 - 400, 1990.

[5] Ahlers G., Cannell D.S., Dennin M.: Spatiotemporal chaos in electroconvection. *Science*, **272**: 388 – 390, 1996.

XXI ICTAM, 15–21 August 2004, Warsaw, Poland

MULTIPLICITY OF PATTERNS IN CYLINDRICAL CONVECTION

Katarzyna Boronska*, Laurette S. Tuckerman*
*Laboratoire d'Informatique pour la Mécanique et les Sciences de l'Ingénieur (LIMSI-CNRS), B.P. 133, 91403 Orsay, France

Summary The experiments of Hof, Mullin and Lucas on Rayleigh-Bénard convection in a cylindrical system are simulated numerically using a pseudospectral three-dimensional code. We confirm that for their parameter values, there exist multiple stable solutions. Starting from a perturbed conductive state, we obtain different final patterns, depending on the Rayleigh number. We then use these flows to initialize the simulations for other Rayleigh numbers. In this way we obtain many different stable solutions for the same Rayleigh number – two, three or four parallel rolls, a three-spoke pattern and even an axisymmetric state.

CYLINDRICAL RAYLEIGH-BÉNARD CONVECTION

The Rayleigh-Bénard instability in a fluid layer heated from below and cooled from above is one of the most ancient and well-known prototypes of pattern formation. When the horizontal dimensions are comparable to the height of the fluid, the shape of the container plays a crucial role in determining the patterns formed. In a vertical cylinder, the Rayleigh number thresholds for onset of convection from the motionless conductive state have been already well described [1]. Secondary bifurcations leading to other patterns have been studied numerically for a few cases [2, 3, 4, 5]. Experiments by Hof *et al.*[6] produced a large number of convective patterns by increasing and decreasing the Rayleigh number in a variety of ways. For example, five different patterns could be obtained at $Ra = 14200$. Our aim is to reproduce, understand, and extend these results.

NUMERICAL SIMULATION

In our numerical code [7], the Navier-Stokes equations are integrated by a classical pseudospectral method, where the velocity and temperature fields are represented using Chebyshev polynomials in the radial and vertical directions and Fourier series in the azimuthal direction. The number of gridpoints or modes is 36 in the radial, 80 in the azimuthal and 18 in the vertical direction. The time-stepping scheme is the Adams-Bashforth formula for the nonlinear term and Crank-Nicolson formula for the linear term. An influence matrix method was used to impose incompressibility.
Matching the parameters in [6], we set the Prandtl number $Pr \equiv viscosity/thermal\ diffusion$ to 6.7 (that of water) and the aspect ratio $\Gamma \equiv radius/height$ to 2.0. We have performed a sequence of simulations, varying the initial state and the Rayleigh number, in order to find the asymptotic state for each configuration.

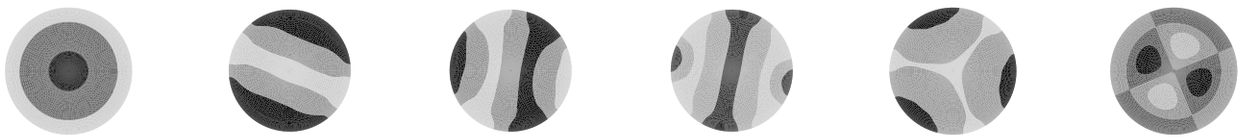
RESULTS

Sudden start from a quasi-conductive state

We initialized the simulations with a perturbed conductive solution satisfying the boundary conditions. Depending on the Rayleigh number, this state evolves towards different flows – see the left part of the diagram on fig. 2.
For $Ra \lesssim 1900$, the initial perturbation decays to zero, resulting in the conductive state. For Ra near 2000, the final state is a convective state with symmetry D_2, which we will call the 'pizza state' (see fig. 1f). For Ra between 3000 and 9000, the system evolves towards a four-roll state. For Rayleigh numbers between 10000 and 20000, the final solution is always a three-roll state, whose roll boundaries become thinner and more curved with increasing Ra. Finally, for $Ra \approx 23000$, the final pattern consists of three radial spokes that we will refer to as the 'mercedes pattern'.

Evolution from convective states

We now use the convective states described above as initial states and change the Rayleigh number. The results of the simulations are represented on fig. 2. For example, we used the mercedes pattern obtained for $Ra = 23000$ as an initial field at $Ra = 15000$. The resulting final solution was still of mercedes form. In other words, the Rayleigh number



(a) torus (b) 2 rolls (c) 3 rolls (d) 4 rolls (e) mercedes (f) pizza

Figure 1. Stable steady flows obtained by the nonlinear simulation. Temperature variation on a horizontal slice at mid-height of the cylinder. Dark areas represent hotter ascending fluid and bright areas colder descending fluid. For each flow, there also exists an equivalent form, in which the signs of the temperature variation and vertical velocity are reversed.

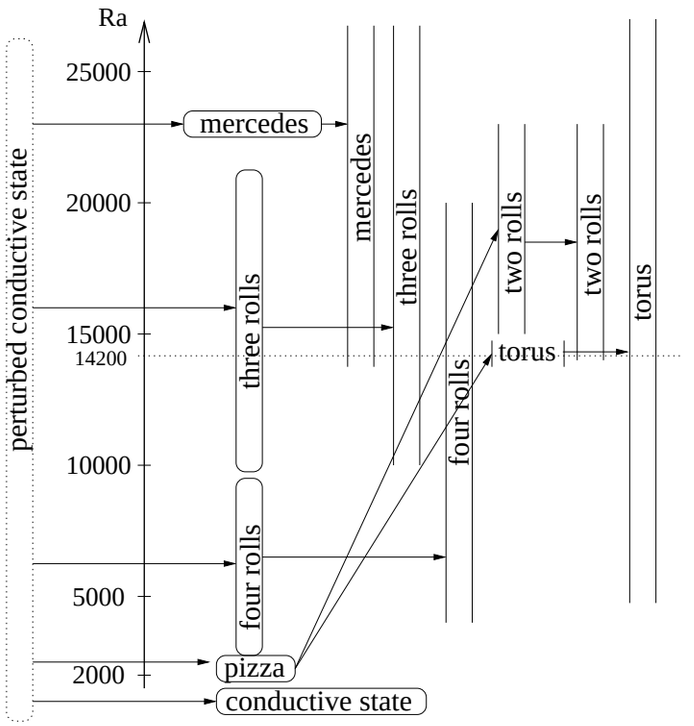


Figure 2. Schematic diagram of the dependence of the final flow pattern on Rayleigh number and on initial state. A first series of simulations used a perturbed conductive state as initial condition over a range of Ra to obtain the patterns listed in the first column. A second series used these patterns as initial conditions, altering the value of Ra. For $Ra = 14200$ we obtain five different final states, including an axisymmetric flow.

range over which the mercedes pattern remains stable is much larger than the range over which this pattern is obtained via evolution from the perturbed conductive state. The same is true for the three-roll and four-roll states. We have not ascertained the stability range for the pizza pattern. However, a large increase of Ra above 15000 leads to a transition to a two-roll state and, interestingly, for $Ra \approx 14000$, to an axisymmetric state consisting of one toroidal roll. This toroidal state remains stable over a very large Rayleigh-number range.

CONCLUSION

We have successfully simulated numerically all of the steady patterns obtained experimentally by Hof. For the same Rayleigh number ($Ra = 14200$) we observed five stable steady solutions: a toroidal roll; two, three and four parallel rolls; and a three-spoke (‘mercedes’) pattern. An additional ’pizza’ pattern is observed at lower Ra. Despite the great variety of flows we have obtained, we are far from an exhaustive study even for this specific configuration of control parameters. It is very likely that other stable solutions exist which we did not observe because they were topologically too far from any of our initial conditions. We also found many transitional patterns that should be described in the future.
There is still much work to be done in classifying the patterns and determining their exact stability limits. Our nonlinear simulations should be refined by a linear analysis, in order to insure that a long-lived pattern is really asymptotically stable. Finally, we hope to construct a bifurcation diagram detailing and organizing the various patterns.

Computations were performed on the NEC-SX5 at the IDRIS-CNRS supercomputer center, project 1119.

References

[1] J.C. Buell and I. Catton. The effect of wall conduction on the stability of a fluid in a right circular cylinder heated from below. *Journal of Heat Transfer*, 105:255, 1983.
[2] M. Wanschura, H. C. Kuhlmann, and H. J. Rath. Three-dimensional instability of axisymmetric buoyant convection in cylinders heated from below. *J. Fluid Mech.*, 326:399–415, 1996.
[3] R. Touihri, H. Ben Hadid, and D. Henry. On the onset of convective instabilities in cylindrical cavities heated from below. i. pure thermal case. *Phys. Fluids*, 11:2078–2088, 1999.
[4] Sten Rüdiger and Fred Feudel. Pattern formation in Rayleigh Bénard convection in a cylindrical container. *Phys. Rev. E*, 62:4927–4931, 2000.
[5] S. S. Leong. Numerical study of Rayleigh-Bénard convection in a cylinder. *Numerical Heat Transfer, Part A*, 41:673–683, 2002.
[6] B. Hof, G. J. Lucas, and T. Mullin. Flow state multiplicity in convection. *Phys. Fluids*, 11:2815–2817, 1999.
[7] L.S. Tuckerman. Divergence-free velocity fields in nonperiodic geometries. *J. Comput. Phys.*, 80:403–441, 1989.

XXI ICTAM, 15–21 August 2004, Warsaw, Poland

LARGE-SCALE SEMI-ORGANIZED STRUCTURES IN GEOPHYSICAL TURBULENT CONVECTION

Tov Elperin*, Nathan Kleeorin*, Igor Rogachevskii*, Sergej Zilitinkevich**
*Department of Mechanical Engineering, Ben-Gurion University of Negev, POB 653, 84105 Beer-Sheva, Israel
**Department of Earth Sciences, Meteorology, Uppsala University, Uppsala, Sweden

Summary A new mean-field theory of turbulent convection is developed. In a shear-free turbulent convection the theory predicts the convective wind instability which causes formation of large-scale semi-organized fluid motions in the form of cells. The theory predicts also the convective-shear instability in a sheared turbulent convection which results in appearance of large-scale semi-organized convective rolls. This instability can cause also a generation of convective-shear waves which have a nonzero hydrodynamic helicity. The increase of shear promotes excitation of the convective-shear instability. Predictions of this theory are in a good agreement with the modern knowledge about the atmospheric convective boundary layer and observed semi-organized structures.

In the last decades it has been recognized that the very high Rayleigh number atmospheric convective boundary layer (CBL) has more complex nature than might be reckoned. Besides the fully organized component naturally considered as the mean flow and the chaotic small-scale fluctuations, one more type of motion has been discovered, namely, long-lived large-scale structures, which are neither turbulent nor deterministic [1,2]. These semi-organized structures considerably enhance the vertical transport and render it essentially non-local in nature. In the atmospheric shear-free convection, the structures represent three-dimensional Benard-type cells (cloud cells) composed of narrow uprising plumes and wide downdraughts. They embrace the entire convective boundary layer (~ 2 km in height) and include pronounced large-scale (~ 3 km in diameter) convergent flow patterns close to the surface [1,2]. In sheared convection, the structures represent CBL-scale rolls (cloud streets) stretched along the mean wind. Life-times of the semi-organized structures are much larger than the turbulent time scales [1,2]. Thus, these structures can be treated as comparatively stable, quasi-stationary motions, playing the same role with respect to a small-scale turbulence as the mean flow.

In spite of a number of studies, the nature of large-scale semi-organized structures is poorly understood. The Rayleigh numbers, Ra, based on the molecular transport coefficients are very large (of the order of $10^{11} - 10^{13}$). This corresponds to fully developed turbulent convection in atmospheric flows. At the same time the effective Rayleigh numbers, based on the turbulent transport coefficients are not high, e.g., they are less than the critical Rayleigh numbers required for the excitation of large-scale convection. Therefore, the emergence of large-scale structures which are observed in the atmospheric flows seems puzzling.

The main goal of this study is to suggest a mechanism for formation of large-scale semi-organized structures. Traditional theoretical models of the boundary-layer turbulence, such as the Kolmogorov-type closures and similarity theories (e.g., the Monin-Obukhov surface-layer similarity theory) imply two assumptions: (i) Turbulent flows can be decomposed into two components of principally different nature: fully organized (mean-flow) and fully turbulent flows. (ii) Turbulent fluxes are uniquely determined by the local mean gradients. For example, the turbulent flux of entropy (or potential temperature) is given by $\langle s\mathbf{u}\rangle = -\kappa_T \boldsymbol{\nabla}\bar{S}$, where κ_T is the turbulent thermal conductivity, $\bar{S}$ is the mean entropy, $\mathbf{u}$ and s are fluctuations of the velocity and entropy, respectively. However, the mean velocity gradients can affect the turbulent flux of entropy. The reason is that additional essentially anisotropic velocity fluctuations can be generated by tangling of the mean-velocity gradients with the Kolmogorov-type turbulence. The source of energy of this "tangling turbulence" is the energy of the Kolmogorov turbulence. The tangling turbulence is strongly anisotropic and has a steeper spectrum ($\propto k^{-7/3}$) than a Kolmogorov turbulence. The anisotropic velocity fluctuations of tangling turbulence were studied in the first by Lumley (1967). It is shown in this study that the tangling turbulence can cause formation of semi-organized structures due to the excitation of large-scale instability. In particular, the tangling turbulence contributes to the turbulent flux of entropy. Calculations based on the Navier-Stokes equation and the entropy evolution equation formulated in the Boussinesq approximation yield the following expression for the turbulent flux of entropy $\boldsymbol{\Phi} \equiv \langle s\mathbf{u}\rangle$:

$$\boldsymbol{\Phi} \;=\; \boldsymbol{\Phi}^* - (\tau_0/6)[5\alpha(\boldsymbol{\nabla}\cdot\bar{\mathbf{U}}_\perp)\boldsymbol{\Phi}^*_\parallel - (\alpha+3/2)(\bar{\boldsymbol{\omega}}\times\boldsymbol{\Phi}^*_\parallel) - 3(\bar{\boldsymbol{\omega}}_\parallel\times\boldsymbol{\Phi}^*)]\,, \tag{1}$$

where $\bar{\mathbf{U}} = \bar{\mathbf{U}}_\perp + \bar{U}_z\mathbf{e}$ is the mean velocity, $\mathbf{e}$ is the vertical unit vector, $\bar{\boldsymbol{\omega}} = \boldsymbol{\nabla}\times\bar{\mathbf{U}}$ is the mean vorticity, $\bar{\boldsymbol{\omega}}_\parallel = \bar{\omega}_z\mathbf{e}$ is the vertical mean vorticity, τ_0 is the correlation time of the Kolmogorov turbulence corresponding to the maximum scale of turbulent motions, $\boldsymbol{\Phi}^*$ is the turbulent flux of entropy which is caused by the contribution of the Kolmogorov turbulence and it is independent of the mean velocity gradients $\nabla_i\bar{U}_j$, $\boldsymbol{\Phi}^*_\parallel = \Phi^*_z\mathbf{e} = -\kappa_T\boldsymbol{\nabla}_z\bar{S}$, $\alpha = (1+4\xi)/(1+\xi/3)$ is the degree of thermal anisotropy of the background turbulent convection (without mean-velocity gradients), $\xi = (l_\perp/l_z)^{2/3} - 1$. The turbulent flux of entropy can be obtained even from simple symmetry reasoning. Here $l_\perp$ and l_z are the horizontal and vertical scales in which the correlation function $\Phi^{(0)}_z(\mathbf{r}) = \langle s(\mathbf{x})\,u_z(\mathbf{x}+\mathbf{r})\rangle$ tends to zero. In the isotropic case, $l_\perp = l_z$ the parameter $\xi = 0$ and $\alpha = 1$. For $l_\perp \ll l_z$ the parameter $\xi = -1$ and $\alpha = -9/2$. The maximum value $\xi_{\max}$ of the parameter ξ is $\xi_{\max} = 2/3$ for $\alpha = 3$. Thus, for $\alpha < 1$ the thermal structures have the form of columns or thermal jets ($l_\perp < l_z$), and for $\alpha > 1$ there exist the ‘’pancake” thermal structures ($l_\perp > l_z$) in the background turbulent convection.

Now let us discuss the mechanisms of formation of semi-organized structures by a large-scale instability. The mechanism of the convective wind instability, associated with the second term $\boldsymbol{\Phi} \propto -\tau_0\alpha(\boldsymbol{\nabla}\cdot\bar{\mathbf{U}}_\perp)\boldsymbol{\Phi}^*_\parallel$ in the expression for the turbulent flux of entropy [see Eq. (1)], in the shear-free turbulent convection at $\alpha > 0$ is as follows. Perturbations of the vertical mean velocity $\bar{U}_z$ with $\partial\bar{U}_z/\partial z > 0$ have negative divergence of the horizontal velocity , i.e., $\mathrm{div}\,\bar{\mathbf{U}}_\perp < 0$ (provided that $\mathrm{div}\,\bar{\mathbf{U}} \approx 0$). This results in the vertical turbulent flux of entropy and causes an increase of the mean entropy. On the other hand, the increase of the mean entropy increases the buoyancy force and results in the increase of the vertical velocity $\bar{U}_z$ and excitation of the large-scale instability. Similar phenomenon occurs in the regions with $\partial\bar{U}_z/\partial z < 0$ whereby $\mathrm{div}\,\bar{\mathbf{U}}_\perp > 0$. This causes a downward flux of the entropy and the decrease of the mean entropy. The latter enhances the downward flow and results in the instability which also causes formation of a large-scale semi-organized convective cell structure (convective wind). Thus, nonzero $\mathrm{div}\,\bar{\mathbf{U}}_\perp$ causes redistribution of the vertical turbulent flux of entropy and formation of regions with large vertical fluxes of entropy. Thereby the regions with

$\mathrm{div}\,\bar{\mathbf{U}}_\perp < 0$ are separated by the regions with low vertical flux of entropy with $\mathrm{div}\,\bar{\mathbf{U}}_\perp > 0$. This results in a formation of a large-scale circulation of the velocity field. Another mechanism of the convective wind instability is associated with the third term [proportional to $(\alpha + 3/2)(\bar{\boldsymbol{\omega}} \times \boldsymbol{\Phi}^*_\parallel)$] in the expression (1) for the turbulent flux of entropy when $\alpha < -3/2$. This term describes the horizontal flux of the mean entropy. The latter results in increase (decrease) of the mean entropy in the regions with upward (downward) fluid flows. On the other hand, the increase of the mean entropy causes the increase of the buoyancy force, the mean vertical velocity $\bar{U}_z$ and the mean vorticity $\bar{\boldsymbol{\omega}}$. Hence the large-scale convective wind instability is excited. The second term in the turbulent flux of entropy at $\alpha < -3/2$ causes a decrease of the growth rate of the instability because, when $\alpha < -3/2$, it implies a downward turbulent flux of entropy in the upward flow. This decreases both, the mean entropy and the buoyancy force. Note that, when $\alpha < -3/2$, the thermal structure of the background turbulence has the form of a thermal column. Our analysis, based on the linearized momentum equation and the equation for the entropy with the derived expression for the turbulent flux of entropy (1), showed that the growth rate $\gamma_{\rm inst}$ of the convective wind instability of long-wave perturbations $[\beta \equiv (l_0 K)^{-2} \gg 1]$ is given by $\gamma_{\rm inst} \propto \nu_T K^2 \sqrt{\beta}\,|\sin\theta|\,[\alpha - 3/8 - (5\alpha/4)\sin^2\theta]^{1/2}$, where θ is the angle between $\mathbf{e}$ and the large-scale wave vector $\mathbf{K}$ of small perturbations, ν_T is the turbulent viscosity and l_0 is the maximum scale of turbulent motions. We considered here an isentropic basic reference state. For large β the growth rate of the instability is proportional to the wave number K (i.e., $\gamma_{\rm inst} \propto K u_0$) and the instability occurs when $\alpha(5\cos^2\theta - 1) > 3/2$. Here u_0 is the characteristic turbulent velocity in the maximum scale of turbulent motions. Thus there are two ranges for the excitation of the instability, i.e., the first range is for $\alpha_* < \alpha < 3$ and the second range is for $-9/2 < \alpha < \alpha_*$, where $\alpha_* = 3/[2(5\cos^2\theta - 1)]$, and we took into account that the parameter α varies in the interval $-9/2 < \alpha < 3$. The first range for the instability corresponds to the angles $3/10 \le \cos^2\theta \le 1$ (the aspect ratio $0 < L_z/L_\perp < 1.5$), and the second range for the instability corresponds to the angles $0 \le \cos^2\theta < 2/15$ (the aspect ratio $2.6 < L_z/L_\perp < \infty$), where $L_z/L_\perp \equiv K_\perp/K_z = \tan\theta$. Our analysis showed that the maximum growth rate of the instability is attained at the scale of perturbations $L_m \approx 10\,l_0$, and the characteristic time of excitation of this instability is of the order of $(20 - 30)\tau_0$. Thus the typical length and time scales of the convective-wind motions are much larger than the turbulence scales. This justifies separation of scales which is required for the description of the semi-organized structures in terms of a mean flow.

In a sheared turbulent convection the mechanism of the convective-shear instability is associated with the last term in the expression (1) for the turbulent flux of entropy $[\boldsymbol{\Phi} \propto \tau_0(\bar{\boldsymbol{\omega}}_\parallel \times \boldsymbol{\Phi}^*)]$. Here $\boldsymbol{\Phi}^* = \Phi^*_z \mathbf{e} - \tau_0 \Phi^*_z (d\bar{\mathbf{U}}^{(0)}(z)/dz)$, the second term in the expression for $\boldsymbol{\Phi}^*$ describes the counter-wind heat flux and $\bar{\mathbf{U}}^{(0)}(z)$ is the imposed horizontal large-scale flow velocity (e.g., a wind velocity). The mechanism of the convective-shear instability is as follows. The vorticity perturbations generate perturbations of entropy. Indeed, for two vortices with opposite directions of the vorticity $\bar{\boldsymbol{\omega}}_\parallel$, the turbulent flux of entropy is directed towards the boundary between the vortices. The latter increases the mean entropy between the vortices. Such redistribution of the mean entropy causes increase of the buoyancy force and formation of upward flows between the vortices. These vertical flows generate vorticity. Thus the convective-shear instability is excited. The growth rate of the instability of long-wave perturbations is given by $\gamma_{\rm inst} \simeq \nu_T K^2 (\beta\lambda \sin^2\theta)^{2/3}$, where we considered turbulent convection with a linear shear $\bar{\mathbf{U}}^{(0)} = (\lambda/\tau_0)\, z\, \mathbf{e}_y$ and a nonzero vertical flux of entropy $\boldsymbol{\Phi} = \Phi^*_z\, \mathbf{e}$. Here λ is a dimensionless parameter which characterizes the shear. This instability causes formation of large-scale semi-organized fluid motions in the form of rolls align along the imposed mean velocity $\bar{\mathbf{U}}^{(0)}$. The instability can also result in generation of the convective-shear waves with the frequency $\Omega \simeq \sqrt{3}\nu_T K^2 (\beta\lambda \sin^2\theta)^{2/3}$. These convective-shear waves propagate perpendicular to convective rolls. This finding is in agreement with observations in the atmospheric convective boundary layer, whereby the waves propagating perpendicular to cloud streets have been detected [3]. Remarkably, that the flow in the convective-shear wave has a nonzero hydrodynamic helicity. For perturbations with $K_x = 0$ the convective-shear instability does nor occur. However, for the perturbations with $K_x = 0$, the convective wind instability can be excited, and it is not accompanied by the generation of the convective-shear waves. Our analysis showed that there are two ranges for the excitation of the instability. However, even a small shear causes an overlapping of these two ranges, and the increase of shear (λ) promotes the convective-shear instability with the growth rate $\gamma_{\rm inst} \propto K^{2/3}$, and the frequency of the generated convective-shear waves is $\Omega \propto K^{2/3}$.

Now let us compare the obtained results with the properties of semi-organized structures observed in the atmospheric convective boundary layer. The semi-organized structures are observed in the form of rolls (cloud streets) or three-dimensional convective cells (cloud cells). Rolls usually align along or at angles of up to 10° with the mean horizontal wind of the convective layer, their lengths vary from 20 to 200 km, the widths from 2 to 10 km, and convective depths from 2 to 3 km [1,2]. The typical value of the aspect ratio $L_z/L_\perp \approx 0.14 - 1$. The ratio of the minimal size of the structure to the maximum scale of turbulent motions $L/l_0 = 10 - 100$. The characteristic life time of rolls varies from 1 to 72 hours. Rolls may occur over water surface or land surfaces. The suggested theory predicts the following parameters of the convective rolls: the aspect ratio $L_z/L_\perp$ ranges from very small to 1, and $L/l_0 = 10 - 100$. The characteristic time of formation of the rolls $\sim \tau_0/\gamma_{\rm inst}$ varies from 1 to 3 hours. The life time of the convective rolls is determined by a nonlinear evolution of the convective-shear instability. The latter is a subject of a separate ongoing study. Convective cells may be divided into two types: open and closed [1]. Open-cell circulation has downward motion and clear sky in the cell center, surrounded by cloud associated with upward motion. Closed cells have the opposite circulation. Both types of cells have diameters ranging from 10 to 40 km and aspect ratios $L_z/L_\perp \approx 0.05 - 1$, and both occur in a convective layer with a depth of about 1 to 3 km [1,2]. The ratio of the minimum size of the structure to maximum scale of turbulent motions $L/l_0 = 5 - 20$. The developed theory predicts the following parameters of the convective cells: the aspect ratio $L_z/L_\perp$ ranges from very small to 1, and $L/l_0 = 5 - 15$. The characteristic time of formation of the convective cells $\sim \tau_0/\gamma_{\rm inst}$ varies from 1 to 3 hours. Therefore the predictions of the developed theory are in a good agreement with observations of the semi-organized structures in the atmospheric convective boundary layer.

References

[1] Atkinson B. W. and Wu Zhang J.: Mesoscale Shallow Convection in the Atmosphere. *Rev. Geophys.* **34**, 403–431, 1996.

[2] Etling D. & Brown R. A.: Roll Vortices in the Planetary Boundary Layer: a Review. *Boundary-Layer Meteorol.* 65, 215–248, 1993.

[3] Brümmer B.: Roll and Cell Convection in Winter-Time Arctic Cold-Air Outbreaks. *J. Atmosph. Sci.*, **56**, 2613–2636, 1999.

NATURAL CONVECTION FOR ANOMALOUS DENSITY VARIATION OF WATER : NUMERICAL BENCHMARK

Tomasz Michałek[*], Tomasz A. Kowalewski[*], Bozidar Šarler[**]
[*] *Polish Academy of Sciences IPPT PAN, Swietokrzyska 21, PL 00-049 Warszawa, Poland*
[**] *Nova Gorica Polytechnic, Laboratory for Multiphase Processes, SI-5000 Nova Gorica, Vipavska 13, Slovenia*

Summary: A steady state natural convection in a differentially heated cavity for temperatures in a vicinity of the freezing point is used to investigate and compare performance of four different numerical methods: finite differences, finite volume, finite elements and mesh-free diffuse approximation method. A primary aim of the exercise is to define a new numerical benchmark solution for natural convection problems, which includes challenging configuration of strongly non-linear buoyancy term. This configuration is used to test performance of two popular commercial codes (Fluent and Fidap) and to compare them with two "classical" finite difference codes and the new promising mesh-free implementation.

PROBLEM FORMULATION

The accurate solution of natural convection flow in enclosures is a crucial task in a goal of achieving precise modelling of solidification problems. Serious discrepancies between numerical and experimental results encountered for a *simple* problem of ice formation in a differentially heated cavity [1] motivated us to revise reliability and performance of typical solvers used form simulating heat transfer phenomena. Traditionally such solvers are verified using reference solution defined by Graham de Vahl Davis [2] over 20 years ago. It describes steady state natural convection of a low Prandtl number (Pr=0.71), Boussinesq fluid in a differentially heated square cavity, with two isothermal and two adiabatic walls. It appears that this largely idealized configuration does not permit to depict bad performing schemes, especially for strong non-linear variation of the fluid density function.

The aim of this work is to formulate a new benchmark solution for verification of numerical codes employed for modelling ice formation problems. The proposed benchmark configuration concerns steady-state natural convection of water in the differentially heated square cavity. By setting the temperature range of isothermal walls close to the freezing point ($T_H = 10^oC$, $T_C = 0^oC$) and by adopting non-linear variation of the water density with temperature a challenging flow configuration with two counter-rotating re-circulation zones is obtained. The competing effects of positive and negative buoyancy force, and interacting layers of hot and cold liquid, create interesting and difficult to model flow pattern. The two circulations create nearly vertical stratification, separating fluid in the cavity into two regions separated by the density maximum. An interesting configuration for studying heat transfer in a thin, well defined mixing zone separating hot and cold region of the same fluid is obtained. The Rayleigh (Ra) and Prandtl (Pr) numbers describing investigated configuration are based on the fluid properties taken at the reference temperature and the cavity height (L=0.038m). Their values are $Ra=1.503 \cdot 10^6$, Pr=13.31. This configuration was employed in our previous studies of freezing of water [1].

Details of the benchmark solution are given elsewhere [3]. In the following, we present numerical results obtained for this configuration with two commercial codes, finite volume code Fluent (FLU) and finite element code Fidap (FID) [4], and compare them with the reference finite difference approximation code FRECON3V [5], being a revised, variable properties version of the classical FRECON (FRE) [2]. Finally performance of the new mesh-free numerical approach based on diffuse approximation method [6,7] is investigated and compared with the defined benchmark solutions. For sake of completeness of the most frequently used numerical methodologies, the benchmark is also used to verify performance of a second-order, finite difference, vorticity – streamfunction code SOLVSTR (STR).

NUMERCIAL ALGORITHMS AND SELCTION OF REFERENCE SOLUTIONS

Extensive mesh-sensitivity tests were performed for each of the five investigated codes and the result of the best performing algorithm are selected as a reference solution. Usual practice of comparing values of flow field parameters at few selected points is not adequate for verifying ability of a code to reproduce fine details of the flow structure. Our tests revealed that even small deviations (2% - 5%) from the reference solution, usually reported as *reasonable* or even *excellent* agreement, correspond to distinct changes of the flow pattern. Such changes become responsible for differences in the local mass and heat transfer in the system, and are not tolerable when phase change processes are present (e.g. freezing of water).

Hence, to obtain better insight into differences or similarities of the flow structures obtained from the different solvers, the second step of the verification procedure is proposed. It is based on calculating deviation of the velocity profiles extracted along three selected lines: horizontal and vertical centrelines, and the vertical line passing through the mixing zone at the cold wall (x=0.9). The mesh sensitivity analysis performed for five investigated codes led us to select as a reference, flow field obtained for the finite difference code FRECON3V on the uniform 201x201 mesh. The velocity and temperature profiles extracted along above mentioned lines are approximated with the high order polynomial and treated as a benchmark solution. The numerical values of the polynomial coefficients obtained permit to perform standard error analysis. An assessment on the accuracy of the solution is obtained calculating relative differences in terms of defined below standard deviations σ, evaluated for the polynomials describing benchmark profiles and corresponding values extracted from the interrogated solution. Nine indicators are defined and used to evaluate accuracy of the solutions: σ_{u1}, σ_{w1}, σ_{t1}, σ_{u2}, σ_{w2}, σ_{t2}, σ_{u3}, σ_{w3} and σ_{t3}. They describe standard deviations calculated for two

velocity components *U,W* and temperature *T* for profiles extracted at centre-lines Y=0.5, X=0.5, and vertical line X=0.9.

The proposed accuracy indicators can be easily used to assess performance of any numerical solutions, regardless of dimension of the mesh size, as well as to estimate the rate of convergence of successive solutions. Comparison of all tested algorithms was done. Figures 1 and 2 show mesh dependence of σ_{u1}, σ_{w1} for U,W velocity profiles at Y=0.5 and σ_{u2},σ_{w2} for U,W velocity profiles at X=0.5, respectively.

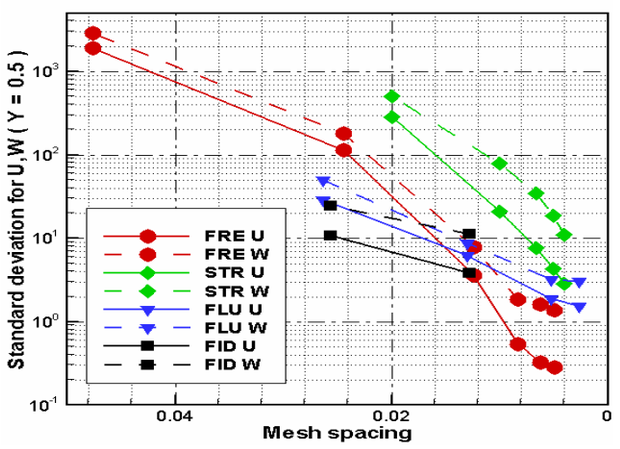


Figure 1

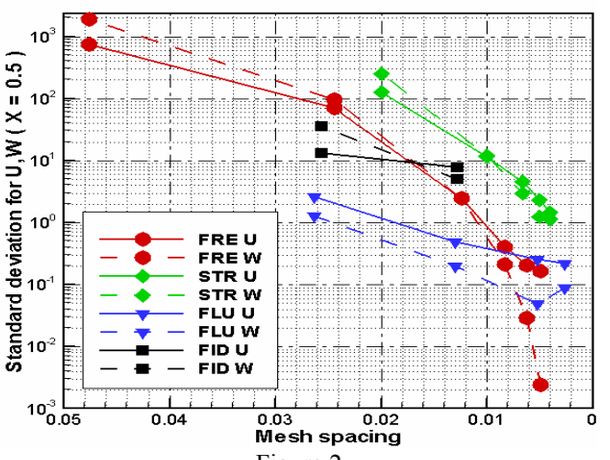


Figure 2

The value of σ_{u1} , σ_{w1} , σ_{u2} σ_{w2} , σ_{u3} , σ_{w3} , σ_{t1} ,σ_{t2} ,σ_{t3} for the finest mesh FRECON3V (red circle in Figure 1 and 2) was taken as a reference error indicator. Generously setting cut-off value for standard deviation equal 3 we are able in clear and straightforward manner decide whether an interrogated solution is close enough to the reference solution to be accepted.

CONCLUSIONS

New reference solution for testing numerical codes dealing with the natural convection is proposed. The solution is obtained for very fine mesh and used for competition with four other codes. Nine velocity profiles are extracted and given in form of high order polynomials. The measure of performance of the solutions in question is investigated in terms of the standard deviation of the corresponding velocity profiles.

Two commercial codes are verified using above method, along with a new mesh-free numerical approach as well as the classical finite difference approximation code. It appears that the defined measure of the code accuracy is very sensitive, allowing to detect minute deviations occurring in the velocity profiles. The precise analysis of defined convergence indicators allowed to ascertain that among tested four codes, only finest Fluent solution (blue triangle in Figure 1 and 2) was close enough to the reference solution to be acceptable. It is noteworthy that the Fluent solution was obtained on the mesh of 380x380 nodes, almost twice as dense as the reference solution. All other solutions even obtained for very fine meshes, appeared to be inaccurate, according to the defined measure.

The new, promising approach based on diffuse approximation in mesh-free method turned out to perform intolerable slow in comparison with classical method. Obviously due to the simple geometry we could not observe any advantages of mesh-free approach. The aim of this comparison was solely verification of performance of the method applied to natural convection problem. Future work is necessary to improve initial phase of this methodology, including application of randomly generated collocation points or its generation using predefined measure of sensitivity as well as application of more sophisticated solvers.

References

[1] T.A. Kowalewski, M. Rebow "Freezing of water in a Differentially Heated Cubic Cavity", Int. J. of Comp. Fluid Dyn, 11:193-210, 1999.

[2] G. de Vahl Davis "Natural convection of air in a square cavity: a bench mark numerical solution" Int. Journal for Numerical Methods in Fluids, 3:249-264, 1983

[3] T. Michalek, T. Kowalewski, B. Sarler „Natural Convection for Anomalous Density Variation of Water : Numerical Benchmark", Progress in Computational Fluid Dynamics, 2004 (in print)

[4] Fluent Inc. Lebanon, NH 2002

[5] E. Leonardi, T.A. Kowalewski, V. Timchenko, G. de Vahl Davis "Effects of Finite Wall Conductivity on Flow Structures in Natural Convection", CHMT99, Cyprus, pp. 182-188, EM University Printinghouse, 1999

[6] H. Sadat and S. Couturier "Performance and Accuracy of a Meshless Method For Laminar Natural Convection" Numerical Heat Transfer, Part B, 37:455-467, 2000

[7] I. Kovacevic, A. Poredos, B. Sarler, "Solving the Stefan problem with the radial basis function collocation method". Numerical Heat Transfer, Part B,44:1-24,2003.

3D FLOW TRANSITION BEHIND A HEATED CYLINDER

Maosheng Ren, Camilo C.M. Rindt & Anton A. van Steenhoven
Department of Mechanical Engineering, Eindhoven University of Technology, P.O.Box 513, Eindhoven 5600 MB, The Netherlands

Summary: In the present study the 3D transition behind a **heated** cylinder is investigated at low Reynolds numbers: $Re = \mathcal{O}(100)$. For a Richardson number $Ri \geq 1.0$, the 3D transition manifests itself in the form of escaping thermal plumes in the far wake. From a numerical simulation at $Re = 85$ and $Ri = 1.0$, it is observed that the formation of the plumes is associated with pairs of streamwise-vortices occurring close behind the cylinder.

INTRODUCTION

Over the last ten years, a lot of attention has been paid to the 3D transition of the wake flow behind a cylinder. Experimental, numerical and theoretical studies significantly contributed to the understanding of the dynamics. From a fundamental point of view, studies on the instability mechanisms resulting in the formation of 3D vortical structures, can contribute to a better understanding of laminar-turbulent transition and may lead to ways to actively control the features of the flow.

For the unheated case, the wake flow is characterized by the Reynolds number. For a Reynolds number around $180 - 190$, a 3D transition occurs with a spanwise wavelength of 3-4 cylinder diameters. For a Reynolds number around $230 - 260$, 3D structures occur with a spanwise wavelength of 1 cylinder diameter.

The effect of a heat input on the behavior of the shed coherent structures received very less attention until the recent studies by Kieft *et al.* [1]. He investigated the wake structure behind a heated horizontal cylinder in cross-flow with water as the working fluid. For low Reynolds numbers, Kieft *et al.* [1] found that by heating the cylinder, the vortices in the upper and lower rows acquire different strengths due to baroclinic vorticity production. This strength difference increases for increasing Richardson numbers. It was observed that for small Richardson numbers the shed vortices move slightly downwards. A more extensive literature review and a summary of earlier results on the wake behavior behind a heated cylinder of our research group is given in van Steenhoven and Rindt [2].

THERMAL PLUMES IN THE FAR WAKE

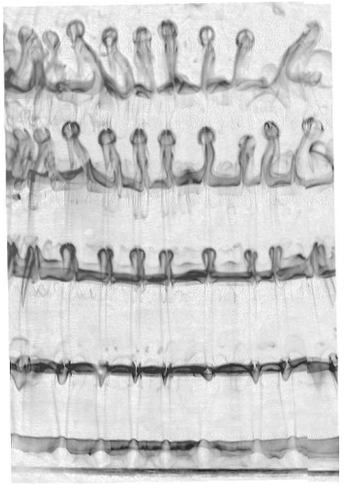
In the present study the 3D transition of the wake flow behind a **heated** cylinder is investigated at a Reynolds number $Re = \mathcal{O}(100)$. In Figure 1 (a), for $Ri = 0$, the wake flow manifests itself as the von Kármán vortex street. If one increases the heat input, for $Ri \geq 1$ a 3D transition manifests itself in the form of escaping thermal plumes [3], see Figure 1 (b). The spanwise distance of the plumes is around 2 cylinder diameters, as shown in Figure 1 (c).



(a) side view $Ri = 0$



(b) side view $Ri = 1.0$



(c) top view $Ri = 1.0$

Figure 1: Visualization of the wake flow at $Re = 117$ and $Ri = 0$, $Ri = 1$.

STREAMWISE VORTICITY IN THE NEAR WAKE

To understand the flow structures observed from the experiments, Spectral Element calculations are carried out for $Re = 85$ and $Ri = 1.0$. Numerical simulations provide more detailed insight into the occurrence of the 3D transition.

In Figure 2, iso-vorticity surface $\omega_x = \pm 0.4$ (vorticity component in streamwise direction) and iso-temperature surface $\Theta = 0.2$ are presented. In Figure 2 (a), the flow is from left to right. It is observed that pairs of streamwise vortices appear close behind the cylinder. The streamwise-vortices-pair has a spanwise distance of around 2 cylinder diameters. In Figure 2 (b), the flow is pointing towards the observer. The fluid at the center region of the streamwise-vortices-pair has a high temperature (Ren *et al.* [4]). Due to the non-uniform temperature distribution in spanwise direction, streamwise vorticity ω_x is generated due to the baroclinic vorticity torque $-\partial_z \Theta \times \mathbf{g}$.

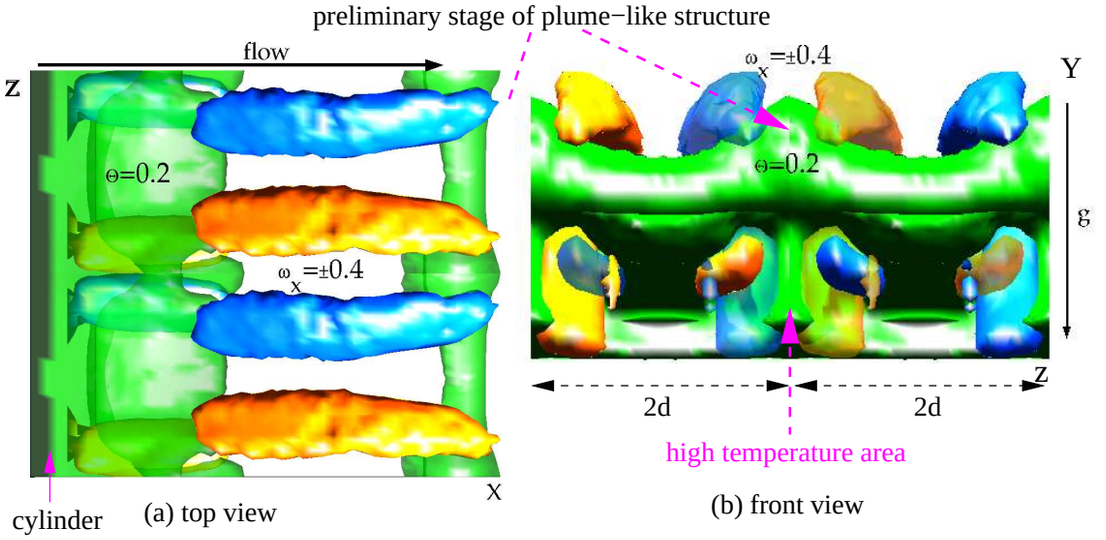


Figure 2: Snap-shot of calculated iso-vorticity $\omega_x = \pm 0.4$ surfaces and iso-temperature $\Theta = 0.2$ surface at $Ri = 1.0$, $Re = 85$. The spanwise distance of the streamwise-vortices-pair is around 2d, d is the cylinder diameters.

Furthermore, we observe the preliminary stage of plume-like structures in the upper vortices, as indicated in Figure 2. From the numerical calculations, the formation of the plume-like structures is associated with the streamwise-vortices-pair 'curling' around the upper vortices.

AIM AND PLAN

The evolution of the streamwise-vortices-pair and the formation of the escaping plumes will be studied as function of the Richardson number. From a fundamental point of view, a detailed study on the origin of the streamwise vorticity in the near wake and the thermal plumes in the far wake will contribute to a better understanding of 3D transition behind heated bluff bodies. This will be the goal of the current research.

References

[1] R. N. Kieft, C. C. M. Rindt, A. A. van Steenhoven, and G. J. F. van Heijst. On the wake structure behind a heated horizontal cylinder in cross-flow. *J. Fluid Mech.*, 486:189, 2003.

[2] A. A. van Steenhoven and C. C. M. Rindt. Flow transition behind a heated cylinder. *Int. J. Heat Fluid Flow*, 24:322, 2003.

[3] W. J. P. M. Maas, C. C. M. Rindt, and A. A. van Steenhoven. The influence of heat on the 3d-transition of the von kármán-vortex street. *Int. J. Heat Mass Transfer*, 46:3069, 2003.

[4] M. Ren, C. C. M. Rindt, and A. A. van Steenhoven. Buoyancy induced 3d-transition behind a heated cylinder. *Proc. Third International Symposium on Turbulence and Shear Flow Phenomena*, page 717, 2003.

EXPERIMENTAL STUDIES OF PLANETARY CORE CONVECTION AND DYNAMO PROCESSES

Jonathan M. Aurnou*
*Department of Earth & Space Sciences, University of California, Los Angeles, USA

Summary Here we will present a basic review of planetary core processes and then discuss experimental means for studying core convection dynamics and dynamo processes, focussing on the rotating magnetoconvection experiment presently being set up at UCLA.

INTRODUCTION

Planetary magnetic fields are generated by convectively driven dynamo processes occurring within the electrically conductive fluid regions of deep planetary interiors. In the terrestrial planets, dynamo generation occurs within the planet's iron-rich molten core [1]. In the giant planets, dynamo generation occurs either below the depth where pressure-induced metallization of hydrogen occurs on Jupiter and Saturn or in the interior region of relatively high ionic conductivity on Uranus and Neptune [1]. Because dynamo generation occurs in deep planetary interiors, the effects of these processes can only be detected via remote techniques, such as satellite magnetometry. Thus, workers use theoretical, numerical and experimental studies to determine the possible dynamo mechanisms that can explain the planetary magnetic field observations.

The fluid motions in planetary cores are affected at first order by buoyancy, Coriolis and Lorentz forces. Linear stability analysis predicts that the onset of thermal convection is facilitated in the regime where Lorentz and Coriolis forces are comparable [2,3], i.e., in the regime where the Elsasser number Λ = (Lorentz force/Coriolis force) ~ 1. Thus, the interaction of strong magnetic fields and strong rotation allows convection to occur more easily, whereas, if these forces were to each act alone, convection would be strongly suppressed. This has lead to the idea that convection-driven dynamos will naturally function most efficiently in the regime where the convection itself is most efficient, again, in the $\Lambda \sim 1$ regime. However, this scaling concept for dynamo field saturation has not been clearly and quantitatively substantiated.

Experimental and numerical studies provide excellent means by which to test this $\Lambda \sim 1$ scaling concept. These methods each have their strengths and weaknesses. A difficulty facing numerical dynamo approaches is that they are presently unable to be carried out using realistic fluid properties [4]. On the other hand, numerical simulations are able to generate dynamo action precisely because they are able to use highly artificial fluid properties that lead to strong magnetic induction (i.e., large magnetic Reynolds numbers, $\boldsymbol{Re}_m$) in weakly driven, nearly laminar convective flows (i.e., at relatively low values of the Rayleigh number, $\boldsymbol{Ra}$).

In the laboratory, it is possible to use liquid metals, such as liquid sodium and gallium, which have physical properties similar to core fluids [5]. Experimental groups are taking two different approaches for improving our understanding of the geodynamo: mechanically-driven dynamo experiments and thermally-driven rotating magnetoconvection experiments. These approaches are complementary ways of studying convectively-driven dynamo generation, which cannot presently be achieved in the laboratory; each type of experiment isolates a different part of the dynamo process. The mechanically-driven experiments impose a velocity field in hopes of producing dynamo-generated magnetic fields. In contrast, the thermally-driven experiments impose a magnetic field and study how the convective velocity field is altered.

Mechanically-driven laboratory dynamo experiments are presently being designed and built by the groups at the University of Maryland, College Park; University of Wisconsin, Madison; CNRS, Cadarache, France; Universite Joseph Fourier and CNRS, Grenoble, France; and at the New Mexico Institute of Mining and Technology, Socorro. These devices will study magnetic induction processes at $\boldsymbol{Re}_m \sim 10^2$. In order to reach such high $\boldsymbol{Re}_m$ in the laboratory, these devices use large mechanical motors to drive electrically-conducting fluids to high velocities where dynamo generation may occur. These mechanically-forced flows are not realistic analogs to flows in planetary cores. Yet should dynamo generation come about, their experimental results will provide an excellent opportunity to determine how dynamo-generated fields equilibrate and whether this nonlinear saturation process occurs in the $\Lambda \sim O(1)$ regime.

Alternatively, in rotating magnetoconvection experiments, the flows are thermally-driven and, in addition to the rotation, the magnetic field is imposed. This forces the convection to occur in the externally imposed $\Lambda \sim 1$ regime. Diagnostic measurements can then determine how the convection varies with Λ. These convective flows are far less energetic than mechanically-driven flows. Thus, the convection-driven induction processes are weak ($\boldsymbol{Re}_m < 1$), and dynamo action cannot be achieved in such devices. The strength of these experiments is that the thermally-driven convection is geophysically realistic and the dynamics, controlled by Λ, are similar to those of the Earth's core.

THE UCLA ROTATING MAGNETOCONVECTION EXPERIMENT

We are presently setting up a large volume rotating magnetoconvection experiment at UCLA. No large volume, plane layer rotating magnetoconvection experiments have been carried out since those made nearly 50 years ago by Nakagawa [6,7]. Smaller volume experiments were recently carried out by Aurnou and Olson [8]. Their experiments, which were made using liquid gallium as the working fluid, agreed with Chandrasekhar's basic predictions for relatively weak Coriolis and Lorentz forces. Thus, their experiments act as a small-scale feasibility study for the large volume device that is now being fabricated.

Figure 1 shows design drawings of the rotating magnetoconvection device presently being set up at UCLA. In order to study the $\Omega \sim 1$ regime, it is necessary that the experimental geometry requires strong Lorentz and Coriolis forces to simultaneously affect the convective motions. Thus, we have chosen a horizontal plane layer geometry, which satisfies this criterion by having the gravity vector, the magnetic field vector and the rotation axis all aligned in the vertical. The design consists of three major sections: 1) the convection tank, 2) the rotary table and 3) the solenoidal magnet coil. Figure 1a shows the cylindrical convection tank and rotary table. Figure 1b also includes the solenoidal electromagnet, shown in its lowered position in which it surrounds the convection tank. The working fluid for these experiments will be gallium-indium-tin eutectic alloy, which has a melting temperature of 10.7°C. The alloy will be heated from below by a non-inductively wound heat pad, allowing us to reach $\boldsymbol{Ra} \sim 5\text{x}10^7$ in non-rotating, non-magnetic, Rayleigh-Benard convection experiments. Rotation rates up to 2Ω rad/s (i.e., 60 rpm) will allow us to reach Taylor numbers of $\boldsymbol{Ta} \sim 10^{12}$ without strongly deflecting the gravitational equipotential surfaces within the fluid layer. The magnetic field will be uniform to 0.5% over the entire volume of the fluid layer and will attain a maximum intensity of 1300 gauss. This will allow us to reach Chandrasekhar numbers of $\boldsymbol{Q} \sim 10^5$. Our inability to produce a much stronger, uniform magnetic field is the limiting factor in this experimental design.

This rotating magnetoconvection device will greatly benefit from an acoustic Doppler velocimetry system that will provide non-invasive measurements of convective velocities in the opaque liquid gallium alloy [8]. These measurements, as well as temperature and magnetic field measurements, will allow us to test the linear predictions for rotating magnetoconvection in the $\Omega \sim 1$ regime and, for the first time, to study strongly nonlinear, turbulent rotating magnetoconvection in order to determine whether the linear results are also valid for fully-developed convective flows. Our experimental findings will be relevant to those studying core convection processes and to the broader fluid mechanics community as well.

References

[1] Stevenson, D.J.: Planetary magnetic fields. *Earth Planet. Sci. Lett,* **208**:1-11, 2003.

[2] Chandrasekhar, S.: Hydrodynamic and Hydromagnetic Stability. Oxford University Press, Oxford, 1961.

[3] Eltayeb, I. A., Roberts, P.H.: On the hydromagnetics of rotating fluids, *Astrophys. J.*, **162**: 699-701, 1970.

[4] Glatzmaier, G.A.: Geodynamo simulations: How realistic are they? *Annu. Rev. Earth Planet. Sci.,* **30**:237-257, 2002.

[5] Poirier, J.P.: Introduction to the Physics of the Earth's Interior, 2nd Ed., Cambridge University Press, Cambridge, 2000.

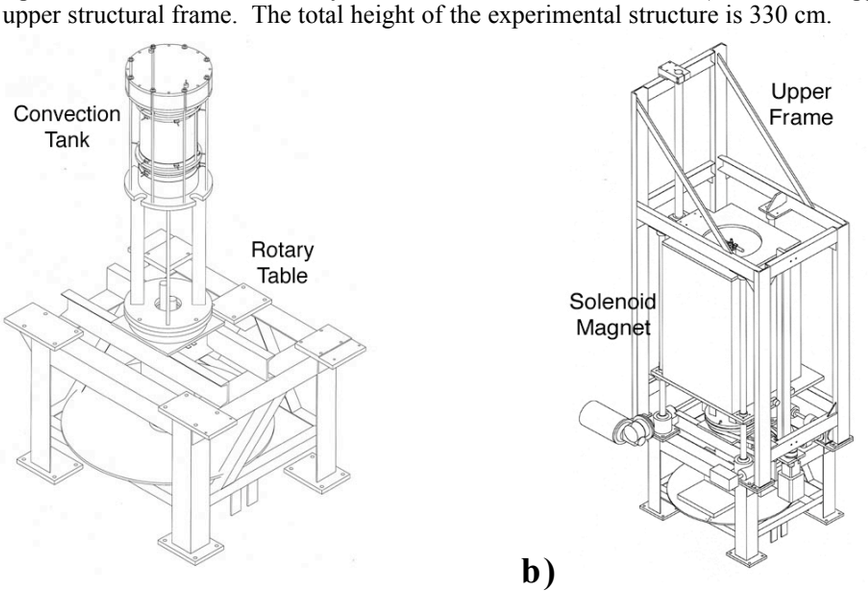
[6] Nakagawa, Y.: Experiments on the instability of a layer of mercury heated from below and subject to the simultaneous action of a magnetic field and rotation, *Proc. R. Soc. Lond. A,* **242**:81-88, 1957.

[7] Nakagawa, Y.: Experiments on the instability of a layer of mercury heated from below and subject to the simultaneous action of a magnetic field and rotation. II., *Proc. R. Soc. Lond. A,* **249**:138-145, 1958.

[8] Aurnou, J.M., Olson, P.L.: Experiments on Rayleigh-Benard convection, magnetoconvection and rotating magnetoconvection in liquid gallium, *J. Fluid Mech.,* **430**:283-307, 2001.

[9] Brito, D., et al.: Ultrasonic Doppler velocimetry in liquid gallium, *Expts. Fluids,* **31**:653-663, 2001.

Figure 1: **a)** Close-up of the convection tank, rotary table and lower structural frame. **b)** The entire apparatus including the magnet and its upper structural frame. The total height of the experimental structure is 330 cm.



PENETRATIVE CONVECTION IN STRATIFIED FLUID: VELOCITY MEASUREMENTS BY IMAGE ANALYSIS

CENEDESE ANTONIO AND MORONI MONICA

Department of Hydraulics, Transportations and Roads, University of Rome "La Sapienza"
Rome, Via Eudossiana 18 - 00184, Italy
Tel: +39-0644585638 / Fax: +39-0644585094
E-mail: monica.moroni@uniroma1.it

1. Introduction

Penetrative convection concerns the advance of a *turbulent* fluid into a fluid layer of stable stratification. The phenomenon is organized in domes, space regions with prevailing vertical motion. Domes springing up the heating surface stress the stable layer causing the generation of internal waves. These ubiquitous motions take many forms, and they must be invoked to explain phenomena ranging from temperature fluctuations in the deep ocean to the formation of clouds in the lee of a mountain. Within the unstable layer, the fluid temperature, density and velocity change with time. Further, it is separated from the rest of the fluid through an interface where large gradients of quantity of interest occur. The investigation of penetrative convection is of importance in several areas of geophysical fluid dynamics, since it occurs in the upper oceans, lower atmosphere and upper lakes. In this regard, we must recall that natural fluid bodies are characteristically stably stratified: that is, in most regions and for most of the time the average density decreases as one goes upwards.
The phenomenon interests the atmosphere when a *turbulent* convective fluid covers a large horizontal area, and gradually deepens and incorporates a stable fluid layer above it. This phenomenon is observed when, owing to surface heating, a growing unstable layer adjacent to the ground replaces from below a nocturnal inversion. In this case, the initially stable environment near the ground is affected by the convection, and full interaction between the two regions occurs. The convection is termed penetrative because the front of the advancing unstable layer presents domes that penetrate small distances into the stable layer (Deardorff *et al.*, 1969).

In most lakes and in the oceans, an analogous phenomenon occurs, starting from the upper, free surface and eroding with time the daily but mostly the seasonally stably stratified lake waters.

The present paper describes the application of PTV to a laboratory model simulating the evolution of a convective boundary layer. The basic idea behind Particle Tracking Velocimetry is to disperse the seeding particles homogeneously in the working fluid and tracking them during their motion. The resulting description of the velocity field is intrinsically Lagrangian. Visualization experiments through LIF are presented as well in order to visualize the evolution and shape of the interface between the stable and unstable layers. Townsend (1964), Deardorff *et al.* (1969), Kato and Phillips (1969), Cenedese and Querzoli (1994), Querzoli (1996), Cenedese and Querzoli (1997) and Mancini and Cenedese (2000) present laboratory investigations on penetrative convection. A larger set of boundary conditions and a refined PTV algorithm differentiate the present contribution.

2. Experimental Set-up

The laboratory model consists of a convection chamber heated from below. The heating simulates the solar radiation effects and causes penetrative convection. The working fluid is distilled water. Pollen is used as passive tracer. The test section, shown in Figure 1, is a cylindrical tank square cross-section. The insulation is kept while the tank is filled with the density-stratified fluid, and carried out from the side facing the camera, to allow its optical access. The lower boundary can be kept to a given nearly constant temperature by means of a circulating water bath, separated from the fluid through a metal sheet. A stable stratification, e.g. a positive vertical temperature gradient, is obtained by means of two connected tanks. The fluid is initially equally distributed into two identical tanks

The thermal convection is started at time $t = 0$ upon replacing the cool water circulating behind the lower boundary with water at temperature almost equal to the larger achieved within the test section. Within 2 minutes, the temperature at the bottom, increases rapidly to at least 82% of its final value and thereafter gradually approached this value.

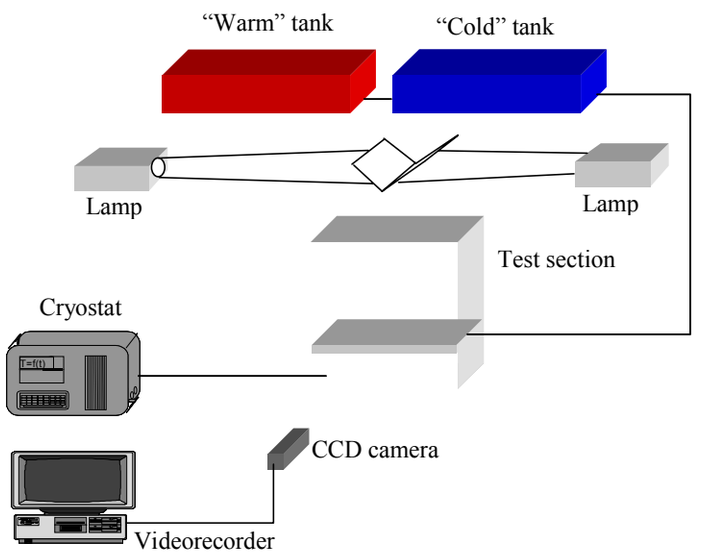


Figure 1 - Experimental set-up

3. Preliminary Results

During each experiment, a thermocouple is cycled repeatedly to obtain successive mean temperature profiles. Different sets of initial conditions are investigated. The mean initial temperature gradient, is determined by taking the best fitting straight line of the initial mean profile

Figure 2 displays the evolution of the temperature along the vertical direction and as a function of time for one of the performed experiments.

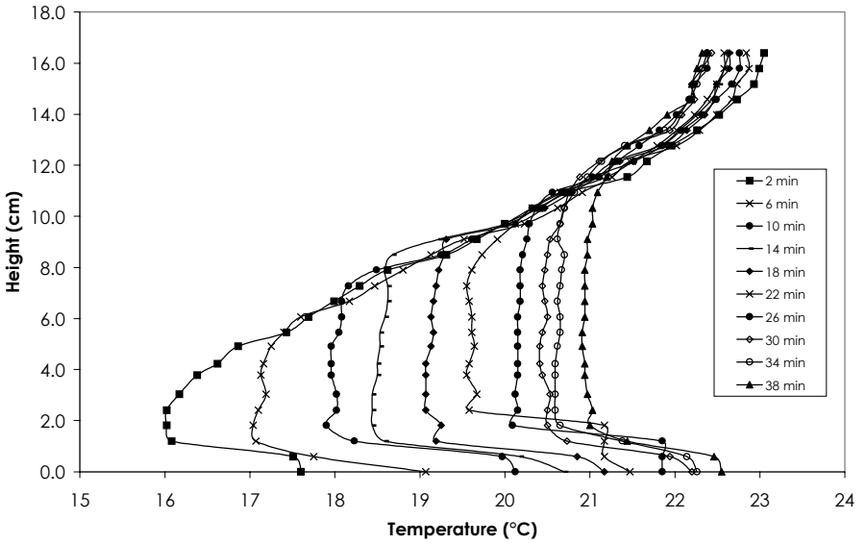


Figure 2 - Vertical profiles of temperature for experiments 3

Figure 3 shows typical images of the mixing layer and of the interface, acquired during an experiment when fluorescina was placed within the convective layer.

The mixing layer evolution can be described in terms of the Rayleigh number:

$$Ra = \frac{\beta g \Delta T (z^*)^3}{\lambda \nu} \tag{2}$$

where: β is the thermal expansion coefficient, λ the thermal diffusivity, ν the fluid cinematic viscosity, g the gravity acceleration, ΔT the difference between the temperature at the boundary where the heat is supplied and the temperature of the mixing layer and z^* is the mixing layer height. During the convection phenomenon evolution, Ra increases, mostly because of z^* increasing. At first, for low values of Ra, convection is organized in coherent structures, remaining over time. Subsequently, for larger values of Ra, the flow becomes turbulent and the coherent structures spring up and break up continuously in different positions. The horizontal surface is smaller for the upward portions than for the downward ones, having the latter a higher velocity. Their characteristic dimensions are of the same order of magnitude as the mixing layer height, while their lifetime is less or equal to the time a fluid particle needs to complete a whole revolution. At times, the following structures occur: growing domes or turrets with an extremely sharp interface at their top, flat regions of rather large extent occurring after a dome or other structure has spread out or receded, cusp-shaped regions of entrainment pointing into the convective fluid. The images above are analyzed to determine the growth of the mixing layer with time. Each image is characterized by a stable layer (color black) and a mixing layer (lighted-colored). After determining the luminosity vertical profile (averaging the gray level of pixels belonging to each row of the image), the luminosity vertical gradient is computed. The gradient is different than zero at a height corresponding to the interface position.

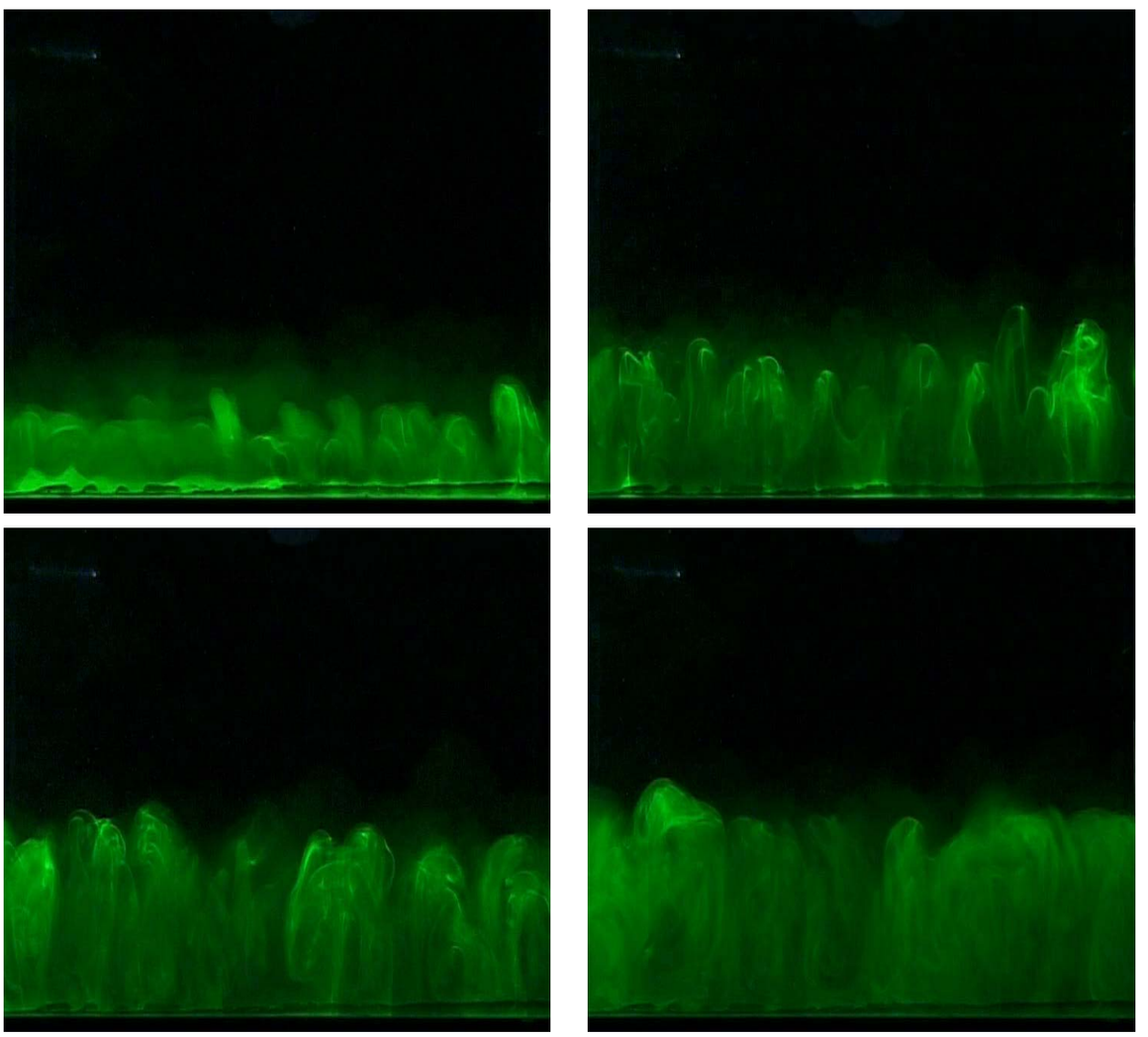


Figure 3 - Visualization of the mixing layer evolution

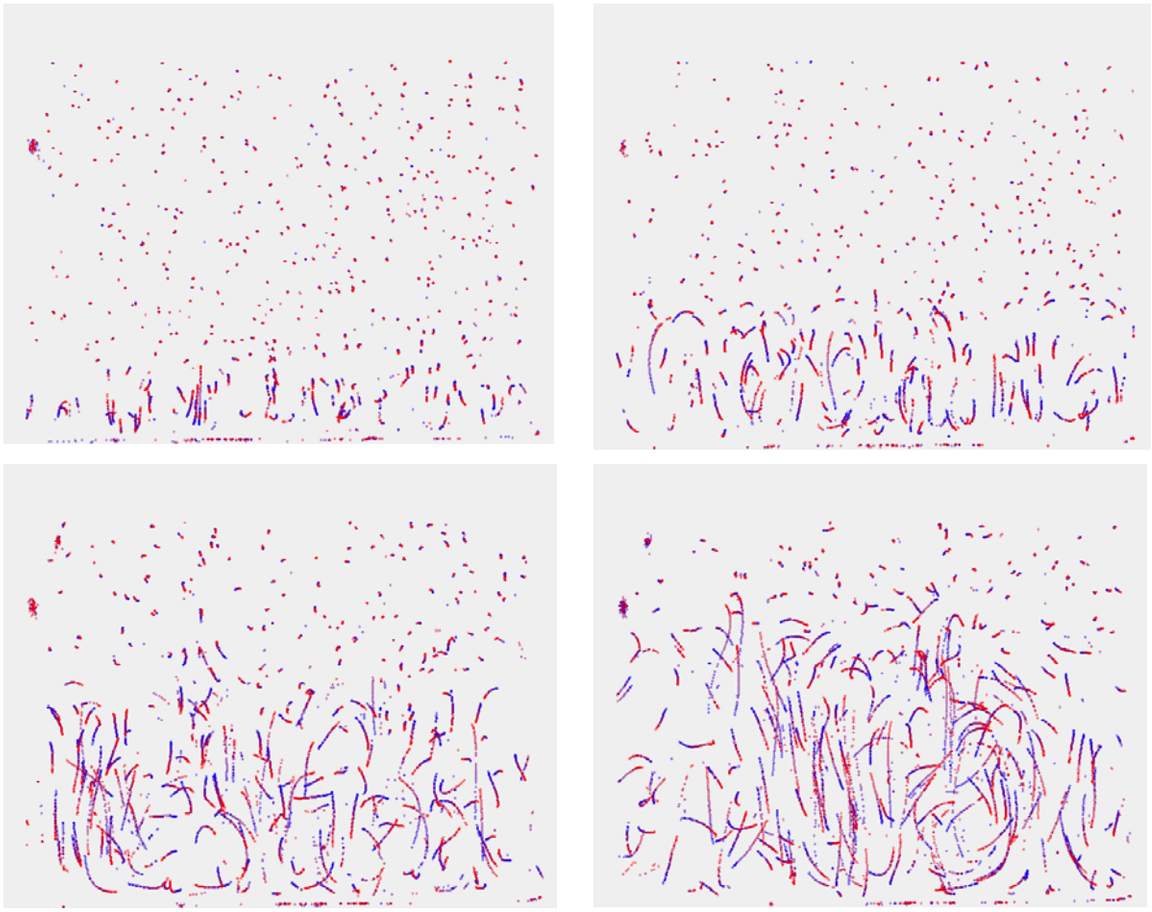


Figure 4 – Centroids reconstructed during the mixing phenomenon (both the effects of penetrative convection and internal waves are depicted)

PTV is employed to individuate barycenters and to reconstruct tracer particle trajectories inside the test section.

The particle detection algorithm is based on image thresholding (based on the image histogram) and labeling of lighted pixels. The barycenter location is determined with a sub-pixel accuracy. The set of particle image locations is used as input data for the tracking algorithm. The first two points belonging to a trajectory are chosen within a circle of fixed radius. This condition is equivalent to assuming a maximum velocity in the investigated flow. To add spots to the two-point trajectory the nearest neighbor principle is employed. When ambiguities arise, the criterion of "minimum acceleration" along the trajectory passing through the points in question is employed. Figure 4 displays centroids reconstructed inside both the stable and the unstable layers as they evolve with time. Each picture presents the centroids reconstructed analyzing 50 frames. Different pictures refer to different instant of times, being time zero the beginning of the mixing process. Looking at Figure 4 we can conclude that the convective motions grow starting from the lower warm boundary and give rise to upward domes. They coalesce one with the others, forming larger structures with higher velocity. Tracking fluid particle motion, its features can be observed. After a particle leaves the boundary, it travels an upward portion till the inversion layer is reached. At this point, the velocity vertical component goes to zero and changes sign. The particle will now travel the mixing layer downward. Fluid particles belonging to the mixing layer remain trapped within it. After the turbulent region has reached a consistent height, the tracer particles belonging to the interface between the stable and unstable layers start moving along oscillating trajectories (internal waves). As time passes, internal waves are present overall the stable layer. The same particles describing oscillating trajectories

are later entrained inside the turbulent fluid.

The Brunt Vaisala frequency of internal wave in the stable layer (Townsend, 1996) and Transilient Matrix, which describes the mass exchange in a given amount of time, will be also determined from the analysis of the velocity field in the lagrangiano framework (Mancini & Cenedese, 2000).

References

Califano, F., Mangeney A., 1994, "Mixed layer in a stably stratified fluid," Nonlinear Processes in Geophysics, Vol. 1, 199.

Cenedese, A., Querzoli G., 1994, "A laboratory model of turbulent convection in the atmospheric boundary layer, " Atmospheric Environment, Vol. 28, No.11, 1901.

Cenedese, A., Querzoli G., 1997, "Lagrangian statistics and transilient matrix measurements by PTV in a convective boundary layer," Meas. Sci. Technol., Vol. 8, 1553.

Cenedese, A., Moroni M. and Querzoli G., "Application of 3D-PTV to the Study of Penetrative Convection", 10th International Symposium on Flow Visualization, Kyoto (Japan), August, 26-29, 2002.

Deardorff, J.W., Willis G.E., Lilly D.K., 1968, "Laboratory investigation of non-steady penetrative convection," J. Fluid Mech., Vol. 35, No.1, 7.

Kato, H., Phillips O.M., 1969, "On the penetration of a turbulent layer into stratified fluid," J. Fluid Mech., Vol. 37, No.4, 643.

Mancini, G., Cenedese A., "Entrainment measurements at a density interface", 5th International Symposium on Stratified Flows, Vancouver, Canada, July 2000.

Querzoli, G., 1996, "A Lagrangian study of particle dispersion in the unstable boundary layer," Atmospheric Environment, Vol. 30, No.16, 2821.

Townsend, A.A., 1966, "Internal waves produced by a convective layer," J. Fluid Mech., Vol. 24, No.2, 307.

EXPERIMENTAL AND NUMERICAL STUDIES OF CONVECTION FLOW IN A CYLINDRICAL-CONICAL FERMENTING TANK

H. Meironke, J. A. Szymczyk
Fachhochschule Stralsund-University of Applied Sciences - Department of Thermofluiddynamics and Turbo Machines

Summary: In this paper the experimental and numerical investigations of the convection flow in a real cylindrical-conical fermenting tank for beer production are described. The experimental investigations were conducted using a two-dimensional ultrasonic Doppler velocity measurement method to measure the flow field during a real fermentation process in opaque wort. In further investigations the fermentation process was simulated with a model-fluid by heating and cooling the outside of the fermenter. In a numerical study the convection flow of the simulated fermentation process was analysed.

INTRODUCTION

Today the fermentation, maturation and storage of beer during the manufacturing process are mostly carried out in cylindrical-conical fermenting and storage tanks. These tanks are made of stainless steel with separated cooling spirals for the different processing steps. The fluid mechanics inside of these tanks has not been recorded satisfactorily from a scientific point of view.
Optimal conditions, i.e. the homogeneous distribution of yeast particles, during fermentation, maturation and storage are achieved by means of controlling the transport mechanisms regarding momentum, heat and mass transfer. The multiphase flow in the tank generated by the fermenting process is three-dimensional and turbulent. The medium “wort” is composed of several phases and components. In the wort, heat and mass transfer processes take place and there is an interrelationship between the biological matter and the carrier liquid.

EXPERIMENTAL ARRANGEMENT

For the analysis of the fluid mechanics inside the fermenting and storage tank a model tank was developed, which was equipped with eight separately controlled cooling zones. The volume flows in these zones were adjustable to the various test conditions and process requirements. The cooling energy was supplied by a chiller with a power of 10 kW. The cooling medium was a glycol/water mixture, which was able to supply the eight cooling panels with a temperature down to minus 7 °C. For the simulation of the fermentation process, these zones could be heated by means of a heating unit, so that different temperature levels in the zones outside the model tank to simulate the process with a model fluid could be obtained. The test facility can work in two different modes: a real fermentation and storage process mode and a mode that simulates the real process by means of a model fluid. This experimental simulation mode allows the comparison with the numerical simulation. For controlling the test facility, a software was created on the basis of the software tool “HP-VEE” with a view to managing the continuous data logging of temperature and volume flows during the fermentation, maturation and storage processes. For the velocity field measurement inside of the fermenting tank an ultrasound Doppler measuring technique is used. The operating principle of this measurement technique is to use ultrasound pulse waves to detect the Doppler frequencies in 128 measurement volumes along the measurement axis. The spatial information of these measurement volumes is determined by the time delay between pulse emission and echo reception. The velocities at each measurement volume are calculated from the Doppler frequencies. For the measurement of two-dimensional velocity fields it is necessary to measure two velocity components at one spatial point in order to calculate a vector. In the intersection point of measuring lines of two transducers the velocity vector can be determined. For this reason a measurement field with a vertical and horizontal arrangement of 16 transducers was installed.

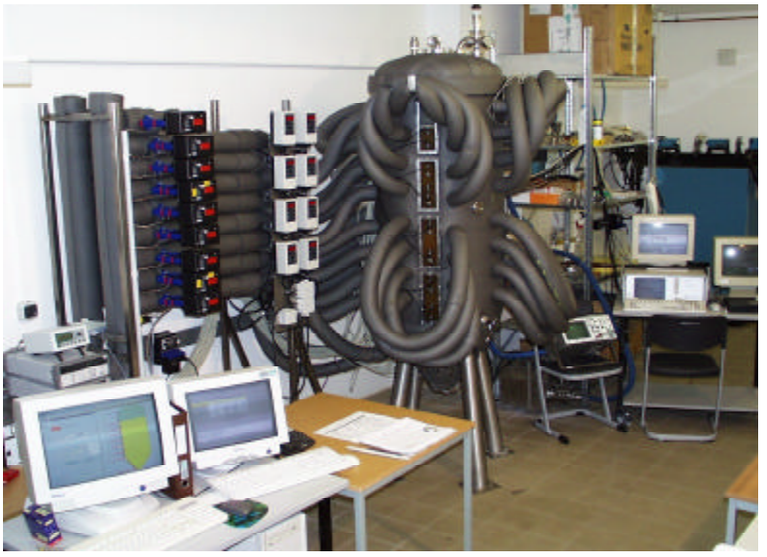


Figure 1: Experimental arrangement

PRESENTATION OF RESULTS

Experimental results

The flow field was measured continuously several times during the eight days of fermentation. The temperature in the cooling zones was set at 5 °C in order to achieve a constant temperature (8 °C) of the interior of the fermenting tank in compliance with the fermenting procedure. In figure 2, an example of the velocity field taken on the 8th day of fermentation is shown. The heat transfer of the fermenting heat took place in the upper two cooling zones. On the first day of fermentation, no convection areas had developed inside the tank. Velocities of 15 mm/s were measured. In the bottom part of the tank, an upward flow, with a velocity of about 4 mm/s, was observed through the windows. On the third day of fermentation the flow activity strongly increased due to the increase of the fermentation process. On the fifth day the velocity field was nearly symmetrical. In the upper part of the tank, a radial flow directed at the cooling zones was detected. In the central area an upward flow was measured with velocities up to 130 mm/s. The warmer liquid in the cone area rises to the upper part, turns to the cooling zones, and sinks at the border area of the tank back to the bottom part due to the fact of continuity. This re-flow is not very intensive. Video recordings show that even at the end of the fermentation process (8th day) a very turbulent three-dimensional flow in the upper part of the tank, below the foam, occurs. In the bottom part a constant downward flow with a velocity of about 4 mm/s could be observed. Inside this flow precipitate yeast agglomerates were observed.

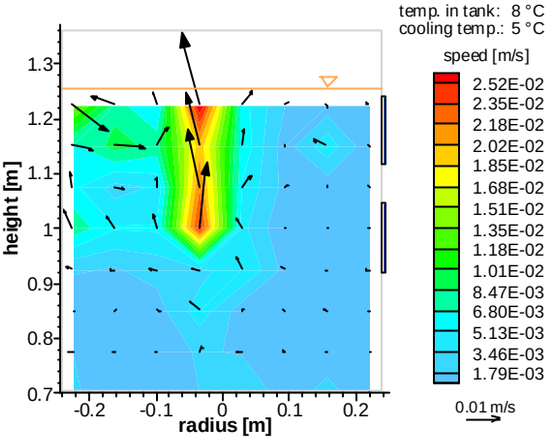


Figure 2: Measurement of velocity field (8th day)

Numerical results

The numerical simulation of heat and momentum transfers in the model fluid in the fermenting tank was conducted by means of the CFD software tool “Fluent”. Water was used as the model fluid, because it is single-phase and incompressible. The geometry of the tank assumed was three-dimensional. The real local heat input through the yeast particles was neglected and substituted by a heated cone wall, with the heat dissipation taking place in the upper two cooling zones. In figure 3 the computed flow field of a simulated fermentation is presented. Mass transfer is neglected in the present computation. A comparison between the computation and the simulated fermentation showed that the numerical results offer a good prediction of the flow fields observed in the experimental simulation.

Further experimental investigations will aim at increasing the accuracy of measuring by means of collecting more experimental data. In addition, the influence of rising CO_2-bubbles during fermentation on the velocity measurements will be investigated.

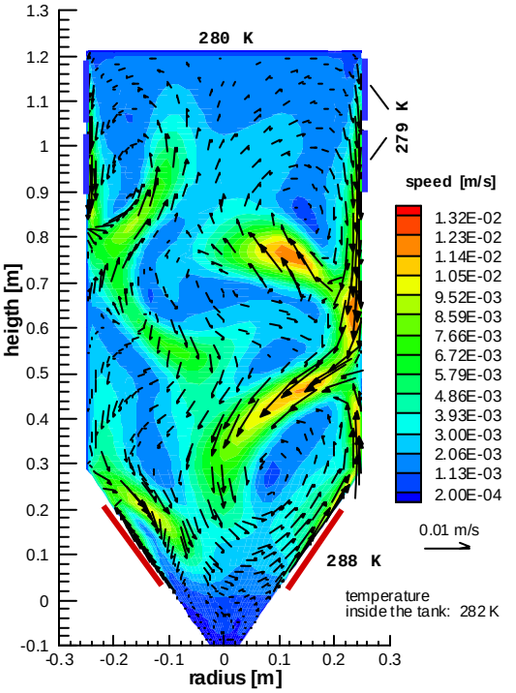


Figure 3: Computation of simulated fermentation

Acknowledgement

The authors gratfully acknowledge the financial support of the Federal Ministry of Economics and Labour FKZ.: KF 0242801 KRF1 and the project executing organisation AiF office Berlin

References

[1] Schuch, C: Bewegungsvorgänge in zylindrokonischen Tanks während Gärung und Reifung, Fortschrittberichte VDI, Reihe 17, Nr. 146, 1996
[2] Denk, V., Enders, T., Peters, U., Hege, U., Schuch, C. : Entwicklung eines Verfahrens zur Regelung und Optimierung der Gärung und Reifung von Bier, Brauwelt Nr. 36, 1995
[3] Meironke, H., Szymczyk, J. A., Leder, A.: Untersuchung der Strömungsvorgänge in einem Gär- und Lagertank mittels der Ultraschall Doppler Messtechnik, Lasermethoden in der Strömungsmesstechnik, Shaker Verlag, Aachen, 2003
[4] Meironke, H., Szymczyk, J. A.: Untersuchung der Geschwindigkeitsverteilung in einem Gär- und Lagertank mittels der Ultraschall Doppler Anemometrie, Proceedings in Applied Mathematics and Mechanics, Wiley VCH Verlag, 2003

XXI ICTAM, 15–21 August 2004, Warsaw, Poland

SEA CONVECTIVE MOTIONS DRIVEN BY RANDOM BUOYANCY INPUTS

V.Bouché
Physics Department,"La Sapienza" University , Rome,Italy

Summary A model for the dynamics of uncorrelated dense water plumes, perturbed by the Coriolis force, and the conditions for their generation, is presented here. A Lagrangian rapresentation allows their time evolution till the initial collective rotating chimney formation to be obtained. Scale relations are examined, depending on the surface air-sea interaction statistics involved; their dependence on buoyancy fluctuations more than mean values is shown

Introduction- The model

Sudden cooling and evaporative events occur on the sea surface during the winter in several regions, inducing buoyancy instabilities and convective mixing, an important mechanism responsible for deep water formation (DWF). A recent review and references are given in Maxworthy (1997) and in Marshall and Schott (1998). The known experimental observations of these phenomena in an open sea can be summed up in:1)a preconditioning phase during all the winter;2)a violent sudden plume very short (2h)formation phase;3) a plume mixing and rotating formation phase,4) a chimney baroclinic instability phase untill the chimney finally breaks off as the external forcing dies down.

The object of the present work is to discuss the plume formation process in a homogeneous ($N^2 = \frac{g}{\rho_0}\frac{\partial \rho}{\partial z} = 0$), and a slowly stratified ($N \approx 10^{-3} - 10^{-4} sec^{-1}$)sea, like it is the MEDOC region or the RED sea, DWF sites; for a sake of semplicity the depth dependence of the vertical stratification and the horizontal stratification are ignored: the extension of the model to this more physical situation will be object of future work. The observation of wind data (Zecchetto et al.2001) measured (a)on $11 November 1994$ at $22:02$ (during the initial preconditioning phase), and (b)on $18 March 1997$ at $22:08$ (during the initial DWF event phase) show transverse winds, symmetric around a central axis, very slowly variable along their motion direction in (a), and transverse winds, but radially symmetric around the center of the doming in (b), when the sea site is baroclinic and slowly rotating ($\omega << f$); this radial winds symmetry would mean a strong surface air-sea momentum transfer and a strong wind stress; but the mechanical mixing due to the winds would be so deep that the convective motion generated occurs at $1/\lambda \geq 100m$, where the wind stress is anyway not important.

I examine an initially still sea, perturbed at the surface by sudden transversal dry, cool winds, that appear as a large series of random events, short range space correlated, occurring in a short time period, whose result is equivalent to sudden space and time non homogeneous surface cooling, as suggested by Maxworthy about the $1Km$ large uncorrelated plumes measured by Schott and Leaman (1991) in the Gulf of Lion. By assuming a correlation between the wind speed and the surface buoyancy flux symmetries, I examine a threedimensional Navier-Stokes model, in (a)a rectangular and (b) a cylindrical frame; in (a) a very slow dependence on y (the winds direction) of the surface buoyancy flux and of the plumes evolution, while in (b) a very slow dependence on the angular polar variable are assumed. It is so possible for both the cases to semplify the threedimensional model into a couple of equations (for the transversal vorticity $\nabla^2_\perp \psi$ and the transversal velocity v ((b) u_θ), uncoupled for short times ($t < 1/f$); i.e. I identify two time scales such that, for $t < 1/f$, a twodimensional convective motion is generated, but perturbed (for $t \geq 1/f$)by the Coriolis force, such that the full evolution is the combination between a twodimensional convective motion and a linear tranverse one.

The basic model equations (scaled with the horizontal dimension L, and the Coriolis parameter f) are, in Boussinesq approximation:

$$\frac{D\nabla^2_\perp \psi}{Dt} = s_b + s_v + s_N + \mathcal{E}\frac{\partial^2 \nabla^2_\perp \psi}{\partial z^2} \quad ; \quad \frac{Dv}{Dt} = -\frac{\partial \psi}{\partial z} + \mathcal{E}\frac{\partial^2 v}{\partial z^2} \quad ; \quad \frac{Db}{Dt} + \mathcal{N}_b w(\frac{b}{g} - 1) = \frac{db_s}{dt}$$

where b is the buoyancy, the viscosity term $\mathcal{E} = \frac{\nu}{L^2 f} \approx 3 \cdot 10^{-7}$ is negligible, $t = ft$, $s_b = -\frac{\partial b}{\partial x}$, $s_v = \frac{\partial v}{\partial z}$, $s_N = -\mathcal{N}_b \frac{\partial P}{\partial x}$ are point vorticity sources; s_b is the primary vorticity source, an antisymmetric x function depending on the horizontal buoyancy gradient produced by the air-sea interaction: $\frac{db_s}{dt} = \frac{db_s(x,t)}{dt} e^{-\lambda z} e^{-y^2/2}$ ($\lambda \approx 1/100 m^{-1}$) is the external input, a symmetric x function, random in x and in t; it is thought off as essentially concentrated near the central axis, and periodically near a set of axes rightly spaced out: a critical distance between them and a suitable decaying range a for each of them are being identified for plumes generation; a stochastic model of a set of short space correlated buoyancy inputs is created such as to have this average periodicity; s_N is a countervorticity source due to stratification (P is the scaled pressure); s_v is a correction term to the vorticity generation due to Coriolis effects: it may be split off into $s_v^b + s_v^N$, working, on long time scales ($t \geq O(1)$), on the horizontal velocities $u(\psi(s_b))$ and $u(\psi(s_N))$ respectively ; moreover it is $u = -\frac{\partial \psi}{\partial z}, w = \frac{\partial \psi}{\partial x}$;((b)a similar set of equations is given in cylindrical symmetry, with b_s not dependent on θ, $u_r = -\frac{\partial r\psi}{r\partial z}, w = \frac{\partial r\psi}{r\partial r}$)

The method

The Boussinesq approximation allows the solution of the vorticity equation to be considered a single Dirichelet problem ($\psi = 0$ on the boundary), solvable by image charge method, by using a transformation to Lagrangian variables $\xi = x - \int_0^\tau u(\xi,\eta,\tau')d\tau'$, $\eta = z - \int_0^\tau w(\xi,\eta,\tau')d\tau'$, $\tau = t$, such that: $\frac{D}{Dt} = \frac{\partial}{\partial\tau}$, $\frac{\partial}{\partial x} = a_{11}\frac{\partial}{\partial\xi} + a_{12}\frac{\partial}{\partial\eta}$, $\frac{\partial}{\partial z} = a_{21}\frac{\partial}{\partial\xi} + a_{22}\frac{\partial}{\partial\eta}$; so : $\frac{D\psi}{Dt} = \frac{\partial\psi}{\partial\tau} = \sum_{k=0}^{\frac{R_0}{na}} \int_0^{\frac{na}{2}} dx' \int_0^h dz_0 s(x',z_0) g_k(x,z,x',z_0) = \sum_{k=0}^{\frac{R_0}{na}} \int dq(x',z_0) g_k(x,z,x',z_0)$ where na is the plumes periodicity, $g_0 = log\frac{r_2 r_3}{r_1 r_4}$, $(r_i = ((x \pm x')^2 + (z \pm z_0)^2)^{1/2})$, $g_{k\neq 0} = log\frac{r_{2k}^+ r_{4k}^-}{r_{2k}^- r_{4k}^+}$, $r_{ik} = ((x \pm x' - nka)^2 + (z \pm z_0)^2)^{1/2}$ and the antysimmetric far dypole depending on $r_{ik} = ((x \pm x' + nka)^2 + (z \pm z_0)^2)^{1/2}$ has been neglected. It is known that $g_k \rightarrow \frac{x' z_0}{(x'^2 + z_0^2)^2} \mid x \mid z$ for $x, z \rightarrow 0, (x = x - nka)$ i.e g_k is hyperbolic near each of the axes; moreover: $b(x,z,t) = b(\xi + \int^\tau u(\xi,\eta,\tau')d\tau', \eta + \int^\tau w(\xi,\eta,\tau')d\tau', \tau) + b_s(x,z,t) - \int^\tau (\frac{b}{g} - 1)\mathcal{N}_b w d\tau'$; $\rho(x,z,t) = \rho(\xi + \int u(\xi,\eta,\tau')d\tau', \eta + \int^\tau w(\xi,\eta,\tau')d\tau', \tau) + \rho_s(x,z,t)$ and, for $t \geq O(1)$, $v(x,z,t) = \int^\tau u(\xi,\eta,\tau')d\tau' + v(\xi + \int^\tau u(\xi,\eta,\tau')d\tau', \eta + \int^\tau w(\xi,\eta,\tau')d\tau', \tau)$. The non linear problem can be linearized if we note that the envelope of all the closed streamfunctions generated by each dq is essentially summed up near the axes where the buoyancy is really mostly concentrated, i.e where an hyperbolic approximation is good, so that $a_{11} = a_{22} = 1$, $a_{12} = a_{21} = 0$ all the time. The consequence is that the buoyancy is dragged along the streamfunction produced by the space integrated vorticity sources situated in 'centers' $(P_k \equiv (\Delta_i^k(t), \zeta_i^k(t))$ such that $\frac{q_i^k}{2} = \int^{\zeta_i^k} dq_i^k(x=0,z)$; $\frac{q_i^k}{2} = \int^{\Delta_i^k} dq_i^k(\zeta,x)$, following the equation $\frac{d^2\zeta_{q_b}^k}{dt^2} = \frac{\partial^2\psi_k}{\partial\tau\partial x}^{hyp}_{z=\zeta_{q_b}^k}$, with the initial condition: $\zeta_{q_b}^k(t=0) = \frac{1}{\lambda} log 2$, $\zeta_{q_N}^k(t=0) = \frac{h}{2}$, $\Delta_{q_b}^k(t=0) = \Delta_{q_N}^k(t=0) = a\sqrt{2(log 2 - log(1 + 2e^{-n^2/8}))}$, soluble for long times, such that $\Delta_i << \zeta_i$.

Results-one plume

1)In order to have a sinking plume it is necessary a steep buoyancy gradient, i.e. a has to be $<< 1$, otherwise only a very slow, not sinking, flow perturbation is visible. 2)A scale invariance with λ is obtained. A single $\delta(t)$ external input, such as $b_s(x) = b_a e^{-\frac{x^2}{2a^2}}$, generates (for times $t < 1/f$), a single sinking plume, following the law $\zeta(t) = (C < B_0 > t^3)^{\frac{1}{2}}$ (B_0 is the surface buoyancy flux) ; a numerical calculation verifies this Marshall scale law with $C \approx (3.2 \pm 1.2)\lambda^{-2}$, got for $t \approx 0.3 f^{-1} >> 1.4 \cdot 10^{-2} f^{-1}$. A stochastic time set of such external inputs, with random b_a, generates a single sinking plume following a higher law power ($t^{5/2}$), or the same, depending on the probability $1/\tau$ of each random event; these 'scaling' laws depend on the mean value B_0 or on its time fluctuations $(< B_0^2 > - < B_0 >^2)^{1/2}$, depending on the air-sea interaction statistics. A surface buoyancy produced by a slowly time continuous variable summed to a stochastic set of such events leads, for large values of τ,to small amplitude variance oscillations, whose frequency is dependent on time. A constant surface buoyancy flux leads to Marshall scale laws. 3)An analysis of the internal randomness leads to intermittent plumes, but internal randomness is anyway hidden by the external randomness 4)The stratification has a perturbative decreasing in time effect on the homogeneous sea vorticity dynamics, depending to the external statistics. 5)For long time scales the Coriolis effect generates a transverse shear (antisymmetric around x ((b)r)$= \sqrt{3}z$): the buoyancy,mostly trapped in the hyperbolic region, is driven along the y((b) θ) direction; but the slow dependence on y((b)θ) allows each surface $y = c$((b) $\theta = c$) to have the same behaviour, so that the buoyancy evolution is not affected directly in average.The vorticity source s_v lets the perturbation to be horizontally propagated; in a stratified sea for long times this propagation is such as to change the sinking evolution law.

Results-more plumes

1)The sinking plume laws depend on the maximum values of the buoyancy and on the steepness of the gradient, not on its mean values. Statistically they depend on buoyancy space fluctuations. 2)A critical distance $l_c = 2\sqrt{2}a$ is identified. For $l \geq 6a$ a set of independent 'one plume' motions like before, for $2\sqrt{2}a < r < 6a$ a set of independent plumes, with the same time power laws as before, (C depending on the buoyancy gradient), are identified. 3)A short space correlation range between a set of surface buoyancy inputs is identified, such as to have this kind of periodicity. 4)For $t = O(1)$ the collective effect of the transversal shear ((b)of the rotation) is a final rotation on the boundary ((b)a collective chimney rotation).5)In a stratified sea the before told propagation lets the single plumes to interact in time.

References

[1] Marshall J.,Schott F.:Open Ocean convection;observations,theory and models.*Rev.Geoph.***37-1**:1–64,1997

[2] Maxworthy T.:Convection into Domains with Open Boundaries*Ann.Rev.Fluid Mech.***29**:327–371,1997

[3] Schott F.,Leaman K.:Obser. with MADCP in the Convection Regime in the Golfe du Lion.*J.Phys.Ocean.***21**:558–574,1991

[4] Zecchetto S.,Cappa C.:The spatial structure of the Medit.Sea revealed by ESR-1 scatt.*Int.J.Rem.sens.***22-1**:45-70,2001

[5] Bouché V.:Stat.conv. down motion driven by random inputs of localized buoyancy in a hom. sea.*N.Cim.***23C,5**:469-485,2000

[6] Bouché V.:About process times in some deepwater formation events in the Mediterranean Sea.*Jour.of Mar.Sys.***38**:305-321,2003

XXI ICTAM, 15-21 August 2004, Warsaw, Poland

THERMOCHEMICAL CONVECTION IN TWO SUPERIMPOSED MISCIBLE VISCOUS FLUIDS

Michael Le Bars*, Anne Davaille**
*Department of Applied Mathematics and Theoretical Physics, Cambridge, UK
**Laboratoire de Dynamique des Systèmes Géologiques, IPGP, France

Summary Marginal stability analysis and laboratory experiments have been performed to investigate thermal convection in two superimposed layers of miscible fluids. Two different regimes are observed: a whole-layer regime, where the interface deforms and convecting patterns develop over the whole depth of the system, and a stratified regime, where convection develops above and below a stable interface. Various behaviours are described and scaling laws determined.

INTRODUCTION

The interest in two-layer thermal convection has been largely inspired by natural problems, in particular the dynamics of the Earth's mantle [1]; besides, it has also been a theoretical challenge, because of the possibility of Hopf bifurcation and time-dependence at marginal stability [2]. The simple fact of adding a second layer considerably complicates the problem of thermal convection and opens up a very large parameter space that has not yet been fully explored.
In our study, we consider two superimposed layers of miscible fluids, with different densities, viscosities and depths, which are heated from below and cooled from above. All other properties of the fluids are equal. Besides, only the case where the initial density stratification is stable is studied; this configuration can however be reversed by thermal effects.

MARGINAL STABILITY ANALYSIS

Equations of motion correspond to Navier-Stokes equations in each fluid, coupled at the deformable interface. Apart from the Prandtl number (taken as infinite), four dimensionless numbers are necessary to fully describe the system: the viscosity ratio γ and the layer depth ratio a characterize the differences between the two layers, the Rayleigh number Ra measures the strength of convection, and the buoyancy number B, ratio of stabilizing chemical to destabilizing thermal density anomalies, determines the stability of the whole system and the ability of the interface to deform.
Linear stability analysis [3] points out the possible occurrence of two different regimes depending on B (see figure 1): i) when B is larger than a critical value B_c depending both on viscosity and layer depth ratios, a stratified regime takes place, with convecting patterns developing above and below a stable interface; ii) when B is lower than the critical value, a whole-layer regime takes place, with a deformed interface and convecting patterns developing over the whole depth of the system.

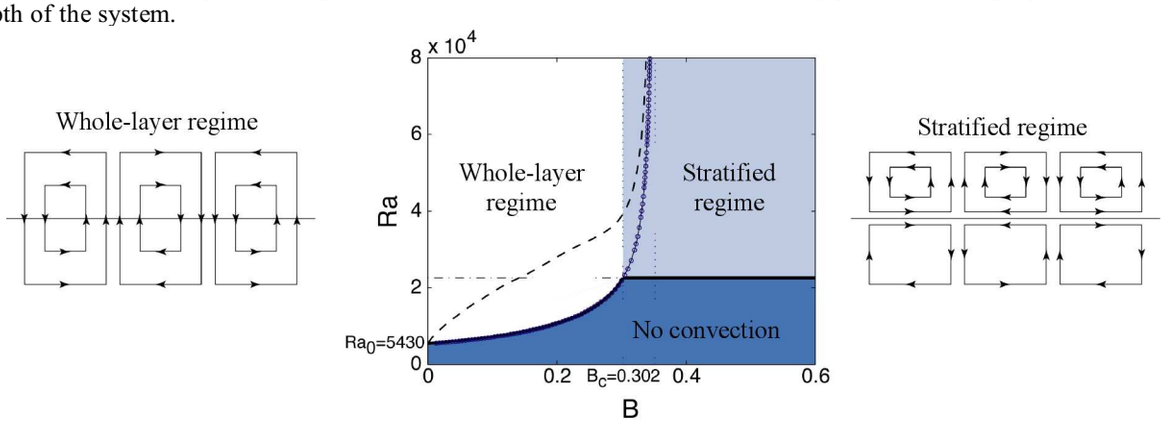


Figure 1: marginal stability analysis for γ=6.7 and a=0.5

EXPERIMENTAL STUDY

Using laboratory experiments [4-5], we have explored large ranges of buoyancy and Rayleigh numbers in order to characterize all possible behaviors ($0.048<B<4.4$ and $32<Ra<6.1\times10^8$). Close to marginal stability, the early scales of convection are well predicted by the linear analysis. At large Rayleigh number Ra, the situation is complicated by the superimposition of various types of convective features: only looking at one of the two fluids, the destabilization of its outer thermal boundary layer possibly leads to the formation of small-scale plumes as in classical Rayleigh-Benard convection, thus referred as 'purely thermal'; but purely thermal features from hot and cold plates also interact at the interface, where they induce a large-scale thermochemical regime, either with a stable interface (even if partly deformed), thus corresponding to the stratified regime, or with a fully destabilized interface, thus corresponding to the whole-layer regime. When $1/5<\gamma<5$ typically, the whole-layer regime takes the form of large convective features developing through the whole depth of the tank. The interface is distorted in all directions, and the two-layer initial system is never

reconstructed: overturning and immediate mixing operates. When $\gamma>5$ or $\gamma<1/5$ typically, the whole-layer regime gives rise to large-scale oscillations: the two fluids conserve their own identity, and the initial two-layer system is periodically reconstructed. The number of observed pulsations rapidly increases with γ. Two mechanisms of initial system reconstruction are possible (figure 2):

- vertical oscillations: starting from a stratified system, the lower fluid is progressively heated and becomes lighter, whereas the upper fluid is cooled and becomes heavier. Once the chemical density anomaly is cancelled by thermal effects, the interface deforms in large domes that rapidly propagate until they reach the opposite boundary: fluid 1 near the cold plate becomes heavier whereas fluid 2 near the hot plate becomes lighter. The initial stratification finally reappears and the system goes back to its initial configuration. A new oscillation can begin. Stirring between the two layers of course slowly works by advection, but more than 10 successive pulsations have been observed.
- initial configuration reversals: the whole invading layer is progressively emptied, until the initial configuration is totally reversed, with fluid 1 lying above fluid 2. Then, fluid 1 cools down, fluid 2 heats up, and the system finally goes back to initial state. In this case, stirring also works by advection, but several successive reversals can be observed.

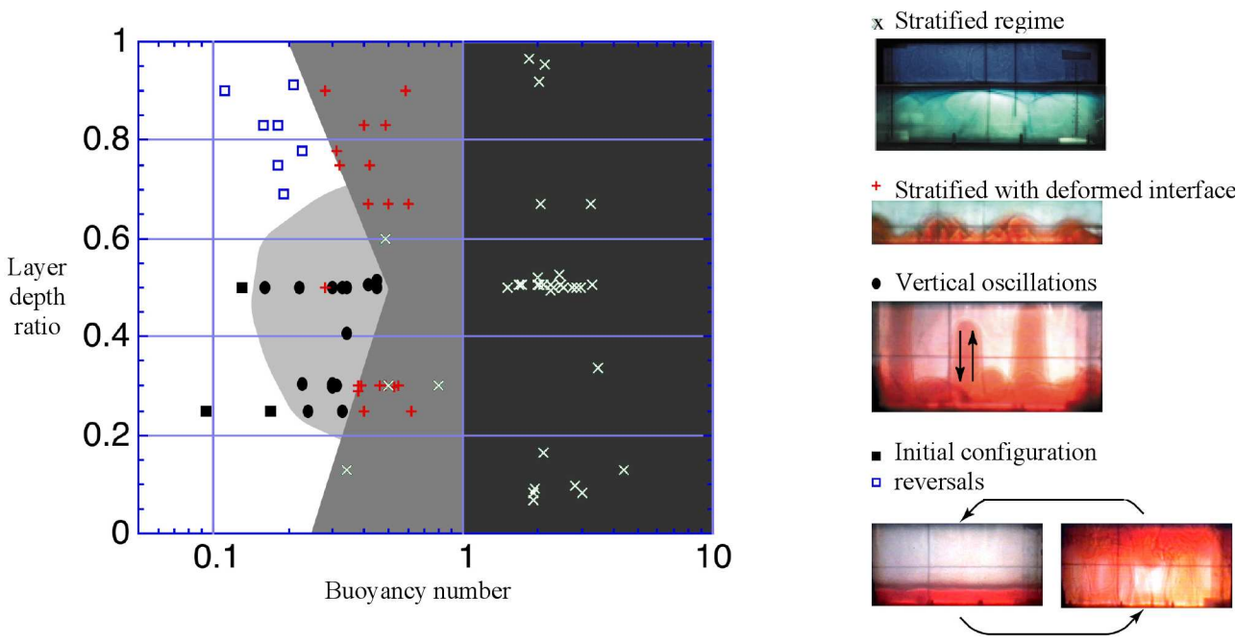


Figure 2: observed regimes depending on the buoyancy number and layer depth ratio.

Initial configuration reversals take place when the chemical stratification is low compared to the thermal buoyancy ($B<0.2$ typically and/or large Ra), but also when the invading layer is small and thus rapidly emptied ($a<0.3$ or $a>0.7$). Vertical oscillations take place otherwise. In all cases, the characteristics of domes (speed, size, period) are mainly controlled by the most viscous layer, which slows down motions over the whole depth of the tank.

CONCLUSION AND IMPLICATIONS FOR EARTH'S MANTLE

All described regimes are transient and the system systematically evolves towards one-fluid Rayleigh-Bénard convection because of stirring. However, the two isolated fluids can persist for very long time compared to the characteristic time-scale of thermal convection. Of particular interest for Earth's mantle are the vertical oscillations [6]: according to the scaling laws derived from the experiments, such a mechanism could indeed provide a simple and single physical explanation for the long-term periodicity (i.e. periods of hundreds millions years) observed in volcanic activity at the surface and magnetic activity in the core.

References

[1] Tackley P. J. Mantle convection and plate tectonics: Towards an integrated physical and chemical theory. *Science* **288**: 2002-2007, 2000.

[2] Richter F.M. & Johnson C.E. Stability of a chemically layered mantle. *J. Geophys. Res.* **79**: 1635–1639, 1974.

[3] Le Bars M. & Davaille A. Stability of thermal convection in two superimposed miscible viscous fluids. *J. Fluid Mech.* **471**: 339-363, 2002.

[4] Davaille A. Two-layer thermal convection in miscible fluids. *J. Fluid Mech.* **379**: 223–253, 1999

[5] Le Bars M. & Davaille A. Large interface deformation in two-layer thermal convection of miscible viscous fluids. *J. Fluid Mech.* **499**: 75-110, 2004.

[6] Le Bars M. & Davaille A. Whole-layer convection in a heterogeneous planetary mantle. *J. Geophys. Res.* In press.

XXI ICTAM, 15–21 August 2004, Warsaw, Poland

NONLINEAR CONVECTIVE PATTERNS IN SPHERICAL RAYLEIGH-BÉNARD SYSTEMS

Xinhao Liao*, Keke Zhang**
*Shanghai Astronomical Observatory, Chinese Academy of Sciences, Shanghai 200030, China
**School of Mathematical Sciences, University of Exeter EX4 4QJ, UK

Summary Nonlinear thermal convection in a spherical fluid layer in the presence of spherically symmetric gravity, spherical Rayleigh-Bénard convection, is investigated. At the onset of spherical Rayleigh-Bénard convection, there exists the (2l+1)-fold degeneracy of the linear solution, where l is the degree of a spherical harmonics. Nonlinear convection is studied through fully three-dimensional numerical simulations. Several new spherical patterns of nonlinear convection are found. In particular, a steadily drifting pattern in the form of a single giant spiral roll covering the whole spherical surface without defects is discovered for various Prandtl numbers for the first time.

INTRODUCTION

Thermal convection in a spherical fluid layer subject to a spherically symmetric radial gravity force and a spherically symmetric boundary condition, which will be referred to as spherical Rayleigh-Bénard convection, is associated with many natural phenomena in geophysical and astrophysical fluid systems (for example, Schubert, 1979; Zhang and Busse, 1998). Spherical Rayleigh-Bénard convection also represents an extensively studied exemplary fluid system involving the pattern and orientational degeneracies (for example, Busse, 1975; Chossat, 1979).
We consider a Boussinesq fluid spherical shell with constant thermal diffusivity κ, thermal expansion coefficient α and kinematic viscosity ν in the presence of its own gravitational field

$$\mathbf{g} = -\gamma \mathbf{r},$$

where γ is a constant. A traditional heating model (Chandrasekhar, 1961) is adopted, in which the basic temperature gradient,

$$\nabla T_s = -\beta \mathbf{r},$$

where β is constant, assumes a uniform distribution of heat sources. The problem of thermal convection, which was first formulated by Chandrasekhar (1961), is governed by the dimensionless equations

$$\frac{\partial \mathbf{u}}{\partial t} + (\mathbf{u}\cdot\nabla\mathbf{u}) = -\nabla p + R\Theta\mathbf{r} + \nabla^2\mathbf{u}, \tag{1}$$

$$P_r\left(\frac{\partial \Theta}{\partial t} + \mathbf{u}\cdot\nabla\Theta\right) = \mathbf{u}\cdot\mathbf{r} + \nabla^2\Theta, \tag{2}$$

$$\nabla\cdot\mathbf{u} = 0, \tag{3}$$

Where $\mathbf{u}$ is the flow velocity and Θ is the temperature perturbation. We have employed the thickness of the spherical shell, $d = (r_o - r_i)$, as the length scale , d^2/ν as the unit of time, and $\beta d^2\nu/\kappa$ as the unit of temperature fluctuation of the system, which lead to the two non-dimensional parameters, the Rayleigh number R and the Prandtl number P_r.

PATTERNS OF NONLINEAR CONVECTION

In the limit of large aspect ratio $\eta \to \infty$, the mathematical problem of spherical Rayleigh-Bénard convection becomes identical to that of the classical Rayleigh-Bénard convection in an infinitely extended horizontal fluid layer heated from below. The plane-layer Rayleigh-Bénard convection is perhaps the most intensively studied nonlinear system in the understanding of its pattern formation (for example, Veronis, 1959; Cross and Hohenberg, 1993; Bodenschatz, 2000). Thermal convection occurs when the Rayleigh number R reaches its critical value $R_c = 1708$. Near the onset of convection, roll, triangular, hexagonal and square patterns can exist. When aspect ratio η is finite, the effect of spherical geometry plays an essential role and the selection of nonlinear pattern bifurcating from a spherical symmetric basic state poses a complicated and difficult mathematical problem (Busse, 1975; Chossat, 1979). At the onset of spherical Rayleigh-Bénard convection, $R = R_c$, the general linear solution may be written, for example, as

$$u_r = f_l(r)\sum_{m=0}^{m=l}(C_m\cos m\phi + S_m\sin m\phi)P_l^m(\cos\theta), \tag{4}$$

where (r,θ,ϕ) are spherical polar coordinates, u_r is the radial flow, $f_l(r)$ represents a radial eigenfunction, $P_l^m(\cos\theta)$ denotes standard spherical harmonics of degree l and $C_m, S_m, m = 0, 1, ..., l$ are $(2l+1)$ arbitrary constants. The value of l corresponds to the minimum Rayleigh number required to initiate convection. Equation (4) indicates that there exists the (2l+1)-fold degeneracy of the solution. A complete elimination of the (2l+1)-fold degeneracy by nonlinearity proves

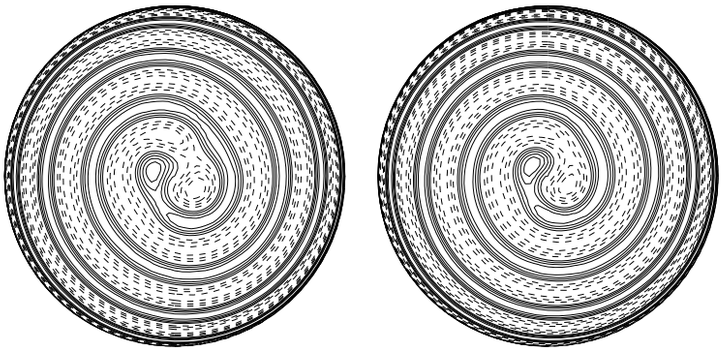


Figure 1. Contours of radial flow u_r at the middle surface of the spherical shell for $\epsilon = (R/R_c) - 1 = 0.28(R_c = 1712)$ and $Pr = 7.0$. Dashed contours indicate radially inward flow $u_r < 0$ and solid contours correspond to radially outward flow $u_r > 0$. The top (middle) panel shows the contours viewed from the north (south) pole.

determined by the size of aspect ratio η. Our linear analysis reveals that the critical Rayleigh number at $\eta = 41.2$ is given by $R_c = 1712$ with $l = 10$, which is slightly larger than that for the plane-layer Rayleigh-Bénard convection $R_c = 1708$ at $\eta \to \infty$. It follows that the convection solution at the bifurcation point has the 21-fold degeneracy.

Our numerical simulation starts with different combination of spherical harmonics as an arbitrary initial condition near the onset of convection for a fixed Rayleigh number $\epsilon = (R/R_c) - 1 = 0.28$. Convection simulations for a moderate $\epsilon = 0.28$ usually takes several viscous-diffusion-time scales to reach a steady equilibrium. We have carried out an extensive numerical simulations using various initial conditions, demonstrating that the final patterns of steady or periodic equilibriums are strongly dependent upon the initial condition used in simulations. In particular, we have discovered a new pattern in the form of a single, giant spiral roll extending from the north pole to the south pole without defects and covering the whole spherical surface. The giant spiral roll is slowly drifting with a constant amplitude which is shown in Figure 1. Of course the position of the pole at which the spiral roll starts or ends is arbitrary because of orientational degeneracy. We shall also report many other patterns of nonlinear equilibriums obtained using different initial conditions at various Prandtl numbers.

CONCLUSION

This is the first time that a single, giant, perfect spiral roll is found in the problem of spherical Rayleigh-Bénard convection. The discovery of the giant spherical spiral roll suggests the importance of plane asymmetric coefficients S_m in equation (4). In fact, the plane symmetry assumption used in the previous theories excludes the possibility of convection patterns in the form of a single giant spherical spiral roll shown in Figure 1.

References

[1] Busse, F. H. (1975) Patterns of convection in spherical shells. *J. Fluid Mech.* **72**, 67-85.
[2] Bodenschatz E. (2000) Recent developments in Rayleigh-Bénard Convection, *Annu. Rev. Fluid Mech.*32:709-778.
[3] Chossat P. 1979 Bifurcation and stability of convective flows in a rotating or not rotating spherical shell *SIAM J. Appl. Math.* 37:627-647.
[4] Chandrasekhar, S. (1961) *Hydrodynamic and hydromagnetic stability.* Clarendon Press, Oxford.
[5] Cross, M. C. and Hohenberg, P. C. (1993) Pattern formation outside of equilibrium, *Rev. Mod. Phys.* **65**,851-1112.
[6] Schubert G. (1979) Subsolidus convection in the mantle of terrestrial planets *Annu. Rev. Fluid Mech.* 7:289-342.
[7] Veronis, G. (1959) Cellular convection with finite amplitude in a rotating fluid. *J. Fluid Mech.* **5**: 410-435.
[8] Zhang, K. and Busse, F. H.(1998) Recent developments in the theory of convection in rotating systems. *Adv. in Fluid Mechanics* **20**:17-70.

VISUALIZATION OF THE FLOW STRUCTURE AND TEMPERATURE FIELD IN THE REGION OF MIXED CONVECTION

Elzbieta Fornalik[*], Wolfgang Leiner [**], Janusz S. Szmyd [*], Tomasz A. Kowalewski [***] and Hiroyuki Ozoe [****]

[*]*AGH University of Science and Technology, PL 30-059 Krakow, Poland*

[**]*Ruhr University of Bochum, D 44780 Bochum, Germany*

[***]*Polish Academy of Sciences, IPPT PAN, Swietokrzyska 21, PL 00-049 Warszawa, Poland*

[*****]*Kyushu University, 6-1 Kasuga Koen, Kasuga, 816 – 8580 Fukuoka, Japan*

Summary The results of experimental simulation of mixed convection in the process of single-crystal growth by Czochralski method are presented. Visualizations were done by dispersed encapsulated liquid crystals, which enable simultaneous measurements of the velocity and temperature fields. Experimental analysis was done for the cylindrical vessel kept in the isothermal conditions. Velocity fields showed appearance of vertical structures, whose number, shape and movement depend strongly on the Reynolds number. Velocity vectors maps are compared with the isotherms.

INTRODUCTION

Developments of microelectronic industry for modern applications require rigorous size and quality control of crystalline materials. The Czochralski method together with the Bridgman method is one of the crystal growth techniques for large-scale production, especially for oxide and semiconductor materials [1]. The convection in the melts during single crystal growth of semiconductors and oxides significantly affects the quality of the crystal grown from the melts in Czochralski crystal growth systems [2]. Therefore it is very important to understand melt motion and fluctuation of temperature in the melt for higher quality and larger size of single crystals.

The process of crystal growth by Czochralski method is widely discussed in the scientific literature. There are many areas of interests in both fields the numerical simulation and the experimental analysis of that process. The numerical simulation is more often discussed, for example Basu et al. [3], Akamatsu et al. [4], Enger et al. [5], who described the process under different conditions. The publications based on the experiments were rarely found in the past, but it can be said that lately their number increased [5], [6], [7], [8]. The authors of presented paper concentrated on the detailed structure of the flow field and the corresponding temperature field in the region of mixed convection, which can lead to better understanding of the phenomenon and to predict the optimal conditions.

EXPERIMENTAL APPARATUS AND PROCEDURE

Experimental apparatus is presented in figure 1. The mixed convection phenomenon was studied in the cylindrical glass vessel (crucible) **(6)** of inner diameter D = 0.094 m, placed into the glass cubic container **(5)**. The space between the crucible and the outer wall was filled by a thermostatic fluid maintaining the system in constant temperature. The cylindrical vessel **(6)** was filled by the mixture of glycerol and water, which was studied as an experimental fluid. To the free surface of mixture the copper cylinder **(4)** of diameter d = 0.022 m was attached. It was supplied from above by a vertical rotating shaft, which was driven by a DC-motor **(1)** provided by an adjustable power supply. A Peltier element **(3)** was fitted between the shaft and the copper cylinder simulating the crystal (4) served to maintain a temperature difference between these both and consequently equally between the inner pool simulating the melt and the copper cylinder simulating the crystal. The upper part of apparatus was covered by a cooling jacket **(2)**.

Essential Parameters

The physical similarity of the experiment was kept as close to the original process of crystal growth as possible, therefore in the present studies the fundamental parameters are the non-dimensional numbers: the Prandtl number (Pr = 14.8), the Grashof number (Gr = 115 555) and the Reynolds number (Re = 0, 5, 10) (eqs. 1)

$$\mathrm{Pr} = \frac{\nu}{a}, \qquad \mathrm{Gr} = \frac{g\beta\Delta T R^3}{\nu^2}, \qquad \mathrm{Re} = \frac{R_x^2 \Omega_x}{\nu} \tag{1}$$

where ν - kinematic viscosity, a – thermal diffusivity, g – gravitational acceleration, β - thermal expansion, ΔT – temperature difference, R – "crucible" inner radius, R_x – "crystal" radius, Ω_x – angular velocity.

Experimental methods

In the experiment the liquid crystals were applied for the velocity and temperature measurements. The velocity field was measured by DPIV method. The liquid crystals slurries were added into the mixture of glycerol and water in the crucible. They cover the temperature range of colour indication from 26.1 ^{o}C to 43.3 ^{o}C. To obtain the colour temperature field, the particular cross-section was illuminated by the white light sheet generated by the halogen lamp.

The digital image processing was applied to transform the colour images into the velocity vectors maps and data representing temperature fields.

RESULTS

The typical structure of the flow in a region of natural convection (Re = 0, temperature difference is set-up to be 5 K) is presented in figure 2. Two vortical counter-rotating structures can be observed. Just below the "crystal-simulating cylinder" the experimental fluid was cooled and it moved toward a crucible bottom. Then the stream of cooled fluid spread toward the side walls. In the vicinity of the side walls the fluid was warmed up and its ascending movement could be observed. In figure 3 velocity vectors map for Re = 10 is presented. The flow field showed very characteristic shape – two very large vortical structures in the central part of crucible, two vortices near side walls due to natural convection and just below the "crystal" two very small vortices. The fluid near the walls moved upward while the descending movement of cooled fluid was observed not below the "crystal" but on its sides. Just below the crystal fluid changed direction and moved upward. Whole structure is very complicated and it is difficult to present it in 2D. The temperature field is not presented here because of the place shortage.

CONCLUSIONS

In this paper the experimental simulation of mixed convection in the case of single crystal growth by Czochralski method was presented. The visualisation of the temperature and velocity field was done by dispersed encapsulated liquid crystals. The temperature images were compared to the velocity fields obtained by DPIV method. Interaction between the natural and forced convection generated very complicated structures, which are not symmetrical. In the central part of crucible, direction of fluid flow was changed, which can have an influence on the mass transfer. The temperature field became more homogeneous than in the case of natural convection.

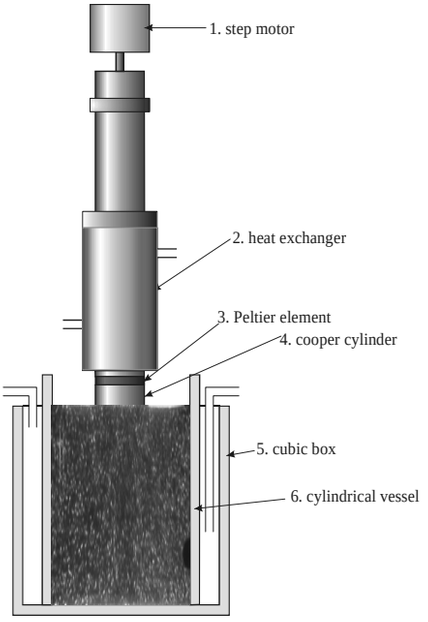


Figure 1. Schematic view of experimental equipment.

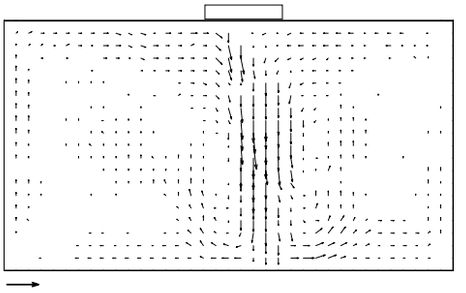


Figure 2. Velocity vectors map, Re = 0.

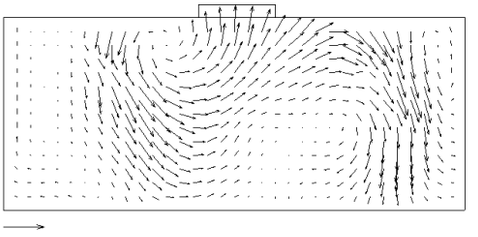


Figure 3. Velocity vectors map, Re = 10.

References

[1] Yoon J. K., Yi K. W.: Modelling of Transport Phenomena in Crystal Growth. WIT Press, Southampton 2000.

[2] Kakimoto K.: Modelling of Transport Phenomena in Crystal Growth. WIT Press, Southampton 2000.

[3] Basu B., Enger S., Breuer M., Durst F.: Effect of rotation on the three-dimensional mixed convection in the oxide melt for Czochralski growth. *J. Crystal Growth*, **230**: 148-154, 2001.

[4] Akamatsu M., Higano M., Ozoe H.: Elliptic temperature contours under a transverse magnetic field computed for a Czochralski melt. *Int. J. Heat and Mass Transfer*, **44**: 3253-3264, 2001.

[5] Enger S., Basu B., Breuer M., Durst F.: Numerical study of three-dimensional mixed convection due to buoyancy and centrifugal force in an oxide melt for Czochralski growth. *J. Crystal Growth*, **219**: 144-164, 2000.

[6] Aleksic J., Szymczyk J.A., Leder A., Kowalewski T.A.: Experimental investigations on thermal, thermocapillary and forced convection in Czochralski crystal growth configuration. Computational Methods and Experimental Measures. WIT Press, 2001.

[7] Hintz P., Schwabe D.: Convection in a Czochralski crucible – Part 2: rotating crystal. *J. Crystal Growth*, **222**: 356-364, 2001.

[8] Ozoe H., Toh K., Inoue T.: Transition mechanism of flow modes in Czochralski convection. *J. Crystal Growth*, **110**: 472-480, 1991.

XXI ICTAM, 15–21 August 2004, Warsaw, Poland

LARGE EDDY SIMULATION OF RAYLEIGH-BÉNARD CONVECTION IN AN INFINITE FLUID LAYER

A. Sergent*, P. Joubert**, P. Le Quéré*
*LIMSI, CNRS, BP 133, 91403 Orsay, France
**LEPTAB, Université de La Rochelle, Avenue M. Crépeau, 17042 La Rochelle cedex 1, France

Summary A numerical study of Rayleigh-Benard convection in an infinite fluid layer (Pr=0.71) is performed using large eddy simulation (LES) of the Navier-Stokes equations with the Boussinesq approximation. We present results in the 'hard turbulence' regime ($2.10^5 < Ra < 2.10^9$). The LES modelling uses the mixed scale diffusivity model, that we have originally developed in the case of the differentially heated cavity. The main observation is the ability of the computations to reproduce the 2/7 scaling behavior over a large Ra range ($2.10^5 < Ra < 2.10^8$). Moreover the regime transition towards the 'ultra-hard regime' is observed at $Ra = 2.10^9$.

INTRODUCTION

Much controversy surrounds the physics of turbulent Rayleigh-Bénard convection, especially at high Rayleigh numbers with recent experiments [1] [2] [3] or computations [4] [5]. The focus is on the Nusselt number correlations ($Nu \propto Ra^n$) and the successive transitions towards a steeper power laws.

As a transition of the mean flow is considered to be probably responsible of the turbulent regime transition between the 2/7 and steeper power law regime[1][4], numerical studies can be seen as an interesting complement to experiments in order to provide a physical picture of the large scale flow. However, because of the need to resolve accurately the thin wall boundary layer and the wall heat transfer, the direct numerical simulations (DNS) are limited to relatively low Rayleigh number ($Ra \propto 10^7$ for the most recent computations in a fluid layer[6]). An alternative way is to resolve in time and space the large coherent eddy structures while the unresolved scales are modelled. In this way, a transient (T-) RANS approach[5] or large eddy simulations (LES)[7] [8] [9] were applied to predict the Rayleigh-Bénard flow or to validate subgrid models. These two turbulence modelling approaches are very appealed insofar as they are potentially able to reach the highest Rayleigh numbers of experimentations ($Ra \sim 10^{15}$).

The present work investigates the Rayleigh-Bénard convection flow in a fluid layer in the hard turbulent regime using large eddy simulation. The main purpose concerns the ability of the LES modelling to provide the 2/7 scaling law in order to explore eventually higher regime.

NUMERICAL SET-UP

We consider the air-flow ($Pr = 0.71$) developing in a large aspect ratio cell (larger than 4) with periodic lateral boundary conditions. The fluid is heated from below and cooled from above by two isothermal no-slip walls. The large aspect ratio cells present several advantages: a lower Rayleigh number range for hard turbulence regime and an improvement in the convergence of statistical properties[10]. The flow is solved by integrating the three-dimensional filtered Navier-Stokes equations with the Boussinesq approximation. The unknown subgrid-scale (SGS) stresses and heat fluxes, which represent the effect of the subgrid scales on the large eddies, have to be modelled. However, using an *a priori* test, it has been shown[11] that the numerical dissipation from the advective term discretization scheme (QUICK) is able to reproduce correctly the energy transfer between resolved and unresolved kinetic scales of the flow, which can be quantified by the time-averaged production of subgrid kinetic energy. Therefore, we chose not to model the SGS stresses, but only the SGS heat fluxes. We used the mixed scale diffusivity model, that we have developed and applied with success in the differentially heated cavity[11]. This original model is based on its own time-scale, so that the Reynolds analogy, which connects the SGS diffusivity with the kinetic scales through a SGS Prandtl number, is not assumed. The equations are discretized on a staggered mesh by second-order accurate finite volume approximations. The resulting system is solved by a splitting procedure with a direct solver in each direction. Incompressibility is imposed by a projection method. The code has been validated by comparison with the DNS data[6] available at $Ra = 2.10^7$. Due to the need to resolve accurately the thin wall boundary layer, we used a non-uniform mesh size in the vertical direction with grids ranging from 26×98^2 up to 82×216^2, respectively in the vertical and horizontal directions. All the simulations have been run for a time long enough to compute reliable statistics for the heat transfer and the second order moments, that require an averaging time from 300 to 100 T_L (T_L: large eddy turnover time) for the Rayleigh number $2.10^5 < Ra < 2.10^9$.

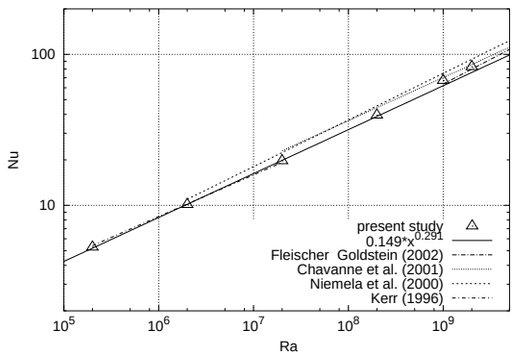


Figure 1. Comparison of the computed $Nu(Ra)$ results with several experimental and DNS correlations.

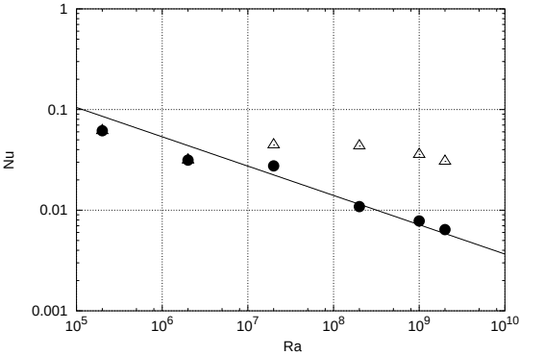


Figure 2. Viscous (△) and thermal (●) boundary layer thicknesses vs Ra. Line is power law $\delta \sim Ra^{-0.291}$.

RESULTS

In figure 1 we report the non-dimensional heat transfer as a function of Rayleigh number with some experimental results [3][1][2] for comparison, and DNS data[6] for validation, with which a good agreement is obtained. From $Ra = 2.10^5$ up to $Ra = 2.10^8$ the points seem to fit narrowly the 2/7 power law, with a best fit to our data given by $Nu = 0.149Nu^{0.291}$. Previous studies[1] have proposed different characteristics to describe the hard turbulent regime: (i) the $\sim 2/7$ power law Ra dependance for different variables, (ii) a mean large scale flow, (iii) an exponential-shaped curve for the histogram of the temperature fluctuations in the center. Now, assuming the distance from wall of the peak of the r.m.s. vertical profile as the boundary layer thickness, we observe effectively the Ra scaling law of the thermal boundary layer (Fig. 2). Moreover the histograms of the temperature fluctuations (no presented here) exhibits the exponential shaped curve for $Ra \geq 2.10^5$ instead of a Gaussian one at $Ra = 2.10^4$. Consequently, we presume to observe the hard turbulent regime for $2.10^5 \leq Ra \leq 2.10^8$.

Above $Ra = 10^9$, $Nu \sim Ra^{2/7}$ trend does not stand anymore, and a steeper curve seems to appear. This transition was also observed experimentally [1] or numerically [4] but for a higher Rayleigh number, due to their smaller aspect ratio cell. However our data present a good agreement with experimentation performed in an horizontal enclosure[3]. Besides it can be noted that a small bump is present in the decrease of the thermal boundary layer around $Ra = 2.10^7$, while the viscous boundary layer gets thicker for $2.10^7 \leq Ra \leq 2.10^9$ instead of decreasing with a constant slope. This behaviour has been also showed by previous studies and interpreted as an effect of laminar-turbulent transition of the viscous boundary layer induced by the large scale flow near the walls[1]. Further computations are needed to describe this new regime.

CONCLUSIONS

A numerical study of Rayleigh-Benard convection in an infinite fluid layer (Pr=0.71) is performed using large eddy simulation (LES) of the Navier-Stokes equations with the Boussinesq approximation. The main observation is the ability of the computations to reproduce the 2/7 scaling behavior over a large Ra range ($2.10^5 < Ra < 2.10^8$). Moreover the regime transition towards the 'ultra-hard regime' is observed at $Ra = 2.10^9$.

References

[1] X. Chavanne, F. Chilla, B. Chabaud, B. Castaing, and B. Hébral. Turbulent Rayleigh-Bénard convection in gaseous and liquid he. *Phys. Fluids*, 13(5):1300–1320, 2001.
[2] J.J. Niemela and Sreenivasan K.R. Confined turbulent convection. *J. Fluid Mech.*, 481:355–384, 2003.
[3] A.S. Fleischer and R.J. Goldstein. High-Rayleigh-number convection of pressurized gases in a horizontal enclosure. *J. Fluid Mech.*, 469:1–12, 2002.
[4] R. Verzicco and R. Camussi. Numerical experiments on strongly turbulent thermal convection ins slender cylinder cell. *J. Fluid Mech.*, 477:19–49, 2003.
[5] S. Kenjeres and K. Hanjalic. Numerical insight into flow structure in ultra-turbulent thermal convection. *Phys. Rev. E*, 66(036307):1–5, 2002.
[6] R.M. Kerr. Rayleigh numberscaling in numerical convection. *J. Fluid Mech.*, 310:139–179, 1996.
[7] T. Eidson. Numerical simulation of the turbulent Rayleigh-Bénard problem using subgrid modelling. *J. Fluid Mech.*, 158:245–268, 1985.
[8] V.C. Wong and D.K. Lilly. A comparison of two dynamic subgrid closure methods for tubulent thermal convection. *Phys. Fluids*, 6(2):1016–1023, 1994.
[9] S.J. Kimmel and J.A. Domaradzki. Large eddy simulation of rayleigh-bénard convection using subgrid scale estimation model. *Phys. Fluids*, 12(1):169–184, 2000.
[10] X.Z. Wu and A. Libchaber. Scaling relations in thermal turbulence: the aspect ratio dependence. *Phys. Rev. A*, 45:842–845, 1992.
[11] A. Sergent, P. Joubert, and P. Le Quéré. Development of a local subgrid diffusivity model for large eddy simulation of buoyancy driven flows: application to a square differentially heated cavity. *Num. Heat Transfer Part. A*, 44(8):789–810, 2003.

THE INFLUENCE OF TRANSLATIONAL VIBRATIONS OF CIRCULAR POLARIZATION ON FLUID CONVECTIVE INSTABILITY AND FLOW PATTERNS

Aleksander A. Kozlov, Igor A. Babushkin, Gennady F.Putin
Department of General Physics, Perm State University, Bukyreva 15, 614600 Perm, Russia

Summary The stability of the mechanical equilibrium, heat transfer and currents of movements fluidy in horizontal plane layer subject to circular translational vibration is investigated experimentally. The ground experimental modeling of thermovibrative currents in the field of translational inertial accelerations with reference to dynamic conditions on space vehicles is planned also. The map of convection modes is constructing. The heat-mass transfer in cavity, both at heating from below and from above were investigated.

In the stratification of density media (gases, liquids, etc.) and under certain external conditions convective movement caused by Archimedean force can arise. The amplified attention to studying convective processes in non-stationary force fields, with reference to conditions of orbital flight, is caused by the development of space technologies, such as the growth of semi-conductor and biological crystals, the reception of especially pure and composite materials, electrophoresis, etc. [2,3] The analysis of weightlessness in real conditions on a space vehicle has shown a necessity to take into account the influence on technological processes not only concerning the gravitational mechanism of convection but also varying in inertial accelerations [3,4]. Measurements of variables inertial accelerations onboard orbital stations " MIR " and "SALUT - 6", and also the " Space Shuttle " show that up to 95 % of capacity accelerations is concentrated in a range of frequencies of 0.1-14 Hz [4,5]. The specified interval corresponds to a range of own frequencies convective systems that determines an opportunity of dynamic excitation convection in microgravity conditions [1]. The performance of necessary researches on space vehicles (SV) is connected to the complexity and the cost of experiments. Therefore it is expedient to carry out laboratory modelling of the phenomena in ground conditions before first-hand experiences on space vehicles.
At laboratory modelling to intensify the vibrational effects in comparison with gravity effects ones it is necessary to create the conditions when Rayleigh vibrational number $Ra_V = (b\beta\omega\theta h)^2/2\nu\chi$ exceeds with gravitational parameter $Ra_G = g\beta\theta h^3/\nu\chi$. Here ν, χ, a are , kinematic viscosity, thermal conductivity of fluid, θ - temperature difference across the layer, h – layer thickness, g and β - acceleration due to gravity and thermal expansion coefficient, b –amplitude and ω - frequency of the vibration The ratio $Ra_V/Ra_G \sim (b\omega)^2\beta\theta/2h$ shows that it is need to use the layers with small thickness, the great temperature difference and mechanical vibrator that the higher vibration velocity is provide.

The stability of the mechanical equilibrium

The threshold curves of mechanical equilibrium are presents in fig. 1(h = 2 *mm*, heptane). The value of the Ra>0 is account heating from below and $Ra_G < 0$ – heating from above. The line a is represents theoretical border of instability, which cuts on a horizontal axis a piece value Ra_G * = $1.7*10^3$, that appropriate to a threshold of occurrence thrmogravitational convection. On a vertical axis the piece Ra_V =$2{,}1*10^3$, that appropriate to a threshold of excitation vibroconvection in conditions of weightlessness is cut. The border of stability quasiequilibrium for "high" frequencies is served a curve "b". For "low" frequencies, curve "c", the border of stability quasiequilibrium is displaced in area of higher numbers Ra_v. According to experimental data, it is possible to consider frequencies above 5.5 Hz "high", and is lower 5.2 Hz "low". The results of experiment indicate that of the inertial acceleration, polarized on a circle, decrease the threshold of mechanical equilibrium stability in a flat horizontal layer of a liquid at $Ra_G > 0$. Convective current arises at smaller numbers Ra_G, than critical number Ra_G * in a static case. Besides the given vibrations raise convective movemenent at heating from above – in a situation, absolutely steady in absence of oscillation of a layer, and the threshold curves depends on frequency of external influences.

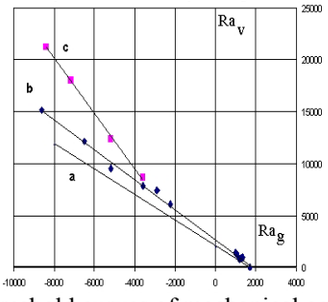


Fig. 1 The threshold curves of mechanical equilibrium a – high frequency line (theory), b – high frequency line (exper-t.), c low frequency line (exper-t.).

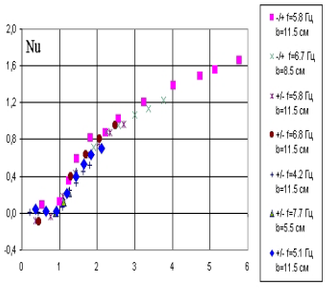


Fig. 2 The dependence of number *Nu* from supercriticality μ.

In figure 2 the dependence of a dimensionless thermal flow - number Nusselta Nu from supercriticality μ is submitted. As it is visible from the diagram, in researched area of parameters experimental value, within the limits of an error, it is good overlay on one curve. The specified behaviour will well be coordinated to root dependence $Nu \sim$ Rag1/2, having a place in many convection tasks. It is necessary to notice also that, according to the diagram in figure 3.5, the number Нуссельта at supercriticality equal 4 accepts value 1,4. For comparison, at convection in a static field of weight the number Nu for $Ra_G/Ra_G^* = 4$ accepts value 1. It testifies to substantial growth heat transfer, caused by the vibrating mechanism of the convection, in comparison with a heat transfer caused by the gravitational mechanism of the convection.

Conclusions

The influence polarized on a circle inertial acceleration on stability of mechanical equilibrium of a liquid in a flat horizontal layer is investigated. Is established, that the circular vibrations lower a threshold of occurrence convective of current of a not isothermal liquid. The dependence of a dimensionless thermal flow - number Nu is investigated depending on conditions heating and intensity of vibrations. Influence of forward vibrations of the mentioned above polarization on structures convection also is investigated. Are found out near-threshold oscillatory modes of convection such as "zipper"- state.

The research described in this publication was made possible in part by Russian Foundation for Basic Research and Administration of Perm Region, Russia, under grant 04-02-96038 and Award No PE-009-0 of the U.S. Civilian Research & Development Foundation for the Independent States of the Former Soviet Union (CRDF).

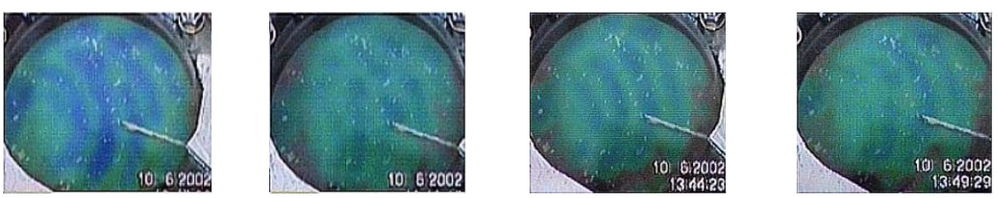


Fig. 3 It is near-threshold oscillations. $Ra_G = 2{,}2*10^3$, $b = 11{,}5$ cm, $\omega = 4{,}5$ Hz

References

[1] Gershuni G.Z., Zhuhovitsky E.M. The convective instability of the incompressible fluid, Moscow, Science, 1972.
[2] Dubovik K.G. , Nikitin S.A., Polezhaev V. I. The convective processes in the weightlessness and theirs significance in the tasks of the space technology. Hydrodynamics and heat-mass transfer in the weightlessness, Moscow, 1982.
[3] Grishin S.D., Leskov L.V., Space industrialization. Problems and prospects. Moscow, Science, 1987.
[4] Barmin I.V., Bezdenezhnyh N.A. The experiments program on the setup for investigations of the hydrodynamics phenomenon in the weightlessness conditions. Lts. SA USSR, MLG, № 4, 1985.
[5] Grishin S.D., Dubovskiy V.B., Obydennikov S.S., Savichev V.V. The investigation of the smaller accelerations on board Of orbital science station «Salut-6". The technological experiments in space. Sverdlovsk, ESC SA USSR, 1983.

XXI ICTAM, 15-21 August 2004, Warsaw, Poland

THERMAL BUOYANCY CONVECTION IN SYSTEMS WITH DEFORMABLE INTERFACES

Dmitriy V. Lyubimov[*], Nicolay I. Lobov[*], Tanyana P. Lyubimova[**], Nikita A. Ospennikov[*], Sergey V. Shklyaev[*]

[*]*Perm State University, Perm, Russia*

[**]*Institute of Continuous Media Mechanics UB RAS, Perm, Russia*

Summary Thermal convection in a two-layer system with deformable interface heated from below is investigated. The generalized Boussinesq approximation is applied. Long-wave and cellular disturbances are investigated in the framework of linear stability theory. Non-linear equation describing the long-wave disturbances with large amplitude is derived and investigated. Numerical simulation of supercritical convective regimes is conducted.

The paper deals with the investigation of thermal buoyancy convection in a two-layer system with deformable interface. It is well known that interface deformability assumption is incompatible with the conventional Boussinesq approximation. Formally it is related to the fact that Rayleigh number, which is the governing parameter in the Boussinesq theory, can be represented as the product of Galilee number Ga and Boussinesq parameter, characterizing relative density variations due to the temperature inhomogeneities. The Boussinesq approximation uses the limit transition, when Galilee number tends to infinity and Boussinesq parameter tends to zero whereas Rayleigh number remains finite. However, when the Galilee number increases, the deformations of fluid interface tend to zero. At the same time there are situations where deformations of interface could be important. One an example is the case of interface between the fluids with close densities. In this case effective description is possible in the framework of generalized Boussinesq approach, in which not only the Boussinesq parameter but also the relative density difference is assumed to be small. In the present work, in the framework of this model the buoyancy convection of a system of two fluids filling the infinite horizontal layer heated from below is considered. The problem allows the solutions which correspond to the conductive state with motionless fluids and horizontal interface.

The stability of this state is investigated analytically and numerically. For small long-wave disturbances analytical investigation is carried out by the expansion into the wave number series. The stability to the disturbances with finite wave-length in the case of thermally conductive layer boundaries is determined by fundamental partial solution system construction. The substitution of the solutions into the boundary conditions allows to obtain the characteristic equation for the disturbances growth rate.

The calculations show that if the density difference of two fluids is large enough (it is convenient to characterize the density difference by the dimensionless parameter *G*, which has the meaning of the Galilee number defined through the density difference) the interface does not practically deform and the threshold of instability coincides with the well known value for the case of non-deformable interface. With *G* decrease the role of interface deformations grows and the critical Rayleigh number corresponding to the most dangerous disturbances increases, i.e. the stability of the system is also raising. However, at small enough values of *G* the crisis of the conductive state does not correspond to the cellular disturbances, but to the long-wave ones and the critical Raleigh number dependence on *G* is different. Namely, with *G* decreasing the critical Rayleigh number decreases up to the zero value by linear low.

Under assumption of small amplitudes of the long-wave interface disturbances, the finite-amplitude excitation of convection is found to be realized at small supercriticalities in a wide range of parameters. However, the problem under consideration is specially interesting by the possibility to study analytically the case of strong deformations of interface. The point is that if the fluid densities are extremely close then even weak flow leads to the strong deformations of the interface. In this way it was possible to derive the amplitude equation

$$\frac{\partial \zeta}{\partial t} = \frac{\partial}{\partial x}\left(f(\zeta)\frac{\partial \zeta}{\partial x}\right) - C\frac{\partial}{\partial x}\left(f_G(\zeta)\frac{\partial^3 \zeta}{\partial x^3}\right)$$

$$f(\zeta) = Ra\, f_R(\zeta) - G f_G(\zeta)$$

where ζ is the deviation of interface from horizontal position, C is the capillary parameter, $f_G(\zeta)$ and $f_R(\zeta)$ are complicated functions in general case; these functions turn to zero at $\zeta = \pm 1$. The first function is positive at $|\zeta| < 1$, and the second function does not have a definite sign. In the limit case, when the viscosity and thermal expansion coefficients of both fluids are the same, the expression for these functions is simplified:

$$f_R = \frac{[\kappa]\left(1-\zeta^2\right)^2}{240}\,\frac{[\kappa]\left(4\zeta^4 - 9\zeta^2 - 7\right) - 10\zeta^3 + 34\zeta}{\left(2 - [\kappa]\zeta\right)^2}, \quad f_G = \frac{1}{24}\left(1-\zeta^2\right)^3$$

Here $[\kappa]$ denotes the difference of thermal conductivity coefficients divided by their half-sum.

In the framework of this equation the stability of conductive state is investigated (conductive temperature distribution, planar interface). It is shown that direct or inverse bifurcations are possible depending on the parameter values.

The periodical stationary solutions of amplitude equation are investigated numerically. Solutions, corresponding to two-dimensional convective flows in the system with deformed interface, are discovered. These solutions exist in a rather narrow range of parameters. In the other cases one of the fluids splits into the drops. In the case of heating from below the drops of fluid with higher thermal conductivity surrounded by less thermally conductive fluid are formed. Under heating from above the opposite situation is observed: the drops of less thermally conductive fluid are surrounded by higher thermally conductive fluid.

In the parameters range where the cellular disturbances are more dangerous, the investigation of supercritical convective regimes is made numerically by finite difference method using level-set approach for a concrete pair of fluids.

CONVECTIVE PHENOMENA IN ROTATING ANNULI HEATED ON PERIPHERY

Vladimir V. Ris[*], Evgueni M. Smirnov[**], Alexander A. Smirnovskii[**]
[*]*SPb State Polytecnic University, Department of Theoretical Fundamentals of Thermoengineering, 195251 St.-Petersburg, Russia*
[**]*SPb State Polytecnic University, Department of Aerodynamics, 195251 St.-Petersburg, Russia*

Summary Results of numerical simulation of 2D and 3D time-dependent free convection in rotating annular air-filled cavities heated on the periphery and cooled at the inner radius are presented. The cavity radial aspect ratio is equal to 0.35, the centrifugal Rayleigh number is ranged from $2\cdot10^4$ to $5\cdot10^7$. In the middle of this *Ra*-range, stable flow regimes with two, four or six vortices can be obtained with the 2D formulation for an unlimited annulus. In a 3D configuration, with two bounding adiabatic discs, the two-vortex regime is inhibited.

INTRODUCTION

Rapidly rotating cavity heated on the periphery are typical elements of gas turbine rotors. A sealed annular cavity formed by two discs and two cylindrical walls is considered as a generic configuration for studies of convective phenomena induced by centrifugal buoyancy [1]. An experimental study of free convection with a radial heat flow in rotating air-filled cavities was performed by Bohn et al. [2] at the Rayleigh numbers exceeding 10^7. Theoretical analysis of buoyancy-induced convection in rotating cavities faces the difficulties associated with three-dimensional and unstable behaviour of the flow, similar to that one has for the Rayleigh-Bénard convection in a fluid layer confined between two horizontal plates, the lower of which is hotter than the upper one. Numerical simulation of 3D convective phenomena in rotating cavities heated on the periphery is very time-consuming. Known attempts were limited by cases of segmented cavities with sectors of 45 degrees [2] or 60 degrees [3]. Note that in the case of segmented cavities the radial partitions stabilise the convection and result in a considerable reduction of the computational grid size. A simplified 2D formulation of the buoyancy-induced convection, assuming rotating annuli are unlimited in the axial direction, were used in [4] for a numerical analysis based on the Boussinesq's approximation. The present contribution covers a numerical analysis of time-dependent air convection flows induced by the centrifugal buoyancy both in an annulus unlimited in the axial direction and in an annular cavity bounded by two adiabatic discs.

STATEMENT OF THE PROBLEM AND COMPUTATIONAL ASPECTS

For the present 3D numerical simulation, following the experimental study [2], we have chosen a rotating annular cavity with the radial ratio, r_i / r_o, equal to 0.352, and the axial ratio, s / r_o, equal to 0.338. Here r_o is the outer radius of the cavity, and s is the cavity axial size. The Rayleigh number is defined as $Ra = Pr\, r_m \Omega^2 (\Delta r)^3 T_m^{-1} (T_o - T_i) / \nu^2$, where Ω is the angular velocity, $T_m = (T_o + T_i)/2$, $r_m = (r_o + r_i)/2$, $\Delta r = r_o - r_i$. According to [2], we set the temperature of the inner cylinder, T_i, equal to 283K, and the outer cylinder temperature, T_o, equal to 373K. The air pressure level is taken as 1 bar. The Prandtl number, *Pr*, is set to 0.71.
We consider also the 2D formulation of the problem, assuming the annulus of $r_i / r_o = 0.352$ is unlimited in the axial direction ($s \to \infty$). The thermal conditions on the cylindrical walls are kept the same as in the 3D case.
The computations on the base of the full Navier-Stokes equations and the energy equation written with the low-speed flow approximation were performed using the well-validated in-house code SINF, which is under long-time development at the Department of Aerodynamics of the St.-Petersburg State Polytechnic University. This advanced 3D Navier-Stokes solver is based on the second-order finite-volume spatial discretization using the cell-centred variable arrangement and body-fitted block-structured grids. A low-dissipative scheme blending the fourth-order central and the second-order upwind techniques is used for convective flux evaluation. The discretization of time derivatives is done with a three-time-level, second-order implicit scheme. In the case of low-speed flows, the artificial-compressibility method is applied at each time step. Additional details of the solver can be found elsewhere [5].
Results presented were obtained using a non-uniform grid consisting of 56×144 cells in the rotation plane and 56 cells in the axial direction (for the 3D analysis). The grid was clustered both to the cylindrical walls and to the bounding discs.

RESULTS AND DISCUSSION

Multiple regimes of 2D convection

Parametric computations on the base of the 2D formulation were performed for the Rayleigh number ranging from $2\cdot10^4$ to 10^8. It has been established that at the Rayleigh numbers ranged from (approximately) $2\cdot10^4$ to 10^5 one is

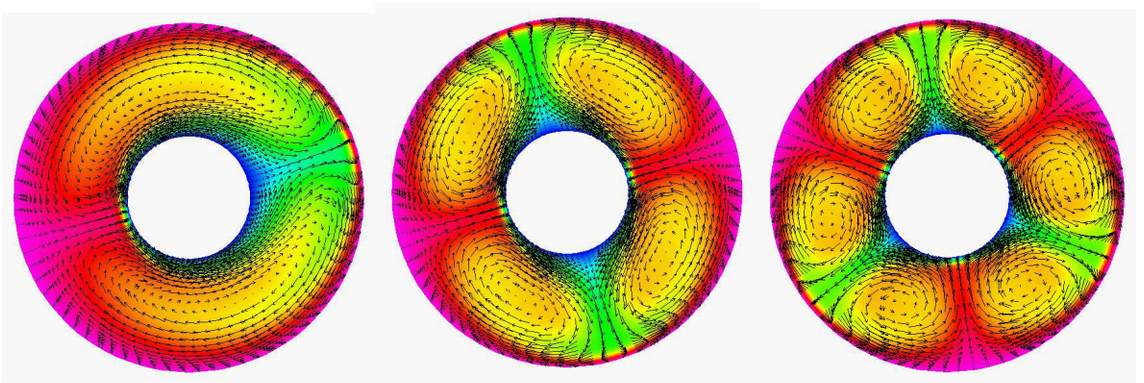


Fig. 1. Three possible regimes of buoyancy-induced 2D convection in an air-filled rotating annulus heated on periphery. Results of unsteady computations with a grid of 56×144 cells at $Ra = 10^5$: rarefied patterns of velocity vectors are imposed on color maps of temperature distributions (scales are common for all the regimes).

able to obtain three stable convection regimes that differ in the number of large-scale vortices. The first regime is characterized by the two-vortex structure of the convection, one of the vortices is cyclonic, and the other is anticyclonic. Respectively, for the second and the third regime, four-vortex and six-vortex convection patterns are observed, as illustrated in Figure 1 for $Ra = 10^5$. The vortices can drift in the circumferential direction. One or another regime develops depending on initial velocity and temperature fields used for a computational run. The two-vortex regime has the narrowest attraction area. In fact we were able to obtain this regime by an artificial way only, generating an initial two-vortex structure via solving the problem of gravity-induced convection in a horizontal annulus. The four-vortex regime exists at the Rayleigh numbers ranged from (approximately) $2\cdot10^4$ to 10^7, and solutions for the six-vortex regime can be obtained for the whole *Ra*-range considered.

Specifics of 3D convection

Results of the 3D numerical analysis performed have led to the conclusion that flow phenomena near the bounding discs suppress the two-vortex regime. This regime degenerates even if initial fields are obtained by translation of a 2D two-vortex solution in the axial direction. Possible regimes with four-vortex or six-vortex large-scale structures manifest a pronounced chaotic behavior at $Ra>10^6$, so that the unsteady convection becomes a "conglomeration" of ordered structures and chaotic components. In the middle plane, between the discs, the flow patterns are similar to those obtained with the 2D approach. Near the discs one can observe formation of the Ekman-type layers [1] which are permanently disturbed by perturbations coming from the corner regions. The vortices are in a relative circumferential motion (drift) and the direction of this drift is opposite to the direction of rotation. A whole turn of the vortex structure takes approximately 230 periods of rotation.

Heat transfer data

Computational data obtained for the heat rate transported from the outer to the inner cylinder show that the Nusselt numbers, *Nu*, for 2D four-vortex convection regimes are by about 25% higher than those for the two-vortex convection, if the latter exists, and by 5 to 15% lower than *Nu*-values in the six-vortex case. For the 3D configuration, the Nusselt numbers are by about 15% lower than those for correspondent 2D solutions. So, one may conclude that the 2D formulation is a fruitful approach for express evaluations of heat transfer in rotating cavities bounded by adiabatic discs, at least for the *Ra*-range examined. Note finally that at $Ra > 10^5$ the Nusselt numbers computed for the six-vortex regimes are in a good agreement with values evaluated with the correlation, $Nu \sim Ra^{0.228}$, given in [2].

The work was supported by the Russian Basic Research Foundation, grant 04-02-16531.

References

[1] Owen J. M., Rogers R. H.: Flow and Heat Transfer in Rotating-Disc Systems. Vol. 2: Rotating Cavities, RS Press, Taunton, U.K., 1995.

[2] Bohn D.E, Deuker E., Emunds R., Gorzelitz V. *ASME Journal of Turbomachinery*, 117:175-183, 1995.

[3] Kirillov A.I., Kitanina E.E., Ris V.V., Smirnov E.M. *Proc. 12th International Heat Transfer Conference*, Grenoble, France, 2002, Aug 18-23, V. 2, pp. 105-110, 2002.

[4] King M. P., Wilson M. *Proc. 12th International Heat Transfer Conference*, Grenoble, France, 2002, Aug 18-23, V. 2, pp. 465-470, 2002.

[5] Smirnov E. M., Abramov A. G., Ivanov N. G., Korsakov A. B., Zajtsev D. K. *Proc. 7th Int. Conf. on Advanced Comp. Methods in Heat Transfer*, Sunden & Brebbia (Eds), WIT Press, pp. 107-116, 2002.

ON THE RAYLEIGH-BÉNARD PROBLEM IN THE CONTINUUM LIMIT

Avshalom Manela*, Itzchak Frankel*
Faculty of Aerospace Engineering, Technion-Israel Institute of Technology, Haifa 32000, Israel

Summary The transition to convection in the Rayleigh-Bénard problem at small Knudsen numbers is studied via a linear stability analysis of the compressible 'slip-flow' problem. No restrictions are imposed on the magnitudes of temperature difference and compressibility-induced density variations. Comparison of the results with existing DSMC and continuum non-linear simulations demonstrates that the present analysis correctly predicts the boundaries of the convection domain. This offers the linear temporal stability analysis as a viable means of studying the effects of the various parameters on the onset of convection.

INTRODUCTION

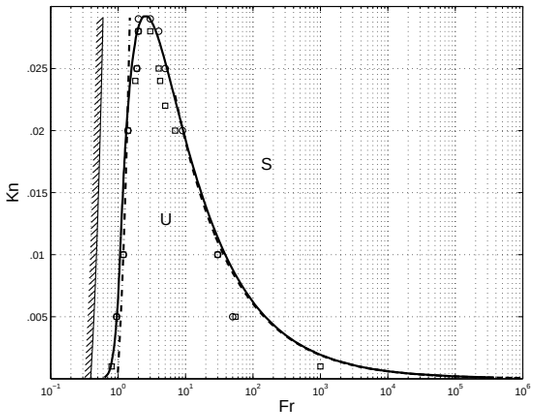
The onset of convection in an initially quiescent fluid confined between parallel horizontal walls and heated from below is a classical problem in hydrodynamic stability theory (Chandrasekhar 1961). This problem has been investigated extensively within the framework of the Boussinesq approximation where fluid-density variations are only considered in the buoyancy term of the equation of motion. This approximation is based on the assumptions that relative temperature differences and density variations owing to compressibility are both small. Each of the relatively few analyses which have hitherto addressed the corresponding compressible-flow problem have relaxed either one but not both of these assumptions. Thus, Fröhlich, Laure and Peyret (1992) studied the effects of large temperature differences while retaining the assumption that compressibility-induced density variations were negligible. Bormann (2001), among others, considered compressibility effects assuming small temperature differences and hence constant transport (i.e. viscosity and thermal conductivity) coefficients. In both cases the results indicate that the compressible-fluid system is less unstable than the comparable predictions based on the Boussinesq approximation. To the best of our knowledge, no comprehensive treatment of compressible-fluid stability problem exists in the literature even within the context of continuum gas-dynamics. Thus, addressing this problem without a priori restricting the relative temperature differences or compressibility-induced density variations is one of the main objectives of the present contribution.

The Rayleigh-Bénard (RB) problem for rarefied gases has been studied in recent years principally by means of the Direct Simulation Monte Carlo (DSMC) method (see Stefanov, Roussinov & Cercignani 2002, hereafter referred to as SRC, and references cited therein). These numerical simulations follow the evolution of the macroscopic (hydrodynamic) fields through their terminal states. The results demonstrate that significant convection only occurs in the continuum limit of small $O(10)^{-2}$ Knudsen numbers. However, 'noisy' elements inherent in DSMC make it difficult to characterize the final states, particularly for parameters combinations in the vicinity of the transition to convection. Furthermore, these simulations become extremely time consuming in the continuum limit, which obstruct an accurate delineation of the domain of instability. An alternative approximate analysis of the onset of RB convection at small Kn numbers thus constitutes our main goal.

PROBLEM STATEMENT AND ANALYSIS

In view of the above we focus on the continuum limit. The commonly-accepted model in this limit is the 'slip-flow' problem consisting of the familiar continuum (i.e. continuity, Navier-Stokes and energy) equations in conjunction with first-order velocity-slip and temperature-jump conditions at the boundaries (which represent the effects of slight rarefaction). The parameters governing this problem are the Knudsen (Kn) number representing the ratio of the microscopic (the mean free path) and macroscopic (the distance between the walls) scales, the Froude (Fr) number characterizing the relative magnitude of the thermal-inertial and gravitational effects, and R_T, the ratio of the upper (cold)- and lower (hot)-wall temperatures. This is in marked contrast to the above-mentioned Boussinesq problem which is exclusively governed by the Rayleigh number (which in the present notation is inversely proportional to $FrKn^2$). No assumptions restricting the respective magnitudes of the temperature differences and compressibility effects are made. This allows us to consider the relevant (according to existing DSMC results) domain of parameters.

In a simple monatomic gas consisting of hard-sphere molecules the viscosity and thermal conductivity are both proportional to the square root of the absolute temperature. For this law of molecular interaction we make use of the closed-form expressions obtained by SRC for the reference 'pure conduction' state. A linear temporal stability analysis is performed assuming small three-dimensional perturbations which are spatially harmonic in planes parallel to the walls and linearizing the governing equations and boundary conditions about the above reference state. However, owing to symmetry , the resulting problem is essentially two-dimensional in a vertical plane parallel to the wave-number vector. The dispersion relation providing the growth rate of perturbations ω as a function of their wave-number k and the above set of parameters (Kn, Fr and R_T) is calculated by transforming the system of ordinary differential perturbation equations into an algebraic eigenvalue problem via application of the Chebyshev collocation method.



Division of the plane of parameters (Fr, Kn) into unstable (U) and stable (S) domains for $R_T = 0.1$ according to the present theory (solid line) together with DSMC (circles) and continuum (squares) results of SRC. Also marked are the large-Fr asymptote $Ra \approx 1773$ (dashed line), the initial appearance of non-monotonical density distribution (dash-dotted line) and the necessary condition for the onset of convection (cross-hatched line).

RESULTS AND DISCUSSION

Throughout the entire domain of parameters our calculations invariably yield real-valued ω. Accordingly, the onset of convection takes place via "exchange of stabilities" (Chandrasekhar 1961), i.e. $\omega = 0$. In the following we focus on a temperature ratio $R_T = 0.1$ so as to facilitate comparison with the results of SRC.

The solid line in the attached figure separates the plane of parameters (Fr, Kn) into respective domains of stable (S), $\omega < 0$, and unstable (U), $\omega > 0$, response. Also presented are the corresponding DSMC (circles) and continuum finite-difference (squares) results of SRC, the large-Fr asymptote ($FrKn^2 \approx 3.65 \times 10^{-3}$, dashed line), the dash-dotted line marking the locus of states where non-monotonical density distributions initially appear in the pure-conduction reference state and the cross-hatched line corresponding to the necessary condition for instability related to compressibility-induced density variations (see the discussion below).

For all $Kn > 0$ the convection domain is confined to a finite interval of Froude numbers. The extent of this interval is rapidly diminishing with increasing Kn, vanishing entirely for $Kn >\approx 0.029$. When $Kn \approx< 0.01$ (and $Fr \gg 1$), the right branch of the U-domain boundary is approaching the dashed line. In this limit compressibility effects are negligible and the asymptote corresponds to a constant Rayleigh number (based on the arithmetic mean of wall temperatures) $Ra \approx 1773$. This coincidence with a critical value of Ra which is larger than the Boussinesq value (≈ 1708) is in qualitative agreement with the results of Frölich *et al.* (1992).

Considering the left branch of the U-domain boundary, we note that for all $Kn <\approx 0.02$ this boundary is disposed to the left of the dash-dotted line. Indeed, transition to convection may take place in a compressible fluid even when the fluid density in the reference state is monotonically decreasing (Bormann 2001). Thus, convection may set in provided that adiabatic expansion of a fluid element rising through the reference hydrostatic pressure field reduces its density below the ambient reference density (Landau and Lifshitz 1959). The cross-hatched line in the figure presents the locus of points where this condition is initially satisfied. The analysis leading to this criterion does not consider the retarding effects of fluid viscosity and heat conductivity, hence it is in fact only a necessary condition for the onset of convection.

In view of the vastly different methods of calculation (a linearized eigenvalue problem as opposed to a non-linear initial value problem), the close agreement between the present results and those of SRC is gratifying. The largest differences between the respective results appear at the lower portion of the right branch of the boundary of the convection domain and may be attributed to non-linear (hysteresis) phenomena which are obviously absent from the present linear analysis. Traversing the rest of the boundary of the U domain we observe that the differences between the present line and the results of SRC are comparable to the differences between their various schemes. The linear analysis thus offers a useful alternative in studying the effects of various parameters and models of molecular interaction on the onset of convection.

References

[1] Chandrasekhar, S.: *Hydrodynamic and hydromagnetic stability*. Clarendon Press, 1961.

[2] Frölich J., Laure P., Peyret, R.: Large departures from Boussinesq approximation in the Rayleigh-Bénard problem. *Phys. Fluids* A **4**:1355–1372, 1992.

[3] Bormann, A.S.: The onset of convection in Rayleigh-Bénard problem for compressible fluids. *Continuum Mech. Thermodyn.* **13**:9-23, 2001.

[4] Stefanov S., Roussinov V., Cercignani C.: Rayleigh-Bénard flow of a rarefied gas and its attractors. I. Convection regime. *Phys. Fluids* **14**:2255–2269, 2002.

[5] Landau L.D., Lifshitz E.M.: *Fluid Mechanics*. Pergamon Press, 1959.

THE INFLUENCE OF VIBRATION ON THE ONSET OF MARANGONI CONVECTION IN HORIZONTAL FLUID LAYER

Zenkovskaya S.M. [*], Shleykel A.L. [*], Novosiadliy V.A. [*]
[*] *RSU, Dep. of Numerical Meth. and Math. Physics, 5 Zorge, Rostov-on-Don, Russia*

Summary The problem of influence of parametric oscillations on dynamic systems has two particularly interesting cases – the case of high-frequency vibrations and parametric resonance. In the case of high frequency vibration the application of averaging method allowed us to make a conclusion that the vibration smoothes the free boundary if the direction of oscillation is not longitudinal. In the case of finite frequency and transversal influence the continued fractions approach made possible to avoid the conventional restriction to the case of small viscosity and almost-resonant frequencies and effectively calculate the areas of parametric resonances. Our numerical results cover a wide range of the parameters (Marangoni number, viscosity, amplitude and frequency of the oscillation).

PROBLEM FORMULATION

We consider fluid flow in a viscid incompressible homogenous fluid layer, bounded from above by a free surface $x_3 = \xi(x_1, x_2, t)$, and by hard or "soft" (free undeformable) wall from below, which is performing oscillations governed by the law $\tilde{b}\cos\tilde{\omega}t$ along the vector $s = (\cos\varphi, 0, \sin\varphi)$. The governing equations are Oberbek-Boussinesq equations of convective motion in the moving coordinate system.

HIGH-FREQUENCY CASE

The first case studied is the case of high-frequency vibration. The amplitude is considered of order *O(1/ω)*, that is we assume b=*a/ω*, *a* is of order *O(1)*. The averaging method is applied, as it was done in [1,2]. The unknown variables are represented as the sum of smooth and fast components:

$$\mathrm{v} = \mathrm{v}'(x,t) + \tilde{\mathrm{v}}(x,t,\tau), \quad p = p'(x,t) + \omega\tilde{p}(x,t,\tau), \quad T = T'(x,t) + \frac{1}{\omega}\tilde{T}(x,t,\tau), \quad \xi = \xi'(x,t) + \frac{1}{\omega}\tilde{\xi}(x,t,\tau) \tag{1}$$

It is possible to express fast components through smooth ones. Substitution of achieved solutions into governing equations leads to appearance of new terms – the vibration-induced mass force (in the case of homogenous fluid they vanish) and vibration-induced stresses [1,2]. The resulting problem can be linearized near quasiequilibrium, resulting in the following eigenvalue problem for the amplitudes of normal perturbations:

$$\begin{gathered}
\sigma(D^2-\alpha^2)\mathrm{v} = (D^2-\alpha^2)^2\mathrm{v}, \quad \sigma\mathrm{Pr}\,\theta = (D^2-\alpha^2)\theta - \mathrm{v} \\
z = 0: \mathrm{v} = \sigma\mathrm{Pr}\,\delta, \quad \mathrm{D}^2\mathrm{v} + \alpha^2\mathrm{v} = Ma\alpha^2(\theta+\delta) \\
(3\alpha^2+\sigma)D\mathrm{v} - D^3\mathrm{v} = \mathrm{Pr}\,\alpha^2(C\alpha^2 + Ga + \mu_s\alpha th\alpha)\delta \\
D\theta - Bi(\theta+\delta) = 0, \\
z = 1: \mathrm{v} = \mathrm{Dv}(\mathrm{D}^2\mathrm{v}) = 0, \quad \mathrm{D}\theta = \mathrm{B}_0\theta = 0
\end{gathered} \tag{2}$$

These equations have the single vibrational parameter $\mu_s = (\mathrm{Re}\sin\varphi)^2/2$, which increases the effective surface tension $C_s = C + Ga/\alpha^2 + \mu_s th\alpha/\alpha$, if the angle of vibration $\varphi \neq 0$. Here $\mathrm{Re} = ah/\nu$ - the vibrational Rayleigh number.
The long-wave asymptotics ($\alpha \to 0$) was also considered. In this case it is possible to represent unknown values as series in powers of α^2 and obtain the terms of asymptotic form of the Marangoni number [1,2].

CASE OF FINITE FREQUENCY

For the same Oberbek-Boussinesq equations the analysis of influence of vibrations of arbitrary frequency and amplitude was made when $\varphi = \pi/2$. For detailed description refer to [3]. The problem has a quasiequilibrium:

$$\mathrm{v}^0 = 0, p^0 = \rho_0 g(t) z, \xi^0 = 0, T^0 = Az + B \tag{3}$$

The system for normal disturbances can be achieved, by separating variable x, excluding pressure, and introducing flow function ψ:

$$\begin{gathered}
(D^2-\alpha^2)\psi_t = (D^2-\alpha^2)^2\psi, \theta_t = \mathrm{Pr}^{-1}(D^2-\alpha^2)\theta - \alpha^2\psi, \\
z = 0: \eta_t = \alpha^2\psi, D^2\psi + \alpha^2\psi = \mathrm{Ma}\,\mathrm{Pr}^{-1}(\theta+\eta), \\
D\psi_t - (D^2-\alpha^2)D\psi + 2\alpha^2 D\psi - (Ga + b\omega^2\cos(\omega t) + C\alpha^2)\eta = 0, D\theta - \mathrm{Bi}(\theta+\eta) = 0, \\
z = h: \psi = 0, D\psi(D^2\psi) = 0, D\theta + B\theta = 0.
\end{gathered} \tag{4}$$

The Floquet solutions of these system are searched as an infinite sum:

$$\psi(z,t)=e^{\sigma t}\sum_{n=-\infty}^{+\infty}\psi_n(z)e^{in\omega t},\ \theta(z,t)=e^{\sigma t}\sum_{n=-\infty}^{+\infty}\theta_n(z)e^{in\omega t},\ \eta(t)=e^{\sigma t}\sum_{n=-\infty}^{+\infty}\eta_n e^{in\omega t}. \tag{5}$$

Here σ is the Floquet multiplier. Expressing ψ_n,θ_n through c_n we can obtain infinite three-diagonal system for coefficients c_n, which can be written as follows:

$$M_n c_n=-q(c_{n-1}+c_{n+1}),\quad 2q=b\omega^2\alpha \tag{6}$$

From this system of equations it is possible to derive a dispersion relation in continuous fractions form:

$$-M_0+\cfrac{-q^2}{-M_1+\cfrac{-q^2}{-M_2+\ldots}}=\cfrac{-q^2}{M_{-1}+\cfrac{-q^2}{M_{-2}+\ldots}} \tag{7}$$

For the case of synchronous and subharmonic loss of stability these equations can be reduced to real form. When $\sigma=0$, that is, the synchronous loss of stability, (7) can be written as:

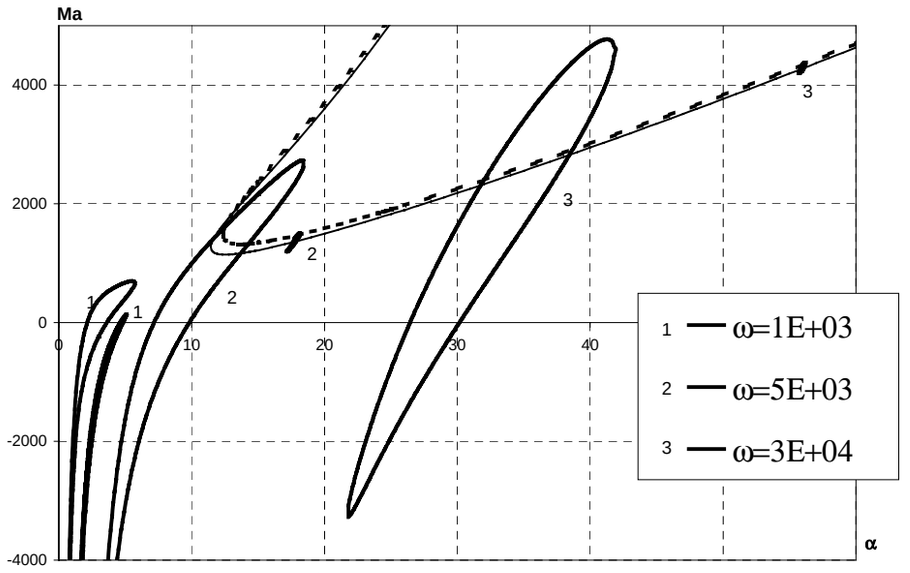
$$\mathrm{Re}\cfrac{q^2}{M_1-\cfrac{q^2}{M_2+\ldots}}=\frac{M_0}{2} \tag{8}$$

If $\sigma=i\omega/2$ we get the following equation:

$$\left|M_0-\cfrac{q^2}{M_1-\cfrac{q^2}{M_2-\ldots}}\right|^2=q^2 \tag{9}$$

These equations allow for a fast and effective numerical stability computation, including the areas of parametric resonance.

NUMERICAL RESULTS



C=10^4, Pr=0.01, Ga=0, Bi=0, B=0, μ$_s$=10^4

By solving dispersion equations (7)-(9) it is possible to obtain the neutral curves corresponding to different instability types.

One of the most interesting results for the arbitrary frequency computation was the discovery of enclosed areas of parametric resonance and their behaviour. These curves do not disappear with frequency increase, but move up and right along the curve of oscillatory instability, which is illustrated on the figure to the left.

Also, the values of frequency ω were computed, for which the results coincide with high-frequency asymptotics [1,2].

References

[1] Zenkovskaya S.M., Shleykel A.L. Effect of High-Frequency Vibration on the Onset of Convection in a Horizontal Fluid Layer. Doklady Physics, Vol. 47, No. 2, 2002, pp. 148-152.

[2] Zenkovskaya S.M., Shleykel A.L. Influence of High-Frequency Vibration on the Onset of Marangoni Convection in Horizontal Fluid Layer. PMM, 2002, Vol. 66, pp. 573-583.

[3] Zenkovskaya S.M., Shleykel A.L., Novosiadliy V.A. Influence of Vertical Vibrations of Finite Frequency on the Onset of Thermocapillary Convection in Horizontal Layer. Preprint VINITI 27.07.03. N 1440 – 20003. 36 p.

AIR CONVECTION IN A CUBIC ENCLOSURE WITH LATERALLY SHIFTED ELECTRIC COIL WITHOUT A GRAVITY FIELD

Tomasz Bednarz*, Toshio Tagawa*, Masayuki Kaneda*, Hiroyuki Ozoe*, Janusz S.Szmyd**
* *Interdisciplinary Graduate School of Engineering Sciences, Kyushu University, Kasuga Koen 6-1, Kasuga, 816-8580, Fukuoka, Japan*
** *AGH University of Science and Technology, 30 Mickiewicz Ave, 30-059 Krakow, Poland*

Summary Magnetizing convection of air in a cubic enclosure with laterally shifted coil is considered in the present work. It is shown that character of convection strongly depends on the distribution of the magnetic field and heat transfer rate can be easily controlled by employing the present characteristics.

INTRODUCTION

The convection of air due to the presence of high magnetic field is expected to have many applications. Air is known as a paramagnetic substance and the driving force for the convective motion is given by the magnetizing force. Air is attracted towards a stronger magnetic field. In the present work, numerical calculations were carried out for the magnetizing convection of air in a cubic enclosure with one electric coil shifted in the Z and X directions.

MODEL EQUATIONS

The model equations for the magnetizing convection of air are based on the work of Tagawa et al. [1] and are given in dimensionless form as follows:

continuity equation: $\vec{\nabla}\cdot\vec{U}=0$, momentum equation: $\dfrac{D\vec{U}}{D\tau}=-\vec{\nabla}P+\mathrm{Pr}\nabla^2\vec{U}-\gamma\mathrm{Ra}\,\mathrm{Pr}\,T\vec{\nabla}B^2$,

energy equation: $\dfrac{DT}{D\tau}=\nabla^2T$, Biot-Savart's law: $\vec{B}=\dfrac{1}{4\pi}\oint_{coil}\dfrac{d\vec{S}\times\vec{R}}{R^3}$

The dimensionless variables and parameters are defined as follows:

$X=x/x_0,\ Y=y/y_0,\ Z=z/z_0,\ U=u/u_0,\ V=v/v_0,\ W=w/w_0,\ \tau=t/t_0,\ P=p/p_0,\ \vec{B}=\vec{b}/b_0,$
$T=(\theta-\theta_0)/(\theta_h-\theta_c),\ x_0=y_0=z_0=l,\ u_0=v_0=w_0=\alpha/l,\ t_0=l^2/\alpha,\ b_0=\mu_m i/l,\ p_0=\rho_0\alpha^2/l^2,$
$\mathrm{Pr}=\nu/\alpha,\ \mathrm{Ra}=g\beta(\theta_h-\theta_c)l^3/(\alpha\nu),\ \gamma=(\chi_0 b_0{}^2\zeta)/(\mu_m g l),\ \gamma\mathrm{Ra}=\chi_0 b_0{}^2\zeta\beta(\theta_h-\theta_c)l^2/(\mu_m\alpha\nu)$

The boundary conditions are:

at $\tau<0$, initial condition is a heat conduction state: $U=V=W=0,\ T=-X\ (-0.5\le X\le 0.5)$,
at the left-hand side vertical wall: $T=0.5$, at the right-hand side vertical wall: $T=-0.5$,
at the vertical adiabatic walls: $\partial T/\partial Y=0$, at the horizontal adiabatic walls: $\partial T/\partial Z=0$,
at all walls: $U=V=W=0$.

These dimensionless equations were approximated by finite difference equations and numerically solved with the HSMAC [2] scheme for a staggered mesh system. The number of meshes is 40×40×40. Distribution of the magnetic field was calculated using Biot-Savart's law.

MODEL SYSTEM AND COMPUTED RESULTS

Model system is shown in Figure 1. The cubic enclosure which is heated isothermally from one vertical wall and cooled from opposite one and with other four walls thermally insulated is considered to be placed in a bore space of a superconducting magnet. In our numerical computations the magnetic field is generated by a single electric coil which is placed in a horizontal plane at various elevations Zc and further shifted in the X direction at Xc. The magnetic buoyancy force which drives the fluid has been known to be proportional to the gradient of the square of the magnetic induction and is determined by the magnitude of the electric current flowing through the coil but not the current direction. In the present computations the dimensional combinations are as follows: the length of the cubic enclosure is set as 0.032[m] and the diameter of the electric coil as 0.1[m].

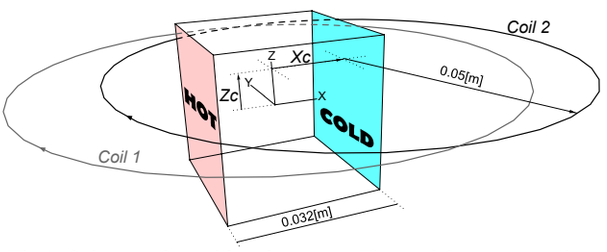


Fig.1. Schema of considered system. The *coil 1* represents the coil at the elevation $Zc=0.25$ while *coil 2* is additionally shifted in the X direction ($Xc=0.5$).

At $g=0$, γ parameter becomes infinity and Ra number becomes zero, and the finite product γRa is used to describe convection at non-gravity cases. Figure 2 shows computed results at $\gamma\mathrm{Ra}=4.53\times10^5$ and $\mathrm{Pr}=0.71$ for various elevations of the coil Zc and for various Xc. At $Zc=0$ the boost effect of the heat transfer rate is largest with Xc.

The average Nusselt number 1.678 at $Xc = -0.5$ increases to 5.17 at $Xc = 0.75$. At $Zc = 0.25$ and 0.5 the character of the plots is alike and the local minimum of the average Nusselt number is observed at $Xc = -0.5$ and maximum at $Xc = 0.75$. When the coil is placed in a horizontal plane in a distance $Zc = 1.0$ from the mid-plane (Z=0), the average Nusselt varies from 3.025 to 3.205. Computed results show that the heat transfer rate can be significantly increased especially with the coil shifted close to the left-hand side vertical hot wall.

Figure 3 shows two extreme cases: the upper ones at $Xc = -0.75$ and the lower ones at $Xc = 0.75$, both at the same value of $Zc = 0$. The coil is placed in a horizontal plane in both cases at $Z = 0$ and only difference is in the coil's position: once the coil is closer to the right-hand side cold wall ($Xc = -0.75$) and another closer to the left-hand side hot wall ($Xc = 0.75$).

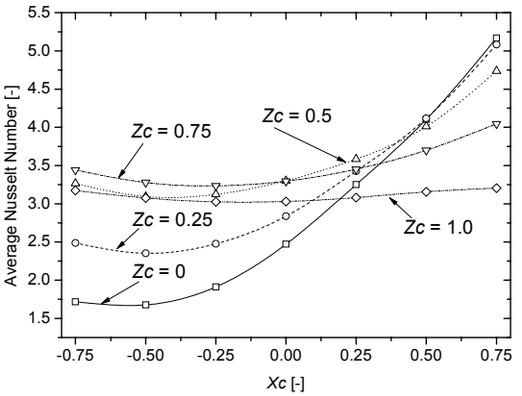


Fig.2. The average Nusselt numbers versus the Xc parameter at various elevations Zc at Pr *= 0.71,* γRa = 4.53×10^5 without a gravity field.

At $Xc = -0.75$ the magnetic buoyancy force vectors seen in Figure 3(b) have larger magnitude close to the cold wall. The force in this region is acting to attract the colder air toward the coil's wire with accordance to the gradient of the square of the magnetic induction and proportionally to local temperature. As seen in Figure 3(d) the colder air is going downward along the cold wall in the upper part of the enclosure ($Z > 0$) and going upward in the lower part of the enclosure ($Z < 0$) and later due to the continuity law goes toward the hot wall. The strongest flow seems to be in the mid-height along the front and back adiabatic walls. Reaching the hot wall, fluid is going from the mid-plane along the hot wall toward top ceiling and bottom floor and then returns to the cold wall. Final and stable temperature distribution is shown in Figure 3(c). The flow mode observed for the case at $Xc = 0.75$ seems to be very similar. However the strongest flow is generated along the hot wall due to the close position of coil's wire. Hot air is strongly repelled from the coil's plane first along the hot wall and later along the top and bottom adiabatic walls. The cold air is squeezed out by the coming fluid and as seen in Figure 3(c) creates very strong flow mostly along the front and back vertical adiabatic walls. This flow mode causes such high heat transfer rate.

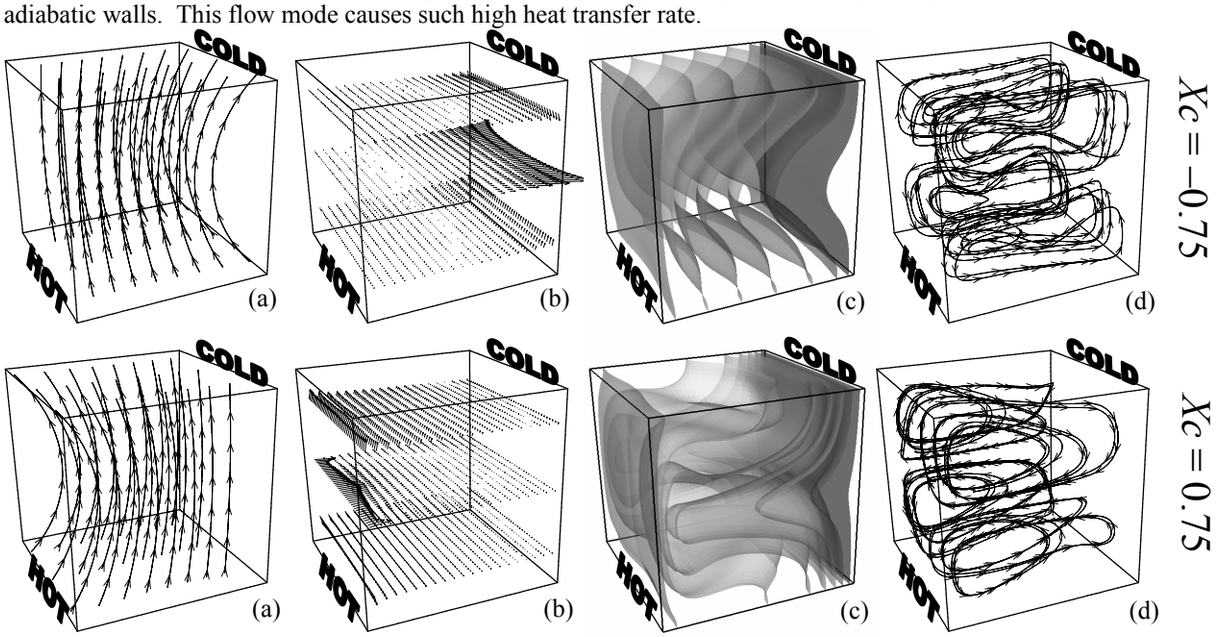


Fig.3. Computed results for two different values of parameter Xc at γRa = 4.53×10^5, $Zc = 0$ and Pr = 0.71: (a) magnetic field distribution, (b) vectors of magnetic buoyancy force, (c) isothermal contours and (d) longtime streak lines.

CONCLUSIONS

Numerical calculations were carried out for the magnetizing convection of air in a cubic enclosure with the coil laterally shifted in positive or negative directions of Xc and Zc. Most efficient configuration at γRa = 4.53×10^5 were obtained for the coil shifted horizontally to have a close location of the coil with the hot wall. It was shown that character of convection and the average Nusselt number depends strongly on the horizontal position of the coil. This work also shows that it is possible to control heat transfer rate by the manipulation of the magnetic field.

References

[1] Tagawa T., Shigemitsu R., Ozoe H.: Magnetizing Force Modeled and Numerically Solved for Natural Convection of Air in a Cubic Enclosure: Effect of the Direction of the Magnetic Field, *Int. J. Heat Mass Transfer*, vol. 45, pp. 267-277, 2002.

[2] Hirt C.W., Nichols B.D., Romero N.: A Numerical Solution Algorithm for Transient Fluid Flow, Los Alamos Scientific Laboratory, LA-5852, 1975.

XXI ICTAM, 15-21 August 2004, Warsaw, Poland

ID 10580

METHOD FOR SOLVING NONLINEAR PROBLEMS ON UNSTEADY FREE-BOUNDARY FLOWS

Yuriy A. Semenov,
Institute of Technical Mechanics of the NAS and NSA of Ukraine, 15 Leshko-Popel' Street, Dniepropetrovsk, 49005, Ukraine, e-mail: relcom@semenov.dp.ua

Summary *A direct method of finding a flow potential of 2-D inverse boundary-value problems is proposed. The method potentialities are illustrated by solving various new water impact problems.*

Historically, a progress in solving the problems of free boundary potential flows in an exact mathematical formulation is based on the development of the complex variable functions theory. Since any analytical function meets the requirements of a fluid incompressibility and zero vorticity the problem is to find such analytical function, which satisfy to given boundary conditions. The problems of free boundary flows lead to mixed boundary conditions. A velocity modulus on the free boundary is known from Bernoulli/Cauchy–Lagrange integral, and a body shape determines the velocity direction. A conformal mapping method proposed by Helmholtz and Kirchhoff and methods developed by Zhykovsky, Levi-Chivita, Chaplygin are applicable for solving the problems on steady free boundary flows. Nonlinear problems of unsteady free flows remain intricate problems. Only few peculiar examples are presented in literature. The first is a problem of an unsteady cavity flow past a flat plate solved by Karman (1949) under condition of a fixed free boundary in time. The second is a self similar problem of water entry of a wedge solved by Dobrovol'skaya (1969).

We propose a way of determination of a complex function on its modulus and argument or its real part and argument, which are given on the boundary of a simply connected domain. In combination with Chaplygin's singular point method it makes possible to determine the expressions of a complex velocity and a derivative of the complex potential of an arbitrary unsteady free boundary flow. These expressions contain in explicit form the modulus and the argument of the velocity as functions of a parameter variable and time. The dynamic and kinematic boundary conditions lead to a system of the integral and integro-differential equations for determination of these unknown functions.

At the first stage we apply this method for solving various water impact problems. This kind of problems contains such important features as nonlinearity, unsteadiness and three phase contact points.

Oblique water entry of a wedge. The self-similar solution that characterizes the flow about a wedge entering a liquid surface, originally at rest, is here considered as a reverse flow in a frame of reference attached to the impacting body. Let *x, y* be Cartesian co-ordinates with their origin ***O*** located at the contact point of the right wedge side with the free surface. The half-space of the ideal weightless incompressible fluid has an inflow velocity v_∞ and an angle γ with the *y*-axis. The sketches of the fluid domain and of the parameter space are shown in Figure *1a* and *1b*, respectively. The deadrise angles on the right and left hand sides are $\beta_R = \pi/2 - \alpha + \delta$ and $\beta_L = \pi/2 - \alpha - \delta$, where 2α is the wedge angle and δ is the deviation angle, that is the angle between the *y*-axis and symmetry axis of the wedge. In the case of a constant entry velocity the self-similar variables $\tilde{x} = x/(v_0 t)$, $\tilde{y} = y/(v_0 t)$ can be introduced so that the time dependent fluid domain in the physical plane is mapped into a stationary domain in the $\tilde{x}, \tilde{y}$ plane and the complex velocity potential $W(z,t) = \phi(z,t) + i\psi(z,t)$ takes the form

$$W(z,t) = \phi(z,t) + i\psi(z,t) = v_0^2 t\left[\tilde{\phi}(\tilde{z}) + i\tilde{\psi}(\tilde{z})\right] \quad (1)$$

where $\tilde{\phi}$ are the velocity potential and $\tilde{\psi}$ the stream function in the stationary plane $\tilde{z} = \tilde{x} + i\tilde{y}$.

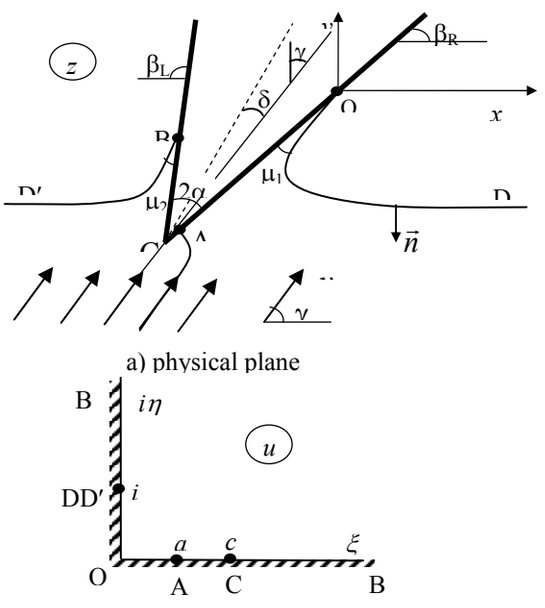


Fig.1. Inflow of a half-plane of the liquid on an inclined wedge

The expression of the complex velocity potential $\tilde{W}$ can be found by constructing the expression of the complex velocity and derivation of the complex potential in the parameter domain. Using the proposed method the final expression of the complex velocity takes the form

$$\frac{d\tilde{W}}{d\tilde{z}} = e^{-i(\gamma_\infty + \alpha + \delta)}\left(\frac{u-a}{u+a}\right)\left(\frac{u+c}{u-c}\right)^{(1-2\alpha/\pi)} \times \exp\left[-\frac{i}{\pi}\int_0^\infty \frac{d\ln v}{d\eta}\ln\left(\frac{i\eta - u}{i\eta + u}\right)d\eta\right] \quad (2)$$

Setting $u = \xi$ in equation (2), along the wetted part of the wedge it is $\arg\left(d\tilde{W}/d\tilde{z}\right) = -\beta_R$ for $0 < \xi < c$,

ID 10580

and $\arg\left(d\widetilde{W}/d\widetilde{z}\right)=-(\pi-\beta_L)$ for $c<\xi<\infty$. On the free surface ($u=i\eta$) the modulus of equation (2) equals the function $v(\eta)$ which is determined later on by using the dynamic boundary condition.

Analyzing the singularities of the complex potential we can construct the expression of derivative of the complex potential

$$\frac{d\widetilde{W}}{du}=Nu^{(2\mu_1/\pi-1)}\frac{u^2-a^2}{\left(1+u^2\right)^2}\exp\left[-\frac{1}{\pi}\int_0^\infty\frac{d\theta}{d\eta}\ln\left(\eta^2+u^2\right)d\eta\right]. \quad (3)$$

where N is the scale factor, and the function $\theta(\eta)=\arctan\left(v_s/v_n\right)$ is expressed via the tangential $v_s(\eta)$ and normal $v_n(\eta)$ velocity components on the free boundary. From equation (3) it follows that, on the wedge sides ($u=\xi$), the imaginary part of the complex potential is equal to zero while along the free boundary ($u=i\eta$) it holds $\dfrac{\mathrm{Im}\,d\widetilde{W}}{\mathrm{Re}\,d\widetilde{W}}=\dfrac{v_n}{v_s}$. Thus, equation (3) satisfies the definition of the complex potential.

The following conditions: the inflow velocity, the length of the wetted part of the wedge side, the y-coordinate at the infinity at the right equals one at the left make it possible to determine the parameters a, c, N. The unknown functions $v(\eta)$ and $\theta(\eta)$ is determining form the dynamic and kinematic boundary conditions.

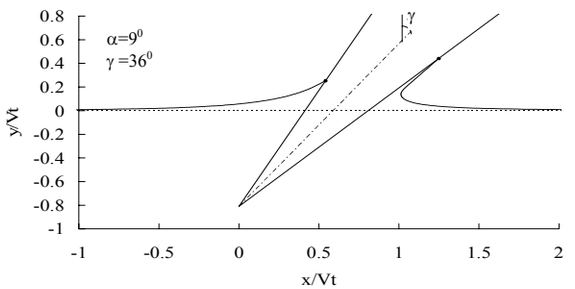


Fig.2 Solution for oblique entry of the wedge case with $\alpha=9^0$ $\gamma=36^0$

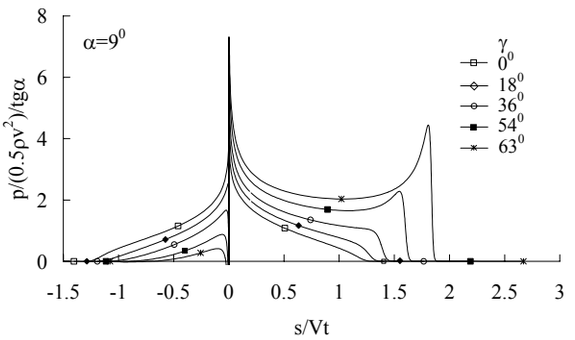


Fig.3 Pressure distribution on the right side (s>0) and on the left side (s<0) of the wedge

Oblique entry of a flat plate. This self-similar problem also was solved by the same way. Analyzing the flow singularities the expression of the complex velocity and the derivative of the complex potential were constructed. These expressions are similar to the Eq.(1) and (2). In Fig. 3 and Fig.4 are shown the free surface shape and pressure distribution along the flat plate. The black line in Fig.4 corresponds to the D.P.Wang's linear theory. When the angle of attack tends to zero the obtained results and the results of the linear theory are very closely.

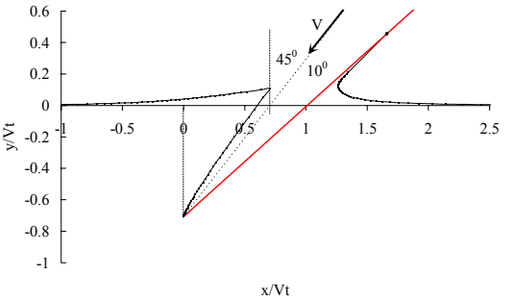


Fig.3 Solution for oblique entry of the flat plate case of the angle of attack $\alpha=10^0$ and the velocity inclination $\gamma=45^0$

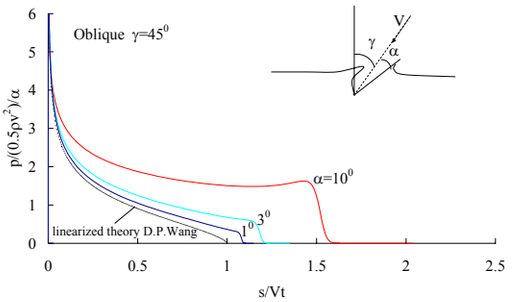


Fig.4. Pressure distribution on the flat plate

Liquid wedge impacting a solid wall. The self-similar problem was solved by the same way. This is a first obtained complete solution of the nonlinear problem.

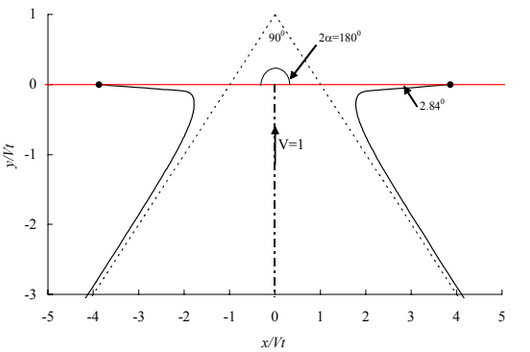


Fig.5. Free boundary of a liquid wedge impacting the solid wall

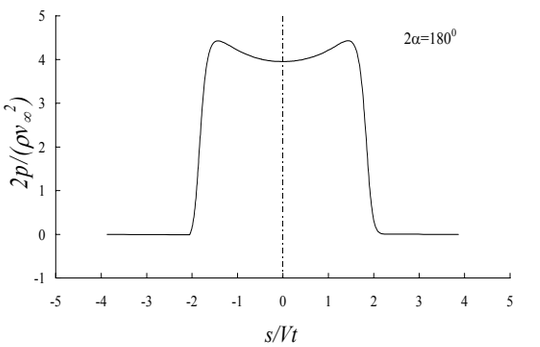


Fig.6. Pressure distribution along the wall

Bubble wall and bubble pair interaction using potential flow theory

M. Moctezuma R. Zenit R. Lima Instituto de Investigaciones en Materiales
Universidad Nacional Autonoma de Mexico

Abstract

In this study the motion and interaction of a bubble with a vertical wall is analyzed in the high Reynolds and low Weber number limit. On this dual limit the inertial effects dominate, and bubbles remain spherical. There are experiments that confirm that this approach is valid. The velocity of the fluid was obtained by expanding the potential in a series of spherical harmonics. The motion equations were obtained using an energy approach.

1 Introduction

We study the motion and interaction of a bubble with a vertical wall in the high Reynolds number limit. We consider small Weber number, for which the deformation of the bubble is negligible. The motion of a pair of bubbles has been investigated by several author [3, 1]. In this study, Laplace's equation is solved in terms of spherical harmonics with a method similar to that used by [1]. In figure (1) photographs of experiments are shown. Bubbles moving near a wall, for the same regime as that considered in the theory, move to the wall and bounce repeatedly as they move upwards. We want to analyze this effect with potential flow theory.

2 Theoretical framework

We have to solve the problem of two spheres in motion with velocity U_1 and U_2, moving in a nearly inviscid fluid. The velocity is decomposed in two components, one mean velocity V=U1+U2, and a difference of velocities component W=W1-W2. Laplace's

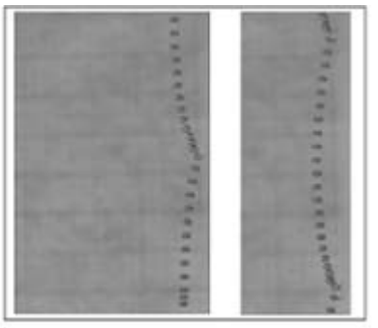


Figure 1: Photographs of experiments of a bubble moving near a wall. The bubble positions for different instants were superimposed into the same plate to show the bubble trajectory

equation must be solved:

$$\nabla^2 \phi = 0 \tag{1}$$

The potential can be expanded in a double series of harmonical spherics centered in each sphere:

$$\Phi_{V_k} = \sum_{i=1}^{n} V_k \cdot a_1 \{ g^1_{mn} \left(\frac{R}{r_1} \right)^{n+1} Y^k_n(\cos\theta_1, \mu) \tag{2}$$

$$+ g^2_{mn} \left(\frac{R}{r_2} \right)^{n+1} Y^k_n(\cos\theta_1, \mu) \} \tag{3}$$

The next step was to calculate the multipole coefficients using the boundary conditions. This was done equating the normal velocity of the fluid in the sphere surface with the normal velocity of the spheres. The coefficients g_{mn} and f_{mn} were obtained in terms of

a powers series of the rate radius-bubble separation (R/s).

$$g_m n = 1/2 \sum_{p=0}^{\infty} K_{mnp}(R/s)^p \qquad (4)$$

3 Equations of motion for two bubbles

Equations of motion can be obtained using an energy method, in which the kinetic energy of the system is calculated. As the energy of the system of spheres and fluid in motion will not change, the equations of motion can be obtained with Lagrange equations.

$$T = 1/2 \rho_l V a_{ij} u_i u_j \qquad (5)$$

Thus the kinetic energy is dependent of the velocities Uk and Wk. The system can be transformed to a system with two absolute velocities : x' and y', and two reltive velocities between the bubbles s' and θ'. Motions equation were find by appliying Lagrange equations to the system of particles and the fluid:

$$\frac{d}{dt}[\frac{\partial T}{\partial \dot{q}^i}] - \frac{\partial T}{\partial q^i} = F_i \qquad (6)$$

4 Results

The motion equations obtained in the last section were solved numerically using a Runge Kutta scheme. For our simulation we selected a fixed radius R, and an initial distance to the wall, s= 4R. With the viscosity and g acceleration of gravity, we calculated a terminal velocity $U = gR^2/9\nu$. Simulations were conducted for a wide range of bubble radii and initial bubble-to-wall distances. In figure (2) two typical trajectories are shown. These are in good qualitative agreement with our experiment observations. A complete recount of results can be found in [4].

When we simulate without drag, then the initial distance of the bubble to the wall is recovered and also the velocity of the bubble recovers its initial value. When including a drag in the bubbles, the motion of the bubbles was damped in each rebound. This work was based on a master Thesis en (IIM,UNAM)[4].

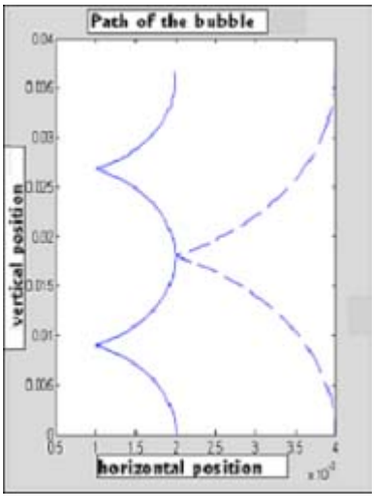


Figure 2: Numerical solution of equation (6) showing the path of the bubble interacting with a wall. Two typical cases, for different radii, are shown.

References

[1] Biesheuvel,A. and Van Vijngaarden,L.,1982. The motion of a pair of bubbles in a liquid, Journal of engineering Mathematics 16,349-365.

[2] Duineveld, P.C., 1995. The rise velocity and shape of bubbles in pure water.., Journal of Fluid Mechanics 292,325.

[3] Lamb, H., 1957. Hydrodinamics, 6th Edition, Cambridge university Press.

[4] Moctezuma, M., 2003. Interaccion y movimiento de pares de burbujas en flujo Potencial, Tesis de Maestria, IIM, UNAM.

LOCOMOTION OF A VISCOUS DROP, INDUCED BY THE INTERNAL SECRETION: BOUNDARY EFFECTS

Olga M. Lavrenteva, Dina Tsemakh, Avinoam Nir
TECHNION, Department of Chemical Engineering, 32000 Haifa, Israel

Summary A theoretical model for the locomotion of the drop induced by the internal secretion of a surfactant is presented. The effect of nearby solid walls or non-deformable liquid-liquid interfaces on the motion has been studied. Cases of plane and spherical boundaries. The dependence of the drop migration velocity on the location of the source and on the separation distance between the drop and the outer boundary as well as on the physical parameters of the system is reported. The dynamics of the drop is studied in the cases of a fixed location of the source inside the drop, and in the case when it passively moves with the internal circulation.

INTRODUCTION

Many modern industrial applications involve drops motion in liquid matrix accompanied by heat or mass transfer between the phases. These include, e.g. direct heat exchange or liquid-liquid extraction. Exchange of active species with an ambient media is one of the most characteristic features of living biological bodies as well. Most of the theoretical studies of such processes were based so far on the assumption of a uniform concentration/temperature inside the drops. This assumption does not hold in the case when a dissolved substance is secreted from some internal source within a drop, e.g. an encapsulated smaller drop in the course of technological processes involving compound drops or from certain organelles in a living cell. For an off-center location of the internal source, the diffusive mass transfer results in a non-uniform distribution of surfactant along the outer surface that, in turn, results in interfacial stress variation that ultimately induce a surface motion and the locomotion of the drop.

We present here a theoretical study of the motion of a drop due to the internal secretion of a surface-active substance. In our model we consider a viscous drop that contains another smaller droplet or a point source of a surface-active substance. The system is embedded in an immiscible viscous fluid that is either unbounded or confined by plane or or within spherical boundaries. A brief description and preliminary results for the motion of a complex drop in unbounded media can be found in Nir & Lavrenteva (2003). In the present work we report a detailed study of the locomotion of drops for a variety of physical parameters. We consider the motion in an unbounded liquid as well as more relevant cases when the flow domains are confined by boundaries of various physical nature. The cases of solid-liquid and liquid-liquid boundaries with various boundary conditions for the concentration are studied. The dependence of the drop migration velocity on the location of the source and on the separation distance between the drop and the outer boundary as well as on the physical parameters is reported. The focus of the study is on the case of a locomotion induced solely by the Marangoni effect. For completeness, the combined action of buoyancy and Marangoni effect is also considered.

PROBLEM DEFINITION AND METHOD OF SOLUTION

Consider a spherical drop containing a source of a soluble weak surfactant, which is submerged into an immiscible viscous fluid. The outer fluid is either unbounded or confined by a flat or spherical boundary. Three different types of outer boundary are considered: solid wall, free surface and liquid-liquid interface, as well as two different types of boundary conditions for the concentration at these boundaries: zero mass flux or given uniform concentration. All physical properties of the fluids are assumed to be constant except for the interfacial tensions, which are assumed to depend on the surface concentration. At the outset, we introduce dimensionless variables based on the size of the larger drop and the physical properties of the ambient fluid. The system is governed by the following set of dimensionless parameters: Reynolds number, Peclet number, two capillary numbers, the Bond number, the ratios of physical characteristics of the phases (viscosity, diffusivity), and the geometry of the system. When the drop moves under the action of gravity force, numbers characterizing the relative influence of gravity and Marangoni effect are also considered.

For simplicity, we consider the cases when inertia, convective transport and deformation effects can be neglected. i.e. Reynolds, Peclet and the capillary numbers are assumed to be zero. Under these conditions the quasi-steady approximation is valid, i.e. the concentration and velocity fields can be somewhat decoupled and found from stationary equations (Laplace and Stokes, respectively). The problems remain coupled only through the dependence of interfacial stress conditions on the variation of surfactant concentration at the surface.

The velocity and pressure fields in each phase satisfy the quasi-stationary Stokes equations with the following boundary conditions: The fluid is at rest at infinity. No-slip conditions are imposed on solid walls. The velocity field is continuous across drops interface, while the drops do not deform. The difference of tangential stresses at the interfaces is balanced by the gradient of the surface tension. The problem definition is complemented by the balance of the forces acting on each of the drops from which the dynamics is extracted, and by the equations for temporal evolution of the positions of the drop and the internal source. The latter may be either fixed within the drop or passively migrate with the internal circulation.

The above problem is solved for axisymmetric configurations using conformal mapping techniques. In this procedure we first calculate the concentration distribution and the Stokes stream function from which the force on the drop can be obtained as a sum of Marangoni force, Stokes drug and buoyancy. Balancing these forces provides an equation on the

drop's migration velocity that is used to advance the geometry of the system.

RESULTS OF CALCULATIONS AND CONCLUSIONS

The dependence of the drop migration velocity on the location of the source and on the separation distance between the drop and the outer boundary as well as on the physical parameters of the system is reported. The various flow patterns are described The dynamics of the drop is studied for the cases of the fixed location of the source inside the drop and in the case, when it passively moves with the internal circulation.

For the case of a motion in an unbounded fluid, the internal source was modeled as a smaller droplet with a uniform concentration of a surfactant. Our computations revealed that the internal secretion from the inner droplet induces locomotion of the compound viscous drop and that the flow generated by the interface of the large drop causes the migration of the internal droplet in the same direction. In general it was found that the velocity of the inner droplet exceeds that of the large drop. With the passage of time, the droplet approaches the interface of the drop and the eccentricity of the system is increased. When the distance between the centers increases, the relative velocity first grows, but as the droplet approaches to the interface, its relative motion is retarded by the strong viscous resistance. At the limiting configuration of the touching droplets the aggregate will move with a constant velocity. When the dimension of the inner droplet is much less than that of the large one, it is natural to model it by a point mass source with a given strength. This model is adopted for the computation of the drops locomotion is confined domains.

The combined effect of the buoyancy and spontaneous Marangoni motion is studied as well. It is shown that a rich variety of interaction patterns may occur, which exhibits separation of flow in the outer fluid and within the large drop. In some particular cases both drops remain suspended motionless in the laboratory reference frame with the fluid circulating in a steady manner. A pair of drops may have several equilibrium positions, with one or two of them being stable.

The presence of nearby boundaries normally increase the hydrodynamic resistance and, thus, fluid flow near the boundary has lower velocity as compared to those in unbounded medium for the same external forcing. On the other hand, for the surface induced flow, a nearby boundary affects the concentration at the drops surface and hence the Marangoni flow. Our calculations revealed that the boundary with constant concentration has a repulsive effect on the drop, while an insulated boundary tends to attract a drop. For a large separation distance, the motion of the drop is similar to that in an unbounded fluid, while for smaller separations it is considerably retarded and, in some cases, can be even reverted.

The effect of liquid-liquid and liquid-gas interface on the hydrodynamic resistance of a nearby particle is much weaker than that of the solid wall. On the other hand, a Marangoni flow is induced on such an interface as well as on the surface of the drop itself. This effect is shown to be quite strong being able to change the flow pattern and the direction of the drops migration.

The dynamics of the drop is calculated for a fixed location of the course inside the drop as well as when it passively moves with the internal circulation for all the types of external boundaries mentioned above.

ACKNOWLEDGEMENT

The research was supported by ISF grant 74/01. DTs and OML acknowledge the support of the Israel Ministry for Immigrant Absorption.

References

[1] Nir A., Lavrenteva O. M.: Capsule dynamics and interfacial transport, in Modeling and Simulation of Capsules and Biological Cells, Chapman & Hall/CRC Mathematical Biology and Medicine Series, 2003.

[2] Tsemakh D., Lavrentea O.M., NirA.: On the locomotion of drops induced by the internal secretion of surfactants. *Int. J. Multiphase Flow (2004) to appear.*

Theoretical Studies of Flow-Induced Coalescence

L. Gary Leal, Fabio Baldessari, Marcos Borrell, and Yosang Yoon
Dept of Chemical Engineering
University of California at Santa Barbara
Santa Barbara, California 93106, USA

We study the dynamics of collision and film drainage that leads to coalescence of two drops in a flow. The objective is a comparison with experimental observations from our laboratory, which have been carried out using small Newtonian drops (20-40 micron), with and without surfactant, in a computer controlled four-roll mill. These measurements include detailed trajectories, the coalescence angle as a function of capillary number, viscosity ratio, drop size and the collision trajectory as specified by the offset at "large" separations. The four-roll mill allows two types of collisions: head-on collisions in which the drops stay in a head-on configuration until coalescence occurs; and glancing collisions in which the drops rotate around one another and either coalesce or are eventually separated by the flow. In the latter case, the critical parameter is the "critical capillary number" above which coalescence is not possible. In the case of head-on collisions for the range of parameters we have considered, the drops always coalesce eventually and the primary experimental measurement is then the "collision time"; namely the time from initial "contact" to coalescence. This provides an indication of the efficiency of the film drainage process.

Existing theory has mainly been carried out for capillary numbers that are in the range 0.1-0.01, which is significantly larger than the capillary numbers observed experimentally. As a consequence of this (at least in part), and possibly also inadequate resolution of the thin film geometry (especially for a fully 3D collision), the existing theories are only in partial agreement with our observations. It may be noted that the resolution problem is severe since the film thickness just prior to coalescence may be as small as 100 angstroms for a drop that is 40 microns in radius.

The present study is focused on theoretical studies of head-on collisions, but with a time-dependent force along the line of centers of the drops that varies with time in the same way that the force along line of centers varies with time in a "normal" glancing collision. Experiments carried out with the computer-controlled version of the 4-roll mill have demonstrated that the coalescence process in such a head-on collision is identical to that in the corresponding glancing collision for low capillary numbers. This includes even cases where it is observed that coalescence occurs after the force along the line of centers has changed sign (i.e. the external flow is pulling the drops apart at the point of coalescence). It is, of course, clear that the collision process for a glancing collision could be decomposed into a motion along the line of centers plus a rotation of the line of centers if the drops were not deformed (i.e. Ca=0). However, it is somewhat of a surprised that the same decomposition remains at least a very good approximation for small but nonzero capillary numbers where it is clear that deformation of the drop is an important part of the coalescence process.

Based on the experimental results mentioned in the preceding paragraph, we therefore focus on head-on collisions with a time-dependent force as mentioned previously. This focus on head-on collisions allows a much greater degree of spatial resolution than is possible in a fully 3D collision. Two types of theory are discussed: thin-film theory based on the asymptotic limit Ca<<1; and boundary integral calculations. The former follows closely the preceding theories of Davis and coworkers, but with several critical differences which follow from the asymptotic nature of the problem at low Ca (as well as the more accurate "retarded" version of the van der Waals force). The boundary integral calculations use a automatically generated mesh refinement to provide adequate resolution within the thin film. We find that the degree of resolution required is greater than has typically been applied in previous studies of the 3D collision process. With these changes, the theories agree in a number of respects with the experimental data. However, there are still some remaining puzzles and issues that we discuss at the end of the talk.

OCUURRENCE OF MICRO-BUBBLES DURING COALESCENT MOTIONS OF GAS-BUBBLES IN LIQUID

Teruo Kumagai, Kazuyuki Yokota, Shingo Saida and Masaki Shimizu
Science University of Tokyo, Noda City(278-8510), Japan

Summary A new superposition method of Oseen's flow fields which is proposed here as a kind of the previous reflection method succeeds to estimate approaching motions of two equal-sized deformable gas-bubbles located vertically in series in a viscous liquid considering the hydrodynamic interactions between the gas-bubbles. The following phenomena are newly recognized by using high-speed video-camera and microscopes: (1) an occurrence of several number of micro-bubbles during a coalescent motion of two gas-bubbles observed at the final stage of the approaching motion of gas-bubbles rising freely in the viscous liquids, (2) an occurrence of several number of micro-bubbles during a coalescent motion of freely-rising motion of two bubbles between two sheets of vertically-set parallel plates in the viscous liquids, and (3) an occurrence of several micro-water-drops and micro-bubbles caused by a bursting motion of a single air-bubble at water surface.

INTRODUCTION

The motion of gas-bubbles in liquid flows are not only a classical subject, but is directly related to many problems in industrial applications. Thus this subject has been treated theoretically and experimentally. However there are left rooms to study the motion of a cluster of deformable gas-bubbles in liquid considering the hydrodynamic interactions among gas-bubbles even if assuming at low Reynolds numbers.

RESULTS

FREELY-RISING MOTION OF GAS-BUBBLES IN LIQUID

A superposition method of Oseen's flow fields around deformable gas-bubbles is newly proposed here as a kind of the usual reflection method considering hydrodynamic interactions among gas-bubbles in liquid. This method succeeds to estimate the freely-rising motions of two equal-sized air-bubbles located vertically in series in a quiescent glycerol as shown in Figure 1. During this motion the following air-bubble approaches the preceding air-bubble even if they are equal-sized at the initial time. When the center-to-center distance reaches three times the equivalent diameter of the air-bubbles, the shape of the preceding air-bubble becomes oblate, while the following air-bubble becomes prolate. Then the two air-bubbles touch and coalesce finally. It should be noted that the numerical results obtained by using the usual Stokes's approximation fails to estimate this freely-rising motion even at the low Reynolds numbers such as Re=0.191.

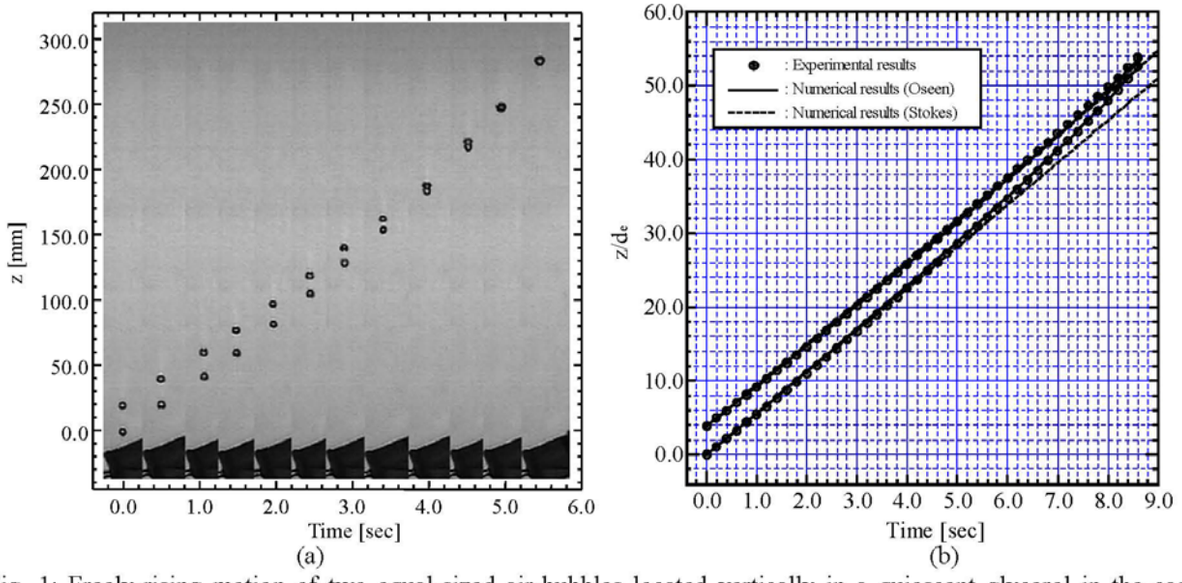


Fig. 1: Freely-rising motion of two equal-sized air-bubbles located vertically in a quiescent glycerol in the case of M=73.4, Eo=7.39(Re=0.191, de=6.1mm); Fig.1(a) shows the video picture, while Fig.1(b) shows the experimental and numerical results.

OCCURRENCE OF MICRO-BUBBLES DURING THE COALESCENCE OF TWO BUBBLES

In the coalescent motion of the two air-bubbles, a crack occurs on the interfacial plane between the two air-bubbles. Then several number of micro-bubbles are left behind the coalesced air-bubble as shown in Fig.2. Fig.2 is obtained by using high-speed video-camera with 10000 frames/s which is moved vertically with the same speed as the rising speed of the center of the two air-bubbles.



Fig.2 Occurrence of micro-bubbles during coalescence of two air-bubbles in glycerol

OCCURRENCE OF MICRO-BUBBLES DURING COALESCENCE OF TWO AIR-BUBBLES IN GLYCEROL BETWEEN TWO PARALLEL PLATES WITH NARROW SPACING

Several number of micro-bubbles are generated from the trailing edges of the upper air-bubble at the final stage of the coalescent motion as shown in Fig.3.

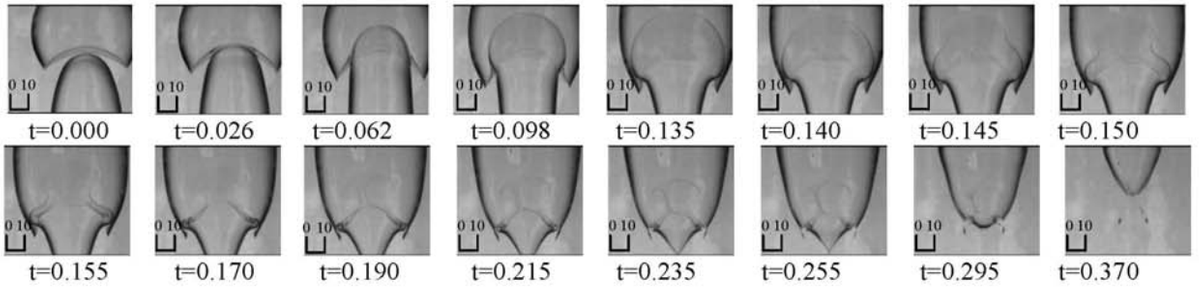


Fig.3: Occurrence of several micro-bubbles during the coalescent motion of two air-bubbles in glycerol between two parallel plates with narrow spacing (Re=0.314, We=0.870)

OCCURRENCE OF SEVERAL NUMBER OF MICRO-DROPS AND MICRO-BUBBLES IN THE BURST OF A SINGLE AIR-BUBBLE AT LIQUID SURFACE

Several number of micro-drops and micro-bubbles occur after a single air-bubble is bursted at water surface as shown in Fig.4, while only several micro-bubbles occur at glycerol surface as shown in Fig.5.

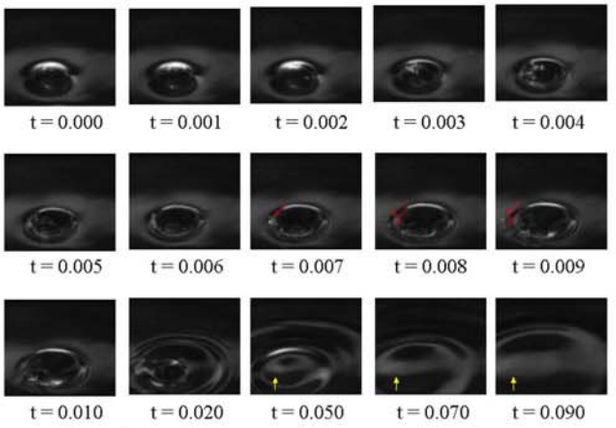


Fig.4 Occurrence of micro-water-drops and micro-bubbles at water surface (d=9.88mm, We=2.94, Re=2.91)

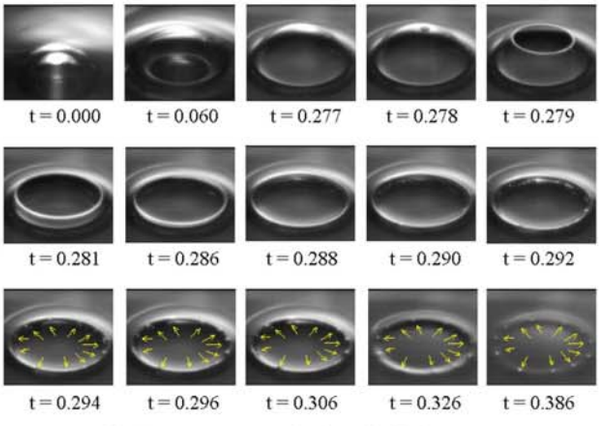


Fig.5 Occurrence of micro-bubbles at glycerol surface (d=23.41mm, We=3.91, Re=2.61)

CONCLUSIONS

The superposition method of Oseen's flow fields describes well the approaching motion of two equal-sized gas-bubbles rising freely in series in the viscous liquid at low Reynolds numbers. The phenomena of occurrence of micro-bubbles are recognized in the coalescence of two gas-bubbles in viscous liquids and in the burst of a single gas-bubble at water surface.

ATOMIZATION OF AN UNDULATING LIQUID SHEET

Nicolas Bremond[1,2], Christophe Clanet [1], Emmanuel Villermaux [1]
[1] *IRPHE, 49 rue Joliot-Curie, BP 146, 13384 Marseille, France*
[2] *Physics of Fluids, University of Twente, P.O. Box 217, 7500 AE Enschede, The Netherlands*

Summary This paper presents an experimental study devoted to the understanding of break-up mechanisms of liquid sheets. A shear instability develops at the interface liquid/gas resulting in an undulated motion of the liquid sheet. These undulations trig a Rayleigh-Taylor instability leading to azimuthal thickness modulations. A model including the development of both instabilities allows us to predict the sheet and drops sizes.

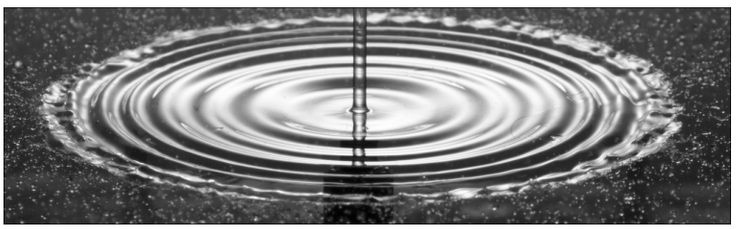


Figure 1: Snapshot of a liquid sheet formed by the impact of a round jet on a vertically vibrating solid rod.

INTRODUCTION

The atomization of a liquid sheet into dispersed droplets is a widespread phenomenon embracing many natural and industrial processes [1]. The main questions of the atomization are the following: how does a compact volume of liquid become a set of drops and what is the resultant drops size distribution ? Here, we focus on the break-up mechanisms of a laminar liquid sheet expanding in air initially at rest. In this case, two regimes exist: a smooth regime, without interaction with the surrounding medium, and an undulated regime corresponding to the development of a shear instability at the interface liquid/gas [3]. For the second regime, the role played by the undulations in the atomization process is not yet well defined. We first describe the experimental set-up used for control the surface oscillations and present the observations on the liquid sheet features. Then a model is suggested for explain this fragmentation regime in presence of undulations and finally compared with experiments.

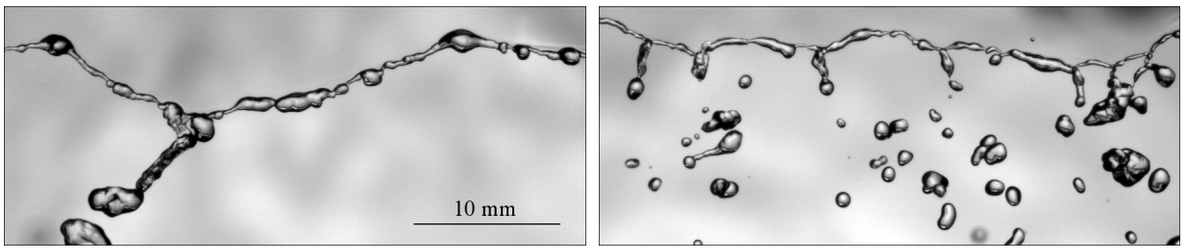
EXPERIMENTS

Experimental set-up

The studied liquid sheet is formed by the normal collision of a water jet on a solid rod. The impact rod diameter is twice larger than the jet diameter d_j which is equal to 3 mm. After the collision, the liquid expands radially forming a sheet shaped like a disk. The velocity in the sheet is constant and equal to the jet velocity u_j. The sheet thickness h decreases like $1/r$, where r is the radial location.
For low jet Weber numbers $We = \rho d_j u_j^2/\sigma$ where ρ is the liquid density and σ is the surface tension, the sheet stays flat, it is the smooth regime. If the Weber number increases, by enhancing the jet velocities in the present experiment, the sheet becomes unstable and flaps like a flag, it is the flapping regime. The critical Weber number is about 1000 in presence of air. In order to study this second regime, the impact rod is fixed on a vibrator which oscillates vertically. We perturb the initially stable sheet (smooth regime) with an amplitude a_0 and a frequency f independently controlled. An example is shown on figure 1.

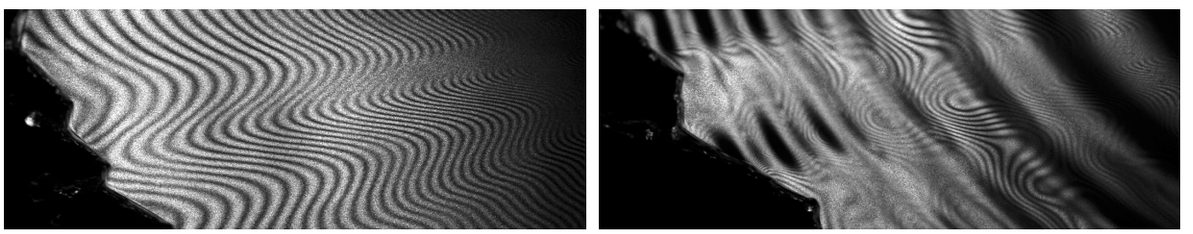
Observations

As we can see on figure 1, the oscillation of the impact rod creates circular waves. These waves propagate towards the free rim of the sheet with a decreasing wavelength. The wave frequency is equal to the imposed one and the wave velocity decreases during their propagation. This means that the contrast velocity between the liquid and the waves increases with r, this will be crucial in the fragmentation scenario. Below a critical frequency, which increases with u_j, the wave amplitude is constant along a radius and nearly equal to the vibrator amplitude. Above this critical frequency, the amplitude is amplified and can reach a value 40 times larger than a_0 for the highest jet velocity.
The sheet size increases with the jet velocity in the smooth regime then decreases in the flapping as noted by the Savart [2] in 1833. In our experiments, whatever the jet velocity the sheet extension decreases when the frequency or the amplitude of the perturbation are enhanced. An other consequence of the surface undulations



(a) (b)

Figure 2: Top views of the free rim of a smooth liquid sheet (a) and a perturbed liquid sheet (b). The length scale is the same on each picture.



(a) (b)

Figure 3: Thickness profiles revealed by a laser interferometric method of a liquid sheet without rod vibration (a) and with rod vibration (b).

is to diminish the drops size. The sheet is bounded by a set of cusps at the tip of which ligaments emerge and break, figure 2 . The distribution of the drops size normalized by the mean drops size has an unique shape independent of the control parameters (u_j, f and a_0). Therefore, if we can predict the mean drops size we know how the sizes are distributed in the spray.
The figure 3 presents the thickness field revealed by an interferometric method. The free case on figure 3a shows an azimuthal modulations of the interference fringes interpreted by a transverse thickness variation. The undulations enhance the initial thickness inhomogeneities, figure 3b.

ATOMIZATION SCENARIO

Because of the velocity difference between the air and the liquid, the sheet develops a shear instability. The features of the waves (frequency,velocity, amplitude) are well described by a linear stability analysis [3]. The velocity contrast between the liquid and the waves induces an acceleration of the fluid particles as they move through the undulations. Higher the contrast is, larger the acceleration. This situation trigs a Rayleigh-Taylor type of instability [4] which amplifies initial thickness inhomogeneities observed on figure 3a.
The position of the rim can be deduced by a local balance between inertia of the fluid an capillary force which pulls back the rim. This balance depends on the local sheet thickness. The thickness field is deduced from the linear analysis of the development of the primary and secondary instabilities. The evolutions of the sheet size with the control parameters are well predicted by this scenario.
As shown on figure 2, the drops are the product of ligaments break-up which are formed at the tip of cusps bounding the sheet. The ligament formation is interpreted as a collision with coalescence of two jets representing both side of a cusp. The shape and the diameter of the free rim depend on the field thickness and impose the ligaments diameter and so the drops size. This model predicts a mean drops size in a good accordance with the experimental data.

[1] for example: Bayvel, L. and Orzechowski, Z.1993 *Liquid atomization.*Taylor & Francis.
[2] Savart, F. (1833) Mémoire sur le choc de deux veines liquides animées de mouvements directement opposés. *Ann. de chim.* **55**, 257-310.
[3] Squire, H.B. (1953) Investigation of the stability of a moving liquid film. *Brit. J. Appl. Phys.* **4**,167-169.
[4] Taylor, G.I. (1950) The instability of liquid surfaces when accelerated in a direction perpendicular to their plane. I *Proc. R. Soc. Lond. A* **201**,192-196.

EVAPORATION-DRIVEN ASSEMBLY OF COLLOIDAL PARTICLES

Eric Lauga & Michael P. Brenner
Division of Engineering and Applied Sciences, Harvard University,
29 Oxford Street, Cambridge, MA 02138.

Summary We use a combination of numerical simulations and theoretical models to study the packing selection problem for the experiment of Manoharan *et al.* [1].

INTRODUCTION

In a recent experiment by Manoharan *et al.* [1], a small number N of spherical particles (diameter of about one micron) located at the surface of an oil droplet self-assemble due to the evaporation of the droplet. Such process leads to final packings of spheres which are unique and, for $N \leq 11$, equivalent to the minimal second moment clusters as studied by Sloane *et al.* [2]. Because such simple experimental process could be used to generate building blocks of a given number of particles at the micron or even nanometer scale, it is of fundamental interest to determine the parameters responsible for the packing selection.

NUMERICAL SIMULATIONS

We first use numerical simulations to reproduce the packings of Manoharan et al [1]. The simulations are performed using The Surface Evolver [3], program designed to calculate minimum energy configurations of deformable surfaces. The N solid spheres are modeled by N droplets of large surface tension, typically 10 to 100 times larger than that of main droplet, in order to penalize deformation of their interface and effectively force them to remain spherical throughout the drying process. Steric constraints are enforced by adding a repulsive part to the energy, acting between the centers of gravity of each sphere; the final packings are found to be independent of the details of such repulsive energy. Finally, the contact angle condition on each sphere is explicitly enforced by choosing the unique value of the droplet-particle interfacial tension which is appropriate in order to satisfy Young's law at the contact line. A typical initial condition is illustrated in Figure 1 in the case of 12 spheres.

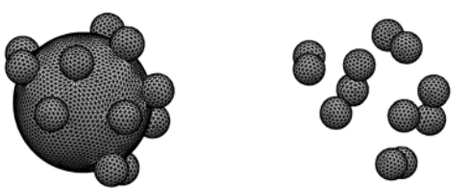


Figure 1: Typical initial configuration for the numerical simulations in the case of 12 spheres. Left: both the spherical particles and the droplet are visualized; right: only the particles are shown. The contact angle in this case is 90°.

Finally, we reproduce the effect of droplet evaporation by decreasing the volume of the droplet in a quasi-static fashion. The results of the simulations, which take up to almost a week for $N = 11$, are presented in Figure 2 [4]. The simulations are found to reproduce well the final packings of Manoharan [1]. However, contrary to what observed experimentally in [1], we observe a smooth evolution of the sphere packings towards the minimum-moment packings of [2]. We attribute such difference to friction between spheres and contact angle hysteresis in the experiments.

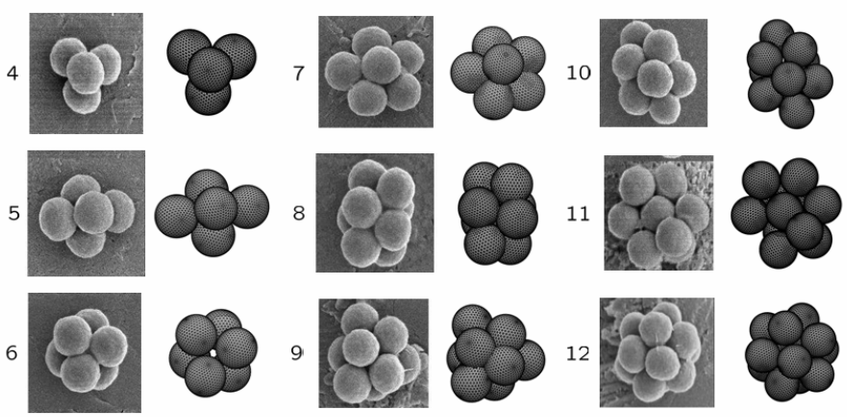


Figure 2: Comparison between the experimental packings of Manoharan et al (2003) [1] (left) with the results of our simulations (right) as a function of the number of spheres.

THEORETICAL CONSIDERATIONS

We now study theoretically the packing selection problem.

Critical packing. If $N = 1$, the droplet shape will trivially remain that of a spherical cap throughout the drying process and there is never any capillary force on the colloidal sphere. If $N \geq 2$, the droplet shape will be spherical as long as its volume is large enough (Figure 3a) but there exists a critical volume V_C below which excluded-volume interactions can no longer be ignored (Figure 3b). The volume of the spherical droplet at this point can be characterized in the following fashion. The steric interactions between particles located on the surface of a sphere can also be thought as the steric interactions between (1) the ``cone of influence'' of each particle, defined as the cone originating from the droplet center and tangent to the particle (illustrated in Figure 3b), or (2) the interactions between the intersection of each of these cones with the spherical cap droplet, i.e. circles. Consequently, packing spherical particles on the surface of a sphere is essentially equivalent to packing circles on a sphere, which is a mathematical problem with a rich history [5,6]: for small N, the circle packings are unique and correspond therefore to unique packings of particles at the critical volume. Furthermore, by geometrical arguments, it is easy to show that the corresponding critical packing of particles are also independent of the solid-liquid contact angle [7]; in contrast, the droplet volume at this critical packing depends naturally on the contact angle.

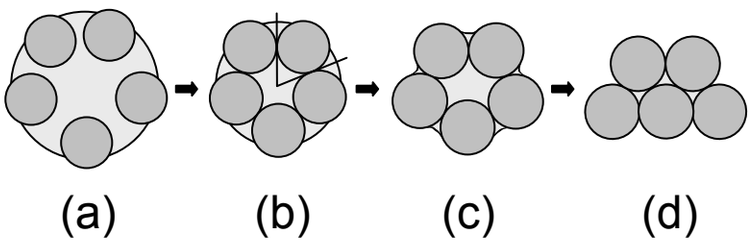


Figure 3: Schematic representation of the drying process for $N \geq 2$.

Deformations below the critical packing. Below the critical volume V_C characterized above, deviations of the droplet interface from a spherical cap lead to the appearance of capillary forces on each particle (Figure 3c). In the limit where the drying rate is small, each particle will be remain at equilibrium throughout the drying process and contact forces need to exist between pair of particles in order to balance instantaneously the capillary forces. The main theoretical question to be answered is: how do the spheres rearrange when the droplet volume is reduced below its critical value? Although intuitively one might think that in order to the answer this question, the full surface energy minimization problem has to be solved, we have found that in fact the various constraints associated with the spherical packings are sufficient to entirely determine the sphere rearrangements. Indeed, suppose the droplet volume is reduced by a small amount. The spheres will rearrange in a way that satisfy (1) the droplet volume constraint (one equation), (2) the contact condition for each touching pair of spheres (n_C equations, where n_C is the number of contacts) and (3) force balance on each sphere. The latter give rise to nontrivial constraints; since there are fewer contact forces (n_C) that there are components of the capillary forces ($3N$), the latter cannot be arbitrary and only a few of the capillary forces can be chosen independently [7]. Counting the number of constraint equations, we found that the number of constraints is exactly equal to the number of unknowns up to N=18, and therefore the rearrangement of the particles is unique and completely determined by the geometry of the spherical packing. Using such procedure, we were then able to construct a model program which starts from the spherical packing, decrease the droplet volume by small increments and calculates the corresponding incremental particle rearrangement consistent with all the constraint until final equilibrium is reached. This model successfully reproduces most of the final packings illustrated in Figure 2, but at a much lower computational cost than the full simulations.

CONCLUSION

We have presented a study of the packing selection problem for the experimental results of Manoharan et al. [1] using a combination of numerical and theoretical analysis. Further work on this problem will concentrate on packings obtained with spheres having variations in their wetting characteristics.

References

[1] Manoharan V.N., Elsesser M.T. & Pine D.J.: Dense Packing and Symmetry in Small Clusters of Microspheres. *Science* **301**: 483-487, 2003.
[2] Sloane N.J.A., Hardin R.H., Duff T.S. & Conway J.H.: Minimal-Energy Clusters of Hard Spheres**.** *Disc. Comp. Geom.*, **14**, 237-259 1995.
[3] Brakke K.: The Surface Evolver. Exp Math. **1** (2) 141-165 1992.
[4] The copyright for the experimental pictures in Figure 1 from ref. [1] has not been obtained yet but will be obtained by May 1st 2004.
[5] Clare B.W. & Kepert D.L.: The closest packing of equal circles on a sphere. *Proc. Roy. Soc.* A **405** 1986.
[6] Kottwitz D.A.: The densest packing of equal circles on a sphere. *Acta. Cryst.* A **47**, 1991.
[7] Lauga E. & Brenner M.P.: Evaporation-driven assembly of colloidal particles (in preparation).

HIGH-FREQUENCY LINEAR VISCOSITY OF EMULSIONS COMPOSED OF TWO VISCOELASTIC FLUIDS

J. Blawzdziewicz*, E. Wajnryb**
*Department of Mechanical Engineering, Yale University, P.O. Box 208286, New Haven, CT 06520-8286
**Polish Academy of Sciences, IPPT PAN, Swietokrzyska 21, PL 00-049 Warszawa, Poland

Summary
The high-frequency linear response to an oscillatory flow is studied for an emulsion of viscoelastic droplets suspended in another viscoelastic fluid. Our analysis applies when the frequency of the imposed flow is much higher than the inverse capillary-relaxation time of the drops. However, the imposed frequency can be comparable to the inverse timescales associated with the response of the component fluids. In our approach, the complex, frequency-dependent effective viscosity of the emulsion is described using the Bergman spectral representation. It allows us to characterize the response of the system in the complex domain by a single real function, i.e. the spectral density. Moreover, the spectral representation enables construction of rapidly converging continued-fraction approximations. We find that the emulsion response is accurately described by several coefficients of the expansion. Numerical results for the spectrum and the continued-fraction coefficients are presented at different volume fractions for emulsions of randomly distributed drops.

Introduction

We consider high-frequency linear viscoelastic response of an emulsion composed of viscoelastic drops suspended in another viscoelastic fluid. Typical examples of such systems include polymer blends and emulsions of polymeric solutions. Due to importance of viscoelastic fluids in chemical, pharmacological, and food industries, viscoelastic emulsion properties have been intensively studied theoretically and experimentally. For moderate drop volume fractions and viscosity ratios between the drop and continuous fluids simple analytical expressions for the effective viscosity of an emulsion have been developed. However, such approximations are inaccurate at high volume fractions of highly viscous drops.

In this work we focus on the frequency regime where the timescale ω^{-1} associated with the frequency ω of the imposed flow is much smaller than the drop capillary relaxation time $\tau_{\rm d} = \eta a/\sigma$,

$$\omega\tau_{\rm d} \gg 1, \tag{1}$$

Here a is drop radius, σ is the interfacial tension, and η is the average viscosity of the fluids. The imposed timescale ω^{-1} may, however, be comparable to the internal relaxation timescales characterizing the component fluids. In this frequency regime the effect of the interfacial tension on drop dynamics can be neglected; yet, the system has nontrivial viscoelastic response due to the viscoelasticity of the component fluids. The drop deformation is assumed to be small at all times, and the response of the component fluids is linear.

Under the high-frequency assumption (1) and small-deformation conditions the drops behave as nearly-spherical viscoelastic fluid blobs with complex viscosity ratio $\lambda(\omega) = \eta^{\rm in}(\omega)/\eta^{\rm out}(\omega)$, where $\eta^{\rm in}(\omega)$ and $\eta^{\rm out}(\omega)$ are complex, frequency-dependent viscosities of the drop and continuous-phase fluids. Due to the long capillary relaxation time (1) the drops passively react to the imposed flow, and the dependence of $\eta^{\rm eff}$ on ω stems entirely from the viscoelasticity of the component fluids, i.e.,

$$\eta^{\rm eff}(\omega) = \eta^{\rm out}(\omega)\bar{\eta}^{\rm eff}(\lambda(\omega)). \tag{2}$$

Bergman representation

The structure of the function $\bar{\eta}^{\rm eff}(\lambda)$ is analyzed using the Bergman spectral representation [1]. The representation, corresponding to a pole expansion of the linear operator describing propagation of the microscopic field in the system, has the form

$$\chi_{\rm S} = \phi \int_0^1 \frac{g(q)}{q-s}\,{\rm d}q, \tag{3}$$

where $\chi_{\rm S} = (\bar{\eta}^{\rm eff}-1)/(\bar{\eta}^{\rm eff}+\frac{3}{2})$ is a normalized susceptibility of a spherical emulsion sample subject to an external flow, and ϕ is the volume fraction of drops. The spectral density $g(q)$ is a real function that depends only on the microscopic geometry (the distribution of the drops for the system considered herein), but is independent of the viscosities of the component fluids. The viscosity ratio in the above expression enters only through the Bergman variable

$$s = 1/(1-\lambda). \tag{4}$$

Thus the complex effective viscosity (2) is represented in equation (4) via a real function of real variable $g(q)$.

We have derived explicit expressions for the function $g(q)$ in terms of the spectrum of the operators characterizing hydrodynamic interactions of spherical drops. The expressions have been evaluated numerically for different volume fractions of randomly distributed drops. Sample results of our calculations are presented in figure 1.

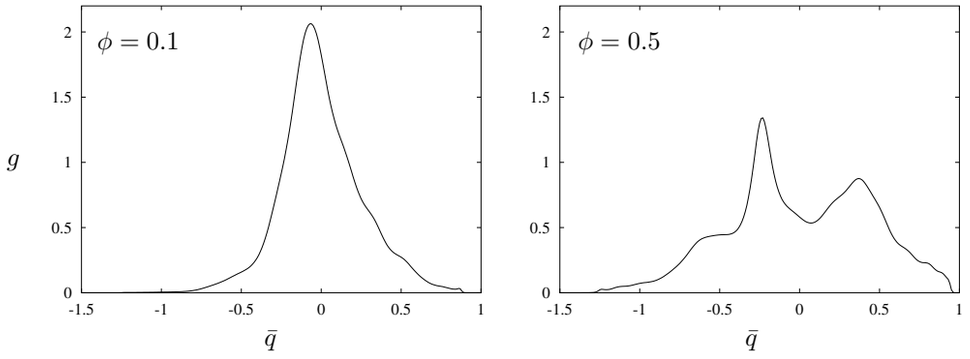


Figure 1. Spectral density g versus $\bar{q} = 1 - \frac{5}{2}q$ for two volume fractions ϕ (as labeled).

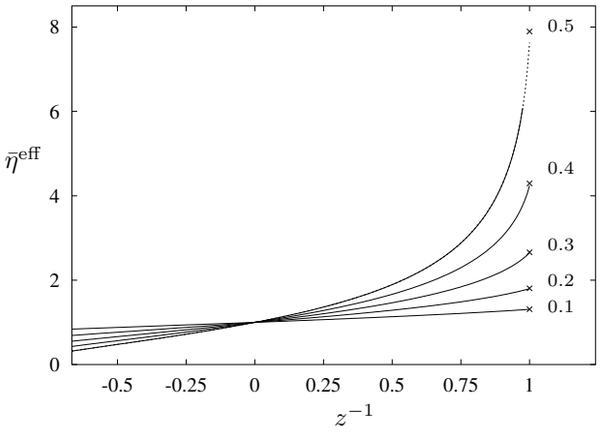


Figure 2. High frequency effective viscosity $\bar{\eta}^{\mathrm{eff}}$ versus $z^{-1} = (\lambda - 1)/(\lambda + \frac{3}{2})$ for different volume fractions ϕ (as labeled). Solid lines correspond to the parameter region where results are accurate within 1 %. Crosses denote results for hard spheres ($\lambda = \infty$), obtained using a different method.

Continued-fraction expansion

The spectral representation not only reduces the amount of information needed to characterize linear response of the system, but it can also be used to construct a set of rapidly converging Padé approximants that form a sequence of increasingly tight rigorous bounds. Following the method used by [2], the Padé approximants are obtained here in a continued-fraction form

$$\tfrac{5}{2}\chi_{\mathrm{S}} = \cfrac{1}{s + \frac{2}{5} - \cfrac{a_1}{s + b_2 - \ldots}} \tag{5}$$

with the expansion coefficients evaluated numerically. Only several levels of the expansion (5) are needed to obtain the effective emulsion viscosity with high accuracy. Our results for the effective viscosity of an emulsion with real values of the viscosity ratio are shown in figure 2.

Conclusions

Using Bergman spectral representation, we have developed a complete description of high-frequency effective viscosity for an emulsion of viscoelastic fluids. We have evaluated numerically the spectral density and the coefficients of the continued-fraction expansion. With only several expansion levels, the continued fraction provides a very accurate analytical representation of the effective viscosity. The work is underway to extend this approach to the frequency regime $\omega\tau_{\mathrm{d}} \gg 1$, where the interfacial-tension effects are important.

References

[1] D. J. Bergman. Physical properties of macroscopically inhomogeneous media. In H. Ehrenreich and D. Turnbull, editors, *Solid State Physics, vol. 46*, page 37. Academic Press, New York, 1992.

[2] B. Cichocki and B. U. Felderhof. Periodic fundamental solution of the linear Navier-Stokes equations. *Physica A*, 159:19–27, 1989.

KBN grant No 5T07A05224 and CONEX project supports are gratefully acknowledged

XXI ICTAM, 15–21 August 2004, Warsaw, Poland

BUBBLE FORMATION IN A CO-FLOWING AIR-WATER STREAM

A. Sevilla, J. M. Gordillo, C. Martínez-Bazán
Área de Mecánica de Fluidos, Universidad Carlos III de Madrid,
Avda. de la Universidad 30, 28911, Leganés, Madrid, Spain

Summary The present work investigates the generation of bubbles in a co-flowing air-water stream from the analytical as well as the experimental point of view. We first study the effect of the outer shear layer on the stability properties of two co-flowing streams of different density moving with different velocities. On the second part of the work we concentrate on the non-linear mechanisms leading to the formation of bubbles. The analytical results given by a model proposed here are compared with experiments.

Laminar co-flowing streams are present in many natural processes as well as engineering applications such those taking place in chemical reactors and modern material manufacturing among others. In particular, the present study focuses on some new aspects related to the formation and stability of laminar, coaxial gas-liquid jets of great relevance in bubble generation processes. Several mechanisms, previously unexplored in the literature, are expected to influence the formation of bubbles in a submerged coaxial air-water jet configuration. More precisely, we study the influence of the outer shear layer generated by the difference of velocity between the external co-flowing liquid stream and the quiescent surrounding liquid from the analytical as well as the experimental point of view. The variety of mechanisms appearing in the bubble generation problem suggests the idea of isolating and exploring them separately. Thus the different aspects analyzed in this work are summarized as follows.

We first studied the stability of two coflowing streams with finite crosstream extent in a cylindrical geometry. Transition curves from convective to absolute instability were obtained in terms of the control parameters, namely, inner to outer fluid density ratio, S, outer fluid to inner fluid velocity ratio, Λ, and, more importantly, external to internal nozzle diameter ratio, a. A new mode of instability caused by the external shear layer included in the velocity profile was identified. It was also found that this mode was responsible for triggering the absolute instability of configurations considered convectively unstable in the limit $a \to \infty$. Moreover, it was shown that, when $\Lambda = 1$, the critical density ratio necessary to sustain absolute instability in axisymmetric jets decreases with the diameter ratio as $S_c \propto a^{-4}$. In more general situations, where $\Lambda \neq 1$, two modes of instability associated respectively with the inner and the outer shear layers coexist. The analysis revealed that the outer shear layer has a significant effect on the stability of the internal interface, especially for light jets, corresponding to $S < 1$, when a is sufficiently close to unity. Furthermore, a new region of absolute instability was described in the a–Λ–S parameter space.

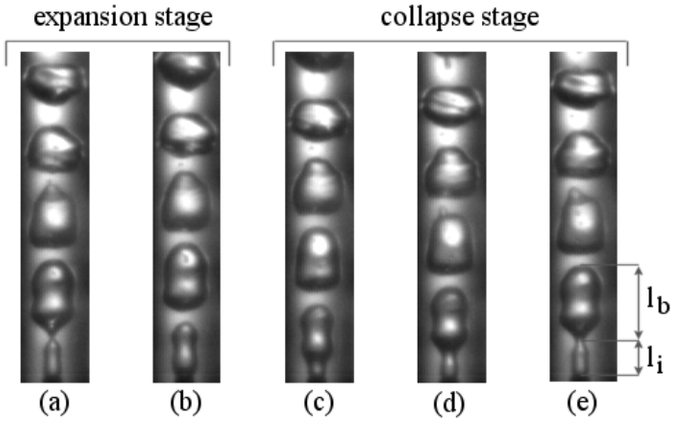


Figure 1. Temporal sequence of images illustrating the two different stages of the bubble formation process, namely *expansion stage* and *collapse stage*. Here l_i and l_b indicate the length of the intact ligament and the bubble respectively.

Once the effect of the external shear layer was described, we concentrated on the formation of bubbles in a co-flowing stream of water, $S = 10^{-3}$, without external shear layer. In this particular problem, the experiments were performed by discharging a water co-flow, which surrounded an air stream, directly into a stagnant air atmosphere. This simplified problem revealed different features which, to our knowledge, had never been reported before. More precisely, two different flow regimes were identified depending on the liquid (outer fluid) to gas (inner fluid) velocity ratio, $u_l/u_g = \Lambda$. For small values of Λ, a *bubbling regime*, characterized by a periodic bubble formation, was found. On the other hand, for values of the velocity ratio larger than a critical one which depends on the gas Weber number, $\Lambda > \Lambda_c$, a *jetting regime* with a long, stable gas jet forming inside the core of the liquid stream was observed. The transition between both regimes

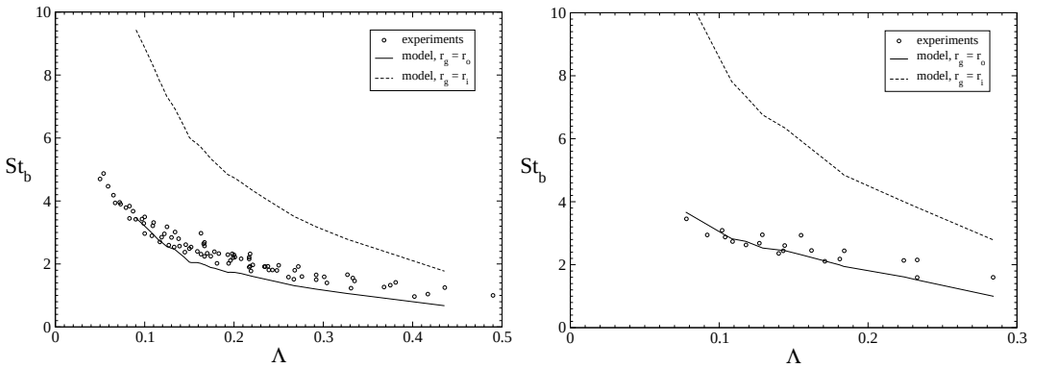


Figure 2. Comparison between the experimentally measured bubble formation frequency and that obtained by the developed model.

was satisfactorily explained in terms of a change in the absolute or convective nature of the instabilities. Regarding the bubbling regime, systematic experiments were performed to characterize the bubbling frequency and the gas ligament intact length, l_i. It was shown, both through experimental evidence and theoretically, that gas compressibility effects were essential during the initial stages of the bubble formation process. Thus, the process was divided into two different stages, namely the *expansion stage* and the *collapse stage*. A sequence of a bubble growth and pinch-off, including the expansion and the collapse stages, is depicted in figure 1. The first stage was theoretically studied by means of the compressible, one-dimensional Navier-Stokes equations for the gas flow, both inside the needle and the bubble. The study revealed that, similar to what happens in a water-hammer phenomenon, the gas pressure inside the bubble initially increased to values of the order of $\Delta p = \rho_g c_0 u_g (1-\Lambda)$ caused by the rapid pinch-off of the previous bubble. Here ρ_g is the gas density, c_0 is the sound speed at the air injection conditions and u_g is the gas injection velocity. Furthermore, the initial overpressure Δp decreased with time due to the bubble growth caused by the liquid acceleration. Since it was observed that compressible effects only took place during the expansion stage, the gas flow inside the bubble could be treated as being approximately incompressible during the rest of the process. In addition, a model to determine the bubbling frequency was developed taking into account the liquid inertia thanks to the use of the Rayleigh-Plesset equation in a cylindrical geometry. It has to be pointed out that the condition that determined the numerical frequency in our model was the neck collapse. This approximation was significantly different from that followed in other related works such those of [2], [1] or [3], where the bubble detachment was imposed as an ad-hoc condition. Experimental results of the dimensionless break-up frequency, St_b, is shown in figure 2 along with the results given by our one-dimensional model.

To conclude, once the different experimentally observed features of the simplified problem were satisfactorily explained, we faced the more complex problem of considering the influence of the external shear layer in the bubble generation process. For this purpose, we injected the co-flowing liquid stream into a stagnant liquid vessel. Similarly to what was observed in the previous simplified problem, two different flow regimes were obtained. In the first regime, occurring for low enough values of the velocity ratio, the flow was observed to be highly periodic due to the non-linear expansion-collapse mechanism described above. Although, in the second regime, which appeared for higher values of the velocity ratio, the flow was also nearly periodic, its presence was qualitatively well explained by the existence of an absolute instability in the system triggered by the external shear layer formed between the liquid coflow and the stagnant surrounding liquid atmosphere.

CONCLUSIONS

The formation of bubbles in a cylindrical co-flowing configuration was investigated here. It was determined that the outer shear layer caused by the difference of velocity between the outer water stream and the stagnant water of the reservoir could trigger the formation of bubbles if the outer diameter of the co-axial nozzle was not sufficiently larger than the inner one. In addition the characteristic of an air-water stream under the assumption of infinitely large outer to inner jet diameter ratio was studied. Under those conditions, two different regimes were described, namely *bubbling* and *jetting*. Furthermore, similar to what happens in a water hammer phenomenon, the bubbling regime was observed to be initially influenced by the overpressure generated by the rapid pinch-off of the previous bubble. The analytical results were satisfactorily compared with the experimental ones.

References

[1] CHUANG, S. & GOLDSCHMIDT, V. 1970 Bubble formation due to a submerged capillary tube in quiescent and coflowing streams. *Trans. ASME D: J. Basic Engng.* **92**, 705–711.

[2] KUMAR, R. & KULOOR, N. 1970 The formation of bubbles and drops. *Adv. Chem. Engng.* pp. 256–368.

[3] OĞUZ, H. & PROSPERETTI, A. 1993 Dynamics of bubble growth and detachment from a needle. *J. Fluid Mech.* **257**, 111–145.

MOLECULE CONFIGURATIONS IN A DROPLET DETACHEMNT PROCESS OF A SEMDILUTE XANTHAN SOLUTIONS

ChristianWagner* and Andriy Kityk**
*Experimentalphysik, Universität des Saarlandes, Postfach 151150, 66041 Saarbrücken, Germany
**Institute for Computer Science, Technical University of Czestochowa, Armii Krajowej 17, 42-200 Czestochowa POLAND

Summary The detachment process of a droplet of an elastic liquid is characterized by the suppression of the pinch off finite time singularity and the formation of a cylindrical filament between the droplet and the nozzle. The flow in this filament is purely elongational. The resistance to such a flow is macroscopically described by the elongational viscosity. However, a sound understanding of the functional connection between the microscopic configurations of the macromolecules and the macroscopic flow is still missing. We present birefringence data that are taken simultaneously to the macroscopic flow measurements. By changing the ionic strength of the solvent we can tune the flexibility of our polyelectrolytic macromolecules and correlate them with the microscopic polymer configurations and the measurements of the elongational viscosity.

SUMMARY

The detachment process of a droplet of a simple liquid is characterized by a finite time singularity of the minimum neck diameter[1]. However, the addition of a tiny amount of flexible polymers can lead to the suppression of the finite time singularity[2]. At a given moment t_c the flow - or strictly speaking its elongational parts - becomes strong enough to deform the polymers and a sharp transition from the self similar power law to a much slower exponential dynamic takes place. A cylindrical filament connecting the droplet and the reservoir is formed and the according flow profile is purely elongational. The resistance to such a flow is macroscopically quantified by the elongational viscosity η_e. It is known that flexible polymers have a higher elongational viscosity than stiff molecules, but the underlying physical mechanisms are only poorly understood. It is thus reasonable to study both the microscopic confirmation and the macroscopic flow response as a function of the chain flexibility. This is possible by using polyelectrolytic polymers, for which the chain flexibility can be tuned by the addition of salt to the solvent[3]. In that way the chain flexibility is altered *without* changing either the polymer chemistry or the chain length (the effects of which on the elongational viscosity are still ill understood).
The polymer we use is Xanthan (Sigma-Aldrich, Mw:~3Mio) at a weight concentration of 500ppm dissolved in 80wt% glycerol-water. The ionic strength of the solvent is tuned by the addition of KaCl at concentrations ranging from 0 to 0.1wt%. Xanthan has a high optical anisotropy and due to its shear thinning effects (and its biological digestibility) it is used largely in the food, pharmaceutical, oil and cosmetic industry.
The experimental setup is sketched in figure 1. The sample solution is quasistatically driven by a syringe pump through a nozzle with a diameter of d=2mm. In a distance D=7cm below the nozzle a plate is mounted in order to omit gravitational effects in the thinning process of the filament. The Retardation δ is measured by use of the optical train consisting of a 5mW HeNe Laser, a Polarizer P, a photo acoustic modulator PAM, the sample liquid, an Analyzer A, a bright field lens system and a photo diode connected to two Lock-Ins.. The polarizer is fixed at and angle of 45° relative to the photoelastic modulator. The photo acoustic modulator allows for a Lock-In technique for the detection of the retardation signal. The bright field lens system (figure 1 B) in front of the detector prevents any light that has not passed the filament from reaching the detector by blocking the parallel components with a mask M in the focal point of lens L1[4]. The lens L2 collects the light that is diffused by the cylindrical filament into the detector.

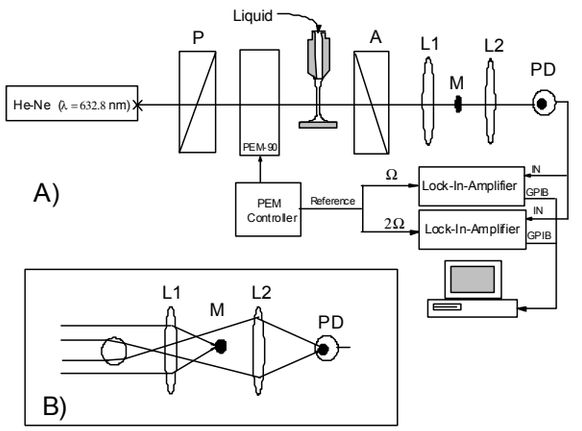
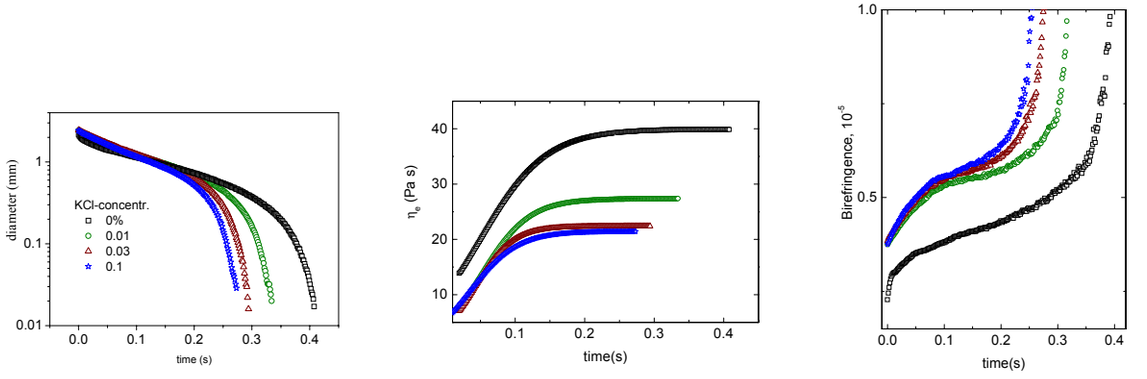


Figure 1
The experimental setup. See text for explanation.

To calculate the birefringence form the retardation signal the instantaneous thickness h(t) of the filament must be known. Therefore the thinning process of the minimum filament diameter h is measured with a high speed camera (encore mac PCI 1000S) that is placed perpendicular to the optical train. The camera is equipped with a 2 times magnification objective and the image capturing is synchronized to the data collection of the two Lock-In´s. The data of h(t) for different salinities are shown in figure 2 a). A decrease in salinity leads to a faster dynamic, hence to a lower resistance of the polymers to the flow. The data can be directly used to calculate the elongational viscosity η_e by equating the capillary pressure with the elastic stresses. Recently Anna and Mc Kinley have shown that "filament thinning studies and filament stretching form complementary experiments" that lead to consistent measures of the transient extensional viscosity of the fluid"[5]. The elongational viscosity η_e is time dependent because in the course of the experiment the polymers are more and more stretched by the flow. The experiments reveal that the temporal behavior of h(t) is first exponential, implying that the elongational rate $\dot{\varepsilon} = -2\partial_t h / h$ remains constant. This indicates a subtle interplay between the polymer and the flow dynamic. For large times of course a steady state value of the elongational viscosity η_e =const will be reached that depends only on the elongation rate $\dot{\varepsilon}$. Figure 2 b) shows that the elongational viscosity decreases with increasing salinity. This correlates with a decrease in flexibility of the polymer chains. Different than most polyelectrolytes Xanthan stiffens with increasing ionic strength due to a collapse of the sugar-backbone.

The microscopic confirmation of the macromolecules can be studied by use of the birefringence data. The birefringence signal is proportional to the end to end elongation of the molecules, to their orientation and to the concentration. In elongational flow the polymer should be elongated along the flow and thus the birefringence is proportional to the elongation of the polymers and the concentration. In that way we could test our method by performing several runs at different polymer concentrations and the birefringence signal was always proportional to the concentration.

The data in figure 3 c) were taken for different salinities and one observes that the birefringence at higher salinities and thus for stiffer polymers is larger than for more flexible ones. This confirms the physical picture that stiffer polymers are already at equilibrium more elongated. However, they perform a lower resistance against the flow as we have shown in figure 2 b). The functional behavior of the birefringence signal shows a monotonic increase that correlates with the uncoiling of the polymer. However at the final stage of the experiment, we observe a divergence in the birefringence signal. This divergence is very robust and takes place at stages of the filament thinning process when the filament diameter is still large enough to render the analysis unambiguous. While the polymers should be completely uncoiled at this stage of constant steady state elongational viscosity we can attribute this behavior only to a concentration enhancement. This explanation is supported also by the fact that eventually the filament might not break at the final stages of the thinning process but a very thin polymer fiber remains between the nozzle and the ground plate.



a) b) c)

Figure 2

a) The filament diameter versus time. b) The time dependent elongational viscosity. C) The birefringence. All plots show data from runs at different ionic strengths of the solvent.

[1] For a review see: J. Eggers , Rev. Mod. Phys. 69, 865 (1997)

[2] Y. Amarouchene, D. Bonn, J. Meunier, and H. Kellay, Phys. Rev. Lett. **86**, 3558 (2001)

[3] C.G. Bauman, S.B. Smith, V.A. Bloomfield, C. Bustamante, P.N.A.S. **94**, 6185 (1997)

[4] T.Sridhar, D.A.Nguyen and G.G. Fuller, J. Non-Newt. Fluid-Mech. **90**, 299 (2000)

[5] S. L. Anna, G. H. McKinley, J. Rheol. **45**, 115 (2001)

SPREADING AND RETRACTION OF IMPACTING DROPS

Christophe Josserand, Stéphane Zaleski
Laboratoire de Modélisation en Mécanique
CNRS-Université P. & M. Curie
Case 162, 4 place Jussieu F-75252 Paris Cedex 05, France

Summary We consider theoretically and numerically the axisymmetric dynamics of drop impacts on a hydrophobic solid surface. For reasonable Weber and Reynolds numbers the dynamics shows an initial spreading of the drop on the substrate followed by a retraction phase due to capillary forces. We perform a parametric study to investigate both capillary and viscosity influences on this dynamics. We particularly focus on the film thickness during the spreading. At early times of impact the ejected liquid lamella is determined for low Weber number by the capillary length. On the contrary for large Weber numbers we observe that the residual liquid film in the center of the impact at maximum spreading is controlled by viscous effects. The retraction dynamics is also captured and is clearly dependant on the liquid film thickness at the center. A simple Taylor-Cullick theory for receeding liquid film on solid substrate will be derived and compare to the numerical results for this hydrophobic case. More general situations with non trivial contact angle will be discussed.

INTRODUCTION

Drops impacting a wet or dry surface are a frequent and common process encountered in many geophysical, industrial and everyday-life situations. It is also well known to produce terrific pictures icons following the work of Worthington[1]. When the surface is perfectly dry and poorly hydrophilic, the drop first spreads on the substrate until it reaches a maximum radius. Then surface tension drives the retraction of the expanded film. Often a partial or complete rebond of the drop is observed creating a secondary droplet[2, 3]. The knowledge and the understanding of the maximum spreading radius and of the retraction dynamics for varying Weber and reynolds present important challenges both for fundamental mechanics and applications. Ink-jet printers need to control the maximum radius while the retraction dynamics is crucial for agricultural soil treatments[3]. Here we investigate numerically the dependance of these quantities with the Weber and Reynolds number for the specific case of hydrophobic surfaces.

NUMERICAL METHOD

We seek to solve the Navier-Stokes for axi-symetrical free surface flows:

$$\rho(\frac{\partial \mathbf{u}}{\partial t} + \mathbf{u}\cdot\nabla\mathbf{u}) = -\nabla p + \nabla\cdot(2\mu\mathbf{D}) + \sigma\kappa\delta_s\mathbf{n}$$

where ρ is the liquid density, $\mathbf{u}$ the velocity field, and p the pressure. μ and σ are respectively the viscosity and the surface tension. κ is the axisymetric curvature, $\mathbf{n}$ the normal to the interface and $\mathbf{D}$ the rate of deformation tensor. The velocity field is divergent free and the outer gas is neglected through free surface boundary conditions. The interface is tracked via a markers chains method developped by Popinet and Zaleski[4]. Two different boundary conditions will be taken at the wall. Firstly, the usual no-slip velocity condition on the wall is considered with $\theta = 180\circ$ constant contact angle. In that case, no typical moving contact line divergence is expected and would be if any suppressed by the numerical grid cut-off. On the other hand, following[2] we consider free-slip velocity conditions on the wall. The interface is captured through a marker-chain which is advected by the local velocity field. Multigrid technics are used to solve the mass conservation.

IMPACT DYNAMICS

Typical drop shapes during the impact are shown on figure (1) for no-slip velocity boundary conditions and for high Weber and Reynolds number. The two first pictures show the drop spreading into a flan thin pancakes. Between the third and fourth pictures, we observe the film retraction driven by surface tension. On the other hand, the dynamics between pictures 2 and 3 occurs almost at constant spread radius. The liquid from the center of the drop is there continuously feeding the rim torus.

The maximum spreading radius is parametrically studied when Re and We vary. In particular we have isolated viscous and capillary effects through fixed Weber or fixed Reynolds numbers study. Although the viscous influence on the radius is hard to determine, it is relevant for low Reynolds number and the maximum radius shows only a weak dependance with the viscosity at high Reynolds number. However, a precise study of the residual film thickness at the impact center shows a typical viscous layer dependance of this length. The capillary influence on the maximum spreading radius is stronger. For high Reynolds number, we compare our numerical results with two asymptotical theories predicting $We^{1/2}$ and $We^{1/4}$ dependance for high Weber numbers. We also discuss a phenomenological transition between small (order one) and high Weber numbers: at small Webers, we have shown[2] that capillary waves propagating along the surface determine the drop deformation. On the opposite case, for high Weber numbers these waves cannot propagate since they are slower than the impacting speed. The transition between these two behaviors will be discussed as a transsonic transition.

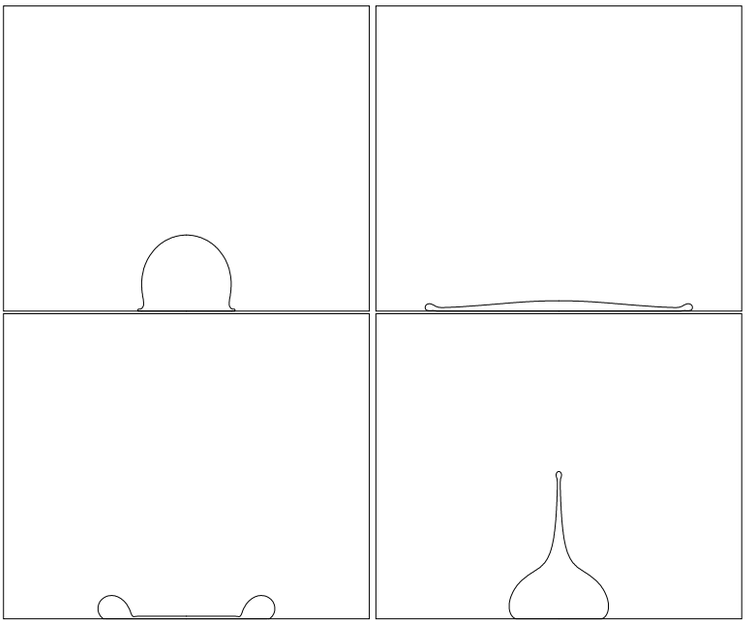


Figure 1. Drop shapes during the impact of a 3 mm water drop ($\mathrm{We} = 540$ and $\mathrm{Re} = 900$).

FILM RETRACTION

The dynamics of film retraction correspond for this hydrophobic situation to a particular dewetting dynamics. We are led to write a Taylor-Culick like theory of retracting film on a solid substrate. This theory accounts for viscous dissipation in the fluid by assuming that velocity gradients are determined by the film thickness. Comparison with 2D numerical simulation will be shown and an extension to non-hydrophobic will be discussed. Retraction speed dependance with capillary number will be calculated and compared with experimental situations.

CONCLUSIONS

The impact of droplets on dry solid surface is studied here following the inspiring hydrophobic case. Numerical simulations are compared with experimental results. We try to obtain consistant theories for the maximum radius expansion of the drop and for the retraction dynamics.

References

[1] A.M. Worthington: "On the form assumed by drops of liquids falling vertically on a horizontal plate", Proc. R. Soc. Lond. **25**, 261-271 (1876).
[2] Y. Renardy, S. Popinet, L. Duchemin, M. Renardy, S. Zaleski, C. Josserand, M.A. Drumright-Clarke, D. Richard, C. Clanet and D. Quéré: "Pyramidal and toroidal water drops after impact on a solid surface", J. Fluid Mech. **484**, 69-83 (2003).
[3] V. Bergeron, D. Bonn, J.-Y. Martin and L. Vovelle: "Controlling droplet deposition with polymer additives", Nature **405**, 772-775 (2000).
[4] S. Popinet and S. Zaleski: "A front-tracking algorithm for accurate representation of surface tension", Int. J. Numer. Meth. Fluids **30**, 775-793 (1999).

Main Factors Controlling the Emulsification Process under Turbulent Conditions. 2. Experiment and data interpretation

S. Tcholakova[1], N. D. Denkov[1], I. B. Ivanov[1] and T. Danner[2]

[1]*Laboratory of Chemical Physics & Engineering,Faculty of Chemistry, Sofia University, 1164 Sofia, Bulgaria*

[2]*BASF Aktiengesellschaft, GCT/P, L549, Ludwigshafen, Germany*

The emulsification was performed by a narrow-gap homogenizer [1]. Three different types of surfactant were studied: anionic SDS, nonionic Brij 58, and protein WPC. Soybean oil was used as oil phases. The electrolyte concentration was varied by addition of 10 or 150 mM NaCl to the surfactant solutions.

For all studied emulsifiers (protein, non-ionic and anionic surfactants; at high and low electrolyte concentrations) we observe two well-defined regions in the dependence of the mean drop size, d_{32}, on the initial surfactant concentration, C_S^{INI}. A considerable decrease of drop size is observed at low surfactant concentrations (Region 1, $C_S^{INI} < 0.1$ wt %), followed by a plateau region at high surfactant concentrations (Region 2, $C_S^{INI} > 0.1$ wt %) - see Figure 1 for illustration of these trends.

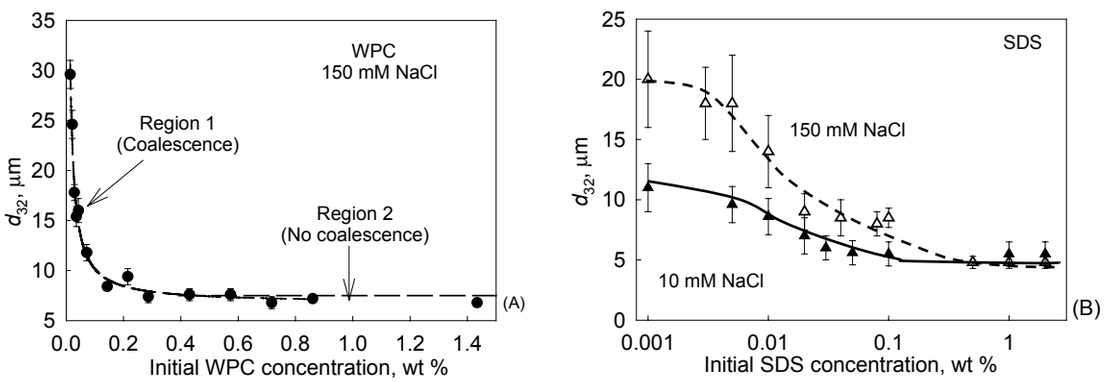


Figure 1. Mean volume-surface diameter, d_{32}, as a function of the initial emulsifier concentration, for emulsions stabilized by (A) WPC and (B) SDS.

At high emulsifier concentrations (in the plateau regions), the experimental data for d_{32} are described very well by the Kolmogorov-Hinze theory of emulsification, which states that the drop size is given by:

$$d_K \sim \varepsilon^{-2/5}\sigma^{3/5}\rho^{-1/5} \tag{1}$$

where σ is the interfacial tension, ρ is the mass density of the continuos phase, and ε is the average power density (rate of energy dissipation per unit volume) in the emulsification chamber. The agreement between eq 1 and the experimental data is illustrated in Figure 2 with two series of experiments: (1) at fixed σ_{OW} and different hydrodynamic conditions; (2) at fixed hydrodynamic conditions and different σ_{OW}.

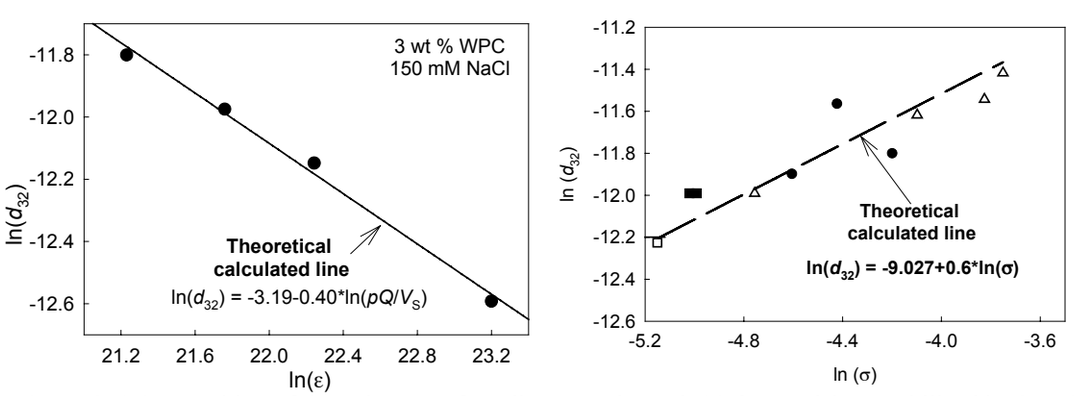


Figure 2. (A) Logarithm of the volume-surface diameter, d_{32}, vs ln(ε) for emulsions stabilized by 3 wt % WPC when σ = 10 mN/m. (B) ln(d_{32}) vs ln(σ), for emulsions prepared under equivalent hydrodynamic conditions, ε = 2.5×10^8 J/(m^3.s). In all experiments the oil volume fraction Φ = 0.28. The symbols represent experimental data, whereas the continuous line is calculated by eq 1.

At lower emulsifier concentration, two qualitatively different cases were recognized. In the case of suppressed electrostatic repulsion (nonionic and protein type of emulsifier in presence of 150 mM NaCl) we found that d_{32} is a linear function of $1/C_S$, see Figure 3. This result can be explained [1] by making a mass balance of the protein initially dissolved in the aqueous phase (before starting the emulsification) and the protein adsorbed on the drop surface (after accomplishing the emulsification). This mass balance predicts that the slope of the dependence $d_{32}(1-\Phi)/\Phi$ vs. $1/C_S$ corresponds to a threshold value of the surfactant adsorption, Γ^*, which is needed to stabilize the drops against coalescence [1]. From the best linear fit through the experimental data, we determined $\Gamma^* = 1.9$ mg/m^2 for WPC solutions and $\Gamma^* = 1.4$ mg/m^2 for Brij 58 solutions, see Figure 3. As shown in Ref. [1], Γ^* does not depend on the oil volume fraction and on ε, which means that Γ^* can be considered as a characteristic of the used emulsifier. This is the typical case when no significant electrostatic repulsion occurs between the drops. In such systems, the drops coalesce during emulsification until Γ becomes equal to Γ^*. Once a sufficiently dense layer is formed, it ensures a strong steric repulsion, which stabilizes the drops against further coalescence.

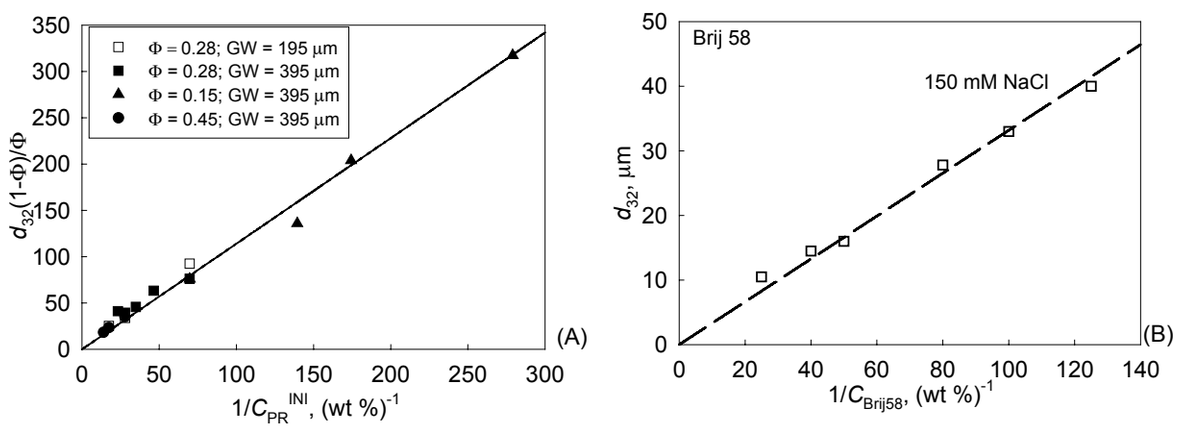


Figure 3. Mean diameter, d_{32}, as a function of the inverse initial surfactant concentration for emulsions stabilized by: (A) WPC, (B) Brij 58.

Our attempts to estimate the threshold emulsifier adsorption, Γ^*, in the systems with significant electrostatic repulsion between the drops (SDS + 10 or 150 mM NaCl), were unsuccessful. To reveal what is the interrelation between surfactant concentration and adsorption, on one side, and the mean drop size, on the other side, we analyzed the role of drop-drop interactions during emulsification [2]. The performed theoretical analysis showed that, for SDS + 150 mM NaCl, there is a threshold surface potential, $\Psi^* = -22$ mV, ensuring electrostatic stabilization of the emulsion drops during emulsification. This means that the emulsion drops would coalesce until the surface electric potential increases in magnitude, as a result of SDS adsorption, from 0 to ca. 22 mV. For emulsions stabilized by SDS + 10 mM NaCl, the theoretical estimates predict that no coalescence is expected to occur, even at very low surface coverage with surfactant, due to the strong electrostatic repulsion between the drops. These theoretical predictions were found to agree well with the experimental data for SDS stabilized emulsions [2].

References:

1. S. Tcholakova, N. D. Denkov, D. Sidzhakova, I. B. Ivanov, B. Campbell, "Interrelation of drop size and protein adsorption at various emulsification conditions", *Langmuir 19* (**2003**) 3084.
2. S. Tcholakova, N. D. Denkov, I. Ivanov, T. Danner, "Role of surfactant type and concentration for the mean drop size during emulsification in turbulent flow", *Langmuir, submitted*.

WATER MIST BEHAVIOR AS FLAME SUPRESSANT

M. T. Parra, F. Castro, J. M. Villafruela, C. Méndez, M. A. Rodríguez
Department of Energy and Fluid Mechanics Engineering, University of Valladolid, Spain

Summary The present work focuses on the numerical simulation of the interaction of a water spray barrier and a premixed methane-air flame inside a closed tube. The water mist is modelled as an uniform cloud of monodispersed droplets. The principal mechanisms of interaction of the water spray against the flame are: the break-up, drag, heating and evaporation of the droplets. The final goal is to determine its effectiveness as extinction mechanism.

INTRODUCTION

The fire suppression effects of water mist are attributed to physical effects more than chemical effects. When the water droplets contact hot or burning gas mixture, the water droplet changes from liquid to steam, which means an increase of 1700 times its volume. The expansion of volume reduces the concentration of oxygen in the flame surroundings. The droplet evaporation removes heat from the burning mixture because of the sensible heat of water vapour. Optimum water droplet sizes ranges from 50 to 200 microns of mean diameter. Droplets must be large enough to avoid the drag and small enough to evaporate quickly. Experiments have shown that water spray can be very effective in quenching strong flames.

It is possible to summarize the mechanisms of energy transfer between the flame front and the water spray barrier as: the surface tension energy necessary to break-up the droplets, momentum to accelerate the droplets due to the velocity of the ambient gases, energy to increase the temperature of the droplets due to the ambient temperature and the latent heat energy involved with steam generation, [1].

NUMERICAL MODEL

Drag model

Regarding the momentum interaction between the gas mixture and the water barrier the gaseous flow exerts a drag force on the water droplets. The drag force is a function of the relative velocity between the gas mixture and the droplets: $F_D = -C_D 0.5\,\rho V_{rel}^2 A_P$ where C_D is the drag coefficient, evaluated with different correlations for Reynolds ranging from 0 to $3\,10^5$ and A_P is the projected area of the droplet, assuming that the water droplets maintain a spherical shape.

Break-up model

It is commonly known that the break-up of a droplet is originated by a deformation of its surface due to the aerodynamic forces imposed by the gas flow. The break-up criterion can be expressed in terms of relative velocity between the droplet and the gas flow, Weber number $We = \rho V_{rel}^2 D/\sigma$, [2]. In the case of water spherical droplets, when the Weber number is bigger than 12 there is bag type break-up, if the ratio of Weber and square root of Reynolds is bigger than 0.5, there is stripping type break-up, [3]. Ranger and Nicholls proposed an empirical expression for the break-up time, [1].

In presence of pressure waves, the break-up criterion comes expressed in terms of the instantaneous acceleration, Eötvös number $Eo = \rho_W (dV/dt) D^2/\sigma$, [4]. There is bag break-up if the Eötvös number is bigger than 16 and stripping break-up if the Eötvös number is bigger than 100, talking of water droplets.

Vaporization model

It was considered that vaporization can occur according two regimes: mass diffusion transfer and boiling conditions, any of them behaves according the widely used Spalding model, [5].

When the droplet temperature is lower than the saturation temperature, then the vaporization is due to diffusion transport from the droplet to the gas mixture, being the mass transfer from one droplet:

$$\frac{dm_W}{dt} = \pi D\,\rho D_W Sh B_M \tag{1}$$

The thermal energy received by one droplet from the surrounding ambient is:

$$\dot{Q} = \pi D\,K Nu (T_G - T_W) \tag{2}$$

D_W is the mass diffusion of water vapour in gas mixture, B_M is the Spalding mass transfer number, K is the thermal conductivity of the gas mixture. The Sherwood number, Sh, and the Nusselt number, Nu, are evaluated from the Ranz and Marshall correlation, [6]. The increase of the droplet temperature can be obtained from:

$$m_W c_W \frac{dT_W}{dt} = \dot{Q} - \frac{dm_W}{dt} L \tag{3}$$

When the droplet temperature is around its boiling point, the vaporisation regime is the boiling. In that case, there is not droplet heating and the total energy is employed to vaporize the water, being the new rate of vaporisation evaluated from equation 3.

DISCUSSIONS OF RESULTS

In the calculations described here, an adaptive mesh was used to represent a tube 18 m length with one locked end, the initial temperature in the unbumed gas mixture is 300 K and the temperature on the locked end is 1800 K to provide the ignition of the flame. The initial composition is the stoichiometric methane/air mixture. The flame will propagate through

the tube. The water barrier is located at L = 3 m from the ignition zone and is characterised by droplets of diameter D = 50 μm being the liquid volume fraction F = 0.05%.

The figure 1 represents the temporal evolution of: temperature and diameter of the droplet and the liquid water volume, on the location x = 4 m. In order to compare simultaneously the three variables, they have been made nondimensional, they are the rate of the temporary value with reference to the initial value. The water volume, increases due to the drag from upwind sections and decreases with the time because of the vaporization. When the water temperature increases, the diffusion vaporization regime occurs. As soon the water temperature reaches the saturation temperature, then the boiling regime begins with an important decrease of the water volume. The important decrease of the diameter is due to the break-up by effects of the pressure waves while the slow reduction is due to the steam generation. The boiling regime begins when the droplet diameter is small enough and therefore has a high surface/volume ratio.

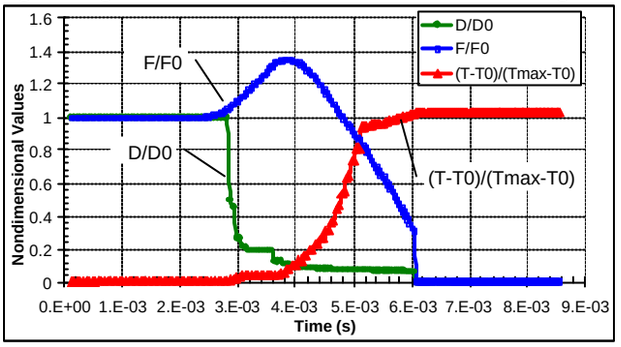


fig. 1. Temporal evolution of the water barrier on x = 4m. Barrier of D = 50 mm, F = 0,05% and L = 3m

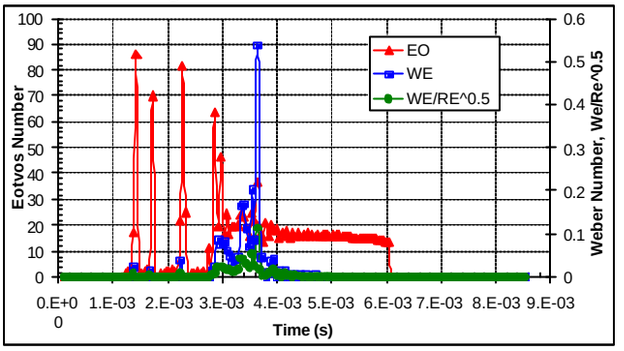


fig. 2. Temporal evolution of break-up parameters on x = 4m. Barrier of D = 50 mm, F = 0,05% and L = 3m

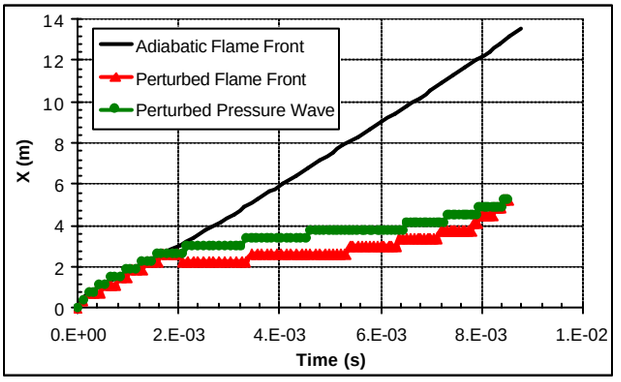


fig. 3. Propagation of the free flame and the flame with the barrier of D = 50 mm, F = 0,05% and L = 3m

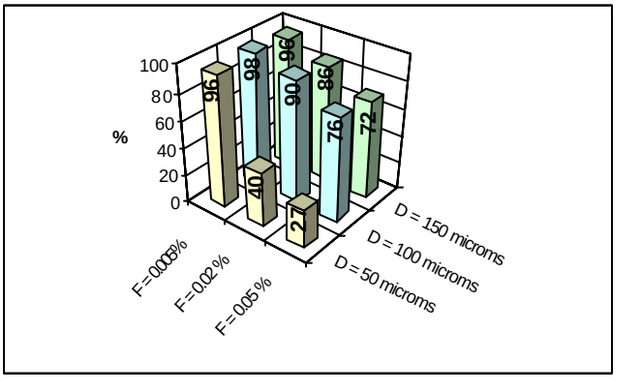


fig. 4. Propagation velocity of the perturbed flame expressed on percentage of the one free flame

Figure 2 shows the Weber and the Eötvös numbers as well as the $We/Re^{0.5}$ on x = 4 m. From the pictures, its possible to see that the Weber number takes values lower than 0.54, the $We/Re^{0.5}$ lower than 0.11 while the Eötvös number takes values up to 86. That means that the main break-up agent is the instantaneous acceleration instead of the relative velocity, and there is bag break-up regime.

The figure 3 represents the propagation of the front of a flame without water barrier (adiabatic flame) and a flame interacting with a water barrier. It is clear the important decrease of its velocity of propagation. On figure 4, there is a parametric analysis of the influence of the droplet diameter and liquid fraction of the barrier. The results are the velocity of propagation of different flames expressed as a percentage of the adiabatic velocity of propagation.

CONCLUSIONS

The interaction of a monodispersed water barrier of droplets with a premixed methane/air flame that propagates in a confined domain has been simulated. The main interaction agents taken into account are: the vaporisation: diffusion and boiling regimes, as well as the droplet break-up based on the Weber and Eötvös number. The results show a reasonable behaviour. The parametric analysis reveals the important decrease of the flame propagation velocity for small droplets and large liquid fractions.

Acknowledgements

We thank the Spanish Ministry of Science and Technology for supporting this work, grant REN2002-1598.

References

[1] Thomas G. O., Edwards M. J. and Edwards D. H., (1990). Studies of detonation quenching by water sprays, Combust. Sci. Tech. Vol. 71, pp.233-245.

[2] Wierzba A., (1990). Deformation and breakup of liquid drops in a gas stream at nearly critical Weber numbers, Experiments in Fluids 9, pp. 59-64.

[3] Nicholls J. A., (1972). Stream and droplets breakup by shock waves, Liquid propellant rockets combustion instability, pp. 126-127, NASA SP-194.

[4] Catlin C. A., Gregory C. A. J., Johnson D. M. and Walker D. G., (1993). Explosion mitigation in offshore modules by general area deluge, Trans IchemE, Vol. 71.

[5] Reitz R. D., (1987). Modeling atomization processes in high-pressure vaporizing sprays, Atomisation and Spray Technology 3, pp. 309-337.

[6] Sirignano W. A., (1993). Fluid dynamics of sprays - 1992 Freeman scholar lecture, Journal of Fluid Engineering, Vol. 115, pp. 345-378.

NUMERICAL SIMULATION OF LIQUID-GAS INTERFACES WITH APPLICATIONS TO ATOMIZATION

Thomas Boeck, Stéphane Zaleski
Laboratoire de Modélisation en Mécanique
4 place Jussieu, 75005 Paris
Email: zaleski@lmm.jussieu.fr

Summary
We investigate the two-phase mixing layer between high speed liquid and gas jets. This flow leads to the breakup of the interface into small droplets and is the basic mechanism in atomization processes. We use Volume of Fluid methods to investigate this flow numerically. Some recent versions of the Volume of Fluid method conserve momentum exactly, which is an advantage for the robust simulation of very small droplets. To validate the use of these methods for the computation of the instability, we have investigated in depth the linear stability theory. Good agreement is obtained between simulations and stability theory. We then report simulations of the non-linear development of the instability in 3D. We use boundary conditions that allow the study of the spatial development of the instability. The simulations show the convective character of the instability and the influence of small upstream perturbations on droplet formation.

INTRODUCTION: THE ATOMIZATION PROBLEM

Atomization phenomena are important in combustion engines as well as in many other processes. Several mechanisms lead to atomisation, such as upstream turbulence, cavitation and the Kelvin-Helmholtz instability in the sheared liquid-gas interface [1, 2, 3]. The development of this instability leads to very complex structures, the study of which is the focus of this lecture. Numerical simulation of these flows is a major challenge for large scale computational fluid dynamics. The LMM group has developped a number of interface tracking methods, among which Volume of Fluid is particularly of interest. Some versions of the Volume of Fluid methods conserve momentum exactly [4], which is an advantage for the simulation of small droplets. However fundamental difficulties remain with the use of these methods. One is that it is very difficult to simulate flows which are simultaneously at (i) large Reynolds number Re (ii) large Weber number We (iii) large values of the density ratio ρ_l/ρ_g and (iv) large values of the viscosity ratio μ_l/μ_g. While it is possible to tune the codes so that large values of all the numbers are reached, doubts may reasonably remain on the accuracy of the result. Thus it is very important to find validation cases. The comparison between linear theory and predictions of the numerical simulations is particularly of interest here. Very few such validations exist with the exception of the work of Tauber, Unverdi and Tryggvason [5]. Moreover, the in-depth investigation of linear theory is interesting in its own right as it sheds light on the mechanisms of the Kelvin-Helmholtz instability.

LINEAR STABILITY THEORY

The simplest version of linear instability theory assumes a staircase-like velocity profile and the temporal development of the instability. Viscosity is neglected. This version predicts a critical Weber number above which instability develops [6].
A more realistic theory is obtained assuming a piecewise-linear velocity profile. These profiles represent schematically the boundary layers in the gas and in the liquid. The gas boundary layer forms in the upstream flow inside the nozzle. After the nozzle exit, both boundary layers evolve under the action of viscosity [7, 8]. The piecewise linear profiles were employed in the theoretical work of E. Villermaux and coworkers. The experimental and theoretical power laws agree but the prefactors do not for axially symmetric flow [9], a result still not understood. It is interesting to note that until now quantitative agreement was very difficult to find between linear theory and numerical simulations as well.
Recently a much more realistic linear theory of atomization was developed by Phil Yecko and one of the authors [10, 11]. It uses smoothly varying boundary layer profiles and solves the full linearized viscous equations, i.e. the Orr-Sommerfeld equations. The error function profiles have advantages in the comparison with numerical simulation as they are slowly varying in time at small viscosity. Excellent agreement is then obtained with the full numerical simulation for relatively small values of the viscosity ratio. There is a large difference with the inviscid theory (Fig. 1a).
An interesting feature of the Orr-Sommerfeld theory is that one obtains, for sufficiently large Reynolds numbers, several new instability modes [10, 11]. These modes are in some sense similar to Tollmien-Schlichting modes: some of them tend to disappear albeit slowly for large Reynolds numbers, while one of them remains and converges very slowly to the inviscid modes. Some of the modes are clearly related to viscous effects and seem for large We to be a continuation of the "Hinch modes" [12].

NUMERICAL METHODS

To solve the fully nonlinear problem, we use a version of the Volume of Fluid method. The method has been thoroughly described in several recent references [13, 4, 14]. In short, we use a volume fraction C_{ij} to describe the fraction of liquid filling a cell ij. The interface is reconstructed and advected at each time step. The Navier-Stokes equations with variable

viscosity and surface tension are solved for an incompressible fluid using a finite volume method on a square lattice. Surface tension is treated by a "Continuous Surface Force" method, smoothing the surface tension term in the equations over two or three grid cells. The incompressibility constraint is obtained using a projection method, with a multigrid algorithm for the pressure. Details will be given in the full lecture. Agreement with linear theory is excellent when the viscosity ratio is small. When the viscosity ratio is large, however, one needs to pay attention to the viscosity in mixed cells. The correct exponential behavior is obtained for a mixed-cell viscosity given by the harmonic mean

$$\mu_{ij} = [\mu_l^{-1} C_{ij} + \mu_g^{-1}(1 - C_{ij})]^{-1} \tag{1}$$

This expression for the mixed cell viscosity had already been proposed by Patankar and used in [15], however it is here shown for the first time to have a large effect on the linear growth regime.

NONLINEAR DEVELOPMENT OF THE INSTABILITY

The nonlinear stages of the instability show the development of 2D sheets, followed by the growth of 3D filaments or fingers. An example of the temporal development is shown in Figure 1a. We also use entry and exit conditions and study the spatial development of the instability. Small perturbations are imposed near the flow entrance. These pertubations create velocity fluctuations of the order of 10 % of the mean flow. When these perturbations are present the instability develops in a manner similar to the experimental observations. In the absence of perturbations the nonlinear development does not occur. This is interpreted as an effect of the convective character of the instability. We measure the size of the detached droplets at various times in the simulation. The observed distribution of droplet sizes is exponential as observed in the experiments.

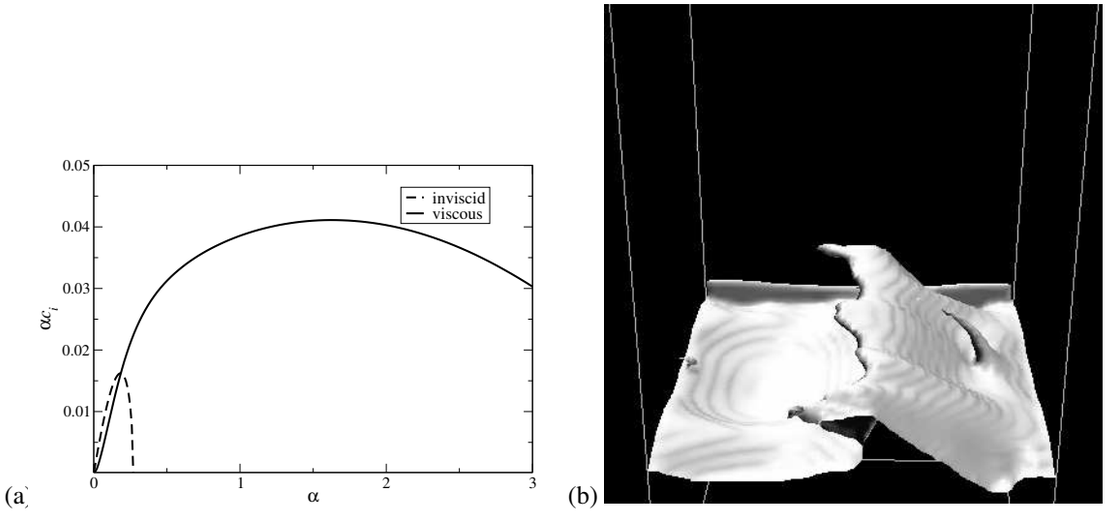


Figure 1. (a) Comparison of inviscid and viscous results, the parameters are $We_g = 200$, $Re_g = 1000$, $\mu_g/\mu_l = 0.025$, $\rho_g/\rho_l = 0.02$ (b) 3D temporal growth of the instability. $\rho_g/\rho_l = 0.1, We_g = 200$, $Re_g = 1000$, the grid size is 128^3.

References

[1] J. W. Hoyt and J.J. Taylor. Waves on water jets. *J. Fluid Mech.*, 83:119–127, 1977.

[2] D.R. Reitz and F. Bracco. Mechanism of atomisation of a liquid jet. *Physics of Fluids*, 25:1730–1742, 1982.

[3] J. C. Lasheras and E. J. Hopfinger. Liquid jet instability and atomization in a coaxial gas stream. *Annu. Rev. Fluid Mech.*, 32:275–308, 2000.

[4] R. Scardovelli and S. Zaleski. Interface reconstruction with least-square fit and split lagrangian-eulerian advection. *Int J. Numer. Meth. Fluids*, 41:251–274, 2002.

[5] W. Tauber, S. O. Unverdi, and G. Tryggvason. The non-linear behavior of a sheared immiscible fluid interface. *Phys. Fluids*, 14:2871, 2002.

[6] S. Chandrasekhar. *Hydrodynamic and hydromagnetic stability*. Oxford Univ. Press, Oxford, 1961.

[7] E. Villermaux. On the role of viscosity in shear instabilities. *Physics of Fluids*, 10(2):368–73, 1998.

[8] E. Villermaux. Mixing and spray formation in coaxial jets. *J. Propulsion and Power*, 14:807–817, 1998.

[9] P. Marmottant and E. Villermaux. Atomisation primaire dans les jets coaxiaux. *Combustion (Revue des Sciences et Techniques de Combustion)*, 2:89–126, 2002.

[10] P. Yecko and S. Zaleski. Two-phase shear instability: waves, fingers and drops. *Annals of the New York Academy of Sciences*, 898:127–143, 1999.

[11] P. Yecko, S. Zaleski, and J.-M. Fullana. Viscous modes in two-phase mixing layers. *Phys.Fluids*, 14:4115–4122, 2002.

[12] E.J. Hinch. A note on the mechanism of the instability at the interface between two shearing fluids. *J. Fluid Mech.*, pages 463–465, 1984.

[13] R. Scardovelli and S. Zaleski. Direct numerical simulation of free-surface and interfacial flow. *Annu. Rev. Fluid Mech.*, 31:567–603, 1999.

[14] E. Aulisa, S. Manservisi, R. Scardovelli, and S. Zaleski. A geometrical area-preserving volume of fluid method. *J. Comput. Phys*, 192:355–364, 2003.

[15] A. V. Coward, Y. Y. Renardy, M. Renardy, and J. R. Richards. Temporal evolution of periodic disturbances in two-layer couette flow. *J. Comput. Phys.*, 132:346–361, 1997.

VISCOUS EXTENSIONAL FLOW AND DROP BREAK-OFF UNDER GRAVITY

Ernest O. Tuck*, Yvonne M. Stokes*
*Applied Mathematics, The University of Adelaide, Australia 5005

Summary
This paper concerns finite drops of very viscous Newtonian fluids falling under gravity in an extensional flow, starting from rest in contact with a solid boundary. Emphasis is on the role of initial conditions, together with balances between forces such as inertia, gravity, viscosity and surface tension. Under gravity and viscosity alone, break-up occurs in finite time, but inertia makes that time formally infinite, and surface tension will further modify this conclusion. A slender-filament theory is used to illustrate these effects.

INTRODUCTION

We seek further understanding of the mechanisms governing gravity-driven extensional flows of viscous liquids which, like honey dripping from an up-turned spoon, exhibit elongation, necking to form a drop suspended by a thin filament and, finally, pinch-off of the drop and further breakup of the filament.

Extensional flow is seen in the dripping of a tap and web spinning by spiders and insects, as well as in important technologies such as ink-jet printing, polymer and glass fibre spinning, blow moulding, soldering and rheological measurement.

Ink-jet printing in particular has driven much recent research in this area, and continues to do so [1,2]. This technology is not only used in the well-known ink-jet printer, but also in biochip arraying and fabrication of transistors [1]. The size and shape of drops impacts on printing quality, as does the formation of satellite drops.

An application area of particular interest is industrial glass moulding, where the first stage is the gravity-driven formation of a drop of molten glass. The size and shape of this drop can be important, as in the production of large CRT screens where it affects the quality of the screen pressed from it [5]. In blow moulding of containers, elongational stretching due to gravity, and the resulting necking of the glass, may lead to unacceptable non-uniformity of container wall thickness. Similarly, in fibre spinning, pulling of the fibre may lead to a non-uniform cross-section.

Extensional flows and the mechanisms which cause breakup into drops have long been of scientific interest [2]. Development of theoretical ideas to explain the observations and computer codes to simulate the free-surface flows has been relatively slow, much of the literature appearing in the last two decades.

By far most attention in the literature has been given to surface-tension driven pinch-off of a Newtonian liquid drop and the subsequent formation of satellite drops. One-dimensional approximations are common [3] and, since the work of Keller and Miksis [4] and Peregrine et al. [6], much focus has been on finding similarity solutions in the neighbourhood in space and time of the pinch-off, motivated by the experimental observation that breakup of a fluid thread appears in some cases to be largely independent of initial conditions, but strongly dependent on fluid properties such as viscosity [7]. The extent of dependence of break-up behaviour on initial conditions is however still an open problem that has been little probed.

This study concerns high-viscosity gravity-driven drops and filaments before pinch-off, when initial conditions and forces other than surface tension do influence the flow. For highly viscous Newtonian fluids subject to an external pull (e.g. smooth honey dripping under gravity), very long filaments can develop and persist well beyond breakup times that would be predicted by current surface-tension dominated theories. Hence “this remains an extremely interesting problem to be studied in more detail” [2]. Previous research by the present authors ([8, 9] shows pinch-off features even with surface tension neglected, and has led us to make the suggestion that, at least for very viscous Newtonian fluids, inertial and viscous forces rather than surface tension forces are dominant in the early stages of pinch-off, with surface tension playing the dominant role only later when the thread diameter becomes very small. The present paper will test this suggestion by explicit inclusion of surface tension in the models.

The present research is innovative in taking a less surface-tension dominated approach than that of most other researchers in this area. Studies neglecting both surface tension and inertia are reported in [8] and [10]. In a recent [9] extension of the work of [8], we have included inertia, while still for the time being neglecting surface tension. Our new results then show flow features not previously recognised that we believe provide a pre-cursor to drop pinch-off, with actual pinch-off occurring later through the action of surface tension, once the local length scales become sufficiently small. Most interestingly, one of these features is some initial pinching, which is usually but perhaps erroneously attributed to the action of surface tension. This behaviour is not properly understood, and calls for a more detailed investigation.

SUMMARY OF SLENDER-DROP THEORY

Although we have also used a finite-element direct solution of the axisymmetric Navier-Stokes equations for drops of arbitrary initial profile, in the present paper we discuss only a one-dimensional approximate theory for slender drops. That is, we assume that initially the fluid occupies a region which is of small width relative to its length, and is at rest in contact with and beneath a given boundary, here taken as a plane horizontal wall. The subsequent motion will then be dominated by the downward velocity component, and will be of an extensional nature.

In the absence of surface tension, the one-dimensional Lagrangian equations of motion can be written [9]

$$X(\xi,t) = \int_0^{\xi} \frac{A_0(\xi_1)}{A(\xi_1,t)}\, d\xi_1$$

and

$$A(\xi,t) = A_0(\xi) - \frac{\rho}{\mu^*}\int_{\xi}^{L_0} A_0(\xi_1)\,[gt - X_t(\xi_1,t)]\, d\xi_1$$

where $x = X(\xi,t)$ is the position at time t of the fluid particle that was at $x = \xi$ at time $t = 0$, and $A(\xi,t)$ is the section area of the drop, starting at $A_0(\xi) = A(\xi,0)$ with initial length L_0. The term "X_t" in the second equation represents inertia, neglected in [8], and $\mu^* = 3\mu$ is the extensional or Trouton viscosity, g is the acceleration of gravity in the positive x-direction, and ρ is (constant) density.

If the inertia term is neglected, these equations provide an explicit solution by quadratures for any initial shape $A_0(\xi)$. This solution in general exhibits finite-time blow-up, with length $L(t) = X(L_0,t) \to \infty$ at a finite time $t = t^* \propto \mu^*/(\rho g L_0)$, the constant of proportionality depending on the initial shape $A_0(\xi)$. At the same time, the section area $A(\xi,t)$ goes to zero at some station $\xi = \xi^*$ (which is often at the wall $\xi^* = 0$), a signal that break-off will occur at that time and place. This conclusion is similar to that of Wilson [10] for a viscous fluid dripping slowly out of a capillary tube.

If inertia is retained, the problem can be recast as a nonlinear diffusion equation for $X(\xi,t)$, and numerical solutions were given in [9]. These solutions have the property that it takes an infinite time for the length $L(t)$ to approach infinity, but for large effective Reynolds number $\rho^2 g L_0^3/\mu^{*2}$, there is a very rapid increase in extension close to time $t = t^*$. There is no actual break-off of the drop, the area $A(\xi,t)$ remaining positive for all ξ and t. However, $A(\xi,t) \to 0$ as $t \to \infty$, at the particular station $\xi = \xi^*$ where the inertia-less drop would have broken at $t = t^*$. Meanwhile the remainder of the drop approaches free fall with acceleration g. Thus as $t \to \infty$, an almost rigid drop forms, together with an ever-thinning filament connecting it to the original boundary. Because of neglect of surface tension, the shape of the final freely falling drop depends critically (and only) on the initial shape $A_0(\xi)$.

We now propose to include surface tension in this model and results will be reported at ICTAM04. Such an inclusion is necessary when the filament diameter becomes comparable to the meniscus scale, which will certainly happen very near to the time of drop pinch-off, if not before. We expect that these results will show a continuous transition from the drop-formation history described above, toward the usual one dominated by surface tension for large time, where the connecting filament has actually broken, and the free drop is asymptotically spherical.

CONCLUDING REMARKS

Our studies [9] including inertia and neglecting surface tension also revealed some interesting and unexpected features of the flow that require further investigation, especially with surface tension included in the model. First, both numerical (finite-element) direct solutions of the Navier-Stokes equations for drops of arbitrary initial aspect ratio, and semi-analytic solutions of the above one-dimensional equations for initially-slender drops show that the acceleration exceeds g for a period of time at a point in the interior of the drop. Second, finite-width numerical simulations show the beginnings of drop pinch-off at this point, which is in the transition region between the main drop and the filament. In the absence of surface tension, this incipient pinch-off is surprising and leads us to suggest that initial conditions along with viscous and inertial forces initiate pinch-off and dictate its position, with surface tension taking over as the dominant force only later, when the local length scales become very small, comparable to the meniscus scale, due to this pinching.

ACKNOWLEDGEMENT

This research is supported by the Australian Research Council.

References

[1] A.U. Chen and O.A. Basaran, A new method for significantly reducing drop radius without reducing nozzle radius in drop-on-demand drop production, *Phys. Fluids* (2002) 14(1), L1–L4.
[2] J. Eggers, Nonlinear dynamics and breakup of free-surface flows, *Rev. Mod. Phys.* (1997) 69(3), 865–929.
[3] F.J. Garcı́a and A. Castellanos, One-dimensional models for slender axisymmetric viscous liquid jets, *Phys. Fluids* (1994) 6(8), 2676–2689.
[4] J.B. Keller and M.J. Miksis, Surface tension driven flows, *SIAM J. Appl. Math.* (1983) 43(2), 268–277.
[5] R.M.M. Mattheij, Personal communication (2001).
[6] D.H. Peregrine, G. Shoker and A. Symon, The bifurcation of liquid bridges, *J. Fluid Mech.* (1990) 212, 25–39.
[7] X.D. Shi, M.P. Brenner and S.R. Nagel, A cascade of structure in a drop falling from a faucet, *Science* (1994) 265, 157 & 219–222.
[8] Y.M. Stokes, E.O. Tuck and L.W. Schwartz, Extensional fall of a very viscous fluid drop, *Q. Jl. Mech. appl. Math.* (2000) 53(4), 565–582.
[9] Y.M. Stokes and E.O. Tuck, The role of inertia in extensional fall of a viscous drop, *J. Fluid Mech.*, (2004) 498, 205–225.
[10] S.D.R. Wilson, The slow dripping of a viscous fluid, *J. Fluid Mech.* (1988) 190, 561–570.

EVOLUTION OF A PAIR OF SPHERICAL BUBBLES RISING SIDE BY SIDE AT MODERATE REYNOLDS NUMBER

Jacques Magnaudet, Dominique Legendre
Institut de Mécanique des Fluides de Toulouse, UMR CNRS/INPT/UPS 5502,
2, Allée Camille Soula, 31400 Toulouse, France

Summary An extensive numerical investigation of the interaction between two spherical shear-free bubbles rising side by side in a viscous liquid has been carried out. The results show that the effect of the vorticity generated on the bubble surface changes dramatically the characteristics of the interaction process, especially by allowing the transverse force to be repulsive for low enough Reynolds number and separation distances, which results in the existence of a stable equilibrium separation distance.

Bubbly flows with moderate-to-large bubble concentration (typically from some percents to 20% in volume fraction) occur in many natural and industrial processes. However the current understanding of these flows and the models used to predict their evolution are far from satisfactory because of the difficulty in describing direct hydrodynamic interactions between bubbles, the effect of which is expected to influence greatly the spatial distribution of the dispersed phase in regions where the bubble concentration is significant. Up to now, most of the detailed theoretical investigations of these hydrodynamic interactions have been carried out either in the Stokes flow limit (following the pioneering papers by Batchelor [1],[2]) or in the potential flow approximation (eg. [3]). Nevertheless, several predictions of the latter two approaches conflict with the results displayed by finite-Reynolds-number experiments. For instance no transverse (lift) force can take place between the bubbles in the Stokes flow limit. Similarly, whereas the potential approximation predicts that when rising under the effect of buoyancy bubbly suspensions tend to organize themselves in the form of horizontal clusters ([4],[5]), experiments reveal much more homogeneous spatial distributions of bubbles.

To get some insight into the microphysics of the hydrodynamic interaction process at finite Reynolds number, we solve numerically the full Navier-Stokes equations and boundary conditions describing the three-dimensional flow past two spherical shear-free bubbles moving side by side in a viscous fluid, the distance between the two bubbles being set fixed. This is achieved by using an orthogonal boundary-fitted grid combined with a second-order accurate incompressible Navier-Stokes code based on a finite-volume discretization. Extensive tests of the influence of the grid parameters were carried out in order to make sure that the results are grid-independent and agree with potential predictions at short time, ie. before vorticity has diffused significantly from the bubble surface [6].

Using this numerical tool, we analyze the interaction between the two bubbles over a wide range of Reynolds number ($0.02 \leq Re \leq 500$, Re being based on the bubble diameter and rise velocity) and separation distance S ($2.25 \leq S \leq 20$, S being the distance between the bubbles centres normalised by the bubble radius). The computations shed light on the role of the vorticity generated at the bubble surface in the interaction process. When Re or S is large enough for the vorticity to remain confined in a boundary layer whose thickness is small compared to the distance between the two bubbles, the interaction is dominated by the irrotational mechanism that results in a maximum of the vertical velocity located in the gap between the two bubbles (Fig. 1, left). Following Bernoulli theorem, the transverse force is then attractive. In contrast, when viscous effects are large enough, the vorticity spreads out about each bubble until it is blocked in the gap by the vorticity existing about the other bubble. This interaction reduces the magnitude of the vertical velocity in the gap, resulting in a repulsive transverse force for small enough values of Re or S (Fig. 1, right). We confirm theoretically the existence of a repulsive force at low-but-finite Re by extending the asymptotic evaluation of the transverse force performed by Vasseur & Cox [7] to the case of shear-free bubbles.

When we set the separation S to a given value and vary Re, we observe that for any S the sign of the transverse force is reversed when the Reynolds number crosses a certain critical value Re_c, being attractive (resp. repulsive) for larger (resp. smaller) Re, in line with the mechanism described above. The value of Re_c depends on S and lies approximately in the range $30 \leq Re_c \leq 100$ for the range of separations covered by the computations. In contrast, if we set Re to a given value and vary S, different situations may happen. If Re is selected to be lower than a critical value of the order of 30, the two bubbles are found to be repelled from each other up to infinity, however large S (left part of the grey area in Fig. 2). For higher values of Re, the two bubbles are repelled only if S is either smaller than a critical value $S_1(Re)$, or larger than another critical value $S_2(Re)$, with $S_2(Re)>S_1(Re)$. To undertand this somewhat complex behavior, we consider the evolution of a pair of *freely moving* bubbles rising under the effect of buoyancy. As such bubbles have to maintain a constant vertical drag force, they cannot follow arbitrary paths in the (Re,S) plane once released with an initial separation S_i. By examining the stability of the equilibrium separation of such pairs of bubbles near the two critical curves $S_1(Re)$ and $S_2(Re)$, we show that only the first of these corresponds to a stable position. Hence, if the initial separation S_i is larger than $S_2(Re)$, the two bubbles are repelled from each other up to infinity (right part of the grey area in Fig. 2). In the opposite case $S_i<S_2(Re)$, they tend to reach the stable equilibrium configuration corresponding to $S=S_1(Re)$. As shown in Fig. 2, $S_1(Re)$ is a decreasing function of the Reynolds number which is about 3 (corresponding to a gap thickness about one bubble radius) for Re=30.

The results of this investigation demonstrate that interaction effects arising between two clean spherical bubbles rising side by side at Reynolds numbers less than about 250 (i.e. the upper limit for which deformation effects

may reasonably be neglected in water) differ significantly from the picture provided by the potential flow approximation since the latter predicts that the interaction force is attractive whatever S. In particular, in contrast with the systematic formation of stable horizontal clusters observed in the potential simulations [3], [4], existence of a repulsive interaction force for small-to-moderate rise Reynolds numbers and of an equilibrium (admittedly small) separation distance for higher Reynolds numbers favours a more homogeneous spatial distribution of the bubbles. We indeed find that the interaction force is positive for Re larger than 50-100 (depending on S), so that horizontal clustering is likely to occur in the range $100 \leq Re \leq 250$. However the actual attractive force is significantly smaller than predicted by assuming an irrotational flow everywhere, suggesting that the clustering process requires a longer time and is less stable to external perturbations than one may infer from the potential flow theory.

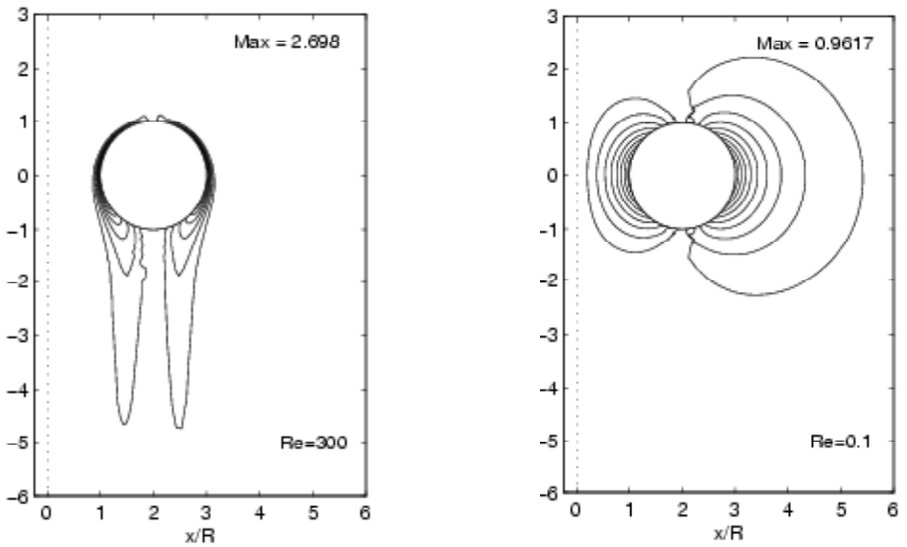


Figure 1. Iso-contours of the z-component of the vorticity in the symmetry plane z=0 for a separation S=4.
Left: Re=300; right: Re=0.1; the dotted line on the left indicates the symmetry plane between the two bubbles.

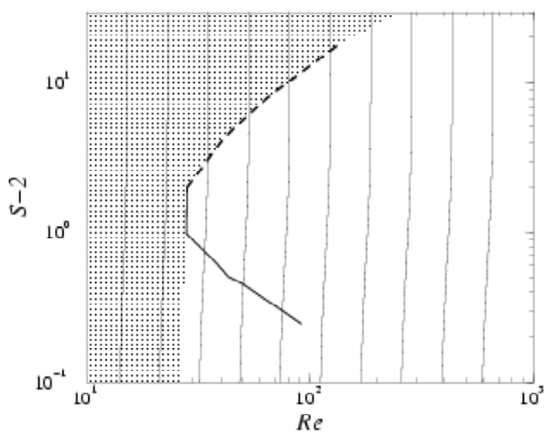


Figure 2. Evolution of the equilibrium separation of a pair of freely rising bubbles in the (Re, S) plane.
——$S_1(Re)$; ------- $S_2(Re)$; ——iso-drag curves; the grey area indicates the sub-region of initial separations S_i for which the bubbles subsequently separate up to infinity, while the white area is the basin of attraction of the stable equilibrium position $S_1(Re)$.

References

[1] Batchelor G. K.: The stress generated in a non-dilute suspension of elongated particles by pure straining motion. *J. Fluid Mech.* **46**:813-829, 1971.
[2] Batchelor G. K.: Sedimentation in a dilute dispersion of spheres. *J. Fluid Mech.* **52**:245-268, 1972.
[3] Sangani A. S. & Didwania A. K.: Dynamic simulations of flows of bubby liquids at large Reynolds numbers. *J. Fluid Mech.* **250**:307-437, 1993.
[4] Smereka P.: On the motion of bubbles in a periodic box. *J. Fluid Mech.* **254**:79-112, 1993.
[5] Van Wijngaarden L.: Hydrodynamic interaction between gas bubbles in liquid. *J. Fluid Mech.* **77**:27-44, 1976.
[6] Legendre D., Magnaudet J. & Mougin G. Hydrodynamic interactions between two spherical bubbles rising side by side in a viscous liquid. *J. Fluid Mech.* **497**:133-166, 2003.
[7] Vasseur P. & Cox R. G.: The lateral migration of spherical particles sedimenting in a stagnant bounded fluid. *J. Fluid Mech.* **80**:561-591, 1977.

XXI ICTAM, 15–21 August 2004, Warsaw, Poland

ON THE NUMERICAL SIMULATION OF TWO PHASE LIQUID-VAPOR PHENOMENA

Damir Juric*, Patrick Le Quéré*, Virginie Daru**, Marie-Christine Duluc*
*LIMSI-CNRS, BP 133, 91404 Orsay Cedex, France
**SINUMEF, ENSAM, Boulevard de l'Hôpital, 75013, Paris, France

Summary The computation of boiling phenomena raises several difficult issues, one of them being the necessity of accounting for both incompressible and compressible phases in the same computational domain. We have developed two different numerical approaches for dealing with such a situation. One of them makes use of a single pressure which has the status of a thermodynamic pressure and obeys a Helmholtz type equation. The other method is of the Low Mach number type where the pressure is split into a mean thermodynamic pressure defined in the gas phase, and an additional field which ensures mass conservation and which obeys a Poisson equation with an inhomogeneous source term in the gas. These two methods are compared in two simplified configurations consisting of an enclosure subjected to sudden heating at its walls and initially containing either solely a perfect gas or a combination of both an incompressible liquid and a perfect gas.

INTRODUCTION

The numerical simulation of boiling flows and phenomena raises many different and difficult issues, from both modelling and computational standpoints. Several of these difficulties, such as implementing surface tension, dealing with the interface between two phases, tracking of the interface, coalescence, etc. are common to the simulation of flows of isothermal and incompressible multiphase fluids. They have received much attention in the recent past and are still the subject of intensive ongoing research [1]. One specific issue in the simulation of boiling phenomena is the coexistence of a liquid and a gas phase in a non-isothermal environment, the gas being made up totally or partially of the liquid vapor. This necessitates the development of algorithms capable of handling both an incompressible and a compressible fluid in the same computational domain. Indeed although the liquid phase may be considered as incompressible, the vapor phase should be necessarily modelled as compressible. This is particularly true if one considers boiling in a closed vessel such as a steam engine or a pressure cooker. In such devices it is the fact that the mean pressure in the gas can rise above the atmospheric pressure that allows the liquid-vapor phase change to take place at temperatures well above $100C$, improving the Carnot efficiency or reducing the cooking time.

Handling the coexistence of both incompressible and compressible phases in the same domain raises specific difficulties. This is due to the fact that computational techniques for dealing with either phase are very different in nature and while efficient for dealing with the phase they were developed for become very inefficient if applicable at all in the other limit. Indeed, numerical methods for compressible flows become very inefficient when dealing with very low speed flows. Explicit methods are faced with stability criteria that prevent simulations over the time scales of interest while implicit methods suffer from convergence difficulties due to the poor conditioning of the Jacobian matrices. On the other hand standard incompressible methods cannot handle compressibility effects at all.

The central question for dealing with such configurations is the status of the variable called pressure. In classical compressible flows the pressure is the thermodynamic pressure satisfying the equation of state while the pressure that appears in the incompressible equations is defined up to an arbitrary constant and is just a Lagrange multiplier of the divergence free condition. Furthermore it is known that the variations of the pressure corresponding to flow speeds of velocity V are of order ρV^2 which can be very small for flows of light low speed fluids and this raises the issue of finite precision arithmetic used in digital computers. For instance air flow velocities of $10^{-2}ms^{-1}$ correspond to differences in pressure of $10^{-4}Pa$, which cannot be represented in single precision arithmetic within a pressure field whose mean value is equal to the atmospheric pressure $\simeq 10^5Pa$, independently of the poor conditioning of the Jacobian matrix.

The inefficiency of compressible algorithms in the low speed limit and the unavailability of well suited equations of state for the liquid phase have promoted the development of specific methods of the low Mach number type. Such methods were initially designed to handle low speed gas flows which can experience large variations of the mean pressure such as discharging flows from pressurized vessels [2] or natural convection flows due to very large temperature differences for which the Boussinesq approximation is no longer valid [3, 4]. In these methods the pressure is split into a mean pressure that can evolve in time and an additional component which is responsible for satisfying the continuity equation. This pressure splitting inhibits the local coupling between pressure and density, thus avoiding the simulation of acoustic waves and alleviating the corresponding stability criteria.

To shed some light on these issues, we have developed two different numerical algorithms aimed at the numerical simulation of these phase change liquid-vapor phenomena. One of them makes use of a single pressure variable, which has the status of a thermodynamic pressure. Defining a generalized equation of state by means of the characteristic function of the gaseous phase, it can be shown that this thermodynamic pressure obeys a Helmholtz type equation [5]. The other one follows the low Mach number approach and the pressure is split into a mean value which needs to be defined in the compressible phase and a small correction responsible for satisfying the continuity equation defined in the whole computational domain. This results in a Poisson equation for this correction, whose source term is inhomogeneous in the gaseous phase.

RESULTS

In the paper we will describe the two methods and compare them in two test cases thereby allowing us to check the effectiveness and efficiency of these methods for addressing such configurations. Both test cases consist of a closed vessel subjected to heating at the walls. In the first case we consider a medium consisting of a single homogeneous fluid which is a perfect gas. In the second case we consider a two-phase medium: a circular bubble of air (considered to be a perfect gas) trapped in the middle of a hundred micron square container of water (treated as an incompressible liquid). To isolate the phenomena of interest buoyancy effects are neglected in both cases. Some results for the second test case are presented in figures (1) and (2). The time variation of the mean pressure in Figure (1) clearly shows the mean pressure rise in the container as a result of the corresponding increase in the temperature of the air bubble. Interesting to note is the initially constant mean pressure during the phase of heat diffusion in the liquid. Figure (2) shows the velocity field at a time of 2.7 ms. The water is completely immobile while the flow in the interior of the air bubble, although quite small, is a result of the compression of the gas.

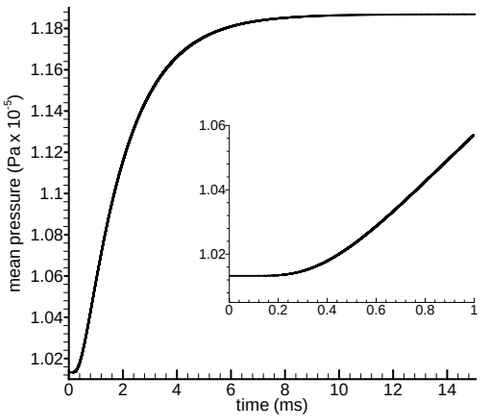


Figure 1. Case 2 : mean pressure vs. time

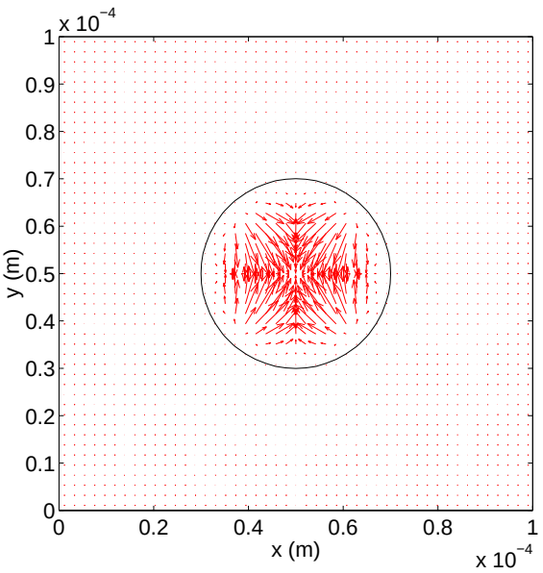


Figure 2. Case 2 : velocity field at $t = 2,5ms$

References

[1] Shin S., Juric D., *J. Comput. Phys.*, **180**:427-470, 2002.
[2] Forester C.K., Emery A.F., *J. Comp. Physics* **10**:487-502, 1972.
[3] Paolucci S., *Sandia National lab. Report SAND 82-8257*, (unpublished), 1982.
[4] Le Quéré P., Masson R., Perrot P., *J. Comp. Physics* **103**:320-335, 1992.
[5] Juric D., Daru V., Duluc M.C., *Proc. of Congrès Français de Thermique*, 2004.

CAVITATION INCEPTION ON MICRO-PARTICLES: A SELF PROPELLED PARTICLE ACCELERATOR

Manish Arora*, Claus-Dieter Ohl*, Knud Aage Mørch**
*Physics of Fluids,TNW, University of Twente, Postbus 217, 7500 AE Enschede, The Netherlands
**Department of Physics and Center of Quantum Protein, Technical University of Denmark, DK-2800 Lyngby

Summary Corrugated, hydrophilic particles with diameters between $30\,\mu$m and $150\,\mu$m are found to cause cavitation inception at their surfaces when they are exposed to a short, intensive tensile stress wave. The growth of cavity and its interaction with the original nucleating particle is recorded by means of digital imaging. The growing cavity accelerates the particle into translatory motion until the tensile stress decreases, and subsequently the particle separates from the cavity. The cavity growth and particle detachment are modeled by considering the momentum of the particle and the displaced liquid. The analysis suggests that all particles which cause cavitation are accelerated into translatory motion, and separate from the cavities they themselves nucleate.

INTRODUCTION

Cavitation (rupture of liquid under tenssile pressure) at much lower values of tensile pressure than thermodynamic estimates is often explained by weak spots -cavitaion nuclei- being present in the liqiuid. The nuclei might be free gas bubbles that are stabilized [1], or interfacial voids at solid surfaces of particles or surrounding walls [2]. The existence of such nuclei has received substantial experimental and also theoretical support [3, 4, 5, 6]. However the actual sequence of events which takes place during the inception of cavitation and interaction of cavity with the nucleating body has not been reported in an experimental or theoretical study. In this work we not only show that the artificially introduced corrugated particlies act as cavitation nuclei by means of direct photographic evidence but also that they are accelarated away from the cavities which originate on them. The process is modeled with a simple force balance model for cavity particle system which explains some of the basic features observed in the experiment.

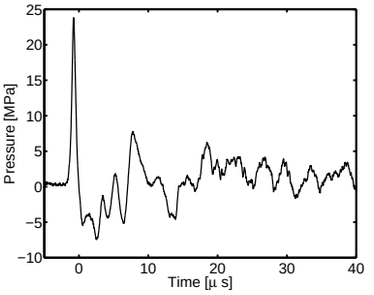


Figure 1. Pressure profile at the acoustic focus

EXPERIMENT

A flask containing filtered and degassed water is seeded with globally spherical particle (hydrophilic polystyrene particles -Copolymer:Divinylbenzol- with a diameter distribution between $30\,\mu$m and $150\,\mu$m) is placed at the acoustic focus of a pizoelectric shockwave device (a slightly modified commercial extracorporeal lithotripter). The pressure signal at the acoustic focus of the device at a dischagre voltage of 5kV is shown in Fig. 1. The cavitaions nuclei expand to form vaporous cavities during the tensile phase of the pressure.

The pictures are taken with a sensitive slow scan CCD camera equipped with a long distance microscope from a working distance of 45mm. The CCD camera is operated in a double-frame mode, which allows two images to be taken in rapid succession before they are transferred to a computer. Both frames are strobe illuminated with a LED for exposure times of $1.8\,\mu$s. All devices are triggered from a digital delay generator.

A typical sequence with the particle and an explosively expanding cavity is presented in Fig. 2: The undisturbed particle is depicted in frame 1. The tensile wave act on the particle $8\,\mu$s before frame 2 where an attached cavity of radius $150\,\mu$m has developed. The particle has been accelerated to the right, the cavity to the left. In frame 3 of Fig. 2 taken $24.2\,\mu$s after the impact of the shock wave the cavity has expanded to a radius of $170\,\mu$m. The neck between the particle and the cavity in frame 2 eventually breaks exciting the surface wave propagating on the cavity surface in frame 3

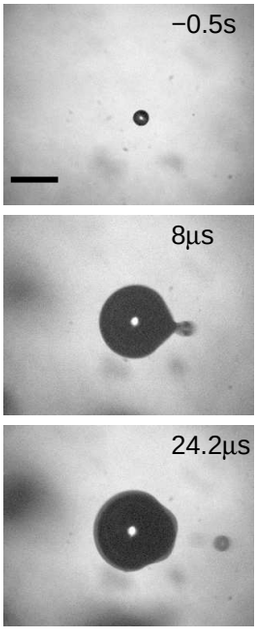


Figure 2. A three frame sequence depicting the explosive growth of a cavitation bubble from a particle, and its later separation.(length of the bar is $200\,\mu$m).

FORCE BALANCE MODEL

Since no external force acts on the particle cavity system the dynamics of the system can be adequately explained by a simple momentum a balance model. When the tensile stress passes below the critical pressure cavitation nuclei begins to expand explosively as a vaporous cavity. The expansion of the cavity is assumed to be

governed by the well known Rayleigh equation:

$$R_c \frac{d^2 R_c}{dt^2} + \frac{3}{2}\left(\frac{dR_c}{dt}\right)^2 = \rho_l^{-1}\left(P_v - \frac{2\sigma}{R_c} - P_\infty\right) \quad (1)$$

where $\rho_l = 10^3\,\mathrm{kg/m^3}$ is the density of the liquid, $\sigma = 7.3 \cdot 10^{-2}\,\mathrm{kg/s^2}$ is the surface tension, and $P_v = 3.2\,\mathrm{kPa}$ is the vapor pressure. P_∞ is far field pressure which is approximated with the measured value.

As long as the far field tensile stress increases, the particle moves with the velocity of the cavity surface at the contact point. However, at the time t_{sep} when the rate of expansion of the cavity passes its maximum, the particle detaches from the cavity and moves on through the liquid, though motion is attunuated first by the detachment process and second by viscous drag.

From cavitation inception at critical tensile stress when $t = t_{\mathrm{crit}}$ until the moment of separation of the particle from the cavity at $t = t_{\mathrm{sep}}$ momentum balance demands that

$$\frac{d}{dt}\left[u_c\left(\frac{1}{2}\rho_l \frac{4}{3}\pi {R_c}^3\right) + u_p\left(\rho_p \frac{4}{3}\pi {R_p}^3\right)\right] = 0 \quad . \quad (2)$$

where u_c and u_p are translation velocities of the centers of cavity and nucleating particle.

The particle-cavity contact condition gives

$$u_c + \frac{dR_c}{dt} = u_p \quad . \quad (3)$$

When the radial expansion of the cavity decelerates, the particle is no longer pushed by the cavity wall, but detaches with the momentum gained. Hence, from this time the analysis of the forces due to drag and added mass acting on the particle need to be incorporated.

Figure 3 presents the calculated motions of the cavity and the particle of Fig. 2 under above considerations.

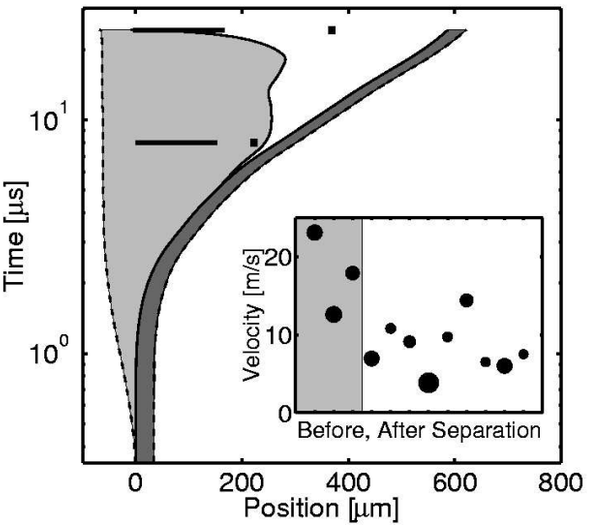


Figure 3. Position and size of the particle-cavity system versus time (note the logarithmic scale). The black squares and bars correspond to the particle and cavity radii, respectively, in the two lower frames of Fig. 2. Left and right dotted lines show the cavity and particle centers, respectively; left and right full lines show the right cavity and left particle surface positions, respectively from the calculations. The inset shows the measurements of the instanteous velocity of the particle before and after separation from the cavity from other experimental runs. The size of the disk symbol scales linearly with the particle diamater from 56 μm to 108 μm.

This model predicts that particle cavity seperation takes place at $t_{\mathrm{sep}} = 5.0\,\mu$s after start of tensile pressure phase and subsequently the particle moves away at speed of 38 m/s. During the initial growth of the cavity (left) its center moves approximately 62 μm to the left due to the conservation of momentum, and the cavity collapses at $t \approx 24\,\mu$s. Qualitative agreement is seen, but quantitatively only the order of magnitude is correct. This is not unexpected as we assume a too simple model for the inception and bubble dynamics. In the experiments, the bubble growth is affected by the presence of nearby expanding bubbles which may explain the lower translatory velocity of the particle measured after separation.

DISCUSSION AND CONCLUSIONS

The finding that a self propelled particle accelerator results from cavitation nucleation can be considered a generic process: Whenever a cavity grows rapidly from the surface of a small particle, the particle eventually detaches at high speed from the cavity which it has itself nucleated. This is a result that is pertinent in connection with the study of cavitation nuclei. Further, the particle ejection suggests that accelerated particles may penetrate into nearby soft surfaces, e.g. biological tissue or cells during exposure to strong, focused sound fields. A possible beneficial application might be the acceleration of micro- or nanometer sized particles, for drug delivery applications. However, for smaller sized particles the energy needed to form the gaseous neck (see second frame in Fig. 2) could be higher than the kinetic energy of the particle, thus preventing the particle from separating from the cavity.

References

[1] F.E. Fox, K.F. Herzfeld, J. Acoust. Soc. Am. **26**, 984 (1954).
[2] E.N. Harvey, D.K. Barnes, W.D. McElroy, A.H. Whiteley, D.C. Pease, K.W. Cooper, J. Cell Comp. Physiol. **24**, 1 (1944).
[3] R.E. Apfel, Ultrasonics **22**, 167 (1984).
[4] R.E. Apfel, J.Acoust. Soc. Am. **48**, 1179 (1970).
[5] K.A. Mørch, J. Fluids. Eng. **122**, 494 (2000).
[6] H. Marschall, K.A. Mørch, A.P. Keller, M. Kjeldsen, Phys. Fluids **15**, 545 (2003).

XXI ICTAM, 15–21 August 2004, Warsaw, Poland

LEVEL-SET SIMULATIONS OF SHEAR FLOW WITH INERTIA PAST A DROPLET ADHERING TO A WALL WITH MOVING CONTACT LINES

Peter D. M. Spelt*
Theoretical Mechanics, University of Nottingham, Nottingham NG7 2RD, United Kingdom

Summary A level-set method for the numerical simulation of incompressible two-phase flow is developed for flows with moving contact lines. The method is used to study shear flow past a two-dimensional droplet that adheres to a solid substrate. Cases with pinned and moving contact lines can be simulated. Previous work on this problem assumed Stokes flow, whereas the present method is suitable for flow with significant Reynolds number.

INTRODUCTION

The deformation of droplets adhering to a wall in shear flow has practical applications in cleaning processes, and serves as a model of a cell adhering to a blood vessel. Of practical interest is for instance the determination of conditions beyond which part of a droplet will be sheared off. The creeping flow case with fixed contact lines has been studied thoroughly in two and three dimensions; results available for moving contact lines are restricted to creeping flow in 2D [3]. We present here results from numerical simulations for the corresponding flow with inertia, in two dimensions. For this purpose, a level-set method is adapted such that multiple contact points can be simulated.

Results are presented for cases in which the contact points are allowed to move. In order to avoid the stress singularity at moving contact lines, the usual no-slip condition is replaced by the Navier condition for the velocity component U_1 along the wall, $U_1 = \lambda \partial U_1/\partial x_2$, where the sliplength λ is small. The contact-line speed will be prescribed through $U_{cl} = \kappa(\theta - \theta_s)$, where θ and θ_s are the dynamic and static contact angle, respectively. More complicated expressions for U_{cl} (Dussan V. 1979) can be implemented in a straightforward manner.

NUMERICAL METHOD

Level set is an efficient numerical method for tracking interfaces. In [4], a level-set method is developed for the simulation of incompressible two-phase flows. In this approach, the level-set function ϕ at a point is the distance from the interface, such that an interface corresponds to a surface where $\phi = 0$. The equations of motion for both fluids involved are combined into a single continuity and momentum equation with variable density and viscosity; surface tension is represented as a sink term in the momentum equation. Required variables such as the density, viscosity and curvature are expressed explicitly in terms of ϕ. At each timestep, ϕ is advected by the fluid velocity field. To ensure that ϕ remains the signed distance function (at least close to interfaces), a redistance step is subsequently required. In order to guarentee mass conservation, the subcell fix of [2] has been implemented, and ϕ is scaled at each timestep in the way proposed in [5]. Conventional methods are used to solve the velocity and pressure fields.

Level set has been used for many flows that do not involve intersections of interfaces with solid boundaries (contact lines). In order to use level set for flows with contact lines, boundary conditions for ϕ are required, instead of using an extrapolation from the fluid interior for the value of ϕ in ghostcells. In [5], the axisymmetric spreading of oil under ice is simulated using level set (involving a single contact point). The interface is extrapolated through the wall, and the value of ϕ at ghostcells is either the signed-distance function corresponding to this extrapolated interface, or (if a normal cannot be drawn from the ghostpoint to the extrapolated interface) an extrapolation of ϕ from the fluid interior.

For more complicated problems, such as a droplet adhering to a wall, the approach in [5] must be generalized. The position of contact points is obtained by integrating the adopted expression for the contact-line speed U_{cl}. The boundary conditions for ϕ are determined as follows (Fig. 1). For points left of the left contact line shown in Fig. 1, a boundary condition (obtained from the distance to $\mathcal{L}_1$) at ghostpoints is required. For points far to the right of the right contact line, it is not possible to draw a normal to the nearest imaginary interfaces (dashed part of $\mathcal{L}_2$), the distance to be used should correspond to that from the solid part of the interface $\mathcal{L}_2$, and no boundary condition should be imposed on ϕ (the value of ϕ in ghostcells is therefore obtained from second-order extrapolation). The two points P and Q indicate possible ghost-point locations between two contact lines. At P, a boundary condition is required for ϕ, obtained from the distance to the nearest imaginary interface. At Q, the minimum distance to an interface may be that to the solid part of $\mathcal{L}_1$, which can be obtained from extrapolation of ϕ from the interior. These boundary conditions are imposed during the redistance step.

RESULTS

In Fig. 1b, the contact angles and perimeter of a droplet relaxing towards static contact angles of 120^o are shown as a function of time. The initial contact angles are 30^o, and there is no imposed shear flow. The capillary number is small: at $t = 0$, $\mu U_{cl}(t = 0)/\gamma = 3.4 \cdot 10^{-3}$ (the Reynolds number $\rho H U_{cl}/\mu = 13.3$, where $H =$ initial droplet height). Hence

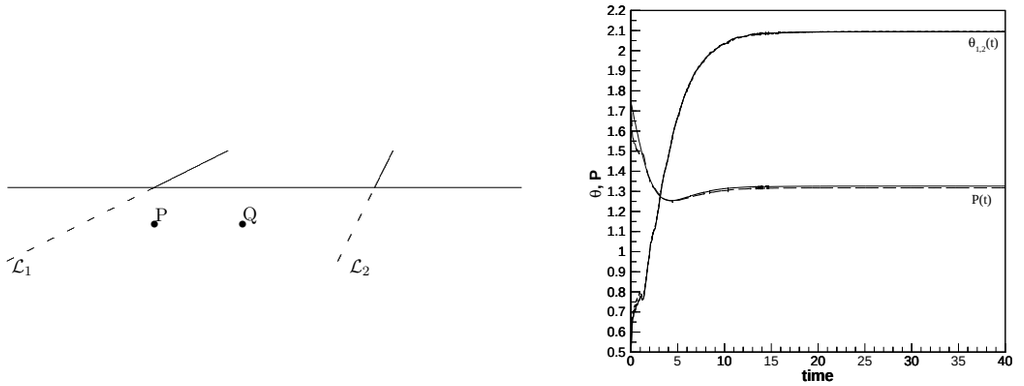


Figure 1. *(a).* Definition sketch for boundary conditions for ϕ imposed. *(b).* Droplet with moving contact lines in a fluid without external flow. Relaxation from initial contact angles of 30^o, to static contact angle of 120^o. Perimeter P and contact angles as a function of time. The long-dashed line represents the perimeter for an exact circular interface with contact angles corresponding to the values resulting from the simulations. To show the influence of slip, results for the contact angles with $\lambda = 0.01$ are indicated by short dashes.

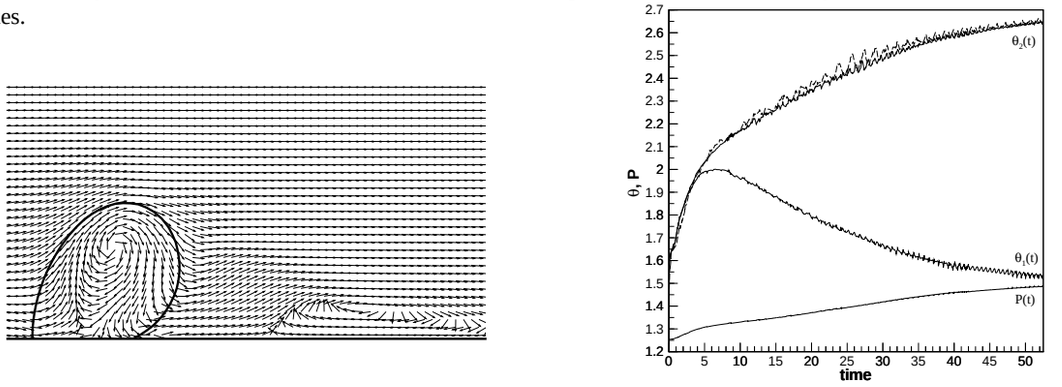


Figure 2. *(a).* Velocity flags (indicating local direction of fluid velocity) for a drop with moving contact lines in a shear flow with $\rho_1 = 1$, $\rho_2 = 20$, $\mu_1 = \mu_2 = 0.1592$, $\gamma = 3.175$. Initial contact angles are $\pi/2$; $\theta_s = 2\pi/3$. Simulations have approached a quasi-steady state, in which the drop moves at constant speed without further deformation. *(b).* Perimeter P and contact angles as a function of time, for a 128×32 mesh. The dashed line corresponds to θ_2 when using a 64×16 mesh.

with that determined from assuming a circular-cap shape and using the contact angles as a function of time. Results were also found to compare well with the boundary-element simulations of [3] for creeping shear flow past a drop on a wall.

Fig. 2 shows a droplet that is deformed by an imposed shear flow. The contact lines are allowed to move, with $\kappa = 0.1$, $\lambda = 0.01$. The droplet has approached a quasi steady state, in which it moves at almost constant speed and does not deform further. The contact angles and perimeter are shown as a function of time in Fig. 2b. A small oscillation is observed in the contact angles, that decreases with increasing mesh size. It is seen from Fig. 2a that a wake has formed downstream of the drop; this moves together with the drop. Due to the direction of rotation inside the drop and the wake, the fluid that shears just over the droplet is seen to make a U-turn between the drop and its wake; this effect was found to be especially prominent in cases of pinned contact lines, where the wake is closer to the droplet.

CONCLUSIONS AND FUTURE WORK

The level-set method proposed in [4,5] has been extended to allow for the presence of multiple contact lines that can move. The method has been used to simulate the motion and deformation of a 2D droplet adhering to a wall in a shear flow. The method is currently extended to allow for contact-line hysteresis, and is being used to determine critical values of dimensionless parameters, beyond which droplets are displaced from an adhering surface by a shear flow with inertia.

References

[1] Dussan V., E. B.: On the spreading of liquids on solid surfaces: static and dynamic contact lines. *Annu. Rev. Fluid Mech.* **11**:371-400, 1979.
[2] Russo, G. and Smereka, P.: A remark on computing distance functions. *J. Comp. Phys.* **163**:51-67, 2000.
[3] Schleizer, A. D. and Bonnecaze, R. T.: Displacement of a two-dimensional immiscible droplet adhering to a wall in shear and pressure-driven flows. *J. Fluid Mech.* **383**:29-54, 1999.
[4] Sussman, M., Almgren, A. S., Bell, J. B., Colella, P., Howell, L. H. and Welcome, M. L.: An adaptive level set approach for incompressible two-phase flows. *J. Comp. Phys.* **148**:81-124, 1999.
[5] Sussman, M. and Uto, S.: A computational study of the spreading of oil underneath a sheet of ice. *CAM Report* 98-32, 1998.

MODELLING SURFACE TENSION USING A GHOST FLUID TECHNIQUE WITHIN A VOLUME OF FLUID FORMULATION

Marianne M. Francois, Douglas B. Kothe, Sharen J. Cummins
Computer and Computational Sciences Division, Los Alamos National Laboratory, Los Alamos, NM 87545, U.S.A.

Summary We investigate a ghost fluid method in a volume of fluid formulation to model the surface tension force along the normal direction at an interface between two fluids of different properties. We compare it with the Continuum Surface Tension Force (CSF) method using numerical results to support our findings.

MODELING SURFACE TENSION

The continuum surface tension force (CSF) of Brackbill et al. [1] has been widely used over the past twelve years to model surface tension in multiphase flow in volume of fluid (VOF), level-set (LS) and front tracking (FT) methods. Surface tension forces acting on the interface are transformed to volume forces in regions near to the interface via delta functions, leading to ideally discontinuous interface jump conditions being modelled as smooth. Recently, ghost fluid methods (GFM) were presented in [3, 4] to impose 'sharper' boundary conditions on embedded boundaries. GFM have been employed to model surface tension in conjunction with LS techniques, since GFM require knowledge of the distance from the interface, which is the information natural for LS methods. We denote VOF-GFM as an underlying VOF method that employs GFM for surface tension, VOF-CSF as an underlying VOF method that employs the CSF method for surface tension, and LS-GFM as an underlying LS approach that employs GFM to model surface tension. VOF-GFM is an interesting alternative to LS-GFM because of the superiority of VOF methods in mass conservation over LS methods. However, since in VOF methods volume fractions are employed to track the interface, a distance function is not naturally available. We have therefore devised a novel technique [5] to reconstruct distance functions from volume fractions, allowing one to combine GFM with VOF. We now address whether or not there are advantages in using a VOF-GFM to model surface tension flows over the widely-used, classical VOF-CSF method. To aid our comparison, we consider the case of a static drop in equilibrium. The jump condition in pressure along the normal direction is $[P]=\sigma\kappa$, where σ is the surface tension coefficient and κ is the interfacial curvature. In VOF methods, a discountinous Heaviside function (volume fractions) f on a fixed grid is employed to track the interface. In cells filled with fluid 1, f is equal to 1, and in cells filled with fluid 2, f is equal to 0. For cells containing the interface, f is between 0 and 1. In VOF, a single set of governing equations are considered with an additional evolution equation to track the interface. In our case, the VOF is initialized using a recursive local mesh refinement technique for cells that contains the interface. We consider the fluid inviscid and the flow incompressible. The governing equations are:

$$\nabla.\vec{u} = 0 \qquad (1)\,, \qquad \frac{\partial(r\vec{u})}{\partial t} + \nabla.(r\vec{u}\vec{u}) = -\nabla P \qquad (2)\,, \qquad \frac{\partial f}{\partial t} + \vec{u}.\nabla f = 0 \qquad (3)$$

where $\vec{u}$ is the velocity, r the fluid density assigned as $r = r_1 f + r_2(1-f)$. The above conservation equations are solved using the projection method and the VOF advection equation is solved with a PLIC (piecewise linear calculation) algorithm [6]. Next, we present how we can apply the surface tension with the CSF and GFM method. To simplify the presentation, we consider a static case with zero velocity.

Continuum Surface Tension Force (CSF) [1], [2]

In the CSF method, the surface tension force is represented as a continuum force per unit volume in regions along and near to the interface. This force $\vec{F}_S = sk\nabla f$ appears as a source term in the momentum equation. Recently a consistent formulation [2] was proposed in which the surface tension force appears in the right hand side of the pressure equation and gradients are discretized at faces:

$$\nabla.\left(\frac{1}{r_{face}}(\nabla P)_{face}\right) = \nabla.\left(\frac{s\,k(\nabla f)_{face}}{r_{face}}\right). \qquad (4)$$

Ghost Fluid Methods (GFM) [3], [4]

In GFM, the pressure jump condition is applied as rigorously on the interface as the distance function f allows. The distance function is zero on the interface, negative inside the interface (fluid 1) and positive outside the interface (fluid 2). Since we are in the context of the VOF method, where we only store volume fractions, we need to reconstruct a distance function. For that we have used our reconstruction distance function (RDF) technique [5]. First, normal distances from the piecewise linear segments are computed using simple geometrical relations to all nearby cells. The piecewise linear segments are constructed based on volume fractions [6] and are part of the VOF technique. The normal distances to the nearby interfacial cells are then weighted to obtain the distance function. The weights are function of the angle made by the interfacial normal and the vector between the cell center and the linear segment centroid (the

smaller the angle, the greater the contribution). In GFM, the pressure stencil is modified to apply the jump condition at the interface due to surface tension. The modifications appear in the right hand side of the pressure equation:

$$\nabla\cdot\left(\frac{1}{r_{face}}(\nabla P)_{face}\right)=F^{L}+F^{R}+F^{T}+F^{B}, \tag{5}$$

where F^L, F^R, F^T and F^B are source terms. Nonzero terms are only those at faces across which the distance function change signs. L is for left stencil (*i-1*,*i*), R for right stencil (*i*,*i+1*), T for top stencil (*j*,*j+1*) and B for bottom (*j-1*,*j*). For example, the left stencil, if $f_{i,j}\le 0$ and $f_{i-1,j}>0$, becomes:

$$F^{L}=\frac{(1/r)_{(i-1/2,j)}(s\,k)_{I}}{(\Delta x)^2} \tag{6}$$

Note that GFM require a series of tedious logical tests, which are not required in CSF method.

Curvature Estimation

To estimate interfacial curvature, a height function method is used, which has been found in [5] to be more accurate than techniques using a distance function or volume fraction convolution.

RESULTS

To illustrate the difference between CSF and GFM we present here the results of a static computation, with dynamic results forthcoming in the full paper. We consider a 2D drop of radius 0.25 in a unit square domain. The surface tension is 1 and the curvature is imposed to its exact value 4 for not introducing error coming from its computation. The pressure equations are solved using an iterative method Line SOR. Both methods recover the exact jump in pressure $\Delta P=4$. However, with the CSF method, the profile is smoother than the GFM result (see Figure 1). GFM are more accurate because it takes account the exact interface position. Interestingly, both GFM and CSF results are independent of the density ratio, as can easily be shown in their formulation.

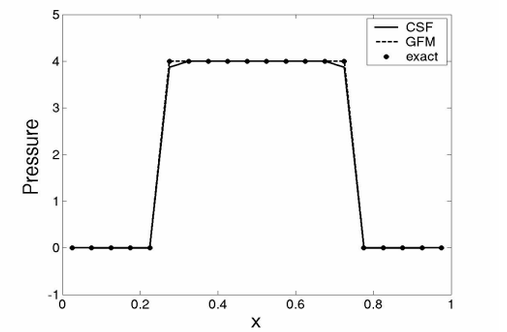


Figure 1: Pressure profile using VOF-GFM and VOF-CSF along the x direction at y=0.5. Grid is resolution 20x20.

CONCLUSIONS

We have investigated the difference between the CSF and GFM to model the jump in pressure due to surface tension at an interface. The GFM achieves a sharp jump in pressure, whereas the CSF method achieves a smooth transition. We have demonstrated that we can combine the VOF and GFM by reconstructing distance functions from volume fractions without solving an equation for the evolution of the distance function as in level-set techniques providing an alternative to the CSF method. Further scrutiny of these two methods will be made with dynamical simulations.

ACKNOWLEDGEMENTS

This work is supported by the Advanced Simulation and Computing (ASC) Program in the U.S. Department of Energy.

References

[1] Brackbill J.U., Kothe D.B., Zemach C., A Continuum Method for Modelling Surface Tension, *J. Comput. Phys.*, **100**: 335-354, 1992.

[2] Francois M.M., Kothe D.B., Dendy E.D., Sicilian J.M., Williams M.W., Balanced Force Implementation of the Continuum Surface Tension Force Method into a Pressure Correction Algorithm, *Proc. of the FEDSM'03, 4th ASME-JSME Joint Fluids Engineering Conference*, 2003.

[3] Liu X.-D., Fedkiw R.P., Kang M., A Boundary Condition Capturing Method for Poisson's Equation on Irregular Domains, *J. Comput. Phys.*, **160**: 151-178, 2000.

[4] Kang M., Fedkiw R.P., Liu X.-D., A Boundary Condition Capturing Method for Multiphase Incompressible Flow, *J. Sci. Comput.*, **15:**, 323-360, 2000.

[5] Cummins S.J., Francois M.M., Kothe D.B., Reconstructing Distance Functions from Volume Fractions: A Better Way to Estimate Interface Topology ?, accepted for publication in *Computers and Structures*, LA-UR-03-7234, 2003.

[6] Rider W.J., Kothe D.B., Reconstructing Volume Tracking, *J. Comput. Phys.*, **141**: 112-152, 1998.

XXI ICTAM, 15–21 August 2004, Warsaw, Poland

DYNAMICS OF BUBBLE SUPERCOMPRESSION IN ORGANIC LIQUIDS

Robert I. Nigmatulin, Raisa Kh. Bolotnova, Nailya K. Vakhitova, Andrei S. Topolnikov
Institute of Mechanics Ufa Branch of Russian Academy of Sciences, K.Marx Str. 12-6, 450000 Ufa, Russia

Summary Theoretical research of vapor bubbles in deuterated acetone and benzol is conducted. On the basis of the developed models of a single bubble and bubble cluster the dynamics of bubbles formed during maximum rarefaction in the liquid is investigated. It is shown that during the rapid contraction of a bubble a shock wave is formed inside it. Shock wave focusing in its center leads to violent rise in density (10^4 kg/m^3), pressure (10^{10}–10^{11} bar) and temperature (10^8–10^9 K), high enough to produce nuclear reactions. The diameter of the neutron emission zone is about 100 nm. It has been found out that the intensity of the bubble collapse and the number of emitted neutrons increase if one varies the phase of nucleation, the positive pressure wave amplitude, the liquid temperature, and when one switches on the mechanism of bubbles coagulation in the cluster during its simultaneous explosion.

INTRODUCTION

According to experimental data [1] neutron emission and tritium production can be observed during acoustic cavitation in D-acetone, that means the achievement of supercompressed state of matter inside bubbles at collapse. For theoretical confirmation and explanation of the phenomenon systematic research on the compression of vapor bubbles oscillating in a cluster, by the force of large amplitude standing acoustic wave, is carried out.
Two model problems are considered. The first deals with the research on the dynamics of a single bubble enforced by the given pressure field to model pressure in the bubble cluster. Parametric investigations are carried out in such a setting to obtain main features of the process of bubble collapse. The second problem joins together the dynamics of a single bubble and the dynamics of a bubble system on the basis of the developed model of bubble cluster.

THE MATHEMATICAL MODEL OF A SINGLE VAPOR BUBBLE

To model the dynamics of a single bubble the spherically symmetric mathematical model is employed, which accounts for vapor and liquid compressibility, and also for heat and mass transfer [2]. Time interval from the moment of bubble nucleation till the final collapse is divided into two stages: slow or low Mach stage, at which the homobaric assumption for gas and incompressible liquid condition are used, and rapid stage, at which the set of differential equations presenting the laws of conservation of mass, momentum and energy is solved simultaneously for vapor inside the bubble and liquid outside it. The second stage, which is principal from the viewpoint of values of the achieved temperatures and neutron production is modeled on the basis of the equation of state in Mie–Gruneisen form with Born–Mayer potential.

THE EQUATIONS OF STATE OF ACETONE AND BENZOL

To describe and analyze the thermodynamic parameters of organic compounds on the basis of acetone and benzol a wide range equation of state is constructed, which gives satisfactory description of vapor and liquid phases. The well-known Mie–Gruneisen form of the equation of state is used as the sum of potential, or cold, and heat components of the internal energy and pressure. The derivation of the equation of state assumes a simplified approximation when the Gruneisen coefficient depends on density only and the heat capacity is set to be constant.

THE MATHEMATICAL MODEL OF BUBBLE CLUSTER ACCOUNTING FOR WAVE PROCESSES

To model the cluster dynamics the scheme is realized, which allows to investigate wave spreading in bubble liquid accounting for compressibility of carrying phase and high amplitude oscillations of the bubbles. To describe the wave processes a single–speed two–pressure model of the bubble system is introduced where the bubble oscillations are described by Rayleigh–Plesset equation with acoustic radiation. It is thought that the bubble medium placed inside the spherical cluster is centered in the limited spherical volume of compressible liquid, at which boundary the spherically symmetric acoustic field is produced. To describe parameters inside the bubbles the simple model is applied, which does not account for heat and mass transfer in phases and on the interface.

THE RESULTS OF NUMERICAL MODELING

On the basis of the mathematical model of single bubble and bubble cluster the numerical research of the bubble dynamics during acoustic cavitation in deuterated liquid is carried out.
As the basic variant the single vapor bubble is considered, which oscillates in deuterated acetone (C_3D_6O) influenced by a sinusoidal acoustic field with the amplitude of 15 bar and frequency of 19.3 kHz at liquid temperature to be 0 ^{o}C. It is shown that the bubble dynamics during slow stage is determined by the processes of heat and mass transfer in vapor and liquid. As acetone has high speed of evaporation and condensation (its accommodation coefficient $\alpha = 1$),

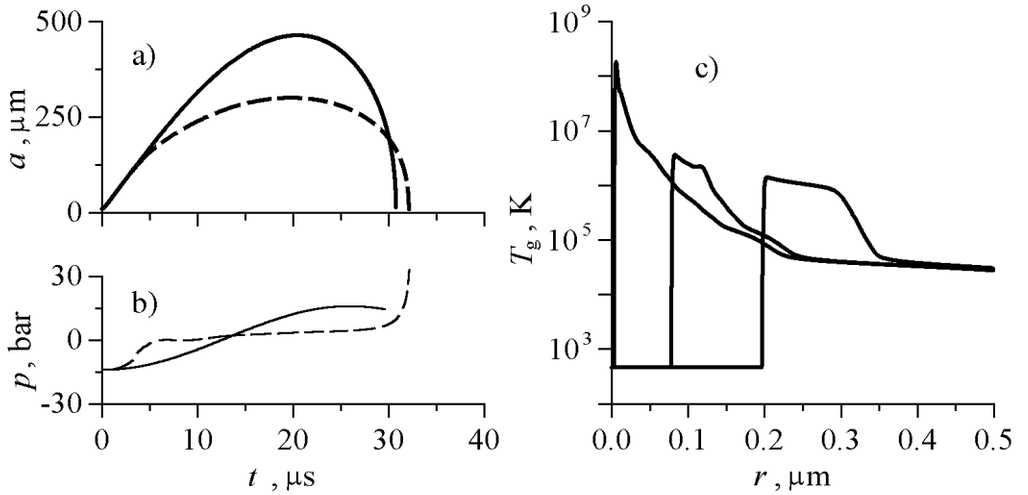


Figure 1. Bubble radius (a) and liquid pressure (b) evolution in time. Solid line – single bubble, dashed line – bubble in 20-bubbles cluster. Focusing of a shock wave near the bubble center (c).

the counterpressure of vapor in the bubble rises slowly, and this makes the collapse very intensive. During the rapid contraction the shock wave is formed inside the bubble (see Figure 1), which focusing in center leads to violent rise in density (10^4 kg/m^3), pressure (10^{10}–10^{11} bar) and temperature (10^8–10^9 K), high enough to produce nuclear reactions. The diameter of the neutron emission zone is about 100 nm with high peak at 3 nm. The average neutron number per collapse of the single bubble is estimated as 0.03 that gives about of 10^5 neutrons per second concerning the whole cluster.

The research of the influence of nucleation phase on the bubble dynamics in D-acetone is carried out. It is shown that the early bubble formation leads to the rise of radius change amplitude, which involves double increase in the number of emitted neutrons. The numerical investigation of positive pressure wave amplitude during bubble collapse is done. Two variants are considered: 50 and 100 bar, and it is obtained that the rise of compression amplitude leads to increase in speed of bubble contraction and, as the sequence, to enlargement of focusing shock wave. As compared with sinusoidal law the number of neutrons increases about ten times.

For three different liquid temperatures (253, 273 and 293 K) a comparative investigation of intensity of bubble collapse is conducted. It is obtained that the temperature decrease leads to the rise of the velocity of bubble contraction, but as the minimum radius also decreases the addition of the emitted neutrons becomes insignificant. The coagulation mechanism accompanied with additional enforcement at the contraction stage is considered. As the result of compression of the large gas volume the total number of emitted neutrons achieved the value of 1–2 per collapse.

The calculations with deuterated benzol (C_6D_6) are performed. It is posed that the collapse intensity and the matter heat up and also the number of emitted neutrons depend on the thermodynamic properties of the matter, in particular on the equation of state parameters.

The numerical simulation of the dynamics of vapor bubbles oscillating in the cluster dependent on the number of bubbles is carried out accounting for pressure waves evolution (see Figure 1). It is obtained that during the spreading of pressure waves in bubble liquid it is possible to get the enlargement of the amplitude that gives additional impulse during bubble contraction. The numerical calculations of the bubble dynamics in the cluster accounting for the pressure waves evolution and complex bubble model are carried out. It is shown that the collapse of the bubble in the cluster is less intensive compared with single bubble collapse. As the result of decrease in maximum and minimum values of bubble radius the shock wave, which leads to heat up of the matter in the bubble, becomes weak and causes the drop of the number of emitted neutrons of about 1–2 orders compared with single bubble.

References

[1] Taleyarkhan R.P., West C.D., Cho J.S., Lahey R.T. Jr., Nigmatulin R.I., Block R.C.: Evidence for nuclear emissions during acoustic cavitation. *Science* **295**:1868–1873, 2002.

[2] Akhatov I., Lindau O., Topolnikov A., Mettin R., Vakhitova N., Lauterborn W.: Collapse and rebound of a laser-induced cavitation bubble.*Phys. Fluids* **13(10)**:2805–2819, 2001.

HYDRODYNAMICS OF GAS BUBBLING THROUGH ORGANIC LIQUIDS

Ryszard Pohorecki, Władysław Moniuk, Paweł Bielski
Faculty of Chemical and Process Engineering, Warsaw University of Technology, Warynskiego 1, PL 00-645 Warszawa, Poland; pohorecki@ichip.pw.edu.pl

Summary The bubble diameter values were calculated from theoretical model. The model has been based on the original approach by Prince and Blanch. It assumes an equilibrium between the coalescence and redispersion processes, and uses a simplified method of solution of the population balance equations. The experiments were carried out with different organic liquids in two bubble columns. A numerical experiment enabling simple calculation of the influence of the properties of liquids on the bubble size is presented.

Bubbling of a gas through a layer of liquid is frequently used for contacting the two phases. It is widely applied in chemical, pharmaceutical and food industries, as well as in biotechnology and environmental protection.
Most of the experimental work described in the literature was carried out with air–water system, at ambient temperature and pressure. For this reason extrapolation of the existing correlations to non-aqueous liquids and/or elevated temperature or pressure is always risky. Only recently a general theoretical approach has been attempted by several workers([1], [2]).
The present work has the following aims:

- to develop a general theoretically based description of the process;
- to verify the proposed model for a wide range of temperature and pressure, using different gas-liquid systems and equipment of different scale;
- to use the verified model for a numerical experiment, enabling simple calculation of the hydrodynamic parameters of gas bubbling through liquids in various conditions.

To achieve the above aims a research program has been carried out, comprising the development of a theoretical model and its experimental verification. The model has been based on the original approach by Prince and Blanch [1]. It assumes an equilibrium between the coalescence and redispersion processes, and uses a simplified method of solution of the population balance equations. The experiments were carried out with different organic liquids in two bubble columns:

- a glass laboratory column 9 cm diameter and 200 cm high with different gas distributors (porous gas distributor and spargers with holes) operated at atmospheric pressure and low temperature, with seven liquids: acetaldehyde, acetone, cyclohexane, isopropanol, methanol, n-heptane and toluene.
- a stainless steel pilot plant column 30.4 cm diameter and 400 cm high (gas distributor – spargers with holes) operated at elevated pressure (up to 1.1 MPa) and temperature (up to 160^{o}C), with cyclohexane as a liquid.

The measurements have been carried out at different heights from the sparger and for a range of gas velocities, in the homogenous flow regime. The bubble diameters were measured by photographic method, with at least 500 bubbles measured for each experimental point. It has been established that in the dynamic equilibrium region the bubble size distribution was independent of both the axial and the radial position in the column.
Very good agreement of the calculated and experimental data has been found. The agreement is better than that between the experimental values of the average bubble size and those obtained from the existing correlations (see Figs. 1 and 2).

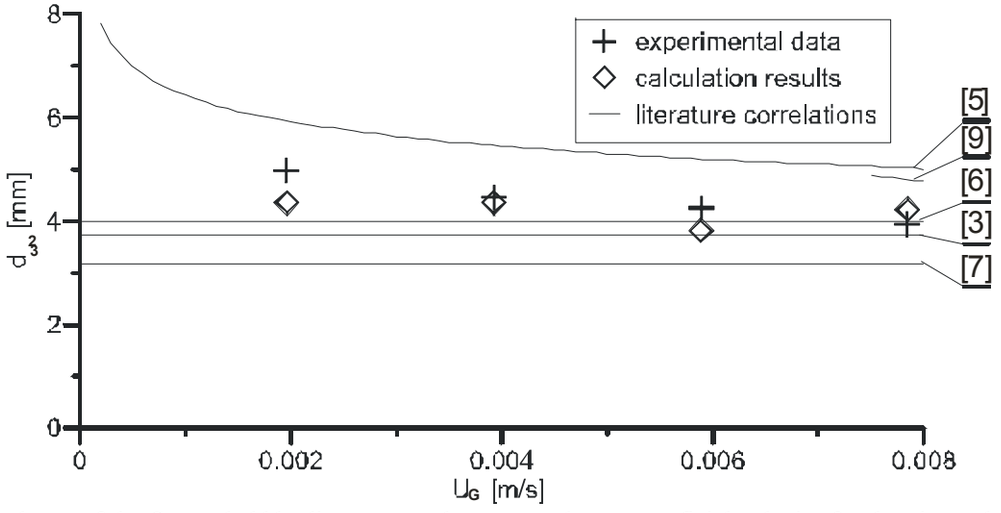


Fig.1 Dependence of the Sauter bubble diameter on the saturated gas superficial velocity for the air – toluene system (laboratory column).

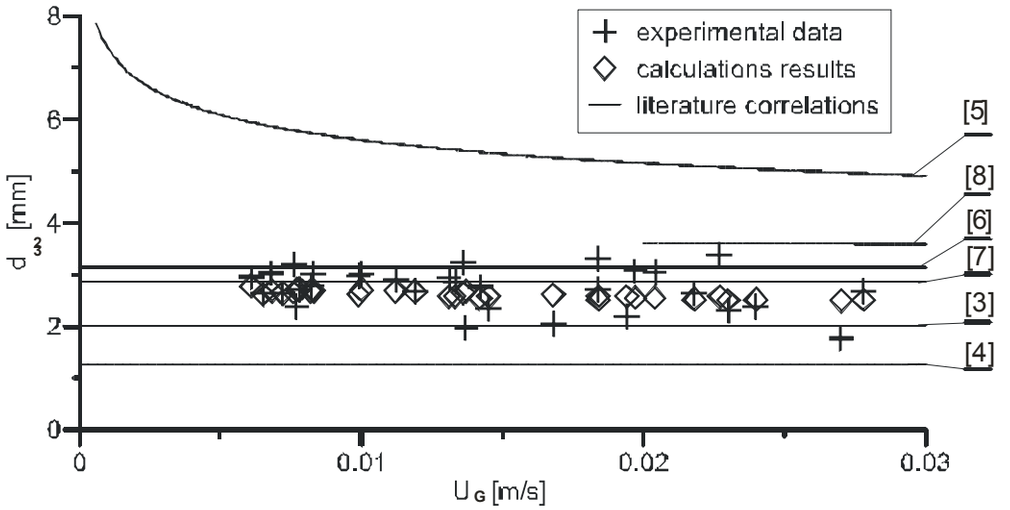


Fig.2 Dependence of the Sauter bubble diameter on the saturated gas superficial velocity for the nitrogen-cyclohexane system (pilot plant column, t=160^{o}C; P=1.0 MPa).

A numerical experiment has been carried out find a theoretically sound correlation relating mean bubble diameter in the main section of the bubble column with the liquid physicochemical properties (density, viscosity, surface tension), and the superficial gas velocity. A correlation has been proposed in an approximate, dimensionless form:

$$Fr = A \cdot \left[\frac{u_G^4 \cdot \rho}{g \cdot \sigma} \right]^{1/2}$$

where: A – constant,
Fr – Froude number,
g – gravity acceleration,
u_G – superficial gas velocity,
ρ – density,
σ – surface tension.

References

[1] Prince M.J., Blanch H.W.: AIChEJ., **36**, 1485, 1990.
[2] Shimizu K., Takada S., Minekawa K., Kawase Y., Chem. Eng. J., **78**, 21, 2000.
[3] Hughmark G.A.: Ind.& Eng. Chem., Process Des. Dev., **6**, 218, 1967.
[4] van Dierendonck L.L.: *PhD. Thesis*, University of Twente, Enschede, 1970.
[5] Akita K., Yoshida F.: Ind. & Eng. Chem., Process Des. Dev., **13**, 84, 1974.
[6] Idogawa K., Ikeda K., Fukuda T., Morooka S.: Int. Chem. Eng, **26**, 468, 1986.
[7] Idogawa K., Ikeda K., Fukuda T., Morooka S.: Int. Chem. Eng, **27**, 93, 1987.
[8] Wilkinson P.M.: *PhD. Thesis*, University of Groningen, Groningen, 1991.
[9] Kumar A., Degaleesan T. E., Laddha G. S., Hoelscher H. E.: Can. J. Chem. Eng., **54**, 503, 1976.

XXI ICTAM, 15–21 August 2004, Warsaw, Poland

SURFACTANT EFFECTS ON BUOYANCY-DRIVEN COALESCENCE OF SPHERICAL DROPS

Michael A. Rother, Alexander Z. Zinchenko Robert H. Davis
Department of Chemical and Biological Engineering, University of Colorado, Boulder, CO 80309-0424, USA

Summary Collision efficiencies are calculated by a trajectory analysis for two contaminated spherical drops in buoyancy at low Reynolds number. The full convective-diffusion equation for the surfactant surface concentration is solved by expansion in spherical harmonics with Lamb's singular series used for the velocity field. A highly efficient algorithm is developed to allow very small surface separations.

INTRODUCTION

Whether present by design or by accident, surfactants are nearly ubiquitous. A proper understanding of the effect of surfactants on the behavior of emulsions, a problem of enormous everyday significance, requires fundamental investigation into their role in the interactions of two or more drops. We consider motion due to gravity of two spherical drops of one liquid immersed in a second immiscible liquid in the presence of bulk-insoluble surfactant when the Reynolds number $Re = \rho_e V_2^{(0)} a_2/\mu_e$ is small. Because the drops do not deform, the capillary number $Ca = \mu_e V_2^{(0)}/\sigma$ is zero. As shown in Fig. 1, the quantities ρ_e and μ_e are the surrounding liquid density and viscosity, respectively, and σ is the interfacial tension, where dimensionless parameters are based on the larger drop radius, a_2.

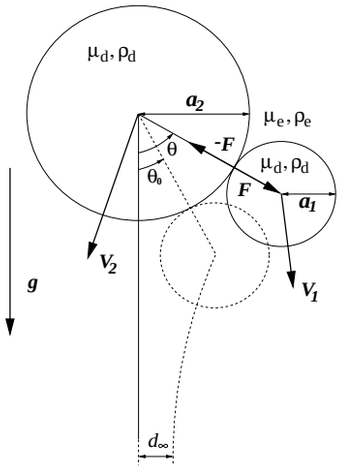


Figure 1. Relative trajectory of two contaminated drops in buoyancy.

Although analytical values for the isolated velocity of the larger drop $V_2^{(0)}$ are not possible in buoyancy for arbitrary surfactant surface coverage in Stokes flow, scaling values can be used. For typical uncontaminated hydrosol systems, Re and Ca are both small, when the drop radius is $O(10 - 50\ \mu\mathrm{m})$.

In the current work, collision efficiencies are determined for two contaminated spherical drops. In an arbitrary trajectory, as in Fig. 1, the drops have an initial horizontal offset d_∞ when well separated, and when the larger drop catches up to the smaller one, the drops will either collide and coalesce, or eventually separate. The collision efficiency E_{12} is determined through the critical horizontal offset d_∞^* demarcating trajectories which lead to coalescence and separation, as follows:

$$E_{12} = \left[d_\infty^*/(a_1 + a_2)\right]^2, \tag{1}$$

where a_1 is the smaller drop radius.

NEARLY UNIFORM SURFACE COVERAGE

Previous work to determine collision efficiencies for two contaminated spherical drops in linear flows [1] and buoyancy [2] has focused on the special case of small deviation from uniform surfactant coverage. In this limiting case, the only effect of the surfactant is on the tangential stress boundary condition, and it is not necessary to solve the convective-diffusion equation for the surfactant concentration. Moreover, the problem remains linear and can be solved by decoupling motion normal and parallel to the drops' line of centers to determine mobility functions.

In Figure 2, the gravitational collision efficiency for nearly uniform coverage is graphed versus the drop-to-medium viscosity ratio at a fixed drop-radius ratio of 0.5 for various values of the retardation parameter $A = B\Gamma_0 a_2/(\mu_e D_s)$, where $B = -\partial\sigma/\partial\Gamma$ is assumed constant, D_s is the surface diffusivity, and Γ_0 is the initial surfactant concentration [2].

An interesting feature of Fig. 2 is that E_{12} increases slightly with viscosity ratio $\hat{\mu}$ at large A and moderate $\hat{\mu}$ because the

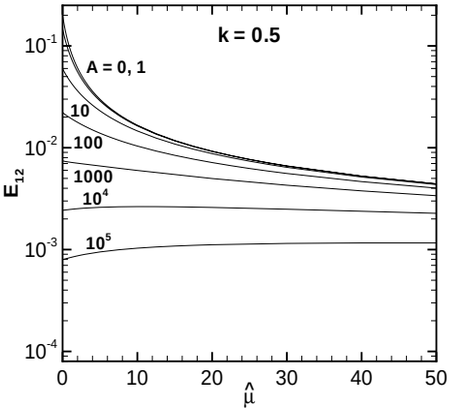


Figure 2. Collision efficiency E_{12} as a function of the drop-to-medium viscosity ratio $\hat{\mu} = \mu_d/\mu_e$ with size ratio $k = a_1/a_2$ = 0.5 at various values of the retardation parameter A for two contaminated spherical drops in buoyancy in the limit of nearly uniform surface coverage. Adapted from [2].

ARBITRARY SURFACE COVERAGE

In general, scaling [1] shows that nearly uniform surface coverage is often a satisfactory assumption for spherical drops. However, when the drops are in close approach, the squeezing flow can cause significant deviation in the surfactant concentration, a fact ignored in earlier studies. Moreover, the solutions of [1,2] show that collision efficiencies depend on the retardation parameter $A = MaPe_s$, where $Ma = B\Gamma_0/(|\rho_e - \rho_d|ga_2^2)$ with g being the magnitude of the gravitational acceleration is the Marangoni number, and $Pe_s = A/Ma$ is the surface Péclet number. On the other hand, existing experiments for small drops in shear flow [3] demonstrate a more complex dependence, with E_{12} being a function of Ma and Pe_s separately. In addition, if the surfactant concentration is dilute [4], redistribution is possible even for larger separations. Therefore, we solve the full time-dependent convective-diffusion equation for the surfactant surface concentration Γ:

$$\frac{\partial \Gamma}{\partial t} = -\nabla_s \cdot (\Gamma \mathbf{u_s}) + \frac{1}{Pe_s}\nabla_s^2 \Gamma, \tag{2}$$

where $\mathbf{u_s}$ is the interfacial velocity and ∇_s is the surface gradient operator. The advantage of our less restrictive solution is that it has very few non-dimensional parameters, making it easy to compare with experiments and avoiding the many additional dimensionless quantities of bulk-soluble surfactant models.

The expansion of the solution of the surfactant equation into spherical harmonics is done similar to [4], which considers single-drop rheology. With surfactant concentration expanded into spherical harmonics, the velocity field is sought *via* Lamb's singular series; boundary conditions are satisfied using biconjugate-gradient iterations to solve the resulting series of nonlinear ordinary differential equations and rotation-based reexpansions of Lamb's series for maximum efficiency [5]. In this problem, it is crucial to extend the dynamical simulation to very small surface separations, with a large number of 3D harmonics/multipoles in the expansions, which requires a highly efficient algorithm. It is anticipated that, under conditions when the surfactant concentration remains nearly uniform when the drops are well separated, significant deviation in coverage may occur in the region of close approach for weak diffusion, causing the interfaces to become immobile. Film drainage would be retarded, considerably decreasing the collision efficiency from spherical-drop results for nearly uniform coverage [2].

References

[1] Blawzdziewicz J., Wajnryb E., Loewenberg, M.: Hydrodynamic Interactions and Collision Efficiencies of Spherical Drops Covered with an Incompressible Surfactant Film. *J. Fluid Mech.* **395**: 29–59, 1998.

[2] Rother M.A., Davis R.H.: Buoyancy-driven Coalescence of Spherical Drops Covered with Incompressible Surfactant at Arbitrary Péclet Number. *J. Colloid Interface Sci.* **270**: 205–220, 2004.

[3] Hudson S.D., Jamieson A.M., Burkhart B.E.: The Effect of Surfactant on the Efficiency of Shear-induced Drop Coalescence. *J. Colloid Interface Sci.* **265**: 409–421, 2003.

[4] Blawzdziewicz J., Vlahovska P., Loewenberg, M.: Rheology of a Dilute Emulsion of Surfactant-covered Spherical Drops. *Physica A*, **276**: 50–85, 2000.

[5] Zinchenko A. Z., Davis R.H.: An Efficient Algorithm for Hydrodynamical Interaction of Many Deformable Drops. *J. Comput. Phys.* **157**: 539–587, 2000.

XXI ICTAM, 15–21 August 2004, Warsaw, Poland

STATIC SHAPES OF LEVITATING VISCOUS DROPS

L. Duchemin*, U. Lange**, J. Lister*
*Department of Applied Mathematics and Theoretical Physics, Cambridge, United Kingdom
**SCHOTT Glas, Mainz, Germany

Summary A lubrication model for the levitation of a drop of molten glass above a spherical porous mould is described, and used to find static shapes of the drop. Comparison with full Navier-Stokes simulations is excellent, and a condition is deduced for the stability of these solutions.

INTRODUCTION

We consider the levitation of a drop of molten glass above a spherical porous mould, through which air is injected with a constant velocity v. In the present context, we assume that the glass is so viscous compared to the air that we can neglect the motion in the drop. Therefore, if static shapes of the drop exist, these shapes are completely determined by the coupling between the equations of motion in the air cushion and the Young-Laplace equation. In what follows, all the lengths are made dimensionless with the capillary length $\sqrt{\sigma/\rho g}$, where σ is the surface tension coefficient of a glass-air interface, ρ is the density of the glass, and g the acceleration due to gravity.

LUBRICATION MODEL

The sessile top surface

The computation of these static shapes can be split into two parts. The first consists in solving the equations for the upper surface, on which the pressure is atmospheric. Taking account of the surface tension, the equation governing this sessile solution is

$$\kappa(r) - z(r) = C^{ste} = \kappa(0), \tag{1}$$

where r is the distance to the axis of symmetry and the curvature $\kappa(r)$ can be approximated by the full 2D curvature

$$\kappa(r) = \frac{z''(r)}{[1 + z'^2(r)]^{3/2}}, \tag{2}$$

owing to the large aspect ratio of a flat-lying drop. This equation is subject to the boundary conditions

$$z'(0) = 0 \qquad \kappa(0) = \kappa_0.$$

Introducing the arclength s and the angle φ between the normal vector to the interface and the vertical, we can split equation (1) into three first-order ordinary differential equations for $\varphi(s)$, $r(s)$ and $z(s)$. These equations are integrated using a fifth-order adaptative Runge-Kutta method, from the top of the drop to a point $r = R$ near where the drop approaches the mould.

The lubrication problem

Once the top surface is known, we match this solution to a lubrication solution in the air film, starting at $r = R$. Let v denote the inlet velocity through the porous mould and μ the dynamic viscosity of the air. Assuming the mould to be almost flat, the lubrication approximation links the depth integrated flux Q at a distance r from the axis of symmetry to the pressure gradient in the r direction [1] :

$$Q = -\frac{h^3}{12\mu}\frac{\partial p}{\partial r}$$

By mass conservation, $Q = rv/2$. In this study, we assume that the motion in the glass can be neglected, so that the non-dimensional pressure in the gas (independent of z, as a consequence of lubrication theory) is

$$p(r) = p_0 - (f(r) + h(r)) - \kappa(r),$$

where $f(r) + h(r)$ is the hydrostatic pressure in the glass, $h(r)$ is the mould shape and the curvature is again taken to be the full 2D curvature (2). Therefore, the non-dimensional steady lubrication equation is

$$6Ca = \frac{h^3}{r}\left(f + h + \frac{f'' + h''}{[1 + (f' + h')^2]^{3/2}}\right)', \tag{3}$$

where $Ca = \mu v/\sigma$ is the capillary number. Once again, we split equation (3) into three first-order ordinary differential equations for $h(r)$, $h'(r)$ and $h''(r)$, where $h'(R)$ and $h''(R)$ are given by the sessile solution and $h(R)$ is a shooting parameter chosen such that the slope on the axis of symmetry is equal to zero.

COMPARISON WITH NAVIER-STOKES SIMULATIONS

Some simulations of the full set of Navier-Stokes equations have been made with an industrial code (POLYFLOW) [2]. Figure 1 shows the comparison between four of these simulations and our lubrication model. The gray patches correspond to the POLYFLOW computations, and the solid lines to the lubrication model. In this example, the radius of curvature of the spherical mould R_M is equal to $4.76V^{1/3}$, where V is the volume of the drop. Some of the Navier-Stokes simulations

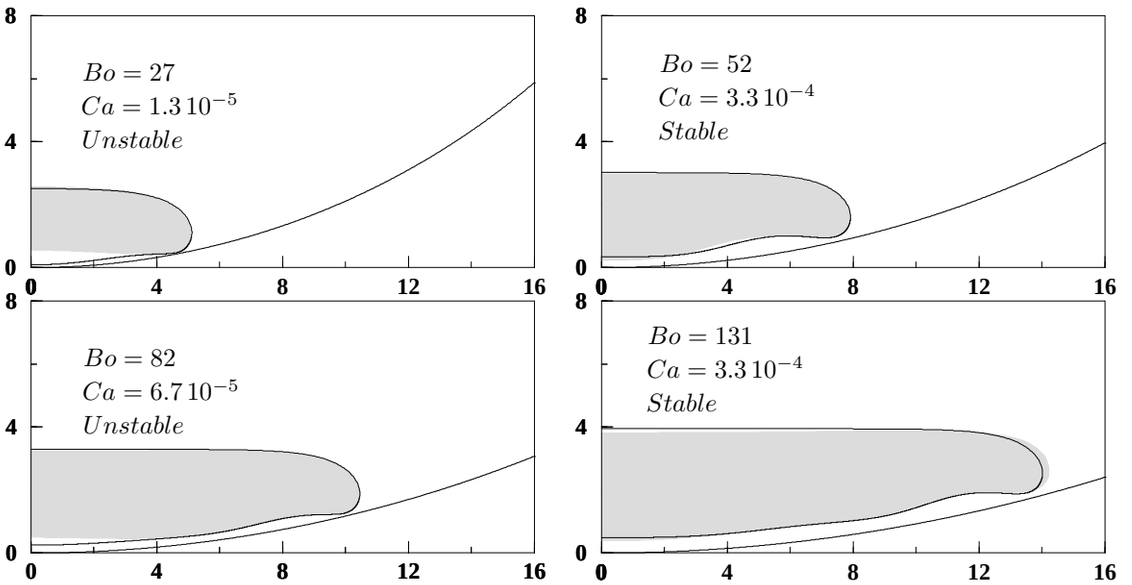


Figure 1.

are stable (the two on the right), and some are unstable (the two on the left). Figure 2 shows, on the left, the stability diagram corresponding to the POLYFLOW simulations [2], according to the Bond number $\rho g V^{2/3}/\sigma$ and the capillary number $\mu v/\sigma$. On the right of the graph are shown some of the lubrication results, for a constant radius of the mould equal to 50 : the points correspond to simulations for which the thickness of the thin film never reaches 1 (which is the capillary length). These results show clearly two regions in which there isn't any realistic solution. This may be a starting point for understanding the stability.

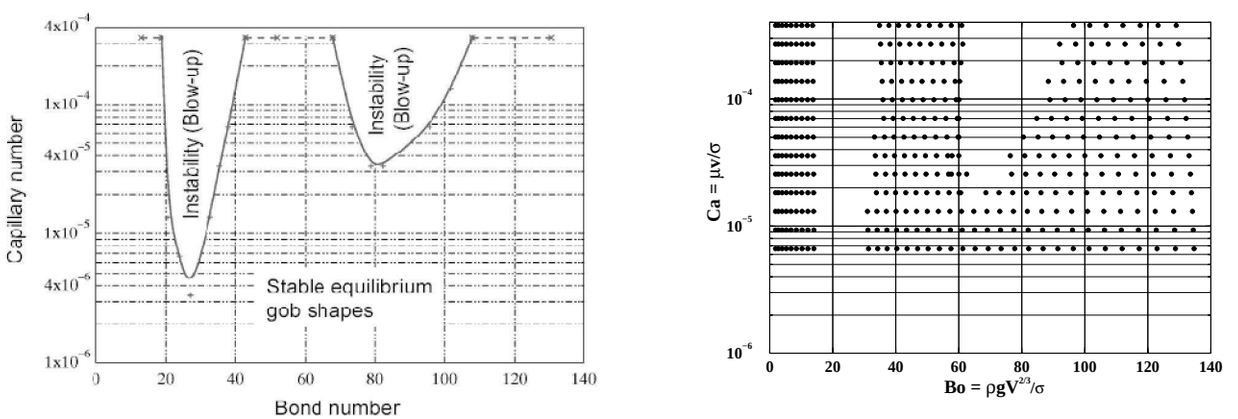


Figure 2.

References

[1] Hinch E.J., Lemaitre J.: The effect of viscosity on the height of disks floating above an air table. *J. Fluid Mech* **273**:313–322, 1994.

[2] Lange, U.: Gas-Film Levitation of Viscous Glass Droplets, ECMI Glass Days, Wattens, Austria, 21/11/2002

A LONG-WAVELENGTH MODEL OF VISCOUS ENTRAINMENT

Wendy W. Zhang

Physics Department & James Franck Institute
University of Chicago Chicago IL 60637

Summary When a large air bubble rises in syrup, it often leaves behind a thin trailing tendril in which air is entrained into the syrup. This is a familiar example of how viscous entrainment can create a long and slender structure on a liquid surface. We derive a simplified model of viscous entrainment in the limit when the entrained fluid is far less viscous than the entraining fluid. Results suggest there exists a class of macroscopic conditions which allow local, scale-invariant entrainment dynamics, thus raising the possibility of that infinitely thin liquid spouts in the continuum model are realizable in practice.

INTRODUCTION

If you turn a half-empty jar of honey upside down, (with the lid closed, of course), you will see a large air bubble form and rise slowly through the honey. If the jar is large, this air bubble will rise for a considerable distance before reaching the top. As it rises, the trailing end of the bubble becomes tapered and eventually leaves a tendril of air behind. Similar phenomena occur when a less viscous liquid is entrained by flow in a more viscous fluid, as relevant in a variety of physical contexts, such as oil recovery, mixing in chemical reactors, and has been proposed as a possible mechanism for the formation and the stability of localized upwelling of hot materials from deep mantle, i.e. hot-spots [1].
Here we ask what determines the volume flux of fluid left behind when a moving liquid drop is deformed sufficiently to just begin to leak at its trailing edge? This question is inspired by a series of experiments on viscous withdrawal by Cohen & Nagel [2]. We are particularly interested in the possibility that the entrainment flux goes to 0 continuously at a critical value of the imposed withdrawal rate, since it corresponds to the steady-state interface undergoing a continuous evolution from a hump to a spout as the withdrawal rate is tuned across the critical value. Fundamentally, the existence of such a continuous transition in the steady-state shape is unusual, because the two fluid layers are immiscible and therefore the interface has a finite surface tension. As a consequence, there exists a Laplace pressure across the interface which is proportional to a product of surface tension and mean curvature. If the curvature becomes infinite at a point, the Laplace pressure also becomes infinite, and stresses in the vicinity of the singularity balance if and only if the viscous stresses also diverge. This corresponds to the formation of a steady-state singularity.

PROBLEM FORMULATION

We design a simple, experimentally realizable model problem (figure 1a) to investigate the possible formation of a steady-state singularity. We consider the entrainment of a thin cylindrical spout of less viscous fluid from a nozzle by an imposed axial straining flow in an exterior fluid $\mathbf{U}_\infty(r,\theta,z) = \left(-\frac{Er}{2},\ 0,\ Ez\right)$. Inertial effects are taken to be negligible everywhere. The nozzle fluid is taken to be far less viscous than the exterior fluid so that the spout surface is well approximated by a surface of zero tangential stress. Most importantly, we assume that the spout profile is long and slender everywhere and look for a long-wavelength model.

In deriving a long-wavelength equation for the case where the interior viscosity μ_{int} is much less than the exterior viscosity μ_{ext}, we follow Taylor [3, 4] in modeling the effect of the free-stress surface on the exterior flow as a radial flow, $q(z)/(2\pi r)$, corresponding to a line of point sources which are situated along the drop centerline. The strength of the volume flux, $q(z)$, is determined by the kinematic condition. Since Taylor's model was for the steady-state shape of a drop in an axial straining flow, the entrainment flux Q_{spout} is always 0 for his case. Moreover global volume conservation for the drop requires that the interior pressure P_{int} for Taylor's problem satisfy an integral constraint. In our case, we assume the nozzle is connected to an extremely large reservoir, so that P_{int} is determined by local stresses. In steady-state the spout profile $R(z)$ satisfies the nonlinear ordinary differential equation

$$Q_{\text{spout}} = 2\pi\left\{\frac{EzR^2(z)}{2} - \frac{R^4(z)}{16\mu_{\text{int}}}\frac{\mathrm{d}}{\mathrm{d}z}\left[2\mu_{\text{ext}}E\left(1+\frac{z}{R(z)}\frac{\mathrm{d}R}{\mathrm{d}z}\right)+\gamma\left(\frac{1}{R}-\frac{\mathrm{d}^2R}{\mathrm{d}z^2}\right)\right]\right\} \tag{1}$$

where Q_{spout} is an unknown quantity and γ the surface tension. The idea is that for a given imposed strain rate E only a specific value of Q_{spout} can satisfy upstream boundary conditions at the nozzle and the condition that a spout be entrained downstream, i.e. that the equation for $R(z)$ supports a solution which extends to positive infinity. Equation (1) can be recast into a simpler, nondimensional form by the nondimensionalizations $\hat{r} = R_N$, $\hat{z} = \frac{\hat{r}}{2\sqrt{\lambda}}$,

$\hat{P} = \frac{\gamma}{\hat{r}}$ and $\hat{U} = \frac{\gamma}{\mu_{\text{ext}}}$ where R_N is the nozzle radius. In our model problem the entrainment dynamics is characterized by two dimensionless parameters, the viscosity contrast $\lambda = \mu_{\text{int}}/\mu_{\text{ext}}$, assumed to be far less than 1, and related only to the material properties and a capillary number $Ca = (2\mu_{\text{ext}}ER_N)/\gamma$ where $Ca \gg 1$ corresponds to the limit of strong flow and weak surface tension. From this point on all the variables are dimensionless unless otherwise specified.

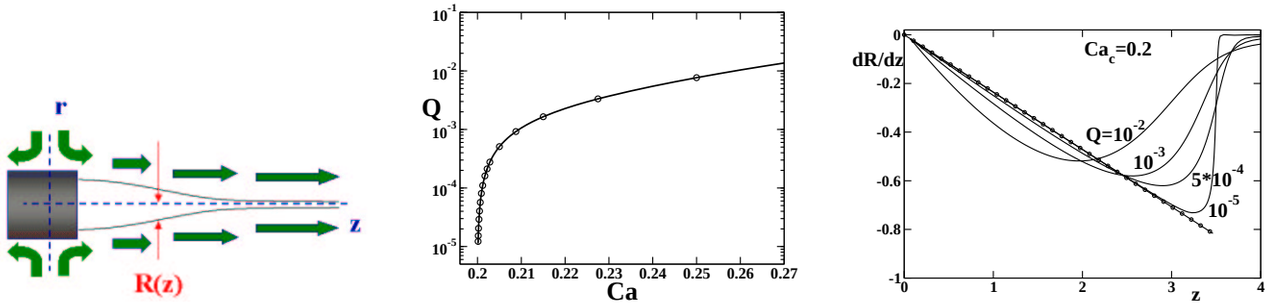


FIG. 1: a) An imposed axial straining flow entrains a steady-state spout from a fluid filled nozzle connected to a large reservoir. b) Steady-state entrainment flux Q versus Ca for nozzle boundary conditions with $Ca_c = 0.2$. The viscosity contrast λ is 1/80. c) Slope profile of full solutions for $Ca_c = 0.2$ at $Q = 10^{-2}$, 10^{-3}, $5 \cdot 10^{-4}$, and $Q_{\min} = 10^{-6}$. The solid line with circles corresponds to $\mathrm{d}R_D/\mathrm{d}z$.

RESULTS

There exists a special class of nozzle boundary conditions which correspond to continuous entrainment transitions in (1). Fundamentally this is because the equation supports a family of exact solutions

$$R_D(z) = 1 - \left(\frac{z}{z_D}\right)^2 \qquad z_D = 2\sqrt{\frac{1}{2Ca_c} - 1} \tag{2}$$

which correspond to $Q = 0$ solutions which end in a cone. From similarity solutions of (1), we know that such conical profiles correspond precisely to the upstream profiles needed for an infinitely thin liquid spout to be entrained [5]. Thus specifying boundary conditions at the nozzle consistent with the existence of (2) at $Ca = Ca_c$ makes it possible for the entrainment volume flux Q to vanish continuously as $Ca \to Ca_c$. Numerical solutions of (1) show indeed this continuous transition, as illustrated by figure 1b. The entrainment flux Q scales linearly with $Ca - Ca_c$ over several decades in Q. For more details, see [5]. Figure 1c shows that the upstream spout profiles at finite, but small Q, converge towards (2) as Q becomes small. In conclusion, full solutions of the long-wavelength model and similarity solutions suggest that liquid spouts of atomic thickness and macroscopic extent can indeed be created at a viscous entrainment transition when appropriate upstream boundary conditions are imposed.

Acknowledgement The work described here grew out of many conversations with Sidney R. Nagel. I am indebted to Todd F. Dupont and Leo P. Kadanoff for good suggestions. I have also benefitted from discussions with and encouragements from Michael P. Brenner, Itai Cohen, Peter Constantin, Jens Eggers, David Quere, Howard A. Stone, Shankar Venkataramani, Thomas A. Witten and Jason Wyman.

[1] A. Davaille, "Two-layer thermal convection in miscible viscous fluids ", J. Fluid Mech. **379**, 223 (1999).
[2] I. Cohen and S. R. Nagel, "Scaling at the selective withdrawal transition through a tube suspended above the fluid surface ", Phys. Rev. Lett. **88**, 074501 (2002).
[3] G. I. Taylor, "The formation of emulsions in definable fields of flow ", Proc. R. Soc. Lond. **146**, 501 (1934).
[4] A. Arivos and T. S. Lo, "Deformation and breakup of a single slender drop in an extensional flow ", J. Fluid Mech. **86**, 641 (1978).
[5] W. W. Zhang, "Viscous entrainment from a nozzle: singular liquid spouts ", (2004), submitted to Phys. Rev. Lett.

XXI ICTAM, 15–21 August 2004, Warsaw, Poland

ENTRAINMENT OF AIR BUBBLES DURING STRONG VORTICITY–FREE-SURFACE INTERACTION

Alessandro Iafrati, Emilio F. Campana, Ulderico P. Bulgarelli,
INSEAN - Italian Ship Model Basin - 00128 - Rome, Italy

Summary The air entraiment induced by vorticity–free-surface interaction is here numerically investigated using a two-fluid model which describes the flow in air and water as that of a single incompressible fluid whose density and viscosity vary smoothly across the interface. The numerical approach is used for the simulation of a viscous vortex pair vertically rising toward the free surface. Several flow conditions are studied aimed at understanding the role played by vortex intensity, surface tension and gravity forces on the amount of entrained air and the mechanisms for its entrainment.

INTRODUCTION

The problem of air entrainment generated by free surface dynamics has several important implications in nature and in the technical context as well. In the naval field interest in air bubble entrainment is connected to the design of stealth ships: the long bubbly wake developing past fast ships, makes them visible through Sintetic Aperture Radar (SAR) images of the ocean surface. In addition to visibility problems, the dynamics of air bubbles entrained in the bow region is responsible for noise generation which alters the response of the Sonar.

On the basis of the above consideration, a research activity has been undertaken aimed at studying some of the mechanisms leading to air entraiment and understanding the dynamics of the entrapped bubbles. A two-fluids numerical approach has been initially developed to study the complex flow generated by the breaking of free surface waves [3]. At large scales wave breaking is characterized by the formation of a plunging jet which leads to the encompassment and to the successive entrainment of a significant amount of air. At shorter scales, owing to the increased role played by the surface tension, the breaking event takes place in a more gentle way with the plunging jet being replaced by a bulge which slides down along the forward face of the wave thus leading to the formation of a strong shear layer beneath the free surface which originates at the toe of the bulge and propagates downstream [4]. In this condition the total amount of entrained air is significantly reduced and the vorticity–free-surface interaction becomes the leading mechanism for the entrainment of air.

In order to study this mechanism for air entrainment, the simpler problem of a vortex dipole rising below a free surface is here considered. This problem has been studied in the past by several authors either experimentally or numerically. In [7] the three dimensional effects are experimentally investigated showing that free surface striations are caused by short wavelength instability of the vortex pair. The free surface deformation caused by a rising vortex pair has been studied in [8] in the framework of an inviscid assumption. Ohring & Lugt did a careful numerical study of both the vertical [6] and oblique [5] ascent of a viscous vortex pair toward the free surface. In their study, which assumes a two-dimensional flow, different intensities of the vortex pair have been analysed and different values of the surface tension and of the gravity force have been used to vary the free surface "stiffness". The role of the free surface stiffness on the generation of secondary vorticity and on the path of the primary vortex are investigated. Since Navier-Stokes equations were solved on a boundary-fitted grid, their study couldn't get too close to the incipient condition for air entrainment when a too strong grid deformation takes place.

In the present paper the same study is carried out with the help of a two-fluid approach which allows to go closer and also further than the incipient conditions for air entraiment. The two-dimensional assumption is still retained for the sake of the computational effort. Ratio among physical quantities, like density and viscosity, are assumed to be the same as for air and water. Some of the conditions used in [6] are analysed for the purpose of the code validation. For a mild vorticity–free-surface interaction a rather good agreement is obtained. For a stronger interaction, in contrast with results presented in [6], air entrainment is found. A deeper verification of the results is currently running aimed at better understanding the reason for the differences in the results.

NUMERICAL MODEL

The flow in air and water is numerically computed with the help of a Navier-Stokes solver for a single incompressible fluid whose density and viscosity values vary smoothly across the interface. The system of Navier-Stokes equation is written in curvilinear coordinates and discretized on a non staggered grid layout by using a numerical approach based on that originally proposed in [9] suitably modified to deal with the two-fluid system in [2]. The method makes use of a fractional step approach: the momentum equation is first advanced in time by neglecting the pressure contribution (predictor step) which is successively reintroduced by enforcing the continuity of the velocity field (corrector step). The diagonal part of the dominating diffusive terms are computed with a Crank-Nicolson scheme whereas all other contributions are treated explicitly with a three-step Runge-Kutta method.

The location of the air-water interface is captured as the zero level of a function $d(\boldsymbol{x}, t)$ which is initialized as the signed normal distance from the interface with $d > 0$ in water and $d < 0$ in air. During the motion the function d is transported with the flow and the new interface location is reconstructed as the level $d = 0$. Hence, the function d is reinitialized as the signed normal distance from the new interface configuration.

As proposed in [1], surface tension effects are included in the momentum equation as a continuum force acting on a neighborhood about the interface whose thickness is $2\delta_T$. To avoid troubles when evaluating derivatives numerically, the jump in density and viscosity is also smeared on a small region about the interface whose width is $2\delta_P$. Numerical tests, aimed at understanding how the two parameters δ_T and δ_P affects the solution, have shown that both of them should be at least three grid cells to guarantee stability of the calculation but should not be too large for the sake of the accuracy.

PRELIMINARY RESULTS

The numerical model discussed above is used for the simulation of the vertical rising of a vortex pair toward the free surface. The study is carried out for different values of the Reynolds (Re), Froude (Fr) and Weber (We) numbers. Initial and boundary conditions are assumed equal to that used in [6]. In order to validate the numerical procedure, a mild interaction is analysed by first. Flow parameters are assumed as $Re = 100, Fr = 0.2, We = 0$ and results, shown in Fig. 1, are in rather good agreement with those reported in [6].
By reducing the gravity, that is for $Fr = 0.4$, the free surface stiffness is reduced and a stronger interaction takes place. For this condition, the results obtained by the present model, reported in Fig. 2, seem to differ from those reported in [6]. In particular, the present model predict some entrainment of air which was not shown in [6]. A deeper verification of the results is currently running aimed at clarifing this point.

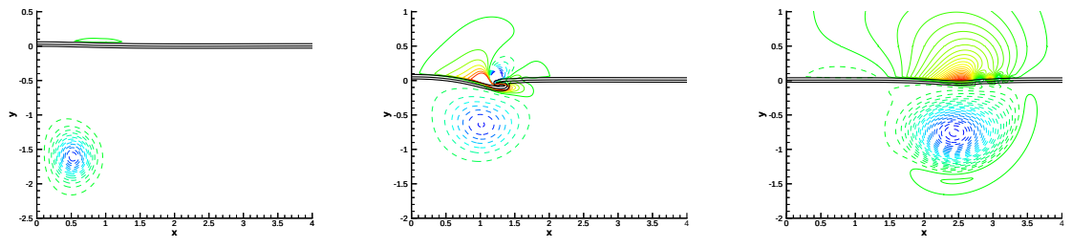


Figure 1. For a mild vorticity–free-surface interaction no air is entrained. Three density levels are plotted with black lines ($\varrho/\varrho_w = 0.03, 0.50, 0.95$). Vorticity contours are also shown with dashed lines used for negative levels.

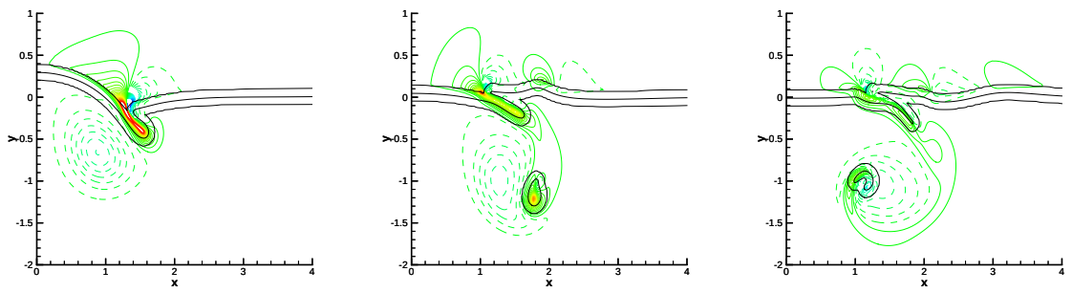


Figure 2. Three different stages of a stronger vorticity–free-surface interaction leading to air bubble entrainment.

References

[1] Brackbill J.U., Kothe D.B., Zemach C.: A continuum method for modeling surface tension. *J. Comput. Phys.*, **100**:335-354, 1992.
[2] Iafrati A., Di Mascio A., Campana E.F.: A level-set technique applied to unsteady free surface flows. *Int. J. Numer. Meth. Fluids*, **35**:281–297, 2001.
[3] Iafrati A., Campana E.F.: A domain decomposition approach to compute wave breaking. *Int. J. Numer. Meth. Fluids*, **41**:419–445, 2003.
[4] Iafrati A., Campana E.F.: Flow field evolution beneath microbreakers. Submitted for publication on *J. Fluid Mech*, 2003.
[5] Lugt H.J., Ohring S.: The oblique ascent of a viscous vortex pair toward a free surface. *J. Fluid Mech*, **236**:461–476, 1992.
[6] Ohring S., Lugt H.J.: Interaction of a viscous vortex pair with a free surface. *J. Fluid Mech*, **227**:47–70, 1991.
[7] Sarpkaya T., Suthon P.: Interaction of a vortex couple with a free surface. *Exp. Fluids*, **11**:205–217, 1991.
[8] Yu D., Tryggvason G.: The free surface signature of unsteady, two-dimensional vortex flows. *J. Fluid Mech*, **218**:547–572, 1990.
[9] Zang Y., Street R.L., Koseff J.R.: A non-staggered grid, fractional step method for time dependent incompressible Navier-Stokes equations in curvilinear coordinates. *J. Comput. Phys.*, **114**:18-33, 1994.

XXI ICTAM, 15–21 August 2004, Warsaw, Poland

SPREADING OF CHARGED MICRODROPLETS

Santiago I. Betelú*, Marco A. Fontelos**
*Department of Mathematics, University of North Texas, P.O. Box 311430, Denton, TX 76203-1430, U.S.A.
**Departamento de Matemática Aplicada, Universidad Rey Juan Carlos, Móstoles, Madrid 28933, Spain

Summary We consider the spreading of a charged conducting droplet on a flat dielectric surface. Two forces drive the spreading: surface tension and electrostatic repulsion. By using the lubrication approximation we derive a fourth order nonlinear partial differential equation that describes the evolution of the height profile. We find that the equation has a two-parameter family of selfsimilar solutions. Some of the solutions are explicitly computed while the other solutions are studied numerically. We show that the solutions have moving contact lines and the radius of the drop is a power law of time with exponent one-tenth. We also construct explicit solutions corresponding to non-circular drops, whose interfaces are ellipses with constant focal length.

MAIN RESULTS

The interaction between a droplet and an electric field has received intense attention in the last few years in connection to its potential technological applications in microfluidics, inkjet printing and electrospray ionization. Here we study spreading drops placed on a dielectric plane surface in the absence of any other external charges or conductors. In particular, we are interested on the influence of the electric charge on the spreading rate and the shape of the drop.
We derive a model based on the thin film approximation and find the following results:

1. For circular drops, there are self-similar solutions that describe the advanced stage of the spreading. We find a two-parameter family of compactly supported self-similar solutions showing that the radius $a(t)$ of the drop is given by a power law of the form
$$a(t) = \zeta(X, Z) \left(\frac{V^3 \gamma}{\mu} t \right)^{1/10}, \tag{1}$$
where μ is the viscosity, γ the surface tension coefficient, V the volume of fluid, t is the time measured since the beginning of the spreading and X, Z are dimensionless parameters.

2. One of these parameters,
$$X = \frac{\varepsilon_0}{V\gamma} \left(\frac{Q}{4\pi\varepsilon_0} \right)^2, \tag{2}$$
where Q is the electric charge of the drop and ε_0 is the permittivity of the gas above the drop, is identical up to a constant to Lord Rayleigh's fissibility parameter (cf. [2], [1]) and measures the ratio between electrostatic and capillary forces controlling the dynamics. The ratio between these forces does not depend on the radius of the drop and remains constant through the whole spreading process. The other parameter Z controls the speed of the spreading and the shape of the drop.

3. One of these solutions is computed explicitly. In this solution the capillarity does not affect the shape of the drop. The other solutions, whose drop shapes are affected by capillarity, are computed numerically by solving a third order boundary value problem. The self-similar solutions have two possible different shapes: convex drops and drops with an annular bump around the center of the drop.

4. We construct explicit solutions for drops with elliptical interfaces, describing the spreading of a liquid initially concentrated on a finite segment. The subsequent shapes of the interface are a family of confocal ellipses that asymptotically approach a circle.

LUBRICATION APPROXIMATION AND SELF-SIMILAR SPREADING

We shall assume that the drop is thin enough to allow the use of the so-called "lubrication approximation". That is, if h_0 is the height of the drop and a its radius, then $h_0/a \ll 1$. Under this approximation, the velocity field is mostly horizontal and its derivatives with respect to the vertical direction are dominant respect to the derivatives on the other directions.
Let the free surface of the drop be described by the graph $z = h(x, y, t)$. If we impose the no-slip boundary condition at the substrate ($z = 0$) as well as zero tangential stresses at the free surface ($z = h$) then it is well know (cf. for instance [3]) that, for a Newtonian fluid, the velocity averaged on the vertical direction is given by:
$$\overline{v} = -\frac{1}{3\mu} h^2 \overline{\nabla} p, \tag{3}$$
where $\overline{\nabla} p$ is the gradient of the pressure at (x, y), which under the given approximation is independent of z. The equation for the interface follows from mass conservation and reads as:

At the free surface the normal stress balance yields the following relationship between pressure, electrostatic stress and capillary pressure:

$$p = -\sigma E_n + \gamma k, \tag{5}$$

where σ is the induced surface charge, E_n is the component of the electric field normal to the surface ($E_n = \overline{E} \cdot \overline{n}$), γ is the surface tension coefficient and k is the mean curvature of the free surface. When the lubrication approximation holds we have

$$k \simeq -\Delta h. \tag{6}$$

After computing the electric field for a circular flat drop and inserting it into the previous equations we arrive at the following lubrication equation:

$$h_t + \frac{1}{r}\left[r \frac{1}{3\mu} h^3 \left(\frac{Q^2}{\varepsilon_0 \left(4\pi a(t)\right)^2} \frac{1}{a^2(t) - r^2} + \gamma \left(h_{rr} + \frac{h_r}{r} \right) \right)_r \right]_r = 0. \tag{7}$$

This equation is defined for $0 \leq r \leq a(t)$. The initial condition is $h(r, t_0) = h_0(r)$ for $r \in [0, a(t_0)]$ and the boundary conditions are

$$h'(0,t) = h'''(0,t) = 0 \text{ (circular symmetry)}, \; h(a(t),t) = 0 \text{ for } t \geq t_0 \tag{8}$$

together with the condition that no mass is lost at the rim of the drop implying that the limit of the term within brackets in (7) is zero at $r = a(t)$.

Selfsimilar solutions are of the form

$$h = \frac{1}{t^{\frac{1}{5}}} H\left(\frac{r}{t^{\frac{1}{10}}} \right) \tag{9}$$

with $H(\rho)$ satisfying:

$$-Z(\rho H_\rho + 2H) + \frac{1}{\rho}\left[\rho H^3 \left(\frac{XY}{1-\rho^2} + H_{\rho\rho} + \frac{H_\rho}{\rho} \right)_\rho \right]_\rho = 0, \tag{10}$$

where X, Y and Z are dimensionless parameters. We find an explicit solution

$$H(\rho) = 1 - \rho^2 \tag{11}$$

provided $Z = 2XY$, $Y = \pi/2$ and broader families of solutions with interesting geometric properties.

References

[1] D. Duft, T. Achtzehn, R. Müller, B. A. Huber and T. Leisner, ”Rayleigh jets from levitated microdroplets”, Nature, Vol. 421 (2003), pg. 9.
[2] Lord Rayleigh, ”On the equilibrium of liquid conducting masses charged with electricity”, Phil. Mag. 14 (1882), pp. 184-186.
[3] T. G. Myers, ”Thin films with high surface tension”, SIAM Rev. 40, no.3 (1998), 441-462.

Multiple Bubbles Dynamics using Level Set Indirect Boundary Element Method

C.Wang*, Fong Siew Wan**, Khoo Boo Cheong***, Hung Kin Chew **
*Shanghai JiaoTong University, 800 Dong Chuan Road, Shanghai 200240
**Institute of High Performance Computing, Science Park Road, #01-01 The Capricorn, Singapore Science Park II, Singapore 117528
*** National University of Singapore, Dept of Mechanical Engineering, Kent Ridge, Singapore

Summary We present a new method for simulating bubble dynamics called Level Set Indirect Boundary Element Method (LSBEM). This method combines the advantages of LSM with BEM. As we know, the Level Set Method (LSM), which is a well known computational technique used for tracking a propagating interface over time, has the strength in accurately handling topological complexities and changes. The Boundary Element Method (BEM), on the other hand, is known to serve well in conserving computational effort by reducing the dimensions of the problem by one. The essence of this work is that while keeping this advantage of BEM, LSBEM simplifies the representation of the interface of multi-bubbles by using LSM. Thus advantages from both methods are utilised. A number of techniques are applied to ensure solution convergence and numerical accuracy. For instance, effort is made to avoid singularities in calculation by defining two sets of source and control points on the mesh which will never overlap one another; also work is done to ensure solution accuracy by reinitializing the level set function using Fast Marching Method (FMM) after every two time-steps.

INTRODUCTION

Boundary Element Method (BEM) is commonly applied in the simulation of bubble(s) dynamics as seen in the works of Blake & Gibson [1], Oguz & Prosperetti [2], and Zhang et al [3]. Most of these works were based on the so-called Direct Boundary Element Method (DBEM) in which the potential or its normal derivative is the primary unknown to be solved first. The method employed here, known as Indirect Boundary Element Method (IBEM), takes the source or dipole distributions as the primary unknown to be solved first, and then evaluate the potential and material velocity in the flow field. Another component to LSBEM is the Level Set Method which was introduced by Osher and Sethian in 1988 [4]. LSM traces the deformation of the interface, in this case the bubble surface, by advecting the level set function. This function is a scale function defined in the space with one dimension higher then that of the interface and the interface coincides with the zero level set. Therefore the LSBEM tries to combine both methods while retaining their respective strengths.

COMPUTATIONAL METHOD DEVELOPMENT

A background uniform mesh covering all the computational domain of the given problem is constructed. Then the level set function is defined on it with source points and control points along the interface (the zero level set). The source points are defined as grid points that are located inside the bubble with at least one neighbouring point that is not inside the bubble. The control points, however, are defined as the middle points of the segments whose two nodes are located in the different sides of the interface. In IBEM, the potential distribution is approximated as the sum of source strength at every source points, which is in turn decided by enforcing the potential value at each control point to be equal to the given boundary condition of the potential. Since the bubble is a close object, the total number of control points will always be larger than that of source points. Therefore, no exact solution can be found; but a least square type of solution can always be obtained.

After getting the source strength on each source point, the velocity distribution of the computational domain is generated. However, it must be noted that the velocity distribution inside the bubble is still unknown and thus has to be calculated by extending the velocity field into the bubble via interpolation. Once this is done, the level set function is shifted to the next time step for the new interface location. Based on the location, source and control points are updated by evaluating the Bernoulli's equation. In order to maintain the accuracy of the results, the level set function is reinitialized after two time-steps with the use of the Fast Marching Method (FMM) [5].

PRELIMINARY RESULTS

We have obtained results for one, two and three bubbles simulations. In this summary, we will show the results from three bubbles simulations. Fig.1 shows the three bubbles in an infinite medium without gravity at three different time-steps.

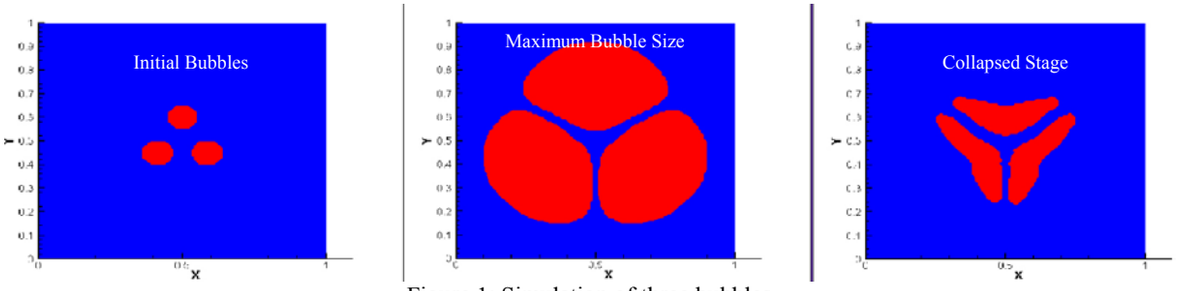


Figure 1: Simulation of three bubbles

Then we proceed to simulate three bubbles with the inclusion of a free surface (Fig.2) and also the simulation with gravity taken into consideration (Fig. 3).

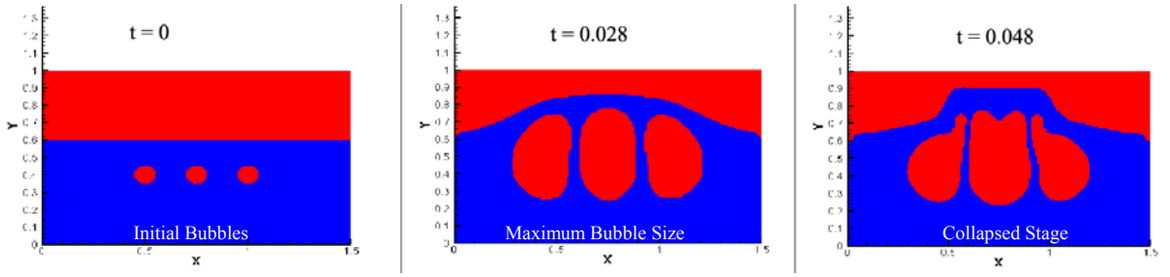


Figure 2: Simulation of three bubbles with a free surface on top

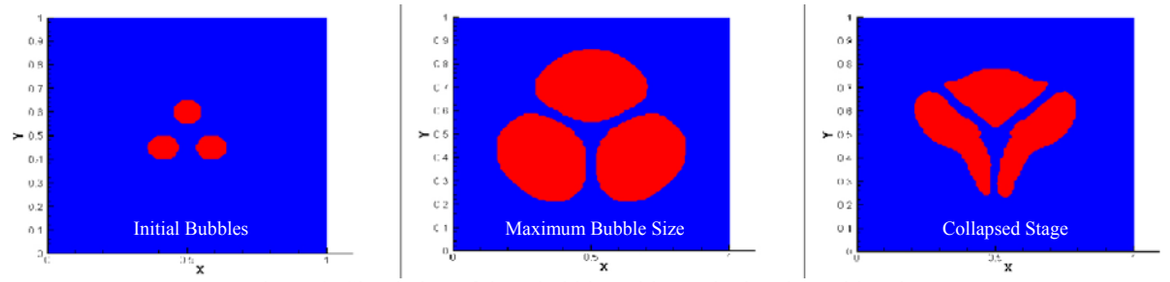


Figure 3: Simulation of three bubbles with gravitational consideration

CONCLUSIONS

Since the size of the matrix involved is determined by the number of source points generated, it is therefore still much less than the total number of grid points of the background mesh. This implies that the advantage of BEM is still kept in the LSBEM method. The representation of the interface by the level set functions simplifies the representation of the interface of multi-bubbles; again utilizing the strength of LSM. It is believed that LSBEM is ideal for simulating bubble dynamics involving topological changes in the multiple bubbles.

References

[1] Blake J. R. and Gibson D. C.: Growth and collapse of a vapour cavity near a free surface. J. Fluid Mech. 111, 123-140 (1981).

[2] Oguz H. N. and Prosperetti A.: Bubble entrainment by the impact of drops on liquid surfaces. J. Fluid Mech. 219, 143-179 (1990).

[3] Zhang Y. L., Yeo K. S., Khoo B. C. and Chong W. K.: Simulation of three-dimensional bubbles using desingularized boundary integral method. Int. J. Num. Methods Fluids. 31(8) 1311-1320 (1999).

[4] Osher, S., and Sethian, J.A., Fronts Propagating with Curvature-Dependent Speed: Algorithms Based on Hamilton--Jacobi Formulations, Journal of Computational Physics, 79, pp. 12--49, 1988.

[5] Sethian J. A., A Fast Marching Level Set Method for Monotonically Advancing Fronts Proc. Nat. Acad. Sci., v93, 4, pp. 1591-1595, 1996.

LOW-REYNOLDS-NUMBER MOTION OF A DROP BETWEEN TWO PARALLEL PLANE WALLS

Andrew J. Griggs, Alexander Z. Zinchenko, Robert H. Davis
Department of Chemical and Biological Engineering, University of Colorado, Boulder, Colorado 80309-0424, USA

Summary The motion of a deformable drop between two parallel plane walls in Poiseuille flow at low Reynolds number is examined using a novel boundary-integral method (BIM). Three-dimensional results are presented for neutrally-buoyant drops of arbitrary fluid-to-drop viscosity ratio, drop size, and position within the channel.

INTRODUCTION

An emulsion consists of drops of one fluid dispersed in a second, immiscible fluid. Many applications, found in areas of biotechnology, food science, geology, and pharmaceutical processing, among others, involve the flow of emulsions through pipes, channels, or porous media. When the droplet and container or pore sizes are comparable, effective-fluid or volume-averaging schemes fail, which provides motivation for developing microstructural flow models.

In the present work, the motion of a deformable drop through another immiscible fluid between two parallel walls is examined. Literature addressing the motion of a single or collection of drops using BIMs are plentiful[1,2]. Previous works give results for a two-dimensional drop in an inclined channel[3] and an array of drops through a cylindrical tube[4]. Closely related to the present work is a study of the motion of a rigid particle in Stokes flow[5], where a BIM is used to solve for the velocity of spherical and ellipsoidal particles as a function particle size and position in the channel. Neutrally-buoyant, rigid spheres in Stokes flow are incapable of crossing streamlines, as can be argued by reversibility. In contrast, a deformable drop is capable of crossing streamlines due exclusively to deformation, such that the assessment of particle deformation and migration requires dynamical simulation.

THEORETICAL AND NUMERICAL METHOD

Consider an incompressible, Newtonian fluid of viscosity μ and density ρ, moving with a velocity **u**. The Stokes equations are valid at low Reynolds numbers (e.g. very slow fluid velocity, high fluid viscosity or minute flow domains). For the case of two immiscible fluids, the Stokes equations are subject to two boundary conditions: equality of interfacial velocities and continuity of the stress vector. The drops can be buoyant and the interfaces are assumed devoid of surfactants.

The fundamental solution for the Stokes velocity is given by the Green's function. The Green's function for the geometry of interest may be represented as sum of each contribution: $\mathbf{G}^k_{WALL} = \mathbf{G}^k_o + \mathbf{G}^k_{LW} + \mathbf{G}^k_{UW} + \mathbf{G}^k_{\varepsilon}$, for the free-space, lower-wall, upper-wall and numerical terms, respectively. The numerical term accounts for the presence of both walls. An advantageous property of this particular Green's function is that it does not require discretization of the walls or the surrounding fluid, but instead only discretization of the particle or drop surface.

The form of the boundary-integral equation, made amenable for numerical calculations by deflation, is given by:

$$\mathbf{w}(\mathbf{y}) = \frac{2}{\lambda+1}\mathbf{u}^{\infty}(\mathbf{y}) + \kappa\left[2\int_S \mathbf{w}(\mathbf{x})\cdot\boldsymbol{\tau}^k(\mathbf{x};\mathbf{y})\cdot\mathbf{n}(\mathbf{x})dS_{\mathbf{x}} - \mathbf{w}'(\mathbf{y}) + \frac{\mathbf{n}(\mathbf{y})}{S}\int_S \mathbf{w}(\mathbf{x})\cdot\mathbf{n}(\mathbf{x})dS_{\mathbf{x}}\right] + \mathbf{F}(\mathbf{y}) \tag{1}$$

$$\mathbf{F}(\mathbf{y}) = \frac{2}{(\lambda+1)}\left(\int_S [\frac{2k(\mathbf{x})}{\mathrm{Ca}} - \frac{\mathrm{Bo}}{\mathrm{Ca}}\mathbf{g}_o\cdot\mathbf{x}]\mathbf{G}^k(\mathbf{x};\mathbf{y})\cdot\mathbf{n}(\mathbf{x})dS_{\mathbf{x}} + \mathbf{u}^{\infty}(\mathbf{y})\right) \qquad \mathbf{y}\in S \tag{2}$$

where S is the interface of the two immiscible fluids, the deflated velocity is **w**(**y**) = **u** - κ**u'**, where **u** is the physical velocity on S, $\lambda = \mu_{\mathrm{drop}}/\mu_{\mathrm{fluid}}$, $\kappa = (\lambda\text{-}1)/(\lambda+1)$, $\mathbf{u}_\infty$ is the undisturbed ambient fluid velocity, $k(\mathbf{x})$ is the mean curvature, γ is the surface tension, and $\boldsymbol{\tau}^k$ is the stress tensor corresponding to the fundamental solution $\mathbf{G}^k$. Two dimensionless quantities of physical interest are the capillary and Bond numbers. The capillary number, $\mathrm{Ca} = \mu_{drop}U_c/\gamma$, gives the ratio of the viscous to interfacial forces, where U_c is the centerline velocity of the parabolic flow (used as the reference velocity). The Bond number, $\mathrm{Bo} = \Delta\rho g_c H^2/\gamma$, where $\Delta\rho$ is the density difference between the two fluids, H is the channel height, and g_c is the magnitude of the gravitational force. Bo incorporates gravitational forces into (2) and is an indication of the ratio of body to interfacial forces. Following singularity subtraction, (1) becomes suitable for efficient numerical integration. Our algorithm involves discretization of the drop surface, followed by evaluation of (1) and a subsequent passive mesh stabilization technique, for every timestep. Discretization of the initially spherical drop is performed by division of the surface into a number of triangles (N_Δ), by inscription of either a dodecahedron or an icosaedron. Equation (1) is then solved at every triangle vertex. For $\lambda \neq 1$, the velocity is obtained by an iterative procedure using simple iterations. When $\lambda = 1$, only (2) requires calculation and the iterative procedure is not required.

RESULTS

When Ca→0, the drop shape does not change and the problem simplifies to the analysis of a spherical drop moving between two parallel walls. The drops cannot deform and therefore, cannot cross streamlines. Steady-state calculations for the velocity of spherical drops are given in Figure 1 for flow along the centerline at various λ. Simulation results for large λ agree well with previous results for rigid spheres[5]. The lateral migration of a single drop between two parallel walls has been examined at finite Reynolds number[6]. Figure 2 shows low-Reynolds number results for the case when the initially spherical drop is placed near the lower wall and allowed to deform and migrate. The drop reaches a steady-state shape and velocity in the center of the channel for the conditions shown.

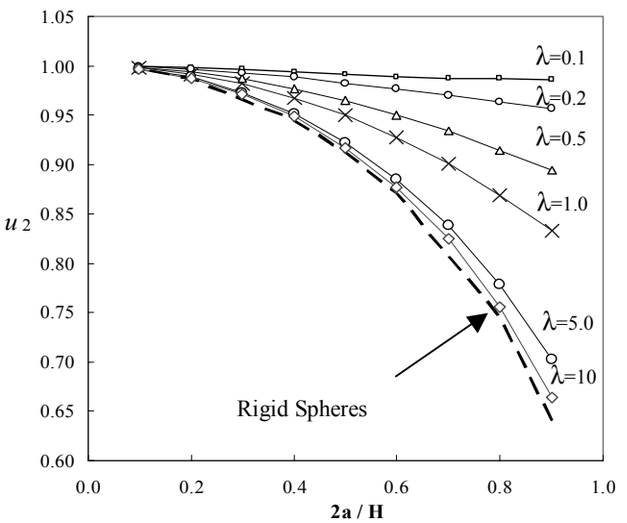


Figure 1. Translational velocities along the channel (u_2) of spherical drops for various viscosity ratios as a function of relative drop size, 2a/H, where a is the drop radius. The dashed line represents data for rigid spheres. The corresponding viscosity ratios are indicated above the curves.

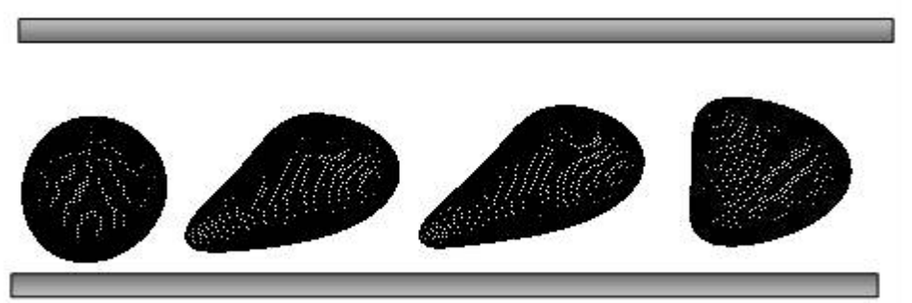


Figure 2. Evolution of a deforming drop initially placed near the lower wall. Migration of the drop across streamlines occurs. Here, Ca =1.0, λ = 1.0, Bo = 0, and N_Δ = 8640.

REFERENCES

[1] Kennedy M.R., Pozrikidis C., Skalak R.: Motion and Deformation of Liquid Drops, and the Rheology of Dilute Emulsions in Simple Shear Flow. Comput. Fluids **23**: 251-278, 1994.
[2] Zinchenko A.Z., Rother M.A., Davis R.H.: A Novel Boundary-Integral Algorithm for Viscous Interaction of Deformable Drops. Phys. Fluids **9**: 1493-1511, 1997.
[3] Coulliette C. and Pozrikidis C.: Motion of an Array of Drops through a Cylindrical Tube. J. Fluid Mech. **358**: 1-28, 1998.
[4] DeBisschop K.M., Miksis M.J., Eckmann D.M.: Bubble Rising in an Inclined Channel. Phys. Fluids **14**: 93-106, 2002.
[5] Zinchenko A. Z., Staben M.E., Davis R.H.: Motion of a Particle Between Two Parallel Plane Walls in Low-Reynolds Number Poiseuille Flow. Phys. Fluids **15**: 1711-1733, 2003.
[6] Mortazavi S., Tryggvasson G.: A Numerical Study of the Motion of Drops in Poiseuille Flow. Part 1. Lateral Migration of One Drop. J. Fluid Mech. **411**: 325-350, 2000.

THERMODYNAMIC PARAMETERS OF VAPOUR BUBBLE GROWTH BY IMAGE ANALYSIS

A. Zachara[*], J. Pakleza[**], S. Blonski[*], R. Trzcinski[*], T.A. Kowalewski[*]

[*] *Polish Academy of Sciences, IPPT PAN, Swietokrzyska 21, PL 00-049 Warszawa, Poland*
[**] *LIMSI-CNRS, BP 133, 91403 Orsay Cedex, France*

Summary: Using high speed video camera and numerical processing of the digital images transient description of the geometry and the interface velocity for vapour bubble growing at the heated surface is achieved. Particle Image Velocimetry and Thermometry are applied to obtain details about velocity and temperature in the surrounding flow field.

INTRODUCTION

From the recent numerical simulations it is possible to generate solutions describing bubble growth from inception to departure without any assumption being made about the bubble shape but axial symmetry and more or less realistic modelling of the wall contact line. To validate these simulations suitable experimental data are required. The bubble shape, the growth rate or the radius of the dried area that are usually employed for comparison are still useful but need to be completed by measurements of additional quantities. In the following we describe summary of experimental investigations of vapour bubble growth performed in our two laboratories. An image analysis is performed and yields an accurate determination of several relevant parameters. Specific attention is devoted to describe dynamics of the moving bubble. Deformation of the interface and frequently observed shape oscillations are analysed to estimate the interface temperature. Velocity and temperature fields in the liquid phase are also visualised seeding the fluid with thermochromic liquid crystals.

EXPERIMENTAL APPARATUS AND PROCEDURE

Isolated bubbles are generated on a horizontal surface inside a 30 cm^3 cube shaped cavity. The working fluid is water boiling under sub-atmospheric pressure. Some experiments are performed for methyl alcohol and PP1 under normal atmospheric pressure. All six walls of the cube are equipped with optical openings for observation or illumination of the internal chamber. In the present experiments the bottom opening is used to mount an electrical heater of a brass plate used for bubbles generation. The technical details can be found in [1].

A typical image of the bubble observed in the bright field of the parallel light shows dark shadow of the central cross-section with an additional bright spot at the centre. To describe properly the bubble shape, the edge extracting technique is applied to distinguish the external contour and its contact with the heating surface, to connect extracted points and to find a smooth functional representation of the pixel set for the further analysis. This description is used to define the bubble shape and contact angles and assuming axial symmetry of the bubble to calculate its volume. After departure vapour bubbles usually exhibit ellipsoidal shape, which can be well approximated by series of Legendre polynomials. Their coefficients describe degree of deformation for each oscillation mode. The main oblate-prolate deformation of the sphere is given by the amplitude $a_2(t)$ of the fundamental oscillation mode. This method of shape description, already successfully applied to oscillating liquid droplets [2], allows for direct comparison of the shape dynamics with analytical models for free oscillating bubbles. Frequency of the bubble oscillations delivers information about variation of the surface tension and indirectly indicate variation of the interface temperature.

Shape of the bubble contour may deliver most of essential thermodynamic parameters of the interface. The local curvature of the interface depends on the balance of pressure, local surface tension and buoyancy. Solving reverse problem the local surface tension can be evaluated and used to obtain local temperature of the interface. For this purpose interpolation of the bubble shape with help of Bézier polynomials is used to obtain smooth (up to the second derivative) representation of the bubble cross-section. It is used to describe local interface velocity (tangential and normal components of the velocity vector) and to evaluate the thermodynamic state of the interface.

The flow visualization around the bubble is performed seeding the fluid with thermochromic liquid crystals. These images are used for the temperature and velocity evaluation (Particle Image Thermometry and Velocimetry [1], [3]).

SELECTED RESULTS

Figure 1 shows typical history of the single vapour bubble observed at low pressure conditions using high speed video imaging. The bubble generation starts at the nucleation site of the wall in the superheated layer of liquid. Due to the back light illumination, cross section of the bubble appears as a dark shadow. The first observable bubbles have diameter of about 30 μm, far above the inertia controlled growth range, described by the simplified Rayleigh model. The initial growth time is much shorter than the temporal resolution of our system, and measured growth time is close to the total growth time. The bubble presented in Figure 1 displays a hemispherical shape then turns very rapidly (≈0.7 ms) to a truncated spheroid. Afterwards, the bubble grows regularly without any significant modification of its form. At time of about 6 ms, the bubble base shrinks that finally leads to the departure process. The whole bubble growth, from time inception to lift-off from the

wall takes about 10 ms. Temperature of fluid above the wall boundary layer is about 4K below saturation temperature. Intensified by the bubble motion cooling of the interface initiates rapid vapour condensation and finally bubble collapses almost completely. The remaining small residual vapour bubbles have diameter of about 15 μm, close to the system spatial resolution. But before the final bubble implosion takes place a few volumetric oscillations can be observed. Such oscillations can be responsible for generation of acoustic waves. Figure 2 collects characteristics of this experiment depicted form the sequence of images. The bubble volume is computed assuming an axial symmetry and D_0 – diameter of the equivalent sphere is plotted together with its base diameter D_b and distance from the bottom for the bubble centre of mass H.

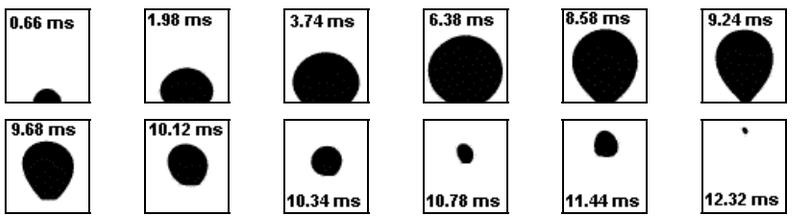


Figure 1. Growth process of a vapour bubble (water P = 4 kPa, T_l = 25.1 °C, T_s = 46.8 °C) observed at 4500 frames/s by high speed camera. Frames shown at few selected time steps. The frame width corresponds to 2.9 mm.

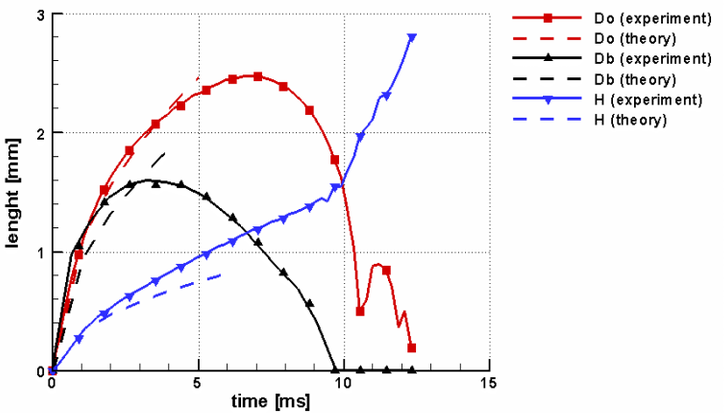


Figure 2. Time history of the experimental and theoretical bubble equivalent diameter D_0, base diameter D_b and height H of the bubble centre of mass evaluated from the sequence of 56 images of the experiment shown in Figure 1.

The other geometric parameters such as maximum and minimum diameter or height of the bubble have also been measured but are not included into the Figure. The experimental results are compared with the theoretical prediction obtained with the aid of a simple mathematical model based on the works of Mei *et al.* [4], Gentile and Pakleza [5], Banerjee and Dhir [6] and other authors. The growth of the bubble may be divided into three main stages. A first one where all quantities increase with time. This corresponds to the early period ($0 < t \leq 2.5$ ms) where strong vaporization is observed, associated with a hemispherical growth. In this stage we observe the best agreement between experimental and theoretical results, especially for the equivalent diameter D_0. A second one where D_b gets smaller while D_0 still increases (2.5 ms $\leq t \leq$ 7.2 ms). Afterwards the bubble base starts to shrink, the vapour production is not strong enough to balance the deficit at the base, and the bubble diameter D_0 decreases. One may see that only during the first 6ms evaporation exceeds condensation and the net volume of the bubble grows. During this time history of the bubble diameter D_0 follows very closely $t^{1/2}$ diffusion controlled regime. In further stages the agreement of experimental and theoretical results is no longer observed. To obtain satisfactory solution the numerical simulation should be applied as it was declared in the Introduction. Evaluation of the local temperature distribution based on previously described methods gives us the opportunity to correct assumption of the isothermal interface correcting heat balance used in the model.

References

[1] Kowalewski T.A., Pakleza J., Chalfen J.-B., Duluc M.-C., Cybulski A., Visualization of vapor bubble growth, 9th International symposium on flow visualization, CD-ROM Proceedings, pp. 176.1-9, Edinburgh 2000.

[2] Becker E., Hiller W.J., Kowalewski T.A., Experimental and theoretical investigations of large amplitude oscillations of liquid droplets, J. Fluid Mech. 231, pp. 189-210, 1991.

[3] Quénot G., Pakleza J., Kowalewski T.A., Particle image velocimetry with optical flow, Exp. in Fluids 25, pp. 177-189, 1998.

[4] Mei R., Chen W.C., Klausner J.F., Vapor Bubble Growth in Heterogeneous Boiling, I – Formulation, Int. J. Heat Mass Transfer, **38**, 909 – 919 (1995).

[5] Gentile D., Pakleza J., A Numerical Simulation of the Boiling Crisis Phenomen (private communication).

[6] Banerjee D., Dhir K.K., Study of Subcooled Film Boiling on a Horizontal Disc, Part I-Analysis, J. Heat Transfer, Trans. ASME, **123**, 271-284, (2001).

Singular droplets

Daniel Bonn, Salima Rafaï, Arezki Boudaoud

ENS-LPS, 24 Rue Lhomond, 75231 Paris cedex 05, France

Summary We study droplets of complex fluids, having either surfactants or polymers dissolved in the fluid. We study the spreading at low Reynolds number. It turns out that both polymers and surfactants slow down the spreading. A special type of surfactants (trisiloxanes), however, leads to "superspreading", in which the droplet spreads out orders of magnitude quicker than with usual surfactants. We provide quantitative explanations for the slowing down of the spreading; however, the mechanism of the speeding up remains a puzzle. At high Reynolds number, we study the impact and subsequent retraction of aqueous droplets on hydrophobic surfaces. Here, the polymer and surfactant additives slow down the retraction, leading to improved deposition. The mechanisms are however very different: the surfactants act on the surface tension, whereas the polymers change the bulk rheology.

1. Introduction

Drops spreading over solid surfaces represent a basic phenomenon important to a wide variety of coating and deposition processes. Efficient deposition is critical to most painting, coating and solution delivery applications. The obvious solution to improve deposition is to add surface-active agents to the droplets to improve the spreading ability of the solutions. However, a full quantitative understanding of the influence of surfactant addition on the spreading dynamics is still lacking. In addition, one can modify the bulk rheology by adding polymers. We study here the deposition of surfactant- and polymer-laden liquids, and see how these additives modify the droplet dynamics both at low and high Reynolds number.

2. Low Reynolds number: spreading of droplets

2.1 Spreading with surfactants

We study the spreading of aqueous surfactant solutions drops onto a hydrophobic surface. The addition of small amounts of trisiloxane surfactants leads to a very rapid ‘super’-spreading of the droplets, faster than that of a simple liquid with the same surface tension and viscosity. On the other hand, classical surfactants are shown to slow down the spreading relative to that of the reference system without surfactants. The latter is linked to the dynamic surface tension of the solutions. For the superspreading surfactant, Marangoni effects are suggested to provide a supplementary different driving force for the spreading that leads to the fast dynamics.

2.1 Spreading with polymers

We study the spreading of aqueous droplets on a hydrophilic surface in two different dilute or semi-dilute polymer solutions. The different solutions exhibit only a single non-Newtonian property, in the sense that other non-Newtonian effects can be neglected. Solutions of stiff polymers have a strong shear rate dependence of the viscosity. Relative to Newtonian fluids the spreading is slowed down For solutions of flexible polymers, elastic effects such as normal stresses are dominant, whereas the shear viscosity is almost constant. Again, a slower spreading is found in this case. We

characterize the non-Newtonian flow properties of these polymer solutions completely, allowing for separate and quantitative investigation of the influence of the two most common non-Newtonian properties on the spreading of droplets

3. High Reynolds number: impact and retraction

3.1 Polymers

Drops impacting onto solid surfaces are important for many applications. An important example being the treatment of plants with herbicides and pesticides, which require precise targeting to meet stringent toxicological regulations. However, the outer wax-like layer of the plant produces a non-wetting interface that causes sprayed droplets to rebound off the foliar surfaces. The plant retains often less than 50% of the initial spray. Our study focuses on the impact and subsequent retraction of non-wetting aqueous drops onto a hydrophobic surface, for which rebound of the droplets limits their deposition. Although extensive experimental and theoretical work has been dedicated to this phenomenon, non-Newtonian rheological effects have not been considered in any detail. Here we show that by adding very small amounts of a flexible polymer to the aqueous phase, we are able to inhibit droplet rebound and dramatically improve deposition without significantly altering the shear viscosity of the solutions. Instead, the results can be understood by taking into account the non-Newtonian elongational viscosity, high values of which provide resistance to drop retraction after impact, that in turn prevent droplet-rebound.

3.2 Surfactants

The behaviour of surfactant-laden droplets turns out to be remarkably similar to that of the polymers: the retraction is almost completely suppressed, and therefore droplet rebound also. The mechanism of the slowing down is however very different: for the surfactants the driving force of the retraction, the surface tension of the liquid-vapour interface, is much smaller. This becomes evident when solutions with different dynamic surface tensions are studied: if the surfactant molecules arrive too slowly at the free surface, rebound may still occur.

References

[1] S. Rafaï, A. Boudaoud, D. Bonn, *Spreading of non-Newtonian fluids on hydrophilic surfaces*, J. Fluid Mech., **513**, 77 (2004)

[2] V. Bergeron, D. Bonn, J.-Y. Martin, L. Vovelle *"Impact and retraction of viscoelastic drops "* Nature, **405**, 772 (2000)

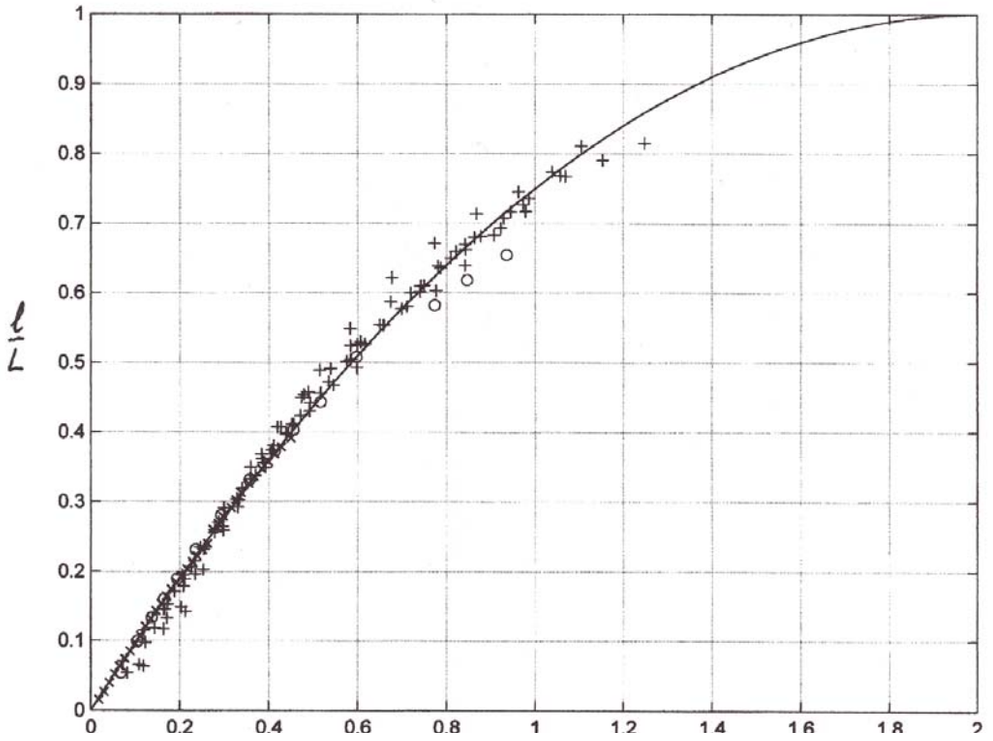
Extended Summary

The growth and structure of double-diffusive cells adjacent to a side-wall in a salt-stratified environment. O. M. Phillips, Department of Earth & Planetary Sciences, The Johns Hopkins University, Baltimore, MD 21218, USA, L. Malki-Epshtein and H. E. Huppert, Institute of Theoretical Geophysics, Centre for Mathematical Sciences, University of Cambridge, CB3 0WA, UK.

Observations and measurements are reported on the patterns and the rates of growth in time of the doubly-diffusive cells that form adjacent to a cooled side-wall in a salt-stratified environment. Fluid near to the wall is cooled and sinks a distance h where its density, increased by cooling, matches that of the salt-stratified ambient. It is observed to separate from the wall, moving outwards as a cool, fresher layer beneath a warmer, more saline region. This leads to growing double-diffusive cells that advance outward at a rate, found by dimensional reasoning to be proportional to Nh, where N is the stability frequency in the cell and h is its vertical thickness. Near the wall at the top of each cell, the sinking colder fluid is continually replaced by selective withdrawal from the ambient 'far field'. The fluid being withdrawn from the ambient is always the least dense in the cell, and as the experiment proceeds, the straining of the fluid in the ambient region reduces the stratification. The vertical density gradient inside the cell relaxes by continuous hydrostatic adjustment (CHA) to match the ambient and the speed of advance reduces proportionately. Measurements of the rate of advance of the cell nose were made in tanks of different lengths L with a range of initial salinity gradients and cell heights h. A simple model is developed to describe the rate of extension of the cells and the internal density gradient as functions of time in which the tank length appears as an important parameter throughout each experiment. This effect does not seem to have been recognized previously. The rates of evolution in each run involve the time scale $\tau = L(C_H h N_0)$, where L is the tank length, $C_H \approx 10^{-2}$ is a heat transfer coefficient, and N_0 the initial stability frequency. The mean length of the cells $\bar{l}(t)$ and the internal stability frequency are given by

$$\frac{\bar{l}(t)}{L} = \frac{t}{\tau} - \left(\frac{t}{2\tau}\right)^2 \qquad \text{and} \qquad N = N_0(1 - t/2\tau)$$

Inversion of the first of these expresses $1 - \left\{1 - (\bar{l}/L)\right\}^{1/2}$ as a linear function of time with slope $(2\tau)^{-1}$. The measurements from individual runs when plotted in this way, do produce remarkably accurate straight lines as the model predicts, from which C_H is found. This should be approximately the same for each run; the mean over all runs was found to be 9.29×10^{-3} with standard deviation 1.77×10^{-3}.



A summary plot of the experiments, showing $l(t)/L$ vs t/τ , incorporating results from tanks of three different lengths: + L = 48.2 cm; o L = 116.5 cm, and x L = 147 cm. The last set of points, difficult to see, is clustered close to the origin.

FLOW AND DISPERSION IN THE ATMOSPHERIC BOUNDARY LAYER INVESTIGATION BY PHYSICAL MODELLING

Zbynek Janour*, Klara Bezpalcova*, Zdenek Zelinger**
*Institute of Thermomechanics AS CR
**J. Heyrovsky Institute of Physical Chemistry, AS CR

Summary The method of physical modelling has been adopted, a new environmental wind tunnel was designed and some methods of measurement have been developed at the Institute of Thermomechanics AS CR. The following examples of results are demonstrated: air pollution due to traffic inside a street-canyon, plum of smoke spreading over complex terrain, the surface mean concentrations of lead from point source assessment.

PHYSICAL MODELLING

Air pollution is enacted on various geographical and temporal scales, running from strictly "here and now" problems to global phenomena, which over the next centuries can change the conditions for man and nature entire globe. Study of the dispersion of pollutants in the atmosphere forms a basis for implementation of effective methods to prevent environmental damage. The main source of information for solving of environmental and wind engineering problems is mathematical modelling and a laboratory simulation of the Atmospheric Boundary Layer (ABL) in specialised wind tunnel so called physical modelling. The principle of physical modelling consists in analogy between a boundary layer formed over the floor of a wind-tunnel working section and the Atmospheric Boundary Layer. Following general requirements for similarity of the boundary layer with the Atmospheric Boundary Layer (ABL) have to be fulfilled in order to transfer results from small-scale wind tunnel experiment (model) to full scale (prototype):

- undistorted scaling of geometry,
- equal Reynolds number Re,
- equal Prandtl number Pr,
- equal Richardson number Ri,
- equal Eckert number Ec,
- surface-boundary-conditions similarity,
- similarity of the approach-flow characteristics

EXPERIMENTAL TECHNIQUE

However, the requirements cannot be satisfied simultaneously in existing facilities and a partial or approximate simulation for particular application has been worked out. These methods have been adopted and a new environmental wind tunnel was designed at the Institute of Thermomechanics Academy of Science Czech Republic. The tunnel is designed as an open-circuit facility that is operated as a fan driven one. It has the cross section 1.5 m x 1. 5 m and the length to the working section 25.5 m. The long test section achieve sufficiently thick boundary layer on the wall of the working section (cca 0.3 m) with the necessary dependent variables profiles. The tunnel inlet is formed by elliptic elements inside of a suction tower with 64 m^2 screens and of size 6 m x 6 m x 12 m preventing external disturbances. It follows a corner with 17 vanes with the gap between thin sheet metal vanes h = 0.1248 m and the chord c = 0.312 m. An aluminium honeycomb made for aircraft sandwich and 6 screens with screen open area ratio ß = 0.57 and 0.79 placed behind the corner guarantee that the wind tunnel meet all demands of a first class aerodynamics facility. The working section of the length 2-m with glass sidewalls follows a section of lights and the two corners. A 30 kW centrifugal blower drives the tunnel at the exit. The velocity at the working section is within interval (0,1, 13) ms^{-1} and depends upon number of revolutions per second.

To solve and investigate all necessary flow and dispersion characteristics in aerodynamic wind tunnel, it was necessary to develop and to adapt some new methods of measurement. First of all, there was demand for flow visualisation and for application of such a method for rough introduction and approximation. We were using during that time common system consisting from fog generator, laser light sheet, digital camera/video camera and Pentium based computer for processing. An example of the plume spread visualisation is demonstrated on fig. 1 The turbulence characteristics of the flow field were measured by a 2D fibre-optic Laser Doppler Anemometer (DANTEC) with 500 mm focal distance of the Meteorological Institute Hamburg. The slow Flame-Ionisation-Detector (Rosemount Analytical NGA 2000-TFID) and $C0_2$ laser photoacoustic spectrometry are used for mean concentrations measurements.

RESULTS

A few examples of acquired applications is demonstrated:

- Flow and dispersion on the street scale was investigated in the framework of COST 715 project. The street scale is important for urban air pollution problems because of most urban emissions occur within the canopy layer, where buildings heavily disturb the atmospheric flow. Therefore two main types of tasks have been investigated: simplified, generalized situations of the street canyon and direct solution of geometric complex situations. The methods of the urban type inflow simulation, small-scale flow simulation and dispersion simulation including a modelling with a line source model were developed in both cases in the scale 1:200. An appropriate configuration of roughness elements and spires made the approaching boundary layer flow, which corresponds with the neutrally stratified urban atmospheric boundary layer. The models of a street canyon with one line permeation pollution source developed in this work as an example of the first type of the street scale problem and model of "Podbielski Strasse in Hannover" with two parallel lines sources, an example of the second type, were manufactured. The similarity criteria have been proved at first. It means that our experimental results can be transferred to full scale. The concentration field of passive contaminant was measured inside the model street canyon and inside of "Podbielski Strasse" and dimensionless field of concentrations across the streets were assessed. Comparison demonstrates differences it the concentration fields, e. g. the leeward side of the "Podbielski Strasse" is heavily polluted, etc. The assessed concentration field demonstrates that the living conditions inside the street are out of the proposed EC directives.
- Processes in the ABL over Orlice River basin were investigated using a geometric scale of 1:1000 and Reynolds number independence method was used. Influence of effective high of the stack has been investigated by visualization technique and surface mean concentration from two point sources inside the urban area has been assessed.
- The surface mean concentrations of lead from KOVOHUTE work, the Czech Republic in complex terrain was assessed. The aim of the search was to assess the KOVOHUTE work contribution to air pollution in the region and its development. The heavy polluted area with diameter of 4.5 km was traced and a model of a landscape on scale 1:6000 including the stack model was manufactured and mounted on a turntable into special aerodynamic wind tunnel of the Institute of Thermomechanics. Approximate similarity of flow in which a laminar flow structure is dominated by the surface geometry had been applied for simulation. Qualitative analysis of the plume spread by visualization method demonstrated that the plume direction is not influenced by the morphology. Then the years mean concentrations have been assessed for different emission situations and the surface concentration fields are compared to demonstrate air pollution progress.

CONCLUSION

Processes in the Atmospheric Boundary Layer are complicated by the combined influences of the Earth's rotation, buoyancy forces, surface drag forces, the geometry of topographic features etc. It is extremely difficult to solve this synergetic problem analytically and experiments in situ are expensive and give only particular results. The method of physical modelling becomes a powerful tool in the ABL search. Its application has been demonstrated for some cases investigated in the Institute of Thermomechanics AS CR.



Fig. 1. Plume spread visualization – side view

EXPERIMENTS ON UP-SLOPE TO DOWN-SLOPE TRANSITION IN AN INCLINED BOX FILLED WITH WATER

K. Dekajło[*], T.A. Kowalewski[*], H.J.S. Fernando[**]
[*]*IPPT PAN, Department of Mechanics & Physics of Fluids, PL 00-049 Warszawa, Poland*
[**]*EFDP, Department of Mechanics & Aerospace Eng., Arizona State University, AZ 85287, USA*

Summary The natural convection of water in inclined side-heated rectangular box is investigated experimentally and numerically. The aim is to demonstrate existence and features of the convective front formation typical for the evening transition of the atmospheric boundary layer on gentle slopes. Particle image velocimetry and thermometry allows for quantitative analysis of the temporary velocity and temperature fields generated in a small scale laboratory model. The laboratory experiment is compared with numerical simulations performed with Fluent. Observations confirmed predictions of the evening transition front described for the atmospheric flows by Hunt et al [1].

INTRODUCTION

Thermal circulation in a complex terrain is not yet fully understood and implemented in large scale atmospheric models. Theoretical models [1] and field observations [2] indicate presence of specific for the slope flow instabilities, like bellowing, "peeling off" and formation of stagnation fronts. These phenomena play an important role in a heat balance and mixing properties of the atmosphere in several urban regions, but they are underestimated or completely neglected in mesoscale weather prediction models. One of the least understood phenomenon is the flow transition in the evening. During the day, the flow is up-slope (known as the anabatic flow) and at night the flow occurs down the slope, (known as the katabatic flow). The transition from up-slope flow to down-slope flow occurs from half an hour to a few hours after the cooling of the ground begins. Recently Hunt et al. [1] developed an analytical model for the evening transition. It assumes that a fluid parcel starting at the bottom break of a slope, which is initially heated and supporting an up-slope flow, is subjected to a gradual cooling of the bottom in linear fashion. As the fluid parcels travel up-slope, they become regularly buoyant and finally stop. The stagnation surface of the fluid parcels take the form of a front which subsequently breaks down by heavy fluid parcels which lay above lighter particles behind the front. This new phenomena has amplifications in air pollution dispersion as the fronts can rapidly mix pollutants vertically and dilute them. Further, on bare lands, such fronts can enliven the dust, thus increasing particulate matter concentrations to unhealthy levels. The possibility of such formation was demonstrated in the laboratory by Hunt et al. [1], but they did not present information on how the temperature of fluid parcels vary along the slope and in direction normal to the slope. This gap is filled in the present study, where temperature and velocity are simultaneously measured using thermochromic liquid crystals tracers [3].

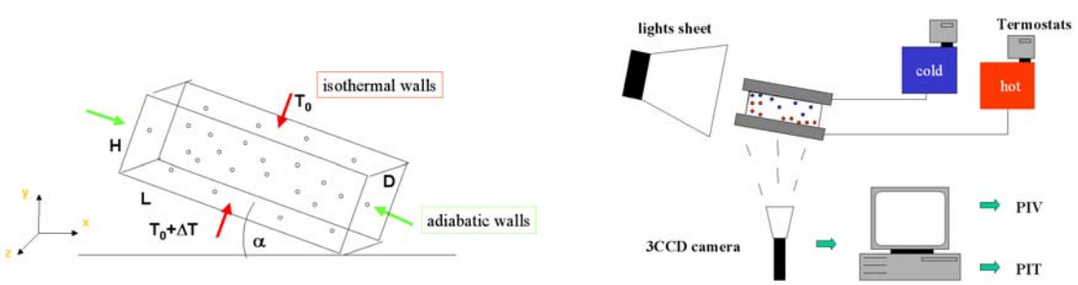


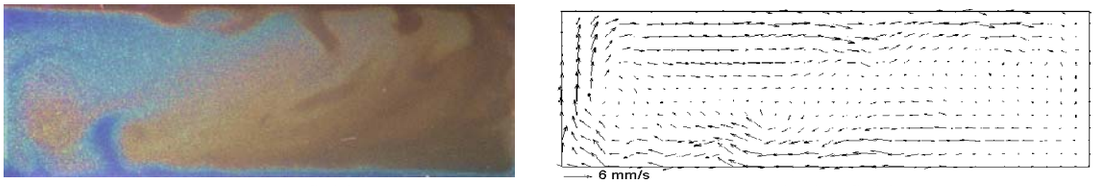
Figure 1. Schematic of the experimental apparatus: (a) – cavity, (b) – basic elements of the experimental rig

We consider natural convection in a rectangular, inclined box filled with water. The cavity has square cross-section 38 mm x 38 mm and is 114 mm high. The two side-walls are made from 7.5 mm thick Plexiglas. The other two isothermal side-walls are made of copper. The temperature of the isothermal walls is kept at 299K and 305K (ΔT=6K) by two heavy duty thermostats. To simulate up-slope flow a negative temperature gradient is set between the lower and upper wall (Fig. 1a). For transition and down-slope flow study the temperature of the walls is reversed by switching coolants settings. In the experiment it takes about 3min to equalize temperature of both walls and the next 3 min to stabilize the reverse temperature setting on the walls. The cavity inclination angle α is varied from 10^o - 30^o (Fig. 1a). The acquisition system (Fig. 1b) consists of a 3CCD colour camera and the 32-bit frame grabber (IC-PCI ITI). The flow field is illuminated with a 2 mm thin sheet of white light from a specially constructed halogen lamp, and observed in the perpendicular direction. Thermochromic Liquid Crystal (TLC) tracers changing colour of refracted light with temperature are employed to measure both temperature and velocity flow fields. The temperature measurements are based on a digital colour analysis of the flow images. The 2D velocity vector distribution is measured by digital particle image velocimetry (DPIV). By this method, the motion of the scattering particles, observed in the plane of the illuminating light sheet, is analysed by cross-correlating pairs of succeeding images. To get a general view of the flow

pattern, several images recorded periodically within a given time interval have been added in the computer memory. Displayed images are similar to the multi-exposed photographs, showing the flow direction and its structure.

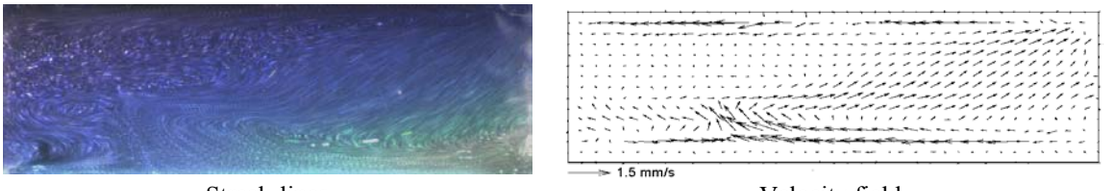
RESULTS

Experiments preformed for higher inclination of the box and larger temperature differences show onset of flow instabilities with periodically rising plums and hot fluid ejections, analogous to that observed for diurnal circulation on long sloping surfaces. Figure 2 shows visualization of the instantaneous temperature and velocity field acquired during ejection of the hot plum (blue colour) at the lower wall. These periodical ejections could be well identified in the experimentally measured velocity fields (Fig.2b) and reproduced in the numerical simulation. By increasing the temperature difference or inclination of the box this instability quickly gave rise to intense bulk flow mixing and equalisation of temperature in the core region. To avoid these effects our study of transition effects is limited to a low Rayleigh number, laminar up-slope flow. It was achieved by limiting the temperature difference to 6K and setting the inclination angle $\alpha = 10^o$. The corresponding Rayleigh number, based on the maximum height of the inclined cavity, is $8 \cdot 10^6$, just below the thermal stability limit. Figure 3 shows appearance of the transition front observed both in temperature field (colour of the tracers) as in the velocity field. The front builds up about 1 min after the reversal of temperature of the walls (4 min after reversal of the thermostats setting) at the distance of 2 cm from the lower edge of the slope, and it disappears about 5 min later, when regular "nocturnal" stratification of temperature and flow pattern develops. Hunt et al. [1] proposed time and length scaling of the front appearance, based on the parcels buoyancy, slope length and mean flow velocity. Using their scale we arrive to approximately 60s for the time scale and 1cm for the length scale. It appears that despite of the absence of turbulent mixing and presence of the flow disturbances created by the confined geometry, this scaling works yet pretty well for the laboratory experiment.



Temperature field Velocity field

Figure 2. Snap-shots of the temperature and velocity fields observed for the up-slope convection in the cavity; $\alpha = 20^o$, ΔT=6K.



Streak-lines Velocity field

Figure 3. Transition front observed 1min after temperature reversal; $\alpha = 10^o$, ΔT=6K.

Numerical simulations of the investigated experimental configurations were performed using finite-volume commercial code Fluent. Spatial derivatives were approximated using QUICK scheme and pressure-velocity coupling was done using SIMPLE algorithm. Solutions were obtained by direct simulation of the flow for two-dimensional, regular mesh with 480000 elements. The main futures of the experimental data like flow structure, temperature distribution, and velocity field appeared to be well reproduced in the numerical results. These initial validation of the numerical model opens possibility to use it for more profound parametric study of the occurrence of the transition front and its dependence on the geometry and temperature, in much wider variation of parameters than it is realizable in the experiment. Specifically numerical scaling of the problem to the environmental configurations will help us to find similarities useful for future building of the parameterisation necessary for weather prediction models.

References

[1] Hunt J. C. R., Fernando H.J.S., M. Princevac, Unsteady Thermally Driven Flows on Gentle Slopes, *J. Atmospheric Sci.* **60**, 2169-2182, 2003

[2] Monti P., Fernando H.J., Princevac M., Kowalewski T.A., Chan W.C., Padyjak E.R., Observations of flow and turbulence in the nocturnal boundary layer, *J. Atmospheric Sci.* **59**, 2513-2534, 2002

[3] T.A. Kowalewski, Application of liquid crystals for full field temperature and velocity measurements, *Proc. of the Inter. Symp. on Envirom. Hydr.*, ASU Tempe 2001, CD-ROM, p.154.1-6, 2001

ANALYSIS OF DOUBLE-FREE SURFACE FLOW THROUGH GATES USING ELEMENT-FREE GALERKIN METHOD

Farhang Daneshmand[*], Mohammad Javad Kazemzadeh-Parsi [**]
[*]*Assistant Professor, Mechanical Engineering Department, Shiraz University, Shiraz 71345, Iran*
[**]*Graduate Student, Mechanical Engineering Department, Shiraz University, Shiraz 71345, Iran*

Summary The goal of the present work is to develop a suitable and accurate numerical procedure based on moving least square method and element-free Galerkin method for the computation of free surface profiles, velocity and pressure distributions and flow rate in a two-dimensional gravity fluid flow through a radial gate. The results of the calculations are compared with those obtained from a hydraulic model test.

PROBLEM STATEMENT AND SOLUTION STRATEGY

In the analysis of free surface flows under gates, computational difficulties arise not only from the non-linear nature of the boundary conditions but also from the fact that the boundary is not known a priori. There are additional difficulties when the problem involves two highly curved unknown free surfaces and arbitrary curved shape boundaries. Fig. 1 shows a typical two-dimensional steady flow from a reservoir through a radial gate as considered in [1]. Geometry of the conduit walls S_2 and S_7 are given and the far upstream and downstream boundaries of the flow domain, denoted by S_1 and S_4, are assumed to be normal to the flow direction. The free surface profiles S_3 and S_5 are not known a priori. In the present study, the flow rate Q is assumed to be unknown and the stagnation level is given as H_E, which is the stagnant fluid level above point A. Flow is assumed to be two-dimensional, steady, incompressible, non-viscous and irrotational in which the stream function ψ must obey the Laplace equation

$$\psi_{,xx} + \psi_{,yy} = 0 \tag{1}$$

On the free surfaces S_5, S_3, two simultaneous conditions should be satisfied; (i) the pressure on the surface must be constant. Using the Bernouli's equation, this condition can be written as

$$\frac{q^2}{2g} + y = H_E \quad \text{or} \quad \frac{\partial \psi}{\partial n} = \sqrt{2g(H_E - y)} \qquad \text{on } S_5,\ S_3 \tag{2}$$

where q is the flow velocity on the free surface, g is the gravity acceleration, y is the free surface elevation, (ii) the velocity normal to the free surface must be zero. This condition can be satisfied through the following procedure based on the algorithm which proposed by Cheng [2] for problems with only one unknown free surface:
(i) Two initial trial free surfaces should be assumed in accordance with the initial trial value of discharge Q^0. (ii) The problem is solved for the resulted fixed domain. (iii) The next trial discharge $Q^{(1)}$, can be evaluated from $Q^{k+1} = Q^k + \alpha\left(Q^k - \overline{\psi}^k_{Surf}\right)$ where $\overline{\psi}^k_{Surf}$ is the average of stream function values on the free surface and α is a constant factor (iv) The following equation is used to adjust the location of the lower free surface profile while the upper free surface is taken to be fixed in the first iteration.

$$\Delta y_i = y_i^{k+1} - y_i^k = -\frac{\psi_i^k}{g\left(y_i^k\right)^2}\left[\left(Q^{k+1} - \psi_i^k\right)\Big/\left(1 - \left(\psi_i^k\right)^2 / g\left(y_i^k\right)^3\right)\right] \tag{3}$$

(v) The problem is solved again while the new position of the lower free surface is fixed and the upper free surface is allowed to vary. (vi)This iteration process is continued until $\left|Q^{(r+1)} - Q^{(r)}\right| \le \varepsilon$, where $Q^{(r)}$ and $Q^{(r+1)}$ are the discharge values at iteration r and r+1, respectively, and ε is the prescribed accuracy. On the other boundaries, these conditions should be applied, $\psi_{,n}(S_1) = \psi_{,n}(S_4) = \psi(S_2) = 0$, $\psi(S_6) = \psi(S_7) = Q$, where *n* denotes the outward normal direction.

Element-Free Galerkin Method (EFG)
The element-free Galerkin method (EFG) as proposed in [3] is used in the present study to obtain the following relations for the solution of Laplace equation (Eq. 1):

$$\psi^h(\mathbf{x}) = \sum_{i=1}^{n} \phi_i(\mathbf{x})\hat{\psi}_i \qquad \phi_i(\mathbf{x}) = \sum_{j=1}^{m} P_j(\mathbf{x})\left[\mathbf{A}^{-1}(\mathbf{x})\mathbf{B}(\mathbf{x})\right]_{ji} \tag{4}$$

$$\mathbf{A}(\mathbf{x}) = \sum_{i=1}^{n} w_i(\mathbf{x})\mathbf{P}(\mathbf{x}_i)\mathbf{P}^T(\mathbf{x}_i) \qquad \mathbf{B}(\mathbf{x}) = \left[w_1(\mathbf{x})\mathbf{P}(\mathbf{x}_1), w_2(\mathbf{x})\mathbf{P}(\mathbf{x}_2), ..., w_n(\mathbf{x})\mathbf{P}(\mathbf{x}_n)\right] \tag{5}$$

where $\mathbf{p}^T(\mathbf{x}) = \left[p_1(\mathbf{x}), p_2(\mathbf{x}), \ldots . p_m(\mathbf{x})\right]$ contains *m* basis function , $w_i(\mathbf{x})$ is the weight function associated with the node *i* and evaluated at point x. In this paper the cubic spline weight function is used,

$$W = \begin{cases} (2 - 12s^2 + 12s^3)/3 & s \le 1/2 \\ (4 - 12s + 12s^2 - 4s^3)/3 & 1/2 \le s \le 1 \\ 0 & s > 1 \end{cases} \tag{6}$$

in which $s=r/R_m$ is a normalized radius and R_m is the support size. Finally,

$$(\mathbf{K}-\mathbf{G})\Psi=\mathbf{q} \tag{7}$$

$$K_{ij}=\int_{\Omega}\left(\phi_{i,x}\,\phi_{j,x}+\phi_{i,y}\,\phi_{j,y}\right)d\Omega\ ,\ G_{ij}=\int_{\Gamma_u}\phi_i\left(\phi_{j,x}n_x+\phi_{j,y}n_y\right)d\Gamma\ ,\ q_i=\int_{\Gamma_q}\phi_i\,\bar{q}\,d\Gamma \tag{8}$$

where $\phi_i(\mathbf{x})$ is the shape function of i^{th} node at point $\mathbf{x}$, and Γ_u and Γ_q are parts of boundary with essential and natural boundary conditions, respectively. As it is seen from the above equations, the essential boundary condition is applied using the method proposed in [4] through the matrix G_{ij}.

RESULTS

The geometric details of the radial gate in are given in Fig. 1 (H_o=3.48 m, gate opening = 30%). To ensure the validity of the results obtained for this example, a hydraulic model test based on Froude law of similarity is also constructed [5]. The pressure distribution in the liner is shown in Fig. 2 and is compared with those obtained from the experiment. Fig. 3 shows the pressure distribution on the radial gate obtained from the numerical and experimental analyses. The shapes of upper and lower free surfaces are plotted in Fig. 4. The computed discharge is 0.470 m^3/s.m that is in good agreement with the experimental result, 0.485 m^3/s.m.

CONCLUSION

This paper demonstrates that the element-free Galerkin method can be successfully used in the free surface flow through the radial gates. It is found that the present procedure can easily handle the problems involving curved shape solid boundaries and is also quite efficient in locating two free surface profiles. It converges rapidly and the results obtained are in good agreement with the experiment.

ACKNOWLEDGMENT

The assistance of Sadid-Tadbir Co. is gratefully acknowledged.

References

[1] F. Daneshmand, S. K. Sharan and M. H. Kadivar: Finite Element Analysis of Double-Free-Surface Flow through Slit in Dam. Journal of Engineering Mechanics, ASCE, Vol. 126, No. 5, 515-523, 2000.

[2] A. H-D. Cheng, J. A. Liggett and P. L-F. Liu: Boundary calculations of Sluice and spillway flows. Journal of Hydraulic Engineering, ASCE 107, HY 10, 1163-1178, 1981.

[3] T. Belytschko, Y. Krongauz, D. Organ, M. Flemming and P. Krysl: Meshless Methods: An Overview and Recent Developments. Computer Methods in Applied Mechanics and Engineering, 139, 3-47, 1996.

[4] F. Daneshamand and M. J. Kazemzadeh Parsi: A Meshless Method for Free Surface Flow Through Sluice Gates. 6th International Conference on Hydro-informatics, Singapore, June 2004 (Submitted).

[5] Hydraulic model test of the Orifice Spillway for Karun III Dam, Report No. KRM-R-002, Sadid-Tadbir Co., Tehran, Iran, 1997.

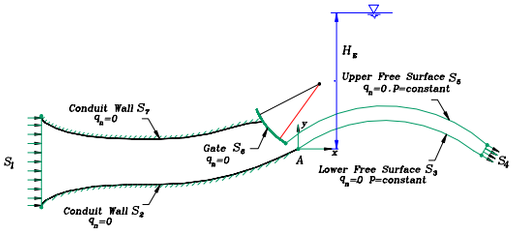


Fig. 1 Flow under the radial gate

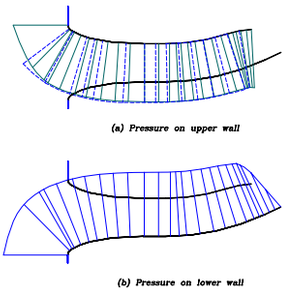


Fig. 2 Pressure in the liner

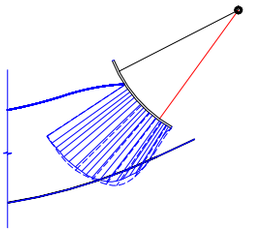


Fig. 3 Pressure on the radial gate

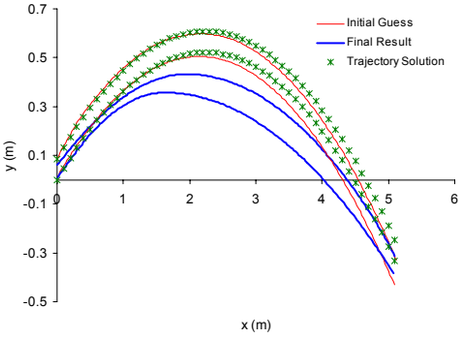


Fig. 4 Free surface Profiles

FREE SURFACE BEHAVIOR IN TURBULENT OPEN-CHANNEL FLOWS

Hitoshi Miyamoto*, Kenji Shimoyama**
*Dept. Architecture and Civil Eng., Kobe University, Rokkodai 1-1, Nada, Kobe 657-8501, Japan
**NEWJEC Co., Ltd., Shima-no-uchi 1-20-19, Chuo, Osaka 542-0082, Japan

Summary Laboratory experiments were conducted to investigate characteristics of the free surface behavior and its influences on turbulence structures in an open-channel shear flow. The results show that the streamwise spectrum of water surface fluctuations follows the –10/3 power low, and that the surface influence layer is approximately less than 20 percent of the mean water depth and its thickness becomes large as the wavelength of the surface fluctuation increases but small as the Froude number increases.

INTRODUCTION

Understanding the roles of turbulent flows around water surfaces is of increasing importance from the perspective of environmental fluid mechanics because turbulence structures near the surfaces may considerably influence free surface phenomena, such as gas transports, momentum exchanges, self-aeration etc., which are essential to aquatic ecosystems. In this study, laboratory experiments were conducted to investigate characteristics of the free surface behavior and its influences on turbulence structures in an open-channel shear flow. A simultaneous image measurement method was used to measure instantaneous velocity vectors and the corresponding water surface profile in a vertical cross section of the open-channel flow. The proper orthogonal decomposition (POD) was applied to the measurement data of the water surface fluctuations to extract their predominant fluctuation patterns. Then, interactions between the predominant water surface fluctuations and the turbulence structures were examined by calculating their space correlations. Based on the knowledge obtained above, the streamwise spectrum of the water surface fluctuations and the influence range of the free surface were discussed.

EXPERIMENTS

Figure 1 shows instantaneous velocity vectors and the corresponding water surface profile measured by the simultaneous image measurement method proposed by Miyamoto and Kanda [1]. In the measurement method, we utilized images, in the same flame of which both the flow field and the water surface profile were visualized by a laser light sheet, an image extracting technique to detect the location of the water surface, and particle image velocimetry (PIV) to measure the velocity vectors. As for the hydraulic conditions, we kept a Reynolds number Re_* based on the friction velocity a constant (= 500), whereas we changed a Froude number Fr based on the mean bulk velocity and the mean water depth from 0.53 to 1.23 (subcritical to supercritical). In this study, since we can obtain both the velocity vectors and the water surface profile, we investigate the 'free surface – turbulence structures' interactions from the viewpoint of the turbulence from the water surface toward the inside fluid.

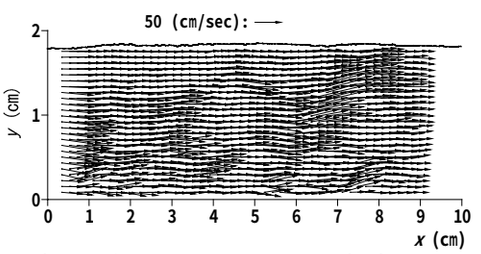


Figure 1 Instantaneous velocity vectors with the corresponding water surface profile (Re_* = 505, Fr = 1.23).

RESULTS AND DISCUSSION

Space correlation structures of predominant water surface fluctuations with turbulence

The POD is applied to the measurement data of the water surface fluctuations to extract their predominant fluctuation patterns. The result of the POD analysis shown in Fig. 2 successfully reveals that most of the principal components are sinusoidal wave shapes. Therefore, the fluctuation distribution of the water surface is almost completely represented by the superposition of the sinusoidal waves. By using the modal amplitudes of the POD eigenvectors, then, we calculate space correlation coefficients between the amplitudes and the velocity fluctuations. Figure 3 shows the contour map of the space correlation coefficients, representing the typical distribution pattern. The result clearly shows that there exists a thin surface influence layer near the water surface in which the turbulent flow seems to be parallel to the wavy surface due to the kinematic

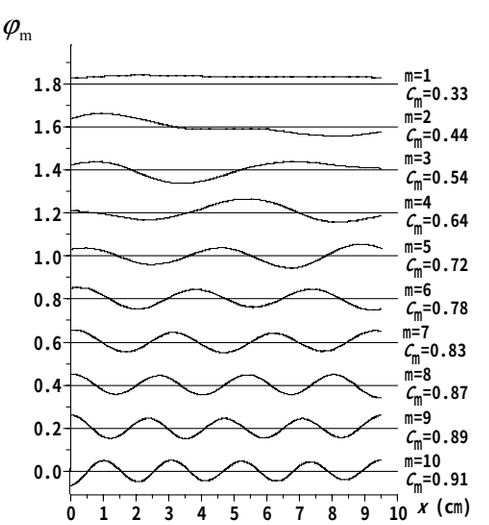


Figure 2 POD eigenvectors of the water surface fluctuations. The vertical axis is modified in 0.2 between two successive modes, m and m+1. Re_* = 505, Fr = 1.23.

boundary condition at the surface, and also that there is the specific interaction between the water surface fluctuations and the large-scale turbulence structures having the same longitudinal scale. The surface influence layer experimentally obtained here is supposed to be almost the same as the blockage layer numerically obtained by Shen et al. [2].

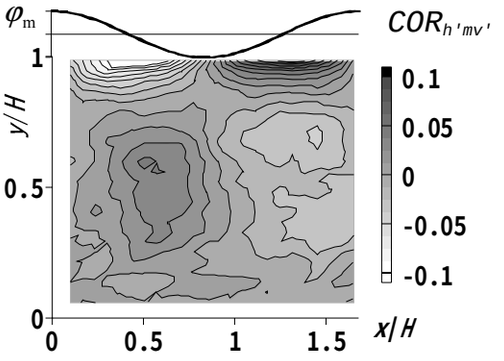


Figure 3 Spatial correlation coefficients of the surface fluctuation component of the eigenvector and the vertical component of the velocity fluctuations. The profile of the corresponding eigenvector is indicated above the contour map. POD mode m = 7, Re_* = 505, Fr = 1.23.

Streamwise spectrum of water surface fluctuations

The POD analysis in the previous subsection is equivalent to the spectrum analysis since most of the eigenvectors are sinusoidal waves with wavelength L_m. Therefore, the POD contribution ratio c_m corresponds to the value of the spectrum at wave number $k_m = 2\pi/L_m$. From the result in Fig. 3, on the other hand, it is revealed that there is a specific interaction between the surface fluctuation h'_m and the large-scale turbulence structure with the same scale L_m. Thus, if we assume a physical mechanism on which the pressure fluctuation p'_{Lm} due to the large scale turbulence u'_{Lm} with L_m makes the surface fluctuation h'_m with the same scale L_m, we can conjecture that in the Fourier space the $\rho\, u'^2_{Lm} \sim p'_{Lm} \sim \rho g h'_m$ have the same slope in the spectral distributions. Consequently, when the spectrum of u'_{Lm} follows the well known –5/3 power low, the streamwise spectrum of h', which is equivalent to c_m in this study, follows the –10/3 power low. Figure 4 shows the streamwise spectrum of h' obtained through the above consideration. It is evident that there exists a range which follows the –10/3 power low in each case and that the range of the –10/3 power low becomes large as the Froude number Fr increases.

Influence range of water surface

From the distribution of the space correlation coefficients in Fig. 3, we evaluate the range of the surface influence layer by defining a vertical scale measure of the layer δ_m. The result shown in Fig. 5 indicates that the surface influence layer is approximately less than 20 percent of the mean water depth H and its thickness δ_m became large as the wavelength of the surface fluctuation L_m increases but small as the Froude number Fr increases.

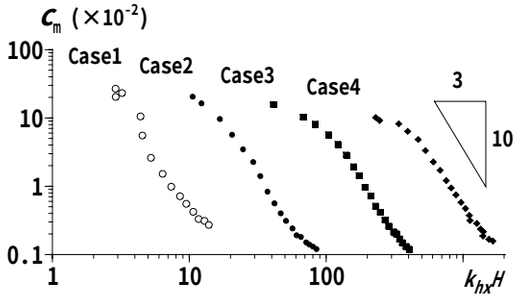


Figure 4 Streamwise spectrum of the water surface fluctuation. The values in horizontal axis are modified by multiplying 5, 5^2, 5^3 in Case2, 3, 4, respectively. Fr = 0.54, 0.64, 0.85, 1.23 in Case1,2,3,4, respectively.

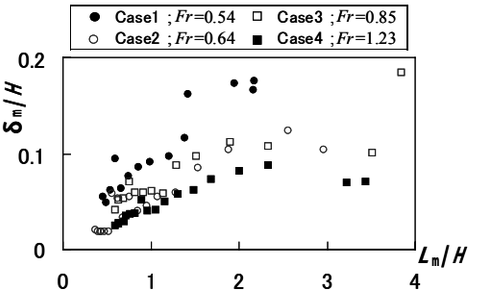


Figure 5 Relationship between the thickness of the surface influence layer and the wavelength of the surface fluctuation. Re_* = 505, Fr = 0.54 – 1.23.

CONCLUSIONS

The main conclusions obtained in this study are as follows. (1) There is a layer near the water surface where the turbulence is strongly affected by the water surface fluctuations. In the surface influence layer, the turbulent flow seems to become parallel to the wavy surface. (2) There is a specific interaction between the surface fluctuation and the large-scale turbulence structure having the same streamwise scale. (3) The streamwise spectrum of water surface fluctuations follows the –10/3 power low. (4) The surface influence layer is approximately less than 20 percent of the mean water depth and its thickness became large as the wavelength of the surface fluctuation increases but small as the Froude number increases.

References

[1] Miyamoto, H. and Kanda, T.: Simultaneous image measurements of velocity field and water-surface wave in open-channel flows, *Proc. Hydraulic Measurement & Experimental Methods Conference 2002*, ASCE, Colorado, 2002.
[2] Shen, L., et al.: The surface layer for free-surface turbulent flow, *J. Fluid Mech.* **386**:167-212, 1999.

INTEGRAL AND LABORATORY MODELLING OF SEDIMENTATION FROM TURBULENT BUOYANT JETS

Gregory F. Lane-Serff
Manchester Centre for Civil and Construction Engineering, UMIST, PO Box 88, Manchester M60 1QD, UK

Summary An integral model has been developed for turbulent, buoyant, particle-carrying jets injected at an angle to the vertical. The model allows particles to leave the jet where their fall-speed is greater than the entrainment speed of ambient fluid into the jet. The remaining particles drop-out once the jet reaches the free surface and spreads as a radial gravity current. The model is compared to laboratory experiments and shows excellent agreement.

INTRODUCTION

Marine outfalls and engine exhausts are examples of buoyant jets (or "forced plumes") injected at some angle to the vertical that may carry particles which subsequently drop out of the flow. The purpose of this work is to model such flows and describe the distribution of the sedimenting particles. In general, the particles can themselves affect the buoyancy but here we consider dilute suspensions, where the particle load has a negligible effect on the jet density. Initially we consider flow into a stationary, uniform ambient fluid, though the effects of ambient flow and stratification can be included later.

MODELLING

Jet model

Figure 1 shows a turbulent buoyant jet (in this case dyed, but with no particles). While the flow is unsteady and turbulent, it is common to work in steady mean flow properties using an integral model. Here we use "top-hat" profiles to describe the properties of the jet, and the basic angled plume model is as described in Lane-Serff et al. (1993)[1]. The local mean jet speed is denoted by U and the radius by R. These are dimensional values - it is usual to non-dimensionalise the equations using the source momentum and buoyancy fluxes.

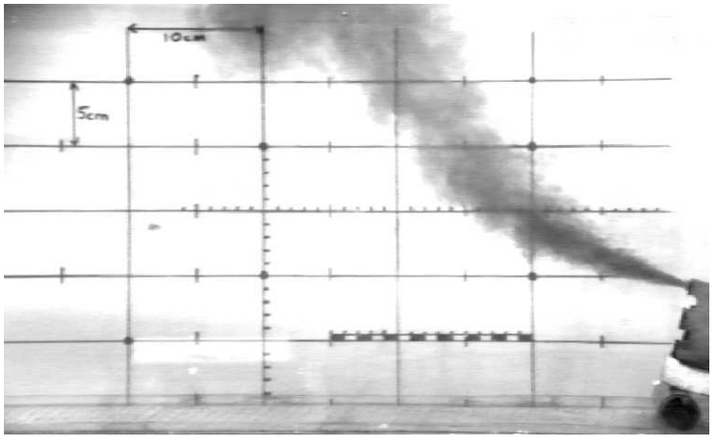


Figure 1. Angled turbulent buoyant jet (no particles), with the source angled slightly above the horizontal. The jet is dyed and the scale of the laboratory experiments is clearly marked. The free surface is just above the top of the picture and some of the spreading surface current can just be seen (especially towards the left).

The particles are assumed to have a single fixed (dimensional) fall speed W_S, and fall out of the jet where the component of fall speed normal to the jet boundary is greater than the entrainment speed of ambient fluid drawn into the jet αU. The model shows that an important parameter is the ratio of the fall speed to a typical entrainment velocity: $w_S = W_S/V_J$. As the jet turns towards the vertical and becomes a buoyant plume the sedimentation ceases. The proportion of sediment dropped in the near-source regions depends only on w_S (which can be regarded as a non-dimensional fall-speed) and the angle of the source. The results for a horizontal source are given in Figure 2a.

Spreading current model

When the buoyant fluid reaches the surface it spreads as a radial gravity current. We can estimate the particle-dropping from this part of flow using the model of Sparks et al. (1991)[2]. However, for our experiments we found that the scale for the predicted Gaussian distribution (R_G, say) is often comparable with or smaller than the radius of the plume at the surface, R_P. Thus we instead use a broader spread for our predictions by simply adding the initial gravity current spread estimate to the radius of the plume at the surface, i.e. $R_S = R_G + R_P$, and using a Gaussian distribution with this larger length-scale.

LABORATORY EXPERIMENTS

Experiments were conducted by injecting fresh water into tanks of salt water, using a simple gravity feed. Fine sand (of various measured size ranges) was mixed into the source water and kept in suspension by stirring. The fall velocity of the sand was determined empirically using tall cylinders of water and timing the falling particles (using video equipment for accuracy). The base of the tank was marked with a grid to determine the distance from the source. Once an experiment was finished, the sand was scraped into piles and collected using a syringe. This was filtered, rinsed with fresh water (to remove the salt), dried and weighed.

RESULTS

From the model, the total deposition is found by summing the near source deposition and the Gaussian distribution from the surface gravity current (Figure 2b-d). The near-source depositon is typically within a jet-length of the source (i.e. non-dimensional distance x = 1 on the figures), while for our experiments the jet reached the surface at approximately x = 2 (different for each experiment depending on the water depth and other parameters).

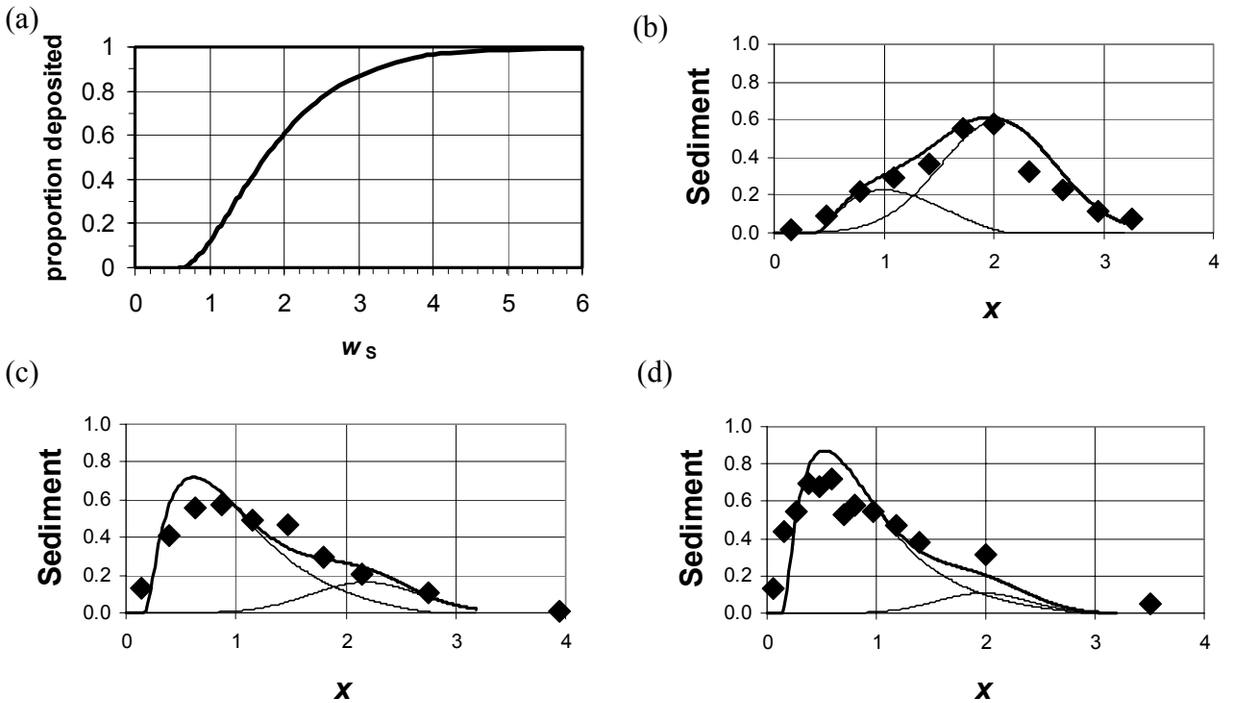


Figure 2 (a) Proportion of sediment dropping out in the near-source region as a function of the non-dimensional fall speed w_S for a horizontal source. (b-d) Theoretical predictions (for horizontal sources) for the sediment dropping out near the source and once the jet has reached the surface (thin lines for the two components, thick line for the sum) with symbols for the experimental measurements, with w_S = (b) 1.21, (c) 2.62 and (d) 3.13.

CONCLUSIONS

As can be seen from the figures, there is remarkably good agreement between the theoretical predictions and the laboratory results. By writing the parameter w_S in terms of the source conditions $w_S = W_S/\sqrt{(\alpha g'_0 D)}$, we find the powerful result that the proportion of sediment deposited in the near-source region is independent of the source flow rate (provided it is large enough that $Fr_0 > 1$).

Further ongoing work (with collaborators in UMIST and Dundee) includes adding the effects of ambient flow (both in the model and laboratory experiments), conducting larger-scale experiments and by developing CFD to include particles in the turbulence modelling. A selection of these results will be presented at the meeting.

References

[1] Lane-Serff, G.F., Linden, P.F., and Hillel, M. "Forced, angled plumes." *J. Hazard. Mater*. **33:** 75-99, 1993.

[2] Sparks, R.S.J., Carey, S.N. and Sigurdsson, H. "Sedimentation from gravity currents generated by turbulent plumes." *Sedimentology,* **38:** 839-856, 1991.

MODIFIED SHALLOW WATER EQUATION FOR INVISCID GRAVITY CURRENTS

Falin Chen and A. C. Ruo
Institute of Applied Mechanics, National Taiwan University, Taipei, Taiwan 107, Taiwan (ROC).

Summary We derive a modified shallow water equation for inviscid gravity currents in which the resistance from ambient fluid is taken into account. The resultant equations are highly nonlinear, which can be solved by a similarity transformation when the gravity current moving with a constant speed is considered. The similarity solutions are shown to be exactly the same with previous solutions obtained by traditional approach that the tradition shallow water equation is solved with the front condition. This result confirms the properness of the modified shallow water equation that it can govern the motion of inviscid gravity current with a resistance imposed by the ambient fluid.

DERIVATION OF MODIFIED SHALLOW WATER EQUATIONS

To analyze the motion of gravity currents, a common approach was to solve the hyperbolic shallow water equations together with the boundary conditions at both the current source at upstream and the current front at downstream [1]. The use of the front condition is a "logical reconciliation" [2] because this condition accounts for the force balance between the static pressure of the current and the resistance from the ambient fluid, which, nevertheless, is missed in the shallow water equations. In the present study, we start from the continuity and inviscid momentum equation and apply the shallow water approximation to derive the so-called modified shallow water equations, in which the resistance from ambient fluid is taken into account so that the consideration of the front condition becomes non-necessary. After applying both the kinematic and kinetic boundary conditions on the interface between the gravity current and the ambient fluid, we obtain the continuity and modified shallow water equations as follows

$$\frac{\partial h}{\partial t}+\frac{\partial (uh)}{\partial x}=0\,,\quad \frac{\partial u}{\partial t}+u\frac{\partial u}{\partial x}+g_r\frac{\partial h}{\partial x}=\frac{\gamma}{2}\frac{\partial}{\partial x}\left[\frac{(\partial uh/\partial x)^2}{1+(\partial h/\partial x)^2}\right]+\gamma\frac{\partial}{\partial t}\left(\frac{(\partial uh/\partial x)(\partial h/\partial x)}{1+(\partial h/\partial x)^2}\right) \tag{1,2}$$

where $u=u(x,t)$ is the flow velocity, $h=h(x,t)$ is the height of the current, $\gamma=\rho_2/\rho_1$, $g_r=(1-\gamma)g$ is the reduced gravitational acceleration, and ρ_1 and ρ_2 are densities of the current and the ambient fluid, respecitvely. It is noted that the right hand side of Eq. (2) vanishes when $\partial h/\partial x\approx 0$, implying that it accounts for the resistance force in terms of a form drag imposed by the ambient fluid on the current head where $\partial h/\partial x>0$ This term vanishes also for $\gamma\to 0$, or the non-Boussinesq gravity current whose density is much larger than the ambient fluid is considered.

THE SIMILARITY SOLUTION FOR A SPECIAL CASE

Equations (1) and (2) are highly nonlinear partial differential equations, being very difficult to solve even numerically. But, fortunately, for a special case that the gravity current moving with a constant speed and the shape of the gravity current remains similar all the time, they can be transformed by the similarity transformation, $\eta=x-Ut$, $u=U\tilde{u}(\eta)$ and $h=H\tilde{h}(\eta)$ into the following ordinary differential equations

$$-\frac{d\tilde{h}}{d\eta}+\frac{d\tilde{u}\tilde{h}}{d\eta}=0\,,\quad -\frac{d\tilde{u}}{d\eta}+\tilde{u}\frac{d\tilde{u}}{d\eta}+\frac{g_rH}{U^2}\frac{d\tilde{h}}{d\eta}=-\frac{\gamma}{2}\frac{d}{d\eta}\{(H\frac{d\tilde{h}}{d\eta})^2/[1+(H\frac{d\tilde{h}}{d\eta})^2\}\,. \tag{3,4}$$

We integrate Eqs. (3) and (4) once and apply relevant boundary conditions to determine the integral constants, and end up with the implicit relation of the current profile $\tilde{h}$ as follows

$$\frac{\eta}{H} = (\tilde{h}_f - \tilde{h})\sqrt{\frac{\gamma}{2(\tilde{h}_f - \tilde{h})} - 1} - \frac{\gamma}{4}\tan^{-1}[1 + \frac{\gamma}{4(\tilde{h}_f - \tilde{h}) - 2\gamma}]\sqrt{\frac{\gamma}{2(\tilde{h}_f - \tilde{h})} - 1} \tag{5}$$

where h_f is the current height far away from the front. A numerical solution of Eq. (6) for $\gamma = 1.1$ is shown in Fig. 1, in which one can see the current profile is more like those observed in experiments than previous similarity solutions obtained by solving the tradition shallow water equation [1,2].

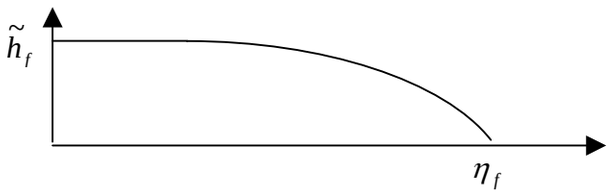


Fig. 1 A example of the current profile of present solution

To compare with previous results quantitatively, we employed the front condition $U^2 = \beta^2 g_r h_f$ [3] to rearrange Eq. (5) further and end up with the following simplified equation

$$H\frac{d\tilde{h}}{d\eta} = -\sqrt{\frac{2 - 2\beta^2\tilde{h}}{2\beta^2\tilde{h} - 2 + \beta^2\gamma}}\ . \tag{6}$$

Due to the fact that the current height is zero at the foremost point of the current head and the slope of the current profile near the head is highly steep, namely, $d\tilde{h}/d\eta \to \infty$, we obtain

$$\beta = \sqrt{2/\gamma}\ , \tag{7}$$

which is exactly the same with the formula provided by Simpson and Britter [3].

CONCLUSIONS

We have derived a modified shallow water equation in which the resistance in terms of the form drag imposed by the ambient fluid on the current head is included. The resultant equations are highly nonlinear, which, for the gravity current moving with a constant speed, can be solved by a similarity transformation, and the similarity solution is shown to be exactly the same with the formula derived by Simpson and Britter [3]. This comparison supports that the present modified shallow water equation can govern the motion of the inviscid gravity currents resisted by the form drag imposed by ambient fluid.

References

[1] Benjamin, T. B.: Gravity currents and related phenomena, *J. Fluid Mech.* **31**, 209, 1968

[2] Klemp, J. B., Rotunno, R., Skamarock, W. C.: On the dynamics of gravity currents in a channel, J. Fluid Mech. **269**, 169, 1994.

[3] Simpson, J. E., Britter, R. E.: The dynamics of the head of a gravity current advancing over a horizontal surface, J. Fluid Mech. **94**, 477, 1979.

XXI ICTAM, 15–21 August 2004, Warsaw, Poland

DAM-BREAK FLOW FOR ARBITRARY SLOPE OF THE BOTTOM

R. Fernandez-Feria
E.T.S. Ingenieros Industriales, University of Málaga, Spain

Summary The dam-break flow problem in the shallow-water approximation on an inclined bed for arbitrary slopes of the bottom is considered. An analytical solution for the spreading of the water fronts at the initial stages is given. A self-similar solution asymptotically valid for large times is also found. For intermediate times the problem is solved numerically by the method of characteristics.

FORMULATION OF THE PROBLEM

Consider the one-dimensional shallow-water equations for the flow over a constant slope bed,

$$\frac{\partial \eta}{\partial t} + \frac{\partial \eta U}{\partial X} = 0\,, \tag{1}$$

$$\frac{\partial U}{\partial t} + U\frac{\partial U}{\partial X} + \cos\theta \frac{\partial \eta}{\partial X} = \sin\theta\,, \tag{2}$$

where θ is the angle between the bed and the horizontal, t is the time, X is the coordinate along the bed, η is the depth of the water measured along the coordinate Y perpendicular to the bed, and U is the depth-averaged velocity component along X [see Fig. 1]. All the magnitudes in the above equations are dimensionless, and have been non-dimensionalized with respect to a length scale η_0, corresponding to some initial depth, and a velocity scale $U_0 = \sqrt{g\eta_0}$, where g is the acceleration due to gravity. These equations can be derived from the Euler equations for an incompressible fluid under the assumption that the characteristic length scale of the flow in the direction of the coordinate X is much greater than the characteristic length scale in the Y direction. According to [1], equations (1)-(2) are valid for any slope $\tan\theta$ of the constant-slope bed, provided that the above assumption is satisfied.

We are interested here in solving these equations for the dam-break problem, i.e., for the flow whose initial condition ($t = 0$) is given by (see Fig. 1)

$$U(0, X) = 0\,, \tag{3}$$

$$\eta(0, X) = \begin{cases} 0 & \text{for } X < -1/e \\ eX + 1 & \text{for } -1/e \le X \le 0 \\ -X/e + 1 & \text{for } 0 < X \le e \\ 0 & \text{for } X > e \end{cases}\,, \tag{4}$$

where $e \equiv \tan\theta$ is the slope of the bed. At $t = 0$, the vertical wall that intersects the bed at $X = e$ is removed instantaneously, causing the fluid to move over the sloping bed under the action of gravity. Note that characteristic length η_0 is the dimensional depth at $X = 0$, $t = 0$.

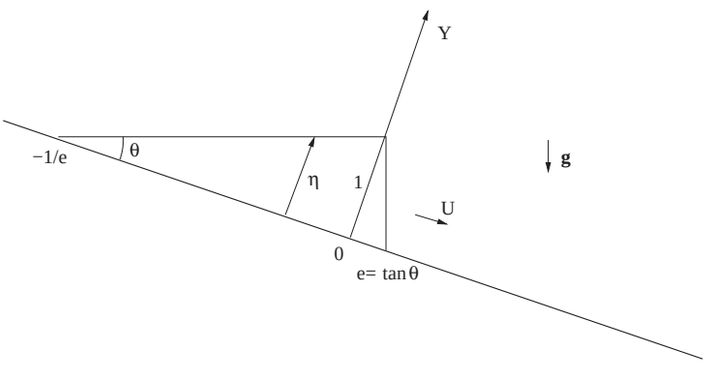


Figure 1. Coordinates and sketch of the initial conditions.

RESULTS

Analytic solution for the advance of the water fronts at the initial stages

Analytic solutions for the advance of the left and right water fronts at the initial stages are found. In fact, it is found that

valid in the region of the (t, X) plane $-1/e \leq X \leq -\sqrt{\cos\theta}\, t$, which means that the left water front remains at rest for $t \leq t_2 \equiv 2\sqrt{\cos\theta}/\sin\theta$. On the other hand, the solution for the advance of the right water front at the initial stages is given by

$$U(t, X) = \frac{t}{\sin\theta}\,, \tag{5}$$

$$\eta(t, X) = \begin{cases} 0 & \text{for } X > e + \frac{1}{\sin\theta}\,\frac{t^2}{2} \\ -\frac{X}{e} + 1 + \frac{1}{e\sin\theta}\,\frac{t^2}{2} & \text{for } X < e + \frac{1}{\sin\theta}\,\frac{t^2}{2} \end{cases}\,, \tag{6}$$

valid in the region of the (t, X) plane $\sqrt{\cos\theta}\, t + [\cos\theta/(2e) + \sin\theta]t^2/2 \leq X \leq e + t^2/(2\sin\theta)$, $t \leq t_1 \equiv 2e/\sqrt{\cos\theta}$. In addition to provide an useful information about the initial water spreading after the breaking of the dam, the above solutions allow the starting of the numerical integration of the equations by the method of characteristics near the singular points $(t = 0, X = -1/e)$ and $(t = 0, X = e)$. Figure 2 shows several profiles of the water depth at different times obtained from the above solutions and the method of characteristics for $e = 0.2$ ($\theta \simeq 11.31^o$; note that for this slope, $t = 1.5$ is between $t_1 \simeq 0.4039$ and $t_2 \simeq 10.0985$).

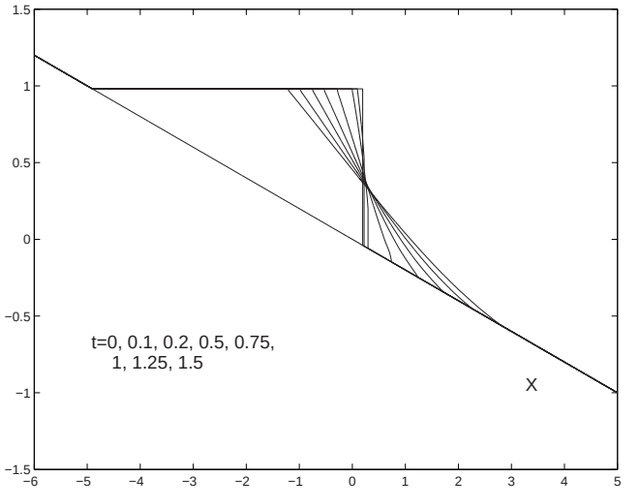


Figure 2. Profiles of the water depth along the sloping bed for $e = 0.2$, and for several instants of time, as indicated

Self-similar solution for large times

For $t \to \infty$, a self-similar solution of the second kind (see [2] for the terminology) is found:

$$\eta(t, X) = \frac{3(\xi - \xi^2)}{\sin\theta\cos\theta\,(u_m t + l_0)}\,, \tag{7}$$

$$U(t, X) = \sin\theta\, t + u_m\,[1 + \phi(t)]\left(\xi - \frac{1}{2}\right)\,, \quad \phi(t) = \frac{6}{u_m \sin\theta\,(u_m t + l_0)}\,, \tag{8}$$

where the self-similar variable is

$$\xi = \frac{X + (u_m t - \sin\theta\, t^2)/2 - l_{02}}{u_m t + l_0}\,, \qquad 0 \leq \xi \leq 1\,, \tag{9}$$

and the constants u_m, l_0, and l_{02} have to be obtained numerically for each initial condition (they depend only on θ; for instance, for $e = \tan\theta = 0.2$, it is found that $u_m \simeq 3.858$, $l_0 \simeq -3.381$, and $l_{02} \simeq 5.191$). At each instant t, the total water extent along X is given by $0 \leq \xi \leq 1$.

References

[1] Keller, J.B.: Shallow-water theory for arbitrary slopes of the bottom. *J. Fluid Mech* **489**:345–346, 2003.
[2] Barenblatt, G.I.: Scaling, self-similarity, and intermediate asymptotics. Cambridge U.P., Cambridge 1996.

EXTENDED NONLINEAR THEORY FOR TOPOGRAPHIC ROSSBY WAVES

Oksana E. Poloukhina[*], Andrey A. Kurkin[**]

[*] *Laboratory of Hydrophysics and Nonlinear Acoustics, Institute of Applied Physics, 46 Ulianov street, 603950 Nizhny Novgorod, Russia*

[**] *Department of Applied Mathematics, Nizhny Novgorod State Technical University, 24 Minin street, 603600 Nizhny Novgorod, Russia*

Summary The nonlinear-dispersive theory is proposed for topographic Rossby waves of small but finite amplitude for the case when external conditions are changed mainly along one direction, and wave is propagating along the orthogonal direction. The theory is based on the asymptotic procedure applied to hydrodynamic equations of frictionless, vertically homogeneous, incompressible, rotating fluid.

The equations of frictionless, vertically homogeneous, incompressible, rotating fluid can be reduced to the only one [1]:

$$\left(\frac{\partial}{\partial t}+u\frac{\partial}{\partial x}+v\frac{\partial}{\partial y}\right)\left(\frac{\omega+\Omega}{h}\right)=0\,, \tag{1}$$

where x, y – are horizontal co-ordinates, t – time, (u, v) – corresponding components of horizontal velocity vector, h – ocean depth, ω - vorticity, Ω - Coriolis parameter. Let us choose Cartesian co-ordinates in such a way that Ω and h are variable mainly in y, and waves are propagating along x-axis. Using relations $\omega=\frac{\partial v}{\partial x}-\frac{\partial u}{\partial y}$, $uh=-\frac{\partial \psi}{\partial y}$, $vh=\frac{\partial \psi}{\partial x}$ and considering nondimensional variables we can transform (1) to:

$$\left(h\frac{\partial}{\partial t}-\varepsilon\frac{\partial \psi}{\partial y}\frac{\partial}{\partial x}+\varepsilon\frac{\partial \psi}{\partial x}\frac{\partial}{\partial y}\right)\left(\frac{1}{h}\left[\mu\varepsilon\frac{\partial}{\partial x}\left(\frac{1}{h}\frac{\partial \psi}{\partial x}\right)+\varepsilon\frac{\partial}{\partial y}\left(\frac{1}{h}\frac{\partial \psi}{\partial y}\right)+\Omega\right]\right)=0\,, \tag{2}$$

where $\mu = (L_y/L_x)^2$ is the small parameter of topographic dispersion (L_y is the characteristic length scale in y-direction, L_x – characteristic wavelength), ε is the small parameter describing wave amplitude.

Let us consider long waves with small, but finite amplitude and put $\mu = \varepsilon$. If c is the speed of linear long wave (yet to be determined) we introduce the new variables [2] $\tilde{t}=t-\int_0^x\frac{d\xi}{c(\xi)}$, $x_i=\varepsilon^i x$ ($i\geq 1$). It follows that

$$\frac{\partial}{\partial t}=\frac{\partial}{\partial \tilde{t}}\,,\qquad \frac{\partial}{\partial x}=\sum_{i=1}^{\infty}\varepsilon^i\frac{\partial}{\partial x_i}-\frac{1}{c(x)}\frac{\partial}{\partial \tilde{t}}\,. \tag{3}$$

Next we assume that our Rossby wave field has the asymptotic expansion

$$\psi(X,y,\tilde{t})=\sum_{i=0}^{\infty}\varepsilon^i\psi_i(X,y,\tilde{t})\,. \tag{4}$$

Here X is a vector representing multiple scales (x_1, x_2, …). After substitution of (3), (4) into (2) and collecting terms of the same order of ε, we obtain the sequence of linear inhomogeneous boundary problems

$$L\frac{\partial \psi_i}{\partial \tilde{t}}=R_i\,, \tag{5}$$

$$\psi_i=0 \text{ at } y=0,l \qquad \text{or} \qquad \psi_i\to 0 \text{ at } y\to\pm\infty. \tag{6}$$

Here L is the linear operator determined by the expression $L\equiv\frac{\partial}{\partial y}\left[\frac{1}{h}\frac{\partial}{\partial y}\right]-\frac{1}{c}\frac{\partial}{\partial y}\left[\frac{\Omega}{h}\right]$. The lowest-order ($i$ = 0) boundary problem (5), (6) is homogeneous, variables can be separated: $\psi_0=A(X,\tilde{t})F(y,X)$, and $F(y,X)$ and $c(X)$ can be found from (5), (6) for any fixed Rossby wave mode. The compatibility conditions for the equation (5) for higher orders let us determine yet unknown slow-variable derivatives from A. For example, in the first order (i = 1) we obtain

$$R_1=C_{11}\frac{\partial A}{\partial x_1}+C_{12}\frac{\partial^3 A}{\partial t^3}+C_{13}A\frac{\partial A}{\partial t}+C_{14}A\,, \tag{7}$$

$$C_{11}=-F\frac{\partial}{\partial y}\left[\frac{\Omega}{h}\right],\ C_{12}=-\frac{F}{c^2h},\ C_{13}=\frac{F^2}{c^2h}\left(\frac{\partial^2}{\partial y^2}\left[\frac{\Omega}{h}\right]-\frac{1}{h}\frac{\partial h}{\partial y}\frac{\partial}{\partial y}\left[\frac{\Omega}{h}\right]\right),\ C_{14}=\frac{\partial F}{\partial y}\frac{\partial}{\partial x}\left[\frac{\Omega}{h}\right]-\frac{\partial F}{\partial x}\frac{\partial}{\partial y}\left[\frac{\Omega}{h}\right] \tag{8}$$

$$\frac{\partial A}{\partial x_1}=-\beta\frac{\partial^3 A}{\partial t^3}-\alpha A\frac{\partial A}{\partial t}-qA \tag{9}$$

$$\psi_1 = \frac{\partial^2 A}{\partial t^2} T^{(d)}(y,X) + A^2 T^{(n)}(y,X) + \int A dt \;\; T^{(x)}(y,X)\,, \tag{10}$$

Here $T^{(d),(n),(x)}(y,X)$ – corrections to the mode $F(y,X)$, they are the solutions of

$$LT^{(d)} = -\beta C_{11} + C_{12}\,, \qquad LT^{(n)} = -\alpha C_{11} + C_{13}\,, \qquad LT^{(x)} = -qC_{11} + C_{14} \tag{11}$$

with boundary conditions similar to (6). Boundary-value problems (11) are solvable if the functions in the right-hand side are orthogonal to eigenfunction F of operator L. It gives us the expressions for α, β and q:

$$\alpha = \frac{\int FC_{13}dy}{\int FC_{11}dy}, \qquad \beta = \frac{\int FC_{12}dy}{\int FC_{11}dy}\,, \qquad q = \frac{\int FC_{14}dy}{\int FC_{11}dy}\,, \tag{12}$$

Now substituting $\partial A/\partial x_1$ (9) with coefficients (12) into series for $\partial A/\partial x$ (3), and keeping the terms up to current order i in ε we obtain the nonlinear evolution equation:

$$\frac{\partial A}{\partial x} + \varepsilon\left(\beta\frac{\partial^3 A}{\partial t^3} + \alpha A\frac{\partial A}{\partial t} + qA\right) = O(\varepsilon^2)\,, \tag{13}$$

which is the generalized Korteweg – de Vries equation with variable coefficients [1].

Continuing the procedure of expansion we obtain in the next order in ε:

$$R_2 = C_{21}\frac{\partial A}{\partial x_2} + C_{22}\frac{\partial^5 A}{\partial t^5} + C_{23}A^2\frac{\partial A}{\partial t} + C_{24}A\frac{\partial^3 A}{\partial t^3} + C_{25}\frac{\partial A}{\partial t}\frac{\partial^2 A}{\partial t^2} + C_{26}\frac{\partial^2 A}{\partial t^2} + C_{27}A^2 + C_{28}\int A dt + C_{29}\frac{\partial A}{\partial t}\int A dt\,, \tag{14}$$

$$\frac{\partial A}{\partial x_2} = -s_2\frac{\partial^5 A}{\partial t^5} - s_3A^2\frac{\partial A}{\partial t} - s_4A\frac{\partial^3 A}{\partial t^3} - s_5\frac{\partial A}{\partial t}\frac{\partial^2 A}{\partial t^2} - s_6\frac{\partial^2 A}{\partial t^2} - s_7A^2 - s_8\int A dt - s_9\frac{\partial A}{\partial t}\int A dt\,, \tag{15}$$

$$\frac{\partial \psi_2}{\partial t} = \frac{\partial^5 A}{\partial t^5}T_2 + A^2\frac{\partial A}{\partial t}T_3 + A\frac{\partial^3 A}{\partial t^3}T_4 + \frac{\partial A}{\partial t}\frac{\partial^2 A}{\partial t^2}T_5 + \frac{\partial^2 A}{\partial t^2}T_6 + A^2T_7 + \int A dt\;\; T_8 + \frac{\partial A}{\partial t}\int A dt\;\; T_9\,, \tag{16}$$

where second-order corrections T_k, k = 2…9, can be found from inhomogeneous boundary-value problems:

$$LT_k = -s_kC_{21} + C_{2k}\,,\ k = 2\ldots9, \tag{17}$$

with boundary conditions similar to (6). Compatibility conditions for problems (17) give the expressions for s_k, k = 2…9:

$$s_k = \frac{\int FC_{2k}dy}{\int FC_{21}dy}\quad. \tag{18}$$

Substitution of $\partial A/\partial x_2$ (15) with coefficients (18) into series for $\partial A/\partial x$ (3) generates the equation:

$$\frac{\partial A}{\partial x} + \varepsilon\left(\beta\frac{\partial^3 A}{\partial t^3} + \alpha A\frac{\partial A}{\partial t} + qA\right) + \varepsilon^2\left(s_2\frac{\partial^5 A}{\partial t^5} + s_3A^2\frac{\partial A}{\partial t} + s_4A\frac{\partial^3 A}{\partial t^3} + s_5\frac{\partial A}{\partial t}\frac{\partial^2 A}{\partial t^2} + s_6\frac{\partial^2 A}{\partial t^2} - s_7A^2 + s_8\int A dt + s_9\frac{\partial A}{\partial t}\int A dt\right) = O(\varepsilon^3) \tag{16}$$

As a result, temporal evolution and spatial transformation of Rossby wave field is described by nonlinear evolution equation (14) of second order in small parameters. This equation contains nonlinear, dispersive, cross nonlinear-dispersive terms, and the terms due to inhomogeneous medium (along the wave propagation axis). Variable coefficients α, β and q (12) and s_k (k = 2..9) of this equation are found in explicit form of integrals (over cross-propagation domain) depending on the wave modal structure, which is determined by a set of boundary-value problems. They are not presented here because they have quite complex form. In the case of homogeneous medium derived equation coincides with the famous second-order Korteweg – de Vries equation. The produced theory is valid for any Rossby wave mode. Because all the formulae derived are rather complicated we have used the symbolic computations for the verification.

The extended evolution equation derived here lets more precisely describe Rossby wave field, but there are some situations when the second order corrections are fundamentally important. Such a situation occurs when the coefficients of the first-order terms in the evolution equation vanish for some medium conditions. In this case nonlinear dynamics of the waves is determined by the next-order terms.

References

[1] Odulo A.B., Pelinovsky E.N. About nonlinear topographic Rosby waves *Oceanology* **18(1)**:16-19, 1978.

[2] Pelinovsky E.N., Fridman V.E., Engelbrecht Yu.K. Nonlinear evolution equations, Tallin, Valgus, 1984.

THE PROPAGATION OF VISCOUS GRAVITY CURRENTS OVER A RIGID CONIC SURFACE

A.A. Osiptsov, A.A. Barmin, O.E. Melnik

Institute of Mechanics, Lomonosov Moscow State University, Michurinskii 1, 119899, Moscow, Russia

Summary Asymptotic models of a thin-film flow of highly viscous heavy fluid with mass supply on a curved rigid surface are constructed. A self-similar solution to the problem of propagation of gravity currents over a conical surface, which can be used for describing extrusive volcano eruptions, is obtained. Non-self-similar flow regimes are investigated numerically.

Formulation of the problem. We consider a non-axisymmetric flow of highly viscous heavy incompressible fluid over a rigid conical surface with local mass supply on the bottom. The problem formulation contains a small parameter ε representing the inverse nondimensional gravity force; accordingly, the solution is sought in the form of asymptotic series in ε. Substituting these series in the governing Navier-Stokes equations and retaining the leading terms, we obtain two fundamentally different systems of equations corresponding to small and finite inclination angles of the surface generatrix to the horizontal. For finite inclinations, the dynamic equation represents the balance between the gravity and the viscous forces, while for small inclination angles the system contains a self-induced longitudinal pressure gradient related with the unknown free-surface shape via the dynamic boundary condition.

Steady-state solutions. The existence of a steady-state solution for the free-surface shape (absent in the case of a horizontal plane) is shown. For small inclination angles, a one-parameter family of solutions on the scale of the mass supply region is obtained for a number of examples. Some of these solutions can be interpreted as a solution of the unsteady problem within the quasi-steady formulation. For finite inclinations and for length scales, much greater than the mass supply region, a unique analytical solution is found. The solutions obtained are generalized for the case of viscoplastic fluid.

Self-similar lava dome growth over a conical surface. We consider an unsteady flow from a point source over a slightly non-axisymmetric conical surface specified by the function $\theta = \theta(\varphi)$ (θ - inclination angle, φ - polar angle in the horizontal plane, $\theta'(\varphi) \ll 1$). For the stretched nondimensional film thickness h, we obtain the hyperbolic partial differential equation (containing φ as a parameter):

$$\frac{\partial h}{\partial t} + \left[\frac{\partial h}{\partial x} + \frac{h}{3x}\right] h^2 \sin\theta(\varphi) = 0 \qquad (1)$$

For a power or an exponential dependence of the entire liquid volume on time, an unique self-similar solution for the free-surface shape and the law of the leading flow front propagation is found analytically. It is shown that Eq. (1) has only two classes of self-similar solutions corresponding to power and exponential laws of mass supply. The families of self-similar solutions describing flows with mass sources or sinks at the leading flow front are also obtained. In the case when the entire fluid volume increases with time as $Qt^{*\gamma}$, the law of flow front propagation in dimensional variables takes the form (dimensional variables are denoted by the asterisk):

$$x_r^* = C(\gamma)\left[\frac{\sin\theta(\varphi)}{\cos^2\theta(\varphi)}\right]^{1/5}\left(\frac{\rho g Q^2}{\mu}\right)^{1/5}(t^*)^{(2\gamma+1)/5}$$

Non-self-similar flow over conical surface with small inclination of the generatrix to the horizontal. For 3D flow over a surface with small inclination angles, a second-order partial differential equation for the free-surface shape is obtained. To compare with the results obtained for finite inclination angles and with the solution for a horizontal plane [1], an axisymmetric flow is studied. It is shown numerically that, in the case of a power law of mass supply, the solution of the evolution equation for h has similarity asymptotics which coincide with the self-similar solution obtained for finite inclination angles. Hence, taking even small inclination angles of the surface generatrix to the horizontal into account leads to the change in the asymptotic law of flow front propagation, as compared with the corresponding law for the horizontal plane.

The solutions obtained can be used for describing extrusive and effusive volcano eruptions on curved substrate surfaces.

References

1. Huppert H.E. The propagation of two-dimensional and axisymmetric viscous gravity currents over a rigid horizontal surface. J. Fluid Mech. 1982. V. 121. P. 43-58.

IUTAM : 21st International Congress of Theoretical and Applied Mechanics
Warsaw, Poland, 15-21 August, 2004

An Alternative Model for "Pingo" Formation in Permafrost Regions

James G A Croll, Department of Civil and Environmental Engineering
University College London

Abstract

Pingos are a characteristic geomorphologic feature of certain Arctic regions in which dome-shaped dimples can form in the permafrost layers of otherwise flat landscapes. It is widely accepted that the formation of a "pingo" results from the development of an excess pore water pressure in the unfrozen ground, the "talik", underlying the permafrost layer. This paper argues that these prevailing models for pingo formation contain some serious mechanical inconsistencies. An alternative model is postulated. It relies upon the development of high levels of in-plane compressive stress in the permafrost layer. These compressions would arise from the restraint to the expansions otherwise occurring when in a thickening of the permafrost layer water turns to ice and/or when the ice in the permafrost layer is subject to a seasonal increase in temperature. An upheaval buckling under these conditions is consistent with the local dimples associated with pingos.

Pingos are a commonly observed geomorphologic formation in areas of permafrost. They take the form of a dome shaped upwelling of the frozen surface ground layers occurring in areas of recent exposure to the effects of permafrost surface penetration. They tend to occur in the beds of lakes that have for some reason been drained of the water that previously insulated the bed layers from permafrost penetration. The generally accepted explanation for their formation is that a hydraulic pressure builds up beneath the recently frozen layer pushing it up into the characteristic dome or sometimes ridge formation. The build-up of pore water pressure in the underlying "talik" is said to result from either ground water flow resulting from a hydrostatic head associated with elevated water tables in the surrounding higher landforms or from the confinement caused by the advancing ice formation within the sealed talik.

While it is almost certainly the case that these pressures contribute to the developments of pingos, the geometry of the pingo has certain characteristics that are not consistent with just this explanation. If a generalised underlying pore pressure were formed the likely response of the frozen surface layer would be a generalised upheaval involving the whole, usually very large, area of the recently frozen permafrost layer. This is not the case. What tends to happen is that a number of seemingly random, relatively small diameter, dimples are formed. These would have to be associated with either highly localised pore water pressure peaks, which is highly unlikely, or localised areas where the permafrost layer is thinner. The latter explanation is the most plausible except for the fact that if they were due to localised thinned areas of permafrost it would be most unlikely that they would exhibit the very regular dome shaped formation which on plan has such a consistently regular circular shape. Much more likely, if this latter consideration were to provide the explanation, the distortions induced by a relatively uniform underlying pore pressure would reflect the inherent irregularity of the thinner than average regions of permafrost. This does not appear to be the case.

This paper will suggest that another mechanism might be at work. In-plane compressions resulting from the restraint to expansion of the ice within the permafrost layer, could induce a thermal uplift buckling. For 2-dimensional sheets subject to a uniform biaxial compression stress, this form of thermal buckling takes the form of a localised dimple closely related to the geometric characteristics of the pingo. The compression needed to generate the buckles could result from the expansion occurring either as the groundwater turns to ice as the thickness of the permafrost layer increases over time, or as the already formed ice sheet experiences an average increase in temperature associated with seasonal cycles. A brief account will be given of the mechanics involved in the thermal uplift buckling and indicative calculations will demonstrate that such a mechanism is consistent with the good deal of recorded observation on pingo formation. It is suggested that this alternative explanation of the formation of pingos will allow some of the physical inconsistencies of the current models to be resolved.

FAST FERRY TRAFFIC AS A NEW FORCING FACTOR OF ENVIRONMENTAL PROCESSES IN NON-TIDAL SEA AREAS

Tarmo Soomere
Marine Systems Institute, Tallinn Technical University Akadeemia tee 21, 12618 Tallinn

Summary The impact of wake wash from high-speed ferries on the coastal environment is analysed in terms of wave energy and power, and properties of the largest waves. Shown is that hydrodynamic loads caused by heavy high-speed traffic may play a decisive role in certain non-tidal areas with high wind wave activity. The main reason of concern is the long periods of wake waves. The leading waves typically have a height of about 1 m and a period of 10-15 s. They cause unusually high hydrodynamic loads in the deeper part of the nearshore. The fast ferry traffic is thus a qualitatively new forcing component of vital impact on the local ecosystem.

INTRODUCTION

The waves from fast ferries have become an environmental problem of growing concern during the last years. Fast ferries do not produce only higher waves than conventional ships, but also fundamentally different wave systems when sailing at supercritical speeds. The influence of ship-generated waves may be critical for certain processes in semi-enclosed estuaries or in areas usually not exposed to swell or severe local windseas [1]. It is generally believed that ship wakes are negligible and that their effect is sporadic in the high-energy coastal areas that are open seawards and where natural waves are frequently much higher than the wakes. This assumption is indeed true for coasts exposed to high tides or large wind waves.

The purpose of the current paper is to demonstrate that ship wakes may nevertheless be of particular importance in certain parts of coasts that are already subject to high hydrodynamic loads and intense beach erosion in natural conditions. The reason is a combination of specific features of the existing hydrodynamic loads (that are restricted, for example, to a particular direction or a certain frequency interval) with a special type of the coastal environment (that has reached a near-equilibrium stage of its evolution) and particularly high anthropogenic wave loads that are qualitatively different from the natural wave loads.

ENERGY AND POWER OF WIND WAVES AND SHIP WAKES IN TALLINN BAY, BALTIC SEA

The study is based on an extensive field study of both wind wave and ship wave properties in different parts of the coastal area of Tallinn Bay [2]. This bay is a semi-enclosed area in the central part of the Gulf of Finland. In recent years, the high-speed ship traffic has increased considerably and amounts up to 70 traverse per day during the high season.

The field results are compared with a long-term reconstruction of wind wave climate based on a high-resolution version of the wave model WAM. The properties of the wave field vary significantly in different areas of the bay. The highest waves occur in the central area of the bay where the 1-year return value of the significant wave height slightly exceeds 2 m and wave heights may reach 4 m during extreme NNW storms.

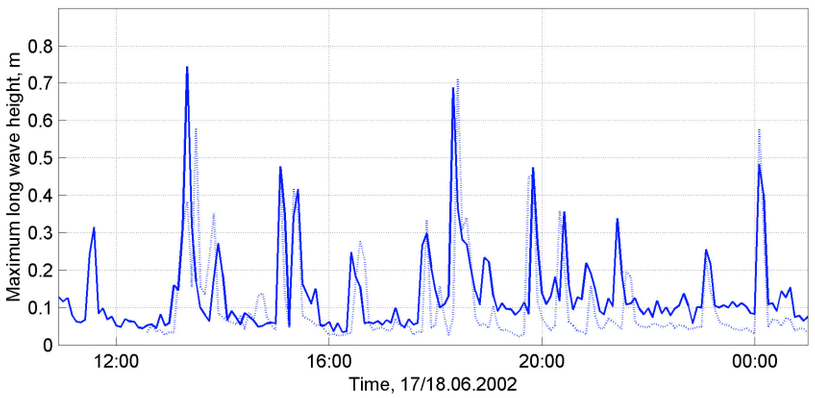


Fig. 1. The maximum height of the long-wave component (waves with periods exceeding 5 s and mostly representing wakes from high speed ships) near the western coast of the island of Aegna at the entrance of Tallinn Bay, at a distance of about 2 km from the ship lane on 17.06.2002 (solid line) and 18.06.2002 (dotted line). The significant height of the wind wave background is 40–60 cm on 17.06 and 30-40 cm on 18.06.

The heights of the wake waves of fast ferries are moderate in the coastal zone of Tallinn Bay and normally do not exceed 1 m (Fig. 1). In particular, they are much smaller than the highest wind waves reaching this area each year: the typical annual maximum significant wave height in the coastal zone is about 1.5 m, therefore, the highest single waves are about 3 m high. However, wind waves of this height occur seldom and the daily highest examples of ship waves mostly belong to the highest 1%–5% of wind waves. The fast ferry traffic is so heavy that the annual mean energy of ship-generated waves is 6-8% from the bulk wave energy and the ship wave power may be as high as 34% from the bulk wave power in the coastal zone of the bay [2].

ENERGY DISTRIBUTION IN WAKE WAVES FROM HIGH-SPEED FERRIES

The reason for such a large difference of the share of ship waves in the wave energy and power suggest that, at least, a part of wake energy is concentrated in wave components with periods greatly exceeding typical periods of wind waves. The daily average wave energy spectra (Fig. 2) indeed show a clear separation of the major portion of the energy of wakes from large high-speed vessels and the energy of wind waves in various natural wave conditions. The separation occurs at different frequencies depending on both the location of the site and the background wave field. The spectrum at Fig. 2a proves that the role of wakes from from conventional vessels and hydrofoils (that mostly exite waves with periods 3-5 s) is negligible in the total energy budget of the ship-generated waves.

A particularly important feature that follows from the spectra in Fig. 2 is that the major part of the energy of wake waves of high-speed vessels lies outside the frequency range of wind waves occurring in typical conditions. The well-defined peak corresponding to the longest waves in the energy spectra in Fig. 2 suggests that, in average, the energy of the leading waves (that are also the longest waves of the wake) considerably exceeds the energy carried by the the rest of the wake. Comparison of Fig.1 and Fig 2 reveals that the leading waves of a ship wake frequently have heights about 1 m and periods of 10-15 s. Waves with such properties do not exist in the natural conditions in the area in question.

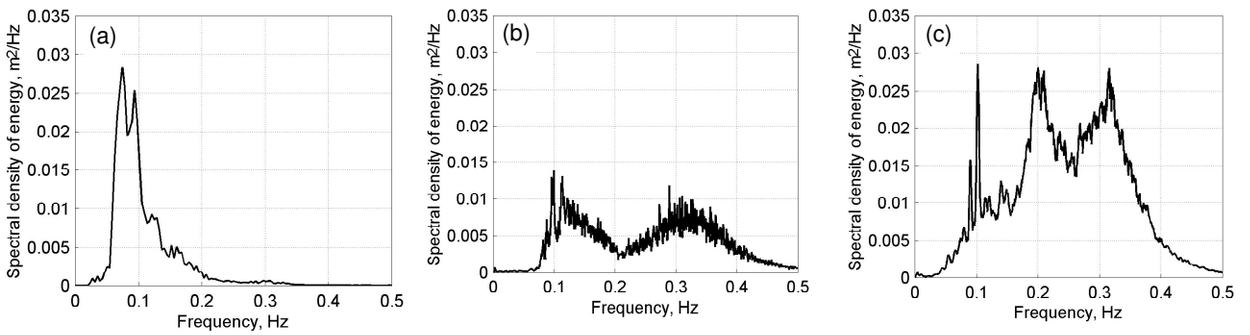


Figure 2. Daily mean joint energy spectra of wind waves and ship wakes in the coastal zone of Tallinn Bay at a distance of about 2 km from the ship lane (a) in perfectly calm conditions; (b) in the moderate wind conditions (the significant height of wind waves is about 40–60 cm, the temporal behaviour of the heights of long waves is given in Fig. 1, solid line); (c) in strong wind conditions (the significant height of wind waves is about 1 m and open sea swell with a period of about 5 s is also present). The measurement site for the panel (b) is located in the area where ships sail at moderate speeds.

ENVIRONMENTAL IMPLICATIONS

The difference of prevailing periods of the highest parts of the ship wash and the windseas is the most critical issue in the Tallinn Bay area. For a fixed wave height, the wave-induced near-bottom velocity depends essentially on the wave period and has the highest variation for the nearshore with the depth of 5-30 m when the wave period increases from 5 s to 8 s. Since the major part of the energy of the wakes from fast ferries is concentrated in the wave components with the periods exceeding 6-7 s [2], the impact of a typical ship wake on bottom sediments and aquatic wildlife at these depths is comparable with or even exceeds the impact of wind waves occurring in the most violent storms. Thus, the wake of fast ferries is a new forcing component of vital impact on the local ecosystem that may cause considerable intensification of beach processes as well as enhanced vertical mixing in the water body, and has a significant influence on the aquatic wildlife.

An abrupt intensification of long-wave activity may cause considerable changes in the existing balance of sediment distribution, because already relatively small levels of long-period wave energy in combination with wind waves can cause greater beach response than an equal amount of energy in the windsea only frequencies [3]. The gross influence of wakes from high-speed ships for a coast with a low hydrodynamic activity and a proper structure of bottom sediments may trigger a new phase of the coastal evolution through fast eroding the seaside part of the nearshore. This process creates a deficit of sediments at certain depths that will be balanced by a more intense transport of material from the vicinity of the shoreline. Another consequence is that after some time the intensity of wind wave breaking may decrease, and more wind wave energy may penetrate to the shoreline [4].

References

[1] Parnell, K.E. and Kofoed-Hansen, H.: Wakes from large high-speed ferries in confined coastal waters: Management approaches with examples from New Zealand and Denmark. *Coastal Manag.*, **29**, 217-237, 2001.

[2] Soomere, T. and Rannat, K.: An experimental study of wind waves and ship wakes in Tallinn Bay. *Proc. Estonian Acad. Sci. Engng*., **9**, 157-184, 2003.

[3] Coates, T.T. and Hawkes P.J.: Beach recharge design and bi-modal wave spectra. In: B.L. Edge (ed.), *Coastal engineering 1998: proceedings of the 26th international conference 22–26 June 1998, Falconer Hotel, Copenhagen*, vol. 3, pp. 3036–3045, American Society of Civil Engineers (ASCE), USA, 1999.

[4] Soomere, T. and Kask, J.: A specific impact of waves of fast ferries on sediment transport processes of Tallinn Bay. *Proc. Estonian Acad. Sci. Biol. Ecol.,* **52,** 319-331, 2003.

Dynamics of separation zone behind the 2D hill in oscillating incident wind.

Alicja Jarza*, Jaroslaw Ciechanowski*
*Institute of Thermal Machinery, Department of Mechanical Engineering and Computer Science, PL 42-200 Czestochowa, Poland

The experimental and numerical simulation of the unsteady wind phenomena around the two-dimensional hill has been performed for different parameters of inflow periodicity.
The study of the turbulent flow over curved surfaces or hills is an excellent way to exploring fundamental aspects of air flow over complex terrain for environmental and meteorological problems such as turbulent transfer and diffusion, which play a critical role in determining the transfer of momentum, heat and moisture in the atmospheric surface layer. An analysis undertaken here were motivated to a considerable extent by potential wind energy applications as well as the guidelines to refine wind estimates in complex terrain especially useful for soil erosion and pollutant dispersion problems.
The dynamics of flow over hills has been an object of great interest of many recent studies [1,2,3] assuming the steady inflow expressed as typical mean velocity profile (exponential or logarithmic) over the terrain of different aerodynamic roughness. These studies provide useful tests for both theoretical analysis and numerical calculations of practically important quantities like the maximum acceleration over the hill summit, surface drag, separation and recirculation position. Far less has been done to take into account the effects of velocity fluctuations in upstream shear boundary layer which can strongly affect the base flow structure downstream the ground object. Especially the unsteady conditions related with periodical gust phenomena or large scale vortices generated in wind environment of the object are the factors of great importance for the overall flow picture around the hill.
In the present paper the formation of wake in the lee of the sinusoidally shaped hill has been simulated by the use both wind tunnel technique and numerical methods. The modelled hill has been immersed in the boundary layer flow formed over the terrain of moderate roughness. To study the effect of periodical disturbances of the approaching wind the oscillating component superimposed on the mean velocity profile has been introduced. (see Fig.1).

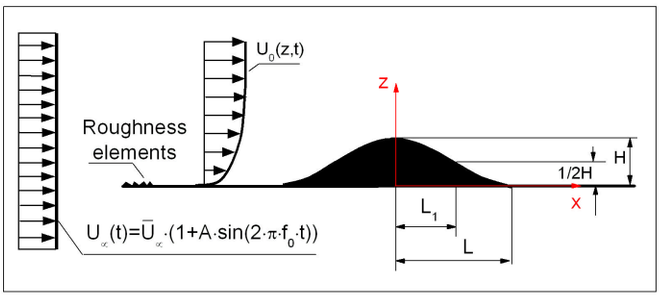


Fig.1. Scheme of the flow over an isolated hill in oscillating wind.

The main parameters of the simulations are specified by the hill slope $s=H/2L_1=0.6$, Reynolds number $Re_\delta=2.6\cdot10^4$, inflow oscillations frequency $f_0=0\div16$Hz, and amplitude $A_\infty=0.2$. Experimental test has been done in wind tunnel equipped with devices generating unsteady wind boundary layer. The fast-scanning acquisition system of X array hot-wire signal was been applied. The numerical simulations, guiding the experimental tests programme, have been performed by the use of phase averaged form of RNG version of k-ε turbulence model. The major findings of the simulations have been illustrated in Figs 2÷5. They reveal the strong dependence between the characteristics of inflow periodicity and vorticity structure of separation region behind the hill (Fig.2).

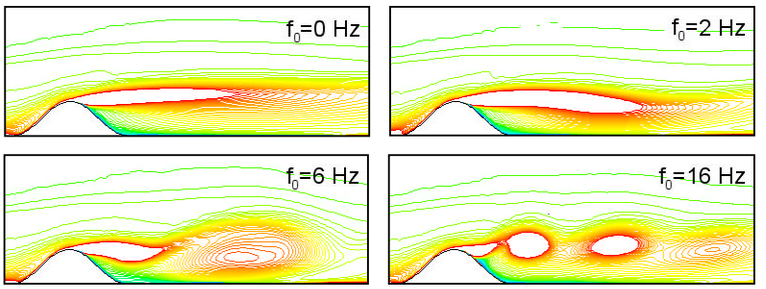


Fig.2. Instantaneous vorticity fields behind the hill for different frequency of incident oscillation (t/T_0=0.25).

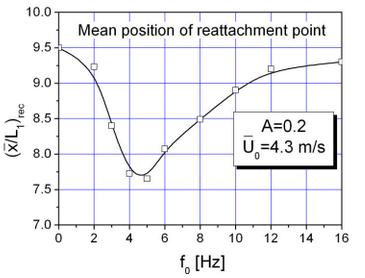


Fig.3. The influence of inflow oscillations on the mean position of downstream attachment

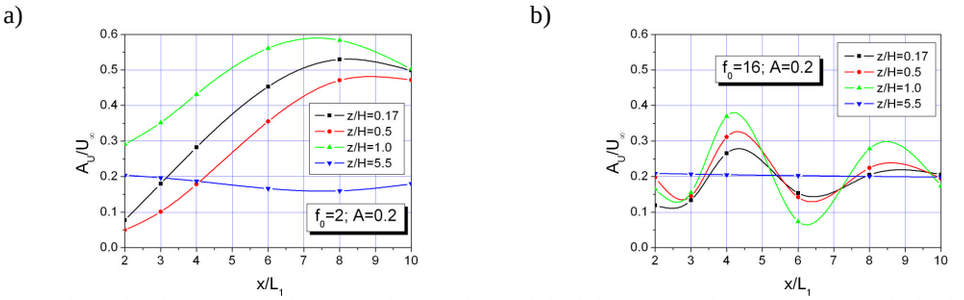


Fig.4. Normalized amplitude of wind velocity oscillations behind the hill for a) the low (f_0=2Hz) and b) high (f_0=16Hz) gust frequency.

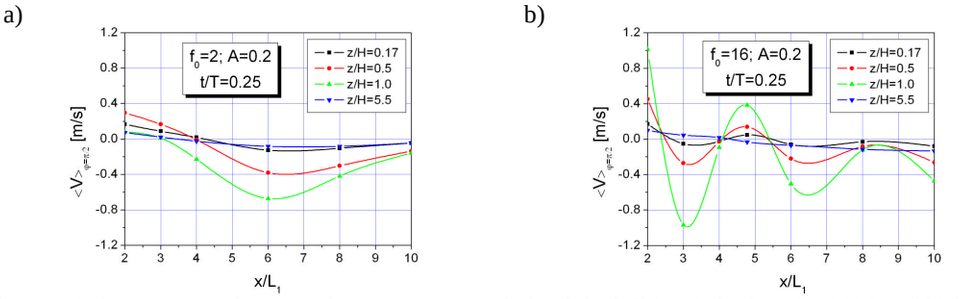


Fig.5. Evolution of phase-averaged cross velocity component behind the hill for a) the low (f_0=2Hz) and b) high (f_0=16Hz) gust frequency.

The mean position of reattachment point is also clearly affected by incident gust frequency (Fig.3). The changes in the wake formation under different inflow periodic conditions are particularly visible in distributions of oscillating velocity amplitude behind the hill (Fig.4.). The phase-averaged traces of cross velocity component shown in Fig.5 reveal the zones of intensive vertical gusts accompanying the process of vorticity decay behind the hill.

References

[1] C.A. Miller, A.G. Davenport, Guidelines for the calculation of wind speed-ups in complex terrain J. Wind Eng. and Ind. Aerodyn. 74-76 (1998) 189-197.

[2] H.G. Kim, V.C. Patel, Test of turbulence models for wind flow over terrain with separation and recirculation, Boundary-Layer Meteorol. 94, 5-21, 2000

[3] Peter A. Taylor Turbulent boundary-layer flow over low and moderate slope hills, J. Wind Eng. and Ind. Aerodyn. 74-76 (1998) 25- 47

XXI ICTAM, 15–21 August 2004, Warsaw, Poland

EFFECTS OF CURVATURE IN AVALANCHE DEFLECTING DAMS

Arne Moe*, Fridtjov Irgens*, Ulrik Domaas** and Carl Bonnevie Harbitz**
*Norwegian University of Science and Technology, Department of Structural Engineering,
Richard Birkelands veg 1a, N-7491 Trondheim, Norway
**Norwegian Geotechnical Institute, P. O. Box 3930 Ullevål Stadion, N-0806 Oslo, Norway

Summary Three different models have been applied to evaluate the centrifugal effects in curved avalanche paths. The objective of this work is to achieve better understanding of how curvature influences avalanche flow. This knowledge is useful for design of deflecting dams; potentially effective and relatively cheap protection measures for changing the course of a slide.

INTRODUCTION

Avalanches and other types of slides represent significant danger to people and property in large parts of the world. Deflecting dams, i.e. dams that change the courses of avalanches to prevent impact upon houses or roads, are used as protection from this hazard. A curved deflecting dam can catch the avalanche at a gentle angle of impact. The flow direction is continuously and gently altered along the whole length of the dam, hence avoiding the more abrupt deflection of a straight dam. As will be shown in the article, spreading the deflection over longer time and distance results in significantly lower run-up heights on the deflecting structure or terrain. A direct consequence of this is that curved deflecting dams may be built lower than straight ones—with less impact to the local environment and at lower cost.

The purpose of the present study is to achieve quantitative knowledge about the effect of curvature on run-up heights. We compare observed behavior to computational results for naturally curved avalanche tracks, applying three models that are described below.

Similar studies have been presented by Irgens, Harbitz and others [5], [2]. The present study, however, involves the improved NIS simulation procedure, as well as the quasi-static run-up model for curved deflecting dams that have not been previously published.

THE APPLIED COMPUTATIONAL MODELS

The quasi-static curved channel model

This model is based on a set of geometrical and kinetic relations, that have been implemented in a spread sheet [6]. An open channel is described by the curvature radii in the horizontal and vertical planes and inclination of the centre line, and by the shape of its cross section. The channel cross section is defined by its inner and outer wall slopes and the width of the channel floor. In addition, the area of the flow cross section is derived either from the volume flux or from the initial flow height, i.e. the flow height without centrifugal displacement of the surface. If the path is in fact a wide area restricted only on one side, the width of the channel is chosen very large, and the cross section area must be given through the volume flux rather than through the initial flow height.

A stationary flow through a fixed cross section is studied. The flow is considered to be inviscid, hence the free surface assumes an inclination perpendicular to the effective body force, consisting of the gravity and the centrifugal forces. These are calculated from the velocity and the shape of the centre line of the channel. Given the orientation of the free surface, we can compute the run-up height on the channel wall.

Though very simplified, this model provides us with information on which properties are most influential given certain conditions: Numerical derivatives of the run-up height with respect to each individual input parameter shows the significance of each of these.

The Schieldrop leading edge model

This model does not, in contrast to the other two, compute run-up on a curved deflecting dam. Instead, the trajectory of the centre of mass of avalanching material arbitrarily hitting a plane deflecting dam wall is computed. This gives us information about which angles of incident that can be handled by a given deflecting dam without the dam being overstepped.

The terrain is described as an inclined plane, with a straight deflecting dam oriented at an oblique angle to the avalanche flow. The inclination, the wall slope and the angle of incidence are the geometrical parameters considered in the computations.

The deflecting dam model is based on the Voellmy-Perla equations, comprising a dynamic drag coefficient and a Coulomb friction. The equations are solved numerically with a fourth order Runge-Kutta procedure.

The Norwegian Geotechnical Institute (NGI) presently use this model as a tool in dam design, and the PCM [8] model is usually applied to provide velocity input and to calibrate material parameters. In this study, however, we have used velocity input from the NIS model, in order to make the comparisons more valid. Domaas and Harbitz [1] showed that the model systematically predicted lower run-up heights than what was observed, and established a best fit relationship between predictions and observations.

The Norem, Irgens and Schieldrop (NIS) model

The NIS model is based on a constitutive model of granular materials and a simplified simulation procedure for the flow. The constitutive model was proposed by Norem et al. [7]. The material properties of the model are specified by a coefficient of Coulomb friction, a shear viscosity, two viscoelasticities, representing the effect of normal stress differences, and a cohesion parameter. The simulation procedure was proposed by Irgens [3] and later improved by Irgens et al. [5] and Irgens [4]. A further improvement is presented in this paper.

The flowing material is assumed to be confined to a channel-like portion of the terrain. The avalanche is approximated by a set of volume elements with varying heights and varying widths, compensating for converging and diverging effects in a real terrain. Horizontal centrifugal effects, due to curvature of the horizontal projection of the flow path, are taken into account. These effects result in an inclination θ of the free surface and a corresponding displacement of the centre line. The centerline of the avalanche is a space curve, which is determined by the terrain and the dynamics of the flowing material.

The cross-sections of the flowing material are approximated by circular segments defined by their radii. The equation of motion in the stream-wise direction and the continuity equation are integrated over the cross-section of the flow. These equations and the geometrical relation between the flow height and the flow width, due to the circular segment approximation, provide three equations for the three unknown: the average flow velocity, the maximum flow height, and the flow width, as functions of time and position. The partial differential equations are solved by a finite difference scheme, with second order central differences in the stream-wise direction and by a fourth order Runge-Kutta procedure with respect to time. The finite difference scheme is Eulerian, requiring a special procedure to make the avalanche progress along the path. Initially the snow is assumed to fill a finite number of volume elements and is at rest. The volume of material passing through the front section fills the downstream volume element ahead of the front. When the accumulated volume exceeds the current value of the volume of that element, partly determined by the current flow height at the front, it is assumed that the avalanche front has advanced one subsegment. A similar procedure is applied to the tail of the avalanche.

In the applied simulation procedure, a new procedure for displacing the centre line is implemented. A differential equation for acceleration perpendicular to the initial path is introduced, giving the displacement a certain inertia. The displacement differential equation is solved for the *centrifugal angle* θ with a second order Runge-Kutta procedure. The following procedure is used for the displacement of the centre line:

1. The velocities of the first run are basis for the initial displacements, but the simulation uses the initial centre line throughout the simulation.
2. The next simulation runs with a centre line that is displaced according to the centrifugal effects of the previous run.
3. The θ values of the two runs are compared.
4. This procedure is repeated until the computed displacement of two subsequent runs are satisfactorily similar.

This improved handling of the centrifugal displacement procedure results in realistic run-up heights, and allows effects of rapidly changing curvature radius to be taken into account.

References

[1] Ulrik Domaas and Carl Bonnevie Harbitz. On avalanche run-up heights on deflecting dams: Centre-of-mass computations compared to observations. In Erik Hestnes, editor, *Norwegian Geotechnical Institute, Publication no. 203*, pages 94–98, Oslo, 1998.

[2] Carl Bonnevie Harbitz, Ulrik Domaas, and Arne Engen. Design of snow avalanche deflecting dams. In *Proceedings of the 9th Interpraevent Congress, June 26–30, 2000*, volume 1, pages 383–396, Villach, Austria, 2000.

[3] Fridtjov Irgens. One dimensional simulation of three-dimensional snow avalanche flow. Paper presented at the 19th International Congress of Theoretical and Applied Mechanics, Kyoto, Japan, August 25–31, 1996.

[4] Fridtjov Irgens. Simplified simulation model of snow avalanches and landslides. Paper presented at the 20th International Congress of Theoretical and Applied Mechanics, Chicago, USA, August 27 – September 2, 2000.

[5] Fridtjov Irgens, Bonsak Schieldrop, Carl Bonnevie Harbitz, Ulrik Domaas, and Runar Opsahl. Simulations of dense-snow avalanches on deflecting dams. *Annals of Glaciology*, 26:265–271, 1998.

[6] Arne Moe. Klatrehøgder av skred på krumma leievoll. Internal report 581200-36, NGI, Oslo, Norway, January 2002. A corrected version in English is planned for 2004.

[7] Harald Norem, Fridtjov Irgens, and Bonsak Schieldrop. A continuum model for calculating snow avalanche velocities. In *Proceedings of Avalanche Formation, Movements and Effects, Davos 1986*, number 162 in IAHS Publication, pages 363–378. IAHS, 1987.

[8] Ron I. Perla, T. T. Cheng, and David M. McClung. A two-parameter model of snow avalanche motion. *Journal of Glaciology*, 26(94):197–207, 1980.

LOBE AND CLEFT FORMATION AT THE HEAD OF A GRAVITY CURRENT

J. N. McElwaine & M. D. Patterson
Department of Applied Mathematics and Theoretical Physics, Centre for Mathematical Sciences, University of Cambridge, Wilberforce Road, Cambridge CB3 0WA, England.

Summary Experiments have been carried out to examine the formation, and subsequent evolution, of lobes and clefts at the head of a gravity current. This has been achieved by calculating the curvature of the level-set of first-arrival times of the front. The results show that there is a weak dynamical linear instability when the radius curvature of the front is similar to the height. The formation and evolution of the clefts is then a nonlinear kinematic phenomenon, caused by the front propagating with a roughly constant normal velocity. Three different mechanisms for the initial instability are discussed and the subsequent evolution of the front is explained in detail.

INTRODUCTION

Gravity currents are a commonly occurring environmental flow and arise in a variety of situations, examples include the buoyancy-driven exchange through an open doorway, the spill of a dense gas, or a pyroclastic flow from a volcano. The density differences driving the flow may have their origins in temperature, composition, or the presence of suspended particles that sediment out of the advancing flow.

The general dynamics of a two-dimensional (2D) gravity current are now thought to be well understood. Laboratory experiments (5) have provided detailed observations of such flows. It was found that the flow arising after the release can be divided into a number of different phases. In the initial phase sometimes referred to as the 'slumping phase' the current develops and forms a head. Somewhat later, the gravity current reaches a second, self-similar phase, where there is a buoyancy-inertia balance. After sufficient time the flow will enter a final phase, in which it is governed by a buoyancy-viscous balance which is well described by shallow water theory.

While the general dynamics of 2D gravity currents are accurately described by relatively simple analysis, no information about the formation of the complicated three-dimensional (3D) lobe and cleft structures at the gravity currents head is provided by these models. Simpson (4) has carried out an experimental study on lobe and cleft formation where he photographed the gravity currents head from below and was thus able to track the clefts as they grew and merged. He suggested that the formation of lobes and clefts is due to the overrunning of less dense fluid by the dense gravity current, which in turn forces itself upward through the gravity current causing a cleft to form. Other work by Härtel (1) used 3D direct numerical simulations (DNS) of a gravity current at relatively low Reynolds number. The simulation exhibited all features typically observed in experimental flows near the gravity current head, including the lobe and cleft structure at the leading edge. The original work was furthered (2) with an examination of the lobe and cleft instability of a gravity current using linear-stability analysis. They concluded that there was a local linear instability at the leading edge of the front caused by the unstable stratification in the flow region between the nose and the stagnation point.

RESULTS

A series of laboratory experiments have been carried out in a glass tank 2.5 m $\times$ 0.7 m $\times$ 0.8 m. In the experiments the tank was filled with fresh water of density $\rho_A = 1000$ kg/m^3 to a depth H. A fixed volume of a denser saline solution of density ρ_L of the same depth, was kept behind a vertical barrier at a distance $L = 0.3$ m from the end of the tank. For visualisation purposes the dense fluid was dyed with food colouring. By lifting the barrier the denser fluid is released into tank. Illumination from behind and above using a diffuse light bank resulted in a sharply defined interface between the gravity current and the ambient fluid.

Video sequences of the experiments were analysed using the method developed in McElwaine (3). The arrival time $T(x, y)$ of the flow is detected for each pixel on the screen. This matrix $T(x, y)$ of first arrival times is a level set, since the contours $T(x, y) = t$ correspond to the front of the flow at a particular time. One such contour is shown in figure 1(a), where the accuracy of the method and the characteristic lobe and cleft structure can be clearly seen. Properties of the flow such as average front position and velocity can then be calculated directly from the contours and the movement of clefts and lobes can also be visualised. However, local features can most easily be tracked working directly with the level set. In general one should account for camera distortion before processing, but a large focal length lens was used and the camera axis was orthogonal to the plane of motion, so the relation between pixel coordinates and world coordinates is accurately represented by a simple scaling. Resampling errors can thus be avoided by working directly with pixel coordinates. The lobes corresponds to large regions of small positive curvature and the clefts to lines of large negative curvature. The curvature is defined as $\kappa = \nabla \cdot \frac{\nabla T}{|\nabla T|}$. Figure 1(b) shows the curvature of the level set from the experiment shown in Figure 1(a).

The structure and motion of the clefts is clearly seen in figure 1(c). The clefts appear and then slowly propagate along the front until they merge with other clefts. The most important point about clefts is that they are a *generic, kinematic* feature of system with evolving fronts that have nothing to do with dynamics. That is any system where the front propagates with approximately constant velocity normal to the front will develop clefts. These clefts correspond to a shock where two

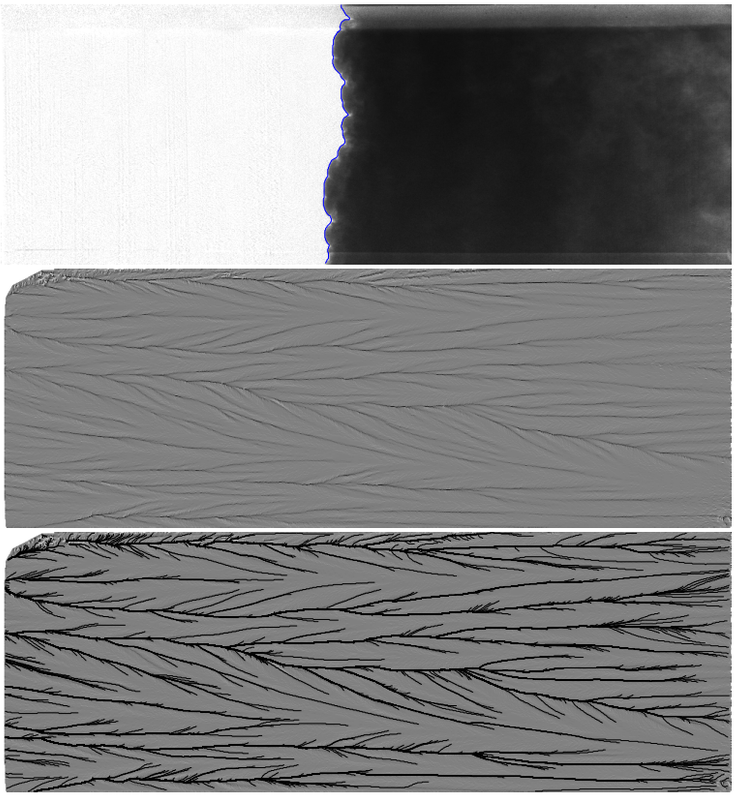


Figure 1. a) Contour mapping. The motion of the gravity current in all figures is right to left. b) Curvature of first arrival time field. Black corresponds to curvatures less than -2 (inverse pixels), white to great than +2, and the intensity is linear in between. c) Position of clefts superimposed on curvature picture

characteristics collide. As the front continues to propagate clefts can merge but never disappear. As the lobes between the clefts increases in size and decrease in curvature they become dynamically unstable and indent smoothly. After propagating a distance of the radius of curvature of the indentation a shock forms and a cleft appears. Thus the overall process is one of clefts continually forming and then merging but never disappearing as can be seen in figure 1(c).

Simpson's previous work states that lobe and cleft instability does not arise in the slip-boundary condition case and hence the instability is due to the overrunning of ambient fluid. This is not necessarily the case however. Compared to environmental flows experiments and simulations are performed at very low Reynolds numbers, where the flows are only barely turbulent. At higher Reynolds numbers the overrunning layer will increase in size relative to trapped ambient layer (scaling as $1/\sqrt{\mathrm{Re}}$) making the trapped layer less important. Since lobes and clefts are still observed for these flows there must at the very least be one other source of instability. An alternative explanation of the results of (4) is that with a slip boundary there is much less turbulence in the flow, and one would have to go to much higher Reynolds number to observe the instability. The scaling of this mechanism also seems wrong. As the flow increases in size and the Reynolds number increases the overrun layer shrink in thickness and one might expect the scale of the instability to scale with this.

Although only one of these seems to have received much attention in the literature. At least three possible mechanisms for generating the initial negative curvature leading to cleft formation appear to be possible, they will be described along with experimental evidence.

References

[1] HÄRTEL, C., MEIBURG, E. & NECKER, F. 2000 alysis and direct numerical simulation of the flow at a gravity-current head. part 1. flow topology and front speed for slip and non-slip boundaries. *J. Fluid Mech.* **418**, 189.

[2] HÄRTEL, C., MEIBURG, E. & NECKER, F. 2000 Analysis and direct numerical simulation of the flow at a gravity-current head. part 2. the lobe and cleft instability. *J. Fluid Mech.* **418**, 213.

[3] MCELWAINE, J. N. 2003 Image analysis for avalanches. To appear. Proceedings of International Seminar on Snow Avalanches Experimental Sites, Grenoble 2001.

[4] SIMPSON, J. E. 1972 Effects of the lower boundary on the head of a gravity current. *J. Fluid Mech.* **53**, 759-768.

[5] SIMPSON, J. E. 1997 *Gravity currents in the environment and the laboratory*. Cambridge University Press.

EXPERIMENTAL AND NUMERICAL SIMULATION OF DENSE WATER OVERFLOWS ON A CONTINENTAL SLOPE

Sabine Décamp, Joël Sommeria
LEGI / Coriolis, 38041 Grenoble, France

Summary We study a gravity current flowing down a uniform slope in a stratified or homogeneous media with rotation. Experiments performed on the large Coriolis turntable (Grenoble) are used to determine the stabilization depth of the main current, to measure the mixing and friction effects in a rotating system and to observe developments of instabilities. Experiments are used to test different turbulent mixing parameterization in numerical models used in oceanography.

Oceanic context

Dense overflows on a continental slope play an important role in renewing deep water as part of the global thermohaline convective cycle. Cold water from Nordic seas or salty water from the Mediterranean Sea descent into the Atlantic ocean over a sill, resulting in mass exchange with high density gradient, instabilities and mesoscale vortices creation. The main objectives of this study are to determine experimentally the principal characteristics of the gravity current (its position, width, thickness, velocity or development of instabilities), to measure the effects of bottom friction, mixing and entrainment in a rotating system and to test the influence of turbulent mixing parameterization in numerical models used in their oceanic configuration.

Experimental simulation

The experiments are performed on the large Coriolis turntable (Grenoble) with the experimental setup described in figure 1. The gravity current is created by salty water injected with a constant flux, which then flows down the incline slope (2m wide, 10m long, 15^o of inclination) with intense turbulent mixing occurring at the interface. In cases of homogeneous media the initial density differences are of 0.75%, 1.5% or 3.0%; and in cases of uniformly stratified environment, the density of the incoming fluid is that of the bottom water. The gravity current is deviated under Coriolis forces along the slopping bottom. The dimensions of the experiment permit to obtain a gravity current both turbulent and strongly influenced by rotation, and allow a good similarity with the oceanic scale with Rossby and Burger numbers conserved. For instance a continental slope of 122km wide and 3km deep can be reproduced. Earlier experiments were done either without rotation (Baines), or in a quasi-laminar regime (Etling).

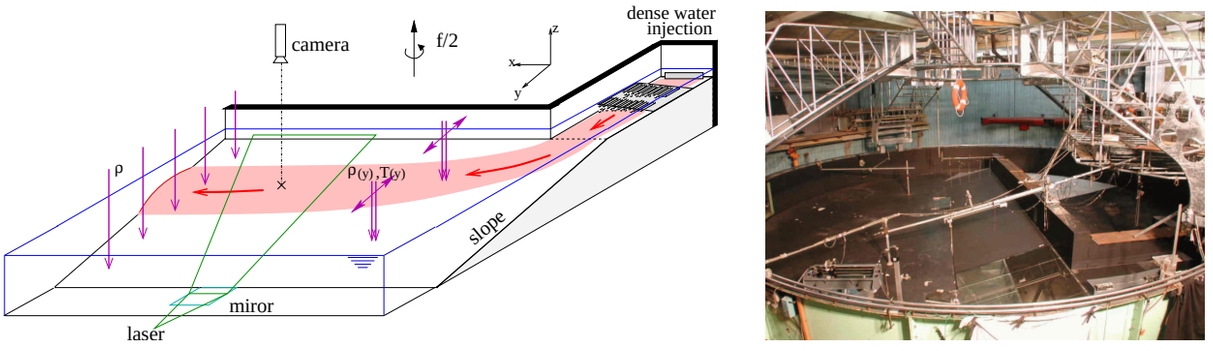


Figure 1. Schematic representation and picture of the experimental setup, with the position of the probes and laser

Velocity fields are measured by particle image velocimetry (PIV). The current is seeded with particles illuminated by a laser sheet directed along the slope at different heights. Probes are also used to record density variations at different locations (Fig 1).

This experimental study allowed trajectory visualisation of the gravity current (Fig 2). From the inlet, the current first flows down the slope as a usual turbulent gravity current, mixing with the ambiant fluid. It is then deflected by the Coriolis force and reaches an equilibrium depth, in a state of geostrophic balance. However a small part of the fluid is moving downward in the bottom viscous boundary layer. It is subject to a friction driven instability, as seen in figure 2a. Another instability, of baroclinic kind, is observed on the main current, generating large vortices stretching over the whole water depth (Fig 2a).

The position of equilibrium can be measured from velocity fields obtained by PIV, as shown on figure 3 in the main current. Density profiles also permit to determine the width, thickness and position of the gravity current, and to measure the mixing occurring mainly at the beginning of the descent. The geostrophically balanced jet flowing along the slope suffers very little mixing.

A global assessment of mixing is obtained 24 hours after an experiment, once the fluid particles of different densities reach their rest state. The global distribution of density probability is calculated from vertical density profiles as shown

in figure 4. The initial density excess of the current in this experiment is 1.5% while the maximal density measured in the main current after mixing is 0.4%,corresponding to the observed peak. The occurrence of higher densities can be attributed to the downward flow in the viscous boundary layer protected from mixing.

Numerical modelling

Global oceanic models don't succeed at representing correctly those dense overflows. The main problem is often due to an excessive mixing of the deep water masses. Models have trouble treating topography, coarse vertical resolutions,and inadequate parameterization of bottom friction and turbulent mixing, especially when rotation is important. These laboratory experiments can be used as test cases to compare the performance of different parameterizations. An isopycnal coordinate model, MICOM, is used here because diapycnal mixing (between layers of different densities) is introduced only by the turbulence parameterization, without numerical contributions. Mixing between the different layers is represented by Hallberg's parameterization (2000) which is based on Turner's turbulent entrainment scheme (1986).

The main features of the gravity current are well reproduced by numerical simulations, but velocities obtained are too high while the current thickness is too small. A thorough analysis of the turbulence parameterization influence is in progress.

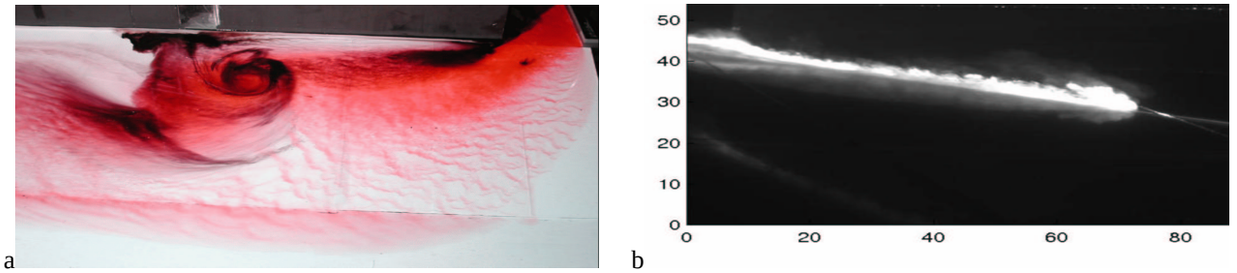


Figure 2. Visualisation of the gravity current behaviour. **a.** The current (red dye) splits into a geostrophically balanced jet flowing along the slope and a thin layer slowed down by viscosity descending the slope. The main current is subject to baroclinic instabilities which induce cyclonic vortices over the gravity current seen by injection of black dye. **b.** The vertical cut (fluorescine illuminated by a vertical laser sheet) shows that the current thickness decreases at the beginning of the slope before growing because of turbulent mixing.

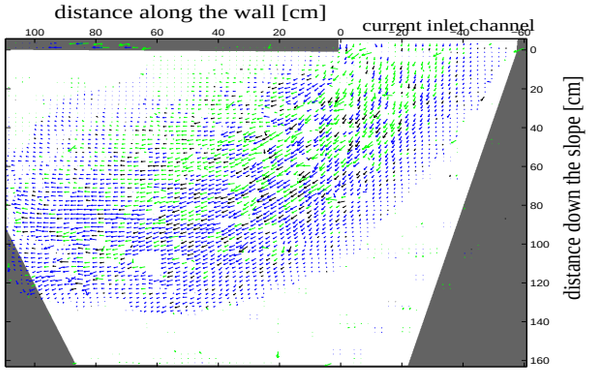


Figure 3. Example of velocity field obtained for the main current by PIV with a laser sheet parallel to the slope at a distance of 2cm.

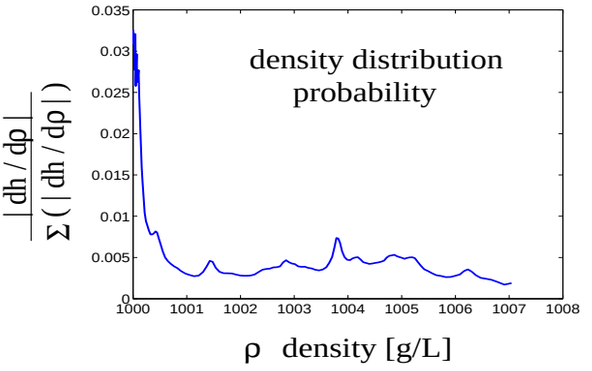


Figure 4. Global density distribution probability obtained by mixing for a current of 1.5% of initial density excess. A peak at 0.4% and A nearly uniform distribution is observed with a peck at 0.4%, the main current density after mixing.

Conclusions

The dynamics of a dense water overflow on a continental slope has been reproduced in laboratory for the first time: effects of rotation and density stratification are reproduced in dynamical similarity, and the gravity current is fully turbulent. The mixing of this current with the surrounding fluid has been characterized, providing support for modelling of turbulence in such systems.

References

[1] Baines P.G.: Mixing in flows down gentle slopes into stratified environments. *J. Fluid Mech.* **443**, 237-270, 2001.
[2] Etling D. et al.: Experiments with density currents on a sloping bottom in a rotating fluid. *Dyn. Atmos. Oceans* **31**, 139-164, 2000.
[3] Hallberg R.: Time integration of diapycnal diffusion and Richardson number dependent mixing in isopycnal coordinate ocean models. *Mon. Wea. Rev.* **128**, 1402-1419, 2000.
[4] Turner J.S.: Turbulent entrainment: the development of the entrainment assumption, and its application to geophysical flows. *J. Fluid Mech.* **173**, 431-471, 1986.

High resolution modelling of atmospheric flow over southern Poland

Jakub Krawczyk[*], Mirosław Andrejczuk[*], Zbigniew Piotrowski[*], Joanna Strużewska[**], Bogumił Jakubiak[***], Szymon Malinowski[*], Lech Łobocki[**]

[*]*Warsaw University, Institute of Geophysics, Pasteura 7, 02-093 Warszawa, Poland.*
[**]*Warsaw University of Technology, Institute of Environmental Engineering Systems, Nowowiejska 20, 00-653Warszawa, Poland*
[***]*Warsaw University, Interdisciplinary Centre for mathematical and Computational Modelling, Pawińskiego 5a, 02-106 Warszawa, Poland*

Summary. A nonhydrostatic model of atmospheric flows EULAG is set up over southern Poland on grid with 1km horizontal resolution. The goal is to test a short-term numerical weather prediction over complicated topography with explicit treatment convective processes. Boundary and initial conditions are interpolated from routine mesoscale hydrostatic UMPL model running at 17km resolution.

OVERVIEW

One of the limitations of contemporary mesoscale numerical weather predition (NWP), resulting from the coarse grid resolution is necessity to parameterize convective processes. Convection is responsible for intense mesoscale phenomena, like thunderstorms, flash-floods, mesoscale convective complexes, gust fronts e.t.c.. Other mesoscale phenomena: valley circulations, gravity waves, forced convection result from interaction of the flow with topography, which at a coarse resolution differs significantly from the reality. This means, that many important intense phenomena, important from the point of weather forecasting are not directly solved by a routine NWP model. In the following we describe an attepmt to overcome these limitations by running a limited area mesoscale model at a high resolution mesh on which many convection/small scale phenomena can be resolved directly.

The high-resolution model was set up over southern Poland covering a square of 200x200x19km with switchable 1km/2km/4km horizontal grid with up to 60 unequally spaced levels in vertical. The area covered by symulations covers three different regions: a hilly terrain 200-450m a.s.l in the northern and middle part of the domain Wisła river valley, with flat bottom 190-250m a.s.l. and front ranges of Carpathian mountains peaking 1300m a.s.l. In the south. The computational area is embedded inside the mesh an operational hydrostatic UMPL NWP model [1], covering central Europe with 17km horizontal resolution.

The analytic equations of motion (in anelastic approximation), thermodynamic energy equation, water substance conservation equation and equations for the cloud water, rain water and ice parameterizations (bulk or detailed) are solved by means of finite-difference approximations using the semi-Lagrangian/Eulerian nonhydrostatic anelastic model EULAG. Sevaral parameterizations of subgrid scale turbulent kinetic energy, cloud and rain microphysics and other meteorological processes (e.g. Heat and humidity flux at the bottom) are available. More information on equations and numerical solutions can be find in [2,3,4,5].

In order to feed high -resolution EULAG with the low resolution UMPL data following operations were made:

1) conversion of UMPL's sigma-p to EULAG's sigma-z vertical coordinate;
2) interpolation of initial and boundary fields from UMPL's 17 km grid to EULAG's 1 km grid;
3) in a border of EULAG domain an interpolated topography with smooth transition from 17km resolution to 1km resolution was introduced;
4) since upper boundary of EULAG mesh is below the upper boundary of UMPL grid, the upper boundary condition has also been interpolated.

   In practice initial/lateral data were interpolated horizontally, using linear or spline interpolation in each level separately, later the data were interpolated vertically in columns to obtain requested number of levels .Vertical interpolation was done together with sigma-p – sigma -z transition.

NUMERICAL SIMULATIONS

The case study presented below is based on meteorological situation from August 26, 2001. NNW inflow of a relatively dry air at the peripheral part of the high pressure system formed good conditions to observe convective clouds forced by topography. Calculations with EULAG began at 8 am, boundary conditions were taken from UMPL's output, heating of the surface by solar radiation was accounted for. Horizontal resolution of the mesh of the presented run was 2 km, the calculations were performed with 60 levels in vertical.

In the course of calculations development of convective clouds forced by NW flow was observed. One band of convective clouds began to form at 10:40 over Jura Krakowsko-Częstochowska. At the same time the second band of Cumulus clouds appeared over the front ranges of Carpathians. Within next three hours the first band grown up and drifted southwards over the Wisła river valley, while the second band was stationary, with some clouds dissipating and new appearing in the same area. A snapshot of this situation at 01:40 local time is presented in the figure on the next page.

At this time comparison of the model output to the satellite image collected at 01:46 by the polar orbiting Sea-Star was made. In the satellite image also two bands of clouds separated with a band of clear air over Wisła valley were visible. More detailed, quantitative comparisons were not possible due to a poor resolution of the available satellite image.

Later during the day both bands of clouds merged over Carpathians, producing small amount of precipitation, which evaporated before reaching the ground level. The calculations were stopped at 16:00 in the afternoon.

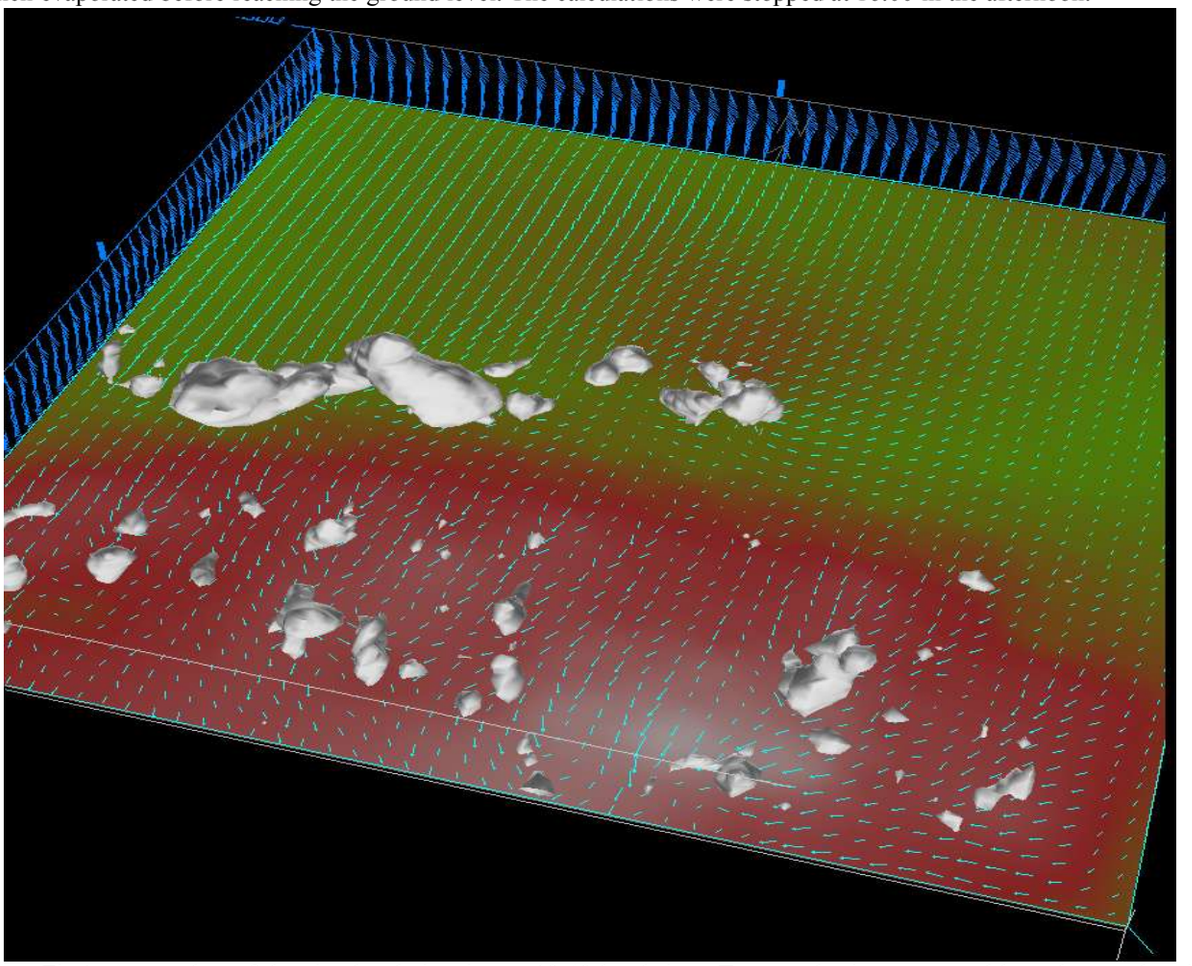


Fig.1. A snapshot of the simulated situation at 13:40 local time. Topography is represented by colour scale with green lowlands in the north and pink highlands in the south of the domain. Airflow at 1500m level is visualized with light blue arrows. Darker arrows at the domain edge show the inflow through the lateral boundary. Clouds are visualized with the isocontour (0.1g/kg) of condensed water.

CONCLUSIONS

The presented case study indicates, that simulations of convective atmospheric processes driven by a local orography at a small (of order kilometer) scale are possible. Even in a case of very complicated topography, careful inretpolation of initial and boundary data and existence of smooth transition region between high-resolution and low-resolution topography makes such a simulations possible.

Acknowledgements:
This research was supported by grant No. 6 P04D 027 19 of the Polish Committee for Scientific Research. Computations with UMPL model were performed at the Interdisciplinary Center for Mathematical and Computational Modeling of Warsaw University.

References.

[1] Niezgódka, M., B. Jakubiak, 2002: Scientific aspects of Numerical Weather Prediction at ICM in 'Research works based on the ICMs UMPL numerical weather prediction system results", ICM, **.ISBN 83-917150-0-0,** pp. 7-13.

[2] Grabowski W.W., P.K. Smolarkiewicz, 2002: A multiscale anelastic model for meteorological research. Mon. Weather Rev. 130, 939-956.

[3] Smolarkiewicz P.K., V. Grubisic, L.G. Margolin, 1997:On forward-in-time differencing for fluids: Stopping criteria for iterative solutions of anelastic pressure equations. Mon. Weather Rev. 125,: 647-654.

[4] Smolarkiewicz P.K.and L.G. Margolin, 1998: MPDATA: A finite-difference solver for geophysical flows. J. Comput. Phys. 140,: 459-480.

[5] Smolarkiewicz P.K, J.M. Prusa, 2002: VLES modelling of geophysical fluids with nonoscillatory forward-in-time schemes. Int. J. Numer .Meth. Fl. 39, 799-819.

FORMATION AND RAPID EXPANSION OF DOUBLE DIFFUSIVE LAYERING IN LAKE NYOS

Alfred Wüest and Martin Schmid
Applied Aquatic Ecology, EAWAG, CH-6047 Kastanienbaum, Switzerland

Summary This contribution addresses a fascinating case of double-diffusion (DD) in lakes. In Dec. 2002, 26 well-mixed layers (thicknesses: 0.2 - 2.1 m) separated by sharp interfaces were discovered in Lake Nyos – the dreaded "Killer Lake" in Cameroon – although no signs of DD have been reported since the catastrophic CO_2 eruption in 1986. The heat fluxes increased by an order of magnitude since the onset of DD convection and continuously reduce the stability, which leads to rapid expansion of the DD zone.

INTRODUCTION

Lake Nyos is a 208 m deep crater lake (surface area: 1.58 km^2) in the north-western part of Cameroon. The water column is divided into two sections by a halocline (steep chemical gradient). The upper section, the "surface-layer", is convectively mixed every year during the dry season, whereas in the lower section, the "deep-water", is not affected by this process and remains permanently stratified. Subaquatic sources introduce warm, salty and CO_2-enriched water into the deepest part of the water column [1]. Due to the high CO_2 concentration, the source water is heavier than the hypolimnetic water and thus increases the overall stability of the water column. These subaquatic sources are the reason for the permanent stratification of the water column.
In August 1986, a large CO_2 cloud erupted from the lake and asphyxiated more than 1700 people. Several processes, which will be shortly mentioned in the presentation, have been proposed as the trigger of the eruption. To prevent a new disaster, a plan for degassing the lake was developed [2]. Currently a degassing pipe with a diameter of 14.5 cm has been installed, which transports water from 203 m depth by a self-sustained fountain to the surface [2].
A characteristic of Lake Nyos is its permanent stratification which is upheld against the destratifying effect of temperature (Figure) by the high concentrations of CO_2 and salinity (whereas CO_2 is more important than salinity). Such stratification with a stabilizing and a destabilizing component, can lead to convective layers by double-diffusion (DD), if the effect of the stabilizing component is not much more than the destabilizing effect of temperature [3, 4]. The susceptibility to DD convection increases as the density ratio R_ρ decreases.

OBSERVATIONS AND RESULTS

The Figure shows a sample section of the DD zone of the CTD profile, collected in December 2002, which revealed a prominent zone of 26 well-identifiable homogeneous layers. The 0.2 to 2.1 m thick layers were distinctly separated by interfaces of strong gradients. The steps are more pronounced in the salinity than in the temperature (Figure). Surprisingly, the DD staircase was never observed before and must have developed a few months back. Before the onset of DD, the temperature at this depth was constant within the measurement resolution of 0.01 ºC, afterwards it decreased almost linearly due to the upward heat flux caused by DD. The DD convection was most probably triggered by the strong seasonal cooling in February 2002, which caused a steep temperature gradient and consequently an increased heat flux at the top of the halocline. In the case of Lake Nyos, the stabilizing factor is not only salt (TDS; Figure), but also CO_2, and subsequently we define the density ratio R_ρ [3] by

$$R_\rho = \frac{\beta_{TDS} \cdot \frac{\partial TDS}{\partial z} + \beta_{CO2} \cdot \frac{\partial [H_2CO_3]}{\partial z}}{\alpha \cdot \left(\frac{\partial T}{\partial z} - \Gamma \right)}$$

Several semi-empirical equations have been proposed to estimate the average thickness H of the steps in DD staircases. Fedorov [5] found that H depends on R_ρ and consequently on the gradients of both the temperature and the dissolved matter. In the DD zone Fedorov [5] provides layer thicknesses between 0.80 m and 1.20 m, slightly increasing with depth. The observed layer thicknesses (average 1.0 m) agree well with Federov's (average 0.9 m). The DD convection leads to an increased transport of heat, salinity and CO_2 out of the deep-water. Several parameterizations for the estimation of the temperature flux F_T have been proposed in literature. We used the semi-empirical equation [6]

$$F_{T,Kelley} = \frac{1}{(13 \pm 6)} \cdot \left(\frac{g \cdot \alpha \cdot \Delta T \cdot H^3}{D_T \cdot \nu} \right)^{0.27 \pm 0.02} \cdot \frac{\Delta T \cdot D_T}{H}$$

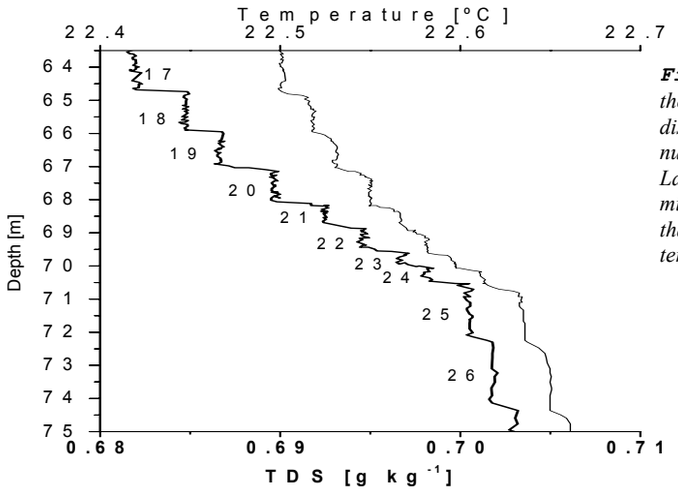


Figure: *Details of an 11-m long section from the profiles of temperature (thin line) and total dissolved solids (TDS) (thick line with layer numbers) measured on 8 December 2002 in Lake Nyos. The observed convectively well-mixed layers are numbered from the top. Note that the interfaces are much steeper for temperature than for TDS.*

and compared it to estimates from the heat budget method. For the flux law the uncertainty of the exponent of ± 0.02 given by [6] was used. The fluxes calculated by the heat budget and using the DD flux laws agree well within the range of the uncertainties and yield about 0.3 W m^{-2}. This agreement was not expected a priori, since the two methods determine the fluxes for completely different time scales. Whereas the heat budget method integrates the heat flux over 260 days, the flux law is a snapshot of the stratification at the end of this period. This agreement indicates, in combination with the nearly linear temperature trend at 62 m depth, that the DD heat flux was approximately constant in time. The heat fluxes following Turner [3] were on average 68% higher than the fluxes of Kelley [6]. The equations of Fernando [7] generally seem to under- (diffusive regime) or overestimate (low stability regime) the heat fluxes. The estimated fluxes of the dissolved components were in the range of 5 - 20 µg m^{-2} s^{-1}, of which more than 80% is CO_2. Integrating over 260 days and the area at 60 m depth, yields a total transport of about 160 t. This is only a small part of the estimated annual CO_2 input of more than 4400 t CO_2 from the deep subaquatic source [1, 8].

CONCLUSIONS

A staircase with 26 well-mixed layers at 53 to 75 m depth was formed by DD convection in Lake Nyos. The temperature profile in this zone is now rapidly transformed: At 62 m depth, the temperature decreased by 0.15 ºC within 9 months. The heat flux caused by the DD convection ranged from 0.1 W m^{-2} in the lower layers to 0.5 W m^{-2} in the upper layers of the staircase. The thicknesses of the observed steps agree well with the semi-empirical equations of Fedorov [5] and Kelley [6].

The heat fluxes based on the heat budget and on the flux laws of DD convection yield the same results within the uncertainty. The semi-empirical equation of Kelley [6] agreed better with the heat budget than Turner [3] and Fernando [7]. Without the DD convection the heat flux is dominated by molecular diffusion. Since the apparent diffusivities caused by DD are about one order of magnitude larger than the molecular diffusion coefficient, we can conclude that DD has increased the heat flux by one order of magnitude and is now the dominant cause for the vertical heat fluxes. They are similar to the heat input of the subaquatic source as estimated by Kusakabe [1] and Schmid [8]. On the contrary, the CO_2 fluxes caused by DD are negligible compared to the subaquatic input.

The current situation, with decreasing heat fluxes as a function of depth, leads to an increase in the destabilizing temperature gradient in the DD zone, which is only to a small part compensated by the CO_2 flux. If the temperature gradient is going to continue to increase, the entire zone could become unstable and a large homogenous layer could be formed within a few years. With the current CO_2 concentrations such a mixing would not be dangerous, but if the CO_2 concentration were near saturation, this process could lead to local supersaturation of CO_2 and subsequently to a new eruption. This mechanism is a possible candidate for having triggered the catastrophic eruption in 1986.

References

[1] Kusakabe M. et al. Journal of Volcanology and Geothermal Research 97, 241-260, 2000
[2] Halbwachs, M. and Sabroux, J.C. Removing CO_2 from Lake Nyos in Cameroon. Science 292, 438-438, 2001 http://perso.wanadoo.fr/mhalb/nyos/nyos.htm
[3] Turner, J.S. Buoyancy Effects in Fluids. Cambridge University Press, Cambridge, 1973
[4] Huppert, H.E. and Linden, P.F. Journal of Fluid Mechanics 95, 431-464, 1979
[5] Fedorov, K.N. In: Nihoul, J.C.J., Jamart, B.M., (Eds.), Small-Scale Turbulence and Mixing in the Ocean. Elsevier, 471-479, 1988
[6] Kelley, D.E. Journal of Geophysical Research 95, 3365- 3371, 1990
[7] Fernando, H.J.S. Journal of Physical Oceanography, 19, 1707-1715, 1989
[8] Schmid M. et al. Ocean Dynamics 53, 288-301, 2003.

XXI ICTAM, 15–21 August 2004, Warsaw, Poland

JOINT URBAN 2003 SURFACE ENERGY BUDGET MEASUREMENTS AND ANALYSIS

J.E. Holeman, M. Princevac, S. Grossman-Clarke, S.M. Lee, H.J.S Fernando, R. Calhoun
EFDP, Department of Mechanical and Aerospace Eng., Arizona State University, AZ 85287, USA

Summary Understanding of the surface energy balance is a critical component of the correct modeling of flow in an urban environment. During the Joint Urban 2003 field campaign, extensive data were collected of the components of the surface energy. These data were analysed in an attempt to close the surface energy budget and to gain an understanding of energy partition.

INTRODUCTION

Research on air flow in urban environments is of considerable importance. Since much of humanity lives in urban settings, it is vitally important from the point of view of public safety to understand the mechanisms through which pollution and other contaminants disperse therein. The Joint Urban 2003 (JU 2003) field campaign was conducted from late June through early August in 2003 to provide data needed to increase our understanding of urban meteorology and dispersion [1, 2]. One of the important aspects that was studied by our group during JU 2003 was the efficacy of current surface energy budget schemes used in meso-scale meteorological models. The surface energy is what drives many of the flows in urban environments [3, 4], and it has been demostrated that surface energy parameterizations of the popular mesoscale meteorological model MM5 needs improvement [5]. During JU 2003, the our group fielded a suite of instruments in order to measure the dominant components of the surface energy budget in a grassy city park located in a suburban area.

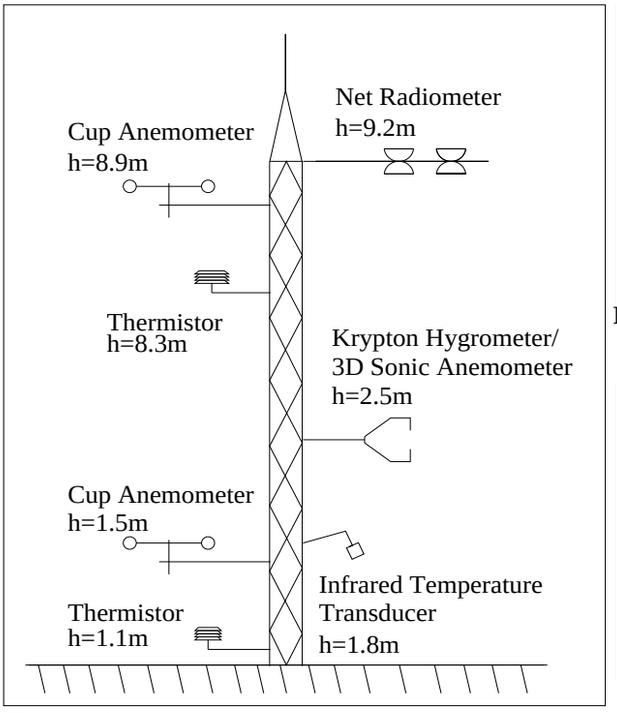


Figure 1: Meteorological Tower Instruments used to measure atmospheric surface energy budget components.

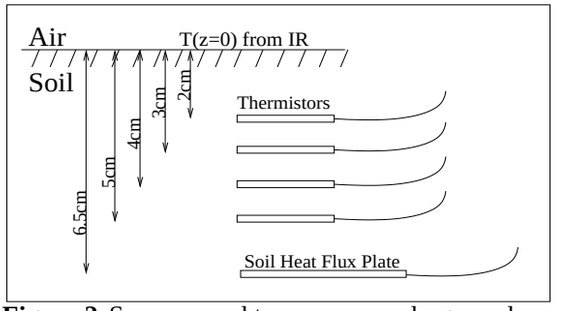


Figure 2: Sensors used to measure underground components of the surface energy budget.

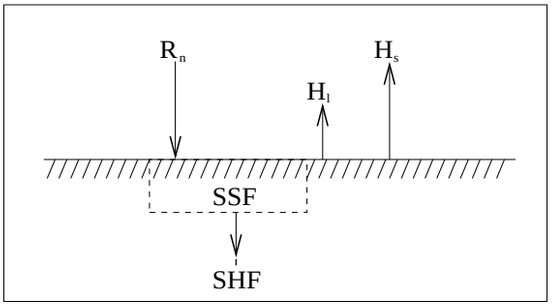


Figure 3: Schematic of the components of the surface energy budget: net raditaion(R_n), sensible heat flux(H_s), latent heat flux(H_l), soil heat flux(SHF), and soil heat storage flux(SSF)

PRELIMINARY RESULTS

Two days in mid-July were chosen for analysis, considering their relatively cloud-free skies on those days. If the assumption of a vertical, one dimensional system is correct, various componants of the surface energy budget (see Figure 3) are expected to be in balance. The net radiometer used is able to measure the shortwave(R_s) and longwave radiation(R_l) both facing up and down. The net radiation present at the Earth's surface is $R_n = R_{l\downarrow} + R_s^{\downarrow} - R_l^{\uparrow} - R_s^{\uparrow}$(Figure 4). The part of the energy, R_n, which is transferred to the atmosphere does so by one of two processes: the sensible heat, and through the evaporation of water into the air, the latent heat. These were measured by turbulent flux instruments near the ground. The sonic anemometer and fine wire thermocouple are used to measure the covariance between vertical velocity (w) and temperature (T), $\overline{w'T'}$ (where $\cdot'$ terms indicate a fluctuation, based on one minute averages). The sensible heat flux is then

$H_s = c_p \rho \overline{w'T'}$, where c_p and ρ are the specific heat at constant pressure and the density, respectively, of dry air. The sonic anemometer is used with a Krypton hygrometer to measure the covariance between vertical velocity (w) and water vapor density (q), $\overline{w'q'}$. Latent heat flux is $H_l = L_v \overline{w'q'}$, where L_v is the latent heat of vaporization (Figure 5). In order to close the energy budget, it is also necessary to measure the heat flux through the bottom of the control surface for the soil layer (SHF) as well as the storage in the control volume (SSF). SHF was measured by a heat flux plate located at a depth of 6.5cm. Integrating the temperature profile of the soil yields energy storage per unit area. Differentiating this with respect to time produces the net flux required to heat or cool the upper soil layer: Soil Storage Flux (SSF) $= \frac{d}{dt} \int_{depth}^{0} c \rho_s T(z) dz$, where c is the specific heat of the soil, ρ_s is the soil density, and $T(z)$ is the temperature profile (Figure 6). The sum $H_s + H_l + SHF + SSF$ is the quantity that should balance the net radiation, R_n. Comparing these quantities as in Figure 7, we see consistancy between the two curves. This is an indication that the measured quantities indeed do a good job of characterizing the surface energy budget in this suburban park. Further, it appears that the assumption of a vertical, one dimensional system may be adequate to describe the surface energy budget at this experiment site.

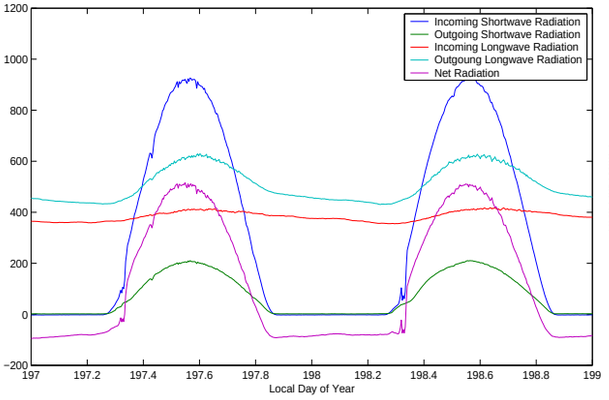


Figure 4: Radiative fluxes for July 16 and 17

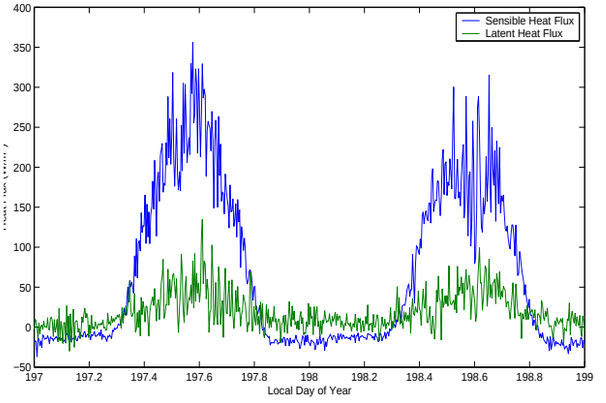


Figure 5: Sensible and latent heat fluxes for July 16 and 17

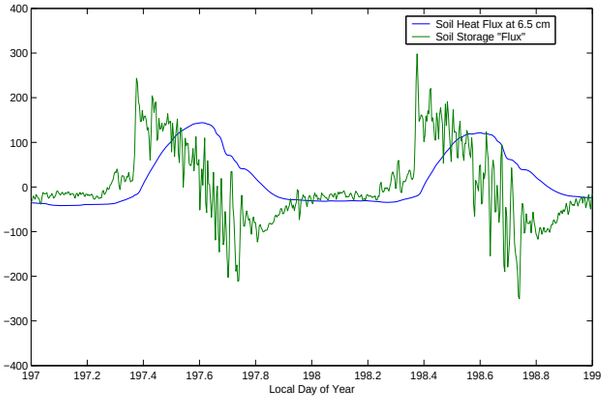


Figure 6: Soil heat fluxes for July 16 and 17

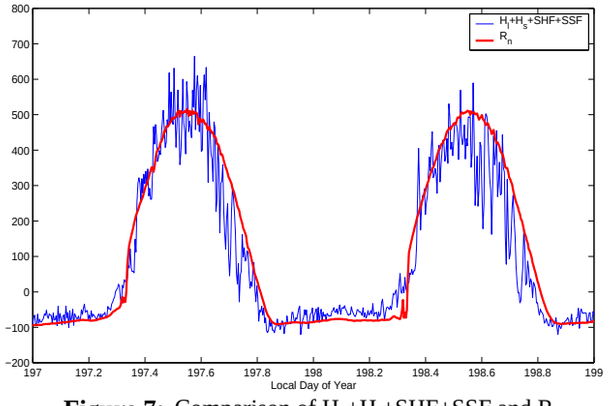


Figure 7: Comparison of H_s+H_l+SHF+SSF and R_n

ACKNOWLEDGEMENTS

Financial support of the Army Research Office and National Science Foundation is gratefully acknowledged.

References

[1] Joint Urban 2003, web site http://ju2003.pnl.gov/

[2] Joint Urban 2003 Atmospheric Dispersion Study, Oklahoma City, Jun-July 2003. Experimental Plan (available from http://ju2003.pnl.gov/study.html)

[3] Fernando H.J.S., S.M. Lee, J. Anderson, M. Princevac, E. Pardyjak and S. Grossman-Clarke: Urban Fluid Mechanics: Air Circulation and Contaminant Dispersion in Cities, *J. Env. Fluid Mech.* **1**: 107-164, 2001

[4] Grimmond C.S.B and T.R. Oke: Turbulent heat fluxes in urban areas: Observations and a Local-scale Urban Meteorological Parameterization Scheme (LUMPS), *J. Appl. Meteor.*, **41(7)**: 792-810, 2002

[5] Zehnder, J.A.: Simple Modifications to Improve Fifth-Generation Pennsylvania State University-National Center for Atmospheric Research Mesoscale Model Performance for the Phoenix, Arizona, Metropolitan Area, *J. Appl. Meteor.* **Vol. 41(9)**:971-979, 2002

NOCTURNAL TEMPERATURE INVERSIONS UNDER CALM CLEAR CONDITIONS: AN ANALYTICAL STUDY

A. S. Vasudeva Murthy and Saji Varghese
TIFR Centre, Indian Institute of Science campus, Bangalore 560 012, India.

Summary The knowledge of inversion height in the nocturnal boundary layer (NBL) under calm clear conditions is crucial in determining the fate of chemical pollutants that are (accidentally or otherwise) released into the atmosphere. A new analytical expression for temperature profiles over bare soil surfaces under calm clear conditions is used to study inversion height and intensity as a function of surface parameters like ground emissivity and cooling rates. Previous analytical expressions available in the literature have ignored these parameters.

INTRODUCTION

On clear days the daily cycle of sun causes a diurnal variation of heating and cooling of the earth's surface which effect the immediate air layers above it creating a boundary layer. While the daytime convective boundary layer has been reasonably well studied (Garrat 1992) the same does not seem to be true for the nocturnal boundary layer (Ha and Mahrt, 2003). One of the main reasons for this is the complex nature of the radiative flux divergence. During the daytime the ground gets hotter quickly than the air because very less solar radiation is absorbed by air. On the other hand during nights the ground cools rapidly by radiating to the cooler space. This rapid cooling of the ground causes cooling of air above it by molecular conduction (because of near zero wind conditions). This results in a temperature profile that increases with height upto some level (say) z_{inv}. Therafter the temperature decreases with the usual adiabatic lapse rate provided all the daytime turbulent convection is eroded. This height z_{inv} is what we refer as the nocturnal inversion (Figure 1). This inversion acts as a lid that stops vertical motion and mixing. Consequently pollutants released within an inversion layer often travel long distances without much mixing and spreading causing severe disasters. One such disaster occured in Bhopal (India) during the early hours of 3, December 1984 when methyl isocyanate (MIC) escaped through a nozzle of 33 m high atmospheric vent-line from the Union Carbide plant. The nocturnal inversion at that time was estimated to be around 250m (Maithili Sharan et al., 1995) which is well above the height at which the lethal MIC got released. This affected about 250,000 people causing death to a significant proportion. Thus the importance of studying nocturnal inversion need not be over emphasized.

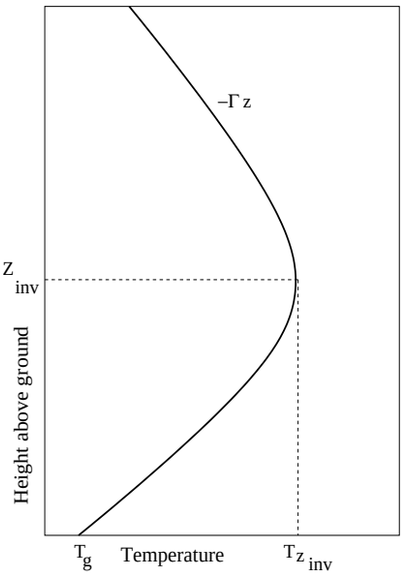


Figure 1. Schematic of typical nocturnal temperature distribution with radiation inversion.

THE ANALYTICAL SOLUTION

Assuming calm clear conditions, so that the nocturnal temperature profile is a function of the vertical height and time alone, Narasimha and Vasudeva Murthy (2003, hereafter NV) derived an approximate analytical solution using singular perturbation techniques. If $T(z,t)$ denotes the temperature at height z and time t the analytical expression is given by

$$T(z,t) = T_{g_0}[1+\Theta] - \Gamma z. \tag{1}$$

Here T_{g_0} is the initial ground temperature (for example, it could be just after sunset). The expression for Θ is

$$\begin{aligned}\Theta &= -\lambda - \epsilon_g\beta\sqrt{t} + \Gamma z + [\lambda - \Gamma z]e^{-\tau e_m(z)} + [\lambda + (\epsilon_g - 1)\beta\sqrt{t}]e^{-\zeta} \\ &\quad -\lambda e^{-\tau} erfc\left(\frac{\zeta}{2\sqrt{\tau}}\right) - \frac{\lambda}{2}\left[e^{-\zeta} erfc\left\{\frac{2\tau-\zeta}{2\sqrt{\tau}}\right\} - e^{\zeta} erfc\left\{\frac{2\tau+\zeta}{2\sqrt{\tau}}\right\}\right]\end{aligned} \tag{2}$$

Here,

$$\lambda = (1-\epsilon_g)(1-\epsilon_s)/4, \tag{3}$$

ϵ_g is the ground emissivty and ϵ_s is the sky emissivity, β is the ground cooling rate and Γ is the adiabatic lapse rate. The function $e_m(z)$ is given by

$$e_m(z) = \frac{\exp(-\delta z)}{1+\alpha z} \tag{4}$$

where δ^{-1} corresponds to the scale height of water vapour mixing ratio and α^{-1} corresponds to the so called emissivity layer or the radiative boundary layer height. Finally ζ and τ are the boundary layer variables

$$\zeta = \epsilon^{-1/2} z, \quad \tau = \epsilon^{-1} t, \tag{5}$$

ϵ is the ratio of radiative to diffusive time scales and is the small parameter in the formulation, typical values are 10 s and 10^5 s (see NV). The smallness of ϵ indicates the dominance of radiative flux divergence in the nocturnal boundary layer.

Several analytical expressions have been proposed by various authors (see Ragothaman et al., 2002, hereafter R02) but none of them take into account surface parameters like $\epsilon_g, \epsilon_s, \alpha$ and β. R02 have also considered these parameters but it was based on numerical simulation. This simple analytical expression explicitly shows how the near surface temperature evolution depends on surface parameters.

RESULTS AND DISCUSSION

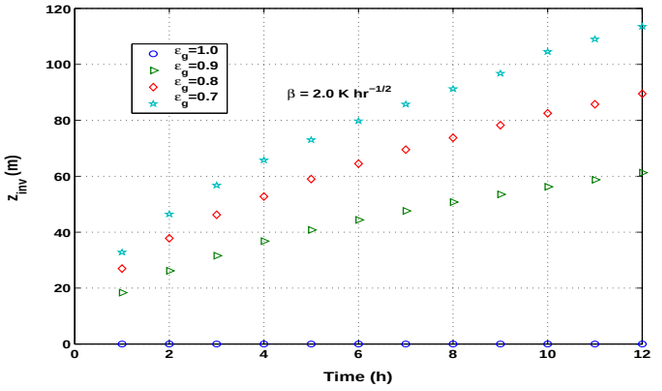


Figure 2. Effect of surface emissivity on the evolution of the inversion depth.

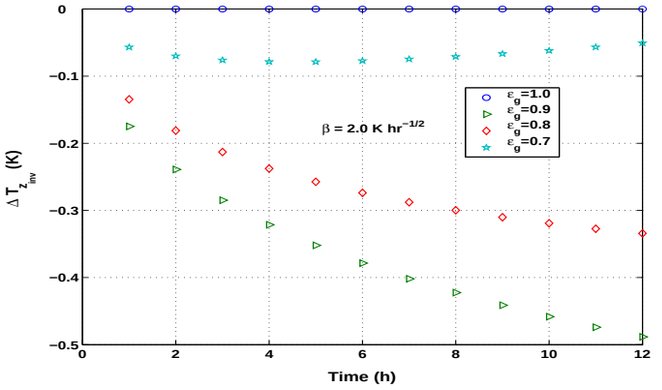


Figure 3. Effect of surface emissivity on the evolution of the temperature difference $\Delta T_{z_{inv}}$.

The above expression is used to compute the inversion height z_{inv} and the intensity of the inversion

$$\Delta T_{z_{inv}}(t) = T_{z_{inv}}(t) - T_g(t) \tag{6}$$

where T_g and $T_{z_{inv}}$ are the ground temperature and the temperature at z_{inv}. Two typical results are given in figure 2 and 3 which show the evolution of the above mentioned quantities for various emissivities of the ground. Except for $\epsilon_g \equiv 1$ the inversion height grows steadily and from the analytical expression it is clear that it grows like $\sqrt{t}$ whereas $\Delta T_{z_{inv}}$ decreases with increase in ϵ_g except at $\epsilon_g \equiv 1$. These results are qualitatively very similar to the results of R02 (for $\epsilon_g < 1$) which was based on numerical simulation of a more complex partial differential equation that included nonlinear integral terms. In deriving (1) NV have simplified the nonlocal nonlinear terms to local linear terms which was then subjected to singular perturbation analysis that yielded an approximate analytical solution. In R02 even for $\epsilon_g \equiv 1$ the inversion height showed a steady growth. Also $\Delta T_{z_{inv}}$ was always positive in R02 which means that the ground temperature is always less than the temperature at inversion height. These two lacunae could be probably due to the above mentioned simplification used in NV.

The importance of ϵ_g and β in the NBL has been recently well studied by Narasimha and his co-workers, see for e.g. Varghese et al. (2003). This was also hinted earlier by Elliot and Stevens (1966).

Acknowledgement

The authors wish to thank the Council of Scientific and Industrial Research, New Delhi for their financial support through the NMITLI project.

References

[1] Elliot W.P., Stevens D.W.: Long-wave radiation exchange near the ground. *Solar Energy*, **10**:5–8, 1966.
[2] Garratt, J. R.: The atmospheric boundary layer. Cambridge Atmospheric and Space Science Series. Cambridge University Press., 316 pp, 1992.
[3] Ha, K.-J., Mahrt L.: Radiative and turbulent fluxes in the nocturnal boundary layer. *Tellus* **55A**: 317–327, 2003.
[4] Maithili, S., Mc Nider R.T., Gopalakrishnan S.G., Singh M.P.: Bhopal gas leak: A numerical simulation of episodic dispersion, *Atmospheric Environment*, **29**: 2061–2074, 1995.
[5] Narasimha, R., Vasudeva Murthy, A.S.: An approximate solution to a simple model for the Ramdas layer. (Preprint), 2003.
[6] Ragothaman, S., Narasimha R., Vasudeva Murthy A.S.: Evolution of nocturnal temperature inversions - A numerical study. *Il Nuovo Cimento*, **25**, 147–163, 2002.
[7] Varghese, S., Vasudeva Murthy, A.S., Narasimha, R.: A fast, accurate method for computation of infrared fluxes and cooling rates in the atmosphere down to the surface. *Journal of Atmospheric Sciences*, **60**: 2869–2886, 2003.

XXI ICTAM, 15–21 August 2004, Warsaw, Poland

ON THE EVAPORATION OF A MONODISPERSE DROPLET STREAM AT HIGH-PRESSURE

Grazia Lamanna*, Han Sun*, Bernhard Weigand*, Davide Magatti**, Pietro Micciché**, Fabio Ferri**
*Institute of Aerospace Thermodynamics, Stuttgart University, D-70569 Stuttgart, Germany
**Department of Chemical, Physical, and Mathematical Sciences, University of Insubria, I-22100 Como, Italy

Summary A new experimental facility has been developed aimed at investigating the evaporation of free falling droplets at high pressure. A monodisperse droplet stream is generated in the upper part of the test rig and is embedded in a gas flow. The droplet speed is determined by means of a video technique and a stroboscope lamp. The droplet size is determined by means of the low- angle light scattering technique.

DROPLET EVAPORATION AT HIGH PRESSURE

Liquid droplet vaporization in a high-pressure, high-temperature environment is of relevance to combustion science and technology, due to the need of developing high-pressure combustion devices such as liquid-propellant rockets, gas turbines, and diesel engines. In all these systems, liquid fuels and/or oxidizer are usually injected into the combustion chamber as a spray of droplets, which undergoes a sequence of vaporization, ignition and combustion processes, at pressures levels well above the thermodynamic critical points of the liquids. Under these conditions, droplets initially injected at subcritical temperature may heat up and experience a thermodynamic state transition into the supercritical regime during their lifetimes. Consequently, for a proper design of the combustor and for an increased combustion efficiency, it is fundamental to model and predict correctly the process of transcritical vaporization. Its potential importance is so well recognized that numerous theoretical and experimental studies aimed at improving the basic understanding of the physics have been pursued [1, 2, 3, 4]. Unfortunately, albeit several evaporation models have been proposed in recent years, which include higher-order non-equilibrium effects and more complicated equation of states, their full validation has been hampered by the absence of reliable experimental data. Aim of our research activities is to develop a new test rig for studying droplet vaporization at high pressure/temperature through simplified and systematic experiments. Since the physics of fluid behaviour in the subcritical and supercritical regime is drastically different, due to the different length scales for heat and mass diffusion between the two regimes [5], we will focus at first on the subcritical regime. To that aim, we are currently developing an appropriate diagnostic tool for the determination of the evaporation rate of single-component droplets embedded in a gas flow.

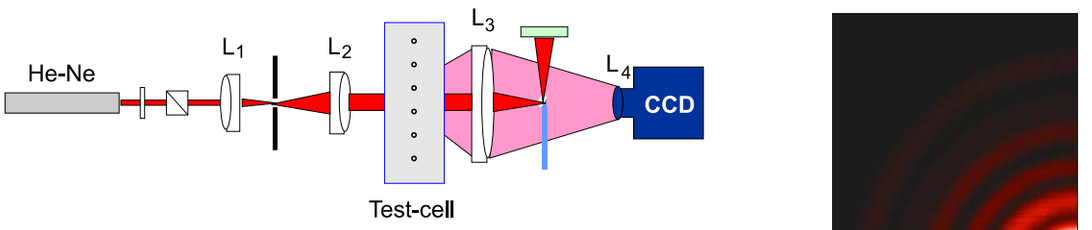
THE EXPERIMENTAL SETUP

High-pressure chamber

A new test rig has been built, where a monodisperse droplet stream evaporates under well defined conditions. The chamber can be pressurised till 80 bar and is thermally insulated to minimise heat losses. The cylindrical test section is $20\,cm$ long and has an internal diameter ϕ of $32\,mm$. The chamber is also equipped with a droplet generator, whose main components are a piezoelectric ceramic and an orifice plate. Upon exciting the piezoelectric element with a suitable frequency, a monodisperse chain of uniformly spaced droplets is obtained. A detailed description of the droplet generator can be found in [6]. The initial droplet temperature can be regulated by a heating/cooling device, and is controlled by a thermocouple. As test gas, nitrogen is used in order to exclude combustion processes. The droplets are falling vertically downwards on the centreline of the chamber and are embedded in a gas flow, in order to prevent condensation at the windows. The nitrogen flow is kept laminar and parallel to the droplet motion. The chamber is mounted on a x-y translator, so that the droplet size can be measured at different axial positions, through a set of two quartz windows $80\,mm$ long. The droplet velocity can be measured simultaneously by a CCD-camera combined with a stroboscope lamp and can be calculated from the known flash frequency of the stroboscope lamp and the distance between two consecutive droplets in the video recording.

Droplet sizing technique

The size history of the droplets is measured by means of the Low Angle Elastic Light Scattering (LAELS) technique, which was successfully applied by Ferri *et al.* [7, 8] to the characterization of large $[0.7 \div 80\,\mu m]$ polystyrene spheres. The method consists in measuring the light scattered by an ensemble of particles at various angles in the forward direction, as schematically illustrated in Fig. 1 (a). As light source, a He-Ne laser is used, whose power can be varied by means of a $\lambda/2$ retardation plate and a Glan-Thompson polarizer. The system of lenses L_1, L_2 creates a collimated beam ($\phi = 5\,mm$), which interacts with the droplet stream. The light scattered by the sample is collected by the lens L_3 and forwarded on the CCD camera. The lens L_4 conjugates the sensor plane with the focal plane of the lens L_3, therefore realizing a one-to-one mapping between scattering angles and pixel positions. A mirror, placed in the focal plane of lens L_3, deviates the transmitted beam upwards. The mirror is positioned in such a way that the focused transmitted beam hits its tip very close to the upper edge, allowing light scattered at very low angle to pass clear. This feature made it possible to use common CCD's as detectors, thus resulting in an increased angular resolution and sensitivity. An example of a typical diffraction pattern generated by a monodisperse droplet stream is shown in Fig. 1 (b).



(a) (b)

Figure 1. (a) Schematic representation of the experimental setup; (b) Typical diffraction pattern produced by a monodisperse droplet stream.

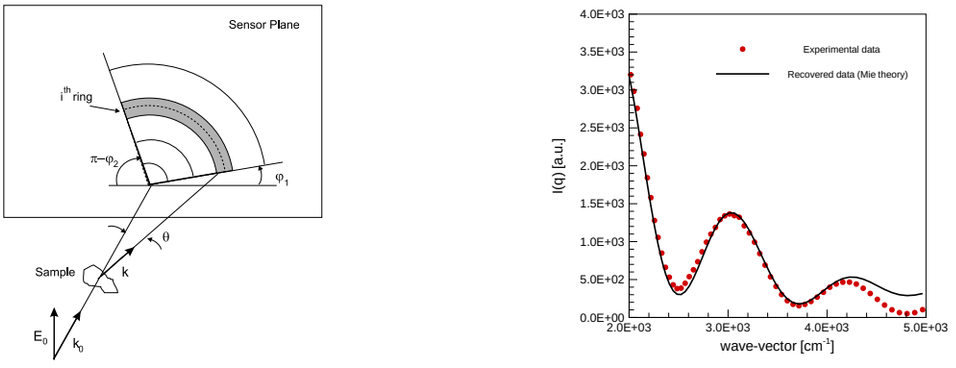
The distribution of light intensity is a function of two angles, the scattering angle θ and the polar angle φ, both defined in Fig. 2 (a). The dependence on θ carries information on the sample structure and size, while the dependence on φ accounts for polarization effects. As customarily done, it is possible to express the scattered intensity as function of the wave vector **q** only, defined as the difference between **k** (scattered wave vector) and k_0 (incident wave vector), i.e. $q = \mathbf{k} - \mathbf{k}_0$. The magnitude of **q** is related to the scattering angle by the relation

$$q = \frac{4\pi n}{\lambda} \sin\left(\frac{\theta}{2}\right), \tag{1}$$

where λ is wavelength of light in vacuum and n is the refractive index of the medium.
When the sample is a monodiperse ensemble of non-interacting droplets, the average scattered intensity is simply given by $I_{exp}(q) = n_d * I_d(q,r)$, where n_d is the number of droplets per cubic centimetre and $I_d(q,r)$ is the intensity scattered by a droplet of radius r:

$$I_d(q,r) = \frac{I_{exp}(q)}{n_d} = \frac{1}{\Omega} \int \mathcal{F}(\theta,\varphi,r)\, d\Omega, \tag{2}$$

averaged over the acceptance solid angle Ω that corresponds to q, $\mathcal{F}(\theta,\varphi,r)$ is the scattered intensity per unit solid angle provided by Mie theory, and the relation between the scattering angle θ and q is provided by Eq. (1). The images are processed by dividing the pixel matrix in concentric rings, centred on the optical axis, so that each ring corresponds to a specific wave-vector associated to the scattering angle θ. For the present experimental configuration, we used 80 concentric contiguous quarter of rings scaled according to a geometrical progression. Equation 2 is inverted by using a nonlinear iterative algorithm, developed by Ferri *et al.* [8]. As an example of the potential of the method, a preliminary result is shown in Fig. 2(b), where the experimental and reconstructed angular intensity distributions are plotted for the case of iso-propanol droplets with an average nominal diameter of $54\,\mu m$.



(a) (b)

Figure 2. (a) Schematic representation of a typical detector for LAELS measurements; (b) Comparison between experimental and reconstructed angular intensity distributions in the case of iso-propanol droplets with an average diameter of $54\,\mu m$.

References

[1] Sato J.: Studies on droplet evaporation and combustion in high pressure. AIAA 93-0813. *31st Aerospace Sciences Meeting*, 11-14 Jan, Reno, NV, 1993.

[2] Nomura H., Ujiie Y., Rath H.J., Sato J., Kono M.: Experimental study on high pressure droplet evaporation using microgravity conditions. *26th International Symposium on Combustion*, pp. 1267–1273, 1996.
[3] Harstad K., Bellan J.: An all-pressure fluid drop model applied to a binary mixture: heptane in nitrogen. *International Journal of Multiphase Flow* **26**: 1675–1706, 2000.
[4] Yang V., Lin N., Shuen J.-S.: Vaporization of liquid oxygen (LOX) droplets in supercritical hydrogen environments. *Combust. Sci. Technol.* **97**:247–270, 1994.
[5] Bellan J.: Supercritical (and subcritical) fluid behavior and modeling: drops, streams, shear and mixing layers, jets and sprays. *Progress in Energy and Combustion Science* **26**:329–366, 2000.
[6] Frohn A., Roth N.: Dynamics of Droplets. Springer Verlag, Berlin 2000.
[7] Ferri F.: Use of a charge coupled device camera for low-angle elastic light scattering. *Rev. Sci. Instrum.* **68**:2265–2274, 1997.
[8] Ferri F., Righini G., Paganini E.: Inversion of low-angle elastic light-scattering data with a new method devised by modification of the Chahine algorithm. *Applied Optics* **36**:7539–7550, 1997.

HPIV USING POLARIZATION MULTIPLEXING HOLOGRAPHY IN BACTERIORHODOPSIN (bR)

Victor S.S. Chan [*], Wouter D. Koek [**], Donald H. Barnhart [***], Christian Poelma [*], Thomas A. Ooms [*], Nandini Bhattacharya [**], Joseph J.M. Braat [**], Jerry Westerweel [*]

[*] *Laboratory for Aero- and Hydrodynamics, Delft University of Technology, Leeghwaterstraat 21, 2628 CA, Delft, The Netherlands*

[**] *Optics Research Group, Delft University of Technology, Lorentzweg 1, 2628 CJ, Delft, The Netherlands*

[***] *Department of Theoretical and Applied Mechanics, University of Illinois at Urbana-Champaign, Urbana, IL 61801-2983, USA*

E-mail[*]: v.chan@wbmt.tudelft.nl

Summary Using an off-axis reference beam and forward-scattered holographic geometry, dual-exposure particle images in a fluid flow has been recorded successfully onto the bR film. This was achieved by photo-induced anisotropy in bR to multiplex two polarization holograms at the same location of the holographic film. Using a sequential holographic read-out method, the two recorded holograms can be retrieved independently during the read-out process. This system allows directional ambiguity to be removed in the HPIV flow data.

INTRODUCTION

Barnhart *et al* (2002) realized the potential of applying bR for holographic particle image velocimetry (HPIV), and subsequently pointed out that a centimeter-square area of bR film has the same information capacity for several hundred state-of-the-art CCD cameras [2]. They have also discussed the advantages and limitations of using bR as a recording medium for HPIV. As has been discussed in Chan *et al* (2004), various multiplexing methods can be used to record multiple holograms onto a same bR film. Polarization multiplexing by photo-induced anisotropies in bR offers the possibility in removing directional ambiguity in the HPIV data [4].

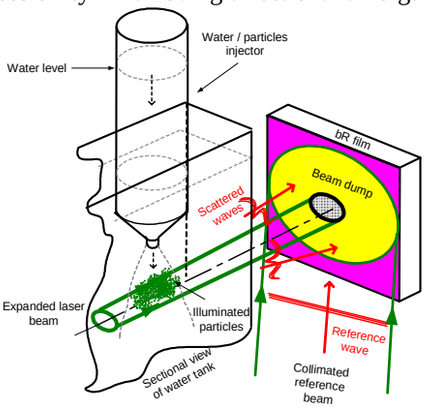


Figure 1: *Schematic of recording a hologram on bR using forward scattering on off axis geometry.*

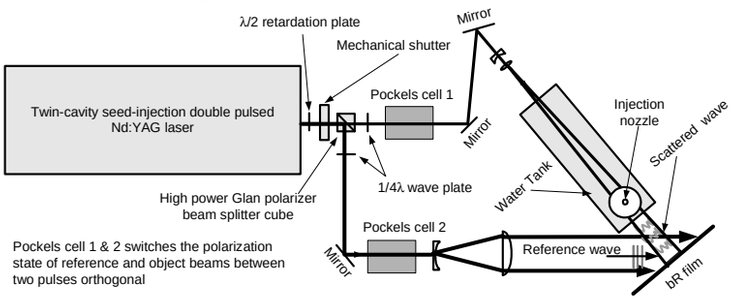


Figure 2: *Schematic of the recording set up for the HPIV experiment.*

EXPERIMENTAL SET UP FOR HOLOGRAPHIC RECORDING

As a proof of principle, an experiment was performed on a water jet seeded with 100µm solid glass sphere. This jet was injected into a clear tank of water through a syringe nozzle. The nozzle has an exit diameter of 2mm. The central position of the measurement control volume was located at six diameters down from the nozzle exit (i.e. X/D=12), which led to a measurement window that was ranging from X/D=8 to X/D=16 along the streamwise direction. In order to maximize the signal to noise ratio of the hologram, we have adopted a forward scattering geometry at a high numerical aperture (NA) configuration. This led to the recording of diffraction-limited particle images [3]. In the current set up as shown in figures 1 and 2, a small expanded laser beam from a dual-cavity seed-injection pulsed Nd:YAG (532nm) with output energy of 300mJ per pulse with pulse duration of 7ns, was used to illuminate the flow volume twice with a pulse separation time of 230µs. The object and reference beam fluences were adjusted to be equal to 80mJ/cm^2 (expanded beam diameter = 9mm) and 5mJ/cm^2 (expanded beam diameter = 80mm) respectively, where it is noted that only a small fraction of the object light scatters onto the bR film. When considering polarization holography in bR for HPIV, the recording of a hologram involves a two-step procedure [3]. During the first exposure both Pockels cells were switched off, such that the object and the reference wavefront would have left hand circular polarization and right hand circular polarization, respectively, at the plane of the hologram. For the second exposures the Pockels cells were supplied with the half wave voltage, resulting in an interchange of the object and reference polarization. With this set up, we have multiplexed two time separated holograms inside a single film.

DATA EXTRACTION RESULTS AND DISCUSSION

The two multiplexed holograms were reconstructed independently using phase conjugated playback geometry [3] as shown in figure 3. The collimated reconstruction beam for the read-out of a hologram has an intensity of 130μW cm^{-2}. Figure 4 shows the two multiplexed holograms that had been retrieved independently by sequentially switching the 1/2λ wave plate in and out (see figure 3). This rotates the incoming circularly polarized wave in the orthogonal orientation. We have reconstructed around 750 particles within a measurement volume of 7x8x9mm^3. The magnified view (top right corner) in figure 4 shows each string as a reconstructed particle. Three-dimensional image intensity analysis (local maxima along the string) was performed to determine all velocity components from the recorded flow hologram. Particle detection was performed by cross-correlating each slice with a particle "mask", a 5x5 Gaussian model particle. Subsequently, the local maxima in the resulting correlation plane were detected (which correspond to particle centers). To extract the velocity vectors, a nearest neighborhood search routine was performed on detected particle centers between the two stacks of images.

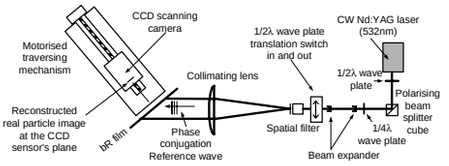


Figure 3: *Reconstruction of two sequentially multiplexed polarization holograms using circular polarization wave.*

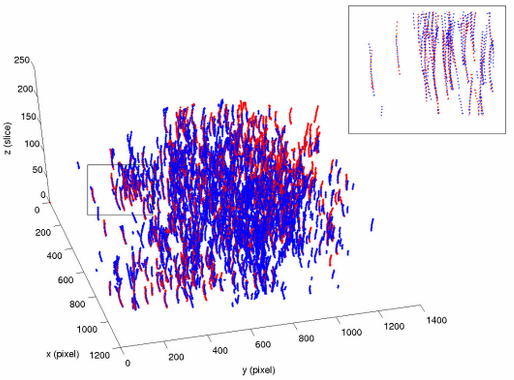


Figure 4: *Two independently reconstructed holographic particle fields superimposed on top of each other.*

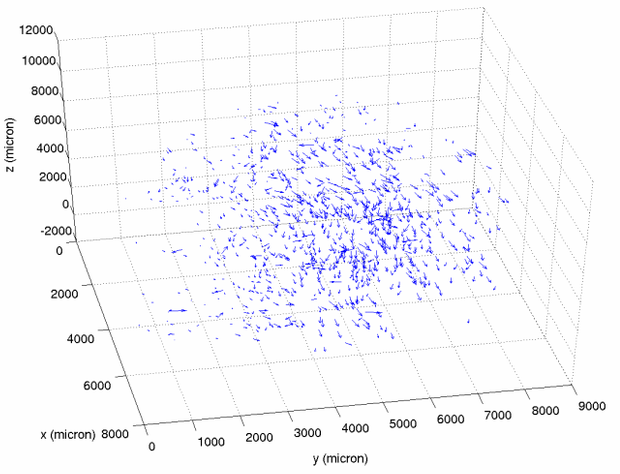


Figure 5: *Extracted HPIV vectors from figure 4, the jet is flowing from top to bottom.*

The directionally resolved data HPIV is presented in figure 5. The vector field exhibits a certain preferential orientation that indicates the jet flowing direction. The obtained maximum flow velocity in the streamwise direction is approximately = 0.5ms^{-1}. It shows a meandering flow profile which could be attributed to the fact that the heavier than water particle was used to seeded the jet.

CONCLUSIONS

As a proof of principal, an experiment was conducted on a particle laden water jet. A dual off-axis transmission hologram was recorded which maximizes the signal to noise ratio of particle images. Volumetric three-dimensional velocity information was extracted from the holograms by tracking the particle positions using the local maxima image intensity analysis with nearest neighborhood search. For the first time, we have demonstrated the feasibility in using bR for the recording of dual-exposure polarization multiplex particulate holograms to remove directional ambiguity in HPIV.

Acknowledgement

The work is financially supported by Foundation for Fundamental Research on Matter (FOM), The Netherlands. We thank Wilco Tax for the technical support of this project.

References

[1] Barnhart D.H, Hampp N, Halliwell N.A & Coupland J.M (2002) Digital holographic velocimetry with bacteriorhodopsin (BR) for real-time recording and numeric reconstruction *11th International Symposium on Applications of Laser Techniques to Fluid Mechanics*, Lisbon, Portugal, Paper 2-6

[2] Barnhart D.H, Koek W.D, Juchem T, Hampp N, Coupland J.M & Halliwell N.A (2004) Bacteriorhodopsin as a high-resolution, high –capacity buffer for digital holographic measurements *Meas. Sci. Technol* **15** 639-646

[3] Chan V.S.S, Koek W.D, Barnhart D.H, Bhattacharya N, Braat J.J.M, & Westerweel J (2004) Application of Holography to Fluid Flow Measurements using Bacteriorhodopsin (bR) *Meas. Sci. Technol* **15** 647-655

[4] Koek W.D, Chan V.S.S, Westerweel J, Bhattacharya N & Braat J.J.M (2004) Holographic simultaneous read-out polarization multiplexing based on photo-induced anisotropies in bacteriorhodopsin *Opt. Lett*. **29** 101-3

TIME-RESOLVED WALL SHEAR STRESS MEASUREMENTS USING MEMS

Alister N. Gibson*, Valery G. Chernoray**, Lennart Löfdahl**, Sjoerd Haasl*** and Göran Stemme***
*The Queen's University of Belfast, School of Aeronautical Engineering, BT7 1NN Belfast, Northern Ireland
**Thermo and Fluid Dynamics, Chalmers University of Technology, SE-412 96 Göteborg, Sweden
***Signals, Sensors and Systems, Microsystem Technology, Royal Institute of Technology, 10044 Stockholm, Sweden

Summary A number of MEMS (Micro Electro Mechanical Systems) wall mounted hot wire sensors have been developed at the Thermo and Fluid Dynamics department (TFD) at Chalmers University of Technology. The sensors were used to investigate the fluctuations of the velocity within the viscous sublayer of a zero-pressure-gradient turbulent boundary layer flow. The measurements performed at Reynolds numbers, R_θ ranging between 1000 and 15000 are discussed and compared to other relevant data collected from literature.

INTRODUCTION

For flow control purposes, wall shear stress is an essential quantity to compute and measure. In a turbulent flow the time-averaged values of this quantity are indicative of the global state of the flow along a surface, while the time-resolved component is a measure of the unsteady structures of the flow field which are responsible for the individual momentum transfer events in the boundary layer. Different methods for the measurement of wall shear stresses have been developed, and most rely on the premise that the mean velocity gradient is proportional to the heat transfer rate at the wall. A general conclusion to be made is that our knowledge of the wall shear stress, and in particular its fluctuating or time-resolved component, is limited. A clear trend in all wall shear stress measurements is that the sensors used have increasingly smaller active sensor areas in order to improve the resolution. In this process, MEMS fabrication technology has in recent years played a central role [1].

The MEMS sensors developed at TFD, Chalmers (final design and production courtesy to the KTH group) are hot wire sensors that are mounted on the wall at a small distance from it. A major advantage of this design is that the performance and accuracy are increased as compared to hot film type sensors. Furthermore, the fixed height of the sensing element from the wall is known precisely at all times, which is not easily achieved with, for example, a standard hot wire attached to a traverse mechanism. Recently, the sensors have been proven to accurately measure the wall shear stress in laminar airflows as is reported in [2]. A first attempt was made at using the sensors to measure the time resolved part of the wall shear stress in turbulent flows in ref. [3]. Due to the design of the MEMS hot wire being wall mounted and to account for near wall effects, the MEMS hot wire is calibrated *in situ* in a turbulent boundary layer against the mean wall shear stress.

While continuing the research into the use of the MEMS sensor in turbulent flows the current tests were designed with the primary aim of increasing the accuracy of the measurements. The relative intensity of the streamwise wall shear stress fluctuations was taken as the primary quantity of interest. The experiments performed by Alfredsson et al. [4] are widely accepted to be the most accurate measurement of the ratio, for which it was claimed that a constant value of 0.4 should be observed. However, an extensive review of papers published since then reveals that this is not necessarily the case as values are found to range from 0.3 to 0.5. This leads to the problem that either the ratio is not a constant value of 0.4 or the other techniques used suffer inadequacies which make their results unreliable. Further investigation of these findings provides an additional motivation for the current research.

EXPERIMENTAL PROCEDURE

Three variations of MEMS sensor wires were utilized for the measurements, a wire measuring $400\times2\times2$ μm^3 at a height of 50 μm from the wall, (one of five shown in figure 1, *left*) and wires with dimensions $200\times1\times2$ μm^3 at heights of 50 μm and 100 μm above the wall (figure 1, *right*). The dimensions of these MEMS sensors give rise to very good spatial resolution within the viscous sublayer of the turbulent boundary layer and this therefore enables them to determine the fluctuating velocity of the flow in this region.

The experiments were conducted in the wind tunnel laboratory of TFD. The closed circuit tunnel has a working test section measuring $3\times1.8\times1.2$ m^3 and has a low turbulence intensity of less than 0.1% of the free-stream velocity. The tests were performed on a zero-pressure gradient flow on a flat plate of dimensions $2500\times1000\times25$ mm^3 with Reynolds number, R_θ, ranging from approximately 1000 to 15000. A wire of 5 mm diameter placed 190 mm from the leading edge was used to trip the flow. The MEMS sensors were positioned on a surface-mounted chuck located 1930 mm from the leading edge of the plate. The sensors were calibrated *in situ* in turbulent boundary layer. This means that near wall effects are accounted for by the calibration.

Twelve independent runs were made using the different wires and great care was taken while conducting the experiments to reduce the errors involved with the measurements. The tests were made at a wide Reynolds number range to observe the effect of this parameter on the fluctuating wall shear stress. A temperature compensation circuit (via a temperature sensitive resistor) was introduced into the constant temperature anemometer bridge to avoid the effect of temperature drift, which can influence the measurements significantly [2].

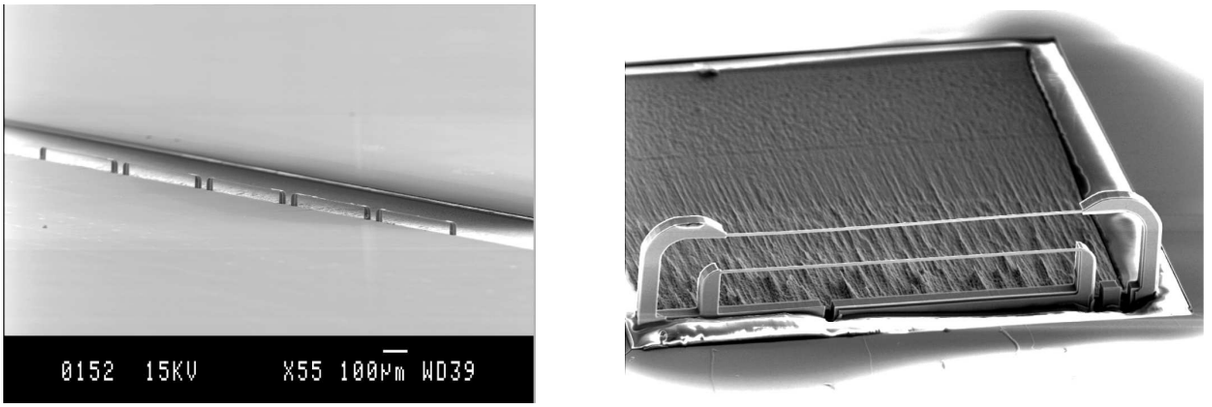


Figure 1. Micrographs of single wire MEMS line rake (*left*) and two-wire MEMS rake (*right*).

A number of methods were also introduced to ensure that the calibration fit was as accurate as possible.

RESULTS AND DISCUSSION

To begin with, extensive measurements were taken using a standard hot wire on the inner and outer regions of the boundary layer to ensure that the flow was of a classical formation at the point on the plate where the MEMS sensors were deployed. The mean shear stress was determined using a Preston tube. The mean velocity close to the wall was proven to be of the form $u^+ = y^+ + c_4 y^{+4} + c_5 y^{+5}$ with $c_4 = -0.0003$ and $c_5 = 1.35 \times 10^{-5}$ up to a value of y^+=11. A comparison between the measurements achieved by employing this distribution for the sensor calibrations and those derived from the calibrations against the Preston tube, was then performed.

The spatial resolution achieved by the sensors employed was taken into account at each Reynolds number range and any measurements made outside the range of $l^+ > 25$ were discarded from the analysis. The calibrations were performed in the range up to $R_\theta \approx$15000 and the time-dependant results were obtained only up to $R_\theta \approx$7500 for spatial resolution reasons. The energy spectrum was analysed and this was found to give a satisfactory distribution with the signal-to-noise ratio being reasonably high. Probability density functions were also calculated and these gave a distribution very close to the lognormal distribution.

An analysis of experimental as well as DNS data available at present was carried out to see if the limiting value of turbulent intensity on the wall of 0.4 was being consistently achieved. A well-known problem encountered during this study was that many of the techniques used to evaluate this parameter have serious flaws when being used in the viscous sublayer of the boundary layer as is discussed e.g. in [4]. From the reliable data available and from the current experiments, it can be deduced that while the value of 0.4 for the limiting ratio is not obtained very often, this figure is indeed a valid approximation as it was to be found at the centre of the spread of data.

References

[1] Löfdahl, L., & Gad-el-Hak, M.: MEMS application in Turbulence and Flow Control, *Progress in Aerospace Sciences*, **35**: 101–203, 1999.

[2] Löfdahl, L., Chernoray, V., Haasl, S., Stemme, G. & Sen, M.: Characteristics of a Hot Wire Microsensor for Time-Dependent Wall Shear Stress Measurements. *Experiments in Fluids* **35**: 240–251, 2003.

[3] Mitchell, G., Chernoray, V., Löfdahl, L., Haasl, S. & Stemme, G.: Measurement of the Turbulence Intensities in a Flat Plate Boundary Layer. *In Proc. of the 4th Int. Symp. on Turbulence, Heat and Mass Transfer*: 261–268, 2003.

[4] Alfredsson, P., Johansson, A., Haritonidis, J. & Eckelmann, H.: The Fluctuating Wall-Shear Stress and the Velocity Field in the Viscous Sublayer. *Physics of Fluids* **31** (5): 1026–1033, 1988.

Void Collapse and Jet Formation:
The impact of a disk on a water surface.

Raymond Bergmann, Mark Stijnman, Devaraj van der Meer, Andrea Prosperetti, and Detlef Lohse
Faculty of Science and J.M. Burgers center for Fluid Dynamics, University of Twente, 7500 AE Enschede, The Netherlands
(January 5, 2004)

Void formation occurs in a large number of real world impact phenomena, ranging from the familiar rain droplets falling into puddles to such large-scale phenomena as asteroids impacting on planets [1]. The large impact velocities of asteroids, typically of the order of ~12 km/s, induce stresses far beyond the point at which any material will yield. In [2] we studied the impact of a steel ball on very fine, soft sand. Here we analyze the impact of a disc on a flat water surface. The formation and collapse of the void created during the impact, is studied both experimentally and numerically.

In the experiments, a disk of radius R is pulled down into a water tank by means of a linear motor. The motor allows for precisely controlled constant velocities of the disk, ranging from U = 0 to 5 m/s. The presence of the free surface and the short duration of the phenomenon suggest that the effects of viscosity can be neglected during the formation and collapse of the void. An inviscid model can therefore be adopted, which is efficiently solved numerically by means of a boundary integral method. Figure 1 shows that the simulations are in excellent agreement with the experimental void formation and collapse. As can be seen in Figure 2, the depth of the void closure divided by the disk radius d_s/R scales with the square root of the Froude number, defined by $Fr = U^2/gR$, for both experiments (blue error bars) and simulations (red dots).

As the walls of the void come together on the axis of symmetry at the end of the collapse, the destruction of the radial liquid momentum produces a large pressure spike which creates two jets of water, one shooting up straight into the air (Figure 3a), and one down, piercing the void enclosed by the collapse (Figure 3b).

[1] H.J. Melosh, *Impact Cratering: A Geologic Process* (Oxford University Press, Oxford, 1989)
[2] D. Lohse, R.P.H.M. Bergmann, R. Mikkelsen, C. Zeilstra, D. v/d Meer, M. Versluis, K. v/d Weele, M.A. v/d Hoef, J.A.M. Kuipers - *Impact*, preprint (2004)
[3] S. Gaudet - *Numerical simulation of circular disks entering the free surface of a fluid*, Phys. Fluids **10**, 2489 (1998)
[4] J.W. Glasheen, T.A. McMahon - *Vertical water entry of disks at low Froude numbers*, Phys. Fluids **8**, 8 (1996)
[5] H.N. Oguz, A. Prosperetti, A.R. Kolaini - *Air Entrapment by a falling water mass*, J. Fluid Mech. **294**, 181 (1995)

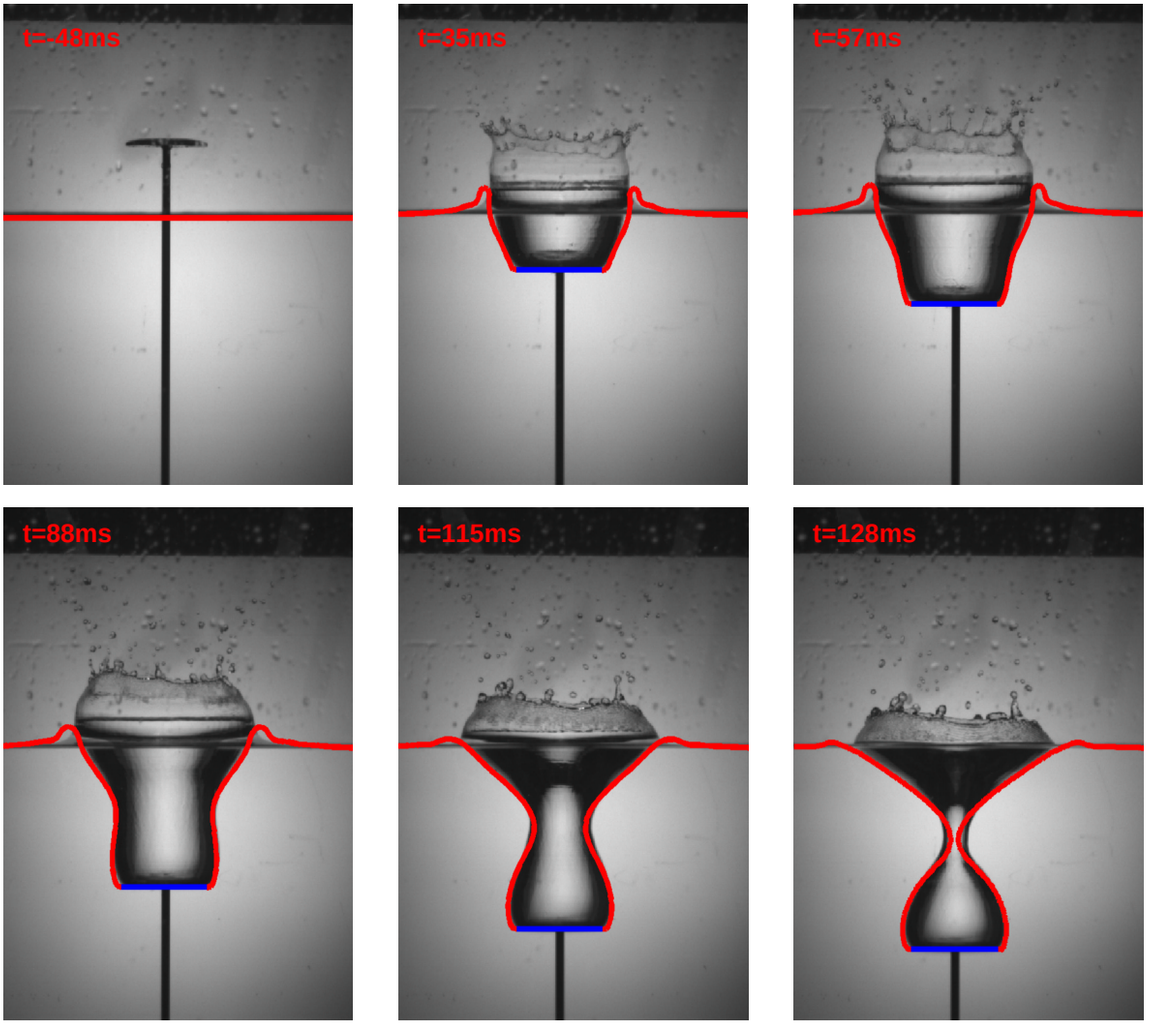


Figure 1: Snapshots from the formation and collapse of the void in an experiment in which a linear motor pulls down a disk of radius R = 3.0 cm through a water surface at a constant velocity U = 1.0 m/s. The overlaying blue/red lines are the numerical results from the boundary integral simulation using the same initial conditions as in the experiment. As can be seen, experiment and simulation are in very good agreement.

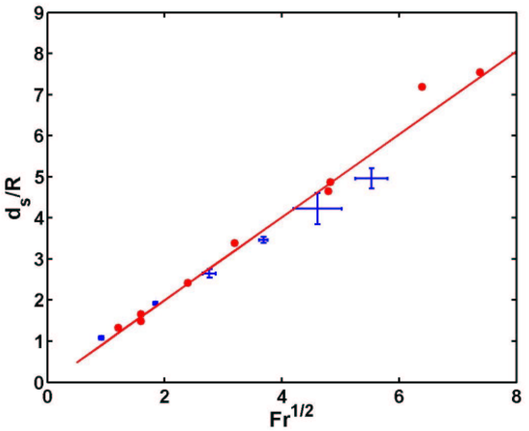


Figure 2: A clear $Fr^{1/2}$ scaling law for d_s/R is observed for experiments (blue error bars) and simulations (red dots).

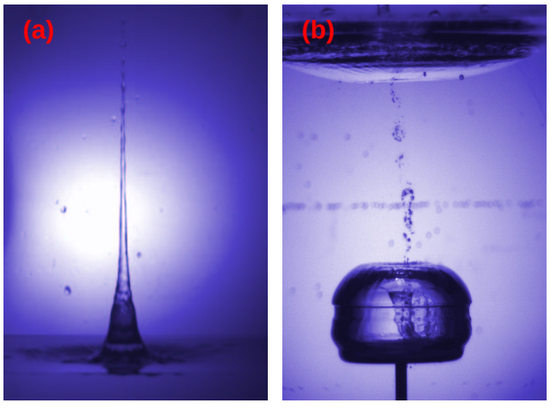


Figure 3: After the collapse of the void (Figure 1) an upward jet (a) shoots straight into the air, and a downward jet (b) pierces the enclosed void.

COMPREHENSIVE EXPERIMENTAL AND COMPUTATIONAL INVESTIGATIONS OF THE UNSTEADY FLOW IN AN AXIAL FLOW LOW SPEED COMPRESSOR STAGE

Andrzej S. Witkowski, Tadeusz J. Chmielniak,
Michał D. Strozik, Mirosław M. Majkut, Jacek M. Żukowski
Silesian Technical University, Insitute of Power Engineering and Turbomachinery,
Konarskiego 18, 44-100 Gliwice, Poland

Summary The objective of the study is experimental and computational investigation of unsteady flow in the axial flow low speed compressor stage with the use of three systems based on totally different principles:

- a five hole pressure probe (FHP),
- a 2-sensor fast response straight and 90 degree triple split fiber probes (TSFP) and,
- commercially available three-dimensional Laser Doppler Anemometer (3D-LDA) system.

Using two measurement system, one being intrusive and the other non-intrusive, in the same complex flow field has been given the opportunity for:

- critical comparison of results and opens the view for further improvements. Attention was focused to the rotor blade wake where both measurements are affected by high tangential shear gradients,
- investigation of the influence vane setting angle on the unsteady flow field in the axial flow compressor stage,
- a concerted application of experimental (LDA) and computational fluid dynamics (CFD) calculations as well as basis for verification of computational results. From a comparison of LDA and CFD data, possible improvements in computational technique can be pointed out.

Experimental Facility and Instrumentation

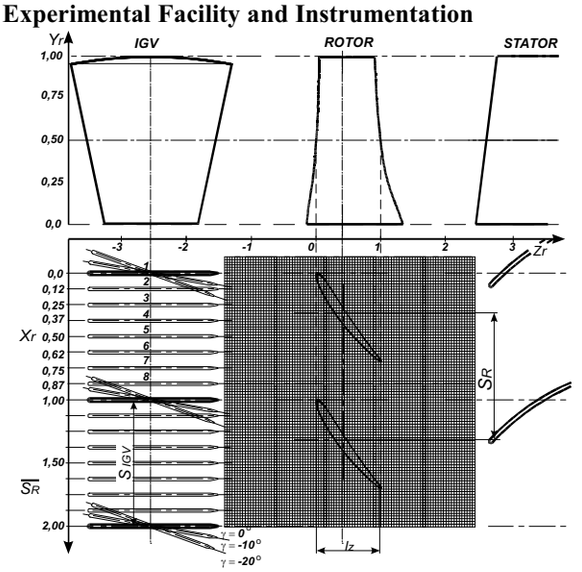


Fig. 1 Measurement locations in spanwise, pitchwise and streamwise direction.

The experiments has been performed in the Axial Flow Low Speed Compressor Stage (AFLSCS) of the Institute of Power Engineering and Turbomachinery at the Technical University in Gliwice which was designed to tests compressor stages over a wide range of parameters and to validate numerical codes [1]. It consists of a rotor with a hub to tip annulus wall diameter ratio 0.56, with outher diameter of 1.0 m, with 16 cambered and twisted blades of British C-4 section, designed for free vortex operation, followed by a 13-vane stator row, and the outflow curvilinear diffuse with the throttling blades. The research compressor stage is connected to the suction side of the measuring collector and consists of a large bellmouth inlet for mass flow measurement. To account for the uniformity of the rotor absolute inlet flow field, measurements have been made at eight tangential locations in the absolute frame equally spaced over one inlet guide vane (IGV) pitch (Fig. 1).

Measurement have been acquired at 40 axial measurement locations from just upstream of the rotor (0.735 chord) to chord downstream of the rotor. Preliminary each measurement location was at midspan. For the measurements with the use of TSFP at each axial or radial location a sequence of 100 real time samples of velocities were recorded over roughly 2 blade passing periods and averaged over 1000 revolutions. In the measurement with the use of LDA system each rotor passage was divided into 50 measurement windows across the rotor pitch. After all instantaneous velocities in both methods were acquired for the particular survey point the velocities is then ensemble averaged and the level of unresolved unsteadiness determined.

Some Results

In the following figures 2 and 3 the results of different axial positions before (Fig. 2) and behind (Fig. 3) the rotor blades were plotted separately to exhibit differences between the three measurement systems in more details The comparison of the circumferential distribution of the axial component of absolute velocities in the IGV and rotor blade wakes normalized by the mean rotor speed (Figs. 2a, 3a) and by the mean velocity $\overline{C}$ (Figs. 2b, 3b) shows good agreement in the vicinities of the center blade wake, in the free stream region the agreement is not so satisfactory. Larger discrepancies in the ensemble average velocity occurred at the rotor

blade wake (Fig. 3), where velocity component value could differ by as much as 7 % at the free stream region. However there is very good agreement in the wakes velocity defect and semiwake width, when the velocity is normalized by the time average velocities $\overline{W}$, determined by the both measuring systems separately.

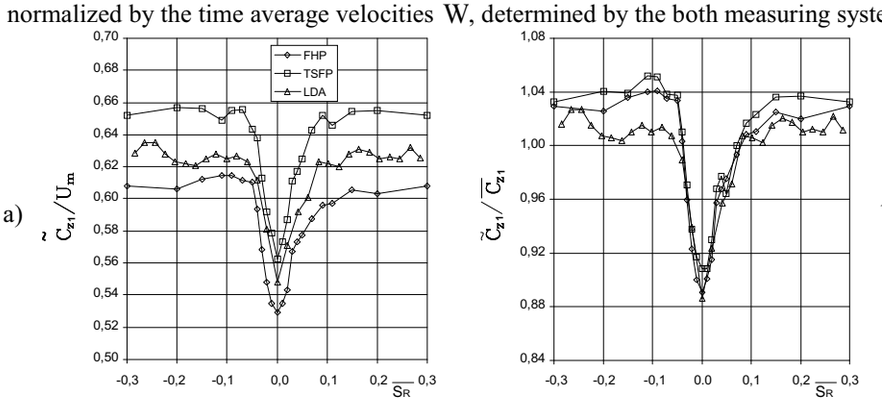


Fig.2 Comparison of the IGV wake velocity profiles normalised by U_m(a) and $\overline{c}_z(b)$ [m/s] with the use of the three measurements systems – just downstream of the IGV

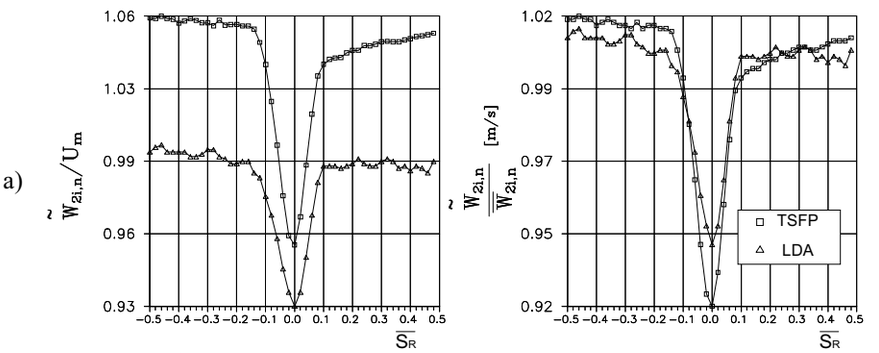


Fig.3 Comparison of the rotor wake relative velocities profiles just downstream of the rotor trailing edge with the use of different measurement systems

A comparison of the numerically obtained [2] the contour plots of the axial components of the relative velocities on the middle radius with experimental data (LDA) is made in Fig.4. This shows that the predictions give good qualitative agreement. The numerical results show some quantitative differences to the measured data. These differences can be due to the turbulence models as well as the grid resolution.

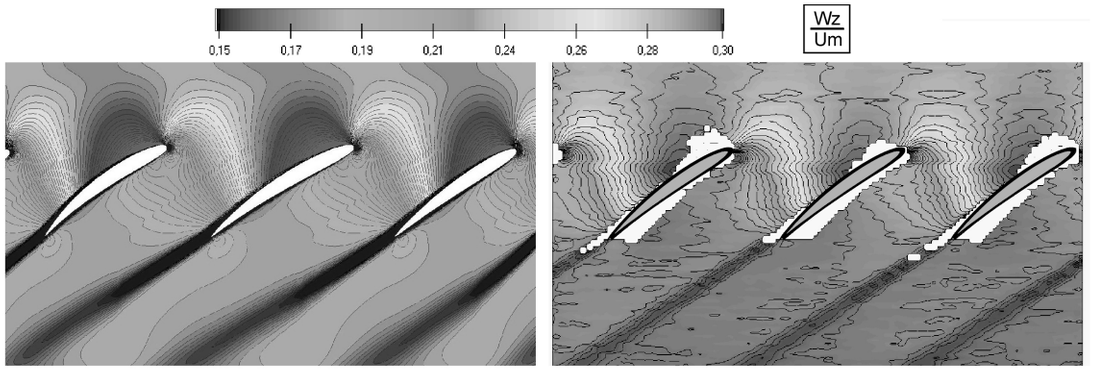


Fig. 4 Contour plots of relative velocities a) CFD data, b) LDA data

Conclusion

- In the present state, the CFD method supplied data giving a fair qualitative characterisation of the flow phenomena in the axial flow compressor stage and pointed out also by the TSFP and LDA measurements.
- In order to obtain a CFD method more capable for simulating flow in compressor stages an improvement must be carried out on the included boundary layer models.
- This comparison of LDA and TSFP technique width CFD method is probably the first on ever made in highly fluctuating and highly turbulent air flow in the axial flow speed turbomachinery channels.

References

[1] Witkowski A., Chmielniak T., Majkut M., Strozik M.: Measurement of the Unsteady Flow Field Due to Inlet Guide Vane Interaction with the Rotor in an Axial Flow Low Speed Compressor Stage., 5 -th European Conference on Turbomachinery, Fluid Dynamics and Thermodynamics, Prague, Czech Republic, 2003.

[2] AEA Technology Engineering Software Limited, Waterloo, Ontario, Canada. CFX-TASCflow, User Documentation, January 1999.

XXI ICTAM, 15–21 August 2004, Warsaw, Poland

EXPERIMENTAL DETECTION OF THE NEW PHENOMENON OF TURBULENT THERMAL DIFFUSION

Alexander Eidelman*, Tov Elperin*, Nathan Kleeorin*, Alexander Krein*, Igor Rogachevskii*,
Julia Buchholz**, Gerd Grünefeld**

*Department of Mechanical Engineering, Ben-Gurion University of Negev, POB 653, 84105 Beer-Sheva, Israel

**Faculty of Mechanical Engineering, RWTH Aachen University, Aachen, Germany

Summary A new phenomenon of turbulent thermal diffusion, which was predicted theoretically in [1,2], has been detected experimentally in oscillating grids turbulence with an imposed mean temperature gradient in air flow with a stable and unstable stratification. This effect implies an additional mean flux of particles in the direction opposite to the mean temperature gradient and results in formation of large-scale inhomogeneities in the spatial distribution of particles. We used Particle Image Velocimetry (PIV) to determine the turbulent velocity field and an Image Processing Technique to determine the spatial distribution of particles. Analysis of the intensity of laser light Mie scattering by particles showed that they are accumulated in the vicinity of the minimum of the mean temperature of the surrounding fluid due to the effect of turbulent thermal diffusion.

Phenomenon of molecular thermal diffusion in gases was predicted by Enskog (1911) and confirmed experimentally by Chapman and Dootson (1917), and thermophoresis of particles was observed by Tyndall (1870). Equation for the number density n of particles taking into account this effect reads $\partial n/\partial t = -\boldsymbol{\nabla}\cdot\mathbf{J}_{_M}$, where the flux of particles $\mathbf{J}_{_M}$ is given by $\mathbf{J}_{_M} = -D(\boldsymbol{\nabla} n + k_t\boldsymbol{\nabla}T/T)$. The first term in the formula for the flux of particles describes molecular diffusion, while the second term accounts for the flux of particles caused by the fluid temperature gradient $\boldsymbol{\nabla}T$ (molecular thermal diffusion). Here D is the coefficient of molecular diffusion, $k_t \propto n$ is the thermal diffusion ratio, and $D_{_M} = Dk_t$ is the coefficient of molecular thermal diffusion. In turbulent fluid flow at large Reynolds and Peclet numbers the nature of diffusion drastically changes, e.g., turbulence results in a sharp increase of the effective diffusion coefficient. It was found in [1,2] that in a low Mach number turbulent fluid flow with a nonzero mean temperature gradient there appears an additional mean flux of particles or gases in the direction opposite to the mean temperature gradient (the phenomenon of turbulent thermal diffusion). For large Reynolds and Peclet numbers the turbulent thermal diffusion is much stronger than the molecular thermal diffusion.

The mechanism of this effect for solid particles is as follows. The inertia causes particles inside the turbulent eddies to drift out to the boundary regions between eddies (i.e., regions with low vorticity or high strain rate and maximum of fluid pressure). Thus, particles are accumulated in regions with the maximum pressure of the turbulent fluid. Similarly, there is an outflow of particles from regions with the minimum pressure of fluid. In a homogeneous and isotropic turbulence without imposed large-scale gradients of temperature a drift from regions with increased (decreased) concentration of particles by a turbulent flow of fluid is equiprobable in all directions. Therefore pressure (temperature) of the surrounding fluid is not correlated with turbulent velocity field and there exists only turbulent diffusion of particles. Situation drastically changes in a turbulent fluid flow with a mean temperature gradient. In this case the mean heat flux $\langle\mathbf{u}\Theta\rangle$ is not zero, i.e., fluctuations of fluid temperature Θ and velocity $\mathbf{u}$ of fluid are correlated. Fluctuations of temperature cause fluctuations of pressure of the fluid, and the pressure fluctuations result in fluctuations of the number density of particles. Indeed, increase (decrease) of the pressure of surrounding fluid is accompanied by accumulation (outflow) of the particles. Therefore, direction of mean flux of particles $\langle\mathbf{u}n\rangle$ coincides with that of heat flux, i.e., $\langle\mathbf{u}n\rangle \propto \langle\mathbf{u}\Theta\rangle \propto -\boldsymbol{\nabla}\bar{T}$, where $\bar{T}$ is the mean fluid temperature. The mean flux of particles is directed to the minimum of the mean temperature $\bar{T}$ and the particles are accumulated in this region.

Evolution of the number density $n(t,\mathbf{r})$ of small particles in a turbulent flow is determined by equation: $\partial n/\partial t + \boldsymbol{\nabla}\cdot(n\mathbf{v}_p) = -\boldsymbol{\nabla}\cdot\mathbf{J}_{_M}$, where $\mathbf{v}_p$ is the velocity field of the particles which they acquire in a turbulent fluid velocity field. Averaging this equation over turbulent velocity field we arrive at the equation for the mean number density of particles $\bar{N} \equiv \langle n\rangle$:

$$\partial\bar{N}/\partial t + \boldsymbol{\nabla}\cdot(\bar{N}\bar{\mathbf{V}}_p) = -\boldsymbol{\nabla}\cdot(\bar{\mathbf{J}}_{_T} + \bar{\mathbf{J}}_{_M})\,, \tag{1}$$

(see [1,2]), where $\bar{\mathbf{J}}_{_T} = \bar{N}\mathbf{V}_{\rm eff} - D_{_T}\boldsymbol{\nabla}\bar{N}$ is the turbulent flux of particles, $D_{_T} = (\tau/3)\langle\mathbf{u}^2\rangle$ is the turbulent diffusion coefficient, τ is the momentum relaxation time of turbulent velocity field, $\mathbf{v}_p = \bar{\mathbf{V}}_p + \mathbf{u}$, $\bar{\mathbf{V}}_p = \langle\mathbf{v}_p\rangle$ is the mean particles velocity, $\mathbf{V}_{\rm eff} = -\langle\tau\mathbf{u}(\boldsymbol{\nabla}\cdot\mathbf{u})\rangle$ is the effective velocity, $\bar{\mathbf{J}}_{_M}$ is the mean molecular flux of particles. The effective mean velocity of particles implies an additional mean nondiffusive flux of particles which can result in formation of large-scale inhomogeneities in particles spatial distribution. Equation (1) was derived by different methods. For noninertial particles advected by a low Mach number turbulent fluid flow, the particles velocity $\mathbf{v}_p$ coincides with the fluid velocity $\mathbf{v}$, and $\boldsymbol{\nabla}\cdot\mathbf{v} \approx -(\mathbf{v}\cdot\boldsymbol{\nabla})\rho/\rho \approx (\mathbf{v}\cdot\boldsymbol{\nabla})T/T$. Thus, the effective velocity is given by $\mathbf{V}_{\rm eff} = -D_{_T}(\boldsymbol{\nabla}\bar{T})/\bar{T}$, where ρ is the density of the fluid. Here we used the equation of state for the ideal gas and we neglected small gradients of a mean fluid pressure. For inertial particles the velocity $\mathbf{v}_p$ depends on the velocity of the surrounding fluid $\mathbf{v}$, and it can be determined from the equation of motion for a particle. Solution of the equation of motion for small particles with $\rho_p \gg \rho$ yields: $\mathbf{v}_p = \mathbf{v} - \tau_p d\mathbf{v}/dt + {\rm O}(\tau_p^2)$, where τ_p is the Stokes time, ρ_p is the material density of particles. Then $\boldsymbol{\nabla}\cdot\mathbf{v}_p = \boldsymbol{\nabla}\cdot\mathbf{v} + \tau_p\Delta P/\rho + {\rm O}(\tau_p^2)$, and the effective velocity is $\mathbf{V}_{\rm eff} = -D_{_T}(1+\kappa)(\boldsymbol{\nabla}\bar{T})/\bar{T}$, where the coefficient κ depends on the particle inertia (m_p/m_μ), the parameters of turbulence (Reynolds number) and the mean fluid temperature, where m_p is the particle mass and m_μ is the mass of molecules of the surrounding fluid. The turbulent flux of particles can be rewritten as $\bar{\mathbf{J}}_{_T} = -D_{_T}[k_{_T}(\boldsymbol{\nabla}\bar{T})/\bar{T} + \boldsymbol{\nabla}\bar{N}]$, where $k_{_T} = (1+\kappa)\bar{N}$ can be interpreted as turbulent thermal diffusion ratio, and $D_{_T}k_{_T}$ is the coefficient of turbulent thermal diffusion. Phenomenon of turbulent thermal diffusion results in large-scale pattern formation whereby initial spatial distribution of particles in a turbulent fluid flow evolves into a large-scale inhomogeneous distribution, i.e., particles are accumulated in the vicinity of the minimum of the mean temperature of the surrounding fluid.

The main goal of this study is to investigate experimentally the effect of turbulent thermal diffusion. Oscillating grids turbulence generator was constructed to study this effect. The test section of the oscillating grids turbulence generator was constructed as rectangular chamber of $29\times29\times58$ cm. Pairs of vertically oriented grids with bars arranged in a square array (with a mesh size 5 cm) are attached to the right and left horizontal rods. Both grids are driven independently with the speed-controlled motors. The grids are positioned at

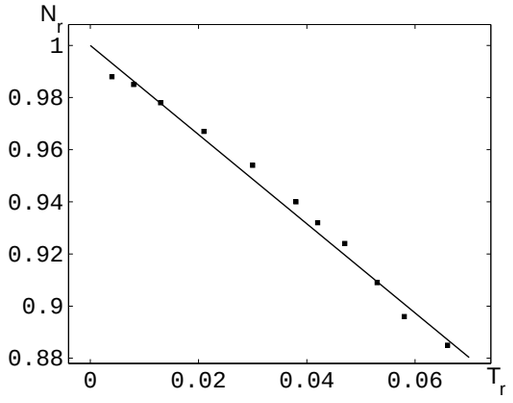


Figure 1. Normalized particles number density $N_r \equiv \bar{N}/\bar{N}_0$ versus normalized temperature difference $T_r \equiv (\bar{T} - \bar{T}_0)/\bar{T}_0$ in the turbulent non-isothermal flow.

a distance of two grid meshes from the chamber walls parallel to them. This two-grid system is capable of oscillating at controllable frequency up to 20 Hz. The grid stroke was adjusted in a range $6 - 10$ cm.

A mean temperature gradient in the turbulent flow with a stable and unstable stratification was formed with two heat exchangers. Temperature measurements were conducted in the oscillating grids turbulence generator. The temperature difference between the heat exchangers varied in the range from 25 up to 50 K. In order to improve heat transfer in the boundary layers at the walls we used heat exchangers with the rectangular fins which allowed us to support a mean temperature gradient in the core of the flow up to 200 K/m at a mean temperature of about 300 K. We determined the mean and r.m.s. velocities, two-point correlation functions and an integral scale of turbulence from the measured velocity fields. Turbulent flow parameters in the oscillating grids turbulence generator are as follows: the Kolmogorov's length scale η is about 0.4 mm, the Taylor's scale is about 5 mm, and the integral scale of turbulence is 15 mm (the vertical size of the chamber is 30 cm). The spatial resolution of the conducted PIV measurements was about 5η. The measured r.m.s. velocity was several times higher than the characteristic mean velocity in the core of the flow.

The effect of Mie light scattering by particles was used to determine the particles spatial distribution in the flow. The scattered light energy flux incident at the CCD camera probe is proportional to the particles mean number density. Analysis of the intensity of laser light Mie scattering by particles in non-isothermal turbulent fluid flows demonstrated that particles are redistributed in the vertical direction in the chamber, they are accumulated in the regions with the minimum mean temperature. The dependence of the normalized particles number density $N_r \equiv \bar{N}/\bar{N}_0$ versus the normalized temperature difference $T_r \equiv (\bar{T} - \bar{T}_0)/\bar{T}_0$, is shown in Fig. 1, where $\bar{T}_0$ is the reference temperature and $\bar{N}_0 = \bar{N}(\bar{T} = \bar{T}_0)$. Figure 1 corresponds to the case of the stable stratification (i.e., for the experiments in the chamber with the cooled bottom wall and heated top wall of the test section).

In order to explain the dependence N_r versus T_r shown in Fig. 1 consider Eqs. (1). If one does not take into account the term $\bar{N}\mathbf{V}_{\rm eff}$ in Eq. (1) for the mean number density of particles, this equation reads $\partial\bar{N}/\partial t = D_T\Delta\bar{N}$, where we neglected a small mean fluid velocity $\bar{\mathbf{V}}_p$ and small molecular mean flux of particles (that corresponds to the conditions in our experiment). The steady-state solution of this equation is $\bar{N}$ =const. However, our measurements demonstrate that the solution $\bar{N}$ =const is valid only for the isothermal turbulent flow, i.e., when $\bar{T}$ =const. Let us take into account the effect of turbulent thermal diffusion, i.e., include the term $\bar{N}\mathbf{V}_{\rm eff}$ in Eq. (1). Now the steady-state solution of this equation for the non-inertial particles reads: $\boldsymbol{\nabla}\bar{N}/\bar{N} = -\boldsymbol{\nabla}\bar{T}/\bar{T}$. This yields $\bar{N}/\bar{N}_0 = 1-(\bar{T}-\bar{T}_0)/\bar{T}_0$, where $\bar{T}-\bar{T}_0 \ll \bar{T}_0$. In our experiments we found that $\bar{N}/\bar{N}_0 = 1-\alpha(\bar{T}-\bar{T}_0)/\bar{T}_0$, where the coefficient $\alpha = 1.71$, i.e., $\alpha > 1$. The deviation of the coefficient α from 1 is caused by a small yet finite inertia of the particles. In all experiments performed for different ranges of parameters and different initial conditions, α was more than 1 in agreement with the theory, which predicts $\alpha = 1$ for the noninertial particles, and $\alpha > 1$ for inertial particles. These experiments were performed for different Reynolds numbers (based on the integral scale of turbulence and r.m.s. velocity) in the range from 150 to 300, and small particles mass loadings. However, the dependence of the parameter α on the Reynolds number in this range is weak. The number density of particles in these experiments was of the order of 10^{10} particles per m^3, so that their collision rate is negligibly small. The effect of the gravitational settling of small particles ($0.5 - 1$ μm) is negligibly small since the terminal fall velocity of these particles is less than 0.01 cm/s.

In the case of unstable stratification (the heated bottom wall and cooled top wall of the test section) particles are accumulated in the vicinity of the top wall of the chamber due to the effect of turbulent thermal diffusion. It was also found that the turbulent thermal diffusion coefficient was larger than that for the turbulent flow with a stable stratification. Note that the total variation of the normalized particles number density due to the effect of turbulent thermal diffusion is more than 10%, and the accuracy of our measurements is less than 0.3%, that is high enough to detect this effect. The obtained experimental results are in a good quantitative agreement with the theoretical predictions [1,2]. Thus, these experiments confirmed the existence of the effect of turbulent thermal diffusion.

References

[1] Elperin T., Kleeorin N. and Rogachevskii I.: Turbulent Thermal Diffusion of Small Inertial Particles. *Phys. Rev. Lett.* **76**: 224–227, 1996.

[2] Elperin T., Kleeorin N. and Rogachevskii I.: Turbulent Barodiffusion, Turbulent Thermal Diffusion and Large-Scale Instability in Gases. *Phys. Rev. E* **55**, 2713–2721, 1997.

3D VORTICS STRUCTURE MONITORING IN TURBULENT FLOWS BY DIGITAL SPECKLE PHOTOGRAPHY

Nikita A. Fomin, Andrey V. Krauklis and Elena I. Lavinskaya
HMTI NANB, Department of Non-Equilibrium Processes, 220072 Minsk, Belarus

Summary 3D vortices structure in complex turbulent flows is reconstructed using computerized speckle tomography. Digital speckle photography (**DSP**) is used for the instantaneous quantitative derivation of a 2D map of deflection angles of the light passing through the flow under study. The macro structures are reconstructed using Radon integral transform and the microscale turbulence structures are determined by using Erbeck-Merzkirch integral transforms.

INTRODUCTION

Digital speckle photography (**DSP**) based on the computer aided acquisition and evaluation of time evolution of dynamic speckle patterns recorded by digital CCD cameras allows the instantaneous quantitative derivation of a 2D map of deflection angles and retardation of the light passing through the flow under study. Even for 3D flows, recent advances in digital optical data storage and analysis make it possible to extract quantitative data from line-of-sight flow visualization techniques [1,2]. Among the most important advantages of **DSP** are its high spatial resolution and the possibility to collect a great amount of experimental information from a single speckle-patterns record. In principle, the resolution can be as high as the diffraction limit of line-of-sight measurements (about 0.2-0.3 *mm)* [2]. For 2D flows the maps of the deflection angles so obtained can be easily transformed into 2D density (temperature) gradient maps using simple calculations and without any calibration. In addition, precise digital multi-projection measurements allow the reconstructing of a 3D vortices structure using computerized tomography approach as below.

SPECKLEGRAM RECORDINGS

The first step of digital specklegram processing is similar to PIV and is performed by evaluation of statistical functions (cross-correlation or structural functions) of the recorded dynamic speckle fields. The record of the whole field is scanned by moving a $N \cdot M$ pixels window across the field. The pattern of the window in a frame 1 taken from the first exposure specklegram is cross-correlated with the pattern of the respective window at the same position in a frame 2 from the second exposure specklegram. Finally, the speckles displacement attributed to the area covered by the window is found from determining the maximum peak of the correlation in quasi-real time operation, see [2,3].

TOMOGRAPHIC RECONSTRUCTION

The general way to obtain interior flow information is to use multidirectional, line- of- sight measurements and reconstruct the 3D data using computer assisted tomography (**CAT**). For a given test object, the quality of the tomographic reconstruction depends on the number of projections taken, the covered total angular range of viewing directions, and the amount of information available from each projection. The integral Radon transformation can be used for data obtained from either laminar or turbulent flow, but an exact determination of the interior flow parameter distributions would need an infinite number of projections. Because of the finite number of projection measurements

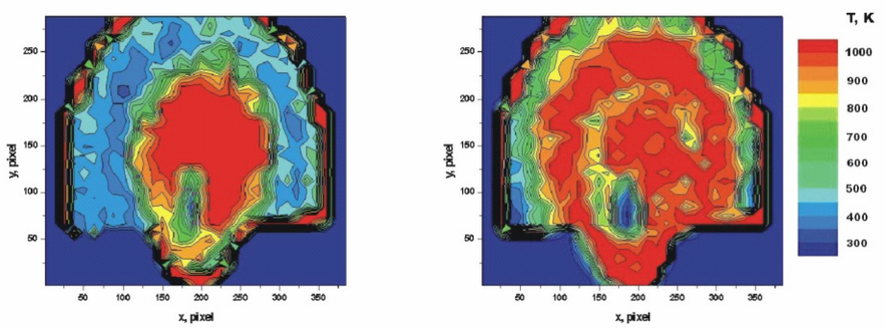


Fig. 1. Instantaneous temperature maps reconstructed by **CAT** with Radon integral equation using two-projectional **DSP**

available the application of the Radon transformation becomes an ill-posed mathematical problem. In practice this means that a small inaccuracy in the experimental data can lead to significantly large errors in the final flow parameter determination. The high data density is particularly advantageous for analyzing complex 3D turbulent flows. In the present paper an iteration technique has been adopted for the calculation of the Radon integral. The noise in the experimental data has been smoothed by a cubic spline technique. This smoothing procedure improves the reconstruction quality, but removes the low-scale variation of the refractive index distribution from the reconstructed

field. For direct recording of the light ray deflection angles, as in **DSP**, the integral Radon transformation simplifies and the optical disturbance (refractive index distribution) can be predicted from the transformation

$$F(x,y) = n(x,y) - n_\infty = -\frac{n_\infty}{2\pi^2}\int_0^\pi d\alpha \int_{-\infty}^{\infty} \frac{\varepsilon(\alpha,p)}{p-p_0}dp \qquad (1)$$

Fig. 1 shows an example of quasi-real time reconstructing the local parameters in an open turbulent flame from data taken in two directions from digital speckle record.

SMALL SCALE VORTICITY EVALUATION

Using the relation between deflection angle and fluid density,

$$\varepsilon_q(p,q) = \mathrm{K}\int_0^L \frac{\partial\rho(p,q,s)}{\partial q}ds \qquad (2)$$

Erbeck and Merzkirch [4] has received a connection between density and deflection angle correlation functions

$$R_{\varepsilon q}(\xi,\eta) = -\mathrm{K}^2 \int_0^L\int_0^L \frac{\partial^2}{\partial\eta^2} R_\rho(\xi,\eta,\zeta)\,dz'dz'' \qquad (3)$$

For the case of isotropic turbulence, this equation can be inverted with respect to density correlation functions:

$$R_\rho(r) = \frac{1}{\pi L\mathrm{K}^2}\int_r^\infty \frac{1}{\sqrt{\tau^2 - r^2}}\left\{\int_0^\tau R_\varepsilon(\tau^*)d\tau^*\right\}d\tau \qquad (4)$$

Using these data, both macro- and micro-scales of turbulence can be determined. Thus, the Erbeck-Merzkirch integral transform is an effective tool for local turbulence parameter determination using digital line-of-sight data. Both macro and micro spatial structures of the turbulent scalar (density) field in compressible flow can be visualized and quantitatively characterized with the applied multi-projectional **DSP** technique. It should be noted that the inversion of this functions to the original one, $R_\rho(r)$, is ill posed mathematical problem and care must be taken performing such calculations. As we can see, the inversion integrals are Abel type integrals, therefore the great experience of solving this equation may be used. The quality of this reconstruction for a small-scale vorticity is rather good with grids of about 200^2.

CONCLUSIONS

Both macro and micro spatial structures of the turbulent scalar (density) field in compressible flow can be visualized and quantitatively characterized with the applied speckle tomography techniques. The macro structures are reconstructed using Radon integral transform. The microscale turbulence structures are determined by using the 3-D density correlation functions evaluated with Erbeck-Merzkirch integral transforms. With "high density" speckle photography data the precision of the turbulence microscale determination using this integral transform for the isotropic turbulence is rather higher. For non-isotropic turbulence the evaluation would require a more correct conversion using multi-angular probing and convolution of Radon and Erbeck-Merzkirch integral transforms.

ACKNOWLEDGEMENTS. The research described in this publication was supported by the Belarusian Fund of Basic Research (grant N T02P-043) and by INTAS (INTAS Project N 00- 0135 ”Novel PIV system for fluid mechanics measurements”, project coordinator Dr. J. Kompenhans).

References

[1] Merzkirch W.: Flow Visualization. Second edition, Academic Press, Orlando, 1987.

[2] Fomin N.: Speckle Photography for Fluid Mechanics Measurements. Springer Verlag, Berlin, 1998.

[3] Fomin N, Lavinskaja E, Merzkirch W, Vitkin D.: Turbulence microscale variations due to interaction with a shock wave. *Shock Waves*, **10**:345-349, 2000

[4] Erbeck R, Merzkirch W.: Speckle photographic measurements of turbulence in air stream with fluctuating temperature. Proc. of the 1st Symposium on Turbulence, University of Missouri-Rolla University Press, 1986.

THERMAL-WAVE RESONATOR CAVITY: MODELING AND APPLICATIONS FOR WATER MIXTURES

Anna Matvienko and Andreas Mandelis
Center for Advanced Diffusion-Wave Technologies, Department of Mechanical & Industrial Engineering, University of Toronto, 5 King's College Road, Toronto, ON, M5S3G8, Canada

Summary A novel technique for ultra-high resolution measurements of the thermal diffusivity of liquid mixtures in a Thermal-Wave Resonator Cavity was developed. This device is very sensitive to thermal diffusivity variations of the intracavity sample by virtue of the exponential dependency of the signal on this quantity. Frequency scan experiments were performed. A theoretical model describing the one-dimensional temperature field within the cavity was developed. Comparison between the theoretical and experimental data (signal amplitude and phase) shows good agreement. To achieve ultra-high sensitivity of the measurements we applied a novel signal baseline suppression technique known as "Common-Mode Rejection Demodulation."

BACKGROUND

In recent years, photothermal techniques have been successfully employed for precise and accurate measurements of thermal properties of aqueous solutions. In this work we developed a photothermal technique for ultra-high resolution measurements of thermal diffusivity of liquid mixtures, namely water-alcohol solutions using a Thermal-Wave Resonator Cavity (TWRC), [1] Fig. 1. One cavity wall is made of metal (aluminum) film. The other wall is the surface of a pyroelectric polyvinylidene fluoride (PVDF) sensor.

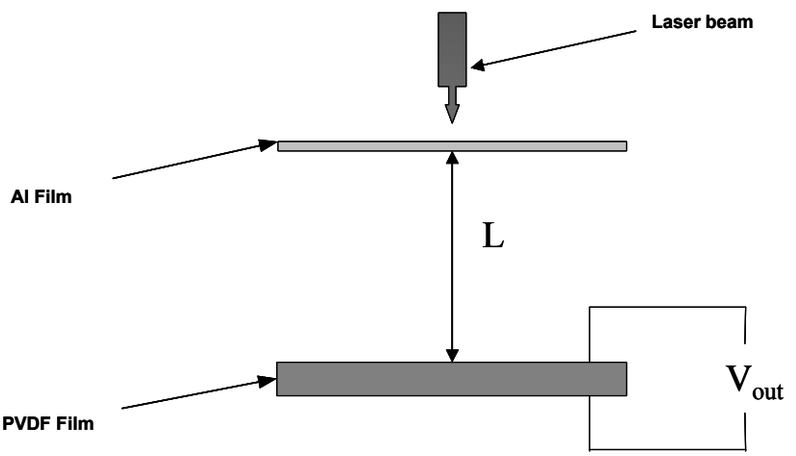


Fig.1. Thermal-Wave Resonator Cavity

The aluminum foil surface exterior to the cavity is slightly sooted to eliminate light reflection and enhance optical absorption and thermal-wave generation from a modulated laser beam. The generated thermal wave field causes temperature oscillations inside the cavity. The PVDF sensor detects the thermal wave launched by the optically heated foil and produces an electrical signal.

The conventional thermal-wave cavity method is very simple and inexpensive. Its high sensitivity to the thermal diffusivity of the intracavity material is due to the exponential dependency of the signal on the thermal diffusivity of the intracavity sample as a function of modulation frequency. However, resolution of minute diffusivity variations is limited by signal baseline (dynamic range). To achieve ultra-high diffusivity resolution in measurements at low concentrations of liquids with water mixtures we applied to the TWRC method the common-mode rejection demodulation (CMRD) scheme.[2]

The CMRD technique involves the launching of two pulses over one modulation period (Fig. 2). In this case, LIA output is the difference between the response waves produced by each one of the two pulses**.** This differential technique improves the limitations of the conventional single square-wave modulation through its ability to suppress the background LIA signal baseline, even in the presence of a strong input signal.[2] Thus, the CMRD increases considerably the dynamic range of the measurement system beyond typical dynamic ranges of modern LIAs and detects small signal variations induced by minute difference in the thermal diffusivity of the intracavity fluid.

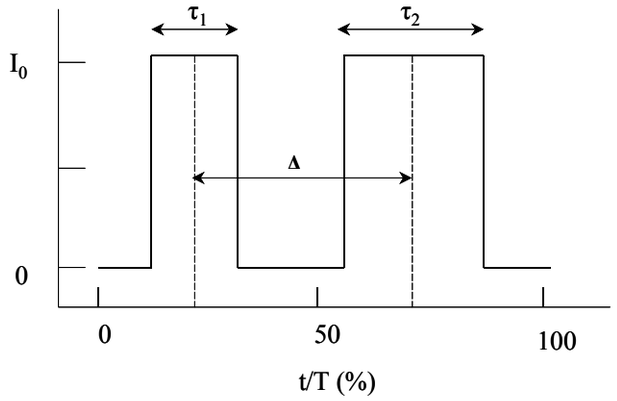


Fig.2. Optical excitation waveform consists of a bimodal pulse applied to TWRC. The horizontal time units are expressed as a percentage of a full repetition period T, τ_1 and τ_2 are the corresponding square pulse width and Δ is center-to-center time delay.

RESULTS

An experimental TWRC set-up was designed for the measurements of thermal diffusivity of liquids. The design involves fixed dimensions of the cavity length at a fixed modulation frequency and a scanned CMRD waveform pulse for obtaining reproducible measurements with various types of water-liquid solutions. Frequency scan experiments with liquid samples were performed. We also found, that accuracy of the measurements is considerably affected by the flatness of the aluminum film (Fig.1). A preliminary theoretical model describing the one-dimensional temperature field within the cavity was developed. The instrumental factor was normalized out by taking the ratio of two signals at the different cavity lengths. Comparison between the theoretical and experimental data for the ratio of signal amplitude (Fig.3) shows good agreement. The analytical model for the thermal-wave cavity response with a liquid intracavity layer permits fitting the theoretical curves to the experimental data to obtain the thermal diffusivity.

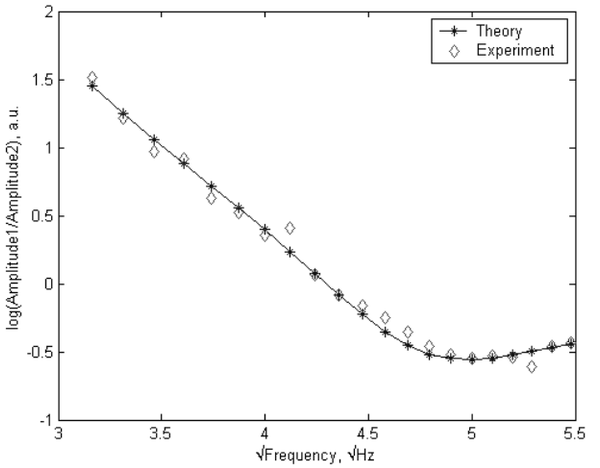


Fig.3. Frequency scan data, water,
$L_1 = 0.42$ mm, $L_2 = 0.65$ mm, $\alpha = 1.462\ 10^{-7}$ m^2/s

The CMRD technique has shown sensitivity of the photothermal signal to methanol in water at the level of 1% by weight. This level is 9% below the lowest reported concentration measurable in this mixture by photothermal techniques.[3] In terms of future applications, environmental pollution concerns require the introduction of simple, robust, inexpensive sensors, which can monitor water quality in remote locations in real time. The proposed system can eventually be implemented into a self-contained in-situ liquid pollution monitor.

References

[1] J.Shen and A. Mandelis, Rev. Sci. Instrum. 66, 4999 (1995).
[2] A. Mandelis, S. Paoloni and L. Nicolaides, Rev. Sci. Instrum. 71, 2440 (2000).
[3] G. Wu, M. Fiebig and A. Leipertz, Int.J.Heat Mass Transfer. 31, 1471 (1988).

PARTICLE IMAGE VELOCIMETRY (PIV) FOR CLOUD DROPLETS – LABORATORY INVESTIGATIONS

Piotr M. Korczyk*, Szymon P. Malinowski**, Tomasz A. Kowalewski*
*IPPT PAN, Department of Mechanics & Physics of Fluids, PL 00-049 Warszawa, Poland
**Warsaw University, Institute of Geophysics, Warszawa, Poland

Summary: Turbulent motion of cloud droplets is observed in a laboratory chamber by means of Particle Image Velocimetry (PIV). A specially developed multi-scale PIV algorithm is used to retrieve two components of velocity of cloud droplets.

INTRODUCTION

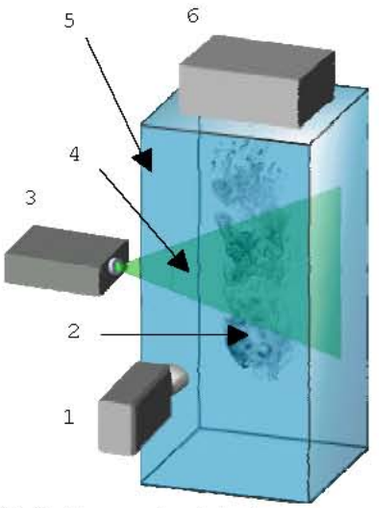


Fig.1. The experimental setup: 1) a camera, 2) a cloud during mixing, 3) a laser, 4) laser sheet, 5) a cloud chamber, 6) a small chamber with the droplet generator inside.

Interaction between small-scale turbulence and cloud particles is a key issue in warm rain formation mechanism, which is an important meteorological and climatological challenge [1],[2]. We investigate this interaction observing motion of cloud droplets in a glass walled chamber 1m deep, 1m wide and 1.8m high [3]. The second smaller chamber, placed above the main one is filled with water droplets of diameters in range from 7 to 25 micrometers. Cloudy air containing water droplets enters the main chamber forming the negatively buoyant, turbulent plume, mixing with unsaturated air in the main chamber and producing additional turbulence by evaporative cooling of droplets.
The plume is illuminated with a 1.2mm thick sheet of laser light (Nd:YAG, λ=532nm), forming the vertical cross-section through the central part of the chamber. Images, formed due to Mie scattering of laser light by cloud droplets are recorded by a high-resolution CCD camera placed outside the chamber, with the optical axis perpendicular to the light sheet. Images are recorded in pairs in order to retrieve information on droplets' velocities. Application of standard PIV algorithms to these pairs resulted in a large amount of errors and artifacts in the retrieved velocity field due to chaotic nature of motion in a chamber. Therefore a special multi-scale algorithm was developed.

MULTI-SCALE PIV PROCESSING

In order to evaluate displacement of a droplet pattern at position (x,y) a square sample from the first exposure centered at this position is taken. Then we search the most similar sample in the second exposure within the interrogation area, also a square centered at (x,y). The size of the interrogation area depends on the expected greatest displacement and on the size of the sample. Images are matrices and each pixel is treated as an element of matrix: an integer representing grey level (brightness) of this pixel. For sample **S** of size M×M and interrogation area **A** of size L×L evaluation function used to process recordings can be defined as:

$$\varphi(m,n)=\sum_{i=1}^{M}\sum_{j=1}^{M}[S(i,j)-<S>][A(i+m,j+n)-<A>]$$

where

$$<S>=\frac{1}{M^2}\sum_{i=1}^{M}\sum_{j=1}^{M}S(i,j) \qquad <A>=\frac{1}{M^2}\sum_{i=1}^{M}\sum_{j=1}^{M}A(i+m,j+n)$$

for

$$m\in[0,L-M] \qquad n\in[0,L-M]$$

The evaluation function can be written as:

$$\varphi(m,n)=\sum_{i=1}^{M}\sum_{j=1}^{M}S(i,j)A(i+m,j+m)-M^2<S><A>$$

which can be efficiently calculated with use o FFT algorithm.
Maximum of ϕ(m,n) corresponds to best similarity between samples from both exposures, from which displacement of the ensemble of droplets contained in **S** is evaluated. In standard PIV algorithms the choice of the size of the sample is a significant technical problem [4]. In the following we propose successive, multi-scale selection of smaller and smaller samples.
In a first step we look for the displacement in the whole image in order to remove the bulk motion of the plume. At the next step the size of the sample is reduced and the position of the interrogation area is determined by the displacement vector evaluated earlier. In this way the displacement is corrected. This algorithm can be repeated few times

decreasing the size of the sample. Due to these operations velocity vector can be evaluated for small patterns containing small number of droplets.
Before application to the experimental the above algorithm was verified in a benchmark pair of images [5]. It implied that average error of the displacement was about 0.5 pixels. The accuracy of retrieval, evaluated on a basis of this benchmark test is significantly better than retrieval by direct correlation.

RESULTS

The new PIV algorithm is employed to investigate properties of a cloud model and provides insight into the cloud structure at scales of centimetres and down. Using laboratory setup consisting the cloud chamber allows us to investigate processes important for initiation of the precipitation.
Observation of the cloud structures falling down through the chamber gives opportunity to study the mixing process of the cloud with an unsaturated environmental air. Application of the multi-scale algorithm provides information on turbulent velocities of the cloud droplets. Due to it, histograms of the velocity fluctuations are acquired. Comparison of histograms of vertical and horizontal fluctuations implies that flow in regions of mixing may not be isotropic with preferred vertical direction. As suggested in [6] it may be caused by negative buoyancy forces produced by droplet evaporation.
The experimental setup and the multi-scale (PIV) algorithm are also used to investigate evolution of spatial distribution of cloud droplets. Flow structure typical for turbulence, like the vortex tube, appears to influence spatial distribution of droplets. Effect of gravity, inertia and drag forces is responsible for clustering of droplets.

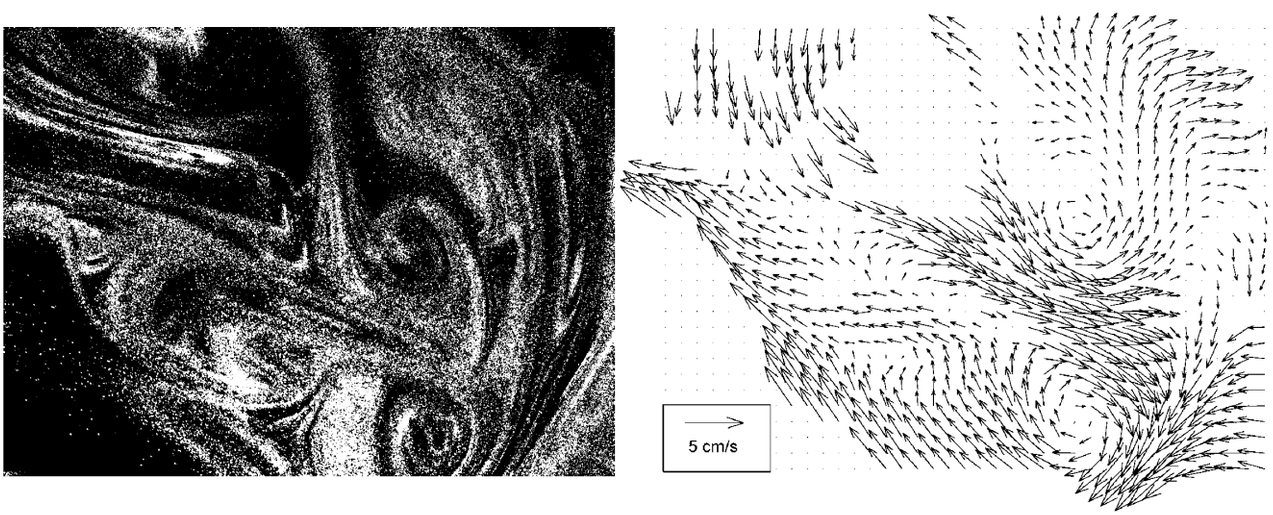


Fig.2. Example of experimental image visualising part of artificial cloud of size about 6cm × 4cm.
Map of velocity fluctuation obtained by processing experimental data and employing mentioned algorithm.

SUMMARY AND FUTURE WORK

A new multi-scale algorithm was introduced and successfully employed to analyse experimental data of complex flow in the turbulent cloud chamber. Further development to increase its accuracy and resolution as well as expanded to use in other application like stereo PIV [7], allowing to retrieval of all three components of velocity vector, will be presented.

Acknowledgments
This research was supported by a research grant No 5 T07A 052 24 of the Polish Committee for Scientific Research.

References

[1] Vailancourt P. A. and Yau M. K.: Review of Particle-Turbulence interactions and Consequences for Cloud Physics. *Bull. Am. Meteorol. Soc.* 81, 285-98, 2000.
[2] Shaw R. A.: Particle-turbulence interactions in atmospheric clouds. *Annu. Rev. Fluid Mech.* 35, 183-227, 2003.
[3] Malinowski S. P., Zawadzki I., and Banat P.: Laboratory observations of cloud-clear air mixing in small scales. *J. Atmos. Oceanic Technol.* 15, 1060
[4] Gui L., Merzkirch W.: Generating arbitrarily sized interrogation windows for correlation-based analysis of particle image velocimetry recordings. *Experiments in Fluids* 24, 66-69, 1998
[5] Quenot G. M., Pakleza J., Kowalewski T. A.: Particle image velocimetry with optical flow. *Experiments in Fluids* 25, 177-189, 1998.
[6] Banat P. and Malinowski S.P.: Properties of the turbulent cloud-clear air interface observed in the laboratory experiment. *Phys. Chem. Earth (B),* 24, 741-745, 1999.
[7] Raffel M., Willert Ch. E., Kompenhans J.: Particle image velocimetry: a practical guide. *Springer* 1998.

OPTICAL DIAGNOSIS SYSTEMS FOR MEASURING THERMOFLUIDDYNAMICALS PHENOMENA IN LIQUID BIOSYSTEMS UNDER ULTRA HIGH PRESSURE

Antonio Delgado*, Özlem Özmutlu*, Christoph Hartmann*, Albert Baars*

Chair of Fluid Dynamics and Process Control, Technische Universität München, Freising, Germany

Summary In modern bioprocess engineering, novel visualization systems for investigating thermofluiddynamical, particularly, phase transition phenomena occurring when liquid systems are pressurized up to 10000 bars, are already presented. Of crucial importance is the observation made for the first time that phase transition causes a substantial convective transport which has been totally ignored in literature till now.

INTRODUCTION

Pressure is a fundamental thermodynamic quantity, comparable to temperature or chemical potential. Thus, the result of application of sufficiently high pressures in bioprocesses proves to be extremely manifold. This reveals pressure as basic tool for fundamental research, for specific biostructure creation and bioprocess design. As a consequence of this, research in the field of high pressure treatment of biomaterials has become recently to an extremely promising and, therefore, worldwide very dynamically developing discipline. Most progress has been achieved in food and biosciences but other disciplines such as medicine have also recognized the high potential of high pressure treatment meanwhile.
In most of the papers in literature the description of biophysical and chemical effects under high pressure occurs assuming validity of thermodynamics for homogeneous matter at rest. It could be shown experimentally and theoretically that this postulation does not hold [1]. In fact, compression is always connected to a forced convection. Furthermore, compression under practical (non-isotherm) conditions generates thermal diffusion and, thus, natural convection in liquid biomaterials. Altogether, it must be stated that the pressurization processes are always heterogeneous even in the case of homogeneous matter available.
Excluding certain biochemical reactions, the inner time scale of running processes during pressurization must be expected to be substantially longer than the sound velocity, which is responsible for the transmission of pressure. Therefore, pressure treatment can be considered as instantaneous but not as homogeneous [1]. The present contribution deals with novel methods suitable for visualizing heterogeneities of the velocity and pressure fields. Particularly, the adaptation of these methods for measuring pressure induced phase transition and corresponding results are presented.

EXPERIMENTAL METHODS

For visualization of velocity and temperature fields microencapsulated thermochromic liquid crystals are used while they can reflect selectively light as a function of temperature. Furthermore, in [2] it was shown for the first time that the wave length of the reflected light also depends on the pressure. Finally, the liquid crystals used are also well suitable as tracer. Thus, they allow determining the temperature distribution by illuminating the liquid crystals with white light and analyzing the reflected light (color or wavelength). Additionally, this facilitate the determination of the velocity field via Particle Image Velocimetry (PIV).
The main experimental setup consists of a tempered high pressure optical cell having a volume of 2 ml, which is equipped with sapphire windows of 6 mm optical width. This high pressure cell is designed to bear pressures up to 700 MPa. This system is illuminated by a sheet of white light from a xenon lamp. The field is recorded by a fixed 3-chip RGB (Red-Green-Blue) CCD camera which is located at a right angle to the incident light sheet. This reflected light is first expressed as HUE values and then related to temperature and pressure by help of digital post-processing. Performing experiments in a wide range of pressure and temperature with different types of liquid crystals have shown that they can be used in a wide temperature range and at pressures at least up to 700 MPa. Thus, High Pressure Particle Image Thermography (HP-DPIT) and High Pressure Particle Image Velocimetry (HP-DPIV) have been developed.

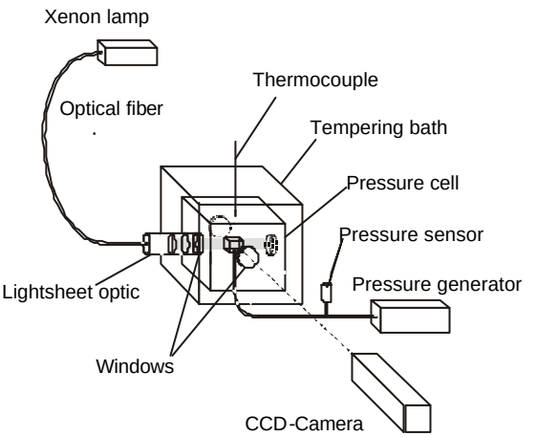


Figure 1: Experimental setup

The liquid crystal particles (having 10-15 µm diameter and 1 g/ml density) used in this study are encapsulated in a polymeric material for protection (from Hallcrest Ltd, BM/R-30C2W/S40).The particles are disposed for tracing the fluid

motion in the substance. Visualizing temperature and velocity fields in liquids necessitates only a low particle concentration of about 10^{-2} to 10^{-3} volume percent. Experimentally, significant difficulties are caused by finding the proper liquid crystals in the region of phase transition. In general, it is possible to have liquid crystal solutions at every start temperature and bandwidth (the temperature where liquid crystals start to reflect and the range in which they change the reflected colour, respectively). But, low temperatures decrease the stability of crystals and therefore it is not possible to produce narrow bandwidths.

RESULTS

Figure 2 and 3 illustrates typical results obtained for the temperature and velocity field in water during pressure induced phase transition to the Ice I conformation [3]. For this process the cell is first cooled down to 263 K and then pressurized to 120 MPa. Then the temperature of the temper bath is set to a temperature around 278 K. In Figure 2 the diffuse streak corresponds to the transition front whereby the rigid phase is placed in the upper part. The blue color corresponds to the higher temperature which decreases with increasing wave length. Thus, red indicate the smallest temperature whereby the detectable temperature difference between blue and red is 1.3 K. This demonstrates the excellent temperature resolution of HP-DPIT. Figure 2 also clearly demonstrates the heterogeneity of temperature distribution in the liquid phase. Most remarkable is the "cold spot " [1] located in the upper right part. In this context it must be taken into consideration that temperature strongly influences biophysical and –chemical processes. Furthermore, the effect of high pressure on microorganisms is strong function of temperature, too.

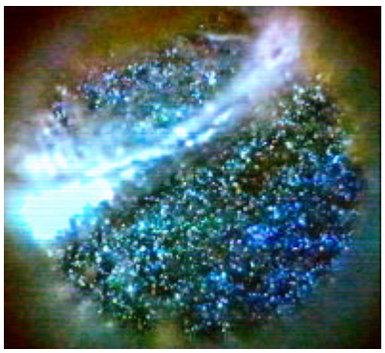


Figure 2: Phase transition of Ice I under high pressure (150 MPa)

The existence of the cold spot mentioned is not only a result of thermal diffusion but mainly of convective transport. Figure 3 illustrates convection during melting of ice. This process starts by melting of ice near the wall region where temperature is maximal. In the presence of liquid ice detaches from the inner wall of the cell. Ice I moves up because of its density is lower than that of water. Movement of the ice block forms two counter rotating vortices in the water layer below it. These vortices have accelerative effect on heat convection: the liquid from near wall region is carried near to the solid-liquid surface and phase transition develops. In PIV image solid body motion can be differentiated with the area located in the upper part of the figure. In the lower fluid part, substantial convection is observed. This is contradictory to the pure diffusive effect of a system in rest assumed in literature. Thus, results for biophysical and –chemical as well as microbiological effects obtained yet have to be checked taking into consideration the coupled momentum and energy transfer found in experiments. Furthermore, the design of high pressure chamber for practical applications of high pressure on biomaterials must include the occurring convective transport processes.

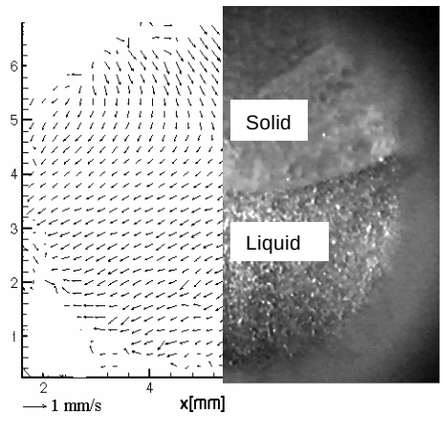


Figure 3: Convective processes during melting of Ice I

CONCLUSIONS

HP-DPIT and HP-DPIV, originally developed for diagnosing temperature and velocity fields in pure one-phase liquids under high pressure, have been further adapted to a method for High Pressure Digital Phase Transition Detection (HP-DPTD). The latter has been shown to be suitable for detecting the transition front as well as the temperature and velocity distribution in its neighborhood. The results found show conclusively that neither the assumption of homogeneity nor of pure diffusive transport in a resting liquid holds. As biosystems are very sensible against mechanical and thermal heterogeneities results published yet are worth to be checked carefully.

References

[1] Delgado, A., Hartmann, C. 2002. Pressure Treatment of Food: Instantaneous but not Homogeneous Effect. *Advances in High Pressure Bioscience and Biotechnology II*, Ed. R. Winter, Springer, Heidelberg.

[2] Pehl, M., Werner, F., Delgado, A. 2000. First Visualization of Temperature Fields in Liquids at High Pressure Using Thermochromic Liquid Crystals. *Experiments in Fluids* **29**: 302-304.

[3] Özmutlu Ö., Hartmann, C., Delgado, A. "Visualization of Temperature and Velocity Fields during Phase Change of Water under High Hydrostatic Pressure" *GALA 2003- Laser Methods in Fluid Mechanics* **(11)**: 29.1-29.6

Liquids: The Holy Grail of Microfluidics Modeling

Mohamed Gad-el-Hak
Virginia Commonwealth University
Richmond, Virginia
<gadelhak@vcu.edu>

Interest in microelectromechanical systems (MEMS) has experienced explosive growth during the past few years. Such small devices typically have characteristic size ranging from 1 mm down to 1 micron, and may include sensors, actuators, motors, pumps, turbines, gears, ducts and valves. Microdevices often involve mass, momentum and energy transport. Modeling gas and liquid flows through MEMS may necessitate including slip, rarefaction, compressibility, intermolecular forces and other unconventional effects. The continuum-based Navier–Stokes equations—with either the traditional no-slip or slip-flow boundary conditions—work only for a limited range of Knudsen numbers above which alternative models must be sought. These include molecular dynamics simulations (MD), Boltzmann equation, Direct Simulation Monte Carlo (DSMC), and other deterministic/probabilistic molecular models. The kinetic theory of gases defines well the boundaries for which the no-slip Navier–Stokes equations can accurately model the flow of a dilute gas. The same cannot be said about dense-gas and liquid flows where intermolecular interactions play a dominant role. Neither type of fluid has a well-advanced molecular-based theory, as is the case for dilute gases. The concept of mean free path is not very useful for liquids and the conditions under which a liquid flow fails to be in quasi-equilibrium state are not well defined. Such complex fluids can only be treated via hybrid continuum–molecular approaches, which approaches are still far from satisfactory at the present time. The present talk will address such issues and outline a blueprint for future developments.

ACTIVE CONTROL OF SHOCK/BOUNDARY LAYER INTERACTION IN TRANSONIC FLOW OVER AIRFOILS

Ramesh K. Agarwal and Jose L. Vadillo
Washington University in St. Louis, Campus Box 1185, 1 Brookings Drive, St. Louis, MO 63130,USA

Summary The objective of this paper is to show, via numerical simulation, the feasibility of weakening the shock wave(s) and reducing the pockets of supersonic and separated flow regions on an airfoil (NACA 0012) in transonic flow at small angles of attack using an active flow control device such as a synthetic jet actuator. The weakening of shock and control of shock/boundary-layer (SBL) interaction can result in both reduced drag and lift, which may be beneficial in achieving rapid altitude change in descent flight.

.

Recently it has been shown experimentally by Amitay et al [1] and computationally by the authors of this paper [2] that the pressure drag of an airfoil at low speeds and small angles of attack can be significantly reduced with a minimum change in lift by modification of the apparent aerodynamic shape of the airfoil. In [1], a small stationary flow interaction domain adjacent to the upper surface of the airfoil was created deliberately by employing a passive small surface mounted obstruction which of course increased the drag appreciably. A synthetic jet actuator was then placed immediately downstream of the obstruction to see its effect on lift and drag of the airfoil; the frequency and momentum coefficient of the synthetic jet were varied in the experiment. It was shown that it was possible to reduce drag with minimal change in lift at higher momentum coefficient and frequencies of the jet. These results have been very encouraging. However, although some computational and experimental work has been done in the application of active control for virtual aeroshaping of an airfoil to reduce drag in subsonic flow, hardly any work has been reported in the literature to date for active control of the strength of shock waves and their unsteadiness, the supersonic regions and shock-induced separation due to shock/boundary layer interaction. This problem is of great relevance for reducing the transonic cruise drag of a transport aircraft and high speed impulsive noise of a rotorcraft.

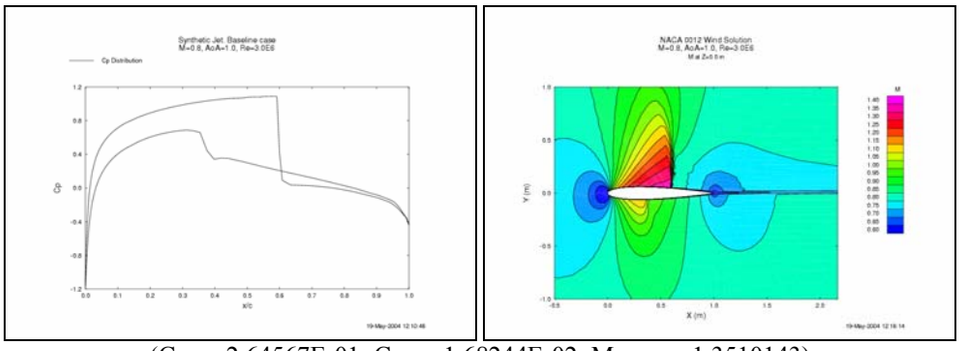
In this paper, CFD simulations are performed by employing an extensively validated well known multi-zone hybrid RANS/LES flow solver WIND. Detached Eddy Simulation (DES) modification of Menter's two-equation Shear Stress Transport (SST) model was employed in the computations. The grid refinement study was performed to ensure that the computed solutions were grid-independent. The uncertainty in the computed solutions due to the numerics (size of computational domain, grid, numerical algorithm and boundary conditions) was minimized. The actual geometry of the control device was included in the simulations. It has been shown by many investigators that the geometry of the control device (e.g. cavity of the synthetic jet) should be included in the computations for accurate simulation of the flowfield; the simplified boundary conditions implemented on the airfoil surface can introduce significant errors.

A large number of numerical simulations were performed for transonic turbulent flow past a NACA 0012 airfoil at small angles of attack by varying various parameters of the synthetic jet such as amplitude of the jet velocity, jet width, momentum coefficient, frequency and jet location on the airfoil surface. Here due to lack of space, we show the results of a typical computation for flow past a NACA 0012 airfoil in transonic flow at Mach 0.8, angle of attack = 1°, chord Reynolds number Re = 3×10^6, with and without a synthetic jet. Figure 1 shows the pressure distribution and Mach contours on the airfoil in the absence of synthetic jet. A synthetic jet of width 0.003c (c = chord of the airfoil), frequency = 1550 Hz, and jet Mach number M_j = 0.3 (maximum amplitude) is applied at the foot of the shock. Figure 2 shows the Mach contours and pressure distributions at three normalized time intervals during one cycle of the synthetic jet. These calculations show reduction in both lift and drag during one cycle of the synthetic jet for this free stream flow condition and the synthetic jet parameters employed. Additional computations will be presented in the complete paper for this case for different amplitudes, frequencies and locations of the synthetic jet. It is concluded that the active control of shock/boundary layer interaction on an airfoil in transonic flow can be achieved, resulting in both reduced drag and lift, for suitably selected parameters of the synthetic jet.

References

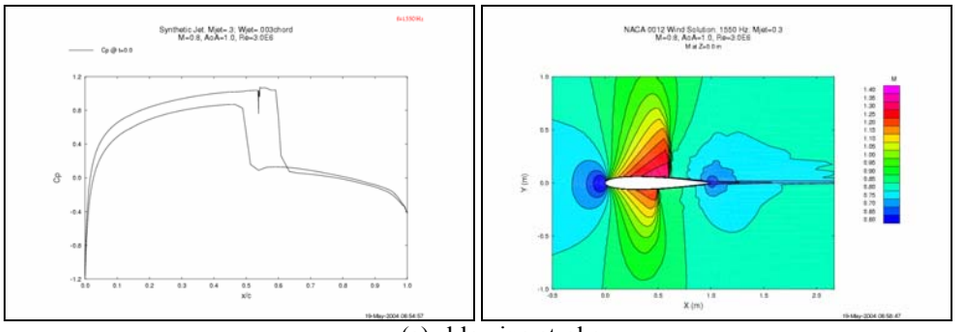
[1] Amitay, M., Horvath, M., Michaux, M., and Glezer, A.: Virtual Aerodynamic Shape Modification at Low Angles of Attack Using Synthetic Jet Actuators. AIAA Paper 2001-2975, 2001,

[2] Vadillo, J.L., Agarwal, R.K., Cary, A.W., and Bower, W.W.: Numerical Study of Virtual Aerodynamic Shape Modification of an Airfoil Using a Synthetic Jet Actuator. AIAA Paper 2003-4158, AIAA 33rd Fluid Dynamics Conference, 23-26 June 2003.



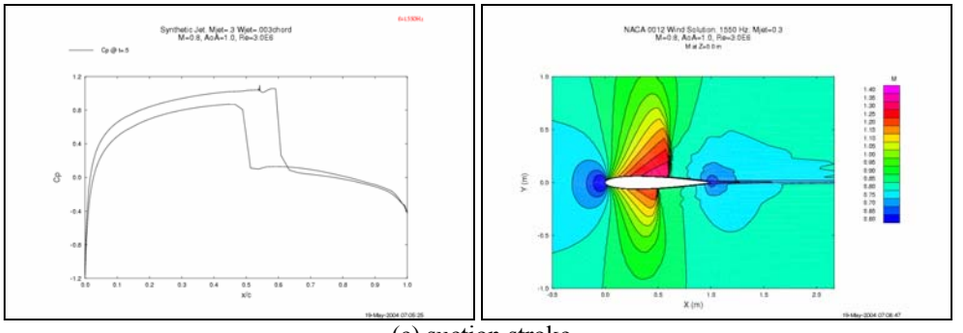
(C_L = 2.64567E-01; C_D = 1.68244E-02; M_{Max} = 1.3510143)

Figure 1: Computed Pressure Distribution and Mach Contours for Flow Past a NACA 0012 Airfoil at M=0.8, Re = 3.0×10^6, α=1.0° without Synthetic Jet.



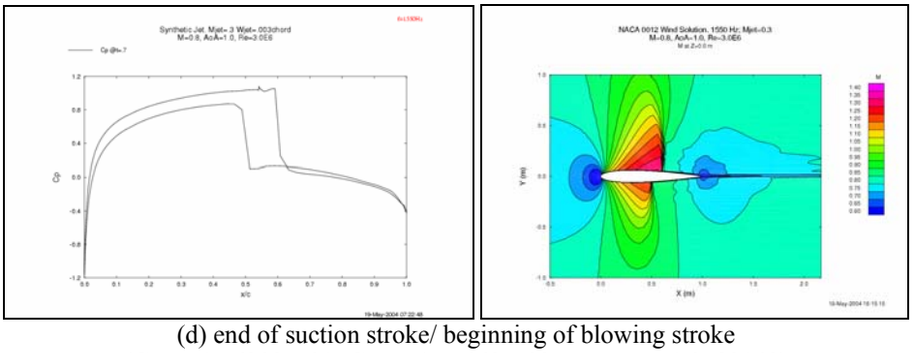
(a) blowing stroke

(C_L = 1.56638E-01; C_D = 1.60760E-02; M_{Max} = 1.3408358)



(c) suction stroke

(C_L = 1.55913E-01; C_D = 1.57559E-02; M_{Max} = 1.3548344)



(d) end of suction stroke/ beginning of blowing stroke

(C_L = 1.56292E-01; C_D = 1.57468E-02; M_{Max} = 1.3583143)

Figure 2: Computed Pressure Distribution and Mach Contours for Flow Past a NACA 0012 Airfoil at M=0.8, Re = 3.0×10^6, α=1.0° with Synthetic Jet, Jet Width = 0.003c, M_j = 0.3, f = 1550 Hz.

MANIPULATING A VEE-SHAPED BLUFF BODY WAKE USING A FLUIDIC OSCILLATOR

Rong F. Huang and Kuo T. Chang
Department of Mechanical Engineering
National Taiwan University of Science and Technology
Taipei, Taiwan 10672, R. O. C.

Summary The vee-shaped bluff body was re-designed by employing the unsteady Coanda effect to induce self-sustained, periodically oscillating jet. The oscillating jet was directed into the near wake of the vee-shaped bluff body to modify the wake characteristics. Oscillating behaviors, frequency characteristics, and turbulence properties of the jet and wake were studied experimentally. Results showed significant enhancement in jet oscillation frequency and wake turbulence.

INTRODUCTION

Bluff body wake is frequently used in various applications due to its fluid mechanics features [1]. The Coanda effect has been discovered for decades by the fluid engineers [2], which is the fundamental physical phenomenon that the jet oscillates through a Hopf bifurcation when the Reynolds number is larger than a critical value. The authors tried to apply the principle of unsteady Coanda effect to the vee-shaped bluff body and develop a periodic jet-injected version in this paper. The self-sustained oscillating jet was directed through passages and then injected into near wake of the vee-shaped bluff body. The oscillating jet and the modulated wake are experimentally examined.

EXPERIMENTALS

The vee-shaped bluff body is made of Plexiglas and installed horizontally in the cross-stream direction in the test section of the wind tunnel, as shown in Fig. 1(a). The side-plates of the vee-shaped bluff body are arranged at 90^o and has an slit width d=3mm at the leading edge, as shown in Fig. 1(b). A target blockage with a horseshoe surface facing the upstream slit is placed in the room between the vee-shaped bluff body side plates. The slit-jet impinges the horseshoe surface of the target block. The horseshoe surface has a radius R originated from the point located on the symmetry axis at a distance h from the virtual vertex of the target block. The geometrical parameters of h, R, and b_{gap} along with the flow parameter Re_d determine the effective regime of design and operation. The flow oscillation process is made observable by using the smoke-wire technique. Streak photography is done via a high speed CCD camera of maximum framing speed at 8000 fps. Frequencies of the unsteady motions in the wake region are detected by a constant temperature hot-wire anemometer. The velocity and turbulence properties are measured by a two-component laser Doppler velocimeter. Evolution process of the jet/wake interaction is detected by PIV.

RESULTS AND DISCUSSION

Flow behaviors

Depending on the values of (h/d, R/d, Re_d), the flows in the cavity enclosed by the vee-shaped bluff body and the target block present different behaviors. For example, Fig. 2 shows the smoke-streak flow patterns at various h/d's as (R/d, Re_d)=(2.33, 339). In Figs. 2(a) and (b) which h/d=0 and 1.00, respectively, the slit-jet goes through the leading-edge slit, impinges the horseshoe surface of the target block, bifurcates into two streams, and forms two counter-rotating vortices. The impinging slit-jet does not oscillate. This flow pattern of bifurcation is usually observed at low values of h/d.
In the instantaneous pictures of Figs. 2(c) and (d) which h/d=1.67 and 2.00, respectively, the slit-jet is neither located at the neutral position, nor stayed at a fixed position. It actually swings back and forth continuously, periodically and proceeds with a self-sustained oscillation. In Figs. 2(e) and (f) for which h/d=2.33 and 2.67, respectively, the slit-jet in the horseshoe cavity is deflected from the central symmetry axis and attached to the inner wall of one of the vee-shaped bluff body walls. Most of the space in the cavity is occupied by a large vortex. No transverse oscillation of the jet is found. If the wind tunnel is restarted or if the jet is subject to a large perturbation, the deflected jet may attach toward the other side wall. This type of flow pattern is usually found at large values of h/d.

Turbulence intensities

The turbulence intensities at various Reynolds numbers increase from the inner region of the near wake, attain peak values, then decrease quickly in the outer region of the wake. Effect of "extra" vortex-stretching induced by the injection jets is apparent. The turbulence intensities in the wake of the fluidic-jet-injected vee-shaped bluff body are significantly high, about 80%, when compared with that of the close-tip vee-gutter, about 50%. Besides, the fluidic jet injection causes the high turbulence region of the jet-injected vee-shaped bluff body to be wider than that of the close-tip vee-gutter. At the downstream stages, the features of high turbulence intensities in the wake remain and the perturbed regions are widened.

Power spectrum, time scale, probability density function and integral length scale

The power spectrum density function in the wake shows two peaks: the shedding frequency of vortices and the

oscillating jet. The frequency of fluidic oscillation in general is about 25 to 40 times higher than its counter part of vortex shedding, depending on the Reynolds number. The oscillation frequency of the presently developed oscillator is about 160 times larger than the previous results for enhancement of heat transfer and about 10 times larger than that of the fluidic flowmeter. The probability density function of the fluctuations displays a dual-peak pattern, which delineates the characteristics of the sinusoidal signals. The Taylor's integral length scale of the fluidic oscillation is about 5% of the large scale vortex shedding. With periodic injection of the jets, the integral turbulence length scales are drastically decreased by one order of magnitude. In view of Kolmogorov's energy cascade process, injecting the fluidic oscillating jets into the low frequency wake may increase the vortex-stretching evolution of the energy flow and play a role in enhancing the transport capability of the turbulence kinetic energy. The increased effect of vortex-stretching in the shear layer finally causes the integral turbulence length scale to reduce.

Evolution process of jet/wake interaction

Topological analysis applied to the PIV measured streak flow patterns in a water tank analogy apparatus shows evolution process of the jet oscillation and interaction between the jet and the wake vortices.

CONCLUSIONS

By inserting the horseshoe target block into the cavity of the vee-shaped guard plates, the slit jet can proceed self-sustained transverse oscillation under some designs of geometric parameters and Reynolds number. The present design pushes the oscillation frequency of the jet to significantly high values. The turbulence are significantly increased so that enhancement of mixing in the wake is expected.

REFERENCES

[1] Hertzberg, J. R. and Shepherd, I. G.: Vortex Shedding Behind Rod Stabilized Flames. *Comb. Flame* **86**:1-11,1991.

[2] Uzol, O. and Camci, C.: Experimental and Computational Visualization and Frequency Measurements of the Jet Oscillation inside a Fluidic Oscillator. J. Visualization, **4**:88-96, 2002.

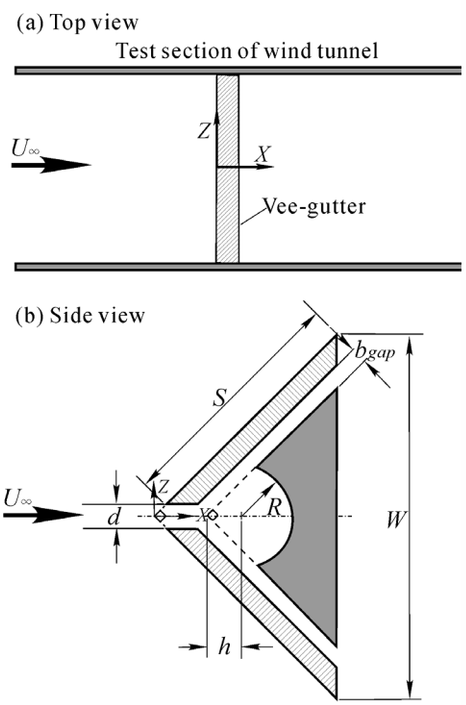


Fig. 1 Experimental setup. (a) vee-gutter in test section; (b) jet-injected vee-gutter.

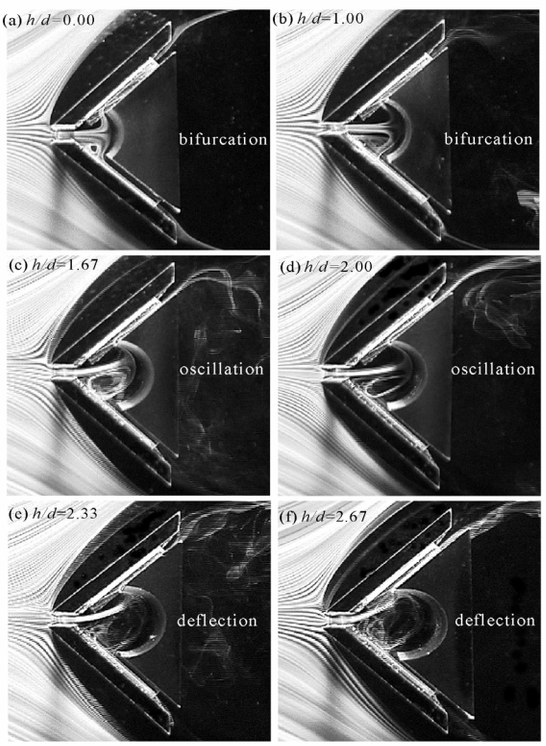


Fig. 2 Behaviors of slit-jet in oscillation cavity. Re_d=339, R/d=2.33, d=3mm, b_{gap}=2mm

RESPONSE OF THE NEAR WALL TURBULENCE TO LOCALIZED UNSTEADY BLOWING PERIODICAL AND DISSYMETRIC IN TIME

Sedat Tardu, Olivier Doche
Laboratoire des Ecoulements Géophysiques et Industriels, LEGI
B.P. 53X 38041 Grenoble Cédex

Key words: Active control, Drag Reduction, Localized Unsteady Time Periodical Blowing

The active control of the near wall turbulence by suboptimal or optimal strategies is plausible, but it requires unfeasibly dense distribution of the sensors and actuators at the wall. One possible way to remedy to this situation is to go through dual control methods. The latter consist of exciting the near wall turbulence locally to render it more predictable and controllable. Such a strategy has been used by Tardu (1998, 2001) who investigated the reaction of the near wall turbulence to a space localized oscillating blowing sinusoidal in time with small severity. He showed that the flow is partly relaminarized during the oscillation cycle until roughly 50 wall units downstream of the slot. This is due to the creation of a positive spanwise vorticity layer that dilutes the negative vorticity existing near the wall. The relaminarized phase is unstable. The diffusion of the induced vorticity layer is constrained into the low buffer layer with limited effect of turbulent mixing, when the frequency of the oscillating blowing is large. Consequently the vorticity concentrates, becomes compact and rolls-up into a coherent spanwise vortex at approximately the beginning of the low buffer layer. It increases the wall shear stress as it is convected downstream, resulting in an important drag penalty compared with steady blowing with the same mean severity.

The relaminarized phase coincides with the accelerating phase (stabilizing) of the injection velocity and the concentrated positive vorticity layer rolls-up during the decelerating (destabilizing) phase. The idea advanced by Tardu (2001), was to use unsteady periodical blowing dissymmetric in time with a rapid acceleration phase followed by deceleration to prevent the destabilization and the set-up of the spanwise vortex that causes the drag increase. Thus a specific new pulsating device was designed and new experiments conducted in the low speed wind tunnel of LEGI. The ensemble of experimental parameters is similar to Tardu (2001). Fig. 1 shows the phase average of the injection velocity. It is seen that the acceleration phase is roughly twice more rapid than the deceleration one. The dissymmetry in blowing is also clearly perceptible through the differences between $< v_0 >$ and its first harmonic. Fig. 2 shows the phase average of the wall shear stress $< \tau >$ normalized by τ_{SBL} of the standard unmanipulated boundary layer at 100 wall units downstream the blowing slot. The results corresponding to the sinusoidal injection velocity are shown by the squares. The large pick value of about 2.5 corresponds to the passage of the coherent vortex. The latter disappears when the blowing is dissymmetric as shown by the circles in the same Fig. Thus, the rapid acceleration followed by a slow deceleration phases prevent the formation of the spanwise vortex and suppresses the drag penalty. These results validate our previous arguments and show how the wall turbulence reaction is sensitive to the temporal waveform of localized blowing. It points at possible alternate ways of drag management. Detailed results related to the velocity profiles and turbulent quantities will be discussed in the Symposium. We are also

performing Direct Numerical Simulations in a fully developed turbulent channel flow and these results will also be presented.

References

1. S. TARDU "Active control of near wall turbulence by local unsteady blowing *J. Fluid Mech*., 43, 217-253, 2001.
2. S. TARDU"Near wall turbulence control by time space periodical blowing and suction. Effect of local time periodical blowing " *Exp. Thermal and Fluid Science* ; 16/1-2; pp. 41-54; 1998.

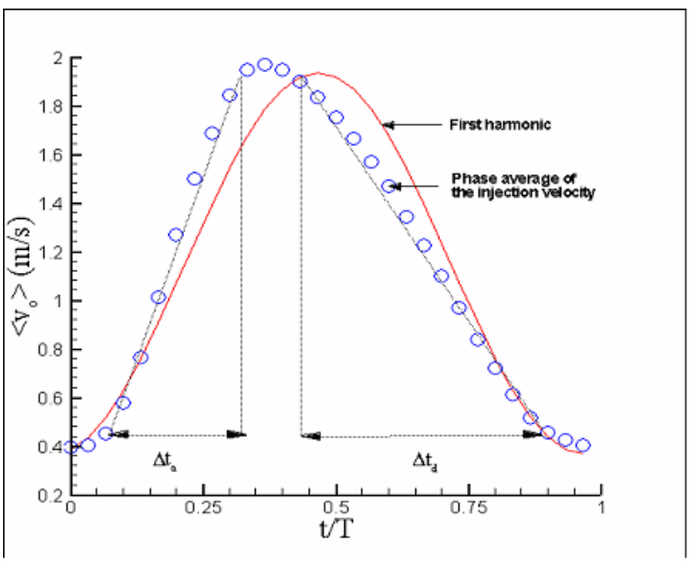


Figure 1 Phase average of the injection velocity.

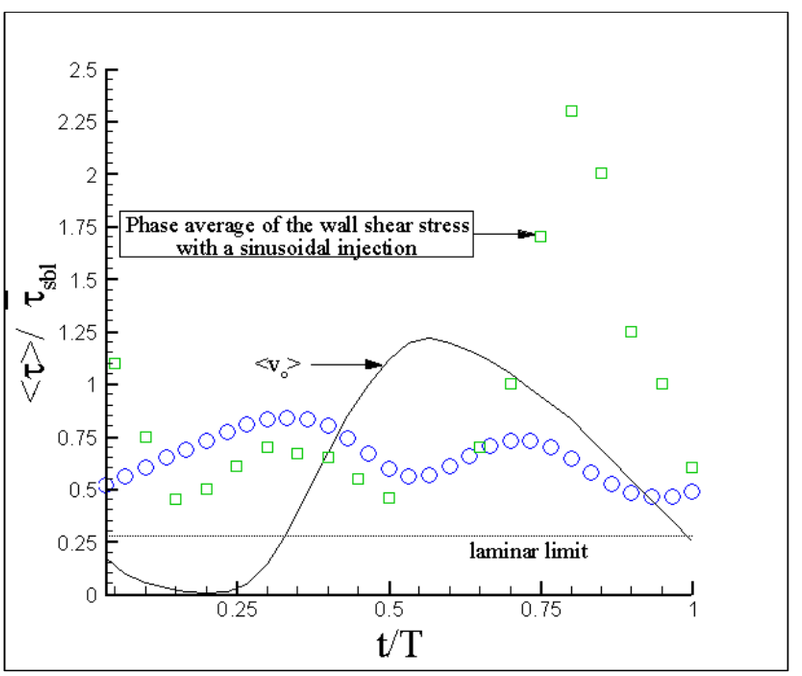


Figure 2 Phase average of the wall shear stress measured at 100 wall units downstream the slot with sinusoidal and dissymmetric blowing velocities oscillating in time.

Passive Control of Turbulent Flow behind a Model Vehicle for Drag Reduction Using Wake Disrupter

Dongkon Lee[*], Jin Choi[*], Woo-Pyung Jeon[**], Jeonglae Kim[*],
Seonghyeon Hahn[**] and Haecheon Choi[*,**]

[*] *School of Mechanical and Aerospace Engineering, Seoul National University, Seoul 151-744, Korea*
[**] *Center for Turbulence and Flow Control Research, Institute of Advanced Machinery and Design, Seoul National University, Seoul 151-744, Korea*

Summary Both wind-tunnel experiment and large eddy simulation are carried out to examine the applicability of a new passive device, wake disrupter, to flow over a model vehicle for drag reduction. The wake disrupter is a small-size rectangular body attached to a part of the trailing edge of the model vehicle, designed to perturb an essentially two-dimensional nature of wake. The wake disrupter significantly changes the wake structures and leads to maximum 23% increase in the base pressure of the model vehicle.

The development of a highly efficient transportation vehicle is one of the most important issues for control of turbulent flow for drag reduction. Generally, for large-scale transportation vehicles, the separation point is fixed at the trailing edge where the flow suddenly changes from a flat-plate boundary layer flow to a wake. Some experiments on control of flow over a model vehicle with a fixed separation point have been conducted for drag reduction using splitter plate and base bleed [1-2]. For a successful drag reduction, however, relatively large-size plate and high blowing rate were required in those studies. The spanwise modifications of the tailing edge such as segmented, curved, M-shaped and sinusoidal edges have also led to significant drag reductions [3,4], but the amounts of shape modification were quite large. Therefore, an effort toward designing a small-size passive device is needed for practical implementation. Very recently, Kim & Choi [5], and Kim et al. [6] suggested an active control method (called distributed forcing) for drag reduction on a circular cylinder and on a two-dimensional model vehicle, respectively, where the forcing (blowing and suction) varied sinusoidally in the spanwise direction but was steady in time. They showed that vortex shedding with the distributed forcing is attenuated for both laminar and turbulent flows and thus drag is significantly reduced. In the present study, a wake disrupter, inspired from the distributed forcing, is proposed as a new passive device to control the turbulent flow behind the model vehicle for drag reduction and its effect is examined by both the wind-tunnel experiment and large eddy simulation (LES).

In our experiment, the model vehicle is made of ABS copolymer and its nose is shaped into a half ellipse with its ratio of the major to minor axis of 8, following Tombazis and Bearman [4] (see Figure 1). A trip wire, which is a chain of spheres with the diameter of 2mm, is attached to both the upper and lower body surfaces at the 100mm downstream location from the nose of the model vehicle. Three different free-stream velocities of 5, 10 and 20 m/s are considered and the corresponding Reynolds numbers are Re_h =20000, 40000 and 80000, respectively. The wake disrupter is a small-size rectangular body attached to a part of the trailing edge of the model vehicle (Figure 1). A pair of wake disrupters is mounted on the mid-span at the upper and lower trailing edges. The l_y and l_z are the sizes of wake disrupter in the wall-normal and spanwise directions, respectively. The 71 cases with the different l_y's and l_z's are tested to determine the optimum-size disrupter for maximum drag reduction. For all the cases, the base pressures are measured on the flat base surface. The momentum and boundary layer thicknesses measured by a hot-wire probe are 1.02mm (Re_q =680) and 13.3mm, respectively, at x/h= -0.033 for Re_h =40000.

Large eddy simulation with a dynamic subgrid-scale model is also carried out for flow over a model vehicle at Re_h =4200. In LES, only the flow field over the rear part of the model vehicle is simulated in a Cartesian coordinate system with a turbulent boundary layer flow of Re_q =670 introduced at the domain inlet. The ratio of the boundary layer thickness at the domain inlet to the body height (d/h = 1.4) is much larger than that in our experiment (d/h = 0.22). An immersed boundary method [7] is used to simulate the flow with the wake disrupter.

The contour plot in Figure 2 shows the percentages of spanwise-averaged base-pressure variation with respect to l_y and l_z at Re_h =40000. Here, l_y and l_z are scaled by the length scales (d and q) of the boundary layer just upstream of the fixed separation point (x/h= -0.033) as well as the height of the model (h). The symbol in this figure corresponds to the actual experimental measurement. For most of disrupters, the base pressure is increased, indicating drag on the model vehicle is decreased except that for $0 < l_y/h < 0.66$ and $0 < l_z/h < 0.033$, where the base pressure is slightly decreased. The maximum increase in the base pressure is about 23% with the optimal wake disrupter having the sizes around $l_y/h = l_z/h = 0.23$. Similar results are obtained at Re_h =20000 and 80000.

As for the LES result, Figure 3 shows the iso-surfaces (top view) of pressure behind the model vehicle for the cases without and with wake disrupter (l_y/h =0.2, l_z/h = 0.2). For the uncontrolled flow, the large-scale two-dimensional Karman vortex cores can be clearly found. However, with wake disrupter, the Karman vortex cores are broken up into some smaller-scale vortices and the wake becomes completely three-dimensional.

In conclusion, the wake disrupter is very effective in reducing drag on a two-dimensional model vehicle at various Reynolds numbers where the separation point is fixed.

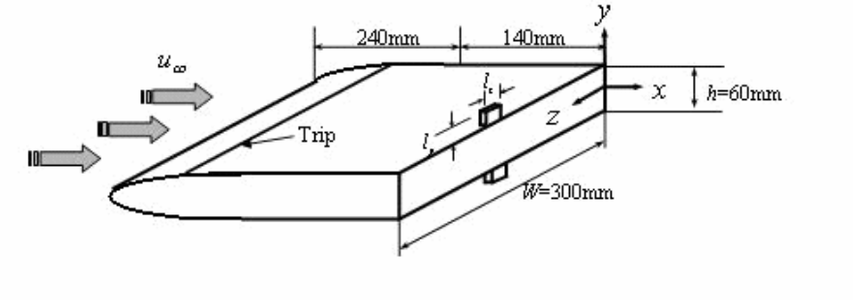


Figure 1 Schematic of the model vehicle and wake disrupter.

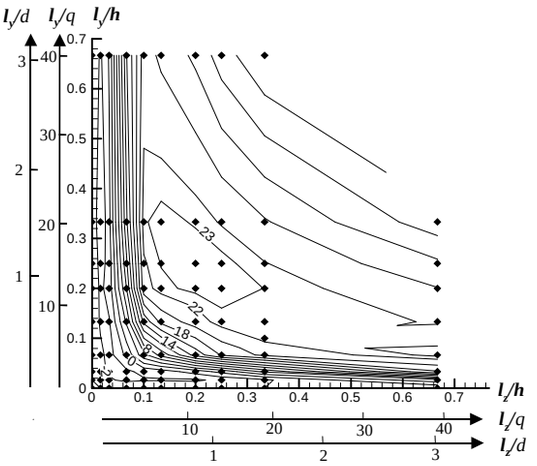
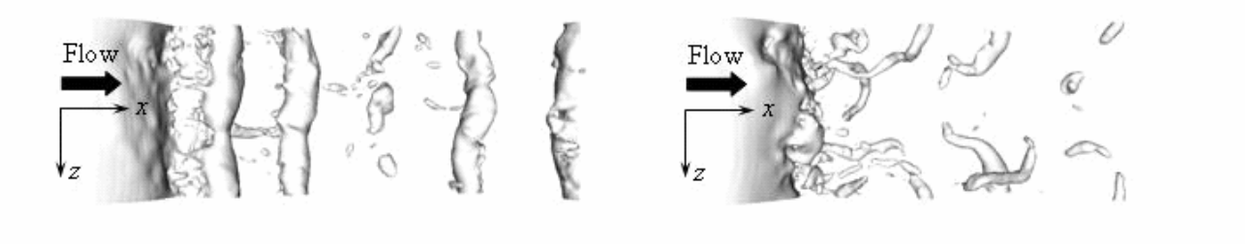


Figure 2 Contours of the spanwise-averaged base-pressure variation (%) with respect to l_y and l_z at Re_h =40000.



Without disrupter With disrupter (l_y/h =0.2, l_z/h = 0.2)

Figure 3 Iso-surfaces of the pressure behind the model vehicle at Re_h =4200.

References

[1] Bearman P. W.: Investigation of the Flow behind a Two-dimensional Model with a Blunt Trailing Edge and Fitted with Splitter Plate. *J. Fluid Mech* **21**:241-55, 1965.

[2] Wood C. J.: The Effect of Base Bleed on a Periodic Wake. *J. R. Aeronaut. Soc.* **68**:477-82, 1964.

[3] Tanner M.: A Method of Reducing the Base Drag of Wings with Blunt Trailing Edges *Aeronaut. Quarts.* **23**:15-23, 1972.

[4] Tombazis N. and Bearman P. W.: A Study of Three-Dimensional Aspects of Vortex Shedding from a Bluff Body with a Mild Geometric Disturbance. *J. Fluid Mech* **330**:85-112, 1997.

[5] Kim J. and Choi H.: Distributed Forcing of Flow over a Circular Cylinder. Third Bluff-Body Wakes and Vortex-Induced Vibration, Port Douglas, Australia, Dec. 17-20, 2002.

[6] Kim J., Hahn S., Kim J., Lee D., Choi J., Jeon W. -P. and Choi H.: Active control of Turbulent Flow over a Model vehicle for Drag Reduction, Third International Symposium on Turbulence and Shear Flow Phenomena, Sendai, Japan, June 2003.

[7] Kim J., Kim D., Choi H.: An Immersed-Boundary Finite Volume Method for Simulations of Flow in Complex Geometries, *J. Comput. Phys* **171:**132-50, 2001.

CONTROL OF INTERNAL SUPERSONIC FLOW SEPARATION

Andrzej Szumowski, Jan Wojciechowski
Warsaw University of Technology. Institute of Aeronautics and Applied Mechanics
ul. Nowowiejska 24, 00-665 Warszawa, Poland

Summary: Separation of turbulent boundary layer in internal supersonic flow along a convex cylindrical contour is controlled by V-letter shape obstacles and swirling jets injected through the wall. Considerable delay of the boundary layer separation and accompanied shock wave have been observed.

The present experiment was aimed to investigate the capability of the boundary layer excitation to delay separation in a supersonic internal flow (Laval nozzle). Because in this case the separation is accompanied by a shock wave, the shock should displace downstream when the upstream boundary layer is excited.

The 2D half-Laval nozzle with a cylindrical contour (Fig.1a) was used . Such a contour was chosen to have a separated flow for any pressure difference through the nozzle. Obstacles and swirling jets were used to excite the boundary layer at the nozzle surface of its divergent section. In the former case a row of oblique half-cylinders paired in form of V-letters (Fig. 1b) were stuck to the nozzle wall. It was noted in the preceding experiment with a V-type obstacle generator located on a flat plate that at the tip of V-obstacle (directed downstream) two stable streamwise vortices occur that rotate in directions opposite one to another. In the latter case the jets from orifices (Fig. 1c) in the nozzle wall were injected into the boundary layer. They were strongly swirled to induce the vortex break down phenomenon. In this effect the air of the jets spread around orifices and disturbed only the flow region close to the nozzle wall.

Figure 2 shows the normalized (by the supply pressure) distributions along the nozzle surface (versus angular coordinate φ - Fig. 1a) and Fig 3 the schlieren photographs of the nozzle flow for unexcited and excited (by V-generators) boundary layer. One can observe that in both the subsonic and the supersonic flow the V-generator induces distinct pressure hill. In the latter case it is accompanied by a shock wave followed by an expansion wave. The waves which are very close to one another are visible in photograph in Fig. 3d as a preceding light strip (at the left upper corner) originating beyond the field of observation. In the supersonic flow the V-generator, causes distinct delay of the flow separation and thereby the shifting downstream the accompanying shock wave. Figures 4 and 5 show the results obtained in case of boundary layer excited by swirling jets. One can note that the swirling jets generator, like the V-generator, disturbs boundary layer sufficiently strong to delay distinctly the supersonic flow separation. Delay of separation occurs due to the secondary flow which appears in the primary one composed of stationary vortices induced by swirling jets, superimposed on uniform (in span direction) flow. In schlieren photograph two distinct strips are visible. The preceding strip visualise disturbance caused by orifices (used to generate swirling jets) in the Laval nozzle wall and the following one the shock wave accompanying separation. The former is weak and does not show any trace in the pressure distributions. (The orifices were located on sides of the symmetry plane – see Fig.2c).
It seems that the swirling jets type generator, in contrast to obstacle one, does not enhance the drag of the wall. Moreover, the delay of separation can be controlled, in some range, by control of the strength of the injected jets.

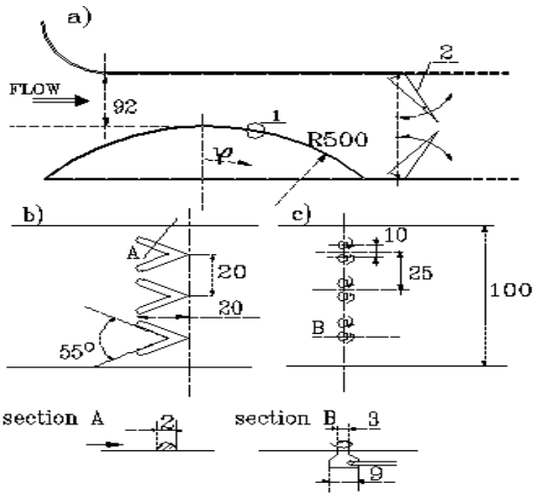


Fig. 1. Test section of wind tunnel (a), obstacle generator (b) and swirling jet generator (c), 1 – generator location, 2 – adjusting valve.

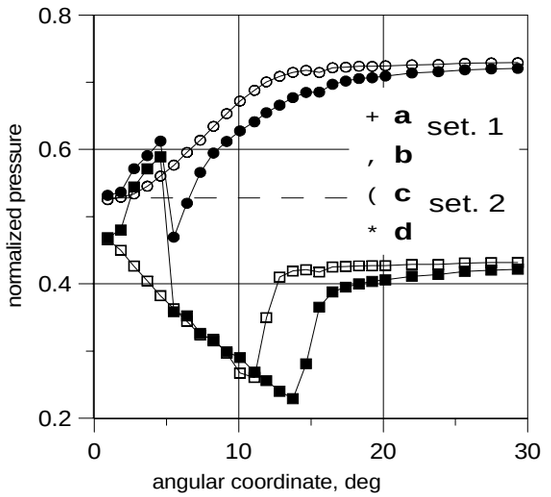


Fig.2. Pressure distributions along nozzle surface for two settings of adjusting valve, without (empty points) and with (filled points) V - generator

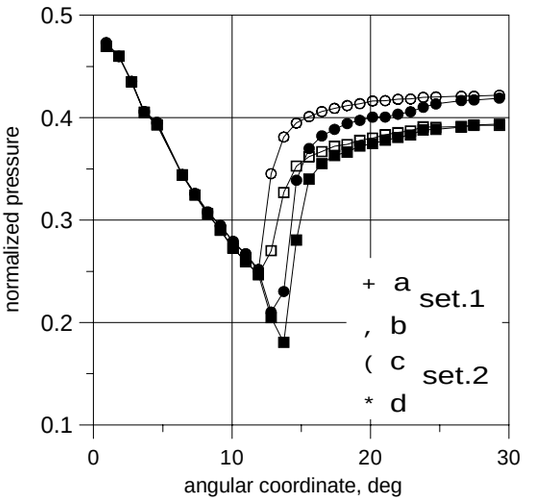


Fig.4. Pressure distributions along nozzle surface for two settings of adjusting valve, without (empty points) and with (filled poets) swirling jet generator

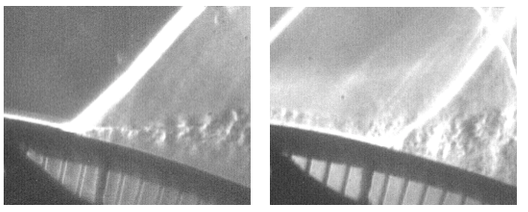


Fig.3. Schlieren photograph of the flow at the nozzle surface corresponding to pressure distributions in Fig. 2

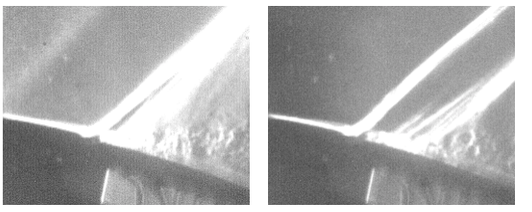


Fig.5. Schlieren photograph of the flow at the nozzle surface corresponding to pressure distributions in Fig. 4

XXI ICTAM, 15–21 August 2004, Warsaw, Poland

A SINGULAR VALUE ANALYSIS OF BOUNDARY LAYER CONTROL

Junwoo Lim*, John Kim**
*Scientific Applications and User Support,Pittsburgh Supercomputing Center, Pittsburgh, PA 15213, USA
**Department of Mechanical and Aerospace Engineering,UCLA, Los Angeles, CA 90095-1597, USA

Summary Several approaches for boundary-layer control are analyzed from a linear system point of view. The singular value decomposition (SVD) is applied to the linearized Navier-Stokes system in the presence of control. The performance of control is examined in terms of the largest singular values, which represent the maximum disturbance energy growth ratio attainable in the linear system under control. The maximum growth ratio is shown to be less in controlled systems than in the uncontrolled system only when control parameters are within a certain range of values. The SVD analysis of various flow controls shows a similarity between the trend observed in the SVD analysis (linear) and that observed in direct numerical simulations (nonlinear), thus reaffirming the importance of linear mechanisms in the near-wall dynamics of turbulent boundary layers. The present study illustrates that the SVD analysis can be used as a guideline for designing controllers for drag reduction in turbulent boundary layers.

INTRODUCTION

There have been increased activities in developing efficient and robust controllers using modern control theory for viscous drag reduction in turbulent boundary layers. Although turbulent flows are in general governed by nonlinear dynamics, some of these new approaches specifically target a linear mechanism that has been identified to be responsible for high-skin friction in turbulent boundary layers. The fact that a linear mechanism plays an important role in this nonlinear turbulent flow allows us to investigate the flow from a linear system theory point of view. Indeed, recently several investigators have reported successful applications of linear controllers derived from linear control theory[1][2], but many fundamental and challenging questions have been raised in the course of applying linear optimal control to turbulent boundary layers.

MATHEMATICAL FORMULATIONS

The traditional linear analysis, which predicts whether a linear system is stable or unstable based on the eigenvalues of the system, is inadequate in explaining transient—nonetheless quite substantial—growth of the kinetic energy of certain disturbances in otherwise a stable system. This transient growth is due to non-normality of the linearized Navier-Stokes system. Eigenfunctions of a non-normal system are not orthogonal to each other, and as such the kinetic energy of certain disturbances can grow before its ultimate decay even in a linear system with no unstable eigenfunctions. Since the transient growth is due to a linear mechanism, its behavior can be analyzed through a singular value decomposition (SVD) of the system operator [3], with which the amplification factor of the so-called optimal disturbance could be determined. We hypothesize that the SVD analysis is also appropriate for examining performance of controllers for turbulent boundary layers. Effective controllers must reduce the non-normality of the flow system, since it is also believed to be responsible for sustaining near-wall turbulence structures, which in turn are responsible for high skin-friction drag in turbulent boundary layers.

State-space representation

The first step to apply the SVD analysis is to formulate the governing equations in terms of the state-space representation as is done for other linear optimal controller design. The linearized Navier-Stokes equations with control input can be written in the following state-space representation:

$$\frac{d\mathbf{x}}{dt} = A\mathbf{x} + B\mathbf{u}, \tag{1}$$

$$\mathbf{u} = -K\mathbf{x}\,, \tag{2}$$

where $\mathbf{x}$ and $\mathbf{u}$ represent the state-space and control input vectors (wall-transpiration in this study), respectively, and A, B and K represent the system, actuation and control-gain matrices, respectively. The control-gain matrix K for an LQR controller is determined by solving an algebraic Riccati equation[1][2], while that for the opposition control suggested by Choi *et al.*[4] is easy to construct (especially when $\mathbf{x}$ represents a collocation vector) once the detection-plane location is known.

Singular Value Decomposition

To analyze the transient energy growth, we consider the ratio of the kinetic energy of a disturbance at a given time (τ) to the disturbance energy at $t = 0$. After a simple mathematical procedure used by Reddy and Henningson[3], we can define the growth ratio function, $G(\tau)$, as

$$G(\tau) = \sup_{\mathbf{x}(\cdot,0)\neq 0} \frac{||\mathbf{x}(\tau)||^2}{||\mathbf{x}(0)||^2} = \sup_{\mathbf{x}(\cdot,0)\neq 0} ||\mathbf{F}\exp[(\mathbf{A}-\mathbf{BK})\tau\,]\mathbf{F}^{-1}||_2^2\,, \tag{3}$$

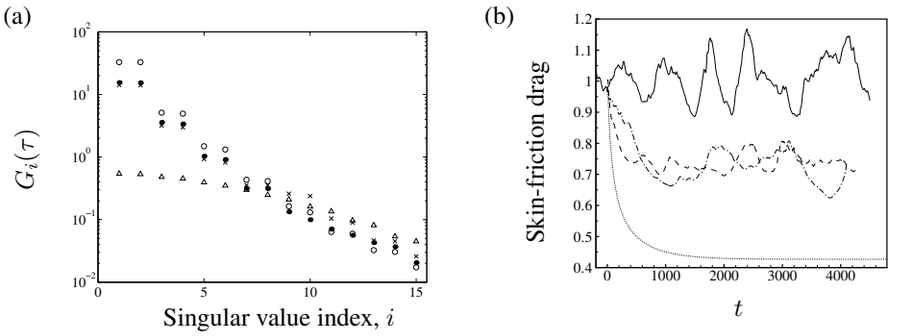


Figure 1. (a) Comparison of singular values for a wavenumber ($k_x = 0, k_z = 6$): ○ , no control; •, opposition control; ×, LQR control; △, virtual flow. (b) Mean skin-friction drag history: ——— , no control; – – – – , opposition control, –·–·– , LQR control; ····· , virtual flow. Here, Re_τ=100.

where the quantity $||\mathbf{x}||^2$ represents the kinetic energy of $\mathbf{x}$, $||\cdot||_2$ is the 2-norm (Euclidian Norm), τ is the given time mentioned above, and the Hermitian matrix $\mathbf{F}$ is defined in terms of the square-root matrix of an inner product in discrete space with sufficient grid points[3]. The 2-norm of a matrix can be easily computed from the SVD of the matrix. The largest $G(\tau)$ value represents the maximum energy growth ratio at τ.

RESULTS

We have performed the SVD analysis of various linear-quadratic-regulator (LQR) controllers we have developed as well as the so-called opposition control used by Choi *et al* [4], in the hope that it could shed new light into these control methods. Note that these methods have been designed to achieve a similar goal, *i.e.*, interfering the interactions between the near-wall streamwise vortices and the wall in order to reduce skin-friction drag in turbulent boundary layers.

Figure 1 (a) shows distributions of singular values for the disturbance energy growth with an appropriate time scale. It can be seen that the singular values corresponding to the opposition control (with the detection-plane location at $y^+ = 15$) and an LQR-controller (minimizing the disturbance energy growth) are much smaller than those corresponding to the uncontrolled system. The singular values corresponding to the opposition-controlled system with different detection-plane locations were higher than those shown here, corroborating with the numerical observation that $y^+ = 15$ is the optimal location. Similarly, an optimal range of control parameters can also be found in LQR control cases [6]. Also, shown are the singular values for a virtual flow [5], in which the linear coupling term between the Orr-Sommerfeld and the Squire equations was removed. Note that all singular values for this case are less than one, indicating that no transient growth in the virtual flow. From these distributions of singular values, one would expect that the virtual flow would be most effective in reducing the skin-friction drag in turbulent boundary layers.

In order to examine the applicability of the above SVD analysis, which is based on the linearized Navier-Stokes system, to fully nonlinear turbulent flows, we applied these controllers to direct numerical simulations of a turbulent channel flow at the same Reynolds number. Figure 1(b) shows the time evolution of mean skin-friction drag in the channel with various controllers. Note that the case without the linear coupling term (virtual flow)results in complete laminarization, consistent with the SVD analysis. Other results are also consistent with the SVD analysis, demonstrating that the SVD analysis is a viable tool in predicting the performance of a controller in the nonlinear turbulent channel flow.

CONCLUSION

We have shown that the SVD analysis could be used to gain useful information on the performance of certain controllers. It could be used in optimizing control parameters without actually performing expensive nonlinear computations. Other issues, such as the effect of using the evolving mean flow as control applied to a nonlinear flow system (also known as gain scheduling) and high Reynolds number limitation, will be investigated through the SVD analysis.

References

[1] Joshi S. S., Speyer J. L., Kim J.: A systems theory approach to the feedback stabilization of infinitesimal and finite-amplitude disturbances in plane Poiseuille flow. *J. Fluid Mech.* **332**, 157–184, 1997.

[2] Lee K. H., Cortelezzi L., Kim J., Speyer J. L.: Application of reduced-order controller to turbulent flows for drag reduction. *Phys. Fluids* **13** (5), 1321–1330, 2001.

[3] Reddy S. C., Henningson D. S.: Energy growth in viscous channel flows. *J. Fluid Mech.* **252**, 209–238, 1993.

[4] Choi H., Moin P., Kim J.: Active turbulence control for drag reduction in wall-bounded flows.*J. Fluid Mech.* **262**, 75–110, 1994.

[5] Kim J., Lim J.: A linear process in wall-bounded turbulent shear flows. *Phys. Fluids* **12** (8), 1885–1888, 2000.

[6] Lim J., Kim J.: A singular value analysis of boundary layer control. *Phys. Fluids* submitted.

XXI ICTAM, 15–21 August 2004, Warsaw, Poland

SEPARATION CONTROL BY STATIONARY AND TIME PERIODIC LORENTZ FORCES

Tom Weier, Gunter Gerbeth, Gerd Mutschke
Forschungszentrum Rossendorf, P.O. Box 51 01 19, 01314 Dresden, Germany

Summary Stationary and time periodic wall parallel Lorentz forces in streamwise direction have been used to control the suction side flow of NACA 0015 and PTL IV hydrofoils. Experimental results, consisting of flow visualizations and force measurements in the low Reynolds number range $Re = 0.5 \ldots 1.5 \times 10^5$ will be presented. Attainable lift gain of both kinds of electromagnetic control is compared and the relation to conventional control by blowing is discussed.

INTRODUCTION

Flow separation and its control is a persistent topic of fluid dynamic research. A wide range of control methods has been investigated [1]. One of the currently investigated areas is the use of periodic addition of momentum [2].

Electromagnetic, i.e. Lorentz forces, may be used to influence the flow of electrically conducting fluids. In the case of liquid metals or semiconductor melts, this control method is already in productive use on an industrial scale. The application of Lorentz forces to fluids of low electrical conductivity like seawater and other electrolytes is less common, although first attempts date back to the 1950s [3].

An electromagnetic body force $\mathbf{F}$ results from the vector product of current density $\mathbf{j}$ and magnetic induction $\mathbf{B}$. The current density is given by Ohm's law: $\mathbf{j} = \sigma(\mathbf{E} + \mathbf{u} \times \mathbf{B})$, where $\mathbf{E}$ denotes the electric field, $\mathbf{u}$ the velocity, and σ the electrical conductivity, respectively. If σ is small (~ 10 S/m), as in the case of seawater and other electrolytes, currents originating from the $\mathbf{u} \times \mathbf{B}$ term in Ohm's law are generally very low for magnetic fields of moderate strength (~ 1 T). Consequently, the Lorentz force due to these currents is negligible. In order to obtain current densities large enough for flow control purposes it is therefore necessary to apply an electric field of magnitude E_0 with $E_0/(U_\infty B_0) \gg 1$, where U_∞ denotes the freestream velocity. This implies that the force density distribution can be determined independently of the flow field. In principle, almost any Lorentz force distribution may be obtained by a suitable combination of electric and magnetic fields. However, practical limitations do exist, e.g. as electrodes and magnets have to be integrated into the given body shape.

There are several distinct features, that make the Lorentz force to an attractive actuator: momentum is directly generated in the fluid without associated mass flux; its frequency response is practically unlimited; virtually any excitation wave form might be realized by feeding the electrodes with an appropriate current. On the other hand, the efficiency of momentum generation by weak magnetic and strong electric fields is generally small since Joule losses dominate in electrically low conducting fluids.

EXPERIMENTS

For the experiments described in the following, an arrangement of flush mounted electrodes and permanent magnets producing a streamwise wall parallel Lorentz force has been used. The Lorentz force decays exponentially with the wall distance. A stationary Lorentz force in downstream direction on the suction side of a stalled hydrofoil acts much like a jet blown over the foils surface. Lift can be increased by two mechanisms: 1) reattaching the separated flow and therefore increasing the critical angle, and 2) introducing circulation due to acceleration of the attached suction side flow. Indeed, it has been shown in [4] that blowing and a steady Lorentz force are comparable even in a quantitative sense. The characteristic parameter to describe the Lorentz force action on the suction side flow is the electromagnetohydrodynamic

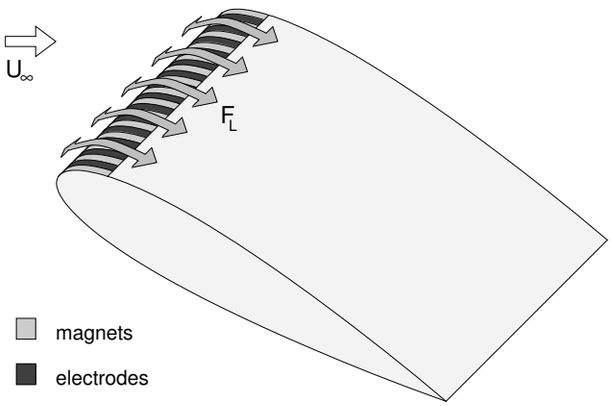


Figure 1. Sketch of the NACA 0015 equipped with the Lorentz force actuator for periodic excitation.

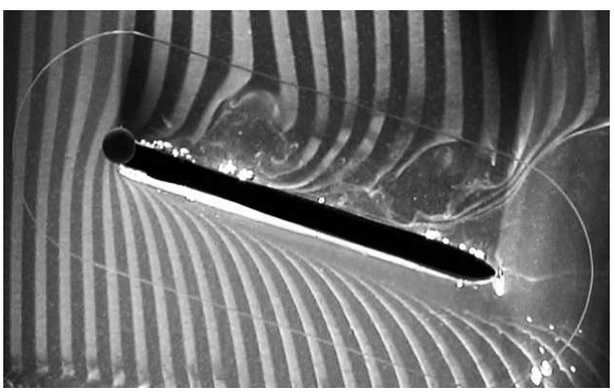


Figure 2. Time periodic Lorentz force at a 15° inclined flat plate, $Re \approx 10^4$, $F^+ = 1.4$, $c'_\mu = 4.4\%$.

(EMHD) momentum coefficient. It relates the momentum injected by the Lorentz force to the freestream dynamic pressure multiplied by the foil area. In the case of steady Lorentz forces, scaling relations for the attainable lift as a function of the EMHD momentum coefficient have been obtained in [4], which result at $Re \sim 10^5$ in lift increments of $\Delta C_{Lmax} \sim 1$ for the various hydrofoils investigated. Such a lift increase is of definite interest for ship components. However, extrapolating the measured data to velocities of typical naval applications reveals that power demand may become a critical issue. Again this situation is not unlike to that found for steady blowing.

During the last decade, a considerable amount of research has been devoted to separation control by periodic addition of momentum [2]. This approach offers a reduction of the cost, in terms of momentum input, by up to two orders of magnitude for the same control effect compared to stationary action. It seems an obvious consequence to apply time periodic Lorentz forces with the expectation of a similar gain in efficiency. Since the mechanism of periodic forcing is supposed to be connected to shear layer excitation, the actuator should be placed near the separation line. A sketch of the NACA 0015 equipped with permanent magnets and electrodes is given in Fig. 1. Flow visualizations on an inclined flat plate (Fig. 2) show that the otherwise fully separated flow can be reattached in an averaged sense by a time periodic Lorentz force acting near the leading edge. A characteristic feature of the flow are the vortices moving along the plate. The strength of the force is denoted by the effective momentum coefficient c'_μ. F^+ is the excitation frequency nondimensionalized by chord length and freestream velocity. Direct force measurements on the stalled NACA 0015 reveal that the maximum lift gain occurs around $F^+ \approx 1$, the forcing effect decays relatively rapidly for higher frequencies. At a constant and effective excitation frequency, the lift increase versus c'_μ is at first steep and than less pronounced. The change in the C_L–c'_μ–curve slope is accompanied by a drag maximum. Fig. 3 gives the lift polar for the NACA 0015 at $F^+ = 0.5$ and $Re = 5 \times 10^4$. Already for small momentum coefficients stall is delayed from 13° to 15° due to a boundary layer transition triggered by the excitation. Lift values in the stalled region are only marginally increased as compared to the unforced flow. The picture changes for larger c'_μ, the abrupt stall merges into a more gentle one. C_L is considerably increased in the post stall region, but the maximum lift increases only due to higher critical angles of attack. Unlike in case of steady forcing, no additional circulation in an already attached flow is generated by periodic excitation. For shipbuilding applications like rudders and stabilizer fins the lift gain relative to the separated flow is less important, the increase of the maximum attainable lift ΔC_{Lmax} is of main interest. This quantity is plotted in Fig. 4 versus c'_μ for the NACA 0015 in a chord length Reynolds number range of $5 \times 10^4 \leq Re \leq 1.5 \times 10^5$. For comparison, corresponding data for oscillatory blowing from [2] have been included. The relative large scatter for electromagnetic excitation is to a great extent owed to the low Reynolds number range used for the experiments. However, the data for oscillatory blowing fit in quite well, despite the difference in foil shape and Reynolds number.

A specific lift increase based on the value for the separated flow can be obtained by oscillatory forcing with fractions of the momentum input necessary for steady Lorentz forces. In contrast, an equal increase of the maximum lift gain ΔC_{Lmax} requires a similar expenditure of momentum for both control methods.

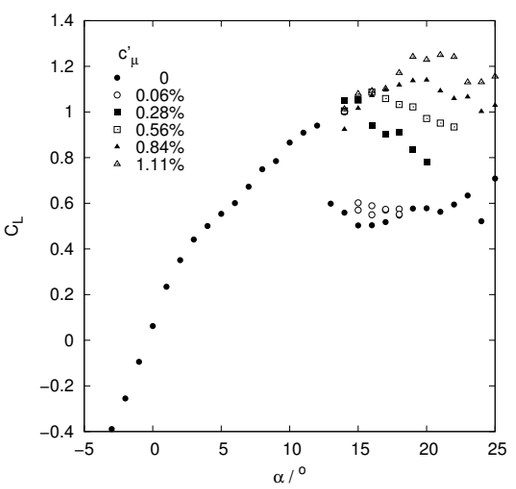


Figure 3. NACA 0015 with periodic Lorentz force: C_L versus α at $Re = 5 \times 10^4$, $F^+ = 0.5$ and different momentum coefficients.

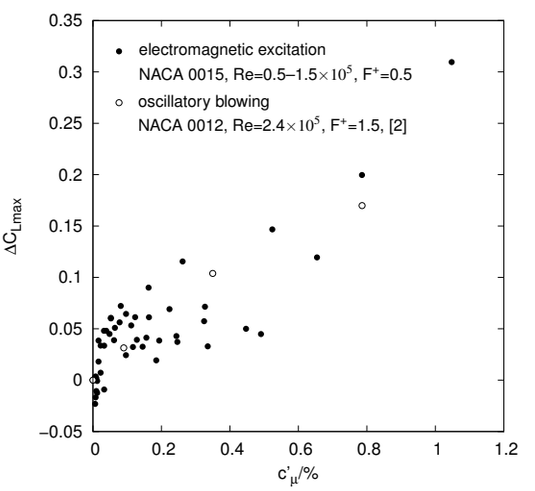


Figure 4. Maximum lift gain for electromagnetic excitation compared to oscillatory blowing.

References

[1] Gad-el-Hak, M., Bushnell, D.: Separation Control: Review. *J. Fluids Engng.*, **113**, 5–30, 1991.

[2] Greenblatt, D., Wygnanski, I.J.: The control of flow separation by periodic excitation. *Prog. Aero. Sci.*, **36**, 487–545, 2000.

[3] Resler, E.L., Sears, W.: The prospects for magneto–aerodynamics. *J. Aero. Sci.* **25**, 235–245, 1958.

[4] Weier, T., Gerbeth, G., Mutschke, G., Lielausis, O., Lammers, G.: Control of Flow Separation Using Electromagnetic Forces. *Flow, Turbulence and Combustion*, to appear.

ON THE POSSIBILITY AND PROSPECTS OF TURBULENT FLOW NOISE CONTROL

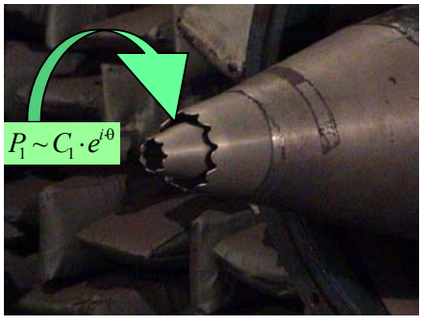
Victor F. Kopiev
TsAGI, Moscow Branch, Acoustic Division, Radio 17, 105005 Moscow, Russia

Summary The main problem of realizing the idea of active noise control rests on the absence of conceptual study of the reduction strategy itself and this, in its turn, reflects our insufficient understanding of the principal mechanisms of noise generation by turbulence, i.e. understanding of the radiating turbulence structure and peculiarities. The situation turns out to fundamentally different for subsonic and supersonic jets. The mechanism of noise generation for supersonic jets is essentially clear and is connected with instability waves developing downstream from the nozzle. This situation is quite different from that for subsonic flows, where a complete understanding of these mechanisms is yet absent. The situation for supersonic and subsonic turbulent jet noise control is considered in some detail.

The intensive development of aviation technique, the advent of passenger transport of the new generation led to a sharp increase of intensive noise sources affecting a human being. The application of turbo-jet by-pass engines permitted improving the acoustic characteristics of aircraft but an active offensive role of ICAO and other international ecology organizations introducing more and more stringent requirements for the current aircrafts and for those being under development requires an intensification of works in this direction. The situation is complicated additionally by the fact that the idea of cardinal noise reduction of advanced aircraft by 20 dB in the nearest future 20 years becomes increasingly popular. Despite the fact that for further noise reduction different sources are to be taken into account (fan noise, airframe noise, etc.), jet noise seems to remain the main stumbling stone in solving this complex task. Therefore the need is felt at present for putting forward new ideas including those that are based on attempts of active controlling the turbulent jet noise in addition to development of traditional approaches to the problem of aviation engine noise reduction.

However the main problem of realizing the idea of active control rests on the absence of conceptual study of the reduction strategy itself and this, in its turn, reflects our insufficient understanding of the principal mechanisms of noise generation since for elimination of the noise cause, i.e. an active action on the radiating part of turbulence, at any case, understanding of the principal mechanisms of this cause occurrence is required, i.e. understanding of the radiating turbulence structure and peculiarities. Here the situation turns out to fundamentally different for subsonic and supersonic jets. The mechanism of noise generation for supersonic jets is essentially clear and is connected with instability waves developing downstream from the nozzle [1]. This situation is quite different from that for subsonic flows, where a complete understanding of these mechanisms is yet absent [2].

Consider first the supersonic jets. It is known that the supersonic jet noise is determined mainly by large-scale disturbances or by wave instabilities developing in the flow. Therefore the task of control can be formulated as the task of reducing the instability wave amplitude and, in particular, of those waves which radiate sound. This task can be formulated in two ways (Fig.1): (i) as a task of non-adaptive control, through introducing the respective stationary devices or surfaces (tabs, chevrons, corrugations, etc.) in the flow, or (ii) a task of adaptive action on the initiating waves, i.e. as a task of generation of the instability waves being in the anti-phase with the most dangerous (from the standpoint of acoustics) waves, naturally appearing and developing downstream from the edge. The main methods of non-adaptive control are made on checking some a priory proposed configurations and on experimental search for the optimum. It is obviously, that this optimum substantially depends on the quantity of the models investigated and on the experimenter's good luck. The adaptive approach is based on the action through production of an anti-wave in the initial part of the mixing layer. We think that the main problem of the adaptive control lies at present, first of all, in development of a suitable elementary basis for anti-wave creation and in elaboration of methods for the experimental separation of that small part of turbulence, which is responsible for radiation in the near field. Exactly the idea of controlling a small part of turbulence (not the whole one) makes this approach attractive and realizable in the case of solving the problem of transducers-actuators.



a)

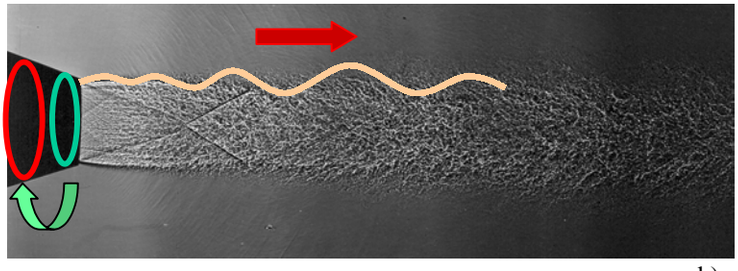

b)

Fig.1 Non-adaptive and adaptive noise control: a) transformation of radiated initial disturbance in non-radiated one; b) creating anti-face initial signal using two rings of transducers and actuators to reduce radiating disturbance amplitude.

The task of noise control in subsonic jets rests, first of all, on the absence of understanding of the radiating turbulence structure itself. Only after a successful solution of this fundamental (and extremely complex) task, one can hope for formulating a reasonable strategy of subsonic jet noise control. Nevertheless, the realization of such an approach "blindly" through multiple investigations of different configurations can appear to be rather useful not only as a possibility of guessing the optimum configuration or the one close to the optimum, but as a way of using this method of control to identify that very structure which cannot yet be identified with using other methods.

References

[1] Tam, C. K. W. (1991) Jet Noise Generated by Large Scale Coherent Motion. *Aeroacoustics of Flight Vehicles Theory and Practice*, *Volume 1: Noise Sources*, H. Hubbard, ed., NASA RP-1258, pp. 311–390.

[2] Kopiev V.F. and Chernyshev S.A. (2000) Vortex ring oscillations, the development of turbulence in vortex rings and generation of sound. *Phusics-Uspehi*, v.43, N7, 663-690 (translated from *Uspehi Fizicheskih Nauk*).

Control of cavity flow by means of a spanwise cylinder

Hervé Illy, Philippe Geffroy & Laurent Jacquin

Introduction

Low frequencies induced by a shear layer cavity resonance are characterized by large dynamic pressure loads and represent an important problem in many aeronautical applications. Recent experiments [1] have shown that efficient amplitude reduction of these oscillations can be produced by a cylindrical rod parallel to the leading edge of the cavity. This passive control method has been applied to the case of the deep cavity flow described in [2]. Schlieren films and pressure signals have been performed for different cylinder diameters and positions in the flow and different Mach numbers. The efficiency of the system is confirmed and the underlying mechanisms are discussed.

Experimentals conditions

The experiments are conducted in a rectangular high-subsonic speed wind-tunnel at Mach numbers M = 0.7 and M = 0.78 . The cavity length is $L = 50\text{mm}$ and its depth, $D = 120\text{mm}$, the aspect ratio being $L/D = 0.42$. The boundary layer at the leading edge of the cavity is turbulent ($Re_{\theta 0} = 10780$ for M = 0.78). One considers spanwise cylinders, with different diameters, parallel to the leading edge of the cavity. The Reynolds number Re_d based on the cylinder's diameter d is subcritical (between 43 000 and 129 000). Two different longitudinal positions of this cylinder, with respect to the leading edge of the cavity, have been also tested. The height of the cylinder above the wall, *z,* has also been varied. So, the effect of the cylinder on the flow is actually a function of the following parameters : Re_d , M , x/L , z/L and d/L . As shown by previous investigations, the effect of the boundary layer thickness on the flow regime is negligible [6].

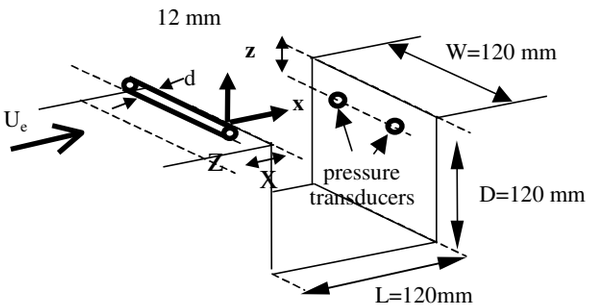


Figure 1 – sketch of the experimental set-up

Results

For z/d<0.7, see Figure 2, the cavity modes are identical to those found without the cylinder device. For z/d ≈ 0.7, a transition occurs from the cavity oscillations to a Von-Karman street regime. Low frequency cavity modes are suppressed and are replaced by oscillations at the cylinder's frequency. This new regimes holds for all values of d/L tested (between 0,05 and 0.15) and it is independent of both Re_d and M . As shown by figure 4, the maximum SPL value decreases from 170 dB to 140 dB and is shifted from 2 000Hz to 20 000Hz. The Strouhal number $St=fd/U_\infty$ of the new mode is 0.21, in accordance with the presence of a Von-Karman street. The same non-dimensional value is found for others diameters.

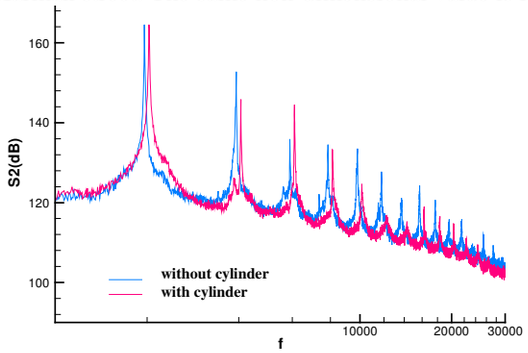


Figure 2 – Pressure spectra with and without control in the case z/d = .2, x/L = -0.1 at M = 0.78

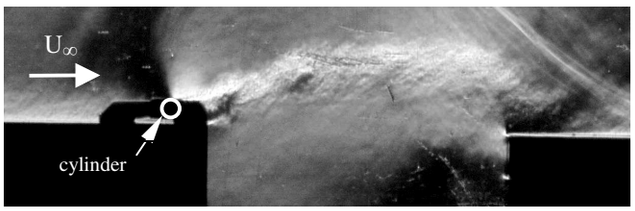


Figure 3 – Schlieren picture (horizontal knife) in the case of Figure 2

In all cases, the separation between the cylinder and the pressure transducers (see figure 1) is such that $L/d \leq 20$. This is a much smaller value compared to $L/d \geq 100$ prescribed in [5] for a change in the cylinder wake dominant frequency. Our results show that the cavity flow is entirely controled by the cylinder for $0.7 \leq z/d \leq 1.6$. Above $z/d \approx 1{,}6$, the cavity tones reappear. Tests have shown that translation of the cylinder upstream increases a little the threshold of *z/d* where the control becomes effective.

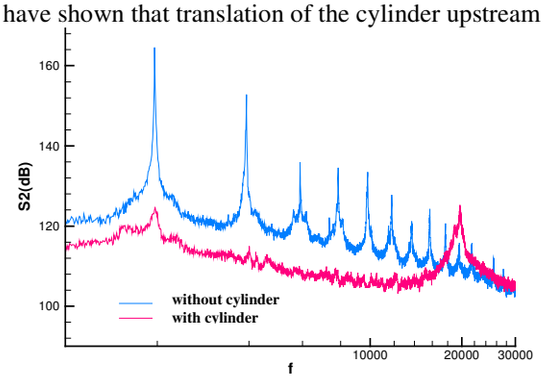


Figure 4 – Pressure spectra with and without cylinder in the case z/d = 1.2, x/L = -0.1 at M = 0.78

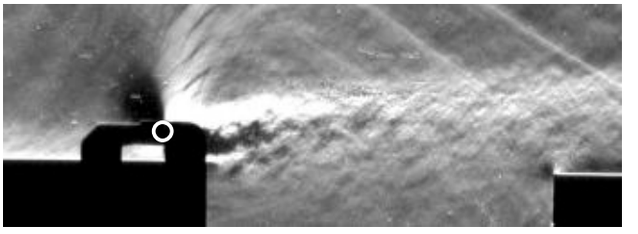


Figure 5 - Schlieren picture (horizontal knife) in the case of Figure 4

Discussion

In ref. [1], it is suggested that the effect of the cylinder could be due to turbulence mechanisms, i.e. to an increase of the rate of energy transfer (or dissipation) within the inertial range of turbulence scales separating the cavity modes ("large scales") from dissipation scales. This interpretation seems not appropriate because a resonant cavity flow does not behave as a standard developed turbulent shear flow. In particular, the Rossiter's modes cannot be considered as large scale turbulent structures. The present results suggest that the perturbations induced by the cylinder break the cavity flow oscillation loop, probably through the cancellation of the vortex formation process which takes place in the very vicinity of the cavity leading edge, as described in [2]. In the presence of the cylinder, two different flow physics are put together. On the one hand, the cylinder flow is driven by a global instability mode, see [4], which is very robust and almost insensitive to external perturbations and which does not feels the acoustics emanating from the cavity. One the other hand, the mixing layer behaves as an amplifier at the dominant forcing frequency. As shown by spectra, the cylinder imposes, by a way or another, its own dynamics when it is immersed in the region of the cavity leading edge. However, following [8] the shear layer could be stabilised due to the change in the mean axial shear layer velocity profiles in presence of the cylinder. This was suggested by LES simulations, see [7]. The modification of the velocity profile could be due to an increase in the diffusion of momentum in the mixing layer forced by the cylinder modes. Further experimental investigations of the mean shear layer profile in presence of the cylinder are in progress to test such proposals. The results will be presented during the symposium.

References

[1] Stanek, M.J., Raman,G., Kibens, V., Ross, J.A., Odreda, J., Peto, J.W., *Control of cavity resonance through very high frequency forcing,* AIAA paper 00-1905 (2000)

[2] Forestier, N.,Geffroy, P. & Jacquin, L., *The mixing layer over a deep cavity at high-subsonic speed,* J. Fluid Mech., Vol. 475, 101-145 (2003)

[3] Glezer A. & Wiltse J.M., *Direct high-frequency excitation of turbulence in free shear flows,* AIAA paper, juanuary 15-18 (1996)

[4] Hammond, D.A. & Redekopp, L.G., *Global dynamics of symmetric and asymmetric wakes,* J. Fluid Mech., Vol. 331,pp 231-260 (1997)

[5] Cimbala J.M., Nagib H.M. & Roshko A., *Large structure in the far wakes of two-dimensional bluff bodies,* J. Fluid Mech., Vol. 190, 265-298 (1988)

[6] Illy, H. , Geffroy, P. & Jacquin, L., *Influence de l'état de la couche limite sur les écoulements de cavité*, RT ONERA (2003)

[7] Arunajatesan, S., Shipman, J.D. & Sinha, N., *Hybrid RANS-LES simulation of cavity flow fields with control*, AIAA-2002-1130

[8] Stanek, M.J., Ross, J.A., Odreda, J. & Peto, J., *High frequency acoustic suppression*, AIAA 2003-0007

SYNTHETIC JET ACTUATION AT THE RESONANCE FREQUENCY

Zdeněk Trávníček[*], František Maršík[*], Tomáš Vít[**], Pieter de Boer[***]
[*]*Institute of Thermomechanics, Academy of Sciences of the Czech Republic, Dolejškova 5, 182 00 Prague 8, Czech Republic*
[**]*Technical University of Liberec, Faculty of Mechanical Engineering, Dept. of Power Engineering Equipment, Hálkova 6, 461 17 Liberec 1, Czech Republic*
[***]*Technical University of Eindhoven, Dept. of Mech. Eng., Divison of Thermo Fluids Engineering, Section of Energy Technology, PO Box 513, WH 3.127, 5600 MB Eindhoven, The Netherlands*

Summary An air round jet was generated by a zero–net–mass–flux actuator. A satisfactory jet synthesis was confirmed experimentally by smoke visualization and hot-wire anemometry. The choice of suitable operating frequency was found near the resonance by means of theoretical as well as experimental approach. In the far field, the streamwise decay of the time-mean velocity is comparable with a conventional (steady) jet.

INTRODUCTION

Synthetic jets are generated by an oscillating force which pushes and pulls a fluid through an orifice (or nozzle) from a cavity [1]. The synthetic jets have many perspective applications such as control of primary flows [1, 2] and a valuable alternative for cooling applications [3].

The synthetic jets are characterized by two length scales: The length scale of the output orifice (diameter D), and the "stroke length" L_O [1]; another name is the "equivalent extruded (fluid) column length", [2]; the L_O is defined by integration of the the orifice velocity over the extrusion (discharge) stroke [1]. The Strouhal number is an only slightly modified ratio of the length scales D and L_O: e.g., at harmonic actuation $St = (1/\pi)\, f D/U_O = (1/\pi)\, D/L_O$ [2], where f is frequency, U_O is the time–mean orifice velocity during the extrusion stroke, i.e. $U_O = L_O/T$, and T is the time period, i.e. $T = 1/f$. There are many possible definitions of the Reynolds number, one of them sounds as $Re = U_O D/\nu$, [1].

RESULTS AND DISCUSSIONS

The present actuator consists of a sealed cavity, which is equipped with an actuating pair of diaphragms $D_D = 66.5$ mm in diameter, and with an emitting orifice $D = 8.0$ mm in diameter. The jet is oriented vertically upwards, a sinusoidal current feeds the actuator. An initiation step of the experiments was made by flow visualization by the smoke–wire technique. Further, the velocity distribution was measured by a hot–wire anemometer (DANTEC: CTA Bridge 56C17, Mean Value Unit 56N22, StreamLine 90N10 Frame, and CA-1000) in the constant temperature mode.

Analysis: resonance frequency of the actuator

From the point of view of energy transformation, the potential energy of the pair of diaphragms is transformed into the kinetic energy of fluid during each period. The oscillating diaphragms are assumed as harmonic motion, and the relationship between the velocities of the actuating diaphragms and the flow in the orifice satisfied the continuity equation (incompressible flow). In the top/bottom dead centers of the diaphragms, the kinetic energy of fluid is zero and the potential energy is maximum. On the other hand, in the neutral position of the diaphragms, the kinetic energy is maximum. The potential energy of the diaphragms can be written as for linear springs, and the resonance frequency can be derived as

$$f = \left(\frac{1}{2\pi}\right)\left(\frac{D}{D_D}\right)\sqrt{\frac{K_P}{2\rho L_e}}\,. \qquad (1)$$

where K_P is the diaphragm (spring) constant (it was evaluated by an auxiliary experiment), ρ is fluid (air) density, and L_e is the "fluid column length" which captures the kinetic energy. For the present geometry, Eq. (1) gives $f = 78.5$ Hz. The "*nominal operating frequency*" has been refined according to the experimental results as $f = 75.0$ Hz.

Experimental results: Flow visualization and hot-wire measurement

Fig. 1 presents the visualization of the typical synthetic jet obtained using multiple exposures at low frequency actuation (30Hz) during 1 s, (it means, 30 superimposed frames were exposed). Fig. 1 shows the so–called "short L_O" (or "high St") synthetic jet, which was generated at $L_O/D = 3.2$, i.e. $St = 0.10$, and $Re = 400$, i.e. $U_O = 0.78$ m/s.

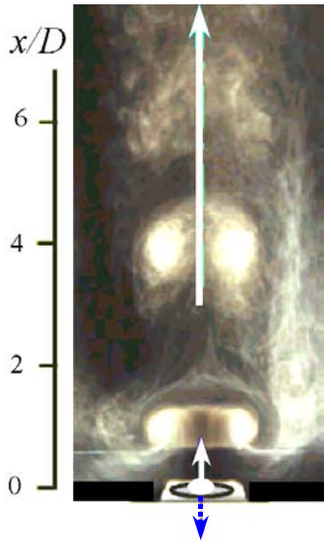


Fig. 1
Synthetic jet visualization, $f = 30$ Hz, $L_O/D = 3.2$.

Counter-rotating vortex pairs are formed at the nozzle exit, and they are distinguishable during their upward motion from the nozzle. According to Fig. 1, the streamwise distances from the nozzle to the first and second vortex pairs are approximately 1 D and 4 D, thus the average pitch of the train of individual vortex pairs is approximately $\Delta x_V = 3\ D$. This Δx_V– value is rather well comparable with the "equivalent extruded column length" $L_O = 3.2\ D$.

Fig. 2 shows results of hot-wire measurements of the "long L_O" (or "low St") synthetic jet, which was generated at the "*nominal operating point*": $f =$ 75 Hz, $L_O/D = 14.3$, i.e., $St = 0.022$, and $Re = 4400$, i.e., $U_O = 8.7$ m/s. Fig. 2 shows the centerline velocities during the actuating cycle namely the phase averaged velocity; U is the time–mean velocity and U_f is the periodic component. This plotting demonstrates a formation of the pulsatile jet when fluid "puff" travels downstream, thus the velocity amplitude moves downstream, and the velocity oscillations gradually diminish. The time–mean velocity U along the centerline is plotted as well. The maximum velocity in the orifice is approximately $3.05U_O$. Behind the orifice, the maximum velocity increases slightly at first, mainly because of the velocity profile formation there; the highest value is nearly $3.5U_O$ at $x = 2.5\ D$. From $x/D = 3.75$, the maximum velocity starts to decrease. In fact, a periodic character of the jet is clearly distinguishable approximately up to $x/D_O = 20$. Further downstream, the initially pulsatile jet remains a conventional (steady) fluid jet with a constant monotonically decreasing streamwise velocity. The streamwise decay of the centerline time-mean velocity of the investigated (originally pulsatile) jet was evaluated as $U \sim x^{-1.04}$. It is very close to the well known proportionality $U \sim x^{-1.0}$ of conventional axisymmetric fully developed turbulent jets.

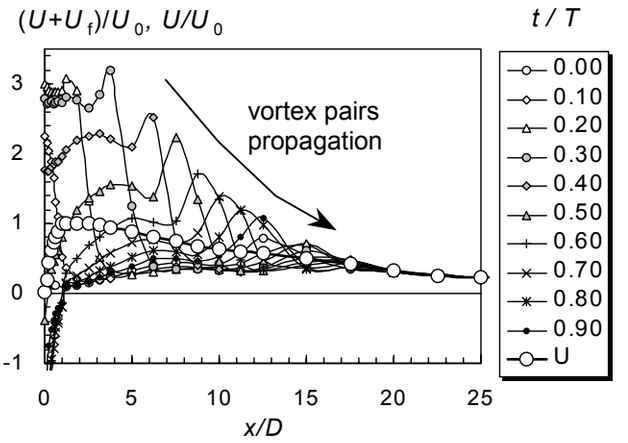


Fig. 2 Phase averaged centerline velocity.

CONCLUSION

A round air jet was generated (synthesized) by means of a zero–net–mass–flux actuator from a train of counter-rotating vortex pairs. The choice of suitable operating frequency was found by means of both theoretical as well as experimental approach: The resonance frequency of the actuator was derived theoretically. In addition, the hot-wire measurement revealed a relationship between the time-mean velocity and the driving frequency. The chosen *"nominal operating frequency", f* = 75.0 Hz, agrees very well with both the theoretical and experimental results.

The expected function of the actuator has been tested experimentally by smoke visualization (using phase–locked multi–expositions) and hot-wire anemometry. The hot-wire data were processed using the phase-averaged technique, and the velocity was decomposed into the time–mean velocity, periodic and fluctuation components. The experiments have confirmed a satisfactory function of the "fluid jet synthesis". Two typical synthetic jets have been presented here, namely the "long–" and "short– extruded columns L_O" cases. The maxima of the centerline local and the time–mean velocities reached approximately 27 m/s and 8.7 m/s, respectively; it was occurred at the *"nominal operating point"* which produces the "long L_O" synthetic jet. The maximum Reynolds number was $Re = 4400$.

The synthetic jet is formed by travelling of fluid "puffs" downstream, thus the velocity amplitude moves downstream and the periodic component of the velocity gradually diminishes. The investigated, originally pulsatile jet resembles a conventional (steady) jet for the axial distance greater than 20 diameters from the orifice, where the streamwise decay of the centerline time-mean velocity was evaluated as $U \sim x^{-1.04}$.

Acknowledgement: We gratefully acknowledge the support by the Academy of Sciences CR (No.6, IT No. 50026).

References

[1] Smith B.L., Glezer A.: The formation and evolution of synthetic jets, *Phys. Fluids* 10 2281–2297, 1998.

[2] Tesař V., Zhong S.: Efficiency of synthetic jets generation, *Transactions of the Aeronautical and Astronautical Society of the Republic of China* 35 (1) 45–53, 2003.

[3] Trávníček Z., Tesař V.: Annular synthetic jet used for impinging flow mass–transfer, *Int. J. Heat Mass Transfer* 46 3291–3297, 2003.

OPTIMAL ENERGY GROWTH AND OPTIMAL CONTROL OF THE SWEPT ATTACHMENT-LINE BOUNDARY LAYER

Alan Guégan*, Peter Schmid**, Patrick Huerre*
*Laboratoire d'Hydrodynamique (LadHyX), CNRS - Ecole Polytechnique, F-91128 Palaiseau Cedex, France
**Department of Applied Mathematics, University of Washington, Seattle, WA 98195-2420, U.S.A.

Summary An adjoint formulation is used to find the optimal perturbation for the swept attachment-line boundary layer in the context of the Görtler-Hämmerlin formulation. Two-dimensional mechanisms in a plane normal to the plate are shown to generate transient energy growth. Optimal control based on wall-normal blowing and suction is demonstrated to be very efficient and to strongly decrease the energy amplification of the optimal perturbation both in the linearly stable and linearly unstable régimes.

INTRODUCTION

The growth of disturbances in the vicinity of the leading-edge of swept wings is known to trigger transition to turbulence over the entire wing surface. It is therefore crucial to develop a control methodology capable of quenching developing disturbances. The three-dimensional swept Hiemenz flow boundary layer along the attachment line (figure 1) is known to become linearly unstable above a Reynolds number of 583 [1]. Furthermore strong transient growth possibly leading to by-pass transition has recently been demonstrated [2] [3].
The objective of the present study is to implement a Lagrangian-based variational optimization scheme [4] in order to first determine optimal perturbations living in swept Hiemenz flow under the Görtler-Hämmerlin assumption. In a second step, the same scheme is adapted to find the optimal control sequence of wall blowing and suction capable of inhibiting the growth of disturbances.

SWEPT HIEMENZ FLOW AND GÖRTLER-HÄMMERLIN FORMULATION

Swept Hiemenz flow is an exact solution of the incompressible Navier-Stokes equations that describes the steady swept attachment-line boundary layer as sketched in figure 1. The velocity components along the $(x,\ y,\ z)$ axes being denoted $(U,\ V,\ W)$, swept Hiemenz flow is obtained by assuming

$$U = xRe^{-1}F'(y)\ , \quad V = -Re^{-1}F(y)\ , \quad W = W(y)\ ,$$

where $\psi = -xRe^{-1}F(y)$ denotes the stream function and Re the Reynolds number based on the freestream spanwise velocity.

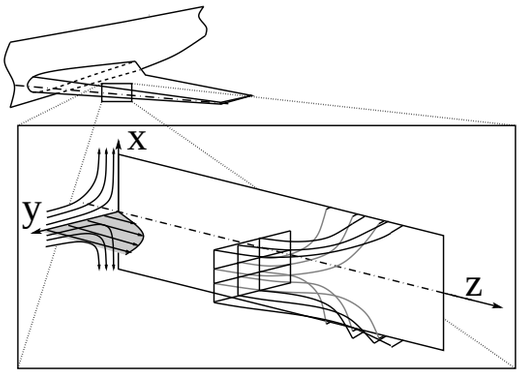


Figure 1. Sketch of swept attachment-line boundary layer.

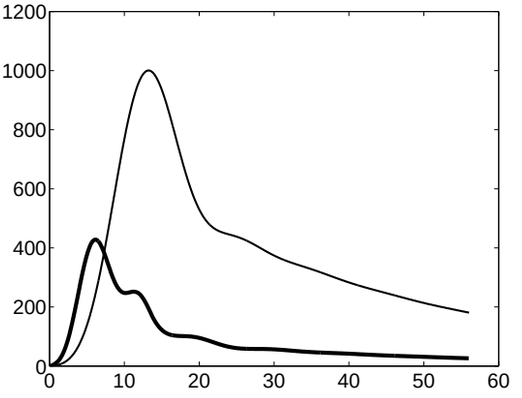


Figure 2. Energy of the optimal perturbation versus time when no control (thin line) or optimal control (thick line) is applied. Parameter settings : $Re = 2000$, $k = 0.1$, $T_p = 14$, $T_c = 14$, $l = 0.5$. Linearly stable base flow.

Under the Görtler-Hämmerlin assumption, small perturbations $(\breve{u}(y,z,t),\ \breve{v}(y,z,t),\ \breve{w}(y,z,t))$ are superimposed on the base flow so as to model the perturbed flow $(u,\ v,\ w) = (U + x\breve{u}, V + \breve{v}, W + \breve{w})$. At leading order, the Navier Stokes equations reduce to a linear system involving $\breve{u}$ and $\breve{v}$. Fourier decomposition in the spanwise direction leads to a linear system of the form

$$(A_{(Re,k)}\partial_t + B_{(Re,k)}) \begin{bmatrix} \hat{u}_k & \hat{v}_k \end{bmatrix}^t = 0 \tag{1}$$

governing the evolution of the Fourier coefficients $(\hat{u}_k,\ \hat{v}_k)$ for a given spanwise wavenumber k. The symbols $A_{(Re,k)}$ and $B_{(Re,k)}$ denote linear differential operators in y only.

OPTIMAL PERTURBATIONS AND OPTIMAL CONTROL

When no wall blowing is applied, the *optimal perturbation* at a given time T_p denotes the initial condition that leads to the maximum kinetic energy at T_p ; the *optimal control* at a given time T_c is the time sequence of wall-normal blowing and suction that leads to the minimum energy at time T_c for a given initial condition. If $E(t)$ denotes the energy of the perturbations at time *t*, the optimal perturbation and the optimal control correspond to extrema of the *cost function* $\mathcal{I} = E(T_{opti})/E(0) + (l^2/2)||\hat{v}(y=0)||^2$, where T_{opti} is either T_p or T_c and l a control parameter weighing the cost of control. A Lagrangian-based variational method, that requires to solve the *adjoint problem* of system (1) is implemented to find these extrema, at fixed $(Re,\ k)$. An example of the transient energy growth of an optimal perturbation is given in figure 2 (thin line) in the linearly stable régime. Under optimal control (figure 2, thick line), the energy amplification at time $T_c = 14$ is seen to be decreased from 1000 to 155.

UNDERLYING PHYSICAL MECHANISMS

At any $(Re,\ k)$, the optimal perturbation (figure 3) consists of vortices aligned in the chordwise direction x and tilted against the sweep W. Depending on the spanwise wavenumber k, two distinct behaviours have been observed, that both lead to transient energy growth : when $k > 0.3$ (figure 3a), the vortices are tilted by the basic shear as in the well-known 'Orr mechanism'. When $k < 0.3$ (figure 3b), the vortices split and re-arrange with their nearest neighbour, in addition to the previous tilting. A parameter study reveals that this mechanism is responsible for the strongest energy growth.

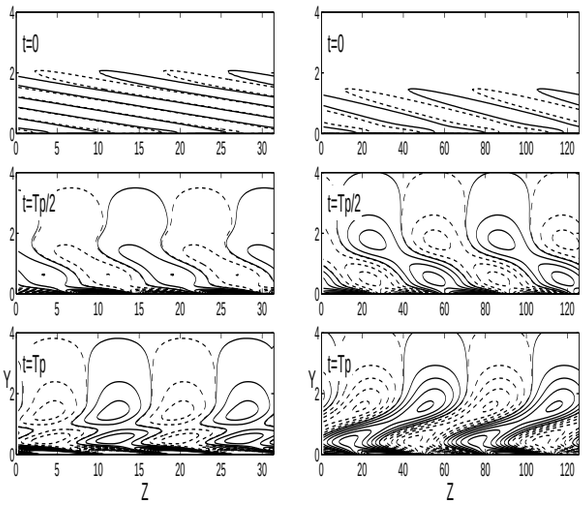


Figure 3. Vorticity contours of the optimal perturbation in the (z, y) plane at time $t = 0,\ T_p/2,\ T_p$. Wall is at the bottom and sweep is from left to right. Parameter settings : $Re = 2000$, (a) $k = 0.4$ and $T_p = 24$, (b) $k = 0.1$ and $T_p = 14$.

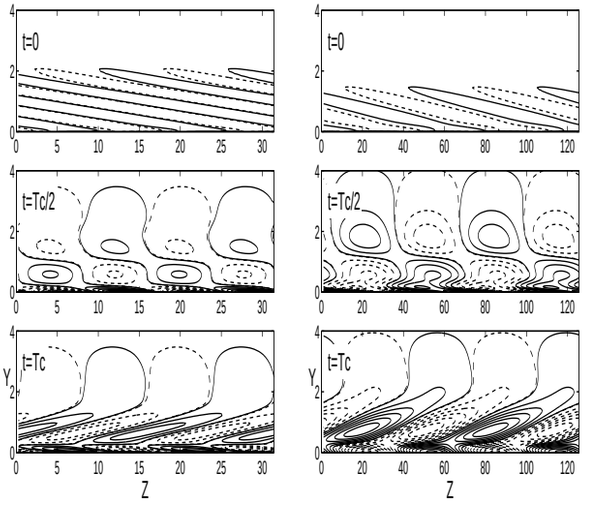


Figure 4. Vorticity contours in the (z, y) plane of the optimal perturbation when control is applied, at $t = 0,\ T_c/2,\ T_c$. Wall is at the bottom and sweep is from left to right. Parameter settings : $l = 0.5$, $Re = 2000$, (a) $k = 0.4$ and $T_c = 24$, (b) $k = 0.1$ and $T_c = 14$.

According to figure 4, optimal control affects the flow in such a way that the vortices evolve faster than they would without wall blowing, so as to lead to a minimum energy at time T_c. This leaves no time for the perturbations to extract energy from the mean flow, and inhibits energy amplification. Such an optimal control is shown to be very similar to opposition control in the linearly unstable régime.

The present study has demonstrated that closed loop active control based on wall-normal blowing and suction effectively damps the energy amplification of perturbations, thereby delaying transition (without control, these disturbances would experience dramatic energy growth).

References

[1] Hall, Malik & Poll. *On the stability of an infinite swept attachment line boundary layer.* Proc. Roy. Soc. Lond. A 395, pp. 229-245, 1984.
[2] Obrist & Schmid. *On the linear stability of swept attachment-line boundary layer flow. Part 1 : spectrum and asymptotic behaviour.* Journal Fluid Mech., Volume 493, pp.1-29, 2003.
[3] Obrist & Schmid. *On the linear stability of swept attachment-line boundary layer flow. Part 2 : non-modal effects and receptivity.* Journal Fluid Mech., Volume 493, pp.31-58, 2003.
[4] Bewley. *Flow control : new challenges for a new Renaissance.* Prog. Aerosp. Sci., Volume 37, pp.31-58, 2001.

FEEDBACK CONTROL OF VORTEX SHEDDING IN A SEPARATED DIFFUSER

Tim Colonius, Takao Suzuki, and Douglas G. MacMartin
Division of Engineering and Applied Science, California Institute of Technology
Pasadena, CA 91024 USA

Summary We propose closed-loop control for vortex shedding in a separated diffuser. Pulses of zero-net-mass injection (consecutive blowing and suction) are issued based on estimates of the circulation of a vortex in the separated region, and a model that suggests an optimal vortex spacing that minimizes stagnation pressure loss. The circulation is estimated using the wall pressure at a limited number of observer points. The closed-loop algorithm improves the robustness of open-loop control when external disturbances are added.

INTRODUCTION

Traditional separation control has relied on steady boundary layer energization (e.g. vortex generators, suction). Recently unsteady zero and positive-net mass injection have been shown to effectively increase lift-to-drag ratio (airfoils) or pressure recovery (diffusers) based on a different principle: spanwise vorticity near the separation point is modulated to produce a more favourable distribution of vorticity [e.g. 1]. In a variety of external and internal flows, it appears to be optimal to oscillate or pulse the injection at roughly twice the frequency of natural vortex shedding [e.g. 2,3,4 for results pertaining to diffusers]. Recently, we proposed a simple model to relate vorticity distribution and performance metrics (e.g.\ airfoil lift/drag or diffuser pressure recovery) [4]. The model allows us to develop a simple, yet effective, feedback control strategy.

Most previous work has focussed on open-loop control, but feedback (on the timescale of the vortex shedding) has the potential to enhance performance and decrease sensitivity to uncertainties and disturbances. Application of feedback requires three elements: effective actuation, sensors that permit identification of key flow events, and a control law that dictates how sensor information is used to modulate the actuation. The past decade has seen rapid advancements to actuator and sensor design, but owing to the complexity of predicting unsteady fluid motion, flow identification and control law development, especially in a form suitable for practical application, have lagged. Techniques currently under development are based on Direct Numerical Simulation [e.g. 5], reduced-order-modeling such as with Proper Orthogonal Decomposition (POD) [e.g. 6], and structure-identification using stochastic estimation [e.g. 7,8]. All of these methods generally require extensive experimental or numerical simulation data as input in their development.

CLOSED-LOOP CONTROL STRATEGY

We present a closed-loop control strategy (see Figure 1) for vortex shedding in a separated diffuser that is based on a much simpler model of the timescale for vortex shedding and its relation to the overall stagnation pressure loss [4]. The model consists of two parts--a vortex pinch-off criterion that yields an estimate for the (natural) vortex shedding frequency of the diffuser, and a control-volume analysis that connects the overall loss in stagnation pressure to the properties of the vortex shedding. The model identifies several parameters that are important in reducing stagnation pressure loss. The most important parameter is the size (or circulation) of the pinched-off vortex near the separation point; other parameters, such as the amount of circulation absorbed at the wall and the convection speed of the shed vortex, are strongly correlated with the size of the pinched-off vortex. We also show that the effects of unsteady mass injection can be understood by their impact on the size of the pinched-off vortex. This leads to the present control strategy: use feedback to pinch-off optimally sized vortices.

In order to exploit the connection between actuation, the size of the shed vortex, and the stagnation pressure loss, we need to be able to estimate the location and circulation of the vortex that is developing near the separation point. For this we introduce an inverse vortex imaging method [9] that detects the position and circulation of a vortex (or vortices) from pressure histories at a limited number of points. The algorithm minimizes a cost function that represents the difference between an inviscid, potential (point) vortex propagating in a diffuser and the measured, time-dependent pressure signal at the wall. In the present study, we use 12 sensors located just downstream of the separation point (see Figure 1). The detection algorithm is implemented using an estimator-corrector approach that averages the measured and predicted vortex trajectories in order to suppress random errors associated with the detection process. Results from a typical detection process are shown in Figure 1. A variety of related implementation issues are discussed in refs. [9] and [10].

To close the loop, we issue a pulse of zero-net mass injection whenever the estimated circulation reaches a pre-defined threshold value. The threshold is defined by varying (in open-loop) the (constant) frequency of pulse injection—the frequency that gives the minimum stagnation pressure loss defines the optimal vortex size and, in turn, the threshold circulation. As noted previously this frequency is approximately twice the natural (no actuation) shedding frequency.

RESULTS FROM NUMERICAL SIMULATIONS

We have designed and implemented the control strategy in a simplified flow using numerical simulation. We solve the Navier-Stokes equations for a laminar, two dimensional (smooth) diffuser with an area ratio of $h_2 / h_1=2$ (see Figure 1). The incoming flow is uniform across the inlet with a laminar boundary layer whose thickness is 10% of the inlet width, h_1. The Reynolds number (based on h_1) is 4000. A synthetic jet actuator is modeled by a distributed source of mass, momentum, and energy in the boundary layer just upstream of separation. Details of the numerical modelling and justifications for the simplified actuator model are given in ref [4]. Without actuation, the laminar boundary layer separates at a stationary location (see Figure 1) and quasi-periodic vortex shedding occurs on a timescale (and with a resulting stagnation pressure loss) that are in good agreement with the aforementioned model. A time history of stagnation pressure at the diffuser exit is given in Figure 2.

Under open-loop operation (but without any external disturbances), periodic pulse injection with sufficient amplitude (results below used a fixed momentum coefficient, $C\mu=1.3\text{x}10^{-3}$) stabilizes vortex shedding over a range of frequencies (i.e induces frequency locking), and leads to the identification of the optimal frequency where the stagnation pressure loss is minimized. This is used to set the threshold circulation ($\Gamma/Uh_1 = 1.26$) at which closed-loop injection should start as noted above.

We investigate both open and closed-loop performance in the presence of inflow disturbances. Disturbances are added by placing a small acoustic source upstream of the separation point. Figure 2 shows significant deterioration in the open-loop performance caused by the disturbances (in this case harmonic disturbances with a frequency five times the natural frequency). The disturbances apparently break the frequency locking and cause vortices of different (non-optimal) sizes to be shed. When closed-loop control is activated, frequency locking is nearly recovered, and stagnation pressure loss is substantially improved (see Table 1). Time-averaged stagnation pressure losses across the diffuser for the different cases are indicated in Figure 2.

DISCUSSION AND FUTURE WORK

We have demonstrated feedback separation control in a simplified two-dimensional diffuser flow. For brevity, we have shown only a few representative results--in the final presentation, additional results, including variation of the temporal waveform of actuation, the addition of random (white noise) disturbances, and further improvements to the vortex detection algorithm, will be given. The control strategy is based on a simple representation of the vortex pinch-off process, and the recognition that optimal performance is obtained (in open loop) at a frequency roughly twice the natural shedding frequency, and when the vortices are shed with nearly equal size and spacing (i.e. when frequency locking occurs). Closing the loop allows this optimal shedding to occur even in the presence of disturbances that significantly deteriorate the open-loop performance. The control law is sufficiently simple and the number of sensors sufficiently small that we expect it could be implemented in real-time in experiments that we hope to complete in future.

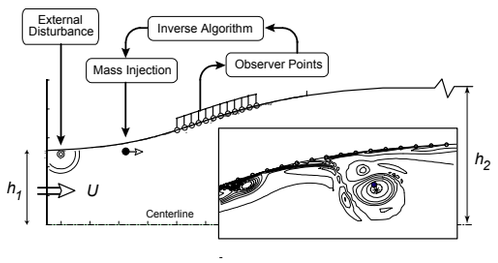


Figure 1. Schematic of control scheme. Inset: contours of vorticity from DNS illustrating the vortex detection algorithm. (*) vorticity maximum from DNS, (●) detected vortex center

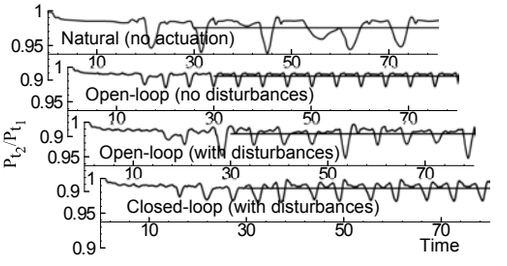


Figure 2. Stagnation pressure ratio across diffuser for different cases. The straight lines are the time averaged values over the period indicated. The average stagnation pressure losses are 2.50,1.23,1.67, and 1.37% (from top to bottom).

References

[1] Greenblatt D., Wygnanski, I.J.: *Progress in Aerospace Sciences* 3**6**:487-545, 2000.
[2] Amitay M., Pitt D., Glezer A.: *AIAA J.* **39**(4):616-620.
[3] Narayanan S., Banaszuk A.: *AIAA Paper 2003-0060*, 2003.
[4] Suzuki T., Colonius T. , Pirrozoli S.: Submitted to *J. Fluid Mech*. See also *AIAA Paper 2003-1138.*
[5] Bewley T.: *Progress in Aerospace Sciences* **37**:21-58, 2001.
[6] Berkooz G. Holmes P. Lumley J.L.*: Annu. Rev. Fluid Mech*. **25:**539-575.
[7] Adrian R.J.: *Appl. Sci. Res*. 53(3-4):291-303. 1994.
[8] Murray N.E. , Ukeiley L.S.: *AIAA J.* **41**(5):969-972. 2003
[9] Suzuki T., Colonius T.: *AIAA J.* **41**(9):1743-1751.
[10] Suzuki T., Colonius T, MacMartin D.G.: *AIAA Paper 2004-0577*.

REDUCTION OF AERODYNAMIC NOISE INDUCED BY FLOW OVER A CAVITY

Seiichiro Izawa*, Masafumi Kuroda*, Ao-Kui Xiong*, Yu Fukunishi*

*Department of Mechanical Engineering, Tohoku University,
Aramaki-Aoba 01, Aoba-ku, Sendai 980-8579 Japan*

Summary An experimental study to develop effective methods to reduce the aerodynamic noise induced by a turbulent flow over a cavity at low Mach numbers is carried out. It is shown that noise reduction can be achieved by both an active flow control method using piezo-ceramic devices and a passive control method inserting a thin plate into the cavity.

INTRODUCTION & EXPERIMENTAL SETUP

The generation of aerodynamic sound at a cavity is a well known phenomenon which can be found in places such as buildings, automobiles with an open sunroof and landing gears on an aircraft. This aerodynamics noise becomes more intense as the velocity of the flow increases, which is currently the limiting factor for the maximum velocity of the high-speed train in Japan. In the process of generation of the cavity noise, a self-sustained mechanism namely the "feedback loop" plays a dominant role. When the cavity is exposed to a flow, the separating boundary layer becomes a free shear layer and rolls-up into series of vortices which repeatedly hit the downstream edge. The periodical pressure-fluctuation travels upstream and affects the shear layer at its origin through the receptivity process, forming a feedback loop. As a result of this feedback loop, the aerodynamic noise from a cavity tends to be a large amplitude single tone. This paper describes the results of series of experiments aimed at developing an efficient method to reduce the aerodynamic noise generated at a cavity when the approaching boundary layer flow is turbulent and is at low Mach numbers.

The experiments were conducted using a low-turbulence wind tunnel of the Institute of Fluid Science (IFS) in Tohoku University, and a large-scale, low-noise wind tunnel of the Railway Technical Research Institute (RTRI). In each case, the test-piece was horizontally mounted in the open-type test section as shown in Figs. 1 and 2. For the IFS experiment, the upstream turbulent boundary layer was created by a combination of a strip of rough surface and a trip wire. In each case, a resonator, long in the streamwise direction, was used to simulate a deep cavity environment. When the boundary layer is turbulent and the Mach number of the flow is small, as in this case, loud peaky noise is not induced by a shallow cavity. So only the deep cavity case becomes important. The naturally dominant frequency of the cavity noise was 523 Hz for IFS (30 [m/s]), and 90 Hz for ITRI (60 m/s). In each case, the operating frequency of the actuators was set to the frequency. The thickness of the approaching turbulent boundary layer was 11mm for the IFS experiment, and 100 mm for RTRI.

In the active control experiment, an array of "bi-morph type" piezo-ceramic actuators attached vertically along the upstream-end vertical wall of the cavity was used. Eight pieces of the actuators were attached side-by-side along the spanwise direction (Fig.1). The idea is move the upstream edge where the receptivity to disturbance is most sensitive. Each "bi-morph type" actuator makes a bending motion, making its top edge to move back an forth in the direction parallel to the freestream. The amplitude of the fluctuation that can be introduced by the actuator is not sufficient to alter the frequency of the tone noise when the flow is turbulent, however the purpose of the control is only to change the phase of the velocity fluctuation along the spanwise direction. In the passive control experiment, a small thin flat plate was inserted vertically into the cavity. The basic idea is to alter the mechanism which the shear layer rolls-up into a series of vortices. Its noise reducing effect was investigated, changing the size and position of the small plate. A single hot-wire and a condenser microphone were used to measure the velocity and the sound, respectively.

RESULTS & DISCUSSION

Fig. 3 shows how the peak height of the dominant frequency component of sound spectrum changes against the voltage supplied to the actuators. Four operation modes were tested: 1) Single-phase - all eight pieces were driven by the same signal, 2) Mode 4 - each group of four pieces were supplied with the same-phase signal, 3) Mode 2 - a couple of two pieces moved together, 4) Mode 1 - each neighbouring piece was manipulated 180 degrees out of phase. It is apparent from Fig.3 that the sound level is suppressed, regardless of the modes, compared to the without-control case. In particular, the maximum value of noise reduction in mode 1 reaches approximately 30dB. Fig.4 shows the contour map of streamwise velocity fluctuation in the *xz*-plane for each mode when the manipulating voltage is 70V. It can be found

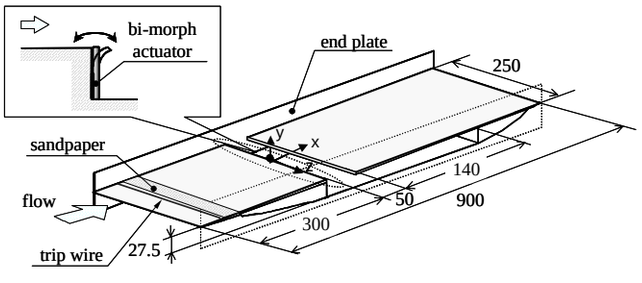


Fig.1 The model with a cavity (IFS)

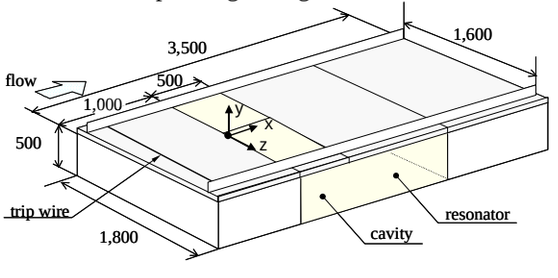


Fig.2 The model with a cavity (RTRI)

that the velocity fluctuation pattern changes sharply at several spanwise locations, which coincide with the boundary of the two actuator pieces that are manipulated 180 degrees out of phase. The results indicate that the active flow field control is successful. And it can be assumed that because the sound waves generated at neighbouring locations were 180 degrees out of phase, the sound waves cancelled each other resulting in the suppression of the peak noise.

The results of the passive control experiment are shown in Fig. 5. The abscissa is the x location of the plate, which corresponds to the distance between the upstream wall of the cavity and the plate. The upper tip of the plate is levelled with the upstream plate surface (y = 0). In the figure, it can be found that the noise suppressing effect becomes more obvious at around x = 15 and near the trailing edge of the cavity. The effect increases with the increase in the vertical length of the plate while it is between 2 and 8 mm. The noise reduction greater than the active control is achieved.

The results of the large wind-tunnel experiment shown in Fig. 6 show the same tendency. However, the noise suppression is not as effective as for the small wind tunnel experiments. When the vertical length of the plate is 30mm, an increase in noise can be found. This may be due to the oscillation of the test pieces itself. Fig. 7 shows the FFT spectra of the sound with and without control. It can be found that when the plate is placed near the leading edge (x = 100 [mm]), not only the peak of the cavity noise around 90 Hz but the energy levels of all frequencies decrease. On the other hand, for the case of x = 450 [mm], the peak noise decrease, but the sound energy levels of some frequency ranges increase instead. This tendency was not observed in the small wind-tunnel experiments.

CONCLUSIONS

Using both methods, the active and the passive flow control, cavity noise suppression experiments were carried out with some promising results. It was found that the "bi-morph type" piezo-ceramic actuators were capable of modifying the phase of the oscillatory flow fluctuation leading to noise suppression. This technique has a possibility to be applied in various flow controlling situations. It was also found that for noise suppression, the passive method to simply insert a thin flat plate into the cavity could be more effective. However, by comparing the experimental results from the two different sized facilities, it was found that the sound suppressing efficiency depends on the scale of the flow field. More research is needed, in order to clarify the reason.

References

[1] Yokokawa Y., Fukunishi Y.: *AIAA Paper* 2000-1931.

[2] Yokokawa Y., Fukunishi Y.: Theoretical and Applied Mechanics, **50** 281-287. 1983.

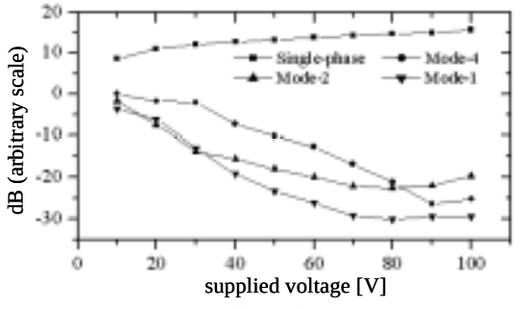
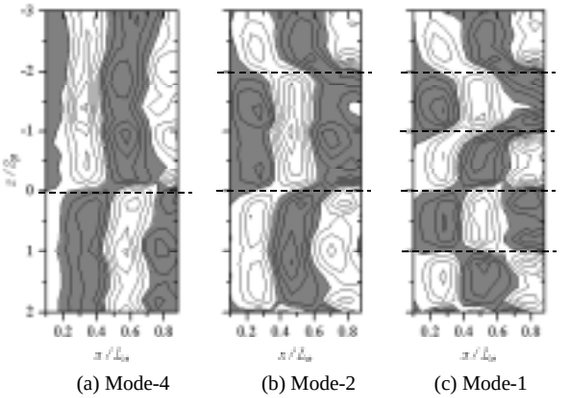


Fig. 3 Noise suppression effect of bimorph actuators (IFS)



(a) Mode-4 (b) Mode-2 (c) Mode-1

Fig.4 Contour maps of streamwise velocity fluctuations in xz-plane at y = 0 and supplied voltage = 70 V (IFS)

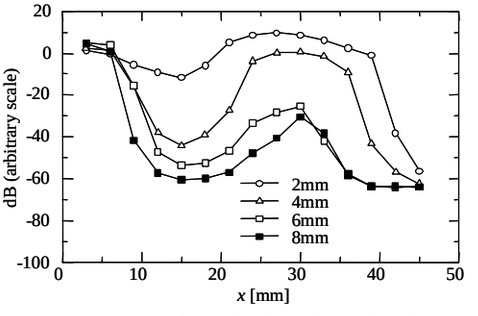


Fig.5 Variation of peak level with plates of different vertical lengths and x locations (IFS)

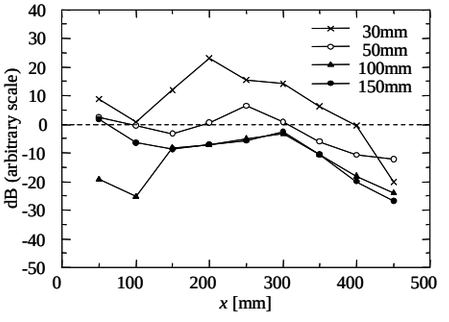


Fig. 6 Variation of peak level with plates of different vertical lengths and x locations (RTRI)

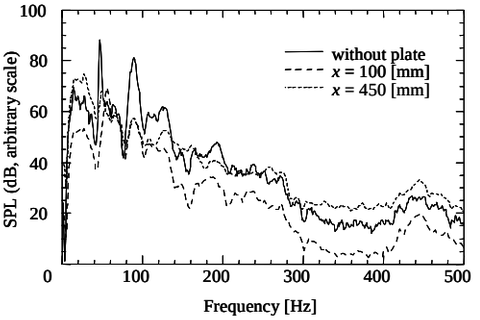


Fig.7 Sound suppressing effect with the plate (vertical length = 100 [mm]) at x = 100 and 450 mm (RTRI)

XXI ICTAM, 15–21 August 2004, Warsaw, Poland

CONTROL OF TURBULENT STREAKS BY ACTIVE WALL MOVEMENT

Philippe Konieczny*, Alexis Renotte**, Bertrand Nogarede**, Alessandro Bottaro*
*IMFT, EMT2 Group, Allée du Professeur Camille Soula, FR 31400 Toulouse, France
**INPT, LEEI, EM^2 Group, Rue Camichel, BP 7122, FR 31071 Toulouse, France

Summary Experimental results on the near-wall structures of turbulent boundary layers subject to a dynamic deformation of the wall are presented. The wall is moved on the basis of computational evidence which shows that a spanwise forcing in the form of a standing or traveling wave of the right amplitude, wave length and frequency can produce a significant turbulent drag reduction. This wave is supposed to act on the near-wall coherent structures, whose dynamics controls the turbulence production. The control is first tested on a model of the near-wall turbulent boundary layer, streamwise vortices and streaks are produced artificially by an array of roughness elements in a Blasius boundary layer. The control in the form of a standing wave has been tested and work is in progress to appraise the effectiveness of a spanwise travelling wave. So far, it has been found that the most effective excitation wave has a period of oscillations close to 50 viscous units of time, in agreement with experimental and theoretical results on similar configurations. Future work will consider the effect of the actuation module in turbulent flows.

INTRODUCTION

The dynamics of turbulent and transitional boundary layers is closely related to the self-sustaining wall-cycle. In the near-wall region, the coherent structures are correctly detected nowadays but if the formation of low and high-speed streaks is well understood, the regeneration of longitudinal vorticity is still under assessment. Linear perturbation analysis reveals that a streak velocity distribution $U(y,z)$, and the process known as the transient growth mechanism, capable of producing large linear amplification by secondary instabilities [2], contribute to the generation of streamwise vortices.
This work aims at finding efficient means to reduce skin friction drag in a turbulent boundary layer. It starts from the realization that a spanwise forcing can significantly reduce the wall shear stress and turbulence intensities. The forcing acts on the streaks hampering the "cycle".

CONTROL STRATEGY

The control procedure by a large-scale spanwise forcing attempts to moderate the streak instability. Forcing through large-scale streamwise vortices induced by vortex generator jets [3] have produced conclusive results. A significant reduction of mean and fluctuating skin friction is observed, that can locally attain 50%. The turbulence production is also hampered by the action of a spanwise volume force, which can be applied in a form of a standing or a travelling wave [4]. The oscillatory force results, with the (sub-)optimal forcing parameters, in a shear stress reduction by more than 30% and by a weakening of the streaks' intensity. Spanwise oscillations of the plate [5] produces similar results to the case of the oscillatory force. The characteristic parameters seem to be the oscillating period and the amplitude of the velocity, around 110 wall time unit and at least $15u_\tau$, respectively, for the optimal case [6]. The effect of a control in the form of a travelling wave are nearly the same, however for a forcing frequency twice, but allowed a vanishing of the streaks. In the present work, the forcing is generated by a moving wall, which is able to induce a spanwise wave.

Control module

To generate the spanwise wave, a control module composed by two arrays of 12 piezo-ceramic actuators is mounted flush at the wall. Each actuator consists of a cantilever beam and is driven by a multilayer piezo-ceramic element. The ceramic elongation induces, via a system of leverage points, a vertical displacement of the beam. The actuators work in pairs and each pair is out of phase with the neighbours, allowing the generation of different wave configurations. The controller active area is 25 cm long and 16 cm wide. To prevent leakage, the module is covered by a thin latex film.

Model system

We aim at producing a scaled-up model of the turbulent viscous layer by artificially generating regular streaks and vortices in a laminar boundary layer, in order to isolate events which appear to be important and to be able to describe more precisely the effect of the wave on the streaks' secondary instabilities. Roughness elements are installed along the span and we introduce "wall" units to scale the model, using the length scale (ν/u_τ), with u_τ the skin friction velocity based on the Blasius velocity distribution at the position corresponding to half-way through the control module. However, the streamwise axis is normalized with the distance of the roughness elements from the leading edge.

Experimental procedure

The experiments are performed in a close circuit low-turbulence-level wind tunnel at a free-stream velocity of $2m/s$. Mean and fluctuating velocity profiles are measured by hot-wire anemometry. Velocity fields have also been taken in the streamwise-spanwise plane by particle image velocimetry (PIV) downstream of the active area, at a fixed vertical position of 3mm, i.e. within the boundary layers thickness. Flow visualization has been carried out by injecting a sheet of smoke through a little slit on the wall placed at the same streamwise position of the roughness elements. This technique is able

to show the artificial streaks undulations and their destabilization by secondary instabilities. The objective is to show the effect of the control, both on the synthetic turbulence model and on the turbulent boundary layer triggered at the leading edge: for this we have carried out a parametric study with the forcing wave characteristics (wavelength λ_z, period T, amplitude A) which will be mostly given in wall units (λ_z^+, T^+, A^+).

RESULTS

Only results in which the control has the form of a standing wave are given here. The case without control and the measurements of artificial streaks are documented in [7] and show a sinuous instability mode. In the same configuration, and for the same roughness elements, a flow velocity of $2m/s$ generates streaks'amplitudes of roughly 10% of the free-stream velocity, at a downstream position of 1.7. The actuation module is located between $x = 1.2$ and $x = 2.0$.

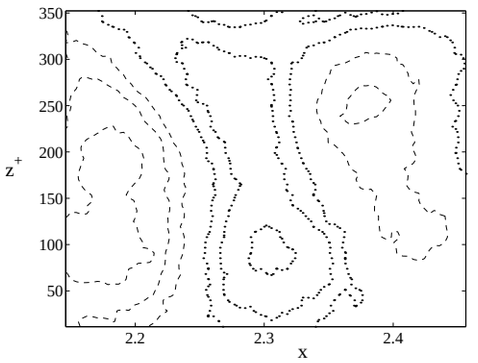


Figure 1. Spanwise velocity induced downstream of the active area generating a standing wave: $\lambda_z^+ = 700$, $T^+ = 30$, $U = 2m/s$. Wave crests are located at $z = 0$ and $z = 350$. Isolines correspond to $\pm 1, \pm 2$ and $\pm 3cm/s$.

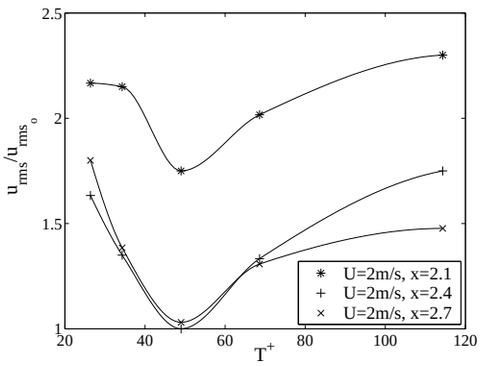


Figure 2. Mean fluctuating velocities in different cross sections along the streamwise direction; u_{rms_0} denotes no action at each given x.

PIV technique is the most efficient mean to measure the transverse forcing produced by the actuators. The largest action is obtained for the wavelength $\lambda_z^+ = 700$ (figure 1), and the velocity induced by the control module does not exceed $5cm/s$ (at $y^+ = 15$) in the window examined. Hot-wire measurements have shown for this case a slight effect (figure 2). Streaks are excited, and the response to the excitation is function of the actuation frequency. Around $T^+ = 50$, the energy of fluctuations reach a minimum. Flow visualizations show that the "wall" wave excite secondary instabilities which depend of the actuating period.
Some measurements by hot-wire and PIV have been taken for a case of a turbulent boundary layer, but no conclusive effects have been discerned yet.

CONCLUSION

Preliminary results seem to indicate that an optimal excitation period close to 50 viscous units of time on the *model flow* yields the most effective control, in agreement with numerical results on similar configuration [4] by a travelling wave. Current work considers the effect of the actuation module in turbulent flows and action in the form of a travelling wave.

References

[1] J. Zhou and R. J. Adrian and S. Balachandar and T. M. Kendall: Mechanisms for generating coherent packets of hairpin vortices in channel flow. *J. Fluid Mech* **387**:353–396, 1999.
[2] W. Schoppa and F. Hussain: Coherent structure generation in near-wall turbulence. *J. Fluid Mech* **453**:57–108, 2002.
[3] G. Iuso and M. Ororato and P.G. Spazzini and G.M. Di Cicca: Wall turbulence manipulation by large-scale streamwise vortices. *J. Fluid Mech.* **473**:23–58, 2002.
[4] Y. Du and V. Symeonidis and G.E. Karniadakis: Drag reduction in wall-bounded turbulence via a transverse travelling wave. *J. Fluid Mech.* **457**:1–34, 2002.
[5] W. J. Jung and N. Mangiavacchi and R. Akhavan: Suppression of turbulence in wall-bounded flows by high-frequency spanwise oscillations. *Phys. Fluids* **4**:1605–1607, 1992.
[6] M. Quadrio and P. Ricco: Initial response of a turbulent channel flow to spanwise oscillation of the walls. *J. Turbulence* **4**, 2003.
[7] P. Konieczny and V. Monturet and B. Nogarede and A. Bottaro: Active control of near-wall coherent structures. *FEDSM 2002-31036*, Montreal, Canada, 2002.

XXI ICTAM, 15–21 August 2004, Warsaw, Poland

MODEL-BASED CONTROL OF SHEAR FLOWS USING LOW-DIMENSIONAL GALERKIN- AND VORTEX MODELS

Mark Pastoor*, Rudibert King*, Bernd R. Noack**, Gilead Tadmor***, Marek Morzyński****
*Institut für Prozesstechnik, Anlagentechnik und Technische Akustik, Technische Universität Berlin P2-1, Hardenbergstr. 36a, D-10623 Berlin, Germany
**Hermann-Föttinger-Institut für Strömungsmechanik, Technische Universität Berlin HF1, Strasse des 17. Juni 135, D-10623 Berlin, Germany
***Department of Electrical and Computer Engineering, Northeastern University, 440 Dana Research Building, Boston, MA 02115, USA
****Institute of Combustion Engines and Basics of Machine Design, Poznań University of Technology, ul. Piotrowo 3, PL 60-965 Poznań, Poland

Summary The present study proposes a model-based flow control strategy using low-dimensional coherent-structure representations. This strategy is applied to the suppression of a von Kármán vortex street and the mixing enhancement of a wall-bounded shear-layer. Here, low-dimensional Galerkin and vortex models are used as a 'plant' for controller and observer design. The control approach is validated against direct numerical simulations.

INTRODUCTION

Low-dimensionsal coherent-structure models of shear flows play an increasing role in industrial and academic research — in addition to experiment and simulation. Low-dimensional models provide deeper understanding of key processes and enable the examination and design of actuators and the application control theory methods.

A model-based strategy of closed-loop flow control is proposed using a low-dimensional coherent-structure model as a plant for observer and controller design. The models are developed with Galerkin and vortex methods. The first approach typically leads to lower dimensions whereupon the latter ansatz is applicable for a larger dynamic range.

GALERKIN MODEL OF THE ACTUATED FLOW AROUND A CIRCULAR CYLINDER

Firstly, our strategy is applied to the flow around a circular cylinder at Reynolds number 100 [1]. At this Reynolds number the von Kármán vortex street is fully developed (see Fig. 1). The control objective is the supression of vortex shedding in the near wake. Two different actuators are investigated in this study:

A) transversal local volume force in the near wake
B) transversal oscillation of the cylinder

Control design is based on a low-dimensional Galerkin model of the natural flow which is approximated by a Galerkin expansion of the velocity field:

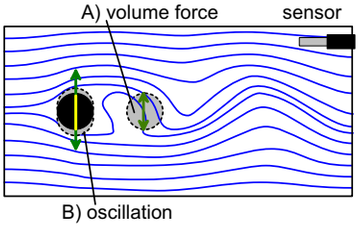


Fig. 1: Streamlines of the von Kármán vortex street in the wake of a circular cylinder at $Re = 100$. Two different actuators are investigated: A) a local volume force, and B) oscillations of the cylinder. The state of the flow is monitored by a single hotwire probe.

$$\mathbf{u}^{[N]}(\mathbf{x},t) \approx \mathbf{u}_0(\mathbf{x}) + \sum_{i=1}^{N} a_i(t)\ \mathbf{u}_i(\mathbf{x}). \qquad (1)$$

The velocity field is decomposed into a basic mode $\mathbf{u}_0$ representing the steady Navier-Stokes solution and N orthonormal modes for the fluctuations. The fluctuations are described by time-dependent Fourier coefficients a_i and spatial POD modes $\mathbf{u}_i$. Low-dimensional Galerkin models usually fail to represent transients, which are essential for control design. To overcome this challenge, a shift-mode $\mathbf{u}_N$ is introduced [2]. This mode is the normalized difference between the steady and mean flow. The shift-mode allows to describe the transient phase. Galerkin projecting (1) onto the Navier-Stokes equation yields the Galerkin system of ordinary differential equations

$$\frac{d}{dt}\ a_i = \frac{1}{Re}\ \sum_{j=0}^{N} l_{ij}\ a_j + \sum_{j,k=0}^{N} q_{ijk}\ a_j\ a_k\,, \qquad a_0 = 1, \qquad (2)$$

with the system coefficients l_{ij} and q_{ijk}. The dimension of the model in (2) is the number of modes N. A minimal Galerkin model with $N = 3$ captures the dominant leading harmonic of the vortex street and resolves 96% of the turbulent kinetic energy.

In case A) the actuator is modelled by an additional term $g\ \mathbf{b}$ in (2), where $g(t)$ is the controller output and $\mathbf{b}$ is the Galerkin representation of the volume force [3]: $d\mathbf{a}/dt = A(\mathbf{a})\ \mathbf{a} + \mathbf{b}\ g$,with $\mathbf{a} = (a_0; \ldots; a_N)$. An energy-based control is designed for this model. Its purpose is to reduce the energy of the fluctuation modes quantified by $r = \sqrt{a_1^2 + a_2^2}$. The controller reduces the turbulent kinetic energy in the near wake by 45%. In addition, an observer is designed to estimate the state of the flow from a single sensor reading. The results are validated against direct numerical simulation. A major task in the design of the controller is to appreciate the validity range of the model and the natural shedding frequency. In this configuration, model-predicted actuated transients reproduce simulations provided that the Fourier coefficients remain near the invariant manifold of natural transients (see Fig. 2).

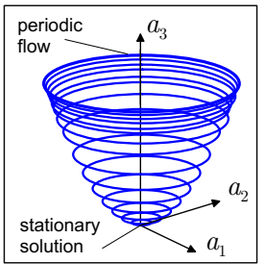


Fig. 2: Invariant manifold of natural transients from the fixed point (steady flow) to the limit cycle (periodic flow).

The oscillating cylinder in case B) is a well-examined actuator. This control generates a transversal cross-flow which is described by an additional actuation mode and its Fourier coefficient a_c. The general form of the Galerkin model for actuation A and B is given by

$$\frac{d}{dt}\,\mathbf{a} = A(\mathbf{a}, g)\ \mathbf{a} + \mathbf{b}\ g + \mathbf{k}_1\ g^2 + \mathbf{k}_2\ \frac{d}{dt}\ g\ . \tag{3}$$

Here, the controller output is equal to the velocity of the cylinder $g = a_c$. The energy-based control method is applied to this model for case B) by using the acceleration of the cylinder instead of the velocity as the controller output ($g = da_c/dt$).

VORTEX MODEL FOR THE FLOW AROUND A BACKWARD-FACING STEP

The 3D flow around a backward-facing step is investigated at a transitional Reynolds number of 4000. The flow separates at the step. In the sequel, the coherent structures are characterized by vortex-shedding and the roll-up of two shear-layer vortices. The flow is controlled by an acoustic actuator located at the upper edge of the step, thus amplifying the Kelvin-Helmholtz-type shear-layer instability. The state is monitored by an array of pressure transducers downstream of the step. The control goal is the regulation of the separation-bubble length. This reattachment length is an indicator of mixing enhancement.

The coherent structures are described by a vortex model [4]. The vorticity is approximated by Oseen vortices in the potential base flow. The dynamics are provided by Biot-Savart's law.

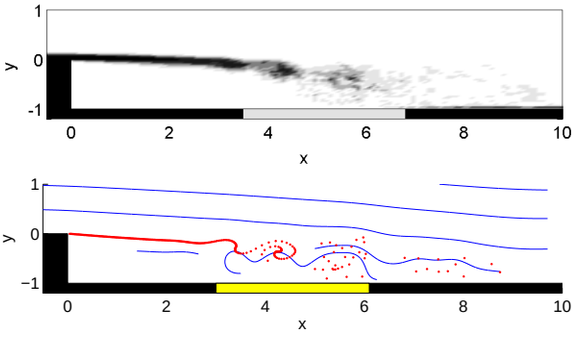


Fig. 3: Numerical simulation (top) and low-dimensional vortex model with $\approx$ 300 vortices (bottom) of the flow around a backward-facing step at $Re_h = 4000$. The top figure illustrates the vorticity distribution of a snapshot. The figure at the bottom indicates vortex locations by red dots. Regions of upstream velocity close to the wall are marked by grey bars.

The manipulation of 2D coherent structures is reproduced with some 300 vortices (see Fig. 3), even for a large dynamic range. As compared to direct numerical simulation, vortex models provide computationally efficient ways for 'rapid prototyping' of coherent structures and the examination of actuation effects. However, the very hybrid nature of this Lagrangian description poses a serious challenge for most control theory methods. This may be overcome by an 'Eulerization' [4].

CONCLUSION AND OUTLOOK

Low-dimensional Galerkin models have been successfully applied to model-based closed-loop control design of a wake instability. Low-dimensional vortex models provide an efficient and ample representation of the coherent structures of shear flows. Hybrid models incorporating the respective strengths of Galerkin and vortex models are pursued as a promising path for more complex configurations.

References

[1] NOACK, B.R. & H. ECKELMANN (1994) A low-dimensional Galerkin method for the three-dimensional flow around a circular cylinder, *Phys. Fluids* **6**, 124–143.

[2] NOACK, B.R., K. AFANASIEV, M. MORZYŃSKI, G. TADMOR & F. THIELE (2003) A hierarchy of low-dimensional models for the transient and post-transient cylinder wake, *J. Fluid Mech.* **497**, 335–363.

[3] GERHARD, J., M. PASTOOR, R. KING, B.R. NOACK, A. DILLMANN, M. MORZYŃSKI & G. TADMOR (2003) Model-based control of vortex shedding using low-dimensional Galerkin models, *AIAA-Paper* **2003-4261**.

[4] PASTOOR, M., R. KING, B.R. NOACK, A. DILLMANN & G. TADMOR Model-based coherent-structure control of turbulent shear flows using low-dimensional vortex models, *AIAA-Paper* **2003-4262**.

XXI ICTAM, 15–21 August 2004, Warsaw, Poland

NUMERICAL ANALYSIS OF THE WAKE CONTROL BEHIND A CIRCULAR CYLINDER WITH OSCILLATORY ROTATION

Marek Morzyński*, Sophie Goujon-Durand**, Bernd R. Noack***, José E. Wesfreid**, Benjamin Thiria**
*Division of Machine Design Methods, Poznan University of Technology Piotrowo 3, 60-965 Poznan, Poland
** Laboratoire de Physique et Mécanique des Milieux Hétérogenes - UMR CNRS 7636, École Supérieure de Physique et de Chimie Industrielles, 10, rue Vauquelin, 75231 Paris Cedex 05, France
***Hermann-Föttinger-Institut für Strömungsmechanik, Technische Universität Berlin, Straße des 17. Juni 135, D-10623 Berlin, Germany

Summary In this study, the wake flow is controlled via open-loop oscillatory rotation of a circular cylinder. The Kármán vortex street is suppressed with this method of control, both, in experiment and in simulation. The results of natural and actuated numerical flow simulations are used as the input for POD analysis. With this approach the spatial distribution of empirical eigenmodes are elucidated. Actuation pushes the Kármán mode downstream if the amplitude and frequency of the rotation are adequately chosen. Thus, the modal energy contains only a fraction of it original value of natural shedding.

INTRODUCTION

Suppression of the flow unsteadiness is of interest in fluid mechanics for many practical reasons. In particular, forces due to the unsteady bluff-body wakes need to be reduced in off-shore oil rigs, high-lift airfoils and other bluff bodies. A benchmark problem for wake control strategies is the flow around circular cylinder. This flow is characterized by a Kármán vortex street at $Re > 47$. This periodic wake dominates the flow even at very large Reynolds numbers. Focus is placed on the investigation of the laminar wake targeting an enhanced understanding and the control of the wake phenomena at high Reynolds numbers. Flow control of the wake is mostly performed with the active methods. These methods can be classified in terms of closed-loop and open-loop control. The real-time implementation of closed-loop control is complicated by the large dimension of the flow problem in many practical situations. However, controller and observer design which is based on low-dimensional Galerkin models of the flow may be successfully implemented in simulations [1] and supposedly soon in experiments. In open-loop forcing of the flow, the lock-in phenomenon is often observed. This phenomenon typically leads to an *increase* of the fluctuation level. In the considered example, however, open-loop control leads to a suppression of the Kármán mode. It should be emphasized that suppression of instabilities typically requires more sophisticated closed-loop strategies.

FLOW SIMULATION

The two-dimensional incompressible flow is simulated with the FEM and penalty formulation as described in [2]. Steady flow solution is used as the input for the disturbance equation:

$$\dot{\acute{V}}_i + \acute{V}_j \bar{V}_{i,j} + \bar{V}_j \acute{V}_{i,j} + \acute{V}_j \acute{V}_{i,j} + \acute{P}_{,i} - \frac{1}{Re}\acute{V}_{i,jj} = 0 \quad (1)$$

$$\acute{V}_{i,i} = 0 \quad (2)$$

The problem is solved as the initial value problem in the rectangular domain$-5 \leq x \leq 15$, $-5 \leq y \leq 15$ with no-slip boundary on the cylinder, uniform inflow $V_x = 1$, $V_y = 0$ and stress-free outflow.

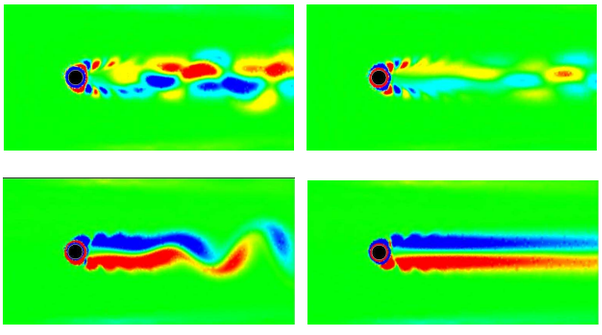


Figure 1. Disturbance vorticity (-5,5) for the fully controlled case ($Re = 100$, $A = 5$, $f/f_{nat} = 4.5$), for time $T = 33.6$ (left) and $T = 200$ (right) and respective sum of the disturbance with the steady flow solution.

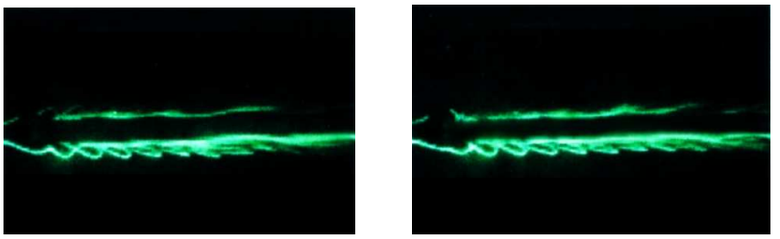


Figure 2. Results of the experiment - flow visualisation for A=5 and $f/f_{nat} = 4$ (left) and for $f/f_{nat} = 5$ (right)

RESULTS OF THE SIMULATION

The results presented here (Fig. 1) are obtained at Re=100, at the amplitude of rotation A=5, and at two frequencies. At $f/f_{nat} = 4.5$ (f_{nat} denotes the frequency of the vortex shedding) the substantial reduction of the Karman mode is obtained. This case we denote as "fully controlled". At $f/f_{nat} = 5$, a large controlled region can be seen behind the cylinder. Vortex shedding emerges only near the outflow. The results of the numerical simulation can be compared with the experimental visualisation depicted in Fig. 2. More details about the experiment can be found in [3].

POD ANALYSIS

In POD analysis is based on a set of "snapshots" of the flow field at different instances. The flow is approximated by a generalized Galerkin ansatz

$$V = \bar{V} + V_s + \sum a_k V_k \tag{3}$$

where $\bar{V}$ is the steady flow solution, V_s is the mean-field correction ("shift mode") and a_k and V_k are the Karhunen-Loéve coefficients and modes, respectively. The results obtained for the optimal values of amplitude and frequency of the cylinder rotation are shown in Fig. 3. The first modes are pairs of the first harmonics. The Kármán mode appears as the 5th and 6th mode with the negligible energy. The first four modes have energy 81.32%, 18.50%, 0.06%, 0.04% respectively. For less favourable amplitudes and frequencies, the Karman mode has much higher energy content and is already present in mode 3 with 9.75% energy. In this case, the fluctuation maximum is located near the outflow and can be seen as the vortex street in the reconstruction.

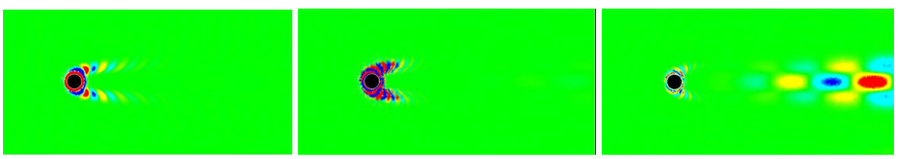


Figure 3. POD mode 1,3 and 5 vorticity (-5,5) for "fully controlled" case

CONCLUSIONS

The wake behind a controlled wake behind a circular cylinder is numerically simulated. The computations are consistent with experimental findings. Active control with adequate frequency and amplitude of the rotation suppresses vortex shedding in the whole computational domain. The Karhunen-Loéve decomposition provides information about the regions of flow dominated by particular modes. Future investigations target the development of Galerkin model for wake control with oscillatory rotation.

References

[1] Tadmor G., Noack B.R., Dillmann A., Pastoor M., Gerhard J., King R., Morzynski M.: Control, observation and energy regulation of wake flow instabilities, Paper **WeM10-4**, p. 2335-2339, *42nd IEEE Conference on Decision and Control*, 2003

[2] Noack B.R, Afanasiev K., Morzynski M., Tadmor G., Thiele F.: A hierarchy of low-dimensional models for the transient and post-transient cylinder wake, *J. Fluid Mech.* **497**, 335-363, 2003.

[3] Thiria B., Wesfreid J.E., Pradal D., Goujon-Durand S., Control actif du sillage autour d'un cylindre oscillant. XVI éme Congres Français de Mécanique, Nice, France (2003).

XXI ICTAM, 15–21 August 2004, Warsaw, Poland

NUMERICAL INVESTIGATION OF CONVECTIVE REGIMES IN A PLANAR FILTRATIONAL CONVECTION PROBLEM

Vasiliy N. Govorukhin*, Igor V. Shevchenko*
*Rostov State University, Department of Mechanics & Mathematics, 344090 Rostov-on-Don, Russia

Summary One-parameter families of steady-state convection regimes developing in the Darcy plane convection problem in a rectangular vessel are investigated numerically with increase of filtrational Rayleigh number and various aspect ratios of the container. The reason of the existence of these families is the cosymmetry. We consider Galerkin systems of various dimensions (up to 1000) for PDE approximation. The qualitative repetition of the bifurcations and consistency of the bifurcation parameter values was established by investigation of Galerkin's models of increasing dimensions for each set of the physical parameters. The loss of stability on a primary family, bifurcations of equilibrium families, periodic and chaotic regimes are studied. The fluid motion and heat transfer by convective regimes are also investigated.

INTRODUCTION AND MATHEMATICAL FORMULATION OF THE PROBLEM

In investigating convective motions of the fluid in a horizontal cylinder with an arbitrary shape of cross-section and with high heat-conducting side walls it had been found [1, 2] that a one-parameter family of equilibria was developed as a result of the first bifurcation. As shown in [2] the cause of the existence of the family was a nontrivial cosymmetry, the theory of which was developed last years. An analytical investigation of the one-parameter family of equilibria in the planar convection problem makes it possible to obtain asymptotics of the family in the neighborhood of its onset. The question about the evolution of the family at increasing the Rayleigh number is out of analytical treatment and requires numerical investigation as well as the analysis of occurrence and development of auto-oscillations.

We consider a rectangular container $D = [0, a] \times [0, b]$ filled with a porous medium and saturated by an incompressible fluid. The dimensionless equations of gravity convection of the fluid in the container uniformly heated from below have the form [1, 2]:

$$\begin{cases} \Delta\psi = \theta_x, \\ \theta_t + \psi_y\theta_x - \psi_x\theta_y = \Delta\theta + \lambda\psi_x. \end{cases} \tag{1}$$

Here $\psi(x, y, t)$ is the stream function, $\theta(x, y, t)$ is the temperature deviation from the equilibrium profile. The parameter λ is the filtrational Rayleigh number. On the boundary of the container the Dirichlet boundary condition is specified

$$\theta\Big|_{\partial D} = \psi\Big|_{\partial D} = 0. \tag{2}$$

We can express ψ in terms of θ by solving the Dirichlet boundary value problem for the Poisson equation

$$\psi = G\theta_x, \tag{3}$$

where G is the corresponding Green's operator. As shown in [2, 3], problem (1), (2) has a cosymmetry determined by the right-hand side of equality (3).

The critical values of the spectral problem for the zero equilibrium are [3]

$$\lambda_{m,n} = 4\pi^2\left(\frac{m^2}{a^2} + \frac{n^2}{b^2}\right), \qquad m, n = 1, 2, \ldots \tag{4}$$

All eigenvalues (4) are at least double and each transition of the bifurcation parameter λ through the value $\lambda_{m,n}$ corresponds to the bifurcation of the origin of a one-parameter family of equilibria. As shown in [2] the first critical value $\lambda_{1,1}$ is always double and a cycle of steady-state regimes branches off the quiescent state at $\lambda = \lambda_{1,1}$. All the equilibria of the family are neutrally stable along the cycle and asymptotically stable in the transversal directions, and their spectrum depends on the equilibrium coordinates and, therefore, this family cannot be an orbit of the action of any symmetry group [3].

In order to approximate problem (1)-(2) the Galerkin method is used. The numerical solution to the problem is found in the form

$$\begin{gathered} \psi = \sum_{i=1}^{nx}\sum_{j=1}^{ny}\psi_{i,j}(t)\phi_{i,j}(x, y), \quad \theta = \sum_{i=1}^{nx}\sum_{j=1}^{ny}\theta_{i,j}(t)\phi_{i,j}(x, y), \\ \phi_{i,j}(x, y) = \tfrac{2}{\sqrt{ab}}\sin\left(m_i\tfrac{\pi x}{a}\right)\sin\left(n_j\tfrac{\pi y}{b}\right). \end{gathered} \tag{5}$$

Substitution (5) into (1) and corresponding projection operations lead to a system of ordinary differential equations of the order $N = nx \times ny$ for the functions $\theta_{i,j}$ [6, 7]. The special technique for calculation of one-parameter families of equilibria was developed in [7] wich based on the cosymmetric version of the implicit function theorem [2, 4] .

NUMERICAL RESULTS

Loss of stability on the family

The loss of stability on a one-parameter family of noncosymmetric equilibria of ordinary differential equations systems is extended on a parameter. It means, that in the beginning on a set there are equilibria with a neutral spectrum. Then these equilibria lose stability, and in their neighborhood there are arcs of unstable equilibria. With a modification of a bifurcation parameter the sizes of unstable arcs are increased, the amount of steady and unstable arcs can vary, both at the expense of origin new, and in an outcome of confluence already existing. We find that the loss of stability on a stable set of stationary regimes depends of vessel size and can be oscillatory or monotone and can happens simultaneously in two, four, six or eight points [5, 6, 10]. After the first loss of stability and further increasing of the parameter λ the set of unstable regimes grow by forming unstable arcs in the families. Further increase of λ may lead to appearence of unstable regimes in new regions of the family both with monotonic and oscillatory instabilities.

Stationary convective regimes

To each point of a one-parameter family of equilibria corresponds stationary driving of a liquid. Is shown, that the character of complication of steady stationary convective regimes depends on geometry of the container [6, 7, 10]. The evolution of convective regimes from the appearance of the family to its instability is the following: for a narrow container increasing of λ makes the structure of existing rolls more complicated, and new convective cells are formed inside the existing ones; for a wide vessel new convective rolls appear. Both local and average heat transfer of the regimes in a wide vessel do not differ much neither qualitatively nor quantitatively. This difference is essential for a narrow vessel since there exist regimes with high and low heat transfer at the top and at the bottom of the vessel.

Bifurcations of families

The series of bifurcations of one-parameter families of equilibria was found out: birth of a new family from already existing, intersection and join of equilibrium curve, origin of a cycle of equilibria 'from an air' etc [6, 7, 10]. The bifurcations of families are connected with different equilibrium families both with primary stable and with unstable. All enumerated bifurcations take place in Galerkin systems of all considered dimensions. We found many variants of bifurcations studied theoretically in [8].

Periodic and chaotic regimes

The periodic and chaotic regimes was founded for different values of λ and sizes of D. The steady periodic regimes can occurs by two ways: as a result of special cosymmetric Hopf bifurcation or as a result of Euler bifurcation that depends on container size. For some values of parameter transition from stationary movement of a liquid at once to chaotic movement is possible. Both periodic and chaotic modes can coexist with steady stationary regimes.

Selection of stable regimes

It is natural to ask which stable stationary regimes of one-parameter family will be realized in a experiment. In the computer experiment, the initial points were distributed uniformly on a small sphere centered on the zero equilibrium for values of λ. We found that two regimes can be realized from the initial conditions near mechanical equilibrium. The selection mechanism was pretty obvious in this case and connected with phase space structure.

References

[1] Lyubimov D.V.: Convective motions in a porous medium heated from below, *Zh. Prikl. Mekh. Tekh. Fiz.* **2**:131-137, 1975.

[2] Yudovich V.I.: Cosymmetry, degeneration of solutions of operator equations, and onset of filtration convection, *Mat. Zametki*, **5, Vol.49**:142-148, 1991.

[3] Yudovich V.I.: Secondary cycle of equilibria in a system with cosymmetry, its creation by bifurcation and impossibility of symmetric treatment of it, *Chaos*, **2, Vol.5**:402-411, 1995.

[4] Yudovich V.I.: Implicit function theorem for cosymmetric equations, *Mat. Zametki*, **2, Vol. 60.**:313-317, 1996.

[5] Govorukhin V.N.: Numerical Simulation of the Loss of Stability for Secondary Steady Regimes in the Darcy Plane-Convection Problem, *Doklady Physics*, **12, Vol.43**:806-808, 1998.

[6] Govorukhin V.N.: Analysis of families of secondary steady-state regimes in the problem of plane flow through a porous medium in a rectangular vessel, *Fluid Dynamics*, **5, Vol.34**:652-659, 1999.

[7] Govorukhin V.N.: Calculation of one-parameter families of stationary regimes in a cosymmetric case and analysis of plane filtrational convection problem, *Notes on Numerical Fluid Mechanics*, **Vol. 74**:133-144, 2000.

[8] Kurakin L.G. and Yudovich V.I.: Bifurcations accompanying monotonic instability of an equilibrium of a cosymmetric dynamical system. *Chaos* **V. 10, N. 2**:311–330, 2000.

[9] Govorukhin V.N. and Schevtschenko I.V.: Numerical solution of Planar Darcy convection problem on a distributed-memory computer, *Computational Technologies*, **1, Vol 6.**:3-12, 2000.

[10] Govorukhin V.N. and Schevtschenko I.V.: Numerical investigation of second bifurcation transitions in a plane filtrational convection problem, *Mech, Zhidkosty i Gaza*, **N5**:115-128, 2003.

DISSOLUTION IN POROUS MEDIA: UPSCALING, INSTABILITIES, AND HETEROGENEITY EFFECTS

F. Golfier[1], B. Bazin[2], R. Lenormand[2], M. Quintard[3]
[1] *Ecole des Mines d'Albi, Campus Jarlard, Route de Teillet, 81013 ALBI CT Cedex 09 – France*
[2] *Institut Français du Pétrole, BP 311, 92506 Rueil-Malmaison Cedex – France*
[3] *Institut de Mécanique des Fluides de Toulouse, Allée du Professeur Camille Soula, 31400 Toulouse – France*

Extended Abstract

Dissolution mechanisms in porous media are of paramount importance in many practical situations. This is the case, for instance, when considering acid injection in reservoirs, or NAPL (Non-Aqueous Phase Liquid) pollutant dissolution in aquifers, salt formation dissolution, …. When trying to model those phenomena, several important theoretical questions must be answered. The major question concerns the possibility of representing by macro-scale equations mass and momentum transfer in such systems. Because dissolution patterns are greatly affected by heterogeneity effects at all scales (pore-scale and small-scale heterogeneities leading to wormholing, large-scale heterogeneities, …) , and because the dissolution process itself leads to transient evolution of the geometrical characteristics of the system, there is a great potential for non-local behavior in space and time.
These questions are reviewed on the basis of recent theoretical, experimental, and numerical evidence. The status of Darcy-Scale and Core-Scale models is discussed based on:

- theoretical arguments using averaging techniques,
- direct numerical simulation of pore-scale and Darcy-scale problems,
- experimental evidence (acid injection, salt dissolution, NAPL dissolution).

Darcy-Scale Model

Darcy-scale models involve most often a dispersion equation with a mass exchange term. The theoretical status of such a macroscopic model is reviewed based on results obtained for the asymptotic regime in a simple case, namely the tube problem, and in a more general case for periodic arrays of particles.

It is shown that Darcy-Scale models have a sufficient potential for reproducing unstable dissolution patterns in porous media (see an example Fig. 1, for heterogeneous porous media), as well as some quantitative characteristics such as the *optimum flow rate* leading to the longest wormhole for a minimum acid consumption. Stability diagrams for the different dissolution patterns (stable front dissolution, conical wormhole, wormhole, ramified wormhole, stable uniform dissolution) have been obtained numerically using the Darcy-scale model, in the case of homogeneous media.

Core-Scale Models

Core-scale models are built through cross-section averages of numerically obtained dissolution patterns. Based on numerical results and theoretical arguments, the possible features of large-scale models is investigated. In particular, one-equation and two-equation models are considered, and effective properties estimated from numerical experiments. The discussion shows that "intrinsic properties" may be expected to some extent for some dissolution regimes, but that historical effects might be important for other regimes.

Impact of heterogeneities

Finally, a weak solution to the problem of the impact of large-scale heterogeneities on dissolution models is presented in the case of NAPL dissolution.

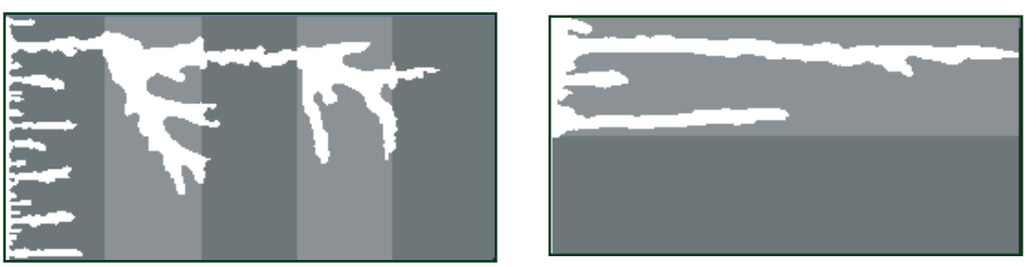


Figure 1. Example of dissolution structures in heterogeneous porous media

References

Golfier, F., C. Zarcone, B. Bazin, R. Lenormand, D. Lasseux, and M. Quintard. 2002. On the ability of a Darcy-scale model to capture wormhole formation during the dissolution of a porous medium. Journal of Fluid Mechanics **457**:213-254.

Golfier, F., M. Quintard, and S. Whitaker. 2002. Heat and mass transfer in tubes: An analysis using the method of volume averaging. Journal of Porous Media **5**:169-185.

INSTABILITY AND DYNAMIC CHAOS OF NON-EQUILIBRIUM FILTRATION OF GASEOUS LIQUID

G.T.Bulgakova and M.M. Khasanov
Ufa State Aviation Technical University, K.Marx 12, 450025, Ufa, Russia

Oil filtration with the pressure head below the bubble point is a classical problem, widely covered due to efforts of many scientists (Wyckoff & Botset 1936; Muskat 1949; Efros 1969; Rosenberg *at al.* 1969). However, experimental data that were recently obtained fall into controversy with the established physical concepts of the process studied (Bolotov *at al.* 1988; Martos 1978). In last papers it is reported that there is an abnormal increase in discharge of gaseous liquid within bubble point pressure ranges, while discharge decreases with further pressure decreasing. Observed phenomenon cannot be explained in the frames of classical approaches. Authors (Bolotov *at al.* 1988; Buyevich 1987) are attributing this effect to the subcritical bubbling (processes of accumulation and discharging of micro gas bubbles in porous media), that results in decreasing of the volumetric viscosity of a gas liquid mixture. However, with the viscosity to decrease up to 10-15%, flow rates have grown up to 2.5-3 fold. From analysis of gas saturation with time, Martos (1978) came to the conclusion of the heterogeneity of flow. On the general background of the gas saturation growth with the throughput volumes, there are observed sporadic fluctuations of the saturation in different sections of the sample.

Experimentally shown (Churaev 1990) that in micro capillaries due to gas absorption, decrease of cohesion forces between a liquid and the inner surface of capillary takes place. With the absorption layer to be about 10 nm only, markedly slippage is registered resulting in a non-monotonous behavior of the relative phase permeability (RPP) of the liquid phase. In this context, it is of great interest to give qualitative, if not quantitative, evaluation of the filtration characteristics of the gaseous liquid flow accounting for a non-monotonous behavior of the RPP.

Let us consider the non-stationary filtration of gaseous liquid in porous medium using the concepts of the theory of filtration of multi component systems. We will focus here on the filtration of oil with dissolved gas.

As a rule, there are considered models of equilibrium filtration of gaseous liquid, with the inter phase mass transfer being described by the known isoterm of the gas solubility in liquid. In particular, Genry solubility isoterm is accepted: $g = g_e = ap$, $a = const$, $g_e(p)$ – equilibrium phase concentration.

On the contrary, we are assuming non-equilibrium phase transitions. In this case, we have the following non-equilibrium model to describe the dependence of the mass concentration of the dissolved gas on the pressure:

$$\frac{dg}{dt} = -\frac{g - g_e(p)}{t},$$

where $\frac{dg}{dt}$ – substantial derivative, $\frac{dg}{dt} = \frac{\partial g}{\partial t} + u_1 \frac{\partial g}{\partial x}$. Velocity u_1 is derived by the Darcy law, t – relaxation time.

From the analysis of the experimental data it follows that the effect of slipping of the liquid is responsible for the nonmonotonic behaviour of the relative permeability of the liquid phase.

We assume that the phase permeability function for the liquid phase has the form shown in Fig. The relative permeability is given by $f_i = k_i / k_{i0}$, where k_{i0} is the permeability measured for the phase *i* when it completely fills the pore volume and k_i is phase permeability.

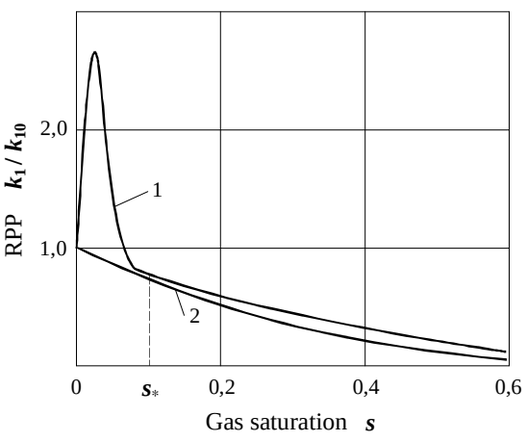


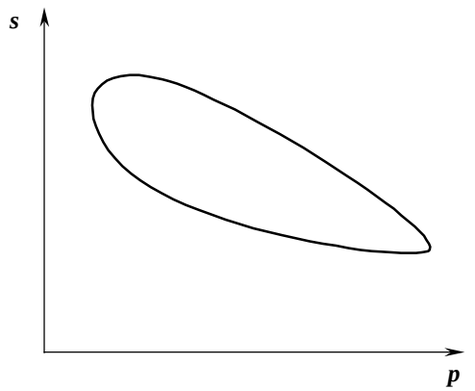
Fig.1. Relative phase permeability versus gas saturation: curves 1 and 2 corresponds to calculations using the method proposed herein and the method of Wyckoff and Botset, respectively.

Experimental studies of the filtration of a gas-liquid mixture through a porous medium show that once the pressure difference becomes critical, steady filtration regimes lose stability and undamped time variation in

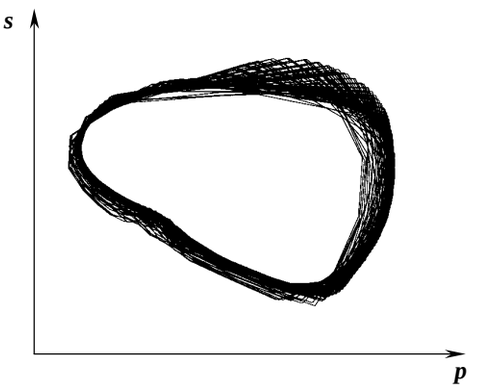
the flow rate of the filtrated liquid are observed. Therefore, we study the stability of steady filtration regimes for the gas-liquid mixture taking into account the nonmonotonic behaviour of the phase permeability for the liquid phase.

The relative permeability of the liquid phase is chosen in such a way that the maximum of the function corresponds to tha gas saturation value *s* for which the involved gas is entirely absorbed by the pore walls. The gas involved acquired mobility, forming a bound phase, at mean gas saturation $s = s_* = 0{,}1$.

By means of numerical investigations it was found out that transition to chaos in the considered system is evolved through destruction of the quasiperiodical movement. Attractor's evolution in the phase plane (p,s) from finite cycle to the strange attractor for the oscillatory regime given on Fig.2.



(a) $\Delta p = 3MPa;\ t = 20\,\text{sec};\ m_0 = 0{,}01$



(b) $\Delta p = 5MPa;\ t = 2000\ \text{sec};\ m_0 = 0{,}001$

CONCLUSIONS

1. We offer a model of non-equilibrium filtration of gaseous liquid within bubble point pressure ranges in the case of non-monotonous dependence of relative phase permeability of fluid on gas saturation.
2. It is shown that in this case two things are possible: stability violation of stationary behaviour of gaseous liquid filtration and regular and stochastic auto oscillations. Oscillations behaviour is determined by pressure drop parameter in a reservoir model, degassing degree, and oil filtration viscosity.
3. We give a numerical solution of oil degassing in a model of porous media taking into account non-equilibrium behaviour of gas releasing and nonmonotonic dependence of relative phase permeability of liquid phase on gas saturation. Calculations show increase in discharge within bubble point pressure ranges and decrease in charge with further pressure decay. The results of numerical investigations satisfactorily coordinate with laboratory experiments data.
4. Numerical solution also shows pressure and gas saturation oscillations during periods of time in particular reservoir section.

REFERENCES

Bolotov A.A., Mirzadganzade A.H. & Nesterov I.I. 1988 Rheological properties of gas solutions in fluid in the range of bubble point pressure. Izvestia Akademii Nauk SSSR. Mekhanica Zhidkosti i Gaza 1, 172-175 (in Russian).

Buyevich Y. A. 1987 Precritical nucleation in fluid with surfactant. Inzhenerno-Fizicheskii Zhurnal 52(3), 394-402 (in Russian).

Churayev N. V. 1990 Physics and chemistry of processes of mass transfer in porous media. Moscow (in Russian).

Efros D.A. 1969 Study of heterogeneous systems filtration. Moscow (in Russian).

Muskat M. 1949 Physical principles of oil production. New York.

Martos V. N. 1978 Some physical regularities of gassy fluid filtration. Filtration, heat transfer and oil-and-gas recovery in complicated reservoirs systems. Moscow, 36-45 (in Russian).

Rosenberg M. D., Kundin S. A. & Kurbanov A.K. et al. 1969 Gassy fluid and other multicomponent mixtures filtration. Moscow (in Russian).

Wyckoff R. D. & Botset H. F. 1936 The Flow of gas fluid mixtures through unconsolidated sands. Physics. 7(9), 325.

DOUBLE-POROSITY SOILS WITH HIGHLY CONDUCTIVE INCLUSIONS: MODELING OF WATER FLOW IN UNSATURATED CONDITIONS

Jolanta Lewandowska[*], Adam Szymkiewicz[**], Jean-Louis Auriault[***]
[*]*Laboratoire LTHE, FR 38041, Grenoble, France*
[**]*Gdansk University of Technology, WBWiIS, PL 80-952 Gdansk, Poland*
[***]*Laboratoire 3S, FR 38041, Grenoble, France*

Summary The homogenization method by asymptotic expansions was used to study water flow in a double-porosity soil. The gravity effect is included. The macroscopic flow model was found to be a single diffusion-type equation with two effective parameters. The effective conductivity tensor is defined as depending on the solution of a local boundary value problem within a period. The effective specific water capacity is found to be the volumetric average. Both parameters are functions of the capillary pressure head. A numerical example of water infiltration into initially dry soil is presented. The results of homogenization show good agreement with the reference fine scale solution.

INTRODUCTION

Double-porosity soils are highly heterogeneous media composed of two porous sub-domains with contrasting hydraulic properties. In this type of media three distinct observation scales exist: (i) the microscopic scale, which corresponds to grains and pores; (ii) local (mesoscopic) scale, which is associated to the characteristic size of heterogeneities (aggregates, inclusions, shales) and (iii) the macroscopic scale, which is the scale of entire soil layers and is most important for practical purposes. Due to the particular structure the modeling of water flow and contaminant transport in double-porosity media requires specially adapted approaches. This paper concerns water flow in an unsaturated double-porosity medium which consists of highly conductive inclusions embedded in a less conductive matrix.

FORMULATION OF THE PROBLEM

We consider a heterogeneous medium of periodic structure, with two characteristic lengths: l (the characteristic size of a period) and L (the characteristic size of the macroscopic domain) (Fig 1a,b). The scale separation is written: $\varepsilon = l / L << 1$. The water flow in unsaturated conditions in both porous sub-domains is described by the Richards equation:

$$C_1 \frac{\partial h_1}{\partial t} - \mathrm{div}_X \left(K_1 \mathrm{grad}_X \left(h_1 + X_3 \right) \right) = 0 \quad \text{in } \Omega_1 \quad \text{and} \quad C_2 \frac{\partial h_2}{\partial t} - \mathrm{div}_X \left(K_2 \mathrm{grad}_X \left(h_2 + X_3 \right) \right) = 0 \quad \text{in } \Omega_2 \tag{1a,b}$$

where h_i is capillary pressure head [L], t is time [T], $\mathbf{X}$ is spatial variable [L] (X_3 oriented vertically upwards), C_i is the specific water capacity [L^{-1}] and $\mathbf{K}_i$ is the hydraulic conductivity tensor [L/T] (i denotes sub-domain 1 or 2). Both C_i and $\mathbf{K}_i$ are highly nonlinear functions of h_i. At the interface Γ the continuity of capillary pressure and flux is satisfied:

$$h_1 = h_2 \quad \text{and} \quad \left(\mathbf{K}_1 \mathrm{grad}_X \left(h_1 + X_3 \right) \right) \mathbf{N} = \left(\mathbf{K}_2 \mathrm{grad}_X \left(h_2 + X_3 \right) \right) \mathbf{N} \tag{2a,b}$$

where $\mathbf{N}$ is a unit vector normal to Γ. Due to the separation of scales two dimensionless spatial variables appear: $\mathbf{x} = \mathbf{X}/L$ and $\mathbf{y} = \mathbf{X}/l$. The following assumptions are introduced: (i) the characteristic time of observation corresponds to the time of flow in sub-domain 2 at the macroscopic scale; (ii) the capillarity dominates over the gravity at the scale of a period, (iii) the ratio of the characteristic diffusivities is of the order of ε: $D_{2C} / D_{1C} = (K_{2C}/C_{2C}) / (K_{1C}/C_{1C}) = O(\varepsilon)$.

HOMOGENIZATION

After normalization of the problem (1)-(2) the dimensionless quantities u^* are presented in form of an asymptotic expansion: $u^* (\mathbf{x},\mathbf{y},t^*) = u^{(0)} (\mathbf{x},\mathbf{y},t^*) + \varepsilon\, u^{(1)} (\mathbf{x},\mathbf{y},t^*) + \varepsilon^2\, u^{(2)} (\mathbf{x},\mathbf{y},t^*) + \ldots$ The homogenization procedure includes three main steps: (i) introduction of the expansions into the normalized equations; (ii) identification of problems at the successive powers of ε; (iii) solution of resulting boundary value problems within the period domain. Only the final results of the homogenization are presented here. The macroscopic model is obtained as a single equation with two effective parameters K_{ij}^{eff} and C^{eff}:

$$C^{eff} \frac{\partial h^{(0)}}{\partial t^*} - \mathrm{div}_x \left(\mathbf{K}^{eff} \mathrm{grad}_x \left(h^{(0)} + X_3 \right) \right) = 0 \tag{3}$$

where $h^{(0)}$ is the macroscopic capillary pressure head. It was found that local equilibrium of capillary pressure exists during the flow. The effective water capacity is defined as: $C^{eff} = w_1 C_1 + w_2 C_2$, where w_i is the volumetric fraction of sub-domain i . The effective conductivity tensor is defined as follows:

$$K_{ij}^{eff} = \frac{1}{|S_i|} \int_{S_i} \left[K_{2ik}^{(0)} \left(I_{kj} - \frac{\partial \chi_j}{\partial y_k} \right) \right] dS \tag{4}$$

where S_i represents the surface of the period normal to i direction. The vector function χ is a solution of the following local boundary value problem:

$$\frac{\partial}{\partial y_i}\left[K_{2ik}^{(0)}\left(I_{kj} - \frac{\partial \chi_j}{\partial y_k} \right)\right] = 0 \quad \text{in } \Omega_2 \quad \text{and} \quad \chi_k = y_k \quad \text{on } \Gamma \tag{5a,b}$$

Moreover, χ should satisfy the periodicity condition. Note that $\mathbf{K}^{eff}$ is not influenced by the conductivity of inclusions.

NUMERICAL EXAMPLE

The numerical simulation concerns infiltration into a soil layer (Fig. 1a). The macroscopic process is 1D, while the local geometry is 2D (Fig. 1b). The scale separation parameter $\varepsilon = 0.01$. For simplicity, the function $C(h)$ is taken the same in both sub-domains, whereas the hydraulic conductivities satisfy: $\mathbf{K}_2(h) / \mathbf{K}_1(h) = 0.01$. The solution of local problem is presented in Fig. 2 and the effective functions in Fig. 3. The soil is initially dry: $h_0 = -100$ cm. At the surface a constant value of h is imposed: $h_S = -2$ cm. At the bottom free drainage condition is applied: $dh/dX_3 = 0$. The macroscopic equation (3) was solved using REMOL_1D numerical code based on the method of lines (DASPK solver). A fine scale solution is also provided, where the local heterogeneous structure of the medium is explicitly represented (SWMS_2D code). The pressure profiles are compared in Fig. 4. It can be seen that the homogenization results are very close to the reference solution. The same holds for the macroscopic water flux (results not shown here).

CONCLUSIONS

The water flow in unsaturated soils with highly conductive inclusions can be described by a single macroscopic equation (local equilibrium conditions) with effective parameters derived by homogenization. The macroscopic conductivity tensor depends on the conductivity of the matrix and the local geometry of the medium and is independent of the inclusions' conductivity. There exists a continuous passage to this solution from the classical approach. Numerical results obtained using homogenization show good agreement with the reference fine scale solution.

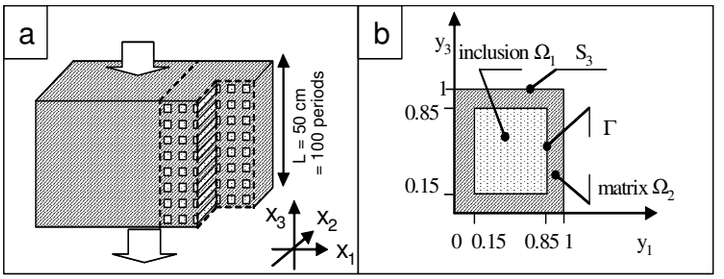


Fig. 1. Macroscopic solution domain and local geometry

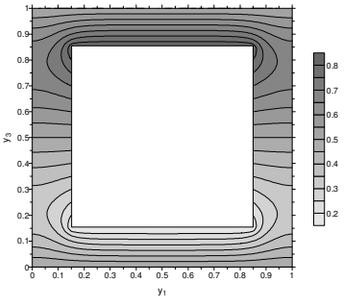


Fig. 2. Distribution of function χ in the period

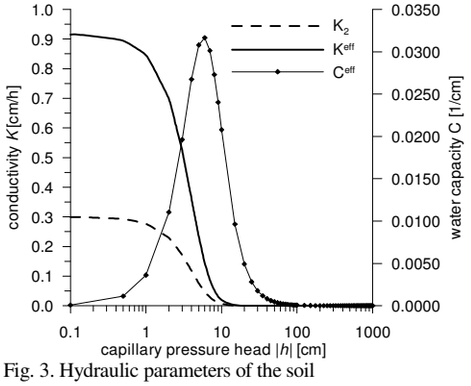


Fig. 3. Hydraulic parameters of the soil

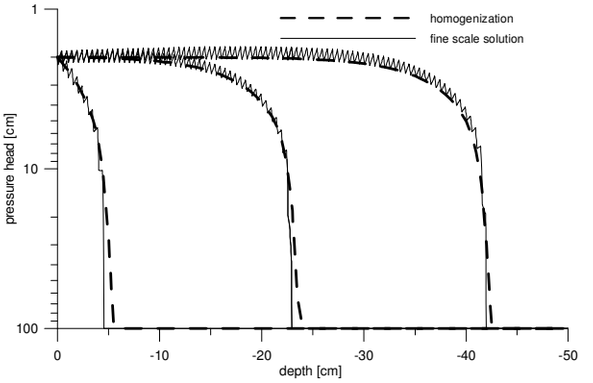


Fig. 4. Pressure profiles obtained from homogenization and reference solution

References

[1] Auriault J.-L.: Heterogeneous medium. Is an equivalent macroscopic description possible? *Int. J. Engng Sci.* **29**(7): 785-795, 1991.

[2] Lewandowska J., Szymkiewicz A., Auriault J.-L.: Modeling of unsaturated water flow in soils with highly conductive inclusions by homogenization. *submitted*, 2003

[3] Panfilov M., Quintard M., Bertin H.: Macroscale two-phase flow through porous media with highly permeable inclusions. in: Dmitrievski A., Panfilov M. (ed.) *Proceedings of the International Conference "Porous Media: Physics, Models, Simulations"*, Moscow 1997.

[4] Sanchez-Palencia E.: Non-homogeneous media and vibration theory. *Lecture Notes in Physics* **127**, Springer-Verlag, Berlin, 1980.

Plastic mass flow of sand under action of pore pressure gradient

Victor N. Nikolaevskiy

The model of poroplasticity has to include the non-associated flow rule, developed (1971) for the Coulomb media with dilatancy in the well-known form. The porous matrix equilibrium is expressed in terms of the effective (Terzaghi) stress σ_{ij} and p - the pore pressure. The Darcy law is sufficient for fluid dynamics description. Let illustrate it for axial symmetry:

$$\frac{\partial \sigma_r}{\partial r}+\frac{\sigma_r-\sigma_q}{r}-\frac{\partial p}{\partial r}=0 \qquad \phi(w-v) = -\frac{k}{\eta}\frac{\partial p}{\partial r} \qquad (1)$$

Here k - the permeability, and η - the fluid viscosity, ϕ - the porosity; w, v - the "true" radial velocity of the fluid and solid phases. The matrix transfer into plastic flow state if $\sigma_q = N\sigma_r - 2Y/(\sigma_s - \alpha)$, $N = \dfrac{q_s + \alpha}{q_s - \alpha}$, $Y_0 = \dfrac{2Y}{\sigma_s - \alpha}$ and $\dfrac{\partial v}{\partial r}+\dfrac{v}{r}=\Lambda q\left(\dfrac{\partial v}{\partial r}-\dfrac{v}{r}\right)$.

The latter is dilatancy relation for plastic rates given in the terms of solid velocities. Besides α, Λ are friction and dilatancy coefficients, Y is cohesion, $\sigma_s = \mathrm{sgn}(\sigma_r - \sigma_q)$, $q = \mathrm{sgn}(\partial v/\partial r - v/r) = \sigma_s$, the matrix tension is positive.

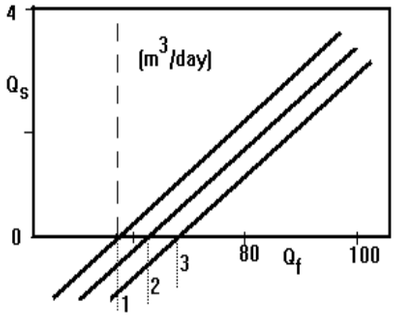


Fig.1. Sand production beginnings Q_f^* (1, 2, 3) depend on cohesion Y_o

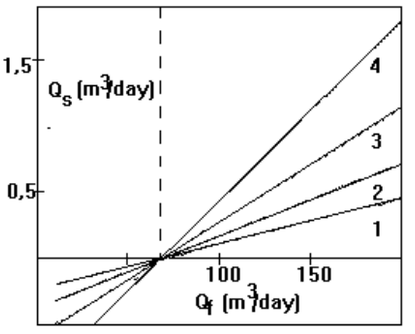


Fig.2. Sand production coefficient (1 – 4) depends on $\boldsymbol{n}$ –dilatancy rate

The mass balances for the fluid and the matrix (ρ_f, ρ_s - the density of fluid and the intact solid material) are given as

$$\frac{\partial}{\partial t}(\phi\rho_f) + \frac{1}{r}\frac{\partial}{\partial r}(r\rho_f\phi w) = 0, \qquad \frac{\partial}{\partial t}(1-\phi)\rho_s + \frac{1}{r}\frac{\partial}{\partial r}\left(r\rho_s(1-\phi)v\right)=0 \quad (2)$$

The simplest stationary problem of "sand production" via well can be solved by assumption of coincidence of the plastic boundary with "feeding contour" R. Then

$$v=\frac{C}{r^n},\ n=\frac{1+q\Lambda}{1-q\Lambda},\qquad v(r)\ =\ -\frac{Q_S}{2\pi hR(1-f)},\ \frac{1-f_R}{1-f}\ =\ \left(\frac{R}{r}\right)^n,\qquad w(r)\ =\ -\frac{Q_f}{2\pi hr f}$$

The connection between sand and fluid rates is calculated and given in Figures 1 and 2.

To avoid the concept of feeding contour is possible if one considered the self-similar problem of the opening of a well drilled to the infinite seam under initial pressure. The solution will depend just on the Boltzman variable:

$$\xi\ =\ \frac{r}{\sqrt{t}},\qquad \frac{\partial}{\partial t}\ =\ -\frac{1}{2t}\xi\frac{d}{d\xi},\qquad \frac{\partial}{\partial r}\ =\ \frac{1}{\sqrt{t}}\frac{d}{d\xi}$$

It is described by the system of ordinary equations but a bit more complicated than in the pore pressure diffusion case.

The ecology rules need in wastes disposal in the underground space. Here the injection of slurry through a well into the artesian seam is considered as plastic flow into a weak layer under high pore pressure. The axial symmetry of the problem assumes frontal stable displacement of masses. The selection of parameters values corresponds to the field data at Alaska experience.

The displacement instability is the main problem of the injection process as happens in the fracpack operation used for injection of gravel into an aquifer potentially dangerous for sand production (a variant of hydrofracturing of brittle rocks, which increases drastically a well productivity). The example of the first adequate calculation done numerically by the same model is shown in Figure 3. Here the stress concentration zones and thickening of a fracture, being filled with gravel (through the cut in a well tube), can be seen.

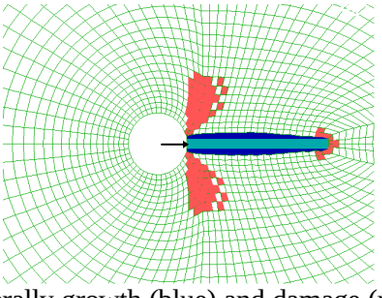


Figure 3. Initial fracture laterally growth (blue) and damage (red) zones under Frac & Pack

Nikolaevskii V.N. (1971) “Governing equations of plastic deformation of a granular medium”. J. Appl. Math. Mech. (PMM), # 6, 1017 – 1029.

Nikolaevskij V.N. (1990). “Mechanics of Porous and Fractured Media.” Singapore: World Scientific Publishers, 472 pp.

Nikolaevskiy V.N. (1996). “Geomechanics and Fluidodynamics. With Applications to Reservoir Engineering”. Dordrecht: Kluwer Acadmic Press, 348 pp.

P-waves behavior at transition from liquid to gas-saturated porous media

Dmitry N. Mikhayalov

Institute the Physics of the Earth, Russian Academy of Sciences, B. Gruzinskaya 10, Moscow, 123810; E-mail: dmikch@uipe-ras.scgis.ru, dmikh@yandex.ru

Summary The comparing of *P*-wave behavior for water and gas - saturated porous media is made. It is shown that in gas-saturated media the 2nd wave has low attenuation. Moreover, in this case at low frequencies the wave characteristics radically differ from ones for water - saturated media. It is obtained that *P*-waves transformation happens if gas pressure exceeds some threshold value, the expression for this value is given.

According to the Frenkel - Biot theory, two *P*-waves can propagate in saturated porous medium [1]. The 1st wave is faster wave and has small attenuation. The 2nd wave is slower, extremely damped wave. But, for gas-saturated media the situation can be changed. As Nikolaevskiy had shown [2], the 2nd wave is determined mainly by rock matrix deformation. For liquid-saturated media, porous matrix can be deformed only if saturating fluid can flow through a pore system, leaving a room for volume repacking. The Darcy resistance creates so high attenuation that this wave can spread at extremely short distances. However, a saturating gas has high compressibility and therefore the matrix volume deformation becomes possible without flow along the pore system. Correspondingly, such 2nd wave can have small attenuation.

The total system of equations of the porous media dynamics in linear approximation looks as [2]:

$$\beta_\Sigma \frac{\partial p}{\partial t} - \beta_1 \frac{\partial \sigma^{eff}}{\partial t} + (1-m_0)\frac{\partial v_1}{\partial x} + m_0 \frac{\partial v_2}{\partial x} = 0 \tag{1}$$

$$(1-m_0)\rho_{10}\frac{\partial v_1}{\partial t} + (1-m_0)\frac{\partial}{\partial x}p = \frac{\partial}{\partial x}\sigma_{eff} + \frac{m_0^2\mu_2}{k}(v_2 - v_1) \tag{2}$$

$$m_0\rho_{20}\frac{\partial v_2}{\partial t} + m_0\frac{\partial}{\partial x}p = -\frac{m_0^2\mu}{k}(v_2 - v_1) \tag{3}$$

$$\sigma_{eff} = K_p e_1 + \varepsilon p \tag{4}$$

here v_i is phase velocity (1 – solid, 2 – saturating fluid); σ_{eff} - effective stress; p - fluid pressure; $K_p = K_b + (4/3)G$, K_b is bulk modulus of a porous skeleton and β_1 is compressibility of its material, G is shear modulus of a skeleton; β_2 is liquid compressibility; m_0 is porosity; μ is viscosity and k is permeability; $\beta = (1-m_0)\cdot\beta_1 + m_0\cdot\beta_2$; $\varepsilon = K_b\beta_1$.

The following parameter values are chosen: $k = 1.8\cdot10^{-11}\ m^2$, $\beta_1 = 2\cdot10^{-10}\ Pa^{-1}$, $K_p = 10^8\ Pa$, $m_0 = 0.25$; and gas parameters $\mu = 2\cdot10^{-5}\ Pa\cdot sec$, $\rho_{20} = 1000\ kg/m^3$, $\beta_2 = 2.4\cdot10^{-6}\ Pa^{-1}$. Let us note that these parameters correspond to "weak" rocks ($\varepsilon << 1$).

The numerical calculations of *P*-wave characteristics on the base of system (1) – (4) confirmed that really in gas-saturated media the 2nd wave has low attenuation, but 1st wave becomes extremely damped. Moreover, for gas-saturated media the wave characteristics depend essentially on frequency (in the contrast to a water - saturated medium). It is important that for gas-saturated media at low frequencies the wave dispersion radically differs from ones for liquid-saturated media. But, at high frequencies the wave behavior does not change. The 2nd wave is "slow" and shows out-of-phase behavior of gas-solid motions only at high frequencies and it becomes "fast" wave and shows in-phase behavior at low frequencies.

On the contrary, gas-bubbles effects on high frequency waves above bubble resonance. It was shown recently by Dunin, Mikhailov and Nikolaevskiy [3].

It is important to note that mentioned effect appears only for "weak" matrix ($\varepsilon << 1$). Calculations made for "cemented" formations, show that wave behavior did not change essentially.

It is also shown that *P*-wave behavior transformation happens only if compressibility of a saturated fluid exceeds some critical value. The expression for this value is obtained:

$$\beta_{2cr}^{-1} = \frac{1-m_0}{m_0}\left\{\frac{\rho_*}{\rho_0}K_p^{-1} - \beta_1\right\} \tag{5}$$

Taking into account that gas compressibility and its density depend on the pressure, and considering the gas behavior as adiabatic, we can find from (5) that at our parameter values, the critical pressure value is approximately $6\cdot10^6\ Pa$. The transformation of wave behavior at variation of the pressure is shown at the **fig. 1**.

The compressibility of saturating fluid also depends on gas fraction. So, for studying of the gas saturation effects on transformation of *P*-waves behavior the generalized system of equations was used. This system takes into account both liquid-solid and gas-solid relative motions (see, for example [2,4,5]). New system consist of mass and momentum balance equations for solid, liquid and gas plus the constitutive laws. The terms, describing the viscous interaction between liquid phase and solid phase (R_2) and gas phase and solid phase (R_3), are introduced according to the generalized Darcy law [2]:

$$R_2 = -\frac{m^2(1-s_0)^2\mu_2}{kf_2(s_0)}(v_2 - v_1); \quad R_3 = -\frac{m^2 s_0^2 \mu_3}{kf_3(s_0)}(v_3 - v_1) \tag{6}$$

here s_0 is gas fraction and $f_i(s_0)$ is phase relative permeability (2 – liquid; 3 - gas).
The numerical calculations of *P*-wave characteristics on the base of the generalized model have shown that the radical changing of wave behavior takes place at high gas fraction $s_0 \sim 90 - 98$ %.
It is also obtained that the phase velocity of the 1st Biot wave sharply decreases as gas fraction changes from zero to 5 – 8% (velocity decreases essentially even at small gas fraction value (~0.01%)).

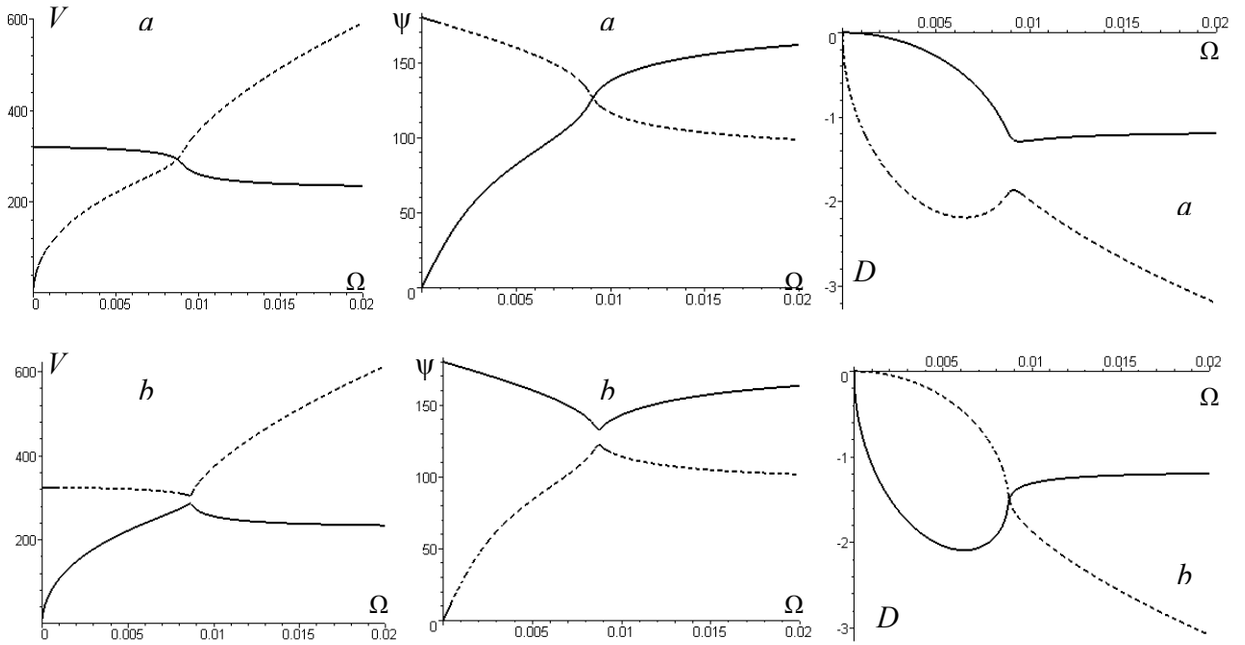


Fig. 1. Change of frequency - depended wave behavior at variation the pressure from $5 \cdot 10^6$ *Pa* (*a*) to $6 \cdot 10^6$ *Pa* (*b*). The firm line corresponds to 2nd wave and dash line corresponds to 1st wave.
Here *V* is wave velocity; *D* is attenuation coefficient; Ψ is "phase shift" between solid and gas relative motions; $\Omega = \omega/\omega_c$ is reduced frequency, ω_c is critical Biot frequency.

References

[1] Biot M.A. Theory of propagation of elastic waves in a fluid-saturated solid. I. Low frequency range *J. Acoust. Soc. Am* **28**:168-178. II. Higher frequency range. *J. Acoust. Soc. Am* **28**:179-191, 1956
[2] Nikolaevskiy V.N. Mechanics of porous and fractured media. Singapore: World Scientific 1990.
[3] Nikolaevskiy V.N., Dunin S.Z., Mikhailov D.N., Stepanova G.S. Vibrate – seismic waves are changing an oil – gas reservoir state *J. Engineering Mechanics,* ASCE, 2004 (in press).
[4] Brutsaert W. The propagation of elastic waves in unconsolidated unsaturated granular medium. *J. Geophysical research* **69**:243 – 257, No. 2, 1964.
[5] Santos J.E., Douglas J., Corbero J.M., Lovera O.M. A model for wave propagation in a porous medium saturated by a two-phase fluid. *J. Acoust. Soc. Am* **87**:1439-1448, 1990.

XXI ICTAM, 15–21 August 2004, Warsaw, Poland

NONSTATIONARY FLOW OF STOKESIAN FLUID THROUGH ELASTIC SKELETON WITH HIERARCHICAL STRUCTURE

Włodzimierz R. Bielski*, Józef Joachim Telega**
*Institute of Geophysics, Polish Academy of Sciences, ul. Księcia Janusza 64, 01-452 Warsaw, Poland
**Institute of Fundamental Technological Research, Polish Academy of Sciences, Świętokrzyska 21, 00-049 Warsaw, Poland

Summary The aim of contribution is to consider the problem of nonstationary flow of v Stokesian fluid through linear elastic porous skeleton. The novelty consists in that the skeleton is deformable and characterized by the so-called double-porosity matrix. The material of the matrix is hierarchical with two *well-separated* scales ε and ε^2. Macroscopic equations were derived by using the method of multiscale convergence. Darcy's law involves both scales and is nonlocal in time.

INTRODUCTION

Porous media theories play an important role in many branches of engineering, including material science, the petroleum industry, chemical engineering and soil mechanics as well as in biomechanics. Powerful tool in the derivation of macroscopic equations describing flows through porous media are offered by homogenization method, cf. [2,5,7,9] and the references therein.

The aim of this contribution is to examine the dynamic flow of Stokesian fluid through elastic porous skeleton. The last is characterized by a hierarchical structure with two *well-separated* scales, cf. Allaire and Briane [1]. For the sake of simplicity these two scale are characterized by ε and ε^2, respectively. To find the macroscopic equations we use the (homogenization) method of three-scale asymptotic convergence, being a specific case of the method of multiscale convergence. To put it briefly, the macroscopic equations, including the Darcy law, are obtained by letting ε tend to zero. This law involves both scales and is nonlocal in time

MICROSCOPIC MODEL: PERIODIC DISTRIBUTION OF MICROPORES

Let Ω be an open domain in $\mathbb{R}^3$. We consider the open domain $\Omega_\varepsilon = \Omega \backslash S^\varepsilon_\Omega$. The closed set S^ε_Ω is obtained as follows: let Y and Z be two fixed reference cells $Y = [0, y^0_1] \times [0, y^0_2] \times [0, y^0_3]$, $Z = [0, z^0_1] \times [0, z^0_2] \times [0, z^0_3]$ and set $y^0 = (y^0_1, y^0_2, y^0_3)$, $z^0 = (z^0_1, z^0_2, z^0_3)$. Denote $F \subset Y$ and $S \subset Z$ two closed subset with smooth boundaries and nonempty interiors. We repeat F and S with "Y-periodicity" and "Z-periodicity", respectively. We assume that for any ε the period Y is exactly covered by a finite number of translated cells of $\frac{\varepsilon^2}{\varepsilon} Z$. The small parameter ε will tend to zero. We set $S^\varepsilon_Y = (Y \setminus F) \cap (\bigcup_{k \in K_\varepsilon} \frac{\varepsilon^2}{\varepsilon}(S + kz^0))$, $Y^\varepsilon = Y \setminus S^\varepsilon_Y$. We assume that $S^\varepsilon_Y \cap F = \emptyset$ for every $\varepsilon > 0$. Hence S^ε_Y is a subset of $Y \backslash F$, composed of closed sets periodically distributed with period $\frac{\varepsilon^2}{\varepsilon}$ and of the same size as the period. We set $S^\varepsilon_\Omega = \bigcup_{h \in H_\varepsilon} \varepsilon(S^\varepsilon_Y + hy^0)$, $F_\varepsilon = \Omega \cap (\bigcup_{k \in \mathbb{Z}^3} \varepsilon(F + ky^0))$, cf. Ene and Saint Jean Paulin [4]. The structure of Ω_ε presents a double periodicity (ε and ε^2). The zones in which the fractions are concentrated are ε-periodic and of size ε.

Let $\Omega^S_\varepsilon = \Omega \setminus \Omega_\varepsilon$ be a domain which is occupied by the elastic matrix and Ω_ε is occupied by the incompressible viscous fluid. The microscopic equations of the problem to be solved are as follows:

$$\varrho^S \ddot{\boldsymbol{u}}^\varepsilon(x,t) = \operatorname{div}\left[\boldsymbol{c} : \boldsymbol{e}(\boldsymbol{u}^\varepsilon(x,t))\right] + \boldsymbol{F}^S(x,t), \qquad (x,t) \in \Omega^S_\varepsilon \times (0,T), \tag{1}$$

$$\varrho^L \dot{\boldsymbol{v}}^\varepsilon(x,t) = \mu\varepsilon^2 \Delta \boldsymbol{v}^\varepsilon(x,t) - \nabla p^\varepsilon(x,t) + \boldsymbol{F}^L(x,t), \qquad (x,t) \in \Omega_\varepsilon \times (0,T), \tag{2}$$

$$\operatorname{div} \boldsymbol{v}^\varepsilon(x,t) = 0, \qquad (x,t) \in \Omega_\varepsilon \times (0,T), \tag{3}$$

$$\dot{\boldsymbol{u}}^\varepsilon(x,t) = \boldsymbol{v}^\varepsilon(x,t), \quad \text{on } \partial\Omega^S_\varepsilon \cap \partial\Omega_\varepsilon \times (0,T). \tag{4}$$

Boundary and initial conditions complete Eqs. (1)-(4). Here $\boldsymbol{e}(\boldsymbol{u}) = 1/2(\nabla \boldsymbol{u} + \nabla \boldsymbol{u}^T)$.

MULTISCALE CONVERGENCE

To derive the macroscopic model and effective coefficients the so-called multiscale convergence method is used, see [1-6]. Double porosity requires exactly the three-scale convergence.

We say that the sequence of functions $\{u^\varepsilon\}$ three-scale converges to $u^0(x,y,z)$ iff

MACROSCOPIC MODEL

As a first step in the process of homogenization we obtain the so-called *three-pressure system* being an extension of two-pressure system in the case of two-scale convergence method and only one porosity. After two step of averaging, first over the basic cell Z and then over Y, we obtain the macroscopic relations. The macroscopic model consists, among others, of the consolidation equation

$$\varrho^S\langle\ddot{\boldsymbol{u}}^0\rangle + \varrho^L\langle\dot{\boldsymbol{v}}^0\rangle = \operatorname{div}\boldsymbol{\sigma} - \nabla_x p^0 - \int_{Y_L}\nabla p^1\,dy - \int_{Y_L}\int_{Z_L}\nabla_z p^2\,dzdy + (1-f)\boldsymbol{F}^S + f\boldsymbol{F}^L,\ \text{in } \Omega\times(0,T). \quad (5)$$

It can be shown that $p^0 = p^0(x,t)$, $p^1 = p^1(x,y,t)$ and $p^2 = p^2(x,y,z,t)$. The three-pressure system is as follows in $\Omega\times Y_L\times Z_L\times(0,T)$

$$\varrho^L\dot{\boldsymbol{v}}^0_{rel}(x,y,z,t) = \mu\Delta_z\boldsymbol{v}^0_{rel} + \boldsymbol{F}^L(x,t) - \varrho^S\ddot{\boldsymbol{u}}^0(x,t) - \nabla_x p^0(x,t) - \nabla_y p^1(x,y,t) - \nabla_z p^2(x,y,z,t), \quad (6)$$

where $\boldsymbol{v}_{rel}(x,y,z,t) = \boldsymbol{v}^0(x,y,z,t) - \dot{\boldsymbol{u}}^0(x,t)$ and f means the porosity. Moreover we obtain

$$\operatorname{div}_z\boldsymbol{v}^0_{rel}(x,y,z,t) = 0 \ \text{ in } \Omega\times Y_L\times Z_L\times(0,T),$$

$$\operatorname{div}_y\int_{Z_L}\boldsymbol{v}^0_{rel}(x,y,z,t)\,dz = \tfrac{1}{|Z|}\int_{\Gamma_Z}\dot{\boldsymbol{u}}^1(x,y,z,t)\cdot\boldsymbol{N}\,ds(z) \quad \text{in } \Omega\times Y_L\times(0,T),$$

$$\operatorname{div}_x\int_{Y_L}\int_{Z_L}\boldsymbol{v}^0_{rel}(x,y,z,t)\,dzdy = \tfrac{1}{|Y|}\int_{\Gamma_Y}\int_Z\dot{\boldsymbol{u}}^1(x,y,z,t)\boldsymbol{n}\,dz\,ds(y) + \int_Y\int_Z\dot{\boldsymbol{u}}^2(x,y,z,t)\cdot\boldsymbol{N}\,dyds(z) \text{ in } \Omega\times(0,T).$$

Here $\boldsymbol{N}$ is the unit normal vector to the boundary of Z_L ($\partial Z_L = \Gamma_Z$) while $\boldsymbol{n}$ is the unit normal vector to ∂Y_L. The three-pressure system is a combination of usual homogenization and cell problem. By eliminating the microscopic variables z and y from Eq. (6) the homogenized Darcy law nonlocal in time is obtained. First, we separate the variables: $p^2(x,y,z,t) = \Pi^{(m)}(z,t)[\boldsymbol{F}^L(x,t) - \varrho^L\ddot{\boldsymbol{u}}^0(x,t) - \frac{\partial p^0(x,t)}{\partial x_m} - \frac{\partial p^1}{\partial y_m}(x,y,t)]$. Then we get

$$\langle v^0_{m\ rel}\rangle_{Z_L} = \frac{1}{\varrho^L}\int_0^t\langle\chi^{(s)}_m(z,t-\tau)\rangle_{Z_L}[F_s - \varrho^L\ddot{u}_s - \frac{\partial p^0}{\partial x_s} - \frac{\partial p^1(x,y,t)}{\partial y_s}]\,d\tau, \quad \text{in } \Omega\times Y_L\times(0,T) \quad (7)$$

where functions $\Pi^{(m)}(z,t)$ and $\chi^{(s)}_m(z,t)$ satisfy the so-called local cell problem posed on $Z_L\times(0,T)$.

$$\mu\Delta_{zz}\chi^{(s)}_m = \varrho^L\dot{\chi}^{(s)}_m - (e^{(s)}_m - \frac{\partial\Pi^{(s)}}{\partial z_m}), \qquad \operatorname{div}_z\boldsymbol{\chi}^{(s)}(z,t) = 0 \quad \text{in } Z_L\times(0,T).$$

Here $\boldsymbol{e}^{(s)}$, $s=1,2,3$ stands for the vector basis in $\mathbb{R}^3$. We observe that in Eq. (7) the local variable y is present. To obtain fully homogenized Darcy law it is sufficient to eliminate y by integration of both sides of Eq. (7) over the cell Y.

To pass to the stationary flow we have to pass with time to infinity ($t\to\infty$).

FINAL REMARKS

To derive macroscopic equations in the case of randomly distributed pores in hierarchical porous deformable medium one can use the method of stochastic multiscale convergence in the mean, cf. [8]. The method of three-scale convergence used in this contribution can be extended to more complex hierarchical media with mixed periodic-random distribution of pores. The approach to macroscopic modelling proposed by us [8] applies not only to geomaterials like fractured porous media, but also to biological tissues (for instance bone tissue).

Acknowledgment. The authors were supported by Ministry of Research and Information Technology through the grants No 3 P04D 007 25 and 8 T07A 052 21. The second author was additionally supported through the grant N0 4 T11F 003 25.

References

[1] G. Allaire, M. Briane, Multi scale convergence and reiterated homogenisation, *Proc. Roy Soc. Edinburgh*, **126A**, 297–342, 1996.
[2] W. R. Bielski, J. J. Telega, *Effective Properties of Geomaterials: Rocks and Porous Media*, Publ. Inst. Geophys. Pol. Acad. Sci., **A-26(285)**, Warszawa 1997.
[3] W. R. Bielski, J. J. Telega, R. Wojnar, Nonstationary flow of a viscous fluid through a porous elastic medium: Asymptotic analysis and two-scale convergence, *Mech. Res. Com.*, **26**, 619–628, 1999.
[4] H. Ene, J. Saint Jean Paulin, On a model of fractured porous media, in: *Mathematical Modelling of Flow Through Porous Media*, eds. by A.P. Bourgeat, C. Carasso, S. Luckhaus, A. Mikelič, World Scientific, Singapore 1995, pp. 402–409.
[5] U. Hornung (ed.), *Homogenization and Porous Media*, Springer, Berlin, 1997
[6] J.L. Lions, *Some methods in the mathematical analysis of systems and their control*, Gordon and Breach, Science Press, Beijing, 1981.
[7] E. Sanchez-Palencia, *Non-Homogeneous Media and Vibration Theory*, Springer-Verlag, New York 1980.
[8] J. J. Telega, W. R. Bielski, Stochastic homogenization and macroscopic modelling of composites and flow through porous media. *Theor. Appl. Mech.*, 28-29, 337-377, 2002.

Confined air-liquid drainage : local analysis and invasion percolation model

F. Plouraboué[1], S. Geoffroy[1,2], F. Flukiger[1], O.Amyot[1], M. Prat[1]
[1] *Institut de Mécanique des Fluides de Toulouse, UMR 5502 CNRS, (France)*
[2] *Laboratoire Génie Mécanique, INSA, 135 av Rangeuil, 31077 Toulouse (France)*

This paper studies drainage of a wetting liquid by non wetting air between two confined rough solid surfaces. From convergence of asymptotic, numerical and experimental analyses, we found simple expressions for the air finger width and total curvature invading a single saddle-point as a function of its aspect ratio. The result of this local analysis is applied to a new invasion percolation numerical model which is compared to experiments involving drainage between complicated rough surfaces.

I. INTRODUCTION

Studying flows between two confined solid surfaces is interesting in different contexts such as fracture flows, microfluidic or water-tightness[2]. We chose to focus on drainage of a wetting liquid by non wetting air in the limit of small Reynolds and capillary numbers. In this limit pressure driven air invasion through the wetting liquid is dominated by capillary forces. Moreover the viscous pressure drop is negligible and the pressure inside the liquid and the air is uniform. In this case the invasion process is controlled by the liquid-gas interface curvature, in keeping with Laplace law. The invasion of air in complicated geometries, is controlled by bottom-neck constrictions that the uniform pressure inside the air finger has to overcome. In section II we begin by examining the air invasion at the local level. From the obtained results section III proposes a new percolation invasion model which is compared with experiments.

II. LOCAL ANALYSIS FOR A SINGLE CHANNEL

This section first analyses the drainage in a longitudinally invariant channel in the x direction — see fig 1a, with associated depth $h(y)$. This analysis will then be complemented by a comparison with a longitudinally constricted channel, with small longitudinal variations along the x direction.

• Experimental description : Mini-channels with $h_0 = 1mm$ have been built with an automatic micro-machining device which has carved a polymeric material, given a specified depth function $h(y)$ with 20 micron precision in every (x, y, z) direction. Experiments were carried out by slowly pumping out a perfectly wetting silicon oil, with associated capillary number smaller than 10^{-3}. The finger width f^∞/ℓ display a very small influence of the capillary number in the range 10^{-3} to 10^{-5}. f^∞ is controlled by the finger tip curvature, because the surface has

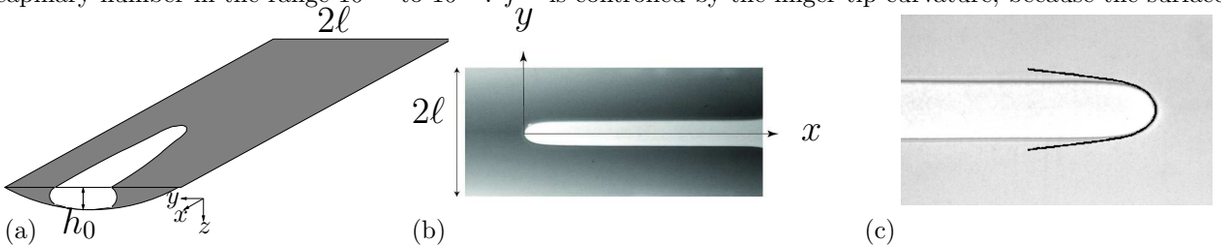


FIG. 1. (a) Perspective view of a sketch of an experimental mini-channel. The air bubble (in white) enters from one side of the mini-channel, while the liquid (in grey) is pumped out from the other side. (b) Top view of the experimental bubble shape in a mini-channel in the (x,y) plane which displays a shape denoted f(x). (c) Superimposition of the experimental finger shapes obtained in a longitudinally uniform channel on constricted one (in black), with a constant vertical to transverse aspect ratio $\epsilon = h_0/\ell$.

a constant curvature, the value of which has to be determined.

• Numerical analysis : we solved the free-boundary problem associated with a perfectly wetting liquid presenting an *a priori* unknown constant mean curvature κ[1]:

$$-\frac{\pi}{4}\frac{\partial_x^2 f}{(1+\partial_x f^2)^{\frac{3}{2}}} + \frac{2}{h(f)} = \frac{2}{h(f^\infty)} = \kappa \tag{1}$$

κ can be decomposed into an horizontal plane curvature which depends on $f(x)$ and the vertical plane principal curvature which is controlled by the local gap h. $f(x)$ presents an horizontal slope at $x \to \infty$, and a vertical one at $x = 0$. These conditions determine the value of κ. The *a priori* unknown asymptotic width f^∞—like the associated κ— is found with a shooting method out of a Runge–Kutta integration procedure. The result is depicted in figure 2.

• Asymptotic analysis : The channel under study presents a small parameter which is the gap to width ratio $\epsilon = h_0/\ell$. Using proper non-dimentionalization, one finds that problem (1) is singular.

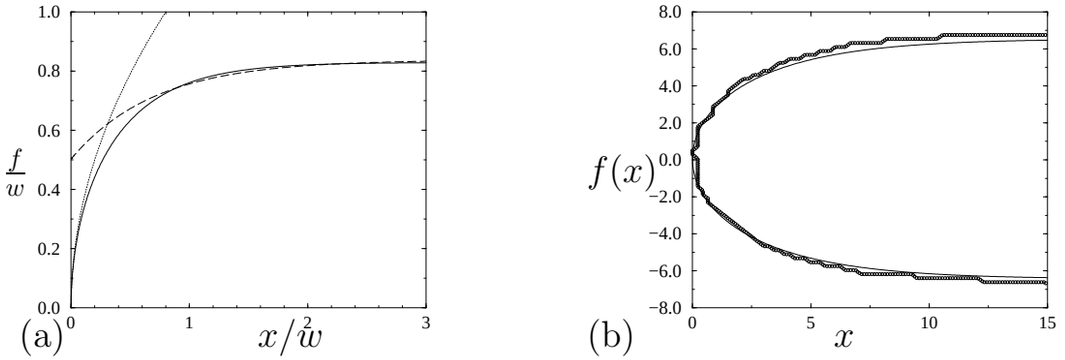


FIG. 2. (a) Numerical computation of in-plane interface shape $f(x)$ in continuous lines compared with asymptotic prediction with a channel aspect ratio $\epsilon = 10^{-2}$. Dotted lines represent the inner asymptotic behavior, dashed lines stand for the exponential decay of the outer solution. The results are non-dimentionalized by an intermediate length-scale which scales as $w = \epsilon^{1/3}\ell$ (b) Superimposition of the numerical computation and the experimental observations inside a quadratic shape $h(y)$ channel depicted in Figure 1a.

Moreover, the typical longitudinal length-scales f and x can be shown to vary with the gap to width ratio ϵ as the intermediate length-scale w defined as $w = \epsilon^{1/3}\ell$. This non-dimensionalization is successfully compared with numerical computation on figure 2a, where it is also observed that asymptotically matched inner and outer solutions satisfactorily compares with the numerical curve. This asymptotic analysis leads to a simple expression for the pressure drop needed to overcome capillary forces associated with surface tension γ :

$$\Delta P = 2\gamma(1 + (\pi/4)^{5/3}(3/4)^{2/3}\epsilon^{2/3})/h_0. \tag{2}$$

This analysis can be directly extended to the case of a longitudinally varying channel. Figure 1c shows that the tip in-plane curvature is very close, for a longitudinally uniform channel or constricted channel having the same gap h_0. Similar conclusions can be drawn from extending previous asymptotic analysis[2].

III. INVASION PERCOLATION

The above analysis is extended to model the air invasion between complicated random surfaces. Experiments are similarly performed on specifically designed micro-channels obtained from numerically generated random surfaces (Fig. 3a). The network of the aperture saddle point is numerically computed (Fig. 3b), so that the invasion percolation rule (2) can be applied (Fig. 3c) using the local ϵ associated with each saddle point.

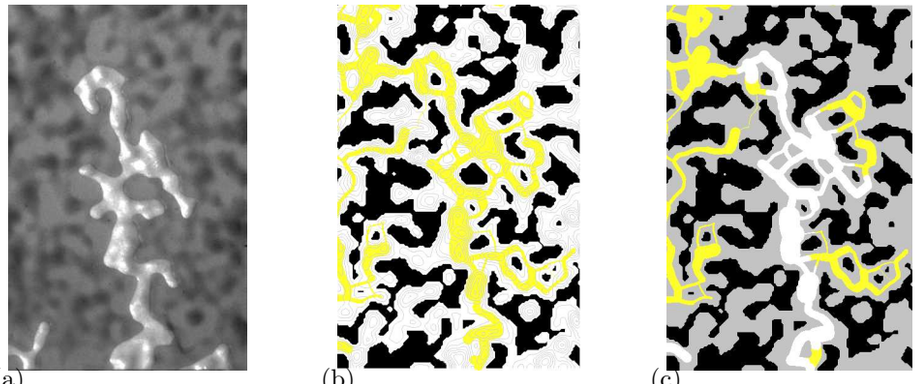


FIG. 3. (a) Drainage experiments between randomly generated surfaces, (b) Numerical extraction of the saddle point network, (c) Predicted invasion is represented in white.

[1] C. W. Park and G.M Homsy, J. Fluid Mech., **139**, 291-308, (1984).
[2] F. Plouraboué, S. Geoffroy, and M. Prat, Phys. Fluid, **16**, 3, 615-624, (2004).

A JOULE-THOMSON PROCESS OF A WETTING FLUID NEAR SATURATION

Thomas Loimer
Institute of Fluid Mechanics and Heat Transfer, Vienna University of Technology, 1040 Wien, Austria

Summary A fluid with positive Joule-Thomson coefficient flows through a porous membrane. Upstream of the membrane, there is saturated vapor. Downstream of the membrane, the fluid is cooler and in the state of unsaturated vapor. The fluid either condenses at the upstream front of the membrane or a liquid film forms in front of the membrane. At an evaporation front within the membrane the fluid evaporates. The process depends on the permeability of the membrane and on surface tension.

INTRODUCTION

The Joule-Thomson process of a real gas is well known in thermodynamics. If a gas flows through a porous plug and there is a pressure loss associated with this process, but the change of kinetic energy is negligible, then the specific enthalpy of the gas is the same at an upstream and a downstream station. A gas with positive Joule-Thomson coefficient is cooler at the downstream station than at the upstream station. However, a saturated vapor with positive Joule-Thomson coefficient cannot simply cool down to reach the downstream state of unsaturated, cooler vapor. Instead, fronts of phase change occur. The process was analyzed previously neglecting capillary pressure [1, 2]. Here, the process is described assuming an ideally wetting liquid phase and accounting for the capillary pressure at a curved meniscus between the liquid and its vapor.

GOVERNING EQUATIONS

The governing equations consist of the balances of mass, momentum, and energy, respectively,

$$\dot{m} = const.,$$
$$\dot{m} = -\frac{\kappa}{\nu}\frac{\mathrm{d}p}{\mathrm{d}z},$$
$$\dot{m}h + \dot{q} = const.,$$

supplemented by Fourier's law of heat conduction and the thermic and caloric equations of state for the fluid. Above, $\dot{m}$ denotes the mass flux, κ is the permeability, z is the coordinate pointing in flow direction and $\dot{q}$ refers to the heat flux. The effective kinematic viscosity and the specific enthalpy of the fluid are given by ν and h, respectively, where the fluid can be a single phase or a two-phase mixture. The pressure difference between liquid and vapor at the evaporation front within the membrane is given by the capillary pressure,

$$\Delta p_{\mathrm{cap}} = \sigma \Big/ \sqrt{3\kappa/\varepsilon}\,,$$

where σ is the surface tension and ε refers to the porosity. At the membrane front the curvature of the menisci is undetermined, therefore the pressure difference can aquire any value between 0 and Δp_{cap}. As boundary conditions upstreams the state of the fluid and downstreams the pressure are given. The upstream state is specified by the temperature and the vapor mass fraction being equal to one. Also, the pressure must be equal to the saturation pressure at the given temperature.

RESULTS

In a previous study [1] it was found that the process depends on the permeability of the membrane with respect to a critical permeability,

$$\kappa_{\mathrm{c}} = \nu_{\mathrm{l}} T_1 (v_{\mathrm{g}} - v_{\mathrm{l}}) k_{\mathrm{l}} / \Delta h_{\mathrm{lg}}^2,$$

where ν_{l} is the kinematic viscosity of the liquid, v_{g} and v_{l} are the specific volumes of the gaseous and the liquid phase, respectively, k_{l} denotes the thermal conductivity of the fluid-filled porous material, T_1 is the absolute temperature upstream of the membrane and Δh_{lg} is the specific evaporation enthalpy.

If the permeability of the membrane lies above the critical value, $\kappa > \kappa_{\mathrm{c}}$, then the saturated vapor condenses partially at the upstream front of the membrane [1, 2]. Due to the condensation it releases heat that is conducted in downstream direction. A two-phase mixture flows through the membrane under decrease of pressure and temperature. The mixture fully evaporates at an evaporation front within the membrane, consuming the heat conducted downstreams. The vapor continues to flow in downstream direction under decrease of pressure, but with nearly constant temperature. The vapor undersaturates and reaches the final, unsaturated state at the downstream front of the membrane. Since the volume fraction of vapor in the two-phase mixture is close to unity even for a very small mass fraction, the capillary pressure between the region containing the two-phase mixture and the vapor is negligible.

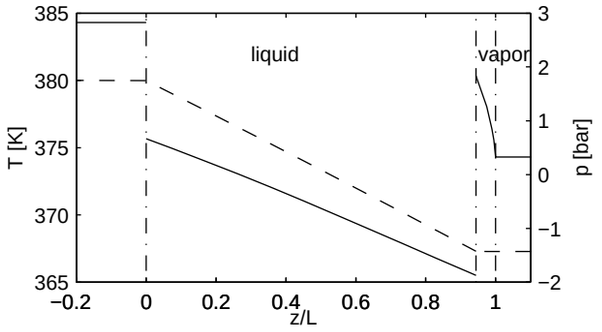


Figure 1. Temperature and pressure distribution for $\kappa/\kappa_c = 0.5$. Solid line: p, dashed line: T, dash-dotted lines: Fronts of phase change and membrane fronts.

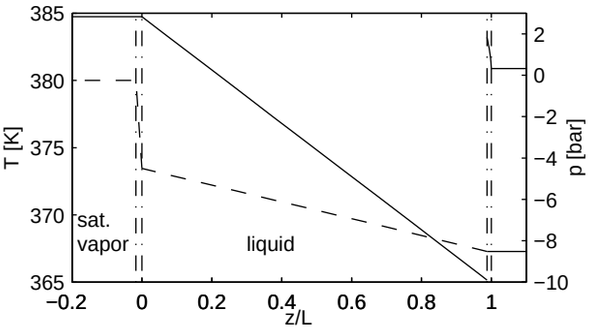


Figure 2. Temperature and pressure distribution for $\kappa/\kappa_c = 0.05$. For definitions of lines see adjacent figure.

If the permeability of the membrane lies below κ_c, the fluid condenses fully. For $\kappa \geq \kappa_f$ the condensation front is located at the upstream front of the membrane. The liquid menisci in the pores of the membrane maintain a pressure difference between the region upstream of the membrane and the liquid in the membrane. For $\kappa < \kappa_f$ a liquid film forms in front of the membrane. The pressure in the film is the same as upstreams of the membrane. The ratio κ_f/κ_c is given by

$$\kappa_f/\kappa_c = 1 - \tfrac{1}{2}\mathrm{Ca}_{JT}^{-2}\left(\sqrt{1 + 4\mathrm{Ca}_{JT}^2} - 1\right), \tag{1}$$

where Ca_{JT} denotes a capillary number,

$$\mathrm{Ca}_{JT} = \mu_{JT}\frac{\mathrm{d}p_s}{\mathrm{d}T}\frac{\Delta p_{12}}{\Delta p_{cap,c}},$$

evaluated at the upstream temperature T_1. Here, μ_{JT} is the Joule-Thomson coefficient, $\mu_{JT} = (\partial T/\partial p)_h$, p_s is the saturation pressure, Δp_{12} is the pressure difference applied to the membrane and $\Delta p_{cap,c}$ denotes the capillary pressure, calculated with the effective pore radius at the critical permeability.

Pressure and temperature distributions for $\kappa_f < \kappa < \kappa_c$ and $\kappa < \kappa_f$ are shown in Figs. 1 and 2, respectively. A system consisting of ethanol and a ceramic membrane with a thermal conductivity $k_m = 23\,\mathrm{W/mK}$ is investigated. The upstream state of the fluid is given by $T_1 = 380\,\mathrm{K}$ and $p_1 = p_s(T_1) = 2.83\,\mathrm{bar}$. A pressure difference of $\Delta p_{12} = 2.5\,\mathrm{bar}$ is applied. For the conditions under consideration, Eq. (1) yields $\kappa_f/\kappa_c = 0.104$.

For $\kappa = 0.5\kappa_c$, see Fig. 1, the condensation front is located at the upstream front of the membrane, $z = 0$. The pressure difference across the condensation front is approximately equal to half the capillary pressure. Liquid permeates through the membrane under decrease of pressure and temperature. At the evaporation front, located close to the downstream front of the membrane, the fluid evaporates. The pressure increases by an amount equal to the capillary pressure. In the remaining part of the membrane the vapor undersaturates nearly isothermically.

For $\kappa = 0.05\kappa_c$ a thin liquid film is formed, see Fig. 2. In the film the pressure remains constant and equal to its upstream value while the temperature decreases. In the liquid flow region in the membrane pressure and temperature decrease. The pressure difference at the evaporation front is much larger than in the previous example because the permeability and hence the pore size is smaller here. Note, that the pressure attains large negative values. This is consistent with experimental observations of a liquid bridge with a concave meniscus of large curvature [3].

CONCLUSIONS

The Joule-Thomson process of a fluid undergoing phase changes is investigated. Extending previous studies [1, 2], the capillary pressure is taken into account. The process depends on the permeability of the membrane with respect to the critical permeability κ_c and on a capillary number Ca_{JT}. Preliminary computations were performed for a fluid with an ideally wetting liquid phase. It is shown that the formation of a liquid film only occurs for $\kappa < \kappa_f$, a value which is much smaller than κ_c.

References

[1] Schneider W.: Vapor flow through a porous membrane — a throttling process with condensation and evaporation. *Acta Mech.* **47**:15–25, 1983.

[2] Loimer T.: A Joule-Thomson process with condensation and evaporation. *Proc. Appl. Math. Mech.* **3**:390–391, 2003.

[3] Fisher L.R., Israelachvili J.N.: Experimental studies on the applicability of the Kelvin equation to highly curved concave menisci. *J. Colloid Interface Sci.* **81**:528–541, 1981.

MICROSCOPIC SIMULATIONS OF THE DISSOLUTION OF ROCK FRACTURES

Piotr Szymczak*, Tony Ladd**
*Institute of Theoretical Physics, Warsaw University, Hoża 69, 00-681 Warsaw, Poland
**Department of Chemical Engineering, University of Florida, Gainesville, Florida 32611-6005

Summary
The results of numerical simulations of dissolution in fractured rocks are reported. The model is microscopic, with a detailed representation of the topography of the fracture. The velocity field in the fracture is assumed to be Stokes flow and is efficiently calculated with an implicit lattice-Boltzmann technique. The transport of dissolved species in the pore spaces is modelled by an innovative random walk algorithm that incorporates the chemical kinetics at the solid surfaces. The simulated morphological changes in a complex fracture are compared with laboratory experiments.

The processes leading to dissolution of a fractured rock by a reactive fluid depend on a subtle interplay between chemical reactions at mineral surfaces and fluid motion in the pores. The complex geometry of a typical fracture makes both numerical and theoretical calculations very demanding. Existing models of fracture dissolution are rarely constructed on a microscopic (pore-scale) level. Instead, various approximations are usually resorted to in order to make the analysis more tractable. For example, instead of computing a three-dimensional velocity field by solving the Navier-Stokes equations, the Reynolds (or lubrication) approximation is used [1, 2, 3], so that the volumetric flow rate is proportional to the cube of the local aperture. It has been shown [4, 5, 6] that the Reynolds equation may significantly overestimate the flow, especially for fractures of high roughness and small apertures. The complicated topography of the fracture is also the reason why the transport of the dissolved material from the walls into the bulk of the fluid is usually accounted for in a simplified way, with the effects of convection assumed to be adequately expressed by a Sherwood number for transport in ducts [1, 2, 7]. However fracture erosion is a complex process involving nonlinear feedback mechanisms. Thus a relatively small change of topography may result in a large variation in permeability, leading to further changes in erosion. These instabilities make it hard to estimate or control the effects of approximations, so there is a need for precise numerical algorithms that allow for a full microscopic simulation of the fracture dissolution process.

In our implementation of the erosion algorithm, the velocity field in the fracture is calculated using the lattice-Boltzmann method with "continuous bounce-back" rules applied at the solid-fluid boundaries [8]. These rules allow information about the solid surface on length scales less than a grid spacing to be resolved. Therefore, it is possible to adequately resolve the flow field with one-half to one-quarter the linear resolution of the traditional lattice Boltzmann method. Furthermore the steady-state solution is determined directly, using conjugate gradients [9], and is at least an order of magnitude faster than time stepping. These improvements allow us to calculate velocity fields in fractures with a characteristic size of several centimeters.

Solute transport in the fracture is modelled by a random walk method, which takes explicit account of the chemical reactions at the pore surfaces. The fracture surface is divided into pixels, typically 200-500 per dimension, and the height of each pixel is eroded in response to contacts by tracer particles. The major drawback of the classical random walk method [10] is that in order to calculate the dissolution fluxes a very large number of particles must be tracked simultaneously so that the concentration in the fluid near the pore surface can be determined accurately. However, there is a considerable simplification in the case of linear dissolution kinetics, where the erosion flux through the interface, J, is given by

$$J = r(c_s - c_0); \tag{1}$$

here c_0 denotes the solute concentration at the interface, c_s is the saturation concentration, and r the rate constant. In this case it is possible to derive a single-particle stochastic propagator which satisfies the boundary condition 1. Using this propagator, one can find the dissolution fluxes in the fracture by tracking a single particle at a time. Such a scheme is several orders of magnitude more efficient computationally and can be used to calculate the concentration profiles in very large fractures. The evolution of the fracture morphology is then determined by removing material from the fracture walls in proportion to the local dissolution flux calculated in the random walk step. The time evolution of the velocity field and local aperture field in the fracture are determined by iterating this procedure, removing small amounts of material at each step.

We have studied the evolution of fracture topography in several different geometries, including artificial fractures created numerically and topographies for which experimental data also exists [11]. The dissolution simulations were performed over a wide range of Peclet and Dämkohler numbers. The Peclet number measures the relative magnitude of convective and diffusive transport of the solute, $Pe = v < h > /D$, where v ia a characteristic fluid velocity, $< h >$ is the mean aperture and D is the solute diffusion coefficient. The Dämkohler number, $Da = k/v$, relates the surface reaction rate to convective transport. In a number of experimental and numerical studies [11, 12] it has been established that the dissolution patterns depend strongly on the values of Pe and Da. These results have been confirmed in the present study. For small values of Peclet number and large values of Dämkohler number the fluid saturates completely at or near the injection face. As a result, after the initial fast dissolution of the rock material at the fluid inlet, the reaction front propagates extremely slowly, as there is almost no unsaturated fluid penetrating inside the fracture. On the other hand, when the flow rate is large and the reaction rate relatively slow, the unsaturated fluid penetrates deep inside the fracture and

the dissolution tends to be uniform throughout the sample. The most interesting phenomena are observed for moderate values of Da and Pe. Here, the nonlinear feedback mechanism mentioned above begins to play an important role. A perturbation in the reaction rate at the advancing dissolution front changes the local permeability which in turn affects solute transport and the dissolution rate. As a result, the front becomes unstable and pronounced channels are formed in which most of the flow is focused while most of the pore space is eventually bypassed. As an example, Fig. 1 present snapshots of the fracture flow field evolution for $Pe = 10$ and $Da = 0.1$. The successive plots show the vertically (fracture normal) averaged momentum flow before dissolution and after 8, 16, 24, 32 and 40 dissolution cycles respectively. In each step, the total volume of material dissolved was equivalent to a layer of about 1% of the mean aperture. The initial fracture geometry was prepared numerically, with a mean aperture equal to 1% of the length. Under these conditions the initially uniform flow is rapidly replaced by a few pronounced dissolution channels. As the dissolution proceeds, the channels compete for the flow and, the growth of the shorter channels eventually ceases. This is in the agreement with the results of Hoefner and Fogler [13] who claimed that the difference in the lengths between two channels is unlikely to exceed the distance between them. After about 30 iterations most of thew flow is focused in the single main channel, which after about 40 iterations connects to the outflow end of the fracture. This breakthrough is accompanied by a huge increase in fracture permeability.

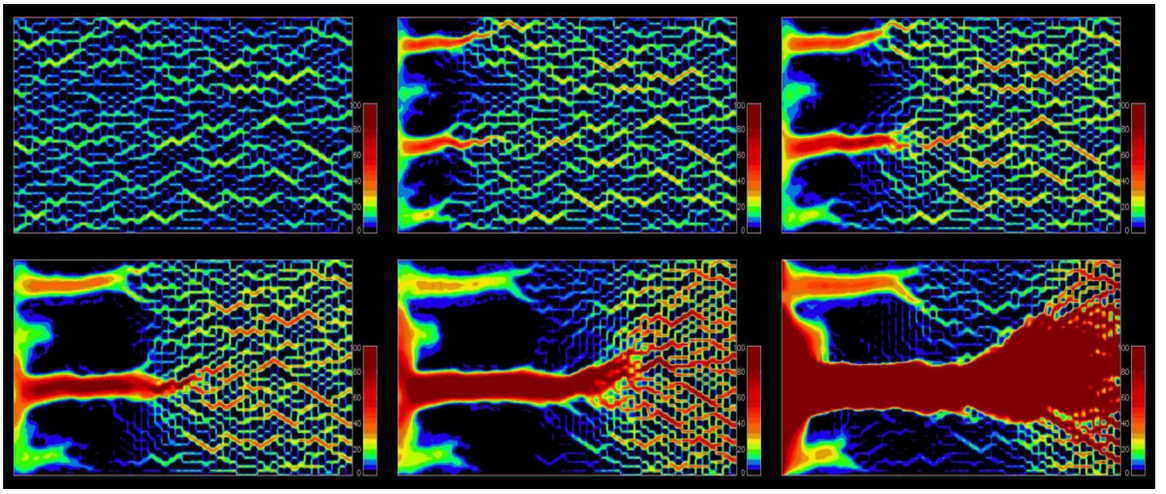


Figure 1. The vertically (fracture normal) averaged momentum flow before dissolution and after 8,16,24,32 and 40 iterations respectively. The colors indicate regions of low (blue), medium (green), and high (red) flow rates. The scale is the same in each picture.

In conclusion, we have developed a fully microscopic numerical method to simulate the dissolution of rock fractures on experimentally relevant length scales. Dissolution morphologies similar to those seen experimentally have been observed. The method may be used not only to analyze the dissolution patterns in various fracture geometries, but also to test the validity of the approximations typically used in fracture erosion models.

References

[1] C. G. Groves and A. D. Howard. Minimum hydrochemical conditions allowing limestone cave development. *Water Resourc. Res.*, 30:607–615, 1994.

[2] R. B. Hanna and H. Rajaram. Dissolution finger growth in variable aperture fractures: Role of the tip-region flow field. *Geophys. Res. Lett.*, 22, 2002.

[3] P. M. Adler and J.-F. Thovert. *Fractures and Fracture Networks*. Kluwer, 2000.

[4] S. R. Brown, H. W. Stockman, and S. J. Reeves. Applicability of the Reynolds equation for modeling fluid flow between rough surfaces. *Geophys. Res. Lett.*, 22:2537–2540, 1995.

[5] M. J. Nicholl, H. Rajaram, R. J. Glass, and R. L. Detwiler. Saturated flow in a single fracture: Evaluation of the Reynolds equation in measured aperture fields. *Water Resour. Res*, 35:3361–3373, 1999.

[6] A. P. Oron and B. Berkowitz. Flow in rock fractures: The local cubic law assumption reexamined. *Water Resour. Res*, 34:2811–2825, 1998.

[7] W. Dreybrodt. Principles of early development of karst conduits under natural and man-made conditions revealed by mathematical analysis of numerical models. *Water Resourc. Res.*, 32:2923–2935, 1996.

[8] R. Verberg and A. J. C. Ladd. Lattice-Boltzmann model with sub-grid scale boundary conditions. *Phys. Rev. Lett.*, 84:2148–2151, 2000.

[9] R. Verberg and A. J. C. Ladd. Simulation of low-Reynolds-number flow via a time-independent lattice-Boltzmann method. *Phys. Rev. E*, 60:3366–3373, 1999.

[10] S. Békri, J.-F. Thovert, and P. M. Adler. Dissolution in porous media. *Chem. Eng. Sci.*, 50:2765–2791, 1995.

[11] R. L. Detwiler, R. J. Glass, and W. L. Bourcier. Experimental observations of fracture dissolution: The role of Peclet number in evolving aperture variability. *Geophys. Res. Lett.*, 30:1648, 2003.

[12] S. Békri, J.-F. Thovert, and P. M. Adler. Dissolution and deposition in fractures. *Eng. Geol.*, 48:283–308, 1997.

[13] M.L. Hoefner and H.S. Fogler. Pore evolution and channel formation during flow and reaction in porous media. *AIChE J.*, 34:45–54, 1988.

FRACTIONAL MODEL FOR SOLUTE SPREADING IN RANDOMLY HETEROGENEOUS POROUS MEDIA

Kira Logvinova, Marie-Christine Néel
Laboratoire d'hydrodynamique complexe, Faculté des Sciences, Université d'Avignon, Avignon, France

Summary Experimental results [4], showed that solute spreading in saturated heterogeneous porous media does not always obey Fourier's law: the second moment of the concentration of a passive tracer dissolved in the saturating fluid may be proportional to a power of time, different from 1. A variety of fractional models are commonly used to account for the possibility, for the solute, to follow preferential paths or to be trapped by obstacles, depending on hypotheses concerning the small scale motion of dissolved particles. One can expect the internal self organization of the pores to influence the general trends of particle motion, at small and at large scale. Therefore we model diffusion, starting from hypotheses concerning the random structure of the heterogeneous porous medium. We consider a medium, which is a collection of tubes, randomly twisted around a general direction, and filled with motionless fluid. Solute spreading is assumed to obey Fick's law. Upon averaging over the tubes, we arrive at a modified version of Fourier's law for the evolution of the solute concentration. Properties of the impulse response of the thus obtained fractional equation are then discussed.

THE MEDIUM

Consider a three dimensional medium, made of a wide collection of tubes (indexed by ω) whose direction depends on the spatial coordinate x, which represents a general trend. As on Figure 1, let $\theta(\omega, x)$ be the angle between the direction x and the sample channel, indexed by ω, so that $\theta(., x)$ is a random variable. Suppose also that the tubes are saturated by motionless fluid. Solute is initially injected in a subset of the medium, which meets all the tubes (at $x = 0$ for instance). The concentration of solute $u(\omega, x, t)$ satisfies

$$\partial_t u(\omega, x, t) = \partial_x (D_0 cos^2\theta(\omega, x)\partial_x u(\omega, x, t)) \tag{1}$$

where D_0 is a coefficient, which also may depend on ω and x. Suppose that $\sqrt{D_0}cos(\omega, x) = \overline{\epsilon} + \tilde{\epsilon}$ is a stochastic process, for instance a Gaussian process with average $\overline{\epsilon}$, and correlation function $a^2 e^{-\nu|x-x'|}$. Moreover a^2 is supposed to be small, while ν is large.

FRACTIONAL DIFFUSION EQUATION FOR THE AVERAGE CONCENTRATION

Upon averaging (1) with respect to ω we obtain

$$\partial_t \langle u(x,t)\rangle - \overline{\epsilon}^2 \partial_{x^2}^2 \langle u(x,t)\rangle = 2\overline{\epsilon}\partial_x \langle \tilde{\epsilon}(\omega, x)\partial_x u(\omega, x, t)\rangle + \partial_x \langle \tilde{\epsilon}^2(\omega, x)\partial_x u(\omega, x, t)\rangle. \tag{2}$$

With $\frac{\delta v(\omega,x,t)}{\delta \tilde{\epsilon}(\omega,x')}$ denoting the functional derivative of v with respect to $\tilde{\epsilon}$ [1] , the Furutsu-Novikov formula [3] yields $\langle \tilde{\epsilon}^2 \partial_x u\rangle = \langle \tilde{\epsilon}(\tilde{\epsilon}\partial_x u)\rangle = a^2 \int_R \langle \frac{\delta(\tilde{\epsilon}\partial_x u)}{\delta \tilde{\epsilon}(x_1)}\rangle e^{-\nu|x-x_1|} dx_1$ and

$$\langle \tilde{\epsilon}^2 \partial_x u\rangle = a^2 \partial_x \langle u\rangle(x,t) + a^4 \int_{R^2} e^{-\nu(|x-x_2|+|x-x_1|)} \langle \frac{\delta^2 \partial_x u}{\delta\tilde{\epsilon}(x_1)\delta\tilde{\epsilon}(x_2)}\rangle dx_1 dx_2. \tag{3}$$

The functional derivative $f(\omega, x, x', t) = \frac{\delta u(\omega,x,t)}{\delta \tilde{\epsilon}(\omega,x')}$ satisfies $\partial_t f(x, x', t) - \partial_x((\overline{\epsilon} + \tilde{\epsilon}^2)\partial_x f(x, x', t)) = 2\overline{\epsilon}\partial_x(\delta(x - x')\partial_x u(\omega, x, t)) + 2\partial_x(\tilde{\epsilon}\partial_x u)$. Disregarding terms of the order of $a^2\langle \partial_x f\rangle$ in (2) and $a^4\langle \frac{\delta \partial_x f}{\delta \tilde{\epsilon}(x_2)}\rangle$ in (3) yields

$$\partial_t \langle f(x, x', t)\rangle - \overline{\epsilon}^2 \partial_{x^2}^2 \langle f(x, x', t)\rangle = 2\overline{\epsilon}\partial_x(\delta(x - x')\partial_x \langle u(x, t)\rangle \tag{4}$$

and

$$\partial_t \langle u(x,t)\rangle - \overline{\epsilon}^2 \partial_{x^2}^2 \langle u(x,t)\rangle = a^2 \langle \partial_{x^2}^2 u(x,t)\rangle + 2\overline{\epsilon}a^2 \partial_x \int_R e^{-\nu|x-x'|} \langle \partial_x f(x, x', t)\rangle dx'. \tag{5}$$

Solving (4) for $\langle f(x, x', t)\rangle$, then setting $\eta = 2a^2/\nu$ and $D' = D - 3a^2$, we obtain that since ν is large $\langle u(x, t)\rangle$ solves the partial differential equation (6):

$$\partial_t \langle u(x,t)\rangle = D' \partial_{x^2}^2 \langle u(x,t)\rangle + \eta \partial_t^{1/2} \partial_{x^2}^2 \langle u(x,t)\rangle. \tag{6}$$

Here the fractional derivative $\partial_t^{1/2}$ is defined by $\partial_t^{1/2} v = \int_0^t \frac{v(\tau)}{\Gamma(1/2)\sqrt{(t-\tau)}} d\tau + \frac{v(0)}{\Gamma(1/2)\sqrt{t}}$, which is intermediate between the Riemann-Liouville derivative and the Caputo fractional derivative [2] of order $1/2$. The total amount of solute $\int_R \langle u(x,t)\rangle dx$ is conserved by (6), whose impulse response differs slightly from the heat equation's when η is small.

IMPULSE RESPONSE TO (6)

With $D' = 1$, the impulse response to (6) is $h(x,\eta,t) = \frac{1}{4\pi}\int_0^\infty e^{-\rho t}\rho^{-1/2}H(\rho,\eta,x)d\rho$, with $H(\rho,\eta,x) = \frac{1}{\sqrt{1-i\eta\rho^{1/2}}}e^{i\frac{\rho^{1/2}|x|}{\sqrt{1-i\eta\rho^{1/2}}}} + c.c.$. For $\eta = 0$ we recover the heat kernel $h(x,0,t) = \frac{1}{2\sqrt{\pi t}}e^{-\frac{x^2}{4t}}$. Setting $\eta \neq 0$ in (6) introduces slight but qualitative modifications of the impulse response, displayed on Figure 2. The behavior of h at $x = 0$ is sensible to $\eta\partial_t^{1/2}\partial_{x^2}^2\langle u(x,t)\rangle$ in (6), even when η is small. Indeed, for $\eta = 0$, the derivative of h with respect to x is zero at $x = 0$. For $\eta \neq 0$, oppositely, the left and right derivatives are non zero and opposite, so that the nose of h is sharper. Nevertheless, the effect is mainly visible at short and intermediate times. The value of η also influences the second moment of h, which is proportional to $t + 2\eta t^{1/2}/\sqrt{\pi}$, so, that non normal diffusive behaviors are visible at short and at intermediate times. At large times, the impulse response corresponding to $\eta \neq 0$ tend to be very similar to the homogeneous case.

CONCLUSION

In a heterogeneous medium, made of randomly twisted tubes where diffusion obeys Fick's law, the averaged concentration of a passive solute was shown to evolve according to a fractional partial differential equation. The fractional equation is a modified version of Fourier's law, including a non local term. Comparing with the bell-shaped Gaussian, the impulse response of the proposed variant has slightly heavier tails, and sharper nose at the point, where solute is initially injected. Nevertheless, the deviation from Fourier's law is less visible at large times.

References

[1] Donsker M.D., Lions J.L., Frechet Volterra variational equations, boundary value problems, and function space integrals, *Acta Mathematica*, **108**: 147–228, 1962.

[2] R.Gorenflo and F.Mainardi, Fractional calculus, integral and differential equations of fractional order, *Fractals and fractional calculus in continuum mechanics, Editors A.Carpinteri, F.Mainardi, CISM courses and lectures N 378, Springer Wien New-York* 223–276, 1997.

[3] Klyatskin V.I., *Izv.vuzov , Radiofisika* **20**,1977.

[4] Matheron G., de Marsily G., Is transport in porous media always diffusive? A counterexample, *Water Resource Research* **16** (5), 901–917, 1980.

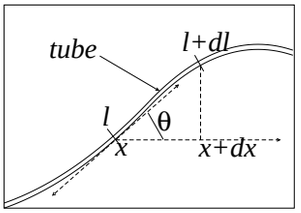


Figure 1. Part of a tube, inside which diffusion occurs. Displacement by dl along the tube increases the x coordinate by dx.

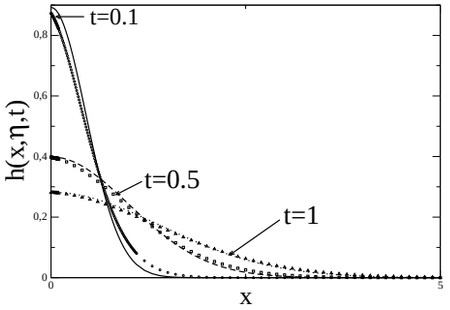


Figure 2. The impulse response of (6), compared with the purely diffusive case $\eta = 0$. Circles, squares and triangles represent the impulse response of (6) for $\eta = 0.1$ at times 0.1, 0.5 and 1. Full, dashed and dotted lines correspond to $\eta = 0$.

OSCILLATORY MODES OF ADSORPTION IN THE FLOW OF MULTICOMPONENT SYSTEMS

Liana Kovaleva, Marat Mavletov
Bashkir State University, Frunze 32, 450074, Russia, Liana@ic.bashedu.ru

Summary A system of equations describing flow of multicomponent mixtures in a porous medium, taking into account the phenomena of competing adsorption is formulated. An equation of sorption kinetics, which describes a series of oscillatory modes for certain of the original parameters, is suggested. A quantitative and qualitative numerical analysis is carried out for formulated problem. A qualitative comparison of the results of calculations and experimental data is given.

Experimental investigations of adsorption phenomena in multicomponent systems show the presence of competing effects, which lead to a non-monotonic distribution of adsorbents on the surface of a solid. A mutual influence of the components on the degree of adsorption of each of them is observed [1]. A system of equations describing flow of multicomponent mixtures in a porous medium includes equation of material balance, sorption kinetics equation, relaxation equation, Darcy's law and piezoconductivity equation [2]. The relaxation equation taking into accounts a non-equilibrium nature o the sorption process. The sorption kinetics equation taking into accounts influence of the components on the degree of adsorption on the surface of a solid.

The formulated initial-boundary-value problem in the special case of two-component sorption was solved numerically by a difference method and using the checkerboard scheme. All the results obtained can be divided into two classes: (1) solutions of the traveling concentration wave type, and (2) solutions corresponding to the various oscillatory processes. Solutions of the first class occur in cases when one of the components clearly predominates over the others either in speed, or in degree of adsorption activity on the surface of the skeleton of the porous medium. Solutions of the second class are if the greatest interest from the point of view of confirming the competitive of the adsorption. Various types of oscillations are possible in the concentration distributions as was shown by the numerical experiment.

The solutions of the problem depend very much on the sorption kinetics equation. In this connection, the stability of the systems of equations of sorption kinetics was analyses for the case of two simultaneously adsorbing components. Region of existence solutions (1) and (2) was founded numerically by the Runge-Kutta method for a wide range of values of its coefficients. An insignificant change in the values of some parameters substantially changes the nature of the process from decaying oscillations, which is due to the presence of singular point of the stable focus, to chaotic oscillations (Fig. 1), connected with occurrence of singular points of the unstable focus type and limiting cycles. Oscillations in the distribution of concentration of adsorbents (a_1, a_2) on the surface of a solid raise the oscillation in the distribution of concentration of components in a moving phase (c_1, c_2).

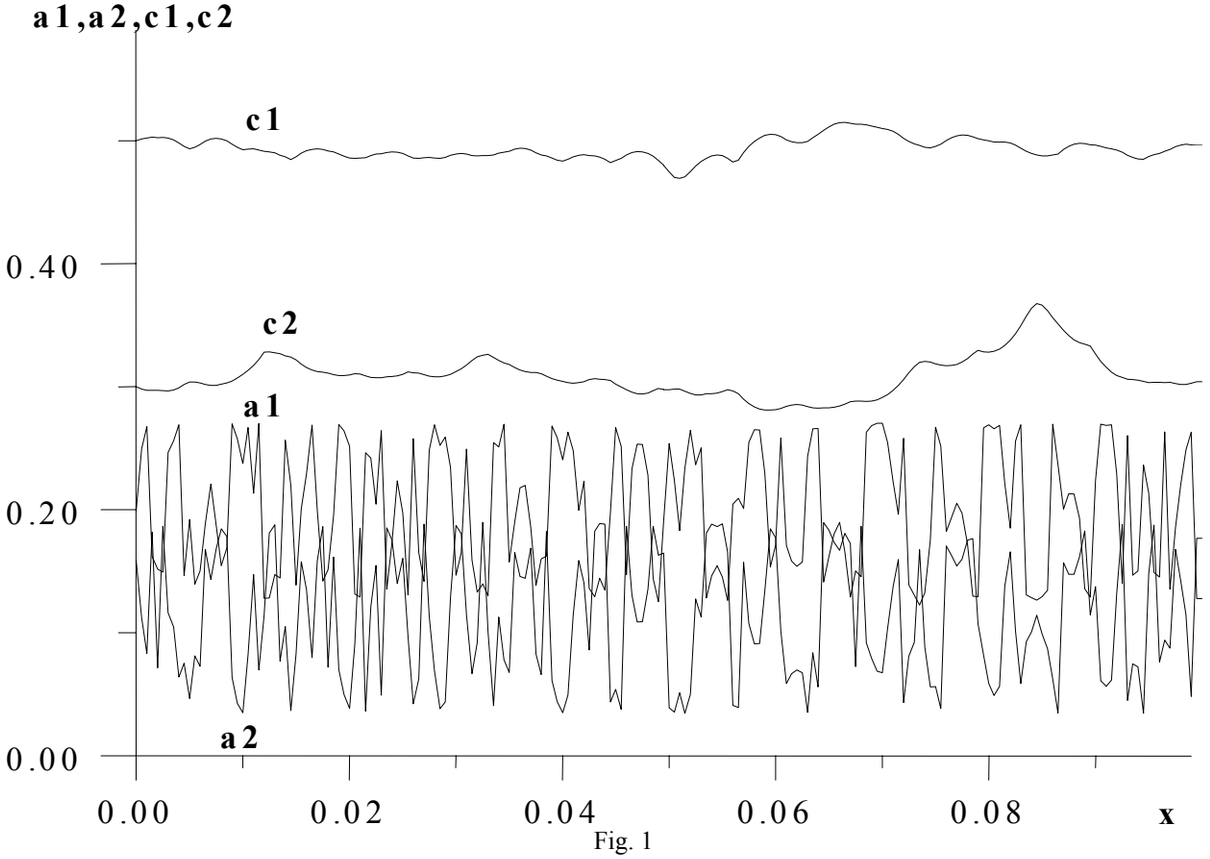


Fig. 1

Phase diagrams in the (c_1, c_2) plane (Fig. 2) show the presence of strange attractor.

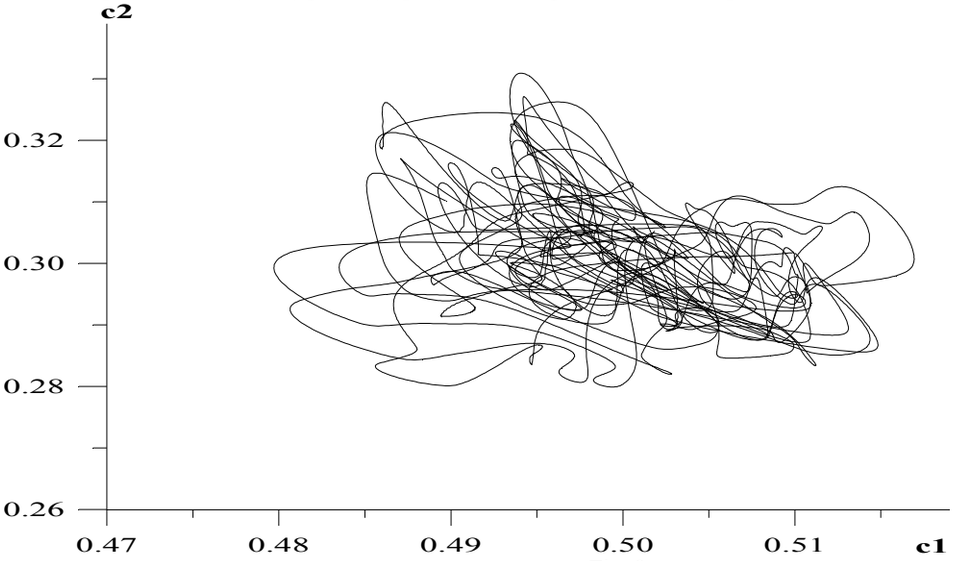


Fig. 2.

The correlation dimension of this attractor is 2.603. This confirms chaotic nature of distribution of adsorbents on the surface of a solid.

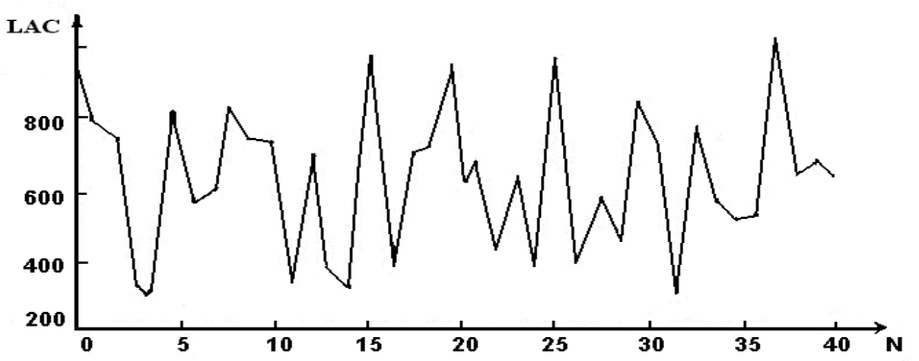


Fig. 3.

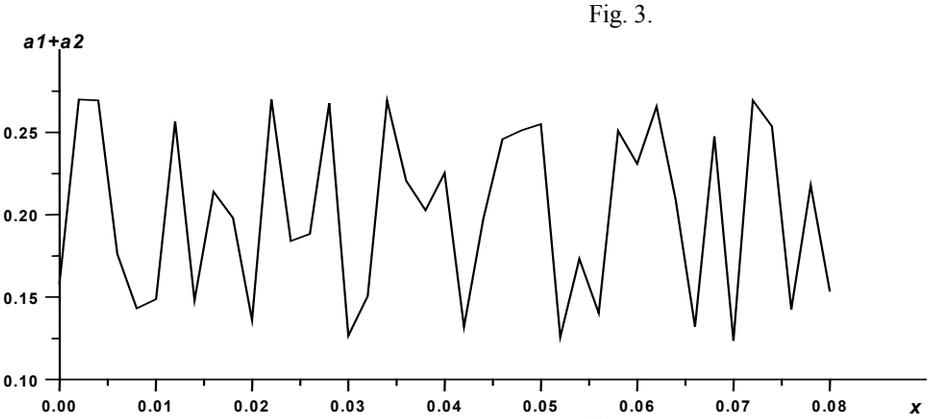


Fig. 4.

The conclusions on the behaviour of the parameters of multicomponent sorption, obtained on the basis of the mathematical model, agree completely with the results of specially conducted experiments [3]. The longitudinal distribution of light adsorption coefficient, which quantitatively characterizes the content of the adsorbent residue, along the model of porous medium was found to be non-linear. The results obtained show good qualitative similarity between the experimental data (Fig. 4) and the numerical calculations (Fig. 3) and the oscillatory nature of the competing adsorption processes.

References

[1] Markhasin I. L., The Physical-Chemical Mechanics of an Oil Stratum. Nedra, Moscow, 1977.
[2] Bochkareva I.V., Kovaleva L.A. Oscillatory modes of adsorption in the seepage of multicomponent systems. *J. Appl. Math. Mechs* **67**. 73-78 2003.
[3] Kovaleva L.A., Ishmurzina N.M. Abstracts of Papers of the Institute of Mechanics and Mathematics. Akad. Nauk AzSSR, Baku, 1990, 74-75.

EXTENDED DESCRIPTION OF PORE SPACE STRUCTURE AND FLUID FLOW THROUGH ANISOTROPIC POROUS MATERIALS

Mieczysław Cieszko
Bydgoszcz University, Institute of Environmental Mechanics and Applied Computer Science
ul. Chodkiewicza 30, 85 064 Bydgoszcz, Poland

Summary The work concerns modelling of mechanical behavior of fluid in porous materials with anisotropic pore space structure. A new macroscopic description is proposed in which the motion of fluid in anisotropic pore space of skeleton is considered as a motion of material continuum in Minkowski (anisotropic) metric space. The generalized equations for wave propagation and for Brinkman and Darcy equations describing fluid flow in porous materials have been derived.

BASIC CONCEPTS

In the paper the fluid motion in a rigid porous medium of anisotropic pore space structure is described. Considerations are based on the new macroscopic model of saturated porous medium in which a fluid flow through porous skeleton of anisotropic pore space structure is described as a motion of the material continuum in the plane anisotropic metric space ([1], [2]). This model takes into account the fundamental fact of kinematics of fluid-saturated porous solid that pore space of permeable skeleton forms the real space for a fluid motion and its structure imposes constraints on that motion.
In such approach the anisotropic pore space of permeable materials is modelled as the affine Minkowski space ([3]-[5]) immersed in the Euclidean space beeing the model of the physical space. The distance u between any two points of the pore space is given by the metric

$$u^2 = \mathbf{u} \cdot \mathbf{M}_{\mathrm{A}}(\mathbf{n}) \cdot \mathbf{u}$$

where $\mathbf{M}_{\mathrm{A}}(\mathbf{n}) \in V^* \otimes V^*$ is the metric tensor of Minkowski space that, in general, depends on the direction $\mathbf{n} = \mathbf{u} / u$ of the measured vector $\mathbf{u} \in V$ and also on its sense $(\mathbf{M}_{\mathrm{A}}(-\mathbf{n}) \neq \mathbf{M}_{\mathrm{A}}(\mathbf{n}))$. The dot in the above relation denotes the bilinear operation (dual multiplication) defined on the dual vector spaces V and V^*.
Tensor $\mathbf{M}_{\mathrm{A}}(\mathbf{n})$ characterizes the anisotropic structure of the skeleton pore space. It determines the measures of any line, surface and volume elements in the pore space and together with the metric tensor $\mathbf{M}$ of the Euclidean space may be applied to define the geometrical parameters of pore structure of porous materials: the tortuosity, the surface and volume porosity.
The concept of plane anisotropic space used as a macroscopic model of the skeleton pore space in which a fluid motion takes place exceeds the framework of fundamental concepts of the mixture theory that is the basis for most theories of multiphase media. Its application to the modelling of porous materials is the new proposition of solution of this problem.
The purpose of this paper is to formulate the balance equations and constitutive relations for fluid filling anisotropic pore space of permeable materials and to discuss the influence of pore structure on mechanical behavior of fluid.

KINEMATICS, BALANCE AND CONSTITUTIVE EQUATIONS

To describe the kinematics of fluid motion in the anisotropic pore space, the existence of continuous fields for fluid mass distribution and mass flux was assumed. It enabled one to define the phase and partial mass densities of fluid and its velocity. Similar requirement formulated for the surface forces as balance quantities results in Cauchy theorem relating the phase stress vector $\mathbf{t} \in V$ and the stress tensor $\mathbf{T} \in V \otimes V$ in a fluid filling anisotropic pore space,

$$\mathbf{t}(\mathbf{x}, \mathbf{t}) = \mathbf{T}(\mathbf{x}, \mathbf{t}) \cdot \mathbf{M}_{\mathrm{A}}(\mathbf{N}) \cdot \mathbf{N} \quad ,$$

where $\mathbf{N} \in V$ is the Minkowski unit vector $(\mathbf{N} \cdot \mathbf{M}_{\mathrm{A}}(\mathbf{N}) \cdot \mathbf{N} = \mathbf{1})$ perpendicular to the surface element.
It was shown that the global and local balance equations for mass and linear momentum written in the vector notation take the classical form and are independent of the pore structure parameters. Such description is a direct consequence of independence of the obtained general expressions for fluxes and for the Gauss-Ostrogradski theorem of any space metric.
The constitutive relations for the phase stress in fluid and for its interaction force with porous skeleton have been formulated. It was assumed that fluid flowing through anisotropic pore space is of the Stockes type and to obtain general expression for the interaction force, the additional tensor $\mathbf{A}(\mathbf{v}) \in V \otimes V^*$ was introduced. This tensor characterizes directional distribution of effective number of pores composing their unit surface in a crossection perpendicular to the given direction.

RESULTS

After reduction the system of equations takes form

$$\frac{\mathrm{D}\rho}{\mathrm{Dt}} + \rho\,\nabla\cdot\mathbf{v} = 0 \ ,$$

$$\boldsymbol{M}(\mathbf{v})\cdot\frac{\mathrm{D}\mathbf{v}}{\mathrm{Dt}} = \overline{\nabla}\left\{-\mathrm{p}(\rho)+\mu'\nabla\cdot\mathbf{v}\right\} + \mu\,\nabla\cdot\mathbf{M}^{-1}\cdot\nabla\{\mathbf{v}\} - \boldsymbol{R}(\mathbf{v})\cdot\mathbf{v} + \boldsymbol{M}(\mathbf{v})\cdot\mathbf{b}$$

where $\overline{\nabla} = \mathbf{M}^{-1}\cdot\nabla$ and $\mathbf{v}$, ρ, p, $\mathbf{b}$ stand for velocity, mass density, pressure and external mass forces in fluid, respectively. The quantity

$$\boldsymbol{R}(\mathbf{v}) = \boldsymbol{M}(\mathbf{v})\cdot\left(\alpha_1\,\mathbf{I} + \alpha_2\,\mathbf{A}(\mathbf{v}) + \alpha_3\,\mathbf{A}^2(\mathbf{v})\right)$$

is the tensorial coefficient of the fluid flow resistance in porous material with anisotropic pore space structure, and

$$\boldsymbol{M}(\mathbf{v}) = \rho\,\mathbf{M}^{-1}\cdot\mathbf{M}_{\mathrm{A}}(\mathbf{v})$$

can be interpreted as the tensor of fluid mass density in anisotropic space. It is seen that in such description the coefficient $\boldsymbol{R}(\mathbf{v})$ is the function of two, in general, independent tensorial characteristics of the pore structure.
The above system for stationary flow of incompressible fluid reduces to generalized form of Brinkman equation,

$$\overline{\nabla}\{\mathbf{p}\} - \boldsymbol{M}(\mathbf{v})\cdot\mathbf{b} = -\boldsymbol{R}(\mathbf{v})\cdot\mathbf{v} + \mu\,\nabla\cdot\mathbf{M}^{-1}\cdot\nabla\{\mathbf{v}\} \ ,$$

or Darcy equation,

$$\overline{\nabla}\{\mathbf{p}\} - \boldsymbol{M}(\mathbf{v})\cdot\mathbf{b} = -\boldsymbol{R}(\mathbf{v})\cdot\mathbf{v} \ ,$$

and for disturbances of small amplitude it takes form of wave equation explicitly dependent on the pore structure parameters

$$\boldsymbol{M}_{\mathrm{o}}(\mathbf{v})\cdot\frac{\partial^2\mathbf{v}}{\partial\mathbf{t}^2} = -a_{\mathrm{o}}^2\,\overline{\nabla}(\nabla\cdot\mathbf{v}) - \boldsymbol{R}_{\mathrm{o}}(\mathbf{v})\cdot\mathbf{v}$$

where a_{o} is the velocity of wave propagation in the bulk fluid, and

$$\boldsymbol{R}_{\mathrm{o}}(\mathbf{v}) = \boldsymbol{M}_{\mathrm{o}}(\mathbf{v})\cdot\left(\alpha_1\,\mathbf{I} + \alpha_2\,\mathbf{A}(\mathbf{v})\right) \ , \qquad \boldsymbol{M}_{\mathrm{o}}(\mathbf{v}) = \rho_{\mathrm{o}}\,\mathbf{M}^{-1}\cdot\mathbf{M}_{\mathrm{A}}(\mathbf{v}) \ .$$

The proposed description allows one to formulate and analyze various problems of fluid flow and wave propagation in porous materials with extended characteristics of pore structure anisotropy and also in materials with nonsymmetric dynamical and filtration properties.

References

[1] M. Cieszko, Minkowski Space as a Model of Anisotropic Pore Space of Permeable Materials. Modelling of the Skeleton Pore Structure. In Proceedings of the International Symposium on *"Trends in Continuum Physics"*, World Scientific, 87-98, 1998.
[2] M. Cieszko, Application of Minkowski Space to Description of Anisotropic Pore Space Structure in Porous Materials, *ZAMM*, **80** S1, 129-132, 2000.
[3] H. Rund, The Differential Geometry of Finsler Spaces, Springer-Verlag, 1959.
[4] A.C. Thompson, Minkowski Geometry, Cambridge University Press, 1996.
[5] D. Bao, S.S. Chern, Z. Shen (2000), An Introduction to Riemann-Finsler Geometry, Springer-Verlag.

ONSET OF CONVECTION FOR A MISCIBLE FLUID IN A POROUS MEDIUM

Robert Behringer, Michael Carey, Mark Steen, and Laurens Howle, Duke University

We present experimental results for the onset of convection in a horizontal layer of porous medium saturated with a miscible binary mixture of ethanol and water. Previous theory[1] indicates a bifurcation to oscillatory convection for negative separation ratio, but we find steady convection at onset. We explore the possibility that enhanced mixing is at the root of these observations.

The experiments were carried out using a variety of different media and two different techniques. The first technique[2] is Magnetic Resonance Imaging (MRI), which allows us to non-invasively probe a variety of porous media. We directly measure the density of fluid in the pore space and the vertical velocity field. With MRI, we explored media constructed from foams and from sphere packings. The second technique[3] is a novel form of a shadowgraph. We construct special media which allow us to transmit light vertically through a porous layer. The media were made by constructing a grid of holes in plastic sheets which were then stacked vertically.

The basic form of the experiment consists of a layer of fluid-saturated porous medium that is heated from below. The control parameters are then the porous Rayleigh number, R, the separation ratio, ψ, the Lewis number, L, and the aspect ratio. R is a dimensionless measure of the vertical temperature difference across the layer. ψ is characterizes the stabilizing influence of the concentration gradient. L is the ratio of diffusion times for mass and heat, and the aspect ratio is the ratio of a typical horizontal dimension and the height of the layer. We used ψ's in the range $-0.2 < \psi < 0$, the Lewis numbers were ~0.01, and the aspect ratios were in the range 5 to 10. The horizontal planform of the convection layers corresponded to disks rectangles, and annuli.

Measurements consisted of MRI velocity maps and temperature differences for MRI imaging. For the shadowgraph, we obtained images of the convective planform, and we also obtained high precision heat transfer data, i.e. data for the Nusselt number, all as functions of R.

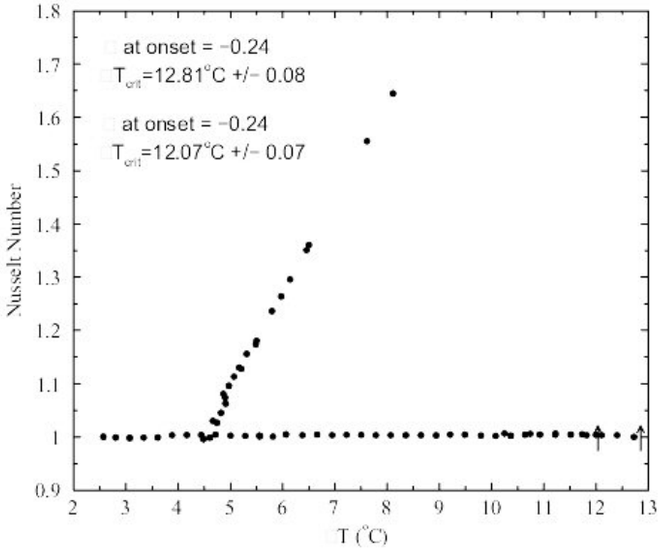


Figure 1. Nusselt Number vs. temperature difference across the layer showing the hysteretic transition to convection. On increasing R, we found that convection was initiated at the arrows, leading to large-amplitude steady convection.

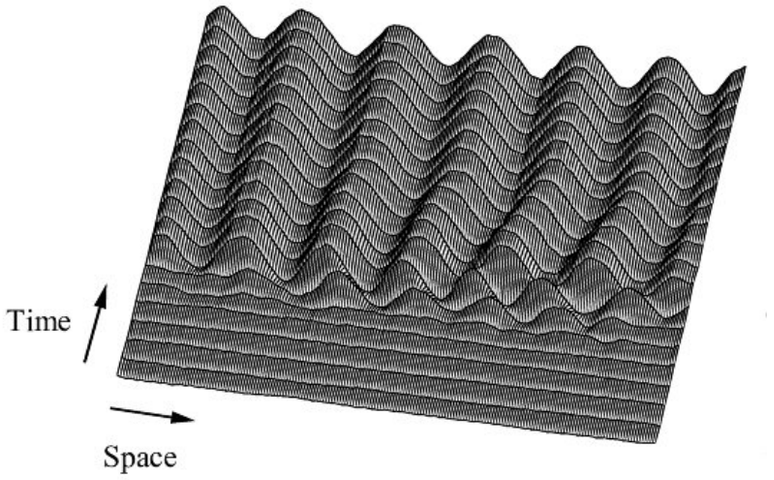


Figure 2. Space-time velocity map showing the vertical fluid velocity after a step change in R. After an initial transient that may be representative of damped oscillatory motion, steady convective rolls persist. In this case, the planform of the layer was a long thin rectangle, and this figure shows data along the long spatial dimension.

Regardless of method, we found that the onset of convection was characterized by a hysteretic transition to steady overturning convection rolls. By contrast, existing theory indicates that the transition to convection should be oscillatory. We note that for the bulk Rayleigh-Benard case, oscillatory phenomena have been routinely observed. Hence, this experimental finding is quite surprising. We show an example in Fig.1, which gives high-precision Nusselt number data for a typical case using the shadowgraph technique. In Fig. 2, we show an example of a transient flow leading to steady convection for a long thin rectangular layer observed with MRI. The transient behavior suggests that oscillatory convection is strongly damped, if it is present at all.

We have pursued the possibility that the difference between previous theory and our observations is due to enhanced mixing. That is, as convection begins, the fluid is mixed as it passes through the solid matrix, thus leading to pure-fluid-like behavior. We have used a Lorentz-model truncation of the full set of equations describing convection in porous media. The momentum equation that we use is Darcy's law plus an additional term for enhanced mixing, as for instance in Bear[4]. Here, however, we assume that the strength of the mixing term grows as the square of the velocity, and assumption that is experimentally justified by direct measurement on our porous media, and that allows for theoretical simplicity. We find that an enhanced mixing term of strength M does change the bifurcation to match the experiments.

We then carried out additional NMR measurements to directly determine the strength of the mixing term for some of our porous media. The experimentally determined values of M were too small by roughly two orders of magnitude to account for our observations. Thus enhanced mixing does not appear to be the explanation for the observed phenomena, which remain unexplained.

References

[1] H. R. Brand, P. C. Hohenberg, and V. Steinberg, Phys. Rev. A **27**:591-59**3,** 1983; Phys. Rev. A **30**:2548-2561, 1984.
[2] L. E. Howle, R. P. Behringer, and J. G. Georgiadis, Nature, **362**:230-232, 1993; J. Fluid Mech. **332**:247-262, 1997.
[3] M.D. Shattuck, R. P. Behringer, G. A. Johnson, and J. G. Georgiadis, Phys. Rev. Lett. **75**:1934-1937; J. Fluid Mech. **332**:215-245, 1997.
[4] Jacob Bear, *Dynamics of Fluids in Porous Media*, Dover, Toronto, 1988.

INSTABILITIES IN A TAYLOR-DEAN OPEN FLOW

A.Ait Aider*, S.Skali and J.P.Brancher**
*Département de Mécanique, Université de Tizi Ouzou,Algérie
**LEMTA,INPL,2Avenue de la Foręt de Haye,54504 Vandoeuvre Cedex

Summary The flow studied hereafter is produced in a system of two coaxial circular cylinders azimuthally opened. It is a combination of the inner cylinder rotation and a flow provided in the gap by external pumping. Our observations, however, indicate that the flow possesses certain distinctive features not present in the pure rotation of closed cylinders (Taylor-Couette flow) neither in the pure pumping (Dean flow). During the laminar-turbulent transition, for a wide range of τ, the ratio of pumping and rotation flow rates, the flow undergoes a series of instabilities giving rise for local or global patterns. These new regimes will be presented.

INTRODUCTION

The stability of a similar flow was first studied experimentally by Brewster et al.[1]. They were interested by the critical conditions of the formation of Taylor vortices and tried to find a common parameter for Dean and Taylor-Couette flows, or any velocity distribution. After then, the effect of a transverse pressure gradient on the stability of a Couette flow was considered theoretically by Di Prima who found an unusual behaviour of the neutral curve. Chandrasekar [2] offered a highly plausible explanation of the very peculiar dependence of the critical Taylor number on τ. Later theoretical studies were focused on the point τ=-0,222 where T.H. Hughes et al. found that the curve of the neutral stability exhibits two loops, due to a discontinuity in the critical wave number. They demonstrate that the two lowest stationary modes do not exist. D.C.Raney showed after them that the stationary modes are replaced by axially nonsymmetric oscillatory modes. On the other hand, these last years, experiments have been performed in the Taylor-Couette system when the cylinders are horizontal and the gap not completely filled. The flow obtained is called the Taylor-Dean flow. Elsewhere, new ideas have been formulated on the stability of open flows and shear flows. The purpose of this study is to investigate experimentally the transition laminar-turbulent of the Taylor-Dean flow with external pumping. The flow is schematised in fig.1. We call it the open Taylor-Dean flow.

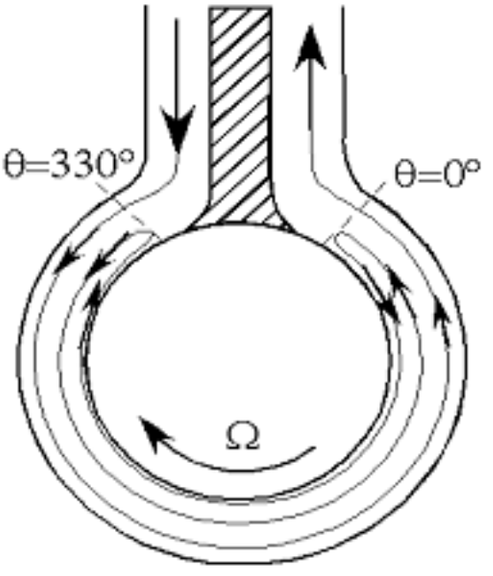


Fig.1 Sketch of the flow system

Experimental set-up and methods

The curved section consists of two concentric cylinders with an inner rotating cylinder of radius R_1 = 3.85cm, a gap d =R_2–R_1=0.6cm, a radius ratio η=0.865 and the cylinders length L=10cm, giving an aspect ratio Γ = L/d = 16,6. We make our observations in a cell delimited axially between 0<z<10cm and azimuthally between 0°<θ<330°. The inner cylinder can rotate in the range–17 rd/s <Ω<17 rd/s. The flow rate varying from 0 to 1000 dm^3/h, is provided by a pump controlled by an electromagnetic flowmeter. The fluid is recycled from a tank. The system is either horizontal or vertical. The fluid is a mixture of water and Emkarox with added Iriodin for the visualisation. Experiments are down for different viscosities to obtain the first instability and the high turbulence in the range of rotation allowing easy observation. The viscosity is varied in the range $10^{-6}<\upsilon<5.10^{-6} m^2 s^{-1}$.

Instabilities

The "entry" and the "exit" of the flow are defined following the direction of the rotating cylinder. The evolution of the flow is described in a two parameter space (Ta, τ), where Ta is the Taylor number. The figure 2 shows the rise and growth of the entry and exit instabilities for τ=0, the so-called Taylor-Dean flow for which the flow is completely reversed : a)longitudinal vortices at the entry and the exit, b)bulb at (z=10, θ=0°), bulbs and thin azimuthal vortices at the exit, c) bulb at (z=0, θ=0°), "necking" cell near θ=330°, d) tangle of the inclined cells propagating axially from z=10 to z=0 and inversely, e) corner vortex and diagonally propagating rolls.

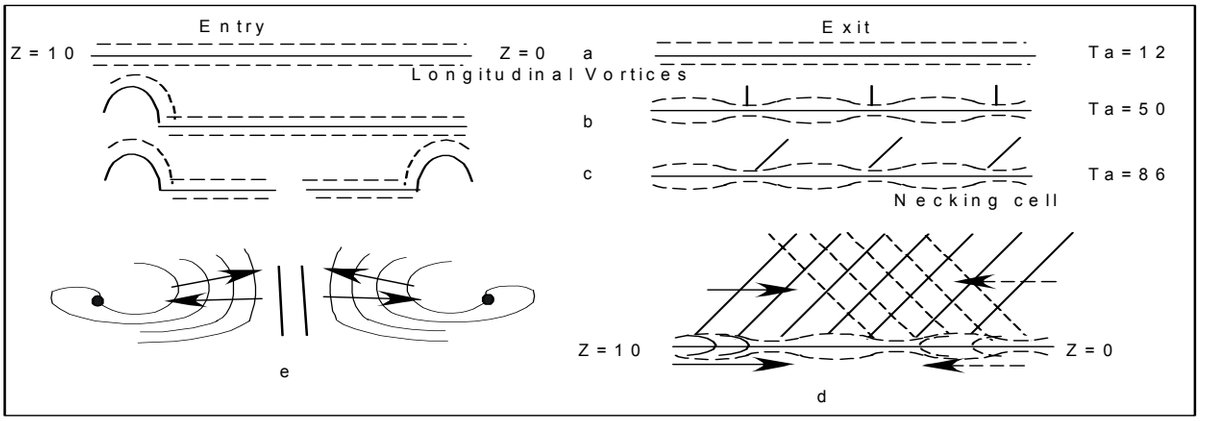


Fig.2 Rise and growth of the entry and exit instabilities for τ=0

Flow regimes

We distinguish two cases:

1) Beyond τ =2/3, the reversed flow is not noticeable. Dean flow dominates.

2) For –2/3<τ<2/3 the flow is partially reversed and gives rise, at the entry and exit zones, to the structures shown in figure 2, ie corner vortex in the entry and "necking" cell with inclined axially propagating rolls in the exit. The flow regimes observed in the core are presented in figure 3. The basic flow, combination of the Couette and Poiseuille flows, is purely azimuthal. At the instability onset, we can observe either axially regularly spaced cells for τ<0 or spirals for τ>0. With increasing Ta for a fixed De, the Dean number, a succession of transitions lead the flow to turbulence: split-merging of the cells, travelling waves with two trains in the same or opposite direction, turbulent bursts, vortex paths due to Kelvin-Helmoltz instability, diagonally travelling rolls, chaos where the different structures coexist and then the stochastic flow where all the structures crumble.

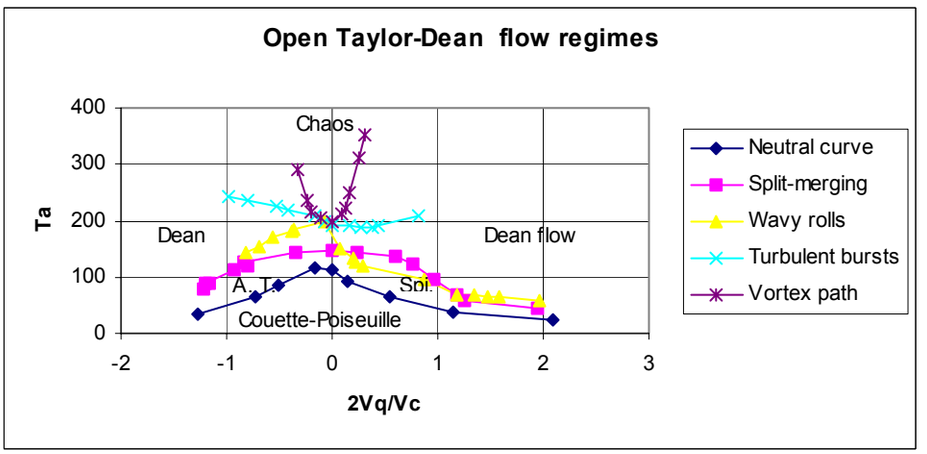


Fig. 3 Open Taylor-Dean flow regimes (A.T.: axially translation motion; Spi.: Spirals)

Conclusion

It is expected that an understanding of the origin of the observed instabilities and their role in the crumble process of the structures of the flow could help to throw some light on the rise of turbulence.

References

[1] D.B., Brewster, P, Grosberg, and A.H Nissan, The stability of viscous flow between horizontal concentric cylinders, Proc. R. Soc. Lond. A Math. Phys. Sci., 251 (1959), 76-91

[2] S.Chandrasekar, Hydrodynamic and Hydromagnetic Stability, Oxford University, London, 1961,343-361

SHEAR LAYER INSTABILITY AND FREQUENCY MODES INSIDE AN OPEN CAVITY

François Lusseyran*, Thierry M. Faure*, Céline Eschenbrenner* and Yann Fraigneau*
*Laboratoire d'Informatique pour la Mécanique et les Sciences de l'Ingénieur, BP 133, 91403 Orsay cedex, France

Summary The dynamic behaviour of the vortex structures occurring in a cavity, in interaction with an upstream wall flow, drives the fluid confinement inside the cavity. This presentation concerns the coupling between the shear instability process and the mechanisms of frequency selection which depend on the size of the cavity. The analysis is based on an experimental exploration of the flow (LDV, PIV) and on direct numerical simulation.

INTRODUCTION

In case of moderate Reynolds number (Re<30000, based on the length of the cavity) the structure of the flow generated by a cavity in interaction with an upstream boundary layer, appears to be more complex (i.e. more unsteady and tri-dimensional) than observed at higher Reynolds number. With the aim to control the exchanges of mass or heat between the cavity and the main flow, it is first necessary to describe the main features of the vortex structures and their physical relationships. This communication concerns the coupling between the shear instability and the mechanisms of frequency selection depending on the size of the cavity. The analysis is based on an experimental investigation (Figure 1) of the flow (LDV, PIV-optical flow [1]) and on 2D and 3D direct numerical simulations (Figure 2).

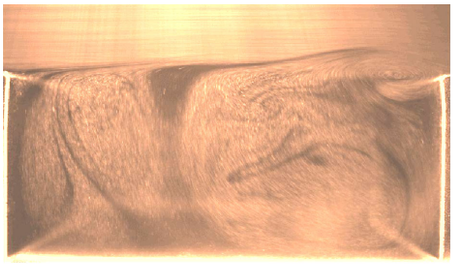


Figure 1: flow inside cavity, light sheet in the plane of symmetry.

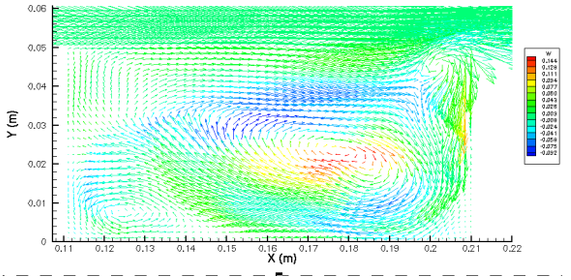


Figure 2: 3D DNS; velocity field in the plane of symmetry.

Following the development of the frequency modes with an increasing flow rate, four main modes appear (Figure 3). The latest one (mode 3) corresponds to oscillation in a turbulent regime flow. The modes 0, 1 and 2 allow a very good comparison between the numerical simulation and the experiment (Figure 4). The mode 2 has been identified with shear instability of the mixing layer above the cavity [2].

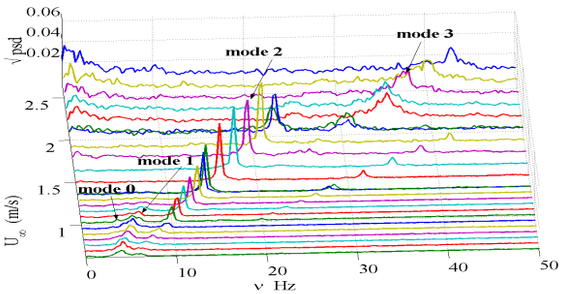


Figure 3: Power spectral density of energy from horizontal velocity component, measured by LDV vs. upstream flow rate

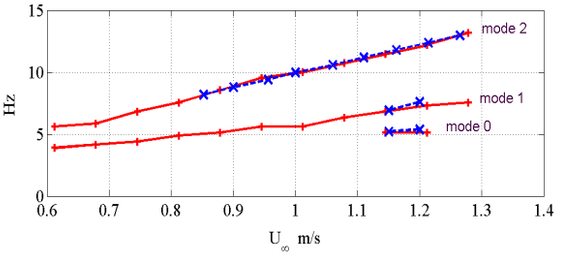


Figure 4: Comparison of numerical simulation (-x-) and experiment (-+-): Frequency modes vs. upstream flow rate.

RESULTS AND CONCLUSIONS

It is essential to stress that the increase of the cavity length L induces a frequency shift of the modes, even for mode 2 corresponding to the shear instability (Figure 5). That shows the existence of selection mechanism acting on the process of shear layer instabilities. This phenomenon is also described in a previous work concerning an open cavity, but at higher Reynolds number [3].

The linear relationship $f^k = f_0^k + \alpha^k U_{ref} = \alpha^k \left(U_{ref} - U_c^k \right)$ between the frequency f^k of each mode k and the flow rate velocity U_{ref} (see Figure 5), allows the construction of a Strouhal number based on the length L:

$$St_L^k = \frac{f^k L}{U_{ref}} = \alpha^k L + \frac{f_0^k L^2/\nu}{\mathrm{Re}_L} = \alpha^k L - \alpha^k U_c^k \frac{L^2/\nu}{\mathrm{Re}_L}$$

with U_c^k a critical flow rate and $\mathrm{Re}_L = U_{ref} L/\nu$. α^k and U_c^k are function of L.

Therefore the Strouhal number becomes asymptotically constant for increasing Reynolds numbers, as actually presented Figure 6. This representation reveals again the three modes and their continuation when the aspect ratio $R = L/h$ is changed. The range of validity of this result is limited one side to $R \geq 1$, value under which the vortex organization inside the cavity changes. On the other side, although we don't explore the aspect ratio bigger than 2, it is known that for high value of R, the flow develops as for a back facing step.

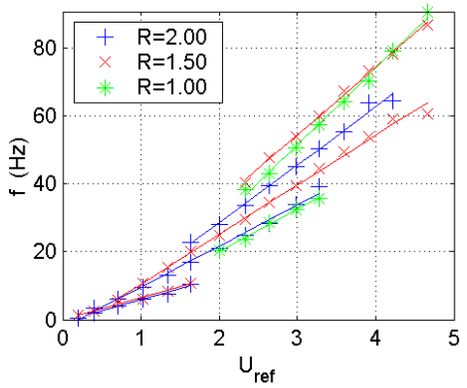


Figure 5:Frequency modes vs. flow rate for three values of the cavity length L; R=L/H the aspect ratio.

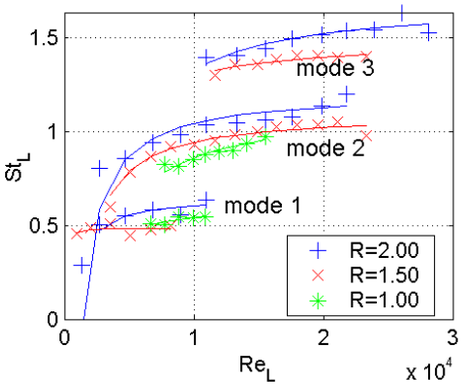


Figure 6: Data of the Figure 5, plotted as Strouhal number vs. Reynolds number (characteristic length L and velocity U_{ref}.): 3 modes grouping effect.

The numerical simulation confirms the persistence and the frequency shift of mode 2, induced by the increase of length L (Figure 7 'circles'). Note that computation is done for a fine step increase of L, even if for a limited range of Reynolds number values.

The discrepancies of the modes grouping and the strong correlated behavior of the different modes have to be discussed.

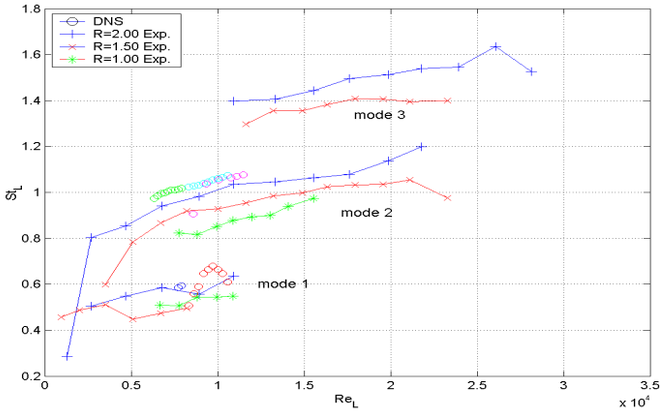


Figure 7: Comparison between the frequencies obtained from the numerical simulation for $1.5 < R \leq 2$ and those obtained from the experimental times series.

References

[1] G.M. Quénot, J. Pakleza, T.A. Kowalewski, "Particle image velocimetry with optical flow", *Exp. In Fluids 25, 1998* pp177-18

[2] Rambert A., Lusseyran F., Gougat P., Fraigneau Y., Elcafsi A., Quénot G., « Relationship between Fourier-modes and spatial-structures in a cavity - boundary layer interaction at moderate Reynolds numbers. » *11th Int. Symp. on Appl. of Laser Techniques to Fluid Mechanics*, Lisbonne (Juillet 2002).

[3] Rockwell D. and Naudasher E., Self-sustained oscillations of impinging free shear layers, *Ann. Rev Fluid Mech.*, **11** : 67-94, 1979.

Travelling waves and transition to turbulence in pipe flow

Bruno Eckhardt and Holger Faisst

Fachbereich Physik, Philipps Universität Marburg
D-35032 Marburg, Germany
e-mail: bruno.eckhardt@physik.uni-marburg.de
Web page: http://www.physik.uni-marburg.de/kosy

ABSTRACT

Hagen-Poiseuille flow through a pipe of circular cross section belongs to the class of shear flows that does not become linearly unstable. The situation is similar to Taylor-Couette flow with the inner cylinder at rest as well as to Taylor-Couette in the limit of large radii where the system approaches plane Couette flow [3]. In these cases the transition to turbulence is not related to series of symmetry-breaking linear instabilities but rather with the formation of nonlinear 3-d states that are not connected to the laminar profile and that seem to form a chaotic saddle.

As indicators for this process we present exact coherent states to pipe flow, we discuss the sensitive dependence on initial conditions quantified by the Lyapunov exponent of turbulent trajectories, and the exponential distribution of life times of the turbulent state. All our findings are consistent with the formation of a strange saddle (repellor) in phase space.

A family of three-dimensional **travelling waves** for flow through a straight pipe of circular cross section has been identified (Fig. 1) [1]. They were found by a Newton-Raphson method which was implemented with a spatial resolution of 21 modes in azimuthal and downstream direction and 44 Legendre polynomials radially. This gives us about 8700 dynamically active velocity coefficients. They originate in saddle-node bifurcations at Reynolds numbers as low as 1250, where Re is based on the mean downstream velocity and the pipe diameter. All states are immediately linearly unstable at the bifurcation.

The travelling waves are dominated by pairs of downstream vortices and streaks (Fig. 1). The high speed streaks near the wall move much less than the low speed streaks closer to the center of the pipe. The dominating structures are streamwise streaks and streamwise vortices that closely resemble coherent states in other shear flows like the wavy-vortex flow in Taylor-Couette or plane Couette flow. The dynamical significance of the exact coherent states is that they provide a skeleton for the formation of a chaotic saddle that can explain the intermittent transition to turbulence and the sensitive dependence on initial conditions in this shear flow [1,2].

For dynamical **lifetime experiments** we follow the experiments of Darbyshire & Mullin [4] and keep the volume flux constant. We extended our numerical investigations to times of 2000 or more (unit of time: mean streamwise velocity/radius), far exceeding the values accessible in the longest currently available laboratory experiment. As initial conditions we used a high amplitude uncorrelated superposition of spectral modes. The spatial structure is so rich and the amplitude so high that the probability to trigger turbulent dynamics is maximal for a wide range of Reynolds numbers. Various conclusions can be drawn from our lifetime experiments: We find a transitional Reynolds number somewhat below $Re = 2000$. The minimum amplitude to trigger a long living turbulent dynamics decreases with Reynolds number. We observe strong sensitivity on initial conditions as well as on parameters which results in large fluctuations in turbulent life times (Fig. 2) [2]. The regions of quickly decaying and long-living trajectories are separated by complicated, fuzzy stability borders. The results are in agreement with experiments by Darbyshire & Mullin [4].

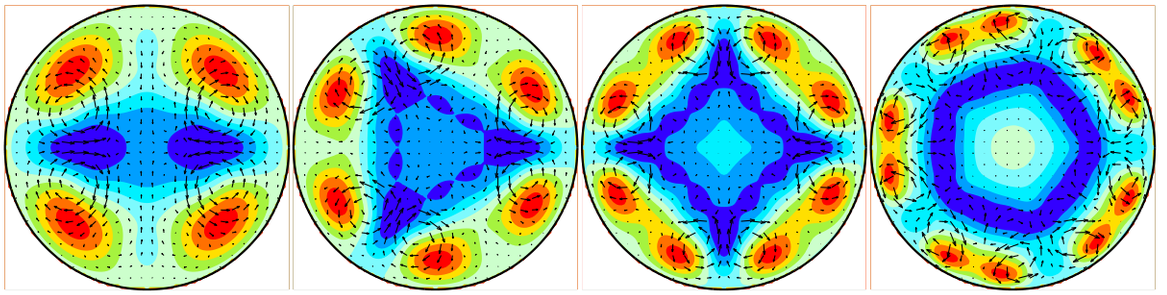


Figure 1: Travelling waves with symmetries C_n with $n = 2$, 3, 4, and 5 (invariance under rotation around the pipe axis by an angle $2\pi/n$). In order to highlight the topology of the states all states are averaged in downstream direction. The representation of the velocity field has vectors for the in-plane motion and color coding for the downstream motion.

The strong sensitivity of lifetimes on initial conditions and on parameters calls for a statistical description of the transition process. Therefore, the distribution of turbulent lifetimes has been calculated and it is shown in Fig. 2.

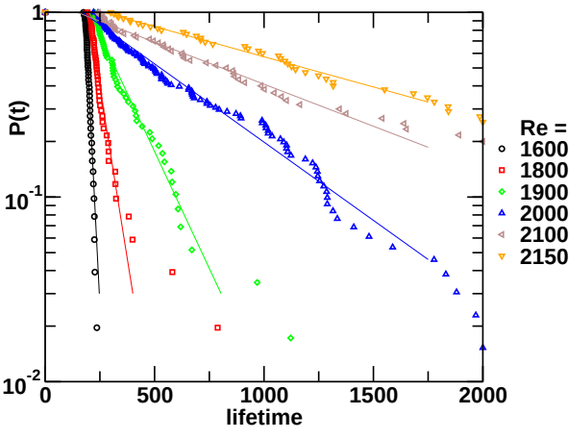


Figure 2: The probability for a single trajectory to still be turbulent after a certain integration time. Between 50 and 100 trajectories have been integrated per Reynolds number.

Although the fluctuations are large an exponential distribution can be identified within the statistical errors. This can be interpreted as a constant rate of escape from the turbulent state which is a major characteristics of a chaotic repellor.

Increasing the Reynolds number up to $\approx$ 2200 the median of the turbulent life times as well as the fluctuations increase rapidly until the median reaches the cut-off life time of 2000. It might even be the case that the escape routes from the repellor are closed and it is turned into a strange attractor.

REFERENCES

[1] H. Faisst, B. Eckhardt, Phys. Rev. Lett. **91**, 224502 (2003)

[2] H. Faisst, B. Eckhardt *Sensitive dependence on initial conditions in transition to turbulence in pipe flow* , J. Fluid Mech., in press

[3] H. Faisst, B. Eckhardt Phys. Rev. E, **61** (2000), 7227

[4] A.G. Darbyshire, T. Mullin. J. Fluid Mech., **289**, 83–114, (1995).

NONLINEAR MECHANICS OF WAVY INSTABILTY OF STEADY LONGITUDINAL VORTICES AND DRAG RISE IN BOUNDARY LAYER FLOW†

J, T. C. Liu*, I. G. Girgis**

*Division of Engineering and the Center for Fluid Mechanics, Brown University, Providence, RI 02912, USA and Laboratoire de Thermocinétique, École polytechnique de l'université de Nantes, Rue Christian Pauc – La Chantrerie – BP 50609 – Nantes Cedex 3 – France

**Department of Mechanical and Aerospace Engineering, Princeton University, Princeton, NJ 08544, USA

Summary Wavy secondary instability of steady longitudinal vortices in boundary layer flow is studied. The nonlinear interaction problem is parabolized through scaling obtained from observations. Emphasis is placed on the nonlinear modification of the steady, averaged problem by the Reynolds stresses of the wavy disturbance. It is found that the skin friction in such a modification process increases well above the local turbulent boundary layer value.

INTRODUCTION

Discussed in a recent paper [1] are the formulation and results for the nonlinear development of steady Taylor-Görtler vortices in the free mixing region after their release from upstream wall bounded flow These steady longitudinal vortices in turn, are susceptible to time-dependent wavy instabilities that are sometimes referred to as secondary instabilities [2],[3,[4]]. They are akinned to the unstable wavy vortices in a Taylor-Couette flow apparatus. At this Congress we will discuss the nonlinear mechanics of time-dependent instabilities of steady three-dimensional longitudinal vortices in the boundary layer. The steady mean flow could be Taylor-Görtler vortices in the boundary layer or artificially induced longitudinal vortices from spanwise-periodic roughness near the leading edge of the boundary layer. Emphasis is placed on the modification of the steady flow by the Reynolds stresses of the nonlinear wavy instabilities, which in turn, causes the skin friction drag to increase. The drag rise induced by the nonlinear wavy instability, a phenomenon which has escaped attention in previous nonlinear studies [5] is of an enormous important consequence in terms of momentum and scalar transport enhancement possibilities

FORMULATION AND METHODOLOGY

It is much more physically illuminating to carry out the analysis in physical rather than in spectral coordinates. The flow is split into a time-independent mean flow and the time-dependent 'high frequency' instabilities; these are nonlinearly coupled via the Reynolds stresses of the unsteady component of flow. The total steady flow consists of longitudinal vortices and the basic steady boundary layer flow. The mechanics of nonlinear interactions between the steady flow component and the wavy instability are recoverable via time and spanwise averaging. Through scaling arguments, the steady flow component continues to be parabolic via scaling in its streamwise development in the viscous sense and devoid of curvature effects, except for the Görtler mechanism, under the assumption of thin boundary layers relative to the radius of curvature. The nonlinear wavy disturbance equations in physical variables are obtained by subtracting the Reynolds-averaged steady flow equations from the total flow quantities before the Reynolds splitting. The nonlinear disturbance equations are thus similar in form as in nonlinear hydrodynamic stability studies (such as in the general formulation in [5], [6]). Under the assumption of small boundary layer thickness relative to local radius of curvature of the wall, curvature effects in advective and viscous diffusion effects are negligible; the Görtler centrifugal mechanism in this case do not arise in the wavy disturbance problem as was found in the linear problem ([7], [2], [4]). Scaling arguments extracted from experiments [8] show that the time-dependent wavy instability velocities, unlike that of the steady flow, are very nearly isotropic; their physical wavy characteristics scale isotropically according to the local shear layer dimensions while their three-dimensional streamwise developing wave envelope would be parabolic, consistent with the steady mean flow. A number of simplifications are thus possible, leading to simpler understanding of the partial differential equations for the disturbances in the present case. The mean flow advection of disturbance momentum is attributed only to the streamwise mean flow velocity. Two dominant mechanisms for instability arises: one is the normal (or vertical) disturbance velocity advection of the three-dimensional structure of spanwise mean flow vorticity, a mechanism familiar in two-dimensional shear flow instabilities [9], the other is the spanwise disturbance velocity advection of the three-dimensional normal or vertical mean flow vorticity. These mechanisms were well identified in earlier linear studies [2], [3] and they remain so with nonlinearities taken into account. The nonlinear generation of higher harmonics is due to the time-dependent excess-Reynolds stresses familiar in nonlinear hydrodynamic stability studies [6].

The system consists of the downstream marching solution of the three-dimensional longitudinal vortex mean flow and of the coupled parabolic partial differential equations for the three-dimensional spectral components of the wavy disturbances, starting from imposed upstream initial conditions. Although the details are very much different, the physical implications of previous work on nonlinear hydrodynamic stability (e.g., [6]) are inferable from the present strongly nonlinear studies; which include the modification of the mean flow, the generation of higher harmonics and

the effect of these on modifications of the fundamental component. These effects are distilled from the partial differential in the present case, reflecting the basic mechanisms depicted by the Stuart constants $k_{1,\,k\,2}$, and $k_{\,3}$ in the Stuart-Landau amplitude equation [6] which was rationally derived from the Navier-Stokes equations under the assumption of weak nonlinearity for parallel flow instabilities.

RESULTS AND CONCLUDING REMARKS

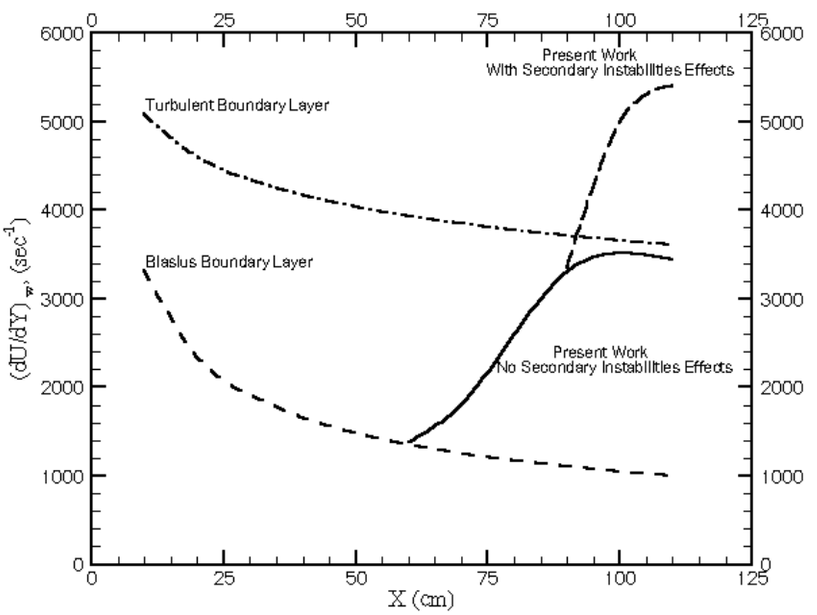
Computational results are obtained for conditions corresponding to experiments [8] for the most amplified steady longitudinal vortex mode and the fundamental wavy instability mode at initial amplitudes consistent with observations. The mushroom shapes of the total steady flow streamwise velocity is shown to be modified as the wavy time-dependent instability amplifies into its nonlinear region. In the absence of wavy disturbance the steady flow skin friction can nearly bridge the transition from laminar values to that of turbulent, which is also the case with experimental measurements [8]. The effect of the wavy instability on the steady values of the skin friction is to increase it well beyond the local turbulent values as the flow develops downstream. This is shown in the accompanying figure.

Although the wavy instability momentum problem does not have the similarity properties with scalar transport as in the steady case [10] because of the streamwise pressure gradient in the wavy instability problem, nevertheless, one can approximately infer that the surface heat (and mass) transfer rates under longitudinal vortices and their wavy instabilities would be similarly augmented as would be found in measurements in progress at the Laboratoire de Thermocinétique in Nantes.

†In memoriam: Henryk Zorski

References

[1] Girgis, I. G., Liu, J. T. C.: Mixing Enhancement via the Release of Strongly Nonlinear Longitudinal Görtler Vortices and their Secondary Instabilities into the Mixing Region. *J. Fluid Mech.* **468**:29-75, 2002.
[2] Yu, X. & Liu, J. T. C.: The Secondary Instability of Görtler Flow. *Phys. Fluids* **A3**:1845-18471991.
[3] Yu, X. & Liu, J. T. C.: On the Mechanism of Sinuous and Varicose Modes in Three-Dimensional Viscous instability of Görtler Rolls. *Phys. Fluids* **6**:736-750, 1994.
[4] Hall, P. & Horseman, N. J.: The Inviscid Secondary Instability of Longitudinal Vortex Structures in Boundary Layers. *J. Fluid Mech.* **232**:357-375, 1991.
[5] Li, F., Malik, R.M.: Fundamental and Subharmonic Secondary Instabilities of Görtler Vortices. *J. Fluid Mech.* **297**:77-100, 1995.
[6] Stuart, J. T.: On the Nonlinear Mechanics of Wave Disturbances in Stable and Unstable Parallel Flows. Part 1. The Basic Behavior in Plane PoiseuilleFlow. *J. Fluid. Mech.* **9**:353-370, 1960.
[7] Sabry, A.S., Yu, X., Liu, J. T. C.: Secondary Instabilities of Three-Dimensional Inflectional Velocity Profiles Resulting from Longitudinal Vorticity Elements in Boundary Layers. IUTAM Symp. Laminar-Turbulent Transition-1989, p. 441. (R. Michel & D. Arnal, Eds.) Springer-Verlag, Berlin, 1990.
[8] Swearingen, J.D., Blackwelder, R.F.: The Growth and Breakdown of Streamwise Vortices in Presence of a Wall. *J. Fluid Mech.***182**: 255-290, 1987.
[9] Lin, C.C.: The Theory of Hydrodynamic Stability. Cambridge University Press, 1955.
[10] Liu, J.T.C., Sabry, A.S.: Concentration and Heat Transfer in Nonlinear Görtler Vortex Flow and the Analogy with Longitudinal Momentum Transfer. *Proc. Royal Soc. London* **A432**:1-12, 1991.



Shear Stress at the Wall

STABILITY OF FLOW IN A ROUGH CHANNEL

J.M.Floryan[*], M Asai[**]
[*]*Department of Mechanical & Materials Engineering, The University of Western Ontario, London, Ontario, N6A 5B9, Canada*
[**]*Department of Aerospace Engineering, Tokyo Metropolitan Institute of Technology, Asahigaoka 6-6, Hino, Tokyo 191-0065, Japan*

Summary Theoretical and experimental investigation of stability of flow in a rough channel has been carried out. The flow destabilization predicted by the theory agrees with the destabilization observed in controlled experiments.

INTRODUCTION

Understanding how surface roughness affects the laminar-turbulent transition process is one of fundamental questions in fluid dynamics. This question has been posed by in 1883 [1] but, in spite of its long history, its rational resolution is still lacking. While this problem is of interest from the fundamental point of view, it is also of considerable practical importance in several application areas, e.g., design of large Reynolds number laminar airfoils, small Reynolds number turbulent airfoils, compact heat exchangers, laminar electrostatic precipitators, etc. The existing experimental investigations show that surface roughness contributes directly to the dynamics of flow only if the wall is hydraulically rough. Precise definition of hydraulical smoothness is not available due to the complex, flow-condition-dependent interaction between the roughness geometry and the moving fluid. The phenomenological effects of the "equivalent roughness" are summarized in the form of friction coefficient [2]. These concepts are being continuously re-evaluated [3,4].

THEORY

This work is focused on the analysis of stability of flow in a rough channel. The roughness geometry is represented in terms of Fourier expansion [5]. The steady flow in the rough channel is determined by solving the Navier-Stokes equations with spectral accuracy. The boundary conditions at the rough wall are enforced using (i) mapping technique [6] and (ii) immersed boundary conditions concept [7]. Both approaches produce the same results. The stability analysis is generalized to account for the spatial modulation of the flow induced by the roughness and is able to deal with disturbances whose structure is related to the roughness structure (the ratio of the respective wave numbers is rational) as well as with disturbances whose structure is not related to the roughness (the ratio of the wave numbers is irrational). Explicit results are given for two case studies, i.e., roughness represented by a single Fourier mode (wavy wall model) and roughness in the form of spanwise grooves (grooved wall model). Figure 1 displays neutral curves obtained for different values of the flow Reynolds number in the case of wavy wall model. It can be seen that the flow becomes unstable at $Re\approx5000$ at this roughness amplitude and that the critical roughness wave number $\alpha\approx10$. Results based on the grooved wall model (not shown) demonstrate that good approximation of the critical Reynolds number can be obtained using only the leading Fourier mode to represent roughness geometry.

EXPERIMENT

Experiments have been carried out in order to confirm theoretical predictions. The wind tunnel used for the measurements is able to produce supercritical laminar Poiseulle flow for Re up to Re=6000 in the case of smooth walls. Controlled disturbances are introduces and their evolution is measured in the streamwise direction. Performance of the facility has been verified by measuring evolution of Tollmien-Schlichting waves in the case of smooth walls. Subsequent measurement have been carried out in the case of corrugated wall with the corrugation described by a single Fourier mode with the corrugation wave number $\alpha=1.02$ and the corrugation amplitude $S=0.04$. Figure 2 displays results of measured growth rates for Re=4000 and Re=5000. It can be seen that the flow is unstable even at Re=4000 in the presence of surface corrugation. The range of unstable disturbance wave numbers is found to be somewhat larger then in the case of smooth channel. Figure 2 also displays predicted growth rates; good agreement between the theory and the experimental measurements is observed.

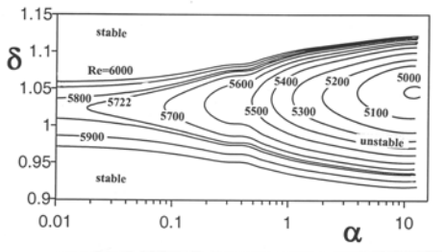


Figure 1 Neutral curves for the wavy wall model with roughness amplitude S=0.017 at different values of the flow Reynolds number Re as a function of the roughness wave number α and the disturbance wave number δ_r. Only two-dimensional disturbances are considered.

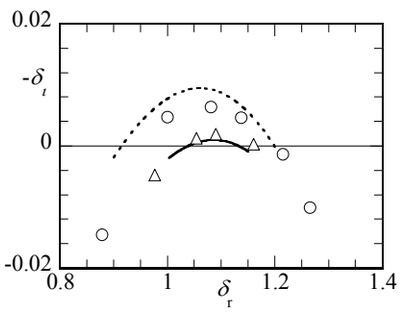


Figure 2. Variations of the amplification rate δ_i of disturbances in a Poiseuille flow at Re=4000 (triangles) and Re=5000 (circles) as a function of the disturbance wave number δ_r. One of the walls is smooth and the other has wavy form with the roughness wave number α=1.02 and the amplitude S=0.04.

SUMMARY

Theoretical and experimental investigation of stability of flow in a channel with distributed surface roughness has been carried out. Fourier expansions were used to model roughness geometry. Explicit results obtained in the case of wavy wall model (single Fourier mode roughness geometry) and grooved wall model (multi-Fourier modes roughness geometry) show that good approximation of the critical Reynolds can be obtained using leading Fourier mode to represent roughness geometry. Experiments carried out in the case of wavy wall model confirm theoretical predictions.

References:

[1] Reynolds, O., 1883, An experimental investigation of the circumstances which determine whether the motion of water shall be direct or sinuous, and of the wall of resistance in parallel channels", *Philos. Trans. R. Soc. London*, v.174, pp.935-82.
[2] Nikuradse, J., 1933, Strömungsgesetze in Rauhen Rohren, *VDI-Forschungscheft #361* (also NACA TM 1292 (1950)).
[3] Bradshaw, P., 2000, A note on "critical roughness" and "transitional roughness", *Phys.Fluids*, v.12, pp.1611-1614.
[4] Waigh, D.R., and Kind, R.J., 1998, Improved aerodynamic characterization of regular three-dimensional roughness, AIAA J., v.36, pp.1117-1119.
[5] Floryan, J.M., 1997, Stability of wall-bounded shear layers in the presence of simulated distributed roughness, *J. Fluid Mech*. v.335, pp.29-55.
[6] Cabal, T., Szumbarski, J. and Floryan, J.M., 2002, Stability of flow in a wavy channel, *J. Fluid Mech.,* v. 457, 2002, pp.191-212.
[7] Floryan, J.M., 2003, Vortex instability in a converging-diverging channel, *J. Fluid Mech*., v.482, 2003, pp.17-50.

XXI ICTAM, 15–21 August 2004, Warsaw, Poland

STABILITY OF LAGRANGIAN IDEAL FLOWS

STÉPHANE LEBLANC
LSEET, Université du Sud Toulon-Var, BP 20132, 83957 La Garde cedex, France

SUMMARY: A general method is presented to investigate the stability of ideal incompressible flows described in Lagrangian representation. Based on the theory of short-wavelength instabilities, the problem is reduced to a transport equation which involves only the distortion matrix of the equilibrium flow. Theory is applied to Gerstner's rotational free-surface gravity waves. It is shown that they are three-dimensionally unstable when their steepness exceeds $1/3$.

INTRODUCTION

The motion of a continuous medium may be described either by the trajectories of its material particles or by the velocity field expressed at any geometric point of space. Although both have been formalized by Euler himself [1], these alternative but equivalent descriptions are called respectively Lagrangian and Eulerian. Both present their own advantages. The Lagrangian description is more convenient to describe the deformations of the medium and is generally used in elasticity theory. Hydrodynamics clearly prefers the Eulerian approach probably because of the extreme complexity of the viscous terms. In ideal flows however, some explicit solutions are known in Lagrangian representation, such as Gerstner's waves discovered in 1802 [1] or unsteady vortices discovered recently [2]. However, it seems that the stability of Lagrangian flows has never been addressed in the past. We propose here a general method based on the theory of short-wave instabilities [3] and apply it to Gerstner's waves [4].

KINEMATICS AND LAGRANGIAN DYNAMICS

Let $\boldsymbol{U}(\boldsymbol{x},t)$ be the Eulerian velocity field of a continuous medium, and $\boldsymbol{X}(t;\boldsymbol{a})$ the trajectories of the material particles, where $\boldsymbol{a}$ is the Lagrangian label. We remind that $\boldsymbol{a}$ is not necessary the initial position of the particle. We assume that the motion is incompressible and smooth. The same notation will be used for any scalar, vector or tensor field f described in either Eulerian or Lagrangian representation: $f(\boldsymbol{X}(t;\boldsymbol{a}),t) \equiv f(t;\boldsymbol{a}) \equiv f(t)$. Material derivative will be noted $\dot{f}$ and initial data f_0. If $\dot{f}=0$, f is a Lagrangian invariant. Trajectories are solutions of $\dot{\boldsymbol{X}} = \boldsymbol{U}$.
Deformations of the medium are characterized by the matrix $\boldsymbol{\mathcal{F}}$ with components [1]:

$$\mathcal{F}_{ij} = \partial X_i/\partial a_j. \tag{1}$$

Continuity and incompressibility assumptions require that $\det \boldsymbol{\mathcal{F}}(t) = \det \boldsymbol{\mathcal{F}}_0 \neq 0$. Therefore $\boldsymbol{\mathcal{G}} = \boldsymbol{\mathcal{F}}^{-1}$ is defined. $\boldsymbol{\mathcal{F}}$ and $\boldsymbol{\mathcal{G}}$ satisfy respectively:

$$\dot{\boldsymbol{\mathcal{F}}} = \boldsymbol{\mathcal{L}}\boldsymbol{\mathcal{F}}, \quad \dot{\boldsymbol{\mathcal{G}}} = -\boldsymbol{\mathcal{G}}\boldsymbol{\mathcal{L}}, \tag{$2a,b$}$$

where $\boldsymbol{\mathcal{L}}$ is the velocity gradient tensor with components $\mathcal{L}_{ij} = \partial U_i/\partial x_j$.
The following kinematical relation may be established from (2):

$$\dot{\boldsymbol{\mathcal{F}}}^T\boldsymbol{\mathcal{F}} - \boldsymbol{\mathcal{F}}^T\dot{\boldsymbol{\mathcal{F}}} = -2\boldsymbol{\mathcal{F}}^T\boldsymbol{\mathcal{A}}\boldsymbol{\mathcal{F}}, \tag{3}$$

where $\boldsymbol{\mathcal{A}} = \frac{1}{2}(\boldsymbol{\mathcal{L}} - \boldsymbol{\mathcal{L}}^T)$ is the skew-symmetric vorticity tensor. In an ideal incompressible flow, it may be shown that the right hand side of (3) is a Lagrangian invariant [2]. The motion of the fluid may be fully described by the evolution of the matrix $\boldsymbol{\mathcal{F}}(t)$, solution of (3) plus incompressibility $\det \boldsymbol{\mathcal{F}} = \det \boldsymbol{\mathcal{F}}_0$ and consistency relations. Exact solutions have been discovered with this formulation, such as precessing or curvilinear vortices [2].

THE THEORY OF SHORT-WAVE INSTABILITIES

The linear stability of an Eulerian equilibrium flow with velocity $\boldsymbol{U}$ is characterized by the growth or decay of infinitesimal disturbances $\boldsymbol{u}$ governed by the linearized Euler equations. The theory of short-wave instabilities consists in considering the evolution of a rapidly-varying WKB wave packet $\boldsymbol{u} = \boldsymbol{v}\mathrm{e}^{\mathrm{i}\phi/\varepsilon}$ with $\varepsilon \ll 1$. By defining the wave vector $\boldsymbol{\xi} = \boldsymbol{\nabla}\phi$, it may be shown that the stability problem is reduced to a system of ordinary differential equations that evolves along the trajectories of the equilibrium flow [3]:

$$\dot{\boldsymbol{X}} = \boldsymbol{U}, \quad \dot{\boldsymbol{\xi}} = -\boldsymbol{\mathcal{L}}^T\boldsymbol{\xi}, \quad \dot{\boldsymbol{v}} = (2\boldsymbol{\xi}\otimes\boldsymbol{\xi}/|\boldsymbol{\xi}|^2 - \boldsymbol{\mathcal{I}})\boldsymbol{\mathcal{L}}\boldsymbol{v}. \tag{$4a,b,c$}$$

Here $\boldsymbol{\mathcal{L}}$ is the basic velocity gradient tensor, $\boldsymbol{\xi}\otimes\boldsymbol{\xi}$ the tensor with components $\xi_i\xi_j$, and $\boldsymbol{\mathcal{I}}$ the identity matrix. This system is completed by initial data for the wave vector and the velocity amplitude: $|\boldsymbol{\xi}_0| = |\boldsymbol{v}_0| = 1$ and $\boldsymbol{\xi}_0 \perp \boldsymbol{v}_0$. It is proved that *the equilibrium flow (steady or not) is unstable if there exists at least one trajectory along which $|\boldsymbol{v}(t)|$ grows unboundedly* [3].
A general solution of (4) is not known, but in some circumstances this set of equations may be locally integrated. Various classical stability results have been recovered and generalized in incompressible or compressible ideal flows (Rayleigh

and Leibovich-Stewartson criteria, hyperbolic and elliptical instabilities), and new instability mechanisms have been discovered in steady or unsteady flows. A review may be found in [3].

The theory of short-wave instabilities is greatly simplified when the equilibrium flow is described in Lagrangian form [4]. Indeed the trajectories being known explicitly, $(4a)$ is already solved. The distortion matrix $\boldsymbol{\mathcal{F}}$ defined in (1), its inverse $\boldsymbol{\mathcal{G}}$, their time derivative and their initial value may then be computed by differentiation. Also, it may be shown from (2) that the wave vector $\boldsymbol{\xi}(t)$ solution of $(4b)$ with initial data $\boldsymbol{\xi}_0$ admits the following explicit expression: $\boldsymbol{\xi}(t) = \boldsymbol{\mathcal{G}}^T(t)\boldsymbol{\mathcal{F}}_0^T\boldsymbol{\xi}_0$. Furthermore the basic velocity gradient $\boldsymbol{\mathcal{L}}$ involved in the amplitude equation $(4c)$ may also be calculated thanks to the kinematical relations (2). As a consequence, instead of system (4), the local stability of a Lagrangian ideal flow is reduced to the study of the following transport equation:

$$\dot{\boldsymbol{v}} = \left(\boldsymbol{\mathcal{F}} - 2\boldsymbol{\mathcal{G}}^T\frac{\boldsymbol{n}_0 \otimes \boldsymbol{n}_0}{\boldsymbol{n}_0^T\boldsymbol{\mathcal{G}}\boldsymbol{\mathcal{G}}^T\boldsymbol{n}_0}\right)\dot{\boldsymbol{\mathcal{G}}}\boldsymbol{v}, \quad \boldsymbol{n}_0 = \boldsymbol{\mathcal{F}}_0^T\boldsymbol{\xi}_0, \tag{5}$$

with initial data verifying $|\boldsymbol{\xi}_0| = |\boldsymbol{v}_0| = 1$ and $\boldsymbol{\xi}_0 \perp \boldsymbol{v}_0$.

APPLICATION TO GERSTNER'S WAVES

Theory is now applied to Gerstner's waves, an exact solution of Euler equations. In the Galilean frame $(O; \boldsymbol{i}, \boldsymbol{j}, \boldsymbol{k})$, let ρ be the density of an incompressible inviscid free-surface flow, subjected to gravity $-g\boldsymbol{j}$. The particle paths in Gerstner's waves are given parametrically by [1]:

$$X(t) = a + k^{-1}\mathrm{e}^{kb}\sin(ka - \omega t), \quad Y(t) = b - k^{-1}\mathrm{e}^{kb}\cos(ka - \omega t), \quad Z(t) = c, \tag{6a, b, c}$$

where $k > 0$ is the spatial wavenumber, $\omega = \sqrt{gk}$ the frequency, and $\boldsymbol{a} = (a, b, c)$ with $b < 0$ is the Lagrangian label. Trajectories are circles of radius e^{kb}/k and center (a, b) in planes $Z = \text{const}$.

Pressure field reads as $P = -\rho g b + \frac{1}{2}\rho\omega^2\mathrm{e}^{2kb}/k^2 + \text{const}$. Surfaces of constant pressure are parametrized by b and are represented on figure 1. They are trochoids with crest-trough amplitude $2\mathrm{e}^{kb}/k$. Any pressure level, say $P(b_0)$, may be chosen as free surface for the flow. The steepness parameter of the free-surface profile thus reads e^{kb_0} (half amplitude multiplied by wave number). When time varies those gravity waves propagate from left to right with celerity ω/k. Contrary to Stokes waves, Gerstner's waves are rotational with vorticity maximum and the free surface and decreasing rapidly with depth. Therefore they cannot be created from a state of rest nor by pressure forces.

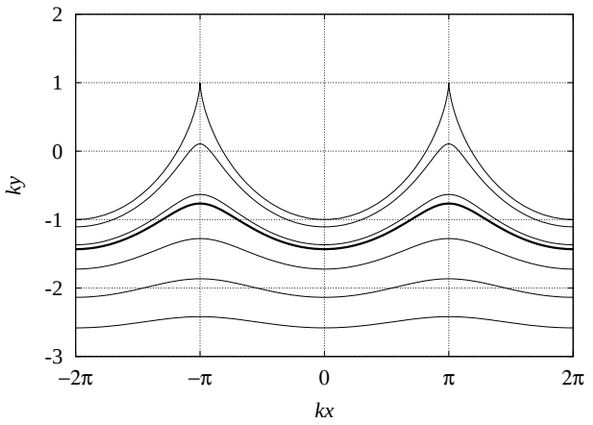


Figure 1. Contour lines of pressure of Gerstner's waves at $t = 0$, plotted for $kb = -2.5$ (lower curve) to $kb = 0$ (upper curve) with increment 0.5. Any level of constant pressure may be considered as the free surface for the flow. The thick line corresponds to $kb = -\ln 3$ above which Gerstner's waves are unstable to short-wavelength disturbances.

The equilibrium flow being two-dimensional in the plane $(O; \boldsymbol{i}, \boldsymbol{j})$, local disturbances characterized by $\boldsymbol{\xi}_0 = \boldsymbol{k}$ lead to the simplified equation $\dot{\boldsymbol{v}} = \boldsymbol{\mathcal{F}}\dot{\boldsymbol{\mathcal{G}}}\boldsymbol{v}$ instead of (5). Both tensors $\boldsymbol{\mathcal{F}}$ and $\dot{\boldsymbol{\mathcal{G}}}$ may be computed explicitly from (6) and the solution may be obtained in closed form [4]. The main result is that *Gerstner's waves are unstable when the free-surface vorticity exceeds* $\omega/4$, *or equivalently when the steepness parameter exceeds* $1/3$. The unstable region is represented on figure 1.

References

[1] SERRIN J.: Mathematical principles of classical fluid mechanics. In *Handbuch der Physik* vol. 8 (ed. S. Flügge & C. Truesdell), pp. 125–263. Springer-Verlag, 1959.

[2] YAKUBOVICH E.I., ZENKOVICH D.A.: Matrix approach to Lagrangian fluid dynamics. *J. Fluid Mech.* **443**, 167–196, 2001.

[3] FRIEDLANDER S., LIPTON-LIFSCHITZ A.: Localized instabilities in fluids. In *Handbook of Mathematical Fluid Dynamics* vol. 2 (ed. S. Friedlander & D. Serre), pp. 289–354. North-Holland, 2003.

[4] LEBLANC S.: Local stability of Gerstner's waves. *J. Fluid Mech.* **506**, 245–254, 2004

INSTABILITY THRESHOLDS OF FLOW BETWEEN EXACTLY COUNTER-ROTATING DISKS

C. Nore[1], M. Tartar[1], O. Daube[2,1], L.S. Tuckerman[1]
[1]*LIMSI-CNRS, BP 133, 91403 Orsay Cedex France*
[2]*Université d'Evry, Val d'Essonne, 40 rue du Pelvoux, 91020 Evry Cedex France*

Summary We present the linear three-dimensional instabilities of the flow between exactly counter-rotating disks over the height-to-radius aspect ratio range $0.5 \leq \Gamma \leq 3$. The lowest Reynolds number threshold always corresponds to a non-axisymmetric and stationary eigenmode and the critical azimuthal wavenumber obeys $m_C \approx 2.2/\Gamma$. The axisymmetric instabilities are quite complicated, and are organized around various codimension-two points.

The von Kármán flow engendered by the differential rotation of the upper and lower bounding disks of a cylinder exhibits a large variety of phenomena, and depends on three parameters, which can be taken to be an angular velocity ratio $s \equiv \Omega_{up}/\Omega_{low}$, an aspect ratio $\Gamma \equiv H/R$, and a Reynolds number $Re \equiv \Omega_{low} R^2/\nu$. This flow is of growing interest to fluid dynamicists, but its three-dimensional patterns and transitions have as yet been explored for only a few parameter combinations, e.g. [1, 2, 3, 4, 5, 6, 7].

We focus on the case $s = -1$ in which the two disks rotate in equal and opposite directions. The system is then not only axisymmetric, but also invariant under simultaneous reflection in z and θ (or any horizontal axis), leading to the symmetry group $O(2)$. For low Re, the solution is unique and axisymmetric. For all values of Γ and Re, there exists an axisymmetric solution called the base state which is connected smoothly to the unique low-Re solution. We calculate the Reynolds numbers at which this solution becomes linearly unstable for $0.5 \leq \Gamma \leq 3.0$.

Newton's method, combined with a streamfunction-vorticity formulation, is used to calculate the base state. To calculate growth rates, we numerically integrate the Navier-Stokes equations linearized about the base state using a 3D code [6, 7] which combines a Fourier decomposition in θ with a staggered non-uniform grid in (r, z). For an axisymmetric base state, the stability computation separates into a family of decoupled subproblems each associated with an azimuthal wavenumber m. The leading eigenvalues are extracted as half the slope of the evolution of the logarithm of the energy corresponding to each m. The thresholds $Re_m(\Gamma)$ are calculated by interpolation and shown in figure 1.

The lowest threshold $Re_C(\Gamma) \equiv \min_m Re_m(\Gamma)$ is achieved for non-axisymmetric eigenmodes over the range $0.5 \leq \Gamma \leq 3.0$ and is shown in figure 3a. The fact that these modes are stationary is a consequence of the $O(2)$ symmetry of the configuration and of the basic flow. This leads to non-axisymmetric eigenmodes which are both stationary and invariant under simultaneous reflection in z and in θ; see figure 2. Figure 3b shows that the critical wavenumber increases approximately linearly with the radius, which is consistent with the idea that this is a generalized Kelvin-Helmholtz instability of an equatorial azimuthal shear layer occupying a constant proportion of the height.

Although the axisymmetric modes are not critical for these parameters, we present their thresholds in order to provide a complete framework which can be continued to other values of Γ or s. Figure 4a shows two pitchfork bifurcations existing for $\Gamma < 0.78$ and disappearing at an isola formation point. Figures 4b,c show two Hopf bifurcations with different frequencies co-existing for $\Gamma < 0.55$, where one of them disappears at a Takens-Bogdanov point. The rapid variation of the axisymmetric Hopf bifurcation threshold seen in figure 1 near $\Gamma = 1.6$ is due to an intersection of two complex eigenvalues. All the codimension-two points, both non-axisymmetric and axisymmetric, are shown in the table.

Competing wavenumbers or bifurcations	Γ	Re	Description
(4,3)	0.63	365	
(3,2)	0.95	310	
(2,1)	1.64	330	
H_1/P_2	0.51	2802	
H_1/H_2	0.535	2602	
H_2/P_2	0.55	2309	Takens-Bogdanov point
P_1/P_2	0.78	700	isola formation point
H_1	1.59	1860	intersection of two complex eigenvalues

References

[1] Y.A. Gelfgat, P.Z. Bar-Yoseph, A. Solan: Three-dimensional instability of axisymmetric flow in a rotating lid–cylinder enclosure, *J. Fluid Mech.* **438**, 363, 2001.
[2] J.M. Lopez, J.E. Hart, F. Marques, S. Kittelman, J. Shen: Instability and mode interactions in a differentially–driven rotating cylinder, *J. Fluid Mech.* **462**, 383, 2002.
[3] L. Schouveiler, P. Le Gal, M.-P. Chauve: Instabilities of the flow between a rotating and a stationary disk, *J. Fluid Mech.* **443**, 329, 2001.
[4] G. Gauthier, P. Gondret, F. Moisy, M. Rabaud.: Instabilities of the flow between co and counter–rotating disks, *J. Fluid Mech.* **473**, 1, 2002.
[5] E. Serre, E. Crespo del Arco, P. Bontoux: Annular and spiral patterns in flows between rotating and stationary disks, *J. Fluid Mech.* **434**, 65, 2001.
[6] C. Nore, L.S. Tuckerman, O. Daube, S. Xin: The 1 : 2 mode interaction in exactly counter-rotating von Kármán swirling flow, *J. Fluid Mech.* **477**, 51, 2003.
[7] C. Nore, M. Tartar, O. Daube, L. S. Tuckerman: Survey of instability thresholds of flow between exactly counter-rotating disks, *J. Fluid Mech.*, to appear.

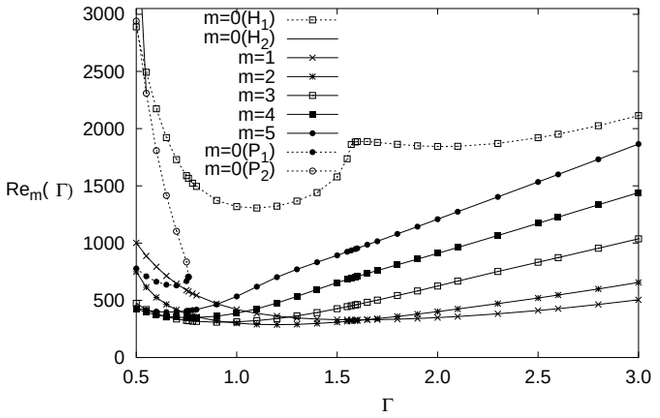


Figure 1. Thresholds $Re_m(\Gamma)$ for azimuthal modes $m = 0$ to 5 as functions of the aspect ratio Γ. The modes $m = 1$ to 5 are stationary while the $m = 0$ mode is stationary for $m = 0$ (P_1) and (P_2) and oscillatory for $m = 0$ (H_1) and (H_2).



Figure 2. Vertical velocity contours of an $m = 3$ eigenvector at $z = \Gamma/4$, $z = 0$, and $z = -\Gamma/4$.

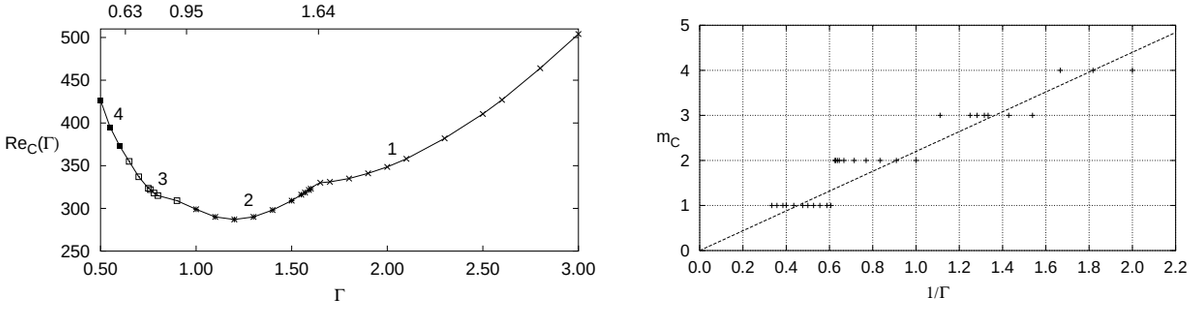


Figure 3. (a) Critical Reynolds number $Re_C(\Gamma)$ as a function of Γ realised for different critical wavenumbers: $m = 1$ ($\times$), $m = 2$ ($*$), $m = 3$ ($\square$), $m = 4$ ($\blacksquare$). (b) Critical wavenumber m_C ($+$) as a function of $1/\Gamma$ with the indicative dashed line $m = 2.2/\Gamma$.

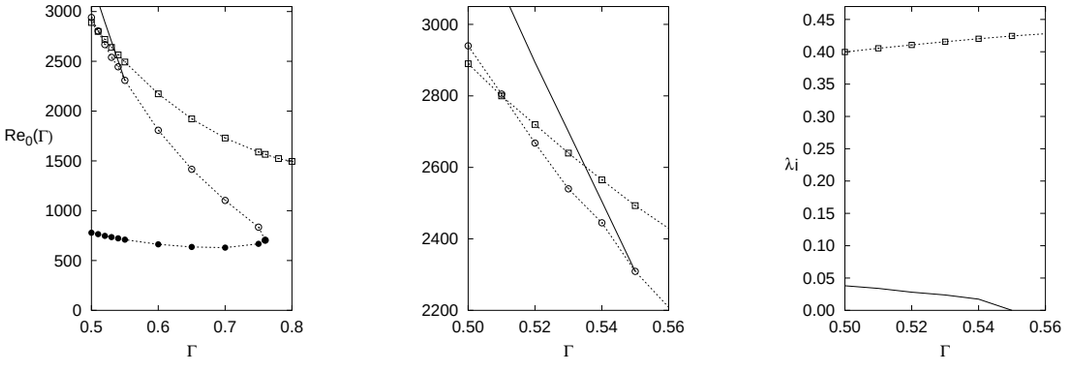


Figure 4. (a) Axisymmetric thresholds: two stationary bifurcations P_1 ($\bullet$) and P_2 ($\circ$) and two Hopf bifurcations H_1 ($\square$) and H_2 (—). P_1 and P_2 disappear at the isolation formation point at $\Gamma = 0.78$. (b) Enlargement of (a) showing the disappearance of H_2 at the Takens-Bogdanov point at $\Gamma = 0.55$. (c) Frequencies for H_1 ($\square$) and H_2 (—).

TRANSIENT GROWTH IN DEVELOPING PLANE AND HAGEN POISEUILLE FLOW

Peter W. Duck
Department of Mathematics, University of Manchester, Manchester, England

Summary The problem of the stability of developing entry flow in both two-dimensional channels and circular pipes is investigated. The basic flow is generated by uniform flow entering a channel/pipe, which then provokes the growth of boundary layers on the walls, until (far downstream) fully developed (Poiseuille) flow is attained; the length for this development to be $\mathcal{O}$(Reynolds number) $\times$ the channel/pipe width/diameter. This enables the use of high-Reynolds-number theory, leading to boundary-layer-type equations; as such there is no need to impose heuristic parallel-flow approximations. The resulting flow is shown to be susceptible to significant, three-dimensional transient (initially algebraic) growth in the streamwise direction, and as such large amplifications to flow disturbances are shown to occur (followed by ultimate decay far downstream). It is suggested that this initial amplification of disturbances is a possible mechanism for flow transition, with steady disturbances being the most 'dangerous'.

INTRODUCTION AND FORMALISM

The stability of Hagen-Poiseuille flow has intrigued scientists for more than a century since Reynolds' experimental investigations. It is reasonably well accepted that *fully developed* Hagen-Poiseuille flow is linearly stable and yet, in practice, most pipe flows are turbulent. In a carefully controlled experimental study of this flow the following sequence of events is usually observed. Below a Reynolds number, Re of $\approx 2,000$ any disturbance introduced into the flow will decay and the flow can be said to be stable in practical terms. Above this value it is possible to maintain laminar flow and the highest recorded Re for laminar flow is $\approx 100,000$ which was achieved with extraordinary amounts of care.

In this paper we consider the stability of developing flow inside two-dimensional channels and circular pipes. At the inlet, the flow is taken to be uniform, and then boundary layers form on the channel/pipe walls, which downstream eventually merge to form fully developed flow. The lengthscale for fully developed flow to become established is very long at large Reynolds numbers - $\mathcal{O}(Re)\times$ width/diameter of the channel/pipe. Close to the inlet the boundary layers resemble flat-plate (Blasius) boundary layers, which are susceptible to streamwise algebraic growth of three-dimensional disturbances ([1], [2]). In this paper it is shown how this class of disturbance is important in the flow development problem.

Consider the two-dimensional channel case (the pipe case develops in an analogous manner). We take coordinates $L(xRe, y, z)$, origin at the leading edge of the lower wall, which lies along $y = 0$, with the flow directed along the positive x direction; z is the crossflow direction. Here L denotes the semi-width of the channel, and the Reynolds number $Re = \frac{U_\infty L}{\nu}$, with U_∞ the incoming (uniform) flow velocity and ν the kinematic viscosity of the fluid (assumed to be incompressible). Throughout it is assumed $Re \gg 1$, enabling the use of the boundary-layer equations to be entirely rational. The flow velocity is then written in the form $\mathbf{u} = U_\infty(U, Re^{-1}V, Re^{-1}W)$, whilst the pressure develops in the form $p = \rho U_\infty^2(P_0(x) + Re^{-1}P_1(x) + Re^{-2}P_2(x, y, z) + \ldots)$, ($\rho$ being the density of the fluid). Taking the leading-order (in Re) terms in the Navier-Stokes equations leads to

$$\begin{aligned} U_x + V_y + W_z = 0 \quad &, \quad U_t + UU_x + VU_y + WU_z = -P_{0x} + U_{yy} + U_{zz}, \\ V_t + UV_x + VV_y + WV_z = -P_{2y} + V_{yy} + V_{zz} \quad &, \quad W_t + UW_x + VW_y + WW_z = -P_{2z} + W_{yy} + W_{zz}, \end{aligned} \tag{1}$$

where $(\frac{L}{U_\infty})t$ denotes dimensional time. Note the y and z components of the momentum equation involve the *third* term in the pressure expansion.

We now decompose the velocity field (U, V, W) into a base flow and a small amplitude ($\mathcal{O}(\delta)$) perturbation, as follows

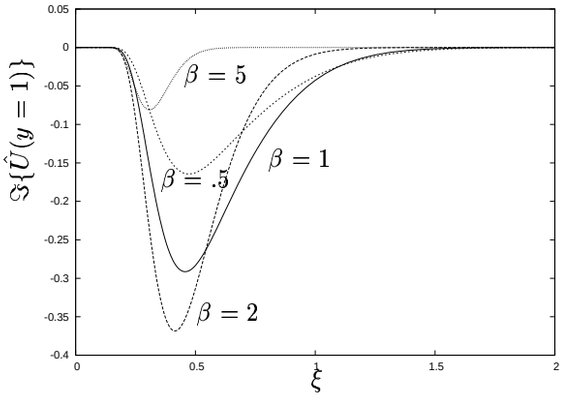
$$(U, V, W, P_2) = (U_0, V_0, 0, 0) + \delta(\hat{U}, \hat{V}, \hat{W}, \hat{P}_2)e^{i\omega t + i\beta z} + \mathcal{O}(\delta^2), \tag{2}$$

ω being the frequency of the disturbance and β the crossflow wavenumber.

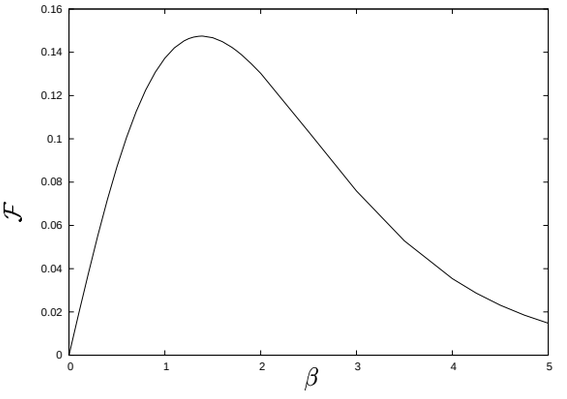
In order to generate accurate results for the disturbance field, it was found necessary to treat both the base flow and the disturbance field with great care, employing a double numerical grid which mimicked the analytic behaviour as $x \to 0$. It is possible to deduce from the analysis that as $x \to 0$, the disturbance field admits streamwise-growing algebraic behaviour, corresponding to that found in [1], [2], [3] and [4], provided the disturbances are three-dimensional (i.e. $\beta \neq 0$). Eigenfunctions corresponding to these modes then provided the initial conditions for the disturbance field, which was then extended downstream using routine parabolic marching techniques (a similar procedure was adopted for the base flow).

RESULTS

Results for the streamwise perturbation velocity along the line of symmetry within the channel are shown in 1(a) for four spanwise wavenumbers (where $\xi = \sqrt{x}$); these results are all for the case of steady disturbances ($\omega = 0$) since it is found that these are generally the most dangerous, i.e. provoke the largest flow response. Of particular note is the value of β that generates the most significant response. This can obviously be measured in a variety of means, but here we define a



(a) Streamwise perturbation velocity along symmetry line



(b) Variation of response function with β

Figure 1. Channel results ($\omega = 0$)

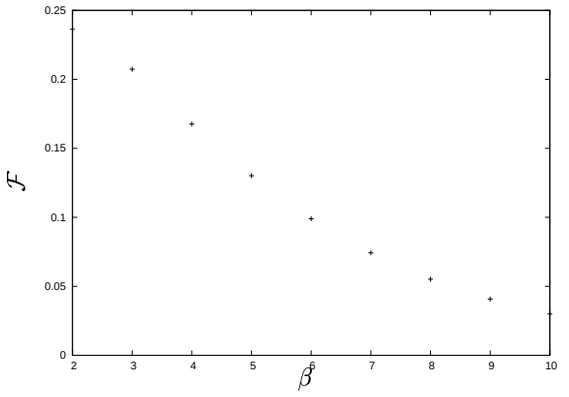


Figure 2. Variation of response function with β, pipe case ($\omega = 0$)

response function $\mathcal{F} = \int_0^\infty |\hat{U}(\xi, y = 1)| d\xi$. Results for the variation of this quantity, as the crossflow wavenumber is varied are shown in figure 1(b), which indicates a maximum at $\beta \approx 1.38$.

There are some interesting similarities and differences in the case of developing flow inside a circular pipe. Firstly if the spanwise wavenumber is replaced by an azimuthal wavenumber β, then this must be restricted to integer values. Second, detailed analysis reveals that $\beta \geq 2$. Again, careful numerical work (including a judicious choice of coordinates) is necessary for accurate stability results. Since (for the permissible values of azimuthal wavenumber) the axial velocity component of the disturbance field is zero, the use of the previous definition of response function is no longer appropriate, and so instead we took $\mathcal{F} = \int_0^\infty |\hat{U}(\xi, r = \sqrt{\frac{1}{2}})| d\xi$, (where r is the non-dimensional radius, such that $0 \leq r \leq 1$). Results for this measure (again, for $\omega = 0$) are shown in figure 2. The largest flow response is seen clearly to occur at the smallest permissible value of azimuthal wavenumber, i.e. $\beta = 2$.

CONCLUSION

Given the significant flow disturbance response that is possible, there is therefore some potential for flow transition to be provoked through the mechanism described in this paper.

References

[1] Luchini, P.: Reynolds-number-independent instability of the boundary layer over a flat surface: optimal perturbations. *J. Fluid Mech* **327** 101, 1996.

[2] Duck, P.W., Stow, S.R. and Dhanak, M.R.: Non-similarity solutions to the corner boundary-layer equations (and the effects of wall transpiration). *J. Fluid Mech* **400** 125, 1999.

[3] Andersson, P., Berggren, M. and Henningson, D.S.: Optimal disturbances and bypass transition in boundary layers. *Phys. Fluids* **11** 134, 1999.

[4] Luchini, P.: Reynolds-number-independent instability of the boundary layer over a flat surface: optimal perturbations. *J. Fluid Mech* **404** 289, 2000.

THREE-DIMENSIONAL GLOBAL MODES IN SPATIALLY VARYING RAYLEIGH–BÉNARD–POISEUILLE CONVECTION

D. Martinand*, Ph. Carrière† and P. A. Monkewitz‡,
* *Department of Aeronautics, Imperial College London, London SW7 2AZ, UNITED KINGDOM*
† *LMFA, École Centrale de Lyon, BP163, F-69131 ECULLY Cedex, FRANCE*
‡ *LMF, École Polytechnique Fédérale de Lausanne, CH-1015 LAUSANNE, SWITZERLAND*

Summary The Rayleigh–Bénard–Poiseuille convection with spatially varying difference of temperatures on the upper and lower plates is the archetype of systems sustaining the growth of synchronised global modes. An analytical construction method and a selection criterion for the most unstable linear instability is proposed in cases of slowly varying systems. The results are in very good agreement with direct numerical simulations.

This study focuses on the instabilities in a laminar Poiseuille flow cooled from its upper plate and heated from its lower one, the latter of which presents a two-dimensional bump of temperature. This flow is representative of systems exhibiting temporally synchronised, or global, instabilities despite a spatial variation of the energy flux transferred to these perturbations — flux imposed by the difference between the temperatures of the lower and upper plates in this case of Rayleigh–Bénard–Poiseuille convection. This tuning to a self-selected frequency cannot be accounted for by a local criterion straightforwardly extended from the homogeneous system. Hence a global selection criterion, taking the inhomogeneity into account, has to be sought. Whereas an arbitrary spatial variation of the basic state is usually only accessible through experimental or numerical stability analysis, the description of slowly varying systems can be coped with analytically. Slow variation indeed allows us to consider local stability properties, such as convective and absolute instability, as the lowest order of a description taking the inhomogeneity into account by means of a Wentzel–Kramers–Brillouin–Jeffreys (WKBJ) expansion. Beyond the local absolute instability threshold, the group velocity of some propagative waves solutions of the local homogeneous stability problem can vanish at some points of the physical domain, called turning points, where the WKBJ expansion breaks down. Our present work aims at extending to two-dimensional situations which present an "island" of instability, i.e. the two-dimensional bump of temperature, the analytical construction of a global mode governed by a double turning point located at the maximum of the local growth rate . The analytical flows and critical conditions obtained by this method are then compared with direct numerical simulations of the Navier–Stokes equations under the Boussinesq approximation.

GLOBAL MODE CONSTRUCTION AND SELECTION

WKBJ expansion

In the inhomogeneous Rayleigh–Bénard–Poiseuille flow, the slow and rapid horizontal variations are separated by the use of slow coordinates $X = \varepsilon x$ and $Y = \varepsilon y$, where ε is a small parameter. The basic steady state is sought as an expansion in powers of ε. The WKBJ expansion of the perturbation is expressed as

$$\boldsymbol{v} = \left(\boldsymbol{v}_0\left(X,Y,z\right) + \varepsilon \boldsymbol{v}_1\left(X,Y,z\right) + O\left(\varepsilon^2\right)\right) \exp\left(\frac{\mathrm{i}}{\varepsilon}\Phi\left(X,Y\right) - \mathrm{i}\omega t\right) + \mathrm{c.c.}, \tag{1}$$

with the complex frequency $\omega = \omega_0 + \varepsilon\omega_1 + O\left(\varepsilon^2\right)$ and wavevector $\boldsymbol{k}\left(X,Y\right) = \boldsymbol{\nabla}\Phi\left(X,Y\right)$. At order $O\left(\varepsilon^0\right)$ of the linearised dynamics equations, the perturbation is sought as a solution of the homogeneous local problem — parameterised by the local Rayleigh number $\mathcal{R}\left(X,Y\right)$ with the frequency ω_0 and the wavevector $\boldsymbol{k}\left(X,Y\right)$ — modulated by an amplitude $A\left(X,Y\right)$. As a consequence the dispersion relation, expressed as

$$\omega\left(\partial_X\Phi, \partial_Y\Phi, \mathcal{R}\left(X,Y\right)\right) = \omega_0, \tag{2}$$

is satisfied by $\Phi\left(X,Y\right)$. At order $O\left(\varepsilon^1\right)$ the solvability condition for the perturbation leads to the amplitude equation satisfied by $A\left(X,Y\right)$:

$$\partial_X A\, \partial_{k_x}\omega + \partial_Y A\, \partial_{k_y}\omega + A\left(-\mathrm{i}\omega_1 + \Gamma\left(X,Y;\omega_0\right)\right) = 0, \tag{3}$$

where $\Gamma\left(X,Y;\omega_0\right)$ gathers terms due to the spatial dependences of the basic state, the wavevector and $\mathcal{R}$. The integration of $\Phi\left(X,Y\right)$ and $A\left(X,Y\right)$, which results in the complete first order of the WKBJ expansion, can be done along the — common — characteristics of equations (2) and (3), whose tangential vector is the group velocity $\left(\partial_{k_x}\omega, \partial_{k_y}\omega\right)$, where the values of ω_0 and ω_1 in these equations must be known and a gauge choice for Φ and A must be given. This can be achieved by means of a two-dimensional double turning point, where $\partial^{\mathrm{t.p.}}_{k_x}\omega = \partial^{\mathrm{t.p.}}_{k_y}\omega = 0$ and $\partial^{\mathrm{t.p.}}_{X}\omega = \partial^{\mathrm{t.p.}}_{Y}\omega = 0$.

Turning point region and selection criterion

Since the WKBJ approximation breaks down at a turning point the perturbation is sought as an expansion in powers of $\varepsilon^{1/2}$. The homogeneous problem recovered at order $O\left(\varepsilon^0\right)$ and the condition $\partial^{\mathrm{t.p.}}_{k_x}\omega = \partial^{\mathrm{t.p.}}_{k_y}\omega = 0$ imposes the solution

$\widehat{\boldsymbol{v}_0}^{\mathrm{t.p.}}(z)$, associated with the frequency $\omega_0^{\mathrm{t.p.}}$ and the wavevector $\left(k_x^{\mathrm{t.p.}}, k_y^{\mathrm{t.p.}}\right)$, of this eigenproblem expressed at the turning point. The condition $\partial_X^{\mathrm{t.p.}}\omega = \partial_Y^{\mathrm{t.p.}}\omega = 0$ imposes the double turning point to be located at the maximum of $\mathcal{R}(x,y)$. The solvability condition at order $O\left(\varepsilon^1\right)$ yields the amplitude of the first order of the perturbation. This first order of the perturbation is then given by:

$$\boldsymbol{v}_0^{\mathrm{inner}}(x,y,z,t) = \widehat{\boldsymbol{v}_0}^{\mathrm{t.p.}}(z)\exp\left(-\frac{\varepsilon\alpha}{2}x^2 - \frac{\varepsilon\beta}{2}y^2 - \varepsilon\delta xy\right)\exp\left(\mathrm{i}\left(k_x^{\mathrm{t}}x + k_y^{\mathrm{t}}y\right) - \mathrm{i}\left(\omega_0^{\mathrm{t.p.}} + \varepsilon\omega_1\right)t\right), \qquad (4)$$

where the coefficients $\varepsilon\alpha$, $\varepsilon\beta$ and $\varepsilon\delta$ and the correction of the complex frequency $\varepsilon\omega_1$ are deduced from the dispersion relation and the $\mathcal{R}(x,y)$ function expressed at the turning point. Furthermore, the first order of the global mode in the turning point region (4) provides a gauge choice for Φ and A.

COMPARISON WITH NUMERICAL SIMULATIONS

For functions $\mathcal{R}(x,y)$ as in figure 1(a), the leading order of the inner expansion of the most unstable mode (4) and its critical conditions flowing from the evaluation of $\omega_0^{\mathrm{t.p.}} + \varepsilon\omega_1$ are compared with the results of a spectral method direct numerical simulations. Rolls orientated transversely with respect to the mean flow, predicted analytically (figure 1(b)) and observed numerically (figure 1(c)), and the very good agreement for their critical conditions underline the relevancy of the analytical selection criterion.

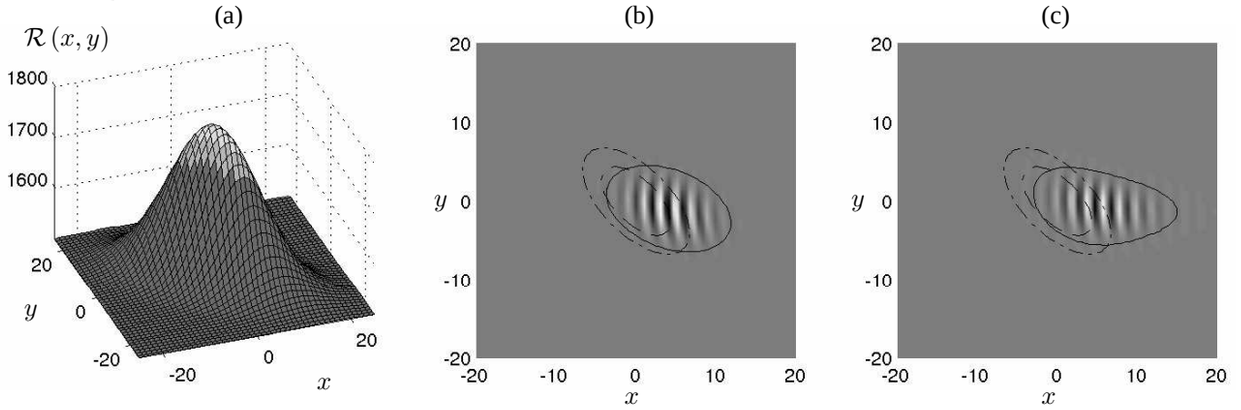


Figure 1. (a): bump of Rayleigh number $\mathcal{R}(x,y)$ with, for increasingly lighter shades of gray, the stable, convectively unstable and absolutely unstable regions obtained for a mean fbw along the x-direction at Reynolds number $R = 0.40$ and a Prandtl number $P = 7$. Comparison between the vertical velocity components of the convection rolls of the analytical approximation (b) and direct numerical simulation at time $t = 125$ (c), with the convectively unstable/stable boundary (dashed-dotted lines), the absolutely/convectively unstable boundary (dashed lines) and the contour where the amplitude of the perturbation reaches fi ve percent of its maximum (solid lines).

Furthermore, the numerical simulations shed light on the nonlinear behaviour of the instabilities. They distinguish situations where the linear mode saturates and preserves its maximum close to the downstream convectively unstable/stable boundary (figure 2(a)) from situations where a front forms at the upstream convectively/absolutely unstable boundary (figure 2(b)), which raise the question of the two-dimensional dynamics of a front.

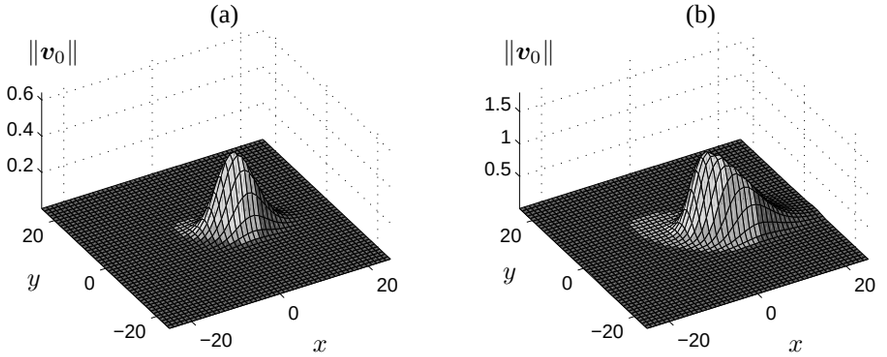


Figure 2. Nonlinear evolution of the amplitude of the instability obtained by numerical simulation for Reynolds numbers $R = 0.4$ (a) and $R = 0.38$ (b), with superimposed local stability properties as in fi gure 1(a).

ELLIPTICAL INSTABILITY IN A ROTATING SPHEROID

Lacaze Laurent, Le Dizès Stéphane and Le Gal Patrice
Institut de Recherche sur les Phénomènes Hors Equilibre, 49 rue F. Joliot Curie, B.P. 146, 13384, Marseille, France.

Summary
This study concerns the elliptical instability of a flow in a rotating deformed sphere. The aim of our work is to observe and measure the characterics of this instability in experiments and to compare them with theorical predictions. For this purpose, an elastic and transparent hollow sphere has been moulded. The flow is visualised using Kalliroscope flakes as the sphere is set into rotation and compressed by two rollers. The elliptical instability occurs by the appearance of the so-called 'spin-over' mode whose growth rates and saturations are measured for different Eckman numbers by video image analysis. These growth rates compare avantageously to theorical calculations which are performed using classical asymptotic expansions. The linear analysis is then completed by a non linear model which predicts correctly the asymptotic regimes for high Eckman numbers. Some results that concern the elliptic instability in a rotating deformed spherical shell or the triangular instability will also be presented.

INTRODUCTION

The elliptical instability is a classical three-dimensionnal instability of fluid dynamics. It is known to affect and even to destroy vortical flows. As described in the review by Kerswell [1], the instability mechanism lies on a resonance phenomenon between inertial (Kelvin) waves and external strain fields. Therefore, this instability appears to be very attractive to explain the three-dimensionnal undulations of non axisymmetric vortices distorted by strain fields [2] as it is the case in turbulence [3] or vortex dynamics [4, 5]. But another major interest of the elliptical instability concerns the behavior of the flows contained in rotating ellipsoids which are laboratory models of astrophysical objects subjected to tidal distorsions of close gravitationnal bodies [6, 7, 8]. More specifically, the occurence of this instability in the motion of the molten iron cores of planets, such as the Earth, would be of prime importance in the understanding of the generation and the dynamics of the magnetic fields of planets [7]. With this aim, Aldridge et al [9] have performed computations and built a rotating deformable shell where they observed some indications of the presence of the elliptical instability in the spherical geometry. Using the technique invented by Malkus [10], and more recently intensively used by Eloy *et al.* [11], we have been able to apply an elliptical constraint to a deformable rotating sphere and measure the characteristics of the flow instabilities by image analysis and finally compared them to the analytical treatment of the instability [12].

EXPERIMENTAL APPARATUS

The hollow sphere is moulded in a cylindrical block of transparent silicone gel. The cylinder is then placed in the device used by Eloy *et al.* [11]. It is set in rotation versus its axis while it is gently compressed by two rollers parallel to the rotation axis. A video camera records the motions of water seeded by kalliroscope particles and enlighted by a laser sheet. A snapshot of the fluid flow is shown on figure 1a.

STABILITY ANALYSIS

The stability of a fluid in a rotating sphere which is slightly elliptically deformed is analysed. It is shown that two linear neutral modes associated with the rotation of the fluid can resonate with the strain induced by the deformation. The condition of resonance can be expressed in term of azimuthal wavenumber and frequency. This resonance leads to a temporal growth of the instability mode amplitude. The so-called spin-over mode is shown to be always the most unstable mode in the range of Ekman number E and deformation rate ε of the experimental flow. This mode is a solid body rotating flow whose rotation axis is perpendicular to the main rotation. The growth rate of this unstable mode can be analytically calculated and a weakly non linear model is developed to predict an observed saturated regime for peculiar values of E.

RESULTS

Figure 1a shows a typical visualisation of the unstable spin-over mode in a meridional plane. The typical S shape of the rotation axis is due to the combination of the main rotation, the spin-over mode and viscous boundary layers. A video analysis permits to measure the tilting angle of the rotation axis as a function of time. Then an estimation of the growth rate can be evaluate and compare to the theoretical prediction (see figure 2).
On figure 1b, one of the experimental video analysis is compared to the weakly non linear model. The model is in agreement with the saturation observed and measured in the experiment. This regime is observed for sufficiently large value of E. If E is smaller than a critical value, small structures destroy the spin-over mode and then more complex dynamic is visualized. For a peculiar value of E, we also observe an intermitent regime between spin-over and peripherical small structures.

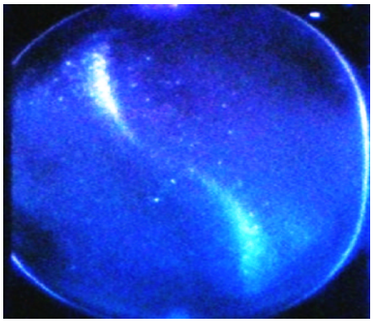
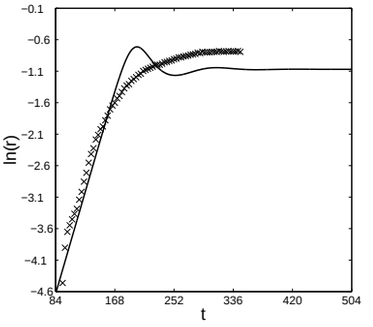
a)  b) 

Figure 1. a) Visualisation of the spin-over mode in a meridional plane. b) Comparison between the experimental results ($\times$) and the nonlinear model. ($E = 2.5\ 10^{-4}$ and $\varepsilon = 0.16$).

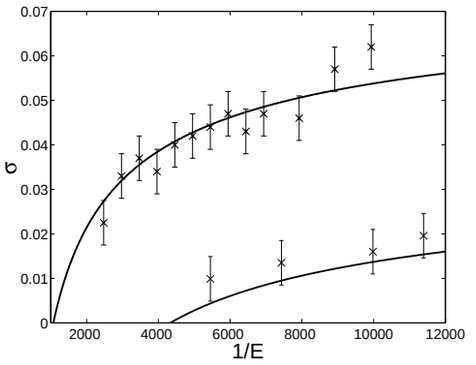


Figure 2. Growth rate versus the inverse of the Ekman number for $\varepsilon = 0.08$ (lower) and $\varepsilon = 0.16$ (upper). Experimental results ($\times$) and linear theory (solid line).

The flow dynamic in a deformed spherical shell has also been investigated. The linear growth rate is in this case measured with laser Doppler anemometry. Comparisons with the linear stability theory have also been carried out for this configuration.

References

[1] R. KERSWELL, Elliptical instability, *Annual Rev. Fluid Mech.*, **34**, 83-113 (2002).

[2] MOORE, D. W. & SAFFMAN, P. G. 1975 The instability of a straight vortex filament in a strain field. *Proc. R. Soc. Lond. A.* **346**, 413–425.

[3] O. CADOT AND S. DOUADY AND Y. COUDER, Characterization of the low pressure filaments in three-dimensional turbulent shear flow, *Phys. Fluids*, **7**, (3), 630-646 (1995).

[4] T.LEWEKE AND C.H.K.WILLIAMSON, Cooperative elliptic instability of a vortex pair, *J. Fluid Mech.*, **360** , 85-119 (1998).

[5] P. MEUNIER AND T. LEWEKE, Three-dimensional instability during vortex merging, *Phys. Fluids*, **13**, (10), 85-119 (2001).

[6] W.V.R. MALKUS, Precession of the Earth as the Cause of Geomagnetism, *Sciences*, **160**, (3825), 259-264 (1968).

[7] KERSWELL, R.R. Tidal excitation of hydromagnetic waves and their damping in the Earth, *J. Fluid Mech.*, **274**, 219-241 (1994).

[8] GLEDZER, E. B. AND PONOMAREV, V. M. Finite dimensional approximation of the motions of an incompressible fluid in an ellipsoidal cavity, *Isv. Atmos. Ocean. Phys.*, **13**, (3825), 565-569 (1977).

[9] ALDRIDGE, A., SEYED-MAHMOUD, B., HENDERSON, G. & VAN WIJNGAARDEN, W. 1997 Elliptical instability of the earth's fluid core. *Phys. Earth Planet. Int.* **103**, 365–374.

[10] W.V.R. MALKUS, An experimental study of global instabilities due to tidal (elliptical) distortion of a rotating elastic cylinder, *Geophys. Astrophys. Fluid Dynamics*, **48**, 123-134 (1989).

[11] ELOY, C. AND LE GAL, P. AND LE DIZÈS, S. Elliptic and triangular instabilities in rotating cylinders, *J. Fluid Mech.*, **476**, 357-388 (2003).

[12] LACAZE, L. AND LE GAL, P. AND LE DIZÈS, S. Elliptical instability in a rotating spheroid, *J. Fluid Mech.*, in press.

THE INSTABILITY OF A LOCALIZED VORTEX DISTURBANCE IN UNIFORM SHEAR FLOW

Jacob Cohen*, Victoria Suponitsky*, Pinhas Z. Bar-Yoseph**
*Faculty of Aerospace Engineering, Technion, Haifa, Israel
**Faculty of Mechanical Engineering, Technion, Haifa, Israel

Introduction

The similarity of the coherent structures (streaks and hairpin vortices) naturally occurring in different fully developed bounded turbulent shear flows as well as in transitional flows suggests the existence of a basic mechanism responsible for the formation of these structures, under various base flow conditions. The common elements for all such flows are the *shear of the base flow* and the presence of a localized vortical disturbance. The objective of the present numerical (and theoretical) study is to examine the capability of a *simple model of interaction, between a localized vortical disturbance and laminar uniform unbounded shear flow*, to reproduce the generation mechanism and characteristics of the coherent structures that naturally occur in turbulent bounded shear flows. This objective is shown schematically in Fig. 1.

Problem statement and methodology

The base flow is characterized by its shear $\boldsymbol{\Omega} = (0, 0, \Omega_z)$ and the localized disturbance by its vorticity field $\boldsymbol{\omega}$. Two geometries of the initial disturbance are considered: (i) a 'spherical' vortex ring (Gaussian vortex), the vorticity field of which is given by $\boldsymbol{\omega} = -\boldsymbol{p} \times \nabla \boldsymbol{F}$, $\boldsymbol{F} = (\pi^{1/2}\delta)^{-3} exp(-r_s^2/\delta^2)$, where $\boldsymbol{p}$ is a vector defining the disturbance magnitude and orientation, δ is a single characteristic disturbance length scale and r_s is a spherical radial coordinate; (ii) a horizontal (xz-plane) torus with a vorticity field: $\boldsymbol{\omega} = \{z, 0, -x\}^T A\, exp(-y^2/\delta^2) exp(-(r - r_o)^2/\delta^2)$, where x, y and z are the streamwise, normal and spanwise directions, respectively, A is a constant defining the strength of the disturbance, $r = \sqrt{x^2 + z^2}$ is a radial cylindrical coordinate and r_o and δ are two characteristic length scales associated with the radius and the thickness of the torus, respectively. The existence of two characteristic length scales allows us to vary the localized properties of the toroidal disturbance by changing the ratio r_o/δ, and to seek 'optimal' aspect ratio, for which the disturbance growth is maximal. (Toroidal disturbance may be considered as a limit of a Gaussian vortex for $r_o = 0$.)

For a given shape of the horizontal initial disturbance, two parameters govern the disturbance evolution: (i) the strength of the initial disturbance (ε) defined by the ratio between the maximum vorticity of the disturbance (ω_{max}) and the shear of the base flow (Ω), i.e. $\varepsilon = \omega_{max}/\Omega$ (for $\varepsilon \ll 1$, the disturbance evolution is governed by the linearized equations); (ii) the Reynolds number based on the characteristic length scale δ, i.e., $Re = \Omega\delta^2/\nu$.

To follow the evolution of the vortical structure, its shape is identified by the iso-surfaces of the vorticity magnitude as well as by the iso-surfaces of the positive second invariant of the velocity gradient tensor, capturing the regions of concentrated vorticity and swirling motion, respectively. The vortical structure is then characterized by its strength, W, measured by integrating the enstrophy over the entire volume, (i.e. $W = \int_V \parallel \boldsymbol{\omega} \parallel^2 dV$); its center, $\bar{X}_i$, defined as the center of its enstrophy (i.e. $\bar{X}_i = \int_V \parallel \boldsymbol{\omega} \parallel^2 x_i dV\ /W$) and by its inclination angle, α, (Fig. 2e) relative to the base flow.

Full unsteady incompressible Navier-Stokes equations were solved using the commercial CFD code 'FLUENT'.

Main results and conclusions

A temporal evolution of a toroidal vortex (with $r_o/\delta = 2$) is shown in Fig. 2. Similar results were obtained for other toroidal and Gaussian vortex disturbances. Accordingly, a small amplitude initial disturbance (linear case) eventually evolves into a streaky structure, whereas a large amplitude disturbance evolves into a hairpin vortex independent of its initial geometry. The main non-linear effects are: (i) the movement of the vortical structure relative to the base flow due to its self-induced motion (the centers of the vortical structure are indicated by the black bullets in Figs. 2 (d) and (e); (ii) the destruction of the vortex streamwise symmetry. In addition, for the small amplitude case, the induced velocity is mainly in a direction opposite to that of the base flow (Fig. 2 d), and therefore the vorticity vector strongly deviates from the direction of the vortical structure. Thus, the vortical structure cannot be represented as a vortex filament. However, as the amplitude of the disturbance is increased the vorticity lines follow more closely the vortical structure (Fig. 2e and other results not shown here).

The qualitative evolution of the disturbance is almost independent of its initial geometry, whereas the quantitative characteristics (i.e. vortex strength, center and inclination angle), strongly depend on the disturbance geometry. The Reynolds number has a negligible effect on the kinematics of the vortical structure, but does have a significant effect on its transient growth. The strength of the vortical structure is governed by the transient growth mechanism, which strongly depends on the disturbance geometry. For the toroidal disturbance there is an 'optimal' range of r_o/δ where the transient growth is maximal (Fig. 3). For this range the spanwise separation ($\approx 2r_o$) of two elongated vortical regions, expressed in terms of wall units, lies within the interval of $63 < y^+ < 88$, which corresponds well to the spanwise spacing of low-speed streaks (as well as the distance between hairpin vortex legs) in turbulent boundary layers. Finally, the above numerical results will be discussed with respect to recent theories concerning the evolution of localized disturbances.

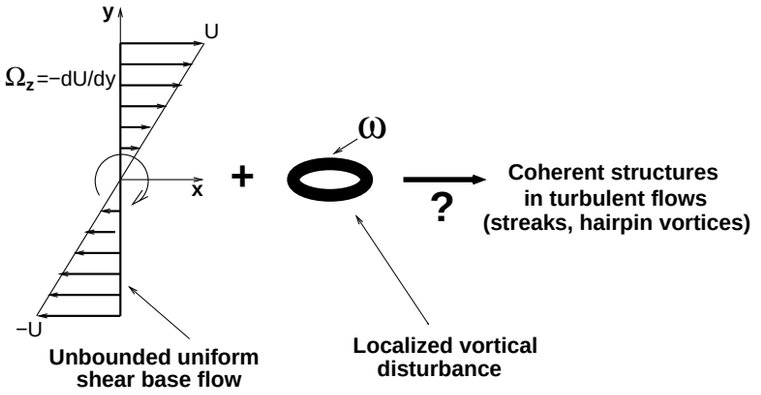


Figure 1. Schematic drawing of the research objective.

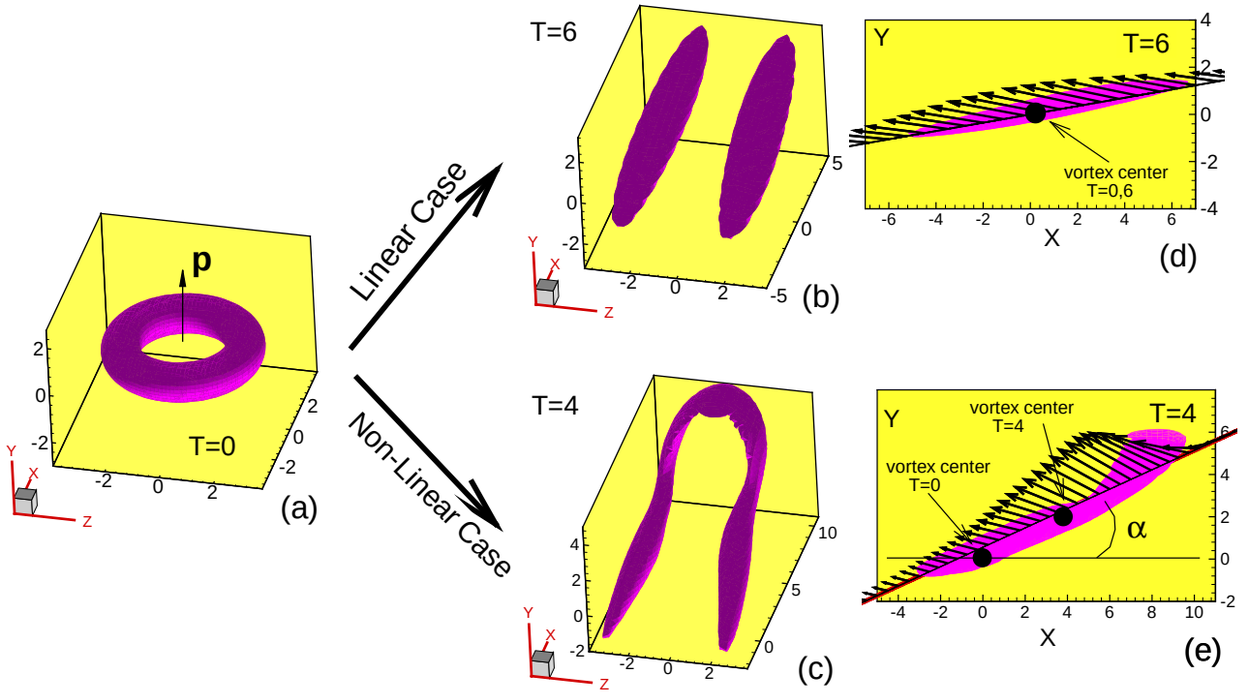


Figure 2. The evolution of a toroidal disturbance with $r_o/\delta = 2$ and $Re = 40$, shown by the iso-surfaces of the vorticity magnitude for $\| \boldsymbol{\omega} \| / \omega_{max} = 0.6$. (a) The initial disturbance, (b) streaky structure evolved from the toroidal disturbance with $\varepsilon = 0.375$, (c) hairpin vortex evolved from the toroidal disturbance with $\varepsilon = 4.5$, (d) & (e) projections on the xy plane of the iso-surfaces shown in (b) and (c), respectively, together with the velocity vectors along the axis of the vortical structure at the plane $Z = 0$ ($T = \Omega t$; $X = x/\delta$, $Y = y/\delta$).

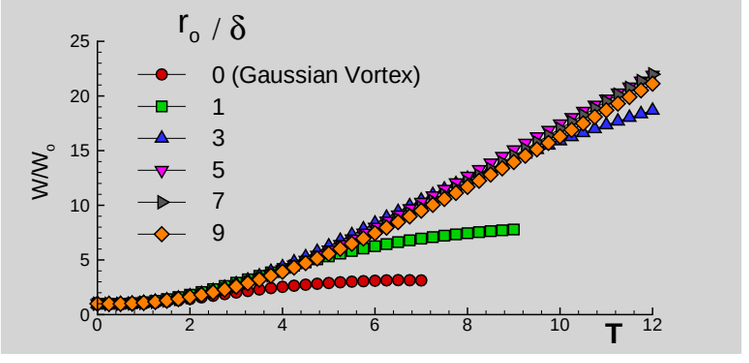


Figure 3. Temporal evolution of the enstrophy integral normalized by its initial value (W/W_o), $\varepsilon = 0.375$, $Re = 40$.

SUBCRITICAL TRANSITION TO TURBULENCE IN PLANE COUETTE FLOW

Maher Lagha, Paul Manneville
LadHyX — Laboratoire d'Hydrodynamique, Ecole polytechnique, 91128 Palaiseau cedex, France

Summary We present numerical simulations of a model of transitional plane Couette flow derived from the Navier–Stokes equations through a Galerkin expansion. Here we focus on the nucleation and development of turbulent domains from spots in the neighborhood of the global stability threshold, hinting at the nature of the transition to turbulence *via* spatio-temporal intermittency.

Plane Couette flow is the flow obtained by shearing a fluid of kinematic viscosity ν between two plates separated by a gap of width $2h$, sliding parallel to each other at speeds $\pm U_{\rm p}$. This flow is linearly stable for all Reynolds numbers $R = U_{\rm p}h/\nu$ but experiences a direct transition to turbulence beyond some global stability threshold $R_{\rm g}$ experimentally found of the order of 325 [1]. Below this value, turbulence is transient with turbulent spots having finite lifetime while, beyond, turbulence is sustained but with a complex behavior involving fluctuating turbulent domains embedded in laminar flow. In experimental set-ups with sufficiently large aspect ratio, at some stage beyond $R_{\rm g}$, turbulent domains evolve into continuous oblique turbulent stripes that ultimately merge when the homogeneous turbulence regime is reached at large R [2]. The transition, though well described experimentally, is far from being completely understood theoretically, which leaves room for modeling attempts. Here we focus on the approach being currently developed at LadHyX.

THE MODEL

The derivation starts from the Navier-Stokes equations in dimensionless form:

$$\partial_t \mathbf{v} + \mathbf{v}\cdot\nabla\mathbf{v} = -\nabla p + R^{-1}\nabla^2\mathbf{v} + \mathbf{f}\,, \qquad \nabla\cdot\mathbf{v} = 0\,.$$

x, y, and z are the streamwise, cross-stream and spanwise coordinates respectively. We assume stress-free boundary conditions and, accordingly, add a bulk force $\mathbf{f}$ to drive the flow. We take: $\mathbf{f}(y) = f\sin(\beta y)\hat{\mathbf{x}}$ with $\beta = \pi/2$ and $f = \beta^2/R$. The total velocity and the pressure field are expanded as:

$$\begin{aligned}
u &= U_0(x,z,t) + [1+U_1(x,z,t)]\sin(\beta y) + U_2(x,z,t)\cos(2\beta y) + ...,\\
w &= W_0(x,z,t) + W_1(x,z,t)\sin(\beta y) + W_2(x,z,t)\cos(2\beta y) + ...,\\
v &= V_1(x,z,t)\cos(\beta y) + V_2(x,z,t)\sin(2\beta y) + ...,\\
p &= P_0(x,z,t) + P_1(x,z,t)\sin(\beta y) + P_2(x,z,t)\cos(2\beta y) + ...,
\end{aligned}$$

Elimination of the pressure is achieved by defining stream functions Ψ_k, velocity potentials Φ_k as follows:

$$\begin{aligned}
\text{mode } 0: &\qquad U_0 = -\partial_z\Psi_0, \quad W_0 = \partial_x\Psi_0,\\
\text{modes } k>0: &\qquad U_k = \partial_x\Phi_k - \partial_z\Psi_k, \quad W_k = \partial_z\Phi_k + \partial_x\Psi_k, \quad (-1)^{k+1}k\beta V_k = \Delta_2\Phi_k,
\end{aligned}$$

with $\Delta_2 = \partial_{xx} + \partial_{zz}$. Here we truncate the model by keeping only the five fields Ψ_0, Ψ_1, Φ_1, Ψ_2 and Φ_2, hence, we get a model in terms of five partial differential equations. Below, we give only the equation for Ψ_0 since it is the most transparent. It reads:

$$\left(\partial_t - R^{-1}\Delta_2\right)\Delta_2\Psi_0 = (\partial_z N_{U_0} - \partial_x N_{W_0}) + \tfrac{1}{2}(\partial_z\Delta_2\Phi_1 - \partial_x\Delta_2\Psi_1)\,, \tag{1}$$

in which the nonlinear terms are given by:

$$\begin{aligned}
N_{U_0} &= U_0\partial_x U_0 + W_0\partial_z U_0 + \tfrac{1}{2}(U_1\partial_x U_1 + \beta V_1 U_1 + W_1\partial_z U_1) + \tfrac{1}{2}(U_2\partial_x U_2 - 2\beta V_2 U_2 + W_2\partial_z U_2),\\
N_{W_0} &= U_0\partial_x W_0 + W_0\partial_z W_0 + \tfrac{1}{2}(U_1\partial_x W_1 + \beta V_1 W_1 + W_1\partial_z W_1) + \tfrac{1}{2}(U_2\partial_x W_2 - 2\beta V_2 W_2 + W_2\partial_z W_2).
\end{aligned}$$

Other equations follow the same pattern, but are much more complicated.
The model reproduces the most important features of plane Couette flow, especially conservation of kinetic energy by nonlinear terms, linear stability for all Reynolds numbers, and a direct transition to turbulence beyond some global stability threshold. As diagnostic variables we use the three local energies $E_0 = U_0^2 + W_0^2$, $E_1 = \frac{1}{2}(U_1^2 + V_1^2 + W_1^2)$, $E_2 = \frac{1}{2}(U_2^2 + V_2^2 + W_2^2)$, defined at each point (x,z), the local total perturbation energy $E_{\rm tot} = E_0 + E_1 + E_2$, and their average values over the (L_x, L_z) domain, $\langle E_0\rangle$, $\langle E_1\rangle$, $\langle E_2\rangle$, and $\langle E_{\rm tot}\rangle$.

NUMERICAL METHOD AND RESULTS

Simulations have been performed using a Fourier pseudo-spectral numerical scheme in a periodic box with exact integration of the dissipation term in R^{-1} and a second order Adams–Bashford scheme for the right hand side, the conservative

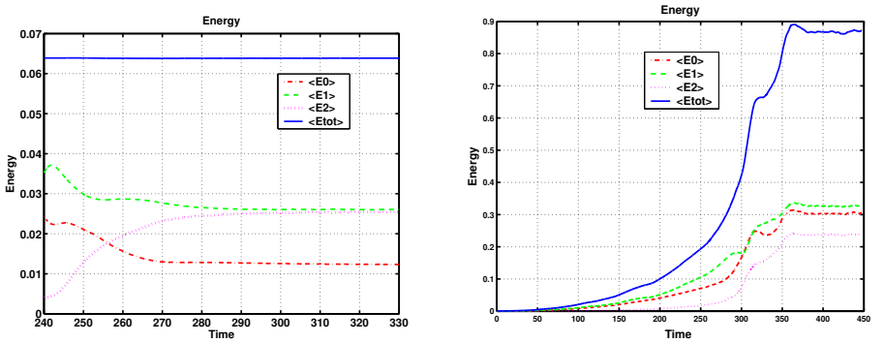


Fig. 1. Left panel: validation of the implementation of nonlinear terms tested from the evolution of average energies $\langle E_0 \rangle$, $\langle E_1 \rangle$, $\langle E_2 \rangle$, and $\langle E_{\rm tot} \rangle$ in an experiment where the production and dissipation terms have been artificially killed. Initial state taken from some turbulent state. Right panel: evolution of the same quantities during the experiment at $R = 75$ producing the snapshots in fig. 2.

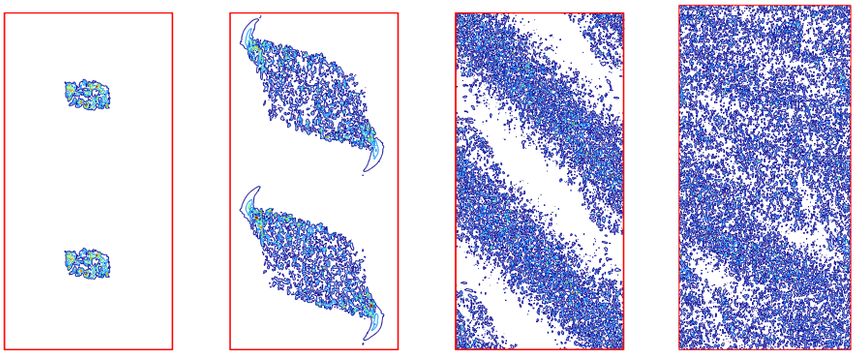


Fig. 2. Left panel: Evolution of a pair of spots into sustained turbulence depicted by the level curves of $E_{\rm tot}$ for $R = 75$; from left to right $t = 93$, $t = 240$, $t = 332.5$, and $t = 352.5$. The streamwise (spanwise) coordinate is along the vertical (horizontal).

nonlinear terms and the linear non-normal energy production terms. The 3/2 unaliasing rule has been used for terms arising from the quadratic advection term and it has been checked that the numerical implementation of the model preserves energy conservation accurately, see Fig. 1 (left panel).

Preliminary studies [3] have shown that the five-field model behaves in the same way as the three-field model obtained when fields Ψ_2 and Φ_2 are ignored [4]. A subcritical transition to turbulence is indeed observed at a global stability threshold $R_{\rm g}$ around 40. This anomalously low value (when compared to experimental results) is attributed to the choice of unrealistic boundary conditions and insufficient dissipation due to low order truncation, but all qualitative features of the transition seem preserved and especially the dynamics of turbulent spots generated by local finite amplitude perturbations.

The development of turbulent domains has been investigated by means of numerical simulations in large aspect-ratio domains ($L_x \times L_z = 512 \times 256$ in unit of h). Such aspect-ratios are still out of reach of direct numerical simulations. In the example shown in the Fig. 1 (right panel) and Fig. 2, the initial condition is made of two small-size (diameter ~ 50) identical turbulent spots. After a period of growth, here illustrated at $t = 93$ and 240, they evolve into oblique turbulent stripes ($t \sim 330$) and after a brief hesitation detected on the evolution curves of the energies (Fig. 1, right panel) they merge into featureless turbulence. This evolution and especially the quantitative characterization of the dynamics of the sharp fronts separating turbulent domains from laminar ones is currently under study. The behavior of these fronts in the vicinity of $R_{\rm g}$ is of special interest in view of the interpretation of the transition to turbulence in terms of spatio-temporal intermittency in extended systems according to seminal ideas put forward by Pomeau [5].

References

[1] For a review see P. MANNEVILLE, O. DAUCHOT, Patterning and transition to turbulence in subcritical systems: the case of plane Couette flow, in *Coherent Structures in Classical Systems*, D. Reguera *et al.* (Springer, 2001).

[2] A.PRIGENT *et al*, Large-scale finite-wavelength modulation within turbulent shear flows, *Phys. Rev. Lett.* **89** (2002) 014501.

[3] M. LAGHA, Transition sous critique à la turbulence: cas de l'écoulement de Couette Plan, web site `http://www.ladhyx.polytechnique.fr/people/maher`.

[4] P. MANNEVILLE, Spots and turbulent domains in a model of transitional plane Couette flow, to appear in *Theor. Comput. Fluid Dyn.*

[5] Y. POMEAU, Front motion, metastability, and subcritical bifurcations in hydrodynamics *Physica D* **23** (1986) 3–11.

THREE-DIMENSIONAL VORTEX BREAKDOWN IN SWIRLING JETS AND WAKES

M.R. Ruith*, P. Chen**, E. Meiburg* and T. Maxworthy**
*Department of Mechanical and Environmental Engineering, University of California at Santa Barbara, Santa Barbara, CA 93106, USA
**Department of Aerospace and Mechanical Engineering, University of Southern California, Los Angeles, CA 90089, USA

Summary DNS simulations of swirling jets and wakes exhibiting vortex breakdown are discussed. The basic form of vortex breakdown is found to be axisymmetric, and the transition to helical and double helical breakdown modes is shown to be caused by a sufficiently large pocket of absolute instability in the wake of the primary breakdown bubble.

Vortex breakdown of nominally axisymmetric, swirling incompressible flows with jet- and wake-like axial velocity distributions issuing into a semi-infinite domain is studied by means of direct numerical simulations. By selecting a two-parametric velocity profile for which the steady, axisymmetric breakdown is well studied (Grabowski and Berger 1976), issues are addressed regarding the role of three-dimensionality and unsteadiness with respect to the existence, mode selection, and internal structure of vortex breakdown, in terms of the two governing parameters and the Reynolds number. Low Reynolds numbers are found to yield flow fields lacking breakdown bubbles or helical breakdown modes even for high swirl. In contrast, highly swirling flows at large Reynolds numbers exhibit bubble, helical (figure 1) or double helical (figure 2) breakdown modes. Here the axisymmetric mode is promoted by a jet-like axial velocity profile, while a wake-like profile renders the flow helically unstable and ultimately yields non-axisymmetric breakdown modes. It is shown that a transition from super- to subcritical flow, as defined by Benjamin (1962), accurately predicts the parameter combination yielding breakdown, if applied locally to flows with supercritical inflow profiles. Thus, the basic form of breakdown is axisymmetric, and a transition to helical breakdown modes is shown to be caused by a sufficiently large pocket of absolute instability in the wake of the bubble, giving rise to a self-excited global mode. Two distinct eigenfunctions corresponding to an azimuthal wavenumber m=-1 (figure 3) and m=-2 have been found to yield a helical or double helical breakdown mode, respectively. Here the minus sign represents the fact that the winding sense of the spiral is opposite to that of the flow.

References

[1] Grabowski, W., Berger, S. Solutions of the Navier-Stokes equations for vortex breakdown. J. Fluid Mech. **75**, 525-544, 1976.
[2] Benjamin, T. Theory of the vortex breakdown phenomenon. J. Fluid Mech. **14**, 593-629, 1962.

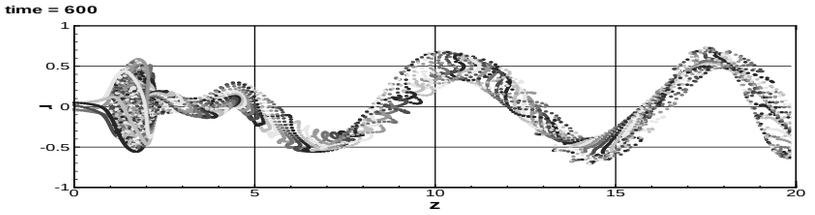


Figure 1: Visualization of flow field with streaklines. Starting from a columnar vortex, a quasi-steady state is reached. It becomes unstable to helical disturbances in the wake of the bubble, so that a helical breakdown mode results.

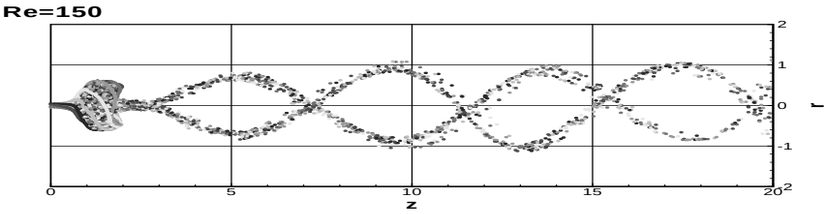


Figure 2: The double helical breakdown mode.

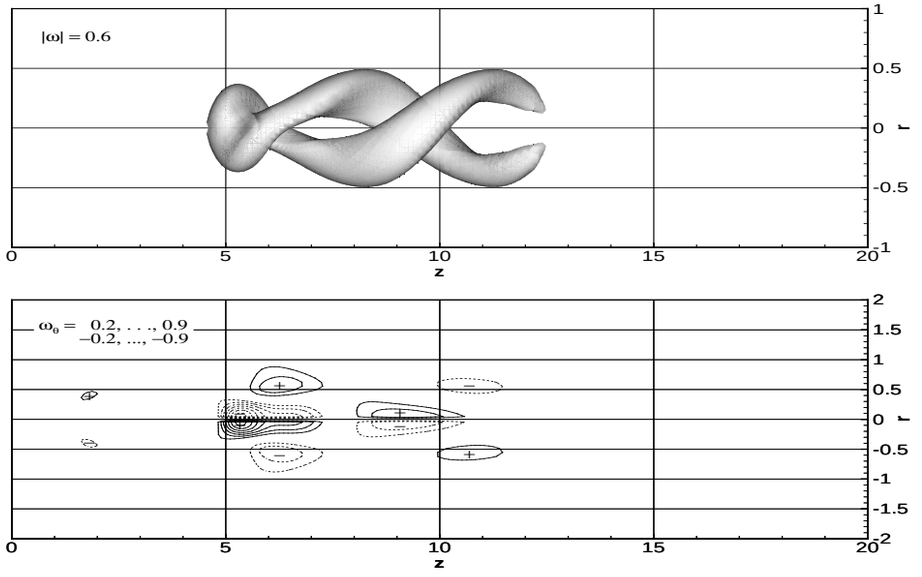


Figure 3: Eigenfunctions of the helical instability mode. The iso-surface of the vorticity (upper frame) reveals an $m = -1$ instability mode which corresponds to alternating signs of the azimuthal vorticity (lower frame).

A NEW CONVECTIVE INSTABILITY WITH GROWTH NORMAL TO A BOUNDARY LAYER

J.J. Healey
Department of Mathematics, Keele University, Keele, Staffs. ST5 5BG, United Kingdom

Summary A localized disturbance to an unstable shear layer might grow in the frame of reference of the source of the disturbance (absolute instability), or in frames moving upstream or downstream of the source (convective instability). However, we have discovered a new type of convective instability in which the disturbance grows as it propagates normal to, i.e. out of, a boundary layer.

INTRODUCTION

If an impulsive disturbance is introduced to an unstable shear layer in which the basic flow is predominantly in one direction (the downstream direction), then the disturbance is likely to grow only as it propagates downstream. As the disturbance propagates away, the region surrounding the source is eventually left undisturbed. Nonlinear behaviour will occur some distance downstream depending on the initial amplitude of the disturbance and the spatial growth rates of the shear layer. This behaviour is called convective instability. Alternatively, if the shear layer contains appreciable basic flow in both downstream and upstream directions then a localized disturbance can grow in the frame of reference of the source, leading eventually to nonlinear behaviour at the position of the source. This is called absolute instability.
This distinction between absolute and convective instability was first recognized by Twiss in 1951 in the field of plasma physics. Absolutely unstable flows act like self-excited oscillators, while convectively unstable flows act as spatial amplifiers, and so the nonlinear dynamics of each can be very different. A method for systematically determining which type of instability is present was developed in the 1960s by Briggs and Bers, and has now been used in many fluid flows.
However, in the present work, we have identified a type of convective instability that is fundamentally different to that described above, though it was discovered using the Briggs-Bers method. It is an instability in the direction normal to the shear layer, with disturbances growing exponentially with distance out into the freestream. This is counter-intuitive behaviour because it means that the growth takes place in a region of zero shear, and therefore where the Reynolds stresses are zero. Energy is transferred from the shear layer to the freestream via exponentially divergent eigenfunctions. Again, this is curious, since these 'eigenfunctions' don't satisfy homogeneous boundary conditions.

METHODOLOGY

The linearized stability equations for parallel shear layers can be most conveniently solved in frequency-wavenumber space, and the physical solution reconstructed from inverse Fourier transforms of the form

$$\hat{v}(x,y,t) = \frac{1}{4\pi^2}\int_A\int_F \frac{f(\omega)v(\alpha,y,\omega)}{\Delta(\alpha,\omega)}\exp \mathrm{i}(\alpha x - \omega t)\,\mathrm{d}\omega\,\mathrm{d}\alpha \qquad (1)$$

where $\hat{v}$ is a disturbance velocity, v is its Fourier transform, f is the transform of the time-dependent forcing ($f = 1$ for the impulsive forcing considered here) and $\Delta = 0$ is the dispersion relation for waves satisfying homogeneous boundary conditions. The shear flow $U(y)$ is in the x-direction, the shear is confined to a layer of finite thickness in y and U rapidly approaches a constant value as $y \to \infty$. The inversion contour F must be placed above any singularities in the complex ω-plane to ensure causality, i.e. $\hat{v} = 0$ for $t < 0$, and A can be placed on the real axis of the complex α-plane.

The Briggs-Bers method allows the propagation properties in physical space to be determined by only considering eigenvalues satisfying $\Delta = 0$, without resorting to the evaluation of the integrals. The roots of α satisfying $\Delta = 0$ are found for a particular value of ω on F. The locii of these values of α as ω moves along F are plotted in the complex α-plane and are called spatial branches. The behaviour of the spatial branches is investigated as F is lowered towards the real axis in the ω-plane. Spatial branches originating above or below the real α axis correspond to downstream or upstream propagating waves respectively. If a spatial branch from the upper half-plane crosses the real α axis as F is lowered, then there is spatial growth in the downstream direction. If this downstream branch coalesces with an upstream branch from the lower half-plane for a value of ω with $\mathrm{Im}(\omega) > 0$, then the flow is absolutely unstable.

THE ROTATING DISC BOUNDARY LAYER

We have investigated the boundary layer flow produced when an infinite disc rotates at constant angular velocity in otherwise stationary fluid. Fluid close to the disc is accelerated in the circumferential direction by viscous stresses. This fluid then spirals outwards due to centrifugal effects, and is replaced by fluid drawn down the axis of rotation. This basic flow is described by von Kármán's similarity solution, and small disturbances are added to this basic flow. The disturbance equations are linearized, a WKB formulation is adopted to account for the weak radial dependence of the basic flow far from the axis of rotation and inverse powers of the Reynolds number are neglected, leading to the Rayleigh equation. Far from the surface of the disc the basic flow is constant and the Rayleigh equation reduces to the Laplace equation with solution

$$w(\alpha,\beta,z,\omega) = C_1 \exp\left(-\sqrt{\gamma^2}z\right) + C_2 \exp\left(\sqrt{\gamma^2}z\right) \tag{2}$$

where C_1 and C_2 are constants of integration, $\gamma^2 = \alpha^2 + \beta^2$ is the square of the total wavenumber, α is the radial wavenumber, β the azimuthal wavenumber, w is the axial velocity component of the disturbance and z is the axial coordinate normal to the disc. The symbol $\sqrt{}$ denotes the square-root with positive real part. Therefore, the homogeneous boundary condition $\lim_{z\to\infty} w = 0$ is obtained by taking $C_1 \neq 0$ and $C_2 = 0$. We consider the solution for given real values of β; our definition of the square-root then implies the existence of branch-cuts along the imaginary axes of the complex α-plane (though the imaginary axis is analytic for $-\beta < \mathrm{Im}(\alpha) < \beta$).

Lingwood [1] has shown that this flow is absolutely unstable for $0 < \beta < 0.2652$. The present study was motivated by the results of our recent, unpublished, longwave theory for this absolute instability, which show that the pinch-point becomes asymptotically close to the imaginary axis of the α-plane as $\beta \to 0$, and that spatial branches cross the imaginary axis. The part of the spatial branch on the 'wrong side' of the imaginary axis can only be accessed by moving the branch-cut due to the square-root away from the imaginary axis, or, equivalently, taking $C_1 = 0$ and $C_2 \neq 0$. We argue that these apparently unphysical solutions correspond to a new convective instability with growth in the wall-normal direction.

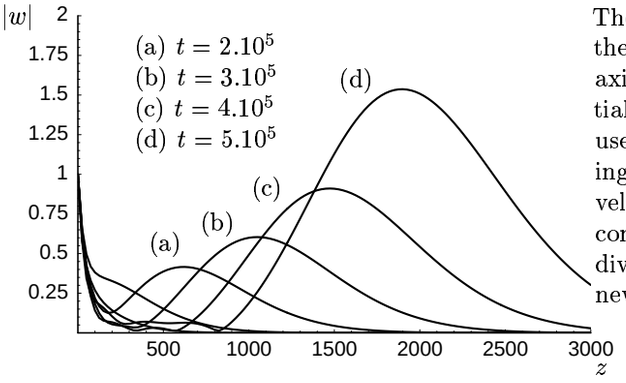
The classic saddle-point analysis for estimating the behaviour of (1) at large times in different reference frames is modified by including the exponential terms from (2) in the phase function:

$$\int_A \int_F \frac{w(\alpha,\beta,z,\omega)}{\Delta(\alpha,\beta,\omega)} \exp \mathrm{i}(\alpha r + \beta\theta - \omega t)\, \mathrm{d}\omega\, \mathrm{d}\alpha = \int_A -\frac{2\pi\mathrm{i}}{\Delta_\omega} \exp\left[\mathrm{i}(\alpha r + \beta\theta - \omega t) - \sqrt{\gamma^2}z\right]\, \mathrm{d}\alpha \tag{3}$$

where the ω integral has been evaluated using the residue theorem and $\omega = \omega(\alpha)$ satisfes the dispersion relation. The saddle point of the exponent is now found from

$$\frac{\mathrm{d}\omega}{\mathrm{d}\alpha} = \frac{r}{t} + \frac{\mathrm{i}\alpha}{\sqrt{\gamma^2}}\frac{z}{t}. \tag{4}$$

We consider frames of reference at fixed radius r, that move away from the disc, i.e. $r/t = 0$ and $z/t \geq 0$. For example, at $\beta = 0.007$ the saddle itself crosses the imaginary axis of the α-plane for a finite range of z/t and the maximum growth rate occurs for $z/t = 0.0042$. But can these saddle-point calculations based on exponentially divergent terms in (2) really be correct?



The figure shows the numerical evaluation of (3) where the path A remains the 'correct side' of the imaginary axis, so that only solutions with decaying exponentials satisfying homogeneous boundary conditions are used during the calculation. The envelope of a growing wavepacket propagating into the freestream at a velocity close to $z/t = 0.0042$ can be clearly seen, confirming that in this problem the exponentially diverging eigenfunctions do indeed correspond to a new type of convective instability.

[1] Lingwood R. J.: Absolute instability of the boundary layer on a rotating disk. *J. Fluid Mech.* **299**; 17–33, 1995.

BY-PASS LAMINAR-TURBULENT TRANSITION OF THE WIND-DRIVEN FREE SURFACE FLOW

Guillemette Caulliez*, Richard Dupont*, Victor I. Shrira**
**Institut de Recherche sur les Phénomènes Hors Equilibre*
163 av. de Luminy, 13009 Marseille, France
***Dept. of Mathematics, Keele University, Keele, Staffordshire, ST5 5BG, UK.*

Summary The laminar-turbulent transition of a wind-driven surface boundary layer is investigated experimentally. Two stages in the development of the perturbations have been clearly identified. First, a slow growth of streamwise longitudinal vortices is followed by rapid development of secondary instabilities. The picture is similar to a by-pass rigid wall transition to turbulence. At the second stage, peculiar to this flow, an explosive deepening of the boundary layer and the fast development of inflexional instabilities occur.

Turbulent motions generated in boundary layers induced by wind at the free surface of natural basins play a key role in heat and mass exchanges at the water-atmosphere interfaces. However, the properties and the origin of this small-scale turbulence as well as its interaction with the atmospheric turbulence above the interface, wind waves, mean shear current or other motions of larger scales present in water are poorly known. This situation is largely due to the fact that all these processes coexist and overlap in space-time domain, making the observations extremely difficult to perform and to interpret. Then, to shed light on the complex structure of the natural free surface boundary layers, a first step may consist in a thorough investigation of the individual basic processes controlling their formation. In that way, the laminar-turbulent transition in wind-driven flows was identified by Okuda et al.[5] and Kawai[3] in an early laboratory study of the temporally-developing boundary layer while a more detailed investigation of the temporal evolution of this boundary layer and its interaction with wind waves was made later by Melville et al[4] and Veron and Melville[6]. Due to the intrinsic difficulties of these temporal measurements, the main processes of the transition to turbulence have not been entirely clarified, in particular the role of waves in this phenomenon. The later was discarded by Tsai[7] on the basis of direct numerical simulations for the temporal case and by Caulliez et al.[2] as a result of a preliminary study of the spatially-developing drift current. The present work is concerned with the laminar-turbulent transition of a spatially-developing boundary layer. Based on precise laboratory experiments performed in steady conditions, it aims at establishing the main features of this phenomenon and at identifying the fundamental mechanisms at the origin of its development.

The observations were carried out in the large and small IRPHE-Luminy wind-wave facilities, for wind speeds ranging from 2.5 to 7 m/s. The structure of the velocity field in the water surface boundary layer was explored at various fetches (distance from the leading edge of the water tank) and depths just downstream the air-water junction plate, using both flow visualisation technique based upon dye injection and laser Doppler velocimeter measurements. The water surface displacements were measured simultaneously by means of a thin wire capacitance wave probe. Special measures were taken to minimise perturbations in the air and the water at the entrance of the tank and the air flow parameters were monitored by pressure and hot-wire probes.

A first description of the overall behaviour of the water flow was provided by means of the dye visualisations (Fig.1). First, just downstream of the air-water junction, the straight marked streamlines parallel to the flat water surface indicate that the surface wind induced current is laminar. Long wavy instabilities appear from time to time but they evolve to a very small extent before vanishing. Then, further downstream, there is a relatively long stage where the perturbations present a consistent tendency to grow. Finally, at a certain fetch, the flow disturbances start to evolve quite rapidly. The dye trajectory first develops instantaneous steep contortions mainly oriented downward. The presence of large oscillations of the residual dye filaments associated with the rapid dye diffusion into a deep layer suggests the formation of turbulent spots. Often after the streamline overturning the resulting turbulent spot disappears, washed up downstream, and the laminar flow is restored until breaking down again, creating an intermittent pattern. Sometimes, the transition to turbulent flow occurs even faster, when the still rectilinear dye filament stops abruptly at a definite fetch and bursts in wreath of dye disseminating into the whole boundary layer. It is also noticeable that small-scale waves ruffling the free surface

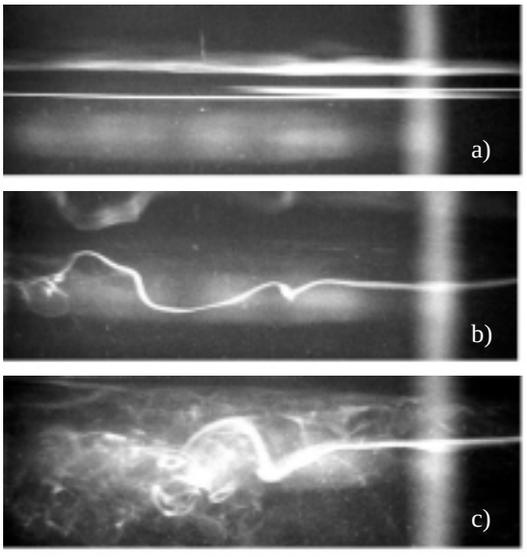


Fig. 1: Sideview of the typical evolution with fetch of the water flow instabilities traced by colored dye injected 30 cm upstream at a depth of 3mm, for a 5m/s wind speed blowing from the right to the left: a) laminar region, b) development of streamwise vortices at the first stage of the transition, c) formation of a turbulent spot at the second stage of the transition.

become visible at the point of the boundary layer breakdown. They mark the downstream regions where the turbulent spots develop and clearly show how the spots slowly expand spanwise until they merge. Thus the characteristic V-shaped streaks are created on the water surface.

Quantitative measurements first show that the thin water boundary layer induced by wind at the leading edge of the water sheet is indeed laminar. The drift current surface velocity and the boundary layer depth increase gradually with fetch, following 1/3 power laws characteristic of the accelerated flat-plate laminar boundary layers. The evolution with fetch of the mean velocity vertical profiles is well described by the self-similar profiles of the Falkner-Skan type. The first low frequency perturbations of the streamwise velocity field observed further downstream are much greater than the vertical one, suggesting the formation and the development of longitudinal vortices within the laminar boundary layer. The laminar-turbulent transition manifests itself by a sudden development of turbulent motions of large amplitude and high frequency localised both in space and time. The critical fetch where the first turbulent spots appear is not linked to any critical Reynolds number, but was found to depend on friction velocity as u^{*-2} (Fig. 2). Then, these turbulent spots evolve with fetch inside longitudinal elongated patches characterised by a slow crosswise expansion, while the boundary layer thickness inside these patches increases with fetch explosively (Fig. 3).

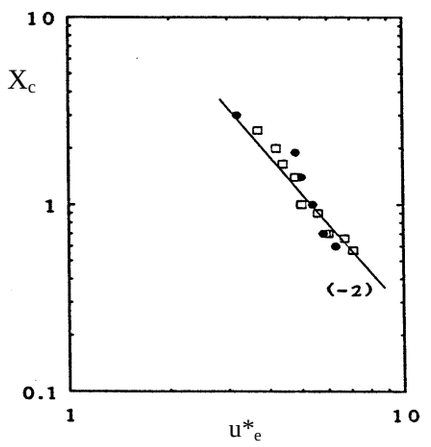


Fig. 2: The critical fetch X_c *vs* the friction velocity u^*_e in water for the different wind conditions observed in the large (open squares) and the small tank (closed circles).

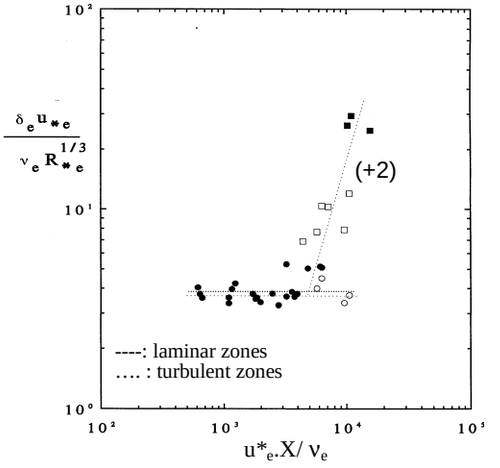


Fig. 3: Boundary layer thickness in water δ_e *vs* non-dimensional fetch ($u^*_e.X/\nu_e = R^*_e$) shown by closed circles in the laminar region, by open symbols in the transitional region, and by closed squares in the fully-developed turbulent region.

These observations then suggest a plausible scenario of the transition to turbulence of the wind-driven boundary layer essentially characterised by two distinct stages. At the first stage, streamwise elongated structures emerge from natural noise disturbances and grow slowly without significant alteration of the mean field flow till their breakdown at a critical fetch. The picture is similar to the scenario of rigid plate laminar-turbulent transition caused a by-pass mechanism as reported by Andersson et al.[1]. In contrast, the second stage, where the turbulent spots created by the collapse of the shear boundary layer expand and merge, differs dramatically from the rigid plate scenario, in particular by the abruptness and the intensity with which the vertical mixing phenomena occur. The observed differences can be attributed to the coexistence of accelerated-decelerated mean flow regions leading to an enhancement of the turbulent diffusion in the vertical direction and its inhibition in the spanwise direction.

References

[1] Andersson P., Brandt L., Bottaro A., Henningson D.S., On the breakdown of boundary layer streaks, J. Fluid Mech. **428**:29-60, 2001.
[2] Caulliez G., Ricci N., Dupont R., The generation of the first visible wind waves, Phys. Fluids **10**, 4:757-759, 1998.
[3] Kawai S., Generation of initial wavelets by instability of a coupled shear flow and their evolution to the wind waves, J. Fluid Mech. **93**:661-703, 1979.
[4] Melville W.K., Shear R., Veron F., Laboratory experiments of the generation and evolution of Langmuir circulations, J. Fluid Mech. **364**:31-58, 1998.
[5] Okuda K., Kawai S., Tokuda M., Toba Y., Detailed observation of the wind-exerted surface flow by use of flow visualisation methods, J. Oceanogr. Soc. Japan, **32**:53-64, 1976.
[6] Veron F., Melville W.K., Experiments on the stability and transition of wind-driven water surfaces, J. Fluid Mech. **446**:25-65, 2001.
[7] Tsai W., On the formation of the streaks on wind-driven water surfaces, Geophys. Res. Lett. **28**, 20:3959-3962, 2001.

LARGE-EDDY SIMULATION OF THE TRANSITIONAL FLOW IN NATURAL CONVECTION IN A HORIZONTAL ANNULUS

Elie Luis M. Padilla, Aristeu Silveira-Neto

School of Mech. Eng. – Federal University of Uberlândia, Uberlândia, MG, Brazil, 38400-902

Summary In the present study three-dimensional analysis of the transitional flow in natural convection in horizontal cylindrical annulus was performed, using Large-Eddy Simulation (LES) methodology with dynamical sub-grid scale model. The beginning of the transition process and the beginning of turbulent regimes is indicated. The characteristics of the oscillatory and the influence on heat transfer coefficient were analyzed. The results showed that coherent structures exist in this type of flow.

Natural convection heat transfer in cylindrical annuli is a very common problem in practical and technological applications. Natural convection in horizontal cylindrical cavity has been studied extensively, both theoretically and experimentally. The majority of these studies are focused on laminar or turbulent regimes. Exist very few works that focalises the phenomenon of transition to turbulence. The problem was first studied by Beckmann [1], who obtained overall heat transfer coefficients using air, hydrogen and carbon dioxide. After, wards other experimental studies have been reported. Several correlations have been proposed using experimental heat transfer data, as reported by Itoh et. al. [2] and McLeod and Bishop [3]. Crawford and Lemlich [4] achieved one of the first numerical solution for natural convection between horizontal concentric cylinders for air using a Gauss-Seidel iterative method. Numerical solutions were presented by many authors, using differents methodologies. However, only three-dimensional results of Fukuda et. al. [5] shows the flow becoming unstable. Physical oscillations appear when the Rayleigh number is increased .

In the present study three-dimensional analysis of the transitional flow in natural convection in horizontal cylindrical annulus was performed, using Large-Eddy Simulation (LES) methodology with dynamical sub-grid scale model. The cavity is formed by two concentric cylinders of radius R_1 and R_2 respectively. The distance between cylinders is L and the axial length is L_{ax}. The inner surface is maintained at temperature T_1 and the outer surface is maintained at temperature T_2 ($T_1 > T_2$) . The flow is considered incompressible, with constant physical proprieties. Buoyancy force is modeled with the Boussinesq approximation. In order to use the LES, the Navier-Stokes and energy equations are filtered. This procedure gives rise to the subgrid-scale Reynolds tensor and the subgrid heat flux that represent the turbulent transport of momentum and heat between the large scale and the subgrid scale. The subgrid-scale Reynolds tensor is modeled with the hypothesis of Boussinesq and the subgrid heat flux ($\dot{q}_t$) with the expression $\dot{q}_t = -\alpha_t \, \partial \overline{T} / \partial x_j$. The thermal diffusivity was estimated from the value of turbulent Prandtl number, $\mathrm{Pr}_t = \nu_t / \alpha_t = 0.6$ (Silveira-Neto et. al. [6]). The eddy viscosity (ν_t) was calculated using the dynamical model of Germano et. al. [7], modified by Lilly [8].

The finite volume method is applied in cylindrical coordinates with an staggered grid. The second order Adams-Bashforth temporal scheme and the second order central-difference spatial scheme were used. The governing equations were solved with a fractional time-step method, employing the following boundary conditions: non-slipping and impermeability in the radial direction and periodicity in the tangential and axial directions. The time-step is conditioned by the CFL criterion. The validation was performed for laminar and transitional natural convection, by comparing with experimental date of Kuehn and Goldstein [9] (Fig. 2) and Fukuda et. al. [5] respectively.

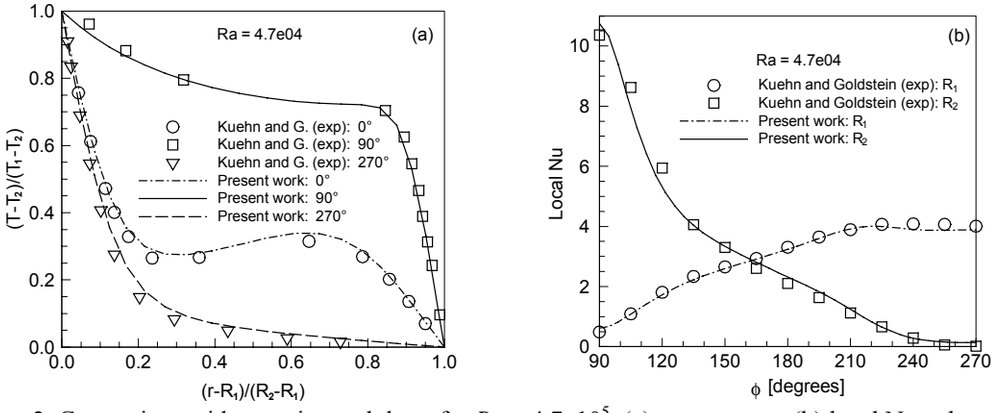


Figure 2. Comparison with experimental dates for $Ra = 4.7\text{x}10^5$, (a) temperature, (b) local Nusselt number.

The numerical analysis was performed for several values of Rayleigh number (Ra), a value of radius ratio ($\eta = R_2/R_1$) and two values of aspect ratio ($\Gamma = L_{ax}/L$). The temperature fields are shown in Fig. 3 and Fig 4. The Rayleigh number for both figures is $Ra = 1.7\text{x}10^5$, $\eta = 2$ and $\Gamma = 2.8$. Fig. 3 shows three planes normal to the z axis, at $z = 0$,

$z = 0.5L_{ax}$, $z = L_{ax}$. The visualization is also presented for three differents times: (a) 29.6 s, (b) 29.8 s and (c) 30 s. In both figures the flow transition is visualized in three directions (r, ϕ, z). It can be seen that the flow presents dynamical oscillations in three directions. For example the oscillation in z direction can be visualized in both figures and presents periodicity. This behavior may be observed clearly in time (Fig. 4(a), 4(b) and 4(c)). Clearly the plume generated at the top of the annulus oscillates right and left, as observed experimentally by McLeod and Bishop [3] and experimentally and numerically by Fukuda et. al. [5]. These authors also observed that the instabilities presents three-dimensional characteristics as we can observe in these figures. The beginning of the transition process and the beginning of turbulent regimes is indicated. The characteristics of the oscillatory flow (such as the variables fluctuations, power spectra and intensity of turbulence) and the influence on heat transfer coefficient were analyzed. The results showed that coherent structures exist in this type of flow.

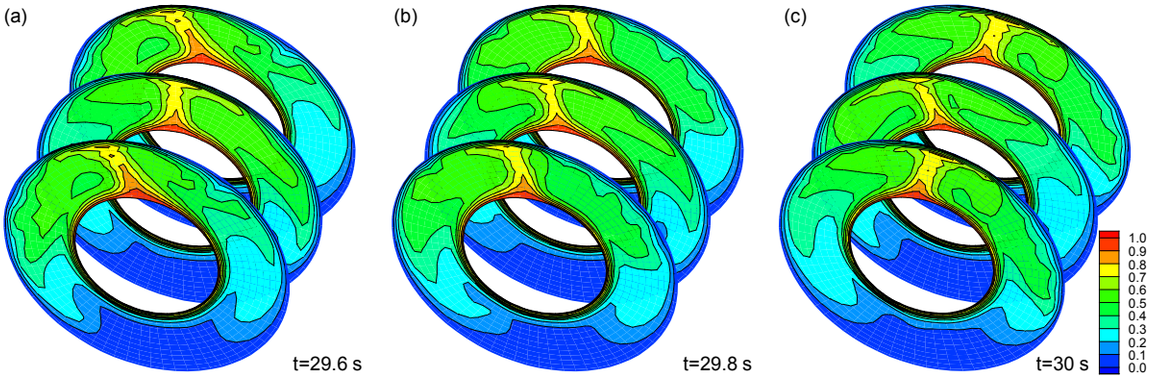


Figure 3. Temperature fields over the planes $z = 0$, $z = 0.5L_{ax}$, and $z = L_{ax}$ for $Ra = 1.7\text{x}10^5$, $\eta = 2$ and $\Gamma = 2.8$.

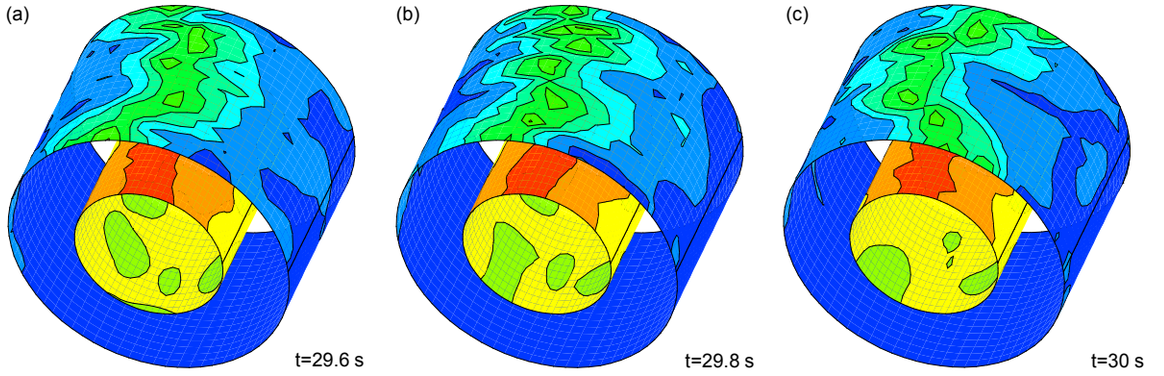


Figure 4. Temperature fields over the planes $r = 1.036L$ (near the inner cylinder) and $r = 1.963L$ (near the outer cylinder) $z = L_{ax}$ for $Ra = 1.7\text{x}10^5$, $\eta = 2$ and $\Gamma = 2.8$.

References

[1] Beckmann, W., Die Warmeubertragung in Zylindrischen Gasschichten bei Naturlicher Konvection, *Forsch. Geb. d. Ingenieurwesen*, Vol. 2, No. 5, pp 165-178, 1931.

[2] Itoh, M., Fujita, T., Nishiwaki, N., and Hirata, M., A New Method of Correlating Heat-Transfer coefficients for Natural Convection in Horizontal Cylindrical Annuli, *Int. J. Heat Mass Transfer*, Vol. 13, pp. 1364-1368, 1970.

[3] McLeod A., and Bishop E. H., Turbulent Natural Convection of Gases in Horizontal Cylindrical Annuli at Cryogenic Temperatures, *Int. J. Heat Mass Transfer*, Vol. 32, No. 10, pp. 1967-1978, 1989.

[4] Crawford, L., and Lemlich, R., Natural Convection in Horizontal Concentric Cylindrical Annuli, *I. E. C. Fundamentals.*, 1(4), pp. 260-264, 1962.

[5] Fukuda, K., Miki, Y., and Hasegawa, S., Analytical and Experimental Study on Turbulent Natural Convection in a Horizontal Annulus, *Int. J. Heat Mass Transfer*, Vol. 33, No. 4, pp. 629-639, 1990.

[6] Silveira-Neto, A. Grand, D., Metais, O., and Lesieur, M., A Numerical Investigation of the Coherent Structures of Turbulence Behind a Backward-Facing Step. *Int. Journal of Fluid Mechanics*, Vol. 256, pp. 1-25, 1993.

[7] Germano, M., Piomelli, U., Moin, P., and Cabot, W. A., A Dynamic Subgrid-Scale Eddy Viscosity Model. *Phys. Fluids*, A3(7), July, pp. 1760-1765, 1991

[8] Lilly, D. K., A Proposed Modification of the Germano Subgrid-Scale Model, *Phys. Fluids*, A4(3), March, pp. 633-635, 1991.

[9] Kuehn, T. H., and Goldstein, R. J., An Experimental and Theoretical Study of Natural Convection in the Annulus Between Horizontal Concentric Cylinder, *J. Fluids Mech.*, Vol. 74, pp.695-719, 1976.

INFLUENCE OF SWIRL VIBRATIONS ON FLOW IN LONG CYLINDER

Denis S. Goldobin, Dmitry V. Lyubimov
Perm State University, Bukireva, 15, 614990, Perm, Russia

Summary We consider stability of azimuthal flow of viscous fluid in infinitely long cylinder involved in swirl vibration. The linear stability thresholds for different classes of perturbations are obtained. Axisymmetric perturbations are found to be most excitable at moderate frequencies. The normal perturbations are classified with respect to their symmetry properties; it allows classifying resonances too.

Introduction. This study is related to the crystal growth by Bridgman method in microgravity conditions. A compound from which the crystal is grown contains some amount of dopants. In the crystallization process these dopants pass to the crystal not so quickly as the main component and due to that the concentration of dopants in the melt grows with the decrease of distance from the crystallization front. To decrease the amount of the dopants in the crystal and to make it more uniform we could create the flow that will remove superfluous amount of dopant from the area close to the crystallization front. For example, such flow can be induced by swirl vibrations of the ampoule containing the melt around its symmetry axis. The required flow can be excited against the background of azimuthal flow arising near the ampoule endwalls or against the background of azimuthal flow developing near the lateral wall of the ampoule. The present study concerns the flows of the second type, namely linear stability of system with respect to these flows.

Stability of periodical regimes is studied for different hydrodynamical systems in many papers, and among them two papers are most closely related to our study [1, 2]. In [1] Patricia Ern and Eduardo Wesfreid studied the flows in an annular gap between coaxial cylinders, the boundaries of which perform rotational motions around its common axis with equal variable angular velocities:

$$\Omega(R_1) = \Omega(R_2) = \Omega_{mon} + \Omega_{osc}\cos\omega t\,.$$

The study was mainly experimental, although there was further numerical analysis. However, the problem was only considered at $R_2 - R_1 \ll R_2$. In [2] Kerczek and Davis studied linear stability of Stokes flow near plane surface. This work is interesting for us too, since in the extreme case of high frequency vibrations, i.e. thin dynamical Stokes layer, our problem turns to the one considered in [2].

Problem formulation and general remarks. Fluid flows within an infinitely long cylinder with radius R are considered (fig. 1). The boundary of the cylinder is involved in swirl vibrations. The speed of the boundary is assumed to vary harmonically with time: $\mathrm{Re}\left(U_0 e^{i\omega t}\right)$.

Behavior of isothermal incompressible fluid with kinetic viscosity ν is governed by two dimensionless parameters: $\tilde{\omega} = \omega R^2 \nu^{-1}$, and $\tilde{U}_0 = U_0 R \nu^{-1}$ (the sign $\tilde{}$ is omitted below). The viscous units ($[x] = R$, and $[t] = R^2/\nu$) and the cylindrical coordinate system are used; the unit tangential vectors of the coordinate map are denoted $\vec{e}_r$, $\vec{e}_\varphi$, and $\vec{e}_z$.

The system admits periodic solution in the form of purely azimuthal axisymmetric flow:

$$\vec{U}(r,t) = \mathrm{Re}\left(U_0 \frac{J_1\left((1-i)r\sqrt{\omega/2}\right)}{J_1\left((1-i)\sqrt{\omega/2}\right)} e^{i\omega t} \right)\vec{e}_\varphi\,.$$

We study the linear stability of this flow.

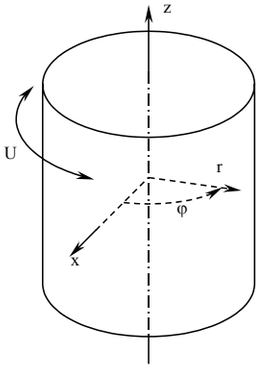


Fig. 1. Problem geometry and coordinate system

The problem has two classes of perturbations that could be most excitable: axisymmetric perturbations (ASPs) and z-uniform non-axisymmetric perturbations (UNSPs). The latter are interesting because at the high-frequency limit the thickness of dynamical Stokes layer and, consequently, spatial scales of flows excited are little in comparison with the surface curvature radius. Thus, the problem turns into the stability problem of Stokes layer near a plane plate [2]. In this problem perturbations with velocities lying on the plane perpendicular to the plate and parallel to its oscillation polarization axis, are most excitable, and perturbations uniform along this polarization axis always decay. The former are the limit of UNSPs, and the latter are the limit of ASPs. UNSPs could be most excitable at some moderate frequencies.

For the both kinds of perturbations, the Floquet solutions are shown to be able to have a negative multiplier only as the particular case of a pair of complex multipliers, and in this case the negative multiplier is doubly degenerate.

Axisymmetric perturbations. To consider ASPs we decompose the velocity field into two components: the planar component being the sum of the radial and z-components, and the azimuthal component. Then the stream function of the planar component can be introduced (stream lines lay on surfaces of constant value of ψ): $\vec{v} \equiv \frac{1}{r}\frac{\partial\psi}{\partial z}\vec{e}_r + v\vec{e}_\varphi - \frac{1}{r}\frac{\partial\psi}{\partial r}\vec{e}_z$. The governing equation systems of normal perturbations ($\sim e^{ikz}$) can be written as:

$$\Omega_t + \frac{i2kU}{r} v = L\Omega ;$$
$$\Omega = -L\phi ;$$
$$v_t + \frac{ik(rU)'}{r}\phi = Lv ;$$
$$r = 1 : \; v = \phi = \phi' = 0 .$$

Here $\Omega \equiv -\partial_z v_r + \partial_r v_z$ is vorticity, $\phi \equiv \psi / r$, $L \equiv \partial_r^2 + r^{-1}\partial_r - r^{-2} - k^2$ is Laplacian, and ' denotes differentiating with respect to radius.

Non-axisymmetric perturbations uniform along the cylinder axis. The most excitable non-axisymmetric perturbations are probably the ones uniform along the cylinder axis. UNSPs can be sorted into two classes: (i) purely shear flows along the cylinder axis, and (ii) flows with a velocity field perpendicular to this axis. We have strictly proved the first-class perturbations to decay always.

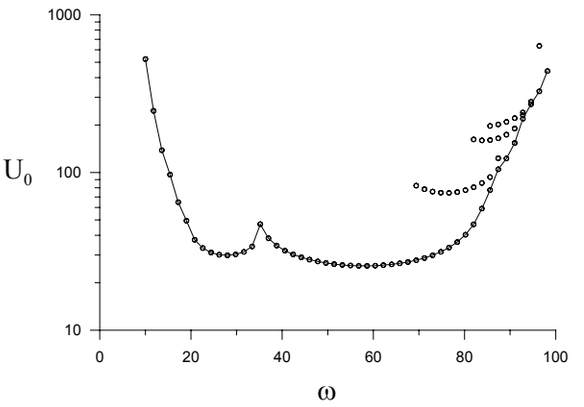


Fig. 2. The boundary of linear stability to ASPs. The circles show the result of local minimizing the critical vibration amplitude with respect to wavenumber; the lines run through the points of the global minima.

Introducing the stream function ($\vec{v} = -\nabla \times (\psi \vec{e}_z)$) for two-dimensional flow uniform along the cylinder axis, we can obtain the governing equation of a perturbation with the quantum azimuthal number m (i.e., the perturbation fields $\sim e^{im\varphi}$) and boundary conditions in the form of

$$L_m \psi_t + \frac{im}{r}\left(\mathrm{Re}(U) L_m \psi + \omega \,\mathrm{Im}(U)\psi\right) = L_m L_m \psi ;$$
$$\psi(r=0) = \psi(r=1) = \psi'(r=1) = 0 .$$

Here $L_m \equiv \partial_r^2 + r^{-1}\partial_r - m^2 r^{-2}$ is Laplacian.

Numerical simulation. The spectral method is convenient for investigating our system. The basis of eigenfunctions of the perturbations behavior problem of the static fluid is used. The numerical simulation of the system shows that the first 15 basic functions are sufficient to get accurate enough (the error ~1%) results on system stability to perturbations of both kinds. The obtained results on the linear-stability threshold of azimuthal flow are presented on the fig. 2.

Results and conclusion. The numerical simulation shows that the most excitable perturbations are ASPs up to the frequencies providing the dynamical Stokes layer thickness $\sim 1/10$ cylinder radius, and the critical vibration amplitudes for UNSPs are much more than the ones for ASPs at moderate and low frequencies. Interest in UNSPs is caused by the high-frequency limit, at which the problem turns into the stability problem of oscillatory Stokes layer near a plane plate. In this problem the perturbations uniform along the vibration direction, which are the limit of ASPs, always decay, while non-uniform ones can be excited [2]. It was the reason for expecting that UNSPs can be most excitable at low and moderate vibration frequencies. This expectation is proved false.

ASPs are found to have the following properties. Firstly, solutions on the stability threshold have been found to correspond to the unit multiplier. Secondly, the planes of zeros of the z -component of the velocity field of the normal perturbation are shifted by the perturbation wavelength quarter from the planes of zeros of the azimuthal component of the same field. Thirdly, different “balloons” on the stability diagram correspond to perturbations of different classes: flows with a purely azimuthal time-averaged velocity field and flows with a purely planar one.

The equation symmetry similar to the one allowing classifying ASPs, results in the following for UNSPs. When one decomposes the periodic velocity field $\vec{v}(\vec{r},t)$ of a critical perturbation into two parts: symmetric $\vec{v}_s(\vec{r},t) = \vec{v}_s(\vec{r},t+\pi/\omega)$ and anti-symmetric $\vec{v}_a(\vec{r},t) = -\vec{v}_a(\vec{r},t+\pi/\omega)$ to the time-shift for the modulation half-period, then the zeros of the azimuthal component of the symmetric velocity field part $\vec{v}_s$ are turned by the angle $\pi/2m$ (a fourth of the angle period) from the zeros of the azimuthal component of the anti-symmetric velocity field part $\vec{v}_a$.

Thus, the linear stability of the azimuthal flow of viscous incompressible fluid in a long cylinder involved into swirl vibrations is studied. The stability threshold is found.

Acknowledgments. The research described was supported by ESA from ESA-ESTEC Contract 15637/01/NL/SH, and by Award No. PE-009-0 of the U.S. Civilian Research & Development Foundation for the Independent States of the Former Soviet Union (CRDF).

Bibliography

[1] Ern, P. & Wesfreid, J. E. 1999 Flow between time-periodically co-rotating cylinders. *J. Fluid Mech.* **397**, 73-98.

[2] Kerczek, C. von & Davis, S. H. 1974 Linear stability theory of oscillatory Stokes layers. *J. Fluid Mech.* **62**, 753-773.

NONLINEAR STABILITY OF ROTATING CHANNEL FLOW

M. Nagata, D. P. Wall,T. Mitsumoji
Dept of Aeronautics & Astronautics, Graduate School of Engineering, Kyoto University, Yoshida-Honmachi, Sakyo-ku, Kyoto. 606-8501 Japan.

Summary The stability of Poiseuille flow in a channel subject to a system rotation about a spanwise axis is considered. Linear stability results show that the basic flow first loses stability to a two-dimensional streamwise-independent disturbance. We find two-dimensional nonlinear secondary flows, and analyse their stability. A rich structure of relationships exists between the secondary flows which does not exist for the equivalent Couette problem. We proceed to find three-dimensional nonlinear travelling-wave tertiary flows which bifurcate from the secondary flows. Three distinct three-dimensional tertiary flows are identified including flows which resemble the twisting vortex flows observed in previous experimental and DNS studies.

INTRODUCTION

The stability of channel fbw subject to system rotation is of relevance to many geophysical and astrophysical problems, as well as having many engineering applications, for example coolant fbw in turbine blades or the fbw inside impellers of centrifugal pumps. The present study investigates channel fbw subject to system rotation about an axis in the spanwise direction. The stability of this fbw is determined by two dimensionless parameters; the rotation number, Ω, and Reynolds number, R. Linear stability analysis [3] predicts a minimum critical Reynolds number, R_c^{ro}, of many orders of magnitude less than the corresponding value for plane Poiseuille fbw. This result has been confirmed experimentally by Alfredsson & Persson [1], who found the setting up of streamwise vortices when $R > R_c^{ro}$ and Ω lies in a certain range. At higher values of R, as Ω is increased a secondary instability occurs which leads to an adjustment of the spanwise wavenumber, while at higher R a three-dimensional travelling-wave tertiary fbw may occur [1].

BASIC FLOW AND LINEAR STABILITY

The governing equations, the Navier-Stokes equations together with the incompressibility condition, are expressed in a rotating frame of reference. Seeking a steady basic solution whose only non-zero velocity component lies in the streamwise direction, we derive a parabolic basic-velocity profile together with a pressure gradient in the wall-normal direction. Consideration of the linear stability of this basic fbw results in a linear differential eigenvalue problem, whose solution was obtained using a Chebyshev collocation-point numerical method. We find good agreement with the well-known results of previous authors for the non-rotating case, and the existing results for the rotating case[1, 3]. For the rotating case, the fbw first becomes unstable to a two-dimensional streamwise-independent mode at the critical Reynolds number $R_c^{ro} = 66.447$ (for R based on maximum speed and half channel width). For larger Reynolds numbers the basic fbw may also lose stability to disturbances of non-zero streamwise wavenumber, α. However, for a given spanwise wavenumber, β, the mode with $\alpha = 0$ is always the most unstable mode. Marginal stability curves for various wavenumber combinations are plotted in Fig. 1.

NONLINEAR TWO-DIMENSIONAL SECONDARY FLOW

Given the results arising from linear stability analysis, and also from DNS and experimental studies [2, 1], we seek a streamwise-independent, steady, nonlinear solution to the governing equations. Nonlinear perturbation equations are solved using the Newton-Raphson algorithm. We find nonlinear solutions which arise from bifurcations from the basic fbw which are of a streamwise-vortex character. In Fig. 2 we plot a measure of the amplitude of the nonlinear solution against R for two different wavenumbers. It may be observed that the $\beta = 2.5$ branch joins with the $\beta = 5$ branch at $R \approx 153$. The secondary stability analysis described in the following section finds that the $\beta = 5$ solution loses stability to the $\beta = 2.5$ solution in a streamwise-independent steady, subharmonic bifurcation. Due to the existence of this type of instability, and the fact that lower-order eigenmodes may become unstable, multiple solution branches may exist for a given wavenumber and a rich structure of relationships exists between the two-dimensional nonlinear solutions.

STABILITY OF SECONDARY FLOWS

It is of interest to analyse the stability of the secondary fbws described in the previous section, both to determine where these fbws may be expected to exist, and also to identify bifurcation points for the tertiary fbws. Since the secondary fbws are periodic in the spanwise direction Floquet theory applies, and we analyse the stability of a given secondary fbw to a linear disturbance with spanwise Floquet parameter, b, and streamwise Floquet parameter, d. Various types of bifurcation have been found which include those which correspond to the steady, spanwise bifurcation described above, and also those which may correspond to the travelling-wave solution described in the introduction. We found that the

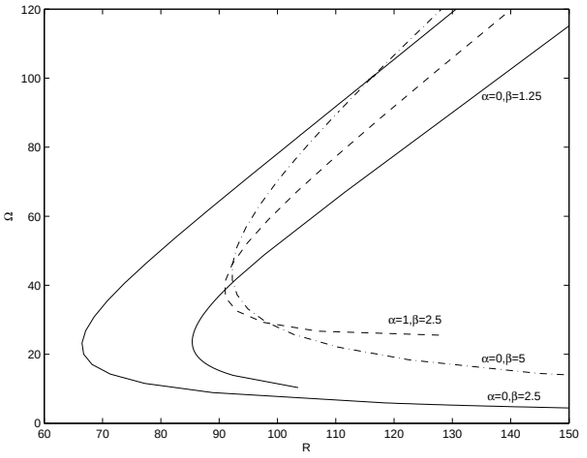


Figure 1. Marginal stability curves corresponding to the most unstable eigenvalue for the values of α and β indicated.

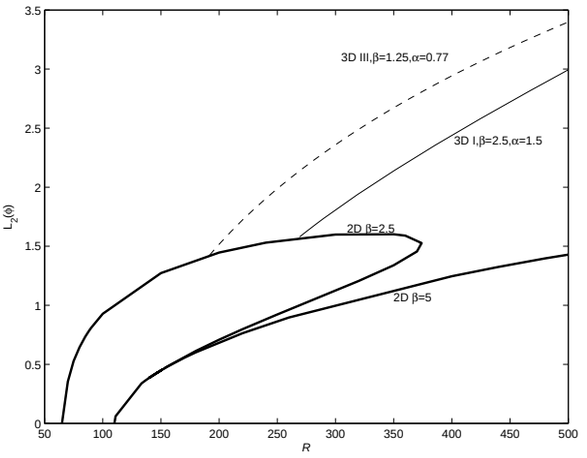


Figure 2. Amplitude of the bifurcating two-dimensional secondary and three-dimensional tertiary flows (I, superharmonic; III, subharmonic) against R when $\Omega = 22.1325$.

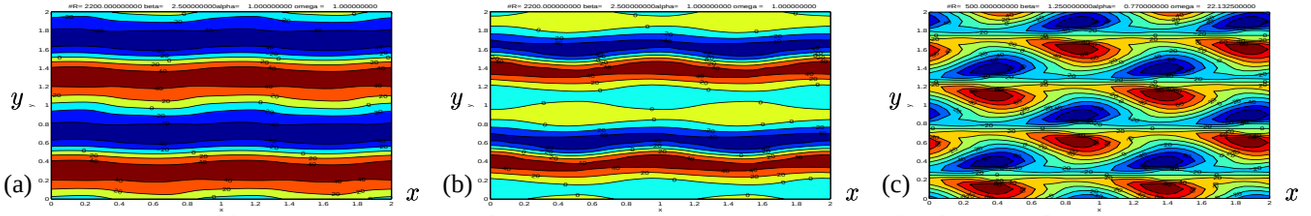


Figure 3. Contours of the streamwise component of vorticity in a streamwise (x) - spanwise(y) slice for tertiary flows (a) superharmonic (I) and (b) superharmonic (II), both for $R = 2200$, $\beta = 2.5$, $\alpha = 1.5$ and $\Omega = 1$, and (c) subharmonic (III) $R = 500$, $\beta = 1.25$, $\alpha = 0.77$ and $\Omega = 22.1325$. The coordinates have been scaled to show two wavelengths in either direction.

flow bifurcating from the minimal critical point is stable to all disturbances for a finite interval beyond the bifurcation point, which is in agreement with the DNS and experimental results [1, 2]. All the flows appear to first lose stability to an Eckhaus disturbance, i.e. disturbances with $d = 0$. However, the secondary flow above the critical point remains stable within a closed Eckhaus region. Excellent agreement is found with the experimental study of Afredsson & Persson [1], both for Eckhaus and travelling-wave instabilities.

THREE-DIMENSIONAL TRAVELLING-WAVE TERTIARY FLOWS

We have solved the governing equations for three-dimensional travelling-wave tertiary flows which arise from a bifurcation from the secondary flows described above. Three distinct tertiary flows have been obtained, two superharmonic flows and one subharmonic flow. The superharmonic flows are characterized by staggered vortices lying either side of low-speed streaks in the streamwise velocity component. One of these flows (I) has one such streak per spanwise wavelength, the other (II) has two. The subharmonic flow (III) also has vortices lying either side of low-speed streamwise streaks, but these vortices are not staggered. An illustration of these flows is provided in Fig. 3, while two of the flows' bifurcations from the secondary flow are shown in Fig. 2.

CONCLUSIONS

We have analysed the linear stability of rotating Poiseuille flow and found the steady, streamwise-independent nonlinear bifurcating secondary flows. The secondary flow bifurcating from the linear critical point is found to be stable to all disturbances for Reynolds numbers in a finite interval above the critical point. A number of possible types of tertiary flow bifurcation points have been identified. Full nonlinear solutions for three different classes of three-dimensional travelling-wave tertiary flows are presented. Good agreement is found with previous experimental and DNS-based studies.

References

[1] P. H. Alfredsson and H. Persson. Instabilities in channel flow with system rotation. *J. Fluid Mech.*, 202:543–557, 1989.
[2] W. H. Finlay. Transition to oscillatory motion in rotating channel flow. *J. Fluid Mech.*, 215:209–227, 1990.
[3] D. K. Lezius and J. P. Johnstone. The structure and stability of turbulent boundary layers in rotating channel flow. *J. Fluid Mech.*, 77:153– 175, 1976.

ON INSTABILITY MECHANISMS IN A SEPARATING BOUNDARY-LAYER FLOW

Matthieu Marquillie, Uwe Ehrenstein, François Gallaire
Lab. J.A. Dieudonné, Université de Nice-Sophia Antipolis,
Parc Valrose, F-06108 Nice Cedex 2, France

Summary The stability of separating boundary-layer flow at the rear of a bump mounted on a flat plate is numerically investigated. It is shown that a geometrically controlled, short separation bubble exhibits a global instability consisting of self-sustained two-dimensional saturated perturbations oscillating at a well defined frequency. Local stability analyses confirm that this instability is triggered by a transition from local convective to local absolute instability in the separation bubble. Solving the three-dimensional Navier-Stokes equations, the flow field is shown to exhibit a three-dimensional steady structure well below the critical Reynolds number for the onset of two-dimensional self-sustained oscillations. Regions subject to centrifugal instability due to streamline curvature are detected, considering the Rayleigh discriminant: some evidence is given that the counter-rotating three-dimensional streamwise vortex structure originates from a potentially unstable region nearby the bump-summit.

INTRODUCTION

Separated flow is known to be subject to powerful instability mechanisms. While a backward-facing step is the most canonical geometry to trigger flow separation, and has received a lot of attention during the last decades, in the present investigation smooth bumps mounted on a flat plate are considered, to trigger adverse pressure gradients (which mimic that on the upper side of an airfoil at high angle of attack). Recirculation bubbles are subject to two-dimensional self-sustained oscillations (cf. [1]) and in the present investigation the asssociated global instabilities are analyzed. Recent global stability investigations of the backward-facing step flow have revealed steady three-dimensional perturbations [2], prior (in terms of the Reynolds number) to the onset of global oscillations. Steady three-dimensional disturbances found in the present flow configuration are analyzed with repect to centrifugal instability criteria [3].

RESULTS

The boundary-layer flow evolving along the bump and the adjacent flat plate is numerically computed solving the three-dimensional Navier-Stokes equations using fourth-order finite differences in the streamwise x-direction, Chebyshev-collocation in the wall-normal y-direction and a Fourier expansion in the homogeneous spanwise z-direction, together with a mapping procedure in order to transform the bump-geometry into a Cartesian one.

Synchronized two-dimensional oscillations in controlled separated flow

In a recent investigation [4], numerical simulation of a blowing-suction device in a backward-facing step flow has been shown to be appropriate to produce two-dimensional, globally synchronized oscillatory instabilities. For the present bump-geometry, and solving the two-dimensional Navier-Stokes equations, the elongated recirculation bubble at the rear of a single bump proved to become unstable *via* aperiodic oscillations [5]. Confining however the recirculation bubble using a second bump downstrean the first one which triggers the separation, it is shown that the bubble undergoes indeed global, synchronized oscillations above a critical Reynolds number, which is based in the present investigation on the displacement thickness at inflow where a Blasius boundary-layer profile is imposed (the dimensionless bump height being $h = 2$).

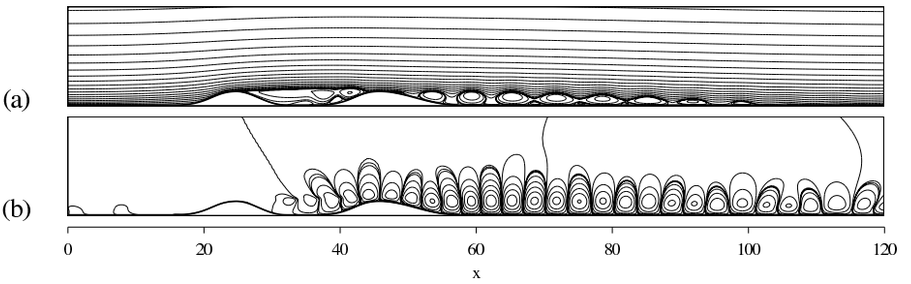


Figure 1: Instantaneous streamlines of (a) the total flow field and (b) the perturbation $\mathbf{u}'$, at $Re = 900$.

The flow field as well as the perturbation are illustrated in figure 1. Local stability analyses, extracting the local velocity profiles from the computed recirculation bubble, have been performed: it is shown that the onset of the global oscillations coincides with the transition from local convective to local absolute instability. As depicted in figure 2(a), the imaginary part of the absolute frequency ω crosses the real axis for increasing Reynolds number, which means that the correponding local profile, shown in figure 2(b), becomes absolutely unstable. The nonlinear frequency-selection criterion for weakly non-parallel flow [6] is shown to predict the computed global frequency.

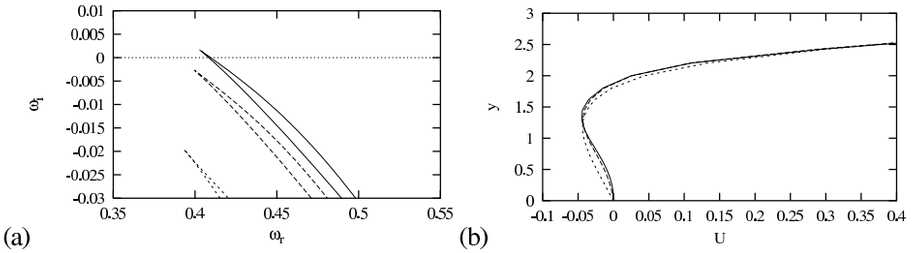


Figure 2:(a) Imaginary part ω_i of complex frequency at the cusp $\frac{\partial \omega}{\partial \alpha}(\alpha_0) = 0$ as function of ω_r and (b) the corresponding profiles, at $x = 33$; ...: $Re = 600$, - - -: $Re = 850$,—: $Re = 900$.

Three-dimensional steady state

Advancing in time solving the three-dimensional Navier-Stokes equations, the flow field converged as expected to a two-dimensional steady state for low inflow Reynolds numbers. However, increasing the Reynolds number, three-dimensional flow structures appear with growing (nonlinear) disturbance amplitudes, well before two-dimensional oscillations set in, similar to backward-facing step flow [2]. Three-dimensional steady disturbances may occur in two-dimensional flow structures which exhibit local vorticity of opposite sign than that of the local algebraic radius of curvature of the streamlines: indeed, classically the Rayleigh dicriminant $R(x, y) = 2U\omega_z/r$ to be negative provides a necessary condition for the corresponding centrifugal instability, where U is the modulus of velocity, ω_z the vorticity of the 2D flow-field (u, v) and r the local radius of the streamlines. Isolines for negative values of the Rayleigh discriminant are depicted in figure 3, for a two-dimensional steady state at $Re = 530$. The upstream part of the bump, where the latter one has concave curvature, exhibits an important region of negative R-values and a second region unstable in Rayleigh's sense appears nearby the summit of the bump. Multiple regions of negative Rayleigh discriminants are also reported in [3] for backward-facing step flow. Figure 4 depicts the three-dimensional flow structure downstream the bump, isosurfaces of the streamwise vorticity being shown. The region of negative R-values is superimposed as well and interestingly the counter-rotating vortex structure is seen to be attached to the potentially unstable region at the summit of the bump.

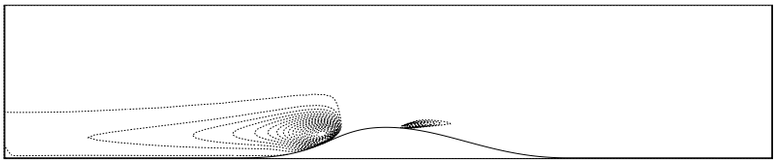


Figure 3: Isolines of negative $R(x, y)$-values indicating regions of possible centrifugal instability.

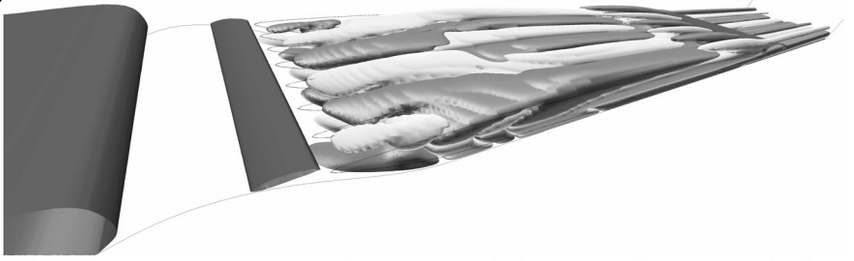


Figure 4: Isosurfaces of $\omega_x = \pm$const.; grey : $\omega_x > 0$; white: $\omega_x < 0$. Black: regions subject to centrifugal instability with $R < 0$.

DISCUSSION

Two different instability mechanisms are identified: while two-dimensional oscillations may clearly be attributed, for confined recirculation bubbles, to local transition from convective to absolute instability, it is conjectured that the global three-dimensional steady states are related to local curvature effects. While the Görtler-type instability mechanism at the upstream part is shown to be inoperative, flow acceleration at the convex part of the bump possibly annihilates the development of perturbations, counter-rotating streamwise vortices originate at the summit of the bump, at the very region where the two-dimensional flow topology satisfies the Rayleigh criterion for (inviscid) centrifugal instability.

References

[1] Dovgal A.V., Kozlov V.V., Michalke A.: Laminar boundary layer separation: instability and associated phenomena. *Prog. Aerospace Sci.* **30**:61–94, 1994.
[2] Barkley D., Gomes M.G., Henderson R.D.: Three-dimensional instability in flow over a backward-facing step. *J. Fluid Mech.* **473**:167–190, 2002.
[3] Beaudoin J.-F., Cadot O., Aider J.-L., Wesfreid J.E.: Three-dimensional stationary flow over a backward-facing step. *Eur. J. Mech. B/Fluids*, in press, 2004.
[4] Kaiktsis L., Monkewitz P.A.: Global destabilization of flow over a backward-facing step. *Phys. Fluids* **15**:3647–3658, 2003.
[5] Marquillie M., Ehrenstein, U.: On the onset of nonlinear oscillations in a separating boundary-layer flow. *J. Fluid Mech.* **490**:169–188, 2003.
[6] Pier B., Huerre P.: Nonlinear self-sustained structures and fronts in spatially developing wake flows. *J. Fluid Mech.* **435**:145–174, 2001.

XXI ICTAM, 15–21 August 2004, Warsaw, Poland

GÖRTLER VORTEX SECONDARY STABILITY: VARICOSE MODE

Leandro F. Souza*, Márcio T. Mendonça**, Marcello A. F. Medeiros*, Markus J. Kloker***
* *EESC-USP, Universidade de São Paulo, São Carlos, Brazil*
** *IAE-CTA, Centro Técnico Aeroespacial, São José dos Campos, Brazil*
*** *IAG, Universität Stuttgart, Stuttgart, Germany*

Summary The varicose mode of Görtler vortex secondary instability was investigated using direct numerical simulation. Root mean square of the streamwise, normal and spanwise secondary instability fluctuation velocity components are presented and compared to previous investigations. The horseshoe structure that evolves due to this secondary instability is also presented showing good qualitative agreement with the structures observed experimentally.

INTRODUCTION

The mushroom type structures that develop due to Görtler vortices result in strongly inflectional streamwise velocity profiles both in the normal and spanwise directions. As a result, secondary instability sets in either as a sinuous or a varicose mode [1]. Hall and Horseman [2] studied both types of secondary instability using an inviscid model and presented the corresponding eigenfunctions. Their results were confirmed by the viscous parallel model of Yu and Liu [3]. A more comprehensive study was presented by Li and Malik [4]. They identified more than one fundamental mode and subharmonic modes that have growth rates comparable to those of the fundamental modes. Their results showed that the sinuous mode is stronger initially, but further downstream the varicose mode has stronger growth rates than the sinuous mode. The present study investigates, through direct numerical simulation, the development of the varicose mode observed in the experiment of Swearingen and Blackwelder [1]. Streamwise, normal and spanwise velocity fluctuations were analyzed and compared to results from previous investigations. The horse-shoe type structure was similar to the structure observed experimentally [1].

FORMULATION AND NUMERICAL METHOD

In the present study the complete Navier-Stokes equations for a constant density and viscosity fluid were rewritten in a vorticity-velocity formulation [5] for the disturbances. The Blasius boundary layer was used as the base flow. The governing equations in non-dimensional form leads to the appearance of the Görtler number, $Go = (k_c\sqrt{Re})^{1/2}$, where k_c is the curvature of the wall. The reference length and reference velocity were L and U_∞, the free-stream velocity. The Reynolds number was given by $Re = U_\infty L/\nu$.

At the wall, no-slip and no penetration boundary conditions were imposed. Disturbances were introduced into the flow field using a suction and blowing function at the wall in a disturbance strip [5]. At the inflow, the velocity and vorticity components were specified based on the Blasius boundary layer. At the upper boundary, the vorticity disturbances were assumed to decay exponentially to zero. A buffer domain technique was implemented in order to avoid wave reflections in the outflow boundary [6].

The equations were solved numerically on an orthogonal uniform grid. The time derivatives were integrated with a classical 4^{th} order Runge-Kutta scheme. The spatial derivatives were calculated using a 6^{th} order compact finite difference scheme. The flow was assumed to be periodic in the spanwise (z) direction and symmetric with respect to $z = 0$. Therefore, the disturbances were expanded in real Fourier cosine and sine series.

RESULTS

In current study the parameters were identical to those used in the experiment of Swearingen e Blackwelder [1]. In their experiment a non stationary disturbance of 130 Hz was observed, and a disturbance with this frequency was introduced in the present numerical simulation. Figures 1 to 3 present the root mean square (rms) of the non stationary disturbance velocity components in the streamwise, normal and spanwise directions at the streamwise position $x = 11.02$ cm. In this figures the mean streamwise velocity profile due to the Görtler vortices is also shown by dashed contour lines, varying from 0.1 to 0.9.

In Figure 1 the largest value of the u_{rms} of about 3.6% is located at the central region ($z = 0$). This u_{rms} peak is located above the wall exactly where the mean flow streamwise velocity is $0.7U_\infty$. This is also the location of the inflection point in the streamwise mean velocity component. This result are in qualitative agreement with the results obtained by [2, 3] and [4] for the first varicose mode, with a single dominant peak at the head of the mushroom. The weaker peaks close to the wall were not capture by Li's [4] inviscid analysis. In the same paper [4] nonlinear, viscous results indicate that the peaks close to the wall grow as the instability develops downstream.

The normal and spanwise disturbance velocity components have more complex structures with stronger v_{rms} peaks located above and inside the mushroom. The w_{rms} has strong peaks on either sides of the mushroom. Figure 2 presents the isolines of v_{rms}. Again, the results are in qualitative agreement with [2] and [3], with a velocity peak at the center.

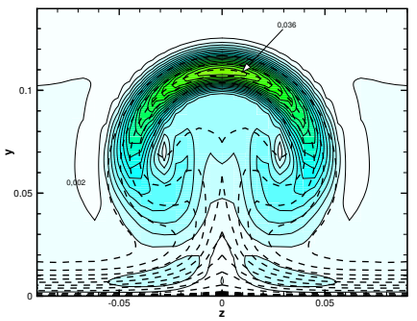


Figure 1. Contour: u_{rms}. Dashed: $\bar{u}$.

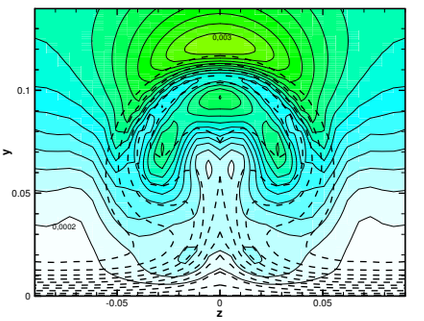


Figure 2. Contour: v_{rms}. Dashed: $\bar{u}$.

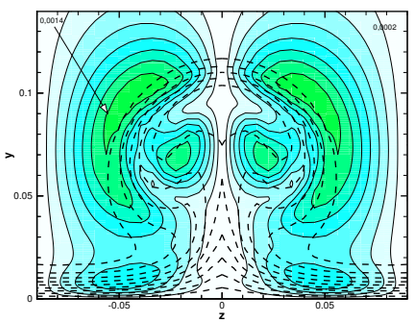


Figure 3. Contour: w_{rms}. Dashed: $\bar{u}$.

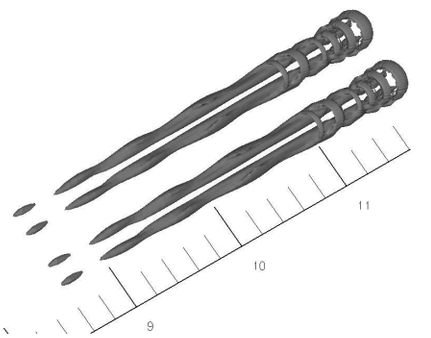


Figure 4. The horseshoe structure.

But in the present study the largest amplitudes of the v_{rms} occurred above the mushroom structure. This difference may be because [2] and [3] considered a parallel mean flow for the secondary stability analysis, discarding the normal and spanwise velocity components of the mushroom.

The results for w_{rm} shown in Figure 3 are also in qualitative agreement with the analysis of [3]. In the present results the two peaks on either side of the mushroom head are farther apart from each other when compared to the results from [3]. These peaks are located at the outer layer of the mushroom, while in [3] they are located inside the mushroom structure. Again, this discrepancy with [3] may be attributed to the parallel assumption used in that work.

In Figure 4 Q isosurfaces are shown for a given time t. The Q isosurfaces are obtained by the method described in [7] and represent the vortical structure of the flow. The streamwise extent covers a region from earlier nonlinear Görtler vortex up to the secondary instability region. These structures were also observed in the experiment of Swearingen and Blackwelder [1].

CONCLUSIONS

In this work the secondary stability of Görtler vortices to non stationary disturbances were analyzed. The results were in good agreement with results from previous investigations. Direct numerical simulation model was able to take into account nonlinear, nonparallel and viscous effects. The mushroom structures observed in the experiment of Swearingen and Blackwelder [1] were recovered in the numerical simulation. Future work will investigate also the sinuous mode and the effect of the spanwise wavelength. The financial support from FAPESP (State of Sao Paulo Research Support Foundation) – Grant numbers 00/04943-7 and 03/05027-2 – is greatly acknowledged.

References

[1] Swearingen J. D., Blackwelder R. F.: The Growth and Breakdown of Streamwise Vortices in the Presence of a Wall. *J. Fluid Mech.*, **182**:255, 1987.

[2] Hall P., Horseman N. J.: The Linear Inviscid Secondary Instability of Longitudinal Vortex Structures in Boundary Layers. *J. Fluid Mech* **232**:357–375, 1991.

[3] Yu X., Liu J. T. C.: On the Mechanism of Sinuous and Varicose Modes in Three-Dimensional Viscous Secondary Instability of Nonlinear Görtler rolls *Physics of Fluids*, **6**:736–750, 1994.

[4] Li F., Malik M. R.: Fundamental and Subharmonic Secondary Instability of Görtler Vortices. *J. Fluid Mech* **297**:77–100, 1995.

[5] Meitz H. L., Fasel H. F.: A compact-difference scheme for the Navier-Stokes equations in vorticity-velocity formulation. *J. Comp. Phys.*, **157**:371–403, 2000.

[6] Kloker M., Konzelmann U., Fasel H. F.: Outflow Boundary Conditions for Spatial Navier-Stokes Simulations of Transition Boundary Layers. *AIAA Journal*, **31**:620–628, 1993.

[7] Dubief Y., Delvayre F.: On coherent-Vortex Identification in Turbulence. *J. of Turbulence*, **11**:1–22, 2000.

SPIRAL VORTEX BREAKDOWN AS A GLOBAL MODE

Michael Ruith*, François Gallaire**, Jean-Marc Chomaz***, Patrick Huerre***, Eckart Meiburg*
*UCSB, Santa Barbara, California, USA
**Laboratoire J.-A. Dieudonné, CNRS-Université Nice-Sophia-Antipolis, France
***Laboratoire d'Hydrodynamique (LadHyX), CNRS, École Polytechnique, F-91128 Palaiseau Cedex, France

Summary The spiral form of vortex breakdown observed in the numerical simulations of Ruith, Chen, Meiburg and Maxworthy[5] is interpreted as the consequence of the development of a so-called nonlinear global mode originating in the convective/absolute transition of the instability in the lee of the vortex breakdown bubble. This local theory gives an excellent prediction of the precession frequency measured in the three-dimensional DNS.

MOTIVATION

Vortex breakdown is a widespread phenomenon affecting swirling jets that is both observed in its axisymmetric form (the bubble) or in its spiral form, as soon as the swirl parameter S, which compares the intensity of the azimuthal velocity component to its axial counterpart, is large enough. These synchronized helical vortex breakdown states (see Escudier [1]) for a review) are characterized by low azimuthal wavenumbers ($m = 1$ or $m = 2$), they rotate in time in the same direction as the swirling base flow but wind in space in the opposite direction.

The aim of the present study is to show that these non-axisymmetric vortex breakdown states observed at moderate Reynolds numbers may be interpreted as the result of local instability of the unstable axisymmetric breakdown serving as a spatially varying base flow. More precisely, according to the initial suggestion of Escudier, Bornstein and Maxworthy[2] and Delbende, Chomaz and Huerre[3], the spiral vortex breakdown is supposed to result from the development of a global mode triggered by the absolutely unstable nature of the $m = 1$ mode in the lee of the breakdown bubble. Yin, Sun, Wei and Wu[4] and Ruith *et al.*[5] have indeed shown that the spatio-temporal stability results associated with the $m = 1$ mode of the Batchelor vortex compare qualitatively well with the experimental characteristics of spiral vortex breakdown states.

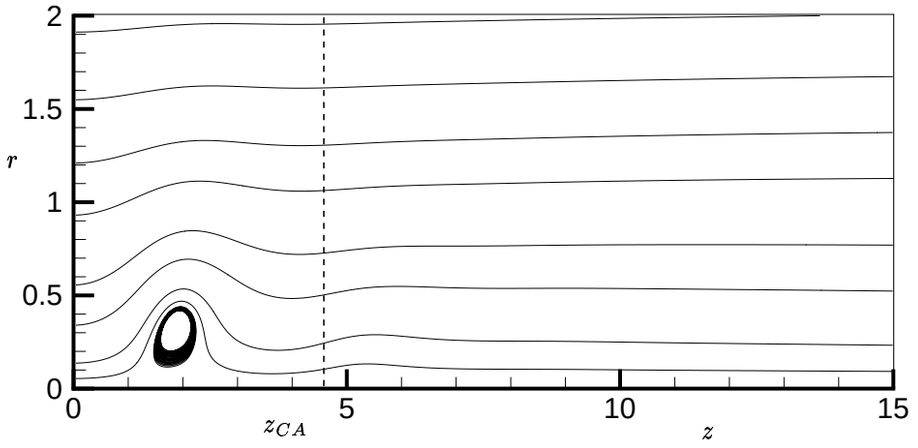


Figure 1. Meridional cut of the streamlines associated to the base flow obtained numerically by imposing the axisymmetry of the flow; $S = 1.095$, $Re = 200$ (Ruith *et al.*[5]).

Our purpose is to validate this hypothesis by using as a base flow the velocity profiles obtained in the numerical simulations of Ruith *et al.*[5] by imposing axisymmetry (see figure 1). As seen in figure 1, vortex breakdown is observed at the swirl number $S = 1.095$, characterized by the typical recirculation zone. At each axial station z along the streamwise axis, the flow is assumed to be weakly non-parallel and the stability study is conducted on a parallel flow basis with the base flow measured locally at the station z. The weakly non-parallel but strongly nonlinear theory of Pier, Huerre and Chomaz[6] suggests that, if there exists a station $z_{C/A}$ where the imaginary part of the absolute frequency ω_0 vanishes and where the flow changes from convective ($\omega_{0,i}(z) < 0$ for $z < z_{C/A}$) into absolute ($\omega_{0,i}(z) > 0$ for $z_{C/A} < z$), then a nonlinear global mode might be triggered with a front located at $z_{C/A}$. This global mode also inherits the real absolute frequency at this point $\omega_0(z_{C/A})$.

COMPARISON BETWEEN WEAKLY NON-PARALLEL STRONGLY NONLINEAR THEORY AND THREE-DIMENSIONAL DNS

For the same parameter setting as in figure 1 but by relaxing the axisymmetry assumption, figure 2 represents the instantaneous streaklines at $t = 1850$ obtained in the DNS with an initial random noise imposed on the base flow of figure 1 at

$t = 0$. The flow settles to a limit cycle oscillating at a well determined frequency ω_G^{NL}.

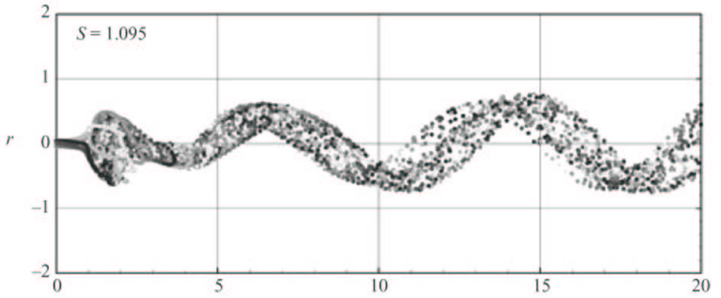


Figure 2. Instantaneous streaklines at $t = 1850$ associated to the three-dimensional flow obtained by DNS at $S = 1.095$ and $Re = 200$ (Ruith *et al.*[5]).

The stability analysis is conducted by numerical means using the method outlined in Delbende *et al.*[3] in a box $1440 \times 196 \times 196$. The results are summarized in figure 3. Two absolutely unstable regions can be distinguished as indicated by the shaded areas. A first region located in the recirculation bubble between $z^1_{C/A} = 1.1$ and $z^1_{A/C} = 3.3$ and a second region in the lee of the bubble for $z \geq z^2_{C/A} = 4.7$.

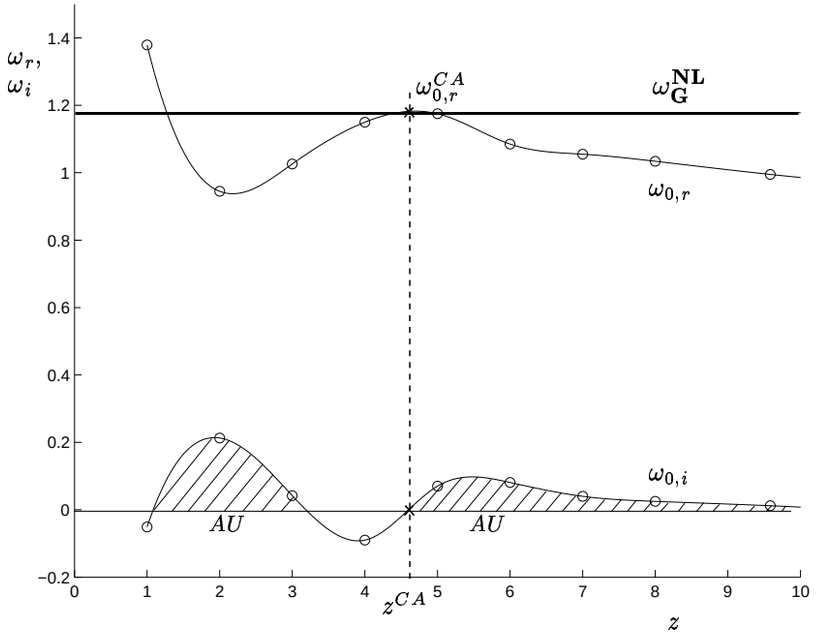


Figure 3. Streamwise evolution of the real $\omega_{0,r}$ and imaginary part $\omega_{0,i}$ of the local absolute frequency as a function of streamwise distance z.

The value of the global frequency ω_G^{NL} measured in the DNS is shown in figure 3 as a horizontal thick line. The agreement between the measured frequency ω_G^{NL} and $\omega^{C/A}_{0,r,2}$ is excellent, whereas it is less satisfactory with $\omega^{C/A}_{0,r,1}$. This shows that the second region is responsible for the global instability and that the transition point $z^2_{C/A}$ plays the role of a wavemaker. The validity of the interpretation of spiral vortex breakdown in terms of a nonlinear global mode with a front located at the transition point $z^2_{C/A}$ is further confirmed by the analysis of the streamwise amplitude distribution and wavenumber variation extracted from the DNS.

References

[1] Escudier M. P. : Vortex breakdown : Observations and explanations. *Prog. in Aerospace Sci.* **25**:189-229, 1988.

[2] Escudier M.P., Bornstein J., Maxworthy T.: The dynamics of confined vortices. *Proc. R. Soc. Lond. Ser. A.* **382**:335-360, 1982.

[3] Delbende I., Chomaz J.-M., Huerre P.: Absolute/convective instabilities in the Batchelor vortex: a numerical study of the linear impulse response. *J. Fluid Mech.* **355**:229-254, 1998.

[4] Yin X.Y., Sun D.J., Wei M.J., Wu J.Z. : Absolute and convective instability character of slender viscous vortices. *Phys. Fluids.* **12**:1062-1072, 2000.

[5] Ruith M., Chen P., Meiburg E., Maxworthy T. : Three-dimensional vortex breakdown in swirling jets and wakes: direct numerical simulation. *J. Fluid Mech.* **486**:331-378, 2003.

[6] Pier B., Huerre P., Chomaz J.-M. : Bifurcation to fully nonlinear synchronized structures in slowly varying media. *Physica D.* **148**:49-96, 2001.

XXI ICTAM, 15–21 August 2004, Warsaw, Poland

COMPUTATIONAL STUDY OF TURBULENT-LAMINAR BANDS IN COUETTE FLOW

Dwight Barkley*, Laurette S. Tuckerman**
*University of Warwick, Coventry CV4 7AL United Kingdom
e-mail: barkley@maths.warwick.ac.uk - Web page: http://www.maths.warwick.ac.uk/∼barkley/
**LIMSI-CNRS, BP 133, 91403 Orsay Cedex France
e-mail: laurette@limsi.fr - Web page: http://www.limsi.fr/Individu/laurette/

Summary
Direct numerical simulations of plane Couette flow are used to study turbulent-laminar patterns similar to the spiral turbulence state known for many years in Taylor-Couette flow. A technique based on minimal flow unit simulations is employed. Turbulent-laminar patterns are found in close agreement with experiment.

Introduction

In Taylor-Couette flow between counter-rotating cylinders it is possible to obtain an intriguing state known as spiral turbulence consisting of alternating regions of turbulent and laminar flow [1]. Because turbulent and laminar flow self-organize into well-defined regions with neither invading the other, this state has attracted much attention over the years [1, 2, 3, 4], but has never been explained. Recently, using a Taylor-Couette apparatus with a very narrow gap, Prigent et al. [5, 6] were able to produce a flow containing several regular repetitions of the turbulent-laminar pattern. Furthermore, they discovered that an analogous state exists in plane Couette systems whose gap is very small compared with the lateral dimensions. In both cases, the pattern is oriented obliquely to the streamwise direction (i.e. the azimuthal direction in the Taylor-Couette case) and the wavelength is on the order of 20–30 times the gapsize. Our work is aimed at understanding the onset and structure of the pattern of laminar and turbulent bands in these Couette flows.

Methods

We use direct numerical simulations (DNS) of plane Couette flow in domains which permit computation of the turbulent-laminar flow at reasonable cost and which allow us to address questions which are not directly accessible to experiment. The simulation domains are illustrated in Fig. 1. Units are chosen such that the plates are separated by a gap of 2 and move at velocities $\pm\mathbf{e_x}$; the Reynolds number is $Re = 1/\nu$. It is known from minimal flow unit (MFU) simulations [7] that a weakly turbulent flow can be sustained in a computational domain with periodic lateral boundaries of size approximately 6 (streamwise) by 4 (spanwise) length units (Fig. 1). The spanwise length is near the minimum streak pair spacing for turbulent Couette flow near $Re = 400$. Here we extend the MFU computations in two ways. First we allow the domain to be tilted with respect to the streamwise direction while still maintaining periodicity of the computational domain and respecting the required streak spacing. This permits us to study patterns which are oblique to the streamwise direction. Secondly, we consider domains which are long in only one direction. Thus we can simulate large length scales and study the effect of angle and domain length on the formation of the turbulent-laminar patterns.

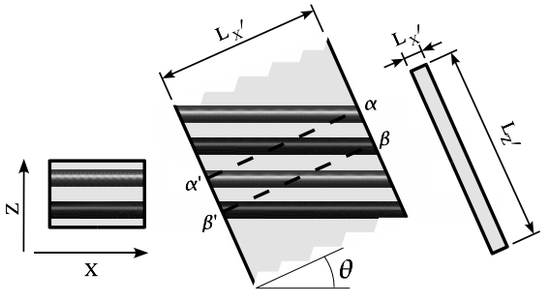


Figure 1. Simulation domains. The streamwise and spanwise directions are x and z; computational domains are aligned in directions x', z', which are tilted at angle θ. The light and dark gray streamwise bars represent streamwise vortices or streaks with a spacing of 4 length units. Left: MFU domain [7]. Middle: tilted domain at angle θ with a short length $L_{x'}$ which respects the streak spacing ($L'_x \sin(\theta) \simeq 4$). Right: domains have a large length $L_{z'}$ in one direction. In all cases $L_y = 2$ (not seen).

Results

Fig. 2 shows the formation of a turbulent-laminar pattern. A turbulent flow is initialized at $Re = 500$. Then Re is decreased, rather quickly, at times indicated. A pattern emerges with three distinct turbulent and laminar regions. This is seen quantitatively in the modulus of the Fourier transform (averaged over 500 time units) by the emergence of a peak at $m = 3$. In the tilted frame the wavelength is 40, agreeing closely with experiment [5, 6]. Re is fixed at 350 long enough to show that the pattern is stable. The flow field is visualized in Fig. 3. Then Re is decreased more slowly. At $Re = 310$ the pattern changes to a two-band structure, seen quantitatively as a rise in the $m = 2$ spectral peak and a decrease in the $m = 3$ peak. Many more simulations have been conducted with different domain sizes and different angles. Fig. 4 shows an isolated turbulent region found at $\theta = 66^o$.

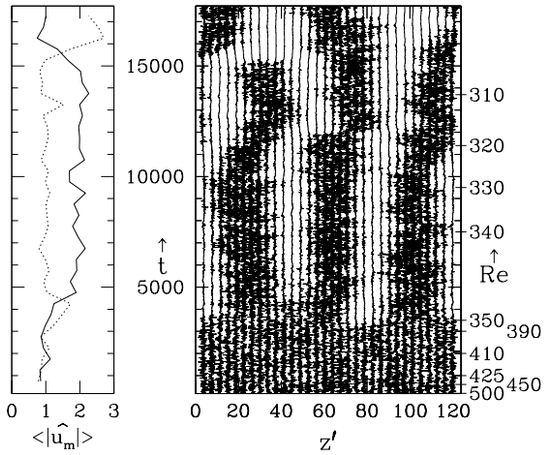


Figure 2. Right: Space-time diagram showing formation of the turbulent-laminar pattern. The domain size is $L_{x'} \times L_{z'} = 10 \times 120$ with a tilt of 24^o. Shown is the spanwise velocity measured at 32 points equally spaced along a line in the middle of the channel ($x' = y' = 0$). Time is shown on the vertical axis with changes in Reynolds number indicated on the right. Left: Time-averaged modulus of the spatial Fourier transform of the data corresponding to modes $m = 3$ (solid) and $m = 2$ (dashed).

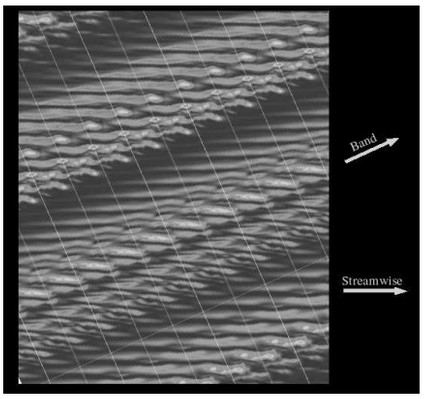


Figure 3. Visualization of the patterned flow at $Re = 350$. The computational domain (outlined in white) is repeated periodically to tile an extended region. Plotted is the streamwise velocity near the upper wall of the channel. The streamwise streaks, typical of turbulent channel flows, can be seen in the turbulent regions. The pattern is oblique to the streamwise direction.

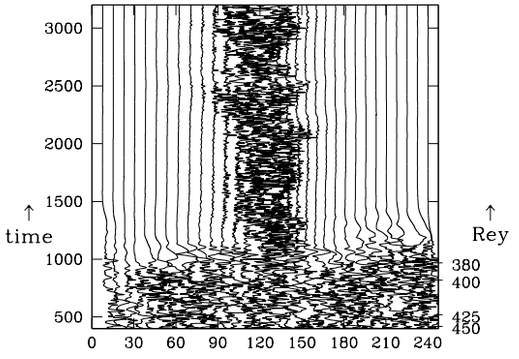


Figure 4. Space-time diagram for $\theta = 66^o$. Here the region of turbulent flow appears isolated. It takes up a relatively small proportion of the domain and its size does not change with changes in domain size. Hence there is no selected periodicity to the pattern.

Conclusions

Our simulations demonstrate that patterns can be generated with only one extended lateral direction ($L_{z'}$). The other dimensions need only be large enough to resolve the inter-plate distance and to contain an integer number of longitudinal vortex pairs or streaks. For a tilt 24^o, the pattern wavelength and onset Reynolds number are in close agreement with experiment. The type of pattern depends on angle and isolated turbulent regions can be found, which may be similar to turbulent spots observed in Couette flows.

Computations were performed on the IBM SP4 computer of the IDRIS-CNRS supercomputer center, project 1119.

References

[1] D. Coles: Transition in circular Couette flow, *J. Fluid Mech.* **21**: 385, 1965.
[2] C.W. Van Atta: Exploratory measurements in spiral turbulence, *J. Fluid Mech.* **25**: 495, 1966.
[3] C.D. Andereck, S.S. Liu & H.L. Swinney: Flow regimes in a circular Couette system with independently rotating cylinders, *J. Fluid Mech.* **164**: 155–183, 1986.
[4] J. Hegseth, C.D. Andereck, F. Hayot & Y. Pomeau: *Phys. Rev. Lett.* **62**: 257-260, 1989.
[5] A. Prigent, G. Grégoire, H. Chaté, O. Dauchot & W. van Saarloos: Large-scale finite-wavelength modulation within turbulent shear flows, *Phys. Rev. Lett.* **89**: 014501, 2002.
[6] A. Prigent, G. Grégoire, H. Chaté, O. Dauchot: Long-wavelength modulation of turbulent shear flows, *Physica D* **174**: 100, 2003.
[7] J. Hamilton, J. Kim & F. Waleffe: Regeneration mechanisms of near-wall turbulence structures, *J. Fluid Mech.* **287**: 317, 1995.

XXI ICTAM, 15–21 August 2004, Warsaw, Poland

A GENERIC MECHANISM FOR BY-PASS TRANSITION IN VORTICES ?

Arnaud Antkowiak* and Pierre Brancher*
Institut de Mécanique des Fluides de Toulouse, Allée du Professeur Camille Soula, 31400 Toulouse, France

Summary Investigation of the energy amplification potential for an axisymmetric vortex is carried out (*optimal perturbation analysis*). Intense amplifications of perturbations are found to occur for various azimuthal wavenumbers m via an original scenario involving both Orr mechanism and vortex induction. Moreover, $m = 1$ optimal perturbation appears to contaminate the core with the formation of a strong bending wave. $m > 1$ optimal perturbations are also capable of core contamination with the creation of a multipolar strain field. This induced field can potentially be the seed for secondary instabilities (by-pass transition). Finally, the ingredients feeding the growth are present in all vortices, revealing the generic nature of the mechanism.

INTRODUCTION

Generic components of a wide diversity of flows, ranging from industrial to geophysical scales, vortices have been the subject of numerous studies since years. Along these, it appeared that without additional ingredients such as an external strain field or the presence of an axial flow, vortices can hardly encounter instabilities. This strong robustness featuring the vortex is well illustrated by its presence and persistence in so much flows, *e.g.* the hazardous wake of an aircraft.

Some theoretical as well as numerical works have switched off these additional effects in order to focus on the dynamics of an isolated vortex (axisymmetric monopole). Particularly, the process of axisymmetrization has been well documented, and it is now well known that an initial random disturbance injected in a vortex will see its own vorticity gradients steepen thanks to the action of differential rotation until the viscous scale is reached, which means the dying of the perturbation. This is the so-called *shear-diffusion* process acting on an $\mathcal{O}(\mathrm{Re}^{1/3})$ timescale.

Nevertheless, monotonic decay of disturbances, although common, is not systematic. Indeed, clues of non trivial behaviours have been reported with rare but violent cases of disruptions. Moreover, analytical works conducted on hollow vortices (plasma columns and hurricanes) have revealed the possibility for algebraic instabilities to occur.

In this context, our objective is to evaluate the potential for transient energy amplification in an axisymmetric monopole.

FORMULATION

The Lamb-Oseen vortex as an archetype of monopole

The monopole under investigation here will be the classical self-similar solution of Lamb-Oseen, with diffusing vorticity $Z(r,t)$ and angular velocity $\Omega(r,t)$ defined as :

$$Z(r,t) = \frac{2}{1+4t/\mathrm{Re}} \exp(-\frac{r^2}{1+4t/\mathrm{Re}}) \; ; \; \Omega(r,t) = \frac{1-\exp(-\frac{r^2}{1+4t/\mathrm{Re}})}{r^2} \tag{1}$$

Here, the initial vortex radius r_0 and initial axis angular velocity Ω_0 have been used to construct the Reynolds number $\mathrm{Re} = \Omega_0 r_0^2/\nu$, where ν denotes the kinematic viscosity.

Non-normality inside

Tracking now the evolution of a disturbance injected in such a flow, we have to solve the governing equations, namely the linearized Navier-Stokes equations, that can be formally written :

$$\mathsf{F}(\boldsymbol{v}) = \mathsf{L}\frac{\partial \boldsymbol{v}}{\partial t} + \mathsf{C}\boldsymbol{v} - \frac{1}{\mathrm{Re}}\mathsf{D}\boldsymbol{v} = \boldsymbol{0}, \tag{2}$$

where L is a normal operator, D a classical self-adjoint diffusion operator and C is an operator where all the couplings between the mean flow and the disturbance concentrate. It is noteworthy that differential rotation breaks the normality for this operator. This mathematical statement has a direct physical translation : a disturbance can experience a transient stage of energy amplification before conforming to the long-time modal prediction (exponential decay in the present case) [1]. But what quantitative redirection of energy from the mean flow to the disturbance can be expected ? This question is addressed in computing the optimal perturbation.

Optimal disturbance

The optimal perturbation is the initial condition which maximizes the energy growth during a finite time interval. Although different techniques exist, it is convenient to use the optimal control theory to compute it [2]. In this theoretical frame, the problem lies in maximizing the energy growth (the *objective*) at a given time τ under the *constraints* of respecting (2) and the associated boundary conditions. The initial condition is used as a *control* to be adjusted in order to meet the objective. This constrained optimization problem can be solved by considering the equivalent unconstrained problem for a Lagrangian functional, whose stationary point can be found using standard methods.

RESULTS

Azimuthal wavenumber-one optimal perturbation ($m = 1$)

The analysis reveals that considerable growths can be reached for $m = 1$ optimal perturbation, even at moderate Reynolds numbers. This amplification follows from an original scenario [3] involving both a local mechanism (an analogue of the Orr mechanism [4]) and the global vortex induction. Figure 1 illustrates the evolution of this perturbation. As can be noticed, another important fact is the ability of the optimal to contaminate the core of the vortex, although initially located at the periphery. The physical mechanisms feeding the energy growth are basically differential rotation and vortex induction. Therefore the mechanism involved is generic; it does not depend on a particular vorticity profile.

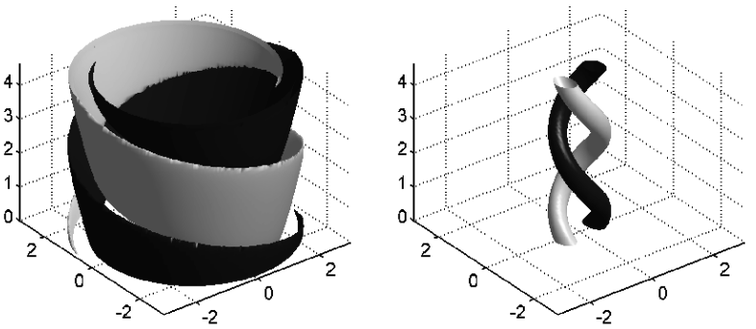


Figure 1. Re = 1000. Initially (left), the optimal perturbation is composed of a set of vorticity sheets lying at the periphery of the vortex. As time flows, the spirals unroll and destructive interference between sheets disappear. Eventually (right), a strong bending wave has been created in the core of the vortex.

Higher wavenumbers optimal perturbations ($m > 1$)

Large growths can still be reached for higher azimuthal wavenumbers (figure 2). Once again, Orr mechanism and vortex induction are associated to the energy amplification. Looking at the evolution of the perturbation, it is found that the main visible difference is due to the role played by vortex induction. For $m = 1$, it results in the creation of a bending wave and for $m > 1$, it produces a transient multipolar strain field in the core of the vortex.

Since secondary instabilities of elliptic kind are known to occur on vortices embedded in an elliptical strain field, it is of interest to look at the nonlinear development of this perturbation. This issue is investigated by means of numerical simulations and preliminary results will be presented, in order to address the relevance of a by-pass transition scenario in vortices.

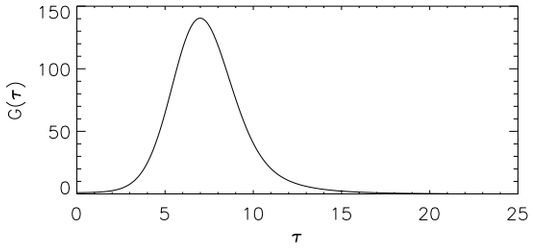


Figure 2. Re = 5000. Typical evolution of the energy growth for a $m = 2$ optimal perturbation.

References

[1] Trefethen L.N., Trefethen A.E., Reddy S.C. and Driscoll T.A.: Hydrodynamic stability without eigenvalues. *Science* **261**, 578, 1993.

[2] Corbett P. and Bottaro A.: Optimal linear growth in swept boundary layers. *J. Fluid Mech.* **435**, 1, 2001.

[3] Antkowiak A. and Brancher P.: Transient energy growth for the Lamb-Oseen vortex. *Phys. Fluids* **16**(1) L1, 2004.

[4] Farrell B.F. and Ioannou P.J.: Optimal excitation of three-dimensional perturbations in viscous constant shear flow. *Phys. Fluids A* **5**, 1390, 1993.

GLOBAL STABILITY OF THE FLOW INDUCED BY WALL INJECTION

Thierry Féraille*, Grégoire Casalis*
*ONERA, Aerodynamics and Energetics Modeling Department, B.P. 4025, 31055 Toulouse Cedex 4, FRANCE

Summary The paper deals with the study of the stability of the plane flow induced by wall injection. The perturbation is in the normal mode form in time and the eigenfunction is described in the (x, y)-plane, where the flow also takes place. This approach allows a better comprehension of the thrust oscillations observed in large solid propellant motors.

PRESENTATION

Large solid propellant motors exhibit oscillations of their thrust certainly due to the coupling of the acoustics and a hydrodynamic instability of the flow inside. In this paper, we only focus on the study of the hydrodynamic instability of the flow. In order to simplify the analysis, compressibility and 3D effects are neglected. The flow is induced by lateral wall injection of fluid, with a constant velocity, in a semi-infinite plane channel.

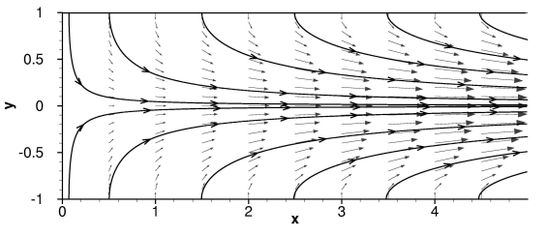


Figure 1. Streamlines and velocity field of the flow induced by wall injection.

The mean flow can be described by a streamfunction $\Psi(x, y)$ whose expression is $\Psi(x, y) = x \sin\left(\frac{\pi}{2} y\right)$ according to the Culick/Taylor relation valid for large Reynolds numbers. The coordinate x is the longitudinal one, with $x \in [0, \infty[$, and y the transverse one, $y \in [-1, 1]$, see figure 1. Both are made dimensionless by half the height of the channel. This mean flow is strongly non-parallel.

The purpose of the present paper is the study of the global behaviour in the (x, y)-plane of any perturbation superimposed to the Taylor/Culick flow. A streamfunction Φ associated with the perturbation is sought in the normal mode form but only in time t, so that Φ can be written as:

$$\Phi(x, y, t) = \phi(x, y) e^{-i\omega t}, \ \omega \in \mathbb{C}.$$

The function ϕ depends on x and y, what is the only acceptable form considering that the mean flow is non-parallel. Classical "quasi-parallel" stability analysis have been previously performed (see [1], [2]), but they are not valid for small values of x in our case (see figure 1).

The linearised Navier-Stokes equations write as a partial differential equation for ϕ with respect to the two variables x and y

$$-\frac{\partial \Psi}{\partial x}\frac{\partial \Delta\phi}{\partial y} - \frac{\partial^3 \Psi}{\partial y^3}\frac{\partial \phi}{\partial x} + \frac{\partial \Psi}{\partial y}\frac{\partial \Delta\phi}{\partial x} + \frac{\partial^3 \Psi}{\partial x \partial y^2}\frac{\partial \phi}{\partial y} - \frac{1}{R}\Delta\Delta\phi = i\omega\Delta\phi,$$

with Δ the Laplacian operator $\Delta = \frac{\partial^2}{\partial x^2} + \frac{\partial^2}{\partial y^2}$ and R the Reynolds number based on half the height and the wall injection velocity. The boundary conditions associated with the previous equation are homogeneous

- At the lateral wall: $\phi(x, \pm 1) = 0$ and $\frac{\partial \phi}{\partial y}(x, \pm 1) = 0$, for all $x \geq 0$,
- At the head of the channel: $\phi(0, y) = 0$ and $\frac{\partial \phi}{\partial x}(0, \pm 1) = 0$, for all $y \in [-1, 1]$.
- An "adequate" output condition for ϕ

what leads to an eigenvalues problem with ω the complex unknown eigenvalue. For its numerical resolution, it is then possible to separate symmetric and antisymmetric solutions in order to divide by two the size of the computational domain. Results are given in the lower half plane $(x, y) \in [0, X_f] \times [-1, 0]$, with X_f the final abscissa of the computational domain. It seems that the "adequate" boundary condition imposed at the exit has nearly no effect on the results.

RESULTS

Two kinds of results can be obtained, first the spectrum of the eigenvalue problem and second the eigenfunctions associated with it. The spectrum gives the value of the pulsation (ω_r, real part of ω) and also the temporal growth rate of the intrinsic perturbation (ω_i, imaginary part). An example (antisymmetric mode for $R = 1000$ and $X_f = 4$) is given figure 2 in the plane (ω_r, ω_i). It can be observed that the spectrum is discrete, so only particular frequencies correspond to intrinsic perturbation of the Taylor/Culick flow. Then, a coupling of the acoustics with the hydrodynamic perturbations is possible when frequencies corresponding to an acoustic mode (a cavity mode) and to a perturbation are the same. It may be a simple way to understand the creation of the thrust oscillations. It can also be observed that the temporal growth rate ω_i of the perturbations is negative, it means that they are vanishing with time t, so a constant source of noise is necessary

in order to observe the perturbations. This seems to agree with direct resolution of Navier-Stokes equations in this case: every one hundred time-steps, noise must be injected at the lateral wall for the oscillations to be observed. In experimental set-up, the noise is provided "naturally". The temporal growth rate ω_i is also decreasing with an increase of the pulsation, this is certainly due to the viscosity of the fluid, the more the phenomenon is varying rapidly, the more it is damped by the viscosity.

If we look at the phase of ϕ, figure 3, a special care must be taken for particular points of these functions. Except on the boundary of the computational domain, the perturbation of the stream-function may present some points Ax ($x = 1, 2, \ldots$, see figure 3) with a modulus equal to zero. For these particular points, the phase of the wave is not defined, and there exist discontinuity lines $\mathcal{L}x$ of the argument of the complex function ϕ, defined in $]-\pi, \pi]$ for figure 3. The lines $\mathcal{L}x$ link the points Ax to a boundary. To each line $\mathcal{L}x$ corresponds a discontinuity line of the phase of Φ which turns in time around each point Ax. These particular points are comparable to amphidromic points when studying the tide of the seas where the amplitude of the tide is always zero-value, and the tide is turning around these points. They are due to the effect of the Coriolis force that curves the stream of the seas and then is responsible for the large amplitude of the tides, much more than the effect of the moon or of the sun that mainly impose the period of the tide (half a day).

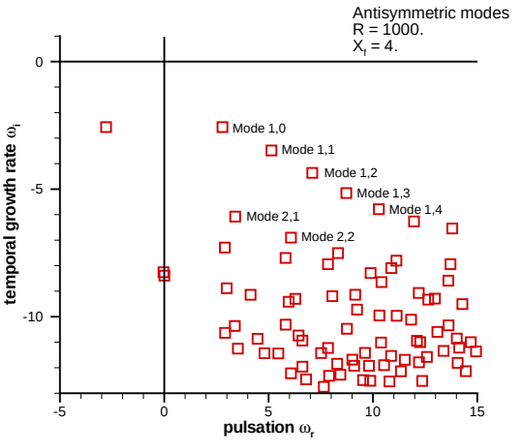


Figure 2. Part of the spectrum of the Taylor/Culick flow for the antisymmetric modes.

By having a look at the first numerically converged modes, enumerated in figure 2, it is possible to classify the modes with the number of amphidromic points of the eigenfunction associated with. Each mode j, i has i amphidromic points. Moreover, except for the mode $i = 0$ whose amplitude is decreasing with x, each mode exhibits a quasi-exponential increase of the amplitude of the function ϕ in the x-direction, see last graphic in figure 3 which represents the real part of ϕ in the (x, y)-plane for the mode 1,2. The increase of the perturbation may be due to the curvature of the streamlines that may act as the Coriolis force on the tide.

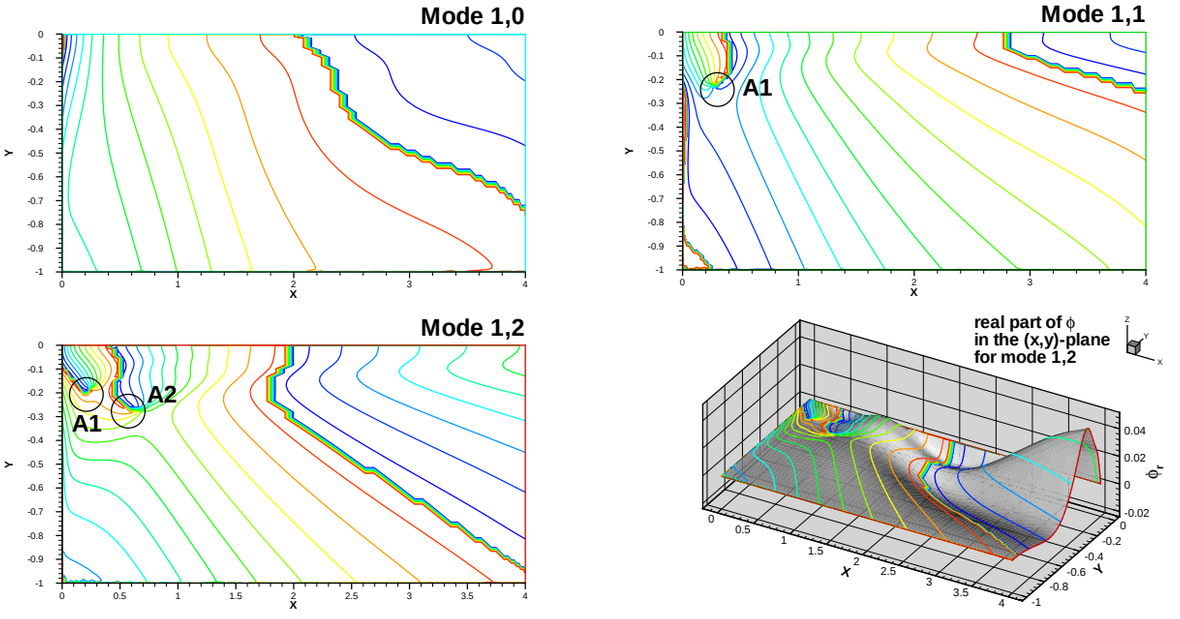


Figure 3. Phase of the eigenfunctions ϕ for modes (1,0), (1,1), (1,2). The number of amphidromic points, Ai, depends on the frequency of the perturbation. The last graphic represents ϕ_r that is oscillating and growing in x.

References

[1] V.N. VARAPAEV, V.I. YAGODKIN: Flow stability in a channel with porous walls. *Izv. AN SSSR. Mekhanika Zhidkosi i Gaza* Vol.4, No.5, 91–95, 1969.

[2] G. CASALIS, G. AVALON, J.-P. PINEAU: Spatial instability of planar channel fbw with fluid injection through porous wall. *Physics of Fluids* Vol.10, No.10. October 1998.

ACOUSTIC FIELD GENERATED BY INSTABILITY WAVES IN THE TRANSONIC REGIME

Christophe Millet*, Stéphane Le Dizès**
*LDG, CEA, BP 12, 91680 Bruyères-le-Châtel, France
**IRPHE, CNRS-UMR 6594, 49 rue Joliot-Curie, BP 146, 13384 Marseille cedex 13, France

Summary We consider the problem of acoustic radiation generated by a spatial instability wave on a weakly-developing two-dimensional mixing layer. Assuming a WKBJ approximation for the instability wave, we compute the far pressure field by using a Fourier transform along the streamwise direction. Approximations for this pressure field are obtained by a steepest descent method when the WKBJ parameter goes to zero. A branch cut and several saddle points are shown possibly to contribute to the approximation. A detailed analysis of these contributions is provided when the instability wave is close to transonic near its maximum amplitude. This permits to explain the modifications of the far pressure field observed during a subsonic-supersonic transition.

INTRODUCTION

The processes by which instability waves generate acoustic radiation have been discussed in the past 20 years (see, for example, Tam [3], Goldstein [2] for review articles, Crighton and Huerre [1] for an asymptotic study of superdirective acoustic sources). Using the wavy wall analogy, it was suggested that the direction of the most intense noise radiation from a supersonic jet or mixing layer can be estimated by using the Mach angle relation based on the speed of the most amplified instability wave. However, Tam and Burton [4, 5] pointed out that the analogy must be modified to account for the growth and decay of the instability wave as it propagates downstream. They demonstrated that the far field should be modified near the location where the instability wave starts to decay but they do not try to fully analyse this transition. For subsonic flows, the noise characteristics are known to be different than their supersonic counterparts as no such transition exists. Yet, the formal solution given by Tam and Burton still applies. The goal of this work is to analyse this solution when we are close to the transonic regime and near the amplitude maximum in order to understand how the supersonic transition occurs.

FAR FIELD IN THE WKBJ FRAMEWORK

We consider a linear compressible instability wave of real frequency ω on a developing two-dimensional mixing layer. In the mixing layer, the perturbation pressure amplitude is assumed to be described, near its maximum, by a WKBJ approximation of the form

$$p_i(X,y) \sim p_o(X,y) \exp\left\{\frac{i}{\epsilon}\int^X \alpha\right\} \tag{1}$$

where y is the transverse coordinate and α is the local (complex) wavenumber which depends on the slow streamwise variable $X = \epsilon x$, characteristic of the evolution length of the mixing layer.
Following Tam and Burton [4], a leading order expression of the pressure far field can be obtained by Fourier transform in terms of the outer variables (X, Y), with $Y = \epsilon y$, as

$$p_f(X,Y) \sim c_\epsilon \int_{-\infty}^{+\infty} q(K) \exp\left\{\frac{\psi(K,X,Y)}{\epsilon}\right\} \,\mathrm{dK}\,, \tag{2}$$

where c_ϵ is an amplitude factor, $q(K)$ a function which is given by Tam and Burton [4] but whose explicit expression is not important here, and

$$\psi(K,X,Y) = i\int^{\overline{X}} \alpha(s)\,\mathrm{ds} - iK(\overline{X} - X) - \lambda(K)Y. \tag{3}$$

In (3), $\overline{X}$ is a function of K defined by $\alpha(\overline{X}) = K$. The function λ can be written, with a suitable choice of non-dimensionalization as

$$\lambda(K) = \sqrt{K^2 - 1}\,. \tag{4}$$

In order to be able to evaluate the function $\overline{X}$ near the branch points $K = \pm 1$ in a general setting, we consider a spatial location X close to the maximum amplitude location X_m defined by $\alpha_i(X_m) = 0$, where α_i is the imaginary part of α, and assume that $\alpha(X_m)$ is also close to 1. This assumption means that we consider an instability wave which is transonic at its maximum. In that way, it can be shown that the phase ψ reduces near $K = 1$ to a "generic" expression of the following form

$$\psi(K,X,Y) \sim \psi(1,X,Y) + i(K-1)(\tilde{X} + a) - b(K-1)^2 + \sqrt{2(K-1)}Y \tag{5}$$

where a is a coefficient proportional to $\alpha(X_m) - 1$, b a coefficient connected to $\alpha'(X_m)$ and $\tilde{X} = X - X_m$.
This "generic" expression permits to understand how the instability field, which is recovered for small Y is transformed into a pure acoustic field for large $\tilde{X}$ and Y.

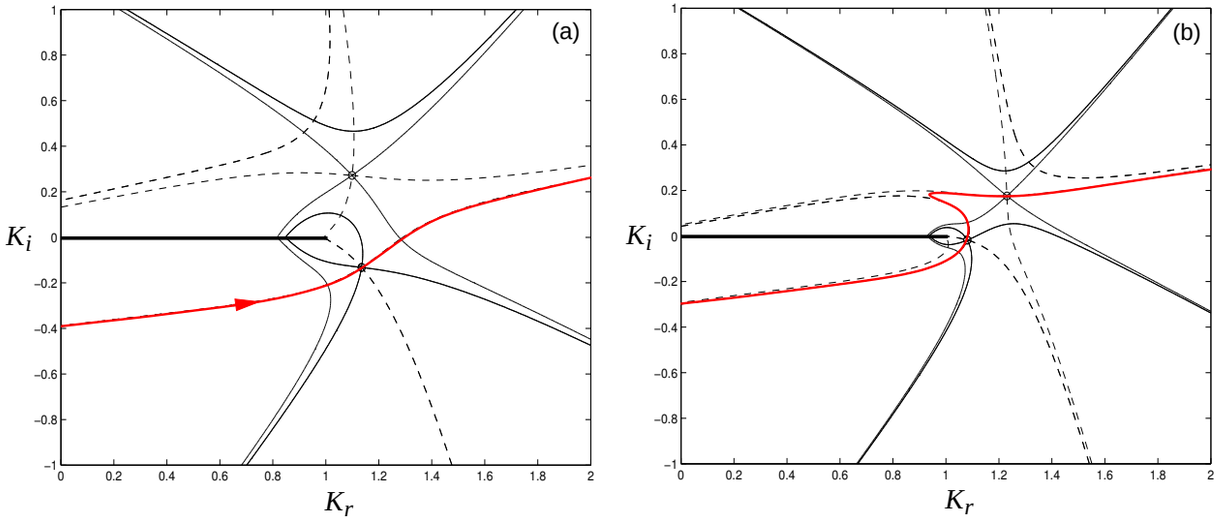


Figure 1. Locus of saddle points (circles) and branch cut (thick black line) in the complex K-plane ($K = K_r + iK_i$). Thin solid lines and thin dashed lines are constant levels of real and imaginary parts of $\psi(K)$, respectively. The thick red line gives the integration contour. Control parameters are given by $a = -i$, $b = e^{-i\pi/8}$ at the location defined by $\tilde{X} = 0$ and $Y = 0.56$ for (a) or $Y = 0.35$ for (b). For $Y \to 0$, it is possible to show that the saddle-point contribution of (a) degenerates into a branch point contribution. The saddle-point of the upper complex half-plane gives the instability wave.

An asymptotic expression of the far pressure field is obtained by the steepest descent method in the limit of small ϵ. The integration contour is deformed in the complex plane in order to go through all the relevant saddle points. Two saddle points are shown to intervene in the analysis, together with the branch point singularity. According the parameters a and b, and the values of the variables $\tilde{X}$ and Y, one or two contributions may be present. In figure 1 are displayed examples of phase contours in the complex K-plane for which there exist one (a) and two (b) saddle-point contributions. The different contributions may also change dominance as the variables are modified. This occurs along particular curves in the $(\tilde{X}, y)$ plane.

When the instability wave is supersonic at its maximum X_m, the main contribution downstream X_m, is found to be associated with the branch point even for Y as small as $O(\sqrt{\epsilon})$. This means that, in some regions, the acoustic field could become dominant over the instability wave that has generated it. It is expected to generate new instability waves in the mixing layer region, downstream X_m. This feedback phenomenon could affect the perturbation field in the mixing layer.

CONCLUSIONS

In this study, we have derived far field approximations for the perturbation field generated by a WKBJ instability wave in a compressible two-dimensional mixing layer. Using a local analysis near the location of perturbation maximum amplitude, we have been able to determine the generic structure of the acoustic far field close to the transonic regime. This has permitted to give a complete description of the subsonic-supersonic transition. It has also demonstrated that the supersonic damped wave continuation described by Tam and Burton [4] is not sufficient to provide the complete structure of pressure fluctuations in the whole physical space. In particular, we have shown that a dominant branch point contribution remains present in the perturbation field downstream the maximum.

Note finally that the analysis, provided here for a mixing layer, can be extended in a straightforward manner to treat the case of axisymmetric jets.

References

[1] Crighton D. G. and Huerre P. : Shear-layer pressure fluctuations and superdirective acoustic sources *J. Fluid Mech.* **220**:355–368, 1990.
[2] Goldstein M. E. : Aeroacoustics of turbulent jet flows. *Ann. Rev. Fluid Mech.* **16**:263–95, 1984.
[3] Tam C. K. W. : Supersonic jet noise. *Ann. Rev. Fluid Mech.* **27**:17–43, 1995.
[4] Tam C. K. W. and Burton D. E. : Sound generated by instability waves of supersonic flows. Part 1. Two dimensional mixing layers. *J. Fluid Mech.* **138**:249–271, 1984.
[5] Tam C. K. W. and Burton D. E. : Sound generated by instability waves of supersonic flows. Part 2. Axisymmetric jets. *J. Fluid Mech.* **138**:273–295, 1984.

XXI ICTAM, 15–21 August 2004, Warsaw, Poland

NONLINEAR TRANSITION OF A FLOW DRIVEN BY A ROTATING MAGNETIC FIELD

Ilmars Grants*, Gunter Gerbeth**
* *Institute of Physics, University of Latvia, Miera 32, LV-2169 Salaspils, Latvia*
** *Forschungszentrum Rossendorf, MHD Department, P.O. Box 510119, 01314 Dresden, Germany*

Summary Results of direct numerical simulation are presented confirming that a linearly stable liquid metal flow driven by a rotating magnetic magnetic field can experience transition to turbulence. This is possible due to a non-normal nonlinear mechanism which governs a transition in several generic shear flows. The employed numerical approach can be used for nonlinear instability analysis of various flows.

INTRODUCTION

Linearly stable shear flows may become turbulent due to finite disturbances. The theoretical explanation of this phenomenon named 'non-normal nonlinear transition' [1] has two ingredients. If the eigenvectors of a linearized system are not orthogonal (non-normal), then some directions in phase space may be very poorly spanned. Consequently, the amplitude of 'misfit' disturbances may grow considerably before getting aligned with the eigendirections. Thus, an initially small initial disturbance may eventually 'catapult' the flow into a nonlinear regime governed by additional subcritical solutions of the Navier–Stokes equations. Such solutions need not to be connected with the basic flow at any finite value of the control parameter. Although unstable [2], these solutions may trap the flow temporarily, at least. It may happen, for instance, if the time-scale of approaching the additional unstable steady state is much less than the characteristic escape time. Besides, the stable manifolds of additional steady states may densely fill the phase space, thus disabling straight return paths. As a result, the disturbance lifetime may be essentially unpredictable and finite as evidenced by direct numerical simulation of the plane Couette flow [2].
The flow due to rotating magnetic field (RMF) is known to have alternative steady solutions [4] very close to the linearly stable basic solution. Experiments [5] have shown that tiny imperfections can cause an irregular onset well below the linear instability threshold. Thus, the linear analysis alone is not sufficient to understand transition of this particular flow. Is this flow so particular or may similar effects take place also in other flows beyond the classical examples? We demonstrate at the example of an RMF driven flow in a cylindrical cavity that the non-normal nonlinear transition can be predicted by direct numerical simulation of the flow response to random forcing.

PROBLEM FORMULATION

The rotating magnetic field is considered in the commonly employed approximation when the skin-effect is neglected and the electromagnetic driving force is flow independent. In this approximation the RMF induces a steady body force with an analytical expression given in [4]. The magnitude of this force in dimensionless terms is the so-called magnetic Taylor number

$$Ta = \frac{\sigma \omega_o B_o^2 H_o^4}{\rho \nu^2},$$

where ω_o and B_o is frequency and the magnetic flux density of the rotating field; σ, ρ and ν is electric conductivity, density and kinematic viscosity of the liquid metal, respectively, but H_o is half-height of the cylinder (assumed equal to the radius in this study). The flow is described by the Navier-Stokes equations with fixed azimuthal body force and by the divergence free constraint. No-slip conditions are applied at the cylinder surface. To simulate noise a random body force is added.

METHOD

The three-dimensional solution $\mathbf{v}$ was decomposed into normal azimuthal modes. Each of these modes was expressed in Chebyshev series of radial and axial coordinates. Symmetries of smooth functions with respect to the radial coordinate were taken into account so that only appropriate parity (even or odd) radial modes were included [6]. The Navier–Stokes equations in primitive variables were integrated in time by a second order implicit scheme. The pressure boundary conditions were evaluated by the so-called spectral dependency matrix. Any of the Chebyshev expansion coefficients of the random body force (representing the noise) were set to a zero mean Gaussian distributed random variable in each time step. The flow response depends on the spatial and temporal resolution in this approximation of noise. Therefore, the timestep and number of decomposition modes were kept constant in all runs. The flow response was expressed in terms of the disturbance energy $\varepsilon = 0.5 \int_V (\mathbf{v} - \mathbf{v}_o)^2 dV$, where $\mathbf{v}_o$ is the basic steady solution. The noise was normalized and scaled by an amplitude factor A in such a way that the disturbance energy $E = 1/T \int_0^T \varepsilon(t) dt = A^2$ for zero basic flow. The integration time was $T = 0.5$ in this study which corresponds to about 50 to 100 revolutions of the core flow depending on *Ta*. The same sequence of random forcing was applied in each run.

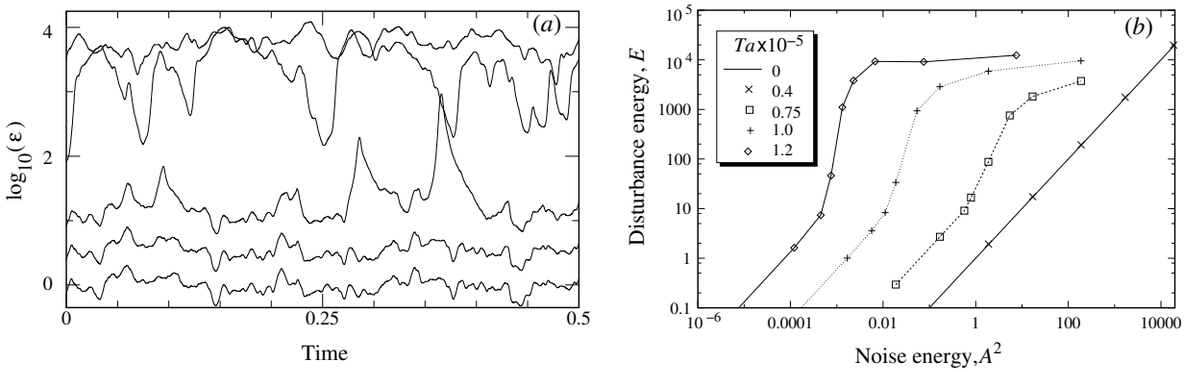


Figure 1. Transient disturbance energy at a variable noise amplitude, $Ta = 10^5$ (*a*) and the response function (*b*).

RESULTS

The azimuthal body force drives an almost rigidly rotating core flow [3] separated from the end walls by the so-called Bödewadt layers. Angular momentum decreases outwards in the side layer supporting a Taylor–Görtler instability there. The meridional flow caused by Ekman pumping, however, instantly deforms and washes away growing Taylor vortices. Thus, the first linear onset at $Ta_c = 1.232 \times 10^5$ is different from the Taylor–Görtler instability [6]. Additional unstable solutions in form of Taylor vortices bifurcate somewhere well above the linear instability limit and continue down to $Ta_g = 0.366 \times 10^5$ [5].

We considered the flow at several fixed values of the forcing parameter $Ta = 0.4, 0.75, 1.0, 1.2 \times 10^5$ from the metastability range $Ta_g < Ta < Ta_c$ and observed four regimes. At the lowest forcing the flow response showed random scatter and did not differ considerably from the response of a motionless state. The energy of response increased at a higher forcing and the time dependency of the response got smoother. The response energy increased linearly with the energy of noise $O(A^2)$ in this second regime. After reaching a certain noise amplitude the flow response experienced a qualitative change characterized by an intermittent nonlinear growth of the disturbance energy. The duration of nonlinear outbursts increased until they merged in a continuous series in the fourth regime (Fig. 1*a*). All four regimes can be recognized in the $E(A^2)$ dependency as shown in Fig. 1*b*. The average response energy scaled with the noise energy $E = kA^2$ with $k = \text{const} \geq 1$ in the first two (linear) regimes. The response grew much faster than $O(A^2)$ in the third regime, and, finally, it was almost insensitive to the noise amplitude in the fourth regime.

DISCUSSION AND CONCLUSIONS

The observations above are in line with two main general features of the non-normal nonlinear transition mechanism [1]. Namely, small disturbances are considerably amplified due to the non-normality of the linearized operator and big enough disturbances are further amplified (temporarily) by nonlinear interactions. The lifetime of the nonlinear structures is often the central issue concerning the nonlinear transition. In our case these nonlinear structures are simply the Taylor vortices born in couples and advected by the basic meridional flow. As soon as the vortices leave the boundary layer they decay linearly. Although the nonlinear structures are not self-sustaining in the RMF flow, their growth is faster than the following linear decay. Consequently, if we consider an instant noise or repeating disturbances, the lifetime of nonlinear structures may only influence the steepness of the response function $E(A^2)$ in the beginning of the nonlinear regime. Assuming that noise is a more appropriate model of natural imperfection than an isolated disturbance, we conclude that a cumulative disturbance amplification factor is practically a more important issue than the lifetime of a single excited state. Note that this factor is always finite as far as we consider the linearly stable flow. In case of the RMF flow this factor can reach values of about 10^6 which explains why hardly visible imperfections could promote onset in the experiment [5].

References

[1] Grossmann, S.: The onset of shear flow turbulence. *Rev. Modern Phys.* **72**, 2, 603–618, 2000.
[2] Schmiegel, A., Eckhardt, B.: Fractal stability border in plane Couette flow. *Phys. Rev. Lett.* **79**, 10, 5250–5253, 1997.
[3] Davidson, P. A.: Swirling flow in an axisymmetric cavity of arbitrary profile, driven by a rotating magnetic field. *J. Fluid Mech.*, **245**, 669–699, 1992
[4] Grants, I., Gerbeth, G.: Stability of axially symmetric flow driven by a rotating magnetic field in a cylindrical cavity. *J. Fluid Mech.* **431**, 407–426, 2000.
[5] Grants, I., Gerbeth, G.: Experimental study of non-normal non-linear transition to turbulence in a rotating magnetic field driven flow *Phys. Fluids* **15**, 2803–2809, 2003.
[6] Grants, I., Gerbeth, G.: Linear three-dimensional instability of a magnetically driven rotating flow. *J. Fluid Mech.* **463**, 229–240, 2002.

XXI ICTAM, 15–21 August 2004, Warsaw, Poland

FULLY NONLINEAR GLOBAL MODES AND TRANSITION TO TURBULENCE IN OPEN FLOWS

Jean-Marc Chomaz
LadHyX, CNRS-École Polytechnique, 91128 Palaiseau Cedex, France

Summary The fully nonlinear theory of global modes in open flows, proposed in recent analyses of amplitude equations, is extended to the case of Navier-Stokes equations using direct numerical simulations. The basic flow under consideration is in a first time, a parallel wake in a finite domain generated by imposing the wake profile at the inlet boundary and by adding a body force to compensate the basic flow diffusion. The link between the global bifurcation, the absolute or convective nature of the local linear instability, and the theory of speed selection for the front separating an unperturbed domain of the flow from a fully saturated solution is elucidated. In particular, thanks to the parallelism of the flow, the bifurcation scenario and the associated scaling laws for the frequency, the healing length, and the slope at the origin predicted by a previous analysis of amplitude equations are recovered with amazing precision. Non-parallel effects are then discussed. Furthermore, new scenarii involving secondary absolute instability are proposed and compared to the dynamics of mixing layers simulations conducted in the same spirit as for the wake.

Mixing layers, jets, wakes, boundary layers over wings or rotating disks, Poiseuille and Couette flows are examples of open shear flows encountered in many industrial or geophysical situations. These flows develop spatially under the combined action of advection and instabilities and eventually undergo a transition to turbulence.
In the eighties [1], the linear concepts of absolute and convective instability succeeded in predicting some aspects of open shear flow dynamics, but a description of their spatio-temporal development including nonlinear effects and secondary instabilities was lacking and even the very fact that a linear criterion describes so well strongly nonlinear flows remains mysterious.

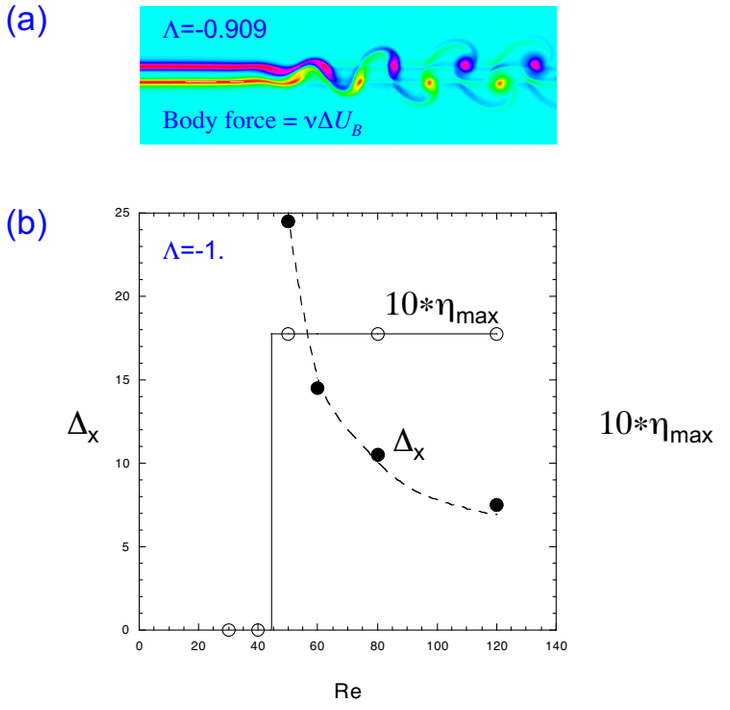


Figure 1. (a) Global Mode of the parallel wake obtained for a Reynolds number $Re = 400$ above the absolute instability threshold, for $\Lambda = -0.909$, $\Lambda = (U_0 - U_\infty)/(U_0 + U_\infty)$ where U_0 is the centre line velocity, U_∞ is the velocity at $y = \infty$. The computational box is 16.8 large and 51.2 long, the wake width being unity.(b) Bifurcation diagram for the wake, showing, for $\Lambda = -1$ (zero backflow) the saturation local enstrophy η_{max}. Following Monkewitz (1988) [9] the instability becomes absolute for Re larger than $Re_A \sim 45$. We observe that, indeed, when the instability becomes absolute the amplitude of the Global Mode measured by η_{max} suddenly increases from zero to a constant finite value as predicted by [8]. The distance Δ_x at which saturation occurs, defined by the location where $\eta(x) = 1$, is also plotted and it is well fitted by $\Delta_x \sim 60.2 * (Re - Re_A)^{-1/2}$ as predicted by the theory.

The present work reports on very recent progress elucidating open shear flow dynamics. By taking advantage of the addition of a body force that compensates the diffusion of the basic flow and makes the flow parallel in the absence of perturbations, we have computed the dynamics of a wake flow and of a mixing layer directly generated at the inlet of the domain [2]. We have established the link between the occurrence of a self-sustained oscillation (a global mode), the linear and the nonlinear transition to absolute instability [3]. First we have shown that the front separating the saturated wake solution from the basic state propagates at the speed of the edge of the linear wave packet [2, 4]. The nonlinear absolute instability as defined by Chomaz (1992) [3] coincides, therefore, with the linear absolute instability for this particular flow. Then, when a homogeneous inlet condition is applied at $x = 0$ (i.e. when the perturbations are assumed to vanish at

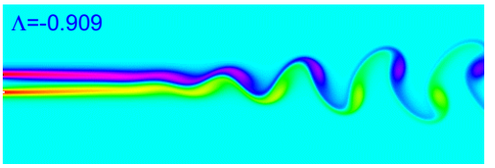


Figure 2. Global Mode of the nonparallel wake obtained for a Reynolds number $Re = 800$ for $\Lambda = -0.909$, i.e. when the inlet flow is everywhere positive. This Reynold number is well above the absolute instability threshold $Re_A \sim 125$ for this particular value of Λ. The computation box is 16.8 large and 51.2 long, the wake width being unity.

$x = 0$) we have shown that the self-sustained oscillation, the nonlinear global mode, is triggered when the flow becomes absolutely unstable. In all the cases studied, the front speed is first shown to be equal to the linear wave packet edge (pulled fronts) [2, 4, 5, 6]. Then, when inlet conditions are introduced a fully nonlinear global mode is shown to appear when the flow is absolutely unstable in the reference frame singled out by the inlet condition (figure 1). The global mode oscillates then at the absolute frequency and is made of a front stop at some distance from the inlet. Both for the wake and the mixing layer, the distance at which saturation occurs, varies as the square of the inverse of the criticality (the departure from threshold) (figure 1b).

For wakes or mixing layers, the parallel basic flow approximation is valid only if the viscosity is nil or compensated by an artificial body force. But in numerical or laboratory experiments, viscosity is finite and the basic flow imposed at the inlet evolves downstream. When the non-parallelism of the real flow is weak enough, i.e. when the scale on which the basic flow varies is large enough compared to the typical scales of the instability (the wavelength, and/or the inverse of the spatial growth rate), the present results may be extended in a straightforward manner. In that case, a nonlinear self-sustained oscillation occurs as soon as a finite domain of absolute instability is present and it is made up of a front located at the most upstream border of the absolutely unstable domain. The oscillation frequency of the Global Mode is then the absolute frequency at the front location. This border may be either a physical boundary of the flow (see [6] for a review) or a location where the flow goes from absolutely unstable to convectively unstable as explained in [7, 8]. Figures 2 shows an example of nonlinear Global Mode in a weakly non-parallel wake obtained by turning on the diffusion of the basic flow in the model. For the wake with co-flow, the instability threshold is postponed to larger values of the Reynolds number but the frequency selection is unchanged.

Since a global mode in a semi-infinite parallel flow reaches finite amplitude saturation at threshold it may itself be unstable. This will occurs when the secondary instability of the uniform saturated wave that follows the front is absolute. But the secondary instability may be absolute either before or after the primary. In the first case a stable global mode will appear first and then, if the control parameter is further increased, it may be destabilized if the secondary instability becomes absolute. In the second case the global mode is already unstable at threshold and an oscillatory or even a chaotic state appears after a single bifurcation. This second scenario involving secondary absolute instability may explain a one step transition to disorder or turbulence as observed for example in rotating disk or mixing layers experiments.

It is worth mentioning that other scenarii should exist that involve a pulled front and for which linear theory should not give a correct prediction. Since the numerical technique introduced by Delbende & Chomaz (1998) [5], allows the direct determination of the linear and nonlinear absolute or convective nature of instabilities, investigations of many different flows are now at hand. Hopefully, some of them will exhibit a nonlinear front velocity selection (pulled front) for which strong departure from linear prediction has already been demonstrated on model equations. In fluid, a nonlinear absolute instability was observed recently for the shear instability in an Hele-Shaw cell [7], the other observations being presently limited to chemical reactions [8].

References

[1] Huerre, P. & Monkewitz, P. A.: *Annu. Rev. Fluid Mech.* **22**: 473-537, 1990.

[2] Chomaz, J.-M.: Fully nonlinear dynamics of parallel wakes. *J. Fluid Mech.* **69**: 57–75, 2003.

[3] Chomaz, J.-M.: Absolute and convective instabilities in nonlinear systems. *Phys. Rev. Lett.* **69**: 1931-1934, 1992.

[4] Couairon, A. & Chomaz, J.-M.: Absolute and convective instabilities, front velocities and Global Modes in nonlinear systems. *Physica D* : **108**: 236-276, 1997.

[5] Delbende, I. & Chomaz, J.-M.: Nonlinear convective/absolute instabilities in parallel two- dimensional wakes. *Phys. Fluids* **10**: 2724-2736, 1998.

[6] Chomaz, J.-M.: Transition to turbulence in open flows: what linear and fully nonlinear local and global theories tell us. *Euro. J. Mech. B* : in press, 2004.

[7] Pier, B., Huerre, P., Chomaz, J.-M. & Couairon, A.: Steep nonlinear Global Modes in spatially developing media. *Phys. Fluids* **10**: 2433-2435, 1998.

[8] Pier, B. & Huerre, P.: Nonlinear self-sustained structures and fronts in spatially developing wake fows. *J. Fluid Mech.* **435**: 145-174, 2001.

[9] Gondret, P., Ern, P., Meignin, L. & Rabaud, M.: Experimental Evidence of a Nonlinear Transition from Convective to Absolute Instability. *Phys. Rev. Lett.* **82**: 11442-1445, 1999.

[10] Hanna, A., Saul, A. & Showalter, K., Detailed studies of propagating fronts in the iodate oxydation of arsenous acid, *J. Am. Chem. Soc.*, **104** (1982) 3838-3845.

[11] Monkewitz, P. A., The absolute and convective nature of instability in two-dimensional wakes at low Reynolds numbers, *Phys. Fluids* **31** (1988) 999-1006.

XXI ICTAM, 15–21 August 2004, Warsaw, Poland

STABILITY OF PLANE POISEUILLE FLOW AND ENERGY GROWTH IN THE CASE OF A BINGHAM FLUID

Cherif NOUAR*, Nadjiba KABOUYA*, Jan DUSEK**, Aziz SALEM***
*LEMTA, 2 Avenue de la Forêt de Haye, 54504 Vandoeuvre-les-Nancy, France
**IMFS, 2 rue Boussingault, 67000 Strasbourg, France
***USTHB, BP 32, El Alia, Bab Ezzouar, 16111 Algiers, Algeria

Summary The present work examines the linear stability of three dimensional perturbations of Poiseuille flow of a Bingham fluid. The principal characteristic of the basic flow is the presence of the plug zone which moves as rigid solid. A Chebychev collocation method is applied to compute eigenvalues and the maximum transient amplification factor. It is found that the Poiseuille flow of a Bingham fluid is linearly stable. Due to the non-normality of the operators, a transient amplification of the kinetic energy of disturbances is observed. The results show that the amplification factor decreases with increasing Bingham number. Critical conditions for the onset of energy growth are also determined. When $B >> 1$, it is shown that the critical Reynolds number Re_c increases as $B^{1/2}$.

INTRODUCTION

We consider the flow of an incompressible Bingham fluid with a yield stress τ_y and a plastic viscosity μ_0 in a plane channel. The non-dimensionalized deviatoric extra-stress tensor is given as :

$$\boldsymbol{\tau} = \frac{1}{Re}\left[1 + \frac{B}{D_{II}}\right]\mathbf{D} \quad \Leftrightarrow \quad \tau_{II} > \frac{B}{Re} \quad \text{and} \quad D_{II} = 0 \quad \Leftrightarrow \quad \tau_{II} \leq \frac{B}{Re}\,, \tag{1}$$

where D_{II} and τ_{II} are respectively the second invariant of the strain rate $\mathbf{D}$ and of the tensor $\boldsymbol{\tau}$. The quantity $(1 + B/D_{II})$ is a dimensionless effective viscosity μ. The dimensionless parameters B and Re are respectively the Bingham and the Reynolds number. They are defined by $B = \tau_y\, H^*/\mu_0\, U_0^*$ and $Re = \rho U_0^*\, H^*/\mu_0$. The flow in the yielded domain is described by Navier-Stokes equations ; in the region where the yield stress is not exceeded (unyielded region), we have $D_{II} = 0$: this region is called the plug zone ; it moves like a rigid solid. The interface between the viscous region and the plug zone is a yield surface where $\tau_{II} = B/Re$. The motion of the plug region is determined by the conservation of linear momentum. For one dimensional shear flow, we have $\mathbf{U} = (\mathrm{U(y)}, 0, 0)$, with :

$$U(y) = \begin{cases} 1, & 0 \leq |y| < y_0, \\ 1 - \left(\dfrac{|y| - y_0}{1 - y_0}\right)^2, & y_0 \leq |y| \leq 1, \end{cases} \tag{2}$$

where, $\pm y_0$ are the positions of the interfaces. The basic flow depends only on B and is represented in Fig. 1.

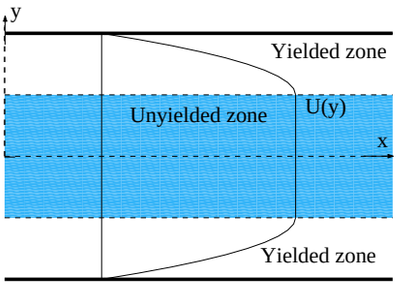


Figure 1. Poiseuille flow of Bingham fluid

LINEAR STABILITY ANALYSIS

Following the usual linear stability analysis, an infinitesimal perturbation $(\epsilon \mathbf{u}', \epsilon \mathrm{p}')$, where $(\epsilon << 1)$ is superimposed on the basic flow $(\mathbf{U}, \mathrm{P})$. Wherever the yield stress is exceeded, the effective viscosity is also perturbed:

$$\mu\,(\mathbf{U} + \epsilon \mathbf{u}') = 1 + \frac{B}{|DU|} - \epsilon\left(\frac{\partial u'}{\partial y} + \frac{\partial v'}{\partial x}\right)\cdot\frac{B}{DU|DU|}\,, \tag{3}$$

The linearized perturbation equation are then derived. Because the streamwise and spanwise directions are uniform, perturbations are assumed to have the form : $A(x, y, z, t) = \hat{A}(y, t) exp[i(\alpha\, x + \beta\, z)]$, where $\hat{A}$ stands for $\hat{u}, \hat{v}, \hat{w}$ and $\hat{p}$. The resulting equations and the boundary conditions can be found in [2]. These equations can be cast in $\hat{u}, \hat{v}$ formulation if $\beta \neq 0$ or $\hat{v}, \hat{w}$ formulation if $\alpha \neq 0$. They can be written as :

$$\mathcal{L}\,\hat{\mathbf{q}} + \frac{\partial}{\partial t}\,\mathcal{M}\,\hat{\mathbf{q}} = 0, \tag{4}$$

where $\hat{\mathbf{q}} = (\hat{u}, \hat{v})^T$ or $(\hat{v}, \hat{w})^T$, $\mathcal{L}$ and $\mathcal{M}$ are 2×2 matrices of linear differential operators. An eigenvalue problem is then derived by assuming $\hat{A}(y, t) = \bar{A}(y) exp(-iCt)$. We obtain : $iC\bar{q} = \mathcal{M}^{-1}\,\mathcal{L}\,\bar{q} = \mathcal{L}_1\,\bar{q}$. The eigenvalues are computed, using a spectral collocation method based on Chebychev polynomials. The least stable mode determines the asymptotic behavior of a perturbation initiated at $t = 0$. The analysis of the transient evolution is performed using kinetic energy of the perturbation. Let $G(t)$ the maximum energy amplification at time t, following the same procedure as in [3], $G(t)$ is :

$$G(t) = max\,\frac{\|\mathbf{q}(\mathrm{t})\|^2}{\|\mathbf{q}_0\|^2} = \|exp(-i\,\mathcal{L}_1\,t\|. \tag{5}$$

RESULTS AND DISCUSSION

The aim of this study is to understand the influence of the Bingham number on the stability problem. For this purpose and by comparison with the Newtonian fluid, one has to note that $B > 0$ induces : (i) a variable effective viscosity in the yielded zone ; (ii) an increase of the viscous dissipation [2] ; (iii) an increase of the velocity gradient near the wall and (iv) a modification of the boundary conditions at the interface.
When $B \to 0$, the plug zone is very thin and the Bingham terms can be neglected in the linearized perturbation equations. The analysis of this particular case denoted after $B \to 0$ permits to assess separately the effect of the boundary conditions at the interface on the stability.
The analysis starts with the eigenvalues spectrum. An example is shown on Fig. 2: it is obtained for $\alpha = 1, Re\ (1 - y_0) = 10^4$ and $B\ (1 - y_0) = 2$. The eigenvalues of the P-family are distributed along two branches, in contrast with the Newtonian fluid, for which it consists in one branch. The splitting of the P-family is actually a consequence of the boundary conditions at the interface $u = v = w = 0$. In the case of three dimensional disturbance a splitting of S-family is also observed (Fig 3). This splitting is probably due the coupling between the velocity components when $B > 0$. The calculation shows that for sufficiently large Reynolds numbers, the least stable mode is an interfacial mode. In addition, in the range of parameters considered here, we have not found any instability. We can also add the fact that B has a stabilizing effect. Concerning the transient growth, Fig. 4 gives the amplification factor for a Newtonian fluid and two values of B : $B = 0.001$ and $B = 2$. We observe that even for moderate values of B, G_{max} is strongly reduced by comparison with the Newtonian fluid.
We conclude this section by the determination of the conditions for no energy growth fig. 5. When $B >> 1$, it is shown that the critical Reynolds number Re_c increases as $B^{1/2}$. This asymptotic behavior is in agreement with the conditional stability based on the energy method [1]

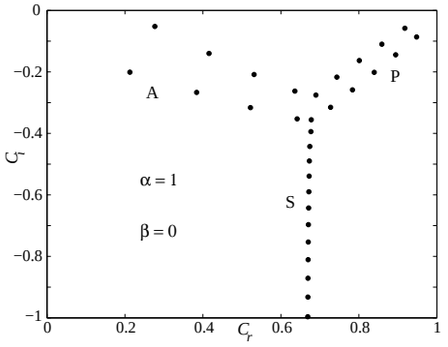


Fig 2 : eigenvalues spectrum for $B \to 0$ and $Re = 10^4$.

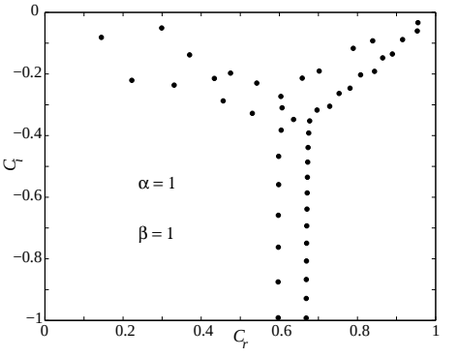


Fig 3 : eigenvalues spectrum for $B = 2$ and $Re = 10^4$.

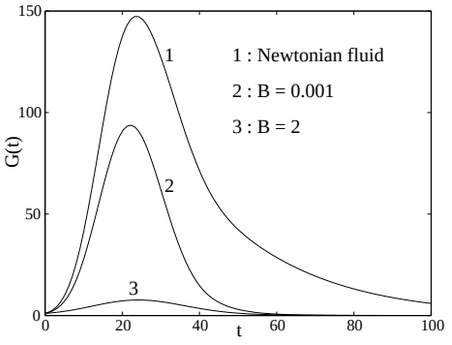


Fig4 : Maximum growth as a function of time.

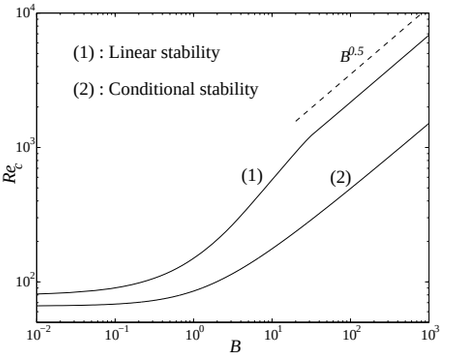


Fig 5 : Critical Reynolds number versus B.

References

[1] Nouar C., Frigaard I.A.: Non linear stability of Poiseuille flow of a Bingham fluid; theoritical results and comparison with phenomenological criteria. *J. Non-Newtonian Fluid Mech* **100**, :127–149, 2001.
[2] Frigaard I.A., Nouar C.: On three dimensional linear stability of Poiseuille flow of Bingham fluids. *Phy Fluids.* **15**, :2843 –2851, 2003.
[3] Shmid. P, Hennigson D.S.: Optimal energy density growth in Hagen-Poiseuille flow. *J Fluid Mech* **277**, :197–225, 1994.

XXI ICTAM, 15-21 August 2004, Warsaw, Poland

INSTABILITY OF THE FAR WAKE BEHIND A WIND TURBINE

Valery L. Okulov*, Jens N. Sorensen**
*Institute of Thermophysics, SB RAS, Lavrentyev Ave. 1, Novosibirsk, 630090, Russia
**Department of Mechanical Engineering, DTU, DK-2800 Lyngby, Denmark

Summary A stability analysis of the far wake behind a N-bladed wind turbine has been carried out. In conflict with experimental data, previous studies based on stability analysis of point vortices predicted instability at all operating conditions. In the present study the wake description is based on a (N+1)-vortex model consisting of N helical tip vortices and a hub vortex, exposed to a constant axial velocity field. As a generalization, the stability problem is reduced to the task of finding a procedure for the evolution of the velocity induced by a helical vortex system. An algebraic solution is obtained that provides for an efficient analysis of motion and stability of the (N+1) vortex systems covering a range of helical pitch variations. The stability properties depend basically on vortex strength, helical pitch and vortex core radius. To relate these properties to the operating conditions of a wind turbine, they are approximately expressed in terms of thrust coefficient and tip speed ratio. In accordance with experiments, the far wake is shown to consist of both stable and unstable flow regimes.

Modern wind turbines are often grouped in parks or "wind farms" in order to provide power to an electrical grid from a large number of turbines at the same site. At some wind conditions, however, one or more turbines may stand in the wakes of other turbines. This causes the loading be dominated by strong periodically varying forces that increase the fatigue loads and hence reduce the lifetime of the turbine. As seen in Fig. 1a the flow behind a wind turbine is dominated by a system of strong trailing tip vortices that forms the dynamics of the far wake. In some cases the vortices become unstable and breaks down, as seen in Fig. 1b. It is clear that if a wind turbine is located in a wake consisting of stable tip vortices, the fatigue loading is more severe that if the vortices break down into a continuous vortex sheet. It is of interest study under which conditions the vortices break down. The present work is focused on studying far-wake features of wind turbines by analyzing stability properties of systems of helical vortices.



Fig. 1.Visualisations of far wake: (*a*) *stable regime* [4] *and* (*b*) *unstable one with the wake decay (data by RISO, Denmark).*

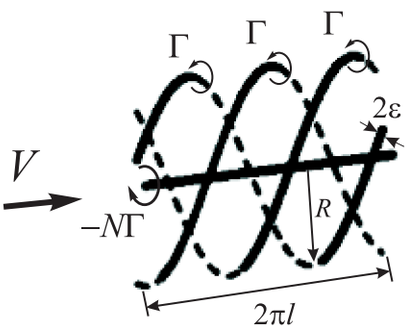


Fig. 2. Scheme of the (N+1) helical vortex structure.

At a sufficiently large distance in the wake behind a wind turbine the vorticity is concentrated in N helical tip vortices that are located on a cylindrical surface of radius R and equally spaced $2\pi/N$ radians apart from each other, where N is the number of blades. Each of the tip vortices has strength Γ and a vortex core radius ε. Further, a hub vortex with strength $(-N\Gamma)$ is lying along the axis of rotation. The stability problem is thus characterized by a system of $(N + 1)$ vortices that are exposed to a constant axial wind field of speed V (see Fig. 2). This $(N + 1)$-vortex system, with constant pitch, $2\pi l$ (or $\tau = l/R$ in dimensionless form) is the simplest possible description of a wake, e.g. Joukowski [1]. Since the axial flow behind a wind turbine has a "wake-like" profile, we consider a system of left-handed helical vortices [2]. Representing the $(N + 1)$-vortex system by point vortices or straight vortex filaments (the limiting case of a helical vortex with infinite pitch) the vortex system (with hub vortex) is absolutely unstable (see, e.g. [3]). This result, obtained as the simplest special case ($\tau = \infty$), is not in agreement with the findings of visualizations of wind turbine wakes, e.g. [4].

In order to study instabilities of the $(N + 1)$ helical vortex system, one turns to the helical variables (r, χ) with corresponding velocity projections $(u_r, u_\chi = u_\theta + u_z/\tau)$. In this context, the problem of stability of the N-vortex configuration without hub vortex was reduced to a two-dimensional case [5, 6]. In the present work the stability analysis is further extended to the general problem of $(N + 1)$ helical vortices with an additional axial translation of the vortex system. To apply the present model to analyze far-wake stability, we need to represent the geometrical and kinematical parameters of the wake model (τ, V and Γ) via typical wind turbine operating characteristics (axial interference coefficient a, and tip speed ratio λ). The

parameter a is defined as the ratio between the axial velocity induced by the helical vortices in the wake and the wind speed. If we neglect of the vortex core size, after averaging axial velocity from [6], we get $a = N\Gamma/2\pi l u_0 = G/\tau$, where $G = N\Gamma/2\pi RV$ is the dimensionless total circulation of the tip vortices. As a next simplification, we present $G = 2a(1-a)/\lambda$ from lifting disk theory. As a result, we get $\tau = 2(1-a)/\lambda$. To replace V we use the defintion of G, i.e. $N/G = 2\pi RV/\Gamma = N\lambda/2a(1-a)$. In terms of these parameters the modified correlation equation from [6] reads

$$\frac{1}{\vartheta(a,\lambda)}\left(2(1-a)+\frac{0.5\lambda^2}{1-a}\left(\ln\left(\frac{2(1-a)}{N\varepsilon\vartheta(a,\lambda)}\right)+\frac{7}{4}\right)\right)+\frac{2(1-a)\lambda^2}{\vartheta^3(a,\lambda)}\left(\ln(N)-\left(1-\frac{\lambda^2}{16(1-a)}\right)\left(\frac{N}{m}-C-\psi\left(-\frac{m}{N}\right)\right)\right)+$$
$$\frac{(1-a)\lambda^6}{\vartheta^7(a,\lambda)}\left(32\left(\frac{\varsigma(3)}{N^2}-1\right)\frac{(1-a)^4}{\lambda^5}-24\left(\frac{\varsigma(3)}{N^2}+1\right)\frac{(1-a)^2}{\lambda^3}+\left(\frac{3\varsigma(3)}{4N^2}-6\right)-\frac{0.5\lambda^2}{(1-a)^2}\right)+\frac{(N-0.5)a-N}{2a(1-a)^2}\lambda^2+$$
$$\frac{(1-a)\lambda^6\left(4(1-a)^2-\lambda^2\right)}{\vartheta^9(a,\lambda)}\left(32\frac{(1-a)^4}{\lambda^4}-24\frac{(1-a)^2}{\lambda^2}+\frac{3}{4}\right)\frac{1-N^2}{N^2}\varsigma(3)+m(N-m)\frac{\vartheta^3(a,\lambda)}{8(1-a)^3}+1=0$$

where $\vartheta(a,\lambda)=\sqrt{4(1-a^2)+\lambda^2}$; $C = 0.577215\ldots$ is the Euler constant. The psi-function $\psi(\cdot)$ for several typical arguments is $\psi(-1/2) = 0.03949\ldots$, $\psi(-1/3) = 1.68177\ldots$, $\psi(-2/3) = -1.63203\ldots$, $\psi(-1/4) = 2.91414\ldots$, and $\psi(-3/4) = -2.89412\ldots$

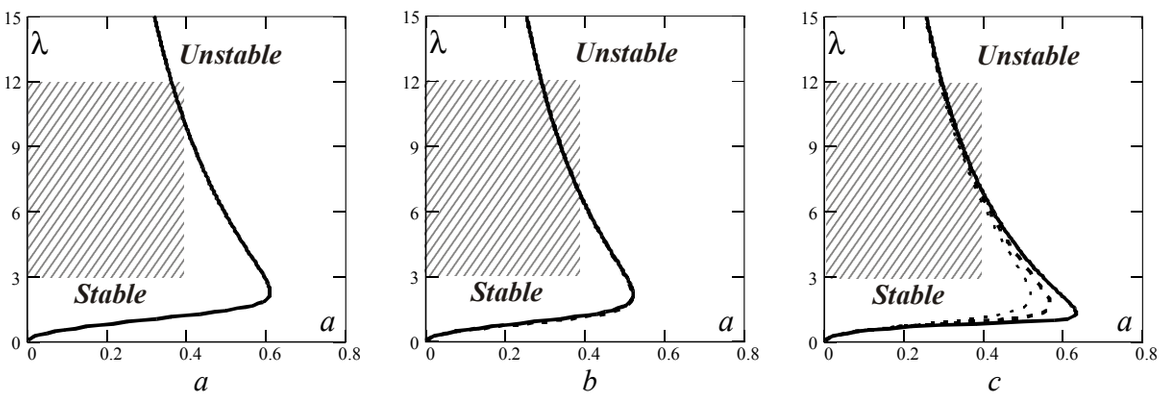


Fig. 3. Diagram of possible operating regimes of wind turbines (crosshatched region) and neutral stability curves for the far wake (a) N = 2; (b) N = 3; (c) influence of vortex core radius - ε on the neutral stability curves for N = 3: ε = 0.1 – solid line, ε = 0.01 – dashed line and ε = 0.001– dotted line.

Figure 3 shows neutral stability curves for the (N + 1) – vortex system model of the far wake as a function of the number of blades, i.e. 2 or 3 blades. Typical wind turbine operating regimes (crosshatched region in Figure 3) are seen to lie mainly in stable domains. However, in some cases wind turbines operate under conditions in which the vortex structure in the wake becomes unstable, in agreement with observations in [7]. Investigation of the influence of the vortex core radius is presented in figure 3*c*. The influence is seen to be small and it may be ignored.

CONCLUSIONS

In conclusion, for the first time an analytical study has of the stability problem of a (N + 1) - vortex system that models the far wake behind a wind turbine has been carried out. Typical operating regimes of wind turbines have been compared to stability characteristics and it was found that, depending on number of blades and operating conditions, both stable and unstable vortical wake structures appear. The analytical form of the correlation equation represents the first step in understanding and controlling wind turbines in parks.

References

[1] Joukowski N.E., "Vortex theory of a rowing screw," Trudy OFNOLE **16**, 1 (1912) (in Russian).
[2] Okulov V.L. Technical Physics Letters, 2002. Vol. 28(12), pp. 1060-1064.
[3] Morikawa G.K., Swenson E.V., Phys. Fluids **14(6)**, 1971, 1058-1073.
[4] Vermeer L.J., Sorensen J.N., Crespo A., 2003, Progress in Aerospace Sciences, vol. 39, pp. 467-510.
[5] Okulov V.L. Technical Physics Letters, 2002. Vol. 28(12), pp. 1060-1064.
[6] Okulov V.L. In book: "Fundamental and applied problems of vortex theory"– Moskow-Izhevsk: ICR, 2003. pp. 392-413 (in Russian).
[7] Pedersen T.F., Antoniou I. Wind Engineering, 1989, Vol. 13, 1989. pp. 239-251.

XXI ICTAM, 15–21 August 2004, Warsaw, Poland

DYNAMICS OF A REACTIVE FALLING FILM AT LARGE PÉCLET NUMBERS

Serafim Kalliadasis, Philip Trevelyan
Department of Chemical Engineering, University of Leeds, Leeds, LS2 9JT, UK

Summary We study the dynamics of a vertically falling film in the presence of a first-order (exothermic or endothermic) chemical reaction. We extend the work by Trevelyan *et al.* [1] on the same problem to large heat/mass transport Péclet numbers and so we take into account the convective terms of the heat/mass transport equations. Our analysis is based on a long-wave expansion and integral-boundary-layer theory of the equations of motion and associated boundary conditions.

FORMULATION

Figure 1 shows the problem definition. We consider a thin viscous film falling down a vertical substrate. The ambient gas phase contains a species A that is absorbed into the liquid where it undergoes a simple first-order decay, $\mathrm{A} \rightarrow \mathrm{B} \pm \mathrm{heat}$. The reaction rate is taken to be temperature dependent so that heat is released into the film or absorbed from the film. Such heat generation gives rise to thermocapillary stresses, which in turn, affect the dynamics of the free surface.

The governing equations, namely equation of motion, energy and concentration equations are

$$u_x + v_y = 0 \tag{1a}$$

$$u_{yy} + 2 = 2\epsilon p_x + \epsilon Re(u_t + uu_x + vu_y) - \epsilon^2 u_{xx} \tag{1b}$$

$$\epsilon v_{yy} = 2p_y + \epsilon^2 Re(v_t + uv_x + vv_y) - \epsilon^3 v_{xx} \tag{1c}$$

$$a_{yy} = (1 + Daa)e^{Da\beta\phi T/(1+Da\phi T)} + \epsilon ReSc(a_t + ua_x + va_y) - \epsilon^2 a_{xx} \tag{1d}$$

$$T_{yy} = -(1 + Daa)e^{Da\beta\phi T/(1+Da\phi T)} + \epsilon RePr(T_t + uT_x + vT_y) - \epsilon^2 T_{xx} \tag{1e}$$

where ϵ the film parameter, Re, Pr and Sc the Reynolds, Prandtl and Schmidt numbers, respectively, and Da the Damköhler number. These equations are subject to the boundary conditions at $y = h(x, t)$

$$p = -\epsilon^2 We(1 - MaDa\phi T)N^{-\frac{3}{2}} h_{xx} + \epsilon N^{-1}(v_y - h_x u_y + \epsilon^2(h_x^2 u_x - h_x v_x)) \tag{2a}$$

$$u_y + \epsilon^2(v_x + 2h_x(v_y - u_x) - h_x^2 u_y) - \epsilon^4 h_x^2 v_x = -2\epsilon WeMaDa\phi(T_x + h_x T_y)N^{\frac{1}{2}} \tag{2b}$$

$$a = 0 \tag{2c}$$

$$T_y - \epsilon^2 h_x T_x = 0 \tag{2d}$$

$$h_t + uh_x = v \tag{2e}$$

and the wall boundary conditions at $y = 0$

$$u = v = 0, \quad a_y = 0, \quad T = 0 \tag{3}$$

where $N = 1 + \epsilon^2 h_x^2$. The thermocapillary effect is modelled by using a linear approximation for the surface tension, $\sigma = \sigma_0 - \gamma(T - T_0)$ with σ_0 the surface tension at the reference temperature T_0 and $\gamma > 0$ for typical liquids. $We = \sigma_0/\rho g h_0^2$ is the Weber number and $Ma = \gamma T_0/\sigma_0$ is the Marangoni number.

A long-wave expansion (LWE) of the above equations for $\epsilon \ll 1$ leads to a single highly nonlinear evolution equation for the film thickness h. Here we extend the previous study by Trevelyan *et al.* on the same problem to the case of large Péclet numbers. As a consequence, the convective effects in both heat and mass transport processes are retained in our LWE formulation.

We construct the solitary wave bifurcation diagrams for a wide range of the pertinent parameters. In all cases the bifurcation diagrams exhibit two branches (a lower one and an upper one). We demonstrate the existence of non-dissipative solitary waves even away from criticality. Time-dependent computations of the fully nonlinear evolution equation show that for large times the interface approaches a train of solitary pulses similar to the lower branch solitary waves. For a given Reynolds numbers and sufficiently small Prandtl and Schmidt numbers the interface is characterized by an irregular row of solitary pulses which interact indefinitely with each other. This complex spatio-temporal behavior is similar to the large-time evolution of a vertically falling film in the absence of Marangoni effects. However, for a sufficiently large Schmidt number or a sufficiently large Prandtl number we observe an intriguing pattern formation process characterized by a regular train of non-dissipative solitary waves (see Fig. 2). This highly ordered state persists indefinitely. Hence, the convective effects associated with the chemical reaction induce a high degree of organization not observed before in falling film studies.

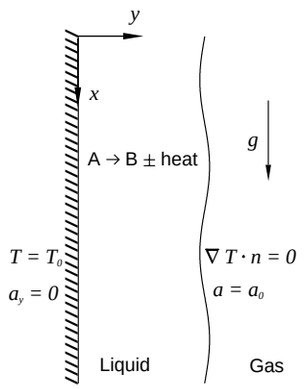


Figure 1. Sketch of the vertically falling film in the presence of a chemical reaction.

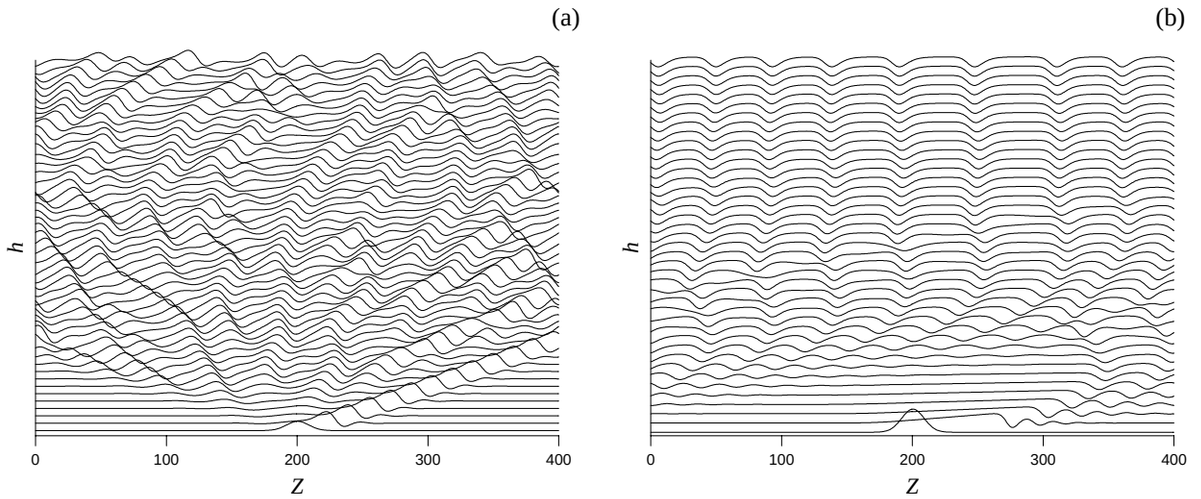


Figure 2. Time evolution of the interface in a moving frame Z for moderate (a) and large (b) heat/mass transport Péclet numbers.

Far from criticality and for moderate Reynolds numbers, the model equation of choise in the absence of Marangoni effects is the Shkadov integral-boundary-layer approximation [2]. However, the Shkadov approach predicts the critical Reynolds number with a 20% error. Here we extend this approximation to the reactive falling film problem and we show that a simple Galerkin projection for the momentum equation corrects the critical Reynolds number obtained from the Shkadov approach. In addition, we develop a hierarchy of IBL models based on high-order Galerkin projections for the concentration and temperature fields onto the set of polymonial test functions. Not only do these models correct the critical Reynolds number, but they also give close to criticality, with an appropriate gradient expansion, the full LWE. We also construct nonlinear solutions of the solitary wave type and we show that unlike LWE, our IBL models predict the continuing existence of solitary pulses for all Reynolds numbers.

CONCLUSIONS

We considered the dynamics of a reactive falling film. Our analysis was based on a long-wave expansion and integral-boundary-layer formulation. Particular emphasis was given to the solitary wave solution branches obtained from the different approaches. Our analysis also indicates that for sufficiently large Prandtl/Schmidt numbers the film can be excited in the form of non-dissipative solitary pulses which close to criticality assume the form of KdV solitons.

References

[1] Trevelyan, P.M.J., Kalliadasis, S., Merkin, J.H., Scott, S.K.: Dynamics of a vertically falling film in the presence of a first-order chemical reaction. *Phys. Fluids* **14**:2402–2421, 2002.

[2] Shkadov, V.Ya.: Wave regimes in the flow of a thin layer of a viscous fluid under the action of gravity. *Izv. Akad. Nauk SSSR, Mekh. Zhidk i Gaza* **1**:43–50, (1967).

LONG-WAVE MARANGONI INSTABILITY IN BINARY-LIQUID FILMS WITH SORET EFFECT

Alexander Oron*, Alexander A. Nepomnyashchy**
Technion-Israel Institute of Technology, Haifa 32000 Israel
**Department of Mechanical Engineering*
*** Department of Mathematics and Minerva Center for Nonlinear Physics of Complex Systems*

Summary We study the onset of Marangoni instability of the quiescent equilibrium in a binary liquid film in the presence of Soret effect. Linear stability analysis shows that both monotonic and oscillatory long-wave instabilities are possible depending on the value of the Soret number χ. Sets of long-wave nonlinear evolution equations are derived for both types of instability. Bifurcation analyses are carried out for both types of instability.

INTRODUCTION

Linear and nonlinear analyses and investigation of pattern formation in long-wave Marangoni instability in a binary liquid layer open to the ambient gas phase are carried out, when the Soret effect is taken into account. The liquid layer is assumed to be sufficiently thin and with sufficiently high surface tension, so that the mathematical model that neglects both buoyancy-driven convection and deformation of the liquid-gas interface is valid

LINEAR STABILITY ANALYSIS

Linear stability analysis in the case of poorly conducting boundaries reveals that both monotonic and oscillatory modes of instability exist here. It is found that monotonic instability sets in when the Soret number χ exceeds the value $\chi_0 = -(1+L^{-1}+L^{-2})^{-1}$, where L^{-1} being the Lewis number, and the critical value of the Marangoni number is $M_{0,mon} = 48[1+\chi(1+L^{-1})]^{-1}$. The oscillatory instability emerges when $-1 < \chi < \chi_0$, and the corresponding critical value of the Marangoni number is $M_{0,osc} = 48(1+L)(1+\chi)^{-1}$.

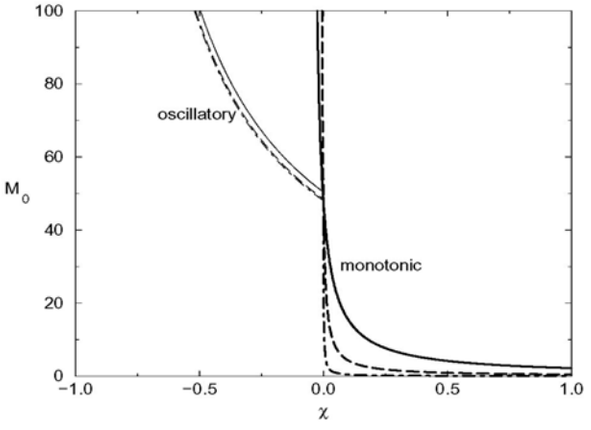


Figure 1. Neutral curves for both long-wave monotonic and oscillatory instabilities and for various values of the inverse Lewis number L^{-1}. The thick and thin curves correspond to the monotonic and oscillatory modes, respectively. The solid, long-dashed and dot-dashed lines correspond to $L^{-1} = 20, 100$ and 1000, respectively.

Figure 1 summarizes the results of linear stability analysis. It displays the neutral curves for both long-wave monotonic and oscillatory instabilities for $L^{-1} = 20, 100$ and 1000. If the value of L^{-1} is fixed long-wave monotonic instability sets in for $\chi > \chi_0$. In the particular case of a pure liquid corresponding to $\chi = 0$ the instability is known to be monotonic with the critical Marangoni number $M_0 = 48$. At $\chi = \chi_0$ the long-wave oscillatory branch bifurcates off the monotonic one and manifests the instability threshold when $-1 < \chi < \chi_0$. This long-wave oscillatory instability disappears when $\chi \le -1$. The bifurcation structure remains the same for any $L^{-1} >> 1$. The critical Marangoni number for the oscillatory mode decreases

with L^{-1} reaching a limiting curve $M_0 = 48(1+\chi)^{-1}$ in the limit of $L^{-1} \to \infty$. On the other hand, the critical Marangoni number for the monotonic mode increases with L^{-1} when $\chi < 0$, and decreases when $\chi > 0$.

NONLINEAR THEORY

Weakly nonlinear analysis of both monotonic and oscillatory instabilities yields sets of two nonlinear evolution equations that govern the spatio-temporal dynamics of the system. In the case of monotonic instability, as in the case of a pure liquid, one of the two equations is of evolution type, while the other is elliptic and describe convective effects in the layer that vanish when the Prandtl number of the liquid is large. Bifurcation analysis based on the evolution equation for a binary liquid with large Prandtl number yields amplitude equations for roll-, square- and hexagon patterns. It is shown that rolls patterns are unstable, while square patterns are stable in the physically relevant limit of large L^{-1}. Hexagonal patterns are found to bifurcate transcritically, and a steady stable hexagonal pattern in the system is possible. It is found that the hexagonal pattern appears in the subcritical region when the distance from criticality is small, and it is replaced by the square pattern at a finite value of this distance. In the case of oscillatory instability the set of nonlinear equations consists of two equations of evolution type. It is found that bifurcation of both standing and traveling waves is supercritical in the range $\chi_1 < \chi < \chi_0$, where $\chi_1 = 3L + O(L^2)$. In this range of the Soret number standing waves are found to be unstable, while travelling waves appear to be stable.

It is found that if finite deformations of the interface are allowed binary-liquid films rupture in a finite time in both settings of prescribed temperature distribution and temperature gradient at the solid substrate. The behavior of the film near rupture is investigated.

ACKNOWLEDGMENTS

The research was partially supported by the Israel Science Foundation founded by the Israel Academy of Sciences through Grant no. 31/03-15.3, ICOPAC Research Network of the European Union (contract HPRN-CT-2000-00136), the Fund for the Promotion of Research at the Technion and Smoler Research Fund. A.A.N. acknowledges the support of the E. and J. Bishop Research Fund.

SOLITARY WAVES ON A LIQUID FILM FLOWING ALONG A PERIODIC WALL

M. Vlachogiannis, K. Argyriadi, V. Bontozoglou
Department of Mechanical & Industrial Engineering,
University of Thessaly, GR-38334 Volos, Greece

Summary Experimental results are reported on the formation and characteristics of solitary waves on liquid films flowing along a periodically corrugated wall. The effect of the wall is manifested in the regularity of the resulting wavetrain and also in the shape of individual humps. At high Re, travelling waves recede in favor of a stationary three-dimensional structure, a phenomenon that has no counterpart in film flow along flat walls.

INTRODUCTION

Film flow along a wavy wall appears to have attracted relatively little attention, despite extensive engineering applications in process equipment aimed at enhancement of heat/mass transfer rates. Asymptotic and numerical studies beyond the limit of creeping flow (Bontozoglou & Papapolymerou 1997, Trifonov 1998, Malamataris & Bontozoglou 1999, Bontozoglou 2000, Wierschem, Scholle & Aksel 2002, Wierschem & Aksel 2003) indicate that significant interaction may occur between the corrugated wall and the free surface. A recent experimental study (Vlachogiannis & Bontozoglou 2002) revealed the establishment of a variety of flow regimes: A statically deformed free surface was observed at low Re, which forms the base flow and is the equivalent of Nusselt parabolic film along a flat wall. With increasing Re and/or inclination angle the base flow was observed to become unstable to traveling disturbances. The aim of the present work is to investigate experimentally the nonlinear evolution and the possible stationary forms of the free surface under these conditions.

EXPERIMENTAL SETUP

The wavy wall used in the experiments has orthogonal corrugations at right angles to the flow direction, with wavelength 12 mm (split into 6 mm of elevation and 6 mm of depression) and height 0.4 mm. Pure water and water-glycerol mixtures are tested at small inclination angles (1º-8º) and Reynolds numbers in the range $10<Re<400$ are used. A fluorescence imaging technique –combined with frame grabbing and image analysis software– is used to record the spatio-temporal evolution of the free surface.

RESULTS AND DISCUSSION

Following the technique of Alekseenko, Nakoryakov & Pokusaev (1985), we introduce at the channel inlet mass disturbances of large amplitude and low frequency. The evolution of the flow is depicted in Fig. 1, in the form of a time-series of the free surface elevation at a fixed downstream location. Each disturbance is observed to disintegrate into a series of waves of striking temporal regularity. Also shown in Fig. 1 is the time-series for flow under similar conditions but along a flat wall, which results in a less populated and more disordered wave train. The higher number and superior ordering of waves along the periodic wall may be interpreted in terms of the regular spatial triggering of each traveling disturbance by the wall corrugations.

For a wide range of Reynolds numbers, traveling disturbances evolve into two-dimensional solitary waves characterized by a steep front and a smooth tail. However, these solitary waves differ from their counterparts along a flat wall, because they are superposed on the base flow with the statically deformed free surface. An example is provided in Fig. 2, which plots instantaneous line profiles of the free surface at the center plane of the channel, along a window of view 90 mm in the flow direction. A solitary wave is observed traveling to the right, preceded by a capillary ripple and followed by a tail with distinct regular undulations. These undulations correspond exactly to the base flow, as is manifested by their appearance at the same absolute locations in the substrate before the solitary hump (lowest line). Of particular importance in the dynamics of the solitary wave is the interaction of the hump with successive crests of the static base flow. An instance of this interaction (which may be described as a weak coalescence) is evident in the upper line profile of Fig. 2.

At high Reynolds numbers a three-dimensional transition occurs, which does not appear in films along a flat wall and is characterized by the formation of a transverse series of depressions along the troughs of the periodic free surface. Surprisingly enough its role is stabilizing, as is indicated by the time-series presented in Fig. 3. More specifically, it is observed that with increasing Re solitary waves are drastically reduced in height and are eventually completely eliminated. It is interesting to note that this three-dimensional transition is a local effect. Thus, before it infects the entire flow field, the 3-D structure temporarily appears on the crests of solitary humps where Re is locally higher. This transient effect leads to the erosion of the crests observed in the upper curves of Fig. 3.

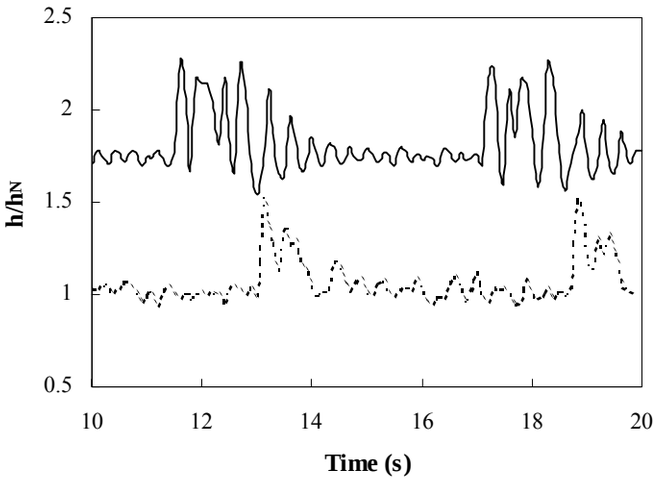


Figure 1: Time-series of free surface elevation at Re=50 and φ=3º, 480 mm downstream of the channel entrance: (—) corrugated wall, (---) flat wall.

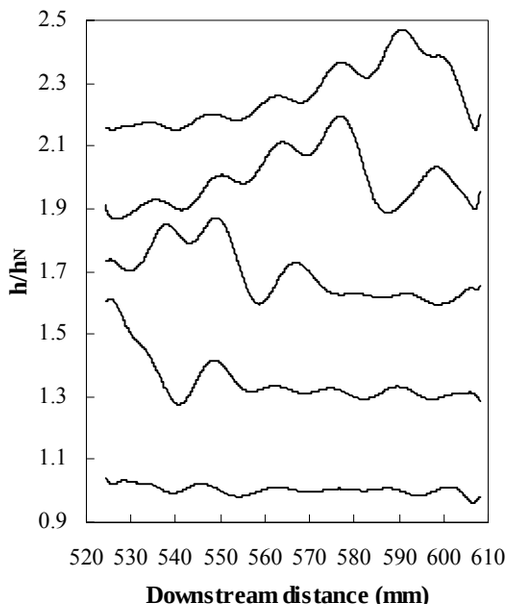


Figure 2: The line profile of a solitary wave traveling from left to right.

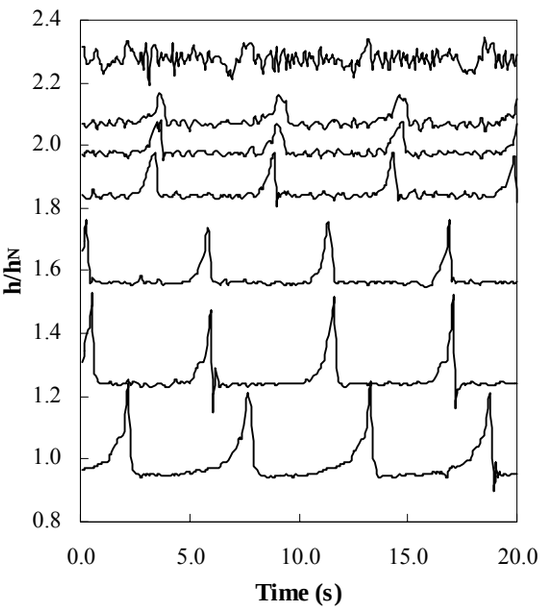


Figure 3: Time-series of free surface elevation at φ=1º, and Re=70, 96, 137, 182, 233, 280, 342 (from bottom to top).

CONCLUSIONS

The characteristics of solitary waves travelling along a wall with orthogonal corrugations are studied experimentally and are set in perspective with their counterparts over a flat wall. One effect of the presence of corrugations is the formation of a more ordered wave train. Solitary waves interact with the statically deformed free surface and thus manifest in their shape the periodicity of the wall. At high Re, a three-dimensional transition occurs, which apparently stabilizes the film and leads to the recession of travelling waves.

References

Alekseenko, S.V.,. Nakoryakov, V. Y and Pokusaev, B. G., *AIChE J.* **31**, 1446 (1985).
Bontozoglou, V. and Papapolymerou, G., *Int. J. Multiphase Flow*, **23**, 69-79 (1997).
Bontozoglou, V., *Computer Modeling Engng. Science*, **1**, 129-138 (2000).
Malamataris, N. A. and Bontozoglou, V., *J. Comp. Phys.*, **154**, 372-392 (1999).
Trifonov, Yu. Ya., *Int. J. Multiphase Flow*, **24**, 1139-1161 (1998).
Vlachogiannis, M. and Bontozoglou, V., *J. Fluid Mech.*, **457**, 133-156 (2002).
Wierschem, A. Scholle, M. and Aksel, N., *Exp. Fluids*, **33**, 429-442 (2002).
Wierschem, A. and Aksel, N., *Physica D*, **186**, 221-237 (2003).

EFFECT OF BOTTOM UNDULATIONS ON THE STABILITY OF FILM FLOW DOWN INCLINED PLANES

Nuri Aksel, Andreas Wierschem
LS Technische Mechanik und Strömungsmechanik, University of Bayreuth, D-95440 Bayreuth, Germany

Summary We study the effect of bottom undulations on the stability of a stationary film flow down inclined planes. Allowing for rather moderate bottom variations, we carry out a linear stability analysis and show how the wavy bottom affects the instability. Contrary to results for weakly undulated bottoms described in literature, where the instability is identical to that over a flat incline, we obtain an increase of the critical Reynolds number and a smaller unstable frequency spectrum with respect to the flat bottom in accordance with experimental observations.

INTRODUCTION

The instability of the steady film flow down an inclined plane has been studied in detail during the last decades [1]. Theoretical studies usually assume idealized conditions such as a perfectly flat incline and disregarding inflow and outflow disturbances. As a deviation from the perfect conditions we consider how moderately wavy bottom variations affect the linear stability of the two-dimensional film flow down inclined planes. As a starting point of our stability analysis, we take the steady flow of thin films over moderately undulated bottoms [2], [3]. By considering moderate bottom variations, our analysis differs from Tougou's who carried out a linear stability analysis for the flow over weakly wavy bottoms [4]. He found that the instability was identical to that over a flat incline without any change of the critical Reynolds number. However, recently, in experiments with rectangular corrugations a higher critical Reynolds number than that for a flat incline has been measured [5]. We show that, different from Tougou's result, the wavy bottom does affect the instability. The bottom waves stabilize the steady flow and increase the critical Reynolds number. The character of the long-wave instability remains but the bottom undulation yields a narrower unstable band than for a flat incline [6].

STABILITY ANALYSIS

Considering two-dimensional flow of a thin film down a sinusoidal bottom of moderate waviness, we carry out a linear stability analysis for the stationary flow using the local coordinate system and the scaling applied in [3]. Especially the perturbation parameter of the linear stability analysis is the same as for the analysis of the stationary flow, i.e. the product of the film thickness and the wave number of the bottom contour. Besides the perturbation parameter, the flow is described by the Reynolds number, the cotangent of the inclination angle, an inverse Bond number, and the waviness of the bottom contour. The Reynolds number is constructed with the film thickness and the maximum velocity of the stationary film flow over a flat incline. The inverse Bond number takes into account the effect of surface tension over the scale of the bottom wavelength: $1/Bo = 1/(Bo*\sin\alpha) = (2\pi l_{Ca}/\lambda)^2/\sin\alpha$, where α, λ, l_{Ca} are the inclination angle, wavelength of the bottom, and capillary length of the fluid, respectively. The waviness is the product of amplitude and wave number of the bottom wave. In the analysis, all these fixed parameters are assumed to be of order one. Thus, the waviness is small enough to avoid the creation of vortices in the valley of the wavy bottom [7].

The analysis is restricted to monotonously falling bottom contours, having, on the other hand, the advantage that the stationary film can be described at leading order essentially as one flowing over a flat plane at the respective local inclination angle. This has important implications. For instance, the film thickness averaged over one bottom wave is larger than for the flat bottom inclined at the mean angle.

The results of the linear stability analysis can be summarized as follows: The instability remains to be one of long-wave type. However, the unstable band is narrower. The instability can be expressed in local terms: The critical Reynolds number is then given in terms of the mean of the local hydrostatic pressure

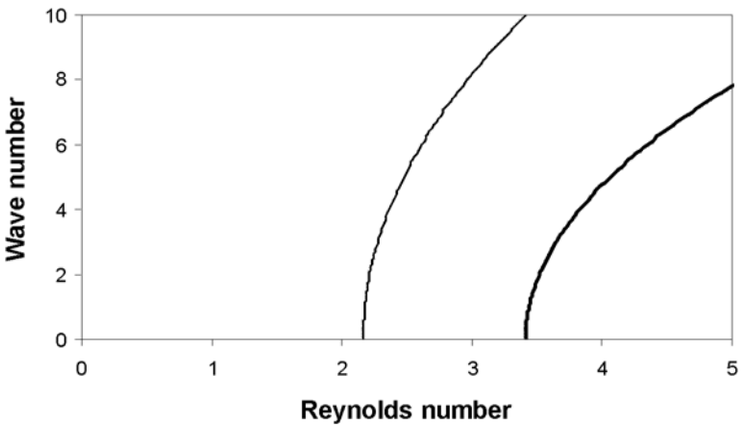


Figure 1: Neutral stability curves. The thin and thick lines represent the marginal curves for the flat plane and a wavy bottom, respectively. Waviness: $2\pi\cdot0.05$, inclination angle: 30°, inverse Bond number: 0.01.

contribution and the local capillary pressure contribution. The hydrostatic pressure contribution, expressed by the mean of the cotangent of the local inclination angle, is always larger than that of the flat bottom. The same holds for the capillary pressure contribution that yields an additional term, also for the long-wavelength limit, due to the bending of the free surface by the bottom contour. An example of the neutral curve comparing the undulated bottom to the flat one is reproduced in Figure 1.

Figure 2 shows that the increase of the critical Reynolds number can be quite important. It not only augments with the waviness of the bottom contour but also with decreasing inclination angle. The latter is due to both, hydrostatic and capillary pressure contributions. Furthermore, the figure indicates why considering weakly wavy bottom contours did not yield any deviations from the results obtained for a flat plane.

CONCLUSIONS

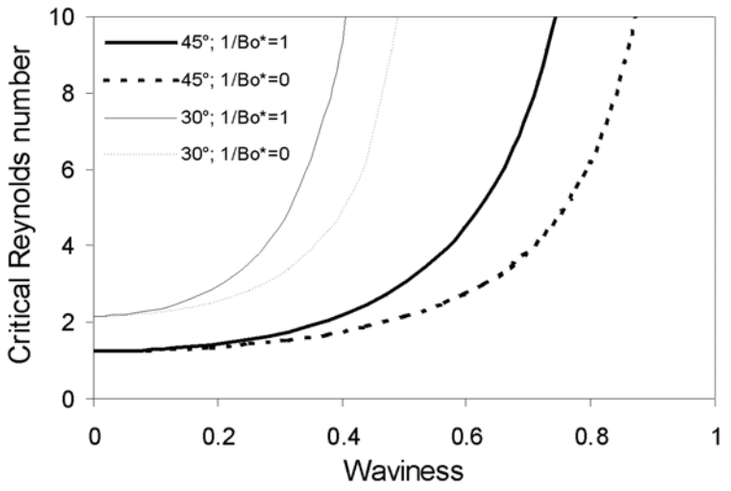


Figure 2: Influence of the waviness and the Bond number on the critical Reynolds number. Inclination angle: 45°.

We carried out a linear stability analysis for the film flow over wavy bottoms. The analysis is restricted to thin films over monotonously falling bottoms, and the Reynolds number and the inverse Bond number are to be of order one or smaller. Within these restrictions, the critical Reynolds number for long surface waves is higher than that for a flat plane. Surface tension alters the minimum critical Reynolds number. It deviates from the flat plane solution with increasing waviness and with decreasing inclination angle. The instability occurs at long wavelength as in the case of a flat bottom. Furthermore, the bottom undulation yields a narrower frequency spectrum than for a flat incline.

REFERENCES

[1] Chang, H.-C., Demekhin, E.A.: Complex wave dynamics on thin films. Elsevier, Amsterdam 2002.
[2] Wang, C.Y.: Thin film flowing down a curved surface. *ZAMP* **35**:533-544, 1984.
[3] Wierschem, A., Scholle, M., Aksel, N.: Comparison of different theoretical approaches to experiments on film flow down an inclined wavy channel, *Exp. Fluids* **33**:429-442, 2002
[4] Tougou, H.: Long Waves on a Film Flow of a Viscous Fluid down an Inclined Uneven Wall, *J. Phys. Soc. Jpn.* **44**:1014-1019, 1978
[5] Vlachogiannis, M., Bontozoglou, V.: Experiments on laminar film flow along a periodic wall, *J. Fluid Mech.*, **457**:133-156, 2002
[6] Wierschem, A., Aksel, N.: Instability of a liquid film flowing down an inclined wavy plane, *Physica D* **186**:221-237, 2003
[7] Wierschem, A., Scholle, M., Aksel, N.: Vortices in film flow over strongly undulated bottom profiles at low Reynolds numbers, Phys. Fluids **15**:426-435, 2003

HYDRAULIC JUMPS AND RESONANCE IN GRAVITY-DRIVEN FLOWS OF LIQUIDS IN INCLINED WAVY CHANNELS: TRANSITION AND HYSTERESIS

Andreas Wierschem, N. Aksel
LS Technische Mechanik und Strömungsmechanik, University of Bayreuth, D-95440 Bayreuth, Germany

Summary We study the flow of a viscous liquid down an inclined channel with a sinusoidal bottom profile of moderate waviness. At low inclination angles, where basins form due to non-monotonous falling bottom slopes, we observe the formation of stationary hydraulic jumps in the form of shock fronts and surface rollers. There exists a bistable region in which both jump phenomena, shock fronts and surface rollers, can occur. At the low end of the bistable region, an instationary regime of a shock with a fingering-like lateral modulation is found. At higher volume flux and inclination angles, the hydraulic jump is suppressed by a standing wave that is generated by a resonance between gravity waves and the wavy bottom. At the transition between surface rollers and standing gravity-waves, periodic switching between the two occur.

INTRODUCTION

Sinusoidal bottom contours seem to be one of the simplest geometries to study the effect of bottom undulations on film and channel flows. The effects of the undulation on the flow increase with the waviness [1], [2] and also qualitatively new phenomena occur: For instance, a resonance of capillary waves with periodic bottom corrugations has been reported [3] and at high waviness, vortices are generated in the valleys of the bottom contour under creeping-flow conditions [4], [5]. For moderate waviness, gravity-driven flow leads to the creation of hydraulic jumps and standing waves once inertia becomes important. This is the region explored here.

EXPERIMENTAL SYSTEM AND SETUP

The experiments were carried out in a channel built from an aluminum bottom and transparent Plexiglas side-walls. It has a width of *170 mm* and is divided into a flat and an undulated section. The undulated part consists of three equal sinusoidal waves. The experiments were carried out around the central wave, which has a wavelength of *300 mm* and *15 mm* amplitude at inclination angles between 5° and 20°, thus in a range where the bottom contour has rising edges. The flat part serves to measure the film thickness. As liquids we chose a silicone oil with a kinematic viscosity *208 mm²/s* and a surface tension of *20.3 mN/m* at *299.15 K*. The surface contour were imaged directly with a CCD camera. For quantitative measurements of the surface contour, we used the PIV-system described in [3].

EXPERIMENTAL RESULTS

We have observed hydraulic jumps as shock fronts and surface rollers. Figure 1 depicts typical examples. Image (a) shows a shock front, which is straight except for bulges close to the wall, which are seen at the borders of the image, and in image (b) a surface roller is presented. At lower flow rate, the surface at the inflow into the basin, which is formed due to the rising edge of the bottom, the surface becomes undulated. With increasing flow rate the first undulation steepens and forms a shock front as shown in Figure 1(a). This shock front remains stable up to a certain flow rate. Beyond that the shock front is replaced by surface rollers. A further increase in the flow rate yields more pronounced surface rollers with surface profiles in flow directions that are more and more curved. Decreasing the flow rate, however, the surface rollers are maintained even below the critical flow rate for their formation, showing the

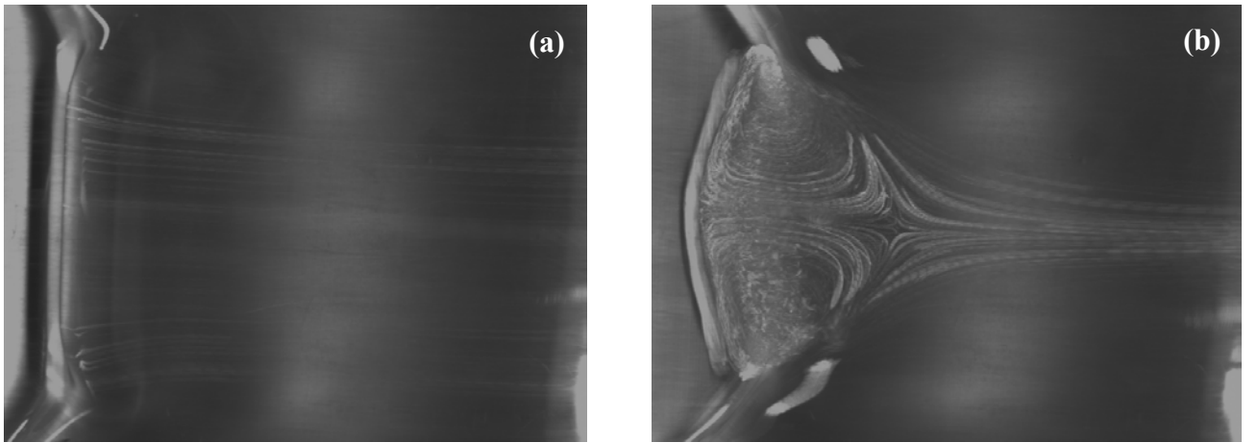


Figure 1: Top-view of the shock front (a) and the surface roller (b). The flow is from the left to the right. The flow is visualized with the air bubbles entrained at the hydraulic jumps. Parameters: Mean inclination angle: 10°; (a): film thickness: 11.5 mm; (b): film thickness: 13.8 mm.

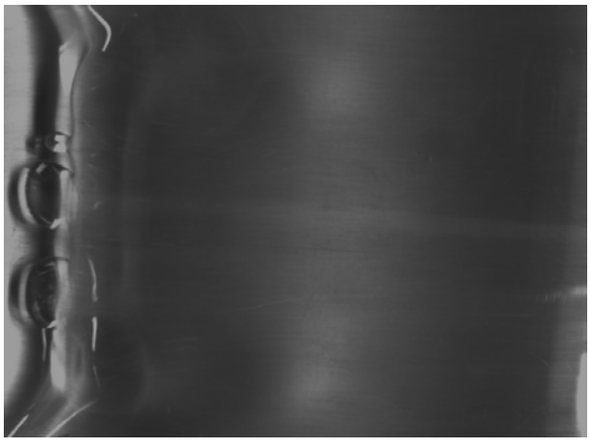


Figure 2: Images of the jump at the lower limit of the bistable. Mean inclination angle: 10°; film thickness: 11.6 mm.

existence of a bistable branch where surface rollers and shock front exist depending on the flow history. Further decreasing the flow rate, at the lower end of the bistable region, the surface rollers degenerate into a shock front with small, generally instationary, fingering-like structures. The latter seem to pour out of the shock-front and surf on the incoming flow as shown in Figure 2. With decreasing flow rate the fraction that is covered by the fingering also decreases. We quantify the bistable range by the position of the local surface indentation and show how the Froude number for the limits of the bistable branch depend on the inclination angle of the sinusoidal bottom.

At high flow rates, the surface roller also looses its stability. It is suppressed by standing waves that are in resonance with the bottom contour. Examples of the latter are shown in Figure 3. The transition between these two structures happens in a small parameter region. Here, the system switches periodically between surface rollers and standing waves. We have observed frequencies of about *0.1 Hz* to *0.2 Hz*, depending on the inclination angle. Although kinematic surface waves come in from the flat incline at the Reynolds numbers where the transition takes place, they do not seem to be responsible for the switching. They rather seem to accelerate or retain the switching as a small perturbation, leading to a broadening in the frequency spectrum.

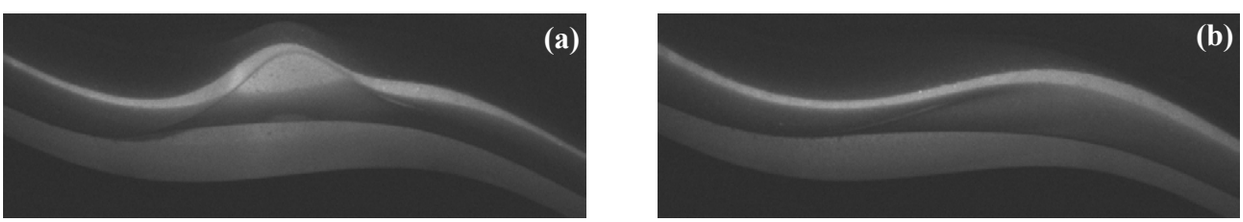


Figure 3: Side-view of resonant standing waves. The free-surface contour corresponds to the upper limit of the bright central part. Mean inclination angle: 12°; film thickness: 13.6 mm (a) and 14.7 mm (b).

CONCLUSIONS

We observed a bistability between shock fronts and surface rollers. At the low end of the bistable region the surface rollers degenerate into an instationary fingering-like structure pouring out of a shock front. It seems to us that surface tension plays an essential role for the existence of the bistability. At higher flow rates the hydraulic jumps loose their stability in favor for standing waves that are in resonance with the bottom contour. At this transition, we observe a switching of low frequency between surface rollers and standing waves.

REFERENCES

[1] Wierschem, A., Scholle, M., Aksel, N.: Comparison of different theoretical approaches to experiments on film flow down an inclined wavy channel, *Exp. Fluids* **33**: 429-442, 2002

[2] Wierschem, A., Aksel, N.: Instability of a liquid film flowing down an inclined wavy plane, *Physica D* **186**: 221-237, 2003

[3] Vlachogiannis, M., Bontozoglou, V.: Experiments on laminar film flow along a periodic wall, *J. Fluid Mech*., **457**:133-156, 2002

[4] Wierschem, A., Scholle, M., Aksel, N.: Vortices in film flow over strongly undulated bottom profiles at low Reynolds numbers, Phys. Fluids **15**:426-435, 2003

[5] Scholle, M., Wierschem, A., Aksel, N.: Creeping films with vortices over strongly undulated bottoms, Acta Mechanica (in press)

HYDRODYNAMIC THEORY OF DE-WETTING

Jens Eggers
School of Mathematics, University of Bristol, University Walk, Bristol BS8 1TW, United Kingdom

Summary A prototypical problem in the study of wetting phenomena is that of a solid plunging into or being withdrawn from a liquid bath. In the latter, de-wetting case, a critical speed exists above which a stationary contact line is no longer sustainable and a liquid film is being deposited on the solid. Demonstrating this behavior to be a hydrodynamic instability close to the contact line, we provide the first theoretical explanation of a classical prediction due to Derjaguin and Levi: instability occurs when the outer, static meniscus approaches the shape corresponding to a perfectly wetting fluid.

INTRODUCTION AND RESULTS

The forced wetting or de-wetting of a solid is an important feature of many environmental and industrial flows. In typical applications such as painting, coating, or oil recovery it is crucial to know whether the solid will be covered by a macroscopic film or not. If a fiber is plunging into a liquid bath to be coated (wetting case), the speed can be quite high (m/sec), while maintaining a stationary contact line. In the opposite case of withdrawal (de-wetting), a stationary contact line is observed only for very low speeds, and a macroscopic film is deposited typically at a speed of only a few cm/sec. Yet no theoretical explanation for this instability exists, or of the fundamental difference between the two cases.

It is well known that viscous forces become very large near a moving contact line, and are controlled only by some microscopic cut-off λ, for example a slip length. As a result of the interplay between viscous and surface tension forces, the interface is highly curved, and the contact line speed U is properly measured by the capillary number $Ca = U\eta/\gamma$, where η is the viscosity of the fluid and γ the surface tension between fluid and gas. It was first proposed by Derjaguin and Levi (1), that instability occurs if this dynamic interface angle reaches *zero*. Apart from the fact that there is no justification for this condition, it does not lead to a unique criterion since the angle depends on the position where it is evaluated. However, it was noted experimentally (2) that the interface profile at the critical speed corresponds to a *static* meniscus with zero equilibrium contact angle, except in the immediate neighborhood of the contact line.

To explain the physical mechanism behind the instability, we note that the interface shape $h(x)$ near the contact line must have the form

$$h(x) = 3\lambda H(\xi), \quad \xi = x\theta_e/(3\lambda), \tag{1}$$

since the cut-off λ is the only available length scale. The dependence on θ_e was put in for later convenience. As expected, the curvature $h''(0) = \theta_e^2/(3\lambda)H''(0)$ becomes very large at the contact line, since λ is in the order of nanometers. As the curvature of the local solution has to match to a value of order unity in the static outer part of the profile, the usual boundary condition for H is one of vanishing curvature for large ξ. In the wetting case this leads to an asymptotic solution first found by Voinov and an expression for the interface angle usually referred to as "Tanner's law".

However, it is a well-known but little appreciated fact that Voinov's solution fails away from the contact line in the de-wetting situation. Instead, the local solution always retains a positive curvature, and will fail to match to an outer solution in the limit of small λ. At the critical speed, the necessary compromise between the inner solution near the contact line and the outer static solution has been pushed to the limit: from all possible inner solutions, the one with the *smallest* possible curvature is selected. The outer solution, on the other hand, realizes the solution with the *largest* curvature, which happens to be the one corresponding to zero contact angle, in agreement with the criterion of Derjaguin and Levi.

To make an explicit comparison between our asymptotic theory and numerical integration of the lubrication equations, we choose a plate being withdrawn from a liquid bath (see Fig.1) as a test case, a geometry which was studied in detail in (3). There it was found numerically that there exists a critical capillary number Ca_{cr}, above which no static solution exists, in agreement with the experimental findings described above. The final result of our theory is then

$$\delta_{cr}^{1/3} \exp[-1/(3\delta_{cr})] = 2^{1/3}\pi(Ai(s_{max}))^2\mu\theta/\theta_e, \tag{2}$$

where $\delta_{cr} = 3Ca_{cr}/\theta_e^3$ is the critical rescaled capillary number, and $\mu = \lambda/\theta_e$ the rescaled slip length.

Our central result (2) is compared in Fig.2 to a numerical solution of the lubrication eqaution. No parameter was adjusted to achieve this comparison.

References

[1] B.V. Derjaguin and S.M. Levi, *Film coating theory*, Focal Press, London (1964).

[2] R.V. Sedev and J.G. Petrov, Colloids and Surfaces, **53**, 147-156 (1991).

[3] L.M. Hocking, Euro. J. Appl. Math. **12**, 195-208 (2001).

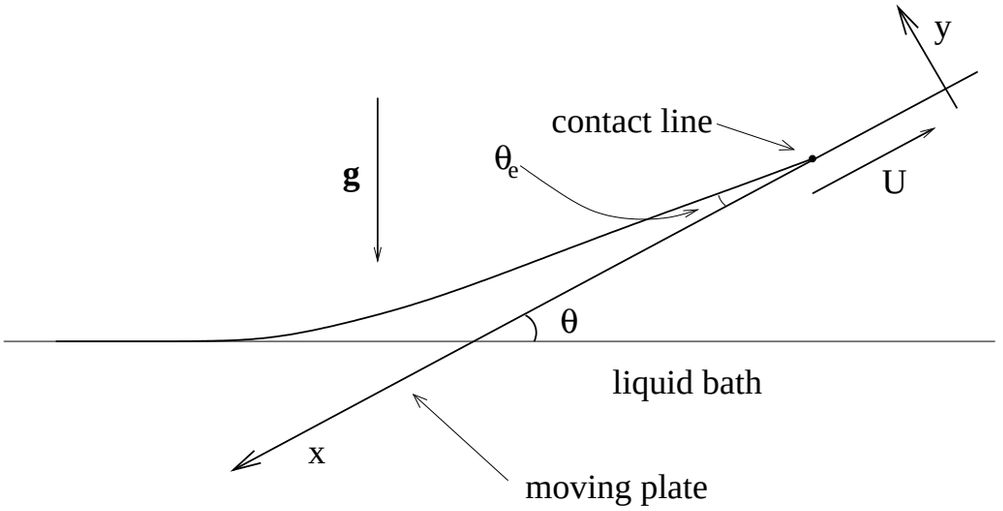


Figure 1. A schematic of the setup. At the contact line, h(0) = 0, and the slope of the interface is θ_e. The plate is being withdrawn at an angle θ.

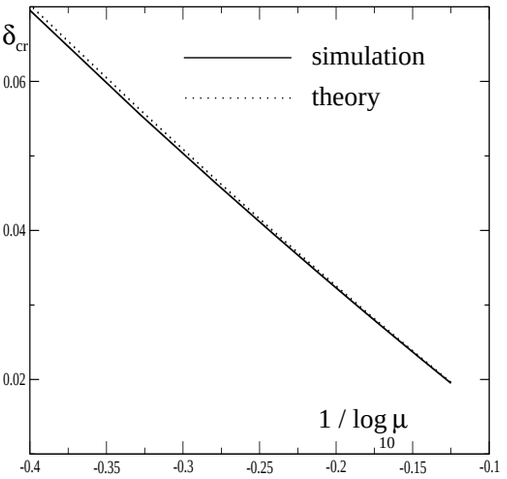


Figure 2. A comparison of δ_{cr} as determined by numerical integration of the lubrication eqaution for $\theta/\theta_e = 1$, and theory, as summarized by equation (2).

XXI ICTAM, 15–21 August 2004, Warsaw, Poland

SURFACTANT-INDUCED FINGERING PHENOMENA IN THIN LIQUID FILMS

M. R. E. Warner *, R. V. Craster *, Omar K. Matar**
*Department of Mathematics, Imperial College London, SW7 2AZ, UK
**Department of Chemical Engineering, Imperial College London, SW7 2AZ, UK

Summary The spreading of surfactant on thin liquid films is accompanied by a fingering instability. We have developed a model, based on lubrication theory, which provides an explanation for this phenomenon. The patterns obtained from our simulations, which undergo tip-splitting and shielding, are in good agreement with those observed experimentally.

INTRODUCTION

Experimental studies involving the spreading of surfactants on thin fluid films by Marangoni stresses have demonstrated that these flows are susceptible to fingering instabilities [1-4]; an example of the fingering patterns from [3] is shown in Fig. 1. Several modeling studies, which have examined the stability of a surfactant monolayer spreading on a film of initially uniform thickness have shown that in the absence of van der Waals forces, growth could not be sustained [5] except in the presence of artifical constant feeding at the origin [6]. More recently, however, Warner *et. al.* [7], focused on the dynamics of an insoluble surfactant deposition of order one thickness spreading over a much thinner liquid film; here the surfactant was present in dilute concentrations. These authors showed [7], that for a sufficiently large disparity in film thickness between the deposition and underlying film thickness, transverse perturbations of intermediate wavenumber grow exponentially targetting the leading edge of the droplet deposition behind the advancing front, in agreement with experimental observations.
Here, we extend the work of Warner *et al.* [7] in an attempt to capture trends associated with solubility and large concentrations observed experimentally [3], which show them to be destabilizing. We use lubrication theory to derive a coupled system of equations for the film thickness and surfactant bulk and surface concentrations in the limit of rapid vertical diffusion. Results from a transient growth analysis and direct numerical simulations show that a combination of surfactant solubility with high surfactant concentrations is in fact destabilizing in agreement with experimental trends. Here, we summarize the results of the numerical simulations only.

FORMULATION

We consider an initially stationary drop of soluble surfactant of constant viscosity μ^* and density ρ^* and of initial thickness $\mathcal{H}^*$ and extent $\mathcal{L}^*$ on a thinner uncontaminated fluid film of thickness $\mathcal{H}_b^*$ and the same physical properties; here, dimensional variables are decorated with an asterisk. The solid substrate underlying the thin film is rigid, horizontal and impermeable and the dynamics of the overlying essentially inviscid gas are neglected. The initially uniform surface and bulk concentrations of the surfactant are denoted by Γ_m^* and C_m^*, respectively; we introduce the ratio $b \equiv \mathcal{H}_b^*/\mathcal{H}^*$: $b \to \infty$ corresponds to a monolayer spreading on an initially uniform film.
The system dynamics are described by the following dimensionless evolution equations for the film thickness and surfactant surface and bulk concentrations, h, Γ and c, in the lubrication approximation [8]:

$$h_t = -\nabla \cdot \left[\frac{\mathcal{C}}{3}h^3\nabla\kappa + \frac{1}{2}h^2\nabla\sigma\right], \quad \Gamma_t = -\nabla \cdot \left[\frac{\mathcal{C}}{2}h^2\Gamma\nabla\kappa + h\Gamma\nabla\sigma\right] + \frac{1}{\mathrm{Pe_s}}\nabla^2\Gamma + K(c-\Gamma), \tag{1}$$

$$c_t = -\left[\frac{\mathcal{C}}{3}h^2\nabla\kappa + \frac{1}{2}h\nabla\sigma\right]\cdot\nabla c + \frac{1}{\mathrm{Pe_b}}\frac{1}{h}\nabla\cdot(h\nabla c) - \frac{\beta K}{h}(c-\Gamma). \tag{2}$$

Here, the surface curvature, is given by $\kappa = \nabla^2 h$ and we have assumed that $\epsilon \ll 1$ and $\epsilon^2\mathrm{Pe_b} \ll 1$ (rapid vertical diffusion). In Eqs. (1) and (2), $\beta \equiv \frac{k_1^*}{\mathcal{H}^* k_2^*}$, $K \equiv \frac{k_2^*\mathcal{L}^*}{\mathcal{U}^*}$, $\mathrm{Pe_b} \equiv \frac{\mathcal{U}^*\mathcal{L}^*}{\mathcal{D}_b^*}$, $\mathrm{Pe_s} \equiv \frac{\mathcal{U}^*\mathcal{L}^*}{\mathcal{D}_s^*}$, $\mathcal{C} \equiv \frac{\epsilon^2\sigma_m}{\mathcal{S}}$, where k_1^* and k_2^* are adsorption and desorption rate constants, respectively; $\mathcal{D}_s$ and $\mathcal{D}_b$ denote the surfactant surface and bulk diffusion coefficients; $\mathcal{U}^* = \mathcal{S}\mathcal{H}^*/\mu^*\mathcal{L}^*$ where $\mathcal{S} = \sigma_0 - \sigma_m$, the surface tension difference between the clean and contaminatedd interfaces. Note that small values of β represent highly soluble surfactants whilst $\beta \to \infty$ represents the insoluble surfactant limit. A dimensionless nonlinear equation of state, is used for closure: $\sigma(\Gamma) = \frac{\alpha+1}{[1+\Theta(\alpha)\Gamma]^3} - \alpha; \Theta(\alpha) = \left(\frac{\alpha+1}{\alpha}\right)^{1/3} - 1$. In the limit $\alpha \to \infty$, $\sigma = 1 - \Gamma$.

RESULTS

We utilize an ADI scheme [7], which is based on operator splitting methods, to perform two-dimensional simulations of Eqs. (1)-(2) on a grid $0 < x < L_x$, $0 < y < L_y$, starting from $h(x,y,0) = (1-x^2+b)H(1-x) + bH(x-1) + A(y)\exp(-5(x-1)^2)$, $\Gamma(x,y,0) = H(1-x)$. Here, $A(y)$ comprises random values chosen from a uniform distribution on $[-0.01, 0.01]$ and $H(x)$ is a smooted Heaviside function. These solutions are subject to the following boundary conditions: $h_x(0,y,t) = h_{xxx}(0,y,t) = 0$, and $h(L_x,y,t) = b$, $h_x(L_x,y,t) = 0$,

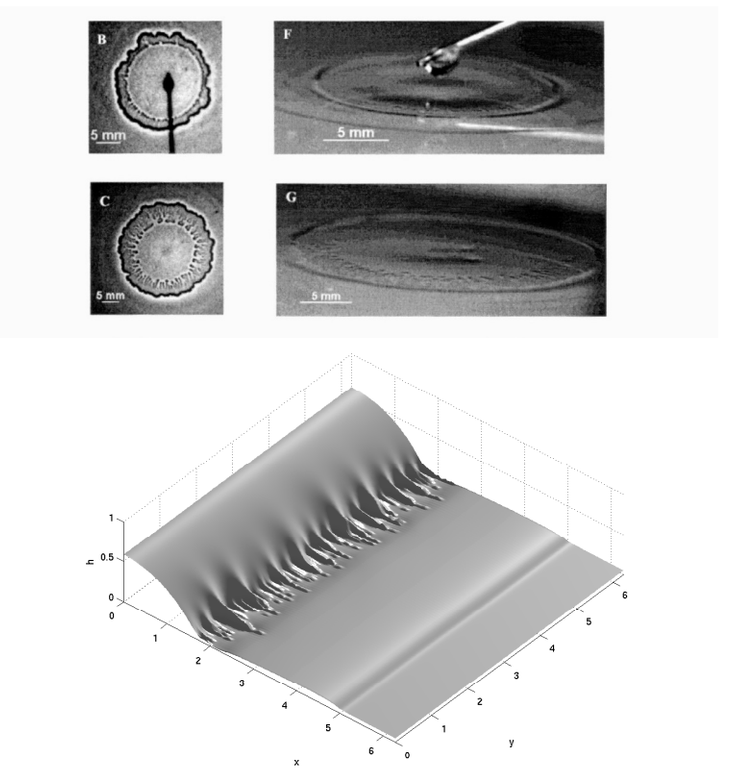


Figure 1. (Top): Fingering patterns at $t = 0.067$ sec ('B') and 0.31 sec ('C') during the spreading of a 9 μl droplet of 1.2 CMC SDS solution on a 25 μm water film [3]; side-views are shown in 'F' and 'G'. (Bottom): Surface plot of h with $\alpha = 0.1$, $\beta = 1$, $b = 0.1$, $K = 1$, $\mathrm{Pe_b} = 100$, $\mathrm{Pe_s} = 10^4$, $\mathcal{C} = 10^{-3}$ and $t = 125$.

$\Gamma_x(0, y, t) = c_x(0, y, t) = 0$ and $\Gamma(L_x, y, t) = c(L_x, y, t) = 0$. Periodic boundary conditions are imposed at $y = 0, L_y$. Typically we utilize a 2π square grid and have a 200×200 mesh. As shown in Fig. 1, the initially noisy disturbances have self-organised into coherent fingering structures, which exhibit splitting and shielding events. The results shown in Fig. 1 demonstrate that the emerging fingering patterns, which are associated with a soluble surfactant are in qualitative agreement with the observed finger formation in many experiments [2,3]. We have also shown [8] that increasing the degree of solubility is destabilizing (except for very small β, for which the Marangoni stresses that drive the instability are very weak).

CONCLUSIONS

We have considered the stability of a drop laden with soluble surfactant spreading on the surface of a thin liquid film within the framework of lubrication theory and rapid vertical diffusion. The results of our numerical simulations of the fully nonlinear governing equations summarised here [8] show the appearance of fingering patterns, which localize at the drop leading edge accompanied by tip-splitting, coalescence and shielding.

References

[1] Marmur A., Lelah M.D.: The spreading of aqueous surfactant solutions on glass. *Chem. Eng. Comm.* **13**:133, 1981.
[2] Cachile M., Schmeelich A., Hamraoui A., Cazabat A.M.: Films driven by surface tension gradients. *Adv. Colloid Interface Sci.* **96**:59, 2002.
[3] Afsar-Siddiqui A., Luckham P.F., Matar, O.K.: Unstable spreading of an anionic surfactant on liquid films. Part II: Highly soluble surfactant. *Langmuir* **19**:703, 2003.
[4] Darhuber A. A., Troian S.M.: Marangoni driven structures in thin film flows. *Phys. Fluids* **15**:59, 2003.
[5] Warner M.R.E., Craster R.V., Matar O.K.: Unstable van der Waals driven line rupture in Marangoni driven thin viscous films. *Phys. Fluids* **14**:1642, 2002.
[6] Fischer B.J., Troian S.M.: Thinning and disturbance growth in liquid films mobilized by continuous surfactant delivery. *Phys. Fluids* **15**:3837, 2003.
[7] Warner M.R.E., Craster R.V., Matar O.K.: Fingering phenomena in surfactant spreading on thin liquid films, under review for *J. Fluid Mech.*
[8] Warner M.R.E., Craster R.V., Matar O.K.: Fingering phenomena created by a soluble surfactant deposition on a thin liquid film, under review for *Phys. Fluids.*

XXI ICTAM, 15–21 August 2004, Warsaw, Poland

LINEAR RESPONSE OF A VISCOUS LIQUID SHEET

Norbert Alleborn*, Hans Raszillier*
*Lehrstuhl für Strömungsmechanik, Universität Erlangen–Nürnberg, Cauerstr. 4, 91058 Erlangen, Germany

Summary The paper investigates the propagation of disturbance signals originating from moving localized sources on a thin viscous liquid sheet of infinite extent. The tool of analysis is the Fourier-Laplace transformation of the linearized perturbation equations, implying an inverse Fourier-Laplace transform to reconstruct the perturbation signal. The development of the signal front from a persistently acting source is investigated in the long time limit by numerical evaluation for varicose and sinuous perturbations.

INTRODUCTION AND PROBLEM FORMULATION

Thin viscous liquid sheets are sensitive to external pressure disturbances, such as pressure fluctuations along their interfaces. In this paper the linear response of a uniform viscous liquid sheet (density ρ, kinematic viscosity ν, surface tension γ) of infinite extent to localized pressure disturbances is investigated. Fig. 1 (a) shows a sketch of the sheet with a passive

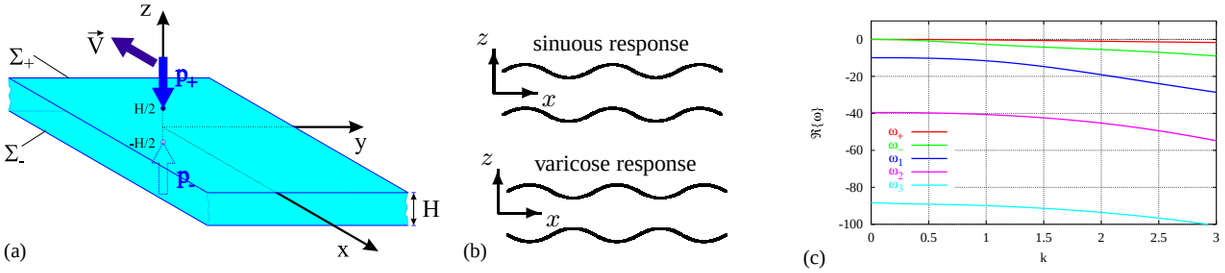


Figure 1. Sketch of a thin viscous liquid sheet (a), perturbation modes (b), varicose spectrum for $\Gamma = 1$ (c).

ambient medium adjacent to it which exerts pressure distributions $p_\pm(\vec{x},t)$, $\vec{x} = (x,y)$, on the sheet interfaces $\Sigma_\pm$. For constant pressures $p_+ = p_- = p_0$ the sheet may be considered at rest with flat interfaces $z_\pm = \pm H/2$. Small local deviations of $p_\pm$ from p_0 induce a flow in the sheet, causing small fluctuations $\eta_\pm$ of the interfaces around its basic state: $z_\pm = \pm(H/2 + \eta_\pm)$. In Fig. 1 (a) (localized) pressure disturbances moving with constant velocity $\vec{V}$ act on the interfaces. A reflection symmetry of the basic state with respect to the plane $z = 0$ allows to consider *varicose* perturbations, that act symmetrically on the interfaces ($p_- = p_+$), and *sinuous* perturbations that act antisymmetrically ($p_- = -p_+$), separately, cf. Fig. 1 (b), with $\eta_- = \eta_+$ and $\eta_- = -\eta_+$, respectively.

RESULTS

The amplitudes η_+ of the varicose and sinuous interface deformations, $\eta_{v,s}$, are obtained by a Fourier–Laplace transform

$$\eta_{v,s}(\vec{x},t) = -\frac{1}{2\pi}\int d\vec{k}\, e^{i\vec{k}\cdot\vec{x}}\ \frac{1}{2\pi i}\int_{c-i\infty}^{c+i\infty} d\omega\ e^{\omega t}\ \frac{k\,\tilde{\mathcal{P}}(\vec{k},\omega)}{D_{v,s}(k,\omega)}\,, \quad c>0\,, \tag{1}$$

from the linear perturbation equations, cf. [2, 3], stated here already dimensionless by normalizing lengths by $H/2$, time by $H^2/(4\nu)$ and pressure by $4\rho\nu^2/H^2$. $\tilde{\mathcal{P}}(\vec{k},\omega)$ denotes the Fourier–Laplace transform of the pressure disturbance $p_+(\vec{x},t)$ and $D_{v,s}(k,\omega)$ the varicose and sinuous dispersion function, respectively:

$$D_v(k,\omega) = \Gamma^2 k^3 + (k^2+l^2)^2\coth(k) - 4k^3 l\coth(l)\,, \tag{2}$$

$$D_s(k,\omega) = \Gamma^2 k^3 + (k^2+l^2)^2\tanh(k) - 4k^3 l\tanh(l)\,, \tag{3}$$

with $k = |\vec{k}|$ and $l^2 = k^2 + \omega$ and with the characteristic number $\Gamma = \sqrt{\gamma H/(2\rho\nu^2)}$. The singularities of the integrand in eq. (1), the zero curves $\omega = \omega(k)$ of $D_{v,s}(k,\omega) = 0$, lie in the left half of the complex ω–plane, i.e. the response modes of the sheet are absorptive. Fig. 1 (c) illustrates the wavenumber dependence of the decay rate $\Re\{\omega\}$ for varicose mode branches, obtained numerically by parameter continuation [1]. For large times the two "soft" branches $\omega_\pm(k)$, for which $\lim_{k\to 0}\omega_\pm(k) = 0$, determine the response signal asymptotically and within the soft branches the long wave part ($k \to 0$) dominates, cf. [3].

A comparison of the decay rates of the soft branches $\omega_\pm(k)$ with their longwave approximations

$$\omega_{v,\pm}(k) \approx \pm\sqrt{4-\Gamma^2}\,k^2 - 2k^2\,, \qquad \omega_{s,\pm}(k) \approx \pm i\,k - \left(\frac{2}{3}+\frac{4}{15}\Gamma^2\right)k^4 \tag{4}$$

in Fig. 2 shows for the sinuous mode that the k^4–dependence of the longwave growth rate approximates the exact solution for the soft branches only in a narrower range of k than the longwave approximation of the varicose modes.

The response (1) of the sheet to steady disturbance of the form $P_{v,s}(\vec{x},t) = P_{0v,s}\,f_{v,s}(x+Vt,y)\theta(t)$, acting for $t > 0$, has been computed numerically in the long time limit ($t \to \infty$) for the axisymmetric form functions $f_v(x,y)$ and

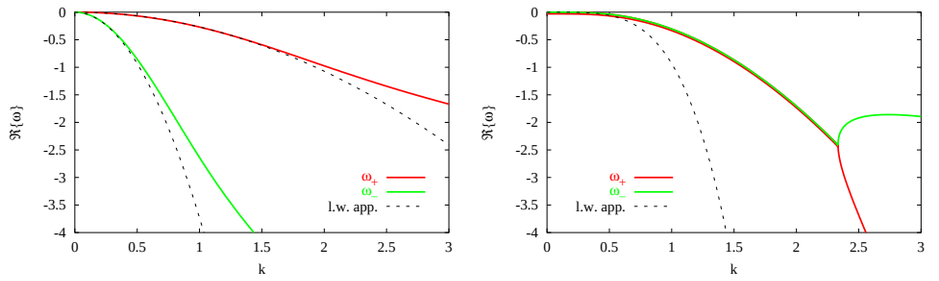
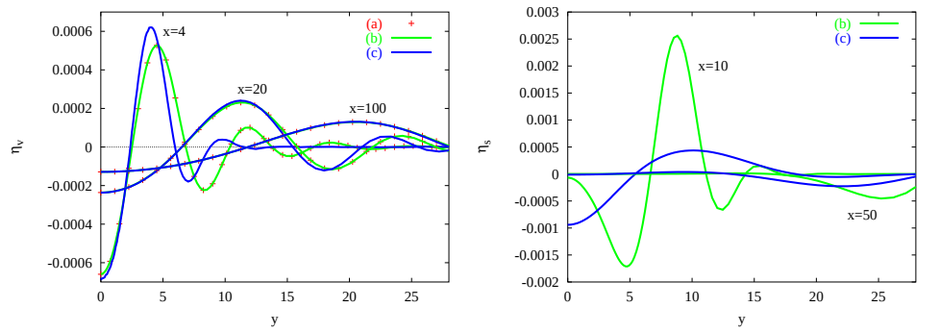


Figure 2. Solution branches of $D_{v,s}(k,\omega)$ for $\Gamma = 1$: Two soft branches $\omega_{\pm}(k)$ and longwave approximation (l.w. approx), for varicose modes (left) and sinuous modes (right).



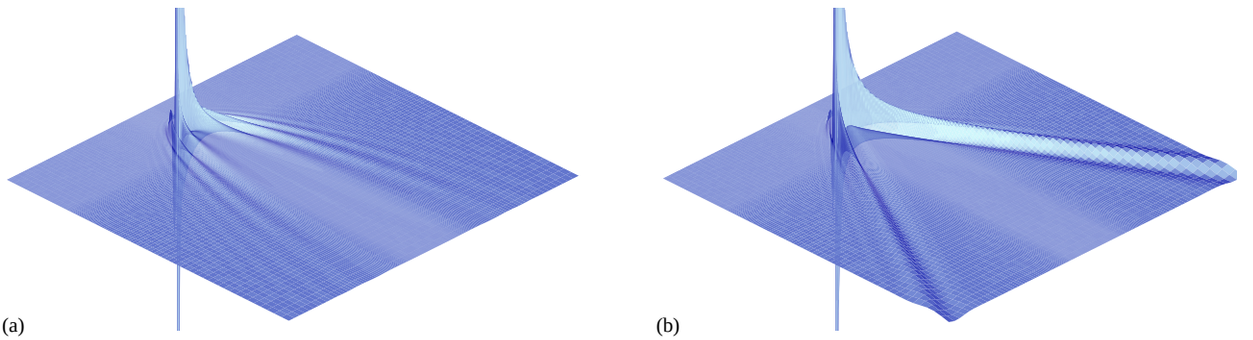
Perturbation form functions:

$$f_v(x,y) = \frac{100}{\pi}\, e^{-100\, r^2}\,,$$

$$f_s(x,y) = \left(1 - 4\, r^2\right)\, e^{-4\, r^2}\,,$$

$$r = \sqrt{x^2 + y^2}\,.$$

Figure 3. Disturbance amplitude $\eta(x,y)$ along the $y-$direction at different distances x from the source, for $\Gamma = 10, V = 2\Gamma$ (rest frame of disturbance): varicose disturbance (left), sinuous disturbance (right). Analytical solution for longwave approximation of varicose disturbance [3] (a), numerical solutions for longwave dispersion functions (b) and for exact dispersion functions (c).



(a) (b)

Figure 4. Propagation of disturbances for the external pressure profiles $P_s(\vec{x},t)$, $\Gamma = 10, V = 2\Gamma$ (rest frame of disturbance): Numerical results for exact dispersion relations, eq. (2) for varicose disturbance (left) and sinuous disturbance (right), with $f_s(r)$ in both cases.

$f_s(x,y)$ shown in Fig. 3. The sinuous disturbance has been chosen in a way that the sheet is statically equilibrated, i.e. $\iint P_s(\vec{x},t)d\vec{x} = 0$. Fig. 3 shows the disturbance amplitudes of the sheet computed numerically, exactly with the dispersion functions, eq. (2) and (3), and in the longwave approximations [3], with eq. (4). For $\Gamma > 2$ the longwave approximation of the varicose soft modes is dispersive, so that the disturbance causes an oscillatory response, cf. Fig. 3 (left). The longwave approximation appears to describe the varicose response behaviour increasingly well with distance from the source, as expected [3]. The longwave sinuous modes are nondispersive and the response of the sheet exhibits therefore only few strongly damped undulations caused by viscous diffusion, whereas the exact evaluation takes into account also the dispersive part of the spectrum and reveals an oscillatory response, cf. Fig. 3 (right). Due to the smaller range of validity of the longwave approximation for sinuous modes, it is expected to give a less good approximation of the response than for varicose disturbances at comparable distances.

The response of the interface to varicose and sinuous disturbances, illustrated in Fig. 4, shows very good qualitative agreement with the experiments of de Luca and Costa [4].

The support of the Deutsche Forschungsgemeinschaft (DFG) is gratefully acknowledged.

References

[1] Alleborn N., Raszillier H., Durst F.: Linear stability of non–Newtonian annular liquid sheets. *Acta Mechanica* **137**:33–42, 1999.

[2] Alleborn N., Raszillier H., Durst F.: Propagation of disturbances in thin viscous liquid sheets. In: *10th International Coating Science and Technology Symposium — Final Program and Extended Abstracts*, ISCST — International Society of Coating Science and Technology, Scottsdale, Arizona, 25–27 September 2000, p. 40–43, 2000.

[3] Alleborn N., Raszillier H.: Linear Response of a Viscous Liquid Sheet to Oscillatory External Pressure Perturbation in the Long Wave Approximation — Varicose Excitation. *Acta Mechanica*, **170**:77–119, 2004.

[4] de Luca L., Costa M.: Stationary waves on plane liquid sheets falling vertically. *Eur. J. Mech. B/Fluids*, **16**:77–88, 1997.

EXPERIMENTAL AND NUMERICAL STUDY OF MARANGONI-NATURAL CONVECTION

L. H. Tan*, E. Leonardi*, T. J. Barber*, S. S. Leong*, T. A. Kowalewski**
*School of Mechanical and Manufacturing Engineering,
University of New South Wales, Sydney 2052, AUSTRALIA
** IPPT PAN, Department of Mechanics & Physics of Fluids, PL 00-049 Warszawa, POLAND

ABSTRACT

An experimental and numerical study of thermal Marangoni - natural convection was carried out to examine the flow behaviour under various conditions of liquid layer depth and heating conditions. Particle Image Velocimetry (PIV) and numerical results using FLUENT V6 are in good agreement. The liquid free surface profile due to the presence of the menisci is shown to be important for validation.

INTRODUCTION

Figure 1 shows the experimental setup of the PIV system. A cylindrical glass container of diameter 56.1 mm is filled with 10 cSt silicone oil to a layer depth of a few millimetres. The shallow depth reduces the strength of natural convection and allows Marangoni convection to dominate [1]. For visualization purposes, the oil is seeded with PSP polyamide particles and a laser diode illuminates the vertical centre plane of the oil. Under steady axisymmetric conditions, the complete flow behavior can be observed on this plane [2]. A CCD camera connected to an image acquisition board records the images for post-processing with PIV software. The container is placed in a water bath to maintain the side and bottom walls at a cooler temperature. A cylindrical copper piece (tip diameter 5 mm) connected with a soldering iron heats up the oil layer at the centre of its free surface. Owing to changes in local surface tension due to the imposed temperature gradient, oil at/near the surface flows out to the cold sidewalls followed by a return bulk flow (Figure 2 and 3).

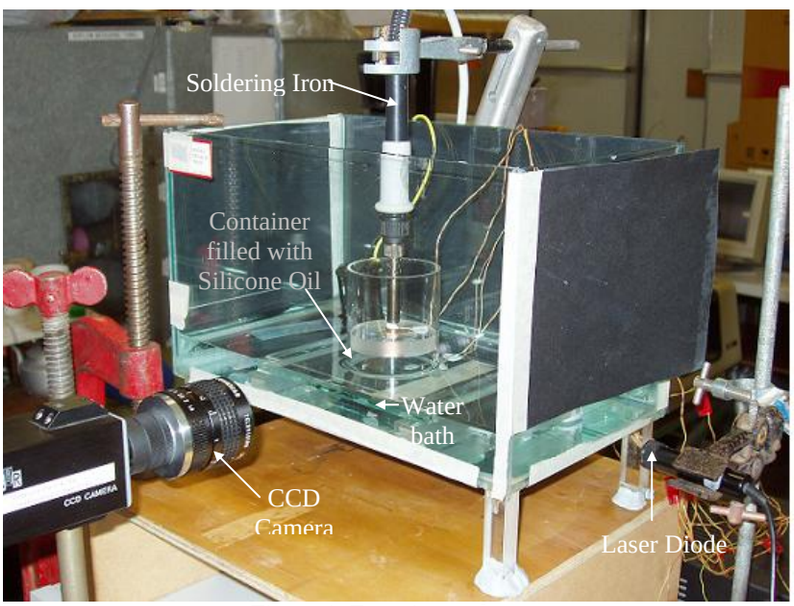


Figure 1. Experimental setup

RESULTS AND CONCLUSIONS

Figure 2 shows the experimental flow patterns at the centre below the hot tip, with a depth of 4 mm and temperature difference of 11.8 K. This corresponds to a Marangoni number, *Ma* = 3624. Figure 3 shows the flow patterns right of centre. A numerical model within FLUENT was constructed for comparison, using the Boussinesq approximation and assuming laminar, axisymmetric flow. Figure 4 shows the streamlines from the numerical predictions, providing comparison with Figure 3. The qualitative agreement is evident between the two.

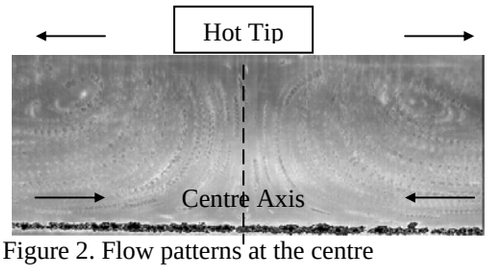


Figure 2. Flow patterns at the centre

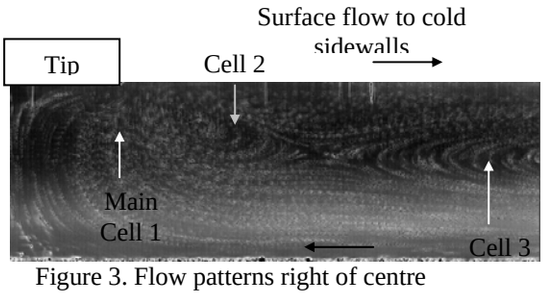


Figure 3. Flow patterns right of centre

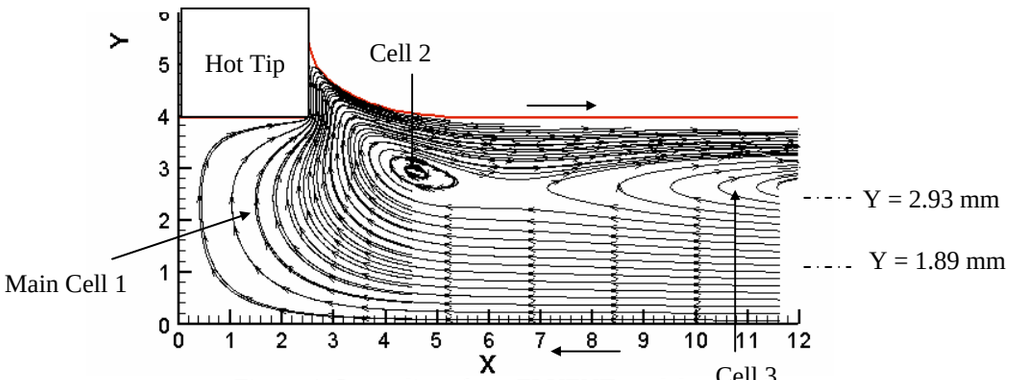


Figure 4. Streamlines from FLUENT model

The presence of two cells (Cell 2 and Cell 3) embedded within the main Cell 1 and rotating in the same direction can be seen in both experimental and numerical results. The meniscus present at the tip is modelled in FLUENT based on captured images to give more accurate quantitative comparisons. Figures 5 and 6 display the experimental and numerical velocity magnitudes across the layer at heights of y = 1.89 mm and y = 2.93 mm, showing good agreement between the two.

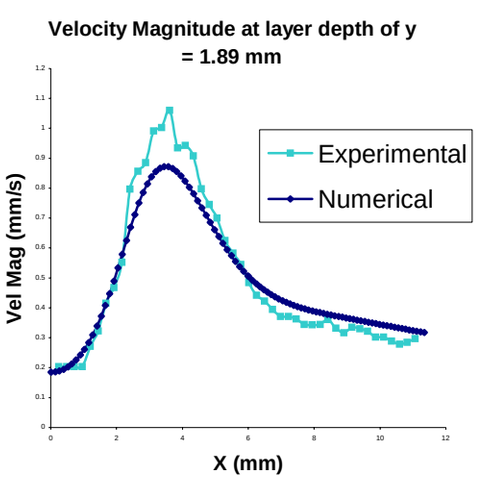


Figure 5. Velocity at y = 1.89 mm

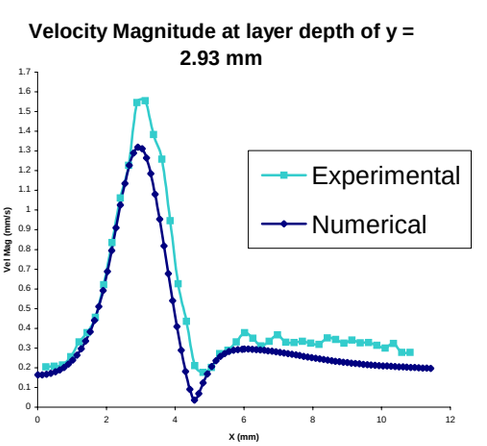


Figure 6. Velocity at y = 2.93 mm

In the paper, experimental and numerical results will be presented with a variation in parameters such as liquid layer depth and temperature differences. The effects of these parameters on the flow patterns and velocities will be presented.

REFERENCES

[1] D. Schwabe, U. Moller, J. Schneider, A. Scharmann, *Instabilities of shallow dynamic thermocapillary liquid layers*, Phys. Fluids A, 4 (11), (1992), 2368-2381.

[2] J. A. Szymczyk, *Interaction between thermocapillary and buoyancy driven convection*, Experiments in Fluids 12, 151-156 (1992)

LAYER THICKNESS DISTRIBUTION OF THIN-FILM INK-JET PRINTED STRUCTURES

Dirkjan B. van Dam
Philips Research, Department Mechanics, Heat and Particle Optics, Prof. Holstlaan 4, 5656 AA Eindhoven, The Netherlands; dirkjan.van.dam@philips.com

Summary We studied the layer formation process of sessile droplets of a colloidal silver suspension, deposited by ink jet printing. An approximate numerical model was developed, and associated scaling laws. The numerical prediction and underlying assumptions of the model were compared with experimental results. They were found to be in reasonable agreement with each other, showing the practical value of the approach.

INTRODUCTION

The drying of ink-jet printed droplets that form thin films of solute is a process that can show various hydrodynamical phenomena, such as Marangoni flow and hydrodynamic instabilities (e.g. [1]). However, even in a relatively simple form that still has practical significance, the description of the drying process already poses significant difficulties. In the case considered here, the processes involved are convective and diffusive transport of solute, coupled with the evolution of the free surface, the evaporation of the solvent, and the viscosity increase of the solution (see figure 1).
Significant work on drying has been performed by Deegan (e.g. [2]), quantifying the surface-tension driven mechanism of convective solute transport initiated by evaporation of droplets of order 1 mm radius. However, for smaller size particles and droplets than Deegan studied, diffusion established by advectively induced concentration gradients can become important. Also, the increase of viscosity as the concentration of the solute increases can become important.
In this study we present a practical and approximate approach towards the drying of an ink-jet printed droplet containing colloidal particles, together with experimental validation. Applications for which this approach is useful are e.g. in the field of printable electronics for displays [3].

MODEL DESCRIPTION

We make the assumption that the solution is well-mixed in the vertical direction, so that the solute concentration only depends on the radial position (valid when $V_c H_c/D \ll 1$ with V_c and H_c being a characteristic respectively evaporation rate and wet layer thickness, and D being the solute's diffusion coefficient). We then write the convection-diffusion equation integrated over the droplet height as:

$$\frac{\partial}{\partial t}(ch) = H\left(1-\frac{c}{c_{cr}}\right)\cdot\left(\frac{1}{r}\frac{\partial}{\partial r}\left(Dhr\frac{\partial c}{\partial r}\right)-\frac{1}{r}\frac{\partial}{\partial r}(rchv)\right) \qquad (1)$$

where t is time, c is the solute volume concentration, h is the wet layer thickness of the droplet, H is the Heaviside step function, r is the radial coordinate, and v is the radial velocity averaged over the droplet height. The use of H expresses a sudden prevention of further solute transport at a critical concentration c_{cr}, as a result of increased viscosity that develops during drying. This approach is motivated by considering a capillary number Ca giving the order of magnitude of the proportion between viscous forces and forces generated by surface-tension in an evaporating sessile droplet:

$$Ca = \frac{\eta v_{e,av}}{\sigma}\left(\frac{r_0}{h_0}\right)^4 \qquad (2)$$

where r_0 and h_0 are the radius and central layer thickness of the droplet during drying, $v_{e,av}$ is the average evaporation rate (defined as evaporating volume per unit of time divided by πr_0^2), η is the viscosity and σ the surface tension of the solution. For practical ink-jet printable fluids and substrates, we usually have $Ca \ll 1$ at the start of drying. For the materials used in this study we found that the viscosity increases sharply with concentration around a critical concentration c_{cr}, so that we can assume that $Ca \ll 1$ if $c < c_{cr}$ and $Ca \gg 1$ if $c > c_{cr}$ and no solute transport occurs.
We assume that the surface evolves as a spherical cap and that the contact line remains pinned, which is the case for many practical situations. Assuming a spherical cap neglects profile changes by gellation or solidification of the material, and unknown development of evaporation rate and material density [4]. Experiments on droplets of 1 mm radius show that this assumption is good for times <80% of the total drying time for the materials in this study.
The continuity equation and evaporation rate model – based on diffusive transport of solvent vapour [2] – read:

$$\frac{d(rvh)}{dr} = -r\left(\frac{dh}{dt}+v_e\right), \qquad v_e = v_{e,av}(1-\lambda)\left(1-\left(\frac{r}{r_0}\right)^2\right)^{-\lambda} \qquad (3), (4)$$

where v_e is the evaporation rate, $\lambda = (\pi-2\theta)/(2\pi-2\theta)$ and θ is the contact angle between fluid and substrate.
We can numerically solve equation (1), (3), (4) and the spherical-cap description for h. We can also infer that the problem is described by three dimensionless numbers and a parameter describing the evaporation rate profile:

$$N_H = \frac{H_0}{R_0}, \qquad N_D = \frac{H_0 D}{v_{e,av} R_0^2}, \qquad N_c = \frac{c_0}{c_{cr}}, \qquad \lambda_0 \tag{5}$$

where H_0, R_0 and λ_0 are the central layer thickness, droplet radius and λ at the start of drying.

COMPARISON WITH EXPERIMENTS

For experimental verification, we used two colloidal suspensions of silver particles in water stabilised with a polymer, obtained from Merck and Nippon-Paint. We printed these on a glass substrate with modified surface energy using a piezo-electric ink jet head. For both solutions we measured the viscosity and diffusion coeffient at the initial concentration c_0, yielding η=1.0 mPa·s, D=2.7·10^{-11} m^{2}s^{-1} and η=1.9 mPa·s, D=1.0·10^{-10} m^{2}s^{-1} respectively. The evaporation rate was measured for droplets with different radius. We also determined the viscosity increase as a function of concentration, at a shear rate of 10 s^{-1}. From this we found that we can estimate c_{cr} as 0.05 and 0.03 for initial silver concentrations of 0.017 and 0.0053 respectively. The sessile droplet radius in the various experiments is between 17 and 96 μm. In checking our model assumptions for the materials, we found that solutal Marangoni effects can be neglected.
Figure 2 shows a direct comparison between an experimentally determined layer thickness profile and the numerical model. The uncertainty in the diffusion coefficient (relative error of 50%) and average evaporation rate (relative error of 30%) determine the error boundaries in the simulation, indicated by the dashed lines. The layer thickness profile was measured after curing the material. A fair agreement is obtained, taking into account the relatively large sensitivity of this specific case to variation in the input parameters of the simulation.
Figures 3 and 4 show the transition from convection-dominated drying (N_D<<1) towards diffusion-dominated drying (N_D>>1), occurring in both the model (for N_H=0.3, N_c=0.3, λ_0=0.4) and the experiments. The model shows that the variation of N_H (0.26<N_H<0.56)) and N_c (0.18<N_c<0.34) in these experiments had a relatively small effect.

CONCLUSIONS

The model and scaling show agreement with experiments using droplets of suspensions of colloidal silver particles. The number of input parameters in the model was kept to a minimum, still describing the relevant physical phenomena for a wide range of solutions. The approximate model and scaling laws provide useful quantitative insight into the drying process of ink-jet printed structures, which can be used in manufacturing of printable inorganic conductors.

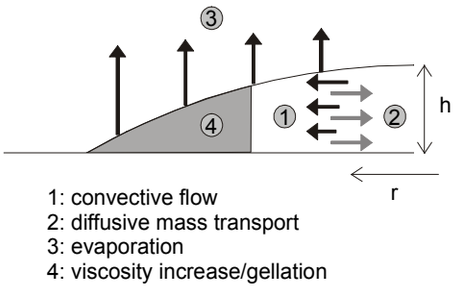


Figure 1. Schematic representation of the model situation.

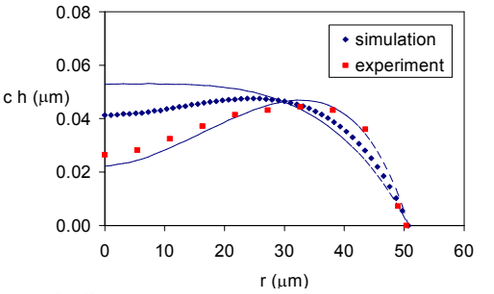


Figure 2. Comparison of experiment and simulation.

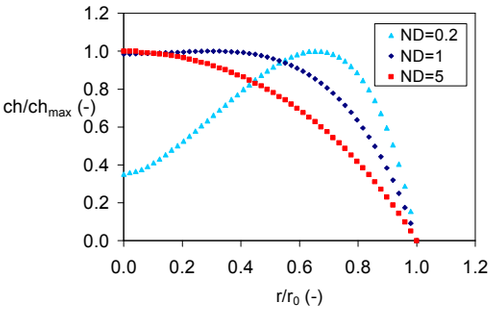


Figure 3. Effect of N_D on dried layer thickness profile.

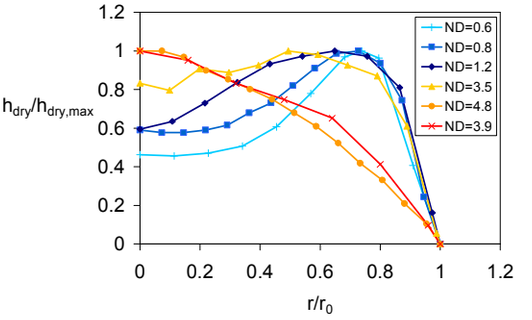


Figure 4. Varied N_D and normalised dry layer thickness.

References

[1] Cuk T., Trojan S.M., Hong C.M., Wagner S.: Using convective flow splitting for the direct printing of fine copper lines, *Applied Physics Letters* **77** (13), 2063, 2000.

[2] Deegan R.D.: Contact line deposits in an evaporating drop, *Physical Review E* **62**(1) 756-765, 2000.

[3] Furusawa M., Hashimoto T., Ishida M., Shimoda T., Hasei H., Hirai T., Kiguchi H., Aruga H., Oda M., Saito N., Iwashige H., Abe N., Fukuta S., Betsui K.: Inkjet-Printed Bus and Address Electrodes for Plasma Display, *SID* 2002.

[4] Parisse F., Allain C.: Drying of Colloidal Suspension Droplets: Experimental Study and Profile Renormalisation, *Langmuir* **13**(14) 3598-3602, 1997.

XXI ICTAM, 15–21 August 2004, Warsaw, Poland

AMPLIFICATION OF NONLINEAR DISTURBANCES ON A FALLING LIQUID SHEET

Takao Yoshinaga, Kentaro Kan
Department of Mechanical Science, Faculty of Engineering Science
Osaka University, Toyonaka, Osaka 560-8531, Japan

Summary We analytically examine behavior of a liquid sheet falling under the action of gravity when liquid viscosity and inertia of surrounding fluids are ignored. Analysis is made based on a set of nonlinear equations for the sheet derived in the gravitational field under the membrane approximation. We numerically find a particular boundary condition for the steady flow whose velocity increases and thickness decreases monotonically as it goes downstream. Weakly nonlinear analysis for unsteady modulational waves shows that only antisymmetric mode of disturbances propagating downstream is amplified and otherwise decayed. Numerical analysis shows that the symmetric mode is locally induced on the antisymmetric mode and it is expected that this induced mode leads to the breakup of the sheet.

INTRODUCTION

Investigations of a liquid sheet are of great importance in scientific and technological applications. In particular, distortion and disintegration of a falling liquid sheet under the action of gravity are important in related problems to the coating technology and it is evident that nonlinearity plays an important role in such behavior of the sheet. As is well known, there can exist two different modes of disturbances on a planar sheet, that is, the antisymmetric (or sinuous) and symmetric (or bulge) modes, and both modes are linearly stable if inertia of surrounding fluids is neglected. On the other hand, for the sheet falling in the gravitational field, it is shown that the antisymmetric mode of infinitesimal disturbances propagating upstream is amplified due to the viscosity. Since the viscosity does not affect on the antisymmetric mode for such a thin sheet, however, this amplification disappears when the sheet thickness becomes thin. In this paper, we show that another amplification is possible if modulational waves are considered on the falling sheet even if the sheet thickness is sufficiently thin. In addition to this, we also show that the nonlinear behavior of the amplified disturbances leads to the breakup of the sheet.

SHEET EQUATIONS AND STEADY SOLUTIONS

We consider a falling liquid sheet in the (x, y) coordinate system as shown in Fig.1, where g denotes the gravitational acceleration, (u, v) the velocity components and p the excess pressure. In addition, the half thickness a and the sheet center plane η are given as $a = (h_+ - h_-)/2$ and $\eta = (h_+ + h_-)/2$ when the sheet boundaries are specified by $y = h_\pm(x, t)$. All dependent variables in the above are normalized by the thickness A_0 and the velocity U_0 at the reference point $x = 0$. According to the membrane approximation where the sheet thickness is so thin that internal structure of the sheet can be ignored, the original full nonlinear two-dimensional equations can be reduced to the following one-dimensional equations:

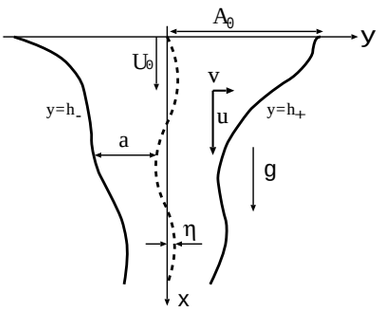


Fig.1 Schematic of a falling liquid sheet.

$$a_t = -(au)_x, \quad \eta_t = v - u\eta_x, \quad v_t = -uv_x - \Delta P/(2a\,\mathrm{We}),$$
$$u_t = -uu_x - [P_x - (\Delta P/2a)\eta_x]/\,\mathrm{We} + 1/(2\,\mathrm{Fr}^2), \qquad (1)$$

where u, v and p are functions of x and t under the approximation, and Fr and We, respectively, denote the Frude number and the Weber number. In the above representations, the mean pressure $P = (P_+ + P_-)/2$ and the pressure difference $\Delta P = P_+ - P_-$ are introduced in terms of $P_\pm = \mp(\eta_{xx} \pm a_{xx})[1 + (\eta_x \pm a_x)^2]^{-3/2}$ on the sheet surfaces $y = h_\pm$. For the steady state, we can assume that only symmetric mode can exist, and so that $\eta = v = 0$ and $\Delta P = 0$ in eqs.(1). Thus, we obtain the following set of equations with respect to $\overline{u}(x)$ and $\overline{a}(x)$ for the steady state:

$$\overline{au} = 1, \quad \overline{a}^{-3}\overline{a}_x + [\overline{a}_{xx}(1 + \overline{a}_x^2)^{-3/2}]_x/\,\mathrm{We} + 1/(2\,\mathrm{Fr}^2) = 0. \qquad (2)$$

The solutions of eqs.(2) are approximately obtained to be $\overline{a} = (x/\,\mathrm{Fr}^2 + 1)^{-1/2}$ for sufficiently large We , while $\overline{a} = (1 + x/\,\mathrm{Fr}^2)^{-1/2} - 3(4\,\mathrm{We}\,\mathrm{Fr}^4)^{-1}[(x/\,\mathrm{Fr}^2 + 1)^{-4} - (x/\,\mathrm{Fr}^2 + 1)^{-3/2}]$ for sufficiently large Fr. On the other hand, eqs.(2) can be numerically integrated for boundary values of $\overline{a}_x$ and $\overline{a}_{xx}$ when $\overline{a}$ is given. We note, however, that these values for the solutions representing the steady flow, whose velocity increases and width decreases monotonically as it goes downstream, should be particularly given for individual values of We and Fr. For example, $\overline{a}_x(0) = -0.049821\cdots$ and $\overline{a}_{xx}(0) = 0.007387\cdots$ when We=10, Fr=$\sqrt{10}$ and $\overline{a}(0) = 1$.

MODULATIONAL INSTABILITY

In order to see unsteady behavior of disturbances on the falling sheet, we assume that rapidly oscillating unsteady disturbances are superposed on the gradually varying steady flow and such solutions can be written as:

$$a = \overline{a}(x_2) + \tilde{a}(x_0, x_1, x_2, \cdots, t_0, t_1, t_2 \cdots), \qquad \eta = \tilde{\eta}(x_0, x_1, x_2, \cdots, t_0, t_1, t_2 \cdots),$$
$$u = \bar{u}(x_2) + \tilde{u}(x_0, x_1, x_2, \cdots, t_0, t_1, t_2 \cdots), \qquad v = \tilde{v}(x_0, x_1, x_2, \cdots, t_0, t_1, t_2 \cdots), \tag{3}$$

where the multiple scales $x_j = \epsilon^j x$ and $t_j = \epsilon^j t$ ($j = 0, 1, 2, \cdots$) are introduced in terms of a small parameter ϵ, in order to differentiate between the phenomena with shorter scales and longer scales. For the steady flow, we choose the approximate solution $\bar{a}(x_2) = (x_2/\,\mathrm{Fr}_0^2 + 1)^{-1/2}$ with longer scale x_2 when $\mathrm{Fr} = \epsilon^{-1}\,\mathrm{Fr}_0$ and $\mathrm{We} \gg 1$, while we set the unsteady disturbance to be:

$$\tilde{a} = \Sigma_{n=1}\epsilon^n A_n(\theta, x_1, x_2, \cdots, t_1, t_2, \cdots) + C.C., \quad \tilde{\eta} = \Sigma_{n=1}\epsilon^n E_n(\theta, x_1, x_2, \cdots, t_1, t_2, \cdots) + C.C., \quad \cdots \tag{4}$$

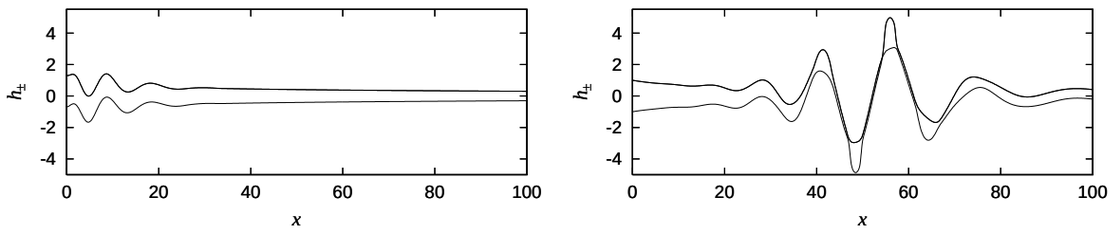
where A_n and E_n are complex amplitudes and $C.C.$ denotes complex conjugate, while we have assumed that the wave number k and angular frequency ω in the rapidly oscillating phase $\theta = kx_0 - \omega t_0$ are functions of x_2 corresponding to $\bar{u}$ and $\bar{a}$. Making use of the derivative expansions $\partial/\partial x = k\partial/\partial\theta + \Sigma_{n=1}\epsilon^n \partial/\partial x_n$ and $\partial/\partial t = -\omega\partial/\partial\theta + \Sigma_{n=1}\epsilon^n\partial/\partial t_n$ into eqs.(1), from the non-secular condition we finally obtain the following amplitude equations for the symmetric and antisymmetric modes, respectively:

$$\mathrm{i}(A_{1t_2} + V_g A_{1x_2}) + P_s A_{1x_1x_1} = Q_s A_1 |A_1|^2 + \mathrm{i}\, T_s A_1, \quad \mathrm{i}(E_{1t_2} + V_g E_{1x_2}) = Q_a E_1 |E_1|^2 + \mathrm{i}\, T_a E_1, \tag{5}$$

where both A_1 and E_1 are including the phase shift and V_g denotes the group velocity. It is found that $T_a > 0$ for the antisymmetric mode of the modulational waves with $V_g > 0$, which means that the disturbances are amplified for the antisymmetric mode propagating to the positive direction of x or downstream.

NUMERICAL RESULTS

In order to confirm above results in the weakly nonlinear analysis and see the effects of larger nonlinearity, we make numerical analysis of eqs.(1) based on the steady solutions which is numerically obtained from eqs.(2). It is then found from Fig.2 for We=100 and Fr=$\sqrt{10}$ that the antisymmetric mode is amplified as the disturbances propagate downstream. It is also found from Fig.2(b) that the symmetric mode is locally induced at every half wave length in the antisymmetric mode and, as a result of this, it is expected that the sheet is disintegrated at the bottlenecks in this induced mode.



(a) $t = 20$ (b) $t = 50$

Fig.2 Propagations of the antisymmetric mode when We=100 and Fr=$\sqrt{10}$.

CONCLUSIONS

Resulting from the weakly nonlinear analysis and numerical analysis based on the sheet equations, we find that the antisymmetric mode of the disturbances propagating downstream is amplified. It is expected that the sheet is disintegrated due to the induced symmetric mode from the amplified antisymmetric mode.

References

[1] Lin,S.P.: Stability of a viscous liquid curtain. J.Fluid Mech.**104**:111–113, 1981.
[2] Mehring, C., Sirignano, W.A.:Nonlinear capillary wave distortion and disintegration of thin planar liquid sheet. J.Fluid Mech.**388**:69–113, 1999.
[3] Yoshinaga, T., Kotani, T.: Modified membrane approximation on a thin liquid sheet.J.Phys.Soc.Jpn. **70**: 372–375, 2001.

THIN FILM FLOWS NEAR ISOLATED HUMPS AND INTERIOR CORNERS

Gregory P. Chini,* Oliver E. Jensen** and John R. King**
* *Mechanical Engineering Department, University of New Hampshire, USA*
** *School of Mathematical Sciences, Nottingham University, Nottingham, UK*

INTRODUCTION

We examine the surface-tension-driven readjustment of a viscous liquid film following a sudden change in the shape of adjacent solid surfaces. Such situations arise widely in industrial contexts, e.g. when geometrical imperfections create defects in coatings. Important physiological applications arise in the lung, when the liquid lining of an airway redistributes following impact of an inhaled particle or contact between the wet walls of a collapsing airway. Here, an initially flat solid substrate is assumed to deform into an *isolated* hump or interior corner. For sufficiently tall humps and sharp corners, a quasi-static puddle connects to a spatially unbounded thin film; the capillary pressure in the film is greater than that in the puddle, causing it to grow. We employ numerical simulations and asymptotic analysis to characterise the induced flows. We then show that flows off humps with maxima less than a critical height have a qualitatively different structure.

MATHEMATICAL MODELS

We model the flow of a two-dimensional incompressible Newtonian fluid of constant viscosity μ bounded above by a passive gas and below by a rigid, possibly curved, stationary substrate. The surface tension σ acting at the free surface is assumed uniform and van der Waals forces are neglected. When gradients in substrate curvature vary over distances large compared to the fluid depth, the standard thin-film equation can be extended in an asymptotically consistent fashion (Schwartz & Weidner 1995), yielding

$$h_t \; + \; \tfrac{1}{3}\left[h^3(h+g)_{xxx}\right]_x \quad = \quad 0, \tag{1}$$

where the substrate and free-surface locations lie at $y = g(x)$ and $y = g(x)+h(x,t)$, respectively, in Cartesian (x, y)-coordinates, and t is time. We employ (1) to model capillary-driven flow off of a Gaussian-shaped hump, $g(x) = g_0 \exp[-(x/2d)^2]$, starting from the uniform initial condition $h(x, 0) = 1$. We examine solutions of (1) on a finite domain $0 \le x \le L$ but select $L \gg 1$ so that the film remains undisturbed near $x = L$. To model flows near an interior corner, where the substrate curvature is singular, we employ an alternative formulation: namely, Heil & White's (2002) modified thin-film equation,

$$\rho_t \; + \; \tfrac{1}{3}\left[h^3 k_s\right]_s \quad = \quad 0, \tag{2}$$

coupled to a parameterisation of the film thickness using spines. s measures distance along the flat substrate from the corner, while h measures the height of the film along certain prescribed directions (spines). The spine angle distribution, $\beta(s)$, is chosen so that the spines do not intersect within the fluid interior and are normal to the substrate where the film is thin. The film density $\rho(s,t) = h\cos\beta + \mathrm{d}\beta/\mathrm{d}s\, h^2/2$ then insures exact mass conservation. By employing the exact curvature of the free surface $k(s,t) = (y_{ss}x_s - x_{ss}y_s)/(x_s^2 + y_s^2)^{3/2}$, (2) enforces the exact Young–Laplace constraint in regions where the film is deep and quasi-steady. In regions where the film is thin, (2) reduces to the standard thin-film equation. Thus, the unsteady dynamics of thin-film regions and, hence, the fluid flux into (or out of) the corner puddle are accurately predicted.

RESULTS

In conjunction with symmetry and no-flux boundary conditions, (1) and (2) were discretised in space using 2nd-order accurate finite differences and advanced in time using an adaptive-step backward-differencing scheme. Most computations were carried out for $O(10^7)$ time units using $O(10^4)$ grid points. Large-hump simulations (e.g. $g_0 = 10$) were conducted with $L = 500$, while small-hump simulations (e.g. $g_0 = 2.8$) were conducted with $L = 5000$. For $d = 0.5$, a nonuniform grid was needed to provide adequate spatial resolution. An equispaced s-grid, however, was found to be adequate for corner simulations with $L = 30$, an initial puddle height (at $s = 0$) of 1.5, an initial far-field film thickness of 0.06 and an interior semi-angle of $\pi/5$. Raw numerical results for both the large-hump and corner simulations are shown in figure 1 [(a),(b)–free-surface locations; (c),(d)–pressure distributions]. Broadly similar behaviour is observed: following a transient phase (not depicted), the film pinches off, separating a quasi-static puddle from a propagating capillary

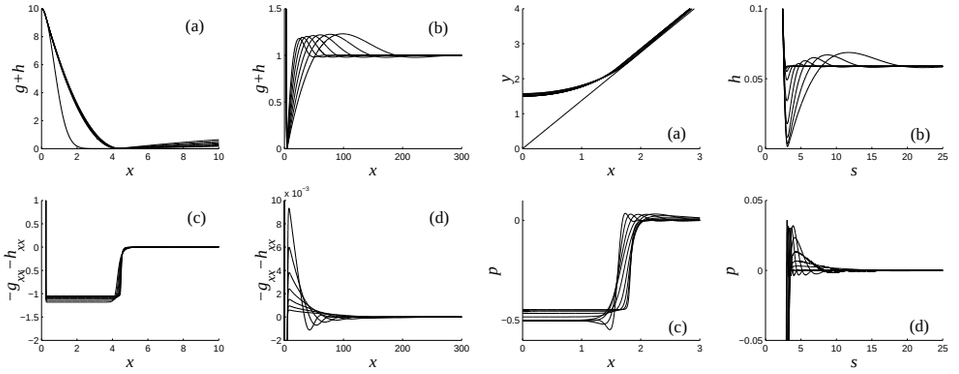


FIGURE 1. Raw simulation data for hump (left subplots) and corner (right subplots).

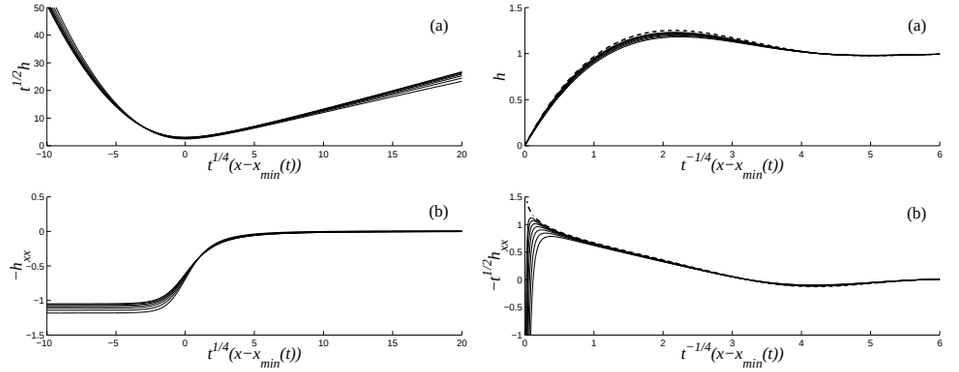


FIGURE 2. Scaled hump film height (upper) and pressure (lower) in regions II (left) and III (right).

wave. Large-time asymptotic analysis reveals that the slowly growing quasi-static puddle (region I) satisfies $h+g \sim \kappa(x-x_0^2)/2$, where κ and, hence, the volume V_I can be related to $g(x)$ and the effective contact line location $x_0(t)$ [$\approx x_{min}(t)$ in figure 2] via matching conditions. The right subplots in figure 2 indicate that the propagating wave (region III) can be captured by seeking a solution of the form $h(x,t) \sim F_0(\xi)+t^{-1/4}MF_1(\xi)$, where $x = x_0(t)+t^{1/4}\xi$ and M is a constant. The dashed lines show the leading-order solution $F_0(\xi)$, which satisfies $-\xi F_{0\xi}/4+(F_0^3F_{0\xi\xi\xi})_\xi/3=0$ (Bowen 1998, Aradian et al. 2001), and its negated second derivative. Since F_1 satisfies a linear equation, we have imposed the normalisation condition $\int_0^\infty F_1 \mathrm{d}\xi \equiv 1$. Region II is a quasi-steady draining region that acts as a valve – note the shock-like pressure distributions in figures 1c. In accord with the left subplots in figure 2 (and following Jones & Wilson 1978), we set $h \sim t^{-1/2}H(\eta)$, $x = x_0(t)+t^{-1/4}\eta$ and obtain $H^3H_{\eta\eta\eta} = -Q$ for some constant flux $Q>0$. Matching H with region I and H_η with region III determines Q in terms of $\kappa(x_0)$. Since $h(x,0)=1$ for $0<x<L$, the total fluid volume $V=L$ for all time. For large t, $V \sim V_I+V_{III}$. Using the equation governing F_0, the leading-order contribution to V_{III} is found to be $L-x_0$. Notably, an $O(1)$ fixed-mass contribution M arises from the F_1 correction, which, although $O(t^{-1/4})$, is spread over an $O(t^{1/4})$ distance. Thus, the volume condition becomes: $x_0 \sim V_I(x_0)+M$, where M – the mass of fluid trapped in (or lost from) region III – is determined by the transient dynamics over intermediate time scales. Following pinch-off, the puddle in region I grows very slowly: x_0 advances according to $V_I'(x_0)x_{0t} \sim Qt^{-5/4}/3$, i.e. $x_{0t} = O(t^{-5/4})$. Finally, simulations for small humps reveal a qualitatively different structure, with a propagating capillary wave attaching *directly* to the top of the hump. To describe this case, we expand $h(x,t)$ as in region III except that $x = t^{1/4}\xi$. We find two solution branches for $1<g_0<g_c$ and no solutions for $g>g_c$, where the critical hump height $g_c \approx 3.36$. Our small-hump numerical simulations converge to the branch of similarity solutions having smaller (negative) slope at the origin. For a given g_0, $M(g_0) = -\int_0^\infty (F_0-1)\mathrm{d}\xi$; i.e. since pinch-off does *not* occur for these small-hump solutions, $M(g_0)$ can be predicted.

GRAVITY- AND SHEAR-DRIVEN THIN FILMS FLOW ON HEATED MICROSTRUCTURED WALLS

Tatiana Gambaryan-Roisman, Alexander Alexeev, Peter Stephan
Darmstadt University of Technology, Chair of Technical Thermodynamics, Petersenstr. 30, 64287 Darmstadt, Germany

Summary A model describing the behaviour of the gravity- and shear-driven liquid films on heated microstructured walls is developed. The hydrodynamic stability of the film flow is investigated using the long-wave theory. It is shown that the longitudinal grooves stabilize the film flow both when the wall is completely or only partially covered by the film. The influence of the thermocapillarity on the film shape and velocity field has been analyzed in the framework of the long-wave theory and numerically using the volume of fluid method.

INTRODUCTION

Thin falling films and shear-driven films are used for cooling of electronic devices and other components, for powders production and for other technological processes. Using microstructured wall surfaces improves the performance of the device and prevents the film dryout. Smooth films flowing down vertical walls are hydrodynamically unstable. The small disturbances are developed into waves, which in many cases possess a three-dimensional structure. Normally, the pure shear-driven flows with linear velocity profile are stable to long-wave disturbances. However, when the gravity- and shear-driven flows are superimposed, the long-wave film instability may appear, leading to development of waves showing a very complicated behaviour [1]. The film waviness drastically changes the heat and mass transfer characteristics of the film. The effect of thermocapillarity (surface tension dependence on temperature) is in many cases a primary reason for the film rupture.
The wall topography may cause the film deformation [2]. It has been shown [3] that, if the wall is completely covered with the liquid, the longitudinal grooves stabilize the isothermal falling film flow.
This work is aimed at investigation of the combined effect of the gravity and the shear stress on long-wave stability of thin liquid films on grooved walls. Another goal of this work is to qualify the effect of the wall structure on the flow induced by thermocapillarity.

FILM STABILITY ANALYSIS

We consider a film flowing down an inclined grooved plate. The grooves axes are oriented in parallel with the gravity-induced flow. The shear stress due to a gas flow over the film acts in the same or opposite direction. The wall temperature is constant and above the gas temperature. The liquid is assumed to be nonvolatile. We assume that the characteristic film thickness h^* is much smaller than the characteristic length of the thickness variation, and the same is applicable to the variation of the wall topography. We also assume that the Reynolds number of the flow is moderate. Under the above assumptions the film dynamics can be described in the framework of the long-wave theory [4]. The film flows under the influence of the gravity, constant shear stress and the surface tension (including the thermocapillarity). We neglect the effect of the film wavyness on the gas pressure and the shear stress.
To perform the film stability analysis, we first determine the shape of an unperturbed film. Then simple harmonic disturbances with small amplitude are applied to this basic state. This disturbed solution is substituted into the evolution equation, which is linearized. The resulting eigenvalue problem is solved to determine the disturbance growth rate and the wave speed depending on the wave number.

SIMULATION OF FILM DYNAMICS

Since the validity conditions of the long-wave theory are rather restrictive, the CFD simulation methods are required. We develop a numerical model for the solution of two-dimensional flow of a liquid film characterized by the gas-liquid interface over a structured wall. The incompressible Navier-Stokes equations are solved for the liquid and gaseous phases, while the free surface is modeled with the Volume of Fluid (VOF) technique. The energy equation is also included into the numerical model allowing calculations of temperature distributions within the film. We use the numerical model to investigate flow of a liquid on a structured wall, when it is caused by a temperature drop between the wall and the ambient gas. This calculation is the first step toward the modeling of a three-dimensional flow of a falling film on a wall with longitudinal grooves.

RESULTS

We have quantified the combined effect of the gravity, the interface shear stress and the groove geometry on the stability characteristics of a film fully covering a wall surface. We have found that in this case, as in the case of falling

films, the grooves have a stabilizing effect on the film flow. The co-current shear stress destabilizes the film, and the counter-current shear stress stabilizes it.
The stability characteristics of the flow with a contact line is illustrated in an example of a flow down a vertical wall in a rectangular groove with a contact angle equal to $\pi/2$. This angle is assumed to be between the receding and the advancing contact angles, so that the contact line is immobile. Figure 1 shows the dependence of the disturbance growth rate, ω, on the wave number, k, values of the groove width, d. The disturbance growth rate on the grooved wall is smaller than that on the smooth wall, which points out at the stabilizing effect of the grooves. Moreover, starting from some value of h^*/d, the film becomes stable for any small disturbance. This behaviour is qualitatively different from that of the thin films on smooth walls.
If the temperature of the wall is higher than that of the gas, the wall structure causes the temperature gradients on the liquid-gas interface. As a result, a thermocapillary flow develops even in the undisturbed state. The interface deforms in such a way, that the liquid tends to accumulate inside the groove. We have shown that, if the grooves are deep enough, dry patches may appear even at moderate temperature drops. But, unlike the case of smooth wall, the location of these dry patches is well defined and corresponds to the grooves crests. The appearance of these dry patches may even improve the heat transfer characteristics [3].
Figure 2 illustrates the thermocapillarity-induced velocity field in a single groove with a depth of 0.5 mm. The calculations have been performed using the VOF method. The temperature drop between the wall and the gas is 10 K. The deformations of the liquid-gas interface are small. The maximal liquid velocity at the interface reaches 1.6 mm/s. The main feature of the velocity field is a vortex in the counter-clockwise direction. This vortex provides an additional mixing of the liquid and may increase the heat transfer rate.

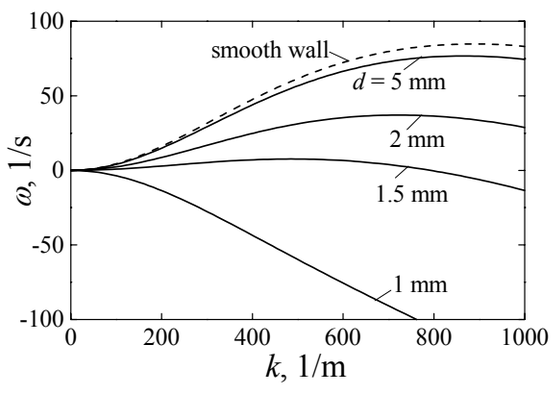


Figure 1. Disturbance growth rate for a film on vertical wall with rectangular grooves. Water, h^*=200 μm, shear stress 1 N/m^2.

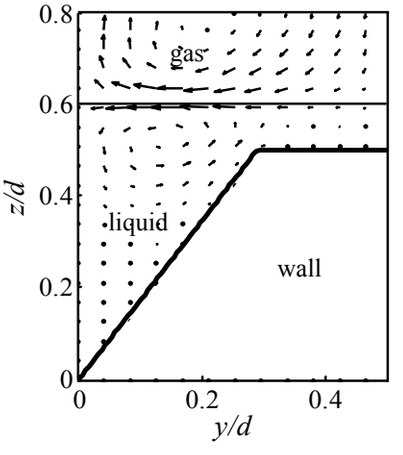


Figure 2. Thermocapillarity-induced velocity field in a film on a grooved wall.

CONCLUSIONS

The foundations for modelling the wavy motion of the gravity- and shear-driven liquid films on structured heated walls have been established. It has been shown that in the case when the wall is completely covered by the liquid the longitudinal grooves have a stabilizing effect on the film flow. The stabilization tendency is also predicted for the cases where the grooves are partly covered by the liquid, and the contact angle is finite.
The thermocapillarity-induced velocity field and liquid-gas interface deformations on the microgrooved wall have been studied in the framework of the long-wave theory and numerically using the VOF method. The thetmocapillary flow pattern is determined by the wall microstructure.

References

[1] Alekseenko S.V., Nakoryakov V.E.: Instability of a liquid film moving under the effect of gravity and gas flow. *Int. J. Heat Mass Transfer* **38**[11]: 2127-2134, 1995.

[2] Pozrikidis C., and Thoroddsen S.T.: The deformation of a liquid film flowing down an inclined plane wall over a small particle arrested on the wall. *Physics of Fluids A* **3**[11]:2546-2558, 1991.

[3] Gambaryan-Roisman T., Stephan P.: Analysis of falling film evaporation on grooved surfaces. *J. Enhanced Heat Transfer* **10**:369-381, 2003.

[4] Oron A., Davis S.H., Bankoff S.G.: Long-scale evolution of thin liquid films. *Rev. Mod. Phys.* **69**[3]:931-980, 1997.

HYDRODYNAMICS OF THE SOLITARY WAVES TRAVELLING DOWN A LIQUID FILM

Jaroslav Tihon
Institute of Chemical Process Fundamentals, AS CR, Rozvojova 135, 16502 Prague, Czech Republic

Summary The regular solitary waves on the surface of a liquid film flowing down an inclined stationary plate were excited by means of the flow rate pulsations. The results of experimental investigations (electrodiffusion flow diagnostics, film thickness measurements, near-wall flow visualization) provided the basic characteristics of surface waves and confirmed the existence of a small backflow region located just in front of the solitary waves.

INTRODUCTION

The wavy film flow down an inclined plane is a typical representative of convective instabilities. The spatio-temporal evolution of waves on the film surface is a complex process and the different kinds of waves can be observed. Small-amplitude waves appearing at the wave inception grow rapidly and develop downstream into the large nonlinear patterns of finite-amplitude, solitary or three-dimensional waves [1]. The large solitary waves are separated by wide regions of the thin liquid film and have the typical shape characterised by a steep front and a gradual tail. Small capillary waves are usually pushed in front of these solitary waves. This region is not easy accessible for the experimental investigation, because rapid flow changes observed there take place inside the thin liquid film. The recent numerical simulation of the wavy film flow [2] has suggested that there is possibly a small backflow region in front of the large solitary waves. It has been a challenge for us to confirm or reject such a surprising finding by the relevant experiments. The electrodiffusion technique [3] using probes flush mounted into a wall has been used to measure local values of the wall shear rate.

DESCRIPTION OF THE EXPERIMENTS

The experimental investigation of the wavy film flow was carried out in an experimental set-up shown in Fig.1. The liquid film was flowing down a long stationary plate (2 m in length and 0.22 m in width). The slope of this stainless steel plate could be changed from the vertical to the horizontal position. A piston mounted into the air chamber produced periodical pulsations of the flow rate with a small amplitude (up to 10% of the mean flow rate) and low frequency (from 0.5 to 2.5 Hz). These low-frequency pulsations excited the regular solitary waves on the liquid film surface. The two-strip electrodiffusion probe was mounted into the wall to detect the wall shear rate under large solitary waves. The capacitance probe, installed at the same distance from the liquid distributor as the electrodiffusion one (x=1.5m), measured simultaneously the instantaneous film thickness. With the aim to measure the wave velocity, two capacitance sensors aligned 20 mm apart in the flow direction were used. The measurements were carried out with water and aqueous solutions of glycerine and Emkarox as the model liquids.

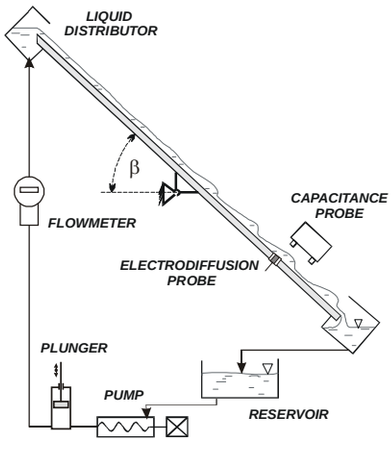


Fig.1 Experimental set-up

To perform the flow visualization the experimental set-up presented in Fig.1 was prolonged with a glass plate. The small glass spheres with a mean diameter of 20 μm were added into the liquid as tracing particles. The high speed camera Kodak Motion Corder SR provided by the telecentric measuring objective Vicotar T10/9.7L was fixed at the working distance about 0.5 m beneath the glass plate. As this microscopic objective (tenfold magnification) was focused on a sign marked on the glass plate, only the particles moving in the near-wall region were seen with sharp contours (depth of the field about 50 μm). The movement of these particles inside the field of view (180 x 190 μm) was recorded with the rate 1000 frames/s. The particle tracking technique was used to analyse changes in the near-wall velocity and to detect the flow reversal.

RESULTS AND DISCUSSION

The typical time courses of the film thickness and the wall shear rate obtained for the solitary wave regime are shown in Fig.2. This regime of regular waves was excited by low-frequency pulsations (f_p=1.8 Hz) of the entrance flow rate. The presented signals, which were simultaneously recorded by the capacitance and electrodiffusion probe, are normalised by their time-average values. The maximum film thickness observed at the wave crests is almost two times higher than the mean film thickness and the peak-to-peak distance between solitary waves is quite long (λ_s=152 mm). The short capillary waves (having λ_c~5 mm and f~53 Hz) are not so clearly seen on the film surface profile, because the signal from the capacitance probe underestimates their amplitudes. This is caused by the averaging effect of the cylindrical probe having the diameter of 3 mm. The wall shear rate profile, obtained after considering the dynamic response of the electrodiffusion probe [4], exhibits the same characteristic features as that obtained from the numerical simulation [2]. Strong fluctuations of the wall shear rate are apparent in the region of capillary waves. Then steep increasing of the wall shear rate is observed with the maximum value located just in front of the large wave crest. It is followed by a rapid

decrease of the wall shear rate just under the wave crest. Finally, gradual relaxation of the wall shear rate takes place in the wave trail region. The most interesting feature is the existence of two small backflow regions characterised by negative values of the wall shear rate. The flow in front of the solitary wave is highly unsteady and that is why the observed near-wall flow reversal takes only several milliseconds.

The movement of the tracing particles in the near-wall region was recorded at the same film flow conditions. The video movie revealed strong pulsations of the near-wall flow velocity in the region of capillary waves. The time sequence of the pictures recorded just before the passage of the solitary wave front is shown in Fig.3. The time changes in particle positions clearly identify their short-time back movement.

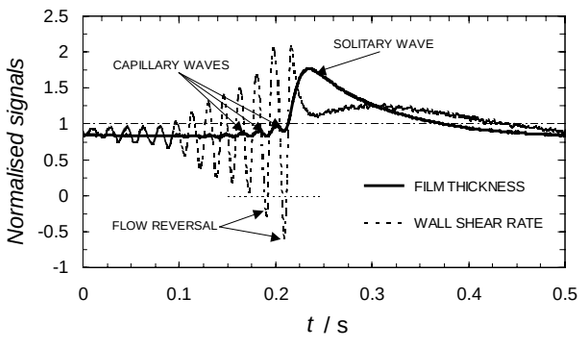


Fig.2 Film thickness and wall shear rate typical for the solitary wave regime (water data measured at f_P=1.8 Hz, Re=91, β=6.5º, x=1.5 m, h=0.63 mm, s=635 s^{-1}, c=0.28 m/s).

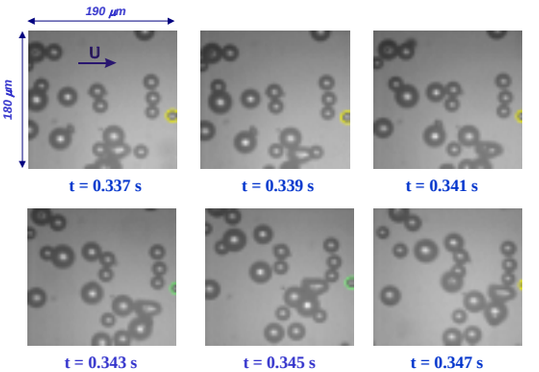


Fig.3 Visualization of the flow in the near-wall region just in front of the solitary wave.

The subsequent measurements carried out with the different model liquids covered the ranges of Re from 10 to 120 and the inclination angle β from 3º to 30º. Their results indicate that the solitary wave regime of the liquid film flow is very sensitive to the excitation conditions. It was found that:

The amplitude of solitary waves, their phase velocity and also peak-to-peak distance as well as the frequency of capillary waves is increased with the Reynolds number and decreased with the excitation frequency. The characteristics of capillary waves are especially sensitive to the operation conditions; e.g. if the excitation frequency is kept constant (f_P=1.2 Hz) and the Reynolds number is increased from 17 to 57, the frequency and wavelength of capillary waves change from 12 Hz and 14 mm to 110 Hz and 3.6 mm, respectively (data for Emkarox 5%: μ=3.9 mPa.s and the plate inclination β=5º).

The proportional relationships between the velocity and amplitude of the solitary waves, which was experimentally confirmed by Alekseenko et al. [1] for vertical films, holds also for the solitary waves appearing on the liquid film flowing down an inclined plate.

The solitary waves are travelling down a thin film substrate. Its thickness changes with the liquid viscosity and the plate inclination, but it is practically independent on the Reynolds number and the wave excitation conditions.

CONCLUSIONS

- The existence of a small backflow region located just in front of the solitary waves was detected by the electrodiffusion measurements of the wall shear rate and then confirmed by the near-wall flow visualization.
- The high-speed camera together with macroscopic objectives proved to be a good tool for near-wall flow visualization.
- The near-wall flow character in the region of capillary waves was found to be very sensitive to the wave excitation conditions, especially the excitation frequency.
- The linear dependence between the solitary wave velocity and amplitude was confirmed also for the wavy film flow along an inclined plane.

Acknowledgement
This work was supported by the Grant Agency of the Czech Republic under the grant No. 101/04/0745.

References

[1] Alekseenko S.V., Nakoryakov V.E., and Pokusaev B.G.: Wave flow of liquid films. Begell House, New York, 1994.

[2] Malamataris N.A., Vlachogiannis M., and Bontozoglou V.: Solitary waves on inclined films: Flow structure and binary interactions. *Phys.Fluids* **14**: 1082-1094, 2002.

[3] Hanratty T.J. and Campbell J.A.: Measurement of wall shear stress, in 'Fluid mechanics measurements' (edited by J.R. Goldstein), Washington, Hemisphere, 1983.

[4] Tihon J., Tovčigrečko V., Sobolík V., and Wein O.: Electrodiffusion detection of the near-wall flow reversal in liquid films at the regime of solitary waves. J.Appl.Electrochem. **33**: 577-587, 2003.

TRANSIENT DISPLACEMENT OF VISCOELASTIC LIQUIDS BY AIR

Yannis Dimakopoulos, John Tsamopoulos
Laboratory of Computational Fluid Dynamics, Department of Chemical Engineering, University of Patras, Greece 26500

Summary We examine the transient displacement by air of viscoelastic liquids, which occupy axisymmetric tubes either completely or partially, as it arises in the Gas-Assisted Injection Molding (GAIM) Process. For the simulations we combine our recently advanced quasi-elliptic grid generation scheme for computing the highly deforming liquid boundaries, the mixed finite element technique and the Discontinuous Galerkin method for computing the viscoelastic stresses. In our parametric study we examine the effects of the elastic and inertia forces, and the solvent to polymer viscosity ratio. Results using the PTT and Giesekus constitutive models show that the thickness of the remaining film increases as the Deborah number increases and remaining fluid fractions greater than 0.60 (the Newtonian limit) arise, in agreement with experiments. Increasing the viscosity ratio decreases the effects of elasticity. Similar is the effect of the Reynolds number which may also result in variable film thickness and a tip splitting instability.

INTRODUCTION

The displacement of a fluid by a gaseous phase is a problem of fundamental and practical importance. There are many engineering applications and physical operations such as the enhanced oil recovery, the pulmonary airway reopening, and the Gas-Assisted Injection Molding, which are based on the displacement of a liquid from a conduit. Apart from its more recent technological importance, the steady displacement of liquids in circular or non circular geometries has attracted the interest of many researchers for a long time and for various basic scientific reasons [1-3]. Quite recently, Dimakopoulos & Tsamopoulos [4-6] initiated a systematic effort in order to examine the transient gas-penetration phenomenon inside straight and suddenly constricted tubes, which are completely filled with a liquid. They examined both Newtonian and viscoplastic materials for a wide range of the dimensionless parameters.
The purpose of this study is to take into consideration the effect of viscoelasticity on the transient displacement process. To this end, we use simple but realistic constitutive equations such as the PTT [7] and Giesekus [8] models, which also allow us to also make simple physical interpretations.

PHYSICAL MODEL

The flow geometry is a cylindrical tube completely or partially filled with a liquid, while in the latter case the rest of the tube towards its right end is occupied by air. The liquid is incompressible and viscoelastic of total dynamic viscosity μ, density ρ and relaxation time λ and sticks to the tube wall, forming a three phase contact line at the left tube entrance. At start up, the air pressure on the left tube entrance is increased abruptly to $\overline{P}_{ext}$ and displacing of the liquid is initiated. The radius and the length of the tube are denoted by *a* and *b*, respectively. Scaling lengths with *a*, pressure with the applied air pressure, $\overline{P}_{ext}$, velocities with $a^2\overline{P}_{ext}/(\mu b)$, the following dimensionless groups arise: the Reynolds number, $Re_p = \rho a^3 \overline{P}_{ext}/(b\mu^2)$, the externally applied pressure, $P_{ext} = a^2\overline{P}_{ext}/(b\sigma)$, where σ is the interfacial tension, the Deborah number, $De_p = a\lambda\overline{P}_{ext}/(b\mu)$, and the solvent to total viscosity ratio, $\beta = \mu_s/\mu\ (<1)$. The transient motion of the liquid within the tube is governed by the momentum balance equations and the mass conservation law in their axisymmetric form. To determine the viscoelastic extra stress, we must introduce a constitutive law to the above set of equations. As such we use a differential model of the general dimensionless form:

$$De_p \overset{\lozenge}{\underline{\underline{\tau}}}_p - 2(1-\beta)\underline{\underline{D}} + \underline{\underline{g}}(\underline{\underline{\tau}}_p) = \underline{\underline{0}} \qquad (1)$$

where $\underline{\underline{g}}(\underline{\underline{\tau}}_p)$ is a function of the polymeric stress, which goes to zero as $\underline{\underline{\tau}}_p$ approaches the same value and $\underline{\underline{D}}$ is the rate of strain tensor. Eq. (1) represents a number of well-known constitutive models including the Oldroyd-B, the Phan-Thien & Tanner (PTT) and the Giesekus models. The symbol $\lozenge$ over the elastic stress tensor denotes the Gordon-Schowalter time-derivative. These equations are subject to the usual boundary conditions on the velocity field. In particular, the velocity field is bounded at the centerline, and (a) in a completely occupied tube, open boundary conditions are applied at the outflow surface and at the tube wall the liquid is assumed to stick on it, while (b) in a partially occupied tube, a seconding moving boundary arises downstream and the liquid follows a Navier-type slip condition to accommodate the singularity at the moving contact line. Along any free surface, the velocity field satisfies a local balance between viscous stresses, surface tension and gaseous pressure and is determined by a kinematic condition.

NUMERICAL APPROACH

The governing equations, the momentum and mass balances, the constitutive equations and the two components of the

indispensable for this problem quasi-elliptic transformation ([6]) are converted to a set of Differential Algebraic Equations (DAEs) by invoking Galerkin's principle. The velocity vector, pressure and position vector are approximated by piecewise continuous basis functions, the velocity by biquadratic Lagrangian polynomials, while the coordinates of the mesh nodes and the pressure unknowns by bilinear functions of the local coordinates in an element. Due to its hyperbolic nature, the polymeric part of the stress is approximated using the Discontinuous Galerkin (DG) method ([9]). The set of DAEs are integrated using the backward Euler method, combined with a forward one for the prediction of solution at the new time instance and the adjustment of the time step. The resulting set of equations ($O(10^5)$) is solved by a Newton-Raphson/Non-linear Gauss-Seidel iteration scheme for separately solving the flow from the mesh generation equations until convergence to a specified tolerance of 10^{-9} for the absolute error norm of the residual vector

RESULTS AND DISCUSSION

The figure depicts the penetrating air bubble and contour lines of τ_{pzz} in the displaced Giesekus liquid which initially occupied completely the undulating tube. The snapshot corresponds to time t´=2.114, when the bubble tip has covered a distance equal to six radii and a thick film of liquid has been deposited on the tube wall. The latter seems to follow the shape of the wall with a small phase difference. We note the smoothness and clarity of the results, despite the discontinuous approximation of the stress tensor confirming the high accuracy of our computations. Due to the moderate value of elasticity and the finite value of β, $\tau_{p,zz}$ takes non-zero values around the front of the bubble and downstream in the whole part of the tube. Examining more closely the stress field around the bubble front we distinguish two different regions, one compressive around the bubble tip, where $\tau_{p,zz}$ attains its minimum value, -0.409, and another one extensional, where $\tau_{p,zz}$ attains its locally maximum value, located at the side of the bubble front. Their absolute values decrease both radially and axially away from these two points (except for the expansive region of the tube walls where it attains its absolutely max value). The compressive region arises because the liquid resists the bubble-imposed deformation, while in the extensional region it tries to give again a flat front to the bubble. For penetration smaller than ~5, velocities and stresses are spatially periodic in each cell due to the absence of inertial forces. We have obtained contour plots of the other stress velocity components for an extended range of parameter values. It is noteworthy that with our numerical scheme and as long as $\beta > 0$ we can compute for as high De_p as 5000, although in such cases we cannot simulate complete displacement of the liquid from the tube because of the appearance of steep boundary layers in stress around the bubble front. The thickness of the remaining film is increased up to 5% by increasing De_p over its Newtonian value, due to the normal stresses that arise in viscoelastic liquids, but not as much as in cases reported for non shear thinning (Boger) fluids and is decreased by increasing β or Re_p.

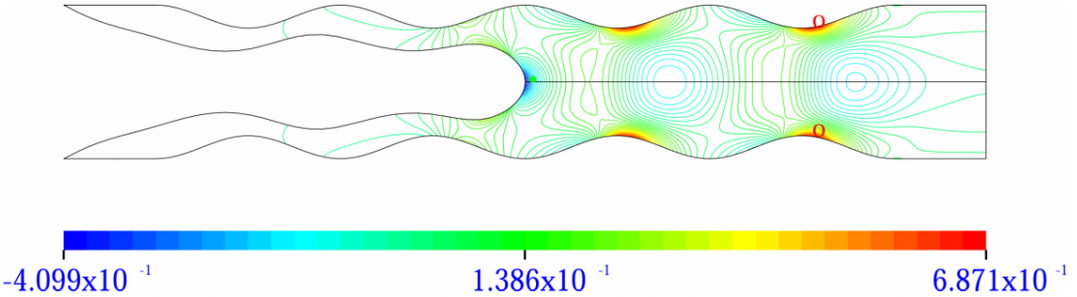


Figure. Contour lines of τ_{zz} in an undulated tube, which is completely filled with a Giesekus fluid at t´=2.114 for $(De_p, Re_p, P_{ext}, b/a, R_{min}/R_{max}, \beta, a_{GS}) = (0.5, 0, 8.33x10^4, 12, 0.7, 0.5, 0.5)$.

References

[1] Taylor G.I.: Deposition of a viscous fluid on the wall of a tube, *J. Fluid Mech.*, **10**: 161-165, 1961.

[2] Giovedoni M.D., Saita F.A.: The axisymmetric and plane cases of a gas phase steadily displacing a Newtonian liquid-A simultaneous solution of the governing equations, *Phys. Fluids*, **9(8):** 2420-2428, 1997.

[3] Gauri V., Koelling K.W.: Gas-assisted displacement of viscoelastic fluids: flow dynamics at the bubble front, *J. Non-Newt. Fluid Mech.*, **83**: 183-203, 1999.

[4] Dimakopoulos Y., Tsamopoulos J.: Transient displacement of a Newtonian fluid by air in straight and suddenly constricted tubes, *Phys. Fluids,* **15(7)**: 1973-1991, 2003a.

[5] Dimakopoulos Y., Tsamopoulos J.: Transient displacement of a viscoplastic material by air in straight and suddenly constricted tubes, *J. Non-Newt. Fluid Mech.*, **112/1**: 43-75, 2003b.

[6] Dimakopoulos Y., Tsamopoulos J.: A quasi-elliptic transformation for moving boundary problems with large anisotropic deformations, *J. Comp. Phys.*, **192**: 494-522, 2003c.

[7] Phan-Thien N., Tanner R.I.: A new constitutive equation derived from network theory, *J. Non-New. Fluid Mech.*, **2**: 353-365, 1977.

[8] Giesekus H.: A simple constitutive equation for polymer fluids based on the concept of deformation-dependent tensorial mobility, *J. Non-Newt. Fluid Mech.*, **11**: 69-109, 1982.

[9] Dimakopoulos Y., Tsamopoulos J.: On the gas-penetration in straight tubes completely filled with a viscoelastic fluid, accepted for publication in *J. Non-Newt. Fluid Mech.*, 2004.

XXI ICTAM, 15–21 August 2004, Warsaw, Poland

ANALYSIS OF FLOW-INDUCED, STEP-BUNCHING INSTABILITIES DURING THE GROWTH OF CRYSTALS FROM LIQUID SOLUTIONS

Bing Dai, Yong-Il Kwon, and Jeffrey J. Derby
Department of Chemical Engineering and Materials Science & Minnesota Supercomputer Institute, University of Minnesota, Minneapolis, MN 55455-0132, U.S.A.

Summary We present a novel multi-scale model of the growth of a vicinal crystal surface from a supersaturated liquid solution that couples bulk fluid dynamics with surface step growth. Of particular interest are the effects of fluid mechanics on morphological crystal growth instabilities, such as macrosteps, step bunches, and inclusions. This model is self-consistently solved by an efficient, moving-boundary, finite element method.

INTRODUCTION

Crystal growth is a prime example of an important materials processing operation which is strongly impacted by fluid mechanics. In this presentation, we address solution crystal growth, i.e., the growth of crystals from a supersaturated liquid, a process which is widely employed to produce large, single crystals of materials not amenable to melt growth techniques. In addition, solution growth is very widely employed in crystallization separations and purification processes for high-value materials such as pharmaceuticals. During solution growth, crystal quality is often compromised by morphological instabilities, such as macrosteps, step bunches, and inclusions, which arise from the coupled effects of fluid dynamics, mass transport, and the growth of atomic layers (steps) across a vicinal crystal surface. The main motivation for the work presented here is the need for a coupled, multi-scale, transport-kinetic model which is sufficiently detailed to capture microscopic step growth kinetics and is in a sufficiently general form to be incorporated in a global transport model of fluid mechanics, such as that employed by Vartak *et al.* [1].

MODEL DESCRIPTION

For the work presented here, we consider relatively simple flows within boundary layers adjacent to the macroscopic, vicinal surface of a crystal growing from a liquid solution. This scenario is depicted schematically in Figure 1(a), where the fluid flow over a crystal surface is shown. There is a depletion of solute due to the crystallization at the surface leading to a concentration boundary layer, which is embedded within the momentum boundary layer. At a still smaller scale, we consider a step source, such as a screw dislocation [2] somewhere along the crystal surface (see the yellow arrow) with a train of steps moving away from it (see the blue box). Within this blue box, which is moving with a group of steps on the crystal surface, we construct a growth model involving a series of elementary transport and kinetic processes, starting from material transport in the bulk phase, adsorption and desorption of growth units to and from terraces between steps, followed by surface diffusion and incorporation at discrete step ledges, as depicted in Figure 1(b). This phenomenological approach to describe step motion was first proposed in the classical model by Burton, Cabrera and Frank (BCF) [2] with later extensions by Chernov [3], Bennema [4], and Gilmer, Ghez, and Cabrera [5] for solution growth.

Of particular interest are scenarios whereby the steps within a group (a step train), which are all initially equally spaced and moving at the same speed, begin moving at different speeds to form a feature known as a step bunch. A step bunch contains many closely spaced steps, surrounded by regions with relatively few steps. It is believed that such step bunches degrade the quality of the growing crystal and are a precursor to the formation of liquid inclusions in the crystal. A number of coupled transport-kinetic models have been applied to address this particular issue of morphological instability, most notably the works of Vekilov and co-workers [7] and Chernov, Coriell, and co-workers [8]. These prior efforts employed a number of idealizations. Our approach, first described in [9], rigorously accounts for the interactions of discrete growth steps through surface diffusion fields, adsorption and desorption events, solute incorporation, and surface convection due to step motion. This model is self-consistently coupled with a bulk model that describes the fluid flow and its effects on the convection and diffusion of solute to the surface. The governing equations are solved numerically by an efficient, moving-boundary, finite element method.

SAMPLE RESULTS

A sample result is shown in Figure 1(c), where a snapshot is displayed of the transient response of a train of 51 growth steps under the influence of a boundary-layer flow directed in the same direction as the step motion. Initially, we impose a perturbation to the inter-step spacing of an equidistant configuration of steps. Under these conditions of flow and growth, the step spacing changes in time, leading to the situation depicted in the figure, which shows a step bunch in the middle of the domain. This step bunch moves with its own phase velocity through the simulation box.

Figure 1(c) also shows the instantaneous bulk concentration of solute in the liquid over the crystal surface. A careful examination of the figure reveals depletion regions around individual steps, as the solute in the bulk liquid diffuses to steps and is incorporated due to step motion (i.e., crystal growth). The action of fluid flow on these concentration variations occurs over longer length scales involving dozens of steps and acts, in this case, to destabilize the step train and form

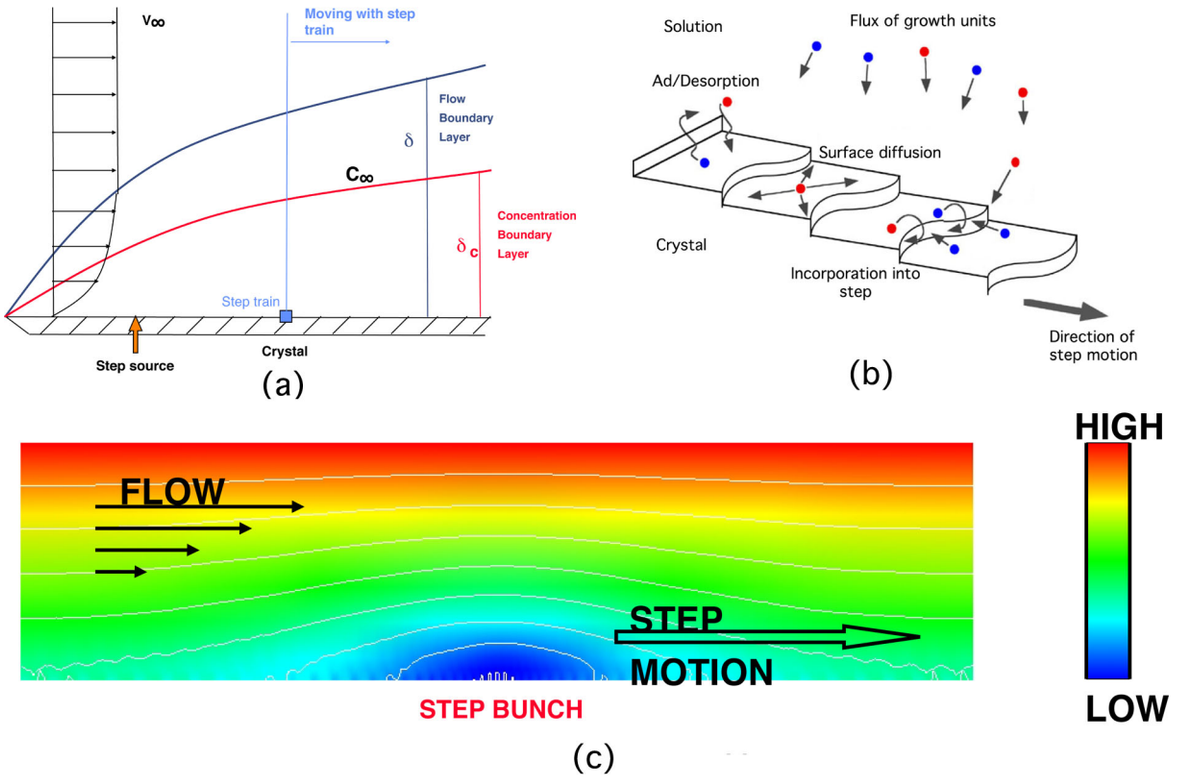


Figure 1. (a) Boundary layer depiction of macroscopic flows and mass transfer across a vicinal crystal surface is shown; the step train is embedded within the blue box moving along the surface. (b) The surface model includes steps, terraces, and growth units. (c) A sample computation of 51 steps under destabilizing conditions. The crystal surface is the bottom of the box; the overlying liquid is colored as a function of its solute concentration. A perturbation in the spacing of the steps results in the evolution of a bunch.

bunches. The lateral concentration profiles across the bulk are in registry with the population of steps along the surface, namely a higher number density of surface steps (a step bunch) is situated below lower-concentration fluid, while higher-concentration fluid regions exists above the surface where there are fewer steps. Thus the lateral variation of the step density couples to the flow, via convection of the bulk solute concentration field, and drives the growth of this step-bunching instability. Under identical conditions, but with the flow direction counter to the direction of step motion, this system is stable to all perturbations and always exhibits equally spaced steps within the train.

SUMMARY

These first-principles computations predict step bunches and allow their underlying mechanisms to be studied. Effects of fluid flow on morphological instability within several growth systems, representing large-molecule organic materials and small-molecule inorganic materials, will be discussed in the presentation and compared to experimental findings.

References

[1] B. Vartak, Y.-I. Kwon, A. Yeckel, and J. J. Derby, "An analysis of flow and mass transfer during the solution growth of potassium titanyl phosphate," *Journal of Crystal Growth*, **210**, 704–718, 2000.
[2] W. K. Burton, N. Cabrera, and F. C. Frank, "The growth of crystals and the equilibrium structure of their surfaces," *Phil. Trans. Roy. Soc. London*, **243**, 299–358, 1951.
[3] A. A. Chernov, "The spiral growth of crystals," *Soviet Physics Uspekhi*, **4**, 116–148, 1961.
[4] P. Bennema, "The importance of surface diffusion for crystal growth from solution," *Journal of Crystal Growth*, **5**, 29–43, 1969.
[5] G. H. Gilmer, R. Ghez, and N. Cabrera, "An analysis of combined surface and volume diffusion processes in crystal growth," *Journal of Crystal Growth*, **8**, 79–93, 1971.
[6] F. Rosenberger, H. Lin, and P. G. Vekilov, "Finite-amplitude instability in growth step trains with overlapping step supply fields," *Phys. Rev. E*, **59**, 3155–3164, 1999.
[7] P. G. Vekilov, F. Rosenberger, H. Lin, and B. R. Thomas, "Nonlinear dynamics of layer growth and consequences for protein crystal perfection," *Journal of Crystal Growth*, **196**, 261–275, 1999.
[8] S. R. Coriell, A. A. Chernov, B. T. Murray, and G. B. McFadden, "Step bunching: generalized kinetics," *Journal of Crystal Growth*, **183**, 669–682, 1998.
[9] Y.-I. Kwon and J.J. Derby, "Modeling the coupled effects of interfacial and bulk phenomena during solution crystal growth," *J. Crystal Growth* **230**, 328–335, 2001.

RELEVANCE OF ALFVEN WAVES IN PROCESS METALLURGY UNDER A HIGH MAGNETIC FIELD

René Moreau*, Kazuhiko Iwai**, Takashi Kameyama**
*Lab. EPM-MADYLAM, ENSHMG, BP 95, 38402 Saint Martin d'Hères Cedex, France
**Department of Materials Processing Engineering, Nagoya University, Furo-cho, Chikusa-ku, Nagoya, Japan 464-8603

Summary Waves are electrically excited at the top free surface and detected at the bottom of a vertical cylinder of liquid gallium, which is located within a vertical superconducting coil generating a 10 Tesla magnetic field. It is shown that, if the frequency is well selected, the pressure disturbance associated to these waves can be detected at the bottom of the apparatus and has all characters of Alfven waves.

INTRODUCTION

It is very common in liquid metal MHD to consider Alfven waves as irrelevant, since their damping time $\mu\sigma L^2$, is usually extremely short (of the order of $10^{-4}\ s$ if the transit length L is $10\ cm$) in comparison with their transit time L/A, where $A=B/\sqrt{\mu\rho}$ is the Alfven celerity. But, with the strong magnetic field delivered by superconducting magnets which now become available, their transit time becomes as short as the damping time, so that the Lundquist number becomes of the order of unity or larger. In this paper, we present a preliminary experiment, performed with liquid gallium at moderate temperature, whose scope is precisely to demonstrate the relevance of these waves. The main characters of such waves, which are derived from an elementary linear theory, are also compared with the measurements. The fairly good agreement between the theoretical predictions and the measurements suggests that this experiment may be considered as a demonstration of the relevance of Alfven waves in liquid metals under high magnetic fields.

THE EXPERIMENT

A $12\ cm$ column of liquid gallium is located in a vertical cylinder made of an electrically insulating material and this vessel is itself centered within a vertical coil, which may generate a $10\ Tesla$ DC magnetic field. A pressure sensor is inserted from below at about $2\ cm$ above the bottom wall and is connected to a noise filter and an oscilloscope. At the top free surface, two cupper electrodes are partially immersed in the liquid metal. They are connected to a power supply capable to generate an AC electric current whose frequency is fixed to $1\ 500\ Hz$ and whose intensity may vary from zero to $90\ Amp$. In the presence of both the vertical magnetic field and the horizontal current passing between the electrodes, the fluid is locally submitted to an oscillating horizontal force, which is itself partially balanced by a pressure force. This results in an unsteady fluid motion, which must be organized as a set of vortices, which propagate and form a traveling wave. According to Ohm's law, associated to the fluid motion, there exists also a set of induced electric current loops. The energy of each vortex and each current loop depends on its distance from the excitation area. With a moderate magnetic field, one would expect that the energy would be damped out rapidly, essentially by Joule effect, since viscosity is quite small whereas the magnetic diffusivity is 10^7 larger, so that this column of vortices would not reach the bottom wall. But, in the presence of the strong DC magnetic field, since the Alfven waves propagate very fast, it may be expected that a significant fraction of this energy should reach the bottom wall. Indeed, the condition to satisfy in order to observe this behavior is to have a Lundquist number $\mu\sigma AL$ at least of the order of unity. This is precisely what we get with a magnetic field of $10\ Tesla$.

The main experimental results, which will be presented, are pressure fluctuations delivered by the pressure sensor. They exhibit the same frequency as the electric current supplied to the electrodes. A spectral analysis of this signal also reveals a second peak at twice that frequency. And it is clearly shown that the height of this second peak varies linearly with the square of the intensity supplied to the electrodes, whereas the height of the first peak varies proportionally to that intensity. This is a specific property of Alfven waves.

A LINEAR THEORY

We start from the usual equations of MHD, and we neglect viscosity since the magnetic Prandtl number of liquid metal is extremely small, so that the ohmic damping is the only remaining dissipation mechanism. We also neglect the non-linear part of inertia in the Navier-Stokes equation, because the energy of the system remains small. The magnetic field

is expressed as $\mathbf{B}=B_0\,\mathbf{i}_z+\mathbf{b}$, $|\mathbf{b}|<<B_0$, where the magnetic field disturbance $\mathbf{b}$ and the fluid velocity are proportional to $exp[i(\mathbf{k}\cdot\mathbf{r}-\omega t)]$. And the wave vector is supposed to be of the form $\mathbf{k}=(k_\perp,0,p+iq)$, where the three quantities $k_\perp, p, q$ are real. This means that the cylindrical vessel is modeled as a 2D rectangular domain. And q represents the attenuation of the wave along the distance from the excitation area, whereas $k_\perp, p$ represent the shape of the vortices in the rectangular plane. The linearized equations obviously lead to a dispersion equation whose analysis yields the typical properties of the waves.

The main theoretical results may be expressed in terms of the Elssaser number $E=\mu\sigma A^2/\omega = \sigma B^2/\rho\omega$ built with the two main data: the applied magnetic field and the frequency of the excitation. They allow to analyze the conditions in which the waves persist all over the domain, in spite of their important and rapid damping. Essentially, it is shown that there exists a range for this number in which the waves are observable without a too strong damping, it is roughly between the two limits 1 and $1/M^2$, where $M=k_\perp/\mu\sigma A$. The smaller value corresponds to the limit below which the skin effect is significant and the excited disturbance does not escape from the skin depth. And the larger value corresponds to a shape factor such that the eddies and the current loops are squeezed between vertical walls too close from each other to allow the development of the induced current without important ohmic losses. Finally, the most efficient value for the Elssaser number appears to be around $\mu\sigma A l_\perp$, where $l_\perp\approx 1/k_\perp$ is the horizontal dimension of the rectangular domain. A numerical application to the case of a gallium experiment suggests a discrete set of frequencies. Each of them corresponds to an entire number of half vortices. And, among them, the frequency $1430\ Hz$, which is remarkably close of the experimental value $1500\ Hz$, can be associated with a flow pattern made of 5 half vortices between the free surface and the bottom wall. In this case, the amplitude of the velocity of the fifth vortex is still 2/3 of that of the vortex present at the free surface.

CONCLUDING REMARKS

The main theoretical conclusion of this work is a prediction of the best conditions to observe Alfven waves in a rectangular domain filled with a liquid metal. It may be illustrated in a quarter plane representing the applied magnetic field versus the frequency of the excitation. The domain where the waves persist is a fraction of this quarter plane, between two curves. One of them gives a minimum magnetic field, such that $E>1$, the other gives a minimum frequency related to the skin effect. Those conditions can easily been applied to metals other than gallium, such as steel or other metallic alloys. In all cases, with the usual physical properties of liquid metals, the minimum magnetic field should be above a critical value of the order of $2\ Tesla$.

And the main conclusion of the experiment, beside the demonstration that the Alfven waves can actually be observed in liquid metals, is indeed a suggestion to repeat and to complement those measurements, with higher magnetic filed and with more sophisticated diagnostic techniques.

EFFECT OF THERMAL BOUNDARY MODULATION IN A RESTRICTED FLUID DOMAIN OF A 3D VERTICAL BRIDGMAN APPARATUS

E. Semma[1], M. El Ganaoui[1], R. Bennacer[2], V. Timchenko[3], and E. Leonardi[3]

1) SPCTS-UMR CNRS 6638, Université de Limoges/Faculté des Sciences, Limoges

2) LEEVAM, Univ. Cergy-Pontoise, 5 mail Gay Lussac, Neuville sur Oise 95031, France

3) The University of New South Wales, Sydney, Australia 2052

Fluids heated from below provide non linear behaviour very rich and interesting in many scientific fields. The classic Rayleigh-Benard problem offers a first approach to this complexity of flow evolving from a conductive to convective regime and a first predictive way of coupling with solid/liquid transition.

Phase change is of great importance in the materials and crystal growth processes. The control of this phenomena permits growth of high quality pure crystals. Stable dynamic solutions are of interest in practice because of their impact on the constitution control. For example, in electronic applications, growth involves convection dominating dopant segregation and influencing interface shape.

Two-dimensional (2D) models are used for predictive investigation of directional solidification configurations based on thermal or solutal control, under full or low gravity conditions. Recently three-dimensional (3D) computations have been limited to high Prandtl number. This study focuses on the three-dimensional character of low Prandtl number flows and on symmetry breaking phenomena which can produce some unsteadiness in the flow and consequently perturb the solid/liquid interface shape and dopant distribution. Only the hydrodynamics in the melt is analyzed in this paper.

In past papers the critical stability limit for the onset of the natural convection in two-dimensional flows was undertaken and the threshold value for breaking symmetry and unsteadiness were identified. In the present work, this problem is studied using three-dimensional simulations thus overcoming the limitation of the 2D assumption. The geometry studied is shown in Figure 1. It has been found that the initially steady symmetric flow in the 3D case becomes asymmetric for lower *Ra* number than for the 2D case. The breaking in symmetry occurs firstly in the transverse plane. For the relatively low *Ra* number we still have no intensification in the global heat transfer but it appears that the heat transfer increases locally on the bottom and decreases on the vertical active walls. The classical spiral flows typical for the 3D effect (in the third direction) is also identified.

Heating conditions varying with time interacts with flow characteristics and the unsteadiness thresholds, such situations are encountered for example for electronic component energized inducing unsteady generation of heat.

The heat and mass transfer regarding the amplitude and the frequency of a given oscillation imposed to the hot wall $T_H = 1 + \varepsilon \sin(2\pi ft)$ exhibits a particular behaviour when compared to the configuration without modulation. Starting with the steady regime for a given low Rayleigh number, modulation can activate a resonant state for which it is possible to predict the next oscillatory state that the system can reach without modulation but only with increasing the intensity of the convection (higher Ra).

2D observation with modulation will be investigated for the 3D case, the steady state regime will be studied on terms of stream function variation an averaged Nusselt number.

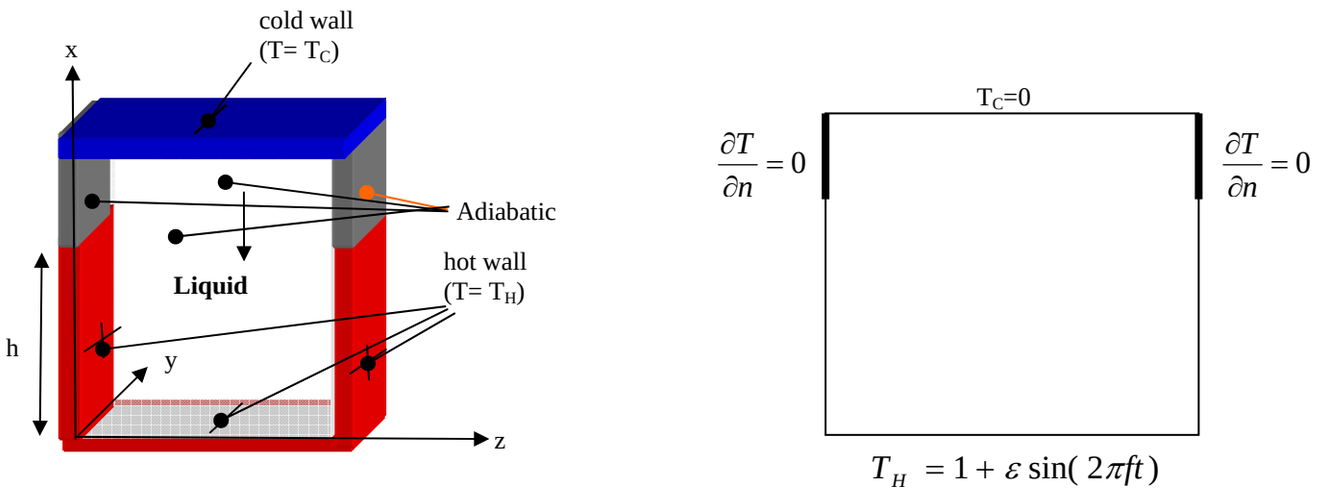


Figure. 1 : Geometrical configuration - 3D full domain and 2D domain.

XXI ICTAM, 15–21 August 2004, Warsaw, Poland

3D COMPUTER SIMULATION OF TIME-DEPENDED SOLUTAL CONVECTION.

Viatcheslav V. Kolmychkov*, O.S. Mazhorova*, Yu.P. Popov*, P.Bontoux**, M.El Ganaoui***
* *Keldysh Institute of Applied Mathematics RAS, 4, Miusskaya pl, Moscow, 125047 Russia*
** *L3M FRE 2405 du CNRS – Les Universités d'Aix–Marseille, 38 rue F. Joliot Curie, 13451 Marseille cedex 20, France*
*** *SPCTS UMR 6638, Universite de Limoges, Lemoges, France*

Summary The paper deals with computer simulation of natural convection in multicomponent solution. Three-dimensional calculations have been done to study the onset of convective motion and correspondent flow patterns. The process is considered for Rayleigh number in range $1 \cdot 10^3 \div 4 \cdot 10^4$. The results are in good agreement with theoretical data on hydrodynamics stability.

MATHEMATICAL MODEL

Computer simulation of mass-transfer in multicomponent systems with phase transition is one of the most challenging problems for modern crystal growth technology. The paper presents the numerical study of natural convection in solidification of ternary nondilute solution. The problem arises in computer simulation of liquid phase epitaxy (LPE) – a crystal growth technique that is widely used for preparation of multi component semiconductor materials with desired structural composition. LPE is classified as a solution growth process. In distinction to solidification of pure materials or dilute alloys phase transition temperature in epitaxial growth depends on the composition of the liquid and solid phases.

The process described by 3D time-dependent fluid flow and mass transport equations. The solution is supposed to be incompressible and Boussinesq approximation is adopted. In cartesian coordiantes (x, y, z) and nondimensional variables the set governing equations is:

$$\begin{cases} \partial_t V + (V\nabla)V = -\nabla p + \Delta V + \sum\limits_{i=1}^{2} Gr_i C_i e_z \\ \nabla V = 0 \\ \partial_t C_i + (V\nabla)C_i = \dfrac{1}{Sc_i}\Delta C_i \end{cases}$$

where $\partial_\xi \equiv \dfrac{\partial}{\partial \xi}$, $\nabla = (\partial_x, \partial_y, \partial_z)$, $\Delta = \nabla^2 = \partial^2_{xx} + \partial^2_{yy} + \partial^2_{zz}$, $(x, y, z) \in \mathcal{D}$, $\mathcal{D} = [0, L] \times [0, L] \times [0, H]$, $L/H \approx 10$, $V = (V_x, V_y, V_z)$ - velocity vector, p - pressure, C_i, $i = 1, 2$ - concentration of the correspondent component, dissolved in the liquid phase, $Gr_{D_i} = \dfrac{g\beta_i H^3 \Delta C_i}{\nu^2}$ is Grashoff number for concentration, $Sc_i = \nu/D_i$ is Schmidt number, $e_z = (0, 0, -1)$. The non - dimensional variables are introduced by scaling the length with the depth of the liquid phase (H), time – with H^2/ν and concentration – with the initial concentration of one of the components in the solution.

The phase transition is going on the substrate that is placed under the solution at $z = 0$. The interface conditions on concentration fields consists of the mass balance between the transported and incorporated solute species:

$$V_{gr} = \frac{\partial_n C_1}{\mathrm{Sc}_1(C_1^s - C_1)} = \frac{\partial_n C_2}{\mathrm{Sc}_2(C_2^s - C_2)}$$

and phase diagram representing the equilibrium between the solution and growing layer: $F_{liq}(C, T) = 0$, $F_{sol}(C^s, C, T) = 0$, where $T(t)$ - temperature of the system, uniform in space and changing in time according a prescribed rule, C_i^s- concentration of the correspondent solute specie in the solid phase. On the rest of the boundary $\partial_n C = 0$. Boundary condition on velocity field is $V = 0$.

The basic principle underlying the growth of epitaxial layers by LPE is similar to that of growth of salt crystals from a saturated saline solution. If the solution is slightly supersaturated dissolved components precipitate out of the solution onto the substrate. Supersaturation is usually maintained by gradually lowering the temperature during the growth . The reduction in the concentration of growth units in the vicinity of the growing layer gives rise to concentration gradients.

The onset of convection in LPE system has a known so far analogy. Neglecting the existence of the component with smaller Grashoff number and supposing linearity of phase diagram we actually obtain the problem concerning convective instability in a horizontal fluid layer with nonlinear conduction temperature profile. In our case instead of temperature the role of active scalar plays concentration. Theoretical analysis of the problem shows, that nonlinear profile gives rise to stable finite amplitude subcritical convective motion in the form of

NUMERICAL RESULTS

The governing equations discretized at staggered grid using control-volume method. Approximation of convective terms ensure kinetic energy conservation and mass balance for dissolved components. The scheme is implicit, has second order in space, first in time. Navier - Stokes equations and equations of mass transfer are solved successively at each time level. To determine velocity and pressure fields we follow predictor -corrector procedure. The calculated velocity field is substituted into the mass transfer equations, that are solved using the extended to 3D case coupled algorithm.

Full scale computer simulation for LPE growth of actual materials under reasonable operating conditions has been done for Rayleight number $Ra = \max_i Gr_i Sc_i$ varying in the range $1.1 \cdot 10^3 < Ra < 1.1 \cdot 10^5$, $Sc_i = 50$.

The onset of finite amplitude subcritical convective motion is observed at $Ra = 1100$. The calculations show a transition from initial non-regular flow pattern to hexagonal planform. The run duration is approximately 25 vertical diffusion times. In the range $1.1 \cdot 10^3 < Ra < 1.4 \cdot 10^4$ a regular cellular convection pattern is obtained. At Rayleight number of $1.4 \cdot 10^4 \div 3 \cdot 10^4$ the transition to skewed-varicose and knot instability is registered. The mean convective structure size increases with Ra while $Ra < 3 \cdot 10^4$. Above $Ra = 3 \cdot 10^4$ chaotic cellular small-scale convection is detected. The mean cell size at $Ra = 3.5 \cdot 10^4$ several times less then at $Ra = 1.8 \cdot 10^4$.

CONCLUSIONS

Three-dimensional numerical simulation for LPE growth of ternary compounds confirm the existence of convective motion at Rayleigh numbers less than critical one measured in two-dimensional calculations and predicted by stability analysis. The planform of subcritical convection and flow direction agree with theoretical data. The evolution of the flow pattern at Ra above the critical value is also consistent with theoretical predictions and experimental results. The numerical procedure is reliable and allows to perform long-time computer simulation of the convective motion in a wide range of operating parameters.

References

[1] *R.Krishnamurti* Finite amplitude convection with changing mean temperature. Part 1. Theory. J. Fluid Mech. (1968), vol. 33, part 3, pp. 457-463

[2] *Mazhorova O.S., Popov Yu.P., Sakharchuk A.S.* , Stability of finite difference schemes for the systems of parabolic equations with non - traditional boundary conditions. Differential equations (trans. from Russian) (1997), v.33, No. 7, pp.946 – 954.

[3] *I.A. Denisov, V.M. Lakeenkov, O.S. Mazhorova, Yu.P. Popov* Numerical study for liquid phase epitaxy of $Cd_xHg_{1-x}Te$ solid solution. J.Crystal Growth (2002), vol. 245, pp. 21-30

[4] *Getling A.V.* Rayleigh - Bernard correction structures and dynamics. Sengapore - New Jersey - London - Hong Kong, World Scientific (1998).

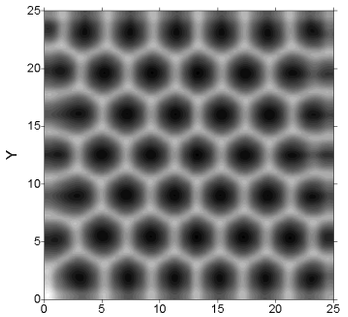


Figure 1. $\overset{\times}{Ra} = 1 \cdot 10^3$

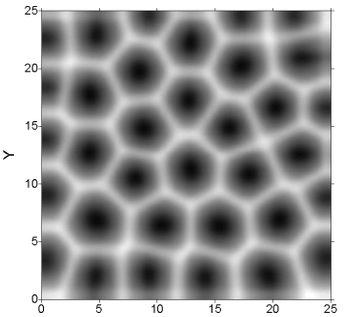


Figure 2. $\overset{\times}{Ra} = 2.5 \cdot 10^3$

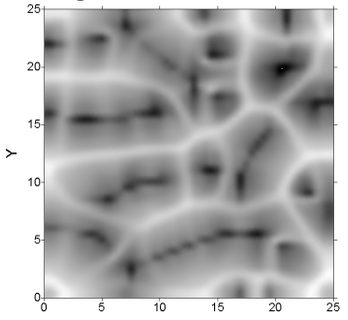


Figure 3. $\overset{\times}{Ra} = 1.8 \cdot 10^4$

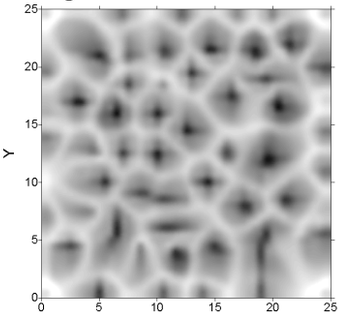


Figure 4. $\overset{\times}{Ra} = 3.5 \cdot 10^4$

LIQUID AND GAS JETS IMPINGING ON A MOVING WETTED SURFACE

Anh V Nguyen , Geoffrey M Evans
Discipline of Chemical Engineering, University of Newcastle, Callaghan, 2308, NSW Australia

Summary In continuous metal processing operations a cooling liquid is often applied to reduce the temperature of the strip. This liquid needs to be removed before downstream rolling operations can be undertaken. This paper contains the theoretical development and predicted results for both analytical and computational models of a combined liquid and gas jet wiping system designed to remove cooling liquid from the surface of a continuous moving strip.

The jetting system, shown in Figure 1, consisted of a liquid jet impinging onto a moving metal strip. A gas jet, located downstream of the liquid jet, is applied to the strip surface to remove undesirable liquid remaining on the strip surface. Both jets are configured in the symmetrical pattern and transversely span over the strip surface. Typical operating conditions are: strip velocity, v_s, of 18 m/s, strip width, W, of 1-2 m, and a plenum chamber clearance, H, of 22 mm.

An analytical approach was used to determine the average cooling liquid height on the moving strip upstream of the jetting assembly. The liquid height was obtained by relating the liquid draining over both sides of the strip to the head of liquid – a discharge coefficient of unity was assumed. It was found that the average height, h_f, varied between 20 – 30 mm as the strip width increased from 1 to 2 metres. This would suggest that the liquid build-up would be at least the same height of the clearance between the nozzle outlets and the top of the strip (i.e. 22 mm). The thickness and velocity profile of the cooling liquid boundary layer was also calculated, based on turbulent flow conditions. It was found that the thickness was in the range 5 – 15 mm, depending on the strip velocity and a cooling liquid injection point 0.5 m upstream from the jetting assembly. The overall cooling liquid velocity profile, therefore, was a moving boundary layer, above which was a pool of relatively stationary liquid.

A momentum balance was carried out to determine if the combined liquid and gas jet momentum were sufficient to prevent the cooling liquid from travelling downstream with the moving strip. Drainage in the direction of strip motion was also included. The analysis showed that the momentum of the liquid jet was an order of magnitude higher than that for the boundary layer flow on the strip, and should provide an adequate "dam" effect against the oncoming stream. It is thought that the action of the gas jet provided mainly a "wiping" effect to remove any gas jet liquid forced to travel in the direction of the strip motion.

Computational Fluid Dynamics (CFD) modelling of the jetting system was successfully developed based on the VOF technique. The governing equations included the continuity and momentum equations formulated in terms of the liquid volume fraction and the flow variables (velocity and pressure). Turbulence was incorporated using the standard k-ε approach in combination with the standard wall function. The finite volume scheme was used to discretise the governing equations which were solved using the commercially available Fluent CFD code. The computational boundary included the wall, the moving wall, the pressure/velocity inlets for the gas and liquid jets, and the pressure outlets. The gas-liquid interface shape was modelled based on the Laplace equation and the contact angle at the interface contact with the wall. The computational domain was meshed non-uniformly by the tetrahedral scheme, with strong grid clustering at the strip surface and along the direction of the liquid jetting.

The two-way coupling, involving an iterative approach, was used to obtain the interaction between the flow fields of the liquid and gas jets, and also the thickness of the liquid film remaining on the moving strip. The computational analysis was undertaken for a number of conditions to determine the effect of liquid and gas jet incident angle and plenum pressure, and strip speed, on the amount of liquid remaining on the strip surface. It was found that when no gas jet was applied a thin film of liquid remained on the strip surface, where the thickness of the film was most strongly influenced by the liquid jet incident angle. When the gas jet was applied it was found that the liquid film was removed in all cases tested (Figure 2). The distance downstream from the liquid jet stagnation point on the strip surface where the film was completely removed (Figure 3) was function of gas jet incident angle and plenum pressure. As expected, the trends observed were directly related to gas jet momentum parallel to the strip surface and opposing the motion of the liquid. Consequently, the optimum conditions to minimise the possibility of liquid remaining on the strip surface include maximising the gas plenum pressure and minimising the jet incident angle.

An insight into the liquid spray generated by the action of the gas jet on the moving liquid film can be gained by considering Figure 4. The boundary between the liquid (jet) and gas phase is shown as an inclined line. The velocity contours highlight the very high velocities generated within the liquid phase at angle not parallel to the moving strip. In practice it is highly likely that the momentum of the fluid would cause the film to breakup and be released from the film in the form of small droplets. A very general estimate of the trajectory angle and quantity of the ensuing liquid spray could be obtained from further analysis of the velocity field.

Finally, the computational analysis indicated significant recirculation of gas within the enclosed region between the two jets. The enclosed region was generated as a result of the two dimensional constraint imposed upon the computational domain. This condition would apply to the longitudinal axis of the strip where there would be little transverse motion of gas. However, the transverse motion would be expected to increase away from the centre of the strip and nearer to the sides. A fully 3D analysis would be needed to create a more realistic description of the flow in this region of the strip.

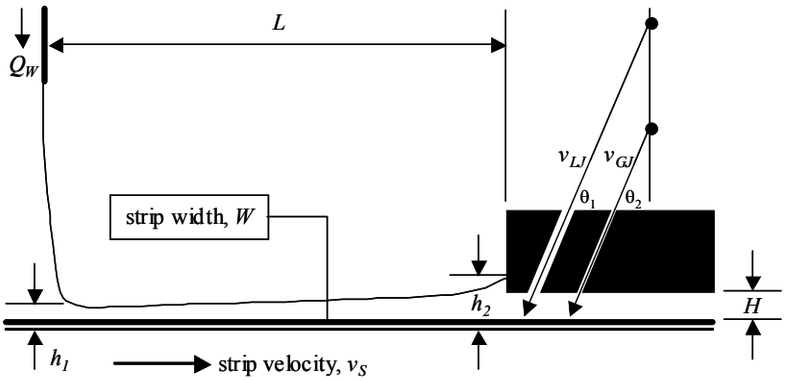


Figure 1: Basic Geometry for the Analytical Model

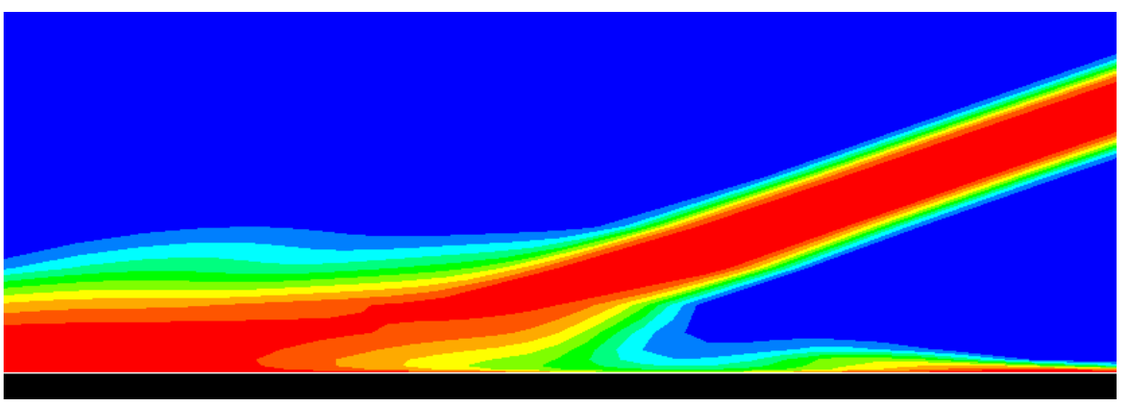


Figure 2: Magnified view of liquid jet with gas jet interaction under normal operating conditions
(Colour contours: liquid fraction = 1 (red), = 0.5 (green) = 0.0 (blue))

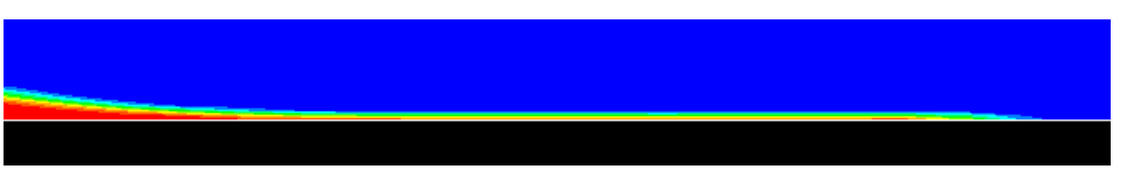


Figure 3: Liquid fraction contour of the residual liquid film left behind the liquid jet
(Colour contours: liquid fraction = 1 (red), = 0.5 (green) = 0.0 (blue))

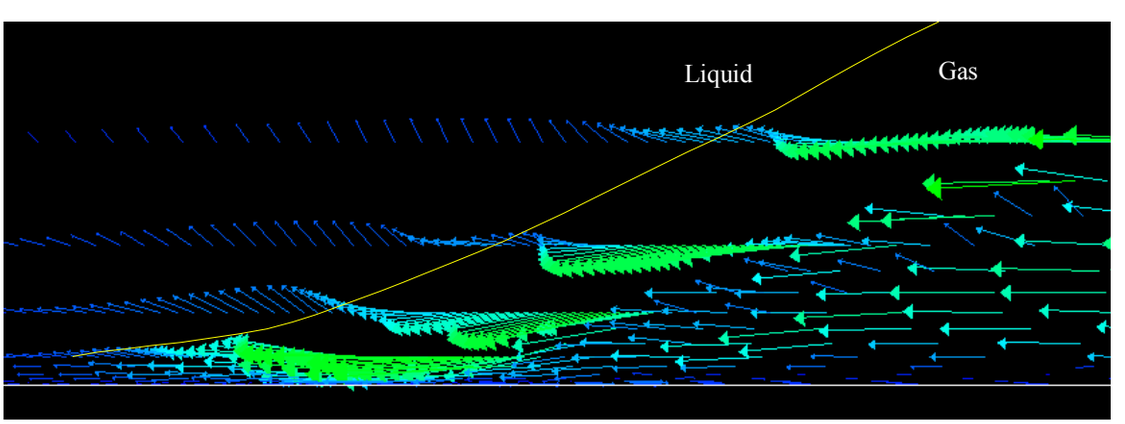


Figure 4: Velocity Vectors for liquid and gas jet system under normal operating conditions
(Colour contours: velocity = 200 m/s (green), = 30 m/s (blue))

CONVECTIVE INSTABILITIES IN CZOCHRALSKI MODEL

V.I.Polezhaev*, N.V.Nikitin**, S.A.Nikitin*
*IPM RAS, Lab. mathematical and physical modeling in fluid dynamics, Vernadskogo 101, b1, 119526 Moscow, Russia
**Institute of Mechanics, Moscow State University, Moscow, Russia

Summary Hydrodynamic Czochralski model as a combination of the classical models buoyancy-driven and Marangoni convection is studied on the basis of three dimensional unsteady Navier-Stokes equations in the Boussinesq approximation. Critical Grashof and Marangoni numbers for axisymmetrical and three dimensional fluid flow were found for different Prandtl numbers and boundary conditions on the melt surface. Role of the buoyancy–driven and Marangoni instabilities in the coupling flows are discussed.

Pulling crystal growth, which is well known as Czochralski growth is the widespread method for electronics and optoelectronics industry [1]. The temperature oscillations in the melt are the main reason of the striation defects in Czochralski crystal growth and studied during more than 25 years [1-5]. Last decade new round of activity was done due to possibility of 3D modeling in fluid dynamics (see [6-10] and references). Although direct three dimensional modeling taking into account all types of convection for the typical for industry high Grashof (Gr) and Marangoni (Mn) numbers are available now (see, for instance [7,11]), critical numbers for onset of instability haven't systematically studied. The validation of the results and control of convection needs more detailed analysis of buoyancy-driven and Marangoni convection, similar as for classical fluid mechanics models [12]. Experimental observations and three dimensional modeling of buoyancy-driven and Marangoni convection in the melt which discussed in above mentioned references show the spatial structures, which are of interest for basic fluid dynamics studies.

We study hydrodynamic Czochralski model (Fig.1), which represents a combination of the classical models of convection with side and bottom heating. The unsteady Navier-Stokes equations in the Boussinesq approximation and the equation for temperature were used. The boundary conditions for the velocity on the melt surface are no-slipping on the crucible wall and bottom and on the crystal. Temperature $\Theta = 0$ on the crystal, $\Theta = 1$ on the

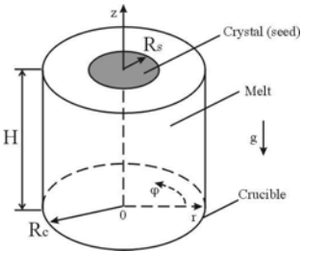


Fig.1. Scheme of hydrodynamic Czochralski model.

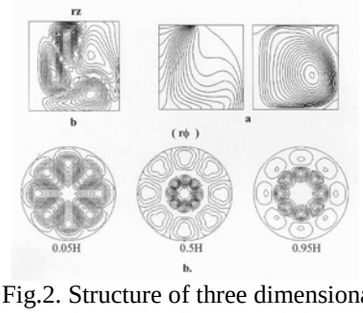


Fig.2. Structure of three dimensional thermocapillary instability.

crucible wall, $\partial\Theta/\partial z = 0$ on the crucible bottom and different thermal boundary conditions on the melt surface are assumed. Even idealized Czochralski model represents nonlinear multi parametrical hydrodynamic system with wide range values of governing parameters. Flow patterns in the melt in the Czochralski model is extremely complex and wasn't well understood, especially the role of Marangoni and it's coupling with buoyancy-driven convection.

A hierarchy of the models and computer codes were developed for the peer analysis of the problem including direct simulation of the transition and turbulent regimes on the basis of 3D Navier-Stokes equations [8-10]. However axisymmetric processes are still of interest in multiparametric analysis.

Three types of the FDM for axisymmertric Czochralski model are used here. The first type is based on the system «INTEX» and includes a variation of geometry, crystal and crucible rotation, gravity-driven and Marangoni convection in vorticity-stream function formulation. The second code is a basis of a novel Computer Laboratory [13]. It includes also 2D flat and axisymmetric problems in the ground-based and microgravity environments. The third type of the axisymmetric codes was used mainly for the calculation of a basic flow for linear stability analysis [9, 10]. For the stability analysis of the axisymmetric steady state flow with respect to 3D perturbations temperature field T is presented in the form,

$$T(t,r,\varphi,z)=T_{2D}(r,z)+\varepsilon T'_n, \qquad T'_n(t,r,\varphi,z)=\mathrm{Re}[T_n(t,r,z)\exp(in\varphi)], \quad n=1,2,\ldots$$

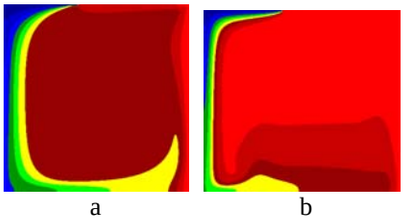
Here, T_{2D} is a given (previously calculated) steady solution of the 2D equations and $\varepsilon T'_n$ is a small 3D perturbation. Substituting this and similar expressions for the velocity components into the governing equations and neglecting $\sim\varepsilon^2$ terms we obtain a set of linear time-dependent problems for perturbations. A general solution for T_n for each azimuthal wave-number *n* has a following form

$$T_n(t,r,z)=\sum_{j=1}^{\infty} T_n^j(r,z)\exp(\lambda_n^j t)$$

Here, λ_n^j are the eigenvalues and T_n^j are the eigenfunctions of the corresponding spectral problem. Solving linear time-dependent equations with some random initial conditions we obtain $T_n(t \to \infty, r, z) \to T_n^1(r, z)\exp(\lambda_n^1 t)$, where λ_n^1 is eigenvalue with the maximal real part. In such a way we may determine the stability or instability of the axisymmetric flow as well as the spatial structure and temporal behavior (monotonic or oscillatory) of the most dangerous 3D perturbations. A focus of the concrete analysis in the paper is natural convection, which includes buoyancy-driven and gradient of the surface tension-driven (Marangoni) convection, which is the major cause of instability. The control function (for instance, amplitude of temperature oscillation, A) seems as follows:

$$A = f(r, z, \varphi, Gr, Mn, Pr, Rs/Rc, H/Rc, \gamma 1, \gamma 2) \qquad (1)$$

Here Gr, Mn – Grashof and Marangoni numbers - criteria of convection, Pr - criteria of the physical properties. Geometrical parameters - non dimensional height of the melt H/Rc = 1.0 and width of the seed Rs/Rc =0.4 for the parameters of the benchmark [7, 9], $\gamma 1$, $\gamma 2$ – thermal boundary and initial conditions. Analysis of the nature and comparison of the 2D and 3D instability phenomena in hydrodynamic Czochralski configuration for buoyancy-driven and thermocapillary convection is done. Systematically comparison of the buoyancy-driven and Marangoni convection including comparison of the impact of the thermal boundary conditions on the melt surface is done. The peculiarities of the convective instability for low and high Pr melt for buoyancy-driven and Marangoni convection are discussed. Fig.2 shows a typical "spoke-type" structure of three dimensional thermocapillary instability for a case of adiabatic melt surface for $Mn_c=5.8x10^5$ and low Prandtl (Pr=0.05). Here a) basic temperature/flow fields, b) structure of 3D disturbances.



a b

Fig.3. Steady state temperature fields for Marangoni (a) and buoyancy-driven (b) convection, Pr=6.5.

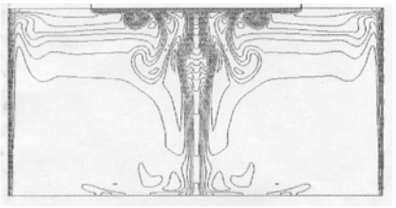


Fig.4. Instantaneous thermal's structure for buoyancy–driven convection, adiabatic melt surface, Pr=6.5, $Gr=4.5\ 10^7$.

Fig.3 shows structure of the temperature fields for high Pr number melt with adiabatic melt surface in axisymmetric case. Here $Mn=10^5$ (a) and buoyancy-driven convection for $Gr < Gr_c$ (b). Critical Gr number for onset of the thermals was found here as $Gr=Gr_c=4.4x10^5$. Fig.4 shows change of the instability mechanism for high Pr melt: instantaneous isotherms for buoyancy-driven convection for $Gr >> Gr_c$ seems as thermals. Such kind of the structures were observed by in experiments with water (see ref. in [1, 7]). Maximum of the Gr_c was found for Pr=0.25 in axisymmetrc case.
Note, that change of instability mechanisms for Marangoni convection in this case wasn't found.
Therefore the nature of Marangoni instability is different from buoyancy-driven one (case of adiabatic melt surface and bottom). It has to be taken into account for control of the temperature oscillations in the melt. Movies 6-8 in URL [http://www.ipmnet.ru/~yarem/paper3] illustrate dynamics of the temperature oscillations in axisymmetric case. Paper presents discussion of the governing parameters where these mechanisms are dominated and summary of the critical Mn and Gr numbers for parameters (1), comments of the coupling phenomena and possibilities for control of the temperature oscillations in the melt using thermal, dynamics (vibrations), magnetic actions as well as microgravity. Because multiparamertric analysis of hydrodynamic Czochralski model needs additional efforts, education and tutorial course were developed [13].

References

[1] Hurle D.T.J.: Crystal pulling from the melt, Springer, 1993.
[2] Carruthers J.R.: Thermal convection instabilities relevant to crystal growth from liquids. In: Preparation and Properties of Solid State Materials. Ed. by W.R. Wilcox and R.A. Lefever. New York - Basel, Marcel Dekker, 1977, v. 3, . 1-121.
[3] Polezhaev V.I.: Hydrodynamics, Heat and Mass Transfer During Crystal Growth, In: Crystals: Growth, Properties and Applications, V.10 (1981), Springer, 81.
[4] Schwabe D.: Surface-tension driven flow in crystal growth melt. In: Crystals: Growth, properties and applications, v. 11, Springer, 1988, 75.
[5] Müller G. and Ostrogorsky A.: Convection in melt growth. In: Handbook of Crystal Growth. Ed. by D.T.J. Hurle. Amsterdam, Elsevier, 1994, v. 2, p. 711-819.
[6] Ristorcelli J.R. and Lumley J.L.: Instabilities, transition and turbulence in the Czochralski crystal melt. J. Crystal Growth, 1992, v. 116, N 3/4, p. 447-460.
[7] Polezhaev V.I.: Modeling of Technologically Important Hydrodynamics and Heart/Mass Transfer Processes during Crystal Growth. In : Crystal Growth Technology (eds) Sheel H.J.,Fyukuda T., Wiley, (2003), 156-186.
[8] Li You-Rong, Peng L. Akyiyama Y., Imaishi N. J.: Crystal Growth, 259, (2003), 374.
[9] Nikitin N.V and .Polezhaev V.I.: J.Crystal Growth, 230, (2001), 30.
[10] Polezhaev V.I. Bessonov, O.A,. Nikitin N.V et al.: J. Crystal Growth, 230, (2001), 40.
[11] Dupret F. and Van Den Bogaert N.: Modelling Bridgman and Czochralski growth. In: Handbook of Crystal Growth. Ed. by D.T.J. Hurle. Amsterdam, Elsevier, 1994. v. 2., 875-1010.
[12] Koshmieder E.L.: Benard cells and Taylor vortices. Cambridge University Press, 1993, 337 p.
[13] Ermakov M.K, Nikitin S.A,.Polezhaev V.I,Yaremchuk V.P.: J. Crystal Growth, 266 (2004), 388-395.

XXI ICTAM, 15–21 August 2004, Warsaw, Poland

NEW POSSIBILITIES FOR VELOCITY MEASUREMENTS AND MODEL EXPERIMENTS IN LIQUID METAL PROCESSING

Andreas Cramer, Kapil Varshney, Gunter Gerbeth
Forschungszentrum Rossendorf, P.O. Box 51 01 19, 01314 Dresden, Germany

Summary Potential difference probes and ultrasound have been employed to investigate liquid metal flows in cylindrical containers. The fluid motion was driven by either a rotating or a pulsating magnetic field. Experimental results containing flow mapping and scaling of mean velocities for very small driving forces will be presented. We report on our new MULTIMAG facility which allows for almost any combination of rotating, traveling, pulsating and d.c. magnetic fields in extended geometries for industrially relevant regimes.

BASIC CONSIDERATIONS

In several branches of materials processing like stirring or casting of metals or crystal growth processes from the melt, large effort is persistently spend on the optimisation of methods and facilities. To achieve an improvement of the final product quality, enhance the process stability, and decrease energy consumption a proper understanding of the underlying fluid flow phenomena is required. Most prominently a better knowledge about the details of the flow structure and the properties of the related heat and mass transport are needed.

During the recent years numerical simulations became an important tool to study these topics. But such calculations alone are often of limited value due to the problems regarding an appropriate modeling, particularly that of turbulence. As a basis for the validation of numerical codes experimental data of the velocity field are indispensable, facing the everlasting problem of the lack of appropriate and available measuring techniques. One of the main problems here is the opaqueness of the liquid metals, almost nothing is available commercially. The potential difference probe (PDP) is mostly applied on laboratory scale. Its functional principle, based on Ohm's law $\mathbf{j} = \sigma(-\nabla\phi + \mathbf{v} \times \mathbf{B})$, where $\phi, \mathbf{B}, \mathbf{v}$ and σ denote the electric potential, magnetic induction of the applied d.c. measuring field, velocity, and the electrical conductivity, reveals already the limitations of this method. Sufficing for measurements of, for example, channel flows of several ten's cm/s in a strong magnetic field the potential difference ϕ becomes formidable small in even medium scale closed flows where the applied magnetic field serves for measurement purposes, only, and must be kept small in order to not disturb the flow.

A new and promising approach is the application of Ultrasonic Doppler Velocimetry (UDV) [1–3]. This non-invasive technique, based on time of flight measurements of short ultrasonic bursts, delivers the complete profile of the velocity component along the direction of sound propagation. However, some serious restrictions always exist to apply the different sensors. Compared to PDP the UDV is slow which may result in less expressive information with respect to turbulence characteristics. Despite the extremely low voltages inherent to PDP a second drawback of UDV is its sensitivity. On the other hand, it delivers spatio-temporal information and is suited to map the whole time-dependent flow field if several sensors are employed, or, as done in the frame of the present work, to map the mean velocity distribution and mean turbulence characteristics if the sensor is traversed.

Industrial scale experiments with hot metallic melts are mostly unaffordable. Often water experiments are used for the validation of numerical simulations. A transformation of these results has to be considered difficult to impossible with regard to meet the relevant characteristic parameters such as Reynolds-, Prandtl-, or Hartmann-number. There exists a multitude of low melting metals which allows for almost any meaningful physical modeling of industrial processes.

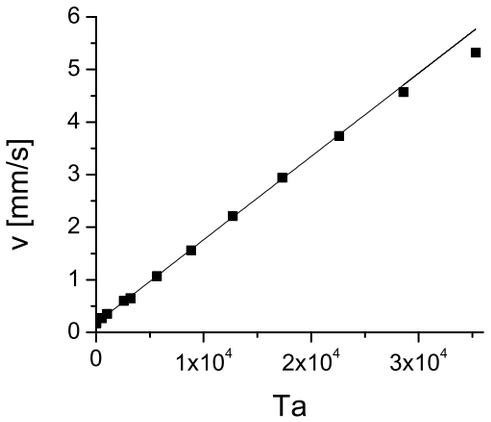


Figure 1. Linear scaling of velocity on the Taylor number below formation of a boundary layer regime

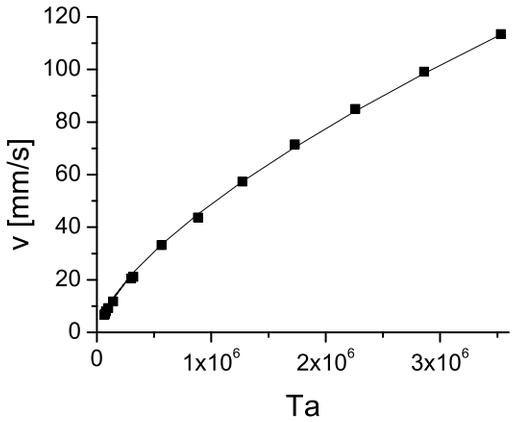


Figure 2. $Ta^{2/3}$ scaling law in the turbulent regime

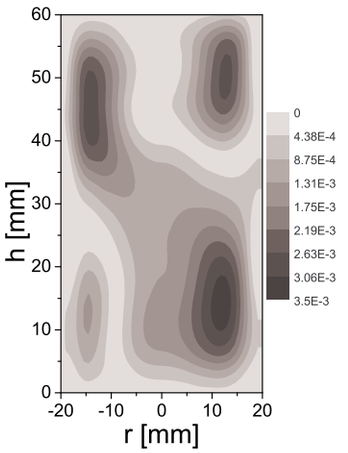


Figure 3. Streamfunction of a pulsating magnetic field driven flow

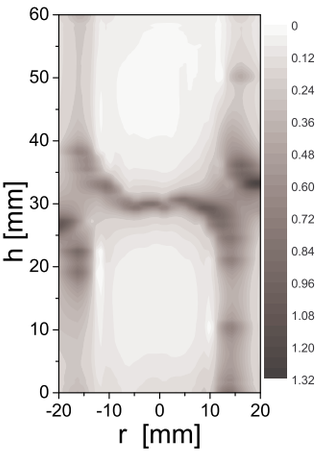


Figure 4. Turbulence degree belonging to the flow in Fig. 3

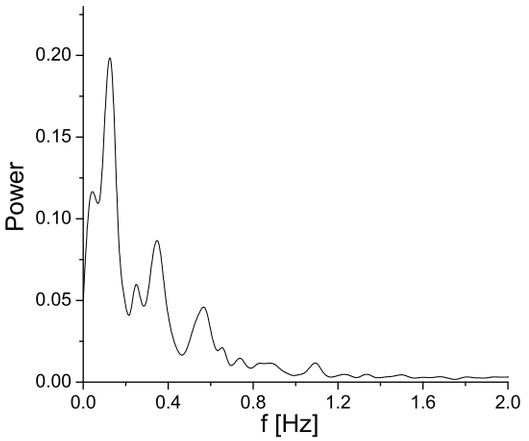


Figure 5. Power spectrum of velocity fluctuations in the center of the vessel

EXPERIMENTS

Modern electronic equipment for data acquisition is able to bridge the gap between the trustworthy direct numerical simulations, capable to cope with a strength of the driving parameters slightly above the instability threshold, and experiment. We employed extremely low-noise amplifiers in combination with steep analog filters to extend the measurable range down to a Taylor number $Ta = \sigma\omega B^2 L^4/(2\rho\nu^2)$ of 32, only, in the case of a rotating magnetic field (RMF) driven flow. Here ω, L, ρ and ν are the frequency, typical dimension, density and viscosity. The PDP measurements in Fig.'s 1 and 2 are in very good agreement with the theoretically predicted scaling laws for different flow regimes. The critical Ta was found to be approx. 1×10^5 which agrees well with theory. For this first time experimental validation of the linear scaling of the viscous controlled regime voltages as low as a few nano-volt have been reliably measured.

A pulsating magnetic field (PMF) was employed to generate fluid motion in a container of 6 cm height and 2 cm radius. From the UDV measurements of the vertical velocity component attained by a 1 mm sensor movement across the whole diameter of the vessel the absolute values of the streamfunction shown in Fig. 3 were calculated. The double vortex structure typical for induction-furnace like configurations can be clearly seen. Fig. 4 depicts the related distribution of the turbulence degree. In [4] PDP measurements and numerical simulations have been done. There the data were acquired at mid-height close to the rim, which turns out from Fig. 4 to be a good position for that purpose. One very low frequency oscillation of $\approx$ 1Hz is reported. The spectrum from UDV measurements in the centre of the container reveals additional frequencies as can be seen in Fig. 5.

MULTIMAG

As shown above, various types of a.c. magnetic fields lead to different flow structures. There are proposals to make use of two field types, for instance, a combination of an RMF and a traveling magnetic field (TMF) to increase the mixing of the metal baths. Nowadays demands may be even one step ahead. Instead of investigating the results of the application of a magnetic system its tailoring with regard to a desired flow structure seems far more promising. With the MULTIple MAGnetic field type facility we set up such a flexible system which permits the independent amplitude variation of RMF, TMF, PMF and the d.c. homogeneous and cusp components, with independent frequency variation for the alternating components. Industrial demands are met with a large experimental volume of 1/2 m in height, diameter of 36 cm and high field strength made possible by a compact design using water-cooled hollow copper profiles in combination with current-controlled 3-phase high power amplifiers. These special developed current sources [5] allow for arbitrary waveforms of $3 \times 160 A_{eff}$ for each of the field types including any phase relation and overlaying of d.c. offsets respectively superpositions of several frequencies.

References

[1] Takeda, Y.: Development of an ultrasound velocity profile monitor. *Nucl. Eng. Design, 126, 277* 1991
[2] Brito, D., Nataf, H.-C., Cardin, Aubert, P.J., Masson, J.P.: Ultrasonic Doppler velocimetry in liquid gallium. *Exp. Fluids, 31, 653* 2001
[3] Eckert, S., Gerbeth, G.: Velocity measurements in liquid sodium by means of ultrasound Doppler velocimetry. *Exp. Fluids, 32, 542* 2002
[4] Baake, E., Nacke, B., Umbrashko, A., Jakovics, A.: LES modelling of heat and mass transfer in turbulent recirculated flows. *Magnetohydrodynamics, 37, 13* 2001
[5] EAAT Ltd., Chemnitz, Germany

DYNAMIC SIMULATION OF THE ENTIRE CRYSTAL GROWTH PROCESS : MULTI-SCALE ANALYSIS OF MELT FLOW TRANSIENTS

V. Regnier, L. Wu, B. Delsaute,
F. Bioul, N. Van den Bogaert, F. Dupret

CESAME, Université catholique de Louvain, E-mail: fd@mema.ucl.ac.be

Abstract

This paper investigates the transient melt flow evolution during a complete Czochralski crystal growth process. Two basic time scales are considered. The short scale concerns the basic transients associated with flow oscillations at different process stages. Accurate understanding of the flow mechanisms at this scale is required to develop an average axisymmetric flow model for complete dynamic simulations. The long time scale is associated with the transients caused by the slower system evolution occurring during the complete growth process. In order to focus on the fundamental effects governing the flow, a model problem is considered where the liquid is placed into a possibly rotating container while a disk of smaller diameter rotates on its top surface. Both the container and the disk are isothermal. Several transient effects are investigated including the effect of disk radius increase or decrease, and abrupt changes of disk or container temperature or rotation rate.

Introduction : dynamic modeling of crystal growth by means of the FEMAG software

There is increasing demand today for robust, reliable and user-friendly software to model bulk growth techniques such as the Czochralski (Cz), Liquid Encapsulated Czochralski (LEC), Floating Zone (FZ) and Vertical Bridgman (VB) processes. The aim is to help predict, design and control the growth processes, and to better understand the factors affecting crystal quality. However, the growth techniques are more and more complex, and optimization can be achieved only by use of suitable numerical modeling that accounts for the severely non-linear physical phenomena involved as well as for the high system thermal inertia. The resulting problem is coupled, global, nonlinear and dynamic. On the other hand, accurate prediction of crystal quality requires both appropriate modeling of the governing physics, and highly accurate dynamic numerical methods for computing the evolution of the solid-liquid interface shape and the temperature field gradient in its vicinity.

The FEMAG simulation software developed in the CESAME center of the University of Louvain is currently used by major crystal growth companies. The numerical model is both global and dynamic, and takes the effect of melt convection into account. Diffuse surface radiation is considered. Geometrical unknowns are dynamically coupled to the other unknowns, i.e. temperature field, velocity field, electrical potential, etc., leading to a complex non-linear system of equations whose solution is found by use of a decoupled scheme at every time step of the simulation. Whereas in its first generation FEMAG already performed global quasi-steady or time-dependent simulations, applications were restricted to top cone, shouldering and body growth stages. Both laminar and non-laminar flow models were considered, including or not the effect of axisymmetric magnetic fields. The objective of launching the FEMAG-2 software generation has been to provide a fully automatic simulator predicting the entire growth process while handling correctly the switches between the growth stages, together with coupling dynamic calculations with accurate melt flow prediction.

A significant difficulty lay in the important evolution of the system geometry during a complete growth process. Indeed, the solidified region is very small during seeding and subsequently becomes larger and larger, while the volume of the molten region decreases continually and can take a complex shape during tail-end stage. The solution adopted combines several approaches based on a representation of the furnace by means of deforming unstructured meshes together with automatic mesh generation. New geometrical methods were designed to allow easy calculation of the different system free surfaces (solidification front, melt/gas interface including crystal/melt and crucible/melt menisci, and crystal/gas surface). These methods allow performing easy time-dependent simulations even for stages of the process where important geometrical changes occur.

Another important difficulty to address in FEMAG-2 development was related to the complexity of dynamic melt flow modeling. Several problems must be solved to accurately couple melt flow predictions with crystal growth process simulation. First, in semi-conductor growth, the melt flow is time-dependent, 3D and weakly turbulent, whereas it can exhibit 3D azimuthal and temporal structured oscillations. The use of an axisymmetric quasi-steady flow model is devoted to average the effect of these oscillations, and the principal issue is to determine reliable average flow models, with the corresponding boundary conditions, above the steady laminar regime. Secondly, due to high nonlinearities, the solution of non-laminar flow problems can be quite difficult while, in most cases, these problems exhibit the numerical stability and convergence issues of transport-dominated systems. To this end, appropriate iterative schemes and stabilization techniques were

introduced into the FEMAG-2 flow module. Thirdly, in order to achieve coupling with global thermal calculations, the melt flow problem is solved in FEMAG-2 at several stages of the simulation by using a quasi-steady model, while long term thermal transients are treated by including appropriate source terms into the momentum and energy equations. Interpolation between the collected results provides the flow pattern and the velocity field at each time step of the dynamic simulation.

Crystal quality can be predicted from the melt flow and temperature histories as long as the physical models are known. Therefore, solid phase simulators are currently developed in FEMAG-2 to calculate defect formation, diffusion and recombination, dislocation generation and motion, etc., on the basis of heat transfer and flow simulation results. A related objective is to develop off-line control algorithms, the ultimate goal being to provide an easy way to determine the evolution of the different process parameters (heater power, pull rate, crystal and crucible rotation rates, crucible lift, magnetic field design and intensity…) in order to optimize selected process variables characterizing crystal shape and quality. For all these reasons it is of the utmost importance to develop accurate and reliable flow models for bulk crystal growth dynamic simulation.

Objectives of the paper in terms of melt flow modelling

The present paper is devoted to investigating the evolution of the melt flow regime and pattern during the complete Cz crystal growth process. To this end, two basic time scales must be considered. The short time scale, which is typically of the order of tens of seconds in silicon growth, concerns the basic transients associated with flow oscillations at different stages of the growth process. Accurate understanding of the flow behaviour at this scale is required to develop the average axisymmetric flow model to be used in global dynamic simulations. The long time scale, which is typically of the order of tens of minutes in Cz silicon growth, is associated with the flow and heat transfer transients caused by the long term system evolution. In particular, the melt height is continually decreasing during the complete growth process. In addition, the crystal radius changes significantly during cone growth and tail-end stages, while simultaneously the heat transfer is strongly affected by the heater power modifications required to obtain a crystal of the prescribed shape – it should be recalled that heater power is slowly decreased during conical growth in order to let crystal radius increase, while it experiences a quick peak during shouldering in order to stop conical growth, and it is progressively increased during tail-end stage in order to let crystal radius decrease to terminate the growth process.

As the aim is here to provide better understanding of the crystal growth melt flow transients at these two time scales, a model problem is considered where the liquid is placed into a possibly rotating cylindrical container while a rotating disk of smaller diameter is placed at the top surface of the liquid. The container and the disk are at uniform, but possibly different, temperatures in order to generate buoyancy forces from radial temperature gradient effect. The advantage of this approach is to allow focusing on the fundamental effects governing the flow by reducing the number of system parameters – the latter being the height of the liquid domain, the container and disk diameters and temperatures, and some material properties of the liquid. Additional parameters can be introduced to characterize the imposed magnetic field if any, but any other effect such as radiation transfer, which is not directly affecting the flow, is removed from the model in order to focus on flow issues only. For validation purpose, this system has been the object of isothermal and non-isothermal experimental investigations by means of a simple apparatus.

In order to capture the particular effects related to the flow behaviour at the short time scale (including the detail of its oscillations in a periodic, quasi-periodic or chaotic regime), a particular simulation technique has been developed where the long term effects are frozen while a laminar flow model is used. Very high mesh and time step refinements are required and therefore short time scale simulations, whose understanding represent a first objective of the paper, are limited to rather small periods of time.

On the other hand, long time scale simulations can only be performed provided an appropriate axisymmetric average flow model is introduced. This non-laminar model is developed by fitting the simulations to short time scale results. The second objective of the paper is to investigate by use of this non-laminar model the importance of the long term flow transients resulting from process parameter changes, such as increase or decrease of disk radius, abrupt change of temperature or rotation rate of the disk or the container, etc. To this end, several examples will be completely analyzed and presented at the conference.

References

F. Dupret, P. Nicodème, Y. Ryckmans, P. Wouters, M.J. Crochet, Int. J. Heat Mass Transfer, 33 (1990), 1849.
F. Dupret & N. Van den Bogaert, in *Handbook of Crystal Growth*, Vol. 2B, Ch. 15, Elsevier, Neth. (1994), 875.
R. Assaker, N. Van den Bogaert, F. Dupret, Magnetohydrodynamics, 31 (1995), 254.
N. Van den Bogaert & F. Dupret, J. Crystal Growth, 166 (1996), 446; 171 (1997), 65; 171 (1997), 77.
R. Assaker, N. Van den Bogaert, F. Dupret, J. Crystal Growth, 180 (1997), 450.
F. Dupret, N. Van den Bogaert, R. Assaker, V. Regnier, in Proc. 8th Int. Symp. on Si Mat. Sc. and Tech., 1998 ECS meeting, Proc. Vol. 98-1 of the Electrochem. Soc., Pennington, NJ (1998), 396.
T. Sinno, E. Dornberger, R.A. Brown, W. von Ammon, F. Dupret, Materials Science and Engineering: R Reports, 28 (2000), 149.

XXI ICTAM, 15–21 August 2004, Warsaw, Poland

SENSITIVE REGIONS AND OPTIMAL PERTURBATIONS IN THE FLOATING ZONE USING THE ADJOINT SYSTEM

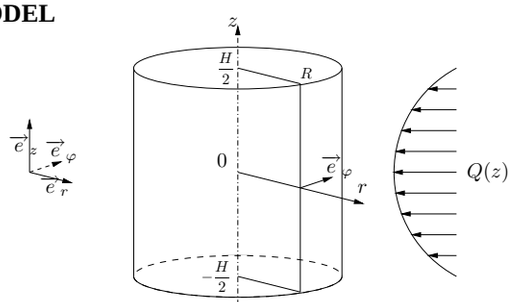
Othman Bouizi, Claudine Dang Vu-Delcarte, Guillaume Kasperski
LIMSI CNRS, Université de Paris-Sud, 91403 Orsay, France

Summary Thermocapillary convection arises in free surface systems, particularly in non-isothermal liquid bridges. In this study, the mechanisms of the growth of instabilities are analysed using an adjoint technique. It allows to determine the most sensitive regions of the flow to local perturbations. The most sensitive regions to thermal perturbations are presented.

INTRODUCTION

The floating zone is a free crucible process used to produce high-quality crystals. A molten zone is created by a lateral heating between a feed and a single crystal rod, and helds by capillary forces. The translation of the material through the heat flux induces the solidification of the crystal. Temperature gradients induce surface tension variations, the source of thermocapillary convection. In order to reduce buoyancy effects, experiments have been performed in a low gravity environment and have demonstrated that thermocapillary convection alone can induce defects in the product due to flow instabilities. A major goal is to identify the mechanisms leading to the growth of those instabilities. A value of interest is the critical Marangoni number of the flow characterizing the transition to instability. The 2D axi-symmetric study of the floating zone performed by [3] has pointed out a symmetry breaking with respect to the midplane for $Pr = 10^{-2}$. The steady-state solution becomes non-symmetric via a subcritical pitchfork bifurcation, followed by a saddle-node bifurcation. This kind of flow is usually studied by direct numerical simulation, continuation method and linear stability analysis. As far as we know, this work is the first attempt to identify the region of the steady thermocapillary flow where a local disturbance has the largest response, by the use of the adjoint technique [4]. This is also the first application of this method to a highly confined geometrical configuration. The floating zone model will be presented, followed by the description of the method. A representation of the most sensitive regions to thermal perturbations are shown.

FLOATING ZONE MODEL



Our model consists of a liquid bridge between two isothermal parallel concentric rigid disks of radius R which are separated by a distance H and which presents a non-deformable heated free surface. The geometry is chosen 2D axi-symmetric in cylindrical coordinates (r, z). The parameters of the model are the Prandtl number Pr, ratio of the characteristic thermal to dynamical diffusion times fixed here to 10^{-2}, the Marangoni number Ma which characterises the thermal convective regime and the aspect ratio $A = H/2R$ fixed to 1. The Navier-Stokes equations, under the Boussinesq approximation in a zero gravity environnement for an incompressible fluid, and the heat equation are used in a non-dimensionnal form:

$$\partial_t \overrightarrow{U} + \left(\overrightarrow{U} \cdot \overrightarrow{\nabla}\right) \overrightarrow{U} = -\overrightarrow{\nabla} P + Pr \Delta \overrightarrow{U} \qquad \partial_t T + \left(\overrightarrow{U} \cdot \overrightarrow{\nabla}\right) T = \Delta T \qquad \overrightarrow{\nabla} \cdot \overrightarrow{U} = 0 \tag{1}$$

together with the boundary conditions

$$U(r=1,z) = 0, \qquad \partial_r W|_{r=1} = -Ma\, f_n(z) \partial_z T|_{r=1}, \qquad \partial_r T|_{r=1} = Q(z)$$

$$U(r, z=\pm A) = 0, \qquad W(r, z=\pm A) = 0, \qquad T(r, z=\pm A) = 0$$

$\overrightarrow{U} = U\overrightarrow{e}_r + W\overrightarrow{e}_z$ is the velocity vector, P the pressure and T the temperature. $Q(z) = (1-z^2)^2$ is the nondimensionnal heat flux. $f_n(z) = (1 - z^{2n})^2$ is a regularizing function of the thermocapillary stress used to avoid a singularity at the junction between the free surface and the solid boundaries. It has been shown that this function has a low impact on the flow behaviour for $n \geq 13$ [2]. The value $n = 13$ has been chosen in this study. The adopted reference scales were based on thermal diffusion. A general notation for flow components is $\mathbb{U} = (U, W, T)$.

LINEARIZED AND ADJOINT SYSTEMS

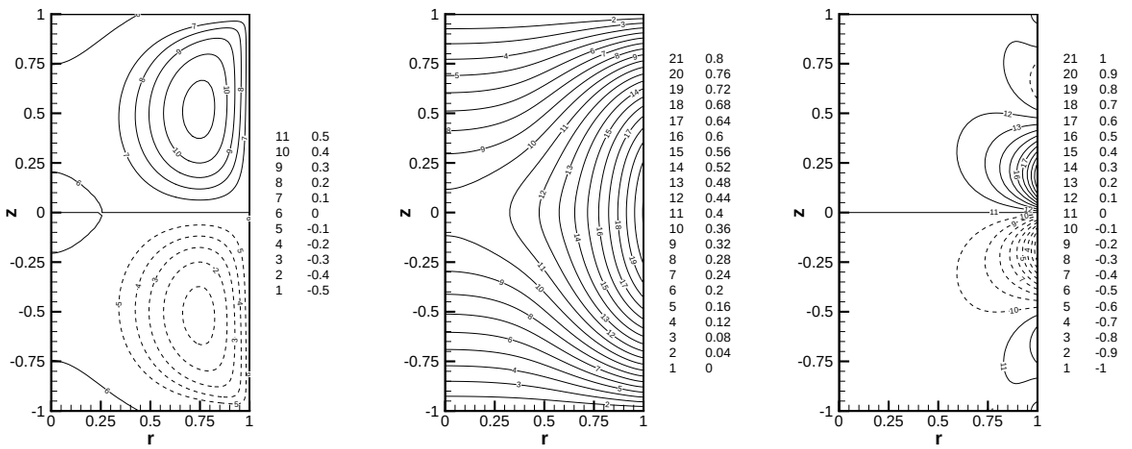
Once a steady flow $\mathbb{U}_0$ has been obtained, we can determine the evolution of a small perturbation $\mathbb{u} = (u, w, \theta)$ around $\mathbb{U}_0$. The evolution equations of $\mathbb{u}$ are obtained by linearizing Eq.(1) and read $\partial_t \mathbb{u} = \mathscr{L}(\mathbb{U}_0, \mathbb{u})$. Let us assume that the linear operator $\mathscr{L}(\mathbb{U}_0, \bullet)$ can be diagonalized and, with a scalar product defined later, that the normalized complex eigenvectors $(\mathbb{u}_i)$ form a basis of the perturbation flow space. The associated eigenvalues (λ_i) are ordered first

by decreasing real part and secondly by increasing imaginary part. Since $\mathscr{L}(\mathbb{U}_0, \mathbb{u}_i) = \lambda_i \mathbb{u}_i$, the evolution of a perturbation $\mathbb{u}$ such that $\mathbb{u}(t=0) = \mathbb{u}_i$ is : $\mathbb{u}(t) = \exp(\lambda_i t)\mathbb{u}_i$. If the initial perturbation $\mathbb{u}$ can be decomposed in the eigenbasis: $\mathbb{u}(t=0) = \sum_{i=1}^{+\infty} a_i \mathbb{u}_i$, its evolution is: $\mathbb{u}(t) = \sum_{i=1}^{+\infty} a_i \exp(\lambda_i t)\mathbb{u}_i$. Considering the case of a real value λ_1, we have, after a sufficiently long time $\mathbb{u}(t) \simeq a_1 \exp(\lambda_1 t)\mathbb{u}_1$. The greater is the value of $|a_1|$, the stronger is the perturbation. To calculate a_1, let us define the scalar product $\left(\mathbb{u}^{(1)}|\mathbb{u}^{(2)}\right) = \int_{-A}^{A}\int_{0}^{1}\left(u^{(1)}\underline{u}^{(2)} + w^{(1)}\underline{w}^{(2)} + \theta^{(1)}\underline{\theta}^{(2)}\right) r\mathrm{d}r\mathrm{d}z$. The adjoint operator $\mathscr{L}^*(\mathbb{U}_0, \bullet)$ of $\mathscr{L}(\mathbb{U}_0, \bullet)$ is defined by $(\mathscr{L}(\mathbb{U}_0, \mathbb{u})|\tilde{\mathbb{u}}) = (\mathbb{u}|\mathscr{L}^*(\mathbb{U}_0, \tilde{\mathbb{u}}))$. The operator $\mathscr{L}^*(\mathbb{U}_0, \bullet)$ having eingenmodes $\left(\tilde{\lambda}_i, \tilde{\mathbb{u}}_i\right)$ such that $\forall (i,j) \in \mathbb{N}^2, \quad (\mathbb{u}_i|\tilde{\mathbb{u}}_j) = \delta_{ij}$ and $\forall i \in \mathbb{N}, \quad \tilde{\lambda}_i = \underline{\lambda_i}$, this leads to $a_1 = (\mathbb{u}(t=0)|\tilde{\mathbb{u}}_1)$.

Let us consider a family $\delta\mathbb{T}(r_p, z_p) = (0, 0, \delta(r-r_p)\delta(z-z_p))$ of initial local temperature perturbations. Their values of a_1 are given by: $a_1(r_p, z_p) = \int_{-A}^{A}\int_{0}^{1} \delta(r-r_p)\delta(z-z_p)\tilde{\theta}_1 r\mathrm{d}r\mathrm{d}z = \tilde{\theta}_1(r_p, z_p) r_p$.

NUMERICAL METHOD AND RESULTS

Calculations were performed with a spectral collocation method on Gauss-Radau points along r and Gauss-Lobatto points along z, using the projection-diffusion method [1]. The steady flow is calculated with a Newton method, the first eigenmodes of $\mathscr{L}$ and $\mathscr{L}^*$ with an Arnoldi method.



Ψ_0 $\qquad$ T_0 $\qquad$ $r\tilde{\theta}_1/max|\tilde{\theta}_1|$

The stream function Ψ_0 and temperature T_0 are represented for the steady flow at $Ma = 106$, the critical Marangoni number being equal to 104.4. The temperature component of the first adjoint eigenmode, normalized and multiplied by r, is displayed on the right. The application of a temperature impulse has maximal efficiency when it is applied on the free surface near the mid plane.

In conclusion, the most sensitive region to thermal perturbation is located on the free surface, that is near the source of motion. It is easily accessible to the experimentation.

Acknowledgements

The authors acknowledge the IDRIS-CNRS and the CRI of University Paris-Sud for their computational ressources.

References

[1] A. Batoul, H. Khallouf, and G. Labrosse. Une méthode de résolution directe (pseudospectrale) du problème de Stokes 2D/3D instationnaire. Application à la cavité entrainée carrée. *C. R. Acad. Sci.*, **IIb**(319):1455–1461, 1994.

[2] E. Chénier, C. Delcarte, G. Kasperski, and G. Labrosse. Sensitivity of the liquid bridge hydrodynamics to local capillary contributions. *Phys. Fluids*, **14**:3109–3117, 2002.

[3] E. Chénier, C. Delcarte, and G. Labrosse. Stability of the axisymmetric buoyant-capillary fbws in a laterally heated liquid bidge. *Phys. Fluids*, **11**(3):527–541, 1999.

[4] D.C. Hill. Adjoint systems and their role in the receptivity problem for boundary layers. *J. Fluid Mech.*, **292**:183–204, 1995.

XXI ICTAM, 15–21 August 2004, Warsaw, Poland

EFFECTIVE VISCOSITY OF AN INHOMOGENEOUS DILUTE SUSPENSION FLOWING ALONG A WALL

Laurentiu Pasol, François Feuillebois
PMMH, UMR 7636 CNRS, ESPCI, 10 rue Vauquelin, 75231 Paris cedex 05, France

Summary The classical result of Einstein for the effective viscosity of a dilute suspension of solid spheres in an arbitrary infinite Stokes flow is extended to account for the effect of a nearby wall. It is found theoretically that the presence of a wall amounts to a slip velocity for the suspension on a macroscopic scale. This slip velocity is obtained in term of the stresslet on a sphere, which is calculated analytically with the method of bipolar coordinates. Because of walls, the effective viscosity is reduced in a homogeneous suspension, in qualitative agreement with experiments. For a bounded suspension, the expression for the viscosity depends on the flow field, even in the first order in volume fraction. Moreover, the sensitivity of the effective viscosity to the inhomogeneity of the suspension is higher for a Poiseuille flow than for a shear flow.

INTRODUCTION

An essential theoretical result for the mechanics of unbounded dilute dispersions of spheres is the expression for the effective viscosity valid at order ϕ, where ϕ is the volume fraction (Einstein [1]). Later experiments performed in tubes showed a surprising result: the effective viscosity is reduced as compared with Einstein's result when the tube diameter decreases (see e.g. [2] and references herein). However, this effect was not fully explained theoretically. Later theories [3] [4] modelled this phenomenon for a homogeneous suspension in a shear flow: they showed that the suspension is slipping on walls on the macro-scale, thereby reducing the effective viscosity. The theory presented here accounts for the more general case of an inhomogeneous suspension in a Poiseuille flow between parallel planes. It will be shown that when the sphere radius is small compared with the distance between planes, considering the effects of the two walls separately provides a good approximation for the effective viscosity.

THEORY FOR THE EFFECTIVE VISCOSITY OF A SUSPENSION NEAR A WALL

Consider a dilute suspension of neutrally buoyant solid spherical particles with radius a flowing along a plane wall. The volume fraction is low: $\phi = (4\pi/3)\, a^3 n_0 << 1$, where n_0 is the number of particles per unit volume in the bulk of the suspension, that is far from the wall. Thus, hydrodynamic interactions between particles will be neglected. On the other hand, interactions between individual particles and the wall will be taken into account. The concentration distribution normal to the wall is general: $n(\mathbf{x}) = n_0 g_W(\mathbf{x}) = n_0 g(\mathbf{x}) H[d(\mathbf{x}) - a]$, where g is an arbitrary function and $d(\mathbf{x})$ is the distance from the particle center at $\mathbf{x}$ to the wall. The Heaviside function H account for the non overlapping of particles with the wall. Equations for the flow $(\mathbf{v}, p)$ valid in each point of a suspension of N particles centered at $\mathbf{x}^\beta$, $(\beta = 1 \cdots N)$ may be written as [5]:

$$\boldsymbol{\nabla} \cdot \mathbf{v} = 0, \quad \mu_f \nabla^2 \mathbf{v} - \boldsymbol{\nabla} p = \sum_{\beta=1}^{N} \mathbf{f}(\mathbf{x}, \mathbf{x}^\beta, W) \tag{1}$$

using induced forces on the surfaces of the particles as defined by $\mathbf{f}(\mathbf{x}, \mathbf{x}^\beta, W) = \left[\boldsymbol{\sigma}^f \cdot \mathbf{n}\right] \delta(|\mathbf{x} - \mathbf{x}^\beta| - a)$, where $\boldsymbol{\sigma}^f$ is the stress tensor, $\mathbf{n}$ the normal outward unit vector on a sphere and δ is the Dirac function. The no-slip condition on the surfaces of particles is taken into account by these forces. The no-slip condition $\mathbf{v} = 0$ on the wall should be applied explicitly . Particles positions are random and effective properties of the suspension are considered here in the sense of ensemble averages. For a distribution (generalized function), this average $< \, . \, >$ is defined for a suspension of non interacting particles as:

$$(< q >, \varphi) = \int_V (q, \varphi)(\mathbf{x}_0) n(\mathbf{x}_0) d\mathbf{x}_0$$

where V is the volume of the whole suspension and φ denotes a test function. This problem is solved using a matched asymptotic expansions approach (like in [6]). In an inner region of order a close to the wall, equations (1) are averaged and the no-slip condition on the wall $< \mathbf{v} >= 0$ applies. In an outer region, far from the wall, induced forces average to zero for neutrally buoyant particles. Then averaging (1) simply gives the Stokes equations and their solution is the fluid velocity profile far from the wall. Only the boundary condition on the wall has to be replaced by a matching condition with the solution in the inner region. It is found that the resulting condition for the outer flow amounts to a slip velocity on the wall. Two different flow profiles are considered here, in view of possible experimental determinations of the effective viscosity: a shear flow and a Poiseuille flow. The Poiseuille flow can be written as the sum of a shear flow $v_x^\infty = k_1 z$ and a quadratic flow $v_x^\infty = k_2 z^2$. As an example, we present here the suspension flow profile as a result of matching for the case of the quadratic flow:

$$V_x(Z) = Z^2 + U_W \quad \text{where} \quad U_W = \frac{3\phi}{4\pi} \int_0^\infty Z \overline{f_x}(Z) dZ$$

All quantities are dimensionless: $V_x = \langle v_x \rangle / k_2 a^2$, $Z = z/a$ and $\overline{f_x}(Z) = \int_{\mathbf{x}\in\Re^3} G_W(Z_1)\widehat{f}_x(\mathbf{X}-\mathbf{X}_1, Z_1)\, d\mathbf{X}_1$, in which $G_W(Z_1) = G(Z_1)H(Z_1-1)$ (where $G(Z_1) = g(aZ_1)$) is the normalized distribution of particles and $\widehat{f}_x(\mathbf{X}-\mathbf{X}_1, Z_1)$ represents the dimensionless stress ($\widehat{f}_x = 1/(\mu_f k_2) f_x$) induced on the surface of a particle with center at the distance Z_1 from the wall. The slip velocity U_W may be expressed in term of the dimensionless stresslet S_{xz} on a particle:

$$U_W = U_0 + U_{HI} = U_0 - \frac{3\phi}{4\pi}\int_1^\infty G(Z_1)[S_{xz}(Z_1) - S_{xz}^\infty(Z_1)]dZ_1 \tag{2}$$

The stresslet was calculated analytically in bipolar coordinates and the integral determined with a 10^{-4} precision. We then obtained for a homogeneous suspension (viz. $G(Z_1) = 1$) in quadratic flow : $U_W^{\text{quadratic}} = 3.586\,\phi$. In a similar way, we found a slip velocity for a suspension in a shear flow: $U_W^{\text{shear}} = u_W^{\text{shear}}/(k_1 a) = 1.4419\,\phi$ which is in agreement with the result of Tözeren and Skalak[3]: $U_W^{\text{TS}} \simeq 1.45\,\phi$. The slip velocity was also calculated for typical inhomogeneous distributions of particles (with accumulation or depletion of particle near the wall) for both flow fields. It was found that the slip velocity is more sensitive to variations in the particle distribution for a quadratic flow than for a shear flow.
The effective viscosity of a inhomogeneous suspension sheared between parallel walls is, by taking in account each wall separately:

$$\langle\mu\rangle = \mu_f\left(1 + \frac{5}{2}\phi - \frac{2a}{h}U_W^{\text{shear}}\right) + O(\phi^2) \tag{3}$$

For the homogeneous case, it reduces to:

$$\langle\mu\rangle = \mu_f\left[1 + \frac{5}{2}\left(1 - 1.1535\frac{a}{h}\right)\phi\right] + O(\phi^2) \tag{4}$$

The effective viscosity of a suspension in Poiseuille flow is defined from the relationship between the pressure drop and the flux of the suspension. The result for an inhomogeneous suspension is:

$$\langle\mu\rangle = \mu_f\left[1 + \frac{5}{2}\phi - 6\frac{a}{h}U_W^{\text{shear}} + 6\left(\frac{a}{h}\right)^2 U_W^{\text{quadratic}}\right] + O(\phi^2) \tag{5}$$

and for the homogeneous case:

$$\langle\mu\rangle = \mu_f\left\{1 + \frac{5}{2}\left[1 - 3.4606\frac{a}{h} + 8.6065\left(\frac{a}{h}\right)^2\right]\phi\right\} + O(\phi^2) \tag{6}$$

Obviously, for $a/h \to 0$, Einstein result [1] is recovered in all cases. Brenner [7] found that a neutrally buoyant particle in a circular tube with radius R in Poiseuille flow induces a $O(a/R)^3$ pressure drop. His calculation uses the method of reflexions and therefore does not take into account the case where the particle is close to the wall. Nevertheless his result allows us to expect that the simultaneous effect of parallel walls on the effective viscosity in a two-dimensional Poiseuille flow will be at most of order $O[\phi(a/h)^3]$.

CONCLUSIONS

All terms involving a/h in the above results for the effective viscosity at order ϕ take into account exactly the interaction of individual particles with a wall. Since these terms are different for a shear flow and a Poiseuille flow, the effective viscosity of a wall bounded suspension is found to be dependent on the flow field, unlike the Einstein result for an unbounded suspension. The effective viscosity found for a suspension in Poiseuille flow is in qualitative agreement with experiments ([8], [9], etc. reviewed in [2]), that is it decreases when the distance h between the plates decreases. The high sensitivity of the effective viscosity to the distribution in particles in Poiseuille flow shows that it is essential to measure the particle distribution at the same time as the viscosity in order to estimate wall effects quantitatively and eventually compare with theory.

References

[1] A. Einstein. *Investigations on the theory of the Brownian movement*. Dover Publications, republication of the translation originally published in the 1926 edition, 1956.
[2] R. G. Cox and S. G. Mason. Suspended particles in fluid flow through tubes. *Ann. Rev. Fluid Mech.*, 3:300–321, 1971.
[3] H. Tözeren and R. Skalak. Stress in a suspension near rigid boundaries. *J. Fluid Mech.*, 82:289–307, 1983.
[4] P. Brunn. The hydrodynamic wall effect for a disperse system. *Int. J. Multiph. Flow (UK)*, 7:221–234, 1981.
[5] U. Geigenmueller and P. Mazur. Sedimentation of homogeneous suspensions in finite vessels. *J. Stat. Phys.*, 53(1/2):137–173, 1988.
[6] F. Feuillebois and J. Bławzdziewicz. Calculation of an effective slip in settling suspension at a vertical wall. *Fluid Mech. Res.*, 22:66–67, 1995.
[7] H. Brenner. Pressure drop due to the motion of neutrally buoyant particles in duct flow. *J. Fluid Mech.*, 43:641–660, 1970.
[8] V. Vand. Viscosity of solutions and suspensions. II. Experimental determination of the viscosity-concentration function of spherical suspensions. *J. Phys. Coll. Chem.*, 52:300–321, 1948.
[9] D. R. Oliver G. H. Higginbotham and S. G. Ward. Studies of the viscosity and sedimentation of suspensions. Part 4.- Capillary-tube viscometry applied to stable suspensions of spherical particles. *British Journal of Applied Physics*, 9:372–377, 1958.

XXI ICTAM, 15–21 August 2004, Warsaw, Poland

VELOCITY FLUCTUATIONS IN NON-BROWNIAN SUSPENSIONS UNDERGOING SIMPLE SHEAR FLOWS

A. Acrivos*, G. Drazer*, J. Koplik * and Boris Khusid**
*The Levich Institute, T-1M, The City College of the City University of New York, New York, NY 10031, USA
**Department of Mechanical Engineering, New Jersey Institute of Technology, University Heights, Newark, New Jersey 07102

Summary The velocity fluctuations present in macroscopically homogeneous suspensions of neutrally buoyant, non-Brownian spheres undergoing simple shear flow, and their dependence on the microstructure developed by the suspensions, are investigated in the limit of vanishingly small Reynolds numbers using Stokesian dynamics simulations. We show that, in the dilute limit, the standard deviation of the velocity fluctuations (the so-called suspension temperature) is proportional to the volume fraction, in both the transverse and the flow directions, and that a theoretical prediction, which considers only the hydrodynamic interactions between isolated pairs of spheres, is in good agreement with the numerical results even up to concentrations $\phi \sim 10\%$.

SUSPENTION TEMPERATURE

The problem of determining the velocity fluctuations in suspensions of non-Brownian solid spheres in Stokes flows is one of long-standing difficulty due to the underlying long-range many-body hydrodynamic interactions between the suspended particles. The variance, or the standard deviation (STD), of the velocity fluctuations is the simplest measure of the magnitude of such fluctuations and is sometimes referred to as the suspension *temperature*, which in the case of an anisotropic motion of the suspended spheres would actually be a tensor (covariance matrix). It is the purpose of this paper to investigate the velocity fluctuations present in a macroscopically homogeneous, unbounded suspension of neutrally buoyant, non-Brownian spheres subject to a simple shear flow in the limit of vanishingly small Reynolds numbers using Stokesian dynamics, as well as their dependence on the suspension microstructure generated by the shear.

The simulations include a non-hydrodynamic repulsive force between the spheres which, although extremely short ranged, leads to the development of fore-aft asymmetric distributions for large enough volume fractions, if the range of that force is kept unchanged. On the other hand, we show that, although the pair distribution function recovers its fore-aft symmetry in dilute suspensions, it remains anisotropic and that this anisotropy can be accurately described by assuming the complete absence of any permanent doublets of spheres.

	$t_{11} = t_{22}$	t_{33}		$t_{11} = t_{22}$	t_{33}
Random Hard Sphere ($g_{\text{HS}}(r)$)	0.3157	0.0811	Simple Shear Flow ($g_{\text{BG}}(r)$)	0.4637	0.1031

Table 1. Temperature tensor in the dilute limit, computed using Eq. 1 for two different pair distribution functions, one for a hard-sphere distribution, and the other given by [1] for a simple shear flow in the dilute limit.

In the dilute limit, the fluctuations in the velocity come from two-particle interactions, and from the far-field form of these interactions it can be shown that any component of the temperature tensor, of the form $\delta v_i \delta v_j$, decays faster than $1/r^3$ and therefore, its average value can be directly computed by averaging the hydrodynamic interaction between a pair of spheres over all possible configurations,

$$T_{ij} = \int d\mathbf{r}\; \delta v_i \delta v_j \, (3\phi/4\pi)\, g(\boldsymbol{r}) = \phi \left[\frac{3}{4\pi} \int d\mathbf{r}\; \delta v_i \delta v_j g(\boldsymbol{r}) \right] = \phi\, t_{ij}, \tag{1}$$

which gives a linear dependence of the temperature components on the volume fraction, $T_{ij} = \phi\, t_{ij}$.

The exact temperature values will depend in general on the pair distribution function. In Table 1, we present the diagonal terms of the temperature tensor in the dilute limit, obtained from the numerical integration of Eq. 1 for two different isotropic pair distribution functions, corresponding to a random distribution of hard spheres, $g_{\text{HS}}(r) = 1$, and to Batchelor & Green's result for a suspension in a simple shear flow, $g_{\text{BG}}(r)$ [1].

In figure 1, we present the diagonal terms of the temperature tensor as a function of the volume fraction, obtained in a simple shear flow by means of Stokesian dynamics simulations [2]. The temperature components T_{11} and T_{22} converge to a common curve in the dilute limit, which is consistent with the existence of an isotropic pair distribution function and indicates that the effect of the particle-depleted region of closed streamlines is not measurable.

In addition, the decay of the velocity fluctuations follows the dilute limit scaling given by Eq. 1, viz. that T_{ij} is proportional to ϕ, even for surprisingly high volume fractions.

On the other hand, at larger concentrations we see that the T_{11} and T_{22} curves separate from each other, which is evidence of the structure developed by the suspension at high concentrations. In fact, in a recent paper we showed that, although we have a very short-ranged interparticle force, $r_c = 10^{-4}$, and that the pair distribution function has fore-aft symmetry

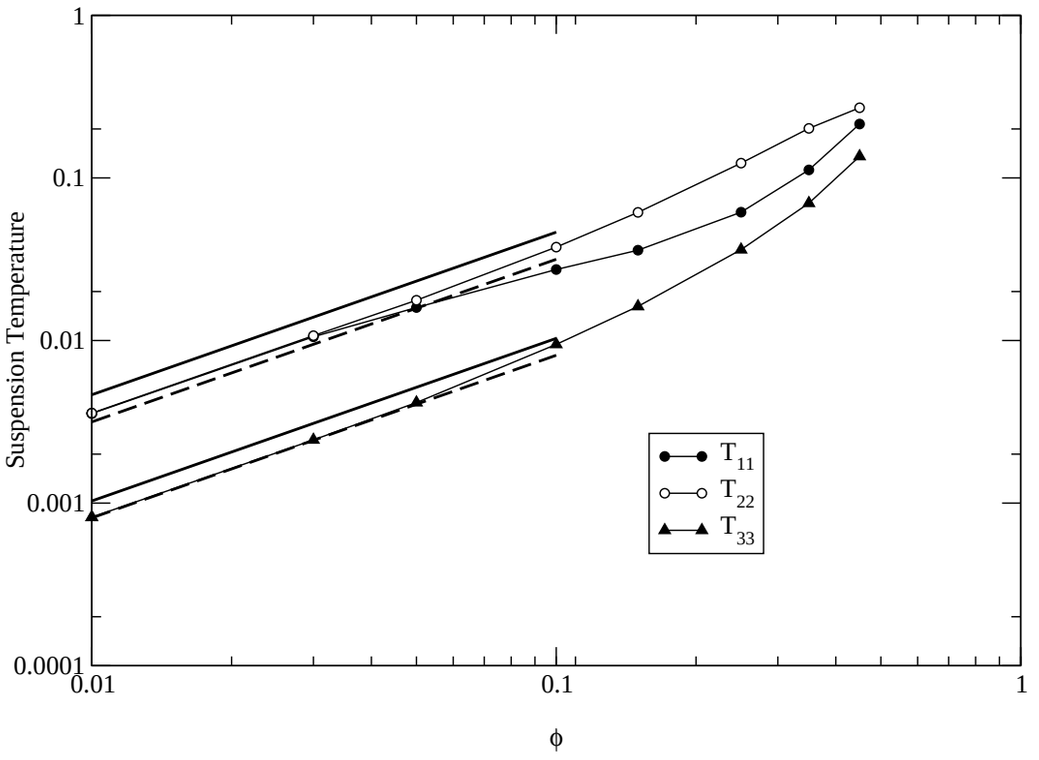


Figure 1. Diagonal components of the temperature tensor as a function of the volume fraction, obtained from the numerical Stokesian dynamics simulations. The solid lines correspond to the dilute limit, i.e. two-sphere, calculation using $g_{\text{BG}}(r)$ for $T_{11;22} = \phi\, t_{11;22}$ and $T_{33} = \phi\, t_{33}$, respectively. The computed values of $t_{11;22}$ and t_{33} are given in the second part of table 1 and the discrepancy between the dilute limit theory and the Stokesian dynamics results is about 25% for $\phi < 0.1$. The dashed lines correspond to the dilute limit calculation for $T_{11;22} = \phi\, t_{11;22}$ and $T_{33} = \phi\, t_{33}$, respectively, assuming a random distribution of hard spheres, i.e. $g_{\text{HS}}(r) = 1$. The computed values of $t_{11;22}$ and t_{33} are given in the first part of table 1 and the discrepancy with the Stokesian dynamics results is about 5%, again for $\phi < 0.1$.

We also show in figure 1 that, the calculations using $g_{\text{HS}}(r) = 1$, provide a surprisingly good estimate to the velocity fluctuations in sheared suspensions, suggesting that, probably, the effect of the microstructure is not measurable in the dilute limit.

This surprising result may be due to the fact that the main difference between the temperature, as obtained from the two-sphere calculations, using either $g_{\text{BG}}(r)$ or $g_{\text{HS}}(r)$, originates in the contribution of the lubrication region, which is negligible in the $g_{\text{HS}}(r) = 1$ case (see table 1).

Thus, a lower bound to the velocity fluctuations in the absence of permanent doublets can be estimated roughly using $g_{\text{HS}}(r) = 1$. Also, due to the slow, $\mathcal{O}(1/r^2)$, decay of the velocity fluctuations with the distance between spheres, the contribution of the lubrication region to the temperature is relatively minor, $\sim 20\%$, for a pair distribution function given by $g_{\text{BG}}(r)$, and should be expected to become even smaller due to the depletion of permanent doublets. However, the observed excellent agreement between the Stokesian dynamics results for the temperature of sheared suspensions and the temperature obtained from the two-sphere calculations using $g_{\text{HS}}(r) = 1$ could not have been expected a priori and is a surprising result.

This work was supported by the Engineering Research Program, Office of Basic Energy Sciences, U.S. Department of Energy under Grant DE-FG02-03ER46068.

References

[1] BATCHELOR, G. K. & GREEN, J. T. 1972*a* The determination of the bulk stress in a suspension of spherical particles to order c^2. *J. Fluid Mech.* **56** (3), 401–427.

[2] BRADY, J. F. 2001 Computer simulation of viscous suspensions. *Chem. Eng. Sci.* **56**, 2921–2926.

[3] DRAZER, G., KOPLIK, J., KHUSID, B. & ACRIVOS, A. 2002 Deterministic and stochastic behaviour of non-brownian spheres in sheared suspensions. *J. Fluid Mech.* **460**, 307–335.

XXI ICTAM, 15–21 August 2004, Warsaw, Poland

THE COLLECTIVE DYNAMICS OF SELF-PROPELLED PARTICLES

Vishwajeet Mehandia, Prabhu R. Nott
Department of Chemical Engineering, Indian Institute of Science, Bangalore 560 012, India

Summary We propose a method that can be used for the dynamic simulation of a collection of self-propelled particles. In our description, each particle is treated as a rigid sphere with a force dipole of constant magnitude. In isolation, it would move at constant velocity set by the magnitude and direction of the force dipole. When it coexists with many such particles, its hydrodynamic interactions with other particles rotates it and therefore changes its direction of motion, and also induces an additional stresslet on it. We have adapted the Stokesian Dynamics technique to simulate up to 80 active particles in unbounded domain. Our simulations show the streaming motion of active particles, similar to that observed in a previous study. The velocity distribution is highly non-guassian, in contrast to that of sheared passive particles.

INTRODUCTION

Self-propelled (or "active") particles, such as bacteria, spermatozoa and other microorganisms, exhibit several intriguing features in the collective dynamics, such as the spontaneous formation of spatio-temporal patterns, convection cells etc. The driving force for the patterms can be a spatial variation in the concentration of chemical species, called chemotaxis, or an external body force such as gravity, called gravitaxis. Bioconvection, is an example of the latter, where the motion of the microorganisms against gravity induces a Raylegh-Benard type instability. Understanding these phenomena is important from a purely scientific viewpoint, but this knowledge is also of potential utility in cell biological applications.

Previous attempts [1] at modelling the collective dynamics of self-propelled particles have either been phenomenological or at a coarse-grained level where the particles are treated as constituting a phase, and hence the concentration field describes the nature of the system. These treatments cannot correctly describe the microstructures that form at the length scale of a few-to-several particle diameters, and may therefore to miss the fluid mechanical phenomena that result from them.

THE MOTION OF AN INDIVIDUAL SELF-PROPELLED PARTICLE

Many studies have investigated the motion of a single active particle, from the point of view of its fluid mechanics [2] as well as its biophysics and biomechanics [3]. Typically, a single microorganism in a fluid medium swims a distance of roughly 3 to 50 times its own size every second, and randomly changes its direction of motion after swimming a distance of roughly 10-100 times its size. The motion of the particle can be driven by the beating of its flagella or cilia, spiral motion of a single flagella, or sometimes even a reversible polymerization/de-polymerization reaction at one end of the organism. However, the mechanism of propulsion is not very important in analysing the fluid mechanics around these particles. As the particles are self-propelled, and not by an external force, far away they appear as point dipoles [4].

COLLECTIVE DYNAMICS

We model a collection of active particles as a collection of hydrodynamically interacting force dipoles. Each particle is treated as a rigid sphere with a force dipole of constant magnitude. In isolation, it moves at constant velocity set by the magnitude and direction of the force dipole. When it coexists with many such particles, its hydrodynamic interactions with them rotates it and therefore changes its direction of motion, and also induces on it an additional stresslet. As a result, interactions between particles tend to randomize the orientation, and hence the velocity, of the particles. We have adapted the Stokesian Dynamics [5] technique to simulate up to 80 active particles in unbounded domain. Our simulations are for a monolayer of active particles, i.e. the particles are constrained to lie in a plane at all time. The sequence of snapshots in the simulations clearly show the streaming motion of active particles, similar to that observed for bacteria in freely suspended film [6].

The velocity distribution of the particles, shown in figure 1, has peaks at $\pm v_0$, the speed of a isolated self propelled particle, a 'crater' at speeds less than v_0, and decays rapidly at velocities larger than v_0. Note that though the distribution is roughly symmetric about $v = 0$, it is is quite different from a Gaussian distribution. This is very different from the distribution of particle velocities in sheared suspensions of "passive" particles, which is approximately Gaussian. The mean square displacement of the particles varies approximately lineary with time for large time (not shown), implying that the collective motion of the particles is diffusive.

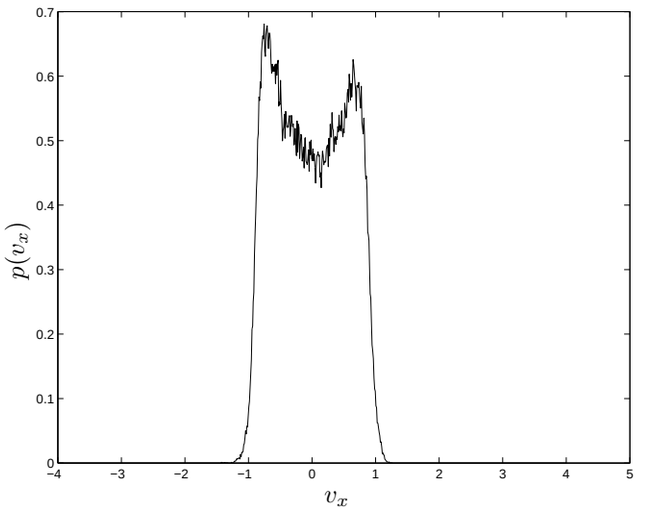


Figure 1. The probability density of the velocity in the x direction for a suspension of active particles of 10% area fraction.

CONCLUSION

Our preliminary results indicate that hydrodynamic interactions alone yield a rich structure in the collective dynamics of self propelled particles. We intend to also incorporate forces on the particles that mimic chemitaxis and gravitaxis, and thereby study physically realistic systems.

References

[1] T. J. Pedley, J. O. Kessler: *Annu. Rev. Fluid Mech.* **24**: 313, 1992
[2] G. I Taylor: *Proc. Roy. Soc. A* **209**: 447, 1951
[3] J. Lighthill: *SIAM Rev.* **18**: 161, 1976
[4] C. Brennen, H. Winet: *Annu. Rev. Fluid Mech.* **9**: 339, 1977.
[5] J.F. Brady, G. Bossis: *Annu. Rev. Fluid Mech.* **20**: 111, 1988.
[6] Wu, Libchaber: *Phys. Rev. Letters* **84(13)**: 3017, 2000.

XXI ICTAM, 15–21 August 2004, Warsaw, Poland

MICROSTRUCTURE OF A DILUTE SEDIMENTING SUSPENSION

Bogdan Cichocki, Krzysztof Sadlej
Institute of Theoretical Physics,Warsaw University, Hoża 69, PL 00-618 Warsaw, Poland

Summary We consider the sedimentation of a dilute suspension of particles in a viscous incompressible fluid at low Reynolds number. Starting from a general Liouville type evolution equation for the particle configuration probability density and assuming finite range of correlations, we are able to explicitly find the two-particle stationary distribution function for a sedimenting suspension in the low particle concentration limit.

INTRODUCTION

Sedimentation is the movement of a suspension under a given external force field acting on the mesoscopic particles suspended in a fluid. The slow sedimentation of a monodisperse, dilute suspension of non-Brownian rigid particles in a viscous fluid where inertial effects can be neglected is one of the basic and fundamental problems in microhydrodynamics of suspensions. However simple it might seem at first glance, it features a myriad of interesting phenomena and questions which are still unresolved and need answering.

A single sphere sedimenting in a viscous fluid falls with the well known constant Stokes velocity. Due to the long range and multi-particle hydrodynamic interactions between an ensemble of sedimenting particles the mean suspension velocity decreases rapidly with increasing particle volume fraction ϕ. The first order correction -6.55ϕ to the single particle sedimenting velocity was first computed incorporating a renormalization procedure by G. K. Batchelor [2]. The calculation assumed: (i) a low particle Reynolds number justifying the neglect of inertia, (ii) consideration of only two-body interactions, (iii) a random (or equilibrium) distribution of particles in configuration space, and (iv) the system infinite in the direction transverse to the force field. But as R .E. Caflisch and J. H. C. Luke [4] pointed out, a random distribution of sedimenting spheres results in velocity fluctuations (variance) which scale linearly with the macroscopic size of the system. The above theoretical predictions have not been seen in experiments. In contradictions [5], [6], [7] [8] experimental measurements of the velocity fluctuations have consistently been interpreted as having a saturation level at some critical and universal system size proportional to the mean interparticle spacing, leading to fluctuation scaling independent of system size. On the other hand, virtually all numerical studies reported [9] have been consistent with the theoretical scaling proportional to the system size.

This obvious discrepancy has attracted a lot of theoretical attention. The first to propose a solution were D. L. Koch and E. S. G. Shaqfeh [10]. Their central idea based on the violation of the assumption (iii). Due to three-particle interactions, the particle were to rearrange in such a way, as to cancel out, or screen, the long rang hydrodynamic interactions. An explicit form of the particle distribution function exhibiting the above property was calculated, but the predicted correlation length scaling turned out not to agree with the experiment.

Several other attempts have been made to crack the mysterious inconsistency. Brenner [11] emphasized the importance of side wall effects on the microscopic evolution, and possible screening of hydrodynamic interactions. Further calculations [12], [13], [14] incorporate the idea of a vertical stratification owing to the broadening of the sediment front. Non of these seem to be experimentally verifiable nor to present a consistent and general picture.

Recent experiments [15] indicate that the particle distribution while sedimenting is not the random or equilibrium one. The explicit determination of the statistical distribution of a steady state sedimenting suspension is still an open problem, with which we are to deal in this work.

METHOD AND MAIN RESULTS

We consider a suspension of N particles sedimenting in a viscous fluid of viscosity η. The radius a of the particles is of the order $10 - 10^2 \mu m$ insuring that the Peclet number is large and that Brownian motion can be neglected.

The basic equation governing the evolution of a suspension is the Navier-Stokes equation, which under the above assumptions can be reduced to the linear Stokes equation. It is further assumed that a given force field $F = (\boldsymbol{F}_1, \boldsymbol{F}_2, \ldots, \boldsymbol{F}_N)$ acts on the particles. Since the problem is linear, the relation between the individual particle velocities and the forces is also linear. This relation can be summarized in a $3N \times 3N$ mobility matrix $\mu(X)$ dependent on the given configuration $X = (\boldsymbol{R}_1, \ldots \boldsymbol{R}_N)$ of particles.

Looking at the problem from a statistical physicists point of view, it is useful to consider the statistical distribution $P(X, t)$ for finding the system in a given configuration X at time t. This distribution satisfies the Liouville equation:

$$\frac{\partial P}{\partial t} + \frac{\partial}{\partial X} \cdot (\mu \cdot FP) = 0. \tag{1}$$

Introducing next the cluster expansion of the general mobility matrix we are able to derive a BBGKY (Bogolubov-Born-Green-Kirkwood-Yvon)-type hierarchy of equations [1] governing the time evolution of reduced s-particle distribution

etc. of particles in given configurations. They are defined by

$$n_s(\boldsymbol{R}_1, \boldsymbol{R}_2, \ldots, \boldsymbol{R}_s; t) = \frac{N!}{(N-s)!} \int d\boldsymbol{R}_{s+1} \ldots d\boldsymbol{R}_N P(X; t), \qquad s = 1, 2, \ldots, N. \tag{2}$$

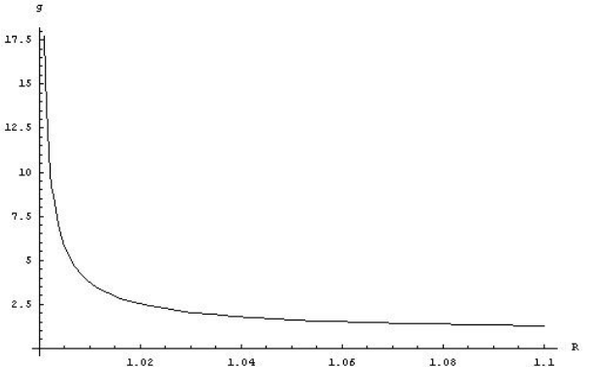
The hierarchy equations give a relation between the time derivative of the s-particle partial distribution function and the spatial derivatives of the mobility matrix and all the consecutive $s, s+1, \ldots$-particle partial distribution functions and their spatial integrals in respect to particle positions with labels $s+1, \ldots$.

In further considerations we focus on stationary states. It can be explicitly shown that the equilibrium state, or random configuration probability density is not a solution of equation (1). Moreover, assuming a random distribution we encounter, discussing the hierarchy equation, similar divergence problems as R .E. Caflisch and J. H. C. Luke [4] came upon while calculating the velocity variance. In this case, due to the very long range character of the hydrodynamic interactions some terms in the hierarchy become infinite in the thermodynamic limit (i.e. the limit of the system volume infinite, number of particles infinite while keeping the particle concentration constant).

The main idea behind this work is to find a particle distribution which despite long range hydrodynamic interactions, will in a self-consistent way keep the correlations length finite (i.e. the correlations will decay faster than $1/r^3$, where r is the interparticle distance) and thus cancel out the otherwise infinite terms in the equations.

We concentrate on the limit of small particle concentrations, when only terms in the lowest order in particle density are taken into consideration and the infinite hierarchy of equations describing the time evolution of the reduced distribution functions becomes a set of closed equations. The first nontrivial equation is the one giving the time evolution of the three-particle reduced distribution function $n_3(\boldsymbol{R}_1, \boldsymbol{R}_2, \boldsymbol{R}_3)$. The requirement to retain a finite correlation length, in spite of long range terms in the interactions between particles, together with the explicit formula for the three-particle mobility matrix given in terms of Green operators [3] lead to a linear partial differential equation for the two-particle reduced distribution function. The received equation is solved, and the explicit form of the two-particle distribution function

Figure 1. The two-particle reduced distribution function $g(R)$ satisfying the finite correlation length criterion



given (fig. 1). The knowledge of that function opens the possibility to recalculate the first order correction in volume fraction to the mean sedimentation velocity. The obtained result is

$$\frac{U}{U_0} = 1 - 3.87\phi + \mathcal{O}(\phi^2). \tag{3}$$

Furthermore the structure factor $S(k=0) = 1 - 1.64\phi + \mathcal{O}(\phi^2)$.

References

[1] R. Balescu, *Equilibrium and Nonequilibrium Statistical Mechanics*, New York, 1975, John Wiley.
[2] G. K. Batchelor, *J. Fluid Mech.* **53**, (245), (1972).
[3] B. Cichocki, M.L. Ekiel-Jeżewska, P.Szymczak, E.Wajnryb, *J. Chem. Phys.* **117**, 1231, (2002).
[4] R. E. Caflisch, J. H. C. Luke *Phys. Fluids* **28**, 259 (1985).
[5] H. Nicolai, E. Guazzelli *Phys. Fluids* **7**, 3 (1995).
[6] H. Nicolai, B. Herzhaft, E.J. Hinch, L. Oger, E. Guazzelli *Phys. Fluids* **7**, 12 (1995).
[7] P. N. Segré, E. Herbolzheimer, P. M. Chaikin *Phys. Rev. Lett* **79**, 2574 (1997).
[8] E. Guazzelli, *Phys. Fluids* **13**, 1573 (2001).
[9] A. J. C. Ladd, *J. Chem. Phys.* **93**, 3484, (1990); *Phys. Fluids* **5**, 299, (1993); *J. Fluid Mech.* **271**, 285, (1994); *Phys. Rev. Lett.* **76**, 1392, (1996); *Phys. Fluids* **9**, 491, (1997); *Phys. Rev. Lett.* **88**, 048301, (2002).
[10] D. L. Koch, E. S. G. Shaqfeh, *J. Fluid Mech.* **224**, (275), (1991).
[11] M. P. Brenner, *Phys. Fluids* **11**, 754, (1999).
[12] J. H. C. Luke, *Phys. Fluids* **12**, 1619, (2000).
[13] S.-Y. Tee, P. J. Mucha, L. Cipelletti, S. Manley, M. P. Brenner, P. N. Segré, D. A. Weitz *Rhys. Rev. Lett.* **89**, 054501, (2002).
[14] P. J. Mucha, M. P. Brenner, *Phys. Fluids* **15**, 1305, (2003).

SEDIMENTATION OF DILUTE SUSPENSIONS

B.U. Felderhof
Institut für Theoretische Physik A, RWTH Aachen, Templergraben 55, 52056 Aachen, Germany

Summary For a class of sedimentation states of a dilute suspension, corresponding to definite values of the mean sedimentation velocity and of the horizontal and vertical velocity variance, the static structure factor and the velocity correlation functions of the suspended particles are calculated and shown to exhibit screening.

The sedimentation of particles in a viscous fluid is still not fully understood, even for settling at low Reynolds number. Batchelor[1] first showed that for disordered suspensions, with complete neglect of correlations in particle positions apart from hard-sphere repulsion, the sedimentation velocity decreases rapidly with volume fraction ϕ, in proportion to $1 - 6.55\ \phi$. However, in his calculation he assumed that the pair distribution of the suspended particles is isotropic, and corresponds to that of a dilute hard-sphere system. The determination of the actual statistical distribution of a sedimenting suspension and the calculation of the corresponding sedimentation velocity is still an open problem.
It is known since the work of Caflisch and Luke[2] that for dilute suspensions, where the point approximation is reliable, the variance of particle velocity diverges with the size of the system if the distribution is random. It has been suggested that a form of hydrodynamic screening is necessary to keep the variance finite[3]. The divergence with the size of the system is not seen in experiment[4][5][6]. Several theoretical explanations have been advanced[7][8] that do not rely on the screening property. Our calculation explores the effect of particle correlations due to hydrodynamic interactions.
Hydrodynamic interactions are simple for dilute suspensions, since then the particles are far apart and a point approximation can be used. We have shown that for sedimentation states that are characterized by a distribution in configuration space of simple form, the horizontal and vertical variance of velocity can be calculated by use of a continuum approximation. The variances tend to finite values in the limit of an infinite system. We have also calculated the corresponding velocity correlation functions, density correlation function, and structure factor. The correlation functions show screening due to an interplay of Boltzmann entropy and hydrodynamic interactions. Parameters of the state can be chosen to obtain agreement with experiment. If the parameters are chosen to be independent of density, then the correlation functions automatically show the scaling with density seen in experiment[6].
Due to the anisotropy of the pair distribution Batchelor's low density result for the friction coefficient must be corrected. We find that to lowest order in density the correction to the Stokes velocity is given by

$$\bar{u}_{z0} = \frac{K}{6\pi\eta a} - \mu_0 \frac{K}{6\pi\eta d} \tag{1}$$

with numerical coefficient $\mu_0 \approx 0.028$. Here K is the force acting on a particle, η is the shear viscosity, a is the particle radius, and $d = (3/4\pi n_0)^{1/3}$ is the mean distance between particles at number density n_0. The velocity variances in the dilute limit are

$$\Delta V_{||0} = \alpha_z \frac{K}{6\pi\eta d}, \qquad \Delta V_{\perp 0} = \alpha_h \frac{K}{6\pi\eta d}, \tag{2}$$

with numerical coefficients $\alpha_z \approx 2.1$ and $\alpha_h \approx 0.9$, as found by comparison with experiment[6]. The quantity $v_K = K/(6\pi\eta d)$ is the velocity scale of the dilute suspension.

References

[1] G. K. Batchelor, J. Fluid Mech. **52**, 245 (1972).

[2] R. E. Caflisch and J. H. C. Luke, Phys. Fluids **28**, 259 (1985).

[3] D. L. Koch and E. S. G. Shaqfeh, J. Fluid Mech. **224**, 275 (1991).

[4] H. Nicolai, B. Herzhaft, E. J. Hinch, L. Oger, and E. Guazzelli, Phys. Fluids **7**, 12 (1995).

[5] H. Nicolai and E. Guazzelli, Phys. Fluids **7**, 3 (1995).

[6] P. N. Segrè, E. Herbolzheimer, and P. M. Chaikin, Phys. Rev. Lett. **79**, 2574 (1997).

[7] M. P. Brenner, Phys. Fluids **11**, 754 (1999).

[8] S.-Y. Tee, P. J. Mucha, L. Cipelletti, S. Manley, M. P. Brenner, P. N. Segrè, and D. A. Weitz, Phys. Rev. Lett. **89**, 054501 (2002).

RELAXATION TIME FOR SEDIMENTING SPHERES OF A SUSPENSION WITH PERIODIC BOUNDARY CONDITIONS

Maria L. Ekiel-Jeżewska*, Eligiusz Wajnryb*
*Institute of Fundamental Technological Research, Polish Academy of Sciences, Świetokrzyska 21, PL 00-049 Warsaw, Poland

Summary We numerically simulate sedimentation of a suspension with periodic boundary conditions. We consider mono-disperse non-Brownian spheres in low-Reynolds-number fluid flow. We analyze how fast a steady state is reached and how the evolution depends on the initial pair distribution.

INTRODUCTION

Sedimentation of suspensions made of spherical mono-disperse non-Brownian particles has been recently extensively investigated experimentally, theoretically and numerically [1]. The main interest has been to investigate the nature of the steady state and to understand how does it differ from equilibrium. Explanation of the observed large correlations of particle velocity fluctuations and theoretical derivation of the relevant pair probability distribution at the steady state are still open problems.

It is of interest to understand how fast and in what way sedimenting suspensions become stationary. The observed relaxation times are long, both in experiments [3, 4] and simulations [5, 6]. Some authors claim that in some cases a steady state is not reached at all [2]. Experiments of Guazzelli et al. [3, 4] indicate that there exist two characteristic time scales in evolution of a sedimenting suspension. First, after several Stokes times only, a big swirl is formed in the container. Later, after a few hundreds of Stokes times, the system becomes stationary. The problem how the relaxation time depends on the size of the system has been raised and investigated [2, 6]. Results of Ref. [7] indicate that time of interaction between sedimenting spheres is sensitive to initial conditions. Therefore in this work, within a toy-model, we investigate qualitatively how does the relaxation time of a sedimenting suspension depend on its initial pair distribution.

INITIAL CONFIGURATIONS – A TOY MODEL

We consider exemplary system with N=8 sedimenting spheres in each periodic cube. We select small volume fraction ϕ=0.003, as in the system investigated experimentally in Refs. [3, 4]. The corresponding size of the periodic cube $L \approx 11.2$. Length is measured in sphere diameters, time and velocity in the Stokes units.

We study the following three classes of initial positions of the sphere centers.

- EQUILIBRIUM – positions are chosen with the most-probable distribution (uniform with no overlap).
- PERTURBED LATTICE (deficit of close pairs) – we perform a random perturbation from cubic lattice with a small amplitude $A = (L-2)/8 \approx 1.1$, with the uniform distribution.
- CLOSE PAIRS (excess of close pairs) – spheres are grouped in pairs, each pair in a separate ball of diameter $D = 4$. We take the most-probable distributions of the spheres within the ball and of the balls within the cube.

The integrated pair distribution $n(r)$ for each class is plotted in Fig. 1. Here $n(r)$ is the mean number of particles in a spherical volume of radius r surrounding a test sphere, minus the average number of particles in the same volume.

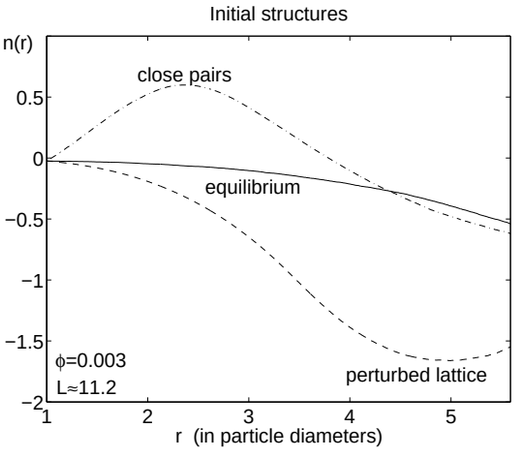


Fig. 1. The initial integrated pair distribution $n(r)$.

METHOD

The fluid is described by the incompressible Stokes equations with periodic boundary conditions and the stick boundary conditions at the surfaces of N spheres immersed in the periodic cube. The Green tensor for such a system has been specified by Hasimoto [8] and expressed in a form suitable for fast numerical computation by Cichocki and Felderhof [9]. Their results are implemented in the numerical codes used in this paper, which are modifications of the previous codes developed for infinite fluids and applied e.g. in Ref. [10]. For given positions of N spheres, the mobility coefficients are evaluated by the multipole method [11], with the lubrication correction [12], which takes care of interactions between close spheres. To get accurate trajectories, we truncate the multipole expansion at the multipole number $l = 3$ (with l defined in Ref. [11]). Equations of motion for N spheres are integrated with the fourth-order Runge-Kutta algorithm. In this way the particle positions and velocities are determined as functions of time.

RESULTS

The averaging is performed over all the particles in the periodic cell and over a number M of random initial configurations, separately within each of three classes listed above. In Figs. 2 and 3, we trace the mean sedimentation velocity U and the mean horizontal and vertical velocity fluctuations, δU $_\perp$ and δU$_{||}$, respectively, as functions of time. Similar analysis is performed for the integrated pair distribution $n(r)$.

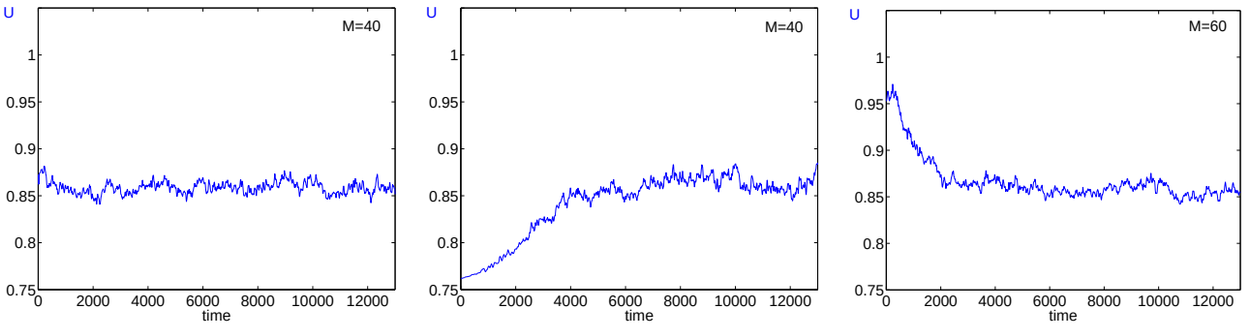


Fig. 2. Evolution of the mean sedimentation velocity U for three classes of initial configurations. Left: equilibrium; center: perturbed lattice; right: close pairs. Time is measured in Stokes times. M is the number of initial configurations.

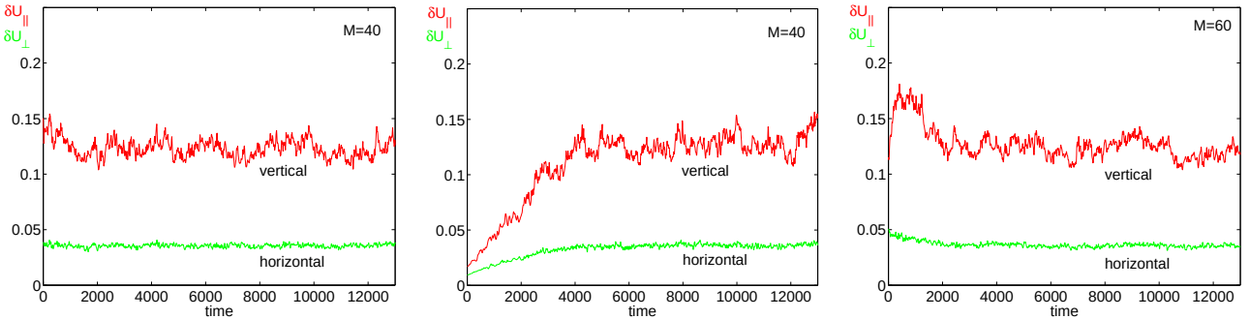


Fig. 3. Evolution of the mean horizontal and vertical velocity fluctuations, δU $_\perp$ and δU$_{||}$, respectively, for three classes of initial configurations. Left: equilibrium; center: perturbed lattice; right: close pairs. Time is measured in Stokes times. M is the number of initial configurations.

Relaxation time to the steady state is of the order of $2000\,\tau_{St}$ for close pairs and $4000\,\tau_{St}$ for perturbed lattice. It increases if the initial deficit (or excess) of particles increases, i.e. if A or D decreases. For initially close pairs, the second much shorter time scale has been observed around $100 - 400\,\tau_{St}$. On this time scale the excess of close pairs, initially concentrated around a given small distance, is redistributed over all the distances. It takes one order of magnitude longer to loose the excess of close pairs, reaching the final steady state.

Acknowledgement. This work was supported in part by Polish KBN grant 5T07C03522.

References

[1] Ramaswamy S.: Issues in the statistical mechanics of steady sedimentation. *Adv. Phys.* **50**:297–341, 2001.
[2] Tee S.Y., Mucha P.J., Cipelletti L., Manley S., Brenner M.P., Segre P.N., Weitz D.A.: Nonuniversal velocity fluctuations of sedimenting particles. *Phys. Rev. Lett.* **89**:054501-1–4, 2002.
[3] Guazzelli E.: Evolution of particle-velocity correlations in sedimentation. *Phys. Fluids* **13**:1537–1540, 2001.
[4] Bergougnoux L., Ghicini S., Guazzelli E., Hinch J.: Spreading fronts and fluctuations in sedimentation. *Phys. Fluids* **15**:1875-1887, 2003.
[5] Ladd A.J.C.: Dynamical simulations of sedimenting spheres. *Phys. Fluids A* **5**:299–310,1993.
[6] Ladd A.J.C.: Effects of container walls on the velocity fluctuations of sedimenting spheres. *Phys. Rev. Lett.* **88**:048301-1–4, 2002.
[7] Janosi I.M., Tel T., Wolf D.E., Galas J.A.C.: Chaotic particle dynamics in viscous flows: The three-particle Stokeslet problem. *Phys. Rev. E* **56**:2858–2868, 1997.
[8] Hasimoto H.: On the periodic fundamental solutions of the Stokes equations and their application to viscous flow past a cubic array of spheres. *J. Fluid Mech.* **5**:317-328, 1959.
[9] Cichocki B., Felderhof B.U.: Periodic fundamental solution of the linear Navier-Stokes equations. *Physica A* **159**:19–27, 1989.
[10] Cichocki B., Ekiel-Jeżewska M.L., Szymczak P., Wajnryb E.: Three-particle contribution to sedimentation and collective diffusion in hard-sphere suspensions. *J.Chem. Phys.* **117**:1231–1241, 2002.
[11] Cichocki B., Felderhof B.U., Hinsen K., Wajnryb E., Bławzdziewicz J.: Friction and mobility of many spheres in Stokes flow. *J. Chem. Phys.* **100**:3780-3790, 1994.
[12] Brady J.F., Bossis G., Stokesian dynamics. *Ann. Rev. Fluid Mech.* **20**:111-157, 1988.

XXI ICTAM, 15–21 August 2004, Warsaw, Poland

NUMERICAL SIMULATIONS OF PARTICLE SUSPENSIONS IN A ROTATING FLOW

Jonghoon Lee and Anthony J.C. Ladd
Chemical Engineering Department, University of Florida, Gainesville, Florida 32611-6005

Summary We have developed an algorithm to simulate the motion of suspended solid particles in a rotating cylinder. The hydrodynamic interactions are calculated from the Stokes-flow generated by a point force, with a Green's function that enforces a zero-velocity boundary condition on the surface of the cylinder. We have implemented a parallel version of the algorithm, which also scales linearly with the number of particles. For the time scales of interest, typically of the order of 100-200 rotations of the tube, simulations of a few thousand particles per processor are feasible. The code has been applied to the investigation of pattern formation in a rotating suspension. In these experiments a cylinder filled with a suspension of heavy particles is rotated about a horizontal axis, and a number of different "phases" or particle patterns have been observed and characterized experimentally. We plan to use numerical simulations to elucidate the hydrodynamic mechanisms leading to pattern formation.

Recent experiments [1] have shown unexpected patterns in the spatial distribution when a suspension of non-neutrally buoyant particles is rotated about a horizontal axis. The combination of gravity and rotational lift produce a variety of interesting and surprising steady states. In Fig. 1 we show results for a small number of particles in a short tube. The tube radius is 0.5cm, the fluid viscosity is 0.58 poise and the particle mass density, corrected for buoyancy, is 1.2 g/cc. The parameters are comparable to the experimental setup except that the tube radius is smaller by a factor of 2. At low rotation speeds the particles are confined to a small volume on the lift side of the tube, as shown by the majority of the particles in the upper left-hand picture of Fig. 1. Particles next to the wall are lifted by the rotation of the tube, but in adjacent layers the gravitational forces exceed the viscous drag from the fluid and they slip down to the bottom so that there is a constant circulation of particles. At the slightly higher rotational velocity shown in the first figure, $\Omega = 0.4\mathrm{Hz}$, particles are ejected into the bulk fluid and fall in a more or less semicircular arc rather than straight down, so that the fluid flow in the upper half of the tube must be predominantly clockwise. This flow sets up a strong shear layer across the center of the cell, so that in the lower half of the tube we see a counter-clockwise flow, lifting particles off the base of the tube and returning them to the wall higher up.

At higher rotation speeds these counter-rotating regions grow and become more symmetrical, filling the tube cross section at the same time, as shown in the upper right picture in Fig 1. At still higher speeds the lower counter-rotating region shrinks (lower left) and eventually disappears altogether (lower right), leaving the particles undergoing a more or less rigid-body motion, produced by a delicate balance of rotational, gravitational and hydrodynamic forces. It should be noted that none of these phenomena occur in the absence of hydrodynamic interactions. A single particle simply rotates about an off-center position, while slowly spiralling to the outside wall, where it eventually reaches a limiting trajectory [2].

At the highest rotation rate we have so far studied, $\Omega = 0.9\mathrm{Hz}$, the particles congregate into weak but stable axial bands as shown in Fig. 2. We have previously proposed an explanation for this axial instability based on a differential centrifuging mechanism [2], but the simulations suggest that a complex combination of rotational and gravitational forces is responsible, and that centrifugal forces do not play a major role. It should be emphasized that all the structures shown here have previously been observed experimentally [1], and so far we have only provided a validation of the computational method rather than a discovery of new physical phenomena. We plan to make a detailed sequence of simulations in the coming year, to try to elucidate the mechanisms underlying the pattern formation.

The numerical method is based on the Green's function for a Stokeslet in a cylindrical tube [3]. We have implemented both the Fourier-Bessel representation and the residue sum detailed in Ref. [3]. We obtain identical results when the particles are more than a few diameters apart, but when they are in near contact there are convergence issues with both methods. We assume that since the suspension is dilute, a typical volume fraction is 2%, the short-range interactions are relatively unimportant, but this remains to be verified. We prefer the Fourier-Bessel representation in our simulations since it enables a linear scaling of the computational time with the number of particles.

In conclusion, we have developed a fast numerical method for simulating the dynamics of suspended particles in a rotational flow. The method can treat of the order of 10^5 particles on a moderately sized cluster (32-64 processors). We have reproduced the key qualitative features of the experimental observations at low rotation rates, within the observed parameter ranges. Future work will be aimed at understanding the mechanisms underlying the pattern formation.

References

[1] W. R. Matson, B. J. Ackerson, and P. Tong. Pattern formation in a rotating suspension of non-Brownian settling particles. *Phys. Rev. E*, 050301:67, 2003.
[2] J. Lee and A. J. C. Ladd. Axial segregation in a cylindrical centrifuge. *Phys. Rev. Lett.*, 89:104301, 2002.
[3] N. Liron and R. Shahar. Stokes flow due to a Stokeslet in a pipe. *J. Fluid Mech.*, 86:727–744, 1978.

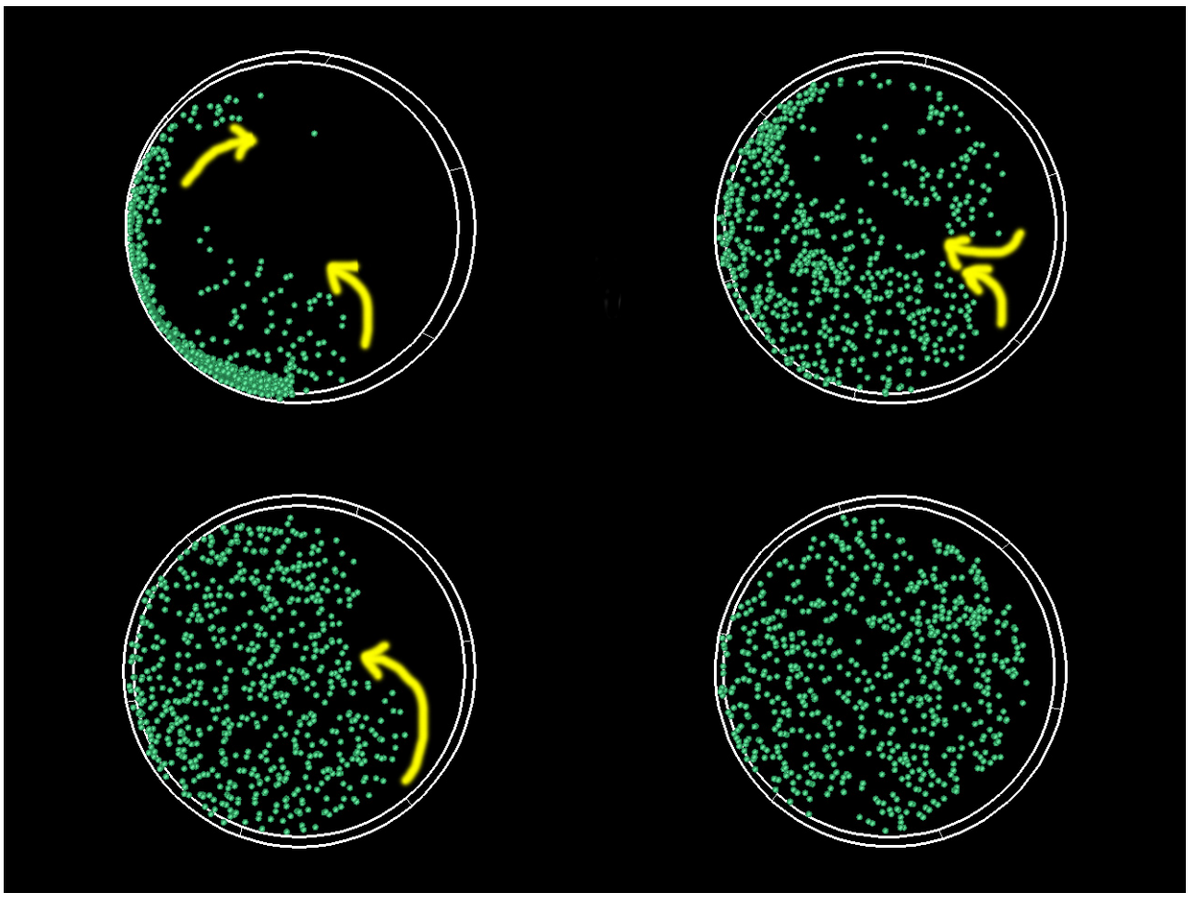


Figure 1. Particle distributions at different rotation rates: $\Omega(\mathrm{Hz}) = 0.4, 0.6, 0.8, 0.9$. At the lowest rotation rate (upper left) a small fraction of the particles are ejected into the bulk fluid by the (clockwise) rotation of the cylinder wall. A counter flow at the base lifts particles in a counter-clockwise flow. At slightly higher rotation rates (upper right) these flows develop into a symmetric pair of semi-circular flows. At higher rates still the lower counter flow becomes small (lower left) and eventually vanishes (lower right) leaving a more or less solid-body rotation of uniformly distributed particles. The yellow arrows are a rough guide to the predominant fluid motions, with respect to the rigid body motion.

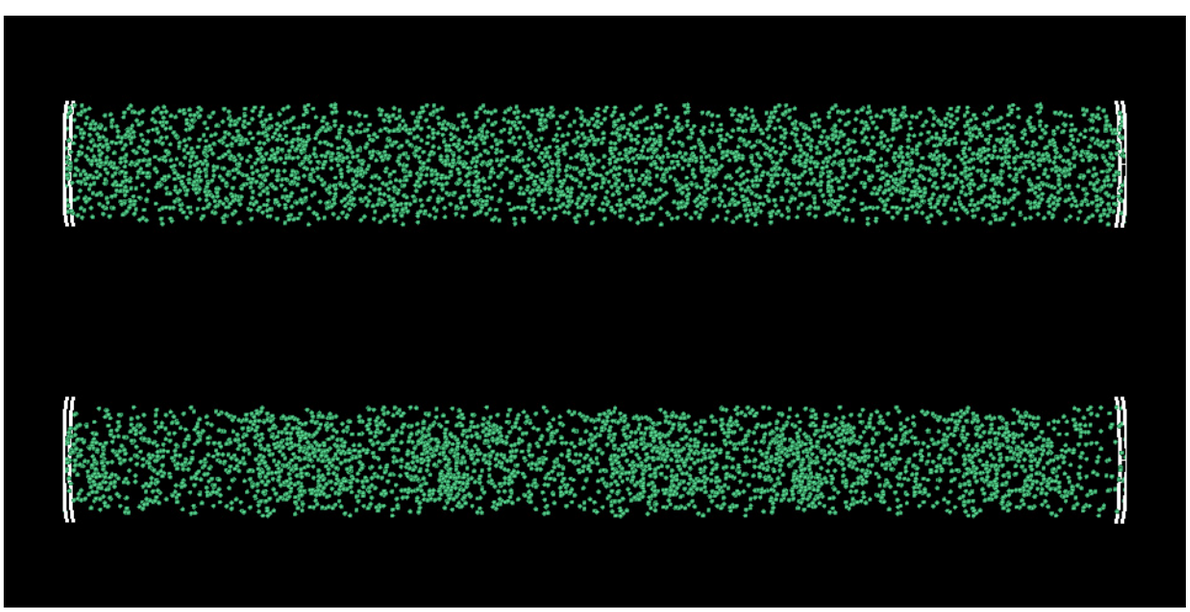


Figure 2. Axial band formation in a rotating suspension. Over a narrow range of rotation rates, $\Omega \approx 1\mathrm{Hz}$, an initially uniform particle distribution (upper) is unstable and permanent axial perturbations develop in the particle concentration. Note that the simulated system been replicated 3 times in the axial direction to allow the eye to pick up the band formation in the lower figure.

A Mode-mode Coupling Scheme of Colloidal Electrolyte Friction

Mathieu G. McPhie and Gerhard Nägele

Institut für Festkörperforschung
Forschungszentrum Jülich
D-52425 Jülich, Germany

The dynamics of charge-stabilized dispersions consisting of highly charged colloidal particles (macroions) dispersed in a solution of weakly charged small counter- and coions (microions) has attracted considerable interest, both experimentally and theoretically. Theoretical work on charge-stabilized colloids has been mostly based on an effective macrofluid model of dressed macroions interacting by an effective pair potential of spherical symmetry, by integrating out the microionic degrees of freedom.

A major drawback of the dressed macroion model is that it does not account for the kinetic influence of the microionic atmosphere on the colloidal dynamics. The theoretical modeling and quantification of electrokinetic effects originating from the non-instantaneous relaxation of the microionic atmosphere is a demanding task even for a single spherical macroion diffusing in an unbounded multi-component electrolyte. In this case, light scattering experiments [1] have revealed that the diffusive motion of the microions relative to the large macroion gives rise to an increase (decrease) in the friction coefficient (sedimentation velocity) of the tracer macroion. As a consequence, the long-time self-diffusion coefficient, D_T^L, of the tracer has a minimal value when the thickness of the microionic cloud, as measured by the screening length κ^{-1}, is comparable to the radius a of the macroion (cf. Fig. 1).

The mean velocity, U, of a slowly sedimenting macroion in the presence of its neutrally buoyant electrolyte atmosphere is related to the long-time self-diffusion coefficient by $D_T^L = k_B T/(6\pi\eta a + \Delta\zeta_T) = D_T^0 U/U^0$, where U^0 and D_T^0 are the Stokesian sedimentation velocity and the diffusion coefficient, respectively, of the tracer, and η denotes the solvent viscosity. The effect of the microion relaxation is embedded in the excess friction contribution $\Delta\zeta_T$. The statistical fluctuations of the microionic atmosphere around the colloidal tracer are coupled to the corresponding hydrodynamic fluctuations through the intervening solvent. Therefore, it is necessary to treat the steric and electrostatic direct interactions, and the hydrodynamic interactions (HI) between tracer and microions on equal footing.

Based on a recently formulated mode-mode coupling scheme for Brownian systems where HI has been included [2], and where the macroion and the microions are treated, equally, as charged hard spheres immersed in an unstructured solvent, we have calculated the long-time self-diffusion coefficient and the sedimentation velocity of the tracer [4]. According to Fig. 1, our mode-mode coupling results are in good agreement with the experimental data for D_T^L. An important conclusion drawn from our theoretical analysis is that the minimum of D_T^L at $\kappa a \approx 0.5$ is due to a combined effect of hydrodynamic and direct forces acting between macroion and microions. This fact should be contrasted with earlier approaches on electrolyte friction where it has been attempted to explain the minimum of D_T^L in terms of direct forces only (cf., e.g., [5,6]). In fact, the neglect of HI gives rise to a charge-independent contribution to $\Delta\zeta_T$. This additional friction contribution, in turn, leads to a monotonic decline of D_T^L with increasing ionic strength, as seen from Fig. 1, in conflict with experimental observation. The charge-independent friction contribution arises from the excluded volume interactions between the tracer and the point-like microions. With HI, the excluded volume contribution becomes quite small, since the microparticles are advected by the hydrodynamic flow field created by the moving tracer sphere.

The theoretical results in Fig. 1 are for point-like microions described by Debye-Hückel-type pair distribution functions. For dispersions of comparably small macroions like charged globular proteins and charged micelles, which are only a few nanometers in size, one needs to account for the finite sizes of the macroions.

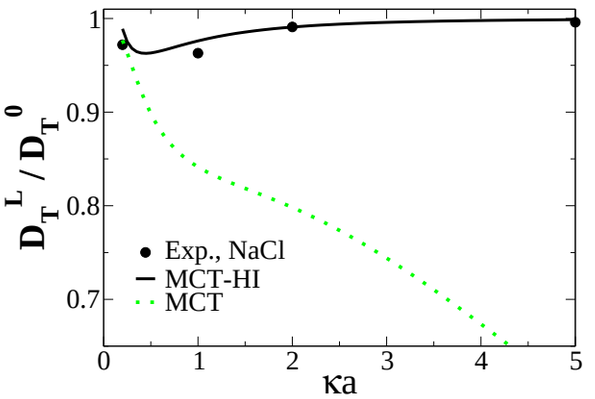


Figure 1: Mode-coupling theory (MCT) results with HI (solid line) and without HI (dotted line) for the normalized long-time self-diffusion coefficient D_T^L/D_T^0 vs. reduced screening parameter κa (from [3]). Without HI, D_T^L/D_T^0 is monotonically decreasing, in conflict with experimental observation. Experimental data points are taken from [1].

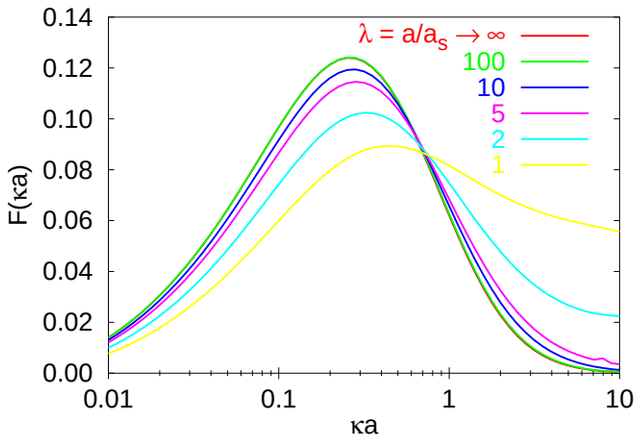


Figure 2: MCT results with HI for the reduced electrostatic part, $F(\kappa a)$, of the electrolyte friction coefficient $\Delta\zeta_T$. Various macroion-microion size ratios $\lambda = a/a_s$ are considered. From [4].

This has been achieved using mean spherical approximation expressions for the static pair correlation functions for differently sized charged spheres. Fig. 2 includes mode-mode coupling results for the reduced electrostatic part, $F(\kappa a)$, of the electrolyte friction coefficient $\Delta\zeta_T$ at various macroion-microion size ratios, $\lambda = a/a_s$, ranging from the colloidal limit $\lambda \to \infty$ to the bare electrolyte limit $\lambda \to 1$. As seen, finite size effects become significant for size asymmetries $\lambda \leq 10$.

[1] G.A. Schumacher and T.G.M. van de Ven, Faraday Discuss. Chem. Soc. **83**, 75 (1987).

[2] G. Nägele and J.K.G. Dhont, J. Chem. Phys. **108**, 9566 (1998).

[3] M. Kollmann and G. Nägele, Europhys. Lett. **52**, 474 (2000).

[4] M. G. McPhie and G. Nägele, work in progress.

[5] A. Vizcarra-Rendón, H. Ruiz-Estrada, M. Medina-Noyola and R. Klein, J. Chem. Phys. **86**, 2976 (1987).

[6] J.M. Schurr, J. Chem. Phys. **45**, 119 (1980).

THE EFFECT OF DIFFERENT PARTICLE CONTACTS ON SUSPENSION RHEOLOGY

Helen J. Wilson*, Robert H. Davis**
*Department of Applied Mathematics, University of Leeds, Leeds, UK
**Department of Chemical and Biological Engineering, University of Colorado, Boulder, CO 80309-0424 USA

Summary In this paper we consider various different models of inter-particle contact in low Reynolds number flow to illustrate the effect of contact on suspension rheology. Experiments have shown that contact between a spherical particle and an inclined plane occur at an effective roughness height that depends on the angle of inclination of the plane. We use two different methods to model this behaviour, and use numerical simulation to investigate the dependence of the suspension properties on the particle contacts.

INTRODUCTION

Many important processes, both natural and technological, involve flowing suspensions and small solid particles transported in a Newtonian liquid. An understanding of the effect of the solid particles on the macroscopic stress of the flowing fluid is critical for applications such as separating solids from liquids by settling, cleaning sediment from pipes by viscous resuspension, and slurry flows.

Recent studies (e.g. [2, 8, 9]) have shown that the small-scale interactions between particles in suspension can have a large effect on the rheology of the macro-scale (apparently homogeneous) fluid. A particular effect which has only recently been considered is that of particle roughness. Perfectly smooth particles without interparticle forces in an inertialess flow should never make contact, and their interactions should be entirely reversible. However, experiments [7] have shown that reversible interactions do occur, and various models of this *contact* interaction have been proposed. In this paper we consider existing and new models of the contact interaction and investigate the effect of contact on suspension rheology, and also the extent to which our results depend on the contact model used.

CONTACT MODELS

Benchmark model

The first model of interparticle contact was introduced by Davis [4] and Hinch [3]: both these papers introduced models which have, as a special case, frictionless roll-slip contact. This is also a special case in models used elsewhere [2, 5]. Particles are assumed to have asperities which do not affect their hydrodynamic interaction. These asperities cause apparent contact between particles when their surfaces reach a specific nominal separation. The contact prevents further approach of the particles, but a contact force can only resist compression, so when the flow acts to separate the particles the roughness ceases to have any effect. This simple one-parameter model (the parameter being ξ, the dimensionless nominal surface separation at contact) is the start-point for most studies of contact effects. Experiments by Smart & Leighton [7] suggest that an appropriate physical range for the dimensionless roughness height is $0.001 \leq \xi \leq 0.01$.

Recent Experimental Observations

The driving force behind the new contact models discussed here is a series of experiments carried out by Zhao, Galvin & Davis [10]. In these experiments, a single sphere travelled down an inclined plane in a viscous fluid at very small Reynolds number. When the apparatus was inverted, the time for the sphere to move away from the plane was measured and used to deduce the sphere's initial separation from the plane. They found that the steeper the angle of inclination of the plane, the larger the measured displacement between sphere and plane during quasi-steady motion down the incline.

First paradigm: multiple roughness heights

The model devised by Zhao *et al.* to reproduce the behaviour described above is based on the idea of sparse asperities with two different effective roughness heights. The fundamental idea behind the model is that a sphere travelling down an inclined plane spends some time in contact with the plane through its large asperities, some in contact through its small asperities and some time falling towards the surface after contact with a large asperity. For a shallow incline, the falling motion is almost directly towards the plane, so the time spent far from the plane is low; for a steep incline the motion after contact with a large asperity is nearly parallel with the plane, so the sphere spends most of its time at a distance from the plane corresponding to the size of the large asperities.

The model has three parameters: the size of the small asperities, the size of the large asperities, and an angle parameter determining the typical spacing between large asperities. A possible generalisation of this model is to consider a Gaussian distribution of asperity heights: again three parameters will suffice, the mean and variance of the distribution and number of asperities per particle. This new model is only accessible via numerical simulation, but is likely to be more realistic than the two-height model.

Second paradigm: compressible asperities

We propose a new way to model the experimental observations above. We treat the asperities as a soft *roughness layer*, which deforms under compression. Thus a sphere on a shallow incline feels a large force (from the normal component of its weight) normal to the incline, which compresses the asperities and yields a low roughness height and large contact force; on a steep incline, the component of gravity normal to the incline is small, so there is little compressive force and a small contact force is sufficient to halt the sphere's approach to the incline, so the roughness layer remains larger.

In order to obtain the simplest possible model that avoids very close approach, we simply treat the compressible layer as a spring, with responds only to compression to under its natural length with a simple nonlinear spring force $\underline{F}$:

$$\underline{F} = \lambda \frac{(\xi - h)}{h\xi} \underline{n} \quad \text{if} \quad h \leq \xi, \qquad \underline{F} = \underline{0} \quad \text{otherwise,}$$

where h is the nominal separation of the sphere surfaces, and ξ and λ are the two spring parameters. The contact force is continuous at $h = \xi$ and diverges as the separation is reduced to zero.

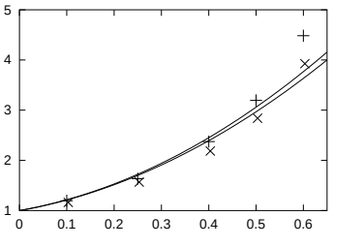
NUMERICAL METHOD

We simulate shear flow of a suspension of solid spheres using a modification of the Stokesian Dynamics (SD) method. In this method, pioneered by Brady & coworkers [1], far-field contributions to the mobility formulation are calculated first, then inverted to calculated a far-field resistance matrix which correctly includes screening; pairwise lubrication interactions are then added directly to the resistance matrix. We use the Accelerated Stokesian Dynamics method [6], which reduces the complexity in return for neglect of lubrication interactions between well-separated particles. In addition, we carry out some simulations in which we neglect far-field interactions completely (which is not too bad an approximation for large dense systems). This reduces the complexity to $O(N)$, where N is the number of particles per periodic box, allowing us to carry out a few calculations at very high concentrations and for very large numbers of particles and to assess the importance of both far-field interactions and box-size. Three-dimensional simulation allows us to calculate the three key rheological quantities of shear viscosity, first and second normal stress differences.

In order to allow for contact forces, we split the time-evolution into two stages. First we calculate the velocities of all spheres in the absence of contact. Then we use this information to approximate the contact forces for each pair of particles, using lubrication theory. Next the particle velocities are calculated numerically with the contact forces acting. In the case of incompressible asperities, the process is iterated to convergence, calculating small corrections to the contact forces.

PRELIMINARY RESULTS AND CONCLUSIONS

Initial two-dimensional studies have been carried out using the original contact model [4] and the full Stokesian Dynamics method. The graph on the right shows the dependence of shear viscosity on area concentration of solids for two different roughness heights, indicating that an increase in ξ decreases the shear viscosity. The curves are theoretical viscosity values from [9], valid for dilute concentrations under certain assumptions. These also predict the trend that increasing contact height will lower the suspension's shear viscosity. The reason for this is that the asperities prevent close approach of the particles, thus limiting the dissipation in lubrication layers between particles.



Suspension viscosity, made dimensionless by fluid viscosity, plotted against particle area fraction. The roughness heights are $\xi = 10^{-3}$ (+) and $\xi = 10^{-2}$ (×).

These preliminary studies also indicate that particle contacts cause a small negative first normal stress difference. We will present further results on the variation of this value with contact height, and on second normal stress differences (for which three-dimensional numerical studies are required).

References

[1] Brady J.F., Bossis G.: Stokesian dynamics. *A. Rev. Fluid Mech.* **20**:111-157, 1988.
[2] Brady J.F., Vicic M.: Normal stresses in colloidal dispersions. *J. Rheol.* **39**:545–566, 1995.
[3] da Cunha F.R., Hinch E.J.: Shear-induced dispersion in a dilute suspension of rough spheres. *J. Fluid Mech.* **309**:211–223, 1996.
[4] Davis R.H.: Effects of surface roughness on a sphere sedimenting through a dilute suspension of neutrally buoyant spheres. *Phys. Fluids A* **12**:2607–2619, 1992.
[5] Ekiel-Jeżewska M.L., Feuillebois F., *et al.*: Hydrodynamic interactions between two spheres at contact. *Phys. Rev. E* **59**:3182–3191, 1999.
[6] Brady J.F., Sierou A.: Accelerated Stokesian Dynamics simulations. *J. Fluid Mech.* **448**:115–146, 2001.
[7] Smart J.R., Leighton D.T.: Measurement of the hydrodynamic surface roughness of noncolloidal spheres. *Phys. Fluids A* **1**:52–60, 1989.
[8] Wilson H.J., Davis R.H.: The viscosity of a dilute suspension of rough spheres. *J. Fluid Mech.* **421**:339–367, 2000.
[9] Wilson H.J., Davis R.H.: Shear stress of a monolayer of rough spheres. *J. Fluid Mech.* **452**:425–441, 2002.
[10] Zhao Y., Galvin K.P., Davis R.H.: Motion of a sphere down a rough plane in a viscous fluid. *Int. J. Multiphase Flow* **28**:1787-1800, 2002.
[11] Zhao Y., Davis R.H.: Interaction of sedimenting spheres with multiple surface roughness scales. *J. Fluid Mech.* **492**:101–129, 2003.

Evolution of suspension sedimenting in a container bounded by horizontal walls

Evgeny S. Asmolov

Central Aero-Hydrodynamic Institute, Zhukovsky, Moscow region, 140180, Russia

Concentration inhomogeneities of the particles sedimenting in the fluid under gravity force with small Reynolds numbers lead to the large-scale velocity disturbances. Caflisch & Luke [1] showed that the velocity fluctuations in a homogeneous suspension with random distribution of particle locations grow linearly with container size. The divergence of fluctuations for infinite system is due to slow decaying, like r^{-1}, of disturbance field far from a particle. Luke [2] studied the evolution of velocity fluctuations in an infinite container with periodic boundary conditions in all directions and particle density stably stratified in vertical direction. He considered the dynamics of linear perturbations followed from the solution of an unsteady continuity equation for the concentration and Stokes equations for the velocity field. As a result a finite variance in the velocity was obtained when $t > 0$ and the container size tends to infinity. The large-scale vortex structures were observed in many recent experiments. Guazzelli [3] studied the transient behavior of the structures at low particle concentration. Their lengthscale is of the order of cell size at short times, and it diminishes at later times. Whether some steady state can be attained is still an open question. Ladd [4] simulated a settling suspension using a lattice-Boltzmann model of the fluid phase. The fluid-velocity fluctuations are found to grow with the cell size in a container with periodical boundary conditions, while in a container bounded at the top and bottom by no-slip walls they saturate.

In the present work the evolution of large-scale disturbances of the particle concentration and fluid velocity in the homogeneous sedimenting suspension is studied. A rectangular container is bounded by rigid walls in vertical direction and periodic in horizontal directions. The continuum model and perturbation methods [2] are applied to obtain solution for any initial distribution of particle concentration as the functions of time and vertical coordinate. The basic flow is a zero fluid-velocity field and constant concentration profile below a sedimentation front which travels with the Stokes velocity. Solution for the linear perturbations is presented in terms of Fourier series. As the Stokes equations governing the fluid flow are linear the evolution of any initial harmonics of concentration disturbances is considered separately.

The concentration inhomogeneities and velocity fluctuations are shown to decay with time. The decay is due to decrease of particles' number because of their deposition on the bottom wall and the variation of sedimentation-front shape. An inhomogeneity with enhanced concentration translates downward faster. After some time the sedimentation front will be lower in this region than the basic-flow position while that for the inhomogeneity with reduced concentration will be higher.

The ensemble-averaged fluctuations and the correlation functions depend on the position of the viewing window. The steady values can not be attained at a fixed position. Fluctuations evaluated in the middle of the cell grow linearly with the height of a cubic container, but saturate or even decrease as the container width grows and the height is fixed. Similar behavior was obtained by simulations [4] of dense suspension in a thin container.

Figure 1 presents the results of calculation of vertical velocity fluctuations in comparison with the experimental values [3] for the particle volume content $\phi = 0.0005$. The fluctuation profile in the container with the aspect ratio $1:1:2$ at short times has the plateau in the middle part (see Fig. 1 (a)). The fluid velocity is very small in the clean fluid, $z > H - U_s t$. The maximum remains approximately in the middle of the suspension layer and decreases only slightly with time. However the fluctuations averaged over the viewing window diminish as the sedimentation front approaches

its upper boundary. The qualitative agreement of the theoretical and experimental time dependences is good (Fig. 1 (*b*)).

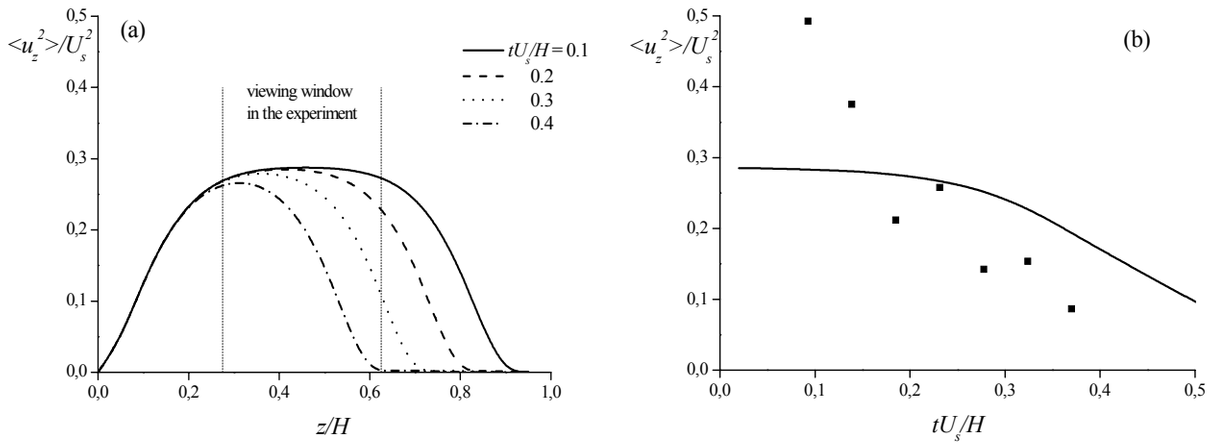


Figure 1

References

[1] R. E. Caflisch and J. H. C. Luke, "Variance in the sedimentation speed of a suspension," Phys. Fluids **28,** 759 (1985).

[2] J. H. C. Luke, "Decay of velocity fluctuations in a stably stratified suspension," Phys. Fluids **12,** 1619 (2000).

[3] E. Guazzelli, "Evolution of particle-velocity correlations in sedimentation," Phys. Fluids **13,** 1537 (2001).

[4] A. J. C. Ladd, "Effects of container walls on the velocity fluctuations of sedimenting spheres," Phys. Rev. Lett. 88 (2002).

XXI ICTAM, 15–21 August 2004, Warsaw, Poland

SPREADING FRONTS AND FLUCTUATIONS IN SEDIMENTATION: PART I EXPERIMENTS

Laurence Bergougnoux*, Sébastien Ghicini*, Élisabeth Guazzelli*, John Hinch**
*IUSTI - CNRS, Polytech'Marseille, Technopôle de Château Gombert, 13453 Marseille Cedex 13, France.
**DAMTP, Centre for Mathematical Sciences, Cambridge CB3 0WA, UK.

Summary The problem of velocity fluctuations in a sedimenting suspension is investigated by laboratory experiments. We examine how the sedimentation front spreads and how this affects the velocity fluctuations. The influence of the size of the container is also examined.

The problem of velocity fluctuations in a sedimenting suspension is still unresolved. Theories [1, 2] with randomly positioned monodisperse particles predict that the fluctuations diverge with the size of the container. Unfortunately experiments find differently [3, 4]. There have been a number of theoretical and numerical attempts to explain this discrepancy [5, 6, 7, 8, 9, 10, 11].

The objective of the present work is to examine by laboratory experiments how the sedimentation front spreads, how this affects the velocity fluctuations, and whether a steady state is reached. Experiments were undertaken at very low Reynolds number ($Re < 10^{-4}$) and volume fraction ($\phi = 0.3\%$) using small but non-Brownian spherical particles (of radius $149 \pm 8\ \mu$m). Two types of experimental measurements were performed. The spreading of the sedimentation front was measured using the attenuation of light through the suspension. The particle velocities were measured using particle image velocimetry (PIV).

First, experiments were performed in a glass walled cell of square cross section 20×20 cm^2 with a filled height of 40 cm [12]. The cell width, L, and height, H, were then large compared to the particle radius and to the mean interparticle spacing.

The width of the front was found to grow linearly in time. Most of the growth could be explained by a polydispersity of the particle size. The extra growth came from a faster fall of the denser iso-concentration planes. No diffusive growth like the square root of time, due to hydrodynamic dispersion, was seen. Hindered settling also played no role in the very dilute suspension.

The behavior of the particles was found different in the front. We observed that the mean particle velocity and its fluctuations decreased as the front arrived in the observation window. Using a window which excluded the front and the sediment, the mean velocity remained constant near to the Stokes value and the fluctuations attained a steady value after an initial rapid transient.

Secondly, the influence of the size of the container was investigated by reducing the lateral size. It was again found that the velocity fluctuations reached a steady state away from the front.

References

[1] Caflisch R. E. and Luke J. H. C.: Variance in the sedimenting speed of a suspension. *Phys. Fluids* **28**:759, 1985.
[2] Hinch E. J.: Sedimentation of small particles, in *Disorder and Mixing* edited by Guyon E, Nadal J. -P. and Pomeau Y. Kluwer Academic, Dordrecht, 1988.
[3] Nicolai H. and Guazzelli E.: Effect of the vessel size on the hydrodynamic diffusion of sedimenting spheres. *Phys. Fluids* **7**:3, 1995.
[4] Segrè P. N., Helbolzheimer E., and Chaikin P. M.: Long-range correlations in sedimentation. *Phys. Rev. Lett.* **79**: 2574, 1997.
[5] Koch D. L. and Shaqfeh E. S. G.: Screening mechanisms in sedimenting suspension. *J. Fluid Mech.* **224**: 275, 1991.
[6] Levine A., Ramaswamy S., Frey E., and Bruinsma R.: Screened and unscreened phases in sedimenting suspensions. *Phys. Rev. Lett.* **81**: 5944, 1998.
[7] Tong P. and Ackerson B. J.: Analogies between colloidal sedimentation and turbulent convection at high Prandtl numbers. *Phys. Rev. E* **58**: R6931, 1998.
[8] Brenner M. P.: Screening mechanisms in sedimentation. *Phys. Fluids* **11**:754, 1999.
[9] Luke J. H. C.: Decay of velocity fluctuations in a stably stratified suspension/ *Phys. Fluids* **11**: 754, 1999.
[10] Ladd A. J. C.: Effect of container walls on the velocity fluctuations of sedimenting spheres. *Phys. Rev. Lett.* **88**: 048301, 2002.
[11] Tee S.-Y., Mucha P. J., Cipelletti L., Manley S., Brenner M. P., Segrè P. N., and Weitz D. A.:Nonuniversal velocity fluctuations of sedimenting particles. *Phys. Rev. Lett.* **89**: 054501, 2002.
[12] Bergougnoux L., Ghicini S., Guazzelli É., and Hinch J. E.: Spreading fronts and fluctuations in sedimentation. *Phys. Fluids.* **15**: 1875, 2003.

CONSTANT FORCE AND CONSTANT VELOCITY MOMENTUM TRACERS IN CONCENTRATED SUSPENSIONS

Patrick T. Reardon*, Alan L. Graham*, James R. Abbott**, Howard Brenner***
* *Los Alamos National Laboratory, Los Alamos, NM 87545*
** *Department of Chemical Engineering, Texas Tech University, Lubbock, TX 79409*
*** *Department of Chemical Engineering, Massachusetts Institute of Technology, Cambridge, MA 02139*

Summary Measurements were made of the apparent viscosity, η_r, of a suspension (relative to that of the pure fluid) using either a settling ball animated by a constant gravitational force (η_r^F) or a towed ball translating with a constant velocity (η_r^V). Over the range of suspension concentrations examined $(0.1 \le \phi \le 0.5)$, η_r^V was found to be significantly larger than η_r^F.

INTRODUCTION

Homogeneous materials are characterized by intrinsic material properties such as density and viscosity that are independent of sample size and of the state of stress of the material. In particular, viscosity is a material property of a Newtonian fluid. For example, a rheological experiment conducted with a test sphere traversing a homogeneous Newtonian fluid would yield the same viscosity whether the experiment involved measuring the force on the test sphere when towed at a constant velocity or the velocity of the test sphere when moving under the influence of a constant force. A series of experiments were performed to explore the difference between the apparent viscosity of a suspension as determined by a constant gravitational force applied to a test sphere (falling-ball rheometry) and the apparent viscosity of the same suspension measured with a test sphere towed (pulling-ball rheometry) with uniform velocity through the suspension. The relative viscosities in both the falling-ball, η_r^F, and towed-ball experiments, η_r^V, were determined by normalizing the suspension results to those obtained in identical experiments in the pure suspending fluid.

EXPERIMENTAL SETUP

The suspending fluid used for these experiments matches the density and refractive index of the particles. Suspensions made using this fluid are neutrally buoyant and transparent. This allows optical techniques to be used in experiments where there are only a limited number of particle interfaces to look through. The suspending fluid consists of a solution of 1,1,2,2, tetrabromethane (TBE, Eastman Kodak, Rochester, NY), polyethylene glycol (90,000 and 9,500 UCON oil, Union Carbide Corp., Danbury, CT), and alkylaryl polyether alcohol (Triton X-100, J.T. Baker, Phillipsburg, NJ). The suspending particles were polymethyl methacrylate (PMMA) spheres obtained from three separate manufacturers in order to obtain the wide range of sizes used in the experiments. All the particles were large enough that colloidal and Brownian forces were not expected to exert an appreciable effect on the suspension behavior [1]. Suspensions of these particles were prepared with solid fractions of ϕ = 0.1, 0.2, 0.3, and 0.5.

In the constant force experiments, test spheres settling in the transparent suspensions were timed with stopwatches through pre-measured zones in the cylinder. The beginning of the first measurement zone was approximately one cylinder diameter from the fluid level in the cylinder, and the last zone ended at the bottom of the cylinder. The mean velocity for the falling balls at the midpoint between adjacent lines was calculated from the interval time and the known distance. In order to obtain a reproducible average, each interval velocity was then averaged over 5-10 ball drops [2]. The suspension was slowly and thoroughly stirred before each ball drop in order to randomize the microstructure and to maintain uniform concentration in each experiment.

For the constant velocity experiments, a motor with constant velocity settings was used to pull the test sphere through the suspension. After stirring the suspension, the test sphere was allowed to sink to the bottom of the cylinder (away from the centerline) pulling the line down with it. Then, the sphere was centered a small distance off the bottom of the cylinder. A scale registered the force required to pull the test sphere through the fluid system. This information was used to calculate the relative viscosities of the fluids and suspensions. The line passed through a rubber gasket fixed at the free surface to ensure that fluid

dragging on the line did not leave the system. The suspensions were slowly and thoroughly stirred after each ball drop or pull.

RESULTS

The effect of ϕ on η_r^V/η_r^F was examined. Over the range of suspension concentrations examined ($0.1 \le \phi \le 0.5$), η_r^V was found to be significantly larger than η_r^F, and the difference increases linearly as ϕ increases from 0.1 to 0.5. This is shown in Fig. 1. It is interesting that $\eta_r^V/\eta_r^F > 1$ in even the most dilute of the suspensions studied. Many non-Newtonian effects are not detectable in dilute and moderately concentrated suspensions, $\phi \le 0.2$ [2], but η_r^V/η_r^F is greater than one in all the suspensions studied ($0.1 \le \phi \le 0.5$). Hence, the results of this investigation support the conclusion that apparent viscosities of both dilute and concentrated suspensions are non-Newtonian and are not material properties [3]. The dimensionless parameter $\lambda = a_s/a_b$ is also used in the theoretical analysis of the reduced viscosities [3]. Test spheres of several sizes were used in the falling-ball and towed-ball experiments on the suspensions. In Fig. 2, η_r^V/η_r^F is shown as a function of λ over the range of our data. There was a statistically supportable effect of λ over the experimental range of this investigation $(0.11 \le \lambda \le 1.00)$.

Figure 1

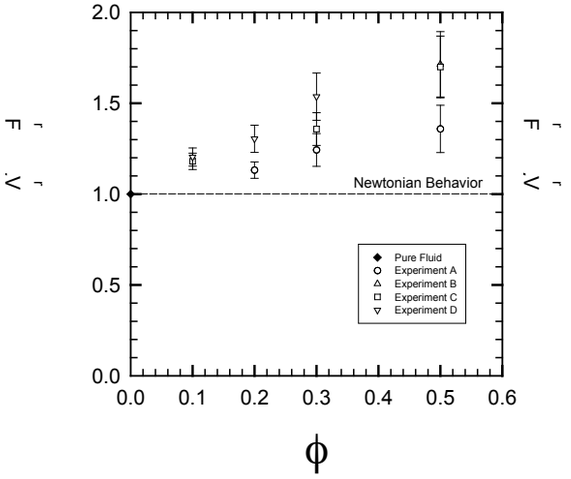
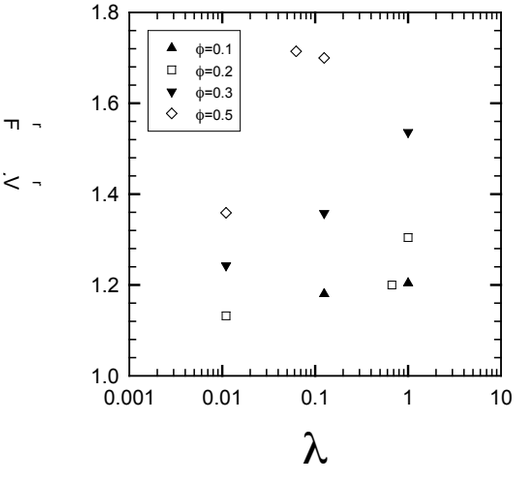


Figure 2



CONCLUSIONS

The objective of this study was to experimentally explore the difference between the apparent viscosity of a suspension as determined by a constant gravitational force applied to a test sphere (falling-ball rheometry) and the apparent viscosity of the same suspension measured with a non-rotating test sphere towed (towed-ball rheometry) with uniform velocity through the suspension. One of the primary results of this paper is the conclusion that the apparent viscosity of the suspension is always larger for the constant velocity case than for the constant force case. The experimental results of this study show a strong linear dependence of the ratio of η_r^V/η_r^F on ϕ over the entire range of our data. Past studies had indicated that dilute suspensions ($\phi \le 0.2$) exhibited essentially Newtonian behavior, and the non-linear effects were observed at higher concentrations [2]. In this study, the towed-ball tests exhibit non-Newtonian behavior for the suspensions for the entire range $(0.1 \le \phi \le 0.5)$.

References

[1] J.R. Abbott, N. Tetlow, A.L. Graham, S.A. Altobelli, E. Fukushima, L.A. Mondy, and T.S. Stephens, "Experimental observations of particle migration in concentrated suspensions: couette flow," J. Rheol. **35**, 773 (1991).

[2] W.J. Milliken, L.A. Mondy, M. Gottlieb, A.L. Graham and R.L. Powell, "The effect of the diameter of falling balls on the apparent viscosity of suspensions of spheres and rods," PhysicoChem. Hydrodyn. **11**, 341 (1989).

[3] Y. Almog and H. Brenner, "Non-continuum anomalies in the apparent viscosity experienced by a test sphere moving through an otherwise quiescent suspension," Phys. Fluids **9**, 16 (1997).

XXI ICTAM, 15–21 August 2004, Warsaw, Poland

FLOW OF A CONCENTRATED SUSPENSION DOWN A ROUGH PLANE

Cyril Cassar, Maxime Nicolas,Olivier Pouliquen
*Groupe Écoulement de Particules, Institut Universitaire des Systèmes Thermiques Industriels
UMR 6595 CNRS-Université de Provence, 5 rue Fermi 13453 Marseille cedex 13 France

Summary Submarine landslides have a great importance in geophysics because of their consequences (submarine canyons, tidal waves). They occur when a large amount of granular material (sand) flows downslope. But the rheology of the sand and water mixture is still not well understood. We lead experiments of submerged granular flows in a water tank. The particles are spherical glass beads and flow down a rough inclined plane from a reservoir with a controlled opening. Thickness, velocity and interstitial fluid pressure of the avalanche are measured, as well as the deposit thickness when the flow is over. Results show that the flow behavior changes abruptly for a small angle variation. Indeed, for a small variation of inclination angle above 36 degrees, the avalanche velocity increases rapidly. We suspect that a transition between a contact regime and a suspension regime occurs.

EXPERIMENTAL SETUP AND MEASUREMENTS

A sketch of the experimental setup is shown on Fig. 1a. We use a rectangular 49×14 cm^2 PVC plate roughened by glued glass beads. The flow starts from a 1120 cm^3 parallepipedic reservoir. The opening of the reservoir is a rectangle with controlled height h_g. The glass beads are similar to those used for the flow : spherical glass beads with a mean diameter of $d = 112 \pm 20$ μm and a density $\rho = 2.47 \pm 0.01$ g.cm^{-3}.

A 5 mm pressure hose was drilled at 25 cm from the reservoir gate. The hole was covered with a 50 μm metallic mesh to prevent particles from falling in the hose. A second pressure hose was placed beside the rough plane at the same depth from the water surface. Both hoses were connected to a differential pressure transducer with 5mm inner diameter flexible tubes.

The plane was lightened with a He-Ne laser sheet with a small angle from the rough plane. When the flow occurred, the laser line was distorted, and its horizontal displacement was proportional to the flow thickness after calibration with an object of known thickness. The flow was recorded using a DV camera and a DV recorder placed above the water tank. Image analysis of the movie gave measurements of the front velocity $u(t)$ and the flow thickness $h(x,t)$.

After filling of the reservoir with wetted particles, the gate of the reservoir was then opened gently to avoid surface waves which could perturb pressure acquisition and flow visualization. Once the reservoir was empty, a small layer of particles remained on the rough plane. Its thickness $h_s =< h(x) >_x$ was measured with the same technique.

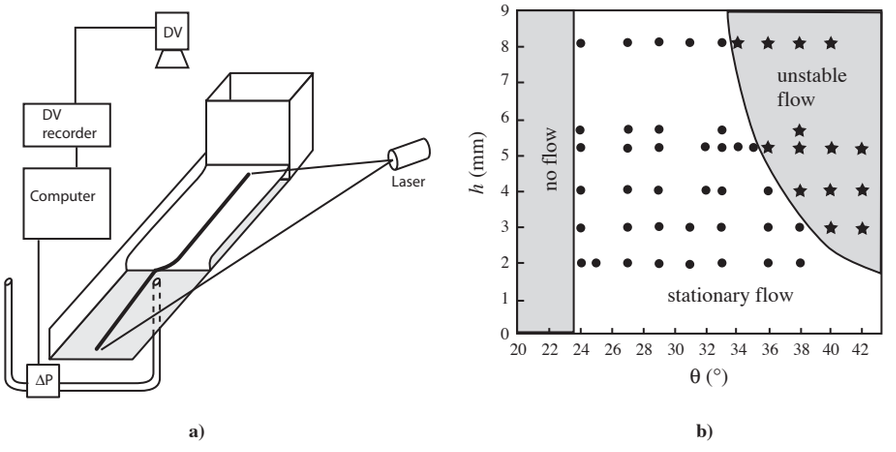


Figure 1. Experimental setup (a) and map of flow regimes (b).

RESULTS

Three different regimes were observed depending on the inclination angle θ and the gate opening h_g (see Fig. 1b). No flow could be observed for an inclination angle θ below 24°. A stationary flow was observed for θ in the [24°;36°] range and an unstable flow was observed for $\theta \geqslant 38°$. The unstable flow is characterized by a wavy free surface and a sudden increase of the front velocity for an angle varying from 36° to 38°.

The front velocity increases with inclination angle, and experiences a sudden increases when the flow becomes unstable. This is clearly shown on Fig. 2a for a gate opening $h_g = 5.22$ mm. Moreover, in the instability regime, velocity measurements are not reproducible. This suggests a transition between a frictional regime and a suspension regime where basal friction is reduced.

Careful measurements of the pressure shows that the basal pressure is strongly correlated with the flow thickness. Fig. 2b shows that in the basal pressure is linear with the flow thickness h. However, the linear trend is different for very slow flows ($\theta = 24°$) than for more rapid flows ($28° < \theta < 38°$). It must be noted that the basal pressure vanishes when the thickness is equal to the static layer thickness h_s. Thus the basal pressure can be scaled as

$$\Delta p \propto \phi(\rho - \rho_{water})g(h - h_s)$$

where ϕ is the rate of suspended particles during the flow.

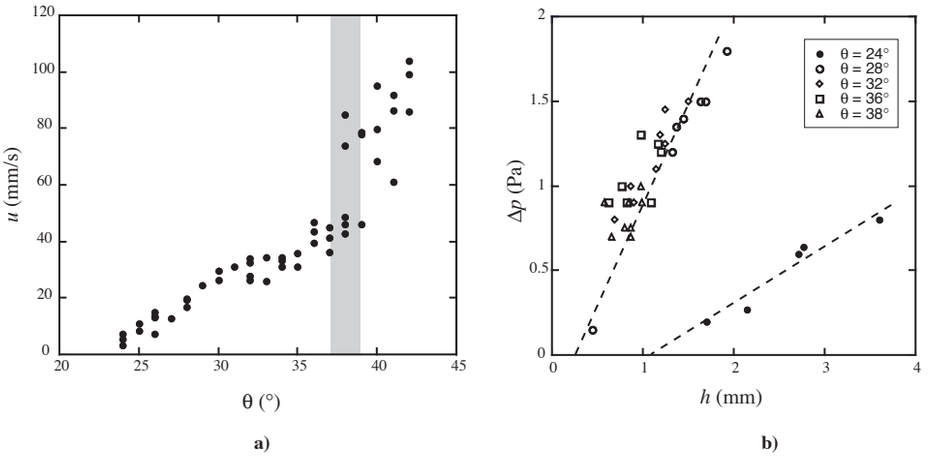


Figure 2. Front velocity versus inclination angle for $h_g = 5.22$ mm (a) and pressure versus thickness for various angles and gate openings (b).

CONCLUSION

Through measurements of basal pressure under an imerged grain flow, this experimental study gives a new sight on concentrated suspension flows. Two different flow regimes can be present at the same time : a contact regime and a suspension regime which contributes to a non zero basal pressure and a reduction of the friction coefficient.

XXI ICTAM, 15–21 August 2004, Warsaw, Poland

INERTIAL MIGRATION OF RIGID SPHERICAL PARTICLES IN POISEUILLE FLOW

J.-P. Matas*, J. F. Morris**, and É. Guazzelli*
*IUSTI, Technopôle de Château-Gombert, 13453 Marseille Cedex 13, France
**Halliburton, Houston TX 77032 USA

Summary A neutrally buoyant particle in pipe flow is known to undergo a radial migration for finite Reynolds number flows. This effect was first observed by Segré and Silberberg (1962), who noted a radial equilibrium position at a radius $r = 0.6R$ in a pipe of radius R, in conditions of finite but low Re. These results have been extended to show that the equilibrium position of the particles is moved toward the wall as Re increases. Moreover a new equilibrium position closer to the center was observed to become dominant at elevated Re. A comparison with asymptotic theories is provided.

In this work, we have examined the influence of inertia upon the radial migration of particles in Poiseuille flow in a tube. We have extended the work of Segré & Silberberg [1] for neutrally buoyant particles up to $Re \approx 2000$. Our results show that the equilibrium radial position for this case, which we have termed the Segré-Silberberg annulus, moves toward the wall as Re is increased. This general trend is illustrated by Figure 1. Also seen on this figure is that our data for large particles, with ratio of tube diameter D to particle diameter d of $D/d < 10$ are in agreement with those of the Segré & Silberberg experiments performed for particles at similar D/d. The results for small particles, $D/d = 42$, are in good agreement with predictions of asymptotic theory [2–5] up to $Re \approx 500$. Note that the results for large particles do not agree with the asymptotic theory: in particular, the experimentally observed equilibrium position is moved toward the center of the pipe relative to the predictions of this theory. This deviation from theory increases as D/d becomes smaller (increasing particle size for fixed tube diameter). The discrepancy can be explained as a particle size effect, as the theory is strictly valid only for $Re_p \ll 1$, a condition which is not met in our experiments. In addition, the theory was developed for a channel flow, and the curvature of the pipe in the experiments cannot be neglected for small D/d. A further source of discrepancy is that the theory may break down for an equilibrium position too close to the wall.

In these experiments, we have observed an accumulation of particles on an inner annulus, i.e. at smaller radial position than the Segré-Silberberg annulus. This occurs for $Re > 600$ for all particles except the smallest set studied here of $D/d = 42$, for which this inner annulus was observed only for $Re > 1200$. This inner annulus coincides with the change in concavity of the force profile predicted by asymptotic theory for channel flow at large Re. In this work, we have probed whether this inner annulus corresponds to a true zero of the force or is a transient feature. Simulations of the trajectories of particles using the force deduced from the asymptotic theory show an inner annulus as a transient feature, meaning particles are seen on the inner annulus at intermediate axial locations before completion of migration to the Segré-Silberberg annulus further downstream. However, this inner annulus is very robust at large Re in the sense that it is even observed to survive through the transition to intermittency, despite the fact that the entry length becomes much smaller than the pipe length at these large values of Re according to existing theory. Also, the distribution is found to change from one centered at the Segré-Silberberg annulus to one with the particles primarily on the inner annulus when Re is increased. This change is seen between in Figure 2, where the distribution at the measurement cross-section and the histogram showing probability of lying at a dimensionless radius are shown for $Re = 1000$, 1650, and 2400 (the last is above transition to intermittent turbulence). In the results from $Re = 1000$ note that the particles are divided between the inner and Segré-Silberberg annuli, while at the larger Re only the inner annulus is populated. This transition depends upon Re in the same way for all particles except the smallest set, a finding in complete contradiction with the theoretical prediction of entry length varying as $(D/d)^3$. These findings lead us to believe that the inner annulus is not a transient feature but is a genuine equilibrium position not predicted by the asymptotic theory for Poiseuille flow in a channel. As noted above, this theory lacks two key features, the curvature of the pipe and the finite size of the particles, which if included may provide insight into the appearance of the inner annulus.

We have investigated the influence of buoyancy in two cases, one being a slight dispersion of particle density about that of the fluid, and the second for a set of particles all slightly heavier than the fluid. For the case of a dispersion in density, we observe an accumulation at the top and bottom of the cross section. This accumulation disappears as the ratio of inertia to buoyancy is increased through an increase of the Reynolds number. In the second case, the inertial migration competes with settling above the tube centerline while the two act in concert below, and this results in a strong asymmetry of the distribution. In both cases, simulation of the particle trajectories based on asymptotic theory captures the general features observed in the experiments.

References

[1] G. SEGRÉ & A. SILBERBERG 1962 Behaviour of macroscopic rigid spheres in Poiseuille flow Part 2. Experimental results and interpretation, *J. Fluid Mech.* **14**, 136-157.
[2] B. P. HO & L. G. LEAL 1974 Inertial migration of rigid spheres in two-dimensional unidirectional flows, *J. Fluid Mech.* **65**, 365-400.
[3] A. J. HOGG 1994 The inertial migration of non-neutrally buoyant spherical particles in two-dimensional shear flows, *J. Fluid Mech.* **272**, 285-318.
[4] J. A. SCHONBERG & E. J. HINCH 1989 Inertial migration of a sphere in Poiseuille flow, *J. Fluid Mech* **203**, 517-524.
[5] E. S. ASMOLOV 1999 The inertial lift on a spherical particle in a plane Poiseuille flow at large channel Reynolds number, *J. Fluid Mech* **381**, 63-87.

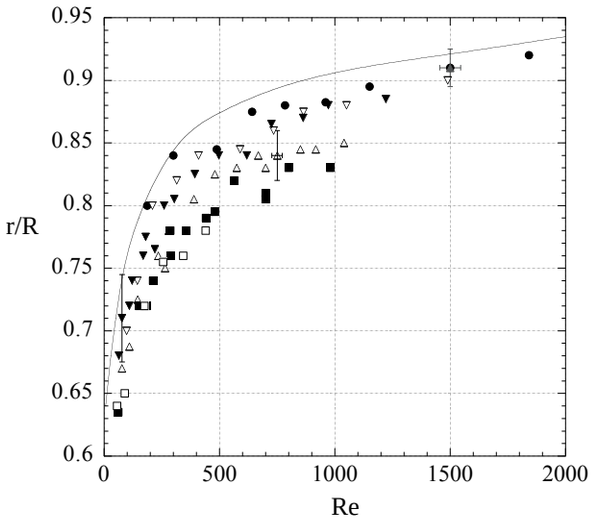


Figure 1. Segré-Silberberg equilibrium position of a rigid spherical particle as a function of Reynolds number for different particle sizes: • $D/d = 42$, ▽ $D/d = 17$, ▼ $D/d = 15$, △ $D/d = 10.5$, ■ $D/d = 9$, □ $D/d = 8$. The solid curve represents the prediction of the asymptotic theory.

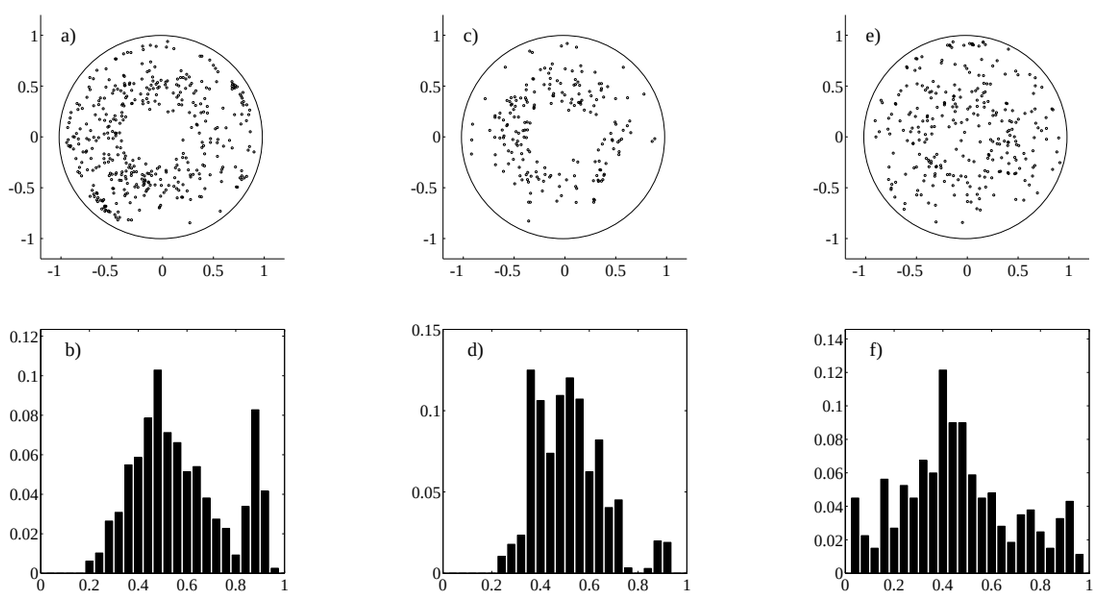


Figure 2. Particle distributions over a cross section for $D/d = 17$ at a) $Re = 1000$, c) $Re = 1650$ and e) $Re = 2400$ and the respective histograms b), d), and f) showing the probability of finding a particle at a given dimernsionless radius, $p(r)$. In a), c), and e), both axes are labeled with lengths scaled by the tube radius. Note that at $Re = 2400$ the flow is intermittent.

SEGREGATION OF SUSPENDED PARTICLES IN A ROTATING FLUID-FILLED HORIZONTAL CYLINDER – EXPERIMENT AND THEORY

G. Seiden[1], S. G. Lipson[1], M. Ungarish[2] and J. Franklin[3]
[1]Department of physics, Technion-Israel Institute of Technology, 32000 Haifa, Israel
[2]Department of Computer Science, Technion-Israel Institute of Technology, 32000 Haifa, Israel
[3] Department of physics, Temple University, Philadelphia, Pennsylvania 19122, USA

Summary An extensive experimental investigation into the segregation phenomenon of suspended particles in a rotating fluid-filled horizontal cylinder is presented as well as a theoretical approach to the underlying physics, based on the assumptions of small Ekman and Rossby numbers. The theoretical predictions agree well with experimental findings. The influence of non-linearity and viscosity on the phenomenon will be discussed as well.

The phenomenon of spontaneous banding of suspended particles in an almost inviscid fluid-filled rotating horizontal cylinder is part of a family of seemingly similar segregation phenomena occurring when two or more phases are embodied in a rotating horizontal tube. Other related phenomena are the axial segregation in a mixture of granular materials placed in a rotating horizontal cylinder [1] and the segregation of neutrally buoyant particles in a partially filled rotating horizontal cylinder [2].

The phenomenon was first observed several years ago as part of a study on the influence of anisotropy on the character of dendritic crystals [3]. In order to prevent interaction with any substrate a supersaturated solution of NH_4Cl was put in a closed horizontal cylinder and rotated about its axis - thus attaining microgravity conditions by which the growth could be examined. As the crystals nucleated a most curious and counterintuitive scene was observed – the crystals tended to accumulate in specific periodic bands perpendicular to the axis of rotation (FIG.1).



FIG.1 Banding phenomenon of NH_4Cl crystals in a supersaturated solution

In order to investigate the main features of the, as yet, mainly unexplored phenomenon we performed several experiments in which we checked the dependence of the periodic spacing between bands on tube length and the dependence of the phenomenon on the size and shape of the particles, as well as on the tube diameter. The experimental apparatus used was a basic mechanical system designed to rotate glass tubes about their horizontal axis.

The surprising results, presented in the generic graph of FIG. 2, indicate a robust phenomenon, independent of particle size or shape as well as of the bounding cylinder diameter. Moreover, a preference of a constant periodic length equal to 3.6R (R being the tube's radius) is observed throughout the experiments.

In addition, an extraordinary phenomenon of oscillation between two possible band configurations was observed. These oscillations, resembling the well-known oscillations between two coupled pendulums from classical mechanics and the Rabi oscillations between two coupled states in quantum mechanics, were investigated as well in order to understand the underlying physics.

An attempt was made to explain the phenomenon of segregation, based on the linear Navier-Stokes equation [4]. Here we assumed the suspended particles to be the source of a periodic disturbance (in the rotating frame of reference) to the otherwise rigidly rotating fluid. This assumption, together with the assumption that in the interior the effect of viscosity is negligible, led to the conclusion that traveling inertial waves, having a unique flow pattern, which could cause the observed axial segregation into bands, are excited.
Our approach is essentially different from a recently published approach [5], which accompanied the report of the occurrence of the same phenomenon, but with more viscous fluids, and which is based on the assumption that the inertial terms are negligible (creeping flow approach).

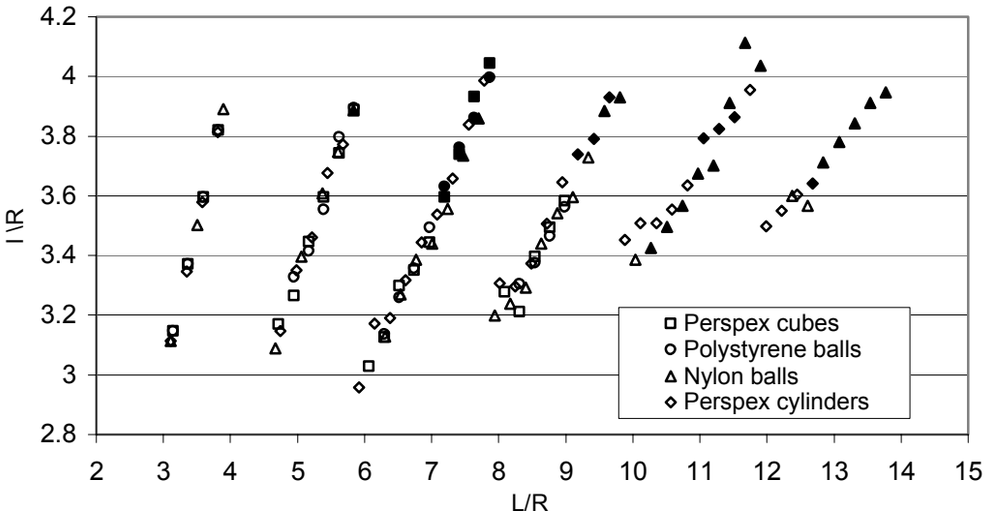


FIG. 2 A compendium of all data gathered in the investigation of the dependence of periodic length (l) on tube length (L) for particles suspended in water (full markers represent observed oscillations between two possible band patterns). The coordinates are scaled by tube radius in-order to manifest general features of the banding phenomenon.

We intend to present the results of the experimental investigation as well as the theoretical approach, the predictions of which well correlate the experimental findings.
We also will discuss the effects of non-linearity and viscosity, which were neglected in the theory, on the phenomenon.
A video clip, illustrating the dynamical evolution of the oscillations between two interleaving band patterns will be presented.

References

1. O. Zik et al., Phys Rev Lett., 73, 644-7 (1994).
2. M. Titumkudulu et al., Phys. Fluids 12, 1615-8 (2000).
3. S. G. Lipson, J. Phys. Condes. Matter 13 (2001).
4. G. Seiden, S. G. Lipson and J. Franklin, Phys. Rev. E 69, Preprint (2004).
5. J. Lee and J. C. Ladd, Phys. Rev. Lett. 89, 104301 (2001).

MIGRATION OF BUOYANT MONO- AND BI-DISPERSE SUSPENSIONS IN LOW REYNOLDS NUMBER PRESSURE-DRIVEN PIPE FLOW

Jay T. Norman, Hebri V. Nayak, Roger T. Bonnecaze
Department of Chemical Engineering, The University of Texas at Austin, Austin, TX, USA 78712

Summary: Suspensions of neutrally buoyant particles in low Reynolds number, pressure-driven flows migrate from regions of high to low shear. When the particle density does not match that of the suspending fluid, buoyancy forces, as quantified by a dimensionless buoyancy number, determines the particle distribution. We use electrical resistance tomography (ERT) to visualize and quantify particle migration in pressure-driven pipe flow of monodisperse suspensions of dense or light particles and bidisperse suspensions of heavy and almost neutrally buoyant particles. The images reveal greater particle segregation for the suspensions at higher buoyancy numbers. Experiments with bidisperse suspensions reveal enhanced resuspension of the heavier particles. In addition for some flow conditions an adverse density gradient is observed with heavy suspension above light. Additionally, ERT imaging captured the developing concentration profile, revealing a complex evolution to fully developed flow. The particle distributions are reasonably well-predicted by a suspension transport model.

INTRODUCTION

Particles in highly viscous suspension flows fall in the Stokes regime, where inertial effects are negligible. A unique property of these flows is the migration of particles away from areas of high shear [1-4]. For example, neutrally buoyant particles in pressure-driven flow in a pipe have been observed to migrate to the centre of the pipe [3,4], and this has been modelled with the so-called suspension balance model[5].

In the case of heavy or light particles, there is a competition between the buoyancy forces, which tend to segregate the particles to the top or bottom of a horizontal pipe, and the migration to the centre of the flow, as quantified by a buoyancy number. This problem for flow between parallel plates has been solved theoretically[6], but there is, however, little experimental data for low Reynolds number, pressure-driven suspension flows with buoyant particles. One exception is a study by Altobelli, Givler and Fukushima using nuclear magnetic resonance imaging [3]. Although, they were able to obtain excellent velocity profiles, the concentration profiles were only qualitative in nature, and they had difficulty resolving the concentration of particles near the surface of the pipe.

The purpose of this study is to make quantitative measurements of the concentration profiles of suspensions where buoyancy forces are important. Here, the concentration profiles of monodisperse suspensions of heavy or light particles and bidisperse suspensions of heavy and almost neutrally buoyant particles in pressure-driven pipe flow are determined using non-invasive ERT imaging. All of the experiments are performed at low pipe-Reynolds numbers, and vanishing particle-Reynolds numbers. The experimental results of this study are then compared to the predictions of the suspension balance model

ELECTRICAL RESISTANCE TOMOGRAPHY IMAGING

ERT is a non-invasive imaging technique with many applications in the medical field and industrial processes. ERT has also been applied to several industrial applications. For example, ERT has been used successfully to monitor mixing tanks at a pilot plant scale [7]. Additionally, ERT has been used to determine concentration profiles of neutrally buoyant particles in a viscous, pressure-driven pipe flow [4] and to monitor pulp consistency in paper processing [8].

ERT imaging is based on the variation in potential fields due to the applied current through a material with varying impedance. A potential field, which is determined by the conductivity distribution in the imaging plane, is produced by introducing a current through a series of electrodes surrounding the plane of interest. The resulting potentials are measured at the electrodes surrounding the image plane. A non-linear inverse algorithm is used to convert these potential measurements into the previously unknown conductivity field. Finally, the computed conductivity profiles are transformed to concentration fields of the multiphase flows using established correlations.

EXPERIMENTAL CONDITIONS

The suspending fluid consisted of UCON lubricant 75-H-90000 to which an aqueous NaI solution was added to produce the desired viscosity, density and conductivity. Silver or PMMA particles were added to the suspending fluid to the desired volume fraction and the suspension was thoroughly mixed at a moderate speed. To measure buoyancy effects in low Reynolds number, pressure-driven pipe flow, the suspensions were pumped at a controlled flow rate through a flow loop. Four ERT sensor arrays are placed at predetermined lengths, and a pressure gauge is used to obtain the average pressure gradient in each experiment.

Table 1 summarizes the volumetric flow rate, pressure gradient, particle-Reynolds number, pipe-Reynolds number and buoyancy number for all experiments. The experimental buoyancy number is defined as $N_b=2(\rho_p-\rho_f)gR^2/9\eta U$, where ρ_p is the density of the particles, ρ_f is the density of the fluid, g is gravity, R is the radius of the pipe, η is the kinematic viscosity and U is the average velocity.

Table 1. Experimental Parameters

Experiment		Q (cm^3s^{-1})	$\Delta P/L$ ($g\ cm^{-2}s^{-2}$)	$Re_{particle}$	Re_{pipe}	N_b
Heavy	1	37.1	986	6.3×10^{-3}	2.12	4.9
	2	18.9	552	3.2×10^{-3}	1.08	9.5
	3	9.7	268	1.6×10^{-3}	0.55	18.6
Light	4	10.8	613	3.7×10^{-3}	0.35	-2.1
	5	5.4	355	1.8×10^{-3}	0.18	-4.2
	6	2.6	199	8.9×10^{-4}	0.09	-8.7

Table 1. Summary of experimental conditions. The volumetric flow rate is given by Q, the average pressure gradient $\Delta P/L$, the particle-Reynolds number $Re_{particle}$, the pipe-Reynolds number Re_{pipe}, and the buoyancy number N_b.

RESULTS

Typical results of the experimental measurements are illustrated in Figure 1, which presents the particle distribution with increasing buoyancy number for light particles. For high flow rates (low absolute N_b) there is significant resuspension and for low flow rates (high absolute N_b) there is more particle segregation to the top of the pipe. Surprisingly, pressure gradient measurements are found to undergo a minimum before reaching a plateau at fully developed flow, which can be explained by the evolution of the concentration profile. Experiments with bidisperse suspensions (not shown here) reveal enhanced resuspension of the heavier particles. In addition for some flow conditions an adverse density gradient is observed with heavy suspension above light. All the experiments are compared to the theoretical predictions of the suspension balance model (not shown here), which is found to predict the experimental observations reasonably well.

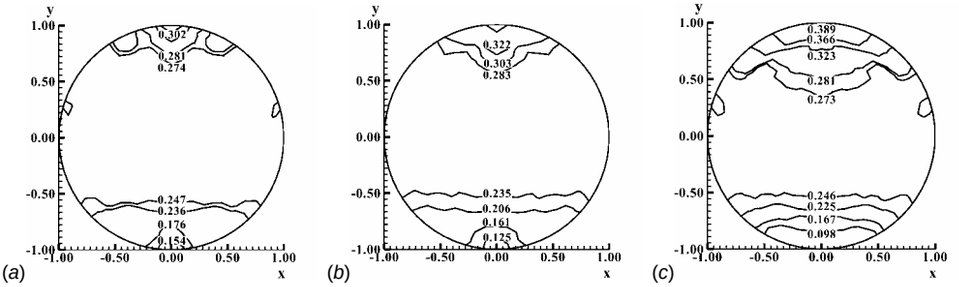


Figure 1. Contour plots of the concentration profile at 9.8 m downstream of the inline mixer for ϕ_b=0.20 and for experimental buoyancy numbers. (*a*) N_b = -2.1; (*b*) N_b = -4.2; (*c*) N_b = -8.7.

CONCLUSIONS

We have made the first quantitative measurements of the particle distribution of low Reynolds number mono- and bi-disperse buoyant suspensions in pressure-driven flow in a pipe. Viscous resuspension is shown to occur, and indeed in some cases to the extent that adverse density gradients can exist in the pipe. The suspension balance model of Nott & Brady is shown to predict the particle distribution reasonably well.

References

[1] GADALA-MARIA, F. AND ACRIVOS, A. (1980) *J. Rheol*., **24**, 799-814.
[2] LEIGHTON, D. AND ACRIVOS A. (1987) *J. Fluid Mech.*, **181**, 415-439.
[3] ALTOBELLI, S.A., GIVLER, R.C. AND FUKUSHIMA, E. (1991) *J. Rheol.,* **35**, 721-734.
[4] BUTLER, J.E. AND BONNECAZE, R.T. (1999) *Phys. Fluids*, **111**,1982-1994.
[5] NOTT, P.R. AND BRADY, J.F. (1994) *J. Fluid Mech*., **275**, 157-199.
[6] MORRIS, J.F. AND BRADY, J.F. (1998) *Int. J. Multiphase Flow*, **24**,105-130.
[7] DICKIN, F. AND WANG, M. (1996) *Meas. Sci. Technol*., **7**, 247-260.
[8] ETUKE E.O., BONNECAZE, R.T. AND BUTLER, J.E. (1999) *TAPPI 1999 Engineering/Process & Product Quality Conference Proceedings.*

DYNAMIC SIMULATIONS OF THE INSTABILITY OF SEDIMENTING FIBERS

David Saintillan[*], Eric Darve[*], Eric S. G. Shaqfeh[**]
[*]*Department of Mechanical Engineering, Stanford University, Stanford CA 94305, USA*
[**]*Departments of Chemical and Mechanical Engineering, Stanford University, Stanford CA 94305, USA*

Summary The concentration instability of sedimenting fiber suspensions at zero Reynolds number is investigated by means of large-scale numerical simulations. Large systems are simulated, allowing the capture of several inhomogeneities. The structure of the suspension is studied in both the vertical and horizontal directions, providing new insight into the formation and dynamics of the inhomogeneities, as well as the mechanisms behind the wavenumber selection process of the instability.

INTRODUCTION

It has been known for over a decade that sedimenting suspensions of non-spherical particles such as fibers undergo a concentration instability, by which an initially homogeneous suspension evolves towards a very inhomogeneous state where high-concentration streamers are surrounded by clarified fluid. The instability was first predicted theoretically by Koch and Shaqfeh [1] as a consequence of a coupling between the fluctuations of the mean flow and the anisotropic mobility of the particles. It was subsequently observed both in experiments [2] and in numerical simulations [3]. While the origin of the instability is now fairly well understood, several important questions remain unanswered: what are the mechanisms behind the wavenumber selection of the instability? And what therefore determines the size of and spacing between the inhomogeneities in the suspension, which have a strong influence on the sedimentation rate?
In their previous simulations, Butler and Shaqfeh [3] captured most of the qualitative features of the instability; however only fairly small systems were typically simulated and the wavenumber selection could not be observed. In this paper we use a fast summation algorithm to perform simulations of larger systems in order to study the suspension microstructure in more detail.

METHOD OF SIMULATION

The simulation method used here follows the previous work by Butler and Shaqfeh [3]. The motion of the fibers is described using Batchelor's slender-body theory, which represents the disturbance of the fibers on the flow as line distributions of point forces or Stokeslets [4]. The force distributions are expanded in a Legendre polynomial along the fiber length in which only the first two moments are retained, namely the total force and dipole term, which can be expressed in terms of the total torque and particle stresslet [5]. The lubrication approximation is used to capture close particle pair interactions [6].
Periodic boundary conditions are used to simulate infinite suspensions, and the velocity disturbance created by the fibers is calculated using the periodic Green's function for Stokes flow [7]. The evaluation of this velocity disturbance constitutes the most time-consuming part of the simulations, and is accelerated using a Smooth Particle-Mesh Ewald (SPME) method previously used in molecular dynamics simulations [8]. The SPME algorithm is similar in many ways to the Accelerated Stokesian Dynamics method of Sierou and Brady [9], and is based on a decomposition of the slowly decaying Green's function into two fast-converging sums: the first one involves the distribution of point forces and is evaluated rapidly over close particle pairs, while the second one is expressed in terms of the Fourier transform of the force distribution and is computed efficiently on a Cartesian grid using Cardinal B-spline interpolation and the Fast Fourier Transform algorithm. The total cost of the algorithm scales as $O(N \log N)$, and therefore results in a significant speedup.

SIMULATION RESULTS

Suspension microstructure and cluster formation

Figure 1 shows the evolution of a suspension of 512 fibers of aspect ratio $A = 11$ and average volume fraction $nl^3 = 0.05$ for a simulation box of high aspect ratio. Starting from a well-mixed suspension, small clusters form and converge towards a high-density streamer. The streamer is composed of several inhomogeneities, with new fibers constantly entering and leaving the clusters. A procedure was implemented to systematically determine the number and size of the clusters inside the streamer (where we define clusters as regions where the local concentration peaks beyond 1.3 times the average concentration). Statistics could therefore be performed, and the graph in Figure 1 shows the evolution of the numbers of small and large clusters (i.e. containing more or fewer than 30 fibers) inside the streamer. The two curves initially present slow oscillations, which are easily interpreted: during the transient phase of the instability, a periodic mechanism is observed by which small clusters merge into larger clusters, which again break up into small clusters. After a while the oscillations subside and a steady state is reached where a combination of clusters of different sizes coexist on average. The average spacing between clusters in the vertical direction at steady state can be estimated at 10 fiber lengths.
Increasing one of the lateral dimensions of the box also allowed to observe several high-concentration streamers as shown in Figure 2. The structure of the suspension is quite interesting as it exhibits large regions of shear between the streamers and the clarified fluid where the fibers are aligned with gravity and slowly converge towards the streamers as

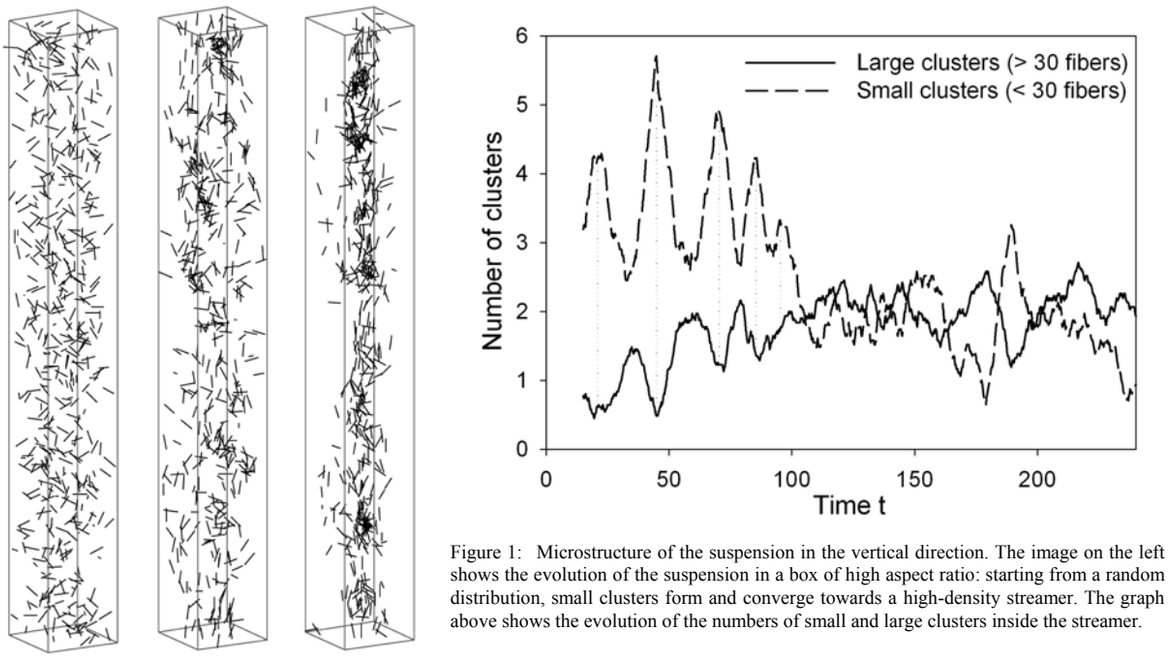


Figure 1: Microstructure of the suspension in the vertical direction. The image on the left shows the evolution of the suspension in a box of high aspect ratio: starting from a random distribution, small clusters form and converge towards a high-density streamer. The graph above shows the evolution of the numbers of small and large clusters inside the streamer.

a result of hydrodynamic dispersion. The average spacing between the streamers is typically quite large, on the order of 20 fiber lengths or higher, and seems to be determined to a large extent by the concentration fluctuations in the initial distribution. More precisely, low-wavenumber concentration fluctuations create backflows in the disturbance velocity field, which seem to act like barriers for the fibers. Because of the quasi one-dimensionality of these simulations in wide boxes, one should be prudent however in extending these conclusions to full-scale suspensions.

Orientation and velocity statistics

Statistics were also obtained for the orientations and velocities of the fibers, and were compared to the experimental results of Herzhaft and Guazzelli [2]. Using very wide boxes in the horizontal direction (such as in Figure 2) allows to obtain very good orientation statistics, where a very large portion of the fibers is essentially aligned in the vertical direction. The fiber velocities and the average sedimentation rate however still greatly depend on the dimensions of the simulation box, and are typically better in very high boxes (such as in Figure 1). We hope that simulations in large boxes in the both the horizontal and vertical directions using parallel computing will allow to reconcile the statistics for orientations and velocities.

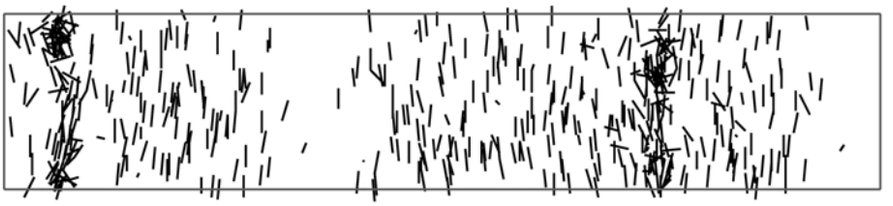


Figure 2: Distribution of fibers at t = 140 for a very elongated box in the lateral direction. Two distinct streamers separated by clarified regions can be observed. Between the streamers and the clarified fluid, fibers are aligned with gravity and slowly migrate towards the streamers as a consequence of velocity fluctuations.

References

[1] Koch D. L., Shaqfeh, E. S. G.: The instability of a dispersion of sedimenting spheroids. *J. Fluid Mech.* **209**:512-542, 1989.
[2] Herzhaft B., Guazzelli E.: Experimental study of the sedimentation of dilute and semi-dilute suspensions of fibres. *J. Fluid Mech.* **384**:133-158, 1999.
[3] Butler J.E., Shaqfeh E. S. G.: Dynamic simulations of the inhomogeneous sedimentation of rigid fibres. *J. Fluid Mech.* **468**:205-237, 2002.
[4] Batchelor G. K.: Slender-body theory for particles of arbitrary cross-section in Stokes flow. *J. Fluid Mech.* **44**:419-440, 1970.
[5] Harlen O. G., Sundararajakumar R. R., Koch D. L.: Numerical simulations of a sphere settling through a suspension of neutrally buoyant fibres. *J. Fluid Mech.* **388**:355-388, 1999.
[6] Claeys I. L., Brady J. F.: Lubrication singularities of the grand resistance tensor for two arbitrary particles. *PhysicoChem. Hydrodyn.* **11**:261-293, 1989.
[7] Hasimoto H.: On the periodic fundamental solution of the Stokes equations and their application to viscous flow past a cubic array of spheres. *J. Fluid Mech.* **5**:317-328, 1959.
[8] Essmann U., Perera L., Berkowitz M. L., Darden T., Lee H., Pedersen L.G.: A smooth particle mesh Ewald method. *J. Chem. Phys.* **103**:8577-8583, 1995.
[9] Sierou A., Brady J. F.: Accelerated Stokesian Dynamics simulations. *J. Fluid Mech.* **448**:115-146, 2001.

MOBILITY OF MEMBRANE-TRAPPED PARTICLES: PROTRUSION INTO THE SURROUNDING FLUID

Howard A. Stone, Division of Engineering and Applied Sciences, Harvard University, Cambridge, MA 02138

Short summary: Rheological and transport studies of model thin films and membranes, often inspired by biological systems, make use of translational or rotational motion or diffusion of particles trapped in the surface film. Here, the mobility of a disk-shaped particle, trapped in a Newtonian surface film and bounded on one side by a viscous Newtonian fluid, is determined for when the particle protrudes into the subphase.

DYNAMICS OF MEMBRANE-TRAPPED PARTICLES

The translation of particles along membranes and interfaces is of interest because it is a model system for describing basic features of interfacial hydrodynamics, it is important in cellular signalling in biology and (Alberts et al. 1994), and it is potentially applicable for understanding dynamics of structured materials. The theoretical investigation of such motions of membrane-trapped particles began with the study of the Brownian motion of a thin *disk-shaped* object at a flat viscous interface bounded on one or both sides by a viscous Newtonian fluid (Saffman 1976; Saffman & Delbruck 1975). The case of a sphere at a surfactant-coated interface was treated numerically by Danov et al. (1995). The hydrodynamics of these two different shapes differ since the protrusion of the sphere into the subphase changes the relative contributions of the surface and subphase resistances. Recent experiments by Sickert & Rondelez (2003) with spherical particles as tracers in monolayers in the liquid-expanded phase motivated our work, which treats protrusions intermediate between the previously studied cases of a thin disk (no protrusion) and a sphere.

The mathematical problem considered originally by Saffman was that of a flat, disk-shaped particle of radius R that spans the thickness of the fluid layer (a monolayer or bilayer) at a fluid-air or fluid-fluid interface (see figure 1). The object is assumed to move at a constant speed U and the force F on the object is calculated in the low Reynolds number limit. The ratio F/U is the particle resistivity, which is related to the measurable translational diffusivity D by a Stokes-Einstein relation, $D=k_BT/(F/U)$. The resistance comes from both the sub- and surface phases and the dynamics are conveniently characterized in terms of a dimensionless parameter $L=Rm/hm_m$, where m is the fluid viscosity, m_m is the viscosity of the membrane fluid, and h is the thickness of the surface layer. The commonly discussed surface viscosity $m_s = m_m h$. Saffman was interested in small proteins so $L \ll 1$. On the other hand, frequently membrane-trapped objects (e.g. phase separated domains) are large in which case $L \gg 1$ (e.g. Klinger \& McConnell 1993; Sickert & Rondelez 2003).

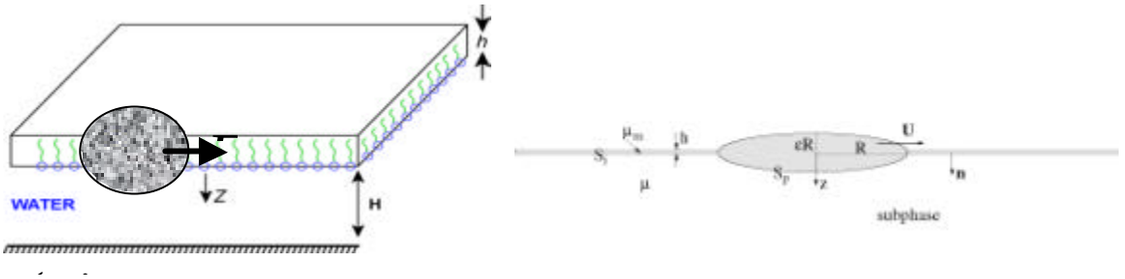


Figure 1: Left – A sphere straddling an interface and translating along the interface. Right – The mathematical characterization of an oblate ellipsoid, with aspect ratio e, straddling the interface.

THE INFLUENCE OF PROTRUSION INTO THE SUBPHASE

We ask ``what if the surface motion is generated by an object that protrudes into the subphase?'' The protrusion causes the flow to be fully three dimensional, unlike the treatment of disk-shaped objects (Saffman 1975; Hughes, Pailthorpe & White 1981; Stone & McConnell 1995; Stone & Ajdari 1998). Danov et al. (1995) considered numerically the case of a sphere straddling a surfactant-coated interface and

for the limit $L >>1$, obtained a drag that is the same as if the spherical particle were translating in a unbounded Newtonian fluid, i.e. $F/F^{\text{Stokes}} = 1$; the influence of the incompressible surface film was negligible. This limiting result is consistent with that given above for a flat disk if the velocity gradients associated with the three-dimensional flow dominate any influences associated with the surface film.

OUR CONTRIBUTION

We consider the intermediate case of a disk-shaped particle that protrudes into the subphase and seek to quantify the variation of the force as the degree of protrusion changes. We assume the shape is a nearly flat oblate spheroid with degree of oblateness indicated by e; $e=0$ is a flat disk and $e=1$ is a sphere. We first illustrate for an oblate spheroid translating in an unbounded fluid that just one term of an expansion in e is an excellent agreement for all $0<e<1$ with an exact result (Happel & Brenner 1983). Hence, for the membrane-bound particle problem we expect, or at least suggest, that just one term of a perturbation expansion in ε should similarly be expected to provide a good description.

Our calculation uses a domain perturbation to relate the oblate spheroid, for which results are unknown, to a disk shape, for which results are known. Hence, we expand the velocity field as $\boldsymbol{u}(\boldsymbol{r};\varepsilon) = \boldsymbol{u}^{(0)}(\boldsymbol{r}) + \varepsilon\boldsymbol{u}^{(1)}(\boldsymbol{r}) + \cdots$ with a similar equation for the force $\boldsymbol{F}$ on the membrane-trapped object; the leading-order velocity field $\boldsymbol{u}^{(0)}(\boldsymbol{r})$ corresponds to that of a thin-disk. Using the Reciprocal Theorem from low-Reynolds-number hydrodynamics, suitably modified to handle the interfacial flow and boundary conditions, and denoting the particle shape by $f(r)$, we arrive at the correction to the force $\boldsymbol{F}^{(1)}$,

$$\boldsymbol{F}^{(1)} \cdot \boldsymbol{U} = -2\int_{r=0}^{1}\int_{\theta=0}^{2\pi} f(r)\left(\frac{\partial \boldsymbol{u}^{(0)}}{\partial z}\right)^2 r\,\mathrm{d}\theta\,\mathrm{d}r\,,$$

which can be evaluated numerically using known results for the leading-order velocity field. Finally, we discuss how these results may be useful for interpreting recent experiments by Sickert & Rondelez (2003).

Acknowledgments

I thank F. Rondelez and M. Sickert for bringing this problem to his attention. ESPCI, the Laboratoire PCT, and the City of Paris are thanked for their support during a visit when much of this work was completed.

References

Alberts, B., Bray, D., Lewis, J., Raff, M., Roberts, K., Watson, J.D.: Molecular biology of the cell. Garland Publishing, Inc., New York 1994.

Danov, K., Aust, R., Durst, F., Lange, U.: Influence of the surface viscosity on the hydrodynamic resistance and surface diffusivity of a large Brownian particle. *J. Coll. & Int. Sci*. 175:36-45, 1995.

Happel, J., Brenner, H.: Low Reynolds Number Hydrodynamics. Martinus Nijhoff Publishers, 1983.

Hughes, B.D., Pailthorpe, B.A., White, L.R.: The translational and rotational drag on a cylinder moving in a membrane. *J. Fluid Mech*. 110:349-372, 1981.

Klinger, J.F., McConnell, H.M.: Brownian motion and fluid mechanics of lipid monolayer domains. *J. Phys. Chem*. 97:6096-6100, 1993.

Saffman, P.G.: Brownian motion in thin sheets of viscous fluid. J. Fluid Mech. 73:593-602, 1976.

Saffman, P.G., Delbruck, M.: Brownian motion in biological membranes. *Proc. Nat. Acad. Sci*. 72:3111-3113, 1975.

Sickert, M., Rondelez, F.: Shear viscosity of Langmuir monolayers in the low density limit. *Phys. Rev. Lett*. 90:126104, 2001.

Stone, H.A., McConnell, H.M.: Hydrodynamics of quantized shape transitions of lipid domains. *Proc. Roy. Soc. Lond.* A448:97-111, 1995.

Stone, H.A., Ajdari, A.: Hydrodynamics of particles embedded in a flat surfactant layer overlying a subphase of finite depth. *J. Fluid Mech*. 369:151-173, 1998.

SPREADING FRONTS AND FLUCTUATIONS IN SEDIMENTATION: PART II COMPUTER SIMULATIONS

Laurence Bergougnoux*, Sébastien Ghicini*, Élisabeth Guazzelli*, John Hinch**
*IUSTI - CNRS, Polytech'Marseille, Technopôle de Château Gombert, 13453 Marseille Cedex 13, France.
**DAMTP, Centre for Mathematical Sciences, Cambridge CB3 0WA, UK.

Summary Following on from the experimental part I, Part II uses computer simulations to examine the spreading of the front and the velocity fluctuations, and how these depend on the concentration and size of the container.

The computer simulations [1] represent the flow with a limited number of Fourier modes which are driven by the fluctuations in the density of the particles. By setting the number of modes equal to the number of particles, varying between 750 and 10368, the flow is well resolved for length scales between the size of the container and the average interparticle separation.

Results for the variance of velocity of the particles scale with the size of the container and the concentration of the particles, and decay in time as heavy clusters fall to the bottom. Restricting observations to a central region, far from the sediment below and from the front above, finds the level of velocity fluctuations constant in time.

The width of the sedimentation front is found to grow linearly in time, like $1.5\phi^{1/3}V_s t$, due to heavy clusters falling out of the front. An alternative model [2] involving nonlinear hydrodynamic dispersion, which gives an alternative prediction for the width of the front as $2.85a\phi^{1/7}(V_s t/a)^{5/7}$, also agrees with the currently available numerical simulations.

References

[1] Bergougnoux L., Ghicini S., Guazzelli É., and Hinch E. J.: Spreading fronts and fluctuations in sedimentation. *Phys. Fluids.* **15**: 1875, 2003.

[2] Tee S.-Y., Mucha P. J., Cipelletti L., Manley S., Brenner M. P., Segrè P. N., and Weitz D. A.:Nonuniversal velocity fluctuations of sedimenting particles. *Phys. Rev. Lett.* **89**: 054501, 2002.

THE ROLE OF COHESIVE FORCES ON THE FLUIDIZATION BEHAVIOR OF FINE POWDERS

J. M. Valverde, A. Castellanos, and M. A. S. Quintanilla
Department of Electronics and Electromagnetism. University of Seville. Avda. Reina Mercedes s/n. 41012 Seville. Spain.

Gas-fluidized beds display three main regimes of behavior: bubbling, fluidlike, and solidlike. At large gas velocities there is a continuous bubbling process in which the bed looses memory of previous states. If the gas velocity is decreased below a critical value bubbles disappear and the bed acts as a low viscosity liquid. Due to interparticle attractive forces, particles aggregate and aggregates interact hydrodynamically with the gas. By means of settling experiments we characterize aggregates. Optical probe measurements reveal the existence of mesoscale pseudoturbulent structures, responsible for an enhanced effective diffusion process, and short-lived voids. As the gas velocity is decreased there comes a point at which aggregates are brought together to a loose packing structure and the bed gets a solidlike appearance. The extension of the fluidlike regime decreases as particle size is increased and shrinks to zero when the particle weight is comparable to the interparticle attractive force.

In the past few decades there has been a strong debate about the structure of stable gas-fluidized beds of powders. R. Jackson [1] proposed a hydrodynamic criterion for the stability of a fluidized bed. Since then theoretical and numerical works have appeared that put emphasis on the hydrodynamic interaction between the solid and the fluid phases as a keystone for the stable structure of a gas-fluidized bed [2]. One decade after the work of Jackson, K. Rietema [3] suggested that interparticle cohesive forces were the responsible for the stabilization of the fluidized bed. These contact forces were assumed to give an effective elastic modulus to the bed that could stabilize the system against small disturbances. In that state the bed would behave like a weak solid rather than a fluid. Menon and Durian [4] reported on measurements by diffusion-wave spectroscopy of the reflection of laser light from fluidized glass beads. They found no fluctuations in the interval of uniform fluidization. Fluctuations were initiated by the instability to bubbling. This finding led them to the conclusion that "the uniformly fluidized state was a completely static state". Remarkably, in these experiments the powders used consisted of particles larger than ~50μm. Smaller particles are very cohesive and cannot usually be fluidized in the conventional sense; they form channels, or lift as a plug in the bed. For particles >~50 μm however the interval of uniform fluidization is very short or even absent, gas bubbles form at or slightly above the minimum gas fluidizing velocity and bed expansion is small. We have used xerographic toners with typical particle size d_p~10 μm. The reduction of cohesiveness by means of surface additives allows for a wide interval of non-bubbling fluidization and with a considerable bed expansion (with up to ~0.9 of free volume), enabling us to explore in detail the transitions between the different regimes of behavior exhibited by our gas-fluidized beds.

The first of our series of experiments [5] demonstrated that both regimes, the solidlike, for gas velocities V_g below a critical value V_c, and the fluidlike, for $V_g > V_c$, could be found in a non-bubbling gas-fluidized bed. In the solidlike regime, the fluidized color samples could not mix. Toner particles remained in a stationary static state. Accordingly we could measure a non-vanishing tensile strength. A confirmation of the existence of a mechanical strength could be obtained by slowly tilting the fluidized bed. In agreement with Rietema's experiments the bed remained stable while the top surface was tilted as well. When the gas velocity was increased above the critical value V_c, a radically different behavior was found. In this fluidlike regime there was no yield stress. Stresses in this state were carried by particle collisions due to fluctuations in their motion. The powder then took on many of the properties of a low-viscosity liquid, its upper surface remaining horizontal when the container was tilted. Color samples mixed successfully and the mixing process could be described by an effective self-diffusion coefficient. The fluid-to-solid transition became also clear when we investigated the response of the fluidized bed to vertical vibration [6]. In the fluidlike regime the bed expanded reversibly as vibration amplitude was increased. On the contrary in the solidlike regime the bed behaved like a weak granular solid relaxing irreversibly toward a more compact state by eliminating low-density metastable configurations.

When the gas velocity was further increased above a critical value $V_b > V_c$ large gas bubbles appeared. Even though the only existence of a fluidlike regime denied that the source of macroscopic bubbling could be the loss of mechanical strength, our results merely showed that, for sufficiently small particles, macroscopic bubbling was inhibited by some complex hydrodynamic mechanism over an extended fluidlike interval. In fact careful measurements by Tsinontides and Jackson [7] on glass beads and cracking catalyst of particle size >~ 50 μm had clearly demonstrated that there was no interval of bubble free expansion beyond the point where the yield strength became zero. We carried out a new series of experiments indicating that the extension of the fluidlike interval shortened as the particle size was increased [8]. Plotting the width of this interval as a function of the granular Bond number Bo_g of the particles (defined as the ratio of the interparticle attractive force to particle weight) we predicted that the fluidlike interval should shrink to zero for Bo_g<~10. A rough estimation yielded that for d_p >~ 40μm bubbling should be only restrained by the solidlike behavior of the fluidized bed in agreement with Rietema. Our results should therefore serve to put an end to arguments about hydrodynamics versus contact forces as stabilizing mechanisms.

The relationship between the settling velocity in sedimentation V_s and the particle volume fraction ϕ for fluidized noncohesive spheres has been well described by the phenomenological Richardson-Zaki (R-Z) law, $V_s = V_{p0}(1-f)^n$, where V_{p0} is the settling velocity of a single particle, n~5 (low Reynolds number limit), and ϕ is the particle volume fraction. When we came to measure [9] the sedimentation velocity of nonbubbling fluidized beds just after the gas supply was suddenly stopped, we found that the top free surface settled initially at a constant velocity. Not surprisingly

we found that for solidlike states ($\phi>\phi_J$) the experimental V_s was lower than the R-Z prediction since settling was hindered by permanent contacts. On the other hand, for fluidlike states ($\phi<\phi_J$) V_s exceeded the R-Z prediction. Indeed fine particles are expected to aggregate since the interparticle attractive force is much larger than particle weight. Our approach was to consider an ideal system of mono-sized aggregates each one consisting of N particles and with a radius of gyration equal to the hydrodynamic radius k (relative to particle size). Settling could then be well described by a modified R-Z law $V_s = V^*(1-f^*)^n$, where $V^*=V_{p0}\ N/k$ is the settling velocity of an individual aggregate and $\phi^*=f\ k^3/N$ is the volume fraction filled by the aggregates. The fractal dimension of the aggregates was $D\sim \ln N/\ln k\sim 2.5$ as predicted by the diffusion-limited-aggregation (DLA) model, where self-similar fractal ramified patterns are grown via irreversible sticking of particles in a random motion. The characteristic screening effect of DLA aggregates justified our assumption that the hydrodynamic and the gyration radius of the aggregates are similar. As expected we found that N and k decreased as Bo_g was decreased. The trend suggested that particles should behave as individuals in the limit $Bo_g \sim 1$, which is close to the border limiting the existence of a fluidlike interval of fluidization. Thus aggregation seemed to play a main role in preventing the growth of large bubbles along an extended fluidlike interval. As a matter of fact the fluidlike interval also shortened when the size of the aggregates was decreased either by increasing the surface additive concentration or by vibrating the bed, thus breaking aggregates.

The fluidlike regime is an interval of non-bubbling expansion. Nonetheless and since bubbles are well-developed instabilities, we might wonder whether the fluidized bed is really linearly stable in this interval. From our measurements of the effective self-diffusion constant [5] we could infer mean fluctuation velocities for the particles as large as two orders of magnitude greater than the gas velocity. It cannot be conceived any purely hydrodynamic diffusive mechanism by which such huge velocities could be generated in a uniform suspension. We should therefore conclude that fast diffusion must arise from the growth of an instability that does not develop into large visible bubbles. This was confirmed when we looked at the time signals of backscattered light from a fiber optic reflection probe [10], providing us a measure of the local concentration of solids. The results, along with visual observation of the free surface, indicated the existence of mesoscopic structures as well as the development of local voids. The number of local voids detected per unit time increased with gas flow until large amplitude bubbles developed and a clear segregation of gas and solid phases occurred. In the nonbubbling regime the measurements indicated that the local voids growth saturated at a certain height whereas at incipient bubbling the local voids continued to grow up to reach a macroscopic size. This behavior is strikingly similar to the behavior of liquid-fluidized beds of dense beads with a Froude number $Fr=V_b^2/(gd_p)\sim 10^{-2}$ [11]. In fact we estimate for our gas fluidized beds $Fr\sim 10^{-1}$-10^{-2} if we use the effective size of aggregates instead of the particle size. This value contrasts with the Froude number of gas-fluidized beds of coarse beads, typically $Fr>1$.

The fluid-to-solid transition parallels non-equilibrium kinetic transitions exhibited by disparate systems such us supercooled liquids, foams, emulsions and colloidal suspensions [12] (usually referred to as jamming). For noncohesive hard spheres $\phi_J \approx$ 0.56-0.59 [12], which is comparable to the random loose packing measured in the limit of zero gravitational force (0.56) but is well below the random close packing theoretical limit (0.64). Our fluidized bed experiments [13] indicated that aggregates jam at volume fractions ϕ_J^* independent of the primary particle size, but dependent on the interparticle attractive force F. ϕ_J^* approached the limit of noncohesive spheres as F was artificially decreased by means of surface additives. Moreover in the close vicinity of jamming the stress- (volume fraction) relationship could be well fitted to a critical-like functional form $\sigma\sim(\phi-\phi_J)^\beta$ as predicted by simulations of dry noncohesive spheres, and where $\beta\sim 1$ is close to the experimental values measured for foams and emulsions. Indeed the ratio of the attractive force to aggregate weight is independent of primary particle size and only slightly above one, which roughly signals the border between cohesive systems and free flowing granular materials. Therefore aggregates might behave effectively as low cohesive spheres also in the weak solid, at least in the close vicinity of jamming. As soon as the consolidation stress became $\sigma>\sim 20$ Pa (depending on the interparticle force), the experimental data deviated from the power law behavior and crossed over to a logarithmic trend $\Delta\phi\sim\ln\sigma$, as typically measured on soils. Like the gelation transition of colloids, the colloidal glass transition and the melting transition of foams, the jamming of our fine powders is extremely sensitive to the applied stress. Our measurements of the local reflectance showed the local nucleation of transient (avalanchelike) fluid structures driving the relaxation time of the system to diverge.

References

[1] R. Jackson, Trans. Inst. Chem. Engrs. Vol. 41, p. 13 (1963).

[2] P. U. Foscolo and L. G. Gibilaro, Chem. Engng. Sci., vol. 39, p. 1667 (1984).

[3] K. Rietema, Chem. Engng. Sci., vol. 28, p. 1493 (1973).

[4] N. Menon and D. J. Durian, Phys. Rev. Lett., vol. 79, p. 3407 (1997).

[5] J. M. Valverde A. Castellanos., and M.A.S. Quintanilla, Phys. Rev. Lett., vol. 86, p. 3020 (2001).

[6] J. M. Valverde A. Castellanos., and M.A.S. Quintanilla, Phys. Rev. E, vol. 64, 021302 (2001).

[7] C. Tsinontides and R. Jackson, J. Fluid Mech., vol. 255, p. 237 (1993).

[8] J. M. Valverde A. Castellanos, P. Mills and M. A. S. Quintanilla, Phys. Rev. E, vol. 67, p. 051305 (2003).

[9] A. Castellanos, J. M. Valverde and M. A. S. Quintanilla, Phys. Rev. E, vol. 64, p. 041304 (2001).

[10] J. M. Valverde , M. A. S. Quintanilla, A. Castellanos, and P. Mills, Phys. Rev. E, vol. 67, p. 016303 (2003).

[11] P. Duru and E. Guazelli, J. Fluid Mech., vol. 470, p. 359 (2002).

[12] V. Trappe et al., Nature, vol. 411, p. 772 (2001). P. N. Pusey and W. van Megen, Phys. Rev. Lett., vol. 59, p. 2083 (1987).

[13] J.M. Valverde, M.A.S. Quintanilla, and A. Castellanos., submitted to PRL.

XXI ICTAM, 15–21 August 2004, Warsaw, Poland

SINGLE PARTICLE MOTION IN COLLOIDAL DISPERSIONS

Ileana C. Carpen*, Todd M. Squires**, & John F. Brady*
*California Institute of Technology, Division of Chemistry and Chemical Engineering, Pasadena, CA 91125, United States
**California Institute of Technology, Depts. of Applied and Computational Mathematics and Physics, Pasadena, CA 91125, United States

Summary Microrheology uses the motion of tracer particles to infer the properties of a surrounding medium. Most applications have limited themselves to examining motion due to thermal fluctuations, with minimal impact upon the structure of that medium. We investigate the forced motion of a particle through a colloidal suspension, which is affected by both the viscous drag and the force resulting from the microstructural deformation, and thus study the departure of the system from the linear viscoelastic regime.

BACKGROUND

In the last decade microrheology has burst onto the scene as a novel experimental technique to study the properties of materials at the microscopic scale, and is particularly well-suited for examining the properties of soft, heterogeneous materials, especially biological materials. Among the collection of techniques known as microrheology, most involve tracking the movement of a colloidal particle or set of particles in order to determine the properties of the surrounding environment [1]. There are two main types of particle-tracking microrheology: passive—tracking the random motion due to thermal fluctuations—and active—applying a constant or oscillatory force to the particles, for example by using optical tweezers or magnetic fields. Due to the small length scales involved, microrheology became most practical after recent improvements in imaging technology. Unlike conventional rheometry, which measures bulk properties, microrheology allows the measurement of local viscoelastic properties and needs much smaller material samples, a particular bonus for scarce biomaterials and small systems such as individual cells; for gels, microrheology also avoids the problem of slip at the walls, common for rheometers. Microrheological techniques have been used to study a diverse set of systems: cells, actin networks, gelatin, DNA and polyethylene oxide solutions, and the behavior of colloids near the glass transition, as well as fundamental interactions between pairs of colloidal spheres and entropic forces in binary colloids. Microrheology has also been proposed as a tool for fundamental physics or for high-throughput material screening.

A cornerstone of particle-tracking microrheology is the application of the Stokes-Einstein relation for a sphere in a homogeneous, incompressible fluid. For single particle tracking experiments, this takes the form (after a Laplace transform):

$$\tilde{r}^2(s) = \frac{kT}{\pi s a \tilde{G}(s)}, \tag{1}$$

where s is the Laplace frequency, $\tilde{r}^2(s)$ is the mean-squared-displacement of the particle, $\tilde{G}(s)$ is a frequency-dependent modulus (Stokes-Einstein generalized for a viscoelastic medium), k is Boltzmann's constant, T is the absolute temperature, and a is the particle radius. A similar equation applies for two-point microrheology, for which the correlated motion of pairs of particles is used instead of the single-particle mean-squared-displacement [2]. The Stokes-Einstein relation translates the microrheological measurement (mean-squared-displacement) into the macroscopic measurement (viscosity or complex modulus), and is therefore crucial to any type of micro-macro comparison. Most applications of microrheology have been in the 'passive' regime where the tracked particle's motion is induced by the thermal fluctuations in the medium and the applicability (or lack thereof) of the generalized Stokes-Einstein equation (1) has been examined in detail [2]. By contrast, much less work has been done on 'active' microrheology, where the tracked particle is driven by an external force. By its very nature the passive regime is limited to the *linear* viscoelastic behavior of the material, while the active regime can be used to drive the system out of equilibrium and investigate the material's *nonlinear* response. The purpose of this work has been to study analytically and numerically the 'active' system, and its transition from linear to nonlinear behavior.

ANALYSIS

In experiments, particle movement can be induced through the use of magnetic fields or optical tweezers, or alternatively, by having one heavy particle suspended amidst neutrally-buoyant particles. The basic problem reduces to examining the motion of a single particle under the action of an imposed external force and how this motion is affected by the response of the medium. We have chosen to investigate (analytically and numerically) the motion of a particle through a colloidal dispersion. Colloids are ubiquitous and can serve as an example of non-Newtonian media.

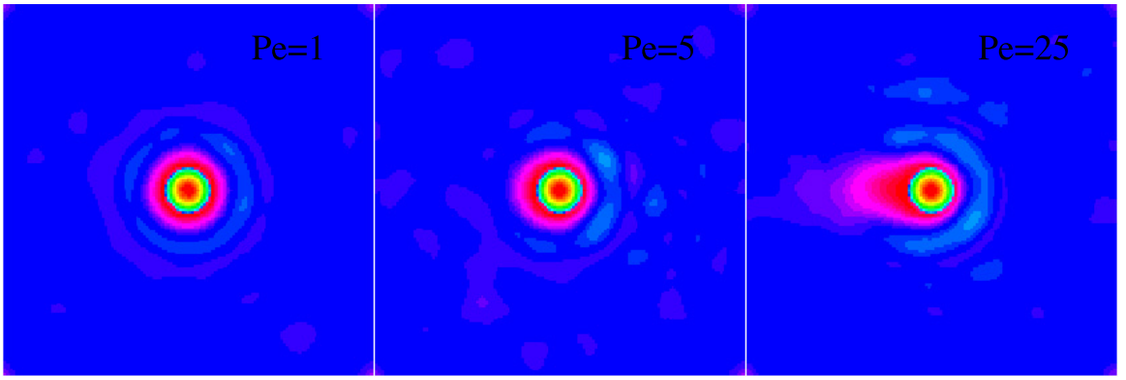


Figure 1. Brownian Dynamics results for the microstructure about a single forced particle in a Brownian suspension at a volume fraction of 35%. The particle generates a discernible wake region as the imposed force is increased beyond O(kT/a) (red regions correspond to low particle density), and a boundary layer of higher density on the 'front' (the direction of the force is left to right). The Péclet numbers based on the applied force, $Pe = Fa/kT$, are 1, 5 and 25, respectively. The total number of particles in the cubic unit cell is $N = 300$.

The particle's translational velocity is determined by a balance between the externally imposed force and the reactive force of the colloidal dispersion, which consists of the familiar viscous Stokes drag and a Brownian force caused by the deformation of the microstructure. For a particle of size a, the Péclet number, $Pe = Fa/kT$, gives the ratio of the external force (F) to the Brownian force (kT/a) and governs the distortion of the microstructure, which is determined from the solution of the Smoluchowski equation. For dilute suspensions in the absence of hydrodynamic interactions a closed form analytical expression can be obtained for all values of the Péclet number. However, consideration of suspensions of appreciable density requires the use of simulations (Brownian Dynamics or, if including hydrodynamics, Accelerated Stokesian Dynamics with Brownian motion (ASDB) [3]). Some results are shown in figure 1.

For small imposed forces (small Pe) the response is found to be viscous, with a linear relation between the imposed force and the velocity of the particle. The system is still in the linear regime for these small Pe (as with 'passive' microrheology) but transitions out of it as the Péclet number is increased. As the force on the particle is increased (increasing the Péclet number) the velocity of the particle decreases with increasing Pe until it reaches a viscous plateau at infinite Pe. This 'shear thinning' of the particle's velocity is reminiscent of the shear thinning of the colloidal dispersion's viscosity and a comparison between the two can be made.

CONCLUSIONS

This research examines the relation between micro and macro-rheology through a combination of theoretical and computational analysis, with an emphasis on the 'active' and nonlinear regime. Most microrheology research and analysis has been performed in the linear regime, with few experiments in the nonlinear regime, despite the great practical interest in the nonlinear problem. The results of this study may be used to both provide insight into currently available results as well as a guide for the design of new experiments.

References

[1] MacKintosh, F. C. & Schmidt, C. F.: Microrheology. *Curr. Op. Colloid Interf. Sci.* **4**:300–307, 1999.
[2] Crocker, J. C., Valentine, M. T., Weeks, E. R., Gisler, T., Kaplan, P. D., Yodh, A. G., & Weitz, D. A.: Two-point microrheology of inhomogeneous soft materials. *Phys. Rev. Lett.* **85**:888–891, 2000.
[3] Banchio, A. J. & Brady, J. F.: Accelerated Stokesian dynamics: Brownian motion. *J. Chem. Phys* **118**:10323–10332, 2003.

SLIP AND FLOW IN PASTES

Michel Cloitre[*], Roger T. Bonnecaze[**]
[*] *Laboratoire Matière Molle et Chimie, ESPCI, 10 rue Vauquelin, 75231 Paris, France*
[**] *Department of Chemical Engineering and Texas Materials Institute, The University of Texas at Austin, Austin, TX 78712, USA*

Summary Slip in soft particle pastes is dominant at low shear rates. By directly imaging the flow of pastes using video-microscopy, we show that slip is characterized by universal properties, which depend on solvent viscosity, bulk elasticity and particle size. A generic slip model based on elasto-hydrodynamic lubrication between the squeezed particles and the wall explains these properties quantitatively.

INTRODUCTION

Concentrated dispersions and pastes of soft particles are ubiquitous in everyday life (mayonnaise), in biology (biological fluids and tissues) and in geology (lava and mud). These materials share in common many properties. At high concentration, steric constraints are so important that the motion of individual particles is drastically reduced unless a finite external force is applied. This is at the origin of many fascinating bulk properties such as yield stress, shear thinning, aging and memory. In practice however, the motion of pastes is often dominated by wall slip, with dramatic effects when they move within confined smooth surfaces. This can have a dramatic effect on the rheology and the processing of yield stress materials.
Wall effects in dispersion flows have often been described in terms of an apparent slip [1]. Slip is generally inferred from macroscopic rheology, and very few studies have tried to correlate the rheology with direct flow visualizations [2]. Slip is believed to arise from particle depletion at the shearing surface. Many mechanisms have been evoked to cause particle depletion; they can be static (*e.g.,* steric, physico-chemical interactions between the particle and the surface) or dynamic (*e.g.,* shear rate gradients, hydrodynamic interactions) in origin. Several important questions remain open. What are the microscopic mechanisms at work when concentrated dispersions flow along surfaces? How are wall phenomena coupled to the bulk rheology? Is there any underlying universality? During the talk, we will answer these questions for the case of soft particle pastes.

SLIP PROPERTIES IN SOFT PARTICLE PASTES

Microgel pastes and emulsions

We have studied pastes of microgel particles and emulsions. A microgel particle consists of a cross-linked polymer network of acrylate chains bearing ionized methacrylic acid groups, which is swollen by a solvent [3]. The bulk rheology of microgel pastes can be tuned by changing the solvent viscosity, the cross-link density of the particles, the total polymer concentration. The emulsions are dispersions of silicon oil in water, stabilized by a surfactant. In dilute suspensions the particles have a spherical shape with a radius R ($R \cong$100-250 nm for microgels and $R \cong 1.5 \pm 1$ μm for emulsions). At high volume fraction, they pack into concentrated pastes and emulsions with solid-like properties. In essence both systems, whilst very different in composition, can be considered as dispersions of soft, elastic spheres. The elasticity of the microgel particles is due to the osmotic pressure of the counter-ions associated with the fixed charges borne by the polymer network. The elasticity of the emulsion droplets comes from the interfacial energy of the oil-water interface.

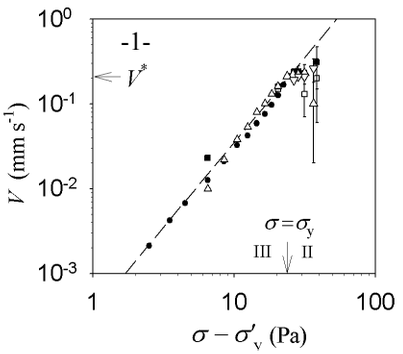
Direct measurements of slip velocity

We have measured simultaneously the non-linear rheology and the local velocity profiles for smooth and rough shearing surfaces. The rheometer is a stress-controlled apparatus with cone and plate geometries. The flow profiles are obtained using video microscopy. The pastes, which are translucent, are seeded at very low concentration with small glass spheres with a diameter of about 10 μm, which reflect light when illuminated. They are observed from the side using a CCD camera equipped with a high magnification zoom lens. Local velocities are obtained by tracking the successive positions of the tracers and by measuring their displacement during time. The spatial resolution is ~ 20 μm and the range of measurable velocities is $1\mu m\ s^{-1} \leq v \leq 3\ mm\ s^{-1}$.
When sheared with rough surfaces, pastes and emulsions flow homogeneously in the whole range of stresses and shear rates accessible by our experimental set-up. When one or both of the shearing surfaces are smooth, wall slip occurs. The slip layer is not resolvable in our set-up. The bulk flow is homogeneous but the actual shear rate to which the paste is subjected is much smaller then the apparent shear rate deduced from rheology. The relative importance of slip depends on the shear stress σ. We can distinguish three regimes of slip. At shear stress much larger than the yield stress σ_y ($\sigma/\sigma_y \geq 1.5$), slip is negligible compared to the bulk flow. Just above the yield

stress ($1 < \sigma/\sigma_y < 1.5$), slip becomes significant and the total deformation of the pastes result from a combination of bulk flow and slip. At and below the yield stress ($\sigma/\sigma_y \leq 1$), the bulk flow is negligible and the apparent motion is entirely to the slipping of the paste.

Scaling properties of slip

Direct measurements of the slip velocity for a typical paste are presented in Fig. 1 as a function of the excess stress $\sigma - \sigma'_y$, where σ'_y is the apparent yield stress in the presence of slip. In regime III ($\sigma/\sigma_y \leq 1$), the slip velocity decreases as the applied stress is decreased. The data are well represented by the quadratic form $V/V^* \sim (\sigma/\sigma_y)^2$. In regime II ($1 < \sigma/\sigma_y < 1.5$) the slip velocity remains equal to a plateau value V^*. V^* is a characteristic velocity that depends only on the solvent viscosity, η_S, on the shear modulus of the paste, G_0, and on the particle radius R. Interestingly, Fig. 2 shows that V^* is of the form: $V^* \sim G_0 R/\eta_S$ for all except the most concentrated pastes.



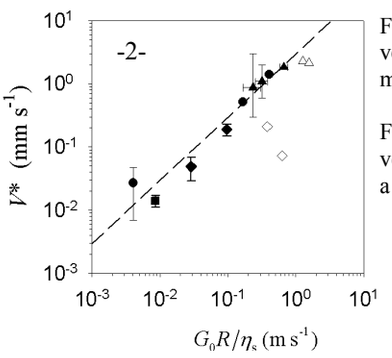


Fig.1: scaling of the slip velocity versus the excess stress for a microgel paste.

Fig.2: scaling of the characteristic velocity V^*. Each symbol refers to a paste or emulsion

ELASTO-HYDRODYNAMIC MODEL OF SLIP

For concentrated suspensions of soft particles, we propose that elasto-hydrodynamic lubrication is responsible for the slip [4,5]. Elasto-hydrodynamic slip can be described qualitatively as follows. At rest, the osmotic pressure of the compressed suspension or emulsion forces the particle into contact with the bounding surfaces. If these contacts were to persist during flow, no-slip behavior would be expected. However, a thin layer of fluid between a soft particle and a smooth surface in relative motion can be maintained due to the non-linear coupling of the flow in the lubrication layer and the elastic deformation of the particle. Indeed, under motion, the particle deforms asymmetrically and the resulting pressure field creates a force pushing the particle away from the wall. This force must balance the osmotic force due to the compressed suspension or emulsion acting on the particle to maintain the lubricated layer, and this balance determines the thickness of the lubricated gap, and ultimately the drag between the particle and smooth surface. These arguments can be formalized with a scaling analysis of the elasto-hydrodynamic lubrication equations. The predictions are in excellent agreement with the experimental results, in particular with the variations depicted in Figs 1 and 2.

CONCLUSIONS

Soft particles pastes exhibit a generic slip behavior near smooth surfaces. A model, which is based on elasto-hydrodynamic lubrication between the squeezed particles and the wall, explains quantitatively the slip properties when stresses are small enough that there is no bulk flow. We think that this elasto-hydrodynamic slip mechanism should apply to many concentrated dispersions of soft particles. Moreover, since jammed particles must 'slip' past one another in order to move, similar mechanisms are likely to occur in the bulk of the material.

References

[1] Barnes H. A., *J. Non-Newtonian Fluid Mech.* **81,** 133, 1999.
[2] Princen H. M., *J. Colloid Interface Sci.* **105**, 150-171, 1985.
[3] Borrega R., Cloitre M., Betremieux I., Ernst B., Leibler L., *Europhys. Lett.* **47**, 729-735, 1999.
[4] Meeker S.P., Bonnecaze R.T., Cloitre M., *Phys. Rev. Lett.* **92**, 198302, 2004.
[5] Meeker S.P., Bonnecaze R.T., Cloitre M., *J. Rheol.*, to appear.

IMPACT

Detlef Lohse, Raymond Bergmann, Rene Mikkelsen, Christiaan Zeilstra, Devaraj van der Meer, Michel Versluis, Ko van der Weele, Martin van der Hoef, and Hans Kuipers
Faculty of Science and J. M. Burgers Centre for Fluid Dynamics, University of Twente, 7500 AE Enschede, The Netherlands
(January 5, 2004)

According to Shoemaker, the "impact of solid bodies is the most fundamental process that has taken place on the terrestrial planets" [1], as they shape the surfaces of all solar system bodies. A lot of information on this process has been extracted from remote observations of impact craters on planetary surfaces [2]; experiments however with large enough impact energies as compared to the energy stored in the ground are difficult. We approach this problem by *downscaled* experiments and by corresponding discrete particle numerical simulations: The idea is to fully *decompactify* very fine sand which then at impact of a steel ball behaves fluid-like. Thus, we are in the gravity-dominated regime. The series of events is as follows: On impact of the ball, sand is blown away in all directions ("splash") and an impact crater forms. When this cavity collapses, a *granular jet* [3, 4] emerges and is driven straight into the air. A second jet goes downwards into the air bubble entrained during the process, thus pushing surface material deep into the ground. The downward jet will therefore considerably change the layering of the sediments underneath a crater, as it provides a mechanism how surface material can be transported deep into the ground. This suggested mechanism may shed new light on the sediment layering data found underneath the Chicxulub crater, which is a source of major controversy [7, 8]. The entrained air bubble rises slowly towards the surface, causing a granular eruption. In many cases the collapsing jet leaves a *central peak* in the crater, just as observed in craters of the terrestrial planets. The upward jet will strongly contribute to the transfer of planetary matter into space [5]. In addition to the experiments and discrete particle simulations, we present a simple continuum theory to account for the void collapse leading to the formation of the upward and downward jets. We show that the phenomenon is robust and even works for *oblique* impacts: the upward jet is then shooting *backwards*, in the direction where the projectile came from.

---

[1] E. M. Shoemaker, in *Impact and Explosion Cratering*, edited by D. J. Roddy, R. O. Pepin, and R. B. Meril (Pergamon Press, New York, 1977), pp. 1–10.
[2] E. Pierazzo and H. J. Melosh, Ann. Rev. Earth Planet. Sci. **28**, 141 (2000).
[3] S. T. Thoroddsen and A. Q. Shen, Phys. Fluids **13**, 4 (1996).
[4] R. Mikkelsen *et al.*, Phys. Fluids **14**, S14 (2002).
[5] J. D. O'Keefe and T. J. Ahrens, Science **198**, 1249 (1977).
[6] A. M. Walsh, K. E. Holloway, P. Habdas, and J. R. de Bruyn, Phys. Rev. Lett. **91**, 104301 (2003).
[7] J. Smit, Ann. Rev. Earth Plan. Sci. **27**, 75 (1999).
[8] G. Keller *et al.*, J. Geol. Soc. **160**, 783 (2003).

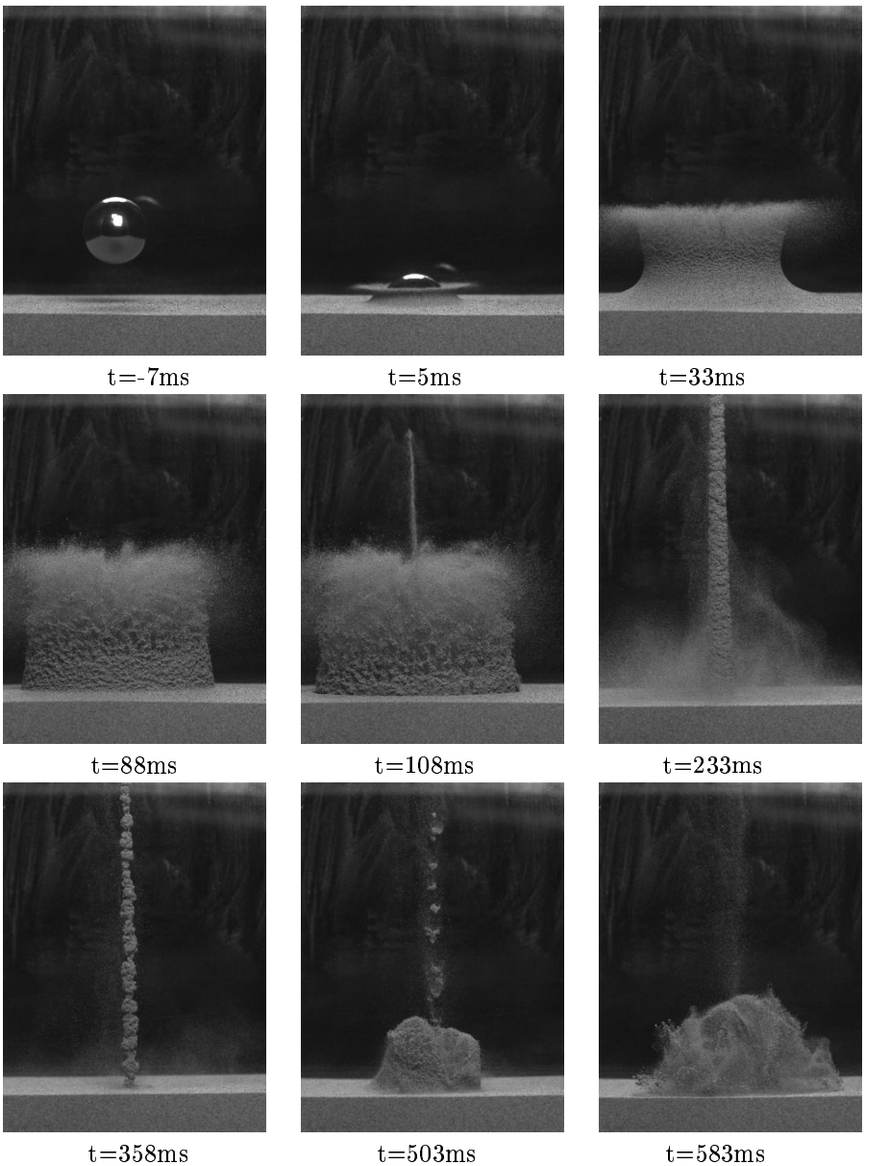


FIG. 1. Jet formation after the impact ($v_0 = 2.43m/s$) of a steel ball of $R_0 = 1.25cm$ on loose very fine sand. The jet in this experiment exceeds the release height of the ball. Frames 2-4: splash; frames 5-6: a jet emerges; frame 7: clustering within the jet; frames 8-9: granular eruption at the surface.

XXI ICTAM, 15–21 August 2004, Warsaw, Poland

MAXIMUM-ENTROPY ESTIMATES AND VIRTUAL THERMOMECHANICS FOR GRANULAR ASSEMBLIES

J.D. Goddard
Department of Mechanical and Aerospace Engineering
University of California, San Diego
9500 Gilman Drive
La Jolla, CA 92093-0411 USA

Summary This is an extension of previous work by others, dating back some thirty years on more (1), on maximum-entropy estimates of the statistical distribution of quasi-static contact forces in granular assemblies.
The precise form of the probability density is shown to depend on the statistical weight assigned to elements in the state space of contact forces or displacements. A brief review is given of comparisons with experiment and computer simulations. The formal methods of statistical thermodynamics are employed to establish a virtual thermomechanics. without reference to a granular temperature. This leads to an elastoplastic work function, of the type appearing in various phenomenological models of complex solids and fluids. The possibility of non-convexity, leading to continuum- and meso-scale material instability, is discussed.

EXTENDED SUMMARY

A major challenge in granular mechanics is to establish reliable connections between continuum-level phenomenological models and micromechanical models, which is essentially a problem in statistical mechanics. This accounts in part for the long-standing efforts to apply the maximum-entropy principle, not only to granular dynamics with large kinetic energy, but also to granular statics (11; 1). In systems devoid of a classical thermodynamic structure, the entropy can be taken as information-theoretic Shannon entropy, and the maximum-entropy principle provides one type of maximum-liklihood estimate for the statistics of systems with prescribed macroscopic averages as global constraints . The purpose of the present article is to establish certain qualifications and ramifications anticipated in previous articles by this author (4; 2).
Bagi's (1) maximum-entropy estimates for the interparticle contact-force distribution exhibit the exponential behavior at large force observed in numerous experiments and numerical simulations (10; 9). Hence, the exponential distribution may be a robust statistical feature of static granular packings, independently of the precise details of force transmission, in which case it cannot be taken as an unequivocal confirmation of various load-diffusion models proposed in the soil-mechanics and physics literature. This conclusion is further supported by the maximum-entropy estimates of (7) on contact forces in granular assemblies subject to the Coulomb condition ($\mu f_n \geq |f_t|$) at particle contacts. It can be shown that local mechanical constraints of this type can be treated as a restriction on state-space weight, without jeopardy to the exponential distribution of large forces (2)

Maximum Entropy with Constant Stress

With the standard expression for (Cauchy) stress (1; 7; 4)

$$\mathbf{T} = n_c \langle \mathbf{M}(\mathbf{f},\mathbf{l}) \rangle, \ \text{ with } \ \mathbf{M}(\mathbf{f},\mathbf{l}) := -\mathbf{f} \otimes \mathbf{l}, \tag{1}$$

where n_c denotes contact number density, $\mathbf{f}$ the vectorial contact force, $\mathbf{l}$ the branch vector connecting centroids of adjacent grains, and $\mathbf{M}$ the associated force dipole.
The maximization of entropy:

$$S[P] = -\langle \log P \rangle = -\int_\Omega P \log P d\Omega \tag{2}$$

based on a state-space measure $d\Omega$ and subject to stationarity of Eq. (1) yields the canonical distribution

$$P(\mathbf{f},\mathbf{l}) = Z^{-1} \exp\{\mathbf{\Lambda}:\mathbf{M}\} = Z^{-1} \exp\{-\mathbf{f}\cdot\mathbf{\Lambda}\cdot\mathbf{l}\}, \tag{3}$$

where the colon denotes contracton of a tensor product and Z the *partition function*

$$Z(\mathbf{\Lambda}) = \int_\Omega \exp\{-\mathbf{f}\cdot\mathbf{\Lambda}\cdot\mathbf{l}\}\, d\Omega(\mathbf{f},\mathbf{l}), \tag{4}$$

a function of the Lagrange multiplier (tensor) $\mathbf{\Lambda} = (\lambda_{ij})$.
As discussed by the present author (4; 2), the actual probability distribution in $\mathbf{f},\mathbf{l}$ depends on the statistical weight factor J connecting $d\Omega$ and the cartesian volume element $d\mathbf{f}d\mathbf{l}$. Employing an argument based on conservation of power-law elastic contact energy $d\Omega \propto f^{\nu-1}df$, one finds a Poisson distribution of force magnitude f for frictionless spheres (4; 2):

$$\rho(F) = \nu \frac{(\nu F)^{\nu-1}}{\Gamma(\nu)} e^{-\nu F}, \ \text{ where } \ F = \frac{f}{\langle f \rangle}, \tag{5}$$

previously obtained by Bagi (1). Figure 1 of (4) shows a favorable comparison of Eq. (5) to experiment and numerical simulation, except for a troubling discrepancy arising from "dead" contacts with zero force in experiment and simulation.

Virtual Thermodynamics

The standard thermodynamic approach (6), according to which all macroscopic properties are derivable from Z, gives

$$\mathbf{T} = \partial_{\mathbf{\Lambda}}\psi, \quad \text{with} \quad \psi(\mathbf{\Lambda}) = -n_c \log Z, \tag{6}$$

with ψ and $\mathbf{\Lambda}$ assuming the respective roles of free energy and (infinitesimal) displacement or velocity gradient.

Eq. (6) represents a "virtual" thermodynamics involving no explicit reference to temperature. In the limit of perfectly rigid particles the energy ψ must be regarded as purely extrinsic, arising from external work done by particle rearrangement.

For frictional sphere assemblies, the real (as opposed virtual) thermodynamic validity of Eq. (6) appears to hinge on some type of elastic-plastic decomposition analogous to that employed in well-known incremental plasticity theories. For example, if we assume that the contact force can be written as a linear combination $\mathbf{f} = \mathbf{f}^E + \mathbf{f}^D$ of elastic and dissipative forces and that the state space measure factors as

$$d\Omega(\mathbf{f}^E, \mathbf{f}^D, \ldots) = d\Omega(\mathbf{f}^E, \ldots) d\Omega(\mathbf{f}^D, \ldots) \tag{7}$$

then Eq. (6) decomposes linearly into an elastic strain energy and a dissipation function, of the form assumed in certain phenomenological treatments of inelasticity (3; 5). However, the standard elastic-plastic version requires a treatment of kinematics like that given in (1), which results in a complimentary energy function (2) resembling that employed for plastic flow rules. Given the highly nonlinear nature of frictional-elastic contacts, it is not clear that the necessary statistical decoupling of force or displacement is realized in the typical granular medium.

There is a further interesting interesting question as to the possible non-convexity of relations such as Eq. (6). In particular, he associated bifurcations might serve to describe strain localization, in the form of shear bands, or stress localization in the form of force chains (4; 2), as a kind of virtual-thermodynamic phase transition.

Given the success of the maximum-entropy method in describing certain aspects of the force distribution in granular assemblies, further investigation of the validity of the above thermodynamic formalism would seem to warranted.

References

[1] K. Bagi. Analysis of micro-variables through entropy principle. In R. Behringer and J. T. Jenkins, editors, *Powders and Grains*, pages 251–4, Durham, NC, USA, 1997. Balkema.

[2] J. .D. Goddard. On Entropy Estimates of Contact Forces in Static Granular Assemblies. Submitted for publication, 2003.

[3] I. F. Collins and G. T. Houlsby. Application of thermomechanical principles to the modelling of geotechnical materials. *Proceedings of the Royal Society of London A*, 453(1964):1975–2001, 1997.

[4] J. D. Goddard. Material instability with stress localization. In J.F. Labuz and A. Drescher, editors, *Bifurcations and Instabilities in Geomechanics*, pages 57–64, Balkema, Lisse, 2002.

[5] M. Grmela. A framework for elasto-plastic hydrodynamics. *Physics Letters A*, 312(3-4):136–46, 2003.

[6] T. L. Hill. *An introduction to statistical thermodynamics*. Addison-Wesley, Reading, Mass., 1960.

[7] N. P. Kruyt and L. Rothenburg. Probability density functions of contact forces for cohesionless frictional granular materials. *International Journal of Solids & Structures*, 39(3):571–583, 2002.

[8] D. M. Mueth, H. M. Jaeger, and S. R. Nagel. Force distribution in a granular medium. *Physical Review E*, 57(3):3164–9, 1998.

[9] C. S. O´Hern, S. A. Langer, A. J. Liu, and S. R. Nagel. Force distributions near jamming and glass transitions. *Physical Review Letters*, 86(1):111–14, 2001.

[10] F. Radjai, D. E. Wolf, M. Jean, and J. J. Moreau. Bimodal character of stress transmission in granular packings. *Physical Review Letters*, 80(1):61–4, 1998.

[11] M. Shahinpoor. Statistical mechanical considerations on the random packing of granular materials. *Powder Technology*, 25(2):163–76, 1980.

XXI ICTAM, 15–21 August 2004, Warsaw, Poland

GRANULAR COLUMN COLLAPSE

Gert Lube*, Herbert E. Huppert**, R. Stephen Sparks*, Mark A. Hallworth**
*Department of Earth Sciences, Bristol University, Bristol BS8 1RJ
**Institute of Theoretical Geophysics, DAMTP, CMS, Wilberforce Road, Cambridge CB3 0WA

Summary We present a study of initially vertical cylinders of granular material collapsing onto a horizontal base. We describe the spreading in terms of three regimes dependent on the aspect ratio $a = h_i/r_i$, where the initial cylinder of material has radius r_i and height h_i. The motion is described by the same scaling relationships for all the materials, independent of internal friction due to interactions between grains. Only at the end of flow, when there is an abrupt halt, is internal friction important.

We conducted a series of experiments in which various granular materials, initially contained in a vertical cylinder, were rapidly released onto a horizontal surface to spread out unhindered over it. The main materials were dry sand and salt, but, for comparison purposes, we also conducted experiments with couscous, rice and sugar, all of which have a quite different size and shape. Nevertheless there was no difference in the resulting spreading relationships. The horizontal plane used was either wood, a smooth surface of baize lying on wood, a smooth transparent Plexiglas plane or a rough plane of sandpaper. The detailed spread of the granular material was also independent of these surfaces. Eight different cylinders, ranging in radius, r_i, from 1.7 to 9.7 cm, were used. The volume of granular material varied from 125 to 13,000 cm^3. Some experiments were recorded and later analysed on a digital high-speed video at 500 frames per second. After all motion had ceased, the profile of the resultant deposit was measured, to find the final runout radius, r_∞, central cone height, h_∞, and the steepest incline, α, of the upper surface.

For all values of a there was a central undisturbed cone of material which did not partake in the motion, whose angle was close to 60°, corresponding to an aspect ratio of 1.7. This can be interpreted as an internal friction angle for the material. At the base, three different regions were captured by video during the collapse: a stationary circular region, of radius r_i; a ring of previously deposited particles; and an outer ring of material which was still flowing. These last two regions were divided by a moving interface that propagated outwards until the flow front came to rest.

Observations from the high-speed photography indicate that other aspects of the motion naturally divide themselves into three different regimes dependent of the initial aspect ratio $a = h_i/r_i$. For initial aspect ratios $a < 1.7$, the upper surface of the released material was divided into an inner stationary circle (which remained at the initial height, h_i) outside of which was flowing material. After the flow front had ceased propagating, a moving interface on the upper free surface appeared, which separated static from flowing particles and which propagated inward from the stationary front. For $a < 1$ the final deposit consisted of an inner, undisturbed central region beyond which there was an axisymmetric, tapering frontal region with α in the range of the angle of repose. For $1 < a < 1.7$ the avalanching which occured after the flow front had stopped moving removed the undisturbed central region.

For $a > 1.7$ the entire upper surface flowed from the beginning of each experiment. Initially, the upper free surface remained undeformed and horizontal. After the column had lost some height, deformation of the top occurred, to form a dome whose radius of curvature decreased with time. The final deposit had a steep central zone and an axisymmetric tapering frontal region with α less than the angle of repose.

A transition in behaviour of collapse was evident from the video analyses to occur when a exceeds about ten. Immediately upon lifting the container the entire free surface began to flow. A flow front developed at the base of the column and propagated outwards while removing material from the centre. In contrast to lower initial aspect ratios, the upper surface of the column remained undeformed until its height sank to that of the neighbouring flat frontal region. Also, once the flow at the base had ceased, an interface between moving and stationary material appeared on the upper free surface but propagated outward from the centre to the flow front. The value of α decreased monotonically with increasing a.

The quality of the observational data and the similarity of the results for the different materials suggest that, with the use of dimensional analysis, the data can be collapsed in a systematic way. The initial experimental set up is uniquely determined by r_i, a and g, the acceleration due to gravity. Our ability to collapse all the data using only this input, and not any material properties, is a robust test for the assumption that no additional material property, such as the friction between individual grains, is needed to describe the motion. This is because, as described in more detail below, the motion stops rapidly at the end, in a very small fraction of the total time of the runout.

The difference between the initial and final radius, $\delta r = r_\infty - r_i$, must be expressible as $\delta r = r_i f(a)$. A plot of $\delta r/r_i$ makes up figure 1. For $a < 1.7$, because there is no motion of the inner region, the resultant expression must be independent of r_i, which requires that $f(a) \propto a$. From figure 1 we determine that the constant of proportionality which best fits the data is 1.3. For $a > 1.7$ the best fit power law to the data for all grains is given by $f(a) = 1.6a^{1/2}$.

The final height at the centre is similarly expressible as $h_\infty = r_i \eta(a)$. Figure 1 also presents all the data for h_∞/r_i as a function of a. For $a < 1.7$, $h_\infty = h_i$, and so $\eta(a) = a$, as indicated by the data. For $1.7 < a <$ c.10 the best fit power

a. This is in response to the wave that originates from the centre and removes material outwards. Unfortunately, the data are a little too scattered to be quantitatively analysed with confidence.

Fig 1

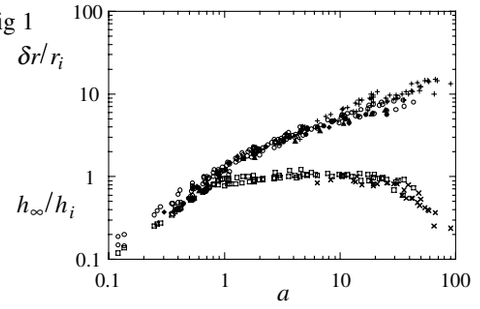


Fig 2

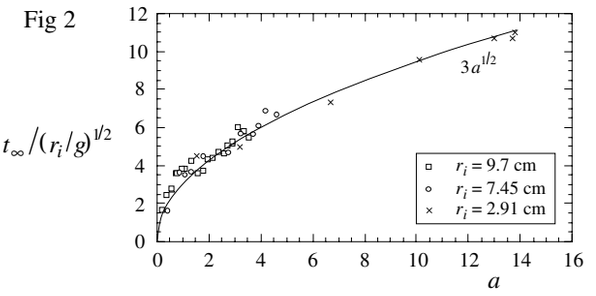


Figure 1. Nondimensional radial displacement and height at centre of pile. Points marked with a cross are for experiments in which the cylinder was raised height H from the base before releasing grains, and aspect ratio is defined as $(H+h_i)/r_i$. This shows that in the final runout distance only maximum initial height is relevant (and initial radius).

Figure 2. Nondimensional time until the grain front ceased motion as a function of a.

So far the parameter g has not entered our expressions because it is the only input parameter for which time is involved in its dimensions, and $\delta r, h_\infty/r_i$ are both independent of time. The value of g will affect the total time for collapse, t_∞, which is defined as the time between the initiation of the experiment and that at which the flow front stops propagating. The high speed video, used on all the experiments with sand, allowed us to determine t_∞ reasonably accurately. By dimensions, it must be of the form $t_\infty = (r_i/g)^{1/2}\psi(a)$, for some function $\psi(a)$. A plot of $t_\infty/(r_i/g)^{1/2}$ as a function of a is presented in figure 2. As before, for $a < 1.7$, an expression independent of r_i requires $\psi(a) \propto a^{1/2}$, which is consistent with the data for a constant of proportionality of 3.8. For $a > 1.7$ thebest fit power law through the data yields $\psi(a) = 3a^{1/2}$, which indicates that $t_\infty = 3(h_i/g)^{1/2}$. Note that the time taken for a particle to fall a height h_i under gravity is $(2h_i/g)^{1/2}$, which is just less than a half of t_∞.

Further insight on the flow characteristics is obtained by an analysis of our kinematic data on the radius of the flow front as a function of time, $r(t)$. For all flows there was a primary acceleration phase during which the acceleration was approximately constant between 0.25 g and 0.3 g. For $a < 1.7$ this acceleration phase was followed by a phase of deceleration which came quite abruptly to a halt. For $a > 1.7$ these two phases were separated by a phase of constant velocity of the flow front whose duration increased with increasing a. This phase of constant velocity has an analogue with the evolution of a fluid axisymmetric gravity current spreading at high Reynolds number, which also goes through a stage of constant velocity [1]. A fluid current then adjusts under a balance between buoyancy and inertial forces, spreading like $t^{1/2}$[2] – the same result as obtained for the granular collapse described here. This analogy, which uses quantitative relationships to describe the motion of the granular medium that are closely analogous to those used to describe the motion of density currents of Newtonian liquids, further strengthens our argument that intergranular frictional effects play a negligible role until the abrupt halt commences.

Obtaining the spreading relationships that our experiments have indicated remains a challenge for the future. In the meantime a clue to understanding the emplacement we have observed may come from an interpretation of the final stages, when the spreading pile comes to a rapid halt. It has been suggested that granular materials can be considered in two states [3]: a static solid state, where intergranular forces at particle faces give the material strength; and a liquid state, exemplified by granular flows and fluidised beds, where the particles are in an agitated state and the system has negligible strength. The abrupt cessation of the motion of the granular flows that we observed can be likened to a phase change between two states [4]. In accord with the characterisation put forward in [3], the change of state can be envisaged as a kinetic process analogous to solidification of a true liquid. In the case of a granular medium, we suggest that as the flow decelerates, the granular temperature falls below a threshold value and frictional interactions between particles become dominant and the granular material converts to a static solid (or deposit).

References

[1] H.E. Huppert, J.E. Simpson, *J. Fluid Mech.* **99**: 785, 1980.
[2] D.P Hoult, *Ann. Rev. Fluid Mech.* **4**: 341, 1972.
[3] H.M. Jaeger, S.R. Nagel, *Rev. Mod. Phys* **68**: 1259, 1996.
[4] H.E. Huppert, *J. Fluid Mech.* **212**: 209, 1990.

GRAVITY FLOW OF A DENSELY-PACKED GRANULAR MATERIAL.

Jean Rajchenbach[1]
Laboratoire de Physique de la Matière Condensée (CNRS UMR 6622),
Université de Nice-Sophia Antipolis, Parc Valrose, 06108 Nice Cedex 02

Summary We present experimental results concerning the rapid flow of a densely-packed grain collection down a bumpy inclined channel. We show that the results do not agree with the predictions of the standard kinetic theory, relying on the binary collision hypothesis. Emphasizing the role played by multicontact collisions in the dense limit, we propose a new approach relying on a long range dissipation scheme. Our model succeeds in accounting qualitatively and quantitatively for the linear profile of velocity found in experiments on dense gravity-driven flows.

INTRODUCTION

So far, there is a reasonable qualitative agreement between the results of experiments conducted on dilute granular media and the predictions of kinetic models inspired from the hard sphere gas theory [1]. However, experiments conducted on dense rapid granular flows lead to drastically different results, results which appear to lie beyond the domain of validity of standard hydrodynamic descriptions [2]. The reason is likely that for dense media, there are long-lasting contacts between grains, and that the basis hypothesis of binary collisions does not hold. Contrary to dilute granular gases, for which the transport of momentum proceeds from balistic flights and interparticle collisions, the most efficient channel to transport momentum and energy through dense granular media is supported by the continuous paths of contacts.

EXPERIMENTAL RESULTS

We have performed experiments in a two-dimensional inclined channel, sloping between 20° and 30°. The bottom is constituted of a saw blade which ensures non-slipping boundary conditions at the bottom for weak enough slopes. The granular material is comprised of monodisperse aluminum spheres of 1.5 mm diameter, with elastic restitution coefficient e =0.6 and friction coefficient μ=0.6. The flows are filmed with a high speed digital camera (250 frames/sec) and then pictures are analysed to access grain position and velocity fields. A typical picture of the flow is shown in Fig. 1. Corresponding solid fraction and velocity profiles are shown in Fig. 2. The salient features are the followings. Firstly the solid fraction appears as nearly constant in the flowing layer (Fig. 2), with value $\nu \cong 0.8$ corresponding to the random close packing (except for the very upper region, owing to the unevenness of the free surface) in two dimensions. Secondly, the shear rate $\dot{\gamma}$ is found to be independent of the depth, i.e. the velocity profile is linear (Fig. 2), and its order of magnitude is given by $\sqrt{g/d}$, where g is the gravity constant and d is the grain diameter. Interestingly, using other materials (as steel beads), the rheological behavior is found to be insensitive to the value of the restitution coefficient e. As for the instantaneous velocity fluctuations in densely-packed materials, it is important to realize that reliable data are very difficult to obtain experimentally. Real experiments can access to grain trajectories only to within the experimental time resolution, and the ostensible velocity fluctuations result more from sliding of grains over adjacent corrugated layers of particles than from the ballistic flight of grains punctuated by distinct collisions. Sampling of grain displacements over a time very short compared with the characteristic shear time $(\nabla v)^{-1}$ indicates an approximatively constant value for the velocity fluctuations through the flow.

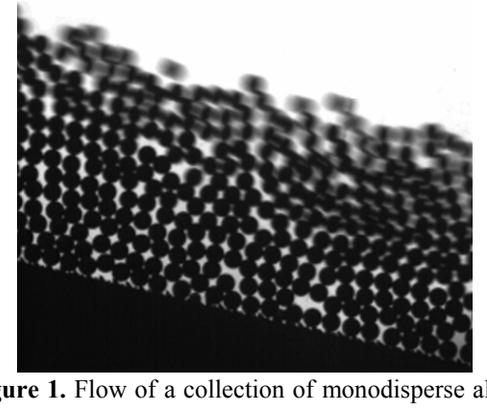


Figure 1. Flow of a collection of monodisperse aluminum spheres (restitution coefficient e=0.6, flow rate 1100 grains/sec, exposure time of the photograph : 1/125 sec). .

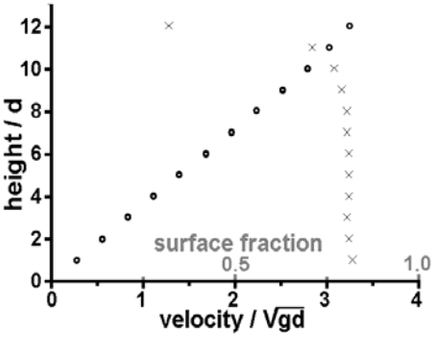


Figure 2. Corresponding adimensioned velocity profile and solid fraction (averaged over 100 samplings).

[1]On leave from LMDH (CNRS UMR 7603), Université P. et M. Curie, 75252 Paris Cedex 05

The above observations cannot be accounted for by kinetic theory. Indeed, for such constant-density, isothermal flows, the kinetic theory recovers the Bagnoldian quadratic dependence of the shear stress on shear rate [3], and hence leads to the following stress balance $(\partial v_x/\partial z)^2 \propto \rho g z \sin\theta$ (where z is oriented downwards, normal to the flow and x is the direction of the flow) in the steady regime . One therefore obtains $v_x \propto (\rho g h^3 \sin\theta)^{1/2} [1 - (z/h)^{3/2}]$ and the 3/2-power law with respect to the depth disagrees the linear velocity profiles found experimentally in dense media.

PROPOSED INTERPRETATION

As mentioned above, this discrepancy likely proceeds from the inadequacy of the binary collision picture in the case of dense materials. Collisions of solids involve various phenomena such as deformations, waves, heating, etc...[4]. The *coefficient of restitution* is well defined only for direct collisions of free, unconstrained spheres, and this is improper to extend it to the case of multibody collisions [5]. It is worth noting that in the case of multibody collisions, the apparent restitution cefficient can be considerably smaller than the one defined from binary collisions.Recently, Falcon *et al.* [6] showed experimentally (in a 1-d geometry) that a column of spherical grains colliding as a whole with a bottom wall, displayed a bounce height decreasing strongly as increasing the number of grains constituting the column. For such *multibody collisions* (with grains subjected to unilateral constraints, owing to noncohesiveness), the apparent restitution coefficient is seen to be zero as the number of the close-packed grains overpasses a threshold value. The reason is that a mechanical wave propagates through the chains of grains in contact, and experiences partial reflection and dissipation through each grain interfaces. Over a certain size (depending on the dimensionality) both momentum and kinetic energy are fully damped in a finite time τ_{damp}, so that the *apparent restitution coefficient* of the impacting column *appears equal to zero*. This result meets the inelastic collapse phenomenon which arises from the modeling of collision waves experiencing dissipative impacts [7]. We advance that taking into account multicontact collisions and the subsequent apparent decrease to zero of the apparent restitution coefficient observed in thick granular bed, are crucial to explain the behavior observed in densely packed gravity flow. We do not plan here to describe in detail the propagation of deformation waves through the bulk. We just specify that the relative momentum and the kinetic energy gained by each grains between two consecutive collisions are fully dissipated, consistently with the result of Falcon *et al.,* through the bulk in a very short time τ_{damp}, compared to the shearing time $(\partial v_x/\partial z)^{-1}$. The spirit of our reasoning is the following. Let us adopt a Lagrangian description, and consider a pair of virtually colliding particles belonging to two adjacent layers. The time-averaged increment of velocity $\bar{\nabla}v$ gained by the upper grain between two successive collisions reads as $\sqrt{gd\sin\theta}$ (where θ is the slope). We derive readily $\partial v_x/\partial z = \bar{\nabla}v/d = \sqrt{g \sin\theta /d}$. Note that this steady state solution results from the following momentum equation (per unit mass) $Dv/Dt = g \sin\theta - d (\nabla v)^2$ (D/Dt is the material derivative) where the damping force $F = -d (\nabla v)^2$ results from the averaged momentum given in to the bulk. Then, introducing the Coulomb friction term between layers, we get the following momentum equation: $Dv/Dt = g \sin\theta - kg \cos\theta - d (\nabla v)^2$ (where $k = \tan\theta_c$ is the coefficient of friction of the material), and the shear rate in the steady regime consequently reads as

$$\frac{\partial v_x}{\partial z} = \left[\frac{\sin(\theta-\theta_c)}{\cos\theta_c} \right]^{1/2} \sqrt{\frac{g}{d}}$$

in agreement with the observed linear profile of velocity, and with a prefactor of correct magnitude. Note that the previous dependence of the shear rate was also recognized experimentally by Orpe and Khakhar in the rotating drum geometry [8]. It is worth noting that the paradoxical nonzero shear rate which is experimentally observed at the vicinity of the free surface, opposes the predictions of standard hydrodynamic theories, but is recovered within our approach. The reason is that, for *constrained* collisions, the momentum is not conserved in the center-of-mass frame of the virtually colliding particles [5].

References

[1] For recent reviews, see Goldhirsch, I. *in* Physics of Dry Granular Media, page 371, H.H. Herrmann, J.P. Hovi & S. Luding Editors., Kluwer, Dordrecht 1997, Jenkins, J.T. *ibitem,* page 353, or Rajchenbach J.: *Advances in Physics,* **49**:229-256, 2000.
[2] Rajchenbach J.: Dense, rapid flows of inelastic grains under gravity*, Phys. Rev. Lett.* **90**:144302, 2003.
[3] Bagnold, R.G.: Experiments of gravity-free dispersion of large solid spheres in a Newtonian fluid under shear, *Proc. Roy. Soc. London, Ser. A* **255:**49 1954.
[4] Goldsmith W.: Impact, Edward Arnold, London 1960.
[5] Ivanov A. P.: The problem of constrained impact, *J. Appl. Maths Mechs* **61**:342-353, 1997.
[6] Falcon E., Laroche C., Fauve S., Coste C.: Collision of a 1D column of beads with a wall, *Eur. Phys. J. B* **5**:111, 1998.
[7] Bernu B., Mazighi R.: One-dimensional bounce of inelastically colliding marbles on a wall: *J. Phys. A* **23**:5745,
[8] Orpe D.V., Khakhar A.V., Scaling relations for granular flow in quasi two-dimensional rotating cylinders. Phys. Rev. E **64**: 031202, 2001.

Flow Dynamics of Dense Granular Materials Subjected to Vertical Vibration

Azita Soleymani,[1] Vesa Tanskanen,[1] Piroz Zamankhan,[1] and William Polashenski, Jr.[2]

[1]Laboratory of Computational Fluid Dynamics, Lappeenranta University of Technology, Finland

[2] Lomic, Inc., 100 N. Patterson St., State College, PA 16801

Results are presented from a numerical study examining the flow dynamics of dense granular materials in a narrow gap between two concentric cylindrical buckets subjected to sinusoidal oscillation in the vertical direction $z = A\sin(\omega t)$, where the parameter $\Gamma = A\omega^2/g$ exceeds a critical value, Γ_C , above which the system becomes fluidized. Using a recently developed expression for the stress tensor of dense granular materials, a set of conservation equations were derived for the particle and fluid phases interacting via an interfacial drag force. Numerical integration of the equations for the granular material in buckets revealed that above Γ_C , granular materials may exhibit liquid-like behavior and convection can occur creating a heap similar to that previously observed experimentally.

As a means of fluidizing granular materials, vibrated beds are widely used in the solid processing, food, and agricultural industries. In vibrated beds, granular materials behave like both continuous and discrete media [1], yielding interesting phenomena such as heap formation and convective roll patterns [2]. Note that by using relatively small grains, namely $d < 1\,\text{mm}$, friction with the container walls can be greatly reduced. For these conditions, the presence of interstitial gas was shown to result in the formation of a heap [3]. Behringer et al. [4] concluded that the vanishing of the heap at low pressure namely 0.01 torr, may be caused primarily due to the onset of a Knudsen regime as well as a lack of a sufficient gas flow to sustain the flow of grains. In light of the above discussion, a model is needed to capture the key role of the ambient gas on dense flows of granular material. Recently within the frame of continuum mechanics, Zamankhan et al. [5] have proposed a model for gas-particle flow in which an effective rate-dependent viscosity was introduced for a slowly deforming dense granular assembly. Their approach could successfully predict the continuous flow of grains in a spinning bucket at high rotational frequencies, in which an evolution of surface shape from cusp to depression near the axis of rotation was predicted similar to that observed experimentally [5].

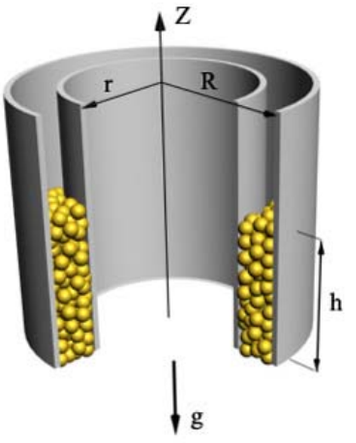


Fig. 1. *Cut-away view of three-dimensional dense granular flow in a bucket whose base is subject to vertical sinusoidal oscillation along the Z axis.*

In this paper a numerical investigation is presented of the flow dynamics of grains and heap formation in a dense granular bed under vertical vibration, $z = A\sin(\omega t)$, as shown in Fig. 1, using the above-mentioned model described in [5]. The granular materials are composed of rough, inelastic, identical spherical glass particles of diameter $\sigma = 0.2mm$. The container is sealed and only its base is oscillated. Note that gravity and the vibration act in the direction of the cylindrical axis. As the relaxation in this system is logarithmically slow, the equations have been normalized in order to decrease the simulation time [6].

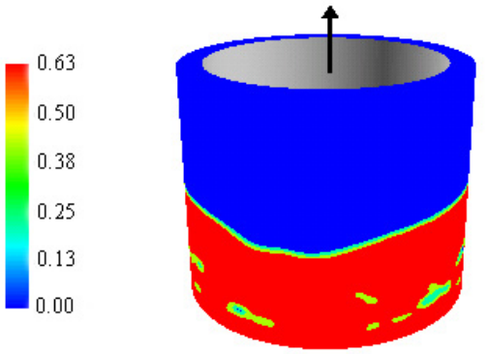


Fig. 2. *Contours of the volume fraction of the particle phase resulting from a vertical sinusoidal oscillation* $z = A\sin(\omega t)$ *of the base of the bucket. Here* $\Gamma = 1.30$*, the granular mean depth* $h = 5$ *cm,* $A = 0.534$ *cm and frequency* $f = 7.78$ *Hz.*

As Γ is varied, the layer undergoes a backward bifurcation between a solid-like state and a liquid-like state that typically consists of a moving layer of maximum depth H riding on the top of a solid layer [7], as depicted in Fig. 2. For $h/d >> 1$ where the relevant control parameter, $\Gamma = A\omega^2/g$ is larger than the critical value Γ_{C-h}, steady convective motion evolves in the form of two counter-rotating rolls, downward along the vertical side walls and upward in the middle, leading to a single heap, as depicted in Fig. 2, making a dynamic angle of repose with the horizontal [3].

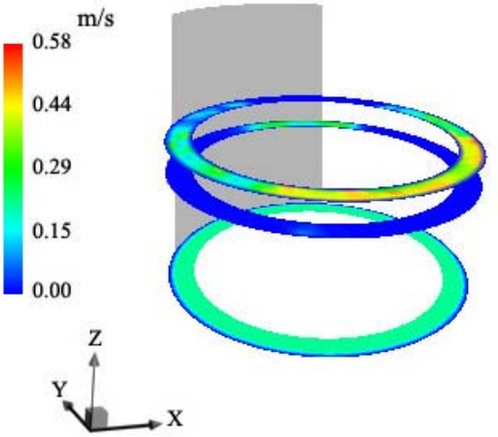


Fig. 3. *Contours of particle phase velocity at three different elevations calculated during a numerical simulation. Here* $\Gamma = 1.30$*, the mean height = 5 cm,* $A = 0.534$ *cm and frequency* $f = 7.78$ *Hz.*

To conclude, we have shown that by using a rate-dependent effective viscosity for a highly concentrated granular flow, the presence of a heap and convective roll patterns can be predicted at Γ slightly higher than unity. The role of ambient gas is taken into account in our simulation. The sample results are presented for the case in which $\Gamma = 1.30$, $\sigma = 0.2mm$, the granular mean depth $h = 5cm$, $A = 0.534cm$ and frequency $f = 7.78$ Hz.

[1] H.M. Jaeger and S.R. Nagel, Science **255**, 1523 (1992).
[2] H.K. Pak, E. Van Doorn, and R. P. Behringer, Phys. Rev. Lett., **74**, 4643 (1994).
[3] H.M. Jaeger, S.R. Nagel, and R.P. Behringer, Rev. of Mod. Phys, **68**, 1259 (1996).
[4] R.P. Behringer, E. Van Doorn, R.R. Hartley, and H.K. Pak, Granular Matter, **4**, 9 (2002).
[5] P. Zamankhan, W. Polashenski Jr., A. Soleymani, Phys. Rev. E, submitted.
[6] J.B. Knight, C.G. Fandrich, C.N. Lau, H.M. Jaeger, and S.R. Nagel, Phys. Rev. E. **51**, 3957 (1995).
[7] G. Metcalfe, S.G.K. Tennakoon, L. Kondic, D.G. Schaeffer, and R.P. Behringer, Phys. Rev. E., **65**, 031302-1 (2002).

PARTICLE IMAGE VELOCIMETRY ANALYSIS OF GRANULAR MATERIAL FLOWS

Irena Sielamowicz[*], Slawomir Blonski[**]

[*] *Bialystok Technical University, Civil Engineering Department, PL-15-351 Bialystok, Poland*
[**] *Polish Academy of Sciences IPPT PAN, Swietokrzyska 21, PL 00-049 Warszawa, Poland*

Summary: Digital Particle Image Velocimetry (DPIV) technique, well know in fluid mechanics, has been applied to evaluate main flow characteristics for granular material (amarantus seed) sliding between parallel walls of a Plexiglas model of a silo. The development and evolution of the consecutive stages of the flow will be demonstrated. The vertical velocity functions on the horizontal sections of the model are used to describe different flow regimes. Velocity fields are used to calculate particle tracks, lines representing main flow structure.

INTRODUCTION

Particle Image Velocimetry technique is a well established experimental method in fluid mechanics, allowing for quantitative measurement of two-dimensional flow structure. It enables measurement of the instantaneous in-plane velocity vector fields within a planar section of the flow field. This method is of great interest to researches and engineers allowing them the calculation of spatial gradients, dissipation of turbulent energy, spatial correlations, and the like. The typical DPIV evaluation procedure is based on the analysis of two successive images of the flow. One of the main drawbacks of classical DPIV is its inability to accurately resolve flow regions characterized by large velocity gradients. Several alternative evaluation methods have been proposed to remove the above limitation. This paper is our effort to apply the optical flow based on DPIV technique (OP-DPIV) [1] in granular material flows to measure flow boundaries, velocity fields and stresses in a model of a silo made of Plexiglas.

Early attempts to describe the plug and funnel flows in bins/hoppers and in different models of silos – plane, conical, wedge-shaped were based on assumption of plasticity, predicted the existence of stagnant zones in the flowing material. But later it was found that radial velocity field predicted theoretically in the flowing zone is far narrower than that observed in practice. Many observations of batch discharge show that the position of the stagnant zone boundary occurs during the flow changes quite slowly with time. Watson and Rotter [2] defined the stagnant zone boundary to be the position at which the velocity was equal to 1% of the centreline velocity at the same height. It is found as a satisfactory approximation for the steady state. Mathematical models of the flow assume the constancy of material density throughout the bin/hopper and describe that the velocity distribution is given by the simple differential equation:

$$\frac{\partial \upsilon}{\partial y} = B\frac{\partial^2 \upsilon}{\partial x^2} \tag{1}$$

where υ is the vertical velocity and x and y are horizontal and vertical distances and B is the kinematic constant and is often of the order of particle diameter. Modification of the kinematic model for unsteady discharge based on the assumption of incompressible radial velocity field resulting from kinematic theory was presented by Nedderman [3], Waters and Drescher [4] and others. An additional assumption that volume changes take place only across the boundary of the expanding flow region was equivalent to identifying the boundary as a dilatational wave or a propagating density shock. The predicted velocities are higher along the center line and decrease gradually towards the boundary, whose shape resembles a growing candlelight [4].

Our paper concerns semi-mass flow in a model of silo made of Plexiglas. The width of the outlet is 1 cm and the dimensions of the model are: 80 cm height, 26 cm width and 5 cm in depth, with a value of inclination of the walls to the vertical 90^o. The model was placed on a stand and granular material was supplied through a box suspended above the model. The box was equipped with a bottom of a wire net. Material discharged into the box scatters producing a uniform granular rain. The material develops negligible static electricity when flowing and sliding over Plexiglas. Uniform and repeatable packing of the materials with no particle segregation was obtained. The model was filled with 75 cm-high column of material. The velocity fields , the evolution of the flow region and the traces of flowing particles were measured and registered with a digital experimental setup. The pictures were registered at a time step 0.266 sec. We present experimental measurements of the stagnant boundary as a function of time, predicted positions of stagnant zone boundary as a function of time and the evolution of the flow during free gravitational discharge.

PIV technique is employed to measure two-dimensional velocity fields. The evaluated fields are used to calculate development and evolution of the flow in the model and the flow paths showing main flow structure. It was found that the mass discharge is not constant, decreasing as the material flows.

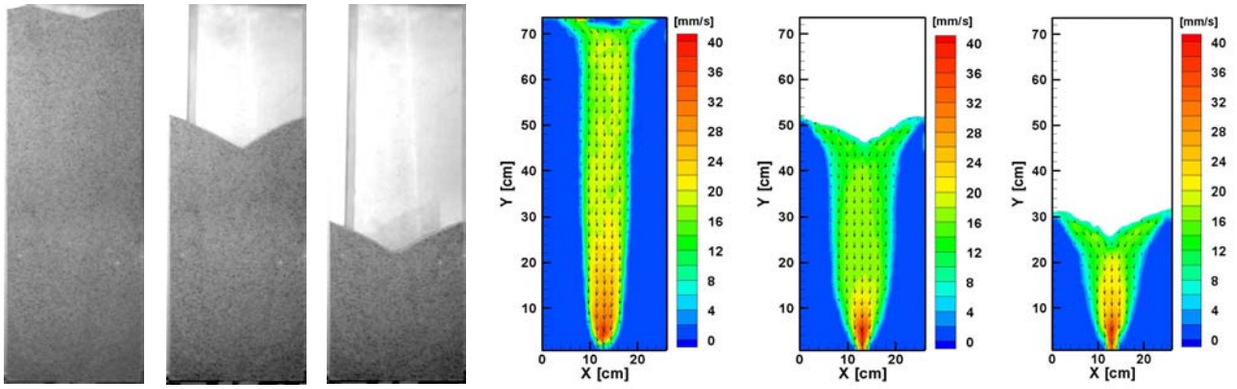


Figure 1. Example of the flow images of the amarantus and the evaluated velocity fields at time steps: 3.75 sec, 30 sec and 52.5 sec.

Figures 1 show the evolution of the flow during free gravitational discharge. The upper plane surface becomes lower and then concaves. With progressing discharge, the upper surface lowers and the flow region increases reaching the top of the material. It was observed in vector fields that the boundaries of the flow zone away from the outlet are vertical and the instantaneous velocities in this zone appear also vertical and decrease with time. Near the outlet the velocity vectors are directed towards the outlet.

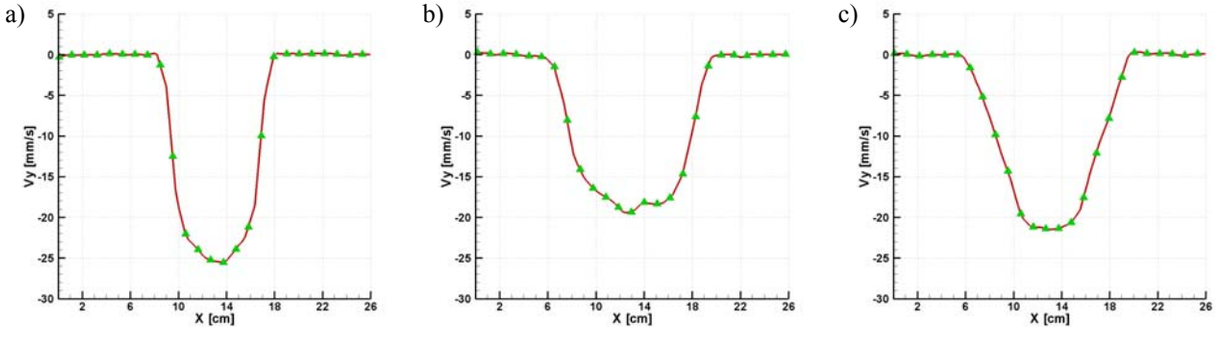


Figure 2. Profiles of the vertical velocity component across the cavity obtained at height h=15cm at time steps 3.75 sec (a), 30 sec (b) and 52.5 sec (c) after beginning of the experiment. Points of the profiles are extracted from the PIV measured velocity vector fields and smoothed with splines (solid line).

Figures 2 show examples the velocity distributions extracted from the full field measurements for a selected cross-sections in the model of silo. It is seen that a quasi-symmetrical flow structure builds up shortly after the flow starts. However, in some cases initial asymmetry was present due to non-uniform packing of the seed in the silo.

CONCLUSIONS

The PIV technique enables measurements velocity fields and the velocity distributions in the flowing granular material. The method offers unique possibility to compare instantaneous full field measurements with theoretical formulations and numerical models. Information gained can be easily converted to calculate local stresses and predict regions of non-uniformity and delayed empting of the silo.

References

[1] G. M. Quenot, J. Pakleza, T. A. Kowalewski: Particle image velocimetry with optical flow, Experiments in Fluids. Vol. 25 (1998), 177-189
[2] G.R. Watson, J. M. Rotter: A finite element kinematic analysiss of planar granular solids flow, Chemical Engineering Sciences. No 51 (1996) 3967-3978
[3] R. M. Nedderman: The use of the kinematic model to predict the development of the stagnant zone boundary in the batch discharge of a bunker, Chemical Engineering Science. Vol.50 (1995) 959-965
[4] A.J. Waters, A. Drescher: Modeling plug flow in bins/hoppers, Powder Technology. Vol. 113 (2000) 168-175

XXI ICTAM, 15–21 August 2004, Warsaw, Poland

PORE PRESSURE RELAXATION DURING GRANULAR COMPACTION

Maxime Nicolas, Max Belzons, Olivier Pouliquen
IUSTI, UMR 6595 CNRS-Polytech Marseille, 5 rue Fermi 13453 Marseille cedex 13 France

Summary The compaction of a granular assembly immerged in a fluid implies complex interactions between viscous forces and grain contact forces. We present the study of the compaction under tapping of a granular packing fully immerged in water. In order to follow the interaction between the grains and the fluid, we measured the pore pressure at the base. A simple model is proposed to understand the time relaxation of the pore pressure.

INTRODUCTION

Powder compaction is an old subject that has recently attracted the attention of physicists as the propotype of non thermal disordered systems. The complex evolution of an initially loose granular packing submitted to external perturbations like vibration has been precisely studied [1, 2, 3]. In all the previous studies the role of the interstitial fluid is negligible. However, the fluid can play an important role in the compaction dynamics as shown for example by the liquefaction phenomena. Grains in a fluid can interact both by direct frictional contact and by viscous forces though the fluid. Dense granular packing in a fluid can then behave like a granular material or a suspension, and the transition between both behaviors is not clearly understood. An initialy loose sand saturated with water can liquefied when submitted to vibration (an earthquake for exemple). As the material compacts, the fluid has to escape developing pressure gradients enough to carry the weight of the grains.
In this work, we investigate a simple configuration where both viscous and contact interaction are present. A granular packing fully immerged in water is compacted under vertical tapping. In order to determine the role of the liquid we measure the time evolution of the pore pressure under the packing during compaction.

EXPERIMENTAL SETUP

The experimental set up is presented in Figure 1. A rectangular box separated in two is fixed on top of an electromagnetic vibrating device. Both sides of the box are full of water, but grains are placed on one side only. The particles are 112 ± 20 μm diameter spherical glass particles. A differential pressure sensor measures the water pressure difference between the two sides of the box and an accelerometer is attached at the bottom of the tank. Before the experiment starts, the granular material is stirred in order to create a suspension. We then wait until all the material is settled at the bottom of the container. The pressure difference between the two side is then zero, as the weight of the grains is carried by the box. We then impose a vertical controled acceleration and measure the time evolution of the pressure. These signals are digitized at 10 kHz using an acquisition board.

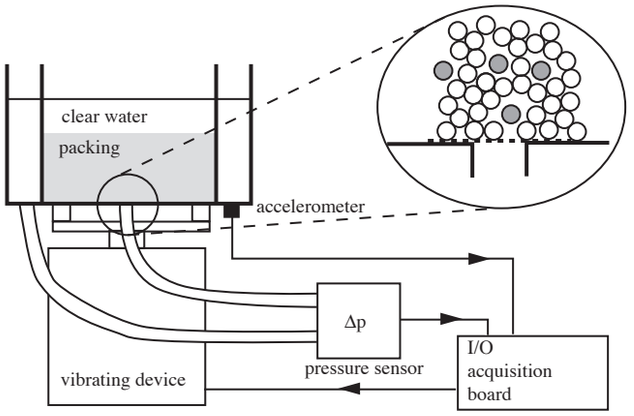


Figure 1. Experimental setup.

PORE PRESSURE MEASUREMENTS

A typical pore pressure relaxation is shown on Fig. 2 for a maximum acceleration of 19 m/s^2 and a « tapping time » of

the height of the packing in the most compact configuration, and h the height in a loose configuration, the pore pressure may be written as an hydrostatic pressure due do suspended particles in the packing (see insert of Fig. 1 for a schematic view) :

$$\Delta P = \phi \Delta \rho g (h - h_c) \tag{1}$$

where ϕ is the particle volume fraction and $\Delta\rho$ the density difference between the particles and the liquid.
This pressure induces a flow inside the deformable porous packing of permeability k. Using Darcy's law, the governing equation for the height is then

$$\frac{dh}{dt} = -\frac{k}{\eta}\phi_c h_c \Delta\rho g \frac{h - h_c}{h^2} \tag{2}$$

where η is the liquid dynamic viscosity and ϕ_c is the random close packing volume fraction. This model is in qualitative agreement with the experimental results and helps understand why pressure relaxation is a slow process compared to the typical time scale of the tapping.

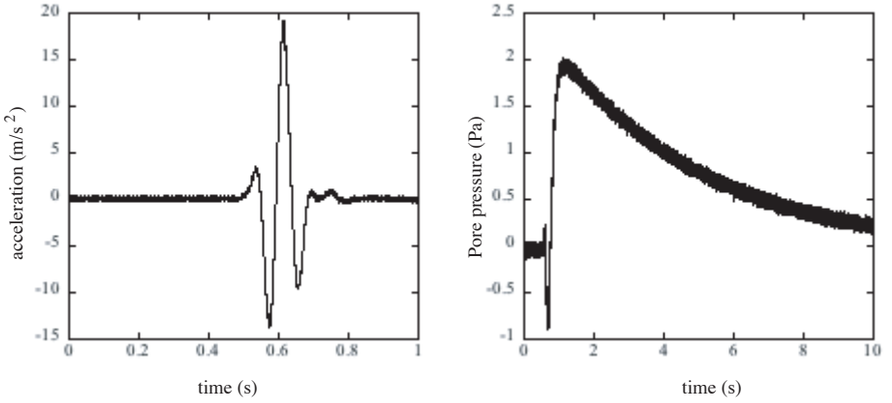


Figure 2. Acceleration (left) and pore pressure relaxation (right) versus time for a 2 cm high packing of 112 μm glass spheres.

CONCLUSIONS AND PERSPECTIVES

We show that the pore pressure inside a packing relaxes exponentially when the material is submitted to a rapid solicitation such as a vertical tapping. If the time between two successive solicitations is shorter than the typical relaxation time, then the pressure may build up until it balances the weight of particles, leading to liquefaction of the liquid/particles mixture.

References

[1] Nowak E.R., Knight J.B., Ben-Naim E., Jaeger H.M., Nagel, S. Phys. Rev. E **51**, 3957 (1995).
[2] Josserand C., Tkatchenko A., Mueth D., Jaeger H.M. Phys. Rev. Lett. **85**, 3632 (2000).
[3] Nicolas M., Duru P., Pouliquen O. Eur. Phys. J. E **3**, 309 (2000).

XXI ICTAM, 15–21 August 2004, Warsaw, Poland

GRANULAR FLOWS ON A HEAP

Pierre Jop, Yoël Forterre, Olivier Pouliquen
IUSTI, Université de Provence, CNRS UMR 6595, 5 rue Enrico Fermi, 13453 Marseille cedex 13, France

Summary Flows of granular material on a heap is experimentally investigated. A layer of granular material is flowing from a hopper on top of a static pile in a channel. We study the role of the side walls and show that it has a dramatic influence on the dynamics of the flow. The angle of the free surface increases with flow rate for narrow channels but remains constant when the side walls are far enough. The systematic study of the flowing thickness for different flow rates and different widths of the channel is also investigated.

INTRODUCTION

The flow of granular matters is often encountered in engineering applications involving the transport of materials such as minerals, cereals, but also in geophysical situations. One of the difficulties in describing such complex flows lies in the uncertainty in the constitutive equations. An important effort has been made in the last few years to study steady uniform flows in various configurations in order to understand the main ingredients necessary for the rheology of granular material [1]. In the case of free surface flows (flow on a pile or flow in a rotating drum) the difficulty is the coexistence of both a liquid and solid behavior of the material: a thin layer of granular material is flowing on top of a static pile. An important question is the selection of the flowing thickness. Previous studies in both rotating drums and flows on piles have shown that the velocity profile in the flowing layer is linear with an exponential tail [2]. The interesting result is that the shear rate seems to be constant independent of the flow rate, implying that the thickness of the flow increases like the square root of the flow rate. However, most of the studies reported in the literature are carried out in narrow channels for which the distance between side walls is less than 50 particles diameters. In this paper we present results about the influence of the width of the channel up to very wide channels and show that side walls dramatically change the dynamics of the flow.

EXPERIMENTAL SET-UP

The set-up is a long channel (1.5 m) with two smooth side walls made of glass and a rough bottom (Fig. 1a). We can change the width of the channel (W) from 10 particle diameters to 600. The channel is partially closed at the bottom end by a 10 cm plate. The whole channel is inclined at an angle less than the angle of repose of the material, such that a static pile can be trapped in the box. The flow is obtained by injecting the granular material (0.53 mm glass beads) from a hopper at the top of the box (Fig. 1a). When starting the experiment, the box is initially empty. When the hopper gate is opened, the material first fills the box, before flowing over the end plate. A steady regime is then reached with a layer flowing on top of a static pile. In this regime, the injected flow rate is exactly equal to the outlet flow rate. It should be noticed that once the width (W) is fixed, the flow rate is the only control parameter. The inclination of the free surfacec and the flow depth are not prescribed *a priori* but selected by the system.

Once the steady regime is obtained, we perform measurements of the free surface inclination and of the velocity profile at the side wall using PIV method. In order to get information of the flowing thickness far from the wall we have developed a weakly intrusive method based on the erosion of a thin powder deposed on a thin obstacle.

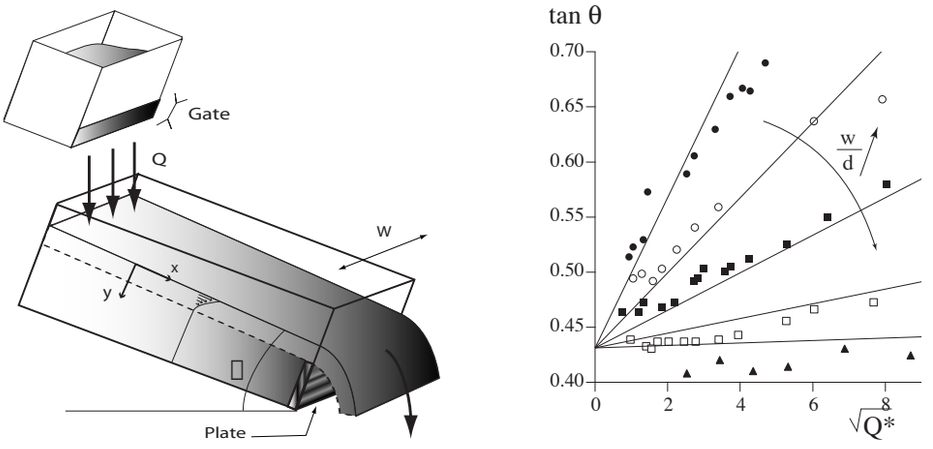


Figure 1. (a) Sketch of the experimental set-up. **(b)** Surface slope as a function of the square root of the dimensionless flow rate for different channel widths (W/d from 10 to 600)

RESULTS

Slope of the free surface

The first result concerns the free surface inclination (Fig 1b). For narrow channels, the inclination increases when increasing the flow rate as reported in the literature [3, 4]. However, when the width of the channel is larger than 500 particle diameters, this effect vanishes and the slope of the flow remains constant independent of the flow rate. These measurements show that the increases of the slope is linked to the additional friction induced by the walls and can be easily understood in the framework of a Coulomb model. This result is compatible with recent measurements carried out on avalanche angles in rotating drum of various widths [5] and on inclined rough plane for high flow rates [6].

Flowing thickness

The measurement of the flowing thickness h in the middle of the channel using the erosion method shows a dramatic influence of the channel width. For example, at a fixed flow rate per unit of width, the thickness h is found to be twice larger for wide channel ($W/d > 500$) than for thin channel ($W/d = 20$). This result raises the question of the role of the boundary in the selection of the boundary between flowing and static region.

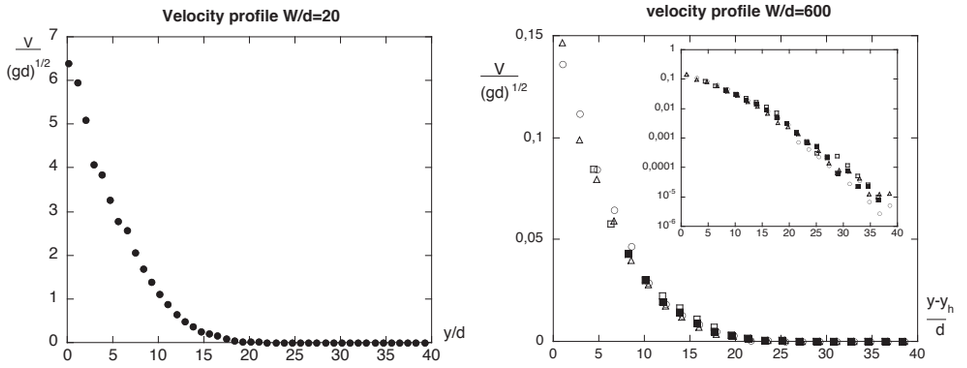


Figure 2. (a) Velocity profile for W/d=20 (Q=30 g/s/cm). **(b)** Velocity profile for $W/d = 600$ and different flow rates plotted to follow the fastest profile. Q=2.9 (black square), 5.4 (white square), 12.8 (triangle) and 25.5 (circle) g/s/cm. Inset : same as b in log-lin

Velocity profiles

Unfortunately we are unable to measure velocity profile in the bulk to get ride of wall effect. The only profile accessible with classical imaging method are at the side wall. A typical velocity profile obtained for thin channels is plotted in Fig. 2a. We can see the linear part at the surface followed by a cut-off. For large width (Fig. 2b) the shape of profiles seems to change. The convex part is larger. An interesting result is that the different profiles obtained for different flow rates can be collapse when shifted along the y direction.

CONCLUSIONS

By studying the flow of granular material on a pile in channel of different widths, we have been able to show that side wall friction has a great influence. One important result is that for wide channel, when side wall effect are negligible, the surface slope is constant, showing that the material choose a single critical inclination. Moreover, the flowing thickness in this case is larger than what has been observed before in narrow channel.

References

[1] GdR Midi : submitted to *Europ. Phys. J. E*
[2] Komatsu T.S, Inagaki S., Nakagawa N., Nasumo S. : Creep motion in a granular pile exhibiting steady surface flow. *Phys. Rev. Let.* **86**:1757-1760, 2001.
[3] Khakhar D. V., A. V. Orpe, P. Andersen, J. M. Ottino: Surface flow of granular materials: model and experiments in heap formation. *J. Fluid Mech.* **441**:255-264, 2001.
[4] Lemieux P.-A., Durian D. J.: From avalanches to fluid flow: A continuous picture of grain dynamics down a heap. *Phys. Rev. Let.* **85**,4273-6, 2003
[5] Courrech du Pont S., Gondret P., Perrin B., Rabaud M.: Wall effects on granular heap stability. *Europh. Let.* **61** (4), 2003.
[6] N. Taberlet, P. Richard, A. Valance, R. Delannay, W. Losert, J. M. Pasini, and J. T. Jenkins: Super stable granular heap in thin channel. *Phys. Rev. Lett.* **91**, 264301 (2003)

COLLAPSE, GROWTH AND MERGING OF CAVITY REGIONS IN A GRANULAR MATERIAL DUE TO VISCOUS FLOW

O.Sano*, Y.Kaneko * and G.P.RajaSekhar **
*Dept. Appl. Phys., Tokyo Univ. Agri. Tech., Koganei, Tokyo 184-8588, Japan
**Dept. Math., Indian Inst. Tech., Kharagpur 721 302,India

Summary Experimental and theoretical studies of viscous flow are made on the effect of macroscopic cavity regions in an otherwise homogeneous granular material. The presence of a cavity enhances local velocity, which leads to collapse of the cavity boundary. The mutual interaction leads to faster growth of fluidized region, which plays an important role in network formation of water channel and onset of landslide.

VISCOUS FLOW THROUGH CAVITIES IN GRANULAR MATERIAL

The presence of a macroscopic cavity in an otherwise homogeneous granular material changes the flow field, which has great influence on the deformation and/or migration of a cavity, as well as merging of two or more cavities [1]-[7]. Here an important parameter is $\zeta_0 (= R_0/\sqrt{k})$, where R_0 and $\sqrt{k}$ are the characteristic sizes of the cavity and the interstices in the granular material, respectively, and k is the permeability. The term "macroscopic" means that $\zeta_0 \gg 1$ in this paper. In our previous analysis on the viscous flow assuming the Stokes equation inside a cavity and generalized Darcy equation outside, we have shown that the volume flow rate into a circular cavity increases as much as 2 times, whereas the velocity at the center of the hole amounts to 3 times of the velocity without that hole for sufficiently large ζ_0 case [1][8]. In the presence of a spherical cavity, they become 3 times and 6 times, respectively[2]. These situations raise a question of accurate estimation of underground water flow in *natural condition*, because velocity measurement necessarily introduces a hole for the detector.

Flow through a cavity of fixed boundary

We first extend our theoretical study to a *slightly but arbitrarily deformed* macroscopic cavity [3]-[5], in view of applying the theory to practical situations where the hole drilled is not a complete circle or where the hole deforms into non-spherical shape (see Fig.1). Our analysis shows that the volume flux into the cavity becomes maximum for an elliptic cavity with inclination angle of about 50 degrees, the detailed angle of which depends on the eccentricity of the cavity.

Flow through two cavities of fixed boundary

Our second extension is to study the *interaction of two macroscopic circular cavities* of different center-to-center distance l and different orientation α of them with respect to the undisturbed uniform flow (see Fig.2)[6][9]. Our experiment revealed that at a certain range of l less than about $3R_0$ and α less than about 30°, the volume flux into the downstream-side cavity increases, whereas it decreases for l less than about $3R_0$ and α around 90°. We shall compare these results with our calculation.

COLLAPSE OF CAVITIES DUE TO VISCOUS FLOW

The enhanced viscous stress has greater possibility of destroying the cavity boundary in the local scale, which leads to global deformation and/or migration of the cavity.

Collapse of a cavity due to viscous flow

Here we shall focus our attention to *collapse of a cavity region* by the viscous flow. To do this we set an initially circular cavity, and experimentally observed its deformation with given velocity at infinity U_∞. When U_∞ exceeds a certain critical value $U_{\rm cr}$, the upstream-side boundary collapses, constituent granular material of which is carried to the other side of the boundary, so that the initial cavity region is filled up by the latter. At the same time, the fluidized region develops towards upstream direction. The growth of the fluidized region resembles an ascent of a bubble under gravity, but front of the former is not so clearly defined as that of the latter.

Collapse of cavities due to viscous flow

The *collapse of two initially circular cavities* is tested for their different arrangement. When two circular

cavities are arranged in tandem, the downstream-side cavity is destroyed even below $U_{\rm cr}$, as a result of enhancement of the velocity by upstream-side cavity. This phenomenon shows a remarkable contrast to the case of two solid cylinders placed in a viscous flow, where downstream-side one in the wake of the other experiences smaller drag. Dependency of center-to-center distance and orientation of the cavities is examined, which reveals the presence of optimum growth rate of void fingers (see Fig.3). Finally the growth of randomly distributed mesoscopic cavities is simulated on the basis of the model taking account of fundamental processes mentioned above, which suggests *macroscopic waterway network formation* as well as sheet-like discontinuity in the granular region. The latter can explain the onset of *landslides* at the time of heavy rainfall.

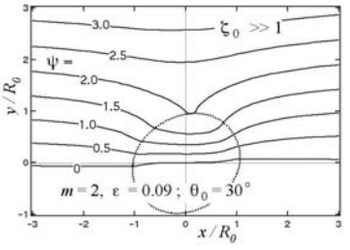


Fig.1. Streamlines around a slightly deformed cylindrical cavity: $r = R_0[1 + \epsilon\cos[m(\theta - \theta_0)]$, $m = 2, \epsilon = 0.09$, angle of attack $\theta_0 = 30^\circ, \zeta_0 \gg 1$.

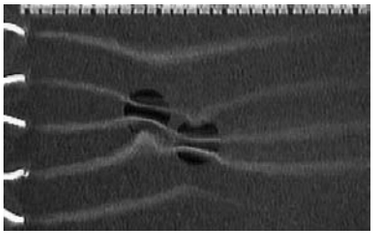


Fig.2. Interaction of two fixed circular cavities of an equal radius $R_0 = 18$ mm, center-to-center distance $l = 2.5R_0$, and angle of attack 30°. Granular material is glass beads of a diameter 1mm. Flow visualization by sodium fluorescein.



Fig.3. Collapse of two circular cavities. Initial radius $R_0 = 18$mm, center-to-center distance $l = 3R_0$, and angle of attack 30°. Granular material is glass beads of a diameter 1mm.

References

[1] O.Sano: Viscous flow past a cylindrical hole bored inside porous media —— with Application to Measurement of the Velocity of Subterranean Water by the Single Boring Method. *Nagare* **2** (1983) 252-259 (in Japanese).
[2] G.P.RajaSekhar & O.Sano: Viscous flow past a circular/spherical void in porous media —— an application to measurement of the velocity of groundwater by single boring method. *J. Phys. Soc. Jpn.* **69** (2000) 2479-2484.
[3] G.P.RajaSekhar & O.Sano: Two-dimensional viscous flow past a slightly deformed circular cavity in a porous medium. *Fluid Dyn. Res.* **28** (2001) 281-293.
[4] O.Sano & G.P.RajaSekhar: Collapse of Void Region and Network Formation of Water in a Granular Material Due to Viscous Fluid. *Proc. Nineth Asian Cong. Fluid Mech.*(Isfahan, Iran, 2002)
[5] G.P.RajaSekhar & O.Sano: Two-Dimensional Viscous Flow in a Granular Material with a Void of Arbitrary Shape. *Phys. Fluids* **15** (2003) 554-567.
[6] Y.Kaneko & O.Sano: Experimental Study on the Interaction of Two Two-Dimensional Circular Holes Placed in a Uniform Viscous Flow in a Porous Medium. *Fluid Dyn. Res.* **32** (2003) 15-27.
[7] O.Sano: Collapse and Growth of Cavity in a Granular Material due to Viscous Flow. *Theor. Appl. Mech.* **52** (2003) 91-96.
[8] K.Momii, K.Jinno & F.Hirano: Laboratory Studies on a New Laser Doppler Velocimeter System for Horizontal Groundwater Velocity Measurements in a Borehole. *Water Resources Res.* **29** (1993) 283-291.
[9] H.Yano, A.Kieda & I.Mizuno: The fundamental solution of Brinkman's equation in two dimensions. *Fluid Dyn. Res.* **7** (1991) 109-118.

UNDULATIONS AND RIPPLES OF A THIN GRANULAR LAYER DUE TO VERTICAL VIBRATION

Akiko UGAWA* and Osamu SANO
*VBL Department of Applied Physics, Tokyo University of Agriculture and Technology, Koganei, Tokyo 184-8588
Department of Applied Physics, Tokyo University of Agriculture and Technology, Koganei, Tokyo 184-8588

Summary We performed an experiment of vertically oscillated granular layer and observed the global patterns, "undulations". Several eigen modes are observed, which is reminiscent of the buckling and bending waves in an elastic rod. In our experiment "undulations" seem to be explained by continuum theory on the bending wave of an elastic plate, irrespective of material of the layer.

EXPERIMENT

Pattern formations of granular layer due to vertical vibration have been extensively studied since pioneering work by Faraday. Later there were many studies of pattern formation in vibrated granular layer [1] ∼ [13]. Here we consider global patterns of a granular layer, "undulations" as well as local patterns, "ripples".

We performed an experiment of the ripples and undulations of a granular layer of thickness h in a vessel, which is a thin vertical acrylic container of width W(=8mm), height H(=91mm), and horizontal dimension L(=146, 91, 60, 46, and 30mm). We used several type of granular particles, sesame, glass beads, lead and steal particles, whose diameters d are 0.2mm ∼1.1mm. The observation was made by means of a high-speed camera. The vertical oscillation of the container was given by $z = a\sin(2\pi ft)$, where the frequency f and amplitude a were given by a function synthesizer and an amplifier under atmospheric pressure.

RESULT

Our observations are as follows: (i) When the acceleration amplitude $\Gamma = (2\pi f)^2 a/g$ (g: acceleration of gravity) is less than $\Gamma_0(\approx 2)$, no motion of granular particles relative to the container was observed. (ii) For $\Gamma = \Gamma_0 \sim \Gamma_1(\approx 4)$, the particles move up and down almost rigidly, where some convective motion is superposed, or ripples appear in a thin layer. (iii) At $\Gamma \approx \Gamma_1$, the upper free surface of the layer reveals undulations, but convective motion is still recognized. (iv) For Γ larger than Γ_1, a standing-wave-like motion of the granular layer is generated, with larger wave number for larger Γ or smaller $\eta \equiv h/d$. (v) Further increase of Γ yields a sequence of wave modes, as is shown in Fig. 1. We classify these typical patterns as A_n and S_n for anti-symmetric and symmetric deformations, respectively. Letters "S" and "A" denote patterns which are symmetric and anti-symmetric, respectively, with respect to the mid-point of the layer, and the subscripts reflect the number of undulations of the layer. The type S_0 denotes approximately rigid-body up-and-down motion. (vi) For Γ larger than $\Gamma_b(\approx 10)$, part of the layer shows burst-like behavior, whose position is not regularly spaced. From images of particle displacement$(g(t_1 + \delta t) - g(t_1))$, we observed the density waves.

DISCUSSION

Undulations are reminiscent of the buckling and bending waves (or flexural waves) of a thin elastic plate of Young's modulus E [14]. In the case of noncohesive discrete systems, like those dealt with in this paper, the features of E needs a caution. However, the vibrating granular layer of moderate thickness suggests the presence of elastic property, which is manifested as density waves. All the data are plotted in Fig. 2, where the ordinate is the wave number and abscissa is a parameter which is derived from bending and buckling theory. From this we can see the sequence of data points seems to be fitted by a single curve $L/\lambda \propto \sqrt{a/h}e_n$, where λ is the wave length and e_n is the eigen value of the system that corresponds to each modes. Estimated Young's modulus of the granular layer $E \approx 2.7 \times 10^4$Pa, which is quite small compared with that of the ordinary solids (i. e. $E \approx 2 \times 10^{11}$Pa for iron and $E \approx 3 \times 10^6$Pa for rubber.)

The above results can be qualitatively explained as follows. When the vertical vibration is applied to the granular layer the disturbance propagates both in the vertical and in the horizontal directions. If the dissipation in the vertical direction is small and the external Γ is small, the global patterns or "ripples" appear. On the contrary, If the energy dissipation in the vertical direction is large and external Γ is large, dilation would occur in the layer, and global patterns or "undulations" appear.

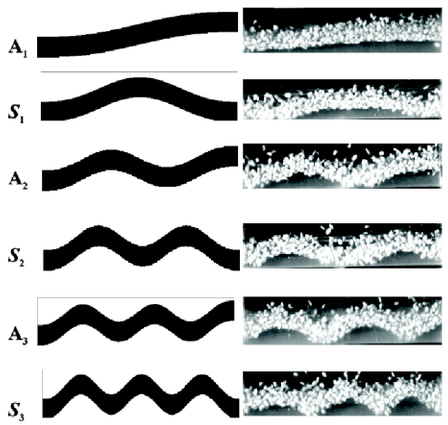


Fig. 1 Undulation of a thin granular layer. Right colimn is a corresponding example observed for an h=6.8mm layer of sesame : $(A_1) f = 20$ Hz, $a = 2.6$ mm, $\Gamma = 4.2$; $(S_1) f = 27$ Hz , $a = 2.5$ mm, $\Gamma = 7.4$; $(A_2) f = 30$ Hz , $a = 1.4$ mm, $\Gamma = 5.1$; $(S_2) f = 30$ Hz , $a = 2.0$ mm, $\Gamma = 7.3$; $(A_3) f = 30$ Hz , $a = 2.3$ mm, $\Gamma = 8.4$; $(S_3) f = 30$ Hz , $a = 2.6$ mm, $\Gamma = 9.6$. Mode S_0 is an almost rigid-body up-and-down motion.

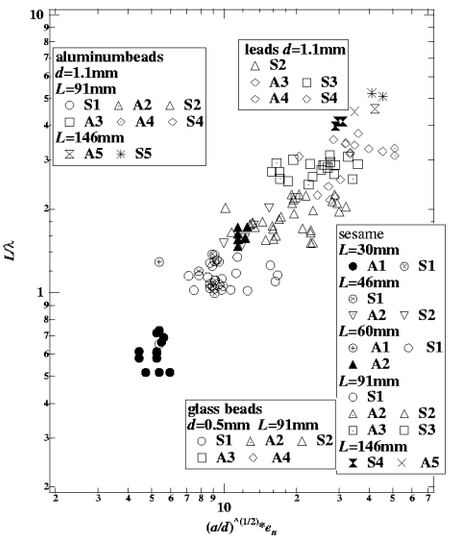


Fig. 2 Mode map of undulations.

References

[1] P.B.Umbanhowar & H.L.Swinney: *Physica* **A288** (2000) 344.

[2] E. Clément & L. Labous : *Phys.Rev. E* **62** (2000) 8314.

[3] A.Ugawa & O.Sano : *J. Phys. Soc. Jpn.* **71** (2002) 2815.

[4] S. Douady, S.Fauve & C.Laroche : *Europhys.Lett.* **8** (1989) 621.

[5] F. Melo, P. Umbanhower & H. L. Swinney : *Phys. Rev. Lett.* **72** (1994) 172.

[6] W.S. Edwards & S.Fauve : J.Fluid Mech. **278** (1994) 123.

[7] F. Melo, P. Umbanhower & H. L. Swinney : *Phys. Rev. Lett.* **75** (1995) 3838.

[8] E. Clément, L.Vanel, J.Rajchenbach & J.Duran : *Phys.Rev. E* **53** (1996) 2972.

[9] K. M. Aoki, & T.Akiyama : *Phys. Rev. Lett.* **77** (1996) 4166.

[10] C. Bizon, M.D.Shattuck, J.B.Swift, W.D.Mc Cormick & H.L.Swinney : *Phys. Rev. Lett.* **80** (1998) 57.

[11] C. Bizon, M.D.Shattuck & J.B.Swift : *Phys.Rev. E* **60** (1999) 7210.

[12] Sung Joon Moon, M.D.Shattuck, C. Bizon, Daniel I. Goldman, J.B.Swift, & H. L. Swinney : *Phys.Rev. E* **65** (2002) 011301.

[13] Sung Joon Moon, Daniel I. Goldman, J.B.Swift, & H. L. Swinney : *Phys.Rev. Lett* **91** (2003) 0134301.

[14] S. Timoshenko & J. N. Goodier : *Theory of Elasticity* (McGraw-Hill, New York, 1951)

SPECIES SEGREGATION DRIVEN BY A GRANULAR TEMPERATURE GRADIENT

Janine E. Galvin, Steven R. Dahl, Christine M. Hrenya
University of Colorado, Department of Chemical and Biological Engineering, Boulder, CO, USA

Granular systems are typically characterized by some degree of polydispersity, which may lead to species segregation. A careful analysis of the equation governing segregation shows that lifting the equipartition-of-energy assumption gives rise to a previously unidentified driving force for segregation: gradient in species temperature. MD simulations, together with kinetic theory, indicate that this new driving force is significant for moderate values of mass differences and restitution coefficients.

IINTRODUCTION

Solid particulate flows occur in a wide variety of geological and engineering systems, such as in landslides, planetary rings, and pharmaceutical processing. Such flows may contain particles of varying sizes and densities. This non-uniformity may lead to species segregation, which is a complex phenomenon of importance to many industrial processes. The separation of dissimilar particles may be either desirable (as in mining operations) or detrimental (as in the mixing of pharmaceutical powders).

The focus of this work is on segregation in rapid granular flows (flows with nearly instantaneous collisions between grains in which the role of interstitial fluid is negligible). Continuum modeling based on dense-gas kinetic theory provides a means of investigating the different behaviors in rapid granular flow. For the case of binary granular mixtures, several kinetic based theories are available. Differences in these theories arise from the various assumptions used in the derivation process. Two simplifying assumptions are a Maxwellian velocity distribution and an equipartition of energy between unlike particles. Previous investigations show that a Maxwellian velocity distribution is not strictly upheld, and that a non-Maxwellian distribution is necessary for reliable stress predictions. Previous studies also indicate that an equipartition of energy is not strictly upheld, though the impact of incorporating a non-equipartition treatment on predictions is not as clear. Furthermore, no current theory exists in which both of these assumptions are lifted.

Of interest is how the equipartition assumption affects the predictive abilities of these models for systems in which segregation occurs. Previous theoretical investigations into the driving forces for segregation [1,2] are based on models in which equipartition of energy is assumed. These studies reveal several driving forces for segregation: external forces, pressure gradient (∇P_1, ∇P_2), species concentration gradient (∇n_1, ∇n_2), and mixture granular temperature gradient (∇T). In the current effort, a similar analysis based on a non-equipartition theory indicates that an additional driving force arises due to non-equipartition effects, namely a gradient in species temperature (∇P_{1n}, ∇P_{2n}). To evaluate the importance of this new driving force, results from molecular-dynamics simulations are applied to a segregating flow system and used together with Jenkins and Mancini [3] kinetic theory, which does not include an equipartition assumption. Segregation in binary mixtures is explored for various diameter ratios, density (mass) ratios, solids fractions, solids fraction ratios, and restitution coefficients. Results indicate that the new driving force is of similar magnitude to other driving forces for systems with moderate values of mass differences and restitution coefficients.

DISCRETE-PARTICLE SIMULATION

Two-dimensional, molecular-dynamics simulations are used to mimic the segregation of a binary mixture driven by a granular temperature gradient. The gravity-free domain is periodic in the y-direction and is bounded by 'walls' of a specified temperature in the x-direction. To establish a temperature gradient, the walls are set to unequal temperatures.

The simulation proceeds through time via a hard-sphere/overlap algorithm, where particle collisions are detected by searching for overlaps after each time step. The maximum allowed overlap between any two particles or a particle and a wall is 1% of either particle radius. After each successful step, collisions are resolved for particles exhibiting overlap. The post-collision speed of a particle colliding with a wall is taken from a Maxwellian distribution consistent with the set temperature of the given wall. The post-collision trajectory of the particle is reversed in the x-direction and unchanged or reversed in the y-direction. Correspondingly, a granular temperature gradient develops in the y-direction.

The simulation proceeds until a statistical steady state is reached. At this point data collection begins, during which 200,000 evenly spaced measurements of solids fraction, and granular temperature are made as a function of x-position by dividing the domain into a set number of vertical strips (parallel to the constant-temperature walls). The average of these 200,000 measurements is then reported for each parameter in a given data collection strip.

The dimensionless quantities that characterize the system include overall solids fraction (ϕ), solids fraction ratio of species 1 to species 2 (ϕ_1/ϕ_2), diameter ratio (d_1/d_2), material density ratio (ρ_{p1}/ρ_{p2}), restitution coefficient (e), granular temperature ratio of the hot wall to the cold wall (T_H/T_C), and ratio of domain size in the x and y direction to the diameter of species 1 (L_x/d_1) and (L_y/d_1). For all simulations, L_y/d_1 is set large enough such that the results are box-size independent. In the case where $L_y = L_x$, the characteristic dimension is simply referred to as L.

RESULTS AND DISCUSSION

Molecular dynamics simulations were used to investigate the behavior of a binary mixture in the presence of a granular temperature gradient. Previous investigations into such "thermal diffusion" indicate that larger particles tend to congregate in the cooler regions of the domain. The current simulations reveal similar findings. Namely, under the influence of a granular temperature gradient, all particles tend to concentrate in the coolest region though the more massive particles have a higher affinity for this region (i.e., species segregation occurs). A quantitative measure of segregation is provided by the local solids fraction of a species over that of the expected species solids fraction in a homogeneous mixture (ϕ/ϕ_E). For example, for ϕ = 0.1, ϕ_1/ϕ_2 = 4, d_1/d_2 = 2, ρ_{p1}/ρ_{p2} = 8.0, e = 0.9, T_H/T_C = 10, and L/d_1 = 62.6, the solids fraction of the large particles is found to be 4.7 times greater than would be expected in a homogenous mixture at x/L = 0.15 (near the cold/left wall), but 0.13 times less than would be expected at x/L = 0.85 (near the hot/right wall). In contrast, the solids fraction of the small particles stays more homogenous across the domain with ϕ_2/ϕ_E = 2.1 at x/L = 0.15 and ϕ_2/ϕ_E = 0.45 at x/L = 0.85.

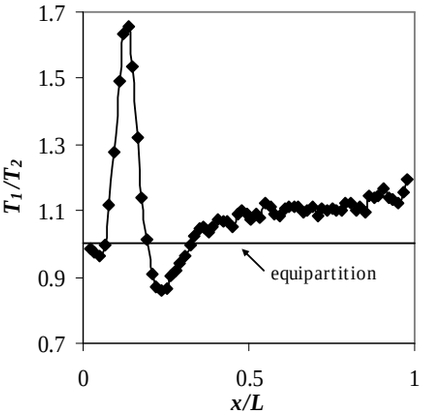


Figure 1. Granular temperature ratio of species 1 to species 2 (T_1/T_2). Relevant parameters: ϕ = 0.1, ϕ_1/ϕ_2 = 4.0, d_1/d_2 = 2.0, ρ_{p1}/ρ_{p2}, = 8.0, e = 0.9, T_H/T_C = 10, and L/d_1 = 62.6

The newly-identified driving force for segregation arises from the presence of non-equipartition. The degree of non-equipartition is demonstrated in figure 1, which displays the granular temperature ratio (T_1/T_2) as a function of x-position. Non-equipartition is seen to exist near the cold wall, specifically in the region around x/L = 0.14 where T_1/T_2 = 1.66. It is also worthwhile to note the non-equipartition is atypical at x/L ~ 0.23; namely $T_1/T_2 < 1$, which implies that the more massive particle is cooler than its lighter counterpart.

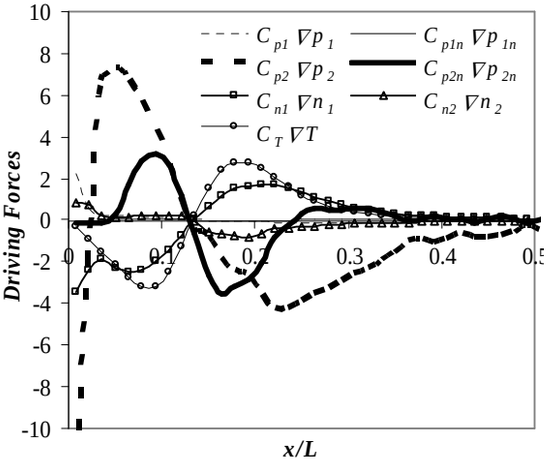


Figure 2. Driving forces for segregation using a form of Jenkins and Mancini [3] diffusion of velocity equation and simulation results. Relevant parameters: ϕ = 0.1, ϕ_1/ϕ_2 = 4.0, d_1/d_2 = 2.0, ρ_{p1}/ρ_{p2}, = 8.0, e = 0.9, T_H/T_C = 10, and L/d_1 = 62.6

A new aspect of this work concerns the presence of non-equipartition driving forces ($CP_{1n}\nabla P_{1n}$ and $CP_{2n}\nabla P_{2n}$) and their magnitude relative to previously identified driving forces ($Cn_1\nabla n_1$, $Cn_2\nabla n_2$, $CT\nabla T$, $CP_1\nabla P_1$ and $CP_2\nabla P_2$). The 'C' terms represent the transport coefficients associated with the segregation driving forces (for details see [3]). Simulation with theory was used to evaluate the importance of the new driving forces. Specifically, the profiles in species number density, species temperature, and mixture temperature obtained from the simulations were used to evaluate the magnitude of the driving forces in the diffusion equation from [3]. An examination of figure 2 reveals that the larger of the two newly identified driving forces arising from non-equipartition is that associated with the lighter particle ($CP_{2n}\nabla P_{2n}$). More importantly, the magnitude of this driving force is similar to that of the other driving forces

CONCLUSIONS

Discrete-particle simulations were employed to simulate segregation of a binary granular mixture driven by a granular temperature gradient. The results from these simulations were then used in conjunction with Jenkins and Mancini [3] theory to assess the various driving forces for segregation. Specifically, the magnitude of a newly identified driving force arising from a non-equipartition of energy was evaluated. Results indicate that the new driving force is of similar magnitude to other driving forces for systems with moderate values of mass differences and restitution coefficients. In many cases, a non-equipartition driving force was the second largest driving force present.

References

[1] Hsiau, S. S. and Hunt, M. L.: Granular thermal diffusion in flows of binary-sized mixtures. *Acta Mechanica* **114**:121-137, 1996.

[2] Arnarson, B. O. and Willits J. T.: Thermal diffusion in binary mixtures of smooth, nearly elastic spheres with and without gravity. *Phys. Fluids* **10**:1324-1328, 1998.

[3] Jenkins, J. T. and Mancini, F.: Balance laws and constitutive relations for plane flows of dense, binary mixture of smooth, nearly elastic, circular disks. *J. Appl. Mech-Trans. ASME* **54**:27-34, 1987.

XXI ICTAM, 15–21 August 2004, Warsaw, Poland

KINETICS OF WEAKLY FRICTIONAL GRANULAR GASES

Isaac Goldhirsch*, S. Henri Noskowicz*, O. Bar-Lev**
*Department of Fluid Mechanics and Heat Transfer, Faculty of Engineering, Tel-Aviv University, Ramat-Aviv, Tel-Aviv, 69978, Israel
**School of Mathematics, Tel-Aviv University, Ramat-Aviv, Tel-Aviv, 69978, Israel.

Summary Although all macroscopic grains are frictional, most of the theoretical studies of granular gases have focused on models of frictionless spheres. The success of these models in explaining many experimental results raises the question of the role of frictional restitution in the dynamics of granular gases. The weak frictional limit is explored here. Using the pertinent Boltzmann equation we derive hydrodynamic equations of motion (as it turns out, one needs to extend the list of hydrodynamic fields for this purpose) and study some of their consequences. One of these consequences is that the homogeneous cooling state is highly non-Gaussian. Another consequence is the long memory associated with the rotational degrees of freedom, when weakly coupled to translation.

EXTENDED DESCRIPTION

In spite of the omnipresence and undeniable importance of friction in granular matter (see e.g., [1]), most models of granular gases consist of frictionless particles, mostly spherical in shape. Although frictional particles have been considered in simulations of granular gases, cf. e.g., [2] and references therein, very few theoretical studies of frictional granular gases can be found in the literature, cf. e.g., [3, 4, 5, 6]. Perhaps the fact that frictionless models have been rather successful in explaining many of the observed phenomena in granular gases [7], or the difficulties one encounters in the theoretical study of frictional granular gases are responsible for this state of affairs, and perhaps there are other reasons. In any case, we believe it is important to study the full kinetics and hydrodynamics of frictional granular gases.

In previous kinetic theoretical based studies of the of granular hydrodynamics [3, 5] it is assumed that the basic distribution function is Maxwellian in both the velocity and angular velocity (and usually different rotational and translational temperatures are allowed for), and corrections due to gradients are identified (on the basis of symmetry). The assumed distribution function is substituted in the Enskog equations, resulting in a closure for the constitutive relations. The above Maxwellian distribution corresponds (when both the rotational and translation temperature are taken to be equal) to the limit of rough molecules, in which there is equipartition between the rotational and translational kinetic energies. Our goal here is to study granular gases near a different limit, i.e., the smooth limit (as frictionless grains comprise the model most studied in the literature), and develop a systematic approach to the problem, i.e., a perturbative scheme

The model considered here is a monodisperse systems of spherical grains. In addition to the velocities of the particles we define a 'spin variable', $\mathbf{s}_i$, whose dimension is that of velocity, by $\mathbf{s}_i \equiv \frac{d}{2}\omega_i$, where d is the diameter of a sphere and ω_i is its angular velocity. The binary collisions of these spheres are defined similarly to refs. [5, 8]. The single particle distribution function, f, depends on space ($\mathbf{r}$), time, t, the velocity, $\mathbf{v}$, and spin, $\mathbf{s}$, degrees of freedom, and it satisfies and appropriate Boltzmann equation. The latter can be studied by employing the Champman-Enskog expansion in order to obtain hydrodynamic equations of motion. The basic premise of this expansion is that the dependence of the single particle distribution function on space and time can be replaced by a dependence on the 'slow' fields. In other words, when the temporal resolution exceeds a few mean free times, and the spatial resolution exceeds a few mean free paths, the (local) dynamics of the particles is only constrained by the slowly changing fields. Therefore, the slow (or hydrodynamic) fields should be those that correspond to conserved (or nearly conserved) entities. In the case at hand, the momentum and the number of particles (or the total mass) are conserved, hence the momentum density and the particle number (or mass) density are hydrodynamic fields. The granular temperature corresponding to the translational degrees of freedom is not conserved, but it is nearly conserved in the near-elastic, near-frictionless case, and is therefore a hydrodynamic field. In the same limit the spin degrees of freedom are decoupled from the translational degrees of freedom and the number density corresponding to each value of the spin, $\mathbf{s}$, is conserved as well, hence the infinite set of spin dependent number densities should be taken as hydrodynamic fields. In the rough limit rotation is strongly coupled to translation and the total (translational plus rotational) energy is conserved in each collision. Therefore, in the latter case one only needs the total energy, momentum and mass densities as hydrodynamic fields. However, no harm is done by exaggerating the number of hydrodynamic fields, hence even in this case one can use the above set of spin dependent densities (which can be used to calculate the rotational temperature as the average of the square of the of the fluctuating spin), and in this case one can retain the translational granular temperature as well. All in all, the general set of hydrodynamic fields that is appropriate for all cases is that corresponding to the smooth elastic limit.

There are several ways to design a perturbative expansion for the distribution function in the present case; each of the expansions uses a different zeroth order limit, around which it is defined. It is preferred that this limit is an exact solution of the Boltzmann equation. In the realm of smooth frictionless granular systems there have been two such expansions. One was [9] the equilibrium state corresponding to the limit of zero inelasticity ($e = 1$) and no-gradients (i.e., the Knudsen number, K, was taken to be zero) and, the other [10] employed the (local) homogeneous cooling state (with $K = 0$) as a zeroth order. These two approaches agree with each other in the common domain of validity (near elastic collisions) and both can be used as zeroth order solutions in the presence of weak friction. Another limit at which a solution of the

rotational and translational temperature are equal to each other. The latter has been employed to describe molecules, cf. [11]. One of the important differences between the smooth particle limit and the rough limit is that in the former the spin degrees of freedom are decoupled from the translational degrees of freedom to zeroth order in the interaction, and serve as independent variables, whereas in the latter case the spin degrees of freedom are strongly coupled to the translational degrees of freedom (the conserved energy in collisions is the sum of the translational and rotational energies) and thus the spin degrees of freedom are not independent. For this reason, and since the smooth limit is the most studied case, we chose to focus on the smooth equilibrium limit. This choice still leaves several possibilities. Below, we choose to study the case of finite Coulomb friction and near frictionless coefficient of tangential restitution. In this case, the small parameters are: the degree of normal inelasticity [9], the degree of tangential inelasticity, and the Knudsen number. Notice that the studied systems can be regarded as a mixture of particles characterized by their respective spins.

The results of the application of the Chapman-Enskog expansion yield constitutive relations, which we have developed to second order in the small parameters. These will be presented elsewhere. Here we specialize to a simple case, the near frictionless homogeneous cooling (i.e., unforced) state. In this case the hydrodynamics equations reduce to:

$$\begin{aligned} \frac{dT}{d\tau} &= -\alpha T + \beta T_{\rm rot} + 2\beta S^2 \\ \frac{dT_{\rm rot}}{d\tau} &= \frac{3}{\kappa^2}\beta T - \left(\delta - \frac{1}{4}\mu - \frac{3}{2\kappa^2}\beta\right) T_{\rm rot} + \mu S^2 \\ \frac{dS^2}{d\tau} &= -\delta S^2 \end{aligned} \tag{1}$$

where, T is the granular temperature, $T_{\rm rot}$ is the rotational granular temperature, $\mathbf{S}$ is the average spin field, and τ measures time in units of accumulated collisions. . Eq. (1) is linear in T, $T_{\rm rot}$ and S^2. The three eigenvalues of this system are negative. The long-time decay rate of T and $T_{\rm rot}$ follows Haff's law, and: $\lim_{t\to\infty} \frac{T_{\rm rot}}{T} = r$, where r the value of the number r depends on the parameters in Eq.(1). Also: $\lim_{t\to\infty} \frac{S^2}{T} = 0$. Since S^2 decays to zero faster than T and $T_{\rm rot}$ it is justified to consider the asymptotic time dynamics for the case $\mathbf{S} = 0$. To simplify matters even further, we shall assume that the spin distribution, $n(\mathbf{s}, t)$, is isotropic, i.e., $n(\mathbf{s}, t)$ depends on the scalar s (and time) alone. It is convenient to define a spin density, $N(s,t)$, by $N(s,t) \equiv 4\pi s^2 n(s,t)$. Clearly: $\int N(s,t)ds = n$, and $\frac{1}{n}\int s^2 N(s,t)ds = T_{\rm rot}(t)$. One can show that N satisfies a spin diffusion equation: $\frac{\partial N}{\partial \tau} = \frac{\partial}{\partial s}\left[A_1 sN + (2T + T_{\rm rot}) A_2 \left(\frac{\partial N}{\partial s} - \frac{2N}{s}\right) + A_3\left(s^2 \frac{\partial N}{\partial s} - 2sN\right)\right]$. In the large time limit, this equation possesses a scaling solution of the form $N(s,\tau) = \frac{n}{\sqrt{T}} F(\zeta)$ where $\zeta = \frac{s}{\sqrt{T}}$, with $T_{\rm rot}/T$ replaced by its asymptotic value r. In this limit the above equation reduces to $F_{\zeta\zeta} + \frac{F_\zeta}{\zeta} C + \frac{F}{\zeta^2}(C-2) = 0$, where C is a fixed parameter. It is easy to check that the normalizable solution of the last equation satisfies $F(\zeta) \sim \zeta^{2-C}$ i.e. the distribution decays as a power law: $n(s) \sim \frac{n}{4\pi T^{3/2}} \left(\frac{s}{\sqrt{T}}\right)^{-C}$. For instance for a degree of inelasticity, $\epsilon = 0.1$ and a similar degree of frictional inelasticity, $F(\zeta) \sim \zeta^{-5.935}$. Therefore, contrary to assumptions in most theories of frictional granular matter, the spin distribution function in the considered case is very different from Maxwellian. As the hydrodynamics was developed on the basis of the Boltzmann equation, (dilute case), the stress tensor (being the average of a symmetric entity) is symmetric, i.e., one does not obtain a micropolar theory. Finite density corrections will be considered elsewhere. Many open questions still remain, among them the effects of friction on shear and vibrated flows, the matching of the expansion presented above with results obtained from an expansion around the rough limit, and, in general, the effects of friction in many types of granular flows.

ACKNOWLEDGMENTS

One of us (I.G.) would like to gratefully acknowledge support from the Israel Science Foundation, grant no. 53-01, the US-Israel Binational Science Foundation, grant no. 1999-417, and INTAS, grant no. 577.

.

References

[1] S. J. Moon, J. B. Swift, and H. L. Swinney. Role of friction in pattern formation in oscillated granular layers. *cond-mat/0308541*, 2003.

[2] R. Cafiero, S. Luding, and H. J. Herrmann. Rotationally driven gas of inelastic rough spheres. *Europhys. Lett.*, 60(6):854–860, 2002.

[3] C. K. K. Lun. Kinetic theory for granular flow of dense, slightly inelastic, slightly rough spheres. *J. Fluid Mech.*, 233:539–559, 1991.

[4] M. Huthmann and A. Zippelius. Dynamics of inelastically colliding rough spheres: Relaxation of translational and rotational energy. *Phys. Rev. E*, 56(6):6275–6278, 1998.

[5] J. T. Jenkins and C. Zhang. Kinetic theory for identical, frictional, nearly elastic spheres. *Physics of Fluids*, 14(3):1228–1235, 2002.

[6] H. Hayakawa N. Mitarai and H. Nakanishi. Collisional granular flow as a micropolar fluid. *Phys. Rev. Lett.*, 88(17):174301–1–4, 2002.

[7] I. Goldhirsch. Rapid granular flows. *Annual Reviews of Fluid Mechanics*, 35:267–293, 2003.

[8] O. Herbst, M. Huthmann, and A. Zippelius. Dynamics of inelastically colliding spheres with Coulomb friction: relaxation of translational and rotational energy. *Granular Matter*, 2(4):211–219, 2000.

[9] N. Sela and I. Goldhirsch. Hydrodynamic equations for rapid flows of smooth inelastic spheres to Burnett order. *J. Fluid Mech.*, 361:41–74, 1998.

[10] J. J. Brey, J. W. Dufty, C. S. Kim, and A. Santos. Hydrodynamics for granular flow at low density. *Phys. Rev. E*, 58(4):4638–4653, 1998.

Morphology and scaling of impact craters in granular media

Amanda M. Walsh and John R. de Bruyn
Department of Physics and Physical Oceanography
Memorial University of Newfoundland
St. John's, Newfoundland, Canada A1B 3X7

We study the size and morphology of impact craters formed when a steel ball is dropped into a container of small glass beads. We find that both the depth (measured from the original surface) and diameter of the crater are proportional to the 1/4 power of energy. This is as expected if the energy of impact goes into excavating the crater and material strength is unimportant. We observe a variety of crater morphologies as a function of impact energy and grain size: simple craters, craters with a central peak, craters with slump terraces around the perimeter, and multi-ringed craters. The progression of these changes in morphology is similar to that observed in lunar craters.

Craters on the moon and planets form as a result of meteor impacts. Various crater morphologies are observed, with features such as central peaks, slump terraces, and multiple rings appearing as the crater size increases [1, 2]. Power-law scaling laws relating crater diameter w and the energy of impact E can be derived in certain limits [3]. If the kinetic energy of the projectile goes into excavating the crater against gravity one can show that $w \propto E^{1/4}$, while if the strength of the target material is important, $w \propto E^{1/3}$ [1, 3]. Craters formed by nuclear explosions follow an intermediate scaling, but gravity dominated scaling is expected to hold for large lunar craters. Laboratory studies of impact crater formation typically involve firing projectiles into a target at speeds of several kilometers per second [4], but experiments on crater formation in granular materials have also been reported [5–7].

We studied the formation of craters by dropping a steel ball into loosely packed glass beads. Balls with diameters 2.54 cm and 1.27 cm and masses 66.0 g and 8.35 g respectively were dropped into a large container of glass beads with diameters D_g ranging from 45-90 μm up to 300-425 μm. The beads were poured evenly into the experimental container prior to each run, with the two smallest sized beads being poured through a sieve. The surface was smoothed with a straight edge but otherwise the beads were used "as poured," with no shaking. The packing fraction of the beads ranged from 56% for the smallest beads up to 62% for the largest. The impact energy E is equal to mgh, where m is the mass of the ball and h is the release height. h was varied in the range 2 to 90 cm, corresponding to $10^5 \leq E \leq 6 \times 10^6$ ergs. In most cases, the steel ball was completely buried in the target material after the impact [8].

Figure 1 shows examples of the craters observed. At low energies and with large beads, simple bowl-shaped craters surrounded by a uniform rim are formed (Fig. 1(a)). For larger E or smaller D_g, a central peak appears (Fig. 1(b)). This peak is associated with the appearance of granular jets [9–11] which result from the inward rebound of displaced grains after passage of the projectile. At still higher energy and with the smallest beads, the craters have less well defined rims, flat bottoms, and terraces around the perimeter (Fig. 1(c)). The terraces result when the original crater walls are so steep that they collapse under gravity. Terracing was observed only for the smallest beads, and since the formation of terraces requires the granular medium to have some material strength, this indicates that these beads are slightly cohesive. At the highest energies studied, craters with multiple rings and a complex central morphology form. Figure 1(d) shows the range of E and D_g over which the different morphologies are observed. This sequence of crater morphologies is the same as that observed on the moon and elsewhere [1, 2].

We measured the crater diameter w at the top of the crater rim, as well as two versions of the crater depth: d, measured from the level of the original surface to the lowest point on the crater floor and the depth, and d_t, measured from the top of the rim to the crater floor. We non-dimensionalized our data by scaling distances by the bead diameter D_g and energy by the energy required to raise one bead a distance D_g against gravity. Fig. 2 is a log-log plot of the scaled crater width w' as a function of scaled energy E' for five different bead sizes and two ball diameters. The data for the four larger bead sizes are well described by a 1/4 power law over more than three orders of magnitude in scaled energy, as expected in the gravity-limited regime. The diameters of craters in the smallest beads (diamonds) fall significantly below the other data and show a weaker dependence on E'. This is mainly due to the fact that with the smallest beads, a significant fraction of the impact energy goes into the formation of large granular jets. This implies a smaller w for a given E for these beads, as observed, and in fact if *all* the energy goes into the jet, a simple argument predicts that $w =$ constant, consistent with the observed slow variation of w with E. These beads are also significantly influenced by air drag and cohesion, which likely arises due to atmospheric humidity.

The scaled crater depth d', measured from the original surface level to the lowest point in the crater, was also studied. The data sets for the different bead sizes are each well described by a 1/4 power law in E'. However, while

the power law *exponent* does not depend on D_g within our uncertainties, our scaling does not completely account for the effects of particle size here, and the data do not collapse onto a single line. Craters in smaller beads are slightly shallower than for larger beads, likely due to the increased effects of air drag and cohesion.

The rim-to-floor depth d_t differs from d due to the height of the crater rim and to compaction of the target material during impact. d_t is also well described by a power law with an exponent close to 1/4 at low E' but flattens out at higher energies, suggesting a change in the details of the crater formation process at high E'. As a result of this, the ratio w'/d'_t of crater diameter to rim-to-floor depth is constant and equal to 8.4 ± 0.4 at low E', in the regime where all crater dimensions scale as $E'^{1/4}$, but increases at higher E' as the behavior of d'_t changes. This ratio has been measured for lunar craters: it is approximately 5 for simple craters (i.e., low energies) but becomes larger for complex craters (high energies) [1]. Our low energy value is slightly higher than for lunar craters, probably due to differences in material properties, but the same trend is observed as E' is increased — craters formed in high energy impacts are relatively wider and flatter than low energy craters.

This research was supported by NSERC of Canada. We are grateful to P. Habdas and K. Holloway for their contributions to this work.

[1] H. J. Melosh, Impact Cratering: A Geologic Process (Oxford University Press, New York, 1989).
[2] H. J. Melosh and B. A. Ivanov, Annu. Rev. Earth Planet. Sci. **27**, 385 (1999).
[3] K. A. Holsapple, Annu. Rev. Earth Planet. Sci. **21**, 333 (1993).
[4] P. H. Schultz, Int. J. Impact Engng. **5**, 569 (1987).
[5] J. C. Amato and R. E. Williams, Am. J. Phys. **66**, 141 (1998).
[6] J. S. Uehara, M. A. Ambroso, R. P. Ojha, and D. J. Durian, Phys. Rev. Lett. **90**, 194301 (2003).
[7] A. M. Walsh, K. A. Holloway, P. Habdas, and J. R. de Bruyn, Phys. Rev. Lett. **91**, 104301 (2003).
[8] J. R. de Bruyn and A. Walsh, Phys. Rev. E, to be published.
[9] A. Walsh and J. R. de Bruyn, unpublished.
[10] S. T. Thoroddsen and A. Q. Shen, Phys. Fluids **13**, 4 (2001).
[11] R. Mikkelsen, M. Versluis, E. Koene, G.-W. Bruggert, D. van der Meer, K. van der Weele, and D. Lohse, Phys. Fluids **14**, S14 (2002).

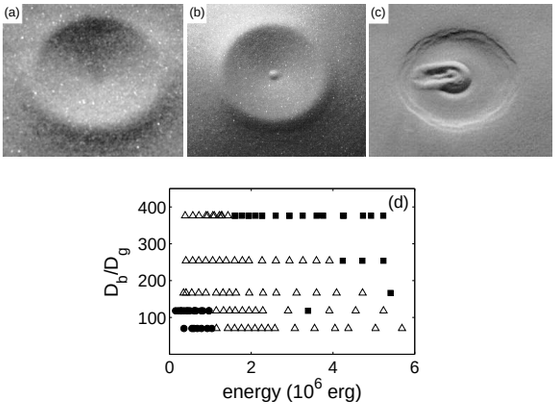


FIG. 1: Impact craters formed by dropping a 2.54 cm diameter, 66.0 g steel ball vertically into a container of small glass beads. (a) A simple crater formed in beads of diameter $D_g = 180$-250 μm when the ball was released from a height h of 14.8 cm. The rim-to-rim crater diameter w is 6.62 cm. (b) A crater with a small central peak and $w = 8.08$ cm. Here $h = 32.5$ cm and $D_g = 180$-250 μm. (c) A complex crater with $w = 5.66$ cm formed in beads with $D_g = 45$-90 μm for $h = 40.1$ cm. (d) The range of existence of the different crater morphologies in terms of the impact energy and the ratio of the ball diameter to the bead diameter, D_b/D_g. Circles: simple craters; triangles: craters with a central peak; squares: craters with multiple rings.

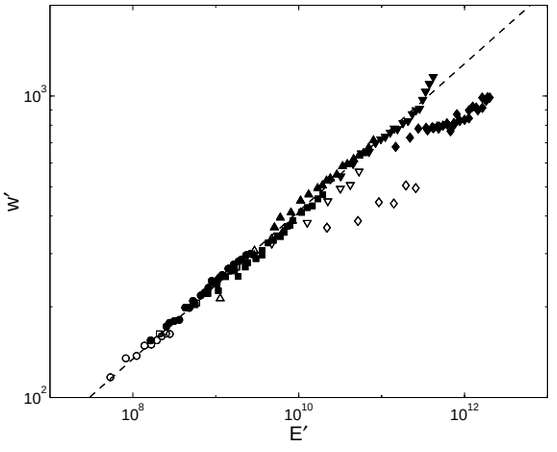


FIG. 2: The scaled crater diameter as a function of scaled energy. Solid symbols are for craters formed with a 2.54 cm diameter steel ball and open symbols for a 1.27 cm ball. The different symbols indicate different sized glass beads: diamonds, 45-90 μm, downward-pointing triangles, 75-125 μm, upward-pointing triangles, 125-180 μm, squares, 180-250 μm, and circles, 300-425 μm. The dashed line is a fit to the data for the four larger bead sizes and the large ball, and has a slope of 0.245 ± 0.002.

EXTENDED GRANULAR TEMPERATURE

Lou Kondic* and Robert P. Behringer**
* *Department of Mathematical Sciences & Center for Applied Mathematics & Statistics*
New Jersey Institute of Technology, Newark, NJ 07102, USA
** *Department of Physics & Center for Nonlinear and Complex Systems*
Duke University, Durham NC, 27708, USA

Summary We consider the role of elastic energy in the context of granular materials undergoing shear flow. Depending on the ratio of pressure to Young's modulus of the material from which grains are made and the typical velocity of shearing, there is a transition from a regime in which the fluctuations of kinetic energy are dominant to the regime where the fluctuations of elastic energy are dominant. This regime has likely been reached in recent experiments. We then consider a generalization of the granular temperature that includes both types of energy fluctuations and that changes smoothly from one regime to the other. We conclude by discussing related energy distributions and the degree to which the zeroth law of thermodynamics is satisfied by this new generalized temperature.

OVERVIEW

We explore the role of elasticity in the energy and energy fluctuations of sheared dense granular systems. For dilated gas-like granular states, energy fluctuations are frequently described in terms of a temperature, defined as the fluctuating part of the kinetic energy, $T_k \equiv m < v^2 > /2$. Here, v is the local random component of the velocity. This definition is predicated on assumptions such as molecular chaos, absence of correlations, and short-lived collisions, that do not always apply. For dense systems, a very different concept, Edwards entropy, has been proposed [1].

Both of these pictures assume that minimal energy is stored in compressional modes of the particles. This assumption is valid when the pressure is small compared to the Young's modulus. However, it can easily be shown that in particular for slow shearing, there are many physical situations when this need not be the case. In such a setting, neither T_k nor T_E is likely to provide a good measure of the random nature of the system.

The main goal of this work is to analyze via discrete element simulations (DES) the storage of energy and energy fluctuations for dense granular material subject to shearing. In this context, we propose an extension of granular "temperature" that contains information on fluctuations of the elastic energy, and then compare this extension to a temperature drawn from statistical mechanics. (A somewhat similar approach of applying equilibrium statistical theory to out-of-equilibrium systems has been recently used by other authors [4, 5].)

The generalization of "temperature" that we consider is based on the classical idea that for a lattice of elastic particles, the average fluctuating energy/particle is $3k_BT$. Using this as a heuristic guide, we define a generalized temperature that is roughly $T_g = m < v^2 > /2 + k < x^2 > /2$, where v corresponds to the fluctuating part of the velocity, and x to the fluctuating part of the compression of a particle. Note that this definition provides a simple bridge between the extremes of a gas-like state and a highly compressed slowly evolving state.

In the simulation, particles are confined between two inpenetrable straight parallel boundaries. The top boundary, which is 50 mean particle diameters (d_m) long, moves at a steady speed, and induces shearing in the system. The boundary conditions in the shearing direction are periodic. These simulations closely follow the soft-disk/sphere model (see [7, 8] and references therein), and are performed with approximately 2000 polydisperse particles, with a radius variability of 10%. The results that follow use t, the time it takes the shearing wall to travel once across the domain, as a time scale, and l/t ($l = 50d_m$) as a velocity scale. The quantities below are calculated using space-time averaging, see [8]. In particular, the elastic energy is obtained by averaging *per collision*, not per particle. The difference between the two is significant for dense granular systems considered here, since particles typically experience multiple collisions.

DISCUSSION OF THE RESULTS

By analyzing the elastic energy and kinetic temperature, as the volume fraction ν is slowly increased, we observe in our simulations that there is a transition region (about $\nu_c = 80\%$) where the energy stored in the internal degrees of freedom (elastic energy) becomes more relevant than the kinetic energy. In order to have a quantity that might play the same role as T_k in a dense granular system we propose a generalized granular 'temperature' by

$$T_g = T_k + T_e, \tag{1}$$

as a sum of T_k, and the 'elastic' part T_e. T_e is defined as the mean fluctuation of *elastic* energy, in a manner similar to T_k, which is the mean fluctuation of *kinetic* energy. This definition follows the classical statistical mechanics result where the mean fluctuations in the combined elastic and kinetic energy of an oscillator are proportional to the temperature. However, unlike this classical case, there is no reason to expect equipartition between elastic and kinetic modes. Rather, the ratio $T_e/(T_e + T_k)$ varies from 0 in the dilute limit, to 1 in the dense limit.

Figure 1 shows T_k, T_e, and average elastic energy, E_e vs. time, for four different ν's. For higher ν's, clearly $T_e \gg T_k$. Interestingly, there are rather large fluctuations of the results with ν just above $\nu_c \approx 80\%$, corresponding to the regime

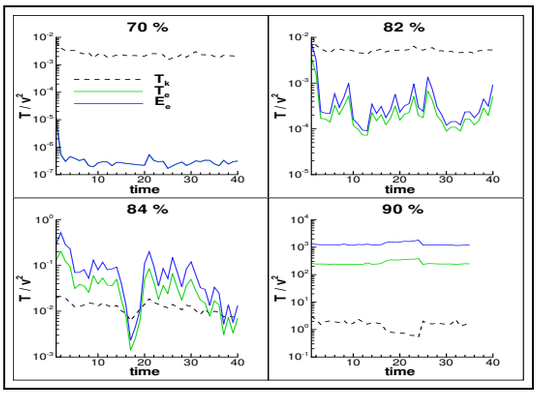


Figure 1. Elastic energy, kinetic and elastic temperatures for various ν's, scaled by v^2.

where elastic energy becomes predominant. Also, experiments have indicated a phase transition for comparable densities which may be related [2]. Generally, one might expect both glassy and/or jamming phenomena to dominate this regime.
We further interpret T_g by comparing it to an alternative definition from statistical mechanics. We consider the standard relation [6] $dU/dT = \delta U^2/T^2$ where U is the total energy in the (usually conservative) system, T is the temperature, and $\delta U^2 = \langle U^2 \rangle - \langle U \rangle^2$. We then ask whether it makes sense to define $T = T_g = T_k + T_e$. To check this idea, we now think of the relation above as a defining equation for $T_m = \sqrt{\delta U^2}/(dU/dT_g)$. The agreement between T_m and T_g will provide some indication of the utility of the definition for T_g. Note that we should not expect perfect or possibly even any agreement, since we are considering a strongly dissipative system far from equilibrium.

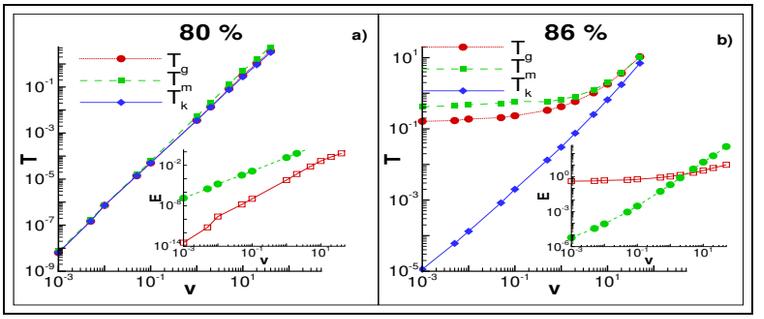


Figure 2. Generalized, kinetic, and 'model' temperature (see the text) for two volume fractions. The insets show kinetic energy (filled circles) and average elastic energy (squares).

Figure 2 contains a summary of the various types of temperatures considered in this study for two ν's. As already noted, for $\nu = 80\%$, most of the energy is still kinetic, while for $\nu = 86\%$, elastic energy is essential. For $\nu = 80\%$, T_k is dominant, and also it satisfies the model above since $T_k \approx T_m$. However, for $\nu = 86\%$ and for slow shearing, T_k is smaller by 4 orders of magnitude than T_g and T_m. Thus, T_k cannot be used to even approximately describe a dense slowly sheared granular system. This difference decreases for higher shearing rates, but only at very high shearing is there good agreement. We note that the presented results apply to any confined, sheared, granular system.
The agreement between T_g and T_m is not perfect; however prefect agreement is not to be expected. These studies demonstrate the clear need to incorporate elastic energy and elastic fluctuations, and that T_g has utility as a generalized granular temperature. Clearly, there remain many open questions regarding the extent to which the various temperatures serve similar functions to their molecular counterpart.
We acknowledge support by NASA NAG3-2367, NAG3-2372, NAG3-2372-05 and NNC04GA98G. RPB acknowledges support by NSF grants DMR-0137119, DMS-0204677 and DMS-0244492.

References

[1] S. F. Edwards. In A. Mehta, editor, *Granular Matter: An Interdisciplinary Approach*, 121, Springer,New York 1994.
[2] D. Howell, C. Veje, and R. P. Behringer. *Phys. Rev. Lett.*, 82:5241, 1999.
[3] W. Losert, J.-C. Geminard, S. Nasuno, and J. P. Gollub. *Phys. Rev. E*, 61:4060, 2000.
[4] I. K. Ono etal. *Phys. Rev. Lett.*, 89:095703, 2002.
[5] H. A. Makse and J. Kurchan. *Nature*, 415:614, 2002.
[6] D. A. McQuarrie. *Statistical Mechanics*. University Science Books, Sausalito, 2000.
[7] L. Kondic. *Phys. Rev. E*, 60:751, 1999.
[8] L. Kondic and R.P. Behringer. *cond-mat/0307555*, 2003.

Evolution of internal structure of sheared dense granular flows: crystallization transition and non-unique final states

J.-C. Tsai and J. P. Gollub
Physics Department, Haverford College, Haverford, PA 19041, USA
Physics Department, Univ. of Pennsylvania, Philadelphia, PA 19104, USA

It is known that uniformly sheared particle suspensions often exhibit ordering that leads to significant rheological changes [1-3]. Can a sheared dense granular flow, whose velocity profile is highly non-uniform, also exhibit spatial order? How does the internal order influence the flow profiles and the shear forces? And how does the shearing process influence the state of internal order? Previous investigations of granular shear flow have sometimes noted layering of particles in the interior [4]. However, the consequences of internal order for the rheology of sheared granular flows have not been fully explored.

In our initial work on this problem [5], we discovered that shearing can trigger a crystallization transition accompanied by a step compaction event. The delay preceding the transition depends strongly on the layer thickness and can require a translation of about 10^5 particle diameters. The internal velocity fields are qualitatively altered by this transition.

In further work to be reported here, we use the simultaneous measurement of shear force, volume changes and internal imaging to elucidate the connection between internal order and rheology. We also investigate the role of boundary conditions and the shearing protocol in the ordering process. Several striking features are found. The shear force declines significantly as a consequence of the crystallization. Furthermore, the transition can be influenced by the boundary conditions imposed even far from the shearing surface. Most importantly, sheared flow can exhibit non-unique final states; the stability of the disordered state depends on prior shearing history.

APPARATUS (Fig.1)

Spherical glass beads of diameter d = 0.6mm fill the annular channel formed by two concentric smooth stationary cylinders. Glass beads are driven by the floating upper boundary, which rotates at a constant speed while exerting a fixed normal load on the beads; the contact surface is roughened by a glued mono-layer of 0.6mm glass beads. Three different lower boundaries are available: (1) flat bottom (2) mono-layer bottom, and (3) bumpy bottom – a mixture of 0.6mm and 1.0mm beads. The inter-particle space is filled with fluorescent fluid whose refractive index matches that of the glass beads; when illuminated by a laser sheet, internal image slices can be created and captured by CCD cameras. The gap between the driving upper surface and the sidewalls is less than 0.5d; this allows the fluid to enter and exit freely while the particles are confined. The vertical displacement of the upper surface indicates the change of granular volume. Meanwhile, the boundary shear force can be determined by measuring the torque exerted by the driving motor.

CRYSTALLIZATION TRANSITION (Fig.2,3)

Long-term shearing can lead to a sharp crystallization transition. This is shown in Fig.2(a): images of a vertical slice along the center-line of the channel before and after the transition, with a Fourier measure of spatial periodicity showing a step rise at the transition time. The image on the right clearly exhibits a 24-layer structure.

In addition to structural change, the granular volume and shear force decline significantly [Fig.2(b,c)] at the time of the transition. Tracking the speed of particles in the lower region of the flow (marked as Γ in the upper right image) indicates that particles here translate more slowly after crystallization [Fig.2(d)]. The velocity profile (Fig.3) shows quantitatively that particle speed decays more rapidly with depth in the crystallized state. These facts suggest that in the crystallized state, downward transfer of horizontal momentum is less effective than in the disordered state, even though the crystallized state is denser.

Effect of the bottom boundary condition – The long-term shearing induces a sharp ordering transition in the case of flat or mono-layer bottom. The use of a bumpy lower boundary can inhibit the crystallization everywhere. When pure unidirectional shear is applied, the system consistently selects a disordered final state.

NON-UNIQUE FINAL STATES (Fig.4)

If a few cycles of oscillatory shear are applied prior to the long-term shearing, the route of the evolution of a disordered packing (with a bumpy bottom) shows stochastic features. The system can *either* crystallize *or* approach a final state whose interior remains disordered; in this case, specifying the boundary condition and shearing protocol does not uniquely determine the outcome of the evolution.

History-dependent stability of the disordered state – The disordered state, after being sufficient compacted by long-term unidirectional shearing, is found to become stable against oscillatory boundary driving (previous paragraph).

CONCLUSIONS

The evolution of a continuously sheared dense granular packing can be non-unique. Compared to a disordered flow, a crystallized flow requires less shear force and shows a more rapid decline of grain speed with depth. Boundary conditions can significantly influence the spontaneous crystallization under long-term shearing. Meanwhile, a theoretical explanation of the history-dependent stability of the disordered state is an open question.

This work is supported by the US-NSF under grants DMR-0072203 and DMR-0079909.

References

[1] Haw M.D. et al. Colloidal Glasses under Shear Strain. *Phys.Rev. E* **58**: 4673-4682, 1998.

[2] Paulin S, Ackerson B.,Wolfe M.: Microstructure-Dependent Viscosity in Concentrated Suspensions of Soft Spheres. *Phys.Rev.E* **55**:5812-19, 1997.

[3] Sierou A, Brady J: Rheology and Microstructure in Concentrated Noncolloidal Suspensions. *J. Rheol.*,**46**:1031-56, 2002.

[4] Mueth D et al. Signatures of Granular Microstructure in Dense Shear Flows. *Nature*, **406**: 385-9, 2000.

[5] Tsai J.-C., Voth G.A., Gollub J.P.: Internal Granular Dynamics, Shear-Induced Crystallization, and Compaction Steps. *Phys.Rev.Lett.***91**: 064301,2003.

Figures

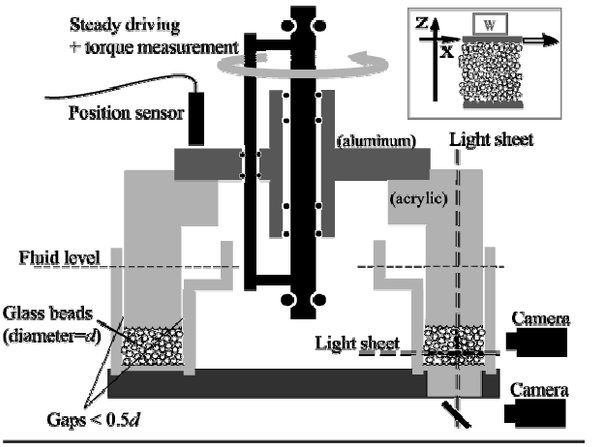


Fig. 1. Cross-section of the annular plane shear flow. The shear and normal load are provided by a rotating aluminum-acrylic assembly that is free to move vertically while maintaining constant rotation rate. The channel width is about 30*d* (*d*=bead diameter) and its circumference is about 800*d*. (The weight of the upper boundary assembly provides a constant normal load, which is more than ten times the total weight of the grains at the typical filling height of 24*d*.)

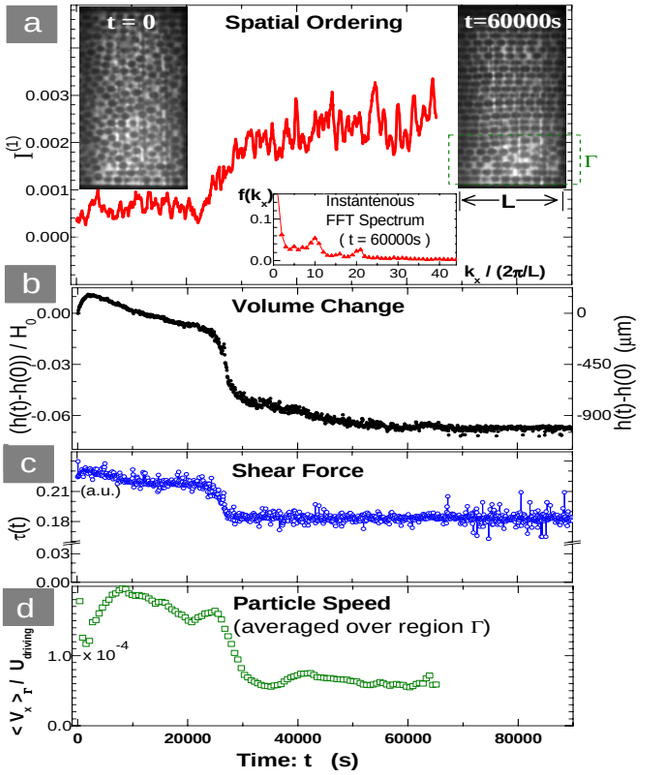


Fig.2. (color) Simultaneous measurement of internal ordering, volume change, shear force, and particle speed, as functions of time. Glass beads are driven at a speed of 12*d*/s from above. (a) Vertical image slices before and after the crystallization, with $I^{(1)}$ showing the Fourier intensity corresponding to a spatial period of 1d in the horizontal direction. (b) Fractional change of total height, as an indicator of total volume change. (c). Shear force (d) Particle speed averaged over the lower region Γ, marked on the upper right image.

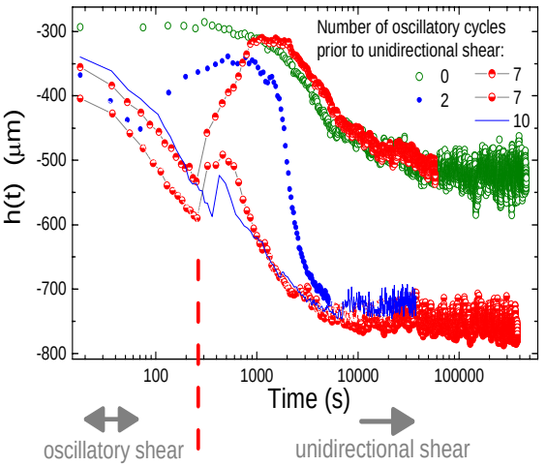


Fig. 4. (color) The height h(t) indicates the final state of internal ordering. With pure unidirectional shearing (labeled empty circles), the system always approaches a disordered final state (joining curves at the top right). On the other hand, oscillatory shearing for a few cycles causes the system to evolve stochastically into either a disordered state, or a denser crystallized state (curves at the bottom right).

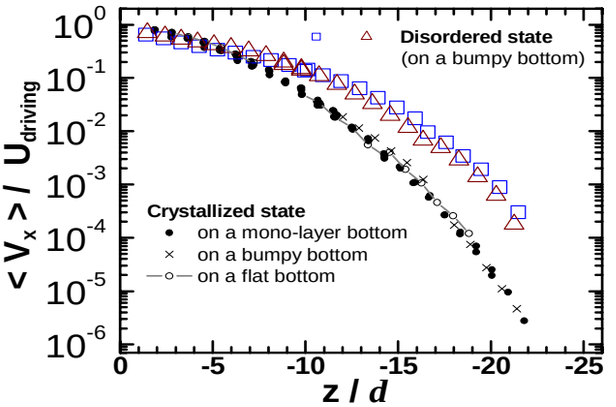


Fig. 3. (color) Comparison of the asymptotic mean velocity profiles for different final states. (The triangles and squares represent velocity profiles measured at different vertical planes of the disordered state.)

ARCHING IN GRANULAR MEDIA

Radoslaw L. Michalowski[*], Namgyu Park[**]

[*] *Dept. Civil & Env. Eng., University of Michigan, Ann Arbor, MI, U.S.A.*

[**] *Texas A&M University,College Station, TX, U.S.A.*

Summary Arching in sand piles can cause a counterintuitive stress depression (a 'dip') at the center of a conical or a wedge-shaped pile. However, predictions of the degree to which the granular material will arch are not easily made. A framework of plasticity analysis is used to shed some light on the issue of arching in granular media.

EXPERIMENTAL EVIDENCE FOR ARCHING IN SAND PILES

The early tests on conical and prismatic piles of sand conducted by Hummel and Finnan [1] revealed very distinct pressure 'dips' under sand piles of both geometries. They also made an observation that clearly links the depression in the base stress to arching: "When the sand was removed at the end of the experiment, it was found that about one-third the height of the cone could be taken away without altering the reading of the centre gauge."

Experiments on conical piles of sand and granular fertilizer by Smid and Novosad [2] confirmed the presence of a stress depression under the center of a conical mass. The heaps were prepared by pouring the granular material through a funnel over a steel platform.

A set of recent laboratory measurements of stress distributions by Vanel et al. [3] beneath both the conical and prismatic heaps indicated the influence of the construction process (or history of sand deposition) on the formation of a pressure 'dip'. The heaps formed by pouring the sand from a point source (conical piles) or a line source (prismatic piles) exhibited a dip, whereas the piles produced by uniform 'raining' did not.

MODELING

Efforts toward description of the distribution of stress in granular piles include both the discrete and continuum approaches (e.g., [4,5] and for a comprehensive review see [6]). The authors' interest in the subject is primarily in the context of the limit state analysis. Solving for stresses under sand heaps is not a typical problem of limit analysis since sand piles are inherently stable, but we are making the argument that the static theorem of limit analysis is useful in assessing fields that promote arching. When this approach is applied to "standard" problems, admissible stress fields are sought to provide a lower bound on an active force causing incipient failure (or an upper bound on a reaction). Although this approach does not guarantee finding the true stress distribution, it shows the correlation of the stress 'dip' and the arching phenomenon.

Radial stress field

We invoke the concept of the plastic radial stress field [7], and we use it as a means of constructing admissible stress distributions in a prismatic sand pile. Irreversible deformation of granular rate-independent materials becomes possible once the plastic stress state is reached. When the incipient failure is of interest (rather than an advanced process of plastic deformation), perfect plasticity is a common assumption, with the Mohr-Coulomb yield condition (f = 0) describing the stress state at failure. Statically admissible stress fields satisfy the stress boundary conditions, are in equilibrium, and do not violate the yield condition. The last requirement indicates that the stress field can be at the limit, as prescribed by: $f = 0$, or the stress state can be below the yielding level: $f < 0$. Therefore, to widen the class of admissible stress fields we introduce a stress function similar to Mohr-Coulomb condition, but with internal friction angle ϕ replaced with variable ϕ^* that is less or equal to ϕ

$$\frac{\sigma_1}{\sigma_3} = \frac{1+\sin\phi^*}{1-\sin\phi^*}, \qquad \phi^* = \phi^*(\theta) \;\le\; \phi \tag{1}$$

We now consider that ϕ^* can be a function of space, and in the special problem of a prismatic pile of sand we assume that ϕ^* is a function of coordinate θ (but not r) of a polar coordinate system with the origin at the apex of the pile. Combining the closure in eq. (1) with differential equations of equilibrium and postulating radial stress field one arrives at the set of two ordinary differential equations for stress distribution

$$\frac{d\chi}{d\theta} = \frac{\cos(2\psi'+\theta) + \chi\left(\sin 2\psi' + \dfrac{d\phi^*}{d\theta}\cos\phi^*\right)}{\cos 2\psi' - \sin\phi^*}, \qquad \frac{d\psi'}{d\theta} = \frac{\sin\theta - \sin\phi^*\sin(2\psi'+\theta) - \chi\cos\phi\left(\cos\phi^* + \dfrac{d\phi^*}{d\theta}\sin 2\psi'\right)}{2\chi\sin\phi^*(\cos 2\psi' - \sin\phi^*)} - 1 \tag{2}$$

When ϕ^* is constant ($d\phi^*/d\theta = 0$) and equal to ϕ, these equations become identical to classical Sokolovskii radial stress equations.

Arching stress distribution in a prismatic sand pile

Equations (2) were used to calculate the admissible stress state in a sand pile with a distribution of ϕ^* governed by an exponential function of θ, where the soil reaches yielding in the 'outer regions' but it is in elastic range in the middle

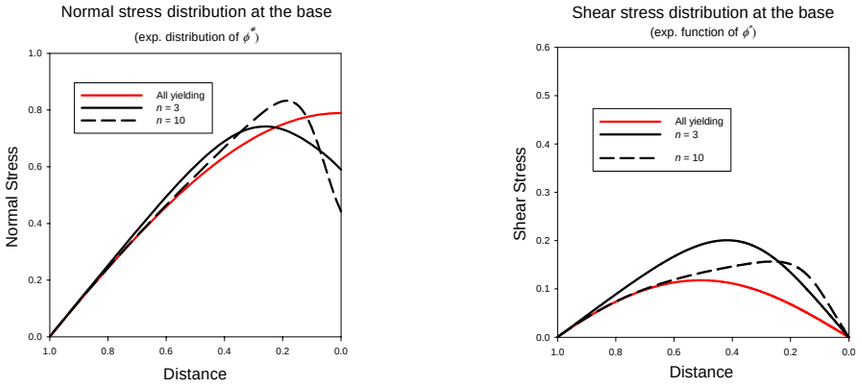


Figure 1. Normalized stress under wedge-shaped sand pile: (a) normal, and (b) shear stress.

part of the pile. The distribution of the base stress underneath the sand pile is illustrated in Fig. 1, along with a distribution for an all-in-failure assumption. Clearly, when the sand is all at yielding, no stress 'dip' occurs, whereas a clear depression is seen when the stress is in the elastic state in the core of the pile.

CONCLUSIONS

Construction of statically admissible stress fields is a standard method in limit analysis for finding a lower bound to an active limit load, or an upper bound to a reaction. Here, the method was modified to indicate the tendency of the stress distribution within the structure to arching. A pile of sand reaches the state closest to failure (consistent with a "spreading" mechanism) when the horizontal component of the reaction under a symmetric half of the pile reaches its minimum. Of different radial stress fields considered, the one with fully plastic stress appeared to yield the minimum of the shear force at the base. Once the stress fields were modified to include below-yielding regions, the horizontal reaction increased, and arching stress fields were found, distinguished by a characteristic 'dip' in the distribution of the normal stress at the base.

The theorems of limit analysis can be rephrased to assess the likelihood of arching occurrence. The static theorem then indicates that *arching may occur and failure will not take place if a statically admissible stress field supporting arching can be found*. Of course, proving that an admissible arching stress field exists does not exclude "non-arching" stress fields from occurring. The second theorem then states that *arching will not occur and collapse is imminent if a kinematically admissible mechanism can be found where the work rate of external loads exceeds the rate of internal work.*

Acknowledgements
The work presented in this paper was carried out while the first author was supported by the National Science Foundation, grant No. CMS-0096167, and the Army Research Office, grant No. DAAD19-03-1-0063. This support is greatly appreciated.

References

[1] Hummel, F.H., Finnan, E.J.: The distribution of pressure on surfaces supporting a mass of granular material. *Minutes of Proc. Inst. Civil Eng.*, Session 1920-1921, Part II.
[2] Smid, J., Novosad, J.: Pressure distribution under heaped bulk solids. *Proc. Powtech 1981*.
[3] Vanel, L., Howell, D., Clark, D., Behringer, R.P., Clement, E.: Memories in sand: Experimental tests of construction history on stress distributions under sandpiles. *Physical Review E* **60**, No. 5,1999.
[4] Wittmer, J.P., Cates, M.E., Claudin, P.: Stress propagation and arching in static sandpiles. *J. Phys. I France* **7**, 39-80, 1997.
[5] Didwania, A.K., Cantelaube, F., Goddard, J.D.: Static multiplicity of stress states in granular heaps. *Proc. Roy. Soc. London* **A 456**, 2569-2588, 2000.
[6] Savage, S.B.: Modeling and granular material boundary value problems. In: *Physics of Dry Granular Media.* Kluwer Acad. Press, 25-95, 1998.
[7] Sokolovskii, V.V.: *Statics of Granular Media*. Oxford: Pergamon, 1965.

TRANSVERSE MOTION, SEGREGATION AND ROTATIONS IN 2D GRANULAR FLOWS

Renaud Delannay*,Alexandre Valance*,Patrick Richard*,Weitao Bi*,Gaelle Berton**Nicolas Taberlet*
*Groupe Matière Condensée et Matériaux, UMR 6626, Université Rennes 1, F35042 Rennes Cedex, France
**Laboratoire de Mécanique et Rhéologie, EA 2640, Université de Tours, 37200 Tours, France

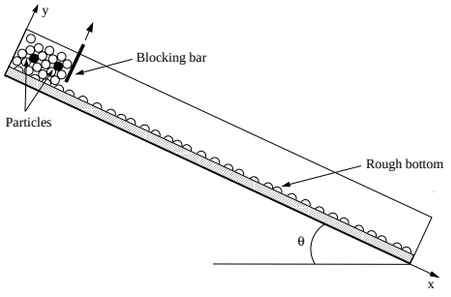
Summary We present an experimental study of 2D dense flows consisting of both monodisperse and bidisperse disks. We have analyzed the trajectories of the particles within the flow in a steady regime. In monodisperse flows, particles are arranged in layers that are in motion relative to one another. The particle transfer between layers can be interpreted as a transverse motion of diffusive nature. The diffusion coefficient associated to each layer increases linearly with the layer height. In polydisperse flows consisting of a few percentage of small disks among large ones, the small particles have a net downward motion on which a fluctuating behavior is superimposed. At short time, the small particle motion can be described as a biased Brownian motion. The ratio of the characteristic time of diffusion to that of convection is found to increase with the layer height, indicating that the segregation process is more efficient in the upper layers of the flow. At longer time, the transverse motion of the small particles seems to differ greatly from a classical biased Brownian motion.

INTRODUCTION

It is crucial to better understand the physical mechanisms which drive granular flows especially since they occur in geophysical context (rock avalanches, landslides) and in industrial applications. Granular flows generally belong to a regime where both friction between particles and collision play important roles. In this regime, no sound convincing constitutive law has been proposed despite the numerous experimental [1, 2, 3, 4, 5, 6], numerical [7] and theoretical [9, 10, 11] works devoted to granular flows. To avoid the experimental difficulties encountered in the case of 3D flows, Drake [3] proposed to use a two-dimensional geometry where particles are confined between two glass walls. This geometry is well suited to a detailed analysis of the micro-structure and the kinematics of the flow via a high speed camera. The purpose of the present work is to analyze in a 2D inclined granular chute flow the process of particle layer transfer. This study is motivated by the understanding and modeling of the segregation phenomenon in granular chute flows.

Experimental Set-up

The chute flow experiments have been performed using the set-up sketched in the Figure. The flowing particles are confined between two smooth glass side walls. Unlike most granular chute experiments, particles used here are not spheres but disks. Although the use of disks instead spheres enhance the friction with the side wall, it allows to work with mono-sized assemblies as well as with binary mixtures.

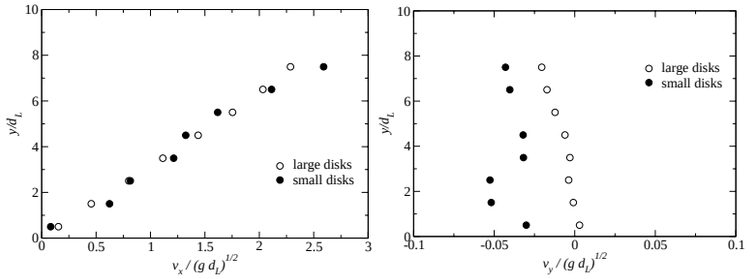


Flow experiments are recorded by a high speed video camera at a frequency high enough to track the motion of each grain of the flow. An image processing software computes the position of the center of mass of the disks on each image, therefore allowing one to extract the trajectories and calculate the kinematic properties of the particles. The binary mixtures were made of large and small polystyrene disks giving a diameter ratio of 2. We worked only with very dilute mixtures (e.g. less than 1% of fine particles). Strictly speaking, the flow is not fully developed since during the chute the segregation process occurs: the small disks migrate progressively towards the lower layer of the flow. However, as the mixture is dilute, the flow of large disks remains stationary and homogeneous along the longitudinal direction. The flow, characterized by a constant height, is dense : the packing fraction is rather constant in the bulk flow and is about 0.7. Within the flow, a stratification develops: layers of one particle width are built up and slide over each other. Close to the top free surface, the layers are less structured, the medium is more fluidized and therefore the packing fraction is lower.

Some results

We have measured the mean velocity of the small particles in the flow and compared it to the mean velocity of large disks. We have plotted the mean longitudinal velocity V_x of each species as a function of the height measured from the bottom. There exists no difference between small and large disks concerning the mean longitudinal velocities. In contrast, the

mean transverse velocity profile is different, whereas the mean transverse velocity of large particles is almost equal to zero, small particles have a significant downward velocity. The examination of the transverse displacements of the small particles allows us to bring some insights about the segregation process. The mean displacements of the small disks are shown in Figure 1.a.



One can note again that the small disks have a net downward motion, except for those which are located in the bottom layer. The mean displacement of the particles varies roughly linearly with time. Furthermore, the particles from the upper layers exhibit a greater downward displacement than those from the lower layers.

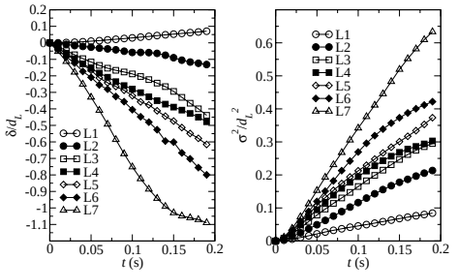


Figure 1. (a) mean transverse displacements and (b) displacement fluctuations as a function of time according the particle position.

We have also calculated the fluctuations of the transverse particle displacements according to their initial position in the flow (see Figure 1.b). The variance of the particle displacement increases linearly with time. The small particles have therefore a diffusive motion superimposed on a net downward motion. We have compared the diffusion coefficient associated to the small particles to that associated to the large ones. The diffusion behavior seems independent of the particle size. For both particle sizes, the diffusion coefficient is of the same order of magnitude and is an increasing function of the layer height.

CONCLUSION

At short time scale, we have put to the fore the existence of two competing processes driving the motion of the small particles diluted among large particles: a transverse downward convective motion which is a gravity-induced, size dependent, void-filling mechanism as described by Savage and Lun [12] and a diffusive process which is not size preferential and has no preferential direction for the layer transfer. The segregation process in dense flows is far from being comprehensively understood and we are performing additional experimental (on air table and chute flows)and theoretical efforts. Our next objective is to fully characterize the particle motion, including rotations of particles.

References

[1] S.B. Savage, J. Fluid Mech. **92**, 53 (1979).
[2] O. Hungr and N.R. Morgenstern, Geotechnique **34**, 405 (1984).
[3] T.J. Drake, J. Geophys. Res. **95**, 8681 (1990).
[4] P.C. Johnson, P. Nott, and R. Jackson, J. Fluid Mech. **210**, 501 (1990).
[5] E. Azanza, F. Chevoir and P. Moucheront, J. Fluid Mech. **400**, 199-227 (1999).
[6] Pouliquen O., Phys. of Fluids **11**, 542-548 (1999).
[7] C.S. Campbell and C.E. Brennen, ASME J. Appl. Mech. **52**, 172 (1985)
[8] S.B. Savage, "Granular flows down rough inclines – review and extension" in *Mechanics of Granular Material: New Models and Constitutive Relations*, edited by J.T. Jenkins and M. Satake (Elsevier, Amsterdam, 1983).
[9] S.B. Savage, "The mechanics of rapid granular flows" in *Advances in Applied Mechanics*,
[10] K.G. Anderson and R. Jackson, J. Fluid Mech. **241**, 145 (1992).
[11] Savage S.B. and Lun C.K.K., J. Fluid Mech. **189**, 311-335 (1988).

VELOCITY PROFILES DURING GRANULAR AVALANCHES

Marc Rabaud*, Sylvain Courrech du Pont*, Philippe Gondret* and Bernard Perrin**
*FAST, Bât. 502, Campus Universitaire, 91405 Orsay Cedex, France
** LPMC de l'ENS, 24 rue Lhomond, 75431 Paris Cedex 05, France

Summary Instantaneous velocity profiles of grain motion during glass beads avalanches are obtained with a high speed camera and by Particle Image Velocimetry (PIV) in a rotating drum set-up. When the pile is seen from above the surface velocity profile is curved with a strong slip on the two lateral smooth walls. When observed from the side, the in-depth velocity profile at the wall is found exponential with a characteristic length of two grain diameters. These profiles are time resolved (1/250 sec.) and show that their shapes are determined as soon as the avalanches start. Velocity measurements are in good agreements with global flow rate measurement deduced from the pile angle decrease.

INTRODUCTION

Understanding the rheology of granular flows is a challenging problem. One of the tool is flow visualization, however visualization of flowing granular particles is usually restricted to the outer surfaces of the piles except when using limiting MRI techniques [1] or if one limits to 2D flow [2], [3]. In the present study of intermittent avalanche flow we show that one can be confident to the surface measurements to evaluate precisely the 3D profiles.

EXPERIMENTAL SET-UP

In order to observe successive avalanches a rotating drum set-up is used. Glass spheres of diameter $d = 1$ mm half fill an horizontal cylinder of diameter $D = 17$ cm and thickness $b = 25$ mm (Figure 1). The drum is put in rotation at a very slow rotation rate ($\Omega \sim 10^{-3}$ rpm) in order to observe well separate avalanches. The drum is then almost motionless during the avalanche. During an avalanche, the mean angle of the pile decreases of about 3 degrees from the maximum angle of stability to a minimum angle in about 1 second. A high speed digital camera (500 im/s) films the pile along the cylinder axis or from above. Two successive images are processed with a PIV software in order to obtain the in-plane velocity of the grains in a close vicinity of the cylinder axis (central part of the avalanches). More details on the experimental set-up can be found in Ref. [4]. In this experiment grains are large and moves in air so we can neglect any effect of the surrounding fluid on the avalanche dynamics [5]. The finite number b/d of grains in the width of the cell affect slightly the amplitude of the avalanches as described in Ref. [6].

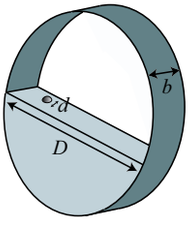


Figure 1. Scheme of the rotating drum.

INSTANTANEOUS VELOCITY PROFILES AND FLOW RATE EVALUATION

Figure 2 shows images from the side (a) and from above (b) of the grain pile together with the corresponding velocity profiles obtained by PIV and averaged on the image width.

At the lateral wall the velocity of the grains decreases rapidly below the free surface (Fig. 2a). The profile is very well fitted by an exponential with a characteristic length of the order of 2 bead diameters, and this at any time, from the very beginning to the final stop of the avalanches. No linear profile as described in Ref [2] is observed.

In the transverse direction (Fig. 2b) we observe an effect of the lateral glass wall: the velocity profile is curved, it presents a maximum in the middle plan and a large slip velocity on the boundaries. This profile can also be fitted by the sum of two exponential functions but experiments with larger gaps are necessary to demonstrate clearly this point.

The maximum velocity during an avalanche occurs in the middle plane and at the pile surface. This velocity increases progressively since the beginning of the avalanche then decreases during the second part of the avalanche. No permanent regime with constant velocity is observed in between. Typical value of the maximum velocity for the present set-up is 100 cm/s which corresponds in dimensionless form to a Froude number $u/\sqrt{gd} \approx 1$.

When the avalanche starts the profiles present very rapidly a self-similar shape and only the maximum velocity in surface or in the middle plan between the walls rescales the profiles.

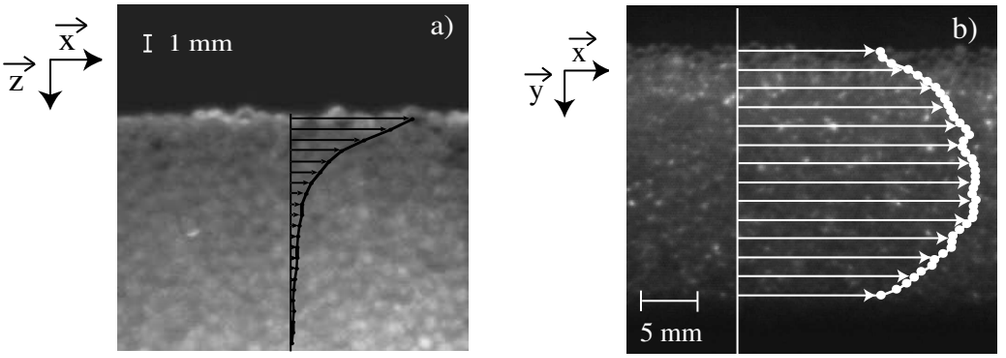


Figure 2. Images of the pile and corresponding instantaneous velocity profiles during an avalanche. (a) From the side at the front wall, (b) from above in between the walls.

From the previous measurement of the lateral and surface velocity profiles and assuming that no unexpected behavior occurs in the bulk of the avalanche, the 3D velocity profile can be written as:

$$u(y,z) = u_0(t)\ \exp(-z/\delta)\, f(y) \tag{1}$$

Integrating this profile in z and in y gives us the flow rate $Q_u(t)$ across the plane $x = 0$ perpendicular to the avalanche. This flow rate is plotted on Figure 3 as well as the macroscopic flow rate deduced from the time decrease of the pile angle θ during the avalanche and of the size of the set-up ($Q_\theta = \frac{D^2 b}{8}\,\dot{\theta}$). The agreement is excellent which indicates that the velocity profiles obtained at a lateral wall reflect well what occurs in the bulk of the avalanche.

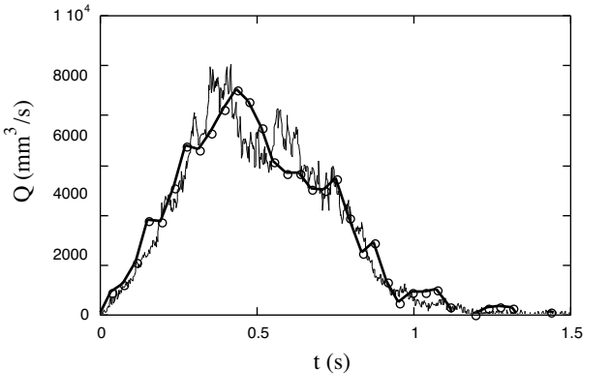


Figure 3. Time evolution of the avalanche flow rate Q based either on velocity profile (Q_u, thin continuous line) or on the time decrease of the macroscopic pile angle (Q_θ, thick line).

CONCLUSION

Velocity measurements of confined avalanches show that avalanches build an exponential velocity profile in the depth of the pile. This velocity field sets-up deeper and deeper during the flow, preserving the exponential shape. In the present set-up no saturation of the shear is observed contrary to others experiments with permanent flows [2], however it is possible that for larger set-up such linear profile near the surface would be observed even in the discrete regime of avalanche.
Furthermore we here demonstrate that flow rate measurements warrant the use of velocity fields observed at a wall to extrapolate the behavior of the grains in the bulk of a flow.

References

[1] Jaeger H.M., Nagel S.R., Behringer R.P.: Granular Solids, Liquids, and Gases. *Rev. Mod. Phys.* **68**: 1259, 1996.
[2] Bonamy D., Daviaud F., Laurent L.: Experimental study of granular surface flows via a fast camera: A continuous description. *Phys. Fluids* **14**:1666, 2002.
[3] Rachenbach J.: Granular Flows. *Adv. Phys.* **49**:229, 2000.
[4] Courrech du Pont S.: Avalanches granulaires en milieu fluide. *PhD Thesis, University Paris-XI* 2003.
[5] Courrech du Pont S., Gondret P., Perrin B., Rabaud M.: Granular avalanches in Fluid. *Phys. Rev. Lett.* **90**:044301, 2003.
[6] Courrech du Pont S., Gondret P., Perrin B., Rabaud M.: Wall effects on granular heap stability. *Europhys. Letters* **61**:492, 2003.

RADIALLY SYMMETRIC POLAR ICE SHEET FLOW WITH EVOLVING ANISOTROPIC FABRIC

Ryszard Staroszczyk*, Leslie W. Morland**
*Institute of Hydroengineering, Polish Academy of Sciences, ul. Waryńskiego 17, 71-310 Szczecin, Poland
**School of Mathematics, University of East Anglia, Norwich NR4 7TJ, United Kingdom

Summary A radially symmetric, gravity-driven, steady flow of a grounded polar ice sheet with a prescribed temperature field is considered. The ice is modelled as an incompressible, non-linearly viscous and anisotropic fluid with evolving orthotropic fabric. To describe the evolution of the fabric as an initially isotropic free surface ice descends to depth in an ice sheet, a constitutive law relating the deviatoric stress to the strain-rate and strain is applied. The solution is constructed as a leading order approximation derived from asymptotic expansions in a small parameter that reflects the small ratio of stress and velocity gradients in the longitudinal direction to those in the thickness direction. Results of calculations show the effects of a bed topography on the ice sheet thickness profile and the velocity components. Additionally, the influence of the temperature field and the free surface snow accumulation rates on the flow is illustrated.

EXTENDED SUMMARY

Ice cores retrieved from large polar ice caps in Antarctica and Greenland reveal strong anisotropic fabrics, with individual ice grain c-axes aligned along some preferential directions (Thorsteinsson *et al.*, 1997). These fabrics develop and evolve in the material in its response to changing stress and deformation states which ice experiences during its passage through the depth of an ice sheet. In current numerical models used to simulate the flow of polar ice sheets on geophysical scales the mechanism of evolving (induced) anisotropy is ignored and, for the sake of simplicity of the analysis, ice is treated as an isotropic material. In order to account for local changes in viscous properties of ice, resulting from its anisotropy, the material rheology is commonly described in terms of ad hoc adopted so-called enhancement factors for compression and shear (Budd and Jacka, 1989). In recent years, however, first attempts have been made to incorporate the ice fabric anisotropy in large polar ice sheet models, but so far they have essentially been restricted to the problems in which a flow field is determined for a given (that is observed in the field) fabric (Mangeney *et al.*, 1997). In this work we make a step further and consider a more general problem in which the effect of the flow field itself on the fabric formation and its subsequent evolution is also taken into account, so that the fabric determination constitutes an integral part of the problem solution.

We investigate a steady, radially symmetric, gravity-driven flow of a grounded ice sheet, with sliding conditions on the bedrock. A temperature field within the glacier is prescribed so that the mass and momentum balance equations are uncoupled from the energy balance equation. Ice is assumed to be an incompressible and non-linearly viscous fluid. The rheology of ice is described by an orthotropic constitutive law formulated in Staroszczyk and Morland (2001) and Morland and Staroszczyk (2003). This law, of an additive form to account for isotropic and anisotropic parts of the ice response, expresses the deviatoric stress in terms of the strain-rate, strain and three structure tensors based on the current (evolving) principal stretch axes, and involves two fabric response coefficient functions which determine the strength of the anisotropy. Furthermore, the strong effects of the temperature and the deviatoric stress magnitudes on the isotropic ice viscosity are taken into account.

In view of the complexity of the computations of the full model equations for a grounded ice sheet, the current application is based on a simplified *reduced model* (Morland, 1997) which exploits the large aspect ratio of polar ice masses, an approach known in theoretical glaciology as the 'shallow ice approximation' (Hutter, 1983). Hence, leading order balances are derived from asymptotic expansions in a small parameter (of a typical magnitude between 10^{-3} and 10^{-2}) which reflects the small ratio of the stress gradients and velocity components in the longitudinal direction to those in the thickness direction. The momentum balance equations are integrated through the ice thickness to eliminate one spatial coordinate, and an asymptotic analysis is carried out to determine a unique free surface slope at the sheet margin for a chosen form of a sliding law. Consequently, the problem is reduced to the solution of a second order parabolic differential equation for the ice sheet thickness profile, forming a two-point boundary-value problem to determine the free surface elevation of the ice sheet. In the case of isotropic ice this completes the solution of the problem. However, when the anisotropy of ice is involved, additional equations are required to account for changing properties of ice particles as they move from the free surface of an ice sheet to its depth. Thus, evolution equations of the hyperbolic type for five deformation gradient components involved are solved, adding substantially to the complexity of calculations. Results of numerical simulations show how the ice fabric changes within the ice sheet, from the isotropic fabric in the accumulation zone on the free surface of the glacier to strongly anisotropic fabrics in regions of high compression or shearing. Furthermore, the effects of the bed topography on both the ice sheet thickness profile (particularly on the ice sheet span) and the velocity and stress components are investigated. Also, comparisons for different temperature profiles and different forms of the functions defining the snow accumulation and ablation rates on the free surface of the glacier are carried out.

References

Budd W.F. and Jacka T.H. (1989) A review of ice rheology for ice sheet modelling. *Cold Reg. Sci. Technol.* **16** (2), 107–144.

Hutter K. (1983) *Theoretical Glaciology. Material Science of Ice and the Mechanics of Glaciers and Ice Sheets*. Reidel, Dordrecht.

Mangeney A., Califano F. and Hutter K. (1997) A numerical study of anisotropic, low Reynolds number, free surface flow for ice sheet modeling. *J. Geophys. Res.* **102** (B10), 22,749–22,764.

Morland L.W. (1997) Radially symmetric ice sheet flow. *Phil. Trans. R. Soc. Lond.* A **355**, 1873–1904.

Morland L.W. and Staroszczyk R. (2003) Stress and strain-rate formulations for fabric evolution in polar ice. *Continuum Mech. Thermodyn.* **15** (1), 55–71.

Staroszczyk R. and Morland L.W. (2001) Strengthening and weakening of induced anisotropy in polar ice. *Proc. R. Soc. Lond.* A **457** (2014), 2419–2440.

Thorsteinsson T., Kipfstuhl J. and Miller H. (1997) Textures and fabrics in the GRIP ice core. *J. Geophys. Res.* **102** (C12), 26,583–26,599.

XXI ICTAM, 15–21 August 2004, Warsaw, Poland

HYDRODYNAMIC INTERACTION OF A SPHERICAL PARTICLE IN POISEUILLE FLOW BETWEEN PLANAR WALLS

R. B. Jones*,
*Department of Physics, Queen Mary, University of London, Mile End Road, London E1 4NS, United Kingdom

Summary By using a two-dimensional Fourier representation of the Green tensor for Stokes flow between parallel walls, we calculate all friction and mobility functions for a single spherical particle moving between two walls subject to Poiseuille flow. The method readily generalises to N particles. For a channel narrow with respect to particle size, superposition of one-wall results is not an accurate approximation for the two-wall problem. Translation-rotation coupling is significant and changes its sign as the lateral position of the particle ranges across the channel. We illustrate these two-wall effects by calculating the trajectories of a magnetic colloid particle in Poiseuille flow subject to an external magnetic field.

INTRODUCTION

Hydrodynamic forces between particles play an important role in determining the dynamics of bulk suspensions of mesoscopic particles [1]. In addition to particle-particle forces, hydrodynamic interactions between particles and surrounding walls can play a significant role in sedimentation [2] and in the dynamics of bound particle clusters [3]. In recent years the development of optical tweezers and confocal microscopy has enabled one to measure directly some of the hydrodynamic interactions between one particle and a single wall [4] or between one particle and two parallel walls [5, 6] as well as hydrodynamic interactions between two particles in the presence of plane walls [7]. These experimental advances and the possibility of technological applications to biological sensors and catalysis based on mesoscopic particles flowing in suspension near walls means that there is need of a better understanding of particle-wall hydrodynamic interactions in channel flow.

TWO-WALL GREEN TENSOR

For a spherical particle near a single wall we have shown earlier that friction functions and mobilities may be calculated from the matrix elements with respect to a complete set of vector harmonics of the Green tensor for the Stokes flow equations in the presence of the wall [9]. Inversion and projection of this matrix gives the grand resistance matrix whose inverse defines the mobility matrix. The same formal scheme works also for two walls, however, the difficulty lies in obtaining a tractable form of the Green tensor. In earlier single wall studies we used an image technique [8, 9] to calculate the Green tensor. For two walls, the Green tensor has been obtained some time ago by a mixture of image methods and two-dimensional Fourier transformation [10]. More recently a scheme has been proposed which builds on the one wall image technique but involves infinite sums of images in the two walls [11]. By use of a two-dimensional Fourier representation without recourse to image summation we have obtained the exact Green tensor for Stokes flow between parallel walls in a representation which is much more symmetric than the earlier calculation [10].

ONE-PARTICLE FRICTION MATRIX

Our Fourier decomposition makes it possible to reduce to one-dimensional quadrature the calculation of all matrix elements of the Green tensor with respect to a complete set of vector harmonics. In obtaining this essentially exact result we derive exact formulae for a class of integrals which involve a scalar spherical harmonic weighted with a complex exponential function. By inversion of this Green tensor matrix followed by projection onto a finite dimensional space of low-order harmonics we obtain the grand resistance matrix for the spherical particle in the presence of the two walls. We determine the Cartesian form of the grand resistance matrix in the presence of an imposed Poiseuille flow between the two walls and relate the Cartesian representation to the harmonic representation. From the grand resistance matrix and its inverse we obtain all scalar friction and mobility functions for a single spherical particle between two walls and subject to an incident Poiseuille flow.

NUMERICAL CALCULATION

The numerical evaluation of the friction and mobility functions involves numerical integration followed by numerical matrix inversion. By comparison with the numerical boundary collocation calculations of Ganatos et al [12, 13] we show the rapid convergence of our scheme. We compare the exact two-wall result with the result for a single wall and with a superposition approximation. When the ratio of wall spacing to particle diameter is less than about five we find that simple superposition of single wall results is not an accurate approximation. The translation-rotation coupling changes sign as the lateral position of the particle ranges between the walls. We show the scalar translation-rotation friction function $\psi^{\mathrm{tr}}(R_z/a)$ below for a ratio of wall spacing to particle diameter equal to two. Here the two walls are located at $R_z = \pm W$ where R_z is the lateral distance of the sphere centre from the centre of the channel and a is the sphere radius.

APPLICATIONS AND CONCLUSIONS

From the friction and mobility functions we can carry out Stokesian dynamics studies of the trajectory of a particle in Poiseuille flow and subject to external fields. In particular, for polar particles subject to external electric or magnetic fields the translation-rotation coupling converts external torque into translational motion. We have studied this effect for a range of field strengths and field orientations. The single particle results are quite interesting in their own right but an important advantage of our method is that it can be generalized quite simply to N particles rather than to just one. For the many-particle problem we require matrix elements of the Green tensor between two centres rather than the same centre. The Fourier representation allows us again to reduce the calculation of all matrix elements to quadrature thus opening the way to N-body Stokesian dynamics studies of a suspension between two walls.

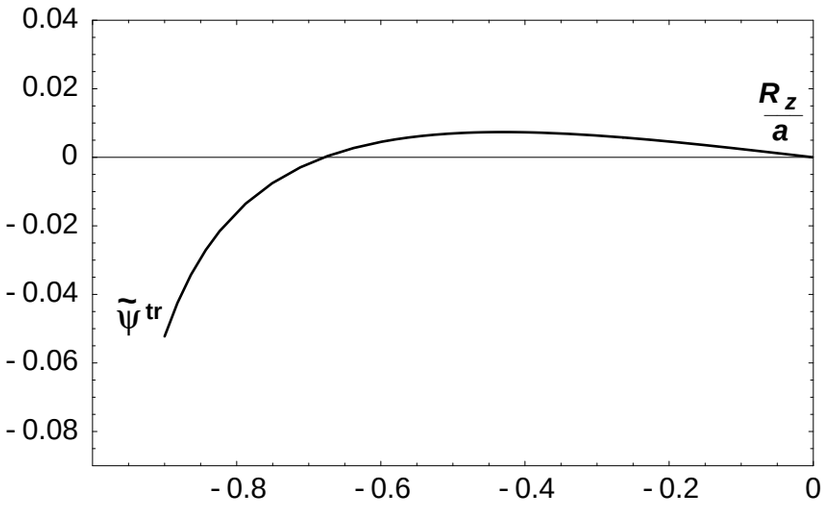


Figure 1. ψ^{tr} as a function of R_z/a for $W = 2a$ and $-0.9 \leq R_z/a \leq 0$.

References

[1] R. B. Jones and P. N. Pusey, Annu. Rev. Phys. Chem. **42**, 137 (1991).
[2] R. B. Jones and R. Kutteh, J. Chem. Phys. **112** 11080 (2000).
[3] R. B. Jones, J. Chem. Phys. **115**, 5319 (2001).
[4] K. H. Lan, N. Ostrowsky and D. Sornette, Phys. Rev. Lett. **57** 17 (1986).
[5] L. Lobry and N. Ostrowsky, Phys. Rev. B **53** 12050 (1996).
[6] Y. Grasselli and L. Lobry, Phys. Fluids **9** 3929 (1997).
[7] E. R. Dufresne, T. M. Squires, M. P. Brenner and D. G. Grier, Phys. Rev. Lett. **85** 3317 (2000).
[8] B. Cichocki and R. B. Jones, Physica A **258**, 273 (1998).
[9] B. Cichocki, R. B. Jones, R. Kutteh, and E. Wajnryb, J. Chem. Phys. **112**, 2548 (2000).
[10] N. Liron and S. Mochon, Journal of Engineering Mathematics, **10**, 287 (1976).
[11] S. Bhattacharya and J. Bławzdziewicz, J. Math. Phys. **43** 5720 (2002).
[12] P. Ganatos, S. Weinbaum and R. Pfeffer , J. Fluid Mech. **99** 739 (1980).
[13] P. Ganatos, R. Pfeffer and S. Weinbaum, J. Fluid Mech. **99** 755 (1980).

Two-layer stagnation point flows

M. G. BLYTH† and C. POZRIKIDIS††

† School of Mathematics, University of East Anglia, Norwich, NR4 7TJ, England, UK
†† Department of Mechanical and Aerospace Engineering, University of California, San Diego, La Jolla, California 92093-0411, USA

SUMMARY: Exact solutions of the Navier-Stokes equations are presented for orthogonal and oblique stagnation-point flow against a flat film resting on a plane wall.

We consider two-dimensional, orthogonal or oblique stagnation-point flow of a semi-infinite fluid with viscosity μ_1 and density ρ_1, against a liquid film with viscosity μ_2 and density ρ_2 resting on a plane wall, as depicted in figure 1. The interface between the two fluids is assumed to be and remain perfectly flat at all times. In the chosen system of coordinates the wall is located at $y = 0$, and the interface is located at $y = h(t)$, where $h(t)$ is the film thickness. The x and y velocity components are denoted by u_j, v_j respectively, where $j = 1$ (2) refers to the lower (upper) fluid.

First, we consider the case of orthogonal stagnation-point flow, wherein the angle β subtended between the incoming dividing streamline and the wall is $\beta = \pi/2$. Pozrikidis & Blyth (2004) showed that, in the limit of Stokes flow, the dividing streamline is straight, and the flow in the film is described by

$$u_1 = 2Gxy \quad v_1 = -Gy^2,$$

with corresponding pressure $p_1 = -(2\mu G + \rho_1 g)(y - h) + P_0(t)$, and the flow in the semi-infinite fluid is described by

$$u_2 = \frac{2G}{\lambda}\, x\, [y + h(\lambda - 1)], \qquad v_2 = -\frac{G}{\lambda}\, [y^2 + h(\lambda - 1)(2y - h)],$$

with corresponding pressure $p_2 = -(2\mu\, G + \rho_2 g)(y - h) + 4\mu h G(1 - \lambda) + P_0(t)$, where $G(t)$ is the strength of the stagnation-point flow, $P_0(t)$ is arbitrary, and $\lambda = \mu_2/\mu_1$ is the viscosity ratio. The Stokes-flow solution is valid when $Re \ll 1$, and breaks down sufficiently far from the origin. where $Re = rGh^2\rho/\mu$, with $r = (x^2 + y^2)^{1/2}$,

The solution at non-zero Reynolds numbers adopts a structure that is similar to that of the classical Hiemenz flow of a homogeneous fluid toward a plane wall. To begin, we write

$$u_j = x\, \frac{\partial f_j}{\partial y}, \qquad v_j = -f_j(y, t), \qquad p_j = x^2 P_j(t) + \phi_j(y, t), \tag{1}$$

where $P_j(t)$ are functions of time, t. Far from the wall, the flow matches the potential-flow solution $u = Gx$, $v = -Gy$, for constant G. Continuity of tangential and normal stresses must be satisfied at the interface, and the no-slip and no-penetration conditions are imposed at the wall. The kinematic condition at the interface yields an evolution equation for the film thickness $h(t)$, $\mathrm{d}h/\mathrm{d}t = -f_1(h)$. Substituting (1) in the Navier-Stokes equation and invoking the quasi-steady approximation to neglect the inertial time derivative on the left-hand side, we obtain a third-order ordinary differential

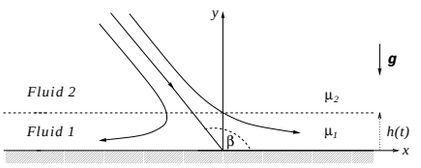


Figure 1: Planar two-fluid stagnation-point flow.

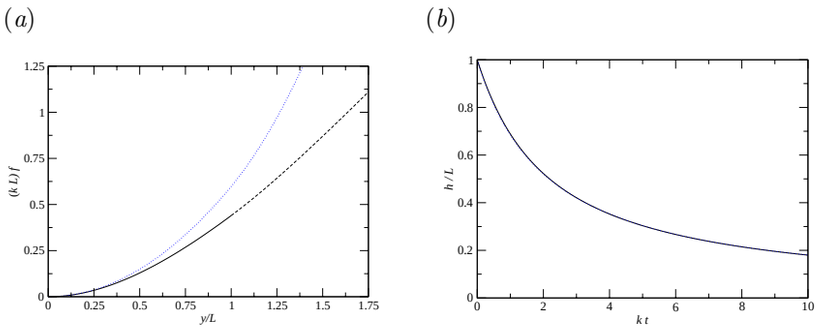


Figure 2: $\lambda = 0.5$, $h(0) = L = 1.0$: (a) The stream function $f_j(y)$ at $kt = 0$. The solid line corresponds to fluid 1, and the broken line corresponds to fluid 2. The dotted line is the Stokes solution. (b) $h(t)$ versus kt for the quasi-steady (solid line) unsteady (dotten line) solutions.

equation to be solved numerically for $f_1(y)$. Alternatively, restoring the unsteady term, we obtain a third-order partial differential equation, which is to be solved numerically for $f_1(y,t)$. Either way, once f_1 is known, the evolution equation for the film thickness may be integrated forward in time using a standard numerical method. Sample results are shown in figure 1.

Next, we consider the case of oblique flow, wherein the incoming dividing streamline makes an angle β with the wall, as shown in figure 2. For a homogeneous fluid, this problem was discussed by Stuart (1959) and Dorrepaal (1986). A solution valid for arbitrary Reynolds number may be sought by writing

$$u_1 = \frac{\partial g_1(y,t)}{\partial y} + x\,\frac{\partial f_1(y,t)}{\partial y}, \quad v_1 = -f_1(y,t), \quad p_1 = x^2 P_1 + x\pi_1(t) + \phi_1(y,t), \tag{2}$$

$$u_2 = \frac{\partial g_2(y,t)}{\partial y} + x\,\frac{\partial f_2(y,t)}{\partial y}, \quad v_2 = -f_2(y,t), \quad p_2 = x^2 P_2 + x\pi_2(t) + \phi_2(y,t), \tag{3}$$

where $g_j(y,t)$, $f_j(y,t)$, P_j, $\pi_j(t)$ and $\phi_j(y,t)$, $j = 1, 2$ are to be found. Conditions similar to those for orthogonal flow must be satisfied at the wall and at the interface. The kinematic condition at the interface yields an evolution equation for the film thickness, which is numerically integrated in time.

CONCLUSIONS

For both the orthogonal and oblique stagnation-point flow, exact solutions to the full Navier-Stokes equations are found in terms of ordinary and one-dimensional partial differential equations. The solutions are exact in the sense that no approximations are needed to simplify the full equations to their reduced form. Numerical simulations reveal that the quasi-steady approximation gives virtually indistinguishable results from the full unsteady calculations. Solutions of this type are also possible for axisymmetric flow.

References

[1] Dorrepaal, J. M.: An exact solution of the Navier-Stokes equation which describes non-orthogonal stagnation-point flow in two dimensions. *J. Fluid Mech.* **98**:161-169, 1986

[2] Pozrikidis, C. & Blyth, M. G.: Effect of stretching on interfacial stability. *Submitted to Acta Mechanica.*

[3] Stuart, J. T.: The viscous flow near a stagnation point when the external flow has uniform vorticity *J. Aero/Space Sci.* **26**: 124-125, 1959.

FREE SURFACE DEFORMATION IN SUSPENSIONS NEAR A ROTATING ROD

L. A. Mondy[*], R. R. Rao[*], M. Hopkins[*], and S. A. Altobelli[**]
[*]*Sandia National Laboratories, Albuquerque, NM USA*
[**]*New Mexico Resonance, Suite C1, 2301 Yale, Albuquerque, NM USA*

Summary Concentrated suspensions of solid spheres suspended in a Newtonian fluid are studied in a rotating concentric cylinder apparatus. Concentration profiles and the shape of the free surface are imaged using magnetic resonance. The experimental data are used to validate a three-dimensional finite element code, which incorporates both free surface models and a continuum constitutive equation for the suspension rheology.

INTRODUCTION

Continuum modelling of low Reynolds number suspension flows has progressed considerably in the last decade based on early work by Leighton and Acrivos [1,2] and Nott & Brady [3] Newer generations of these models capture the demixing of suspensions of spheres in a variety of one- and two-dimensional flows including torsional flows in parallel and cone-and-plate geometries [4,5]. Although there are arguments in favour of either of two main modelling approaches [6,5], the diffusive flux model [7] has the advantage in terms of computational speed. We have incorporated a model based on the diffusive flux arguments into a massively parallel, three-dimensional, general purpose, multi-physics, finite element computer code developed at Sandia, GOMA [8]. In addition to solving the coupled heat and momentum transport equations, GOMA supports fully coupled free- and moving-boundary parameterization, making it ideal for manufacturing process modeling. In order to validate the treatment of free-surface problems involving suspensions, we have studied the free surface near a rotating rod, in a classic "rod climbing" experiment. Experimental data was taken with magnetic resonance imaging, which allows the visualization of suspended particle concentration profiles as well as detailed views of the free surface profile. Concentrated suspensions of up to 50% by volume of uniform spheres were subjected to a variety of rod rotation rates. Results showed good agreement between model and experiment. The results show that the interface dips near the rotating inner rod, in agreement with earlier studies [9], and that our model captures this normal-stress induced behavior.

EXPERIMENTS

Nuclear magnetic resonance (NMR) measurements were performed at 1.9 T in an Oxford horizontal bore superconducting magnet with a clear bore diameter of 310 mm, using a custom-made linearly driven RF birdcage probe tuned to the ^{1}H frequency of 80.35 MHz, and a TecMag Libra spectrometer (TecMag Inc, Houston, TX, USA). The suspensions consisted of polymethyl methacrylate (PMMA) spheres nominally 100 microns in diameter suspended in a Newtonian viscous oil. The suspending oil was made to match the density of the particles at 21 ^{o}C. The fluid consisted of a solution of potassium iodide (KI) salt (Fischer Chemical, Inc) in water mixed with UCON ^{TM} 90,000, a poly-alkylene glycol (Union Carbide Corporation). The fluid produces an NMR signal, whereas the PMMA particles do not; therefore, the particle concentration can be measured quantitatively. Figure 1B shows a typical series of images obtained for a suspension of 50% by volume of solids with the inner rod rotating at 20 rpm. The upper left image depicts the initial condition before the motor attached to the rod is started. Each image is an average of the results over the time it takes to make the image (about 4.5 minutes), and images were taken back to back. The method allows some temporal resolution of the formation of the downward curvature of the interface.

MODEL

A diffusive-flux transport model for particle volume fraction, modified to include anisotropy using a flow-aligned tensor, is used [10]. This tensor is based on a local decomposition of the fluid velocity field into principal flow directions (flow, velocity gradient, and vorticity) and causes anisotropic particle migration. The constitutive equation is implemented in a Navier-Stokes solver based on the Galerkin/finite element method [8], and the problem is solved using a two-dimensional (axisymmetric) geometry with a (swirling) velocity component in the third dimension. A unique feature of the code is the treatment of free interfaces (position unknown) using an Arbitrary-Lagrangian-Eulerian formulation. Figure 1C shows results for a suspension of 50% by volume of 100 micron spheres, at early times during the development of the interface shape.

CONCLUSIONS

A finite element solution to the coupled transport equations using a diffusive-flux-based suspension constitutive equation modified to allow anisotropic diffusion does well in predicting the free surface deformation near a rotating rod due to normal stresses.

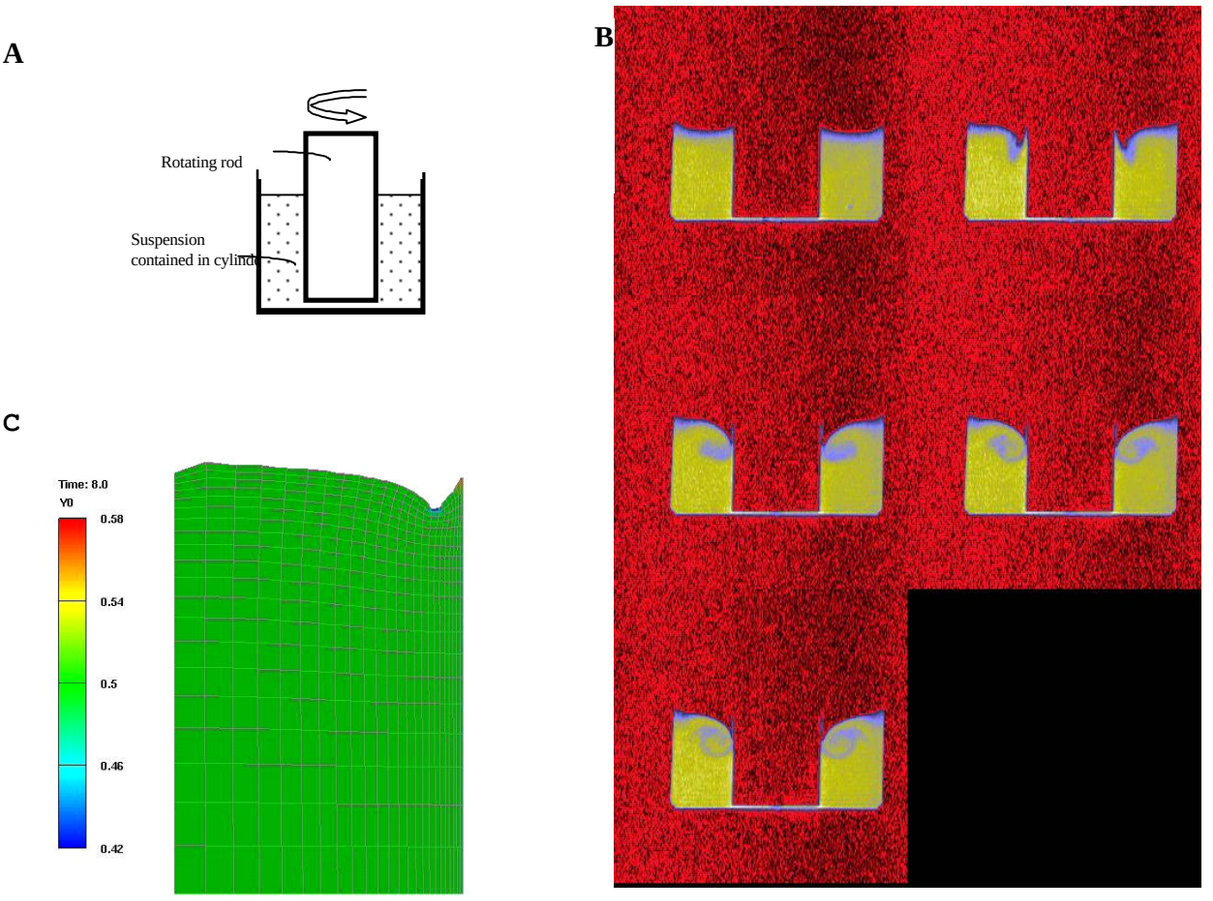


Figure 1. (A) Sketch of rotating rod apparatus. (B) NMR slices of the time evolution (left to right, top to bottom) of suspension liquid concentration. The rotating rod does not produce a signal, so only the suspension is seen. (C) Calculation of half of the domain corresponding to the early time data pictured in (B).

References

[1] Leighton, D., Acrivos, A.: Measurement of Shear-Induced Migration of Particles in Concentrated Suspensions. *J. Fluid Mech.* **177:**109-131, 1987.

[2] Leighton, D., Acrivos, A.: The Shear-Induced Migration of Particles in Concentrated Suspensions. *J. Fluid Mech.* **181:**415-439, 1987.

[3] Nott, P. R., Brady, J. F.: Pressure-Driven Flow of Suspensions: Simulation and Theory. *J. Fluid Mech.* **275**:157-199 (1994).

[4] Morris, J. F., Boulay, F.: Curvilinear Flows of Noncolloidal Suspensions: The Role of Normal Stresses. *J. Rheology* **43**:1213-1237, 1999.

[5] Fang, Z., Mammoli, A., Brady, J. F., Ingber, M. S., Mondy, L. A., Graham, A.L.: Flow-Aligned Tensor Models for Suspension Flows. *Int. J. Multiphase Flow* **28**:137- 166, 2002.

[6] Zarraga, I. E., Leighton, D. T.: Normal stress and diffusion in a dilute suspension of hard spheres undergoing simple shear. *Phys. Fluids* **13**:565-577, 2001.

[7] R. J. Phillips, Armstrong, R. C., Brown, R. A., Graham, A. L., Abbott, J. R.: A Constitutive Equation for Concentrated Suspensions that Accounts for Shear-Induced Particle Migration. *Phys. Fluids A*, **4**: 30-40, 1992.

[8] Schunk, P. R., Sackinger, P. A., Rao, R. R., Chen, K. S., Cairncross, R. A., Baer, T. A., Labreche, D. A.: "GOMA 2.0," Sandia National Laboratories, SAND97-2404, 1997.

[9] Zarraga, I. E., Hill, D. A., Leighton, D. T.: The Characterization of the Total Stress of Concentrated Suspensions of Noncolloidal Spheres in Newtonian Fluids. *J. Rheol*. **44**:185-220, 2000.

[10] Hopkins, M. M., Mondy, L. A., Rao, R., Altobelli, S. A., Fang, Z., Mammoli, A. A., Ingber, M. S.: Three-Dimensional Modeling of Suspension Flows with a Flow-Aligned Tensor Model. Proceedings of the Pacific Rim Rheology Conference, Vancouver, BC, CANADA July 2001.

XXI ICTAM, 15–21 August 2004, Warsaw, Poland

PARTICLES LOCATED ON A PLANAR FREE-SURFACE – HYDRODYNAMIC INTERACTIONS IN QUASI-TWO-DIMENSIONAL SYSTEM

Bogdan Cichocki*, Maria L. Ekiel-Jeżewska**, Gerhard Nägele***, Eligiusz Wajnryb**
*Institute of Theoretical Physics, Warsaw University, Hoża 69, 00-681 Warsaw, Poland
**Institute of Fundamental Technological Research, Polish Academy of Sciences, Świetokrzyska 21, PL 00-049 Warszawa, Poland
***Institut für Festkörperforschung, Forschungszentrum Jülich, IFF, Weiche Materie, D-52425 Jülich, Germany

Summary The friction and mobility matrices are constructed for a quasi-two-dimensional system consisting of spherical particles, which are suspended in a quiescent fluid and which touch a planar free surface. For such a system, the one-sphere resistance operator is calculated numerically. Moreover, the long-distance leading terms of the two-sphere mobility matrix are evaluated up to the order of $1/R^3$, where R is the interparticle distance.

INTRODUCTION

The dynamics of mesoscopically large colloidal particles suspended in a viscous fluid is strongly influenced, in addition to direct interparticle forces, by fluid-mediated hydrodynamics interactions [1]. In the past, research was mainly focused on the microhydrodynamics of three-dimensional bulk dispersions of particles. Meanwhile the center of interest has shifted to properties of colloids near boundaries like a single hard wall, colloids close to a clean or surfactant-covered fluid-fluid interface. In such systems, the particle dynamics is more complicated in comparison to an unbounded bulk suspension, since additional fluid boundary conditions have to be satisfied. Of particular interest are so-called quasi-two-dimensional dispersions, where the particles are confined to move along liquid-gas interfaces [2, 3]. A well-studied example of such a dispersion is given by micron-sized super-paramagnetic colloidal spheres suspended in water next to a water-air interface [4, 5, 6, 7]. By means of an experimental hanging-drop geometry, the spheres are gravitationally confined to lateral motion along the interface. For a quantitative description of particle diffusion in this magnetic model system, it is necessary to know precisely the lateral hydrodynamic mobility tensors of the spheres in presence of the liquid-gas interface. The mobility tensors are thus an essential input in theoretical and Brownian dynamics simulation studies of in-plane diffusion and microstructure.

In this work, we provide a general method to determine the low-Reynolds-number hydrodynamic interactions for such quasi-two-dimensional systems. In particular, we show how to construct the friction and mobility tensors for particles moving along a planar free surface. We give explicit numerical results for the single sphere mobilities in such a system. Finally, we evaluate the long-distance leading terms of the two-sphere quasi-two-dimensional mobility matrix, up to the order of $1/R^3$, where R is the interparticle distance.

THEORETICAL METHOD

The fluid in the half-space is described by the Stokes equations [1], with the free-surface boundary conditions at the planar interface and the stick boundary conditions at the surfaces of the spheres immersed in the fluid. To solve them, the corresponding Green operator, constructed by the method of images is used [8], and expansion in irreducible multipole functions [9] is applied. The mobility matrix is constructed as the multiple scattering series [10].

The essential contribution of this work is the reformulation of the scheme outlined above [8] in the special context of spheres, which touch the interface. In this case, to treat properly the lubrication effects and to avoid a spurious divergence, the symmetry of the system (inherent to the free-surface condition at the planar boundary) has been included into the new multipole functions. To evaluate them explicitly, the displacement theorems from Ref. [11] have been used.

RESULTS

Due to the lubrication forces, a sphere at the interface has only three degrees of freedom: translation along the plane and rotation around the axis perpendicular to it. Therefore the quasi-two-dimensional N-particle mobility is a 3Nx3N tensor, which determines the particle translational and angular velocities, $U_{ix}, U_{iy}, \Omega_{iz}$, for given forces and torques, $\mathcal{F}_{ix}, \mathcal{F}_{iy}, \mathcal{T}_{iz}$, with i=1,...,N. The coordinate system shown in Fig. 1, with z-axis perpendicular to the free surface, and x-axis and y-axis parallel to it.

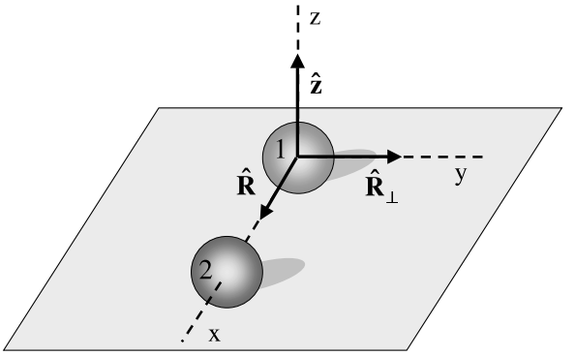


Figure 1. The system of coordinates used to describe the particles at the planar interface.

Single sphere mobilities

The quasi-two-dimensional one-sphere mobility tensor is given as

$$\boldsymbol{\mu}_F = \begin{pmatrix} \mu_F^{tt} & 0 & 0 \\ 0 & \mu_F^{tt} & 0 \\ 0 & 0 & \mu_F^{rr} \end{pmatrix}, \tag{1}$$

with $\mu_F^{tt} = 1.3799554\,/\,(6\pi\eta a)$ and $\mu_F^{rr} = 1.10920983\,/\,(8\pi\eta a^3)$.
These coefficients are equal to the inverse of the drag and turn coefficients for two touching spheres, calculated in Ref. [12] as 1.3801 and $4\,/\,\zeta(3)\,/\,3 = 1.1092098301\ldots$, respectively.
The method developed in this work allows to evaluate numerically with a high precision also other coefficients, which determine the reaction of a single sphere on an external ambient fluid flow.

Two-sphere mobility tensor for large interparticle distance

The quasi-two-dimensional mobility tensor for two spheres is determined by 3x3 Cartesian tensors $\bar{\boldsymbol{\mu}}_{11}$ and $\bar{\boldsymbol{\mu}}_{12}$, which are specified by the relation,

$$\begin{pmatrix} U_{1x} \\ U_{1y} \\ \Omega_{1z} \end{pmatrix} = \bar{\boldsymbol{\mu}}_{11} \begin{pmatrix} \mathcal{F}_{1x} \\ \mathcal{F}_{1y} \\ \mathcal{T}_{1z} \end{pmatrix} + \bar{\boldsymbol{\mu}}_{12} \begin{pmatrix} \mathcal{F}_{2x} \\ \mathcal{F}_{2y} \\ \mathcal{T}_{2z} \end{pmatrix}. \tag{2}$$

The long-distance leading terms of the mobility tensor are given as $\bar{\boldsymbol{\mu}}_{11} = \boldsymbol{\mu}_F + o(1/R^3)$ and

$$\bar{\boldsymbol{\mu}}_{12} = \mu_0^{tt} \left[\frac{1}{R} \begin{pmatrix} \frac{3}{2} & 0 & 0 \\ 0 & \frac{3}{4} & 0 \\ 0 & 0 & 0 \end{pmatrix} - \frac{1}{R^3} \begin{pmatrix} 1.159862... & 0 & 0 \\ 0 & 0.111686... & 0 \\ 0 & 0 & 0 \end{pmatrix} \right] + \frac{\mu_0^{rt}}{4R^2} \begin{pmatrix} 0 & 0 & 0 \\ 0 & 0 & -1 \\ 0 & 1 & 0 \end{pmatrix} - \frac{\mu_0^{rr}}{8R^3} \begin{pmatrix} 0 & 0 & 0 \\ 0 & 0 & 0 \\ 0 & 0 & 1 \end{pmatrix}, \\ + \quad o(1/R^3), \tag{3}$$

where R is the dimensionless interparticle distance, normalized by the particle diameter. Note that x-axis is along versor $\hat{\mathbf{R}}$, parallel to the line of sphere centers, and y-axis is along the perpendicular versor $\hat{\mathbf{R}}_\perp$, as depicted in Fig. 1.

References

[1] Kim S., Karrila S.J.: Microhydrodynamics: Principles and Selected Applications. Butterworth-Heinemann, London, 1991.
[2] Pesché R., Kollmann M., Nägele G.: *J. Chem. Phys.***114**:114, 2001.
[3] Nägele G., Kollmann M., Pesché R., Banchio A.: *Mol. Phys***100**:2921, 2002.
[4] Zahn K., Mendez-Alcaraz J. M., Maret G.: *Phys. Rev. Lett.***79**:175, 1997.
[5] Rinn B., Zahn K., Maass P., Maret G.: *Europhys. Lett.***46**:537, 1999.
[6] Zahn K., Maret G.: *Phys. Rev. Lett.***85**:3656, 2000.
[7] Kollmann M., Hund R., Rinn B., Nägele G., Zahn K., König H., Maret G., Klein R., Dhont J.K.G.: *Europhys. Lett.***58**:919, 2002.
[8] Cichocki B., Jones R.B., Kutteh, R., Wajnryb E.: *J. Chem. Phys.***112**:2548, 2000.
[9] Schmitz R., Felderhof B.U.: *Physica A***113**:90, 1982.
[10] Felderhof B.U.: *Physica A***151**:1, 1988.
[11] Felderhof B.U., Jones R.B.: *J. Math. Phys.* **30**:339, 1989.
[12] Jeffrey D.J., Onishi Y.: *J. Fluid Mech.* **139**:261, 1984.

MICROCAVITATION AND DETACHMENT OF A STOKES PARTICLE IN NEAR-WALL SLOW MOTION

A.N.Prokunin

A near-wall slow motion of a solid spherical particle along the wall in a fluid is studied experimentally. In the theoretical study of such motion within the Stokes approximation [1], the following paradox was revealed: no motion of a smooth heavy particle in contact with a plane wall is possible because the particle hydrodynamic drag is infinite and contactless motion is also impossible due to the absence a hydrodynamic lift. In [1], a number of possible factors which could remove this inconsistency were listed: fluid inertia (Magnus force), surface roughness, shear elasticity of the fluid, anomalous viscosity at high pressures or shear rates, cavitation, violation of the no-slip condition on rigid surfaces, disjoining pressure, etc.

The present experimental study motivated by [1] and aimed at clarifying the paradox was preformed for a spherical particle rolling down along an inclined wall of a tube in a quiescent fluid under the action of gravity (see fig). P is the particle weight in a fluid. We used highly viscous fluids, such as silicone and glycerin, and particles with various densities. The particle diameter d ($\geq$ 1 mm) was much greater than the particle surface roughness (not shown in fig.) which, in turn, was much greater than the wall roughness. At fixed d, different particle surface roughnesses were considered. The particle traveled at constant translational velocity u and angular velocity Ω. The inclination angle of the wall α to the horizontal was variable.

It was shown that, for fairly small roughnesses and fairly large α, the particle can travel without contact with the wall under the action of a lift force F_n different from the Magnus force. The gap h between the particle and the wall attained several micrometers. For fairly high roughnesses, the particle traveled in contact with the wall for all values of α. The influence of roughness on particle motion in contact with the wall was considered in [2,3].

In contactless motion of the particle, we observed a cavity (single microbubble) formed directly behind the particle in the particle-wall gap.

The existence of the cavity results in the onset of a lift force F_n according to the following mechanism. Without taking the cavitation into account [1], directly behind the particle in the lubrication layer in the particle–wall gap a negative pressure can arise, while ahead of the particle the pressure is positive. Such pressure distribution gives zero lift force exerted on the particle. When a bubble is formed, that prevents the occurrence of negative pressures, a lift force appears (see fig).

We demonstrated experimentally that contactless motion of the particle depends on static (atmospheric) pressure P_s and surface tension σ for the fluid-air system. These facts also indicate the existence of cavitation and the related lift force. Using the data on the shape of the cavity, we found nondimensional parameters related with P_s and σ and determining nondimensional particle velocities. The existence of such dependencies was verified experimentally.

CONCLUSION

The new hydrodynamic effect was registrered and explained: a slow contactless motion of a spherical particle along a wall with the formation of a particle—wall clearance due to a lift force of cavitation nature.

REFERENCES

1. Goldman A.J., Cox R.G., Brenner H. Chem. Eng. Sci. 1967. V.22. N4. p. 637.
2. Smart J.R., Beimfohr S., Leighton D.T. Phys. Fluids A. 1993.V5.N1.p13.
3. Calvin K.P., Zhao Y., Davis R.H. Phys. Fluids. 2001. V13. N11.p3108.

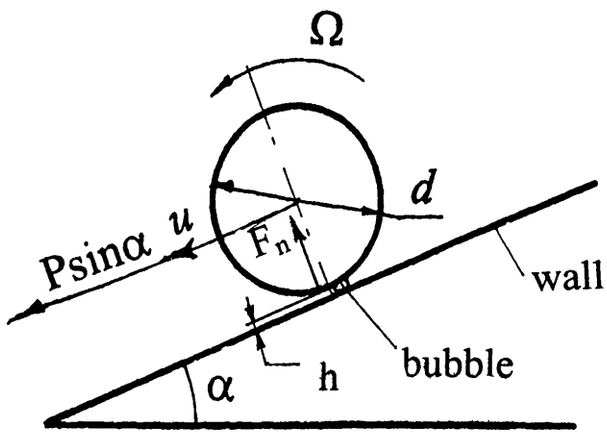


Fig.

FLOW VISUALIZATION EXPERIMENTS OF CELLULAR STOKES FLOWS INDUCED BY ROTATION OF A CYLINDER VARIOUSLY POSITIONED INSIDE CHANNELS

Emin Fuad Kent
Istanbul Technical University, Department of Thermodynamics, 34437, Gumussuyu, Istanbul, Turkey

Summary In this work, flow visualization experiments of cellular Stokes flows induced by rotation of a circular cylinder variously positioned inside channels of different shapes have been performed. Flow visualization experiments have been carried out inside wedge-shaped and rectangular channels. High quality visualization photographs have been presented. The inner cylinder is positioned at different locations inside these channels and many interesting flow patterns have been visualized. The shape of the separating streamline and recirculating eddies are clearly seen and compared for the channels.

INTRODUCTION

Many problems of physical interest involve the flow of fluids at low Reynolds numbers. This type of flow is encountered in many practical application, cited in [1]-[3]. The purpose of the present investigation is to perform flow visualization experiments of cellular Stokes flows induced by rotation of a circular cylinder variously positioned inside channels of different shapes. In the experiments wedge-shaped and rectangular channels are filled with silicon rhodorsil oil of different viscosities (Newtonian fluid) and carboximetilcellulose (CMC) (non-Newtonian fluid). The motion is generated by the uniform rotation of a circular cylinder positioned at different locations inside these channels. Flow visualization experiments are carried out using solid tracers of magnesium for the Newtonian fluid and Rilsan for CMC. They are illuminated by a thin sheet of light coming from a laser device and the visualization photographs are obtained by means of long time exposure photography. A series of experiments have been performed at different rotational speeds varying from 3 rpm to 80 rpm and using silicon rhodorsil oil of viscosities 10 cm^2/s and 300 cm^2/s. Thus the Reynolds number of the flow, defined by $Re=(\omega_0 R_1^2)/\nu$, ranged between 0.001 and 0.84, have been obtained and high quality visualization photographs have been presented at these low Reynolds numbers. The shape of the separating streamline and recirculating eddies are clearly seen on these photographs and some quantitative data (the center of the recirculating eddies, the location of the separating streamlines) are deduced from these pictures. The inner cylinder is positioned at different locations inside these channels and many interesting flow patterns have been visualized.

EXPERIMENTAL RESULTS

In Figure 1, the visualization photographs for the centered and upper position of the cylinder are presented. The exposure times are 15 minutes and 90 minutes, respectively.

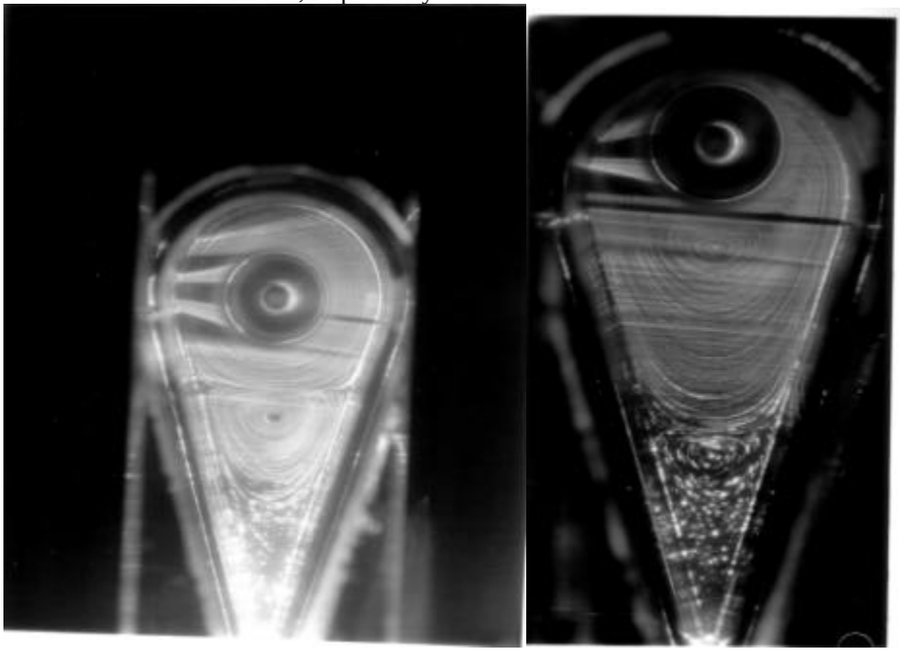


Figure 1- The visualization photographs for the exposure time of 15 (left) and 90 (right) minutes.

In Figure 2 (left) the cylinder is positioned 1 cm ahead along the axis towards the corner. At each side of the cylinder there is a cellular motion. On the right side of Figure 2 the cylinder is shifted 0.5 cm from the centered position towards the right wall.

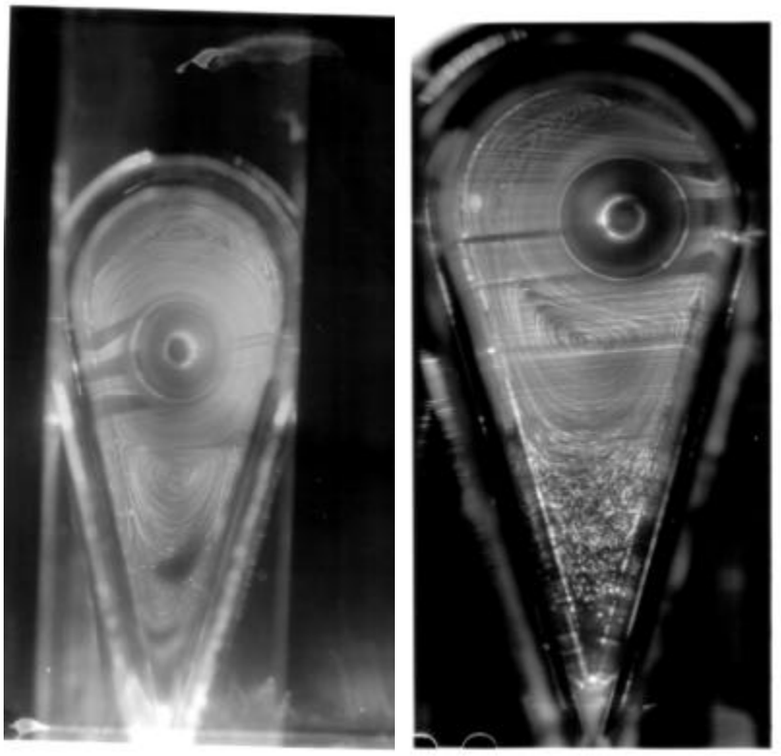


Figure 2- The visualization photographs for different positions of the cylinder.

The experiments are also performed in rectangular channels and compared with wedge-shaped channels. The shape of the separating streamline and recirculating eddies are clearly seen on these photographs and some quantitative data (the center of the recirculating eddies, the location of the separating streamlines, ect.) are deduced from these pictures. The experiments are also carried out with CMC fluid for comparison. The numerical solution of the problem is also obtained and compared with the corresponding visualization photographs. Excellent agreement is found between experimental and numerical results.

CONCLUSIONS

Flow visualization experiments of cellular Stokes flows induced by rotation of a circular cylinder variously positioned inside channels of different shapes have been performed. These experiments have been carried out inside wedge-shaped and rectangular channels and high quality visualization photographs have been presented. The inner cylinder is positioned at different locations inside these channels and many interesting flow patterns at low Reynolds numbers have been visualized. The shape of the separating streamline and recirculating eddies are clearly seen on these photographs and some quantitative data (the center of the recirculating eddies, the location of the separating streamlines) are deduced from these pictures and compared each other.

References

[1] Shen C, Floryan J.M.: Low Reynolds number flow over cavities. *Phys. Fluids* **28**:3191-3202, 1985.

[2] Higdon J.J.L.: Stokes flow in arbitrary two dimensional domains:Shear flow over ridges and cavities. *J. Fluid Mech* **159**:195-226, 1985.

[3] Rybicki A., Floryan, J.M.: Thermocapillary effects in liquid bridges. I Thermocapillary convection. *Phys. Fluids* **30**: 1956-1972, 1987.

Many-sphere hydrodynamic interactions: weak convective inertia effects

I. T. Pieńkowska

Institute of Fundamental Technological Research
Świętokrzyska 21, 00-049 Warsaw, Poland

The motivation for this work is to analyse the effects of weak convective inertia of the fluid on the many-body hydrodynamic interactions. We consider a finite number N of rigid spheres, held rigidly in the incompressible, viscous fluid, having a uniform velocity $\boldsymbol{U}$ at infinity. The paper deals with weak inertia effects, influencing the hydrodynamic forces $\boldsymbol{F}_j$, $j = 1,\ldots,N$, exerted by the fluid on the spheres, in the régime of small Reynolds numbers Re, based on the radius a of the spheres, the kinematic viscosity v of the fluid and the magnitude U of the fluid velocity. In particular, we will examine the violation, due to the inertia effects, of the Stokes symmetry, characterizing the Stokes many-body hydrodynamics interactions and the respective hydrodynamic forces, experienced by the spheres.

The range of the considered hydrodynamic interactions is specified by means of the following parameters:

(i) $\sigma = a/R$, where R is the typical distance between the centres of the spheres, $\sigma < ½$,

(ii) $\mathrm{Re} = aU/v$, $\mathrm{Re} < 1$.

The problem is considered on the basis of the Oseen equations. The presence of the spheres in the flow is taken into account by means of the so-called induced forces $\boldsymbol{f}_j$, distributed on the surfaces of the spheres. The velocity field of the fluid is expressed in terms of the integral equations, involving the inertia-dependent Green tensor. *U*sing the no-slip boundary conditions on the surfaces of the spheres, we have obtained a set of N integral equations, relating the induced forces $\boldsymbol{f}_j$ to the velocities $\boldsymbol{V}_j$ of the spheres with respect to the unperturbed fluid. The many-sphere hydrodynamic interactions are represented in terms of the multiple scattering processes. The multiple scattering events are described by means of the so-called self- and mutual interaction tensors, concerning, respectively, the hydrodynamic interactions of an individual sphere with the surrounding fluid, and the mutual interactions between two spheres. In terms of these interaction tensors, such properties of the hydrodynamic interactions, as the long range, non-locality, and non-additivity, are discussed.

The hydrodynamic forces $\boldsymbol{F}_j$ are obtained in the form of an infinite series, describing the allowed sequences of the hydrodynamic interactions. That series enables us to calculate the regarded forces within the assumed approximation with respect to the small parameters σ , and Re. We have distinguished different régimes of the hydrodynamic interactions and the resulting forces $\boldsymbol{F}_j$ for small, and respectively, large values of the parameter RU/ν (the interactions close to, and far from the Stokes conditions). As examples, we will consider the drag, and side forces, exerted on three spheres, placed in line, in the transversal and parallel directions with respect to $\boldsymbol{U}$.

We will apply the presented solutions to the Oseen boundary value problem to examine the analogous Navier-Stokes boundary value problem, at small data, in the sense of Finn (Robert Finn, ARMA **19**, 363 (1965)).

XXI ICTAM, 15–21 August 2004, Warsaw, Poland

VISCOUS EDDY STRUCTURES IN AN OSCILLATING CYLINDER WITH SHARP CORNERS

M. Branicki and H. K. Moffatt

Department of Applied Mathematics and Theoretical Physics,
University of Cambridge,
Wilberforce Road, Cambridge CB3 0WA, UK

Summary The two-dimensional, unsteady flow of a viscous fluid contained in a cylinder which is subjected to rotational oscillatory motion is considered. It is assumed that the cross-section of the cylinder has sharp corners. The problem is linearised assuming sufficiently small amplitude of oscillations - $\mathrm{Sr} \gg 1$ - and sufficiently large viscosity - $\mathrm{Re} \ll \mathrm{Sr}$. A sufficient condition for the appearance of oscillatory corner eddy structures is obtained.

We consider the two-dimensional motion of a viscous, incompressible fluid contained in an infinitely long cylinder whose cross-section D has sharp corners but is otherwise arbitrary. The flow is driven by rotational oscillations of the cylinder with angular velocity $\Omega = \hat{\Omega}\, e^{i\omega t}$. In the frame of reference rotating with the cylinder, the non-dimensionalised Navier-Stokes equation can be written as

$$\frac{\partial \nabla^2 \psi}{\partial t} - \mathrm{Sr}^{-1} \frac{\partial(\psi, \nabla^2 \psi)}{\partial(x, y)} - \mathrm{Re}^{-1} \nabla^4 \psi = i\, e^{it}\,, \quad \psi = \frac{\partial \psi}{\partial n} = 0 \ \text{ on } \ \partial D\,, \tag{1}$$

where the Poincaré-type force $\dot{\Omega} \sim i\, e^{it}$ provides a uniform rate of production of vorticity. In general, there are two independent parameters in the problem: the Strouhal number $\mathrm{Sr} = \omega / 2\hat{\Omega}$ which is the ratio of the frequency of oscillations ω and the amplitude of oscillations $\hat{\Omega}$, and the oscillatory Reynolds number defined as $\mathrm{Re} = L^2 \omega / \nu$, where L is the characteristic length of the cross-section D and ν is the fluid viscosity.

It is shown that for sufficiently large Strouhal number: $\mathrm{Sr} \gg 1$, $\mathrm{Re} \ll \mathrm{Sr}$, and for certain range of corner angles, there exist very interesting oscillatory eddy structures emerging from the corners. In particular, it is shown that infinite sequences of corner-eddy like structures are present in the instantaneous streamline patterns for N-sided regular polygonal cylinders, provided $3 < N < 11$. An examination of time-evolution of these structures reveals an intricate inertial mechanism of the flow reversal when the cylinder changes its direction of rotation. The appearance of corner eddies in steady Stokes flow problems was considered by Moffatt 1964a,b, 1979 and 1980. Recently, Shankar *et al* 2003 studied certain oscillatory eddy structures in a rectangular cavity with periodically moving lid. However, as regards the infinite sequence of corner eddies, no attempt to determine analytically their existence in an unsteady case was presented.

The presence of the oscillatory eddy structures is determined from separable solutions of the linearised equation (1), where the amplitude $\hat{\psi}$ of the stream function $\psi = \hat{\psi}(x, y)\, e^{it}$ satisfies the inhomogeneous equation

$$\nabla^2 \hat{\psi} - (i\mathrm{Re})^{-1} \nabla^4 \hat{\psi} = 1\,, \quad \hat{\psi} = \frac{\partial \hat{\psi}}{\partial n} = 0 \ \text{ on } \ \partial D\,. \tag{2}$$

The self-adjointness of (2) greatly simplifies derivation of the Green's function for some simple geometries, and allows, for example, for construction of a global solution in a rectangular domain which is of particular interest. For domains with more complex boundaries, determination of a global solution to (2) becomes very difficult, if not impossible. Therefore, the structure of local solutions near a corner is analysed through comparison of the 'driven' component of the flow and the eigenfunction ingredients of the corresponding homogeneous problem which are inevitably present. Using similar techniques to those described in Moffatt 1964a, it is determined that for corner angles α within the range of approximately $82^\circ < \alpha < 146^\circ$, an infinite sequence of corner eddies of decreasing size and rapidly decreasing intensity will be present in the instantaneous streamline pattern. For $\alpha > 146^\circ$ no such eddy structures exist. For $\alpha < 82^\circ$ there might still be a finite number of eddies, but their presence depends on conditions far from the corner, and cannot be determined from local analysis. Numerical simulations are used to investigate these cases.

Our poster will present more detailed analysis of the problem supported by extensive numerical simulations for various geometries of the boundary. Stirring properties of resulting flows will be also discussed.

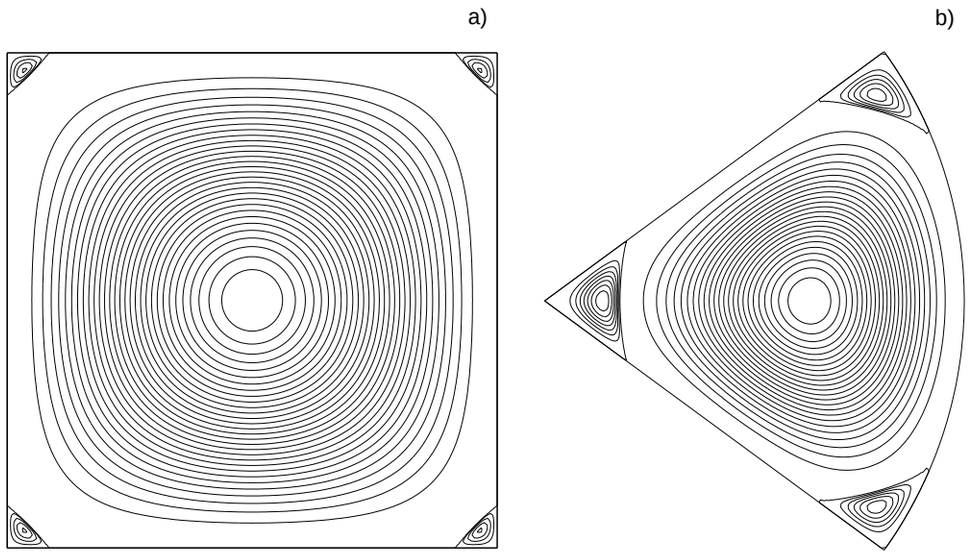


Figure 1. Oscillatory eddy structures in unsteady Stokes flows inside an inifinitely long cylinder subjected to rotational oscillatory motion (in the plane of the figure). Instantaneous streamline patterns are shown in a non-inertial frame oscillating with the cylinder for a) square cross-section, b) section of a circle. Contours represent isolines (not equidistant) of the time-periodic stream function $\Psi = \mathrm{Re}(\hat{\psi}e^{it})$ (see eqn (2)). Only the primary eddies are visualised. The location of the dividing streamlines $\Psi = 0$ changes in time and plays important role during the flow reversal. Streamline patterns for other geometries will be presented and analysed on our poster.

References

[1] Moffatt, H.K. 1964a Viscous and resistive eddies near a sharp corner. J. Fluid Mech. **18**, 1-18.
[2] Moffatt, H.K. 1964b Viscous eddies near a sharp corner. Arch. Mech. Stosowanej **16**, 365-372.
[3] Moffatt, H.K. 1979 The asymptotic behaviour of solutions of the Navier-Stokes equations near sharp corners. *Proc. IUTAM Symp. Approximation Methods for Navier-Stokes Problems. Lecture Notes in Mathematics*, Springer, no. 771,371-380.
[4] Moffatt, H.K. & Duffy, B.R. 1980 Local similarity solutions and their limitations. J. Fluid Mech. **96**, 299-313.
[5] Shankar, P.N. Kidambi, R. Hariharan, J. 2003 Oscillatory eddy structure in a container. J. Fluid Mech. **494**, 163-185.

TRANSIENT SQUEEZE FLOW OF VISCOPLASTIC LIQUIDS

G. Karapetsas, N. Chatzidai, M. Pavlidis, J. Tsamopoulos
Laboratory of Computational Fluid Dynamics, Department of Chemical Engineering, University of Patras, Greece

Summary We examine the axisymmetric squeeze-flow, under creeping flow conditions, of viscoplastic materials placed between two parallel disks using the continuous constitutive model suggested by Papanastasiou and, more recently, the discontinuous Bingham model. This is the first transient simulation of such liquids and allows us to also determine the shape of the liquid/air interface, initially located inside the disks, as it is displaced towards their edge or beyond it. We employ the mixed finite element method coupled with a quasi-elliptic mesh generation scheme in order to follow these large deformations. The material yields in part of the domain as the disks approach each other, departing from the corresponding Newtonian solution. Unyielded material arises around the two stagnation points of flow at the disk centers verifying previous steady state calculations. The unyielded region increases with the Bingham number, but decreases with time. If wall-slip is present, the unyielded region decreases significantly and may even totally disappear.

INTRODUCTION

Viscoplastic materials behave as rigid solids for low stress values, whereas beyond some critical value of stress, called yield stress, they flow with viscosity that depends on the local shear rate. The deformation and flow of such materials is becoming increasingly important, since many multicomponent fluids, such as suspensions, emulsions, paints, foodstuffs, foams, slurries and pastes, which are frequently encountered in industrial processes, are viscoplastic. A typical experiment in order to characterize such materials is squeeze flow, in which a fluid sample is squeezed between two parallel disks. Although several researchers have studied flows of viscoplastic liquids in the past, they restricted it to steady state models [1]-[4]. This is the first truly transient simulation of such liquids and allows us to determine the shape of the liquid/air interface which was impossible with the quasi steady state models. The purpose of this study is to determine the liquid/air interface as well as the unyielded regions that arise as a function of relevant parameters of the problem. To this end, we use the continuous constitutive equation that has been proposed by Papanastasiou for viscoplastic liquids [5] as well as the discontinuous original Bingham model [6].

PHYSICAL MODEL

Liquid is placed in the gap between two parallel disks (see figure). The liquid is viscoplastic of zero shear viscosity η_0 and density ρ. Initially the distance between the two disks is $2L$, the liquid is at rest, under constant pressure and the free surface is flat. For $t>0$ the disks approach each other with constant velocity V, displacing the liquid that exists between them. Scaling lengths with L, velocity with V the following dimensionless groups arise: the Reynolds number, $Re=\rho VL/\eta_0$ and the Bingham number, $Bn=\tau_y L/(\eta_0 V)$, where τ_y is the yield stress. The transient motion of the liquid within the disks is governed by the momentum-balance and the mass conservation law in their axisymmetric form. To determine the extra stress tensor we use the continuous model that has been proposed by Papanastasiou [5] for viscoplastic liquids.

$\underline{\underline{\tau}}=\left[\eta_o+\tau_y\frac{1-e^{-n\dot{\gamma}}}{\dot{\gamma}}\right]\underline{\underline{\dot{\gamma}}}$, where $\underline{\underline{\tau}}$ is the viscous part of the total stress tensor, $\underline{\underline{\dot{\gamma}}}$ is the rate of strain tensor, $\dot{\gamma}$ its second invariant and n a parameter. At large values of n the behavior of an ideal Bingham plastic is approached. As Burgos and Alexandrou [7] have mentioned extremely large values of n must be avoided. In order to determine the unyielded regions the criterion that was used is that fluid yields when the second invariant of the extra stress tensor $\left\|\underline{\underline{\tau}}\right\|$ is larger than the yield stress, $\left\|\underline{\underline{\tau}}\right\|\geq\tau_y$. These equations are subject to the usual boundary conditions on the velocity field. In particular, the velocity field is bounded at the axis and plane of symmetry. At the disk surface the fluid is assumed either to stick on it or wall slip is introduced via a parameter β (the no-slip condition results when $\beta\to\infty$). Along the free surface, the velocity field satisfies a balance between viscous stresses, surface tension and gaseous pressure.

NUMERICAL APPROACH

In order to solve these equations, we have chosen the mixed finite element method to discretize the velocity and pressure fields, together with a system of quasi-elliptic partial differential equations, capable of generating a boundary-fitted finite element discretization of the transient domain occupied by the liquid [8], [9]. The latter is an essential part of our method for capturing the large deformations of the free surface. We approximate the velocity vector with

biquadratic Lagrangian polynomials whereas the pressure and position vector with bilinear ones. The set of differential algebraic equations that arises is integrated using the backward Euler method, preceded by a forward Euler step in order to predict the new solution and then adjust the time step to optimize code performance. The resulting set of equations is solved by a Newton-Raphson/Non-linear Gauss-Seidel (Picard) iteration scheme for separately solving the flow from the mesh generation equations until convergence.

RESULTS

The figure depicts the domain between the upper disk and the plane of symmetry, from the axis of symmetry on the left side to the disk edge. In this example the liquid initially fills completely the space between the disks. Even from the very beginning of the motion of both disks towards the plane of symmetry the viscoplastic material yields everywhere, except for the area around the stagnation points of the flow. The figure also shows contour lines of the axial velocity component in the displaced viscoplastic liquid for $Bn = 100, Re = 0, \beta = 10^5, \varepsilon = 0.1$, where ε is the aspect ratio, $\varepsilon = L/R$. The snapshots correspond to dimensionless times t=0, t=0.2, t=0.4. We observe that the axial velocity u_z has its smallest (negative) values near the upper disk and monotonically increases towards zero at the plane of symmetry. At the axis of symmetry it remains equal to the velocity of the upper disk up to a point fairly close to the plane of symmetry because of the unyielded region that exists there. The size of this region decreases as time passes, because the correspondingly decreased distance between the disks generates a more intense shear field near r=0. In the process, material moves radially outward and emerges outside the domain between the disks while it undergoes apparent "extrudate swelling". Indeed, as the material exits the disks, it experiences smaller and smaller stresses becoming "frozen" and, thus, it retains the thickness it had at the instant it exited and before the disks moved further towards each other. The unyielded region decreases as ε or Bn decrease or the slip on the disk wall increases.

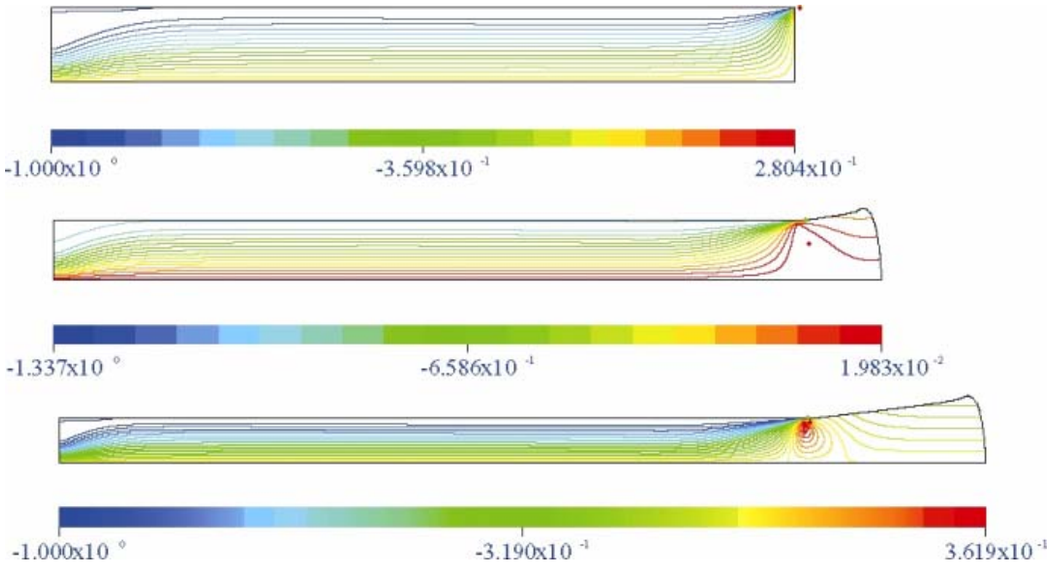


Figure Liquid/air interface shape and contour lines of axial velocity component at t=0, t=0.2, t=0.4 for $Bn = 100, Re = 0, \beta = 10^5, \varepsilon = 0.1$.

References

[1] Smyrnaios D. N., Tsamopoulos J. A., "Squeeze flow of Bingham plastics", J. Non Newtonian Fluid Mech. **100** (2001) 165-190

[2] O'Donovan, E.J., and Tanner, R.I., 'Numerical study of the Bingham squeeze film problem', J. Non-Newt. Fluid Mech., **15**, 75-83 (1984)

[3] Matsoukas A., Mitsoulis E., "Geometry effects in squeeze flow of Bingham plastics", J. Non Newtonian Fluid Mech. **109** (2003) 231-240

[4] Jay, P., Magnin, A., and Piau, J.M., 'Viscoplastic fluid flow through a sudden axisymmetric expansion', AICHE J., **47** (10), 2155-2166 (2001).

[5] Papanastasiou T. C., "Flows of materials with yield", J. Rheol. **36** (1992) 389-407

[6] Bingham, E.C., 'Fluidity and Plasticity', McGraw-Hill (1922)

[7] Burgos G. R. & Alexandrou A. N., "On the determination of yield surfaces in Herschel-Bulkley fluids", J. Rheol**. 43(3)** (1999) 463-483

[8] Dimakopoulos Y. & Tsamopoulos J.A., "Transient displacement of a viscoplastic material by air in straight and suddenly constricted tubes", J. Non Newtonian Fluid Mech. **112** (2003) 43-75

[9] Dimakopoulos Y., Tsamopoulos J.: A quasi-elliptic transformation for moving boundary problems with large anisotropic deformations, J. Comp. Phys., **192**: 494-522, 2003c.

Slow Rotation of a Double Sphere in a Viscous Fluid

D. Palaniappan
Texas A&M University at Qatar, c/o Qatar Foundation, PO Box 5825, Doha, Qatar

Estimating the couple acting on a solid suspended in a viscous fluid is a well-known old problem in hydrodynamics. As explained in the literature, the analytical treatments for such boundary value problems become quite cumbersome for nonspherical bodies owing to their complex geometrical structures. In fact, there is no standard method available todate which could yield solutions for a body of arbitrary profile. Despite this fact, several closed form analytic solutions have been discovered during the last 150 years (see for instance [1]). Although the modern computing schemes could handle a variety of problems, it is of important to have convincing results to support and test the relevent numerical codes. Here, we provide an exact closed form solution for a nonspherical body rotating in Stokesian fluid.

We consider two spheres of radii 'a' and 'b' centered at positions A and B respectively. The two spheres overlap and intersect at an angle $\frac{\pi}{n}, n$ an integer. The distance 'c' between the centers is $c = \left[a^2 + b^2 + 2ab\cos\frac{\pi}{n}\right]^{1/2}$. The composite geometry consisting of two overlapping spheres is called a 'double sphere'. Let A_j, B_j be the successive inverse points lying along the line joining the centers. The first point A_1 is the image of B in sphere A and B_1 is the image of A in sphere B etc. The distances $a_j = AA_j$ and $b_j = BB_j$ satisfy the recurrence relations $a_j = \dfrac{a^2}{c - b_{j-1}}$, $b_j = \dfrac{b^2}{c - a_{j-1}}$ with initial values $a_0 = b_0 = 0$. For the angle of intersection $\frac{\pi}{n}$, with n an integer, one can prove that [2] $a_{n-1} + b_{n-1} = c$. In this case the image points A_{n-1} and B_{n-1} coincide. It can be further shown that the distances A_jP and B_jP (P is the vertex) can be expressed in terms of a_j and b_j by

$$A_jP = \left[a_j^2 + \frac{b^2 - a^2 - c^2}{c}a_j + a^2\right]^{1/2}, \qquad B_jP = \left[b_j^2 + \frac{a^2 - b^2 - c^2}{c}b_j + b^2\right]^{1/2} \tag{1}$$

Let r, r' denote the distances of an arbitrary point with A and B as origins respectively. Similarly, let r_j, r'_j denote the distances of the same point with A_j and B_j as origins. The surface of the double sphere is composed of spheres A and B defined by $r = a$ and $r' = b$, respectively.

It is known that for the axial rotation of an axisymmetry body the function $\Psi(R, \phi, z) = v_\phi(R, z)\sin\phi$, where v_ϕ is the tangential component of velocity, satisfies the Laplace equation $\nabla^2\Psi = 0$. The corresponding boundary value problem is well documented elsewhere [3] and therefore we omit the details here. We now exploit the fact that for a sphere rotating about a diameter in a Stokesian fluid the image is just a rotlet/couplet, the Green's function for rotational flow, located at its center. For two spheres A and B the similar rotation produces two rotlets at their centers. The successive reflections of each rotlet on either sphere generates a series of rotlets on the line of centers and for the vertex angle $\frac{\pi}{n}$, by a direct computation it can be demonstrated that, the resulting series is finite. The final solution for the tangential velocity component reads

$$v_\phi(R, z) = -\omega R\left\{\frac{a^3}{r^3} + \frac{b^3}{r'^2} - \sum_{j-1}^{n-1}{}'(-1)^{j+1}\left[\frac{A_jP^3}{r_j^3} + \frac{B_jP^3}{r'^3_j}\right]\right\}. \tag{2}$$

where $r^2 = R^2 + z^2$ etc. and the prime on the summation indicates that the last term must be divided by 2. It is evident that the image system consists of rotlets of strengths -ωa^3, -$\omega b^3, (-1)^{j+1}\omega A_jP^3$ and $(-1)^{j+1}\omega B_jP^3$ located at A, B, A_j and B_j respectively. The distances A_jP and B_jP may be calculated by the use of the relation (1). The image rotlets also depend on the magnitude of the angular velocity ω. It is now straightforward to extract an expression for the torque/couple from the singularity solution (2), which

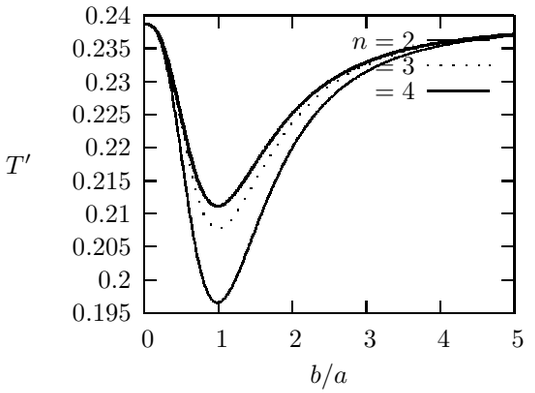


Figure 1: The reduced couple $T' = \frac{T}{8\pi\mu\omega(V_a+V_b)}$ versus b/a for different vertex angles.

is given by

$$T = 8\pi\mu\omega \left[a^3 + b^3 - \sum_{j=1}^{n-1}{}' (-1)^{j+1}(A_j P^3 + B_j P^3) \right]. \tag{3}$$

For $b = 0$, the above expression yields the familiar Kirchhoff's result for an isolated sphere rotating in a viscous fluid. For larger n it can be shown numerically that (3) approaches the value for two touching spheres. The reduced torque $T' = \frac{T}{8\pi\mu\omega(V_a+V_b)}$ (V_a and V_b are the volumes of the spheres A and B) is plotted against the radii ratio b/a in Fig.1 for various vertex angles. It is readily seen that the reduced torque decreases for $b/a < 1$ until it reaches its minimum value. For the values $b/a > 1$, it increases gradually till it becomes a constant. It may be noted that the contact angle has significant influence on the minimum value of the reduced torque. Now, it is not difficult to show that the quantity $\frac{T}{8\pi\mu\omega V_a}$ is always $\geq$ unity. In view of this, it may be conjectured that

$$V_a \leq \frac{T}{8\pi\mu\omega} \leq V_a + V_b$$

The above inequality gives the upper and lower bounds for the torque experienced by the double sphere rotating in a viscous fluid. It should be mentioned that for arbitrary vertex angle, the problem is solved by the use of toroidal coordinates [3] in terms of complicated Mehler conal functions. The corresponding expression for the torque is also given as a quadrature. Our method clearly avoided the use of such special functions and indeed our results could be used to examine those quadratures. Needless to say that the present approach may conveniently be extended to solve other swirling flow problems involving intersecting spheres and their interaction with other particles; however the use of toroidal coordinates method for such flow problems remains to be explored. It is worthmentioning that the results provided here may be useful in validating the numerical algorithms for merging objects [4] in electrostatic as well as in microfluidic environments.

References

[1] C. Pozrikidis, Boundary integral and singularity methods for linearized viscous flow. *Cambridge University press* (1992)

[2] B.U. Felderhof, and D. Palaniappan, Electrostatic capacitance of two unequal overlapping spheres and rate of diffusion-controlled absorption. *J. Appl. Phys.*, **86** 6501-6506 (1999).

[3] J.C. Schneider, M.E. O'Neill and H. Brenner, On the slow viscous rotation of a body straddling the interface between two immiscible semi-infinite fluids. *Mathematika*, **20**, 175-196 (1973)

[4] M.L. Mansfield, J.F. Douglas and E.J. Garboczi, Intrinsic viscosity and the electrical polarizability of arbitrarily shaped objects. *Phys. Rev. E*, **64**, 061401 (2001).

MIGRATION AND INTERACTION OF TWO CONDUCTING PARTICLES FREELY IMMERSED IN A LIQUID METAL

Antoine Sellier
LadHyX, Ecole Polytechnique, 91128 Palaiseau Cédex, France

Summary We determine the rigid-body motions of two solid and conducting particles freely immersed in a liquid metal and subject to uniform ambient electric and magnetic fields. The advocated procedure resorts to a very few boundary-integral equations on the surface of the cluster and circomvents to calculate the electric field and the liquid flow in the unbounded fluid domain. The implemented numerical strategy will be presented together with the numerical results for several two-particle clusters.

MOTIVATIONS AND AIMS

Any solid and conducting particle freely suspended in a liquid metal of uniform conductivity $\sigma_l > 0$ and viscosity μ migrates when subject to uniform ambient electric and magnetic fields $\mathbf{E}$ and $\mathbf{B}$ (Kolin, 1953). Since this phenomenon may receive applications in impurities removal it is worth to determine the translational and angular velocities $\mathbf{U}$ and $\mathbf{\Omega}$ of a particle of prescribed but arbitrary shape and uniform conductivity $\sigma \geq 0$. Whilst a sphere of radius a admits the simple motion (Leenov & Kolin 1954)

$$\mathbf{U} = \frac{\sigma_l(\sigma - \sigma_l)}{3(\sigma + 2\sigma_l)} \frac{a^2}{\mu} (\mathbf{E} \wedge \mathbf{B}) \quad \text{and} \quad \mathbf{\Omega} = \mathbf{0} \tag{1}$$

non-spherical particles in general translate not necessarily parallel to $\mathbf{E} \wedge \mathbf{B}$ and rotate (Moffatt & Sellier 2002; Sellier 2003a, 2004). Because clusters may occur in practice it is also of interest to look at the challenging case of two close (and therefore interacting) particles $\mathcal{P}_1$ and $\mathcal{P}_2$ of uniform conductivity σ_1 and σ_2, respectively. In this direction the boundary formulation established for a single particle in Sellier (2004) has been recently extended to the case of two *insulating spheres* (Sellier 2003b). The present work shows how to cope with the general case of two *conducting and arbitrary-shaped* particles by solely solving a very few boundary-integral equations on the entire surface of the cluster.

GOVERNING EQUATIONS AND ADVOCATED STEPS

We consider, as sketched in figure 1, two solid and conducting particles $\mathcal{P}_1$ and $\mathcal{P}_2$ freely suspended in a Newtonian liquid metal of uniform viscosity μ and conductivity $\sigma_l > 0$.

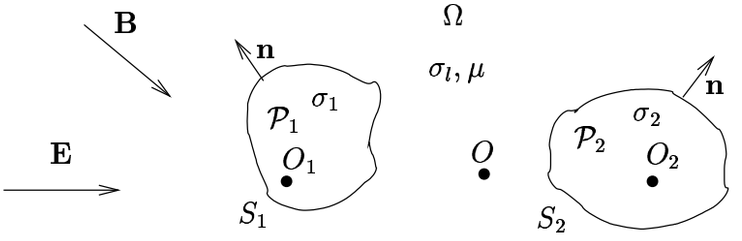


Figure 1. Two solid, conducting and arbitrary-shaped particles $\mathcal{P}_1$ and $\mathcal{P}_2$.

The particle $\mathcal{P}_n$ (n=1,2) has uniform conductivity $\sigma_n \geq 0$ and smooth boundary S_n. We denote by O_n a point attached to $\mathcal{P}_n$ and by $\mathbf{n}$ the unit outward normal on the entire surface $S = S_1 \cup S_2$. The two-particle cluster disturbs the ambient electric field $\mathbf{E}$. More precisely, in $\mathcal{P}_n$ and in the liquid domain Ω the electric field is $\mathbf{E} - \nabla\phi_n$ and $\mathbf{E} - \nabla\phi$, respectively. The unknown functions ϕ_n and ϕ obey the well-posed problem

$$\nabla^2\phi = 0 \ \text{ in } \ \Omega, \ \ \nabla^2\phi_n = 0 \ \text{ in } \ \mathcal{P}_n, \ \ \nabla\phi \to \mathbf{0} \ \text{ as } \ OM \to \infty \tag{2}$$

$$\sigma_l(\mathbf{E} - \nabla\phi).\mathbf{n} = \sigma_n(\mathbf{E} - \nabla\phi_n).\mathbf{n} \ \text{ and } \ \phi = \phi_n \ \text{ on } \ S_n \ \text{ for } \ n = 1, 2. \tag{3}$$

Under the same physical assumptions of Moffatt & Sellier (2002) the liquid experiences a quasi-static creeping flow described by its velocity and pressure fields $\mathbf{u}$ and p such that

$$\nabla.\mathbf{u} = 0, \ \ \mu\nabla^2\mathbf{u} = \nabla p - \sigma_l(\mathbf{E} - \nabla\phi) \wedge \mathbf{B} \ \text{ in } \ \Omega, \tag{4}$$

$$(\mathbf{u}, p) \to (\mathbf{0}, \sigma_l[\mathbf{E} \wedge \mathbf{B}].\mathbf{OM}) \ \text{ as } \ OM \to \infty, \ \ \mathbf{u} = \mathbf{U}^{(n)} + \mathbf{\Omega}^{(n)} \wedge \mathbf{O_nM} \ \text{ on } \ S_n \tag{5}$$

with $\mathbf{U}^{(n)}$ the velocity of O_n and $\mathbf{\Omega}^{(n)}$ the angular velocity of $\mathcal{P}_n$. Since our particles are freely immersed in the liquid we finally supplement (2)-(5) with the additional conditions (taking into account the Lorentz body force inside each particle)

$$\sigma_n \int_{\mathcal{P}_n} (\mathbf{E} - \nabla\phi_n) \wedge \mathbf{B} dv + \int_{S_n} \boldsymbol{\sigma}.\mathbf{n} dS = \mathbf{0} \quad \text{for} \quad n = 1, 2, \tag{6}$$

$$\sigma_n \int_{\mathcal{P}_n} \mathbf{O_n M} \wedge [(\mathbf{E} - \nabla\phi_n) \wedge \mathbf{B}] dv + \int_{S_n} \mathbf{O_n M} \wedge (\boldsymbol{\sigma}.\mathbf{n}) dS = \mathbf{0} \quad \text{for} \quad n = 1, 2 \tag{7}$$

with $\boldsymbol{\sigma}$ the usual stress tensor associated to the liquid flow $(\mathbf{u}, p)$.

Of course, for arbitrary-shaped particles $\mathcal{P}_1$ and $\mathcal{P}_2$ one needs to solve (2)-(7) by a numerical method. At the very first glance, one may also think about determining the unknown rigid-body motions $(\mathbf{U}^{(1)}, \boldsymbol{\Omega}^{(1)})$ and $(\mathbf{U}^{(2)}, \boldsymbol{\Omega}^{(2)})$ by appealing to the following steps (i)-(iii):

(i) Obtain ϕ_n in $\mathcal{P}_n$ and ϕ in Ω by solving (2)-(3).

(ii) Use the previously computed functions ϕ_n and ϕ to deduce the flow $(\mathbf{u}, p)$ solution to (4)-(5) for arbitrarily prescribed values of $(\mathbf{U}^{(1)}, \boldsymbol{\Omega}^{(1)})$ and $(\mathbf{U}^{(2)}, \boldsymbol{\Omega}^{(2)})$.

(iii) Finally, determine the rigid-body motions so that (6)-(7) hold through an iterative procedure appealing to the key step (ii).

Unfortunately, the fluid domain is unbounded and this prevents us from accurately achieving the key steps (i)-(ii) at a reasonable cpu time cost even by using a standard Finite Element solver.

In this work we therefore advocate and present a quite different approach that is free from the above drawbacks. The established procedure circumvents to calculate the functions ϕ_1, ϕ_2, ϕ and the liquid flow $(\mathbf{u}, p)$ in the unbounded fluid domain Ω. It rests on the use of adequately selected boundary-integral equations on the entire surface S of the cluster and permits us to compute the rigid-body motion of two arbitrary-shaped conducting particles at a reasonable cpu time cost. For conciseness, we only describe in this extended abstract the main steps of the work. These steps are:

1) We first establish a whole boundary formulation of the problem, i. e. show how it is indeed possible to obtain the rigid-body motion of each particle by solely solving boundary-integral equations on S.

2) For distant particles such that $\epsilon = (a_1 + a_2)/O_1O_2 \ll 1$ with a_n the length scale of $\mathcal{P}_n$ we asymptotically obtain each rigid-body motion in terms of the small parameter ϵ. This is achieved by appealing to the derived boundary formulation and permits us to quantify the very first correction to the motion of isolated particles.

3) For close particles the asymptotic solutions obtained in Step 2) are not valid any more and we therefore give and implement a suitable numerical strategy to numerically solve each encountered boundary-integral equation.

4) Finally, we present and discuss numerical results for a few two-sphere clusters of equal or inequal spheres for several settings $(\mathbf{E}, \mathbf{B})$ and $(\sigma_1/\sigma_l, \sigma_2/\sigma_l)$.

References

[1] KOLIN A.: An electromagnetokinetic phenomenon involving migration of neutral particles *Science*, **117**, 134–137, 1953.

[2] LEENOV D.,KOLIN A.: Theory of electromagnetophoresis. I. Magnetohydrodynamic forces experienced by spherical and symmetrically oriented cylindrical particles. *J.Chem.Phys.*, **22**, 683–688, 1954.

[3] MOFFATT H. K., SELLIER A.: Migration of an insulating particle under the action of uniform ambient electric and magnetic fields. Part 1. General theory. *J. Fluid Mech.***464**, 279–286, 2002.

[4] SELLIER A.: Migration of an insulating particle under the action of uniform ambient electric and magnetic fields. Part 2. Boundary formulation and ellipsoidal particles. *J. Fluid Mech.***464**, 335–353, 2003a.

[5] SELLIER A.: On particle-particle interactions in impurities removal. 4^{th} International Conference on Electromagnetic Processing of Materials. Lyon, France. 14-17 October 2003b.

[6] SELLIER A.: Migration of an insulating particle under the action of uniform ambient electric and magnetic fields. Part 3. Case of a conducting particle and numerical results. Submitted to *J. Fluid Mech.* 2004.

Extended summary of the proposed ICTAM2004 lecture V. Shtern 7 October 2003

BIFURCATION OF CONICAL MAGNETIC FIELDS

Vladimir Shtern

University of Houston, TX 77204-4006, USA

1. Introduction. According to "anti-dynamo" theorems [1, 2], the axisymmetric dynamo is impossible. This result seems paradoxical because observed magnetic fields are nearly axisymmetric as for stars and planets [3] so for cosmic jets erupting from active galaxy nuclei [4]. The paradox was bypassed in two ways. Braginsky showed that even a slight asymmetry is sufficient for the dynamo to occur [2]. Another bypass is that a flow being unsteady and three-dimensional at small scales can generate a nearly steady and axisymmetric large-scale magnetic field [3].

In contrast to these bypasses, the present study deals with exactly axisymmetric steady states and shows that a magnetic field appears in a magnetic-free conical flow via a pitchfork bifurcation. This seemingly contradicts to the anti-dynamo" theorems, however, there is no contradiction indeed as conditions of the theorems do not hold for conically similarity flows.

Conical similarity is a feature of a wide family of solutions of the Navier-Stokes equations. This family includes the Schlichting, Landau, and Squire swirl-free round jets, the Long swirling, thermal convection near a point source of heat and gravity [5], and many other flows.

Streamlines and magnetic lines are open in a conical flow: they go to and from infinity or the singularity point. This feature is crucial as Cowling [1] emphasized that his anti-dynamo theorem is not applicable for a flow with open lines. Also, the proof by Braginsky [2] based on the condition that the magnetic induction, **H**, decays at infinity as r^{-3} or faster is not applicable to conical flows where both **H** and **v** decay weaker being proportional to r^{-1}; r is the distance from the flow origin.

Thus, on one hand, the theorems do not rule out a possibility of dynamo occurrence in conical flows. On the other hand, an MHD bifurcation in a conical flow can be not necessarily interpreted as dynamo.

2. Reduction to ODDE. An advantage of the conical similarity is the reduction of governing equation to ordinary differential equations (ODE) that radically eases the analysis.

The conical similarity means that

$$\{v_r,v_\theta,v_\phi\} = \nu r^{-1}\{u,u/\sin\theta,\Gamma/\sin\theta\},\ T = T_\infty + \gamma r^{-1}\vartheta,$$

$$p=p_\infty+\rho_\infty\nu^2 r^{-2}q,\ \{H_r,H_\theta,H_\phi\} = h\nu r^{-1}\{R,\Theta/\sin\theta,\Phi/\sin\theta\}, \quad (1)$$

where p is pressure, T is temperature, $\{v_r,v_\theta,v_\phi\}$ and $\{H_r,H_\theta,H_\phi\}$ are the velocity and magnetic field components in spherical coordinates $\{r,\theta,\phi\}$ (Fig. 1), ρ is density, ν is viscosity, h is a scale constant, and γ characterizes the heat flux from the origin. Dimensionless functions u,u,Γ,ϑ, q, R, Θ, and Φ depend only on $x = \cos\theta$.

Suppose that a point source of gravity is located at the coordinate origin and neglect self-gravitation of the ambient fluid. This yields that the acceleration due to gravity is $\mathbf{g} = -\mathbf{e}_r\,\delta/r^2$. Here $\mathbf{e}_r$ indicates the outward radial direction, and δ characterize the strength of **g**. We apply the Boussinesq approximation, $\rho/\rho_\infty = 1-\beta(T-T_\infty)$, β is the coefficient of thermal expansion.

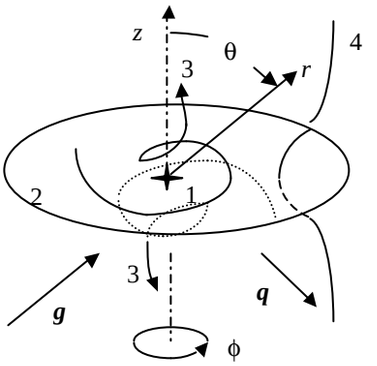


Figure 1. Schematic of a flow near a point source 1 of gravity ***g*** and heat flux ***q*** with accretion plane 2. Typical stream 3 and magnetic 4 lines are shown.

Substituting (1) reduces the MHD equations [1] to:

$$(1-x^2)\psi'+2x\psi-\tfrac{1}{2}\psi^2 = F-\Theta^2/2, \quad (2a)$$
$$(1-x^2)F''' = Ra\,\psi\vartheta+2\Gamma\Gamma'-2\Phi\Phi', \quad (2b)$$
$$(1-x^2)\Gamma'' = \psi\Gamma'-\Theta\Phi', \quad (2c)$$
$$(1-x^2)\vartheta' = Pr\,\psi\vartheta, \quad (2d)$$
$$(1-x^2)\Theta'' = Bt(\psi\Theta'-\psi'\Theta), \quad (2e)$$
$$(1-x^2)\Phi''=Bt[\psi\Phi'-\Theta\Gamma'+2(\psi'\Phi-\Theta'\Gamma)+ 2x(\psi\Phi-\Theta\Gamma)/(1-x^2)], \quad (2f)$$

where $\psi = -u$ ($u = -\psi'$, $R = \Theta'$); $Ra = \beta\gamma\delta/(\kappa\nu)$, $Pr = \nu/\kappa$, and $Bt = \nu/\nu_m$ are the Rayleigh, Prandtl, and Batchelor numbers, respectively; κ and ν_m are the thermal and magnetic diffusivities.

3. MHD bifurcation in the bipolar swirling jet. At Ra=0, consider a *vortex*-sink motion prescribed on the accretion plane (2 in Fig. 1), i.e., the boundary conditions at $x = 0$ are: $u = Re_p$, $u = 0$, and $\Gamma = Re_s$, where Re_p and the swirl Reynolds number, Re_s, characterize the accretion and vortex strengths. The velocity on the axis is bounded if $\psi=F=F\ell=\Gamma=0$ at $x = 1$.

The magnetic field must satisfy the conditions, $\Phi(0)=\Theta'(0)=0$ (symmetry) and $\Phi(1)=\Theta(1)=0$ (regularity).

This problem has a solution with $\Theta=\Phi\equiv 0$, that describes a swirling flow that converges (for $Re_p < 0$) to the axis near the disk and goes away from the origin along the axis (curve 3 in Fig.1). As the accretion ($-Re_p$) increases, a magnetic field appears via the pitchfork bifurcation, as Fig. 3 shows. The abscissa, $Al^{1/2}=0$, is the axis of plot symmetry and solutions with $Al^{1/2}>0$ and $Al^{1/2}<0$ have just opposite direction of the magnetic field; *Al* is the magnetic-to-kinetic energy ratio on the disk

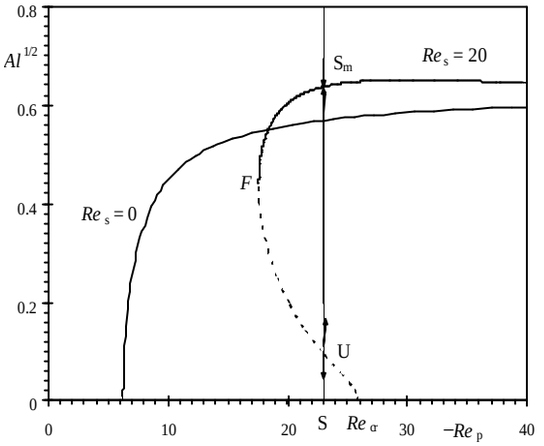


Figure 2. Bifurcation of magnetic field in a vortex-accretion flow.

We see that the MHD bifurcation is supercritical in a swirl-free ($Re_s=0$) flow and becomes subcritical when the swirl is sufficiently strong (e.g. at $Re_s=20$). Arrows show the time-evolution direction of a disturbed magnetic field. The presence of fold point *F* means that as the accretion increases and decreases, transformations between magnetic-free and MHD states occur via hysteretic transition in a flow with a strong swirl.

4. MHD bifurcation in the buoyancy flow. Now consider a bipolar outflow that develops via onset of thermal convection [5]. It appears that not only the convection, but also a magnetic field bifurcates in a converging-to-the-axis flow as Fig. 3 shows at $Bt = 0.18$. Line E corresponds to the equilibrium state of rest. At point *T* ($Ra = 24$), the trans-critical bifurcation of convection occur. No MHD bifurcation occurs in the diverging flow (lower inset and curve *La* at $\psi_{min}<0$). The converging flow (upper inset) is unstable (broken curve *FT*). As ψ_{max} reaches 4 (at fold point *F*), the jet velocity becomes unbounded and the fluid-sink singularity develops on the axis. In this singularity flow (curve *Tu*), the MHD (supercritical pitchfork) bifurcation occur at point *B*. In the MHD flow (curve *MT*), the magnetic field grows, consumes the kinetic energy, and suppresses the sink singularity at point *L* as *Ra* increases.

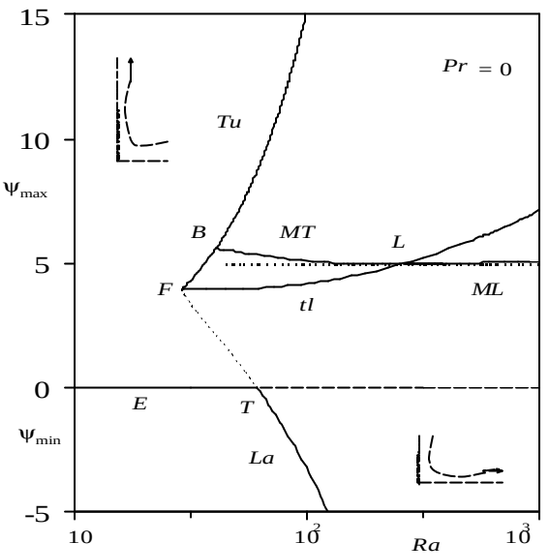


Figure 3. Bifurcations in a buoyancy flow.

Curve *tl* is a boundary between regular (below) and singular (above) flow states. Curve *ML* corresponds to a regular MHD flow. It is interesting that this solution branch is remote from other regular flow states.

5. Conclusions. This study has shown that self-sustained magnetic fields can develop via bifurcation in jet-like flows. A necessary condition for the MHD bifurcation is the presence of accretion in a flow. In the swirl-free accretion flow, the self-induced magnetic field eventually (as $-Re_p$ increases) suppresses the bipolar jet, but the jet can remain strong in the vortex-accretion flow (§3). In the buoyancy-induced flow (§4), the jet remains strong even in s swirl-free MHD state. Thus, our results reveal that the bifurcation of magnetic field is typical of jet-like flows and, therefore, can contribute to the development of long-range magnetic fields in cosmic jets as well.

[1] Cowling, T. G. 1957 *Magnetohydrodynamics*. New York, Interscience.

[2] Braginsky, S. I. 1964 Self-excitation of magnetic field during the motion of a highly conducting fluid. *Sov. Phys. JETP* **48**, 1084-1098.

[3] Moffat, H. K. 1978 *Magnetic field generation in electrically conducting fluids.* Cambridge University Press.

[4] Ferrari A. 1998 Modeling extragalactic jets. *Annu. Rev. Astron. Astrophys.* 36, 539-598.

[5] Shtern, V. & Hussain, F. 2001 Generation of collimated jets by a point source of heat and gravity. *J. Fluid Mech.* **449**, 39-59.

Complementary Experiments at the Karlsruhe Dynamo Test facility

Ulrich Mueller*, Robert Stieglitz**, Sandor Horanyi*** Fritz Busse***

*Universität Karlsruhe, Dpt. Fluid Mech
*Forschungszentrum Karlsruhe, IKET
** KFKI Atomic Energy Research Institute Budapest
**** Universität Bayreuth, Dpt.Theor. Physics IV

Summary The Karlsruhe Dynamo Experiments have demonstrated that a permanent magnetic field of dipole character can be generated by sodium flow in a proper arrangement of helical and axial channels in a cylindrical container. Moreover, it has been shown that the dynamo state originates from the hydrodynamic turbulent state of channel flow as an imperfect bifurcation.(see Mueller, Stieglitz, Horanyi 2004). In a following series of experiments the critical conditions for dynamo action as well as the dynamo behaviour under supercritical conditions has been investigated with regard to the following aspects: **A)** The feedback of the dynamo magnetic field on the velocity of the forced flow in the guide channels of the test module; **B)** The dynamic response of the dynamo to an enforced periodic variation of the volumetric flow rates; **C)** The response of the dynamo magnetic field at supercritical conditions to a variation of electrical conductivity due to a change in the system's temperature.

A) The influence of the growing dynamo field on the velocity distribution in the axial channel of the test module is studied with the help of Compensated Permanent Magnetic Potential Probes (CPMPP) (Knebel, Krebs 1994). Based on Ohm's induction law the particular design of the used probe renders possible the measurement of the velocity in the axial channels located near to the centre of the module. A typical result of such a measurement is shown in figure 1.

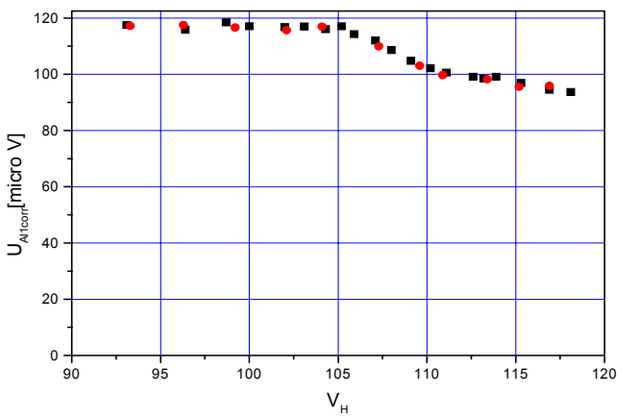


Figure 1:The measured compensated voltage at the Permanent Magnet Potential Probe located in an axial channel near the centre of the test module. One micro Volt (1 micro V) corresponds to a velocity of 0.04 m/s.

The result was obtained for a fixed central flow rate $\dot{V}_c$ = 105 m^2 /h (i.e. at a mean velocity 3.7 m/s) and for varying helical flow rates which were raised from sub-critical to super-critical conditions. The graph shows that the local axial velocity decreases from a plateau value for sub-critical flow rates at onset of dynamo action and saturates at another lower plateau value at higher super-critical flow conditions. This must be interpreted as a transition and redistribution of the turbulent velocity profile without magnetic field at Reynolds numbers 4,1 10^5 to a flat velocity profile at Hartmann number Ha ≈ 500. From this observation we conclude that the saturation of dynamo action at supercritical conditions is substantially governed by the formation of a MHD-core-flow with Hartmann boundary layers in the channel system of the test module.

B) It has been conjectured (Normand 2003, Petrelis & Fauve 2003) that a variation of the volumetric flow rates at time scales comparable to the magnetic diffusion time scale of the module's dimensions could lead to reduced critical flow rates for the onset of dynamo action. This conjecture has been tested by periodically varying the flow rate in the axial channels of the module at periods of 20 s and 7.5 s and an amplitude variation of 10 and 5% respectively to the mean value. The result is shown in figure 2.

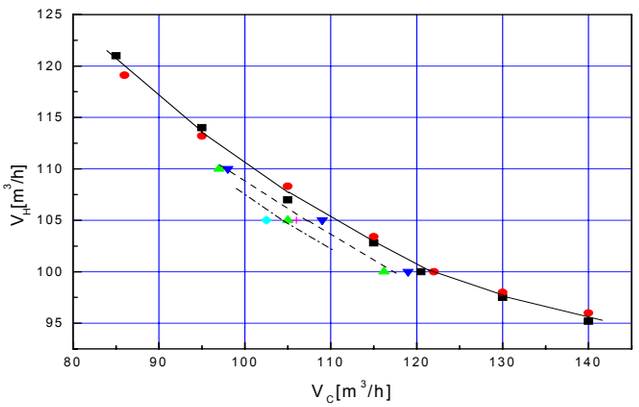


Figure 2: State diagram for dynamo action; steady state flow conditions (□ pressure loss criterion; • energy criterion, - fitting curve); periodic axial flow rates of period τ = 7.5 s and a 5% change in amplitude (▼ pressure loss criterion, ▲ energy criterion, --- fitting curve); periodic axial flow rates of period τ = 20 s and a 10% change in amplitude (+ pressure criterion, ♦ energy criterion, - • - • - conjectured fitted marginal line for dynamo action).

Using the local energy and the integral pressure criteria, developed in previous investigations (Mueller et al. 2004), the phase diagram for dynamo action demonstrates a shift of the critical flow rates towards lower values in the case of oscillatory flow rates, compared to the steady state ones. Moreover, the quantity of reduction seems to increase with the intensity of the fluctuations and with decreasing frequency.

C) The effect of a changing electrical conductivity of the fluid on the intensity of the dynamo magnetic field was studied by varying the system-temperature. We observed for instance at high supercritical flow rates of 115 m^3/h a drastic decrease of the field intensity from about 500 Gauss down to several Gauss when the system-temperature was increased from 125 °C to 145 °C. This can be explained by the enhancement of the critical Reynolds number Rm_c for onset dynamo action and, as a consequence, a reduction of the measure for the system's super criticality, i.e. $Rm - Rm_c$ (with Rm as the actual Reynolds number of the system).

As a result of the outlined experiments we summarize and conclude as follows: The dynamo magnetic field modifies the velocity distribution in the channels from its purely turbulent character to a MHD-core-flow with Hartmann boundary layers. A time periodic modulation of the volumetric flow rate may reduce the critical conditions for onset of dynamo action. The dynamo intensity is very sensitive to a variation of the electrical conductivity of the test fluid.

References:

Mueller U., Stieglitz R., Horanyi S. 2004, A two-scale hydromagnetic dynamo experiment. JFM 498, 31.

Normand Chr. 2003, Ponomarenko dynamo with time-periodic flow. Phys. Fluids 15, 1606.

Petrelis F., Fauve S. 2003,Private communication and 2001,Saturation of the magnetic field above the dynamo threshold. Eur. Phys. J. B. 22, 273.

LIQUID METAL FLOW UNDER INHOMOGENEOUS MAGNETIC FIELD

Oleg Andreev, Yurii Kolesnikov, Andre Thess
Department of Mechanical Engineering, University of Technology, D-98684 Ilmenau, Germany

Summary We experimentally investigate the influence of a vertical inhomogeneous static magnetic field on a liquid metal flow in insulating planer channel. The studies show an existence of three regions of flow formation: before, inside and behind magnetic field. In the first region, flow fluctuations are damped; in the second region, new flow with velocity M-shape profile is formed; in the third region, two shear layers near side walls are developed. Distributions of mean velocity, perturbation intensity of velocity and electrical potential and their spectra are presented. The work relates to experimental MHD modeling and industrial applications.

INTRODUCTION

In an industrial and experimental practice in a majority of MHD situations a flow of an electrically conducting fluid is situated in a sufficiently inhomogeneous magnetic field. Owing to the certain technological or design requirements the poles of a magnet system are performed either with a breach of discontinuity or with dimensions that are smaller than a size of a flow. In some MHD machines and devices the poles of magnets are presented by a number of alternating lugs and cavities that caused a periodical distribution of magnetic field. The problem of molten metal control by a spatially inhomogeneous magnetic fields is getting more important for industrial applications in metallurgy and crystal growth. In an industrial facility a magnetic field is created by an electromagnet mounted in the mould of a slab caster where it controls the flow of the hot metal. This method, also known as electromagnetic brake, for example, in the process of continuous casting. Inhomogeneous magnetic field is applied for suppression of undesirable jet-like structures of liquid metal flows. The process of electromagnetic brake, its advantages and drawbacks are broadly described in special publications [1-3]. In principle, an excessive brake effect redistributes the velocity drastically. The velocity vanishes in the central part and increases near periphery of flow. This flow is known as a M-shape. Such a flow is well investigated theoretically and experimental [4-6,8]. In the present study we consider the effects of a vertical inhomogeneous short extent magnetic field on a liquid metal flow in electrically insulating channel.

BEHAVIOUS OF FLOW IN INHOMOGENEOUS MAGNETIC FIELD

In some place on a length of channel we locate magnetic system which consists of two narrow (along the flow) magnet poles creating vertical magnetic field. Before and behind magnets the magnetic field is down. Interaction of the flow and magnetic field induces potential gradient and electric current according to the Ohm's law. Maximum electric current is concentrated in central area of a gap between magnet poles. By virtue of this effect the electric current is closed in areas of small magnetic field before and behind of the magnetic system.
The Lorentz's breaking force in the liquid, in plane perpendicular to the magnetic field, generated by interaction of the electric current and magnetic field, is higher in the center of the magnetic gap then the force in the vicinity of the side walls. As a result inhomogeneous M-shape velocity profile arises. Such flow formation we present formally as a generation of a vorticity parallel to the vertical component of magnetic field within the magnetic field region [7]. The vorticity is generated not only by viscosity, but it also occurs at given x-component of electric current and magnetic field z-component gradient along the flow. Downstream behind magnetic system two turbulent shear layers similar to wall jet are developed.
In connection with this, we consider three regions of flow development. The region **I** is characterized by an exposure of inhomogeneous magnetic field to the flow and by a damping of perturbations incoming to the magnetic field. The region **II** is between the front of magnetic system and distance where formation of the velocity profile under inhomogeneous magnetic field is completed. Here, in parallel with the non-homogeneity of profile growth, a vortical structures arises by pressure differential in areas between inlet and outlet of the magnetic field. The region **III** is characterized by a further development of flow M-shape velocity profile without magnetic field. Two shear layers issuing from magnetic field region are propagated nearly the channel side walls.

EXPERIMENTAL SET-UP AND MEASUREMENT TECHNIQUES

The experiments are carried out in a rectangular channel of a half meter long made of Plexiglas with a cross-section 100mm×20mm. As working liquid we use the eutectic alloy Ga68%In20%Sn12% which has a melting temperature of +10.5°C. Two permanent magnets of 20×30×100mm are located above and below the channel. An induction of the magnetic field B = 0.504 T is a maximum in the central point of the gap between the poles and essentially changes in x-direction (along the flow).
During the experiments we introduce in flow by alternately a potential probe [4] and a Vives' probe[7]. By application of the first probe we measure averaged and pulsating potential distributions in area of a magnetic field, region II, and by the use of the second probe we measure averaged and pulsating velocity in regions I and III, where magnetic field is absent.
With this actual setup we vary in experiments the Reynolds number within the range Re = 500-16000. The Hartmann number in magnetic gap is Ha = 400 for maximum magnetic field induction. The MHD interaction parameter, as a ratio

of electromagnetic to inertial forces, is varied within the range of N = 10-320. Here, we use a flow rate mean velocity and the height of flow.

RESULTS AND DISCUSSION

The order of results are: (1) profiles of the mean and root-mean-square (rms) velocity in areas of magnetic field absence; (2) distributions of the mean and root-mean-square (rms) local electric field in region of applied magnetic field presence; (3) flow visualization and amplitude-frequency spectra of electrical potential and velocity fluctuations.

Suppression region I

We start with analyzes of a velocity field of flow incoming to the region of magnetic field at Reynolds number Re = 4000. On the axes before magnetic field, the maximum of mean velocity and fluctuations as well take place. In this region, rms magnitude constitutes 6–7% of the flow rate velocity. As the flow is approached to the magnetic field region, the intensity of pulsations reduces 2-fold in the center and 3-fold nearly sidewalls. The reduces are due to a transformation of mean flow and fluctuations damping in this transition region of magnetic field growth.

Vortical region II

In this region the Lorentz force has perceptible effect on the flow. Maximum of the velocity displaces to the sidewalls. In central domain the flow velocity is halved to a flow rate velocity. We emphasize that the crosswise velocity changes the sign to the right and to the left of flow axis, i.e. the flow coming in magnetic field has a tendency to be separated into two flows directed toward the side walls. Downstream both transversal flows nearly the walls again directed toward the axes. Obvious closed lines confirms the existence of two large-scale vortical structures in the immediate region of the magnetic field. Space measurement of potential distributions shows an existence of these vortical structures two-dimensional in plane perpendicular to the magnetic field. In the vicinity of walls the velocity is 3-fold higher then mean flow rate velocity.

Wall jet region III

In this region a pulsation intensity does not exceed of 5% in axial zone, whereas it increases nearly wall up to 27% at Re = 4000. At high the Reynolds number the intensity perceptibly decreases. For instance, at Re = 16000 the intensity declines to a level of 7.5%. A relative decrease of the intensity of longitudinal pulsation is physically explained by growth of more dissipative high-frequency part in spectrum of perturbations generated by the wall shear flow at given the Reynolds number. Notice that profiles hold their M-shape downstream with the resulting formation of two wall planer shear layers. The existence a basic frequency and double one testifies that a double vortical street forms downstream behind magnetic system. We note also that an active interaction between perturbations generated by both wall shear flows takes place.

CONCLUSIONS

The arrangement studied serves as a physical model for the industrial process, where structure and intensity of flow are controlled by magnetic field. The actual set-up allows measurement the mean and fluctuating both local electric field and velocity in area of applied magnetic field and in a regions of magnetic field absence. Three regions of flow development we consider: (I) a damping of perturbations coming in the magnetic field; (II) generation of vortical structures and M-shape profile formation; (III) development of M-shape wall shear flow. As the flow is approached to the magnetic field, the intensity of pulsations reduces 2-fold in the center and 3-fold nearly sidewalls. In region downstream without magnetic field in area of wall shear flow the intensity increases up to 27% at Re = 4000 and up to 7.5% at Re = 16000. Obtained amplitude-frequency spectra show that in central part of the flow determinant vortices develop downstream from magnet system, their combinations arise in the spectra.

References

[1] The EMBR for slab CC-machines, 4th Int. Iron&Steel Conf. 1982.

[2] Steel flow control in a high speed caster using an electromagnetic brake. AISE, 1983.

[3] Kasunuma J., *et al*.: Continuous casting of highly clean steel slab. AIME, 1984.

[4] Kit L. G., *et al*.: Investigation of the influence of fringe effects on a MHD flow in a duct with non-conducting walls. *Magnetohydrodynamics* **6**: 47,1970.

[5] Holroyd R. J.: An experimental study of the effects of wall conductivity, non-uniform magnetic fields and variable area ducts on liquid metal flows at high Hartmann number. Part. 1. Ducts with non-conducting walls. *J. Fluid Mech* **93**: 609, 1979.

[6] Holroyd R. J., Hunt J. C. R.: Theoretical and experimental studies of liquid metals flows in strong non-uniform magnetic fields in ducts with complex geometry. Proc. 2nd Beer-Sheva Int. seminar on MHD flows and turbulence, 1980.

[7] Knebel J.U., Krebs L.: Calibration of a miniature permanent magnet flow meter probe and its application to velocity measurements in liquid sodium. *Exp. Therm. Fluid Sci.* **8**: 135 ,1994.

[8] Bühler L.: Instabilities in quasi-two-dimensional magnetohydrodynamic flows. *J. Fluid Mech* **326**: 125, 1996.

SMALL-SCALE MOTION IN THE CORE OF THE EARTH

P.A. Davidson and F. Siso-Nadal

University of Cambridge, Trumpington Street, Cambridge CB2 1PZ

SUMMARY

In 1996, St Pierre (1996) reported numerical simulations of a buoyant blob migrating across the earth's outer core and subject to the combined effects of rotation and an azimuthal magnetic field. He noted that the blob rapidly fragments into a series of plate-like structures. Quite independently, Davidson (1995, 1997) observed a similar behaviour in the context of low-R_m turbulence (without a Coriolis force) and showed that this phenomenon has its roots in the destruction of angular momentum by the Lorentz force. The purpose of this paper is to pull together these earlier studies and, in particular, to determine whether or not St Pierre's platelets are likely to be a generic feature of small-scale motion in the core of the earth.

Classical theories of the geo-dynamo rest on the assumption that there are two scales of motion in the core. For example, α-Ω dynamos rely on large-scale differential rotation sweeping out an azimuthal field, B_θ, from the observed dipole field, and then on small-scale motion (waves or turbulence) reinforcing the dipole field via the α-effect acting on B_θ. However, the validity of such a picture has recently been questioned, partially because small-scale turbulence is highly dissipative and so α-Ω (or α-α) dynamos are not particularly efficient mechanisms for maintaining the earth's magnetic field. (See, for example, Malkus, 1994). Moreover, recent large-scale numerical simulations, which do not model the small scales, suggest that a dynamo might operate through the action of large-scale motion alone. All of this suggests that the α-effect, if it operates at all, is most active at the intermediate to large scales, and not at the small scales, as classically assumed.

It seems natural, therefore, to examine the small-scale dynamics in order to determine just how dissipative it is, and to assess the validity, or otherwise, of the use of sub-grid models in some of the large-scale simulations. Moreover, recent numerical experiments (St Pierre, 1996) show that small buoyant eddies in the outer core rapidly fragment into plate-like structures aligned with the local **B-Ω** plane, a phenomenon anticipated by Braginsky (1964), Braginsky and Meytlis (1990), and Braginsky and Roberts (1995). It is clearly desirable to understand why this phenomenon occurs and to determine if it is likely to be a generic feature of all small-scale turbulence.

Our starting point is the study of low-R_m turbulence by Davidson (1995, 1997), in which the Coriolis force is absent. It is shown there that the disintegration of eddies into platelets is inevitable whenever the axis of rotation of the eddy is non-parallel to the local magnetic field. Moreover, Davidson shows that this behaviour can be predicted from a simple argument related to the angular momentum of the vortex. The main purpose of this paper is to extend the earlier analysis of Davidson by incorporating the Coriolis force, thus forming a bridge to the work of Braginsky (1964), Braginsky and Meytlis (1990), St Pierre (1996), Shimizu and Loper (1997) and Loper (2001). We conclude that the small scales are both highly dissipative and highly anisotropic.

References

Braginsky, S.I., 'Magnetohydrodynamics of the Earth's core', *Geomag. Aeron.* **4,** 698-712 (1964).

Braginsky, S.I. and Meytlis. V.P., 'Local turbulence in the Earth's core', *Geophys. Astrophys. Fluid Dynam.* **55**, 71-87 (1990).

Braginsky, S.I. and Roberts, P.H., 'Equations governing convection in the Earth's core and the geodynamo', *Geophys. Astro. Dynam.* **79**, 1-97 (1995).

Davidson, P.A., 'Magnetic damping of jets and vortices', *J. Fluid Mech.*, **299**, 153-186 (1995).

Davidson, P.A., 'The role of angular momentum in the magnetic damping of turbulence', *J. Fluid Mech.* **336**, 123-150 (1997).

Loper, D.E., 'On the structure of a Taylor Column driven by a buoyant parcel in an unbounded rotating fluid', *J. Fluid Mech.* **427**, 131-166 (2001).

Malkus, W.V.R., 'Energy sources for planetary dynamos'. In: *Lectures in Solar and Planetary Dynamos* (Eds. M.R.E. Proctor and G.D. Gilbert), Cambridge University Press, Cambridge (1994).

Shimizu, H.S. and Loper, D.E., 'Time and length scales of buoyancy-driven flow structures in a rotating hydromagnetic fluid', *Phy. Earth Planet. Inter.* **104**, 307-329 (1997).

St Pierre, M.G., 'On the local nature of turbulence in the earth's outer core', *Geophys. Astrophys. Fluid Dynam.* **83**, 293-306 (1996).

MAGNETOHYDRODYNAMIC INSTABILITIES OF ASTROPHYSICAL JETS

Hubert Baty*, Rony Keppens**, Pierre Comte***
*Observatoire Astronomique, 11 Rue de l'Université, 67000 Strasbourg, France
**FOM-Institute for Plasma Physics Rijnhuizen, Association Euratom/FOM, P.O. Box 1207, 3430 BE Nieuwegein, The Netherlands
***Institut de Mécanique des Fluides et des Solides, 2 Rue Boussingault, 67000 Strasbourg, France

Summary We present the main findings of recent studies using high-resolution magnetohydrodynamic (MHD) simulations of compressible shear flow layers, with the aim to investigate configurations representative of astrophysical jets. We show how initially weak magnetic fields control the non linear dynamics of Kelvin-Helmholtz instabilities, through magnetic reconnection events and stabilizing mutual interaction with magnetic instabilities.

Astrophysical jets are collimated flows that are observed to propagate over large distances with respect to their radial extents. This is the case of jets emanating from young stellar objects and active galactic nuclei. It is to date an open question how these supersonic jets survive MHD instabilities (Ferrari 1998). Indeed, in high-resolution three dimensional (3D) hydrodynamic simulations, Kelvin-Helmholtz (KH) instabilities are seen to disrupt the flow with a strong turbulent transition. The characteristic time scale of the disruption is too fast by more than one order of magnitude to account for the observations. However, the astrophysical jets are believed to be magnetized although the dominant contribution to the jet energy is the kinetic one. Thus, we investigate the role played by the magnetic field with the aim to examine the issue of large-scale flow coherence and survival.

To that end, we use the Versatile Advection Code (VAC) initiated by Tóth (1996), to solve the full set of non linear MHD equations as an initial value problem. VAC and its recent grid-adaptative variant AMRVAC (Keppens et al. 2003) are general finite-volume based schemes, making use of a second order accurate shock capturing method and employing a Roe-type approximate solver.

In order to model the interface separating the jet from the surrounding medium, we first consider a single two dimensional (2D) shear flow layer embedded in a weak uniform magnetic field that is aligned with the flow (in the longitudinal x direction). We assume periodicity along the longitudinal direction, and we use free outflow boundaries on the lateral sides. Thanks to AMRVAC, we have followed the initial growth of many KH vortices initiated by a white noise perturbation. A strong process of large-scale coalescence is found. It proceeds through continuous pairing/merging events between adjacent vortices up to the point where the final large-scale vortice structure reaches the domain dimensions. This coalescence is also accompanied by small-scale magnetic reconnection events that partially disrupt the vortices at different stages of the evolution, thus releasing a non negligible part of the perturbed energy. The extension of these results (Baty et al. 2003) to a 2D slab jet is actually under current investigation.

Second, we consider a 3D magnetized cylindrical jet configuration. The flow is axial, sheared in the radial direction with an hyperbolic tangent form, and is embedded in an helical magnetic field. We take an axial length equal to the linearly dominant axial wavelengths (the large-scale coalescence is excluded), and the jet surface is perturbed at $m = \pm 1$ azimuthal mode numbers. As predicted by a stability analysis, a $m = -1$ KH mode develops at the interface (dominating the $m = 1$ KH counterpart), while the jet core is affected by the growth of a $m = -1$ magnetic instability that is driven by the electrical current. This simultaneous development of the two types of modes is illustrated in Figure 1. As time proceeds, the magnetic field deformation induced by the current-driven (CD) mode provides a stabilizing effect on the further KH development. The subsequent disruptive effect on the flow (due to a magnetic reconnection process) is shown to be weaker than in magnetized configurations without CD mode (in particular with an axial magnetic field), as illustrated in Figure 2 (see also Baty & Keppens 2002).

We have presented two examples of configurations in which initially weak magnetic fields ultimately control the non linear dynamics of unstable shear flow layers. The long-term disruptive effect on the flow is thereby weaker compared to a 3D purely hydrodynamic configuration, in particular when the jet is embedded in an helical magnetic field. These results provide important clues to understand astrophysical jets survival.

This work was supported in part by the European Community's Human Potential Program under contract HPRN-CT-2000-00153, PLATON.

References

[1] Baty H., Keppens R.: The Astrophysical Journal **580**, 800, 2002.
[2] Baty H., Keppens R., Comte P.: Physics of Plasmas **10**, 4661, 2003.
[3] Ferrari A.: Annual Review of Astronomy and Astrophysics **36**, 539, 1998.
[4] Keppens R., Nool M., Tóth G., Goedbloed J. P.: Computer Physics Communications **153**, 317, 2003.
[5] Tóth G.: Astrophysical Letters and Communications **34**, 245, 1996.

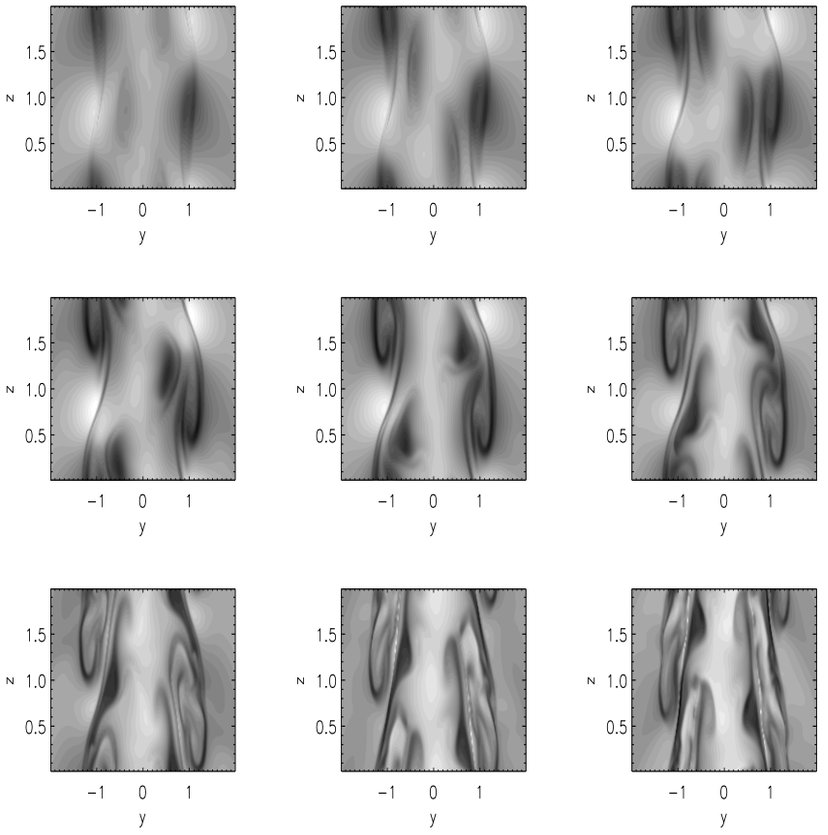


Figure 1. Grey-scale images of the density distribution of a magnetized jet simulation with an helical magnetic field (using VAC), in the $y-z$ plane (using a 2D cut at $x=0$). The times are running from left to right and top to bottom. Dark regions correspond to low values.

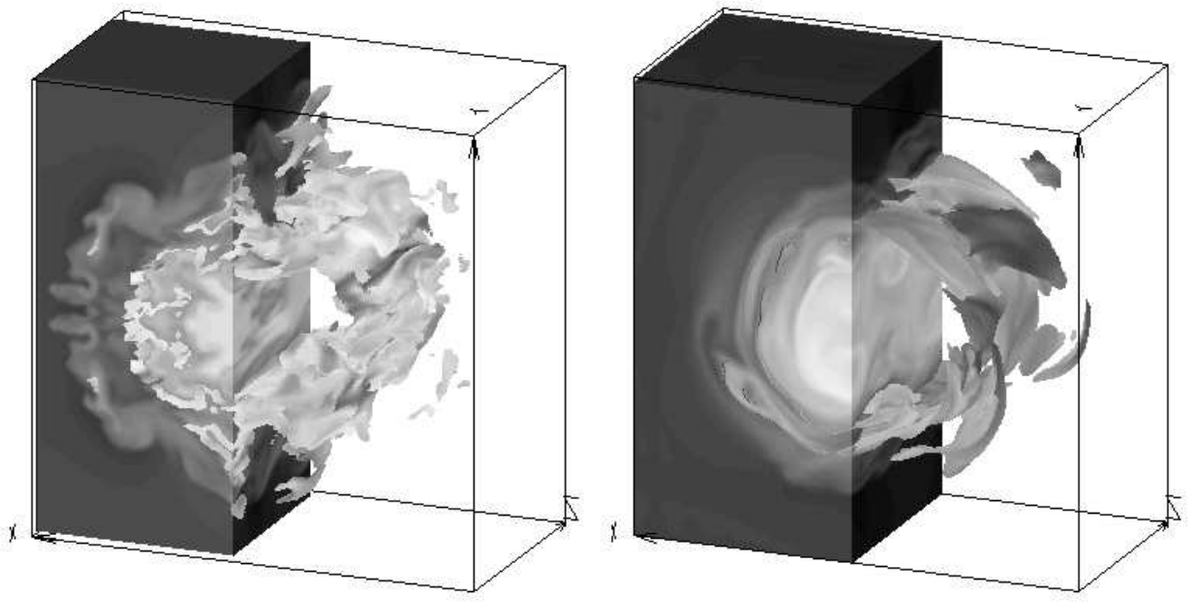


Figure 2. The 3D jet structure at the end of the simulations for magnetized jets in a pure axial (left), and in helical (right) magnetic field. Shown is the axial velocity V_z on various cross-sections, and an isosurface $V_z=0$ corresponding to the jet boundary.

MAGNETOHYDRODYNAMIC MOTION OF TOROIDAL MAGNETIC EDDIES

Y. Hattori*, H. K. Moffatt**
*Division of Computer Aided Science, Kyushu Institute of Technology, Kitakyushu 804-8550, Japan
**DAMTP & CMS, University of Cambridge, Cambridge CB3 0WA, UK

Summary The magnetohydrodynamic motion of toroidal magnetic eddies are studied using a new contour-dynamics formulation. The eddies are assumed to be axisymmetric with purely poloidal velocity and toroidal magnetic fields. Numerical simulation shows that the magnetic energy does not decay to zero against expectation although its lower bound determined by helicity is zero. Spherical heads which are approximated by an exact solution are formed to prevent the magnetic energy from vanishing.

INTRODUCTION

Magnetohydrodynamic (MHD) flows appear in various phenomena in astrophysical and engineering contexts. When dissipation effects are negligible, there exist three invariants of the dynamics: total energy, cross helicity and magnetic helicity. Magnetic helicity, which measures topological complexity of magnetic-field lines, bounds magnetic energy as

$$E_M \geq C|H|, \quad E_M = \frac{1}{2}\int B^2, \quad H = \int \boldsymbol{A}_M \cdot \boldsymbol{B}, \quad \boldsymbol{B} = \boldsymbol{\nabla} \times \boldsymbol{A}_M, \tag{1}$$

where C is a constant determined by the geometry of the region. Thus, magnetic energy cannot vanish if $H \neq 0$.
In this paper, we are concerned with the converse: does magnetic energy vanish when $H = 0$ so that the helicity bound for E_M is zero? In other words, we seek other mechanisms which control magnetic energy. We investigate this problem for toroidal magnetic eddies which have compact cross sections. The toroidal magnetic eddy can be regarded as a simple model of curved magnetic tubes which are observed in, for example, solar flares; we expect the results below are extended and applied to actual phenomena.

CONTOUR DYNAMICS

We consider an axisymmetric MHD flow whose velocity and magnetic fields are purely poloidal and toroidal, respectively: $\boldsymbol{u} = u_r \boldsymbol{e}_r + u_z \boldsymbol{e}_z, \boldsymbol{B} = B_\theta \boldsymbol{e}_\theta$; note that helicity vanishes for this choice. Both viscosity and magnetic diffusivity are assumed to be zero. The toroidal component of magnetic field is further assumed to vanish outside of a compact cross section $f(r, z, t) > 0$ and be proportional to the distance from the axis of symmetry in the inside: $B_\theta = \kappa r H[f(r, z, t)]$, $H[\cdot]$ being the Heaviside function and κ being a constant. The fluid is assumed to be at rest initially. Then the flow is irrotational except on the boundary or contour $f = 0$ where singular vorticity is created because of the Lorentz force:

$$\omega/r = \Omega(r, z, t)\delta[f(r, z, t)]\,|\boldsymbol{\nabla} f|. \tag{2}$$

The MHD equations reduce to the following contour dynamics

$$\frac{\partial \gamma}{\partial t} = \kappa^2 R \frac{\partial R}{\partial s}, \tag{3}$$

$$\frac{\partial R}{\partial t} = u_r(R, Z, t), \quad \frac{\partial Z}{\partial t} = u_z(R, Z, t), \tag{4}$$

$$u_r(r, z) = \frac{1}{r}\oint \gamma \left[\frac{\partial}{\partial z} G(r, z|R, Z)\right] \mathrm{d}s, \quad u_z(r, z) = -\frac{1}{r}\oint \gamma \left[\frac{\partial}{\partial r} G(r, z|R, Z)\right] \mathrm{d}s, \tag{5}$$

$$G(r, z|r', z') = \frac{1}{2\pi}(rr')^{1/2}\left[\left(\frac{2}{k} - k\right)K(k) - \frac{2}{k}E(k)\right], \quad k^2 = \frac{4rr'}{(r + r')^2 + (z - z')^2}. \tag{6}$$

Here $(r, z) = (R(s, t), Z(s, t))$ is a parametric representation of the contour with s as the parameter, γ is related to the strength Ω of the vortex sheet through $\gamma = \Omega R\left[(\partial_s R)^2 + (\partial_s Z)^2\right]^{1/2}$, and $K(k)$ and $E(k)$ are the complete elliptic integrals of the first and second kinds, respectively. The formulation above can be easily extended to multiple contours $B_\theta = r\sum_{i=1}^{m} \Delta\kappa_i H[f_i(r, z, t)]$, which in principle can approximate any continuous toroidal magnetic field with compact support in L^2-norm.
The contour dynamics derived above is closely related with the motion of an interface between two fluids which have different values of density [1]. Under appropriate assumptions, the motion of interface is described by a similar set of equations; buoyancy is the driving force of the motion and creates singular vorticity on the interface. For the present case, the Lorentz force drives the motion.

RESULTS

We have carried out some numerical simulations using the equations of contour dynamics (3) and (4). Standard techniques for related problems [2–4] are employed. The integrals in (5) are evaluated by the trapezoidal formula for discrete points

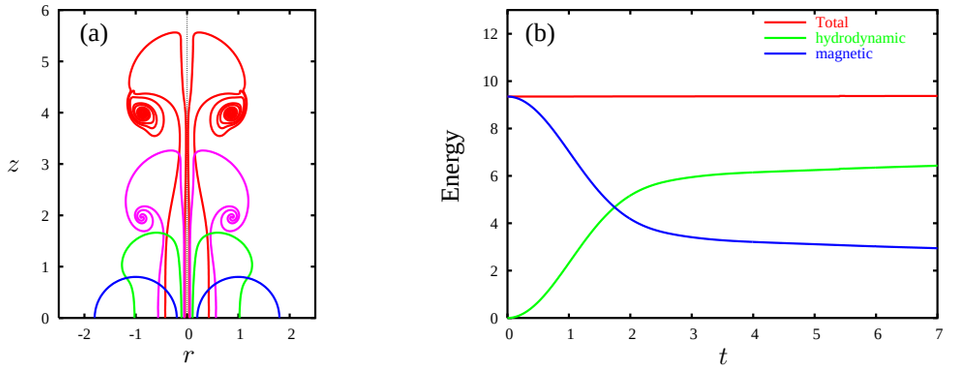


Figure 1. (a) Evolution of magnetic eddies. Cross section. $r_c = 0.8R_0$. $t = 0$ (blue), 2 (green), 4 (pink), 7 (red). (b) Evolution of energy: total energy (red), hydrodynamic energy (green), magnetic energy (blue).

which approximate the contours. They have divergent parts at $(r, z) = (R, Z)$, of which principal values are evaluated analytically [4]. As time proceeds in the numerical simulation, distance between neighbouring points becomes too large or too small depending on the positions to keep sufficient spatial resolution. To overcome this defect we reparametrize s at regular intervals.

The present method, however, suffers singularity which develops on the contours; it is essentially the same singularity that develops on a vortex sheet in non-MHD flow [2]. In order to track the global motion of the eddies for sufficient time, we regularize Green's function by introducing a smoothing parameter ϵ to the Biot-Savart law [3]: $4\pi \boldsymbol{A}_H = \int \boldsymbol{\omega}/x \ \rightarrow \int \boldsymbol{\omega}/\left(x^2+\epsilon^2\right)^{1/2}$.

Figure 1 shows an example of the numerical results. Figure 1(a) shows the evolution of the eddy; its cross sections by a plane $\theta = \text{const.}$ are drawn for selected instants. The initial magnetic eddy is a torus whose cross section is a circle of radius $0.8R_0$ (R_0 is the radius of the torus). Only the upper half ($z > 0$) is shown since there is symmetry with respect to $z = 0$. The Lorentz force acts inward so that the eddy shrinks to z–axis as seen initially; one would expect the eddy eventually collapses to z–axis and correspondingly the magnetic energy vanishes. This is not prohibited since the helicity bound for the magnetic energy is zero in the present case. Two characteristic structures form as time proceeds: one is the spherical head which propagates steadily along z–axis and the other is the roll-up behind it. The number of turns in the roll-up increases with time; as a result fine structures emerge so that the dynamics cannot be pursued further.

Figure 1(b) shows time evolution of energy. The total energy is conserved with sufficient accuracy. The hydrodynamic energy, which is zero initially, starts to grow parabolically; after a stage of linear growth, the rate of growth becomes much smaller so that the magnetic energy appears to approach a constant. Correspondingly, the magnetic energy decreases monotonically and approaches a constant which is not zero although the helicity bound is zero.

This result on magnetic energy is closely related with formation of the spherical head. The head is well approximated by an exact solution which moves along z–axis with a constant speed $U_0 = (2/3)\,\kappa R_0$; it is represented in terms of Stokes' streamfunction as

$$\Psi(r, z_*) \quad = \quad \begin{cases} 0 & \sigma < R_0, \\ (1/2)\,U_0 r^2\left[1-(R_0/\sigma)^3\right] & \sigma > R_0, \end{cases} \tag{7}$$

where $(r, z_*) = (r, z - U_0 t)$ is a moving frame and $\sigma^2 = r^2 + {z_*}^2$. To summarize, the magnetic energy decays as the eddy shrinks to z–axis; however, it cannot decay to zero since a part of the eddy forms a spherical head close to an exact solution which maintains a finite amount of magnetic energy.

The flow field of the exact solution we have found is that of Hill's spherical vortex outside the sphere and is identically zero inside it; the gap between the two sides is compensated by the magnetic field and the vortex sheet. In fact there is a family of exact solutions which includes (7) and Hill's spherical vortex as members. Numerical test of the exact solution (7) shows that a spike like that observed for Hill's spherical vortex [4, 5] develops on the rear side while the front side appears to be stable. In addition to the formation of spike, singular vortex sheet is subject to the Kelvin-Helmholtz instability. Stability analysis in progress would clarify these two mechanisms of instability. Direct numerical simulation using the MHD equations, which is also in progress, will reveal the dynamics in more general cases including the case of non-vanishing helicity.

References

[1] Baker G. R., Meiron D. I., Orszag S. A.: Vortex simulations of the Rayleigh-Taylor instability. *Phys. Fluids* **23**:1485–1490, 1980.
[2] Krasny R.: A study of singularity formation in a vortex sheet by the point-vortex approximation. *J. Fluid Mech.* **167**:65–93, 1986.
[3] Krasny R.: Computation of vortex sheet roll-up in the Trefftz plane. *J. Fluid Mech.* **184**:123–155, 1987.
[4] Pozrikidis C.: The nonlinear instability of Hill's vortex. *J. Fluid Mech.* **168**:337–367, 1986.
[5] Moffatt H. K., Moore D. W.: The response of Hill's spherical vortex to a small axisymmetric disturbance. *J. Fluid Mech.* **87**:749–760, 1978.

FLUID DYNAMOS AND PRECESSION DRIVING

J.Léorat
Observatoire de Paris-Meudon, 92195-Meudon, France

Summary: Experimental fluid dynamos have important power needs. We study the flow generated by the precession motion of a container in a water experiment. The laminar and turbulenct regimes are described. The dissipated power remains relatively small, which implies that flows at Rm of a few hundreds could become feasible.

Introduction

The main motivations for designing experimental fluid dynamos may be found in the numerous non linear problems raised by astrophysical observations of MHD turbulence: estimate of transport coefficients, spectral indexes of kinetic or magnetic energies, spatial and temporal evolution of largest scales (chaotic, periodic or steady?), etc… As for ordinary turbulence, the intrinsic lack of resolution of the numerical approach argues in favor of some kind of MHD wind tunnel. Contrary to the hydrodynamic case, the development of large scale MHD devices is however still in a preliminary stage, possibly due to the amount of technical difficulties to be solved, along with a weak economic impact of most applications of astrophysical interest. Scientific issues seems however sufficiently promising to motivate an increased number of teams at international level involved in such a program [1, 2]: the present work intends to contribute to the design study of such a facility.

Let us state the nature of the challenge to be overcome. Although the problem of dynamo action (conversion of kinetic energy into magnetic energy) may be set as a linear one, no sufficient criterion is available as a general guide to optimize the driving of an experimental fluid dynamo. About 50 years of various analytical and numerical investigations have shown that kinematic (i.e. for a given flow) dynamo action may in some cases take place in a closed container, when the flow magnetic Reynolds number Rm = □□VL (L = typical flow size, V = maximal speed, □ = fluid conductivity, □ = magnetic permeability) exceeds some critical value R_m*, of the order of 100. Using liquid sodium, this condition implies that VL reaches 10 m^2/s and the Reynolds number is then 10^7, which shows that the size and the driving power exceed the standard laboratory means.

Three different strategies may be used for the design of an experimental fluid dynamo:

- realize the flow configuration of a known analytical or numerical kinematic dynamo
- try many driving configuration in various containers and look for successful magnetic signals
- optimize the driving by iterations between measurements from water experiments and kinematic dynamo computations using the mean velocity field

While the first approach has been used by the successful Riga and Karlsruhe experiments in 1999 [1], the second may be justified by the large gap between the information content of a turbulent flow and the numerical reality. To adopt the third one, one has to assume that turbulence itself has a low impact on dynamo action, which is thus due to the time averaged flow used in the kinematic code.

Following this later approach, the design problem may be divided in two stages:

(a) a purely hydrodynamic problem: given a size L and a driving power, what is the driving configuration leading to the maximal speed V?

(b) a numerical computation: what is the critical R_m* of such a flow?

Motivations for precession driving and ATER experiment

In the dynamo problem, there is a competition between the ohmic diffusion and the stretching term and since the experimental magnetic Reynolds number cannot be much greater than the critical value, only the largest scales of the flow are able to convert kinetic into magnetic energy (this remark does not apply to, say, the solar dynamo, where the magnetic Reynolds numbers are huge). To drive a flow at the largest available scale, one is thus led to examine the efficiency of moving the container walls to drive a flow, using for instance composition of rotations. Since a fixed rotation axis leads to solid body rotation (an antidynamo), the next step is to impose an uniform rotation to the instantaneous rotation axis. Although consideration for this type of flow forcing in the dynamo context has been first given more than 30 years ago [3, 4, 5], quantitative information about the achievable flow speed is lacking.

In order to solve the first step indicated above, we have realized a water experiment (ATER = “Agitateur pour la Turbulence en Rotation”), using a cylindrical container rotating around its symmetry axis, for simplicity of realization and equipment. In the container frame, precession is acting through the “Poincaré acceleration “ $\mathbf{a}_P$ = d□/dt ^**r** = (□$_p$^□$_r$) ^ **r**: the instantaneous rotation axis □(t) describes a cone around the cylinder axis. The direction of the precession axis has been chosen orthogonal to the rotation axis and the ratio of precession frequency to rotation frequency fixes the effective aperture of the cone of instantaneous rotation. The radius of the container is 0.15 m. The main parameters of the experiment are the aspect ratio (length/diameter may be chosen between 1 and 4/3, the rotation frequency (up to 10 t/s), the precession frequency (up to 1 t/s). The smallest Eckman number is thus around 10^{-6}.

A torque meter may be mounted on the rotation axis, and a CCD camera for Particle image velocimetry may be placed along the rotation axis (either static or corotating) or along a diameter. To visualize the flow, spherical particles (density close to 0.9) may be introduced in the container. We present here only the mechanical results, awaiting the realization of the lightning device that will allow 2D particle image velocimetry.

Laminar and turbulent flows

We begin by a qualitative account of what is observed visually, as the precession frequency is increased step by step, starting from zero, for a fixed rotation frequency. At zero precession frequency, particles tend to align in the vicinity of the cylinder axis, due to the action of buoyancy in the centrifugal pressure field. A soon as precession is present, the central concentration of particles form a wavy thin tube, quasi steady in the precession frame, showing that the line of zero speed is now a 3D curve, which deviate from the rotation axis as the precession increases. Advected particles outside the wavy core suggest that the tilted streamlines are also steady in the precessing frame. Above a critical precession frequency, the flow becomes suddenly turbulent: the size of the time dependent streamlines drops to a fraction of the radius. This turbulence looks remarkably homogeneous and statistically steady. When decreasing the precession frequency (still keeping a constant rotation rate), one recovers the laminar flow, at a critical precession frequency lower than for the transition from laminar to turbulent (hysteresis).

The rotation torque increases smoothly with the precession rate in the laminar regime and shows a jump at the critical precession frequency, followed by a plateau. When the precession decreases, an hysteresis curve is obtained.

Some insight on the laminar regime may be obtained from the linearised equations, while the stability analysis remains to be done (see for example [6] for the precessing ellipsoid case). The Navier-Stokes equations are adimensionalised using the container radius and the rotation period as units. If the viscous dissipation term is neglected (the Eckman number is small), the only remaining parameter in the dynamical equations is the *precession rate* α, defined by the ratio of the precession frequency to the rotation frequency. Using different rotation speeds to study the transitions from laminar to turbulence (noted +) and back (noted -), one find that the critical rates (α_+ and α_-) are indeed independent of the rotation frequency. They depend on the aspect ratio: for example, they are close to 0.1 when the aspect ratio is 4/3.

The secondary flow induced by precession scales with the precession rate. To get higher speed in the laminar regime, which is potentially efficient for dynamo action (flow at large scale) and less power demanding in term of driving, one has to find higher critical rates. This can be done by exploring different values of the aspect ratio. Another tool has been successfully tested: since the stability of the laminar flow at such high Reynolds numbers could be a consequence of rotation motion, we have fixed four radial blades on one top of the cylindrical container to enforce rotation motion: The blade velocity is parallel to its normal, whereas it is tangent to the wall for the curved cylindrical wall. Rotation is now driven by pressure/inertial forces instead of viscous forces. Using blades with height equal to 1/10 of the container length allows to double the critical precession rates (for aspect ratio = 4/3, $\alpha_+ = 0.215$, $\alpha_- = 0.175$), and thus to double also the maximal speed V in the laminar regime. The gain in driving efficiency is important.

Power scaling

In the turbulent regime, at sufficiently small scales, the influence of rotation becomes negligible, Kolmogorov phenomenology of homogenous isotropic turbulence may apply, and the non-linear energy flux scales as $(\rho V_0^2)/(L_0/V_0)$, where L_0 and V_0 are defining the "energy range". Although they are not directly measurable, they are related to the container geometry (length L, radius R) and the driving design (be it external pump, internal turbines or precession), so that the values of the ratio L_0/R and V_0/V_c are characteristics of each configuration. As a consequence, when viscous dissipation at the smallest scales is fed by a turbulent cascade, the dissipated power per unit volume scales a priori as $P_{diss} = \rho\gamma V_c^3/R$,

where the power coefficient γ represents a concentrate of the driving characteristics. The scaling with container speed of the dissipated power in the turbulent regime cubic law has been verified in the ATER experiment, and the power coefficient γ has been found close to 0.02 for precession driving. In the optimization stage of an MHD wind tunnel, one has to compare power needs for a given magnetic Reynolds number, i.e. a typical flow speed V. In the case of precession with radial blades, V may reach about $2\,\alpha_+\,V_c$ in the laminar regime (with dissipated power lower than in the turbulent regime). Such values may also be extrapolated from numerical studies up to Reynolds number 5000 (cf P. Lallemand, priv. com.), and have to be confirmed with the PIV under realization.

Conclusion

Precession driving looks as a promising tool to get high R_m flows. Since typical powers of a few hundred of kW are considered in the design of experimental fluid dynamos, its power scaling is compatible with the realization of MHD flows at magnetic Reynolds numbers of a few hundreds. Compared to turbine driving, it has also the technical advantage to use a closed container and avoid seals in liquid sodium. To confirm this favorable position and take advantage of it in an experimental fluid dynamo, critical magnetic Reynolds numbers must now be obtained.

References

[1] A.Gailitis, O.Lielausis, E.Platacis, G.Gerbeth, F.Stefani, "Laboratory experiments on hydromagnetic dynamos", Rev. Mod. Physics, **74**, 973-990 (2002)

[2] « Dynamo and Dynamics, A Mathematical Challenge », Cargèse Workshop, August 21-26, 2000, Lecture Notes in Physics, Eds. P. Chossat, D. Armbruster, I. Oprea

[3] W. Malkus, " Precession of the Earth as the cause of geomagnetism", Science, **169**, 259-264 (1968)

[4] R.F. Gans, "On the precession of a resonant cylinder", J. Fluid Mech., **41**, 865-872 (1970)

[5] R.F. Gans, "On hydromagnetic precession in a cylinder", J. Fluid Mech., **45**, 11-130 (1970)

[6] R. Kerswell, "The instability of precessing flows ", Geophys. and Astroph. Fluid Dyn., **72**,107-144, 1993.

XXI ICTAM, 15–21 August 2004, Warsaw, Poland

LARGE EDDY SIMULATION OF MAGNETIC DAMPING OF JET

Jungwoo Kim*, Jeongyoung Park** and Haecheon Choi*
*School of Mechanical and Aerospace Engineering, Seoul National University, Seoul 151-744, Korea
**Applied Technology Research Department, Hyundai Mobis, Gyunggi-Do 449-910, Korea

Summary In the present study, we perform large eddy simulations to investigate the effect of magnetic field on the flow characteristics of a round jet at Re=10000. We consider two different directions of magnetic field. With the axial magnetic field, the shear layer becomes thinner and the potential core becomes longer than those without magnetic field. In case of the transverse magnetic field, the jet progressively spreads along the direction of the magnetic field applied, and the negative axial velocity appears along the direction perpendicular to the magnetic field line.

It has been known that a static magnetic field is able to suppress the turbulent motion of liquid metal. This phenomenon is called magnetic damping. This magnetic damping is useful for metallurgical processes which commonly take the form of submerged jet. Generally, the current induced by the motion of liquid across the magnetic field leads to Joule dissipation and the rise of thermal energy due to Joule dissipation decreases the kinetic energy. As a result, the turbulent motion of liquid metal is suppressed. Sajben & Fay [1] performed an experiment for a turbulent mercury jet in a coaxial magnetic field. They observed that the rate of spreading of the jet and the turbulent intensity decreased with increasing magnetic-field strength. Davidson [2] analytically investigated the evolution of the inviscid jet under the magnetic damping by a transverse magnetic field.

However, the previous studies have not investigated the effect of the magnetic field on the vortical structures of a turbulent jet in detail. In early seventies, Crow & Champagne [3] observed that the turbulence field is made up of the large-scale coherent structure and fine-scale turbulence motion. Since that time, it has been well known that the dynamics in a round jet significantly depends on the coherent structures. Therefore, the change in the coherent structures by the magnetic damping is important to understanding the magnetic damping phenomenon, which is the objective of the present study.

The computation of a round jet is conducted using large eddy simulation (LES) with a dynamic subgrid-scale model (Germano *et al.* [4], Lilly [5]). In the present study, we consider MHD flow at a low magnetic Reynolds number. The governing equations for an electrically conducting and incompressible flow considered in the present study are as follows;

$$\frac{\partial u}{\partial t} + (u \cdot \nabla)u = -\nabla p + \frac{1}{Re}\nabla^2 u + N(-\nabla\phi + u \times B) \times B, \tag{1}$$

$$\nabla^2 \phi = \nabla \cdot (u \times B) = B \cdot \omega, \tag{2}$$

$$\nabla \cdot u = 0, \tag{3}$$

where u is the velocity, p is pressure, $\omega = \nabla \times u$ is the vorticity, B is magnetic field, Re and N are the Reynolds and Stuart numbers, respectively. The Suart number N is the ratio of the electromagnetic force to the inertial force. The numerical method used to solve these equations in a cylindrical coordinate is based on a semi-implicit fractional-step method (Akselvoll & Moin [6]). In the present computation, the Reynolds number based on the jet velocity (U_J) and jet diameter (D) is 10,000. At the jet exit, we imposed a top-hat velocity profile with a laminar blasius profile near the wall. In MHD turbulent flow, the direction of the magnetic field is one of the important parameters of determining the effect of magnetic field on the flow characteristics (Lee & Choi [7]). In the present study, a uniform magnetic field is applied in the axial or transverse direction to a turbulent jet. The Stuart numbers are $N_x = 0.5$ and $N_y = 0.05$ in the cases of axial and transverse magnetic fields, respectively. The computational domain size used is $-3.6 \leq x/D \leq 30$, $0 \leq r/D < 7$ and $0 \leq \theta < 2\pi$.

Figure 1 shows the contours of the instantaneous axial velocity in the cross-sectional plane with and without magnetic fields. With the axial magnetic field, the thickness of shear layer is thinner and the length of potential core is longer than those without magnetic field. In case of the transverse magnetic field, the jet progressively spreads along the magnetic field line with increasing x/D. Also, the negative axial velocity is observed along the direction perpendicular to the magnetic field line, which qualitatively agrees with the results by Davidson [2].

Figure 2 shows the vortical structures with and without magnetic fields. The iso-pressure surface is used to identify the vortical structures. Without magnetic field (Fig. 2a), the shear layer becomes unstable due to the shear layer instability (Kelvin-Helmholtz instability) and large coherent structures are observed due to the vortex pairing at a downstream location. As shown in Fig. 2, the changes in the vortical structures by the magnetic field depend on the direction of magnetic field. With the axial magnetic field, the vortical structures become weak because the magnetic field decreased the turbulence intensity as observed by Sajben & Fay [1]). On the other hand, with the transverse magnetic field, the vortical structures are weakened at a further downstream location because the Stuart number in this case is small as compared to the case of axial magnetic field. Currently, we are conducting LES at larger Stuart numbers. The detailed vortical structures and turbulence statistics with respect to the Stuart number will be shown in final presentation.

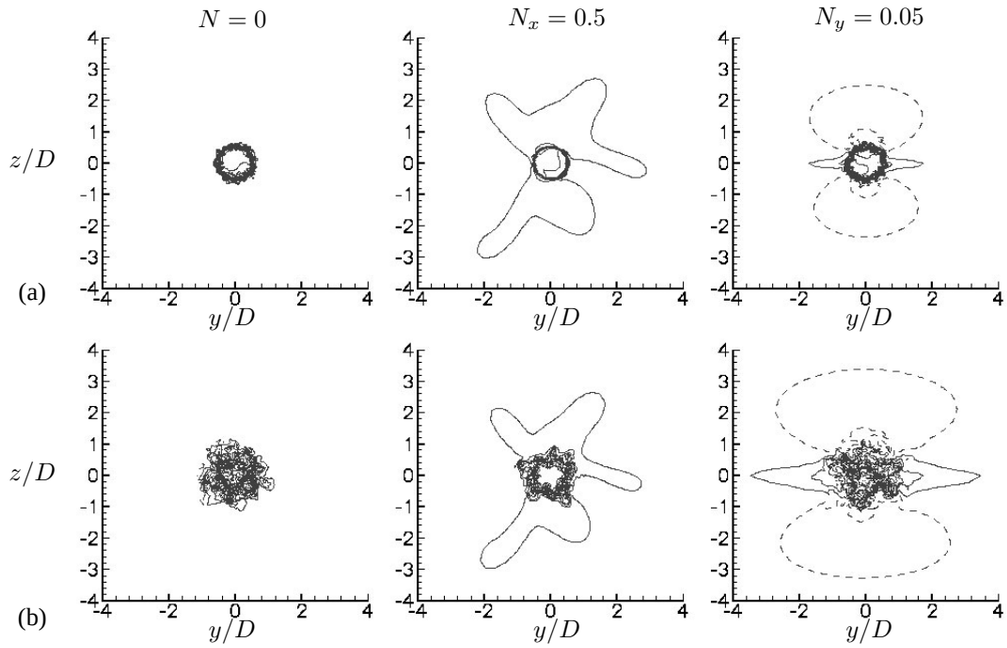


Figure 1. Contours of the instantaneous axial velocity in the cross-sectional plane: (a) $x/D = 1$; (b) $x/D = 5$. Dashed line represents the negative value.

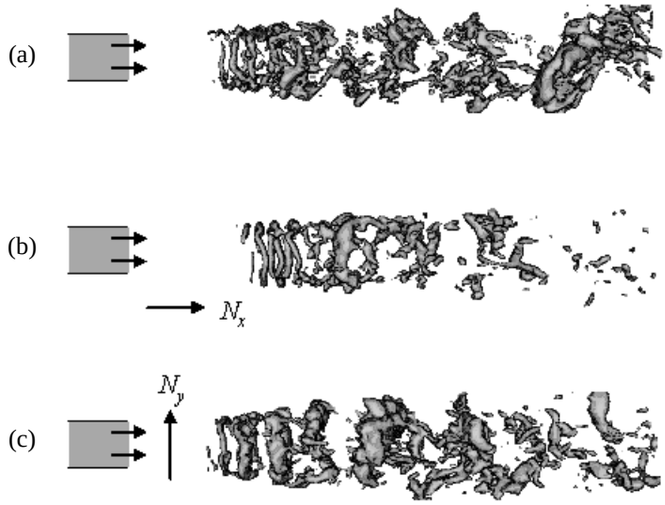


Figure 2. Instantaneous vortical structures: (a) without magnetic field; (b) $N_x = 0.5$; (c) $N_y = 0.05$.

References

[1] Sajben, M., Fay, J.A.: Measurement of the growth of a turbulent mercury jet in a coaxial magnetic field. *J. Fluid Mech* **27**:81–96, 1967.
[2] Davidson, P.A.: Magnetic damping of jets and vortices. *J. Fluid Mech* **299**:153–186, 1995.
[3] Crow, S.C., Champagne, F. H.: Orderly structure in jet turbulence. *J. Fluid Mech* **77**:397–413, 1971.
[4] Germano, M., Piomelli, U., Moin, P., Cabot, W.H.: A dynamic subgrid-scale eddy viscosity model. *Phys. Fluids A* **3**:1760–1765, 1991.
[5] Lilly, D.K.: A proposed modification of the Germano subgrid-scale closure method. *Phys. Fluids A* **4**:633–635, 1992.
[6] Akselvoll, K., Moin, P.: Large eddy simulation of turbulent confined coannular jets and turbulent flow over a backward facing step. *Report No. TF-63*, Thermoscience Division, Department of Mechanical Engineering, Stanford University, Stanford, CA.
[7] Lee, D., Choi, H.: Magnetohydrodynamic turbulent flow in a channel at low magnetic Reynolds number. *J. Fluid Mech* **439**:367–394, 2001.

Observations of the magnetorotational instability in spherical Couette flow

Daniel P. Lathrop
University of Maryland, College Park, MD 20904

January 2, 2004

Experiments conducted in liquid sodium confined between a rotating inner sphere and a concentric stationary outer sphere show a host of magneto- hydrodynamic behavior.

The experimental system consists of a 10 cm diameter copper rotating inner sphere and a 30 cm diameter stainless steel stationary outer sphere. A coaxial external magnetic field is supplied using an external electromagnet. The base state shows a rotation rate profile which is Rayleigh stable (Ωr^2 rising in cylindrical r), and magnetorotationally unstable (Ω falling in cylindrical r) [1]. The rotation rate profiles and oscillations were measured using ultrasound Doppler velocimetry.

With a sufficiently strong external applied field, this system exhibits the magnetorotational instability. The angular momentum transport increases at the instability onset. The primary instability shows a continuous bifurcation to a rotating m=1 pattern in the magnetic field, and concomitant oscillations in the velocity field.

By varying both the rotation rate and the external magnetic field (made dimensionless as the magnetic Reynolds number and the Lundquist number respectively), we have navigated the parameter plane to observe a number of states with distinct dominant wavenumber and parity. These include states with dominant patterns with even and odd symmetry with respect to inversion through the origin. Patterns with dominant azimuthal wavenumbers $m = 0$, $m = 1$, and $m = 2$ have been observed.

The onset conditions compare favorably with expectations from linear stability calculations [2]. This is remarkable considering the significant background turbulence (15

Finally we have explored the suitability of spherical Couette flow to show dynamo action. We conjecture that for a rotating outer sphere and a stationary inner sphere, that (using the notation of Dudley and James [3]) a S_2T_1 velocity pattern suitable for dynamo action can be achieved. We will present measurements of pulse decay measurements for external magnetic fields to test this conjecture.

References

[1] S.A. Balbus, and J.F. Hawley, "Instability, turbulence, and enhanced transport in accretion disks." Rev. Mod. Phys. 70, 1-51 (1998).

[2] J. Goodman, and H. Ji, "Magnetorotational instability of dissipative Couette flow," J. Fluid Mech. 462, 365-382 (2002)

[3] M. L. Dudley and R. W. James, "Time-dependent kinematic dynamos with stationary flows," Proc. R. Soc. Lond. A 425, 407 (1989).

SIMULATING THE ORSZAG-TANG VORTEX USING RSPH

Steinar Børve*, Marianne Omang**, Jan Trulsen*
*Institute of Theoretical Astrophysics, University of Oslo, P.O. Box 1029 Blindern, N-0315 Oslo, Norway
**Norwegian Defence Estates Agency, P.O. Box 405 Sentrum, N-0103 Oslo, Norway

Summary The formation of the compressible Orszag-Tang vortex has become a standard test for multi-dimensional MHD codes. In the present work, the problem is studied using the Lagrangian method Regularized Smoothed Particle Hydrodynamics (RSPH). First, a brief introduction to RSPH is given. Then, test results are presented, both for the case of uniform and non-uniform resolution. The results indicate that RSPH is a fully competitive, Lagrangian alternative to traditional grid-based methods for this type of problem.

INTRODUCTION

Regularized Smoothed Particle Hydrodynamics (RSPH) is an extension to the Lagrangian method Smoothed Particle Hydrodynamics (SPH) [1]. It was developed with the aim of achieving high accuracy modelling of hydrodynamic and magnetohydrodynamic problems using a highly adaptive numerical description [2]. In SPH based methods, a continuous fluid is represented by a discrete set of interacting particles moving with the fluid flow. Based on interpolation theory, the equations of motion can be expressed using integral interpolants, which in the discrete case are approximated by summation interpolants. The key parameter in determining the resolution of the interpolation is referred to as the smoothing length, denoted h [3].

RSPH differs from standard SPH in two important aspects. First, the former method allows h to vary both in time and space by orders of magnitude based on flexible, problem-specific criteria. The h-profile is chosen to be piecewise constant, with each step in space representing a factor of 2 change in h. Secondly, RSPH allows the particle distribution to be redefined at temporal intervals through a mass, momentum, magnetic energy, and total energy conserving process. Highly irregular particle distributions and particle penetration can thus be avoided, leading to reduced numerical errors. In comparison, standard SPH codes typically apply a uniform h-profile, or at best, allow h to vary slowly in time and space as a function of the particle number density. In addition, standard SPH does not provide any mechanism for optimizing the particle distribution during a simulation.

RSPH equations of motion

The ideal MHD model equations are found by neglecting the displacement current as well as the effects of electrical resistivity, viscosity and thermal conduction. The continuous equations are expressed in terms of the Lagrangian derivative $D/Dt = \partial/\partial t + \boldsymbol{v}\cdot\nabla$, and the units of the magnetic field are chosen so that the factor $1/\mu_0$ does not appear explicitly in the equations. For a given particle a, the discrete equations can be written as summations over neighbouring particles b:

$$\frac{d\boldsymbol{r}_a}{dt} = \boldsymbol{v}_a, \tag{1}$$

$$\rho_a = \sum_b m_b \mathcal{W}_{ab}, \tag{2}$$

$$\frac{d\boldsymbol{v}_a}{dt} = \sum_b m_b \left(\frac{\boldsymbol{\mathcal{M}}_b}{\rho_b^2} + \frac{\boldsymbol{\mathcal{M}}_a}{\rho_a^2} + \Pi_{ab} \right) \cdot \nabla_a \mathcal{W}_{ab} - \boldsymbol{B}_a \sum_b m_b \left(\frac{\boldsymbol{B}_b}{\rho_b^2} + \frac{\boldsymbol{B}_a}{\rho_a^2} \right) \cdot \nabla_a \mathcal{W}_{ab}, \tag{3}$$

$$\frac{de_a}{dt} = \sum_b m_b \left(\frac{P_a}{\rho_a^2} + \frac{1}{2}\Pi_{ab} \right) \boldsymbol{v}_{ab} \cdot \nabla_a \mathcal{W}_{ab}, \tag{4}$$

$$\frac{d\boldsymbol{B}_a}{dt} = \frac{1}{\rho_a} \sum_b m_b (\boldsymbol{B}_a \boldsymbol{v}_{ab} - \boldsymbol{v}_{ab} \boldsymbol{B}_a) \cdot \nabla_a \mathcal{W}_{ab}, \tag{5}$$

$$P_a = (\gamma - 1) e_a \rho_a, \tag{6}$$

where m_a, $\boldsymbol{r}_a$, $\boldsymbol{v}_a$, ρ_a, P_a, $\boldsymbol{B}_a$, and e_a are the mass, position, velocity, mass density, thermal pressure, magnetic field strength, and internal energy of particle a. The term $\boldsymbol{\mathcal{M}}_a$ denotes the stress tensor given by

$$\boldsymbol{\mathcal{M}}_a = \boldsymbol{B}_a \boldsymbol{B}_a - \left(\frac{1}{2} \boldsymbol{B}_a{}^2 + P_a \right) \boldsymbol{\mathcal{I}}, \tag{7}$$

where $\boldsymbol{\mathcal{I}}$ is the unity tensor. The weight kernel used in this work, $\mathcal{W}_{ab} = \mathcal{W}(\boldsymbol{r}_a - \boldsymbol{r}_b, h_{ab})$, is the third order central B-spline with the characteristic scale length $h_{ab} = (h_a + h_b)/2$ [3]. The artificial viscosity term, Π_{ab}, is needed when modelling shocks [3]. The ratio of specific heat at constant volume and constant pressure is given by γ.

THE ORSZAG-TANG VORTEX

The 2D Orszag-Tang vortex problem was originally studied in the context of incompressible MHD turbulence [4]. Since then, a supersonic version of the problem has become a frequently used test of compressible MHD codes, see e.g. [5]. The test is set up in a 2D quadratic box with sides 1 length unit and periodic boundary conditions. The initial profiles of velocity and magnetic field are

$$\boldsymbol{v}(x,y) = [-\sin(2\pi y), \sin(2\pi x)] \tag{8}$$

and

$$\boldsymbol{B}(x,y) = \frac{1}{(4\pi)^{1/2}}[-\sin(2\pi y), \sin(4\pi x)], \tag{9}$$

respectively. The mass density and thermal pressure are initially uniform and equal to $25/(36\pi)$ and $5/(12\pi)$, respectively, and $\gamma = 5/3$.

In figure 1 the mass density is plotted at $t = 0.5$ for 4 different simulations. In the first 3 simulations, a uniform h-profile is used with an initial, rectangular lattice particle configuration of 128×128 (case a), 256×256 (case b), and 512×512 (case c) particles. One can see that the resolution is improved by increasing the number of particles and that the results fit well with earlier results [5]. In case d, a variable h-profile with a time-averaged particle number of roughly 47300, is used. Note that the resolution obtained in the central region in case d is comparable to that obtained in the same region in case c, despite the fact that more than 5 times as many particles have been used in case c.

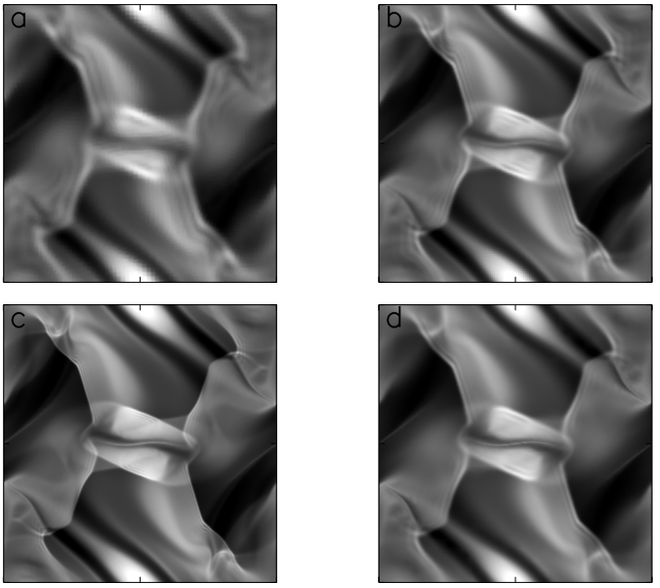


Figure 1. Mass density at $t = 0.5$ obtained from three different simulations using a uniform resolution of 128×128 (a), 256×256 (b), and 512×512 (c) particles, and a nonuniform resolution with a time-averaged particle number of roughly 47300 (d).

CONCLUSIONS

In this paper, the particle method RSPH has been used to study the Orszag-Tang vortex problem. Using a uniform h-profile, the accuracy of the presented results are comparable to that obtained with other methods. It is also shown that using a non-uniform h-profile, the time-averaged particle number can be reduced considerably with little reduction in accuracy. In problems where dominating features are more isolated than what is the case in the current problem, the benefit from using a non-uniform h-profile is expected to be even greater. Based on these results, RSPH appears to be a fully competitive, Lagrangian alternative to traditional grid-based methods when studying a large class of MHD problems.

References

[1] Gingold R.A., Monaghan J.J.: Smoothed particle hydrodynamics: theory and applications to non-spherical stars. *Mon. Not. R. Astron. Soc.* **181**:375–389, 1977.
[2] Børve S., Omang M., Trulsen J.: Regularized smoothed particle hydrodynamics: A new approach to simulating magnetohydrodynamic shocks. *Astrophys. J.* **561**:81–93, 2001.
[3] Monaghan J.J.: Smoothed particle hydrodynamics. *Annu. Rev. Astron. Astrophys.* **30**:543–574, 1992.
[4] Orszag S.A., Tang C.-M.: Small-scale structure of two-dimensional magnetohydrodynamic turbulence. *J. Fluid Mech.* **90**:129–143, 1979.
[5] Dai W., Woodward P.R.: On the divergence-free condition and conservation laws in numerical simulations for supersonic magnetohydrodynamic flows. *Astrophys. J.* **494**:317–335, 1998.

Homogenisation of electrically heated glass melts by Lorentz forces

U. Krieger*, B. Halbedel, D. Hülsenberg, A. Thess

Department of Mechanical Engeneering
Technical University of Ilmenau
P.O. Box 100565
D-98694 Ilmenau
Germany

Abstract:
We report a series of experimental investigations about the stirring effect and the homogenisation of Lorentz forces in glass melts. By variation of the electrical current and the magnetic field the interaction of the electromagnetic force and the temperature gradient driven convection is analysed. We verify the capability of Lorentz forces to effectively stir the glass melt, to redistribute the temperature field and to homogenise the material.

Introduction:
The material qualities of glass are very attractive for many applications in industry as well as for domestic purposes. Specifically, attractive properties are its chemical durability, transparency or high electrical resistance, which mainly depend on the chemical composition of the glass and the processing parameters. The homogeneity of the material before the last manufacturing step significantly affects the quality of the production.
In glass melts occur only slow laminar flows due to their high viscosity η and small Reynolds numbers ($Re \approx 1$). Therefore, insufficient mixing causes high concentration gradients produced by solution residuals of the glass tank, surface evaporation or contaminants of feed material. Viewable defects evolve from this inhomogeneities caused by different refraction index from $\Delta n \approx 10^{-4}$ or changes of ≈0,5% in chemical composition [1].
To provide isotropic properties, mechanical stirring is used, but the corrosion of the stirrer causes material loss and extra impurity in glass melts. The employment of electromagnetic mixing may lead to a new possibility for the homogenisation and processing technique in glass melts.

Experiments:
As stated in the literature [2,3,4] direct electrical heating (by electrodes in the glass melts) enhances the homogeneity of the material due to auxiliary thermal energy and additional effects. With the interaction of an external magnetic field perpendicular to the electrical field Lorentz forces

(1) $$\vec{f}_L = \vec{j} \times \vec{B}$$

are generated (equation 1), which reinforce or counteract the temperature gradient driven convection. Both physical values, the electric current density j, and the magnetic flux density B, have alternating quantities with the same frequency and direction is adjust with phase angle.
The effect of electromagnetic stirring is currently not used in industrial glass manufacturing processes. Hence, our research project aimed at the determination of the stirring activation by Lorentz forces in highly viscous liquids with small electrical conductivities, as well as at the detection of the homogenisation and change of flow characteristics applied to the refining process in special glass melts [5].
We have systematically explored several experiments characterized by different values of the heating electrical current, the intensity of the magnetic field and the direction of the Lorentz forces. Furthermore, the investigation of material from specimens showed an improved homogeneity at similar optical and physical properties (e.g. density, refraction index, transmission). The used glass composition consists of 30% SiO_2 – 49,275% BaO – 20,725% B_2O_3 (wt%) and showed no crystallisation. To verify the results of the hot experiments we analyse model fluids to get visual information about the changes in the convection flow. In addition to that numerical simulations and analytical modelling complete the research.

Conclusions:
We have systematically explored the potential of electromagnetic forces for the enhancement of mixing and homogenisation in glass melts. By variation of different physical parameters in experiments and additional studies we qualified the interaction of bouyancy and Lorentz forces. The application of our findings may lead to significant improvements in the production of glass and show that extensive further research is necessary in order to make full use of capabilities for the electromagnetic processing of materials (EPM) in glass technology.

* Corresponding author: Uwe.Krieger@tu-ilmenau.de

Acknowledgment:
This study is supported by the Deutsche Forschungsgemeindschaft in frame of the „Forschergruppe Magnetofluiddynamik“. We would like to thank all participants and co-workers in the research group for their cooperation and kind assistance in this research.

References:

[1] H. JEBSEN-MARWEDEL, R. BRÜCKNER : *Glastechnische Fabrikationsfehler* : p. 67, Springer Verlag, 1980

[2] G. NÖLLE : *Technik der Glasherstellung* : p. 106, Deutscher Verlag für Grundstoffindustrie, 1997

[3] O.R. HOFMANN, A. THESS : *Elektromagnetische Beeinflussung der Glasbadströmung – ein neues Anwendungsbeispiel der Magnetohydrodynamik* : Glas - Ingenieur, **1**, 39-45, 2002

[4] J. STANEK, : *Electric Melting Of Glass* : pp. 215-220, Elsevier Amsterdam-Oxford-New York, 1977

[5] B. HALBEDEL, G. CONRAD, D. HÜLSENBERG : *Elektromagnetisches Rühren von Glas-schmelzen – Nachweis elektromagnetisch initiierter Strömungen in Glasschmelzen* : Workshop Elektroprozesstechnik: „Elektromagnetische Verfahrenstechniken - Induktives Erwärmen, Schmelzen und Rühren - Kristallisation im Magnetfeld - Elektromagnetische Strahlungstechnologien“, Technische Universität Ilmenau - Fachgebiet Elektrowärme - 25.-26. Sept. 2003

A model for liquid metal electric current limiters

Andre Thess[*], Yurii Kolesnikov[*], T. Boeck[**]
[*]*Department of Mechanical Engineering, Ilmenau University of Technology, P.O. Box 100565, 98684 Ilmena,. Germany*
[**]*Laboratoire de Modelisation en Mecanique, Université Pierre et Marie Curie, 8 rue du Capitain Scott, 75015 Paris, France*

Summary We present a simple model which describes the complex interplay between electromagnetic forces, inertia, and gravity in liquid metal current limiting devices utilizing the electromagnetic pinch effect. The dynamics of this system is described by a nonlinear differential equation for the fluid height. A bifurcation analysis of stationary states shows that for sufficiently high initial fluid levels the fluid height is a discontinuous function of the electrical current. The jump in fluid height above some critical current is accompanied by a strong increase of the total electric resistance of the system and results in the current limiting action of the device. An experimental study of the system confirms the predicted switching behavior. For low electric current the experiment is in quantitative agreement with the theory. Due to its conceptual and numerical simplicity our model enables us to isolate the pertinent parameters and scaling laws of liquid metal current limiters.

SUMMARY

When an electric current passes through an electrically conducting fluid, the interaction of the current with its own magnetic field produces a Lorentz force acting inwardly which can lead to an instability resulting in a reduction of the cross section of the fluid. This phenomenon, called pinch effect, has first been observed in a liquid metal in Northrup's classical experiment [1] and has since received considerable attention in plasma physics ([2] and references therein) as well as in liquid metal magnetohydrodynamics [3], [4].

Recently, the liquid metal pinch effect has found a new application in electrical engineering for current limiting devices in switchgear assemblies [5], [6]. Traditionally, a current limiter (e.g. a fuse) is a device which interrupts the electric current in a network in case of a short-circuit. After removal of the cause of the short-circuit the device has to be replaced or mechanically restored which may incur substantial expenditures, especially in industrial applications characterized by high electric power. In contrast, liquid metal current limiters exploit the pinch effect which reduces the cross section of the fluid and thereby leads to a drastic increase of the resistance via ignition of an electric arc. To effectively limit the maximum current this process has to be very fast (a few ms). An important advantage of a liquid metal current limiter is its "self healing" property. When the short circuit fault is removed, the system returns to its initial state without any external action. In spite of considerable progress in the design of such devices, the understanding of the underlying magnetohydrodynamic (MHD) phenomena is still far from complete. More specifically, no systematic theory is available to date that would be capable of describing the dependence of the critical electric current and of the response time on the geometry and other parameters of the system. Although full-scale numerical simulations of the coupled fluid-dynamic electromagnetic problem for realistic complex geometries provide useful insight, they fail to uncover the basic scaling laws of the system.

The purpose of the present work is to introduce a conceptually simple prototype problem for the current limiting action of the pinch effect in which the mathematical complexity of the governing three-dimensional time-dependent MHD-equations can be reduced to the greatest possible extent, while retaining the intricate interplay between electromagnetic, inertial and gravity forces, respectively. After the definition of our system and a qualitative discussion of its steady state behavior, we will formulate the mathematical model for the general time-dependent case. Further, we report results of a numerical bifurcation analysis supplemented by an analytical treatment in the vicinity of its critical point. We then describe a simple experiment in which we verify the predictions of our model. We finally summarize our conclusions and translate our findings into general scaling relations valid for a broad class of wall-bounded pinch effects under the influence of gravity forces.

References

[1] Northrup E: *Phys Rev* **24** 474-497, 1907.
[2] Biskamp D., 1993 Nonlinear Magnetohydrodynamics, Cambridge University Press.
[3] Bojarevics V., Y. Freibergs, E.I. Shilova, E.V. Shcherbinin: 1988 Electrically Induced Vortical Flows, Kluwer Academic.
[4] Davidson P.A.: Magnetohydrodynamics in Materials Processing. Annu. Rev. Fluid Mech., **31**, 273--300, 1999.
[5] Terhoeven P., Berger F., Krätzschmar A., Freyermuth, T., 2001, German Patent DE0010018564A1.
[6] Thess A., Boeck Th., Terhoeven P., Krätzschmar A., Freyermuth Th. 2004 German Patent DE 102 43 993.1.

THE MAGNETOHYDRODYNAMIC COUETTE FLOW IN A PLANE AND SPHERICAL GEOMETRY WITH SINGULAR HARTMANN BOUNDARY LAYERS

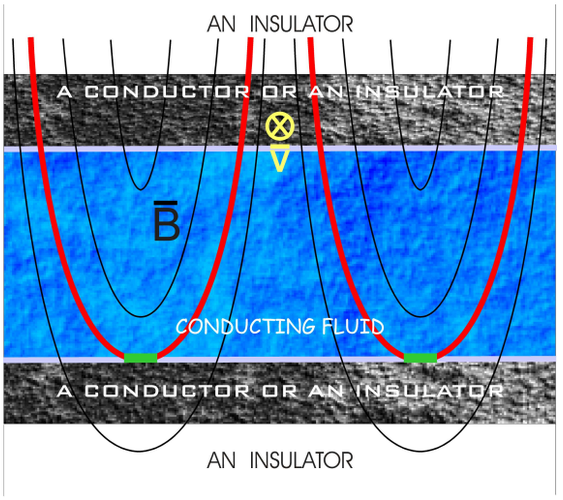
Krzysztof A. Mizerski

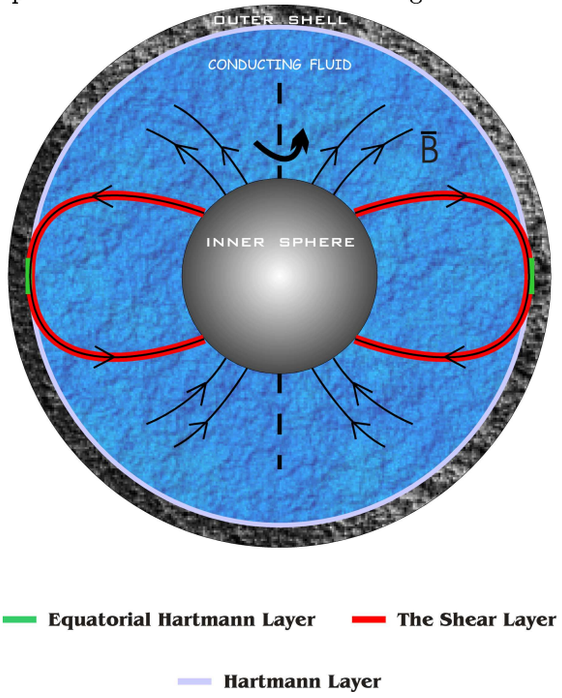
WARSAW UNIVERSITY, Institute of Geophysics, 02-093 Warszawa, Poland

Summary: A magnetohydrodynamic flow between two boundaries one of which is moving with a constant speed is considered here. Two geometries are taken into account: Carthesian and Spherical. The external magnetic field in the system is chosen in such a way that causes the Hartmann boundary layers to become singular at some points. In this configuration the velocity field of the fluid and the infuence of the conductivity of the boundaries on the fluid's movements is studied.

INTRODUCTION AND ASSUMPTIONS

Let's consider a flow of a viscous and conducting fluid between two boundaries which may be either insulating or conducting. One of the boundaries moves *very slowely* at a constant rate what imposes a velocity field in the fluid. The whole system is in *strong* magnetic field chosen in such a way that Hartmann boundary layers which are present in this problem, at some points become singular due to the fact the component of the magnetic field, which is perpendicular to the boundary vanishes. The rest of the space is an insulator.
Two geometries have been taken into account: Carthesian and Spherical what is ilustrated on the figures below:





So the assumptions expressed in terms of the non-dimensional numbers have the form:

$$Re_M = \frac{vL}{\chi} \ll 1 \quad Re = \frac{\rho v L}{\eta} \ll 1 \quad M = \frac{BL}{\sqrt{\mu\eta\chi}} \gg 1$$

where Re and Re_M are the viscous and magnetic Reynolds numbers, v is the velocity of the boundary, L is the thickness of the fluid layer and χ, ρ, η, μ are as follows: the magnetic diffusivity, the density, the viscosity and the magnetic permeability of the fluid.

SOME OF THE RESULTS FOR SPHERICAL FLOW

The solution of the problem stated in the introduction is strongly depended on the character of the boundary - whether it is an insulator, a poor or a good conductor. In this section some of the results for the spherical case (where the external field is assumed to be a dipol field) with slightly conducting outer boundary, meaning that the conductivity of the outer shell is much smaller than the conductivity of the fluid, are presented. Analogical case, but with insulating outer boundary was already resolved by E. Dormy *et al.* (2001), and in this paper I will follow their ideas.

Additional assumptions
In order to make analitical progress some additional assumptions have to be made such as $\epsilon = \frac{\sigma_o}{\sigma} \ll 1$ and $\epsilon M \sim 1$ where σ_o, σ are the electrical conductivities of the outer conductor and the fluid respectively (for simplicity it has been assumed that the conductivity of the inner shere is the same as the conductivity of the fluid).

The summary of results
A boundary layer approximation is used to solve the Navier-Stokes and the induction equations. The boundary layers are of a Hartmann type almost everywhere except for the equatorial region, where the dipol field is tangent to the outer sphere and therefore the boundary layer is singular there. Apart from the boundary layers the velocity and the magnetic field are constant on the dipol field lines therefore the line which is tangent to the outer sphere (red line on the second figure above) has to be treated exceptionally and will be referred to as a critical line.

The influence of the small conductivity of the outer boundary in the Main Flow can be seen only in the magnetic field. The velocity field describes a rigid body rotation with a velocity of the inner sphere due to a strong magnetic interaction between the fluid and the inner conductor.
In the first order of magnitude there is also no influence of the new boundary condition on the solution in the region of the critical dipol field line and in the equatorial Hartmann layer. A non-zero correction to these solutions probably appears in the next order of magnitude.
The most interesting phenomenon in this system are the super-velocities present in the region where the critical dipol field line is tangent to the outer shell. This means that the fluid rotates with the angular velocity greater than the angular velocity of the inner sphere. The solution for these super-velocities is written below:

$$\Omega_S(n) = erf\left(-\frac{n}{\sqrt{8}}\right) - \frac{1}{\sqrt{8\pi}} \int_{-\infty}^{0} \Omega_S(n') \exp\left(-\frac{(n-n')^2}{8}\right) dn' -$$

$$-M^{-\frac{1}{2}} \mathcal{J}_1(1+l, n, M) + M^{-\frac{1}{4}} \mathcal{J}_2(1+l, n, M)$$

where the term $M^{-\frac{1}{4}} \mathcal{J}_2(1+l, n, M)$ is an unknown next order correction outcoming from the fact that the outer boundary is a conductor. Although the precise form of $\mathcal{J}_2(1+l, n, M)$ is not known it can be shown that it is grater than zero, therefore it enlarges the super-rotation, although the factor by which it increases is not evident.

Concluding remarks
This means that the conductivity of the outer boundary has an influence on the magnitude of the super-rotation namely if the conductivity is non-zero the velocities in the equatorial region are larger than in the case of insulating outer boundary.

References:

[1] E. Dormy, D. Jault, A. M. Soward 2001, "A super-rotating shear layer in magnetohydrodynamic spherical Couette flow", *J. Fluid Mech.*

MEAN ELECTROMOTRICE FORCE FOR A RING OF HELICAL VORTICES

Raul A. Avalos-Zuñiga[*], Franck Plunian[*] and Karl-Heinz Rädler[**]
[*]*Laboratoire des Ecoulements Géophysiques et Industriels, BP 53 38041Grenoble CEDEX 9,France*
[**]*Astrophysical Institute Potsdam, An der Stvenwarte 16, D-14482 Potsdam, Germany*

Summary
We study the dynamo mechanism for a flow made of a ring of stationary helical vortices in an electrically conducting media. The choice of this flow is related to the one obtained in thermal convection in a rotating shell which is also expected in the Earth's outer-core. This choice is also related to a sodium experiment, carried out in Grenoble, based on a spherical Taylor-Couette model. Applying the mean field approach and relying on the second order correlation approximation we derive the mean electromotive force (e.m.f.) produced by such a flow. We find that such a ring of helical vortices may produce, from an azimuthal mean magnetic field, an azimuthal mean e.m.f. leading to the generation of a poloidal magnetic field.

INTRODUCTION

A ring of helical vortices is a common feature of thermal convection in a rotating shell. This fluid motion has been reproduced experimentally and numerically [1] for specific ranges of parameters. The question to know if such a flow is relevant to the flow in the Earth's outercore is not answered yet. However there is some interest to investigate further what kind of dynamo mechanism such a flow could produce. Besides, a sodium experiment in preparation in Grenoble is designed to reproduce such a ring of vortices [2][3]. The device is made of a spherical shell in which there is a rotating innercore. Between the innercore and the spherical shell there is liquid sodium, the whole device being in a rotating frame. The difference of rotation between the innercore and the spherical shell produces a shear instability at the innercore tangential cylinder leading to a ring of vortices. These vortices are helical because of Ekman pumping due to the Ekman layers at the top and bottom and also because of the spherical shape of the top and bottom. We want to know what kind of dynamo mechanism such a flow can produce.

DESCRIPTION OF THE WORK

The mean field approach

We assume a given flow ***u***. Instead of calculating directly the magnetic field ***B*** by solving the induction equation

$$\partial B/\partial t = \nabla\times(u\times B) + \eta\nabla^2 B \tag{1}$$

where η is the magnetic diffusivity, we use the mean field approach, decomposing $u = \overline{u} + u'$ and $B = \overline{B} + B'$ into mean and fluctuating parts where the mean is defined as the average in the azimuthal direction φ where (s, φ, z) are the cylindrical coordinates. Then our aim is to calculate the mean electromotive force (mean e.m.f.) defined by $\varepsilon = \overline{u'\times B'}$. We can show (see [4]) that it can be expressed in the form:

$$\varepsilon_\kappa(s) = \breve{a}_{\kappa\lambda}(s)\overline{B}_\lambda(s) + \breve{b}_{\kappa\lambda s}(s)\frac{\partial\overline{B}_\lambda(s)}{\partial s} + \cdots \tag{2}$$

where $\breve{a}$ and $\breve{b}$ are pseudo-tensors of rank 2 and 3. Then knowing $\breve{a}$ and $\breve{b}$ the dynamo problem is reduced to solving the mean part of the induction equation:

$$\frac{\partial\overline{B}}{\partial t} = \nabla\times(\overline{u}\times\overline{B}) + \nabla\times\varepsilon + \eta\nabla^2\overline{B}\ . \tag{3}$$

Assumptions

Let us write the fluctuating part of the induction equation:

$$\frac{\partial B'}{\partial t} = \nabla\times(u'\times\overline{B}) + \nabla\times(\overline{u}\times B') + \nabla\times(u'\times B') - \nabla\times(\overline{u'\times B'}) + \eta\nabla^2 B' \tag{4}$$

Then we consider the low conductivity limit (see [4]), leading to neglecting the term at the left hand side of (4). We also consider that the second order approximation (see [4]) is valid (leading to neglecting the 3rd and 4th terms of the right hand side of (4)). Finally, we consider that the mean e.m.f. does not depend on $\overline{u}$ (see [4]), assuming that it is sufficient to consider $\overline{u}$ in (3) only.
Finally we come out with the following equation to solve:

$$\eta\nabla^2 B' = -\nabla\times(u'\times\overline{B})\,. \tag{5}$$

The velocity field

The flow is considered to be steady, z-independent and harmonic in φ. It is non-zero for $1-\delta \le s/l_0 \le 1+\delta$ where l_0 is a typical length scale defined by the radius of the ring of vortices. The velocity is defined by $u = (u_s(s)\sin m\varphi, u_\varphi(s)\cos m\varphi, u_z(s)\cos m\varphi)$ and a typical example is given in figure 1.

Tensor of second rank

Solving (5) and replacing *B'* in $\varepsilon = \overline{u' \times B'}$, we find that $\breve{a}_{\kappa\lambda} = \frac{\eta}{l_0} R_m^H \begin{pmatrix} R_m^Z \tilde{a}_{ss} & 0 & 0 \\ 0 & R_m^Z \tilde{a}_{\varphi\varphi} & 0 \\ 0 & R_m^H \tilde{a}_{z\varphi} & 0 \end{pmatrix}$ with $R_m^H = \frac{u_0^H l_0}{\eta}$ and

$R_m^Z = \frac{u_0^Z l_0}{\eta}$, u_0^H and u_0^Z being typical horizontal and vertical velocities, and with:

$$\tilde{a}_{ss} = -\frac{1}{2}\int_0^\infty \left(\frac{\partial h_m(s,s')}{\partial s'} u_\varphi(s) u_z(s') + \frac{\partial h_m(s,s')}{\partial s'} u_z(s) u_\varphi(s') \right) s' ds'$$

$$\tilde{a}_{\varphi\varphi} = \frac{m}{2}\int_0^\infty \left(\frac{h_m(s,s')}{s} u_z(s) u_s(s') + \frac{h_m(s,s')}{s'} u_s(s) u_z(s') \right) s' ds'$$

$$\tilde{a}_{z\varphi} = -\frac{1}{2}\int_0^\infty \left(\frac{\partial h_m(s,s')}{\partial s} u_s(s) u_s(s') + m \frac{h_m(s,s')}{s} u_\varphi(s) u_s(s') \right) s' ds'$$

and where $h_m(s,s') = \frac{1}{2m}\left(\frac{s'}{s}\right)^m$ for $s' \le s$ and $h_m(s,s') = \frac{1}{2m}\left(\frac{s}{s'}\right)^m$ for $s \le s'$.

The tensor of third rank has also been calculated but cannot be included in this short summary.

One example

As an example, we consider the velocity profile defined by $u_z / u_0^Z = \frac{15\pi}{16}(1-\xi^2)^2 \cos m\varphi$ and

$(u_s, u_\varphi, 0)/u_0^H = -e_z \times \nabla\psi$ with $\psi = \delta(1-\xi^2)^3 \cos m\varphi$ and $\xi = \frac{s-1}{\delta}$. The *s*-profiles obtained for the three coefficients $\tilde{a}$ are given in figure 2 in the case where $\delta m = \pi/2$, corresponding to helical vortices with similar length scales in the *s* and φ directions.

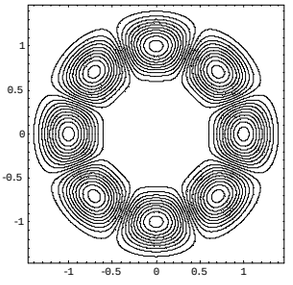


Fig.1. Isolines of u_z for *m*=4.

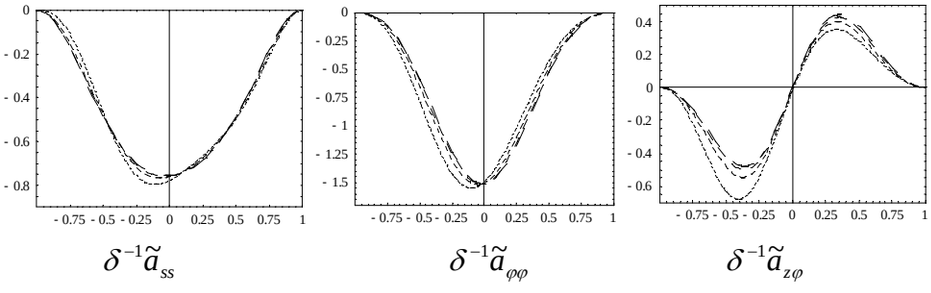


Fig.2. The functions $\delta^{-1}\tilde{a}$ versus $(s-1)/\delta$ for $\delta m = \pi/2$ and *m*=1, 2, 4, 8, 16

CONCLUSIONS AND FURTHER WORK

The coefficient $\breve{a}_{\varphi\varphi}$ being not zero and even dominant compared to the others, we can conclude that from an azimuthal mean magnetic field an azimuthal mean e.m.f. is generated. Then this e.m.f. can generate a poloidal magnetic field. The generation of a azimuthal field from a poloidal field by some differential rotation $\bar{u}$ could then close the loop. We are now considering the case where the flow is z-dependent. In the future we shall examine the influence of $\bar{u}$ onto the mean e.m.f.

References

[1] E. Dormy, A. M. Soward, C. A. Jones, D. Jault & P. Cardin The onset of thermal convection in rotating spherical shells, *J. Fluid Mech* , 2004.

[2] P. Cardin, D. Brito, D. Jault, H.-C. Nataf and J.-P. Masson, Towards a rapidly rotating liquid sodium dynamo experiment, *Magnetohydrodynamics* **38** No. 1-2, 177-189, 2002.

[3] N. Schaeffer, P. Cardin, Boundary driven shear layer instability in a rotating fluid, submitted to *J. Fluid Mech* 2004.

[4] F. Krause F., K.-H. Rädler, Mean-Field Magnetohydrodynamics and Dynamo Theory. Akademie-Verlag, Berlin 1980.

XXI ICTAM, 15–21 August 2004, Warsaw, Poland

NUMERICAL SIMULATIONS OF DYNAMO EXPERIMENTS

Andreas Tilgner
Institute of Geophysics, University of Göttingen, Herberger Landstrasse 180, 37075 Göttingen

Summary Several experimental groups throughout the world have reproduced the dynamo effect on a laboratory scale or are preparing to do so. All experiments rely on numerical simulations, both in the design phase and for data analysis. This talk presents a few examples of how experiments and simulations interact, and where they agree and disagree, in particular for the Karlsruhe experiment. Possible implications for the geodynamo will also be discussed.

An experiment built in Karlsruhe has recently reproduced the dynamo effect on a laboratory scale . In this experiment, liquid sodium is pumped through a vessel which contains 52 cells arranged in a square lattice. Each cell consists of two coaxial pipes and a blade of helical shape inserted in the space between the inner and the outer pipe. The sodium flows straight through the inner pipe but is forced to flow along a right handed helix in between the two pipes of each cell. The flow alternates directions between adjacent cells. Two different length scales characterize the experiment: The size of each cell and the size of the entire sodium vessel. The two length scales differ by a factor somewhat larger than 8. This approximate separation of scales sets the Karlsruhe experiment apart from another successful experiment run in Riga.

In the experiment, the 52 cells are enclosed in a cylinder. However, parts of the piping which lead sodium from one cell to a neighboring cell stick out from the cylindrical container. The real geometry is too complicated to be simulated exactly.

A dynamo in a finite cylinder is cumbersome to handle numerically because of the corners and because there is no analytic expression for a potential field outside a finite cylinder. For the simulations, the cylinder has been embedded in the smallest sphere capable of enclosing the cylinder. The space between the cylinder and the spherical boundary is assumed to be filled with sodium at rest. This surrounding sodium is of course the strongest approximation involved in the simulations presented here. In accompanying computations, the space between cylinder and sphere has been filled with material of magnetic diffusivity 10 times larger than the diffusivity of sodium. These computations have shown that the outer conductor reduces the critical volumetric flow rates and that the general structure of the magnetic field is not affected by the outer conductor.

Another uncertainty concerns the value of the magnetic diffusivity. The simulations use a uniform diffusivity whereas the experiment consists of both sodium and stainless steel structures. Moreover, the spatially averaged resistivity is anisotropic. The resistivities perpendicular and parallel to the cell axis are a factor 1.3 and 1.06 larger than the resistivity of pure sodium, respectively. Turbulence further increases the magnetic diffusivity. However, the turbulent diffusivity can be estimated at $2.5 \times 10^{-3} m^2/s$ which is a negligible contribution compared with the molecular value.

Despite all the approximations involved in the simulations, the central quantities are identical in the experiment and the simulations. The onset of dynamo action and the field morphology outside the sodium are well predicted numerically. Discrepancies still exist in the shape of the interior field and some aspects of the dynamics of the magnetic field are not yet understood.

Peffley et al. have started an experimental investigation of a class of flows originally studied numerically by Dudley and James. Similar flows are currently under study by other groups as well. These flows exist in a sphere and are axisymmetric. Two counterrotating propellers with coaxial shafts set the liquid sodium into motion. The magnetic Reynolds number Rm reached in the experiment is insufficient to obtain self-excitation of the magnetic field $\mathbf{B}$. The approach to the critical Rm is diagnosed by applying an external magnetic field either parallel or perpendicular to the propeller axes and by observing the decay of $\mathbf{B}$ after the external field has been switched off. The radial component of the magnetic field is measured by an array of Hall probes placed on a ring coaxial with the axis of symmetry of the flow. The decay rates of the non-axisymmetric fields excited by an external field perpendicular to the axis of symmetry increase with increasing Rm. On the other hand, a field parallel to the shafts excites predominantly axisymmetric modes. The decay rate of these modes decreases with increasing Rm up to the highest Rm reached in the experiment. Extrapolation of the experimental curve to higher Rm predicts that the growth rate will become positive at sufficiently high Rm (around 160). Peffley et al. conclude that non-axisymmetric components in their flow must be essential to the dynamo mechanism because an axisymmetric velocity field generates a dynamo field without any axisymmetric component according to kinematic dynamo theory.

The second experimental finding of relevance here is the apparent spatial variability of the decay rates. Surprisingly, different decay rates of the magnetic field are measured at different locations. It is not surprising that different decay rates are measured from pulse to pulse if the external magnetic pulse is repeatedly applied to a turbulent flow. However, if the decaying field following a single pulse corresponds to the eigenmode with the smallest decay rate, one expects to find one single decay rate at all positions after an initial transient. The value of that decay rate depends on the actual shape of the (time dependent) velocity field during the decay.

It will be shown in this talk that the experimental data are nonetheless compatible with the assumption that global magnetic eigenmodes of an axisymmetric velocity field are observed. A model based on kinematic dynamo theory reproduces the experimental findings if one assumes that a superposition of eigenmodes is excited by the combined effect of the external field and turbulent fluctuations.

STABILITY OF LIQUID METAL DROPS AFFECTED BY HIGH-FREQUENCY MAGNETIC FIELDS

Václav Kocourek[1], Christian Karcher[2] and Dietmar Schulze[1]

[1]*Department of Electroheat, Technische Universität Ilmenau*
[2]*Department of Mechanical Engineering, Technische Universität Ilmenau*

Summary The dynamic behavior of sessile liquid metal drops submitted to a high-frequency magnetic field is investigated experimentally. The drops are of Galinstan and placed on a curved glass plate. A ring-like inductor fed by an alternating electrical current generates the magnetic field. The free surface contour of the drop is observed using a high-speed camera system. In the experiment we vary the inductor current and the drop volume while the frequency is fixed. Upon increasing the inductor current static axisymmetric squeezing ($0 \le I < I_C$) and following azimuthal waves ($I \ge I_C$) were observed.

INTRODUCTION

Alternating electromagnetic fields can induce Lorentz forces within electrically conducting liquids. Due to the so-called skin effect, at high frequency the Lorentz forces are acting only in a thin layer adjacent to the free surface of the liquid metal. They correspond to magnetic pressure that influences directly the shape and the stability of the surface [1], [2]. Within this context we study experimentally the effects of a high-frequency magnetic field acting on liquid metal drops. The motivation of this work comes from electron beam evaporation where it is favorable to form a liquid metal dome supported by electromagnetic forces only. In this case one may avoid intense contact between the aggressive hot melt with the crucible side walls. Hence, contamination of the melt as well as heat losses are reduced.

EXPERIMENTAL SET-UP

Figure 1 shows a principle sketch of the experimental set-up. It consists of a cylindrical container with an inner diameter of D = 60 mm. A curved glass plate forms the bottom. A slight radius of curvature of r_c = 80 mm is chosen to provide axisymmetric conditions. In the experiments, we place a certain volume of liquid metal on the glass plate. As a test liquid we use a GaInSn alloy of such a composition that its melting point is as low as -19°C (Galinstan). To provide quasi-isothermal conditions, the bottom of the glass plate is water-cooled. During the experiments we cover the drop with hydrochloric acid to avoid oxidation of the free surface.
The electromagnetic field is generated by an inductor arranged at the same height as the drop. This inductor is made of rectangular copper tubes and consists of 10 windings arranged in two layers with an inner radius of r = 48 mm. The inductor is fed by an alternating electrical current of a constant frequency f = 20 kHz.
In the experiments we observe the drop shape from above via a high-speed camera system at a rate of 307.7 frames per second while increasing the feeding current up to 350 A. The drop volume is varied within the range 0.3 ml < V < 11 ml.

RESULTS

Static deformation Upon increasing the inductor current from I = 0 A, we observe a squeezing of the drop due to the induced magnetic pressure acting on its surface. This squeezing effect is characterized by decrease of the drop radius R combined with a mounting-up of the drop in the center. For drop sizes within the range 0.6 ml < V < 11 ml a static squeezing of typically $R/R_0 \approx 0.85$ is possible where R_0 denote the drop radius when the magnetic field is absent. For smaller drops of the size V = 0.3 the squeezing effect is more pronounced as we get $R/R_0 = 0.75$.

Instabilities Upon a further increase of the inductor current to a critical value I_c, the static drop shape become unstable. Depending on drop size, we observe the excitation of axisymmetric waves with azimuthal mode numbers m = 2, 3 and 4. The dependence of I_c on the drop volume is shown in ***Figure 2***. Typically, upon increasing the drop volume, the corresponding critical current decreases while the mode number increases. The stability diagram, i.e. Fig. 2, shows the three parabolas referring to m = 2, 3 and 4, respectively.
For the unstable condition, the drop is oscillating. The measured oscillation frequencies f_m as a function of the drop volume are shown in ***Figure 3.*** The experimental findings are compared to the natural eigenfrequencies defined by [3]

$$f_m = \frac{1}{2\pi}\left(\frac{\sigma m\left(m^2-1\right)}{\rho R^3}\right)^{1/2},$$

where σ and ρ denote the surface tension and the density of the material, respectively, and R is an average value of the radius of the drop in the magnetic field. As obvious from Fig. 3, for each mode number the oscillation frequency decreases with increasing drop volume. The experimental results are in excellent agreement with the prediction of the above equation.

CONCLUSIONS

We have investigated experimentally the effects of a high-frequency magnetic field on (i) the static shape of a liquid metal drop and (ii) the stability of the drop shape. The experiments show that below a certain threshold value of the feeding inductor current, I_c, a static squeezing of the drop is possible. This corresponds to the forming of a stable liquid metal dome in application. However, when $I > I_c$, the drops starts to oscillate with an azimuthal mode number depending on drop volume. The critical inductor current as well as the oscillation frequency decrease with increasing drop volume. The measured oscillation frequencies correspond well with the natural eigenfrequencies of drops based on surface tension.

Acknowledgement This work is sponsored by Deutsche Forschungsgemeinschaft (DFG) under grant FOR 421/1-2 Ka-A3 within the frame of the Forschergruppe Magnetofluiddynamik at Technische Universität Ilmenau.

References

[1] P.A. Davidson: *An Introduction to Magnetofluiddynamics*, Cambridge Academic Press, Cambridge (2001).
[2] R. Moreau: *Magnetohydrodynamics*, Kluwer, Dordrecht (1990).
[3] Y. Fautrelle, J. Etay, and S. Daugan: Free surface horizontal waves generated by low frequency alternating magnetic fields. Fluid Flow Phenomena in Metals Processing, San Diego (1999).

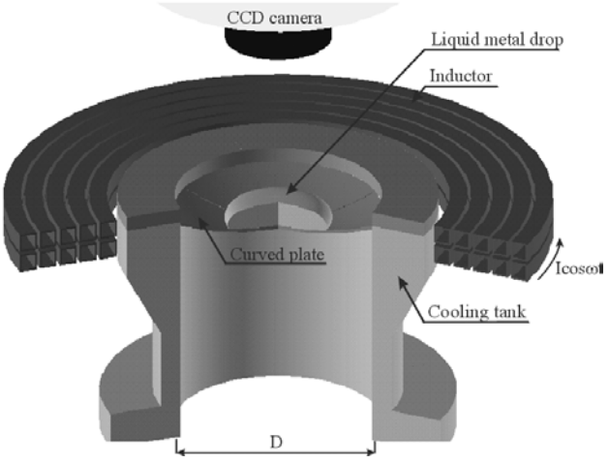


FIG. 1. Sketch of the experimental set-up.

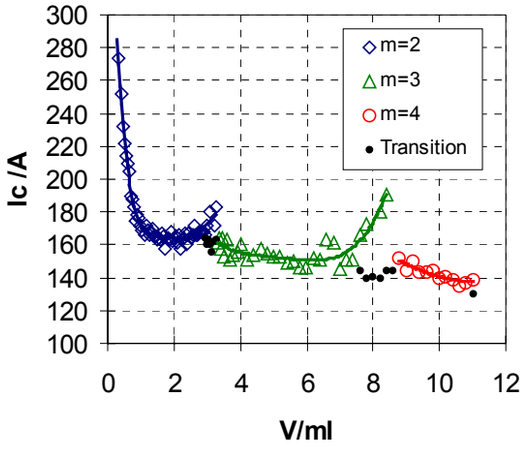


FIG. 2. Stability diagram of a puddle of GaInSn by 20kHz. Critical current for instability.

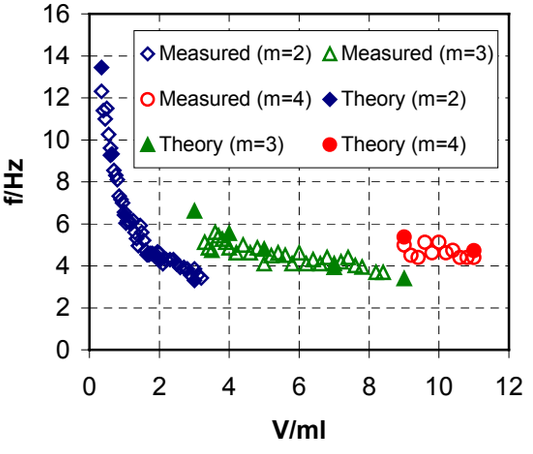


FIG. 3. Comparison between theory and measurement of the drop oscillation frequency.

QUASI-GEOSTROPHIC DYNAMOS

Nathanaël Schaeffer*, Philippe Cardin**
*LGIT, Université Joseph Fourier, Grenoble, France
**LGIT, Université Joseph Fourier, Grenoble, France and CNRS

Summary Taking advantage of the properties of liquid metals and of rapidly rotating flows, we are able to compute dynamos at high Reynolds number ($Re > 10^5$) and low magnetic Prandtl number ($Pm < 10^{-2}$)
We developed a numerical model that uses a quasi-goestrophic approximation to compute the flow (without subgrid scale model), leading to two-dimensional equations. The induction equation for the magnetic field is fully resolved in 3D, in a sphere. This approach proves quite efficient for low magnetic Prandtl number and suitable flows, for which there is a scale separation between magnetic field and velocity field, allowing to compute the magnetic field on a coarser grid and with larger time steps than for the velocity field. We show results of these calculations applied on the turbulent flow produced by the destabilization of a Stewartson shear layer.

INTRODUCTION

The magnetic field of the Earth is produced by a dynamo effect in the metallic liquid core of our rotating planet. Many efforts have been done successfully in the last decade to describe the mechanism of a self induced magnetic field with experimental models and numerical simulations. Both approaches have limitations. No experiment has been done in rotation while rotation is thought as a key ingredient by geophysicists to explain the geometry and the amplitude of the geomagnetic field. All numerical models [4, 5, 6], have introduced the Coriolis force in solving the Navier-Stokes equation, but the prescribed magnetic Prandtl number ($P_m = \nu/\eta$, where ν is the kinematic viscosity and η the magnetic diffusivity) is of order unity, due to current computer capabilities. However, liquid metals exhibit magnetic Prandtl number lower than 10^{-5} in planetary cores [7]. This low value of P_m may indicate a separation, in terms of scales and frequencies, between the velocity and magnetic fields in a metallic dynamo.

NUMERICAL MODEL

We propose an approach that aims to compute very low magnetic Prandtl number dynamo taking advantage of the geostrophic behavior of the velocity field. For very low Ekman number ($E = \nu/\ \Omega R^2$, where Ω is the rotation rate of the spherical container, and R its radius), a quasi-geostrophic (QG) approach model correctly the flow in a rapidly rotating sphere [1, 2, 3]. It consists of the integration of the Navier-Stokes equation along the axis of rotation. Even if the numerical resolution is done with a pseudo current function in the equatorial plane (2D), the top and bottom boundary effect are present through β and Ekman pumping effects in the Coriolis term. We compute the QG flow in the equatorial plane with a fine spatio-temporal resolution, the velocity is extrapolated to a coarse 3D spherical grid where the induction equation is solved. Then, the z-integrated associated Lorentz forces is used to compute the evolution of the velocity field. Even if there is some computation time spent in the conversion between grids, this method is efficient if the scale separation is large enough.

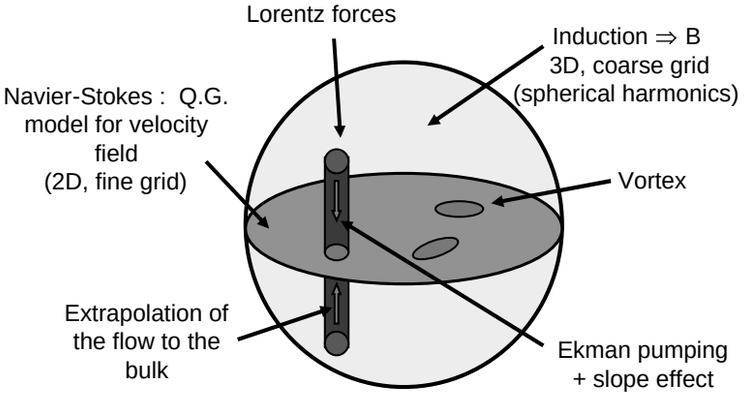


Diagram showing the principles of our quasi-geostrophic dynamo model

TEST CASE : THE STEWARTSON DYNAMO

The forcing

In order to demonstrate the validity of this approach, we decide to apply it to a simple case. Instead of a thermal convective flow where the heat equation has to be solved, we model the flow associated wit the instabilities of an internal geostrophic shear layer. This layer, known as the Stewartson layer, is produced by a differentially rotating inner core in a rotating sphere and consists of two nested viscous shear layers. For large Ro number ($Ro = \Delta\Omega/\Omega$, where $\Delta\Omega$ is the differential

rate of rotation of the inner core), the Stewartson layer may become unstable and generate Rossby waves [8]. For even larger Ro, the flow becomes turbulent. However this turbulence is strongly influenced by the global rotation of the system and is large-scales dominated, with a steep k^{-5} spectrum. This suggest that we can properly neglect the induction due to small scales.

Kinematic dynamo results

For the kinematic dynamo study, we don't compute the Lorentz force, so that the evolution of the flow remains purely hydrodynamic. Some dynamo experiments are reported on the following table. There does not seem to be a limit in Pm or E for driving a dynamo. The only restriction is that the Rossby number remains small enough so that the velocity field can be considered as QG. We will also report some specific features of these dynamos.

E	Ro	Pm	Re
10^{-5}	0.04	5	100
10^{-6}	0.013	0.6	1000
10^{-6}	0.04	0.3	10000
10^{-7}	0.015	0.03	100000
10^{-8}	0.02	0.005	400000

Kinematic dynamos runs for various E,Ro and Pm input parameters. Re is an output parameter.

Lorentz force back-reaction

With the Lorentz force, the magnetic field acts back on the velocity field. However we can show that in the regime of small Rossby numbers, the Elsasser number (measuring the ratio of the Lorentz force by the Coriolis force) remains small, insuring that the Proudman-Taylor constraint is not violated.

References

[1] Aubert J., Gillet N., Cardin P. : Julien Aubert and Nicolas Gillet and Philippe Cardin. *Geochem. Geophys. Geosyst.* **4(7)**,1052 (2003)

[2] Busse F. : Thermal instabilities in rapidly rotating systems. *J. Fluid Mech.* **44**,441-460 (1970)

[3] Cardin P., Olson P. : Chaotic thermal convection in a rapidly rotating spherical shell: consequences for flow in the outer core *Phys. Earth Planet. Inter.* **82**, 235-259 (1994)

[4] Glatzmaier G., Roberts P. : Dynamo model at a turning point. *Nature* **377**,198-199 (1995)

[5] Kageyama A., Sato T. : Generation mechanism of a dipole field by a magnetohydrodynamic dynamo. *Phys. Rev. E* **55**, 4617-4626 (1997)

[6] Kuang W., Bloxham J. : Numerical Modeling of Magnetohydrodynamic Convection in a Rapidly Rotating Spherical Shell: Weak and Strong Field Dynamo Action. *J. Comput. Phys.* **153**,51-81 (1999)

[7] Poirier J-P. : Physical properties of the Earth's core. *C. R. Acad. Sci. Paris* **318**,341-350 (1994)

[8] Schaeffer N., Cardin P. : Boundary driven shear layer instabilities in a rotating fluid. *J. Fluid Mech.* 2004, submitted.

XXI ICTAM, 15–21 August 2004, Warsaw, Poland

MODEL OF GAS FLOW INSIDE A PLASMA THRUSTER

S. Barral*, Z. Peradzyński**, K. Makowski*, M. Dudeck†
*Institute of Fundamental Technological Research - PAS, Warsaw, Poland
**also: Warsaw University, Mathematics Dept., Warsaw, Poland
†CNRS Laboratoire d'Aérothermique, Orléans, France

Summary Stationary Plasma Thrusters (SPT) are high-efficiency electric rocket engines that are ideally suited to spacecraft orbit transfer and positioning missions. By harnessing the power resources available on-board to accelerate a plasma, these engines allow substantial savings on the propellant mass in comparison with chemical rocket engines.

Further improvements of their performance remain hindered, however, by the poor understanding of the underlying physics. With this incentive, a large number of numerical models of the discharge are being developed [1, 2, 3, 4]. In such models, the dynamic of neutral particles (non-ionized propellant) is a key element in the overall description of the discharge. It has been shown in particular that the flow of neutral gas is directly involved in the so called "breathing mode", a low frequency longitudinal mode that strongly affects the operation of the engine.

Because of the complexity of SPT plasmas, many different modeling approaches have been adopted to investigate different time scales and phenomena. In many models of discharge, a fully kinetic description of the gas flow is either not acceptable due to computational constraints or not necessary in view of the low accuracy inherent to the plasma description. Because the Knudsen number of the flow of neutral gas is much larger than one, it is commonly assumed that the mean axial velocity of neutrals is constant through the channel [3, 2]. This assumption is challenged, however, by ionization which acts as a selection process by removing slow neutrals, thus allowing only fast neutrals to reach the exit. Additionally, the diffuse reflections of neutrals on the walls gives rise to a reverse flow and makes the mean axial velocity smaller upstream than downstream.

The goal of this study is to propose a simple, yet more realistic alternative to the classical monokinetic model, using one-dimensional macroscopic equations that account for the phenomena mentioned above.

MAIN ASSUMPTIONS

The annular channel is bounded by two coaxial cylinders of radii R_{in} , R_{out} and of length L. The gas is fed through a circular slit of radius $(R_{in} + R_{out})/2$ located at the closed extremity of the channel (at axial position $z = 0$).

Because the Knudsen number is typically of the order of 100, the flow is supposed collisionless. The gas flow accounts for both ground level and excited neutrals; once a particle is ionized, it is removed from the gas flow. We assume that the distribution function at the gas feed is half-Maxwellian (i.e. consists only of particles with a positive axial velocity) with a temperature T_c equal to that of the channel.

Typical density and mean velocity maps of neutrals in such a channel are represented on Fig. 1.

DERIVATION OF ONE-DIMENSIONAL MACROSCOPIC EQUATIONS

Preliminary result for a stationary flow with smooth walls and ionization

If particles are specularly reflected at the walls and if the ionization frequency ν_i is a function of z only, the distribution of neutrals as a function of their axial velocity integrated over the cross-section evolves along the z axis as

$$f_z(z,\, v_z) = \frac{\dot{M}}{\kappa T_c A} \exp\left(-\frac{m v_z^2}{2\kappa T_c} - \frac{1}{v_z}\int_0^z \nu_i(z)\, dz\right) \qquad \text{with } v_z > 0\,. \tag{1}$$

where $\dot{M}$ is the mass flow rate, m the mass of a neutral, A the cross-section of the channel and T_c the temperature of the channel. Defining now the axial velocity dispersion as $D_z(z) = \frac{1}{n}\int (v_z - V_z)^2\, f_z(z,\, v_z)\, dv_z$ where n is the density and V_z the mean axial velocity of the flow, it can be shown after some manipulations that for any $z > 0$, D_z is bounded by

$$\frac{1}{3}\frac{\kappa T_c}{m} < D_z < \left(1 - \frac{2}{\pi}\right)\frac{\kappa T_c}{m} < 0.364\,\frac{\kappa T_c}{m}\,. \tag{2}$$

Model for rough walls and ionization

Particles which collide with the walls are now assumed to be thermalized. The *primary flow* directly injected by the gas feed and the *secondary flow* of particles thermalized by collisions with the walls are thus distinguished.

The amount of particles transfered at the walls from the primary to the secondary flow can be estimated using view factors [5]. Assumed that in the primary flow and at a given position z the ratio between the axial flux and the flux to the walls is independent of ionization and only given by geometrical factors, this ratio is then $\zeta(z) = z/\left[(R_{out} - R_{in})/4 + z^2\right]$. Additionally, the neutral-wall collision frequency ν_{nw} for the secondary flow is straightforwardly obtained by assuming that it is in thermal equilibrium with the channel walls, i.e. $\nu_{nw} = \sqrt{2\kappa T_c/\pi m}/\,(R_{out} - R_{in})$.

The macroscopic equations for the primary flow are then derived by integration of Boltzmann equations using the approximation $D_z \approx \kappa T_c/3m$ suggested by Eq. (2). For the secondary flow, a reasonable assumption to close the equation system consists in stating that the thermalization with the walls is perfect ($D_z = \kappa T_c/m$).

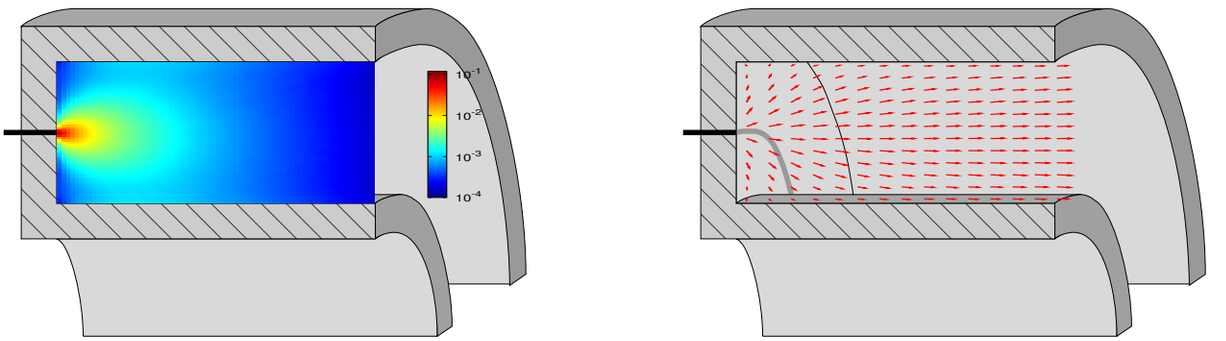


Figure 1. Stationary density (left) and mean velocity (right) maps of neutrals inside the channel for a uniform ionization frequency (results obtained with a fully kinetic Monte-Carlo simulation). $T_c = 800$K and $\nu_i = 30$kHz.

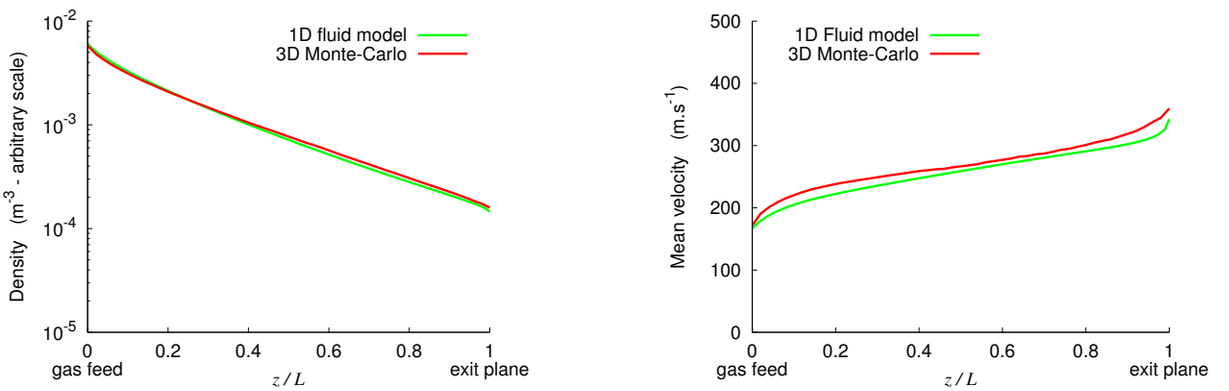


Figure 2. Section-averaged stationary profiles of density (left) and mean velocity (right) in the channel obtained with a 3D fully kinetic simulation and with the macroscopic model, for a uniform ionization frequency. $T_c = 800$K and $\nu_i = 30$kHz.

With these assumptions, the final equations read:

$$\frac{\partial n_1}{\partial t} + \frac{\partial (n_1 V_{1z})}{\partial z} = -\nu_i\, n_1 - \zeta(z)\, n_1 V_{1z}\,, \tag{3}$$

$$\frac{\partial (n_1 V_{1z})}{\partial t} + \frac{\partial (n_1 V_{1z}^2 + n_1 \frac{\kappa T_c}{3m})}{\partial z} = -\nu_i\, n_1 V_{1z} - \zeta(z)\, n_1 V_{1z}^2\,. \tag{4}$$

$$\frac{\partial n_2}{\partial t} + \frac{\partial (n_2 V_{2z})}{\partial z} = -\nu_i\, n_2 + \zeta(z)\, n_1 V_{1z}\,, \tag{5}$$

$$\frac{\partial (n_2 V_{2z})}{\partial t} + \frac{\partial (n_2 V_{2z}^2 + n_2 \frac{\kappa T_c}{m})}{\partial z} = -\nu_i\, n_2 V_{2z} - \nu_{nw} n_2 V_{2z}\,. \tag{6}$$

The exact stationary density and velocity profiles are compared to those obtained with this macroscopic model on Fig. 2.

CONCLUSION

A simple model for the dynamic of neutrals in a SPT has been derived, taking into account kinetic effects induced by ionization as well as the friction due to the roughness of the walls. The model has been tested in the stationary case by comparison with a 3D Monte-Carlo model. A time-dependent test problem (not reported here) has also shown that the assumptions which could potentially be challenged in time-dependent problems were not critical, thus demonstrating the ability of the model to be used within the global transient model of discharge.

References

[1] J. M. Fife, M. Martinez-Sanchez, and J. Szabo. A numerical study of low-frequency discharge oscillations in Hall thrusters. In *Proc. 33rd AIAA Joint Propulsion Conference*, number 97-3051, Seattle, 1997.
[2] J.-P. Boeuf and L. Garrigues. Low frequency oscillations in a stationary plasma thruster. *J. Appl. Phys.*, 84:3541, 1998.
[3] E. Ahedo and F. I. Parra. Model of plasma discharge in a Hall thruster with heat conduction. *Phys. Plasmas*, 9:4061, 2002.
[4] S. Barral, K. Makowski, Z. Peradzyński, N. Gascon, and M. Dudeck. Wall material effects in stationary plasma thrusters. II. near-wall and in-wall conductivity. *Phys. Plasmas*, 10:4137, 2003.
[5] R. Siegel and J. R. Howell. *Thermal Radiative Heat Transfer*. Mac Graw-Hill, 1972.

XXI ICTAM, 15–21 August 2004, Warsaw, Poland

NUMERICAL STUDY OF THE FLOW IN A FINITE CYLINDER DRIVEN BY A ROTATING MAGNETIC FIELD

Karel Fraňa, Jörg Stiller
Institute for Aerospace Engineering (ILR), Dresden University of Technology , D-01062 Dresden, Germany

Summary We present direct numerical simulations (DNS) of the flow in a finite cylinder driven by a rotating magnetic field. The objective of this study is to identify the dominating structures and mechanisms in the transitional and early turbulent flow regimes. The DNS cover a range up to $10\,Ta_{\mathrm{c}}$, where Ta denotes the magnetical Taylor number. The main result of the study is the insight in the formation, evolution and finally dissipation of Taylor-Görtler-like vortices that clearly dominate the turbulence physics and provide an efficient mixing mechanism in this flow.

INTRODUCTION

Electromagnetic stirring provides an appealing method for non-intrusive flow control in metallurgy and crystal growth. In this study we focus on the flow in a finite cylinder driven by a rotating magnetic field. This topic has been subject to extensive research since the pioneering work of Moffat [1]. A review of ealier work is given, e.g. in [2]. Concerning stability of the laminar flow significant progress has been made only recently, e.g. [3,4]. Our knowledge of the turbulent regime, however, relies on quite few experimental data and semi-empiric theories [5].

NUMERICAL APPROACH

Employing the rigid-body and low-frequency approximations the mathematical model reduces to the Navier-Stokes equations with a priori known Lorentz force. A three-dimensional, second-order finite-element method combined with Adams-Bashforth time integration is used for discretization. The direct numerical simulation were performed in parallel on an SGI multiprocessor system. The computations cover a range up to $10\,Ta_{\mathrm{c}}$, where Ta denotes the magnetical Taylor number.

RESULTS

In agreement with the semi-empiric model of Davidson [5] and the little available experimental data, the mean flow is characterized by a homogeneously rotating core. The top and bottom Bödewadt layers drive a weak secondary flow which, however, plays an important role in balancing the Lorentz and friction forces, see Fig. 1.
The most striking result of the study is the insight in the formation, evolution and finally dissipation of Taylor-Görtler-like vortices that clearly dominate the turbulence physics and provide an efficient mixing mechanism in this flow. Typical large structures identified by the second invariant of the fluctuation velocity gradient are shown in presented in Fig. 2. The coloring indicates the orientation of the rotation axis. As might be expected, pairs of Taylor-Görtler-like vortices represent the preferred structure at moderate supercritical flow. Our analysis shows that these vortices survive for several rotations of the mean flow. Near top and bottom they are drawn into the Bödewadt layers where they are finally dissipated. At higher Taylor numbers, the vortices become more unstable and irregular but still provide the dominating turbulence mechanism. In addition to these vortex structures, large scale flow variations in azimuthal direction could be identified. However, as is evident from frequency and wave number spectra, these fluctuations do not contain any harmonic components even in near-critical flow.

CONCLUSION

The transient and early turbulent flow driven by a rotating magnetic field was investigated in detail by numerical computation. Consistently to the model by Davidson, the top and bottom Bödewadt layers drive a weak secondary flow, forcing fluid from the core region to pass the viscous wall layers. Furthermore, the DNS revealed that the turbulent flow is at least up to $10\ Ta_{\mathrm{c}}$ dominated by long-living Taylor-Görtler vortices.

References

[1] Moffatt H.K.: On fluid flow induced by a rotating magnetic field. *J. Fluid Mech.* **22,3**:521–528, 1965.
[2] Gelfgat Yu. M., Priede J.: MHD flows in a rotating magnetic field (a review). *Magnetohydrodynamics* **20,1-2**:521–528, 1965.
[3] Grants I., Gerbeth G.: Linear three-dimensional instability of a magnetically driven rotating flow. *J. Fluid Mech.* **463**:229–239, 2002.
[4] Grants I., Gerbeth G.: Experimental study of non-normal nonlinear transition to turbulence in a rotating magnetic field driven flow. *Physics of Fluids* **15,10**:229–239, 2002.
[5] Davidson P.A.: Swirling flow in an axisymmetric cavity of arbitrary profile, drivenby a rotating magnetic field *J. Fluid Mech.* **245**:669–699, 1992.

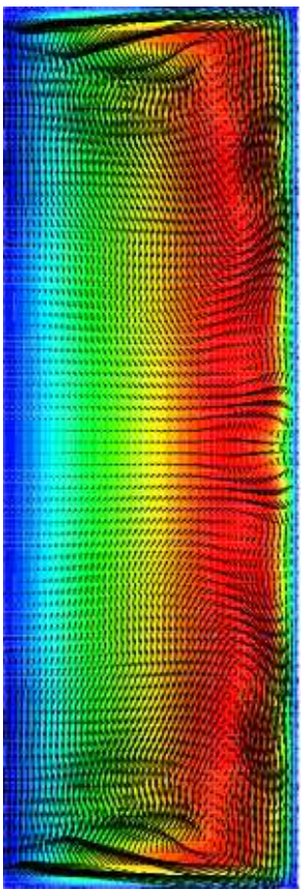


Figure 1. Mean velocity distribution at $Ta = 10^5$

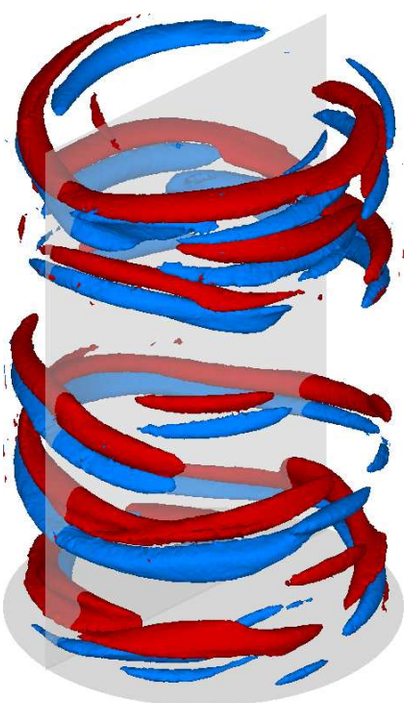


Figure 2. Instantaneuous vortex structures at $Ta = 10^5$

INTERFACE RECONSTRUCTION IN CYLINDRICAL TWO-COMPARTMENT-SYSTEMS USING MAGNETIC FIELD TOMOGRAPHY

Hartmut Brauer[*], Marek Ziolkowski [*,**], Milko Kuilekov[*], Shouqiang Men[***], Christian Resagk[***]
[*]*TU Ilmenau, Dept. Electrical Engineering & Information Technology, D-98684 Ilmenau, Germany*
[**]*TU Szczecin, KETiI, Sikorskiego 37, PL-70313 Szczecin, Poland*
[***]*TU Ilmenau, Dept. Mechanical Engineering, D-98684 Ilmenau, Germany*

Summary In magnetic fluid dynamics appears the problem of reconstruction of free boundary between conducting fluids. The reconstruction problem of the interface between two conducting fluids with different conductivities using external magnetic field measurements in the case of a highly simplified model of an aluminium electrolysis cell has been investigated. In the paper, an interface reconstruction technique based on genetic algorithms is presented, and numerical simulations are compared with some magnetic field measurements.

INTRODUCTION

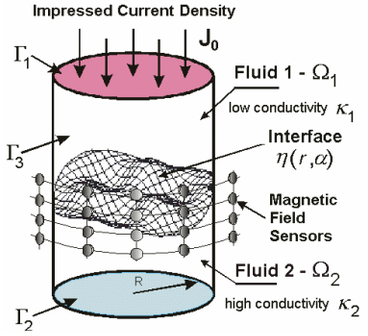
There are a variety of problems in material processing where it would be useful to know the time-dependent distribution of the electrical conductivity of a single fluid or a multiphase flow. For instance, the knowledge of the position of the interface between highly conducting molten aluminium and poorly conducting electrolite (cryolite) is important to prevent unwelcome instabilities in aluminium reduction cells [1]. Recently, it has been demonstrated that the concept of *Magnetic Field Tomography (MFT)* can be successfully used for detection of interfaces between current carrying fluids of different electrical conductivity [2]. We have demonstrated that the external magnetic field generated by the electrical current flowing in a highly simplified model of an aluminium reduction cell provides sufficient information to reconstruct the unknown interface characteristics. In the reconstruction process we have applied genetic algorithms. Genetic algorithms (GAs) – search techniques based on the mechanism of natural evolution and genetics – are particularly effective when the goal is to find an approximate global minimum (or maximum) in a multimodal function domain. In the present work, we show how this technique can be applied to *magnetic fluid dynamics (MFD)*. Therefore, in this paper numerical simulations of the identification of the interface in a cylindrical two-compartment-system are compared with some magnetic field measurements taken from a simple test model.

MAGNETIC FIELD MODELING

If we consider typical figures of aluminum electrolysis cells it must be noticed that the cross section has a length of about L = 10 m, whereas the interface displacement η is very small compared to the lateral extent of the system. Industrial practice shows that already such small interface displacement can perturb significantly the operation of the cell [4]. Consequently, our physical model is characterized by a very small ratio η/L. The considered problem is shown in Fig. 1. Two fluids with different electrical conductivities σ_1 (*top*) and σ_2 (*bottom*) are situated in a long cylinder with the radius R. The cylinder walls are non-conducting. Along the length axis of the cylinder a homogeneous electrical current density $\mathbf{J_0}$ is applied. Then the complete interface perturbation $\eta(r,\alpha)$ can be described [2] as

$$\eta(r,\alpha) = A \sum_{m=-M}^{M} \sum_{n=1}^{N} \eta_{mn} J_m(k_{mn} r) e^{jm\alpha}$$

The value n is called the *radial* mode number and the value m the *azimuthal* mode number. Although the quantity of modes is usually unlimited, the highest modes have the smallest amplitudes and can be neglected. The abbreviation η_{mn} is used for the description of the interface shape. The validity of the above interface representation is limited by the amplitude of the interface deformation. We consider only small deformations because the larger oscillations lead to instabilities due to drop formation.



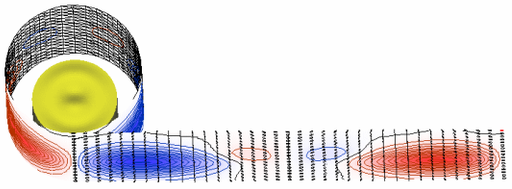


Fig.1: Highly simplified aluminium electrolysis cell model with a non-axisymmetric interface (*left*). Computed sample distribution of the magnetic flux density (B_r component) around cylinder and on the enveloped cylindrical surface (*right*).

If the interface between fluids is flat, the current density **J** is homogeneous everywhere in the cylinder. As soon as the interface deviates from its flat shape due to interfacial waves or an external forcing, the current density **J** will become inhomogeneous near the interface. The inhomogeneity of **J** can be represented by the perturbation current density **j**. If the perturbation of the fluid interface is non-axisymmetric, it leads to a perturbation of the *r*- and *z*-components of the magnetic field outside the cylinder. To model the magnetic field we have to calculate first the current density distribution in the cylinder. This can be done by applying the finite element method. With the distribution of the current density **j** in the cylinder volume, the magnetic flux density around the cylinder is calculated using the Biot-Savart law.

THE INVERSE PROBLEM

The inverse problem is formulated as follows: having the magnetic field flux density distribution (B_r, B_z components) in the sensors positions around the cylinder we would like to reconstruct the interface shape described by (1). The flowchart of the procedure for the interface reconstruction is shown in Fig. 2.

In the current state it enables to identify the modes of the interface between two conducting fluids on the basis of simulated data. It consists of two basic parts: simulation and reconstruction. In the first part for the chosen mode, e.g. mode η_{13}, the magnetic flux density distribution at the sensors positions is calculated using FEM.

In the second step the modes of the interface is identified by means of a modified GA. The goal of the modification is to overcome the problem of the premature convergence in the case of the simple GA [3]. We have applied a multiple optimization loop accompanied by a scaling block which enables to rescale the initial vector of each simple GA run. Thus, the starting point for each run is the same but the parameter vectors are scaled to the best solution of the last step.

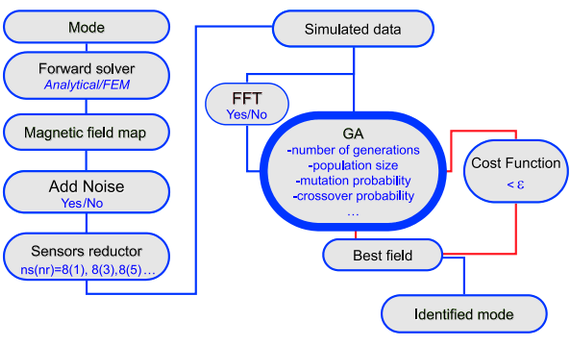


Fig. 2: Flowchart of the mode identification procedure applying a modified GA and FFT

NUMERICAL SIMULATIONS

In our simulations we have assumed that the oscillating interface is in a steady state, i.e. we record the signal from the sensors and then we choose the time instant in which the signal reached the maximum. That time moment corresponds to the maximum of the amplitude of the interface which is identified with the presented procedure.

In the modified reconstruction procedure, we have used a C++ library of genetic algorithm components (GAlib) developed at the M.I.T. [5].

The cost function has been defined as

$$CF = \sqrt{\sum_{i=1}^{Ns} \left(B_{ri} - B_{ro}\right)^2 + \left(B_{zi} - B_{zo}\right)^2} ,$$

where *Ns* denotes the number of sensors, and B_i, B_o are the values of the magnetic flux density for the current generation and the simulated input data, respectively. They were evaluated using a FEM code.

In the presentation the results of the numerical simulations will be given in full details. The comparison with first measurements shows a good agreement, the existing deviations will be discussed.

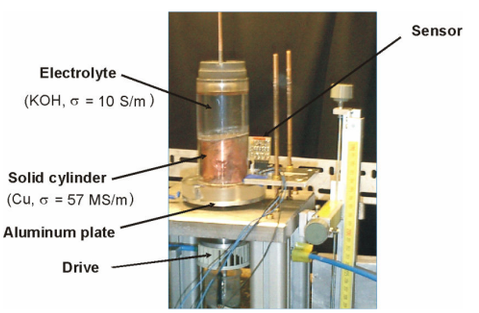


Fig.3: Cylindrical test model of a 2-compartment-system; for the simulation of multi-channel measurements the cylinder was rotating with very low frequency (4-5 Hz).

CONCLUSIONS

We have shown that it is possible to reconstruct the shape of the interface between two conducting fluids on the basis of magnetic flux density simulations with a good quality using genetic algorithms. The new implementation of a modified GA version in the reconstruction procedure improves the quality of reconstruction. Further tests of the algorithm have to be performed to assure proper reconstruction results also in the case of measured data.

References

[1] Davidson, P.A.: "Magnetohydrodynamics in material processing," *Annu. Rev. Fluid Mech.*, vol. 31, pp. 273-300, 1999.

[2] Brauer H., Ziolkowski M., Kuilekov M., Men S., Resagk Ch.: "Surface current reconstruction using magnetic field tomography", *IEEE Transactions on Magnetics*, vol. 40, 2004 (accepted)

[3] Michalewicz, Z.: *Genetic Algorithms + Data Structures = Evolution Programs*, 3rd ed., Springer Verlag, Berlin, Heidelberg, New York, 1996.

[4] Miles, J., Henderson, D.: "Parametrically forced surface waves," *Annu. Rev. Fluid Mech.*,vol. 22, pp. 143-165, 1990.

[5] Wall, M.: "GAlib: A C++ Library of Genetic Algorithm Components". V2.4, 1996, http://lancet.mit.edu/ga/

XXI ICTAM, 15–21 August 2004, Warsaw, Poland

CONTACTLESS INDUCTIVE FLOW TOMOGRAPHY: THEORY AND EXPERIMENT

Frank Stefani, Gunter Gerbeth, Thomas Gundrum
Forschungszentrum Rossendorf, P.O. Box 510119, D-01314 Dresden, Germany

Summary When a moving electrically conducting fluid is exposed to an applied magnetic field, electrical currents are induced that give rise to an additional magnetic field. The ratio of the induced field to the applied field is determined by the magnetic Reynolds number Rm. If Rm is not too small, the induced field can be measured in the exteriour of the fluid. Applying the imposed magnetic fields in different directions and measuring the respective induced fields one can gather sufficient information to reconstruct, at least approximatively, the velocity structure of the fluid. The theory of such a *contactless inductive flow tomography* (CIFT) is delineated, and its practical feasibility is demonstrated in a liquid metal experiment.

MOTIVATION

In many industrial applications, including crystal growth and metallurgy, there is a growing interest in determining the velocity field of metal or semiconductor melt flows. Due to the opaqueness of those fluids, the customary optical methods of flow measurements fail. What is more, the fluids are often very hot or chemically aggressive, hence a contactless measuring technique would be highly desirable. In case of electrically conducting fluids, the velocity dependent magnetic induction can be utilized to establish such a contactless measuring technique.

THEORY

When an electrically conducting fluid, moving with the velocity $\mathbf{v}$, is exposed to a magnetic field $\mathbf{B}$, an electromotive force $\mathbf{u}\times\mathbf{B}$ is induced that drives a current $\mathbf{j}=\sigma(\mathbf{E}+\mathbf{v}\times\mathbf{B})$, with σ denoting the electrical conductivity of the fluid and $\mathbf{E}$ the induced electric field. In the steady case, $\mathbf{E}$ can be expressed as the gradient of the electric potential, $\mathbf{E}=-\nabla\varphi$. For this form of the current, the application of Biot-Savart's law yields the following expression for the induced magnetic field $\mathbf{b}$ [1]:

$$\mathbf{b}(\mathbf{r}) \quad = \quad \frac{\mu_0\sigma}{4\pi}\int\limits_V \frac{(\mathbf{v}(\mathbf{r}')\times\mathbf{B}(\mathbf{r}'))\times(\mathbf{r}-\mathbf{r}')}{|\mathbf{r}-\mathbf{r}'|^3}dV' - \frac{\mu_0\sigma}{4\pi}\int\limits_S \frac{\varphi(\mathbf{s}')\mathbf{n}(\mathbf{s}')\times(\mathbf{r}-\mathbf{s}')}{|\mathbf{r}-\mathbf{s}'|^3}dS' \ . \tag{1}$$

The first term on the r.h.s of Eq. (1) represents the effect of the so-called *impressed* currents, $\sigma\mathbf{v}\times\mathbf{B}$, in the fluid volume V. The second term appears if we convert the volume integral over the $\nabla\varphi$ term into a boundary integral. These so-called *secondary* currents depend on the electric potential φ at the fluid boundary S. The electric potential φ, in turn, has to fulfil the boundary integral equation

$$\varphi(\mathbf{s}) \quad = \quad \frac{1}{2\pi}\int\limits_V \frac{(\mathbf{v}(\mathbf{r}')\times\mathbf{B}(\mathbf{r}'))\cdot(\mathbf{s}-\mathbf{r}')}{|\mathbf{s}-\mathbf{r}'|^3}dV' - \frac{1}{2\pi}\int\limits_S \frac{\varphi(\mathbf{s}')\mathbf{n}(\mathbf{s}')\cdot(\mathbf{s}-\mathbf{s}')}{|\mathbf{s}-\mathbf{s}'|^3}dS' \ , \tag{2}$$

which results from Green's theorem when applied to the solution of the Poisson equation for the case of insulating boundaries. Interestingly, Eqs. (1) and (2) are equivalent to the corresponding equations in magneto- and electroencephalography [2], where only the term $\sigma\mathbf{v}\times\mathbf{B}$ has to be replaced by the impressed currents due to the neuronal activity in the brain.

It is important to note that for a small magnetic Reynolds number Rm, defined as $Rm=\mu_0\sigma lv$ (where l and v denote characteristic length and velocity scales of the fluid), the total $\mathbf{B}$ under the integrals in Eqs. (1) and (2) can be replaced by the applied magnetic field $\mathbf{B_0}$. Under this condition, we get a *linearized* version of the general inverse problem of how to infer the velocity field from measuring the induced magnetic field in the exterior of the fluid and the electric potential at the boundary of the fluid [1]. The considerations in [3] had revealed an intrinsic non-uniqueness of this inverse problem with respect to the depth dependence of the velocity field. This non-uniqueness can only be resolved by applying magnetic fields of varying frequencies, or by the use of appropriate regularization techniques.

In [4] it was shown that the electric potential measurement can be avoided by applying the imposed magnetic field in two, e.g. orthogonal, directions and measuring only the respective induced magnetic field. A necessary ingredient of this method is the implicit treatment of the unknown electric potential at the fluid boundary.

EXPERIMENT

An experiment has been set-up in order to demonstrate the feasibility of the CIFT. The basic problem to be solved prior to any practical application is the sufficiently accurate determination of small induced magnetic fields on the background of much larger imposed magnetic fields. Fig. 1 shows the experimental set-up, both in a schematic view and as a photograph. We use 4.4 litres of the eutectic alloy GaInSn in a cylindrical vessel of 18 cm diameter and approximately the same fill

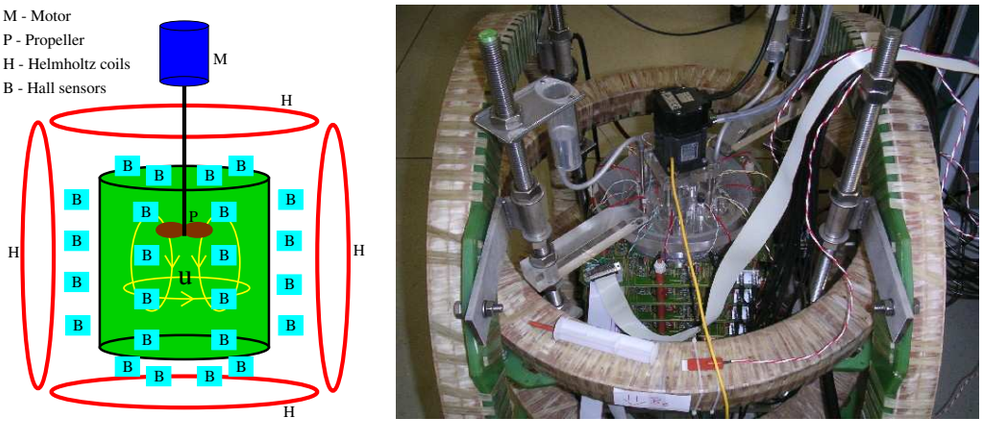


Figure 1. Schematic view (left) and laboratory set-up (right) of the CIFT experiment. The propeller driven flow of a metallic melt is exposed alternately to a transverse and an axial magnetic field, which are produced by two pairs of Helmholtz coils. The respective induced magnetic fields are measured at 49 Hall sensors.

level. A motor driven propeller can reach rotation rates up to 2000 rpm, which corresponds to a magnetic Reynolds number of approximately 0.4.

The measuring procedure of the CIFT is as follows: The current is switched on and off in the two Helmholtz coil pairs, producing alternately a transverse and an axial magnetic field. For either applied field, the respective induced magnetic fields are measured at a total of 49 Hall sensors covering the fluid volume rather homogeneously. Both data sets are put jointly into the inversion solver. After each switching and measuring cycle one gets a global picture of the flow. In the present configuration the flow is monitored every 3-4 seconds.

In Fig. 2 we show the measured induced magnetic fields for transverse (a) and axial (b) field situations, jointly with the reconstructed velocity (c). This measurement was carried out for the case that the propeller pumped upward at a rotation rate of 1200 rpm. Qualitative as well as quantitative changes of the flow field were resolved by the CIFT method in a reasonable and reproducible way. Even the transient start-up of the 2D flows has been resolved in time-steps of about 3 seconds.

Presently, work is under way to include AC fields in order to improve the depth resolution of the method.

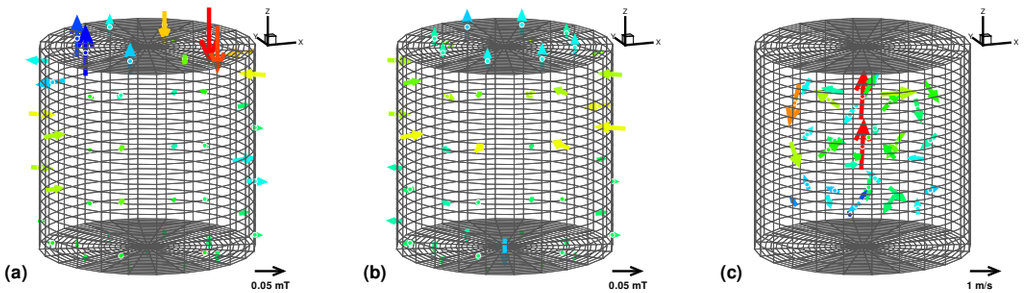


Figure 2. The measured induced magnetic fields for transverse (a) and axial (b) imposed magnetic field. The direction of the arrows indicates the measured field component. The reconstructed velocity field is shown in (c), where the colour indicates the flow speed.

References

[1] Stefani, F., Gerbeth, G.: Velocity reconstruction in conducting fluids from magnetic field and electric potential measurements. *Inverse Problems* **15**: 771–786, 1999.

[2] Hämäläinen, M., Hari, R., Ilmoniemi, R. J., Knuutila, J., Lounasmaa, O. V.: Magnetoencephalography - theory, instrumentation, and application to noninvasive studies of the working human brain. *Rev. Mod. Phys.* **65**: 413–497, 1993.

[3] Stefani, F., Gerbeth, G.: On the uniqueness of velocity reconstruction in conducting fluids from measurements of induced electromagnetic fields. *Inverse Problems* **16**: 1–9, 2000.

[4] Stefani, F., Gerbeth, G.: A contactless method for velocity reconstruction in electrically conducting fluids. *Meas. Sci. Tech.* **11**: 758–765, 2000.

DYNAMO ACTION IN STEADY HELICAL PIPE FLOW

Leszek Zabielski*, A. Jonathan Mestel**
*Mathematics Dept., Warsaw University of Technology, 00-661 Warszawa, Poland
**Mathematics Dept., Imperial College London, SW7 2BZ, UK

Summary The steady, pressure-driven flow of a conducting fluid down a helical pipe of rectangular cross-section is shown to drive a kinematic dynamo at moderate values of the magnetic Reynolds number, R_m. The asymptotic structure of the growing modes is analysed as $R_m \to \infty$. This is the first laminar, pressure-driven dynamo to be found.

INTRODUCTION

A velocity field giving rise to spontaneous magnetic field generation in a conducting fluid is known as a *kinematic dynamo.* Various simple examples of kinematic dynamos are known, but there are very few dynamically self-consistent examples, in which the initial instability grows to a level where it interacts with the driving mechanism. In this paper we consider configurations with helical symmetry, as originally formulated by [1] and [2]. The Ponomarenko [3] kinematic dynamo can be regarded as a special case of helical flow. Here, a fully nonlinear laminar dynamo driven merely by a steady pressure gradient along a pipe is described. The pipe has a helical shape with a rectangular cross-section, as shown in figure 1. The work has relevance to the construction of laboratory dynamos [4]. Further details can be found in [6].

HELICALLY SYMMETRIC PIPE FLOW

Helical symmetry is a natural generalisation of two-dimensionality ($\varepsilon = 0$) and axisymmetry ($\varepsilon \to \infty$.) In terms of cylindrical polar coordinates $(r,\, \theta,\, z)$, a scalar function is helically symmetric if it depends only on r and $\phi = \theta + \varepsilon z$, where ε is a constant. The symmetry direction is designated by the Beltrami vector field, $\mathbf{H}$, which is related to the unit coordinate vectors $\mathbf{e}_\theta$ and $\mathbf{e}_z$ by

$$\mathbf{H} = (\mathbf{e}_z - \varepsilon r \mathbf{e}_\theta)/h^2 \qquad \text{where} \qquad h = (1+\varepsilon^2 r^2)^{1/2} \qquad \text{and} \qquad \nabla \wedge \mathbf{H} = -\frac{2\varepsilon}{h^2}\mathbf{H}.$$

The Navier-Stokes equations and the magnetic induction equation are invariant with respect to this symmetry, and thus helically symmetric solutions to both can be found. The helically symmetric incompressible flow $\mathbf{u}$ can be conveniently represented by two scalar functions $v(r,\phi)$ and $\psi(r,\phi)$ as

$$\mathbf{u} = v\mathbf{H} + \mathbf{H} \wedge \nabla\psi\,.$$

The governing equations for ψ and v are geometrically linked.

Steady, pressure-driven laminar flow down a helical pipe was calculated in [5] as a function of the hydrodynamic Reynolds number, R_e. A solution is shown in figure 2 for an intermediate value of R_e. The two left-hand diagrams show the contours of ψ and v, the cross-pipe and down-pipe flow. An important feature of the flow is that the cross-pipe component has a stagnation point structure, with a weaker, counter-rotating portion in the lower right. The associated field stretching influences dynamo action strongly.

DYNAMO ACTION

Magnetic fields with the same helical symmetry as the flow are sought. For the kinematic problem, the field $\mathbf{B}$ can be decomposed as

$$\mathbf{B} = (B\,\mathbf{H} + \mathbf{H} \wedge \nabla\chi)e^{\lambda t}$$

and the complex growth rate λ determined. Three cases are considered, when the medium outside the pipe is perfectly conducting, perfectly insulating or of the same conductivity as the fluid. Only the perfectly conducting case is presented here. The magnetic field is then zero outside of the pipe region, which has a constraining effect on the dynamo.

Pipes with no dynamo

In many cases the steady, pressure-driven pipe-flows do not in fact drive a dynamo for any R_m, except in the limit as $R_e \to \infty$. This is because the cross-pipe flow is too strong. Such a case is the square pipe $0.5 < r < 1.5$, $0 < \phi < 1$. If however, the cross-pipe flow is artifically set to zero, a kinematic dynamo occurs with a field structure which varies rapidly in the direction tangential to the pipe as shown on the right in figure 1. The asymptotic structure of the modes as $R_m \to \infty$ is analysed and agrees with the numerics.

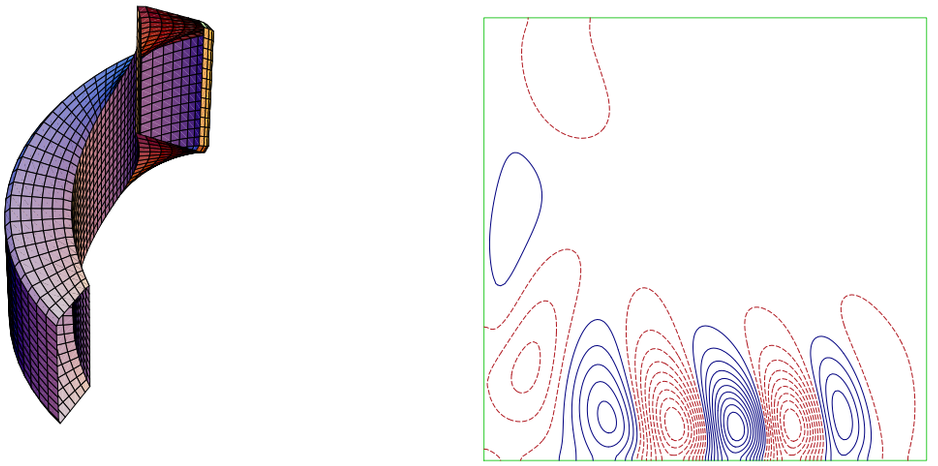


Figure 1. Left: A helical rectangular pipe for $\varepsilon = 1$, $0.5 < r < 1.5$ and $0 < \phi < \frac{2}{3}\pi$.
Right: Kinematic dynamo in a square pipe for a velocity field with $\psi = 0$ and conducting walls.

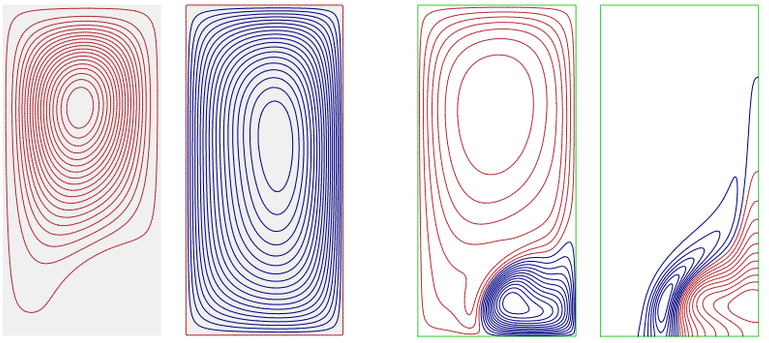


Figure 2. Dynamo for $R_m = 17^3$, $R_e = 2000$ and the pipe of figure 1. From left to right: the cross-pipe flow, ψ, and the down-pipe flow, v, the cross-pipe field, χ, and the down-pipe field, B. The inside of the pipe is on the left. The effect of field-stretching near the separation point is pronounced.

Pipes with dynamos

For the taller pipe drawn in figure 1, with $0.5 < r < 1.5$ and $0 < \phi < \frac{2}{3}\pi$, a dynamo is found for $R_e = 2 \times 10^3$ and $R_m \sim 100$. In figure 2 the growing magnetic field is shown on the right alongside the cross-pipe flow. It is clear that the stretching of the field at the separation line is an important feature of the dynamo process. The other vital ingredients are the shear in the downpipe velocity and the torsional nature of helical symmetry which drives a diffusive term involving B in the χ-part of the induction equation, a “geometrical α-effect."

Computations of the time evolution and saturation of the dynamos described here are in progress and only preliminary results are presented at the meeting. This work was supported by EPSRC grants GR/R71191/01 and GR/S87539/01 .

References

[1] Benton, E.R.: Kinematic dynamo action with helical symmetry in an unbounded fluid conductor. Parts I & II. *Geophys. Astrophys. Fluid Dyn.* **12**: 313–358, 1979.
[2] Lortz, D.: Exact solutions of the hydrodynamic dynamo problem. *Plasma Phys.* **10**: 967–972, 1968.
[3] Ponomarenko Y.B.: On the theory of hydromagnetic dynamos. *Zh. Prikl. Mekh. Tekh. Fiz.* **6**: 47–51, 1973.
[4] Rädler, K.-H. & Cēbers, A.: The special issue: MHD dynamo experiments. *Magnetohydrodynamics* **38**, 2002.
[5] Zabielski, L., & Mestel, A.J.: Steady flow in a helically symmetric pipe. *J. Fluid Mech.* **370**: 297–320, 1998.
[6] Zabielski, L., & Mestel, A.J. Dynamo action in helical pipe flow. *J. Fluid Mech.* (submitted, 2003)

LARGE-EDDY SIMULATION OF PARTICLE DISPERSION IN THE DUCT WITH FLUID INJECTION

Konstantin N. Volkov*
*University of Central Lancashire, Harris Building, Corporation Street, PR1 2HE Preston, UK

Summary Turbulent gas-particle flows in the ducts with fluid injection are simulated using large eddy simulation technique. The constructed computational approach is taking into account the velocity and temperature fluctuations of turbulent duct flow. The influence of inflow conditions, size of particles and place of particles injection on their dispersion pattern in the duct flow are investigated.

INTRODUCTION

Gas-particle flow research has applications to a vast number of technological systems and industrial devices. In technological applications the interaction of the particles with the turbulent structure of the flow is an extremely complex problem. The introduction of new models and improved computer power allows making more accurate computations performed with less empiricism than before. The technique is supposed to make possible studying the physical phenomena that occur in more complex engineering-like applications. Large eddy simulation (LES) methodology corresponds to those purposes.

The application of LES for computation of turbulent flows in the ducts with fluid injection is considered in this paper. Simulation of such flows is of a great significance for the designing and perfection of heat exchangers and solid rocket motors. In these applications exact computation of field of fluid flow plays an important role because it serves as a background for simulation of condensed particles formed during the combustion of solid fuel, their interaction and separation on a wall [1, 2]. The computational domain is shown in the figure 1. The purpose of established calculations is definition of optimal initial parameters of duct flow and lead-in conditions of solid particles.

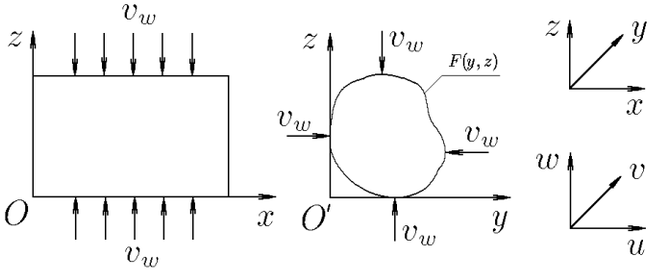


Figure 1. Computational domain

MATHEMATICAL FORMULATION

The numerical calculations are performed by the Eulerian-Lagrangian approach for the fluid and dispersed phases respectively.

Gas phase

The fluid flow calculations are based on filtered Navier-Stokes equations. Subgrid turbulent viscosity is computed with the Smagorinsky's formula and the dynamic model is used for estimating the Smagorinsky's parameter. The subgrid length is assumed to be proportional to the filter width, which then is related to the volume of grid mesh in three dimensions. The present LES implicity applies a box filter in each direction.

Dispersed phase

The solid phase is treated by the Lagrangian approach, which means that particles are followed in time along their trajectories through the flow field. At every given time step, the new position of the particles and the new translational velocity are calculated according to the forces acting on the particles. LES allows obtaining fluctuating components spontaneously from momentum equation unlike approach [1, 3] which uses normal distribution for fluctuating properties of turbulent fluid flow. It is assumed that the particles are undeformable spheres, there is no particle-particle or droplet-droplet interaction, density of dispersed phase is much bigger than density of gaseous phase, the dominant forces acting on the particle are the drag, influence of particle phase on carrying gas flow is negligible.

NUMERICAL METHOD

The filtered equations are solved numerically using a finite volume method on staggered grid with non-uniform cell size. The numerical procedure employs a Chorin-type projection method for the decoupling of momentum and

continuity equations. The second order explicit Adams-Bashforth time integration scheme is used to advance the velocity field. The discretization of diffusive flux is based on the central differences of second order. Concerning numerical method, the most important component is the discretization of the non-linear convective fluxes. The sharp and monotonic algorithm for relative transport (SMART) is used [4]. The Poisson equation for pressure is solved by the bi-conjugate gradients stabilised method (BiCGStab) with preconditioning [5].
The computational domain is divided into several rectangular subdomains for the parallelization. Each process holds some ghost cells, which overlap inner cells of the adjacent process. Values are copied from these to the ghost cells when necessary. To minimise communications, the program divides computational domain in a way that minimises the area of the touching faces and equilibrates the number of cells in the different subdomains. The MPI library is used for organisation of communication between processors.

RESULTS

The presented calculations have been performed for demonstrating the influence of the different physical phenomena on the development of the particles dispersion. In order to underline the particles motion exceptions in the duct, these calculations were performed only for one-way coupling approach.
The grid containing 100 000 cells in the cross section of duct and 300 sections downstream was used in typical variant of computation. Some problematic issues concerning the methodological base of LES were investigated. The main results of the paper are the following: (i) elaboration of convergence criteria of LES (in other words, how filter length influences computational results and how filter kernel influences treatment of computational results); (ii) development of numerical schemes ensuring necessary accuracy; (iii) development of LES for computation of turbulent flows on the basis of general curvilinear grid structures; (iv) development of parallel numerical algorithm for high performance computer systems both with shared and distributed memory.
Fluid flow pattern was investigated depending on intensity of fluid injection. The formation of recycling regions and reverse flow in the duct was discovered with the some of initial data. The computed results are compared with the approximate solutions, the available benchmark solutions and experimental data.
The dispersion of particle is defined by the relation of the particle relaxation time to the dissipation dynamic time scale of the turbulence. The particles with radius r_p<10 μm hit a target in the region with a maximum value of fluid velocity turbulent fluctuations. Such particles are dispersed strongly. The region of increased particles concentration is formed in the vicinity of the centerline of the duct. Inert particles penetrate to the contrary wall, where turbulence level is equal to zero, and are not dispersed.
The obtained results have a good agreement with the results computed on the base of Reynolds averaged Navier-Stokes equations and experimental data [5].

CONCLUSIONS

The simulation of transition processes of momentum and heat in the duct with fluid injection shows that the fluctuations of turbulent flow exercise an essential influence on dispersion and heating of particles. The developed model and obtained results reasonably explain computational and experimental data. In particular, they explain the formation of regions of irregular particles concentration in the turbulent two-phase duct flows.
Successful application of LES for computation of fluid properties in the duct with fluid injection makes possible computations taking into account more complex physical and chemical effects. It requires development subgrid scale models for compressible fluid, connection combustion model to LES concept and elaboration of corresponding computational tools.

References

[1] Volkov K.N., Emelyanov V.N.: Stochastical model of condensed particle motion in the duct with fluid injection. *Mathematical simulation* **11**(3):105-111, 1999.
[2] Volkov K.N., Emelyanov V.N.: Three-dimensional flows in the ducts with fluid injection. *Mordern Problems of Non-Equilibrium Gas and Thermodynamics* 43-63, 2002.
[3] Gosman AD, Ioannides E.: Aspects of computer simulation of liquid-fueled combustors. *AIAA Paper* 81-0323.
[4] Choi S.K., Nam H.Y., Cho M.: A comparison of higher-order bounded convection schemes. *Computational Methods in Applied Mechanics Engineering* **121**:281-301, 1995.
[5] Van der Vorst H.A.: Bi-CGSTAB: A fast and smoothly conversing variant of Bi-CG for the solution of non-symmetric linear systems. *SIAM Journal of Science Statistical Computations* **13**:631-644, 1992.

SIGNS OF FLOODING INSTABILITY IN INCLINED LIQUID FILMS AT HIGH PRESSURE AND MASS TRANSFER IN HIGH DENSITY GAS SLUGS

Maria J. F. Ferreira, João R. F. Guedes de Carvalho
FEUP, Department of Chemical Engineering, 4200-465 Porto, Portugal

Summary The influence of gas density on flooding instability phenomena is investigated experimentally both in long gas slugs of CO_2 rising in vertical tubes filled with water at pressures up to 5.2 MPa, and inside a rectangular column with flat walls positioned in the vertical and at 15º, 45º and 60º from the horizontal, at absolute pressures up to 0.6 MPa with air and up to 1.5 MPa with argon, at Reynolds numbers for the water between 2667 and 26667.

INTRODUCTION

Our team have shown (see Ref. 1 to 7) that when long high density gas slugs rise in vertical tubes filled with liquid, signs of flooding instability of the wetted-wall flow become apparent, if the gas density is raised sufficiently (above about 2-3 MPa with argon, for slugs in 32.8 mm i.d. and in 21 mm i.d. tubes, respectively). The detection of flooding instability was carried out by means of measuring pressure drop (and its rapid fluctuation) along the gas slugs[8].
Despite the considerable evidence provided, for tubes with 21 mm and 32.8 mm i.d., there is some scepticism about the possibility of flooding instability occurring with the low gas velocities reported. However, it should be remembered that the drag force exerted by the gas on the descending waves, that leads to flooding instability is directly proportional to the density of the gas.

Experiments in inclined liquid films at high pressures
In order to investigate further the influence of gas density and the inclination of the column on flooding phenomena, a new study was performed based both in visualization and on the measurement of pressure gradients inside a rectangular column, 3.0 m long, with cross section 25 × 30 mm, positioned in the vertical and at 15º, 45º and 60º from the horizontal, at absolute pressures up to 0.6 MPa with air and up to 1.5 MPa with argon, at Reynolds numbers for the water between 2667 and 26667. The technique adopted follows closely that originally presented by the authors (see Ref. 1 to 7).

Experiments in high density gas slugs
In an independent study, on long gas slugs at high pressure, Nakazatomi *et al.*[9] measured the velocity of the waves moving along the falling film as well as the average thickness of the film and, it may be concluded, that flooding instability was obtained with slugs of nitrogen in water, in a 19.2 mm i.d. column, for gas pressures above 5 MPa.
In the present work we provide additional evidence of flooding instability by means of the measurement of mass transfer rates for long slugs of CO_2, at pressures up to 5.2 MPa, rising in water. The mass transfer coefficients were measured by the constant volume method[10,11], in which the pressure variation is followed inside a tightly closed tube along which a single long slug of CO_2 is allowed to rise. Under these circumstances, mass transfer is totally determined by conditions on the liquid side and therefore, the value of the mass transfer coefficient gives a significant indication of the flow pattern on the liquid film. For laminar film flow the original theory of Higbie[12] is valid, but where transition to turbulent film flow occurs, there is a steep increase in the mass transfer coefficient.
The experiments performed in this work show that for pressures above a certain threshold (corresponding to flooding instability), there is a further substantial increase in the mass transfer coefficient, which results from the gas-liquid interface being severely disrupted. This is strong additional evidence in favor of our claim that flooding instability is observed with high gas densities. We conducted our experiments at up to 5.2 MPa, in tubes with internal diameters of 21, 32.8 and 40.5 mm.

CONCLUSIONS

The experiments in high density gas slugs rising in vertical tubes filled with water at pressures up to 5.2 MPa and inside a rectangular column with flat walls positioned in the vertical and at 15º, 45º and 60º from the horizontal operanting at high pressures (up to 0.6 MPa with air and up to 1.5 MPa with argon), have shown that there is a critical value of $\rho_g (u + u_i)^2$ above which flooding instability sets in, for a given liquid at a given flow rate in a given column (where ρ_g is the density of gas, u the average velocity of gas and u_i is the liquid velocity on gas-liquid interface).

References

[1] Guedes de Carvalho, J.R.F., Talaia, M.A.R. and Ferreira, M.J.F.: Flooding of High Density Gas Slugs Rising in Viscous Liquids. *Proceedings of the 2nd International Symposium on Two-Phase Flow Modelling and Experimentation*, Pisa-Italy, **2**, 771-778, 1999.

[2] Guedes de Carvalho, J.R.F., Talaia, M.A.R. and Ferreira, M.J.F.: Flooding Instability of High Density Gas Slugs Rising in Vertical Tubes Filled with Water. *Chem. Engng Sci.*, **55**, 3785-3802, 2000.

[3] Guedes de Carvalho, J.R.F. and Ferreira, M.J.F.: Pressure Drop in Gas Slugs in Vertical Tubes and the Hypothesis of Flooding. *AIChE J.*, **4**, 707-723, 2000.

[4] Guedes de Carvalho, J.R.F., Ferreira, M.J.F. and Talaia, M.A.R.: The Phenomenon of Flooding Instability in Wetted-Wall Tubes Operating with High Density Gas. *Proceedings of* 3rd European Thermal Sciences Conference, Heidelberg-Germany, **2**, 1033-1039, 2000.

[5] Guedes de Carvalho, J.R.F. and Ferreira, M.J.F.: Visualization of Flooding Instability in Counter-Current Gas-Liquid Flow Along Vertical Flat Walls. *Proceedings of the 5th World Conference on Experimental Heat Transfer, Fluid Mechanics and Thermodynamic*, Thessaloniki-Greece, **2**, 1423-1428, 2001.

[6] Ferreira, M.J.F.: Flooding Instability in a Rectangular Column Operating at High Pressures. *Proceedings of the 3rd International Conference on Transport Phenomena in Multiphase Systems*, Kielce-Poland, 285-292, 2002.

[7] Ferreira, M.J.F. and Guedes de Carvalho, J.R.F.: Flooding Instability Phenomena at High Pressures. *Book of Abstracts of the* 5th *Euromech Fluid Mechanics Conference*, Toulouse-France, 85, 2003.

[8] Dukler, A.E., Smith, L. and Chopra, A.: Flooding and Upward Film fFow in Tubes – I: Experimental Studies. *Int. J. Multiphase Flow*, **10**, 585-597, 1984.

[9] Nakazatomi, M., Shimizu, H., Miyake, G. and Sekoguchi, K.: Rising Characteristics of a Single Measure of Gas in Stagnant Liquid-Effect of Pressure. *J.S.M.E. International Journal*, series II, **35**, 388-394, 1992.

[10] Niranjan, K., Hashim, M.A., Pandit, A.B. and Davidson, J.F.: Liquid Phase Controlled Mass Transfer From a Gas Slug. *Chem. Engng Sci.*, **43**, 1247-1252, 1988.

[11] Sena Esteves, M.T. and Guedes de Carvalho, J.R.G.: Liquid-side Mass Transfer Coefficient for Gas Slugs Rising in Liquids. *Chem. Engng Sci.*, **48**, 3497-3506, 1993.

[12] Higbie, R.M.: The Rate of Absorption of a Pure Gas into a Still Liquid During Short Periods of Exposure. *Trans. Amer. Instn Chem. Engrs*, **31**, 365-389, 1935.

VISCOUS AND VISCOELASTIC POTENTIAL FLOW

Daniel D. Joseph
University of Minnesota

Abstract

Recent results will be reviewed and new results presented which establish that in all cases in which potential flow satisfies the equations of motion for viscous (or viscoelastic) fluids, it is neither necessary nor useful to put the viscosity to zero. Stated more severely these results suggest that the inviscid part of potential flow theory may be deleted.

Extended Summary

It is well known that the Navier-Stokes equations are satisfied by potential flow; the viscous term is identically zero when the vorticity is zero but the viscous stresses are not zero (Joseph & Liao 1994). It is not possible to satisfy the no-slip condition at a solid boundary or the continuity of the tangential component of velocity and shear stress at a fluid-.fluid boundary when the velocity is given by a potential. The viscous stresses enter into the viscous potential flow analysis of free surface problems through the normal stress balance at the interface. Viscous potential flow is an approximation to viscous flow which neglects the effects of vorticity and friction at the boundary. Two questions are immediately suggested by such an approximation. Is viscous potential flow a better approximation than inviscid potential flow? (1) Under what circumstances is viscous potential flow a better approximation than inviscid potential flow? (2) Under what circumstances is viscous potential flow a good approximation to viscous flow? The answer to the first question is yes; general answers to the second question are not yet known; the subject is new and under development.

Up to now, the utility of the theory of potential flow of a viscous fluid has been suggested by the comparison of potential and viscous flow solutions and experiments and some partial results from flow fundamentals. The examples show that when considering potential flow, it is never necessary nor useful to put the viscosity to zero.

The entry “potential flow” in search on Google yields 8,770,000 hits. Of these, the number of academic studies of potential flows of viscous fluids is perhaps less than twenty. These studies may be divided into applications using the dissipation method and to the direct application to interface problems, especially to stability problems of the type considered here. The dissipation method has been applied to the calculation of drag on gas bubbles of different shapes rising in viscous liquids and to computation of the rates of decay of waves on gas-liquid surfaces discussed by Lamb 1932 (see Joseph & Wang 2003 for a recent review together with new results). Harper 1972 argued that the dissipation method works well for the drag on a spherical gas bubble at large Re because, unlike the solid sphere, an increasing fraction of the dissipation occurs in the irrotational bulk liquid relative to the dissipation in the vorticity layer at the boundary. The boundary layer at a solid surface resolves a discontinuity of velocity. At a gas surface it resolves a discontinuity in the vorticity. Harper’s idea is plausible though details have not been given. On the other hand, stability limits for capillary instability of jets of viscous liquids into viscous liquids using the potential flow approximation is very close to exact results for moderately large Reynolds numbers (Funada & Joseph 2002). In other words, there are cases for which viscous potential flow works well at liquid-liquid surfaces where Harper’s 1972 arguments do not apply; it is a surprise and not well understood.

Uncompensated irrotational shear stresses arise at stress free surfaces when the flow is irrotational, Joseph & Wang 2003 argued that irrotational flow of a viscous fluid is a good approximation when the uncompensated irrotational shear stress is zero or small. The Rayleigh-Plesset bubble executes purely radial motions in a viscous liquid; the motion of the liquid is exactly described by irrotational flow; it depends on viscosity through the viscous normal stress at the gas-liquid surface. There are no uncompensated shear stresses there and the solution is exact. The rise of a spherical cap bubble is a case where the uncompensated shear stress near the stagnation point is small. It is very well approximated by the potential flow of a viscous fluid (Joseph 2003). Joseph, Belanger & Beavers 1999 constructed a viscous potential flow analysis of the Rayleigh-Taylor instability which gives results which are almost indistinguishable from those obtained from the exact fully viscous analysis. The basic flow whose stability is studied is free of shear stresses.

Other stability studies using potential flow of a viscous fluid are not uniformly excellent approximations of exact results, but the errors are small for some parameter regions, with large errors less than about 40% in the worst cases. In all cases, viscous potential flow gives a much better approximation to exact results and experiments, than inviscid potential flow.

Funada & Joseph 2002 constructed a viscous potential flow analysis of capillary instability of a liquid cylinder which was in excellent agreement with the exact fully viscous analysis. Funada & Joseph 2001 constructed a viscous potential flow analysis of Kelvin-Helmholtz instability in a channel. A fully viscous flow analysis is not available because the basic flow which postulates two uniform streams with different velocities is incompatible with the requirement that the shear stress and tangential component of velocity should be continuous and the no-slip conditions at the channel wall. The analysis of Funada & Joseph 2001 is in much better agreement with experiments reviewed by Mata, Pereyra, Trallero & Joseph 2002 than with other theories which account for the shear of the gas using different empirical correlations.

The excellent and well known book on stability theory by Drazin & Reid 1981 starts with an analysis of Rayleigh-Taylor, Kelvin-Helmholtz and capillary instability of an inviscid fluid. The potential flow analyses are not more difficult, but have a much richer content when the viscous contribution to the normal stress is not put to zero.

Irrotational flows of viscous fluids are not good approximations for flows with distributed vorticity. The diffusion of vorticity from the boundary is important. For stability problems, the time for instability could be smaller than a typical time of diffusion. However, there are flows such as rising gas bubbles in which the diffusion of vorticity is not an important factor.

Here, we study the potential flow of a second order fluid over a sphere or an ellipse. The normal stress at the surface of the body is calculated and has contributions from the inertia, viscous and viscoelastic effects. We investigate the effects of different Reynolds numbers and body sizes on the normal stress; for the ellipse, various angles of attack and aspect ratios are also studied. The effect of the viscoelastic terms is opposite to that of inertia; the normal stress at a point of stagnation can change from compression to tension. This causes long bodies to turn into the stream and causes spherical bodies to chain. For a rising gas bubble, the effect of the viscoelastic and viscous terms in the normal stress is to extend the rear end so that it tends to the cusped trailing edge observed in experiments.

References

1. Drazin, P.G. & Reid, W.H. 1981. *Hydrodynamic Stability*. Cambridge University Press.
2. Harper, J.F. 1972. The motion of bubbles and drops through liquids, *Adv. Appl. Mech.* **12** 59-129.
3. Funada, T. & Joseph, D.D. 2001. Viscous potential flow analysis of Kelvin-Helmholtz instability in a channel, *J. Fluid Mech.*, **445**, 263-283.
4. Funada, T. & Joseph, D.D. 2002. Viscous potential flow analysis of capillary instability, *Int. J. Multiphase Flow*, **28**, 1459-1478.
5. Joseph, D.D., Belanger, J. & Beavers, G.S. 1999. Breakup of a liquid drop suddenly exposed to a high-speed airstream, *Int. J. Multiphase Flow*, **25**, 1263-1303.
6. Joseph, D.D. & Liao, T.Y. 1994. Potential flows of viscous and viscoelastic fluids, *J. Fluid Mech.*, **265**, 1-23.
7. Joseph, D.D. & Wang, J. 2003. The dissipation approximation and viscous potential flow, submitted to *J. Fluid Mech*. A PDF file of this paper can be downloaded from *http://www.aem.umn.edu/people/faculty/joseph/ViscousPotentialFlow/*
8. Mata, C., Pereyra, E., Trallero, J.L., Joseph, D.D. 2002. Stability of stratified gas-liquid flows, *Int. J. Multiphase Flow*, **28**, 1249-1268.

SEPARATION AND SORTING OF HEAVY PARTICLES SUSPENDED IN A FLUID BY SETTLING IN A PERIODIC VORTICITY FIELD

Urbano Sánchez*, Maria José Moreno**
*Fluid Mechanics Division, Huelva University ,Campus La Rábida, Huelva (spain) urbano.sanchez@dcaf.uhu.es
**Chemical Engineering Department, Huelva University, Campus El Carmen, Huelva (Spain) moreno@uhu.es

Summary: We propose a new procedure for particle-fluid separation which differentiates particles with different inertia values. We simulate a velocity field which allows us to sort heavy particles suspended in a fluid depending on their inertia values.

Disperse multiphase flows are very common in the environment and many industrial processes, as mining or mechanical and thermal process technology (e.g. erosion phenomena, coal combustion, gas-particle or gas-droplet flow). The agglomeration of particles in a turbulent gas flow is also very important for many chemical engineering processes, e.g. the production of particles by gas phase reaction. Furthermore processes for the separation of solid particles from fluids and its classification are an important field to study [1].
Frequent processes for dust control include suppressing dust production, accelerating particle sedimentation, separating dust from the air stream with air cleaning devices and ventilation [2]. To accelerate the dust sedimentation some options have been studied as air ionization systems. Any mechanical strategies for dust control have been suggested, as fiber filters, water or oil scrubbers electrostatic precipitators, cyclone type dedusters [3].
All those procedures do not differentiate particles with different features. Here we propose a method for particle-fluid separation which differentiates particles with different inertia values. For that purpose we have simulated a velocity field generated by a 2D array of vortices periodically repeated in space.
In order to show the main features of the dynamics of heavy particles in vortex flows we consider the Rankine vortex, defined by a smooth transition from solid rotation close to its centre to an irrotational flow from it. The normalised 3-D velocity field in cartesian co-ordinates relatives to the axis of the vortex is given by $u_x^*=-2y^*\Gamma^*/(R_v^{*2}+x^{*2}+y^{*2})$, $u_y^*=2x^*\Gamma^*/(R_v^{*2}+x^{*2}+y^{*2})$, $u_z^*=0$ with Γ^* the circulation of the vortex and R_v^* the radius of the vortex, so the maximum value of the velocity $|u^*|=U^*$ is given on $r^*= R_v^*= \Gamma^*/U^*$.
The motion of small spherical particles in a fluid is governed by a balance between the particle inertia, gravity and drag and buoyancy forces from the relative motion of particle and fluid. If the particle density is greater than the fluid density buoyancy and acceleration forces are not important and Newton's Second Law determines:

$$m_p^* \frac{d\mathbf{v}^*(t^*)}{dt^*} = 6\pi a^* \mu^* \left[\mathbf{u}^*(\mathbf{x}^*, t^*) - \mathbf{v}^*(t^*)\right] + m_p^* \mathbf{g}^* \,, \qquad (1)$$

with m_p^* particle mass, a^* particle radius, μ^* fluid viscosity, $\boldsymbol{g}^*$ gravitational acceleration and $\mathbf{u}^*(\mathbf{x}^*,t^*)$ local fluid velocity. Here, d/dt^* is the derivative following the particle**.** We have to write equations (1) in dimensionless form introducing the suitable dimensionless parameters. If the Reynolds number of the particles, based on their diameter and their terminal velocity, is small only two dimensionless parameters are enough to describe the motion of small spherical particles: a gravitational and an inertial parameter. The gravitational parameter could be the ratio of the terminal velocity of the particles in still flow V_t^* to the characteristic velocity of the fluid U^*: $V_t=V_t^*/U^*=m_p^*g^*/6\pi a^*\mu^*$. In the case of turbulent flows, if the time that the particles need to escape from regions of intense vorticity is much greater than the life time of those vortex structures, the inertia of the particles is characterised by the Stokes number $St=\tau_p^*/\tau_r^*$, where $\tau_p^*= m_p^*/6\pi a^*\mu^*=V_t^*/g^*=(\beta-1)d_p^{*2}/(18\nu^*)$ is the viscous response time of the particles and $\tau_r^*=R_v^*/U^*$ is the characteristic residence time of the fluid flow. Here β is the ratio between the particle density and the fluid density, d_p^* is the particle diameter and ν^* is the kinematic viscosity of the fluid. Considering $\mathbf{x}=\mathbf{x}^*/R_v^*$, $\mathbf{v}=\mathbf{v}^*/U^*$, $t=t^*U^*/R_v^*$ the scaled nondimensional equations of motion are:

$$\frac{d\mathbf{x}(t)}{dt} = \mathbf{v}(t) \,, \qquad (2.a)$$

$$\frac{d\mathbf{v}(t)}{dt} = \left(\frac{1}{St}\right)\left[\mathbf{u}(\mathbf{x},t) - \mathbf{v}(t) + \mathbf{V_t}\right]. \qquad (2.b)$$

The trajectories of particles are obtained integrating equations (2) using a fourth order variable step size Runge-Kutta method. The initial condition at the position $\boldsymbol{x_o}$ is that the particles have the velocity of the fluid at $\boldsymbol{x_o}$.
We have simulated two cases. Firtsly the neighbouring vortices were swirling alternatively cyclonically and anticyclonically. For inertial particles there is not possibility of particle trapping due to the centrifugal inertial force, therefore there are not closed trajectories. Figure 1 shows that for small particle inertia the particles follow the flow streamlines surrounding the vortices, but for larger stokes number i.e. for larger particle inertia values figure 2 shows a surprising behaviour; every time the distance between the particle and the vertical row of vortices is greater and at last the particles settle in the central region of low vorticity situated between two vertical rows of vortices due to an inertial bias. It is similar to something observed by Wang and Maxey [4] in an homogeneous turbulent flow generated with direct numerical simulation: the particles group in the "canal" between neighbouring regions of vorticity. The particles tend to regions of high strain rate or low vorticity.

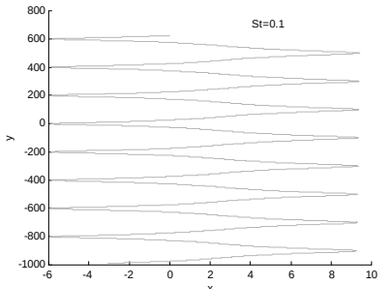


Figure 1: trajectories of inertial particles with neighbouring vortices swirling alternatively cyclonically and anticyclonically for small particle inertia.

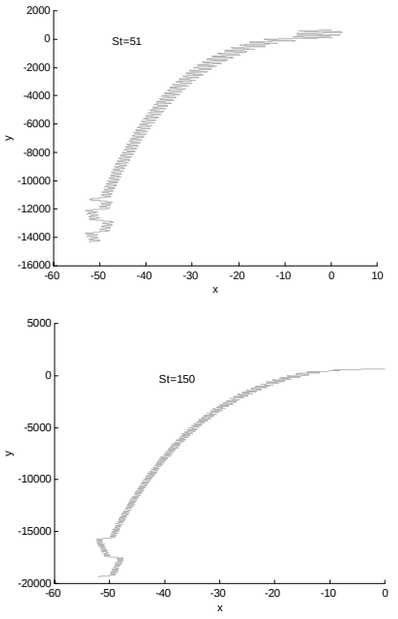


Figure 2: trajectories of inertial particles with neighbouring vortices swirling alternatively cyclonically and anticyclonically for moderate particle inertia.

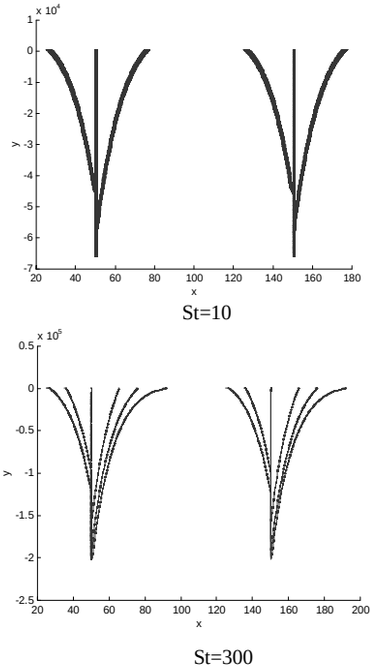
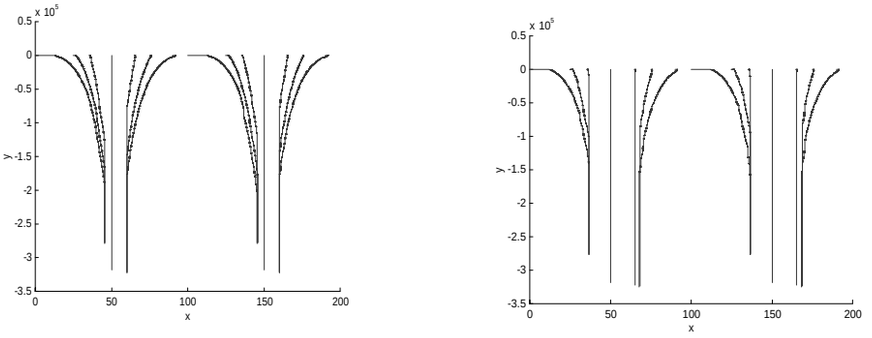


Figure 3: trajectories of inertial particles with neighbouring vortices swirling anticyclonically for small or moderate particle inertia.

Secondly all the vortices were swirling anticyclonically. In figure 3 we can see that for small or moderate particle inertia values all the particles settle in the central region of low vorticity situated between two vertical rows of vortices. The behaviour of the particles is the same as in the previous case (figure 2). Nevertheless, figure 4 shows a different behaviour for larger particle inertia values, an unexpected and surprising behaviour: for sufficiently large particle inertia the particles do not settle in the central region of low vorticity, they settle on some isolated curves which limit some regions of low vorticity where particles can not enter if they were initially outside those regions. As greater is the particle inertia greater is the width of those regions. At the same time, some empty regions situated under each vertical row of vortices appear. As greater is the particle inertia smaller is the width of these empty regions because the influence of the vorticity field is smaller.



St=600 St=1000

Figure 4: trajectories of inertial particles with neighbouring vortices swirling anticyclonically for large particle inertia.

Therefore is we know the particle inertia we will know the position in which it will settle and vice versa, so this fact suggest to develop a mechanism to sort particles with different inertia values materializing the velocity field mentioned above.

[1] Frank, Th., Wassen, Q. Yu. E. & Schneider, J. (1999). Experimental and numerical investigation of particle separation in a symmetrical double cyclone separator. Proceedings of the 3rd ASME/JSME Joint Fluids Engineering Conferences, San Francisco, California, USA.

[2] Dawson J.R. (1990). Minimizing dust in livestock buildongs-A review of possible alternatives to mechanical separation. J. Agricultural Eng. Res. 47:235-248.

[3] Owen, J.E. (1982). Dust-filtration solutions and their cost. Farm building programs, 68,19-23.

[4] Wang, L.P. & Maxey, M.R. (1993). Settling velocity and concentration distribution of heavy particles in homogeneous isotropic turbulence. J. Fluid Mech., 256, 27-68.

GAS-LIQUID INTERFACIAL DISTRIBUTION IN INCLINED DOWNWARD PIPE FLOW

Elena Trostinetsky, Lev Shemer and Dvora Barnea
Faculty of Engineering, Tel-Aviv University, Tel-Aviv 69978, Israel.

Summary. Two-phase air-water flow experiments for a wide range of pipe inclinations and flow rates are reported. Digital video camera connected to a boroscope is used to visualize phase distribution in the pipe cross-section illuminated by a laser light sheet. Advantages and limitations of the boroscope technique applied for two-phase flow are discussed. Simultaneously, wave gauges are used to measure the instantaneous surface changes. The main goal of this work is to investigate the transition from stratified to annular and to slug flow. Simultaneous video images and wave gauge records provide extensive information on the instantaneous and statistical properties of the phase distributions in the pipe.

Introduction

Two-phase (gas-liquid) flow in horizontal or downward inclined pipes is often stratified with the liquid film occupying the bottom part of the pipe. This flow regime is usually observed when gas and liquid flow rates are sufficiently low. One of the most intriguing problems in two-phase stratified flow is the distribution of the liquid film around the circumference in horizontal and inclined pipes. Transition from stratified flow to non-stratified slug or annular flow depends strongly on the film thickness and on the film shape. Experimental measurements of these parameters, especially near the transition zone, are quite rare. Calculations of the film thickness distribution in the pipe cross-section are usually complicated and require application of phenomenological models. For horizontal and slightly downward inclined flow, stratified – slug transition takes place at relatively high liquid flow rates, whereas stratified – annular transition occurs at high gas flow rates. At downward steep inclinations, stratified – annular transition is observed even at very low gas flow rates. The knowledge of the gradual variation of the average and the instantaneous film thickness and of the interfacial shape up to the transition to annular or slug flow is of utmost importance for understanding the mechanism of the flow pattern transition. In addition, the knowledge of the film shape for various operational conditions is required for pressure drop and heat and mass transfer calculations. The purpose of this study is to perform quantitative measurements of the distribution of the liquid and gas phases in the pipe cross-section in downward flow. Measurements are carried out for pipe inclination angles ranging from horizontal to nearly vertical (80^0).

Experimental facility and methods

Experimental investigation of the instantaneous cross-sectional distribution of the void fraction within a downward inclined pipe is carried out. The experimental facility consists of a 10 m long pipe with an internal diameter of 2.4 cm, built of 2 m long sections, that is placed on a steel frame and can be fixed at any desired angle of inclination. Water and air are used as the working fluids. The gas and the liquid superficial velocities are measured by a set of rotameters. In the current research we attempt to apply a novel and seemingly attractive approach to perform instantaneous void fraction measurements in the whole cross-section under various operational conditions. Two independent measuring techniques are employed. The first method uses a combination of a borescope based on fiber optic technology and a light-sheet illumination by a laser. This is a non-intrusive technique that practically does not interfere with the flow. The boroscope is inserted into the upper part of the pipe at an angle of about 20^0 relative to the pipe axis. To this end, a special module has been constructed. The boroscope is connected to a digital video camera using a special adapter. Calibration of the image is necessary to account for the optical distortions that arise from the slant angle at which the boroscope is introduced. The images recorded by the camera provide the necessary input to obtain the instantaneous cross-sectional void fraction distribution. Digital image processing of sequences of continuously recorded boroscope images makes it possible to calculate the appropriate statistical parameters.

Selection of the boroscope location and geometry is based on preliminary experiments that were carried out in our laboratory. These experiments demonstrated that when dispersed liquid drops or gas bubbles exist in the flow, the boroscope images become distorted. Moreover, in these cases optical distortions may be induced by liquid drops or gas bubbles that settle at the boroscope itself. Effective use of the boroscope technique seems to be limited to the cases where a single phase (either gas or liquid) exists at the boroscope lens. This limitation allows to study in detail separated gas-liquid flow, such as stratified flow (either smooth or wavy), annular flow, or the shape of elongated bubbles in slug flow.

Since the boroscope technique is quite new in two-phase flow studies, it is important to validate the results by more conventional methods. Measurements were therefore simultaneously performed using an alternative experimental method: capacitance wave gauges that are routinely used for studies of gravity-capillary waves on the water surface were applied to validate of the boroscope results. Up to four gauges can be used simultaneously. Here again, construction of a special module to introduce wave gauges into the pipe and to enable the gauge calibration is required. The probes are made of 0.6 mm tantalum wire which underwent an anodizing procedure to uniform coat it with a thin dielectric tantalum oxide layer. The probes are introduced into the measuring module at various angles relative to the vertical. The instantaneous wetted length measured by the probes allows capturing data at different points along the pipe.

Each measuring module is built of 20 cm long sections of 2.4 cm ID pipe. The modules can be placed at any connection between the 2 m long pipe sections. Most measurements in this study were carried out when the measuring modules were located at adjacent positions close to the exit from pipe (at about 8 m from the pipe inlet).

Results

A typical sequence snapshots recorded by the camera in stratified flow regime is presented in Fig. 1. According to the flow pattern map (Barnea et al. 1982), stratified flow in downward pipe flow is wavy. The unsteady character of the flow is indeed clearly visible in variation of the instantaneous shape of the interface in the illuminated by the laser sheet pipe cross-section.

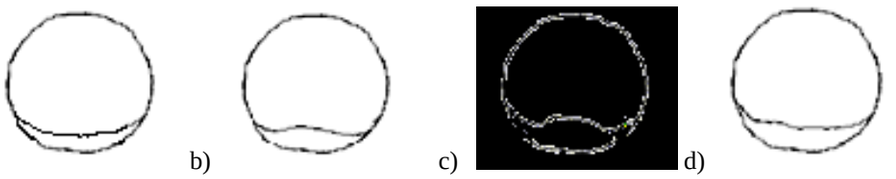


Figure 1: Sequence of instantaneous interface shapes. Pipe inclination 10^o, U_{LS} =0.1m/sec, U_{GS} =0.1 m/sec.

Increase of the inclination angle strongly affects the interface shape which varies from a smooth for zero inclination to wavy-stratified at higher inclinations and to nearly axially-symmetric annular flow for inclination angles approaching the vertical. The variation of the mean interface shape with the inclination angle is studied for various flow conditions. The transition between from stratified to non-stratified flow patterns is compared with the model predictions given in Barnea et al (1982). It is observed that the temporal variation of the instantaneous film thickness depends strongly on the pipe inclination angle. This is demonstrated in Fig. 2. A comparison is carried out between the instantaneous water depth measured at the vertical diameter of the pipe cross-section by the wave gauge, and that derived from a sequence of the video images. Good agreement is obtained between the two measuring techniques. The mean film thickness for given flow rates decreases with increasing inclination angle. The wave amplitudes and frequencies dependence on pipe inclination and on the gas and liquid flow rates is studied in detail.

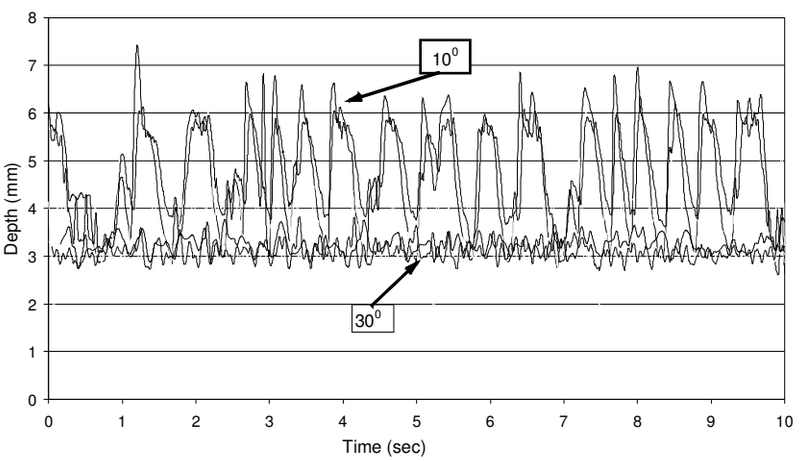


Figure 2: Instantaneous liquid film depth at the vertical diameter in the pipe cross-section derived from the recorded boroscope images (thin line) and measured by a capacitance probe (thick line). Flow rates as in Fig. 1.

Measurements were also performed in the slug flow regime, which is obtained for higher gas and liquid flow rates. Results of the shape of the elongated bubbles, as well as slug unit propagation velocities and the mean lengths of the liquid slugs and elongated bubbles, are obtained for various flow conditions. Transitions between the flow patterns observed in the present study are compared with those reported before. The present results demonstrate the potential of the experimental approach adopted in this study for two-phase flow measurements.

Acknowledgement

This study was supported by a grant from the Israel Science Foundation.

Reference

Barnea D., Shoham O. and Taitel Y. (1982) Flow pattern transition for downward inclined two phase flow; horizontal to vertical. Chem. Eng. Sci. 37, 735-740.

VIDEOGRAMETRY IN FLUIDIZED BED REACTORS

Stanisław Anweiler, Roman Ulbrich
Politechnika Opolska, KTCiAP, ul. Mikołajczyka 5, 45-271 Opole, Poland

Summary The main task of this research work was to develop and then apply method for evaluation of the homogeneity of the fluidized bed, based on digital image analysis for different types of fluidization, and to compare and correlate the results. Various types of fluidization was recorded with the use of high speed CCD video camera and frame sequences of recorded two-phase flow were put under digital image analysis on the basis of brightness level of the image measurement.

Experiments on identification and evaluation of two-phase gas-solid flow pattern in fluidized bed model apparatuses were carried out. The main task of this research work was to evaluate the homogeneity of the fluidized bed for different types of fluidization in different types of fluidized bed reactors. The dynamics of homogeneity changes have been expressed as change of brightness level value of the image in time and space domain. By the analysis of brightness level of each pixel of each image in the frame sequence, the grey level fluctuation function is drawn (Figure 1). The grey level function is base signal for further analysis in stochastic manner (Figure 2). Functions such as autocorrelation and probability density have been used for that analysis. The experimentation was held in different fluidization columns with transparent walls. Various types of fluidization was examined with the use of high speed CCD video camera.

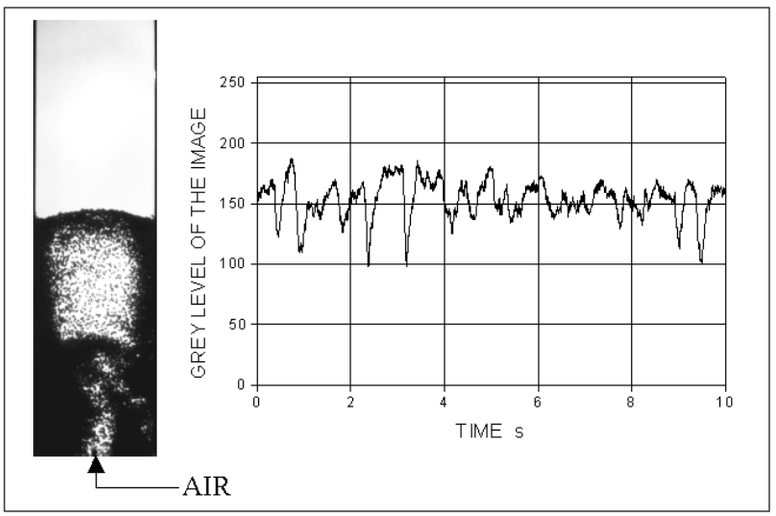


Figure 1. Example image of bubbling fluidization and example graph of grey level of the image fluctuation.

Technology of the fluidization of solid particles with gas stream is known for almost 100 years, but behaviour description of such two-phase mixture still causes problems. This is because of the huge amount of particles, which interacts between themselves, walls and other obstacles inside the reactor. The influence of the geometrical structure of the vessel on the flow pattern intensifies with the increase of the complicity of the flow geometry of the apparatus. Dynamic description of movement of such set of particles requires detailed information about factors responsible for particular two-phase flow structure and needs application of image and stochastic process analysis.
New measurement method for two-phase gas-solid flow, called videogrametry, was carried out. This method allows dynamic space and time analysis of phase concentration distribution inside the fluidization apparatus, on the basis of image analysis of brightness of pixels of the image in specified area. Method was applied for estimation of the vessel structure influence on distribution of phase concentration for different types of fluidization.
Experiment was carried out on three different two-dimensional models of fluidization apparatus with rectangular cross section. First for bubbling fluidization – a chamber with a grill. Second for jet spouted fluidization – chamber with conical section and vertical conveying riser mounted axially inside the vessel. Third for fast fluidization – vertical riser with recirculating solid particles. The subject of investigation was two-phase gas-solid flow structure estimation in dependence of geometry of the fluidization chamber. Void fraction was measured in different places inside the vessel. Solid particles with diameter of 1 to 10 millimetres and density of 1000 kg/m^3 were fluidized with air. Air velocity inside the flow channels was in range of 1,5 to 17,0 m/s. All velocities were calculated for empty vessels.
Visualization of the process was possible due to application of transparent materials for building the apparatus models, and digital video camera for high speed capturing of high resolution images. Used CCD camera is capable of getting up to 1800 frames per second and the resolution of the images is 1024/1024 pixels. These features of the applied video camera enable recording of very fast processes.The values of such parameters as heat, mass and momentum transfers are

strongly dependent on hydrodynamic condition of the bed, it causes that the flow pattern of two-phase flow is the criterion of similarity for comparing processes held in different constructed reactors.
There are many various measurement methods for investigation of two-phase flow systems. One of them, worked out by our research team – videogrametry – is an optical method based on analysis of the recorded images of the flow. These images are bitmaps with recorded distribution of solid phase concentration in the form of brightness level distribution. With the use of dynamic image analysis of brightness level of each pixel in every image in the sequence, space and time characteristic of brightness level fluctuation were obtained. Brightness level is also called grey level. Change of grey level is time and space depending function. Brightness level of pixel or image was measured in range of 0 – 255, where 0 means black or 100% solid phase, and 255 means white or 100% gas phase. Results between these boundaries are grey levels. Using simple transposition functions allows calculating the grey level to void fraction. Additional stochastic analysis was made for brightness level functions to get information on the process in frequency domain. Correlation of the results shows that each classified two-phase flow structure has its own and original pattern of the grey level changes. Different types of flow regimes have their own original sets of grey level fluctuation patterns.
On figure 2 there are shown results of stochastic analysis of the grey level fluctuation signals for two types of flow regime. Figure 2A presents three graphs for plug two-phase gas-solid flow. The images grey level fluctuation pattern (top graph). Below there are probability density function (PDF) and autocorrelation function (ACF). In the same manner figure 2B shows result of digital image analysis for turbulent flow regime.

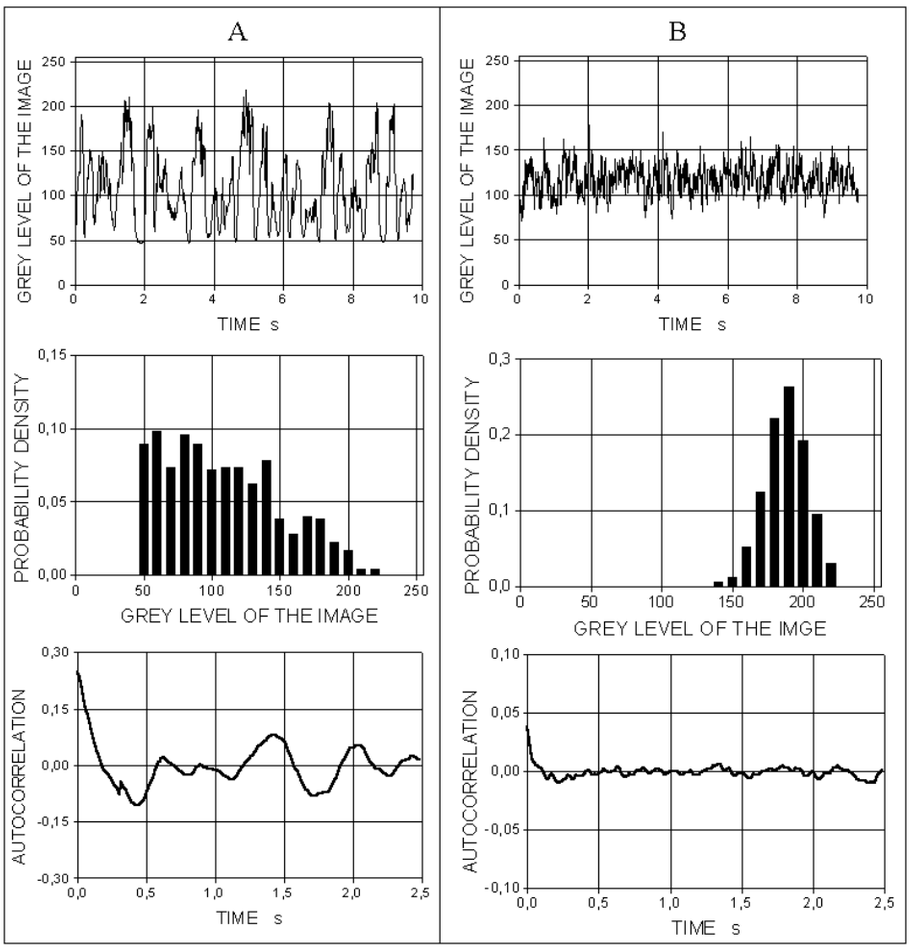


Figure 2. Example results of digital image analysis for A – plug flow regime and B – turbulent flow regime.

In multiphase systems research, experiments are led mostly in laboratory models of apparatuses with simple shape. It is often a vertical riser. But the chambers and flow channels of real devices are not so simple. They frequently change diameter and direction and the two-phase stream reacts with various obstacles.
Digital imaging and analysis of fluidization phenomena – videogrametry – provides a non-invasive measurement tool for recognition of two-phase flow structure, i.e. evaluation of dead zones inside the vessel, tracing trajectories of particles, examination of local void fraction, and for validation of numerical simulations developed in recent years, and much more. Building models of various types of fluidized bed reactors and examining them with the use of videogrametry helps finding specific features of fluidized bed constructions.

XXI ICTAM, 15–21 August 2004, Warsaw, Poland

GRAVITY INDUCED MIXING OF MISCIBLE FLUIDS IN VERTICAL AND INCLINED TUBES

Thomas Séon*, Bernard Perrin**, Dominique Salin*, Jean-Pierre Hulin*
*Laboratoire FAST, UMR 7608 Bâtiment 502, Campus Universitaire, 91405 Orsay Cedex (France)
**LPA, UMR 8551, Département de Physique de l'ENS, 24 rue Lhomond, 75231 Paris Cedex 05 (France)

Summary Gravity induced mixing of two miscible fluids in a long tube is studied as a function of the tube tilt angle from vertical θ and of the density contrast characterized by the Atwood number At. At high At values and/or low θvalues, the relative concentration of the two fluids follows a macroscopic diffusion law characterized by a diffusion coefficient D increasing strongly with the tube tilting (by a factor of 100 between 0 and 70^o). At higher θ values and/or for low density contrasts, a segregation of the two fluids in the tube section is induced by gravity resulting in a stable counterflow with little mixing at the interface. The value of At at the transition between the diffusive and counterflow regimes increases with the θ from $At = 10^{-4}$ for $\theta = 0^o$ to $At = 5 \times 10^{-2}$ for $\theta = 80^o$.

OBJECTIVES AND PRINCIPLE OF EXPERIMENT

Buoyant mixing of miscible fluids of different densities ρ_1 and ρ_2 in gravitationally unstable configurations in vertical or inclined channels is frequently encountered in chemical and petroleum engineering[1] as well as in fire propagation in shafts[2] : in the present work we study experimentally the influence of the tilt angle on these mixing processes.

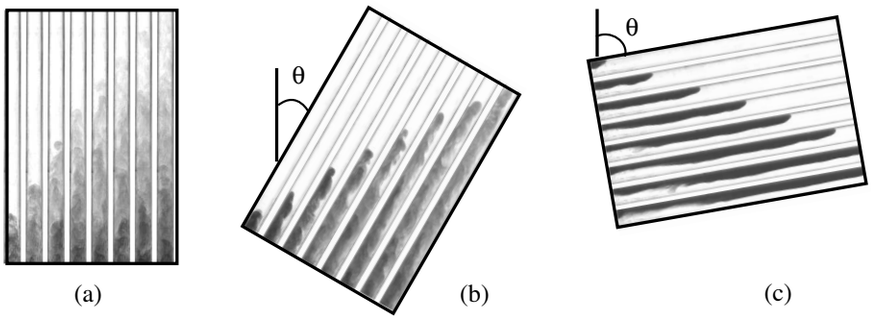


Figure 1. Sequences of pictures obtained right after beginning of experiments for three different tilt angles $\theta = 0, 30, 80^o$. Atwood number $At = 4 \times 10^{-3}$. Respective durations of sequences = $50\,s, 20\,s$ and $20\,s$.

Experiments are realized in a $4\,m$ long transparent tube of diameter $d = 20\,mm$ with a slot valve in the middle[3, 4]. The tilt angle θ varies from 0 to 90^o. The lighter fluid is dyed water and the heavy fluid is a solution of water and $CaCl_2$ salt. Density contrasts are characterized by the Atwood number $At = (\rho_2 - \rho_1)/(\rho_2 + \rho_1)$ varying from 2×10^{-5} to 10^{-1}. The upper and lower halves of the tube are initially filled with the heavy and light solutions and mixing is initiated by opening the slot valve. Figure 1 displays the flow above the slot valve for three different angles θ. Increasing θ results in a transition from weakly turbulent mixing to fully stratified flow with no transverse mixing.

EXPERIMENTAL RESULTS

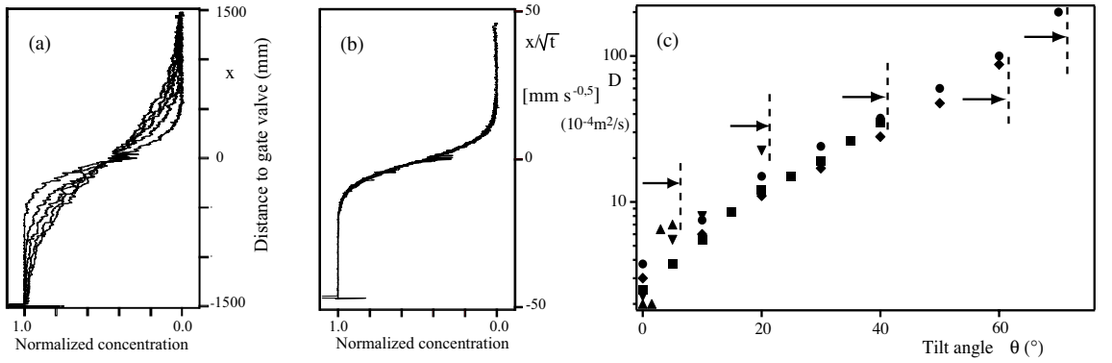


Figure 2. Normalized concentration profiles obtained at successive times $t = 100, 300, 500, 700$ and $900s$ for $\theta = 0^o$ and $At = 4 \times 10^{-3}$ - (a) profiles plotted vs distance x from slot valve. - (b) profiles plotted vs $x/\sqrt{t}$. - (c) Variation of diffusion coefficient D with the tilt angle θ for different density contrasts. • : $At = 3.5 \times 10^{-2}$, ♦ : $At = 10^{-2}$, ■ : $At = 4 \times 10^{-3}$, ▼ : $At = 10^{-3}$, ▲ : $At = 4 \times 10^{-4}$). Arrows mark the values of θ corresponding to the upper limits of the diffusive domains for the various contrasts.

The tube is illuminated from the back and digital images are recorded at regular intervals. They are translated into normalized concentration maps and averaged over the width of the tube to obtain mean concentration profiles $\overline{C}(x,t)$. Figure 2a displays such profiles measured at regular time intervals in a weakly turbulent regime in a vertical tube. All profiles overlay perfectly when plotted as a function of $x/\sqrt{t}$ (Figure 2b) and are well fitted by an error function (continuous line). The mixing process is therefore diffusive and the fit provides the value of the corresponding macroscopic diffusion coefficient D. These diffusive characteristics are only observed up to a limiting tilt angle which gets larger as At increases.

The variation of D with the tilt angle θ is plotted in Figure 2c for different density contrasts. A key feature is the very strong increase of D with θ (by a factor of 100 between $\theta = 0^o$ and 70^o). On the contrary, for a given tilt angle, D increases only weakly with At. For tilt angles higher than the limit of the diffusive domain, the instabilities of the interface beween the two fluids do not develop : this reduces transverse mixing across the tube section. At very large tilt angles, one reaches a final state in which the two fluids are segregated in a *stable* configuration.

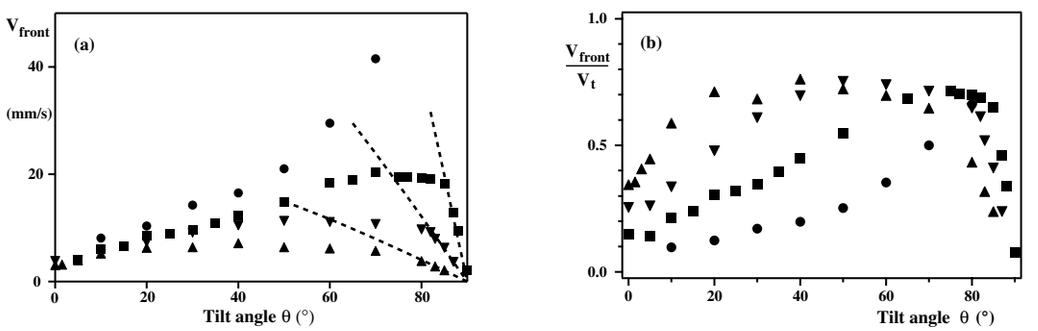


Figure 3. (a) Mixing front velocity variation as a function of tilt angle θ - (b) Normalized velocity V_{front}/V_t as a function of θ. $\bullet$: $At = 3.5 \times 10^{-2}$, $\blacksquare$: $At = 4 \times 10^{-3}$, $\blacktriangledown$: $At = 10^{-3}$ $\blacktriangle$: $At = 4 \times 10^{-4}$.

Another important parameter is the velocity V_{front} of the upper and lower fronts marking the limit of the penetration of each fluid into the other. Figure 3a displays the variation of V_{front} with the tilt angle θ for several values of the Atwood number At. A clear-cut feature is the strong initial increase of V_{front} with θ. On the contrary, for very large tilt angles close to 90^o, V_{front} decreases sharply : it is likely that, in this latter domain, the potential energy gained from buoyancy forces just compensates for viscous dissipation in the counterflow of the two fluids (dotted lines in Figure 3a are the corresponding theoretical velocity variations). At the low θ values, flow is determined by a balance between inertia and buoyancy forces : the characteristic velocity of this mechanism is $V_t = \sqrt{Atgd}$. Figure 3b shows that the ratio V_{front}/V_t is at first lower than 1, indicating a lower effective density contrast at the front due to local mixing and becomes of the order of 1 when the two fluids are segregated. The increase of V_{front}/V_t is much slower at the largest density contrasts - also due to a stronger mixing.

CONCLUSION

These experiments illustrate that tilting the tube slows down transverse mixing across the flow section and influences strongly the interpenetration of the fluids. For moderate tilt angles θ and high enough Atwood numbers At, mixing is diffusive : the diffusion coefficient D increases very fast with θ but is almost independent of At. At larger angles, a stable counterflow of the fluids with almost no transverse mixing takes place. The transition between these regimes occurs at larger angles whenAt increases. Both the variation of D and that of the mixing front velocity depend strongly on the *local* density contrasts in the flow and not only on At. These local contrasts are very much influenced by the efficiency of mixing and then by the tilt angle. A full understanding of these processes requires therefore a small scale analysis of the spatial and temporal characteristics of the velocity and concentration fluctuations in the flow.

Acknowlegments : We thank C. Saurine, G. Chauvin, and R. Pidoux who designed and realized the experimental set-up and E.J. Hinch for illuminating discussions.

References

[1] M.H.I. Baird, K. Aravamudan, N.V. Rama Rao, J. Chadam and A.P. Peirce. "Unsteady axial mixing by natural convection in vertical column" *AIChE J.***38**, 1825 (1992).

[2] E.E. Zukoski "A review of flows driven by natural convection in adiabatic shafts" NIST report NIST-GCR-95-679 (1995) and references therein.

[3] M. Debacq, V. Fanguet, J.P. Hulin, D. Salin and B. Perrin "Self-similar concentration profiles in buoyant mixing of miscible fluids in a vertical tube", *Phys. Fluids* **13**, 3097 (2001).

[4] M. Debacq, J.P. Hulin, D. Salin, B. Perrin and E.J. Hinch "Buoyant mixing of miscible fluids of varying viscosities in vertical tubes", *Phys. Fluids* **15**, 3846 (2003).

OSCILLATORY MOTION OF FREELY-MOVING LIGHT BODIES: FROM CYLINDERS TO DISKS

P. Cordeiro Fernandes, P. Ern, F. Risso and J. Magnaudet
Institut de Mécanique des Fluides, UMR 5502 CNRS-INP-UPS
Allée C. Soula, 31400 Toulouse, France

Summary We report on an experimental investigation of the oscillatory motions of flat cylinders rising in a low-viscosity fluid otherwise at rest. Original results are presented concerning the vertical velocity and the horizontal oscillations of the body velocity and orientation (amplitude, frequency and phase difference), underlining the crucial effect of the body aspect-ratio on the complex coupling between body rotation and translation.

In many situations, free falling or rising particles at moderate-to-large Reynolds numbers exhibit oscillatory motions: spiral, zigzag or tumbling. Our general concern is to determine the causes of these oscillations for particles moving under the effect of buoyancy in a fluid otherwise at rest. Consider first a fixed sphere of radius r in a uniform flow of velocity V of a fluid of viscosity ν. Beyond a certain Reynolds number ($Re = 2rV/\nu$), the wake becomes unstable and unsteady drag and lift forces act on the body. For a freely-moving buoyant sphere [1], these forces represent a first possible cause of path oscillations. When the sphere moves freely, its velocity V is *a priori* unknown and the Reynolds number is replaced by the Archimedes number, $Ar = r\sqrt{\frac{\Delta\rho}{\rho_l} gr}/\nu$ (where g is the acceleration of gravity and $\Delta\rho$ the density difference). As the amplitude of the oscillations is significant only if the body is light enough, the solid-to-fluid density ratio ρ_s/ρ_l is an important parameter. For a non-spherical body, the anisotropy of the added-inertia tensors can also produce path oscillations because it couples the equations for translation and rotation. Moreover, the viscous drag also depends on the direction of the velocity with respect to the body orientation. Therefore, the body shape is also of major importance.
We carried out an experimental study on the rise of light flat cylinders (diameter d, thickness h and equivalent radius $R_{eq} = \left(\frac{3}{16} h d^2\right)^{\frac{1}{3}}$) in a 1.70 m high tank of salted water. Since our objective is to investigate the range of moderate Archimedes numbers, we used very small density differences ($10^{-3} \leq \Delta\rho/\rho_l \leq 10^{-2}$) determined with an accuracy of 5×10^{-4} kg/dm^3. Consequently, ρ_l/ρ_s is very close to unity. Experiments were performed for various aspect ratios d/h ranging from 1.5 to 10 and Ar between 50 and 100 ($150 \leq Re \leq 300$). The vertical mean velocity, V_z, ranges between 10 to 35 mm/s and the amplitude of horizontal body-centre displacements lies between 0.15 and 3 mm, which corresponds to velocities between 0.5 and 5 mm/s. The rise of the body is followed by two moving cameras; its location and orientation are then determined by image processing with an accuracy of ± 0.15 mm (see figure 1). We observe that in all cases orientation and horizontal velocity experience harmonic oscillations at the same frequency ω, the vertical velocity oscillating at 2ω. The frequency ($0.1 \leq \omega \leq 0.35$ Hz) is an increasing (resp. decreasing) function of Ar (resp. d/h). However, the Strouhal number, $St = R_{eq}\,\omega/V_z$, is approximately independent of Ar and remains close to 0.06 for $d/h \geq 4$.
We consider now the amplitudes of the oscillations. From a top view, the trajectory is an ellipse, the principal axes of which we denote by X and Y. The displacements in the X- and Y-directions are described by sine functions (with amplitudes A_X and A_Y) that are $\pi/2$ out of phase. The ratio A_Y/A_X is observed to vary from 0 (plane zigzag trajectories) to 1 (circular helix). For Ar larger than 70, A_Y/A_X first increases from 0 to 0.35 when d/h is increased from 1 to 4 and then decreases towards 0 when d/h is further increased. For lower values of Ar, A_Y/A_X seems to be an increasing function of d/h over the whole range of aspect ratio investigated but the conclusion is uncertain for d/h larger than 8 because the amplitude of oscillations becomes very small.

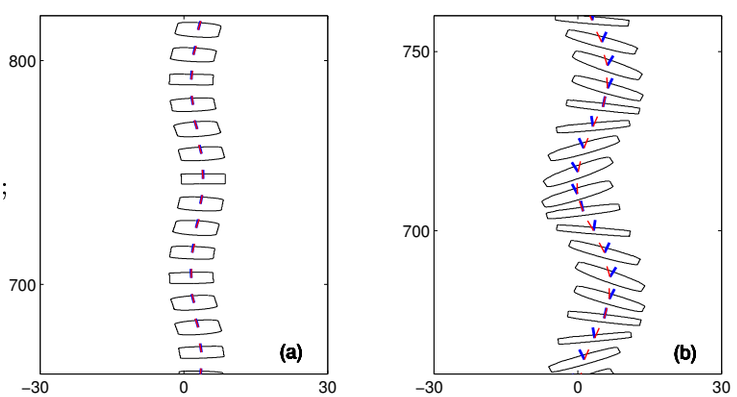


Figure 1. Typical body motions ($Ar = 85$). Thick blue line: body axis; Thin red line: velocity direction. (a) $d/h = 2$; (b) $d/h = 10$.

The amplitude of the horizontal displacement is represented on figure 2(a) by the maximum angle, θ_{max}, made

by the body-center velocity and the vertical direction. The amplitude θ_{max} increases with Ar but exhibits two different behaviors depending on d/h being larger or smaller than 4. Here all the aspect ratios investigated correspond to oblate bodies, the axis of which oscillates about the vertical direction. Note that the limit $d/h \to 0$ corresponds to a strongly different behavior since a stable prolate body (as a rod) moves with its axis perpendicular to its velocity. It is thus not surprising to observe a monotonic evolution towards the disk limit ($d/h \to \infty$) only beyond $d/h = 4$; after this value θ_{max} increases strongly. The same behavior is observed for vertical velocity fluctuations which are negligible for d/h less than 4 and then increase regularly with d/h. However, the amplitude of the vertical oscillations is smaller (at least 5 times) than the horizontal one which itself is smaller (at least 3 times) than the mean rise velocity V_z. It is thus relevant to examine the drag coefficient C_d based on the mean velocity. At a given Ar, the two regimes are again observed: C_d first increases and keeps a constant value beyond $d/h = 4$. More interesting is the fact that for given d/h, C_d is an increasing function of Ar and consequently of Re. This seems in contradiction with results concerning fixed bodies. On the other hand, experiments [2] and numerical simulations [3] concerning rising bubbles show that the drag coefficient is an increasing function of the amplitudes of path oscillations. This is also observed here.

Figure 2(a) also shows the evolution of the maximum angle, α_{max}, made by the body axis and the vertical direction. The two distinct regions separated by $d/h = 4$ are again observed but at variance with velocity oscillations, α_{max} is approximately constant for $d/h \geq 4$. In other words, we observe that when the body becomes thinner the amplitude of the horizontal displacement increases whereas its maximal inclination remains almost constant. An important feature of figure 2(a) is that the instantaneous velocity is not parallel to the body axis. The drift angle between the velocity and the body axis is crucial for a non-isotropic body since it couples translation and rotation. However, the difference between α_{max} and θ_{max} is not sufficient to characterize this drift angle, since the phase difference between the harmonic oscillations of the velocity and those of the body orientation depends on d/h. Indeed, figure 1(a) shows that for a thick body ($d/h = 2$) velocity and orientation are almost in phase whereas figure 1(b) shows that for the thinnest body ($d/h = 10$), they are about $\pi/2$ out-of-phase. In figure 2(b) one sees that the phase difference varies continuously with d/h between these two limits and is almost independent of Ar.

The detailed description of the oscillatory motion of rising flat cylinders carried out in this work for a wide range of aspect ratio and Archimedes number underlines the complexity and diversity of the dynamics of rising bodies. Concerning the mean rise velocity, it appears that the drag coefficient is not a simple function of the mean Reynolds number, as for a fixed body, but is strongly influenced by the oscillatory motion. When d/h is increased the amplitude of body orientation oscillations reaches a constant value while that of velocity oscillations continues to increase. Moreover, the phase difference between the body velocity and orientation oscillations evolves from about 0 (bubble-like behavior) to a value close to 90^o (disk-like behavior) when the aspect ratio is increased. However, the orientation and the velocity oscillate at the same frequency, characterised by a Strouhal number rather independent of both Ar and d/h for $d/h \geq 4$ and have amplitudes that increase with Ar. This suggests that the wake instability mechanism, which is related to the production of vorticity at the body surface and generates the oscillations, is rather independent of the body shape (for $d/h \geq 4$) and drives the body velocity and rotation to which it imposes its frequency. The body velocity and rotation respond to this forcing with their respective dynamics, which strongly depend on the body aspect ratio and determine their own amplitude and phase. To check this interpretation, our future work will focus on the determination of the different hydrodynamical forces and couples that act on the body, the present experimental techniques being sufficiently accurate to determine the linear and angular accelerations of the body.

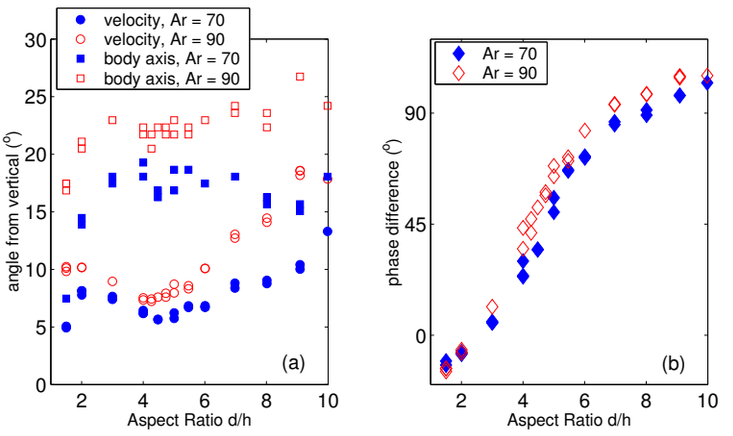


Figure 2. Comparison between body axis and horizontal velocity oscillations: (a) amplitudes measured by maximum angles from the vertical direction; (b) temporal phase difference.

References

[1] Jenny M., Bouchet G., Dusek J.: *Phys. Fluids* **15**(1):L9-L12, 2003.
[2] Ellingsen K., Risso F.: *J. Fluid. Mech.* **440**:235-268, 2001.
[3] Mougin G., Magnaudet J.: *Phys. Rev. Lett.* **88**(1):14502, 2002.

XXI ICTAM, 15–21 August 2004, Warsaw, Poland

PARTICLE TURBULENCE INTERACTION

S. Balachandar[1], P. Bagchi[2], L. Wakaba[1], L. Zeng[1]
1: Department of Theoretical & Applied Mechanics, University of Illinois, Urbana, IL, USA.
2: Department of Mechanical & Aerospace Engineering, Rutgers University, USA.

The interaction between the carrier and the dispersed phases is bi-directional: the carrier-phase turbulence influences the dispersion and preferential accumulation of particles and bubbles, and particles and bubbles in turn modulate the fluid turbulence. At the level of a single particle, the effect of freestream turbulence is to modify the drag force compared to that in a steady uniform flow. On the other hand, the particle can modify freestream turbulence by the formation of a wake, periodic shedding of vortices, and wake turbulence. The collective effect of a distribution of particles can further modify the effective drag force on a particle due to the screening effect and thereby influence the mean settling and dispersion characteristics. Similarly, the collective effect of the dispersion of particles will determine the attenuation or augmentation of the turbulence intensity. Thus, many of the mechanisms of multiphase flow turbulence are quite distinct from those that have been well established in single-phase turbulence and therefore deserve detailed investigation.

Here we present results from fully-resolved direct numerical simulations (DNS) of turbulent multiphase flow. In addition to resolving the wide range of length and time scales associated with turbulence, which would exist even in the absence of the particles, we now need to resolve all the length scales associated with the particles and the small-scale flow features generated by them. Thus, direct numerical simulations of multiphase flow turbulence pose greater challenge than the DNS of corresponding single-phase turbulence. Here we plan to present results for the interaction of a single spherical with ambient turbulence. We will consider the cases of both isotropic freestream turbulence and wall-bounded channel flow turbulence.

For the case of isotropic turbulence the particle Reynolds number is varied from about 50 to 600, and the particle diameter is about 1.5 to 10 times the Kolmogorov scale of the undisturbed turbulent flow. The Taylor microscale of the freestream turbulent flow is 164 and the relative intensity of freestream turbulence to mean crossflow is varies from 10% to 25%. The DNS technique employed here resolves both the smallest scales in freestream turbulence and the thin shear layers and complex vortical structures associated the particle wake. The present DNS study is similar to the experimental study by Wu & Faeth (1994a, 1994b), and agreement between the DNS results and the experimental measurement are presented.

Figure 1a summarizes the drag coefficient for a sphere in the presence of freestream isotropic turbulence compiled from many different experimental measurements. Also plotted for reference as the solid line is the standard Schiller-Neumann drag law corresponding to a turbulence-free uniform flow. The scatter in the experimental data clearly illustrates the large discrepancy between the different results. Also plotted in the figure are the DNS results which show that freestream isotropic turbulence does not have a substantial and systematic effect on the time-averaged mean drag on the particle. Standard drag correlation based on instantaneous relative velocity between the particle and the undisturbed fluid velocity at the center of the particle results in a reasonable prediction of the mean drag. However, the accuracy of prediction of the instantaneous drag decreases with increasing particle size. For the smaller particles, the low frequency oscillations in the DNS drag are well captured by the standard drag, but for the larger particles significant differences exist even for the low frequency components. Inclusion of the added-mass and history terms, computed based on the undisturbed ambient flow at the center of the particle, does not improve the prediction of instantaneous forces. Fluctuations in the drag and lift forces are shown to scale with the mean drag as well as the freestream turbulence intensity (see figure 1b).

The effect of freestream turbulence on the mean and instantaneous wake structure is studied. The mean wake in a turbulent flow shows reduced velocity deficit and a flatter profile. However, the mean wake in a turbulent flow behaves like a self–preserving laminar wake. At low Reynolds numbers the wake in a turbulent flow oscillates strongly without any vortex shedding, but at higher Reynolds numbers vortex shedding starts. The nature of the vortices are very different from that in a uniform flow. Increasing the freestream turbulence intensity suppresses the process of vortex shedding, and only marginally increases the wake oscillation. The modulation of freestream turbulence in the wake is studied in terms of the distribution of the distribution of the kinetic energy and RMS of velocity fluctuation. The freestream energy lost in the wake is recovered faster in a turbulent flow than in a uniform flow. The energy of the velocity fluctuation is enhanced in the wake at low freestream intensities, and is damped or marginally increased at higher intensities. The fluctuation energy is not equi-partitioned among the streamwise and cross-stream components. The RMS of the streamwise fluctuation is always enhanced, whereas the RMS of the cross-stream fluctuation is enhanced only at low freestream intensities, and damped at higher intensities.

We are currently extending the above results in several significant ways. For a given ambient turbulent flow, the particle Reynolds number can be expressed in terms of the other two parameters: the relative turbulence intensity and the ratio of particle diameter to freestream turbulence. Here we explore in greater detail the independent role of these different parameters on turbulence modulation. The above DNS approach is also being used to address the influence of freestream turbulence on the mean settling (or rise) velocity of heavier-than-fluid particles (or lighter-than-fluid bubbles). Unlike the earlier simulations, here the particle is allowed to freely move in response to hydrodynamic forces acting on it.

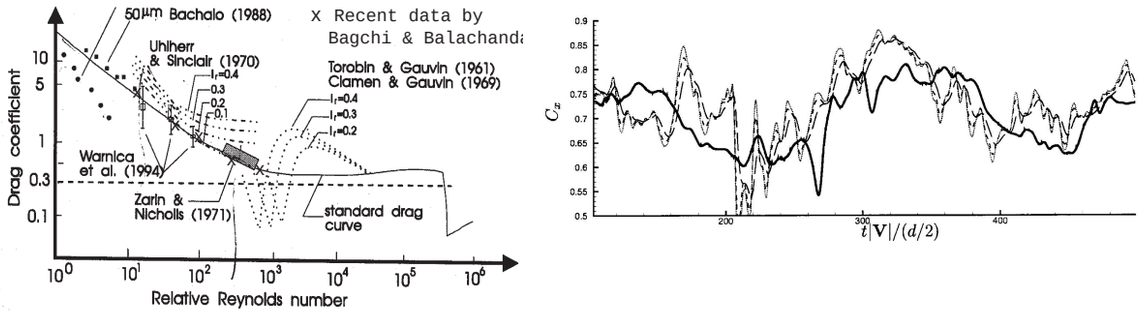


Figure 1. (a) Data on the effect of freestream turbulence on mean drag coefficient for varying Re obtained from several different experiments. Shown in the plot is the standard drag curve valid for a rigid sphere in a turbulence-free uniform cross-flow. Also shown are the recent DNS results of Bagchi & Balachandar (2003b). (b) Time variation in the streamwise component of the drag coefficient due to freestream turbulence. For the case shown here the ratio of particle diameter to Kolmogorov scale is 4, turbulence intensity is 10% and $Re = 261$. Thick solid line: DNS result, thin solid line: standard drag law (SDL), dash line: SDL plus added-mass force, dash-dot line: SDL plus added-mass and Basset history force.

We are also in the process of investigating the interaction of a single isolated particle with wall turbulence. We consider the case of a spherical particle embedded in a channel formed between two parallel plates. Inflow to the computational domain is specified as a fully developed turbulent channel flow (at a specified Reynolds number based on friction velocity) obtained from an auxiliary turbulent channel flow simulation. The computational grid for the present simulation is chosen such that it resolves all the scales of the turbulent inflow across the entire width of the channel as well as the unsteady boundary layers, shear layers and the wake behind the particle. A high accuracy spectral element numerical methodology is used for simulating the turbulent flow around the sphere within the channel. Of particular interest is the interaction of the turbulent wake with the nearby wall. The key parameters of the problem are the relative size of the particle compared to the channel height, and the relative distance of the particle center from the nearby wall. We plan to vary these two parameters and accordingly the particle Reynolds number.

As with the isotropic turbulence, we plan to first study the effect of wall turbulence on the mean and fluctuating components of drag on the particle. The asymmetric effect of the nearby wall is to introduce a lift force on the particle. We will also investigate the effect of wall turbulence on the mean and fluctuating components of the lift force. We will then study the effect of the particle on the wall turbulence by focusing attention on the wake region downstream of the particle. The back-effect of the particle on the structure of turbulence will be first investigated in terms of interaction between wall-vortical wake-vortical structures. The turbulence statistics in the wake region will be compared with the undisturbed channel flow statistics to assess the influence of the particle. Particular attention will be focused on the effect of the particle on modifying the mean drag on the nearby flat plate.

References

[1] Wu, J.S. & Faeth G.M.: Sphere wakes at moderate Reynolds numbers in a turbulent environment, *AIAA Journal*, **32**, 535–541, 1994a.

[2] Wu, J.S. & Faeth G.M.: Effect of ambient turbulence intensity on sphere wakes at intermediate Reynolds numbers, *AIAA Journal*, **32**, 535–541, 1994b.

Non-Uniform Flow Hydrodynamics of Deformable Shapes

T. Miloh
Faculty of Engineering,
Tel-Aviv University,
ISRAEL, 69978
(miloh@eng.tau.ac.il)

January 21, 2004

This contribution is motivated by the recent works of Moffatt and Sellier (2002), Sellier (2003), Shin and Kang (2002) and Kang et al. (2002). Moffatt and Sellier examined the low Reynolds number migration of an insulating rigid particle in a viscous liquid metal which is subject to uniform electric and magnetic fields E and B in the Stokes realm. Complementary to these studies, Shin and Kang considered the effect of a uniform magnetic field on the shape of a deformable bubble embedded in an homogeneous weakly viscous conducting fluid in a uniaxial straining flow. In the present paper, we consider a much broader class of practical multiphase problems, namely the trajectories of arbitrary 3-D deformable shapes which move with six degrees of freedom in a conducting viscous liquid in a pure ambient shearing flow. In order to obtain analytic expressions for the pressure-induced force and moment exerted on the moving body, we assume for simplicity that the linear ambient flow field can be represented by

$$\boldsymbol{u}(\boldsymbol{r},t) = \boldsymbol{V}(t) + \mathsf{G}(t)\boldsymbol{r} + \frac{1}{2}\,\boldsymbol{\omega}(t) \times \boldsymbol{r} \tag{1}$$

where $\boldsymbol{V}$ is a uniform stream, $\mathsf{G}(t)$ is a second-rank symmetric tensor with zero trace and $\boldsymbol{\omega}(t) = \nabla \times \boldsymbol{u}$ is the ambient vorticity field. The pressure field is determined from the governing Navier-Stokes equation which includes the Lorentz term, i.e.,

$$\rho \frac{D\boldsymbol{u}}{Dt} = -\nabla p + \boldsymbol{J} \times \boldsymbol{B} + \nu \nabla^2 \boldsymbol{u} \tag{2}$$

The time-dependent magnetic field $B(t)$ which evolves with time according to Maxwell's equation also depends on the ambient vorticity. The electric current density in the case of a

low magnetic Reynolds number can be obtained from Ohm's law as

$$\boldsymbol{J} = \sigma(\boldsymbol{E} + \boldsymbol{u} \times \boldsymbol{B}) \tag{3}$$

where $\boldsymbol{E}$ is the ambient electric field and σ is the electric conductivity. It is next assumed that a general deformable moving body is impulsively introduced into the ambient flow field and our goal is to first derive analytic expressions for the forces and moments acting on the body. Limiting the analysis to clean bubble surfaces (Magnaudet and Eames, 2000), it can be rigorously shown that at least during a short time after introducing the body, viscous effects can be neglected and the induced velocity field in the viscous conducting field, (due to the motion of the body) is essentially of an irrotational nature. The analytic expressions for the pressure loads can be next integrated so as to render the complete trajectories of the deformable shape. If the ambient fluid is non-conductive, the present analysis reduces to that given in Miloh (2003, 2004).

References

1. Kang K.H, Kang I.S and Lee C.M.
   Physics of Fluids, 14. pp. 29-40, 2002.

2. Magnaudet J and Eames I,
   Annual Review of Fluid Mechanics, 32, pp. 659 - 2002.

3. Miloh T.
   Journal Fluid Mechanics, 479, pp. 287-305, 2003.

4. Miloh T.
   Physics of Fluids, 16, 22-28, 2004.

5. Moffatt H.K. and Sellier A.
   Journal of Fluid Mechanics, 464, pp. 279-286, 2002.

6. Sellier A.
   Journal of Fluid Mechanics, 488, pp. 335-353, 2003.

7. Shin S.M. and Kang I.S.
   International Journal of Multiphase, pp. 105-125, 2002.

Mean motion induced in a liquid by rising bubbles

Véronique ROIG, Amaury LARUE DE TOURNEMINE
Institut de Mécanique des fluides de Toulouse, UMR 5502 CNRS-INPT-UPS,
Avenue du Professeur Camille Soula 31400 Toulouse, France

Summary We report experiments on the mean motion generated by a uniform injection of bubbles in a uniform liquid flow. The Reynolds number of the relative motion is high, the Weber number is moderated and the void fraction is varied up to 15%. With a newly developed methodology, we estimate the statistics of the liquid velocity conditioned or not by the presence of the bubbles. We therefore discuss the displacement of liquid induced by the relative motion of the bubbles. We discuss drift flux models as developed by Kowe *et al* (1988) and more recently by Eames *et al* (2003). An attempt to take into account wakes effects in such models is also presented.

INTRODUCTION

The present problem is related to the characterisation of the mean motion induced in the liquid phase of a homogeneous flow by the relative movements of a swarm of ascending bubbles. Our purpose is to get insight into the complex mechanisms of transport in the liquid phase of a bubbly flow, using precise and well suited definitions of the statistical properties of the flow. We focus on the analysis of inertial bubbly flows at large Re (typically Re=200), and moderate We (We=0.4-0.6). In this work we distinguish between statistics in the liquid conditioned or not by the presence of the bubbles. We develop a global methodology to define the separation between the statistics of the local velocity field perturbed by an individual bubble (strongly controlled by the local boundary condition even though it can also be influenced by hydrodynamics interactions), and the far-field statistics where hydrodynamic interactions entirely control the velocity field. Such a distinction allows us to analyze drift mechanisms, and to discuss the definition of the mean relative velocity between both phases. We examine the mechanistic drift flux model developed by Kowe *et al*. (1988), and the recent analysis by Eames *et al*. (2003). We present a comparison between new experimental results and model predictions. An attempt to take into account the effect of entrainment by the wakes in such models is also discussed.
The experimental set-up is described into details in Larue de Tournemine (2001). A uniform bubbly flow is generated in a vertical channel of 3.1 m height and 0.3 x 0.15 m^2 cross-sectional area. The gas flow rate can be varied from $Q_G = 2.52\ 10^{-4}$ m^3s^{-1} to $Q_G = 3.6\ 10^{-3}$ m^3s^{-1}. While the liquid flow rate is maintained constant all along the experiments ($Q_L = 18.2\ 10^{-3}$ m^3s^{-1}), we vary the void fraction from 0.3 % to about 14 %, by varying the gas flow rate. We have used hot film anemometry to measure the velocity of the liquid. Precise tests proved that we can be self-confident in the meaning of the hot film anemometry signal in the vicinity of the interfaces. The mean bubble diameter varies from 1.14 mm to 2.38 mm depending on Q_G . Double optical fibber probes (OFP) were used to measure bubble sizes and bubbles velocities.

MOTION OF THE LIQUID IN THE VICINITY OF THE BUBBLES

Phase average

We have calculated the average form of the velocity field in the liquid phase in the neighborhood of the bubbles by a phase averaging of the velocity signals obtained from hot film anemometry around each detected bubble. We use two phase averages, a downstream one and an upstream one, denoted $<U(\tau)>$,with the upstream and downstream detected interfaces respectively as reference points of these averages. Whatever the void fraction, the phase average shows that the perturbation of the velocity field due to bubble passage is mainly potential at the front and controlled by the wake at the back of the bubble (Figure 1). The distance necessary to recover the asymptotic level at infinity is higher in the rear field than in the upstream field. Far away from the bubble interfaces, the velocity reaches an asymptotic level, independent of the distance from the bubble. The far field is, thus, not controlled by the action of the test bubble, and controlled by hydrodynamic interactions.

Characteristic length scales of the flow around the bubbles

It is difficult to compare the profiles of the phase averages with models of relative motion around an isolated bubble because the phase average integrates combined effects of several random processes (piercing, random angle between vertical and trajectory, diameter). Nevertheless we have defined characteristic time (or length) scales for the decrease of the perturbation on each side of the bubble. While the time scale upstream is quite independent of the void fraction, the time scale downstream decreases when the void fraction increases. The decrease is consistent with the observation made by Risso & Ellingsen (2001), who found, at low void fraction, that the hydrodynamic interactions make the liquid velocity decrease faster downstream of a bubble in a suspension than in the wake of an isolated bubble. It is also consistent with a recent theoretical analysis of Hunt & Eames (2002) showing that the external strain exerted on the wake due to the blockage effect of the neighboring bodies leads to a rapid disappearance of this wake in two-phase flows.

CONDITIONAL AVERAGES

These time scales give the extend of the perturbation induced by the bubble passages. The analysis of the phase average thus allows us to define conditional averaging of the velocity of the liquid in the near field and in the far field of the bubbles passing across the point of measurement. The near field average (U_{NF}) is taken over the ensemble of measurements in the liquid phase around each bubble in the part of the signal limited by the relaxation times of the phase average. The far field average (U_{FF}) is taken over the residual signal. The far field average is interesting because it represents the interstitial velocity. It is a concept present in the drift flux models and it allows the estimation of a more significant relative velocity.

DISCUSSION OF DRIFT FLUX MODELS

The eulerian mean velocity U_L which is measured, as well as the measured void fraction, allows to estimate $U = (1-\alpha)U_L$ the local superficial velocity of the liquid. In our experiments, we have also measured the eulerian interstitial mean velocity U_{FF}. We have also measured the velocities of the bubbles. So we can test the predicted links between the variables given by Kowe *et al* (1988) (equation (1)) or by Eames *et al* (2003) (eq. (2)).

$$\frac{(U-U_{FF})}{(V_B-U_{FF})} = \alpha C_M - \frac{\alpha U_{FF}}{V_B-U_{FF}} \qquad (1)$$

$$\frac{(U-U_{FF})}{(V_B-U_{FF})} = \alpha(1+C_M) \qquad (2)$$

where C_M is the added mass coefficient.

The comparison with the model developed by Eames *et al* shows a very good agreement at low void fraction (Figure 2). The model of Kowe *et al* is less satisfactory, may be because it neglects the hydrodynamic interactions. At higher void fraction, the comparison is less satisfactory, because wakes effects cannot be neglected and they are not present in the model of Eames *et al*. built on potential flow approximation. A preliminary attempt to take into account the effects of the vanishing wakes observed in our experimental conditions has been made. The vanishing wakes may be represented in the potential calculus of Eames *et al*. as dipoles whose strength is calculated with the measured relaxation lengths of the wakes. The corrective effect seems quite promising.

CONCLUSIONS

We have developed a method for the analysis of conditional statistics of the velocity in the liquid phase of a bubbly flow. We have defined statistics far away from the interfaces from one-point measurements. This method is quite general and allows a discussion of fluid displacement models. The drift concept and models which up to now had been tested in relatively pure situations of isolated bubbles has been examined in this work in a more complex situation.

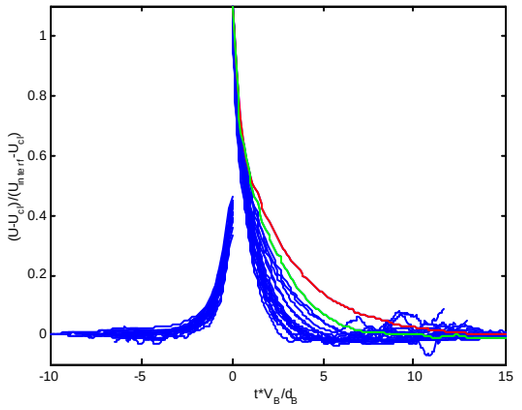


Figure 1 : Phase average of the velocity around the bubbles (red : minimum void fraction ; green, then blue : void fraction increases)

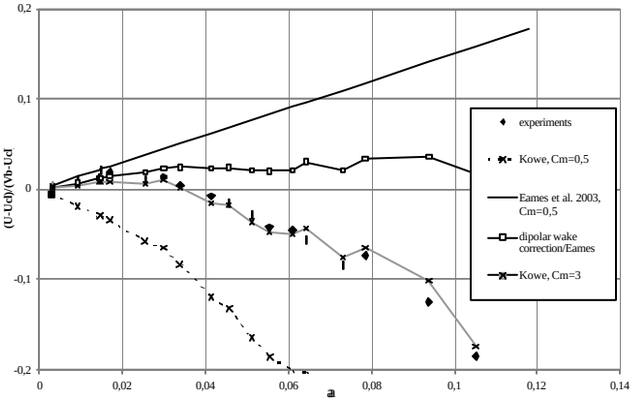


Figure 2 : Comparison between drift models and experimental results (Ucl denotes U_{FF})

(V_b velocity of the bubbles, d_B their diameter , U_{interf} :velocity of the liquid at interface, U_{cl} :at infinity, α void fraction)

References

[1] RISSO F., ELLINGSEN K., 2001, Velocity fluctuations in a homogeneous dilute dispersion of high-Reynolds-number rising bubbles, J. Fluid Mech., vol.

[2] LARUE DE TOURNEMINE A., 2001, "Etude expérimentale de l'effet du taux de vide en écoulements diphasiques à bulles", Thèse INPT, Toulouse, France.

[3] KOWE R., HUNT J. C. R., HUNT A., COUET B., 1988, The effects of bubbles on the volume fluxes and the pressure gradients in unsteady and non-uniform flow of liquids, Int. J. Multiphase Flow, Vol. 14, n°5, pp. 587-606.

[4] EAMES I., HUNT J. C. R., BELCHER S. E., 2003, General theory for inviscid flow through “clouds” of bodies, under consideration for publication in J. Fluid Mech.

[5] HUNT J. C. R., EAMES I., 2002, The disappearance of laminar and turbulent wakes in complex flows, J. Fluid Mech., vol. 457, pp. 111-132.

Plane Couette flow of dense liquid-particle suspensions

Jos Derksen* & Sankaran Sundaresan
Department of Chemical Engineering, Princeton University,
Princeton, NJ 08544, USA

Dense solid-liquid suspensions are encountered in numerous situations in nature (e.g. sediment transport in rivers and oceans) and in industry (e.g. fluidized beds, slurry reactors). The specific flow problem that we study is inspired by the classical experimental study of Bagnold [1], who employed a cylindrical Couette device to measure shear and normal stresses in neutrally buoyant suspensions as functions of apparent shear rate and volume fraction of solids. He concluded from his experiments that at high shear rates both shear and normal stresses manifested a quadratic dependence on apparent shear rate, labeled this as a grain-inertia regime, and attributed the stresses in this regime to particle-particle interactions. Recently, Hunt et al. [2] critically assessed the design of Bagnold's experiments and the single-phase flow that would occur in this geometry, and raised troubling uncertainties about his interpretation. To address some of the issues raised by Hunt et al. [2], and to study the role of solid particle motion, we have simulated the behavior of dense (solids volume fractions of 25-60%) solid-liquid suspensions undergoing simple shear.

Our simulation procedure, which is three-dimensional and time-dependent, applies lattice-Boltzmann discretization of the Navier-Stokes equations to solve the fluid flow in between the particles [3]. The solid particles are represented by an immersed boundary technique [4]. This method directly provides the hydrodynamic forces acting on the particles. Particles are allowed to interact through hard-sphere, inelastic, frictional collisions. We include lubrication forces between solid surfaces, when the gap between the surfaces is smaller than the lattice spacing [5].

The flow domain in our simulations is bounded by two flat walls, which create a shearing motion by moving in opposite directions. At the remaining four bounding planes, periodic boundary conditions are imposed. Just as in Bagnold's experiments, the gap width amounts to 8 particle diameters. In the examples shown below, the lengths of the domain in streamwise and spanwise directions are 16 and 8 particle diameters respectively. We have performed simulations at different resolutions to ascertain that a particle diameter of 16 lattice spacing is adequate to get essentially grid-spacing independent results. At this resolution, the size of the flow domain is 256x128x128 lattice units. From our simulations, we determine how the time-averaged particle concentration, fluid and particle velocities, fluid-particle interaction force, shear and normal stresses due to particle-particle interactions, fluid phase viscous and pseudo-turbulent stresses vary across the gap.

In Figure 1, we present some of our results in a qualitative manner. At particle volume fractions of 0.50 (Figure 1D) and 0.55 (Figure 1E), the shear orders particles in strings along the flow direction (shear induced crystallization). This effect has been observed in colloidal systems, where the Stokes number is very small [6]. In the cases presented in Figure 1, however, the Stokes number (defined as $St = \frac{\rho_s}{\rho_l}\frac{\dot{\gamma} d_p^2}{\nu}$ where $\dot{\gamma}$ is the apparent shear rate, d_p is the particle diameter, ν is the fluid's viscosity; and the density ratio is taken to be 1 to obtain a neutrally buoyant system) amounts to 375. At 59% solids (Figure 1F) the ordering is much less pronounced. The ordering largely disappears when we introduce a little polydispersity (Figure 1G). At relatively low solids volume fractions (see Figure 1A), particles tend to avoid wall regions and hardly ever collide with the walls.

Quantitative analysis of the 46% solids cases (see Figure 2) reveals the presence of a granular regime (with the dimensionless normal stress approximately proportional to Ba^2). No evidence for the macro-viscous regime in which the stress is proportional to Ba was found even at Ba as small as 10. Further

* Permanent address: Kramers Laboratorium , Delft University of Technology, Prins Bernhardlaan 6, 2628 BW Delft, Netherlands

analysis showed that in most of the flow domain momentum is mainly transferred by particle-particle collisions, and that lubrication forces play a minor role in this process.

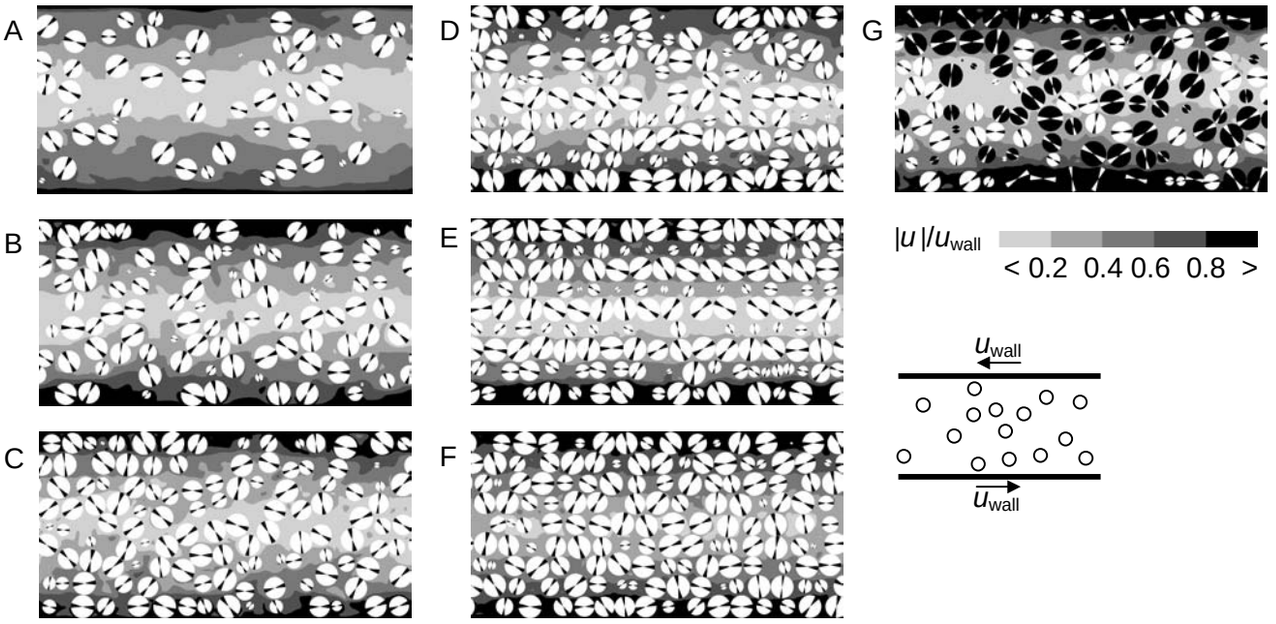


Figure 1. Cross-sections of single realizations of the solid-liquid flow. In cases A-F the particles have uniform size and *St*=375 (*St* is defined in the text). The solids volume fractions in cases A-F are 0.26, 0.37, 0.46, 0.50, 0.55, and 0.59 respectively. Case G has the same solids volume fraction as case D, except that in case G there are two particle diameters: one 0.9 times (white), and one 1.1 times (black) the diameter of case D. The gray scale denotes the absolute value of the liquid velocity. The collisions are elastic and frictionless.

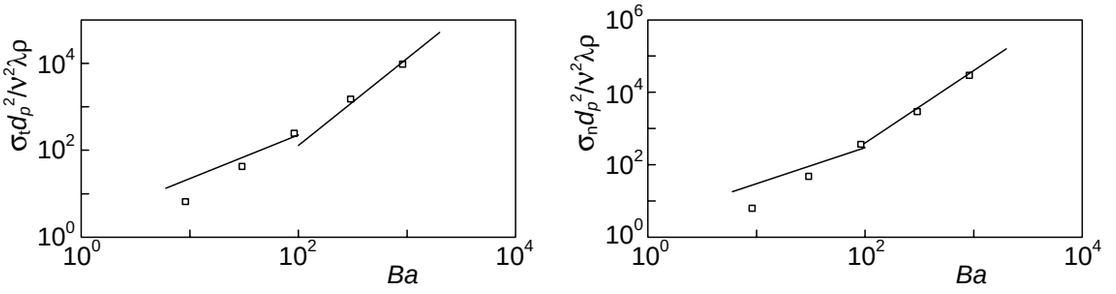


Figure 2. Non-dimensional shear (left) and normal (right) stress as a function of the Bagnold number ($Ba=St\cdot\lambda^{1/2}$ if $\rho_s=\rho_l$, with $\lambda=1/[(\phi_0/\phi)^{1/3}-1]$, and $\phi_0=0.74$ the closest packing of spheres volume fraction). The solid lines are the empirical correlations due to Bagnold [1], the symbols are simulation results for $\phi=0.46$ ($\lambda=5.8$).

References

[1] R.A. Bagnold: Experiments on a gravity-free dispersion of large solid spheres in a Newtonian fluid under shear. *Proc. R. Soc. Lond. A* **225**, 49 (1954).

[2] M.L. Hunt, R. Zenit, C.S. Campbell, and C.E. Brennen: Revisiting the 1954 suspension experiments of R.A. Bagnold. *J. Fluid. Mech*. **452**, 1 (2002).

[3] S. Chen, and G.D. Doolen: Lattice-Boltzmann method for fluid flows. *Annu. Rev. Fluid Mech*. **30**, 329 (1998).

[4] J. Derksen, and H.E.A. van den Akker: Large-eddy simulations on the flow driven by a Rushton turbine. *AIChE J*. **45**, 209 (1999).

[5] N.-Q. Nguyen, and A.J.C. Ladd: Lubrication corrections for lattice-Boltzmann simulations of particle suspensions. *Phys. Rev. E* **66**, 046708-1 (2002).

[6] G. Bossis, and J.F. Brady: Dynamic simulation of sheared suspensions. I. General method. *J. Chem. Phys*. **80**, 5141 (1984).

Simulation of planar wave instabilities in liquid-fluidized beds

Jos Derksen* & Sankaran Sundaresan
Department of Chemical Engineering, Princeton University,
Princeton, NJ 08544, USA

It is well known that dense fluidized beds exhibit a rich variety of complex, inhomogeneous flow structures, ranging from one-dimensional traveling waves to bubble-like voids, and the hierarchy of these structures has been a subject of many theoretical and experimental studies [1, 2]. An Eulerian two-phase flow model, which treats the fluid and particle phases as interpenetrating continua, coupled with simple phenomenological closures for the effective stresses and the fluid-particle interaction force, seems to capture the experimentally observed structures in a qualitatively correct manner; however, quantitative predictions remain elusive [1]. Much effort is in progress to develop more accurate closures through computational simulations of flows involving homogeneous assemblies of particles [e.g., see 3, 4].

In the present study, we first demonstrate that the transition from homogeneous fluidization (worming regime) to an inhomogeneous system with traveling, one-dimensional waves observed experimentally in fluidized beds of limited lateral extent at relatively low fluidization velocities [2] can be captured through detailed discrete particle simulations. From our simulations, we then determine how the particle concentration, fluid and particle velocities, fluid-particle interaction force, stress due to particle-particle interactions, fluid phase viscous and pseudo-turbulent stresses vary in the traveling wave. Such detailed information not only allows us to examine the importance of various terms in the continuum model and various microphysics such as lubrication force, but also assess whether closures developed from simulations of homogeneous suspensions should be supplemented for non-local effects in inhomogeneous systems.

The flow domain that we consider in our simulations is fully periodic. It contains spherical, solid particles (all having the same diameter d_p). The size of the domain in the examples illustrated below is $6d_p$ in the two lateral directions, and $20d_p$ in the flow direction. A body force exerted on the fluid drives the flow. This body force is balanced by a force acting on the solids in the opposite direction. We apply lattice-Boltzmann discretization of the Navier-Stokes equations to solve the liquid flow in between the particles [5]. The particles (which were given a diameter of 10 grid-spacing) are represented by means of an immersed boundary technique [6]. Their motion is controlled by the hydrodynamic force emerging from the lattice-Boltzmann method, by the leading order term of the radial lubrication force that acts as a sub-grid force when particle surfaces are in close proximity (less than one grid-spacing apart), and by hard-sphere collisions (that in this study are assumed to be elastic, and frictionless).

The operating conditions can be fully characterized by three dimensionless parameters: the average solids volume fraction ϕ_0, the density ratio ρ_s/ρ_f, and the Reynolds number of a single particle, freely falling in the working fluid: $Re_t = \frac{u_t d_p}{\nu}$. These three parameters are used to translate physical units into lattice-Boltzmann units. The simulations are designed to mimic one of the cases defined by Duru et al. [2], more specifically their Combination #7 (with ϕ_0=0.488, Re_t=120 and ρ_s/ρ_f =4.1).

In Figure 1, we show snapshots of our flow system operating in the worming (1A), and in the planar wave regime (1B). In order to reach the latter regime, we had to operate the bed at a significantly lower volume fraction compared to the experiment (0.43 versus 0.488). This is most probably due to the hydrodynamic diameter of the particles being larger than their given diameter on which ϕ_0 is based [7]. The space-time graphs in Figure 2 show the transition from the worming to the planer-wave regime. The homogeneous cases (A and B) have much less volume fraction fluctuations than the other cases that are in the planar wave regime. The wave speed that can be derived from the space-time graphs corresponds

* Permanent address: Kramers Laboratorium , Delft University of Technology, Prins Bernhardlaan 6, 2628 BW Delft, Netherlands

very well with the experimentally observed wave speed: $0.24u_t$ in the experiment, $0.25u_t$ in the simulation. Time-averaged waveforms are given in Figure 3. These waves are quite noisy, and the simulation must be run for a much longer duration to obtain a smoother one-dimensional wave. Comparison of Figures 1D and 1E, and the waveforms in Figure 3 suggest that the lubrication force is not important in this example.

In this presentation, we will describe and discuss further details concerning spatial variation of various quantities such as fluid-particle interaction force and particle phase pressure.

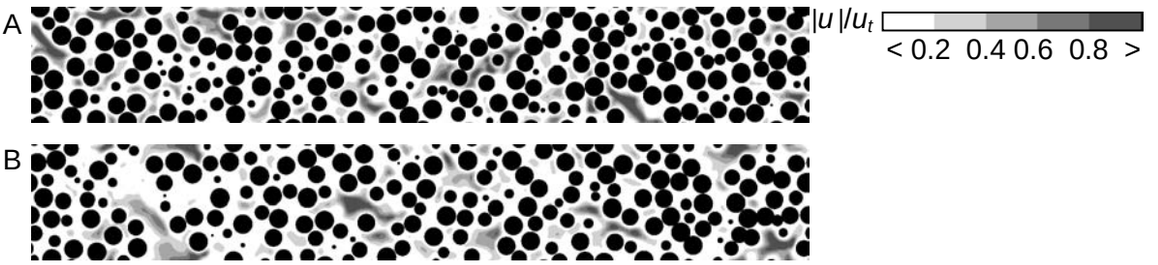


Figure 1. Cross-sections of single realizations of the solid-liquid flow. In both cases Re_t=120 and ρ_s/ρ_f =4.1. Case A has ϕ_0=0.48, case B has ϕ_0=0.41. The gray scale indicates the absolute value of the liquid velocity.

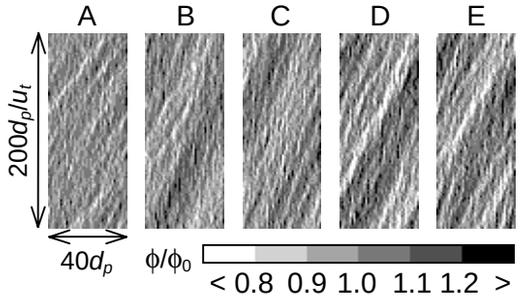


Figure 2. Space (horizontal) – time (vertical) plots of the solids phase volume fraction. Case A-D have ϕ_0=0.48, 0.46, 0.43, and 0.41 respectively, and do not take into account the radial lubrication force. Case E is the same as case D, but now with lubrication.

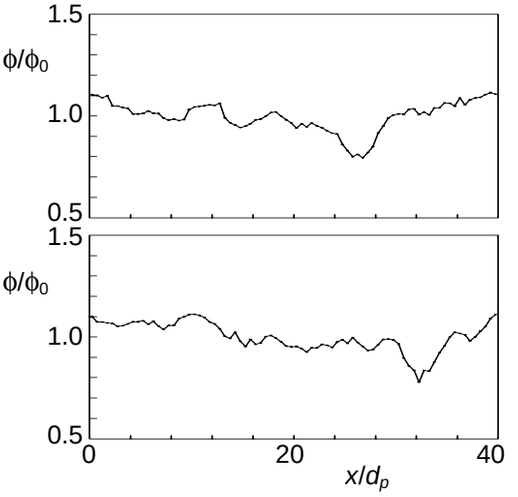


Figure 3. Time-averaged wave form of cases D (bottom) and E (top) as defined in Figure 2.

References

[1] S. Sundaresan: Instabilities in fluidized beds. *Annu. Rev. Fluid Mech*. **35**, 63 (2003).
[2] P. Duru, M. Nicolas, J. Hinch, and E. Guazelli: Constitutive laws in liquid-fluidized beds. *J. Fluid Mech*. **452**, 371 (2002).
[3] R.J. Hill, D.L. Koch, and A.J.C. Ladd: Moderate-Reynolds-number flows in ordered and random arrays of spheres. *J. Fluid Mech*. **243**, 448 (2001).
[4] J.J. Wylie, D.L. Koch, and A.J.C. Ladd: Rheology of suspensions with high particle inertia and moderate fluid inertia. *J. Fluid Mech*. **480**, 95 (2003).
[5] S. Chen, and G.D. Doolen: Lattice-Boltzmann method for fluid flows. *Annu. Rev. Fluid Mech*. **30**, 329 (1998).
[6] J. Derksen, and H.E.A. van den Akker: Large-eddy simulations on the flow driven by a Rushton turbine. *AIChE J*. **45**, 209 (1999).
[7] A.J.C. Ladd: Numerical simulations of particulate suspensions via a discretized Boltzmann equation, Part 1: Numerical results. *J. Fluid Mech*. **271**, 311 (1994).

IMAGE PROCESSING METHOD IN ESTIMATION OF BUBBLE COLUMN'S WORK

Daniel Zając*, Roman Ulbrich*
*Technical University of Opole,KTCiAP, PL 45-271 Opole, Poland

Summary This paper presents an experimental study of identification and analysis of two phase gas-liquid flow using image processing method. The process of two phase flow has been realized in bubble column. The continuous and dispersed phases were water and air, respectively. The gray level value of the obtained recordings from gas-liquid flow was the basic parameter for process investigation. Based on this parameter it was possible to calculate and determine many important statistical characteristics of two phase gas-liquid flow.

This paper presents an experimental study of identification and analysis of two phase gas-liquid flow using image processing method. The process of two phase flow has been realized in two dimensional bubble column (1300/300/20mm). The continuous and dispersed phases were water and air, respectively. Recorded realizations (by CCD camera), were put into analysis either by the use of own software and commercial product (MATLAB). The gray level value of the obtained recordings from gas-liquid flow was the basic parameter for process investigation. Based on this parameter it was possible to calculate and determine many important characteristics of two phase gas-liquid flow.

Authors presents modified version of the bed expansion method, due to volume fraction calculation. This method was supported by image analysis technique. On the recorded images edge detection filters was used. This allowed for calculation of the area of both the dispersed bed and static column which directly led to volume fraction determination.

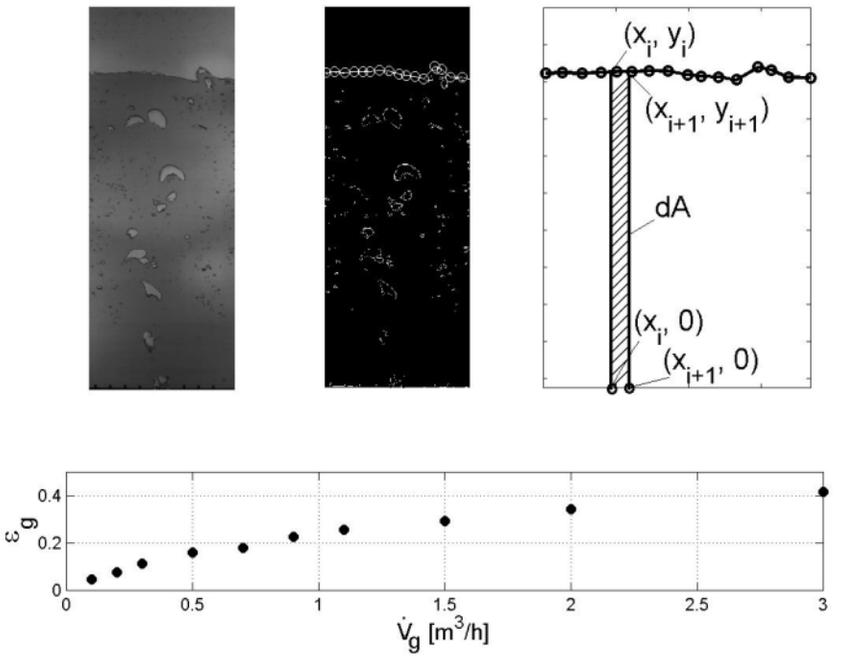


Fig.1. Volume fraction's determination method. This parameter is calculated strictly from the area of the two phase bed.

Another primary parameter which was calculated was the velocity of the gas phase. In this part of the research the particle image velocimetry (PIV) technique was applied. Mentioned method is based on calculating of displacement of bubbles between two consecutive images, which were captured with camera, in known time interval. Captured images are divided into interrogation areas. For every interrogation area, the average bubble displacement between two images is calculated with a numerical procedure based on cross correlation. The results are velocity fields for gas phase and graphs representing bubble trajectories (figure 2).

The gray level value is representing the discrete distribution of the illumination in the area of bubble column. The range of this parameter can change from 0 (black) to 255 (white). For better contrast between water and air, the first one was colored by inert dye. After this procedure both phases had representative range of the gray level value. Based on this fact authors showed the change of volume fraction along and broadwise the bubble column. Analyzing the change of the gray level value in time (calculated from various interrogation areas) the pattern recognition in bubbly flow regime was possible (figure 3).

The last part of this research is the stochastic analysis. The change of the gray level value was taken into consideration. From each obtained courses authors determined a series of statistical parameters such as amplitude, minimum, maximum, standard deviation, skewness, kurtosis and average value. Those values helped in pattern recognition in bubbly flow regime. Except statistical parameters also stochastic functions have been calculated (PDF, PSD, ACF).

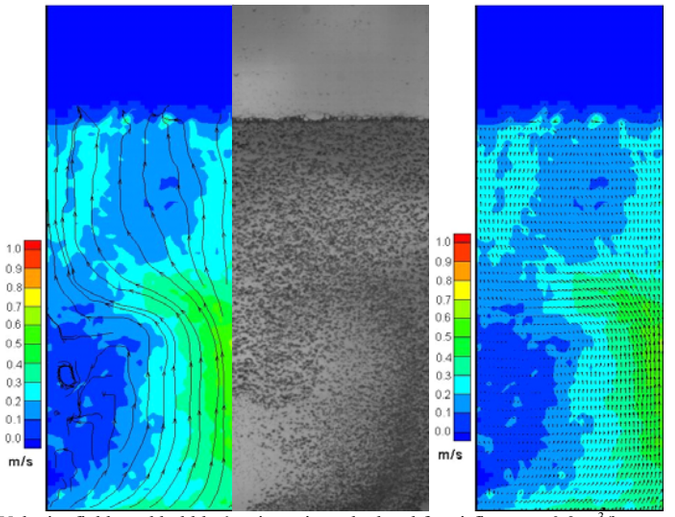


Fig.2 Velocity fields and bubbles' trajectories calculated for airflow rate 0,3 m^3/h

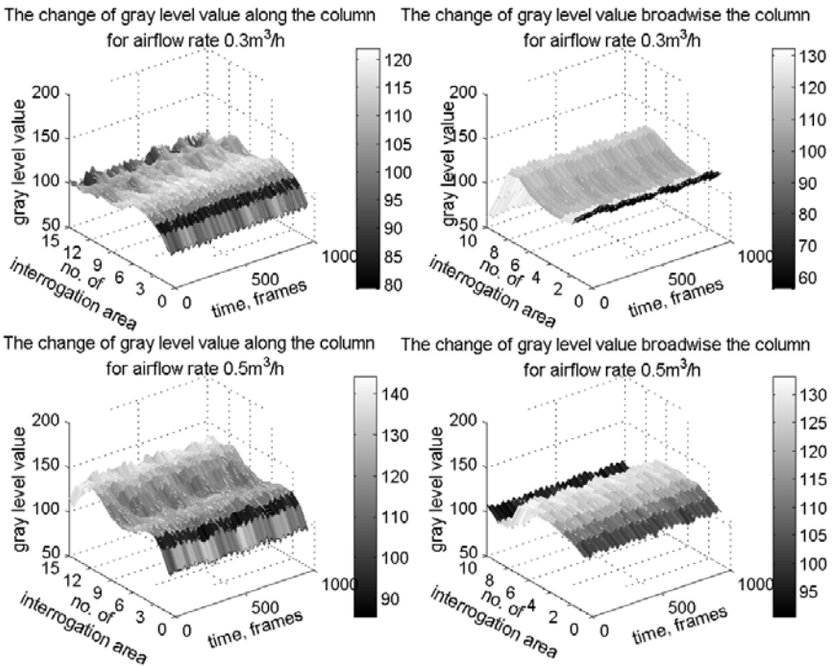


Fig. 3 The change of the gray level in time in airflow range 0.3÷0.5 m^3/h. Diagrams on the left illustrates the change along the apparatus (interrogation area no. 1 – bottom, no. 15 – top of two-phase bed) and diagrams on the right illustrates the change broadwise the column (1 – left side, 10 – right side of the bed). 1000 frames=9.7 s.

To sum up, the gray level value showed to be suitable parameter for two-phase flow conducted in bubble column analysis. The DIP method allowed obtaining many very important statistical characteristics of the flow. The results illustrate the change of volume fraction in time and plane (in both; along and broadwise the column) for the whole airflow range. This allows for the analysis of the dispersion's behaviour as well as for distributor's work assessment (because in bubble column's work, as a result the uniform air phase distribution is desirable). Additionally stochastic parameters and functions showed to be a good tool for two-phase flow pattern recognition.

Statistics and preferential distribution of micro-particles in turbulent boundary layer: implications for resuspension mechanisms

Maurizio Picciotto, Andrea Giusti, Cristian Marchioli and Alfredo Soldati *
Centro Interdipartimentale di Fluidodinamica e Idraulica and Dipartimento di Energetica e Macchine, Università di Udine, Udine, 33100, Italy

Abstract

The distribution of inertial particles dispersed in turbulent flows is highly non-homogeneous and may exhibit a complex pattern which is driven by the structures of the turbulent flow field. Fluid motions in turbulent flows are intermittent and have a strongly organized and coherent nature represented by the large scale coherent motions.

In this work, we simulate a turbulent channel flow of air laden with a dilute dispersion of inertial micro-particles for different values of their inertial parameter (the relaxation time). We study a turbulent channel, calculated for a shear Reynolds number based on the half-width equal to 150, using a pseudo-spectral Direct Numerical Simulation. The domain is $1885 \times 942 \times 300$ in the streamwise (x), spanwise (y), and wall-normal (z) directions, respectively, and is discretized into $128 \times 128 \times 129$ Fourier/Chebichev modes. The dispersion dynamics is simulated using Lagrangian tracking of swarms of $O(10^5)$ particles characterized by different values of their inertia parameter (Stokes numbers equal to 0.2, 1, 5). We run simulations considering different sets of forces acting on particles (Drag, inertia, gravity and lift) and different modelling approaches: one-way and two-way coupling.

The object of the paper is to examine in detail the influence of the inertia on particle transfer mechanisms and specifically on reentrainment mechanisms. In particular, we focus on the unbalance between transfer fluxes toward and away from the wall which causes the well known phenomenon of *turbophoresis* (Caporaloni, et al., 1975, and Reeks, 1983).

In our previous works (Marchioli and Soldati, 2002, and Marchioli et al., 2003), we concluded that particle transfer fluxes away from the wall are limited by the time and space causal relationships among the different events characterizing turbulence regeneration cycle in the wall region *i.e.* the causal relationship between strongly coherent sweeps and ejections, quasi-streamwise vortices and low speed streaks. Specifically, we observed that particles which are driven to the wall by a sweep and are not re-entrained to the outer flow by the corresponding ejection on the opposite side of the quasi-streamwise vortex are bound to remain in the viscous wall layer for long times and slowly diffuse to the wall (Narayanan et al., 2003).

We examine first the role of quasi-streamwise structures on reentraining particles from the viscous sublayer. In Figure 1, we show the probability density function of the time spent by the swept-and-reentrained particle in the viscous sublayer (*i.e.* the wall region between $z^+ = 0$ and $z^+ = 5$). We calculated the pdf by recording the time spent by each particle which enters the viscous sublayer (threshold level $z^+ = 5$) coming from the outer region ($z^+ > 5$) before the same particle crosses next the same threshold coming from the inner region ($z^+ < 5$). We observe that the pdfs have a maximum in the range $7 < t^+ < 12$ for the different time scales of the particles investigated. If we consider that the inverse of the streamwise vorticity (*i.e.* the average time scale of the vortical structures) peaks sharply at $z^+ = 5$ where it has a value of $t^+_{\omega_x} = 14$, we can infer the following: i) first, we can confirm that the quasi-streamwise vortical structures dominate particle transfer toward and away from the wall; ii) second, the particles with the highest probability of being reentrained are those which enter and exit the viscous sublayer riding the same quasi-streamwise vortical structure.

A relevant issue in boundary layer turbulence is the modulation of turbulence structures by the presence of dispersed particles. We examine how the particle wall transfer fluxes are modified due to the action of particles themselves in modulating turbulence. In Figure 2, we compare the time evolution of the $\tau_p^+ = 5$

*Corresponding author. E-mail: soldati@uniud.it

particles number distribution profiles as a function of the wall normal direction. We can observe that if particles have a feedback on the flow field (two-way coupling), the concentration peak is reduced thus decreasing the importance of turbophoresis. Apparently, particles modulate turbulence at the wall such to reduce selectively the action of the quasi-streamwise structures.

In the full paper, we will present complete results describing thoroughly the interactions among particles and turbulence structures in the wall region.

References

1. M. Caporaloni, F. Tampieri, F. Trombetti & O. Vittori, Transfer of particles in nonisotropic air turbulence, *J. Atmos. Sci.*, vol. 32, 565-568.
2. C. Marchioli, A. Giusti, M.V. Salvetti & A. Soldati, Direct numerical simulation of particle wall transfer and deposition in upward turbulent pipe flow, *Intl J. Multiphase Flow*, vol. 29, 1017-1038, 2003.
3. C. Marchioli & A. Soldati, Mechanisms for particle transfer and segregation in turbulent boundary layer, *J. Fluid Mech.*, vol. 468, 283-315, 2002.
4. C. Narayanan ,D. Lakehal, L. Botto & A. Soldati, Mechanisms of particle deposition in a fully-developed turbulent open channel flow. *Phys. Fluids*, vol. 15, 763-775, 2003.
5. M.W. Reeks, The transport of discrete particles in inhomogeneous turbulence. *J. Aerosol Sci.* vol. 14, 729-739, 2003.

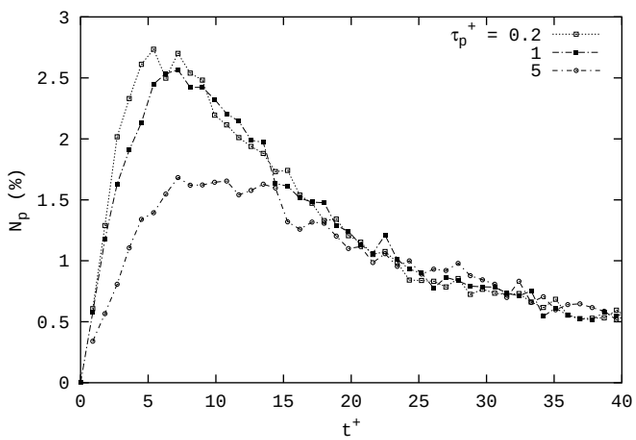


Figure 1: PDF of the time spent by the swept-and-reentrained particle in the viscous sublayer ($z^+ < 5$).

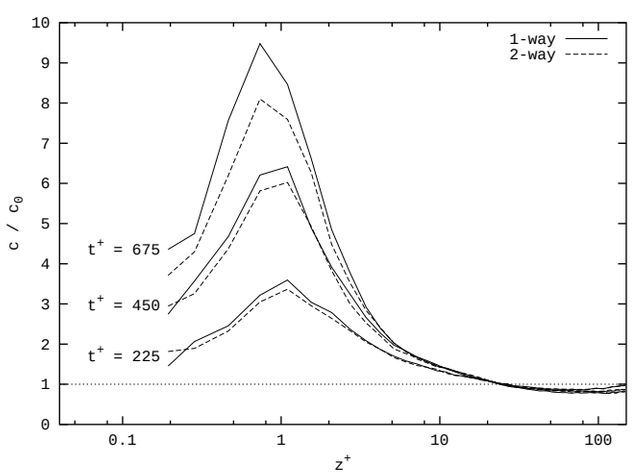


Figure 2: Time evolution of the $\tau_p^+ = 5$ particles number distribution profiles as a function of the wall normal direction.

EXPERIMENTAL OBSERVATIONS OF HYDRATE FORMATION IN A CONVECTION TANK

C. F. Chen and Cho Lik Chan
Department of Aerospace and Mechanical Engineering
University of Arizona, Tucson, AZ 85721, USA

Summary Experiments were carried out to study the hydrate formation in water and the refrigerant R141b (CH_3CCl_2F) contained in a convection tank. Experiments were performed both in the quiescent and convection mode. A thin hydrate film forms on the interface between the two fluids after seeding. Then a mushy layer forms above the hydrate film and grows in time. In a test tank with copper sidewalls, hydrates also grow from these walls at a faster rate than those at the interface. Under the convection mode, growth of hydrates in the mushy layer is very much affected by the convection current.

INTRODUCTION

Clathrate hydrates are crystalline compounds formed by cage-like structure of hydrogen bonded water molecules enclosing a guest molecule of a hydrate forming substance. Many substances such as gases and fluorocarbon refrigerants are hydrate formers. Hydrates of SO_2 was discovered by Priestley in 1790, and that of chlorine gas independently by Davy in 1811. Natural gas hydrates became industrially important in 1930's when they were found to form blockages in gas pipelines, thus prompting much research in their formation and dissolution, see recent reviews of Makogan [1] and Sloan [2]. Ohmura et al [3]were the first to perform experiments on hydrate formation on a drop of liquid R141b immersed in water. Kato et al [4] studied hydrate formation on a jet of R141b entering into a flowing water stream. Kobayashi et al [5] and Ito et al [6] made microscopic observations of the growth of R141b hydrates. We have carried out experiments to study the growth of such hydrates in a convection tank.

EXPERIMENTAL APPARATUS AND PROCEDURE

Our experiments were carried out in two different test tanks both were 3cm wide. The first tank has 9.5cm square sidewalls made of chrome-plated copper, with passages provided for the circulation of fluids from two different constant-temperature baths. All other walls were made of Plexiglas. The other tank is smaller and is made of Plexiglas throughout with 5cm square sidewalls equipped with coolant passages. Both tanks are well insulated by polystyrene boards. The test procedure is to fill the lower half of the tank with liquid R141b (heavier and hydrophobic) and the upper half with water. After the fluids have been cooled to the desire temperature, a slurry consisting of water and tiny hydrate particles prepared beforehand is introduced in the water to initiate hydrate formation process. The growth of the hydrate layer is recorded by photographs at regular intervals up to 24 hours.

RESULTS

The first experiment was carried out in the tank with copper sidewalls at a quiescent state of 2°C with R141b and water pre-saturated with R141b. Hydrates formed into a film on the interface soon after seeding. Thereafter hydrates continued to form and they appeared as a mushy layer consisting of tiny crystal whiskers immersed in water just above the interfacial film. No growth of hydrates appear on the under side of the film. At the same time, hydrates started to grow from the two copper sidewalls with a growth rate much larger than that at the interfacial film. The hydrates grown from the walls were similar to the methane hydrates observed by Makogon (1997). No growth was observed from the Plexiglas walls. Two hours after seeding, hydrates grown from the sidewalls reached the middle of the tank and the hydrate mushy layer became thicker as shown in a head-on view of the interface, Fig. 1a. The view from below at the same time, Fig. 1b, clearly shows the nature of the crystals in the mushy layer above the interface and the comparatively smooth crystal surface below the interface. Experiments with plain water and R141b under the same conditions show similar results except the growth rate is slower. In order to study the growth at the interface clearly, the next two experiments were conducted in the all Plexiglas test tank.

(a) (b)

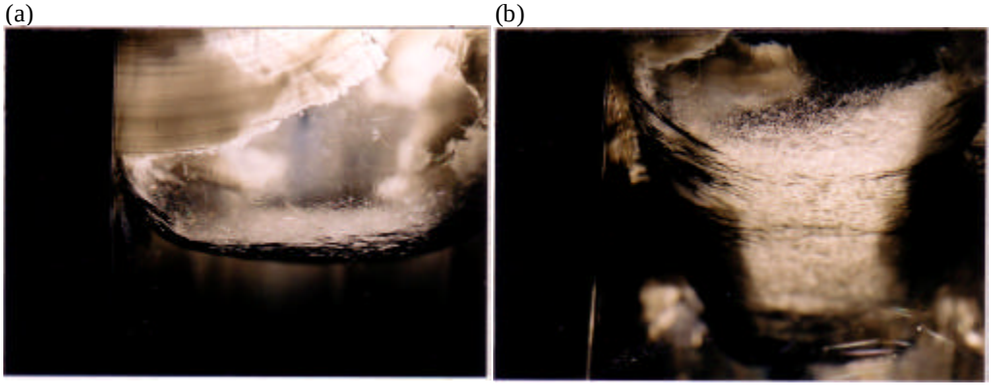


Fig. 1 Experiment in tank with copper sidewalls at 2°C quiescent state 2 hrs after seeding. (a) Head-on view of the interface. Note hydrate mushy layer above interfacial hydrate film, and growth from the sidewalls. (b) View of interface from below showing loose crystal structure of the mushy layer.

Experiment 2 was conducted at 2°C in quiescent state with plain water. The interfacial hydrate crystal film formed quickly after seeding. The hydrate mushy layer above the interface grew in time, at 5 hours after seeding; its thickness was approximately 4mm as show in Fig. 2a. It can be seen from this photo that the mushy layer thickness is quite uniform, and that there is no hydrate formation at either of the sidewalls.

(a) (b)

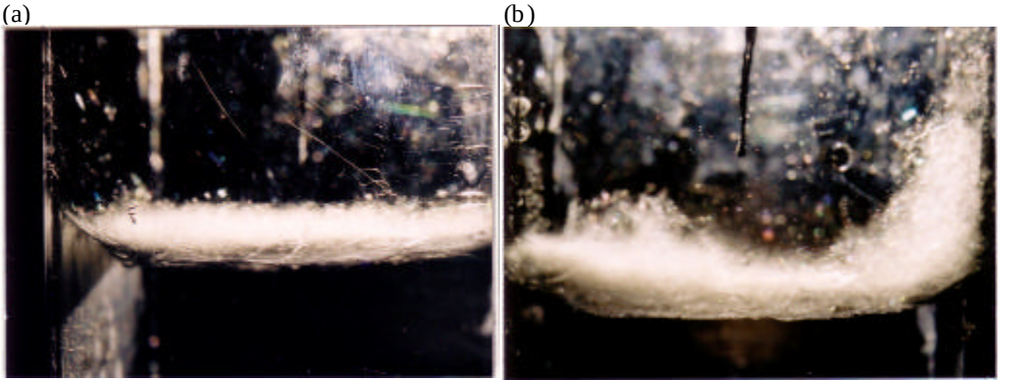


Fig. 2 Experiments in all Plexiglas tank. (a) Interfacial hydrate layer at 5 hrs after seeding under 2°C quiescent state. (b) Convection state with 3.3°C at left and 1.9°C at right with counterclockwise circulation. View of the hydrate interfacial layer at 4 hrs after seeding.

Experiment 3 was a convection experiment with the left wall at 3.3°C and the right wall at 1.9°C. Circulation in the water is counter-clockwise. A photo taken at 4 hours after seeding is shown in Fig. 2b, and the effect of convection is clearly visible. Not only the hydrates were nonuniformly distributed with large accumulations along the right wall and at the foot of the left wall, but also the hydrate growth rate, as compared to the previous experiment, was enhanced by convection. The results of these experiments show that convection has an important effect on the growth of hydrates.

References

[1] Makogan, Y. F.: Hydrates of Hydrocarbons. PennWell Publications, Tulsa OK 1997
[2] Sloan, E. D.: Clathrate Hydrates of Natural Gases. 2nd Ed, Marcel Dekker, New York 1998
[3] Ohmura, R., Shigetomi, T. & Mori, Y. H.: *J. Crystal Growth* **196**:164-173, 1999
[4] Kato, M., Iida, T. & Mori, Y. H.: *J. Fluid Mech* **414**:367-378, 2000
[5] Kobayashi, I, Ito, Y. & Mori, Y. H.: *Chem Eng Sci* **56**: 4331-4338, 2001
[6] Ito, Y., Kamakura, R., Obi, S. & Mori, Y.H.: *Chem Eng Sci* **58**:107-114, 2003

MORPHOLOGICAL STABILITY OF DIRECTIONAL SOLIDIFICATION UNDER TEMPERATURE MODULATIONS

C. A. Chung, K. H. Ho and W. Z. Chien

Department of Mechanical Engineering, National Central University, Jhongli, Taiwan 320

Summary We study the instability of a planar solid-melt interface during directional solidification of a binary mixture. The molten zone is oscillated by an imposed temperature modulation. The basic state is solved analytically with the bulk melt quiescent by expanding the governing equations in terms of the small amplitude of modulation. A preliminary investigation on the morphological instability of the basic state is presented.

INTRODUCTION

The possibility of processing crystal growths in space is attractive because the buoyancy-driven convection may be eliminated in such a low-level background of gravitation. However other physical factors may in turn dominate the casting conditions. For example, the g-jitter due to the inherent mechanical vibrations may itself induce buoyant convection, and the related problems have been drawn a great deal of research efforts [1]. In this paper, we consider another potential factor, the temperature fluctuations. Such a time-dependent variation may result from the orbital maneuvers; the space laboratory may periodically face the sun leading to fluctuations of the laboratory temperature. In addition earth based experiments have also shown the molten region can undergo significant temperature oscillations induced by such as the thermo-capillary instability of the floating zone [2]. We therefore study the stability of a planar solid-melt boundary during directional solidification of a binary alloy assuming the temperature is being modulated in a sinusoidal way. We hope the present study will gain an insight into the morphological instability of oscillatory molten zones.

MATHEMATICAL FORMULATION AND ASSUMPTIONS

The system considered consists of a binary alloy solidifying from below. The solid-melt interface is described by $z = h(x, y, t)$. The interface is assumed to advance into the bulk melt at a time-mean constant pulling rate V and have a planar shape before the instability occurs. We choose the coordinates fixed at the interface moving upward at the same speed V. The governing equations are the continuity equation, the momentum equation and the concentration equation [3]:

$$\nabla\cdot\boldsymbol{u}=0,\quad S_c^{-1}\left(\frac{\partial}{\partial t}-\frac{\partial}{\partial z}+\boldsymbol{u}\cdot\nabla\right)\boldsymbol{u}=-\nabla p+\nabla^2\boldsymbol{u}+R_cC\hat{e}_z,\quad \left(\frac{\partial}{\partial t}-\frac{\partial}{\partial z}+\boldsymbol{u}\cdot\nabla\right)C=\nabla^2C\,.$$

At the solid-melt interface $z = h(x, y, t)$, the boundary conditions are

$$\boldsymbol{u}\times\boldsymbol{n}=\boldsymbol{0},\quad \boldsymbol{u}\cdot\boldsymbol{n}=0,\quad (k-1)C\left(1+\frac{\partial h}{\partial t}\right)\hat{e}_z\cdot\boldsymbol{n}=\nabla C\cdot\boldsymbol{n},\quad T=MC-UK$$

These equations represent respectively the no-slip condition, the no-penetration condition, the conservation of solute at the interface, and the thermodynamic relation between the melting temperature and composition. Note that the surface energy effect (the Gibbs-Thompson effect) is also included in the thermodynamic condition, where U is the dimensionless capillary length and K the curvature of the interface (assumed negative for a concave projection into the melt). The molten zone is assumed to have a time-mean constant height H, where the melt is motionless and the solute concentration is fixed at an imposed value. Therefore the corresponding boundary conditions at $z = H$ are,

$$\boldsymbol{u}=\boldsymbol{0},\quad C=1\,.$$

The governing equations and boundary conditions have been made dimensionless with the solute-field scales: V for velocity, D/V for length, (where D is the solute diffusivity), D/V^2 for time, the concentration value at $z = H$ for concentration, and the freezing temperature of the pure solvent for temperature. The two dimensionless parameters appearing in the governing equations are the Schmidt number S_c and the solutal Rayleigh number R_c. To simplify the analysis, the frozen temperature assumption is adopted by which the temperature is assumed fixed at its imposed value. We assume the temperature is modulated by

$$T = T_0(1+\delta\cos\Omega t)+Gz\,,$$

where δ is the amplitude of the temperature oscillation, Ω is the input frequency of modulation, and G is the temperature gradient assumed to be a constant.

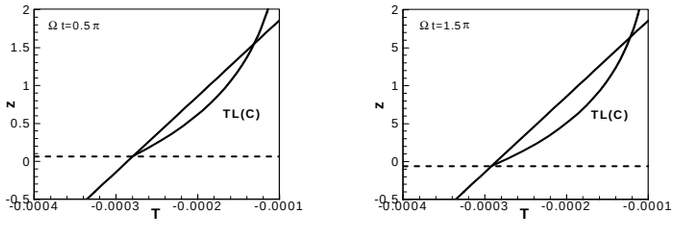


Figure 1. The instantaneous temperature T and melting temperature T_L at two phases of a period: (a) $\Omega t = 0.5\pi$, (b) $\Omega t = 1.5\pi$.

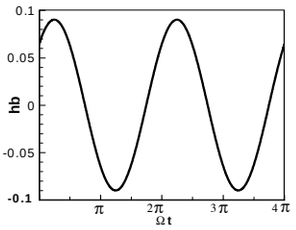


Figure 2. The interface position oscillates as a function of time.

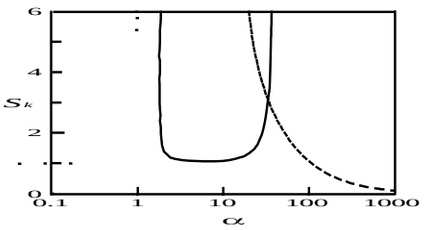


Figure 3. The neutral curves in terms of the Sekerka number S_k and the wave number α. The left curve corresponds to the synchronous mode and the right curve the subharmonic mode.

RESULTS

Basic state

Before the onset of morphological instability, the melt is quiescent relative to the laboratory frame and the solid-melt interface remains flat. We call this state the basic state. The basic state is solved by expanding the governing equations in term of δ, which is assumed to be small. The basic-state interface position and concentration have the form

$$h_b = \delta h_1(t) + ...$$

$$C_b = C_0(z,t) + \delta C_1(z,t) + ...$$

Shown in figure 1 are the instantaneous temperature T and the melting temperature $T_L(C)$ at two phases of a period: (a) $\Omega t = \pi/2$ and (b) $\Omega t = 3\pi/2$. Because the melting temperature is a function of the concentration C, the melting temperature curve implies the existence of a concentration boundary layer near the interface. The depth as well as the strength of the supercooling region varies in a sinusoidal way. The time dependence of the interface position h_b is shown in figure 2. The interface moves back and forth sinusoidally relative to the moving frame. We found the amplitude of the interface position decreases as the input frequency is increased.

Linear stability analysis

A preliminary linear stability analysis on the basic state is performed assuming $R_c = 0$. Namely, we have neglected the gravitational effects. Two morphological instability modes are found. Their neutral curves are shown in figure 3 in terms of the Sekerka number S_k and the wave number α for the case of $\Omega = 0.3$ and $\delta = 0.01$. The left curve of smaller values of the wave numbers is the synchronous mode having the same oscillatory frequency as that of the input temperature modulation. The right curve is the subharmonic mode that has the frequency half the input frequency. As shown, the subharmonic mode is likely to be more critical and dominant.

CONCLUSIONS

We consider in this paper the directional solidification of a binary mixture undergoing temperature modulations. The solid-melt interface moves back and forth in a sinusoidal way. The interfacial instability tends to occur with a subharmonic mode whose oscillatory frequency is half the input frequency. The wavelengths of the subharmonic mode are much smaller than that of the synchronous mode.

References

[1] Murray, B. T., Coriell, S. R., McFadden, G. B.: The Effect of Gravity Modulation on Solutal Convection during Directional Solidification. *J. Crystal Growth.* 110: 713-723, 1991.

[2] Hu, C. C., Chen, J. C., Huang, C. H.: Effect of Pulling Rates on the quality of YIG Single Crystal Fibers. *J. Crystal Growth.* 225: 257-263, 2001.

[3] Chung, C. A., Chen, F.: Instability in Directional Solidification under Inclined Rotation. *J. Fluid Mech.* **477**: 381-408, 2003.

NONLINEAR OSCILLATORY CONVECTION IN MUSHY LAYERS

Peter Guba, M. Grae Worster
Institute of Theoretical Geophysics, DAMTP, Centre for Mathematical Sciences, University of Cambridge, Wilberforce Road, Cambridge CB3 0WA, UK

Summary The nonlinear development of two-dimensional oscillatory convection in a mushy layer during solidification of a binary mixture is studied. A comprehensive investigation of the nonlinear stability of travelling and standing waves, including the relative stability between the two wave patterns, is provided. The relevance of our results to recent laboratory experiments is discussed.

INTRODUCTION

When a binary alloy solidifies directionally, a planar solidification front can become morphologically unstable owing to compositional supercooling. Consequently, regions of coexisting liquid and solid phases, referred to as 'mushy' regions, are often formed. The solidification of a binary alloy in a mushy layer can be profoundly influenced by fluid flow. The flow in mushy layers can be driven by a variety of different mechanisms, though buoyancy-driven convection has received most attention in recent years [1]. As a result of a complex interaction with solidification, convection can be oscillatory at onset [2]. It is the nonlinear evolution of this oscillatory instability which we shall elucidate here.

FORMULATION

The physical system under consideration consists of a horizontal mushy layer lying between semi-infinite solid and liquid regions. The system is cooled from below with the rate of freezing being constant in time, so that the solid–mush and mush–liquid interfaces advance upward with a constant solidification speed. The dimensionless equations for the temperature (or equivalently composition), the local solid fraction and the Darcy fluid velocity assume the form given in [3]. Convective instability is controlled principally by the Rayleigh number R, mediated by the Stefan number S and the compositional ratio $\mathcal{C}$.

In order to pose an analytically tractable problem, we suppose that the system is close to the eutectic point [4], which amounts to considering the limit of small mushy-layer thickness compared to the thermal-diffusion lengthscale $\delta \ll 1$, with $\mathcal{C} = O(1/\delta)$. We assume also that the Stefan number is large, $S = O(1/\delta)$, which allows a destabilization of the system to the oscillatory mode of convection [2]. In this limit, a function relating the permeability of the mushy layer to the local solid fraction can be approximated by $K(\phi) \sim 1 + K_1\phi + K_2\phi^2$, where K_1 and K_2 are positive constants.

BIFURCATION ANALYSIS

Oscillatory instability

From a linear stability analysis of the steady, motionless basic state [5], it is known that the onset of convection in the mushy layer can be oscillatory, even though the stabilizing thermal buoyancy is set equal to zero and no double-diffusive effects are present in the model. In physical terms, this oscillatory instability is linked with a phase lag between the background macroscopic solidification and the local dissolution caused by the fluid motion.

Weakly-nonlinear oscillatory convection

A key result of our analysis is a set of coupled evolution equations

$$a\dot{\mathcal{A}} = b\mathcal{A} + c\mathcal{A}|\mathcal{A}|^2 + d\mathcal{A}|\mathcal{B}|^2, \tag{1}$$

$$a\dot{\mathcal{B}} = b\mathcal{B} + c\mathcal{B}|\mathcal{B}|^2 + d\mathcal{B}|\mathcal{A}|^2, \tag{2}$$

for the complex amplitudes $\mathcal{A}$ and $\mathcal{B}$ of left- and right-travelling waves, respectively. These equations describe the nonlinear interaction between the two counter-propagating waves near a Hopf bifurcation point [6] and can be used to determine the stability of, and the relative stability between, the travelling and standing waves.

The structure of the bifurcation diagrams in the vicinity of the linear Rayleigh number for the onset of oscillatory convection $R = R^{(\mathrm{o})}$ is illustrated in figure 1. Both travelling and standing waves bifurcate simultaneously. Stable solutions are present provided both oscillatory branches bifurcate supercritically. Furthermore, the stable solution is the one with the larger Nusselt number ($\sim 1 + \epsilon^2(|\mathcal{A}|^2 + |\mathcal{B}|^2)$, where ϵ measures a perturbation amplitude).

The explicit predictions for the mushy-layer system can be established on the basis of the complex coefficients a–d. The presence of oscillations is controlled by the parameters S, $\mathcal{C}$ and δ, as can be inferred from [5]. Our analysis reveals that a preference for distinct wave patterns, and hence the possibility of their realization in the experiments, is determined by particular values of the permeability coefficients K_1 and K_2, as indicated in figure 2. Thus, the pattern selection process is dominated by a nonlinear effect associated with permeability variations due to perturbations to the solid fraction.

Recently, Solomon & Hartley [7] performed experiments on an aqueous solution of ammonium chloride, and were able to observe a periodic convective behaviour. However, the sense of the convective motion did not reverse during evolution, indicating that the observed behaviour should not be related to the standing roll state studied here. Instead, we anticipate that it is a manifestation of a secondary Hopf bifurcation, arising from an intricate nonlinear interaction between steady and oscillatory convection. The present study forms the basis for future investigation of this problem.

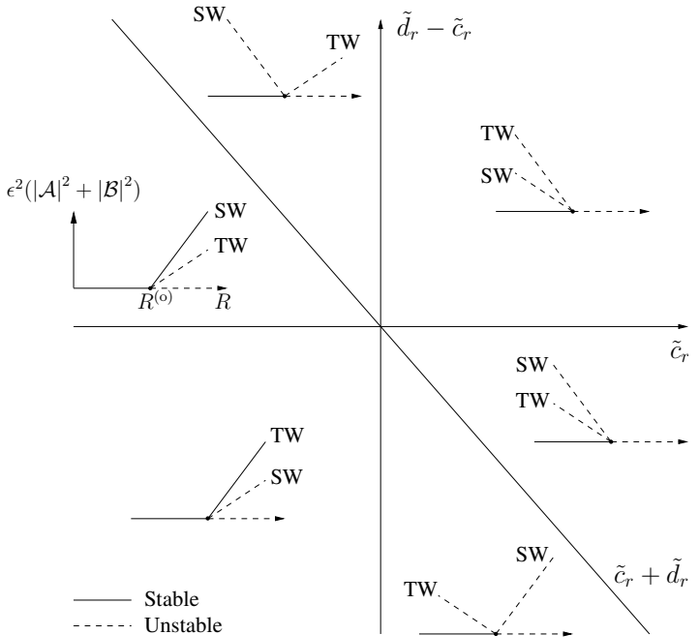


Figure 1. Bifurcation diagrams in the $(\tilde{c}_r, \tilde{d}_r - \tilde{c}_r)$ plane, showing the amplitude $\epsilon^2(|\mathcal{A}|^2 + |\mathcal{B}|^2)$ of travelling waves (TW) and standing waves (SW) as a function of the Rayleigh number R. Here, $\tilde{c}_r = (c/a)_r$, $\tilde{d}_r = (d/a)_r$, and the subscript r indicates the real part.

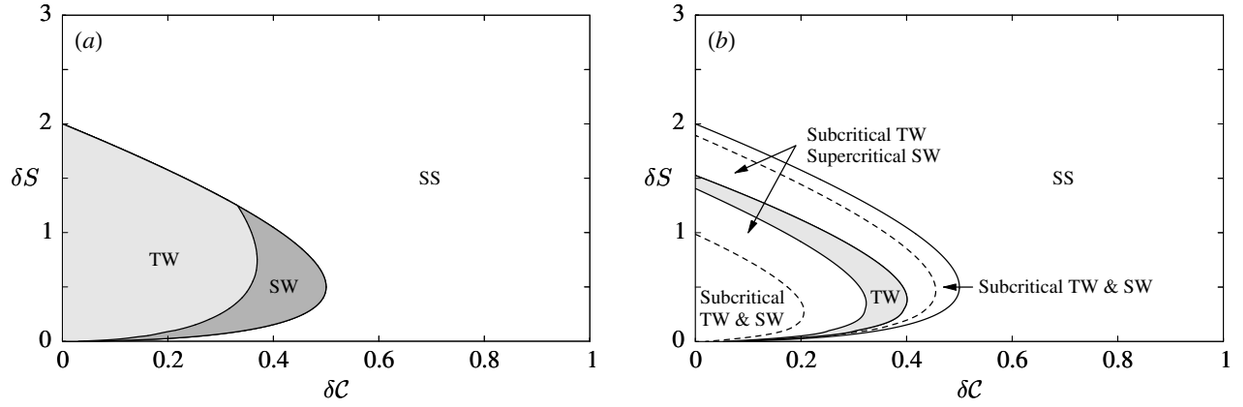


Figure 2. Stability regions. A diagram showing the regions in the $(\delta S, \delta \mathcal{C})$ parameter space where various features of oscillatory convection can be identified. The light-shaded portion corresponds to those parameter values where stable travelling waves are predicted, while the dark-shaded portions indicate where stable standing waves are expected to appear. The outermost solid curve represents the boundary between steady (SS) and oscillatory behaviour. The dashed lines separate the domains in which either oscillatory bifurcation is subcritical. Two representative cases are shown: (*a*) $K_1 = 0$, $K_2 = 0.05$; (*b*) $K_1 = 3$, $K_2 = 6$.

CONCLUSIONS

We have studied the nonlinear development of the oscillatory convecting states in mushy layers. Depending on parameter values, either travelling waves or standing waves can be stable at onset. Our analysis emphasizes the importance of a specific form of the constitutive relationship in selecting the oscillatory convection pattern. The overstable convective motions in the mushy layer leave a signature in the solid in the form of striation of its texture and local bulk composition. Quantification of these issues, currently under way, promises to provide a useful insight into the nonlinear aspects of segregation in cast alloys.

References

[1] Worster M. G., *Ann. Rev. Fluid Mech.* **29**: 91–122, 1997.
[2] Anderson, D. M., Worster, M. G., *J. Fluid Mech.* **302**: 307–331, 1995.
[3] Amberg, G., Homsy, G. M., *J. Fluid Mech.* **252**: 79–98, 1993.
[4] Fowler, A. C., *IMA J. Appl. Maths* **35**: 159–174, 1985.
[5] Anderson, D. M., Worster, M. G., *J. Fluid Mech.* **307**: 245–267, 1996.
[6] Crawford, J. D., Knobloch, E., *Ann. Rev. Fluid Mech.* **23**: 341–382, 1991.
[7] Solomon, T. H., Hartley, R. R., *J. Fluid Mech.* **358**: 87–106, 1998.

XXI ICTAM, 15–21 August 2004, Warsaw, Poland

MAGNETIC RESONANCE IMAGING OF STRUCTURE AND CONVECTION IN SOLIDIFYING MUSHY LAYERS

P. Aussillous*, A. J. Sederman**, L. F. Gladden **, H. E. Huppert* , M. G. Worster*
* *Institute of Theoretical Geophysics , DAMTP, Cambridge University*
** *Magnetic Resonance Research Center, Dept. Chem. Eng., Cambridge University*

Summary We use Magnetic Resonance Imaging to study the structure and convection inside a solidifying mushy layer formed from a binary alloy cooled from above. We focus especially on systems in which defects known as chimneys are observed. We obtain high-resolution images and have direct access to a number of measurements (chimney behaviour, porosity, etc.). The mushy layer is seen to grow in a self-similar manner until internal convection begins, when the solid fraction increases in the lower part of the layer.

INTRODUCTION

Many modern technological components are cast from metallic alloys that are poured into a mould in a molten state then cooled and solidified to form the final product. During solidification, the constituents of the alloy become segregated: one or more of the constituents preferentially form the first solid to precipitate, which usually creates a matrix of crystals (often dendritic), while the other constituents are left behind in the melt between these crystals, where they solidify later, at lower temperatures. The two-phase region comprising the matrix of primary crystals and interstitial, residual melt is called a mushy layer. One of the common defects observed during this process is the formation of so-called freckles, channel segregates or chimneys [1]. Such defects can result in the component being discarded, at huge cost in terms of wasted production time and reprocessing of materials. This phenomenon is also observed in sea ice and may occur in magma chambers and in the Earth's core.

We aimed principally at determining the conditions under which the chimneys occur. Until now, experimental studies [2-5] have tried to describe what is happening inside the mushy layer during solidification by indirect means such as studying the evolution of the bulk liquid properties (such as concentration, volume, etc.) to deduce the mean evolution of the mush. Observations have also been made of the mushy layer / liquid interface to study the crystal matrix properties or the onset of appearance of the chimneys. Most studies have been made *a posteriori*, once the solidification stopped (for example, to obtain the local porosity, the mushy layer is cut in slices; or more sophisticated techniques are used such as X-rays). But this gives information only at one instant. In our work, using a Magnetic Resonance Imaging technique, we obtain direct observations and quantitative measurements inside the mushy layer during solidification.

EXPERIMENTAL SET UP

The experimental set up consists of a cylindrical tank of internal diameter 3.5cm and depth 18cm, filled with a mixture of sugar and water; typically a 20 %wt sugar solution (figure 1). We cool it from the top at -20C, well below the liquidus temperature. A mushy layer then develops with a solid phase made of pure ice. The liquid phase corresponds to a mixture of sucrose and water more concentrated in sucrose than initially in the bulk. As the liquid density increases with sugar concentration this system convects, which leads to the formation of the channels free of crystals, called chimneys.

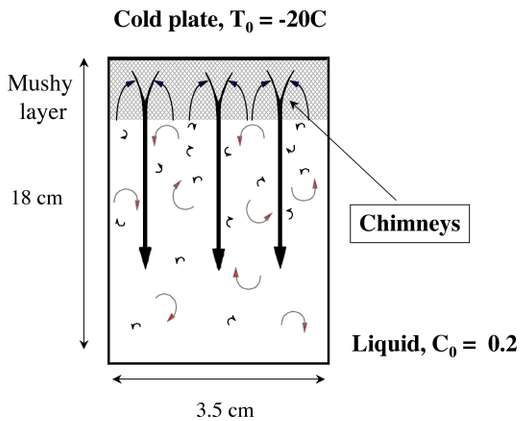


Figure 1. experimental set up.

The experimental set up is placed inside a magnet with a cooled jacket to insure thermal insulation. In contrast with previous experiments, we can obtain continuous data during solidification. The data consist of images of vertical and

horizontal slices across the sample. The slices are typically 2mm thick with 4mm between two slices. The solid phase doesn't yield any MRI signal so the intensity of signal received for each pixel corresponds to the liquid fraction.

RESULTS

Structure

With the MRI technique, we obtain information on the structure of the mushy layer. First, with the highest resolution, which is about 100 μm, we distinguish the ice matrix platelet structure inside the mushy layer, as can be seen in the figure 2a in a horizontal slice. In the horizontal slices the chimneys appear as white disks (see figure 2a). From time and position sequences we can study the chimneys' size and distribution. We also observe that the chimneys do not penetrate the whole mushy layer. Using the vertical slices, we can follow the time evolution of particular chimneys with time. In figure 2b one can see such a vertical slice after 14h (6cm of growing mushy layer). We then observe that chimney appears to get a complex structure with a lot of branches.

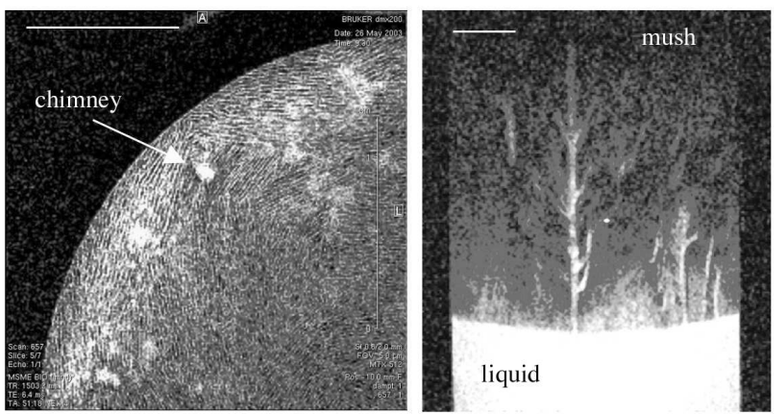


Figure 2. a) platelet structure of the ice matrix and chimneys observed in an horizontal slice. b) branched chimney in a vertical slice. In both case the white line represents 1cm.

Local porosity

We also obtain more quantitative data such as the local porosity as a function of time. These data are obtained locally for the first time and allow comparison with theoretical models [6-9]. For example we can show that initially the vertical mean porosity (averaged across a horizontal slice) follows a similarity law. This is consistent with there being little or no convection inside the mushy layer. We show that this similarity law is valid until a certain critical Rayleigh number is exceeded, as predicted previously, and is correlated with the appearance of chimneys. Thus knowledge of the local porosity and its time evolution gives direct information on the convection inside the mushy layer.

CONCLUSIONS

Using a powerful Magnetic Resonance Imaging technique, we have obtained for the first time measurements of the evolution of structure within a solidifying mushy layer. Quantitative measurements such as local porosity have been made and are shown to provide direct information on the convection which occurs inside the mushy layer.

References

[1] Kurz W., Fisher D.J. : Fundamentals of Solidification. *Trans. Tech. Publication*, 1986.
[2] Chen C. F., Falin Chen : Experimental study of directional solidification of aqueous ammonium chloride solution. *J. Fluid Mech* **227**:567–586, 1991.
[3] Tait S., Jaupart C. : Compositional convection in a reactive crystalline mush and melt differentiation.*J. Geo. Res.* **97**:6735–6756, 1992.
[4] Chen C. F. : Experimental study of convection in a mushy layer during directional solidification. *J. Fluid Mech* **293**:81–98, 1995.
[5] Wettlaufer J. S., Worster M. G., Huppert H.E. : Natural convection during solidification of an alloy from above with application to the evolution of sea ice. *J. Fluid Mech* **344**:291–316, 1997.
[6] Huppert, H.E. : The fluid mechanics of solidification. *J. Fluid Mech* **212**:209–240,1990 .
[7] Huppert, H.E.: Bulk models of solidification. The Handbook of Crystal Growth, D.T.J.Hurle, North Holland 1993.
[8] Worster, M.G.: Convection in mushy layers. *Ann. Rev. Fluid Mech.* **29**:91–122, 1997.
[9] Worster, M.G.: Solidification of fluids. Perspectives in Fluid Dynamics, G.K. Batchelor, H.K. Moffatt and M.G. Worster, CUP, 393–446, 2000.

SOLIDIFICATION AND COMPOSITIONAL CONVECTION OF A TERNARY ALLOY

Andrew F. Thompson[*], Herbert E. Huppert[**], M. Grae Worster[**], Anneli Aitta[**]
[*]*Scripps Institution of Oceanography, UCSD, La Jolla, CA 92093, USA*
[**]*Institute of Theoretical Geophysics, DAMTP, University of Cambridge, Wilberforce Road, Cambridge CB3 0WA, UK*

Summary We describe an experimental study where an aqueous solution of potassium nitrate and sodium nitrate is cooled from below resulting in the formation of two mushy layers. A density reversal is observed that leads to a transition from a convective regime to a diffusive regime and significantly alters the structure and growth rate of the mushes.

INTRODUCTION

The formation of solids from a liquid melt often generates fluid flows due to convection, which can effectively transfer heat and mass and significantly influence the structure and growth rate of the solid phase. Preferential incorporation of some components into the solid and rejection of others gives rise to one or more mushy layers between the melt and composite solid. Solidification of a ternary alloy reveals dynamics not observed in well-studied binary alloys. One such process is a density reversal, which we consider here.

Aitta, Huppert and Worster [1] initiated an experimental study of ternary alloys by cooling from below a simple alloy of two salts dissolved in water. In these experiments the initial concentrations of the alloy were chosen so that the compositional fields were stably stratified at all times. Convection was absent and the growth of the mushy layers and composite solid were diffusion-limited. In our experiments we considered initial conditions such that there was a transient period during which convection influenced the growth rate of the mushes.

METHODS

The alloy selected consisted of two salts, potassium nitrate (KNO_3) and sodium nitrate ($NaNO_3$) dissolved in water. This system was chosen principally because it conforms to a simple phase diagram with liquidus temperatures easily reached with typical lab equipment. Concentration measurements of KNO_3 and $NaNO_3$ in water were made using a Varian SpectrAA flame atomic absorption spectrometer. Experiments were conducted in a rectangular Perspex tank with internal dimension 20 cm by 20 cm, which was filled with solution to a depth of 35 cm. The walls and roof were insulated while the brass base allowed coolant to flow through it and cool the plate evenly.

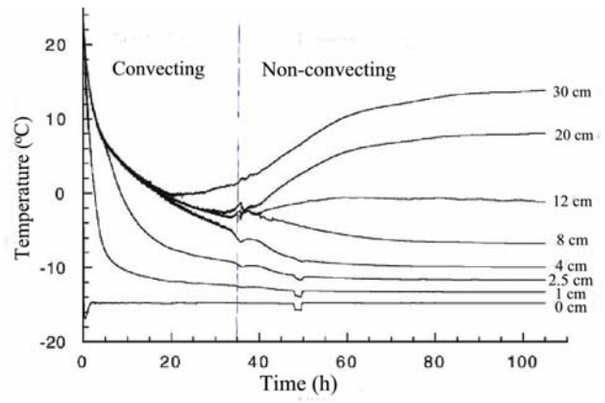
Initial concentrations were chosen so that KNO_3 solidified in the upper, primary, mush and KNO_3 and H_2O solidified in the lower, cotectic mush. The baseplate could be maintained at a constant temperature below the cotectic temperature, but above the eutectic temperature so that in the experiments discussed here no composite solid formed. Temperature measurements were made at various heights near the center of the tank using glass bead thermistors, including one embedded in the baseplate. Convection was monitored using a shadowgraph technique and the heights of the two mushy layers were determined by visual observations.

OBSERVATIONS AND MEASUREMENTS

Crystal formation began approximately one minute after coolant entered the baseplate, and the plate was completely covered with crystals after two minutes. Strong convection that kept the entire tank well mixed developed within the first five minutes of each experiment. The crystals initially had a thick fiber-like structure that evolved into a thinner shape after one or two hours. The mushes remained flush against the side of the tank while the system was convecting, and no chimneys were observed.

After a few hours the cotectic mush grew faster than the primary mush, thus reducing the depth of the upper mush layer. As the primary mush became thin, convection weakened and no longer kept the entire depth of the tank well mixed. Eventually the cotectic mush overtook the primary mush and convection ceased completely. This transition took 1 to 2 hours compared with a total convection time of 25 to 35 hours. As the single mush that remained continued to grow, a visible interface identifiable by a change in crystal structure or solid fraction remained visible at the height where the cotectic mush overtook the primary mush. Above this interface a gap developed between the mush and the side of the tank that was probably due to external heating from the lab.

Figure 1 shows the temperature traces at various heights above the baseplate in an experiment where the baseplate was maintained at a temperature of -14.75 ± 0.05 °C. Convection kept the liquid well mixed and the temperature uniform in the melt. As thermistors entered the mush the traces fell away from the uniform temperature. Convection stopped completely after 35 hours and as diffusion started to govern the dynamics, the melt became thermally stratified. The sharp drop in temperature seen around 48 hours was due to accidental error in the control setting. Figure 2 shows the heights of the primary and cotectic mushes from the same experiment as in figure 1. This plot shows the cotectic mush overtaking the primary mush and altering the growth rate of the remaining mush layer. Concentration measurements (not shown here) of samples removed from the melt during convection fall on the tie line between the liquidus point and the cotectic curve with concentrations moving towards the cotectic curve with increasing time. Concentration measurements of samples removed from within the cotectic mush after convection stopped collapsed on the cotectic curve with concentrations moving towards the eutectic point with increasing depth in the mush.



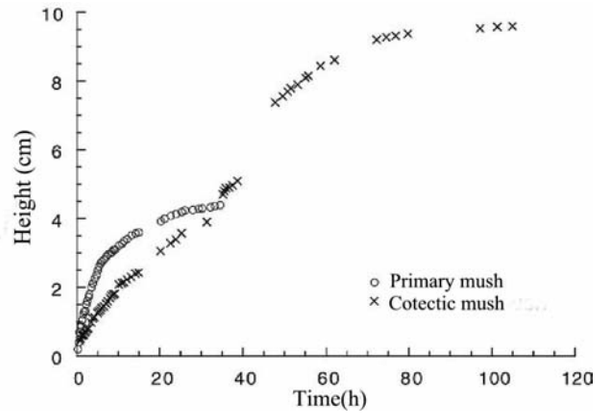


Figure 1 (*left*). Temperature traces of the residual liquid from various heights above the baseplate. The dashed vertical line marks the end of convection at approximately 35 hours. The drop in temperature at 48 hours is due to personal error.

Figure 2 (*right*). The height of the primary and cotectic mushes from the same experiment as in figure 1. Convection stopped at approximately 35 hours when the cotectic mush overtook the primary mush.

GLOBAL CONSERVATION MODEL

To describe our experiments we adopt a one-dimensional, global conservation model that is an extension of the binary model [2] including convection [3]. As opposed to the diffusion-limited model, the inclusion of convection implies that the solid fractions in the two mush layers are time-dependent. The model begins with equations for the conservation of heat and exact integral equations for conservation of solute in each layer. Then a shape assumption is applied to the solid fractions to simplify the system. Here we assume that the solid fractions are depth-averaged values so that they are independent of height. We further assume that local thermodynamic equilibrium holds throughout the mushy layers so that temperature and solute concentrations conform to the linear liquidus relationships. This assumption further allows us to neglect solutal diffusion in the mushes. Boundary conditions are provided at the interfaces by using the ternary phase diagram, and the growth rates are coupled by conservation of heat at the interfaces.

The model is initiated with empirical values for the solute and heat fluxes, which are determined by the time rate of change of concentration and temperature in the melt. The Stefan condition is introduced at the interfaces, which describes a balance between the latent heat release upon solidification, heat conduction through the solid and, in the case of the upper mush layer, a convective heat flux. The model was found to give good results for the interface positions of the two mushy layers up until the point where the cotectic mush overtakes the primary mush. Further work is required to accurately model the dynamics of the transition from a convective to a diffusive regime. The reader is referred to Thompson *et al.* [4] for the full derivation of the global conservation model.

CONCLUSIONS

We have shown experimentally that a density reversal can lead to the reduction of the number of distinct mushy layers in a solidifying alloy. This transition can have profound effects on the structure and growth rate of the solidifying components, and plays an important role in dynamics of more complex multi-component alloys.

References

[1] Aitta, A., Huppert, H.E., Worster, M.G.: Diffusion-controlled solidification of a ternary melt from a cooled boundary. *J. Fluid Mech.* **432**:201-217, 2001.
[2] Huppert, H.E., Worster, M.G.: Dynamic solidification of a binary melt. *Nature* **314**, 703-707.
[3] Kerr, R.C., *et al.*: Solidification of an alloy cooled from above. Part 2. Non-equilibrium interfacial kinetics. *J. Fluid Mech.* **217**:331,348, 1990.
[4] Thompson, A.F., *et al.*: Solidification and compositional convection of a ternary alloy. *J. Fluid Mech.*

AHP SETUP FOR LOW LAMINAR MELT FLOW STUDY IN CRYSTAL GROWTH

Michael A. Gonik*, Janusz A. Szymczyk **, Tomasz A. Kowalewski ***
* *CTR "Thermo", Department of Crystal Growth, 601650 Alexandrov, Russia*
** *University of Applied Sciences, Department of Engineering, 18445 Stralsund, Germany*
*** *IPPT PAN, Department of Mechanics & Physics of Fluids, PL 00-049 Warszawa, Poland*

Summary For verification of numeric methods and development of experimental benchmarks for 2D and 3D models of heat and mass transfer in crystal growth, the experimental AHP setup based on a novel AHP crystal growth method is designed to conduct experiments with $NaNO_3$ and ice. It is equipped with PIV and PVT visualizations systems to provide finding of field of flow velocity and temperature distribution in the fluid. Preliminary investigations have proved the possibility to suppress natural convection and to create low melt flow similar to micro gravity conditions and shown good coincidence of calculated data on mass transfer with those observed in the experiment.

INTRODUCTION

Solid-liquid phase-change phenomena are present in a large number of industrial applications and natural processes. Numerical modelling of such strongly non-linear, moving boundary, thermal and fluid flow problems is not a trivial task. In the case of solidification, the planar interface appears to be unstable depending on environment conditions, creating different structures, such as cells or dendrites. These local mechanisms have drastic consequences at a larger scale and convective motion in the interdendritic melt is a primary cause for a macrosegregation that is the variation in composition of a solidified alloy for instance. In the microgravity environment, despite the absence of natural convection, problems arising from the effects of Marangoni convection or g-jitter effects seriously damped initial enthusiasm on using space labs for crystal growth.

Computer simulation has a major relevance as a tool of analysis of the experimental studies or for the design of engineering hardware. In order to assess a satisfactory level of confidence of the simulation tools, both the model and the procedure have to be tested through properly designed validation experiments, reproducing the basic features of the simulated phenomena. Therefore, experimental benchmarks for code validation have gained a special attention in the recent years.

In the prevailing growth methods, when a strong forced or thermocapillary convection takes place, a complex flow unstable by its nature is formed. Under such conditions, it is extremely difficult to realize quantitative correlation between experimental and calculated data. In this connection, special interest presents solidification from a thin melt layer [1,2] when low laminar flows are initiated. Employing modern visualization tools, which provide a way for thermometric and velocimetry measurements, and expanding a number of model liquids, it is possible to carry out researches in heat and mass transfer during solidification within a wide range of determining parameters.

SETUP AND EXPERIMENTAL TECHNIQUE

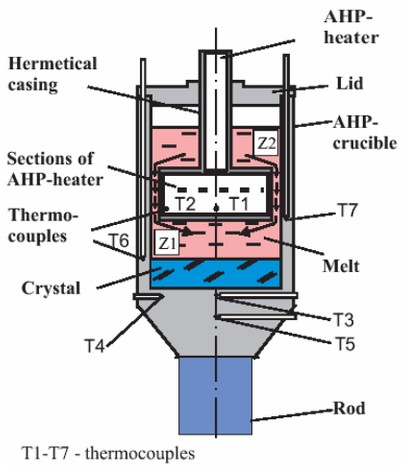


Figure 1. Schematics of AHP crystal growth

A novel AHP method of crystal growth under conditions of Axial Heat flux close to Phase interface characterized by an additional heater placed inside in the melt close to the solid-liquid interface was previously proposed [2]. Functioning as a baffle [1], a submerged heater divides the melt into two zones Z1 and Z2 (Fig. 1). The zone above the AHP-heater, Z2, serves for feeding the solidification zone Z1 with the melt (under the heater). Processes in these zones do not affect each other. In zone Z1, the natural convection of the melt is suppressed and a low melt flow, arising due to movement of the crystal with the crucible relatively to the AHP-heater, is laminar and steady-state. In case when thermocouples are installed along all boundary surfaces, it is possible to control during the growth cycle the basic technological parameters: position and shape of the solid-liquid interface, actual growth rate of a crystal, and temperature gradient at the solidification front.

With the aim to observe the behavior of low AHP flow, an experimental AHP setup for visualization of $NaNO_3$ crystal growth [3], employing 20 μm particles of aluminum powder as tracers, was designed. The fragment of crystallizer is presented in Fig. 2. The $NaNO_3$ charge was completely molten with the background heater, the AHP-heater was submerged into the melt, and thermal conditions were established under which a part of the melt was solidified. In this case, the solid-liquid interface was formed at a certain distance within 5-20 mm from the AHP-heater bottom. Varying power of the background and AHP-heater sections, the planar shape of the phase interface was established. The crucible was pulled down, while the AHP-heater was stationary.

Another type of crystallizer is designed for visualization of fields of velocities and temperature distribution in the liquid, as well as for investigation of faceted growth effect on heat and mass transfer and origin of morphological instability in ice growth.

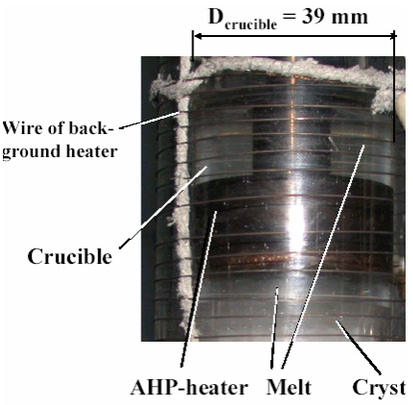


Figure 2. $NaNO_3$ solidification in AHP method

Particle image velocimetry (PIV) as well as particle image thermometry (PIT) are used as a quantitative determination of the velocity and temperature map in a convective flow field. PIT is based on the property of certain thermochromic liquid crystals (TLCs), with diameter of 10-100 μm, to reflect light of various colors depending on their temperatures and the observation angle. In PIV, flow is illuminated by a xenon flash or a halogen lamp and observed at 90 ^{0} by a high-resolution 3-CCD color camera (see Fig. 3). The evolution methods and their software were successfully developed in house [4]. Being applied to ice solidification, the flow images are used to evaluate the shape and location of the phase front. These measurements are performed using image analysis software. As for the solidification front, the edge detection, supported by manual intervention, appeared to be the most efficient way to find the interfacial profiles [5].

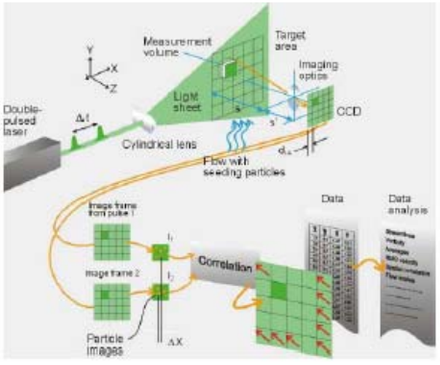


Figure 3. Schematics of visualization system

RESULTS

Setup examination was carried out in growth of $NaNO_3$ crystals at 7 mm/h rate. The axial temperature gradient in the melt was 20-40 K/cm and the radial temperature gradient was 1.2-1.3 K/cm. The solid-liquid interface was planar in all experiments. Depending on thickness of the set melt layer, the Rayleigh number did not exceed 30000. The laminar character of convection, varied from pronounced natural one with two vortexes, located close to the solid-liquid interface, up to, practically, pure forced convection [6], was well observed. Performed numerical computations have shown a good quantitative coincidence. It has been found that the natural convection is completely suppressed (Fig. 4) at the melt layer of 2 mm (Ra_{radial}=900), and heat and mass transfer becomes similar to that under microgravity conditions.

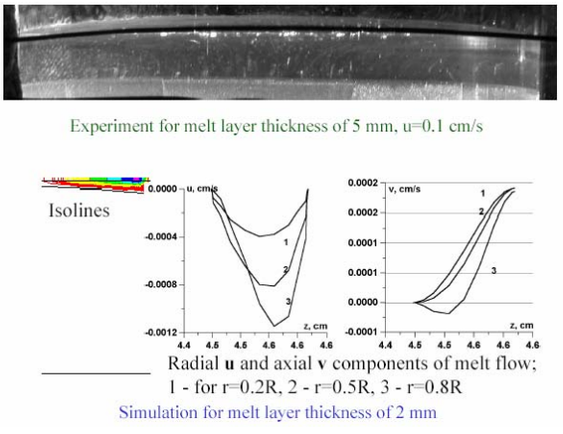


Figure 4. Forced low melt flow during $NaNO_3$ solidification

CONCLUSIONS

It has been shown that crystal growth by the AHP method is characterized by low laminar flows. This allows obtaining experimental benchmarks and testing of 2D and 3D codes for simulation of convection under conditions of phase change. Due to selection of the melt layer, it is possible to create conditions at which forced convection plays a dominant role. Such flows can be considered as benchmark ones and employed as tools for studying the effect of convection nature on growth of a crystal and formation of its structure. The research was sponsored by INTAS-99-01814 and by CRDF RE1-2480.

References

[1] Ostrogorsky, A. Diffusion-controlled distribution of solute in Sn-1%Bi specimens solidified by the submerged heater method. Journal of Crystal Growth, **110**, 950-954, 1991.

[2] V.D. Golyshev, M.A. Gonik, A temperature field investigation in case of crystal growth from the melt with a plane interface on exact determination thermal conditions, Cryst. Prop. and Preparation, **36-38,** 623-630, 1991.

[3] V.D. Golyshev, M.A. Gonik, A.N. Kovalenko, E.V. Zharikov. Study of low melt flows during $NaNO_3$ solidification by AHP method. Abstracts of Int. Symp. on Visualization and Imagining in Transport Penomena, May 5-10, 2002, Antalya, Turkey, p. 61-63., 2002.

[4] J. Aleksic, P. Zielke and J. A. Szymczyk. Temperature and flow visualization in a simulation of the Czochralski process using temperature-sensitive liquid crystals. Visualization and imaging in transport phenomena. Annals of the N.Y. Acad. of Sci., vol. 972, 2002, 158-163.

[5] T. A. Kowalewski. Particle image velocimetry and thermometry for two-phase flow problems. Visualization and imaging in transport phenomena. Annals of the N.Y. Acad. of Sci., vol. 972, 2002, 213-222.

[6] V.D. Golyshev, M.A. Gonik, A.N. Kovalenko, M.P. Marchenko and E.V. Zharikov. Experimental and numerical study of low laminar melt flows in crystal growth of $NaNO_3$ by AHP method. Int. J. of Heat and Mass Transfer (in preparation).

OPTIMIZATION OF THE GROWTH CONDITIONS OF A $Nd:YVO_4$ CYLINDRICAL BAR

Liliana Braescu*, Agneta M. Balint**, Robert Szabo***, Stefan Balint****
*,***,**** Department of Applied Mathematics, The West University of Timisoara
Bd. V. Parvan No. 4, 300223 - Timisoara, Romania
** Department of Physics, The West University of Timisoara
Bd. V. Parvan No. 4, 300223 - Timisoara, Romania

ABSTRACT

The main purpose of this paper is to find those values of the growth process parameters (pulling rate v, temperature at the meniscus basis T_0, die radius r_0) which assure the growth of a $Nd:YVO_4$ cylindrical bar with a prescribed diameter $2r_f$ and for which the non-uniformities of the surface of the bar, due to small uncontrollable oscillations of the pulling rate and the melt temperature at the meniscus basis, are minimum possible. Numerical results ar given for cylindrical bar of 5 (mm) diameter, grown in a furnace in which the vertical temperature gradient is $k = 33$ (K/mm) for the following three type of uncontrollable oscillations: $\Delta v = 0.001$ (mm/s), $\Delta T = 1$ (K); $\Delta v = 0.01$ (mm/s), $\Delta T = 10$ (K) and $\Delta v = 0.02$ (mm/s), $\Delta T = 20$ (K), respectively.

INTRODUCTION

Oxide cylindrical monocrystals grown from the melt by dege-defined film-fed growth (E. F. G.) method are used as solid-state laser hosts and materials for acousto-opto-electronic devices. The shape and the quality of the crystal grown by E. F. G. method are determined by the shape of the meniscus (the liquid bridge retained between the crystal and the die) and its behavior during the growth. In the last 20 years many experimental and theoretical studies have been reported regarding this growth process (Refs. [1, 5]). The E.F.G. method is performed to achieve crystals with constant radius when the pulling rate v and the melt temperature T_0 at the meniscus basis are constant and the bottom line of the melt/gas meniscus on the die is fixed to the inner or outer edge (Refs. [6]). In reality the pulling rate v and the melt temperature T_0 can have small uncontrollable oscillations around an average value.

THE MATHEMATICAL MODEL

In this paper we consider the nonlinear mathematical model:

$$\begin{cases} \frac{dr}{dt} = -v\tan\left(\alpha(r,h,r_0) - \alpha_1\right) \\ \frac{dh}{dt} = v - \frac{1}{\Lambda\rho_2}[\lambda_1 G_1(r,h) - \lambda_2 G_2(r,h)] \end{cases} \tag{1}$$

which permits to compute the evolution in time of the radius $r = r(t)$ and the meniscus height $h = h(t)$.
In Eqs. (1): v - pulling rate; α_e - growth angle, $\alpha_e = \pi/2 - \alpha_1$; $G_{1,2}$ - temperature gradients in the melt and in the crystal, respectively; Λ - latent heat; $\rho_{1,2}$ - density of the melt and of the crystal, respectively; $\lambda_{1,2}$ - thermal conductivity coefficients in the melt and in the crystal, respectively; $\alpha(r,h) < \pi/2$ - the angle between the Or axis and the tangent to the meniscus in the point (r,h).

In order to grow a cylindrical bar with constant radius, the following system:

$$\begin{cases} -v\tan\left(\alpha(r,h,r_0)-\alpha_1\right)=0 \\ v-\frac{1}{\Lambda\rho_2}[\lambda_1 G_1(r,h)-\lambda_2 G_2(r,h)]=0 \end{cases} \tag{2}$$

has to be satisfied. System (2) has two solutions (r_1,h_1) and (r_2,h_2) with $r_1<r_2$. The steady state (r_1,h_1) is not stable but the steady state (r_2,h_2) is asymptotically stable. In the following the asymptotically stable steady-state (r_2,h_2) will be denoted by (r^*,h^*). The asymptotically stable steady-state (r^*,h^*) depends on v, on T_0, and on r_0. In order to determine these dependences we consider several values of the die radii r_0 in the range $(r_f;1.6r_f]$ and for each of them we find the set $S(r_0)$ of those couples (v,T_0) for which the grown crystal radius is equal to a desired radius r_f . For each die radius r_0 we find that couple (v,T_0) from $S(r_0)$ for which the amplitude A of the change of r_f, due to small oscillations of v and T_0, is minimum. Finally we identify that die radius r_0 and that (v,T_0) couple for which the amplitude A is minimum possible.

NUMERICAL RESULTS

Numerical results are given for a $Nd:YVO_4$ cylindrical bar of 5 (mm) diameter, grown in a furnace in which the vertical temperature gradient is $k=33$ (K/mm) for the following three type of uncontrollable oscillations: $\Delta v=0.001$ (mm/s), $\Delta T=1$ (K); $\Delta v=0.01$ (mm/s), $\Delta T=10$ (K) and $\Delta v=0.02$ (mm/s), $\Delta T=20$ (K), respectively.

CONCLUSIONS

In the above model it is possible to predict those values of r_0, v, T_0, for which small uncontrollable oscillations of v and T_0 cause minimal variations of the desired crystal radius r_f.

References

[1] M. Kobayashi, T. Tsukada, M. Hozawa // J. Crystal Growth 249 (1-2) (2003) 230.

[2] V. A. Tatarchenko - Handbook of Crystal Growth, D. T. J. Hurle Editor, North-Holland, Amsterdam 1994, pp.1017-1048.

[3] V. A. Tatarchenko - Shaped Crystal Growth, Kluwer Academic Publishers, Dordecht, 1993, pp.19-145.

[4] M. Kobayashi, T. Tsukada, M. Hozawa - Journal of Crystal Growth 249 (1-2) (2003) 230.

[5] L. Braescu, A. M. Balint,I Jadaneantu, St. Balint - Journal of Crystal Growth, Nr. 240 (2002) 305.

[6] B. M. Epelbaum - personal communications

[7] Kaslik, A. M. Balint, St. Balint - Nonlinear Studies, Vol. 10, 1 (2003) 67.

[8] B. M. Epelbaum, K. Shimamura, K. Inaba, S. Uda, V. V. Kochurikhin, H. Machida, Y. Terada, T. Fukuda - Cryst. Res. Technol. 34 (1999) 301.

FRONT TRACKING TECHNIQUE ON A FIXED GRID IN MODELLING OF BINARY MIXTURE SOLIDIFICATION WITH NATURAL CONVECTION

Jerzy Banaszek*, David J. Browne**, Marek Rebow* and Mariusz Proczek*

* Institute of Heat Engineering, Warsaw University of Technology, Warsaw, Poland

** University College Dublin, Dublin, Ireland

Summary. A novel front tracking method is presented in calculations of binary mixture solidification driven by conduction and natural convection. The method based on the local dendrite tip kinetics enables the detection of the under-cooled liquid zone in front of a curve joining the dendrite tips. Its results have been verified and validated through detailed comparisons with both: the predictions of the enthalpy-porous medium model and the PIV experimental findings.

Nowadays, it is commonly appreciated that natural convection plays a crucial role in formation of local micro- and macro-structures during solidification of binary systems. For over two decades various validate computer simulations of these two coupled and complex phenomena have become a fundamental tool for prediction of local flow patterns, temperature and concentration fields, supplementing or even replacing cumbersome time-consuming and expensive experimental findings.

The most popular macroscopic representation of transport phenomena in the two-phase region ('mushy zone') is based on the single domain approach (valid for liquid, solid and mushy zones), where this region is macroscopically represented by the enthalpy–porous medium model and underlying micro-structural evolution is incorporated via a map of solid fraction throughout the domain.

Yet, a novel front tracking technique on a fixed Cartesian grid, based on the kinetics of dendritic growth was developed recently [1,2,3,4]. Its results have been compared with the ones got from the enthalpy-porous medium model - in details for the case of solidification driven only by conduction [1,2,4] and preliminary when the thermal natural convection also occurs [3] - showing the superiority of the front tracking technique in the detection of the under-cooled zone and, thus, in potentially modelling of columnar/equiaxed grain structures [1,4].

The paper presents further development of this numerical technique in calculations of binary mixtures solidification driven by both conduction and natural convection as well as in the model verification and validation through its comparisons with both: the theoretical predictions by the enthalpy-porous medium approach and the experimental results got through the use of the PIV (Particle Image Velocimetry) technique [5].

A novel model of the advance of a columnar front and the growth of equiaxed grains, proposed in [1,3,4], is based on a front-tracking technique on a fixed grid and on the kinetics of dendrite growth. Mass-less marker particles are used to determine the interface evolution as a function of the local under-cooling. An initial position of each marker is assumed in accordance with both an initial state and thermal boundary conditions. A new position of each marker is then calculated from the time interval Δt and the growth velocity, which is a function of local under-cooling determined from a current temperature field. This dendrite kinetics relationship, which is fundamental in the model, can result from the theoretical considerations (e.g. [6]) or from experimental findings. A new interface position is then obtained by linear interpolation between each successive marker. So, it is assumed that the columnar front is a line joining dendrite tips. Next, the points at which this representation of the front intersects the grid-lines of the computational mesh are calculated. These points now become the new marker particles. Like in the classical single-domain approach, the single set of mass, momentum and energy conservation equations is used to get the velocity, pressure and temperature fields. But the commonly used total enthalpy concept is not applied here. Instead, the latent heat effect is considered by a careful definition of the source terms in the energy equation accounting for both: the advance of solidification front and subsequent thickening of the mushy zone within a control volume [1,3,4].

The fact that the kinetics of dendrite tips is exploited in the model, enables it to identify two regions between the equilibrium solidus and liquidus isotherms within a control volume that containing the interface, namely the columnar dendrite zone behind the dendrite tips and the under-cooled zone in front, where equiaxed structure can be formed. To show that the temporal shapes of all zones are given in Fig.1 for solidification of Al_2%wgt-Cu in a sand mould (interface heat transfer coefficient equal to $500 W/(m^2K)$) driven by pure conduction (the first three left columns) and also by thermal natural convection, showing the flow pattern (the remaining columns). Here the kinematics of dendrite tips is a theoretical parabolic function of the local under-cooling [6].

The verification and validation procedures for the front tracking model were further conducted through the detailed comparisons of its results with both: the enthalpy-porous medium model calculations and the experimental velocity field along with the front position identified from the PIV technique.

As an example problem the solidification, in a differentially heated square cavity, of 3.5%wgt NH_4Cl in water was simulated. The left vertical wall was kept at the initial temperature of $9.5^{O}C$ whereas the right one had a temperature of $-10^{O}C$. Figure 2 shows shapes and positions of the interface at four different times of the process, whereas the Figure 3 depicts the corresponding results from the enthalpy-porous medium model calculations.

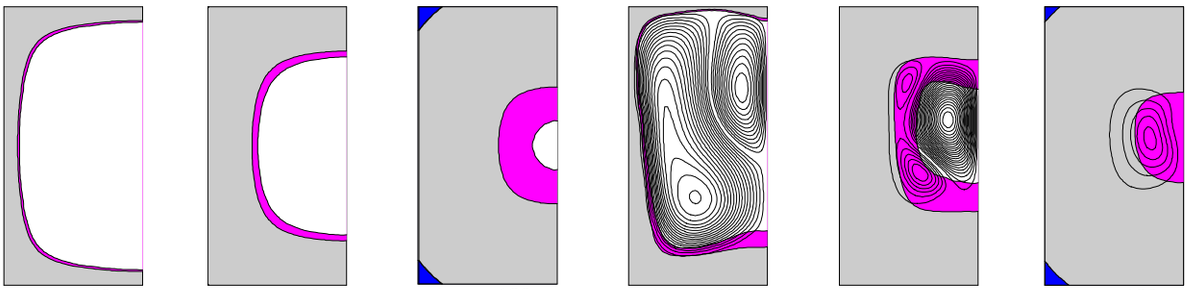


Fig.1. Solidification of Al_2%wgt_Cu in a sand mould: white – liquid phase, pink – under-cooled liquid zone, grey – mushy zone, dark blue- solid phase.

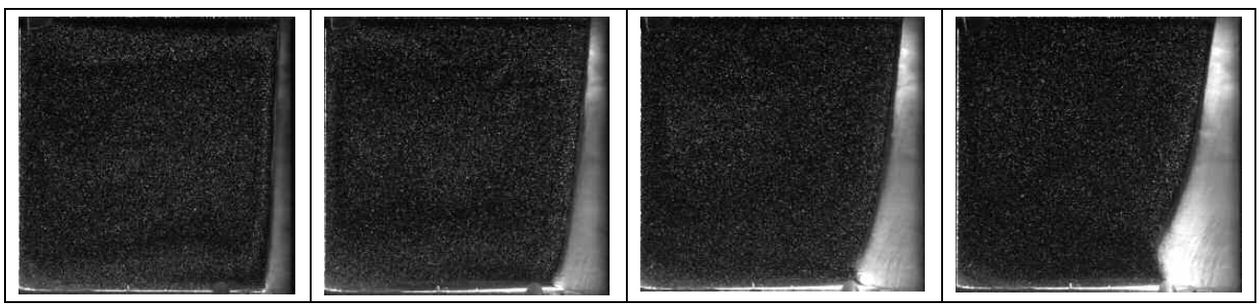


Fig.2. Experimental pictures: the seed and the temporal solid-liquid front position after 100s, 500s, 1000s and 2000s (from left to right) of solidification of 3.5%wgt aqueous solution of NH_4Cl.

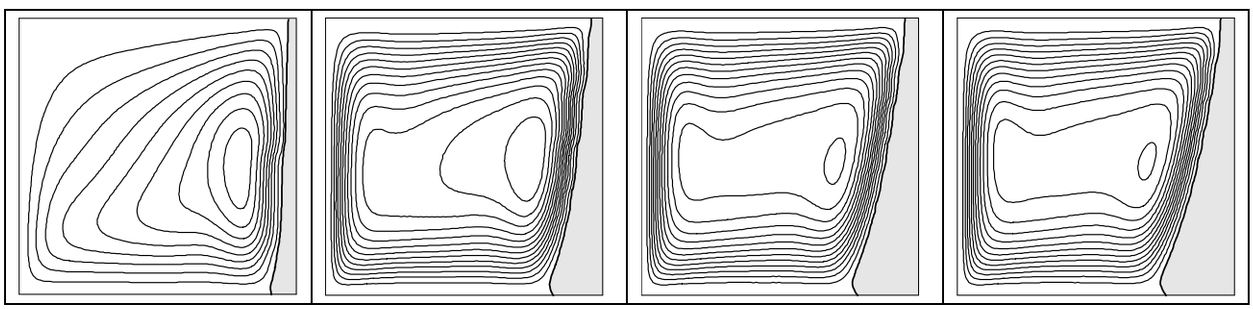


Fig.3 Enthalpy-porous medium model: the calculated flow pattern and solid phase shape after 100s, 500s, 1000s and 2000s (from left to right) of solidification of 3.5%wgt aqueous solution of NH_4Cl..

Kinematics of dendrite tips, used in the front tracking technique, has been obtained experimentally, i.e. from pictures of the temporal front shapes taken at short even time intervals using a high resolution camera. This allows specifying the local dendrite tips velocity as a function of time and position.

Detailed comparisons of the velocity field and front positions calculated by the front tracking technique with those presented above will be given in the paper. They will be followed by a short discussion concerning the physics of phenomena and the results of the validation procedure performed.

Acknowledgements

The work was supported by the State Committee for Scientific Research, Poland, Grant No. 8T10B07220, the European Space Agency, contracts 14585/00/NL/SFe(IC) and 14313/01/NL/SH(CCN002).

References

1. Browne D.J.: Modelling columnar and equiaxed growth. D. Phil. Thesis, Oxford, 2002
2. Banaszek J., Browne D.J, Furmanski P.: Eulerian equilibrium and non-equilibrium macroscopic modelling of binary system solidification. Archives of Thermodynamics, vol.24, no. 1, pp. 37-57, 2003.
3. Browne, D.J., Banaszek, J. and Hunt. J.D.: Front tracking on a fixed grid versus enthalpy approach in modelling of binary alloy solidification. Proceedings of the ASME International Mechanical Engineering Congress and Exhibition, New Orleans, USA, paper IMECE2002-32871, 2002.Browne, D.J. and Hunt, J.D.: A fixed grid front-tracking model of the growth of a columnar front and an equiaxed grain during solidification of an alloy. Numerical Heat Transfer, Part B: Fundamentals, in press.
5. Banaszek J.,Rebow M., Proczek M.: Study of reliability of numerical predictions for buoyancy-induced transport processes in pure water and dilute aqueous solutions of sodium chloride. 9thInternational Conference on Thermal Energy Storage, FUTURESTOCK'2003, pp.503-510, 2003.
6. Burden M., Hunt, J. D., Cellular and dendritic growth, Journal of Crystal Growth, vol.22, pp. 99-116, 1974.

SALT PRECIPITATION IN GEOTHERMAL RESERVOIRS

George G. Tsypkin [*], Andrew W. Woods [**]
[*] *Institute for Problems in Mechanics RAS, Ave. Vernadskogo 101, 119526 Moscow, Russia*
[**] *BP Institute for Multiphase Flow,Madingley Rise,Madingley Road,Cambridge CB3 0EZ, UK*

Summary We model the motion of the boiling front which develops when hot saline solution migrates towards a low pressure well from a geothermal reservoir which is initially saturated with hot saline solution. We derive a family of self-similar solutions which describe the motion of the liquid and vapour towards the well, as the boiling front migrates out into the reservoir. These solutions take into account the reduction in permeability and porosity due to salt precipitation at the boiling front. We find that for low reservoir pressure or small salt concentration there are two distinct branches of self-similar solutions. For each salt concentration, these branches coincide at a critical reservoir pressure. For larger reservoir pressure, the self-similar solutions cease to exist and we propose that in this regime, the pore space becomes fully clogged with salt precipitate.

PROBLEM FORMULATION

We consider the extraction of vapour from a low pressure well embedded in a hot porous rock saturated with aqueous saline solution. As the fluid evaporates, the salt concentration of the residual liquid increases leading to precipitation of salt in the porous space and hence a reduction of rock porosity and permeability [1-3]. The primary objective is to investigate this salt precipitation process; for the sake of simplicity we focus on the idealized isothermal problem in which the reservoir temperature is equal to the initial value $T = T_0$. This hypothesis implies that there is a cross-layer heat flux which maintains the temperature in the permeable layer from a neighbouring impermeable layer. Vaporization occurs within a geothermal reservoir if the pressure P_w in the well-bore is less than the saturation pressure $P_f(T_0)$ at the vaporization front. In the water and vapour zones, the pressure evolves according to Darcy's law combined with the local mass-conservation equations, leading to the governing equations for the liquid and vapour regions

$$\frac{\partial P}{\partial t} = \kappa_1 \Delta P, \quad \kappa_1 = \frac{k}{\phi \alpha \mu_w}; \qquad (\text{grad } P)^2 + P \Delta P = 0; \tag{1}$$

where k is the permeability, ϕ the porosity, μ the viscosity and α the water compressibility coefficient. As the boiling front migrates away from the extracting well, the pressure distribution in the vapour zone is quasi-stationary owing to the low density of the vapour [4]. The solid salt precipitate occupies some part of the volume of porous space in the vapour zone. This part we denote as the unknown function S_{pr}. We assume that the vaporization front coincides with the precipitation front. The boundary condition for the mass of solution includes the reduction in the porosity and permeability of the vapour region due to the formation of salt deposit with density ρ_{salt} and has the form

$$\phi[\rho_w - S_{pr}\rho_{salt} - (1 - S_{pr})\rho_v]V_n = -Q_{vn-} + Q_{wn+} \tag{2}$$

where V is the front velocity and the mass fluxes in the water and vapour regions are defined by the formulas

$$Q_w = -\rho_w \frac{k_0}{\mu_w} \text{grad } P, \quad Q_v = -\rho_v \frac{k_0 K(S_{pr})}{\mu_v} \text{grad } P \tag{3}$$

We assume that the advective transport of salt dominates the diffusive transport and conservation of salt across the front has the form

$$\phi(S_{pr}\rho_{salt} - c_+\rho_w)V_n = -c_+ Q_{wn+} \tag{4}$$

where c is the salt concentration in the fluid ahead of the boiling front. The mass-conservation equation for the salt in the water region can be written as

$$\frac{\partial c}{\partial t} - \frac{k}{\phi \mu_w} \text{grad } P \text{ grad } c = 0 \tag{5}$$

We consider one-dimensional flow in an unbounded constant temperature reservoir, $x>0$, and assume that at the extraction well, $x=0$, the pressure has value P_w. Thus, the boundary and initial conditions have the form $t = 0$: $P=P_0$, $c=c_0$; $x=0$: $P=P_w$. If the initial and boundary values are constants the problem admits a similarity solution $P = P(\xi)$, $c = c(\xi)$, $X = \beta\sqrt{t}, \xi = xt^{-1/2}, V = \dot{X}(t)$. The exact solutions for the water ($x>0$) and vapour ($0<x<X(t)$) regions are obtained from the equations (1) and (5) together with a low for the change in permeability associated with the precipitation. Here we use a parametric relation to describe the change in permeability as a function of the mass of precipitate, given by

$$k_- = k_0 \frac{1 - \exp[\vartheta\phi(1 - S_{pr})]}{1 - \exp(\vartheta\phi)} = k_0 K(S_{pr})$$

where ϑ is a coefficient which accounts for different changes in the permeability as a result of precipitation.

The unknown functions β and S_{pr} can be found if we substitute the similarity solutions into boundary conditions (2) and (4) at the vaporization front, leading to a system of transcendental equations.

EXISTENCE OF MULTIPLE SOLUTIONS

Numerical solutions of the transcendental system for the typical values of the main parameters, namely the far-field reservoir pressure and the salt concentration in solution are presented in figure 1 (c_0=0.1, 1-$P_w = 4\cdot10^5$ *Pa*, 2-$P_w = 6\cdot10^5$ *Pa*, 1-$P_w = 8\cdot10^5$ *Pa*). We have found that there are two solutions (solid and dashed lines) for small values of the far-field pressure and hence liquid flux, but that as the reservoir pressure increases, these two solutions eventually meet, and for large values of the pressure, there is no solution. Instead, we expect the pore space to be fully clogged with precipitate. It has been shown in [4] that in the limit of high reservoir pressure and hence large liquid flow from the far filed, the motion of the boiling front is suppressed and $V \to 0$. From equation (2), we expect that in this limit, the approximate balance $Q_w = Q_v$ applies. If the front velocity V is sufficiently small then salt precipitate accumulates owing to the advective transport of fluid to the well-bore. For a self-similar flow, for which the boiling front advances at a rate $V_0\, t^{-1/2}$ and the fluxes decay at a rate $Q_0\, t^{-1/2}$, then using equations (3) and (4) we find that

$$Q_{v0}^2 = \frac{\phi \rho_v \rho_{salt} k_0 \delta P}{c_0 \mu_v} S_{pr} K(S_{pr})$$

where δP is the fixed difference in pressure between the boiling front and the well and we have used the result that $S_{pr}\rho_{salt} >> c_0\rho_w$. Since the permeability decreases as the mass of salt precipitated increases, then quantity $S_{pr}K(S_{pr})$ may vary non-monotonically with S_{pr}. Indeed, it is likely to be very small for both small and large value of S_{pr} corresponding to the case of a very small mass of precipitate and a large mass of precipitate which nearly clogs the matrix. For intermediate values, the value of $S_{pr}K(S_{pr})$ is likely to be larger and there is some intermediate value S^*_{pr} at which is attains a local maximum. For $Q_{v0} < Q_{v0}(S^*_{pr})$, we expect two solutions for S_{pr} and hence V_0 for the given value of Q_{v0}, with the other parameters fixed; this is consistent with the full numerical calculations (figure 1). In figure 2, the curve $S_{pr}K(S_{pr})$ is shown as a function of S_{pr}, and the critical value for S^*_{pr} is equal approximately 0.24. In this figure we also show the critical value as calculated from the complete similarity solution for three values of the salt concentration. It is seen that the exact value depends on the initial salt concentration. For small initial concentration, a large flow rate is needed to clog up the porous space, but for such flow rates the velocity of the boiling front is small and the effect of front motion is negligible. Therefore the water flux is equal approximately to the vapour flux and the exact numerically-computed critical value practically coincides with our simple asymptotic estimate.

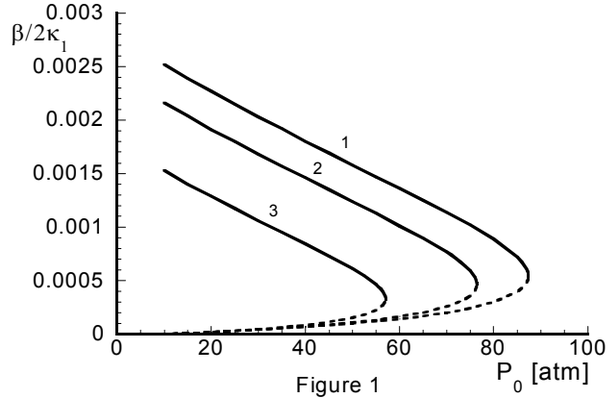


Figure 1

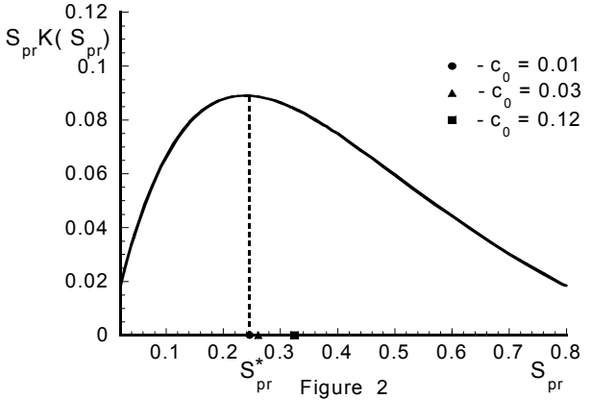


Figure 2

CONCLUSIONS

Our analysis has established that if there is some salt precipitation associated with the boiling of the liquid, there are typically two possible self-similar solution branches. These two branches coincide for a critical value of the liquid flux, and above this value, the self-similar solution ceases to exist. Instead, the rock becomes clogged with salt.

We are grateful for funding from the BPI which supported GT as a senior visiting fellow.

References

[1] Battistelli, A., Calore, C., Pruess K.: Analysis of salt effects on the depletion of fractured reservoir blocks. World Geothermal Congress, Florence, *Proceedings*, 1613-1618, 1995.

[2] Battistelli, A., Calore, C., Pruess K.: The simulator TOUGH2/EWASG for modelling geothermal reservoirs with brines and a noncondensible gas. *Geothermics*. **26**, 437-464, 1997.

[3] Phillips, O. M.: Flow and Reactions in Permeable Rocks. Cambridge University Press, 1991.

[4] Tsypkin, G.G., Woods A.W.: Vapour extraction from a water saturated geothermal reservoir. *J. Fluid Mech* 2004 (in press).

XXI ICTAM, 15–21 August 2004, Warsaw, Poland

BOUNDARY-LAYER ANALYSIS OF CHIMNEY STRUCTURES IN MUSHY LAYERS

Jacqueline Ashmore, M. Grae Worster
ITG, DAMTP, University of Cambridge, UK

Summary The presence of chimneys has a significant effect on the transport of heat and solute through a mushy layer. Coupled nonlinear partial differential equations govern the flow, pressure, temperature, solute concentration and solid fraction in the mushy layer. We use boundary-layer analysis to find a similarity solution and thereby determine predictions of chimney width as well as the fluid, heat and solute fluxes through it.

Background

During solidification of a multicomponent liquid, a morphological instability can occur that results in solid crystals of one component developing, forming a porous medium, with interstitial liquid that is rich in the other components. This is referred to as a mushy layer. When density differences due to concentration variations cause convection, the solid crystals of the porous matrix can be dissolved in the region where the fluid upwells. These cylindrical liquid-filled channels are called "chimneys." Mushy layers and chimneys occur in industrial processes when binary alloys are solidified, and in geophysical situations when saline water is frozen, for example (Worster, 1997).

Main assumptions

We consider a system in which the compositional buoyancy variations are destabilizing, and dominate over thermal buoyancy effects, which we neglect. Since the thermal diffusion coefficient is much larger than the solute diffusion coefficient, we neglect solute diffusion macroscopically. Also we assume that the mushy layer is in thermodynamic equilibrium so that the temperature and concentration are related by the liquidus condition, and we assume that the liquidus relationship can be approximated as being linear. Finally, we neglect changes of density on solidification.

Equations and boundary conditions

We consider the case that the solidifying system is moved at constant speed V through heat exchangers when a steady state has been attained with respect to the heat exchangers. Such conditions are representative of industrial casting processes, and are convenient for mathematical analysis. We denote pressure by p, the Darcy velocity in the moving frame by $\mathbf{u}$, the rescaled temperature by θ and the solid fraction by ϕ. $\Pi(\phi)$ represents the permeability of the mushy layer, and we define the direction of motion to be in the z-direction.

In the mushy layer, we assume that the temperature and solute concentration are related by the liquidus condition. Then the flow, pressure, temperature and solid fraction are determined by the following coupled nonlinear partial differential equations:

$$\begin{aligned} \mathbf{u} = -\mathcal{R}\Pi(\nabla p + \theta \mathbf{e}_z), \quad \text{with} \quad \nabla \cdot \mathbf{u} = 0 \\ \mathbf{u}\cdot\nabla\theta + \mathcal{S}\phi_z \quad = \quad \nabla^2\theta + \theta_z \\ \mathbf{u}\cdot\nabla\theta + (\phi\,\theta)_z \quad = \quad \theta_z + \mathcal{C}\phi_z. \end{aligned} \tag{1}$$

An important parameter in the problem we consider is the Rayleigh number $\mathcal{R} = \beta(C_0 - C_E)g\Pi_0/\nu V$, where $\beta = \rho^{-1}\partial\rho/\partial C$, C_0 is the far-field solute concentration, C_E is the solute concentration at the eutectic point, g is the acceleration due to gravity and ν is the kinematic viscosity. Two other parameters which also appear in the basic equations are the Stefan number $\mathcal{S} = \mathcal{L}/c\Delta T$, where $\mathcal{L}$ is the latent heat per unit mass, c is the specific heat and ΔT is the difference between the liquidus temperature far away and the eutectic temperature; and $\mathcal{C} = (C_S - C_0)/(C_0 - C_E)$, where C_S is the solute concentration in the solid phase, which quantifies how much solute is incorporated on solidification.

The boundary conditions on the chimney wall are found using a lubrication analysis of the flow in the chimney region, as performed by Chung and Worster (2002), plus the condition of marginal equilibrium formulated by Schulze and Worster (1998). We impose that the solution far away from the chimney (i.e. at large x) must decay to a specified far-field temperature distribution of the form cz^b, where c and b are specified positive constants. Another important parameter that enters the boundary conditions is the Darcy number $\mathcal{D} = \Pi_0 V^2/\kappa^2$, where Π_0 represents a typical permeability and κ is the thermal diffusion coefficient.

Solutions

We consider a two-dimensional flow and use the streamfunction formulation. In numerical simulations (Schulze and Worster, 1998) it has been observed that a thermal boundary layer structure develops around the chimney. We focus on this region of the flow. A scaling analysis shows that the mushy layer depth scales as $\mathcal{R}^{-1/3}$, the chimney width scales as $\mathcal{D}^{1/3}/\mathcal{R}^{2/9}$ and the thermal boundary layer width scales as $\mathcal{R}^{-2/3}$ (Schulze and Worster, 1988). We assume that $\mathcal{D}^{1/3}\mathcal{R}^{4/9} \ll 1$ so that the chimney width is small compared to the boundary layer width, and find a solution that is valid in the asymptotic limit that $\mathcal{R} \gg 1$.

Neglecting variations in the permeability and using a lubrication approximation to equations (1), we find similarity solu-

tions in the variables x and z for the streamfunction, the temperature and the solid fraction, that are valid in the thermal boundary layer. The equation that governs the function of the similarity variable is a third order nonlinear differential equation, which is solved by a numerical shooting method. The horizontal velocity $u(x,z)$ varies as $z^{-\frac{1}{2}(1-b)}U(\eta)$, the vertical velocity $w(x,z)$ varies as $z^b W(\eta)$ and the temperature field $\theta(x,z)$ varies as $z^b\Theta(\eta)$, where the similarity variable $\eta = x/z^{\frac{1}{2}(1-\beta)}$ and the functions W and Θ are plotted in Figure 1.

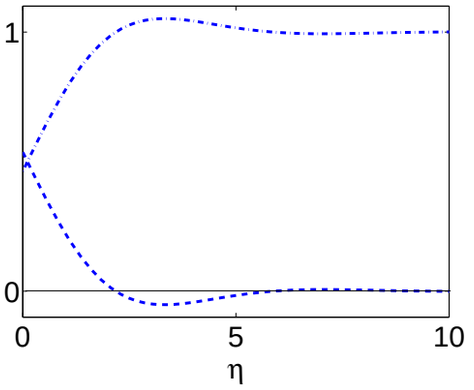


Figure 1. The vertical velocity function $W(\eta)$ (dash line) and temperature function $\Theta(\eta)$ (dash-dot line) as a function of $\eta = x/z^{\frac{1}{2}(1-\beta)}$, for $b = 1$ and $c = 1$.

We also determine numerical results for the fluid flux, the heat and solute flux through the chimney, and the chimney width. The rescaled chimney width varies as $z^{\frac{1}{6}(1-b)}$; the mass flux varies as $z^{\frac{1}{2}(1+b)}$; and the heat flux varies as z^b. Some results for the prefactors, which depend on the far-field boundary condition, are shown in Figure 2. This theoretical study follows from and complements previous numerical studies of chimneys (e.g. Schulze and Worster, 1998; Chung and Worster, 2002). It is also related to studies of the temperature field near a heated plate submerged in a saturated porous medium (e.g. Johnson and Cheng, 1978).

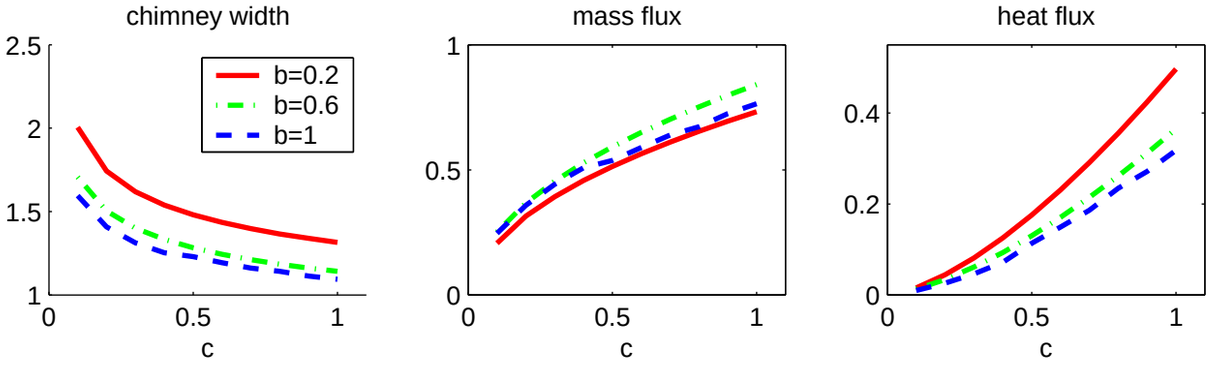


Figure 2. Numerical results for rescaled chimney width, mass flux and heat flux through the chimney. The far-field temperature boundary condition is cz^b.

Conclusions

Our study provides a theoretical prediction of a steady-state chimney. Although the analysis does not incorporate the finite depth of the mushy layer, since it is based on a boundary layer analysis, a suitably truncated solution may be expected to provide a reasonable prediction of experimental results. In addition, the analytical results for a steady-state isolated chimney may be a useful foundation for studies of the dynamics of multiple chimneys.

References

[1] Chung C.A. and Worster M.G., "Steady-state chimneys in a mushy layer," *J. Fluid Mech.* **455**, 387–411 (2002).
[2] Johnson C.H. and Cheng P., "Possible similarity solutions for free convection boundary layers adjacent to flat plates in porous media," *Int. J. Heat Mass Transfer* **21**, 709–718 (1978).
[3] Schulze T.P. and Worster M.G., "A numerical investigation of steady convection in mushy layers during the directional solidification of binary alloys," *J. Fluid Mech.* **356**, 199–220 (1998).
[4] Worster M.G., "Convection in mushy layers," *Ann. Rev. Fluid Mech.* **29**, 91–122 (1997).

XXI ICTAM, 15-21 August 2004, Warsaw, Poland

TRAVELLING MAGNETIC FIELD INFLUENCE ON CRYSTAL GROWTH BY BRIDGMAN METHOD

Irina S. Fayzrakhmanova, Tatyana P. Lyubimova,
ICMM UB RAS, Institute of Continuous Media Mechanics, Korolev str. 1, 614013, Perm, Russia

Summary The paper presents the results of fully unsteady numerical simulation of travelling magnetic field (TMF) influence on semiconductor crystal growth by vertical Bridgman method. We obtained the fields of stream function, temperature, dopant distribution in melt and in grown crystal with and without TMF, and analysed the influence of TMF on crystal growth.

PROBLEM FORMULATION

The usage of magnetic fields is known to be an efficient way to control the flows of electrically conductive fluids and therefore allowing to control heat and mass transfer in the melt and, in turn, in the resulting crystal. Bridgman method is employed both under microgravity conditions and at the Earth. In the present paper we consider the growth under terrestrial conditions.

The following model is used in the numerical simulations. A cylindrical domain is filled with two phases of a semiconductor: the melt is on top, the crystal is at the bottom. The solid-liquid interface is curved and is subjected to determination along the simulation process. The position and shape of interface are determined from the temperature distribution in both melt and crystal.

Both the experimental observation and numerical simulation indicate that the Bridgman growth is greatly influenced by buoyancy-induced convection. The application of magnetic field during the growth gives an instrument for the convective flow control.

Governing equations and boundary conditions

The melt is assumed to be Newtonian and isothermally incompressible; hence it is possible to use time-dependent Navier-Stokes equations in the Boussinesq approximation. We use the following boundary conditions. On the lateral wall of ampoule the Biot law is imposed. The top and lateral wall of the domain, and the interface are impermeable for the liquid as well as for the dopant; the no-slip boundary conditions are applied there as well. The position and shape of interface are determined front velocity from the temperature balance condition on the crystal/melt interface. Latent heat and the difference in heat conductivities of phases are taken into account. For the detailed description of the model and method we refer to [1,2]. Application of TMF could significantly influence the flow structure. It can even establish meridional flow, directed opposite to the buoyancy convection, which seems attractive for crystal growth. The low frequency approximation is adopted for the calculation. In this approximation, induced magnetic field is neglected. The average Lorentz force for the non-zero motion of the medium contains terms linear in velocity. Theoretical basis for TMF application technique with substantiation of all approximation is described in details in [3]. The frequency of the applied voltage is 50 Hz. Other ampoule and material parameters are taken from [1,2].

ALGORITHM AND NUMERICAL PROCEDURE

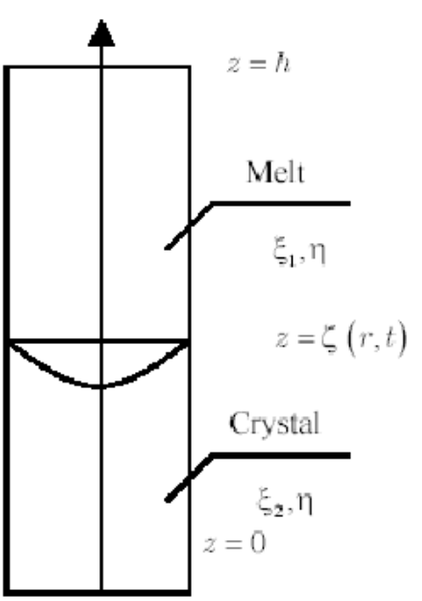
We solve the problem in 2-d approximation using stream function - vorticity formulation. However, the geometry of problem is still very complex due to the moving curved melt/crystal interface.

In this situation it is convenient to make coordinate transformation:

$\eta = r$, $\xi_2 = \frac{zf}{\zeta} z$, $\xi_1 = h + a(z - h)$;

where $a = \frac{zf - h}{\zeta - h}$, zf - front position.

Here r, z is physical curvilinear coordinate, ξ_1, ξ_2, η are computational rectangular orthogonal coordinates in computational domain with unmoving flat interface. Expressions for derivatives are not written here because of their complexity. The equations and boundary conditions were rewritten in new coordinates and solved by finite difference method.



Computational procedure:

1. Temperature & solid/liquid interface setup (go to 2).
2. Momentum equation for vorticity, Poisson equation for stream function, equation for solute concentration (go to 1), while characteristics will be settled.
3. Temperature & solid/liquid interface setup. Calculate new position of moving heater (go to 4).
4. Momentum equation for vorticity, Poisson equation for stream function, equation for concentration. Go to next time step while heater arrive at the top of ampoule. (go to 3)

NUMERICAL RESULTS

Numerical results obtained for GaAs growth under TMF at different intensity are presented in Figs.1-3. Fig.4 demonstrates longitudinal crystal slices. In our case TMF intensify upper vortex and weaken down vortex. From the figs it is shown that TMF flows leads to interface decreasing.

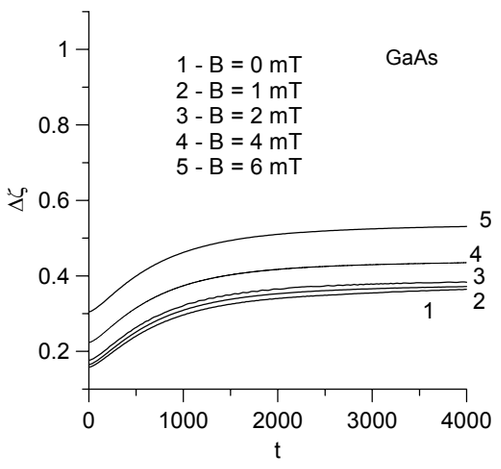


Fig.1. Effect of TMF on the temporal evolution of interface deflection GaAs

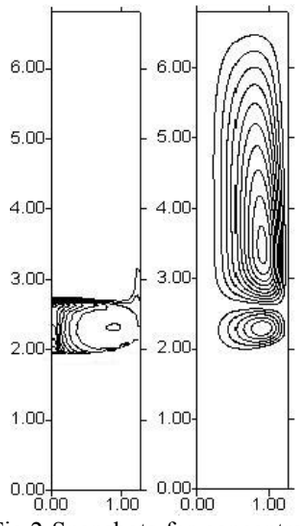


Fig.2 Snapshots for concentration and stream function was taken at t=800 s, B=0mT

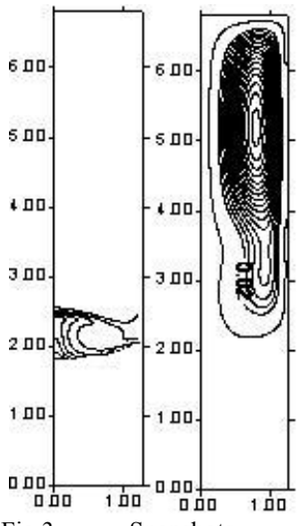
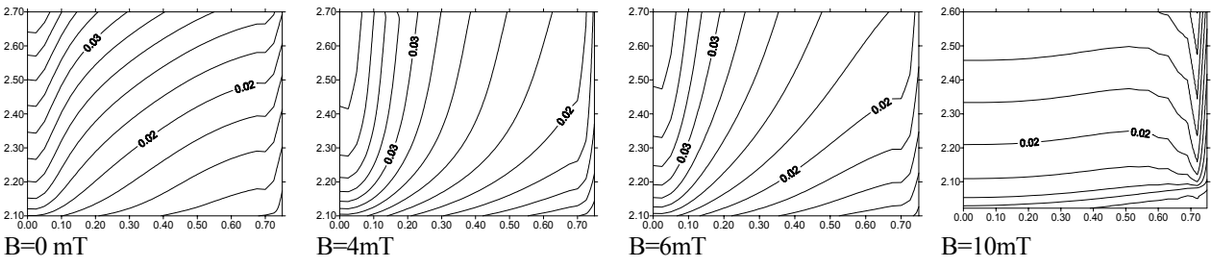


Fig.3. Snapshots for concentration and stream function was taken at t=800 s, B=4mT



B=0 mT B=4mT B=6mT B=10mT

Fig.4

CONCLUSION

We can resume that, in contrast to alternating axial magnetic field, TMF even of not very high intensity greatly influences the melt flow structure, and hence the dopant distribution in the resultant crystal. Under the influence axisymmetric traveling magnetic field intensity of buoyancy-induced flow increases and interface deflection decreases, which is favorable for crystal growth.

References

[1] Adornato P.M., Brown R.A.. J. Cryst.Growth 80 155-190, 1987.
[2] Lan C.W., Ting C.C. J. Cryst.Growth 149 175-186, 1995.
[3] Mazuruk K. Adv. Space Res. 29, 4, 541-548, 2002.

XXI ICTAM, 15–21 August 2004, Warsaw, Poland

A SEMI-SHARP PHASE FIELD METHOD FOR QUANTITATIVE PHASE CHANGE SIMULATIONS

Gustav Amberg
Department of Mechanics, KTH, S-100 44 Stockholm, Sweden

Summary The standard phase field model for simulation of phase change requires an asymptotic analysis in a vanishing interface width, in order to connect the model parameters to the sharp interface parameters, which has hampered the quantitative usefulness of the method. In this talk a modification of the method is presented, that allows the sharp and phase field parameters to be identified, in principle without restrictions on the model parameters.

INTRODUCTION

The phase-field method [1, 2, 3] has become very popular for simulations of the evolution of microstructures in solidification and other phase change problems, such as dendritic growth of crystals in an undercooled melt. The governing equations are derived from the thermodynamic potentials of the system, together with the assumption of a surface energy associated with a diffuse solid/liquid interface. It is thus possible to consider different physical situations with relative ease, such as grain boundaries, mixtures, etc. The phase is represented by introducing a scalar variable that has different constant values in the solid and liquid, and a steep transition between the two in the diffuse interface.

The problem with the method is that in its original form, the width of the diffuse interface must be prohibitively small for the results to match the proper interface kinetics, [4, 5], typically $W^* << d_0^*$, where W^* is the interface width, and $d_0^* = cT_m\gamma/L^2$ is the capillary length, which in typical cases can be in the order of nanometers (c is specific heat, T_m temperature of a flat interface at equilibrium, γ surface energy, and L latent heat). As a remedy to this, Karma and Rappel [6, 7], introduced the thin interface version of the method, whereby the asymptotic analysis of the phase field equations is taken to second order in interface width, allowing the kinetics to be identified under less stringent conditions [6, 7]. Also, in the thin interface limit the kinetic term can be eliminated from the undercooling, if that is desired. However, the seemingly modest extension of this analysis to nonhomogeneous properties, such as different diffusion coefficients in the solid and liquid, requires nontrivial modifications of the model equations, [8, 9].

In this talk the standard phase field method is simplified to the point that a relevant reduced problem can be solved analytically. Contact can thus be made between the phase field and the sharp interface descriptions, in principle without restrictions on the model parameters, other than the inevitable condition that the interface width is small compared to local radius of curvature.

MATHEMATICAL MODEL

For clarity we will describe the model for the simple situation of thermal solidification of a pure material with isotropic Gibbs-Thomson kinetics at the interface,

$$-\theta_i = \frac{V}{\mu} + \frac{d_0}{R} \tag{1}$$

Here V denotes the normal speed of the interface, μ the kinetic coefficient, R the local radius of curvature, and d_0 the capillary length. Here, and in the following, we have nondimensionalized temperature according to $\theta = c(T - T_m)/L$, lengths with an (arbitrary) reference length H, time with H^2/κ, where κ is the heat diffusivity.

As a starting point, the phase field model is written as

$$\tau\frac{\partial\phi}{\partial t} = W^2\nabla^2\phi - f'(\phi) - g'_\delta(\phi)\cdot h(\lambda\theta) \tag{2}$$

Here ϕ is the phase field variable which is $+1$ in the solid and -1 in the liquid. W denotes the interface width parameter, τ will be linked to the kinetic undercooling, and λ to the capillary length.

The conservation of heat takes the form:

$$\frac{\partial\theta}{\partial t} = \nabla^2\theta + \frac{\partial g_\delta(\phi)}{\partial t} \tag{3}$$

The function $f(\phi)$ should be a double well, with minima at $\phi = \pm 1$, $g_\delta(\phi)$ accounts for the change in internal energy on phase change and should increase from 0 to 1 as ϕ goes from -1 to $+1$. A standard choice is $f(\phi) = (1-\phi)^2(1+\phi)^2$ and $g_\delta(\phi) = 15/16(\phi^5/5 - 2\phi^3/3 + \phi) + 1/2$. We note that the two functions $f(\phi)$ and $g_\delta(\phi)$ are independent, and that there is a considerable degree of freedom in choosing these. Here we have also introduced a function $h(\lambda\theta)$ in the last term of equation (2), which in the standard model is $h(\lambda\theta) = \lambda\theta$.

We now introduce the following modifications:

i) The function $g_\delta(\phi)$ is chosen as a smoothed step function, $g_\delta(\phi) = (1 + \phi\sqrt{(1+\delta^2)/(\phi^2+\delta^2)})/2$, that jumps from 0 to 1 over an interval of width $\sim\delta$ at $\phi = 0$. The model we are interested in is then obtained in the limit $\delta = 0$.

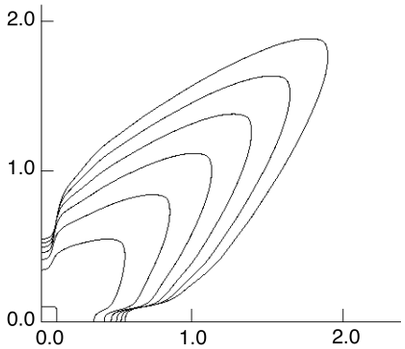


Figure 1. Sequence of interfaces for a developing needle crystal, $t = 0, 0.1, ..., 0.6$. The total size of the domain is 10 x 10.

ii) In order to evaluate the kinetics of the model exactly, we choose a simpler form of $f(\phi)$, i.e $f(\phi) = (\phi - 1)^2$ for $\phi > 0$, and $f(\phi) = (\phi + 1)^2$ for $\phi < 0$.
iii) With these choices of $f(\phi)$ and $g_\delta(\phi)$, an explicit function $h(\lambda\theta_i) = \frac{1}{2}\lambda\theta_i\sqrt{8 + (\lambda\theta_i)^2}$, will give linear Gibbs-Thomson kinetics, also for large values of $\lambda\theta$.
We will view the interface as being given by the contour generated by $\phi = 0$, i.e. the interface is 'sharp' in this sense. With the choices in i)-iii), a reduced problem can be formulated, see [10], assuming a profile of ϕ that is translating with a quasi-constant shape, in the presence of mild curvature, i.e. $R >> W$. This can be solved exactly to yield a relation between interface temperature, curvature and speed at the position where $\phi = 0$. By comparing with Gibbs-Thomson kinetics, eq (1), we can now identify the phase field and the sharp interface parameters as $\mu = W\lambda/\tau$, $d_0 = W/\lambda$.

SAMPLE COMPUTATION

To illustrate the practical use of the method, we simulated a typical case of solidification with an undercooling of 0.5, i.e. $\theta_\infty = -0.5$, and the sharp interface parameters $\mu = 117.5$ and $d_0 = 0.001191$. We also included anisotropy by letting the surface energy vary by a factor $(1 + \epsilon cos(4\beta))$, with β being the angle between an interface normal and the preferred growth direction. The value of the anisotropy parameter was $\epsilon = 0.04$. The phase field parameters λ and τ are determined from μ and d_0 and a desired width of the transition region, here $W = 0.02$, which gives $\lambda = 16.792$ and $\tau = 0.002858$. This case was deliberately chosen with a quite thick interface, i.e., λ considerably larger than unity. Figure 1 shows the interface obtained with $W = 0.02$ as it develops for times from 0 to 0.6. The shape evolves into a typical needle crystal, where the tip attains a nearly parabolic shape and a constant speed. A direct comparison of the temperature obtained at the interface and that predicted from equation (1) shows a very good agreement. This computation was made using adaptive finite elements implemented using our toolbox femLego [11]. In the talk additional examples and applications will be presented as time and results allow.

CONCLUSION

In summary, we have presented a few simple modifications of the standard phase field model that will allow the correct kinetics to be simulated with quite thick interfaces. The only restrictions are in terms of numerical resolution, and that radii of curvature should be larger than interface widths. The model presented retains its connection to the thermodynamic derivation of phase fields, giving hope that it can be applied to many different situations. The presented method can perhaps also be viewed as an intermediate between diffuse interface phase-field formulations and proper sharp interface or level set methods.

References

[1] R. Kobayashi, Bull. Jpn. Soc. Ind. Appl. Math. **1**, 22 (1991).
[2] O. Penrose and P. Fife, Physica D **43**, 44 (1990).
[3] S. H. Davis, *Theory of Solidification* (Cambridge University Press, 2001).
[4] G. Caginalp and J. Xie, Phys. Rev. A **48**, 1897 (1993).
[5] G. Caginalp and J. Jones, Ann. Phys. **237**, 66 (1995).
[6] A. Karma and W.-J. Rappel, Physical Review Letters **77**, 4050 (1996a).
[7] A. Karma and W.-J. Rappel, Physical Review E **53**, R3017 (1996b).
[8] A. Karma, Phys. Rev. Letters **87**, 115701 (2001).
[9] J. Ramirez and C. Beckermann, in *41st AIAA Aerospace Sciences Meeting, Reno, Nevada. Jan 6-9. 2003* (2003).
[10] G. Amberg, Physical Review Letters **91**, 265505 (2003).
[11] G. Amberg, R. Tönhardt, and C. Winkler, Mathematics and Computers in Simulation **49**, 149 (1999).

DIRECTIONAL SOLIDIFICATION OF PB-SN ALLOYS AFFECTED BY A ROTATING MAGNETIC FIELD

Sven Eckert[1], *Bernd Willers*[1], *Ulf Michel*[2], *Gustav Zouhar*[2], *Petr A. Nikrityuk*[3], *Kerstin Eckert*[3]
[1] *MHD Department, Forschungszentrum Rossendorf, 01314 Dresden, Germany*
[2] *Institute of Material Science, Technische Universität Dresden, 01062 Dresden, Germany*
[3] *Institute of Aerospace Engineering, Technische Universität Dresden, 01062 Dresden, Germany*

Summary An experimental and numerical study with respect to the influence of a rotating magnetic field (RMF) on the directional solidification of Pb85wt%Sn and Pb25wt%Sn alloys will be presented. The effect of the electromagnetically driven convection on solidification parameters such as the cooling rate, the temperature gradient G_L or the growth velocity of the liquidus isotherm V_T was investigated. Significant effects of the flow on the macro- and microstructure of the solidified ingots are evident.

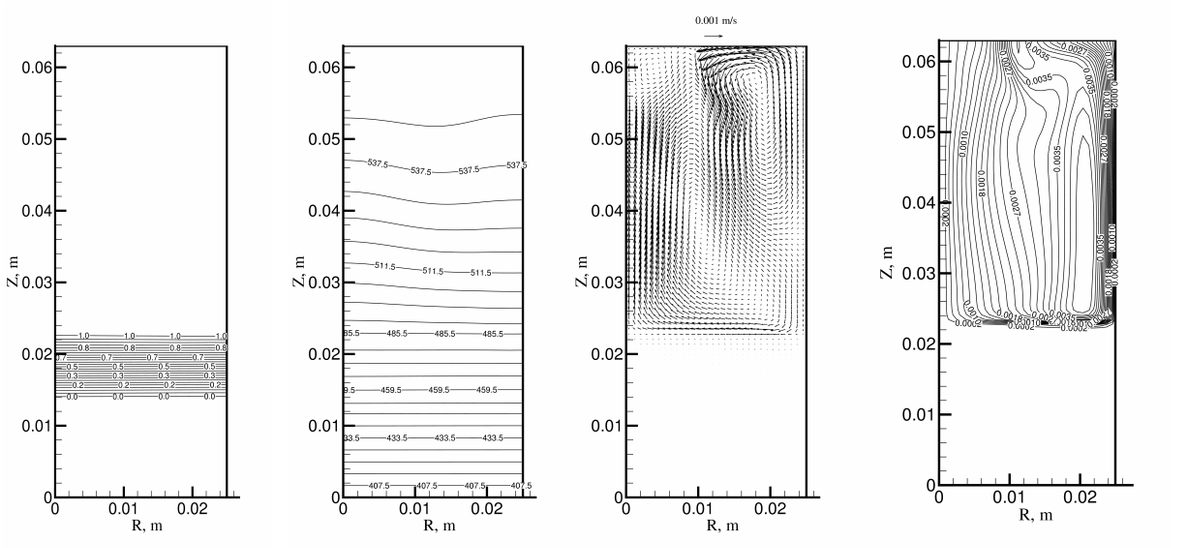
Introduction

Many references from the cast metal literature are known discussing the effect of melt convection during the early stages of solidification on the grain structure. The application of mechanical or electromagnetic stirring, ultrasonic or sonic vibrations promotes the formation of fine, equiaxed grains [1,2]. However, there has been much speculation about the mechanism of this process. The prevalent interpretation favoured during the last decades is that the grain refinement results from a fragmentation of primary dendrites. The macrostructure of chill cast ingots generally consists of a columnar and an equiaxed zone. The occurrence and position of the transition between both zones was found to be influenced by casting parameters, including the temperature gradient, the cooling rate or the probe composition, respectively [3, 4]. Fluid flow occurring in the liquid phase was also found to affect the structure and position of CET [5]. Therefore, we studied the dependence of the CET on the Taylor number

$$Ta = \frac{s w B^2 R^4}{2 r n^2} \qquad (1)$$

of the applied RMF with the field intensity B and the frequency $f=w/2p$ for a fluid container with radius R where σ, ρ and ν denote the electrical conductivity, the density and the kinematic viscosity of the fluid. The application of time varying magnetic fields can be considered as an effective tool to organize a well-defined flow structure in the liquid phase affecting the nucleation and solidification parameters. Main goal of our activities is to find a strategy for refining the microstructure of castings by an optimal combination of magnetic field intensity, field frequency and cooling rate.

Numerical calculations



(a) (b) (c) (d)

Figure 1. Predicted solidification behavior at t=60 sec for Taylor number $5.8 \cdot 10^4$. (a) volume fraction of liquid, (b) temperature field, (c) the meridional velocity field and (d) contour plot of the azimuthal velocity

A continuum formulation based model [6] has been adopted to study the solidification of binary alloys using the following assumptions: all transport properties of each phase, such as thermal and electrical conductivity or viscosity, are constant; the density of the solid phase equals the density of the liquid phase; the phases are in local thermodynamic equilibrium; buoyancy effects are negligible; the velocity of solid phase is zero. The Lorentz force term F_L has been included into the momentum conservation equation in order to take into account the effect of the applied magnetic field.

The predicted and measured temperature curves are in good agreement. *Figure 1* presents the spatial distributions of the volume fraction of liquid, the temperature and the velocity field 60 sec after the start of the solidification at the bottom of the container. It can be seen that fluid motion caused by the RMF at such small Taylor number has no influence on the shape of the mushy zone front due to the high cooling rate. The arising secondary flow in the radial-meridional plane was found to have a significant influence on the mass and heat transfer at the solidification front. Time-dependent calculations revealed that this secondary flow structure is strongly influenced by the advancement of the solidification front. The resulting permanent change of the aspect ratio of the fluid volume prevents the development of the double-vortex structure being well known for the isothermal case. These findings were confirmed by fluid velocity measurements during solidification.

Experimental results

The Pb-Sn alloys were solidified directionally from the bottom in a cylindrical stainless steel mold having an internal diameter of 50 mm, a height of 100 mm and a wall thickness of 3 mm. The side walls were covered by a 5 mm heat insulation to prevent a radial heat transfer from the mold. The filling height for each charge was 60 mm. During solidification continuous temperature measurements were performed by means of a set of six thermocouples installed in the center of the mold at vertical positions of 1.5, 11.5, 22, 32, 41.5 and 51.5 mm measured from the base of the ingot. The ultrasound Doppler velocimetry (UDV) was used to measure the velocity inside the liquid phase as well as the position of the solidification front. Selected transverse and longitudinal sections of the solidified specimens were polished and etched for microscopic examination.

The RMF drives a convection in the bulk liquid showing a distinct influence on the solidification parameters and the properties of the microstructure of the ingots. The fluid flow increases the heat transfer rate and decreases the temperature gradients in the melt. Such small temperature gradients reduce the probability of remelting of solid fragments ahead of the solidification front required for the promotion of the CET. Moreover, the temperature measurements also revealed the occurrence of strong temperature fluctuations arising from the turbulent flow in the vicinity of the solidification front. These fluctuations may promote a localized remelting of dendrites and thus the creation of solid fragments. Velocity measurements have been obtained in the melt during solidification with applied RMF by means of UDV. If the temperature falls below the liquidus isotherm, a strong decrease of the velocity amplitude was observed indicating a rapid increase of the fluid viscosity due to an increase of the solid fraction. The position where the velocity becomes zero can be approximately identified with the position of the solidification front as long as a columnar front grows.

If the ingot is solidified under the influence of forced bulk flow induced by RMF a CET can be observed. As shown in *Figure 2* the CET position is affected by the convection. An enhancement of the magnetic Taylor number *Ta* results in a reduction of the length of the columnar region. The distribution of the eutectic in the microstructure is not homogeneous. In the equiaxed domain an up to 10% higher eutectic content is observed as compared to the columnar region. The highest concentration of eutectic is found directly at the CET position (*Figure 3*).

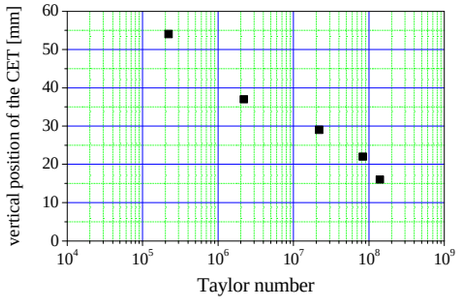


Figure 2. Position of the CET as function of the magnetic Taylor number *Ta*

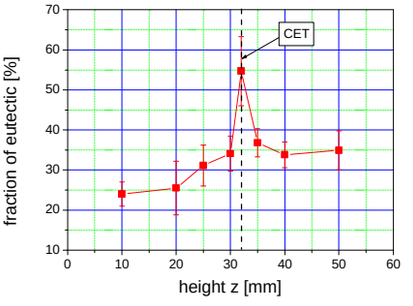


Figure 3. Volume fraction of the eutectic along the axis of the ingot for $Ta = 8 \cdot 10^6$

References

[1] D.B. Spencer, R. Mehrabian, M.C. Flemings: Rheological Behaviour of Sn-15 Pct Pb in the Crystallization Range. *Met. Trans.* **3**: 1925-1932, 1972

[2] W.C. Johnston, G.R. Kofler, S. O'Hara, H.V. Ashcom, W.A. Tiller: Grain Refinement via Electromagnetic Stirring During Solidification. *Trans. Met. Soc. AIME* **233**: 1856-1860, 1965

[3] R.B. Mahapatra, F. Weinberg: The Columnar to Equiaxed Transition in Tin-Lead Alloys. *Metall. Trans.* **18B**: 425-432, 1987

[4] A.E. Ares, C.E. Schvezov: Solidification parameters during the Columnar-to-Equiaxed Transition in Lead-Tin Alloys, Metall. *Mat. Trans.* **31A:** 1611-1625, 2000

[5] W.D. Griffiths, D.G. McCartney: The effect of electromagnetic stirring during solidification on the structure of Al-Si alloys. *Mat. Sci. Techn.* **A216**: 47-60, 1996

[6] W.D. Bennon and F.P. Incropera: A continuum model for momentum, heat and species transport in binary solid-liquid phase change systems I: Model formulation. *Int. J. Heat and Mass Transfer* **30**: 2161-2170, 1987

CELL SHAPES IN DIRECTIONAL SOLIDIFICATION : A GLOBAL STUDY

Marc Georgelin, Alain Pocheau
IRPHE,Université Aix-Marseille I, 49 rue Joliot-Curie, BP 146, F-13384 Marseille cedex13 France

Summary We experimentally characterize the *whole* shape of growth cells in directional solidification, from their tip to their grooves, and in a large *domain* of control parameter. For this a library of cell shapes is determined and fitted to a class of definite shape functions. This first global characterization of cell geometry in both the real space and the control parameter space provides a firm ground for testing or improving theories or simulations of directional growth in the cellular to near dendritic regime.

INTRODUCTION

Far from eutectic composition, nearly pure alloys solidifying in a thermal gradient undergo, above a critical pulling velocity, a morphological instability which makes a planar front restabilize onto a non-linear growth solution: a cellular array (Fig.1). The shape of these cells is important in many different issues. It first monitors micro-segregation with important consequences on the resulting properties of the solid material. It also conditions the subsequent instabilities that may develop on each cell (sidebranching, tip-splitting) or on the cell array (2λ-O modes, cell elimination) [1,2]. It finally stands as a relevant test of models or simulations and thus, as a valuable challenge for improving our understanding of directional growth or our ability in adressing more complex regimes.

However, despite long-standing efforts, only a partial understanding or determination of cell shapes have been achieved. For instance, although different models have been developed for treating cell tips or cell grooves [1,3], one still lacks a global model capable of handling the *whole* cell shape. Also, on the experimental side, attention has been devoted to the characterization of the local geometry at cell tip or of the asymptotic features in cell grooves [1], but no global observation or treatment of the cell geometry taken as a *whole* has been achieved to date.

The present study is devoted to determine the global shape of cells displayed in the directional solidification of an alloy and to characterize its evolution with the control parameters. For this, we experimentally scan a large range of thermal gradient G, pulling velocity V and cell spacing L. We then characterize the geometry of this family of cell shapes by fitting each of them to a class of non-linear functions. This class is chosen so that its parameters are geometrically meaningful and display coherent variations with the control parameters (L,V,G). We thus obtain the first global characterization of cell shape both in the real space and in the control parameter space. This provides a firm ground for testing or improving models or simulations of directional growth in the cellular regime.

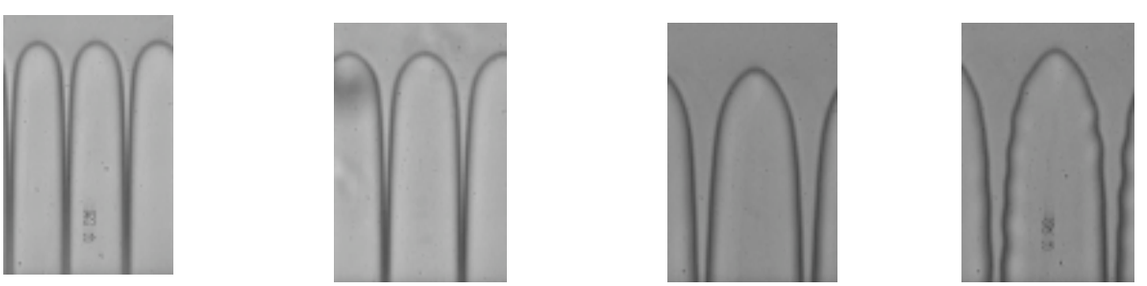


Fig 1 : Snapshots of cell shapes in the cellular or near dendritic regime. The width of each picture is about 180 μm.

EXPERIMENTAL CONFIGURATION AND RESULTS

The experiment is driven in thin samples so as to avoid buoyancy effects. The solidified material is an impure transparent plastic crystal (succinonitrile) which behavior may be considered similar to that of a dilute metal alloy. The experimental range extends from the cellular to the near-dendritic regime of solidification. Control parameters are the thermal gradient G ($50<G<140$ K/cm), the pulling velocity V ($8<V<24$ μm/s) and the local cell spacing L ($50<L<200$ μm). Due to an hysteretic behavior of the system, L has been proven to be a real independent control parameter that could be monitored experimentally [4]. Observations are made by using a microscope with a large frontal distance and the experimental pictures are treated by image processing.

The choice of the family of fitting functions has been guided by the following requirements: i) the fit parameters must be geometrically significant, ii) their number is restricted to the minimum in order that their variation from shape to shape be relevant, iii) the geometry near the cell tips must be parabolic., iv) the shape must involve asymptots in the grooves. This led us to chose a family of fitting functions involving two free parameters only, each being physically

relevant to the description of either the tip region or the grooves. Taking the z-coordinate parallel to thermal gradient and pointing towards the liquid zone, and the second coordinate x in the sample plane, the generating function of the chosen family may be written : $\underline{z} = - b/(2a)\ \mathrm{atanh}(\underline{x}^2)$, where atanh is the inverse hyperbolic tangent and where z and x have been rendered non dimensional : $\underline{z} = z/b$ and $\underline{x} = x/b$. Parameter a corresponds physically to the tip curvature radius ρ, whereas 2b stands for the effective cell width at the bottom of the cell image. Each shape of the cell library could be finely fitted this way as a *whole*, i.e. from the tip to the grooves. Evolution of their geometry is displayed in figure 2, together with the variation of tip-undercooling, i.e. of tip position, with the control parameters.

Interestingly, it is found that the parameters a and b vary very smoothly with the control parameters (L,V,G) with no discontinuity or slope breaking, even at the onset of sidebranching. This makes the fit parameters (a,b) easily linked to the control parameters by power laws : $a = 0.097\ L^{3/4}V^{-1/4}G^{1/2}$ and $b = 0.43\ L$, where the units of a, b and L are μm and where V and G are expressed in μm/s and in K/cm.

The absence of shape transition at the occurrence of sidebranching confirms that sidebranching does not refer to a change of branch of solution [4]. The variation of parameter a with cell spacing ($a \approx L^{3/4}$) deviates from the pure geometrical similarity expected at zero Péclet number. Its variation with velocity ($a \approx V^{-1/4}$) also significantly differs from the well-known relationship $\rho^2 V$ = constant that is well documented in free growth [6] and which is actually expected in directional growth at infinite Péclet number.

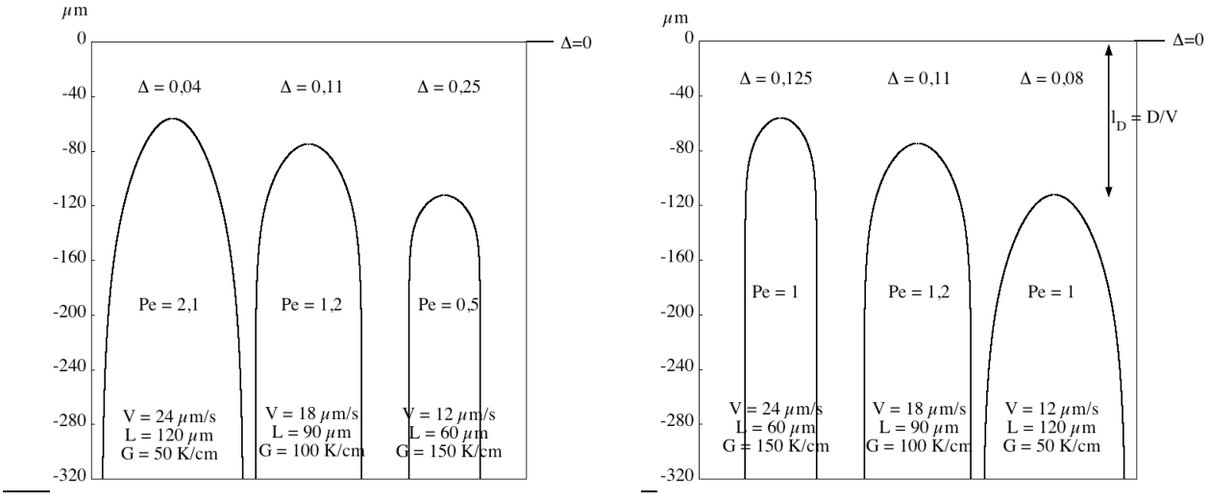


Fig 2 : Examples of cell geometries ranging from large sharp shapes to thin rounded shapes. Lines correspond to the shapes recovered by the fitted function with adequate parameters. The position of cell tips have been set so as to correspond to the undercooling relationship determined in [5], The Péclet number and the solutal diffusivity are denoted Pe=LV/D and D respectively.

CONCLUSION

We have achieved the first characterization of the *whole* geometry of cells in directional solidification both in the real space and in the control parameter space. This determination would worth be recovered by simulation or theories, not only on a given cell, but also on the whole cell library, so as to improve our understanding of directional growth. In addition, applying theoretical or numerical stability analysis to these cell profiles would help us better clarify cell stability, in particular regarding sidebranching.

References

[1] Billia B., Trivedi R.: Handbook of Crystal Growth **1** Chapter 14, Elsevier Science Publishers, 1993

[2] Kopczynski P., Rappel W.-J., Karma A.: Critical Role of Crystalline Anisotropy in the Stability of Cellular Array Structures in Directional Solidification. *Phys. Rev. Lett.* **77**:3387-3390 , 1996.

[3] Pelcé P. , Pumir A. : Cell shape in directional solidifcation in the small Péclet number limit. *J.Cryst.Growth* **73**: 337-442, 1985.

[4] Georgelin M., Pocheau A.: Onset of sidebranching in directional solidification. *Phys Rev. E* **57**:3189-3203, 1998.

[5] Pocheau A., Georgelin M.: Cell tip undercooling in directional solidifcation. *J. Cryst. Growth* **206**:215-229, 1999.

[6] Huang S.C., Glicksman M.E.: Fundamentals of dendritic solidifcation. *Acta metall* **35**:701-734,1981.

Convection driven by tidal heating: numerical model and parameterized theory

Leszek Czechowski
Institute of Geophysics
ul. Pasteura 7
02-093 Warszawa, POLAND
email: lczech@fuw.edu.pl

1. Introduction

The role of solid state convection in the planet's interior is recognized for the Earth. The convection in the Earth's mantle is a driving force of tectonic and volcanic processes described by the plate tectonics theory (e.g. Czechowski, 1993a). There is no plate tectonics in the same form on the other planets and satellites but large-scale tectonic structures on other planetary bodies are probably a result of thermal convection in the bodies' interior (e.g. Schubert et al., 2001; McKinnon, 1998).

Thermal convection requires a source of heat. The main source of heat in the terrestrial planets is a decay of long-time living radioactive elements (U, Th and radioactive isotope of K). However, the radiogenic heating is not intensive enough to give rise convection in small bodies like medium size icy satellites (MIS) of giant planets. This group of bodies have radii in the range form 200km (Mimas, satellite of Saturn) to 780 km (Titania, satellite of Uranus). Czechowski and Leliwa-Kopystynski (2003) have found a strong correlation of the value of tidal parameters with the existence of large-scale tectonic structures on MIS. There are also others observational as well as theoretical indications that the tidal heating is the only possible source of heating that could lead to solid state convection in the interiors of MIS.

2. Numerical model and its basic results

To investigate the problem author developed 3D numerical model of convection driven by both: uniform radiogenic heating and non-uniform and non-spherically-symmetric tidal heating. The numerical model is based on the following system of equations: Navier-Stokes equation, equation of thermal conductivity, equation of continuity and equation of state. The Oberbeck-Boussinesq approximation of the equations is used (e.g. Czechowski, 1993 b), i.e. fluid is assumed to be incompressible and all parameters of the fluid (i.e. density, coefficient of thermal expansion, specific heat and thermal conductivity) are assumed to be constant with the exception of density in the gravity force term in the Navier-Stokes equation. For more details of the model see: Czechowski and Leliwa-Kopystyński, 2003) .

Rate of heat generation is the sum of two terms representing two different physical phenomena responsible for the heating: decay of radioactive elements and tidal deformations. The radiogenic heating is assumed to be constant. The tidal heating is not uniform and depends on the position inside the satellite. The distribution of tidal heat generation is calculated using numerical model developed by L. Czechowski. The model is based on the methods presented by Kaula (1963), Peale and Cassen (1978) and Poirier et al. (1983). Tensor of tidal deformations in a satellite is expressed by truncated series of spherical functions. The rheology of the satellite interior is assumed to be of Kelvin-Voigt type and the eccentricity of the orbit is included as the only source of deformations. The adopted approximation makes possible to scale the distribution of the tidal heating. It means that the same distribution after multiplying by a constant coefficient could be used for different values of eccentricity.

Steady state solutions of the convective flow are obtained using the numerical model for low and moderate Rayleigh number ($0<Ra<500\ 000$). The results indicate that convection patterns specific for the tidal heating are strongly oriented in respect to the near and the far sides of the satellite. The pattern of convection consists usually of 2 cells, but for some cases 1 cell pattern is also observed (for more details of the results see: Czechowski and Leliwa-Kopystyński, 2003) .

3. Function Nu(Ra)

The Rayleigh number is the main parameter that could serve as a measure of intensity of convection. The role of convection for heat transfer is determined by Nusselt number Nu. For considered here problem of steady state convection in volumetrically heated body, the Nusselt number could be defined as: $Nu=DTcond/DTconv$ where DTcond is the average temperature difference in the body without convection (the surface temperature is chosen to be a reference temperature) and DTconv is the average temperature difference in the body with convection. If convection is absent then thermal regime is determined by conduction only and Nusselt number is equal to 1. If convection operates in the body, the heat transfer is more efficient comparing to the heat transfer without convection, DTconv is lower than DTcond and consequently the values of Nu greater than 1 are characteristic for convection. Generally the Nusselt number is an increasing function of the Rayleigh number

but scrutiny of the function Nu(Ra) indicates also some exceptions from the above rule, especially close to bifurcations.

The function Nu(Ra) is usually approximated with some kind of the power function. For considered here case the situation is a little more complicated because the critical value of the Rayleigh number is zero, but power function is still useful with some modifications. Eventually the following approximation is chosen: Nu(Ra)=(Ra-A)^M where A and M are determined by fitting data obtained from the numerical model. Both values: A and M depend on ratio of tidal to radiogenic heating.

4. Parameterized theory

Parameterized theory of convection is used successfully for convection driven by radiogenic heating. The basic assumptions of this method is presented in many papers: e.g. Schubert et al. 2001. Some modification of the theory is necessary for convection driven by tidal heating. In the present research the parameterized theory is based on the following system of equations: function Nu(Ra) (see discussion above), viscosity of water ice as a function of temperature (taken from McKinnon, 1998), efficiency of tidal heating (according to the results of Poirier et al. 1983), thermal conductivity and specific heat of ice as a function of temperature (both taken from Leliwa-Kopystyński and Kossacki, 2000). The main unknown of the system is average temperature of the body's interior.

5. Discussion

The main result of the presented parameterized theory is determining the existence of a few steady state solutions for convection with significantly different energies. Each of the satellites has a low temperature solution that corresponds to low tidal heating and slow convective flow. A given satellite could be in any state, but beside Enceladus all other Saturnian medium sized icy satellites seem to be in the low energy state.

The answer why Enceladus is in the high energy state is beyond the scope of the present paper. Large impact in the past could be a source of additional energy. This energy could increased the temperature and consequently the efficiency of tidal heating. The absence of signs of such catastrophic event makes this hypotheses doubtful. Therefore the author prefers rather that the present state of Enceladus is an effect of specific evolution of the satellite's orbit.

6. Conclusions

1. The parameterized theory indicates the existence of a few steady states of convection with significantly different energies for some satellites.
2. Enceladus is in high energy state. All other medium sized Saturnian icy satellites seem to be in the basic, low energy state.
3. The average rate of tidal heat production for basic state is comparable to the radiogenic rate for a low energy state. For a high energy state the rate of tidal heating is 10 to 100 higher than radiogenic heating.
4. The Rayleigh number is so sensitive function of parameters that its reliable estimation cannot be achieved by the parameterized theory. Theory could be used for determining some less sensitive rheological parameters.

7. References

Czechowski, L.: 1993a, 'Plate Tectonics', In: R. Teisseyre, L. Czechowski and J. Leliwa-Kopystyński (eds), *Dynamics of The Earth's Evolution*,. Elsevier, Amsterdam, pp. 1-50.

Czechowski, L.: 1993b, 'Theoretical Approach to Mantle Convection', In R. Teisseyre, L. Czechowski and J. Leliwa-Kopystyński (eds), *Dynamics of The Earth's Evolution*, Elsevier, Amsterdam, pp. 161-271.

Czechowski, L. and Leliwa-Kopystyński, J.: 2003, 'Tidal heating and convection in medium sized icy satellites'. Celestial Mechanics and Dynamical Astronomy, **87**, 157-169.

Kaula W. M.: 1963, 'Tidal dissipation in the Moon', *J. Geophys. Res.*, **68,** 4959-4966.

Leliwa-Kopystyński, J. and Kossacki, K. J.; 2000, 'Evolution of porosity in small icy bodies'. *Planet. Space Sci.*, **48,** 727-745.

McKinnon, W.B., Geodynamics of Icy Satellites, in *Solar System Ices*, eds. B. Schmitt et al., 525-550, Kluwer Academic Publishers, 1998.

Peale S. J. and Cassen, P.: 1978, 'Contribution of tidal dissipation to Lunar thermal history', *Icarus,* **36,** 245-269.

Poirier, J. P., Bloch, L. and Chambon, P.: 1983. 'Tidal dissipation in small viscoelastic ice moons: the case of Enceladus'. *Icarus,* **55,** 218-230.

Schubert, G., Spohn, T. and Reynolds, R. T.: 1986, 'Thermal histories, compositions and internal structures of the moons of the solar system', In: J. A. Burns and M. S. Matthews, (eds), *Satellites*, The University of Arizona Press, Tucson, pp. 224-292.

Schubert, G., Turcotte D.L., and Olson P. , 2001, Mantle convection in the Earth and Planets, Cambridge Univ. Press, Cambridge, UK, pp 940.

Ternary Alloy Convection in Mushy Layers: Extended Summary

D.M. Anderson
Department of Mathematical Sciences
George Mason University
Fairfax, VA 22030, USA

T.P. Schulze
Department of Mathematics
University of Tennessee
Knoxville, TN 37996, USA

January 9, 2004

Much has been learned over the past several decades on convection and solidification in binary alloy mushy layers (for reviews see Worster[1, 2]). However, many industrial applications and geological processes involve multicomponent alloys. We are motivated by this and the success of the binary alloy models to extend the modeling efforts to ternary alloy systems.

The presence of multiple chemical species complicates even the equilibrium characterization of the known material phases. The complexities of the thermochemistry for common industrial multi-component superalloys leaves little room for mathematical analyses of these systems. Typically, one must resort almost immediately to numerical solution of the models to make headway. Recently, however, a window of opportunity has been identified by Aitta *et al.*[3, 4] who performed an experimental investigation on the solidification of the aqueous solution of potassium nitrate ($KN0_3$) and sodium nitrate ($NaN0_3$). This ternary alloy system has a relatively simple equilibrium thermochemistry, at least in comparison to its metallurgical counterparts, that is characterized well enough to merit theoretical investigation. In particular, it was found that a ternary eutectic phase diagram with complete solid immiscibility was suitable to describe the phases formed during solidification. Their experimental system has proved not only feasible for mathematical investigation but also of great scientific interest, as a number of interesting phenomena have been identified and are as yet not completely understood.

In the experiments of Aitta *et al.*, H_2O–$KN0_3$–$NaN0_3$ was solidified from below by a cold, planar boundary at $z = 0$. The operating state was in a diffusion-controlled regime; convection, including that due to thermal and solutal buoyancy, was absent. Their experiments showed the formation of two distinguishable mushy layers between a

liquid layer above and a ternary eutectic solid layer below. Due to the complexities of the double mushy layer geometry, this system has convecting regimes about which very little is known.

We describe here recent work on a diffusion-controlled model of the solidification of ternary alloys in mushy layers[5]. In particular, we identify one-dimensional similarity solutions describing the temperature and composition profiles through the layers, as well as the solid fraction profiles through the mushy layers for non-convecting scenarios. Detailed investigations of how the growth characteristics, such as the layer thicknesses, depend on the system control parameters are given. These results compare well with the experimental work of Aitta *et al.*

The double mushy layer geometry in the ternary alloy system gives rise to convective scenarios that are not present during binary alloy solidification. As described by Aitta *et al.*[4] and Anderson[5] the ternary system can develop two mushy layers in which compositional convection occurs in (i) neither mushy layer, (ii) the primary layer only, (iii) the secondary layer only, or (iv) both layers. These guidelines offer clues to the likely convection in the ternary system but they do not address how convection in one layer may influence that in another layer. We investigate these issues in more detail by identifying convecting solutions in the double mushy layer geometry and analyzing their stability properties.

References

[1] Worster, M.G. 1997 Convection in mushy layers. *Ann. Rev. Fluid Mech.* **29** 91–122.

[2] Worster, M.G. 2000 Solidification of Fluids. In *Perspectives in Fluid Dynamics*, (ed. G.K. Batchelor, H.K. Moffatt & M.G. Worster) pp. 393–446. Cambridge University Press.

[3] Aitta, A., Huppert, H.E. & Worster, M.G. 2001a Diffusion-controlled solidification of a ternary melt from a cooled boundary. *J. Fluid Mech.* **432**, 201–217.

[4] Aitta, A., Huppert, H.E. & Worster, M.G. 2001b Solidification in ternary systems. In *Interactive Dynamics of Convection and Solidification*, (ed. P. Ehrhard, D.S. Riley and P.H. Steen) pp. 113–122. Kluwer.

[5] Anderson, D.M. 2003 A model for diffusion-controlled solidification of ternary alloys in mushy layers. *J. Fluid Mech.* **483** 165–197.

CONVECTIVE INSTABILITIES DURING SOLIDIFICATION OF A MUSHY LAYER

In G. Hwang*, Chang K. Choi**
*Department of Chemical Engineering, The University of Suwon, Suwon 440-600, Korea
**School of Chemical Engineering, Seoul National University, Seoul 151-742, Korea

Summary The convective instabilities of binary alloys solidified from a bottom boundary are analyzed under linear stability theory. By using a similarity variable, the time-dependent disturbance equations for the liquid and mushy layers are transformed to the self-similar stability equations. The critical conditions at the onset of convection in the mushy layer are found numerically for the solidification of aqueous ammonium chloride solution.

INTRODUCTION

Convective instability during solidification causes freckles in a resultant solid and often controls the quality of solid products in the processes of crystal growth and castings of metallic alloys. In binary solidification, a mushy layer of dendritic crystals is often formed by constitutional supercooling. When a binary alloy is solidified in a gravitational field, an unstable density profile induced by concentration and temperature gradient may occur buoyancy-driven convection in the mushy layer.
In the present study, the onset of convective instabilities in the mushy layer during time-dependent solidification of binary alloys is analyzed based on propagation theory we have developed. By using a similarity variable, the time-dependent disturbance equations for the liquid and mushy layers are transformed to the self-similar stability equations. The present study suggests the critical conditions to mark the convective motion in the liquid and mushy layers of the solidification system in which the mushy-layer thickness and the density profile vary with time.
The system considered here is shown in Fig. 1. The supereutectic melt is initially quiescent at a constant temperature T_∞ and a constant solute concentration C_∞. For time $t \geq 0$ the bottom boundary of the melt is supercooled at a constant temperature, which is lower than the eutectic temperature T_E. The mushy layer grows above a eutectic solid layer, and compositional convection of light residual liquid may be induced. It is assumed that the mush-solid interface is at the eutectic concentration C_E and the solid-layer thickness at the bottom is very small. The position of the mush-liquid interface $H\ (=2\lambda\sqrt{\kappa t})$ is moving upward, where λ is the phase-change rate and κ is the thermal diffusivity.

SELF-SIMILAR STABILITY EQUATIONS

The governing equations for convection during solidification of binary alloys are described well by Worster [1] and Emms and Fowler [2]. In the present study, the non-dimensional time-dependent disturbance equations are transformed to functions of a similarity variable $\zeta\ (= z/h = z/(2\lambda\sqrt{\tau}))$, where h is the mushy-layer thickness scaled by an arbitrary length L, and τ is the time scaled by L^2/κ. The self-similar stability equations in the mushy layer are given in the previous work [3]:

$$(\bar{\mathrm{D}}^2 + 2\lambda^2\zeta\bar{\mathrm{D}} - a^{*2})\theta_m^* = R_m^* w_m^* \bar{\mathrm{D}}\theta_{m0} - 2\lambda^2 St\zeta\bar{\mathrm{D}}\chi^*,$$

$$2\lambda^2\zeta[\chi^*\bar{\mathrm{D}}\theta_{m0} + \chi_0\bar{\mathrm{D}}\theta_m^* + (\theta_{m0} - \gamma)\bar{\mathrm{D}}\chi^* + \theta_m^*\bar{\mathrm{D}}\chi_0] = R_m^* w_m^* \bar{\mathrm{D}}\theta_{m0},$$

$$(\bar{\mathrm{D}}^2 - a^{*2})w_m^* = a^{*2}\theta_m^*,$$

where $\bar{\mathrm{D}} = \mathrm{d}/\mathrm{d}\zeta$ and a^* is the wave number. The amplitude of velocity disturbance w_m^* has the scale of $\kappa\Pi/L^3$, where Π is the permeability of the mushy layer. In the liquid layer, the amplitude of velocity disturbance is rescaled by a non-dimensional time-dependent scaling factor $h^2\ (=4\lambda^2\tau)$ based on propagation theory, and w^* has the scale of $\kappa H^2/L^3$. The self-similar stability equations in the liquid layer are given by

$$(\bar{\mathrm{D}}^2 + 2\lambda^2\zeta\bar{\mathrm{D}} - a^{*2})\theta^* = R_T^* w^* \bar{\mathrm{D}}\theta_0,$$

$$(Le\bar{\mathrm{D}}^2 + 2\lambda^2\zeta\bar{\mathrm{D}} - Lea^{*2})c^* = R_S^* w^* \bar{\mathrm{D}}c_0,$$

$$[(\bar{\mathrm{D}}^2 - a^{*2})^2 + \frac{2\lambda^2}{Pr}(\zeta\bar{\mathrm{D}}^3 - a^{*2}\zeta\bar{\mathrm{D}} + 2a^{*2})]w^* = a^{*2}(\theta^* - c^*).$$

The Darcy-Rayleigh number $R_m^*\ (=\mathrm{g}\beta_m\Delta C\Gamma\Pi H/(\kappa\nu))$ is based on the mushy-layer thickness H, where $\beta_m = \beta - \alpha\Gamma$, $\Delta T = \Gamma\Delta C = T_L(C_\infty) - T_E$, $\Delta C = C_\infty - C_E$, and Γ is the slope of the liquidus curve. The thermal Rayleigh number R_T^* and the solutal Rayleigh number R_S^* are defined as $R_T^* = \mathrm{g}\alpha\Delta TH^3/(\kappa\nu)$ and $R_S^* = \mathrm{g}\beta\Delta CH^3/(\kappa\nu)$, respectively. The parameter St is the Stefan number $(=\bar{L}/(C_p\Delta T))$, and γ is the concentration ratio $(=(C_s - C_\infty)/\Delta C)$, where $\bar{L}$ denotes the latent heat of fusion, C_p the

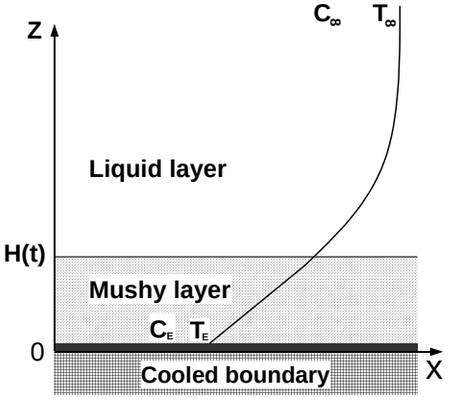


Fig. 1. Schematic diagram of liquid and mushy layers during time-dependent solidification.

specific heat, and C_s the solute concentration in solid. The parameter *Le* is the Lewis number ($=D/\kappa$), and *Pr* is the Prandtl number ($=\nu/\kappa$), where *D* is the solute diffusivity, and ν is the kinematic viscosity. In the mushy layer, the basic-state equation is given by

$$\overline{\mathrm{D}}^2\theta_{\mathrm{m0}} + 2\lambda^2\zeta\left(1+St\frac{\gamma-\theta_{\mathrm{i}}}{(\gamma-\theta_{\mathrm{m0}})^2}\right)\overline{\mathrm{D}}\theta_{\mathrm{m0}} = 0,$$

with $\theta_0 = \theta_{\mathrm{m0}}$, $\overline{\mathrm{D}}\theta_0 = \overline{\mathrm{D}}\theta_{\mathrm{m0}}$ at ζ=1, and $\theta_{\mathrm{m0}} = -1$ at ζ=0. In the liquid layer, the basic-state temperature and concentration fields are given by $\theta_0 = \theta_\infty + (\theta_{\mathrm{i}} - \theta_\infty)\mathrm{erfc}(\lambda\zeta)/\mathrm{erfc}(\lambda)$ and $\mathrm{c}_0 = \theta_{\mathrm{i}}\mathrm{erfc}(\lambda\zeta/\sqrt{Le})/\mathrm{erfc}(\lambda/\sqrt{Le})$, respectively, where θ_{i} $(=(T_{\mathrm{i}} - T_{\mathrm{L}}(C_\infty))/\Delta T)$ is the temperature at the liquid-mush interface, and θ_∞ $(=(T_\infty - T_{\mathrm{L}}(C_\infty))/\Delta T)$ is the superheat.

The following boundary conditions are applied to the self-similar stability equations:

for $\zeta\to\infty$, $\theta^* = 0$, $c^* = 0$, $w^* = 0$, $\overline{\mathrm{D}}w^* = 0$,

at ζ=1,

$$\theta^* = \frac{R_{\mathrm{T}}^*}{R_{\mathrm{S}}^*}c^*, \quad \overline{\mathrm{D}}\theta^* = R_{\mathrm{T}}^*\left[\frac{\overline{\mathrm{D}}c^*}{R_{\mathrm{S}}^*} - 2\lambda^2\left(\frac{1-Le}{Le}\right)\overline{\mathrm{D}}\theta_0 h^*\right], \quad \theta^* = \frac{\Pi^* R_{\mathrm{T}}^*}{R_{\mathrm{m}}^*}\theta_{\mathrm{m}}^*, \quad \overline{\mathrm{D}}\theta^* = R_{\mathrm{T}}^*\left[\frac{\Pi^*}{R_{\mathrm{m}}^*}\overline{\mathrm{D}}\theta_{\mathrm{m}}^* + 2\lambda^2\left(\frac{St}{\theta_{\mathrm{i}}-\gamma}\right)\overline{\mathrm{D}}\theta_0 h^*\right],$$

$$w^* = w_{\mathrm{m}}^*\Pi^*, \quad \overline{\mathrm{D}}w^* = 0, \quad \overline{\mathrm{D}}w_{\mathrm{m}}^* = -\left[\overline{\mathrm{D}}^3 w^* - a^{*2}\overline{\mathrm{D}}w^* - \frac{2\lambda^2}{Pr}(\overline{\mathrm{D}}w^* - \overline{\mathrm{D}}^2 w^*)\right], \quad \chi^* = \frac{\overline{\mathrm{D}}\theta_{\mathrm{m0}}^*}{\theta_{\mathrm{i}}-\gamma}h^*\frac{R_{\mathrm{m}}^*}{\Pi^*},$$

at ζ=0, $\theta_{\mathrm{m}}^* = 0$, $w_{\mathrm{m}}^* = 0$,

where Π^* $(=\Pi/H^2)$ denotes the Darcy number. The Rayleigh numbers have the relations of $R_{\mathrm{T}}^* = AR_{\mathrm{m}}^*/\Pi^*$ and $R_{\mathrm{S}}^* = (1+A)R_{\mathrm{m}}^*/\Pi^*$, where A $(=\Gamma\alpha/\beta_{\mathrm{m}})$ is the buoyancy ratio.

RESULTS AND DISCUSSION

The shooting method is employed to solve the self-similar stability equations [3]. We investigate the stability criteria for $A\to 0$, *St*=5, γ =20, $\Pi^* = 10^{-5}$, and *Pr*=10. These values are relevant to solidification of aqueous ammonium chloride solution. The marginal stability curves for various Lewis numbers with θ_∞=0.5 are shown in Fig. 2. The critical Darcy-Rayleigh number $R_{\mathrm{m,c}}^*$ for mushy-layer-mode convection is found to be 19 for $\theta_\infty = 0.1$ and $Le = 0.013$, and 7.6 for $\theta_\infty = 1$ and $Le = 0.007$. These $R_{\mathrm{m,c}}^*$-values compare with the existing results [1,2,4]. The critical mushy-layer thickness H_{c} is predicted to be 0.8~2 cm for the onset of mushy-layer-mode convection, which is consistent with the existing experimental data [5].

The present results show that the Prandtl number, the Lewis number, and the superheat are destabilizing parameters for convective instabilities. With increasing the Darcy number Π^*, the critical Rayleigh numbers increase and mushy-layer mode convection becomes dominant. However, when Π^* is small, boundary-layer-mode convection becomes dominant, since the permeability of the mushy layer is small and the resistance to mushy-layer-mode convection is large. The critical time t_{c} to mark the onset of mushy-layer-mode convection is predicted from the relation of $t_{\mathrm{c}} = H_{\mathrm{c}}^2/4\lambda^2\kappa$. It is found that t_{c} has a minimum point with varying θ_∞ and that t_{c} decreases with increasing θ_∞ for $\theta_\infty < 0.3$, while it increases for $\theta_\infty > 0.3$.

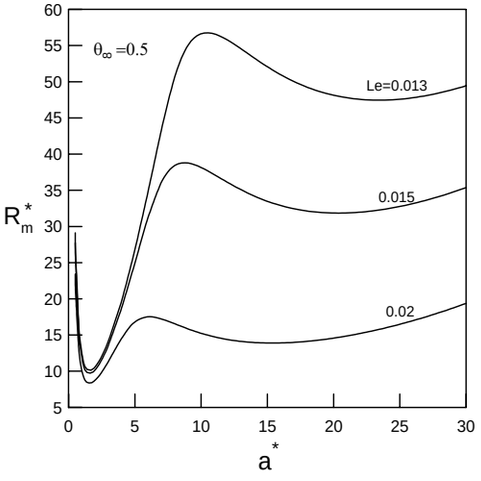


Fig. 2. Marginal stability curves for various Lewis numbers *Le* with θ_∞=0.5.

References

[1] Worster M. G.: Instabilities of the Liquid and Mushy Regions During Solidification of Alloys. *J. Fluid Mech*. **237**: 649-669, 1992.

[2] Emms P. W., Fowler A. C.: Compositional Convection in the Solidification of Binary Alloys. *J. Fluid Mech*. **262**: 111-139, 1994.

[3] Hwang I. G., Choi C. K.: The Onset of Mushy-Layer-Mode Instabilities During Solidification in Ammonium Chloride Solution. *J. Crystal Growth* **220**: 326-335, 2000.

[4] Tait, S., Jaupart, C.: Compositional Convection in a Reactive Crystalline Mush and the Evolution of Porosity. *J. Geophys. Res*. **97**: 6735-6756, 1992.

[5] Chen, C. F., Chen, F: Experimental Study of Directional Solidification of Aqueous Ammonium Chloride Solution. *J. Fluid Mech*. **227**: 567-586, 1991.

Development of the fractal dimension of material elements in homogeneous isotropic turbulence using Kinematic Simulation

F. Nicolleau and A. El Maihy
University of Sheffield, Department of Mechanical Engineering

Kinematic Simulation is a unified model for one- or multi-particle turbulent diffusion. It relies on the integration of

$$\frac{d\vec{x}}{dt} = \vec{u}(\vec{x}(t), t)$$

where $\vec{x}$ is the position of the fluid particle and $\vec{u}$ a turbulent-like Eulerian velocity field. In this contribution we only study the case of a $k^{-5/3}$ energy spectrum defined over the range $[L_1, \eta]$.

The evolution of the fractal dimension of material elements (lines, surfaces and 3-D objects) as a function of time in homogeneous isotropic turbulence is investigated using Kinematic Simulation in which high Reynolds numbers can be achieved.

KS are used to track 10^4 particles which are released from a straight line. The fractal dimension of this set of particles is calculated for different ratios L_1 / η using the Modified Box Counting Method of Buczkowski (1998). The fractal dimension is found to increase with time, the larger the Reynolds number the larger the increasing rate. KS predict a maximum value of the fractal dimension equal to 2.37 at a Reynolds number of 4000. We find that the fractal dimension of the line obeys the equation

$$D = 1 + 0.088\Gamma\left(\frac{L}{\eta}\right)^{2/3}\left(\frac{L}{u'}\right)$$

as can be seen in figure (1), where L is the turbulence integral length scale and u' the turbulence rms velocity. This result is very similar to the one obtained theoretically and experimentally by Villermaux et al (1994) and by LES (Nicolleau 1996) at small Reynolds numbers except for the factor Γ=5.5 which accounts for the differences between the spectrum used in experimental work and the spectrum used in KS. The comparison between our results and Villermaux's leads to an exact relation between experimental and KS Reynolds numbers in the form

$$\mathrm{Re}^{KS} = \left(\Gamma\left[\frac{L}{\eta}\right]^{2/3}\right)^2 = \left(5.5\left[\frac{L_1}{6.28\eta}\right]^{2/3}\right)^2 = 2.611\left(\frac{L_1}{\eta}\right)^{4/3}$$

We also study the evolution of 10^4 particles released from a horizontal square of size L. The fractal dimension is found to increase with time, the larger the Reynolds number the larger the increasing rate. KS predict a maximum value of the fractal dimension equal to 2.4 at a Reynolds number of 10^4. We find that the surface fractal dimension of an initial square obeys the equation

$$\frac{D-2}{0.088(\mathrm{Re}^{KS})^{1/2}} = \frac{1}{2}\frac{tu`}{L}$$

as shown in figure (2). That is for a given Reynolds number its increase if half that of the line.

Finally we release 8000 particles from a cube of size 0.2 L, use KS to track the particles and then measure the fractal dimension of the set of particles as a function of time for different Reynolds numbers. The fractal dimension of the cube is found to decrease regularly towards 2 reflecting the fact that the volume, initially a thick compact object, is progressively converted into a set of elongated sheets. The cube's fractal dimension is found to be independent of the Reynolds number in agreement with Villermaux et al (1999). However, the cube's fractal dimension increases with the increase of its initial size (S). A universal formula governing the evolution of the fractal dimension of a cube with time is found in the form

$$\frac{S(3-D)}{tu`} = 0.3\left(\frac{tu`}{L}\right)^{-2/3}$$

as shown in figure (3).

References

Buczkowski, S., Kyriacos, S., Nekka, F., and Cartilier, L.: The Modified Box-Counting Method: Analysis of Some Characteristic Parameters. *Pattern Recognition*, 31(4), 411-418. 1998.
Nicolleau, F.: Numerical Determination of Turbulent Fractal Dimension." *Physics of Fluid*, 8(10), 2661-2670. 1996.
Villermaux, E., and Gagne, Y.: Line Dispersion in Homogeneous Turbulence: Stretching, Fractal Dimension, and Micromixing." *Physical Review Letters*, 73(2), 252-255. 1994.
Villermaux, E., and Innocenti, E.: On the Geometry of Turbulent Mixing." *Journal of Fluid Mechanics*, 393, 123-147. 1999.

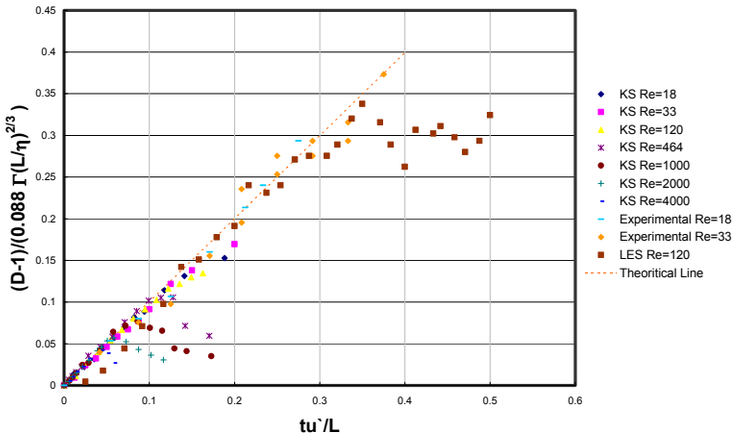


Figure (1): $[(D-1)/0.088Re^{1/2}]$ as a function of (t/t_d) for experimental, LES and KS results.

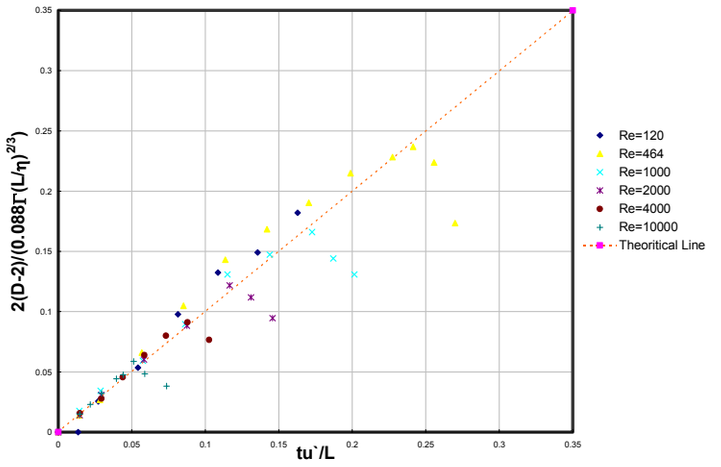


Figure (2): $[2(D-1)/0.088\ \Gamma(L/\eta)^{2/3}]$ as a function of (t/t_d) for different Reynolds numbers.

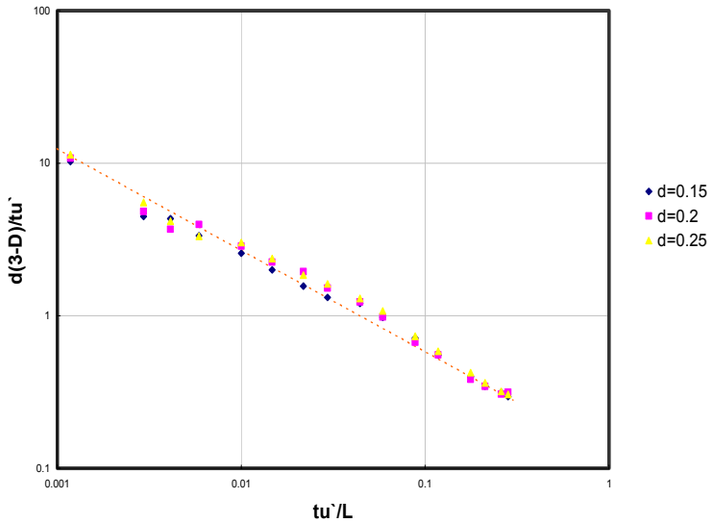


Figure (3): $\dfrac{d(3-D)}{tu`}$ as a function of tu`/L for different source diameters.

CHAOTIC ADVECTION IN A MIXER WITH CHANGING GEOMETRY

Stephen M. Cox*, Matthew D. Finn**
*School of Applied Mathematics, University of Adelaide, Adelaide 5005, Australia
**School of Mathematical Sciences, University of Nottingham, Nottingham NG7 2RD, UK

Summary Chaotic advection is examined in a mixer consisting of a circular vat full of fluid, stirred by an arbitrary number N of stirring rods. The fluid is assumed to be highly viscous, and the flow two-dimensional. A series solution for the velocity field permits an extremely precise computation of the paths of passive fluid particles under motion of the stirring rods. Of particular note is the case $N > 2$, which allows the generation of 'topological chaos' provided the stirring rods move with appropriate topology. To date, the stirring rods have had circular cross-section; it is shown here how the series-solution approach can be modified to accommodate other cross-sectional profiles, and that stirring can be made more effective using elliptical paddles rather than circular ones.

INTRODUCTION

Over the past twenty years or so [1, 2], it has become well established that fluids can be stirred effectively even in simple two-dimensional laminar flows. The key to effective stirring in such flows is the generation of chaotic paths for fluid particles. The position $(x(t), y(t))$ of a fluid particle is given by $\dot{x} = u(x,y,t)$, $\dot{y} = v(x,y,t)$, where (u,v) is the fluid velocity, and particle paths can readily be made chaotic if the time-dependence of the velocity field is chosen appropriately.
The first, pedagogical examples of flows exhibiting the chaotic advection of fluid particles were inviscid flows, driven by various forms of singularities (vortices, sources, sinks) – see, for example, [1]. Soon afterwards the opposite limit, of Stokes flow in a highly viscous fluid, was investigated, for example the flow in an eccentric annular space, driven by successive rotations of each boundary. The essential motivation behind the choice of either inviscid or highly viscous fluids was the desire for an exact expression for the fluid velocity field. Such an expression could generally be computed in all the cases studied. With an exact expression for $u(x,y,t)$ and $v(x,y,t)$, it is possible to carry out numerical integrations of fluid particle advection with extreme precision, and this is a prerequisite to tracking faithfully the particle paths (a significant computational inconvenience is that of course errors grow exponentially in a chaotic flow).
Most of the viscous-flow devices that possess an exact expression for the velocity field contain no genuinely moving parts – time-dependence in the flow is generated by motion of the boundaries of the flow domain parallel to themselves in time-dependent fashion. A consequence of this restriction is that the geometry of the device remains fixed, which is not ideal in a model for a mixer, but, crucially, permits an exact solution to the problem. One exception to this rule of fixed geometry is the 'TRM' [3], which models slow viscous flow in a vat of circular cross-section driven by the motion of a single stirring rod, also of circular cross-section. The streamfunction is readily derived for general motion of the stirring rod, and, in fact, can be constructed from a superposition of results from the fluid and solid mechanics literature dating back to the 1940's. The stirring rod in the TRM is driven by a planetary gear and it is a straightforward matter to choose the gear ratios so as to provide a highly effective stirring protocol. This is achieved largely by trial and error, and careful tuning of the system parameters.

STIRRING WITH PADDLES

Although the TRM has a genuinely time-dependent geometry, it has only one stirring rod. Clearly one would like to have at one's disposal an arbitrary number (N, say) of stirring rods, moving simultaneously through the vat, rather than only one. The case $N > 1$ provides a more realistic model for any industrial planetary mixer. However, it seems unlikely that an exact expression for either inviscid flow or Stokes flow could be found in the case of general N. But for the purposes of numerically tracking the evolution of fluid particles it is not the existence of an exact expression for (u,v) that matters, just the means to compute the velocity with extreme (preferably machine) accuracy. Fortunately, a series solution for the streamfunction of the motion can be developed [4, 5], which gives very rapid convergence and sufficient accuracy that it may be considered effectively 'exact'. The coefficients in the series are obtained numerically by minimizing the residual squared error in the boundary conditions.

Non-circular paddle cross-section

The very rapid convergence of the series is undermined if one attempts to model stirring rods whose cross-section is other than circular. However, we show that the method is readily adapted to accommodate simple paddles, provided one can find a conformal mapping $w(z)$ from the paddle to a circle. The series are then written in terms of the mapping function w rather than in z. For example, elliptical paddles are easily modelled, since the requisite conformal map is well known, and by varying the aspect ratio of the ellipse we span the spectrum of cases from circular paddles to flat paddles. We have been able to simulate paddles down to aspect ratios of around 10^{-7} with no computational difficulties.
The method of solution is highly efficient. Since an exact expression is posed for the streamfunction (and similar expressions for the velocity components are readily obtained), all that needs to be computed and stored is the corresponding set of coefficients of the sums involved. It is also a simple matter to compute various other quantities of physical interest, such as the energy usage of the device.

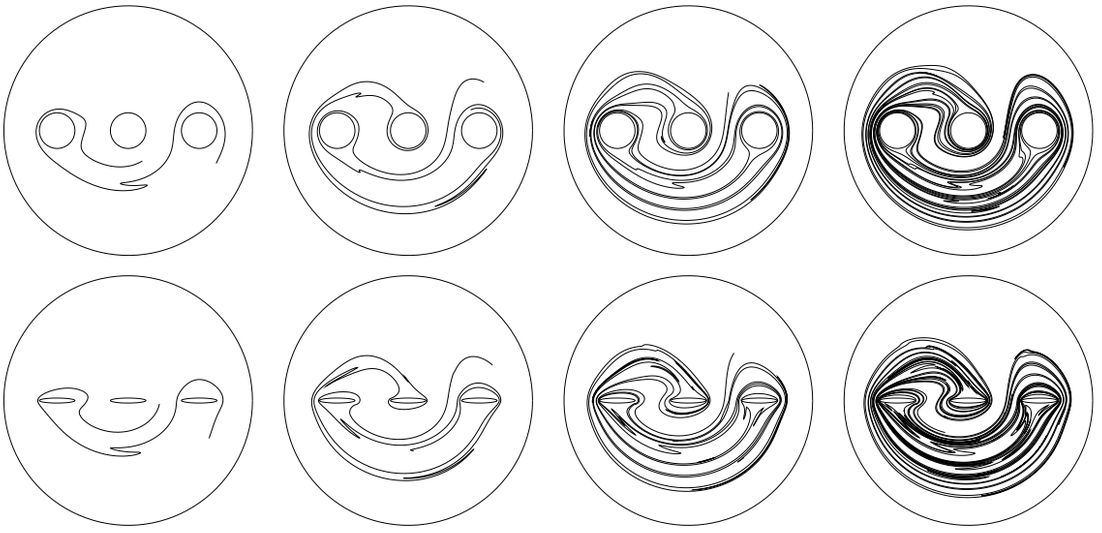


Figure 1: Top: evolution of a line element, stirred by circular paddles. Bottom: as top, but with elliptical paddles of aspect ratio 0.14. The line element grows by a factor 95.3 (top) or 123 (bottom), indicating greater stretching by the elliptical paddles.

Topological chaos

Not only does a mixer with multiple stirring rods accord more closely to everyday notions of a mixing device and to industrial planetary mixers, it also permits the generation of 'topological chaos' [6] – if the stirring rods are braided around one another in a topologically nontrivial way, there is a region of the flow domain in which a certain degree of chaos is guaranteed. Striking experiments by Boyland, Aref and Stremler [6] have shown that careful consideration of the topology of the motion of three circular stirring rods leads to a dramatic improvement in the stirring effectiveness, and that superficially similar stirring protocols can generate very different results. Using our series solution we have simulated their experiments [4] and find excellent qualitative agreement.

Results

We have simulated topological chaos in a batch mixer with $N = 3$ stirring rods generating Stokes flow in a circular vat. The rods are moved according to the following protocol: first the right-hand pair are interchanged, in a counterclockwise motion, then the new left-hand pair are interchanged, but clockwise. The evolution of a line element whose length is initially equal to the radius of the vat is shown in Figure 1, after one, two, three and four applications of this protocol. One might expect flat paddles to stir rather better than circular ones: the figure illustrates results for both circular and elliptical paddles, and shows that, at least in the specific case considered, this is indeed the case.

CONCLUSIONS

Stirring of a highly viscous fluid by an arbitrary number of stirring rods of arbitrary cross-section is readily described with high accuracy, sufficient for the tracking of chaotic fluid particle paths. The solution method easily accommodates elliptical paddles of aspect ratio ranging from unity (circular paddles) to extremely small values (e.g. 10^{-7}, very flat paddles). Topological chaos is readily simulated and we find some empirical evidence that elliptical paddles stir the fluid more effectively than circular ones.

References

[1] Aref, H.: Stirring by chaotic advection. *J. Fluid Mech.* **143**:1–21, 1984.

[2] Aref, H.: The development of chaotic advection. *Phys Fluids* **14**:1315–1325, 2002.

[3] Finn, M. D. and Cox, S. M.: Stokes flow in a mixer with changing geometry. *J. Eng. Math.* **41**:75–99, 2001.

[4] Finn, M. D., Cox, S. M. and Byrne, H. M.: Topological chaos in inviscid and viscous mixers. *J. Fluid Mech.* **493**:345–361, 2003.

[5] Price, T. J., Mullin, T. and Kobine, J. J.: Numerical and experimental characterization of a family of two-roll-mill flows. *Proc. R. Soc. Lond. A* **459**:117–135, 2003.

[6] Boyland, P. L., Aref, H. and Stremler, M. A.: Topological fluid mechanics of stirring. *J. Fluid Mech.* **403**:277–304, 2000.

XXI ICTAM, 15-21 August 2004, Warsaw, Poland

ENHANCED MIXING BY VORTICES

Patrice Meunier, Emmanuel Villermaux
Institut de Recherche sur les Phénomènes Hors Equilibre
49, av. Joliot-Curie, 13364 Marseille, France

Summary The mixing of a passive scalar blob by the simple stirring protocol realized in the deformation field of an axisymmetric vortex is investigated. The complete transient concentration field exhibits an accelerated diffusion of the scalar, due to its stretching in a spiral surrounding the vortex. The concentration histogram of the scalar presents an unexpected cusp at early stages. The long time properties of the histogram and the scalar dissipation rate are also examined.

INTRODUCTION

A central question in scalar mixing is the description of the histogram or probability distribution function (PDF) $P(c)$ of the concentration level c of a substance being mixed. In the presence of a velocity field, the diffusion is altered by the stirring of the substrate and is usually enhanced, as for example in a straining field [1] or in a vortex [2,3]. However, experimental and theoretical works addressing the structure and origin of the scalar PDF are scarce. Based on a spatially and temporally resolved experiment, we study the mixing chronology of a blob of dye embedded in the displacement field of a Lamb-Oseen vortex, from the initial segregation of the blob to the state where it is almost completely diluted in the medium [4].

ACCELERATED DIFFUSION IN A VORTEX

A blob of dye (dark patch on Fig. 1) with initial size s_0, concentration c_0 and diffusivity D is placed far from the vortex center of initial size a_0 . The vortex can therefore be considered as a point vortex, with azimuthal velocity $v_\theta=\Gamma/2\pi r$ (Γ=14 cm^2/s being its circulation). The passive blob rolls up around the vortex in a spiral, and its length increases linearly in time. By a local analysis in a frame of reference aligned with the spiral, the search for $c(r,t)$ is reduced to a simple problem of diffusion in a stretching field whose amplitude depends on the radius from the vortex center, and which can be solved by a classical change of variable [1], leading to an exact solution of the concentration field [4]. A simple expression for the maximal concentration c_M at each radius follows:

$$c_M(r,t) = c_0 \; erf\left[\frac{1}{4}\left(\frac{Dt}{s_0^2}+\frac{D\Gamma^2 t^3}{3\pi^2 r^4 s_0^2}\right)^{-1/2}\right]$$

The maximal concentration has two different behaviours whether the fluid particles in the spiral have lived less or more than a mixing time t_s, obtained when the term inside the error function equals unity:

$$t_s(r) = \frac{r^2}{\Gamma}\left(\frac{3\pi^2}{16}\right)^{1/3}\left(\frac{s_0}{r}\right)^{2/3}\left(\frac{\Gamma}{D}\right)^{1/3}$$

Before the mixing time, the striation thickness is larger than the diffusion length and the maximal concentration c_M is constant. After the mixing time, enhanced diffusion is observed, for which c_M decreases as $t^{-3/2}$ instead of $t^{-1/2}$. This is due to the stretching of the spiral as t added to a normal diffusion in the contracting coordinates. This prediction contains no fitting constant and is plotted on Fig. 2a for a fixed radial location together with the experimental measurements.



Fig. 1: Roll-up of a blob of fluorescent dye in a point vortex at t = 0, 2 and 10 s. The field of view is 4.8 cm wide.

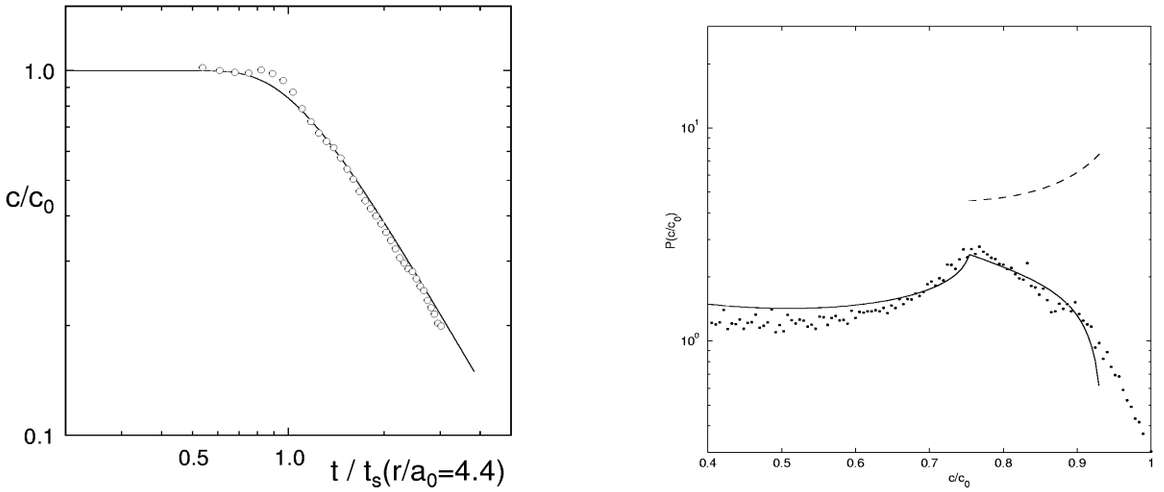


Fig. 2: (a) Maximal concentration of the dye obtained experimentally (symbols) and theoretically (solid line) at a radius r=4.4 a_0. (b) Probability density function of the dye concentration at t =13 s. Theoretical prediction is made for the global scalar field (solid line) and for the maximum dye concentration of the spiral (dashed line).

HISTOGRAM OF THE PASSIVE SCALAR

After the mixing time, the transverse concentration profile across the spiral arms is a Gaussian function parametrized by c_M. By extracting the shape of the iso-concentration lines, it is possible to derive an analytical solution of the PDF of the concentration $P(c)$ at any time [4]. An example is shown on Fig. 2(b) at a given intermediate stage. The PDF of the maximal concentration c_M is also shown as a dashed line on Fig. 2(b). The global PDF can be understood as the sum of U shaped histograms based on each maximal concentration. This superposition introduces a cusp at the minimum of the maximal concentration, obtained for the minimum radius of the blob of dye. When this radius is small, or at late stages, the cusp vanishes and the PDF tends to a pure power law

$$P(c) \sim c^{-3/2}$$

at late stages.

SCALAR DISSIPATION RATE

The exact solution of the concentration field also provides the scalar dissipation rate $\chi=-(d/dt)\langle c^2\rangle$. If all the elements of the spiral have not reached the mixing time, χ scales as $t^{1/2}$, as shown by Flohr and Vassilicos [2]. However, if all the elements of the spiral have reached the mixing time, *i.e.* when there is no dye with the initial concentration, the dissipation rate scales as $t^{-5/2}$.

CONCLUSIONS

The simple stirring protocol considered here allows to reach an exact solution of the concentration field and of the PDF of the concentration, in close agreement with the experimental data. Useful scalings are derived at late stages for the PDF of concentration and for the scalar dissipation rate.
The evolution of the concentration field during the merging of two independent vortices will be analyzed as well.

References

Ranz W. E.: Application of stretch model to mixing, diffusion and reaction in laminar and turbulent flows. *AIChE J.* **25**:41-47, 1979.
Flohr P., Vassilicos J. C. : Accelerated Scalar Dissipation in a Vortex. *J. Fluid Mech.* **348**:295-317, 1997.
Bajer K., Bassom A. P., Gilbert A. D. : Accelerated Diffusion in the Centre of a Vortex. *J. Fluid Mech.* **437**:395-411, 2001.
Rhines P. B., Young W. R. : How Rapidly is a Passive Scalar Mixed within Closed Streamlines. *J. Fluid Mech.* **133**:133-145, 1983.
Meunier P., Villermaux E.: How Vortices Mix. *J. Fluid Mech.* **476**:213-222, 2003.

GEOMETRIC FEATURES OF HIGH-SCHMIDT NUMBER SCALAR MIXING

Jörg Schumacher*, Katepalli R. Sreenivasan**
*Department of Physics, Philipps University, D-35032 Marburg, Germany
**International Centre for Theoretical Physics, I-34100 Trieste, Italy

Summary The mixing of passive scalars of decreasing diffusivity, advected in each case by the same three-dimensional Navier-Stokes turbulence, is studied. It becomes more isotropic with decreasing diffusivity. The local flow in the vicinity of steepest negative and positive scalar gradients are in general different, and its behavior is studied for various values of the scalar diffusivity. Mixing approaches monofractal properties with diminishing diffusivity.

MOTIVATION AND NUMERICAL MODEL

Turbulent mixing of dyes or macromolecular substances can be understood by analyzing how these scalar substances are advected and diffused in a fluid medium. For small concentrations, the admixture, or scalar, is passive, or has no dynamic feedback on the flow—which is therefore determined independent of the scalar. Often, the scalar diffusivity is small compared with the viscosity of the fluid, so that their ratio, the so-called Schmidt number, $Sc = \nu/\kappa$, is large. Our interest here lies in the advection and diffusion of passive scalars for large values of Sc. In particular, we wish to understand the recent result from numerical simulations that turbulent mixing becomes more isotropic when Sc is increased [1]. This approach to isotropic state is evident from the fact that deviations from it, as quantified by odd moments of the scalar derivative along a mean scalar gradient, $\partial_\parallel \theta$, decrease as Sc increases from 1 to 64 for a fixed Reynolds number of the turbulent flow [1].

The reason for the anisotropy for $Sc = O(1)$ has long been known to be the presence of ramp-cliff structures in the signature of the scalar field whenever there is a mean gradient in the scalar alone or in both scalar and velocity. These cliff structures of the scalar field are related to sharp fronts of the scalar gradient distribution in three-dimensional space and can be found in the positive far tail of the probability density function (PDF) of the scalar gradient fields.

Analytical approaches to understanding the features are difficult. Significant progress has been made for the so-called Kraichnan model of passive scalars in which the advecting velocity field is assumed to be Gaussian and to vary infinitely rapidly in time; for a review see [2]. However, even for the synthetic Kraichnan velocity field, a systematic study of anisotropy with Sc has not been made. Another approach [3], which follows Batchelor's original model of quasistatic straining motion, provides upper bounds for scalar derivative moments as functions of Sc. However, the problem still contains numerous open questions. For instance, it is unclear as to what changes occur in and around the ramp-cliff structures as $Sc \to \infty$.

Some of these changes were quantified via high-resolution numerical simulations of turbulent mixing [4]. We particularly considered level sets of the steep gradients and related them to the local structure of the advecting flow. Furthermore, the multifractal approach is known to sample efficiently the "singular" structures at small scales [5]. Therefore, we also studied the scalar dissipation field in high-Sc cases.

Our numerical results were obtained in a homogeneously sheared flow [6] with $\langle u_x \rangle = Cy$, where C is a constant, at a Taylor-microscale Reynolds number R_λ of 87 in which the scalar field of constant mean gradient was allowed to evolve according to the advection-diffusion equation. The Schmidt number was varied from 1 to 64. The pseudospectral simulations were done with resolutions of $512 \times 257 \times 512$ grid points for a box of size $2\pi : \pi : 2\pi$. We ensure that the scalar fluctuations are properly resolved by requiring that $k_{max}\eta_B \geq 1.3$ with $k_{max} = \sqrt{2}N_{max}/3$, where $N_{max} = 512$; the Batchelor scale $\eta_B \equiv \eta/\sqrt{Sc}$ and the Kolmogorov scale $\eta \equiv (\nu^3/\epsilon)^{1/4}$. The scalar gradient $\mathbf{G} = \mathbf{e}_y/\pi$ for all runs.

RESULTS

To shed some on the return to isotropic mixing, we show in Figure 1 three slices of the scalar field at the same moment of evolution, each slice corresponding to a different value of Sc. It is clear that the large structure, and the front associated with it, do not change with Sc but internal striations of finer scale accompany larger Sc. These striations increase the relative population of negative gradients. This is what causes the tail of the PDF for the positive gradient values to be effectively unchanged, whereas the events with negative gradients, shows higher probability as Sc increases, thus rendering the PDFs increasingly symmetric.

The question that immediately arises is what type of flow causes the steepest negative scalar gradients, and their increase with increasing Sc? To answer these questions, we have performed an eigenvalue analysis of the local velocity gradients in the vicinity of the largest scalar gradients. Here, pure straining motion corresponds with three real eigenvalues and local vortical motion with a conjugate complex pair and a real third eigenvalue. We performed this analysis in the vicinity of the steepest positive and negative scalar gradients only. For positive gradients, i.e. for the cliffs, local straining becomes somewhat more dominant with growing Sc, while, for the negative tails, the swirling and straining motion contribute in almost equal parts for large Sc. This is consistent with the view that the cliffs are associated with the front stagnation point of a moving fluid parcel, where the velocity field is predominantly straining, while the negative slopes come from

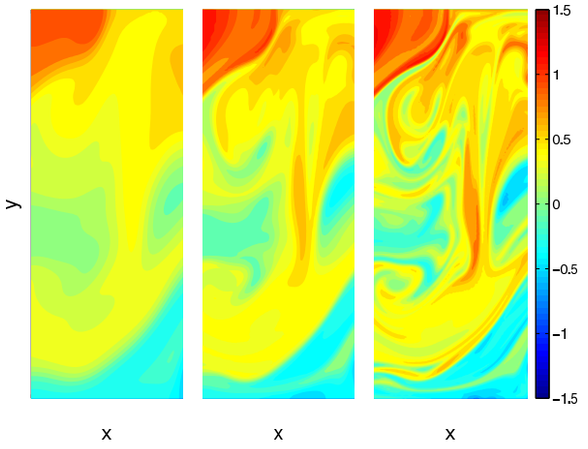


Figure 1. Slices of the total scalar field (mean plus fluctuation) for $Sc = 1$ (left), 8 (middle), and 64 (right), all of which are advected by the same flow. Only a fraction of the simulation domain is shown.

the wake region behind such parcels where the fluid motion is both vortical and straining.

The geometric properties of the scalar gradient level sets were also studied by means of box-counting analysis. The box counting dimension D_0 of a level set F, embedded in the three-dimensional space, is defined as the scaling exponent of $N_\delta(F) = N_0\delta^{-D_0}$ where $N_\delta(F)$ is the number of cubes of size δ that are needed to cover F. While for lower Sc differences between the positive level set and its negative counterpart were detected, they disappear more and more with increasing Schmidt number.

The variation of the level set threshold at fixed Schmidt numbers clearly indicates the multifractal character of the gradient fields. For operational purposes, it is more convenient to consider the scalar dissipation field, $\epsilon_\theta(\mathbf{x},t) = \kappa\sum_{j=1}^{3}(\partial_j\theta)^2$. We define the measure

$$\mu_r^{(i)} = \frac{X_r^{(i)}}{X_L} = \frac{\int_{V_r^{(i)}}\epsilon_\theta(\mathbf{x}+\mathbf{x}_i,t)\mathrm{d}^3\mathbf{x}}{\int_V \epsilon_\theta(\mathbf{x},t)\mathrm{d}^3\mathbf{x}} \tag{1}$$

where $V_r^{(i)}$ is the ith cube with length r. The spectrum of generalized dimensions [5], $D_q(q)$, obeys the following scaling relation

$$\sum_i \left(\mu_r^{(i)}\right)^q \sim r^{(q-1)D_q}\,. \tag{2}$$

It was found that the spectrum of generalized dimensions gets flatter with increasing Sc means that in the limit of very large Sc the scalar dissipation rate becomes a monofractal, i.e. $D_q = D_0$ for all q. The physical picture is as follows: large "singular" spikes of the scalar dissipation rate fill out the whole space more and more, so that the "quiet" regions in-between become less prevalent. The degree of spatial and temporal intermittency decreases, which is just the property to which the spectrum is sensitive. We can quantify this result also by fitting a bimodal multifractal cascade model to the data. For $Sc = 8$ we obtain $p = 0.86$, for $Sc = 64$ a value of $p = 0.81$, decreasing to 0.58 for experimental data at $Sc = 1900$. The model would yield a monofractal dissipation field for equidistributed energy flux, i.e. $p = 0.5$.

Acknowledgements

The computations were carried out on the IBM Blue Horizon at the San Diego Supercomputer Center within the NPACI program of the US National Science Foundation. JS was supported by the Deutsche Forschungsgemeinschaft and KRS by the National Science Foundation with grant CTS-0121007.

References

[1] Yeung, P.K., Xu, S., Sreenivasan, K.R.: Schmidt number effects on turbulent transport with uniform mean scalar gradient. *Phys. Fluids* **14**:4178–4191, 2002.
[2] Falkovich, G., Gawędzki, K., Vergassola, M.: Particles and fields in fluid turbulence. *Rev. Mod. Phys.* **73**:913–975, 2001.
[3] Schumacher, J., Sreenivasan, K.R., Yeung, P.K.: Schmidt number dependence of derivative moments for quasi-static straining motion. *J. Fluid Mech.* **479**:221–230, 2003.
[4] Schumacher, J., Sreenivasan, K.R.: Geometric features of the mixing of passive scalars at high Schmidt numbers. *Phys. Rev. Lett.* **91**:174501 (4 pages), 2003.
[5] Ott, E.: Chaos in Dynamical Systems. Cambridge University Press, Cambridge, 2002.
[6] Schumacher, J.: Derivative moments in stationary homogeneous shear turbulence. *J. Fluid Mech.* **441**:109–118, 2001.

FRONT PROPAGATION IN LAMINAR CELLULAR FLOWS : AN EXPERIMENTAL STUDY

Alain Pocheau, Fabien Harambat
IRPHE, Universités Aix-Marseille I & II, 49 rue Joliot-Curie, B.P. 146, F-13384 Marseille, France

Summary Front propagation in different kinds of laminar flows is investigated experimentally. Images of front propagation as well as data on their mean velocity show that a kinematic model of propagation is more relevant here than models based on homogeneization procedures.

This work is devoted to study experimentally the propagation of reaction fronts in laminar flows. This issue may concern chemical reactions in microfluidic or biological environments, chemical engineering, combustion, and more generally propagation of reactions in poorly stirred environment as found in populations dynamics or in planetary sciences (e.g. dynamics of the ozone hole) for instance. Our main objective is to model this issue in order to identify the most relevant picture of the corresponding process and its most valuable modelization. For this, we have designed different experiments in which a front propagates in a liquid medium that involves simple prescribed steady flows. The difference between experiments relies on the geometry of the flows. The comparison between the resulting front behaviour will be used to identify the salient features of the process.

EXPERIMENTAL CONFIGURATION

The experimental configuration is designed so as to study front propagation in flows created either by thermal means (i.e. thermoconvection) or by electromagnetic means (i.e. electroconvection). For this the reaction must take place in an aqueous solution [1]. We have chosen to work here on the chlorite-iodide reaction [2]. This autocatalytic oxydo-reduction reaction yields iodide I^- to be oxidized in iodine I_2. Addition of a starch indicator makes the presence of iodide visible as a blue colour. Thus, oxydation of iodine as the wave passes through leaves a colourless medium whose frontier with the blue medium localizes the front. Front is initiated by contact with an electrode. Its velocity is about $U_L \approx 2mm/mn$ at ph=5. It varies with temperature or electric current in a way which has been monitored.

From the images and the velocity of the front, we have deduced its thickness $\delta \approx 1mm$, the reaction time $\tau_r \approx 6s$, and the form of the reaction term $f(\theta)$ of the corresponding 1-d reaction-diffusion equation $\partial_t\theta = D\partial_x^2\theta + f(\theta)/\tau_r$. This term takes a polynomial shape $|f(\theta)| = \theta(1-\theta)(1-0.39\theta)$ which corresponds to a KPP wave.

The convective flows are generated by electrical heating from below and by cooling from above by water circulation. To allow front visualization, an optical access is made in the cooling device and a mirror is fixed in between the fluid and the heating plate. The depth of the convective layer is $d = 5.8mm$, its width is $l = 6mm$ and its length $X = 20cm$. This yields a chain of about 30 steady rolls to appear beyond onset. The flow intensity U depends on the distance to onset. However, to accurately determine it, care has been taken of the finite thermal conductivities of the boundary plates and of the temperature variation of water physical properties. The range of flow intensity scanned was : $12 < U < 60mm/mn$.

The electroconvective flows are produced by generating a current along a similar channel below which a chain of magnets, $2*2cm$ wide, has been placed with alternating directions of their magnetic field. The flow intensity $3 < U < 35mm/mn$ is proportionnal to the current intensity, the layer depth is $d = 3mm$, its width is $l = 12mm$ and its length is $X = 20cm$.

According to the above values, our experiment involves high Péclet numbers $Pe = UL/D > 600$ where L corresponds to the vortex size ($L \approx d$ in convection and $L = 20mm$ in electroconvection). On the other hand, the Damhköhler number $Da = L/U\tau_r$ is : $2 < Da < 7$ in convection ; $5 < Da < 48$ in electroconvection. This means that advection dominates diffusion but that advection and reaction have similar importances.

OBSERVATIONS AND RESULTS

Either in convective flows or in electroconvective flows, the front was rolled up by vortices, but it always succeeded in keeping its structure locally unchanged (Fig.1). In particular, no increase in front thickness has been noticed. Once contaminated by the fronts, the vortices were "burnt" at a speed roughly equal to the laminar velocity U_L. This is easily understood since perpendicularly to the flow streamlines, no advection can help the front to propagate.

The interesting phenomena come from the contamination of vortices. It arises from the "burnt" medium adjacent to the still "fresh" vortex, near the separatrix between both (Fig.1). This contamination sets the overall reaction rate since, once established, the vortex will burn in a prescribed time. It appears that the contamination is quick and roughly proportionnal to the flow intensity U. It then yields a mean relative front velocity U_f/U_L nearly proportionnal to the relative flow intensity U/U_L for both the convective and the electroconvective case (Fig.2).

The similarity between the propagation in the two kinds of flows stops here. In particular, the paths followed by the front inside a vortex and when crossing the separatrix with its neighbor are different in both flows. It is actually more 3-dimensionnal with convective flows than with electroconvective flows (Fig.1). In the former case, the front directly invades the middle of the vortex from the separatrix ; in the latter case, it gently rolls along the boundaries before uniformly propagating towards the center. This spatial difference is surprising since both flows are *a priori* designed to be 2-d

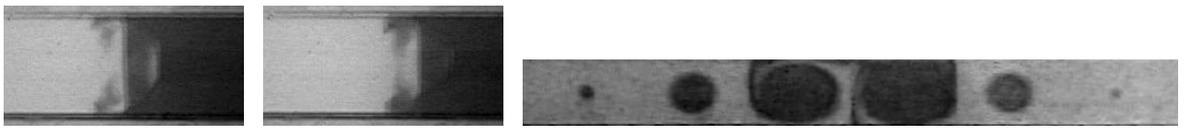


Figure 1. Images of front propagation in convective flows (left, view normal to the roll axis) and electroconvective flows (right, view along the roll axis).

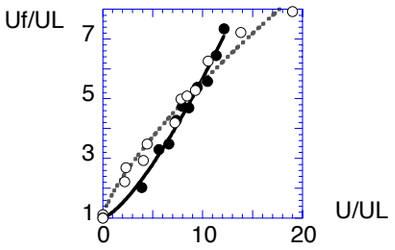


Figure 2. Relative increase of front velocity U_f/U_L as a function of the relative flow intensity U/U_L in convective flows (full circles) and in electroconvective flows (open circles).

cellular flows. We attribute it to the secondary flows (similar to Rossby flows) that develop when the vortex boundary layers separate one from the other. This occurs sooner in the convective case due to a weaker relative confinement of vortices on their axis direction. Beyond this, convection becomes quickly more efficient in increasing front propagation than electroconvection (Fig.2). This stresses the importance of the fine details of flow geometry on front propagation.

MODELS AND INTERPRETATION

The models of front propagation in a stirred medium proposed in literature rely either on the advection-reaction-diffusion-equation or on the G-equation (which describes the eikonal dynamics of a self-propagating wave surface in an advecting flow) [3, 4]. Most of them seek to determine the resulting mean front velocity U_f as the propagation velocity of an effective reaction-diffusion *wave* with renormalized diffusion coefficient D' and reaction time τ_r' : $U_f = (D'/\tau_r')^{1/2}$. The way these renormalized variables vary with U and U_L sets the final dependence of the mean front velocity with the flow intensity, i.e. at large Pe : $U_f \approx U^{1/4}$ for $Da << 1$ and $U_f \approx U^{3/4}$ for $Da >> 1$.

None of these tendencies are recovered in our experiments, whatever the kind of flows. Moreover, direct observation of the way fronts propagate in the cellular structure reveals the essential role played by their leading edge, in contrast with the above wave picture. In particular, the mean propagation velocity is actually set by the rate of propagation of the *most advanced part* of the front, whatever the state of contamination behind it. This statement asks for viewing the process of front propagation more as the propagation of local objects (i.e. "particles") than as the propagation of a global object (i.e. a "wave"). The implications on the modelization is to turn attention to kinematic models (e.g. [5]) treating the front as an assembly of local parts, the quickest of them setting the average propagation speed in the system.

We have derived such a kinematic model for electroconvective flows and obtained a good agreement. We have not yet achieved it for the convective case because the geometry of their flows (especially their secondary flows) deserves a special attention. However, we have looked to another kind of flows produced by alternating supercritical zones and subcritical zones of convection, i.e. by alternating convection and conduction. Here too, a kinematic model based on flow geometry enabled us to recover the experimental data.

CONCLUSION

Looking experimentally to front propagation in different cellular flows at moderate Damköhler numbers led us to conclude, both from qualitative and quantitative observations, that a kinematic modelization is much more relevant than a homogeneization procedure. This means that fronts behave, in average, not as a wave but as a set of dynamically independent parts, the mean velocity being set by the fastest one. Following this, front propagation in laminar flows appears as an optimization problem instead of an homogeneization problem.

References

[1] Ronney P.D., Haslam B.D. and Rhys. N.O.: Front propagation rates in randomly stirred media *Phys.Rev.Lett* **74**:3804, 1995.
[2] Weitz D.M., Epstein I.R.: Spatial waves in the reaction of chlorite with iodide. *J. Phys. Chem.* **88**:5300–5304, 1984.
999:999–996, 1999.
propagation in laminar flows. Phys.Rev.E 64:046307-1-13, 2001 propagation in steady and unsteady cellular flows. Phys. Fluids 15:679-688, 2003. R.J. and Burger M., John Wiley and sons, 1985
[3] Audoly B., Berestycki H., Pomeau Y.: Réaction diffusion en écoulement stationnaire rapide. *C.R. Acad.Sci.* Ser.IIb **328**: 255, 2000.
[4] Abel M., Celani A., Vegni D. and Vulpiani A.: Front propagation in laminar flows. *Phys.Rev.E* **64**:046307-1-13, 2001
[5] Cencini M., Torcini A., Vergni D. and Vulpiani A.: Thin front propagation in steady and unsteady cellular flows. *Phys. Fluids* **15**:679-688, 2003.

XXI ICTAM, 15–21 August 2004, Warsaw, Poland

ON THE DESIGN OF 3D MICROMIXERS HAVING THE BERNOULLI PROPERTY

Stephen Wiggins*, Julio M. Ottino**
*School of Mathematics, University of Bristol, Bristol BS8 1TW, UK
**R. R. McCormick School of Engineering and Applied Sciences, Northwestern University, Evanston, Illinois 60208, USA

Summary In dynamical systems theory a hierarchy of characterisations of mixing exist Bernoulli -> mixing ->ergodic, ordered according to the quality of mixing (the strongest first). We consider micromixers whose flows take one of two forms: 2D "blinking flows", or 3D duct flows. We show that these types of flows can be reduced to so-called linked twist maps (LTMs). LTMs can be shown to possess the Bernoulli property of mixing under certain conditions. Hence, conditions can be specified for a large class of micromixers guaranteeing the best quality mixing. Extensions of these concepts lead to first principle-based designs without resorting to lengthy computations.

INTRODUCTION

Microfluidics is the recently coined term to describe the study of fluid flows in devices having dimensions ranging from millimeters to micrometers . The volumes of fluid involved range from nanoliters (10^{-9} liters) to picoliters (10^{-12} liters). The applications of such fluid flows have literally exploded on the past few years.

Because of the length scales associated with the flow of fluids in microchannels the flow is characterized by a low Reynolds number (Re), and is therefore laminar (smooth in space, as opposed to turbulent). Hence, there is a need to understand transport, stirring, and mixing, in low Reynolds number, laminar flows. From the point of view of fluid mechanics, many aspects of this subject are well-developed and quite mature. However, the problems posed by applications at the microscale introduce some new difficulties. The channel lengths and flow speeds in “micromixers” are not sufficient to allow for the mixing effects of molecular diffusion. In this case, it is critical to understand the details of particle paths in the fluid flow over relatively short time scales (compared to the molecular diffusive time scale). This is precisely the subject area of what has been broadly termed “chaotic advection” ([1], [2]).

OPTIMAL DESIGN OF 3-DIMENSIONAL MICROMIXERS HAVING THE BERNOULLI PROPERTY

A dynamical system having the *Bernoulli property* on some invariant set of its domain possesses the “mathematically optimal” form of mixing on that domain. The obvious question then is "how do we design a mixer so that it has the Bernoulli property on as large a domain as possible?" To a mathematician, this might seem a naïve question since rigorous proofs that maps possess the Bernoulli property on regions of nonzero volume are notoriously difficult. Few examples are known, the Baker’s transformation being one of them. To a physicist or engineer, the known examples have a rather artificial flavour, epitomized by the Baker’s transformation, and consequently, tend not to provide inspiration for digging out "useful" concepts from the difficult and often less than user-friendly mathematics. The situation is not bleak however; we describe a new (from the point of view of applications to fluid mixing) type of map, or advection cycle, that has been rigorously shown to possess the Bernoulli property. Most surprisingly (and very fortuitous for the design purposes) many previously built micromixers, as well as a variety of potentially new micromixers, can be optimised for the Bernoulli property if they are designed so that the flow patterns give rise to a linked twist map (LTM). In order to show how this can be done we begin by describing precisely what a LTM is and, most importantly, its mixing properties. The material presented here is based on a series of papers by [3], [4], [5] published in the pure mathematics literature.

Linked Twist Maps

Let $S_1(r,\theta) = (r, \theta + g_1(r))$ be a twist map defined on the annulus A_1 (see Fig. 1) with $\frac{dg_1}{dr} \neq 0$ and $g_1(r_i^1) = 2\pi n$, for some integer n. Then r_o^1 is chosen such that $g_1(r_o^1) = 2\pi n + k_1$, where k_1 is an integer whose value will be discussed shortly.

Let $S_2(r,\theta) = (r, \theta + g_2(r))$ be a twist map defined on A_2 (see Fig. 1) with and $g_2(r_i^2) = 2\pi m$, for some integer m, and $g_2(r_o^2) = 2\pi m + k_2$. Furthermore, we suppose that the annuli intersect transversally in two disjoint components in the sense that $r_i^1 \cap r_i^2 \neq \emptyset$ and $r_o^1 \cap r_o^2 \neq \emptyset$ (see Fig. 1). The map defined by $S_2 \circ S_1$ on $A_1 \cup A_2$ is referred to as a *linked twist map* (LTM). Let $\alpha_i = \sup_{r_i^i \leq r \leq r_o^i} \frac{dg_i}{dr}$. The value of α_i is a measure of the strength of the differential winding of the map. $\alpha_i > 0$ is just referred to as the "twist condition". Regarding the annuli as chosen and fixed, there are four important parameters for the linked twist map: k_1 and k_2, which describe the number of twists for each twist map, and α_1 and α_2 , which describe the strength of each twist.

We can now state the main results on mixing. There are two cases to consider. One is where the annuli rotate in the same sense. This corresponds to k_1 and k_2 having the same sign (the co-rotating case). In this case if each map is at least a double twist ($|k_i| \geq 2$) and $\alpha_1\alpha_2 > 0$, then on $A_1 \cup A_2$ the linked twist map has the Bernoulli property.

Interestingly, if the annuli rotate in the opposite sense, i.e., k_1 and k_2 have opposite signs (the counter-rotating case), then the conditions that the linked twist map has the Bernoulli property on $A_1 \cup A_2$ are more restrictive. If the product of

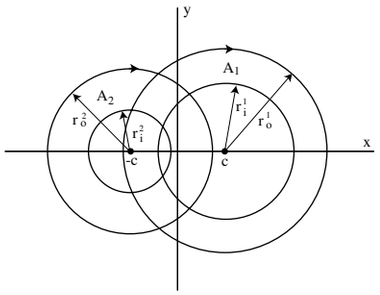


Figure 1. Geometry of the annuli from each half cycle of the advection cycle that make up the linked twist map.

α_1 and α_2 are negative then we must have $\alpha_1\alpha_2 < C_0 \approx 17.24445$. These results also indicate that, all things being equal, it is easier to achieve the Bernoulli property in the co-rotating case, as opposed to the counter-rotating case. It is then apparent that in designing a flow for optimal mixing the key quantities we need to understand are $g_i(r)$, $i = 1, 2$, on the annuli of choice, since these functions determines the rotation properties of the annuli, the radii of the annuli, and the strength of the twist. This is significant because the design of a mixer with the Bernoulli property boils down to the properties of one function describing closed streamlines in each half cycle of the advection cycle.

How to Make a LTM from a Duct Flow

Now we describe how to obtain a linked twist map (LTM) from a duct flow. By *duct flow* we mean a three-dimensional, steady, spatially periodic flow where the axial flow does not depend on the axial coordinate. We refer to each spatial period as a *cell*, and the flow is described by a mapping from the beginning of a cell to the end of a cell. This mapping is the composition of two mappings, each a twist map. The first twist map is the mapping of particles from the beginning of the cell to the half cell. The second twist map is the mapping of particles from the end of the half cell to the end of the cell. The cell to cell LTM obtained in this way will be discontinuous in the sense that each twist map is computed separately and continuity at the half cell is not enforced. Details of the computations required to go from a duct flow of this type to a linked twist map can be found in [6] and [7].

EXAMPLES OF MIXERS THAT CAN BE ANALYZED AS LTMS

Many mixers fit within the linked twist map framework. This is significant because LTMs provide an analytical approach to the design of devices producing a mathematically optimal, and precisely defined, type of mixing, depending on the geometry of the streamlines in the cross-section of the flow at the end of each half cell. Two comments first. The first example of a chaotic flow, the blinking vortex flow [1], is also the most transparent and the most immediately analyzable example of a flow that can be put in the form of a LTM. In this case the flow itself is already in the form of a linked twist map and the functions can be controlled at will. It is remarkable that, in some sense, this example encompasses, if not all, a large number of other examples. It is also important to stress that the most conceptually efficient way to think about mixing is in terms of maps and not in the terms of deviations for integrability. The most useful heuristic, is "streamline crossing", i.e. streamlines in a bounded domain at two different times must intersect. This precisely the central message of the LTMs.

Recently there have been a number of studies of micromixers appearing in the literature that can be analyzed in terms of LTMs. Two examples are the 2D electroosmostically driven “blinking flow” in [8] and the 3D pressure driven micromixer in a channel with patterned walls in [9].

References

[1] Aref, H. Stirring by chaotic advection, *J. Fluid Mech.*, **86**, 1-21, 1984.
[2] Ottino, J.M. The Kinematics of Mixing: Stretching, Chaos, and Transport, Cambridge University Press, Cambridge, England, 1989
[3] Burton, R. and Easton, R. Ergodicity of linked twist mappings. Global theory of dynamical systems (Proc. Internat. Conf., Northwestern Univ., Evanston, Ill., 1979), pp. 35–49, Lecture Notes in Math., 819, Springer, Berlin,1980.
[4] Wojtkowski, M. Linked twist mappings have the K-property. Nonlinear dynamics (Internat. Conf., New York, 1979), pp. 65–76, Ann. New York Acad. Sci., 357, New York, 1980.
[5] Przytycki, F. Ergodicity of toral linked twist mappings. *Ann. Sci. Ecole Norm. Sup. (4)*, **16**, 345-354, 1983.
[6] Mezic, I., and Wiggins, S. On the integrability and perturbation of three-dimensional fluid flows with symmetry. *J. Nonlinear Sci.*, **4**, 157-194, 1994.
[7] Wiggins, S., and Ottino, J. M. Foundations of Chaotic Mixing. *Phil. Trans. Roy. Soc*., to appear.
[8] Qian, S. and Bau, H. H. A chaotic electroosmotic stirrer. *Anal. Chem.*, **74**, 3616-3625, 2002.
[9] Stroock, A. D., Dertinger, S. K. W., Ajdari, A., Mezic, I., Stone, H. A. and Whitesides, G. M. Chaotic mixer for microchannels. *Science*, **295**, 647-65, 2002.

INTERMITTENT DISTRIBUTION OF HEAVY INERTIAL PARTICLES IN TURBULENT FLOWS

Alain Pumir [*], Gregory Falkovich [**]
[*] *Institut Non Linéaire de Nice, 1361, route des Lucioles, F-06560, Valbonne, France*
[**] *Physics of Complex Systems, The Weizmann Institute of Sciences, Rehovot 76100, Israel*

Summary The phenomenon of preferential concentration of inertial particles is studied by following lagrangian trajectories. Elementary properties of the coarse-grained distribution of heavy particles in simple turbulent flows are investigated by direct numerical simulations. In the small Stokes number case, we compute the coarse-grained particle distribution, $\overline{n}_r$, and we demonstrate that the second moment $\langle \overline{n}_r^2 \rangle$ behaves as an approximate power law : $\langle \overline{n}_r^2 \rangle \sim r^\alpha$. The dependence of the exponent α as a function of the Reynolds and of the Stokes number is studied in the small Stokes number limit. Our results show a strong dependence of the level of fluctuation of the particle distribution as a function of the Reynolds number.

INTRODUCTION

Inertial particles advected by a turbulent flow are known to have very inhomogeneous distributions [1]. In clouds, the clustering of water droplets is known to have several important consequences [2],in particular in enhancing the collision rate between droplets, thus dramatically accelerating the formation of rain [3]. The origin of this effect is due to particle inertia : particles are advected by an effective velocity field $\mathbf{v}$, which is *compressible* ($\nabla \cdot \mathbf{v} \neq 0$) even when the surrounding fluid motion, $\mathbf{u}$ is incompressible ($\nabla \cdot \mathbf{u} = 0$). This effect is often refered to as preferential concentration.
In the limit of weak particle concentration, the density of particles, n, obeys :

$$\partial_t n + \nabla \cdot (\mathbf{v} n) = 0 \tag{1}$$

In an incompressible turbulent flow, with a Kolmogorov scale η, the divergence of the particles' velocity field $\mathbf{v}$ acts as a source term of density fluctuations at scales $\sim \eta$ [1]. As fluid elements get squashed by turbulence, the particle distribution reaches finer and finer scales, down to a cutoff length scale, r_d, determined by the diffusive process and/or by the size of the inertial particles. The clustering of particles is characterized here by the coarse-grained density of particles over a volume of size r, $\overline{n}_r$. This quantity can be expressed in terms of the properties of the trajectories of particles in the flow, conditioned by the stretching occuring along the trajectory [1, 3].
Using direct numerical simulations (DNS) of turbulent flows, we compute the properties of the second moment of the fluctuating quantity $\overline{n}_r$: $\langle \overline{n}_r^2 \rangle$ and its dependence as a function of the parameters in the problems, such as the Reynolds number, R_λ, the Stokes number, St, and size, r. A power law dependence is found numerically : $\langle \overline{n}_r^2 \rangle \propto r^\alpha$. In the limited range ($R_\lambda \leq 130$) studied here, a strong variation of the exponent is found.

LAGRANGIAN APPROACH

Inertial particles of density ρ_0, of radius a, evolve in a fluid of density ρ and of viscosity ν subject to an incompressible turbulent motion, described by an eulerian velocity field $\mathbf{u}(\mathbf{x}, t)$. In the low concentration case, particles can be considered as purely passive. Introducing $\beta = 3\rho/(\rho + 2\rho_0)$ and the Stokes time, $\tau_s = a^2/3\nu\beta$, the velocity $\mathbf{v}$ of inertial particles satisfies [2] :

$$\frac{d\mathbf{v}}{dt} - \beta \frac{d\mathbf{u}}{dt} = (\mathbf{u} - \mathbf{v})/\tau_s \tag{2}$$

We restrict ourselves here to the case where the time τ_s is short compared to the Kolmogorov time scale, $\tau_K = \langle \omega^2 \rangle^{1/2}$, so the Stokes number, $St \equiv \tau_s/\tau_K$ is small. The velocity is well approximated by $\mathbf{v} = \mathbf{u} - \tau_s \frac{d\mathbf{u}}{dt}$, where $\frac{d\mathbf{u}}{dt}$ is the lagrangian derivative of the velocity field : $\frac{d\mathbf{u}}{dt} \equiv \partial_t \mathbf{u} + (\mathbf{u} \cdot \nabla)\mathbf{u}$. The velocity field $\mathbf{v}$ is *compressible* : $\nabla \cdot \mathbf{v} = -\tau_s \nabla \cdot (\mathbf{u} \cdot \nabla)\mathbf{u} = -\tau_s tr(m^2)$, where m is the velocity derivative tensor : $m_{ij} = (\partial u_j/\partial x_i)$. The source of concentration fluctuations is related to the compressibility of the velocity field $\mathbf{v}$; it acts therefore most strongly at the Kolmogorov size, η [1, 3]. To estimate the coarse-grained distribution of particles over a size r, $\overline{n}_r$, at location $\mathbf{x}$ and time t, one has to trace back in time to the previous time $-t_r$, and to the location $\mathbf{x}_r$, such that the trajectory starting at $-t_r$, and location $\mathbf{x}_r$ ends up at $t = 0$ at location $\mathbf{x}$. The flow maps a small volume of characteristic size r at $t = 0$ to a volume whose largest scale is η at time $t = -t_r$. The intuitive picture is that particle concentration fluctuations accumulate at a scale r as long as it takes to expand the volume to a size $\sim \eta$ as the trajectory evolves backwards in time. The coarse-grained particle concentration is [1] :

$$\overline{n}_r(\mathbf{x}, t) = n_0 \exp\Big(\tau_s \int_{-t_r}^{0} tr(m^2)(t')dt'\Big) \tag{3}$$

The statistical weight associated with each trajectory is $\propto 1/n$. As a consequence, the second moment of the distribution of $\overline{n}_r$ is simply $\langle \overline{n}_r^2 \rangle_E = \langle n_0 \exp\Big(\tau_s \int_{-t_r}^{0} tr(m^2)(t')dt'\Big) \rangle_{Lag}$, where $\langle ... \rangle_E$ ($\langle ... \rangle_{Lag}$) refers to eulerian average (average over a set of trajectories).
In the small Stokes number limit, the difference $|\mathbf{v} - \mathbf{u}| \sim St|\mathbf{u}| << |\mathbf{u}|$ is small. We thus simply follow the compression along lagrangian trajectories of the flow to obtain an estimate of the quantity $\langle \overline{n}_r^2 \rangle$.

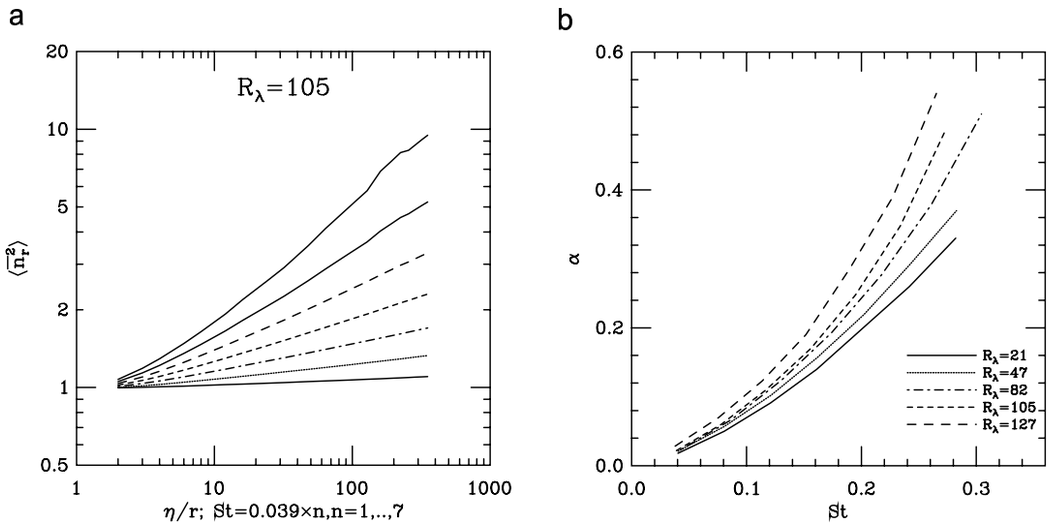


Figure 1. The variance of the concentration fluctuation $\langle \overline{n}_r^2 \rangle$ as a function of r, at $R_\lambda = 105$ and for $St = n \times 0.039$ (1a), and the exponent α as a function of St for several values of R_λ (1b).

NUMERICAL METHODS

A turbulent velocity field is generated by standard DNS methods [4]. At a given time, a set of N_l lagrangian trajectories is released. Along with the locations and velocities of the particles, we follow the tensor W describing the deformation of small (infinitesimal) fluid elements, as well as its inverse : $\frac{dW_{ij}}{dt} = m_{ik} W_{kj}$ and $\frac{dW_{ij}^{-1}}{dt} = -W_{ik}^{-1} m_{kj}$. The compression between time $-t_r$ and 0 of a fluid parcel of size η to a small scale r implies that the norm of W^{-1} grows by a factor (η/r) during this lapse of time. By monitoring the tensor W^{-1}, we are therefore able to determine the final location $\mathbf{x}$ of a trajectory, starting at $\mathbf{x}_0$, such that the compression of a fluid element between the initial $t = 0$ and the final time $t = t_r$ is equal to a given value (η/r). This allows us to determine the quantities X_r and $\overline{n}_r$ without having to integrate the equation of motion for the fluid particles backwards in time.

The number of grid points was varied in the range $32^3 - 256^3$. The product $k_{max}\eta$, where k_{max} is the highest wavenumber represented in the simulation is maintained in the range $1.4 \leq k_{max}\eta \leq 2$, thus assuring that the small scales are adequately resolved. The Reynolds number is varied in the range $20 \leq R_\lambda \leq 130$. Lagrangian trajectories are followed using the algorithm developped in the tensor W and W^{-1} are integrated according to the method introduced in [5].

SCALE DEPENDENCE OF THE COARSE-GRAINED DENSITY FLUCTUATION

Fig.1a shows a typical example of the r-dependence of $\overline{n}_r^2$ as a function of r, at $R_\lambda = 105$, and at a value of the Stokes number $St = 0.0390 \times n$, $n = 1, ..., 7$. Away from the values of r close to $\eta/r = 1$, $\langle \overline{n}_r^2 \rangle$ behaves almost as a power law, as revealed by the straight lines seen on the log-log plot. The curves however show a slight convexity.

The exponent can be computed directly from the numerical data by finite differences. Our numerical results demonstrate that a power law dependence is a very good approximation of the experimental data. The exponent was systematically measured at a value of $\eta/r = 200$. Fig.1b shows the exponents as a function of the Stokes numbers for several values of the Reynolds numbers. Remarkably, it is found that the exponent α grows strongly when the Reynolds number increases.

DISCUSSION

We have analysed the phenomenon of preferential concentrations by following, along individual particle trajectories, the quantity $tr(m^2)$. Our results show that the effect of preferential concentration is strongly dependent on the properties of the turbulence. The very small scale, intermittent structures of turbulence, such as vortex tubes, thus have a direct and important impact on the distribution of heavy particles in turbulent flows.

References

[1] Balkovsky E.,Falkovich G., Fouxon A., Phys. Rev. Lett. **86**, 2790, 2001.
[2] Shaw, R.A., Annu. Rev. Fluid Mech. **35**, 183, 2003.
[3] Falkovich G., Fouxon A., Stepanov M., Nature **419**, 151, 2002.
[4] Pumir A., Phys. Fluids, **6**, 2071, 1994.
[5] Yeung P.K., Pope S., J. Comp. Phys. **79**, 373, 1988 and Girimaji S.,Pope S., J. Fluid Mech. **220**, 427, 1990.

CHAOTIC STIRRING OF PASSIVE FLUID BY A VORTEX PAIR IN CIRCULAR DOMAIN

Alexandre A. GOURJII[*], Vyacheslav V.MELESHKO[**], and GertJan F. van HEIJST[***]

[*]*Institute of Hydromechanics, National Academy of Science, 01057 Kiev, Ukraine*
[**]*Kiev National Taras Shevchenko University, 01033 Kiev, Ukraine*
[***]*Eindhoven University of Technology, 5600 MB Eindhoven, the Netherlands*

Summary The advection problem of a passive fluid in 2D velocity field induced by two point vortex pair in an inviscid incompressible fluid inside a circular domain is considered. It is shown that the motion of fluid particles can demonstrate chaotic properties which result under certain initial conditions in an intensive stirring regime. Various criteria and methods were proposed in order to identify these regions, including: an analysis of phase trajectories, spectral and correlation analyses, construction of Poincaré sections, calculation of largest Lyapunov exponents. Some additional criteria are offered, namely: definition of the changes of length of border of investigated contours in time, analysis local stretching maps of passive contours and some statistical methods adapted to 2D fluid flows. Comparative analysis of various stirring criteria and methods in a velocity field induced by two and three point vortices in a circular domain is presented.

The stirring of a passive fluid domain with arbitrary borders in known velocity field induced by two point vortices is discussed. This problem has relations with various practical applications in chemical, pharmaceutical and food industries, and also in ecology. On the other hand, mixing phenomenon represents a fundamental scientific problem closely connected to the modern concepts of chaotic and regular dynamics [1].

It is known that laminar flows can result in intensive stirring regimes under certain conditions. Such regimes, which usually are called in the literature as chaotic ones, are a subject of intensive research both from theoretical, and from the experimental points of view. The main importance in these researches is that the velocity field in some laminar flows can be presented in analytical forms.

An advection problem is limited to the analysis of the trajectories of Lagrangian fluid particles (markers), which form borders of the region under investigation, in Eulerian velocity field. Every fluid particle can be treated as a passive fluid particle governed by vector equation

$$d\mathbf{x}/dt = \mathbf{U}(\mathbf{x},t), \qquad \mathbf{x}(0) = \mathbf{x}^0. \tag{1}$$

Here $\mathbf{x}^0(t)$ is the position of fluid particles (markers) and $\mathbf{U}(\mathbf{x},t)$ is the velocity field. The investigation is reduced to the study of an evolution of fluid particles in the flow. Every such particle moves along its own trajectory, and the equations (1) can predict particle positions at any moment. If we analyse evolution of an arbitrary contour presented by system of markers, then ordered connection of markers provides the boundary of the domain for a given moment of time.

The goal of the present study is a comparative analysis of various criteria of stirring processes in 2D bounded domains. We illustrate our analyses and main results using an example of fluid flow generated by N point vortices in a circular cavity. The achieved results allow to formulate the main peculiarities of stirring processes of a passive impurity.

Let us consider a system of N point vortices of intensities k_α at positions (x_α, y_α), $\alpha = 1,...,N$, in a circular cavity of radius a. Motion of vortices described by [2]

$$k_\alpha \frac{dx_\alpha}{dt} = \frac{\partial H}{\partial y_\alpha}, \qquad k_\alpha \frac{dy_\alpha}{dt} = -\frac{\partial H}{\partial x_\alpha}, \qquad H = -\frac{1}{4\pi}\sum_{\alpha=1}^{N} k_\alpha \left[\sum_{\beta=1}^{N}{}' k_\beta \ln r_{\alpha\beta} - \sum_{\beta=1}^{N} k_\beta \ln \rho_{\alpha\beta} \right], \tag{2}$$

where $r_{\alpha\beta}^2 = (x_\alpha - x_\beta)^2 + (y_\alpha - y_\beta)^2$, $\rho_{\alpha\beta}^2 = (x_\alpha - a^2 x_\beta / R_\beta^2)^2 + (y_\alpha - a^2 y_\beta / R_\beta^2)^2$, $R_\beta^2 = x_\beta^2 + y_\beta^2$.

The introduction of the stream function Ψ permits to present equations (1) for every markers with coordinates (X, Y) in Hamiltonian form

$$\frac{dX}{dt} = \frac{\partial \Psi}{\partial Y}, \qquad \frac{dY}{dt} = -\frac{\partial \Psi}{\partial X}, \qquad \text{with} \qquad X(0) = X^0, \qquad Y(0) = Y^0 \tag{3}$$

where $$\Psi = -\frac{1}{2\pi}\sum_{\alpha=1}^{N} k_\alpha \ln \frac{(X - x_\alpha)^2 + (Y - y_\alpha)^2}{(X - a^2 x_\alpha / R_\alpha^2)^2 + (Y - a^2 y_\alpha / R_\alpha^2)^2}.$$

Here the prime denotes omission of the singular term $\alpha = \beta$.

Consider an example of a periodic motion of two point vortices (vortex pair, $k_1 = -k_2 = k = 1.0$) initially located at $x_1^0 = 0.7$, $x_2^0 = -0.3$ and $y_1^0 = y_2^0 = 0.0$ inside a circular domain of radius $a = 1.0$. Here and in what follows we use non-dimensional length with a and non-dimensional time scale at a^2/k. In this case vortices move periodically with a period $T = 23.53$. Fig.1 shows trajectories of vortices, and fig.2 illustrates the Poincaré section for passive fluid markers.

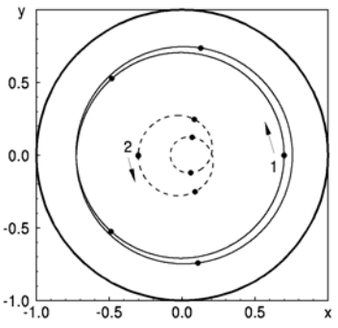


Fig.1 Trajectories of vortices.

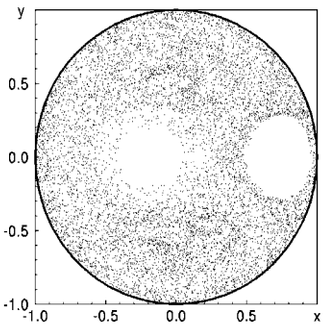


Fig.2 Poincaré section for marker.

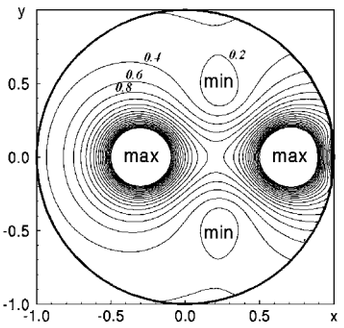


Fig.3 Local stretching map for T=0.

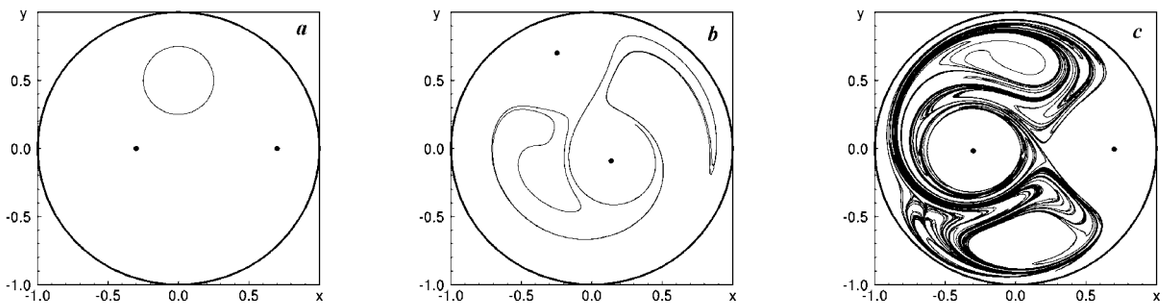


Fig4. Deformation of a passive contour by two point vortices at: (a) $t = 0$, (b) $t = T$, and (c) $t = 3T$.

Although two vortices have regular trajectories, the movement of passive markers in a given velocity field can be both regular and chaotic. The Poincaré section shows that the flow contains two regular zones located near point vortices. The fluid particle located in other part of circular domain, participates in chaotic motion. The similar results give other criteria, namely: spectral and correlation analysis of trajectories, values of the largest Lyapunov exponent for chosen markers both from regular and from chaotic zones of Poincaré section.

However, stretching of contour borders in the chaotic regions of marker motion demonstrates different stirring properties. Local stretching maps [3], which show a degree of exponential stirring of fragments of the contour placed at a point (x, y) of given velocity field for the default moment, and testify that those parts of a contour, which have an intensive stretching, are located near point vortices. There are even regions in the chaotic zone of motion, in which stretching appears insignificant (the region marked "min" in fig. 3). It is interesting to note that zones of moderate stirring are inside of chaotic motion of markers identified by Poincaré section (fig. 2).

Let us consider a deformation of a passive fluid contour formed by circular domain of radius $r_0 = 0.25$ with the centre placed at $(0.0,0.5)$, fig.4a. Vortices move in counter-clockwise direction. Positions of border contour, which correspond to moments $t = T$ and $t = 3T$, are plotted in figs.4b and 4c, respectively. The comparative analysis shows that in the top and bottom parts (in order to the initial vortex position) the flow forms two boundary regions. These zones are near the wall, where the normal component of velocity field is equal to zero, and form a region of an intensive stirring, which is approximately in the central part of the circular domain.

The comparative analysis of criteria shows that there is no universal criteria among a wide set of criteria of regular and chaotic motion of passive fluid particles. Each of the considered criteria is directed to the analysis of the certain peculiarities of evolution. It is possible to conclude that it is necessary to use a complex of criteria to detect the stirring regime. In some cases using separate criterion can result in erroneous results.

References

[1] Aref H.: Chaotic advection of fluid particles. *Phil. Trans. R. Soc. London*. **333**: 273-288, 1990.

[2] Lamb H.: Hydrodynamics. Cambridge University Press, 1932.

[3] Gourjii A.A.: Intensive and weak mixing in the chaotic region of a velocity field / in "Tubes, Sheets and Singularities in Fluid Dynamics", eds. K.Bajer and H.K.Moffatt / Kluwer Acad. Pub.: 87-92, 2002.

XXI ICTAM, 15–21 August 2004, Warsaw, Poland

CHAOTIC ADVECTION AND MIXING IN PULSED SOURCE–SINK SYSTEMS

Mark A. Stremler, Baratunde A. Cola
Department of Mechanical Engineering, Vanderbilt University
VU Station B 351592, Nashville, TN 37235, USA

Summary Laminar mixing in high-aspect-ratio volumes can be achieved by pulsing an arrangement of source–sinks pairs. We will present a chaotic advection analysis for pulsed source–sink systems in unbounded, circular, and rectangular domains. This analysis will be used to identify the optimal operating parameters for producing chaos.

INTRODUCTION

Achieving efficient and uniform mixing of laminar flows in high-aspect-ratio volumes is of practical interest in the design of many micro- and meso-scale fluid systems. One example of particular importance is DNA microarray analysis, a biological tool used widely in genomic research [1]. The typical microarray implementation uses DNA molecules suspended in a fluid volume that is approximately 7.5 cm by 2.5 cm by 50 μm, which we can view as a Hele–Shaw cell. The success of this tool depends in large part on having the suspended molecules uniformly sample as much of the surface as possible. Standard usage relies solely on molecular diffusion of the DNA and thus requires long sample times (at least 12 hours) and high DNA concentrations; both of these requirements limit the incredible potential of this technology. One would expect that improved results can be obtained by transporting the molecules with an imposed flow, and that significant enhancement is achieved when the flow produces chaotic advection. We refer to this process of building a system to mix by chaotic advection as 'designing for chaos' [2].

Under the Stokes flow approximation, the depth-averaged velocity in a Hele–Shaw flow can be represented by a velocity potential. Thus, assuming that the transport of molecules across the surface is determined by the depth-averaged velocity, an effective mixing system can be designed by considering chaotic advection in a two-dimensional potential flow. The flows of interest will transport molecules on a time scale much shorter than that of diffusion, so we expect the flow kinematics to provide a good representation of the overall molecule dynamics.

A potential flow that generates chaotic advection and can be implemented in a practical device [3] is produced by pulsing an arrangement of sources and sinks. Jones and Aref [4] present a comprehensive analysis of chaotic advection in a system consisting of one point source and one point sink in the unbounded plane. The source and sink each have strength q and are operated alternately, with switching between the singularities occurring periodically with frequency $1/T$. An important component of this system is the procedure whereby fluid extracted at the sink is subsequently reinjected at the source. The analysis in [4] concentrates primarily on a 'first out–first in' protocol that can be realized physically by collecting the extracted fluid in a tube beneath the sink, then turning the tube over and reinjecting the fluid at the source. It is shown in [4] that the flow is dominated by chaotic advection over a wide range of operating parameters. The details of the chaos change with the reinjection procedure, but the occurrence of chaotic advection persists.

The results for the unbounded plane provide a reasonable basis for designing a high-aspect-ratio mixing device. A variation on this system has been applied to enhancing microarray analysis [5], with preliminary results demonstrating that increased signal levels can be achieved an order of magnitude faster with pulsed source–sink mixing than with the traditional method. In contrast to the existing chaotic advection analysis [4], the real flow is bounded and the sources and sinks must operate in pairs in order to conserve volume. These are substantial changes that will impact the extent and character of the chaos, and thus an optimization of mixing in this system must be based on an analysis of chaotic advection in a bounded domain with source–sink pairs. Analytic solutions exist for source–sink pairs in unbounded and various bounded domains, making it possible to carry out a comprehensive analysis similar to that in [4]. We will present the results of this analysis for pulsed source–sink pairs in unbounded, circular, and rectangular domains.

MATHEMATICAL FORMULATION

Consider first the flow due to a source–sink pair in the unbounded plane. Superposition of a point source with strength q located at $z_{\mathrm{p}} = x_{\mathrm{p}} + \mathrm{i}y_{\mathrm{p}}$ in the complex plane and a sink with strength q at z_{n} produces a flow with complex potential

$$F(z) = (q/2\pi)\,\big[\log(z - z_{\mathrm{p}}) - \log(z - z_{\mathrm{n}})\big]. \tag{1}$$

Time dependence, and hence the opportunity for chaotic advection to occur, is introduced into the system by periodically switching operation among a set of source–sink pairs. Here we will consider only two source–sink pairs, $(z_{\mathrm{p}1}, z_{\mathrm{n}1})$ and $(z_{\mathrm{p}2}, z_{\mathrm{n}2})$, but more complex arrangments are obviously possible. For a period of time T the motion of a particle in the plane is governed by (1) with $(z_{\mathrm{p}}, z_{\mathrm{n}}) = (z_{\mathrm{p}1}, z_{\mathrm{n}1})$. This flow is then stopped, and the particle is advected for time T with $(z_{\mathrm{p}}, z_{\mathrm{n}}) = (z_{\mathrm{p}2}, z_{\mathrm{n}2})$. Switching between the two pairs is continued periodically. Particles extracted from the domain through a sink are reinjected through a source during the next cycle of operation. Thus, for example, particles extracted through $z_{\mathrm{n}1}$ are reinjected through $z_{\mathrm{p}2}$.

The motion of a particle at z in the upper half plane due to a point source with strength q at z_{p} and a point source with

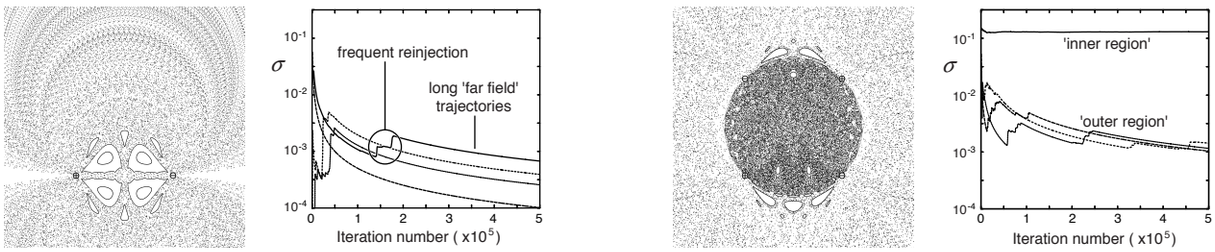


Figure 1. Chaos diagnostics for two pulsed source-sink systems in the unbounded plane. Sources are indicated by $\oplus$ and sinks by $\ominus$. Panels (a) and (c) show Poincaré maps, and (b) and (d) show convergence of the positive Lyapunov exponent for different initial positions. The system in (a)–(b) consists of one source and one sink operated alternately as in [4]. In (c)–(d) the right source and sink are operated as a pair, and then the left source and sink are operated as a pair. The dark circular area in (c) is the 'inner region'.

strength q at $z_{\rm n}$ is governed by the complex potential

$$F(z) = (q/2\pi)\,\big[\log(z - z_{\rm p}) + \log(z - \overline{z_{\rm p}}) - \log(z - z_{\rm n}) - \log(z - \overline{z_{\rm n}})\big], \tag{2}$$

where the overbar denotes complex conjugation. A variety of bounded domains can be obtained from (2) by conformal mapping of the z-plane to the w-plane. Circular and rectangular domains are given by the mappings

$$w = (\mathrm{i} - z)/(\mathrm{i} + z) \qquad \text{and} \qquad w = \big[1 + \mathrm{sn}^{-1}\big(K(k)\,z, k\big)\big]/2, \tag{3 a, b}$$

respectively, where $\mathrm{sn}(z, k)$ is the Jacobian elliptic sine, $K(k)$ is the complete elliptic integral of the first kind, and the parameter k is determined by the aspect ratio α of the domain through

$$\alpha = \big[K\big(\sqrt{1 - k^2}\big)\big]/[2\,K(k)].$$

Operation of these systems is the same as described for the unbounded plane.

RESULTS AND OUTLOOK

Chaos diagnostics such as Poincaré maps and Lyapunov exponents are computed by numerically integrating a given particle forward in time under the constraint that during a cycle of operation the particle remain on its streamline, given by $\psi(x, y) = \mathrm{Im}[F(z)] =$ constant. Some illustrative results are shown in Figure 1 for the unbounded plane.

Panel (a) shows a Poincaré map for a case with only one source and one sink, as analyzed in [4]. There are several elliptic islands close to the source and sink, but much of the domain is occupied by the chaotic sea. The motion of a particle in the chaotic sea is characterized by periods of frequent extraction and reinjection interspersed with long forays away from the singularities along essentially curved paths. The convergence of the Lyapunov exponents in Panel (b) clearly indicates that the rapid stretching associated with chaos is caused by frequent reinjection, while the long far-field trajectories are essentially regular.

Panel (c) shows a Poincaré map for a case with two source-sink pairs arranged on the vertices of a square. The scale of the system and the operation time T are the same as in Panel (a). Particles in the far field experience long, essentially regular trajectories similar to those above. The influence of the source–sink pairs is seen in the 'inner region'. For the choice of parameters used in Panel (c), a particle in the inner region is trapped there for all time and avoids being carried into the far field. Thus this inner region experiences a sustained level of rapid stretching, as shown in Panel (d).

Bounding the domain on a scale similar to the source–sink separations forces all of the particles to remain near the sinks, eliminating the far-field trajectories and causing almost all particles to experience frequent reinjection and high levels of chaos. Pulsed source–sink pairs in a bounded domain are thus expected to mix even better than the original unbounded analysis suggests.

The details of the chaotic advection in bounded domains depend upon the domain shape and size, the source–sink configuration, the reinjection procedure, and the operation time T. We will present the results of an analysis that identifies the optimal operating parameters for producing chaos in pulsed source–sink systems.

References

[1] DeRisi J.L., Iyer V.R.: Genomics and array technology. *Curr. Opin. Oncol.* **11**:76–79, 1999.
[2] Stremler M.A., Haselton F.R., Aref H.: Designing for chaos: Applications of chaotic advection at the microscale. *Phil. Trans. Roy. Soc. London* A, in press.
[3] Evans J., Liepmann D., Pisano A.P.: Planar laminar mixer. In *Proc. IEEE Int. Workshop Micro Electro Mech. Sys., Nagoya, Japan, Jan. 26–30*, pp. 96–101, 1997.
[4] Jones S.W., Aref H.: Chaotic advection in pulsed source-sink systems. *Phys. Fluids* **31**:469–485, 1988.
[5] McQuain M.K., Seale K., Peek J., Fisher T., Levy S., Stremler M.A., Haselton F.R.: Chaotic mixer improves microarray hybridization. *Anal. Biochem.*, in press.

ON DISSIPATIVE STRUCTURES OF STIRRING-GRIDS TURBULENCE

L. J. Jiang, S. S. Shy, and T. H. Yuan
Department of Mechanical Engineering, National Central University, Chung-Li 32054, Taiwan

Summary The spatiotemporal scalar and kinetic energy dissipation rates were measured in a stationary near-isotropic turbulence generated by a pair of vertically stirring grids in a water tank. Results reveal the complexity of dissipative scales containing line, blob, and sheet-like structures at which essentially all dissipations are concentrated. These fine structures are found ranging in scale from 0.4 to 5 Kolmogorov scale, η, with a mean of about 1 and 3 η for scalar and kinetic energy dissipative structures, respectively.

INTRODUCTION

Isotropic turbulence is the simplest turbulence that has long been used in theoretical treatments of turbulence, as a crucial building block for understanding more complex, real turbulent flows [1]. Most experimental studies on isotropic turbulence were conducted in wind and water tunnels, where a mean flow was passed through a grid and turbulence was in a rapidly decaying state. An alternative to water- or wind-tunnel decaying isotropic turbulence was a vibrating-grid turbulence (VGT) created in a water tank by a pair of vertically vibrating-grids, in which a near-isotropic stationary turbulence may be generated in the core region between the two grids [2]. This work presents measurements of kinetic energy (KE) and scalar dissipation rates in VGT flow using a four-dimensional particle image velocimetry (PIV) and a full spatial laser-induced fluorescence technique, so that fine-scale structures can be investigated. Fine-scale turbulence is central to the understanding of turbulent mixing [3]. Ever since 1948, Burgers and Townsend independently proposed three canonical structures of the dissipative scales for the vorticity field in turbulence, the line-like, sheet-like, and blob-like elements, respectively. The line-like and/or sheet-like structures have respectively one major dimension much greater and/or smaller than the other two. There is still no consensus on which canonical structure dominates fine-scale turbulence. For instance, some experiments found that finest scales were more to be line-like than sheet-like in a fully turbulent flow [4], while some reported that the sheet-like structure was the only underlying canonical element of for turbulent flows [5]. Furthermore, direct numerical simulations [6] concluded that the highest values of the vorticity were concentrated in line-like structures in homogenous isotropic turbulence. Hence, there is a need to further study the true dissipative structures, in particular, the full spatial KE dissipation rate field in statistically stationary isotropic turbulence, as the one presented here. We will show and compare the probability density functions of the sizes of both KE and scalar dissipative structures in the VGT flow for the first time.

EXPERIMENTAL

Figure 1 presents the experimental setup, including the VGT apparatus and the associated 4-D PIV arrangements. Vertically vibrating a pair of horizontally-oriented grids in a water tank of an inside dimension of 15x15x30 cm height can generate near-isotropic stationary turbulence in the core region between the two grids, please see [2] for details. The experimental conditions are: the distance between the two grids is fixed to be 10.56 ± 2 cm and the grid stroke, mesh size, and oscillation frequency are set to be S=2 cm, M=3 cm, and f=6 Hz, respectively, yielding a grid turbulent Reynolds number $Re_g=fSM/\nu$=3,600. The method uses a high-speed successive sweeping 5-W Argon-ion laser sheet and two synchronous high-speed stereo CCD cameras (up to 8,000 frames/s) combined with a fast image processing system, so that the underlying full spatial velocity field in near-isotropic region of the VGT flow can be extracted (see Fig. 1), where the seeding particles used are polyethylene with a mean diameter of 15 μm and with a density of 1.03 g/cm^3. Each measuring image (1.4x1.2 cm^2) contains 480x420 pixels in which the resolution reaches beyond the local Kolmogorov scale and may resolve the local strain-limited molecular diffusion scale of turbulence. Note that in this work the temporal separation between successive data planes is 4 ms and the spatial resolution is about 29 μm, which are respectively much smaller than the estimated Kolmogorov time (42 ms) and length (0.21 mm) scales. The resulting four-dimensional data can be thus differentiated directly in all three space dimensions and in time to extract the true dissipation rates. Due to the space limit, the reader is directed to [7] for a detailed treatment concerning measurements of the scalar dissipation rate in the same VGT flow.

RESULTS AND DISCUSSION

Figure 1 also shows three typical 3-D velocity maps at three different z positions, where the axes are normalized by the local strain-limited viscous diffusion scale $\lambda_v \approx 5.9\ \eta$, the color bar represents the magnitude and direction of z-component velocity, and the reference arrow of 1.44 cm/s that is the energy-weighted r.m.s. turbulent intensity for the VGT flow at f = 6 Hz [2] is also plotted. Thus, the true KE dissipation rate field can be determined by differentiation of these data planes in all three directions. Figure 2a displays a typical example of a fully resolved three-dimensional (420^{2}x210 pixels) spatial data volume, revealing the kinetic energy dissipation rate field $\varepsilon(\boldsymbol{x},t)=2\nu\boldsymbol{s}:\boldsymbol{s}$, where $s = 0.5(\partial u_i / \partial x_j + \partial u_j / \partial x_i)$ is the strain rate tensor in index notation.. A typical scalar dissipation rate field, $\chi=\nabla\zeta\cdot\nabla\zeta$,

is shown on Fig. 2b, where the experimental conditions are the same as Fig. 2a, ζ is the conserved scalar, and ζ_m is the mean value in such data plane. It is found that fine-scale mixing occurs in both sheet-like layers and line-like tubes (roughly circular) for the present VGT flow. The distribution of the dissipation rate field is a highly intermittent phenomenon, in which high dissipation rates occur very infrequently, similar to that found by Sreenivasan & Antonia [3]. Regions of high kinetic energy dissipation rate are well correlated with regions of high principal strain rate. We found that the fine structures of the kinetic energy dissipation rate field in the present VGT flow are complex, containing sheet-like, line-like, and blob-like structures at which all dissipations are concentrated. This result is different from [5] in which only the sheet-like structure is observed in a free shear turbulent jet flow, probably due to different types of turbulence applied. In order to estimate the sizes of these fine structures, we plot only highest values of KE dissipation rate data for $\log_{10}\varepsilon/\langle\varepsilon\rangle \geq 0.66$ (less than 2 % of volume fraction). As can be seen from Fig. 2c, these fine structures are found ranging in scale from 0.4 to 5 η with a mean of about 1 and 3 η for scalar and kinetic energy dissipative structures, respectively. The important scaling properties of 3-D velocity data are also discussed.

References

[1] Hinze, J. O.: Turbulence. McGraw-Hill, New York, 1975.

[2] Shy, S. S., and Breidenthal, R. E.: Turbulent Stratified Interfaces. *Phys. Fluids A* **3**, pp. 1278-1285, 1991; Shy, S. S., Tang, C. Y., and Fann, S. Y..: A Nearly Isotropic Turbulence Generated by A Pair of Vibrating Grids. *Exp. Thermal Fluid Sci.* **14**, pp. 251-262, 1997; Yang, T. S., and Shy, S. S.: The Settling Velocity of Heavy Particles in an Aqueous Near-Isotropic Turbulence. *Phys. Fluids* **15**, No. 4, pp. 868-880, 2003.

[3] Sreenivasan, K. R., and Antonia, R. A.: The Phenomenology of Small-scale Turbulence. *Ann. Rev. Fluid Mech.* **29**, pp. 435-472, 1997.

[4] Kuo, A. Y., and Corrsin, S.: Experiments on the Geometry of the Fine-structure Regions in Fully Turbulent Fluid. *J. Fluid Mech*. **56**, pp. 447-479, 1972.

[5] Dahm, W. J. A., Southerland, K. B. and Buch, K. A.: Direct, High-resolution, Four-dimensional Measurements of the Fine Scale Structure of *Sc* >> 1 Molecular Mixing in Turbulent Flows. *Phys. Fluids A* **3**, pp. 1115-1127, 1991.

[6] She, Z. S., Jackson, E., and Orszag, S. A.: Intermittent Vortex Structures in Homogeneous Isotropic Turbulence, *Nature* **344**, pp. 226-228, 1990.

[7] Shy, S. S., Gee, K. L., and Lee, E. I.: Three-dimensional Measurements of Scalar Dissipation Rates in a Zero-Mean-Shear Turbulence. *J. Flow Visual. Image Process.* **6**, pp. 177-187, 1999.

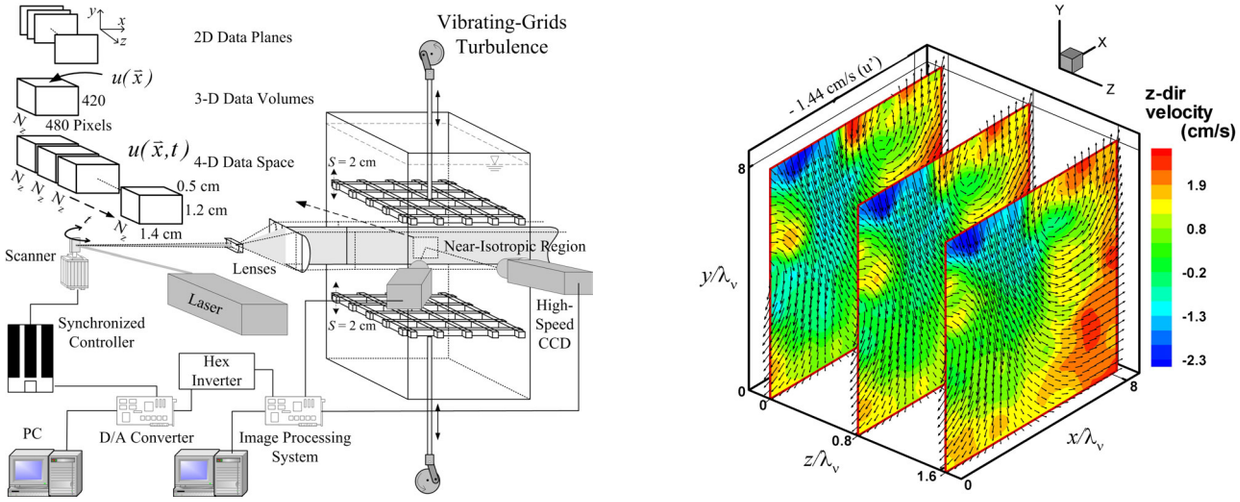
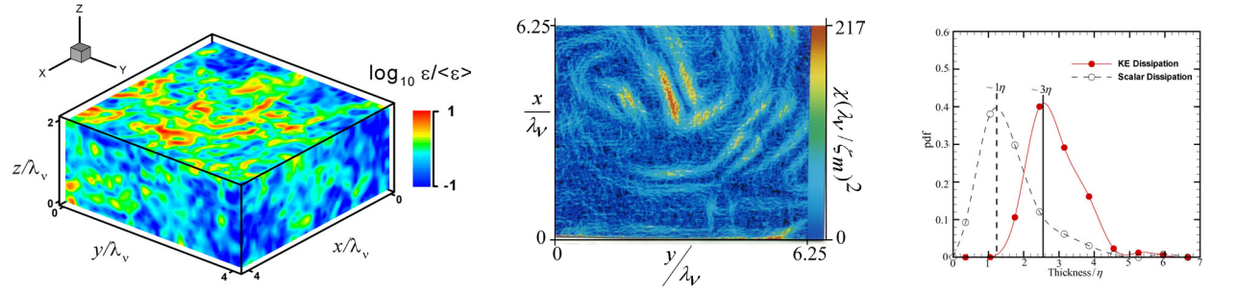


Fig. 1. Schematic of the setup and 3-D velocity maps, where the local strain-limited viscous diffusion scale $\lambda_v \approx 5.9\eta$ (the Kolmogorov length scale).



(a) KE Dissipation Rate (b) Scalar Dissipation Rate (c) PDF of Fine Structure Sizes

Fig. 2. (a) Typical logarithmic plot of kinetic energy dissipation rate field, where $\langle\varepsilon\rangle$ is the mean kinetic energy dissipation rate averaged from the corresponding data volume. (b) Typical scalar dissipation rate field $\chi = \nabla\zeta\cdot\nabla\zeta$, where ζ is the conserved scalar and ζ_m is the mean value in such data plane. (c) The probability density function of the thickness of both scalar and kinetic energy dissipative structures.

EVALUATION OF TRANSPORT PROPERTIES BY EXCHANGE MATRIX METHOD

Tatyana S. Krasnopolskaya[*], Vyacheslav V. Meleshko[**]
[*]*IHM NASU, Department of Vortex Motion, Zhelyabov 8/4, 03680 Kiev, Ukraine*
[**]*Kiev National Taras Shevchenko University, Volodymirska 64, 01033 Kiev, Ukraine*

Summary This work is devoted to the study of transport properties of materials in chaotic two-dimensional stirring, using Spencer & Wiley matrix method. This study is important for applying in problems of pollutant transport (such as petroleum patches) in tidal flows. In order to construct this special exchange matrix we use an approximation of such flows suggested by Zimmerman, who adopted the idea of chaotic advection, first put forward by Aref. Then for a quantitative estimation of the transport properties we explore a coarse-grained density description introduced by Gibbs and Welander. Such coarse-grained representations over an investigation area show a "residence place" for the pollutant material at any instant. The exchange matrix can show transport of patches or particles from any place in the area under consideration to an arbitrary location in the tidal sea and time if it happens.

.

INTRODUCTION

The study of transport of pollutants is an important issue. This work deals with exchange matrix method described by Spencer & Wiley [1] and in the paper [2]. We apply this method to problems of pollutant transport, for example, of petroleum patches in tidal flows. A good approximation of such flows was suggested by Zimmerman [3]. He deviated from earlier attempts at modeling tidal flows by means of turbulence theory and adopted the idea of chaotic advection, first put forward by Aref [4]. In this pioneering paper it was shown that chaotic mixing of a passive tracer (which in our case will be the petroleum patch) may occur even in deceptively simple flow systems. Zimmerman [3] realized that the macroscale flow in a tidal sea is not much more complicated than chaotic advection model and so should lead to similar phenomena. In particular, he suggested that the many fine striations often observed in scalar dispersal were due to chaotic motion driven by the macroscale, rather than microscale turbulent mixing. By numerical simulations he demonstrated that the patterns formed by dispersed passive particles were very similar to field observations. In the recently published tutorial paper Aref [5] described numerous applications of chaotic advection in fluid mechanics, in general, and in geophysical and geological flows, in particular. It was shown in many other works [6,7] how important it is to identify the parameters and conditions that lead to widespread chaotic advection. In the course of flow evolution an initially designated interface of any petroleum patch may become extremely convoluted, and it appears difficult to follow pattern structures in full detail. In this study we use the special algorithm developed in our previous paper [7], in which extra contour (surface) points are automatically added when needed. Attention will also be given to a quantitative estimation of the transport quality based upon measures first suggested by Gibbs [8] and Welander [9], such as coarse-grained density. Such coarse-grained representations over an investigation area, show a "residence place" for the pollutant material at any instant. If initially it occupies any box *ij* of the whole marine zone, divided by square boxes, nonzero elements of the exchange matrix show places where pollutant particles go.

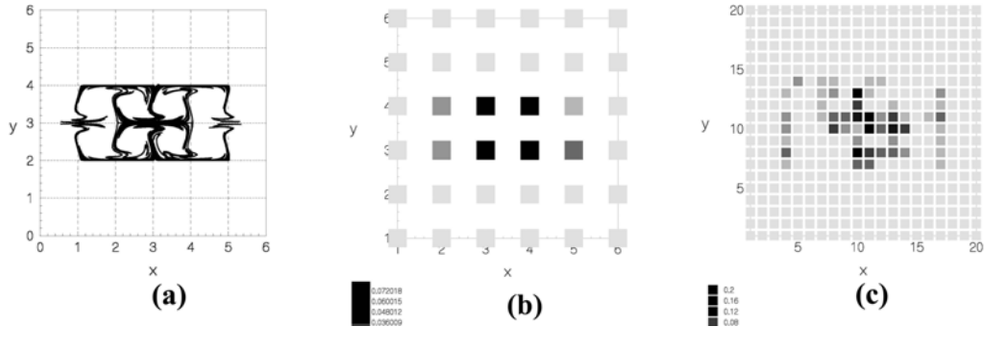
EVALUATION OF CHAOTIC TRANSPORT

In the present study of the petroleum patch transport in tidal areas we use Zimmerman's kinematical model [3, 6] which is based upon a superposition of a tidal and a residual current flow field. The kinematical model describes a motion of a mathematical point that moves at each instant with the velocity corresponding to its instant position. The petroleum particle is supposed to be inertialess, not subjected to diffusion or interfacial tension. The residual time independent current field is an infinite sequence of clockwise and anticlockwise rotating eddies. Streamlines of the residual velocity field divide the whole area into square cells of equal area, with elliptic points in the centers and hyperbolic points in the corners of cells. The tidal field plays a role of a pertubation of the Hamiltonian system (the stream function is the Hamiltonian for the residual flow). In general this pertubation leads to chaotic dynamics and could be studied in different ways, for example, by means of Poincaré sections. However, in pollutant spreading problems, we are interested in the short term history of pollutant transport. Poincaré sections present the history of motion of points in some area during a long time interval, say, during a thousand periods of a tidal flow. (For the problem of petroleum patch transport this corresponds to the history of one point during almost one and a half year.) On the contrary, ecological considerations demand that disastrous spread of pollution has to be stopped in days or weeks. Therefore, we need to know which part of the Eulerian space will be polluted in a short time and, more importantly, how much petroleum will leak to some specific part of a sea. The orbit expansion method [6], developed for a quantification of the chaotic transport and exploited an assumption that the contributions of tidal and residual currents are of different orders (the tidal is much stronger), does not give answers to those questions. In our case, it is important to know not the mixing region (where presumably mixing is instantaneous) obtained by the long time tool – Poincaré sections, -- or the rate of material exchange (which could be high in a very narrow domain), but how uniformly this mixing region is

distributed over the whole area during a specific finite interval of time. We suggest a different approach for an estimation and quantification of pollutant transport.

Here we briefly present a methodology for the quantification of the chaotic transport [7] based on the statistical quantities such as a coarse-grained density. First step is to present a petroleum patch, for example, as a circular blob continuously occupying some part in marine or coastal zone. Then we use a contour tracking algorithm that conserves both area and topological properties (connectedness and non-self-intersection) to find the blob's boundary in Eulerian space at any moment of time. In our algorithm the key idea is the use of a non-uniform distribution of points at the initial contour to present this interface in such a way that (i) the distance between neighbouring points remains between some chosen values (for that points are added when the distance becomes long enough and points are removed when it becomes too short) and (ii) the angle between any neighbouring straight lines is larger than some prescribed value. The principal advantage of our algorithm is that area preservation of the blob enclosed by the contour is guaranteed even after high stretching and complicated folding. Knowing the position of the contour line (the boundary of the petroleum patch) we can construct an Eulerian description of the mixing process, giving an opportunity to quantify mixing at any moment of time.

The next step is dividing the whole area of investigating marine zone S into N square boxes of a side size δ with an area $s = \delta^2$ each, then the marine zone area can be written as $S = Ns$. The conservation of petroleum area enclosed by the contour line permits us to introduce a probability function for the petroleum distribution inside a box with number k as proportional to value of area P_k occupied by petroleum in this box. A ratio of P_k and s can be called a probability density or a coarse-grained density. Figure shows the highly ramified petroleum patch (a) and the coarse-grained representations (with (b) δ=1 and (c) δ=0.3) of the mixing pattern after 9 periods of the tidal flow in the zone with 6 cells of the residual current in x and in y directions. The lightest boxes correspond to areas without petroleum.



At any instant the coarse-grained representation of the petroleum patch distribution clearly demonstrates which boxes are empty, and which have the petroleum material and how much. It may also be used to show the exchange of material inside boxes, if we study this process and construct a special exchange matrix for the tidal flow in the area under consideration. Then using this matrix we can predict transport of petroleum from any place (any box) in the area to an arbitrary location in the tidal sea and determine the time when it happens.

References

[1] Spencer R.S., Wiley R.M.: The mixing of very viscous liquids. *J. Colloid Sc* **6**:133-145, 1951.

[2] Kruijt P.G.M., Galaktionov O.S., Anderson P.D., Peters G.W.M., Meijer H.E.H.: Analyzing mixing in periodic flows by distribution matrices: Mapping method, *AIChE Journal* **47**(5):1005-1015, 2001.

[3] Zimmerman J.T.F.: The tidal whirlpool: a review of horizontal dispersion by tidal and residual currents, *Neth. J. Sea Res.* **20**:133-154, 1986.

[4] Aref, H.: Stirring by chaotic advection. *J. Fluid Mech* **143**:1-24, 1984.

[5] Aref, H.: The development of chaotic advection, *Phys. Fluids* **14**:1315-1325, 2002.

[6] Beerens S. P., Ridderinkhof, H., Zimmerman J. T. F.: An analytical study of chaotic stirring in tidal areas. In: *Chaos Applied to Fluid Mixing* (ed. H. Aref & M. S. El Naschie) Pergamon Press :267-285, 1995.

[7] Krasnopolskaya T.S., Meleshko V.V., Peters G.W.M., Meijer H.E.H.: Mixing in Stokes flow in an annular wedge cavity. *Eur.J. Mech.B/Fluids* **18**: 793-822, 1999.

[8] Gibbs J.W.: Elementary Principles in Statistical Mechanics. New Haven, Scribner 1902.

[9] Welander, P.: Studies of the general development of motion in a two-dimensional ideal fluid. *Tellus* **7**:141-156, 1955.

XXI ICTAM, 15–21 August 2004, Warsaw, Poland

MIXING IS AN AGGREGATION PROCESS

E. Villermaux*, J. Duplat**
*Université de Provence & Institut Universitaire de France, IRPHE, 13384 Marseille Cedex 13, France
**Université de Provence, IUSTI, 13453 Marseille Cedex 13, France

Summary Experiments show how a stirred scalar mixture relaxes towards uniformity through an aggregation process. The elementary bricks are stretched sheets whose rates of diffusive smoothing and coalescence build up the overall mixture concentration distribution. The cases studied in particular include mixtures in two and three dimensions, with different stirring protocols and Reynolds numbers which all lead to a unique family of concentration distributions stable by self-convolution, the signature of the aggregation mechanism from which they originate.

INTRODUCTION AND OBSERVATIONS

A mixture is a transient state between the initial segregation of the constituents, and their ultimate homogeneity. The overall mixing process of a drop of dyed fluid in a stirred medium involves two phenomena : a process of dispersion of the drop in the diluting medium by which the phases interpenetrate, and a process of interaction between the dispersed elements from which homogeneity arises. It is shown here that the mixture's evolution is directed by a random aggregation process essentially independent of the detailed stirring mechanism. In a first experiment (Fig.1a), a turbulent jet of water plus dye discharge in a square, transparent, long duct at $Re \simeq 10^4$. A second experiment consists in stirring a blob of dye with a rod in a thin layer of very viscous fluid at $Re \simeq 10^{-1}$, by a two-dimensional, quasi-periodic protocol (Fig. 1b).

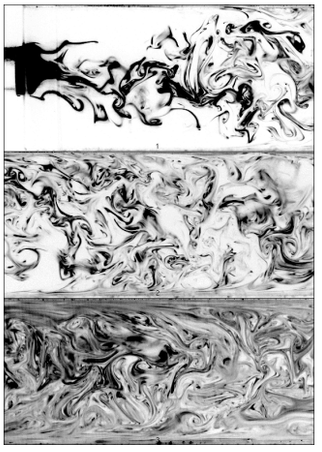
a)  b) 

Figure 1. a) Successive mixing states of a dye discharging from a jet in a square duct. b) Mixture realized by stirring a dye in a viscous two-dimensional layer by a periodic protocol.

In both cases, the distribution $P(C)$ presents a skewed, bell shape which gets narrower around $\langle C \rangle$, very well described by a family of one parameter distributions, namely Gamma distributions

$$P(X = C/\langle C \rangle) = \frac{n^n}{\Gamma(n)}\, X^{n-1}\, e^{-nX}. \qquad (1)$$

The fairness of the fit holds for the whole concentration range, down to quite low probability levels, and accounts for the deformation of $P(C)$ through the single parameter n which depends on the protocol: it increases like the power 5/2 of time (or downstream location) in the channel case, and like the power 3/2 of the number of stirring cycles in the two-dimensional case (Fig.2).

STRETCHING ENHANCED DIFFUSION AND MIXTURE COMPOSITION

Stirring motions progressively convert a compact blob in a set of sheets of increasing surface and decreasing thickness [1]. Let $s(t)$ be the distance between two material particles in the direction z perpendicular to a sheet, and $\sigma(t) = \partial \ln s(t)/\partial t$ its rate of compression. The concentration profile $c(z,t)$ across the sheet results from an equilibrium between stretching induced compression and diffusive spreading. The thickness reduction process goes on until $\sigma(t)$ is balanced by the rate of diffusive spreading $D/s(t)^2$. This defines the mixing time t_s of the sheet. If for instance the sheet thickness is $s(t) = s_0(1+\gamma t)^{-\beta}$ where γ is an elongation rate, then $\gamma t_s \sim (\gamma s_0^2/D)^{\frac{1}{2\beta+1}}$.

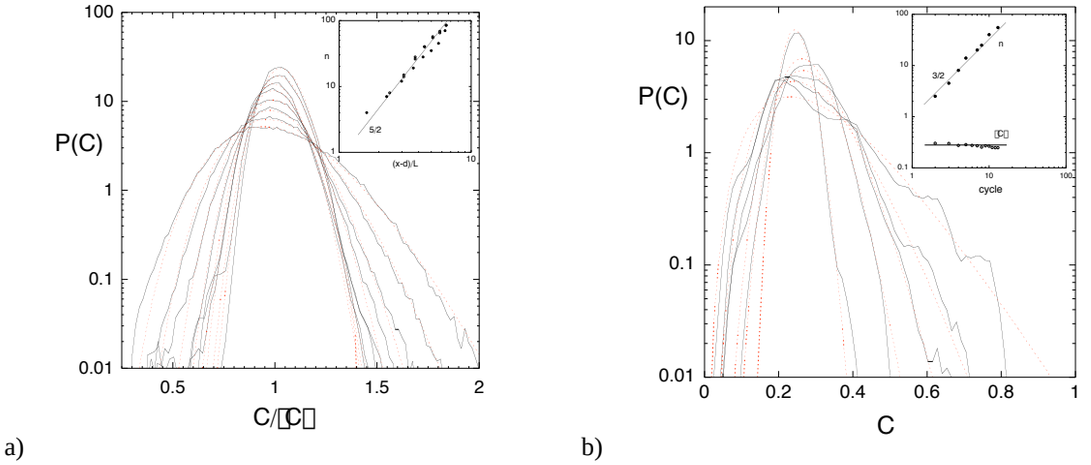


Figure 2. a) Downstream evolution of the concentration distribution $P(C)$ as the dye progresses along the duct as shown on Fig. 1 and fitting parameter n of the distributions of Eq. 1 as a function of the downstream distance $(x-d)/L$. $\circ$: $Re = 10^4$, $\bullet$: $Re = 5 \times 10^3$. b) Concentration distributions for the two-dimensional protocol as a function of the number of stirring cycles, and fitting parameter n. $Re \simeq 10^{-1}$.

Beyond this characteristic time, the maximal concentration in the sheet $c(0,t)$ which is such that $c(0,t)(Dt)^{1/2}/s(t)$ is, by mass conservation, constant, decays as $c(0,t) \sim (\gamma t)^{-\beta-1/2}$. In incompressible two-dimensional flows where the length of material lines grow like γt [2], the mean transverse thickness of the scalar sheet decrease as $s(t) = s_0/\sqrt{1+(\gamma t)^2}$, providing $c(0,t) \sim (t/t_s)^{-3/2}$ for $t > t_s$, with $t_s \sim \frac{1}{\gamma} Pe^{1/3}$, where $Pe = \gamma s_0^2/D$ is a Péclet number. If material surfaces in three dimensions grow like $(\gamma t)^2$, then [3], $s(t) = s_0/(1+(\gamma t)^2)$, providing $c(0,t) \sim (t/t_s)^{-5/2}$ for $t > t_s$, with $t_s \sim \frac{1}{\gamma} Pe^{1/5}$. These timescales are the relevant mixing times as soon as the inverse of the elongation rate γ^{-1} is smaller than the diffusive time of the sheet constructed on its initial size s_0^2/D, that is for $Pe \gg 1$.
However, the sheets interact as they move in the flow so that their diffusive boundaries interpenetrate to give rise to new sheets whose concentration profile is the *addition* of the original ones owing to the linearity of the diffusion process. Because of the irregular stirring motions, the addition of the concentration levels is made at random among those available in the population $P(C)$ at time t which therefore evolves by self-convolution as [4]

$$\frac{\partial P}{\partial t} = -\frac{\partial}{\partial C}\left(\left\langle \frac{\mathrm{d}c}{\mathrm{d}t}\right\rangle P\right) + \frac{\mathrm{d}n}{\mathrm{d}t}\left(-P + P^{\otimes(1+1/n)}\right), \tag{2}$$

whose asymptotic solution is a Gamma distribution of order n. The piling-up of the concentration levels by coalescence contributes, through the second term of Eq. 2, to the increase of the average concentration by a factor given by $\exp\{\int \mathrm{d}n/n\} = n$ and is balanced by the damping factor when $n = 1/c(0,t)$. Stretching motions in 3D form sheets whose maximal concentration $c(0,t)$ decays like $t^{-5/2}$ whereas 2D motions form filaments whose maximal concentration decays like $t^{-3/2}$. The coalescence mechanism giving rise to Eq. (1), will therefore make the average concentration $\langle C \rangle$ constant if

$$n \sim t^{-3/2} \quad \text{in 2D, and} \quad n \sim t^{-5/2} \quad \text{in 3D}, \tag{3}$$

as expected from Fig. 2. The mechanism building-up the concentration distribution $P(C)$ solely relies on *random additions* of concentration levels, independently of the *rate* at which these additions are made.

CONCLUSIONS

Composition fields obtained at a very low Reynolds number are very similar to those obtained at much larger Reynolds number. The reason is that the evolution mechanism is the same. The motion of the rod in the two-dimensional viscous fluid plays the role of the random stirring motions in higher Reynolds number flows. Their role is to ensure the independence –in the statistical sense of Eq. (2)– of the concentration levels additions giving rise to the self-convolutive construction of the mixture composition; a particularly simple paradigm for the impact of turbulence on mixing.

References

[1] Duplat, J. and Villermaux, E. 2000 Persistency of material element deformation in isotropic flows and growth rate of lines and surfaces. *Eur. Phys. J. B* **18**, 353–361.
[2] Meunier, P. and Villermaux, E. 2003 How vortices mix *J. Fluid Mech.* **476**, 213–222.
[3] Villermaux, E. and Rehab, H. 2000 Mixing in coaxial jets. *J. Fluid Mech.* **425**, 161–185.
[4] Villermaux, E. and Duplat, J. 2003 Mixing as an aggregation process. *Phys. Rev. Letters* **91**, (18), 184501.

STIRRING AND MIXING EFFECTS IN AGGLOMERATIVE PRECIPITATION

Jerzy Bałdyga, Magdalena Jasińska
Warsaw University of Technology, Faculty of Chemical and Process Engineering, Waryńskiego 1, PL 00-645 Warszawa, Poland

Summary Precipitation of a solid product from liquid ionic solutions includes mixing, fast chemical reaction, nucleation, growth and agglomeration of crystals. At high supersaturation precipitation is dominated by agglomeration of particles that are much smaller than the Kolmogorov microscale. Modeling of particle agglomeration includes effects of bulk fluid motion, Brownian diffusion (both with hydrodynamic interaction), colloidal forces and mixing. Mixing determines chemical environment of colliding particles.

INTRODUCTION

Consider the complex process of agglomerative precipitation of solid products from two liquid ionic solutions A and B:

$$A^{n+} + B^{n-} \rightarrow C\downarrow \qquad (1)$$

involving instantaneous (mixing controlled) chemical reaction, subsequent crystallization of the product (i.e. nucleation and growth of crystals) and its agglomeration. At low supersaturation there are usually negligible effects of agglomeration, and the crystals size distribution is mainly affected by competition between nucleation and growth of crystal, which results from the competition between creation and consumption of supersaturation. Supersaturation is created by mixing controlled chemical reaction, and is consumed by precipitation; it also decreases due to mixing with the less supersaturated environment. At high supersaturation the process is dominated by agglomeration. Modeling of the agglomerative precipitation process requires a complete knowledge of the spatial distribution of instantaneous, local concentrations of all ions and molecules involved in the process and resulting distribution of supersaturation. Supersaturation distribution determines the local rates of nucleation and growth of particles and affects strongly agglomeration process; effect on agglomeration results from the fact that the supersaturated solution supplies material necessary to bond colliding particles and form agglomerates. Local concentrations determine also electrical interaction between small colloidal particles, because most particles in aqueous media are charged, and resulting repulsion force depends on solution composition. Identification of concentration distributions requires application of mixing models. In what follows PDF approach is used to model mixing, whereas the agglomeration rate is expressed as the product of expressions describing collision rate and probability of agglomeration.

THEORY AND MODELLING OF AGGLOMERATION

Collision of particles

We consider small particles of collision diameter smaller than the Kolmogorov length microscale. We further assume that particles are so small that their relaxation time is much smaller than the Kolmogorov time microscale. Under such assumptions the effect of inertial forces on the micro-motions of the fluid and particles can be neglected and the creeping flow can be assumed. New formed nuclei have the size of the order of nanometer and they grow due to crystal growth and agglomeration up to several micrometers size. Hence, to follow nucleation, growth and agglomeration of particles, one needs to model simultaneously the perikinetic (Brownian diffusion), orthokinetic (convective transport due to fluid motion) as well as an intermediate regime of collision and to include effects of the colloidal forces on relative particle velocity. The model applied in this work is based on the convective-diffusion equation for the probability of finding two particles at a given relative position, similarly as in models presented in ref. [1, 2]. The Batchelor-Green [3] relation is used for the relative particle velocity**,** and the turbulent flow at scales smaller than the Kolmogorov microscale is represented by assuming an axisymmetrical extensional flow with the mean value of an extension rate given by Batchelor [4]. The tensor of Brownian diffusion is expressed using the method of Batchelor [5] and the hydrodynamic functions $A(\rho,\lambda)$, $B(\rho,\lambda)$, $G(\rho,\lambda)$, $H(\rho,\lambda)$ that describe the disturbance of the ambient fluid velocity by presence of two colliding particles are determined by solving analytically the Stokes and continuity equations following the method proposed by Lin et al. [6]. For a very small distance between particles instead of an exact analytical solution the near-contact asymptotics are used following O'Neill and Majumdar [7]. The colloidal interaction forces that induce particle velocity in the radial direction result from attractive and repulsive potentials; the potentials are calculated from equations proposed by Hamaker and Hogg respectively. The repulsive potential is identified with the diffuse layer potential and calculated from the Gouy-Stern-Grahame double layer model [8] using the surface potential resulting from the Nernst equation. The Nernst equation shows that composition of the solution including ionic strength and ion concentration affects the surface potential the resulting collision rate. This means that also mixing, by affecting concentration distribution, has indirect effect on the agglomeration rate. Fig. 1 presents distribution of the pair probability function computed for spherical particles. One can see increased concentration of small particles in the neighbourhood of the larger one; this results from slowing down of particles due to action of both repulsive forces and hydrodynamic interactions. Once the pair probability function distribution is determined, the collision rate constant (collision kernel) can be computed by integrating the particle flux over the entire particle surface.

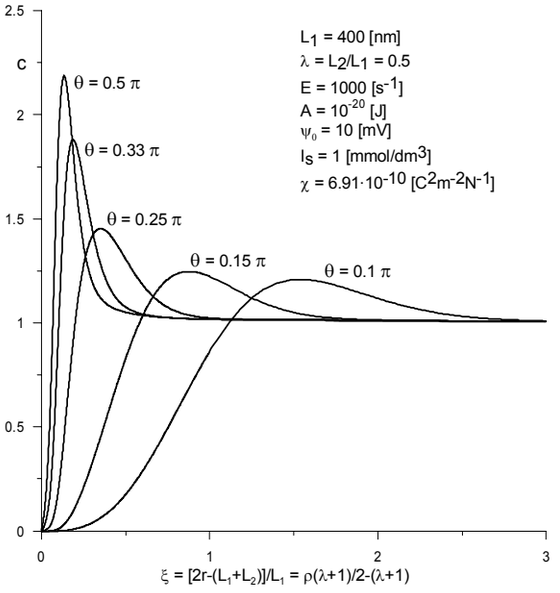


Fig.1.Pair probability function distribution

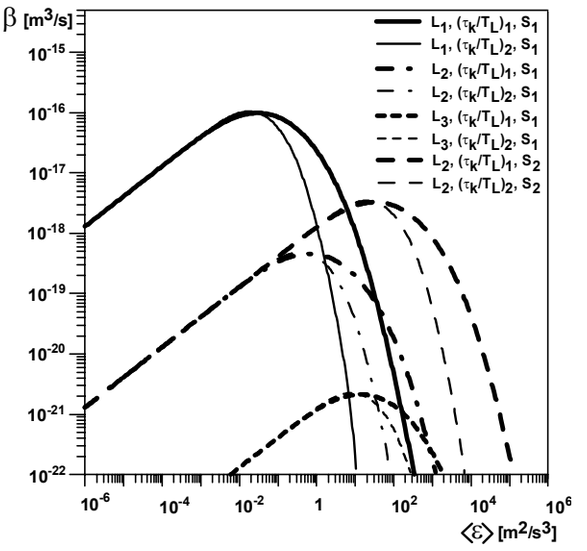


Fig.2. Effect of the rate of energy dissipation $\langle \varepsilon \rangle$ on the rate of aggregation. $L_1 = 10^{-6}$ m, $L_2 = 10^{-7}$ m, $L_3 = 10^{-8}$ m, $(\tau_k/T_L)_1 = 10^{-4}$, $(\tau_k/T_L)_2 = 0.01$, $S_1 = 2800$, $S_2 = 14400$.

Probability of agglomeration

In the previous section the collision rate of particles was modeled. However, especially in the case of large particles not every collision leads to agglomeration. That is why the concept of agglomeration probability has to be introduced. Agglomeration probability function expresses probability that during particle collision there will be enough time to build the crystalline bridge strong enough to resist the hydrodynamic stresses generated by turbulence.

In this presentation the probability of agglomeration is related to the fine scale structure of turbulence and expressed using multifractal formalism; we apply to this end the Lagrangian approach worked out by Borgas [9]. The multifractal model of turbulence is used as the subgrid closure for the rate of strain and related stresses when the RANS based CFD code is used to simulate the process. Multifractal formalism enables prediction of the form of the agglomeration probability function that is specific for each collision kernel, which distinguishes presented method from the other ones applying presumed forms of this function.

RESULTS AND CNCLUSIONS

The model predicts that the process of agglomeration is scale dependent, which means the scale-up methods employing the constant value of the rate of energy dissipation in the systems of different size that are used by chemical engineers are of limited universality. Fig. 2 illustrates this feature of agglomeration observed in the case of orthokinetic agglomeration in homogeneous, isotropic turbulence for particles of size L_i, in the solution of supersaturation S_i and for two different values of the ratio of the Kolmogorov time microscale τ_K to the Lagrangian time macroscale T_L. The time scale ratio reflects effect of the scale of the system on the process. The agglomeration model was combined with the PDF method for modeling mixing and linked to the CFD code. The computations were carried out with the CFD package Fluent 6 employing the k-ε model. Results of computations were compared with experimental data obtained for barium sulphate precipitation carried out in the 4 m long tubular reactor of diameter equal to 0.0320 m for the pipe Reynolds number varied from 40000 to 70000. The model predicts trends observed in experiments.

References

[1] Zinchenko A. Z., Davis R.H.: Collision rates of spherical drops or particles in a shear flow at arbitrary Peclet numbers. *Phys. Fluids* **7**: 2310-2327, 1995
[2] Melis S., Verduyn M, Storti G., Morbidelli, M., Baldyga J.: Effect of fluid motion on the aggregation of small particles subject to interaction forces. *AIChEJ* **45:** 1383-1393, 1999
[3] Batchelor G. K., Green J. T.: The hydrodynamic interaction of two small freely-moving spheres in a linear flow field. J. Fluid Mech. **56**, 375-400, 1972
[4] Batchelor G. K.: Mass transfer from small particles suspended in turbulent fluid. *J. Fluid Mech* **98,** 609-623, 1980
[5] Batchelor G. K.: Brownian diffusion of particles with hydrodynamic interaction. J. Fluid Mech **74,** 1-29, 1976
[6] Lin C. J., Lee K. J., Sather N. J.: Slow motion of two spheres in a shear field. *J. Fluid Mech* **43,** 45-47, 1970
[7] O'Neill M., Majumdar S.: Asymmetrical slow viscous fluid motions caused by the translation or rotation of two spheres. Part II: Asymptotic forms of the solutions when the minimum clearance between the spheres approaches zero. *Zeit. Angew. Math. Phys*., **21**, 180-187, 1970
[8] Elimelech M., Gregory J., Jia X., Williams R. A., Particle Deposition and Aggregation. Butterworth-Heinemann, 1995
[9] Borgas M. S.: The multifractal nature of turbulent dispersion. Advances in Turbulence 3, Springer-Verlag, Berin, 1991

XXI ICTAM, 15–21 August 2004, Warsaw, Poland

RESONANCES AND MIXING IN STOKES FLOWS

Dmitri Vainchtein*, Igor Mezić**, Anatoly Neishtadt***
*Department of Mechanical and Environmental Engineering
University of California Santa Barbara, USA
**Department of Mechanical and Environmental Engineering,
Department of Mathematics,
University of California Santa Barbara, USA
***Space Research Institute, Moscow, Russia

Summary In the present paper we study chaotic advection and mixing in a stationary incompressible Stokes flow between two co-axial counter-rotating cylinders. The velocity field of the flow is a result of a small perturbation of an integrable velocity field. Under arbitrarily small perturbations of a certain kind a domain of chaotic advection within the gap between the cylinders arises. We show that this phenomenon is a consequence of quasi-random changes in the adiabatic invariant of the flow, which occur as a streamline crosses the two-dimensional resonance surface of the unperturbed flow. We derive an asymptotic formula for the change in the adiabatic invariant due to the passages through the resonance and describe the diffusion of the adiabatic invariant due to multiple passages through the resonance.

Problems of chaotic advection in incompressible Stokes flows attract much interest in connection with impurity transport and mixing (see e.g. [1]). It was first shown numerically in [2], that the presence of a special singular surface (separatrix) leads to the appearance of a domain of chaotic dynamics in near-integrable flows. Similar phenomena was later studied analytically, [3], and experimentally, [4]. In the present study we investigate the mixing in steady Stokes flows in the presence of a different kind of singular surfaces: the resonance. As a model problem we chose a stationary flow between two co-axial counter-rotating cylinders, the outer being of a periodically varying diameter (see Fig. 1a). We consider the case when the variations of the diameter of the outer cylinder are small compared with the separation between the cylinders. In the original (unperturbed) system the flow is regular. It possesses two integrals of motion and all the streamlines are closed curves. The perturbation (assumed to be small) consists of two parts: the vertical flow due to the motion of the inner cylinder and the additional flow due to the noncircularity of the outer cylinder. By itself, either perturbation does not break the approximate regularity of the flow. However, when both of the perturbations are present, regardless of how small those perturbations are, the dynamics becomes more complicated. The space is divided into three regions: in the vicinity of either cylinder the flow is still almost regular, while near the middle of the gap streamlines are chaotic and the mixing occurs (see Fig. 1b). The objective of the present paper is to describe the size and the position of the chaotic domain and the rate of mixing.

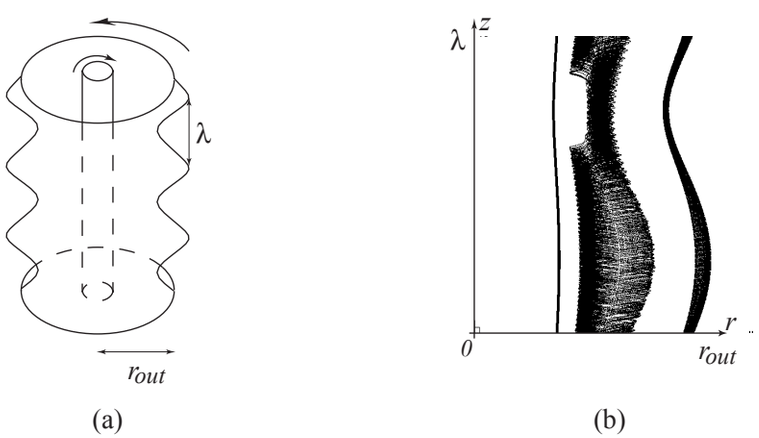


Figure 1. (a) The flow setup. (b) Projection of three streamlines on the (r, z) plane (periodic boundary conditions in z were imposed). The right and left streamlines are regular, the middle one is chaotic.

For a small magnitude of the perturbation, the system possesses two distinct time scales. Streamlines wind fast around the inner cylinder (in clockwise or counterclockwise direction depending on the distance from the axis) while r and

z coordinates of a streamline change much slower. Therefore, in the first approximation we can average equations of motion over the fast (angular) variable and consider the averaged system instead of the exact one. The averaged system gets one new invariant of motion (that is an adiabatic invariant of the exact system) and recovers the regularity of the streamlines.

The exact system follows the averaged one for a very long time everywhere, where the time scales are well separated and averaging is possible. These conditions are satisfied away from a special (*resonance*) surface, where the angular velocity of the unperturbed system vanishes. And it is the vicinity of the resonance surface where the Lagrangian chaos (divergence of initially close streamlines) and mixing are localized. We demonstrate that Lagrangian chaos is a consequence of abrupt changes of the adiabatic invariant, that occur when a streamline crosses the resonance surface.

To describe the processes occurring in the vicinity of resonance we apply the theory developed in [5], [6] for Hamiltonian systems. We show that there are two major phenomena that take place near the resonance. The first is the *scattering on resonance*, a phenomenon that happens on almost every crossing of the resonance surface, but changes a value of the adiabatic invariant and the shape of a streamline only slightly. The second phenomenon is the *capture into resonance*, that changes a value of the adiabatic invariant significantly forcing the exact streamline to abandon the corresponding streamline of the averaged system and to start following the resonance surface. Unlike scattering, capture occurs only for a small measure of the initial conditions. We derive formulas for changes in adiabatic invariants due to both phenomena and compare them with numerical simulations.

The extreme sensitivity of the above phenomena on tiny changes of the initial conditions makes it reasonable (for multiple passages through the resonance) to consider both scattering and capture as probabilistic phenomena. The accumulation of changes of the adiabatic invariant after multiple passages results in destruction of adiabatic invariancy and leads to Lagrangian chaos and mixing. We estimate characteristic time of mixing based on the statistical properties of the resonance phenomena. We show that while the rate of mixing depends on the magnitude of the perturbation, in the first approximation the size of chaotic domain is independent of it, depending only on the extend of variations of the diameter of the outer cylinder. To describe the overall mixing we compute the finite-time Lyapunov exponents and compare the theoretically predicted rate of mixing with results of numerical simulations of the exact system.

References

[1] Aref H.: Stirring by chaotic advection. *J. Fluid Mech.*, **143**: 1-21, 1984.

[2] Bajer K., Moffatt H.K.: On a class of steady confined Stokes flows with chaotic streamlines. *J. Fluid Mech.*, **212**; 337-363, 1990.

[3] Vainshtein D.L., Vasiliev A.A., Neishtadt A.I.: Changes in the adiabatic invariant and streamline chaos in confined incompressible Stokes flow. *Chaos*, **6**: 67-77, 1996.

[4] Ward T., Homsy G.M.: Electrohydrodynamically driven chaotic mixing in a translating drop. II. Experiments. *Physics of Fluids* **15**: 2987-2994, 2003.

[5] Neishtadt A.I.: Scattering by resonances. *Celestial Mechanics and Dynamical Astronomy*, **65**: 1-20, 1997.

[6] Neishtadt A.I.: On adiabatic invariance in two-frequency systems. In: Hamiltonian systems with 3 or more degrees of freedom, *NATO ASI Series C*, **533**: 193-213, Kluwer Academic Publishers, 1999.

XXI ICTAM, 15–21 August 2004, Warsaw, Poland

MIXING IN MULTICONNECTED PLANAR DOMAINS

Philip Boyland
Department of Mathematics, University of Florida, Gainesville, FL, 32611-8105, USA

Summary We study the stirring of two-dimensional fluids in multi-connected domains with moving boundaries using analytic and numerical tools. For time-periodic Euler flows, the classical Helmholtz-Kelvin Theorem shows that for typical initial vorticity such flows are not chaotic. On the other hand, it is shown that for constant initial vorticity there are stirring protocols which always yield chaotic time-periodic Euler flows. These protocols are those that generate flow maps in pseudoAnosov isotopy classes. These classes are a basic ingredient of the Thurston-Nielsen theory and a further application of that theory shows that pseudoAnosov stirring protocols with generic initial vorticity always yield solutions to Euler's equations for which the sup norm of the gradient of the vorticity grows exponentially in time.

We also investigate Stoke's flow with the same stirring geometry. Numerical and experimental results have shown that the flow maps under pseudoAnosv protocols appear to lack elliptic islands on a visible scale and thus are very thorough stirring procedures. Our investigations center on the connection between the classical Helmhotz characterization of Stoke's flow as minimizing the L^2-norm of the deformation tensor and the quasiconformal distortion of the flow map. Minimization of the latter under the appropriate conditions is known to imply global hyperbolicity.

INTRODUCTION

We study the stirring of two-dimensional fluids in multi-connected regions with moving boundaries using analytic and numerical tools. The outer boundary is fixed and the inner boundaries or "strirrers" are moved in a T-periodic protocol. We usually restrict to the case that the resulting velocity field is also periodic and study the time T-flow (or Poincaré) map f. As has been well established, the methods of dynamical systems theory can be used to analyze the map f and thus gain basic insights into the kinematic template underlying the fluid stirring.

Our analysis centers on the way in which the topology of the motion of the stirrers influences the stirring of the flow map. This topology is described by assigning a braid to each stirring protocol by visualizing its motion in three dimensional space-time. This braid determines the isotopy class of the flow map and the isotopy class information is then used in the Thurston-Nielsen Theory. In the case of stirring protocols of pseudoAnosov type, this theory provides *a priori* lower bounds on such quantities as the stretching of material lines and the topological entropy. These bounds depend only on the braid of the stirring protocol and not the details of the stirrer motion, and further, are valid for any fluid model, eg. ideal flow or Stokes flow, as long as the fluid region is maintained as connected continuum.

This circle of ideas was introduced in [2] and has been studied in [4] and [5]. In this paper we examine the implications of the stirring topology on the dynamics of the flow map under the assumption of a specific fluid model. We restrict attention here to incompressible, constant density flow and examine the two extreme cases of inviscid (Euler) flow and quasi-stationary Stokes flow.

EULER FLOW

We first investigate the dynamics of time-periodic Euler flows in multi-connected, planar fluid regions which are "stirred" by the moving boundaries. The classical Helmholtz-Kelvin theorem on the transport of vorticity implies that if the initial vorticity of such a flow is generic among real-valued functions in the C^k-topology ($k \geq 2$) or is C^ω and nonconstant, then the flow has zero topological entropy (the C^ω case is equivalent to Remark 4 in [3]).

Amongst the Euler flows with non-generic vorticity those with constant vorticity are of particular interest. Using standard potential theory, a proposition shows that systems with constant vorticity and periodic stirring protocols always give rise to periodic Euler fluid motions. Further, if the stirring protocol is of pseudoAnosov type, then the resulting flow maps always have positive topological entropy and thus are chaotic. Since conditions that ensure periodic solutions to the Euler equations are very rare, this result is useful in guaranteeing the existence of at least one interesting class of time T-Euler flow maps.

Using these results in the real analytic case yields a dichotomy that is somewhat similar to that of Arnol'd for steady 3D Euler flows. For 2D time-periodic Euler flows, if the vorticity is nonconstant, then the dynamics are "integrable" and the entropy is zero. One may have chaotic dynamics in the constant vorticity case, but only if the fluid is stirred.

As another consequence of the Thurston-Nielsen theory of surface automorphisms, we also show that for generic initial vorticity there are large classes of periodic stirring protocols which never give rise to periodic Euler fluid motions. Further, these stirring protocols result in exponential growth of the sup norm of the gradient of the vorticity. As a consequence of the preservation of vorticity one expects this general type of behavior in any chaotic Euler flow with generic smooth vorticity. The attractive feature of the theorem is that the topology of the stirrer motion allows one to get concrete results on the exponential growth.

[4]

QUASI-STATIONARY STOKES FLOW

One of the striking feature of the viscous flow maps reported from experiment in [2] and numerical computations in [4] and [5] is the apparent lack of elliptic islands. Elliptic islands are regions of the fluid associated with periodic points whose multipliers are on the unit circle. Since the region enclosed by the invariant circles is invariant under the action of the flow map, elliptic islands give patches of fluid that do not mix with the surrounding fluid. The apparent lack of elliptic islands thus indicates a highly thorough stirring protocol.

We present an analytic and numerical investigation of this phenomenon using quasi-Stationary Stokes flow as a model. We give evidence that the lack of elliptic islands can be explained using the classic Helmholtz variational principle in which Stoke's flow is characterized amongst divergence-free vector fields with given boundary values as minimizing the rate of energy dissipation as measured by the L^2-norm of the deformation tensor. This property is, in turn, connected to properties of the flow map, with particular importance given to the quasi-conformal (qc) distortion. The qc-distortion measures how much infinitesimal circles are distorted by the map, and it is, in many ways, the analog for maps of the rate of energy dissipation for a velocity field. It is known that the global minimization (in the appropriate class of maps and metrics) of the qc-distortion is connected to hyperbolicity and in fact can be used to characterize pseudoAnosov maps ([1]). While we have not been able to make these connections rigorous, and in fact have counterexamples to various conjectured connections. we do have numerical evidence for the connection of the two measures of distortion on certain "scales" and use it to provide a plausible explanation for the lack of elliptic islands above a certain length scale.

References

[1] Bers, L., An extremal problem for quasiconformal mappings, *Acta. Math.*, **141**, 1978, 73–98.
[2] Boyland, P., Aref, H. and Stremler, M., Topological fluid mechanics of stirring, *J. Fluid Mech.*, **403**, 277–304, 2000.
[3] Brown, M. & Samelson, R., Particle motion in vorticity- conserving, two-dimensional incompressible flows, *Phys. Fluids*, **6**, 2875–2876, 1994.
[4] Finn, M., Cox, S. & Byrne, H., Topological chaos in inviscid and viscous mixers, *J. Fluid Mech.*, **493**, 345–361, 2003.
[5] Vikhansky, A., Simulation of topological chaos in laminar flow, *Chaos*, 2004 (in press).

XXI ICTAM, 15–21 August 2004, Warsaw, Poland

EULERIAN MEASURES FOR LAGRANGIAN STIRRING IN A THERMALLY DRIVEN FLOW

R. J. Keane*, P. L. Read *, G. P. King**
*Atmospheric, Oceanic and Planetary Physics, Department of Physics, University of Oxford, UK
**Fluid Dynamics Research Centre, School of Engineering, University of Warwick, UK

Summary Lagrangian stirring in a thermally driven rotating annulus is investigated numerically. The stirring is quantified using Eulerian symmetry measures, as well as more commonly used Lagrangian measures. The ability of the measures to identify transport barriers and regions of well and poorly stirred flow is investigated, and space and time averages of the Eulerian symmetry measures are compared to those of the Lagrangian measures for various flow regimes.

Introduction

Tracer transport in fluid flows, particularly atmospheric fluid flows, is commonly studied using analysed wind (velocity), temperature and pressure fields. Tracer trajectories are integrated forward in time, using the velocities defined on a grid, and interpolating them to the required point at each step of the integration. This technique has provided many useful insights, particularly in the stratosphere, where the Lagrangian motion can be almost entirely determined by the large scale wind structure. However, integrating many such trajectories is computationally expensive and is less accurate in other areas of the atmosphere, particularly where the wind fields are known only on a sparse grid. It is therefore of benefit to discover connections between Eulerian velocity fields and the Lagrangian structure produced by such fields without the need to carry out detailed integrations of tracer transport. Additionally, such connections are arguably of interest at a fundamental level, and may reasonably be expected to find applications in many areas of fluid mechanics.

Recently [1] discovered that integrated values of a suitably chosen Eulerian measure of the local three dimensionality of the phase space were strongly correlated with the extent of stirring in the flow, as measured by an effective diffusion coefficient. An objective of our work is to evaluate Eulerian symmetry measures for thermally driven rotating annulus flows and to compare them with Lagrangian measures of stirring, such as finite time and finite scale Lyapunov exponents.

The Flow and Methods

The flow considered is that of a viscous, thermally conducting fluid in a differentially heated rotating annulus, with rigid sidewalls and lower endwall, and a stress-free upper endwall. The flow is held to be axisymmetric but the sidewall heating is time dependent. The two numerical codes used are a Navier Stokes field model, and a particle path tracking code similar to that used by [1]. Because the Navier Stokes model is axisymmetric, the velocity fields produced by it are constrained to be two dimensional.

The velocity field in the r-z plane, (u, w), is used to find tracer trajectories in r and z using the particle path tracking code, which integrates the equations $(\dot{r}, \dot{z}) = (u, w)$ for a predetermined starting position for each tracer. The integration is done using a 2nd order Runge-Kutta routine in either direction. For each integration step, the velocity fields are interpolated to the position of the tracer, and to the intermediate point required for the Runge-Kutta integration, from the nearest grid points using a bicubic interpolation in space and a linear interpolation in time.

In the absence of time dependence in the temperature forcing, the flow does not produce chaotic tracer trajectories, since the number of phase space dimensions is two. Introducing the time dependence increases the number of phase space dimensions to three (two space and time), so it is possible to observe chaotic tracer trajectories and hence enhanced stirring.

A motivation for seeking Eulerian measures for enhanced stirring comes from a consideration of the Hamiltonian formulation of the governing equations of motion. For example, a two dimensional incompressible flow can be written in terms of a streamfunction, which can be considered to play the role of the Hamiltonian. If the streamfunction is time independent then, the flow is integrable, whereas if the streamfunction is time dependent then a function F satisfying $\frac{\mathrm{d}F}{\mathrm{d}t} = 0$ is required for integrability. If it can be written $\frac{\mathrm{d}F}{\mathrm{d}t} = \phi(\mathbf{V})$ where $\mathbf{V}$ is the velocity field, then ϕ provides a measure of departure from dynamical symmetry. Similarly, the time dependence of the streamfunction provides a measure of departure from geometrical symmetry. For a time dependent two dimensional flow field, then, regions of the flow where ϕ or $\frac{\partial \psi}{\partial t}$ is zero will give rise to integrable trajectories. Physically, tracer particles in regions of zero ϕ or $\frac{\partial \psi}{\partial t}$ will be constrained to two dimensional surfaces, and will therefore not be well mixed in these regions. The value of these quantities may therefore be expected to provide some idea of how well mixed tracers advected due to the flow will become in a given region, since, for lower values, trajectories will be more closely constrained to two dimensional surfaces.

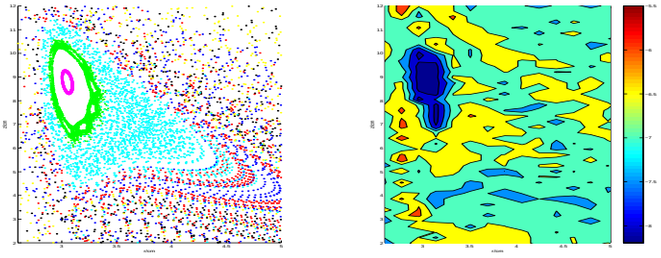
While studying the axisymmetric annulus flows, some Lagrangian measures of mixing have been identified, mainly to provide a 'control parameter' to which to compare the Eulerian symmetry measures. However, it is interesting to investigate how well these Lagrangian measures themselves can quantify how well mixed the flow is in different regions, for both the axisymmetric and the non-axisymmetric cases.

Results

Box counting dimensions, finite time Lyapunov exponents and finite scale Lyapunov exponents were calculated for various flow regimes, with a rotation rate of $1\,\mathrm{rad\,s^{-1}}$ and a mean temperature difference between the inner and outer wall of $4\,\mathrm{K}$,

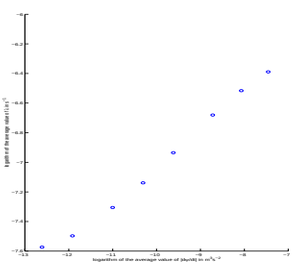
and various forcing amplitudes and frequencies. These Lagrangian measures were found to predict poorly mixed regions, and transport barriers in particular, rather well. A contour plot of the finite scale Lyapunov exponent λ, and the Poincaré section for the same region of the flow, are shown in figure 1. The forcing amplitude and frequency are $1\,\mathrm{K}$ and $2\pi/100\,\mathrm{s}^{-1}$ respectively. The exponent is calculated by taking two tracers a distance $x(0)$ apart, and integrating their trajectories until they have reached a separation $x(\tau) = Rx(0)$. The exponent is given by $\lambda(r,z) = \frac{1}{\tau}\ln R$, where τ is the time at which the separation reaches $Rx(0)$ and (r,z) is the initial position of one of the tracers. The value of R used in the figure is 1000.

Figure 1. Comparason of Poincaré section and contour plot of logarithms of the value of λ in s^{-1}, for a region of the flow



This lyapunov exponent was calculated for eight different flow regimes, all with forcing frequency $\pi/100\,\mathrm{s}^{-1}$ and various amplitudes. The exponent was averaged over the phase space for each flow regime, to give an average value $\bar{\lambda}$. This is compared with the corresponding average value of the geometrical symmetry measure $\frac{\partial\bar{\psi}}{\partial t}$, which measures the extent of the time dependence of the Hamiltonian (the streamfunction) governing the flow. A log-log plot of the two measures is shown in figure 2 and there is a slope of about 0.24, suggesting that $\bar{\lambda} \propto \left(\left|\frac{\partial\bar{\psi}}{\partial t}\right|\right)^{0.24}$. The geometrical symmetry measure thus seems to be able to predict the extent of the mixing in a given flow as a whole, when the amplitude of the forcing is varied with constant frequency of forcing.

Figure 2. Correlation between logarithms of geometrical symmetry and finite scale Lyapunov exponent



Conclusions

The Lagrangian measures accurately predict the locations of transport barriers.The Eulerian symmetry measures seem to provide a way of efficiently predicting the broader mixing characteristics of a flow, although they are not sufficiently sharp to predict the exact locations of transport barriers.

The next part of this study will be to look at fully three dimensional thermally driven rotating annulus flows, which will provide an opportunity to evaluate the methods in the context of a more dynamically consistent flow regime. It will also be possible then to compare the results with laboratory experiments.

References

[1] King G. P., Rowlands G., Rudman M., Yannacopoulos, A. N.: Predicting chaotic dispersion with Eulerian symmetry measures: Wavy Taylor-vortex flow. *Physics of Fluids* **15**(9):2522–2528,2001

AN ANALYSIS OF MIXING PROCESS IN A STATIC MIXER

Marek Jaszczur*, Janusz Szmyd*, Marcus Petermann **
*AGH University of Science and Technology, Mickiewicza 30, 30-059 Kraków, Poland
** Ruhr-Universität Bochum, Inst. of Thermo- and Fluid Dynamics, 44780 Bochum, Germany

Summary In the present study flow mixing process in a static mixer for two immiscible viscous fluids has been treated numerically. A comparison of numerical results and measured data for flow mixing process in circular duct has been made to check the results of numerical simulations. The mixing efficiency function has been proposed to performed process optimisation and obtain most efficient conditions for industrial mixing process.

Introduction

In many industrial applications static mixers are easy used for homogenisation of different liquid, gas or grain components. Advantage of this mixing technology is very small maintenance, which is a result of the absence of any dynamic devices. Despite the numerous applications of static mixers, the fundamental understanding of the process is so far described insufficiently (Godfrey 1992). Some researchers have reported pressure drop data (Chen 1973, Shah&Kale 1991, Fasol 1997), resident time distributions (Nauman 1991, Fasol 1997, Li 1998), friction factor (Moranicais 1999), mixing pattern "frieze" by solidification of coloured components. Recently computational investigations of mixing analysis have been carried out for different mixers. Byre&Sawley[1] and Muzzio performed three-dimensional analysis; however those studies did not provide detailed analysis of mixing performance. Also comparisons of computed mixing pattern with experimental one have not been reported. A prediction or calculation of quality of mixing process of two streams with different viscosities, densities and phase ratios which are homogenised in a static mixer do not have been reported in open literature. This study presents results for a SMX (and SMR) static mixer and compare mixing pattern with experimental visualisation. The paper focus on the mixing quantities In the mixing process of two different flow streams with similar or different properties as well as flow rates.

Formulation of the problem

Geometries of SMX and SMR static mixers used in analysis are shown on Fig.1. Geometrically the Sulzer SMX and SMR mixers are very similar in design, and main differences are in the shape of inserts - round or rectangular cross-section duct. Detailed information can be found in Sultzer, Chemtech.

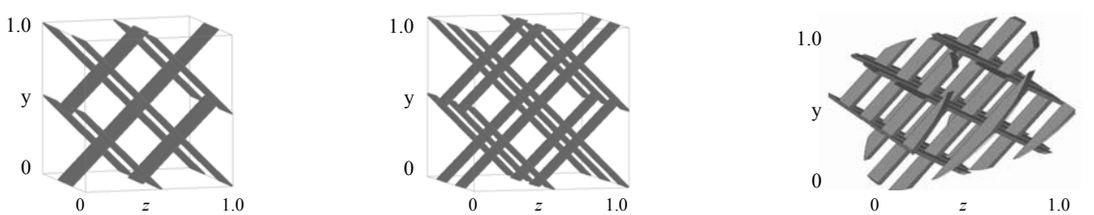


Fig.1. Applied geometries of one mixing element with 3,5-sections for rectangular duct and 8-sections for round duct.

The mathematical model for the flow mixing processes of n-fluids is given by the continuity and momentum equations. Assumed the fluid is considered to be incompressible, Newtonian and properties (for each fluid) are constant these equations are as follows:

$$\nabla \cdot V = 0 \quad (1) \qquad \frac{\mathrm{D}\boldsymbol{V}}{\mathrm{D}t} = -\frac{1}{\rho}\nabla P + \frac{\mu}{\rho}\nabla^2 \boldsymbol{V} + \boldsymbol{F} \quad (2) \qquad \frac{\partial f_n}{\partial t} + \nabla \cdot (f_n V) = 0 \quad (3)$$

Equation (3) has been used for analysis mixture of more than one fluid with different properties. Function f_n has been used in VOF (Volume of Fluid) method to specify amount of n-th fluid mixture in each computational control volume. For two different fluids mixture $f_1 + f_2 = 1$. Base on that information fluid properties in each CV can be easily calculated as follows: $\rho = f_1 * \rho_1 + f_2 * \rho_2$ and $\mu = f_1 * \mu_1 + f_2 * \mu_2$ where subscript (1) and (2) denote constant properties of fluids at duct inlet. For constant mesh (Fig.2) geometrical approximation has to be introduced also. Proposed method was adopted from phase-change solidification problems on constant grid.

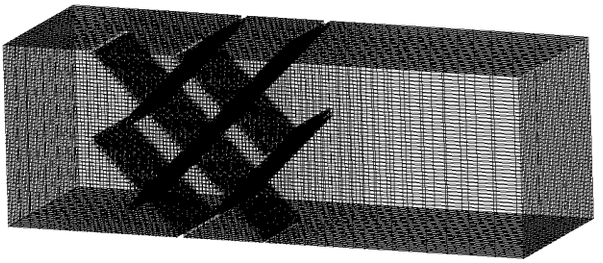


Fig.2. Simplify grid for square cross-section duct with one mixing element with 2-sections.

The flow in mixing process was calculated numerically by the control volume method, solving the finite-difference equivalent of equations (1)-(3). Staggered grids were used for the velocity components. The SIMPLE-C algorithm was used to solve the pressure. The central finite-difference approximation was applied for the diffusion terms while, for the convection terms the QUICK scheme was used. The present scheme was based on fully implicit discretisation schemes taking into account the unsteady terms of governing equations. The grid points were non-uniformly allocated and total number of grids was 50x50x200 up to 100x100x400. Properties of a working fluid was based on water properties but in same cases the density and viscosity was set one order higher to analyse mixing process of fluids with different properties. A condition examined here was determined by Re number (base on duct diameter). At the duct inlet one fluid entrance was located in the upper half of the cross-section and second one in lower half. To investigate mixing properties a total 250.000 massless passive tracers was distributed uniformly located in the upper or lower half cross-section.

Results

The evolution of the mixing pattern in the SMX static mixer for different cross-section and Re=1 for each fluids has been compared with experimental visualisation form Sulzer (Chemtech)

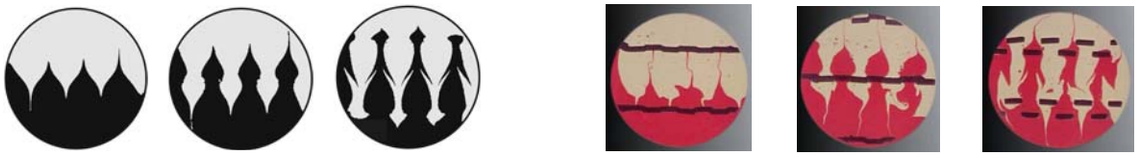


Fig.3. Computed and observed mixing pattern for Re=1 and mixing element length z*=0.25, 0.5, 0.75

One of the most important parameter in mixing analysis is segregation, pressure drop and particles resident time. In present work two primary parameters segregation [2] and pressure drop (with reference to pressure in empty duct) has been link to one parameter mixing efficiency $E = \frac{-\log(S)}{Z}$. Examine of that parameter E allow us to obtain most efficient conditions for mixing process.

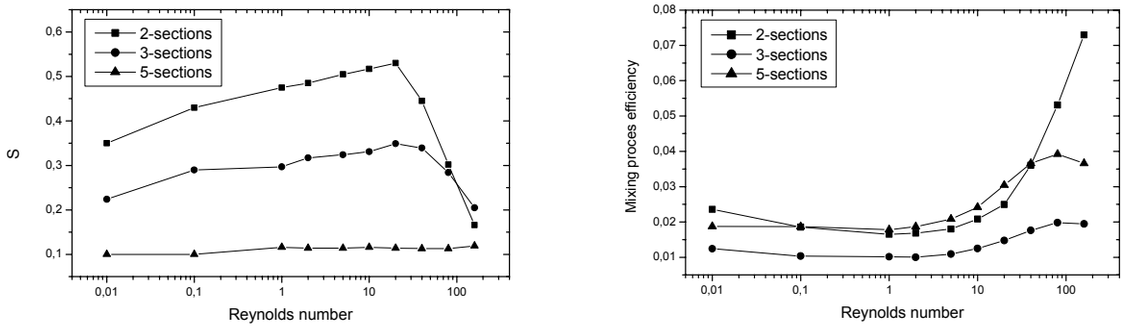


Fig.4. Mixing segregation and mixing efficiency versus Reynolds number for 2,3,5-sections element in square duct

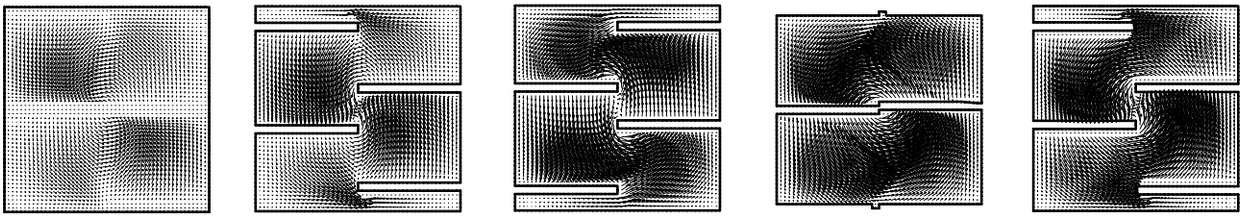


Fig.5. Velocity vectors for 2-section mixing element and Re=10 (for XY plane and z*=0.0; 0.2; 0.4; 0.5; 0.6)

Fig.5 shows velocity components (u,v) of the flow fields in XY cross-section planes. It can be seen big differences in velocity magnitude at points near to the element wall and wall of a duct. In configuration with 3,5-sections element velocity magnitude is more uniformly distributed over XY duct cross-section.

Conclusions

Flow characteristic in SMX static mixer agree well with experimental visualisation. The effect of Re number on segregation and mixing efficiency was analysed. It has been found that irrational increasing of flow rate (Re number) can decrease mixing segregation .i.e. higher flow rate produce less effective mixing but required energy is very high.

References

[1] Byre O., Sawley M.: Parallel computation and analysis of the flow in static mixer, *Chem. Eng. J*., 70, 93-104,1998.
[2] Bednarz T., Analiza numeryczna procesu mieszania płynów newtonowskich w mikserze statycznym, proc. of XV KKMP, Augustów,PL, 2002.

XXI ICTAM, 15–21 August 2004, Warsaw, Poland

STIRRING BY BLINKING ROTLETS IN A BOUNDED STOKES FLOW

Dennis van der Woude*, Herman Clercx*, GertJan van Heijst*, Vyacheslav V. Meleshko**
*Physics Department, Eindhoven University of Technology, The Netherlands
**Department of Theoretical and Applied Mechanics, Kiev National Taras Shevchenko University, Ukraine

Summary A blinking rotlet model is used for the analysis of stirring in a Stokes flow in a rectangular domain. After the two-dimensional biharmonic equation is solved analytically, the associated velocity field of a pair of blinking rotlets positioned symmetrically on the y-axis, is used studying the stirring qualities of this blinking rotlet model. Contour kinematic simulations are performed in order to obtain information about the chaotic behaviour of a blob of passive tracer material put in this flow field.

INTRODUCTION

The way in which passive tracer material will be distributed in an ambient fluid depends basically upon two processes: advection due to the presence of an imposed velocity field and secondly upon mass-diffusion. Although mixing is essentially a combination of both mechanisms, only the effects of advection are considered. Strictly speaking, with this limitation one does not deal with mixing anymore, but with stirring.
The spreading of tracer particles through advection becomes more efficient when the flow has a chaotic nature. This chaotic nature is characterized by an exponential growth in time of the contact length of a patch of tracer material with its surroundings. Time-dependency is in 2D an essential ingredient towards 'good stirring' [1] — what is meant by this, not to mention how to quantify it, is not just of importance for a good understanding of stirring, but also of mixing.
In this study the behaviour of tracer material is considered when put in an incompressible, highly viscous fluid. The velocity field is driven by two, independently adjustable rotlets. In order to advect the tracer material chaotically, a blinking rotlet model is used, by which a time-dependent laminar flow is obtained. This blinking rotlet model was studied before by Aref & Meleshko [2]; they considered the stirring effects of two rotlets in a circular domain.

PROBLEM FORMULATION AND SOLUTION APPROACH

A highly viscous, incompressible fluid is captured in a rectangular domain Π: $\Pi = \{\mathbf{x} \in \mathbb{R} | -a < x < a, -b < y < b\}$, and is stirred by two individually adjustable rotlets. The resulting velocity field is described by an overall stream function Ψ; letting the rotlets blink, implies that Ψ is actually a function of time, although not continuously.
The position of the rotlets are restricted such that they are confined along the y-axis: rotlet A is positioned at $(0, c_0)$ and rotlet B at $(0, -c_0)$; $\pm c_0$ are stagnation points which depends on a and b. Thus a blinking rotlet model of two rotlets can be constructed in which the rotlet that is "off", does not disturb the flow. So, one writes

$$\Psi(t, \mathbf{x}) = \varepsilon_A(t)\Psi_A(\mathbf{x}) + \varepsilon_B(t)\Psi_B(\mathbf{x}), \qquad (t, \mathbf{x}) \in \mathbb{R}^+ \times \Pi, \tag{1}$$

where the time-dependent functions $\varepsilon_{A,B}(t)$ are periodic square waves used to adjust the intensity of the rotlets and to switch the rotlets "on" and "off". The time-independent contributions Ψ_A and Ψ_B satisfy the biharmonic equation and can be decomposed into two, what might be called, elemental stream functions $\Psi_1(\mathbf{x})$ and $\Psi_2(\mathbf{x})$, in such a way that

$$\Psi_A(\mathbf{x}) = [\Psi_1(\mathbf{x}) + \Psi_2(\mathbf{x})], \tag{2}$$

$$\Psi_B(\mathbf{x}) = [\Psi_1(\mathbf{x}) - \Psi_2(\mathbf{x})]. \tag{3}$$

Due to the linearity of the biharmonic equation, both Ψ_1 and Ψ_2 have to be solutions of the biharmonic equation. The main objective therefore is to find the analytical expressions for these elemental functions satisfying the appropriate, with no-slip associated, boundary conditions.
The underlying idea solving the biharmonic equation is that the elemental stream functions Ψ_i $(i = 1, 2)$ are written as a sum of two contributions

$$\Psi_i(\mathbf{x}) = \psi_i^{(\sigma)}(\mathbf{x}) + \psi_i(\mathbf{x}), \quad i = 1, 2. \tag{4}$$

The first contribution takes the effects into account of two imaginary rotlets, positioned at $(0, \pm c)$. In the case where $i = 1$, the rotlets rotates in the same direction; in the other case where $i = 2$, the rotlets rotate in opposite directions. The second contribution, ψ_i, is due to the presence of the boundaries: it indicates the effect of the boundaries on the interior flow field.
Since $\nabla^2 \psi_i^{(\sigma)} = 0$, the unknown functions ψ_i are solutions of the biharmonic equation as well. The required no-slip boundary condition can be translated into Neumann boundary conditions for ψ_i. One important feature of the construction of the solution is the appearance of a system of infinite series, which is solved using the method of reduction [3]. Some mathematical background can also be found in Ref. [4].

SOME RESULTS

The velocity field $\mathbf{u} = -\nabla \times (\mathbf{e}_z \Psi)$, calculated from the overall stream function Ψ (eq.(1)), is used in a contour kinematics simulation to follow the time evolution of an initially circular blob of tracer material placed in the centre of the rectangular domain. In the two cases here presented, the individual adjustable rotlets are positioned at $(0, \pm c)$, where $c = 0.6$, and the rotlet intensity σ is set equal to 1. The main difference is the position of the walls with respect to the position of the rotlets. This makes it possible to study the effects of the walls on the interior flow field and therefore the effects of the walls on the chaotic behaviour of the tracer particles.

Rectangular domain

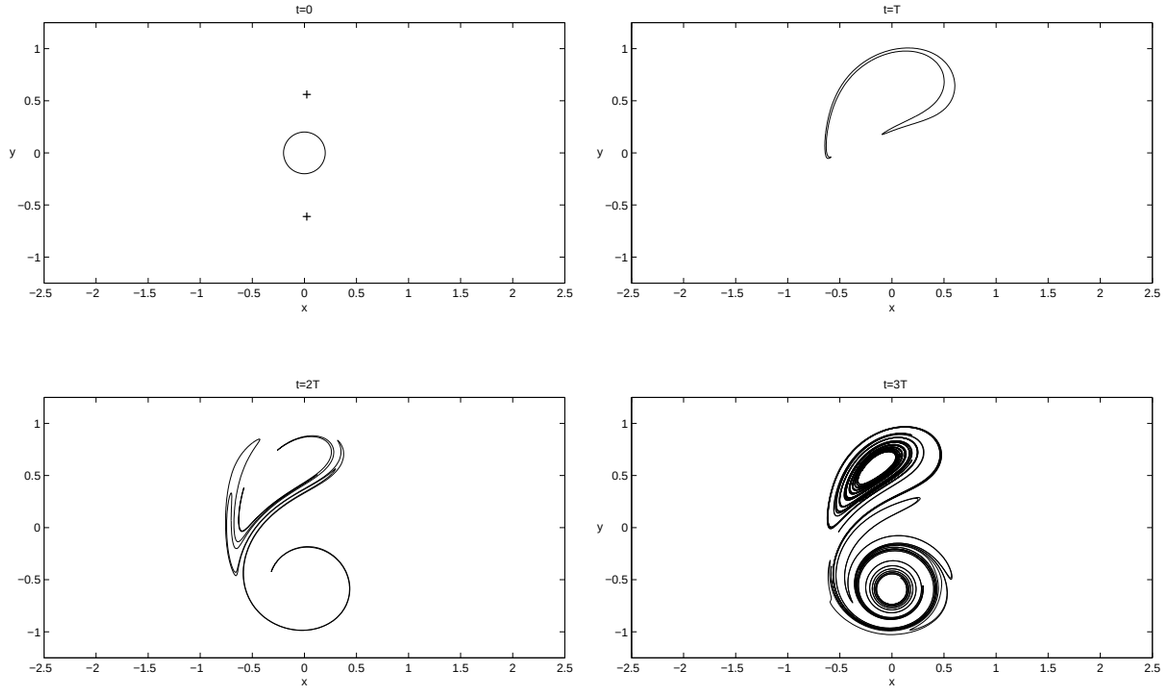


Figure 1. Advection of a patch tracer material due to two blinking rotlets ($c = \pm 0.6$, $\sigma_A = \sigma_B = 1$, $a = 2b = 2.5$).

Square domain

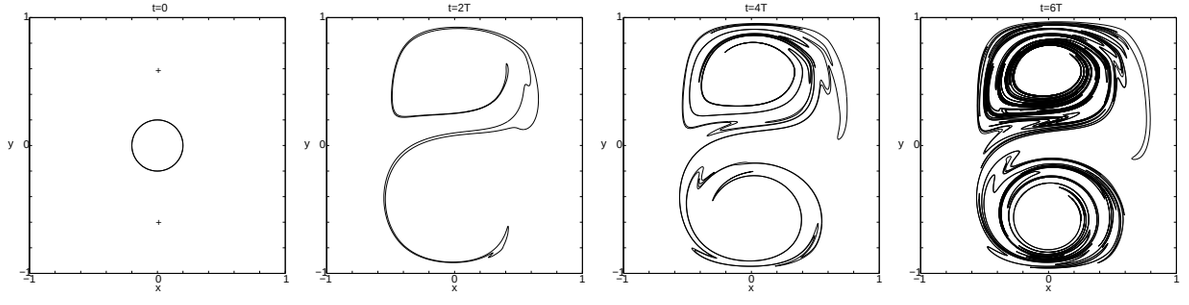


Figure 2. Advection of a patch tracer material due to two blinking rotlets ($c = \pm 0.6$, $\sigma_A = \sigma_B = 1$, $a = b = 1$).

References

[1] Aref, H.: Stirring by chaotic advection. *J. Fluid Mech.* **143**: 1–23, 1984.
[2] Meleshko, V.V., Aref H.: A blinking rotlet model for chaotic advection. *Phys. Fluids* **8**: 3215–3217, 1996
[3] Kantorovich, L.V., Krylov, V.I.: *Approximate methods of higher analysis.* Noordhoff, Groningen 1958
[4] Meleshko, V.V.,Gomilko, A.M.: Infinite systems for a biharmonic problem in a rectangle. *Proc. R. Soc. Lond. A*: 2139–2159, 1997

XXI ICTAM, 15–21 August 2004, Warsaw, Poland

WEAK INERTIA AND MIXING BETWEEN ROUGH SURFACES

David Lo Jacono[1], Franck Plouraboué[2], Alain Bergeon[2], Pauline Assemat[2]
[1] *Laboratory of Fluid Mechanics, Swiss Federal Institute of Technology Lausanne (EPFL), CH-1015 Lausanne, Switzerland.*
[2] *IMFT UMR 5502 / UPS, Allées du Pr. C. Soula 31400 Toulouse, France.*

INTRODUCTION

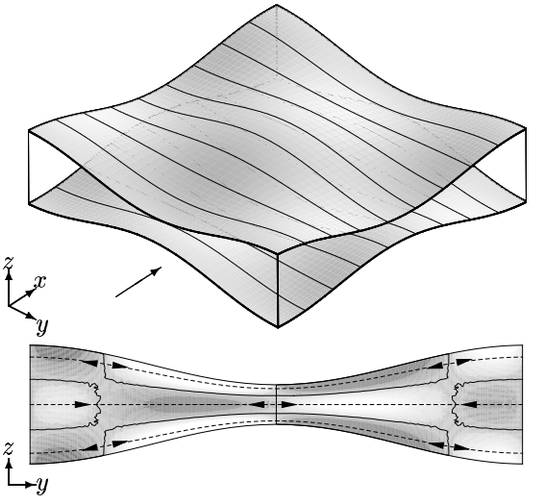


Figure 1. Top: tridimensional view of a patterned channel, the arrow indicates the mean flow direction. Periodic boundary conditions are used longitudinally whereas a Neumann impermeable flux is taken transversely. Arrow indicates the passive scalar displacement. Bottom: Lagrangian displacement map in a Poincaré section (y, z) of the flow.

Weak inertial effects in flows between two rough surfaces may lead to significant effects in various situations such as fracture flow or micro-fluidic. In the latter, Reynolds numbers are generally small and the flow is laminar. Recent experimental results [1] have shown that proper surface patterning could produce vortex which are transverse to the longitudinal mean flow and could be used to produce chaotic stirring [2]. Results of these experiments have been analyzed successfully in the context of Stokes flows in the limit of small patterning amplitude [3]. The question of finding optimal patterning for mixing remains an important issue for many practical applications. It requires theoretical investigations to avoid expensive computations of three dimensional Navier-Stokes equations in complex geometries. Hence, another interesting limit for surface patterning is the case of smooth variations of the aperture field between the two solid surfaces. If the Reynolds number is zero, the lubrication approximation is valid. The flow has a zero helicity and transverse mixing does not occur. Nevertheless including inertia could lead to efficient transverse mixing. Different works have focused on the impact of inertia on mixing issues in some related context [4, 5]. The present study concerns the influence of weak-inertia effects produced by a smooth surface patterning on the flow field and the streamline geometries. The analysis presented here is a first step towards optimization of the surface patterning associated with inertially driven stirring. First section describes an asymptotic treatment of the Navier-Stokes equation that leads to inertial corrections to lubrication equations. Second section gives some example of inertial influence on the flow field properties that are relevant for mixing.

ASYMPTOTIC ANALYSIS OF INERTIAL EFFECTS

We consider two surfaces with relative vertical distance $2Z_-(x, y)$ where (x, y) are the horizontal Cartesian coordinates. An example of such surface patterning is depicted in figure 1. We assume that the surfaces are smooth, so that the local slopes of each surfaces are of order $\epsilon \ll 1$. The Reynolds number Re is considered to be larger than one, whereas the "lubricated" Reynolds number $Re\epsilon$ is considered to be small. Expanding the pressure p (non dimensionalyzed by the viscous pressure) and the velocity field $\mathbf{U} = (u, v, \epsilon w)$ (non dimensionalized by the mean velocity) in powers of ϵ in the Navier-Stokes equations leads to the following development:

$$\begin{array}{rcccccl} p & = & \epsilon^{-1} p_0 & + & Re\, p_1 & + & O(\epsilon^2, Re^2\epsilon), \\ \mathbf{U} & = & \mathbf{U}_0 & + & Re\epsilon\, \mathbf{U}_1 & + & O(\epsilon^2, Re^2\epsilon^2). \end{array} \tag{1}$$

The zeroth order gives the lubrication approximation with uniform pressure $p_0(x, y)$ along the vertical direction for which the mean flux $\mathbf{q_0}$ – the integrated horizontal in-plane velocity $\mathbf{u_0} = (u_0, v_0)$ in between the surfaces – is proportional to the pressure gradient: $\mathbf{q_0} = -2\nabla p_0 Z_-^3/3$. The leading order lubrication velocity field $\mathbf{u_0} = -1/2\nabla p_0(z^2 - Z_-^2)$ is also proportional to the pressure gradient so that the helicity $H_0 = \mathbf{U_0} \cdot \nabla \times \mathbf{U_0}$ of the associated flow field is zero ($H_0 = 0$), while self-consistently neglecting $O(\epsilon)$. The inertial correction gives a non-zero $O(Re)$ contribution to the helicity, so that transverse mixing perpendicular to the mean flow becomes possible. Inserting (1) in the Navier Stokes equations leads to the following in-plane correction to the flow field:

$$\mathbf{u_1} = -(z^2 - Z_-^2)\left(\frac{1}{2}\nabla p_1 + Re\varepsilon(z^4 - 4z^2 Z_-^2 + 11 Z_-^4)\left(\frac{1}{240}\nabla(\nabla p_0)^2 + \frac{1}{60 Z_-}\nabla p_0(\nabla p_0 \cdot \nabla Z_-)\right)\right), \tag{2}$$

the integration of which, associated with the divergence-free flux condition, gives the two-dimensional equation for the pressure correction $p_1(x,y)$:

$$\nabla \cdot \left(Z_-^3 \nabla p_1 \right) = -\frac{6}{5} Re\epsilon \nabla \cdot \left(\nabla (\nabla p_0)^2 \frac{Z_-^7}{63} + 4 \nabla p_0 (\nabla p_0 \cdot \nabla Z_-) \frac{Z_-^6}{3} \right) \tag{3}$$

We call equation (3) Oseen-Poiseuille equations as it gives the first in-plane inertial correction to the lubrication Darcy-Poiseuille flux. Beside two-dimensional, inertial effects are not simply related to the lubrication pressure field $p_0(x,y)$ and the aperture field $2Z_-(x,y)$. The high polynomial order dependence associated with the right hand side of equation (3) requires the use of a high order numerical method to solve it.

MIXING ISSUE

We use a spectral element method to solved the simplified boundary layer equations introduced in the preceding section. Figure 2 shows the computed stream-lines mean flux $\mathbf{q}$ of the velocity field in the horizontal plane. When changing the sign of the mean applied pressure difference, the zero Reynolds number flow shows no difference due to the Stokes flow reversibility.

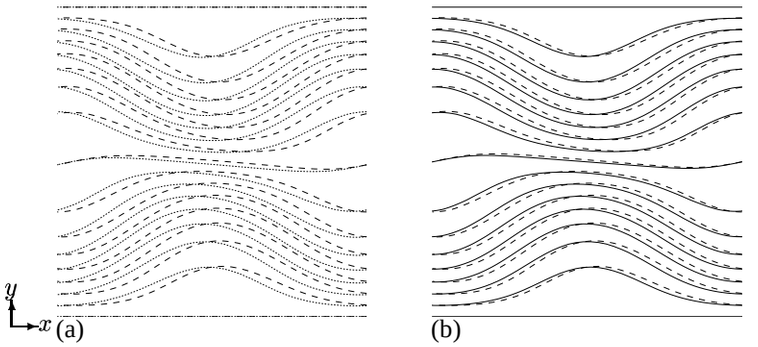


Figure 2. Mean in-plane flux $\mathbf{q}$ stream-lines are displayed. ——: $\mathbf{q_0}$, - - -: $\mathbf{q_0} + (\epsilon \mathbf{Re}) \mathbf{q_1}$. The direction of the mean applied pressure gradient has been switched from left to right in (a), to right to left in (b)

On the contrary, when inertia corrections are taken into account, the stream-lines structure is no more reversible. Some symmetries of the non-inertial stream-lines geometry are broken and the two inertial streamlines associated with opposite pressure gradient are symmetric with respect to the broken symmetry. Another interesting feature of the flow field appears when examining Poincaré sections in the (y,z) plane as represented in figure 1. When $Re = 0$, there is no transverse mixing. When weak inertia is added, the vertical dependence of the flow field is no longer spatially uniform leading to a Lagrangian transverse displacement presented in figure with a grey scale. The continuous lines drawned onto the grey scales are the zero-displacement level sets in the transverse direction. The arrow indicates the *stability* associated with fixed points with zero-displacement. The rich set of attracting and repulsing regions observed in this figure illustrates that a proper succession of surfaces patterning induces a succession of stretching/folding which are necessary for Lagrangian chaos.

References

[1] Stroock A.D., Dertinger S.K.W., Ajdari A., Mezic L., Stone H.A., Whitesides G.M.: Chaotic mixer for microchannels. *Sciences* **295**(5555):647–651, 2002.

[2] Aref H.: Stirring by chaotic advection. *J. Fluid Mech.* **143**:1–21, 1984.

[3] Stroock A.D., Dertinger S.K., Whitesides G.M., Ajdari A.: Patterning flows using grooved surfaces. *Anal. Chem.*, **74**(20):5306–5312, 2002.

[4] Jones S.W., Thomas O.M., Aref H.: Chaotic advection by laminar-flow in a twisted pipe. *J. Fluid Mech.* **209**:335–357, 1989.

[5] Sobey I.J.: Dispersion caused by separation during oscillatory flow through a furrowed channel. *Chem. Eng. Science*, **40**(11):2129–2134, 1985.

ACTIVE SHEAR SUPERPOSITON MICROMIXER

Frederic Bottausci, Caroline Cardonne, Igor Mezic and Carl Meinhart
UCSB, Department of Mechanical and Environmental Engineering, California USA

Summary We present a theoretical and experimental study of the mixing in a Micro Electro Mechanical System (MEMS). The mixer is an active micromixer. Its design consists of a main mixing channel where the main flow is perturbed by jet flows emanating from a series of secondary channels. The lateral flows oscillate in time and reorient the lamination of passive tracers from streamwise to cross-stream. The micromixer is a silicon-etched device where the main channel is 2h wide, 13h long and h deep (h = 100 microns). The secondary channels are 5h long and h/2 wide. The parameters (flow rate, frequency, and amplitude of oscillation) are accurately controlled. The mixing process is studied numerically and experimentally using flow visualizations techniques. The numerical simulations are performed for the 3-D flow. We present some flow properties using the Mixing Variance Coefficient (MVC).

Introduction

Mixing time of two fluids can be enhanced when the interface area between the fluids is increased by stretching and folding, so that diffusion between the fluids has to occur over a relatively small distance. At the microscale, the Reynolds number Re = UL/ν, where U is the characteristic velocity, L the characteristic lengthscale and ν the kinematic viscosity, is close to unity or smaller. The flow cannot be turbulent. A solution to enhance the mixing is to create a chaotic advection (Aref 1984, Ottino 1989) based strategy which has the advantage of producing an exponential rate of mixing, as opposed to an algebraic rate (e.g. t^{-1}), which is achieved e.g. by inducing vertical motion. Thus advective stretching and folding is still desirable in order to improve the effective diffusion coefficient.
The microscale mixers can be divided in two broad classifications: the active and the passive micromixers. If there are no moving parts used to produce the mixing, the mixer is defined as passive micromixer (Miyake et al. 1993, Stroock et al. 2002, Song et al. 2003). These passive designs are such that the flow in the channel is fully three-dimensional, which is a necessary condition for a laminar steady flow to have chaotic trajectories. The first active micromixer developed by (Evans et al. 1997) is based on chaotic advection resulting from a source/sink system, where unmixed fluids are pumped into a mixing chamber, and then two source/sink systems are alternately pulsing the flow.
The current design of the micromixer studied here, called “shear superposition micromixer”, was developed at UCSB in 1998 (Volpert et al. 1999). This is a continuous through-flow micromixer consisting of a main channel with three cross-flow side channels that are capable of producing time-dependent shear flow in the direction transverse to the main stream (see figure 1). A micromixer design with one transversal secondary channel has been presented recently in Lee et al. 2001. A configuration with multiple side channels is mathematically investigated in Niu and Lee 2003.
The choices of frequencies and phase shifts for optimal mixing previously discussed in Volpert et al. 1999 are not obvious and are the subject of current investigations for the three-dimensional configuration. We evaluate the mixing using the mixing variance coefficient function (MVC) (Mathew et al. 2003) both in the experiments and in the numerical simulation. We present a study where the velocity in the side channel is large compare to the main flow.

Micromixer Design and Experimental Methods

The micromixer design is shown in Figure 1. Flow in the main channel is manipulated by controlling time-dependent oscillating flow from three pairs of secondary channels. The secondary channels induce time-dependent cross-stream momentum on the main channel flow which affects the fluid motion. A top view picture of the experimental chip is shown in Figure 1a and a description of the fluid motion in the mixer is shown in Figure 1b. The effectiveness of the mixer is evaluated using several different flow configurations by varying the frequencies and the amplitude of oscillation within the secondary channels.

A 3-D Poiseuille profile is specified at the entrance of the main channel, which is eventually perturbed by the secondary channels. The pressure at the entrances of the secondary channels, far from the main channel, is specified to be sinusoidal in time, with each pair having independent frequencies. The numerical simulations are performed with the mmercial CFD software FLUENT.

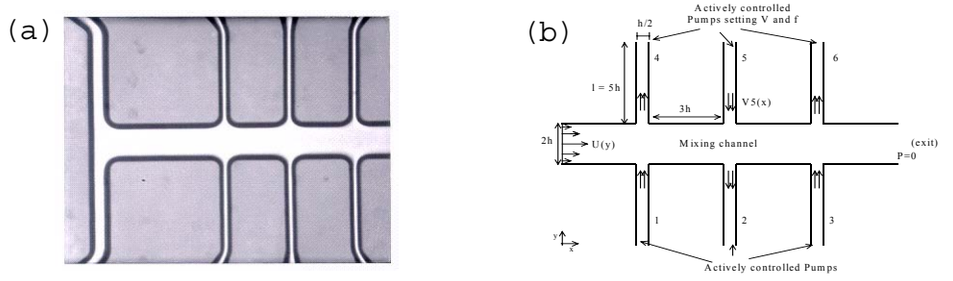


Figure 1. (a) micrograph of the mixing chip, (b) schematic showing one possible flow configuration.

RESULTS

Modeling

The velocity in the plane (x,y, z = *h*/2) for the main channel is measured by PIV (Particle Image Velocimetry) and is compared with the analytical solution and the numerical simulations. By solving the Navier-Stokes equation using the Fourier series expansion, we fund the solution of the time-dependent flow in the side channels which has been validated by the PIV measurements. The flow behavior at the junction of the main channel and the side channel is experimentally studied in details (figure 2(a,b)). We propose a simple model for the flow in the micromixer which is the superimposing of both analytical solutions. This model provides an estimation of the mixing based on the residence time of the fluid particle.

Mixing Variance Coefficient measurements

We are interested in the distribution of the fluid particles in the micromixer mainly at the exit of the channel. We used the so-called mixing variance coefficient (MVC) function to quantify a homogenous particles distribution of the two fluids initially unmixed at different scales. The MVC is defined as follows $MVC = \frac{1}{S^2}\sum_{1}^{S^2}\left(\rho_k - 0.5\right)^2$ where S^2 is the total number of boxes and ρ_k is the average particle label in the box *k*. S defines the size at which we look at the mixing. The best mixing is achieved when the mixing variance coefficient is equal to zero. The MVC definition can be extended to the experimental measurements. In this case, the mixing is analyzed by taking pictures of the channel through a microscope. At the entrance of the main channel, the water appears dark and the dye white.

We analyze the flow behavior at the intersection of the main channel and the side channels for different amplitudes and frequencies. At large amplitude and frequency the flow visualization and the PIVmeasurements show two recirculation regions (figure2) on each side of the side channel axis. These recirculation regions are not symmetric due to the main flow and depend on the velocity in the side channel

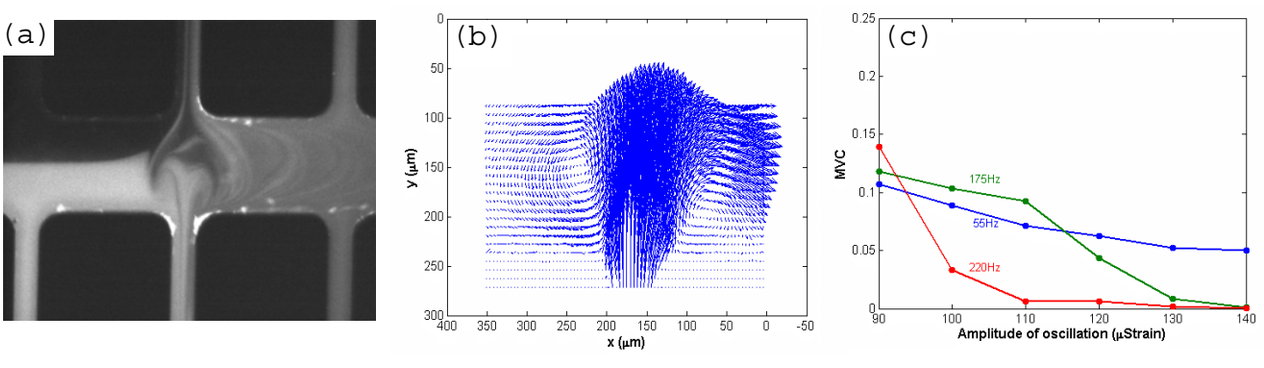


Figure2: (a) flow visualization for large amplitude of oscillation and large frequency in the middle plane. (b) PIVmeasurement in the same configuration. (c) MVC for different frequencies and amplitudes.

Figure 2c shows the MVC for different amplitudes of oscillation and different frequencies when one pair of side channels is activated. The re-circulations improve the mixing by adding some stretching and folding in the main flow.

CONCLUSION

The results presented here correspond to an analysis of the mass transport in an active micromixer. An analytical solution for the steady flow in the main channel and for the unsteady flow in the side channel is compared successfully with the experimental measurements obtained by micro-PIV and a simple model is proposed. Flow visualizations and PIV measurements show two non-symmetric recirculation regions when the velocity in the side channels is larger than in the main channel. Measurements of the mixing using the MVC function for one pair of side channels activated show a mixing increasing with the amplitude and the frequency of the oscillations.

STREAMLINE TOPOLOGY OF THE NEAR WAKE OF A CIRCULAR CYLINDER AT LOW REYNOLDS NUMBERS

Morten Brøns*, Kristine Niss**, Bo Jakobsen**, Lars K. Voigt***,
Rune Petersen*, Anders Bisgaard*

* *MAT, Technical University of Denmark, DK-2800 Kongens Lyngby, Denmark*
** *IMFUFA, Roskilde University, DK-4000 Roskilde, Denmark*
*** *HV Turbo, DK-3000 Helsingør, Denmark*

Summary Using methods from bifurcation theory, we find all possible instantaneous streamline patterns in the wake of a cylinder at Reynolds numbers close to the onset of vortex shedding and close to the cylinder. The analysis indicates that two different regimes are to be expected. Using numerical simulations, we verify the existence of these regimes.

The basic features of the flow around a circular cylinder of diameter D are well known. For low values of the Reynolds number $Re = UD/\nu$ the flow is attached to the cylinder. At $Re \approx 5$ the flow separates, and two counter-rotating steady vortices are created behind the cylinder. At $Re \approx 50$ the steady flow becomes unstable, and the vortices are shed periodically from the cylinder, resulting in the celebrated von Kármán vortex street. The transition to periodicity is a Hopf bifurcation, see e.g. [6]. For higher values of Re the flow becomes three-dimensional and turbulent.

The purpose of the present paper is to analyze the transition from steady flow to periodic flow on the basis of the streamline patterns. An attempt of such an analysis on the basis of numerous visualization experiments was performed by Perry *et al.* [5]. The result is shown in figure 1. The basic mechanism in the creation of new vortices is the merging of two dividing streamlines at the cylinder surface, as shown in the transition between panel (d) and (e) and again between (h) and (a). In this process, an attached vortex and a free stagnation point are created.

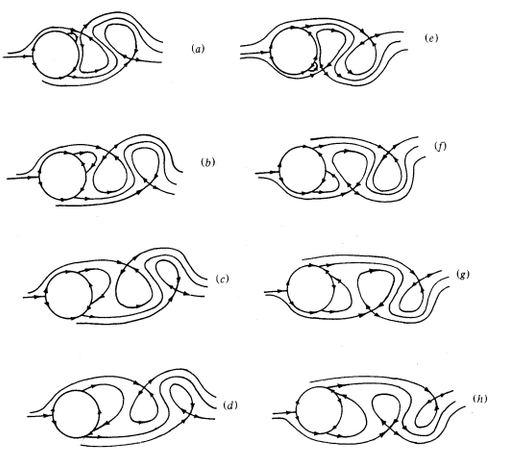


Figure 1: Instantaneous streamline pattern during a shedding cycle proposed by Perry et al. *[5].*

In the present paper we consider the equations for the instantaneous streamlines at time t_0, $\dot{\mathbf{x}} = \mathbf{v}(\mathbf{x}, t_0, Re)$, as a dynamical system, depending on a parameter Re, and, in the unsteady case, the time t_0. For certain values of the parameters the streamline pattern may be degenerate or structurally unstable, and arbitrarily small changes in the parameters give rise to qualitative changes in the streamline patterns. Using bifurcation theory, classification of the possible patterns close to a degenerate configuration may be obtained. For the present case, the flow close to a fixed wall with no-slip boundary conditions, the basic theory is established in [1] and [4]. Applications of this approach to the analysis of numerical simulations are given in e.g. [3].

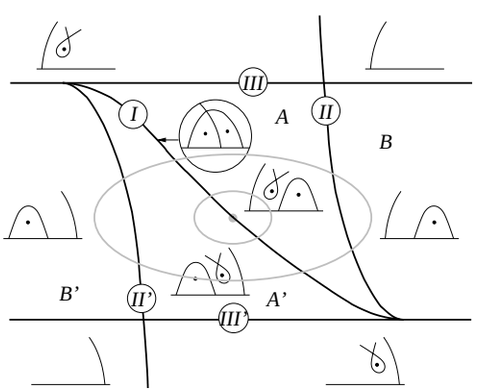


Figure 2: Bifurcation diagram. A slice in the parameter space is partitioned into regimes with different streamline patterns. In each region, the pattern is sketched. The horizontal lines correspond to the cylinder wall.

Taking the flow at the creation at $Re \approx 5$ of the two steady vortices as the degenerate configuration from which we perform the bifurcation analysis, we can prove the following

Theorem *Any velocity field which is a perturbation of the field at the creation of two symmetric vortices is locally equivalent to a member of the three-parameter family of velocity fields generated from the normal form streamfunction*

$$\psi = y^2(c_{0,2} + c_{1,2}x + c_{0,3}y + xy - x^3).$$

Here x denotes a coordinate along the cylinder surface, y is a coordinate orthogonal to the surface, and $c_{0,2}, c_{1,2}, c_{0,3}$ are free parameters.

The theorem is proved with methods from normal form theory. For proofs of similar theorems, see e.g. [2, 4]. The analysis of the normal form streamfunction results in a three-dimensional bifurcation diagram in the $c_{0,2}, c_{1,2}, c_{0,3}$ parameter space.

An interesting two-dimensional slice is shown in figure 2. The space is partitioned into regions *A, A'*, ... with different streamline topologies. The regions are bounded by bifurcation curves, shown heavy. The curve *I* is a global bifurcation curve. Here the streamlines has the topology of the steady vortex pair, but possibly with the symmetry broken.

To connect this result with the vortex shedding, we assume that the transition to periodic flow occurs at a Reynolds number so close to the creation of the steady vortices, that the flow patterns can be considered perturbations of the degenerate flow, and hence must be contained in the bifucation diagram. With this assumption, we can follow the development of the topology of the wake in the diagram as *R*eis increased. The steady state corresponds to the grey point on the global bifurcation curve *I*. As the flow becomes periodic, the temporal development of the streamfunction must be represented by a closed curve in the bifurcation diagram. Right after the bifurcation the amplitude is small, and is represented by the small ellipse in figure 2. Hence the theory predicts that right after the Hopf bifurcation, two different structurally stable streamline patters will prevail, namely *A* and its mirror image *A'*. At exactly two time instants during the cycle, the topology of the steady vortices will exist, as the bifurcation curve *I* is crossed.

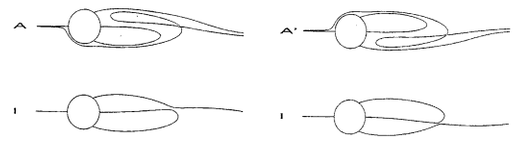


Figure 3: Numerical simulations for $Re = 45$, right after the Hopf bifurcation. The panels show instantaneous streamline patterns at different times during the shedding cycle.

Increasing *R*e, it is expected that the amplitude of the limit cycle will grow, resulting in a larger closed orbit in the bifurcation diagram. Hence, there is the possibility, that beyond a certain critical *R*e, further bifurcation curves can be crossed, as indicated by the large ellipse in figure 2.

The analysis above is of a purely qualitative nature, and relies only on the existence of a streamfunction for the flow. Hence, one cannot on this basis predict actual Reynolds numbers where transitions between different sequences occur. We have verified the scenarios by numerical simulations using a finite volume code. The code finds the Hopf bifurcation at $Re = 43$, in reasonable agreement with experiments. At $Re = 45$ a sequence of patterns corresponding to the small ellipsis in figure 2 is obtained. This sequence persists only until $Re \approx 45.8$, where the limit cycle intersects the bifurcation curves *II* and *II'*, and the streamline patterns *B* and *B'* appear during the cycle. No further changes are observed up to $Re = 200$.

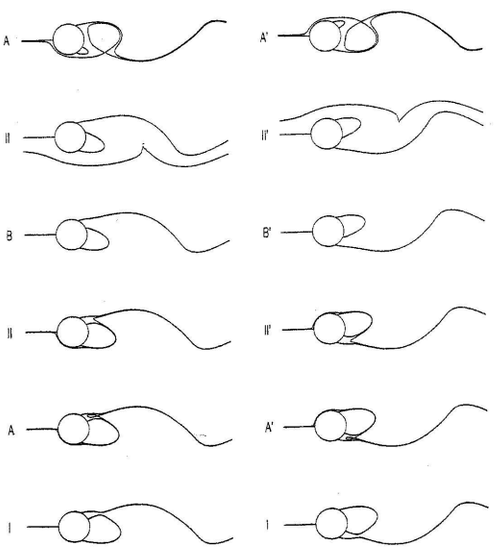


Figure 4: As figure 3, but for $Re = 100$.

Note, that the sequence in figure 1 is not obtained. It is a perfectly legitimate sequence, and Hartnack [4] shows that the sequence is in fact the simplest possible which can account for creation and destruction of attached vortices. However, it does not include the topology of the steady vortices, and the present analysis shows that this cannot be avoided generically.

The present qualitative analysis does not depend on the specific shape of the fixed body. For more general shapes such as ellipses the same bifurcation diagram will be relevant, as long as the streamline pattern of the steady vortex pair is of relevance.

References

[1] P. G. Bakker. *Bifurcations in Flow Patterns*. Klüver Academic Publishers, Dordrecht, 1991.

[2] M. Brøns. Topological fluid mechanics of axisymmetric flows. In J. N. Sørensen, E. J. Hopfinger, and N. Aubry, editors, *Simulation and Identification of Organized Structures in Flows*, pages 213–222. Kluwer, 1999.

[3] M. Brøns, L. K. Voigt, and J. N. Sørensen. Streamline topology of steady axisymmetric vortex breakdown in a cylinder with co- and counter-rotating end-covers. *Journal of Fluid Mechanics*, 401:275–292, 1999.

[4] J. N. Hartnack. Streamline topologies near a fixed wall using normal forms. *Acta Mechanica*, 136(1-2):55–75, 1999.

[5] A. E. Perry, M. S. Chong, and T. T. Lim. The vortex-shedding process behind two-dimensional bluff bodies. *Journal of Fluid Mechanics*, 116:77–90, 1982.

[6] M. Provansal, C. Mathis, and L. Boyer. Bénard-von Kármán instability: Transient and forced regimes. *Journal of Fluid Mechanics*, 182:1–22, 1987.

NAVIER-STOKES TURBULENCE

Koji Ohkitani* and Peter Constantin**

*RIMS, Kyoto University, Kyoto 606-8502, Japan
**Department of Mathematics, The University of Chicago, Chicago, Il 60637, USA

Summary Numerical study of Eulerian-Lagrangian analysis of Navier-Stokes turbulence is presented. Near identity transformations associated with diffusive Lagrangian labels capture a time scale of small scale motion. A novel characterization of the singular perturbation nature as $\nu \to 0$ is proposed as connection anomaly.

INTRODUCTION

One of the important properties of the the Navier-Stokes flows is that in the limit of vanishing viscosity their behavior differs from that of corresponding Euler equations. For example, in the inviscid case the total energy is conserved, whereas in slightly viscous Navier-Stokes flows it is observed to be dissipated in a nontrivial fashion. This anomalous behavior, finite energy dissipation in the limit of small viscosity is the fundamental premise of Kolmogorov's theory of turbulence. Another example is the phenomenon of vortex reconnection in slightly viscous flows, as opposed to frozen vortex lines in inviscid fluids.
Recently, a framework of the Navier-Stokes equations suitable for studying the singular perturbation nature and/or topological properties of vortex lines in viscous flow has been developed by one of the authors [1, 2]. It has been applied to numerical simulations of the Navier-Stokes equations and its usefulness for monitoring vortex reconnection has been shown. The purpose of this paper is to apply it to fully-developed turbulence to quantify its anomalous behavior.

THE EULERIAN-LAGRANGIAN FORMULATION

The incompressible Navier-Stokes equations read with standard notations

$$\frac{\partial \boldsymbol{u}}{\partial t} + (\boldsymbol{u}\cdot\nabla)\boldsymbol{u} = -\nabla p + \nu\triangle\boldsymbol{u}, \ \ \mathrm{div}\ \boldsymbol{u} = 0 \tag{1}$$

We recast them using impulse $\boldsymbol{w}$, e.g. [3]

$$\frac{\partial \boldsymbol{w}}{\partial t} + (\boldsymbol{u}\cdot\nabla)\boldsymbol{w} = -(\nabla\boldsymbol{u})^T\boldsymbol{w} + \nu\triangle\boldsymbol{w}, \tag{2}$$

where T means matrix transpose. The velocity $\boldsymbol{u}$ is obtained by solenoidal projection $\boldsymbol{u} = \boldsymbol{P}[\boldsymbol{w}]$. The crux of the Eulerian-Lagrangian formalism is the introduction of diffusive Lagrangian label as

$$\frac{\partial \boldsymbol{A}}{\partial t} + (\boldsymbol{u}\cdot\nabla)\boldsymbol{A} = \nu\triangle\boldsymbol{A}, \tag{3}$$

and velocity decomposition $\boldsymbol{u} = \boldsymbol{P}[(\nabla\boldsymbol{A})^T\boldsymbol{v}]$, much like Weber formula in the inviscid case.
For consistency with the Navier-Stokes equations, virtual velocity $\boldsymbol{v}$ was shown to obey [1]

$$\frac{\partial \boldsymbol{v}}{\partial t} + (\boldsymbol{u}\cdot\nabla)\boldsymbol{v} = 2\nu\boldsymbol{C} : \nabla\boldsymbol{v} + \nu\triangle\boldsymbol{v}, \tag{4}$$

where $i-$th component of $\boldsymbol{C} : \nabla\boldsymbol{v}$ is $C_{m,k;i}\dfrac{\partial v_m}{\partial x_k}$ and $C_{m,k;i} \equiv \dfrac{\partial x_j}{\partial A_i}\dfrac{\partial^2 A_m}{\partial x_j \partial x_k}$. Connection $\boldsymbol{C}$ measures non-commutativity between the Euler and Euler-Lagrange derivatives; $[\nabla_A^i, \nabla_E^k] = C_{m,k;i}\nabla_A^m$. Practically, in stead of $\boldsymbol{v}$, we solve for displacement vector $\boldsymbol{\ell} = \boldsymbol{A} - \boldsymbol{x}$ which satisfies a passive equation of the form

$$\frac{\partial \boldsymbol{\ell}}{\partial t} + (\boldsymbol{u}\cdot\nabla)\boldsymbol{\ell} = -\boldsymbol{u} + \nu\triangle\boldsymbol{\ell}. \tag{5}$$

Once $\boldsymbol{\ell}$ is obtained, $\boldsymbol{C}$ and all other quantities of interest can be obtained *a posteori* by matrix inversion and by $\nabla\boldsymbol{A} = \nabla\boldsymbol{\ell} + \boldsymbol{I}$.
In inviscid fluids $\boldsymbol{A}$ remains invertible under smooth evolution because $\det(\nabla\boldsymbol{A})$ is constant. In viscous fluids the determinant is not preserved in general. In [4] it was found that the matrix becomes non-invertible in time and this phenomenon is related with vortex reconnection. It is necessary to reset $\boldsymbol{\ell} = 0$ if $|\det(\nabla\boldsymbol{A})| \le \epsilon$, where ϵ is a small parameter.

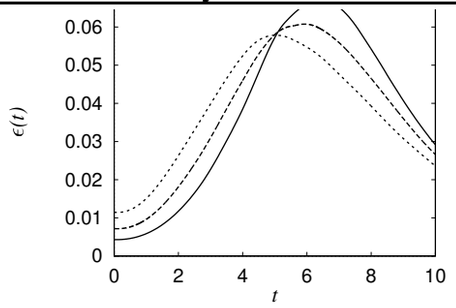


Figure 1: Time evoultion of the energy disspation rate for $\nu = 4 \times 10^{-3}$(dotted), 2.5×10^{-3}(dashed) and 1.5×10^{-3}(solid)

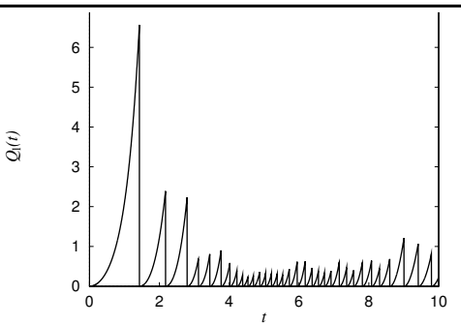


Figure 2: Time evoultion of enstrophy of displacement for the case of $\nu = 2.5 \times 10^{-3}$.

APPLICATION TO DECAYING TURBULENCE

A 2/3−dealiased pseudo-spectral method was employed under periodic boundary conditions with grid points typically 256^3. Time marching was performed with a fourth-order Runge-Kutta scheme. The initial condition has an energy spectrum of the form

$$E(k) \propto k^2 \exp(-k^2), \text{ with } \left\langle |\boldsymbol{u}|^2 \right\rangle = 1.$$

Numerical parameters used are $\nu = 4 \times 10^{-3}, 2.5 \times 10^{-3}$ and 1.5×10^{-3} with $\Delta t = 2 \times 10^{-3}$ and with $\epsilon = 0.01$. The energy dissipation rate $\epsilon(t)$ attains its maximum around $t = 6$ in Fig.1. We show time development of

$$Q_{\boldsymbol{\ell}}(t) = \frac{1}{2} \left\langle |\nabla \times \boldsymbol{\ell}|^2 \right\rangle .$$

in Fig.2. In the developed stage the resetting time interval is found to be comparable to Kolmogorov's time scale or less. Occurrence of resetting implies that the first term on the RHS of (4) is not negligible in the limit of small viscosity. To quantify the anomaly of connection we are led to the following hypothesis: for consecutive resetting times $t_j,\ t_{j+1}$ there are positive constants A_p independent of ν such that

$$\lim_{\nu \to 0} \nu \int_{t_j}^{t_{j+1}} ||C||_p^2 \mathrm{d}t > A_p > 0, \quad ||\boldsymbol{C}||_p \equiv \left(\frac{1}{(2\pi)^3} \int |\boldsymbol{C}|^p \boldsymbol{dx} \right)^{1/p}. \tag{6}$$

The nondimensional integral is observed to be bounded from below by positive constants of order 10^{-1}, 10^{-1} and 10^2 for $p = 1, 2$ and ∞, respectively. The connection anomaly is a characterization of singular nature of the limit $\nu \to 0$.

References

[1] Constantin, P. 2001 An Eulerian-Lagrangian Approach to the Navier-Stokes Equations *Commun. Math. Phys.* **216**, 663–686.

[2] Constantin, P. 2003 Near identity transformations for the Navier-Stokes equations in *Handbook of Mathematical Fluid Dynamics* (ed. S. Friedlander, D. Serre). vol. 2, pp. 117–141. Elsevier.

[3] Buttke, T.& Chorin, A. 1993 Turbulence calculations in magnetization variables *Appl. Num. Math.* **12**, 47–54.

[4] Ohkitani, K. & Constantin, P. 2003 Numerical study of the Eulerian-Lagrangian formulation of the Navier-Stokes equations *Phys. Fluids* **15**, 3251–3254.

TOPOLOGICAL CHAOS IN SIMPLE MIXERS

Matthew D. Finn*, Stephen M. Cox**, Helen M. Byrne*
*School of Mathematical Sciences, University of Nottingham, Nottingham NG7 2RD, UK
**School of Applied Mathematics, University of Adelaide, Adelaide 5005, Australia

Summary Topological chaos is discussed in a two-dimensional batch mixer and a three-dimensional static mixer, under very viscous flow conditions. Topological ideas may be used to calculate a minimum stretch rate for certain flows, but cannot predict the size of the region in which this stretching is achieved. Numerical simulations of dye advection are used to test whether topological ideas can be used to practically enhance mixing quality. In two dimensions it is found that material stretch rates are in tight accordance with theoretically predicted values dependent on flow topology. Furthermore, effective mixing is readily achieved in a useful sized domain. However, in three dimensions we find flow features which make topological arguments less practical for improving mixing quality.

INTRODUCTION

A mixing regime commonly studied in the last twenty years, and exploited in industries such as polymer manufacturing, is slow viscous flow, or Stokes flow, in which simple stretching and folding mechanisms are employed to generate chaotic particle paths [1, 2]. Although chaotic advection is readily created, optimising mixing parameters for a given purpose is extremely difficult because chaotic flow simulations are computationally expensive and usually prohibit exhaustive parameter-space searches. A further stumbling block for many optimisation procedures is that mixing performance can depend sensitively on geometrical parameters (e.g. the size of a stirring impeller), and on the fluid properties. However, very recently, an elegant idea has emerged which potentially allows one particular mixing measure, material stretch rate, to be robustly built-in to a mixer. The concept is Topological Chaos, as described in a remarkable theoretical and experimental paper by Boyland, Aref and Stremler [3]. Topologically chaotic flows are a subset of chaotic flows in which the flow topology alone is responsible for achieving a guaranteed minimum theoretical material stretch rate, in some part of the domain, regardless of the exact geometry or fluid details (viscosity, compressibility, rheology, etc). The topological approach, however, while widely applicable, cannot predict the size of the region in which this stretch rate is achieved. A careful investigation is needed into whether topological ideas can generate good mixing *in practice*.

STIRRING IN TWO DIMENSIONS

A requirement for topologically chaotic flow is that a batch mixing device must contain at least three moving stirrers [3]. Surprisingly, therefore, very few industrial batch mixers are equipped to exploit topological chaos. Those that are appear to employ it almost accidentally, as they are not marketed as possessing any special topological flow properties. Almost all mixing devices which have so far been modelled mathematically are incapable of producing topological chaos. However, such flows are readily generated in a two-dimensional model batch stirring device (BSD) [3, 4], which is the subject of our study. The BSD is a generalisation of the translating, rotating mixer [5], consisting of a circular cylinder in which the fluid is stirred by an arbitrary number of moving stirring rods. In order to perform meaningful simulations of the chaotic flow, accurate expressions for the velocity field are needed because numerical errors grow exponentially in time. Although we cannot determine an exact solution for the BSD velocity, we have developed a computationally cheap, spectrally accurate, series expression for the streamfunction, which allows high-precision simulations of tracer advection experiments. Some sample advection simulation results are shown in Figure 1.

A key question we have addressed is whether topological ideas may be useful in practice for guiding mixer design, paying particular attention to whether stretch rates predicted by the topological theory are achieved in a physically useful area of the mixing domain [6]. Our form of solution may be used to calculate accurately other physical quantities of interest, such as the energy input required for mixing, allowing studies of mixing efficiency. The effect of stirrer shape on mixing quality is also discussed, because stirrers of ‘paddle’ shape cross-section, for instance, might be better, intuitively, than the mathematically simpler circular cross-sections. Non-circular stirrers may be considered by using appropriate conformal transformations in the series solution for the velocity field. Although the change in stirrer cross-section has no influence on the flow topology, it may have an impact on energy usage, or be used to enhance stretching rate above that predicted by the topological theory, allowing a more economical, or a higher performance mixer, respectively.

STIRRING IN THREE DIMENSIONS

Although batch mixers are used in industry, continuous-throughput mixing in three dimensions is more widely used. An extra spatial dimension to the flow means that static mixing is possible, i.e. no time dependence is required in the velocity field in order to achieve chaotic particle advection [7]. Time-dependence commonly is employed, but many successful patented static mixer designs exist (e.g. by Kenics, Mixtec, TAH Industries and Sulzer–Chemtech). These static mixers generally consist of a circular cylindrical pipe containing a judiciously designed insert that causes fluid in the cylinder to be ‘cut and folded’ in the cross-section as it is pumped axially. We study a static mixer called the braided pipe mixer (BPM) inspired by the two-dimensional BSD [8]. The BPM consists of a circular cylindrical pipe containing smaller

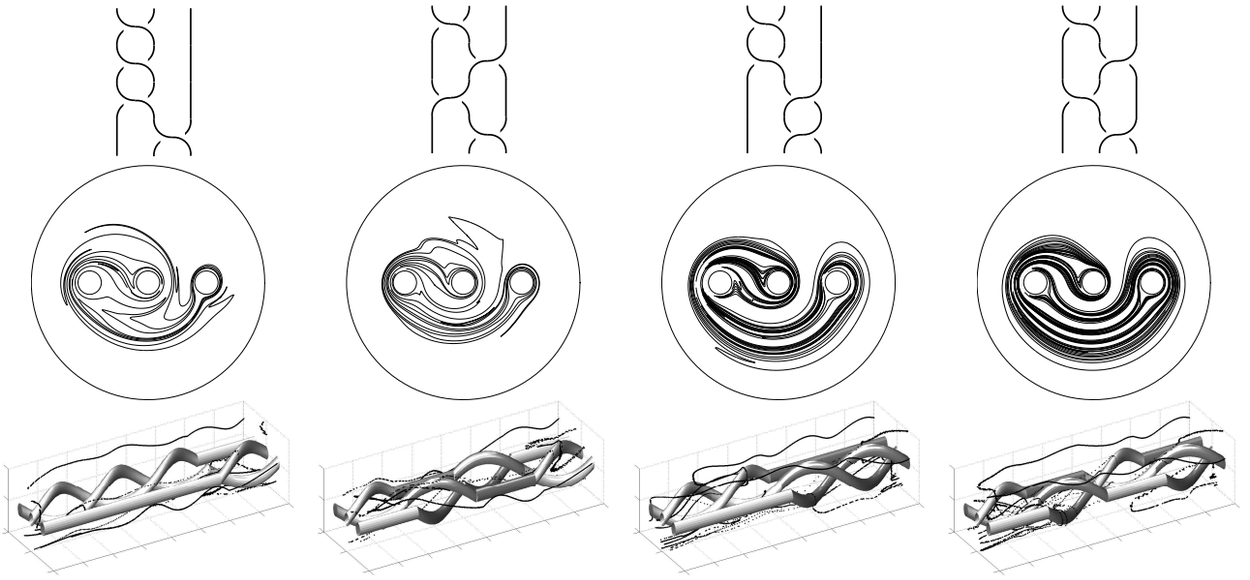


Figure 1. Example results of dye advection in the BSD (middle row) and BPM (bottom row), with stirring regimes corresponding to different braid topologies (top row). In the BSD the flow topology refers to how the stirring rods are moved around each other; in the BPM the topology describes how the internal pipes are intertwined. The images show the fate of a straight line initial dye blob after a 'moderate' stirring time.

twisted pipes that cause the fluid to mix as it is driven along by an imposed pressure gradient. In such static mixers the axial coordinate occupies the role played by time in the two-dimensional BSD. The correspondence is not exact, however, because different fluid particles travel at different axial speeds, and some even come to rest on the internal pipes. The velocity field for the BPM is constructed using a series approach, as with the BSD. Sample BPM dye advection results are shown in Figure 1 (the outer pipe is not shown). It was recently suggested that the obstacles in the pipe could be braided to generate effective chaotic mixing in three dimensions [3, 9]. Furthermore, it was conjectured that these pipes could be reduced in thickness and still generate good mixing. By direct comparison with the two-dimensional work, we discuss whether topological ideas for two-dimensional flows may be applied to improve mixing in steady three-dimensional flows.

CONCLUSIONS

The two-dimensional BSD, containing three or more stirring rods, is capable of generating topologically chaotic flow. We provide numerical evidence to support the observation of Boyland *et al.* [3] that the region of high stretch is comparable with that through which the stirring elements move during operation of the device. Calculated material stretch rates were found to be in close agreement with the corresponding theoretical predictions. The theoretical stretch rates were achieved in the BSD even as the radii of the stirring rods were reduced, although the stretching became more localised around the trajectories of the rods. In the three-dimensional BPM we found that it was difficult to distinguish between the mixing performance of different braid topologies according to material stretch rate and measures based on the axial distribution of tracer, in contrast with the BSD where braid performances were clearly ordered and in agreement with topological theory. Although one might intuitively expect static mixer design could be improved using topological considerations, there is no formal topological chaos theory for three-dimensional flows. By considering particle advection in an artificial two-dimensional flow using the axial coordinate as 'time', we find that topological chaos *is* present in the BPM; however, in this system, the regions of high material stretch rate corresponded exactly with those regions where particle advection along the device was very slow using the real time. On a practical time scale the fast stretching is not seen, and topological chaos appears to offer no significant benefit to the mixer design.

References

[1] Aref, H.: Stirring by chaotic advection. *J. Fluid Mech.* **143**:1–21, 1984.
[2] Aref, H.: The development of chaotic advection. *Phys. Fluids* **14**:1315–1325, 2002.
[3] Boyland, P.L., Aref, H. and Stremler, M.A.: Topological fluid mechanics of stirring. *J. Fluid Mech.* **403**:277–304, 2000.
[4] Vikhansky, A.: Simulation of topological chaos by immersed boundary method. Preprint, University of the Negev, 2003.
[5] Finn, M.D. and Cox, S.M.: Stokes flow in a mixer with changing geometry. *J. Eng. Math.* **41**:75–99, 2001.
[6] Finn, M.D., Cox, S.M. and Byrne, H.M.: Topological chaos in inviscid and viscous mixers. *J. Fluid Mech.* **493**:345–361, 2003.
[7] Jones, S.W., Thomas, O.M. and Aref, H.: Chaotic advection by laminar flow in a twisted pipe. *J. Fluid Mech.* **209**:335–357, 1989.
[8] Finn, M.D., Cox, S.M. and Byrne, H.M.: Chaotic advection in a braided pipe mixer. *Phys. Fluids* **15**:77–80, 2003.
[9] Mackay, R.S.: Complicated dynamics from simple topological hypotheses. *Phil. Trans. R. Soc. Lond. A* **359**:1479–1496, 2001.

GAUGE PRINCIPLE FOR IDEAL FLUIDS AND VARIATIONAL PRINCIPLE

Tsutomu Kambe[1]
IDS, Higashi-yama 2-11-3, Meguro-ku, Tokyo 153-0043, Japan

Summary A variational formulation is given for flows of a compressible ideal fluid by defining a Galilei-invariant Lagrangian. Variations are required to be gauge-invariant with respect to both translation and rotation groups. Carrying out variations by using a covariant derivative defined in terms of gauge fields, we deduce the Euler's equation of motion. Noether's theorem results in the conservation laws of momentum and angular momentum.

INTRODUCTION: FLUID FLOWS AND FIELD THEORY

Study of fluid flows is considered to be a field theory in Newtonian mechanics. In other words, it is a *field theory of mass flow* subject to Galilei transformation. It is well-known that there are various similarities between fluid mechanics and electromagnetism. For example, the functional relation between velocity and vorticity fields is the same as the Biot-Savart law known in the electromagnetism between magnetic field and electric current. One may ask whether the similarity is mere an analogy, or has a solid theoretical background.

In the theory of *gauge field*, a guiding principle is that laws of physics should be expressed in a form that is independent of any particular coordinate system. In the quantum field theory, a free-particle Lagrangian is defined first in such a way as having an invariance under Lorenz transformation. Next, a gauge principle is applied to the Lagrangian, requiring it to have a *symmetry*, *i.e.* the gauge invariance. As a result, a gauge field such as the elecromagnetic field is introduced to satisfy *local* gauge invariance. In regard to the fluid flows, relevant symmetry groups are *translation group* and *rotation group* [3].

We seek a scenario which has a formal equivalence with the gauge theory in the quantum field theory. To that end, we define a Galilei-invariant Lagrangian for fluid flows which has also global gauge invariance. The *global* means that transformations are uniform at all points and times. Next, we examine whether it has *local* gauge invariance. Applying the gauge principle to the Lagrangian first with respect to translational transformations, the action principle results in the equation of motion for *irrotational flows*. That is, the velocity field thus obtained from the translation invariance must have a potential. This corresponds to *superfluid* flows.

Next, we consider an additional transformation with respect to the gauge group $SO(3)$, a *rotation group* in the three-dimensional Euclidean space. The gauge transformation introduces a new *rotational* component in the velocity field (*i.e.* the vorticity), even though the original field is irrotational. In complying with the local gauge invariance, a gauge-covariant derivative is defined by introducing a new gauge field Ω. Galilei invariance of the covariant derivative requires that the *gauge field* Ω should coincide with the *vorticity* [1, 2]. As a result, the covariant derivative of velocity is found to be the so-called *material* derivative of velocity, and the Euler's equation of motion for an ideal fluid is derived from the Hamilton's principle. The Noether's theorem leads to conservation laws associated with gauge invariances: *i.e.* conservation equations of momentum and angular momentum. Furthermore, the Lagrangian has a symmetry with respect to particle permutation, which leads to a local law of vorticity conservation, *i.e.* the vorticity equation [2, 3].

The flow fields are characterized by two gauge groups: a translation group and a rotation group. The former is abelian and the latter is non-abelian. Thus, the flow fields are governed by two characteristically different transformation laws.

HAMILTON'S PRINCIPLE FOR AN IDEAL FLUID

Constitutive conditions and definitions

We carry out the material variations under the following conditions and definitions.
(*i*) *Kinematic condition*: The $\boldsymbol{x}$-space trajectory of a material particle, specified by the Lagrangian coordinte $\boldsymbol{a}$, is denoted by $\boldsymbol{x}_a(\tau) = \boldsymbol{x}(\tau, \boldsymbol{a})$ and the time $t = \tau$, and the particle velocity is

$$\boldsymbol{v}(\boldsymbol{x}, t) = \partial_\tau \boldsymbol{x}(\tau, \boldsymbol{a})\,. \tag{1}$$

All the variations are taken so as to follow such trajectories of material particles. In addition, all the analyses are carried out by keeping mass fixed. As a consequence, the equation of continuity must be satisfied always.
(*ii*) *Gauge-covariance*: All the expressions must satisfy both global and local gauge invariance.
(*iii*) *Hamilton's principle*: Lagrangian for flows of an ideal fluid is defined by

$$L_{\rm F} := \int_M \tfrac{1}{2}\,\langle\, \boldsymbol{v}, \boldsymbol{v}\,\rangle\,\rho\,{\rm d}V - \int_M \epsilon(\rho, s)\,\rho\,{\rm d}V\,, \qquad \langle \boldsymbol{v},\, \boldsymbol{v}\rangle = \sum v_k v_k, \tag{2}$$

where $\boldsymbol{v} = (v_k)$ is the fluid velocity, ρ the density, and ϵ the internal energy per unit fluid mass, with ${\rm d}V$ a volume element, and M is a bounded space under consideration with $\boldsymbol{x} \in M \subset \mathbb{R}^3$. The action principle is given by $\delta\mathcal{A} = 0$, where the action is defined by $\mathcal{A} = \int_{t_0}^{t_1} L_{\rm F}[\boldsymbol{v}, \rho, \epsilon]\ {\rm d}t$.

[1]kambe@gate01.com Visiting Professor, Nankai Institute of Mathematics (China)

(*iv*) *Covariant derivative*: Gauge-covariant derivative $\nabla_t \boldsymbol{v}$ must be used for the variation, where

$$\nabla_t \boldsymbol{v} = \partial_t \boldsymbol{v} + \mathrm{grad}(\tfrac{1}{2}\, v^2) + \boldsymbol{\omega} \times \boldsymbol{v} = \partial_t \boldsymbol{v} + (\boldsymbol{v} \cdot \nabla)\, \boldsymbol{v}\,, \qquad (\boldsymbol{\omega} = \mathrm{curl}\, \boldsymbol{v}). \tag{3}$$

(*v*) *Physical material*: An ideal fluid is defined by the property that there is no disspative mechanism within it such as viscous dissipation or thermal conduction. As a consequence, the fluid motion is *isentropic*, *i.e.* the entropy s per unit mass remains constant following the motion of each material particle. The entropy is not necessarily constant at every material particle, *i.e.* not necessarily homentropic.

We carry out an *isentropic material variation* satisfying local gauge invariance, under the above conditions.

Gauge principle

For the gauge transformations, it is important to recognize that the velocity $\boldsymbol{v}$ in the Lagrangian (2) must be represented by the form (1). According to the gauge principle, the partial time derivative $\partial/\partial t$ must be modified so that all the variations as well as the Lagrangian L_{F} are gauge-invariant. The above form of the covariant derivative $\nabla_t \boldsymbol{v}$ can be deduced on this basis of the gauge principle.

Suppose that the time derivative of velocity $\boldsymbol{v}$ is represented such that

$$\nabla_t \boldsymbol{v} = \mathrm{D}_t \boldsymbol{v} + \Omega \boldsymbol{v} = \partial_t \boldsymbol{v} + A\boldsymbol{v} + \Omega \boldsymbol{v}, \qquad \mathrm{D}_t \boldsymbol{v}_* = \partial_t \boldsymbol{v}_* + A\boldsymbol{v}_*.$$

where $\boldsymbol{v}_* = \mathrm{grad} f$, and A and Ω are linear operators called *gauge fields*, and the velocity field $\boldsymbol{v}(\boldsymbol{x}, t)$ can be represented with a linear combination of irrotational and rotational parts: $\boldsymbol{v}(\boldsymbol{x}, t) = \mathrm{grad} f + \mathrm{curl}\, \boldsymbol{B}$ for $f(\boldsymbol{x})$, $\boldsymbol{B}(\boldsymbol{x}) \in C^\infty[M]$. First, concerning an irrotational flow field $\boldsymbol{v}_* = \mathrm{grad} f$, we require that the covariant derivative $\mathrm{D}_t \boldsymbol{v}_* = \partial_t \boldsymbol{v}_* + A\boldsymbol{v}_*$ is invariant with respect to *translational* gauge transformation, both global and local. Furthermore, $\mathrm{D}_t \boldsymbol{v}_*$ is required to be invariant with respect to Galilei transformation. This determines the gauge operator A such that $A\boldsymbol{v}_* = (\boldsymbol{v}_* \cdot \nabla)\boldsymbol{v}_* = \frac{1}{2}\, \mathrm{grad}(\boldsymbol{v}_*)^2$, where $(\boldsymbol{v}_* \cdot \nabla)(\boldsymbol{v}_*)_k = (\partial_i f)\partial_i(\partial_k f) = (\partial_i f)\partial_k(\partial_i f) = \frac{1}{2}\, \partial_k (\boldsymbol{v}_*)^2$.

Next, it is required that the covariant derivative $\nabla_t \boldsymbol{v} = \mathrm{D}_t \boldsymbol{v} + \Omega \boldsymbol{v}$ is invariant with respect to *rotational* transformation $SO(3)$, both global and local. Furthermore, requirement of Galilei invariance of $\mathrm{D}_t \boldsymbol{v} + \Omega \boldsymbol{v}$ determines the gauge operator Ω which is represented as a skew-symmetric matrix (an element of Lie algebra $\mathbf{so}(3)$). Then, the $\Omega \boldsymbol{v}$ is expressed by a vector product $\hat{\Omega} \times \boldsymbol{v}$, where

$$\hat{\Omega} = \nabla \times \boldsymbol{v} = \boldsymbol{\omega}$$

is the **vorticity**. It is found that the vorticity $\boldsymbol{\omega}$ is the gauge field with espect to the gauge group $SO(3)$. Thus, the covariant derivative (3) is deduced. It should be noted that the covariant derivative $\nabla_t \boldsymbol{v}$, *i.e.* the *Lagrange derivative* of velocity vector, is invariant with respect to the two gauge transformations: both translational and rotational. Thus it is verified that the Lagrange derivative of velocity has a *gauge-theoretic* significance.

Variation of the action $\mathcal{A}$ is given by

$$\delta\, \mathcal{A} = \Big[\int_M \langle \boldsymbol{v}, \boldsymbol{\xi} \rangle\, \rho\, \mathrm{d}V \Big]_{t_0}^{t_1} + \int_{t_0}^{t_1} \mathrm{d}t \oint_S p\, \langle \boldsymbol{n}, \boldsymbol{\xi} \rangle\, \mathrm{d}S - \int_{t_0}^{t_1} \mathrm{d}t \int_M \big\langle \big(\nabla_t \boldsymbol{v} + \rho^{-1} \mathrm{grad}\, p\big),\, \boldsymbol{\xi}\, \big\rangle\, \rho\, \mathrm{d}V,$$

where p is the pressure. The first two terms vanish owing to the boundary conditions of *vanishing* of the variation $\boldsymbol{\xi}$. Thus, the action principle $\delta\, \mathcal{A} = 0$ for arbitrary variation $\boldsymbol{\xi}$ leads to

$$\nabla_t \boldsymbol{v} + \rho^{-1}\, \nabla\, p = 0\,, \tag{4}$$

This is the *Euler's equation of motion*. Using (3), we have $\partial_t \boldsymbol{v} + (\boldsymbol{v} \cdot \nabla)\, \boldsymbol{v} = -\rho^{-1}\, \nabla\, p$, or equivalently $\partial_t \boldsymbol{v} + \boldsymbol{\omega} \times \boldsymbol{v} + \nabla(\frac{1}{2}\, v^2) = -\nabla\, h$, where $(1/\rho)\nabla p = \nabla h$ (h: enthalpy). The Euler's equation (4) must be supplemented by the equation of continuity and the isentropic equation:

$$\partial_t \rho + \mathrm{div}(\rho \boldsymbol{v}) = 0, \qquad \mathrm{D}_t s = \partial_t s + \boldsymbol{v} \cdot \nabla\, s = 0\,.$$

CONCLUSION

Thus, guided by the gauge principle in the quantum field theory, one can carry out a gauge-covariant variational formulation of ideal fluid flows consistently.

References

[1] Kambe, T., 2003. Gauge principle for flows of a perfect fluid. *Fluid Dyn. Res.* **32**, 193-199.

[2] Kambe, T., 2003. Gauge principle and variational formulation for flows of an ideal fluid. *Acta Mechanica Sinica* **19** (5), 437-452.

[3] Kambe T., 2004. Gauge principle and variational formulation of ideal fluid flows, *Preprint* TK2004a. **http://hw001.gate01.com/˜kambe** .

XXI ICTAM, 15–21 August 2004, Warsaw, Poland

PARTICLE TRANSPORT BY A VORTEX SOLITON

Yoshi Kimura*, Souji Koikari**
*Graduate School of Mathematics, Nagoya University, Furo-cho, Chikusa-ku, Nagoya, 464-8602, Japan
**Theory and Computer Simulation Center, National Institute for Fusion Science, Oroshi-cho 322-6, Toki 509-5292, Japan

Summary Motions of fluid particles advected by a vortex soliton are studied. In the moving frame which makes the vortex soliton steady in space, particle motions are confined in a torus near the loop for a wide range of three parameters that characterize the shape and strength of the vortex soliton. To extract the essential mechanism of the transport properties, an ODE model is proposed, which is named the chopsticks model.

INTRODUCTION

Transport of fluid particles by an isolated vortex has been a fundamental problem which, particularly if a vortex moves steadily, provides a direct example of long-surviving advection of materials in fluids. The main objective of this paper is to demonstrate an example of finite volume transport by a 3D thin steady vortex tube, called vortex soliton named after Hasimoto [1]. The vortex soliton is one of few steady solutions for a vortex filament under the local induction approximation moving without changing its shape [2]. The original observation of vortex soliton in a rotating tank experiment implies that a vortex soliton is endowed with an ability to transport physical quantities, such as mass, kinetic energy, and linear and angular momenta, from a turbulent region to a laminar one [3][4]. Among others, mass is the most fundamental and important quantities in the transport phenomena of the vortex soliton, which in this paper is investigated by scrutinizing the flow field near the vortex soliton numerically [5] .

While the flow structure around the vortex soliton is quite convoluted, we could observe that some particles are confined in a torus near the loop of the vortex soliton. If the Poincaré section is taken for the torus, we see each particle inside the torus moves on an invariant surface which wraps a periodic orbit at the center of the torus. Similarity is also found for the structure of the torus with the KAM torus for non-integrable Hamiltonian systems. Figure 1 shows an example of the torus for the vortex soliton with a certain set of parameters for the shape and the strength of the soliton. The surface of the torus is weaved by a single particle trajectory in a moving frame which makes the vortex soliton steady. The edge of the torus marks a boundary in the flow field; outside particles are repelled into the flow while particles are continuously trapped inside. Thus the vortex soliton transports a finite volume of fluid in the form of a torus, and we are concerned with the transported volume as a function of the parameters for the properties of the vortex soliton.

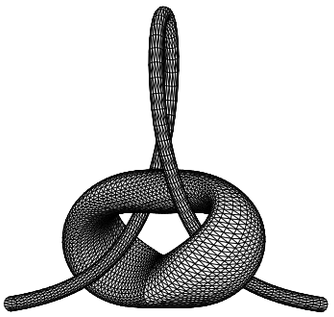


Figure 1. Torus with the vortex soliton.

FORMULATION

Hasimoto-vortex soliton is a solitary wave type solution of the Localized Induction Equation(LIE) for the motion of an isolated vortex filament,

$$\frac{\partial \mathbf{X}}{\partial t} = G\,\frac{\partial \mathbf{X}}{\partial s} \times \frac{\partial^2 \mathbf{X}}{\partial s^2}. \tag{1}$$

In the above equation $G = \frac{\Gamma}{4\pi}\log\left(\frac{L}{\epsilon}\right)$ is the self-induction constant where L and ϵ are two cut-off lengths, large and small, and Γ is the circulation. Usually G is absorbed by scaling the time variable, but we leave it here to have a specific time scale both for the vortex soliton and fluid particles. Following Hasimoto [1], the soliton solution for the above equation is given with two additional parameters $\nu > 0$ and τ, where ν is related with the curvature of a soliton $\kappa(s)$ by the formula $\kappa(s) = 2\nu\,\mathrm{sech}(\nu s)$ and τ is a constant torsion of a soliton. By denoting $\mathbf{X}(s,t) = {}^t\,[X_f(s,t), Y_f(s,t), Z_f(s,t)]$, we obtain

$$\begin{aligned} X_f(s,t) &= \frac{2\mu}{\nu}\,\mathrm{sech}\left\{\nu(s-2\tau G t)\right\}\cos\left\{\tau(s-2\tau G t)+(\nu^2+\tau^2)Gt\right\} \\ Y_f(s,t) &= \frac{2\mu}{\nu}\,\mathrm{sech}\left\{\nu(s-2\tau G t)\right\}\sin\left\{\tau(s-2\tau G t)+(\nu^2+\tau^2)Gt\right\} \\ Z_f(s,t) &= s - \frac{2\mu}{\nu}\tanh\left\{\nu(s-2\tau G t)\right\} \end{aligned} \tag{2}$$

where $\mu = \nu^2/\left(\nu^2+\tau^2\right)$.

For the particle motion we assume that fluid particles are advected by the velocity induced by the vortex soliton through the Biot-Savart's integral taken over the centerline of the vortex tube. Under this assumptions, the equation of the motion

of a fluid particle at $\mathbf{r}(t) =^t [x(t), y(t), z(t)]$ in the frame which makes the vortex soliton steady is given as,

$$\frac{\mathrm{d}\mathbf{r}}{\mathrm{d}t} = \frac{1}{4\pi}\int_{-\infty}^{\infty} \frac{\mathbf{x}'(s)\times(\mathbf{r}-\mathbf{x}(s))}{|\mathbf{r}-\mathbf{x}(s)|^3}\mathrm{d}s + (\nu^2+\tau^2)G\begin{bmatrix} y \\ -x \\ 0 \end{bmatrix} + \begin{bmatrix} 0 \\ 0 \\ -2\tau G \end{bmatrix}, \tag{3}$$

where $\mathbf{x}(s) = \mathbf{X}(s,0)$ is the coordinates of the vortex soliton steady in time, and the time variable t and G are re-scaled by the circulation. A certain congruent transformation is introduced to derive the second and the third terms in the right hand side to compensate the rotation about the z-axis and the translation in the z-direction. We use (3) as an autonomous dynamical system for the motion of particles around the vortex soliton. The solution to (3) with an initial condition $(x(0), y(0), z(0))$ provides a triplet $(x(t), y(t), z(t))$ which defines a trajectory in the 3D phase space.

NUMERICAL RESULTS

As a canonical tool to analyze trajectories in a phase space of higher dimension than two, the Poincaré section is quite well-known. Figure 2 shows the Poincaré sections for the trajectories of (3) with a various initial conditions for two different values of G, ((a): 0.1832, (b): 0.3113). The Poincaré plane is located at $y = 0$, and a dot is placed at a point on the plane every time when a trajectory passes the plane transversally at the point. On both the Poincaré sections, we can observe that there are two large islands of groups of nested curves (composed with continuous and broken lines) surrounded by small islands and scattered points. Each large island has a center which corresponds to a single periodic orbit in the original 3D space.

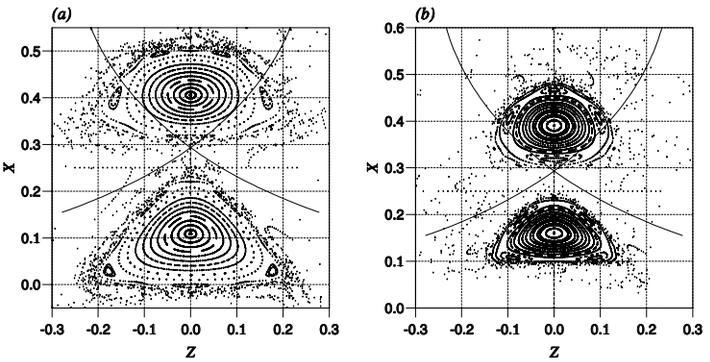


Figure 2. Poincaré sections for trajectories of (3) with various initial conditions. Poincaré plane is located at $y = 0$. The parameter values are $(\nu, \tau) = (1.924, 0.3827)$ and (a): $G = 0.1832$, (b): $G = 0.3113$.

Each nested curve around the center point, on the other hand, corresponds to an invariant surface of a torus around the periodic orbit. The scattered points outside the islands mean trajectories of particles repelled from the loop by the uniform translational flow in the moving frame. While (3) is not a Hamiltonian, very similar features are observed with the KAM torus for non-integrable Hamiltonian systems.

The most interesting and fundamental quantity about the transport by the vortex soliton is the fluid mass which can be estimated by calculating the volume surrounded by the outmost torus. Figure 3(a) shows the volume of the torus as a function of G for some pairs of ν and τ. As the Poincaré sections above suggest, a torus has a larger volume for smaller G for any combination of ν and τ. For a given G, a smaller value of τ gives always a larger values of the volume.

To understand and extract the essential mechanism of the formation of tori and the transport of volume, we propose a simplified toy model, in which the vortex soliton is replaced with two infinite straight line vortices in 3D space, and we call it the chopsticks model.

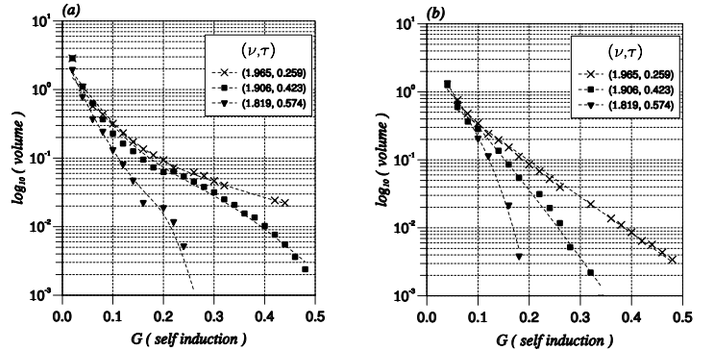


Figure 3. Comparison of the volume of the outmost torus as a function of G for three different combinations of ν and τ. (a) vortex soliton, (b) chopsticks model

This model successfully provides a similar torus structure and the dependence of the volume on the parameters. Figure 3(b) shows the volume obtained with the chopsticks model for the same parameter sets with Figure 3(a).

References

[1] Hasimoto H.: A soliton on a vortex fi lament. *J. Fluid Mech.* **51**: 477–485, 1972.
[2] Kida, S.: A vortex fi lament moving without change of form. *J. Fluid Mech.* **112**: 397–409, 1981.
[3] Hopfi nger, E.J. & Browand, F. K.: Vortex solitary waves in a rotating, turbulent fbw. *Nature* **295**: 393–395, 1982.
[4] Hopfi nger, E.J., Browand, F. K. & Gagne, Y.: Turbulence and waves in a rotating tank. *J. Fluid Mech.* **125**: 505–534, 1982.
[5] Kimura, Y. & Koikari, S.: Particle transport by a vortex soliton, submitted to *J. Fluid Mech.*

XXI ICTAM, 15–21 August 2004, Warsaw, Poland

GENERIC HYDRODYNAMIC INSTABILITY

Robert W. Ghrist*, John B. Etnyre**
*Department of Mathematics, University of Illinois, Urbana, IL 61801, USA
**Department of Mathematics, University of Pennsylvania, Philadelphia, PA 19104, USA

Summary Every fluid dynamicist knows that almost all 3-d steady incompressible inviscid fluid flows are unstable; however, very few rigorous results about generic instability exist. Our idea is to use the geometry of the flow domain as a parameter. We prove that for generic geometry, *all* of the curl-eigenfield solutions to the steady Euler equations on R^3 (with periodic boundary conditions) are hydrodynamically unstable (linear instability, L^2 norm), with the possible exception of the zero-eigenvalue solution. The proof involves a marriage of topological methods with the instability criteria of Lifshitz-Hameiri and Friedlander-Vishik. An application of a new homology theory in symplectic geometry is the crucial step.

STATEMENT OF RESULTS

The problem of linear hydrodynamic instability for steady Euler flows on three-dimensional domains is classical in nature and foundational in implication [7, 9]. It is universally asserted that in dimension three such flows are almost always unstable, though the precise definition of *"almost always"* is an issue left undiscussed. The small literature on generic properties of fluid flows [6, 13] focuses on the Navier-Stokes setting and uses external forcing or Dirichlet data as a parameter.

We present a clear formulation of the problem and prove a generic instability theorem for a large class of flows — the curl eigenfields — which form the most fascinating and challenging steady solutions to the Euler equations. The chief difficulty with genericity issues for curl eigenfields is that the "space of all eigenfields" on a typical Riemannian three-manifold is a "discrete" space and is not amenable to perturbations. Our idea in formulating a well-defined genericity statement is to use the geometry of the domain as a parameter.

Theorem 1: *For a generic set of C^r Riemannian metrics on R^3 (for each $2 \leq r < \infty$) with periodic boundary conditions, all of the curl-eigenfield solutions to the Euler equations (with nonzero eigenvalue) are linearly hydrodynamically unstable in energy (L^2) norm.*

THE TOPOLOGY OF CURL EIGENFIELDS

The following technical result provides the basis for the instability theorem.

Theorem 2: *For generic choice of C^r metric (for each $2 \leq r < \infty$), all of the curl-eigenfields on a compact three-manifold M with non-zero eigenvalue have all fixed points nondegenerate. In addition, if any eigenfield does not possess any fixed points, then all its periodic orbits are nondegenerate.*

By nondegenerate fixed point, we mean that the linearization of the vector field about the fixed point has all eigenvalues nonzero. Nondegenerate periodic orbits are those whose Floquet multipliers are never equal to one.

The proof of Theorem 2 for fixed points is a combination of transversality theory with some machinery of K. Uhlenbeck [14]. The proof for periodic orbits is more delicate, using techniques from symplectic geometry and a theorem of C. Robinson [12].

Dealing with the case of curl-eigenfields without fixed points leads very naturally to a type of object in symplectic geometry called a *contact structure*. A contact structure on a 3-d domain is a plane field distribution which is maximally nonintegrable: it "twists" in all tangent directions.

The relationship between curl-eigenfields and contact structures is dual: the orthogonal plane field to any fixed-point-free curl eigenfield is a contact structure, and all contact structures arise as orthogonal plane fields of some curl eigenfield. The general version of this correspondence theorem can be used to understand the existence and qualitative behavior of steady solutions to the Euler equations [3, 4, 5]. For example, by exploiting the flexibility of contact structures, one can construct steady Euler flows on a compact 3-d domain which possesses periodic flowlines exhibiting all knot and link types [5].

OUTLINE OF PROOF

Thanks to an insight of Arnold and the analysis of Friedlander-Vishik [8] (who used the technique developed by Lifshitz-Hameiri [11]), it is now known that the underlying dynamics of the flowlines of the steady velocity field u can force linear instability. In particular, we rely on the following:

Instability Criterion: [8] *The presence of a nondegenerate periodic orbit of saddle-type in a steady Euler flow induces linear instability in the energy norm.*

By saddle-type, it is meant that there is are both expanding and contracting directions associated to the local flow about the orbit. Nondegenerate fixed points are always of saddle type in an incompressible flow; however, nondegenerate periodic orbits can be of *elliptic type*, with the flow rotating about the flowline. Such orbits foil the instability criterion.

The outline of the proof of the Theorem 1 is as follows: For a generic geometry, Theorem 2 guarantees that all fixed points

present are hyperbolic. These are of saddle type and thus force instability. This, then, provides a quick proof of generic instability for invariant flow domains such as $S^2 \times [0,1]$ which are forced to have fixed points on the boundaries. The case of R^3 with periodic boundary conditions has vanishing Euler characteristic, and therefore admits flows without fixed points. The crux of the difficulty is determining when an eigenfield without fixed points possesses a saddle-type periodic orbit. Theorem 2 guarantees that all periodic flowlines are either of elliptic or saddle type: but how does one determine if periodic orbits exist and are of saddle type?

To answer this last, most difficult question, we turn to contact topological methods, including the recent *contact homology* of Eliashberg, Givental, and Hofer [2]. For an introduction to contact topological techniques in fluid dynamics, see [10]. Translated to the context of this application, contact homology is a method for counting periodic orbits of curl-eigenfields using topological properties of the orthogonal plane field. A delicate computation of the homology groups demonstrates that there must *always* exist a periodic orbit of saddle type in a curl eigenfield with nonzero eigenvalue.

Theorem 3: *Any nondegenerate nonvanishing curl-eigenfield on R^3 with periodic boundary conditions always possesses a closed flowline of saddle type.*

The proof of this is a very delicate computation using the methods of [1]. Combining these ingredients yields Theorem 1. These techniques are an example of how topological methods can yield rigorous results about fluid flows without the need for restrictive hypotheses.

References

[1] F. Bourgeois, *A Morse-Bott approach to contact homology*, PhD Thesis, Stanford 2002.

[2] Y. Eliashberg, A. Givental and H. Hofer, *Introduction to symplectic field theory*, GAFA 2000 (Tel Aviv, 1999), Geom. Funct. Anal. (2000), Special Volume, Part II, 560–673.

[3] J. Etnyre and R. Ghrist, *Contact topology and hydrodynamics I. Beltrami fields and the Seifert conjecture.* Nonlinearity 13 (2000), no. 2, 441–458.

[4] J. Etnyre and R. Ghrist, *Contact topology and hydrodynamics II. Solid tori.* Ergodic Theory Dynam. Systems 22 (2002), no. 3, 819–833.

[5] J. Etnyre and R. Ghrist, *Contact topology and hydrodynamics III. Knotted flowlines.* Trans. Amer. Math. Soc. 352 (2000), 5781–5794.

[6] C. Foias and R. Temam, *Structure of the set of stationary solutions of the Navier-Stokes equations*, Comm. Pure & Appl. Math. XXX (1977) 149–164.

[7] S. Friedlander, *Lectures on stability and instability of an ideal fluid*, in Hyperbolic equations and frequency interactions (Park City, UT, 1995), 227–304, IAS/Park City Math. Ser., 5, Amer. Math. Soc., Providence, RI, 1999.

[8] S. Friedlander and M. Vishik, *Instability criteria for steady flows of a perfect fluid.* Chaos 2 (1992), no. 3, 455–460.

[9] S. Friedlander and V. Yudovich, *Instabilities in fluid motion.* Notices Amer. Math. Soc. 46 (1999), no. 11, 1358–1367.

[10] R. Ghrist and R. Komendarczyk, *Topological features of inviscid flows*, in Geometry and Topology of Fluids, NATO ASI Series II vol. 47, Kluwer Press, 183–202.

[11] A. Lifshitz and E. Hameiri, *Localized instabilities of vortex rings with swirl.* Comm. Pure Appl. Math. 46 (1993), no. 10, 1379–1408.

[12] C. Robinson, *Generic properties of conservative systems.* Amer. J. Math. 92 (1970), 562–603.

[13] J. Saut and R. Temam, *Generic properties of Navier-Stokes equations: genericity with respect to the boundary values*, Indiana Univ. Math. J. 29 (1980), no. 3, 427–446.

[14] K. Uhlenbeck, *Generic properties of eigenfunctions*, Amer. J. Math., 98 (1976), no. 4, 1059–1078.

SUBMITTED TO *Proceedings of ICTAM 2004* December 29, 2003

Helicity Dynamics of Vortex Filaments

Darryl D. Holm[1,2] and **Samuel N. Stechmann**[1,3]

[1]Theoretical Division and Center for Nonlinear Studies
Los Alamos National Laboratory, MS B284
Los Alamos, NM 87545 USA
email: dholm@lanl.gov

[2]Mathematics Department
Imperial College London
SW7 2AZ, UK
email: d.holm@imperial.ac.uk

[3]Courant Institute of Mathematical Sciences
New York University, New York, NY 10025
email: stechman@cims.nyu.edu

Abstract

We determine the Hamiltonian dynamics in the Lagrangian fluid description describing a massless filament of vorticity $\boldsymbol{\omega} = \operatorname{curl}\mathbf{u}$ supported along a space curve $\mathbf{x} = \mathbf{R}(\mathbf{a},t)$ that moves without slipping in the incompressible flow induced by its own helicity.

Singular Lagrangian vortex filament solutions induced by the helicity

The Lagrange-to-Euler map for a vorticity filament is, $\boldsymbol{\omega}(\mathbf{x},t) = \int \frac{1}{J}\,\mathbf{R}_s(\mathbf{a},t)\delta\big(\mathbf{x}-\mathbf{R}(\mathbf{a},t)\big)d^3a\,,$ with $J = \det(\partial\mathbf{R}/\partial\mathbf{a})$, and its helicity is,

$$H = \frac{1}{2}\int \mathbf{u}\cdot\operatorname{curl}\mathbf{u}\,d^3x \;=\; \frac{1}{8\pi}\int \frac{\mathbf{R}(\mathbf{a},t)-\mathbf{Q}(\mathbf{a}',t)}{|\mathbf{R}(\mathbf{a},t)-\mathbf{Q}(\mathbf{a}',t)|^3}\cdot\frac{d\mathbf{R}}{ds}\times\frac{d\mathbf{Q}}{ds'}\,d^3a\,d^3a'\,, \tag{1}$$

as obtained by using the Biot-Savart Law for vorticity filaments,

$$\mathbf{u}(\mathbf{x}) = \frac{1}{4\pi}\nabla\times\int\frac{J\boldsymbol{\omega}(\mathbf{R})\,d^3R}{|\mathbf{x}-\mathbf{R}|} = \frac{1}{4\pi}\nabla\times\int\frac{\mathbf{R}_s\,d^3a}{|\mathbf{x}-\mathbf{R}(\mathbf{a},t)|}\,. \tag{2}$$

Here $d/ds' = \boldsymbol{\omega}_{(0)}(\mathbf{a}')\cdot\partial/\partial\mathbf{a}'$ is the derivative along the filament in the primed Lagrangian coordinates and the vectors $\mathbf{R}$ and $\mathbf{Q}$ denote spatial positions either on the same, or different filaments.

The Lagrangian filament dynamics generated by the helicity H in equation (1) may be computed using the Rasetti-Regge Dirac bracket (RRDB) $\{\cdot\,,\cdot\}$ derived in [6]. See also [3, 4] for additional discussions and reviews of the RRDB. Hence, the induced Lagrangian filament velocity is found to be,

$$\dot{\mathbf{R}}(s,t) = \{\mathbf{R}\,,\,H\} \;=\; \frac{1}{|\mathbf{R}_s|^2}\,\mathbf{R}_s\times\frac{\partial}{\partial s}\frac{\delta H}{\delta\mathbf{R}_s} = \frac{-1}{4\pi}\,\frac{1}{|\mathbf{R}_s|^2}\,\mathbf{R}_s\times\frac{\partial}{\partial s}\bigg(\int\frac{\mathbf{R}(s)-\mathbf{R}(s')}{|\mathbf{R}(s)-\mathbf{R}(s')|^3}\times\frac{d\mathbf{R}}{ds'}\,ds'\bigg)\,.$$

We apply the local induction approximation (LIA) to the integral in this expression by following the Arms-Hammer procedure [1] as explained, for example, in [5]. Hence, we find the following approximate equation, in which the LIA logarithmic cutoff constant is denoted as $c = \log(L/\sigma)$,

$$\dot{\mathbf{R}}(s,t) = \{\mathbf{R}\,,\,H\} \;=\; \frac{c}{4\pi}\,\frac{1}{|\mathbf{R}_s|^2}\,\mathbf{R}_s\times\frac{\partial}{\partial s}\Big(\mathbf{R}_s\times\mathbf{R}_{ss}\Big) = \frac{-c}{4\pi}\,\hat{P}\,\mathbf{R}_{sss}\,, \tag{3}$$

with projection operator $\hat{P} = -\hat{\mathbf{t}} \times \hat{\mathbf{t}} \times$, where $\hat{\mathbf{t}} \equiv \mathbf{R}_s/|\mathbf{R}_s|$ is the tangent vector. Equation (3) gives the LIA dynamics of vorticity filament solutions on the space curve $\mathbf{x} = \mathbf{R}(s,t)$ obtained by using the helicity (1) as the Hamiltonian H in the RRDB. When the parameter s is transformed into arclength along the curve, by $d\ell = |\mathbf{R}_s|ds$, so that $\partial_s = |\mathbf{R}_s|\partial_\ell$, equation (3) may be put into "intrinsic" form,

$$\dot{\mathbf{R}}(s,t) \;=\; \frac{-c}{4\pi}\,\hat{P}\,\mathbf{R}_{sss} = \frac{-c}{4\pi}\left(\tilde{\kappa}'\hat{\mathbf{n}} + \tau\tilde{\kappa}\,\hat{\mathbf{b}}\right). \tag{4}$$

Here $\hat{\mathbf{t}}$, $\hat{\mathbf{n}}$, $\hat{\mathbf{b}}$ are the Serret-Frenet unit vectors for the space curve, and τ and κ are torsion and curvature, respectively. We define $\tilde{\kappa} \equiv \kappa|\mathbf{R}_s|^2$ and $\tilde{\kappa}' \equiv d\tilde{\kappa}/d\ell$. Note that $\mathbf{R}_s \cdot \dot{\mathbf{R}}_s = -\dot{\mathbf{R}} \cdot \mathbf{R}_{ss} = (c\,/4\pi)\,\tilde{\kappa}'\kappa \neq 0$. Hence, equation (4) allows self stretching by an isolated filament with curvature, so that $|\mathbf{R}_s|^2$ does not remain constant, even in the LIA. We compare this with the da Rios-Betchov equation, [3, 7, 8]

$$\dot{\mathbf{R}}(s,t) = (1/|\mathbf{R}_s|^2)\,(\mathbf{R}_s \times \hat{\mathbf{t}}_s) = \kappa\,\hat{\mathbf{b}}\,.$$

This is generated by RRDB with Hamiltonian $H_{dRB} = \int |\mathbf{R}_s|ds$ and it does not allow self stretching.

Outlook We have determined the Hamiltonian dynamics for the singular solutions generated by the helicity invariant of the divergenceless vorticity vector field. Conservation laws and other natural directions remain to be explored. For example, one should investigate whether the Hasimoto transformation [2] for Kelvin-wave solitons on vortex filaments also leads to interesting phenomena in the present situation. In particular, applying the Hasimoto transformation to the intrinsic equation (4) for the Hamiltonian motion of vortex filaments induced by the helicity (1) leads to yet another generalization of the nonlinear Schrödinger equation which may have interesting dynamics.

Acknowledgements We are grateful to P. K. Newton and B. N. Shashikanth for helpful remarks and prompt correspondence during the course of this work. The research reported here was supported by US DOE, from contract W-7405-ENG-36 and from US DOE, Office of Science ASCAR/AMS/MICS.

References

[1] Arms, R. J. and F. R. Hama [1965] Localized induction concept on a curved vortex and motion of an elliptic vortex ring. *Phys. Fluids* **8**, 553–559.

[2] Hasimoto, R. [1972] *J. Fluid Mech.* **51** 477.

[3] Holm, D. D. [2003] Rasetti-Regge Dirac bracket formulation of Lagrangian dynamics of vortex filaments. *Mathematics and Computers in Simulation* **62**, 53-63.

[4] Kuznetsov, E. A. & V. P. Ruban [2000b] Hamiltonian dynamics of vortex and magnetic lines in hydrodynamic type systems. *Phys. Rev. E* **61** 831-841.

[5] Newton, P. K. [2001] *The N-Vortex Problem: Analytical Techniques*. Springer: New York.

[6] Rasetti, M. & T. Regge [1975] Vortices and current algebra. *Physica A* **80** 217–233.

[7] Ricca, R. L. [1996] The contributions of Da Rios and Levi-Civita to asymptotic potential theory and vortex filament dynamics. *Fluid Dyn. Res.* bf 18 245-268.

[8] Ricca, R. L. [1998] Applications of knot theory in fluid mechanics. In *Knot Theory* (ed. V. F. R. Jones et al.), vol. 42, pp. 321-346. Banach Center Publications, Institute of Mathematics, Polish Academy of Sciences, Warszawa.

RELATION BETWEEN MIXING EFFICIENCY AND GEOMETRICAL PROPERTY OF STABLE MANIFOLDS

Mitsuaki Funakoshi*, Hiroshi Kawazoe*
*Department of Applied Analysis & Complex Dynamical Systems, Graduate School of Informatics, Kyoto University, Yoshida-Honmachi, Sakyo-ku, Kyoto, 606-8501, JAPAN

Summary We examine the mixing of fluids associated with the chaotic motion of fluid particles due to the time-periodic flow between two eccentric cylinders caused by the time-periodic slow rotation of these cylinders. We examine the relation between the geomtrical property of the stable manifold of the unstable periodic points of the Poincaré map and the efficiency of the mixing. We find that the maximum stretching rate of fluid elements in a short time is large in the region where the density of the stable manifold is high, and that this stretching rate is small in the region where the curvature of this manifold is large. We also find that small blobs initially located at the region of high density of the stable manifold are mixed well in a short time.

INTRODUCTION

The motion of fluid particles in a flow of an incompressible fluid can be chaotic even if the velocity field of the fluid is steady or time-periodic. The efficient mixing of fluids caused by this chaotic motion is often called the chaotic mixing. There has been many researches on the chaotic motion of fluid particles (Lagrangian chaos) and the chaotic mixing due to two-dimensional time-periodic flows or three-dimensional steady flows since 1980's [1–3].
In the present study, we examine the chaotic mixing due to the time-periodic flow between two eccentric cylinders caused by the time-periodic slow rotation of these cylinders. The main purpose of the present study is to examine what information on the mixing efficiency is obtained from the geometrical property of the stable and unstable manifolds of the unstable periodic points of the Poincaré map which maps the location of a fluid particle onto its location after one period of the flow.

TIME-PERIODIC FLOW BETWEEN TWO ECCENTRIC CYLINDERS

When two eccentric cylinders of sufficiently long length rotate at small angular velocities, we can assume that the flow of an incompressible fluid between these cylinders caused by this rotation is a two-dimensional Stokes flow on the (x, y) plane. Therefore, if we introduce streamfunction ψ satisfying $u = \partial\psi/\partial y$ and $v = -\partial\psi/\partial x$, where ($u$,$v$) is the ($x$,$y$) component of fluid velocity $\boldsymbol{u}$, then ψ satisfies

$$\Delta^2\psi = 0, \tag{1}$$

and non-ship condition on the walls of the cylinders, where Δ denotes the Laplacian operator. The solution of this differential equation can be written in the following form :

$$\psi = \Omega_i(t) f_i(\boldsymbol{x}) + \Omega_o(t) f_o(\boldsymbol{x}), \tag{2}$$

where $f_i(\boldsymbol{x})$ and $f_o(\boldsymbol{x})$ are certain functions of spatial coordinate $\boldsymbol{x}$, and $\Omega_i(t)$ and $\Omega_o(t)$ are angular velocities of inner and outer cylinders of radii R_i and R_o, respectively. Here t is the time. It is assumed that the motion of the cylinders is time-periodic and that the outer cylinder alone rotates first by angle πT_o, then the inner one alone by angle $2\pi T_i$, and finally the outer one alone by angle πT_o in one period T. The parameters of this problem are T_i, T_o, radius ratio $\alpha = R_i/R_o$, and the eccentricity $\varepsilon = \ell/(R_o - R_i)$. Here ℓ is the distance between the centers of the cylinders, and then ε ranges from 0 to 1.
When both $\Omega_i(t)$ and $\Omega_o(t)$ are periodic functions of period T, ψ is also a time-periodic function. The time evolution of the location $(x, y) = (X(t), Y(t))$ of a fluid particle is governed by

$$\frac{dX}{dt} = \frac{\partial\psi(X, Y, t)}{\partial Y}, \quad \frac{dY}{dt} = -\frac{\partial\psi(X, Y, t)}{\partial X}. \tag{3}$$

POINCARÉ MAP AND POINCARÉ PLOT

Since ψ is time-periodic with period T, we can define a two-dimensional area-preserving map M that maps $\boldsymbol{X}(t) = (X(t), Y(t))$ onto $\boldsymbol{X}(t + T)$, called the Poincaré map. Furthermore, by plotting the values of $\boldsymbol{X}(nT) = M^n\boldsymbol{X}(0)$ $(n = 0, 1, 2, \cdots)$ for a few initial positions $\boldsymbol{X}(0)$ of fluid particles, we obtain the Poincaré plot.
Since Poincaré map M is area-preserving, the periodic points (including fixed points) of map M are either hyperbolic (saddle type) or elliptic (center type) depending on their eigenvalues. It is commonly observed in the Poincaré plots that if $\boldsymbol{X}(0)$ is sufficiently close to one of the p elliptic periodic points of period p, $\boldsymbol{X}(nT)$ are on one of the closed curves encircling these points for all n. The region around elliptic periodic points where $\boldsymbol{X}(nT)$ of each fluid particle moves regularly on the curves encircling these points is called the regular region or island region.

Moreover, since (3) is a non-antonomous conservative system with respect to two variables, it is possible that this equation has the chaotic solution. Furtheremore, the fluid region between the cylinders is divided into the chaotic region in which each fluid particle moves chaotically and the regular region. The fluid particle starting from the regular (chaotic) region cannot enter the chaotic (regular) region. Therefore, it is better for the efficientmixing to have smaller regular region.
Many unstable hyperbolic periodic points of map M are usually imbedded in the chaotic region. Each unstable periodic point has its stable and unstable manifolds. Any fluid particle starting from a location on the stable (unstable) manifold approaches this periodic point as $t \to \infty(-\infty)$.

GEOMTRICAL PROPERTY OF STABLE MANIFOLDS

In the present study, we examine only the case in which almost all the fluid region is the chaotic region. Therefore, the efficientmixing of fluids after many periods is generally expected. However, in the mixing of fluids at the industries, the efficiencyof mixing in a relatively small time is also important. Therefore, it may be useful if we can obtain information on this efficiencyfrom the geomtrical property of the stable manifolds of the unstable periodic points of Poincaré map M. Examination of this problem is the main purpose of the present study.

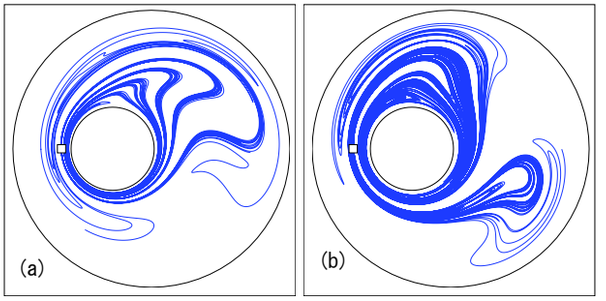


Fig.1 Stable manifolds of unstable fixedpoints denoted by squares. $\alpha = 0.3, \varepsilon = 0.4$. (a) $T_o = 1.0, T_i = 6.0$, (b) $T_o = 0.5, T_i = 3.0$.

Figure 1 shows examples of parts of the stable manifolds of unstable fixedpoints. For the parameters of Fig.1, almost all the fluid region is the chaotic region. Therefore, there is no recognizable difference between the Poincaré plots for the parameters of Figs.1 (a) and (b). Although stable manifolds are expected to cover almost all the fluid regions, the manifolds in Fig.1 obtained by inversely mapping for finitetimes of small line elements directing the stable direction from the fixedpoints are considerably localized. We findthat the density of the manifolds can be closely related to the maximum stretching rate of line elements in a relatively small time. That is, this stretching rate is large at the location where this density is high. From the computation of the evolution of small blobs, we obtain the result that the blob starting from the high-density region is mixed well within a relatively small time, whereas the mixing of the blob starting from the low-density region is bad in a relatively small time, although this blob is also expected to be mixed well after a long time. We also findthat the elongation of a line element is suppressed at the location of large curvature of the stable manifold because the direction of the maximum stretching rate at this location in one period is not consistent with the corresponding direction at the points of relatively small curvature on the manifold. There were a few studies on the curvature of material lines in chaotic fbws [4–5]. The relation between the results of these studies and the present study also will be discussed.

CONCLUSIONS

The relation between the geomtrical property of the stable manifold of the unstable periodic points of the Poincaré map and the efficiencyof the mixing is examined. In conclusion, we findthat if a small fluid blob has to be mixed well with a surrounding fluid in a relatively short time, it should be located at the region where the density of the stable manifold is high, and should not be located at the points from which fluid particles move to the region where the curvature of the manifold is high after a short time.

References

[1] Aref H.: Chaotic Advection of Fluid Particles. *Phil. Trans. Roy. Soc. Lond. A* **333**:273–288, 1990.
[2] Ottino J.M.: The Kinematics of Mixing : Stretching, Chaos, and Transport. Cambridge Univ. Press, 1989.
[3] Ottino J.M.: Mixing, Chaotic Advection, and Turbulence. *Annu. Rev. Fluid Mech.* **22**:207–253, 1990.
[4] Liu M., Muzzio F.J.: The Curvature of Material Lines in Chaotic Cavity Flows. *Phys. Fluids* **8**:75–83, 1996.
[5] Cerbelli S., Zalc J.M., Muzzio F.J.: The Evolution of Material Lines Curvature in Deterministic Chaotic Flows. *Chem. Eng. Sci.* **55**:363–371, 2000.

TOPOLOGICAL ASPECTS OF THE TORNADO PROBLEM

Dmytro I. Cherniy [*], Vyacheslav V. Meleshko[*], Stanislav A. Dovgiy[**]

[*] *Kiev National Taras Shevchenko University,01033 Kiev, Ukraine*
[**] *Institute of Hydromechanics NASU,03057 Kiev, Ukraine*

Summary We examine the topological aspects of a concentrated vortex structure, a tornado, in inviscid fluid. A laboratory study is complemented by numerical simulations of vortex dynamics taking into account the topological structures of vortex knots. Natural observation performed in Kazakhstan (August 2002) agree reasonably well with laboratory experiments.

TORNADO VORTEX PROBLEMS

We have considered three-dimensional concentrated vortex problem related to the topological properties of intensive tornado structures.



Fig. 1
Tornado in Kazakhstan (August 2002)

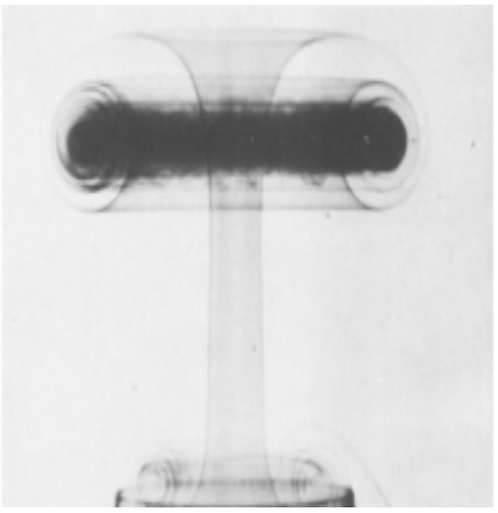
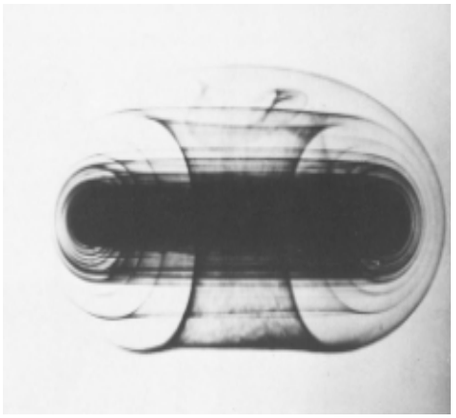
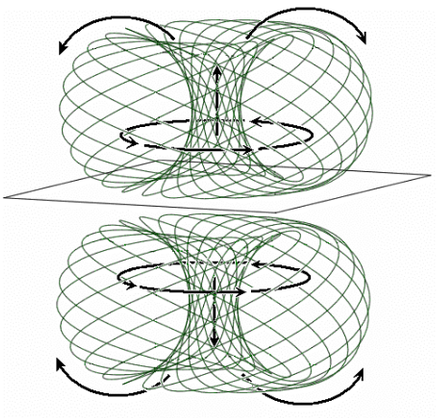


Fig. 2
Vortex ring experiments (Weyer)

It is assumed that initially the tornado can be modelled as a torus (two-dimensional closed manifold) over a rigid surface. The mirror image of the torus (Figure 1) provides the possibility to consider the development of this vortex structure in an unbounded domain.





The mathematical statement of the problem for the potential flow outside the vortex core is:

$$t \geq t_0: \qquad \Delta\phi = 0 \qquad \textbf{in} \quad D^+ \tag{1}$$

$$\frac{\partial\phi}{\partial n} = W_n \qquad \textbf{on} \quad L_d \tag{2}$$

$$\left(\frac{\partial\phi}{\partial n}\right)^+ = \left(\frac{\partial\phi}{\partial n}\right)^-, \quad p^+ = p^- \qquad \textbf{on} \quad L_v \tag{3}$$

$$\left|\nabla\phi\right| = V_\infty < \infty \qquad \textbf{at} \quad \infty \tag{4}$$

$$\frac{\partial\phi}{\partial t} + \frac{1}{2}(\nabla\phi)^2 = p \tag{5}$$

$$t = t_0: \qquad L_0, \quad \phi^+\big|_{t=0} = \phi_0^+ \tag{6}$$

We have performed the experimental studies of the tornado-like structures using the idea suggested by Weyer (1889). The phenomenon of vortex hysteresis is experimentally observed.

We have presented a system of ordinary differential equations describing concentrated vortex dynamics that allow for efficient numerical simulation.

$$\frac{d\vec{r}_v}{dt} = \vec{V}(\vec{r}_v(t), t)$$

$$\vec{r}_v(t_0) = \vec{r}_{v0}$$

The numerical model [2] may be readily extended to describe more complex physical situation.

The Lyapunov stability conditions is essential while studying the Euler characteristic of the vorticity field. The possibility of effective stirring by a steady motion in the vortex core is pointed out. These problems might be benchmark ones for various numerical schemes in the vortex dynamics.

References

[1] Cherniy D. I.: Approximation of solution of initial boundary problem with moving boundaries. *J. Comput. Appl. Math* . 82 :112-123, 1997.

[2] Dovgiy S.A., Cherniy D. I.: About topology of the boundary of MDV. *IX Int. Symp. "Discrete Singularities Methods in Mathematical Physics-2000"*, OSU, Orel, 2000, 465-467.

XXI ICTAM, 15– 21 August 2004, Warsaw, Poland

LARGE EDDY SIMULATIONS OF DECAYING ROTATING TURBULENCE

J. Andrzej Domaradzki, Xiaolong Yang
Department of Aerospace and Mechanical Engineering, University of Southern California, Los Angeles, CA 90089-1191, U.S.A.

Summary Large eddy simulations of decaying, homogenous turbulence subjected to system rotation were performed using the Truncated Navier-Stokes method. It is observed that the nonlinear energy transfer from large to small scales is reduced by rotation, the energy decay is inhibited, the energy spectrum departs from the classical $k^{-5/3}$ form, and initially isotropic turbulence becomes anisotropic, with the anisotropy reflected in longitudinal integral length scales and directional stress tensors. We found that the latter effect is strongest at moderate rotation rates. At high Reynolds numbers and for sufficiently long times the Reynolds stress tensor and its invariants also become anisotropic, contrary to commonly reported results at low Reynolds numbers. The anisotropy may be responsible for the energy spectrum having k^{-3} rather than k^{-2} form found under the assumption of isotropy.

THE GOVERNING EQUATIONS AND THE NUMERICAL METHOD

The Navier-Stokes equations in a frame of reference rotating with an angular velocity Ω in the x_3 direction are:

$$\frac{\partial}{\partial t}u_i + \frac{\partial}{\partial x_j}u_i\, u_j = -\frac{1}{\rho}\frac{\partial}{\partial x_i}p + \nu\frac{\partial^2 u_i}{\partial x_j \partial x_j} - 2\Omega\varepsilon_{i3l}u_l, \tag{1}$$

where $\mathbf{u}$, p, ρ, and ν are the fluid velocity, pressure, density, and kinematic viscosity, respectively. Rotation considerably affects the dynamics and structure of these flows through the Coriolis force but classical turbulence models, developed for non-rotating flows, perform poorly in the presence of rotation. We have performed large eddy simulations of rotating turbulence using the truncated Navier-Stokes (TNS) approach, which is appropriate for rotating turbulence [1, 2]. TNS is effectively a sequence of low resolution direct numerical simulation (DNS) runs with a periodic processing of the solution that provides SGS dissipation, and between processing instants, the energy transfer from the physical scales is accomplished by the nonlinear interactions with the small, estimated scales. The method is easy to implement, does not use the concept of a SGS stress tensor and since only Navier-Stokes equations are solved, TNS satisfies all transformation properties of the Navier-Stokes equations.

For homogenous turbulence, we apply periodic boundary conditions in all three Cartesian directions and use a Fourier representation for all dependent variables. The N-S equation (1) transformed to spectral space is solved numerically using a well-known pseudo-spectral method with an explicit second-order predictor-corrector time stepping scheme. To alleviate time step restrictions viscous and Coriolis terms are integrated analytically using the integrating factor technique [3].

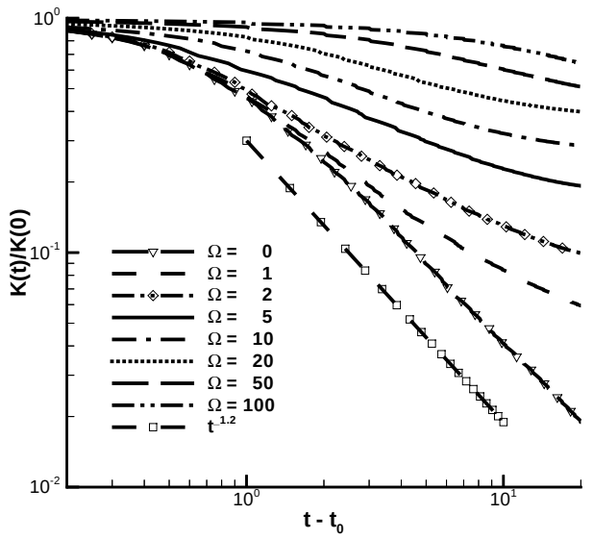


Figure 1. TNS: History of energy decay on a log-log scale for nominally infinite Re. Long dashed line with gradients: $\Omega = 0$; dashed-dotted-dotted line with diamonds: $\Omega = 1$; dashed line: $\Omega = 2$; solid line: $\Omega = 5$; dashed-dotted line: $\Omega = 10$; dotted line: $\Omega = 20$; long dashed line: $\Omega = 50$; dashed-dotted-dotted line: $\Omega = 100$; dashed line with squares: $t^{-1.2}$ law.

RESULTS

The TNS model was used to perform simulations at two Reynolds numbers for rotating turbulence using the same initial condition of Horiuti [4]. For low Reynolds number, TNS provides results in agreement with theoretical analysis, DNS and other LES data for cases with and without rotation. We confirmed that the energy decay is inhibited by rotation. The $k^{-5/3}$ form appeared for the non-rotating case but a spectrum close to k^{-2} was observed for moderate rotation rate $\Omega = 10$. At high rotation rates, the energy spectrum obeyed a linear viscous decay law. The coupling effect between nonlinear interaction and rotation triggers the anisotropy which is reflected in longitudinal integral length scales and a directional stress tensor. The presence of anisotropy is conveniently quantified using macro- and micro-Rossby numbers Ro^L and Ro^ω, respectively, defined as follows: $Ro^L = u'/(2\Omega L)$, where L is the integral length scale and u' is the rms turbulent velocity; $Ro^\omega = \omega'/(2\Omega)$, where ω' is the rms vorticity. We found that anisotropy effects are strongest at moderate rotation rates for Rossby numbers approximately in the range between $Ro^L < 1$ and $Ro^\omega > 0.1$.

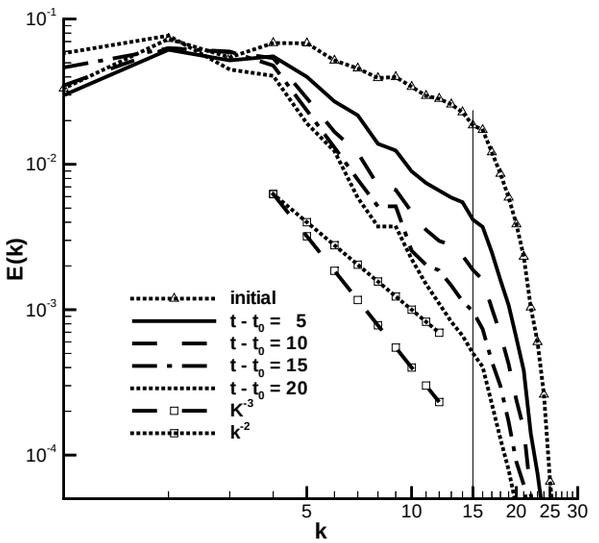


Figure 2. TNS: Energy spectrum at different time for $Re = 4 \times 10^{15}$, $\Omega = 20$. Dotted line with deltas: initial condition; solid line: $t - t_0 = 5$; dashed line: $t - t_0 = 10$; dashed-dotted line: $t - t_0 = 15$; dotted line: $t - t_0 = 20$; dashed line with squares: k^{-3} spectrum; dotted line with squares: k^{-2} spectrum.

At high Reynolds numbers, the energy decay in a case without rotation is consistent with $t^{-1.2}$ decay law but, in general, the rotation effects are stronger than at low Reynolds numbers . The energy decay is inhibited more for all rotation rates considered (Fig. 1). Even for very rapid rotation $\Omega = 100$, the evidence of nonlinear interactions modified by rotation was obvious and its behavior differed from the simple linear viscous decay observed at lower Reynolds number. For sufficiently long calculation time, we found that the Reynolds stress tensors and their invariants also became anisotropic, which is different from the results obtained in the short time, low Reynolds number runs. At high Reynolds numbers, the energy spectra close to k^{-2} and k^{-3} are observed, depending on the level of anisotropy (Fig. 2). At earlier times, when anisotropy is weak, the spectral slope is -2, consistent with phenomenological theories of rotating turbulence [5]. At later times, anisotropy is strong and the spectral slope tends toward value of -3. The latter result is consistent with analysis of Cambon [6] who showed that a k^{-3} spectrum can be derived in the asymptotic limit of quasi-infinite Reynolds number and quasi-zero Rossby number by using a wave-turbulence statistical model derived from a generalized EDQNM theory.

References

[1] J. A. Domaradzki and K. Horiuti, "Similarity modeling on an expanded mesh applied to rotating turbulence", Phys. Fluids **13**, 3510 (2001).
[2] J. A. Domaradzki, K. C. Loh and P. P. Yee, "Large Eddy Simulation Using the Subgrid-Scale Estimation Model and Truncated Navier-Stokes Dynamics", Theoret. Comput. Fluid Dynamics **16**, 1-30 (2002).
[3] P. K. Yeung and Y. Zhou, "Numerical study of rotating turbulence with external forcing", Phys. Fluids **10**, 2895 (1998).
[4] K. Horiuti, "Rotation tansformation and geometrical correlation of SGS models", in *Modern Simulations Strategies for Turbulent Flw*, edited by B. J. Geurts (R. T. Edwards, Philadelphia, 2001).
[5] Y. Zhou, "A phenomenological treatment of rotating turbulence", Phys. Fluids **7**, 2092 (1995).
[6] C. Cambon, personal communication, 2003.

XXI ICTAM, 15–21 August 2004, Warsaw, Poland

LARGE-EDDY SIMULATION OF SHOCK-WAVE / TURBULENT-BOUNDARY-LAYER INTERACTION

M.S. Loginov* **, N.A. Adams*, A.A. Zheltovodov**

*Institute of Fluid Mechanics, Dresden University of Technology, George-Bähr Str. 3c, 01062 Dresden, Germany

**Institute of Theoretical and Applied Mechanics, Institutskaya Str. 4/1, 630090 Novosibirsk, Russia

Summary A Large-Eddy Simulation (LES) is conducted to investigate the characteristics of the mean flow and the turbulence structure of the boundary layer along a compression corner. The compression corner has a deflection angle $\beta = 25^0$, and the mean free-stream Mach number is $M_\infty = 2.95$. The Reynolds number based on the incoming boundary layer thickness is $Re_{\delta 0} = 63560$ in accordance with reference experiments. An analysis of the flow computation shows a good agreement with the experiment in terms of mean quantities (shock position, separation zone length, skin friction and surface pressure distributions) and turbulence characteristics. A mechanism of turbulence amplification in the external flow by travelling compression waves is proposed. The existence of three-dimensional large-scale structures (Görtler-type vortices) is shown .

INTRODUCTION

Shock-wave / turbulent-boundary-layer interaction for compression corner flow is a canonical test case for turbulence modelling. Although numerous RANS computations were performed, most of them failed to predict some crucial characteristics. On the other hand DNS computations are too expensive to be applicable for practical configurations. LES is the most appropriate numerical tool since it gives an accurate instantaneous flow representation. Although different subgrid-scale models have been extensively tested throughout the world, most LES computations are still limited to Reynolds numbers which are significantly lower then their experimental counterparts.

The current numerical investigation is aimed at a direct comparison with an available experiment. For this purpose all flow parameters and the flow geometry are matched with the experiment [1]: the free-stream Mach number is $M_\infty = 2.95$, the Reynolds number based on the incoming boundary layer thickness is $Re_{\delta 0} = 63560$, the ramp deflection angle is $\beta = 25^0$. By matching directly the experimental parameters the prediction quality of the employed subgrid-scale model can be assessed without further assumptions. Given a successful validation, the computational results provide an important source to analyse the flow physics in detail.

NUMERICAL TECHNIQUE

For current LES we employ the Approximate Deconvolution Model (ADM) [2] for modelling the sub-grid scales. The conservation equations for the filtered density, momentum and total energy are solved in curvilinear coordinates. A 6-th order compact finite-difference scheme is used for spatial discretization and an explicit low-storage 3-rd order Runge-Kutta scheme is applied for time advancement. Boundary conditions are applied as follows: periodic conditions in the spanwise direction, sponge technique at the outflow [3], non-reflecting condition with sponge layer at the upper boundary, and isothermal condition at the wall. The wall temperature distribution along the streamwise direction in the interaction region is taken from the experiment [1]. The inflow conditions have been generated by a separate flat-plate boundary-layer simulation using the rescaling and recycling procedure described in [4].

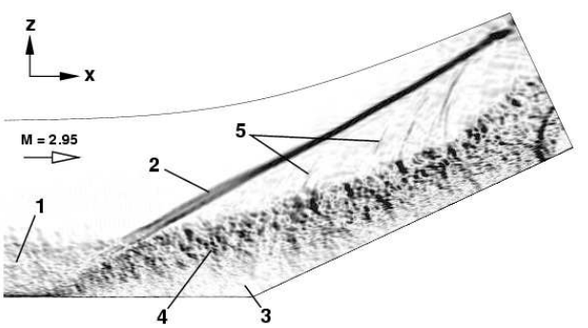


Figure 1. Density gradient averaged in spanwise $\|\nabla\rho\|$ (computed imitation of Schlieren visualization)

The computational domain has a size of $26.6\delta_0 \times 4.2\delta_0 \times 4.1\delta_0$ in streamwise, spanwise and wall normal direction respectively (δ_0 is the boundary layer thickness at inflow) and $701 \times 132 \times 201$ points. The simulation was running over 144 δ_0/U_∞ characteristic time scales. For statistical analysis, the field was sampled 265 times. To further improve statistical data the collection of samples is still in progress.

SIMULATION RESULTS

On Fig. 1 one can clearly identify the main flow field structures in the considered configuration: the undisturbed incoming turbulent boundary layer (1) interacts with the shock wave (2) resulting in the appearance of a separation zone near the corner (3) and a containing shear layer (4). All these flow features were also found in the experiment [1] and all calculated scales (separation zone length, shock position and slope) agree well with the experimental data. Another interesting feature is the existence of weak compression waves (5) above the reattached shear layer. Such waves were observed also

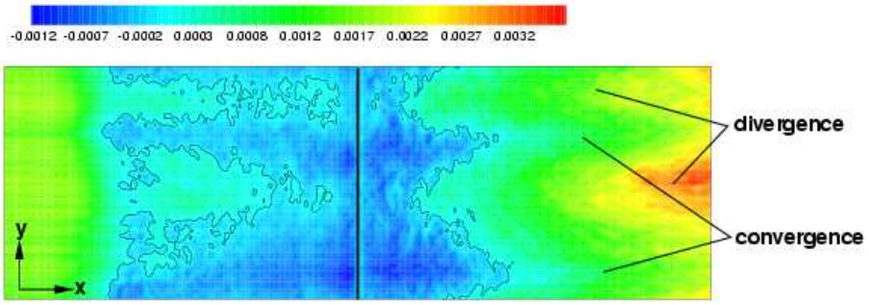


Figure 2. Time-averaged skin friction coefficient distribution at the wall

in previous DNS [3]. Experiments also exhibit compression waves in the described area. The compression waves are probably caused by unsteady motion of the shock wave. They emerge from the shock foot and travel further downstream. It seems that these waves are responsible for the amplification of turbulence levels in the external flow after passing the shock. The shock system unsteadiness itself is a crucial issue for wall loads: due to random shock motion the root mean square of the pressure fluctuations at the wall can reach 20% of mean pressure near the separation line, which agrees with experimentally observed values.

A detailed consideration of the flow field shows indications of large three-dimensional structures. In Figure 2 a time-averaged skin friction coefficient distribution at the wall is shown near the corner. The thin black line indicates $C_f = 0$, the thick vertical line indicates the compression corner position. Two divergence and two convergence lines after reattachment can be clearly seen. Similar oil-flow patterns observed in experiments are associated with Görtler-type vortices. In both cases the vortex width is about $2\delta_0$. Large-scale vortical structures influence mass, turbulence and heat transfer from external flow towards the wall. Eventually, these vortices strongly affect the skin friction distribution: in the reattachment region skin friction can vary along spanwise direction with the amplitude equal to the flat-plate boundary-layer value.

In Figure 3 the skin-friction-coefficient distribution in streamwise direction is shown, open dots denote experimental values, first vertical dotted line indicates the compression corner position, the second vertical dotted line that of the rarefaction corner (not considered in the present simulation). The skin friction coefficient averaged in time and in spanwise direction is denoted by solid line, minimum and maximum values over the spanwise direction are indicated as dashed lines (only in the interaction region). Unfortunately, the spanwise position of the experimental data probes with respect to the large-scale streamwise vortices is unknown.

So far, the turbulence statistics have been analyzed only qualitatively and will be presented more comprehensively durin the conference. Relative growth of density, momentum and velocity fluctuations after interaction were found to agree experimentall data.

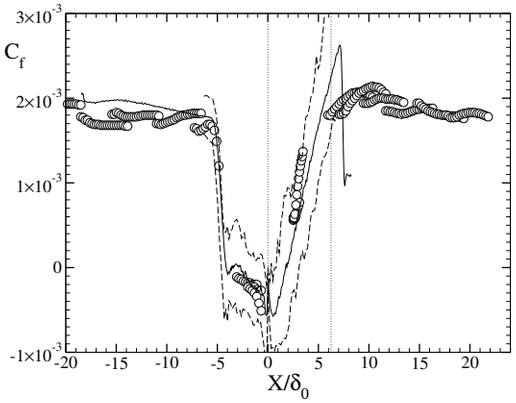


Figure 3. Skin friction coefficient at the wall

CONCLUSIONS

The Large-Eddy Simulation which was performed for flow parameters matching a reference experiment proves the possibility of a correct numerical prediction of shock-wave / turbulent-boundary-layer interaction at compression corners. Its analysis also imposes new requirements for the experiments which should take into account three-dimensional effects. A study of subsequent boundary-layer acceleration in a Prandtl-Meyer rarefaction is currently in progress.

This research is supported by DFG under grant AD 162/1. Travel funding for A.Zheltovodov was provided by SNF under the SCOPES program.

References

[1] Zheltovodov A. A., Trofimov V. M., Schulein E., Yakovlev V. N.: An experimental documentation of supersonic turbulent flows in the vicinity of forward- and backward-facing ramps. *Report N 2030* Institute of Theoretical and Applied Mechanics, USSR Academy of Sciences, Novosibirsk, 1990

[2] Stolz S., Adams N. A., Kleiser L.: The approximate deconvolution model for large eddy simulation of compressible flows and its application to shock-turbulent-boundary-layer interaction. *Phys. Fluids* **13**:2985–3001, 2001

[3] Adams N. A.: Direct simulation of the turbulent boundary layer along a compression ramp at M=3 and Re=1685 *J. Fluid Mech* **429**:187-216, 2000

[4] Stolz S. and Adams N.A.: Large-eddy simulation of high-Reynolds-number supersonic boundary layers using the approximate deconvolution model and a rescaling and recycling technique *Phys. Fluids* **15**:2398–2412, 2003

EXPERIMENTAL STUDY OF ROTOR-STATOR FLOWS WITH CENTRIPETAL FLUXES

Sébastien Poncet, Marie-Pierre Chauve, Patrice Le Gal
IRPHE UMR 6594-CNRS / Université d'Aix-Marseille I et II, Technopôle Château Gombert, 49 rue F. Joliot Curie B.P.146, 13384 Marseille cédex 13, France

Summary The evolution of the entrainment coefficient K of the rotating fluid in a rotor-stator cavity, is studied with an imposed centripetal flux and according to the flow control parameters. Measurements are realised by a two component laser Doppler anemometry (L.D.A.). It is shown that the coefficient K depends on a local flow rate coefficient Cq_r of the fluid according to a $5/7$ power law whose coefficients depend on the value of the velocity at the entry of the cavity. A theoretical analysis confirms the asymptotic behavior.

INTRODUCTION

Rotating flows are studied since more than one century [2] because they are present in many rotating machines. Of prime importance for these flows is the rate of rotation K (or entrainment coefficient) of the fluid in the rotor-stator cavity. The values taken by this coefficient determine in fact the rotating machine operating conditions. Following the analysis performed by R. Gassiat in his thesis [3], our study relates to the determination of K when a centripetal flux is added on the rotating flow. We show that a local flow rate coefficient Cq_r is the similarity parameter of the flow and can be used directly to calculate K. As these values are connected to the pressure gradient across the cavity, the knowledge of K is particulary interesting from an industrial point of view.

EXPERIMENTAL SET-UP

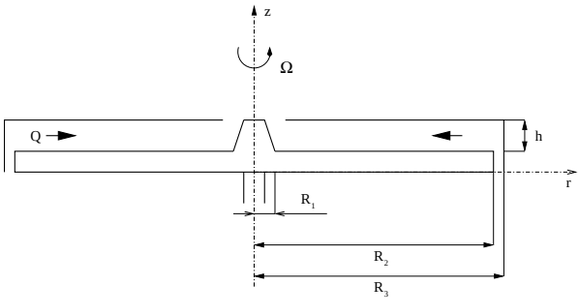


Figure 1. Annular cavity with $\Omega = 0 - 63\ rad.s^{-1}$, $Q = 0 - 4\ l.s^{-1}$, $h = 0 - 12\ mm$, $R_1 = 37.5\ mm$, $R_2 = 250\ mm$, $R_3 = 253\ mm$

The cavity consists of a fixed disk (stator) and of a rotating disk (rotor) which rotates at the uniform angular velocity Ω. The height of the cavity h is variable. The flow depends mainly on three control parameters which are : the Reynolds number $Re = \Omega r^2/\nu$ (r the local radius, ν the water kinematic viscosity), the Rossby number $Ro = Q/(2\pi\rho\Omega R_2^2 h)$ (ρ the water density) and the aspect ratio $G = h/R_2$. A centripetal and variable flux Q is imposed on the basic flow. At the cavity entry, the fluid rotation is ensured by a complementary device linked to the rotor. At rest, the cavity is maintained with a pressure of 2 bars to avoid cavitation effects. The temperature is also maintained constant by a special water cooling device. The flow is supposed to be axisymmetric. By L.D.A., the two velocities components, radial velocity V_r and tangential velocity V_θ are measured in the frame (r, z). For a given radius the rate of rotation K of the fluid is defined by the ratio of the tangential velocity of the fluid in the rotating core and the disk velocity at the same radius position ($K = V_\theta(r)/(\Omega r)$).

RESULTS

The challenge is to find a relation giving the rate of rotation of the fluid K versus h, Ω and Q by using a new coefficient called the local flow rate coefficient whose expression will be determined in the following.

Definition of the local flow rate coefficient Cq_r

It is recalled that we consider a flow with two boundary layers separated by a central rotating core : the Ekman layer on the rotor and the Bödewadt layer on the stator. First we seek an expression for the thickness of the Ekman layer [5]. We consider a volume element of δ_E in height and dS in surface inside the boundary layer of the rotating disk. In this volume element the balance between the centrifugal force and the shearing stress is expressed by :

$$\tau_0 \sin\alpha\, dS = \rho\, r\, \Omega^2\, \delta_E\, dS \tag{1}$$

where α is the angle formed by the shearing stress at the wall τ_0 and the tangential direction.
If it is supposed that the velocity profile evolves according to a $1/7$ power law, the tangential component of shearing stress is given by (The external velocity of the boundary layer is the core velocity decreased by the disk velocity) :

$$\tau_0 \cos\alpha = \rho\,((K-1)r\,\Omega)^{7/4}\,(\nu/\delta_E)^{1/4} \tag{2}$$

By supposing that the angle α of stream lines inclination remains constant along the radius r, we find the expression of the Ekman layer thickness : $\delta_E \sim r\,(K-1)^{7/5}\,(\Omega r^2/\nu)^{-1/5}$.

Secondly we seek an expression for the Bödewadt layer thickness. Contrary to [1], it is supposed that the radial friction is controlled in this boundary layer by the radial flux :

$$\tau_0 \sin\alpha = \rho\,(Q/(2\pi r\delta_{Bo}))^{7/4}\,(\nu/\delta_{Bo})^{1/4} \tag{3}$$

$$\tau_0 \cos\alpha = \rho\,(K\,r\,\Omega)^{7/4}\,(\nu/\delta_{Bo})^{1/4} \tag{4}$$

The combination of these two last relations gives the expression of the Bödewadt layer thickness $\delta_{Bo} \sim Q/(2\pi r^2 \Omega K)$. Now by considering that radial velocity in the rotating core is zero (that is experimentally verified), the continuity equation reads:

$$\overline{V_{Bo}}\,\delta_{Bo} + \overline{V_E}\,\delta_E = Q/(2\pi r) \tag{5}$$

$\overline{V_{Bo}}$ and $\overline{V_E}$ are mean velocities proportional to the maximum values of the boundary layers velocities (for large K) :

$$\overline{V_{Bo}} = \gamma Q/(2\pi r\delta_{Bo}) = \gamma\,K\,\Omega\,r \qquad \overline{V_E} = \beta r\Omega \tag{6}$$

By using (5) and (6), we get: $K \sim (\frac{Q}{2\pi r^3\Omega}(\frac{\Omega r^2}{\nu})^{1/5})^{5/7}$, which gives finally the required expression of the similarity parameter Cq_r :

$$Cq_r = \frac{Q}{2\pi r^3\Omega}(\Omega r^2/\nu)^{1/5} \tag{7}$$

Under these conditions we can write $K = (a \times Cq_r + b)^{5/7}$, where a and b are constants determined experimentaly. It can be noticed that for $r = R_2$, we find the same expression for Cq_r that in [4].

Experimental results

The experimental device previously described have been used to test relation (7) by determining K for many values of Q, Ω and r and for two values of the gap h. The whole of the experimental results are in good agreement (see fig.2) with the $5/7$ power law with $a = 11.1$ and $b = 0.31$. For our experiment, this law is validated in the range of Reynolds number $[6.92 \times 10^5 - 4.15 \times 10^6]$ and of Rossby number $[2 \times 10^{-6} - 6.6 \times 10^{-5}]$.

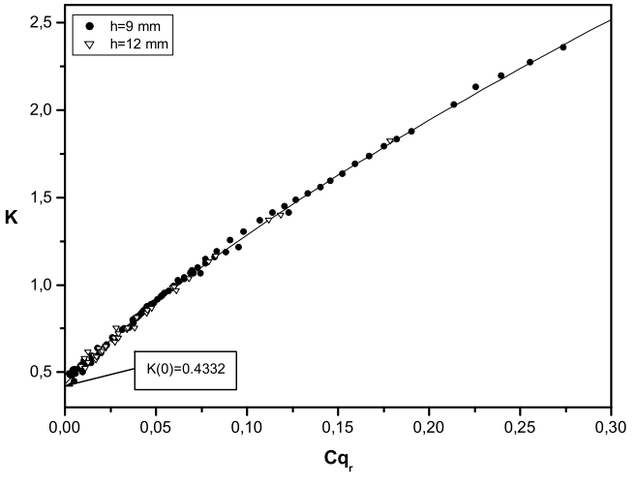


Figure 2. $5/7$ power law giving K versus Cq_r.

References

[1] Daily J.W., Nece R.E. : Chamber dimension effects on induced flow and frictional resistance of enclosed rotating disks. *A.S.M.E. J. Basic Eng.* **82**:217–232, 1960

[2] Ekman V.W.: On the influence of the Earth's rotation on ocean currents. *Arkiv. Mat. Astr. Fys.* **2**(11):1–52, 1905.

[3] Gassiat, M.R.: Etude expérimentale d'écoulements centripètes avec prérotation d'un fluide confiné entre un disque tournant et un carter fixe. *PhD Thesis*, Univ. Aix-Marseille II, Marseille, 2000.

[4] Kurokawa J., Toyokura T. : Axial thrust, discfriction torque and leakage loss of radial flow turbomachinery. *Int. Conference on pump and turbine design and development*, Glasgow, 1976

[5] Schlichting H.: Boundary-Layer Theory. McGraw-Hill, NY 1979.

XXI ICTAM, 15–21 August 2004, Warsaw, Poland

PDF COMPUTATION OF TURBULENT FLOWS WITH A NEW NEAR-WALL MODEL

Marta Wacławczyk*, Jacek Pozorski*, Jean-Pierre Minier**
*Institute of Fluid-Flow Machinery, Polish Academy of Sciences, Fiszera 14, 80952 Gdańsk, Poland
**Research & Development Division, Electricité de France, 6 quai Watier, 78400 Chatou, France

Summary The modeling and computation of near-wall turbulent flows is addressed with the probability density function (PDF) method for velocity and the turbulent frequency. A new model for viscous transport is proposed and a method of elliptic relaxation for a blending function is applied to model the pressure-strain term. The PDF equation is solved by a Monte Carlo method and the whole approach appears as a self-contained Lagrangian simulation using stochastic particles. For the sake of numerical example, the fully developed channel flow is computed; results are compared with the available DNS data.

PDF modelling of the near-wall effects

From a practical point of view, a sound modeling of near-wall turbulence is of utmost importance, for the overall characteristics of momentum and heat transfer are mostly controlled and determined by a relatively thin near-wall region. At the same time the near-wall treatment in turbulent flows remains a notorious difficulty for statistical modeling. In the wall proximity a strong inhomogeneity due to the mean shear and considerable gradients of turbulence statistics are observed. The turbulence in this region is also highly anisotropic, with the wall-normal direction definitely distinct from others; this effect is felt also at larger distances from the wall through the pressure field. In the near-wall region, the molecular transport (viscosity, thermal conductivity) has to be accounted for explicitly.

The present work addresses the modeling and computation of turbulent wall-bounded flows. Approach followed here is the stand-alone PDF method, cf. [7], which is extended to account for wall effects. This is also the continuation of the previous work of the authors [5], [8], where the wall function approach was applied in the PDF method. The work differs in a few aspects from the study of Dreeben and Pope [1]. First, a new model for viscous transport is proposed, which operates with only first-order derivatives of the mean velocity field. In order to model the non-local wall effects we implement in the PDF approach the elliptic relaxation method [2] in its efficient one-equation variant [3]. In order to deal with numerical problems arising in the modeling of the viscous sublayer, a new integration scheme for the stochastic differential equations is proposed.

In the Lagrangian approach the viscous effects are modelled through the Brownian motion in the equation for the stochastic particle position and additional terms in equation for velocity increment [1]. The alternative model presented below retains the same structure of the velocity increment equation as the model for high Reynolds numbers [7]:

$$\begin{aligned} d\mathcal{X}_i &= \mathcal{U}_i dt + \sqrt{2\nu}\, dW_i^X, \\ d\mathcal{U}_i &= -\frac{\partial \langle P\rangle}{\partial x_i}\, dt - (A_{ij}+G_{ij})\,(\mathcal{U}_j - \langle U_j\rangle)\, dt - \frac{1}{2}\frac{\epsilon}{k}\,(\mathcal{U}_i - \langle U_i\rangle)\, dt + \sqrt{D}\, dW_i \end{aligned} \tag{1}$$

where $\langle\cdot\rangle$ denotes the ensemble average, P is the kinematic pressure, $\boldsymbol{\mathcal{U}}(t)$ is the velocity of a particle, defined as the Eulerian fluid velocity $\mathbf{U}(\mathbf{x},t)$ evaluated at the particle position, i.e. $\boldsymbol{\mathcal{U}}(t) = \mathbf{U}\,[\boldsymbol{\mathcal{X}}(t),t]$; $d\mathbf{W}$ and $d\mathbf{W}^X$ denote the increments of the Wiener process, ϵ is the dissipation rate of the turbulent kinetic energy k, and $D = (2/3)G_{kl}\langle u_k u_l\rangle$. The tensor A_{ij} is determined from the requirement

$$A_{il}\langle u_l u_j\rangle = \nu \frac{\partial\langle U_i\rangle}{\partial x_k}\frac{\partial\langle U_j\rangle}{\partial x_k}. \tag{2}$$

The LHS of the above expression has the physical interpretation: it is the dissipation rate of the kinetic energy connected with the mean motion. The form (2) assures that in the Reynolds stress equations corresponding to the stochastic model (1) the viscous transport term is exact.

In the vicinity of the wall the effects of kinematic damping of the wall-normal velocity component and pressure scrambling can be modeled by a proper form of the tensor G_{ij}. Here, the components of this tensor are computed as the interpolation of their known near-wall form G_{ij}^w and a standard quasi-homogeneous model G_{ij}^h (eg. the basic pressure-strain model) used far from walls: $G_{ij} = (1-\alpha\epsilon T)G_{ij}^w + \alpha\epsilon T\; G_{ij}^h$, where $T = 1/\langle\omega\rangle$ is the time scale, $\langle\omega\rangle$ is the mean turbulent frequency and α is the elliptic blending function to be determined from the Helmholz equation [3]:

$$L^2\nabla^2\alpha - \alpha = -\frac{1}{\epsilon T} \tag{3}$$

with the length scale $L = C_L \max\{\frac{k^{3/2}}{\epsilon}, C_\eta \frac{\nu^{3/4}}{\epsilon^{1/4}}\}$. In the Lagrangian formulation the equation for the turbulent frequency ω is solved and ϵ is computed from the formula $\epsilon = k\langle\omega\rangle + \nu C_T^2\langle\omega\rangle^2$ (see [1]).

The dissipation rate ϵ has a non-zero value at the wall while the kinetic energy $k \sim y^2$ in the wall vicinity. Hence, some expressions present in the stochastic differential equations (1) are unbounded when discretized with the Euler scheme: $(\epsilon/k)u_i\Delta t \sim 1/y$ for $i \neq 2$. For the purpose a new numerical scheme has been developed [4]. It is based on the exponential solution of the stochastic equations (1) (details are not shown here).

PDF computation results for channel flow

Another objective of the work is to report computational results from the velocity PDF code for the case of fully developed channel flow. Computations are done to match the numerical experiment (DNS) [6] at $Re_\tau = 395$ and 590. The statistics (cf. Fig. 1) fit reasonably well the DNS data, although the mean velocity profile show a discrepancy in the buffer layer. This can be a consequence of the simple one-equation elliptic blending model used. Figure 2 presents probability density functions of the fluctuating streamwise velocity computed at different distances from the wall. As it is seen, even the definitely non-Gaussian behavior of the probability density functions near the wall can be reproduced correctly by the PDF method.

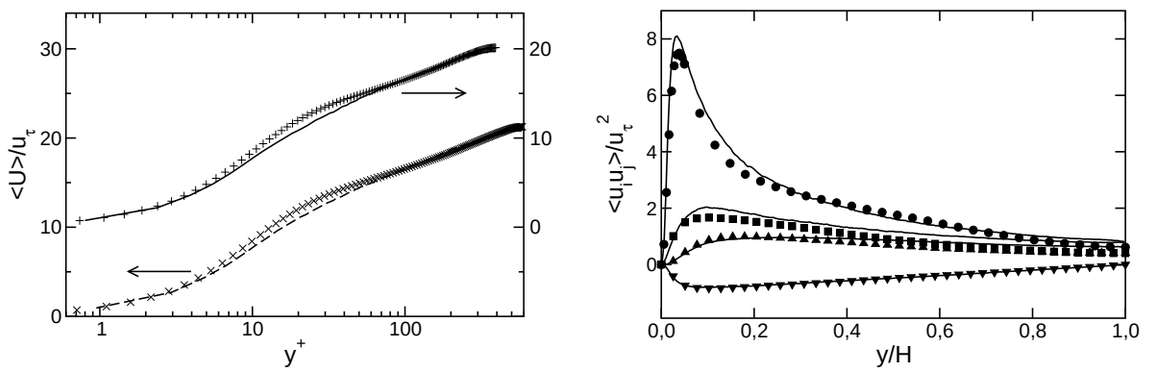


Figure 1. a) Mean velocity profiles in the turbulent channel flow at $Re_\tau = 590$ and $Re_\tau = 395$ (data sets shifted upward by 10); PDF computations: lines, DNS results[6]: symbols. b) the Reynolds stresses at $Re_\tau = 395$, PDF computations (——); DNS data: $\langle u^2 \rangle$ •, $\langle v^2 \rangle$ ▲, $\langle w^2 \rangle$ ■, $\langle uv \rangle$ ▼.

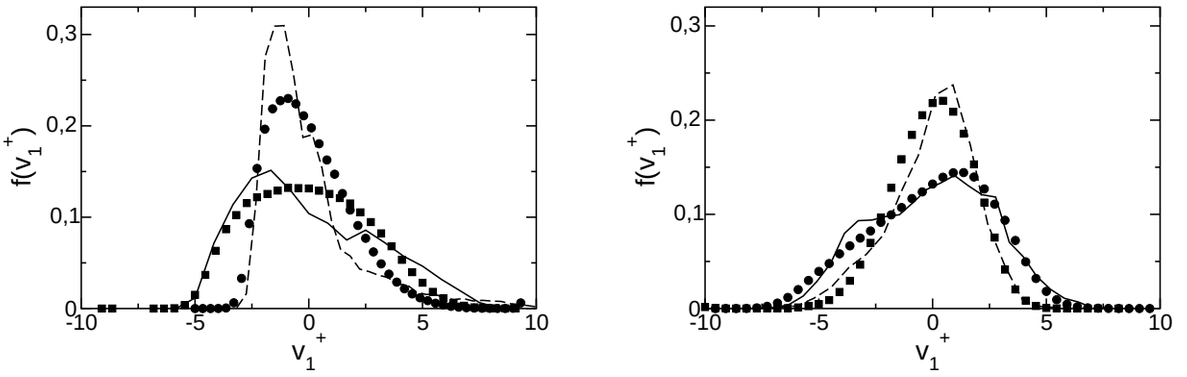


Figure 2. PDFs of the streamwise velocity fluctuations at $Re_\tau = 395$. a) PDF computations at $y^+ = 5$ (— —) and $y^+ = 10$ (——). b) PDF computations at $y^+ = 20$ (——) and $y^+ = 80$ (— —). DNS: symbols.

Conclusions

The main thrust of the work has been the development of a complete near-wall stochastic model with a new proposal for viscous transport. Unlike the previous model [1] no second order derivatives need to be computed. Moreover, the Lagrangian equation for velocity increment retains the same simple structure as for the high-Re case. The elliptic relaxation approach has been applied in the Lagrangian PDF setting in its simple and computationally efficient variant [3] with only one additional elliptic equation solved. When supplemented with a suitable scalar transport equation, the approach presented here can readily be applied to the case of near-wall turbulence with heat transfer to model the thermal fluctuations in the immediate vicinity of the wall.

References

[1] Dreeben T. D., Pope S. B.: PDF/Monte Carlo simulation of near-wall turbulent flows. *J. Fluid Mech.* **357**:141–166, 1998.
[2] Durbin P. A.: A Reynolds-stress model for near-wall turbulence. *J. Fluid Mech.* **249**:465–498, 1993.
[3] Manceau R., Hanjalić K.: Elliptic blending model: a new near-wall Reynolds-stress turbulence closure. *Phys. Fluids* **14**:744–754, 2002.
[4] Minier J.-P., Peirano E., Talay D.: Schémas numériques faibles pour les équations différentielles stochastiques intervenant dans les modèles diphasiques Lagrangiens, EDF R&D Report No. HI-81/01/026/A 2001.
[5] Minier J.-P., Pozorski J.: Wall boundary conditions in PDF methods and application to a turbulent channel flow, *Phys. Fluids* **11**:2632–2644, 1999.
[6] Moser R. D., Kim J., Mansour N. N.: Direct numerical simulation of turbulent channel flow up to $Re_\tau = 590$. *Phys. Fluids* **11**:943–945, 1999.
[7] Pope S. B., Turbulent Flows. Cambridge University Press, 2000.
[8] Pozorski J., Wacławczyk M., Minier J.-P.: Full velocity-scalar PDF computation of heated channel flow with wall function approach. *Phys. Fluids* **15**:1220–1232, 2003.

INTERACTION BETWEEN A COLUMNAR VORTEX AND EXTERNAL TURBULENCE

Naoya Takahashi, Takeshi Miyazaki
Department of Mechanical Engineering and Intelligent Systems, University of Electro-Communications, 182-8585, JAPAN

Summary The interaction between a columnar vortex and external turbulence is investigated numerically. As the columnar vortex, the Lamb-Oseen vortex and the q-vortex are used. The columnar vortex is immersed in an initially isotropic homogeneous turbulence field, which itself is produced by a direct numerical simulation of decaying turbulence. Using visualization techniques, we investigate the formation of inhomogeneous fine turbulent eddies around the columnar vortex, the vortex-core deformations and the dynamical evolution in the passive scalar field.

INTRODUCTION

Interactions between intense elongated vortices and surrounding turbulent motion often occur in engineering and environmental flows, and they occur naturally in most homogeneous and sheared turbulent flows. Several experimental and computational studies have been undertaken on the instability of vortices interacting with background turbulence. These interactions are thought to play an important role in the three-dimensionalization of the flow fields. It is also of practical interest to estimate the lifetime of trailing vortices under the influence of atmospheric turbulence. In this paper, we investigate the dynamical evolution of the vortex structure and the passive scalar structure, appeared due to the isotropic homogeneous turbulence interacting with the columnar vortex. The characteristics of the flow field are analyzed by using several flow-visualization techniques. The statistics of the turbulence around the columnar vortex are investigated by computing the two-point energy spectrum tensors, and they are compared with the results of a linear rapid distortion theory (RDT) [1]. The growth of the velocity and vorticity disturbances are proportional to $t^{0.9}$ and t^1 respectively. Although the results are qualitatively consistent with RDT, that do not agree quantitatively with the prediction of RDT($\propto t^2$).

NUMERICAL METHOD

We solve the Navier-Stokes equation for incompressible fluids and the transport equation for the passive scalar (such as a passive temperature field or a dye) under periodic boundary conditions with period 4π. A spectral method is used to solve the equations. The time integration is performed using the fourth order Runge-Kutta-Gill method. The simulations are done with resolutions of 256^3 and 512^3.

The columnar vortex is immersed in an initially isotropic homogeneous turbulence field, which itself is produced numerically by a direct numerical simulation of decaying turbulence.

The initial condition is set up with an energy spectrum of $k^4\mathrm{e}^{-2k^2}$. Its Reynolds number is 500, based on the velocity as the root mean square of the field, and the length of the inverse of the wavenumber k at which the initial energy spectrum is maximal and based on the kinematic viscosity ν. The initial turbulent field is produced as decaying turbulence. The Reynolds number based on the Taylor micro scale is about 126. In these initial fields, a coherent fine scale structure of 'worms' is observed.

As the columnar vortex, we use the q-vortex, which is a model for trailing vortices. The q-vortex is defined by

$$(U_r, U_\theta, U_z) = \left(0, \frac{\Gamma_0}{2\pi r}\left\{1 - \exp\left(-\frac{r^2}{r_0^2}\right)\right\}, \frac{\Gamma_0}{2\pi r_0 q}\exp\left\{-\frac{r^2}{r_0^2}\right\}\right), \tag{1}$$

where U_r, U_θ and U_z are the radial, azimuthal and axial components of the velocity field, and q is the swirling parameter. In this paper, r_0, the initial radius of the columnar vortex, and $T = 2\pi r_0/(\Gamma_0/2\pi r_0)$, the time period for a fluid particle on the surface of the vortex core to make one revolution, are used as the characteristic length and time scales to render the results dimensionless. The initial circulation Γ_0 is an arbitrary parameter, so we set the circulation strong enough to dominate the vortex dynamics of the flow field as $\Gamma_0 = 40r_0^2\omega_{r.m.s.}$ where $\omega_{r.m.s.}$ is the root mean square of the vorticity of the initial turbulence. Then the Reynolds number of the columnar vortex Γ_0/ν becomes about $20,000$ to $80,000$. We consider three values of q, that is $-\infty$ (a.k.a. Lamb-Oseen vortex), -0.45 (unstable case) and -1.5 (marginally stable case).

RESULTS

The Lamb-Oseen vortex ($q = -\infty$)

In this case, the columnar vortex corresponds to the Lamb-Oseen vortex, which is an exact solution of the Navier-Stokes equation. The linear stable columnar (Lamb-Oseen) vortex undergoes a deformation due to the interaction, and the vortex wraps worms around its surface in a spiral structure (Fig. 1(a)). On the surface, external velocity disturbances are blocked by the vortex and they cannot penetrate into the vortex core directly ('blocking effect'), whereas various types of vortex

waves (Kelvin waves) are excited. The disturbances in the axial direction were suppressed. This result is consistent with the Taylor-Proudman's theorem.

Scalar advection of the interaction ($q = -\infty$)

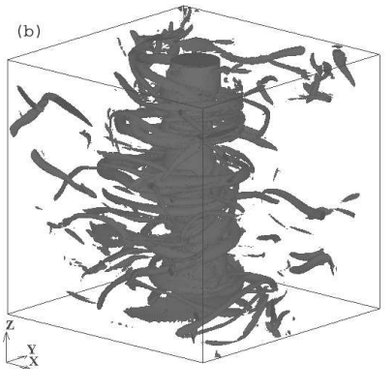
The initial scalar field is initialized with the profile $s_0(z)$, which depends only on the axial component of z and has a Gaussian profile. Figure 1(b) is an instantaneous snapshot of the scalar field with enstrophy. This figure shows noticeable advection of the passive scalar field around the surface of the vortex core. This phenomenon may be due to the fact that the blocking effect of the velocity field is excited where the mean axial gradient of the scalar field is large. Another characteristic advection is observed separated from the vortex core. The coherent fine scale structure (worm) wrapps the passive scalar; i.e., the only swirling motion of the vortical structure becomes important in the scalar advection.

Unstable case of q-vortex($q = -0.45$)

The q-vortex with $q = -0.45$ is most unstable against the bending disturbance with $m = 1$[2]. The vortex core tends to form helical structures with two blades. The structure corresponds to the linear instability. At about the time of the saturation of the linear instability, small vortex ring-like structures occur around the surface of the blades as shown in Fig. 2(a). After a short time, the columnar vortex disolves abruptly, which indicates that the small vortex rings may correspond to the secondary instability.

Less stable case of q-vortex ($q = -1.5$)

We investigate the less unstable case in which the q-vortex has the swirl parameter $q = -1.5$. This parameter is selected so that the q-vortex is almost neutrally stable, and the q-vortex with $|q| > \sqrt{2}$ is stable for disturbances (WKB modes) at the smallest wave numbers. Fig. 2(b) shows the isosurface of the vorticity. Inside the vortex core, the emergence of thin and strong spiral structures, that are different structures of worm, are observed. This indicates that the nonlinear interaction is concentrated inside the core. These structures generated around the surface of the core are wound up by the columnar vortex, which stretches and thins the structure.



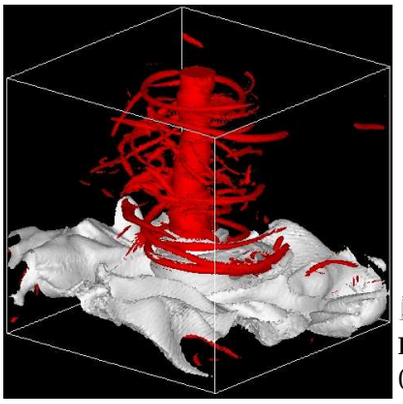


Fig. 1 (a) Iso-surfaces of vorticity. (b) Iso-surfaces of vorticity (red) and passive scalar (white). ($q = -\infty$, Lamb-Oseen vortex).

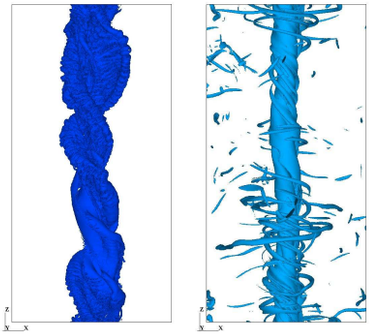


Fig. 2 (a)Iso-surfaces of vorticity (q-vortex, $q = -0.45$ (unstable case)). (b)Iso-surfaces of vorticity (q-vortex, $q = -1.5$ (less stable case)).

CONCLUSION

We investigated the interaction between a columnar vortex and external turbulence using direct numerical simulations.

The linear stable columnar (Lamb-Oseen vortex, $q = -\infty$) vortex underwent a deformation due to the interaction. The vortex wraps worms around itself to form spiral structures. Inside the vortex core, axisymmetric and bending vortex waves are excited. The interaction promotes scalar advection on the surface of the vortex core.

In the case of the unstable columnar vortex (q-vortex, $q = -0.45$), helical structures occur due to the linear instability. At the saturation of the linear instability, the secondary instability sets in and the columnar vortex disolves abruptly.

In the case of the marginally stable columnar vortex (q-vortex, $q = -1.5$), thin and strong spirals form inside the vortex core. These structures are stretched by the differential rotation around the columnar vortex, and they are dissipated gradually.

References

[1] Miyazaki, T. and Hunt, J. C. R.: Linear and nonlinear interactions between a columnar vortex and external turbulence, *J. Fluid Mech.* **402**: 349, 2000.
[2] Mayer, E. W. and Powell, K. G.: Viscous and inviscid instabilities of a trailing vortex, *J. Fluid Mech.* **245**: 91, 1992.
[3] Takahashi, N., Ishii, H. and Miyazaki, T.: The Influence of Turbulence on a Columnar Vortex, *Phys. Fluids* (submitted), 2003.

TURBULENCE SCALINGS IN SUPERSONIC CHANNEL FLOW

Rainer Friedrich[*], Holger Foysi[*], Sutanu Sarkar[**]
[*]*TU München, Fachgebiet Strömungsmechanik,D-85748 Garching, Germany*
[**]*UCSD, Mechanical & Aerospace Engineering, La Jolla, CA 92093-0411, U.S.A.*

Summary Direct numerical simulations of compressible channel flow have been performed at subsonic and supersonic Mach numbers with the aim to better understand effects of compressibility. The ability of outer and inner scalings to collapse profiles of turbulence stresses on to their incompressible counterparts is investigated. It turns out that such collapse is possible with outer scaling when sufficiently far from the wall, but not with inner scaling. Compressibility effects on the turbulent stresses, their anisotropy and their balance equations are identified. A reduction in the near-wall pressure-strain, is explained using a Green's function-based analysis of the pressure field.

INTRODUCTION

Supersonic channel flow is a prototypical example of a high-speed internal flow that allows for a systematic study of compressibility effects in wall-bounded turbulence. Pioneering investigations of this flow have been made by Coleman et al. [1] and Huang et al. [2]. Coleman et al. [1] performed DNS of supersonic channel flow between cold isothermal walls with Mach numbers up to M = 3. They found that Morkovin's hypothesis, "the flow dynamics follows an incompressible pattern", holds for the most part, and that the Van-Driest log-law is valid. Huang et al. [2] observed that the turbulent stresses, $\overline{\rho} R_{ij}$, scale with the wall shear stress, τ_w, and that semi-local scaling is useful. Lechner et al. [3], in their study of M = 1.5 channel flow, reported that the anisotropy of the Reynolds stresses was changed relative to the corresponding incompressible values, but they did not provide any explanation. Morinishi et al. [4] simulated supersonic channel flow at M = 1.5 with one wall isothermal and the other wall adiabatic, and found significant differences between the flows in the two halves of the channel. Based on this literature survey it appears that there are open issues regarding the behaviour of the turbulent stresses. The first objective of the current work is to evaluate the applicability of the incompressible fluctuating velocity scale (the friction velocity) and the inner and outer length scales to compressible flow where the density and viscosity are functions of position, and the second objective is to provide an explanation for the systematic change of the turbulent stresses with increasing Mach number.

DETAILS OF DNS

The compressible Navier-Stokes equations are numerically solved using a pressure-velocity-entropy formulation following the algorithm of Sesterhenn [5]. The mean pressure gradient that drives the channel flow is replaced by a uniform body force. Both channel walls are cooled and kept at a temperature of T_w = 500 K. Periodic boundary conditions are applied in stream- and spanwise directions. The compact 5th-order upwind scheme of Adams & Shariff [6] is used to discretize the Euler terms, the compact 6th-order scheme of Lele [7] for the molecular terms, and a 3rd-order low-storage Runge-Kutta scheme for the time advancement.
The numerical algorithm has been validated in [3] for a M = 1.5 case and excellent agreement with data of [1] has been found. In the present work the mean mass flow rate is systematically increased so that the Mach number $M = u_{av} / c_w$ based on the Reynolds cross-sectionally averaged velocity and the sound speed at wall temperature takes values between 0.3 and 3.0. The bulk Reynolds number $Re = \rho_m \, u_{av} \, h / \mu_w$ is based on the cross-sectionally averaged mean density. It increases with M. The friction Reynolds number $Re_\tau = \rho_w \, u_\tau \, h / \mu_w$, with $u_\tau = (\tau_w / \rho_w)^{1/2}$ is a result of the simulation. Table 1 summarizes the flow parameters, computational box sizes and number of grid points used in the different compressible cases M0.3 to M3.0. Equidistant grids are taken in streamwise x_1- and spanwise x_3-directions. In the wall-normal x_2-direction, points are clustered using tanh-functions [3]. The compressible flow results are compared with the incompressible data of Moser et al. [8] at various Reynolds numbers: Re_τ = 180, 395, and 590, denoted by cases I1, I2, I3, respectively.

Case	M	Re	Re_τ	L_{x1}/h	L_{x2}/h	L_{x3}/h	N_{x1}	N_{x2}	N_{x3}	Δx_1^+	$\Delta x_2^+{}_{min}$	$\Delta x_2^+{}_{max}$	Δx_3^+
M0.3	0.3	2820	181	9.6	2	6	192	129	160	9.12	1.02	4.21	6.84
M1.5	1.5	3000	221	4π	2	4π/3	192	151	128	14.46	0.84	5.02	7.23
M2.5	2.5	5000	455	2π	2	2π/3	256	201	128	11.16	1.17	7.46	7.44
M3.0	3.0	6000	560	2π	2	2π/3	256	221	128	13.37	0.89	9.38	8.91

TABLE 1. Flow and computational parameters

The flow physics in compressible channel flow with isothermal cold walls is different from that in incompressible channel flow mainly because of the large change in fluid properties. The mean temperature increases in the core of the channel due to viscous heating and, since $\mu \sim T^{0.7}$, so does the mean viscosity. The mean density, being inversely proportional to the mean temperature, decreases from its wall value with increasing x_2.

PRESSURE-STRAIN CORRELATION

The pressure-strain correlation, Π_{ij}, plays a key role in changing the turbulent stresses and associated anisotropy. It is observed that the pressure-strain profiles for all incompressible and compressible cases collapse in the outer region, $x_2/h > 0.35$ when scaled with $\tau_w\, u_{av} / h$ (outer scaling). In the inner region, Π_{ij} is reduced in compressible channel flow as compared to the incompressible counterpart. In an attempt to explain the underlying mechanism, an equation for the pressure fluctuations is derived taking the divergence of the momentum equation, and using mass conservation. After some algebraic manipulation, the following equation results for channel flow:

$$\nabla^2 p' = A_1 + A_2 + A_3 + B_1 + B_2 + C_1 + C_2 + C_3\,, \tag{1}$$

with

$$A_1 = -\,\overline{\rho}\,(u_i''u_j'' - \overline{u_i''u_j''})_{,ij}\,; \quad A_2 = -2\,\overline{\rho}\,\tilde{u}_{1,2}\,u_{2,1}''\,; \quad A_3 = \sigma'_{ij,ij}\,; \quad B_1 = -2\,\overline{\rho}_{,2}\,(u_2''u_j'' - \overline{u_2''u_j''})_{,j}\,. \tag{2}$$

In incompressible flow, the terms A_1 to A_2 describe effects by nonlinear fluctuations and mean shear, respectively. In compressible flow, the additional terms involve effects by viscosity (A_3),mean density gradients (B_1, B_2) and by density fluctuations (C_1, C_2, C_3). Neglecting the density fluctuations, eq. (1) can be interpreted as a Poisson equation for the pressure which accounts solely for mean density variations. In this case the rhs of (1) is replaced by $\overline{\rho}f'$ and a Green's function analysis is performed. It turns out that the Green's function G is the same as that given by Kim [9] for incompressible channel flow. An extra inhomogeneous fluctuating term B', however, appears in compressible flow due to nonzero wall-normal pressure gradient fluctuations. The pressure-strain correlation can finally be expressed in the form

$$\Pi_{ij}(x_2) = \int_{-1}^{1} \overline{\rho}(x_2')\,\overline{(G * f'(x_1,x_2,x_3,x_2')s_{ij}')}\,dx_2' + \overline{(B's_{ij}')} \tag{3}$$

Fig. 1 shows a comparison of the analytical solution, eq. (3), and the DNS data for cases M0.3 and M1.5.The overall agreement is very good, confirming our ansatz that a variable-density extension of the Poisson equation is sufficient for obtaining the pressure-strain term in wall-bounded flows.

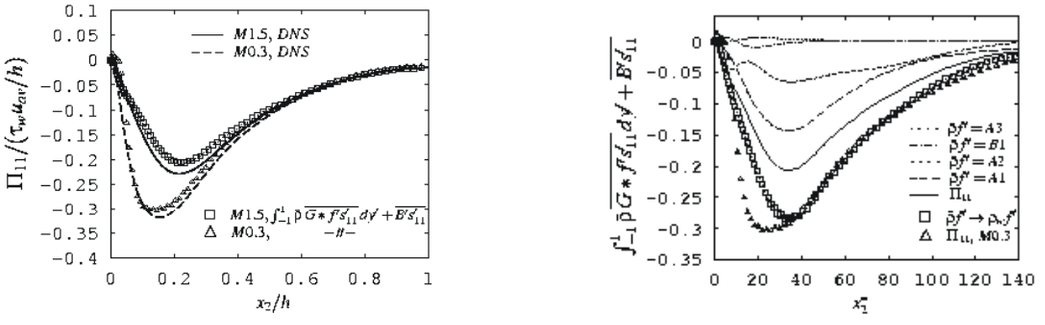


Figure 1. Left: Comparison of the DNS data with results using eq. (3) for the pressure-strain correlation. Right: Contribution of source terms, A_1- A_3, B_1 to eq. (3) in the case of Π_{11} are shown by lines for case M1.5.

CONCLUSIONS

Conventional outer scaling of the turbulent stresses with τ_w collapses all compressible and incompressible profiles for $x_2/h > 0.35$. Similarly, $\tau_w\, u_{av} / h$ is the proper outer scale for the pressure-strain correlation, Π_{ij}. The significant difference of compressible and incompressible turbulent stresses in the near-wall region is linked to a reduction in the pressure-strain correlation. A variable-density ansatz, neglecting wave-propagation in the pressure equation, leads to a simplified Green's function solution which identifies the reduction of $\overline{\rho}$ with respect to its wall value as the primary reason for the observed decrease in Π_{ij}.

References

[1] Coleman G., Kim J., Moser R.: Turbulent Supersonic Isothermal-Wall Channel Flow. *J. Fluid Mech* **305**:159-183, 1995.

[2] Huang P., Coleman G., Bradshaw P.: Compressible Turbulent Channel Flows: DNS Results and Modeling. *J. Fluid Mech* **305**:185-218, 1995.

[3] Lechner R., Sesterhenn, J., Friedrich, R.: Turbulent Supersonic Channel Flow. *J. Turbulence* **2**:1-25, 2001.

[4] Morinishi Y., Tamano S., Nakabayashi K.: A DNS Algorithm Using B-Spline Collocation Method for Compressible Turbulent Channel Flow. *Comput. Fluids* **32**:751-776, 2003.

[5] Sesterhenn J.: A Characteristic-Type Formulation of the Navier-Stokes Equations for High Order Upwind Schemes. *Comput. Fluids* **30**:37, 2001.

[6] Adams N.A., Shariff K.: A High-Resolution Hybrid Compact-ENO Scheme for Shock-Turbulence Interaction Problems. *J. Comp. Phys.* **127**: 27, 1996.

[7] Lele S.K.: Compact Finite Difference Schemes with Spectral-Like Resolution. *J. Comp. Phys.* **103**: 16-42, 1992.

[8] Moser R., Kim J., Mansour N.N.: Direct Numerical Simulation of Turbulent Channel Flow up to $Re_\tau = 590$. *Phys. Fluids* **9**: 943-945, 1999.

[9] Kim J.: On the Structure of Pressure Fluctuations in Simulated Turbulent Channel Flow. *J. Fluid Mech* **205**:421-451, 1989.

ON THE SCALE SIMILARITY IN LARGE EDDY SIMULATION.

F. Gallerano, G. Cannata e E. Pasero

Dipartimento di Ingegneria Idraulica, Trasporti e Strade, Università degli Studi di Roma "La Sapienza

Email: *e.pasero@tin.it*

Among the most common LES models present in literature there are Eddy Viscosity-type models.
In these models the subgrid scale (SGS) stress tensor is related to the resolved strain rate tensor through a scalar eddy viscosity coefficient.
These models are affected by two fundamental drawbacks: they are purely dissipative, i.e. they cannot account for back scatter; they assume that the principal axes of the resolved strain rate tensor and SGS stress tensor are aligned.
Several authors, by means of both numerical and experimental tests, have proved that backscatter occurs and is significant, even in equilibrium flows, and there is no alignment between the strain rate tensor and the SGS stress tensor.
Scale similarity models (SSM) were created to overcome the drawbacks of eddy viscosity-type models. The SSM models, such as that of Bardina et al. and that of Liu et al., assume that scales adjacent in wave number space present similar hydrodynamic features.
This similarity allows to effectively relate the unresolved scales, represented by the Modified Cross tensor and the Modified Reynolds tensor, to smallest resolved scales represented by the modified Leonard tensor (Bardina et al.) or by a term obtained through multiple filtering operations at different scales (Liu et al.).
The SSM models unlike the eddy viscosity-type models, assume neither the local alignment of the resolved strain rate tensor to the SGS stress tensor nor the local balance between production and dissipation of SGS kinetic energy.
The models of Bardina et al. and Liu et al. are affected, however, by a fundamental drawback: they are not dissipative enough, i.e. they are not able to assure a sufficient energy drain from resolved scales of the motion to unresolved ones.
In this paper it is shown that such drawback is due to the fact that such models do not take into account the smallest unresolved scales where the most dissipation of turbulent SGS energy takes place.
Indeed in the Bardina Model. the principle of material Frame indifference imposes that the SGS stress tensor should be represented only by the modified Leonard tensor.
Thus the modified Cross tensor an modified Reynolds tensor are not taken into account and thus neither are the unresolved scales, where the most viscous dissipation occurs.
The Liu et al. model assumes that the SGS stress tensor is equal to the product of a scalar and a resolved stress tensor obtained performing a double filtering operation on the grid scale and on the test scale. Such scalar is computed by means of a Germano identity operated on a grid scale and on a test scale whose dimensions are four times as big.
Consequently the Liu et al. model represents the SGS stress tensor only through terms that are associated to a limited range of small resolved scales, lying between the SGS

kinetic energy production scales range and the SGS kinetic energy dissipation scales range.
In this paper a scale similarity LES model that is able to grant an adequate drain of energy from resolved scales to unresolved ones.
The SGS stress tensor is aligned with the modified Leonard tensor.
The coefficient of proportionality is expressed in terms of the trace of the modified Leonard tensor and in terms of the SGS kinetic energy (computed by solving its balance equation).
The validity of the proposed model was tested through channel flow simulations with friction-velocity-based Reynolds numbers ranging from 180 to 2340.

Two scale approach to anisotropic turbulence in He II

Tomasz Lipniacki
Institute of Fundamental Technological Research - Polish Academy of Sciences

Superfluid ^{4}He may be regarded as a mixture of normal fluid and superfluid, described by the velocity fields $\mathbf{V}_s$ and $\mathbf{V}_n$, and the density fields ρ_n and ρ_s, respectively. The rotation of superfluid is confined to one dimensional singularities called quantum vortices. Due to existence of these singularities, the superfluid component is coupled dissipatively to the normal one by the so-called mutual friction force $\mathbf{F}_{ns}$, which is proportional to the density of superfluid vortices L, and to the magnitude of counterflow $\mathbf{V}_{ns} = \mathbf{V}_n - \mathbf{V}_s$. At very low velocities the flows of normal and superfluid components are laminar and the quantum vortices form an ordered array of locally parallel lines; the whole system is described by the Hall Vinen Bakarevich Khalatnikov (HBVK) equations. At higher velocities the superfluid laminar flow develops into a superfluid turbulent flow in which quantum vortices form a chaotic tangle. The quasi isotropic tangle, which may be generated under the thermal counterflow, is described by the Vinen equation. There remain outstanding questions concerning highly anisotropic quantum turbulence, which may be produced mechanically (e.g. in Couette flow or spin-up), and which may not be described by either HBVK equations or Vinen equation. The theoretical difficulty in modeling anisotropic turbulence has been overcome recently be extensive numerical simulations in which the dynamics of quantized vortices is described by Biot-Savart law. Despite such simulation provide accurate description, they are restricted to relatively weak turbulence with low L.

In this study we propose an alternate approach: In macroscale scale we use the two-fluid model equations; the Euler equation for the superfluid component and the Navier Stokes equation for the normal component. These two equations are coupled by the mutual friction force $\mathbf{F}_{ns}$, which depends on the local line-length density L. The vortex density L at given point, say p, is calculated in a small volume Ω around p, based on the Vinen equation, which is modified to describe the evolution of line-length density of quantum tangle with net macroscopic vorticity. The generalized equation includes the drift of the anisotropic tangle caused by Magnus force. The volume Ω, must be enough large to contain a large number of vortex lines, but small when compared with the integral scale of the flow. It is assumed that the normal and superfluid velocity fields $\mathbf{V}_n$,$\mathbf{V}_s$, given in macroscale by Euler and Navier-Stokes equations, respectively, are constant in microscale, across small volume Ω. The proposed approach is, to some extent, similar to the non-local approximation (NLA), the numerical method proposed by Barenghi *et al.* (1997) to calculate the growth of the quantum tangle in imposed ABC flow of normal component. According to NLA the motion of vortex filaments is calculated using LIA, but in the superfluid velocity field, which is calculated in relatively small number of points using Biot-Savart law. In the incompressible approximation $\mathrm{div}\mathbf{V}_n = \mathrm{div}\mathbf{V}_s = 0$, the derived equations (after neglecting two terms in expressions for $\mathbf{F}_{ns}$ and $\mathbf{V}_L$) add up to the following closed system;

$$\rho_s\left(\frac{\partial \mathbf{V_s}}{\partial t} + \mathbf{V}_s \cdot \nabla \mathbf{V}_s\right) = -\nabla p_s - \mathbf{F}_{ns} \ , \tag{1}$$

$$\rho_n\left(\frac{\partial \mathbf{V}_n}{\partial t} + \mathbf{V}_n \cdot \nabla \mathbf{V}_n\right) = -\nabla p_n + \mathbf{F}_{ns} + \eta \Delta^2 \mathbf{V_n} \ , \tag{2}$$

with mutual friction force $\mathbf{F}_{ns}$ and local line-length density L given by

$$\mathbf{F}_{ns} = \alpha\ \kappa\ \rho_s\ L\ \Big(\mathbf{q} \times (\mathbf{q} \times \mathbf{V}_{ns}) - \frac{2}{3}\mathbf{V}_{ns}(1-q^2)\ \Big) \ , \tag{3}$$

$$\frac{\partial L}{\partial t} = \alpha\ I_0\ c_1\ (1-q^2)\ |\mathbf{V}_{ns}|\ L^{3/2} - \beta\ \alpha\ {c_2}^2\ (1-q^2)^2\ L^2 - \mathrm{div}\big(L\mathbf{V}_L\big) \ , \tag{4}$$

where $\mathbf{V}_L$ is the tangle drift velocity and $\mathbf{q}$, $|\mathbf{q}| = q \le 1$, the vector of tangle polarization

$$\mathbf{V}_L = \mathbf{V}_s + \alpha\ \mathbf{q} \times \mathbf{V}_{ns} \ , \qquad \mathbf{q} = \frac{\nabla \times \mathbf{V_s}}{\kappa L} \, . \tag{5}$$

In the above α is the nondimensional coefficient of mutual friction, β depends logarithmically to the tangle density, but in most cases remains of order of quantized circulation $\kappa = 9.97 * 10^{-4}\mathrm{cm}^2/\mathrm{s}$, c_1, c_2, I_0 are geometric measures of quasi isotropic tangle (with $\mathbf{q} = 0$) adopted after Schwarz (1998), corresponding, respectively, to the average curvature of vortex lines, average curvature squared, and averaged anisotropy of the binormal. To derive expressions for mutual friction force $\mathbf{F}_{ns}$ and local line-length density L we follow the method proposed by Lipniacki (2001) and assume that the distribution of the unit tangent to vortex lines in the tangle is the most probable distribution which results in a given tangle polarization $\mathbf{q}$. In simple words, our assumption implies that macroscopic vorticity is absorbed into the tangle and causes its directional polarization, which is consistent with simulation of rotating turbulence using Biot-Savart law description by Tsubota *et al.* (2003). In the case of stationary rotating turbulence Eq. (4) gives the line-length density with respect to cylinder angular velocity $\Omega = \omega_s/2$ and counterflow velocity $\mathbf{V}_{ns}$ in implicit form

$$L = \frac{L_H}{(1-q^2)^2}\ , \qquad L_H = V_{ns}^2 \Big(\frac{c_1\ I_0}{\beta\ c_2^2}\Big)^2, \tag{6}$$

where L_H is the steady-state line-length density resulting from same counterflow V_{ns} and $q = 0$. Anisotropy parameter q can be written as $q = L_\omega/L$, where $L_\omega = \omega_s/\kappa$ is the line-length density associated with rotation ω_s and zero counterflow. This prediction is the satisfactory agreement with Swanson *et al.* (1983) experimental data and simulations of Tsubota *et al.* (2003).

Equations (1-5) are supplemented by the boundary conditions for normal and superfluid velocity components, which in the simplest case, when there is no thermally induced flow, simplify to

$$\mathbf{n} \cdot \mathbf{V}_s|_{\partial U} = 0\ , \quad \mathbf{V}_n|_{\partial U} = 0. \tag{7}$$

Eq. (5) implies that when $\nabla \times \mathbf{V_s} \neq 0$, the vortex tangle (and the superfluid vorticity) moves across the counterflow. This implies that the boundary conditions must include additional condition connected with the rate of generation (or annihilation) of vortex lines at the wall. This condition must include some information about surface roughness. If the wall is perfectly smooth, the vortices can slip over and, provided that (7) is satisfied, there is no vorticity production at the wall; however, if the tangle drifts towards the wall, the line-length may annihilate. If the boundary is not perfectly smooth, pinning leads to the elongation of vortices, which results in a boundary production term proportional to the tangle density at the boundary.

The system of equations (1-5) was tested by applying it to the problem of formation of the shear flow between two parallel infinite material surfaces $z = 0$ and $z = D$. We consider the case, in which for $t < 0$ both material surfaces remain at rest, and then at $t = 0$, one of them starts moving along x axis with constant velocity V. We assumed that there is some initial density of remnant vortices L_0. The following scenario is observed. The normal component starts moving due to the viscosity forces, this introduces the velocity difference between normal and superfluids components $\mathbf{V}_{ns}$. The counterflow $\mathbf{V}_{ns}$ makes that the line-length density grows up (Eq. 4), and the two components become coupled by the mutual friction. The fact that superfluid velocity tends to match with normal velocity makes that $\boldsymbol{\omega}_s \neq 0$, which implies the polarization and drift of the tangle. After sufficiently long time the shear flow is formed.

There are three characteristic regimes with respect to the value of $D\ V$:
I - For large $D\ V$ the characteristic time of tangle generation is shorter than the drift time, in which the vortices can propagate across the vessel. This implies that the drift can be neglected. Moreover, until the components are not locked together, the tangle is almost anisotropic.
II - For small $D\ V$ the line generation is slow and the tangle is highly polarized. The drift term makes that vortex lines are efficiently swept out of the region where the counterflow exists. As the result there are two characteristic regions in the flow. In one of them the counterflow is almost zero and the quantum vortices form an ordered array of lines, and in the second region counterflow is non-zero, but there are few vortices.
III - For intermediate $D\ V$ the drift term in the modified Vinen equation is comparable with the generation term. There are three regions; of high tangle polarization in which the components are locked together, of intensive vortex generation, and of relatively dilute tangle, where the superfluid velocity is almost constant.

References

Barenghi, C. F., Samuels, D.C., Bauer, G. H. & Donnelly, R. J. *Phys. Fluids* **9** (9), 2631 (1997).
Lipniacki, T., *Phys. Rev.* B **64**, 214516 (2001).
Schwarz, K. W. *Phys. Rev.* B, **38** 2398 (1988).
Swanson, C.E. Barenghi, C. F. & Donnelly, R. J. *Phys. Rev. Lett* **50**, 190 (1983).
Tsubota, M., Araki, T. & Barenghi, C. F. Phys. Rev. Lett. **90**, 205301-1 (2003).

OPTIMIZATION OF AN IMPLICIT SUBGRID-SCALE MODEL FOR LES

S. Hickel*, S. Franz*, N.A. Adams*, P. Koumoutsakos**
*Dresden University of Technology, Institute of Fluid Mechanics, 010162 Dresden, Germany
**ETH Zürich, Institute of Computational Sciences, Switzerland

Summary We give a summary of the derivation of an implicit subgrid-scale model for LES which is obtained from a new approach for the approximation of hyperbolic conservation laws. Adaptive local deconvolution is performed using a quasi-linear solution-adaptive combination of local interpolation polynomials. The physical flux function is substituted by a suitable numerical flux function. The truncation error has physical significance and effectively acts as subgrid-scale model. It can be determined by a modified-differential-equation analysis and is adjustable through free parameters. Computational results for Burgers equation show that the model with parameters identified by evolutionary optimization give significantly better results than other models.

INTRODUCTION

The key idea of implicit subgrid-scale (SGS) modeling is that the truncation error of an under-resolved discretization can be utilized to model the effects of the unresolved scales. In order to reveal the connection of implicit to explicit SGS models the differential equation has to be analysed [1, e.g.]. Without loss of generality we initially focus on a generic scalar conservation law $\partial_t u + \partial_x F(u) = 0$. The finite-volume semi-discretization

$$\partial_t \bar{u}_N + G * \partial_x F_N(u_N) = \varepsilon_{SGS} \tag{1}$$

is based on applying an explicit spatial filtering $\bar{u} = G * u$, where G is the top-hat function with the spatial averaging scale h. The grid function $\bar{u}_N = \{\bar{u}_j\}$ results from the spectrally accurate projection $\bar{u}_j \approx \bar{u}(x_j)$. The cutoff frequency $\xi_C = \pi/\Delta$ is linked to the spatial grid spacing Δ and to the spatial filter scale $h = \Delta$. In the case of LES, characterized by (under-resolved) finite grid spacing, a non-closed subgrid-scale error $\varepsilon_{SGS} = G * \partial_x F_N(u_N) - G * \partial_x F_N(u)$ remains on the right hand side due to the nonlinearity of $F(u)$. Common practice is to close (1) by an explicit model of the SGS stresses τ which approximates $\varepsilon_{SGS} = -\partial_x \tau$.

CONSTRUCTION OF THE IMPLICIT SGS MODEL

As shown in [2] it is desirable to exploit the deconvolved solution $u_N = G^{-1} * \bar{u}_N$. Since the used top-hat filter is not fully invertible the application of any approximate inverse $\tilde{u}_N = \tilde{G}_N^{-1} * \bar{u}_N$ results in an additional error term. Finally, we replace the physical flux function by a more suitable numerical flux function $\tilde{F}_N$. If the resulting cumulative numerical truncation error $\varepsilon_N = G * \partial_x F_N(u_N) - G * \partial_x \tilde{F}_N(\tilde{G}_N^{-1} * \bar{u}_N)$ approximates ε_{SGS}, the implicit SGS model contained in the numerical discretization

$$\partial_t \bar{u}_N + G * \partial_x \tilde{F}_N(\tilde{u}_N) = 0 \tag{2}$$

substitutes the explicit model. Thus the construction of an implicit SGS model amounts to devise an appropriate adaptive deconvolution operator and a suitable numerical flux function. Consistently with the framing finite-volume approach, the top-hat filtering of the one-dimensional flux divergence in (2) returns the difference of the flux trough the cell faces $x_{j\mp 1/2}$, while the filtered solution $\bar{u}_N$ is known at the cell centers only. Following the suggestion in [3] intended for Essentially-Non-Oscillatory (ENO) schemes, the required reconstruction of point values of the deconvolved solution can be determined by the interpolation polynomials $u(x_{j\pm 1/2}) = \sum_{l=0}^{k-1} c^{\mp}_{j,k,r,l} \bar{u}_N(x_{j-r+l}) + \mathcal{O}(h^k)$, where the coefficients $c^{\mp}_{j,k,r,l}$ contain the grid-dependend deconvolution and interpolation operator which can be computed with a rule given by [3]. The shift $r = 0, \ldots, (k-1)$ characterises the treated stencil. The main idea of weighted ENO is the linear combination of reconstructions of a single order $k \equiv K$ to obtain a approximation of order $2K-1$ in smooth regions. We extend this scheme by also including the computationally cheaper reconstructions of order $k = 1, ..., K$

$$\tilde{u}^{\mp}_N(x_{j\pm 1/2}) = \sum_{k=1}^{K} \sum_{r=0}^{k-1} \omega^{\mp}_{k,r}(x_j) p^{\mp}_{k,r}(x_{j\pm 1/2}) \qquad \text{with} \qquad p^{\mp}_{k,r}(x_{j\pm 1/2}) = \sum_{l=0}^{k-1} c^{\mp}_{j,k,r,l} \bar{u}_N(x_{j-r+l}). \tag{3}$$

Since highest possible order of accuracy is not required, free parameters can be introduced. The weights $\omega^{\mp}_{k,r}(x_j)$ are computed from a solution-dependend function $\beta_{k,r}(x_j)$ which is used as smoothness measure and from a set of constant parameters $\gamma^{\mp}_{k,r}$ which denote stencil-selection preferences in particular allow to adjust the truncation error [4] .

REPRODUCTION OF EXPLICIT SGS MODELS

Since the model should depend on the kind of nonlinearity, the following analysis is limited to the viscous Burgers equation $F(u) = u^2/2 - 1/Re\ \partial_x u$, which is the relevant model for the Navier-Stokes equation. As mentioned above, the dominating terms of the implicit SGS model are identified by comparing the modified differential equation (2) with

the exact LES equation (1). The model parameters can be adjusted in order to reproduce approved explicit SGS models. We found a set of parameters for $K = 3$ that matches with the standard Smagorinsky model $-\partial_x \tau = 2C_S h^2 |\partial_x \bar{u}| \partial_x^2 \bar{u}$ up to order $\mathcal{O}\left(h^3\right)$

$$\varepsilon_N = 2\, C_S\ |\partial_x \bar{u}|\ \partial_x^2 \bar{u}\, h^2 - \frac{1}{6}\, C_S\ |\partial_x \bar{u}|\ \partial_x^4 \bar{u}\, h^4 + \mathcal{O}\left(h^6\right)\ . \tag{4}$$

For validation, simulations of statistically forced and decaying turbulence of the viscous Burgers equation were performed with this implicit model. In both cases we observe a good agreement with the reference data computed with a de-aliased spectral discretization where the Smagorinsky SGS model is added explicitly (Fig. 1).

OPTIMIZATION OF THE IMPLICIT SGS MODEL

If computations with the implicit model produce results of comparable quality as common explicit models, the benefit is in the implicit character which removes computational overheads of explicit SGS models. Other parameters, however, may yield much better results than those matched to explicit models. In order to identify them, one has to evaluate the implicit model by defining a cost function for every test case. For the stochastically forced Burgers equation a suitable criterion is the grade of agreement of the inertial range of the time-averaged energy spectrum with theoretical predictions. There are, however, two major difficulties: First the dependency of parameters and spectra is unknown, and second, the effects of random forcing result in an ambiguous cost function. Therefore traditional optimization strategies are not applicable. The idea of Evolutionary Optimization (EO) adopts concepts with random components as selection, recombination and mutation [5]. The application on the above mentioned test case shows nearly monotone convergence which slows down after 200 generations and leads to a set of parameters that results in the effective model

$$\varepsilon_N = \left(-0.11108\ \left(\partial_x^2 \bar{u} \partial_x \bar{u} + \partial_x^3 \bar{u} \bar{u}\right) + 0.66667\, |\partial_x \bar{u}| \partial_x^2 \bar{u}\right) h^2 + \mathcal{O}\left(h^4\right)\ . \tag{5}$$

Computational results for stochastically forced Burgers equation show that these model parameters give significantly better results than parameters from other models (Fig. 1).

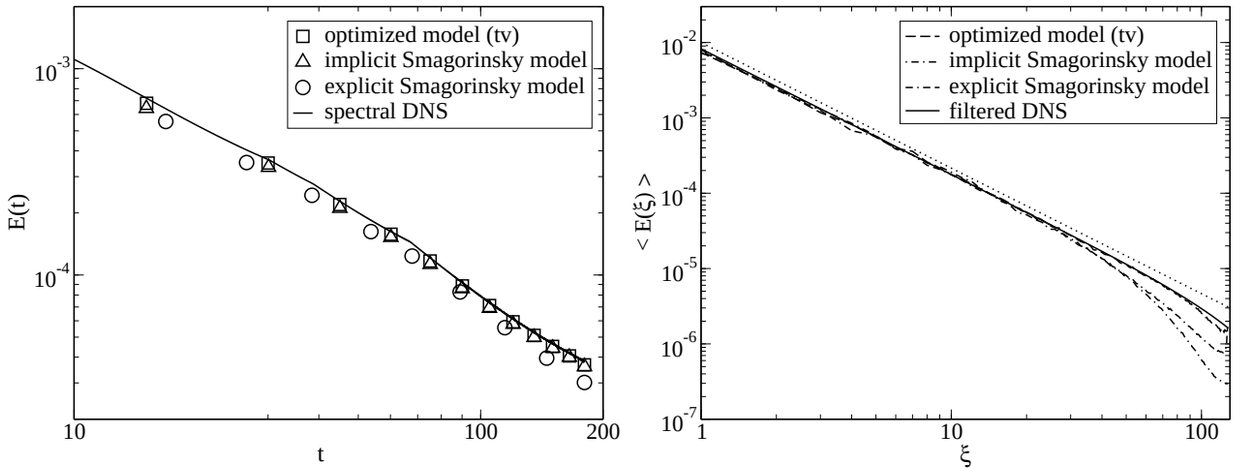


Figure 1. *Left:* decaying turbulence: temporal evolution of total energy; *Right:* forced turbulence: time-averaged energy spectra

CONCLUSIONS

Subgrid-scale model and discretization of a conservation law can be merged. Systematical optimization of the presented implicit SGS model results in an superior model, which has been successfully applied to the one-dimensional Burgers equation. The extension of the optimization to three-dimensional Navier-Stokes equation is subject of ongoing work.

References

[1] Margolin, L.G. ; Rider, W.J. (2002) A rationale for implicid turbulence modelling. Int. J. Numer. Meth. Fluids 39 : 821-841
[2] Adams, N.A. ; Stolz, S. (2002) A subgrid-scale deconvolution approach for shock capturing. J. Comput. Phys. 178 : 391-426
[3] Shu, C.W. (1997) Essentially non-oscillatory and weighted essentially non-oscillatory schemes for hyperbolic conservation laws. Technical Report 97-65, NASA Langley Research Center, Hampton, Virginia
[4] Adams, N.A. ; Hickel, S. ; Franz, S. (2004) Implicit subgrid-scale modeling by adaplive deconvolution. J. Comput. Phys. (in press)
[5] Beasley, D. ; Bull, D., Martin, R. (1993) Overview of Genetic Algorithms Part I and II. University Computing

XXI ICTAM, 15–21 August 2004, Warsaw, Poland

STUDY OF THE TURBULENT ENERGY SPECTRUM BUILD UP IN AN EXPERIMENTAL VORTEX BURST

Yannis Cuypers †, Agnès Maurel ‡ & Philippe Petitjeans †
† *Laboratoire de Physique et de Mécanique des Milieux Hétérogènes*
‡ *Laboratoire Ondes et Acoustique*
Ecole Supérieure de Physique et de Chimie Industrielles,
10 rue Vauquelin, 75005 Paris - France.

Summary We present an experiment where a stretched vortex is experiencing quasi-periodical turbulent bursts inside a laminar environment. We characterize the vortex bursts by hot film measurements. It is shown that the turbulent bursts are responsible for the build up of a Kolmogorov $k^{-5/3}$ energy spectrum over one decade. The build up of this turbulent spectrum with time is investigated and compared with the Lundgren mechanism for the energy transfer towards small scales [1].

INTRODUCTION

In 1982 Lundgren has proposed a model of turbulent fine scales in the form of a stretched spiral vortex. The main result of this model is that the time averaged spectrum of the structure shows a Kolmogorov $k^{-5/3}$ fall off. The Lundgren's mechanism for the built up of the energy cascade has initiated a field of research whose results show nice predictions for turbulent flows. However, experimental evidences validating this model are still lacking. In our experiment we investigate the energy cascade build up resulting of a vortex burst. We show some common features with the Lundgren mechanism for the energy cascade [2].

EXPERIMENTAL SET UP

A stretched vortex is generated in a low velocity hydrodynamic channel. A small step added to a laminar boundary layer profile in the bottom wall produces the initial vorticity that is strongly enhanced by the stretching produced by sucking the flow through slots on each lateral wall (Fig.1). Varying the experimental parameters make two regimes occur: in the first one, the vortex is stable (Fig.2 a,b), in the second one the vortex is experiencing periodical bursts (Fig.2 c,d). The flow is characterized by the following experimental values: $Re = 4000, R = 3$cm (lateral extension of the burst), a=[1-10 s^{-1}] (stretching)

AN EXPERIMENTAL VORTEX WITH A TURBULENT BEHAVIOR, COMPARISON WITH THE LUNDGREN VORTEX

We focused on the second regime, where we characterize the vortex evolution via hot film and PIV measurements. The hot film probe is set parallel to the z axis and measure $U = \sqrt{u_r^2 + u_\theta^2}$. A typical signal obtained from hot film measurements shows the quasi-periodical character of the bursts (Fig3). Each cycle is composed of two parts: a laminar part, for which the vortex is still coherent, showing a smooth increase of the velocity, and a turbulent part associated to the vortex burst, showing rapid fluctuations of the velocity.

Using an appropriate rescaling of the hot film data and a local Taylor hypothesis to obtain spatial scales, we compute the velocity spectra of the turbulent parts. When the spectrum is calculated over the whole lifetime of the burst, a turbulent behavior with Kolmogorov $k^{-5/3}$ spectrum is obtained near the place where the vortex explodes (Fig.4). An inertial range is found between $k_m = 0.2$ cm^{-1} and $k_M = 2$ cm $^{-1}$. The estimation of the inertial range of a Lundgren vortex for our experimental values of a, Re, R gives $k_m \simeq 0.3$ cm^{-1} and 10 cm^{-1} $\leq k_M \leq$ 34 cm^{-1} that reasonably compare with experimental inertial range.

Instantaneously a spiral vortex give a $k^{-\sigma}$ energy spectrum, where σ is dependant on the flow field characteristics. It is one remarkable property of the Lundgren vortex that the time averaging over the lifetime of the vortex always results in the $k^{-5/3}$ spectrum, independently of the spiral structure considered. To better understand the energy cascade build up and to go further in the comparison with the Lundgren model, we focus on the temporal evolution of the velocity spectra during the vortex burst. In order to observe an evolution in the spectra slopes, we compute the spectra over small windows $(t, t + \Delta t)$ within the turbulent parts, so that each spectrum gives a quasi-instantaneous picture of the vortex bust energy distribution among scales at different times. We find that the slope of the spectra is time dependant and varies between a value close to -1 at the beginning of the burst to a value close to -2 at the end of the burst (Fig5). However spectrum built over the whole burst lifetime results in the $k^{-5/3}$ spectrum, as it is the case for the Lundgren vortex.

References

[1] T. S. Lundgren, Phys. Fluids, **25**: 2193–2203 (1982).

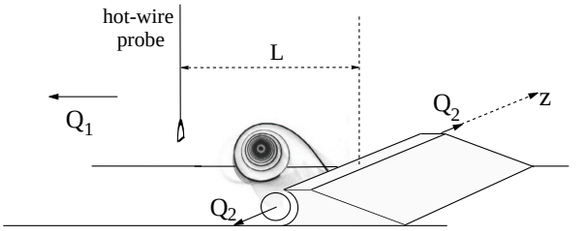


Figure 1. Experimental set-up.

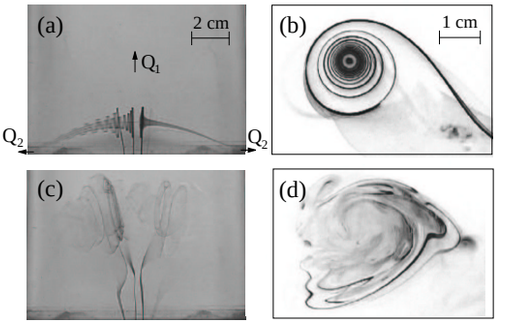


Figure 2. Sketch of the vortex cycle at $Q > Q_c$: (a-b) first stage of the cycle, the vortex is still coherent (a) side view and (b) top view; (c-d) second stage of the cycle, the vortex breaks into a turbulent burst (c) top view and (d) side view.

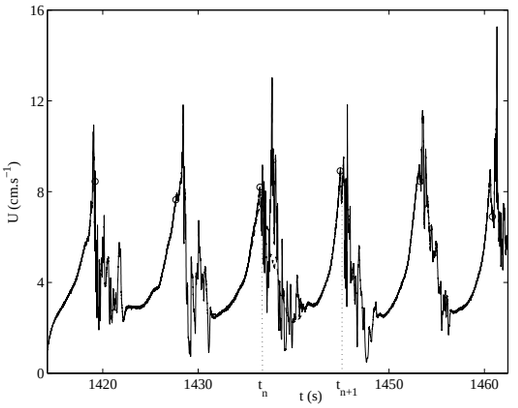


Figure 3. Close up of the temporal recording over several vortex cycles $U(t_a)$, $\circ$ indicates the times t_n at which the vortex breaks on each cycle;

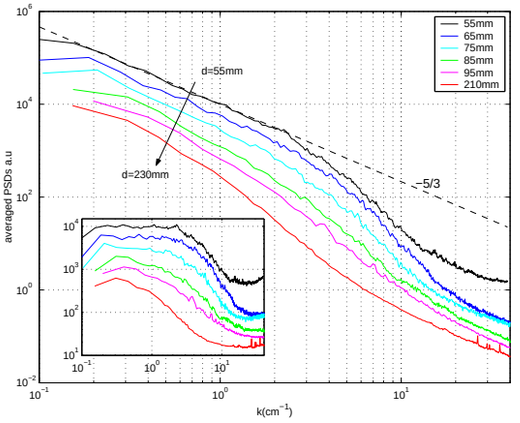


Figure 4. Experimental velocity PSD's averaged over the whole cycle for various distances d of the probe from the z-axis (d = 55, 65, 75, 85, 95, 135 and 230 mm). Subplot shows the compensated spectra $k^{5/3}E(k)$

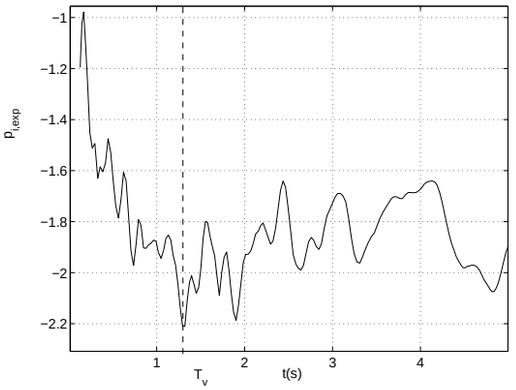


Figure 5. k-slope p of the quasi-instantaneous velocity PSDs as a function of time , T_v is the burst lifetime.

XXI ICTAM, 15–21 August 2004, Warsaw, Poland

EMPIRICAL GALERKIN MODELS FOR INCOMPRESSIBLE FLOW — PRESSURE-TERM AND 'SUBGRID' TURBULENCE REPRESENTATIONS

Bernd R. Noack*, Paul Papas**, Peter A. Monkewitz**, Marek Morzyński*** & Gilead Tadmor****
*Hermann-Föttinger-Institut für Strömungsmechanik, Technische Universität Berlin HF1, Strasse des 17. Juni 135, D-10623 Berlin, Germany
**Fluid Mechanics Laboratory (LMF), Swiss Federal Institute of Technology (EPFL), CH-1015 Lausanne, Switzerland
***Institute of Combustion Engines and Basics of Machine Design, Poznań University of Technology, ul. Piotrowo 3, PL 60-965 Poznań, Poland
****Department of Electrical and Computer Engineering, Northeastern University, 440 Dana Research Building, Boston, MA 02115, U.S.A.

Summary Necessary ingredients of *accurate* empirical Galerkin models for incompressible free and wall-bounded shear flows are discussed. These models are based on the Karhunen-Loève (K-L) decomposition of a Navier-Stokes simulation and a Galerkin projection on the Navier-Stokes equation. Specifically, a novel analytical pressure-term representation is first developed and shown to be necessary for accurate Galerkin systems of near-field wakes and of mixing layers. Secondly, a hierarchy of 'subgrid' turbulence models based on Rempfer's (1991) modal eddy viscosities is presented and shown to be helpful if a low-dimensional K-L ansatz does not resolve a significant portion of the fluctuation energy. Finally, the role of 'missing' phase space directions in the K-L ansatz is revisited and additional modes are proposed. The proposed generalizations and improvements have been integrated in a modular Galerkin 'tool-box' with a hierarchy of procedures to determine model coefficients.

INTRODUCTION

Most 'empirical' Galerkin models are based on Karhunen-Loève (K-L) decompositions of numerical simulations or experimental data [1]. Low-dimensional Galerkin models of coherent structures are often helpful for testing physical understanding. More recently, many low-dimensional modelling efforts are also targeting flow control applications for two main reasons: Such 'plant models' allow the use of all the powerful tools of control theory and their simplicity allows quick exploratory actuation studies.

FRAME-WORK OF THE EMPIRICAL GALERKIN METHOD

The frame-work of the empirical Galerkin method [1] is generalized by adding physical modes to the K-L decomposition and by incorporating additional physical processes in the Galerkin system. The generalized Galerkin approximation for the velocity field of an incompressible flow is taken to be

$$\mathbf{u} = \sum_{i=0}^{N_{KL}} a_i \, \mathbf{u}_i + \sum_{i=N_{KL}+1}^{N} a_i \, \mathbf{u}_i \tag{1}$$

where $a_0 = 1$ and $i = 0, \ldots, N_{KL}$ are indices of the K-L modes $\mathbf{u}_i$ and their Fourier coefficients a_i. Non-empirical modes may be added and are indicated by the index $i = N_{KL}+1, \ldots, N$. The Galerkin system is given by

$$\frac{d}{dt} a_i = \sum_{j=0}^{N} (\nu \, l_{ij} + l_{ij}^{+}) \, a_j + \sum_{j=0}^{N} \sum_{k=0}^{N} (q_{ijk} + q_{ijk}^{+}) \, a_j \, a_k \tag{2}$$

where $\nu = 1/Re$. The coefficients l_{ij} arise from the viscous term, and q_{ijk} from the convection term. Coefficients with the superscript '$+$' may be added to incorporate the effect of the pressure term and to represent non-resolved 'subgrid' fluctuations. The 'standard' model is defined by $N = N_{KL}$, $l_{ij}^{+} \equiv 0$, and $q_{ijk}^{+} \equiv 0$.

RESULTS FOR FREE AND WALL-BOUNDED SHEAR FLOWS

Pressure-term representation

A pressure-term representation has been analytically derived from the pressure Poisson equation [2]. The main ingredients are the correct implementation of the boundary conditions and a computationally manageable algorithm. This pressure model leads to an additional quadratic term q_{ijk}^{+} in Eq. (2). This improvement can have a drastic effect on the accuracy of the Galerkin model for convectively unstable shear flows (see Fig. 1) — even if the fluctuation energy is fully resolved by the standard Galerkin approximation with $N = N_{KL}$. On the other hand, incorporating the pressure term in models of self-excited flows, such as near-wakes, appears less important.

Unresolved 'subgrid' turbulence representation

At higher Reynolds-numbers, a low-dimensional ansatz (1) can only resolve a fraction of the fluctuation energy. The effect of the neglected 'subgrid' fluctuations on the resolved coherent structures is modelled by an ansatz of the form

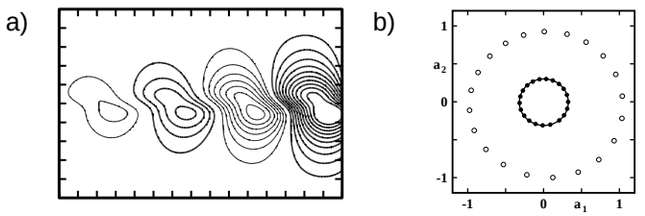


Figure 1. 4-dimensional Galerkin model of a 2D Kelvin-Helmholtz instability with the inlet profile $u = 2/3 + 1/3 \tanh y$. (a) Streamlines of the fluctuation in the computational domain. The tick marks are separated by the vorticity thickness. (b) Phase portraits of the Navier-Stokes simulation and Galerkin models based on the first two Fourier coefficients a_1, a_2 of the Galerkin approximation (1). They show that the limit cycle of the Galerkin model with pressure-term representation ('•') essentially coincides with the Navier-Stokes attractor (solid curve), whereas the omission of the pressure term ('○') gives rise to amplitudes which are far too large.

$l_{ij}^{+} = \nu_{T,i} l_{ij}$ [3]. This ansatz has been generalized by a hierarchy of algorithms for the determination of the modal eddy viscosities $\nu_{T,i}$ directly from simulation data and without solution matching [4]. Fig. 2 shows the improvements achieved for a transitional wall-bounded shear-layer — including also a pressure-term representation.

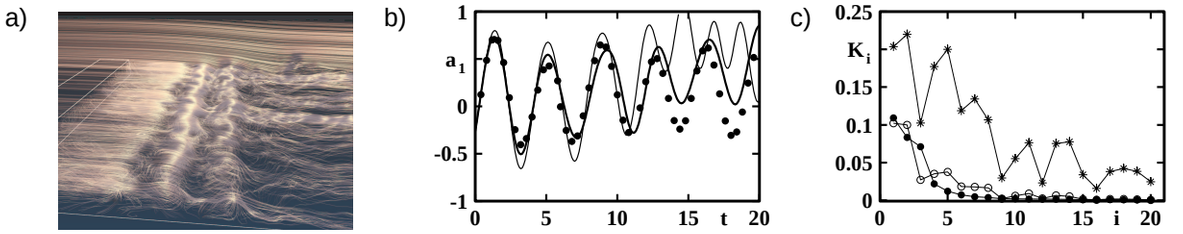


Figure 2. 20-dimensional Galerkin model of the transitional flow over a back-ward facing step at $Re_h = 3000$. (a) Snapshot of the streamlines (the step is indicated by a white frame) [5]. (b) The Galerkin model with the turbulence representation (thick curve) follows the LES simulation (•) over on a longer time than the model without turbulence representation (thin curve). (c) Modal energy distribution K_i (i being the mode index). The LES results (•) are significantly better predicted with the enhanced turbulence model (○) than without it (∗).

Re-construction of missing phase-space directions

Finally, the range of validity of the Galerkin model is enhanced to not only capture the post-transient perturbation dynamics but also to incorporate the basic (unstable) steady Navier-Stokes solution and the transient dynamics. This is achieved by adding non-empirical modes obtained from a weakly non-linear stability analysis [6].

CONCLUSIONS

The proposed generalisations and improvements of the empirical Galerkin method include (i) a pressure-term representation for open flows, (ii) a representation of unresolved 'subgrid' turbulence at high-Reynolds numbers and (iii) the addition of non-empirical modes for non-equilibrium conditions. These improvements are additive and therefore it has been possible to incorporate them in a modular 'tool-box' with different levels of simplifications. This tool-box significantly enlarges the class of flows for which Galerkin models can be usefully constructed. In addition, the dynamic range of the Galerkin system has been markedly enhanced by the proposed improvements. This effect is exploited in flow control applications [7] which shall be presented in another contribution at this conference.

References

[1] HOLMES, P., J. LUMLEY & G. BERKOOZ (1998) *Turbulence, Coherent Structures, Dynamical Systems and Symmetry*, Cambridge University Press, Cambridge.

[2] NOACK, B.R., P. PAPAS & P.A. MONKEWITZ (2004) "The need for a pressure-term representation in empirical Galerkin models of incompressible shear flows", accepted for publication in *J. Fluid Mech.*

[3] REMPFER, D. (1991) *Kohärente Strukturen und Chaos beim laminar-turbulenten Grenzschichtumschlag* (transl.: coherent structures and chaos in the laminar-turbulent boundary-layer transition), PhD thesis, Universität Stuttgart.

[4] TADMOR, G. & B.R. NOACK (2004) "Dynamic estimation for reduced Galerkin models of fluid flows", Paper **WeM18.1**, *2004 American Control Conference*, Boston, MA, U.S.A.

[5] WEINKAUF, T., H.-C. HEGE, B.R. NOACK, M. SCHLEGEL & A. DILLMANN (2003) Coherent structures in a transitional flow around a backward-facing step, *Phys. Fluids* **15**, S3.

[6] NOACK, B.R., K. AFANASIEV, M. MORZYŃSKI, G. TADMOR & F. THIELE (2003) A hierarchy of low-dimensional models for the transient and post-transient cylinder wake, *J. Fluid Mech.* **497**, 335–363.

[7] GERHARD, J., M. PASTOOR, R. KING, B.R. NOACK A. DILLMANN, M. MORZYŃSKI & G. TADMOR (2003*a*) Model-based control of vortex shedding using low-dimensional Galerkin models, *AIAA Paper* **2003-4262**.

Orthonormal Wavelet Analysis of CGT in Fully Developed Asymmetric Turbulent Channel Flow

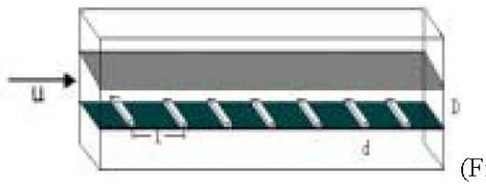
(Shanghai University, Shanghai Institute of Applied Mathematics and Mechanics, Shanghai 200072)

1. **Introduction** One of fundamental characteristics of turbulence is its stronger transport than laminar flows. In most of turbulent models, gradient transport assumption is adopted, which assumes that momentum, scalar flux and energy flux are transported towards the direction where mean velocity or scalar decreases. In fact, underlying of gradient transport is Fourier law. However it is well known in laboratory and engineering that counter gradient transport (abbr. CGT) phenomena exist (Jiang et al 2000). For example, there exists a region in the central region of fully developed asymmetric channel where $< uv >$ and $\partial U / \partial y$ have the same sign, that means momentum is counter gradient transported. Traditional cascade theory （Kolmogorov 1941） can't explain these phenomena. Mechanisms and reasons of CGT phenomena still remain open. Results obtained till now only show that coherent structures may be one of many reasons.

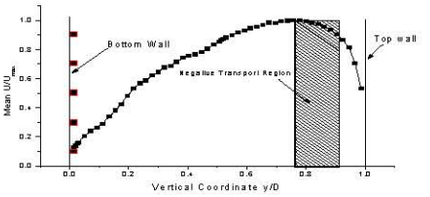
In this paper, four families of orthogonal wavelets are applied to investigate CGT phenomena in the fully developed asymmetric flow. Comparing to continuous wavelets, orthogonal wavelets are mutual orthogonal to each other and remain the original information. So orthogonal wavelets are more reliable to use when investigating the statistics of turbulent flows (Yamada & Ohkitani 1990, Meneveau 1991, Mouri et al 1999).

2. **Analytical method** Due to the uncertainty principle, the spatial localization and temporal localization are affected each other. So in this paper, following the work of Mouri et al (1999), four families of orthogonal wavelets are used: Haar wavelet, Db20 wavelet, Meyer wavelet, Harmonic wavelet. It has been stated in Mouri et al (1999) that most spatial localization is obtained for Haar wavelet, while most scale (frequency) localization is obtained for Harmonic wavelet. The localization of other two wavelets lie between Haar and Harmonic wavelets.

3. **Experiment** The experimental scheme is shown in fig.1 (Lu et al 2001). The asymmetry is introduced by roughening the bottom wall while top wall remains smooth. By roughening the wall, small ribs with length d=0.003m and width 0.22m are glued on the bottom wall. The measuring instrument is TSI9100－9 laser Doppler velocimetry made by TSI company. Data collection and analysis are completed by the accompany software FIND (Flow Information Display).



(Fig.1)

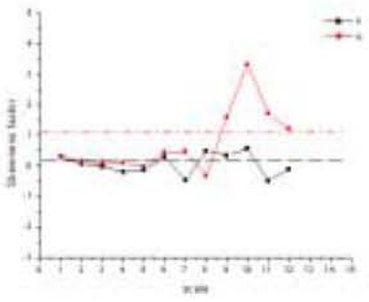


(Fig.2)

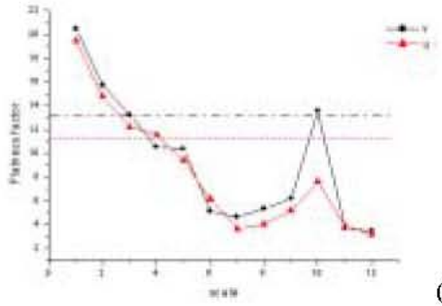
CGT region in fully developed section is sketched in fig. 2

4. **Main Results (**Statistical Characteristics, turbulent structure**)**

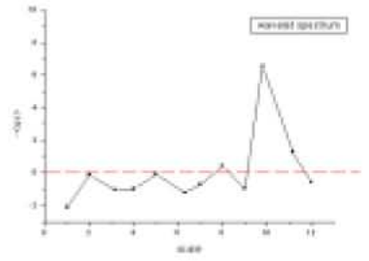
Fig 3a shows the skewness factor on each scale of streamwise and longitudinal velocity using four families wavelets (same results) in CGT region. It is evident that the skewness factors are functions of scales and aren't zero on each. It should be emphasized that skewness factor on scale 10 deviates zero more. Fig3b gives the flatness factors on each scale. For flatness factors, we could see that flatness factors decrease before scale 6, but begin to increase from scale 7 and reach the maximum at scale 10. From scale 11, they decrease again. There sre some difference between present results and those of Meneveau(1991), Lili (2001), Mouri et al(1999). Our observations show that intermittency between scale 6 and 10 is increased. The results of PDFs (not listed here) for each scale also indicate that intermittency increases with the scale. Furthermore when scale is increasing, PDF is approaching Gaussian distribution. But scale 9,10 and 11 needs more attention: scales 9,11 approaches distribution Gaussian distribution more than scale 10. Combining the results for skewness and flatness factors, it could be seen that in CGT region, the intermittency of small scales are generally stronger than larger scales, but CGT causes intermediate scale(s) more intermittent than larger and smaller scales.



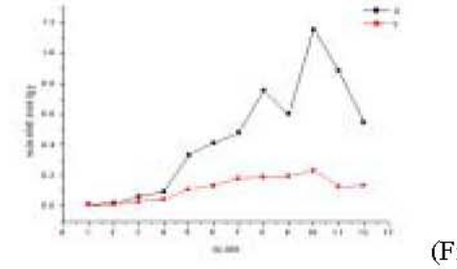
(Fig.3a)



(Fig.3b)



(Fig.4)



(Fig.5)

Fig4 gives the wavelet cross spectrum for Reynolds shear stress at the point in CGT region. It is evident that different scales make different contributions to Reynolds shear stress. The maximum contribution comes from scale at 10 and is positive, which means momentum transport is local CGT. Other scales give negative contributions to Reynolds stress, which means that momentum transport is gradient transport. Reminding that Reynolds stress is positive here, so it is evident that structures with scale 10 lead to CGT phenomena. For other points, although local CGT and gradient transport coexist, but total momentum transport is gradient transport. For example, for Ansym3 where $\partial U/\partial y < 0$, $-uv > 0$. Scales 8 and 11 give negative contributions to Reynolds stress while other scales give positive contributions. But total contributions are positive, which means total transport is gradient transport.

There still exist many opinions about principal scale of coherent structures, including maximal energy method (Jiang Nan et al 1998), energy method (Liandrat et al 1990), energy method (Farge 1992) and de-noising method (Szilagyi et al 1999). In this section, we will extend the maximal energy method for CWT to DWT.

By using the method given above, the ration is constant on all scales for white noise. Fig 5 gives the principal scale of coherent structures. Here only the results for Db20 are given. It could be observed that the principal scales are scale 10 in CGT, 5 in asym2, 5 in asym3 and 7 in asym1. It should be noted that scale 10 for CGT region is just the scale that determines the global CGT phenomena.

5. Conclusion

It is well known that random, multiple scale and structures are most essential characteristics of turbulence. Thus wavelet analysis is a suitable tool to investigate turbulence. In this paper orthogonal wavelets are applied to study the counter gradient transport phenomena in fully developed asymmetric channel flow. We study on each scale the flatness, skewness factors, probability density functions, scale-scale and velocity-velocity correlations, the principal scale of coherent structures. Finally we investigate the relationship between CGT phenomena, principal scale of coherent structures and Non-Gaussian characteristics of turbulence.

The results show that in CGT region, skewness and flatness factors deviate strongly the corresponding values of Gaussian distribution on certain scale(s). PDFs on each scale confirm this observation. Scale-scale correlation and velocity-velocity correlation give further support that CGT phenomena will cause certain scale more intermittent. Cross wavelet spectra indicate that local CGT phenomena could be present at different scales.

Investigation of principal scale of turbulent coherent structures shows that, when that scale contributes most to Reynolds stress and causes local CGT phenomena at the same time , the total momentum is global counter gradient transported.

XXI ICTAM, 15–21 August 2004, Warsaw, Poland

THE CELLULAR STRUCTURE AND ITS TRACKS OF A $\mathrm{H_2/O_2/AR}$ DETONATION WAVES

X. Y. Hu*, J. Czerwinska* N. Adams*, B. C. Khoo**
*Technical University of Dresden, Dresden 01062, Germany
**National University of Singapore, Singapore 119260, Singapore

Summary In this paper, the cellular structure and its tracks of a two-dimensional ordinary detonation wave in low pressure $\mathrm{H_2/O_2/Ar}$ mixture simulated with detailed chemical reaction model, high order scheme and high resolution grids are investigated. The regular cellular structure is produced by introducing perturbations in the reaction zone of a steady one-dimensional detonation wave. The calculated structure shows a double-Mach like strong type configuration, in which strong ignition is observed behind the transverse wave. It is also observed that there are three different structure tracks associated with different triple points or the kink on the transverse wave. The comparisons with previous experiments indicates the presence of strong structure for an ordinary detonation.

INTRODUCTION

It is well known that gaseous detonation wave has cellular structure. The tracks of structure recorded on smoke foils have been observed in experiments, and the regions enclosed by these tracks are called detonation cells. The structure usually involves triple-wave/Mach configuration with the combination of incident shock wave (I), Mach stem (M) and transverse wave (T). Two types of structure, i.e the weak structure and the strong structure, are observed in experiments. The weak structure is characterized by single-Mach configuration with the associated transverse wave being merely shock wave, while the strong structure is characterized by multi-Mach configuration with much stronger transverse wave leading to strong ignition. It is widely accepted that, in a marginal detonation, the cellular structure is of the strong type. As much smaller detonation cell size and the associated structure can not be resolved easily and directly by experiments, it is still quite an open issue whether an ordinary detonation possesses a strong structure (Fickett and Davis 1979). From the late 1970's, numerical simulation has been employed and increasingly so to study the cellular structure to reveal details that can not be determined easily in experiments. Recently, the multi-step, detailed reaction model has been employed with some success. With this model Oran et al (1998) calculated the cellular structure tracks for the low pressure $\mathrm{H_2/O_2/Ar}$ mixture. However, the coarser resolution employed may have led to unclear structure and tracks which are difficult to verify the actual structure type. In this paper, the cellular structure and its tracks are investigated by two dimensional numerical simulations with both detailed reaction model and high resolution.

MODELING AND COMPUTATIONAL INITIALIZATION

This simulation models an ordinary detonation propagating in a two-dimensional channel with stoichiometric $\mathrm{H_2/O_2}$ diluted by 70% argon at initial pressure and temperature given as 6.67kPa and 298K, respectively. A 9 species, 19 elementary reactions model is used for hydrogen-oxygen combustion. The 5th order WENO-LF scheme, which is able to resolve the different discontinuities accurately and has small numerical dissipation, is employed. The time discretization for the fluid dynamic terms is the 3rd order TVD Runge-Kutta method which is combined with an stiff ODE solver. The initial condition, which is an one-dimensional steady detonation wave, is perturbed by introducing random disturbances for the first time-step of chemical kinetic integrations.

HIGH RESOLUTION REGULAR CELLULAR STRUCTURE

Figure 1 shows the detailed structure with $0.025mm$ grid size, which is about $1/200$ of the reaction zone length. One can find that the wave configuration resembles to some extent that of a double-Mach reflection of a shock wave. The main difference between them is the second triple wave configuration in the cellular structure is transitional-Mach like. Hence, the whole structure shows stronger strength than a merely double-Mach configuration. The ignition front, which is approximately defined by the concentration discontinuity, suggested that all the ignitions after the Mach stem, the incident wave, and transverse wave are associated with strong shock induced ignition processes. The structure shows clearly multi-Mach configuration with more than one triple points and the presence of strong transverse wave ignition. Therefore, one can conclude that the cellular structure is of the strong type.

CELLULAR STRUCTURE TRACKS

In the present work, the structure tracks are obtained by recording the maximum flow velocities on all grid nodes in the time history. Figures 2 and 3 show the numerical detonation cells as an analogue of smoke foil tracks and how the tracks are left after the sweeping of the structure, respectively. Generally, it can be observed that there are three tracks left by the structure (see Fig. 2). The first track is left by tangential velocity discontinuity on the first slip line S. The second track is left by the tangential velocity discontinuity on the second slip line S'. The third track is left by the region near the kink point c to the extending transverse wave. Table 1 shows the details of comparisons between the numerics and experiments

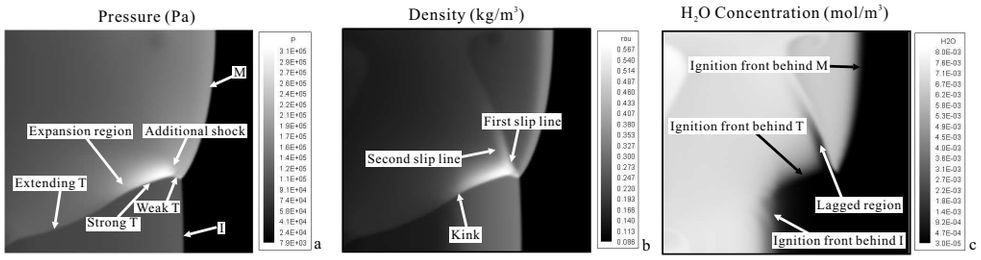


Fig. 1 Cellular tructure with one transverse wave with 0.025mm grid size
a)pressure, b)density, c)d)H_2Oconcentration

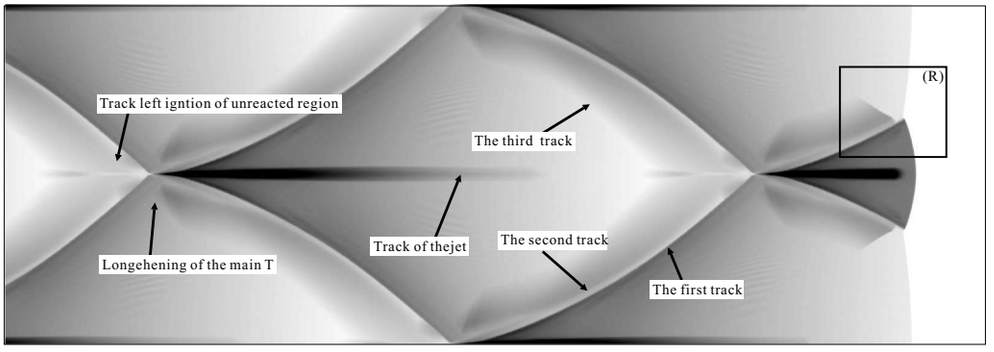


Fig. 2 Numerical detonation cells in a 8mm channel (region (R) is produced schematically in Fig. 3

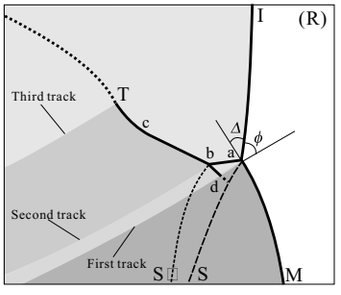


Fig. 3 The making of structural tracks
in a numerical detonation cell

Table 1 Comparison of cell geometries
between simulation and experiments

Cell geometries	Current results	Experiments [a]
Width/length (d/l)	0.55	$0.5 \sim 0.6$
Exit angle (β)	$< 10^o$	$5^o \sim 10^o$
Entrance angle (α)	40^o	$32^o \sim 40^o$
Track angle (ω)	30^o	$\sim 30^o$

[a] From Strehlow (1968)

(Strehlow 1968). Strehlow's (1969) argument for the presence of weak structures in ordinary detonations is based on the ground that the observed structure tracks are "single lines". However, if the experimental smoke foil tracks in Strehlow (1968) are analyzed further, the "single line" is actually a narrow band. In this band, less soot is removed compared to the neighboring regions. This narrow band is very similar to the narrow band reflected in Figs. 2 and 3 and recorded by by region lying between the first and the second tracks. This concurrence of the simulation and experiment suggests the presence of a strong structure for the ordinary detonation in $H_2/O_2/Ar$ mixture. As many experimental smoke foil data (Fickett and Davis, 1979) for *different* ordinary detonations show that the structure tracks are actually narrow bands too, it may be surmised that strong structures exist for other reactive systems.

CONCLUDING REMARKS

In this paper, the cellular structure and its tracks of an ordinary detonation in $H_2/O_2/Ar$ mixture are investigated by a two-dimensional simulation. The calculated high resolution results suggested a strong structure which left three different tracks associated with different triple points or the kink on the transverse wave. The comparisons with previous experiments indicates the presence of strong structure for an ordinary detonation.

References

[1] W. Fickett, W.C. Davis: *Detonation* (University of California, Berkeley, 1979)
[2] .S. Oran, J.E. Weber, E.I. Stefaniw, M.H. Lefebvre, J.D. Anderson: *Combust. Flame* **113** 147-163, 1998
[3] R.A. Strehlow: *Combust. Flame* **12** 81-101, 1968
[4] R.A. Strehlow RA: *Astronaut Acta* **14** 539-548, 1969

XXI ICTAM, 15–21 August 2004, Warsaw, Poland

ENERGY SPECTRUM IN ROTATING TURBULENCE

Frédéric Moisy, Cyprien Morize, Marc Rabaud
FAST, Bât. 502, Campus Universitaire, 91405 Orsay Cedex, France

Summary
The transition between three-dimensional and quasi-two-dimensional turbulence in a rotating frame is experimentally investigated. Turbulence is generated by rapidly towing a grid in a rotating water tank, and the velocity field in a plane perpendicular to the rotation axis is measured by means of particle image velocimetry. During the decay, the power spectrum shows a power law $E(k) \sim k^{-n}$, with an exponent n that continuously increases from $n = 5/3$, as expected for the 3D Kolmogorov regime at large Rossby number, up to $n \simeq 2.2$ for the lowest Rossby number. This trend is consistent with the spectrum of the enstrophy cascade regime, $E(k) \sim k^{-3}$, in the limit of zero Rossby number.

INTRODUCTION

Turbulence subjected to system rotation, a situation present in a wide range of applications, from engineering to geophysics and astrophysics, is a complex problem which is not completely understood. The limit of very small Rossby numbers is expected to give rise to two-dimensional turbulence, where inverse energy cascade and enstrophy cascade may eventually take place. In the case of moderate rotation, the usual description in terms of direct energy cascade should be modified to account for the effect of the Coriolis force.
Adding rotation to an otherwise 3D homogeneous turbulence introduces a new characteristic time, Ω^{-1}, that may affect the largest scales associated with low levels of vorticity compared to the background vorticity 2Ω. On this phenomenological ground, Zhou (1995) [1] proposes to use the timescale Ω^{-1} instead of the characteristic turn-over time based on the Kolmogorov estimate, leading to a k^{-2} power law spectrum for the small wavenumbers instead of the classical $k^{-5/3}$ law. However, taking account of the anisotropy leads to a k^{-3} law, in accordance with the enstrophy cascade regime expected at large wavenumbers in the limit of zero Rossby number [2].

EXPERIMENTAL SET-UP

The experimental cell, similar to the one from Hopfinger *et al.* (1982) [3], is sketched in figure 1(a). It consists of a square water tank, 55 cm in height and 35 cm in side, mounted on a rotating turntable, whose angular velocity Ω can be adjusted between 0 and 4.5 rad/s. A cover is placed below the free surface to avoid surface waves and unwanted β-effects. A turbulent velocity field is generated by rapidly towing a grid through the height of the tank. The grid consists of 1 cm square bars with a mesh $M = 39$ mm. Typical velocity fluctuations $u' \simeq 0.1$ m/s are obtained by imposing a grid velocity of order of 1 m/s. During the turbulence decay, the background rotation gradually affects the entire flow in an homogeneous way.

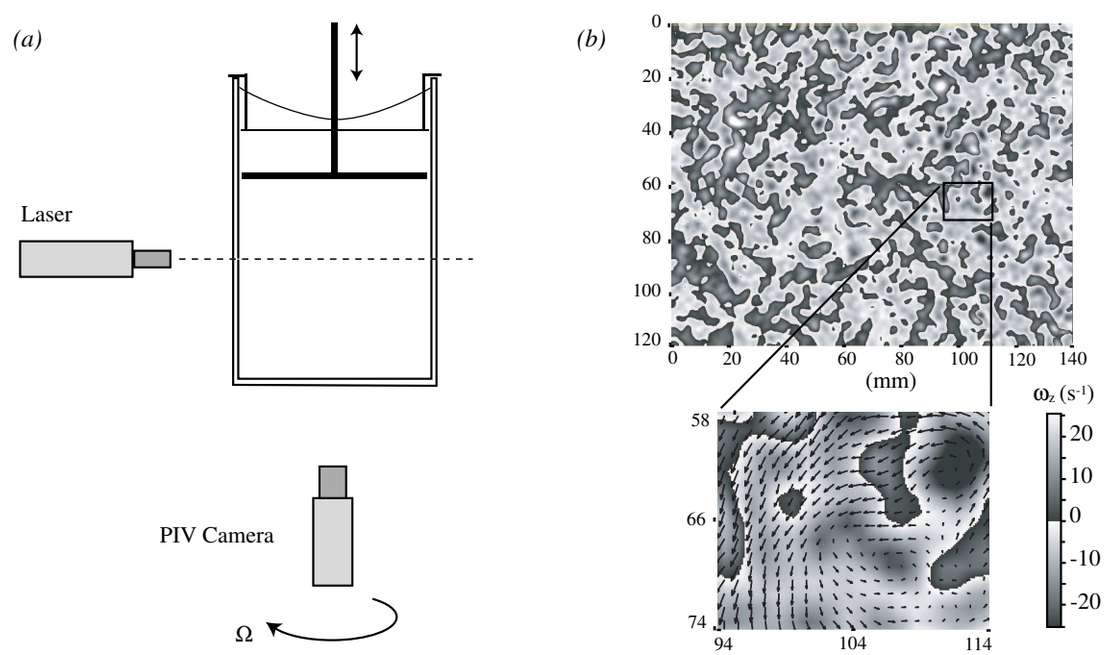


Figure 1. (a) Schematic of the experimental set-up. The water tank, the oscillating grid and the camera are in the rotating frame, while the pulsed laser remains in the laboratory frame. (b) Example of vertical vorticity field measured by PIV.

Instantaneous velocity fields in the horizontal plane (x, y) are obtained using a particle image velocimetry (PIV) system. The flow is seeded with small glass spheres, and illuminated by a horizontal laser sheet produced by a double pulsed laser. Images are acquired with a double-buffer high resolution camera in the rotating frame, synchronized with the laser at a maximum rate of 4 frames pair per second.

The instantaneous velocity fields may be characterized by the Reynolds number, $\mathrm{Re}_M = u'M/\nu$, and the *macro* Rossby number, $\mathrm{Ro}_M = u'/2\Omega M$, based on the velocity fluctuation u' and the mesh size M. As the turbulence decays, both numbers decrease, with the ratio $\mathrm{Ro}/\mathrm{Re} = \nu/2\Omega M^2$ remaining constant. In addition, a *micro* Rossby number, $\mathrm{Ro}_\omega = \omega'/2\Omega$ is introduced. We are interested in the regime $\mathrm{Ro}_M < 1$ and $\mathrm{Ro}_\omega > 1$, i.e. the intermediate regime where the large scales are strongly affected by the background rotation, whereas the small scales remain essentially three-dimensional.

RESULTS

Figure 2(a) shows three power spectra, measured in the horizontal plane, during the decay of the turbulence, for $\Omega = 4.5$ rad s^{-1} and a grid velocity of $V_g = 0.8$ m s^{-1}. For the first spectrum, the Rossby number is $\mathrm{Ro}_\omega = 1.1$, and a pure Kolmogorov scaling law can be seen, $k^{-5/3}$, indicating a weak influence of the rotation. As the Rossby number decreases in time ($\mathrm{Ro}_\omega = 0.53$ and 0.29), the spectra show a steeper slope, k^{-n} with $n > 5/3$.

The exponent n of the power spectrum is shown in figure 2(b) as a function of Ro_ω. The collapse of the curves for the different data sets, corresponding to various initial Reynolds numbers, is remarkable, indicating that the micro Rossby number is the relevant local parameter for the energy spectrum. The exponent is found to continuously increase for $\mathrm{Ro}_\omega < 1$. The value $n = 2$ is observed, but it only appears as a transient state in the route towards the bidimensionalization of the flow. The trend is found consistent with the $n = 3$ limit, expected for purely 2D turbulence in the enstrophy cascade regime.

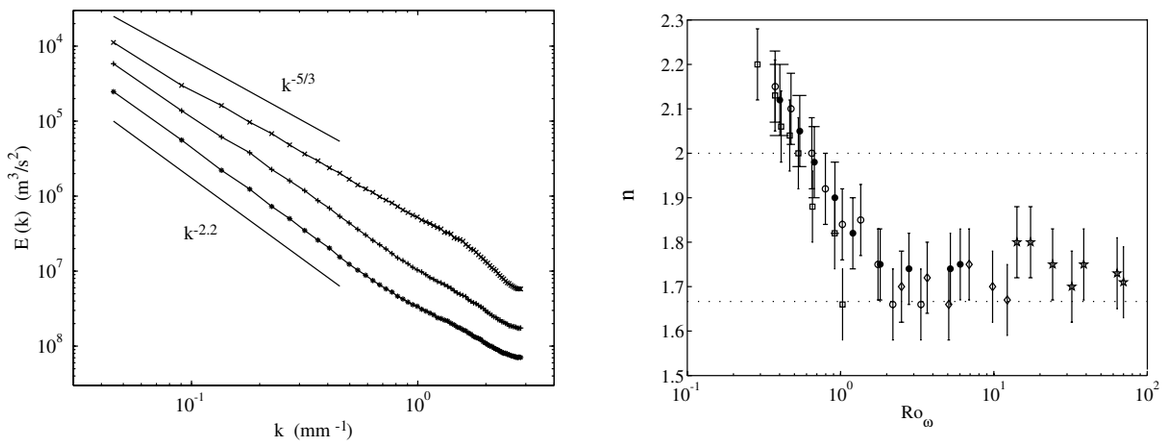


Figure 2. (a) Power spectra in the horizontal plane. (b) Exponent n of the power spectrum as a function of the micro Rossby number $Ro_\omega = \omega'/2\Omega$.

References

[1] Zhou Y.: A phenomenological treatment of rotating turbulence. *Phys. Fluids* **7**:2092, 1995.
[2] Cambon C., Rubinstein R., Godeferd F. S.: Advances in wave turbulence: rapidly rotating flows. *New J. Phys.* **6**:73, 2004.
[3] Hopfinger E. J., Browand F. K., Gagne Y.: Turbulence and waves in a rotating tank. *J. Fluid Mech.* **125**:505, 1982.

THREE-DIMENSIONAL TURBULENT STRUCTURES OF DIFFERENT SCALES

Akira Rinoshika*, Yu Zhou**
*Department of Mechanical Systems Engineering, Yamagata University, Yamagata, Japan
**Department of Mechanical Engineering, The Hong Kong Polytechnic University, Hong Kong

Summary An orthogonal vector wavelet multi-resolution technique has been developed and applied to decomposing the measured velocity data of a three-dimensional turbulent near-wake into a number of wavelet components based on their central frequencies or scales. The spanwise vorticity contours of the wavelet component at f_0 (the vortex shedding frequency) display a secondary spanwise structure near the saddle point, whose vorticity is opposite-signed to that of the Kàrmàn vortices. The wavelet components of f_0 or $2f_0$ make a predominant contribution to the Reynolds normal stresses and account for most of the shear stress. On the other hand, the relatively small-scale turbulent structures contribute most to vorticity variance.

INTRODUCTION

The turbulent near-wake of a circular cylinder is characterised by a high degree of organisation, thus being attractive for studying turbulent structures in terms of their organised aspects and clarifying their role in the transport process. In this flow, turbulent structures consist of a wide range of scales, including large-scale spanwise structures and relatively small-scale structures such as the secondary vortices, Kelvin-Helmholtz vortices and longitudinal rib-like structures. Previous studies [1], [2] of the organised motion mostly focused on large-scale structures; investigations of other scales have been relatively scarce since it is difficult to extract the structures of these scales using conventional vortex-detection techniques. The purpose of the present work aims to develop an orthogonal vector wavelet multi-resolution technique for decomposing the turbulent structures of different scales and provides both quantitative and qualitative information on the structures of individual scales. The turbulent structures of various scales are examined in detail, including their instantaneous streamline patterns and vortcity contours, and contributions to Reynolds stresses and root mean square (rms) vorticity from each scale.

ORTHOGONAL VECTOR WAVELET MULTI-RESOLUTION TECHNIQUE

For any one-dimensional vector data $\vec{v}$, the vector discrete wavelet transform, $\vec{S} = W\vec{v}$, is first carried out. Here $\boldsymbol{S}$ and $\boldsymbol{W}$ are called discrete wavelet coefficient matrix and the analysing wavelet matrix of $\vec{v}$. $\boldsymbol{W}$ is orthogonal and satisfies $\boldsymbol{W}^T\boldsymbol{W} = \boldsymbol{I}$, where $\boldsymbol{I}$ is a unit matrix, usually constructed based on a cascade algorithm of an orthogonal wavelet basis function. In the present study, the Daubechies wavelet basis with an order of 20 is used. Then the inverse vector discrete wavelet transform is applied to the wavelet coefficient of each wavelet level and the wavelet components of vector data are constructed. Therefore, a non-linear vector data can be convert to an infinite summation of vector wavelet components at different wavelet level or central frequencies, i.e., $\vec{v} = \sum_{i=1}^{N} \vec{v}_i$, where the vector wavelet components are normal to each other, given by $\vec{v}_i = W^T \vec{S}_i$. The first term $\vec{v}_1$ and the last $\vec{v}_N$ represent the wavelet components at level 1 (the lowest frequency) and level N (the highest frequency), respectively. Evidently, the sum of all wavelet level or frequency components is a reconstruction of the original vector data.

EXPERIMENTAL CONDITIONS

A circular cylinder (d = 12.5 mm) was used to generate a turbulent wake. Measurements were conducted at x/d = 20 (x is the streamwise distance downstream of the cylinder) and a constant free stream velocity (U_∞ = 6.7 m/s). The corresponding Reynolds number Re ($\equiv U_\infty d/\nu$) was 5600. The Kolmogorove length scale at this x/d was estimated to be about 0.16 mm. Two orthogonal arrays, each of eight X-wires, were used. Eight X-wires were aligned in the (x, y)-plane, i.e. the plane of mean shear, and eight in the (x, z)-plane, which is parallel to both the cylinder axis and the streamwise direction. The sixteen X-wires allow velocity fluctuations u and v in the (x, y)-plane and u and w in the (x, z)-plane to be obtained simultaneously. The sampling frequency was 3.5 kHz.

INSTANTANEOUS TURBULENT STRUCTURES OF VARIOUS SCALES

The dominant frequency f_0 of large-scale structures (i.e. Kàrmàn vortices) is selected as the 'fundamental central frequency' for the wavelet multi-resolution analysis, and the central frequencies of wavelet components are given by f_0, $2f_0$, $4f_0$ and $8f_0$. This range of frequencies is of major concern in the present investigation. In order to better 'visualise data', sectional streamlines [3] were constructed for velocity of each scale as well as for measured velocities. The streamlines are viewed in a reference frame translating at the convection velocity of the large-scale structures, which is $U_C = 0.87U_\infty$. Vorticity was approximated based on instantaneous wavelet components of velocity using the central difference approximation [1]. Figures 1 and 2 show instantaneous streamlines and corresponding normalised vorticity contours of different scales in the (x, y)- and (x, z)-plane, calculated from the wavelet components of velocity at the central frequencies of f_0 and $2f_0$, respectively. The solid and broken lines in the vorticity contours represent positive and negative levels, respectively. Structures at f_0 represent the large-scale organised motion and appear better organised and exhibit a much stronger periodicity. The foci and saddle points are marked by F and S, respectively. A number of more

observations can be made from Fig.1. Firstly, the focus in general coincides with the local peak of $(\omega_z)_{f_0} d/U_\infty$ (negative), while the saddle point occurs at the minimum of $(\omega_z)_{f_0} d/U_\infty$. Secondly, the saddle point is mostly associated with the up-down concentrations of positive vorticity, e.g. at $tU_c/d \approx$ -8, -4, 0.8 and 5.2 in Fig.1 (c). The positive vorticity concentration below the saddle point is apparently part of positive-sign vortices, which occur below the centreline. On the other hand, the vorticity concentration above the saddle point probably results from interactions between two consecutive spanwise structures of negative sign; its positive sign is further consistent with the fact that the vorticity strength of a spanwise vortex is higher than that of the neighbouring downstream one because of a fast decay in the vortex strength as *x/d* increases. This secondary structure of positive vorticity (or negative-sign vorticity if below the centreline) has not been observed from previous conditional method [1], [2].

As the central frequency increases to $2f_0$ (Fig.2), the vorticity strength in both planes almost doubles that at the central frequency of f_0, though this strength in the (*x*, *z*)-plane is still significantly weaker than in the (*x*, *y*)-plane, the maximum contour level of $(\omega_y)_{2f_0} d/U_\infty$ being 0.7, significantly smaller than that (1.2) of $(\omega_z)_{2f_0} d/U_\infty$. The difference reflects the fact that the structures in the (*x*, *y*)-plane are connected to primary or secondary spanwise structures, while those in the (*x*, *z*)-plane result from the three dimensionality of primary spanwise structures and rib structures. Furthermore, the vorticity concentrations of opposite sign tend to occur alternately in the longitudinal direction, irrespective of the (*x*, *y*)- or (*x*, *z*)-plane. The alternate occurrence of opposite-sign vorticity concentrations, mostly associated with the saddle points, is also observed in the spanwise direction. The spanwise spacing between these concentrations is in the order of 1*d*. The observation is again linked to the behaviour of the rib structures.

The contributions to the Reynolds stresses from the wavelet components are also quantified. The wavelet components of f_0 and $2f_0$ contribute most to the Reynolds normal stresses, accounting for about 45% of $\overline{u^2}$ and 80% of $\overline{v^2}$, respectively. The contribution from the wavelet component of $4f_0$ declines quite sharply, by up to 30% of $\overline{v^2}$, compared with that of f_0 or $2f_0$, and further reduces for a higher central frequency. The Reynolds shear stress is largely attributed to the wavelet components of lower central frequencies. The components of f_0 and $2f_0$ are responsible for almost 70% of $\overline{uv}$, the latter two components contributing about 35% to $\overline{uv}$.

As to the root mean square vorticity of each scale, the wavelet component of f_0 makes a small contribution to spanwise vorticity variance, accounting for about 10% of $\overline{\omega_z^2}$. The contribution climbs as the central frequency increases; the component of $8f_0$ contributes about 22% to $\overline{\omega_z^2}$, suggesting that vorticity tends to reside in the small-scale structures.

CONCLUSIONS

(1) The spanwise vorticity contours at f_0 display a secondary spanwise structure above the saddle point, whose vorticity is opposite-signed to that of the spanwise structures. This structure is observed for the first time and probably results from the strong interactions between the consecutive spanwise structures of the same sign. Its occurrence and vorticity sign is consistent with the downstream decay in the vorticity strength of the spanwise structures.

(2) The wavelet components of f_0 or $2f_0$ make a predominant contribution to the Reynolds stresses.

(3) The relatively small-scale turbulent structures contribute most to vorticity variance.

References

[1] Hussain A.K.M.F., Hayakawa M.: Education of large-scale organized structures in a turbulent plane wake. *J. Fluid Mech* **180**: 193-229, 1987.

[2] Zhou Y., Antonia R.A.: A critical points in a turbulent near-wake. *J. Fluid Mech* **275**: 59-81, 1994.

[3] Perry, A. E., Chong, M. S.: A description of eddy motions and flow patterns using critical-point concepts. *Ann. Rev. Fluid Mech* **19**: 125-155, 1987.

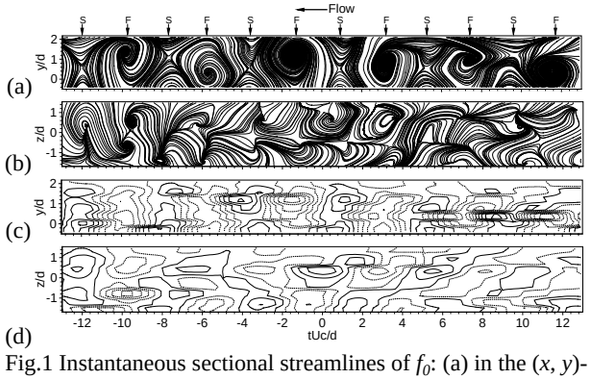


Fig.1 Instantaneous sectional streamlines of f_0: (a) in the (*x*, *y*)-plane; (b) in the (*x*, *z*)-plane of *y/d*=0.2. Vorticity contours of f_0: (c) $(\omega_z)_{f_0} d/U_\infty$ in the (*x*, *y*)-plane (Max: 0.45, Min: -0.65, Increment: 0.1); (d) $(\omega_y)_{f_0} d/U_\infty$ in the (*x*, *z*)-plane of *y/d*=0.2 (Max: 0.35, Min: -0.35, Increment: 0.1)

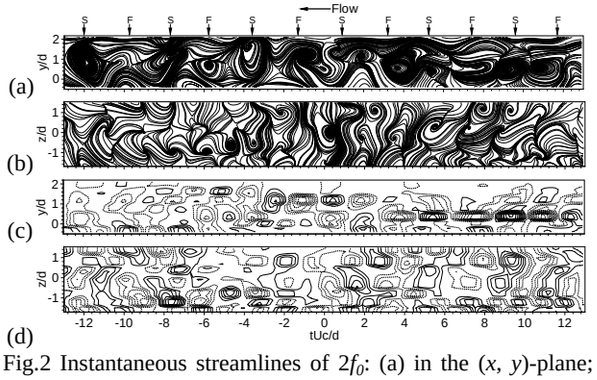


Fig.2 Instantaneous streamlines of $2f_0$: (a) in the (*x*, *y*)-plane; (b) in the (*x*, *z*)-plane of *y/d*=0.2. Vorticity contours of $2f_0$: (c) $(\omega_z)_{2f_0} d/U_\infty$ in the (*x*, *y*)-plane (Max: 1.0, Min: -1.2, Increment: 0.1); (d) $(\omega_y)_{2f_0} d/U_\infty$ in the (*x*, *z*)-plane of *y/d*=0.2 (Max: 0.7, Min: -0.6, Increment: 0.1).

INERTIAL SIMILARITY OF VELOCITY DISTRIBUTIONS IN HOMOGENEOUS ISOTROPIC TURBULENCE

Tomomasa Tatsumi*, Takahiro Yoshimura**
*International Institute for Advanced Studies, Kyoto 619-0225, Japan
**Toyota Techno Service Co. Tokyo 135-0091, Japan

Summary The one- and two-point velocity distributions of homogeneous isotropic turbulence are obtained as the solutions of the closed set of equations, which are derived from the Lundgren-Monin (1967) equations using the the cross-independence hypothesis. This problem was first reported by Tatsumi (2000) in ICTAM 2000, and new concrete results and strengthend physical arguments are presented in the present version.

CROSS-INDEPENDENCE HYPOTHESIS

Cross-Independence

The cross-independence of two velocities $\mathbf{u}_1 = \mathbf{u}(\mathbf{x}_1, t)$ and $\mathbf{u}_2 = \mathbf{u}(\mathbf{x}_2, t)$ is defined as the independence of their sum $\mathbf{u}_+ = (\mathbf{u}_1 + \mathbf{u}_2)/2$ and difference $\mathbf{u}_- = (\mathbf{u}_2 - \mathbf{u}_1)/2$. Unlike the ordinary independence of $\mathbf{u}_1$ and $\mathbf{u}_2$ which is only valid for large values of the distance $\mathbf{r} = \mathbf{x}_2 - \mathbf{x}_1$, the *cross-independence* is shown to be valid for both large and small values of the distance $\mathbf{r}$. This may be understood from a simple example: $\langle XY \rangle = \langle ((X+Y)/2)^2 \rangle - \langle ((X-Y)/2)^2 \rangle$.

Independence of Small and Large Eddies

It is interesting to note that the cross-independence is essentially identical with Kolmogorov's (1941) basic premise that small-scale eddies characterized by the velocity difference $2\mathbf{u}_-$ are independent from large-scale eddies characterized by $\mathbf{u}_1$ and $\mathbf{u}_2$. Experimental and numerical supports have been given by Sreenivasan et al. (1998) showing that the cross independence is accurately satisfied for the distance $\mathbf{r}$ of order of the inertial range.

ONE-POINT VELOCITY DISTRIBUTION

Cross-Velocity Distributions

For homogeneous turbulence, we define the one- and two-point velocity distributions of the velocities $\mathbf{u}_1$ and $\mathbf{u}_2$ by $f(\mathbf{u}_1, t)$ and $f^{(2)}(\mathbf{u}_1, \mathbf{u}_2; \mathbf{r}, t)$ respectively, likewise for the velocity $\mathbf{u}_+$ by $g_+(\mathbf{u}_+, \mathbf{r}, t)$, for $\mathbf{u}_-$ by $g_-(\mathbf{u}_-, \mathbf{r}, t)$, and for the pair of $\mathbf{u}_+$ and $\mathbf{u}_-$ by $g^{(2)}(\mathbf{u}_+, \mathbf{u}_-; \mathbf{r}, t)$. Then, the cross-independence of $\mathbf{u}_1$ and $\mathbf{u}_2$ gives the relationship,

$$f^{(2)}(\mathbf{u}_1, \mathbf{u}_2; \mathbf{r}, t)\, d\mathbf{u}_1 d\mathbf{u}_2 = g^{(2)}(\mathbf{u}_+, \mathbf{u}_-; \mathbf{r}, t)\, d\mathbf{u}_+ d\mathbf{u}_- \quad (1)$$

$$g^{(2)}(\mathbf{u}_+, \mathbf{u}_-; \mathbf{r}, t) = g_+(\mathbf{u}_+, \mathbf{r}, t)\, g_-(\mathbf{u}_-, \mathbf{r}, t) \quad (2)$$

One-Point Velocity Distribution

On substitution of the cross-independence relations (1) and (2), the Lundgren-Monin equation for the one-point velocity distribution $f(\mathbf{u}_1, t)$ is simplified as

$$[\partial/\partial t + \alpha(t)\, |\, \partial/\partial \mathbf{u}_1\, |^2]\, f(\mathbf{u}_1, t) = 0 \quad (3)$$

$$\alpha(t) = (2/3)\, \nu \lim_{|\mathbf{r}| \to 0} |\, \partial/\partial \mathbf{r}\, |^2 \int |\, \mathbf{u}_-\, |^2 g_-(\mathbf{u}_-, \mathbf{r}, t)\, d\mathbf{u}_- \quad (4)$$

where $\alpha(t)$ is the inverse diffusion constant. It can be shown further that $\alpha(t)$ is related with the mean energy dissipation rate $\overline{\varepsilon}(t)$ and the energy of turbulence $\overline{E}(t)$ as

$$\alpha(t) = (1/3)\, \overline{\varepsilon}(t) \quad (5)$$

$$\overline{\varepsilon}(t) = \langle \varepsilon(\mathbf{x}, t) \rangle = \nu \sum_{i,j=1}^{3} \langle (\partial u_i(\mathbf{x}, t)/\partial x_j)^2 \rangle = -\, d\overline{E}(t)/dt. \quad (6)$$

$$\overline{E}(t) = \langle E(\mathbf{x}, t) \rangle = (1/2) \langle |\, \mathbf{u}(\mathbf{x}, t)\, |^2 \rangle \quad (7)$$

Eq. (3) permits a self-similar solution for the one-point velocity distribution.

$$f(\mathbf{u}_1, t) = f_0(\mathbf{u}_1, t) = (t/4\pi\alpha_0)^{3/2} \exp[-\, |\, \mathbf{u}_1\, |^2 t/4\alpha_0] \quad (8)$$

$$\alpha(t) = \alpha_0 t^{-2}, \quad \overline{\varepsilon}(t) = \varepsilon_0 t^{-2}, \quad \overline{E}(t) = E_0 t^{-1}, \quad \alpha_0 = (1/3)\, \varepsilon_0 = (1/3) E_0 \quad (9)$$

which represents the three-dimensional *normal distribution*.

Inertial Similarity

The equation (3) and the solution (8) of the one-point velocity distribution clearly indicate that it depends upon only one parameter $\alpha(t) = (1/3)\, \overline{\varepsilon}(t)$ and not on the viscosity ν explicitly. This means that the one-point velocity distribution of homogeneous isotropic turbulence obeys the *inertial similarity* of Kolmogorov's sense.

The *inertial normality* of the velocity distribution was first pointed out by Hopf (1952) as a particular solution representing the velocity distribution functional but does not seem to have drawn attention of later researchers. It will be shown below that the two-point velocity distributions also obey the normal distribution, so that the *inertial normality* seems to be a universal character of the statistics of homogeneous turbulence.

It may be interesting to note that the energy dissipation $\alpha(t)$ is expressed in terms of the integral of turbulent fluctuation, so that it actually satisfies the *fluctuation-dissipation* relationship of statistical physics.

Viscous Similarity

It should be noted that the inertial similarity is not a unique consequence of eq. (4) since it permits another limit,

$$\alpha(t) = \nu\,\gamma(t), \quad \gamma(t) = (2/3)\lim_{|\mathbf{r}|\to 0} |\partial/\partial\,\mathbf{r}|^2 \int |\underline{\mathbf{u}}_-|^2 g_-(\mathbf{u}_-, \mathbf{r}, t)\,d\mathbf{u}_- \tag{10}$$

with finite $\gamma(t)$. This similarity associated with the finite energy dissipation $\varepsilon(t)$ and the viscosity ν constitutes the full-set of Kolmogorov's local equilibrium and may be called the *viscous similarity*.

The *viscous normal distribution* (8) associated with the energy dissipation (10) proportional to the viscosity ν is already familiar for us as the normality of weak turbulence composed of large number of independent small eddies.

TWO-POINT VELOCITY DISTRIBUTIONS

Velocity-Sum Distribution

On substitution of the cross-independence relations into the Lundgren-Monin equation for the two-point velocity distribution, we obtain a closed equation for $f^{(2)}(\mathbf{u}_1, \mathbf{u}_2; \mathbf{r}, t) = 2^{-3} g^{(2)}(\mathbf{u}_+, \mathbf{u}_-; \mathbf{r}, t)$. Then, on substitution of (2) and integration with respect to $\mathbf{u}_-$, this equation is reduced to the following equation for the velocity-sum distribution:

$$[\partial/\partial\,t + (1/2)\,\alpha(t)\,|\partial/\partial\,\mathbf{u}_+|^2]\,g_+(\mathbf{u}_+, \mathbf{r}, t) = 0 \tag{11}$$

This equation is identical to eq. (3) for the one-point velocity distribution except for the factor 1/2 of $\alpha(t)$. Thus, its solution is immediately given from eq. (8) as

$$g_+(\mathbf{u}_+, \mathbf{r}, t) = g_0(\mathbf{u}_+, t) = (t/2\pi\alpha_0)^{3/2} \exp[-|\mathbf{u}_+|^2 t/2\alpha_0] \tag{12}$$

Comparison of this result with eq. (8) clearly shows that the velocity-sum distribution (12) is given by the convolution of two independent velocity distributions (8) at the points $\mathbf{x}_1$ and $\mathbf{x}_2$.

Although the *inertial normal distribution* (12) is valid for all values of $\mathbf{r} > 0$, it must coincide with (8) in the limit of $\mathbf{r} \to 0$ since $g_+(\mathbf{u}_+, \mathbf{r}, t) \to f(\mathbf{u}_1, t)$ in this limit. This implies an abrupt change of $g_+(\mathbf{u}_+, \mathbf{r}, t)$ at $\mathbf{r} = 0$, but such a discontinuity is replaced by the continuous change under the viscous similarity mentioned above.

Lateral Velocity-Difference Distribution

Integration of the closed equation for $f^{(2)}(\mathbf{u}_1, \mathbf{u}_2; \mathbf{r}, t) = 2^{-3} g^{(2)}(\mathbf{u}_+, \mathbf{u}_-; \mathbf{r}, t)$ with respect to $\mathbf{u}_+$ gives the equation for the velocity-difference distribution $g_-(\mathbf{u}_-, \mathbf{r}, t)$. If we define the variables as $\mathbf{u}_- = (u_-, v_-, w_-)$, $\mathbf{r} = (r, 0, 0)$, we can derive the following equation for the lateral velocity-difference distribution:

$$[\partial/\partial\,t + (1/2)\,\alpha(t)\,\partial^2/\partial\,v_-^2]\,g_\perp(v_-, r, t) = 0 \tag{13}$$

Since this equation is the one-dimensional version of eq. (11), its solution is immediately given from (12) as

$$g_\perp(v_-, r, t) = g_0(v_-, t) = (t/2\pi\alpha_0)^{1/2} \exp[-v_-^2 t/2\alpha_0] \tag{14}$$

The same physical arguments as those for the solution (12) are applied to the *inertial normal distribution* (14). In particular, since the distribution $g_\perp(v_-, r, t)$ has to reduce to the delta distribution in the limit of $r \to 0$, its abrupt change should take place more drastically compared with the velocity-sum distribution. This discontinuity is again resolved by taking account of the viscous similarity.

Longitudinal Velocity-Difference Distribution

Following the same process as for the lateral distribution, we obtain the equation,

$$[\partial/\partial\,t + (1/2)\,\alpha(t)\,\partial^2/\partial\,u_-^2 + (1/3)\,(8u_- + u_-^2\,\partial/\partial\,u_-)\,\partial/\partial\,r]\,g_\parallel(u_-, r, t) = 0 \tag{15}$$

for the longitudinal velocity-difference distribution. Obviously, this equation permits the *inertial normal distribution*,

$$g_\parallel(u_-, r, t) = g_0(u_-, t) = (t/2\pi\alpha_0)^{1/2} \exp[-u_-^2 t/2\alpha_0] \tag{16}$$

for large distance r. However, it also has an *inertial range* solution which is obtained from the self-similar equation,

$$(1 - (2/9)\,\zeta^3)K'' - (20/9)\,\zeta^2 K' - (16/9)\,\zeta K = 0 \tag{17}$$

$$\zeta = u_-\,r^{-1/3}(t^2/\alpha_0)^{1/3}, \quad g_\parallel(u_-, r, t) = r^{-1/3}(t^2/\alpha_0)^{1/3} K(\zeta) \tag{18}$$

The solution $K(\zeta)$ satisfies the inertial-range similarity $u_- \propto r^{1/3}$ and takes asymmetric form with a cusp-like singularity at $\zeta = (9/2)^{1/3}$ and algebraic tails.

CONCLUSION

The *inertial normality* of the velocity distributions in homogeneous isotropic turbulence seems to have been established so far as the one- and two-point statistics. This provides us with good scope for the study of *viscous similarity* of this turbulence and the extension of the present approach to more complex turbulent motions.

References

Hopf, E. (1952) *J. Rat. Mech. Anal.* **1**, 87-123.

Kolmogorov, A. N. (1941) *Dokl. Akad. Nauk. SSSR*, **30**, 301-305.

Lundgren, T. S, (1967) *Phys. Fluids*, **10**, 969-975.

Monin, A. S. (1967) *PMM J. Appl. Math.* **31**, 1057-1068.

Sreenivasan, K. R. & Dhruva, B. (1998) *Progr. Theor. Phys. Suppl.* No. 130, 103-120.

A new mixed nonlinear LES models for boundary layers

R.M. Kerr and P.G. Tucker
School of Engineering, University of Warwick, Coventry CV4 7AL UK

In 1970, Clark et al. [1] introduced a nonlinear model for the subgrid stress terms to complement linear dissipation such as the Smagorinsky eddy viscosity [13]. However, since then this simple formulation for adding more of the nonlinearity of the grid scales has been largely ignored by the turbulence modelling community. This is largely because it was not recognised that such nonlinear terms for a simple way to introduce backscatter effects, that is the energy from the subgrid scales that can appear in the resolved scales. This can be demonstrated by *a priori* analysis of interaction of filtered and sub-filtered scales in direct numerical simulations [6] Other approaches such as dynamically determining the coefficient in the Smagorinsky model C_s [11] and stochastical backscatter. [10] suffer from inherent problems in strong shears.

We will take the goal of LES research to be finding a formulation for the subgrid scales with the following properties:

- easy to implement
- dissipates approximately the correct energy,
- has roughly the correct transport properties,
- generates approximately the correct small-scale instabilities,
- and consistently does all of these for a variety of flow geometries.

This contribution will discuss comparisons between new large-eddy simulations (LES) and benchline flows (sophisticated LES and DNS) for two flows, primarily a pressure driven channel flow and secondarily decaying, isotropic turbulence. The channel flow is particularly challenging for LES because it has both a strong shear in the boundary layer and an interior that resembles isotropic turbulence. The classical LES approach [12] is to make the coefficient in the Smagorinsky eddy viscosity smaller in the boundary layer. The reason is that the value for homogeneous, isotropic turbulence, $C_s = 0.2$, creates too much dissipation in the boundary layer and suppresses the instabilities required to generate turbulence. The objective is either to effectively reduce C_s in the boundary or introduce fluctuations that could overcome the eddy-viscosity and drive the instabilities.

Figure 1 shows the profiles for several mixed non-linear models for the velocity profile in a classical, pressure-driven plane channel flow. The model that gave the best results is an existing LES model [14] plus a filtered nonlinear model based upon the Leray regularization of the Navier-Stokes equations [9]. The comparison with a sophisticated benchline LES [11] at $Re_\tau = 1050$, which in turn was based on comparisons with a high-resolution DNS [7], is nearly perfect, Direct comparisons with our own high-resolution DNS are in progress. Profiles of all components of the kinetic energy are also better than the competing mixed non-linear models [8, 15]. Coefficients for the eddy viscosity and nonlinear terms were determined by theoretical considerations of the energy cascade and discretization on the grid-scale, then checked by comparing an LES to a DNS of the energy decay and spectra for isotropic decaying turbulence,

The underlying LES channel model uses an eddy viscosity based on a URANS turbulent kinetic energy with a length scale damping function near the wall [15]. The (x,y,z) domain size of $2\pi \times 2 \times \pi$ is discretized on a 33 x 65 x 33 grid involving a cross-stream (y) geometric grid expansion factor of 1.15. This factor ensures y_+ values at 1st off-wall nodes are around unity. The grid is such that $Dx_+ \approx 200$ and $Dz_+ \approx 100$.

The decaying isotropic DNS is a higher Re version of a case [4, 5] that contains a strong initial transient. All the underlying decaying LES calculations were on a 64^3 mesh using the classical Smagorinsky eddy viscosity [13]. When a small physical viscosity is added for stability, the basic model agrees with the DNS decay rate as does the spectra of the LES until near the wavenumber cutoff, at which point there is a small anamolous at the high wavenumber end of the LES spectrum.

To each of these LES models, a filtered non-linear Leray model [3] is added. This filters non-linear advection terms and adds the following filtered non-linear term at the grid scales:

$$\frac{1}{1+\alpha^2 k^2}\mathrm{FFT}\left\{\alpha^2(u_{i,k}u_{j,k} + u_{i,k}u_{k,j})\right\} \text{ with } \alpha^2 = \Delta^2. \text{ where } \Delta \text{ is the mesh.} \quad (1)$$

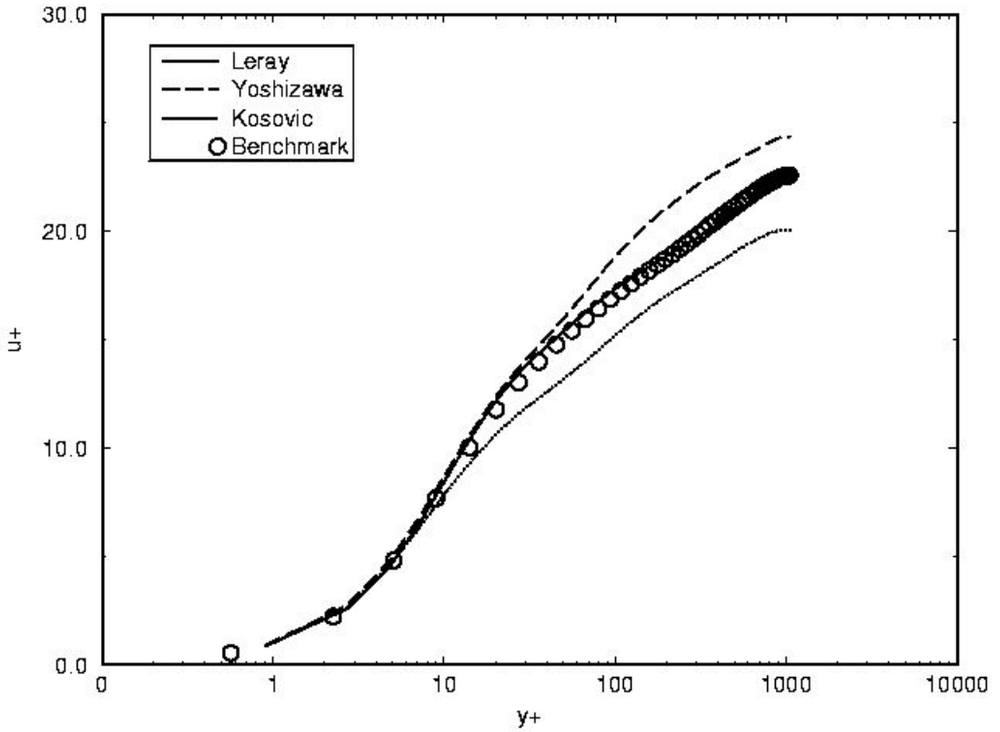


Figure 1: Mean profile for plane channel flow produced by several mixed nonlinear models [8, 15], including ours (Leray). Benchmark is dynamic LES [11]

The indicated Helmholtz filter is used with the decaying calculations and the channel code uses a multi-grid filter. This non-linear term is very similar to that proposed by Clark et al. [1], whose form reduces to the first term of (1) with a coefficient of $(1/12)\Delta^2$. Doing these operations succeeds in eliminating the anamolously high energies near the wavenumber cutoff in the pure Smagorinsky case. The non-linear terms of Clark et al. and LANS-α [2] were also tested, yielding worse results for the mean velocity profile.

References

[1] R.A.,Clark,J.H.,Ferziger,and W.C.,Reynolds J. Fluid Mech. **91**, 1 (1979). '
[2] C.,Foias,D.D.,Holm,and E.,Titi Physica D **152**, 505 (2001).
[3] B.J.,Geurts,and D.D.,Holm Phys. Fluids **15**, L13 (2003).
[4] J.R.,Herring,and R. M.,Kerr Phys. Fluids A**5**, 2792 (1993).
[5] D.D.,Holm,and R.M.,Kerr Phys. Rev. Lett. **88**, 244501 (2002).
[6] Kerr, R. M., J.A. Domaradzki, & G. Barbier 1996: Small-scale properties of nonlinear interactions and subgrid-scale energy transfer in isotropic turbulence. *Phys. Fluids* **8**, 197.
[7] J.,Kim,P.,Moin,and R.D.,Moser J. Fluid Mech. **177**, 133 (1987).
[8] B.,Kosović J. Fluid Mech. **336**, 151 (1997).
[9] J.,Leray Acta Mathematica **64**, 193 (1934).
[10] P.J.,Mason,and D.J.,Thomson J. Fluid Mech. **242**, 51 (1992).
[11] U.,Piomelli Phys. Fluids A**5**, 1484 (1993).
[12] U.,Schumann J. Comp. Phys. **18**, 376 (1975).
[13] J.,Smagorinsky Mon. Weath. Rev. **93**, 99 (1963).
[14] P.G,Tucker,and L.,Davidson Computers and Fluids **33**, 267 (2003).
[15] A.,Yoshizawa Phys. Fluids A**1**, 1293 (1989).

XXI ICTAM, 15–21 August 2004, Warsaw, Poland

NONLINEAR SCALE-FREE CASCADES AND THEIR STATIONARY SPECTRA

Dmitri O. Pushkin*, Hassan Aref**

* *University of Illinois at Urbana-Champaign, Department of Theoretical and Applied Mechanics, Urbana, IL 61801, USA*

** *Virginia Polytechnic Institute and State University, Blacksburg, Va 24061-0217, USA*

The cascade idea is central to our understanding of an amazingly broad scope of natural phenomena. One of the earliest mathematical cascade models, the Galton-Watson process [1], was suggested in 1874 as a solution to the "problem of the extinction of families." This kind of branching cascades was later used for theoretical treatment of chemical and nuclear chain reactions, electron multipliers, and statistics of polymers among other problems. These cascades are linear, as the agents are assumed to not interfere with each other.

Studies of turbulence provided a wealth of examples of nonlinear cascade processes. Among them are the Richardson cascade of energy in the inertial range that underlies the now classical approach of Kolmogorov [2], the Kraichnan reverse enstrophy cascade for two-dimensional turbulence [3], and various random cascade models suggested as theoretical explanations of the unsolved problem of turbulence intermittency.

We propose that many other complex multi-scale mechanical phenomena can be viewed as nonlinear cascades. They include coagulating particles in multiphase flows, coalescing drops in clouds and cracks in solids; the asteroid size distributions due to collisional fragmentation, etc.

Nonlinear cascades are characterized by strong interaction between the agents. Unlike linear cascades, they are are poorly understood. Their studies have relied on system-specific features and assumptions. As a result, the general picture remained unknown. Our purpose is to turn the attention to a broad class of nonlinear scale-free conservative cascades, and to show that seemingly different systems reveal common features when considered from this unifying viewpoint. In particular, we derive a nonlinear conservative cascade equation, and demonstrate how it can give rise to stationary power-law spectra. We show that the power-law exponent depends only on three indices characterizing a particular cascade: the 'conservation law' index m, the *scale homogeneity index* α, and the *nonlinearity index* h. This result is illustrated by Table 1.

Let us set up the stage. We think of cascades as statistical collective systems of interacting agents of different type. As a result of an interaction of two or more agents, 'new' agents form, whereas 'old' agents annihilate. For instance, the result of hydrodynamic interactions between turbulent eddies leading to exchange of their energies, is viewed as annihilation of 'old' eddies and creation of 'new' eddies having altered energies in their place.

A cascade state is specified by the agent distribution, also called spectrum, $n(t,s)$, which equals the average number of agents of the type s at the time t:

$$n(t,s) = \langle N(t,s) \rangle \,. \tag{1}$$

Here $N(t,s)$ is the instantaneous value for the number of agents. When s is continuous, $n(t,s)ds$ must be interpreted as the average number of agents in the interval $(s, s+ds)$. Common examples of agent distributions are the turbulent energy spectrum $E(t,k)$ in homogeneous isotropic turbulence, where the scalar wavenumber k plays the role of s; and the distribution $n(t,m)$ of masses of particle clusters formed due to cluster coagulation or/and fragmentation. Here we will assume s to be a real number, and refer to it as size.

The primary goal of a cascade theory is to predict the spectrum n. From the master equation for statistical systems [4], we derive a novel formal *nonlinear cascade equation*, which describes temporal evolution of n for a general nonlinear cascade:

$$\dot{n}(t,s) = \langle\langle\, \nu(s,\{s_i\})\, \rangle\rangle \,, \tag{2}$$

Table 1. Some scale-free conservative cascades with power-law spectra, $n(s) \propto s^{-\tau}$, discovered in various contexts. For all of them $\tau = 1 + (m+\alpha)/h$.

Cascade type	h	p	α	τ	Notes
Turbulence energy	$3/2$	0	1	$5/3$	Kolmogorov (1941)
Enstrophy	$3/2$	2	1	3	Kraichnan (1967)
Passive tracer	1	0	0	1	Batchelor (1959)
Cluster Coagulation (Aggregation)	2	1	α	$(3+\alpha)/2$	Pushkin & Aref (2002)
1D-Diffusion Limited Cluster Aggregation	3	1	0	$4/3$	Takayasu (1988)
'Spontaneous' fragmentation	1	1	1	3	Bem-Naim & Krapivsky (2000)
Collisional fragmentation	2	1	$2/3$	$11/6$	Dohnanyi (1969)
Percolation	2	1	2	$5/2$	
Scale-free networks	1	1	1	3	Barabasi & Albert (1999)

where the following notation has been introduced: for any function $f(\{s_i\})$,

$$\langle\langle\ f(\{s_i\})\ \rangle\rangle\,(t) \equiv \sum_{\{s_i\}} f(\{s_i\})\,\langle\, W(\{s_i\},[N])\,\rangle\,. \tag{3}$$

Here $\nu(s,\{s_i\})$ is the number of agents of size s created due to an "elementary" interaction of agents of sizes $\{s_i\}$; $W(\{s_i\},[N])$ is the probability of this interaction per unit time, the square brackets emphasize dependence on the whole distribution N. The summation in (3) is carried over all sets $\{s_i\}$.

As an example, we show that both the turbulent energy transfer equation [5] and the Smoluchowski coagulation equation [6] can be written in this form. At this point equation (2) is not closed, as the interaction strength depends on microdistribution N. However, for a wide class of conservative scale-free cascades the asymptotic spectra can be found without solving the closure problem.

The condition that a processes is scale free has several consequences: first, interactions have no characteristic size. In mathematical terms: if $s_i' = \lambda s_i,\ N' = \lambda^{-1}N$, then

$$\langle\, W(\{s_i'\},[N'])\,\rangle = \lambda^{\alpha}\,\langle\, W(\{s_i\},[N])\,\rangle\,. \tag{4}$$

For instance, for homogeneous isotropic turbulence $\alpha = 1$ and this value can be traced to the gradient operator in the Navier-Stokes equations. For coagulation, α is the homogeneity degree of the coagulation kernel.

Next, the interactions must be scalable in agent density. Thus, if $s_i' = s_i,\ N' = \lambda N$,

$$\langle\, W(\{s_i'\},[N'])\,\rangle = \lambda^{h}\,\langle\, W(\{s_i\},[N])\,\rangle\,. \tag{5}$$

For example, for homogeneous isotropic turbulence $h = 3/2$, because the interactions depend on the third order velocity correlation function, and velocity scales as square root of energy. For coagulation $h = 2$ due to binary collisions.

Let the conservation law read:

$$\sum_{s_j} \nu(s_j,\{s_i\}) s_j^m = 0,\ \text{for any set } \{s_i\}. \tag{6}$$

For instance, the energy conservation law for turbulence yields $m = 0$, while enstrophy conservation for 2D turbulence results in $m = 2$. Mass conservation in coagulation and fragmentation cascades yields $m = 1$.

A cascade can be maintained in a stationary state by constant 'forcing' through an influx of the conserved quantity E at some scale s_0. Then, we demonstrate that steady spectrum has the form:

$$n(s,s_0,E) = E^{1/h} s^{-\tau} f(s_0/s),\ \ \tau = 1 + \frac{m+\alpha}{h}. \tag{7}$$

We show that for wide classes of interactions the system completely "forgets" the small scale s_0 at much larger s. This is referred to as *similarity of the first kind* or *complete similarity* [7]. Then,

$$\lim_{x\to 0} f(x) = C,\ \text{and, thus, } n(s) \approx C E^{1/h} s^{-\tau}. \tag{8}$$

Such interaction classes depend on asymptotic properties of the interactions. They have been determined for cluster coagulation [8] and the weak wave approximation in turbulence ('locality conditions') [9]. The constant C was first introduced by Kolmogorov [2], and is often denoted as C_2. It is clearly interaction-dependent and, therefore, non-universal. For cluster coagulation an expression for C was found in [8].

The important relation (8) is our central result. It includes as particular cases the Kolmogorov spectrum, the Kraichnan spectrum for two-dimensional turbulence, the Batchelor spectrum for a passive tracer, and other cascades, including some fractal models of intermittency. Table 1 confirms that (7) has, in fact, much broader applicability. It can also serve as a powerful tool for analyzing new power-law spectra generated by cascade processes, due to the clear physical meaning of the indices α, h, and m.

References

[1] Watson, H. W., Galton F. On the probability of the extinction of families. *J. Antropol Inst. Great Britain and Ireland* **4**: 138, 1874.

[2] Kolmogorov, A. N. The local structure of turbulence in incompressible viscous fluid for very large Reynolds numbers. *Dokl. Acad. Nauk SSSR* **31**:538, 1941.

[3] Kraichnan, R. H. Inertial ranges in two-dimensional turbulence. *Phys. Fluids* **10** (7):1417, 1967.

[4] van Kampen, N. G. Stochastic processes in Physics and Chemistry, North-Holland, Amstredam, 1981.

[5] Frisch, U. Turbulence. Cambridge University Press, Cambridge, 1995.

[6] Smoluchowski v. M., Drei Vorträge über Diffusion, Brownische Bewegung und Koagulation von Kolloidteilchen. *Phys. Z.* **17**: 557, 1916

[7] Barenblatt, G. I.: Scaling, self-similarity and intermediate asymptotics. Cambridge University Press, Cambridge, 1996.

[8] Pushkin, D. O., Aref, H.: Self-similarity theory of stationary coagulation. *Phys. Fluids* **14** (2):694, 2002.

[9] Zakharov, V. E., L'vov, V. S., Falkovich G. E. Kolmogorov spectra of turbulence. Springer-Verlag, 1992.

3D-MEASUREMENTS IN AN ADVERSE-PRESSURE-GRADIENT TURBULENT BOUNDARY LAYER OVER SMOOTH AND RIBBED SURFACES

Thomas Indinger, Stefan Hickel, Nikolaus A. Adams
Technische Universität Dresden, Institut für Strömungsmechanik, 01062 Dresden, Germany

Summary 3D-PIV and 2D-LDA measurements in a fully turbulent boundary with adverse pressure gradient have been performed. Two types of surfaces were investigated: a smooth surface and a surface with riblets aligned in main flow direction. Particle image velocimetry was used to determine the influence of the surface structure on large-scale structures in the near wall region whereas profiles of mean and fluctuating velocity inside the boundary layer were acquired by laser Doppler anemometry. Significant changes of size and location of near-wall vortex structures were found ongoing with a deformation of the mean-velocity profile due to the riblet surface.

INTRODUCTION

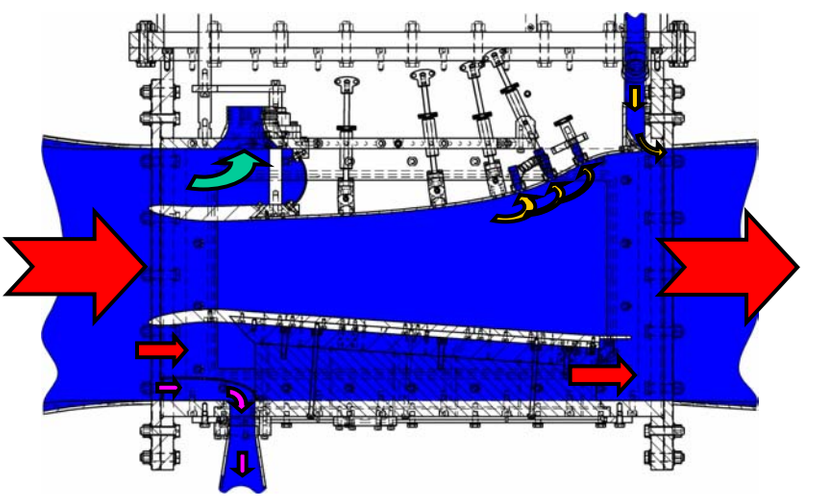
E. g. for optimal efficiency of turbo machines a strong deceleration of boundary layer flow is required which promotes, however, the tendency of the boundary layer to separate. Turbulent boundary layers are known to be less likely to separate than laminar ones. The main disadvantage of turbulent boundary layers are higher friction losses. Passive devices to reduce these losses resulting are so-called riblets, microscopic grooves aligned with mean-flow direction. Numerous investigations showed their properties and have helped to design optimal shapes and dimensions [1]. A yet unsolved issue is their influence on an adverse-pressure-gradient turbulent boundary layer.

The presented research has two objectives. First, beneficial the determination of vortex structure, mean and fluctuating velocity distributions inside a turbulent boundary layer over differently rough surfaces subjected to a pressure gradient, in order to examine the influence of riblets on the attached and separated flow. Second, the verification of a new method of particle image velocimetry (PIV) which is well-suited for measuring three-dimensional flows [2].

DISCRIPTION OF TEST FACILITY AND MEASUREMENT TECHNIQUES

The experiments have been carried out in a closed circuit water channel with a special designed test section, described in detail below. The medium water has been selected since the comparably large riblet dimensions facilitate manufacturing. Also, the developed boundary layer has a sufficient thickness for high resolution PIV and LDA measurements.

Test section of closed circuit water channel



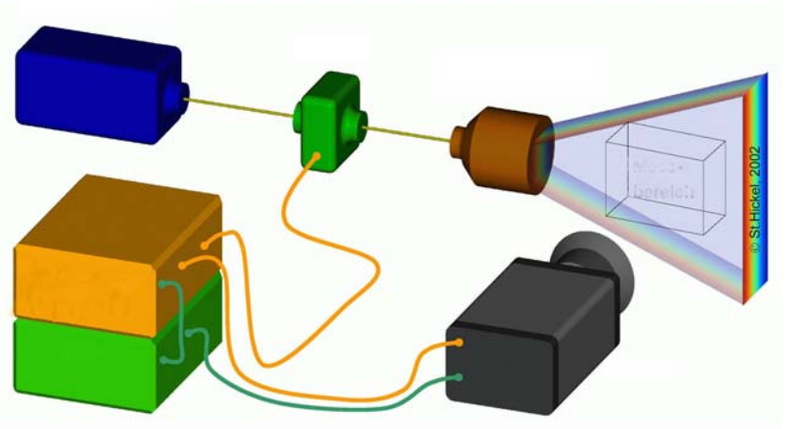
The test section made of stainless steel has a cross section of 0,4 x 0,4 m² and an overall length of 0,8 m. Installed is a flat plate of 0,725 m length with elliptical leading edge which allows to be lined with exchangeable surfaces. The reference surface is mirrored polished glass which improves measurements in the near wall region. The riblet surface has been manufactured by wire-cut EDM of a master and cloning by a silicon-vacuum-casting process. Based on previous investigations trapezoidal grooves were selected with a height to spacing ratio h/s = 0,5 and a tip angle of 30°. On the trailing edge of the plate an additional flap was installed in order to prevent back flow. To obtain a constant adverse pressure gradient in mean-flow direction a flexible and adjustable ceiling made from special plastics is installed. This contour is also translucent for optical access from top. For an controlled boundary layer development within the measurement section three additional suction taps are installed. Suction-tap one is located near the leading edge to avoid blockage and to control the stagnation point flow. A second tap is used for removing the entire flow above the upper wall. This is necessary because channel is of closed-circuit type without open surface. A third tap is located at the upper contoured wall in order to avoid separation due to curvature effects. Optical access is possible through a Plexiglas window on each side of the test section.

Conventional measurement techniques

Mean-velocity profiles were measured by a commercial LDA system by DANTEC Dynamics. Because of coincidence problems in the standard 2D-configuration a simple 1D-setup has to been used. Therefore three independent measurements at each location in streamwise direction were necessary in order to obtain profiles of all mean and fluctuating velocities.

To measure the pressure gradient 12 static pressure holes are installed on the flat plate. Wall shear stress was measured by means of a Preston tube. A reference point was defined right at the beginning of flow deceleration. At this location the velocity can be evaluated by a Prandtl tube, the free-stream turbulence level by a 1D-CTA probe.

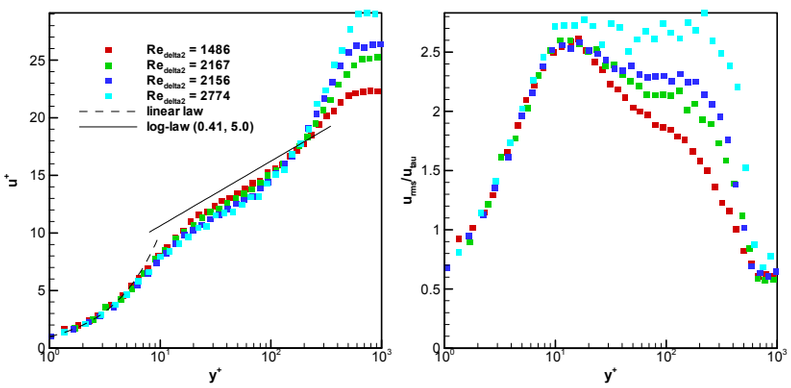
Fully 3D-PIV System



A newly developed 3D-PIV technology combines classical PIV with a color-coded light-sheet and with a new principle of three-dimensional cross-correlation of probability-density fields. To achieve a high-resolution measurement of three coordinates of position and displacement, a multi-color light sheet with a typical thickness of 1 up to 10 centimeters is used. The local wavelength is a (quasi-) continuous and invertible function of the coordinate in perpendicular direction across the light sheet. The particles which move with the flow scatter light elastically. So the frequency noted by the PIV colour camera permits the allocation of the particle to a certain plane in the light sheet. On the basis of the functional characteristics of the light sheet, the most probable position of each particle, visible on the color photographs, can be determined from the frequency of the scattered light. The probability density in the surrounding three-dimensional area of this point can not be calculated exactly, so we assume a log-normal distribution depending on luminance and the size of the particle's image. The superposition of the probability densities of all available particles results in a three-dimensional scalar field, which forms the data base for the cross-correlation instead of the usual two-dimensional black-and-white pictures. These fields are decomposed into cubical parts called “interrogation cubes”. The 3D cross-correlation of corresponding partitions performed in frequency domain is the core of the interrogation process and yields three components of displacement directly. Because the data base was cut into several layers of interrogation cubes not only in x and y direction but also in z direction, we obtain a true 3D measured field.

RESULTS

Mean-velocity profiles and profiles of root-mean-square fluctuating velocities for different Reynolds numbers obtained by LDA measurements (smooth surface) are shown in the figures on the right. The pressure gradient parameter β is 0.93 (red), 2.18 (green), 3.30 (blue) and 6.49 (turquoise), respectively. Whereas the linear part of the mean velocity profile is well recovered, the values of the von-Kármán constant κ and the integration constant C deviate from their zero-pressure-gradient values.



Results of the boundary layer quantities over the riblet surface and 3D-PIV measurements of coherent structures for both surface cases will be presented during the oral session of the meeting.

References

[1] Walsh, M. J.: Riblets, in: Viscous Drag Reduction in Boundary Layers, Bushnell, D. M., Hefner, J. N. (Editors), Progress in astronautics and aeronautics (Vol. 123), 1990

[2] Hickel, S.: Entwicklung einer neuen echt dreidimensionalen Particle Image Velocimetry, Thesis (in German), Brandenburg University of Technology, Cottbus, 2003.

POD ANALYSIS OF COHERENT STRUCTURES IN TURBULENT FLOWS

Song Fu, Min Tang, Jiang He
Department of Engineering Mechanics, Tsinghua Univ., Beijing, 100084, China

Abstract POD (proper orthogonal decompositions) is an efficient method to extract turbulent coherent structures. In this paper, POD technique is applied to the study of turbulent natural thermal convection between two vertical plates and the study of planar compressible mixing layer flow, based on DNS database. Both the direct POD method and the snapshots method are applied in the present work. The distribution of energy among POD modes has been closely examined. The most energetic structures are extracted, respectively spiral structures and streamwise vortexes in natural convection and span-wise vortices, turbulence structure etc in mixing layer. It has been observed that the flow structures in experiment match well with the ones in POD, and these structures are the essential characteristic of natural convection and mixing layer flow. The direct method and the snapshots method have also been compared in this paper.
Keywords Coherent structures, POD, natural convection, planar compressible mixing layer

INTRODUCTION

Though the coherent structures have been widely observed, there are many different methods to extract these structures. Among them, the Proper Orthogonal Decomposition (POD) method, which was first introduced in the fluid mechanics community by Lumley[1], has great influence in the turbulence study. From the point of energy, POD method can capture the most energetic structures that are dominant in the flow. Applying this method, many typical flows have been successfully studied such as the flow in a channel, plane boundary and Rayleigh-Benard convection. It has been proved efficient to analyze the dynamics of coherent structures. Now the POD method is applied here to identify the structures in the turbulent natural convection between two vertical plates and also the mixing layer flow.
POD method has also derived from the origin approaches to this so-called snapshots (strobes) method. Comparison of these specific processing methods is also mentioned.
(Due to the limited length of this extended summary, only the research on the structures in the turbulent natural convection between two vertical plates will be specifically described here.)

POD METHOD THEORY

POD extracts objectively optimal basis functions from experimental or DNS data to describe the characteristic of the data set. This basis is optimal in the sense that a finite number of these orthogonal modes represent more of energy than any other set of orthogonal modes.
Speaking of POD method, the origin way that Lumley introduced has met some difficulties in the determination of the basis functions from a practical point of view, incase of dealing with large-scale database. To solve this problem, Sirovich[3] brings forward a the method of snapshots or strobes. Both the two method is wildly used today in data analysis. Because of the different scale of our databases of these two different flows, we respectively applied these two methods.

Direct method

To gain the set of POD basis, an eigenvalue function is to be calculated. And this eigenfunction's order is up to $J \times N$, while J is the dim of the constants to be determined and N is the number of the components to be used as basis functions. So if a realistic count of the number functions in a realistic simulation gives a number of quite large, the caculation of eigen-problem will be out of the question.

Method of snapshots or strobes

Order of eigen-problem by means of snapshots is only correlate to the number of snapshots you chosen. We are interested in choosing a set of coherent structures that capture most of the energy. So we could confirm a minims number of snapshots considering how many energy we want to catch abstractly. The question of whether to ues the direct method or the snapshots method approach rests on a comparison of $J \times N$ and the minims number of snapshots.

DATA SET (NATURAL CONVECTION PART)

Natural convection

POD modes are obtained using 200 snapshots from a well-resolved DNS of natural convection between vertical plates at $Ra = 5.4 \times 10^5$ and $\Pr = 0.71$[2]. The computational domain is of the size $L_1 \times L_2 \times L_3 = 2\pi \times 1 \times \pi$ (gridding size $N_1 \times N_2 \times N_3 = 180 \times 48 \times 90$) in the streamwise, wall normal and spanwise directions.

Mixing layer

POD modes are obtained using 200 snapshots from a well-resolved DNS of mixing layer flow at $M_1 = 2.9, M_2 = 1.3, M_c = 0.8$, $\mathrm{Re} = 400, \mathrm{Re}_c = 525$ [4]. The computational domain is of the size $L_1 \times L_2 \times L_3 = 350 \times 120 \times 30$ (gridding size $N_1 \times N_2 \times N_3 = 875 \times 140 \times 80$) in the streamwise, wall normal and spanwise directions.

RESULT (NATURAL CONVECTION PART)

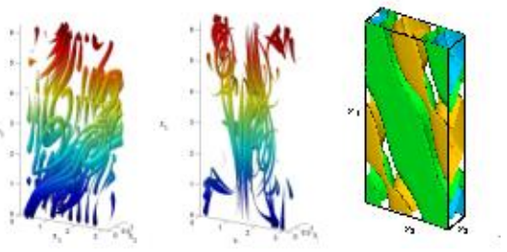
In Fig. 1 to Fig. 3, flow structures with and without mean flow are shown. Since in the real flow field the typical structures are all observed in the background of mean flow, the mode structures with mean flow are more consistent with the spiral structures observed in the DNS flow field. In Fig.2 to Fig. 3, the temperature field is displayed at the same time. It can be observed that the temperature structures match with spiral velocity structures, which implies that large-scale structures are always accompanied with heat transport. This is an essential characteristic of natural convection.

In Fig. 4, time series of coefficients associated with some modes are shown. We can see that large-scale structures, which contain more energy, have longer time scale than the small structures. It corresponds with the common sense to coherent structures.

CONCLUSIONS (NATURAL CONVECTION PART)

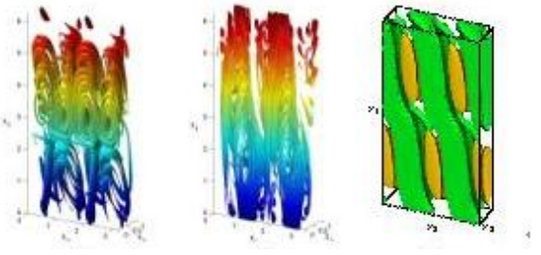
1). Via POD method, the distribution of energy can be known. The energy converge fast enough to do low dimension model research.

2). The modes implying spiral structure contain most of fluctuating energy. They are the main style of coherent structures in the turbulent natural convection between two vertical plates.



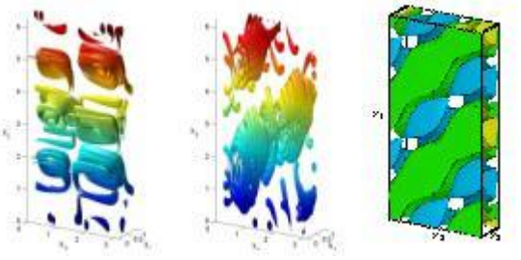
(a) (b) (c)

Fig. 1. Flow field associated with 2nd mode (a) streamtube without mean velocity. (b) streamtube with mean velocity. (c) temperature isosurface.



(a) (b) (c)

Fig. 2. Flow field associated with 4th mode (a) streamtube without mean velocity. (b) streamtube with mean velocity. (c) temperature isosurface.



(a) (b) (c)

Fig. 3. Flow field associated with 5th mode. (a) streamtube without mean velocity. (b) streamtube with mean velocity. (c) temperature isosurface. isosurface.

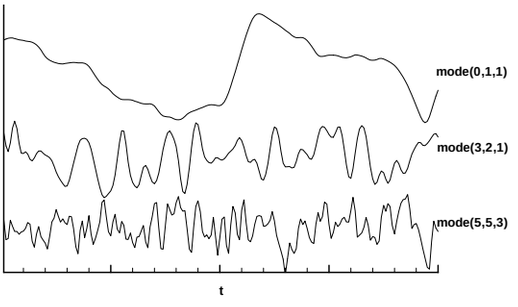


Fig. 4. Time series of coefficients associated with some typical modes.

References

[1] Lumley, J. L., The structure of inhomogeneous turbulence. In Atmospheric Turbulence and Wave Propagation. ed. A. M. Yaglom, V. I. Tatarski, 166-178. Moscow: Nauka, 1967

[2] Wang M.H., Fu S., Zhang G. H., Large-Scale Spiral Structures in Turbulent Thermal Convection Between Two Vertical Plates, *Physical Review E*, 2002, 66

[3] Sirovich, L., Turbulent and the dynamics of coherent structures Part I: coherent structures. *Q. Appl. Math.,*. **XLV** (3), 561-571,1987

[4] Li Q.B., Numerical study of compressible mixing layer with BGK scheme, disquisition of Doctor's degree. Tsinghua Univ. 2002

RESONANT INTERACTIONS OF 3D INSTABILITY WAVES IN AN AIRFOIL BOUNDARY LAYER FOR HARMONIC AND BROADBAND PERTURBATIONS

D. Sartorius[*], W. Würz[*], S. Wagner[*], V.I. Borodulin[**], Y.S. Kachanov[**]
[*]*Institut für Aerodynamik und Gasdynamik (IAG), Universität Stuttgart, Pfaffenwaldring 21, 70550 Stuttgart, Germany*
[**]*Institute of Theoretical and Applied Mechanics (ITAM), Russian Academy of Sciences, 630090 Novosibirsk, Russia*

Summary This paper is devoted to a systematic experimental investigation of resonant interactions of Tollmien-Schlichting (TS) waves occurred at weakly-nonlinear stages of the laminar-turbulent transition in an essentially non-self-similar boundary layer on an airfoil with a long laminar run. The paper is aimed to analyze the importance of the TS-wave interactions in dependence on the base-flow and disturbance parameters in order to clarify two main questions: (i) how the base flow non-uniformity influence the efficiency of the resonant interaction and (ii) when these interactions are significant for the transition prediction.

MOTIVATION OF THE STUDY

For the design of subsonic, natural laminar flow airfoils usually some half-empirical transition prediction methods are applied, which are based on the linear stability theory (the *N*-factor method for instance). This approach gives reliable results as long as the streamwise extent of the nonlinear disturbance growth is short in comparison with the linear part. However, previous experimental and theoretical studies (see e.g. [1]) have shown that even at rather low TS-wave amplitudes (0.1% or even lower) the linear disturbance growth can be modified quite significantly by some resonant interactions of instability waves. In this case the application of the transition prediction methods based purely on the linear stability theory becomes questionable and some nonlinear interactions of instability waves have to be taken into account. The present paper is devoted to the detailed experimental study of resonant weakly-nonlinear interactions of TS-waves occurred in a specially designed 2D airfoil with a long laminar run where the boundary layer is essentially non-self-similar.

EXPERIMENTAL SETUP AND REGIMES OF MEASUREMENTS

Experimental model and base flow

The experiments were conducted in the Laminar Wind Tunnel of the IAG. The lower surface of the WW03BL106 airfoil section was specially designed to provide a constant threshold of the *N*-factor of $N = \ln[A(f)/A_o(f)] = 6$ at an angle of attack of 2 degree and the chord Reynolds number of 700000. All necessary base flow parameters were measured in detail by means of pressure taps and hot-wire anemometry. Very good agreement with calculations was found. The boundary layer under investigation was essentially non-self-similar at its initial part and the corresponding shape factor H_{12} decreased downstream within the region of main measurements from 2.9 to 2.6. The mean flow stability characteristics measured for both 2D and 3D TS-waves in a range of frequencies from 200 to 600 Hz, were found to agree very well with the linear stability theory.

Excitation of disturbances

The experiments were carried out at controlled disturbance conditions. The TS-waves were excited in the boundary layer by a specially designed slit disturbance source, which was mounted flush with the surface at $s/s_{max} = 0.13$ (where $s_{max} = 604$ mm is the arclength measured from the leading edge). The slit was 0.2 mm wide and extended 290 mm in spanwise direction. Below the slit, 116 equally spaced pneumatic tubes were connected to 32 micro loudspeakers, which were driven by power amplifiers and a 16-channel signal generator. This disturbance source enabled to generate a great variety of initial disturbance spectra consisted of various combinations of 2D and 3D TS-waves with desirable frequencies and spanwise wavenumbers, including broadband perturbations.

Main regimes of measurements

In total, several dozens of initial disturbance spectra (and regimes of excitation) were examined. The following most important regimes have been studied. First of all the resonant interactions in symmetric tuned TS-wave triplets were investigated. Every triplet consisted of a 2D fundamental wave and a pair of 3D subharmonic waves with amplitudes of about one order lower than the fundamental one. The dependence of the tuned resonance on the fundamental wave frequency and amplitude was studied in a wide range, as well as the dependence on the initial phase shift between the fundamental wave and the subharmonic-wave pair, which was measured either directly or by means of a method of 'extremely small' (–1%) subharmonic frequency detuning. The influence of frequency detunings Δf_s of the subharmonic-wave frequency f_s was examined in a range of detuning parameter $\Delta f_s/f_s$ from –80 to +80% for four different frequencies of the 2D fundamental wave, when the 3D quasi-subharmonic wave pairs were excited at spanwise wavenumbers, which corresponded to the resonance condition at the position of the disturbance source. The influence of the spanwise wavenumber detunings was investigated for two fundamental frequencies. The case of the

strongest resonant interaction (found for the highest, of studied, fundamental frequency) was measured in detail in a range of spanwise wavenumber detunings $\Delta\beta/\beta_r$ from –100 to +100% (where β_r is the resonant spanwise wavenumber at the disturbance source location). A case of a joint interaction of a quasi-subharmonic 3D wave pair with two 2D fundamental waves was studied for fundamental-wave frequencies f_{f1} = 610 Hz and f_{f2} = 510 Hz, while the quasi-subharmonic modes had a frequency of f_s = 311 Hz. This case is regarded as an important first step for investigation of resonant interactions of continuous-spectrum (broadband) disturbances, which would simulate the conditions of a "natural" boundary-layer transition. A first case of such broadband perturbation was investigated as well. For most of the studied cases, separate development of subharmonic wave pairs in absence of the fundamental wave was also investigated for comparison. All measurements were performed for TS-wave maxima in their wall-normal profiles. The shapes of wall-normal and spanwise distributions of the disturbance amplitudes and phases were studied as well.

MOST IMPORTANT RESULTS

Tuned resonant triplets

It is found, in particular, that similar to the self-similar boundary layers (see e.g. [1]) the resonant amplification in tuned wave triplets is the double-exponential but depends significantly on the subharmonic/fundamental phase shift. A resonant suppression of the subharmonic-wave linear growth is observed when this shift is orthogonal to the resonant one. In contrast to the self-similar flows, the efficiency of the resonant interaction turned out to be strongly dependant on the fundamental-wave frequency. The interaction is very strong at high frequencies and is nearly absent at very low frequencies. This fact seems to be explained by a streamwise variation of the TS-wave dispersion characteristics associated with the base flow non-uniformity.

Frequency- and wavenumber-detuned resonances

It is found that the subharmonic-type resonant interactions have very large spectral width in the frequency spectrum and in the spanwise-wavenumber spectrum. The frequency detuned resonances turned out to be weaker (in general) than the tuned ones at the highest of studied frequency. However, for lower frequencies the strongest resonant interactions were observed in the wave triplets having positive frequency detunings with the detuning parameter $\Delta f_s/f_s$ varied from nearly zero (for fundamental frequency f_f = 610 Hz) to approximately +80% for f_f = 255 Hz. A 'cumulative effect' was found for a set of frequency detuned resonances, which led to a concentration of efforts of resonant interactions in several different wave triplets (with different fundamental frequencies) in a narrow range of subharmonic frequencies. The resonance turned out to amplify always two quasi-subharmonic modes: the excited one (f_{sexc}) and a symmetric mode (with frequency $f_{ssym} = f_f - f_{sexc}$). It is found that the mode, which has the lowest frequency (either f_{sexc} or f_{ssym}) reaches always the largest amplitudes in the end of the parametric stage of the resonant interaction. This effect is observed for all studied subharmonic-frequency detunings and fundamental-wave frequencies, regardless of the presence or absence of the predominance of frequency detuned resonances over the tuned ones. The resonances with spanwise-wavenumber detunings turned out to be weaker, in general, than those in the tuned case. At the same time, the subharmonic growth rates were found to depend significantly on the streamwise position and changed together with the base flow characteristics. In particular, the growth rate observed for $\Delta\beta/\beta_r$ = –54% close to the source was the same as that for $\Delta\beta = 0$, while in the end of the region of measurements the strongest amplification was found for $\Delta\beta/\beta_r$ = +50%. The resonant interaction with the 2D subharmonic wave ($\Delta\beta/\beta_r$ = –100%) is found to be very weak and the measured subharmonic growth corresponded to that due to the linear instability mechanism.

Multi-wave and broadband resonant interactions

It is found that in the case of joint resonant interaction of a quasi-subharmonic wave pair with two fundamental waves a superposition principle is satisfied approximately (in a certain sense) for efforts of these two resonances and the cumulative effect leads to a very rapid growth of quasi-subharmonic waves with increments, which are as large (or even somewhat greater) as those observed in the same two resonances when they occur separately. This property leads to a very strong resonant interaction of broadband instability waves observed in a case of a white-noise-like initial spectrum simulating a kind of "natural transition". In this case a rapid resonant growth of very-low-frequency disturbances was observed, while in absence of the interaction these perturbations attenuated in agreement with the linear stability theory.

ACKNOWLEDGEMENTS

This paper is supported by a joint international grant of Deutsche Forschungsgemeinschaft (N 436 RUS 113/749/0-1) and the Russian Foundation for Basic Research (N 03-01-04003).

References

[1] Borodulin V.I., Kachanov Y.S. and Koptsev D.B.: Experimental study of resonant interactions of instability waves in a self-similar boundary layer with an adverse pressure gradient: I Tuned resonances. *Journal of Turbulence* N.3:062, 2002.

XXI ICTAM, 15–21 August 2004, Warsaw, Poland

COMPRESSIBILITY EFFECTS AND SOUND PROPAGATION IN TURBULENT CHANNEL FLOW

Pierre Comte*, Christophe Brun**, Marie Haberkorn*,
Gilles Bouchet*, V. Pagneux***, Y. Aurégan***.
* *IMFS, 2 rue Boussingault, F67000 Strasbourg, France*
** *Polytech'Orléans/LME, 8 rue Léonard de Vinci, F45072 Orléans, France*
*** *LAUM, av. Olivier Messiaen, F72085 Le Mans, France*

Summary Large-Eddy Simulations of supersonic channel flow and the advection of a passive scalar oscillating at the walls are presented. A new and non-local scaling of the wall co-ordinate y^+ is proposed. In the quasi-incompressible regime, the oscillating passive scalar obeys the laminar Stokes law at high driving frequencies and exhibits increasing wall shear at decreasing frequency below $\omega^+ \sim 0.01$.

Direct and Large-Eddy Simulations of plane channel flows have proved helpful to better understand wall-bounded turbulence, in particular in supersonic and unsteady cases (see e.g. [1] and [2], resp.), in which the streamwise and spanwise homogeneity helped the interpretation. We have attempted to continue these investigations with a two-fold motivation:
a) reach higher Mach numbers to clarify the scaling of statistics with the Mach number, with particular interest in the spanwise correlations and the streak spacing, which is of crucial interest for the design of riblets for future supersonic transport aircraft;
b) understand the most basic mechanisms through which turbulence affects sound propagation. The advection by a quasi-incompressible channel flow of a passive scalar oscillating at the walls is considered here, as a starting point.

In both cases, LES are carried out with the macro-temperature closure of the compressible equations in conservation formulation [3], with the same subgrid-scale model and numerical methods as in [4], namely, the *filtered structure-function model* and an explicit McCormack scheme with 4th order accurate discretization of the inviscid fluxes. All calculations presented here have been performed at bulk Reynolds number $Re_b = 3000$, in a domain of size $(L_x/h, L_y/h, L_z/h) = (4\pi, 2, 4/3\pi)$ as in the DNS in [1], with $128 \times 65 \times 80$ grid points, instead of $144 \times 80 \times 119$. The subsequent friction Reynolds number $Re_\tau = \rho_w h u_\tau/\mu_w$ ranges from 180 for Mach number $M = u_b/\sqrt{\gamma R T_w} = 0.3$ to 522 for $M = 5$. However, the level of turbulence is found to decrease as M increases, as can be seen from Figure 1. This confirms that Re_τ is not the appropriate scaling parameter. Indeed, it has been known since [5] that no locally defined wall unit is satisfactory. Among the possible choices, that proposed as the best in [6], viz., $\rho(\tau_w/\rho)^{1/2} y/\mu$ yields corresponding Reynolds numbers h^+ decreasing from 180 for $M = 0.3$ to 84 for $M = 5$. Attempts to scale the mean velocity and temperature profiles lead one of us (C.B.) to propose an alternative to the van Driest transformation. It stems from the near-wall law $du^+ = (\mu_w/\mu) y^+$, integrated in the form $\overline{U}^+ = \int_0^{y^+} \frac{\mu_w}{\mu} dy^+ = y_c^+$. It yields an improved scaling of the mean profiles in the buffer region (Figure 2), and the spanwise correlation of the velocity fluctuations (Figure 3). It thus appears that the preferential spanwise streak spacing $\lambda_{z_c}^+$ settles around 130 for M between 0.3 and 2. This is consistent with [1], in which λ_z/h and $\lambda_{z_c}^+$ (approximately evaluated by us), hardly vary between $M = 1.5$ and $M = 3$.

The transport equation of a passive scalar oscillating at the walls is solved for several pulsations ω^+ at $M = 0.3$, for which compressibility is negligible. Figure 4 shows the evolution with ω^+ of the phase-averaged scalar gradient at the wall $\langle \left(\frac{dc}{dy}\right)_w \rangle = A_\tau(y) \cos[\omega t + \Phi_\tau(y)]$, compared with experimental and numerical counterparts in pulsating flows ([2],[7],[8]). The general trends are recovered, namely, negligible departure from the laminar Stokes solution at high frequencies, and increasing shear with decreasing phase shift at low frequencies. The dip of A_τ below its Stokes value, whose origin is controversial, is not recovered in this linearized scalar approach. Note that, in these calculations, the scalar's diffusivity has been set in such a way that the Stokes thickness $l_s^+ = \sqrt{2/(Sc\,\omega^+)}$ is kept constant ($l_s^+ = 30$, which is expected to be large enough for the shear wave to reach the buffer region). Other choices are under investigation.

Acknowledgements: part of the CPU time was allocated free by IDRIS, the CNRS supercomputing center.

References

[1] Coleman, G.N., Kim, J., Moser, R.D.: A numerical study of turbulent supersonic isothermal-wall channel flow. *J. Fluid Mech.* **305**:159-183, 1995.
[2] Scotti, A., Piomelli, U.: Numerical simulation of pulsating turbulent channel flow. *Phys. Fluids.* **13**(5):1367–1384, 2001.
[3] Lesieur, M., Comte, P.: Favre filtering and macro-temperature in large-eddy simulations of compressible turbulence. *C. R. Acad. Sci.* **329**IIb:363–368, 2001.
[4] Ducros, F., Comte, P., Lesieur M.: Large-Eddy Simulation of transition to turbulence in a boundary layer developing spatially over a flat plate. *J. Fluid Mech.* **326**:1–36, 1996.
[5] Bradshaw, P.: Compressible turbulent shear layers. *Ann. Rev. Fluid Mech.* **9**:33–54, 1977.
[6] Huang, P.G., Coleman, G.N., Bradshaw, P.: Compressible turbulent channel flows: DNS results and modelling. *J. Fluid Mech.* **305**:185–218, 1995.
[7] Ronneberger, D., Ahrens, C.D.: Wall shear stress caused by small amplitude perturbations of turbulent boundary-layer flow: an experimental investigation. *J. Fluid Mech.* **83**:433–464, 1977.
[8] Tardu, S., Binder, G.: Wall shear stress modulation in unsteady turbulent channel flow with high imposed frequencies. *Phys. Fluids. A* **5**:2028–2037, 1993.

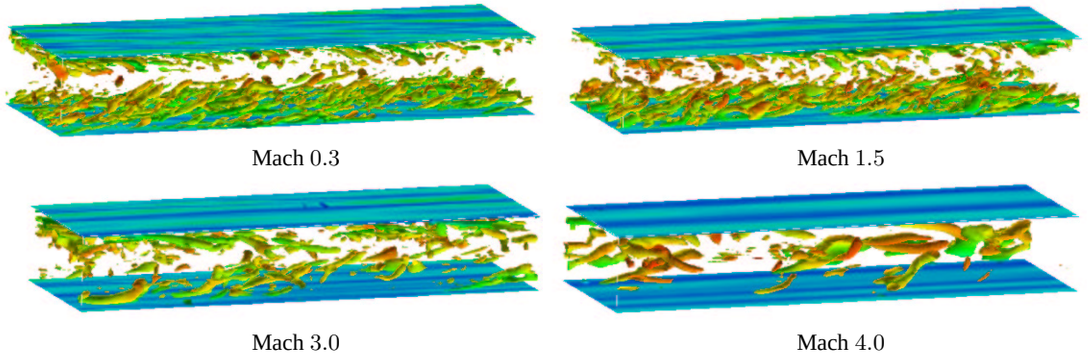


Figure 1. Coherent structures materialized by the isosurface $Q = 6\frac{u_\tau}{h}$ and slices of streamwise velocity near the walls.

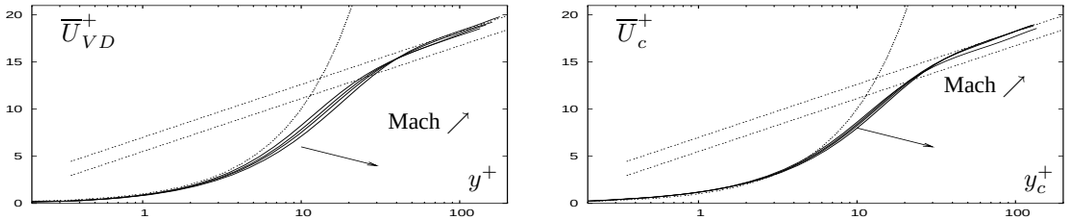


Figure 2. Mean velocity profiles after van Driest transformation (left) and the propoosed scaling (right).

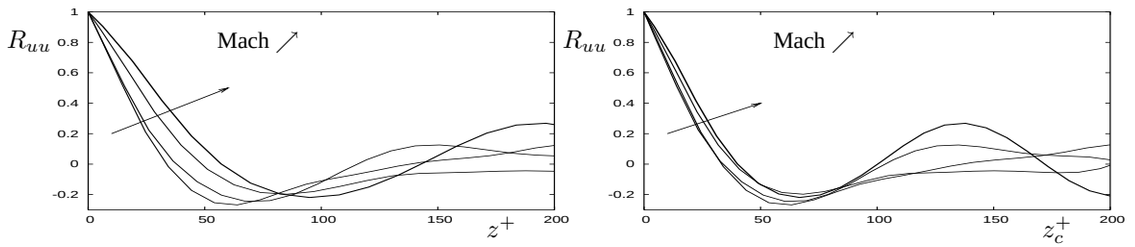


Figure 3. Spanwise correlations of the streamwise velocity fluctuations in the near-wall region ($y_c^+ = 2.5$) in standard scaling (left) and with modified wall unit (right), for $0.3 \leq M \leq 2$.

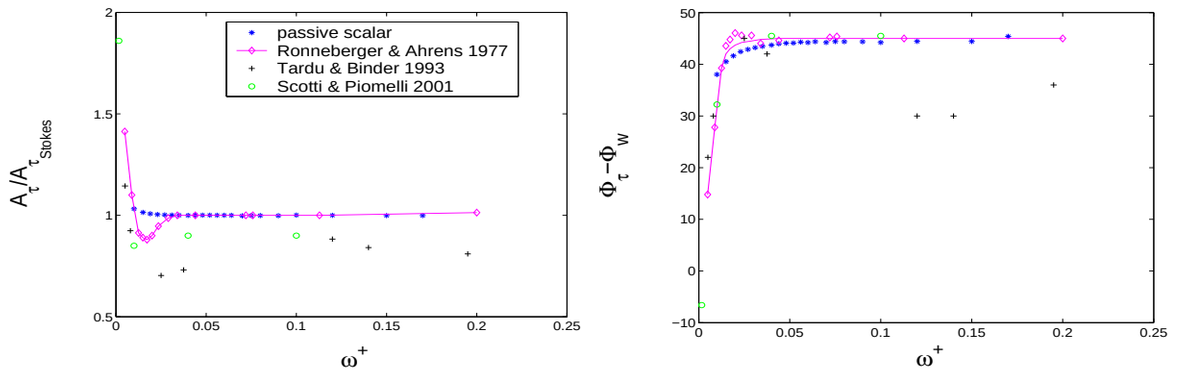


Figure 4. Normalized wall shear impedance as a function of the pulsation ω^+. **Left:** amplitude normalized by the laminar Stokes value $A_{\tau_{\text{Stokes}}}$. **Right:** phase shift between the shear and the forcing at the wall. The laminar Stokes solution corresponds to 45° $\forall\omega^+$.

ON THE STRUCTURE OF TURBULENCE AND REYNOLDS STRESS DISTRIBUTION IN THE BOTTOM BOUNDARY LAYER OF THE COASTAL OCEAN

Luksa Luznik[*], Roi Gurka[*], W.A.M. Nimmo Smith[**], Weihong Zhu[*], Joseph Katz[*], Thomas Osborn[***]

[*] *Department of Mechanical Engineering, The Johns Hopkins University, Baltimore, USA*
[**] *School of Earth, Ocean and Environmental Sciences, University of Plymouth, Plymouth, UK*
[***] *Department of Earth and Planetary Science, The Johns Hopkins University, Baltimore, USA*

Summary Turbulent flow measurements were performed in the bottom boundary layer on the U.S. Southeastern continental shelf using PIV. The experiments were performed within 2 m above the bottom, during half of a tidal cycle. A log layer was identified from the obtained velocity field realizations. The bottom boundary layer consists of powerful vortical structures ("gusts"), separated by periods of quiescent flow. In addition, the profiles of Reynolds stresses are estimated using the second order structure function of the velocity fluctuations.

INTRODUCTION

In the coastal ocean, the momentum and energy balances are influenced by several parameters, among which the bottom shear stress and the dissipation rate are of particular significance [1]. The bottom shear stress affects the circulation directly and also generates turbulence that diffuses into the flow. The dissipation rate is a controlling mechanism for the entire turbulent energy budget. Thus, understanding and modeling of ocean flows, sediment transport, pollutant dispersal, and biological processes rely on knowledge of the turbulence characteristics near the ocean bottom. Turbulent flow measurements were performed in the bottom boundary layer on the U.S. Southeastern continental shelf using particle image velocimetry (PIV). The measurements covered half of a tidal cycle within 2 meters from the ocean bed. The results include the mean velocity profile, vorticity contours as well as distribution of Reynolds stresses and dissipation rate, along with the turbulence spectra.

EXPERIMENTAL SET-UP AND DEPLOYMENTS CHARACTERISTICS

The submersible PIV system was deployed in the vicinity of the South Atlantic Bight Synoptic Offshore Observational Network (SABSOON) in a water depth of 23m. Images were recorded using two 2Kx2K digital cameras. The light sheets were produced by a dual-head, pulsed, dye lasers and transmitted via optical fibers to the submerged optical probes. Other environmental sensors were also deployed with the submersible PIV system. All the instruments were rigidly mounted on a telescopic platform with a maximum profiling range of 10 m. The platform also aligned the light sheets with the mean flow. Cameras were focused onto two sample areas of 35x35 cm^2 in vertical plane, and separated horizontally by 31 cm. Correlation analysis with 64x64 pixels (corresponding to 1.1x1.1cm^2 area in the fluid) interrogation areas, and 50% overlap between adjacent windows, yielded 63x63 2D vectors per individual instantaneous realization. Depending on natural seeding, only 85 to 90% of the interrogation areas have a sufficient number of particles to calculate the velocity. During one of the SABSOON deployments, the system was submerged continuously for 5 hours, and images were recorded at 3Hz for 20 minutes, generating 3600 realizations per run. Then the elevation was changed and another series was recorded.
The aim of this experiment was to acquire data covering accelerating, peak, and decelerating phase of the tidal cycle, and at the same time traverse the water column. Tidal currents ranged from 17 to 27 cm/sec at the lowest elevation, and up to 40 cm/sec at the highest measurement site. Surface waves signature was present in all records with streamwise wave induced flow amplitude ranging from 7 to 10 cm/sec, and a typical period of 8 seconds.

RESULTS AND DISCUSSION

The mean streamwise velocity profiles are constructed from seven data sets within 2 m above the bottom. The velocity values are normalized by the mean current speed (figure 1) obtained independently from the ship's ADCP. The data demonstrate the existence of a "log layer" within a mixed oscillatory motion and a mean current flow. Clearly, the slope of the log layer varies, presumably due to effects of acceleration and deceleration.
A major challenge is to separate between waves induced motion and turbulence while calculating the Reynolds stresses. To estimate the Reynolds stresses, we use 2nd order structure function of the velocity fluctuations. The methodology is introduced in [2] and has already been applied to ocean data by [3]. The magnitude of the structure function asymptotically approaches that of the Reynolds stress when the separation between the scale of the measured flow field is larger than the integral length scale of turbulence, but is still much smaller than the wavelength of the surface waves. The PIV data enables us to calculate the structure function as a function of the separation distance. Vertical profiles of the shear stresses are obtained by dividing the vector maps into horizontal strips and applying the structure function separately on each of them. The final manuscript will contain a comparison between the shear stress estimate from the log layer profile and the Reynolds stress calculated from the structure function.

The turbulent flow in the bottom boundary layer consists of domains with powerful vortical structures ("gusts"), separated by periods of quiescent flow as illustrated by the time series of vorticity magnitude (figure 2). For the subsequent analyses, the flow is classified into categories of high (figure 3), intermediate, and low (figure 4) instantaneous mean vorticity magnitude. Conditional sampling of the Reynolds shear stresses based on the vorticity magnitude shows that almost all the contribution to the Reynolds stresses are made by the high and intermediate vorticity magnitude events. This trend is consistent with previous observations at lower current speed [4]. During periods of low vorticity magnitude, the shear stresses are essentially zero. Thus, shear stresses, and as a result turbulent production, are generated only in flow domains containing large vortex structures, i.e. during periods of gusts. On the other hand, the dissipation rates estimated from the spectra and by direct calculation of local velocity gradients indicate that dissipation occurs continuously and increases only slightly during gusts [1]. This trend is consistent with the shapes of the conditionally sampled turbulent spectra, showing that the gusts affect mostly the large scales, and have much less effect on the small scales. Consequently, the intermittent passage of large-scale vortical structures has a weak effect on the local dissipation rate, which is dominated by the more uniform distributions of the background small-scale turbulence. Data analysis that will be presented in the final manuscript will also examine the occurrence of bursting, ejection and sweeps, and their effects on production and dissipation.

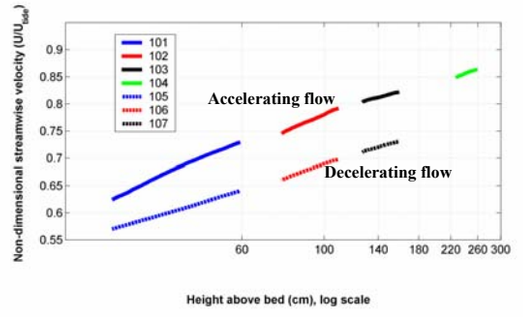


Figure 1: Mean velocity profile in the ocean bottom on a semi-log scale, normalized by the mean current speed

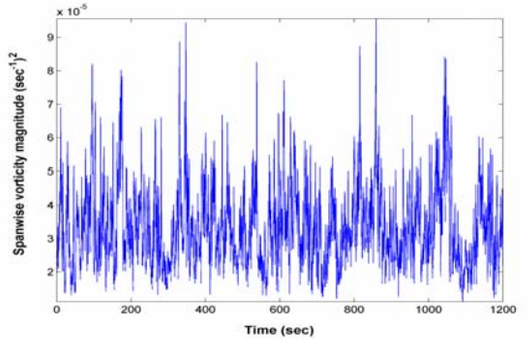


Figure 2: Time series of the mean vorticity magnitude over an entire vector map

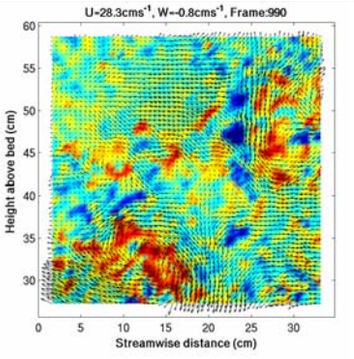


Figure 3: Instantaneous vorticity contour plot demonstrating the presence of strong vortical motion

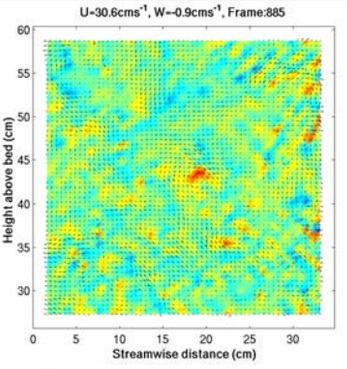


Figure 4: Instantaneous vorticity contour plot demonstrating the presence of a quiescence flow

References

[1] Doron, P., L. L. Bertuccioli, J. Katz, and T. R. Osborn,: Turbulence Characteristics and Dissipation Estimates in the Coastal Ocean Bottom Boundary Layer from PIV Data. J. of Phys. Oceanogr., **31**:2108-2134, 2001.

[2] Trowbridge J.H.: On a Technique for Measurement of Turbulent Shear Stress in the Presence of Surface Waves, J. of Atmos. Oceanic Tech., **15**: 290-298, 1998.

[3] Nimmo Smith W.A.M, Atsavapranee P., Katz J. and Osborn T.R.: PIV Measurements in the Bottom Boundary Layer of the Coastal Ocean, Exp. in Fluids, **33**:962-971, 2002.

[4] Nimmo Smith W.A.M, Katz J. and Osborn T.R.:. On the Structure of Turbulence in the Bottom Boundary Layer of the Coastal Ocean, submitted to J. of Phys. Oceanogr., 2003.

Numerical Modelling of Small-Scale Turbulence in clouds

Mirosław Andrejczuk*, Szymon P. Malinowski*
Wojciech W. Grabowski** and Piotr K. Smolarkiewicz**
*Warsaw University, Institute of Geophysics, Pasteura 7, 02-093 Warszawa, Poland.
**National Center for Atmospheric Research, Boulder, CO, USA

Summary. High-resolution modelling of small-scale turbulent mixing of clouds and clear air was performed. A substantial production of TKE by negative buoyancy resulting from evaporation of cloud water occured at centimeter scale. Anisotropy of turbulence due to buoyancy effects appeared to be an important feature of the simulations, even when TKE produced by evaporation was small in comparision to TKE cascading down from larger scales.

Introduction.

Despite recent progress in cloud physics, the understanding of key issues such as spatial distribution of cloud particles, turbulent mixing of clouds with the environment, or interaction of turbulence and microphysics, is still far from being complete. These issues are important - beyond fundamental understanding - in applications such as radiative transfer through clouds, initiation of precipitation in warm (i.e. ice-free) clouds, and parameterization of small-scale and microscale processes in models resolving larger scales.

This paper discusses results from a series of idealized numerical simulations of moist 3D turbulence accompanying the small-scale cloud/clear-air mixing. In the moist case, kinetic energy of small-scale motions comes not only from the classical downscale energy cascade, but it can also be generated internally due to the evaporation of cloud droplets.

We simulate directly the interfacial mixing, in order to study the impact of the evaporative cooling and cloud droplets' sedimentation on the generation of the turbulent kinetic energy (TKE). Our numerical model is set up to simulate the crux of the laboratory experiment described in [1]. Insofar as the initial and boundary conditions are concerned, we do not strive to mirror the laboratory case - the latter would be both computationally demanding and mathematically complex - but tend rather to capture key physical features of the problem at hand. This is in the spirit of DNS turbulence studies which assume heavily idealized initial and boundary conditions, while focusing on an accurate representation of the evolving flow.

Numerical model setup.

The analytic equations of motion (in anelastic approximation), thermodynamic energy equation, water substance conservation equation and equations for the cloud water parameterizations (bulk and detailed, accounting for droplet sedimentation) are solved by means of finite-difference approximations using the semi-Lagrangian/Eulerian nonhydrostatic anelastic model EULAG, broadly documented in the literature ([2-6] and references therein).

Taking into account all physical and numerical limitations of the approach, we compromised on using a relatively coarse grid length 0.01 m and modest computational grid 64^3 , for all simulations reported here. In effect, the simulations reported fall into the gray area between poorly resolved DNS and well resolved LES.

The initial velocity field has the same spatial distribution for three series of experiments corresponding to high, moderate and low TKE level in clouds. The initial air temperature is set to 293K everywhere and the water vapor mixing ratio outside the cloud is 9.9g/kg ; this corresponds to the relative humidity of 65%). The initial cloud water is specified to form filaments, with the same temperature as in the environment, 100% relative humidity, and the cloud water mixing ratio around 3.2g/kg defined such that cloudy filaments are neutrally buoyant.

In all detailed microphysics simulations, 16 classes of cloud droplets are used with the droplet sizes linearly distributed in the range from 0.78 μm to 24 μm.

Results and conclusions.

Our simulations suggest that, at high initial values of the large-scale TKE, moist processes have minor impact on the small-scale dynamics of mixing and homogenization. In particular, the evolutions of TKE and dissipation rate (proportional to enstrophy) differ between moist and dry simulations only at the final stage of mixing, when most of the TKE has already been dissipated.

There are, however, significant differences related to the small-scale anisotropy. Moist turbulence is anisotropic even for high values of the TKE input, with turbulent filaments elongated in the vertical, consistent with the laboratory experiment [7].

For moderate and low initial values of TKE, the influence of moist processes on small-scale mixing and homogenization is substantial. Especially, for low initial TKE, the energy/enstrophy evolutions are dominated by moist processes, and the impact of cloud droplet sedimentation is the largest. Relative differences between simulations with the bulk and detailed microphysics appear not big even for low TKE input. However, coarse spatial resolution afforded in this study tends to overestimate the role of the temperature and moisture diffusion compared to the cloud droplet sedimentation, across the cloud/clear-air interface. More detailed numerical experimentation at higher resolutions (e.g., 128^3 ,256^3 , etc.), whatever possible is necessary

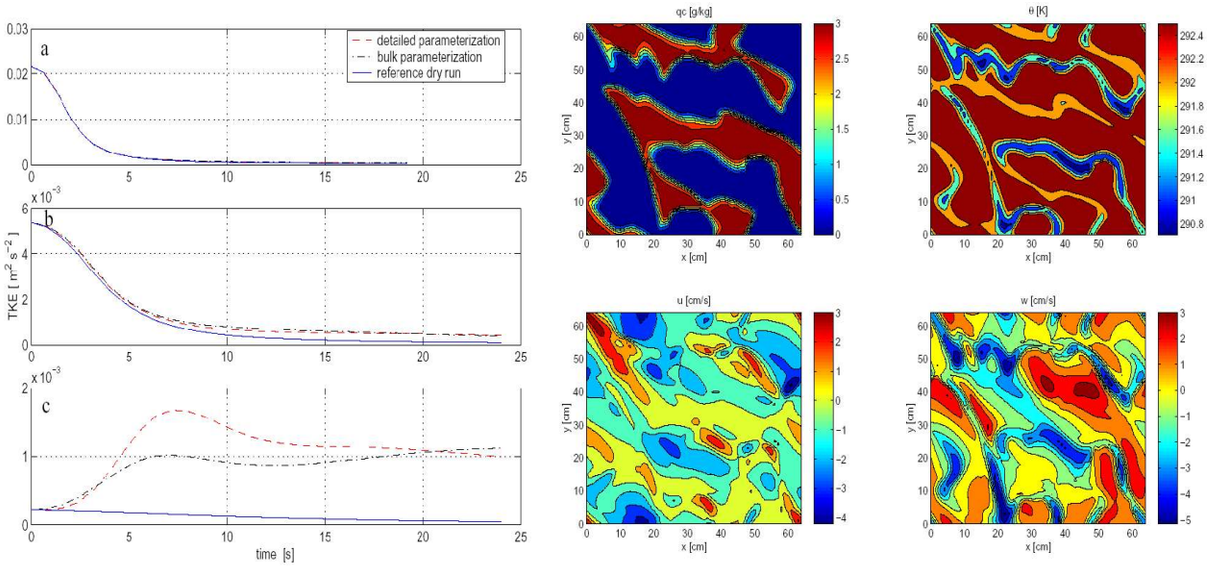


Fig.1. On the left: temporal evolution of TKE for three initial values: (a) – high, (b) moderate, (c) low. On the right: vertical cross section through the computational domain after 3.6 seconds of simulations with low initial TKE and detailed microphysics. Clockwise from the upper left panel: cloud water, potential temperature (visible cooling due to evaporation of sedimenting droplets), horizontal (u) and vertical (w) velocity components.

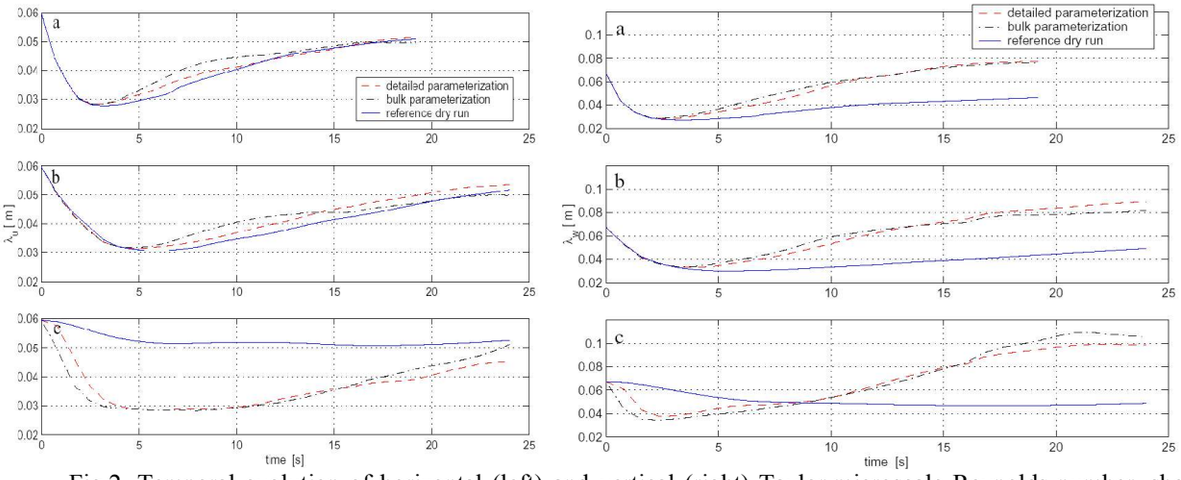


Fig.2. Temporal evolution of horizontal (left) and vertical (right) Taylor microscale Reynolds number, showing anisotropy in smallest scales of resolved motions.

Acknowledgements:

This research was supported by grant No. 6 P04D 027 19 of the Polish Committee for Scientific Research. The National Center for Atmospheric Research is sponsored by the National Science Foundation.

References:

[1] Malinowski, S.P., I. Zawadzki and P. Banat, 1998: Laboratory observations of cloud-clear air mixing at small scales, J.Atmos.Ocean.Technol. 15, 1060-1065.

[2] Grabowski W.W., P.K. Smolarkiewicz, 1996: Two-time-level semi-Lagrangian modeling of precipitating clouds. Mon. Weather Rev. 124,: 487-49.

[3] Grabowski W.W., P.K. Smolarkiewicz, 2002: A multiscale anelastic model for meteorological research. Mon. Weather Rev. 130, 939-956.

[4] Smolarkiewicz P.K., V. Grubisic, L.G. Margolin, 1997: On forward-in-time differencing for fluids: Stopping criteria for iterative solutions of anelastic pressure equations. Mon. Weather Rev. 125,: 647-654.

[5] Smolarkiewicz P.K.and L.G. Margolin, 1998: MPDATA: A finite-difference solver for geophysical flows. J. Comput. Phys. 140,: 459-480.

[6] Smolarkiewicz P.K.,J.M. Prusa, 2002: VLES modeling of geophysical fluids with nonoscillatory forward-in-time schemes. Int. J. Numer .Meth. Fl. 39, 799-819.Banat P. and S.P. Malinowski, 1999: Properties of the turbulent cloud-clear air interface observed in the laboratory experiment, Phys. Chem. Earth, B 24, 741-745.

[7] Andrejczuk, M., W.W. Grabowski, S.P. Malinowski and P.K. Smolarkiewicz, 2003: Numerical simulation of cloud/clear-air interfacial mixing. J. Atmos. Sci., in press.

IMPACT OF PRESSURE-GRADIENT CONDITIONS ON HIGH REYNOLDS NUMBER TURBULENT BOUNDARY LAYERS

Hassan Nagib[*], Chris Christophorou*, and Peter Monkewitz[**]
[*]*Illinois Institute of Technology (I I T), Chicago, IL 60616, USA*
[**]*Swiss Federal Institute of Technology Lausanne (EPFL), CH-1015, Lausanne, Switzerland*

Summary Mean velocity distributions in the overlap region, over the range of Reynolds numbers 10,000 < Re_q < 70,000, under five different pressure-gradient conditions are accurately described by a log law. The pressure-gradient conditions include adverse, zero, favorable and strongly favorable. The wall-shear stress was measured using oil-film interferometry, and hot-wire sensors were used to measure velocity profiles. Parameters of the logarithmic overlap region developed from these higher Reynolds number boundary layers continue to be consistent with our recent findings and to remain independent of Reynolds number. The best estimate of the log-law parameters from the zero-pressure gradient boundary layers is k = 0.38, B = 4.1. However, the Kármán "coefficient" (k) is found to vary considerably for the non-equilibrium boundary layers under the various pressure gradients. The results highlight the variation with pressure gradient not only in the outer region of the boundary layer but also within the inner region.

INTRODUCTION & EXPERIMENTAL ARRANGEMENT

Two independent experimental investigations of the behavior of turbulent boundary layers with increasing Reynolds number (Re_q) were recently completed [1]. The experiments were performed in two facilities, the MTL wind tunnel at KTH and the NDF wind tunnel at IIT. While the KTH experiments were carried out on a flat plate, the model used in the NDF was a long cylinder with its axis aligned in the flow direction. Both experiments were conducted in a zero-pressure gradient, covered the range of Reynolds numbers based on the momentum thickness from 2,500 to 27,000, and utilized oil-film interferometry to obtain an independent measure of the wall-shear stress. Contrary to the conclusions of some earlier publications, careful analysis of the data revealed no significant Reynolds number dependence for the parameters describing the overlap region using the classical logarithmic relation. The parameters of the logarithmic overlap region were found to be constant and were estimated to be: k = 0.38, B = 4.1. These two experiments have been recently extended to Reynolds numbers based on momentum thickness exceeding 70,000. The current experiments were also carried out in the National Diagnostic Facility (NDF) at IIT on a 10 m long and 1.5 m wide flat plate using free-stream velocities ranging from 30 to 85 m/s. Again, hot-wire anemometry and oil-film interferometry were used to measure the velocity profiles and the wall-shear stress, respectively. The design of the experiments, and in particular the location and spacing of the velocity profiles in the downstream direction and the hot-wire sensor in the wall-normal direction, developed to facilitate the evaluation of wall-normal *and* streamwise derivatives. The arrangement of the NDF was designed to allow the adjustment of the test-section ceiling to impart various pressure gradients. Several conditions were investigated so far, including: Adverse Pressure Gradient (APG), Zero Pressure Gradient (ZPG), Favorable Pressure Gradient (FPG), Strongly Favorable Pressure Gradient (SFPG), and Complex Pressure Gradient (CPG) as displayed in Figure 1.

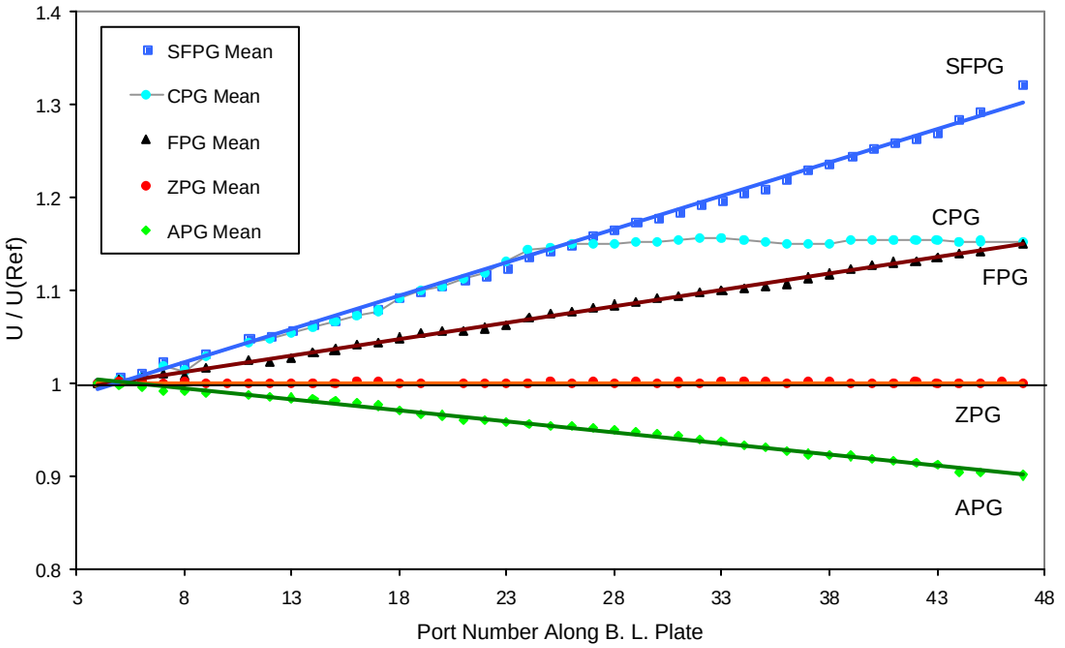


Figure 1. Variation of free-stream velocity along 10 m long boundary layer plate for various pressure-gradient conditions

RESULTS

One of the cornerstones of our approach to measurements of turbulent wall-bounded flows is the *independent* and accurate measurement of the wall shear stress with oil-film interferometry. We believe the only wall-bounded flow that may not require such measurements is the *fully developed* pipe flow, where the careful measurement of pressure gradient can lead to an accurate determination of the friction velocity. For the non-equilibrium boundary layers under various pressure-gradient conditions, one can be dramatically misled by other indirect techniques for the determination of wall-shear stress. Figure 2 compares our recent ZPG measurements with the recent two sets of measurements of Hites and Österlund. The value of the Kármán constant extracted using the correlation proposed by Fernholz [2] and all three sets of data is approximately 0.38.

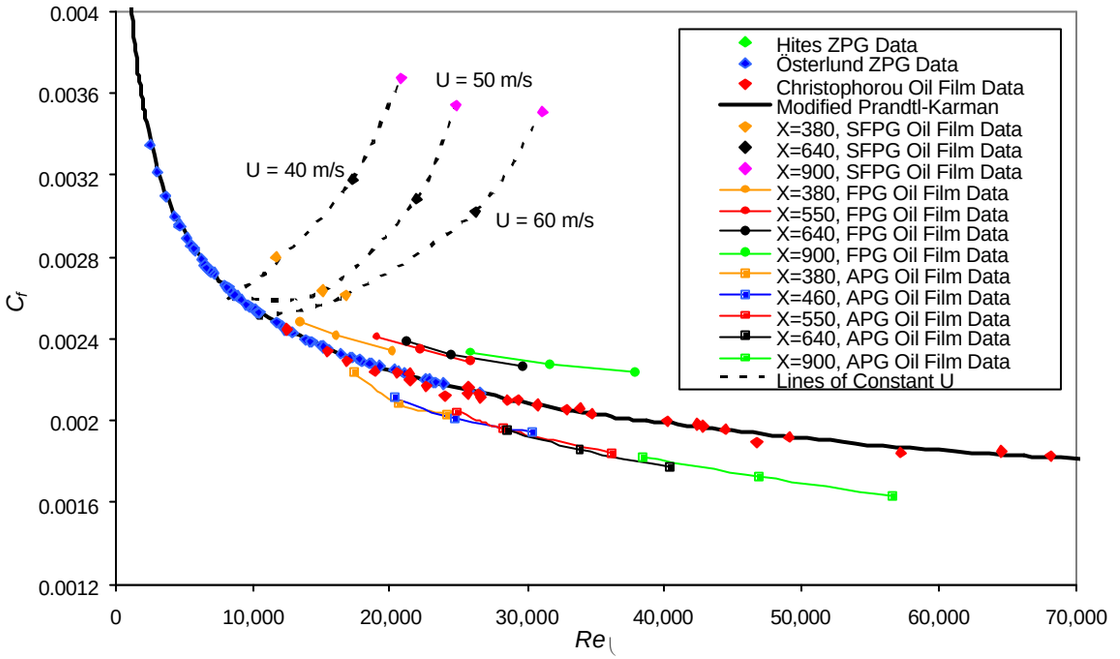


Figure 2. Variation of skin friction with momentum-thickness Reynolds number for different streamwise positions and free stream velocities.

A few samples of pressure-gradient data are included in Figure 2. In particular, the behaviour of the non-equilibrium layers with the SFPG is most revealing when contrasted to the equilibrium ZPG data where the resulting skin friction is independent of whether Re_q is varried by changing the free-stream velocity or the downstream distance. As in our earlier work [1], profiles of the mean and rms streamwise component of the velocity and their spatial derivatives are used to examine the effects of the pressure gradient on the inner and outer layers as well as their overlap region. The results demonstrate that the pressure gradient causes significant changes not only in the outer region of the boundary layer but also within the inner region; i.e., the buffer layer. The effect of these changes on Coles' outer layer parameter and the behavior of the maximum turbulence stress have also been documented.

CONCLUSIONS

A number of yet unexplained differences between wall-bounded turbulent flows in pipes [3], channels [4] and boundary layers are discussed and clarified based on the comparison between our recent measurements in ZPG boundary layers and the present results for different pressure gradients. The variation of the Kármán "coefficient" (k) from generally accepted values is revealed by these measurements in both equilibrium and non-equilibrium wall-bounded shear flows.

References

[1] J.M. Österlund, A.V. Johansson, H. M. Nagib, and M. H. Hites, A note on the overlap region in turbulent boundary layers, Phys. Fluids, 12:1 - 4, 2000.

[2] H. H. Fernholz, Ein halbempirisches Gezetz fuer die Wandreibung in kompressiblen turbulenten Grenzschichten bei isothermer und adiabater Wand. ZAMM, 51: 148 - 149, 1971.

[3] A. E. Perry, S. Hafez, and M. S. Chong, A Possible Reinterpretation of the Princeton Superpipe Data, J. Fluid Mech., v. 439, 2001.

[4] E-S Zanoun, F. Durst, and H. Nagib, Evaluating the law of the wall in two-dimensional, fully-developed turbulent channel flow, Fluids, 15:10 - 3079, 2003.

Extended summary of the proposed ICTAM2004 lecture M. Herrasda & V. Shtern 8 September 2003

NEW MEANS OF VORTEX BREAKDOWN CONTROL

Miguel A. Herrada [1] and Vladimir Shtern[2]

[1] Universidad de Sevilla, 41092 Sevilla, SPAIN
[2] University of Houston, TX 77204-4006, USA

Vortex breakdown (VB) is an intriguing effect of practical and fundamental interest, occurring, e.g., in tornadoes, above delta-wing aircraft, and in vortex devices. Depending on application, VB is either beneficiary or harmful and therefore requires a proper control. This study shows that VB can be efficiently controlled by an additional near-axis swirl, temperature gradients, and their combination. To explore the underlying mechanism, we address a flow in a cylindrical container driven by a rotating bottom disk. This model flow has been extensively studied being well suited for understanding both the VB mechanism and its control. Our numerical analysis explains experimentally observed effects of control co- and counter-rotation (with no temperature gradient) and reveals some flaws of dye visualization. Next, we explore the effects of temperature gradients with no additional swirl on VB enhancement and suppression. Finally, we apply both the temperature gradient and additional swirl and demonstrate that a moderate negative (positive) axial gradient of temperature can significantly enforce (diminish) the VB enhancement by the counter-rotation. A strong positive temperature gradient stimulates the centrifugal instability and time oscillations in the flow with counter-rotation. A new efficient time-evolution code for axisymmetric compressible flows has facilitated the numerical study.

We use the Navier-Stokes equations for an axisymmetric flow of an ideal viscous and heat conducting gas. The parameters of the base flow—$h = H/R$, $\mathrm{Re} = \rho_0 \Omega R^2/\mu$, $\mathrm{Ma} = \Omega R(\rho_0 R_g T_0)^{-1/2}$, $\mathrm{Pr} = \rho_0 c_p/\lambda$, and $\gamma = c_p/c_v$—are the aspect ratio, the Reynolds, Mach and Prandtl numbers, and specific heat ratio, respectively. Here H and R are the cylinder height and radius (Fig. 1), ρ_0 and T_0 are the reference density and temperature, Ω is the angular velocity of the rotating disk, $R_g = (c_p - c_v)$ is the gas constant. Viscosity μ, thermal conductivity λ, and the specific heats, c_p and c_v, are kept constant in our analysis. We take $\mathrm{Pr} = 0.72$ and $\gamma = 1.4$ as values typical of gases.

The base flow is controlled by a rotation of the central rod and the axial gradient of temperature. The control rotation is characterized by the Reynolds number $\mathrm{Re}_i = \rho_0 \Omega_i R_i^2/\mu$ based on the radius, R_i, and on the angular velocity, Ω_i, of the rotating rod. The thermal control is characterized by the dimensionless temperature difference, $\varepsilon = (T_{bot} - T_{top})/(T_{bot} + T_{top})$, where T_{bot} and T_{top} are temperature of the bottom and top disks; $T_0 = (T_{bot} + T_{top})/2$.

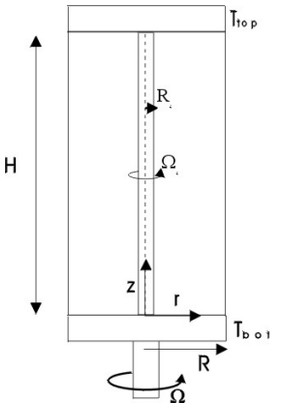


Figure 1.

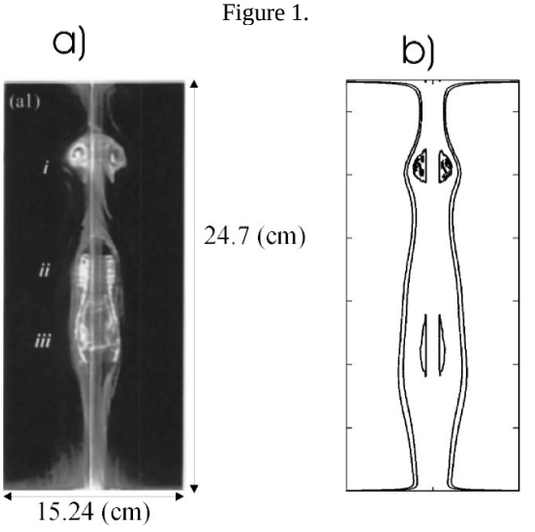


Figure 2.

Figure 2 shows streamline patterns by (a) flow visualization [1] and (b) numerical simulations of the flow where the rod is at rest ($\mathrm{Re}_i = 0$). A minor difference is that the visualization seems to show three vortex rings (Fig.

2a) while the numerical results reveal only two vortex rings (Fig. 2b).

Figure 3 and 4 show the flow at $Re_i = 21$ (co-rotating rod) and $Re_i = -12$ (counter-rotating rod). Comparing Fig. 3 (Fig. 4) with Fig 2, we see that the co-rotation (counter-rotation) suppresses (enhances) VB.

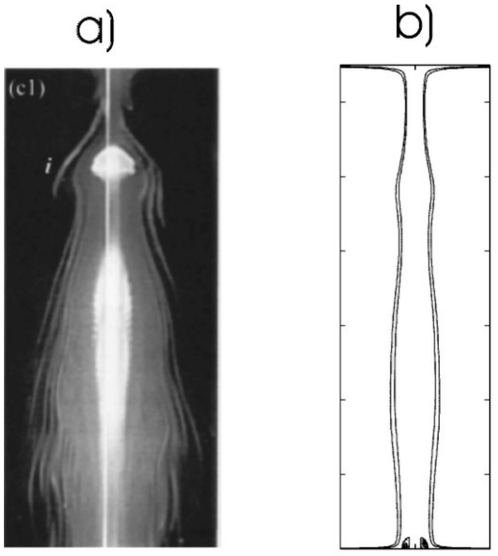


Figure 3.

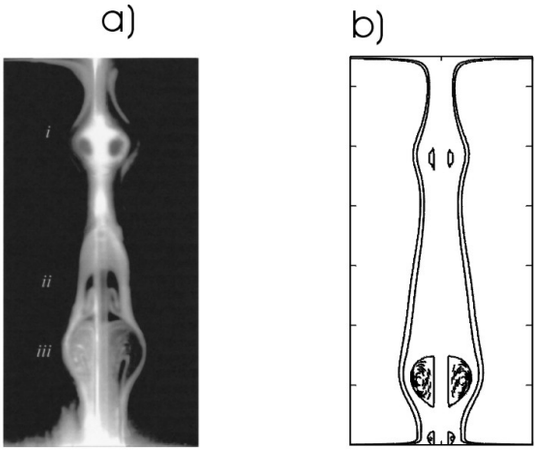


Figure 4.

Figure 5 shows the effect of the temperature gradient in the flow with no rod. VB occurring at $\varepsilon = 0$ (a) is totally suppressed at $\varepsilon = 0.7$ (b).

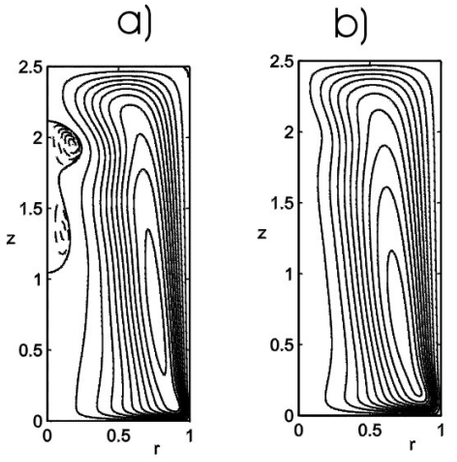


Figure 5.

Figure 6 shows the combined effect of the counter-rotation and the temperature gradient: (a) $Re_i = -12$, $\varepsilon = -0$, and (b) $Re_i = -12$, $\varepsilon = -0.6$. The negative temperature gradient enlarges VB "bubbles" and makes the flow unsteady.

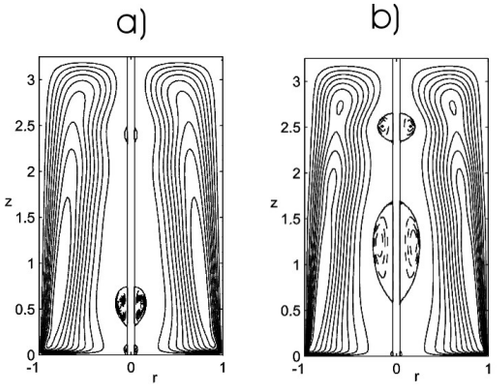


Figure 6.

These results indicate that an additional co-rotating cold (counter-rotating hot) swirling jet can help to suppress (enhance) VB in practical flows, e.g. over delta-wing aircraft and vortex burners.

[1] H. S. Husain, V. Shtern and F. Hussain, Physics of Fluids **15**, 271 (2003).

INSTABILITIES OF A VORTEX PAIR IN A STRATIFIED AND ROTATING FLUID

Paul Billant*, Augustin Colette** and Jean-Marc Chomaz*
*LadHyX, Ecole Polytechnique, CNRS, 91128 Palaiseau Cedex, France,
**CNRM, Météo-France, 42 Av Coriolis, 31057 Toulouse, France

Summary We present laboratory experiments on the three-dimensional instabilities developing on a counter-rotating vertical vortex pair in a stratified and rotating fluid. Four distinct types of instability have been identified on the cyclone or the anticyclone: the zigzag instability, the elliptic instability, the centrifugal instability and a new oscillatory instability. Numerical and theoretical stability analyses demonstrate that the latter oscillatory instability is a non-axisymmetric centrifugal instability.

INTRODUCTION

The three-dimensional stability of vortices in the atmosphere and the oceans is crucially controlled by the planetary rotation and the stable stratification. The rotation is indeed known to enhance both the centrifugal instability and the elliptic instability on anticyclonic vortices[1, 2]. Stratification effects are also responsible for the development of the zigzag instability[3].
Here, we present an experimental investigation of the three-dimensional instabilities developing on a counter-rotating vertical vortex pair in a stratified and rotating fluid. This work extends previous studies that have been conducted in the presence of either rotation [4] or stratification [3]. Four distinct types of instabilities have been observed on the cyclone or the anticyclone: the zigzag instability, the elliptic instability, the centrifugal instability and an oscillatory asymmetric instability. Numerical and theoretical stability analyses have been further conducted to determine the origin of the latter oscillatory instability which seems to have never been observed before.

EXPERIMENTAL SET-UP AND BASIC STATE

The vertical vortex pair is generated by computer-controlled flaps (i.e. by closing quickly two rotating vertical plates hinged to a vertical base) inside a 140cm×140cm×100cm tank mounted on a turntable which is 2.5m in diameter. The tank is filled with a stably stratified fluid with a working depth of 60cm.
PIV measurements have shown that the initial vortex pair can be well modeled by two Lamb-Oseen vortices separated by a fixed distance $b = 4$cm and with individual azimuthal velocity profile $v_\theta = \zeta a^2(1 - exp(-r^2/a^2))/2r$. The core radius a is always $a = 1$cm while the core vorticity ζ is controlled by varying the speed of closure of the flaps.

EXPERIMENTAL OBSERVATIONS

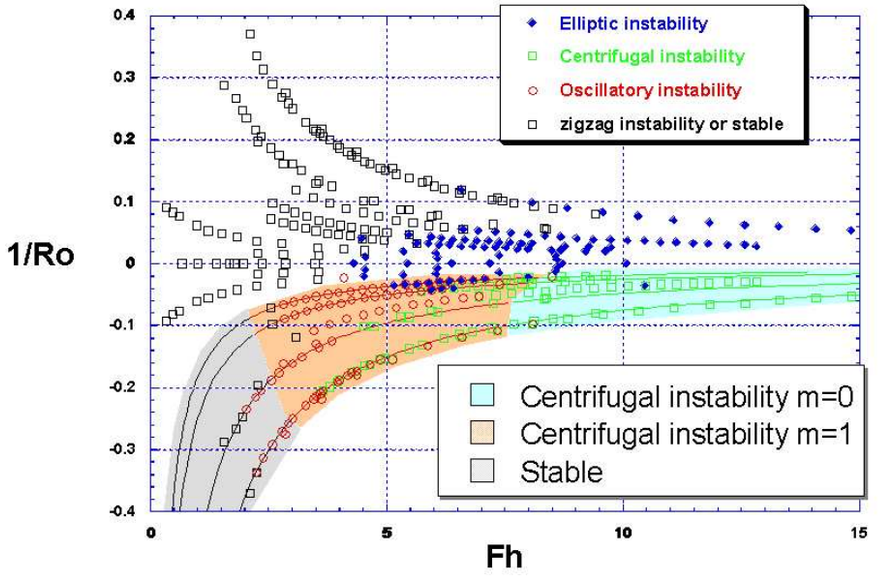


Figure 1. Experimental map of the instabilities in the parameter space $(F_h, 1/Ro)$. The symbols indicate the instability observed on the cyclone ($Ro > 0$) and the anticyclone ($Ro < 0$) for each experiment. The shaded regions show the results of the numerical stability analysis of the Lamb-Oseen vortex. See the text for more details.

The figure 1 shows the domains of existence of the different three-dimensional instabilities in the parameter space



(a) (b)

Figure 2. Instabilities of the anticyclone (on the left of each picture): (a) Axisymmetric centrifugal instability, (b) Oscillatory instability ($m = 1$ centrifugal instability). The cyclone (on the right) is stable in both cases.

$(F_h, 1/Ro)$ where $F_h = \zeta/N$ is the horizontal Froude number and $Ro = \zeta/2\Omega$ is the Rossby number, N being the Brunt–Väisälä frequency and Ω the angular velocity of the rotating table. In this diagram, the instabilities observed in each experiment is reported by two symbols: for positive Rossby number, we indicate the instability observed on the cyclonic vortex, while for negative Rossby number the instability observed on the anticyclone is indicated.

For small rotation of the table (i.e. small $1/Ro$), we have observed the zigzag instability at small Froude number and the elliptic instability at large Froude number on both vortices as in [3]. As $1/|Ro|$ is increased, the elliptic instability develops with different wavelength and growth rate on the cyclone and the anticyclone. For larger $1/Ro$, the elliptic instability continues to be observed on the cyclone but tends to be stabilized by rotation effects for a given Froude number. In contrast, the anticyclone becomes subjected to two other types of instability: a centrifugal instability for large Froude number and an oscillatory instability for moderate Froude number. The centrifugal instability (figure 2(a)) produces axisymmetric toroidal vortices which are reminiscent of those of the Taylor-Couette instability. The oscillatory instability (figure 2(b)) is asymmetric and exhibits a standing oscillation. Horizontal cross-sections in the vortex pair have shown that the perturbation has an azimuthal wavenumber $m = 1$ that rotates in the same sense of rotation as the basic vortex.

NUMERICAL AND THEORETICAL STABILITY ANALYSIS

The observation of the centrifugal instability was predictable from the generalized Rayleigh criterion. In contrast, the oscillatory asymmetric instability is quite unexpected. To determine the physical origin of this new instability, the stability of an axisymmetric Lamb-Oseen vortex in a stratified and rotating viscous fluid has been investigated numerically for the same Reynolds number as in the experiments. In agreement with the generalized Rayleigh criterion, we have found that this vortex is centrifugally unstable for negative Rossby number: $Ro < -1$. However, the classical axisymmetric mode ($m = 0$) is the most unstable perturbation only for large Froude number : $F_h > 7$ (figure 1). In the range $3 < F_h < 7$, the most unstable centrifugal mode is the $m = 1$ azimuthal mode like the oscillatory instability observed in the experiments. Furthermore, as seen on figure 1, the domains of existence of the $m = 1$ centrifugal instability and the oscillatory instability are in very good agreement. The oscillatory instability is therefore of centrifugal nature. This conclusion is corroborated by the fact that the properties of the oscillatory instability are not in agreement with other possible candidates, namely the elliptic instability[2] or the Gent & McWilliams instability[5].

In order to explain further why a centrifugal mode with an azimuthal wavenumber $m = 1$ is selected for intermediate Froude numbers, we have conducted a WKB stability analysis for large vertical wavenumber. This approach leads to a generalization of the Rayleigh criterion to stratified rotating fluids and to non-axisymmetric perturbations. It clearly shows that the combination of stratification and viscous effects stabilize the $m = 0$ mode leaving room for the $m = 1$ mode to be the most unstable.

References

[1] Hopfinger E.J., Heijst G.J.F. van: Vortices in rotating fluids. *Annu. Rev. Fluid Mech.* **25**:241–289, 1993.

[2] Kerswell R.R.: Elliptical instability. *Annu. Rev. Fluid Mech.* **34**:83–113, 2002.

[3] Billant P., Chomaz J.-M.: Experimental evidence for a new instability of a vertical columnar vortex pair in a strongly stratified fluid. *J. Fluid Mech.* **418**:167–188, 2000.

[4] Afanasyev Y.: Experiments on instability of columnar vortex pairs in rotating fluid. *Geophys. Astrophys. Fluid Dynamics* **96**:31–48, 2002.

[5] Gent P.R., McWilliams J.C.: The instability of barotropic circular vortices. *Geophys. Astrophys. Fluid Dynamics* **35**:209-6233, 1986.

ON THE STABILITY OF OCEANIC VORTICES: A SOLUTION TO THE PROBLEM

E.S. Benilov
University of Limerick, Ireland

INTRODUCTION

The contradiction between observational and theoretical estimates of the lifespan of oceanic vortices (rings) has been identified more than two decades ago. Observations (e.g. Olson 1991) suggest that rings exist for years, whereas theoretical studies (see Benilov 2003 and references therein) indicate that they are unstable.

An attempt to resolve the contradiction has been made by Dewar & Killworth (1995), who considered a two-layer ocean with a Gaussian vortex in the upper layer and a weak co-rotating circulation in the lower layer ("deep flow"). It turned out that the latter could stabilize the vortex, or at least considerably reduce the growth rate of instability. This result has been later extended to other vortex shapes by Katsman *et al.* (2003): in all examples considered, a co-rotating deep flow reduced the growth rate (although no profile other than the Gaussian one would become entirely stable).

Before we describe the results of the present paper, note that Dewar & Killworth (1995) and Katsman *et al.* (2003) assumed that the deep circulation has the same shape as the upper-layer vortex. We shall use a different approach: the profile of the deep flow will be derived from the assumption that potential vorticity (PV) in the lower layer is constant. Such model is suggested by the fact that most oceanic vortices are shed by unstable frontal currents: when a vortex moves away from the current and arrives to a new location, the PV field below it cannot change and remains equal to its initial, background value. Observe also that the interface displacement, caused by the vortex, contributes to the lower-layer PV – hence, to maintain its initial value, the lower layer spins up. Remarkably, the resulting circulation is always *co-*, and never *counter-*, rotating!

The present paper examines, numerically and analytically, vortices in a two-layer ocean. It is demonstrated that vortices with uniform PV in the lower layer are baroclinically stable, regardless of their profiles in the upper layer.

FORMULATION

Consider a vortex in a two-layer ocean with rigid lid and flat bottom, with $H_{1,2}$ being the depths of the layers ($_1$ marks the upper layer). The vortex will be characterized by the swirl velocities, $V_{1,2}(r)$, where r is the radial coordinate. Various profiles of the upper-layer velocity $V_1(r)$ have been examined and yielded similar results – here, we shall present those for the Gaussian vortex,

$$V_1 = V_* \frac{r}{r_*} \exp\left(-\frac{r^2}{2r_*^2}\right),$$

where V_* and r_* are the amplitude and radius of the vortex. With regards to the lower layer, we shall consider two particular cases: compensated vortices, for which the lower layer is at rest, $V_2 = 0$; and vortices with uniform lower-layer PV, for which V_2 satisfies

$$\frac{d}{dr}\left[\frac{1}{r}\frac{d}{dr}(rV_2)\right] - \frac{f^2}{g'H_2}(V_2 - V_1) = 0 \tag{1}$$

(f is the Coriolis parameter and g' is the reduced gravity). Both types of vortices were examined for stability through the usual linear normal-mode analysis, which yields the following eigenvalue problem:

$$(cr - V_1)\left[\frac{1}{r}\frac{d}{dr}\left(r\frac{d\psi_1}{dr}\right) - \frac{k^2}{r^2}\psi_1 - \frac{f^2}{g'H_1}(\psi_1 - \psi_2)\right] + Q_1'\psi_1 = 0, \tag{2}$$

$$(cr - V_2)\left[\frac{1}{r}\frac{d}{dr}\left(r\frac{d\psi_2}{dr}\right) - \frac{k^2}{r^2}\psi_2 - \frac{f^2}{g'H_2}(\psi_2 - \psi_1)\right] + Q_2'\psi_2 = 0, \tag{3}$$

$$\psi_{1,2}(0) = \psi_{1,2}(\infty) = 0, \tag{4}$$

where $\psi_{1,2}(r)$ describe the spatial structure of the mode, k and c are the mode's azimuthal wavenumber and phase speed (if $\mathrm{Im}\, c > 0$, the vortex is unstable), and

$$Q_1' = \frac{d}{dr}\left[\frac{1}{r}\frac{d}{dr}(rV_1)\right] - \frac{f^2}{g'H_1}(V_1 - V_2), \qquad Q_2' = \frac{d}{dr}\left[\frac{1}{r}\frac{d}{dr}(rV_2)\right] - \frac{f^2}{g'H_2}(V_2 - V_1)$$

are the PV gradients (observe that equation (1) is equivalent to $Q_2' = 0$).

NUMERICAL RESULTS

First, the eigenvalue problem (2)-(4) was solved numerically. We computed the marginal stability curve on the (ε, r_0)-plane, where

$$\varepsilon = H_1/H_2, \qquad r_0 = r_*/R_d$$

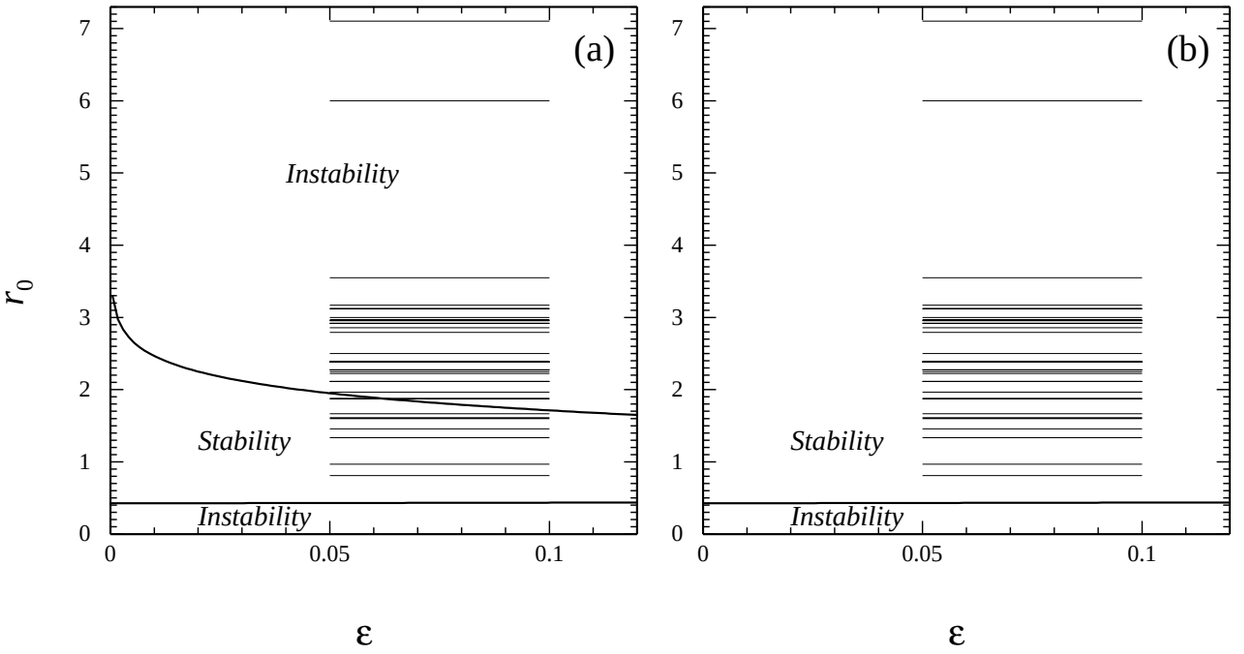


Figure 1. Stability of (a) compensated vortices, and (b) vortices with uniform PV in the lower layer, on the (ε, r_0)-plane (ε is the depth ratio of the ocean, r_0 is the nondimensional radius of the vortex). Horizontal segments show the rings catalogued by Olson (1991).

are the depth ratio of the ocean and nondimensional radius of the vortex ($R_d = \sqrt{g'H_1}/f$ is the Rossby radius).

The results for compensated vortices are shown in Fig. 1a. One can see that there are two regions of instability: vortices with small r_0 are unstable due to horizontal shear (*equivalent-barotropic* instability), while vortices with large r_0 are unstable with respect to vertical shear (*baroclinic* instability). We also show, on the same figure, the parameters of real-ocean rings catalogued by Olson (1991)[1]. One can see that only 7 out of Olson's 35 rings appear to be stable, which proportion is far too low to account for observations. It is also worth noting that none of the real rings is unstable barotropically, as their radii are two large for that.

The same computation has also been performed for vortices with uniform PV in the lower layer (see Fig. 1b). Remarkably, the entire region of baroclinic instability has disappeared, and all of Olson's (1991) rings are now stable.

ASYMPTOTIC RESULTS

The numerical results have been confirmed and complemented by an asymptotic analysis of the eigenvalue problem (2)-(4) under the assumption that the upper layer of the ocean is thin, i.e. $H_1 \ll H_2$. This assumption is not very restrictive as most oceanic rings are indeed localized in a thin layer (the only exceptions are the Southern Ocean rings, for which $H_1 \sim H_2$).

It has been shown that, if the "deep flow" satisfies (1), all vortices, not only the Gaussian ones, are baroclinically stable (for more details, see Benilov 2004).

CONCLUSION

We conclude that the model based on a vortex with uniform PV in the lower layer consistently describes the observed lifespans of oceanic rings.

References

[1] Benilov E.S.: Instability of quasigeostrophic vortices in a two-layer ocean with thin upper layer. *J. Fluid Mech.* **475**: 303–331, 2003.
[2] Benilov E.S.: Stability of vortices in a two-layer ocean with uniform potential vorticity in the lower layer. *To appear in J. Fluid Mech.*, 2004.
[3] Katsman C.A., Van der Vaart P.C.F., Dijkstra H.A., de Ruijter W.P.M.: On the stability of multi-layer ocean vortices: a parameter study including realistic Gulf Stream and Agulhas rings. *J. Phys. Oceanogr.* **33**: 1197–1218, 2003.
[4] Killworth P.D., Blundell J.R., Dewar W.K.: Primitive equation instability of wide oceanic rings. Part 1: linear theory. *J. Phys. Oceanogr.* **27**: 941–962, 1997.
[5] Olson D.B.: Rings in the ocean. *Ann. Rev. Earth Planet. Sci.* **19**: 283-311, 1991.

[1] Unfortunately, Olson (1991) presents no data on the thickness of the upper (active) layer of the ocean. Since most of oceanic vortices are localized in a thin layer, we assumed $0.05 < \varepsilon < 0.1$. As a result, vortices in Fig. 1 are represented by segments, not points.

CURVATURE INSTABILITY OF A VORTEX RING

Yasuhide Fukumoto*, Yuji Hattori**
*Graduate School of Mathematics, Kyushu University, Japan
**Faculty of Engineering, Kyushu Institute of Technology, Japan

Summary A new instability mechanism is found for Kelvin's vortex ring, which may surpass the Widnall instability. The effect of ring curvature emerges at $O(\epsilon)$ in the asymptotic solution of the Euler equations in powers ϵ, the ratio of core to ring radii. We show that the $O(\epsilon)$ field causes a parametric resonance between a pair of Kelvin waves whose azimuthal wavenumbers are separated by 1. A closed-form solution enables us to calculate the maximum growth rate to be $165/256\epsilon$ and to make headway to nonlinear stability.

MOTIVATION AND MAIN RESULT

Vortex rings are invariably susceptible to wavy distortions, leading to violent wiggles and sometimes to disruption. It has been widely accepted that the *Moore-Saffman-Tsai-Widnall instability* (the *MSTW instability*) is responsible for genesis of unstable waves [1]–[5]. Remember that this is an instability for a straight vortex tube subjected to a straining field.

When viewed locally, a thin vortex ring looks like a straight tube. Because of circular-cylindrical symmetry, the *Rankine vortex*, a circular core of uniform vorticity, is neutrally stable and supports a family of three-dimensional oscillations called the *Kelvin waves*. The vortex ring induces, on itself, not only a local uniform flow that drives itself but also a local straining field akin to a pure shear [1]. This is a quadrupole field proportional to $\cos 2\theta$ and $\sin 2\theta$, in terms of local polar coordinates (r, θ) in the meridional plane, with its origin at the core center and with $\theta = 0$ along the traveling direction . This field breaks the circular symmetry of the core by deforming it into ellipse, and feeds parametric resonance between two Kelvin waves whose azimuthal wavenumbers are separated by 2.

However this might be a oversimplified picture. The asymptotic solution of the Navier-Stokes or the Euler equations for a thin vortex ring in powers of a small parameter ϵ, the ratio of core- to ring-radii, starts with a circular-cylindrical tube at $O(\epsilon^0)$. A vortex ring is featured by vortex-lines curvature This feature manifests itself, at $O(\epsilon^1)$, as a local *dipole field* proportional to $\cos\theta$ and $\sin\theta$. The quadrupole field comes merely as a correction at $O(\epsilon^2)$ [3, 6, 7]. The dipole field also acts as a symmetry-breaking perturbation. Despite its dominance, this has not attracted as much attention as it deserves.

In the present investigation, we explore a possible instability that the dipole field can trigger. We show that the dipole field causes a parametric resonance between two Kelvin waves whose azimuthal wavenumbers differ by 1.

Remarkably we have succeeded in constructing *an explicit solution* of the linearized Euler equations, in terms of the Bessel and the modified Bessel functions. Thereby, an accurate computation of the growth rate becomes feasible for all azimuthal wavenumber combinations $(m, m+1)$ of Kelvin waves. The closed-form solution is amenable to an asymptotic analysis. We reveal that that the most unstable mode occurs in the short-wave limit with radial are azimuthal wavenumbers being of the same magnitude, with the maximum growth rate $165/256\,\epsilon$. The same value has been reached by the geometric optics method [8]. Contrary to the MSTW instability, all of multiple eigenvalues do not result in resonance. This discrepancy is accounted for by Krein's theory of Hamiltonian spectra [9], with the aid of the formula for energy of Kelvin waves [5].

SETTING OF LINEAR STABILITY PROBLEM

A formulation of the linear stability analysis was performed by Widnall & Tsai [3], but the dipole effect has gone untouched.
The center circle penetrating inside the toroidal ring is parameterized by the arclength s. Kelvin's vortex ring is an axisymmetric solution of the Euler equations valid to $O(\epsilon)$. The r and θ components of velocity field inside the core are written, after an appropriate nondimensionalization, as

$$U = \epsilon U_1(r,\theta) + \cdots\,,\;\; V = V_0(r) + \epsilon V_1(r,\theta) + \cdots\,;\quad V_0 = r\,,\;\; U_1 = \frac{5}{8}(1-r^2)\cos\theta\,,\;\; V_1 = \left(-\frac{5}{8} + \frac{7}{8}r^2\right)\sin\theta\,.$$

Upon this, we superimpose the following form of the disturbance velocity

$$\tilde{\boldsymbol{v}} = (\boldsymbol{v}_0 + \epsilon\boldsymbol{v}_1 + \cdots)e^{i(ks-\omega t)}\,; \qquad k = k_0 + \epsilon k_1 + \cdots\,, \quad \omega = \omega_0 + \epsilon\omega_1 + \cdots\,.$$

Suppose that a pair of Kelvin waves whose azimuthal wavenumbers differ by 1 are simultaneously excited to $O(\epsilon^0)$:

$$\boldsymbol{v}_0 = \boldsymbol{v}_0^{(1)} e^{im\theta} + \boldsymbol{v}_0^{(2)} e^{i(m+1)\theta}\,.$$

Then the wave excited at $O(\epsilon)$ is found from the linearized Euler equations to possess the following angular dependence

$$\boldsymbol{v}_1 = \boldsymbol{v}_1^{(1)} e^{im\theta} + \boldsymbol{v}_1^{(2)} e^{i(m+1)\theta} + \boldsymbol{v}_1^{(3)} e^{i(m-1)\theta} + \boldsymbol{v}_1^{(4)} e^{i(m+2)\theta}\,.$$

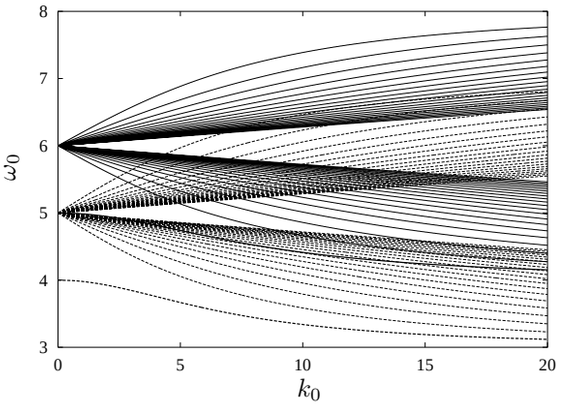


Figure 1. Dispersion relation of Kelvin waves of $m = 5$ (dashed lines) and $m = 6$ (solid lines).

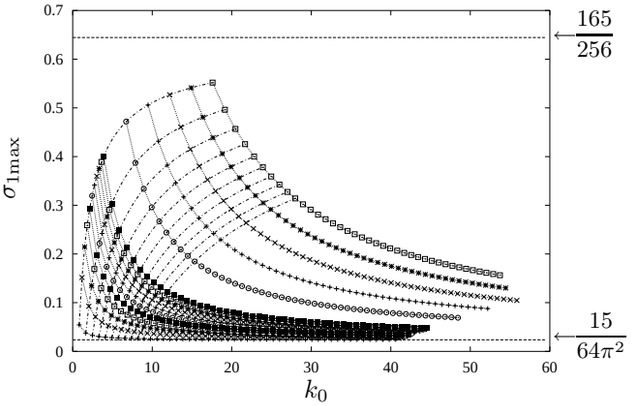


Figure 2. Growth rate of the principal modes.

Excitation, at $O(\epsilon)$, of a pair of waves with the same azimuthal wavenumbers as at $O(\epsilon^0)$ implies a possibility of parametric resonance. In practice, imposition of the boundary conditions at the edge of the core ($r = 1$) yields solvability conditions including the amplitude of the m and the $m + 1$ waves of $O(\epsilon^0)$. Simultaneous excitation of both waves are requisite for instability ($\mathrm{Im}\,\omega_1 > 0$), and a combination of the conditions for the m and the $m + 1$ waves give rise to the growth rate $\sigma_1 = |\mathrm{Im}\,\omega_1|$.

NUMERICAL RESULTS AND SHORT-WAVELENGTH ASYMPTOTICS

Instability is permissible only at the intersection points, in the (k_0, ω_0) plane, of the dispersion curves of the m and the $m+1$ waves. In case of instability, resonance occurs in a small wavenumber band of width of $O(\epsilon)$ around the intersection point $k = k_0$ and the growth rate takes its local maximum value $\sigma_{1\max}$ at $k = k_0$.

Figure 1 illustrates the dispersion relation of Kelvin waves of $m = 5$ (dashed lines) and $m = 6$ (solid lines). Both waves consist of infinitely many branches. The growth rate $\sigma_{1\max}$ is calculated at many of the intersection points. Destabilization occurs only at the intersection points between upgoing modes of $m = 5$ and downgoing modes of $m = 6$. Relatively large growth rate is maintained to short wavelengths at intersection points of branches with the same labels, which we call the *principal mode*.

Calculation of the growth rate for the principal modes is extended to a large azimuthal wavenumber m in figure 2. The same symbol is used for the same azimuthal wavenumber pair $(m, m + 1)$, and the lowest sequence (symbol $+$) corresponds to $m = 0$. Given $(m, m + 1)$, the growth rate decreases with k_0 and tends to $\sigma_{1\max} = 15/64\pi^2 \approx 0.02374715242$ as $k_0 \to \infty$. On the other hand, given the branch label, the growth rate increases monotonically with m and approaches the common value $\sigma_{1\max} = 165/256 = 0.64453125$ as $m \to \infty$. By virtue of the closed-form solution for $\boldsymbol{v}_1^{(1)}$ and $\boldsymbol{v}_1^{(2)}$, the asymptotics for the first principal mode (the leftmost curve) is deduced as

$$\sigma_{1\max} \approx 0.64453125 - 1.548698742/m^{2/3}.$$

This is the most dominant mode over the all possible resonance pairs. This mode outweighs, for the entire range of ϵ ($0 < \epsilon \lesssim 1$), the Widnall instability which is of $O(\epsilon^2)$.

The disturbance vorticity field is calculated and its correlation with the local strain is examined. The instability mechanism is traced to stretching of disturbance vortex lines in the toroidal direction. Discussions are also given to the effects of viscosity and nonlinearity.

References

[1] Widnall, S. E., Bliss, D. B., Tsai, C.-Y.: The instability of short waves on a vortex ring. *J. Fluid Mech.* **66**: 35–47, 1974.

[2] Moore, D. W., Saffman, P. G.: The instability of a straight vortex filament in a strain field. *Proc. R. Soc. Lond. A* **346**: 413–425, 1975.

[3] Widnall, S. E., Tsai, C.-Y.: The instability of the thin vortex ring of constant vorticity. *Phil. Trans. R. Soc. Lond. A* **287**: 273–305, 1977.

[4] Eloy, C. & Le Dizès, S.: Stability of the Rankine vortex in a multipolar strain field. *Phys. Fluids* **13**: 660–676, 2001.

[5] Fukumoto, Y.: The three-dimensional instability of a strained vortex tube revisited. *J. Fluid Mech.* **493**: 287–318, 2003.

[6] Fukumoto, Y., Moffatt, H. K.: Motion and expansion of a viscous vortex ring. Part 1. A higher-order asymptotic formula for the velocity. *J. Fluid Mech.* **417**: 1–45, 2000.

[7] Fukumoto, Y.: Higher-order asymptotic theory for the velocity field induced by an inviscid vortex ring. *Fluid Dyn. Res.* **30**: 67–95, 2002.

[8] Hattori, Y., Fukumoto, Y.: Short-wavelength stability analysis of thin vortex rings. *Phys. Fluids*. **15**: 3151–3163, 2003.

[9] Arnold, V. I.: Mathematical Methods of Classical Mechanics, 2nd ed., Springer-Verlag, 1989.

NUMERICAL EXPERIMENTS ON VORTEX SHEDDING FROM AN OSCILLATING CYLINDER

Fernando Ponta[*], Hassan Aref[**]
[*] *Department of Theoretical and Applied Mechanics, University of Illinois at Urbana-Champaign, Urbana, IL 61801, USA*
[**] *Virginia Polytechnic Institute & State University, Blacksburg, Virginia, 24061-0217, USA*

Summary Vortex street wakes behind oscillating cylinders have been studied experimentally and numerically by several authors. Williamson and Roshko attempted a classification of the various wake patterns observed as a function of two dimensionless parameters, the wavelength and amplitude of the undulatory motion of the cylinder scaled by the cylinder diameter. Several qualitatively distinct wake regimes were observed experimentally. These were classified in terms of the vortex patterns, e.g., two singlets, two pairs, pair and singlet, and so on. We have performed a number of numerical experiments for Re=140 and established several points of correspondence with the experiments. Our simulation results also shed light on the classification scheme of Williamson and Roshko and suggest how this classification may change with Reynolds number. We find remarkable sensitivity to details of the oscillation of the cylinder, in particular whether the oscillation takes place at fixed streamwise velocity or at fixed cylinder speed along its trajectory.

INTRODUCTION

In addition to the familiar Kármán vortex street behind a stationary cylinder in a uniform stream several more complex vortex patterns have been observed in the wakes of oscillating cylinders. There is a large body of literature on experimental studies of vortex wakes behind cylinders oscillating either perpendicularly to or in-line with the uniform stream (see [2] for further references). An attempt at classifying such vortex patterns has been made by Williamson and Roshko [3], henceforth referred to as WR, using a symbolic code of letters and numbers that describes the combination of pairs and single vortices shed during each cycle of the forced oscillation of the cylinder. For example, 2S indicates two single vortices shed per cycle, 2P indicates two vortex pairs shed per cycle, P+S signifies a pattern in which one pair and a single vortex are shed in each cycle, and so on. WR gave a map of when the various vortex patterns would occur using a non-dimensional wavelength-amplitude plane. We have used their classification and map as a basis for our computational study. Besides the experimental work referenced above, there is some analytical and computational work on complex wake structures of forced and freely oscillating cylinders. Aref and Stremler [1] applied their analysis of the motion of three point vortices with net zero circulation in a periodic strip to the observations of WR of the P+S wake and were able to find reasonable correspondence with the experimental results although several parameters (e.g., the vortex circulations) could be adjusted. This analysis suggested that many additional possibilities, so far not observed experimentally, exist for the vortex structure of the wake behind an oscillating cylinder. We have begun referring to such vortex patterns as *exotic wakes*. Several direct numerical simulation studies have been performed on freely oscillating cylinders for Re up to 350 (see [2] for a list of references). In this paper we primarily study the periodic vortex structures produced in the wake of a cylinder subject to forced oscillations at low Re, exploring in particular the phenomenon of the P+S structure. To this end, we have developed a new numerical approach that we briefly introduce in the next Section. Using this code, we experiment with wakes of oscillating cylinders, exploring a section of the WR map at Re=140 and identifying similarities and differences with the higher Re results reported in WR.

THE KINEMATIC LAPLACIAN EQUATION METHOD

In this section we briefly introduce the main features of our method for computing the time-dependent flow in the wake of an oscillating cylinder. Our method can be seen as a vorticity creation algorithm or, alternatively, as a time-space split method to solve the time-dependent viscous flow around moving bodies. This new type of vorticity creation method is based on a space-time splitting of the problem that solves the time evolution of the vorticity as an ODE on each node of the spatial discretization, using at each step of the time discretization the spatial solution for the velocity field provided by a new PDE expression that we call the *Kinematic Laplacian Equation* (KLE). The idea is based on a kinematic relation that solves the Laplacian of the velocity field for a given distribution of vorticity and rate of expansion. The vorticity distribution is provided by the ODE solution and the rate of expansion is zero due to incompressibility. The KLE is intended to work within non-linear time-evolving schemes providing a quick, linear, spatial solution to the velocity field for successive time-steps. For time integration we used a variable-order Adams-Bashforth-Moulton predictor-corrector solver with adaptive stepsize control, which proved to be quite efficient for this application. For the discretization of the KLE we used unstructured meshes of isoparametric finite elements.

NUMERICAL EXPERIMENTS ON VORTEX WAKES OF AN OSCILLATING CYLINDER

In this section we report on our results regarding the formation, shedding and further evolution of vortex patterns produced in the wake of a cylinder executing forced oscillations for the range of Reynolds number below 180. This is,

approximately, the periodic laminar wake regime for the usual, Kármán vortex street case. We concentrated on the case of Re=140 since this case is representative of the range and shows a variety of arrangements of vortex structures. Figure 1(a) shows the non-dimensional vorticity field for wavelength=7.5 and amplitude=1 (both in units of the cylinder diameter), which produced the clearest P+S arrangement. We checked that for each triplet the sum of the circulation of the two positive vortices equals the opposite of the circulation of the negative vortex, so the complete circulation produced in one cycle is very close to zero. We see how the positive (lower) half of the near wake is stretched by the strain rate field of the neighboring vortices until it breaks into two separated vortices. If we follow the evolution of the negative (upper) half of the near wake, we notice that it also starts to split in two but, contrary to what happens to its positive counterpart, a major portion of the shed vorticity remains together, and this vorticity forms a vortex that is strong enough to recover its "tail". This process can be followed in the successive triplet structures as they progress and evolve downstream. In an attempt to assess the effects of the fluctuations of the speed of the cylinder along its trajectory, we moved the cylinder along a new path in which the speed of motion relative to the fluid is kept constant. Although this motion nominally has the same values of frequency and amplitude as before, the cylinder really has acquired a slight streamwise oscillation relative to the steady translation of the earlier motion. Figure 1(b) shows the non-dimensional vorticity field for the constant-speed path. In this case, we have two single vortices shed in each cycle and the wake initially shows a relatively well-defined and close-packed Kármán arrangement that extends downstream for a distance of about 10 diameters. Later, however, a process of merging of neighboring vortices within either row takes place. This process forms a set of larger vortices with twice the downstream and cross-stream spacing of the original street and that we may call a "hyper-Kármán vortex-street".

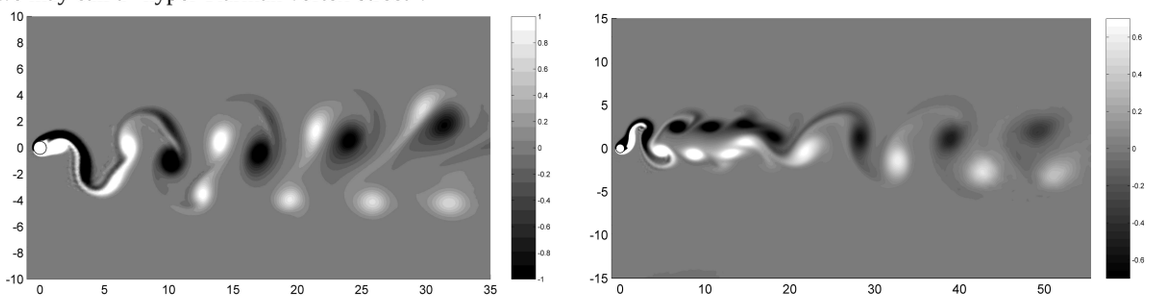


Figure 1: (a) Vorticity field for the P+S case (b) Vorticity field for the "hyper-Kármán vortex-street"

CONCLUSIONS

We have introduced a mathematical-computational approach to solving flows in a frame of reference attached to a moving body and we have used this tool to explore the vortex synchronization regions in the amplitude-wavelength map of WR for low Reynolds number, focusing on the process of splitting which characterizes the formation of the P+S and 2P structures. The formation of a secondary vortex street in the wake of a stationary cylinder in a uniform stream was observed by several researchers by using flow visualization techniques and hot-wire measurements on acoustically-forced cylinder wakes. In these experiments the primary Kármán vortex street decays downstream, and the secondary vortex street is formed with a larger scale of vortices (and thus a lower frequency) than those in the primary Kármán street. WR observed coalescence into a large-scale, Kármán-like arrangement of a large number of small vortices produced at high frequencies of the forced oscillation for sinusoidal trajectories. Working with constant-speed trajectories, we found the "hyper-Kármán vortex street" arrangement. This phenomenon, characterized by a pairwise merging process at low frequency that produces a duplication of the period, is, to the best of our knowledge, reported here for the first time for a moving, vertically oscillating cylinder. The synchronization of our primary vortex street with the vertical forced oscillation instead of with the Kármán shedding suggests that the pairwise merging phenomenon itself is related to the structure of the primary street (through the spacing of the vortices) rather than to the original process that generated the primary street. Based on point vortex models we are convinced that there exist a multitude of more complex vortex wake patterns (exotic wakes) that have not so far been seen in experiments. Although we understand how to "set these up" if we had complete control over how to distribute the vorticity in the flow, we do not yet fully understand how to produce such vortex wakes by oscillation and rotation of a wake-producing bluff body. We hope to use the numerical tool developed here for such explorations in the future and plan to report our most recent findings in this regard at the Congress.

References

[1] Aref, H., Stremler, M. A.: On the motion of three point vortices in a periodic strip. *J. Fluid Mech* **314**: 1-25, 1996.

[2] Khalak, A., Williamson, C. H. K.: Motion forces and mode transitions in vortex-induced vibration at low mass-damping. *J. Fluids Struct.* **13**: 813-851, 1999.

[3] Williamson, C. H. K., Roshko, A.: Vortex formation in the wake of an oscillating cylinder. *J. Fluids Struct.* **2**: 355-381, 1988.

BIFURCATION OF MOTIONS OF THREE VORTICES AND APPLICATIONS

Lu Ting*, Denis Blackmore**

* *Courant Institute of Mathematical Sciences, New York Univ., New York, NY 10012, USA.*
** *Department of Mathematical Sciences, New Jersey Institute of Tech. Newark, NJ 07102, USA*

Summary With the motion of three point vortices reduced to a problem of two variables, the ratios of the sides of the triangle formed by the vortices, there are stationary points, where the triangles will remain similar. We show the bifurcation from a stationary point of contracting similar triangles ending at the stationary point for expanding triangles. The study is extended to the motion of three coaxial slender vortex rings.

BACKGROUND

The motion of three free point vortices in a planar incompressible inviscid flow was first studied by Groebi in 1877 for specialized vortex strengths and by Synge in 1949 [1], giving a qualitative classifications of all possible motions in terms of the sum of the products of the vortex strengths, $K = k_1k_2 + k_2k_3 + k_3k_1$. It is called elliptic, parabolic or hyperbolic for K greater, equal to or less than 0, respectively. The analysis of Synge was continued in 1988 [2], presenting quantitative results. Figure 1 shows the triangle $\mathcal{G}$ formed by three vortices, at $z_j = Re\ z_j + i\ Im\ z_j$ at instant t, in the complex z-plane, with circulations $2\pi k_j$, and the opposite sides R_j, $j = 1, 2, 3$. With the conservation of linear and angular momentums, the motion was reduced to the variation of the sides of the triangle $\mathcal{G}$, i. e., the trajectory of point $\mathbf{R}(t)$ in space. Synge projected the trajectory radially onto point $\mathbf{x}$ on the $\alpha\beta$ plane, $R_1+R_2+R_3 = \sqrt{2/3}$ and introduced the trilinear coordinates $x_j = R_j/(R_1 + R_2 + R_3)$ as shown in Figure 2. The $\alpha\beta$ plane in the first octant is equilateral triangle $\mathcal{P}$ with vertices P_j of unit heights and the distances of point $\mathbf{x}$ from the sides opposite to P_j, as shown by the dotted line, yield x_j fulfilling the condition, $x_1 + x_2 + x_3 = 1$. Because of the triangle inequality, the point $\mathbf{x}$ has to lie inside or on the boundary of the equilateral triangle, $\mathcal{Q}$, formed by the mid-points Q_j of the sides of $\mathcal{P}$. An vertex of $\mathcal{Q}$, say Q_1 where $R_1 = 0$ or $z_2 = z_1$, represents the coalescence of two vortices, A point on an edge,

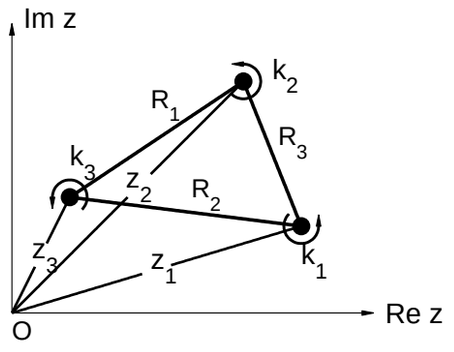


Fig. 1. Configulation of three vortices

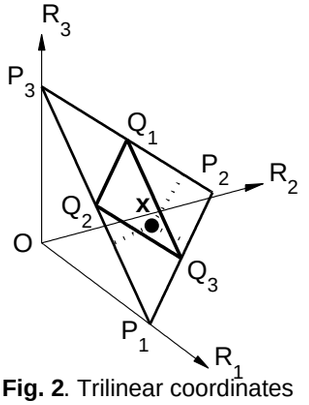


Fig. 2. Trilinear coordinates

say Q_2Q_3 where $x_1 = x_2 + x_3 = 1/2$, the vortices are collinear. Corresponding to a point $\mathbf{R}$, there are two congruent triangles, $\mathcal{G}_\pm$ with the vortices in opposite orientation. Figure 1 shows $\mathcal{G}_+$, with the vortices z_1, z_2, z_3 oriented counterclockwise. We shall set the orientation by assuming $k_1 \geq k_2 = 1 \geq k_3$. When the triangle $\mathcal{Q}$ in the $\alpha\beta$ plane is considered as a disc with faces $\mathcal{Q}_+$ and $\mathcal{Q}_-$, having normal vectors pointing away or toward the origin respectively. Thus a point $\mathbf{x}$ on face $\mathcal{Q}_+$ or or its image on $\mathcal{Q}_-$ represents the trilinear coordinates of the vortices in the counterclockwise or clockwise orientation. The vortices change their orientation only when they cross over an common edge of $\mathcal{Q}_\pm$. When the three vortices move as a rigid body, we have $\mathbf{R}$ stationary or being a critical point. To each configuration defined by a point $\mathbf{R}$ in space there is a unique $\mathbf{x}$ on the $\alpha\beta$ plane. The converse is true for $K \neq 0$. In addition to the vertices of Q_j, there are critical points Q_{j+3} on each edge of $\mathcal{Q}$ and at the centroids $E^\pm$, of $\mathcal{Q}^\pm$. The stabilities of these eight critical points were analyzed in [1] and [2]. The three equations for the variations of $R_j(t)$ are $k_j^{-1}R_j\dot{R}_J = 2A(R_{j+1}^{-2} - R_{j+2}^{-2})$, $j = 1, 2, 3$ with $R_{j+3} = R_j$, γA denoting the area of the triangle $\mathcal{G}$ and $\gamma = \pm 1$ its orientation. They were reduced to two invariants for R_j in [1] defining the integral curves in space. The curves plus the direction of $\dot{\mathbf{R}}(t)$ yield the trajectories. These two invariants were combined to one invariant for the trilinear coordinates [2],

$$I = \{\sum_{j=1}^{3} \frac{x_j^2}{k_j}\}\{x_1^{k_2k_3}x_2^{k_3k_1}x_3^{k_1k_2}\}^{2/K} = \text{const.} \quad K \neq 0 \quad \text{and} \quad I_0 = (\frac{x_1}{x_3})^{2k_1}(\frac{x_2}{x_3})^{2k_2} = \text{const.}\,, \quad K = 0. \qquad (1)$$

When we set the origin of $\alpha\beta$ plane at the vertex Q_3 the α-axes along Q_3P_2 amd β-axis along Q_3P_3, we have $\beta = x_3$ and $\alpha = (x_2 - x_1)/\sqrt{3}$. From the above invariants and the direction of $\dot{\mathbf{x}}$ or $\dot{\mathbf{R}}$, the trajectories of $\mathbf{x}$ in the $\alpha\beta$ plane were presented in [2] for various values of k_j's for the elliptic, parabolic and hyperbolic cases.
For the parabolic case, with $k_3 = -k_1k_2/(k_1 + k_2) < 0$, in addition to the eight critical points $\mathbf{x}$ corresponding to those of $\mathbf{R}$ mentioned before, there are stationary points $\mathbf{x}$ along an arc in $\mathcal{Q}_+$ from critical point Q_4 on the edge Q_2Q_3 passing through the centroid E to point Q_5 on Q_3Q_1, and also on the image of the arc in $\mathcal{Q}_-$. A point $\mathbf{x}$ in the segment Q_4E (EQ_5) represents expanding (contracting) similar triangles $\mathcal{G}_+$. For the image in $\mathcal{Q}_-$, we interchange expanding and contracting for $\mathcal{G}_-$ The contraction of similar triangles to the final collision of three vortices looks like an interesting solution but the solution was shown to be unstable in [2] while the expanding one are stable. Now we shall study the deviation or bifurcation from a contracting similar solution due to instability.

CURRENT RESEARCH

For a parabolic case, the invariant I_0 in (1) decreases from ∞ at the vertex Q_3 where $\beta = x_3 = 0$ to 1 at the centroid E, $\beta = 1/2$ and finally to 0 at the vertex Q_1 or Q_2 where $\beta = 1$. The arc Q_4EQ_5 in $\mathcal{Q}_+$, the loci of stationary points, is defined by $H = k_2x_1^2 + k_1x_2^2 - (k_1 + k_2)\beta^2 = 0$. Crossing the arc from below, H changes sign from negative to positive. Along the arc, $H = 0$, the invariant I_0 decreases from its maximum at E towards its end points. With $k_1 > k_2$, we have $I_0(E) = 1 > I_0(Q_4) > I_0(Q_5)$. The vertex Q_3 is a center and the invariant curves move away from Q_3 as I_0 decreases from ∞ to 1, with the curve $I_0 = 1$ tangent to the arc $H = 0$ at E from below. The trajectory or the separatrix from Q_4 lies above the arc $H = 0$ and ends on the arc at point S_4 between E and Q_5. The separatrix from Q_5 lies above that from Q_4, across over the edge Q_2Q_3 at point S_5 and return to Q_5 along the image of S_5Q_5 in $\mathcal{Q}_-$. The unstable branch EQ_5 is partitioned by point S_4 to two segments. For a point $\mathbf{x}$ in the unstable segment ES_4, the trajectory bifurcates from the point along $I_0 \in (I_0(Q_4), 1)$ above the arc with x_1 increasing while x_2 decreasing, ending at a point in the stable segment Q_4E of the arc representing stable expanding triangle $\mathcal{G}$. For a point $\mathbf{x}$ in the unstable segment S_4Q_5, the trajectory bifurcates from the point along $I_0 \in (I_0(Q_5), I_0(Q_4))$ above the arc with x_2 decreasing to and then crossing over the edge Q_2Q_3 above point Q_4 and returning along the image trajectory to $\mathbf{x}$ in stable segment $S_4^*Q_5$ in $\mathcal{Q}_-$. For a point $\mathbf{x}$ in the entire unstable segment EQ_5, the trajectory bifurcates along $I_0 \in (I_0(Q_5), 1)$ below the arc with x_1 decreasing to and then crossing over the edge Q_3Q_1 to $\mathcal{Q}_-$ and ending at the image of $\mathbf{x}$ in the stable segment E^*S_5. Similarly, we can trace the trajectories bifurcating from the unstable segment Q_4E^* in $\mathcal{Q}_-$ for $I_0 \in (I_0(Q_4), 1)$. Thus completes the description of the trajectories for $I_0 \in (I_0(Q_5), 1)$ in $\mathcal{Q}_\pm$. Note that the centroid E (also E^*) is unstable and looks like a saddle point below the arc $H = 0$ but like a center above.
In addition to the above analyses, bifurcations of three vortex motions are also studied using a Hamiltonian approach thereby providing further insights into the nature of the dynamics. As is well known, the governing equations of motion of three vortices in a plane can be written in a three-degree-of-freedom Hamiltonian form. This system has three independent integrals in involution, including the Hamiltonian function H, and is therefore completely integrable. Two of these integrals can be used to reduce the number of degrees-of-freedom of the system by two. By choosing the reduction properly, this system can be used to obtain the bifurcation results described above and also provide some additional information concerning the motions.
The planar motion of three vortices serves as the leading order approximation of three slender coaxial vortex rings in a meridian plane [3] having radii much larger than the distances between the rings, The approach was used in [4] to analyze certain qualitative features of the motion of three coaxial vortex rings. In particular, they showed, using the KAM and Poincaré-Birkhoff theorems, for vortex strengths having the same sign (the elliptic case), there is a region of initial positions of positive area in a meridian plane for which the relative motion of the rings is quasiperiodic on invariant tori or periodic. A similar formulation shall be employed to investigate the bifurcations of motions of three coaxial vortex rings in the parabolic case.

References

[1] Synge, J. I.: On the Motion of Three Vortices. *Can. J. Math.* **1**: 257-270, 1949.
[2] Tanvantzis J., Ting L.: The Dynamics of Vortices Revisited. *Phys. Fluids* **31**: 1392-1409, 1988.
[3] Ting L., Klein R., Viscous Vortical Flows. Lecture Notes in Physics **374**, Springer-Verlag, NY 1991.
[4] Blackmore D., Knio O., KAM Theory Analysis of the Dynamics of Three Coaxial Vortex Rings. *Physica D*, **140**: 321-348 2000.

STRONG CYCLONIC VORTICES OVER TOPOGRAPHY ON A BETA-PLANE

Hung-Cheng Chen, Chin-Chou Chu and Chien-Cheng Chang
Institute of Applied Mechanics, National Taiwan University, Taipei 106, Taiwan, R.O.C.

Summary Strong cyclonic vortices over topography on a beta-plane were investigated by a joint analytical, experimental and numerical approach. The motion of the vortices shows complicated track deflections associated with meandering Rossby wave wakes. The track deflections can be further explored by a dynamic model which predicts similar results to those observed from the experiments, numerical calculations and some historical typhoon trajectories encountering the Island of Taiwan.

BASIC EQUATIONS AND THE DYNAMIC MODEL

A rotating *shallow water model* (SWM) is employed to simulate the behaviour of strong cyclonic vortices (Ro ~ O(1)-O(10)) over topography on a beta-plane. The bottom topographies considered in the present study include (i) an elliptical-shape topography, (ii) a gently sloping bottom and (iii) a paraboloidal free surface. The paraboloidal free surface is induced from the tank rotation, while the sloping bottom is implemented to represent a planetary beta effect. A gradient-wind balanced vortex model is adopted as the initial conditions which are the distributions of the surface depression and the azimuthal velocity. In order to take care of the viscous dissipation, an internal dissipation term is also incorporated in the momentum equations as suggested by Schär and Smith (1993).

The dynamic model of the strong vortices

According to the principle of conservation of potential vorticity (PV), and assume small variations of surface depression η^* and the bottom topography h_B^*, a non-dimensional PV conservation relationship for strong cyclonic vortices can be written

$$\frac{D}{Dt}\left(\beta_0 y + \beta_B h_B - \beta_v \eta + \varsigma\left(1 + Ro\left(\beta_B h_B - \beta_v \eta\right)\right)\right) = 0, \tag{1}$$

where the non-dimensional beta parameters β_0, β_B and β_v, respectively, account for the planetary beta effect, elliptical-shape topography and the vortex depression. The proposed dynamic model predicts that at any instant, the velocity of the vortex

$$\vec{V} = \vec{V_c} + \vec{V_y} + \vec{V_B} \tag{2}$$

consists of three contributions: $\vec{V_c}$, the component without planetary beta and topographic effect, and two other components $\vec{V_y}$ and $\vec{V_B}$ as explained below. During a small time interval, assume that the surface depression and the relative vorticity at the vortex centre are approximately unchanged. From Eq. (1), we can derive a *meridional adjusting velocity (MAV)* $\vec{V_y}$ of the vortex moving across the isobaths

$$\vec{V_y} = -\alpha\left(dh_B/dt\right)\vec{e_y} \text{ along the direction of } \vec{V_c}, \tag{3}$$

where the topography-adjusting factor α is defined to be $\alpha \equiv \left(1 + Ro\varsigma_c\right)\beta_B/\beta_y$, where ς_c is the relative vorticity at the vortex centre. In the meanwhile, another *topography-adjusting velocity (TAV)* $\vec{V_B}$ is also induced as the vortex moving across the isobaths of the topography,

$$\vec{V_B} = \frac{1}{\left|\nabla h_B\right|}\left(dh_B/dt\right)\vec{e}_B \text{ along the direction of } \vec{V_c}, \tag{4}$$

where $\vec{e}_B$ represents the non-dimensional unit vector along the topographic gradient.

EXPERIMENTAL SETUP

The experiments were performed in a rectangular glass water tank of horizontal dimensions 135 cm × 135 cm and 40 cm in depth rotating with a slow angular speed varying from 0.3 to 10 rpm. The generation of a cyclonic vortex was conducted by a 4-cm-diameter solid cylinder rotating in parallel to the axis of the rotating table. In the present experiment, the slope of the bottom was approximately 0.0538. Flow visualizations were performed by the horizontal streak photography and to measure the local surface depression by a vertical laser light sheet. A light sheet was generated from a 4-Watt Argon-ion laser, and the laser beam was reflected by an 8-facet rotating prism onto a thin light sheet of a fan region. The vertical light sheet was generated by a diode laser and was mounted directly on the tank. With careful manipulation on the position of the light sheet on the passage of the vortex, the surface profiles were recorded slice by slice during the passage of the vortex. Then, the actual vortex depression can be obtained by subtracting the corresponding profile with a reference frame. A particle track velocimetry (PTV) technique was also implemented to extract the horizontal distribution of velocity of the vortex.

NUMERICAL CALCULATIONS

The numerical method used in the present study closely related to Helfrich et al. (1999). The rotating shallow water model was numerically integrated using a public-domain, finite volume code CLAWPACK by LeVeque (1998). The main feature of CLAWPACK is a Godnov-type finite volume method in which the Riemann problems are solved at cell interfaces to properly resolve the wave structure. The SWM calculations were performed with a grid of size 320×320. All the calculations were performed on a Cray J916 machine at a non-dimensional time step 0.016 and approximately 11.6 CPU seconds were required for a single time step.

RESULTS AND DISCUSSION

Figure 1 shows the experimental streaklines photographs. Figures 2(a)-(d) shows a sequence of vorticity contours of the numerical simulation for a typhoon-like vortex on a beta-plane impinging upon a mountain with 2500 m height. The vortex moves to northwest due to the topographic beta effect and sheds secondary wakes at the downstream. Fig. 2(e) showes the comparisons of the vortex tracks obtained from the shallow water model (circles) and the proposed dynamic model (solid lines); the results are in close agreement with each other. Figure 3(a) showes some historical typhoons passing over Taiwan as reported by Wang (1980). Fig. 3(b) shows that qualitatively similar tracks were observed from the dynamic model calculations. From the time series of the vortex speed as shown in Fig. 3(c), we discover an unsteady motion of *deceleration-acceleration-deceleration-acceleration* (D-A-D-A) alternative type of motion.

CONCLUDING REMARKS

In summary, this study proposes a dynamic model which predicts the vortex speed under the influence of the planetary beta and topographic effect. The velocity $\vec{V}$ of the vortex in the proposed model consists of (i) the component without the planetary beta and topographic effect $\vec{V_c}$, (ii) the meridional adjusting velocity $\vec{V_y}$ and (iii) the topographic adjusting velocity $\vec{V_B}$. The results predicted by the model compare very well with experiments and numerical calculations based on the SWM. Further application of the proposed model to typhoon vortices encountering the island of Taiwan also shows very interesting comparison in the vortex trajectories.

References

[1] Helfrich K. R., Kuo A. C., and Pratt L. J.: Nonlinear Rossby adjustment in a channel. *J. Fluid Mech.* **390**:187-222, 1999.

[2] LeVeque R. J.:Balancing source terms and flux gradients in high-resolution Godnove method: The quasi-steady wave propagation algorithm. *J. Comput. Phys.* **146:** 346-365, 1998.

[3] Schär C. and Smith R. B.: Shallow-water flow past isolated topography. Part I: vorticity production and wake formation. *J. Atmos. Sci.* **50:** 1373-1400, 1993.

[4] Wang S. T.: Prediction of the behaviours and intensity of typhoons in Taiwan and its vicinity. *Chinese NSC Res. Rep.* **18,** 100pp., 1980.

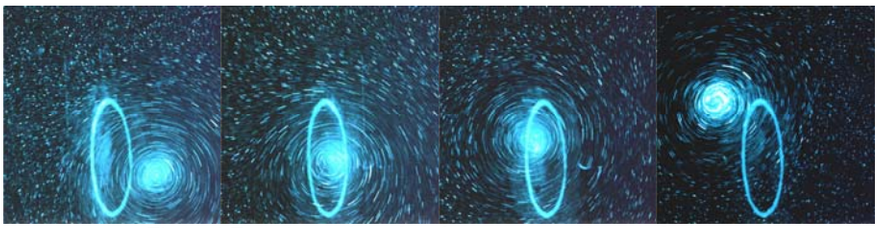


Figure 1 Experimental results of vortex streamlines evolutions.

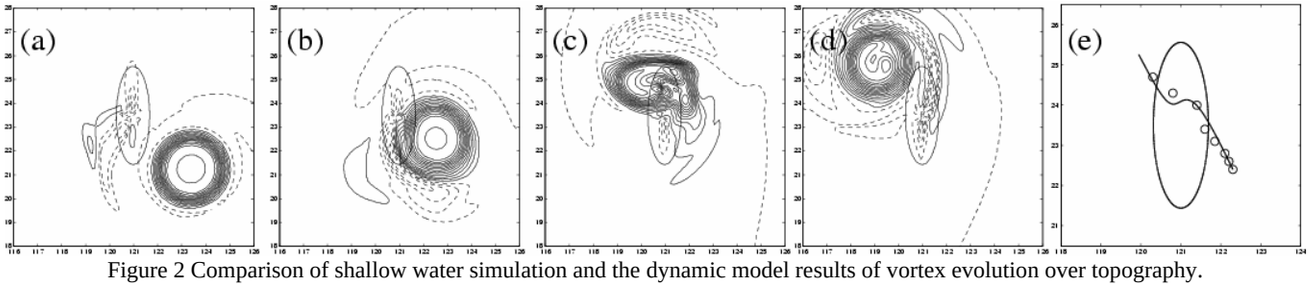


Figure 2 Comparison of shallow water simulation and the dynamic model results of vortex evolution over topography.

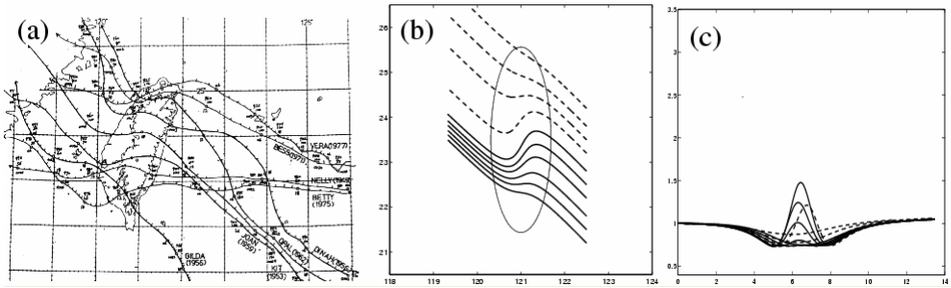


Figure 3 (a) Historical typhoon tracks, (b) vortex tracks calculated by the dynamic model and (c) time evolution of the drifting velocity of the vortex.

XXI ICTAM, 15–21 August 2004, Warsaw, Poland

SPONTANEOUS SIGN REVERSALS IN SELF-ORGANIZED STATES OF FORCED TWO-DIMENSIONAL TURBULENCE ON A BOUNDED SQUARE DOMAIN

David Molenaar, Herman J.H. Clercx, GertJan F. van Heijst
Eindhoven University of Technology PO Box 513, 5600 MB Eindhoven, The Netherlands

Summary The inverse energy cascade present in two-dimensional (2D) turbulence leads to the formation of large-scale flow structures. In the case of decaying 2D turbulence on a square domain with no-slip walls the flow usually shows self-organization into a single domain-filling circulation cell with an associated increase in the total angular momentum of the flow — a process referred to as 'spontaneous spin-up'. Subsequently, this organized state may persist until all energy is depleted by viscous dissipation and the fluid eventually comes to rest. In contrast, if the energy of the flow is maintained by some external forcing mechanism, a spectacularly different behaviour may be observed. Boundary layers present at the domain walls can destabilize the organized state, such that the dominating circulation cell collapses, and the self-organization process may start anew. Most strikingly, the circulation may even show sign reversal. This flow behaviour has been investigated by high-resolution numerical simulations based on spectral techniques.

DECAYING 2D TURBULENCE

A well-known feature of two-dimensional (2D) turbulence is the inverse energy cascade, according to which energy is passed from small to large scales of motion. It is generally assumed that the inverse cascade is linked to the formation of vortex structures. In the case of slowly decaying turbulence, these structures show complicated interactions, resulting in a decreasing number of vortices of increasing size. Numerical simulations carried out for a turbulent flow on a double periodic square domain have revealed that the flow eventually becomes organized in the form of a combination of two cells of positive and negative circulations [1]. In contrast, the 'final state' of decaying 2D turbulence on a square domain with no-slip boundaries consists of a large central cell with either positive or negative circulation, surrounded by a shielding ring of negative or positive vorticity, respectively, such that the total circulation of the flow is zero (as dictated by the no-slip condition at the domain boundaries). This long-time behaviour has been found both in laboratory experiments and in high-resolution numerical flow simulations. A remarkable observation was that in many cases the total angular momentum $L(t)$ of the flow, which is initialized randomly, with $L(t=0) \simeq 0$ shows a sudden change to non-zero values — a feature termed 'spontaneous spin-up' [2]. This total spin-up of the fluid is directly associated with the self-organization of the flow into a single larger vortex structure that fills the domain almost completely. In the next stage of the flow evolution, the absolute angular momentum $|L(t)|$ shows a very slow decay to zero for very late times. It is important to note that the no-slip boundary condition is a prerequisite for the spin-up, as the angular momentum $L(t)$ is an irrelevant quantity for the flow evolution on a double-periodic domain. Also, the square domain geometry is important, spin-up being virtually absent on a circular domain [3] or on a long rectangular domain in which the 'final state' consists of a linear (domain-filling) array of counter-rotating cells [4]. Obviously, the change of the total angular momentum during the spontaneous spin-up is connected with the action of forces at the domain boundaries. Numerical simulations have revealed that — for the case of a square geometry — the contribution of the inviscid normal stress (i.e., the pressure) is much larger than the effects of viscous shear and normal stresses.

FORCED 2D TURBULENCE

In recent direct numerical simulations of stochastically forced 2D turbulent flow on a square domain with no-slip boundary conditions we also observed spontaneous spin-up behaviour, although remarkably different from the decaying case. In these forced turbulence experiments one observes several consecutive events of rapid increase and decrease of $|L(t)|$, often with sign reversal of $L(t)$ between neighbouring peaks in $|L(t)|$.

The evolution of the flow is governed by the vorticity equation

$$\frac{\partial \omega}{\partial t} + (\mathbf{v} \cdot \nabla)\omega = \nu \nabla^2 \omega + q \tag{1}$$

with $\mathbf{v}(\mathbf{r},t) = (u,v)$ the velocity vector and $\mathbf{r} = (x,y)$ the position vector on a square domain $\mathcal{D}$ defined by $\{-1 \leq x \leq 1; -1 \leq y \leq 1\}$; furthermore, $\omega(\mathbf{r},t) \equiv \hat{\mathbf{z}} \cdot \nabla \times \mathbf{v} = \frac{\partial v}{\partial x} - \frac{\partial u}{\partial y}$ is the vorticity component perpendicular to the flow field, ν is the kinematic viscosity, and q represents the stochastic external forcing of the flow. Subject to the no-slip condition $\mathbf{v} = 0$ on domain boundary $\partial\mathcal{D}$, and initially, $\omega(\mathbf{r},0) = 0$ on $\mathcal{D}$, equation (1) is solved numerically using a pseudo-spectral code based on Chebyshev expansions and a semi-implicit Adams-Bashforth Crank-Nicolson time integration scheme [5]. The forcing q is modelled as a first order Markov process [6]. The total angular momentum $L(t)$ of the flow with respect to the domain centre is defined as

$$L(t) = \int_{\mathcal{D}} (\mathbf{r} \times \mathbf{v}) \cdot \hat{\mathbf{z}} dA \, . \tag{2}$$

A typical example of the evolution of the normalised angular momentum $L'(t) = L(t)/L_u(t)$ — where $L_u(t)$ is the angular momentum associated with a uniform rotation with kinetic energy $E(t)$ — during a simulation with integral scale

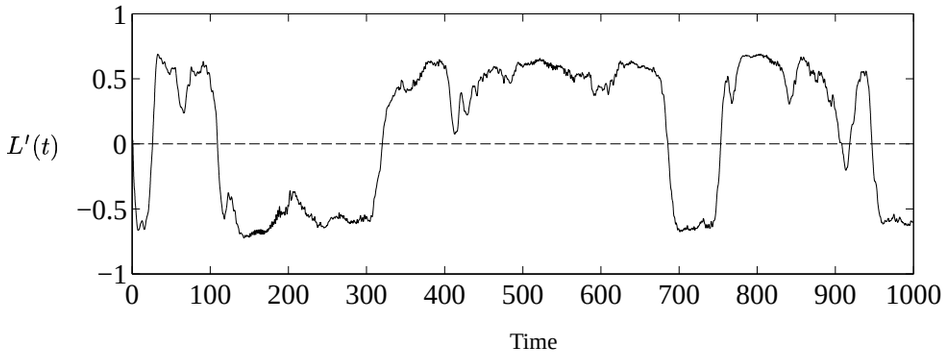


Figure 1. *Evolution of the normalized angular momentum $L'(t)$, showing distinct phases of spin-up.*

Reynolds number $Re = (Ud/\nu) \simeq 3000$ (where U is the root-mean-square velocity and d the domain size) is shown in Figure 1. It is clearly seen that — although being equal to zero initially — the angular momentum tends to reach a non-zero value, i.e. the flow exhibits spontaneous spin-up. Moreover, several sign changes in L' are observed to occur: apparently the flow reverses abruptly in those cases.

In fact, a few different stages can be distinguished in the flow evolution: first the flow is showing evidence of self-organization or spin-up, as can be observed from the build-up of a larger circulation cell and the associated angular momentum, followed by a relatively rapid destruction of the cell and a dramatic decrease of the flow's total angular momentum. Subsequently, the flow becomes organized again into a larger circulation cell — either with the same or with opposite rotation direction as the previous cell. The no-slip boundaries enclosing the flow domain play a crucial role in the repeated destruction of the organized flow state. The viscous layers at the walls contain oppositely-signed vorticity, as a consequence of the no-slip condition. Once the larger cell is established, the boundary layers detach, giving rise to the formation of smaller vortices in the corners of the domain. The corner vortices gradually grow in size and strength, and subsequently start to interact with the flow in the interior. The central cell is thus progressively eroded, it soon becomes unstable, and then breaks down rapidly. At that stage, the flow has become irregular, consisting of filamentary structures without any overall coherence. Subsequently the self-organization process may start anew, possibly leading to a flow cell with oppositely signed circulation.

References

[1] Matthaeus, W.H., Stribling, W.T., Martinez, D., Oughton, S. & Montgomery, D.: Decaying, two-dimensional, Navier-Stokes turbulence at very long times. *Physica D* **51**, 531–538, 1991.

[2] Clercx, H.J.H., Maassen, S.R. & van Heijst, G.J.F.: Spontaneous spin-up during the decay of 2D turbulence in a square container with rigid boundaries. *Phys. Rev. Lett.* **80**, 5129 – 5132, 1998.

[3] Li, S., Montgomery, D. & Jones, W.B.: Two-dimensional turbulence with rigid circular walls. *Theor. Comput. Fluid Dyn.* **9**, 167 – 181, 1997.

[4] Maassen, S.R., Clercx, H.J.H. & van Heijst, G.J.F.: Self-organization of quasi-2D turbulence in stratified fluids in rectangular containers. *J. Fluid Mech.* **495**, 19 – 23, 2003.

[5] Clercx, H.J.H.: A spectral solver for the Navier-Stokes equations in velocity-vorticity formulation for flows with two non-periodic directions. *J. Comput. Phys.* **137**, 186 – 211, 1997.

[6] Maltrud, M.E. & Vallis, G.K.: Energy spectra and coherent structures in forced two-dimensional and beta-plane turbulence. *J. Fluid Mech.* **228**, 321 – 342, 1991.

A MODEL FOR THE FORMATION OF 'OPTIMAL' VORTEX RINGS WITH TAKING INTO ACCOUNT VISCOSITY

Felix B. Kaplanski and Ylo A. Rudi
Tallinn University of Technology, Laboratory of Multiphase Media Physics,
Akadeemia tee 23A, Tallinn 12618, Estonia

Summary The paper presents the model for formation of an axisymmetric vortex ring based on the viscous analogy to the Norbury vortices. By using the matching procedure suggested earlier and the obtained properties of the viscous vortex ring, it is found that when the limiting stroke value L/D ('formation number') reaches the value 4.0, the appropriate limiting values of the normalized energy and circulation become around 0.3 and 2.0, respectively. The predicted values are in agreement with the experimental data. An approach that enables to predict the 'formation number' is proposed.

INTRODUCTION

Vortex ring formation process was reproduced many times in the laboratory experiments Relatively recently, much attention has been paid to a structures produced for large piston stroke to the diameter ratios, L/D. The experiments by Gharib *et al.* [1] have shown that in this case the generated flow consists of the leading vortex ring followed by a trailing jet. The vorticity field of the leading vortex ring is disconnected from the trailing jet at a critical value of L/D (Gharib *et al.* refer to this as the "formation number"), at which time the vortex ring attains maximum volume, circulation and energy. The limiting value of the "formation number" follows from the direct experimental measurements by Gharib *et al*. who reported the values close to L/D=4 with a range of 3.6 to 4.5 for a variety of exit diameters, exit plane geometries, and non-impulsive piston velocities. Also the limiting values of the normalized energy and circulations were found experimentally as 0.3 and 2.0, respectively. The predictive models of the "optimal " vortex rings formation (Mohseni and Gharib [2]and Linden and Turner [3]) were developed by equating the motion invariants in the idealized slug-flow model with the corresponding properties of the Norbury vortices. However, real physical vortex rings have peakier vorticity distributions in contrast with the uniform vorticity density of the Norbury vortices. The model for the prediction of the optimal vortex ring formation on the base of the viscous analogy to Norbury vortices is discussed in this paper.

THE DIMENSIONLESS ENERGY AND CIRCULATION

The expressions for the circulation Γ_m, kinetic energy E_m and translation velocity U_m of the viscous vortex ring are given by (Kaplanski and Rudi[4])

$$\Gamma_m = \frac{M}{\pi R_0^2}\left(1-\exp\left(-\tau^2\right)\right),\ E_m = \frac{M^2\rho\tau}{2\pi^2 R_0^3}\left(\frac{1}{12}(\pi)^{1/2}\tau^2\ {}_2F_2\left[\left\{\frac{3}{2},\frac{3}{2}\right\},\left\{\frac{5}{2},3\right\},-\tau^2\right]\right),$$

$$U_m = \frac{M\tau}{4\pi^2 R_0^3}\left\{3(\pi)^{1/2}\exp\left(-\frac{\tau^2}{2}\right)I_1\left(\frac{\tau^2}{2}\right)+\frac{1}{12}(\pi)^{1/2}\tau^2\ {}_2F_2\left[\left\{\frac{3}{2},\frac{3}{2}\right\},\left\{\frac{5}{2},3\right\},-\tau^2\right]-\frac{3(\pi)^{1/2}}{5}\tau^2\ {}_2F_2\left[\left\{\frac{3}{2},\frac{5}{2}\right\},\left\{2,\frac{7}{2}\right\},-\tau^2\right]\right\}.$$

Here I_1 is the modified Bessel function of order one, ${}_2F_2$ is the generalized hypergeometric function, R_0 is the initial radius of the vortex ring and $\tau = R_0/\ell$ is the ratio of the outer radius to the diffusivity scale of the ring's core ℓ identified as the ring's inner radius. These invariants are found on the basis of the solution for the vorticity distribution

$$\omega_m = \exp\left(-\frac{1}{2}\left(\sigma^2+\eta^2+\tau^2\right)\right)I_1(\sigma\tau), \qquad (1)$$

$$\omega = \frac{\varsigma}{\varsigma_0},\ \sigma = \frac{r}{\ell}, \eta = \frac{x-x_o(t)}{\ell}, \tau = \frac{R_o}{\ell}.$$

Following the idea by Monseni and Gharib [2](see also Linden and Turner [3]), we use the dimensionless stroke length in the form

$$\frac{L}{D} = \sqrt{\frac{\pi}{2}}\frac{\Gamma^{3/2} I^{1/2}}{E}$$

This allows us to establish the dependence of the value of L/D on τ by equating the values of the impulse $I_m = M\rho$, circulation, and kinetic energy of the injected plug to the above-mentioned values of the viscous vortex ring. It is then possible to obtain the dimensionless energy and circulation for L/D=4

$$\widetilde{E} = \frac{E_m}{\Gamma_m^{3/2} I_m^{1/2}} = 0.3,\ \widetilde{\Gamma} = \frac{\Gamma_m}{I_m^{1/3} U_m^{2/3}} = 2.1.$$

The evaluated values are in agreement with the experimental data. [1] However, unlike the Norbury vortices, the vorticity distribution (1) at short-time limit tends to the Gaussian form and is consistent with that observed experimentally.

THE 'FORMATION' NUMBER

The method of entrainment diagrams reported by Cantwell is applied. [5] For this purpose the equations for streamlines are determined by

$$\frac{dx}{dt} = \frac{1}{r}\frac{\partial \Psi}{\partial r} + U(t),\ \frac{dr}{dt} = -\frac{1}{r}\frac{\partial \Psi}{\partial x},$$

The appropriate autonomous system in dimensionless variables σ, η, with two parameters $Re_0 = \Gamma_0 / \nu$ and τ, can be written as

$$\frac{d\eta}{ds} = -\frac{\eta}{2} + \frac{2\sqrt{2}}{\sqrt{\pi}}\frac{Re_0\,\tau}{8}u_t,\ \frac{d\sigma}{ds} = -\frac{\sigma}{2} + \frac{2\sqrt{2}}{\sqrt{\pi}}\frac{Re_0\,\tau}{8}v_t. \qquad (2)$$

Here $s = \ln(t)$ and u_t, v_t are given by

$$u_t = \frac{1}{\sigma}\frac{\partial \Phi}{\partial \sigma} = \frac{\sqrt{\pi}}{2\sqrt{2}}\int_0^\infty \mu^2 F(\mu,\eta) J_1(\tau\mu) J_0(\sigma\mu)\,d\mu,\ v_t = -\frac{1}{\sigma}\frac{\partial \Phi}{\partial \eta} = -\frac{\sqrt{\pi}}{2\sqrt{2}}\int_0^\infty \mu\{-G(\mu,-\eta) + G(\mu,\eta)\} J_1(\tau\mu) J_1(\sigma\mu)\,d\mu,$$

where $F(\mu,\eta) = G(\mu,\eta) + G(\mu,-\eta), G(\mu,\eta) = \exp(\eta\mu)\left(1 - \mathrm{erf}\left(\frac{\mu+\eta}{\sqrt{2}}\right)\right)$.

The analysis is focused on various isocline patterns of this dynamical system and on critical points (σ_0, η_0), where $d\eta/ds = 0, d\sigma/ds = 0$. The presented study is motivated by the hypothesis that analyzing of the system (2) can reveal properties of the nonlinear solution although the Stokes solution is used. Observing the particle trajectories for relatively high value of τ=10 versus Re_0, we recognize three regimes. In the first regime ($Re_0 < 150$), the particle trajectories converge to a single node, which lies on the axis η. In the second regime ($150 < Re_0 < 700$), particle trajectories are divided into two parts: some of trajectories converge to a node on the axis η, while other trajectories include the core of the ring. In the third regime ($Re_0 > 700$) all trajectories turn towards the center of the ring. The first transition can be interpreted as the transformation of the jet structure into the structure corresponding to the combination of a wake and a vortex ring. The appearing of these structures at the formation stage is consistent with the numerical studies. The solution (1) for high value of τ tends to the Gaussian distribution. When this solution is incorporated into the system (2) it shows the formation of the wake, i.e. indicates the nonlinear behaviour. We assume that the defined pattern with the second regime of the particle trajectories corresponds to the presence of a Gaussian distribution of vorticity inside the ring core. In this connection it is also natural to ask: 'What is the largest volume a vortex ring can achieve with the Gaussian distribution of vorticity in the ring core?' The boundaries for the flows consisting of the combination of a wake and a vortex ring in the parameter space (τ and Re_0) for $\tau \le 10.$ are computed. This enables us to estimate the critical value of τ for which the above-mentioned structures disappear (for any Re_0). It lies in the range $3 < \tau < 4$. Since R_0 is fixed, the reduction of τ leads to the increasing of the ring inner radius and volume. Thus, the corresponding range of the limiting values of L/D for those the vortex ring has the largest volume can be estimated as $4.0 < L/D < 5.5$. Even though the above attempt includes heuristic arguments it gives the estimation of the 'formation' number. An estimation of this value, to our knowledge, not yet been suggested.

References

[1] Gharib M., Rambod E. and Shariff K.: A universal time scale for vortex ring formation. *J. Fluid Mech.* 360, 121,1998.

[2] Monseni K. and M. Gharib M.: A model for universal time scale of vortex ring formation. *Phys. Fluids* **10**, 2436, 1998.

[3] Linden P. E. and Turner J. S.: The formation of 'optimal' vortex rings, and the efficiency of propulsion devices. *J. Fluid Mech.* **427**, 61,2001.

[4] Kaplanski F. and Rudi Y.: Dynamics of a viscous vortex ring, *Int. J. Fluid Mech. Res.* **26**, Nos.5&6, 618,1999.

[5] Cantwell B. J. Organized motion in turbulent flow," *Ann. Rev. Fluid Mech*., **13**, 1981, 457,1981

NUMERICAL SIMULATION OF VORTICAL FLOWS USING A HIGHLY ACCURATE FINITE DIFFERENCE SCHEME

Katsuya Ishii[*], Tomonori Nihei[**], Shizuko Adachi[**]
[*]*ITC, Nagoya University, Nagoya, 464-8601, Japan*
[**]*Dept. of CSE, Nagoya University, Nagoya 464-8603, Japan*
[***]*RIKEN, Wako, 351-0198, Japan*

Summary A combined compact finite difference (CCD) scheme with high accuracy and high resolution is proposed for numerical simulation of incompressible vortical flow fields. The CCD scheme has eighth-order accuracy and spectral-like resolution for the first derivative except for the boundary. The Poisson equation is also solved accurately by using the CCD scheme and the ADI method. The vortical flows in the three-dimensional lid-driven square cavities with different spanwise aspect ratios are studied using this new scheme.

INTRODUCTION

Numerical simulations of vortical flows need high accuracy and high resolution, since vortices with different spatial scales are found in the flow. The combined compact finite difference (CCD) scheme proposed by the authors has high accuracy with comparatively low computational cost and it is a promising scheme for large-scale computation with high accuracy[1]. A class of combined compact difference schemes was proposed by Chu and Fan [2]. In the schemes, the derivatives of a function are evaluated by means of the values and derivatives at the two adjacent points. Our CCD scheme has eighth-order accuracy and spectral-like resolution for the first order derivative in the problem with periodic boundary conditions. The order of computational cost for the CCD scheme is the same as that of the ordinary difference scheme.

In this paper, the incompressible vortical flow field in a three-dimensional lid-driven cavity is considered. We modify the CCD scheme for the incompressible flow fields. For solving the Poisson equation, a new iterative method using the ADI method and the CCD formulation is proposed, and it gives highly accurate numerical solutions of the 3D Poisson equation. We also discuss the CCD scheme with Dirichlet and/or Neumann boundary conditions and the parallelization of the scheme.

The flow in the lid-driven cavity has been extensively studied as a fundamental model for separated flows and for the vortex dynamics in the closed systems with simple geometry and boundary conditions. There are two aspect ratios in the three dimensional flows in finite domains : $\Gamma = d/h$ and $\Lambda = l/h$ where d, h and l are the width, height and span length of cavity respectively . We consider the square cavity ($\Gamma = 1$) with different spanwise aspect ratio Λ's and study the side boundary effect for the overall flow structure and the Taylor-Görtler-like vortex pair in the secondary flow.

NUMERICAL SCHEME

Consider a function $f(x)$ defined on the interval where N grid points are located with a uniform spacing h. Let f_i, f'_i, f''_i and f'''_i be the values of the function and its first, second and third derivatives at i-th grid point x_i respectively. The CCD scheme evaluates these derivatives implicitly from the following relations:

$$f'_i = a_1(f_{i+1} - f_{i-1}) + a_2(f'_{i+1} + f'_{i-1}) + a_3(f''_{i+1} - f''_{i-1}) + a_4(f'''_{i+1} + f'''_{i-1})$$

$$f''_i = b_1(f_{i+1} + f_{i-1} - 2f_i) + b_2(f'_{i+1} - f'_{i-1}) + b_3(f''_{i+1} + f''_{i-1}) + b_4(f'''_{i+1} - f'''_{i-1})$$

$$f'''_i = c_1(f_{i+1} - f_{i-1}) + c_2(f'_{i+1} + f'_{i-1}) + c_3(f''_{i+1} - f''_{i-1}) + c_4(f'''_{i+1} + f'''_{i-1})$$

The formal accuracy of the scheme is determined by the parameters a_j, b_j and c_j. By relaxing the requirement for the highest formal accuracy, we have free parameters. The values of the free parameters are chosen to minimize errors in the wavenumber space for most waves except very short waves [1,3].

The Poisson equation usually needs to be solved in incompressible fluid flow problems, and its finite difference solver generally takes a large portion of the entire computation time. Since CCD schemes implicitly evaluate the derivatives, a method such as SOR, which is often used, is hard to apply to the Poisson equation solver that uses a CCD scheme. Chu and Fan [2] proposed an algorithm for a CCD scheme which solves the 2D elliptic partial differential equation by the ADI method using the modified Poisson equation and the CCD derivatives. However, their method is not effective for the accurate calculation with many grid points. We developed a new ADI method using the original Poisson equation. This algorithm can be parallelized easily.

The incompressible Navier-Stokes equations in conservation form are numerically solved by the well-known MAC method and the fourth order Runge-Kutta method for the time integration. The derivatives in the equations are evaluated by the CCD scheme, in which the first and the second derivatives have eighth-order accuracy except for the boundary and the third derivative has fourth-order accuracy. At the boundary, the first and the second derivatives have sixth-order accuracy. In the case of the cubic cavity(Λ=1) at Re=100 to 400, the numerical results using this new scheme with 33x33x33 uniform grid points are in good agreement with the previous results[4] with 81x81x81 non-uniform grid points. For the study of the wall effect, the 100x100x 100Λ uniform grid system is used in the calculation, in which Λ is a spanwise aspect ratio.

RESULTS

We focus on the flows in a square driven-cavity with spanwise aspect ratios Λ from 1 to 6.55 at the Reynolds number $Re=Ud/\nu$=850, where U is the speed of the sliding upper wall and ν is the kinematic viscosity. In this Reynolds number, we got steady state solutions. We show the streamline using the projected velocity on the vertical plane near the upstream end wall at Λ=4 and Λ=6.55 in Fig.1 and Fig. 2 respectively. While Fig. 1 shows one symmetric flow structure and the upper corner vortex, Fig.2 shows 2.5 cell structures in the central region and the other cell structure near the side wall. These results agree with the experimental result [5]. These patterns are strongly related to the Taylor-Görtler-like vortex pairs in the secondary flow of the overall flow structure. We can discuss the bifurcation of flows in the lid-driven cavity with different spanwise aspect ratios Λ.

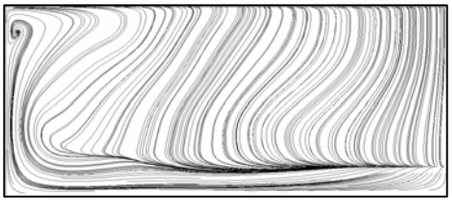


Fig.1 streamlines using the projected velocity near the upstream end wall (left half plane, Λ =4)

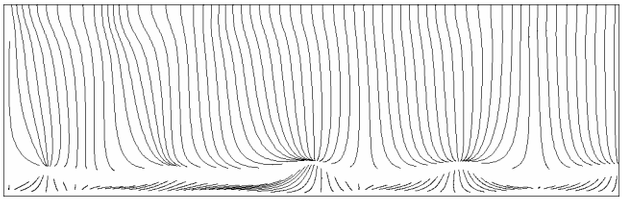


Fig.2 streamlines using the projected velocity near the upstream end wall (left half plane, Λ=6.55)

CONLUDING REMARKS

We have developed the highly accurate combined compact finite difference scheme for the incompressible flow. The application to the flow shows the efficiency of the new scheme. The numerical results clearly show the bifurcation of flow structures in a lid-driven cavity with different spanwise aspect ratios

Reference

[1] Nihei ,T. and Ishii, K:A Fast Solver of the Shallow Water Equations on a Sphere using a Combined Compact Difference Scheme.*J. Comput. Phys.* **187**, 639—659,2003

[2] Chu, P.C. and Fan, C.: A Three-point Combined Compact Difference Scheme, *J. Comput. Phys.* **140**, 370-399,1998.

[3] Lele, S.K.:Compact Finite Difference Schemes with Spectral-like Resolution. *J. Comput. Phys.* **103**, 1992, pp. 16—42, 1992.

[4] Iwatsu, R., Ishii, K., Kawamura, K. Kuwahara, K. Hyun, J. M: Numerical Simulation of Three-dimensional Flow Structure in a Driven Cavity, *Fluid Dyn Res* **5**,173-189, 1989..

[5] Albensoeder, S., Kuhlmann, H. C., and Rath, H.J. : Three-dimensional Centrifugal-flow Instabilities in the Lid-driven-cavity Problem. *Phys. of Fluid* .**13,** 121-135,2001.

THE DEVELOPMENT OF AN AXISYMMETRIC GRAVITY CURRENT

M. D. Patterson*, J. E. Simpson* S. B. Dalziel* & G. J. F. van Heijst**
*Department of Applied Mathematics and Theoretical Physics, Centre for Mathematical Sciences, University of Cambridge, Wilberforce Road, Cambridge CB3 0WA, England.
**Fluid Dynamics Laboratory, Department of Physics, Eindhoven University of Technology, PO Box 513, 5600MB Eindhoven, The Netherlands

Summary Three-dimensional releases of fixed volumes of saline fluids into fresh water and their radial spread have been examined experimentally. At high Reynolds numbers three distinct regimes have been identified. A short initial phase, a secondary phase where the frontal speed is constant and a final stage where the front speed is reduced. In the secondary stage the gravity current's head is dominated by the presence of a ring vortex above the front. This stage of the flow propagation comes to an abrupt end with the breakdown of the ring vortex at a clearly defined point. The experimental results have been compared to 2D and 3D numerical simulations. The simulations compare well with the experimental data for the early stages of the flow. The results show the development of a complex flow field and highlight the unsuitability of shallow water modelling for axisymmetric lock releases.

INTRODUCTION

Gravity currents have been studied extensively in different configurations because of their importance to a large number of industrial and environmental situations. An example of particular interest is the spread of a dense gas due to the rupture of a chemical storage tank. Understanding the dynamics of the gravity current arising after such an accidental release is crucial for a better risk assessment.

Previous work has revealed that gravity currents due to a fixed volume release into a parallel-sided channel behave differently from those allowed to spread radially. Numerical simulations of axisymmetric dam-break problems based on the shallow-water approximation were first presented by Rottman & Simpson (2) (3) for both the two-dimensional plane-flow case and the axisymmetric case discussed here. Solutions were obtained for the depth profiles of the dense fluid in both cases. In the axisymmetric case most of the heavy fluid appears to become concentrated in a ring between the front and a backward facing hydraulic jump behind the front that propagates from the centre: this jump propagates radially outward more rapidly that the front itself. Rottman & Simpson (2) proposed that the catch-up of the rear bore is the mechanism that is responsible for the formation of the frontal ring.

In this paper we examine the axisymmetric spreading gravity current in some detail, this study consists of laboratory experiments and numerical simulations.

METHODOLOGY

Three different types of laboratory experiment have been carried out in a sector-shaped tank 2.35 m long, with a sector angle measuring approximately 10°. In the first set of experiments the sector tank was filled with fresh water of density $\rho_A = 1000$ kg/m^3 to a depth $H = 0.3$ m. A fixed volume of denser fluid, density $\rho_L = 1013.5$ kg/m^3, was kept behind a vertical barrier at a radial distance $R = R_0$ and at a depth h_0, where $h_0 \leq H$, with fluid of density ρ_A above. By lifting the barrier the denser fluid is released into the widening part of the tank. For visualisation purposes the dense fluid was dyed with potassium permanganate. Illumination from behind using a diffuse light bank resulted in a sharply defined interface between the gravity current and the ambient fluid. The evolution of the resulting gravity current was recorded using a high resolution digital video camera with the movies saved to a computer. A mirror placed above the experiment allowed plan-view information of the gravity current's propagation to be recorded simultaneously using a single camera.

The flow is characterised by the following parameters: the reduced gravity $g' = \Delta\rho g/\rho$, the fractional depth $\phi = h_0/H$, and the aspect ratio $\gamma = h_0/R_0$. In order to investigate the role of the fractional depth of the lock release on the front speed a number of experiments were carried out for different values of this parameter. In total four differrent experiments were carried out.

A second series of experiments to examine the effects of aspect ratio on a gravity current have also been carried out in this study. To create initial conditions that are as close to identical as possible the position of the lock gate, the reduced gravity g', the heights H and h_0 have been kept constant. To vary the aspect ratio a barrier has been inserted into the lock at a distance R_1 from the centre, where $R_1 < R_0$. Data from these experiments has been obtained in exactly the same fashion as in the first set of experiments. The experiments have been analysed to investigate how variation of the aspect ratio γ effects the fronts propagation speed. The temporal evolution of the concentration field when γ is varied is also examined.

In the third set of experiments a Particle Image Velocimetry (PIV) technique has been used to examine the temporal and spatial development of the gravity current's head. Pattern matching algorithms have been adapted for this purpose. For this set of experiments both the lock and the ambient fluid were seeded with a mixture of particles of differing densities. The flow was illuminated using a 5 mm vertical light sheet created using a 300 W arc lamp with a parabolic reflector to collimate the light. The use of a light sheet implies that three-dimensional movements could be filtered out as only the particles that remained in the light sheet are bright enough to be detected by the camera.

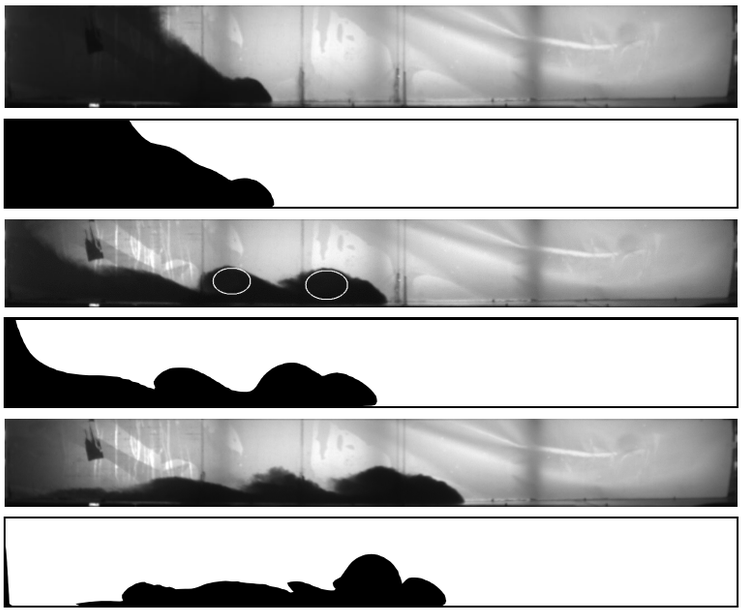


Figure 1. Experimental (upper picture) and numerical (lower picture) results showing the evolution the radially spreading gravity current for an axisymmetric lock release with $\phi = 1.0$, $g' = 13.2$ cm/s^2 for times $t = 2.59$ s (a), 6.19 s (b), 8.70 s and (c).

Three-dimensional numerical flow simulations have been carried out with a code based on the Monotone Integrated Large Eddy Simulation (MILES) method described in Almgren *et al.* (1). The scheme is an incompressible variable density Navier-Stokes solver. The main difference between this MILES based code and other Navier-Stokes solvers is that there are no explicit closure schemes applied to solve for turbulence. The simulations are used to resolve the macroscopic scales in the problem and it is assumed that the flux-limiting monotone algorithms used for solving the set of coupled equations have a high frequency filter that inherently maintains physically reasonable behaviour near the grid scale cut–off.

RESULTS

The development of a full-depth gravity current $\phi = 1.0$, can be observed in figures 1 (a)-(c), which present experimental snapshots of the flow, together with the corresponding density plots from a two-dimensional axisymmetric numerical simulation. The figures clearly show a frontal bulge starting to develop shortly after the lock release (a). Then during the collapse of the dense fluid volume, vorticity is created mainly at the interface between the lighter and denser fluids. While being advected by the radially spreading fluid, the vorticity accumulates near the front, contributing to the formation of a gradually expanding leading ring vortex, a secondary ring vortex is also generated and the locations of the ring vortices are marked as white circles in (b). Vortex stretching appears to stabilise the rings (c) and these ring vortices become more intense. At a later stage the vortical flow can no longer be maintained and it vanishes abruptly. The front then continues to propagate outward without such a clearly defined structure. Comparison of the experimental and numerical results shows an excellent agreement for the initial stages of the flow (before vortex breakdown), with the front position and the form of the gravity current being accurately predicted.
Results from three-dimensional simulations have also be compared with two-dimensional numerical simulations.

References

[1] A. S. Almgren, J. B. Bell, and W. G. Szymczak, "A numerical method for the incompressible Navier-Stokes equations based on an approximate solver," SIAM J. Sci. Comput., **17:2**, (1996).

[2] J. W. Rottman, and J. E. Simpson, "Gravity currents produced by instantaneous releases of a heavy fluid in a rectangular channel," J. Fluid Mech. **135**, 95 (1983).

[3] J. W. Rottman, and J. E. Simpson, "The initial development of gravity currents from fixed volume releases of heavy fluids," Atmospheric Dispersion of Heavy Gases and Small Particles (eds G. Ooms and H. Tennekes), Proc. IUTAM Symposium, Delft, The Netherlands, 1983. Springer-Verlag (1984).

[]

NUMERICAL INVESTIGATION OF THE LAMINAR-TURBULENT TRANSITION OF THE FLOW IN A ROTOR-STATOR CAVITY

Ewa Tuliszka-Sznitko [*], *Eric Serre, Patrick Bontoux* [**]
[*] *Institute of Thermal Engineering, Technical University of Poznan, 60-965 Poznan, Poland*
[**] *LMSNM CNRS-FRE 2405, IMT Château-Gombert, Université de la Méditerranée ,Marseille, France*

Summary Incompressible fluid flow in a rotor-stator configurations has been numerically investigated for cylindrical and annular cavity. The numerical computations are based on a pseudo spectral Chebyshev-Fourier method for solving 3D Navier-Stokes equations. The nature of the transition to unsteadiness is investigated as well as the influence of the shaft and shroud boundary layers on the transitional process. A linear stability analysis is also performed in order to enlighten the DNS results with respect to type I and type II instability. Moreover, the absolute instability regions are theoretically identified.

INTRODUCTION

Flow in rotting disks systems is not only a subject of fundamental interest but is also a topic of practical importance. Typical configurations are cavities between compressors and turbines disks. Numerous works have been recently devoted to the investigation of the instabilities associated to a single disk flow [1] and to a differentially rotating disks flow. [2-5] Identification and characterization of mechanisms related to this process should improve the prediction methods and lead to new more efficient control strategies. In the present work the incompressible fluid flow in a stator/rotor cavity (cylindrical and annular) is numerically investigated using direct numerical simulation (DNS) and theoretical method (LSA). The nature of the transition to unsteadiness as well as the influence of the end-walls boundary conditions (the influence of the attachment of the shroud and shaft to the rotor or to the stator and the influence of the approximation of the end-walls azimuthal profiles) on the stability of the flow have been investigated.

MATHEMATICAL MODEL AND NUMERICAL METHOD (DNS)

The geometrical configuration consists of a closed cylindrical and annular cavity (Fig.1a). The rotor rotates at uniform angular velocity $\Omega = \Omega\, e_z$, e_z being the unit vector. The flow is controlled by three physical parameters which are the Reynolds number based on the outer radius $Re_R = R_1^2\Omega/\nu$, the aspect ratio $L=(R_1-R_0)/2h$ (R_0 is the inner radius) and the curvature parameter $R_m = (R_1+R_0)/(R_1-R_0)$. The governing equations are 3D Navier-Stokes equations. The numerical solution is based on a pseudospectral collocation Chebyshev-Fourier Galerkin approximation. The approximation of the flow variables $\Psi = (u, w, v, p)$ is given by a development in truncated series:

$$\Psi_{NMK}(r,z,\varphi,t) = \sum_{p=-K/2}^{K/2-1}\sum_{n=0}^{N}\sum_{m=0}^{M}\tilde{\Psi}_{nmp}(t)T_n(r)T_m(z)e^{ip\varphi} \quad \text{for} \quad \begin{matrix} -1 \le r, z \le 1 \\ 0 \le \varphi \le 2\pi \end{matrix}$$

The time scheme is semi-implicit and second-order accurate. It corresponds to a combination of the second-order backward differentiation formula for the viscous diffusion term and the Adams-Bashforth scheme for the non-linear terms. The method uses a projection scheme to maintain the incompressibility constrain. No slip boundary conditions apply at all rigid walls, then u = w = 0. For the azimuthal velocity component, the boundary conditions are v=0 on the stator and v = (1+r)/2 on the top rotating disk. For the cylindrical cavity the end-wall cylinder is also at rest, then v=0. However, in order to eliminate singularity the of the azimuthal velocity at the junction between the stationary end-wall and the rotating disk, this boundary condition is smoothed using an exponential azimuthal velocity profile v = exp((z-1)/0.006) which approximates well the thin gap between the edge of the rotating disk and the stationary end-wall. For the annular geometry we considered the following cases: a) the linear profiles for the shaft and shroud, b) the exponential profiles with the both end-walls attached to the stator, c) the exponential profiles with the shaft attached to the rotor and with the shroud attached to the stator. The initial condition is as follows: u=0, v = (1+r)(z+1)/4, w=0.

RESULTS AND DISCUSSION

In the case of cylindrical geometry computations have been performed using the LSA method for a two disk flow and using the DNS method for a rotor-stator cavity of aspect ratio L=5 in order to accurately investigate the transition to unsteadiness. Surprisingly, no transition from a steady Batchelor state to an unstable oscillatory flow has been numerically emphasized till now, except in cavities of small aspect ratio $L \le 2$. Starting from a base state at $Re_R=3000$ and increasing very slowly the disk rotation, this study has emphasized a supercritical Hopf bifurcation to an oscillatory solution of frequency $\sigma \approx 1.1$, and at a critical Reynolds number estimated between $11500 \le Re_R \le 12300$. As expected, for the cylindrical cavity the unsteadiness first develops in the stator boundary layer while the rotor boundary has remained stable for the rotation rates considered in this work. Three-dimensional structures related to the stationary disk boundary layer instabilities have been accurately emphasized by DNS and studied using LSA results.

Spiral arms with positive and negative angles have been observed in the stationary disk layer flow(Fig.1b) in good agreement with the LSA results. Taylor-Görtler-like vortices have been also observed at the junction between the stationary shroud and the stator expanding in near end-wall flow region under the form of large spiral arms. Computations have been repeated for the flow additionally disturbed by superimposing on the initial condition for every consecutive Re_R the disturbance of the form $\eta \sin(\pi\varphi/2)$ $(0.0 \le \eta \le 3.5)$. For the cylindrical cavity the absolute/convective character of the instability of the both boundary layer has been also investigated using LSA. The computations performed for the annular geometry have shown the dramatic influence of the end-walls boundary conditions on the stability of the stationary and rotating disk boundary layers. Figs.2a, b and c show the exemplary iso-lines of the fluctuations of the azimuthal velocity component obtained for Re_R =60000, L=5 and R_m =4 for three different end-walls boundary conditions. Calculations have shown that the most unstable is the case with the shroud attached to the stator and the shaft attached to the rotor. For the annular geometry as well as for cylindrical geometry the nature of the transition to unsteadiness has been investigated.

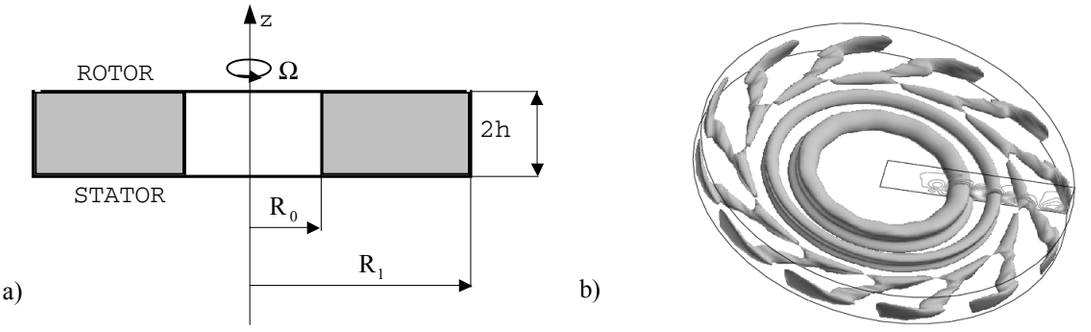


Fig. 1. a) Schematic picture of the rotating annular cavity (in the case of the cylindrical cavity $R_0 = 0$). b) Iso surface of the fluctuations of the axial component of the velocity at Re_R= 13200. Coexistence of annular and spiral structures related to stationary disk layer instability during the transient time t=60.

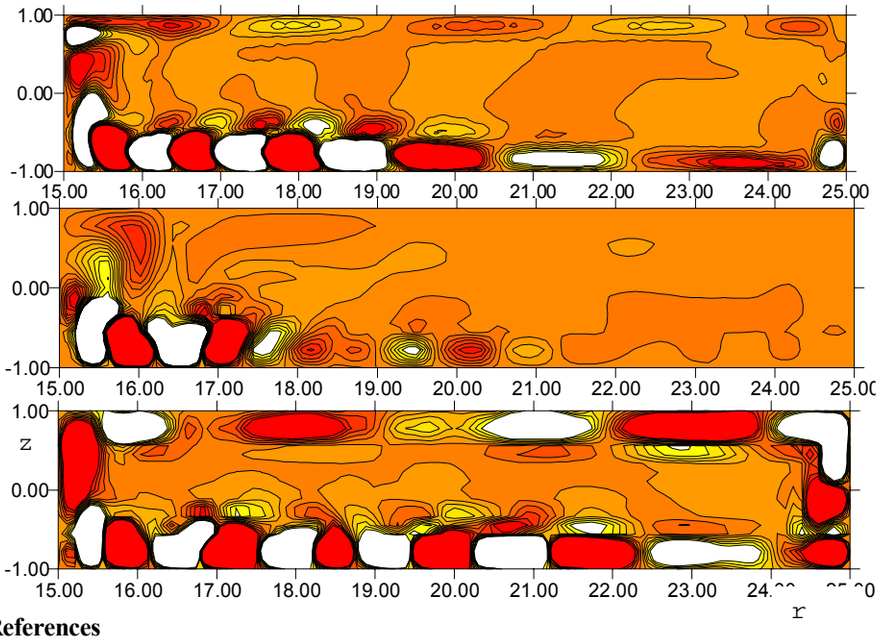


Fig.2 Time dependent axisymmetric instability at Re_R =60000, L=5, R_m =4. Iso-lines of the azimuthar velocity component in the (r,z) plane obtained for the different end-walls boundary conditions. From the top to the bottom: a) the linear profiles for the shaft and shroud, b) the exponential profiles with the both end-walls attached to the stator, c) the exponential profiles with the shaft attached to the rotor and with the shroud attached to the stator.

References

[1] Lingwood R.: Absolute instability of the boundary layer on a rotating disk,J. Fluid. Mech. **299**, 1, 1995
[2] Tuliszka-Sznitko E., Soong C.Y.: Instability of non-isothermal flow between coaxial rotating disks, Proceedings of European Congress on Computational Methods in Applied Sciences and Engineering, Barcelona, 2000.
[3] Serre E., Bontoux P.:Vortex breakdown in a three-dimensional swirling flow, J. Fluid Mech. **459**, 347, 2002.
[4] Serre E., Tuliszka-Sznitko E., and Bontoux P., 2004, ''Coupled numerical and theoretical study of the flow transition between a rotating and a stationary disk'', Phys. of Fluids (in print).
[5] Tuliszka-Sznitko E., Serre E. and Bontoux P., 2002, "On the nature of the boundary layers instabilities in a flow between a rotating and a stationary disc", C.R. Mecanique **30**, 90.

VISCOUS VERTICAL LENGTH SCALE SELECTION IN STRATIFIED FLUIDS

Ramiro Godoy-Diana, Jean-Marc Chomaz and Paul Billant
LadHyX, CNRS–École Polytechnique, F-91128 Palaiseau Cedex, France

Summary The evolution of pancake dipoles of different aspect ratios is studied in a stratified tank experiment. When the vertical Reynolds number is large enough, the vertical size of the dipole is shown to decrease whereas its horizontal circulation is conserved. This decrease of the dipole thickness is due to the peeling off of two boundary layers, on top and bottom of the dipole, where the fluid is slowed down by viscosity. The thickness of the dipole diminishes until a viscous length scale δ, defined by the vertical size of these boundary layers, is reached. Viscosity is therefore responsible for a fast vertical decorrelation of the flow. The mechanism that we evidence may play a significant role in the determination of the vertical length scale in strongly stratified flows.

GEOPHYSICAL CONTEXT

The emergence and evolution of pancake vortices in strongly stratified fluids have been studied intensely recently because of their role in the dynamics of geophysical flows. Of particular interest is the vertical length scale selection that constrains the energy and momentum exchanges determining for instance the turbulence spectra observed in the atmosphere and in the ocean.

EXPERIMENTAL SETUP AND OBSERVATIONS

The experiments are carried out in a tank of 1m x 2m base and 0.6m height filled with salt-stratified water. The dipole is generated by a pair of parallel vertical flaps as described in [1]. The experimental setup differs from [1] by the fact that the initial dipole is partially blocked by a vertical screen perpendicular to the moving direction of the dipole (figure 1). A single horizontal slice of the vortex column goes through the screen and forms a pancake dipole with an initial thickness that may be varied simply by adjusting the aperture on the screen.

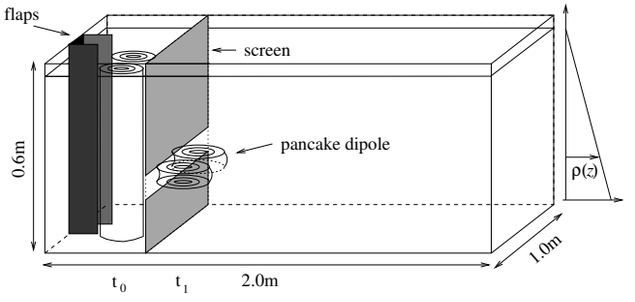


Figure 1. Experimental setup.

Three nondimensional control parameters can be defined for the dipole coming out of the screen: the Reynolds number $Re_0 = U_0 L_{h0}/\nu$, the horizontal Froude number $F_{h0} = U_0/NL_{h0}$ and the aspect ratio $\alpha_0 = L_{v0}/L_{h0}$, where U_0, L_{h0} and L_{v0} are, respectively, the initial translation speed and the horizontal and vertical length scales of the dipole, ν is the kinematic viscosity and N the Brunt-Väisälä frequency. Measurements of the velocity field were obtained by Particle Image Velocimetry (PIV).

In figure 2 we show two instants that depict the first stages of the evolution of a pancake dipole with initial control parameters $F_{h0} = 0.18$, $Re_0 = 182$ and $\alpha_0 = 1.27$. The velocity field in figure 2.b exhibits a horizontal V shape, the layers on top and bottom of the dipole being swept away generating two "wakes" in the upper and lower layers where the velocity is horizontal. A decrease on the vertical length scale is thus caused by the top and bottom layers that are slowed down and left behind. The present results contrast with the usual decay scenario for a dipolar structure in a stratified fluid, where the thickness of the layered flow slowly increases by diffusion while the circulation decays (e.g. [3]).

VISCOUS PEEL-OFF MODEL

We propose a model based on the low-Froude number theory first proposed by [4] where a scaling analysis of the equations for a stratified viscous fluid in the Boussinesq approximation gives at leading order the momentum equation in terms of the vertical vorticity

$$\frac{\partial \omega_z}{\partial t} + (\mathbf{u}_h \cdot \nabla_h)\omega_z = \frac{1}{\alpha^2 Re}\frac{\partial^2 \omega_z}{\partial z^2} \tag{1}$$

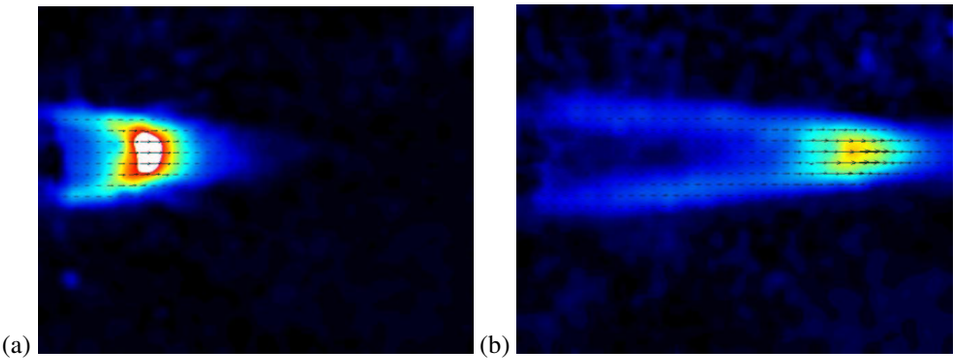


Figure 2. PIV measurements on a vertical cross-section through the dipole symmetry axis of the velocity modulus $|V|$. The initial instant immediately after the dipole has come out of the screen is shown in (a). In (b) the same frame 90 seconds later.

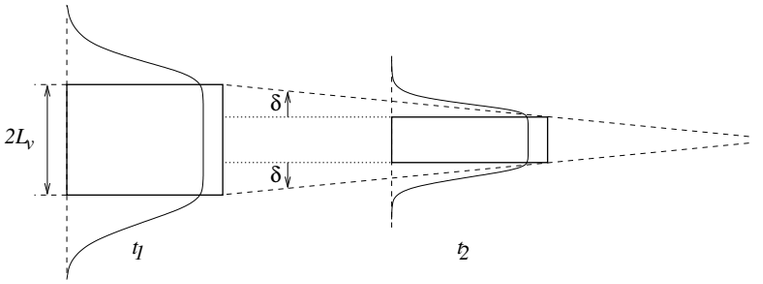


Figure 3. Schematic diagram of the two boundary layers during the slimdown regime.

where the subscript h denotes the horizontal field and α is the aspect ratio of the layer considered. In the boundary layer, the dominant balance principle imposes that the vertical length scale L_v should be such that $\alpha^2 Re = 1$ and the vertical scale

$$L_v = \delta \equiv L_h Re^{-1/2} \tag{2}$$

independent of N. In the core regions between the boundary layers $\alpha^2 Re$ is initially large and the motion may be assumed inviscid with a constant circulation. The height of the core region diminishes as the outer layers are slowed down —diffusing momentum to the still regions on top and bottom of the dipole— until it reaches the scale δ for which diffusion cannot be ignored. This scenario is shown schematically in figure 3. The two "boundary" layers of thickness δ on each side of the pancake dipole are left behind as the dipole moves until the core region vanishes. It should be noted that the mechanism described above relies on equation (1) which gives the leading order dynamics if $\delta \gg U/N$. This insures that vertical transport is negligible compared to diffusion. The other limit case when δ is smaller than U/N has been described by [2] and leads to a vertical scale proportional to the buoyancy scale $L_B = U/N$. The present theory completes this previous work in the case where viscous effect dominate over vertical transport.

CONCLUSIONS

The experimental observations on the present work give evidence of a new mechanism responsible for the formation of small-scale vertical structure in strongly stratified fluids. The creation of free "boundary" layers of thickness $\delta = L_h Re^{-1/2}$ observed in the experiments should occur when the ratio of the buoyancy length scale U/N to the viscous length scale δ is small, and whenever initially L_v is larger than δ, because there are no forces that counteract the viscous strain force. The present results manifest the need to consider viscous effects in any attempt of predicting the final vertical length scale of strongly stratified flows when the Reynolds number is lower than F_h^{-2} (i.e. when $\delta \gg U/N$).

References

[1] P. Billant and J.M. Chomaz. Experimental evidence for a zigzag instability of a vertical columnar vortex pair in a strongly stratified fluid. *J. Fluid Mech.*, 418:167–188, 2000.

[2] P. Billant and J.M. Chomaz. Self-similarity of strongly stratified inviscid flows. *Phys. Fluids*, 13:1645–1651, 2001.

[3] J.B. Flor, G.J.F. van Heijst, and R. Delfos. Decay of dipolar vortex structures in a stratified fluid. *Phys. Fluids*, 7:374–383, 1995.

[4] J.J. Riley, R.W. Metcalfe, and M.A. Weissman. Direct numerical simulations of homogeneous turbulence in density stratified fluids. In B.J. West, editor, *Proc. AIP Conf. Nonlinear properties of internal waves*, pages 79–112, La Jolla Institute, 1981.

ON LOCAL VORTEX IDENTIFICATION

Pinaki Chakraborty, S. Balachandar, Ronald J. Adrian
Department of Theoretical & Applied Mechanics, University of Illinois at Urbana-Champaign, Urbana, IL, USA.

We explore the question of identifying vortical filaments in flow using a local criterion with two kinematic parameters. Based on the kinematic properties the vortex filament is required to satisfy the following requirements:

- The local flow in the frame of reference translating with the vortex should be swirling.
- The identified core geometry should be Galilean invariant.
- The separation between the swirling material points inside the vortex core remains small in the plane of the vortex, i.e. orbits of the material points are compact.

We follow the critical point approach [1] by adopting a frame of reference translating with the local fluid velocity. In this reference frame, the variation in the local velocity to the linear order is captured by the velocity gradient tensor $\boldsymbol{\nabla v}$. Using a similarity transformation it can be shown that in a local curvilinear coordinates spanned by the eigenvectors of $\boldsymbol{\nabla v}$ the local behavior of streamlines is governed by the eigenvalues of $\boldsymbol{\nabla v}$ [2].
The local swirling rate is determined by the imaginary part of the complex conjugate eigenvalue i.e. λ_{ci}. The time period for one complete revolution of the projected motion of the pathline in the plane spanned by the complex conjugate eigenvectors is given by $2\pi/\lambda_{ci}$. The second parameter is given by the ratio of the real to imaginary part of the complex conjugate eigenvalue and it measures the orbital compactness. In other words, in the plane of the vortex spanned by the complex conjugate eigenvectors the ratio of final to initial radial location of the spiraling path after one complete revolution increases as $exp(2\pi\lambda_{cr}/\lambda_{ci})$. In this regard, we identify $\lambda_{cr}/\lambda_{ci}$ to be the inverse spiraling compactness. Hence, these two parameters have unambiguous mathematical interpretation in terms of the local kinematics of the flow. These two kinematic parameters form the basis of our local vortex identification criteria. We identify the vortical region to be points in the flow that satisfy the dual requirement: $\lambda_{ci} > \epsilon$ and $\lambda_{cr}/\lambda_{ci} < \delta$, where ϵ and δ are positive thresholds and are determined from physical considerations of the problem.
We explore the relationships between these parameters and other commonly used local vortex identification methodologies, namely Q, Δ and λ_2 criteria. For the case of Q and Δ we get the following closed form relations:

$$Q = \lambda_{ci}^2 \left(1 - 3\left(\frac{\lambda_{cr}}{\lambda_{ci}}\right)^2\right) \tag{1a}$$

$$\Delta = \frac{\lambda_{ci}^6}{27}\left[1 + 9\left(\frac{\lambda_{cr}}{\lambda_{ci}}\right)^2\right]^2. \tag{1b}$$

A significant aspect of the present approach is that regions of inward and outward swirling motion can be distinguished through the sign of $\lambda_{cr}/\lambda_{ci}$. For incompressible flows, inward swirling translates to stretching along the axial direction, hence the vortex can be interpreted as being in the process of intensification. Large positive values for the ratio $\lambda_{cr}/\lambda_{ci}$ above a set threshold corresponrs to a rapid outward spiral and thus will not qualify as a vortex filament.
It is clear from the above equations that $\Delta = 0$ criterion corresponds to $\lambda_{ci} = 0$ and similarly $Q = 0$ criterion corresponds to $\lambda_{cr}/\lambda_{ci} = 1/\sqrt{3}$. No similar simple relation exists between the $\lambda_2 = 0$ criterion and the rest. Here we interpret the $\lambda_2 = 0$ criterion in terms of λ_{ci} and the ratio $\lambda_{cr}/\lambda_{ci}$ for all possible configurations of the local velocity gradient tensor, $\boldsymbol{\nabla v}$. The key result is that $\lambda_2 = 0$ corresponds to a small range of value for the ratio $\lambda_{cr}/\lambda_{ci}$. Furthermore, except for a very small window in the configuration space, $\lambda_{ci} = 0$ criterion corresponds to the largest vortex core.
The above different criteria have been used in the past for a variety of flow fields. In some applications the vortical structures obtained by the different criteria have been observed to be remarkably similar [3], while in other applications significant differences between the different criteria have been highlighted [4]. Resolving such apparent contradiction has been an objective of the present study. Toward this end, we investigate the relationship between the different criteria at finite amplitude thresholds. The ease of local kinematic interpretation of the present criterion makes the choice of thresholds to be based on physical considerations. The time scale of the vortex filaments to be identified determines the value of ϵ and the orbital compactness of the desired vortex filaments determines δ. Here we explore the relation between the different criteria in the context of five different flows: Laminar Burger's vortex, swirling jet, isotropic turbulence, uniform flow over a sphere at moderate Re and turbulent channel flow. From these examples it becomes clear that in case of a strong vortex core, corresponding to a large positive threshold, the differences in the vortex core structure extracted by the different criteria is minimal. Significant differences emerge only in case of identifying weakly spiraling regions corresponding to small values of λ_{ci}.
For locating the intense vortices, we address the question: given the thresholds for λ_{ci} and the ratio $\lambda_{cr}/\lambda_{ci}$, what are the thresholds for the different criteria so that the vortical regions educed are comparable? Based on simple analysis we

propose the following equivalent threshold for the Q, Δ and λ_2 criteria, for extracting nearly identical intense vortical structures from the different criteria:

$$Q \geq Q_{th} = \epsilon^2 \tag{2a}$$

$$\Delta \geq \Delta_{th} = \frac{1}{27}\epsilon^6 \tag{2b}$$

$$\lambda_2 \leq (\lambda_2)_{th} = -\epsilon^2. \tag{2c}$$

We observe that for the case of Burger's vortex the difference in the size of the vortex core, as extracted by the different criteria, is significant at lower Re. With increasing Reynolds number, however, the differences between the different criteria rapidly decrease. In the case of isotropic turbulence, the well accepted worm-like intense vortical structures extracted by the different criteria with the equivalent threshold are nearly identical. The only exception is the Δ criterion, whose vortical structure includes additional "debris" as compared to the other criteria. We observe that these debris have high values of $\lambda_{cr}/\lambda_{ci}$, hence do not qualify as vortices. As can be observed from (1b) large values of the ratio $\lambda_{cr}/\lambda_{ci}$ also contributes to large values of Δ and thus erroneously misconstrued as intense vortical regions. Similar results were also observed for the case of wake flow over a sphere and the turbulence channel flow, with nearly identical vortex structures extracted by the different criteria using the equivalent threshold (except for the Δ criterion which also includes additional vortical debris).

We explore the question of interacting vortices with the model problem of a vortex ring. The strength and radius of a vortex ring are varied and the resulting vortex structure is educed using our identification criteria. For small radius and large strength, the vortex is subjected to self induced strain. Using our two parameters for identification of vortices, we explore the resolution of the criteria, i.e. its ability to distinguish the interacting vortex cores. This identification is compared with the other local schemes.

References

[1] Chong, M. S., Perry, A. E., Cantwell, B. J.: A general classifi cation of three-dimensional flow fi elds. *Phys. Fluids* **A 2**:765-777, 1990.

[2] Zhou, J., Adrian, R. J., Balachandar, S., Kendall, T. M.: Mechanisms for generating coherent packets of hairpin vortices in channel flow. *J. Fluid Mech.* **387**: 353-396. 1999.

[3] Dubief, Y., Delcayre, F.: On coherent-vortex identifi cation in turbulence. *J. Turbulence* **1**: 1-22, 2000.

[4] Jeong, J., Hussain,F.: On the identifi cation of a vortex *J. Fluid Mech.* **285**: 69-94, 1995.

THE MODELLING OF THE DYNAMICS OF HAIRPIN VORTEX PACKETS IN WALL TURBULENCE

Vyacheslav V. Meleshko[*], Eugene I. Nikiforovich[**], Alexandre A. Gourjii[**], Ronald J. Adrian[***]
[*] *Department of Theoretical and Applied Mechanics, Kiev National Taras Shevchenko University, 01033 Kiev, Ukraine*
[**] *Institute of Hydromechanics NASU, 03057 Kiev, Ukraine*
[***] *Department of Theoretical and Applied Mechanics, University of Illinois at Urbana-Champaign, Urbana, 61801 IL, USA*

Summary The talk addresses the experimental, analytical and numerical modelling of the dynamics of concentrated vortex packets over a rigid smooth plane. To answer the principal question why and how does fluid in outer region of the turbulent boundary layer organize itself into hairpin streamwise vortex packets with low-speed convective velocity we developed the vortex filament model of hierarchy of hairpin packets.

INTRODUCTION

The coherent structure of the turbulent boundary layer has been studied for about fifty years. Based on a combination of analysis and physical insight, Theodorsen in 1952 proposed a simple vortex model as the central element of the turbulence generation process in shear flows. It took the form of a hairpin (or horseshoe)-shaped vertical structure inclined in the direction of mean shear (see Fig. 1). Since that time a large amount of turbulence structure models has been proposed by numerous investigators, see e.g. [1] for a review. These models typically involve similar single or multiple configurations of hairpin vortical structures. Probably the most convincing evidence of the existence of such vertical structures embedded in fully developed turbulent boundary layers has come from recent experimental [2] and computational (e.g.[3, 4]) studies. The idea is to explore the flow of effectively inviscid fluid with embedded vorticity, with topology change allowed upon close encounters of vortical fluid regions.

VORTEX FILAMENT ε-MODEL

We consider thin vortex filaments over a flat rigid plane (with no-penetration conditions) embedded into a shear flow of an effectively inviscid fluid. Virtual mirror filaments maintains no-penetration condition. The induced velocity field is defined by means of the Biot-Savart law:

$$U_x = \frac{1}{4\pi}\int_L \Gamma(x',y',z')\frac{(y-y')dz'-(z-z')dy'}{\{(x-x')^2+(y-y')^2+(z-z')^2\}^3},$$

$$U_y = \frac{1}{4\pi}\int_L \Gamma(x',y',z')\frac{(z-z')dx'-(x-x')dz'}{\{(x-x')^2+(y-y')^2+(z-z')^2\}^3},$$

$$U_z = \frac{1}{4\pi}\int_L \Gamma(x',y',z')\frac{(x-x')dy'-(y-y')dx'}{\{(x-x')^2+(y-y')^2+(z-z')^2\}^3}.$$

The main difference from traditional models is that we consider the strength of the filament dependent on its position. Lagrangian vortex models track fluid elements containing vorticity. The kinematics is governed by geometric relations.

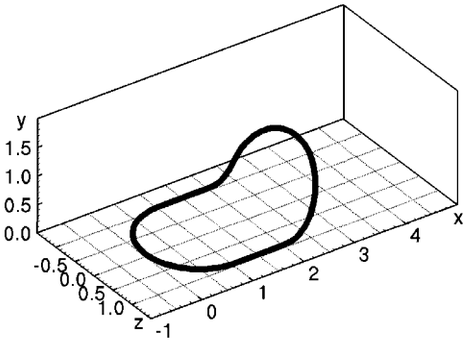


Fig.1 Representation of hairpin vortex by a vortex filament

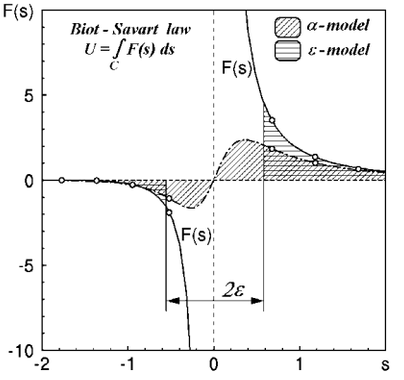


Fig.2 Integration according to the Biot-Savart law

Advantages of the model

- Numerical integration by the formulas of the various order,
- It accounts the cross-section size of the vortex tube,
- Representation of the vortex tube by a smooth curve,
- Description of vortex tube by small number of markers.

Disadvantages of the model

- Increasing the order of integration methods leads to longer calculation.

RESULTS

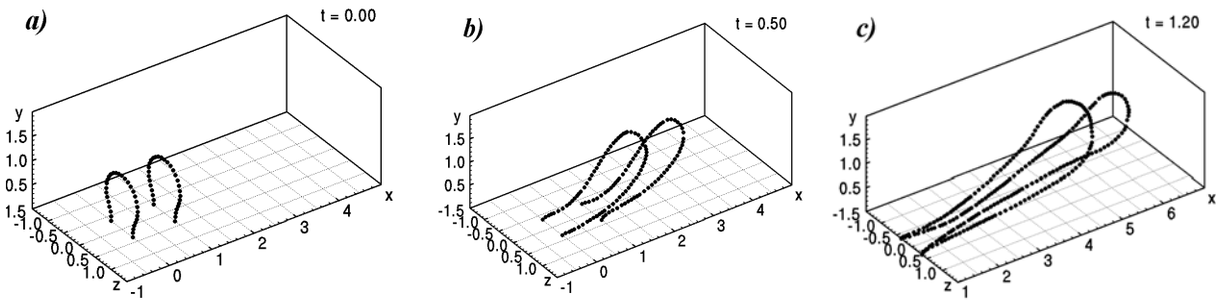


Fig.3 Dynamics of two hairpin vortices above a rigid wall in a shear flow

CONCLUSION

We addressed the global vorticity dynamics by representing each hairpin vortex as a filament with a `core parameter', interacting via the Biot-Savart law. The contour kinematic spline method for tracing the vortex filaments in a shear flow over a rigid wall was developed. Special attention is paid to the soliton-like behaviour of the vortex filaments over the rigid plane. Comparisons with experimental results and DNS data show a good correspondence. Although an extreme idealization, the analytical model of vortex filaments appears to shed considerable light on what to expect in the laboratory experiments. The results obtained for the concentrated hairpin vortex structures confirm von Kármán [5] words that "many peculiarities of real flow can be understood based on the notion of existence of separated vortices in the flow and the laws of motion of such vortices in an ideal fluid."

References

[1] Robinson S. K.: Coherent motion in the turbulent boundary layer. *Annu. Rev. Fluid Mech* **23**:601-639, 1991.

[2] Adrian R. J., Meinhart C.D., Tomkins C.D.: Vortex organization in the outer region of the turbulent boundary layer. *J. Fluid Mech* **422**:1-54, 2000.

[3] Perry A. E., Chong M.S.: On the mechanism of wall turbulence. *J. Fluid Mech* **119**:173-217, 1982.

[4] Spalart P. R.: Direct simulation of a turbulent boundary layer up to Re_θ =1410. *J. Fluid Mech* **187**:61-98, 1988.

[5] Kármán Th. von: Mechanische Ähnlichkeit und Turbulenz. *Nachr. Ges. Wissen. Göttingen. Math-Phys.Kl*:17-25, 1930.

Coherent structure of point vortices influenced by uniform straining flow

Marcin Kurowski, Konrad Bajer
Institute of Geophysics, Warsaw Uniwersity, Pasteura 7, PL 02-093 Warszawa, Poland

Summary

Two-dimentional numerical simulations of motion of an elliptic vortex patch modelled by a group of identical point vortices in an inviscid uniform straining flow is described. The behaviour of the patch as a function of strain rate in the external flow is presented. It is shown that for strong strain the cloud may come apart or survive as a remnant of the initial one. Moreover, we observe disturbances created at the edge of the patch that penetrate into the structure and destroy its internal order.

Introduction

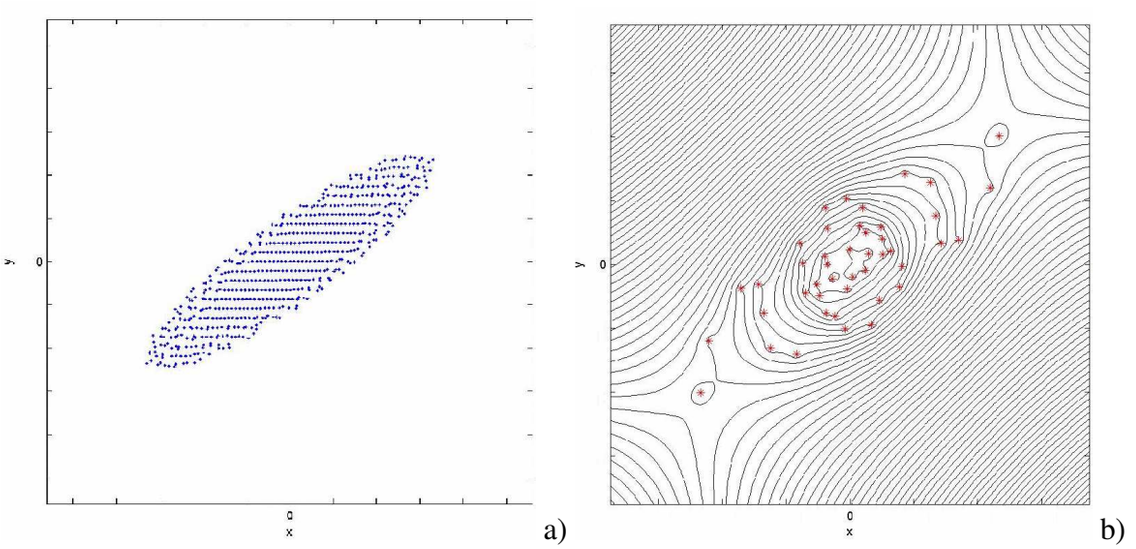
The theory of point vortices is well developed [1]. When a two-dimensional straining flow is applied it still remains a Hamiltonian system. For a coherent structure in an external flow dispersion is not an invariant of motion, so there are no restrictions on the positions of the vortices, and the patch can decay. We simulate it by the method of point vortices which also gives us the information about the internal processes. The external strain models the influence of other distant vortices. It is stronger when the distant vortices are closer to the patch.

Results of the numerical experiments

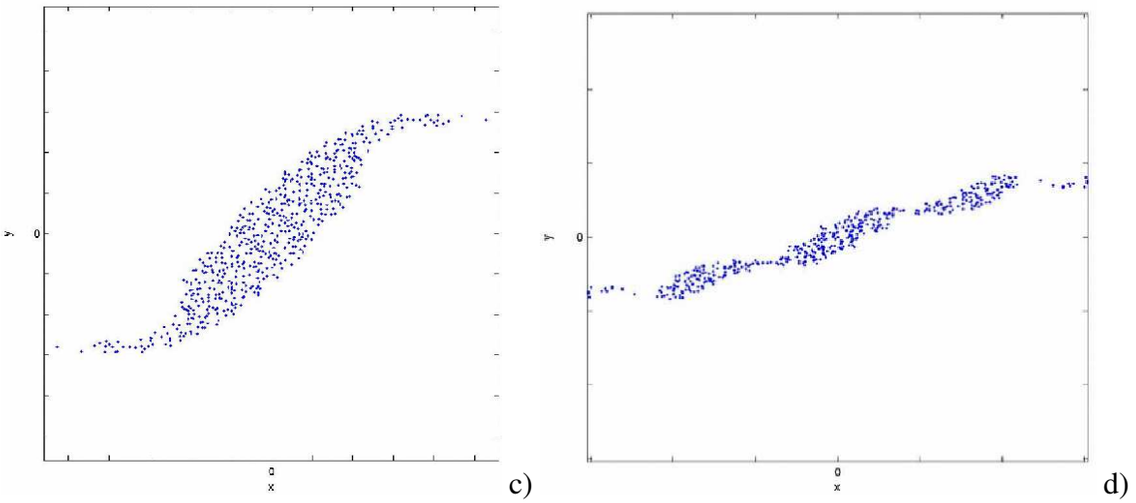
The initial condition is a homogeneous elliptical structure of identical point vortices, which represents a patch of a constant vorticity. The cloud of vortices in a straining flow rotates around its center of vorticity and its ellipticity oscillates. The stronger flow increases the amplitude of oscillations. It also changes an angular velocity of the patch into non-uniform. The internal structure, unlike to its shape, rotates with constant angular velocity, independently on a strain. Disturbances created at the edge of the patch penetrate into the structure and gradually destroy its internal order (fig. a). Density of point vortices within the patch becomes non-uniform. The stronger flow causes a ”mixing” process more effective and a chaos expands faster. Typical forms of heterogeneity are little groups, lines and pairs of vortices rotating around the local centers of vorticity. Fluctuations of density strongly depend on a strain rate and can trigger loss of small groups of vortices. That situation in terms of streamlines is presented in a fig. b. The decay of the cloud can proceed slowly (single vortices are being ”scraped” by the flow) or rapidly (vortices leave the structure and the flow can penetrate the cloud deeper to pull out more vortices). The elliptic shape of the cloud can change into a spiral. At a critical strain the axes are rotated by $\pi/4$ and two little streaks of vortices flow out from the cloud (quasi-steady state) (fig. c). It is possible that fluctuations of density can stop the leakage of vortices and the structure can survive as a remnant of the initial one. As a consequence of the Kelvin-Helmholtz instability the cloud comes apart and a big structure turns into a vortex street (fig d).

Conclusions

Two-dimensional numerical analysis of interactions between coherent structure of point vortices and an external straining flow is presented. At the first approximation that flow is the influence of other distant vortices, so we can treat it as an example of interactions between



a) Disturbances formed at the edge of the patch penetrating into the structure.
b) Single vortices pulled out by the flow (lines are temporary streamlines).



c) Leakage of vortices through the "gates" of two main stagnation points.
d) Remnant of an initial elliptical structure as a vortex street.

vortices. The external strain causes the behaviour of the patch more irregular and the stronger one increases fluctuations of density and a mixing time (see above). Close to the critical value the patch can lose vortices and finally transform into a vortex street.

References:

[1] H. Aref, Integrable, chaotic and turbulent vortex motion in two-dimensional flows. *Ann. Rev. Fluid Mech.* 15 (1983) 345-89.

[2] H. Aref, Chaos and the dynamics of a few vortices - fundamentals and applications. *Proceedings of IUTAM 1985* Elsevier Science Publishers B.V. (North-Holland).

[3] S. Kida, Motion of an elliptic vortex in an uniform shear flow. *J. Phys. Soc. of Japan* 10 (1981) 3517-3520.

STRONG SHOCK - VORTEX INTERACTION – A NUMERICAL STUDY

W. Schröder, O. Thomer, E. Krause
Aerodynamisches Institut, RWTH Aachen, Aachen, Germany

Summary: The intersection of a longitudinal vortex by a normal shock is studied with a numerical solution of the Euler and Navier-Stokes equations for time-dependent, three-dimensional, laminar flow. The study is concerned with the destruction of the vortex core, usually referred to as vortex breakdown or bursting, by letting the shock intersect the vortex normal to its axis. Results are presented for a Mach number $Ma_\infty = 1.6$. The calculations were performed on a Cartesian mesh with approximately 2 millions grid points. The computations show noticeable differences between the two solutions, and viscous forces become important in the burst part of the vortex. Visualization studies clearly reveal the time-dependent, three-dimensional nature of the flow after breakdown.

INTRODUCTION

Vortex breakdown is observed in technical applications, for example, in decelerated pipe flows as studied by Sarpkaya and Novak in [1] and by Brücker in [2] in incompressible flow. Schlechtriem and Lötzerich conjectured in [3], that vortex breakdown might also occur in compressible flow in turbine engines. When compressors are operated near their stability limit, breakdown of the tip leakage vortex, caused by an intersecting shock in the supersonic flow, might be responsible for rotating instabilities and subsequent stall. Breakdown caused by the interaction of a vortex with a strong shock is also encountered on delta wings in supersonic flight near the trailing edge. Depending on the flow conditions the vortex can burst and cause rolling motions of the aircraft as a direct result of the local loss of lift. Breakdown also occurs on delta wings with leading-edge extension, and severe vertical tail buffeting may result, when the burst part of the vortices hits the vertical tails. There are marked differences between breakdown in supersonic and subsonic flow, and for this reason the investigation is restricted to the problem of strong shock-vortex interaction. Earlier numerical studies of compressible vortical flows interacting with shocks were reported by Kandil et al. in [4]. Erlebacher et al. in [5], Mahesh in [6]. Nedungadi and Lewis in [7], and Kandil et al. in [8]. In this paper results obtained with a numerical solution for the Euler and Navier-Stokes equations will be presented for time-dependent, three-dimensional, supersonic flows.

NUMERICAL SOLUTION OF THE EULER AND NAVIER-STOKES EQUATIONS

The governing equations are introduced in dimensionless form, written in a Cartesian frame of reference The system is closed with the thermal equation of state and with relations defining the viscosity, the thermal conductivity, and the specific heats at constant pressure and constant volume. The integration is carried out in a rectangular domain. The boundary conditions in the inflow cross-section are prescribed by a Burgers vortex. The kinematic flow condition is employed on thE side boundaries. The gradient of the vector of the conservative variables normal to the boundaries is assumed to vanish on the top and on both sides of the computational domain. The pressure on the boundaries is obtained from the momentum equations. The boundary condition for the outflow cross-section is given by the assumption that there is no back-flow into the computational domain. The approximation for non-reflecting boundary conditions is used for inviscid flows and for viscous flows the approximation described by Poinsot and Lele [9]. For the initial conditions the Burgers vortex is used for the entire domain of integration. At the beginning of the integration the Rankine-Hugoniot conditions are imposed at a certain location on the bottom of the computational DOMAIN. In a second approximation, a normal shock is imposed across the entire flow field. Then a Burgers vortex is prescribed upstream of the shock, and uniform flow downstream. Comparison of the numerical results for long computational times did not reveal any noticeable differences. The time integration of the governing equations was carried out with a 5-step Runge-Kutta scheme. The details of it may be found in [10]. The spatial integration employed a node-centered scheme. An adapted cell-vertex scheme was used for the discretization of the diffusive fluxes. The computational domain is a rectangular box containing a Cartesian grid with 99 x 99 x 199 points which are clustered in the vicinity of the shock and near the *z*-axis to ensure a sufficient resolution of the vortex core. Further details of the solution see [10].

EXAMPLATORY RESULTS OF RECENT COMPUTATIONS

Interaction patterns were computed for a free-stream Mach number $Ma_\infty = 1.6$. An examplatory result of the calculations of normal shock-vortex interaction is shown in Fig. 1. Although the shock-vortex interaction is dominated by pressure forces, the flow structure inside of the bubble is markedly influenced by viscous forces.

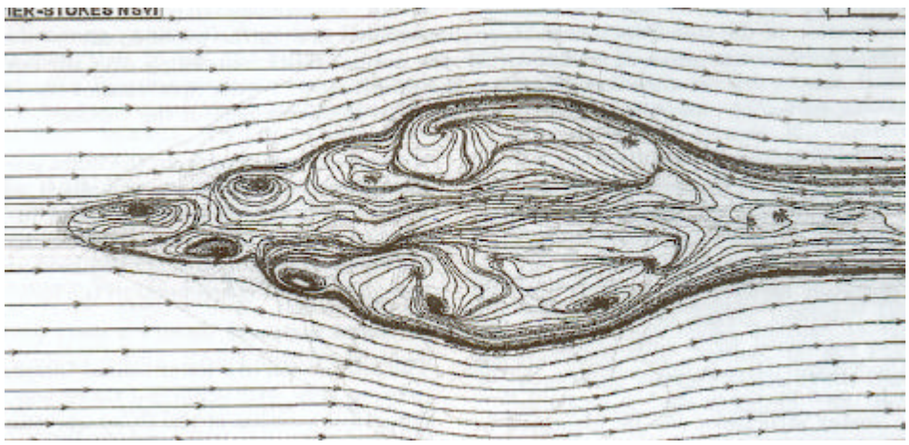


Fig. 1: Streamlines for normal shock-vortex interaction for $Ma_\infty = 1.6$ and $Re_\infty = 1.5.\ 10^3$; obtained with solution of Navier-Stokes equations.

CONCLUSIONS

The interaction of a longitudinal Burgers vortex in supersonic flow with a normal shock was studied with a numerical solution of the Euler and the Navier-Stokes equations. In the simulations only a strong shock was considered, which resulted in a bursting of the vortex. Examplatory results of computations were presented for a free-stream Mach number $Ma_\infty = 1.6$. The computations of both solutions showed that a cone-like bubble was formed by the interaction with the shock, which enforced a marked redistribution of vorticity in the recirculation region. It is pointed out, that the Navier-Stokes solution showed more small vortical structures in the burst part of the vortex than did the Euler solution. The visualization studies revealed, that vortex rings were shed periodically from the recirculation region, which in addition to two periodically generated and shed ring vortices, also contained supersonic nozzle flow, entering the recirculation region from the back Also small shocks were detected by the comp utation inside of the burst part of the vortex.

.

REFERENCES

[1] Sarpkaya, T., Novak, F.: Turbulent Vortex Breakdown: Experiments in Tubes at high Reynolds Numbers. In: IUTAM Symposium on Dynamics of Slender Vortices, Aachen, Aug. 31-Sept. 3, Krause, E., Gersten, K. (Eds.), Kluwer Academic Pub., pp. 287-296, (1997).

[2] Brücker, C. H.: Breakdown of Spinning Tube Flows. In: IUTAM Symposium on Dynamics of Slender Vortices, Aachen, Aug. 31-Sept. 3, Krause, E., Gersten, K. (Eds.), Kluwer Academic Pub., pp. 321-330, (1997).

[3] Schlechtriem, S., Lötzerich, M.: Breakdown of tip leakage vortices in compressors at flow conditions close to stall, IGTI-Asme Conference, Orlando, Florida, (1997)

[4] Kandil, O. A., Kandil, H. A., Liu, C. H.: Shock-Vortex Interaction and Vortex-Breakdown Modes. In: IUTAM Symposium of Fluid Dynamics of High Angle of Attack, Tokyo, Sep. 13-17, Schumann et. al. (Ed.), Springer Verlag. (1992).

[5] Erlebacher, G., Hussaini, M. Y., Shu, C.-W.: Interaction of a Shock with a Longitudinal Vortex, ICASE Report, No. 96-31, (1996).

[6] Mahesh, K.: A Model for the Onset of Breakdown in an Axisymmetric Compressible Vortex (PHF), vol.8, no.12, pp. 3338-3345, (1996).

[7] Nedungadi A., Lewis, M. J.: Computational Study of the Flow fields Associated with Oblique Shock-Vortex Interactions, AIAA-Journal, vol. 34, no. 12, (1996).

[8] Kandil, O. A., Kandil, H. A., Massey, S. J.: Simulation of Tail Buffet Using Delta Wing-Vertical Tail Configuration, AIAA Paper No 93-3688-CP, AIAA Atmospheric Flight Mechanics Conference, Monterey, CA, 566-577, (1993).

[9] Poinsot, T. J., Lele, S. K.: Boundary Conditions for Direct Simulations of Compressible Viscous Flows, 101, pp. 104-129, Journal of Computational Physics, (1992).

[10] Thomer, O.: Computation of vortex breakdown in supersonic flow. Diss. RWTH Aachen. (2003).

XXI ICTAM, 15–21 August 2004, Warsaw, Poland

ISOLATED VORTICES OVER SEAMOUNTS: LABORATORY EXPERIMENTS AND NUMERICAL SIMULATIONS

O.U. Velasco Fuentes
Departamento de Oceanografía Física, CICESE, Ensenada, México

Summary We study the competition between the instability of isolated vortices and the nearly geostrophic balance in a rotating fluid of varying depth. The laboratory experiments were performed in a water tank placed on top of a rotating table and the numerical simulations were done with a vortex-in-cell method. The intrinsic vortex instability produces horizontally elongated vortex structures while the nearly geostrophic balance forces the vortices to remain on top of the seamount where they are generated. It was found that the condition for the topographic confinement of the laboratory vortices (which have a Rossby number of order one) is that the semount height be at least one half of the total fluid depth. This condition was confirmed by the numerical simulations.

EXTENDED SUMMARY

Seamounts are ubiquitous features of the ocean floor. They generate and trap eddies, enhance biological productivity and improve fish catch [1]. It is well known that the flow of a stream over topography may generate vortices: anticyclonic vortices form over seamounts, whereas cyclonic vortices form over seavalleys. It is also well known that a monopolar vortex over uneven topography is not steady: anticyclonic vortices migrate towards deeper water, whereas cyclonic vortices migrate towards shallower water.

Here we study the evolution of an isolated vortex over a seamount in a fluid which is otherwise at rest. Over a flat bottom the intrinsic instability would produce vortices with a horizontal extent which is substantially larger than that of the original vortex. The nearly geostrophic balance, however, prevents motion across isobaths and thus would force the vortices to remain on top of the seamount. The purpose of this study is to determine the conditions under which the vortex is trapped on top of seamounts of circular and square shapes.

The experiments were carried out in a square tank of 100 cm side and 50 cm depth mounted on a rotating table. In the center of the tank we placed circular or square mounts with horizontal extent (diameter or side length, respectively) of 20 cm and various heights (2.5, 5 and 10 cm). The tank was filled up to a depth of 20 cm and the whole system was set to rotate with a period of 7.5 s. Once the water reached a state of solid body rotation, a vortex was generated by cyclonically stirring the water inside a bottomless cylinder placed on top of the seamount. Dye was added after the stirring was stopped in order to visualize the flow. The vortex was released into the ambient fluid by vertically lifting the bottomless cylinder (Figure 1a). Owing to its vorticity distribution the vortex is unstable [2], and the anticyclonic vorticity accumulates on two opposite sides of the core vortex to form a tripolar vortex (Figure 1b). Over a flat bottom the tripole would slowly grow until an elongated shape would be reached; under certain conditions the tripole itself could become unstable and the whole structure would translate while performing a complicated unsteady motion [3]. In this case, however, the seamount was sufficiently high to keep the tripole confined within the water column located above the seamount (Figure 1d).

It was found that the vortices were effectively confined over the seamount when this had a height equal or larger than half the total fluid depth. This result is valid for circular as well as for square mountains. There is, however, a large difference in the evolution of a vortex confined by a circular mount and that confined by a square mount. The former reaches a nearly steady state, whereas the latter remains highly unsteady during the whole evolution. The unsteady motion of the core and the satellite vortices leads to intense stirring. This produces the numerous interlaced bands of dyed and clear water that are visible in the last stages (Figures 2c and 2d).

Numerical simulations with a vortex-in-cell model confirm the main experimental results, namely, the condition for the vortex to remain trapped and the effect of the seamount shape on the stirring properties of the vortex.

References

[1] Roden, G.I. 1987 Effects of seamounts and seamount chains on ocean circulation and termohaline structure. In *Seamounts, Islands and Atolls*, Geophys. Monogr. Ser. 43, (B.H. Keating et al. eds.). AGU, Washington, D.C.

[2] van Heijst, G.J.F., Kloosterziel, R.C. & Williams, C.W.M. 1991 Laboratory experiments on the tripolar vortex in a rotating fluid. *Journal of Fluid Mechanics* **225**, 301-331.

[3] Velasco Fuentes, O.U., van Heijst, G.J.F. & van Lipzig, N.P.M. 1996 Unsteady behaviour of a topography-modulated tripole. *Journal of Fluid Mechanics* **307**, 11-41.

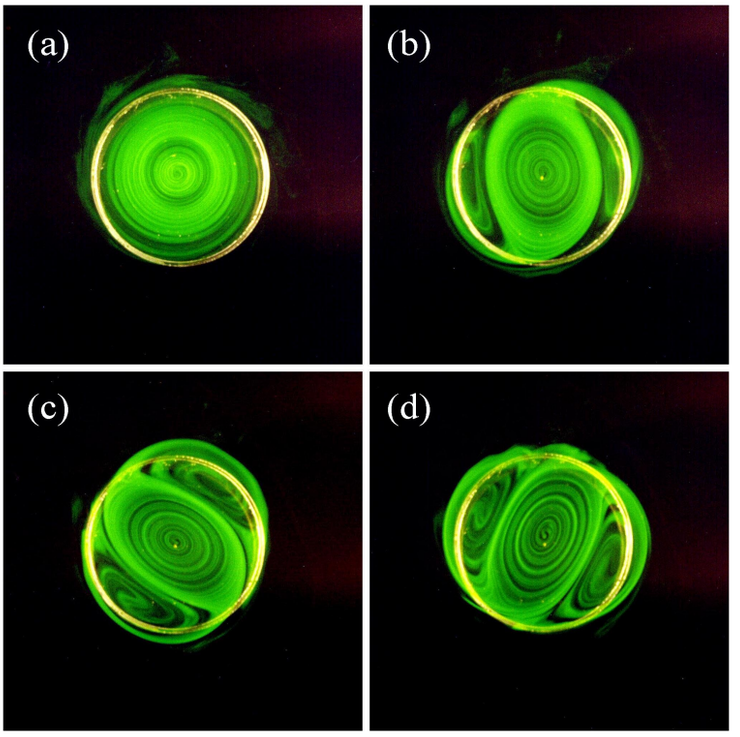


Figure 1. Experimental sequence showing the evolution of an unstable vortex on top of a circular seamount (the border is indicated by a bright circle). Pictures were taken at times $t = 8\tau/3$ (a), $t = 28\tau/3$ (b), $t = 12\tau$ (c), and $t = 16\tau$ (d), where τ=7.5 s is the rotation period of the water tank.

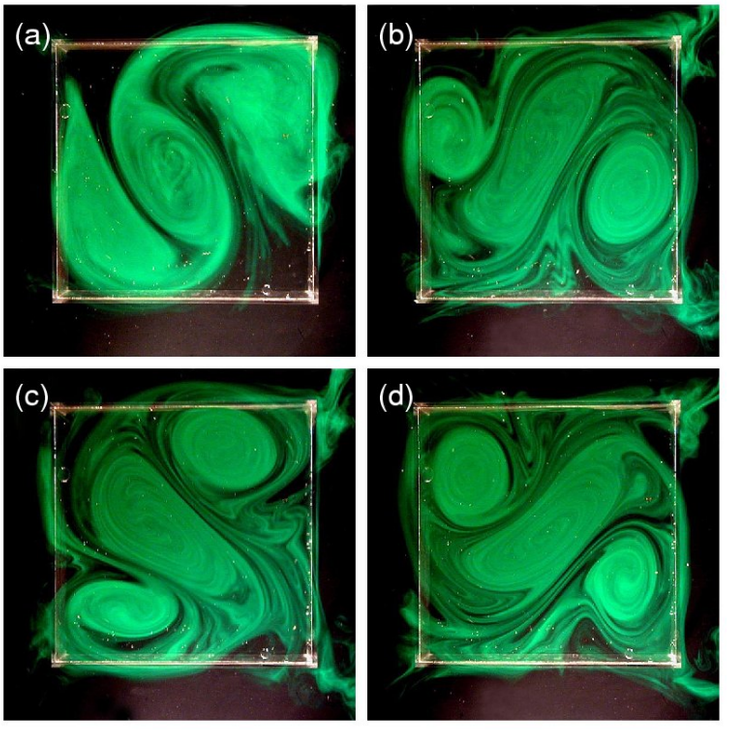


Figure 2. Same as figure 1, but now for a square seamount. Pictures were taken at times $t = 3\tau/$ (a), $t = 11\tau$ (b), $t = 14\tau$ (c), and $t = 19\tau$ (d).

THREE DIMENSIONAL VELOCITY FIELD OF VORTICES IMPINGING ON A WALL OBTAINED BY SCANNING PARTICLE TRACKING VELOCIMETRY.

K. W. Hoyer, Institute of Hydromechanics and Water Resources Management, ETHZ, CH-8093 Zurich.

MOTIVATION

Vortex wall interactions are omnipresent in wall-bounded turbulent flows and are therefore of fundamental interest for understanding such flows. In this study SPTV was used to quantitatively measure the rapid changes in flow topology of vortex rings directed towards a rigid boundary. The 3D velocity vector fields generated on impact are dependant on the angle of the vortex propagation direction to the wall. If the vortex ring approaches the wall perpendicularly the vortex first stretches due to the mean strain induced from the stagnation point type flow, then builds up a shear layer of opposite sign close to the wall. This shear layer rolls up into vortices while being subject to the induction from the still strong original vortex. Subsequently, the first of the rolled up shear layer vortices is entrained into the original vortex in a complex three dimensional fashion which leads to multiple breakdown events along the vortex core and to the very rapid destruction of the originally coherent vortex. This is in contrast to the case when the angle of propagation is inclined with regard to the wall. Here, upon approach of the vortex ring to the wall, this interaction also first stagnates in the region of closest contact, and a similar shear layer entrainment develops locally. Now, since this interaction originates where the vortex is close to the wall, two symmetric vortex breakdown events develop and travel along the vortex core towards the less perturbed part of the vortex ring which has not jet felt the presence of the wall. During this process, strong flows develop along the vortex core due to the pressure gradient between the strongly rotating and weakly rotating regions. Chang et al.[1] (1997) have numerically simulated a similar setup, where an elliptical vortex propagated parallel to the wall and interacted when first approaching with the long principal axis.
Two main questions are addressed in this study.
First, for vortices that impact with an inclined angle, we want to focus the attention on the region initiating the symmetric vortex breakdown to obtain estimates for the increase in the local maximum vorticity, and azimutal strain rate. Since the symmetric vortex breakdown can be interpreted as a “terminal” Kelvin wave, this type of vortex wall interaction is relevant to turbulent transition and energy exchange. It is speculated that turbulent drag reduction by addition of polymers is caused by interference with this breakdown process. Kerr[2] (1993) shows evidence for a developing singularity in vorticity magnitude when simulating such an event using the incompressible Euler equations.
Second, for vortices impacting a wall perpendicularly we want to elucidate the complex mechanisms at work when we have the main ingredients of a turbulent flow (e.g. vortex filament, shear layer, and strain) interacting in a strongly dynamic fashion and leading to the rapid dissipation of the introduced energy.

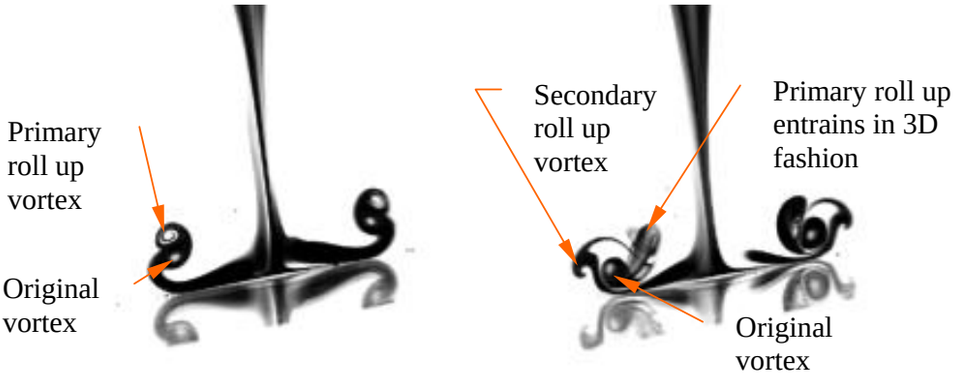


Figure 1: Flow visualization using Laser Induced Fluorescence in the center plane of a vortex ring impinging perpendicular onto a wall. The light sheet is 4 mm thick and the diameter of the original vortex torus ca 50 mm wide. Two instances in time are shown. Left image is shortly before 3D breakdown; right image is at the instant of the 3D entrainment of the primary roll up vortex into the original vortex.

METHODS

3D Particle Tracking velocimetry[3,4] has been developed as a full flow field measurement tool at our institute in collaboration with the Institute of Geodesy and Fotogrammetry over the last decade and has yielded numerous publications and dissertations. In the classical system, a four-camera setup records images of tracer particles being convected through an illuminated observation volume with similar dimensions in the three spatial directions. Stereoscopic matching identifies a number of individual particles in the different image frames, and allows determining

the 3D position in physical space from the previously in situ calibrated setup. A tracking algorithm then repeatedly identifies and follows the individual particles in time to obtain the particle paths. The system however has an inherent limit to the seeding density because of the long optical path through the observation volume. Practically an upper limit to the number of particles is of $O(10^3)$ independent on the absolute size of the observation volume. Applying a higher density leads to an unacceptable number of overlapping particles in each image space so that the yield of stereoscopic matches decreases and the overall performance degrades.
One possible solution is to scan a thinner illuminated volume (with regard to the optical path) through the region of interest and record images correspondingly faster. In a first approximation, one is able to increase the particle density linearly with the reduction in the thickness of the scanned volume. The motivation for the increase in particle density lies in the need to resolve small scales with sufficient accuracy while at the same time having a large enough observation volume to realize the large-scale flow topology.
A sketch of the scanning optical setup is given below. A laser light sheet is generated with appropriate thickness and scanned horizontally by passing through a quadratic prism. On the receiving end, a four-way image splitter projects the different views onto a single chip of a high-speed image acquisition system (Photron Ultima APX). The image trigger is provided by an optical gate together with a hole-disk mounted to the rotating prism.

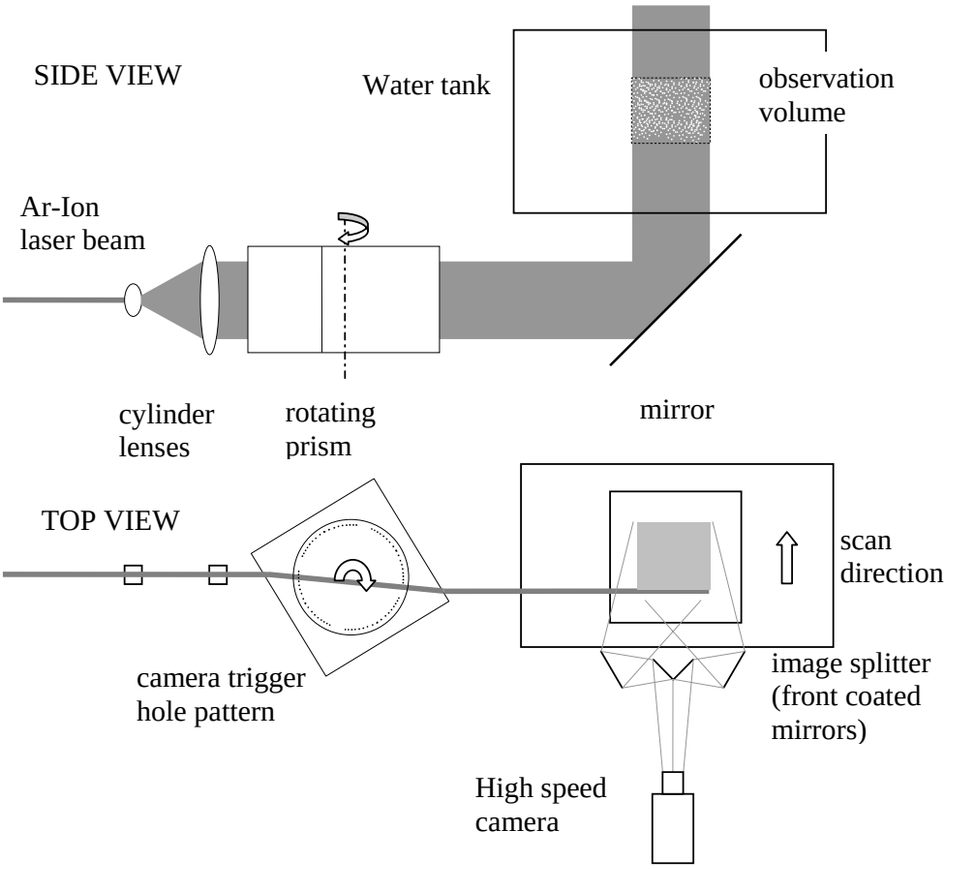


Figure 2: Optical setup of the scanning PTV system used to increase the particle density in the observation volume. The light sheet undergoes parallel displacement depending on the rotation angle of the prism.

It is planned to maximize the particle density sufficiently to obtain velocity gradient information throughout the observation volume and apply newly developed analysis through the availability of the velocity gradient tensor.

1 Chang et al., Three-dimensional vortex/wall interaction: Entrainment in numerical simulation and experiment, Phys. Fluids 9, 57 (1997)

2 Kerr RM. 1993. Evidence for a singularity of the3-dimensional, incompressible Euler equations. Phys. Fluids A 7:1725–46

3 Maas, H.-G., 1992: Digitale Photogrammetrie in der dreidimensionalen Stroemungsmesstechnik ETH Zurich - Dissertation Nr. 9665

4 Marko Virant, Anwendung des dreidimensionalen "Particle-Tracking-Velocimetry" auf die Untersuchung von Dispersionsvorgängen in Kanalströmungen, ETH Zürich Dissertation Nr.11678, 1996

XXI ICTAM, 15–21 August 2004, Warsaw, Poland

STUDY OF THE VORTEX RINGS INTERACTION BY 3D VORTICITY PARTICLE–IN–CELL METHOD

Henryk Kudela*, Paweł Regucki*
*Wrocław University of Technology, Department of Numerical Modelling of Flows,
Wybrzeże Wyspiańskiego 27, PL 50-350 Wrocław, Poland

Summary The vortex rings interactions were studied. At first the leap–frogging phenomenon for inviscid flow was investigated. It was shown that dynamics of the vortex rings is very sensitive to the initial parameters like diameters of the rings, their mutual positions and circulations. For viscous flow the vortex rings reconnection was studied. The vorticity particle–in–cell method for three-dimensional, viscous flow was used.

VORTEX RINGS INTERACTION

The vortex rings are the simplest 3D vortex structure that can be observed in the turbulence flow. It is the structure that is relatively easy reproduced in the laboratory. The interaction of two vortex rings gives an interesting and good example of non–linear interaction of the regions with concentrated vorticity and it may serve as a clue to understanding them. Despite of the simple geometry the dynamics of the integrations of two rings are very reach and complex. It is very sensitive on initial parameters and circulation. One of the most fascinating phenomena relates to the interaction of two vortex rings moving along a common axis of symmetry in the same direction. In this case the effects of the mutual influence of two vortex rings consist in enlargement of the diameter and retardation of the former ring, and simultaneously, in contraction of the diameter and acceleration of the other one (leap–frogging phenomenon) [3]. The small changes in the initial in parameters produced different behavior of the vortex rings. The „vortex game" numerically can be demonstrated for inviscid fluid (Fig. 1).

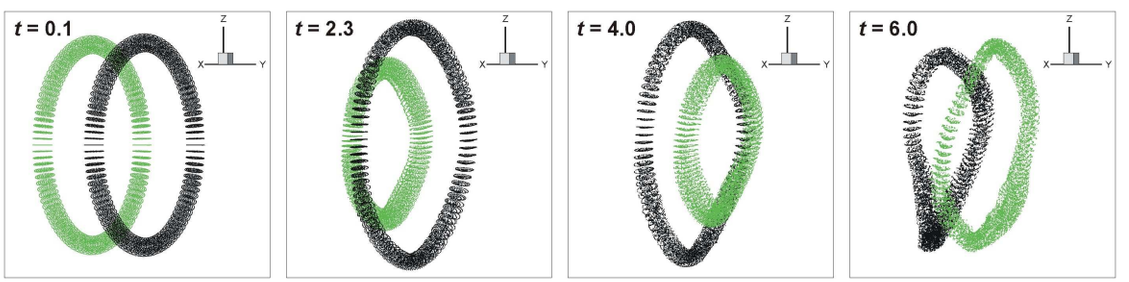


Figure 1. The sequence of the time position of the vortex particles for the leap–frogging phenomenon in the inviscid flow

One can observed „pure" form of the vortex game but also the appearance of the tail structure (Fig. 2) and some times the rearward ring becomes entrained into forward one.

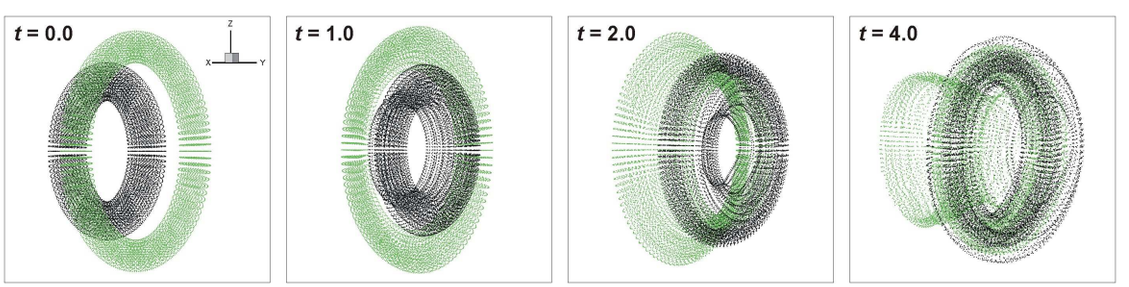


Figure 2. The sequence of the time position of the vortex particles for the tail structure in the inviscid flow

When the viscosity is taken into account the vortex ring reconnection can be observed [2, 5]. The term „reconnection" signifies a distinct change in the connectivity of configuration of two rings with opposite circulation that collide with each other (Fig. 3).

VORTICITY PARTICLE–IN–CELL METHOD

For the study of the vortex ring interactions we used the vorticity particle method that in 2D version is known as a vortex–in–cell method [1]. One can distinguish two different types of vortex methods: the direct method based on the Biot-Savart

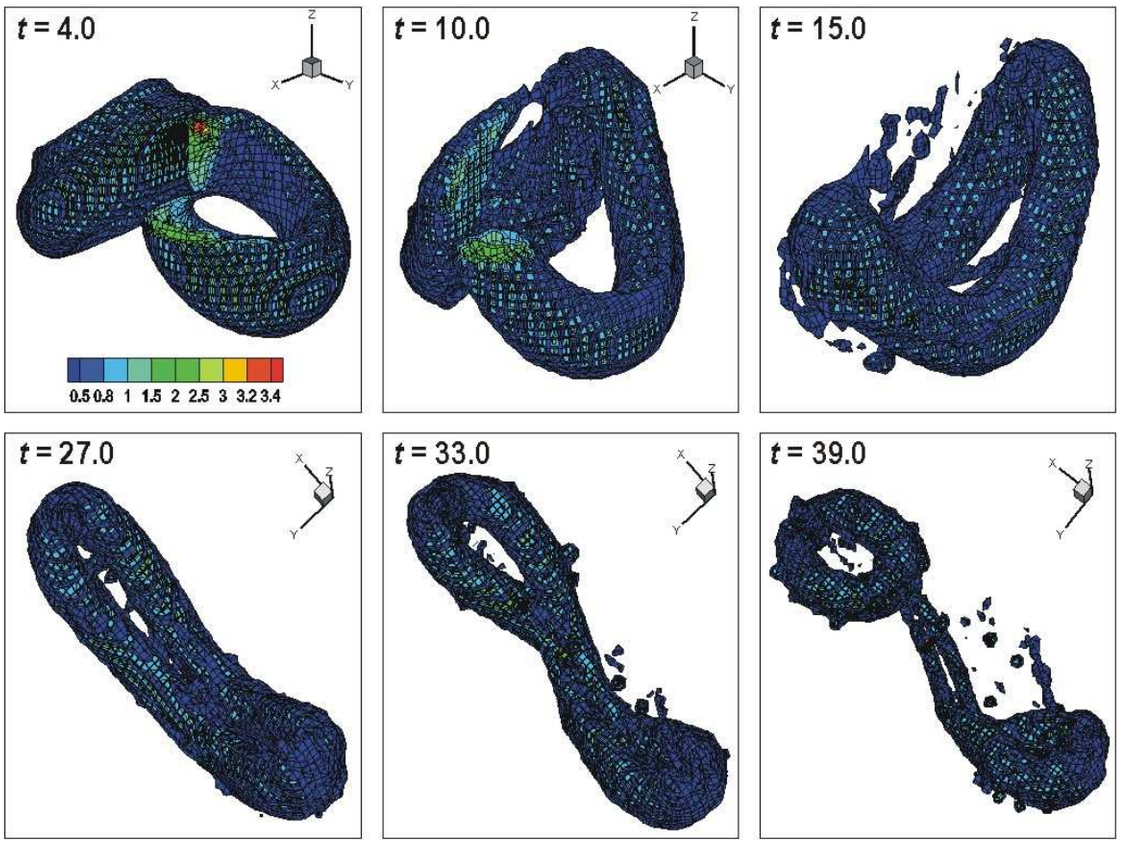


Figure 3. Time evolution of $|\omega|$ surface during the reconnection phenomenon of two vortex rings. For better viewing, the bottom diagrams show the vorticity field from a different direction than the top ones do

law where the velocity of each vortex element is calculated by summing up the contribution of the all particles in the domain, and the vortex–in–cell method where the velocity is obtained on the grid nodes by solving Poisson equations for the vector potential [4]. Then the vector potential is differentiated numerically by the finite difference method in order to obtain the velocity on the grid nodes and interpolate its value to the particle position. Most of the published results relate to the 2D VIC method and one can find very few application of this method for 3D flows. Despite the fact that vorticity is divergence free we introduced to the computation a vector particle that carries the „mass" of the vorticity. Due to that fact during the computation we monitored the divergence of the vorticity, velocity and vector potential fields. We also monitored invariants of the motion like kinetic energy, helicity and enstrophy. To simulate the viscous effect we used the viscous splitting algorithm: at first we solved the Euler equations by VIC method and next the viscous effect was taken into account by particle strength exchange method.

References

[1] Cottet G-H., Koumoutsakos P.: Vortex Methods: Theory and Practice. Cambridge University Press, Cambridge 2000.
[2] Kida S., Takaoka M.: Vortex Reconnection. *Ann. Rev. Fluid Mech.* **26**:169–189, 1994.
[3] Lim T.T., Nickels T.B.: Vortex Rings. *Fluid Vortices*, Kluwer Academic Publisher, Dordrecht, 95–153, 1995.
[4] Kudela H., Regucki P.: The Vortex–in–Cell Method for the Study of Three-Dimensional Vortex Structures. *Tubes, Sheets and Singularities in Fluid Dynamics* vol. **71** series *Fluid Mechanics and Its Applications*, Kluwer Academic Publisher, Dordrecht, 49–54, 2002.
[5] Schatzle P.: An Experimental Study of Fusion of Vortex Rings. *PhD Thesis*, California Institute of Technology, 1987.

XXI ICTAM, 15–21 August 2004, Warsaw, Poland

NONLINEAR LONG WAVES ON THE INTERFACE OF A TWO-LAYERED HORIZONTAL FLOW OF VISCOUS LIQUIDS

Dmitry G. Arkhipov*, Georgy A. Khabakhpashev **
*Novosibirsk State University, Pirogov Str. 2, Novosibirsk 630090, Russia
**Institute of Thermophysics SB RAS, Academician Lavrentyev Ave. 1, Novosibirsk 630090, Russia

Summary This paper deals with the theoretical study of plane waves with small but finite amplitude in the two-layer system bounded by the horizontal lid and bottom. The evolution equation for the interface disturbances, which takes into account long-wave contributions of the layers inertia, weakly non-linearity of waves and non-stationary shear stresses at all boundaries of the system is obtained. It is found that amount and direction of a steady unperturbed flow may change not only lengths of disturbances but its polarity too.

In last half a century the dynamics of gravitational waves on surfaces of the liquid shallow currents with shear of longitudinal velocity was studied rather sufficiently (e. g., [1–7]). Recently more attention was paid to such investigations. For instance, model equations for internal waves, which taking into account stationary flows of ideal liquids with piecewise constant dependence of velocity on depth, were suggested in the work [7]. The evolution equation for the interface perturbations in a two-layered system subject to dissipation but failing a steady-state current was deduced in the paper [8]. We note also the analysis [6], where, in particular, it was shown analytically that the two-layered Poiseuille flow is stable in the wide-ranging of the system parameters, and the experiment [5], in which the flow stability for the interface disturbances up to a initiation of a turbulence was demonstrated for the same current of mineral oil and water in the plane one-inch channel. The purposes of the present paper are a derivation of the corresponding model equation which is able to describe a transformation of long nonlinear waves on the interface of two viscous liquids in the presence of a stationary flow in the horizontal channel and an investigation of some its solutions.

It is supposed that two incompressible and immiscible liquids bounded by the rigid fixed lid $z = h_1$ and bottom $z = -h_2$ (unperturbed interface is at $z = 0$), characteristic horizontal lengths of disturbances λ are sufficiently larger and its amplitudes η_a are much less than the layers depths h_l ($h_l/\lambda \sim \varepsilon^{1/2}$ and $\eta_a/h_l \sim \varepsilon$, where ε is a small parameter). Moreover, the capillary effects are assumed to be moderate (the Bond number $\mathrm{Bo} = (\rho_2 - \rho_1)\, g\, h_1 h_2/\sigma > 1$, here ρ is the liquid density, g is the acceleration of the free fall, and σ is the surface tension). Finally, the non-stationary laminar boundary layers remain thin, that is the time required for the boundary layer to develop over the entire thickness of the liquid is proposed to be much greater than the characteristic time of the wave process τ (the hydrodynamic homochronicity number $\mathrm{Ho}_{\nu l} = \nu_l \tau/h_l^2 \sim \varepsilon^2$, where ν is the kinematical viscosity of the fluid). Below the variable values relating to the stationary flow are marked by the subscript 0 and relating to the interface are marked by the subscript i.

Let c is the phase velocity of linear perturbations in the two-layered system. Than for very long nondissipative waves if $\max u_{0l}(z) < c$ solutions of the motion equations for disturbances of the velocity vertical component have the forms

$$w_{lz} = u_{0i}\,\frac{b_l}{D}(c-u_{0l})\frac{4A_l}{\sqrt{D}}\,\arctan\left((2A_l z + B_l)\frac{u_{0i}}{\sqrt{D}}\right) + u_{0i}\,\frac{b_l}{D}(2A_l z + B_l) + C_l(c-u_{0l}), \qquad (1)$$

here $D = 4A_l u_{0i}(c-u_{0i}) - B_l^2 u_{0i}^2$. We used the kinematical boundary conditions $w_1(h_1) = w_2(-h_2) = 0$ and $w_{lz}(0) = \omega\eta_a(1-u_{0i}/c)$, where ω is the cyclic frequency of waves. Some these solutions are shown in the Figure 1*a*. Dissipation affects distinctly on a vertical motion at relatively high velocities of the unperturbed flow (see Figure 1*b*).

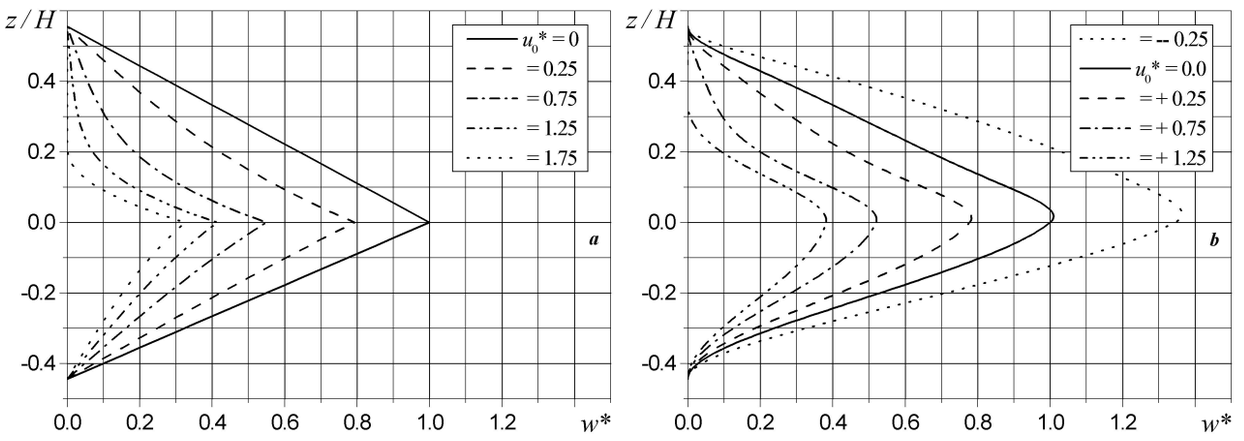


Figure 1. Vertical profiles ($H = h_1 + h_2$) for the dimensionless normal component of the liquid velocity ($w^* = w_z/\omega\eta_a$) calculated by formulas (1) and taking into account a dissipation of linear very long disturbances (cases *a* and *b*, respectively) at $\rho_1/\rho_2 = 0.98$, $h_1 = 1.5$ cm, $h_2/h_1 = 1.25$, $\nu_1 = 10^{-4}$ St, $\nu_1/\nu_2 = 0.83$, $\omega/2\pi = 1$ Hz, and different values of the flow velocities ($u_0^* = u_{0i}/c$).

Due to the linear approximations of $w_{lz}(z)$ for small values of the flow velocity, the ordinary boundary conditions and an integration over the z-coordinate the initial system of equations was reduced to following one evolution equation:

$$\frac{\partial^2\eta}{\partial t^2} + u_{0i}(1+S_f)\frac{\partial^2\eta}{\partial t\partial x} - (c_0^2 - u_{0i}^2\,S_f)\frac{\partial^2\eta}{\partial x^2} - C_d\,\frac{\partial^4\eta}{\partial t^2\partial x^2} - C_n\,\frac{\partial^2\eta^2}{\partial x^2} + C_b\int\limits_0^t \frac{\partial^2\eta}{\partial x^2}\frac{dt'}{\sqrt{t-t'}} = 0 \qquad (2)$$

Here all the coefficients C_b, C_d, C_n, S_f, and c_0^2 are depended only on the physical (g, ρ_1, ρ_2, ν_1, ν_2, σ, and u_{0i}) and the geometric (h_1, h_2) parameters of the system. If we may neglect a dissipation of perturbations ($C_b = 0$) the model equation has steady-state solutions, which contain Jacobi eliptic functions (the periodic conidal and the solitary waves):

$$\eta = \eta_{cn}\,\mathrm{cn}^2(\xi/L_{cn},\,m), \qquad \xi = x - Ut,$$

where $L_{cn} = m\,U\,\sqrt{6\,C_d/(\eta_{cn}C_n)}$, $U = U_{cn} = u_{0i}(1+S_f)/2 + \sqrt{u_{0i}^2(1-S_f)^2/4 + c_0^2 + 2\,\eta_{cn}C_n(2-1/m^2)/3}$;

$$\eta = \frac{\eta_s}{\cosh^2(\xi/L_s)}, \qquad L_s = U\sqrt{\frac{6\,C_d}{\eta_s C_n}}, \qquad U = U_s = \frac{u_{0i}(1+S_f)}{2} + \sqrt{\frac{u_{0i}^2(1-S_f)^2}{4} + c_0^2 + \frac{2}{3}\,\eta_s C_n}.$$

Some periodic and solitary solutions as well as the behavior of the coefficient C_d are represented in the Figure 2. It is shown that amount and direction of an unperturbed flow may change not only lengths of disturbances but its polarity too.

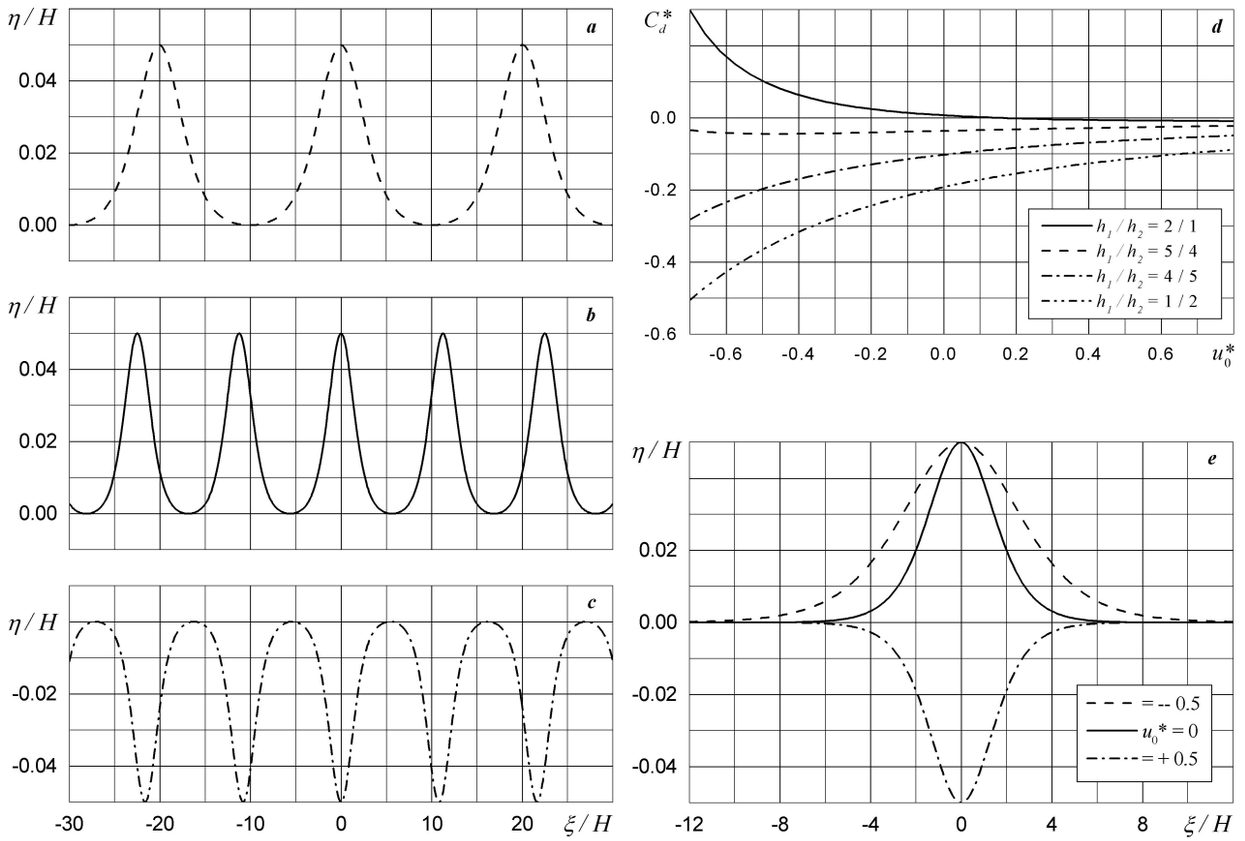


Figure 2. Nonlinear periodical (*a*, *b*, *c*) and solitary (*e*) waves as well as coefficient C_d (*d*) at $m = 0.96$, $\eta_{cn}/H = 0.05$ (*a*, *b*, *c*), $\eta_s/H = 0.05$ (*e*), $\rho_1/\rho_2 = 0.98$, $\nu_1/\nu_2 = 0.23$, $h_1/h_2 = 2$, $h_2 = 2$ cm, $\sigma = 45$ dyn/cm and $u_0^* = -0.5\,(a),\ 0\,(b),\ 0.5\,(c)$.

This work is supported by the Russian Foundation for Basic Research (Proj. 04-01-00183) and SB RAS (Progr. 4.2-04).

References

[1] Burns J.C.: Long waves in running water. *Proc. Camb. Phil. Soc* **49**:695–706, 1953.
[2] Hunt J.N.: Gravity waves in flowing water. *Proc. Roy. Soc. London* **A231**:496–504, 1955.
[3] Miles J.W.: On the generation of surface waves by shear flow. *J. Fluid Mech* **3**:185–204, 1957.
[4] Velthuizen H.G.M., van Wijngaarden L.: Gravity waves over a non-uniform flow. *J. Fluid Mech* **39**:817–829, 1969.
[5] Kao T.W., Park C.: Experimental investigation of the stability of channel flow. Part 2. *J. Fluid Mech* **52**:401–423, 1972.
[6] Hooper A.P., Grimshaw R.: Nonlinear instability at the interface between two viscous fluids. *Phys. Fluids* **28**:37–45, 1985.
[7] Pelinovskii E.N., Polukhina O.E., Lamb K.: Nonlinear internal waves in the ocean stratified in density and current. *Oceanology* **40**:757-766, 2000.

UNIDIRECTIONAL STEEP WAVES IN WAVE TANKS

L. Shemer, K. Goulitski, E. Kit

Faculty of Engineering, Tel-Aviv University, Tel-Aviv 69978, Israel.

Summary A nonlinear focusing process in which a single unidirectional steep wave emerges from an initially wide amplitude- and frequency-modulated wave group at a predicted position in the laboratory wave tank is studied both theoretically and experimentally. The spatial version of the Zakharov equation was applied in the numerical simulations. Experiments were carried out in two facilities which have substantially different scales: in the Tel-Aviv University wave tank, which is 18 m long, and in the Large Wave Channel in Hanover, which is 330 m long. Comparison between the experimental studies in both facilities and the corresponding numerical results is carried out. Good agreement was obtained between experiments and calculations. The effect of dissipation and bound waves is discussed.

Introduction

An ability to produce a single steep wave at a prescribed location in a laboratory wave tank of constant depth is often required for model testing in coastal and ocean engineering. Such waves can be generated by a superposition of a large number of waves at a given location and instant. This implies that effective focusing requires that the spectrum of the initial wave group generated at the wavemaker is wide. Dispersive properties of deep or intermediate-depth surface gravity waves can be utilized for this purpose. Since longer gravity waves propagate faster, a wave group generated at the wave maker in which wave length increases from the front to the tail may be designed to focus the wave energy at a desired location. Such a wave sequence can be seen as a group that is modulated both in amplitude and in frequency. The essentially nonlinear behavior of wave groups with high maximum wave steepness has been demonstrated in a number of studies. Due to nonlinear interactions, considerable variation of the wave spectrum along the tank is observed. The width of the spectrum in the current study precludes application of theoretical models that have severe limitations on the spectral width, like the cubic Schrödinger equation or its modification due to Dysthe (1979). An alternative theoretical model that is free of bandwidth constraints is the Zakharov (1968) equation. Unidirectional spatial version of this equation was derived and has been applied successfully in Shemer et al. (2001) to describe the evolution of nonlinear wave groups in the tank. The Zakharov equation is based on Hamiltonian formulation of the water-wave problem and does not account for non-conservative effects. The limits of applicability of the model equation are studied with respect to the problem of generation of a single steep unidirectional water wave. An experimental study of propagation of steep wave groups with wide spectrum is carried out in two laboratory wave tanks of different sizes. The experimental study is accompanied by numerical simulations based on the spatial version of the Zakharov equation.

Theory

The purpose of the present study is to obtain at a prescribed distance from the wave maker, $x = x_0$, a steep unidirectional wave group with a narrow, Gaussian-shaped envelope with the surface elevation variation in time, $\eta(t)$, given by

$$z(t) = z_o \exp-(t/mT_0)^2 \cos(w_o t), \tag{1}$$

where $w_0=2p/T_0$ is the carrier wave frequency, η_0 is the maximum wave amplitude in the group. The small parameter representing the magnitude of nonlinearity e is the maximum wave steepness $e = \eta_0 k_0$. The parameter m determines the width of the group; higher values of m correspond to wider groups and consequently narrower spectra. The spectrum of the surface elevation given by (1) is also Gaussian. The wave field at earlier locations, $x < x_0$ is obtained from the computed complex surface elevation frequency spectrum at this location. To this end, the unidirectional discrete spatial version of the Zakharov equation is used:

$$i \cdot c_g \frac{\partial B_j(x)}{\partial x} = \sum_{w_j + w_l = w_m + w_n} V(w_j, w_l, w_m, w_n) B_l^* B_m B_n \, e^{-i(k_j + k_l - k_m - k_n)x}, \tag{2}$$

where c_g is the group velocity, V is the interaction coefficient and * denotes complex conjugate. This equation describes the slow evolution along the tank of every free spectral component $B_j = B(w_j)$ of the surface elevation spectrum in inviscid fluid of constant (infinite or finite) depth and accounts for Class I, or quartet, nonlinear interactions among various components. The dependent variables $B_j(x)$ representing the free components in the wave field, are related to the generalized complex 'amplitudes' $b_j = b(w_j, x)$ that are composed of the Fourier transforms of the surface elevation $\hat{z}(w_j, x)$ and of the velocity potential at the free surface $\hat{f}^s(w_j, x)$. The amplitudes b_j represent a sum of the free and the bound waves. The bound higher order components can be computed at each location once the free wave solution $B_j(x)$ is known. The spectrum corresponding to (1) is integrated using (2) from the planned focusing location x_0 backwards up to the wavemaker at $x = 0$. The waveforms derived from the computed spectra serve as the wavemaker driving signals, with corrections that account for the actual response of the wavemakers of both facilities.

Experimental Facilities and Procedure

The first facility is the Large Wave Channel (GWK) in Hanover, which is 330 m long, 5 m wide and 7 m deep. About 25 wave gauges are installed along the tank. The gauges are concentrated at the distance of 120 m from the wavemaker, where the steep wave emerges. In parallel, a similar study is carried out in the Tel-Aviv University wave tank which is

18 m long, 1.2 m wide and 0.9 m deep. In these experiments, the steep wave is tuned to appear at distances ranging from 5 m to 8 m from the wavemaker. Up to four wave gauges are used simultaneously. The gauges are placed on a carriage that can be moved along the tank. In both wave tanks wide spectrum short wave groups given by (1) with m=0.6 are studied. Numerical simulations are performed for 100 free modes and various amplitudes and carrier wave periods

Results

Am example of the measured and the computed variation of the spectral shape along the tank is given in Fig. 1 for the Hanover experimental facility. Corresponding variation of the surface elevation along the tank is presented in Fig. 2. Good agreement between the measurements and computations is clearly seen in these Figures. A single steep wave indeed appears in the tank at the planned location x_0 = 120 m, Fig. 2b. The effect of bound waves can be noticed in Fig. 1b where low and high harmonics in the amplitude spectra arise.

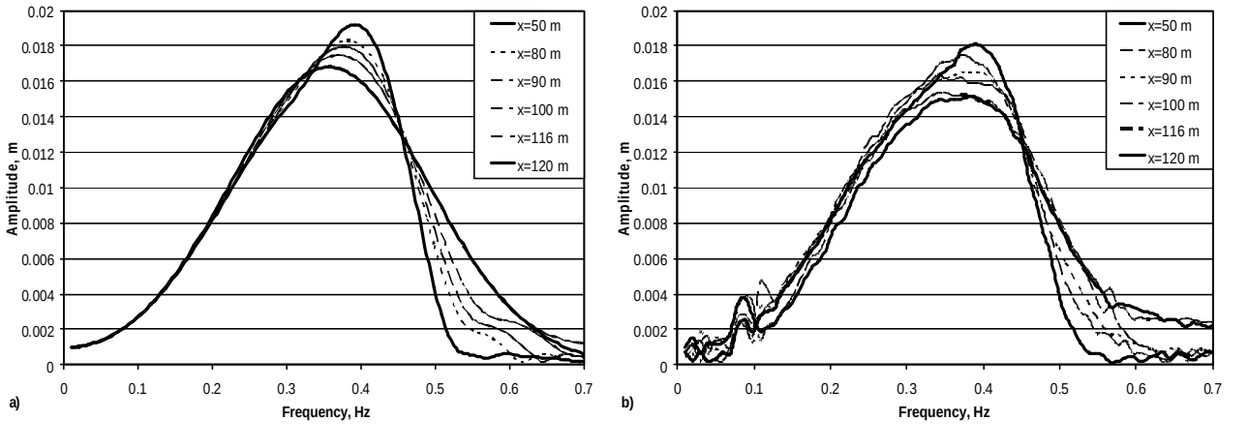


Figure 1. Amplitude spectra of wave group evolution for T_0=2.8 s, m=0.6 and the maximum wave steepness at the focusing location x=120 m, e=0.3: a) computation b) Hanover experiment.

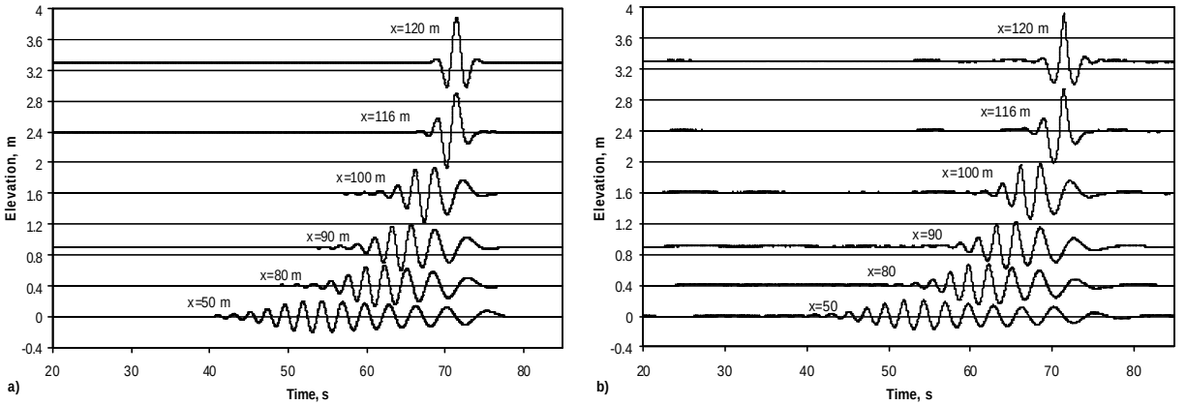


Figure 2. Wave elevation of wave group propagating along the large wave tank for T_0=2.8 s, m=0.6 and the maximum steepness at the focusing location x=120 m, ε=0.3: a) computation b) Hanover experiment.

The advantages and the limitations of application of the spatial Zakharov nonlinear water-wave model for simulations of wave field evolution in deep or intermediate-depth water are discussed based on the experiments carried out in both facilities. In particular, effects of evanescent modes, bound waves and dissipation are considered.

Acknowledgements

The authors acknowledge the support provided by HPRI-Programme that made possible experiments at FZK in Hanover. The support of INTAS is gratefully acknowledged.

Reference

1. Dysthe, K.B. (1979) Note on a modification to the nonlinear Schrödinger equation for application to deep water waves. Proc. Roy. Soc. London A369, 105-114.

2. Shemer, L., Jiao, Haiying, Kit, E., and Agnon, Y. (2001) Evolution of a nonlinear wave field along a tank: experiments and numerical simulations based on the spatial Zakharov equation. J. Fluid Mech. 427, 107-129.

3. Zakharov, V.E. (1968) Stability of periodic waves of finite amplitude on the surface of deep fluid. J. Appl. Mech. Tech. Phys. (English transl.) 2, 190-194.

XXI ICTAM, 15–21 August 2004, Warsaw, Poland

WAVE BREAKING AND EQUILIBRIUM SURFACE WAVE SPECTRA

Tetsu Hara*, Stephen E. Belcher**
*University of Rhode Island, Graduate School of Oceanography, USA
**University of Reading, Department of Meteorology, UK

Summary Breaking waves enhance energy and momentum fluxes from wind to surface waves. The breaking wave effect on the form of the equilibrium range of surface wave spectra is investigated. The theory is based on the conservation of momentum and energy in the wave boundary layer together with the conservation of the wave action spectrum. The results show that the breaking wave effect is not very strong for fully-developed wave spectra but may be significant for the spectra of growing seas.

INTRODUCTION

Under given wind forcing the spectra of ocean surface gravity waves attain an equilibrium state at frequencies much higher than the peak frequency. Knowledge of the equilibrium range of the wave spectrum is of practical importance since existing numerical wave prediction models cannot solve right down to the smallest gravity waves. Instead they resolve explicitly only to a fixed maximum wavenumber and then patch on to the spectrum a 'tail' to represent the equilibrium range. Therefore these models need to know the solution for the equilibrium range before being integrated. Although many observational and theoretical studies were performed to investigate the equilibrium spectra, there remain discrepancies in the form of the equilibrium spectra among different studies.
The evolution of surface waves are described in terms of the spectral density of wave action $N(\vec{k})$,

$$\frac{dN}{dt} = -\nabla_k \cdot T(\vec{k}) + S_w - D \tag{1}$$

where $\vec{k}$ is the wavenumber vector, S_w is the wind input, $T(\vec{k})$ is the flux of the wave action by nonlinear wave interactions (∇_k is the gradient operator in $\vec{k}$) and D is the dissipation due to wave breaking. Within the equilibrium range the sum of the three forcing terms must vanish. Phillips [1] assumed that in the equilibrium range the three input terms to the wave action conservation equation are all of the same order of magnitude and balance one another, and that the divergence of the wave action flux is proportional to the cube of the local wave spectrum. Phillips [1] further assumed that the wave growth rate is determined by the total wind stress τ_{tot} for the entire equilibrium range, and predicted that the equilibrium wavenumber spectrum is proportional to $k^{-7/2}$ ($k = |\vec{k}|$) and the friction velocity u_*.
Hara and Belcher [2] extended Phillips' [1] theory by accounting for the overall conservation of momentum. Waves exert a drag on the airflow so that they support a fraction of the applied wind stress, which thus leaves a smaller turbulent stress near the surface to force growth of shorter wavelength waves. Formulation of the momentum budget accounting for this *sheltering* constrains the overall conservation of momentum and leads to a local turbulent stress that reduces as the wavenumber increases. This local turbulent stress then forces wind-induced wave growth. Hara and Belcher [2] predicted that the equilibrium degree of saturation is expressed in a simple analytical form:

$$B(k) = \frac{k^4}{c} N(k) = \frac{1}{c_\beta c'_\theta} \left[1 + \left(\frac{k_s}{k} \right)^{\frac{1}{2}} \right]^{-1}, \tag{2}$$

where c is the wave phase speed and c_β and c'_θ are coefficients determined from the form of the wave growth rate. The sheltering wavenumber, k_s, represents the wavenumber at which the local turbulent stress begins to be affected by sheltering by the longer wavelength waves. At low wavenumbers $k \ll k_s$, $B(k)$ is proportional to $k^{1/2}$ as in Phillips [1], but $B(k)$ becomes constant at high wavenumbers $k \gg k_s$.
The theory of Hara and Belcher [2] assumes that the wave induced stress is entirely due to nonbreaking waves, that is, the airflow is always attached to the wavy water surface. However, at high winds a significant portion of waves breaks and causes airflow separation and enhancement of the wave drag [3]. The objective of this paper is to examine the effect of breaking waves on the form of the equilibrium surface wave spectra.

THEORY

Momentum conservation in wave boundary layer

We begin by assuming that the total wind stress is a sum of the turbulent stress, the (nonbreaking) wave induced stress, and the breaking wave induced stress;

$$\tau_{tot} = \tau_t(z) + \tau_w(z) + \tau_b(z), \tag{3}$$

where z is the height above the water surface. As in Hara and Belcher [1] the wave induced stress $\tau_w(z)$ is obtained by integrating the momentum input to waves in all angles and up to a wavenumber $k = \delta/z$, where δ is the normalized depth of the inner region [4]. The local turbulent stress $\tau_t^l(k)$, which forces waves at a wavenumber k, is then set equal to $\tau_t(z = \delta/k)$, that is, the turbulent stress evaluated at the top of the inner region.

It is assumed that the wave drag (momentum flux) due to a single breaking wave of a wavenumber k is determined by the length of its breaking crest and the wind speed evaluated at $z = \delta'/k$ (height that is equal to a set fraction of the wavelength) relative to the wave phase speed. The breaking statistic Λ is defined such that $\Lambda(\vec{k})d\vec{k}$ is the total length of breaking wave crests with wavenumbers between $\vec{k}$ and $\vec{k} + d\vec{k}$ per unit surface area. The breaking wave induced stress $\tau_b(z)$ is obtained by integrating the momentum input to breaking wave crests in all angles and up to a wavenumber $k = \delta'/z$.

Energy conservation in wave boundary layer

Since the braking wave induced stress depends on the wind speed rather than the local turbulent stress, it is necessary to obtain the vertical wind profile $u(z)$ together with the equilibrium wave spectrum. Following Hara and Belcher [5], the wind profile is determined from the energy conservation in the wave boundary layer:

$$\tau_{tot}\frac{du}{dz} + \frac{d\Pi}{dz} - \rho_a\varepsilon = 0. \tag{4}$$

Here, the vertical energy flux Π due to wave induced motion is set equal to a sum of the energy flux into nonbreaking surface waves integrated up to the wavenumber $k < \delta/z$ and the energy flux into breaking waves integrated up to the wavenumber $k < \delta'/z$. The viscous dissipation rate $\rho_a\varepsilon$ of the turbulent kinetic energy is parameterized in terms of the local turbulent stress following the approach used in one-equation models of turbulence.

Conservation of wave action spectrum

Within the equilibrium range the sum of the three forcing terms in (1) vanishes. The wind input term S_w is expressed as a sum of the input into nonbreaking waves and the input into breaking waves. The dissipation term D is set proportional to the breaking statistic Λ following Phillips [1]. All three forcing terms are assumed to be proportional to the cube of the degree of saturation.

RESULTS

The combination of the above three conservation constraints yields a coupled integral equations for the mean wind speed u and the degree of saturation B. After normalization the equations contain three nondimensional parameters: the wave age, the sheltering wave age (this parameter was defined by Hara and Belcher [5] and is proportional to Phillips' [1] constant of the equilibrium spectra), and a single new parameter that determines the breaking effect. The numerical solutions are then obtained with realistic values of these parameters.

The results of fully developed (mature) spectra show that the effect of breaking is relatively weak. The breaking effect is confined in an intermediate wavenumber range since both very long and very short waves propagate faster than the wind speed at the corresponding heights and therefore do not experience enhancement of the wind input.

With growing seas the breaking effect may be enhanced because breaking waves near the spectral peak receive enhanced momentum and energy fluxes from wind. Consequently, the wind profile is also modified significantly and the Charnock coefficient (normalized equivalent surface roughness) may increase by a factor or 2 or more due to breaking.

This theoretical model of the equilibrium wave spectra may be combined with a numerical wave prediction model to investigate the drag coefficient over complex seas.

References

[1] Phillips O.M.: Spectral and statistical properties of the equilibrium range in wind-generated gravity waves. *J. Fluid Mech* **156**:505–531, 1985.
[2] Hara T., Belcher S.E.: Wind forcing in the equilibrium range of wind-wave spectra. *J. Fluid Mech* **470**:223–245, 2002.
[3] Kudryavtsev V.N., Makin V.K.: The impact of air-flow separation on the drag of the sea surface. *Bound.-Layer Meteor.* **98**:155-171, 2001.
[4] Belcher S.E., Hunt J.C.R.: Turbulent shear flow over slowly moving waves. *J. Fluid Mech* **251**:109–148, 1993.
[5] Hara T., Belcher S.E.: Wind profile and drag coefficient over mature ocean surface wave spectra *J. Phys. Oceanogr.* under review.

XXI ICTAM, 15–21 August 2004, Warsaw, Poland

PROPAGATION AND INTERACTIONS OF NONLINEAR INTERNAL GRAVITY WAVE BEAMS

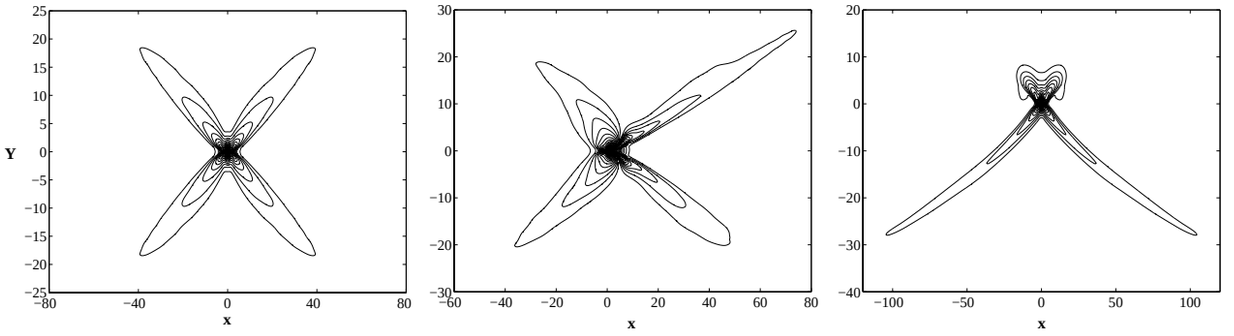
T. R. Akylas*, Ali Tabaei**
*Department of Mechanical Engineering, Massachusetts Institute of Technology, Cambridge, MA 02139, USA
**Department of Civil & Environmental Engineering, Massachusetts Institute of Technology, Cambridge, MA 02139, USA

Summary A locally confined source oscillating with frequency below the buoyancy frequency in a stratified fluid generates beam-like wave structures propagating along specific directions. A theoretical study is made of nonlinear effects in such wave beams. Nonlinearity is found to be particularly important in the reflection of a wave beam from a sloping wall and in collisions of two beams propagating along different directions.

PROPAGATION OF NONLINEAR WAVE BEAMS

Based on linear inviscid theory, a two-dimensional source oscillating with frequency ω_0 in a uniformly stratified (constant buoyancy frequency N_0) Boussinesq fluid induces a steady-state wave pattern, also known as St Andrew's Cross, that features four straight wave beams stretching radially outwards from the source at angles $\pm\cos^{-1}(\omega_0/N_0)$ relative to the vertical. Similar wave beams are generated by oscillatory stratified flow over topography. In addition, there is now evidence from numerical simulations and field observations that a significant component of thunderstorm-generated gravity waves in the atmosphere is in the form of beam-like structures. Dewan et al (1998), in particular, were able to link internal wave beams in satellite images of the upper stratosphere to isolated thunderstorms.

All existing theoretical models of the St Andrew's Cross and previous discussions of internal gravity wave beams are based on the linearized equations of motion, valid for small-amplitude disturbances. In the present study, exploiting the fact that uniform plane-wave beams of infinite extent happen to be exact solutions of the nonlinear inviscid equations of motion, we study the propagation of finite-amplitude wave beams taking into account weak viscous and refraction effects. Oblique beams ($\omega_0 < N_0$) are considered first and an amplitude-evolution equation is derived assuming gradual variations along the beam direction. Remarkably, the leading-order nonlinear terms cancel out in this evolution equation and, as a result, the steady-state similarity solution of Thomas & Stevenson (1972) for linear viscous beams is also valid in the nonlinear régime. Moreover, for the same reason, nonlinear effects are found to be relatively unimportant for nearly-vertically propagating ($\omega_0 \approx N_0$) beams. This explains the success of previous studies interpreting results from fully numerical simulations and field observations on the basis of linear theory. Owing to the fact that the group velocity vanishes when $\omega_0 = N_0$, however, the transient evolution of nearly vertical beams takes place on a slower time scale than that of oblique beams; this is shown to account for the discrepancies between the steady-state similarity solution of Gordon & Stevenson (1972) and their experimental observations. Based on the present asymptotic theory, we also study the refraction of nearly vertical nonlinear beams in the presence of background shear and variations in the buoyancy frequency. Figure 1(a) shows a wave-beam pattern generated by a locally confined source oscillating with dimensionless frequency $\omega_0 = 1$ in a uniformly stratified Boussinesq flow. Refraction of this wave pattern due to background shear and variations in the buoyancy frequency are shown in figures 1(b) and 1(c), respectively.



(a) (b) (c)

Figure 1. Contour plot of the amplitude of the vertical velocity at time $T = 4$ for wave pattern generated by oscillatory forcing at the origin $x = Y = 0$: (a) uniformly stratified flow with dimensionless buoyancy frequency $N^2 = 1 + 0.04$; (b) uniformly stratified flow with the same buoyancy frequency as in (a) in the presence of background shear $\overline{u} = 2 + 0.1Y$; (c) non-uniformly stratified flow with $N^2 = 1 + 0.01(4 - \frac{3}{4}Y)$ and $\overline{u} = 0$.

REFLECTIONS AND INTERACTIONS

While the effects of nonlinearity are relatively insignificant in the propagation of an isolated finite-amplitude beam, nonlinear effects turn out to be particularly important when two wave beams propagating along different directions interact. We study two examples of such interactions: the reflection of an incident wave beam from a sloping wall and the collision of two beams propagating in different directions.

In the case of reflection from a sloping wall, nonlinear interactions are confined solely in the vicinity of the sloping wall where the incident and reflected beams meet, as each of these beams is an exact nonlinear solution. At higher orders, this interaction region then acts as a source of a mean and higher-harmonic disturbances, and the latter are capable of radiating in the far field, forming additional reflected beams. Depending on the flow geometry, higher-harmonic beams can be found on the opposite side to the vertical than the primary reflected beam (see figure 2). Similarly, when two oblique beams collide, nonlinear interactions in the vicinity of the collision region induce secondary beams with frequencies equal to the sum and difference of those of the colliding beams. The theoretical results are consistent with numerical simulations and experiments.

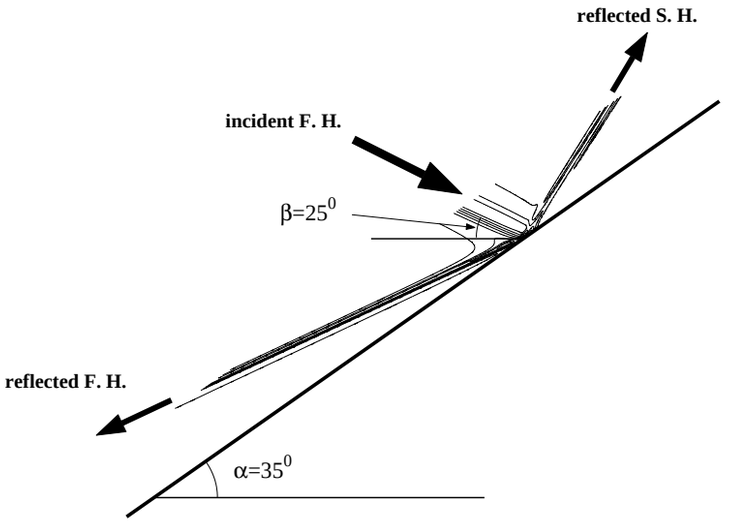


Figure 2. Contour plot of the stream function ψ for incident wave beam of angle $\beta = 25^0$ reflecting from a slope of angle $\alpha = 35^0$. F.H. and S.H. denote first harmonic and second harmonic, respectively.

References

[1] Dewan E.M., Picard R.H., O'Neil R.R., Gardiner H.A., Gibson J.: MSX Satellite Observations of Thunderstorm-generated Gravity Waves in Mid-wave Infrared Images of the Upper Stratosphere. *Geophysical Research Letters* **25**:939–942, 1998.

[2] Gordon D., Stevenson T.N.: Viscous Effects in a Vertically Propagating Internal Wave. *J. Fluid Mech* **56**:629–639, 1972.

[3] Thomas N.H., Stevenson T.N.: A Similarity Solution for Viscous Internal Waves. *J. Fluid Mech* **54**:495–506, 1972.

XXI ICTAM, 15–21 August 2004, Warsaw, Poland

WEAK-TURBULENT THEORY OF WIND-DRIVEN SEA

Vladimir E. Zakharov*
*Landau Institute for Theoretical Physics, Moscow 119334, Russia;
Department of Mathematics, University of Arizona, Tucson, AZ 85721, USA

Summary We developed a weak turbulent theory of the wind-driven sea, based on the assumption that the main physical process is the resonant nonlinear four-wave interaction. This model far developed analytically, supported by the massive numerical experiments is possible to explain from the first principles the balk of experimental facts on the wind-driven surface wave turbulence collected in physical oceanography.

Physical oceanography collected a huge amount of experimental data on the wind-driven sea. These data include frequency and angular-frequency spectra of surface elevation as well as spatial spectra measured from planes and satellites. A lot of collected data present fetch and duration dependance of such sea integral characteristics as energy $\epsilon =< \eta^2 >$ and the peak frequency ω_p. This variety of experimental data can be essentially reduced by the use of Kitaigorodskii similarity conjecture [1], stating that the major features of wind-driven sea can be expressed in terms of dimensionless variables (here U is wind velocity):

$$\nu = \frac{\omega_p U}{g}, \qquad e = \frac{\epsilon g^2}{U^4}, \qquad \chi = \frac{xg}{U^2}.$$

Experiments show that e, ν are powerlike functions on the dimensionless fetch χ:

$$e = u\chi^p, \qquad \nu = v\chi^{-q} \tag{1}$$

Here $0.75 < p < 1.0$, $0.24 < q < 0.3$ and $u = (5 \sim 10) \cdot 10^{-7}$, $v \simeq 10$ are constants, which vary in different studies. Omnidirectional frequency spectra can be presented in the universal form:

$$F(\omega) = \frac{g^2}{\omega^5} F\left(\frac{\omega}{\omega_p}, \nu\right)$$

The dependance on $\nu = 1/c$ (c is a "wave age") is relatively slow.

Since the seminal works of Hasselmann [2], it is widely accepted that the wind-driven sea can be described by the kinetic wave equation imposed to the spatial spectrum of wave action $N(\vec{k})$:

$$\frac{\partial N_k}{\partial t} + \frac{\partial \omega}{\partial \vec{k}} \frac{\partial N_k}{\partial \vec{r}} = S_{nl} + S_{in} + S_{ds} \tag{2}$$

Here S_{in} is the wind input, S_{ds} is dissipation term, and S_{nl} is nonlinear transfer term describing exchange of wave energy due to four-wave resonant nonlinear processes. S_{nl} can be calculated exactly from the Euler equation for potential flow of the fluid with free surface in presence of gravity. The term S_{in} cannot be found analytically due to a strong turbulence in the atmospheric boundary layer. The excitation of waves by wind is the Cherenkov-type instability. It leads to the following phenomenological form of S_{in}:

$$S_{in} = \beta \cdot N_k, \qquad \beta \simeq \mu \frac{\rho_a}{\rho_w} \omega f(\xi), \qquad \xi = \frac{U\omega \cos\theta}{g}$$

Here $f(\xi) = 0$ if $\xi < 1$, and $\mu \simeq 0.1$ is an empiric small parameter, appearing due to turbulence of atmosphere, ρ_a, ρ_ω are densities of air and water. For $\xi \gg 1$, we have $F(\xi) \simeq \xi^\kappa, 1 < \kappa < 2$. The term S_{in} is known from the experiments with poor accuracy (scatter of S_{in} has the same order as S_{in}).

The most important mechanism of wave energy dissipation is generation of parasitic capillary harmonics on the breaking wave crests. This process takes place uniformly on the whole ocean surface. At high wind velocities it turns to the "microbreaking" process. This process leads to absorption of energy in the high-frequency part of wave spectra. The direct white-capping on the crests of leading waves is the dissipation mechanism of secondary importance, responsible for slow saturation of the downshift process for waves moving faster than wind. There are neither analytical nor serious experimental studies making possible to derive a well-justified expression for S_{ds}. Some hand-woven forms of S_{ds} are used worldwide in the operational models of wave prediction (WAM, SWAN, *etc.*) Mostly they are constructed in a way to provide the local in frequency energy balance, i.e.

$$S_{in} + S_{ds} = 0$$

In these scenario S_{nl} terms plays an auxiliary role. In our report we offer a completely different approach [3-6]. In accordance with all summary of experimental facts we assume that S_{ds} is essential only in the region of high wave numbers, where it plays the role of a "universal sink" and does not affect essentially spectral dynamics in the area of spectral peak. In the leading order the wind-driven sea can be described by the conservative kinetic equation

$$\frac{\partial N_k}{\partial t} + \frac{\partial \omega}{\partial \vec{k}} \frac{\partial N_k}{\partial \vec{r}}$$

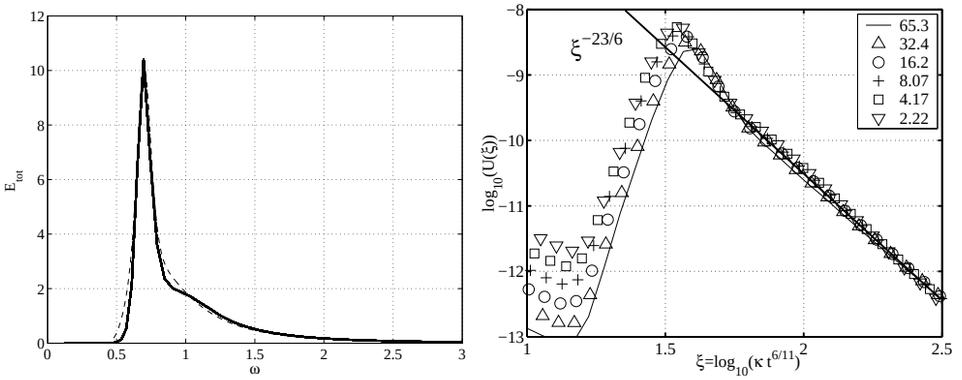


Figure 1. Left panel — comparison of numerical solutions (hard line) for the kinetic equation with JONSWAP approximation (dash) for wave age 1.42 (time 5.3 hours). Generation is given by Hsiao & Shemdin (1983) formula, wave speed is 20m/s. Dependence of α on wave age follows Babanin & Soloviev (1998) with the exponent $\kappa = 1$ and $\alpha_0 = 0.00127$. Right — self-similar function $U(\xi)$ ($\xi = |\mathbf{k}|t^{6/11}$) for different times (see legend, in hours). Bold line is the Kolmogorov inverse cascade solution $U \sim \xi^{-23/6}$. Wave input is given by Hsiao & Shemdin formula for wind speed 10 m/sec

together with the wave-action balance equation

$$\left\langle \frac{\partial N_k}{\partial t} \right\rangle + \left\langle \frac{\partial \omega}{\partial \vec{k}} \frac{\partial N_k}{\partial \vec{r}} \right\rangle = \langle S_{nl} \rangle \tag{4}$$

The brackets presume integration over the $\vec{k}$-space. Eq.(2) describes weak turbulence that is governed by the direct cascade of energy and the inverse cascade of wave action. Both uniform

$$\frac{\partial N_k}{\partial t} = S_{nl} \tag{5}$$

and stationary

$$\frac{\partial \omega}{\partial \vec{k}} \frac{\partial N_k}{\partial \vec{r}} = S_{nl} \tag{6}$$

versions of Eq.(1) have two-parameter families of self-similar solutions. The parameters could be found from balance Eq.(2). The self-similar solution of Eq.(6) in dimensionless variables reads:

$$n(\kappa, \chi, \theta) = b^5 \chi^{5\beta - 1/2} P_\beta \left(b\chi^\beta \kappa, \theta \right), \tag{7}$$

where b, β are free constants. Eq.(6) presumes that for Eq.(1)

$$q = \frac{2p+1}{10}, \qquad v = u^{1/5} C_\beta, \qquad C_\beta \simeq 1 \tag{8}$$

Relations (8) are very well confirmed by experimental data. Eq. (5) has following self-similar solutions

$$n(\kappa, \tau, \theta) = b^{19/4} \tau^{\frac{19\beta - 2}{4}} P_\beta (b\kappa\tau^\beta, \theta) \tag{9}$$

Here $\tau = tg/u$ is a dimensionless duration. Solution (9) is in accordance with the experimental data that in the case of duration-limited studies are scant. However for Eq. (5), asymptotic self-similarity of its solution is confirmed very well by massive numerical experiments [4,6]. It is remarkable that the shape of frequency spectra, obtained in these computations, almost perfectly fits the experimental data collected in the fetch-limited studies (Fig.1).

References

[1] Kitaigorodskii S.A.:Application of the theory of similarity to the analysis of wind-generated waves as a stochastic process.*Bull.Acad.Sci.USSR.Geophys.Ser*, 1962.

[2] Hasselmann K.: On the non-linear energy transfer in a gravity-wave spectrum. *J. Fluid Mech*, **12**:481–500, 1962;**15**:273–281, 1963.

[3] Zakharov V.E., Filonenko N.N.: Weak turbulence of capillary waves. *J.Appl.Meck.Tech.Phys.*, **4**:506–515, 1967.

[4] Pushkarev A., Resio D., Zakharov V.: Weak Turbulent Theory of the Wind-generated Gravity Sea Waves. *Physica D: Nonlinear Phenomena*, **184**:29–63, 2003.

[5] Zakharov V.E.: Theoretical Interpretation of Fetch Limited Observations of Wind–Driven Sea. Preprints 7th Int. Workshop on Wave Hindcasting and Forecasting, Banff, Alberta, Canada: 286–294, 2002.

[6] Badulin S., Pushkarev A., Resio D., Zakharov V.: Direct and Inverse Cascade of Energy, Momentum and Wave Action in the Wind-Driven Sea.

SHALLOW-WATER THEORY FOR WAVE-CURRENT-BOTTOM INTERACTIONS

Hu Huang
Shanghai Institute of Applied Mathematics and Mechanics, Shanghai University, Shanghai 200072, P R China

Summary A new shallow-water theory valid for wave-current-bottom interactions with arbitrary depth and unsteady horizontal currents is derived by Hamilton's canonical equations for surface waves, which constitutes a systematic hierarchy of partial differential equations for linear gravity waves in the near shore region. The first and second members of this hierarchy, the Helmholtz equation and the mild-slope equations of Berkhoff (1972) for pure waves and of Kirby (1984) with current, are second order. The third member is fourth order but may be approximated by Miles & Chamberlain's (1998) explicit fourth-order partial differential equation for pure waves which contains as a special case Chamberlain & Porter's (1995) modified mild-slope equation .

INTRODUCTION

Wave-current-bottom interactions have all along received a widespread attention as main dynamical mechanism in coastal area. On the background of the mild-slope equation[1], Miles & Chamberlain[2] recently obtained a systematic hierarchy of partial differential equations for linear pure gravity waves in water of variable depth by using the expansion of the average Lagrangian, the resulting explicit forth-order partial differential equation is time-independent. Constructing the new structure of the unknown potential field, a more systematic hierarchy of time-dependent partial differential equation for wave-current-bottom interactions is developed by way of Hamilton's canonical equations[3], which effectively extends the system of Miles & Chamberlain[2].

FORMULATION

We suppose that inviscid, incompressible fluid is in irrotational motion over a bed of varying depth $h(\mathbf{x})$, $\mathbf{x}\equiv(x,y)$ denoting horizontal Cartesian coordinates. The vertical coordinate, z, is measured positively upwards with the free surface $z=\zeta(\mathbf{x},t)$, $z=0$ denoting the undisturbed free surface. Now a new determination of the structure of the unknown potential field $\Phi(\mathbf{x},z,t)$ and $\zeta(\mathbf{x},t)$ for wave-current-bottom interactions can be given as follows

$$\zeta=\zeta_0(\mathbf{x},t)+\varepsilon\zeta_1(\mathbf{x},t)\ ,\quad \Phi=\phi_0(\mathbf{x},t)+\varepsilon\left[\cosh \mathrm{k}(z-\zeta_0)+\kappa \mathrm{k}^{-1}\sinh \mathrm{k}(z-\zeta_0)\right]\phi_1(\mathbf{x},t)\equiv\Re(\mathrm{k}^2,z)\phi_1 \tag{1}$$

where $\mathrm{k}^2\equiv-\nabla^2\equiv\left(-\partial^2/\partial x^2,-\partial^2/\partial y^2\right)$, $\nabla\equiv(\partial/\partial x,\partial/\partial y)$, ζ_0 and ϕ_0 are the surface elevation due to presence of current and the velocity potential of the current, $\boldsymbol{U}=\nabla\phi_0$, ε denotes the wave slope, κ is determined by the relation

$$\kappa=k\tanh q=\omega_r^{\,2}/g\qquad (q=k(h+\zeta_0)) \tag{2}$$

in which k is the wavenumber and ω_r the relative frequency. The operators $\cosh \mathrm{k}(z-\zeta_0)$ and $\mathrm{k}^{-1}\sinh \mathrm{k}(z-\zeta_0)$ are defined by their power-series expansions in k^2, and expand the operator $\Re$ in powers of the Helmholtz operator

$$\mathcal{H}\equiv\nabla^2+k^2=-\left(\mathrm{k}^2-k^2\right) \tag{3}$$

Introducing the truncated expansion

$$\Phi(\mathbf{x},z,t)=\left[\Re(k^2,z)-\left(\partial\Re/\partial \mathrm{k}^2\right)_{\mathrm{k}=k}\mathcal{H}+O(\mathcal{H}^2)\right]\phi_1(\mathbf{x},t) \tag{4}$$

The classical Berkhoff mild-slope equation[1] for pure wave motion can be given as

$$\left(\nabla^2+k^2\right)\psi=-A^{-1}\nabla A\cdot\nabla\psi \tag{5}$$

where $\Phi(\mathbf{x},z,t)=\mathrm{Re}\left[f(h,z)\psi(\mathbf{x})\mathrm{e}^{-i\omega t}\right]$ with frequency ω, $A=(1/2k)\left[B+kh\left(1-B^2\right)\right]$, $B=\tanh kh$, $f(h,z)=\cosh Q/\cosh kh$, $Q=k(z+h)$. (5) suggests that

$$\mathcal{H}\phi_1=-R^{-1}\nabla R\cdot\nabla\phi_1\qquad \left(R=(1/2k)\left[T+q\left(1-T^2\right)\right],T=\tanh q\right) \tag{6}$$

From (4) and (6), we obtain

$$\Phi(\mathbf{x},z,t)=\phi_0+\varepsilon\left[F(h,z)\phi_1+G_1(h,z)\Psi_1+G_2(h,z)\Psi_2+G_3(h,z)\Psi_3+O\left(|\nabla h|^2\right)\right] \tag{7}$$

where $F=\dfrac{\cosh Q}{\cosh q}$, $\Psi_1=\nabla h\cdot\nabla\phi_1$, $\Psi_2=\nabla k\cdot\nabla\phi_1$, $\Psi_3=\nabla\zeta_0\cdot\nabla\phi_1$, $G_1=\left(\dfrac{\partial\Re}{\partial \mathrm{k}^2}\right)_{\mathrm{k}=k}\dfrac{\partial R/\partial h}{R}=$

$\dfrac{1}{2}\left[\dfrac{(Q-q)\sinh Q-\sinh q\sinh(Q-q)}{k^2\cosh q}\right]\dfrac{\partial R/\partial h}{R}$, $G_2=\left(\dfrac{\partial\Re}{\partial \mathrm{k}^2}\right)_{\mathrm{k}=k}\dfrac{\partial R/\partial k}{R}$, $G_3=\left(\dfrac{\partial\Re}{\partial \mathrm{k}^2}\right)_{\mathrm{k}=k}\dfrac{\partial R/\partial\zeta_0}{R}$.

Notice that $R = \int_{-h}^{\zeta_0} F^2 dz$. The total energy of the fluid H is written as

$$\mathrm{H} = (1/2)\rho \iint d\mathbf{x} \left\{ g\zeta^2 + \int_{-h}^{\zeta} dz \left[(\nabla\Phi)^2 + \Phi_z^2 \right] \right\} = \mathrm{H}_0 + \varepsilon \mathrm{H}_1 + \varepsilon^2 \mathrm{H}_2 \qquad (\partial\Phi/\partial z \equiv \Phi_z) \tag{8}$$

From Hamilton's canonical equations for surface waves[3] ,we have

$$\rho\, \partial\zeta_1/\partial t = \delta \mathrm{H}_2/\delta\phi_1 \quad , \qquad \rho\, \partial\phi_1/\partial t = -\delta \mathrm{H}_2/\delta\zeta_1 \tag{9}$$

where δ denotes a variational derivative and ρ fluid mass density.

THE SHALLOW-WATER THEORY

Substituting (8) into (9) yields

$$\begin{aligned} \partial\zeta_1/\partial t &= -\zeta_1 \left[k(\nabla\zeta_0 \cdot \boldsymbol{U}) \tanh q + \nabla \cdot \boldsymbol{U} \right] - \nabla\zeta_1 \cdot \boldsymbol{U} + \int_{-h}^{\zeta_0} L dz - \nabla \cdot \int_{-h}^{\zeta_0} N dz + \delta P/\delta\phi_1 \\ \partial\phi_1/\partial t &= -g\zeta_1 - \nabla\phi_1 \cdot \boldsymbol{U} + \phi_1 k(\nabla\zeta_0 \cdot \boldsymbol{U}) \tanh q \end{aligned} \tag{10}$$

where the detailed expressions for L, N, and P are given in Appendix. Elimination ζ_1 from (10) leads to the time-dependent equation for the new shallow-water theory for wave-current-bottom interactions

$$\begin{aligned} &\frac{D^2\phi_1}{Dt^2} + (\nabla \cdot \boldsymbol{U}) \frac{D\phi_1}{Dt} - \left\{ \frac{D}{Dt} \left[k(\nabla\zeta_0 \cdot \boldsymbol{U}) \tanh q \right] + \left[k(\nabla\zeta_0 \cdot \boldsymbol{U}) \tanh q \right] \left[k(\nabla\zeta_0 \cdot \boldsymbol{U}) \tanh q + \nabla \cdot \boldsymbol{U} \right] \right\} \phi_1 \\ &\qquad + g \left[\int_{-h}^{\zeta_0} L dz - \nabla \cdot \int_{-h}^{\zeta_0} N dz + \frac{\delta P}{\delta\phi_1} \right] = 0 \qquad \left(\frac{D}{Dt} = \frac{\partial}{\partial t} + \boldsymbol{U} \cdot \nabla \right) \end{aligned} \tag{11}$$

Accepting the common assumption for the mild-slope equation that terms with ∇F, ∇h, ∇k, and $\nabla\zeta_0$ can be ignored, (11) reduced to the well-known Kirby mild-slope equation with current[4] which includes (5). When neglecting current $\boldsymbol{U}$ and ζ_0, and considering purely harmonic motion, $\phi_1(\mathbf{x}, t) = \mathrm{Re}\left[\Phi_0(\mathbf{x}) \mathrm{e}^{-i\omega t} \right]$, (11) leads to Mile & Chamberlain's explicit forth-order partial differential equation[2]

$$\begin{aligned} &(k^2 A - K)\Phi_0 + \nabla \cdot \left\{ A\nabla\Phi_0 + \langle fG \rangle \nabla(\nabla h \cdot \nabla\Phi_0) + \left[M(\nabla h \cdot \nabla\Phi_0) - \right. \right. \\ &\qquad \left. \left. \nabla \cdot \left(\langle G^2 \rangle \nabla(\nabla h \cdot \nabla\Phi_0) + \langle fG \rangle \nabla\Phi_0 \right) \right] \nabla h \right\} = 0 \end{aligned} \tag{12}$$

($A \equiv H$ and $f = F$ in Mile & Chamberlain's notation). The detailed expressions for K, M, G and $\langle\langle\ \ \rangle\rangle$ are given in [2]. Discarding all terms of G reduces (12) to Chamberlain & Porter's modified mild-slope equation[5].

This work was supported by the National Natural Science Foundation of China (10272072) and Shanghai Key Subject Program. The author wishes to thank Professor H. Zhang of Shanghai Library for her great help over 5 years.

APPENDIX: EXPRESSIONS FOR L, N AND P IN (10) AND (11)

$$\begin{aligned} L &= \phi_1 (\nabla F)^2 + \nabla F \cdot \left(F\nabla\phi_1 + \Psi_1 \nabla G_1 + \Psi_2 \nabla G_2 + \Psi_3 \nabla G_3 \right) + \phi_1 F_z^2 + F_z \left(\Psi_1 G_{1z} + \Psi_2 G_{2z} + \Psi_3 G_{3z} \right), \\ N &= F^2 \nabla\phi_1 + F\left(\phi_1 \nabla F + \Psi_1 \nabla G_1 + \Psi_2 \nabla G_2 + \Psi_3 \nabla G_3 \right) + \nabla(F\phi_1) \cdot \left(\nabla h \nabla G_1 + \nabla k \nabla G_2 + \nabla\zeta_0 \nabla G_3 \right) + \\ &\quad \left\{ \Psi_1 \left[(\nabla G_1)^2 + G_{1z}^2 \right] + \Psi_2 G_{1z} G_{2z} + \Psi_3 G_{1z} G_{3z} \right\} \nabla h + \left\{ \Psi_2 \left[(\nabla G_2)^2 + G_{2z}^2 \right] + \Psi_1 G_{1z} G_{2z} + \right. \\ &\quad \left. \Psi_3 G_{2z} G_{3z} \right\} \nabla k + \left\{ \Psi_3 \left[(\nabla G_3)^2 + G_{3z}^2 \right] + \Psi_1 G_{1z} G_{3z} + \Psi_2 G_{2z} G_{3z} \right\} \nabla\zeta_0 + \nabla h \nabla G_1 \cdot \left(\Psi_2 \nabla G_2 + \Psi_3 \nabla G_3 \right) + \\ &\quad \nabla k \nabla G_2 \cdot \left(\Psi_1 \nabla G_1 + \Psi_3 \nabla G_3 \right) + \nabla\zeta_0 \nabla G_3 \cdot \left(\Psi_1 \nabla G_1 + \Psi_2 \nabla G_2 \right), \\ P &= \iint d\boldsymbol{x} \int_{-h}^{\zeta_0} dz \left\{ (1/2) \left[G_1^2 (\nabla\Psi_1)^2 + G_2^2 (\nabla\Psi_2)^2 + G_3^2 (\nabla\Psi_3)^2 \right] + G_1 G_2 \nabla\Psi_1 \cdot \nabla\Psi_2 + G_1 G_3 \nabla\Psi_1 \cdot \nabla\Psi_3 + \right. \\ &\quad \left. G_2 G_3 \nabla\Psi_2 \cdot \nabla\Psi_3 + \left(G_1 \nabla\Psi_1 + G_2 \nabla\Psi_2 + G_3 \nabla\Psi_3 \right) \cdot \left[\nabla(\phi_1 F) + \Psi_1 \nabla G_1 + \Psi_2 \nabla G_2 + \Psi_3 \nabla G_3 \right] \right\}. \end{aligned}$$

References

[1] Berkhoff J. C. W.: Computation of Combined Refraction-Diffraction. *Proc 13th Int Conf on Coastal Engng, Vancouver, Canada,* ASCE, 471−490, 1972.
[2] Miles J.W., Chamberlain P.G.: Topography Scattering of Gravity waves. *J. Fluid Mech* **361**:175-188, 1998.
[3] Miles J.W.: On Hamilton's Principle for Surface Waves. *J. Fluid Mech* **83**: 153-158, 1977.
[4] Kirby J. T.: A Note on Linear Surface Wave-Current Interaction. *J. Geophys. Res* **89**(C1):745-747, 1984.
[5] Chamberlain P. G., Porter D.: The Modified Mild-Slope Equation . *J. Fluid Mech* **291**: 393-412, 1995.

XXI ICTAM, 15–21 August 2004, Warsaw, Poland

UNSTEADY UNDULAR BORE TRANSITION IN FULLY NONLINEAR DISPERSIVE WAVE DYNAMICS

Gennady El
School of Mathematical and Information Sciences, Coventry University,
Priory Street, Coventry CV1 5FB, UK

Summary A complete set of conditions describing the expanding undular bore transition in nonlinear conservative wave dynamics is derived. The transition conditions are obtained in a general form by employing the asymptotic formulation of the problem based on the Whitham modulation equations and allow, in particular, determination of the lead solitary wave amplitude as a function of the initial jump in (generally) non-integrable systems. Several examples pertaining to the shallow water dynamics and collisionless plasma physics are considered.

BACKGROUND

Undular bores (in diffrent contexts also called dispersive, or collisionless shocks) represent regions of rapidly oscillating nonlinear wave structures evolving out of smooth initial or boundary conditions of nonlinear dispersive wave equations. In the presence of small dissipation, the undular bores despite their oscillatory structure exhibit global properties characteristic for classical, turbulent bores or shock waves: they have steady, though wavy, profile and constant width such that the speed of the bore propagation and the transition conditions can be derived within the classical theory of hyperbolic conservation laws. The qualitative theory of such undular bores has been first developed by Benjamin and Lighthill [1] for shallow water waves and by Sagdeev [2] for rarefied plasma flows.

This classical theory of steady undular bores, however, is valid only for the regime, when nonlinearity, dispersion and dissipation are in balance. Contrastingly, in the case when dispersive effects dominate dissipation, the traditional analysis of the mass, the momentum and the energy balance across the undular bore transition can not be applied directly. The reason for that is that *the boundaries of the dissipationless undular bore diverge with time*, i.e instead of the single shock speed U defined by the mass balance one has now two different speeds $s_1 > s_2$ determining motion of the undular bore boundaries. These speeds, however, can not be obtained without the analysis of the nonlinear oscillatory structure of the undular bore because in the conservative dynamics, in contrast to the steady, dispersion-dissipative case, dispersion not only dramatically modifies the fine structure of the flow in the bore region but also, along with nonlinearity, determines the undular bore location.

In a weakly nonlinear case, when the original system can be approximated by one of the exactly integrable equations, such as Korteweg – de Vries or nonlinear Schrödinger equation, the undular bore solutions can be found using semi-classical asymptotic of the inverse scatering transform method [3]. Fully nonlinear dispersive waves, however, are often described by non-integrable systems, for which exact solutions of the Cauchy problem are not available in principle. In this case determination of the transition conditions allows one to put the entire problem of the dissipationless undular bore dynamics into the classical hydrodynamic setting, so that the expanding undular bore is 'embedded' into the solution of the dispersionless inviscid Euler equations bypassing the analysis of its fine structure.

GENERAL SETTING AND FORMULATION OF THE PROBLEM

We consider the system describing fully nonlinear flows in a dissipationless dispersive medium. In a symbolic form such a system can be represented as

$$\mathbf{K}_{M,N}(\mathbf{U}; \partial_t \mathbf{U}, \partial_{tt}^2 \mathbf{U}, \ldots; \partial_x \mathbf{U}, \partial_{xx}^2 \mathbf{U}, \ldots) = 0\,, \tag{1}$$

where $\mathbf{U}$ and $\mathbf{K}$ are vectors and M and N are the orders of the system with respect to the t- and x- derivatives respectively. In this study, we restrict ourselves with the important subclass of such systems with $M = 2$, $N = 4$ and the real-valued linear dispersion relation $\omega = \omega_0(k)$, where ω, is the frequency and k is the wavenumber. We assume that the system (1) supports nonlinear single-phase travelling wave solutions $f(kx - \omega t)$ and possesses at least four independent conservation laws of the form $\partial_t P_j + \partial_x Q_j = 0$.

We define the dispersionless limit of the system (1) by introducing $X = \epsilon x$ and $T = \epsilon t$ instead of x and t, and then by tending $\epsilon \to 0$. Let this limit have the form of the Euler equations of ideal gas dynamics

$$\partial_T \rho + \partial_X(\rho u) = 0\,, \qquad \partial_T u + u\partial_X u + c_s^2(\rho)\rho^{-1}\partial_X \rho = 0, \tag{2}$$

where ρ is the 'flow density', u is the 'flow velocity', and $c_s(\rho)$ is the 'sound speed'.

The described class of systems is quite broad and includes some known integrable models such as defocusing nonlinear Schrödinger equation and Kaup-Boussinesq system. As a typical (and important) non-integrable example one can indicate the Green-Naghdi system for fully nonlinear shallow water gravity waves [4] which also appears in such different physical contexts as bubbly fluid dynamics and magnetohydrodynamics of solar tachocline:

$$\partial_t h + \partial_x(hu) = 0\,, \qquad \partial_t u + u\partial_x u + \partial_x h = (3h)^{-1}\partial_x[h^3(u_{xt} + uu_{xx} - {u_x}^2)]\,. \tag{3}$$

Here h is total liquid depth and u is horisontal velocity averaged over depth (in the traditional shallow water terms).
The requirement of the particular form (2) for the dispersionless limit is, actually, not necessary for our theory to be valid, it is chosen solely for a greater transparency of presentation.
The problem formulation: *to derive a set of conditions determining transition for the solutions of the system (1) from one constant state* $(\rho, u) \to (\rho_2, u_2)$ *as* $x \to -\infty$ *to another constant state* $(\rho, u) \to (\rho_1, u_1)$ *as* $x \to +\infty$ provided $\rho_2 > \rho_1$.

RESULTS

The sought set of conditions is found by adopting the approach to the description of undular bores established in the integrable systems theory. The main assumptions we make are the following: (i) asymptotic as $t \to \infty$ description of the undular bore with the aid of the modulated travelling wave solutions of (1) $f(kx - \omega t; X, T)$ where $X = \epsilon x$ and $T = \epsilon t$, $\epsilon \ll 1$; (ii) hyperbolicity of the corresponding modulation (Whitham) equations $\partial_T \bar{P}_j + \partial_X \bar{Q}_j = 0$, $j = 1, \dots, 4$, where the bar denotes averaging over the family (1) [6].
We introduce the "extended" linear dispersion relation $\omega = \omega_0(k, \bar{\rho}, \bar{u})$ for the system (1) by linearizing it about the slowly changing mean state $\rho = \bar{\rho}(X, T)$, $u = \bar{u}(X, T)$. Then, analysis of the natural matching of the characteristics for the solutions of the Whitham and Euler equations at the (unknown at the onset) boundaries of the undular bore leads to the following description of the undular bore transition. The undular bore asymptotically as $t \to \infty$ occupies the self-similarly expanding zone $[s_2, s_1]$, where $s = X/T$, such that the following conditions hold.
(i) Relationship between admissible values of the boundary parameters $\rho_{1,2}$, $u_{1,2}$:

$$u_2 - u_1 = \int_{\rho_1}^{\rho_2} \frac{c_s(\rho)}{\rho} d\rho \,. \tag{4}$$

(ii) Location of the undular bore edges $s_{1,2}$ in self-similar co-ordinate $s = X/T$ is determined from:

$$s_2 = \frac{\partial \Omega_0}{\partial k}(k_2, \rho_2) \,, \qquad s_1 = \frac{\tilde{\Omega}_s(k_1, \rho_1)}{k_1} \,, \tag{5}$$

where

$$\Omega_0(k, \bar{\rho}) = \omega_0(k, \bar{\rho}, \bar{u}(\bar{\rho})) \qquad \tilde{\Omega}_s(\tilde{k}, \bar{\rho}) = -i\Omega_0(i\tilde{k}, \bar{\rho}) \,, \tag{6}$$

$$\bar{u}(\bar{\rho}) = u_1 + \int_{\rho_1}^{\bar{\rho}} \frac{c_s(\rho)}{\rho} d\rho \,, \qquad k_2 = k(\rho_2) \,, \;\; \tilde{k}_1 = \tilde{k}(\rho_1) \,. \tag{7}$$

The functions $k(\bar{\rho})$ and $\tilde{k}(\bar{\rho})$ are found from the ordinary diffrential equations:

$$\frac{dk}{d\bar{\rho}} = \frac{\partial \Omega_0 / \partial \bar{\rho}}{\bar{u}(\bar{\rho}) + c_s(\bar{\rho}) - \partial \Omega_0 / \partial k} \,, \qquad k(\rho_1) = 0 \,. \tag{8}$$

$$\frac{d\tilde{k}}{d\bar{\rho}} = \frac{\partial \tilde{\Omega}_s / \partial \bar{\rho}}{\bar{u}(\bar{\rho}) + c_s(\bar{\rho}) - \partial \tilde{\Omega}_s / \partial \tilde{k}} \,, \qquad \tilde{k}(\rho_2) = 0 \,. \tag{9}$$

(iii) Inequalities providing consistency of (i) and (ii) should be satisfied:

$$u_2 - c_s(\rho_2) < s_2 < u_2 + c_s(\rho_2) \,, \qquad s_1 > u_1 + c_s(\rho_1) \,. \tag{10}$$

Remarkably, the conditions (i) – (iii) are determined by the dispersonless limit (2), which is characterised by the 'sound speed' $c_s(\rho)$, and the linear dispersion relation $\omega_0(k; \bar{\rho}, \bar{u})$ and thus, do not rely on the integrability of the system (1). We also note that the condition (i) has been for the first time proposed [7]in the context of the dissipationless dispersive shocks in plasma.
We apply conditions (i) – (iii) to the systems where undular bore solutions have been obtained earlier using either exact analytic methods (the integrable Kaup-Boussinesq system for the dispersive shallow water waves [5]) or numerically (fully nonlinear ion-acoustic waves in collisionless plasma [7]). In both cases a complete agreement of our conditions with the earlier results is shown. We then apply the undular bore conditions (i)– (iii) to the Green – Naghdi system (3) to obtain the lead solitary wave amplitude in the fully nonlinear shallow water undular bore as a function of the initial jump.

References

[1] Benjamin, T.B & Lighthill, M.J. 1954 Proc. Roy. Soc. A **254**, 448 - 460
[2] Sagdeev, R.Z. 1968 in: Leontovich, M.A. ed. *Reviews of Plasma Physics*, Volume 4, p. 20. Consultants Bureau. New York
[3] Lax, P.D. & Levermore, C.D. 1983 The small dispersion limit of the Korteweg – de Vries equation I, II, III. *Comm. Pure Appl. Math.* **36**, 253-290, 571-593, 809-829.
[4] Green, A.E. & Naghdi, P.M. 1976 A derivation of equations for wave propagation in water of variable depth. *J.Fluid Mech.* **78**, 237 - 246.
[5] El, G.A., Grimshaw, R.H.J. & Pavlov, M.V. 2001 Integrable shallow water equations and undular bores. *Stud. Appl. Math.* **106**, 157-186.
[6] Whitham, G.B. 1965 Non-linear dispersive waves *Proc. Roy. Soc.* **A283**, 238-291.
[7] Gurevich, A. V. & Meshcherkin, A. P. 1984 Expanding self-similar discontinuities and shock waves in dispersive hydrodynamics *Sov. Phys. JETP* **60**, 732.

The theory of travelling deformation waves and its applications in biomechanics, engineering, and geophysics

A.I. Dobrolyubov
United Institute of Information Problem, Surganov st. 6, Minsk, 220012, Belarus,
dobr@newman.bas-net.by

Our theoretical and experimental researches of the *travelling waves of deformation* in solid, liquid, and gaseous bodies have resulted in an establishment of some unknown before wave phenomena and effects. With help of natural examples from biomechanics, engineering mechanics, and geophysics this report introduces these widespread different wavelike phenomena. On descriptive and mathematical levels the different in physical state, dimensions, and shapes travelling deformation waves are presented. Developed mathematical expressions which give main kinematics and masstransfer parameters of the travelling deformation waves are presented and explained. The travelling deformation wave is defined as a size limited deformed region which is moving along some lengthy deformable body. It was established, that the travelling waves of deformation play an important role both in living organisms and in inanimate nature and act in various physical matter in micro- and macrocosm. The created theory of travelling waves of deformation and wave masstransfer has allowed to receive new scientific results and to make inventions in such areas as the theoretical mechanics, the theory of mechanisms and machines, the biomechanics and medicine, the Earth's and planets' sciences. These results were recognized as fundamental by various experts in our republic and abroad. Our results on a competitive basis were awarded with grants of Fund of basic researches of Belarus, the American Physical Society, the International Soros scientific fund.

New scientific results were received:

- ***In the field of the biomechanics and medicine:***

- From positions of the theory of travelling waves of deformation and wave masstransfer the non-conventional explanation of locomotion of such living creatures as garden caterpillar, earthworm, snake, and snail was received and mathematical model of these phenomena was created. From the same mathematical model positions the non-conventional explanations of such medical and biologic mechanisms as peristaltic in digestive system, work of urethra, biomechanics of labour were given.

- ***In engineering area:***

– Wave mechanisms and machines of new type, which use a biomechanical wave principle of movement (wave reducers of continuous and step-by-step rotation, linear and rotational step-by-step electric motors), which are characterized by simplicity of structure, the technical and economic advantages in comparing to traditional analogous mechanisms.

– The transport and transport-tractive machines which use new biomechanical wheel-stepping method of movement posses such advantages as simplicity of design and high tractive force in comparison with traditional machines of the same purpose. The wheel-stepping machines are perspective for use in such areas as an agriculture, machines for work in mines, building of roads and tunnels, a forestry works etc. Now the International Science and Technology Centre has examined our submitted project "Design and production of the experimental pattern of transport device which uses biomechanical wheel-stepping principles of motion " which was submitted by UIIP together with the Minsk tractor plant.

- ***In the field of the Earth's sciences:***

It was supposed and proved that the travelling tidal waves which are continually arising in all layers of the Earth play role main generators of global geophysical processes in all geospheres. From positions of the theory of travelling tidal waves and wave masstransfer the non-conventional scientific explanations of following global geophysical processes were given:

- Tectonics of lithosphere plates;
- The tidal mechanism of generation and accumulation of strains in the Earth's crust as a driving mechanism of the "earthquake machine";
- Generation of the large-scale ocean currents;
- Superrotation of the top layers of an atmosphere of the Earth and planets;
- Superrotation of photosphere of the equatorial belt (zone) of the Sun;
- The mechanism of formation and maintenance of the magnetic field of the Earth and planets.

The mentioned results were approved at native and international scientific seminars and conferences, published in the special literature and were recognized as new in these areas of science. Mechanical and hydraulic models and visual computer models and animations for demonstration of the laws of wave processes and wave masstransfer in solid, liquid, and gaseous environments were developed. The patents for some wave mechanisms and machines and physical devices are received.

We hope, that these report will promote establishment of scientific communications in joint International scientific projects. With the same purpose the specialists from UIIP are ready to read before the interested audience the lectures in Russian or English "The travelling waves of deformation in nature, engineering, and medicine ", concerning the above theme on mechanics, biology, medicine, physics, and sciences about the Earth. Lectures will be accompanied by demonstration of new wave models and mechanisms, physical demonstration devices, video and computer films.

SELECTED OUR PUBLICATIONS

Dobrolyubov A.I. Mechanisms with flexible and elastic elements. – Minsk, "Science and Technology", 1984. – 118 pages. (In Russian)

Dodrolubov A.I., Kusmin A.V. Neue Wellenschrittmechanismen. Feingeratetechnik, Berlin, 1986, N 1, s. 19-20. (In German)

Dobrolyubov A.I. The Mechanism of Locomotion of Some Terrestrial Animals by Travelling Waves of Deformation. London, Journal Theor. Biology, 1986, v. 119, pp. 457-466.

Dobrolyubov A.I. Wave Motions in Deformable Solids and Liquids (Kinematics and masstransfer), – Minsk, "Science and Technology", 1989. – 95 pages. (In Russian)

Dobrolyubov A.I. Sliding, Rolling and Waving Motions of Deformable Bodies (Biomechanical and engineering applications).- Moscow, "Science, Physmatlit", 1991.- 176 pages. (In Russian)

Dobrolyubov A.I. Travelling Deformation Waves: A Tutorial Review. - New-York, Applied Mechanics Reviews, 1991, N 5, pp. 215-255.

Dobrolyubov A.I. Stepping Wave Mechanisms. - London, Mechanisms and Machines Theory, 1990, v.25, N 4, pp.449-456.

Dobrolyubov A.I. Wave transfer of matter. - Minsk, "Belarus science", 1996. – 304 pages. (In Russian)

Dobrolyubov A.I. Travelling deformation waves as a generator of the large-scale geophysics processes, – Minsk, Lithosphere, 1996, №4 pp. 22-49. (In Russian).

A. I. Dobrolyubov, S. K. Shumak Wheel-stepping transport vehicles – The report at the International seminar Conversion of scientific researches in Byelorussia within the framework of ISTC activity, Minsk, May, 17-22, 1999.

Dobrolyubov A.I. To the theory of superrotation of Venus atmosphere, – Minsk, Doklady of Belorussian Accademy of Sciences. 2001, Vol. 41, № 1, p. 120-123. (In Russian)

Dobrolyubov A.I., Shumak S.K. Travelling Deformation Waves as a Transport Mechanism in Biological Systems. – Minsk, Proceedings of Belorussian Academy of Sciences, Biology series. 2001, №.3, p102-104.(In Russian)

Dobrolyubov A. I. The travelling deformation waves as a biological transport mechanism. -- Russian Journal of Biomechanics. Russia, Perm. 2001, Vol. 5, #3, pp. 55-69. (In English)

Dobrolyubov A.I., Douchy G. Peristaltic transport as the Travelling Deformation Waves. -London, Journal Theor. Biology., 2002, v. 119, pp. 455-461

Dobrolyubov A.I Travelling Deformation Waves. 2-nd ed., – Moscow, Editorial URSS, 2003. – 144p. (In Russian)/

In the web site Dobrolyubov A.I., Kolesnik A.A. Travelling Deformation Waves. Website, http://pages.sbcglobal.net/akolesnik/ there are animations and pictures related to the report.

THE SPACING OF LANGMUIR CIRCULATION IN STRONG WAVY SHEAR

William R.C. Phillips

Department of Theoretical and Applied Mechanics,
University of Illinois at Urbana Champaign, Illinois, U.S.A.

The inviscid instability of $O(\epsilon)$ two-dimensional free surface gravity waves propagating along an $O(1)$ parallel shear flow is considered. The modes of instability involve spanwise-periodic longitudinal vortices resembling oceanic Langmuir circulation. Here, not only are wave-induced mean effects important but also wave modulation, caused by developing mean streamwise-velocity anomalies. The former is described by the generalized Lagrangian-mean formulation of Andrews & McIntyre and the latter by a modified Rayleigh equation given by Craik. Since both effects are essential, the instability is called "generalized" Craik-Leibovich (CLg) to distinguish it from the related but fundamentally different CL2 instability. Motivation for the work stems from interest in the air-sea interface and in particular in modeling Langmuir circulations. These occur in open water bodies in the presence of moderate winds and play an important role in the transfer of heat, mass and momentum between the atmosphere and the ocean. CL2 is a leading candidate mechanism to describe this occurrence but there is as yet no proof that CL2 is realizable in the ocean or laboratory.

According to the Craik-Phillips-Shen criterion, wave mean interactions are unstable to longitudinal vortex form if, from the reference frame of the waves, and in the direction of increasing mean flow, the relative increase in mean flow exceeds the relative increase in wave amplitude. So, the flow under consideration is unstable to longitudinal vortex form provided the amplitude of the waves diminishes with depth. Of specific interest is whether spanwise distortion of the wave field acts to enhance or inhibit instability to longitudinal vortices. Also of interest is whether the instability gives rise to a preferred spacing for the vortices and whether that spacing concurs well or poorly with experiment.

The layer depth is varied from much less than the e-folding depth of the $O(\epsilon)$ wave motion, to infinity. Relative to an identical shear flow with rigid though wavy top boundary, it is found that wave modulation acts to increase the maximum growth rate of the instability. It is further found that, while mean streamwise-velocity anomalies in layers of finite depth are typically a maximum at the free surface and of single sign with depth, anomalies of mixed sign are common when the depth is infinite. Mixed sign is associated with multiple, vertically stacked vortices, a feature expected to enhance mixing. Finally, the preferred spacings calculated herein concur well with those observed in laboratory experiments, with the implication that the instability acting in the experiments very likely is CLg.

This work was supported by National Science Foundation grants OCE-9818092 and OCE-0116921.

EXPERIMENTS ON ROTATING AND REFLECTING INTERNAL WAVE BEAMS

Thomas Peacock*, Patrick Weidman**, Ali Tabaei*
*Massachusetts Institute of Technology, Cambridge, Massachusetts, 02139, USA
**University of Colorado, Boulder, Colorado, 80309, USA

Summary : We present new results for two sets of experiments on internal wave beams. For conical beams in a rotating system, we confirm the dependence of the beam angle on the rotation rate and identify the cut-off frequencies. For reflected beams, we provide the first experimental observations of second harmonic beams generated by nonlinear interactions at the wall. The synthetic schlieren method of visualisation was used for both experiments.

INTERNAL WAVE BEAMS

Internal waves arise as a result of disturbances in a stratified fluid. If gravity is assumed to be in the vertical direction, the dispersion relation is such that disturbances generated by a localised source propagate as beams. The angle of the beams with respect to the horizontal is

$$\theta = \sin^{-1}(\omega/N), \tag{1}$$

where ω is the excitation frequency and N is the Brunt-Vaisala frequency of the stratification. There is thus a cut off frequency ($\omega = N$) above which disturbances cannot propagate. This fascinating phenomenon was first investigated by Mowbray & Rarity [1] and has been the subject of a wide variety of research relevant to both the oceans and the atmosphere. Recently, the novel "synthetic schlieren" experimental technique [2] has enabled detailed quantitative investigations of the beam structure.

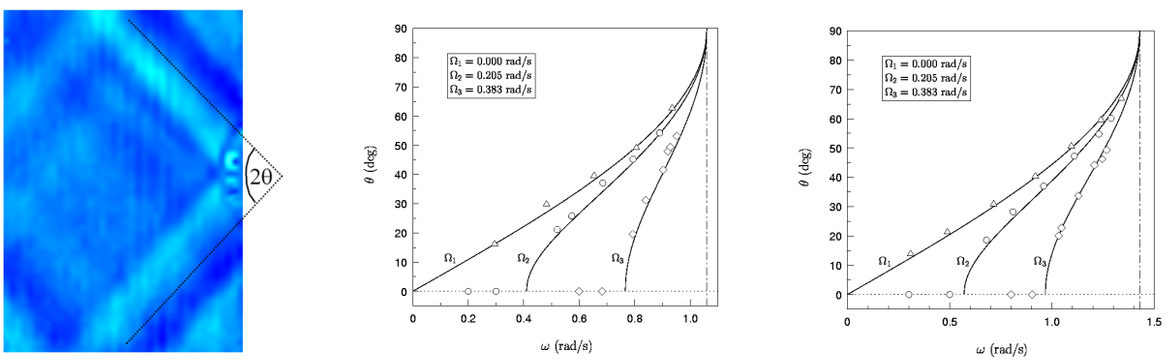
Rotating internal wave beams

The influence of rotation on the orientation of internal wave beams is documented by LeBlond & Mysak [3]. Disturbances from a point source generate a conical wave-beam structure whose angle to the horizontal is given by the dispersion relation

$$\theta = \sin^{-1}\sqrt{\frac{\omega^2 - 4\Omega^2}{N^2 - 4\Omega^2}}, \tag{2}$$

where Ω is the angular rotation rate of the system, that is oriented anti-parallel to gravity. In contrast to the non-rotating case, there are both lower (2Ω) and upper (N) cut-off frequencies, outside of which no disturbances can propagate. This dispersion relation has never previously been verified experimentally.

The experiment comprised an acrylic tank of diameter 1 meter mounted on a rotating table. Two stable salinity stratifications ($N = 1.06, 1.43 \pm 0.01\text{s}^{-1}$) were established by filling the tank using the double bucket method. The density gradient was measured using a calibrated salinity probe. A sphere of radius 2.54±0.02 cm was fixed to a thin rod and positioned at the center of the tank. The sphere was oscillated vertically with an amplitude of 1.50±0.01cm over a range of frequencies. Through the arrangement of a video camera, a mirror and a back lit pattern of dots the resulting conical wave beams were visualised using the "synthetic schlieren" method [2]. A beam cross section for which $N = 1.43\text{s}^{-1}$, $\Omega = 0.285 \pm 0.007\text{s}^{-1}$ and $\omega = 1.11 \pm 0.01\text{s}^{-1}$ is presented in Figure 1(a). The beam angles were objectively measured using the Radon transform of images such as that in Figure 1(a). Results for $N = 1.06$ and $N = 1.43$ are presented in Figures 1(b) and 1(c). The agreement between experiment and theory is very good, and for the rotating systems one can see the existence of a lower cut off frequency, below which no beams could propagate.



(a) (b) (c)

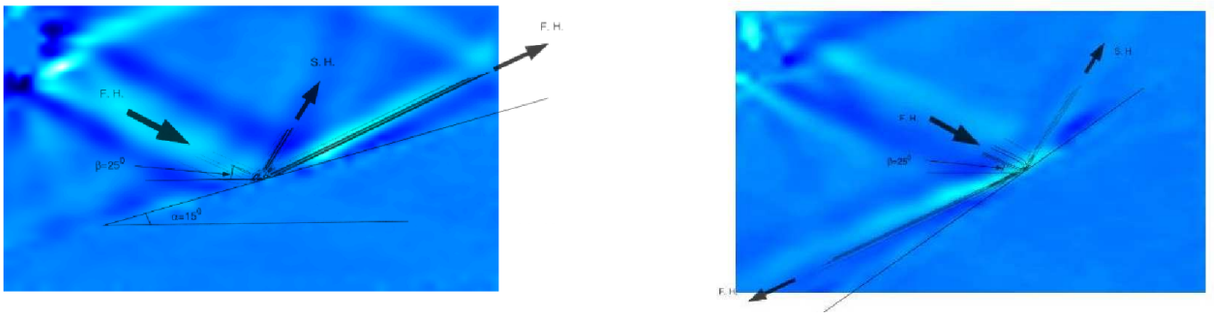
FIGURE 1 : (a) Cross section of a pair of conical wave beams originating from a sphere (center-right). $N = 1.43\text{s}^{-1}$, $\Omega = 0.285\text{s}^{-1}$, $\omega = 1.11\text{s}^{-1}$ (b) Experimental results for $N = 1.06\text{s}^{-1}$ (c) Experimental results for $N = 1.43\text{s}^{-1}$.

Reflecting internal wave beams.

It has recently been realised that the linearised solutions for internal wave beams are, in fact, solutions of the full nonlinear problem [4]. The effect of nonlinear interactions between two such beams may be calculated using these linear solutions [5]. Such a situation arises when two distinct beams bisect within the body of a stratified fluid. Alternatively, interaction can arise when an individual beam is reflected from a boundary, in which case the incoming beam interacts with its reflected counterpart. These interactions have been predicted to generate additional beams, of different harmonics, whose angle of propagation is determined by the dispersion relation (1). If the interaction takes place at a sidewall, propagation of the reflected beams is also directed by the the angle of inclination of the wall ϕ.

The experiments were performed in a tank 30cm deep, 40cm high and 40cm wide. An acrylic cylinder 2.54±0.02cm in radius and 30cm long was attached to a slender rod and positioned across the center of the tank. A stable salinity stratification was obtained by filling the tank from below using a double bucket method. The cylinder was oscillated with an amplitude of 0.5 ± 0.01cm to generate planar internal wave beams emanating at an angle of 25.0 ± 0.1^o along the length of the cylinder. The arrangement was such that one of the beams was reflected from an inclined surface, and the reflections were observed using the synthetic schlieren set-up.

The visualisations for two experimental arrangements are shown in Figures 2(a) and 2(b). The beams originate from the cylinder in the top right hand corner of each image. Superimposed on top of the images are the results of complementary numerical simulations, which indicate the orientation of the incoming and reflected beams. The arrangement for Figure 2(a) was $\theta = 25.0 \pm 0.1^o$ and $\phi = 15.0 \pm 0.1^o$. The reflected first harmonic and the generated second harmonic, making an angle of 57.7^o to the horizontal, are both oriented towards the top right of the image. It is impossible for a reflected first harmonic or second harmonic to go in any other direction, because the wall prevents this. In contrast, the arrangement for Figure 2(b) was $\theta = 25.0 \pm 0.1^o$ and $\phi = 35.0 \pm 0.1^o$, so that the reflected first harmonic is directed towards the bottom left of the image. The second harmonic beam still proceeds towards the top right, as its progress is not blocked by the wall. It was not possible to realise a third scenario, in which both beams are directed towards the lower left corner. Numerical simulations demonstrated that this is due to the fact that the energy of the generated second harmonic beam is too weak to be detected with the current experimental set-up.



(a) (b)

FIGURE 2 : Reflected internal wave beams. (a) $\theta = 25^o, \phi = 15^o$. (b) $\theta = 25^o, \phi = 35^o$.

CONCLUSIONS

We have performed two careful sets of experiments in which "synthetic schlieren" was used to obtain new results on the dynamics of rotating and reflecting internal wave beams. The results agree very well with both theory and numerical simulations, and are relevant to atmospheric and oceanic dynamics.

Bibliography

[1] Mowbray D.E. , Rarity, B.S.H : A theoretical and experimental investigation of the phase configuration of internal waves of small amplitude in a density stratified fluid. *J. Fluid Mech.* **28**:1–16, 1967.

[2] Sutherland B.R. ,Dalziel S.B. , Hughes, G.O. , Linden P.F. : Visualisation and measurement of internal waves by "synthetic schlieren". Part 1: Vertically Oscillating Cylinder. *J. Fluid Mech.* **390**:93–1226, 1999.

[3] LeBlond P.H. , Mysak L.A. : Waves in the ocean, Elsevier, 1978.

[4] Tabaei A. , Akylas, T.R. : Nonlinear internal gravity wave beams. *J. Fluid Mech.* **482**:141–161, 2003.

[5] Tabaei A.ł,, Akylas, T.R. : Nonlinear effects in reflecting and colliding internal wave beams . To be submitted.

SPATIO-TEMPORAL MEASUREMENTS OF CAPILLARY-GRAVITY WAVES

Paul A. Hwang[1], David W. Wang[1], Guillemette Caulliez[2], and Vladimir K.Makin[3]

[1]*Oceanography Division, Naval Research Laboratory, Stennis Space Center, MS, USA*
[2]*Air-Sea Interaction Laboratory, IRPHE-IOA, Marseille, France*
[3]*Royal Netherlands Meteorological Institute (KNMI), De Bilt, The Netherlands*

Summary Small scale surface waves in the capillary-gravity region can be easily advected by surface currents from all sources. Temporal measurements using fixed-point wave probes, therefore, cannot resolve reliably the spatial or wavenumber structure of short waves unless the surface currents are also monitored, which is an even more difficult task than surface wave measurement. A two-dimensional scanning slope sensor system is developed to perform 4D measurements [$\nabla h(x,y,t)$] of small scale surface waves. The data yield 3D spectrum [$B(k_x,k_y,w)$] covering the capillary-gravity wave scales. The directional properties of small scale waves can be quantified by such data to a great detail. These data can be used to investigate the balance of source functions in the wave action conservation equation following the approach suggested by Phillips (1984, 1985).

A series of laboratory experiment is carried out to study the spectral properties of wind-generated waves in the capillary-gravity length scale. Two instruments are used for the wave measurements. The first is a two-dimensional laser scanning slope sensing system (SSS) similar to the one described by Hwang et al. (1993, 1996). The device scans a laser beam upward from underwater to cover a surface area of about 0.1 m × 0.1 m. The spatial resolution is 2 mm in both upwind and crosswind directions, and the temporal resolution is 50 frames per second. The second instrument is a linear array of 40 capacitance wave gauges (WGA) spaced 0.0508 m (2") apart, placed in the middle of the tank and with the gauges aligned in the downwind direction. The vertical resolution of the wave gauges is 2.3×10^{-4} m. The wave gauges are simultaneously sampled with 40 analog-to-digital circuits at a rate of 50 Hz for each gauge.

An example of the slope topography obtained from the laser scanning system is shown in Fig. 1a for the upwind slopes. The spatio-temporal measurements can be analyzed to yield 3D saturation spectrum (Phillips 1985) of the surface waves $B(k_x,k_y,w)$, from which, 1D and 2D spectra can be calculated. Fig. 1b shows the 2D wavenumber spectrum $B(k_x,k_y)$ produced from integrating the 3D spectrum over frequency. The forward and backward propagating wave components can be clearly detected from $B(k_x,k_y)$. This is a significant improvement over the 2D wavenumber spectrum derived from individual images (denoted as $B'(k_x,k_y)$ here), in which the forward/backward and left/right information are not distinguishable due to the inherent axi-symmetric property of the Fourier transformation (Fig. 1c). The forward and backward propagating components appear in pairs within the resolution range of the instrument (k<1600 rad/m), with the upwind propagating waves having generally shorter wavelengths. The apparent upwind propagating components were originally thought to be the reflection of short waves in oscillating currents as described by Shyu and Phillips (1990). Unfortunately, later analysis indicates that they are a result of frequency aliasing because the sample rate (50 frames per second) is too slow and wave components with wavenumber greater than 500 rad/m may be misrepresented in the 3D spectrum. More quantitative analysis of the wave properties can be obtained from frequency slices of the 3D spectrum, an example is shown in Fig. 1d.

Phillips (1984) describes an approach to establish the dissipation function in the equilibrium region of gravity waves from the functional dependence of B on u_*/c, where u_* is the wind friction velocity and c is the wave phase speed. In particular, if B can be expressed as a power-law function of u_*/c, $B = A_0(u_*/c)^{a_0}$, and the dissipation function can be expressed as a power-law function of B, $D = A_d B^{a_d}$, then the coefficient and exponent of the dissipation function can be obtained from A_0 and a_0, assuming local balance between the wind input and dissipation functions in the equilibrium region, and employing an empirically established wind input function. For shorter waves that are influenced by both gravity and surface tension, the balance of source/sink terms is much more complicated. For example, other generation and dissipation mechanisms, such as three-wave interaction, parasitic capillary wave generation, capillary wave reflection by orbital currents, micro scale breaking and viscous dissipation, may all be of the same order of importance in the energy and momentum balance of capillary-gravity waves. Phillips' approach, however, can still be applied to the analysis of the dynamic balance between the wind input and the D function, which is now treated as the sum of the remaining source/sink functions.

We examine the dependence of B on u_*/c in the capillary to short gravity wave region using both sets of SSS and WGA data. Indeed, the results appear to fit the power-law function nicely (Fig. 2a-b). The coefficient A_0 and exponent a_0 can be obtained from least square fitting of the measured data. The coefficient and exponent of the D function are calculated by A_d=0.04/A_0, and a_d=1+2/a_0. Fig. 2c shows the data-fitted a_0 as a function of the dimensionless wavenumber (normalized by k_m, the wavenumber of the wave component that gravitational force and surface tension force serve equally as the restoring force of the wave motion), and Fig. 2d shows the calculated a_d. Interestingly, the exponent of the D function varies only slightly in the capillary-gravity range. The average a_d is 1.54±0.37 from the SSS in the range of k/k_m>0.5, 1.38±0.16 from the WGA in the range of 1.2>k/k_m>0.4, and it gradually decreases to about 1 at k/k_m about

0.1. Compiling a dataset spliced from WGA measurements for $k/k_m<0.9$ and SSS measurements for $k/k_m>1.1$, and their average in the range $0.9<k/k_m<1.1$, a set of empirical equations is suggested for A_0 and a_0 for the convenience of computing the D function by $A_d=0.04/A_0$, and $a_d=1+2/a_0$ (application range is approximately $5>k/k_m>0.1$):

$$A_0=\begin{cases}1.3\times10^{-2}, & k/k_m<0.3\\ 8.4\times10^{-4}(k/k_m)^{-2.3}, & 0.3\le k/k_m<1.6\\ 2.7\times10^{-4}, & k/k_m\ge1.6\end{cases}$$

$$a_0=\begin{cases}1, & k/k_m<0.3\\ \log[1.26(k/k_m)^{-3}], & 0.3\le k/k_m<0.4\\ 1.5, & k/k_m\ge0.4\end{cases}.$$

Phillips' (1984) approach is applied to short scale wave measurements collected in the ocean to study the source function balance of wind waves. The results suggest that the dissipation function is localized in the wavenumber space rather than the broadband distribution commonly assumed. The detail is described by Hwang and Wang (2004).

References

[1] Hwang, P. A., Trizna, D. B., Wu, J.: *Dyna. Atmos. and Oceans* **20**:1-23, 1993.
[2] Hwang, P. A., Atakturk, S., Sletten, M., Trizna, D. B.: *J. Phys. Oceanogr* **26**:1266-1285, 1996.
[3] Hwang, P. A., Wang, D. W.: *Geophys. Res. Lett* **31**:L15301, doi:10.1029/2004GL020080, 2004
[4] Phillips, O. M.: *J. Phys. Oceanogr* **24**:1425-1433, 1984.
[5] Phillips, O. M.: *J. Fluid Mech* **156**:505-531, 1985.
[6] Shyu, J.-H., Phillips, O. M.: *J. Fluid Mech* **217**:115-141, 1990.

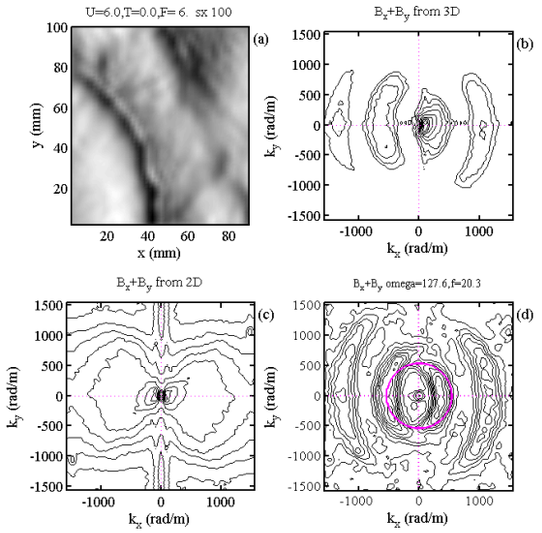


Fig. 1.
Examples of the results from space-time measurements of capillary gravity waves using a laser scanning slope sensor system: (a) downwind slopes, (b) $B(k_x,k_y)$ integrated from 3D spectrum $B(k_x,k_y,w)$, (c) $B'(k_x,k_y)$ calculated from 2D images, and (d) the frequency slice of the 3D spectrum $B(k_x,k_y,w)$ at 20.3 Hz. In (d), the circle represents the linear dispersion relation for the given frequency. The spectra shown here are based on 30-s (1500 frames) average of the wave data collected at a fetch of 6 m, and the wind speed is 6 m/s. Contours plotted are 3 dB (about a factor of 2) apart. Positive k_x is in the downwind direction.

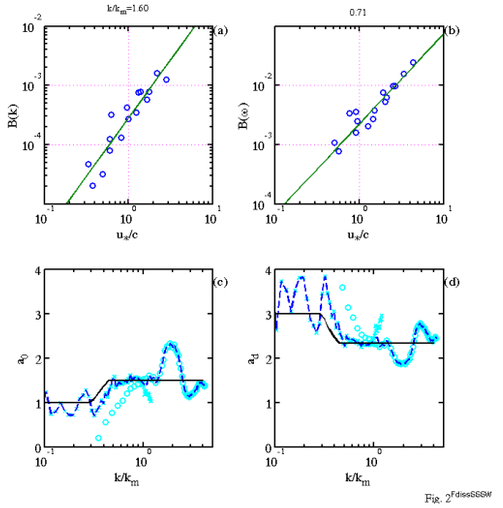


Fig. 2.
Top row: Dependence of B on u_*/c, the solid curve is calculated from least square fitting. (a) From the scanning slope sensor data, (b) from the wave gauge array data. The results are obtained from 16 different combinations of wind speeds and fetches.
Bottom row: Empirically derived exponents of (c) $B(u_*/c)$, and (d) $D(B)$. Circles are from SSS; crosses are from WGA. The spliced data are illustrated by the dashed curve and the suggested parameterization equations are shown by the solid curve.

STANDING GRAVITY WAVES IN DEEP WATER

Gérard Iooss*, Pavel Plotnikov†, John F.Toland‡,
* *IUF, INLN UMR CNRS-UNSA 6618, 1361, route des Lucioles, 06560 Valbonne, France*
† *Lavryentyev Inst. of Hydrodynamics, Lavryentyev pr. 15, Novosibirsk 630090, Russia*
‡ *Dept. of Mathematical Sciences, University of Bath, Bath BA2 7AY, UK*

Summary The two dimensional standing gravity wave problem, for an infinitely deep layer, is considered, based on the formulation of the problem as a second order non local PDE (see (1)). Despite the infinitely many resonances in the linearized problem we use the Nash-Moser implicit function theorem for proving the existence of standing waves corresponding to values of the amplitude ε having 0 as a Lebesgue point.

INTRODUCTION

We consider an infinitely deep layer of a perfect incompressible fluid, in two-dimensional potential motion under gravity, with a free surface without surface tension. We are interested in *solutions which are periodic in time and in the horizontal direction, and invariant under reflexion in the vertical axis.* The existence of solutions in the finite depth case were proved recently by Plotnikov and Toland in [5]. The problem we consider below has the additional difficulty to be infinitely degenerate at the linearized level, as noticed a long time ago (Poisson (1816), Boussinesq (1877), Rayleigh (1915)).

The formulation we take for the standing wave problem is the one introduced in Dyachenko et al [2], where w is a function of (x,t), both even and $2\pi-$ periodic in x and t. In the following we denote by $\mathcal{H}$ the spatial periodic Hilbert transform. The equation satisfied by w is a *second order nonlocal partial differential equation*, which may be written as follows (see [2] and [4])

$$\mathcal{F}(w,\mu) \stackrel{def}{=} \partial_t(L_{w'}\dot{w}) - \mu\mathcal{H}w' + \mathcal{H}\partial_x\left\{\frac{1}{D}\mathcal{H}(L_{w'}\dot{w}\mathcal{H}L_{w'}\dot{w}) + (\mathcal{H}L_{w'}\dot{w})\mathcal{H}\left(\frac{1}{D}L_{w'}\dot{w}\right)\right\} = 0, \tag{1}$$

where a dot means a partial time (t) derivative, and a prime means a partial space (x) derivative ∂_x, and where

$$L_{w'}f = (1+\mathcal{H}w')f - w'\mathcal{H}f, \quad D = (1+\mathcal{H}w')^2 + w'^2,$$

and μ is the bifurcation parameter $\mu = gT^2/2\pi\lambda$, where T is the time period, λ is the spatial period, and g is the gravitational acceleration. With these equations, the free surface is given parametrically in physical coordinates (ξ,η) by

$$(\xi,\eta) = (x+\mathcal{H}w(x,t), -w(x,t)); \quad (x,t)\in\mathbb{R}^2.$$

The formulation (1) is equivalent to the classical formulation for sufficiently smooth solutions. We notice that $w = const$ is always a solution, and that we can look for solutions of (1) with zero average. Let us define for $m \geq 0$ suitable (Sobolev) spaces of doubly periodic functions

$$H^{m,ee}_{\natural\natural} = \{w \in H^m\{(\mathbb{R}/2\pi\mathbb{Z})^2\};\ w \text{ is even in } x \text{ and in } t,\ w \text{ has zero average}\},$$

Then, for $m \geq 3$, $\mathcal{F}$ is an analytic map from $H^{m,ee}_{\natural\natural}\times\mathbb{R}$ to $H^{m-2,ee}_{\natural\natural}$ and the linearization of (1) at the origin reads

$$\mathcal{L}_\mu u \stackrel{def}{=} D_w\mathcal{F}(0,\mu)u = \ddot{u} - \mu\mathcal{H}\partial_x u.$$

If μ is irrational, the kernel of $\mathcal{L}_\mu$ in $H^{m,ee}_{\natural\natural}$ is $\{0\}$. For $\mu = 1$ the kernel of $\mathcal{L}_1$ in $H^{m,ee}_{\natural\natural}$ is the *infinite-dimensional subspace* $E_0 \cap H^{m,ee}_{\natural\natural}$, with $E_0 = span\{A_q\cos q^2x\cos qt; A_q\in\mathbb{R},\ \ q\in\mathbb{N}\}$. For other rational values of μ, the infinite dimensional kernel of $\mathcal{L}_\mu$ is easily deduced from E_0. For $f \in H^{m,ee}_{\natural\natural}$ which is orthogonal to E_0 in $L^2_{\natural\natural}$, there is a unique $u \in H^{m,ee}_{\natural\natural}$, orthogonal to E_0 in $L^2_{\natural\natural}$, which is solution of $\mathcal{L}_1 u = f$.

Since the pseudo-inverse of $\mathcal{L}_1$ is not regularizing and since the nonlinear terms in (1) lose 2 degrees of regularity, we need to adapt the Nash-Moser implicit function theorem for the bifurcation problem.

MAIN RESULTS

A suitable choice of scales allows to only consider μ close to 1. It is then known that approximate solutions of the standing wave problem exist up to an arbitrary power of ε, where $\mu = 1+\varepsilon^2/4$. More precisely we have the following

Theorem 1 *There are infinitely many approximate solutions w of (1) under the form of asymptotic expansions in powers of the amplitude ε of the wave*

$$w_\varepsilon^{(N)} = \sum_{1\leq n\leq N} \varepsilon^n w^{(n)},\ \mu = 1+\varepsilon^2/4,\ w^{(1)} = \sum_{q\in I} \frac{\varepsilon_q}{q^2}\cos q^2 x \cos qt,\ \varepsilon_q = \pm 1,\ I\subset \mathbb{N},$$

with any finite subset I of $\mathbb{N}$, moreover $w_\varepsilon^{(N)}$ is such that $\mathcal{F}(w_\varepsilon^{(N)}, 1+\varepsilon^2/4) = \varepsilon^{N+1}Q_\varepsilon$, where Q_ε is bounded in any $H^{m,ee}_{\natural\natural}$ when $\varepsilon\to 0$ (see [1] for $I=\{1\}$, [3] for the general result).

Our main result is the following

Theorem 2 *For $m\geq 17$, $N\geq 4$ and $\varepsilon_0>0$ small enough, there is a measurable set $\mathcal{E}\subset(0,\varepsilon_0)$, with 0 as a Lebesgue point (hence dense at 0), i.e.*

$$(1/r)meas\{\mathcal{E}\cap(0,r)\}\to 1 \text{ as } r\to 0, \tag{2}$$

such that for any $\varepsilon\in\mathcal{E}$ and $\mu = 1+\varepsilon^2/4$, there exists a solution w of $\mathcal{F}(w,\mu)=0$ in $H^{m,ee}_{\natural\natural}$, whose asymptotic expansion is $w_\varepsilon^{(N)}$, with $w^{(1)}=\cos x\cos t$ and $||w-w_\varepsilon^{(N)}||_{H^m} = O(\varepsilon^{N-1})$ (see the complete proof in [6]).

Remark 1: Same theorem holds when we take any rational value of μ, instead of 1.

Remark 2: Theorem 2 also holds for most of the other type of asymptotic form $w_\varepsilon^{(N)}$ of the solution w, indicated at theorem 1, provided that a generally satisfied algebraic condition holds on the subset I of integers. Notice that in this case the set $\mathcal{E}$ of "good values" of ε may depend on the form of $w^{(1)}$ (see [7]).

SKETCH OF PROOF

Since there are infinitely many formal solutions, we need to specialize the solution we are looking for in searching for $\underline{w}$ of order 1, defined by

$$w = w_\varepsilon^{(N)} + \varepsilon^{N-1}\underline{w},\ N\geq 4,\ \mu = 1+\varepsilon^2/4 \tag{3}$$

and the equation to solve is now

$$\mathcal{F}(w_\varepsilon^{(N)} + \varepsilon^{N-1}\underline{w}, 1+\varepsilon^2/4) = 0. \tag{4}$$

The proof of Theorem 2 relies on the possibility to invert the linear operator $\mathcal{A}_w$ (approximate linearized operator at a non zero point), defined for any u in $H^{s,ee}_{\natural\natural}$ by

$$\partial_w\mathcal{F}(w,1+\varepsilon^2/4)u = \mathcal{A}_w u + \Gamma(\mathcal{F},u)$$

where $\Gamma(\mathcal{F},u)$ cancels when w is a solution of $\mathcal{F}(w,1+\varepsilon^2/4)=0$. The main result is that we are able to invert $\mathcal{A}_w$ for $\underline{w}$ bounded in $H^{m,ee}_{\natural\natural}$, $m\geq 17$, in controling a *diophantine condition on* two functions of ε arising after averaging, along the Newton iteration scheme used in the Nash-Moser theorem. This inverse operator satisfies

$$||\mathcal{A}_w^{-1}||\leq c/\varepsilon^2 \tag{5}$$

in the space $\mathcal{L}(H^{s,ee}_{\natural\natural}, H^{s-2,ee}_{\natural\natural})$, $s\geq 2$, which shows a loss of two derivatives and a bound which grows like ε^{-2} as $\varepsilon\to 0$. For obtaining such a result, suitable for proving theorem 2, we manage a succession of change of coordinates and change of variables in the spirit of the work [5], except the first change of coordinates which reduces all second order derivatives occuring in $\mathcal{A}_w$ to a single second order derivative in t. The other key point is that we are able to invert explicitely the main order ε^2 of the "bifurcation part" of the linear equation $\mathcal{A}_w u = f$ in the infinite dimensional subspace $E_0\cap H^{m,ee}_{\natural\natural}$, which introduces the factor $1/\varepsilon^2$ in the bound (5) of $\mathcal{A}_w^{-1}$, while the control of the diophantine condition leads to the loss of the two derivatives.

References

[1] C.J.Amick, J.F.Toland. The semi-analytic theory of standing waves. Proc. Roy. Soc. Lond. A 411 (1987), 123-138.
[2] A.I.Dyachenko, E.A.Kuznetsov, M.D.Spector, V.E.Zakharov. Physics Lett. A **221** (1996), 73-79.
[3] G.Iooss. On the standing wave problem in deep water. J.Math. Fluid Mech. 4 (2002), 155-185.
[4] G.Iooss, J.F.Toland. Riemann-Hilbert and variational structure for standing waves. Far East J. Appl. Math., 15 (2004) 3, 345-376.
[5] P.I.Plotnikov, J.F.Toland. Nash-Moser theory for standing water waves. Arch. Rat. Mech. Anal. **159**, (2001) 1-83.
[6] G.Iooss, P.I.Plotnikov, J.F.Toland. Standing waves on an infinitely deep perfect fluid under gravity. Preprint INLN, 03/ 2004 (112 p.).
[7] G.Iooss, P.I.Plotnikov. Existence of multimodal standing gravity waves. Preprint 07/2004.

NONLINEAR THREE-DIMENSIONAL FREE SURFACE FLOWS IN FINITE AND INFINITE DEPTH

Emilian Părău*, Jean-Marc Vanden-Broeck*, Mark J. Cooker*
*School of Mathematics, University of East Anglia, Norwich, NR4 7TJ, UK

Summary Boundary integral equation methods are used to calculate steady three-dimensional potential free surface flows. The formulation uses Green's functions and generalises the work of Forbes [1] to finite depth. Accurate numerical results are presented for free surface flows generated by moving disturbances such as distributions of pressure, ships and submerged objects.

INTRODUCTION

In the last hundred years, important progress has been achieved in the calculation of two dimensional free surface flows. Numerical solutions to nonlinear three dimensional potential free surface flows have also been calculated, but most of them solve model equations or use algorithms which solve the time dependent formulation of the problem. An extensive review of the computations of nonlinear free-surface flows is given by Tsai & Yue [2]. Here iterative methods are presented to solve directly the steady fully nonlinear problem.

FORMULATION

We present the method in the case of a three-dimensional distribution of pressure moving at a constant velocity U at the surface of a fluid of finite depth h. We choose a frame of reference moving with the pressure distribution and assume that the flow is steady. We introduce cartesian coordinates x, y, z with the z-axis directed vertically upwards and the x-axis in the opposite direction of the velocity U. We denote by $z = \zeta(x, y)$ the equation of the free surface. The potential function $\Phi(x, y, z)$ satisfies Laplace equation

$$\nabla^2 \Phi = 0, \qquad x, y \in \mathbf{R}, z < \zeta(x, y), \tag{1}$$

in the flow domain.

The kinematic boundary condition, the dynamic boundary condition, the bottom boundary condition and the radiation condition can be written as

$$\Phi_x \zeta_x + \Phi_y \zeta_y = \Phi_z, \quad z = \zeta(x, y), \tag{2}$$

$$\frac{1}{2}(\Phi_x^2 + \Phi_y^2 + \Phi_z^2) + g\zeta + \frac{p}{\rho} = \frac{U^2}{2}, \quad z = \zeta(x, y), \tag{3}$$

$$\Phi_z = 0 \qquad \text{on } z = -h. \tag{4}$$

$$\text{no waves} \quad \text{as} \quad x \to -\infty. \tag{5}$$

Green's second identity holds in three dimensions, where V represents a volume bounded by the surface δV

$$\int_V (\alpha \Delta\beta - \beta \Delta\alpha) dV = \int_{\delta V} (\alpha \frac{\partial \beta}{\partial n} - \beta \frac{\partial \alpha}{\partial n}) ds. \tag{6}$$

By using the three-dimensional Green function which satisfies (4)

$$G(P, Q) = \frac{1}{4\pi} \left(\frac{1}{((x - x^*)^2 + (y - y^*)^2 + (z - z^*)^2)^{1/2}} + \frac{1}{((x - x^*)^2 + (y - y^*)^2 + (z + z^* + 2h)^2)^{1/2}} \right) \tag{7}$$

where $P = (x, y, z), Q = (x^*, y^*, z^*)$, we obtain

$$2\pi(\Phi(Q) - x^*) = \int\int_{S_F} ((\Phi(P) - x) \frac{\partial G(P, Q)}{\partial n_P} - G(P, Q) \frac{\partial}{\partial n_P} (\Phi(P) - x)\, ds_P \tag{8}$$

where S_F is the free surface. This equation is projected in the $x - y$ plane.

We present results by choosing the pressure as $p(x, y) = \begin{cases} P_0 e^{\frac{L^2}{(x^2 - L^2)} + \frac{L^2}{(y^2 - L^2)}}, & |x| < L \text{ and } |y| < L \\ 0, & \text{otherwise} \end{cases}$.

We introduce dimensionless variables by using U as the unit velocity and L as the unit length. Combining equations (2) and (3) and using the chain rule of calculus we obtain

$$\frac{1}{2} \frac{(1 + \zeta_x^2)\phi_y^2 + (1 + \zeta_y^2)\phi_x^2 - 2\zeta_x \zeta_y \phi_x \phi_y}{1 + \zeta_x^2 + \zeta_y^2} + \frac{\zeta}{F_L^2} + \varepsilon P = \frac{1}{2} \tag{9}$$

where $F_L = U/(gL)^{1/2}$ and $\varepsilon = \frac{P_0}{\rho U^2}$. When the depth is finite we use the Froude number based on depth $F = U/(gh)^{1/2} = F_L/\sqrt{H}$ where $H = h/L$.

The singularities in the equation (8) can be isolated and evaluated in closed form (see Forbes [1]). The numerical sheme to solve the equations (9) and (8) is similar to the one used in Părău and Vanden-Broeck [3], where the problem is discretized by using finite differences and the resulting algebraic equations are solved by Newton's method. Extensions of the numerical procedure to other disturbances (ships and submerged objects) will be discussed in the talk.

RESULTS

Various numerical results will be presented. We include here examples for the free surface flow generated by a moving distribution of pressure. In infinite depth the wake and the two different families of waves (transverse waves and short-length divergent waves) can be easily observed. The transverse waves are perpendicular to the direction of the velocity (i.e. the x-axis). The divergent waves have crests roughly parallel to the direction of velocity, moving outward. When F_L increases the amplitude of the divergent waves becomes more important than that of the transverse waves. The wavelength of the transverse waves increases with the Froude number. Nonlinear solutions can be calculated close to the maximum height of waves allowed by Bernoulli's equation.

In finite depth, when $F < 1$, the wave–pattern is similar to the case of infinite depth, but when $F > 1$ the transverse waves disappear and the angle of the outer waves decreases with F (see Fig. 1).

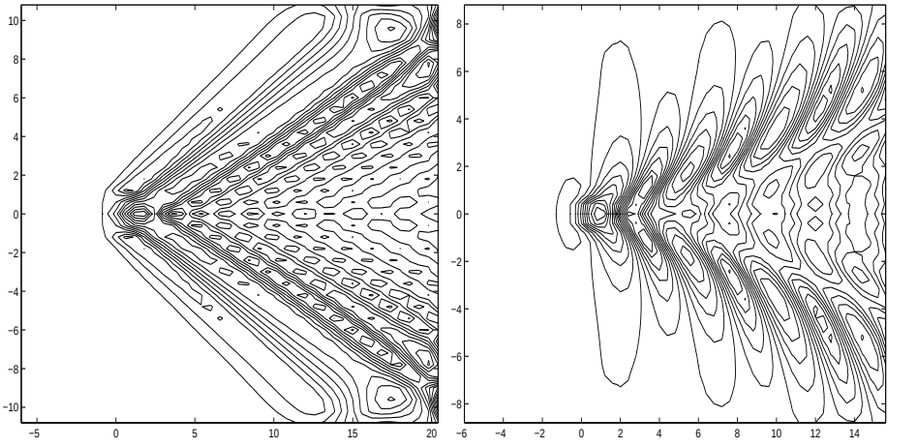


Figure 1: The wake in the cases $F > 1$ (left) and $F < 1$(right). In both cases $\varepsilon = 1$.

The algorithm can be easily modified to include two or more pressure distributions and to study the interaction of the wakes produced by each of them. The V-shape of the waves downstream becomes in that case a W-shape. This can be viewed as the wave interactions between ships moving in parallel in deep water.

CONCLUSION

We have calculated three-dimensional free surface flows generated by moving disturbances in a fluid of finite or infinite depth. Accurate fully nonlinear solutions have been obtained.

References

[1] L. K. Forbes, An Algorithm for 3-Dimensional Free-Surface Problems in Hydrodynamics, *Journal of Computational Physics* 82 (1989) 330-347.

[2] W. T. Tsai, D. K. Yue, Computation of nonlinear free-surface flows, *Ann. Rev. Fluid Mech.* 28 (1996) 249-278.

[3] E. Părău, J.-M. Vanden-Broeck – Nonlinear two- and three- dimensional free surface flows due to moving disturbances, *Eur. J. Mechanics B/Fluids*, **21**, 6 (2002), 643-656.

XXI ICTAM, 15–21 August 2004, Warsaw, Poland

DYNAMICS OF CRESCENT WAVE PATTERNS IN A CHANNEL

D. Fructus*, C. Kharif**, D. Clamond*, M. Francius**, Ø. Kristiansen*, J. Grue*
*Mechanics Division, Department of Mathematics, University of Oslo, Norway
**Institut de Recherche sur les Phénomènes Hors-Equilibre, Technopôle de Château-Gombert, 49 Rue Frédéric Joliot-Curie, B.P 146, 13384 Marseille Cedex 13, France.

Summary Solving the full set of water wave equations, we perform numerical simulations of evolution of class II instabilities. We reproduce the well known steady horse-shoe patterns and the oscillating ones. For small initial steepness, we identify the existence of a recurrence cycle. We further study the feasibility of experimental observation of such patterns and give an explanation for the selection mechanism.

INTRODUCTION

Instabilities of plane Stokes wave have been studied for many decades. For infinite water depth, modulational instability is dominant for small to moderate initial steepness $(ak)_0$ and leads to a recurrence phenomena for small initial wave steepness $(ak)_0$ and to breaking otherwise[1]. While another class of instability characterized by its three-dimensionality (Mc Lean class II) dominates for larger values of $(ak)_0$ [5,6,7]. This instability leads usually to wave breaking through formation of spilling breakers[9]. The presence of surfactants on the free surface of the flow may cancel the modulational instability, however. Making possible the development of class II instabilities even for small $(ak)_0$. Similarly, for shallow water cases, instabilities of a plane Stokes wave may be dominated by class II [6].

We use hence a numerical model to solve the full set of water wave equations and focus our attention onto the evolution of class II instabilities in the absence of modulational instabilities. We give numerical evidence that the class II instabilities may give rise to a recurrence phenomena similar to the Fermi-Pasta-Ulam recurrence, for small $(ak)_0$, and to breaking otherwise. Analysis of the evolution of several class II perturbation allows us a close comparison with experimental data, including the well known steady horse-shoe patterns[9] and the newly discovered oscillating horse-shoe[2].

The match is impressively good and a further study of the last patterns allows us to suggest an explanation for the selection mechanism that may be responsible for trigging this instability in the case of the Collard and Caulliez[2] experiment (this resonant quintet is theoretically never the dominant one over the class II). We give explanation of the selection mechanism and simulate the experiment.

NUMERICAL EXPERIMENTS

We compute the elevation η of non-overturning surface waves in water of infinite depth using a three-dimensional fully nonlinear method [3,4]. Application of potential theory is assumed. The resulting Laplace equation is inverted by use of Green's theorem and Fourier transform, resulting in a fast numerical algorithm that solve the full set of equations. A special attention is put upon identification of breaking.

In the first step, we compute the elevation $\bar{\eta}$ of an exact plane Stokes waves of steepness $(ak)_0$, where $2a$ is the distance from trough to crest. The frequency of the waves is $\omega_0 = \omega(k_0)$. A small perturbation, $\widehat{\eta}$ of the wave surface, taking the form $\widehat{\eta} = \epsilon a \sin[(1+p)k_0 x]\cos(qk_0 y)$, is added to the Stokes wave train. Here, ϵ is a small number, making the amplitude of the initial perturbation field a fraction of the Stokes waves. $(1+p,q)k_0$ denotes the wavevector. A perturbation velocity potential corresponding to the perturbation surface is computed and added to the initial potential field.

RESULTS

The chosen perturbation corresponds to one of the class II unstable modes according to the McLean diagram for the considered wave amplitude. A three dimensional horse-shoe pattern develops in the numerical tank. Depending on the wave amplitude and on the chosen initial perturbation, either the steady horse-shoes or oscillating patterns appear. While the steady horse-shoe pattern exhibits a steady shape, organized in chess-like order, the new one is characterized by aligned crescents oscillating in time (fig. 2). The spectrum of the wave field shows wave frequencies for the steady wave pattern with $n\omega_0$ and $(2n-1)\omega_0/2$, $n = 1, 2, ...,$. The wave frequencies of the new wave pattern are: $n\omega_0$, and $\sim \frac{4}{3}\omega_0$, $\sim \frac{5}{3}\omega_0$,$\sim \frac{7}{3}\omega_0$,$\sim \frac{8}{3}\omega_0$, etc. Those results together with geometrical comparisons agree well with experimental observations of Su[9] and of Collard and Caulliez[2].

When considering several initial perturbations, all corresponding unstable modes develop and coexist together, the importance of each one depending on its initial amplitude, leading to a chaotic behavior and eventually to breaking.

For small values of $(ak)_0$ (typically $(ak)_0 < 0.17$), the patterns are characterized by a periodic evolution from plane stokes waves into crescent shaped patterns. This recurrence phenomena is similar to the Fermi-Pasta-Ulam recurrence for modulational instability (fig. 1 illustrates this recurrence for the steady patterns). For larger value of $(ak)_0$, the evolution of the perturbation leads to wave breaking.

A further analysis of Collard and Caulliez[2] experiments bring us to suggest a scenario for the appearance of the oscillating patterns. The effect of the wavemaker in a confined channel may generate, through parametric resonance, cross-waves[8]. Nonlinear self-interaction yield to the excitation of high harmonics of the cross-waves. Unstable modes of the class II lying on those eigenmodes are then trigged. An important point is the role of high transverse wavenumbers.

We numerically reproduce the development of steady horse-shoe patterns for an initial steepness $(ak)_0 = 0.13$ and of oscillating patterns for $(ak)_0 = 0.17$ in the same channel while taking the same initial perturbations, in perfect agreement with experimental setup and results.

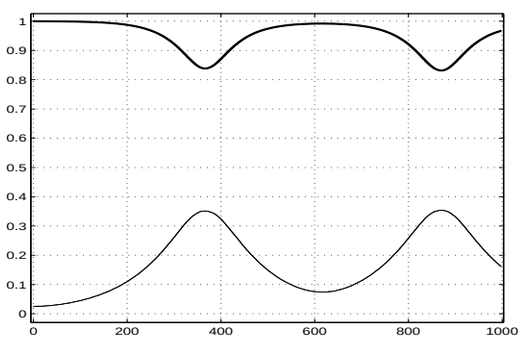


Figure 1. Typical energy evolution for the main modes corresponding to a recurrence cycle ($(ak)_0 = 0.13$), fundamental (thick line) $(k_0, 0)$ and perturbation $(1.5k_0, q)$.

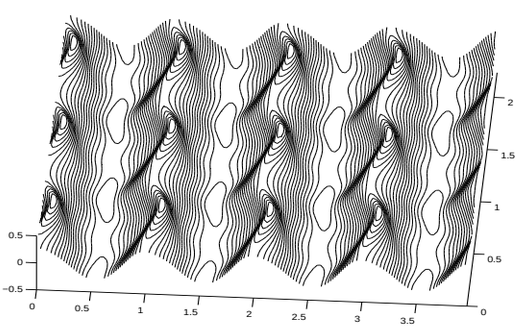


Figure 2. Free surface elevation of oscillating horse-shoe pattern.

References

[1] M. Banner and X. Tian, *J. Fluid Mech.*, 1998, **367**, 107
[2] F. Collard and G. Caulliez, *Phys. Fluids, Letters*, 1999, **11**, 3195-3197
[3] D. Clamond and J. Grue, *J. Fluid Mech.*, 2001, **447**, 337
[4] J. Grue, *Applied Ocean Res.*, 2002, **24**, 261-274
[5] C. Kharif, R. Pontier and C. Skandrani, *Personal communication*, 2000.
[6] C. Kharif and M. Francius, *Proc. conf. geophys. turb.*, Univ. de Toulon et du Var, 2003.
[7] J. W. McLean, *J. Fluid Mech.*, 1982, **114**, 315
[8] J. Miles and J. Becker, *J. Fluid Mech.*, 1988, **186**, 129
[9] M. Y. Su *J. Fluid Mech.*, 1982, **124**, 73-108

EVOLUTION OF PACKETS OF SURFACE GRAVITY WAVES OVER SMOOTH TOPOGRAPHY

E.S. Benilov, J.D. Flanagan, C.P. Howlin
University of Limerick, Ireland

INTRODUCTION

The dynamics of surface gravity waves over bottom topography is one of the classical problems of fluid mechanics. It has been thoroughly studied in various formulations, including linear/weakly-nonlinear monochromatic waves and shallow-water solitons (see Mei 1983 and references therein). However, an important particular case has been overlooked, as there seems to be virtually no results on shoaling of wave packets – which omission seems even stranger, if one recalls the significance of this problem for oceanography. The only exception is the paper by Barnes & Peregrine (1995), who showed that the behaviour of a shoaling packet is quite different to that of a monochromatic wave. It turned out that the amplitude of the former is much lower than that of the latter, as the packet tends to spread out – and this effect is more marked for slowly-varying topography. However, no quantitative results were obtained, which would link the parameters of the packet to the bottom topography over which it travels.

The present paper addresses this omission.

SURFACE WAVES OVER SMOOTH TOPOGRAPHY

Consider surface gravity waves in a channel with an uneven bottom. We shall assume that both topography and waves are one-dimensional, i.e. the depth H of the basin and the elevation η of the surface depend on a single horizontal coordinate, x (η also depends on the time t). We shall further assume that all our variables are non-dimensionalized using the mean depth H_0 and the acceleration due to gravity, g.

In this paper, we are concerned with weakly nonlinear, quasi-monochromatic waves (packets), which can be characterized by a frequency ω. If the bottom was flat, ω would correspond to a certain value of the wavenumber k, determined by the dispersion relation of surface gravity waves,

$$\omega^2 = k \tanh kH. \tag{1}$$

If H depends on x (uneven bottom), (1) can still be used as a means of determining k – which, however, will now depend on x (i.e. the frequency of the wave is fixed, while its wavenumber changes as it propagates over topography, see Djordjevic & Redecopp 1978). To justify the use of (1) for an uneven bottom, $H(x)$ should be a slowly-changing function of x, i.e. its spatial scale should be much larger than the wavelength $2\pi k^{-1}$.

Under these assumptions, the packet can be represented by

$$\eta(x,t) = \mathrm{Re}\left\{A(x,t)\,\exp\left[i\int k(x)\,dx - i\omega t\right]\right\},$$

where $A(x,t)$ is a slowly-varying function, governed by a modified nonlinear Schrödinger (MNS) equation (Djordjevic & Redecopp 1978):

$$i\left(\frac{\partial A}{\partial x} + \frac{1}{c_g}\frac{\partial A}{\partial t} + \mu A\right) + \alpha\frac{\partial^2 A}{\partial t^2} + \beta A\left|A\right|^2 = 0. \tag{2}$$

In this equation, c_g is the group velocity of surface gravity waves and

$$\alpha = \frac{1}{2\omega c_g}\left(\frac{2\omega H\tanh kH}{c_g} + 1 - \frac{H}{c_g^2}\right), \qquad \beta = \frac{1}{2\omega^3 c_g}\left\{3k^4 + 2\omega^4 k^2 - \omega^8 - \frac{\left[2\omega k - c_g\left(\omega^4 - k^2\right)\right]^2}{H - c_g^2}\right\},$$

$$\mu = \frac{\left(1-\tanh^2 kH\right)\left(1 - kH\tanh kH\right)}{\tanh kH + kH\left(1-\tanh^2 kH\right)}\frac{d\left(kH\right)}{dx}.$$

Observe also that the MNS equation (2) is written in the form, where the spatial coordinate x is the "evolutionary" variable (which role is usually played by t).

ASYMPTOTIC ANALYSIS

If the bottom is flat, the coefficients of (2) become constant and, provided that $\alpha\beta > 0$, (2) admits an exact solution describing steadily propagating envelop soliton,

$$A = \sqrt{\frac{2\alpha}{\beta}}\lambda\,\mathrm{sech}\,\lambda\tau\,\exp\left(\frac{iv\tau}{2\alpha} + \frac{4i\lambda^2 x}{4+v^2}\right), \tag{3}$$

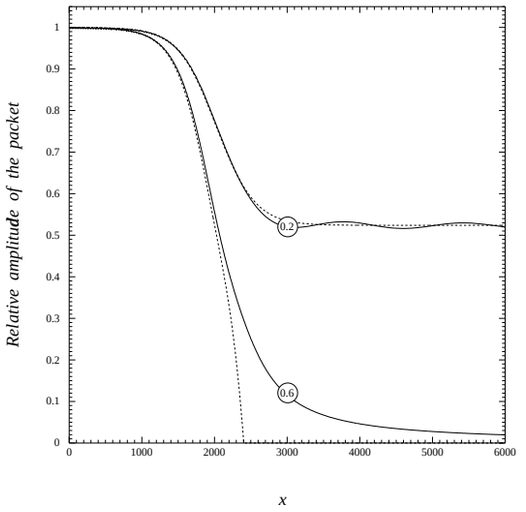


Figure 1. The evolution of wave packet over topography (5) (the curves are marked with the corresponding values of ΔH). The numerical solution of equation (2) is shown in solid line, the asymptotic solution (4) is shown in dotted line.

where $\tau = t - \left(c_g^{-1} + v\right) x$, and λ and v are arbitrary parameters. Observe that the amplitude of the wave packet is proportional to λ, whereas λ^{-1} is the width of the packet. Finally, v characterizes the packet's translation speed.

If the depth of the channel varies with x, but the horizontal scale of this variability is larger than the width of the packet, we can still assume the solution of (2) to be close to (3), but the parameters of (3), λ and v, should depend now on x. A straightforward asymptotic procedure results in the following "conservation law" for λ:

$$\frac{4\alpha\lambda}{\beta}\left(\tanh kH + kH\,\mathrm{sech}^2\, kH\right) = \mathrm{const}\,. \tag{4}$$

EXAMPLES AND DISCUSSION

We shall illustrate the use of (4) by the following example. Let the depth of the channel be

$$H(x) = 1 - \Delta H\ \tanh\left[0.002\ (x - 2000)\right], \tag{5}$$

which describes a step-like depth variation, of amplitude ΔH and width $(0.002)^{-1}$, located at $x = 2000$. The initial values of the packet are $k = 2$, $\lambda = 0.1$ at $x = 0$. First, we shall consider a small depth variation, $\Delta H = 0.2$, and calculate the evolution of the packet's amplitude using formula (4) – see Fig. 1. Remarkably – unlike linear waves or shallow-water solitons (see Mei 1983) – the amplitude of the shoaling packet decreases! This tendency was observed in all examples considered.

We have also present the results for a stronger depth variation, $\Delta H = 0.6$ (see Fig. 1), with all other parameters being the same as before. In this case, the asymptotic formula (4) predicts that, at $x \approx 2400$, the packet's amplitude vanishes and its width becomes infinite – which essentially means that the packet disintegrates.

To understand why this occurs, note that, at $kH = 1.363$, the nonlinearity coefficient β of the MNS equation vanishes. Note also that, as follows from (4), λ must vanish together with β. Hence, if $H(x)$ becomes sufficiently small, kH reaches the critical value, and the amplitude of the packet vanishes. Beyond this point, $\alpha\beta < 0$ – and the packet may no longer exist as a coherent solitary wave. Not dwelling on the details, we remark that a simple formula can be derived, relating the critical depth to the frequency of the packet: $H_{cr} \approx 1.195\,\omega^{-2}$. Thus if $H(x) > H_{cr}$, the packet passes over the depth variation as a coherent solitary wave – and disintegrates otherwise.

To verify the above conclusions, the exact MNS equation (2) has been simulated numerically using the psedospectral method. The results demonstrated that the agreement between the asymptotic and numerical solution is quite good (see Fig. 1). Finally, note that, strictly speaking, the asymptotic equation (4) is not applicable near the critical point. We shall not discuss this question in further detail, but refer the reader to the paper by Malomed & Shrira (1991).

References

[1] Barnes T., Peregrine D.H.: Wave groups approaching a beach: Full irrotational flow computations. *Proc. Coast. Dyn.*: 950–962, 1995.
[2] Djordjevic V.D., Redecopp L.G.: On the development of packets of surface gravity waves moving over an uneven bottom. *J. Appl. Math. Phys. (ZAMP)* **29**: 950-962, 1978.
[3] Malomed B.A., Shrira V.I. Soliton caustics. *Physica D* **53**: 1–12, 1991.
[4] Mei C.C. *The Applied Dynamics of Ocean Surface Waves*, Wiley, 1983.

Three dimensional gravity water waves

Walter Craig *
Department of Mathematics and Statistics
McMaster University, Hamilton L8S 4K1, Canada

Abstract

Three dimensional gravity water waves are ubiquitous, and of importance to physical oceanography and marine engineering. Yet being a complex nonlinear process the study of water waves remains a rich source of mathematical problems, whose answers can be of relevance to ocean scientists. My presentation concerns the form of three dimensional traveling water waves, contrasting the geometry of waves over deep water with the shallow water regime. In particular, solutions typically occur in two-parameter bifurcation families, which can have complex secondary bifurcations in resonant situations. The rigorous mathematical theory will be compared with numerical computations and controlled laboratory experiments. I will also discuss the existing stability theory, especially of the deep water case.

This paper is concerned with stationary patterns in free surface water waves, which is a classical topic in the fluid dynamics of the ocean surface. Descriptions of two dimensional progressive wavetrains date to at least the time of Stokes, and a rigorous mathematical existence theory was initiated by Levi-Civita [7]. The relevence of these wave forms to observation depends upon their stability to three dimensional perturbations, a topic which is taken up in McLean's two fundamental papers [8][9]. A two dimensional solution of the water wave problem gives rise of course to a three dimensional pattern, namely one which is constant in a second horizontal independent variable. More interesting cases are given by genuinely three dimensional patterns, which is a topic of current research interest, addressed in part in the papers [2][3] of Craig & Nicholls. Solutions arise in two dimensional parameter families, in a bifurcation problem for surfaces whose two governing parameters are the components of the horizontal phase velocity of the solution. An interesting variety of wave patterns emerges, with a distinct change in character between deep water progressive watetrains and wave patterns in shallow water [10]. Again the relevance of these solutions to observations depends upon their stability. Recent experimental observations of such three dimensional wave patterns in deep water are described by Hammack, Henderson & Segur [5]. The goal of the present paper is to describe analytical and numerical results on the stability, or indeed the metastability of the progressive wave patterns given in [2][3][10], as a functions of the principal parameters, namely the mean depth, the aspect ratio of the fundamental horizontal period, steepness, and perhaps most importantly, the particular bifurcation component of the solution. Related stability results in those of Ioualalen, Roberts and Kharif [6].

Our analysis is based on the description of the water waves problem as a Hamiltonian system given by Zakharov [12]. Using the Dirichlet-Neumann operator to express the equations of motion, a convenient form of the Hamiltonian is given in Craig & Sulem [4],

$$H(\eta,\xi) = \int_{\mathbf{T}^2} \tfrac{1}{2}\xi G(\eta)\xi + \tfrac{g}{2}\eta^2\, dx \ , \tag{1}$$

where g is the acceleration due to gravity, $y = \eta(x,t)$ gives the free surface, $\xi(x,t) = \varphi(x,\eta(x,t),t)$ represents the boundary values of the velocity potential on the free surface, and the Dirichlet-Neumann operator [1] is expressed by $G(\eta)\xi dx = N \cdot \nabla\varphi dS$. The torus $\mathbf{T}^2 = \mathbf{R}^2/\Gamma$ is the periodic

*Research partially supported by the Canada Research Chairs Program and the NSERC through grant number 238452-01

fundamental domain of the wave pattern in question. The components of the horizontal momenta for $j = 1, 2$ are given by

$$I_j(\eta, \xi) = \int_{\mathbf{T}^2} \eta \partial_{x_j} \xi \, dx \ . \tag{2}$$

Because the evolution equations take Hamilton's canonical form $\partial_t \eta = \delta_\xi H$, $\partial_t \xi = -\delta_\eta H$, progressive wave patterns follow the classical Lagrange multiplier rule that

$$\delta H = c \cdot \delta I \tag{3}$$

which is to say that the traveling wave patterns are critical points of the Hamiltonian functional (1) for fixed horizontal momenta (2). This forms the basis for a theory of multiplicity of solution branches of progressive waves [3], and in the presence of surface tension a rigorous existence theory [2].

Questions of linear stability involve the linearization of (3) about a traveling wave solution, in a frame of reference moving with the wavetrain. Writing $(\delta\eta, \delta\xi)^T = \exp(\sigma t) v(x)$, $v(x) = (w, z)^T(x)$, the linearization is written

$$\sigma \begin{pmatrix} w \\ z \end{pmatrix} = \begin{pmatrix} \delta^2_{\eta\xi} H & \delta^2_{\eta\eta} H \\ -\delta^2_{\eta\eta} & -\delta^2_{\eta\xi} \end{pmatrix} \begin{pmatrix} w \\ z \end{pmatrix} \ . \tag{4}$$

This is an eigenvalue problem for pairs v, σ analogous to the Floquet-Bloch band theory of quantum electrons in a crystal lattice. Setting boundary conditions on the fundamental domain $\mathbf{T}^2$ to be $v(x + \gamma) = \exp(ip \cdot \gamma) v(x)$ for all $\gamma \in \Gamma$, we obtain band functions $(v(x; p), \sigma(p)), p \in (\mathbf{T}^2)' = \mathbf{R}^2/\Gamma'$ as solutions to the eigenvalue problem (4). Here Γ' is the dual lattice to $\Gamma \subseteq \mathbf{R}^2$ which determines the periodic fundamental domain. Band functions $\sigma(p)$ with nontrivial real components signify instabilities of the progressive wave pattern at wavenumber p. Given a numerically computed progressive wave pattern, the band functions $\sigma(p)$ and their associates eigenfunctions $v(x; p)$ are computed numerically for indications of such three dimensional instabilities.

References

[1] R. Coifman and Y. Meyer. Nonlinear harmonic analysis and analytic dependence. In *Pseudodifferential operators and applications (Notre Dame, Ind., 1984)*, pp. 71–78. Amer. Math. Soc., 1985.

[2] W. Craig and D. Nicholls. Traveling two and three dimensional capillary gravity water waves. *SIAM: Mathematical Analysis* 32:323–359, 2000.

[3] W. Craig and D. Nicholls. Traveling gravity water waves in two and three dimensions. *Euro. J. Mech. B - Fluids* 21-6:615–641, 2002.

[4] W. Craig and C. Sulem. Numerical simulation of gravity waves. *J. Comp. Phys.*, 108:73+, 1993.

[5] J. Hammack, D. Henderson and H. Segur. Deep-water waves with persistent two-dimensional surface patterns. submitted to J. Fluid Mech. (2003).

[6] M. Ioualalen, A. J. Roberts and C. Kharif. On the observability of finite-depth short-crested water waves. *J. Fluid Mech.* 322:1–19, 1996.

[7] T. Levi-Civita. Détermination rigoreuse des ondes permanentes d'ampleure finie *Math. Annalen*, 93:264–314, 1925.

[8] J.W. McLean. Instabilities of finite amplitude water waves. *J. Fluid Mech.* 114:315–330, 1982.

[9] J.W. McLean. Instabilities of finite amplitude gravity waves on water of finite depth. *J. Fluid Mech.* 114:331–341, 1982.

[10] D. Nicholls. On Hexagonal Gravity Water Waves. *Mathematics and Computers in Simulation* 55:567–575, 2001.

[11] P. Plotnikov. Nonuniqueness of solutions of the problem of solitary waves and bifurcation of critical points of smooth functionals. *Math USSR Izv.* 38:333-57, 1992.

[12] V. E. Zakharov. Stability of periodic waves of finite amplitude on the surface of a deep fluid. *Journal of Applied Mechanics and Technical Physics*, 9:190+, 1968.

SHARPENING AND BREAKING OF SUBHARMONIC GRAVITY WAVES ON DEEP WATER

Vasyl P. Lukomsky[1], Ivan S. Gandzha[1], Yaroslav V. Tsekhmister[2]

[1] *Institute of Physics, National Academy of Sciences, Kyiv, Ukraine*;
[2] *Bogomoletz National Medical University, Kyiv, Ukraine*;
lukom@iop.kiev.ua / Fax: 38–044–2651589

The purpose of the present work is to investigate the process of sharpening and formation of singular flows in symmetric and non-symmetric subharmonic gravity waves that have a period m times greater than the period of Stokes waves. Subharmonic waves are excited due to subharmonic instabilities of Stokes waves and have the crests of different height, as was at first established by Chen and Saffman [1] for symmetric waves and by Zufiria [3] for non-symmetric waves.

Potential two-dimensional gravity waves and related fluid flows in the case of ideal fluid are governed by the following set of equations

Laplace equation: $$\Delta\Phi = 0\,;\quad -\infty < y < \eta(\theta)\;; \tag{1}$$

Bernoulli equation: $$-c\Phi_\theta + \frac{1}{2}(\Phi_\theta^2 + \Phi_y^2) + \eta = 0\,,\quad y = \eta(\theta)\,; \tag{2}$$

Kinematic condition: $$-c\eta_\theta - \Phi_y + \eta_\theta\Phi_\theta = 0\,,\quad y = \eta(\theta)\,; \tag{3}$$

$$\Phi_y = 0\,,\quad y = -\infty\,; \tag{4}$$

where $\Phi = \Phi(\theta, y)$ is the velocity potential, $\eta(\theta)$ is the elevation of the free surface, c is the phase speed, $\theta = x - ct$ is the wave phase.

The velocity potential and the elevation of the free surface are looked for in the form of the following truncated Fourier series:

$$R(\theta, y) = \sum_{n=1}^{mN} \xi_{\frac{n}{m}} \exp\left(\frac{n}{m}(y + i\theta)\right),\quad \Phi = -ic(R - R^*)\,; \tag{5}$$

$$\eta(\theta) = \sum_{n=-mM}^{mM} \eta_{\frac{n}{m}}\, e^{i\frac{n}{m}\theta}\,,\ \eta_{-\frac{n}{m}} = \eta_{\frac{n}{m}}^*\,; \tag{6}$$

the coefficients $\eta_{n/m}$ and $\xi_{n/m}$ being real for symmetric waves and complex for non-symmetric waves. The equations of motion are thereby reduced to a system of non-linear algebraic equations for the coefficients of the expansions and the wave phase speed, which is solved by Newton's iterations.

The following results were obtained.

1. The calculations of Chen and Saffman [1] and Simmen and Saffman [2], where integrodifferential equation in the inverse plane formulation was solved, were reproduced using Fourier expansions in the plane of physical variables, the bifurcation points from the Stokes branch having been calculated up to m = 10. Then the subharmonic branches for m = 2, 3, 5 were traced up to limiting subharmonic waves.

2. Irregular flows beyond limiting subharmonic waves were investigated. These are the flows with stagnation point inside the flow domain and discontinuous streamlines near the wave crests. The horizontal water velocities in such wave crests exceed the speed of the crests themselves, as was established by the authors in the case of Stokes waves [4]. Irregular subharmonic flows were found to originate in the following way. Streamlines become discontinuous only in the highest sharp crests while the flow in all other crests (that are still rounded and have much lesser amplitude) remains regular (see Figure 1 for the case m = 2). Irregular flows produce a simple model for describing the initial stage of the formation of spilling breakers when a localized jet is formed at the crest following by generating whitecaps.

The following two alternatives for the exact solutions associated with approximate irregular flows were singled out [5]: (i) the profile of an exact solution is continuous with sharp corner at the crest (a discontinuous first derivative) similar to the limiting Stokes wave but is of lesser steepness; (ii) the profile of an exact solution has two symmetric finite discontinuities in the vicinity of the wave crest and is not single-valued. An additional set of stagnation points is found to exist above the crest area of almost limiting waves supporting the conjecture of Grant [6] that the 120° singularity of the limiting wave is formed of several coalescing 90° singularities.

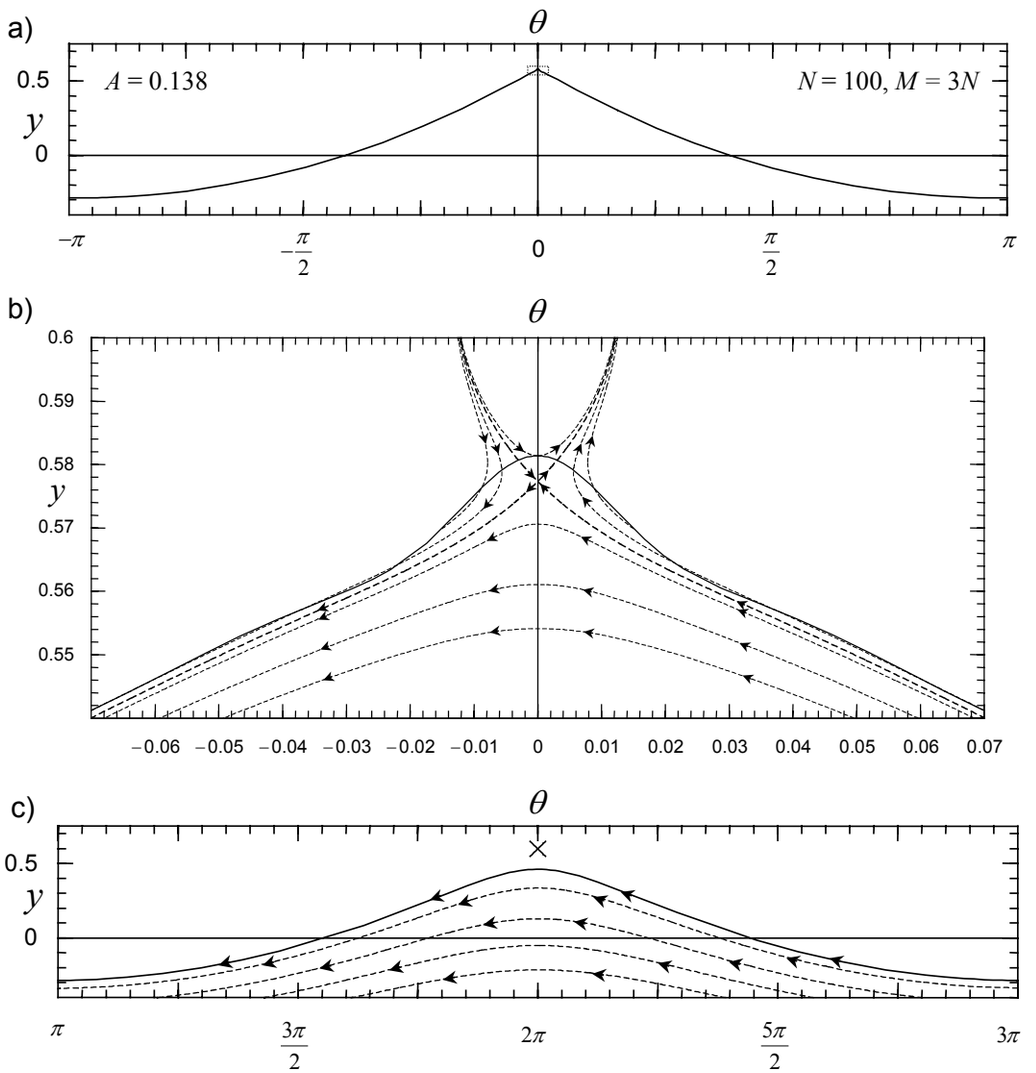


Figure 1. The subharmonic irregular flow of order $m = 2$: a) an *irregular* sharp crest; b) the irregular flow in the vicinity of the irregular crest; c) a *regular* rounded crest.

3. The effect of non-symmetry of subharmonic waves was found to be more essential with wave sharpening. Non-symmetry can lead directly to wave breaking and formation of subharmonic irregular flows. This produces a good model for describing storm waves with crests of variable height (a ninth roll). In such waves, large-amplitude breaking crests are usually preceded by a number of rounded gentle crests of lesser amplitude.

References

[1] B. Chen and P. G. Saffman. Numerical evidence for the existence of new types of gravity waves of permanent form on deep water, *Stud. Appl. Math.*, 1980, **62**, 1–21.

[2] J. A. Simmen and P. G. Saffman. Steady deep-water waves on a linear shear current, *Stud. Appl. Math.*, 1985, **73**, 35–57.

[3] Z. Zufiria. Non-symmetric gravity waves on water of infinite depth, *J. Fluid Mech.*, 1987, **181**, 17–39.

[4] V. P. Lukomsky, I. S. Gandzha, D. V. Lukomsky. Steep sharp-crested gravity waves on deep water, *Phys. Rev. Lett.*, 2002, **89**, 164502.

[5] V. P. Lukomsky, I. S. Gandzha. Fractional Fourier approximations for potential gravity waves on deep water, *Nonlinear Processes in Geophysics*, 2003, **10**, 599–614.

[6] M. A. Grant, The singularity at the crest of a finite amplitude progressive Stokes wave, *J. Fluid Mech.*, 1973, **59**, 257–262.

SHORT WIND WAVES AND SURFACE WIND DRIFT

Xin Zhang

Institution of Oceanography,UCSD, La Jolla, CA92093-0213, USA

Summary The problem of short wind waves propagate on surface wind drift is considered here. The convergence of piecewise linear approximation for solving Rayleigh instability equation is proved. The method is numerically efficient and highly accurate. Applying this method, linear stability diagrams of various boundary flows are examined. It is also used to validate the applicability of other approximate approaches to the problem of propagation of short waves on wind drift shear. (*Acknowledgment:* This work is supported by the National Science Foundation. OCE0118028).

Under the assumption of small monochromatic surface waves on a steady horizontally uniform surface shear of an inviscid fluid, the governing equation becomes the well-known Rayleigh equation. The exact analytical solutions are found for a very limited number of current profiles. For arbitrary current profiles, approximate solutions are used[1,2]. The conditions for these approximations may be violated in the case of short wind waves on wind drift shear. As an alternative approach, the piecewise linear approximation (PLA) is explored.

THE CONVERGENCE OF THE PIECEWISE LINEAR APPROXIMATION

A continuous shear profile is approximated by constant vorticity layers. It is convenient to assume an uniform layer thickness, Δz. At the layer interfaces, the piecewise linear velocities are chosen to match the corresponding continuous shear velocities. Our PLA solution to the Rayleigh equation is an expansion series in powers of the layer thickness:

$$W(z) = W^{(0)}(z) + (\Delta z)^1 W^{(1)}(z) + (\Delta z)^2 W^{(2)}(z) + \ldots$$

The boundary conditions at free surface and the bottom are the same for all the orders[2], so does the velocity continuity across the layer interfaces. At the zeroth order, the vorticity jump condition holds at layer interfaces. However, at the higher orders, there is an additional term from lower order residue as underlined below:

$$(c-\gamma U_i)[W^{(m)}'(z_i+\frac{\Delta z}{2}) - W^{(m)}'(z_i-\frac{\Delta z}{2}) + \underline{W^{(m-1)}}] = -\gamma[U'(z_i+\frac{\Delta z}{2}) - U'(z_i-\frac{\Delta z}{2})]W^{(m)}(z_i), \quad m>0, \ \Delta z \to 0$$

where γ is a non-dimensional scaling factor, c is the surface wave speed, z_i is the position of a layer interface, and U_i is the velocity value at z_i. $'$ denotes for vertical differentiation. The difference between finite difference of U' of PL velocity and that of $\mathcal{U}'(z)$ of the continuous profile is at an order of $(\Delta z)^2$:

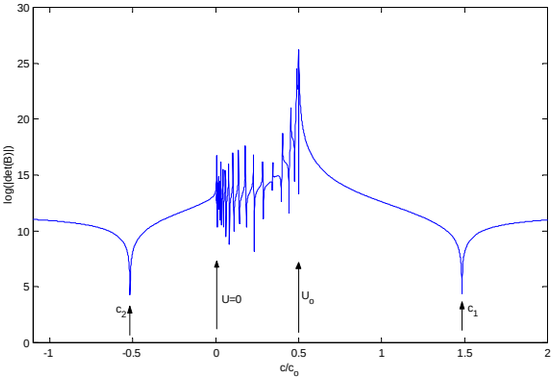
$$[U'(z_i+\frac{\Delta z}{2}) - U'(z_i-\frac{\Delta z}{2})] = [\mathcal{U}'(z_i+\frac{\Delta z}{2}) - \mathcal{U}'(z_i-\frac{\Delta z}{2})] + \mathcal{O}\left(\Delta z^2\right)$$

If $W^{(m)}'(z)$ is continuous at $z=z_i$ as $\Delta z \to 0$, and the second derivative, $W^{(m)}''(z)$, at the layer interfaces also becomes well-defined at the limit, then, we can show:

$$(c-\gamma\mathcal{U})\left(W^{(0)}''+W^{(0)}\right) + \gamma\mathcal{U}''W^{(0)} = 0 \quad z=z_i$$

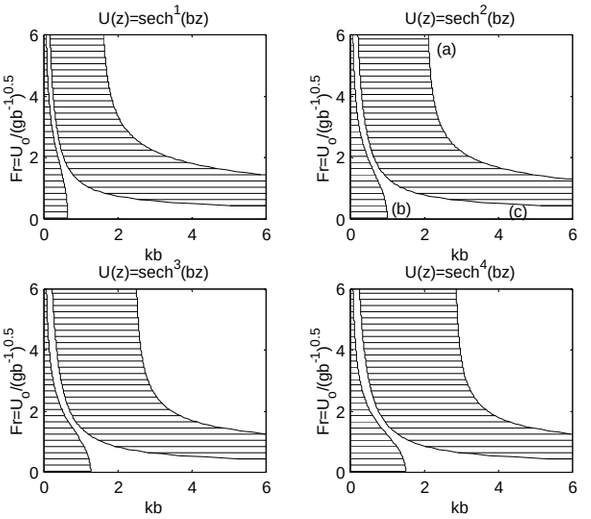
Although, the higher order terms become insignificant as $\Delta z \to 0$, they are necessary only to uphold the convergence. For an eigen value problem, if c is an eigen value admitted for both of the continuous and PL systems, then, the solution is unique subject to the same surface and bottom boundary conditions.

The PLA solution can be found by solving a homogenous algebra equation: $[B]W = 0$, and the dispersion relation is defined by $\det[B] = 0$. The left figure shows the logarithm of absolute value of $\det[B]$ evaluated at real values of wave speed c for a $\mathrm{sech}^2(z)$ surface shear profile. In the figure, $c = \pm 1$ correspond the wave speeds of linear waves in still water (normalized). The roots of the dispersion relation are at the dips in the figure where the determinant changes sigh when it crosses zero. The shear current is in the range of [0 .5]. Normally, there are two roots that are associated with nature surface waves, c_1, c_2, with c_1 travels along and c_2 travels against the current. The other roots are those modes whose phase speeds equal the current speed at some depth, $c-\gamma U(z_c) = 0$.



$U'' = 0$ everywhere except at the layer interfaces for PLA, while there are normaly only a limited number of inflection points for a realistic shear profile. It has been shown by Yih[3] that neutral solutions are not allowed at non-inflection points for most of the boundary flows. Many neutral solutions from the PLA are artificial because of the real $\mathcal{U}''(z_c) \neq 0$. One has to be very cautious in applying the PLA in the range of $U_{\min} \le c \le U_{\max}$.

THE NEUTRAL MODES OF CERTAIN SURFACE SHEAR FLOWS



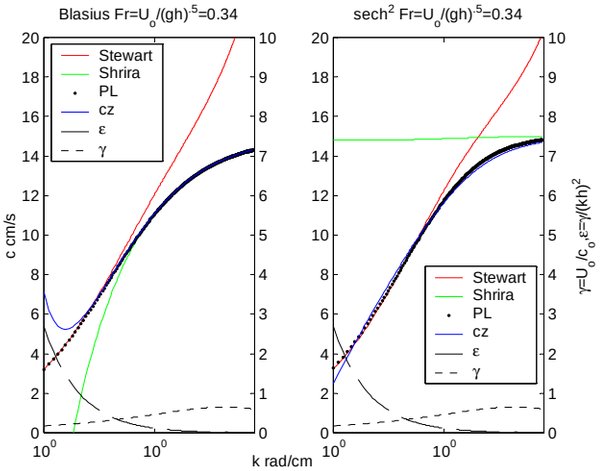
The instability of a horizontal shear flow with a free surface has important applications to the study of surface wakes of ships or near water surface bodies; to the stability of the crest of a spilling wave breaker; and to wind-drift currents. There are only a few cases that analytic solutions are found, thus, it largely depends on elaborated numerical calculations to solve for realistic surface shear profiles.
A well-studied case is the linear instability of a shear flow with a velocity profile in the form of $\mathcal{U}=\mathcal{U}_o\mathrm{sech}^2(bz)$. This profile has been numerically studied [4,5] to fit experimental data of the surface shear flow in a wake of a hydrofoil. For the linear instability analysis, the neutral modes form the stability boundaries in the wavenumber and Froude number space (k, Fr). In addition, an analytic solution is found for neutral modes at the inflection points[6]. Knowing the valid eigen value c_s for the continuous current profiles, the corresponding wavenumber and waveform can be very precisely calculated by PLA. In the figure above, the linear stability diagram for surface gravity waves are shown for the family profiles of $\mathcal{U}=\mathcal{U}_o\mathrm{sech}^n(bz)$. For $n=2$, PLA accurately matches with the analytic calculation[6]. Here the Froude number is defined as $Fr=\mathcal{U}_o/\sqrt{gD}$, $D=b^{-1}$. The curves (a) and (b) are the lico of the neutral solution associated with velocity $c=\gamma\mathrm{sech}^n\left[\tanh^{-1}\left(\sqrt{1/n}\right)\right]$, and the curve (c) the locus of the neutral solution with $c=0$. The shaded regions are the unstable regions. The linear stability diagrams for other boundary shear flows, such as $\mathcal{U}=\mathcal{U}_o(1-\tanh(b(y/D)^2)$, exponential, error function, and Blasius profile, are also examined with and without including surface tension.

PROPAGATION OF SHORT WIND WAVES ON WIND DRIFT

The mechanism that modifies the propagation of surface waves by currents is well understood. However, the applications are so far still limited to the simple velocity profiles. First of all, it is not an easy task to measure the profile of the surface currents in most cases. Secondly, our calculations on propagation speed rely heavily on the perturbation approximations which may not hold for short waves. With PLA, we are able to calculate the wave propagation speed accurately for a given realistic surface flow profile, thereby, to test perturbation approximations.
Also, an implicit expression for the wave speed can be found by integrate the equation from the bottom to the surface:

$$c=U_o-c_o\frac{k}{\kappa}\left[\frac{U_o'}{2c_ok}\pm\sqrt{\frac{\kappa}{k}+\left(\frac{U_o'}{2c_ok}\right)^2}\right] \quad \text{where } \kappa=\int_{-\infty}^{0}dz\left[\left(\frac{W'}{W(0)}\right)^2+\left(\frac{W}{W(0)}\right)^2\left(k^2+\frac{U''}{U-c}\right)\right].$$

A suitable trail function is $W\doteq W(0)e^{kz}$, which yields: $\kappa=k+\int_{-\infty}^{0}dz\left(e^{2kz}\frac{U''}{U-c}\right)$. Figure below is an example of different shear profiles with their Froude numbers close to the case of 5 m/s wind speed estimated from Wu's laboratory measurements[7]. Stewart approximation holds well for long waves while Shrira's approximation is good for high wavenumbers (the first order approximation only). Our approximation fits well in a wider wavenumber range. However, a better physical justification is needed.



References

[1] Stewart, R. H. & Joy, J. W. *Deep-Sea Res.* 21, 1039-1049,1974.
[2] Shrira, V. I. *JFM* 252, 565-584, 1993.
[3] Yin, C. S. *JFM* 51, 209-220, 1972
[4] Triantyfallou, G. S. & Dimas, A. A. *Fhys. Fluids* A 1, 1813-1821, 1989
[5] Dimas, A. A. & Triantyfallou, G. S. *JFM* 260, 211-246, 1994
[6] Engevik, L. *JFM* 406, 337-346, 2000
[7] Wu, J. *JFM* 68, 49-70, 1975

TRANSVERSE INSTABILITY OF SURFACE SOLITARY WAVES

Takeshi KATAOKA , Michihisa TSUTAHARA
Graduate School of Science and Technology, Kobe University, Rokkodai, Nada, Kobe 657-8501, Japan

Summary The linear stability of finite-amplitude surface solitary waves with respect to long-wavelength transverse perturbations is examined by the asymptotic analysis for small wavenumbers of perturbations. The instability criterion is explicitly derived, and it is newly found that there exist transversely unstable surface solitary waves for the amplitude-to-depth ratio of over 0.713. This critical ratio is well below that for the one-dimensional instability (=0.781) obtained by Tanaka [1].

INTRODUCTION

The one-dimensional stability (stability to perturbations that depend only on the main wave's travelling direction) of small-amplitude solitary waves without surface-tension effects was first examined by Jeffrey & Kakutani[2] in the framework of the celebrated Koreweg-de Vries (KdV) equation. Then, these waves were found to be one-dimensionally stable. The transverse stability (stability to perturbations that depend both on the main wave's travelling direction and its transverse direction) was examined first by Kadomtsev & Petviashvili[3]. Then it was found that the small-amplitude solitary waves are also stable to transverse perturbations (see Refs.[4-6]).

The stability of finite-amplitude solitary waves was first examined by Tanaka[1]. He investigated the one-dimensional stability of surface solitary waves numerically, and found that an exchange of stability occurs at their first stationary point of the total energy. The critical amplitude-to-depth ratio is 0.781. Tanaka et al.[4] also conducted numerical simulation of the time development of perturbed solitary waves, and the growth rate of sufficiently small perturbations was found to agree with that of the linear stability analysis.

In contrast, it is only recently that the study on the transverse stability of finite-amplitude solitary waves was initiated. Bridges[7] examined the linear stability of surface solitary waves to long-wavelength transverse perturbations, and found no solitary waves that are transversely unstable. According to his analysis, the surface solitary waves are at the neutral stability to transverse perturbations of small wavenumbers. However, his analysis is based on the leading-order effect of the small wavenumbers only. The higher-order effects therefore, determine the stability.

In the present study, these higher-order effects are investigated. Then, we newly reveal that there exist transversely unstable surface solitary waves. The critical amplitude-to-depth ratio for the transverse stability is found to be 0.713, which is well below that for the one-dimensional stability (=0.781).

LINEAR STABILITY ANALYSIS

Basic equations

Consider the irrotational flow of an incompressible ideal fluid of undisturbed depth D with free surface under the uniform gravitational acceleration g. The set of basic equations is the usual Laplace equation for the velocity potential under the boundary conditions at the bottom (the impermeable condition) and those on the free surface (the kinetic and dynamic conditions). The effects of surface tension are neglected. In what follows, all variables are non-dimensionalized using D and g. Introducing the Cartesian coordinate $x-y-z$ with z pointed vertically upward and its origin placed on the undisturbed free surface, we seek a solution of the following form:

$$\phi = -\mathrm{v}\xi + \Phi_s(\xi, z) + \hat{\phi}(\xi, z)\exp(\lambda t + \mathrm{i}\varepsilon y), \qquad (\xi = x - \mathrm{v}t) \tag{1a}$$

$$\eta = \eta_s(\xi) + \hat{\eta}(\xi)\exp(\lambda t + \mathrm{i}\varepsilon y), \tag{1b}$$

where ϕ is the velocity potential and η is the vertical displacement of the free surface. $-\mathrm{v}\xi + \Phi_s$ and η_s represent the steady propagation of solitary wave solution at constant speed v in the positive x direction against a uniform flow of constant velocity $-\mathrm{v}$. The remaining terms in (1a,b) represent linear perturbations, where ε is a given real constant and λ is a real or a complex constant. The value of λ is determined by solving the following eigenvalue problem for the linear perturbations $\hat{\phi}$ and $\hat{\eta}$, which is obtained by substituting (1a,b) into the basic equations and linearizing with respect to $\hat{\phi}$ and $\hat{\eta}$:

$$\partial^2\hat{\phi}/\partial\xi^2 + \partial^2\hat{\phi}/\partial z^2 = 0, \tag{2a}$$

with the boundary conditions:

$$\partial\hat{\phi}/\partial z = 0 \quad \text{at} \quad z = -1, \tag{2b}$$

$$\left(-\frac{\partial}{\partial z} + \frac{d\eta_s}{d\xi}\frac{\partial}{\partial\xi}\right)\hat{\phi} + \left[\frac{\partial^2\Phi_s}{\partial\xi^2} + \frac{\partial^2\Phi_s}{\partial\xi\partial z}\frac{d\eta_s}{d\xi} + \left(-\mathrm{v} + \frac{\partial\Phi_s}{\partial\xi}\right)\frac{d}{d\xi}\right]\hat{\eta} = -\lambda\hat{\eta} \quad \text{at} \quad z = \eta_s, \tag{2c}$$

$$\left[\left(-\mathrm{v} + \frac{\partial\Phi_s}{\partial\xi}\right)\frac{\partial}{\partial\xi} + \frac{\partial\Phi_s}{\partial z}\frac{\partial}{\partial z}\right]\hat{\phi} + \left[\left(-\mathrm{v} + \frac{\partial\Phi_s}{\partial\xi}\right)\frac{\partial^2\Phi_s}{\partial\xi\partial z} + \frac{\partial\Phi_s}{\partial z}\frac{\partial^2\Phi_s}{\partial z^2} + 1\right]\hat{\eta} = -\lambda\hat{\phi} \quad \text{at} \quad z = \eta_s. \tag{2d}$$

Note that the solitary wave solution is unstable if there exists a localized solution of (2a-d) whose λ possesses the real positive part. In prior study, the stability with respect to perturbations that have no dependence on y (the case of

$\varepsilon = 0$), or the one-dimensional stability was examined numerically by Tanaka[1] as mentioned in the introduction. According to his study, the condition for the solitary waves to be one-dimensionally stable is to satisfy

$$dE/d\mathrm{v} > 0\,, \tag{3}$$

where E is the total energy of the solitary wave.

Here we investigate the transverse stability, or the stability with respect to perturbations that depend not only on the ξ direction but also on the y direction, of one-dimensionally stable solitary wave that satisfies the condition (3). For the sake of analytical convenience, we make an asymptotic analysis for small ε to examine the stability to long-wavelength transverse perturbations.

Stability analysis to long-wavelength transverse perturbations

We seek an asymptotic solution of (2a-d) for small ε in the following power series of ε :

$$\hat{\phi} = \hat{\phi}_0 + \varepsilon\hat{\phi}_1 + \varepsilon^2\hat{\phi}_2 + \cdots, \quad \hat{\eta} = \hat{\eta}_0 + \varepsilon\hat{\eta}_1 + \varepsilon^2\hat{\eta}_2 + \cdots, \quad \lambda = \varepsilon\lambda_1 + \varepsilon^2\lambda_2\,. \tag{4}$$

Substituting the series (4) into (2a-d) and arranging the same-order terms in ε , we obtain a series of equations for $\hat{\phi}_n$ and $\hat{\eta}_n$ ($n = 0,1,2,\cdots$). At the leading-order (or $n = 0$), the equations are homogeneous and they possess the following leading-order solution: $\hat{\phi}_0 = \partial\Phi_s/\partial\xi$, $\hat{\eta}_0 = d\eta_s/d\xi$.

From the next orders (or $n = 1,2,3,\cdots$), the equations for $\hat{\phi}_n$ and $\hat{\eta}_n$ are inhomogeneous. Since their homogeneous part has the nontrivial solution $(\hat{\phi}_0, \hat{\eta}_0)$, their inhomogeneous terms must satisfy the solvability condition to have a solution. From this condition, the values of λ_1 and λ_2 are determined. Specifically, at $n = 1$, the solvability condition is identically satisfied. At $n = 2$, it becomes

$$\left(\lambda_1^2/\mathrm{v}\right)dE/d\mathrm{v} = -\int_{-\infty}^{\infty} d\xi \int_{-1}^{\eta_s} \left(\partial\Phi_s/\partial\xi\right)^2 dz\,. \tag{5}$$

This corresponds with the first-order criterion used by Bridges[7]. Recalling that we have assumed that the solitary wave solution satisfies the condition (3), the real part of λ_1 is zero from (5) so that the stability of the solitary wave solution is not determined at this order. To know the stability, we must proceed to the next order.

At $n = 3$, the solvability condition gives

$$\lambda_2 = \begin{cases} \pm Q & \text{if } Q < 0, \\ \text{no solution} & \text{if } Q > 0, \end{cases}' \tag{6}$$

where

$$Q = \frac{\mathrm{v}}{2}\left[I + \lambda_1^2 \frac{d}{d\mathrm{v}}\left(\frac{I}{\mathrm{v}}\right)\right]\frac{d}{dE}\left(I - \frac{2T}{\mathrm{v}}\right), \tag{7}$$

and I is the impulse, and T is the kinetic energy of the solitary wave. Thus, we have a solution of the eigenvalue problem (2a-d) whose λ possesses the real positive part (or $\lambda_2 = -Q$) when $Q < 0$. That is, the solitary wave solution is unstable to long-wavelength transverse perturbations when $Q < 0$.

Now we apply the instability criterion $Q < 0$ to the solitary wave solution, which is calculated by the numerical method described in Ref.[1]. We found that the function $I + \lambda_1^2 d(I/\mathrm{v})/d\mathrm{v}$ included in Q is always positive. In Fig.1, therefore, $I - 2T/\mathrm{v}$ is plotted as a function of E . If this function takes negative gradient for the one-dimensionally stable range of $dE/d\mathrm{v} > 0$, the corresponding wave is transversely unstable. The circle in the figure represents the point of $dE/d\mathrm{v} = 0$, or the amplitude-to-depth ratio $z_{\max}$ of 0.781, and the solitary wave is one-dimensionally stable for v smaller than that of the circle (or the upper branch from the circle in Fig.1). We see that the function $I - 2T/\mathrm{v}$ takes negative gradient from the cross to the circle. Therefore, there exist solitary waves that are one-dimensionally stable but are transversely unstable in this range. The cross in Fig.1 represents the critical point for the transverse stability, and its amplitude-to-depth ratio $z_{\max}$ is 0.713, which is well below that for the one-dimensional stability $z_{\max} = 0.781$.

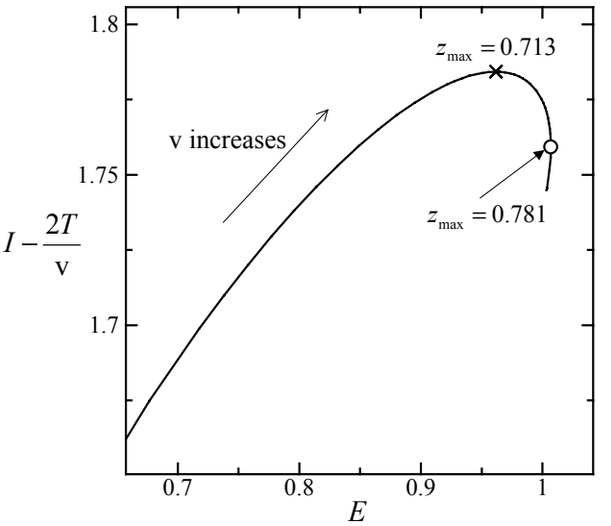


Fig.1 $I - 2T/\mathrm{v}$ as a function of E .

References

[1] Tanaka, M: *Phys. Fluids* **29**:650-655, 1986.
[2] Jeffrey, A., Kakutani, T.: *Indiana Univ. Math.* **20**: 463-468, 1970.
[3] Kadomtsev, B.B., Petviashvili, V.I.: *Sov. Phys. Dokl*. **15**: 539-541, 1970.
[4] Tanaka, M. et al.: *J. Fluid Mech.* **185**, 235-248, 1987.
[5] Zakharov, V.E.: *JETP Lett.* **22**: 172-173, 1975.
[6] Alexander et al.: *Phys. Lett. A* **226**: 187-192, 1997.
[7] Bridges, T.J.: *J. Fluid Mech.* **439**: 255-278, 2001.

A LAGRANGIAN APPROACH TO WAVE-INDUCED OCEANIC MASS TRANSPORT

Jan Erik Weber
Department of Geosciences, University of Oslo
P. O. Box 1022, Blindern, N-0315 Oslo, Norway

Summary The mean mass transport induced by surface gravity waves is investigated theoretically for a deep, rotating ocean with a constant eddy viscosity. The waves are periodic in space, and have amplitudes that grow or decay slowly in time. The analysis is based on a Lagrangian description of motion, and the results are valid to second order in the wave steepness. Various oceanic applications are discussed.

INTRODUCTION

It is well-known that surface water waves carry mean momentum [1]. For monochromatic waves in a viscous non-rotating fluid, the pioneering paper is [2]. For a direct Lagrangian approach to wave drift in a rotating ocean, earlier treatments of this problem are found in papers such as [3], [4], and [5]. Also the generalized Lagrangian-mean formulation in [6] can be applied to this problem. When the wind is blowing over the sea, it exerts a mean stress along the sea surface. This stress may balance the Coriolis force to yield an Ekman transport in the oceanic surface layer. The Ekman transport, and the vertical motion associated with the horizontal convergence or divergence of this transport, is crucial for the understanding of the general ocean circulation. However, the wind will also generate surface waves, and with the present-day modeling tools, e.g. [7], the surface wind wave spectrum is well resolved. One of the remaining problems, as far as the ocean circulation is concerned, is to determine in a realistic way the mass flux induced by the wind waves. In [8] this problem has been investigated for time-periodic waves with spatially-varying amplitudes. We here study the similar problem for surface waves with amplitudes that decay or grow slowly in time.

MATHEMATICAL FORMULATION

Wave momentum is related to particle motion in waves, and is most conveniently discussed by using a Lagrangian description of motion. We consider plane waves that propagate along the x-axis in a Cartesian coordinate system, where the x- and y-axes are situated at the undisturbed horizontal sea surface. The z-axis is vertical, and directed upwards. Our system rotates with constant angular velocity $f/2$ about the vertical axis, where f is the Coriolis parameter. The ocean is incompressible, and we apply an eddy assumption for the turbulent Reynolds stresses. We here consider deep-water surface gravity waves. A fluid particle is associated with its initial coordinates (a, b, c). The particle position at later times (X, Y, Z) and the pressure P will then be functions of a, b, c, and time t. Velocity components and accelerations are given by (X_t, Y_t, Z_t), and (X_{tt}, Y_{tt}, Z_{tt}), respectively, where subscripts denote partial differentiation. In a Lagrangian description the free material surface is given by $c = 0$. For plane waves along the x-axis, the deviations (x, y, z, p) from the initial state will not depend on b. We then may write

$$X = a + x(a,c,t),\ Y = b + y(a,c,t),\ Z = c + z(a,c,t),\ P = -\rho g c + p(a,c,t),$$

where ρ denotes the constant density and g is the acceleration due to gravity. For convenience, we introduce a complex horizontal velocity $W = x_t + iy_t$, where i is the imaginary unit. With the present notation, the momentum equations become to second order in wave steepness

$$W_t + ifW - \nu\nabla_L^2 W = -\frac{1}{\rho}(p+\rho g z)_a - \frac{1}{\rho}J(p,z) + \nu\{J(W_a,z) + J(x,W_c) + J(W,z)_a + J(x,W)_c\},$$

$$z_{tt} - \nu\nabla_L^2 z_t = -\frac{1}{\rho}(p+\rho g z)_c - \frac{1}{\rho}J(x,p) - gJ(x,z) + \nu\{J(z_{ta},z) + J(x,z_{tc}) + J(z_t,z)_a + J(x,z_t)_c\}.$$

Here ν is the constant turbulent eddy viscosity, and $\nabla_L^2 \equiv \partial^2/\partial a^2 + \partial^2/\partial c^2$ is the Laplacian operator in Lagrangian coordinates. Furthermore, $J(A,B) \equiv A_a B_c - A_c B_a$ is the Jacobian. Finally, the conservation of mass (here volume) leads to

$$x_a + z_c = -J(x,z).$$

We consider wave motion that is periodic in space, and average our variables over one wavelength. When we generalize, and move from considering a single wave component to a fully developed wind sea, this process must be understood as an ensemble mean. Denoting the averaging process by an over-bar, and integrating the averaged horizontal momentum equations from a depth *H*, where the motion and the stresses vanish, to the surface, we obtain

$$\frac{d}{dt}\int_{-H}^{0}\rho\overline{W}dc + if\int_{-H}^{0}\rho\overline{W}dc = \rho\nu\overline{W}_c(c=0) - F_w \,. \qquad \text{(I)}$$

Here $\overline{W}_c(c=0)$ depends on the external stresses and the physical conditions at the sea surface [9]. When the viscous effect of the air is neglected, we find that $\overline{W}_c(c=0)=0$, e.g. [2]. F_w in (I) contains all the nonlinear terms in the horizontal momentum equation. For wind waves with frequencies much higher than *f*, we may write

$$F_w = \int_{-H}^{0}\{(\overline{p}+\rho g\overline{z})_a + \overline{J(p,z)} - \rho\nu(\overline{J(x_{ta},z)} + \overline{J(x,x_{tc})} + \overline{J(x_t,z)}_a + \overline{J(x,x_t)}_c)\}dc.$$

MAIN RESULT AND DISCUSSION

Inserting for the linear, real, deep-water wave field (denoted by the symbol ~), with frequency ω, growth rate β, wave number k and initial amplitude ζ_0 [9] (neglecting the effect of the fluctuating tangential wind stress) into the right-hand side of (I), we find for the wind- and wave-induced complex Lagrangian mean mass transport

$$\frac{d}{dt}\int_{-H}^{0}\rho\overline{W}dc + if\int_{-H}^{0}\rho\overline{W}dc = \tau_E + \tau_D \,. \qquad \text{(II)}$$

Here τ_E denotes the mean tangential (Ekman) wind stress component, and τ_D is the form drag given by

$$\tau_D \equiv -\overline{\tilde{\sigma}\tilde{z}_a}, \quad c=0 \,,$$

where $\tilde{\sigma}$ is the real part of the fluctuating wind-stress normal to the sea surface. In the present formulation we find

$$\tau_D = \frac{d}{dt}M + 2\rho\nu k^2\omega\zeta_0^2\exp(2\beta t) \,. \qquad \text{(III)}$$

Here $M = \frac{1}{2}\rho\omega\zeta_0^2\exp(2\beta t)$ is the total horizontal wave momentum. (It may be obtained by integrating the Stokes drift in the vertical, [2]). We note that in the absence of wind, we have $\tau_D = 0$, or $\beta = -2\nu k^2$ for temporally decaying waves, and hence the total wave-induced mass transport is zero when averaged over the inertial period [9]. Various aspects of (II) related to growing and decaying (breaking) waves are discussed. For example, when generalized to a statistically steady sea state $(\beta = 0)$, empirical models for τ_D in (III) can be used to relate the turbulent bulk eddy viscosity in the water to the properties of the wave spectrum and the wind speed.

References

[1] Stokes, G. G.: On the theory of oscillatory waves. *Trans. Cambridge Phil. Soc*. **8**: 441-455, 1847.

[2] Longuet-Higgins, M. S.: Mass transport in water waves. *Phil. Trans. R. Soc. Lond*. **A 245**: 535-581, 1953.

[3] Chang, M.-S.: Mass transport in deep-water long-crested random gravity waves. *J. Geophys. Res.* **74**: 1515-1536, 1969.

[4] Ünlüata, Ü., Mei, C. C.: Mass transport in water waves. *J. Geophys. Res*. **75**: 7611-7618, 1970.

[5] Weber, J. E.: Attenuated wave-induced drift in a viscous rotating ocean. *J. Fluid Mech*. **137**: 115-129, 1983.

[6] Andrews, D. G., McIntyre, M. E.: An exact theory of nonlinear waves on a Lagrangian-mean flow. *J. Fluid Mech*. **89**: 607-646, 1978.

[7] WAMDI Group: The WAM model - A third-generation ocean wave prediction model. *J. Phys. Oceanogr*. **18**: 1775-1810, 1988.

[8] Weber, J. E.: Wave-induced mass transport in the oceanic surface layer. *J. Phys. Oceanogr*. **33**: 2527-2533, 2003.

[9] Weber, J. E., Melsom, A.: Transient ocean currents induced by wind and growing waves. *J. Phys. Oceanogr*. **23**: 193-206, 1993.

XXI ICTAM, 15–21 August 2004, Warsaw, Poland

EFFECT OF HORIZONTAL COMPONENT OF THE CORIOLIS FORCE ON PROPAGATION OF NEAR-INERTIAL WAVES IN THE OCEAN

Theo Gerkema*, Victor I. Shrira**
*NIOZ, PO Box 59, 1790 AB Den Burg, The Netherlands; & IMG,University of Grenoble
**Department of Mathematics, Keele University, Keele, Staffordshire, ST5 5BG, UK

Summary Oceanic motions of scales small compared to the Earth's radius are commonly described as if the rotating Earth were locally ¤at with the horizontal component of the Coriolis force being neglected (the so-called "traditional approximation"). We show that taking into account the horizontal component of the Coriolis force changes dramatically dynamics of near-inertial waves.

A new family of sub-inertial waves, which are absent under the "traditional approximation", is found to play a crucial role: On the "non-traditional" beta-plane inertial waves propagating poleward and reaching their inertial latitude are not re¤ected at this latitude, as is the case under the "traditional approximation", but turn into subinertial waves which propagate further poleward trapped within near bottom and near surface wave-guides around the minima of the buoyancy frequency. Their horizontal and vertical scales rapidly decrease and tend to zero at a critical latitude. There is no re¤ection and, thus, inertial waves are absorbed contributing to deep ocean mixing.

Oceanic motions of scales small compared to the Earth's radius are commonly described as if the rotating Earth were locally ¤at with the horizontal component of the Coriolis force being neglected (the so-called "traditional approximation"). We show that taking into account the horizontal component of the Coriolis force changes dramatically propagation of near-inertial waves and has major implications for dynamics of deep ocean.

We begin with the standard linear equations on the non-traditional f-plane under the Boussinesq approximation, which can be reduced to a single equation for vertical velocity w

$$\nabla^2 w_{tt} + (\vec{f}\cdot\nabla)^2 w + N^2\nabla_h^2 w = 0 \tag{1}$$

We employ the following Cartesian frame: x (west-east), y (south-north); z (vertical, positive upward); u, v and w are the corresponding velocity components; $\vec{f} = (0, \tilde{f}, f)$, and ∇_h^2 denotes the horizontal Laplacian. We allow the buoyancy frequency N to depend on z. In the traditional approximation one would take $\tilde{f} = 0$.
For plane monochromatic ($w = W\exp(i\sigma t)$) waves travelling in the $\chi = x\cos\alpha + y\sin\alpha$ direction, we £nd

$$(N^2 - \sigma^2 + f_s^2)W_{\chi\chi} + 2ff_sW_{\chi z} - (\sigma^2 - f^2)W_{zz} = 0\,, \tag{2}$$

where $f_s = \tilde{f}\sin\alpha$. Equation (2) is the starting point of our study.
On employing the standard boundary conditions at the surface and the bottom the substitution of $W = \psi(z)\exp i(k\chi + \delta z)$, with $\delta = -kff_s/(\sigma^2 - f^2)$ leads to the following BVP for ψ

$$\psi'' + k^2\Big[\frac{N^2(z) - \sigma^2}{\sigma^2 - f^2} + \Big(\frac{\sigma f_s}{\sigma^2 - f^2}\Big)^2\Big]\psi = 0\,, \qquad \psi(0) = \psi(H) = 0, \tag{3}$$

Note, that from purely mathematical perspective the "non-traditional term" containing f_s, does not pose any dif£culty, as it produces merely an additive constant. However it results in the following qualitative effects. In the vicinity of the inertial frequency the solution becomes independent on $N(z)$ and can be readily found for the $n-$th mode

$$(\sigma^2 - f^2)/\sigma = \pm\frac{f_sH}{2\pi n}k, \qquad k > 0 \tag{4}$$

In contrast to the "traditional" boundary-value problem where for all eigenmodes $\sigma^2 - f^2 > 0$, we, in addition, have another family of *sub-inertial* modes with $\sigma^2 - f^2 < 0$, which being con£ned to a narrow $O((f_s/N)^2)$ frequency range are trapped in the waveguides around minima of $N(z)$, i.e near surface and bottom of the ocean. In the longwave limit frequencies of the modes of both families tend to f with £nite group velocity $d\sigma/dk = f_sH/2\pi n$.

The importance of the new family of sub-inertial waves, which are absent under the "traditional approximation", becomes apparent if the beta effect or any kind of large scale nonuniformity is taken into account. On the "non-traditional" beta-plane near inertial waves are described by the equation

$$(N(z)^2 - \sigma^2 + \tilde{f}^2)W_{yy} + 2f\tilde{f}W_{yz} - (\sigma^2 - f^2 - 2f\beta y)W_{zz} = 0\,, \quad W(0) = W(H) = 0 \tag{5}$$

which is the starting point of further analysis.
Under the "traditional approximation" inertial waves propagating poleward slow down approaching their inertial latitude and then are totally re¤ected back. On the "non-traditional" beta-plane the picture of wave evolution is entirely different: near inertial waves propagating poleward do not slow down on reaching the inertial latitude, they pass it with £nite group

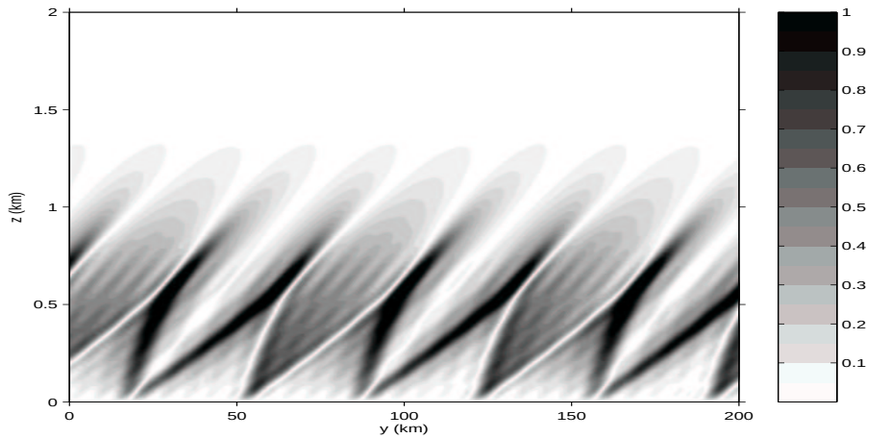


Figure 1. An example of a bottom-trapped sub-inertial wave ($\sigma = 0.99f$), given by a superposition of the £rst £ve modes. The strati£cation is given by the realistic values $N_0 = 5 \times 10^{-4}\text{rad}\,\text{s}^{-1}$, gradient $\gamma = 4 \times 10^{-10}\text{rad}^2\,\text{m}^{-1}\text{s}^{-2}$; latitude $\phi = 45^o$ and propagation is in the meridional direction: $\alpha = \pi/2$ (poleward to the right).

velocity and propagate further poleward turning into sub-inertial modes trapped within near bottom and near surface wave-guides. On passing the inertial latitudes the horizontal and vertical scales of waves rapidly decrease and tend to zero at a critical latitude, beyond which there is no wave propagation. The critical latitude is located at a distance a few hundred kilometres from the inertial latitude. The picture resembles wave propagating in a wedge. There is no re¤ection and, thus, inertial waves are absorbed contributing to ocean mixing. Since the main sub-inertial guide is near the bottom, it is expected that the outlined mechanism might be the key one in the so far unexplained mixing in deep ocean.

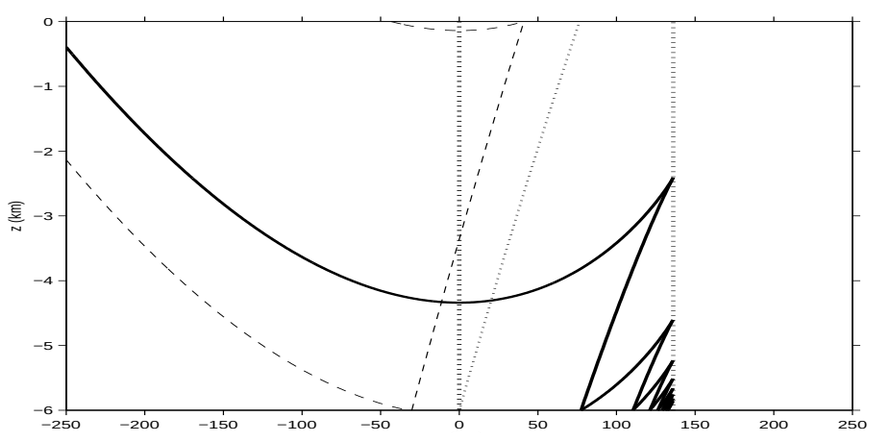


Figure 2. Behaviour of the characteristic curves $\xi_\pm = const$ for the model $N = const$.

The sub-inertial regime is entered via ξ_+ (solid line), which connects to ξ_- as it re¤ects at the critical latitude. The alternation between ξ_+ and ξ_- continues upon each re¤ection at bottom or critical latitude. Inertial and critical latitudes are again indicated by the vertical dotted lines at $y = 0$ and $y = 136$km. A ξ_+-curve that has passed the diagonal dotted line cannot escape anymore from the sub-inertial domain. The dashed line represents an example of an equatorward returning path.The dotted diagonal line representing a $\xi_- = const$ characteristic, marks a borderline: any characteristic $\xi_+ = const$ that re¤ects at the surface to the left of this curve will return equatorward, as is illustrated by the dashed path; all others will get trapped in the lower-right corner of the sub-inertial domain. It thus appears that *most* of the poleward propagating energy will get trapped into this corner.

GENERALIZED INTERNAL SOLITARY WAVES AND FRONTS

Frédéric Dias*, Christophe Fochesato*
*CMLA, Ecole Normale Supérieure de Cachan, France

Summary It was shown in [1] that waves in a two-layer system with free-surface boundary conditions (or in a three-layer system) can be modelled by a system of two coupled long wave equations. The study of the resonance between a solitary wave of one of the two equations and a copropagating periodic wave of the other equation is carried out numerically. The resulting wave is a generalized solitary wave. It is shown that in the case of a thick solitary wave (solution of a modified Korteweg–de Vries equation with a cubic nonlinearity), the generalized solitary waves do not behave like common sech^2 generalized solitary waves. Simplified models are introduced, which allow a better understanding of these stationary and time-dependent long wave solutions.

Introduction

This work deals with a particular case of long waves, which arise for example in the physical context of multi-layer flows of inviscid fluids. For instance, two superposed fluids with both a free surface and an interface, or three superposed fluids with two interfaces and a rigid top, are typical configurations of interest here. We are dealing with systems having two wave modes which admit generalized solitary waves. These are nonlinear long wave solutions consisting of a localized central pulse and periodic non decaying oscillations at infinity. These solutions do not only occur in this context. In fact most existing results have been obtained in the framework of the classical water-wave problem with surface tension [2]. It has been proved that, in a specific region of the parameter space, pure solitary waves cannot exist because periodic oscillations, eventually exponentially small, get caught on the solitary pulse.

When dealing with interfacial waves, the amplitude of the solitary pulse can be bounded by the configuration. In the case of classical solitary waves, it is known that when the wave speed approaches a critical value, the solution is best modelled by an extended Korteweg-de Vries (KdV) equation, i.e. a KdV equation with a cubic nonlinear term. The solitary wave reaches its limiting amplitude by infinite broadening. In the limit, one has to consider fronts, which are related to conjugate flows [3]. Some questions arise when dealing with generalized solitary waves: Do oscillations appear on top of the flat part of the wave? Do oscillations only appear on the sides? What are their properties? The objective of this work is to learn more about these new solutions. Rather than proving their existence in a particular context, the idea is to derive models to describe and compare them with common generalized solitary waves.

Dias and Il'ichev [1] derived a system based on two KdV equations with cubic nonlinear and coupling terms. They briefly considered analytically the case with small oscillations on top of a front. A system of two coupled KdV equations was also derived by Grimshaw [4] for three layers with two interfaces, but without emphasis on generalized solitary waves. His point of view consists in treating generically the phenomenon of resonance between two wave modes, in the weakly nonlinear long wave limit. Generalized solitary waves, which are solitary waves with resonant periodic oscillations copropagating with the long wave, appear naturally. Grimshaw's system has been studied by Grimshaw and Iooss [5], who show the existence of such nonlocal solutions. We consider a similar system to study generalized thick solitary waves:

$$u_t + \Delta u_x + \alpha_1 u u_x + \beta_1 u^2 u_x + \lambda_1 u_{xxx} + \kappa_1 v_x = 0$$
$$v_t - \Delta v_x + \alpha_2 v v_x + \beta_2 v^2 v_x + \lambda_2 v_{xxx} + \kappa_2 u_x = 0,$$

where u and v are the wave amplitudes. All the coefficients are real.

First we look for stationary solutions. Their properties are discussed and compared with well-known generalized solitary waves. The study of the stationary system provides an approximation for the initial data used when integrating the time-dependent system. The non-stationary solutions are described in terms of the characteristics underlined in the stationary study. In both cases, it is useful to solve analytically a simpler model which clarifies the results.

Stationary solutions

When the coupling is weak and v of the same order as the coupling, a good approximation of the system is a modified KdV equation in u, whose solution forces a linear equation in v. This forced equation is certainly the simpler model describing generalized solitary waves. It is completely solvable, so it can be used to get explicit information on the solutions we are interested in. Since we are looking (numerically) for periodic solutions, we choose periodic boundary conditions. Then the domain length is the wavelength of the long periodic wave, which is essentially a solitary wave. In [6], it was shown that the forcing by a flat solitary wave is quite different from the forcing by a sech^2 solitary wave. It is due to the fact that a flat forcing has simple poles outside the imaginary axis in the complex plane. As a consequence, there are isolated parameter values for which the flat solitary wave tends to zero at infinity. If the forcing was the solution of a classical KdV equation, the amplitude of the ripples would never vanish.

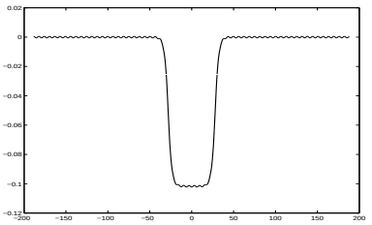


Fig1. *A stationary solution, with ripples on the sides and in the middle part*

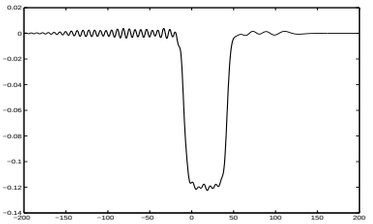


Fig2. *A non-stationary solution*

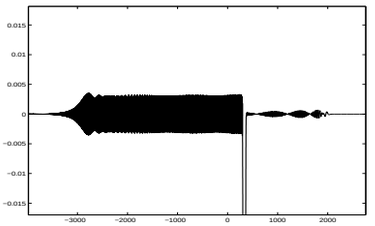


Fig3. *A non-stationary solution after a long time*

Next we compute stationary solutions of the full system numerically (Figure 1). Using spectral methods, we get solutions similar to those of the simplified model. By varying the soliton width, we were able to confirm the previous results on the possibility to kill the ripples.

Time-dependent solutions

This part deals with the evolution of an initial perturbation. In particular, we want to know if we can get a generalized thick solitary wave. If so, what are its characteristics? As expected, the long wave radiates only on one side as it was discovered for usual generalized solitary waves. The solution after a long time can be compared with stationary solutions of the previous section. On one hand, numerical computations on the whole system are carried out. On the other hand, we use again the forced linear equation ($\alpha_2 = \beta_2 = 0$) to obtain information at very large times.

The numerical scheme combines a spectral method in space with a Runge Kutta time stepping scheme. In order to allow for larger time steps, the integrating factor technique is used. It consists in multiplying each equation by an exponential factor so that the dispersive term no longer appears in the system to be solved. Then the classical fourth order Runge Kutta method is applied (nonlinear terms are computed with the fast Fourier transform and its inverse). The initial perturbation is the thick solitary wave solution of the extended Korteweg-de Vries equation. It gives a good approximation to the core of the expected generalized solitary wave. Indeed, Figure 2 shows such a solution. Note that an initial wave which does not have the proper width splits into several solitary waves. As expected, the ripples radiate only on one side (behind the long wave). We notice the presence of small waves on top of the central pulse. For this moderate time, the wave radiation is not of constant amplitude.

The presence of small oscillations requires small time steps, and so solutions for very long time are difficult to obtain. This is why the simpler model is used again to compare with stationary solutions. This approximation available for weak coupling is solvable in time and leads to an integral formulation of the solution. From this expression, we can plot the solution for any desired time through a numerical evaluation of the integral by fast Fourier transforms. This way, we can check if the stationary solution can be reached. Figure 3 shows a zoom of a solution which underlines the resonance phenomenon. We observe that the envelope modulation is attenuated and slightly oscillates around a constant value. On the other side of the central pulse, there are also some waves which propagate under the form of wave packets. Most likely they correspond to the faster branch of the relation dispersion curve. Their precise origin is still under investigation. If we specify a parameter set such that the stationary solution has vanishing oscillations on the sides as shown in the previous section, we note that the long wave is located just at a trough between two wave packets: therefore the resonance does not occur, or rather occurs with zero amplitude ripples.

Conclusion

This study is a first step in the study of generalized internal solitary waves and fronts. The time evolution of generalized fronts appears to be quite different from the behaviour of generalized solitary waves.

References

[1] Dias F., Il'ichev A.: Interfacial waves with free-surface boundary conditions : an approach via a model equation. *Physica D* **150**:278–300, 2001.
[2] Lombardi E.: Oscillatory integrals and phenomena beyond all algebraic orders. Lecture Notes in Mathematics 1741, Springer-Verlag, 2000.
[3] Dias F., Vanden-Broeck J.-M.: On internal fronts. *J. Fluid Mech.* **479**:145–154, 2003.
[4] Grimshaw R.: Models for long-wave instability due to a resonance between two waves. in Trends in Applications of Mathematics to Mechanics, ed. Iooss, Guès, Nouri, Chapman & Hall/CRC, 2000.
[5] Grimshaw R., Iooss G.: Solitary waves of a coupled Korteweg-de Vries system. *Math. and Computers in Simulation* **62**:31–40, 2003.
[6] Fochesato C., Dias F.: Amplitude des oscillations d'ondes solitaires généralisées. *C. R. Acad. Sci. Paris, Ser. I* **337**:137–142, 2003.

INTERMITTENT MIXING BY MULTISCALE BREAKING OF WIND WAVES: IMPLICATIONS FOR OIL DISPERSION

Igor A. Brovchenko*, Vladimir S. Maderich*
*Institute of Mathematical Machine and System Problems NANU, Department of Marine and River Systems, Glushkov pr. 42, 03187 Kiev, Ukraine

Summary We simulated the intermittent mixing by breaking waves with the use of non-stationary 1D two-equation turbulence model. The wave-breaking layer with thickness of half significant wave height was included into consideration. An injection of turbulence by penetrating breakers in this layer was parameterized by source term in the turbulent kinetic energy and dissipation equations. The Monte-Carlo simulations of intermittent mixing were carried out. They support assumption that observed log normal distribution of dissipation rate is associated with breaking of waves in many scales. An intermittent mixing effects on the scales of breakup and dispersion in water of oil droplets in the wave breaking layer. The detailed results of simulations of turbulence and droplet spectre and concentration in the wave enhanced layer for stormy conditions by linked model of surface turbulent layer and 3D Lagrangian model of oil spill are presented.

INTRODUCTION

Breaking serves to limiting height of surface waves, dissipating surface-wave energy, some of which is available for turbulent mixing [1]. Breaking is multi-scale process: from large-scale breaking waves and smaller-scale waves breaking on longer waves to micro-scale breaking. Direct measurements show that breaking generates spectre of the intensive outbursts of turbulence with dissipation rate that is orders of magnitude larger than the mean value. These events result in the roughly log normal probability distribution of the dissipation rate [2]. Oil spilled at sea often entrained by breaking waves in stormy conditions and forms clouds of oil droplets that are dispersed by subsurface turbulence and shear currents. Aim of this paper is to clarify role of turbulence injected by breaking waves in mixing of near-surface layer and to estimate effects of intermittent injection of oil by highly energetic breaking wave events.

INTERMITTENT MIXING BY WAVE BREAKING

We simulated an intermittent mixing by breaking waves by non-stationary 1D two-equation turbulence model. The wave-breaking layer with thickness of half significant wave height was included into consideration (Fig. 1). An injection of turbulence by penetrating breakers in this layer was parameterized by source term in the turbulent kinetic energy and dissipation rate equations. The Monte-Carlo simulations of intermittent mixing were carried out. Example of time series of kinetic turbulent energy flux in wave-breaking layer is given in Fig. 2. Both simulated (curve 2) and observed [2] (curve 1) distribution of near-surface dissipation in Fig. 3 support assumption that observed quasi-lognormal distribution of dissipation rate is associated with breaking of waves in many scales. Time averaged profiles of dissipation rate (curve 7) agree with measurements (1-3) and stationary solutions (curve 4) in Fig. 4. Curves 5-6 show limits in the variability of the dissipation rate. However, temporally intermittent mixing effects on the scales of breakup and dispersion in water of air bubbles and oil droplets in the wave-breaking layer.

OIL DISPERSION IN WAVE ENHANCED LAYER

To simulate breakup and oil dispersion the 3D Lagrangian oil dispersion model was developed [4]. It describes entrainment of oil in the water by breaking waves and resurfacing entrained droplets. The turbulent diffusion processes are simulated by use Lagrangian stochastic simulation technique based on the random walk method for Gaussian "spillets". It was shown that almost all statistical models of break-up of an immiscible fluid immersed into a turbulent flow [5] were not able reproduce observed distribution of oil droplet size. Instead, the new model of the breakup based on Kolmogorov approach [6] was proposed to reproduce observed log normal distribution of oil droplet sizes (Fig.5). The detailed results of simulations of turbulence and droplet concentration in the wave enhanced layer for stormy conditions by linked model of surface turbulent layer and 3D Lagrangian model of oil spill are presented. The hypothetical scenario of oil spill 75,000 tons of crude oil on the north-western shelf of the Black Sea 25.09 2002 at distance around 50 km from Odessa oil terminal was considered. As seen in Fig.6 the model reproduces processes of surface slick entrainment by the breaking waves, generation of oil droplets, diffusion by subsurface turbulence and gradual resurfacing of droplets by buoyancy forces that contributes in the forming of frequently observed thin oil film tail ("sheen") behind the thick slick area. The calculations show that knowledge of mean characteristics of breaking wave field wave field such as wave height, length, breaking frequency and whitecapping is not enough to simulate breakup and dispersion of liquid and gas in the surface layer

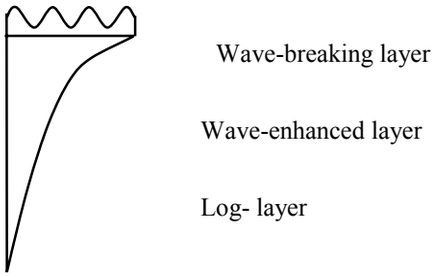


Fig. 1 Vertical structure of surface layer

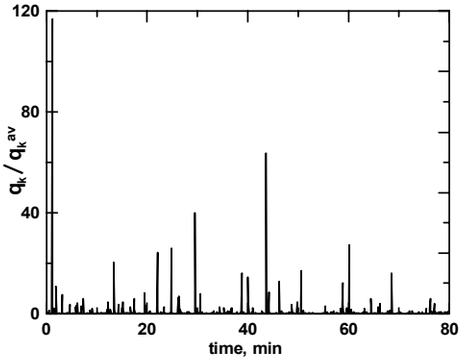


Fig. 2 Simulated by Monte-Carlo method time series of flux of kinetic turbulent energy in wave-breaking layer

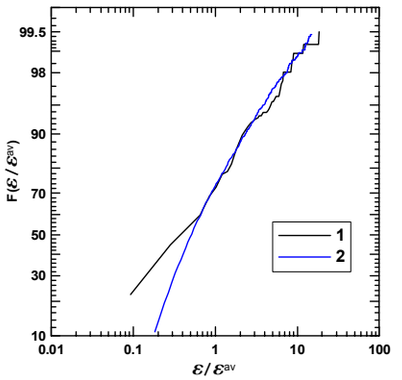


Fig. 3 Simulated (2) vs. observed (1) [2] distribution of near-surface dissipation normalized on time-averaged value

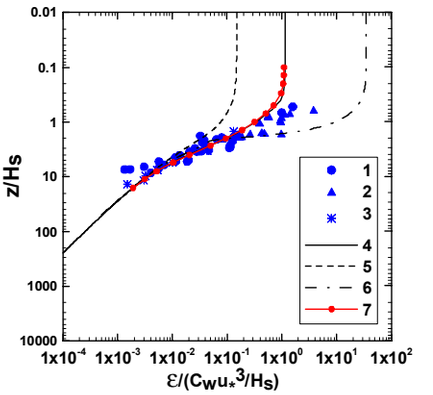


Fig. 4 Profiles of normalized dissipation rate in surface layer.

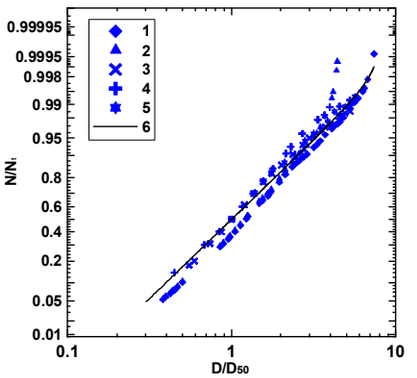


Fig. 5 Simulated (curve 6) vs. measured (1-5) self-similar size distribution of oil droplets.

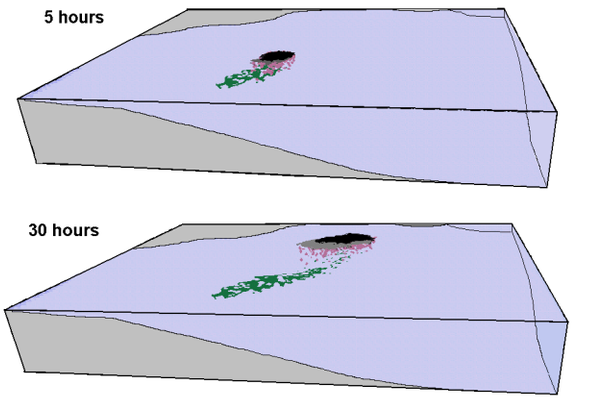


Fig. 6 . 3D representation by interactive visualisation tool of the oil spill at the North-western shelf of the Black Sea. The surface slick, oil-in-water and oil-on-bottom concentrations are shown by black, red and green, respectively.

References

[1] Melville W.C.: The role of surface wave breaking in air-sea interaction. *Annu. Rev. Fluid Mech* **28**:279-321, 1996

[2] Agarwal Y.C. et al.:Enhanced dissipation of kinetic energy beneath surface waves. *Nature* **359:**219-220, 1992

[3] Maderich V. S., Brovchenko I., A.: Effect of the wind wave breaking on the structure of surface turbulent layer in the ocean. *Applied Hydromechanics*, **5(77)** No. 3, 2003.

[4] Brovchenko I. et al.: The modelling system for simulation of the oil spills in the Black Sea. Proc. 3rd EUROGOOS Conference, Elsevier, 2003.

[5] Lasheras J.C. et al.: A review of statistical models for the break-up of an immiscible fluid immersed into a fully developed turbulent flow. *Int. J. Multiphase Flow* **28**: 247-278, 2002.

[6] Kolmogorov A., N.: On lognormal distribution of the particle sizes produced by breakage *Dokl. Akad Nauk* **31**: 99-101, 1941.

Equatorial wave attractors and inertial oscillations

Leo Maas and Uwe Harlander
Netherlands Institute for Sea Research

The Laplace Tidal Equations (LTE) have been extremely succesfull in their description of external waves of Kelvin, Poincaré and Rossby type in thin spherical shells, and local f and β-plane approximations thereof. However, the neglect of the horizontal component of Coriolis terms (traditional approximation) and the use of the hydrostatic approximation in the LTE have been recognized as omitting a class of cellular, hyperbolic type of waves, that may be focused by non-cylindrical geometry onto limit cycles (wave attractors). Here, a very simple stratified, equatorial beta-plane model is introduced,in which the traditional and hydrostatic approximation are defied, which will illustrate analytically certain aspects that have emerged in global models by Friedlander and Siegmann (1982) and Dintrans, Rieutord and Valdettaro (1999). As this is the stratified extension of Stern's (1963) model, it will be referred to as the Stratified Stern Equation. The associated characteristic equation for axially symmetric waves, shows the appearance of bent characteristics (as in the Stern Equation) and turning latitudes, very close to the inertial latitude (as in the global models). Iterating the characteristics, to find webs of connected characteristics, shows the emergence of equatorial wave attractors and, in particular, point attractors, at the intersection of turning latitude and bottom, which are therefore interpreted as (near)inertial oscillations, possibly of relevance to the ubiquitously observed spectral peak at the inertial frequency.

References

Dintrans, B., Rieutord, M. & Valdettaro, L. 1999 Gravito-inertial waves in a rotating stratified sphere or spherical shell. *J. Fluid Mech.* **398**, 271–297.

Friedlander, S. & Siegmann, W. L. 1982 Internal waves in a rotating stratified fluid in an arbitrary gravitational field. *Geophys. Astrophys. Fluid Dynamics* **19**, 267–291.

Stern, M. E. 1963 Trapping of low frequency oscillations in an equatorial 'boundary layer'. *Tellus* **15**, 246–250.

Maas, L. R. M. 2001 Wave focusing and ensuing mean flow due to symmetry breaking in rotating fluids.*J. Fluid Mech.* **437**, 13-28.

FOCUSING OF AN INERTIA-GRAVITY WAVE PACKET BY A BAROCLINIC SHEAR FLOW

Chantal Staquet*, Neil R. Edwards*[1]
*Laboratoire des Ecoulements Géophysiques et Industriels, BP 53, 38041 Grenoble cdx 9, France

Summary
We investigate the interaction of an internal gravity wave packet in a rotating fluid with a baroclinic shear flow, using ray equations and three-dimensional direct numerical simulations (DNS) of the Boussinesq equations. In this problem, the intrinsic frequency of the wave packet increases due to the horizontal shear of the background flow in which it propagates. The packet is trapped at locations where the intrinsic frequency reaches its upper bound and is amplified there. When the horizontal shear of the background flow is low enough, ray equations predict that the packet may further penetrate into that flow through reflection within a wave guide. The DNS show that the packet is actually dissipated before reflecting because of the strong decrease of its horizontal wavelength and group velocity during the interaction. Consequently, the wave packet is not able to penetrate into the shear flow, except when the latter vanishes locally.

INTRODUCTION

The purpose of this paper is to investigate how inertia-gravity waves, *i.e.* internal gravity waves in a rotating medium, may interact with a horizontal flow with both a horizontal and a vertical shear. Such interactions occur everywhere in geophysical flows as soon as inertia-gravity waves propagate in a wind or a current, or encounter a vortical motion such as a large scale vortex. We use a simple model for the wave and the baroclinic flow, described in the next section. We rely on ray theory and also perform direct numerical simulations of the three-dimensional nonlinear Boussinesq equations. The geophysical motivation of this work is to investigate whether some irreversible transport process may occur across the shear flow as a result of its interaction with the wave field.

PHYSICAL MODEL

Let (x, y, z), with z directed upwards, be a Cartesian coordinate system in the rotating reference frame attached to the fluid container. The baroclinic shear flow consists of a velocity field along the x-direction $\mathbf{U}(y, z)$ in thermal wind balance with a buoyancy field $B(y, z)$. The baroclinic current is a horizontal shear layer, centered about $y = y_s$, with a vertical shear: $U(y, z)/U_0 = \left[1 + \tanh\left(\frac{y-y_s}{L_s}\right)\right]\left[1 + \beta \sin\left(\frac{2\pi z}{H_s}\right)\right] - 1$. The velocity scale is U_0 and the parameter β represents the strength of the baroclinicity: the shear flow is barotropic if $\beta = 0$ or $\beta \ll 1$. The buoyancy field B is inferred from the thermal wind balance. This initial condition implies that an inertia-gravity wave packet propagating from a region where $y \ll y_s$ travels, as y increases, from a uniformly translating medium along the x direction with speed $-U_0$, to a moving medium with both a vertical and a horizontal velocity shear. Let $\mathbf{k}$ and $\Omega(\mathbf{k})$ refer to the main wave vector and intrinsic frequency respectively of such a wave packet. We recall that $f \leq \Omega(\mathbf{k}) \leq N$, where f and N are the Coriolis and local buoyancy frequency. A initial time $t = 0$, we assume that the wave induced energy is confined within a two-dimensional Gaussian envelope along the y and z directions.

RAY EQUATIONS AND DIRECT NUMERICAL SIMULATIONS

We solve the classical ray equations (see *f.i.* [1]), which describe how a wave vector is refracted by the gradients of the background flow along a ray. From a practical point of view, the ray equations are initialized by a set of rays starting from points that model the wave packet. The wave vector and intrinsic frequency at each of these starting points are computed using the constancy of k_x and of the absolute frequency along a ray. We also solve the Navier-Stokes equations in the Boussinesq approximation in a parallelepipedic domain. The boundary conditions are periodic along the x and z directions and of free slip type along the y direction, so that a pseudo-spectral method can be used. The equations are integrated in time using a third-order Adams-Bashforth scheme.
We have performed several computations, which are described in [2]. The point of view we have chosen is the following: the wave packet propagates into the current such that its intrinsic frequency increases because of the y-dependency of the shear flow. This means that the wave packet should be trapped in the neighbourhood of the $\Omega = N$ surface and possibly break there, at least when $\beta = 0$ [3], thereby inducing mean flow changes. Our purpose is to investigate the influence of the baroclinicity parameter β on this behavior for $0 < \beta \leq 1$.

RESULTS

We illustrate the wave-shear flow interaction for a background flow with a weak horizontal shear, with Rossby number (close to 0.3) comparable to that of the wave packet at initial time ($simeq 0.85$). The ratio $N_0/f = 4.4$ (where $N_0 = 1$ is the buoyancy frequency of the fluid at rest) and the Prandtl number is equal to 1. Two cases are presented, corresponding to $\beta = 0.5$ and $\beta = 1$.

[1]Present address:Physics Institute, University of Bern, Sidlerstrasse 5, CH-3012 Bern, Switzerland

Ray trajectories predicted from ray theory for $\beta = 0.5$ are displayed in Figure 1a. The rays steepen in the neighbourhood of the $\Omega = N$ surface, are trapped there and travel downwards with the now quasi-vertical group velocity. The intrinsic frequency Ω increases during this stage (Figure 1b). The shear flow we have designed possesses regions where $\partial U/\partial z$ vanishes, U and $\partial U/\partial y$ being minimum there, so that the $\Omega = N$ surface flattens about this region. This is where the rays, which have become quasi-vertical because Ω is close to N, reflect. Figure 1a shows that the rays are able to propagate further in the shear flow, within a wave guide limited by two portions of the $\Omega = N$ surface. Results from DNS for the same run are plotted in Figures 1c to 1e. The wave amplitude first decays because of dispersion. This is an important effect, which the subsequent interaction with the shear flow (through which the wave amplitude increases) does not make up for. As in the ray theory, the wave packet is then steepened by the trapping process (Figure 1d), travels along the $\Omega = N$ surface and meets again that surface when it flattens (Figure 1e). But as opposed to the ray theory predictions, no reflection is clearly observed: the decay of the wavelength along the y-direction and of the group velocity makes the packet very sensitive to viscous effects. It has totally dissipated by the time the rays first reflect ($t \simeq 300$), assuming the ray theory predictions are quantitatively reliable.
When the baroclinicity parameter $\beta = 1$, U and $\partial U/\partial y$ now also vanish in the region where $\partial U/\partial z = 0$. Figure 1f shows that the wave packet now penetrates into the shear flow, because the trapping process has been suppressed, and that this region acts as a wave guide.

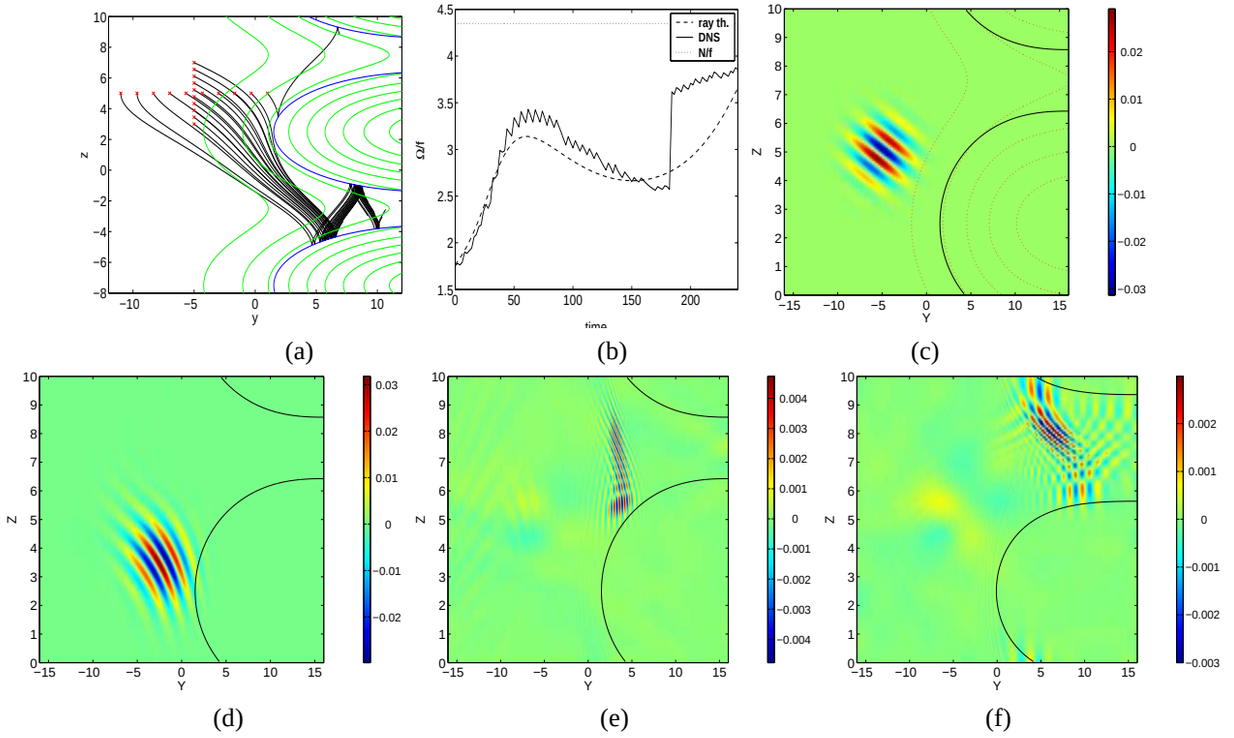


Figure 1. (a) to (e): $\beta = 0.5$. (a) Predictions from ray theory; trajectories of rays starting from points modelling the initial wave packet at $t = 800$. (b) Intrinsic frequency computed at the packet center versus time, from ray theory and DNS. (c) to (f): Constant contours in a vertical (y, z) plane of the fluctuating density field computed from DNS, at $t = 0\ (c),\ 56\ (d),\ 84\ (e),\ 176\ (f)$. (g) Run $\beta = 1$. DNS results at $t = 204$. In all frames (but b)), the surface $\Omega = N$ is displayed with a blue line.

CONCLUSION

When a wave packet propagates in a baroclinic shear flow such that its intrinsic frequency increases due to the horizontal shear, DNS of the Boussinesq equations show that the packet amplitude is first attenuated because of dispersion, then is trapped in the vicinity of the $\Omega = N$ surface and is dissipated there. When the shear flow locally vanishes, both ray theory and DNS results predict that the wave can penetrate into the shear flow through a wave guide. The resulting changes of the background medium are however insignificant if the wave is not forced. Our study suggests that there should be "less" waves inside large scale geophysical vortices than outside.

References

[1] Olbers D.J.: The propagation of internal waves in a geostrophic current. *J. Phys. Oceanogr.* **11**:1224–33, 1981.
[2] Edwards N.R., Staquet C.: Interaction of an inertia-gravity wave packet with a baroclinic shear flow. To appear in *Dyn. Atmos. Oceans*.
[3] Staquet C., Huerre G.: On transport across a barotropic shear flow by breaking inertia-gravity waves. *Phys. Fluids*, **14**(6), 1993–2006, 2002..

STEEP CAPILLARY WAVES IN ELECTRIFIED FLUID SHEETS

Jean-Marc Vanden-Broeck*, Demetrios Papageorgiou **
*School of Mathematics, University of East Anglia, Norwich, NR4 7TJ, UK
**Department of Mathematical Sciences and Center for Applied Mathematics and Statistics, New Jersey Institute of Technology, Newark, NJ 07102, USA

Summary Nonlinear capillary waves propagating on fluid sheets in the presence of electric fields are considered. Both two-dimensional and axisymmetric configurations are investigated. Numerical solutions are obtained by boundary integral equation methods. In addition analytical aprroximations are calculated by long wave asymptotics. The effects of the electric fields on the wave profiles are studied. New families of capillary waves are presented.

Free liquid films arise in different physical and technological applications in chemical and biomedical engineering, for example. The nonlinear phenomena associated with large interfacial deflections and possible rupture, are of interest in the fundamental understanding of such flows. Physical applications have been discussed by Maldarelli et al (1980) and others.

The linear stability of inviscid free liquid sheets to two-dimensional disturbances was considered by Taylor (1959) who derived dispersion relations for both symmetric (varicose) and antisymmetric (sinuous) modes. Viscosity was introduced by Maldarelli at al (1980) and is found to damp the dispersive waves. In these studies gravity is absent and surface tension is present. In the case of a free surface above an infinitely deep inviscid liquid, exact nonlinear traveling capillary waves were found by Crapper (1957). These solutions were extended to layers of finite thickness by Kinnersley (1976) who constructed nonlinear symmetric waves (for inviscid flows these also describe waves over a horizontal solid surface), as well as nonlinear antisymmetric waves.

We first study the effects of horizontal electric fields on Kinnersley's solutions. The governing equations are

$$\nabla^2\phi(x,y;t) = 0, \tag{1}$$
$$\nabla^2 V^{(1,2)}(x,y;t) = 0, \tag{2}$$

where in what follows superscripts 1, 2 denote the regions bounded by and outside of the moving interfaces (see Figure 1). The electric fields are $\mathbf{E}^{(1,2)} = \nabla V^{(1,2)}$.

The boundary conditions at a free surface $y = S(x,t)$ are the kinematic condition, continuity of normal stresses, and the continuity of the normal displacement and tangential components of the electric field. These are:

$$S_t + \phi_x S_x - \phi_y = 0 \tag{3}$$
$$[\mathbf{n}\cdot\mathbf{T}\cdot\mathbf{n}]_2^1 = \sigma \mathrm{div}\mathbf{n} \tag{4}$$
$$[\epsilon\mathbf{E}\cdot\mathbf{n}]_2^1 = 0 \tag{5}$$
$$[\mathbf{E}\cdot\mathbf{t}]_2^1 = 0, \tag{6}$$

where $[\cdot]_2^1$ denotes the jump in the quantity as the interface is crossed from the fluid region, the vectors $\mathbf{n}$, $\mathbf{t}$ are the outward pointing normal and tangent to the interface respectively, and the stress tensor $\mathbf{T}$ is given by

$$T_{ij} = -p\delta_{ij} + \mathcal{E}_{ij}, \qquad \mathcal{E}_{ij} = \epsilon\left(E_iE_j - \frac{1}{2}|\mathbf{E}|^2\delta_{ij}\right). \tag{7}$$

The first term in (7) is the inviscid hydrodynamic contribution and the second term arises from interfacial electric stresses given by the Maxwell stress tensor. The parameters ϵ_1, ϵ_2 are the dielectric constants in regions 1 and 2 respectively. The momentum equations can be integrated to yield a Bernoulli equation at the interface. The pressure in region 2 is ambient and equal to a constant and on elimination of the pressure jump across the interface from (4), we arrive at the following Bernoulli boundary condition:

$$\rho_1\left(\phi_t + \frac{1}{2}|\nabla\phi|^2\right) + \frac{1}{1+S_x^2}\left\{S_x^2\left[\mathcal{E}_{11}\right]_2^1 - 2S_x\left[\mathcal{E}_{12}\right]_2^1 + \left[\mathcal{E}_{22}\right]_2^1\right\} = \frac{\sigma S_{xx}}{(1+S_x^2)^{3/2}} + K_p. \tag{8}$$

The Maxwell stresses appearing in (8) are given by

$$\mathcal{E}_{11} = \frac{\epsilon}{2}\left(V_x^2 - V_y^2\right), \qquad \mathcal{E}_{12} = \epsilon V_xV_y, \qquad \mathcal{E}_{22} = \frac{\epsilon}{2}\left(V_y^2 - V_x^2\right), \tag{9}$$

and superscripts 1 and 2 are implied where appropriate in (9).

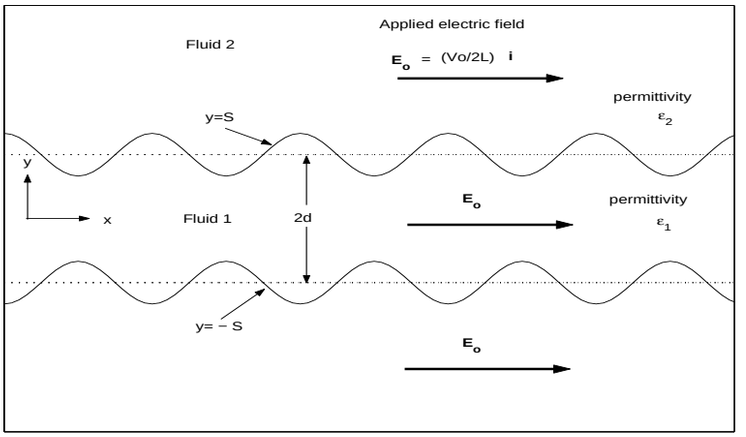


Figure 1: Sketch of the flow configuration. Here the waves are assumed to be symmetric

In the absence of an electric field nonlinear traveling waves (symmetric and antisymmetric) have been constructed analytically by Kinnersley (1976). With electric fields present, we no longer have exact solutions. Therefore we developed weakly nonlinear asymptotic solutions (based on a long wave approximation) and fully nonlinear numerical solutions.

Our numerical method can be described as follows. The three Laplace equations ((1)-(2)) are reformulated as integral equations. This can be done in two ways: (i) using complex variables and Cauchy integral formula, (ii) Green's functions and Green's theorem. Both approaches work equally well in two dimensions, but approach (ii) can be extended to axisymmetric or three-dimensional geometries. The problem is then reduced to one with unknowns on the interfaces. In addition to the shape of the interface, these unknowns are $V^{(1,2)}$ and ϕ. The integral equations are discretized and the resulting nonlinear systems are solved by iteration. The system is more complex than traditional free surface problems due to the additional integral equations and unknowns. The above approach provides a systematic way to derive asymptotic long wave theories. This leads to simpler non-local integro-differential equations which are also addressed numerically. An important finding is that the asymptotic equations give accurate solutions over a long range of system parameters (e.g. imposed electric fields). This is important because the asymptotic models are much faster to solve numerically as compared to the fully nonlinear ones.

Both symmetric and antisymmetric solutions are studied. In addition we show the existence of waves which are neither symmetric or antisymmetric.

The equations (1)-(8) assume a horizontal electric field and non-conducting fluids and neglect the flow in region 2 of Figure 1, for example. Many applications involve vertical electric fields and/or perfectly conducting fluids. For other applications the motion in both regions must be accounted for (in such cases we refer to the free surface as an interface). The last part of the talk will describe some of these extensions.

CONCLUSION

We have developed nonlinear theories to study the effects of electric fields on capillary waves.

References

[1] G. D. Crapper, An exact solution for progressive capillary waves of arbitrary amplitude, *J. Fluid Mech.* 2 (1957) 532-540.

[2] W. Kinnersley, Exact large amplitude capillary waves on sheets of fluid, *J. Fluid Mech.* 77 (1976) 229-241.

[3] C. Maldarelli, R.K. Jain, I.B. Ivanov and E. Ruckenstein, Stability of symmetric and unsymmetric thin liquid films and long wavelength perturbations. *J. Colloid. Interface Sci.*, **78**, (1980), 118.

[4] G.I. Taylor, The dynamics of thin sheets of fluids II. Waves on fluid sheets. *Proc. Roy. Soc. Ser.A.*, **253**, (1959), 296-312.

BI-DIRECTIONAL WATER WAVES AND INTEGRABLE HIGH ORDER KDV EQUATIONS

Georgy I. Burde*
*J. Blaustein Institute for Desert Research, Ben-Gurion University, 84990 Sede-Boker Campus, Israel

Summary It is shown that the Boussinesq system arising in the context of the shallow water wave motion can be decomposed to a set of coupled equations for the right- and left-moving waves in such a way that, to any order, one of the equations is dependent only on the main right-moving wave and has the form of the KdV equation with higher order corrections. Some classes of exact solutions of the right-moving wave equation, which include impacts of all orders of the asymptotic perturbation expansion, are constructed.

BI-DIRECTIONAL WATER WAVES

The irrotational incompressible flow of shallow layer of inviscid incompressible fluid moving under the influence of gravity as well as surface tension is studied. The wave regime is considered where the surface wave motion has small amplitude and long wavelength and the classical Stokes number is of order one so that the amplitude parameter α and the wavelength parameter β may be treated on an equal footing: Expanding the Euler equations and boundary conditions with respect to the small parameter β and retaining terms up to a certain order gives the Boussinesq equations [1]. These equations admit waves travelling in two directions and thus free of the presumption of unidirectionality that is the hallmark of Korteweg-de Vries (KdV)-type equations as models of surface wave propagation. Although the wave theory first introduced solitons as solutions of unidirectional wave equations, it is expected that the Boussinesq equations should have more intrinsic interest than the unidirectional models.

The KdV equation and its extended versions including higher order corrections are commonly derived from the Boussinesq system by specializing to a wave moving to the right. In the present paper, solutions of the Boussinesq system are considered, in which the surface elevation splits into two components u and ζ corresponding to the right- and left-moving waves (In a similar manner, in [2], the first order system of coupled KdV equations for the right- and left-moving waves is derived and, in [3], the interaction of solitary waves at fourth order is considered under the assumption that the amplitude of the left-moving wave is of $O(\beta^3)$). In the present work, it is assumed that the amplitude of the left-moving wave is of $O(\beta)$ as compared with that of the right-moving wave. The procedure, similar to that commonly used for the unidirectional waves to derive the KdV equation and its extended high order versions, is applied to the Boussinesq equations to decompose them to a set of equations consisting of a relation expressing the fluid velocity through u and ζ and a system of two coupled equations for u and ζ. It is shown that a non-uniqueness of such a decomposition can be used to derive a system of equations for u and ζ, in which, to any order, one of the equations is dependent only on the surface elevation u for the main right-moving wave while the second equation includes both u and ζ. In addition, there are freedoms in choosing the form of the equation for u, in particular, to any order, it can be put (at the expense of an appropriate choice of the second equation form) into the form having the same differential structure as the high order KdV equations arising in the unidirectional case but with arbitrary coefficients in the high order differential polynomials.

INTEGRABLE HIGH-ORDER KDV EQUATIONS AND THEIR SOLUTIONS

The freedoms existing in the choice of the equation for the main right-moving wave may be used to make it integrable. For example, it can be chosen to be a member of the KdV family of integrable equations. Those equations have N-soliton solutions which are the same as the KdV N-soliton solutions except for the higher order corrections to the velocity. In the present work, we consider another, more interesting, possibility of constructing exact solutions of the equation for the right-moving wave. It is of interest in that the constructed solutions include impacts of all orders of the expansion and therefore can be treated as a solution of the original problem in a sense. The solutions are constructed using a new approach to the use of the LIe-Bäcklund groups for equations dependent on a small parameter (in the spirit of the approach developed in [4] for point transformations. A central point of the approach is a new integrable equation that is dependent on the parameter β and possesses the following properties: the leading term of its expansion with respect to βrepresents the KdV equation and the higher order terms are differential polynomials of the same weight as those in the corresponding orders of the equation for the right-moving wave. Solutions of the new integrable equations stem, like the solutions of the KdV family of integrable equations, from solutions of the leading order KdV equation but they possess the features that are present neither in the solutions of the leading order KdV equation nor in the solutions of the high-order KdV equations belonging to the KdV family of integrable equations. In particular, a transition from solitons (waves of elevation) to anti-solitons (waves of depression) may occur, when the value of β exceeds some threshold value (this value depends on the soliton parameters and may be rather small). Correspondingly there are solutions that describe an interaction of waves of elevation with waves of depression.

APPLICATIONS IN THE CONTEXT OF ASYMPTOTIC INTEGRABILITY

The new integrable equations constructed via the approach described are also of interest in the context of asymptotic integrability of physical systems.

First, this integrable equation may be used as a reference equation to define conditions for the asymptotic integrability, which provides an approach to the asymptotic integrability problem different from that based on the normal form theory. In the normal form theory, a near identity transformation is sought that converts the original equation at a specific order in β to an equation given by the symmetries of the leading order equation. In the alternative approach, it is required that a near identity transformation applied to the original equation at some order in β convert it to the equation given by the corresponding terms of an asymptotic expansion of the new integrable equation.

Another result obtained with the use of the new integrable equation is that a near identity transformation, applied to define a solution of a high order KdV equation on the basis of the solution of the equation given by the symmetries of the leading order equation, may yield incorrect solutions even for small values of β.

References

[1] Whitham G.B.: Linear and Nonlinear waves. Wiley, NY 1974.

[2] Matioli F. Decomposition of the Boussinesq Equations for Shallow Water Waves into a Set of Coupled Korteweg-de Vries Equations. *Phys. Fluids A* **3**:2355-2359, 1991.

[3] Marshant T.R.: High-Order Interaction of Solitary Waves on Shallow Water. *Studies Appl. Math.* **109**:1-17, 2002.

[4] Burde G.I.: Potential Symmetries of the Nonlinear Wave Equation $u_t = (uu_x)_x$ and related exact and approximate solutions. *J. Phys. A: Math. Gen.* **34**:5355-5371, 2001.

CD-ROM Proceedings

W. Gutkowski and
T. A. Kowalewski (Eds.)

MECHANICS OF 21st CENTURY



PART 3

International Union of
Theoretical and Applied Mechanics

Springer Academic Publishers

ELASTIC-PLASTIC LARGE DEFORMATION ANALYSIS OF 2D FRAME STRUCTURE

Chung-Yue Wang[*], Ren-Zuo Wang[*], Long-Chyuan Kang[**], Edward C. Ting [*]
[*]*Department of Civil Engineering, National Central University, Chungli 32054, Taiwan, ROC*
[**]*Institute of Nuclear Energy Research, P.O. Box 3-7, Lung-tan, 325, Taiwan, ROC*

Summary This paper presents a numerical simulation method, so called vector form intrinsic finite element (VFIFE) method that can conduct the analysis of 2D frame structure under elastic-plastic large deformation. This new method can simultaneously calculate large rigid body motions and large geometrical changes of a structural system consisting of multiple continuous bodies. The essence of the method includes a set of equations of motion for the modeling nodes of the system, an explicit time integration scheme, the use of a deformation coordinate system to dissect rigid body and deformation displacements, and the use of a convected material reference frame to handle the deformation. Numerical examples of frame structure having large elastic-plastic deformation states under static and dynamic excitations are demonstrated to verify the accuracy and effectiveness of this newly proposed method.

INTRODUCTION

The development of the Finite Element Method (FEM) is originated from the matrix analysis and slope deflection method of the structural mechanics. It promoted the concept of member-connection of structure to the continuous medium. The equilibrium condition is satisfied within all the members (elements) according to the deformation modes characterized by the connections (nodes) and a set of linear equations is obtained by equilibrating internal forces assembled from surrounding members (elements) of each connection (node). This intrinsic concept of physically modeling of the structural system obtains good results in analyzing continuous medium by using constant triangle elements. However, this member-connection modeling of linear structure admitted difficulties when it was applied to the higher order finite element, plate/ shell and 3D deformable bodies. The finite element method entered its new era after adopting the theory of the calculus of variation and some numerical techniques of approximation and discretization. The FEM currently known to the researchers can be identified as a mathematical modeling of continuous medium and is a computational modeling of Ritz-Galerkin analysis. Nevertheless, the analysis method based on the theory of the calculus of variation and the balance of energy inside the simply connected continuous medium still has its limitations on solving some real world problems especially with very large rigid body motion and multiple discontinuities.

A VECTOR FORM INTRINSIC FINITE ELEMENT METHOD

A new computational method so called the Vector Form Intrinsic Finite Element (VFIFE) is developed by Ting etc. [1- 4] to handle engineering problems with the following characters: (1) containing multiple deformable bodies and mutual interactions, (2) material non-linearity and discontinuity, (3) large deformation and arbitrary rigid body motions of deformable body. Since the conventional FEM based on variational method requires the total virtual work to be zero but dose not require the balance of forces at nodes. These unbalanced residual forces will do some non-zero work under virtual rigid body motion and cause the inaccuracy and un-convergence of the calculation results. The computation procedure and some concepts of this VFIFE method are similar to the FEM. But the major difference is that the VFIFE does not apply the variational principle on the stress expressed equilibrium equations in its formulation. Instead, VFIFE maintains the intrinsic nature of the finite element method and makes strong form of equilibrium at nodes, the connections of members. All the forces balanced at each node are obtained from the principle of virtual work and the associated deformations are satisfied with the compatibility condition of deformation. In this method (see Fig. 1), explicit formulation is used to avoid the difficulties that are caused by iterations of material non-linearity and an incremental theory based on the material reference frame of current configuration is used to define the stress-strain relations. In the calculation process, the external loads are applied to the deformable body incrementally. These incremental forces apply to a continuous body with stress and motion. All the material properties, stress distribution, particle velocities and geometry are defined from the calculation results of previous time step. The motion path and loading history of material points in the system are independent to the incremental type computational algorithm. The history dependency is inherited in the adjusting of parameters of material model during the calculation. Hence, we can call this explicit calculation is based on the convected material frame. The incremental theory may not be so complete and accurate as the total deformation theory since errors are introduced in every incremental step. But, we are benefited from the simplification and convenience it provides to the code development.

ELASTIC-PLASTIC LARGE DEFORMATION ANALYSIS OF 2D FRAME STRUCTURES

To verify the capabilities of VFIFE method, some problems with large deformation were studied. Consider a cantilever modeled by frame elements, and is subjected to constant end moment. The beam should coil with constant curvature.

Figure 2 shows simulations done by the VFIFE method exactly match the analytical solutions. The elastic-plastic behavior of a free ring subjected to impulse loading on its upper surface is simulated. Figure 3 shows the prediction matches the experimental data very well. Figure 4 shows the shapes and trajectories of fragments after fracture due to impulse loading. It is clear that the VFIFE method can simulate the problems with very large deformation better than the conventional methods.

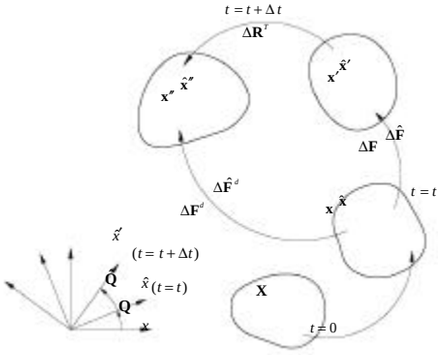


Figure 1.

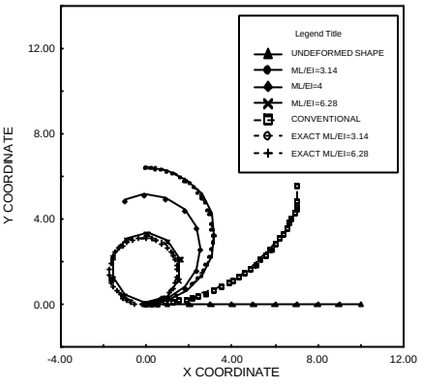


Figure 2.

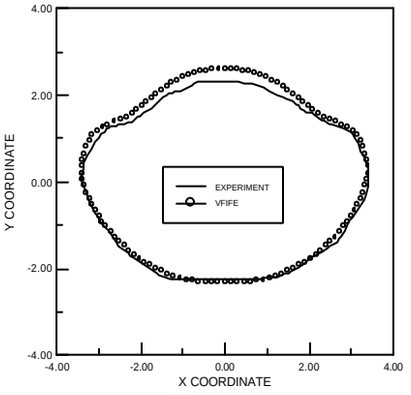


Figure 3.

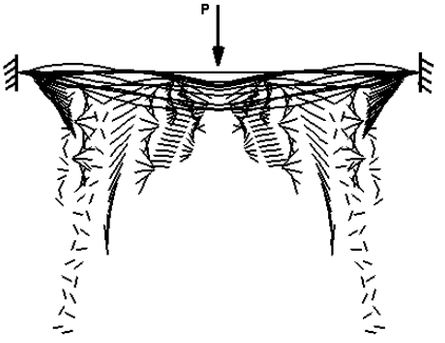


Figure 4.

CONCLUSIONS

In this paper, a convected material frame is used to define strain, stress and virtual work. Based on this frame system, a new incremental analysis procedure is developed for the study of motions that involve very large deformation, displacements and fragmentation behaviors that are difficult to be conducted by the conventional FEM. This explicit procedure is named as vector form intrinsic finite element (VFIFE) method. The stability and accuracy of this method were verified by examples. Since the calculation of the VFIFE method is carried on each discrete node, it is very easy to couple this method with other numerical schemes to study mechanics problems containing solid- fluid- temperature- electromagnetic interactions. Besides, the explicit formulation of the VFIFE method allows it to model the discontinuous and nonlinear dynamic behaviors of material easily.

References

[1] Ting, E. C., Shih, C. and Wang, Y. K.: Fundamentals of A Vector Form Intrinsic Finite Element: Part I. Basic Procedure and A Plane Frame Element. *Chinese Journal of Mechanics* (to appear), 2004

[2] Ting, E. C., Shih, C. and Wang, Y. K.: Fundamentals of A Vector Form Intrinsic Finite Element: Part II. Plane Solid Elements. *Chinese Journal of Mechanics* (to appear), 2004.

[3] Shih, C., Wang, Y. K. and Ting, E. C.: Fundamentals of A Vector Form Intrinsic Finite Element: Part III. Convected Material Frame and Examples. *Chinese Journal of Mechanics* (to appear), 2004.

[4] Wang, C. Y., Wang, R.-Z., Wu, T. Y., Ting, E. C. and Kang, L. C.: Nonlinear Discontinuous Deformation Analysis of Structure. Proceedings of the Sixth International Conference on Analysis of Discontinuous Deformation (ICADD-6), Ming Lu , 79-91, A. A. Balkema Publishers, 2003.

XXI ICT AM, 15–21 August 2004, Warsaw, Poland

MULTISCALE ANALYSIS OF SCATTERED ELASTIC WAVES BASED ON THE LIPPMANN–SCHWINGER EQUATION

Terumi Touhei*

*Dept. of Civil Engineering, Tokyo University of Science, Noda City 278-8510, Japan

Summary A method for the multiscale analysis of scattered elastic waves by means of the Lippmann–Schwinger equation is developed. A multiscale decomposition is defined herein in order to examine how the effects of fluctuations of the wave field are conveyed to the far field by Green's function. The numerical results were found to clarify the scale effects of the wave field on scattering of waves.

INTRODUCTION

Although a great deal of research concerning scattering of elastic waves is in the literature; however, the way in which small-scale fluctuation of the wave field influences the scattering of waves remains unclear. It is convenient to express the solution of the wave field in terms of the Lippmann–Schwinger equation (Colton and Kress, 1998) in cases in which the medium has a small-scale fluctuation. In the present paper, the Lippmann–Schwinger equation together with a multiscale decomposition (for example, Hughes, 1995) is applied in order to examine the scale effects of a medium on scattering of elastic waves.

THEORETICAL FORMULATION

Consider an infinite wave field in which the properties of the field vary continuously. For simplicity, the presence of only the S wave is assumed and the shear modulus in the medium is as follows:

$$\mu(x) = \mu_0 + \mu_1(x), \quad x \in \mathbb{R}^n, \quad \text{supp } \mu_1(x) \subset B \tag{1}$$

where $\mu(x)$ is the shear modulus, μ_0 is a constant and $\mu_1(x)$ is the fluctuation of the shear modulus around μ_0 and B is a compact set in $\mathbb{R}^n$. Let the fluctuation be made up of two parts. Namely,

$$\mu_1(x) = \mu_l(x) + \mu_s(x), \quad \text{supp } \mu_s \subset B_s \subset B \tag{2}$$

where μ_l is the shear modulus showing a large-scale variation, while μ_s is that for the localized small scale variation.

The first step of the formulation is to express the solution of the wave field in the form of the integral equation (the Lippmann–Schwinger equation) as follows:

$$u(x) = f(x) - \int_B a(x,y)u(y)dy, \quad x, y \in \mathbb{R}^n \tag{3}$$

where u is the displacement field, f is the free-field response of the wave field and $a(x,y)$ is the kernel of the integral equation which is constituted by $\mu(y)$ and Green's function for the homogeneous wave field. In the following, Eq. (3) is simply expressed as $u = f - Au$ for convenience.

Next step is the application of the multiscale decomposition to the solution of Eq. (3) such that

$$u(y) = u_l(y) + u_s(y), \quad y \in B, \quad B_s \subset \text{supp } u_s \subset B \tag{4}$$

where u_l is the large-scale solution and u_s is the small-scale solution which covers the area of the small-scale fluctuation. This type of decomposition becomes possible by means of the scaling function and wavelets of compact support. For example, u_l and u_s can be expressed as follows:

$$u_l(y) = \sum_{k\in\mathbb{Z}} \alpha_k \phi_{m,k}(y), \quad u_s(y) = \sum_{m'\geq m} \sum_{k\in\mathbb{Z}} \beta_k \psi_{m',k}(y) \tag{5}$$

where $\phi_{m,k}$ and $\psi_{m',k}$ are the Haar scaling function and wavelet (Williams and Amaratunga, 1994). According to the decomposition, the projections P and Q can be defined such that $u_l = Pu$, $u_s = Qu$ and $P \perp Q$. The decomposition of the displacement field leads to the following two integral equations.

$$u_s + QAu_s = Qf - QAu_l \tag{6}$$

$$u_l + PAu_l = Pf - PAu_s \tag{7}$$

According to Eq. (6), an operator M such that $u_s = M(f, u_l)$ can be defined if $\|QA\| < 1$. Then, Eq. (7) becomes

$$u_l + PAu_l = Pf - PA\ M(f, u_l) \tag{8}$$

from which the large-scale solution is derived.

NUMERICAL EXAMPLES

Figure 1 shows the analyzed model for 1-D wave propagation problem, in which a thin soft layer is embedded in the medium and a plane incident wave is propagating toward the soft layer. Properties of the material for the medium are described in Fig. 1 and the spatial variations of the shear modulus are shown in Fig. 2. The frequency of the analysis is 1 Hz. There are two cases for numerical examples. A small-scale fluctuation of the rigidity of the medium is imposed on Case-2. Figure 3 shows the comparison of the displacement between the two cases. For both cases, the convergence of the solutions using the Haar scaling function and wavelet is preliminarily examined. It was found from the examination that the size of the support of u_s covering the fluctuated area did not affect the total field solution, if the solution converged. The order of the resolution of Eq. (5) for Case-2 was found to be $m' = 7$ for the satisfactory level of accuracy. A difference in the amplitude in the backward side and that of phase lag in the forward side can be seen in Fig. 3. Figure 4 shows the comparison of the components of the scattering of the wave due to the large and small-scale solutions. According to the comparison, the amplitudes of both scale solutions are comparable outside the soft layer, although the amplitude of the small-scale solution is very small inside the layer. The small-scale solution is found to have a significant role outside the soft layer as the large-scale solution has.

CONCLUSIONS

Multiscale decomposition of the wave field was carried out for the Lippmann–Schwinger equation to examine the scale effects of fluctuation of the medium on scattering of waves. The usage of the scaling function and wavelet basis ensured the multiscale additive decomposition here. The numerical results showed that the small-scale solution also had as significant a role for scattering of waves as the large-scale solution.

References

[1] Hughes, T.J.R.: *Computer methods in applied mechanics and engineering*, **127**, pp. 387-401, 1995.
[2] Colton,D. and Kress, R.: *Inverse acoustic and electromagnetic scattering theory*, Berlin, Springer, 1998.
[3] Williams, J.R. and Amaratunga, K.: *Int. J. Num. Method. in Engineering*, **37**, pp. 2365-2388, 1994.

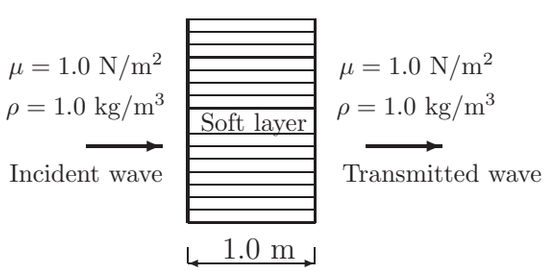


Figure 1. Analyzed model.

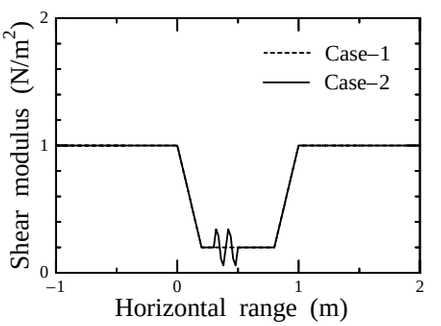


Figure 2. Spatial variation of the shear modulus.

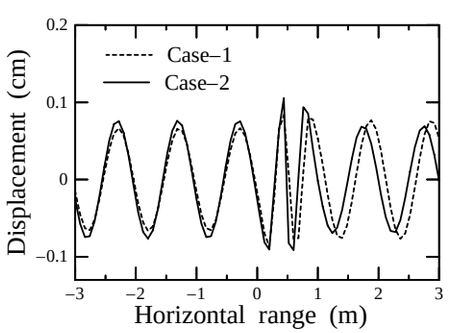


Figure 3. Comparison of displacement between the two cases.

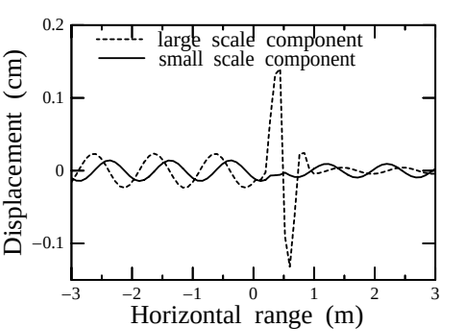


Figure 4. Comparison of the two scale solutions.

MODEL UPDATING A MULTICRITERIA OPTIMIZATION PROCESS IN MECHANICS

Hans H. Müller-Slany
University of Duisburg-Essen, Institute of Mechatronics and Systemdynamics,
D-47057 Duisburg, Germany

Summary Model updating is a widely used area of research in the field of dynamics of elasto-mechanics. The ill-conditioned inverse mathematical problem is mainly solved in a sensitivity based numerical process, considering regularization methods. Here it is shown how additional dynamical properties of the structure can be introduced in the updating procedure. Model updating will be formulated as a constrained multiobjective optimization problem, which can be solved by a hierarchical scalarization method. Applications will be shown.

INTRODUCTION

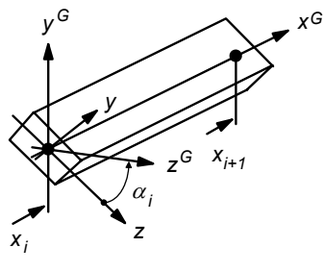
Model updating is the tool for achieving a validated mathematical model of an elasto-mechanical system. The purpose of model updating is to converge the mathematical model of a system upon measurements that are taken from the real structure. Thinking in input/output relations, the goal is to adjust the model parameters by comparing measured dynamical i/o relations of the system with numerical i/o relations of the mathematical model.
Model updating has become a very wide-spread area of research in the field of FE-modelling of structures. The Finite Element method is the tool most used for numerical modelling in structural engineering today. But for many applications, an initial FE-model is often a poor representation of a real structure because of simplifying and idealization while constructing the FE-model. A special issue of the Journal of *Mechanical System and Signal Processing* [1] demonstrated the developments in model updating. Typical examples and benchmark tests include the recently completed COST action [2] (European CO-operation in the field of Scientific and Technical research). Updated and validated mathematical models are of very great importance in the area of industrial developments of mechatronic systems, in the field of optimization of dynamic systems, for structural modification problems and for model based damage detection.
The common way of model updating is based on sensitivity methods. Here, an error function is defined as the difference between the numerical and the measured data of a dynamic system. The errors are defined in the modal domain (natural frequencies and mode shapes) and in the frequency domain (FRFs: frequency response functions). The model updating problem is solved by minimizing a global function of all system errors in an iterative numerical process. Usually this inverse mathematical problem is ill-conditioned. For its solution it is necessary to apply "regularization" methods by using additional constraints.

MODEL UPDATING DESCRIBED BY FUNDAMENTALS OF MECHANICS

Model updating is an ill-conditioned inverse mathematical problem; adjusting of model parameters has to be calculated from the output of the model. Facing this fact, it is necessary to go back to the fundamentals of mechanics. Instead of applying formal regularization methods, we have to deal with invariants of the elasto-mechanical system and with the application of the principles of mechanics.
The goal is the generation of a mathematical model, which is substantially condensed and at the same time highly accurate, regarding dynamical system properties.

Description of the elasto-mechanical structure using FE-super-elements

The updated model is a highly accurate dynamic description of the real system using FE-macro-elements, e. g. macro-beam-elements (see Fig. 1). Due to application in system modification and optimization and model based damage detection, its layout has to be close to reality. It is described by design variables x_i, $i = 1,\ldots, n$. These are: element masses, positions of the element nodes, angles of principal axes of the cross sections and parameters of bending, torsion and axial stiffness. The model will be described by the vector $\boldsymbol{x} = [x_1, \ldots, x_n]^T$ of n design variables. Finally, this design vector is the result of the updating process.



parameters of an element i	
coordinates of element nodes	x_i
	x_{i+1}
mass	m_i
stiffness parameters	EA_i
	EI_{yyi}
	EI_{zzi}
	GI_{pxi}
principal axis	α_i

Fig. 1: Parameters of FE-macro-element (y^G, z^G: global coordinates)

Considered dynamical properties of an elasto-mechanical structure

Regarding the fundamentals of mechanics, model updating means the adaptation of all mechanical invariants and dynamical properties to the mathematical model. Considering more of such properties is equal of making the ill-

Type	Dynamical property	
Mass-geometrical data	Total mass	$m = \sum_{i=1}^{p} m_i$
	Centre of mass	$\boldsymbol{r}_{OS} = [x_{OS}, y_{OS}, z_{OS}]^T$
	Tensor of inertia	$\boldsymbol{I}_S = \begin{bmatrix} I_{xx} & I_{xy} & I_{xz} \\ & I_{yy} & I_{yz} \\ sym. & & I_{zz} \end{bmatrix}$
Modal Data	Nat. frequencies	$\omega_i, \ i = 1, \ldots, k$
	Nat. mode shape	$\boldsymbol{q}_i, \ i = 1, \ldots, k$
Frequency Response function	Selected FRF-data	$h_j(\omega_i), \ \begin{matrix} i = 1, \ldots, k \\ j = 1, \ldots, p \end{matrix}$

Table 1: Dynamical properties for model updating process

conditioned inverse mathematical problem less under-determinated. If we are considering only modal values and FRF-data, that means simply that we are dealing with mathematical models, which are far away from the reality of mechanics. Regularization methods cannot close this gap. They make sense only in numerical adjusting, not in better mechanical modelling.

A reasonable model updating process has to consider at least all mass-geometrical values of the real elasto-mechanical structure, all modal values in a concerned frequency range (natural frequencies f_i and natural mode shapes $\boldsymbol{q}_i$) and all selected FRF-data near to the natural frequencies f_i (see table 1). The updated model will be correct in a mechanical sense, only if the time-variable forces inside of the structure are correctly updated to a state of a vibration. We can construct a vector of *local momentum*, which is composed of the linear momentums of each macro-element of the system in a state of a vibration [3]. Using this vector in the updating procedure means we additionally consider the internal forces of the structure.

MODEL UPDATING: A MULTICRITERIA OPTIMIZATION PROBLEM

All dynamical properties can be formulated as functions of the design vector $\boldsymbol{x}$. The error expressions $\varepsilon_k(\boldsymbol{x})$ between the numerical and measured system properties are elements of the vector objective function $\boldsymbol{f}[\boldsymbol{\varepsilon}(\boldsymbol{x})]$ (1). Finally, the model updating procedure can be formulated as a constrained multiobjective optimization problem (2) Where $\boldsymbol{h}(\boldsymbol{x})$ = equation of constraints; $\boldsymbol{x}_L$ and $\boldsymbol{x}_U$ are the lower and upper bounds, respectively.

$$\boldsymbol{f}(\boldsymbol{x}) = \begin{bmatrix} \varepsilon_1(\boldsymbol{x}) \\ \varepsilon_2(\boldsymbol{x}) \\ \varepsilon_3(\boldsymbol{x}) \\ \varepsilon_4(\boldsymbol{x}) \\ \varepsilon_5(\boldsymbol{x}) \\ \varepsilon_6(\boldsymbol{x}) \end{bmatrix} = \begin{bmatrix} error\ expression\ of: \quad total\ mass \\ \ldots\ position\ of\ centre\ of\ mass \\ \ldots\ elements\ of\ tensor\ of\ inertia \\ \ldots\ natural\ frequencies\ f_1(\boldsymbol{x}) \ldots f_k(\boldsymbol{x}) \\ \ldots natural\ mode\ shapes\ \boldsymbol{q}_1(\boldsymbol{x}) \ldots \boldsymbol{q}_k(\boldsymbol{x}) \\ \ldots selected\ FRF\text{-}datas \end{bmatrix}, \qquad (1)$$

$$\min_{\boldsymbol{x} \in \Sigma} \left\{ \boldsymbol{f}[\varepsilon(\boldsymbol{x})] \,\middle|\, \boldsymbol{h}(\boldsymbol{x}) = \boldsymbol{0} \right\}, \quad \Sigma := \left\{ \boldsymbol{x} \in \Re^n \,\middle|\, \boldsymbol{x}_L \le \boldsymbol{x} \le \boldsymbol{x}_U \right\}. \qquad (2)$$

$$\boldsymbol{f}(\boldsymbol{x}) \quad \Rightarrow \quad \boldsymbol{s}\{\boldsymbol{f}[\varepsilon(\boldsymbol{x})]\} = \begin{bmatrix} s_1[\varepsilon_1(\boldsymbol{x}), \varepsilon_2(\boldsymbol{x}), \varepsilon_3(\boldsymbol{x})] \\ s_2[\varepsilon_4(\boldsymbol{x})] \\ s_3[\varepsilon_5(\boldsymbol{x})] \end{bmatrix}. \qquad (3)$$

This optimization problem can be solved numerically by a hierarchical scalarization strategy in consecutive steps using a SQP algorithm. The elements of the vector objective function (1) are divided in three different groups by scalarization (3): *1st group*: all mass-geometrical values; *2nd group*: the considered eigenfrequencies and mode shapes; *3rd group*: the considered FRF-values. In each step of the hierarchical optimization procedure, one group of dynamical properties of the mathematical model will be adapted to the properties of the real system. Those system properties, which already have been adapted in previous steps of the procedure, must be fixed by additional constraints in the following steps. The final vector $\boldsymbol{x}$ of the design variables creates the updated model for the elasto-mechanical structure considered here. The great advantage of this formulation is the fact that each different system property can be updated in a special process, whereas in sensitivity based methods all errors between model and measurements are regarded simultaneously. This model updating procedure will be shown for several elasto-mechanical structures.

CONCLUSIONS

The creation of updated models can be solved in three main steps. First, the elasto-mechanical system has to be constructed by FE-macro-elements whose lay-out is close to reality. All system parameters are collected in a design vector $\boldsymbol{x}$. Next, a number of dynamic system properties form the basis of the updating procedure. Finally, this process can be formulated as a constrained multiobjective optimization problem, where a vector objective function of system errors will be minimized. A special hierarchical scalarization strategy is shown for the solution of this problem.

References

[1] Mottershead, J.E., Friswell,M.I. (Eds.): *Special Issue: Model Updating*. Mech. Systems & Signal processing, 1998, Vol. 12, No. 1, 223 pp.

[2] Golinval J.-C., Link M. (Eds.): *Special Issue: COST Action.* Mech. Systems & Signal processing, 2003, Vol. 17, No. 1, 254 pp.

[3] Müller-Slany, H.H.: Möglichkeiten und Grenzen der Schwingungsdiagnose für mechanische Systeme auf der Basis numerischer Strukturmodelle. VDI-Berichte, No. 1788, VDI-Verlag, Düsseldorf, 2003, pp. 71-104.

Experiment and Quasicontinuum simulation of nanoindentation of single crystal copper

Yuan Lin, Shan Debin, Guo Bin
School of Materials Sciences and Engineering, Harbin Institute of Technology, Harbin, 150001, China
E-mail: yuanlin@hit.edu.cn

Abstract: Experiment and quasicontinuum simulation [1] of nanoindentation of fcc single crystal copper are performed. Indentation is accommodated by elastic deformation of the surface, up to an indenter displacement of about 4.2 Å, and by nucleation of crystalline defects for deeper indents. The critical load for the event is computed and the nucleation is observed. The result is compared with experimental data. The comparison conveys the conclusion that incipient plasticity is induced at much earlier times and much smaller loads than observed in nanoindentation experiment, and the measured instabilities are collective events involving a large number of pre-existing dislocations.

In load-controlled nanoindentation experiments, after a preliminary elastic stage, a discontinuity in indenter displacement has been captured for the measured load ***P*** versus indentation depth ***h*** response for several crystals. A quantitative understanding of the critical condition for homogeneous dislocation nucleation is still lacking. Experiment and quasicontinuum simulation of nanoindentation in fcc copper are performed. The copper is modeled using the EAM potential [1]. A rigid knife-like flat indenter, 9.31 Å wide, is driven down into the (110) surface of the crystal. Perfect stick conditions between the indenter and crystal are assumed. The model is shown in fig.1. When indented in the [111] direction produces dislocation nucleation from the stress concentration sites at the indenter edge. The critical load for the event is computed and the nucleation is observed. The result is compared with experimental data. The comparison conveys the conclusion that incipient plasticity is induced at much earlier times and much smaller loads than observed in nanoindentation experiment, and the measured instabilities are collective events involving a large number of pre-existing dislocations.

The load versus indentation depth curve for this simulation is plotted in fig. 2. The sudden drop in the load at the instant of dislocation nucleation is clearly visible. The nucleated dislocations are shown by plotting the displacement plots (see fig. 3). Moreover the 22st snap of atoms of nanoindentation by QC simulation is shown (see fig. 4). The dislocations are found.



Figure 1: Nanoindentation model by QC simulation

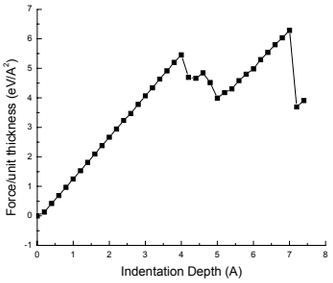
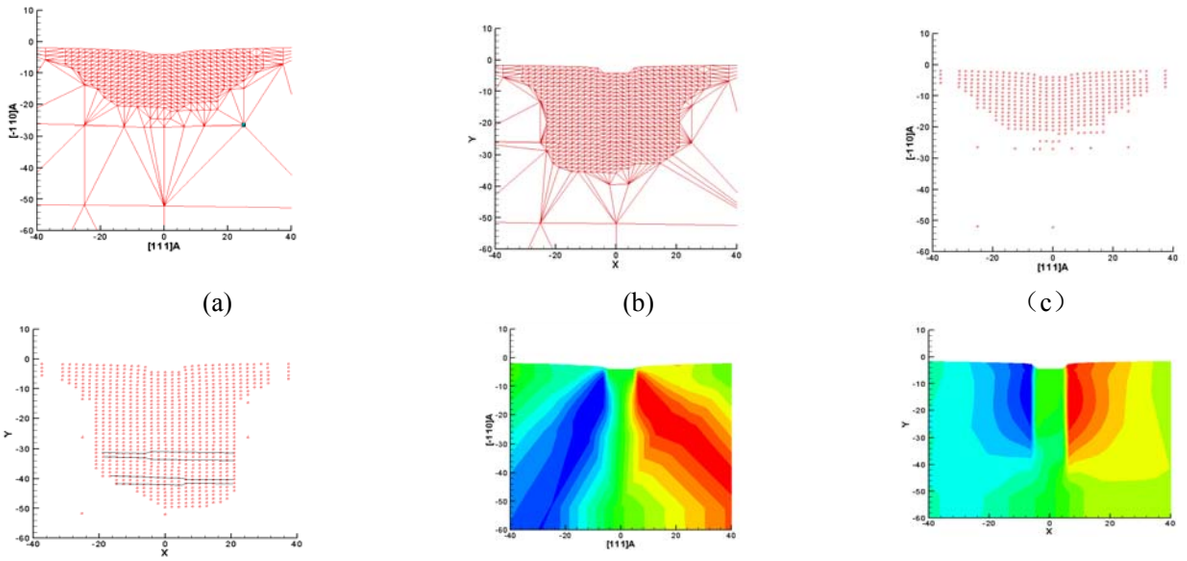


Figure 2: The force per unit thickness versus indentation depth for the nanoindentation simulation



(a) (b) (c)

(d) (e) (f)

Figure 3: Two snapshots of the mesh under indenter (a) immediately before the first emission, (b) after emission of dissociated dislocations from both ends of the indenter and (c) corresponding snap of atoms at 21st steps (d) corresponding snap of atoms at 22st steps. Frames (e) and (f) show the corresponding scatter plots.

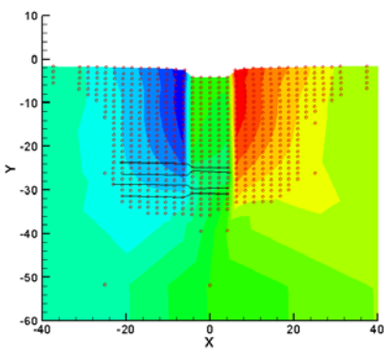


Figure 4: Snap of atoms at 22st steps and contour (UZ)

References:

1. E.B.Tadmor, M. Ortiz, and R. Phillips. Quasicontinuum analysis of defects in solids. Phil. Mag. A, 73(6):1529-1563,1996
2. S.M. Daw and M.I. Baskes. Embedded-atom-method functions for the fcc metals Cu, Ag, Au, Ni, Pd, Pt, and their alloys. Phys. Rev., B, 33(12):7983-7991

A BEM SOLUTION TO TRANSVERSE SHEAR LOADING OF BEAMS

Evangelos J. Sapountzakis*, Vasilios G. Mokos*
*School of Civil Engineering, National Technical University, Zografou Campus, GR-15773 Athens, Greece

Summary In this paper a boundary element method is developed for the evaluation of the transverse shear stresses in beams of arbitrary simply or multiply connected constant cross section subjected in transverse shear loading. The transverse shear loading is applied at the shear center of the cross section, avoiding in this way the induction of a twisting moment. Two boundary value problems that take into account the effect of Poisson's ratio are formulated with respect to harmonic functions and solved employing a pure BEM approach. The evaluation of the transverse shear stresses is accomplished by direct differentiation of these harmonic functions, while both the coordinates of the shear center and the shear deformation coefficients are obtained from these functions using only boundary integration. Numerical examples with great practical interest are worked out to illustrate the efficiency, the accuracy and the range of applications of the developed method.

Statement of the problem

Consider a cylindrical beam of length L with a cross section of arbitrary shape, occupying the two dimensional multiply connected region Ω of the y,z plane bounded by the $K+1$ curves $\Gamma_1,\Gamma_2,...,\Gamma_K,\Gamma_{K+1}$ as shown in Fig.1. Without loss of generality, it may be assumed that the beam end with centroid at point C is fixed, while the x –axis of the coordinate system is the line joining the centroids of the cross sections.

When the beam is subjected to torsionless bending arising from a concentrated load Q applied at the shear center M of its free end cross section, at a distance x from the fixed end the internal forces are the shear forces Q_y, Q_z being the components of the concentrated load Q along y and z axes, respectively and the bending moments M_y, M_z given as

$$M_y = -Q_z\left(L-x\right) \qquad M_z = Q_y\left(L-x\right) \tag{1}$$

Moreover, the normal component of stress acting on the beam cross section made from a homogeneous, isotropic and linearly elastic material is given as

$$\sigma_{xx} = -\left(\frac{M_y I_{yz} + M_z I_{yy}}{I_{yy}I_{zz} - I_{yz}^2}\right) y + \left(\frac{M_y I_{zz} + M_z I_{yz}}{I_{yy}I_{zz} - I_{yz}^2}\right) z \tag{2}$$

The evaluation of the shear stress distributions will be accomplished by regarding the beam subjected separately to Q_y and Q_z shear forces and obtaining the arising shear stress components by superposition.

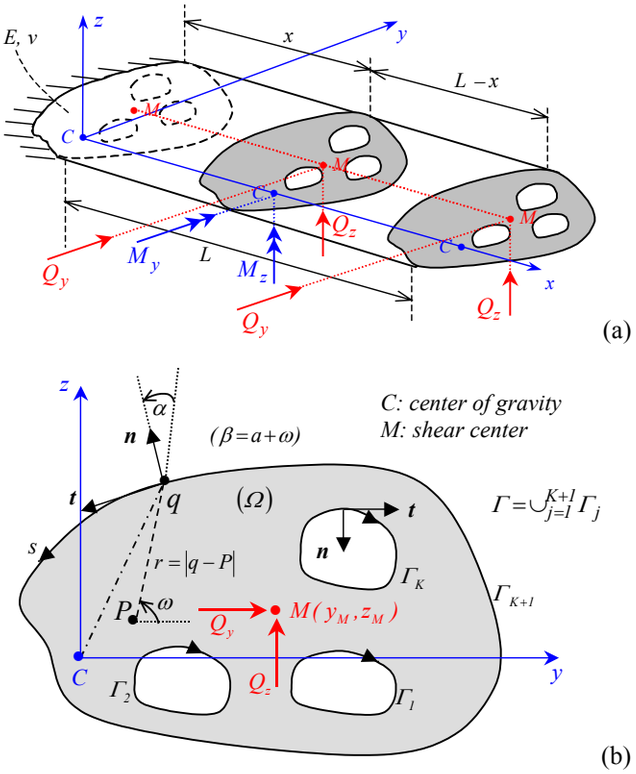


Fig.1. Prismatic bar subjected to torsionless bending (a) and two dimensional region Ω occupied by the cross section (b).

Thus, considering the beam subjected to Q_z shear force and assuming a stress function $\Phi\left(y,z\right)$ having continuous partial derivatives up to the third order such that the compatibility conditions to be identically satisfied the transverse shear stress components τ_{xy}, τ_{xz} are expressed as

$$\tau_{xy} = \frac{Q_z}{B}\left[\frac{\partial \Phi}{\partial y} + \nu\left(I_{yz}\frac{y^2-z^2}{2} - I_{zz}yz\right)\right] \qquad \tau_{xz} = \frac{Q_z}{B}\left[\frac{\partial \Phi}{\partial z} + \nu\left(I_{zz}\frac{y^2-z^2}{2} + I_{yz}yz\right)\right] \tag{3a,b}$$

where it has been set $B = 2\left(1+\nu\right)\left(I_{yy}I_{zz} - I_{yz}^2\right)$. Substituting eqns.(3a,b) in the first equation of equilibrium and vanishing the traction vector normal to the boundary on the free surface of the beam, the partial differential equation governing the stress function $\Phi\left(y,z\right)$ and its boundary condition are obtained as

$$\nabla^2\Phi = 2\left(I_{yz}y - I_{zz}z\right) \quad \text{in } \Omega \qquad \frac{\partial\Phi}{\partial n} = \nu\left(I_{zz}yz - I_{yz}\frac{y^2-z^2}{2}\right)\cos\beta - \nu\left(I_{zz}\frac{y^2-z^2}{2} + I_{yz}yz\right)\sin\beta \quad \text{on } \Gamma \tag{4a,b}$$

while the coordinate y_M of the shear center M can be obtained from

$$y_M = \frac{1}{B}\left[\frac{\nu}{2}\int_\Omega\left(I_{zz}y + I_{yz}z\right)\left(y^2+z^2\right)d\Omega - \int_\Omega\left(z\frac{\partial\Phi}{\partial y} - y\frac{\partial\Phi}{\partial z}\right)d\Omega\right] \tag{5}$$

Similar relations with (3a,b), (4a,b) and (5) can be derived considering the beam subjected to Q_y shear force and defining as $\Theta(y,z)$ the corresponding stress function. Finally, the shear deformation coefficients a_y, a_z and a_{yz} using an energy approach are obtained from

$$a_y = \frac{A}{B^2}\int_\Omega\left[\left(\frac{\partial\Theta}{\partial y} - \nu\left(I_{yy}\frac{y^2-z^2}{2} - I_{yz}yz\right)\right)^2 + \left(\frac{\partial\Theta}{\partial z} - \nu\left(I_{yz}\frac{y^2-z^2}{2} + I_{yy}yz\right)\right)^2\right]d\Omega \tag{6a}$$

$$a_z = \frac{A}{B^2}\int_\Omega\left[\left(\frac{\partial\Phi}{\partial y} + \nu\left(I_{yz}\frac{y^2-z^2}{2} - I_{zz}yz\right)\right)^2 + \left(\frac{\partial\Phi}{\partial z} + \nu\left(I_{zz}\frac{y^2-z^2}{2} + I_{yz}yz\right)\right)^2\right]d\Omega \tag{6b}$$

$$\begin{aligned} a_{yz} = \frac{A}{B^2}\int_\Omega\Bigg[&\left(\frac{\partial\Theta}{\partial y} - \nu\left(I_{yy}\frac{y^2-z^2}{2} - I_{yz}yz\right)\right)\left(\frac{\partial\Phi}{\partial y} + \nu\left(I_{yz}\frac{y^2-z^2}{2} - I_{zz}yz\right)\right) + \\ &\left(\frac{\partial\Theta}{\partial z} - \nu\left(I_{yz}\frac{y^2-z^2}{2} + I_{yy}yz\right)\right)\left(\frac{\partial\Phi}{\partial z} + \nu\left(I_{zz}\frac{y^2-z^2}{2} + I_{yz}yz\right)\right)\Bigg]d\Omega \end{aligned} \tag{6c}$$

Integral Representations - Numerical Solution

The numerical solution of both boundary value problems concerning the stress functions $\Phi(y,z)$ (described by eqns.4a,b) and $\Theta(y,z)$ is similar. Thus, for the stress function $\Phi(y,z)$ employing the Green identity the following integral representation is obtained

$$\begin{aligned} \Phi(P) = &\frac{1}{4\pi}\int_\Gamma\left[\left(I_{yz}y - I_{zz}z\right)\left(2\ln r - 1\right)r\cos a - \left(I_{yz}\cos\beta - I_{zz}\sin\beta\right)\left(\ln r - 1\right)r^2\right]ds + \\ &\frac{1}{2\pi}\int_\Gamma\left[\Phi(q)\frac{\cos a}{r} - \left(\nu\left(I_{zz}yz - I_{yz}\frac{y^2-z^2}{2}\right)\cos\beta - \nu\left(I_{zz}\frac{y^2-z^2}{2} + I_{yz}yz\right)\sin\beta\right)\ln r\right]ds \quad P\in\Omega, q\in\Gamma \end{aligned} \tag{7}$$

The values of the function Φ inside the domain Ω are established from the integral representation (7) after evaluating the boundary values of Φ, which is achieved by writing eqn.(7) for the boundary points, using a special technique to overcome the singular line integrals and solving the resulting linear system of simultaneous algebraic equations.

Numerical examples

Numerical examples with great practical interest such as that presented in Fig.2 are worked out to illustrate the efficiency, the accuracy and the range of applications of the developed method.

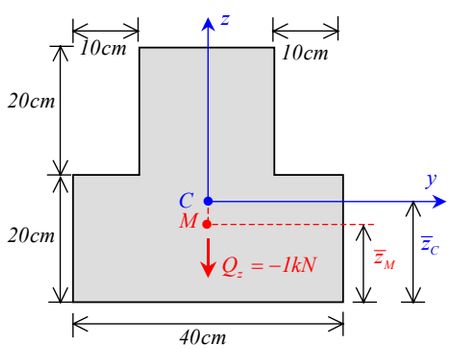
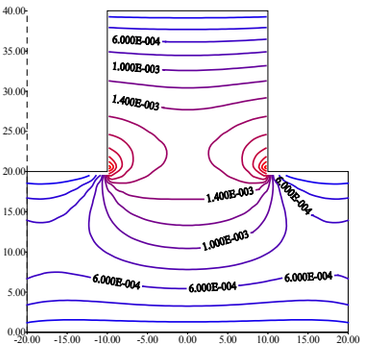
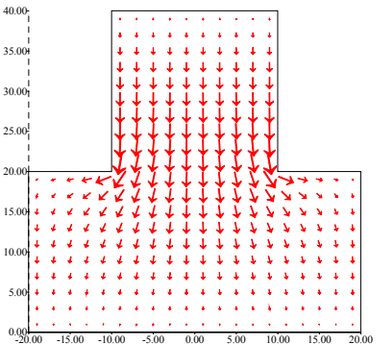


Fig.2. Geometry of the cross section.



Shear stresses τ_{xz} $(\nu = 0.20)$



Distribution of τ_{xz} $(\nu = 0.20)$

References

[1] Gruttmann F.,Wagner W.: Shear correction factors in Timoshenko's beam theory for arbitrary shaped cross-sections. *Computational Mechanics* **27**:199-207, 2001.

[2] Pilkey W.D.: Computer Analysis of Elastic Thin-Walled Beams. Department of Mechanical, Aerospace and Nuclear, Engineering University of Virginia Charlottesville, Virginia 1998.

XXI ICTAM, 15–21 August 2004, Warsaw, Poland

MECHANICAL FEATURES OF PIANO HAMMER FELT

Anatoli Stulov
Centre for Nonlinear Studies, Institute of Cybernetics at Tallinn Technical University, Akadeemia 21, Tallinn 12618, Estonia

Summary Experimental testing of piano hammers, which consist of a wood core covered with several layers of compressed wool felt demonstrates, that all hammers have the hysteretic type of the force-compression characteristics. It is shown, that different mathematical hysteretic models can describe the dynamic behavior of the hammer felt. In addition to the four-parameter nonlinear hysteretic felt model, another new three-parameter hysteretic model was developed. The both models are based on the assumption that the hammer felt made of wool is a microstructured material possessing history-dependent properties. Both of the models are equivalent for the slow loading of the felt.

INTRODUCTION

The dynamics of the hammer - string interaction is one aspect of piano physics that has been the subject of considerable research, beginning with von Helmholtz. The hammers in the early pianos have been made of wooden head covered with leather. Since about 1830, the standard material for piano hammers manufacturing is the felt. In spite of the endless attempts to match a more suitable material for the piano hammer, the felt is a unique coating matter of wooden mallets used up to the present. The modern hammers have a wood core covered with one or two layers of compressed wool felt, whose stiffness increases from heavy bass hammers to light treble hammers to produce a good tone.
First constitutive framework proposed to mathematical model of the hammer felt was made by Ghosh [1], who considered the force-compression characteristic of the felt obeying the power law form

$$F = K\,u^p\,, \tag{1}$$

where F is the acting force, u is felt compression, and constant K has units of N/m^p. Experimental static testing of different hammers by Hall and Askenfelt [2] demonstrate that for hammers taken from pianos the values of p ranging from 2.2 to 3.5 give a good approximation of dependence (1).

SIMPLE HAMMER FELT MODEL

A new geometrical version of the static hammer felt model is proposed in [3]. By deriving of this model it was taking into account that the felt deformation depends only on the stiffness of the felt material, identical for all the hammers of the piano, and on the geometrical configuration of the felt compressed. Assuming that the kinetic energy of the hammer transforms into the energy of the felt deformation and that the energy density is a constant value in the volume of interaction, the simple model of the felt is derived in the form

$$F(y) = E\frac{d^3}{R}\left(1+\frac{d}{2R}\right)^{-1/2} y\,q(y)\,, \tag{2}$$

with a function

$$q(y) = 2\arcsin\phi - 2(1-2y)\phi\,; \qquad \phi = 2\sqrt{y(1-y)}\,.$$

Here $y = u/d$ is a nondimensional compression; E is a Young's modulus of the felt material; d is the string diameter; R is the curvature radius of the hammer head. For small deformation $y \ll 1$, Eq. (2) gives

$$F(u) = \frac{\sqrt{2}E}{R}\left(\frac{rR}{r+R}\right)^{1/2} u^{5/2}\,, \tag{3}$$

which is close analogy to the Hertz's law. The value of the compliance nonlinearity exponent $p = 2.5$ in Eq. (3) is in a good agreement with the experimental results discussed in [2]. At the same time, according to Hertz's Law the force acting on two connected locally Hookean bodies gives p=1.5. The values of p different from 1.5 indicate the non-Hooke or the nonlocal felt properties. Just like these properties of the felt were confirmed experimentally by Yanagisawa, Nakamura and Aiko [4], and by Yanagisawa and Nakamura [5]. Their dynamic experiments demonstrate very important properties of the felt: the nonlinear force-compression characteristic, strong dependence of the slope of the loading curve on the rate of loading, and significant influence of hysteresis, i.e. the loading and unloading of the felt are not alike. These phenomena require that the felt made of wool is a microstructural material possessing history-dependent properties. The dynamic behavior of such solid matter is highly sensitive to characteristic frequency and rate of loading, and for this reason the concept of an almost unique force-compression curve for a given material does not exist. The model that describes the history-dependent properties of the hammer felt was proposed in [6].

HYSTERETIC MODELS OF THE FELT

The new hysteretic model is derived by replacing of the constant parameter K in expression (1) by a time-dependent operator $F_0\ [1 - R(t)*]$, where $*$ denotes the convolution, and the relaxation function given by $R(t) = (\varepsilon/\tau_0)\exp(-t/\tau_0)$. Thus, instead of the simple relation (1) we have the four-parameter hereditary model of the felt in the form

$$F(u(t)) = F_0 \left[u^p(t) - \frac{\varepsilon}{\tau_0} \int_0^t u^p(\xi) \exp\left(\frac{\xi - t}{\tau_0} \right) d\xi \right] . \tag{4}$$

Here the instantaneous stiffness F_0 and compliance nonlinearity exponent p are the elastic parameters of the felt, and hysteresis amplitude ε and relaxation time τ_0 are the hereditary parameters.

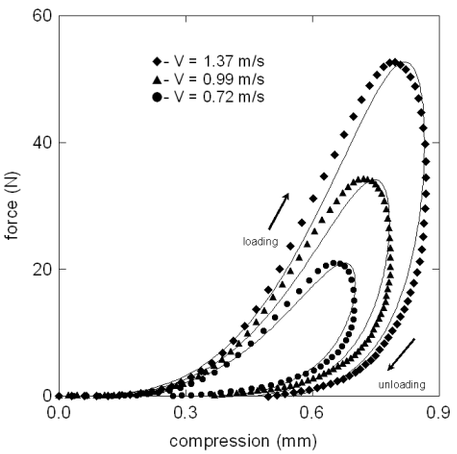


Figure 1. Force-compression characteristics of the felt. Experimental data and numerical simulation.

According to this model, a real piano hammer felt possesses history-dependent properties, or in other words, is a material with memory. For the experimental study of the dynamic felt features the piano hammer testing device described in [7] was used. This device permits to measure the force-time and compression-time dependencies, and investigate the force-compression characteristics of the felt under the different rates of loading. The results of the experimental felt examining are presented in Fig. 1. The arrows indicate the direction of the compression process. The solid lines here represent the numerical simulation of the experiment in according to hysteretic model (4).

The relationships of dynamic force versus felt compression show the significant influence of hysteresis characteristics, so the loading and unloading of the felt (shown by arrows) are not alike. Moreover, the slope of the force-compression characteristics increases with the growth of the hammer velocity, just like the model of the hysteretic hammer predicts. It is evident, that the experiments confirm fairly well the theory. It is also evident that in according to this model each force–compression curve results in a unique combination of felt parameters and vice versa.

However not all is so simple. In spite of this almost evident supposition, the numerical simulation of the felt impact demonstrates that very similar (by eye) force-compression curves can be obtained using the different sets of felt parameters. A close and subtle analysis of this phenomenon results in a new and quite another hysteretic model of the felt.

Usually the hammer velocity not exceeds 5 m/s. This fact corresponds to the non equality $F(t) \gg \tau_0\ dF/dt$, which is valid for all values of τ_0 that are rather small in comparison with the contact duration. Taking into account this non equality and eliminating the integral term in Eq. (4) we can determine the new three-parameter model of the felt in the form

$$Q(u(t)) = Q_0 \left[u^p + \alpha \frac{d(u^p)}{dt} \right] , \tag{5}$$

where $Q(u)$ is the acting force, Q_0 is the static felt stiffness, and α is the retarded time. Similar to model (4), this model of the felt can also be simply proposed by replacing of the constant parameter K in expression (1) by a time-dependent operator $Q_0\ [1 + \alpha\, D]$, where D denotes time differentiation.

Such hysteretic model (5) is very similar to nonlinear Voigt model and permits a description of the felt compression that is consistent also with experiments. Both of the models describe the dynamic felt behavior in a similar way up to the rates of loading 10 m/c. In case of very slow deformation, the both models are complete equivalent. For very fast loading these two models are rather different. Using only the general consideration it is very difficult to choose which model is more physical and reasonable by nature. To decide this problem and to prefer the correct model the additional experiments with a very fast felt loading must be provided.

References

[1] Ghosh, M., “An experimental study of the duration of contact of an elastic hammer striking a damped pianoforte string,” Indian J. Phys., 1932, **7**, pp. 365-382.
[2] Hall, D. E., and Askenfelt, A., “Piano string excitation. V. Spectra for real hammers and strings,” J. Acoust. Soc. Am., 1988, **83**(4), pp. 1627-1638.
[3] Stulov, A., “A simple grand piano hammer felt model,” Proc. Estonian Acad. Sci. Engin., 1996, **5**(2), pp. 155–167.
[4] Yanagisawa, T., Nakamura, K., and Aiko, H., “Experimental study on force-time curve during the contact between hammer and piano string,” J. Acoust. Soc. Jpn., 1981, **37**(12), pp. 627–633.
[5] Yanagisawa, T., and Nakamura, K., “Dynamic compression characteristics of piano hammer felt,” J. Acoust. Soc. Jpn., 1984, **40**(11), pp. 725–729.
[6] Stulov, A., “Hysteretic model of the grand piano hammer felt,” J. Acoust. Soc. Amer., 1995, **97**(4), pp. 2577–2585.
[7] Stulov, A., and Mägi, A., “Piano hammer testing device,” Proc. Estonian Acad. Sci. Engin., 2000, **6**(4), pp. 259–267.

A DUAL PARTICLE COMPUTATIONAL METHOD FOR CONTINUA

L.D. Libersky[*] , P.W. Randles[**]
[*]Los Alamos National Laboratory, Los Alamos, New Mexico 87545
[**]Defense Threat Reduction Agency, Kirtland AFB, New Mexico 87117-5669

Summary A brief history of particle methods will be presented towards assessing the promise offered by these techniques for computational continuum dynamics. We will then discuss recent progress in Dual Particle Dynamics (DPD), a spatially staggered particle discretization of the strong form. Particular attention will be given to stability, boundary conditions, and neighbor searching. We demonstrate stability for Eulerian kernels resulting from the coupling of linear completeness in spatial derivative estimates and two-step Predictor-Corrector time derivative approximations. Boundary conditions are formulated in a unified and consistent way using constrained MLS fits. Several test problems are shown and conclusions drawn.

Stability of Lagrangian numerical methods is a critical and unresolved issue. Important recent contributions have come from [1,2,3] after the original identification of the SPH tensile instability [4]. The tremendous appeal of particle methods is the hope of treating large deformations in a Lagrangian framework. However, if Eulerian kernels which allow for change of connectivity (acquiring new neighbors) cannot be made stable, much of the appeal is lost. It appears that stability can be maintained for Eulerian kernels if certain rules are followed [3]. Fig. 1 results from a stability analysis of DPD and shows a basin of stability in complex eigenvalue space for a Predictor-Corrector time update scheme. The boundary of the basin defines a curve on which the growth rate of the instability is unity. Neighborhoods can be found that allow for a particle time step to satisfy this condition.

Boundary conditions are implemented with constrained moving least squares approximations for derivatives on boundary particles. This can be done quite generally within the context of the particle method used for interior derivatives. Both boundary conditions and neighborhood configurations couple closely with the stability and general accuracy requirements. Complex dynamical interactions occur that are peculiar to the discrete numerical approximations. These issues are addressed to the extent that they are now understood.

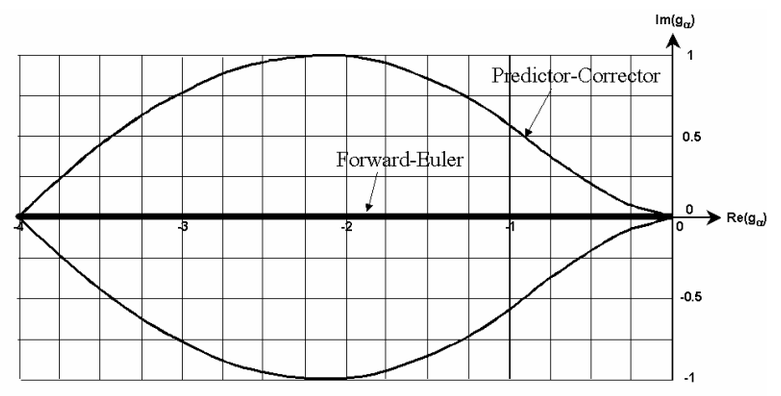


Figure 1. Basins of stability for DPD with Eulerian kernel.

References

[1] T. Belytschko, Y Guo, W.K. Liu, S.P. Xiao, "A Unified Stability Analysis of Meshless Particle Methods," *International Journal for Numerical Methods in Engineering*, v. 48, p. 1359, 2000.
[2] J. Bonet, J. Kulasegaram, "Remarks on Tension Instability of Eulerian and Lagrangian Corrected Smoothed Particle (CSPH) Methods*„ International Journal for Numerical Methods in Engineering,* v. 52, p. 1203, 2001.
[3] P.W. Randles, A.G. Petschek, L.D.Libersky, C.T. Dyka, "Stability of DPD and SPH,"*, Lecture Notes in Computational Science and Engineering,,* Springer, eds., M. Griebel and M. Schweitzer, v. 26, p. 339, 2002.
[4] J.W. Swegle, D.L. Hicks, S.W. Attaway, "Smoothed Particle Hydrodynamics Stability Analysis*," J. Comp. Phys.,* v. 116, p.123, 1995.

XXI ICTAM, 15–21 August 2004, Warsaw, Poland

MESH OPTIMIZATION FOR THE QUASICONTINUUM METHOD: A GENERALIZATION OF VALE

J. Knap, J. Marian and M. Ortiz
Division of Engineering and Applied Science
California Institute of Technology
Pasadena, CA 91125

Summary The current formulation of the quasicontinuum (QC) method relies on a static triangulation of the reference crystal configuration. This computational mesh needs to encompass a wide range of spatial resolutions, from fully atomistic at defect cores, to continuum-like in defect-free regions. Moreover, it must continuously adapt to the structure of the deformation field, so as to return the least possible potential energy for a fixed number of nodes. In the implementations of the QC method to date, the mesh adaption procedure has been based on empirical indicators. We present a variational adaption Lagrangian-Eulerian (VALE) method for the QC method. In this approach, the computational mesh is factored directly into the description of the energetics of the crystal. Therefore, the energy minimizer determines not only the equilibrium configuration of the crystal, but also the optimal configuration of the computational mesh. We apply the VALE-QC method to the investigation of a wide array of problems, from nanoindentation to crack tips.

PROBLEM FORMULATION

We consider a set of N atoms occupying a subset of simple d-dimensional Bravais lattice spanned by lattice vectors $\boldsymbol{a}_i, i = 1, \ldots, d$. The coordinates of atoms in the reference configuration of the crystal are:

$$\boldsymbol{X}(\boldsymbol{l}) = \sum_{i=1}^{d} l^i \boldsymbol{a}_i, \quad \boldsymbol{l} \in \mathcal{L} \subset \mathbb{Z}^d, \tag{1}$$

$\boldsymbol{l}$ denotes the lattice coordinates and $\mathbb{Z}$ is the set of integer numbers. The corresponding atomic coordinates in the current configuration may be conveniently collected in an array $\boldsymbol{x} = \{\boldsymbol{x}(\boldsymbol{l}), \boldsymbol{l} \in \mathcal{L}\} \in X$. The linear space $X \equiv R^{Nd}$ may be referred to as the 'configuration' space of the crystal.
The energy of the crystal is assumed to expressible as a function of the atomic coordinates, i.e. $E(\boldsymbol{x})$. Moreover, any applied loads are considered conservative and to derive from an external potential $\Phi^{\text{ext}}(\boldsymbol{x})$. Therefore, the total potential energy of the crystal is:

$$\Phi(\boldsymbol{x}) = E(\boldsymbol{x}) + \Phi^{\text{ext}}(\boldsymbol{x}). \tag{2}$$

The stable equilibrium configurations of interest are the minimizers of $\Phi(\boldsymbol{x})$ over the space X, i. e., the solutions of the variational problem

$$\min_{\boldsymbol{x} \in X} \Phi(\boldsymbol{x}). \tag{3}$$

A NEW FORM OF QC REDUCTION

The quasicontinuum theory strives to replace Eq. (3) with a reduced problem of finding the total potential energy minimizers over a subspace X_h of X. Within the framework of the 'classical' quasicontinuum [2, 3, 1], a set of atoms, also referred to as 'representative atoms', is introduced to form a basis of X_h. Here instead, we construct X_h by interpolation from an *arbitrary* set T_h of $N_h \ll N$ points, or nodes, not necessarily coincident with atomic sites. Thus, let $\boldsymbol{Q}_h = \{\boldsymbol{Q}_h(i_h), i_h \in T_h\}$ denote an array of nodal coordinates in the reference configuration of the crystal, or referential nodal coordinates. Additionally, let $\mathcal{T}_h$ be a triangulation of T_h and suppose that the crystal lattice $\mathcal{L}$ is contained within the polytope of T_h. The triangulation $\mathcal{T}_h$ supports a collection of shape functions, $\varphi_h(\boldsymbol{l}|i_h), i_h \in T_h$. The positions of all atoms in $\mathcal{L}$ can then be determined by interpolation of the coordinates of all nodes in the set T_h, namely,

$$\boldsymbol{x}_h(\boldsymbol{l}) = \sum_{i_h \in T_h} \varphi_h(\boldsymbol{l}|i_h) \boldsymbol{q}_h(i_h), \tag{4}$$

where $\boldsymbol{q}_h = \{\boldsymbol{q}_h(i_h), i_h \in T_h\}$ is an array containing the nodal coordinates in the current configuration of the crystal, or spatial nodal coordinates, i. e., an element of a linear space X_h of dimension $N_h d$ (c.f. Knap and Ortiz [1]).

REDUCED PROBLEM

Tadmor *et al*. [2, 3] define the reduced counterpart of (3) as

$$\min_{\boldsymbol{q}_h \in X_h} \Phi(\boldsymbol{q}_h). \tag{5}$$

Evidently, the energy minimizers of the reduced problem implicitly depend on the choice of the triangulation $\mathcal{T}_h$ through subspace X_h. As noted by Thoutireddy and Ortiz [4], the *optimal triangulation* is that which delivers the least minimum potential energy. This leads to a reduced problem of the form

$$\min_{\boldsymbol{q}_h, \boldsymbol{Q}_h} \Phi(\boldsymbol{q}_h, \boldsymbol{Q}_h). \tag{6}$$

in which the energy is minimized with respect to *both* spatial and referential nodal coordinates. The stationarity of the total potential energy yields the reduced equilibrium equations

$$\boldsymbol{f}_h(i_h) = \sum_{\boldsymbol{l}\in\mathcal{L}} \boldsymbol{f}(\boldsymbol{l}|\boldsymbol{x}_h)\varphi_h(\boldsymbol{l}|i_h) = \boldsymbol{0}, \tag{7}$$

$$\boldsymbol{F}_h(i_h) = \sum_{\boldsymbol{l}\in\mathcal{L}} \boldsymbol{f}(\boldsymbol{l}|\boldsymbol{x}_h) \sum_{j_h\in T_h} \frac{\partial\varphi_h(\boldsymbol{l}|j_h)}{\partial \boldsymbol{Q}_h(i_h)} \boldsymbol{q}_h(j_h) = \boldsymbol{0}. \tag{8}$$

Here,

$$\boldsymbol{f}(\boldsymbol{x}) = \Phi_{,\boldsymbol{x}}(\boldsymbol{x}) \tag{9}$$

are the forces corresponding to $\boldsymbol{x}$ and $\boldsymbol{f}(\boldsymbol{l}|\boldsymbol{x})$ is the value of $\boldsymbol{f}(\boldsymbol{x})$ at site $\boldsymbol{l}$. The system of equations (7) imposes the mechanical equilibrium of the crystal, whereas the system (8) imposes the configurational equilibrium of the nodes.
As noted by Tadmor *et al.* [2, 3], the practicality of the method requires the application of lattice summations rules in order to circumvent the calculation of the full atomistic force array $\boldsymbol{f}$. Following Knap and Ortiz [1], we employ cluster summation rules, albeit based on a slightly modified definition of the cluster. Specifically, the cluster of lattice sites located within a sphere of radius $r(i_h)$ centered on the node i_h is defined as $\mathcal{C}(i_h) = \{l : |\boldsymbol{X}(\boldsymbol{l}) - \boldsymbol{Q}_h(i_h)| \leq r(i_h)\}$. The application of these summation rules to the reduced equilibrium equations gives

$$\boldsymbol{f}_h(i_h) \approx \sum_{i'_h\in T_h} n_h(i'_h) \left[\sum_{\boldsymbol{l}\in\mathcal{C}(i'_h)} \boldsymbol{f}(\boldsymbol{l}|\boldsymbol{x}_h)\varphi_h(\boldsymbol{l}|i_h) \right] = \boldsymbol{0}, \tag{10}$$

$$\boldsymbol{F}_h(i_h) \approx \sum_{i'_h\in T_h} n_h(i'_h) \left[\sum_{\boldsymbol{l}\in\mathcal{C}(i'_h)} \boldsymbol{f}(\boldsymbol{l}|\boldsymbol{x}_h) \sum_{j_h\in T_h} \frac{\partial\varphi_h(\boldsymbol{l}|j_h)}{\partial \boldsymbol{Q}_h(i_h)} \boldsymbol{q}_h(j_h) \right] = \boldsymbol{0}. \tag{11}$$

where $n(i_h), i_h \in T_h$ are the cluster weights, computed, as before, by requiring that the summation rules be exact for all shape functions.

CONCLUSIONS

We have developed a new formulation of the quasicontinuum method that generalizes the original description of Tadmor *et al.* [2]. The method now incorporates a variational technique [4] that leads to a natural coupling of mechanical and configurational force systems. In this manner, any arbitrariness associated with the initial choice of the reference configuration is removed, and the equilibrium configurations of interest are calculated on an optimal reference mesh. The new formulation results in enhanced computational efficiency and effectively removes *ad hoc* elements from previous implementations of the QC method. Calculations concerned with nano-indentation, straight dislocation cores and crack tips are presented which illustrate the performance and versatility of the method.

References

[1] J. Knap and M. Ortiz. An analysis of the quasicontinuum method. *Journal of the Mechanics and Physics of Solids*, 49(9):1899–1923, 2001.
[2] E.B. Tadmor, M. Ortiz, and R. Phillips. Quasicontinuum analysis of defects in solids. *Philos. Mag. A*, 73:1529–1563, 1996.
[3] E.B. Tadmor, R. Phillips, and M. Ortiz. Mixed atomistic and continuum models of deformation in solids. *Langmuir*, 12(19):4529–4534, 1996.
[4] P. Thoutireddy and M. Ortiz. A variational r-adaption and shape-optimization for finite-deformation elasticity. *International Journal for Numerical Methods in Engineering*, 2004.

DERIVATION OF THE HIGHER-ORDER STIFFNESS MATRIX OF A SPACE FRAME ELEMENT FOR GEOMETRIC NONLINEAR ANALYSIS OF STRUCTRUES

Jiann-Tsair Chang*, I-Dang Huang*
* *Department of Civil Engineering, Vanung University, Chung-Li CIty, Tao-Yuan County, Taiwan, ROC*

Summary A physical concept, the rigid body rule, is applied for the derivation of the higher-order stiffness matrix of a space frame element. The derivation has a physical meaning that is the higher-order stiffness matrix can be derived by regarding there is a set of incremental nodal forces existing on the element, then the element undergoes a small rigid body rotation. The incremental forces should keep their magnitude and follow the rigid body motions. Then taking advantage of the existing geometric stiffness matrix derived by researchers, the higher- order stiffness matrix can be analogy derived without any difficulty. The derived higher-order stiffness matrix has explicit expressions. It can be used at the forces recovery stage in the geometric nonlinear analysis of frame structures. Meanwhile an effective numerical method, the Generalized Displacement Control (GDC) method, was adopted to trace the load-defection curves of the structures. Some numerical examples were tested by taking the proposed higher-order stiffness matrix into consideration in the nonlinear analysis of the structures .

INTRODUCTION

Researchers have paid a lot of attention during the past four decades to conduct the geometrical nonlinear analysis of framed structures (Bathe [1]; Yang and Kuo [2]; Belytschko et al. [3]; Yang, Kuo and Wu, [4]) and others. Most of them have derived the geometric stiffness matrix for the geometrical nonlinear analysis. In this study, the rigid-body-motion concept was used in the derivation of the higher-order stiffness matrix of a frame element. One can use the derived higher-order stiffness matrix combining linear stiffness and geometric stiffness matrices of the element in the force recovery stage to dramatically reduce the iterations in each incremental step during the whole geometrical nonlinear analysis.

In the literature, based on the various variational principles, many geometric nonlinear elements have been generated by researchers, which included truss, frame and plate elements, and so on. When talking about geometric nonlinear analyses, without sayings, linear and geometric stiffness matrices are presented in the formulations no matter what kinds of variational principles were adopted by researchers. In the meanwhile, based on incremental variatonal principles, different forms of geometric stiffness matrices have been generated. But for the higher-order stiffness matrix less attention has been made because of its tedious derivations and lengthy expressions by conventional derivations. In this research an explicit form for the higher-order stiffness matrix will be derived by extension the concept of the so call the rigid body test.

In the nonlinear finite element method for a formulated nonlinear element, a criterion used to qualify the derivation geometric nonlinear elements, so called the rigid body test that was first proposed by Yang and Chiou [5] in 1987. It can be stated as followed: Once an element is in equilibrium with a set of initial forces acted when it undergoes rigid body motions, the forces acted on the element will keep their magnitudes and rotate with the rigid body motions. It is named as rigid body rule that is a physical interpretable concept. Using this concept, an analogy from of the higher-order stiffness can be easily established for nonlinear analysis of structures.

The derived higher-order stiffness matrix has a clear physical meaning that just as to the properties of the geometric stiffness matrix of the element. It can be stated as following. When there is a set of incremental nodal forces existing on the element, let the element undergo a small rigid body motion, the incremental forces should keep their magnitude and following the rigid body motions just as the initial nodal forces acting on the element behave. In this way the higher-order stiffness matrix of the frame element can be derived with the aids of the geometric stiffness matrix. One merely changes the initial forces in the geometric stiffness instead of the incremental forces. The higher-order stiffness matrix of the element can be formed easily. It has the same expression from but different in incremental forces in contrast to the initial forces in the geometric stiffness matrix. This formulation is simple and explainable. It can be seen that most coefficients lying in the higher-order stiffness matrix have explicit expressions just as the geometric stiffness matrix does.

The main purpose of this study is to derive the higher stiffness matrix of a space frame with the aids of widely derived geometric stiffness matrix and the concept of rigid body motions. The derived higher-order stiffness matrix combined the linear stiffness and geometric stiffness matrices to form a tangent stiffness matrix can be used in the force recovery stage in the geometrical nonlinear analysis. It can effectively reduce the number of iterations at each incremental step by use the derived higher-order stiffness matrix can be ensured. Finally some numerical examples were solved by the proposed elements and the generalized displacement control method proposed by Yang and Shieh [6].

NUMERICAL EXAMPLE

A deep circular arch structure was considered herein. The geometry and material properties of the deep circular arch are shown as in Figure 1. The circular arch is subject to a concentrated load on the convex side, as also depicted in Figure 1. One of the edges of the circular arch is hinged and the other is fixed. Herein 36 frame elements were also used

to discrete the deep circular arch. One or two iterations were needed in each incremental step in the analysis. Results of the central deflection versus the applied load have been plotted in Figure 2, with convergent criterion by setting less than one thousandth of the relative norm of the unbalanced forces for per incremental step. The results obtained by the proposed higher-order stiffness matrix agree well with conventional method, i.e., only the linear stiffness matrix and geometric stiffness matrix are included in the tangential stiffness matrix of the element.

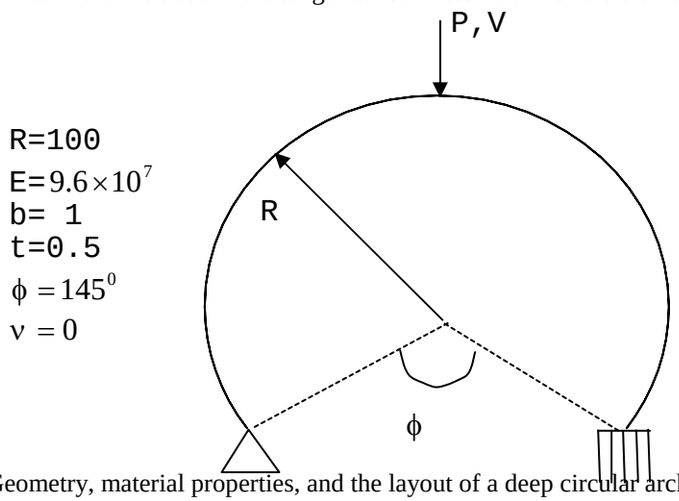


Figure 1. Geometry, material properties, and the layout of a deep circular arch under a concentrated load.

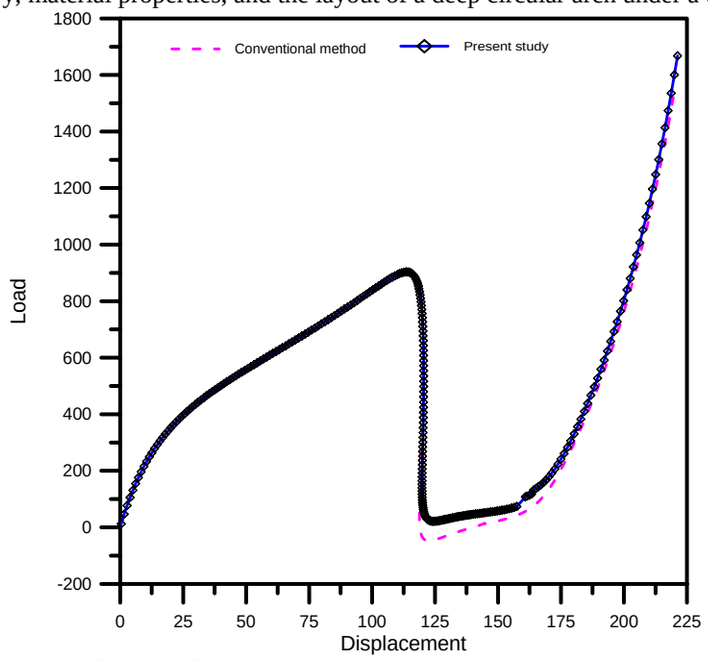


Figure 2. Central deflection of the deep circular arch under a concentrated load at its crown

CONCLUSIONS

From the demonstrated example and its results, it shows the reliable solution of the structure modelled by the proposed elements. This means that the present concept is applicable and has less iteration required in the force recovery stage for all the geometric nonlinear analysis of frame and arch structures. Meanwhile, the solution procedure is quite effective in dealing with limits points, snap through phenomena. The present approach has been referred as an engineer's approach, because the derivation is based on physically intuitive concepts. By the demonstrated example, the concept, i.e., the rigid body rule is power, not only can be adopted to derive a geometric stiffness matrix but also play a key concept for derivation of the almost an exactly tangential stiffness matrix of the frame element for the geometric non-linear analysis of frames and arches.

References

[1] Bathe, K. J.: Finite Element Procedures in Engieering Analysis, Prentice Hall, Englewood Cliffs, N.J., 1979.

[2] Yang, Y. B.: Kuo,S. R. Theory & Analysis of Nonlinear Framed Structures, Prentice Hall, Englewood Cliffs, N.J., 1994.

[3] Belytschko,T. Moran,B. Liu,W. K.: Nonlinear Finite Elements for Continua and Structures, John Wiley & Sons, Third Avenue, N.Y., 2000.

[4] Yang,Y. B. Kuo,S. R. Wu,Y. S.:Incrementally small-deformation theory for nonlinear analysis of structural frames, Engineering Structures, 24:783-798, 2002.

[5] Yang, Y. B., Chiou, H. T.:Rigid body motion test for nonlinear analysis with beam elements,Journal of Engineering Mechanics, ASCE, 113(9): 1404-19, 1987.

[6] Yang, Y. B. Shieh, M. S.:Solution method for nonlinear problems with multiple critical points, AIAA J., 28(12): 2100-16,1990

THE METHOD OF SOLVING OF NON-STATIONARY COUPLED PROBLEMS OF THE THEORY THERMAL-PLASTICITY FOR THE ROTATION SHELLS

Pavlo A. Steblyanko*

* *State Technical University, Dneprostroevskaya 2, 51918 Dneprodzerzhinsk, Ukraine*

Summary The new on-component splitting method of higher accuracy of numerical solving of non-stationary coupled problems of the theory of thermal-plasticity for non-steady loading of the rotation shells is proposed. The numerical solving is reduced to the solution of the systems of differential equation in partial derivatives, consisting of equations of motion, geometrical ratios, equations of physic state and equation of thermal conduction. All unknown values for each step by time are found in the spline-function form.

INTRODUCTION

In the papers [1,2] the method for on-component splitting of higher accuracy is proposed. The space non-stationary problems of theory of thermal-plasticity are solved by this method [7]. All unknown values (velocity of displacements, strains and deformations) are found in form of spline functions (cubic B-splines, strained splines) [1-3]. The application of this method for the solution of non-stationary problems of thermal-plasticity for plates and shells is described in papers [4,5]. The non-stationary two-dimensional and three-dimensional coupled problems of the theory of thermal-plasticity are studied in paper [6]. In present paper this method is applied for the first time for solving of coupled non-stationary problems of the theory of thermal-plasticity for rotation shells. The method proposed by us allows the fourth order of approximation of the method on coordinates.

THE PROBLEM

In the present paper the above-mentioned technique is used for determination of coupled non-stationary thermal-strains-deforming state of thin-walled rotation shells working beyond the limits of the material elasticity. The basic unknown values are velocities of displacements V_1, V_2, V_3, specific efforts Q_1, Q_2, , T_1, T_2, S, specific moments M_1, M_2, H, deformation of a median surface ε_1 ε_2, shifts γ_1, γ_2, angles of rotation ω_1, ω_2, curvatures χ_1, χ_2, torsion τ and temperature T.

The complete set of simultaneous equations consists of:

- the equations of motion of thin-walled element of construction;
- the equations for speeds of the specific efforts and moments change which give the physical ratio (we use the ratio of theory of processes of deformations of mean curvature elaborated by the Academician Y.N.Shevchenko and his disciples [7]);
- the nonlinear geometrical ratio.

The temperature field is constructed by solution of non-stationary two-dimensional equation of heat conduction with account of probable influence of heat emission in the process of loading of rotation shells [3].

The above mentioned simultaneous equations may be reduced to vector form

$$\frac{\partial \vec{W}}{\partial t} = \sum_{i=1}^{2}\left(A_i \frac{\partial \vec{W}}{\partial \alpha_i} \right) + \vec{F} \quad , \tag{1}$$

to which the method of on-component slitting where the unknown values are given in the spline-function form (cubic B-splines and strained splines) may be applied [1].

In general vector $\vec{W}$ has 21 components: $w_1=v_1$; $w_2=v_2$; $w_3=v_3$; $w_4=Q_1$; $w_5=Q_2$; $w_6=T_1$; $w_7=T_2$; $w_8=S$; $w_9=M_1$; $w_{10}=M_2$; $w_{11}=H$; $w_{12}=\varepsilon_1$; $w_{13}=\varepsilon_2$; $w_{14}=\gamma_1$; $w_{15}=\gamma_2$; $w_{16}=\omega_1$; $w_{17}=\omega_2$; $w_{18}=\chi_1$; $w_{19}=\chi_2$; $w_{20}=\tau$; $w_{21}=T$.

The 20 components of vector $\vec{F}$ ($F_i, i=1,2,...,20$) are defined by the expression introduced in paper [5].

For the solution of bound non-stationary problems for F_{21} we use the expression [3]

$$F_{21} = S_{ij}\dot{\Im}_{ij} - \frac{1}{2G}S_{ij}\dot{S}_{ij} + \frac{\sigma_{ii}}{3}\left(\dot{\varepsilon}_{jj} - 3\alpha_T \frac{\partial T}{\partial t}\right) - \frac{\sigma_{ii}}{3K}\dot{\sigma}_{jj} \text{ , } \quad S_{ij} = \sigma_{ij} - \delta_{ij}\sigma \text{, } \Im_{ij} = \varepsilon_{ij} - \delta_{ij}\varepsilon \text{ .}$$

NUMERICAL METHOD

The non-explicit form of the on-component splitting method scheme for equation (1) has form ($\alpha+\beta=1$, $\phi_1+\phi_2=1$, $n=1,2$)

$$\vec{W}^{\,p+\frac{n}{3}} - \alpha\tau\left[A_n\lambda_n(\vec{W})\right]^{p+\frac{n}{3}} = \vec{R}_n\,,\ \vec{R}_n = \vec{W}^{\,p+\frac{n-1}{3}} + \beta\tau\left[A_n\lambda_n(\vec{W})\right]^{p+\frac{n-1}{3}} + \tau\phi_n\vec{F}\,. \qquad (2)$$

Let us rewrite the equation (2) in the form*:*

$$\vec{W}_j^{\,p+\frac{n}{3}} = \alpha\tau\left[A_n\lambda_n(\vec{W})\right]_{j-1}^{p+\frac{n}{3}} = \vec{R}_n\,, \qquad (3)$$

λ_n - the difference operator [1], *j* – number of iteration *(j= 1, 2, 3...).* The initial iteration is the solution of the problem obtained by the explicit scheme. Thus,

$$\vec{W}_0^{\,p+\frac{n}{3}} = \left\{\vec{W} + \tau\left[\phi_n\vec{F} + A_n\lambda_n(\vec{W})\right]\right\}^{p+\frac{n}{3}}. \qquad (4)$$

If $\max(W_m;\lambda_n(W_m)) < \Lambda$, then $(W_m)_{i+1} - (W_m)_i < (\alpha\frac{\tilde{\tau}}{h_k}\Lambda)^i$, $(k = 1,2)$ and, therefore at $\alpha\tilde{\tau}\Lambda < h_k$ the iterative procedure converges.

NUMERICAL RESULTS

We consider the problem of non-stationary loading of previously contracted cylindrical shell ($T_1 = T_{10}$-const) subjected to the cyclic torsion of small amplitude, when the non-zero value of the normal velocity of displacement of a medial surface of a cylindrical shell (V_3 =0,05 and V_3 =0,1) is given for initial time moment. Numerical values of dimensionless velocities of radial displacement for different points in time are given in Table 1.

Table 1.

$V_3=V_3(t)$	$t = 25\tilde{\tau}$	$t = 50\tilde{\tau}$	$t = 75\tilde{\tau}$	$t = 100\tilde{\tau}$
$V_3(0)$=0,05; T=0	-0,021	0,012	0,043	-0,026
$V_3(0)$=0,05; T=T(t)	-0,005	-0,007	0,009	0,008
$V_3(0)$=0,1; T=0	-0,045	0,024	0,089	-0,044
$V_3(0)$=0,1; T=T(t)	-0,012	-0,016	0,023	0,018

lines 3 and 5 are constructed by the on-component splitting method, and lines 2 and 4 represent similar results obtained for the case when temperature equals zero.

The received results show that the emission of heat in the process of cyclic loading beyond the material elasticity limit may considerably influence the strain-deformed state of the cylindrical shell.

CONCLUSIONS

Thus, the on-component splitting method of higher accuracy for solving of non-stationary coupled problems of the theory of thermal-plasticity for rotation shells proposed by us allows to determine the unknown values of velocities of displacements of the medial surface of the shell, specific efforts and specific moments, deformation of the medial surface, shifts, angles of rotation, curvatures, torsion and temperature. The absence of the derivatives of the second order on coordinates in the complete set of simultaneous equations gives the opportunity to get the fourth order of approximation of the method on coordinates which results in higher accuracy of calculations.

References

[1] Steblyanko P.A. The methods of decomposition in space problems of the theory of plasticity. Naukova dumka: Kiev, 1998.

[2] Steblyanko P.A. The method of decomposition in the non-stationary space problems of the theory of plasticity. .: SMC HE: Kiev, 2000.

[3] Steblyanko P., Volosova N. Non-stationary 2D and 3D coupled problems of the theory of thermal-plasticity. *J. System technologies. MPTM* 2001;. **2**(13);174-181.

[4] Steblyanko P.A. Spline-approximating of solution of system of nonlinear PDE. *J. System technologies. MPTM* 2001;. **2**(13);181-189.

[5] Steblyanko P.A. The schemes of abnormally high accuracy solution of non-stationary problems of theory of thermal-elastic-plasticity for plates and shells. *The Fifth International Congress on Thermal Stresses and Related Topics*. Vol.1. Virginia Polytechnic Institute and State University Blacksburg, Virginia, USA, 2003, TM-2-3-1 – TM-2-3-4.

[6] Steblyanko P., Krylov V., Volosova N., Yakimchuk S., Victorov V. The definition non-stationary thermal-elastic-plastic of a station of shallow shells by means of method of component splitting. *J. System technologies. MPTM* 2003;. **4**(27);142-151.

[7] Shevchenko U.N., Savchenko V.G. The mechanics of coupled fields in elements of constructions. Vol. 2. The thermal-viscous plasticity. – .: Naukova dumka: Kiev, 1987.

XXI ICTAM, 15–21 August 2004, Warsaw, Poland

A NEW APPROACH FOR THE FE MODELLING OF COHESIVE CRACKS

Julia Mergheim, Ellen Kuhl, Paul Steinmann
Chair of Applied Mechanics, Department of Mechanical Engineering, University of Kaiserslautern, PO-Box: 3049, 67653 Kaiserslautern, Germany

Summary The present contribution is concerned with the computational modelling of cohesive cracks, whereby the discontinuity is not limited to interelement boundaries, but is allowed to propagate freely through the elements. Inelastic material behaviour is described by discrete constitutive models, formulated in terms of tractions and displacements at the surface. Details on the implementation and numerical examples are given.

INTRODUCTION

The modelling of propagating discontinuities was recently considered by several authors, following different approaches. As an approved method, most similar to the present one, we mention the partition of unity method, which was introduced in [1] and [2] and was applied for the modelling of cohesive cracks, for example, in [3]. In the present work we will follow the approach recently suggested in [4]. Thereby neither the jump nor the strain jump is an explicit variable, but it is only worked with polynomial approximations and displacement degrees of freedom. In the next section the governing equations and the weak formulation are recapitulated, afterwards the idea of constructing elements with internal discontinuities is highlighted. Then some details about the applied discrete constitutive law and the implementation are given and the performance of the method is pointed out by means of numerical examples.

WEAK FORMULATION

Let Ω denote the configuration occupied by an initially linear elastic body. The boundary $\partial\Omega$ with the outward normal vector $\boldsymbol{n}_e$ is subdivided in $\partial\Omega = \Gamma_N \cup \Gamma_D$ with $\Gamma_N \cap \Gamma_D = \emptyset$, where either Neumann or Dirichlet boundary conditions are prescribed. Furthermore Ω exhibits a smooth internal boundary Γ_I, which divides Ω into the parts Ω_1 and Ω_2. The unit normal vector $\boldsymbol{n}$, associated with Γ_I, points from Ω_2 to Ω_1. The jump in the displacement field $\boldsymbol{u}$ along Γ_I is defined by $[\![\boldsymbol{u}]\!] = \boldsymbol{u}_1 - \boldsymbol{u}_2$. The equilibrium equation and boundary conditions read:

$$-\boldsymbol{\nabla}\cdot\boldsymbol{\sigma} = \boldsymbol{b} \text{ in } \Omega, \qquad \boldsymbol{u} = \bar{\boldsymbol{u}} \text{ on } \Gamma_D, \qquad \boldsymbol{\sigma}\cdot\boldsymbol{n}_e = \bar{\boldsymbol{t}} \text{ on } \Gamma_N, \qquad \boldsymbol{\sigma}\cdot\boldsymbol{n} = \boldsymbol{t}([\![\boldsymbol{u}]\!]) \text{ on } \Gamma_I, \tag{1}$$

whereby $\bar{\boldsymbol{t}}$ and $\bar{\boldsymbol{u}}$ are the prescribed tractions and the prescribed displacements, $\boldsymbol{\sigma}$ is the Cauchy stress and $\boldsymbol{b}$ is the body force. For the considered geometrically linear formulation the symmetric strain tensor $\boldsymbol{\epsilon}$ is given by the kinematic equation $\boldsymbol{\epsilon} = \frac{1}{2}[\nabla\boldsymbol{u} + \nabla^t\boldsymbol{u}]$. The constitutive relation in the bulk is given by $\boldsymbol{\sigma} = \boldsymbol{D} : \boldsymbol{\epsilon}$, whereby $\boldsymbol{D}$ is the fourth order constitutive tensor. The description of the inelastic behaviour of the material is completely covered by the discrete constitutive model applied at the internal boundary Γ_I. The weak formulation, which is obtained by multiplication of (1) with a test function $\delta\boldsymbol{u}$ and integrating by parts, possesses an additional contribution due to the tractions $\boldsymbol{t}$ along Γ_I

$$\int_{\Omega_1\cup\Omega_2} \delta\boldsymbol{\epsilon} : \boldsymbol{\sigma}(\boldsymbol{u})\, dV + \int_{\Gamma_I} [\![\delta\boldsymbol{u}]\!]\cdot\boldsymbol{t}([\![\boldsymbol{u}]\!])\, dA = \int_{\Omega_1\cup\Omega_2} \delta\boldsymbol{u}\cdot\boldsymbol{b}\, dV + \int_{\Gamma_N} \delta\boldsymbol{u}\cdot\bar{\boldsymbol{t}}\, dA. \tag{2}$$

Thereby the traction vector $\boldsymbol{t}$ depends on the discrete constitutive law in terms of the displacement jump.

DISCRETIZATION

In this section details about the discretization are given. The weak form (2) will be solved, using finite elements which allow for a discontinuity intersecting the elements, following the approach suggested in [4].
To construct an element E with an internal discontinuity, we consider that E is divided by Γ_I into $E_1 := \Omega_1 \cap E$ and $E_2 := \Omega_2 \cap E$. The displacement field $\boldsymbol{u}$ will be continuous on each part, but discontinuous over Γ_I, therefore $\boldsymbol{u}$ can be represented by

$$\boldsymbol{u} = \begin{cases} \boldsymbol{u}_1 & \text{in} \quad E_1 \\ \boldsymbol{u}_2 & \text{in} \quad E_2 \end{cases} \tag{3}$$

To approximate the function $\boldsymbol{u}_1$ on E_1 one needs the usual number of degrees of freedom, depending on the desired polynomial degree. Even though $\boldsymbol{u}_1$ is only defined on E_1, it can be represented by its nodal values at the existing nodes of the element E and the standard basis functions. The same applies for function $\boldsymbol{u}_2$, which has, due to the discontinuous characteristic of $\boldsymbol{u}$, no relation to $\boldsymbol{u}_1$. That means that for an element intersected by a discontinuity two independent copies of the standard basis functions N are used, whereby one set is put to zero on one side of the discontinuity, while it takes its usual values on the opposite side, and vice versa:

$$N_1^j = \begin{cases} N^j & \text{in} \quad E_1 \\ 0 & \text{in} \quad E_2, \end{cases} \qquad \text{and} \qquad N_2^j = \begin{cases} 0 & \text{in} \quad E_1 \\ N^j & \text{in} \quad E_2. \end{cases} \tag{4}$$

It is recognizable that this set of basis functions with an internal discontinuity can be easily constructed for any standard finite element in 2D or 3D. The additional degrees of freedom are introduced at the existing nodes and the points of intersection between element edges and the interface as well as the geometry of the element parts are only needed for the evaluation of the weak form.

DISCRETE CONSTITUTIVE MODEL

In the proposed method discrete constitutive models are applied to model the inelastic material behaviour. The discrete models are formulated in terms of tractions and displacements and they are applicable at the internal surface. In the following a discrete damage-type model for quasi-brittle materials is introduced, with the tensile stress f_t and the fracture energy G_f being the main parameters. An exponential softening in normal direction and a constant shear stiffness in tangential direction is assumed. The traction vector $\boldsymbol{t}$ is determined by

$$t_n = f_t \, \exp\left(-\frac{f_t}{G_f}\,[\![u_n]\!]\right), \qquad t_m = d\,[\![u_m]\!] \qquad \text{and} \qquad \boldsymbol{t} = t_n\,\boldsymbol{n} + t_m\,\boldsymbol{m}, \tag{5}$$

whereby d is the shear stiffness and $\boldsymbol{m}$ is the tangential vector associated to Γ_I. This discrete constitutive model is chosen because of its simplicity with respect to the implementation. Due to the constant shear stiffness, which is a valid assumption for mode 1 failure only, the tangent stiffness matrix preserves its symmetry. Nevertheless the introduction of a more general constitutive model is straightforward.

IMPLEMENTATION AND NUMERICAL EXAMPLE

To describe a propagating discontinuity we need to propose a failure criterion, a method to determine the alignment of the discontinuity and an adequate integration scheme for the intersected elements. During the calculation the principle stresses in the element ahead of the discontinuity tip are monitored. If the stresses exceed the tensile strength, the discontinuity is introduced as a straight line through the element and is enforced to be geometrically continuous. To determine the right direction of the extension of the discontinuity, non-local stresses are calculated. The non-local stress tensor is computed as the weighted average of the stresses at the gausspoints within an interaction radius around the tip. The discontinuity is extended in the direction perpendicular to the non-local principle stress.
In the elements, intersected by a discontinuity, the same basis functions as in the ordinary elements are used. But since the geometry of the element parts varies, the element fragments are triangulated into sub-domains and standard Gauss quadrature is applied. Additional integration point are inserted along the internal boundary Γ_I, to integrate the contributions depending on the traction vector.
To show that the proposed method allows for the propagation of a discontinuity, independent of the mesh structure, two numerical examples are given. We consider a three-point bending test, whereby a simply supported beam is loaded by an imposed displacement at the center of the top edge. The analysis is performed with linear, three-noded triangles, a full Newton-Raphson solution procedure is used and linear elastic behaviour of the continuum is assumed. Figure (1) shows the propagation of a discontinuity introduced at the center of the beam and figure (2) pictures a discontinuity which is introduced excentric. Both the simpler case of the straight crack and the curved crack are calculated independently of the mesh structure.

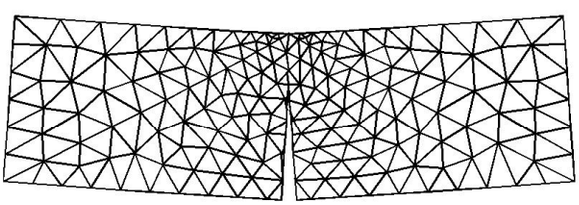


Figure 1: Propagation of centered crack

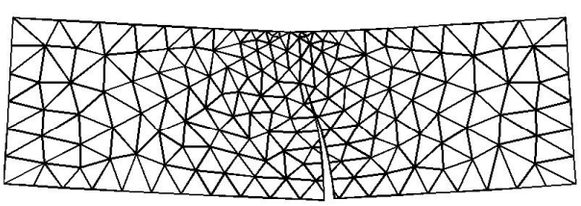


Figure 2: Propagation of excentered crack

CONCLUSIONS

We introduced a finite element method for the modelling of cohesive cracks. The characteristic feature of the method is the construction of the elements with an internal discontinuity, which is independent of the element type and uses only the standard basis functions. The method was applied to model cohesive cracks, making use of a discrete constitutive law. The presented numerical examples point out that the method allows for simulating propagating discontinuities independent of the mesh structure.

References

[1] Belytschko T, Black T. Elastic crack growth in finite elements with minimal remeshing. *International Journal of Numerical Methods in Engineering* 1999; **45**(5): 601-620.

[2] Moës N, Dolbow, J, Belytschko T. A finite element method for crack growth without remeshing. *International Journal of Numerical Methods in Engineering* 1999; **46**(1): 131-150.

[3] Wells GN, Sluys LJ. A new method for modelling cohesive cracks using finite elements. *International Journal of Numerical Methods in Engineering* 2001; **50**(12): 2667-2682.

[4] Hansbo A, Hansbo P. A finite element method for the simulation of strong and weak discontinuities in elasticity. *Computer Methods in Applied Mechanics and Engineering*; to appear.

EFFECTIVE SOLUTION FOR FINITE ELEMENT PROBLEMS WITH NONLINEAR CONSTRAINTS

S.A Lukasiewicz
Department of Mechanical and Manufacturing Engineering
The University of Calgary
2500 University Dr, N.W.
Calgary, AB, Canada T2N1N4
lukasiew@ucalgary.ca
M.H. Hojjati
Department of Mechanical Engineering
The University of Mazandaran
Bobol, Iran
mhojatti@eneme.ucalgary.ca

Introduction

Very often solutions of mechanical problems based on the Finite Element Method are accompanied by a system of nonlinear equations. FEM creates a large number of linear equations but the requirements of laws of physic, optimization techniques, geometrical non-linearity's, adaptive modeling result in nonlinear equations. In this case the whole system is considered nonlinear and is solved using methods for the solution of non-linear equations. The Newton-Raphson iterations is the method most commonly used. This method needs the calculation of first derivatives and the Jacobian matrix for the system. The solution is obtained by means of consecutive iterations. If the functions are differentiable with respect to the unknown variables and behave well, it is possible to find the solution in a reasonable number of iterations. However, this method needs the initial guess for all the variables taken sufficiently close to the simultaneous roots of the nonlinear system. The approach is not effective if the number of equations is large. There are problems with the convergence to correct the solution and problems with the initial guesses for the variables.

Method

This paper presents a new method for the solution of a system of ***m+n*** nonlinear equations when the system of equations can be presented as two groups of equations. The first group of ***m*** equations is linear with respect to the selected ***m*** variables; the second group of ***n*** equations is nonlinear. The solution for the first group does not require any iterative procedures and can be found by means of any method for the system of linear equations. The method uses iterations only for the nonlinear part and needs therefore much fewer number of initial guesses as compared to those needed in Newton-Raphson method.

The general system of equations can be presented in the following form:

$$\mathbf{f}(x,t) = 0,$$

$$\boldsymbol{\varphi}(x,t) = 0,$$

where the system f_i is linear with respect to the variables x_i with the assumption that the values of the variables t_i are known. Equations φ_n are non-linear with respect to the variables x_i and $\mathbf{t}_i$. Suppose that the vector t is the initial guess solution to the nonlinear variables of the system of the equations. Similarly, the vector x is the vector of initial solution for the linear part of the system equations based on t. The vector x can be found by means of any method for the system of linear equations. Let $x+\Delta x$ and $t+\Delta t$ be a better approximate solution.

Representing the functions f and $\boldsymbol{\varphi}$ by Taylor expansions, we have

$$\boldsymbol{\varphi}(x,t) + \frac{\partial \boldsymbol{\varphi}}{\partial x}\Delta x + \frac{\partial \boldsymbol{\varphi}}{\partial t}\Delta t = 0, \qquad \mathbf{f}(x,t) + \frac{\partial \mathbf{f}}{\partial x}\Delta x + \frac{\partial \mathbf{f}}{\partial t}\Delta t = 0. \tag{1}$$

Solving equations (1) and with respect to Δx and Δt gives:

$$\Delta \mathbf{t} = -\left[I - \left(\frac{\partial \boldsymbol{\varphi}}{\partial t}\right)^{-1}\left(\frac{\partial \boldsymbol{\varphi}}{\partial x}\right)\left(\frac{\partial \mathbf{f}}{\partial x}\right)^{-1}\left(\frac{\partial \mathbf{f}}{\partial t}\right)\right]^{-1}\left[\frac{\partial \boldsymbol{\varphi}}{\partial t}\right]^{-1}[\boldsymbol{\varphi}(x,t)], \tag{2}$$

and $$\Delta \mathbf{x} = -\left[\frac{\partial \mathbf{f}}{\partial x}\right]^{-1}\left[\mathbf{f}(x,t) + \frac{\partial \mathbf{f}}{\partial t}\Delta t\right]. \quad (3)$$

The new values of **t** and **x** are calculated as $\mathbf{x_{i+1}} = \mathbf{x_i} + \Delta \mathbf{x_i}$, $\mathbf{t_{i+1}} = \mathbf{t_i} + \Delta \mathbf{t_i}$. Below a simple example is presented to explain the method. Let us consider the following system of algebraic equations. The variables to be found are *x*, *y*, *z* and *t*.

$$\begin{aligned} &tx + 2y - z = 21,\\ &-2x + 3y - z = 0,\\ &2x - y + 5z = 26\\ &tx^2 - 2xy + y^2 - tz^2 = -213. \end{aligned} \quad (4)$$

The first and last equations are clearly nonlinear. However, following the procedure explained in the previous section, if we consider *t* as the variable to be found by iterations, the first three equations will be linear in terms of *x*, *y* and *z* and can be solved for any given ***t***.

$$\mathbf{x}=\begin{bmatrix} x\\ y\\ z\end{bmatrix} = \begin{bmatrix} t & 2 & -1\\ 2 & -1 & 5\\ -2 & 3 & -1\end{bmatrix}^{-1}\begin{bmatrix} 21\\ 26\\ 0\end{bmatrix}. \quad (5)$$

The table presented below provides the record of the number of iterations and corresponding residue of ϕ_1 for different initial guesses t_1. The method found three independent solutions for x, y, z, and t. The most important fact is that it is almost independent on the initial value of the variable **t** and converges quickly to the solution. Three independent solutions were found. The number of iterations is very low, between 1 and 8.

Initial guess for *t*	***x***	***y***	***z***	***t***	No. of iterations	ϕ_1 *(x,y,z,t)* error
0.5	15.6300	10.7900	1.1036	0.0331	6	-0.00004
1	-10.6594	-4.2339	8.6170	-3.5729	8	-0.00013
2	2.0000	3.0000	5.0000	10.0000	4	0.00170.003
5	2.0000	3.0000	5.0000	10.0000	3	0.001
7	2.0000	3.0000	5.0000	10.0000	3	0.000002
9	2.0001	3.0001	5.0000	9.9993	2	0.0232
9.9	2.0000	3.0000	5.0000	10.0000	2	0.0003
10	2.0000	3.0000	5.0000	10.0000	1	0
50	2.0000	3.0000	5.0000	9.9999	3	0.0034
100	2.0000	3.0000	5.0000	9.9998	3	0.0068
1000	2.0001	3.0000	5.0000	9.9996	3	0.0117
10000	2.0001	3.0000	5.0000	9.9996	3	0.0124

Final Remarks and Conclusions

The method was tested on numerous examples with large number of equations and nonlinear unknowns. It has been found that the algorithm is very effective in all cases and is able to find many solutions for **t** with very high accuracy**.** It is especially suitable for the solution of identification problems, adaptive modeling, Adaptive Matrix Filter [2], where the identification and modeling is based on the large number of experimental data and model equations. It eliminates the problems with the convergence and initial guess for the all the variables. The presented approach makes possible to find the solution for many problems that were not solved due to the lack of convergence and effectiveness of the other methods. It gives often more effective solution than the method of neural networks.

References

1. Lukasiewicz, S. A. " Matrix Filter for Correcting Experimental Data", *Communications in Numerical Methods in Engineering*, Vol. 9, 797- 803, (1993).
2. Lukasiewicz, S. A., Hojjati, M. H., "Adaptive Matrix Filter", *Proceedings of CANCAM 2003 (19th)* University of Calgary, Calgary, Canada, June, (2003).

LINGOPTI PROJECT : SEMI-CONTINUOUS CASTING PROCESS OF COPPER-NICKEL ALLOYS

Etienne Pecquet [1], Ralf Volles [2], Jacqueline Lecomte-Beckers [3], Anne Marie Habraken [1]
[1] *ULg, Department of Mechanic of Materials and Structures, B-4000 Liege, Belgium*
[2] *RWTH, Institut für Bildsame Formgebung, 52056 Aachen, Germany*
[3] *ULg, Department ASMA, sector Special Metallic Materials, B-4000 Liege, Belgium*

Summary The following text deals with casting of copper-nickel alloys. They are high added values materials. The research contains two main parts. Laboratory tests (completed with bibliography) that provide thermal and mechanical properties of the ingot and the mould but also heat transfer coefficients between the ingot and its environment (mould, air and water). These parameters are required in the second part : development and validation of numerical modelizations by the finite element method to optimise the industrial process.

INTRODUCTION

The Lingopti project, performed in the University of Liege, is a first Europe research co-financed by the European Social Funds and the Walloon Region. The studied industrial process is the one of LBP factory. It consists in a vertical semi-continuous casting of copper-nickel alloys. The dimensions of an ingot are 7m in height and the section is 960x310mm. After a mould cooling, ingot is submitted to air cooling, water sprays and finally water tank cooling. LBP society makes several alloys. The principle component is the copper, and the content of nickel is between some percents to thirty percents. Sometimes, it can be added some iron or other components. Cupronickels are high added values materials used in very different domains from Euros money to tubes of brakes by Volvo.
The final goal of this research is the optimisation of the mould and the whole casting process of the enterprise to obtain better cast products. In fact, cast products sometimes present long oscillations marks ($\lambda \approx 500$mm) and some ingots have many internal cracks. It will also be examined the influence of the content in Nickel on the thermo mechanical evolution of the ingot during whole the casting process.

LABORATORY TESTS

Laboratory tests have been carried out in several domains. In fact, cupronickel alloys are not so common than steel and we do not dispose in the bibliography of enough data to characterise thermal and mechanical properties up to high temperatures and for the right alloys. Tests allow to determine thermal and mechanical properties of the solid, but in addition, heat transfer coefficients have also been determined for different environment conditions.

Mechanical tests

In casting process, it is essential to know the mechanical behaviour, up to the liquid state. Because of the viscosity is also an important parameter, tests of uniaxial compression has been carried out at different high temperatures and different speeds of deformation. Currently, we dispose of stress-strain curves for two alloys for three temperatures (500,900 and 1100°C) and three speeds of deformation (10^{-2}, 10^{-3} and 10^{-4} s^{-1}) : CuNi 75/25 and CuNi 70/30 with some Iron.

Thermal tests

With these tests, we determine, up to the solidus temperature, four parameters : the specific heat C_p, the thermal expansion coefficient α, the specific mass ρ and the heat conductivity λ. So that, we characterise the thermal behaviour and also dispose of these measurements for the two alloys mentioned here above. Thermal properties are also determined and can be used if we decide to modelize the mould in the numerical simulations.

Heat transfer coefficients

Finally, to be able to simulate numerically whole the casting process, heat transfer coefficient between the ingot and its environment are also necessary. We studied as well exchanges between the mould and the ingot (in case of contact or not) as heat transfer after that, with air, water sprays and water tank. For that purpose, some tests developments have been realised in collaboration with the department IBF of the University of Aachen (RWTH).

NUMERICAL CALCULATIONS

All the parameters determined here above are used in the numerical calculations by the finite element method with the Lagamine code, developed at the department M&S of the University of Liege since 1982. Currently, two 2D models are used and developed. A vertical slice has been first used only in thermal analysis. It allows to see the field of temperatures, but also to check, by a parametric study, the influence of several parameters. So, we verify that the latent heat of fusion or the

exchanges with the mould influence a lot the field temperature. Another important point is that the vertical heat flux is small in comparison with the horizontal one. That allows to consider an horizontal slice (see after). Figure 1 presents the field of temperatures for this vertical slice for whole the cooling process.

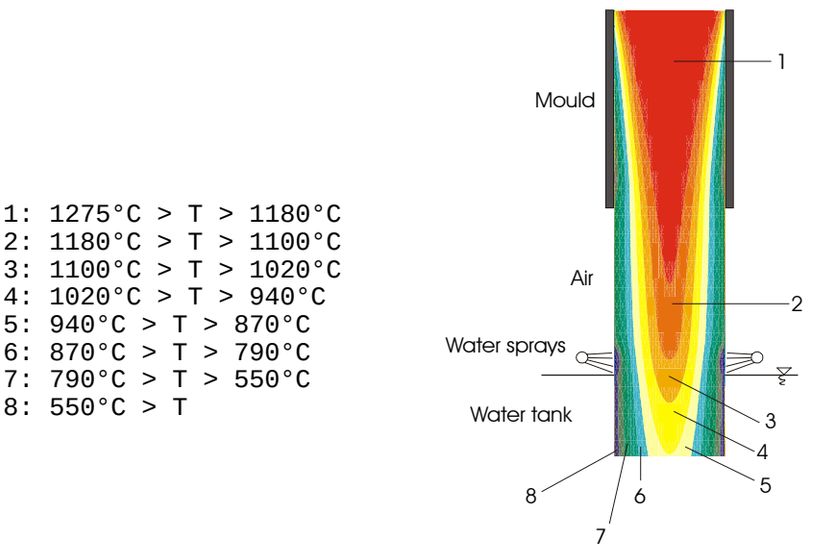


Figure 1 : Field temperature with the vertical slice model

With an horizontal slice model, we perform thermo mechanical analysis. The slice, by progression in the casting process, gives a 3D view of the ingot in stationary situation by a 2D modelization. This model, already developed and used by F.Pascon for continuous casting of steel [1], takes into account, in a simplified way by the concept of generalised plane state, stresses in the casting direction.
For the thermo mechanical analysis, for having convergence, mechanic requires small steps of time and themal behaviour big ones. So, we perform alternatively thermal and mechanical analysis transferring information from one to the other.
Figure 2 gives a view of the different material states obtained by this horizontal slice.

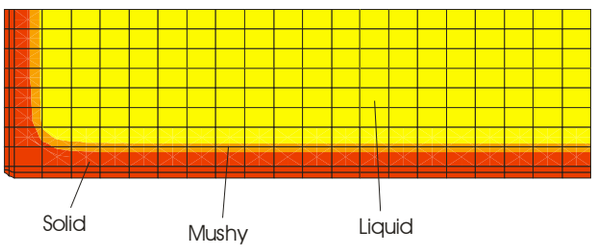


Figure 2 : Material state with the horizontal slice

PERSPECTIVES OF THE RESEARCH

Currently, models continue to be developed and validation has started. In order to compare numerical calculations and experimental measurements on the industrial process, following measurements have to be performed : heat flux extracted with the mould, geometry of the final ingot and surface temperatures just after the mould cooling.
We will also try to explain numerically long oscillation marks obtained on a lot of ingots and examine the ability of the available model to predict ingot shape.
The final goal is the optimisation of the casting process, when alloys composition is modified.

References

[1] Pascon F.: 2D1/2 Thermal-Mechanical model of Continuous Casting of Steel Using Finite Element Method *PhD Thesis*, Department M&S, ULg, 2003.

TWO SCALE FINITE ELEMENT METHOD

George Mejak*
*Department of Mathematics, FMF, University of Ljubljana, Ljubljana, Slovenia

Summary A two scale computational method based on the finite element method is presented. A method is suited for problems with two length scales, macro and micro, where a direct numerical resolution of the micro scale by the standard finite element method is too expensive. At the micro scale a standard finite element method is used, while at the macro scale the Petrov-Galerkin method is used. Problems with several thousand cells and tens of the fibre orientations are readily computed.

INTRODUCTION

Modern materials have quite often two length scales, a macro scale which is proportional to the physical size of the object and a micro scale which is proportional to the fine structure of the material. Considering the material homogeneous at the macro scale its material properties are given by the effective material properties by the homogenization theory. In general, the homogenization theory gives only existence of the effective material properties and only in some particular cases, for example for laminated or periodic structure, gives explicit formula for the effective material properties in terms of the micromechanical material properties. Thus in general case to obtain effective material properties a numerical method must be used. To this end a new computational method is proposed.

DESCRIPTION OF THE METHOD

Partition of the variational problem

Let Ω be an open bounded subset of $\mathbb{R}^d$ with a piecewise regular boundary and let us consider the following macro scale boundary value problem in the variational form: find $u \in H^1_0(\Omega)$ such that $a(u,v) = (f,v)$ for all $v \in H^1_0(\Omega)$. Further, let $\{\Omega_k\}_{k=1,\dots,K}$ be a family of open pair wise disjoint bounded subsets of Ω with piecewise regular boundaries such that $\overline{\Omega} = \cup_{k=1}^N \overline{\Omega}_k$. Restriction of the form $a(\cdot,\cdot)$ to $H^1(\Omega_k) \times H^1(\Omega_k)$ is denoted by $a_k(\cdot,\cdot)$. To each set Ω_k we associate a reference domain $\mathcal{O}_{i(k)}$, $i(k) \in \{1,\dots,I\}$ and a diffeomorphisem $T_k : \mathbf{x}_{i(k)} \mapsto \mathbf{y}_k$ from $\mathcal{O}_{i(k)}$ onto Ω_k. It is expecting that $I << K$. For example, if Ω is made of identical cells, then $I = 1$ and each T_k is a rigid transformation. A mapping T_k pulls back form a_k to the form $a^*_k(\cdot,\cdot)$ defined on $H^1(\mathcal{O}_{i(k)}) \times H^1(\mathcal{O}_{i(k)})$. In particular, if $a(u,v) = \int_\Omega A\nabla u \cdot \nabla v \, d\mathbf{y}$, $A \in \mathbb{R}^{d\times d}$, then $a^*_k(u^*,v^*) = \int_{\mathcal{O}_{i(k)}} A^*_k \nabla u^* \cdot \nabla v^* \, d\mathbf{x}_{i(k)}$, where $A^*_k = \left|\frac{\partial \mathbf{y}_k}{\partial \mathbf{x}_{i(k)}}\right| \left(\frac{\partial \mathbf{x}_{i(k)}}{\partial \mathbf{y}_k} A \left(\frac{\partial \mathbf{x}_{i(k)}}{\partial \mathbf{y}_k}\right)^T\right)^*$. Next we define an equivalence relation $\mathcal{R}$ on the set $\mathcal{K} = \{1,\dots,K\}$ by $k_1 \,\mathcal{R}\, k_2 \iff (A^*_{k_1} = A^*_{k_2} \quad \& \quad i(k_1) = i(k_2))$ and a factor set $\mathcal{K}_0 = \mathcal{K}/\mathcal{R}$. It is expecting that $K_0 = |\mathcal{K}_0|$ is a small number comparing to K. For example, if Ω is a square domain of the unit size and Ω_k are the squares with the sides of length $\frac{1}{n}$, $n \in \mathbb{N}$, aligned with the sides of Ω then $K = n^2$, $I = 1$ and each T_k is a translation from $\mathcal{O}$ to Ω_k. Further, if restriction of A to Ω_k represents material properties of Ω_k and each Ω_k is a composite made of the matrix Ω^{m}_k and the inclusion Ω^{i}_k with the material coefficients $C^{\mathrm{m}}_{j(k)}$ and $C^{\mathrm{i}}_{j(k)}$, $j \in \{1,\dots,J\}$, respectively, then $K_0 = \sum_{j=1}^J m(j)$, where $m(j)$ is a number of different geometrical arrangements of the inclusions Ω^{i}_k with the same material coefficients $C^{\mathrm{i}}_{j(k)}$. Typically, K_0 is of order 10 and K could be of order 10^4 or even of greater order.

Macro and micro finite element discretization

Let $\mathcal{T}_H$ be a finite element triangulation of Ω subordinate to the partition $\overline{\Omega} = \cup_{k=1}^N \overline{\Omega}_k$. In another words, each $\overline{\Omega}_k$ is a finite union of the sets from $\mathcal{T}_H$. The corresponding finite element space with the zero boundary data is denoted by V_{0H} and the basis functions by Ψ. The space V_{0H} is called the macro finite element space. Further, we denote by $\mathcal{T}_{h_k}$ a finite element triangulation of Ω_k and by V_{h_k} the corresponding finite element space. The spaces V_{h_k} are called the micro finite element spaces. It is required that the restrictions of the macro finite element space V_{0H} to Ω_k are contained in the micro finite element spaces V_{h_k}. In another words, micro finite element discretization is finer than the macro element discretization. On each Ω_k we associate to every macro basis function Ψ_p a discrete microscale variational problem : find $M^1_{p,k} \in V_{h_k}$ such that $M^1_{p,k} = \Psi_p$ on $\partial\Omega_k$ and $a_k(M^1_{p,k},\phi) = (f_k,\phi)$ for all $\phi \in V_{h_k}$ and a variational problem independent of Ψ_p: find $M^0_k \in V_{0h_k}$ such that $a_k(M^0_k,\phi) = (f_k,\phi)$ for all $\phi \in V_{0h_k}$. Here V_{0h_k} is a subset of V_{h_k} with the zero boundary data along $\partial\Omega_k$. For given $M^1_{p,k}$ and M^0_k we define microscale basis function $M_{p,k} = M^1_{p,k} + (\alpha_k - 1)M^0_k$ where α_k is yet unspecified parameter. Global microscale basis functions M_p are defined over Ω by combining definitions of $M_{p,k}$ over the supports of Ψ_p and extending by zero outside of them. It should be noted that it suffices to actually compute microscale basis functions only for the indices $k_0 \in \mathcal{K}_0$ since for $k \notin \mathcal{K}_0$ microscale basis functions are obtained by the mapping $T_k \circ T^{-1}_{k_0}$.

Having found microscale basis function we approximate solution of the macro scale variational problem by the linear combination $u_{H,h} = \sum_{p=1}^P u_p M_p$ such that 1) $u_{H,h}$ is a Petrov-Galerkin solution for the finite element triangulation $\mathcal{T}_H$ with the coordinate solutions M_p and the weighting functions Ψ_p and 2) restriction of $u_{H,h}$ to Ω_k is a solution of the microscale variational problem. It follows from the second condition that $\sum_{p\in P(k)} u_p \, \alpha_k = 1$, where $P(k) = \{p :$

supp $\Psi_p \cap \Omega_k \neq \emptyset\}$. Using this equation in the Petrov-Galerkin statement $a(u_{H,h}, \Psi) = (f, \Psi)$ for all $\Psi \in V_{0H}$ we obtain a system of linear equations

$$\sum_{p \in P(q)} \sum_{k \in K(p)} u_p \, a_k(M^1_{p,k} - M^0_k, \Psi_q) = (f, \Psi_q) + \sum_{k \in K(p)} u_p \, a_k(M^0_k, \Psi_q), \tag{1}$$

$q = \{1, \ldots, P\}$, where $P(q) = \{p : \text{supp}\, M_p \cap \text{supp}\, \Psi_k \neq \emptyset\}$ and $K(p) = \{k : \text{supp}\, M_p \cap \Omega_k \neq \emptyset\}$. Rewriting (1) in the compact notation we have $\mathbf{Bu} = \mathbf{b}$. Note that the components B_{qp} of $\mathbf{B}$ and b_q of $\mathbf{b}$ are expressible as the linear combinations of $a_k(\phi_{kr}, \phi_{ks})$ and (f, ϕ_{kr}), where ϕ_{kr}, $\phi_{ks} \in V_{h_k}$ have nonzero boundary values along $\partial\Omega_k$. The matrix $\mathbf{B}$ is sparse but in general unsymmetric. If the bilinear form $a(\cdot, \cdot)$ is coercive, the system $\mathbf{Bu} = \mathbf{b}$ has a unique solution. Due to the construction convergence of the macro finite element is $O(H^\beta)$, where the order of convergence β is given by the global regularity of the solution and the interpolation properties of V_{0H}. It is expected but not yet proved that the solution has certain superconvergence properties of order $O(h^\gamma)$.

Validation of the method

A simple test to validate the two scale finite element computation is to apply the method to the problem with the homogeneous material. To this end, let for a given macro finite element discretization a partition of Ω be coincident with the triangulation $\mathcal{T}_H$. Then the maro/micro finite element solution $u_{H,h}$ has two scale convergence properties, namely, for a fixed h we have $\lim_{H \to 0} u_{H,h} = u$ and for a fixed H we have $\lim_{h \to 0} u_{H,h} = u$. Choosing appropriate mesh parameters H and h a significant reduction of the computational time and space, comparing to the global mesh discretization of the size h can be achieved. Another test is provided by the homogenization theory by comparing solution of the problem with the effective material properties and the solution of the problem with highly oscillating periodic material properties. The proposed two scale finite element method passed both two tests by the predicted accuracy.

NUMERICAL EXAMPLES

Due to the restricted space only a very simple numerical example is given. For Ω is chosen a unit square which is partitioned into N^2 squares Ω_k with the area $\frac{1}{N^2}$. Each Ω_k is a bimaterial composite made of the isotropic matrix and the isotropic elliptical inclusion with a random orientation α_k where α_k is the angle between the major axis of the ellipse and the direction of the chosen side of the square Ω. We assume that α_k take values from the set $\{\alpha_1, \ldots, \alpha_{K_0}\}$ with the same probability. The semi axis of the ellipse are $\frac{a}{N}$ and $\frac{b}{N}$ with the nondimensional numerical values $a = 0.4$ and $b = 0.2$. The nondimensional material matrix of the matrix Ω_k^{m} is the identity matrix $\mathbf{I}$ and the nondimensional material matrix of the inclusion is $\beta\mathbf{I}$. As found by the numerical computation, weak inclusion gives more pronounced dependance upon the orientation and thus results for $\beta = 10^{-3}$ are presented. The nondimensional load vector is $f = 2$. Summarizing, the problem is to find a solution $u \in H^1_0(\Omega)$ such that $\int_\Omega \hat{\beta}, \nabla u \cdot \nabla v \, d\Omega = 2 \int_\Omega v \, d\Omega$ for all $v \in H^1_0(\Omega)$. Here $\hat{\beta} = 1$ on Ω_k^{m} and $\hat{\beta} = \beta$ on Ω_k^{i}. In terms of mechanics, u is either a Prandtl stress function of a torsion problem for a composite cylindrical bar or either a solution of the steady state heat equation with the internal heat source f, see Fig. 1. In the first case nondimensional torsional rigidity $D = 2 \int_\Omega u \, d\Omega$ is of interest, see Table 1.

CONCLUSIONS

The proposed new two scale finite element computation is highly effective. It is capable to accurately resolve the micro scale at the cost of the macro element discretization. Application of the method to the problems with the homogeneous material is considered as an important improvement of the finite element method.

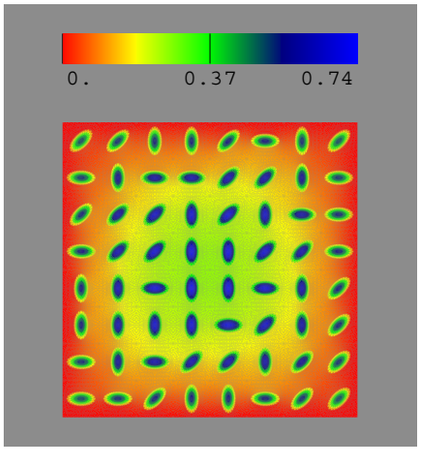


Fig. 1. Temperature distribution within the media with the random oriented inclusions.

Table 1. Dependance of the torsional rigidity upon the number of cells $K = n^2$; D_{p} torsional rigidity of the periodic structure with two orientations $\alpha_1 = 0$ and $\alpha_1 = 90°$, D_{u} torsional rigidity of the unidirectional periodic structure with $\alpha_1 = 0$. Element type : quadratic micro element.

n	h	H	D_{p}	D_{u}
2	$1/16n$	h	2.21001	2.21200
4	$1/16n$	h	0.73591	0.73895
8	$1/16n$	h	0.37091	0.37432
16	$1/16n$	$2h$	0.28006	0.28343
32	$1/16n$	$2h$	0.25747	0.26076
64	$1/16n$	$4h$	0.25147	0.25443
128	$1/16n$	$16h$	0.24872	0.24921

PROBLEMS OF APPLICATION OF HIERARCHICAL MODELLING, DISPLACEMENT FEM AND A POSTERIORI RESIDUAL ERROR ESTIMATION TO STATIC AND DYNAMIC ADAPTIVE ANALYSIS OF COMPLEX STRUCTURES

Grzegorz Zboinski*, Maciej Jasinski *
*Institute of Fluid Flow Machinery, Polish Academy of Sciences, 14 Fiszera Street, PL 80-952 Gdansk, Poland

Summary The paper addresses the main problems of implementation of the idea of hierarchical modelling in the scope of displacement finite element methods and of application of the a posteriori residual error estimation to adaptive analysis of complex structures. These structures consist of solid, thin- and thick-walled parts and transition zones as well. Our presentation is limited to linear static and linear dynamic (modal) analyses. The main source of the problems under consideration is incompatibility of the various mechanical models forming hierarchy of models for complex structures, locking, improper solution limit and boundary effect sensitivity of the displacement finite element formulation, and similar sensitivity of the a posteriori error estimation by the Element Residual Methods. The elaborated methods of overcoming the mentioned problems are elucidated, if available. For those of the problems which have not been resolved yet, the suggested methods are indicated and their potential for overcoming the problems are thoroughly discussed.

GENERAL OVERVIEW OF COMPLEX STRUCTURE ANALYSIS

The main difficulty in complex structures analysis by FEM is that conventionally each part of the structure, i.e. solid, thin- and thick-walled part is described with the different mechanical model. Such models may correspond to various theories, for example: first order shell, higher order shell, hierarchical shell or three-dimensional elasticity one. It is known that for each of the listed theories different field unknowns are used. As a consequence also different degrees of freedom of the corresponding finite element methods are utilised. For this reason analysis of complex structures is usually difficult. That is also why, in comparison to enormous number of works devoted to analysis of solids, shells and plates, the papers concerning all them together as one complex structure are really rare.

Some achievements in adaptive finite element methods for solids and shells [1] as well as recent advances in hierarchical modelling of the first order shells [2] or hierarchical shell models [3, 4] has become an impulse for the authors of this work to extend these potentially promising and powerful ideas into the complex structure description and analysis. The results of the research on hierarchical modelling and adaptive finite element methods for complex structures static analysis has been recently presented in [5]. The idea is now being extended to linear dynamic (modal) problems. The idea utilises hierarchical modelling applied to first order shell, hierarchical shell and three-dimensional elasticity, as well as two-dimensional, three-dimensional or mixed *hp* approximation spaces, which both lead to local (element level) model, *h*-, *p*- and *q*-adaptive finite element methods based on displacement formulation. The numerical parameters *h*, *p* and *q* represent averaged dimension of the element, as well as longitudinal and transverse orders of approximation, respectively. The two-dimensional or three-dimensional isotropic or anisotropic adaptive procedures are controlled through a posteriori total, modelling and approximation error estimation based on the Residual Equilibration Method. The main feature of the proposed approach is overcoming of the problem of different degrees of freedom in various parts of the complex structure by means of application of the three-dimensional approach which consists in utilisation of three-dimensional degrees of freedom only, regardless mechanical models applied. Note that in contrast to other researchers' approach, we managed with our method to build one hierarchy of models including various mechanical models instead of exclusion of the models which do not fit the main hierarchy of the predecessors', i.e. which are not compatible with either hierarchical shells originated from higher order theories or with the first order shell hierarchy or with hierarchy of numerical models conforming three-dimensional elasticity.

For the sake of honesty we should mention also attempts of the other researchers, which could be utilised in analysis of complex structures. These works address only one aspect of adaptive complex structure analysis, i.e. the modelling error issues and are quite rare [6, 7]. The recent contribution of Stein and Ruter [8] suggest many practical hints for proper adaptive modelling within complex structures but seems to propose different methods that could lead to effective complex structure analysis. In this paper we will try to show that some of the problems listed in [8] has already been resolved in [5] partly or completely or can be potentially resolved within our approach.

MAIN PROBLEMS, THEIR SOURCE, AND OVERCOMING THEM

Apart from the main implementation problem of hierarchical modelling of complex structures resulting from different degrees of freedom of different theories used for description of various parts of complex structures there are also other implementation problems. They deal with application to complex structures of the most common displacement formulation of the finite element methods, and with employment of the Residual Equilibration Methods (REM) for error estimation. The displacement FEM is sensitive (in the sense that special approach is necessary) to such phenomena as: the improper solution limit of the 3D elasticity model when transverse order of approximation *q* equals one, shear or shear-membrane lockings, and boundary layers typical for thin- or thick-walled members of the complex structures. Also REM may suffer from the latter two numerical phenomena. It is also sensitive to edge and corner singularities.

Hierarchical modelling

Even though the proposed 3D approach enables usage of the same three-dimensional degrees of freedom within all the complex structure, regardless of the locally applied models, this approach does not remove incompatibility of the first order Reissner-Mindlin model with the hierarchic shell models and with the three-dimensional elasticity. The source of this incompatibility are: the plain stress assumption and kinematic assumption of the theory (no elongation of the normals to the mid-shell surface during deformation). The incompatibility due to the second of the mentioned assumptions can be removed through application of the transition approximations of the displacement field between the first order shell model and hierarchic shell models or three-dimensional elasticity model, while the first one is an inherent feature of the first order shell models and cannot be easily resolved. In our proposition we are not afraid of the latter incompatibility. The method proposed for such situations is controlling the modelling error within the transition zone. This can be done with the same methodology which is used for the first order model itself. Such a control leads to movement of the transition area into the region where this error is acceptable. If such an action is not effective enough then the first order model has to be replaced with the first of the higher order shell models compatible with the description of the remaining part of the complex structure.

Displacement finite element methods

Three phenomena – improper solution limit of the 3D elasticity model (with transverse order of approximation q equal to one), locking, and boundary layers need special treatment within displacement FEM formulation (this is also true for some of these phenomena within other FEM formulations). The approach proposed in this work offers local (element level) a posteriori numerical tools for detection and assessment of the mentioned phenomena. To the best of the authors' knowledge the idea is totally original and has been proposed and implemented first in [5]. For the improper solution limit phenomenon we propose detection numerical tool, for the locking phenomena (either shear or shear-membrane) we present tools for their detection and assessment of their strength, while for boundary layers we have to detect and assess strength and range of the edge effect. The additional advantage is that the proposed tools are compatible with the error estimation procedures that facilitates their implementation. In our proposition two local problems have to be solved for the chosen element of the potentially affected region and the obtained solutions have to compared. Note that with these tools at hand we try to move adaptive solution for the complex structure static or dynamic problems towards the asymptotic convergence region, where adaptivity controlled with error estimation can be performed.

A posteriori error estimation

In contrast to a typical case of simple structures a posteriori error estimation within complex structures has to include not only the approximation error but also the modelling error which results from application of mechanical models simplified with respect to three-dimensional (3D) elasticity. For the purpose of approximation and modelling error estimation we propose application of the Residual Equilibration Method for all mechanical models included, i.e. 3D-based first order and hierarchic shell models and 3D elasticity model as well. The method is applied twice. First we apply it to approximation error estimation for the elements conforming three mentioned models. Note that the global approximation error being a sum of element error indicators possesses upper bound property for these models. For the second time the method is applied for total error estimation within the elements conforming two shell models. The upper bound property of the global total error estimate can be proved for the hierarchic shell models only. Local modelling error indicators are obtained as a difference of the total and approximation indicators.

Some improvement of the estimation in the case of locking, boundary effect and boundary singularities can be gained by constraining local problems or introduction of higher order splitting functions for equilibration instead of linear ones.

CONCLUSIONS

The elaborated general method constitutes an interesting proposition towards obtainment of an effective numerical tool for linear static or dynamic adaptive analysis of complex structures. Some problems await resolution or improvement, however.

References

[1] Szabo B. A., Sahrmann G.J.: Hierarchic plate and shell models based on *p*-extension. Int. J. Num. Methods Engng 26: 1855-1881, 1988.

[2] Chinosi C., Della Croce L., Scapolla T.: Hierarchic finite elements for thin plates and shells. *Comp. Assisted Mech. Engng Sci.* **5**: 151-160, 1998.

[3] Oden J.T., Cho J.R.: Adaptive *hpq* finite element methods of hierarchical models for plate- and shell-like structures. *Comp. Methods Appl. Mech. Engng* **136**: 317-345, 1996.

[4] Actis R.L., Szabo B.A., Schwab C.: Hierarchic models for laminated plates and shells. *Comp. Methods Appl. Mech. Engng* **172**: 79-107, 1999.

[5] Zboinski G.: Hierarchical modelling and finite element method for adaptive analysis of complex structures. *DSc Thesis*, IFFM, Gdansk, 2001.

[6] Stein E., Ohnimus S.: Anisotropic discretization and model-error estimation in solid mechanics by local Newmann problems. *Comp. Methods Appl. Mech. Engng* **176**: 363-385, 1999.

[7] Oden J. T., Prudhomme S., Hammerand D.C., Kuczma M.S.: Modeling error and adaptivity in nonlinear continuum mechanics. *Comp. Methods Appl. Mech. Engng* **190**: 6663-6668, 2001.

[8] Stein E., Ruter M.: Error-controlled adaptive modeling and finite element analysis in the context of European structural codes. *CD-Rom Proc. First Int. Conf. Adaptive Modeling and Simulation ADMOS 2003*, Goeteborg, 2003: 1-28.

STATICS AND KINEMATICS OF SYMMETRIC SWELLING VIRUSES

Flórián Kovács[*], Tibor Tarnai [**], Simon D. Guest[†], Patrick W. Fowler[‡]
[*]*Research Group for Computational Structural Mechanics, Hungarian Academy of Sciences – Budapest University of Technology and Economics, Műegyetem rkp. 3., H-1521 Budapest, Hungary*
[**]*Department of Structural Mechanics, Budapest University of Technology and Economics, Műegyetem rakpart 3., H-1521 Budapest, Hungary*
[†]*Department of Engineering, University of Cambridge, Trumpington Street, Cambridge CB2 1PZ, UK*
[‡]*Department of Chemistry, University of Exeter, Stocker Road, Exeter EX4 4QD, UK*

Summary Some viruses in biology vary their diameter in response to pH change, and retain icosahedral symmetry during its swelling motion. In this research, a mechanical ball-jointed model of the virus was set up, then mobility and self-stresses were analysed with symmetry-adapted techniques. Also investigated was the uniqueness of fully symmetric kinematic paths of swelling, through analytical relationships between geometrical variables of the model.

MODELLING THE COWPEA CHLOROTIC MOTTLE VIRUS

The CCMV (Cowpea Chlorotic Mottle Virus) has recently received much attention, partly because of its icosahedral symmetry, rarely observed in biological systems, but more interestingly because, if there is a change in pH, the virus starts to behave as a mechanism, leading to a symmetric enlargement of the original object [1]. Expansion is produced by screw-like motion of each polygonal morphological unit (capsomere) of the virus coating: pentagonal and hexagonal elements (called pentamers and hexamers) undergo a radial translation and rotation in a way that original symmetry of the structure is preserved. Fig. 1 shows computer-aided image reconstruction of native (a) and swollen (b) form of a CCMV [2].

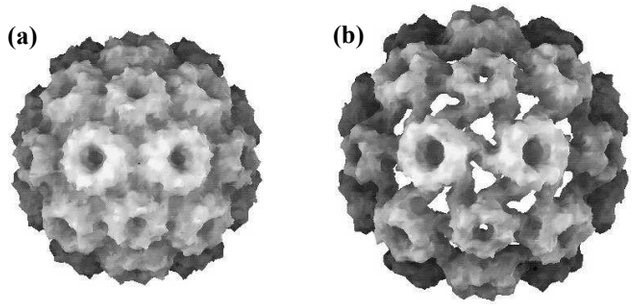


Fig. 1: native and swollen form of a CCMV capsid

Numerical data obtained by cryo-electron microscopy reveals two important factors: (i) there is a double protein chain between adjacent capsomeres; (ii) internal deformations of capsomeres are relatively small compared to the dimension of swelling. It looks therefore plausible to reproduce and analyse the swelling motion by a ball-jointed mechanical model composed of rigid elements.

Mechanical model

In the mechanical model of a CCMV (referred to as 'double-link expandohedron' [3] henceforth), capsomeres are represented by regular pentagons and hexagons forming a truncated icosahedron in the closed configuration. Pairs of rigid bars that substitute protein links are arranged such that two endpoints of each bar lie somewhere in the planes of connected polygons respectively. An additional requirement is that double link connections between hexagons must obey C_2 symmetry, in order to respect overall symmetry conditions. We assume that contact points give a pattern of C_5 and C_6 symmetry on pentagons and hexagons. For example, Fig. 2a represents the closed configuration of a model where connection points are located along the edges of somewhat smaller polygons (for clarity, only these shrunk polygons are displayed instead of original ones).

For the numerical analysis of the model, polygons are represented by position coordinates of their mid-points and another triplet of numbers that characterises the rotation of the polygon. The set of 32 polygons (12 pentagons and 20 hexagons) is constrained by $12\times5 + 20\times6 = 180$ rigid bars. A compatibility matrix is set up which relates the change of length of each bar to the geometric variables describing the position of the polygons. In this way, $6\times(12+20) = 192$ kinematic variables and 180 constraints define a 180-by-192 matrix to be analysed.

Symmetry-adapted analysis

Singular value decomposition (SVD) of a compatibility matrix gives directly all independent states of self-stress and mechanisms, but in a general Cartesian coordinate system; much more progress can be made if they are put into a

symmetry-adapted form. With the help of the Great Orthogonality Theorem of Group Representation Theory, it is possible to generate matrices that transform both states of self-stress (constraints) and mechanisms (variables) into a symmetry-adapted basis where matrices take a block-diagonal form [4].
For the symmetry-adapted compatibility matrix of the CCMV model, performing SVD on each block separately shows that there is a fully symmetric mechanism, but no fully symmetric state of self-stress; a direct proof for the finiteness of that fully symmetric (swelling) mechanism [4]. Therefore the expandohedron described above seems to be an appropriate model for the expanding virus, and a general configuration of the expandohedron is shown in Fig. 2b. We note, however, that in addition there were three states of self-stress and other eight mechanisms of different symmetry properties that implies the existence of other possible inextensional mechanisms that are not investigated here.

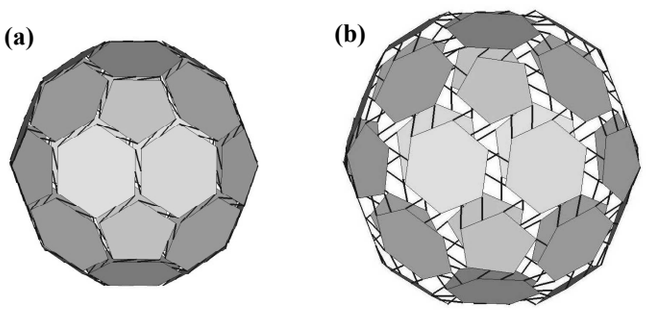


Fig. 2: Closed and general configuration of the expandohedron

POSSIBLE PATHWAYS OF SWELLING

If once the rotation (α) of a hexagon is given for any configuration, the corresponding radius of inscribed sphere (R_6) can be computed from a quadratic polynomial. Therefore there are generally two possible radii for a given angle, and the $R_6 - \alpha$ relationship gives an irregular egg-like diagram. The limit points mark the minimum and maximum rotation allowed, but in fact only a part of the upper curve is physically admissible because of self-intersections (the lower part corresponds to shrinkage rather than expansion).
Once all of the connection points on the polygons and link lengths are defined, the pentagons must fit in a compatible way to their surrounding hexagons – measurements on the CCMV indicate that the radius characterising the translation of the pentagons (R_5) is greater than R_6. Analysis of the expandohedron shows that the explicit formula for R_5 leads to a fourth-order polynomial in α. Numerical experiments revealed that there are possible initial geometrical data that allow for four real roots of this polynomial, even within the physically admissible domain of expansion, while other geometries (and other α) produces two or zero real roots. Detailed analysis showed that changes in number of real roots in several cases occur at the same configurations where there are kinematic bifurcations. Thus even in the fully symmetric mode the expansion is not uniquely determined by the generic model. Instead it will be necessary to refine the initial geometry with parameters (link lengths, node coordinates within polygons) taken from experimental data obtained from electron microscopy. Then it will be possible to have a better insight into the problem: which of the different kinematic pathways is really physically admissible?

CONCLUSIONS

A rigid, ball-jointed mechanical model of a CCMV was found to be appropriate to reproduce some aspects of experimentally observed swelling: double-link expandohedra certainly have a finite symmetric expansion mode. Analytical rotation-translation relationships were determined for hexagons and pentagons that showed limit points and possible bifurcations within the physically admissible kinematic pathway, showing that symmetric expansion can be performed in different ways for a given geometry. Measurements on the exact virus geometry, however, will help to find the correct kinematic path.

References

[1] Speir J. A., Munshi S., Wang G., Baker T. S., Johnson J. E.: Structures of the native and swollen forms of cowpea chlorotic mottle virus determined by X-ray crystallography and cryo-electron microscopy. *Structure* **3**:63-78, 1995.
[2] Reddy V., Natarajan P., Okerberg B., Li K., Damodaran K., Morton R., Brooks III C., Johnson J.: VIrus Particle ExploreR (VIPER), a Website for Virus Capsid Structures and Their Computational Analyses. *J. of Virology* **75**:11943-11947, 2001.
[3] Kovács F., Tarnai T., Guest S. D., Fowler P. W.: Double-link expandohedra: a mechanical model for expansion of a virus, *Proc. R. Soc. Lond. A* (submitted), 2003.
[4] Kangwai R. D., Guest S. D.: Detection of finite mechanisms in symmetric structures. *International Journal of Solids and Structures* **36**:5507–5527, 1999.

A NUMERICAL APPROACH FOR LARGE-SCALE COMPUTATION CEM

Jixin Yang[*], Cheng Wang[**],Chengwu Shen[*]

[*]*College of Transportation, Wuhan University of Technology, 430063 ,Wuhan,China*

[**]*College of Civil Engineering and Mechanics, Huazhong University of Science & Technology, 430074, Wuhan, China*

Summary A new numerical approach for large-scale computation-cellular element method (CEM) is introduced. The similarities and differences among the moment distributed method, finite element method and cellular element method are studied. Its basic principle and computing steps are presented. Several numerical computing examples are given. Based on the numerical results, the feasibility, advantages and disadvantages of cellular element method are discussed.

THE BASIC PRINCIPLE OF CELLULAR ELEMENT METHOD

At setting up the material constitutive relation, there is principle of local action. It isn't necessary to consider the motion of particles outside its vicinal area when you decide the stress of a particle. That is to say, the action of a particle is regarded as being limited in a definite area. Its motion and stress only decide on the motion of its adjacent particles because it is numb to the information of other particles. Material equilibrium is considered an automatic organic phenomenon through the information transmission of each other. The course is very similar to cellular automata (CA).

A cellular automata is a mathematical model dispersed in time and space. According to it, any system consists of disjunctive individuals. It can be used for describing the whole action behaviour and the evolution process of any system displayed by particles' interaction. CA usually describes cell position in scalar at present, and evolves according to a certain rule, finally attains a kind of stable state. We can generalize the basic characteristics of the cellular automatic as follows: (a) A lot of dispersed meshes and nodes called cells constitute a system (one, two and there dimension). (b) All cells' positions are described by discrete parameters or continuous parameters. (c) All cells are only connected with their adjacent area in definite space, and the current position of a cell is decided on the area of its neighbour. (d) The state of a cell will change with a certain regulation (the characteristic of cell).

Therefore, the analysis of the mechanics fits the request of cellular automata's four basic characteristics, and the characteristic (d) is the force-deformation curve that is decided by material constitutive relation. Certainly, the state of each cell must be described by vector or tensor. Because the number of particles in a structure is infinite, it is very difficult to directly study each particle's mechanics behaviour and evolution mechanism. But we can study finite particles instead of infinite particles. It is the same to finite element method in which a structure is regarded as a composite that consists of finite cells. We can attain the approximate solution of all elements or nodes through the way. Previously we must analysis the cells mechanics characteristic by dividing elements and using the discrete techniques on condition that the static equilibrium equations are obeyed.

For a structure, we can disperse it as in finite element method and get cells formed with nodes and elements. A node and its vicinal nodes and elements form a cell. The cell that node N_i is on its center is called cell D_i. Supposing N_i has relation with E_i^j formed by number of m_i elements. Here N_i^k are their adjacent nodes. Then it is describe as

$$D_i = N_i \cup \left\{E_i^1,\cdots,E_i^{m_i};\ N_i^1,\cdots,N_i^{n_i} \mid N_i \in E_i^j;\ N_i^k \in E_i^j,\ j=1,\cdots,m_i\right\} \tag{1}$$

The cell D_i includes vicinal nodes N_i^k (k=1, ..., n) beside N_i and correlative elements E_i^j (j=1,..., m_i). The state V_i of cell D_i is defined as general displacements (u_i) and forces (F_i). Then there is equation:

$$V_i = \{u_i, F_i\} \tag{2}$$

V_i has 2*R* dimension. It may be *R*=2(plane truss, elastic plane problem and axial symmetry structure), *R*=3(plane frame, slab, three-dimension object) or *R*=6(space frame and shell). It will change with various structures.

For cell D_i, the forces on node (F_i) and the restrictions of its neighbour node N_i^k will decide the displacements of node N_i . The relation of forces and deformations can be analysed by two proceedings with the form of its increment:

(1) Nodal force increments ΔF_i will result in displacement increments Δu_i of the node N_i .

(2)With the displacements increments Δu_i , the node N_i may cause its adjacent nodes to have the nodal force increments $\Delta F_i^k (k=1,2,\cdots n_i)$.

All cells of the structure transit force-displacement-force each other. Finally the increments of Δu_i and ΔF_i^k will be nearly equal to zero. This automatic adjusting phenomenon will make the structure equilibrium.

Based on principle of local action, the idea of Cellular Automata and the discrete techniques in finite element method, the new numerical analysis method is called cellular element method (CEM).

THE ALGORITHM OF CELLULAR ELEMENT METHOD

The general solving process of cellular element method can be described as follows:
(1) Divide the structure into a series of elements and nodes by using the discrete techniques in finite element method.
(2) For each node, circular operation as follows is done.

(a) Applying zero-displacement restrictions on the adjacent nodes of the computing node, i.e., make them fixed.

(b) Calculating the displacements of the computing node. The region where the computing node and its adjacent nodes can be seen as a cell, and the restricting condition is that its adjacent nodes are fixed. Only one node (the current computing one) can move. Its displacements can be solved with finite element method (rigidity method). We only have to solve a equation group with 6 linear equations at most, because the number of a node's displacements is not more then six.

(c) Calculating the restriction forces of the adjacent nodes.

We can calculate the nodal forces of the element by using the computing node's displacements and the zero-displacement of its adjacent nodes. In the same time, the restriction forces of the adjacent nodes can be worked out.

(d) Assuming the loads of the computing node are zero, and the restriction forces of the adjacent nodes are added to the nodes negatively.

(e) Accumulating the displacements of the computing node.

(3) At the end of each circulation, check whether the differences (named ε) of every node's displacements in two circulations are in the range of accuracy. If not, we continue the next circulation. Finally, we will attain the approximate value of every node's displacements in balance state.
(4) Computing the stresses and strains of elements with the displacements of nodes, elements' geometric and physical equations.

The method has the following advantages:
(1) It isn't necessary to solve the structural whole balance equation, and has not problems caused by a large quantity of data memory when computing on computer.
(2) It has complete parallel computing ability.

The solving process of cellular element method is similar to the moment distributed method in structure mechanics. In fact, the moment distributed method can be seen as a particular example of cellular element method in solving a rigid frame structure.

But in the classical moment distributed method, each node had only one direction displacement. While moment distributed method can only be suit for continuous beam and plane rigid frame without lateral displacement, cellular element method can be applied to any structure.

NUMERICAL INSTANCES

Three numerical instances were given: a space frame structure, a plane stress problem, and a space entity structure. All results show that when we use the cellular element method to calculate the structures, we can get the same solutions as those worked out by finite element method.

CONCLUSIONS

Cellular element method is a new numerical computing method. In this method the integer analysis of structure is changed into a series of local element analysis by using the idea of Cellular Automata. It may have a good future in the aspect of computing large structure because it hardly has any special request on the capability of computer. Simultaneity, It can be developed into a high parallel arithmetic to suit for the request of parallel computer.

References

[1] Shen Chengwu, Tang Xiaobing, Yang Jixin. An approach to mechanical analysis of plane truss using cellular automata. Journal of Wuhan transporation university.2000, 24(2): 105-108

[2] Yang Jixin.Study on the theory of cellular element method and its program. Doctor扭 degree paper of Wuhan University of technology.2002.6

[3] Yang Jixin, Shen Chengwu, Chen Dingfang. Cellular element method for analysis of spline.Engineering mechanics.2003, 20(2): 142-145

[4] Montheillet F,Gilormini P.Predicting the mechanical behavior of materials with cellular automata. Int.J.plasticity,1996，12(4):561_574

SOME INVESTIGATIONS ON FM BEM IN SOLID MECHANICS

Zhenhan Yao, Haitao Wang, Pengbo Wang
Department of Engineering Mechanics, Tsinghua University, 100084 Beijing, China

Summary A new version algorithm of $O(N)$ FM BEM for 2D elastostatics is presented and applied to the simulation of 2D elastic solid with large number of randomly distributed inclusions. Furthermore, FM BEM is applied to the simulation of 2D elastic solid containing large number of randomly distributed cracks.

INTRODUCTION

As well known, the boundary element methods (BEM) has remarkable advantages of dimension reduction and higher accuracy, but the conventional BEM is not efficient for large scale problems. For the conventional BEM $O(N^3)$ operations and $O(N^2)$ memory are required, where N is the number of DOF.

Fast multipole (FM) methods presented by Rokhlin, Greengard and other mathematicians have reduced the operations and memory requirement tremendously, finally reduced to $O(N)$. The FM BEM becomes an attractive way to solve complex practical scientific and engineering problems with BEM. There are nearly 500 papers so far have been cited by SCI in the field of fast multipole BE. In solid mechanics, especially if the local effects are important in the analysis, the higher accuracy is required, and some further investigations are still required for their application in different large scale problems.

In this presentation, some investigations of authors' group on FM BEM in solid mechanics are presented, including: a new version algorithm of $O(N)$ FM BEM for 2D elastostatics and its application to the simulation of 2D elastic solid with large number of randomly distributed inclusions; application of FM BEM to the simulation of 2D elastic solid containing large number of randomly distributed cracks. Three years ago in authors' group, the largest scale of practical problem solved by conventional BEM was 54,000 DOF, on a parallel PC cluster consisted of 8 PCs. The scale of numerical examples by FM BEM presented in this presentation, already reaches 544,000 DOF and 1,500,000 DOF, calculated on one PC.

A NEW VERSION OF FM BEM FOR 2D ELASTOSTATICS

Original FM BEM of $O(N)$

The **Step 1** of FM BEM for 2D elastostatics is *Multipole Expansion of the Kernels*. The far-field expansion of kernels is performed in terms of complex Taylor series with respect to the field point y around a selected point y_0, which is the center of a small square box A containing y, as shown in Fig.1. The **Step 2** is *Shift of Multipole to Multipole Expansion*. The multipole expansion with respect to the center of smaller square box A is shifted to that with respect to point y_1, the center of larger square box B. The **Step 3** is *Shift of Multipole to Local Expansion*. The multipole expansion with respect to the center of square box B is shifted to the local expansion with respect to point x_0, the center of square box C, which is as the same size as the box B, but containing the source point x. The **Step 4** is Shift of Local to Local Expansion. The local expansion with respect to the center of square box C is shifted to that with respect to point x_1, the center of a smaller square box D including x. The details of the algorithm and the formulas can be found in Ref. [1].

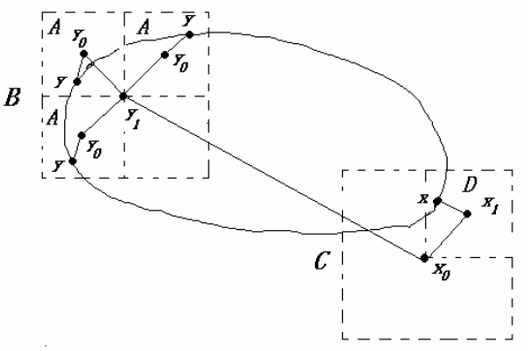
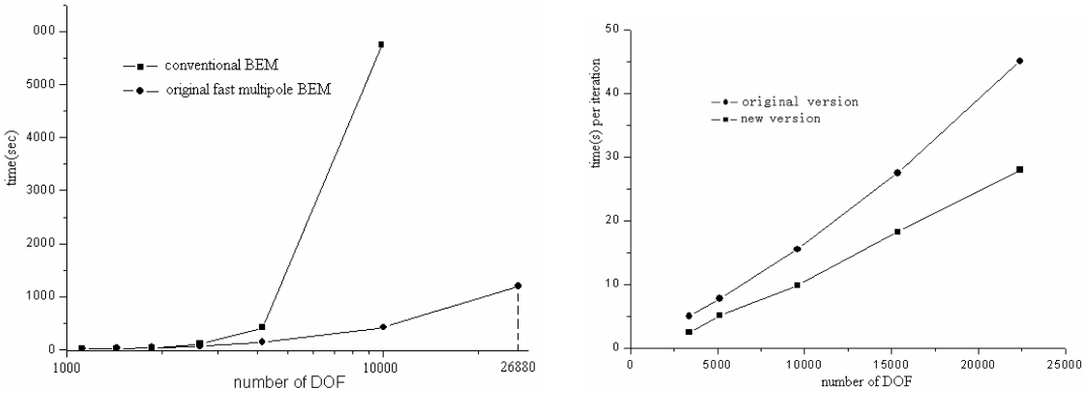


Fig. 1 Main steps of FM BEM

New Version FM BEM

The main idea of the new version FM BEM for 2D elastostatics is to replace the Step 3 of original one by other three sub-steps, which make the translation operator diagonal. The **Step 3.1** is *Shift of Multipole to Exponential Expansion*; the **Step 3.2** is *Shift of Exponential to Exponential Expansion*; and the **Step 3.3** is *Shift of Exponential to Local Expansion*. Although it is more complex, the efficiency is further improved. The comparison of conventional BEM, original FM BEM and new version FM BEM in computational speed can be found in Fig. 2.



a) b)

Fig. 2 Comparison of conventional BEM, original and new version FM BEM in computational speed

SIMULATION OF 2D ELASTIC SOLID WITH LARGE NUMBER OF INCLUSIONS

The FM BEM has been successfully applied to the computation of the effective properties of 2D elastic solid with 1600 randomly distributed circular inclusions as shown in Fig.3. Actually, for such problem, the sample with 100 inclusions is sufficient, and it can be computed by conventional BEM. But the example shown here with 544,000 DOF is a large scale problem, which can not be treated using conventional BEM. For the further investigation of 3D composites it will be a large scale problem as well, only the FM BEM has potential to simulate it successfully.

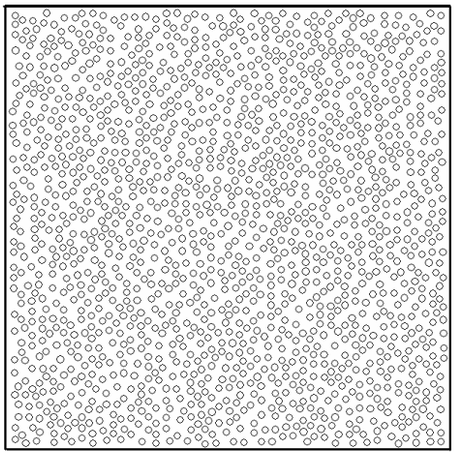


Fig. 3 2D elastic solid with 1,600 randomly distributed inclusions

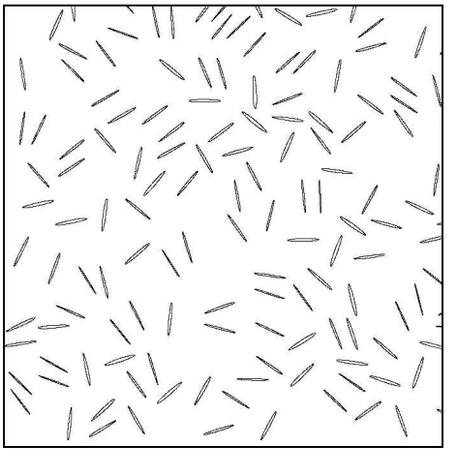


Fig. 4 zoomed deformation pattern of 2D solid containing large number of cracks

SIMULATION OF 2D ELASTIC SOLID WITH LARGE NUMBER OF CRACKS

A new form of complex Taylor series is applied to reduce the number of multipole moments. An improved preconditioner for GMRES is developed for reducing computing time and memory requirement. The FM BEM has also been successfully applied to the computation of 2D infinite elastic solid containing 16384 randomly distributed cracks in a finite region, with 1,572,864 DOF. The computing time on one PC is about 7 hours. The zoomed deformation pattern is shown in Fig. 4.

CONCLUDING REMARKS

The investigations on FM BEM in simulation of 2D elastic solids have shown its attractive advantages. The FM BEM can be applied to some large scale problems. The further investigation in authors' group will be concentrated on 3D elasticity problems, including composites and thin structures, and on the simulation of the failure process of the composite materials.

References

[1] Wang, H.T., Yao, Z.H.: Simulation of 2D elastic solid with large number of inclusions using fast multipole BEM. In: Bathe, K.J. ed. *Computational Fluid and Solid Mechanics 2003*, 732-736, Elsevier, 2003.

XXI ICTAM, 15–21 August 2004, Warsaw, Poland

RADIAL-TYPE APPROXIMATION TECHNIQUE FOR A SPACE-TIME MULTISCALE COMPUTATIONAL STRATEGY

Anthony Nouy*, Pierre Ladevèze*
*LMT-Cachan (ENS Cachan / CNRS / University Paris 6)
61, avenue du Président Wilson, F-94235 Cachan CEDEX, France

Summary A new multiscale computational strategy was introduced recently for the analysis of structures. It involves an automatic homogenization procedure in space and in time. This procedure requires the resolution of a large number of linear evolution equations. Here, we present a robust approximate resolution technique for these equations, based on the concept of radial approximation. It leads to the construction of a relevant reduced basis of space functions and it is particularly suitable for the analysis of composite structures.

INTRODUCTION

The behavior of heterogeneous structures, such as composite structures, often results from complex phenomena taking place on the microscale. Attempts to predict the behavior of such structures have led to the development of increasingly sophisticated models describing the material on a very fine scale compared to the scale of the structure. Therefore, the numerical simulation of these problems requires the development of efficient computational strategies taking into account these multiscale aspects. For the description of local phenomena with short lengths of variation in space as well as in time to be accurate, the calculations must be performed on a fine discretization of the structure and of the time interval being considered. This condition leads to problems with very large numbers of degrees of freedom, whose computation costs with standard calculation codes are generally prohibitive. One of the main objectives in the last few decades has consisted in developing efficient and robust computational strategies suitable for this type of problem.

A new multiscale computational strategy for nonlinear evolution problems was introduced recently. This strategy involves an automatic homogenization technique in space as well as in time [3, 4] which is an extension of previous works limited to space [2]. This strategy, developed in a general framework, makes no *a priori* assumption on the form of the solution and, therefore, does not have the limitations of standard homogenization techniques. Until now, it has been developed in the framework of small disturbances of (visco)plastic structures under possible contact conditions with or without friction.

THE MULTISCALE COMPUTATIONAL STRATEGY

The first characteristic of this strategy consists in partitioning the structure into substructures and interfaces, each of these entities having its own variables and equations. The change of scale takes place only at the interfaces, where forces and displacements are split into ”macro” and ”micro” contributions. The macro quantities have a real physical meaning: they are some mean values of the forces and displacements over space and time. The second characteristic of this strategy is the use of the LATIN method [1], an iterative resolution technique taking into consideration the whole time interval being studied. At each iteration, one must solve a homogenized macro problem defined over the whole space-time domain, and a set of independent micro problems, which are linear evolution problems defined within each substructure, at their boundaries, and over the time interval being studied.

RADIAL APPROXIMATION TECHNIQUE

The resolution of a large number of micro problems at each iteration can lead to prohibitive calculation costs if classical incremental techniques are used. Moreover, when dealing with composite structures containing a large number of similar substructures, the operators and right-hand sides of the micro problems may vary only slightly from one resolution to the next, but classical techniques are unable to take advantage of this characteristic.

A possible answer to this problem is an alternative resolution technique based on the concept of generalized radial approximation [1]. This technique, which relies on strong mechanical bases and is often used in the context of the LATIN method, consists in approximating a solution $u(\underline{x}, t)$ defined over the space-time domain by a sum of radial functions, each of which is the product of a scalar function of the time variable by a function of the space variable, i.e.

$$u(\underline{x}, t) = \sum_i \lambda^i(t) U^i(\underline{x})$$

Both space and time functions are *a priori* unknown. First of all, this approach reduces the computation cost drastically by transforming an evolution problem defined over the space-time domain into a series of uncoupled problems defined either over the space domain or over the time domain. It also reduces the storage cost for the variables defined over the space-time domain. Last but not least, it enables the construction of a relevant reduced basis of space functions which turns out to be particularly suitable for composite structures containing families of many identical substructures.

Of course, the radial approximation is not defined uniquely. The classical approach is to define this approximation using an orthogonality criterion associated with a primal or dual formulation of the evolution equation [1]. This definition leads

to the “best” approximation only for particular cases, and it provides no simple and systematic way to evaluate the quality of this approximation. Still, this classical approach is efficient in the single-scale framework. However, in some special situations, it may lead to non-convergence of the LATIN method. This lack of robustness is particularly notable for the multiscale computational strategy.

Here, we propose a new and extremely robust approach which maintains a completely mixed vision of the evolution problem. In fact, the search directions of the proposed iterative strategy can be interpreted as linearized constitutive relations. A natural and mechanics-based approach then consists in formulating the micro problem as the minimization of the constitutive relation error associated with the search directions. A radial approximation is searched for all the variables on a substructure, static and kinematic. The definition of the best radial functions is simply that they minimize the constitutive relation error. With this new approach, the approximation relates only to the search directions, which are the parameters of the strategy. Compared to the classical method, this approach certainly increases the computational cost, but it also improves the effectiveness and the robustness of the strategy. Moreover, it now provides a simple and relevant error criterion to evaluate the quality of the radial approximation.

The construction of the space functions is by far the most expensive step. Therefore, it can be interesting to store and reuse these functions. The space functions constructed at each iteration can be reused systematically during the subsequent iterations. Moreover, in the case of composite structures, the basis of the space functions is shared by a large number of identical substructures. Therefore, the initialization step of a micro problem on a particular substructure can reuse the space functions defined in other substructures during the previous iterations (or even the current iteration). Then, the resolution of a micro problem begins with an initialization step which consists in seeking a set of time functions associated with an already existing basis of space functions. The operators and the right-hand sides of the micro problems vary little from one iteration to the next, and even from one substructure to another. Therefore, this initialization step is often sufficient to obtain a good approximation of the solution of the micro problem.

Figure 1 shows a 2D problem of a composite structure containing cracks (unilateral contact with friction). The materials are viscoelastic. Figure 2 shows that very few new sets of radial functions were built at each iteration. Moreover, this number decreases as the iterations progress.

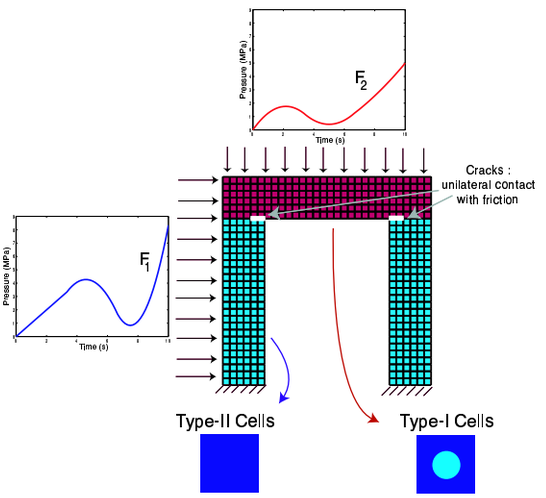


Figure 1. Description of the problem

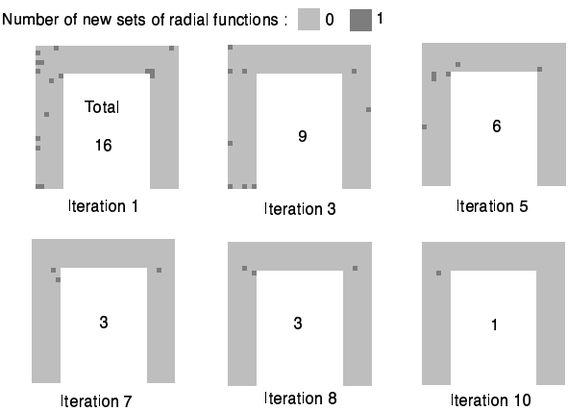


Figure 2. Number of new sets of radial functions per iteration and per substructure

CONCLUSION

The presented approximation technique leads to significant savings in terms of computational and storage costs without affecting the efficiency and the robustness of the multiscale computational strategy. It could also lead to the construction of pertinent reduced models for heterogeneous structures and allow analysis such as parametric analysis, optimizations, which nowadays can not be carried out with experiments or computational techniques.

References

[1] Ladevèze P.: Nonlinear Computational Structural Mechanics - New Approaches and Non-Incremental Methods of Calculation. *Springer Verlag*, 1999.

[2] Ladevèze P., Loiseau O., Dureisseix D.: A micro-macro and parallel computational strategy for highly heterogeneous structures. *Int. J. for Numerical Methods in Engineering*, **52**:121-138,2001.

[3] Ladevèze P., Nouy A.: A multiscale computational method with time and space homogenization. *C. R. Mécanique*, **330**:1-7, 2002.

[4] Ladevèze P., Nouy A.: On a Multiscale Computational Strategy with Time and Space Homogenization for Structural Mechanics. *Computer Methods in Applied Mechanics and Engineering*, **192**:3061-3087,2003.

AN ENERGY CONSERVING SCHEME FOR TIME DEPENDENT PROBLEMS USING THE EXTENDED FINITE ELEMENT METHOD

Réthoré J.*, Gravouil A.* and Combescure A.*
*LaMCoS, INSA Lyon, 20, Av. Albert Einstein 69621 Villeurbanne

Summary Lots of techniques have been developed to take into account discontinuities such as cracks, holes or material interfaces. The eXtended Finite Element Method (X-FEM) for example has first been presented for crack modeling [1] but is also used for arbitrary discontinuities. This paper proposes, with a proof of stability for the numerical scheme in the linear case, a generalization of X-FEM for time dependent problems with an application to dynamic crack propagation.

NUMERICAL STABILITY AND ENRICHMENT STRATEGY

In this paper, we propose a study of Newmark type schemes for problem with evolving discretization. This study, applied for the particular case of dynamic crack growth simulation using XFEM, allowed us to define an enrichement strategy. This strategy is satisfying stabilty conditions and is also energy preserving.

$$[B_\alpha] = \left[\sqrt{r}sin(\frac{\theta}{2}), \sqrt{r}cos(\frac{\theta}{2}), \sqrt{r}sin(\frac{\theta}{2})sin(\theta), \sqrt{r}cos(\frac{\theta}{2})sin(\theta)\right] \quad (1)$$

An enrichment is added to the displacement, velocity and acceleration fields with the same basis of enriched shape functions (discontinuous step function, and singular functions listed in Eq. (1)) using the Partition of Unity Method [2](see Ref.[3] for an other approach). The enrichment strategy for time dependent problems is presented in Fig. 1.

Using X-FEM, new enriched shape functions must be considered to simulate the crack growth. All enrichments are kept from time t_n to t_{n+1} and the initialization of new degrees of freedom is made to zero (Eq. (2)).

This strategy is justified by a theoretical study of Newmark type schemes for problems with evolving discretization. This study is an extension of the energy method from Hughes and Belytschko [4] to dynamic problems with evolving discretization. This approach, called the balance recovery method [5], ensures stability and energy conservation. Using this approach, the discretization can evolve when the crack propagates without any instability or uncontroled energy transfert.

$$\left[U_n^{n+1}\right] = \begin{bmatrix} \frac{U_n^n}{0} \\ \vdots \\ 0 \end{bmatrix} \quad (2)$$

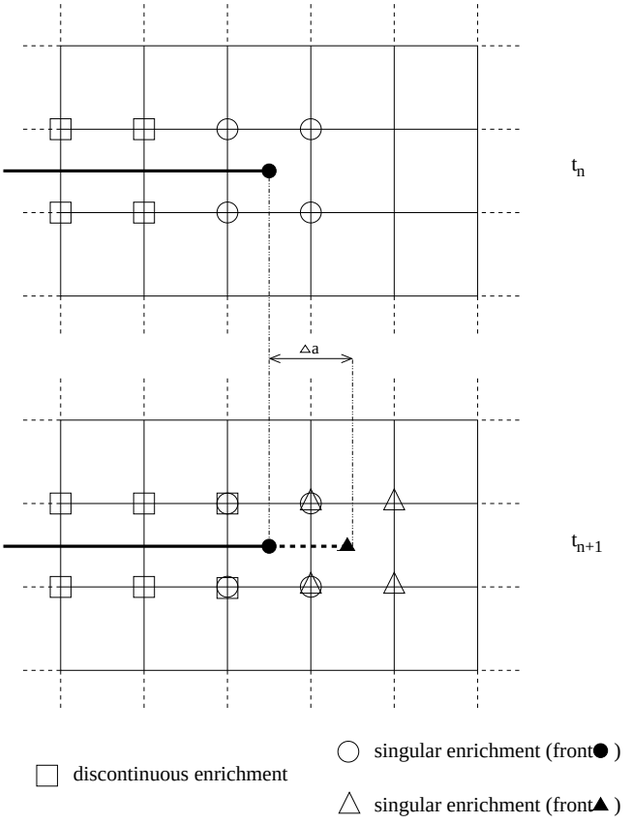


Figure 1. Enrichment strategy

EXAMPLE

To show the capabilities of the method, we calculate the dynamic propagation of a crack in a plate under prescribed displacement (see Fig.3).

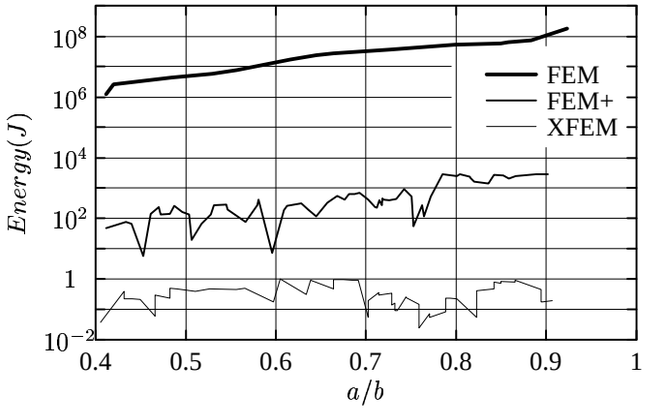


Figure 2. Cumulated energy out of balance

This example has already been calculated by authors in a classical FEM framework [5]. Using FEM, the balance recovery method (FEM+) reduces the cumulated energy out of balance but projections and remeshing needed in this framework still produce uncontroled energy transferts. With X-FEM, the presented enrichment strategy enables us to calculate the crack propagation satisfying energy conservation (see Fig. 2).



Figure 3. Dynamic crack growth in a plate under prescribed displacement

CONCLUSION

An enrichment strategy is developed to satisfy conditions obtained from a theoretical study. This strategy is energy preserving and satisfies the same stability conditions as Newmark type schemes. Numerical results reveal the advantage of X-FEM which avoids numerical problems due to remeshing and projections. This framework is still valid for other time dependent problems and this general enrichment strategy should be applicated to arbitrary moving discontinuities.

References

[1] Moës N, Dolbow J, Belytschko T. A finite element method for crack growth without remeshing *International Journal for Numerical Methods in Engineering* 1999; **46**(1):133–150.
[2] Babuska I, Melenk JM. The Partition of unity method *International Journal for Numerical Methods in Engineering* 1997; **40**:727–758.
[3] Belytschko T, Chen H, Jingxiao X, Goangseup Z. Dynamic crack propagation based on loss of hyperbolicity and a new discontinuous enrichment. *International Journal for Numerical Methods in Engineering* 2003; **58**:1873–1905.
[4] Hughes TJR, Belytschko T. *Nonlinear finite element analysis* ICE Division, Zace Services Ltd., 2000.
[5] Rethore J, Gravouil A, Combescure A. A stable numerical scheme for the finite element simulation of dynamic crack propagation with remeshing. *Computer Methods in Applied Mechanics and Engineering* submited.

XXI ICTAM, 15–21 August 2004, Warsaw, Poland

DEVELOPMENT OF A NOVEL 'CRACK' FINITE ELEMENT FOR PROPAGATION SIMULATION

Young-Sam Cho*, Sukky Jun*, Seyoung Im*
*Department of Mechanical Engineering, KAIST, 373-1, Guseong-dong, Yuseong-gu, Daejeon 305-701, Korea

Summary In this paper, we propose a 2D 'crack' element for the simulation of propagating crack with minimal remeshing. A regular finite element containing the crack tip is replaced with this novel crack element, while the elements which the crack has passed are split into two transition elements. Singular elements can easily be implemented into this crack element to represent the crack-tip singularity without enrichment. Both crack element and transition element proposed in our formulation are mapped from corresponding master elements which are commonly built using the moving least-square (MLS) approximation only in the natural coordinate. In numerical examples, the accuracy of stress intensity factor K_I is demonstrated and the crack propagation in a plate is simulated.

INTRODUCTION

It is well known that FEM has still shortcomings especially in simulating propagating cracks due to the intricacy of continual remeshing procedures. In order to avoid this difficulty of remeshing, enriched meshfree methods have been developed and applied to the crack growth problems. These method do not employ meshes in function approximations, and thus can have advantage in the simulation of moving discontinuity. However, meshfree methods do require the enrichment of basis to accurately represent the singular behavior of strain field around a crack tip, which may lead to immense load of computation. More recently developed is the extended finite element method (XFEM) [1,2] which is based on FEM and does not need the remeshing though. In order to represent the discontinuity, XFEM employs the modification of shape functions for the elements involving crack surface, as well as the enrichment around the crack tip. In this paper, we present a novel 'crack' finite element. Instead of modifying the shape function for discontinuity, we replace cracked elements with two or more transition elements and thus the crack surface naturally fulfills the traction-free boundary conditions, which makes the conventional formulation of FEM unaltered. Furthermore, our approach does not require the enriching procedure because our crack element itself reproduces the singular strain field by the typical FEM way of constructing singular element. These implies that we are able to calculate all the shape functions simply by the mapping from the parent or master elements to the physical elements. We construct the master elements for crack and transition elements by using the moving least-square (MLS) approximation. It means we adopt the MLS approximation in natural coordinates, not in physical coordinates, which are obviously different from the meshfree methods and XFEM. Furthermore, the present methodology is fundamentally different from the interface element method (IEM) recently reported [3] in that no interface elements are introduced nor adaptive meshing is required as crack tip moves. Therefore, it appears to be far more effective for simulating crack propagation than any other methods ever reported.

NUMERICAL EXAMPLES

First of all, a center cracked plate as shown in Fig. 1(a) is demonstrated for calculating stress intensity factor, K_I. The model is constituted with 25 elements including a crack element. The plate is subjected to a uniform tension, $\sigma_0 = 2\times10^4$ N in the y direction at bottom and top of the plate. The dimensions and properties are $H = 12.0$ m, $W = 12.0$ m, $a = 3.0$ m, $E = 1 \times 10^6$ Pa and $\nu = 0.25$. The contour plots of $\sigma_{\rm yy}$ are shown in Fig. 1(a). The errors for stress intensity, $100 \times \frac{K_{\rm exact}-K_{\rm num}}{K_{\rm exact}}$ %, at the tip of crack is 2.809 %. $K_{\rm exact}$ is the exact value of mode I stress intensity factor and $K_{\rm num}$ is the numerically calculated value of mode I stress intensity factor. The exact value of stress intensity is $K_{\rm I} = 1.325\sigma_0(\pi a)^{\frac{1}{2}}$. The mode I stress intensity factor $K_{\rm I}$ is computed from J-integral using domain integration. For simulation of crack propagation, we consider half the plate of Fig. 1(a), as shown in Fig. 2(a). The loading is applied on the upper left corner in the form of a concentrated force, which is oriented 45 degree from the top surface as shown in Fig. 2(a). The bottom edge is simply supported while the remaining edge is free from traction except the upper left loading point. We utilize the maximum circumferential stress criterion with the aid of the two-state conservation integral, which are known to be very effective for the mode decomposition [4-7]. Fig. 2(b)-(g) show the configuration of the crack propagation as the load increases. As shown in this figure, the modification needed for accommodating the varying configuration due to the crack propagation is just to add the nodal points on the crack faces that have been created. So far the present method appears to be far more effective than other existing schemes for modelling moving discontinuity such as a propagating crack.

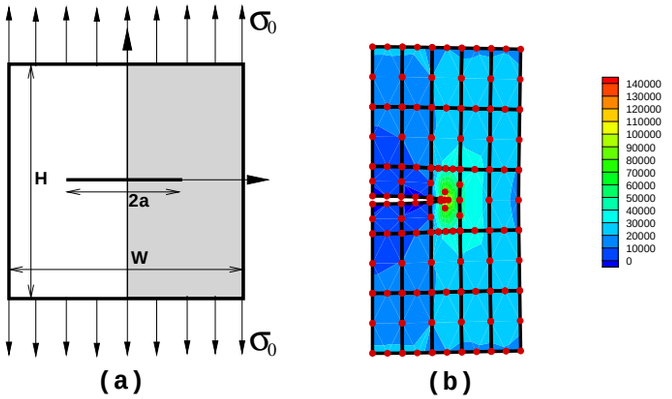


Figure 1. (a) A center cracked plate model, (b)Contour plot of σ_{yy} at the crack tip.

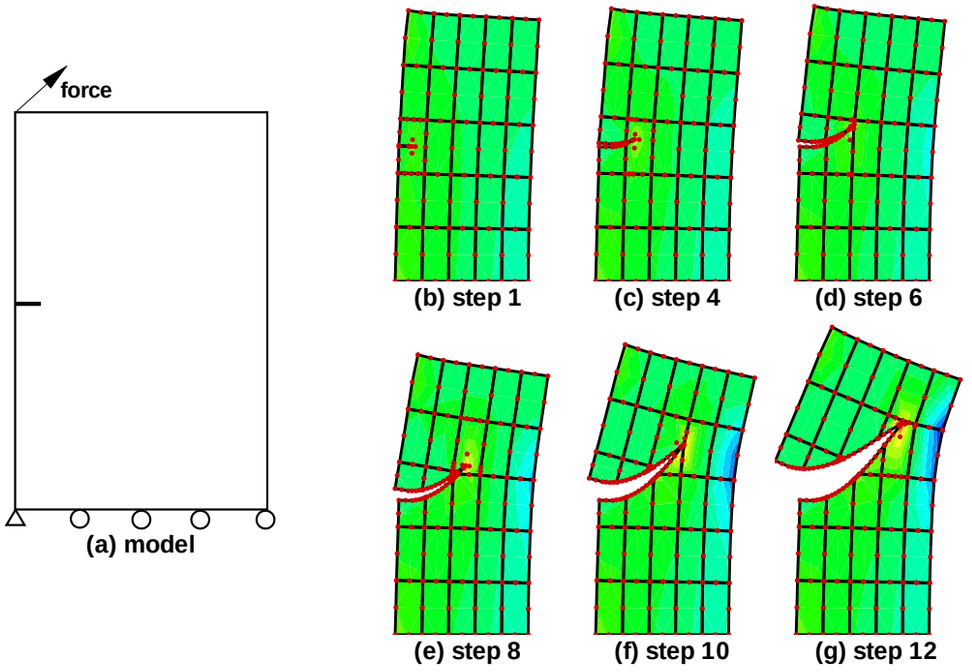


Figure 2. Crack propagation using the proposed method.

References

[1] Belytschko T., Black T.: Elastic crack growth in finite elements with minimal remeshing. *Int. J. for Numer. Meth. in Eng.*, **45**:601–620, 1999.

[2] Moes N., Dolbow J., Belytschko T.: A finite element method for crack growth without remeshing. *Int. J. for Numer. Meth. in Eng.*, **46**:131–150, 1999.

[3] Kim H.-G.: Arbitrary placement of local meshes in a global mesh by the interface-element method (IEM). *Int. J. for Numer. Meth. in Eng.*, **56**:2279–2312, 2003.

[4] Im S., Kim K.-S.: An application of the two-state M-integral for computing an intensity of a singular near-tip field for a generic composite wedge. *J. Mechanics and Physics of Solids.*, **48**:129–151, 2000.

[5] Jeon I., Im S.: The role of higher order eigenfields in elastic-palstic cracks. *J. Mechanics and Physics of Solids.*, **49**:2789–2818, 2001.

[6] Kim Y. J., Kim H.-G., Im S.: Mode Decomposition of Three Dimensional Cracks under mixed mode International Journal of Solids and Structures. *Int. J. of Solids and Structures*, **38**:6405–6426, 2001.

[7] Lee Y., Im S.: On the computation of the near-tip stress intensities for three dimensional wedges via two-state M-integral. *J. Mechanics and Physics of Solids*, **51**:825–850, 2003.

MODELLING OF STATIC AND DYNAMIC PROCESSES OF NANOPARTICLES INTERACTION

Alexander V. Vakhrouchev

Institute of applied mechanics Urals Dep. of the Russian Academy of Science, Izhevsk, Russia

Summary. The problem of dynamic and static of the nanoparticles interaction is considered. Object of research are singl nanoparticles and nanoparticles systems, making composites. By the method of molecular dynamics are investigated the fundamental mechanisms of dynamic and static of the nanoparticles interaction.

INTRODUCTION

. The problem of dynamic and static of the nanoparticles (NP) interaction is urgent for the number of nanotechnology tasks. For example, interaction NP with a surface of materials at the using NP both as modifying agents of a surface of materials and during treating materials, interaction between the NP at forming processes of nanocomposites, interaction NP with environment at the use of nanocomposites, and so on. It will be noted that the investigation of these processes by experimental methods requires substantial material resources and time. Hence the application of mathematical modeling methods allowing carrying out prior investigations of NP interaction save time and economize resources while developing new technologies is quite necessary. The task of modelling of the processes clusters and clusters structures forming was formulated by the author elsewhere [1-4]. The purpose of this work was to develop researches of the author in the field of the analysis of processes of formation and application of powder nanocomposites.

TASK FORMULATION

Problems of a statics NP include two basic tasks: definition of structure of an isolated particle in a quiet, static condition; calculation of parameters NP at its static interaction with an environment and others NP during static formation nanomaterials. Subject of NP dynamics is wider class of problems: formation NP, movement NP in gas and liquid environments,dynamic interaction NP among themselves and with external power (force) fields; division NP on parts and their association, etc. For the problem of modeling of the static and dynamic of NP interaction is present paper the method of molecular dynamics are used. The variant of a method based on use of concept of a power surface of the Bohr – Oppenheimer, being is used by the multivariate space describing energy of system as function of position of atoms nucleus forming it. Numerical integration of the equations of movement of NP atoms was carried out under Verlet method.

NUMERICAL RESULTS

For example, some results of the numerical investigation interaction between nanoparticles are shown in Fig.1-4. Change of a kind of connection cooperating nanoparticles (merging or coupling in larger particles) depending on the its sizes, it is possible to explain on the basis of the analysis of the graph of energy change of connection nanoparticles (fig. 1). From fig 1. follows, that, though with increase in the size of a particle energy of connection E_{np} grows also , its size in comparison with superficial energy of a particle E_S sharply increases at reduction of the sizes nanoparticles. Hence, for fineer particles energy of connection can appear sufficient for destruction of their configuration under action of a mutual attraction and merging in larger particle.

Spatial distribution of particles influences on rate of the forces holding nanostructures, formed from several nanoparticles, also. On fig.2 the chain nanoparticles, formed is resulted at coupling of three nanoparticles (from 512 atoms everyone), located in the initial moment on one line. Calculations have shown, that in this case nanoparticles form a stable chain. Thus particles practically do not change the form and cooperate on « small platforms ». In the same figure the result of connection of three NP, located in the initial moment on a circle and consisting of 256 atoms everyone is submitted. In this case particles incorporate among themselves "densely", contacting on a significant part of the external surface. Distance between particles at which they are in balance it is much less for the particles collected in group: $L^0_{3np} < L^0_{2np}$. It confirms also the graph of forces from which it is visible, that the maximal force of an attraction (F_{3np}) between particles in this case (is designated by a continuous line) in some times more, than at an arrangement of particles in a chain (dashed line) (F_{2np}).

In fig.3 is shown the dependence of strength of a composite on the nanoparticles sizes. It is visible, that at reduction of the sizes of structural elements of a composite (diameter of a nanoparticle) strength of a composite grows.

In fig.4 is shown the interactions of two particles are moving towards each other with different speed. At small speed of moving is formed steady agglomerate (fig.4 right). In a fig. 4(left) is submitted interaction of two particles moving towards each other with the large speed. It is visible, that steady formation in this case is not formed and the particles collapse.

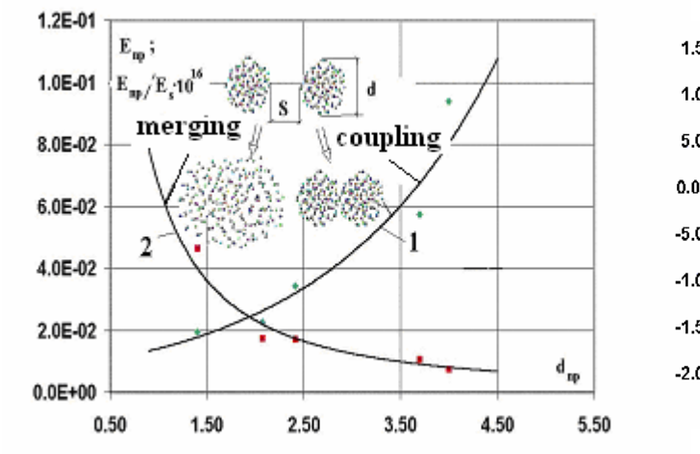


Fig.1

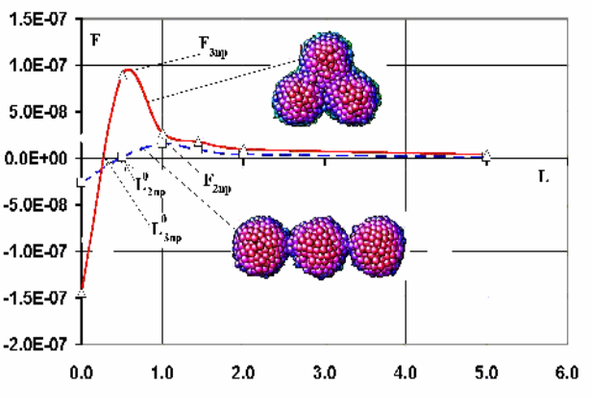


Fig.2

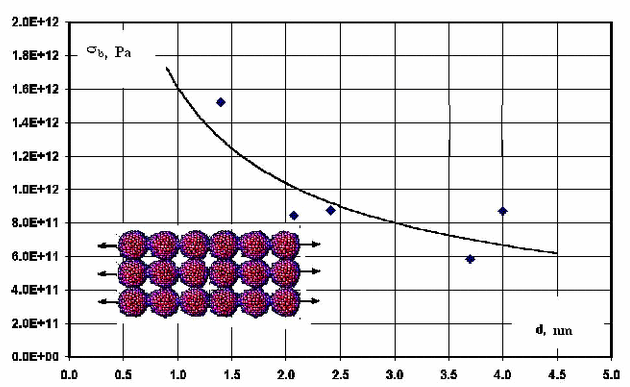


Fig.3

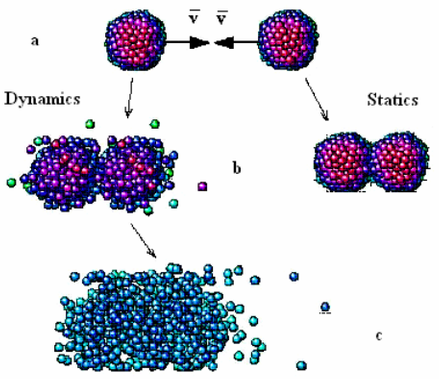


Fig.4

Fig. 1. Kinds of interaction of two nanoparticles and change of energy of their connection (1) and its attitudes to superficial energy (2) depending on nanoparticles diameter. Points designate the calculated values. Continuous lines – approximation

Fig. 2. Change of force of 3 nanoparticles interaction, consisting of 512 atoms everyone, and connected among themselves on a line and on the beams missing under a corner of 120 degrees, accordingly, depending on distance between them

Fig. 3 Dependence of strength of a composite on the nanoparticles sizes

Fig. 4 Pictures of dynamic interaction of two nanoparticles: à) an initial configuration nanoparticles, b) nanoparticles at dynamic interaction, c) the "cloud" of atoms formed as a result of dynamic destruction two nanoparticles

CONCLUSIONS

Thus, the numerical investigation allowed to cover the fundamental mechanisms of NP interaction and to ascertain the basic parameters, defining the conditions of stability NP. In particular, at NP-surface interaction processes nanoparticles can be shattered or dive inside of a material, depending on its drop energy of move, temperature and proportion between ultimate strengths of a material and particle. Depending on thickness of a material nanoparticle can as remain inside a material or pass it through. At low-level energy of move the particle is simple adheres to a surface of a material. At shock of particle at bevel way to a surface it can pull out a slice of a material of a surface, which one can fly away. At interaction nanoparticles among themselves the processes of agglomerate formation, formation of larger particles at merge of particles of the smaller size, absorption by large particles of the smaller ones, dispersion of particles on separate atoms are observed.

References

[1] Vakhrouchev A.V., Lipanov A.M. A numerical analysis of the rupture of powder materials under the power impact influence// Computer & Structures N1, v.44,1992, pp.481-486.

[2] Vakhrouchev A. V., Lipanov A.M. The numerical simulation of the cluster static and dynamics, The proceeding of the international conference," Application of the mathematics modeling in the science and techniques», Izhevsk, p.p. 158-163,1996

[3] Vakhrouchev A.V. Modeling of a static and dynamics of the clusters at macro--, meso- and micro structural levels // Bulletin IzSTU: Periodic scientific-theoretical magazine. - Izhevsk:„2001, ¹ 1, p.p. 25-29.

[4] Vakhrouchev A.V. Physical bases and mathematical modeling of the metal powder composites. *Doctor's Thesis, Institute of applied mechanics Urals Dep. of the Russian Academy of Science* , Izhevsk , 2002.

SINGULARITIES OF THE FOUR-SIDED ANTIPRISM RING

András Lengyel*
*Budapest University of Technology and Economics, Department of Structural Mechanics
H-1521 Budapest, Hungary

Summary An antiprism ring is a simple type of spatial truss structures, which is able to produce finite motions and bifurcation points on their compatibility paths. The structure may, under certain topological and geometric conditions, become both statically and kinematically indeterminate, i.e. an overconstrained mechanism. At singular positions the number of instantaneous degrees-of-freedom can change. The structure is quite sensitive to geometric errors. Depending on the initial geometry and different imperfection parameters, various singularities can occur referring to different cases of mobility of the structure. It may form a rigid structure or produce finite or infinitesimal mechanisms as well.

INTRODUCTION

An antiprism ring is a truss which comprises of two n-sided polygons of vertices. The upper polygon is a closed linkage of bars while the vertices of the lower polygon are foundation nodes. The vertices of the two polygons are interconnected by $2n$ bars in a zigzag layout as illustrated by the four-sided ring in Figure 1a. Generally an antiprism ring is rigid as it satisfies Maxwell's rule for rigidity [1]. However, it can be proved that the existence of a plane of symmetry through a vertex of the upper polygon is a necessary and sufficient condition for mobility if n is even. In this case the truss is both statically and kinematically indeterminate. In this paper the four-sided structure is discussed.

BASIC STRUCTURE

Consider the structure shown in Figure 1a with all bars having a uniform length of 2. The foundation nodes are the corners of a square on the (x, y) plane. In the base position of the structure the upper polygon is also a square. At this position the structure is capable of one finite motion which can be represented by a compatibility path plotted in the space of the variables chosen to describe the geometry of the structure. During the motion the structure can reach a special position shown in Figure 1b where the bars of the upper polygon coincide in pairs. Here the possibility of another motion appears, the compatibility path bifurcates and the structure may change shape to move on a different path. Similar bifurcation phenomena may occur for other mechanisms as well [2, 3, 4].
In our investigation we apply two different sets of variables to describe the bar-assembly. One can assign three Cartesian coordinates for each of the four moving nodes and one constraint condition for each bar setting up the relationship of the variables. Alternatively, one can regard the interconnecting bars rigid and define the position of the moving nodes by one angle each as shown in Figure 1a. Now one constraint condition is formulated for each of the upper bars. A four-dimensional space is required to visualise the compatibility paths. However, as the structure has at least one plane of symmetry during the motion, two of the variables are equal and a three-dimensional plot can be generated. The plot of the paths consists of two intersecting closed loops. The intersection points are bifurcation points.

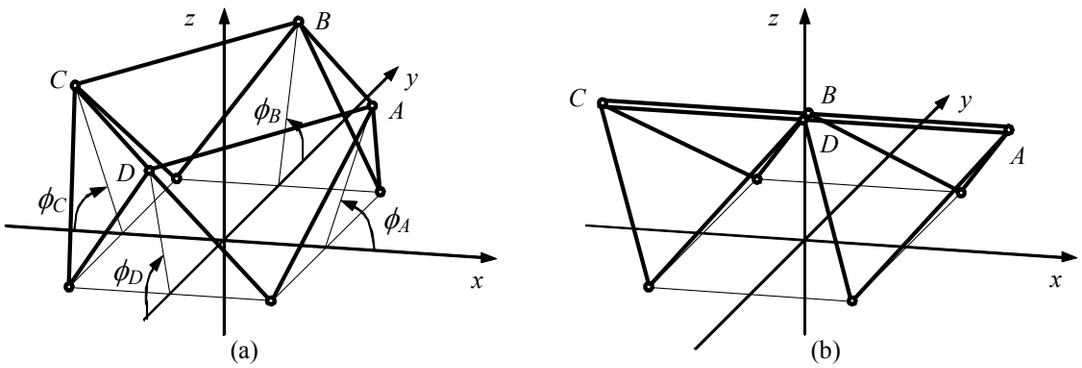


Figure 1: Antiprism ring. (a) Base position. (b) Bifurcation position.

ANALYSIS

In the analysis of the behaviour of the structure we may use either of the variable systems introduced above. Let us regard the structure as a truss and introduce 12 Cartesian coordinates to define the position of the four moving nodes. 12 bars connect the nodes to one another and to the foundations. The equilibrium matrix of the truss can be calculated, which is the basis to determine the static and kinematic determinacy. Now it is a square matrix with 12 rows for the

coordinates of the nodes and 12 columns for the bars. If the matrix is of full rank at a certain position, the structure is rigid. If the row rank decreases by 1 or 2, then 1 or 2 mechanisms become possible. Due to the same number of rows and columns, the column rank will decrease equally corresponding to states of self-stress.
The rank deficiency represents instantaneous degrees-of-freedom. They may correspond to either finite or infinitesimal mechanisms, which cannot be determined by the matrix itself. Finite mechanisms represent motions with no elongations of the bars, while infinitesimal mechanisms cannot be activated without infinitesimal elongations. Compatibility is enforced by applying constraint conditions for the bars, either in terms of Cartesian coordinates or angles. In order to determine whether a mechanism is finite or infinitesimal, it needs to be activated by changing one of the variables. Complying with the all but one of the compatibility conditions, the other variables can be calculated, and the last condition is evaluated. If it is satisfied, the mechanism is finite. If higher than first-order elongations are obtained, the mechanism is infinitesimal.

IMPERFECTIONS

All real structures are subject to geometric imperfections due to manufacturing errors or wear, etc. Such imperfections may have significant effect on the behaviour of the structure, especially if it is an overconstrained mechanism. Imperfections may render a mobile bar-assembly rigid, reduce the finite mobility to an infinitesimal one, or even preserve the finite motion. Imperfections can be defined for all bars as length errors in general. It is beyond the scope of this paper to examine this multi-parameter problem in its entirety, hence here we present a few combinations of imperfections to illustrate different cases of mobility.
Consider first the base configuration shown in Figure 1a without imperfections. The assembly has one finite mechanism and one state of self-stress. The equilibrium matrix has a rank of 11, i.e. a rank deficiency of 1. In the special position shown in Figure 1b the rank decreases to 10 and the compatibility path bifurcates. Now there are two instantaneous degrees-of-freedom, both corresponding to finite mechanisms.
Consider now imperfections applied to the bar-assembly in its base position. An arbitrary set of imperfections will typically make it rigid reducing the compatibility path to a single point. Special combinations can be found, such as a uniform elongation of the upper bars, which will not reduce the mobility.
More cases can be examined in the bifurcation position of the assembly. For brevity, we define a set of imperfections by defining the modified position of the nodes at which the structure is assembled strain-free. Three examples are shown to illustrate different types of mobility. Consider first the case when the four moving nodes are simultaneously shifted by a small extent along axis y keeping the (y, z) plane of symmetry and modifying the supporting bars accordingly. The coincidence of the upper bars is preserved, the rank deficiency remains 2, and both degrees-of-freedom correspond to finite mechanisms, and hence the bifurcation point indeed remains a bifurcation point. However, if the shift is applied in the x direction keeping (x, z) plane of symmetry, one of the finite mechanisms will be reduced to an infinitesimal one. In spite of the singularity of this point, now there is no bifurcation. If shifts are applied in both directions, both mechanisms will become infinitesimal. In this case the compatibility path is a single point though the assembly has no first-order rigidity.

CONCLUSIONS

The examination of the four-sided antiprism ring has shown that the mobility of the assembly is greatly affected by small perturbations. Various types of mobility can be obtained. While the initial structure was statically and kinematically indeterminate, perturbations can render it rigid, i.e. determinate. In the singular position one or both finite mechanisms can be reduced to infinitesimal mechanisms while the assembly is still statically and kinematically indeterminate. That is, the singularity of the system remained while the bifurcation point and compatibility path(s) disappeared, quite contrary to the non-overconstrained linkages, where perturbations typically produce regular paths in the neighbourhood of bifurcation points.

References

[1] Calladine, C. R., Buckminster Fuller's "Tensegrity" structures and Clerk Maxwell's rule for the construction of stiff frames. *International Journal of Solids and Structures* **14**, 161-172, 1978.

[2] Litvin, F. L. Application of theorem of implicit function system existence for analysis and synthesis of linkages. *Mechanism and Machine Theory* **15**, 115-125, 1980.

[3] Tarnai, T. Rigidity and kinematic bifurcation of structures, *40th Anniversary Congress of the International Association for Shell and Spatial Structures* (IASS), CEDEX, Madrid, Spain, Sep 20-24 ,1999; 1: B 2.81-B 2.90.

[4] A. Lengyel, Z. You, Analogy between bifurcations in stability of structures and kinematics of mechanisms. *Mechanics Based Design of Structures and Machines* (accepted for publication)

XXI ICTAM, 15–21 August 2004, Warsaw, Poland

ANALYSIS OF EVOLVING DEFORMATION MICROSTRUCTURES IN INSTABLE INELASTIC SOLIDS BASED ON ENERGY RELAXATION METHODS

Ercan Gürses*, Christian Miehe*
* *Institute of Applied Mechanics (Civil Engineering), University of Stuttgart, D–70550 Stuttgart, Germany*

Summary An incremental variational formulation for the constitutive response of dissipative materials is applied to the stability analysis of inelastic solids. The material stability is governed by weak convexity properties of an incremental stress potential obtained from a local minimization problem. As a result of instability deformation microstructures develop and are resolved by energy relaxation methods. We develop relaxation analyses in terms of rank–one convexifications and make comparisons of results obtained from different orders of lamination as well as different kinematic degrees of freedom of the laminates.

Introduction

In problems of finite inelasticity such as in single–slip plasticity material instabilities may occur due to geometric effects. These instabilities then cause the development of fine scale microstructures. The goal of this lecture is to resolve the development of these deformation microstructures based on an incremental energy minimization method. To this end we define an incremental stress potential function depending on the current deformation $\mathbf{F}_{n+1} := \mathbf{F}(t_{n+1})$ at time t_{n+1} which determines the stresses at t_{n+1} by quasi–hyperelastic function evaluation $\mathbf{F}_{n+1} = \partial_{\mathbf{F}} W(\mathbf{F}_{n+1})$. Here W is defined by a minimization problem proposed in [2]

$$W(\mathbf{F}_{n+1}) = \inf_{\boldsymbol{\mathcal{I}} \in \mathcal{G}} \int_{t_n}^{t_{n+1}} [\,\dot{\psi} + \phi\,]\, dt \quad \text{with} \quad \boldsymbol{\mathcal{I}}(t_n) = \boldsymbol{\mathcal{I}}_n \tag{1}$$

where ψ and φ denote the free energy and dissipation functions, respectively. For a prescribed deformation, this problem defines the incremental stress potential function W as a minimum of the generalized work $\int_{t_n}^{t_{n+1}} [\,\dot{\psi} + \phi\,]\, dt$ with respect to internal variables $\boldsymbol{\mathcal{I}}$ done on the material in the time increment under consideration. The minimization problem is approximated by a finite–step–sized algorithm and serves as the fundamental basis of the subsequent stability analysis.

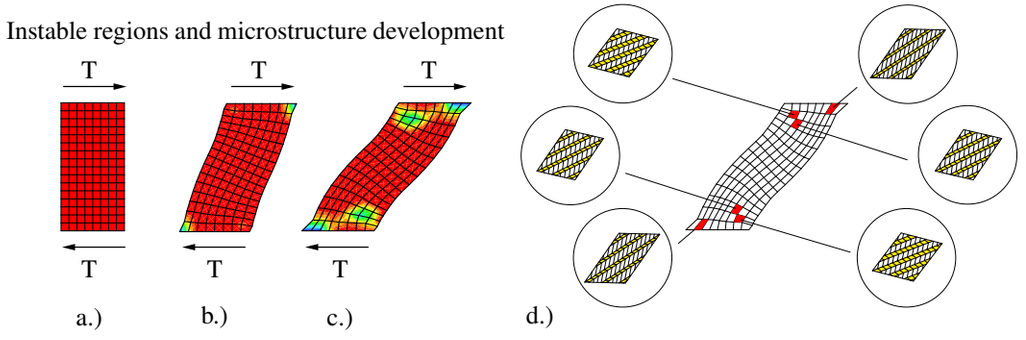


Figure 1. Rectangular specimen in shear. a - c.) Evolution of instable regions, d.) visualization of deformation microstructures.

Material Stability Analysis of Standard Dissipative Solids

As already pointed out in [1, 3, 4, 5], a key advantage of the above mentioned variational formulation is the opportunity to analyze the incremental stability of inelastic solids in terms of terminologies used in finite elasticity. The existence of the constitutive minimization problem (1) allows the introduction of an incremental minimization formulation of the boundary value problem of finite inelasticity for standard dissipative solids in a typical time increment. We consider a displacement functional $I(\boldsymbol{\varphi}_{n+1}) = \int_{\mathcal{B}} W(\mathbf{F}_{n+1}) dV - [\Pi_{ext}(\boldsymbol{\varphi}_{n+1}) + \Pi_{ext}(\boldsymbol{\varphi}_{n})]$ of the current deformation field $\boldsymbol{\varphi}_{n+1}$ with contribution Π coming from body forces and surface tractions. The current deformation map of inelastic standard dissipative materials can then be determined by a principle of minimum incremental energy $I(\boldsymbol{\varphi}^*{}_{n+1}) = \inf_{\boldsymbol{\varphi}_{n+1}} I(\boldsymbol{\varphi}_{n+1})$ subject to essential boundary conditions. This minimization problem governs the response of inelastic solid in the finite increment $[t_n, t_{n+1}]$ in a structure identical to the principle of minimum potential energy in finite elasticity. Extending the results of the existence theory in finite elasticity to the incremental response of standard dissipative solids in the finite step $[t_n, t_{n+1}]$, we consider *quasiconvexity* of the incremental potential W as the fundamental criterion for the incremental material stability of the inelastic solid. W is said to be *quasiconvex* at $\mathbf{F}_{n+1}$ if the condition

$$\frac{1}{|D|} \int_D W(\mathbf{F}_{n+1} + \nabla \mathbf{w}(\mathbf{y})) dV \geq W(\mathbf{F}_{n+1}) \tag{2}$$

with $\mathbf{y} \in \mathcal{D}$ is satisfied for all $\mathbf{w}$ having $\mathbf{w} = \mathbf{0}$ on $\partial\mathcal{D}$. Here, $\mathcal{D} \in \mathcal{R}^3$ is an arbitrarily chosen part of the inelastic solid and $\partial\mathcal{D}$ is its boundary. The quasiconvexity condition states for all fluctuations $\mathbf{w}$ on $\mathcal{D}$ with support on $\partial\mathcal{D}$, the homogeneous deformation $\mathbf{F}_{n+1}$ provides an absolute minimizer of the incremental potential in $\mathcal{D}$. This condition extends results obtained by [7] for continuous rate formulation to a finite–step–sized incremental setting.

Relaxation of Non–Convex Response and Development of Microstructures

If the incremental potential W becomes non–quasiconvex, then material instability is detected at a point of the solid and accordingly the existence of the solutions is not ensured. In order to overcome this problem we consider the *relaxed energy functional* $I_Q(\boldsymbol{\varphi}_{n+1}) = \int_{\mathcal{B}} W_Q(\boldsymbol{\varphi}_{n+1})dV - [\Pi_{ext}(\boldsymbol{\varphi}_{n+1}) - \Pi_{ext}(\boldsymbol{\varphi}_n)]$ where the relaxed potential is obtained by replacing the non–convex integrand W by its *quasiconvex* envelope W_Q. The quasiconvexified incremental stress potential is defined by the minimization problem with respect to the microscopic fluctuation field

$$W_Q(\mathbf{F}_{n+1}) = \inf_{\mathbf{w}\in\mathcal{W}_0} \frac{1}{|D|}\int_D W(\mathbf{F}_{n+1} + \nabla\mathbf{w}(\mathbf{y}))dV. \tag{3}$$

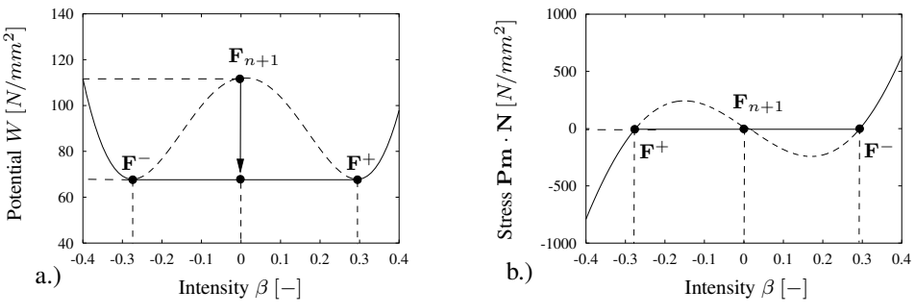


Figure 2. Simple shear test. Details of the rank–one convexification. β parameterizes the intensity of the laminate $\mathbf{F}^{\pm} = \mathbf{F}_{n+1} + \beta^{\pm}\mathbf{m}\otimes\mathbf{N}$. a.) At $\mathbf{F}_{n+1}$ the potential is not rank–one convex (dashed line). $\mathbf{F}_{n+1}$ decomposes into micro–phases $\mathbf{F}^{\pm}$ (solid line). b.) The relaxed stress-strain relation characterizes a snap–through Maxwell–line behavior between the micro–phases $\mathbf{F}^{\pm}$.

The current deformation field of the standard dissipative solid is determined by the relaxed incremental variational problem $I_Q(\boldsymbol{\varphi}^*{}_{n+1}) = \inf_{\boldsymbol{\varphi}_{n+1}} I_Q(\boldsymbol{\varphi}_{n+1})$. The relaxed problem is considered to be a well–posed problem as close as possible the original instable problem. In Figure 2 the non–convex character of the incremental potential and corresponding stress response are visualized for the model problem of single slip plasticity. Since the quasiconvexity is hard to handle in practice, we concentrate on the slightly weaker rank–one–convexification W_R of the potential W for different orders by sequential laminations. The simplest case is a first–order rank–one–convex envelope W_{R_1} of W defined by

$$W_{R_1}(\mathbf{F}_{n+1}) = \inf_{\xi,d,\mathbf{m},\mathbf{N}}\{\xi W(\mathbf{F}^+) + (1-\xi)W(\mathbf{F}^-)\} \tag{4}$$

where $\mathbf{F}^+ = \mathbf{F} + (1-\xi)d\mathbf{m}\otimes\mathbf{N}$, $\mathbf{F}^- = \mathbf{F} - \xi d\mathbf{m}\otimes\mathbf{N}$, ξ and $1-\xi$ represent the rank–one connected deformation phases and the corresponding volume fractions. Higher order relaxed response is obtained by further minimizing of each phase by first–order laminates. The lecture points out mathematical relaxation approaches and discusses the physical relevance of the developing microstructures. This is done by considering

- a first order rank–one relaxation with keeping all the parameters free [5], i.e. minimization of energy is obtained with respect to the set $\mathbf{q} = [\xi, d, \mathbf{m}, \mathbf{N}]$. Figure 1 shows for first–order laminate microstructures developed in a shear test,
- a sequential lamination with fixed laminate orientation motivated by physical observations as conceptually investigated in [6, 3, 4].

References

[1] Lambrecht M., Miehe C. and Dettmar J.: Energy Relaxation of Non-Convex Incremental Stress Potentials in a Strain-Softening Elastic-Plastic Bar. *International Journal of Solids and Structures*, **40**:1369–1391, 2003.

[2] Miehe C., Schotte J. and Lambrecht M.: Homogenization of Inelastic Solid Materials at Finite Strains Based on Incremental Minimization Principles. Application to the Texture Analysis of Polycrystals. *Journal of the Mechanics and Physics of Solids*, **50**:2123–2167, 2002.

[3] Miehe C., Lambrecht, M.: A Two–Scale Finite Element Relaxation Analysis of Shear Bands in Non–Convex Inelastic Solids: Small Strain Theory for Standard Dissipative Materials, *Computer Methods in Applied Mechanics and Engineering*, **192**:473–508, 2003.

[4] Miehe C., Lambrecht M.: Analysis of Microstructure Development in Shearbands by Energy Relaxation of Incremental Stress Potentials: Large–Strain Theory for Generalized Standard Solids, *International Journal for Numerical Methods in Engineering*, **58**:1–41, 2003.

[5] Miehe C., Lambrecht M. and Gürses E.: Analysis of Material Instabilities in Inelastic Solids by Incremental Energy Minimization and Relaxation Methods: Evolving Deformation Microstructures in Finite Plasticity, submitted to the *Journal of the Mechanics and Physics of Solids*.

[6] Ortiz M., Repetto E.A and Stainier L.: A Theory of Subgrain Dislocation Structures, *Journal of the Mechanics and Physics of Solids*, **48**:2077–2114, 2000.

[7] Petryk H.: Material Instability and Strain Rate Discontinuities in Incrementally Nonlinear Continua, *Journal of the Mechanics and Physics of Solids*, **40**:1227–1250, 1992.

XXI ICTAM, 15–21 August 2004, Warsaw, Poland

MICROSTRUCTURAL BEHAVIOUR OF SOLDER JOINTS

René L.J.M. Ubachs*, Piet J.G. Schreurs*, Marc G.D. Geers*
*Eindhoven, University of Technology, WH4.20, PO box 513, 5600MB, Eindhoven, The Netherlands

Summary Mechanical properties of soldered connections, as well as damage initiation and propagation, are strongly influenced by the continuously changing microstructure of the solder. Therefore, in this contribution the microstructure evolution is included in the model by a diffuse interface model that is dependent on a strongly nonlocal parameter. The material behaviour is described by the hyperelasto-viscoplastic Perzyna model. The material parameters are taken to be dependent on the mass fraction.

The model has been implemented within a finite element context. A quantitative comparison has been made between two-dimensional simulations and experiments of the static ageing of a eutectic tin-lead solder. A good agreement was found.

The mechanical response is shown to be sensitive to the coarseness of the microstructure. Furthermore, stress concentrations develop near interfaces, which are known to be crack initiation sites during fatigue failure.

INTRODUCTION

During their life soldered connections are subjected to thermomechanical loading. In combination with the high temperatures at which they operate, they are susceptible to low cycle fatigue. Solder joints are often tested for their thermo-mechanical fatigue properties by subjecting them to accelerated test methods. However, during these accelerated experiments damage mechanisms might be invoked which do not occur during normal usage. Predictions based on accelerated cycling tests are therefore unreliable. Thermo-mechanical modelling can be used during the design process to simulate the real life conditions of a solder joint, and thus give an accurate prediction of its lifetime, with a reduction in cost and design time when compared to prototype testing.

Solder joints are known to behave differently than the bulk solder material because of their high surface to volume ratio and their small size compared to the microstructure. A joint can thus not be regarded as a homogeneous continuum. Moreover, its microstructure and properties will change over time: the high homologous temperature at which solder materials operate provokes microstructural coarsening, resulting in a markedly different microstructure after only a short time after solidification. This coarsening process is in general not homogeneous. Regions which show increased coarsening are known to be crack nucleation sites during thermal cycling. It is also well-known that thermal cycling leads to faster coarsening rates than static thermal aging, possibly due to the mechanical stresses which arise within the material due to differences in thermal expansion coefficients.

In this contribution the mechanical behaviour of solder joints is investigated while taking the microstructure evolution into account.

MODELLING

A nonlocal diffuse interface model

To describe the microstructural evolution, a diffuse interface theory is used where the free energy is supposed to be dependent on local composition, nonlocal composition and stresses and strains. The model can be seen as an extension of the Cahn-Hilliard model [1, 2]. The total system of equations then reads:

$$\rho \frac{\mathrm{d}c}{\mathrm{d}t} = \vec{\nabla} \cdot \left[\rho \boldsymbol{M} \cdot \left(\frac{\partial F(c, \bar{c}, \boldsymbol{\sigma}, \boldsymbol{\varepsilon})}{\partial c} \right) \right] \tag{1}$$

$$\bar{c} - \ell^2 \vec{\nabla}^2 \bar{c} = c \tag{2}$$

$$\vec{\nabla} \cdot \boldsymbol{\sigma} = 0 \tag{3}$$

where ρ denotes mass density, c mass fraction, t time, $\boldsymbol{M}$ mobility, F free energy, $\boldsymbol{\sigma}$ Cauchy stress, $\bar{c}$ nonlocal mass fraction, and $\boldsymbol{\varepsilon}$ the strain. The internal length parameter ℓ determines the size of the area of influence of an interface.

Perzyna hyperelasto-viscoplastic model

Because the elastic energy is an important driving force behind the diffusion process its important that elastic energy is handled correctly in the material model. Therefore a hyperelastic model is used. Furthermore, since the operating temperature of solder alloys is typically close to their melting temperature, the deformation behaviour is governed by high temperature phenomena like creep due to e.g. grain boundary sliding. Therefore the Perzyna viscoplastic material model has been chosen to describe the mechanical behaviour of the solder [3]:

$$\overset{\triangledown}{\boldsymbol{\tau}} = \mathbb{H} : (\boldsymbol{D} - \boldsymbol{D}_{vp}) \qquad \text{with} \qquad \boldsymbol{D}_{vp} = \eta \left(\frac{\tau_{eq} - \tau_y}{\tau_{y0}} \right)^N \boldsymbol{N} \tag{4}$$

Here $\overset{\triangledown}{\boldsymbol{\tau}}$ is the Truesdell time derivative of the Kirchhoff stress, $\boldsymbol{D}$ the strain rate tensor, and $\mathbb{H}$ is the fourth-order material tensor. The direction of the viscoplastic strain rate $\boldsymbol{D}_{vp}$ is $\boldsymbol{N}$, while its magnitude is determined by the fluidity parameter η and the current (τ_y) and initial (τ_{y0}) yield stress of the material.

The parameters used for the Perzyna model are taken to be dependent on the mass fraction field calculated with the microstructure evolution model. In this way the influence of the size and shape of the microstructure is accounted for. The system of equations is solved using the finite element method in a large deformation framework.

RESULTS

Figure 1 shows the microstructure during static ageing of a eutectic tin-lead solder at 150°C for both an experiment and a simulation. This coarsening process has been quantified, the result of which can be seen in figure 2.
Figures 3 and 4 show the mechanical response of an as-cast and an aged microstructure of tin-lead solder under uniaxial tension.

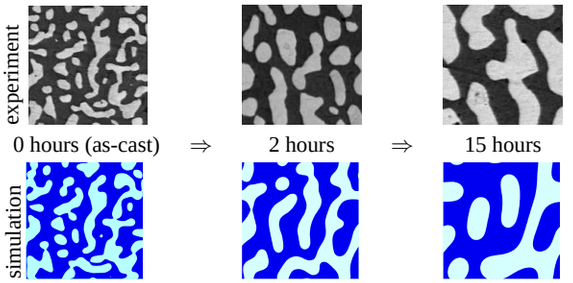


Figure 1. Ageing of tin-lead, size 10×10 μm

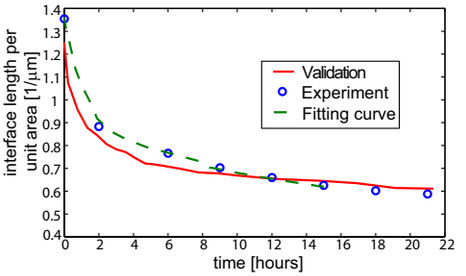


Figure 2. Development of interface area.

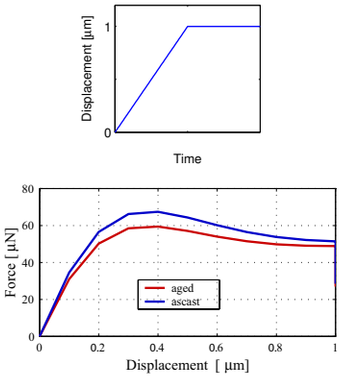


Figure 3. Loading and force-displacement curve.

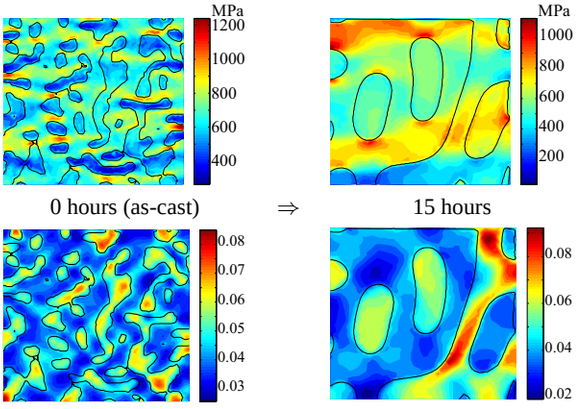


Figure 4. Stress (top) and strain (bottom) distributions at 3% strain.

CONCLUSIONS

An extension of the Cahn-Hilliard model is used to describe the microstructure evolution of tin-lead solder. The free energy density is taken to be a function of the local and a strongly nonlocal mass fraction which in this case is calculated by solving a Helmholtz partial differential equation. The difference between the nonlocal and the local mass fraction is associated with the surface energy. The variation with respect to local mass fraction of this energy acts as a driving force for the coarsening process. Incorporation of additional driving forces into the free energy is straightforward. In this way the effect of stresses on diffusion is also accounted for through the addition of the elastically stored energy.
The numerical implementation of the nonlocal diffuse interface theory is done within the framework of the finite element method in a large deformation setting, which allows for arbitrary geometries to be modelled. The results are found to be in a good quantitative agreement with experimental data.
The mechanical behaviour of the material is described with the hyperelasto-viscoplastic Perzyna model. The material parameters are taken dependent on the mass fraction of the components calculated with the diffusion part of the model. In this way the microstructure is accounted for. The mechanical behaviour is shown to be dependent on the microstructure. Stress concentrations arise within the harder phase and near interfaces. Strains tend to localise in the softer phase.

References

[1] Cahn, J., Hilliard, J.: Free energy of a uniform system, I: Interfacial energy. *J. Chem. Phys.* **28**(2):258–267, 1958.
[2] Dreyer, W., Müller, W.: A study of the coarsening in tin/lead solders. *Int. J. Solids Struct.* **37**:3841–3871, 2000.
[3] Perzyna, P.: Fundamental problems in visco-plasticity. In: *Recent Advances in Applied Mechanics.* Academic Press, New York, 1966.

MOLECULAR MECHANICS SIMULATIONS OF CARBON NANOSTRUCTURES USING MULTI-SCALE BOUNDARY CONDITIONS

Sergey N. Medyanik, Eduard G. Karpov, Wing Kam Liu
Northwestern University, Department of Mechanical Engineering, IL 60208 Evanston, USA

Summary The method of Multi-Scale Boundary Conditions is applied to simulations of carbon nanostructures: graphite sheets and diamond. It allows simulation of a deformable boundary, thus reducing the size of computational domain and, consequently, the cost of computations. This approach is tested on model problems and results are in good agreement with the benchmark full domain solutions. The method can be useful for simulations of real-life experiments on nanoindentation of diamond and layered graphite.

INTRODUCTION

Atomistic simulation methods, such as molecular dynamics and molecular mechanics, are very important and find application in many areas of research providing information about processes happening on microscale level. However applicability and effectiveness of these methods hinge upon ability to fulfil very large scale computations. That makes these methods restricted to solving systems, which are too small even for nano scale problems. Solvable systems are of several orders of magnitude smaller than scales of real-life nanomechanical experiments. This situation is resolved with the usage of the so-called multiscale methods, when atomistic simulations are used only for a reduced domain (fine scale), and continuum finite element or meshless methods are used for the rest of the domain (coarse scale)[1]. Method of Multi-Scale Boundary Conditions (MSBCs) makes it possible to eliminate the coarse scale dimensions of freedom and simulate only the fine scale by imitating the so-called deformable boundary, when the boundary of a reduced domain behaves as if it were a part of a full domain.

MATHEMATICAL FORMULATION

The main idea of the method is based on Fourier analysis of regular atomic lattice structures [2]. For a periodic crystal lattice it is possible to derive displacements of the layer of atoms which is next to the fine scale domain (we denote it as n=1 layer) in terms of the neighboring boundary layer of the fine scale (layer n=0) and the last (boundary) layer of the full domain. We denote the last layer of the full domain as $n=a$, where a is the *coarse scale parameter*. In general form, the MSBCs can be written as $\mathbf{u}_1 = \boldsymbol{\Theta}(\mathbf{u}_0) + \boldsymbol{\Xi}(\mathbf{u}_a)$, where specific forms of operators $\boldsymbol{\Theta}$ and $\boldsymbol{\Xi}$ depend on the geometry of a crystal lattice, interatomic forces between its atoms, and a value of the coarse scale parameter. In case when the boundary of the full domain is fixed, so that displacements of atomic layer $n=a$ are zero, we have left only with the first part of this equation. In a more extended form it can be written as:

$$\mathbf{u}_{1,m} = \sum_{m'=m-m_c}^{m+m_c} \boldsymbol{\Theta}_{m-m'}\, \mathbf{u}_{0,m'} ,$$

where index m is used for numbering of atoms in the layer n (here n=0,1,a) and m_c is a truncation parameter. Typical shape of components of matrices $\boldsymbol{\Theta}_m$, called the *kernel matrices*, is given below at figure 1.

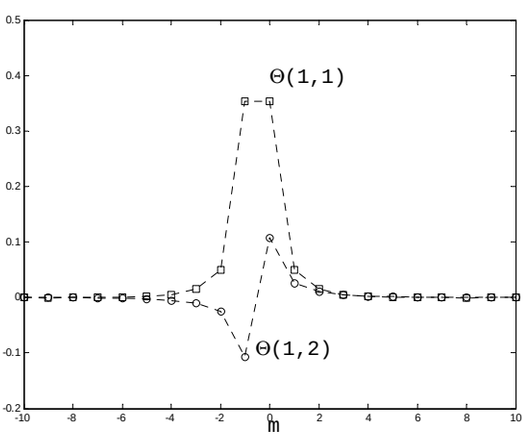


Figure 1.

It is important that the components of the kernel matrices $\boldsymbol{\Theta}_m$ decay fast with the growth of $|m|$. This allows using a small value of the truncation parameter m_c in the above equation. Also, we mention that the assumptions of regular crystal

lattice and linear deformations, which were used for MSBCs derivation, have to hold only in a small vicinity of the deformable boundary, where the MSBCs are applied. At the same time, large deformations (including plasticity) are allowed inside the reduced domain and far enough from the deformable boundaries.

SIMULATION RESULTS

We consider the following model problem (see Figure 2): a rectangular sheet of graphite is fixed at all four sides, and initial displacements are applied in several steps to one of the atoms in the middle of the domain (the loaded atom is circled at the figure) in a direction perpendicular to the plane of the sheet. Here, we apply the MSBCs at two sides – left and right. Value of the coarse scale parameter for both deformable boundaries is a=6. The whole full domain is shown at Figure 2. Filled circles – are atoms belonging to reduced domain (fine scale) and void circles – atoms of coarse scale domain, which are excluded from molecular mechanics calculations.

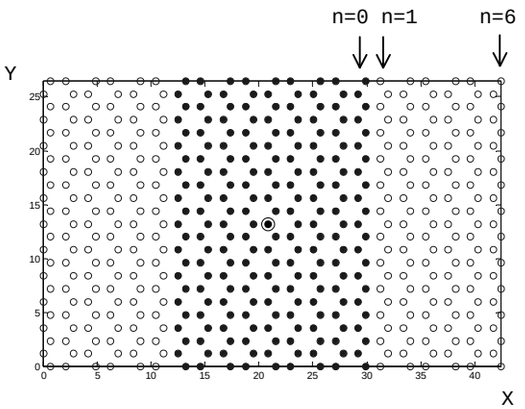


Figure 2.

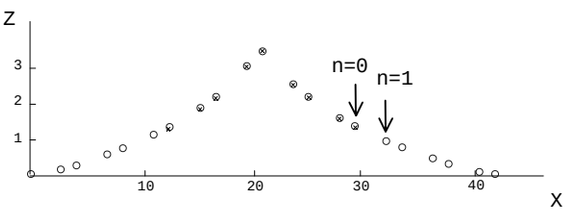


Figure 3.

Results of the computations are presented at Figure 3, where vertical displacements of atoms located along the horizontal middle line are plotted. The circles represent the exact solution for the full domain, which was obtained by regular molecular mechanics simulations. The crosses represent the approximate solution obtained for the reduced domain with the MSBCs applied. Similar results were obtained for a hexagonal domain, where all six boundaries were modeled using the MSBCs. We used hexagonal shape for reduced domain, because, in this case, all the boundaries correspond to an identical crystallographic orientation; that allows using the same kernel matrices as for the rectangular domain. This method was also applied to nanoindentation of diamond. In that case we obtain the kernel matrices for a slab-like boundary layer of atoms. Their behavior is similar to that shown at Figure 1. Application of the method to three-dimensional atomic lattice structures, such as diamond, is tractable, as soon as boundaries of the reduced domain are drawn along a limited number of crystallographic planes.

CONCLUSIONS

The method of Multi-Scale Boundary Conditions helps to overcome the limitations of atomistic simulations, regarding the size of a computational domain. By using sufficiently large values of the coarse scale parameter a it may allow simulations of real-life experiments. Current efforts are being made to apply this method to simulation of experimental results on nanoindentation of diamond and layered graphite presented in [3].

References

[1] Liu W.K., Karpov E.G., Zhang S., Park H.S.: An Introduction to Computational Nano Mechanics and Materials. *Comput. Methods Appl. Mech. Engrg.* (accepted, 2004).

[2] Karpov E.G., Yu H., Park H.S. et al.: Multiscale Boundary Conditions in Crystalline Solids: Theory and Application to Nanoindentation. *Phys. Review B.* (submitted, 2004).

[3] Richter A., Ries R., Smith R. et al.: Nanoindentation of Diamond, Graphite and Fullerene Films. *Diamond and Related Materials*, **9**:170-184, 2000.

MULTISCALE BUCKLING ANALYSES OF CORRUGATED FIBERBOARD

Hirohisa Noguchi [*], Nobutada Ohno [**], and Dai Okumura [**]

[*] *Department of System Design Engineering, Keio University, Kohoku-ku, Yokohama 223-8522, Japan*

[**] *Department of Mechanical Engineering, Nagoya University, Chikusa-ku, Nagoya 464-8603, Japan*

Summary In this paper, multiscale micro-macro interaction analyses of corrugated fiberboard are conducted by the finite element method in conjunction with the homogenization theory. The updated Lagrangian method is adopted for the geometrically nonlinear analyses of microstructure and the scaled corrector method is adopted for detecting the buckling mode. By comparing with the experimental results, the validity of the proposed method is illustrated.

INTRODUCTION

Corrugated fiberboard is frequently used as packing material and, being piled together, it is also utilized as shock absorber because it can assimilate impact energy by large deformation of inner corrugating medium. The mechanical properties of corrugated fiberboard are sometimes unstable due to buckling and very difficult to estimate because of the variety and the complexity of microscopic structure. Macroscopic behavior of corrugated fiberboard is also varied by the change of mechanical properties of microscopic structures undergoing large deformation. In this paper, firstly a focus is placed on the variation of the macroscopic property of corrugated fiberboard caused by the microscopic inner local buckling. Assuming that a piled corrugated fiberboard is composed of periodic structures, the macroscopic equivalent properties are calculated from the microscopic, properties and deformation by using the updated Lagrangian geometrically nonlinear finite element method combined with the homogenization theory. Secondly, the micro-macro interaction analysis based on the homogenization theory is carried out. Macroscopic buckling induced by microscopic buckling is demonstrated and the results are compared with the experimental results.

MICRO-MACRO INTERACTION ANALYSIS BASED ON THE HOMOGENIZATION [1,2]

The rate form of principle of virtual work is written at time t, as

$$\int_{{}^t v} {}_t^t\dot{S}_{ij}\,\delta\,{}_tE_{Lij}\,d\,{}^t v + \int_{{}^t v} {}^tT_{ij}\left(\delta\,{}_tE_{NLij}\right)' d\,{}^t v = \delta\dot{R} \tag{1}$$

$$\delta\,{}_tE_{Lij} = \frac{1}{2}\left(\delta u_{i,j} + \delta u_{j,i}\right) \tag{2}$$

$$\left(\delta\,{}_tE_{NLij}\right)' = \frac{1}{2}\left(\delta u_{k,i}\cdot\dot{u}_{k,j} + \dot{u}_{k,i}\cdot\delta u_{k,j}\right) \tag{3}$$

S_{ij} is the Truesdell rate, E_{ij} the Green-Lagrange strain tensor and T_{ij} is the Cauchy stress tensor. The rate of displacement can be divided into $\dot{u}_i^0$ and $\dot{u}_i^*$ as shown in Eq.(4), which are macroscopic and microscopic components, respectively.

$$\dot{u}_i = \dot{u}_i^0 + \dot{u}_i^* \tag{4}$$

Substituting Eq.(4) into Eq.(1), Eq.(2) and Eq.(3), the following microscopic and macroscopic equations are finally obtained.

$$\int_Y \left({}_t^tC_{ijpq} + \delta_{pi}\,{}^tT_{qj}\right)\chi_{p,q}^{kl}\,\delta u_{i,j}^*\,dY = \int_Y \left({}_t^tC_{ijkl} + \delta_{ki}\,{}^tT_{lj}\right)\delta u_{i,j}^*\,dY \tag{5}$$

$$\int_{{}^t v} D_{ijkl}^{\mathrm{H}}\,{}^t\dot{u}_{k,l}^0\,\delta u_{i,j}^0\,d\,{}^t v + \int_{{}^t v} \delta_{ki}\,{}^tT_{lj}^{\mathrm{H}}\,{}^t\dot{u}_{k,l}^0\,\delta u_{i,j}^0\,d\,{}^t v = \delta\dot{R}^{\mathrm{H}} \tag{6}$$

where D_{ijkl}^{H} is the homogenized stiffness tensor. T_{lj}^{H} is the homogenized Cauchy stress tensor. ${}_t^tC_{ijkl}$ is the constitutive tensor. χ_i^{kl} is the characteristic displacement vector corresponding to ${}_t\dot{\varepsilon}_{kl}^0$ as shown in Eq.(7).

$${}^t\dot{u}_i^* = -\chi_i^{kl}\,{}_t\dot{\varepsilon}_{kl}^0 \tag{7}$$

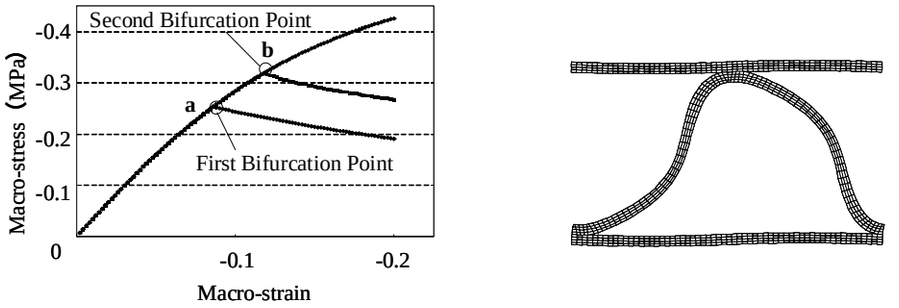
After finite element discretization, Eq.(5) and Eq.(6) are solved alternately by exchanging the macroscopic strain rates and the homogenized stiffness and the Cauchy stress tensor.

NUMERICAL EXAMPLES

The multiscale micro-macro interaction analyses of corrugated fiberboard are conducted. Fig. 1(a), (b) show an obtained homogenized stress-strain curve and bifurcation buckling mode [3] of microscopic structure, respectively. It is noted that this macroscopic stress-strain curve shows strain-softening behavior and it might cause macroscopic instability. The macroscopic structure is illustrated in Fig. 2(a) and each element in macroscopic structure has the same unit cell shown. In the analyses, the following three cases are considered. Case 1: Buckling (in unit cell) does not occur

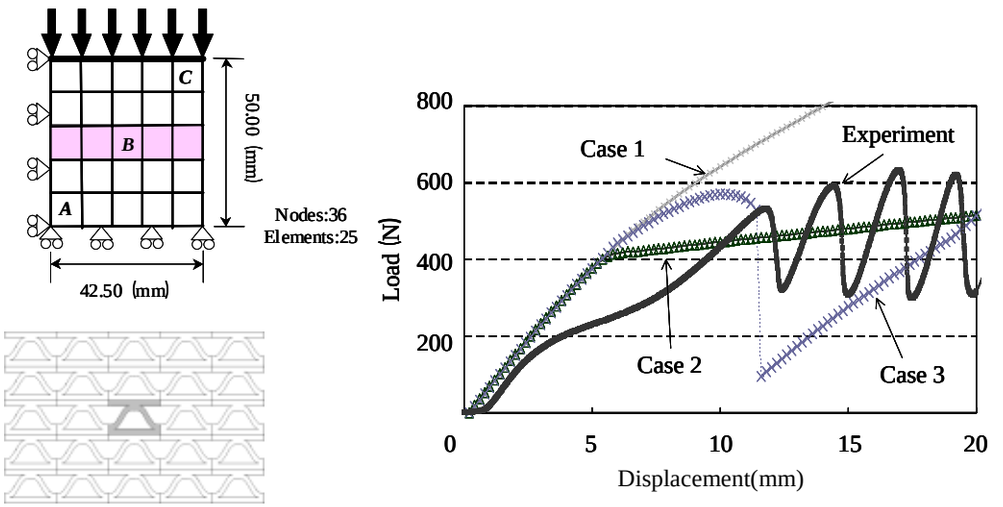
in all macroscopic elements. Case 2: Buckling occurs simultaneously in all macroscopic elements. Case 3: Buckling occurs only in the middle layer of macroscopic elements.

The load-displacement curves are shown in Fig. 2(b) In the experiment, only one layer buckles first, then other layers buckle subsequently one by one. Each local maximum point in Fig. 2(b) corresponds to buckling of each layer. Which layer starts buckling depends on initial irregularity of corrugated fiberboard. On the contrary, in numerical analysis, load-displacement path can be controlled by path switching in bifurcation analysis. The load-displacement curve obtained in Case 1 is the primary path of this structure and no unit cells buckle. In Case 2 that unit cell is controlled to buckle simultaneously at every point of macroscopic structure, the secondary path varies linearly after bifurcation and go between local maximum and minimum points. The total absorption energy seems equivalent to that by the experiment. In Case 3, only the middle layer is controlled to buckle. As shown in Fig. 2(b), the first buckling point is almost equal to that observed in the experiment, however, the recovery of stiffness is slower than the experimental result. This is due to the ignorance of contact condition inside the corrugated fiberboard. From these results, the validity of the present analyses is clarified.



(a) Homogenized Stress-Strain Curve (b) Bifurcation mode at a

Figure 1. Microscopic response of Corrugated Fiberboard



(a) Analysis model (b) Load-Displacement Curve

Figure 2 Macroscopic response of Corrugated Fiberboard

CONCLUSIONS

In this paper, the multiscale micro-macro interaction analysis of corrugated fiberboard based on the homogenization theory is conducted. Firstly, the microscopic bifurcation of unit cell is analyzed and the macroscopic mechanical properties of corrugated fiberboard are investigated. Secondly, the results of micro-macro interaction analysis are compared with the experimental results and the present analyses are validated.

References

[1] Ohno N, Okumura D, Noguchi H.: Microscopic symmetric bifurcation condition of cellular solids based on a homogenization theory of finite deformation. *J. Mech. Phys. Solids* **50** (5), 1125-1153, 2002.

[2] Okumura D, Ohno N, Noguchi H.: Post-buckling analysis of elastic honeycombs subject to in-plane biaxial compression. *Int. J. Solids Struct.* **39** (13-14), 3487-3503, 2002.

[3] Noguchi H., Okazawa S. and Fujii F.: Scaled corrector and branch-switching in necking problems. *Comp. Mech.* **26**, 236-242, 2000.

XXI ICTAM, 15–21 August 2004, Warsaw, Poland

MODIFIED ERROR IN CONSTITUTIVE RELATION AND ITS APPLICATION TO DYNAMIC TESTS WITH CORRUPTED BOUNDARY CONDITIONS

Pierre Feissel*, Olivier Allix*
*LMT-Cachan ENS de CACHAN/CNRS/Université Paris VI 61, avenue du Président Wilson, 94235 Cachan Cedex, France

Summary The aim of this work is to develop an identification strategy suitable for the identification of models dedicated to crash simulation. Due to the experimental difficulties, the method has to take into account the uncertainties on the measurements. Therefore, a method is proposed, based on the modified error in constitutive relation. First developed in the case of homogeneous elasticity, this method appears to be very robust and is extended to the case of heterogeneous elasticity.

INTRODUCTION

The purpose of this study is the prediction of the crash behavior of multi-layered composites. The simulation of tests performed on such absorbing materials involves several difficulties:
(1) the insufficient knowledge of the dynamic behavior and crashworthiness of the materials involved,
(2) the often imperfectly known boundary conditions,
(3) the heterogenous state implied by damage and rupture localization.
The dynamic tests we are considering are dynamic compression tests on laminated plates based on Split Hopkinson Pressure Bar principle. These lead to imprecise measurements of forces and velocities. Thus, Problem (2) is encountered from the very beginning of the identification process. In a first attempt, we have made use of a method proposed in [1] which is based on a comparison between two calculations, one with prescribed displacements and one with prescribed forces. This method was proved to be very efficient for well mastered dynamic tests but appears to be unadapted in the case of strong uncertainties on the boundary conditions. The problem that we have addressed is therefore the following:
How can one formulate an identification problem in dynamics in such a way that the results would be accurate in spite of the great measurement uncertainties?

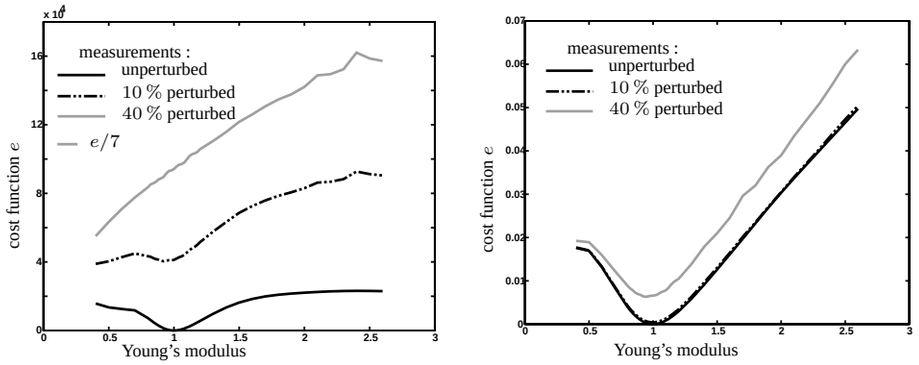
IDENTIFICATION STRATEGY

Our guiding principle, which was directly inspired by studies on model updating in vibration [2], is to verify exactly, during the identification process, the properties which are considered to be reliable. The uncertain quantities are then taken into account by minimizing a modified constitutive relation error [3]. In this first work [4, 5], we are considering the simple problem of an elastic rod with redundant displacement and force conditions at both ends, denoted $\tilde{u}_d$ and $\tilde{f}_d$, which are assumed to be uncertain. The identification of the Young's modulus E is carried out in two steps: for a fixed E, the ill-posed problem is reformulated as the minimization of:

$$e(u,\sigma,u_d,f_d) = \| \sigma - E.\epsilon \|^2 + \alpha \| f_d - \tilde{f}_d \|^2 + \beta \| u_d - \tilde{u}_d \|^2 \tag{1}$$

under the conditions:

$$u \text{ KA to } u_d, \quad \sigma \text{ DA to } f_d, \quad \rho.\ddot{u} - div\sigma = 0 \tag{2}$$



(a) classical approach (b) our method

Figure 1. Variation of the error with E for different perturbation levels

One can note that the boundary conditions u_d and f_d are related to the fields used in the minimization problem and, therefore, can be different from the measured values $\tilde{u}_d$ and $\tilde{f}_d$. This minimization under constraints is performed by introducing an appropriate number of Lagrange multipliers, which leads to the simultaneous resolution of both a direct problem and an adjoint (time-retrograde) problem related to one another. The resolution methods will be discussed during the presentation. The regularization properties of the method will be discussed along with the influence of the weights α and β between the different terms of the error.

Subsequently, the identification of the best E is carried out using the same functional, whose gradient can be calculated directly from the fields which are solutions to the first problem with fixed E. A numerical example, in which the exact measurements were modified by up to 40% on the average, is presented figure 1. The method proposed here, which turns out to be particularly robust, and the one inspired by [1] are compared.

Then, the robustness of the method is studied by introducing two other formulations deduced from the previous one by removing the distance to the measurements in one or two steps of the method. The comparison of the three methods leads to the conclusion that the method is efficient with respect to the perturbations, because it takes the whole experimental information in one calculation and it introduces a distance between the measurements and the calculation.

EXAMPLES IN HETEROGENEOUS CASES

The results of the proposed method in term of robustness led us to extend the method to more complicated cases. The first one, illustrated 2, is the identification of the properties of a heterogeneous beam, where the spatial distribution of the properties is known. Other examples such as the identification of the size of heterogeneities are treated.

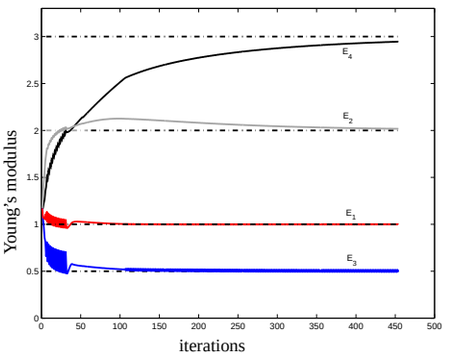


Figure 2. Young's modulus as a function of the iterations

CONCLUSION

The proposed method appears to be very robust with respect to the perturbations on the measurements. Its robustness is due to the taking into account of the whole experimental information in one calculation and the introduction of a distance between the experimental data and the calculation. A first step toward the identification of models suitable for crash simulation has been made by treating examples in heterogeneous elasticity, where the method remains accurate.

References

[1] L. Rota, *"An inverse approach for identification of dynamic constitutive equations"*, Int. Symposium on Inverse Problems, Ed A.A.Balkema, 1994.

[2] P. Ladevèze and A. Chouaki, *"Application of a posteriori error estimation for structural model updating"*, Inverse Problems, 15, 49-58, 1999.

[3] P. Ladevèze, *"A modelling error estimator for dynamical structural model updating"*, in Advances in Adaptive Computational Methods in Mechanics, P. Ladevèze, J.T. Oden eds, Ed Elsevier, 1998.

[4] P. Feissel, O. Allix, *"Identification à partir d'essais dynamiques bruités"*, Rapport contractuel d'avancement, 2001.

[5] O. Allix, P. Feissel, P. Thévenet, *"A delay-damage meso modeling of laminates under dynamic loading: basic aspects and identification issues "*, Computers and structures, 81(12), 1177-1191, 2003.

XXI ICTAM, 15–21 August 2004, Warsaw, Poland

GEOMETRY BASED RATIONAL ENRICHMENT FUNCTIONS FOR TRIANGULAR PLANE ELASTICITY ELEMENT

Juha Mäkipelto*
*Institute of Applied Mechanics and Optimization, Tampere University of Technology,
P.O. Box 589, FIN-33101 Tampere, Finland, e-mail:* juha.makipelto@tut.fi

Summary In this paper the sides of the triangular plane elasticity *p*-element are allowed to be rational Beziér curves, and the geometry is mapped by the blending function method. If typical hierarchic polynomial shape functions are used, the element is not complete. We present how the element can be made complete by enriching the shape function space with rational functions corresponding to the geometry mapping. A numerical example shows that the enriched element is more efficient than the one without enrichments.

INTRODUCTION

Roots of this research lie in the shape optimization, where the *p*-version of the finite element method has many advantages over the *h*-version. If the element geometry is mapped by the blending function method, the boundary curves of the structure can be the boundary curves of the elements, too. In this case the geometries of the structure and the finite element model are exactly the same, which is desirable especially in the shape optimization. Shyy et al. [1] used parametric polynomial curves as *p*-element sides and stated certain requirements that the element has to meet in order to be complete. When Schramm and Pilkey [2] allowed element sides to be also rational curves, they discovered some numerical inaccuracies. This gave rise to the current research, the aim of which was to improve the *p*-element in such a way that it, even with rational parametric curves as sides, is complete and gives reliable results. In this paper we first recapitulate the blending function method, then present the rational enrichment functions, and finally a numerical example shows how the enriched element performs when compared to the one without enrichments.

MAPPING BY THE BLENDING FUNCTION METHOD

In the blending function method [3], the element geometry is controlled by parametric boundary curves. The element geometry follows exactly the geometry of the boundary curves, and therefore the method is well suited for mapping of the complicated geometries. The blending function method for triangular finite elements was presented by Szabó and Babuška [4], and next we rewrite these mapping functions with slight notational modifications. Element sides are represented by rational Beziér curves

$$\mathbf{R}^i(u) = \big(R^i_x(u), R^i_y(u)\big) \qquad u \in [0,1] \qquad i = 1,2,3, \tag{1}$$

which are directed so that an increasing parameter u corresponds movement anticlockwise around the element. Now, the convention of the side curve directions allows us to define difference functions for side 1

$$D^1_x(u) = R^1_x(u) - (1-u)x_1 - ux_2 \qquad D^1_y(u) = R^1_y(u) - (1-u)y_1 - uy_2, \tag{2}$$

where x_i and y_i are the nodal coordinates. The difference functions for sides 2 and 3 are analogous to those in equation (2). We use common triangular coordinates L_1, L_2 and L_3 to define the three blending functions

$$B^1 = \frac{4L_1L_2}{1-(L_2-L_1)^2} \qquad B^2 = \frac{4L_2L_3}{1-(L_3-L_2)^2} \qquad B^3 = \frac{4L_3L_1}{1-(L_1-L_3)^2}. \tag{3}$$

In the blending function method global coordinates are given by equations

$$x = \sum_{i=1}^{3} L_i x_i + \sum_{i=1}^{3} B^i D^i_x(\xi_i) \qquad y = \sum_{i=1}^{3} L_i y_i + \sum_{i=1}^{3} B^i D^i_y(\xi_i), \tag{4}$$

where auxiliary variables are

$$\xi_1 = \frac{L_2 - L_1 + 1}{2} \qquad \xi_2 = \frac{L_3 - L_2 + 1}{2} \qquad \xi_3 = \frac{L_1 - L_3 + 1}{2}. \tag{5}$$

RATIONAL ENRICHMENT FUNCTIONS

In order for the element be complete, the element shape functions must be able to represent the element geometry. If the element has a rational side, clearly the polynomial shape functions can not represent the geometry. However, we can enrich the shape function space with special rational shape functions, corresponding to the geometry mapping, which make the element complete. Consider again for example the side 1, which we assume to be rational. From the mapping equation (4) the products of the blending and the difference functions vanish on sides 2 and 3, and so they can be used as the side shape functions of side 1. Furthermore, these products are the base of the enrichment side shape functions

$$\hat{N}^1_x = c^1 B^1 D^1_x(\xi_1) \qquad \hat{N}^1_y = c^1 B^1 D^1_y(\xi_1). \tag{6}$$

The factor c^1 scales the values of the enrichment functions to fit for the values of the other shape functions. This prevents numerical problems, since the difference function values may vary largely depending on the element size in the global xy coordinate system. The shape function space always includes the triangular coordinates L_1, L_2 and L_3 (they are the nodal shape functions), and when enriched with the functions (6), it clearly is able to represent the geometry given by the mapping (4). A drawback of the enrichments is that they are different for each rational element side of the FE-model.

A numerical example

We consider a plane stress problem, where the modulus of elasticity is $E = 200$ GPa, Poisson's ratio $\nu = 0.3$, and the sheet thickness $t = 10$ mm. The structure is like a cantilever beam with three holes (see Figure 1), supported from the left end and subject to a stress distribution varying linearly from -30 to 30 MPa at the right end. Each hole is modelled with four second degree rational Beziér curves, each of which has a control polygon with three control points and weights $\{1, 8, 1\}$. Due to the high weight of the middle control point, the curves form almost square holes. The mesh consists of 32 elements, 20 of which are straight sided. The rest 12 elements around the holes each have one very curved and rational side. The mesh is fixed, the curved sides are either enriched or not, and the polynomial degree p of the elements is uniformly increased from 1 to 10. The "exact" results for the problem are from an FE-model with the number of degrees of freedom $N > 259000$. The effect of the enrichments on the performance of *p*-extensions is shown in Figure 2, where various relative errors are plotted against the $\sqrt{N}$. Graphs of the true relative error in energy norm with a) normal and b) enriched elements clearly show the benefits of the enrichments; the error is notably smaller and the rate of convergence at lower values of p is faster. *A posteriori* estimates of the exact strain energy were computed from three consecutive FE-solutions with increasing p, and the relative errors of these estimates with c) normal and d) enriched elements are also shown in Figure 2, where we see again that the enriched elements give more accurate results.

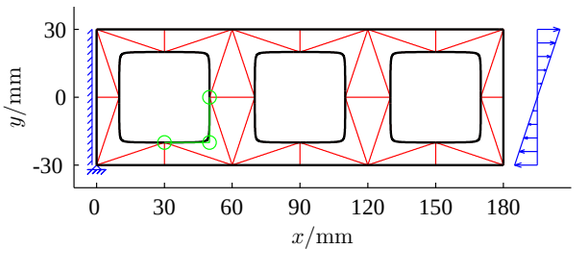


Figure 1. The plane structure (black), its support and loading (blue), the 32 element mesh (red), and an example of a control polygon (green).

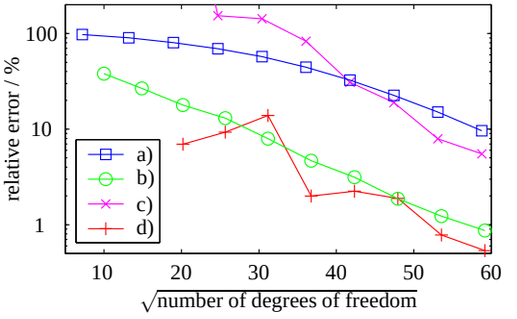


Figure 2. Relative error in energy norm with a) normal and b) enriched elements. Relative error in estimate of exact strain energy with c) normal and d) enriched elements.

CONCLUSIONS

When combined, the *p*-version of the finite element method, rational Beziér curves as element sides, and the blending function method, form an analysis tool suitable for the shape optimization. If the elements are enriched with the rational shape functions as shown in this paper, they will be complete. The numerical example indicates that the enriched element is more efficient and gives more reliable results than the element with no enrichment. A future work might consist of a generalization of the current work for other element types.

ACKNOWLEDGEMENTS

The author wishes to thank Finnish Technological Foundation (Tekniikan edistämissäätiö) for the financial support.

References

[1] Shyy Y.K., Fleury C., Izadpanah K.: Shape optimal design using high-order elements. *Computer Methods in Applied Mechanics and Engineering*, **71**:99–116, 1988.

[2] Schramm U., Pilkey W.D.: The coupling of geometric descriptions and finite elements using NURBs — A study in shape optimization. *Finite Elements in Analysis and Design*, **15**:11–34, 1993.

[3] Gordon W.J.: Blending-function methods of bivariate and multivariate interpolation and approximation. *SIAM Journal on Numerical Analysis*, **8**:158–177, 1971.

[4] Szabó B., Babuška I.: Finite Element Analysis. John Wiley & Sons, Inc., New York, 1991.

SOLVING OF INDIRECT PROBLEMS USING TREFFTZ METHOD

Marek S. Karaś*
*Institute of Mathematics, Jagiellonian University, Reymonta 4, PL 30-069 Kraków, Poland

Summary In indirect problems we can observe distribution of certain quantities inside the considered region of a given structure and, after that, knowing this distribution, we can approximately define the whole boundary-value problem [4]. Usually this is done by virtue of minimization of a special form of a functional that is dependent on the searched, unknown boundary values. Thus this leads to a kind of optimization procedure. Some improvements of such a procedure are proposed. These improvements are based on using the generalized Trefftz method (in which the trial functions identically fulfill the given partial differential equations) and the fact that the shape of considered structure remains unchanged. Also a method of direct solving of such kind of indirect problems is proposed. The methods are illustrated in the series of numerical examples.

INTRODUCTION

Typically engineering problem is formulated as a boundary value problem. Because of complexity of such boundary value problems there are used numerical methods to solve them. The generalized Trefftz method is one of such numerical methods. The main idea of the method is to use, like shape functions, functions analytically fulfilled the governing differential equations, so-called T-functions (or Trefftz functions). Any linear combination of T-functions is an exact solution of the governing equations, so coefficients of this linear combination are chosen such that the boundary conditions are satisfied as well as possible.
There are two main variants of the Trefftz method. The first one is the global method in which we obtain one global solution in the whole considered region. In this version, usually, collocation formulation is used [2,3]. The second one is so-called T-elements method [1,5] in which the solution is glued from the solutions in the subregions of the considered regions. In this version, usually, the hybrid formulation with an internal Trefftz field and a frame functions (given on the boundary of elements) is used.
The main advantage of the Trefftz method against another methods such that Finite Element Method or Boundary Element Method is the CPU time that is needed for numerical calculations (in a single solution of a structure). This is especially important when we must repeat such calculations hundreds of thousands times in the loop, for example, of optimisation procedure. The same situation is when we solve indirect problem.
In this paper we consider the following indirect problem. Assume that we have the structure that occupies the region Ω with the boundary $\partial\Omega = \Gamma_1 \cup \Gamma_2$. Also assume that we have given tractions on the boundary Γ_1 and we do not known the tractions (boundary conditions) on Γ_2. Instead of this we known (from measurement for example) the stresses in the fixed control points $\xi_1,...,\xi_k \in \Omega$. Our problem is to recover tractions (boundary conditions) on Γ_2.

SOLUTION

Main idea of the solution

The main idea of the solution of the above-defined indirect problem is following. We choose any distribution $\hat{t}_2$ of tractions (boundary conditions) on Γ_2, and then we calculate the implicated stresses $\hat{\sigma}_1,...,\hat{\sigma}_k$ in the control points $\xi_1,...,\xi_k$ (in this step we must solve the given boundary problem). And after that we compare $\hat{\sigma}_1,...,\hat{\sigma}_k$ with the given (measured) stresses $\overline{\sigma}_1,...,\overline{\sigma}_k$. The comparison is done (in two dimensional case) by virtue of the calculation of the following functional:

$$I = \sum_{i=1}^{k} \left[\left(\hat{\sigma}_{ix} - \overline{\sigma}_{ix}\right)^2 + \left(\hat{\sigma}_{iy} - \overline{\sigma}_{iy}\right)^2 + \left(\hat{\sigma}_{ixy} - \overline{\sigma}_{ixy}\right)^2 \right]. \tag{1}$$

In the loop of our procedure we try to choose $\hat{t}_2$ such that the value of the functional I is as small as possible. For this purpose a kind of evolutionary algorithm was used, but also other kinds of optimisation algorithm can be used. As an recovered tractions on Γ_2 we take the $\hat{t}_2$ with the minimal value of I.

Trefftz formulation

In the global Trefftz method with collocation formulation we fix the collocation points $\eta_1,...,\eta_r \in \Gamma_2$ and $\eta_{r+1},...,\eta_n \in \Gamma_1$, and, for given boundary conditions we solve the following equation:

$$\mathbf{A} \cdot \mathbf{c} = \mathbf{b}, \tag{2}$$

where $\mathbf{b} = \{t_1^n, t_1^s, ..., t_n^n, t_n^s\}^T$ is a vector consisting of normal and tangential (in two-dimensional case) components of the tractions in the collocations points $\eta_1, ..., \eta_n$, $\mathbf{A}$ is the matrix given by the Trefftz functions $\Phi_1, ..., \Phi_N$ and $\mathbf{c} = \{c_1, ..., c_N\}^T$ is a vector including coefficients of a linear combination of $\Phi_1, ..., \Phi_N$. Eq. (2) is usually solved in the least-square sense, so the solution has the form:

$$\mathbf{c} = \left(\mathbf{A}^T\mathbf{A}\right)^{-1}\mathbf{A}^T\mathbf{b}. \tag{3}$$

Thus $\mathbf{c}$ depends on $\mathbf{b}$ linearly. Let $\hat{\sigma}$ be the vector collecting stresses $\hat{\sigma}_1, ..., \hat{\sigma}_k$, then:

$$\hat{\sigma} = \mathbf{B}\cdot\mathbf{c}, \tag{4}$$

where $\mathbf{B}$ is the matrix given by $\Phi_1, ..., \Phi_N$. From (3) and (4) we obtain:

$$\hat{\sigma} = \mathbf{B}\cdot\left(\mathbf{A}^T\mathbf{A}\right)^{-1}\mathbf{A}^T\mathbf{b}, \tag{5}$$

so $\hat{\sigma}$ also depends on $\mathbf{b}$ linearly.

Improvement of calculations

Let write:

$$\mathbf{b} = t_1^n\cdot\mathbf{e_1} + t_1^s\cdot\mathbf{e_2} + ...t_r^n\cdot\mathbf{e_{2r-1}} + t_r^s\cdot\mathbf{e_{2r}} + \mathbf{b_0} \tag{6},$$

where $\mathbf{e_1}, ..., \mathbf{e_{2r}}$ are elements of the canonical basis of the space $\mathbf{R^{2n}}$ and $\mathbf{b}_0 = \{0, ...0, t_{r+1}^n, t_{r+1}^s, ..., t_n^n, t_n^s\}^T$. Then we can write

$$\hat{\sigma} = \mathbf{C_0} + t_1^n\cdot\mathbf{C_1} + t_1^s\cdot\mathbf{C_2} + ...t_r^n\cdot\mathbf{C_{2r-1}} + t_r^s\cdot\mathbf{C_{2r}}, \tag{7}$$

where $\mathbf{C_0} = \mathbf{B}\cdot\left(\mathbf{A}^T\mathbf{A}\right)^{-1}\mathbf{A}^T\mathbf{b}_0$, $\mathbf{C}_1 = \mathbf{B}\cdot\left(\mathbf{A}^T\mathbf{A}\right)^{-1}\mathbf{A}^T\mathbf{e}_1, \ldots, \mathbf{C}_{2r} = \mathbf{B}\cdot\left(\mathbf{A}^T\mathbf{A}\right)^{-1}\mathbf{A}^T\mathbf{e}_{2r}$. The formulation (7) allows us to improve significantly the procedure of solving our indirect problem. Indeed, we only one time during the whole process calculate the vectors $\mathbf{C}_0, \mathbf{C}_1, ..., \mathbf{C}_{2r}$ and then inside the loop of the procedure we only evaluate the distribution $\hat{t}_2$ in the collocation points $\eta_1, ..., \eta_{r2}$ (the values $t_1^n, t_1^s, ..., t_r^n, t_r^s$), substitute to formula (7), and then evaluate the functional I. This considerably decreases the CPU time needed for calculations inside the single pass of the loop and of course for the whole process.

Direct solutions

The other idea of solving our problem is to solve, with respect to $t_1^n, t_1^s, ..., t_r^n, t_r^s$, the following equation:

$$\mathbf{C_0} + t_1^n\cdot\mathbf{C_1} + t_1^s\cdot\mathbf{C_2} + ... + t_r^n\cdot\mathbf{C_{2r-1}} + t_r^s\cdot\mathbf{C_{2r}} = \overline{\sigma}, \tag{8}$$

where the vector $\overline{\sigma}$ collects the stresses $\overline{\sigma}_1, ..., \overline{\sigma}_k$. The transition of the tractions $t_1^n, t_1^s, ..., t_r^n, t_r^s$ into the distribution $\hat{t}_2$ gives us the solution of our indirect problem. It can be noted that this is a direct form of solution of the indirect problem.

Numerical examples and conclusions

The efficiency of the proposed method was tested in the series of examples in which the real distribution t_2 of the tractions on the boundary Γ_2 was known. The good convergence of the recovered distribution $\hat{t}_2$ to the distribution t_2 showed that the proposed method works good. Also the improvement given by the formula (7) was tested. The measured CPU time spent for the whole calculation then was decreased about hundred times. The direct method proposed above (solution of Eq. 8) is now tasted. Similar improvements can be done when we use T-elements formulation.

Acknowledgement: Grant KBN 4 T11F 012 23 is gratefully acknowledged.

References

[1] J. Jirousek, A. Wróblewski,: T-elements: State of the art and future trends, Arch. Comp. Meth. Eng. **3**, 4, 323-434, 1996.

[2] Karaś M., Zieliński A.P.: Parametric structural shape optimization using the global Trefftz approach. *J. Theor. and Appl. Mech.*, **2**, 38, 285-296, 2000

[3] Karaś, M.: Application of generalized Trefftz method to optimization of elastic structures. *PhD Thesis*, CUT Dept. of Mech., Cracow, 2001.

[4] Liu G.R., Han X.:Computational inverse techniques in non-destructive evaluation, *CRC Press,* Boca Raton, London, 2003.

[5] Qing H. Q.: The Trefftz Finite and Boundary Element Method, *WITPress,* Southampton, Boston, 2000.

XXI ICTAM, 15–21 August 2004, Warsaw, Poland

TENSOR INVARIANTS AND MECHANISMS OF TRANSITION TO CHAOS IN NONHOLONOMIC DYNAMICAL SYSTEMS

Alexey V. Borisov*, Ivan S. Mamaev**
*Institute of Computer Science, Udmurt State University, 1, Universitetskaya str, Izhevsk 426034, Russia.
E-mail: borisov@rcd.ru
**Institute of Computer Science, Udmurt State University, 1, Universitetskaya str, Izhevsk 426034, Russia.
E-mail: mamaev@rcd.ru

We consider nonholonomic systems that describe rolling of a rigid body on a plane and a sphere, as well as rolling of a ball on an arbitrary surface.

Any nonholonomic system has at least one nonintegrable constraint, and in our case this constraint implies that the point of contact of the body with the surface has zero velocity. Therefore, this nonholonomic model differs radically from the Hamiltonian model (with an absolutely smooth plane) and, at the same time, does not incorporate any sliding friction. Obviously, under the no-slip condition, the work done by the friction forces is zero and, therefore, the energy is conserved.

Study of nonholonomic systems goes as far back as to the classical papers by S. A. Chaplygin, P. E. Appell, D. J. Korteweg, E. J. Routh, and today we can see a rapid growth of interest in such systems, due to the latest developments of the theory of dynamical systems. Nonholonomic systems show striking and often quite unusual properties. One of the most well-known examples is a so-called rattleback [1], which is a solid body with a special mass distribution, rolling on a plane (Fig. 1).

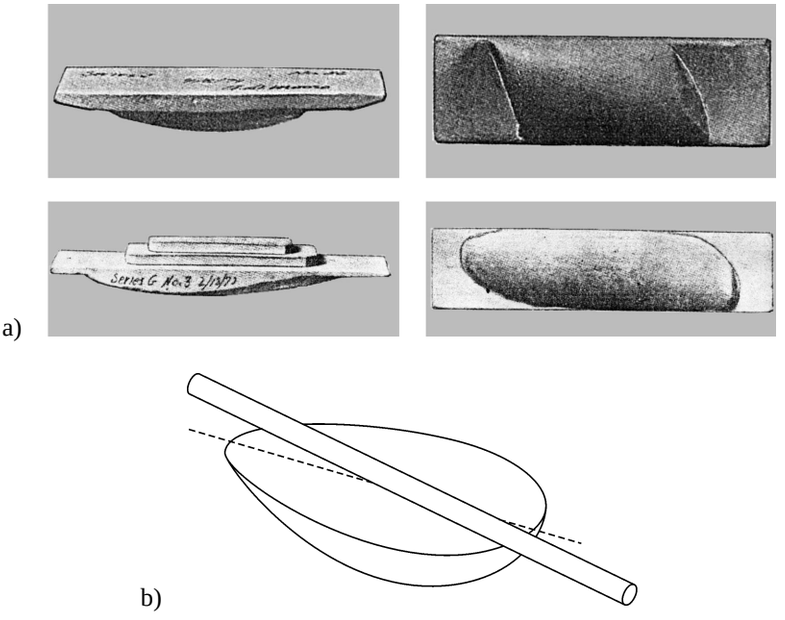


Figure 1. The rattleback models from the paper by J. Walker.

The unusual properties of a rattleback's behavior manifest themselves in the following way. When placed on a horizontal surface and spun in a certain direction about the vertical axis, a rattleback spins freely; if, however, it is then made to rotate in the opposite direction, it soon stops rotating and starts oscillating about the horizontal axis. Some rattlebacks can reverse the direction they were spun initially.

It turns out that this and similar problems can be investigated numerically using the three-dimensional Poincaré cross-section. As such numerical investigations show, the behavior of this system can be very complex. The following theorem (proved with certain computer-assisted techniques) holds:

Theorem 1 (on complex dynamics) *Let a body be bounded with a paraboloid surface, its geometrical axes not coinciding with the axes of the inertia ellipsoid. Then the values of the system's parameters and the inertia ellipsoid are such that*

1) *there are no asymptotically stable periodic solutions in the phase space;*

2) *unstable periodic solutions exist, their stable and unstable invariant manifolds intersect transversally (i. e., a complex dynamics exists);*

3) *there is a domain in the phase space, and a phase flow on its boundaries is inward (i. e., an attractive set exists);*

4) *the Lyapunov exponent of a typical orbit is non-zero.*

Therefore, there is a strange attractor in the phase space.

Besides, we show, using numerical and analytical methods, that these classical problems (rolling of a body on a plane and on a sphere and rolling of a ball on an arbitrary surface) include various new cases when tensor invariants [2] (additional integrals and the invariant measure) exist. And there is a certain hierarchy of possible types of behavior of nonholonomic systems. The extreme cases of this hierarchy are, on one hand, quite integrable systems (according to the Euler–Jacobi theorem), which can have the full set of first integrals and the invariant measure that behave quite regularly, and on the other hand, systems that have neither integrals, nor invariant measure. The latter display chaotic behavior, which can be either Hamiltonian or dissipative (a rattleback is a good example of such a system).

There is one more new mechanical effect discovered from the numerical experiments. We consider the motion of an axisymmetric ellipsoid with special mass distribution, so that the axes of the inertia ellipsoid are rotated, with respect to its geometrical axes, about the axis perpendicular to the ellipsoid's symmetry axis Oz (Fig. 2). Spun about this axis, the body at first shows reversion, like a rattleback, i. e. only the direction of the motion is changed. But this rotation is unstable either, and the body would gradually turn over, like a Chinese top, i. e. its initially upper part would move down, and vice versa.

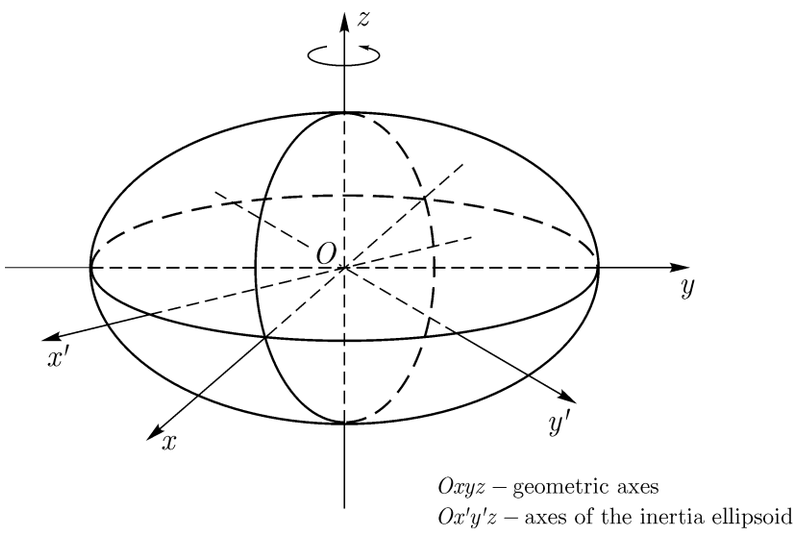


Figure 2.

References

[1] *Walker J.* The mysterious «rattleback»: a stone spins in one direction and then reverses. Scientific American, 1979, No. 10, pp. 144–149.

[2] *Kozlov V. V.* On the integration theory of equations of nonholonomic mechanics. Reg.&Chaot. Dyn. 2002, V. 7, No. 2, pp. 161–176 (in Russian).

XXI ICTAM, 15–21 August 2004, Warsaw, Poland

ANALYSIS OF A STRUCTURAL DETAIL USING A TWO-SCALE APPROACH

M. Cloirec, N. Moës, P. Cartraud
GeM - Institut de Recherche en génie civil et mécanique
Ecole centrale de Nantes / Université de Nantes / CNRS
1 Rue de la Noe, BP 92101, F -44321 Nantes Cedex 3, France

Summary The aim of this work is to solve mechanical problems on large structure containing details. We seperate the scale of the structure from the one of the detail (two-scale analysis). The structural scale is solved using a mesh which does not take into account the detail. The detail is introduced either by an "extended" homogenization or by an enrichment strategy. The homogenization or the enrichment is obtained from a local analysis of the detail on a distinct mesh from the structural one. On this local mesh, the X-FEM approach is used to carry out the analysis. The detail is considered embedded in an infinite media, so that the boundary conditions are not an issue.

The eXtended Finite Element Method (X-FEM) has a wide range of potential applications. We will deal with a new application in the field of multi-scale analysis and particularly the influence of a detail on a large structure. Usually, a detail in a structure is taken into account by a global refined mesh around the detail (often prohibitive) or by a global-local approach (wich may lead to very inaccurate results). In this paper, we suggest a two-scale approach using the capabilities of X-FEM.

The first step is to separate the scales. Two different meshes are needed : one for the discretisation of the detail and another mesh which will be coarse for the structure. We allow these two meshes to be completely independent from each other.

The purpose of the detail analysis is to obtain elementary solutions as a response to imposed "structural" loads. The X-FEM aproach is used to solve this specific detail problem to avoid to mesh complex details or to take into account several detail geometries on the same mesh. With X-FEM, the physical surfaces do not need to be meshed. The detail geometries (or voids) is located on the mesh using the level sets technique [1] [2]. Regarding the boundary conditions for the detail analysis, we consider the detail embedded in an infinite media with zero displacement at infinity (considering the detail has no impact at an infinite distance).

The elementary detail solutions are then used to perturb the structural problem. Two approaches are studied : "extended" homogenization and enrichment strategy using the partition of unity [5]. In the first approach, the regular element stiffness of the structural problem are replaced by the homogenized element stiffness for those elements close to the detail. The homogenized stiffness matrix is deduced from the elementary solutions computed during the resolution of the detail problem. In the second approach, the formulation of the elements close to the detail is enriched using the partition of unity. The classical finite appoximation is enriched by addition of degrees of freedom multiply by specific functions deduced from the detail analysis.

To check the effectiveness of the two-scale method, our solution is compared with the one obtained with an overkill mesh taking into account the detail on several classical benchmark problems.

References

[1] N. Moës, M. Cloirec, P. Cartraud and J.-F. Remacle : A computational approach to handle complex microstructure geometries. Computer Methods in Applied Mechanics and Engineering, 192, 3163-3177, 2003.
[2] N. Sukumar and D. L. Chopp and N. Moës and T. Belytschko : Modeling Holes and Inclusions by Level Sets in the Extended Finite Element Method. Computer Methods in Applied Mechanics and Engineering, 190, 6183-6200, 2001.
[3] A. Nicolet, J.F. Remacle, B. Meys, A. Genon and W. Legros : Transformation methods in computational electromagnetism. J. Appl. Phys. 75 (10), 6036-6038.
[4] P. Ladevèze, O. Loiseau and D. Dureisseix : A micro-macro and parallel computational strategy for highly heterogeneous structures. International Journal for Numericals Methods in Engineering, 52 (1-2), 121 -128,2001.
[5] J.M. Melenk and I. Babuška : The Partition of Unity Finite Element Method : Basic theory and applications, Computer Methods in Applied Mechanics and Engineering, 39, 289-314, 1996.

XXI ICTAM, 15–21 August 2004, Warsaw, Poland

ADAPTIVE DISCONTINUOUS GALERKIN METHOD FOR ELASTODYNAMICS ON UNSTRUCTURED SPACETIME GRIDS

Reza Abedi*, Shuo-Heng Chung**, Yong Fan*, Shripad Thite**, Jeff Erickson**, Robert B. Haber*
*Department of Theoretical & Applied Mechanics, University of Illinois at Urbana-Champaign, 104 S. Wright St., Urbana, IL 61801, USA
**Department of Computer Science, University of Illinois at Urbana-Champaign, Urbana, IL 61801, USA

Summary We present an adaptive spacetime discontinuous Galerkin (SDG) method for linearized elastodynamics. The SDG method uses a simple Bubnov-Galerkin projection that delivers stable and oscillation–free solutions, with $\mathcal{O}(N)$ complexity and exact momentum balance on every spacetime element. An extended version of the Tent Pitcher algorithm generates unstructured spacetime grids that support simultaneous grading in space and time. We present results in 1D and 2D $\times$ time, emphasizing problems with shocks. [1]

INTRODUCTION

Effective numerical methods for elastodynamics are needed in diverse engineering applications, ranging from seismic exploration to automotive design for crashworthiness. Accuracy requires highly refined spatial and temporal discretizations when shocks are present, so the computational expense can be unacceptably large. We present an adaptive procedure for elastodynamic analysis based on a spacetime discontinuous Galerkin (SDG) finite element method [1] that delivers low-dissipation and oscillation-free solutions. The discontinuous SDG basis functions facilitate our adaptive implementation, since nonconforming grids and jumps in polynomial order are automatically supported. We use unstructured spacetime meshes and a direct patch–by–patch solution procedure with O(N) complexity. Extreme refinement is only required along the spacetime trajectory of shocks, and we are not forced to impose global constraints on the time step size. The patch–by–patch solution technique supports local adaptive operations. The following sections outline the SDG formulation, describe the adaptive spacetime meshing procedures, and present some numerical results.

SPACETIME DISCONTINUOUS GALERKIN FORMULATION FOR ELASTODYNAMICS

Consider an open spacetime analysis domain, $D \subset E^d \times R$, where d is the spatial dimension. Let $\mathcal{V}$ denote the space of admissible SDG displacement fields on D which are piecewise H^1, but which may suffer discontinuities across a collection of d–dimensional jump manifolds. The SDG formulation derives from the following Bubnov-Galerkin weighted residual statement. Find a spacetime displacement solution $\mathbf{u} \in \mathcal{V}$ such that

$$\int_Q \mathbf{w} \cdot \mathcal{L}\left(\mathbf{dM} + \rho\mathbf{b}\right) - \int_{\partial Q} \left\{\mathbf{w} \cdot \mathbf{i}\left(\mathbf{dM} + \rho\mathbf{b}\right) + \dot{\mathbf{w}} \cdot \left(\mathbf{M}^* - \mathbf{M}\right) + \left(\boldsymbol{\varepsilon}^* - \boldsymbol{\varepsilon}\right) \wedge \mathbf{i}\hat{\mathbf{M}}\right\} + \int_{\partial Q^-} \mathbf{w}_0 \cdot \kappa\left(\mathbf{u}_\mathbf{0}^* - \mathbf{u}_\mathbf{0}\right) \mathbf{i}\boldsymbol{\Omega} = 0 \tag{1}$$

for all $\mathbf{w} \in \mathcal{V}$, and for all open subdomains $Q \subset D$ such that $\mathbf{u}|_Q \in H^1(Q)$ but where $\mathbf{u}$ may jump across ∂Q. The variables in (1) are differential forms with vector coefficients: $\mathbf{M}$ is the spacetime momentum flux, a d–form comprised of the stress and momentum density; the body force $\mathbf{b}$ is a $(d+1)$–form (ρ is mass density); the strain-velocity $\boldsymbol{\varepsilon}$ is a 1–form; and Ω is the standard basis for $(d+1)$–forms. The notations $\mathcal{L}$ and $\mathbf{i}$ denote the Lie derivative and insertion operators, both defined with respect to the time direction. A superscript '$*$' indicates a Godunov boundary value from a local Riemann problem, and $\hat{\mathbf{M}}$ is the momentum flux associated with the weighting function $\mathbf{w}$. A subscript '0' indicates a mapping into the zero–energy subspace of steady, infinitesimal–rigid displacement fields. Equation (1) enforces momentum balance via the equation of motion, $\mathbf{dM} + \rho\mathbf{b} = \mathbf{0}$, and the momentum flux jump condition, $\mathbf{M}^* - \mathbf{M} = \mathbf{0}$ on ∂Q. Kinematic compatibility is weakly enforced via the jump conditions, $\boldsymbol{\varepsilon}^* - \boldsymbol{\varepsilon} = \mathbf{0}$ on ∂Q and $\mathbf{u}_\mathbf{0}^* - \mathbf{u}_\mathbf{0} = \mathbf{0}$ on the time–inflow boundary, ∂Q^-. Integration by parts using the Cartan identity yields the SDG weak form on Q,

$$\int_Q \left(\mathbf{d}\dot{\mathbf{w}} \wedge \mathbf{M} - \dot{\mathbf{w}} \cdot \rho\mathbf{b}\right) - \int_{\partial Q} \left\{\dot{\mathbf{w}} \cdot \mathbf{M}^* + \left(\boldsymbol{\varepsilon}^* - \boldsymbol{\varepsilon}\right) \wedge \mathbf{i}\hat{\mathbf{M}}\right\} + \int_{\partial Q^-} \mathbf{w}_0 \cdot \kappa\left(\mathbf{u}_\mathbf{0}^* - \mathbf{u}_\mathbf{0}\right) \mathbf{i}\boldsymbol{\Omega} = 0 \;\forall \mathbf{w} \in \mathcal{V} \tag{2}$$

The SDG finite element method is obtained from (2) by associating Q with each element in a spacetime meshing of D, and by equipping each element with an independent set of discrete basis functions. The SDG method has low dissipation and it delivers exact momentum balance on every element in terms of the physically meaningful Godunov fluxes $\mathbf{M}^*$. It requires no stabilization and generates oscillation–free solutions, even when shocks are present.

CAUSALITY AND THE ADAPTIVE TENT-PITCHER ALGORITHM

A mesh is called patch–wise causal if the elements can be grouped into patches such that the wave characteristics at every point on every patch boundary are either all inward or all outward. The causal property establishes a partial ordering of

[1] Work supported by grants NSF DMR 01-21695 and DOE B341494; per–pixel rendering software by Yuan Zhou and Michael Garland.

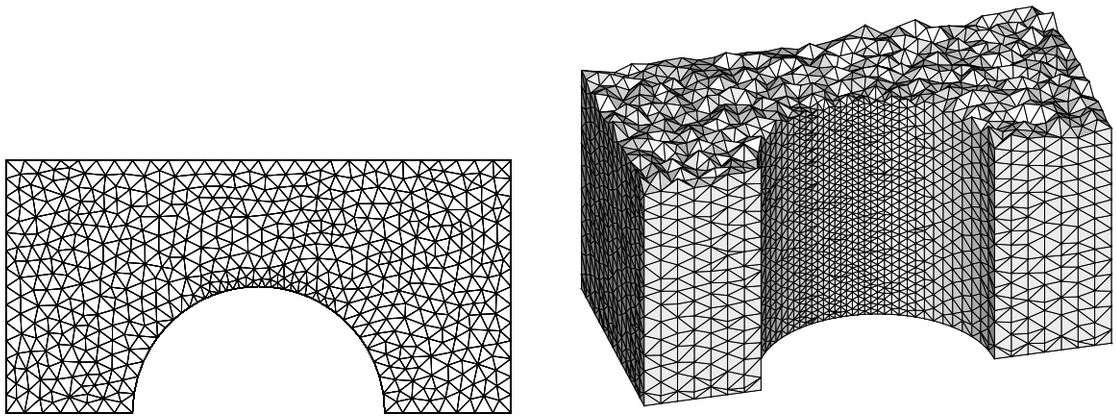


Figure 1. An input space mesh and the resulting spacetime mesh computed by Tent Pitcher [2]

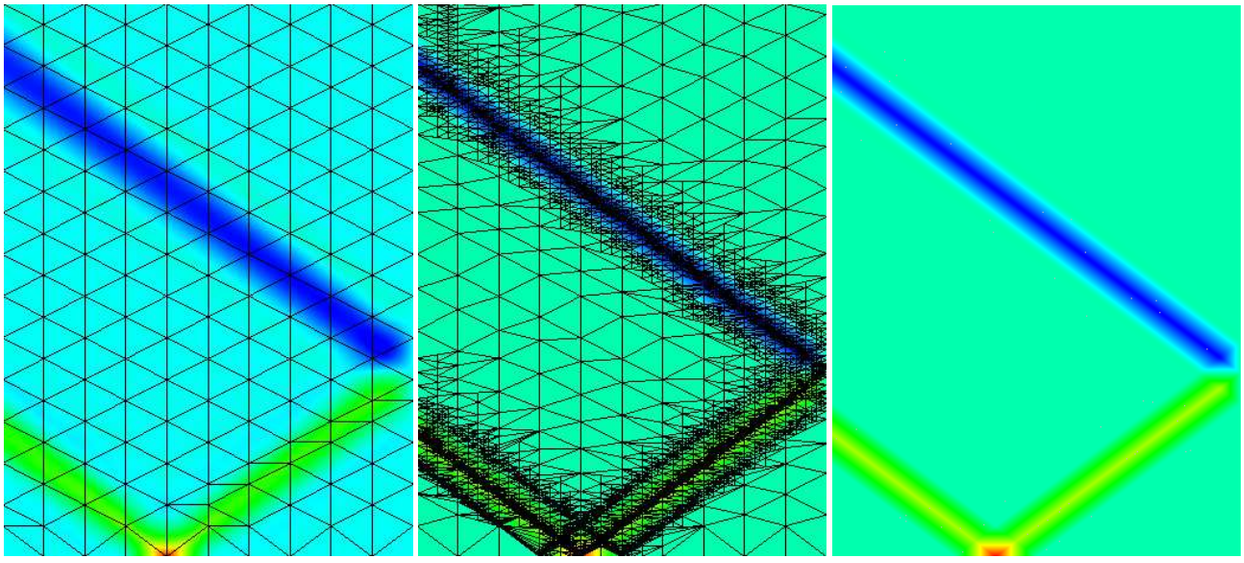


Figure 2. SDG displacement solutions for shock propagation in an elastic rod without adaptivity (left) and with adaptive refinement and coarsening (center and right). The space domain is along the horizontal axis, and time is increasing upwards.

patches where the solution on a given patch is independent of the solutions on all subsequent patches; this enables patch–by–patch solution procedures with $\mathcal{O}(N)$ complexity. Tent Pitcher [2] is an advancing–front meshing procedure that generates patchwise–causal spacetime meshes over an arbitrary spatial triangulation, as shown in Fig. 1. We immediately compute the SDG solution on each new patch generated by Tent Pitcher. Then, based on an appropriate error indicator, we decide whether to accept the patch (with or without a request for coarsening on subsequent patches) or to discard the patch and demand a local h–refinement operation. In the latter case, or when coarsening is requested, an adaptive implementation of Tent-Pitcher [3] exploits the ability of the SDG formulation to accommodate nonconforming meshes in carrying out the adaptation while maintaining the patch–wise causal property.

The adaptive SDG method has been implemented for linear elastodynamics in one and two spatial dimensions. The example depicted in Fig. 2 illustrates the benefits of spacetime adaptivity in a shock propagation problem. Shock loading is applied to an elastic rod, with a transmitting boundary on the left and a fixed boundary on the right. The smearing of the shock bands in the nonadaptive solution indicates numerical error. The strongly graded adaptive mesh resolves the fine details of the shocks with no visible smearing. Restricting the refinement to the shock trajectories reduces the computational expense relative to adaptive procedures constrained by a global time–step size.

References

[1] Yin L., Acharya A., Sobh N., Haber R., Tortorelli D.: A Spacetime Discontinuous Galerkin Method for Elastodynamic Analysis, in Cockburn B., Karniadakis G., and Shu C., eds. *Discontinuous Galerkin Methods: Theory, Computation and Applications*, Springer, 2000.

[2] Erickson J., Guoy D., Sullivan J. M., Üngör" A.: Building Space-Time Meshes over Arbitrary Spatial Domains, Proc. 11th Int. Meshing Roundtable, 391–402, 2002.

[3] Erickson J., Guoy D., Sullivan J. M., Thite T.: Spacetime Meshing with Adaptive Refinement and Coarsening, Proc. Symp. on Comp. Graphics SoCG 2004, to appear.

XXI ICTAM, 15–21 August 2004, Warsaw, Poland

CONTINUUM MECHANICS AND CARBON NANOTUBES

Marino Arroyo
Graduate Aeronautical Laboratories, California Institute of Technology, Pasadena CA 91125

Summary The understanding of the mechanics of atomistic systems greatly benefits from continuum mechanics. One appealing approach aims at deductively constructing continuum theories starting from models of the interatomic interactions. This viewpoint has become extremely popular with the quasicontinuum method. The application of these ideas to carbon nanotubes presents a peculiarity with respect to usual crystalline materials: their structure relies on a two-dimensional curved lattice. This renders the cornerstone of crystal elasticity, the Cauchy-Born rule, insufficient to describe the effect of curvature. We discuss the application of a theory which corrects this deficiency to the mechanics of carbon nanotubes. We review recent large scale simulations based on this theory, which have unveiled the complex nonlinear elastic response of thick multiwalled carbon nanotubes. We also discuss simplifications of the continuum theory, useful for fast engineering computations, and its application to the prediction of nanotube failure, refining other recent analysis.

INTRODUCTION

Continuum mechanics rationalizes the mechanics of materials in terms of irreducible sets of parameters (e.g. elastic moduli, Peierls stress), is amenable to analytical calculations, and affords very efficient simulations (e.g. finite elements). The most classic approach for continuum modelling of atomistic systems adopts a standard continuum theory (e.g. linear elasticity), and adjusts the material parameters to the data available. This phenomenological approach is simple and useful, particularly when the mechanics are well understood *a priori*, and the phenomena are simple enough to be encoded in the model. Another approach aims at deductively constructing continuum theories starting from models of the interatomic interactions as realistic as possible, with a minimal set of assumptions [1]. We are interested in this systematic approach.

The analysis of mechanics of carbon nanotubes by continuum models has attracted the attention of many researchers in the recent years. Let us cite the seminal work of Yakobson and co-workers [2], as the first to fully acknowledge the shell-like behavior of these nanostructures, and the relationship of their mechanics with the buckling of elastic shells. While most of the available works rely on the above mentioned phenomenological approach, some authors have tackled the problem within the framework of finite crystal elasticity. This approach is very attractive for carbon nanotubes given their nearly defect-free crystalline structure, and the very large deformations that they sustain reversibly. In [3], we pointed out the fundamental limitations of the Cauchy-Born rule for curved lattices of reduced dimensionality, and a generalized kinematical rule inspired in the geometric structure of the kinematics of two dimensional continua was proposed. This method consistently derives a hyperelastic surface model from the atomistic interactions. One feature of this model is that the continuum object under consideration is two-dimensional, i.e. a surface without thickness. In our view, this model overcomes the futile issue, so often discussed in the literature, about the appropriate thickness in a thin shell theory for this two-dimensional lattice.

SUMMARY OF THE THEORY AND VALIDATION

The essential idea behind the present theory, as in classical finite crystal elasticity, is to use the Cauchy-Born rule (here the generalized CB rule) to express the geometric quantities characterizing the deformation of the lattice in terms of the deformation of the continuum. For bulk materials, the bond lengths and angles are expressed in terms of a Lagrangian strain measure such as the right Cauchy-Green tensor. In the case of curved two-dimensional continua, such as that required for carbon nanotubes, the geometry of the deformed lattice is explicitly expressed in terms of the stretch (first fundamental form) and the curvature (second fundamental form) of the surface. The discretization of this continuum theory by finite elements yields a coarse-grained simulation method, which very accurately captures the nonlinear mechanics of carbon nanotubes, and can afford huge computational savings as illustrated in the next section.

Figure 1 shows simulations for a twisted (10,10) nanotube. Three representative snapshots of the deformation process are shown. The evolution of the strain energy is presented for both the atomistic and the continuum/finite element calculations. The snapshots demonstrate that, even for these intricate deformed morphologies, the continuum mechanics theory is surprisingly accurate, and the finite element model remarkably fits the atomic positions. When it comes to the energetics, the agreement is also excellent. A comprehensive set of comparisons between atomistic and continuum simulations can be found in [4].

MECHANICS OF THICK MULTI-WALLED CARBON NANOTUBES

The computational method that results from combining the present theory with finite elements allows for simulations of multimillion atom systems to be easily performed at a fraction of the cost. Figure 2(a) shows simulations reproducing the rippling deformations observed in recent experiments. These simulations reveal the three dimensional structure of the rippling deformations, reminiscent of the Yoshimura pattern (b). Furthermore, the analysis of the energetics of these deformations manifests a well-defined genuinely nonlinear response. See [5] for further details.

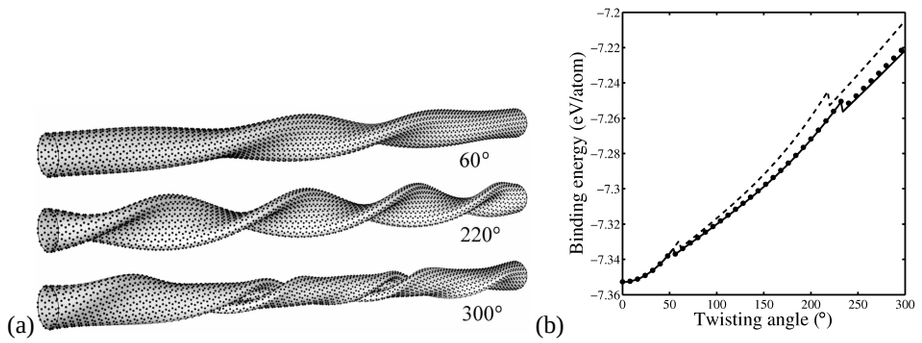


Figure 1. (a) Twisted 25.11 nm long (10,10) nanotube: super-imposed deformed configurations at three twisting angles for atomistic calculation (black spheres) and continuum finite element calculation (gray surface). (b) Comparison of the strain energy as a function of the twisting angle for atomistic calculation (—), and continuum/FE calculation (•), and strain energy evolution for the simplified model (- - -).

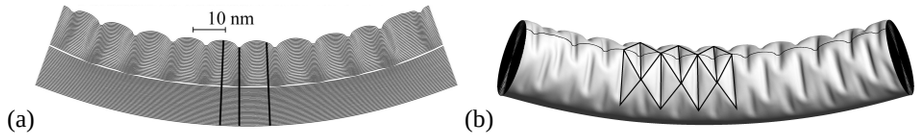


Figure 2. (a) Simulated rippling deformations in a 34-walled carbon nanotube, and (b) three dimensional structure of the deformation.

SIMPLIFIED MODEL

Although the continuum models described above affords very accurate and efficient computations, it is relatively complex and its computational cost is higher than that of standard engineering material models; it is strongly non-linear, its evaluation requires the inner displacement relaxation, and the membrane and bending contributions are tightly coupled. On the other hand, the simulations suggest that the nonlinearity of the mechanical response is mostly geometrical, rather than stemming from the material model. In this section we show that following rational arguments, it is possible to deduct the simplest nonlinear model, capable of reproducing the essential mechanics, and consistent with an irreducible set of elastic parameters.

It is well known that the infinitesimal in-plane elastic response of graphene is isotropic. In [6] we showed that the bending response is also isotropic. By analogy with the Kirchhoff-Saint Venant model of finite elasticity, the simplest isotropic model for a two-dimensional continuum splits the energy into membrane and bending energy, and is of the form

$$W_{\text{approx}} = W_{\text{m}} + W_{\text{b}} = \frac{1}{2}[2\mu\mathbf{E} : \mathbf{E} + \lambda(\text{tr } \mathbf{E})^2] + \frac{1}{2}[a(2H)^2 + bK]$$

where μ and λ are the 2D Lamé coefficients [6], $\mathbf{E}$ is the Green strain tensor, the mean curvature H and the Gaussian curvature K are the invariants of the curvature tensor, and a and b are bending elastic moduli. Since $\int_\Omega K\ dX$ is a topological invariant of the surface, the term involving K can be disregarded from the strain energy density. In [6] we provided explicit expressions for the bending modulus a in terms of the inter-atomic potential, as well as for the Lamé coefficients. Fig 1(b) (dashed line) shows that indeed this simple model captures the essential geometric nonlinearities of the problem, and provides quite good energetics. It also shows that for very large deformations, when presumably the material nonlinearities become more important, this model does not perform as well as the complete model discussed above. Although not shown, the agreement in the deformed configurations is also good for the simplified model.

References

[1] Stakgold I.: The Cauchy relations in a molecular theory of elasticity. *Quarterly Journal of Applied Mathematics* **8**:169–186, 1950.
[2] Yakobson B.I., Brabec C.J., Bernholc J.: Nanomechanics of carbon tubes: Instabilities beyond the linear response. *Phys. Rev. Lett.* **76**:2511–2514, 1996.
[3] Arroyo M., Belytschko T.: An atomistic-based finite deformation membrane for single layer crystalline films. *J. Mech. Phys. Solids* **50**:1941–1977, 2002.
[4] Arroyo M., Belytschko T.: Finite element methods for the non-linear mechanics of crystalline sheets and nanotubes. *Int. J. Numer. Meth. Eng.* **59**:419–456, 2004.
[5] Arroyo M., Belytschko T.: Nonlinear Mechanical Response and Rippling of Thick Multiwalled Carbon Nanotubes. *Phys. Rev. Lett.* **91**:215505, 2003.
[6] Arroyo M., Belytschko T.: Finite crystal elasticity of carbon nanotubes based on the exponential Cauchy-Born rule. *Phys. Rev. B* accepted.

XXI ICTAM, 15–21 August 2004, Warsaw, Poland

TOWARD CONVERGENCE IN INITIALLY RIGID COHESIVE FRACTURE MODELS

Chin-Hang Sam*, Katerina Papoulia*, Pritam Ganguly**
*School of Civil and Environmental Engineering, Cornell University, Ithaca, NY 14853, USA
**Department of Theoretical and Applied Mechanics, Cornell University, Ithaca, NY 14853, USA

Summary We analyze the convergence of finite element methods for cohesive fracture. The focus is on generalized fracture in which finding the crack path or paths is part of the solution process. Initially rigid cohesive models, in which interface elements are inactive until a critical traction is attained, are usually preferred in this context. We show that convergence as the time-step tends to zero is erratic or nonexistent unless the model satisfies a property called "time continuity." We also argue that convergence as the spatial mesh size tends to zero is unlikely unless the mesh is able to represent all possible crack paths without preferred directions. We propose a method to achieve this kind of mesh isotropy in two dimensions based on Radin's pinwheel tiling. The pinwheel tiling in the limit can approximate any plane curve with the correct length.

COHESIVE FINITE ELEMENTS

Cohesive zone modeling, which was originally proposed by Dugdale and Barenblatt, represents fractures with explicit displacement jumps. In such a model, the separation of bulk material is resisted by cohesive forces governed by the corresponding cohesive constitutive model.

It is natural to apply cohesive modeling to problems where defined interfaces exist and, indeed, this approach has been successfully used in problems concerning bi-material interfacial debonding and fracture, delamination of composite materials, and many other settings. A widely used cohesive model is one that consists of an ascending branch and a descending branch, referred to here as "initially elastic."

In the past decade, there are increasing applications of cohesive finite elements in the dynamic fracture arena, including void nucleation, interfacial fracture, branching and fragmentation. In some of these simulations, the crack pattern is not known in advance. This precludes the possibility of prepositioning cohesive surfaces. Alternatively, every edge of the bulk elements is considered as a potential fracture surface. The crack propagation path can then be resolved as part of the solution of the governing equations.

Two different approaches are taken to this end. In the first approach, every edge of each bulk element is the site of an initially elastic cohesive surface. A fundamental problem is that as the spatial discretization is refined, the effective modulus of the material is non-physically decreased ultimately to zero [1].

Trying to solve this problem leads to the second approach, namely an adaptive approach in which cohesive surfaces are only inserted when they are needed. In other words, the effective initial stiffness of the cohesive model is infinite. We denote this type of model as initially rigid. Although the initially rigid model can eliminate some drawbacks of the initially elastic model, special considerations in its finite element implementation are essential to its numerical behavior, and it was pointed out by Papoulia et al. [3] that in explicit dynamics using a rigid model, the correct time convergence rate can be obtained only if a certain condition called "time continuity" is satisfied.

In this paper, we propose an improved model that also satisfies the time-continuity condition. The rigid cohesive modeling methodology and the time-continuity condition are briefly described in Section 2.

Section 3 considers convergence of the initially rigid cohesive model as the spatial mesh size is refined. It is argued that many typical meshes are poorly suited for cohesive zone modeling for generalized fracture because these meshes contain unphysical preferred crack directions. The existence of these preferred directions precludes convergence to the true solution as the mesh size tends to zero. A two-dimensional technique based on Radin's pinwheel tiling is proposed for remedying this problem. Pinwheel tilings have the property that given any piecewise smooth plane curve P and any $\epsilon > 0$, there is a sufficiently fine refinement R of the mesh such that R contains a path P' of mesh edges such that P' lies within distance ϵ of P and such that $|\text{length}(P') - \text{length}(P)| \leq \epsilon$.

TIME CONVERGENCE

In this section, the matter of time continuity and convergence as the time-step tends to zero is analyzed. For this section, regard cohesive fracture as a spatially discretized differential equation in the standard form of nonlinear frictionless mechanics, namely,

$$\mathbf{M}\ddot{\mathbf{u}} = \mathbf{f}^{ext} - \mathbf{f}^{int}(\mathbf{u}, \mathbf{q}) \equiv \mathbf{f}, \tag{1}$$

where $\mathbf{M}$ is a mass matrix, $\mathbf{u}$ is the global nodal displacement vector, $\mathbf{f}^{int}$ is the internal nodal force vector and $\mathbf{f}^{ext}$ the external nodal force vector. $\mathbf{f}^{int}$ can explicitly depend on the displacement vector $\mathbf{u}$ and some history vector $\mathbf{q}$. In order to obtain convergent results as the time step is varied, $\mathbf{f}^{int}(\mathbf{u}, \mathbf{q})$ is required to be

a continuous function of $\mathbf{u}$ for those values of $(\mathbf{u}, \mathbf{q})$ encountered on the solution trajectory of Equation (1). Specifically, quadratic convergence is obtained with the central difference time stepping scheme when time-continuity is observed, whereas lack of convergence or erratic sequences of interface activations are observed when the condition is violated [3]. The source of discontinuities of the internal force vector arise at the time step when a new cohesive surface is inserted. Since the bulk constitutive model and the cohesive constitutive model are chosen independently, continuity of the nodal forces before and after the insertion is not guaranteed. We propose a methodology that converts almost any initially elastic cohesive into a time continuous initially rigid model. The methodology is simpler and more general than the approach to time continuity taken by [3].

The new approach is tested in a mixed mode dynamic fracture experiment of a concrete beam investigated by John and Shah [2] in which a notched specimen supported at two corners is subjected to an impact load. Different time step values Δt_i are used ($\Delta t_i = 2 \times 10^{-7}/2^i$ s, $i = 0 : 5$) and the results from the simulation using the smallest time step (i.e. $i = 5$) is taken as the "exact" solution. The relative error is defined as $\text{error}_i = \| \mathbf{v}_i - \mathbf{v}_{exact} \|_2 / \| \mathbf{v}_{exact} \|_2$, where $\mathbf{v_i}$ is the velocity vector of the simulation using Δt_i. The convergence results of the time-continuous model TCM (marked by 'o') and discontinuous model TDM (marked by 'x') are compared at two different times ($t_1 = 2 \times 10^{-4}$ s as the dashed line, $t_2 = 6.8 \times 10^{-4}$ s as the dotted line) and is shown in Figure 1 with logarithmic scale. For a convergent method, one expects that the error will diminish to zero as the time step size goes to zero, and quadratic convergence means that the rate of decrease will be of second order. Hence, it can be observed that the results of the continuous model shows quadratic convergence for time steps smaller than a certain critical value, but for the discontinuous model, the results are either converging at a very slow rate or not converging at all. In addition, while the activated interfaces in the continuous model have similar patterns for all the different choices of time step, the activated interfaces in the discontinuous model are different for each time step size.

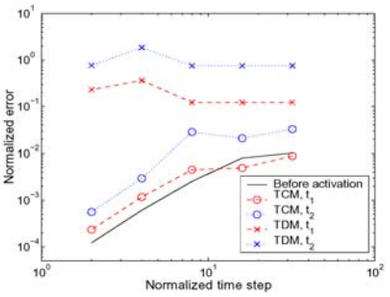


Figure 1. Convergence results of mixed mode beam bending.

SPATIAL CONVERGENCE

Although several researchers have carried out spatial convergence studies with cohesive models, there is no proof available that cohesive finite element models converge to a "true" solution as the spatial mesh size tends to zero. Indeed, we claim that such convergence is not likely unless a special kind of mesh is used. The reason is that standard meshes used in the literature contain preferred fracture paths. Consider, e.g., a cross-triangle quadrilateral mesh in which the quadrilaterals are squares. In both the true solution and the finite element solution, the energy required to form a crack is proportional to its length. If the true crack path is linear and is oriented at 0°, 45°, 90° or 135° with respect to the x-axis, then this crack path is exactly represented in the mesh as the mesh is refined. On the other hand, if the crack has any other orientation, e.g., 22.5°, then its length is not exactly represented as the mesh is refined. In fact, there is a constant $\alpha > 1$ such that the ratio between the length of the mesh's representation of the crack and true crack length is greater than α for all levels of refinement of this mesh. Therefore, the energy to form this crack never converges to the true energy as the spatial mesh is refined. This persistent gap in the energy means that cohesive finite elements will probably never find the true crack solution in this mesh if it is a line oriented at 22.5°.

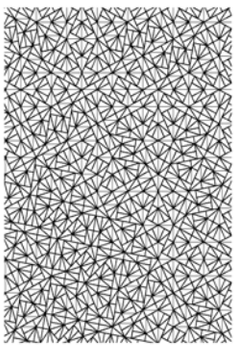


Figure 2. Radin's pinwheel tiling of the plane

We propose a technique to solve this problem based on Radin's pinwheel tiling of the plane [4], a portion of which is depicted in Fig. 2. Radin's tiling has the property that any piecewise smooth curve is represented arbitrarily accurately (including its length) by tile edges as the tiling is refined. Radin's pinwheel tiling is not suitable for use in finite element modeling because it will not conform to boundaries. We present computations using a generalization of the pinwheel tiling for arbitrary 2D domains that preserves the length-approximation property.

References

[1] M. L. Falk, A. Needleman, and J. R. Rice. A critical evaluation of cohesive zone models of dynamic fracture. Journal de Physique IV, Prceedings, Pr-5-43-Pr-5-50, 2001.

[2] R. John and S. P. Shah. Mixed-mode fracture of concrete subjected to impact loading. Journal of Structural Engineering, 116(3):585–602, 1990.

[3] K. Papoulia, C. Sam, and S. Vavasis. Time continuity in cohesive finite element modeling. International Journal for Numerical Methods in Engineering, 58(5):679–701, 2003.

[4] C. Radin. The pinwheel tilings of the plane. Annals of Math., 139:661–702, 1994.

XXI ICTAM, 15–21 August 2004, Warsaw, Poland

COMPUTATIONAL HOMOGENISATION OF MICROHETEROGENEOUS MATERIALS INCLUDING DECOHESION AT FINITE STRAINS

Stefan Loehnert*, Peter Wriggers*
* *IBNM, University of Hanover, Appelstr. 9A, 30167 Hannover, Germany*

Summary In this paper we present some aspects of computational homogenisation procedures of microheterogeneous materials which can show decohesion in a cohesive zone around the particles. Applications to this are e.g. polymer coatings stiffened with sand. Due to the decohesion we get £nite deformations and £nite strains within the RVE. The geometrical and material nonlinearities cause the main dif£culties. The homogenisation procedure leads to an effective stress strain curve for the RVE. Here we set a special focus on the adaptive numerical model, the statistical testing procedure and the different boundary conditions (pure traction, pure displacement and natural boundary conditions) applied on the RVE.

HOMOGENISATION AT FINITE STRAINS

The effective material data of a representative volume element (RVE) is obtained from the relation between the effective strains $\boldsymbol{\varepsilon}$ and the effective stresses $\boldsymbol{\sigma}$. The effective material tensor $\mathbb{E}^*$ maps the volume average of the strains on the volume average of the stresses

$$\langle \boldsymbol{\sigma} \rangle_\Omega = \mathbb{E}^* : \langle \boldsymbol{\varepsilon} \rangle_\Omega \tag{1}$$

with $\langle \cdot \rangle_\Omega = \frac{1}{|\Omega|} \int_\Omega \cdot \, \mathrm{d}\Omega$. Ω is the domain of the regarded RVE. Equation (1) also holds in the nonlinear range where $\mathbb{E}^*$ depends on the deformation and maybe on the deformation path itself. A requirement for the strain measure in (1) is linearity in the displacements, also for the geometrically nonlinear theory.

The average strain theorem states that for a perfectly bonded RVE under uniform displacement boundary conditions the volume average of the deformation is the same as the given deformation on the boundary. Given a constant deformation gradient on the boundary $\boldsymbol{\mathcal{F}}$ it can be shown that

$$\langle \boldsymbol{F} \rangle_{\Omega_0} = \boldsymbol{\mathcal{F}} + \frac{1}{|\Omega_0|} \int\limits_{\partial\Omega_0^1 \cap \partial\Omega_0^2} [\![\boldsymbol{u}]\!] \otimes \boldsymbol{n}_0 \, \mathrm{d}\partial\Omega_0^{1,2} \qquad , \tag{2}$$

where $[\![\boldsymbol{u}]\!]$ is the jump within the displacement £eld in case of a not perfectly bonded microstructure, $\boldsymbol{n}_0$ is the unit normal vector, and Ω_0^1 and Ω_0^2 are the domains of the different materials in the RVE respectively. In case of a perfectly bonded microstructure the displacement jumps vanish. Then $\langle \boldsymbol{F} \rangle_{\Omega_0} = \boldsymbol{\mathcal{F}}$, and similarly $\langle \dot{\boldsymbol{F}} \rangle_{\Omega_0} = \dot{\boldsymbol{\mathcal{F}}}$.

The average stress theorem states that in the absence of body forces and under a uniform load on the boundary the volume average stress is the same as the given stress on the boundary. For £nite deformations one has to distinguish between different con£gurations. Here we restrict ourselves to the mixed con£guration. We assume a constant £rst Piola-Kirchhoff stress tensor $\boldsymbol{\mathcal{P}}$ on the boundary. Using Cauchy's theorem and applying the equations of motion one can show that

$$\langle \boldsymbol{P}^T \rangle_{\Omega_0} = \boldsymbol{\mathcal{P}}^T + \frac{1}{|\Omega_0|} \int\limits_{\Omega_0} \boldsymbol{X} \otimes \boldsymbol{f}_0 \, \mathrm{d}\Omega_0 \tag{3}$$

which for zero body forces yields $\langle \boldsymbol{P} \rangle_{\Omega_0} = \boldsymbol{\mathcal{P}}$.

A commonly accepted criterion for the choice of the size of the RVE is Hill's condition which states that for a perfectly bonded microstructure and no body forces the microenergy is equal to the macroenergy of the RVE. This leads to the fact that the RVE has to be small enough such that from the macroscopic point of view the strain and the stress of the macroscopic body can be assumed to be approximately constant at the location of the RVE. Due to that the RVE can be regarded as one point of the macroscopic structure. On the other hand the RVE has to be large enough such that the boundary £eld ¤uctuations are relatively small. For £nite deformations one can show that in case of Dirichlet boundary conditions and a perfectly bonded microstructure as well as for pure Neumann boundary conditions and no body forces we have

$$\langle \boldsymbol{P} : \dot{\boldsymbol{F}} \rangle_{\Omega_0} = \langle \boldsymbol{P} \rangle_{\Omega_0} : \langle \dot{\boldsymbol{F}} \rangle_{\Omega_0} \qquad . \tag{4}$$

MATERIAL MODEL

The microstructure consists of randomly distributed spherical particles embedded in a binding matrix. The delamination process is restricted to a domain around the particles. This zone is also called "cohesive zone". Further details about the cohesive zone approach can be found for example in [6]. The material law chosen for the binding matrix and the inclusions is a simple compressible Neo-Hooke material with the Lamé parameters $\mu^{(\mathrm{m})}$, $\lambda^{(\mathrm{m})}$ and $\mu^{(\mathrm{p})}$, $\lambda^{(\mathrm{p})}$ respectively. The material model for the cohesive zone is a simple damage model following the suggestion of Zohdi [7]. The undamaged material is also a compressible Neo-Hooke material with the material parameters $\mu_0^{(\mathrm{cz})}$ and $\lambda_0^{(\mathrm{cz})}$. The local degradation

is represented by a variable α with $0 < \alpha \leq 1$ which "weakens" the stiffness of the material. That means, the material constants become

$$\mu^{(\mathrm{cz})} = \alpha \mu_0^{(\mathrm{cz})} \qquad \text{and} \qquad \lambda^{(\mathrm{cz})} = \alpha \lambda_0^{(\mathrm{cz})} \quad . \tag{5}$$

The local constraint condition from which α can be computed is $\Psi(\alpha) = \mathcal{M}(\alpha) - \mathcal{K}(\alpha) \leq 0$ where $\mathcal{M}(\alpha)$ is a scalar valued term representing the stress state of the material point

$$\mathcal{M}(\alpha) = \sqrt{\boldsymbol{g}(\boldsymbol{\sigma}_{\mathrm{deg}}(\alpha)) : \boldsymbol{g}(\boldsymbol{\sigma}_{\mathrm{deg}}(\alpha))} \quad \text{with} \quad \boldsymbol{g}(\boldsymbol{\sigma}_{\mathrm{deg}}(\alpha)) = \eta_1 \frac{\mathrm{tr}(\boldsymbol{\sigma}_{\mathrm{deg}})}{3}\mathbf{1} + \eta_2 \left(\boldsymbol{\sigma}_{\mathrm{deg}} - \frac{\mathrm{tr}(\boldsymbol{\sigma}_{\mathrm{deg}})}{3}\mathbf{1} \right) \tag{6}$$

and η_1 and η_2 are parameters scaling the isochoric and deviatoric parts of $\boldsymbol{g}(\boldsymbol{\sigma}_{\mathrm{deg}}(\alpha))$. $\mathcal{K}(\alpha)$ is a threshold value which depends on the damage variable α itself.

$$\mathcal{K}(\alpha) = \Phi_{\mathrm{lim}} + (\Phi_{\mathrm{crit}} - \Phi_{\mathrm{lim}})\, \alpha^P \tag{7}$$

Φ_{crit} is the initial threshold value, and Φ_{lim} is the threshold value in the limiting case when the material point has degraded completely ($\alpha = 0$). Finally P is an exponent which controls the rate of degradation.

NUMERICAL MODEL AND COMPUTATIONAL TESTING

The RVE is chosen to be a cube with a random distribution of inclusions. In three dimensions it is not easy to generate a mesh of only nicely shaped hexahedra elements for complex geometries. This motivates a different way of discretisation where we use only linear cube shaped elements which approximate the particle boundaries only roughly. In order to increase the accuracy of the discretisation we apply non-conforming elements close to the interfaces between the particles and the cohesive zone and the cohesive zone and the matrix material. An illustration of this discretisation can be seen in £gure 1. To get a representative material response one has to do statistical tests with different random distributions of inclusions. Of special interest is the number of particles needed for each test, the re£nement of the mesh, the number of tests performed and of course the different boundary conditions. The tests done are performed with pure displacement boundary conditions, pure traction boundary conditions and natural boundary conditions. The necessary re£nement of the mesh has been tested in a one particle test. The resulting strain energy as a function of the number of degrees of freedom is shown in £gure 2.

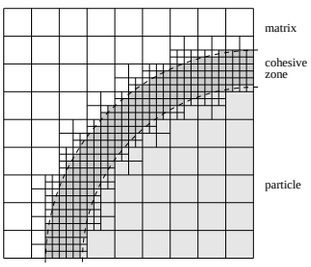


Figure 1: Discretisation with non-conforming cubic elements

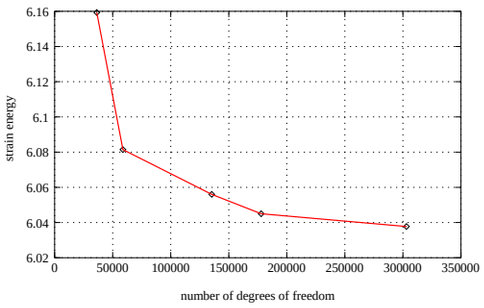


Figure 2: Convergence: overall energy

To £gure out the required number of inclusions we look at the standard deviation of the stress response for multiple tests with the same number of inclusions. This value does not decrease with the number of tests performed. Only the number of inclusions in each test has an in¤uence on it. However, to get a statistical representative response it is necessary to compute the same test many times with a different random distribution of the inclusions. In £gure 3 one can see that a relatively low number of inclusions is suf£cient.

At last the number of tests which have to be computed to get a statistically representative result is important. It is not possible to increase the accuracy of the effective response by computing more tests. But at a higher number of tests performed, the collection of the effective results of each test form a more Gaussian distribution of the effective results. This is shown in the histograms in £gure 4 for 200 tests performed.

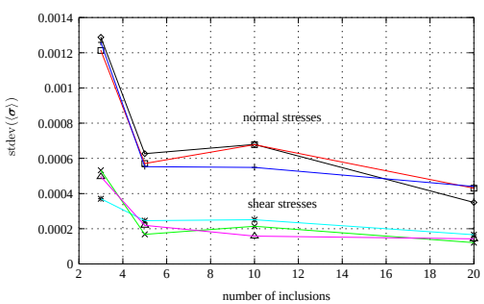


Figure 3: Standard deviation of the effective stresses

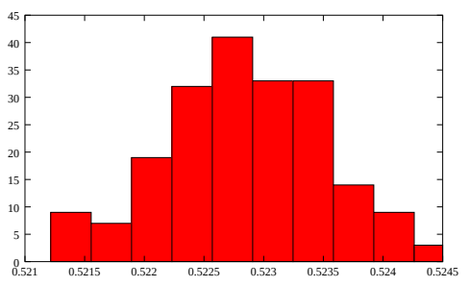


Figure 4: Histogram for effective Cauchy stress component $\langle \sigma_{11} \rangle$

References

[1] Bishop, J.F.W. and Hill, R.: A Theory of the Plastic Distortion of a Polycrystalline Aggregate under Combined Stresses. *Phil. Mag.*, 42, (1951a), 414-427.

[2] Bishop, J.F.W. and Hill, R.: A Theoretical Derivation of the Plastic Properties of a Polycrystalline Face-Centred Metal. *Phil. Mag.*, 42, (1951b), 1298-1307.

[3] Hill, R.: The Elastic Behaviour of a Crystalline Aggregate. In: *Proc. Phys. Soc. (Lond.)*, A65, pages 349-354 (1952).

[4] Reuss, A.: Berechnung der Fliessgrenze von Mischkristallen auf Grund der Plastizitätsbedingung für Einkristalle. *Z. angew. Math. Mech.*, 9, (1929), 49-58

[5] Voigt, W.: Über die Beziehung zwischen den beiden Elastizitätskonstanten isotroper Körper. *Wied. Ann.*, 38, (1889), 573-587.

[6] Needleman, A. et al: Matrix reinforcement, and interfacial failure. In: Suresh, S., Mortensen, A. and Needleman, A.: *Fundamentals of metal matrix composites*, Butterworth-Heineman publishers (1993).

[7] Zohdi, T; Wriggers, P.: Computational micro-macro material testing. *Archives of Computational Methods in Engineering.*, 8, 2, (2001), 131-228.

THE LOAD CASES IN NUMERICAL MODEL OF PELVIC BONE WITH ARTIFICIAL ACETABULUM

A. John*, P. Orantek*, J.J. Telega**
*Silesian University of Technology, Department for Strength of Materials and Computational Mechanics, 44-100 Gliwice, Konarskiego 18A, Poland,
**Institute of Fundamental Technological Research Polish Academy of Science, 00-049 Warszawa, Swietokrzyska 21, Poland

Summary The numerical modelling makes possibilities to account the stress and strain distribution in every points of model. It is particular important when the THA operation is performed and the artificial acetabulum is fitted. Very often before and after operations the knowledge of the stress and strain distribution in the pelvic bone is needed. For checking the influence of the forces acting in acetabulum on the stress and strain distribution in the surroundings of the artificial acetabulum a simple bench-mark was proposed, with force acting in acetabulum by ceramic ball.

INTRODUCTION

Bioengineering concerns many important problems apply to human body. The pelvic joint and its correct working is one of them. The pelvic bone is one of the most important supporting elements in human pelvic joint but it is liable to suffer an injury. Very often before and after operations the knowledge of the stress and strain distribution in the pelvic bone is needed. It is particular important when the THA operation is performed and the artificial acetabulum is fitted. Because the safety of patient should be taken into account there are only two possibilities: model testing and numerical calculations. Before numerical calculations the numerical model should be prepared.
In the paper the numerical model is prepared on the ground of the geometrical data from 3D scanning or CT. The accuracy of geometrical model depends on number of scanning levels. A numerical routine (numerical code) was built to translate the geometrical data (the set of coordinate points) to the Patran/Nastran code. The layer structure of bone tissues is taking into account. Using an in-house numerical code the inner surface in numerical model is implemented (between cortical bone tissue and trabecular bone tissue). Separate solid elements layers are modeled by cortical and trabecular bone. At present homogeneous elastic properties within a certain group of tissue are assumed.

NUMERICAL MODELING

In the aim to creating an artificial acetabulum a few procedures were done. All procedures were written in the C++ language. The procedures create the flange (*width*), the spherical cap (*radius*), and the bolts of artificial acetabulum (*2 angles in spherical coordinates*, *width*, *height*). On the basis of the above parameters the whole geometry of the structure is created. Next on the ground of the geometry, the finite element model is created and put into the bone finite element model. The surfaces are modeled using triangular elements and the solids are modeled using tetrahedral elements.
There is possible to model cemented and cementless acetabulum, with contact element and without. At present MSC.Patran/Nastran and MSC.Patran/Marc systems are applied. Here, boundary conditions are given in two area: in contact area with sacral bone and in pubic symphysis. Stress and strain distribution of human pelvic bone is a result of external load coming from upper body part's weight and muscles forces. Referring to earlier works, the model takes up 23 muscle tensions influencing through pelvic bone and tendons on insertions' surfaces. For checking the influence of the forces acting in acetabulum on the stress and strain distribution in the surroundings of the artificial acetabulum a simple bench-mark was proposed, with force acting in acetabulum by ceramic ball. Fig. 1 shows the model of artificial acetabulum and Fig. 2 shows the model of pelvic bone with fitted artificial acetabulum.

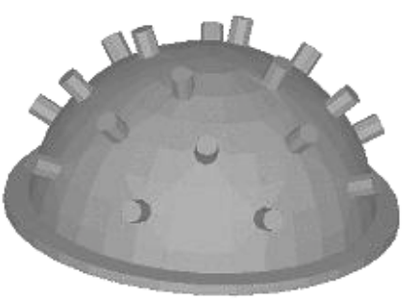


Fig. 1 The artificial acetabulum (model)



Fig. 2 The numerical model of pelvic bone with artificial acetabulum and ceramic ball

NUMERICAL CALCULATIONS

The calculations were performed for 5 schemes of acting forces (Fig. 3). The scheme 1 represents force acting perpendicularly to base plane of artificial acetabulum. The schemes 2 – 5 represent forces acting at an angle of 30° to force from scheme 1, in given direction. All the forces acting in the center of ceramic ball, inwards of acetabulum. The highest effort of constituent elements were obtained for the 5th scheme of load. The stress distribution show the Fig.Fig. 4 – 6 for the cortical bone, artificial acetabulum and cement layer, respectively.
Obtained results can be useful to planning and quality assessment of THA. The surgeons can observe which state of load are dangerous for the patients.

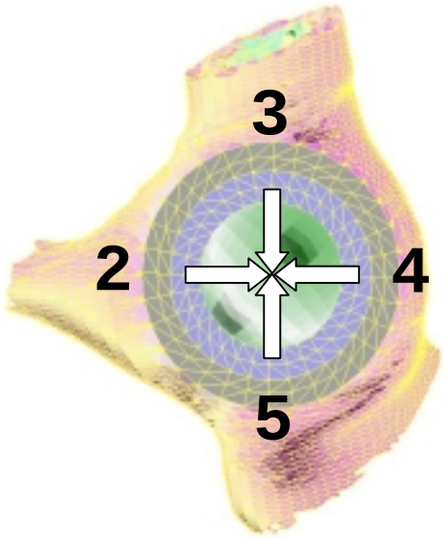


Fig. 3 The Scheme of acting forces

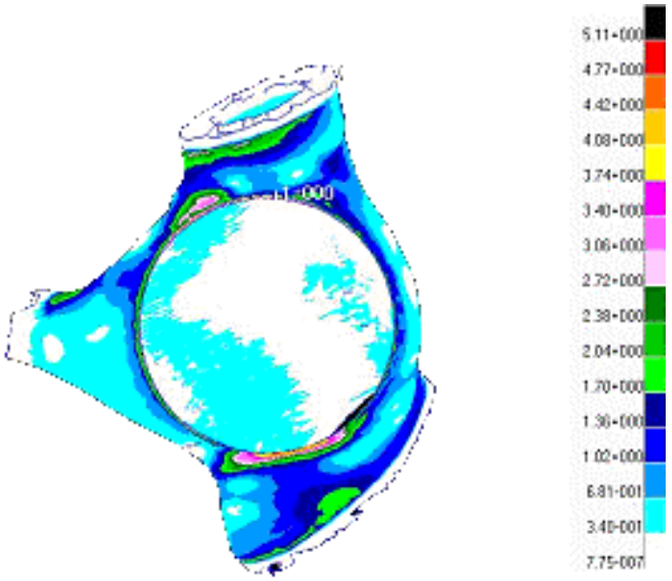


Fig.4 The reduced stress distribution in cortical bone (scheme 5)

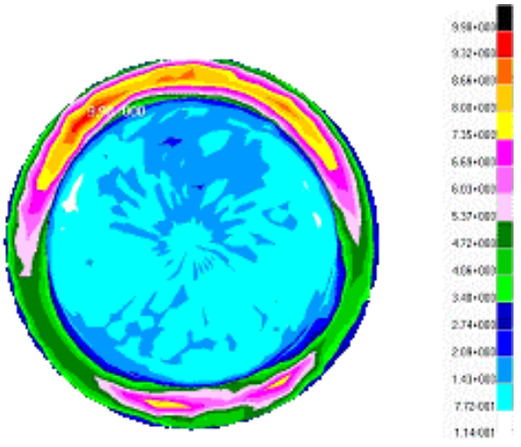


Fig. 5 The reduced stress distribution in artificial acetabulum (scheme 5)

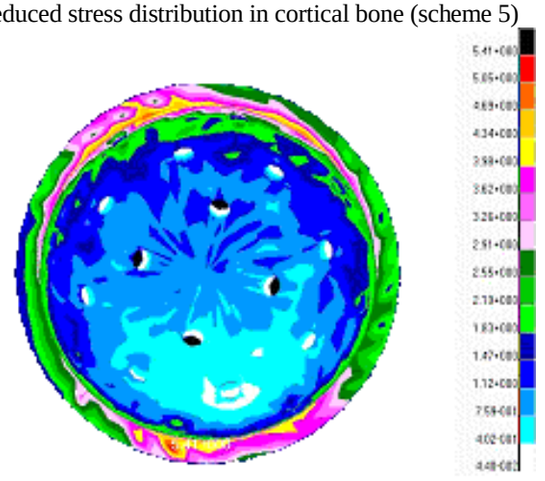


Fig. 6 The reduced stress distribution in cement layer (scheme 5)

References

[1] John A., Orantek P.: Computer aided creation of geometrical model of human pelvic bone. *Acta of Bioengineering and Biomechanics*, 3, Supplement 2, 217-220, 2001.
[2] John A., Orantek P.: Numerical modeling of human pelvic bone. *Proc. Of the 2nd Europian Conference on Computational Mechanics*, Vol. of Abstracts, 2, Kraków, 786-787, 2001.
[3] Stańczyk M., Telega J.J.: The analysis of the PMMA bone cemented polymerisation process within the hip prosthesis fixation – a new approach. *Acta of Bioengineering and Biomechanics*, 5, Supplement 1, 458-463, 2003.

The work was done as a part of research project 4T11F00325 sponsored by Polish Ministry of Science and Information Technology.

SHAKEDOWN SAFETY CRITERION IN RELIABILITY ANALYSIS

Andrzej Siemaszko

Institute of Fundamental Technological Research, PAS; Swietokrzyska 21, PL-00-049 Warsaw, Poland

Summary This paper discusses the problems related to the integration of the shakedown analysis with the reliability analysis. Failure functions with respect to inadaptation (non-shakedown) are defined in the space of random material/geometrical parameters, load multipliers, and directional cosines. Then, a general problem of time-invariant shakedown reliability analysis is formulated. For special cases with low variance of stochastic parameters, simplified formulations are derived and discussed. Separation of load and resistance terms in the failure functions is suggested. The computation can be further simplified since the shakedown response surface may be computed in advance. The problems may be efficiently solved by reliability simulation methods or FORM/SORM combined with a general shakedown analysis algorithm integrated with the Response Surface Method. A practical industrial example of shakedown reliability evaluations is presented.

INTRODUCTION

Inelastic structures such as, for example, pressure vessels and pipelines subjected to variable repeated/cyclic loading may work in four different regimes: elastic, shakedown (adaptation), inadaptation (non-shakedown), and limit (ultimate) state. Since for the elastic regime there are no plastic effects at all, whereas for the adaptation regime the plastic effects are restricted to the initial loading cycles and then they are followed by exclusively elastic behavior, both regimes are considered as safe working ones and they constitute a foundation for the structural design. Hence the shakedown criterion becomes a significant safety criterion for structural design [1].
The structural shakedown takes place due to the development of permanent residual stresses, which, imposed on actual stresses, shift them towards purely elastic behavior. Residual stresses are a result of cinematically inadmissible plastic strains introduced to the structure by overloads or initial pre-stressing. They may avoid any plastic effects in the future, provided that the loads are smaller than the initial overload. Therefore, a memory effect is observed corresponding to maximum loads.

LOADING DOMAINS

Loading is the major factor influencing the structural reliability. Therefore, its proper modeling needs special attention. Unfortunately, the loading history is usually unknown and only its extreme limits are available. Hence, the shakedown approach, for which the knowledge of exact load history is not necessary, provides a powerful analysis platform. It requires stochastic description of maximum loads (envelopes) over each cycle or extreme limits over the lifetime.
The residual stresses assuring the shakedown may be introduced to the structure by initial plastic deformation or, prior to the exploitation, by some technological processes (e.g. heating, test overload) or pre-stressing. Therefore, it is useful to distinguish the induced (inherently) and imposed (externally) shakedown domains [2]. For reliability evaluation the load and above shakedown domains may be compared providing so called failure conditions. We may distinguish the following approaches:

- **shakedown reliability analysis for the imposed shakedown domain** in which the random load domains are compared with the imposed shakedown domain
- **shakedown reliability analysis for the induced shakedown domain** in which the induced shakedown domains (or maximum load domain) are compared with the theoretical maximum (target) domain to which they may be proportionally enlarged still assuring the shakedown.

SHAKEDOWN RELIABILITY PROBLEMS

Besides the loading, also the material and geometrical parameters should be considered as random variables. As a result, the shakedown multiplier, which separates the safe working regime of shakedown from the inadaptation regimes, becomes a random variable. Then, the general structural shakedown reliability problem may be formulated [3]. The probability of failure (or the corresponding reliability index) against inadapatation (non-shakedown) is defined as the probability that the random load multiplier, defined for the maximum loads, does exceed the limits of the target (or the imposed) shakedown multiplier.

For special cases, with low variance of some stochastic parameters, simplified formulations can be derived from the general shakedown reliability problem. They may be conditioned on vector $\boldsymbol{x}$ of geometric/material parameters, in the case they have a very low variance, as well as conditioned on vector $\boldsymbol{a}$ of dominant direction of extreme load domains. It should be noted that they represent the system reliability and may be obtained in a single analysis without the necessity of considering multiple componental reliability subproblems.
The inadapatation (non-shakedown) failure function has a form, which allows to separate, under certain conditions, the load and the shakedown response terms. This allows for computing the shakedown response functions in advance. Moreover, it is shown that the shakedown response function is equivalent to the failure function. It divides the space of parameters into the safe domain and the failure one. It is recommended to apply the Response Surface Method (RSM) to approximate the response functions [4]. Polynomial and exponential approximations are taken into consideration. A numerical code CYCLONE [5] is integrated to compute the shakedown multipliers required in experiments. For illustration, the shakedown reliability problem is solved for a practical example of high-pressure chamber.

CONCLUSIONS

Since obtained by RSM the shakedown response surface is an analytical one and it constitutes simultaneously the failure function, the reliability computation is significantly simplified and extremely efficient. In particular, the simulation or FORM/SORM methods can be used.
Advantages of the presented method, such as working in the X-space, simple formulation in the low-dimensional load space, accounting for global failure criteria corresponding to the system reliability, separate examination of load and strength parameters as well as introduction of response surfaces are discussed in the conclusions. The methodology presented may be easily applied in the reliability design of realistic structures such as pressure systems.

References

[1] König J.A.: Shakedown of elastic-plastic structures. PWN-Elsevier, Warsaw-Amsterdam, 1987.
[2] Siemaszko A.: Shakedown and limit reliability analysis. In: D.Weichert and G.Maier (Eds.), Inelastic behavior of structures under variable repeated loads, Direct analysis methods, CISM Courses and Lectures no. 432, Springer, Wien, New York, 319-376, 2002.
[3] Siemaszko A.: Shakedown and limit reliability analysis. WCCM V Congress on Computational Mechanics, Vienna, 2002.
[4] Knabel J., Bielawski G., Siemaszko A.: Reliability analysis of elastic-plastic structures using response surface methodology. 34 Solid Mechanics Conference, SOLMECH, Zakopane, September 2-7, 2002.
[5] Bielawski G., Siemaszko A., Zwolinski J.: CYCLONE - a system for structural adaptation and limit analysis. In: Inelastic Analysis of Structures under Variable Loads, G.Maier, D.Weichert, Eds., Kluwer, Dordrecht, 135-146, 2000.

XXI ICTAM, 15–21 August 2004, Warsaw, Poland

A NEW FINITE ELEMENT FORMULATION BASED ON THE THEORY OF A COSSERAT POINT

Eiris F. I. Boerner*, Stefan Loehnert*, M. B. Rubin **, Peter Wriggers*
* *IBNM, University of Hanover, Appelstr. 9A, 30167 Hannover, Germany*
** *Technion, Israel Institute of Technology, Haifa 32000, Israel*

Summary A finite element formulation based on the theory of Cosserat points is presented. First attempts reveal, that it is free of showing undesired hourglassing or locking-phenoma and additionally performs well for incompressible materials, large deformations and sensitive geometries. Results of tests of this formulation, that has been developed by [3], are presented, as well as first attempts on how to overcome difficulties with deformed initial meshes.

FE-FORMULATION BASED ON THE THEORY OF A COSSERAT POINT

The theory of Cosserat points is the basis of a finite element formulation, that recently was presented by [3]. Within the theory of Cosserat points, the position vectors $\mathbf{X}$, $\mathbf{x}$ can be described through director vectors $\mathbf{D}_i$, $\mathbf{d}_i$

$$\mathbf{X} = \sum_{i=0}^{7} N^i \mathbf{D}_i, \qquad \mathbf{x} = \sum_{i=0}^{7} N^i \mathbf{d}_i, \tag{1}$$

where N^i are shape functions. The geometry of an 8-node-hexahedral element can henceforth be expressed in terms of eight director vectors in the initial and the current configuration respectively. As opposed to standard shape functions, the functions N^i are here defined as

$$N^0 = 1,\ N^1 = \theta^1,\ N^2 = \theta^2,\ N^3 = \theta^3,\ N^4 = \theta^1\theta^2,\ N^5 = \theta^1\theta^3,\ N^6 = \theta^2\theta^3,\ N^7 = \theta^1\theta^2\theta^3, \tag{2}$$

with θ^i being the coordinates in the reference configuration. The approximation is trilinear as for standard 8-node-hexahedrons, but the resorting of the shape functions enables to split the deformation into homogeneous and inhomogeneous parts. The homogeneous part of the deformation gradient $\mathbf{F}$ is connected to the first three director vectors

$$\mathbf{F} = \sum_{i=1}^{3} \mathbf{d}_i \otimes \mathbf{D}^i. \tag{3}$$

This split requires to find expressions for the material stiffnesses for the homogeneous part of the deformation as well as for each of the inhomogeneous deformation modes. But once this is done, the deformation is decoupled and locking as well as hourglassing-phenomena do not occur. The Cosserat point element does henceforth not require artificial stabilization parameters. Currently, the calculation of the deformation mode related stiffnesses is based on analytical solutions for each of the deformation modes. These analytical solutions however assume a parallelepiped-shaped reference element, with a geometry similar to the initial geometry.

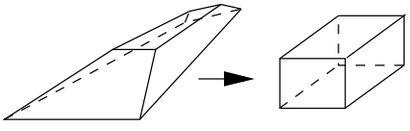


Figure 1: A similar parallelepiped is used to calculate the stiffness of the deformation mode.

This method shows similarities to a class of finite elements using an hour-glass controlled stabilization method, that requires the calculation of artificial stabilization parameters, see e. g. [1], [2], [5] and [4]. Furthermore, stabilized elements require to invert matrices on the element level, which is not necessary for the Cosserat point element.

TESTING THE COSSERAT POINT ELEMENT

The Cosserat point element has been tested concerning a number of different aspects.

- thin structures (beams, shells, plates)
- incompressibility
- distorted elements

These tests have shown, that the performance of the Cosserat point element is excellent for regular shaped elements. It does not show hourglass or locking phenomena but excellent behaviour in case of incompressible materials, for large deformations and in case of sensitive geometries such as shells or plates. One of the tests, which is illustrated in the figure below, is significantly representative for the properties of the Cosserat point element. A cantilever beam is loaded in bending. The beam is discretized with two elements, which are increasingly distorted (Parameter a).

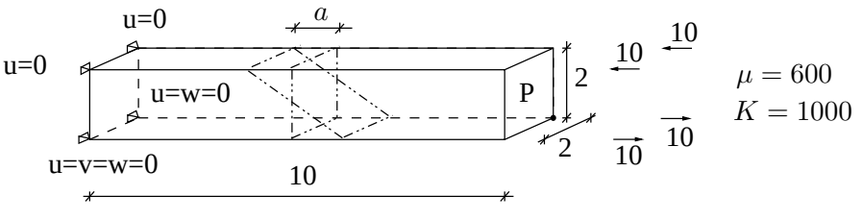


Figure 2: Model of cantilever beam

	Q1	Q1SP	Cosserat	exact
a=0.0	0.28	1.00	1.00	1.00
a=3.0	0.08	0.64	0.16	1.00
a=5.0	0.03	0.03	0.03	1.00

The Cosserat point element gives the exact solution for parallelepiped-shaped elements ($a = 0$), but increasingly wrong results, the more the geometry of the initial mesh differs from a parallelepiped shape. The standard displacement Q1-element locks independently of the shape of the elements.

The difficulty with irregular initial element geometries mainly occurs due to the determination of stiffnesses based on parallelepipeds that are similar to the real element geometry, but might still have an entirely different behaviour in bending or shear. Methods to overcome this difficulty can be based on the numerical analysis of the stiffenss of an irregular shaped element, as well as analytical solutions if those exists.

References

[1] Belytschko, T., Ong, J.S.-J., Liu, W.K. and Kennedy, J.M.: Hourglass control in linear and nonlinear problems. *Computer Methods in Applied Mechanics and Engineering*, 43, (1984), 251-276.

[2] Korelc, J. and Wriggers, P.: Improved enhanced strain 3-D element with taylor expansion of shape functions. *Computational Mechanics*, 19, (1996), 30-40.

[3] Nadler, B. and Rubin, M.B.: A new 3-D finite element for nonlinear elasticity using the theory of a Cosserat point. *International Journal of Solids and Structures*, 40, (2003), 4585-4614.

[4] Reese, S., Wriggers, P. and Reddy, B.D.: A new locking-free brick element technique for large deformation problems in elasticity. *Computers and Structures*, 75, (2000), 291-304.

[5] Wriggers, P. and Korelc, J.: On enahnced strain methods for small and finite deformations of solids. *Computational Mechanics*, 18, (1996), 413-428.

ARC-LENGTH METHOD FOR EXPLICIT DYNAMIC RELAXATION

Ilson P. Pasqualino

Ocean Engineering Department, COPPE – Federal University of Rio de Janeiro, Brazil

Summary The study comprises the use of the arc length method to trace convolute load-deflection paths, typical of buckling problems, in association with dynamic relaxation technique, an explicit iterative method for the static solution of structural mechanics analyses. The work presents some new advances on the combination of these two techniques that are suitable to handle highly nonlinear limit point and snap-through problems.

DYNAMIC RELAXATION

The technique consists of finding the static solution from the transient response of a system excited through a suddenly loading. The dynamic equilibrium equations corresponding to n degrees of freedom of the system are solved for a damping coefficient close to the critical one. After some initial oscillations both velocities and accelerations tend to zero while the vector of displacements approaches to the deformed equilibrium configuration. It is based on the time domain integration of recursive eqs (1) and (2) related to the k^{th} time increment to determine the discrete displacement vector $\boldsymbol{q}$:

$$\dot{\boldsymbol{q}}^{k+1/2} = \frac{(2 - c\Delta t)}{(2 + c\Delta t)}\dot{\boldsymbol{q}}^{k-1/2} + \frac{2\boldsymbol{M}^{-1}\boldsymbol{r}^{k}\Delta t}{(2 + c\Delta t)} \ , \tag{1}$$

$$\boldsymbol{q}^{k+1} = \boldsymbol{q}^{k} + \dot{\boldsymbol{q}}^{k+1/2}\Delta t \qquad \text{and} \tag{2}$$

$$\boldsymbol{r}^{k} = \boldsymbol{P}^{k} - \boldsymbol{F}^{k} \ , \tag{3}$$

where $\boldsymbol{M}$ is a mass diagonal matrix (nxn), $\boldsymbol{r}$ the residual vector, c the damping coefficient and the dot ($\dot{\bullet}$) means derivative in relation to the time t. The residual force vector is the difference between the internal force vector ($\boldsymbol{F}$) and the external load vector ($\boldsymbol{P}$). When the velocity vector $\dot{\boldsymbol{q}}$ approaches to zero the static equilibrium is then assumed. The optimum c, $\boldsymbol{M}$ and Δt parameters may be obtained as proposed by Underwood [1]. A damping coefficient close to the critical one can speed up the convergence that is obtained when $\boldsymbol{r}^{k} \approx 0$.

ARC-LENGTH METHOD

The arc-length method was first introduced by Riks [2] and used by Wempner [3] in order to improve the incremental computations near to limit points. Ramesh and Krishnamoorthy [4] applied the method for the first time in association with the dynamic relaxation to trace load-displacement paths for buckling analyses. A constrain condition based on the norm of the total displacements vector was employed. The method presented good results for truss and beam elements, but was not able to trace the post-buckling behavior of shells, in view of an oscillating response at the unstable equilibrium path. The arc-length method is used to calculate de load increment (δp) that becomes an unknown in the unstable region of the equilibrium path. A constrain condition is added to the n equilibrium equations to obtain the solution of $n+1$ unknowns, the n degrees of freedom and an incremental load intensity factor $\delta\Lambda$. The circular constrain condition proposed by Crisfield [5] was considered suitable to be employed in the dynamic relaxation technique,

$$\left\|\delta\boldsymbol{q}^{k+1}\right\|^{2} + \left(\delta\Lambda^{k+1}\right)^{2} = S^{2} \qquad \text{or} \qquad \sum_{i=1}^{n}\left(\delta q_{m,i}^{k+1}\right)^{2} + \left(\delta\Lambda_{m}^{k+1}\right)^{2} = S^{2} \ , \tag{4a,b}$$

where S means the arc-length and the subscript m the load increment. From eqs. (1) and (2), the components of the incremental vector $\delta\boldsymbol{q}$ may be represented by the following equations:

$$\delta q_{m,i}^{k+1} = \beta\left(\delta q_{m,i}^{k} - \delta q_{m,i}^{k-1}\right) + \delta q_{m,i}^{k} + \frac{\alpha r_{m,i}^{k}}{m_{ii}} \ , \qquad \beta = \frac{(2 - c\Delta t)}{(2 + c\Delta t)} \ , \qquad \text{and} \qquad \alpha = \frac{2\Delta t^{2}}{(2 + c\Delta t)} \ . \tag{5a,b,c}$$

When the theoretical model assumes one single parameter p to represent the applied external force, eq. (6) may be used to represent the external load as a function of a constant reference value (p_{ref}):

$$p_{m}^{k} = \Lambda_{m}^{k+1} p_{ref} \ . \tag{6}$$

If following forces (non-conservative loading) must be considered, the load vector $\boldsymbol{P}$ is given by

$$\boldsymbol{P}_{m}^{k} = \boldsymbol{P}_{m-1} + \delta\boldsymbol{P}_{m}^{k} = p_{m}^{k}\boldsymbol{g}_{m}^{k} \ , \tag{7}$$

where ***g*** is a vector in which the components are displacement functions, therefore

$$\delta \boldsymbol{P}_m^k = \delta p_m^k \boldsymbol{g}_m^k + p_m^k \delta \boldsymbol{g}_m^k = \delta p_m^k \boldsymbol{g}_m^k + \left(p_{m-1} + \delta p_m^k\right)\delta \boldsymbol{g}_m^k = \delta \Lambda_m^{k+1} p_{ref}\left(\boldsymbol{g}_m^k + \delta \boldsymbol{g}_m^k\right) + p_{m-1}\delta \boldsymbol{g}_m^k . \tag{8}$$

Using eqs (3), (7), (8) and (5a), the constrain condition (4b) may be transformed into the following second degree equation:

$$a_1\left(\delta \Lambda_m^{k+1}\right)^2 + a_2 \delta \Lambda_m^{k+1} + a_3 = 0 \ , \qquad \text{where} \tag{9}$$

$$a_1 = \left\|\boldsymbol{a}_m^k\right\|^2 + 1 \ , \qquad a_2 = 2\left(\boldsymbol{a}_m^k \cdot \boldsymbol{b}_m^k\right) \qquad \text{and} \qquad a_3 = \left\|\boldsymbol{b}_m^k\right\|^2 - S^2 \ , \tag{10a,b,c}$$

and the components of the vectors ***a*** and ***b*** are, respectively,

$$a_{m,i}^k = \frac{\alpha}{m_{ii}} p_{ref}\left(g_{m,i}^k + \delta g_{m,i}^k\right) \qquad \text{and} \qquad b_{m,i}^k = \beta\left(\delta q_{m,i}^k - \delta q_{m,i}^{k-1}\right) + \delta q_{m,i}^k - \frac{\alpha}{m_{ii}}\left(P_{m-1,i} + p_{m-1}\delta g_{m,i}^k - F_{m,i}^k\right) . \tag{11a,b}$$

If the discriminant (Δ) of eq. (9) is positive, two real roots will be generated. The correct root must generate the minimum angle (maximum cosine) with the old solution $\delta \boldsymbol{q}_{m-1}$, to prevent the solution from 'doubling back on its tracks' [6]. Therefore, these roots must be used to obtain from eq. (5a) the new incremental displacement vectors $\delta^1 \boldsymbol{q}_m^{k+1}$ and $\delta^2 \boldsymbol{q}_m^{k+1}$. The cosine of the angles θ_1 e θ_2, between the 'new' and the 'old' increments are given by:

$$\cos\theta_1 = \frac{\delta^1 \boldsymbol{q}_m^{k+1} \cdot \delta \boldsymbol{q}_{m-1}}{S^2} \qquad \text{and} \qquad \cos\theta_2 = \frac{\delta^2 \boldsymbol{q}_m^{k+1} \cdot \delta \boldsymbol{q}_{m-1}}{S^2} \ . \tag{12a,b}$$

Unfortunately, near to limit points, the discriminant assumes positive values close to zero and complex roots may occur. To overcome this problem a shift (d) of the constraint condition may be done in the following way

$$\left\|\delta \boldsymbol{q}_m^{k+1}\right\|^2 + \left(\delta \Lambda_m^{k+1} - d\right)^2 = S^2 \ . \tag{13}$$

The correct value of d must generate $\Delta \geq 0$ or

$$\Delta = 4\left(\boldsymbol{a}_m^k \cdot \boldsymbol{b}_m^k - d\right)^2 + 4\left(\left\|\boldsymbol{a}_m^k\right\|^2 + 1\right)\left(S^2 - d^2 - \left\|\boldsymbol{b}_m^k\right\|^2\right) \geq 0 \ . \tag{14}$$

The solution of eq. (14) generates two roots d_1 e d_2 , given by eq. (15). The correct value of d must lie between d_1 and d_2,

$$d_{1,2} = \left\{-\left(\boldsymbol{a}_m^k \cdot \boldsymbol{b}_m^k\right) \pm \sqrt{\left(\left\|\boldsymbol{a}_m^k\right\|^2 + 1\right)\left[\left(\boldsymbol{a}_m^k \cdot \boldsymbol{b}_m^k\right)^2 + \left\|\boldsymbol{a}_m^k\right\|^2\left(S^2 - \left\|\boldsymbol{b}_m^k\right\|^2\right)\right]}\right\} \Big/ \left\|\boldsymbol{a}_m^k\right\|^2 \ . \tag{15}$$

CONCLUSION

The method herein described has been successfully applied to simulate the quasi-static propagation of collapse in submarine pipelines [7]. It was used in combination with the finite difference discretization of the solid structure but applications with the finite element method are also possible [4]. It can be easily adapted to others explicit vector iteration methods and is especially attractive for problems with highly nonlinear geometric and material behavior.

References

[1] Underwood, P.: Dynamic Relaxation. In: Belytschko T., Hughes T.J.R.: Computational Methods for Transient Analysis. North-Holland, Amsterdam, 245-265, 1983.

[2] Riks, E.: On the Numerical Solution of Snapping Problems in the Theory of Elastic Stability. *PhD Thesis*, Dept. Aero/Astronautics, Stanford University, Stanford, 1970

[3] Wempner, G.A.: Discrete Approximations Related to Nonlinear Theories of Solids. *Int. J. Solids Struct.* **7**:1581-1599, 1971.

[4] Ramesh, G., Krishnamoorthy, C.S.: Post-Buckling Analysis of Structures by Dynamic Relaxation. *Int. J. Num. Meth. Eng.* **36**:1339-1364, 1993.

[5] Crisfield, M.A.: A Fast Incremental/Iterative Solution Procedure that Handles Snap-Through. *Computers and Structures* **13**:55-62, 1981.

[6] Crisfield, M.A.: Non-Linear Finite Element Analysis of Solids and Structures. Vol. 1: Essentials. John Wiley & Sons, NY 1991.

[7] Pasqualino, I.P., Estefen, S.F.: A Nonlinear Analysis of the Buckle Propagation Problem in Deepwater Pipelines. *Int. J. Solids Struct.* **38**:8481-8502, 2001.

XXI ICTAM, 15–21 August 2004, Warsaw, Poland

MODELLING OF NON-UNIFORM DEFORMATION OF METALS WITH DISLOCATION CELL STRUCTURE.

E.M. Viatkina*†, W.A.M. Brekelmans*, M.G.D. Geers*†
*Eindhoven University of Technology, Department of Mechanical Engineering, PO Box 513, 5600 MB Eindhoven, the Netherlands
†Netherlands Institute for Metals Research, P.O.Box 5008, 2600 GA Delft, the Netherlands

Summary The hardening behaviour of metals physically originates from a complex microstructure evolution. To describe non-uniform deformation of metals a model of the dislocation cell structure is proposed in this contribution. The material containing cells is modelled to behave like a composite consisting of a periodic array of two types of elements: hard cell walls and soft cell interiors. To ensure compatibility of plastic deformation across the interface between the hard and soft phases, polarised layers of geometrically necessary dislocations are introduced at the interface. The internal stresses created in the material by the geometrically necessary dislocations are taken into account.

The model is capable of describing the material behaviour for monotonic deformation and for deformation with a strain path change. The model predicts the strain path change effect, its dependency on the amount of prestrain and on the amplitude of the strain path change.

INTRODUCTION

The hardening behaviour of metals physically originates from a complex microstructure evolution. This work deals with the contribution of the dislocation cell structure to the mechanical response. The dislocation structure appears at early stages of deformation due to the statistical trapping of dislocations. Cell walls contain dislocation dipoles and multipoles with high dislocation densities and enclose cell-interior regions with a considerable smaller dislocation density. The presence and evolution of such a dislocation arrangement in the material influence the mechanical response of the material and is commonly associated with the transient hardening after strain path changes. The models developed until now to predict the strain path change effects on the basis of the dislocation structure evolution are either too detailed, and thus computationally costly [1], or phemenological [2]. This contribution introduces a continuum model of the dislocation cell structure based on the physics of the dislocation interactions.

CELL STRUCTURE MODEL

As a number of investigators have proposed earlier, e.g. [3], material with a dislocation cell structure is idealised in the present work as a two phase composite of cell walls and cell interiors. The cell wall component represents the phase with the high dislocation density and the cell interior component represents, correspondingly, the areas enveloped by the dislocation walls with the low dislocation density. The cell structure is modelled as a 3D periodic configuration of cuboid cells formed by three mutually perpendicular sets of planar cell walls (Figure 1).

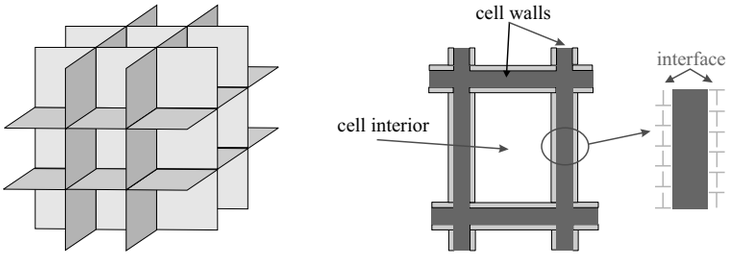


Figure 1. Morphology of the dislocation cell structure: 3D geometry (right), cross section (left).

The heterogeneous distribution of dislocations in the composite structure causes, during external loading, a non-uniform field of plastic strains. To ensure compatibility of the plastic deformation across the interface between the hard and soft phases, polarised layers of geometrically necessary dislocations (GND) will develop at the interface between cell walls and cell interior. It is known that the dislocation network in the material substantially affects the mechanical behaviour by creating internal stresses. In the cell structure model the statistically stored dislocations in the wall and cell interior phases are randomly distributed and therefore induced stress fields will compensate each other. These dislocations do not produce long-range effects. On the contrary the geometrically necessary dislocations are polarised in the interface layers and are, therefore, the source of resulting internal stresses in the material. To compute the internal stresses $\boldsymbol{\beta}$ created by the geometrically necessary dislocations, first, the density of the GND is quantified using the second order Nye's tensor $\boldsymbol{\Lambda}$, and, next,the equilibrium problem for a material with a dislocation distribution $\boldsymbol{\Lambda}(\mathbf{x})$ is solved by the method of Green's functions. In the case of the composite considered here the internal stresses was found analytically as a function of the plastic incompatibility and the composite geometry.

In the presence of the internal stresses the actual stresses $\mathbf{S}$ experienced by the material is the combination of the stresses $\boldsymbol{\sigma}$, applied externally, and the internal stresses $\boldsymbol{\beta}$, induced by the dislocation network. The actual stresses $\mathbf{S}$ are determined by the local material behaviour of the components of the cell structure. As the composite model represents the average behaviour of the entire cell structure developed through a polycrystal, the material behaviour of the cell interior component represents the average material behaviour of all cell interiors in the specimen and the material behaviour in the walls is representative for the average material behaviour of all cell walls. Therefore, the details of the material behaviour as described by dislocation dynamics, slip anisotropy, etc, are assumed to cancel out by averaging and are not taken into account. Thus the material behaviour of the components is modelled to be uniform inside the components and is described by continuum elastoplasticity in the context of geometrical nonlinearity with finite deformations. The material behaviour of the cell and wall components are distinguished by different values of the yield stress related to the local density of dislocations statistically stored in the components.

The macroscopical mechanical behaviour of the entire composite, namely the average applied stress and strain, is determined by spacial averaging of the local quantities. Additional assumptions about the mechanical coupling of the composite components are done to provide deformation compatibility along the interface and stress continuity across the interface.

To summarise, the homogenised mechanical response of the material with the dislocation cell structure can be computed by the following procedure. For a given macroscopic deformation, the actual stresses $\mathbf{S}$ and the plastic deformation of each composite component are determined by the averaging procedure and the elastoplasticity equations for each material component. Then the internal stresses created by the geometrically necessary dislocations are calculated for the found distribution of the plastic deformation. The applied stresses in each composite component can be found by subtracting the internal stresses from the actual stresses and then averaged over the composite to give the macroscopic response of the composite.

RESULTS

To validate the model sequences of two uniaxial tensile tests performed in different directions were considered. The material parameters determining the morphology of the cell structure were identified for copper at room temperature. Calculations proved that significant internal stresses $\boldsymbol{\beta}$ develop through the cell structure and lead to the strain path change effect. The dependence of the reloading yield stress σ^y_Φ (Figure 2) on the amount of prestrain and the angle Φ between the current and previous tension axes are shown in Figure 3.

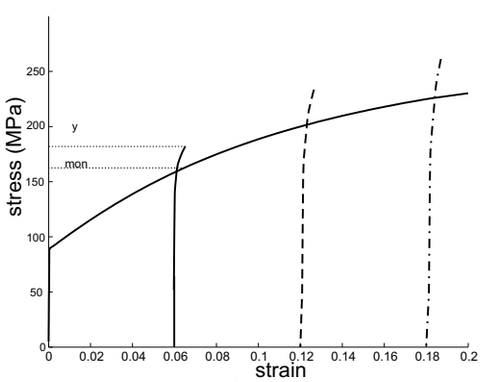


Figure 2 *Calculations of the reloading yield stress. The angle between the two successive tension axes $\Phi = 45°$; prestrain in the first tension $\varepsilon_{pre} = 0.06; 0.12; 0.18$.*

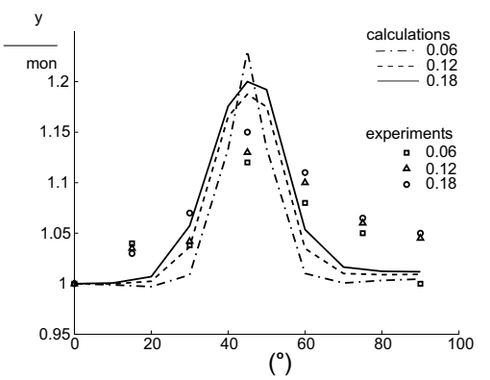


Figure 3 *Strain path change effect. Dependence of the normalised reloading yield stress on the angle between the two successive tension axes Φ. Experimental data from [4].*

CONCLUSIONS

To describe non-uniform deformation of metals a composite model for the dislocation cell structure is proposed. The model takes into account the internal stresses created by the dislocation network during deformation. The model predicts strain path change effects: the increased reloading yield stress, the influence of the direction of the strain change, the influence of the amount of prestrain. To improve the model a physically based evolution of the cell structure geometry should be considered.

References

[1] Peeters B., Seefeldt M., Teodosiu C., Kalidindi S., Van Houtte P., Aernoudt E, *Acta mater.* **49**: 1607-1619, 2001

[2] Teodosiu C., Hu Z.: *in: Simulation of Materials Processeng:Theory, Methods and Applications, Shen & Dawson (eds)*: 1995 Balkema, Rotterdam, 173-182

[3] Mughrabi H.: *Mater. Sci. and Eng.* **85**: 15-87, 1987

[4] Schmitt J.H., Fernandes J.V., Gracio J.J: *Mater. Sci. Eng.* **A147**: 143- 154, 1991.

XXI ICTAM, 15–21 August 2004, Warsaw, Poland

THE NUMERICAL HOMOGENIZATION OF THE CONCRETE BEHAVIOR

Frédéric Grondin[*,**], Hélène Dumontet[**], Abdelwahed Ben Hamida[**], Ghassan Mounajed[*], Hocine Boussa[*]
[*]*Centre Scientifique et Technique du Bâtiment, Division MOCAD, 84 av. Jean Jaurès, 77421 Champs-sur-Marne Cedex 2, France*
[**]*Laboratoire de Modélisation, Matériaux et Structures, CNRS UMR 7143, Université Paris 6, 4 place Jussieu, 75252 Paris Cedex 05, France*

Summary The following extended summary will expose a numerical model using the finite element method to evaluate the concrete homogenized behavior. In this present paper, we describe the model and some results on the damage evolution of a High Strength Concrete subjected to thermal loads.

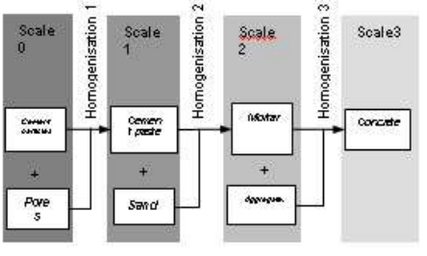
INTRODUCTION

In this research we propose to simulate the cement-based materials behavior subjected to thermal, hydrous and mechanical loads using multi-scales approaches. Multi-scales techniques allow characterizing, from the knowledge of the microstructure, the heterogeneous material behavior by substituting it an equivalent homogeneous material. Using these approaches, it is then possible to reach the local fields and so, to be able to predict and to follow the evolution of the damage within the microstructure. Various homogenization models have been proposed these last years [1]. These models are different of the choice of the Representative Elementary Volume (REV) of the material and the way with which the load is applied. Simplified approaches adopt a REV with simple geometries, and representing only one heterogeneity to give explicitly the equivalent behavior [1]. The homogenization of periodic media is a numerical approach and gives a good approximation of the local fields. It allows to model accurately the microscopic damage [2]. These approaches require, in most of cases, a numerical resolution. Others numerical approaches are based on a more realistic representation of the REV by describing the microstructure of porous media with a random generation of the heterogeneities size distribution [3]. Either by a digital-image-based [3], or by a finite element method [4]. Our numerical method is based on the exploitation of the Digital Concrete model (" Béton Numérique ") [5] developed in the general Finite Element (F.E.) code 'SYMPHONIE'. This model allows the generation of a rich and more realistic REV by considering the heterogeneous microstructure as a multi-phases material. It takes in account the aggregate and pore size distributions. These heterogeneities are generated in a random way inside the REV which is discretized by the finite element method. Here, we present first the numerical aspects concerning the REV grid generation. After, we remind briefly the method of homogenization in the case of a linear thermal-hydro-mechanical problem. The application of the model concerns the study of a High Strength Concrete (HSC) subjected to thermal loads. By using the multi-scales approaches, the global damage is defined by local damages in the microstructure. Finally, the equivalent permeability of the concrete is evaluated as a function of the damage evolution.

THE DIGITAL CONCRETE MODEL

The Digital Concrete implementation

In this method, we consider several scales of modelling: cement paste, mortar, and concrete. The homogenization is needed on each scale to go to the following upper one (scheme below). The local approach is based on the random 'Digital Concrete' model developed by Mounajed [5]. The random character is due to the concrete heterogeneously led by the random aggregate size distribution, and the random pore size distribution in the cement paste. Aggregates and pores have some characteristics different of the solid cement matrix. The proposed approach allows considering the Digital Concrete material as a multi-phases material with successions of n materials phases distributed spatially in a random way. After the model has validated the inclusions position, the finite elements concerning these inclusions are affected by the material characteristics defined by the user. The model verifies that two heterogeneities do not overlap.



Homogenization of a thermal-hydro-mechanical problem

The homogenization principle defines the equivalent homogeneous behavior for heterogeneous materials. The material equivalent homogeneous behavior is given by the following homogenized behavior law [6]: $\boldsymbol{\Sigma} = \mathbf{C}^{\mathbf{hom}} : \left(\mathbf{E} - \alpha^{\mathbf{hom}}\boldsymbol{\Delta}\theta\right)$.

The macroscopic stress field $\mathbf{\Sigma}$ is so defined as the average on the REV of microscopic stresses, solutions of the cellular problem, generated by the imposed macroscopic strain field $\mathbf{E}$. In practice, the rigidity homogenized tensor $\mathbf{C^{hom}}$ and the thermal expansive tensor $\alpha^{\mathbf{hom}}$ are obtained due to the problem linearity. Results obtained appear in good agreement with experimental results [7]. As the same way the equivalent homogeneous permeability tensor ($\mathbf{K^{hom}}$) is then given by the Darcy's law [8].

STUDY OF A HIGH STRENGTH CONCRETE BEHAVIOR

The localization principle constitutes the interest of the homogenization method proposed with regard to certain simplified homogenization approaches. These approaches do not take in account interactions between heterogeneities. In this frame a study of a thermal-mechanical coupling with damage was realized. The Digital Concrete model is coupled with the damage model MODEV developed in SYMPHONIE [9]. The model allows evaluating the global damage according to the local damage evolution in the microstructure. After, the equivalent permeability is calculated and we define a relation between the permeability and the damage of the High Strength Concrete. The localization principle allows evaluating the damage evolution in the microstructure and predicting the failure growth. The follow-up of the drainage at the microscopic scale can turn out of a big interest, in the damage modelling, the role which the water can play in the coupled behavior for these materials. We can imagine this interest to simulate, for example, the microstructure degradation further to high variations in temperature (fires, freeze-thaw . . .).

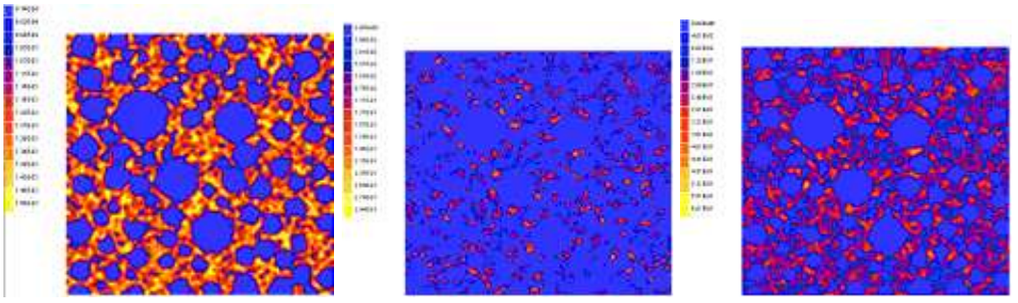


Figure 1. Simulation results for the damage calculus in a HSC under thermal loads (thermal strain fields, damage at $50^{\circ}C$, $120^{\circ}C$)

CONCLUSION

In this research, we adopt a multi-scale approach to identify the thermal-elastic behavior concrete as well as the effect of the damage evolution on the permeability of the material. This is done by using a numerical method based on the Digital Concrete model developed into the general F.E. code SYMPHONIE. It allows characterizing the concrete homogenized behavior under a thermal-mechanical load by a multi-scales approach. We take in account random heterogeneities size distributions at the mortar scale and at the concrete scale. The obtained simulations results confront in a completely encouraging way with experimental results [10]. Furthermore, this method allows reaching the strain fields and the stress fields which reign in the microstructure. The damage evolution is observed with a micro-mechanical analysis. Recent studies allow determining the equivalent permeability of the HSC, from the permeability of material constituents.

References

[1] Bornert M., Bretheau T., Gilormini P.: Homogénéisation en mécanique des matériaux. *Tome 1*. Hermès Sciences Publications, Paris 2001.

[2] Ben Hamida A., Dumontet H., Léné F.: Modelization of the failure surface of syntatic foams by a micro-macro approach. *ICC9*, July 1-6, San Diego 2002.

[3] Bentz D. P., Garboczi E.J., Martys N.S.: Application of Digital-Image-Based Models to Microstructure, Transport Properties, and Degradation of Cement-Based Materials. *Modelling of Microstructure and Its Potential for Studying Transport Properties and Durability*, Kluwer Academic Publishers, Jennings H. Editor, 167-185, 1996.

[4] Breunese A.: Tensile properties of concrete during fi re. *Master's thesis*, Delft University of Technology, 2001.

[5] Mounajed G.: Exploitation du nouveau modèle Béton Numérique dans Symphonie : Concept, homogénéisation du comportement thermomécanique des BHP et simulation de l'endommagement thermique. *Cahiers du CSTB*, **3421**, 2002.

[6] Frankfort G.: Homogeneization and thermoelasticity. *Journal of Mathematics Analysis*, SIAM, **14**: 696-708, 1983.

[7] Ben Hamida A., Dumontet H., Grondin F., Mounajed G.: Le Béton Numérique : Une approche multi-échelles pour le comportement du béton. *Congrès Français de Mécanique 2003*, 1-5 Septembre, Nice 2003.

[8] Gomez-Hernandez J.J.: A stochastic approach to the simulation of block conductivity fi elds conditioned upon data measured at a smaller scale. *Ph.D*, Stanford University, 1991.

[9] Mounajed G., Ung Quoc H., Mesureur B.: New tangent formulation of the concrete damage model " MODEV ". *Werner Fuchs, Hans-Wolf Reinhardt, Rolf Eligehausen au 60ème anniversaire*, Geburtstag, ibidem-Verlag, Stuttgart 2002.

[10] Stabler J., Baker G.: On the form of free energy and specifi c heat in coupled thermo-elasticity with isotropic damage. *International Journal of Solids and Structures*, **37**:4691-4713, 2000.

DISCRETE DISLOCATION CALCULATIONS OF THE STORED ENERGY OF COLD WORK

A. Amine Benzerga*, Yves Bréchet**, Alan Needleman***, Erik van der Giessen+
* *Department of Aerospace Engineering, Texas A&M University, College Station, TX 77843-3141*
** *LTPCM, 1130 Rue de la Piscine, BP 75, Domaine Universitaire, 38402*
*** *Division of Engineering, Brown University, Providence, RI 02912, USA*
+ *Dept. of Appl. Physics, Univ. of Groningen, Nyenborgh 4, 9747 AG Groningen, The Netherlands*

Summary The stored energy of cold work is calculated for single crystals deformed in plane strain tension and bending. Plastic deformation occurs through dislocation glide. Superposition is used to represent the solution of boundary value problems in terms of the infinite fields for discrete dislocations and image fields that enforce boundary conditions. Constitutive rules are used which account for the effects of 3D dislocation dynamics such as dynamic junction formation. The change in free energy with a change in dislocation positions at constant stress can be explicitly calculated with the line energy contribution accounted for. The extent to which the energy stored in the sample depends on the deformation state is analyzed.

INTRODUCTION

When a material sample is cold-worked, most of the mechanical energy expended is converted into heat and the remainder is stored in the sample, thereby altering its free energy. In single crystals, energy storage is essentially due to dislocations. Here the stored energy due to plastic deformation is calculated as the change in free energy with a change in dislocation positions at constant stress. Such calculations are made feasible by solving boundary value problems where plastic behavior results from the motion and interaction of large numbers of dislocations. These are modeled as linear defects in an isotropic elastic solid and superposition is used to accurately account for the image fields which correct for actual boundary conditions [1]. Dislocation interactions at short range are treated as in [2]. 2D plane strain problems are formulated for the sake of computational efficiency as in [1], but account is taken of 3D dynamic processes such as junction formation and destruction and dynamic source operation. The stored energy calculations are illustrated for two deformation states: tension and bending.

FORMULATION

Calculations are carried out for a planar fcc 6μm$\times 2\mu$m crystal. In tension the calculations of [2] are supplemented by unloading sequences at strain intervals of 0.01. In bending a special numerical procedure is used to assure vanishing of the axial force and unloading sequences are carried at rotation intervals of 0.015. The stored energy rate is equal to the free energy rate, which can be readily calculated using the elastic solution of the boundary value problem. Part of that stored energy is recoverable upon unloading and represents the elastic portion of it. The other portion represents the portion of the plastic work that is not converted into heat but stored in the dislocation structure. The stored energy is calculated both in the unloaded state, as in experiments, and in the loaded state. Initial conditions and material parameters correspond to the crystal labeled B in [2].

RESULTS

Loading response

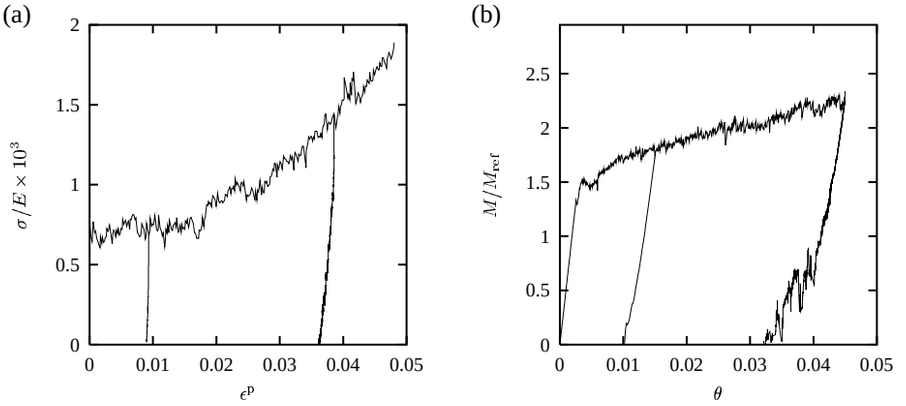


Figure 1. Response in (a) tension and (b) bending ($M_{\rm ref} = 33.3\mu$Nm/m).

The response in tension shown in Fig. 1(a) exhibits a two-stage hardening as is usually the case for crystals oriented so

that only one slip system is initially activated. The figure also illustrates two unloading sequences from a total strain of 0.01 and 0.04. During the linear stage II hardening a rough cell structure develops so that, upon unloading, reverse yielding occurs while the sample is still in tension. This indicates a strong Bauschinger effect, which almost disappears in the absence of a dislocation structure as detailed elsewhere.

Figure 1(b) shows the moment versus rotation response in bending of the same sample including unloading after $\theta = 0.015$ and $\theta = 0.045$. Here hardening is linear throughout and, after a sufficient amount of bending prior to unloading, reverse yielding is clearly seen while the global moment is still positive. A dislocation structure develops regardless of the density of dynamic junctions. Long arrays of like-signed dislocations are formed on each slip system to accommodate the imposed strain gradient. Those arrays define a density of geometrically necessary dislocations. In [3] it was shown that about 80% of the dislocations are GNDs up to a bending angle $\theta = 0.06$. More recent calculations pursued up to $\theta = 0.12$ clearly demonstrate that the GNDs dominate the global moment-rotation response even at higher angles where the GND density becomes as low as 20% of the total density.

Stored energy

In order to compare the behavior under the two deformation states (tension and bending) the stored energy under load, E^{s}, is plotted in Figure 2(a) against the total work, E^{w}, expended in deforming the crystal. For a given supplied E^{w} it appears that the *rate* of energy storage *under load* is independent of the state of deformation. This is remarkable given that the loading response (Fig. 1 above) and the dislocation structure are very different in tension and bending.

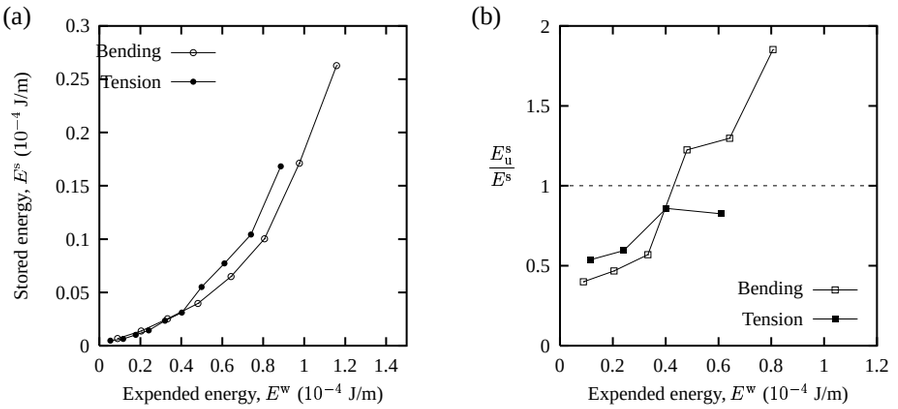


Figure 2. Energy storage under two deformation states, tension and bending. (a) Stored energy, E^{s}, versus expended energy, E^{w}. (b) Ratio of stored energy in the unloaded state, $E^{\mathrm{s}}_{\mathrm{u}}$, to E^{s} versus E^{w}.

Upon unloading, however, the rate of energy storage is found to be dependent upon the deformation state. This is best illustrated by considering the stored energy after load removal, $E^{\mathrm{s}}_{\mathrm{u}}$, relative to the stored energy under load, E^{s}, for a given supplied mechanical energy E^{w}. As shown in Fig. 2(b), a significant fraction of the stored energy is released in tension upon unloading. By way of contrast, energy release after unloading in bending only occurs at low values of the bending angle. Depending on the amount of supplied external energy, the energy stored in the unloaded state can be smaller or higher than that of the loaded state.

CONCLUSIONS

The loading response (flow stress, hardening and unloading) is controlled by the density of statistical dislocations in tension and by the density of GNDs in bending. In bending, however, the build-up of a statistical density strongly affects the magnitude of energy stored in the bent sample after load removal. This suggests important consequences for recrystallization in bending in comparison with tensile loading.

References

[1] Van der Giessen E., Needleman A.: Discrete Dislocation Plasticity: a Simple Planar Model. *Modell. & Sim. Mater. Sci. Engrg.* **3**:689–735, 1995.

[2] Benzerga A.A., Bréchet Y., Needleman A., Van der Giessen E.: Incorporating Three-dimensional Mechanisms into Two-dimensional Dislocation Dynamics. *Modell. & Sim. Mater. Sci. Engrg.* **12**:159–196, 2004.

[3] Benzerga A.A., Needleman A., Bréchet Y., Van der Giessen E.: Discrete Dislocation Predictions of Single Crystal Hardening: Tension vs Bending. Kluwer academic press, 2003.

DEFORMATION ANALYSIS OF INFLATED CYLINDRICAL MEMBRANE OF COMPOSITE MATERIAL WITH RUBBER MATRIX REINFORCED BY CORDS

Tran Huu Nam and Bohdana Marvalová [*]

[*]*Department of Mechanics & Stress Analysis, TU Liberec, Hálkova 6, 461 17 Liberec, Czech Republic*

Summary An orthotropic hyperelastic constitutive model is proposed which can be applied to numerical simulation for the response of the nonlinear anisotropic hyperelastic material of the air-spring sheet used in inhibitive vibration of driver's seat and of the biological soft tissue. The parameters of strain energy function are fitted to the experimental results by the nonlinear least squares method. The deformation field of inflated cylindrical membrane of air-spring sheet is calculated by solving the system of five first-order ordinary differential and by the finite element method (FEM). Stability analysis is carried out in finite element analysis (FEA) to detect limit points by arc-length method.

INTRODUCTION

Recently, classical phenomenological constitutive equations for rubber-like solids, such as Mooney–Rivlin, Neo-Hookean or Ogden models (Holzapfel, 2000; Guo, 2001) are progressively replaced by more physical models based on statistical considerations in various engineering applications.

The main purpose of the authors is the numerical simulation of inflated cylindrical membrane of the composite made of rubber matrix reinforced by textile cords. The deformation field is determined by the method of the numerical integration of the system of the ordinary differential equations described recently for isotropic membrane by Guo (2001) and the FEM described by Shi-Moita (1996) and Verron et al (2001).

MATERIAL DESCRIPTION AND EXPERIMENTAL ANALYSIS

The material of air-spring sheet considered here is created from rubber matrix reinforced by textile cords to be called rubber-textile cord composite. The air-spring sheet is usually made up of four layers – the inner and the outer liner of calandered rubber and the two plies of cord reinforced rubber in which the cords have a specific bias angle to the other arranged symmetrically with respect to the circumferential direction. The cylindrical air-spring is relatively short – the diameter of the tubular sheet is 2R=80 mm, the height is L=120 mm and the wall thickness is H=2mm.

The experimental tests were carried out at five different positions of the air-spring. First the mounting plates of the non-loaded air-spring were fixed at the distance by 15, 20, 30, 40 or 50 mm shorter than the free height of the sheet. Then the air-spring was loaded and unloaded gradually by pressurized air step 0.05MPa in the range 0.1–0.5MPa. Photographs of the deformed sheet were recorded by digital camera, the axial force and the inner pressure were measured and stored at every stage of loading.

AN ORTHOTROPIC HYPERELASTIC CONSTITUTIVE MODEL

The orthotropic hyperelastic materials in this paper are considered incomprresible composite materials with two families of fibers. Let's assume that the isochoric deformation and neglect the dissipation due to irreversible effects. The strain energy function of these materials is considered the combination of scalar-value functions corresponding to energy stored in matrix material (isotropic) and the fibers (anisotropic) parts.

$$\Psi(\lambda_1,\lambda_2)=\sum_{i=1}^{3}\frac{\mu_i}{\alpha_i}\left(\lambda_1^{\alpha_i}+\lambda_2^{\alpha_i}+\lambda_1^{-\alpha_i}\lambda_2^{-\alpha_i}-3\right)+\frac{k_1}{k_2}\left\{\exp[k_2(\lambda_2^2\cos^2\alpha+\lambda_1^2\sin^2\alpha-1)^2]-1\right\} \quad (1)$$

where λ_1 and λ_2 are the axial and circumferential stretches respectively, and the angle of the two families of reinforcing cords α is supposed to be 48.8^o. The parameters μ_i and α_i of Ogden's model of rubber (Holzapfel, 2000) are μ_1 = 630kPa, μ_2 = 1.2kPa, μ_3 = -10kPa, α_1 = 1.3, α_2 = 5, α_3 = -2. The stress-like parameter k_1 and the non-dimensional parameter k_2 are determined from the experimental results.

IDENTIFICATION OF MATERIAL PARAMETERS

The constitutive equations between Cauchy stresses and stretches are represented through strain energy function Ψ as

$$\sigma_1-\sigma_3=\lambda_1\frac{\partial\Psi(\lambda_1,\lambda_2)}{\partial\lambda_1},\ \sigma_2-\sigma_3=\lambda_2\frac{\partial\Psi(\lambda_1,\lambda_2)}{\partial\lambda_2}. \quad (2)$$

The quasi-static equilibrium equations applied to various inflated structures are

$$\frac{d}{ds}(T_1 r)=T_2\frac{dr}{ds},\quad \kappa_1 T_1+\kappa_2 T_2=p\ . \quad (3)$$

where κ_1 and κ_2 are principal curvatures for the deformed membrane surface. T_1 and T_2 are the stress resultant forces per unit length of the meridional and circumferential directions: $T_1=h(\sigma_1-\sigma_3), T_2=h(\sigma_2-\sigma_3)$ (4)

From above constitutive equations and equilibrium equations after some transformations we obtain the system of nonlinear equations for the two variables k_1 and k_2. We solved this system of equations with experimentally measured values of λ_1 and λ_2 and obtained the parameters k_1 = 4.187e+04kPa and k_2 = -23.775.

DEFORMATION ANALYSIS OF INFLATED CYLINDRICAL MEMBRANE COMPOSITE

Determination of deformation of cylindrical membrane by numerical integration

After some substitutions and simplifications we obtained the system of five ordinary differential equations for the principal stretches λ_1 and λ_2, the tangent angle θ, the coordinate x in the deformed configuration and the inner pressure p with respect to the coordinate X of the undeformed configuration. We solved this system of differential equations by the shooting method in Matlab with the boundary condition determined from the experiments. The results are at the Fig. 1 where deformed profiles of membrane are compared with experimental one.

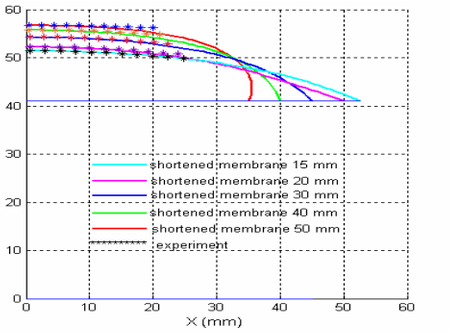


Fig.1 The deformed profiles of cylindrical membrane subjected to inner pressure p=0.5MPa

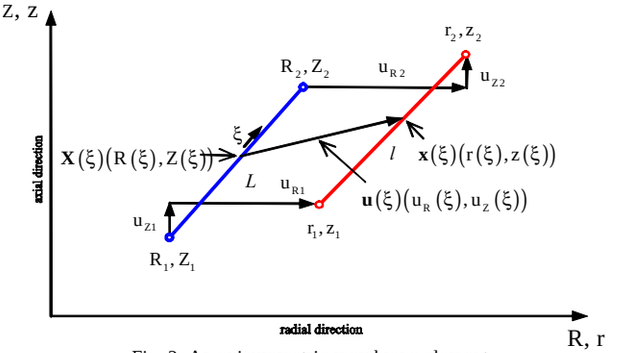


Fig. 2. An axisymmetric membrane element

Determination of deformation of cylindrical membrane by FEM

The axisymmetric membrane element that has length of L and thickness of H in the reference configuration and length of l in the current configuration is presented in Fig.2. This element has two nodes and vector node displacement $\mathbf{u}=\{u_{R1},u_{Z1},u_{R2},u_{Z2}\}^T$. Green-Lagrange (GL) deformation tensor $\mathbf{E}$ and second Piola-Kirchhoff (PK2) strain tensor $\mathbf{S}$ are used in the form of conjugate pair in order to express the formulation of strain energy in the Lagrangian description. The elastic tensor $\mathbb{C}$ is determined from principal components of PK2 (see Holzapfel, 2000, pp. 258).

$$\mathbb{C}=\frac{\partial \mathbf{S}}{\partial \mathbf{E}},\quad \mathbb{C}=\begin{bmatrix} \frac{1}{\lambda_1}\frac{\partial S_{11}}{\partial \lambda_1} & \frac{1}{\lambda_2}\frac{\partial S_{11}}{\partial \lambda_2} \\ \frac{1}{\lambda_1}\frac{\partial S_{22}}{\partial \lambda_1} & \frac{1}{\lambda_2}\frac{\partial S_{22}}{\partial \lambda_2} \end{bmatrix},\quad \mathbf{S}=\mathbb{C}\mathbf{E} \qquad (5)$$

The principle of virtual work can be expressed through introduction of the external load factor λ as

$$R(\mathbf{u},\delta\mathbf{u},\lambda)=\mathbf{R}(\mathbf{u},\lambda)^T\cdot\delta\mathbf{u}=(\mathbf{f}_{\text{int}}(\mathbf{u})-\lambda\mathbf{f}_{\text{ext}}(\mathbf{u}))^T\cdot\delta\mathbf{u} \qquad (6)$$

The stiffness matrix $\mathbf{K}_t$ is expressed in the following form: $\mathbf{K}_t=\left[\frac{\partial \mathbf{f}_{\text{int}}}{\partial \mathbf{u}}-\lambda\frac{\partial \mathbf{f}_{\text{ext}}}{\partial \mathbf{u}}\right]$ (7)

Nonlinear numerical solution: The incremental-iterative approach described here is based on a combination of the modified Newton-Raphson method and the arc-length method, meaning that the tangent stiffness matrix and internal force vector and external force vector are not only updated at the commencement of each load step, but also at every iterative cycles. Numerical simulated results are obtained by predictor-corrector method using Matlab software. The equilibrium path is obtained to overcome the limit points (Fig. 3 and Fig. 4).

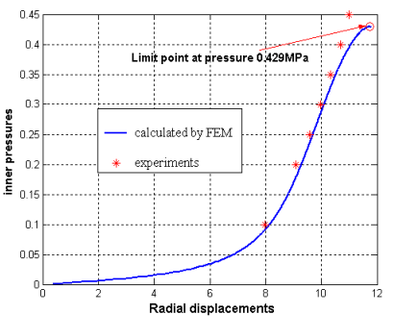


Fig.3 The internal pressure - radial displacement path in the case of free heads

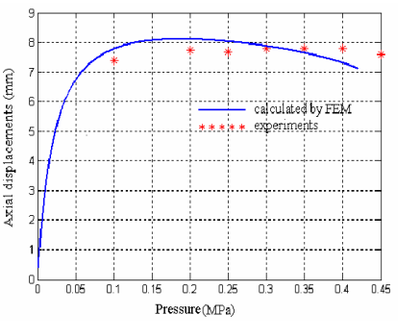


Fig.4 The internal pressure - axial displacement path in the case of free heads

CONCLUSIONS

The deformations of the nonlinear composite membrane were determined experimentally. The problem of the identification material parameters was solved. The deformations were determined by numerical integration based on the membrane theory and by FEM. Numerical results for simulation of the inflated cylindrical membrane are obtained answering by experimental responses.

Acknowledgement

This work was realized in the framework of the project MŠMT CEZ: MSM 242100003 „*Interakce vibroizolačního objektu s člověkem a okolním prostředím*". Financial support was provided by the Czech Ministry of Education, Youth and Sports.

References

[1] Guo, X., (2001), Large deformation analysis for a cylindrical hyperelastic membrane of rubber-like material under internal pressure, Rubber chemistry and technology 74, 100-115.

[2] Holzapfel G.A., (2000), Nonlinear solid mechanics, John Wiley & Sons Ltd, Baffins Lane, Chichester West Sussex PO19 1UD, England.

[3] Shi J., Moita G.F., (1996), The post-critical analysis of axisymmetric hyper-elastic membranes by finite element method, Comput. Methods Appl. Mech. Engrg, 135, 265-281.

[4] Verron E., Marckmann G., (2001), An axisymmetric B-spline model for the non-linear inflation of rubberlike membranes, Comput. Methods Appl. Mech. Engrg., 190, 6271- 6289.

DYNAMIC ANALYSIS OF GRADIENT ELASTIC SOLIDS BY BEM

Demosthenes Polyzos[*], Katerina G. Tsepoura[*], Dimitri E. Beskos[**]
[*]*Department of Mechanical and Aeronautical Engineering, University of Patras, GR-26500 Patras, Greece*
[**]*Department of Civil Engineering, University of Patras, GR-26500 Patras, Greece*

Summary A frequency domain boundary element method is presented for the harmonic and transient dynamic response analysis of three-dimensional solids exhibiting linear elastic material behavior coupled with microstructural effects taken into account with the aid of a simple gradient elastic theory. Numerical examples are presented and the gradient elasticity effect on the response is assessed.

Extended Summary

The classical theory of linear elasticity cannot describe satisfactorily the mechanical behavior of linear elastic materials with microstructure, such as polymers, polycrystals or granular materials. In these materials microstructural effects are important and the state of stress has to be defined in a nonlocal manner. One way of successfully modeling these microstructural effects in a macroscopic manner is by using higher-order strain gradient theories.

In this work a simple form of the strain gradient theory due to Mindlin [1, 2] is employed of the form

$$\tilde{\boldsymbol{\sigma}} = \tilde{\boldsymbol{\tau}} + \tilde{\mathbf{s}} \tag{1}$$

$$\tilde{\boldsymbol{\tau}} = 2\mu\tilde{\mathbf{e}} + \lambda(\nabla\cdot\mathbf{u})\tilde{\mathbf{I}}, \qquad \tilde{\mathbf{e}} = (\nabla\mathbf{u} + \mathbf{u}\nabla)/2 \tag{2}$$

$$\tilde{\mathbf{s}} = -\nabla\cdot\tilde{\boldsymbol{\mu}}, \qquad \tilde{\boldsymbol{\mu}} = g^2\nabla\tilde{\boldsymbol{\tau}} \tag{3}$$

where $\tilde{\boldsymbol{\sigma}}$ is the total stress tensor, $\tilde{\boldsymbol{\tau}}$ and $\tilde{\mathbf{s}}$ are the Cauchy stress and relative stress tensors, respectively, $\tilde{\mathbf{e}}$ is the strain tensor, $\mathbf{u}$ is the displacement vector, $\tilde{\boldsymbol{\mu}}$ is the double stress tensor, g^2 is the volumetric strain gradient energy coefficient and λ and μ are the Lamè constants. The above constitutive model has been successfully used in a boundary element formulation for the static analysis of 2-D and 3-D gradient elastic solids (Polyzos et al [3]). In this work this methodology is extended to the dynamic case.

The frequency domain equation of motion of a gradient elastic body with material behavior described by eqs (1) – (3) takes the form

$$\mu\nabla^2\mathbf{u} + (\lambda+\mu)\nabla\nabla\cdot\mathbf{u} - g^2\nabla^2\left(\mu\nabla^2\mathbf{u} + (\lambda+\mu)\nabla\nabla\cdot\mathbf{u}\right) + \mathbf{f} + \rho\omega^2\mathbf{u} = 0 \tag{4}$$

where $\mathbf{u}$ now represents the displacement amplitude, ω is the excitation frequency, ρ the mass density and $\mathbf{f}$ the body force.

A variational statement is used to re-derive the equation of motion (4) as well as to determine all possible classical and non-classical (due to gradient terms) boundary conditions of the general boundary value problem in the frequency domain.

The gradient frequency domain elastodynanic fundamental solution is explicitly derived and used to construct the boundary integral representation of the problem with the aid of a reciprocal integral identity. In addition to a boundary integral representation for the displacement, a boundary integral representation for its normal derivative is also necessary for the complete formulation of a well posed problem. These two boundary integral equations for zero body forces and a smooth boundary S read

$$\frac{1}{2}\mathbf{u} + \int_S \left(\mathbf{P}^*\cdot\mathbf{u} - \mathbf{U}^*\cdot\mathbf{p}\right)dS = \int_S \left[\mathbf{Q}^*\cdot\mathbf{R} - \mathbf{R}^*\cdot(\partial\mathbf{u}/\partial n)\right]dS \tag{5}$$

$$\begin{aligned}\frac{1}{2}(\partial\mathbf{u}/\partial n) + \int_S \left[\left(\partial\mathbf{P}^*/\partial n\right)\cdot\mathbf{u} - \left(\partial\mathbf{U}^*/\partial n\right)\cdot\mathbf{p}\right]dS = \\ = \int_S \left[\left(\partial\mathbf{Q}^*/\partial n\right)\cdot\mathbf{R} - \left(\partial\mathbf{R}^*/\partial n\right)\cdot(\partial\mathbf{u}/\partial n)\right]dS\end{aligned} \tag{6}$$

where $\mathbf{u}$ and $\mathbf{p}$ are the displacement and traction vector amplitudes, n is the unit normal vector and $\mathbf{U}^*, \mathbf{P}^*, \mathbf{Q}^*$ and $\mathbf{R}^*$ are kernels of the gradient elastodynamic fundamental solution in the frequency domain.

The discretization of the body, restricted only to its boundary, is accomplished with the aid of surface quadratic quadrilateral boundary elements. Thus, eqs (5) and (6) are written in discrete form and after collocation and employment of the boundary conditions, the resulting system of equations is solved numerically for the given operational frequency to obtain the harmonic response. For the transient excitation case, the problem is solved in the frequency domain for a sequence of values of the frequency parameter and the transient response is obtained in the time domain by a numerical inversion of the frequency domain solution through the fast Fourier transform algorithm.

Two numerical examples serve to illustrate the method, demonstrate its accuracy and assess the gradient effect on the response. The two examples deal with the response of a spherical cavity embedded in an infinite gradient elastic medium to a uniform external pressure a) harmonically varying with time and b) of the step pulse type. The accuracy of the numerical results as compared to those of the analytic solution obtained by the authors is excellent. It is also observed that the response decreases with increasing values of the gradient coefficient in both cases.

References

[1] Mindlin R.D.: Microstructure in Linear Elasticity. *Arch. Rat. Mech. Anal.* **10**: 51-78, 1964.

[2] Mindlin R.D.: Second Gradient of Strain and Surface Tension in Linear Elasticity. *Int. J. Solids Struct.* **1**: 417-438, 1965.

[3] Polyzos D., Tsepoura K.G., Tsinopoulos S.V., Beskos D.E.: A Boundary Element Method for Solving 2-D and 3-D Static Gradient Elastic Problems, Pt I: integral formulation, Pt II: numerical implementation. *Comp. Meth. Appl. Mech. Engngn* **192**: 2845-2873 & 2875-2907, 2003.

VARIABLE-ORDER SINGULAR BOUNDARY ELEMENT FOR CALCULATION OF THREE-DIMENSIONAL STRESS INTENSITY FACTORS

Kian-Meng Lim [*], Wei Zhou [**], Andrew A.O. Tay [*]
[*] *Mechanical Engineering Department, National University of Singapore, Singapore*
[**] *R&D, Micron Semiconductor Asia Pte Ltd, Singapore*

Summary A new variable-order singular boundary element has been developed for stress analysis of three-dimensional cracks and multi-material junctions. The singular element shape functions include the variable orders of singularity and the angular profiles of the field variables. The stress intensity factors are formulated as nodal unknowns and are obtained directly from the final system of equations without the need of post processing, such as three-dimensional J-integral.

INTRODUCTION

Stress singularities often occur in cracks and dissimilar material corners. Such singular stress fields are generally three-dimensional in character. The stress intensity factor is a function of the position along the line of singularity and not a constant as commonly determined in two-dimensional solutions. However, three dimensional stress singularity problems are more complicated to analyze compared to their two-dimensional counterparts. The finite element method [1, 2] and boundary element method [3] are commonly used. In this paper, we present a new variable-order singular boundary element that provides efficient and accurate solutions for three-dimensional stress singularity problems.

VARIABLE-ORDER SINGULAR ELEMENT FORMULATION

The formulation for the current three-dimensional singular boundary element is an extension of that of the two-dimensional singular element [4]. The singular field in the vicinity of the line of singularity is assumed to be dominated by a combination of two in-plane and one out-of-plane singular modes, with the stress intensity coefficients varying along the line of singularity. The variable orders and angular field profiles are obtained separately from asymptotic singularity analysis. These asymptotic solutions form the basis of the shape functions in the new singular element. Both asymptotic stress and displacement fields are represented simultaneously for a better accuracy even in a very coarse mesh.

The intrinsic coordinates (ξ, η) of the singular element are chosen such that the singular profiles lie in planes parallel to the η direction, while the stress intensities vary along the ξ direction. The tractions and displacements in the singular element are expressed as a combination of the singular fields and the non-singular polynomials as

$$t_i = \sum_{h=1}^{3}(a_{1h} + a_{2h}\xi + a_{3h}\xi^2)r^{\lambda_h - 1}p_{ih}(\theta) + a_4 + a_5\xi + a_6\eta + a_7\xi\eta + a_8\xi^2 + a_9\xi^2\eta$$

$$u_i = \sum_{h=1}^{3}(b_{1h} + b_{2h}\xi + b_{3h}\xi^2)r^{\lambda_h}q_{ih}(\theta) + b_4 + b_5\xi + b_6\eta + b_7\xi\eta + b_8\xi^2 + b_9\xi^2\eta$$

where t_i and u_i are the i^{th} component of the traction and displacement at the coordinate (ξ, η) respectively, and a_{jh}, a_j, b_{jh}, b_j (j=1 to 9) are independent coefficients to be determined. The first part in the equations represents the contribution from the singular fields in which the stress intensity coefficients are assumed to have a quadratic variation along ξ, and the order of singularity λ_h and the angular profiles $p_{ih}(\theta)$ and $q_{ih}(\theta)$ are assumed to be unchanged along the crack front. The second part includes non-singular polynomial terms which are obtained according to the sequence in the Pascal triangle. The coefficients are subsequently expressed in terms of the displacements, tractions and stress intensity factors at the nodes. The resulting expressions associated with these nodal quantities then give the shape functions for displacement and traction at each node.

The new singular surface elements replace the conventional elements adjacent to the line of singularity. Transition elements are not required because the singular elements are made naturally compatible with adjacent normal quadratic boundary elements. The stress intensity factors are formulated as nodal unknowns along the line of singularity and they can be directly obtained from the solution process of the boundary element method. The post-processing step commonly used in the literature, is not necessary in this case.

NUMERICAL EXAMPLES

First, a penny-shaped crack (radius c=0.08b) in a homogenous cube (Figure 1a) under remote tension is analyzed. Only one-eighth of the cube is modeled and a relatively coarse boundary element mesh is used. In the vicinity of the crack front, only six elements are used on each side of the crack front. The singular element gives accurate results (Figure 1b) for the mode I stress intensity factor K_I which is within 5% of the analytical value K_0 [5].

Next, the versatility of the singular element in handling various orders of singularity is illustrated using a bi-material system with a through-thickness inclusion under remote tension (Figure 2a). Singular fields occur at the fully bonded

internal corner and the various orders of singularities are present: λ_1=0.798, λ_2=0.786 and λ_3=0.732. The equivalent stress intensity factors F are defined here along the horizontal interface: $t_y = r^{\lambda_1 - 1} F_I \sigma_0 + r^{\lambda_2 - 1} F_{II} \sigma_0$ and $t_z = r^{\lambda_3 - 1} F_{III} \sigma_0$. The variations of the stress intensity factors through the thickness are determined. Figure 2b shows the results for the three modes. Plane strain conditions are also simulated by imposing symmetric boundary conditions on both the surfaces z/t=0 and z/t=0.5 and the results are included for comparison. It is found that the three-dimensional results for modes I and II are very close to the plane strain solutions for most part of the internal edge, while the intensity for mode III increases from the mid-plane z/t=0 to the free surface z/t=0.5.

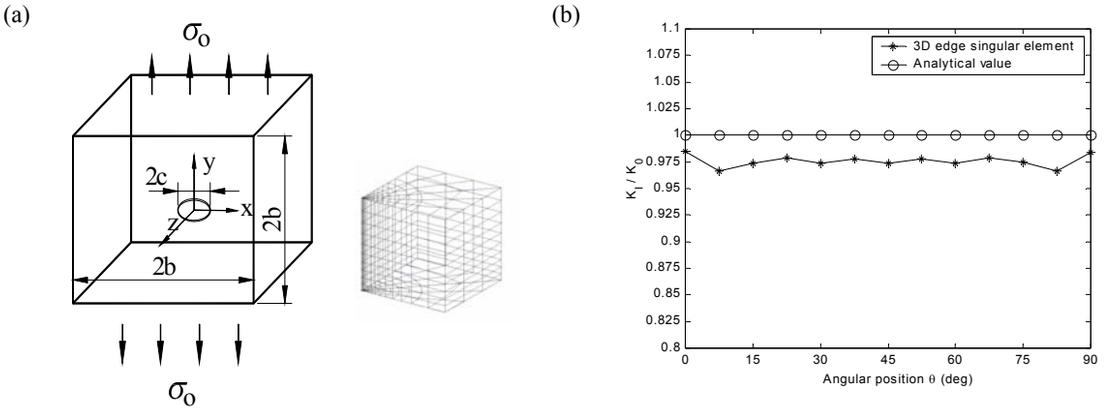


Figure 1: (a) Penny-shaped crack in homogeneous medium and the one-eighth model mesh. (b) Magnitude of stress intensity factor along crack front.

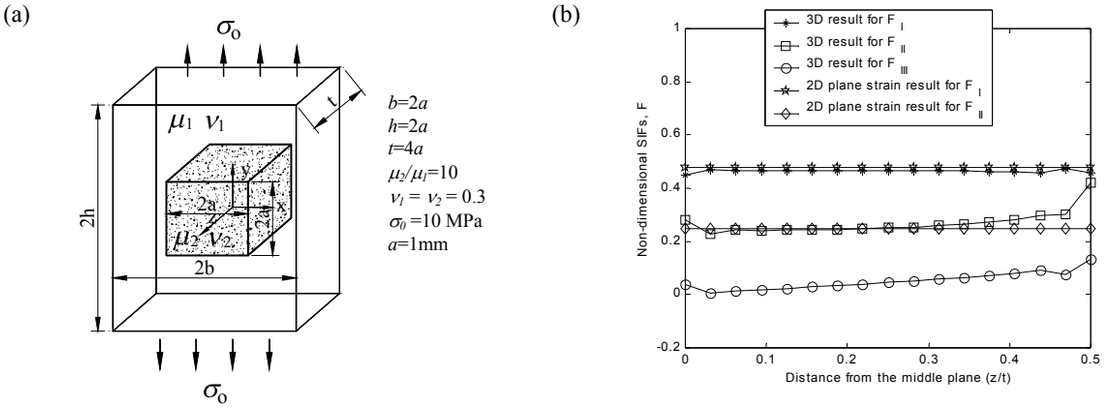


Figure 2: (a) Through-thickness bi-material inclusion. (b) Stress intensity coefficients along bi-material edge.

CONCLUSION

By incorporating both the variable orders and the angular variations, the new singular boundary elements can provide accurate solutions to three-dimensional stress singularity problems. The stress intensity factors which are normally difficult to determine using conventional numerical techniques are hereby easily computed with good accuracy using relatively coarse elements.

References

[1] Moran B., Shih C.F.: A general treatment of crack tip contour integrals. *Int. J. Fracture* **35**:295-310, 1987.

[2] Kwon S.W., Sun C.T.: Characteristics of three-dimensional stress fields in plates with through-the-thickness crack. *Int. J. Fracture* **104**:291-315, 2000.

[3] Aliabadi M.H.: A new generation of boundary element methods in fracture mechanics. *Int. J. Fracture* **86**:91-125, 1997.

[4] Lim K.M., Lee K.H., Tay A.A.O., Zhou W.: A new variable-order singular boundary element for two-dimensional stress analysis. *Int. J. Num. Meth. Engrg.* **55**:293-316, 2002.

[5] Tada H., Paris P.C., Irwin G.R.: The stress analysis of cracks handbook. Del Research Corporation, Hellertown, 1973.

XXI ICTAM, 15–21 August 2004, Warsaw, Poland

APPLICATION OF THE MATERIAL FORCE METHOD TO STRUCTURAL OPTIMIZATION

Swantje Bargmann*, Ellen Kuhl*, Harm Askes**, Paul Steinmann*
*Technical University of Kaiserslautern, Faculty of Mechanical Engineering,
P.O. Box 3049, D-67653 Kaiserslautern, Germany
**Delft University of Technology, Faculty of Civil Engineering and Geosciences,
P.O. Box 5048, NL–2600 Delft, Netherlands

Summary The present contribution aims at deriving a variationally consistent strategy to generate truss structures which are optimal in the sense of energy minimization. Accordingly, not only the spatial node point positions of the individual truss members, but also their material node point positions, i.e. the truss geometry itself, are introduced as primary unknowns. The governing equations follow straightforwardly from the Dirichlet principle for conservative mechanical systems. Thereby, the central idea is the reformulation of the total variation of the potential energy at fixed referential coordinates in terms of its variation at fixed material and at fixed spatial coordinates. The corresponding Euler–Lagrange equations define the spatial and the material motion version of the balance of linear momentum, i.e. the balance of spatial and material forces, in a consistent dual format. The suggested algorithm is then essentially characterized through the discretization and simultaneous solution of both, the spatial and the material motion problem. In this sense, the proposed strategy can be interpreted as a variational ALE formulation which renders not only the deformed truss structure but also an improvement of the node point positions themselves. The suggested algorithm will be discussed by means of illustrative examples.

INTRODUCTION

The material force method has gained an increasing interest over the last decade. The notion of material forces, or rather forces on singularities, dates back to the early work of Eshelby [8], in the honor of whom the mechanics on the material manifold have been termed Eshelbian mechanics. While the classical spatial motion problem typically deals with spatial or Newtonian forces which are essentially conjugate to spatial variations at fixed material positions, material or Eshelbian forces are generated by material variations at fixed positions in the spatial configuration. Classically, material forces were introduced in the context of material inhomogeneities,see e.g the textbooks by Maugin [12] and Gurtin [9] or in the recent work of our own group [1, 10, 11, 14, 15]. However, the application of material forces is not only restricted to physical inhomogeneities. In the finite element context, material forces can be utilized, to locate discrete inhomogeneities introduced by the finite element discretization. The first discussion on discrete material forces dates back to Braun [5], where, for the first time, finite element nodes were interpreted as discrete defects inducing discrete material forces. It was found, that meshing can be improved by moving the nodes in the direction opposite to the corresponding material forces and thus releasing an additional amount of energy, see Mueller & Maugin [13], Askes et al. [1], Kuhl et al. [10], Thoutireddy & Ortiz [16] and Thoutireddy [17]. An alternative application of the material force method was presented recently by Braun [6] who made use of discrete material node point forces to generate optimal truss structures. In the present work, we shall extend these ideas to the geometrically nonlinear theory and elaborate different solution strategies.

GOVERNING EQUATIONS

The underlying relaxation of the material node point position is strongly related to Arbitrary Lagrangian-Eulerian formulations which have traditionally been applied in the context of moving interfaces, e.g. in fluid-structure-interaction. An ALE formulation is basically characterized through the introduction of an independent fixed reference domain $\mathcal{B}_\square$ next to the classical material and spatial domain $\mathcal{B}_0$ and $\mathcal{B}_t$, see e.g. [1–4, 7, 10]. The following considerations are essentially based on two independent mappings, i.e. the referential maps from the referential to the spatial configuration $\boldsymbol{x} = \bar{\boldsymbol{\varphi}}\,(\xi, t)\ : \mathcal{B}_\square \to \mathcal{B}_t$ and from the referential to the material configuration $\boldsymbol{X} = \tilde{\boldsymbol{\Phi}}\,(\xi, t)\ : \mathcal{B}_\square \to \mathcal{B}_0$, with the corresponding deformation gradients $\bar{\boldsymbol{F}} = \nabla_\xi \bar{\boldsymbol{\varphi}}$ and $\tilde{\boldsymbol{f}} = \nabla_\xi \tilde{\boldsymbol{\Phi}}$. In what follows, we shall restrict ourselves to the hyperelastostatic case for conservative systems for which the Dirichlet principle defines the appropriate variational setting. In this context, the conservative mechanical system is essentially characterized through the infimum of the total energy $\mathcal{I}$ or, alternatively, through its vanishing total variation.

$$\mathcal{I}\,(\bar{\boldsymbol{\varphi}}, \tilde{\boldsymbol{\Phi}}) = \int_{\mathcal{B}_\square} W_\square + V_\square \,\mathrm{d}V_\square \to \inf \qquad \delta\mathcal{I} = \delta_{\boldsymbol{x}}\mathcal{I} + \delta_{\boldsymbol{X}}\mathcal{I} \doteq 0 \tag{1}$$

Thereby $\mathcal{I}$ can be understood as the integral over the internal potential energy density $W_\square$ plus the external potential energy density for conservative systems $V_\square$ over the reference domain $\mathcal{B}_\square$. Note, that in equation (1), the total variation with respect to fixed reference coordinates has been reformulated as the sum of the variation with respect to the spatial coordinates at fixed material positions plus the variation with respect to the material coordinates at fixed spatial position.

DISCRETIZATION

The reference domain can then be discretized in n_{el} linear truss elements. Each truss is interpolated by the linear shape functions in terms of the discrete node point positions ξ_i of the $i = 1, 2$ truss nodes. Following the isoparametric concept,

the unknowns $\bar{\boldsymbol{\varphi}}$ and $\tilde{\boldsymbol{\Phi}}$ and their variations $\delta\bar{\boldsymbol{\varphi}}$ and $\delta\tilde{\boldsymbol{\Phi}}$ are interpolated on the element level with the same shape functions N as the element geometry. Recall, that the spatial and the material stretch with respect to the reference truss element of unit length are simply given through the corresponding deformation gradients $\bar{F} = l$ and $\tilde{f} = L$, i.e. the length of the spatial and the material truss element. The discrete spatial and material variation of the total energy $\mathcal{I}$ take the following format

$$\delta_{\boldsymbol{x}}\mathcal{I} = \sum_{I=1}^{n_{\rm nd}} \delta\bar{\boldsymbol{\varphi}}_I \cdot \boldsymbol{R}^I_{\bar{\boldsymbol{\varphi}}} \qquad \delta_{\boldsymbol{X}}\mathcal{I} = \sum_{J=1}^{n_{\rm nd}} \delta\tilde{\boldsymbol{\Phi}}_J \cdot \boldsymbol{R}^J_{\tilde{\boldsymbol{\Phi}}} \tag{2}$$

with the discrete residuals of the spatial and the material motion problem $\boldsymbol{R}^I_{\bar{\boldsymbol{\varphi}}}$ and $\boldsymbol{R}^J_{\tilde{\boldsymbol{\Phi}}}$ defined in the following form.

$$\boldsymbol{R}^I_{\bar{\boldsymbol{\varphi}}} = \mathop{\mathsf{A}}_{e=1}^{n_{\rm el}} \nabla_\xi N_i \, \bar{\Pi} \, A \, \boldsymbol{n}_e \doteq \boldsymbol{0} \qquad \boldsymbol{R}^J_{\tilde{\boldsymbol{\Phi}}} = \mathop{\mathsf{A}}_{e=1}^{n_{\rm el}} \nabla_\xi N_j \, \pi \, A \, \boldsymbol{N}_e \doteq \boldsymbol{0} \tag{3}$$

LINEARIZATION

The above derived discrete residual statements represent a highly nonlinear coupled system of equations which can be solved within the framework of a monolithic incremental iterative Newton–Raphson solution strategy. To this end, we perform a consistent linearization of the governing equations which introduces the following contributions to the overall iteration matrix.

$$\begin{aligned}
\boldsymbol{K}^{IK}_{\bar{\boldsymbol{\varphi}}\bar{\boldsymbol{\varphi}}} &= \mathrm{D}_{\bar{\boldsymbol{\varphi}}_K} \boldsymbol{R}^I_{\bar{\boldsymbol{\varphi}}} = \mathop{\mathsf{A}}_{e=1}^{n_{\rm el}} \nabla_\xi N_I \, \mathrm{D}_{\bar{F}} \bar{\Pi} \, A \, \boldsymbol{n}_e \otimes \boldsymbol{n}_e \, \nabla_\xi N_K + \nabla_\xi N_I \, \bar{\Pi} \, A \, \frac{1}{l} [\, \boldsymbol{I} - \boldsymbol{n}_e \otimes \boldsymbol{n}_e \,] \nabla_\xi N_K \\
\boldsymbol{K}^{IL}_{\bar{\boldsymbol{\varphi}}\tilde{\boldsymbol{\Phi}}} &= \mathrm{D}_{\tilde{\boldsymbol{\Phi}}_L} \boldsymbol{R}^I_{\bar{\boldsymbol{\varphi}}} = \mathop{\mathsf{A}}_{e=1}^{n_{\rm el}} \nabla_\xi N_I \, \mathrm{d}_{\tilde{f}} \bar{\Pi} \, A \, \boldsymbol{n}_e \otimes \boldsymbol{N}_e \, \nabla_\xi N_L \\
\boldsymbol{K}^{JK}_{\tilde{\boldsymbol{\Phi}}\bar{\boldsymbol{\varphi}}} &= \mathrm{D}_{\bar{\boldsymbol{\varphi}}_K} \boldsymbol{R}^J_{\tilde{\boldsymbol{\Phi}}} = \mathop{\mathsf{A}}_{e=1}^{n_{\rm el}} \nabla_\xi N_I \, \mathrm{D}_{\bar{F}} \pi \, A \, \boldsymbol{N}_e \otimes \boldsymbol{n}_e \, \nabla_\xi N_K \\
\boldsymbol{K}^{JL}_{\tilde{\boldsymbol{\Phi}}\tilde{\boldsymbol{\Phi}}} &= \mathrm{D}_{\tilde{\boldsymbol{\Phi}}_L} \boldsymbol{R}^J_{\tilde{\boldsymbol{\Phi}}} = \mathop{\mathsf{A}}_{e=1}^{n_{\rm el}} \nabla_\xi N_J \, \mathrm{d}_{\tilde{f}} \pi \, A \, \boldsymbol{N}_e \otimes \boldsymbol{N}_e \, \nabla_\xi N_L + \nabla_\xi N_J \, \pi \, A \, \frac{1}{L} [\, \boldsymbol{I} - \boldsymbol{N}_e \otimes \boldsymbol{N}_e \,] \nabla_\xi N_L
\end{aligned} \tag{4}$$

The solution of the linearized system of equations finally not only renders the iterative update for the deformed configuration $\bar{\boldsymbol{\varphi}}_K = \bar{\boldsymbol{\varphi}}_K + \mathrm{d}\bar{\boldsymbol{\varphi}}_K$ but also the iterative update for the optimal truss structure $\tilde{\boldsymbol{\Phi}}_L = \tilde{\boldsymbol{\Phi}}_L + \mathrm{d}\tilde{\boldsymbol{\Phi}}_L$. Recall, that alternatively, a staggered solution technique can be applied, which follows straightforwardly from the above algorithm by neglecting the coupling terms $\boldsymbol{K}^{IL}_{\bar{\boldsymbol{\varphi}}\tilde{\boldsymbol{\Phi}}}$ and $\boldsymbol{K}^{JK}_{\tilde{\boldsymbol{\Phi}}\bar{\boldsymbol{\varphi}}}$.

CONCLUSIONS

The key idea of the present contribution was the application of the material force method for the optimization of truss structures. Motivated by a variational Arbitrary Lagrangian Eulerian formulation in combination with a particular parametrization, we derived the spatial and the material motion version of the balance of linear momentum. The solution of the former renders the spatial configuration while the latter defines the related material configuration, i.e. node point positions of the structural elements which are optimal in the sense of energy minimization.

References

[1] H. Askes, E. Kuhl, P. Steinmann, An ALE formulation based on spatial and material settings of continuum mechanics. Part 2: Classification and applications, *Comp. Meth. Appl. Mech. Eng.*, accepted for publication .

[2] T. Belytschko, J. M. Kennedy, Computer models for subassembly simulation, *Nuclear Engineering & Design* **49** 17–38, 1978.

[3] T. Belytschko, W. K. Liu, B. Moran, Nonlinear Finite Element Analysis for Continua and Structures, John Wiley & Sons, 2000.

[4] H. Braess, P. Wriggers, Arbitrary Lagrangian Eulerian finite element analysis for free surface flow, *Comp. Meth. Appl. Mech. Eng.* **190** 95–109, 2000.

[5] M. Braun, Configurational forces induced by finite–element discretization, *Proc. Estonian Acad. Sci. Phys. Math.* **46** 24–31, 1997.

[6] M. Braun, Structural optimization by material forces, in: G. A. Maugin, P. Steinmann (Eds.), Mechanics of Material Forces, Kluwer Academic Press, 2004.

[7] J. Donéa, Arbitrary Lagrangian Eulerian finite element methods, in: T. Belytschko, T. J. R. Hughes (Eds.), Computer Methods for Transient Analysis, Elsevier Science Publishers, pp. 473–516, 1983.

[8] J. D. Eshelby, The force on an elastic singularity, *Philosophical Transactions of the Royal Society of London* **244** 87–112, 1951.

[9] M. E. Gurtin, Configurational Forces as Basic Concepts of Continuum Physics, Springer Verlag, New York – Berlin – Heidelberg, 2000.

[10] E. Kuhl, H. Askes, P. Steinmann, An ALE formulation based on spatial and material settings of continuum mechanics. Part 1: Generic hyperelastic formulation, *Comp. Meth. Appl. Mech. Eng.* accepted for publication.

[11] E. Kuhl, H. Askes, P. Steinmann, Convexity conditions in hyperelasticity – Spatial and material settings, *J. Elasticity.* submitted for publication.

[12] G. A. Maugin, Material Inhomogeneities in Elasticity, Chapman & Hall, London, 1993.

[13] R. Mueller, G. A. Maugin, On material forces and finite element discretizations, *Comp. Mech.* **29** 52–60, 2002.

[14] P. Steinmann, On spatial and material settings of hyperelastodynamics, *Acta Mechanica* **156** 193–218, 2002.

[15] P. Steinmann, On spatial and material settings of thermo–hyperelastodynamics, *J. Elasticity* **66** 109–157, 2002.

[16] P. Thoutireddy, M. Ortiz, A variational Arbitrary Lagrangian–Eulerian (VALE) method of mesh adaption and optimization in static finite–element calculations, *Int. J. Num. Meth. Eng.*, submitted for publication .

[17] P. Thoutireddy, Variational Arbitrary Lagrangian–Eulerian Method, Ph.D. thesis, California Institute of Technology, Passadena, California, 2003.

THERMOCONTACT INTERACTION OF BODIES OF REVOLUTION DURING INDUCTION HEATING

Mykola Shulzhenko[1], Pavlo Gontarowskiy[1], Yuriy Matyukhin[1], Mykhaylo Pantelyat[1], Ivo Doležel[2], Bohuš Ulrych[3]
[1]*Institute of Mechanical EngineeringProblems NASU, Pozharsky str. 2/10, 61046 Kharkov, Ukraine*
[2]*FEL ČVUT, Technická 2, 166 27 Praha 6, Czech Republic*
[3]*FEL ZČU, Sady Pětatřicátníků 14, 306 14 Plzeň, Czech Republic*

Summary A technique of numerical analysis of kinetics of thermal and stress-strain states of bodies of revolution joined with interference at their induction heating-based assembly and disassembly is presented. Theoretical considerations are supplemented with an illustrative example dealing with assembly and disassembly of a joint "chuck-drill" of a drilling machine.

One of effective methods of thermal assembly and disassembly of metal machine joints with interference fit is based on the induction heating. Determination of the assembly and disassembly parameters requires the simultaneous solution of electromagnetic, thermal and thermoelastic problems taking into account contact interactions. In general these problems are coupled because material properties depend on temperature. However, in the case of small temperatures it is possible to neglect its influence on the electromagnetic field. Interrelation between thermal and stress-strain states is essential.

During assembly and disassembly of interference fits of bodies of revolution a thin surface layer of metal of the external body is heated intensively. Heating is carried out by eddy currents induced by harmonic or transient electromagnetic field generated by inductor that surrounds the joint. As during disassembly the internal body is heated by means of heat transfer, it is necessary to carry out the heating sufficiently quickly, otherwise the disassembly may become impossible.

For the finite element analysis a mathematical model based on the variational formulation of axisymmetric problems of electromagnetics, heat conduction and mechanics of deformable bodies is used. In the cylindrical coordinate system $r\theta z$ the functionals for the two first problems read

$$I_1 = \frac{1}{2}\iint_S \left[\frac{1}{\mu}\left(\frac{\partial A}{\partial r}\right)^2 + \frac{1}{\mu}\left(\frac{\partial A}{\partial z}\right)^2 + \frac{1}{\mu}\cdot\frac{A^2}{r^2} + \frac{2}{\mu}\cdot\frac{A}{r}\cdot\frac{\partial A}{\partial r} + 2\gamma A\frac{\partial A}{\partial t} - 2j_0 A \right] rdS + \int_{L_r} \alpha^*\left(\frac{A}{2} - A_\infty\right) ArdL,$$

$$I_2 = \frac{1}{2}\iint_S \left[k_r\left(\frac{\partial T}{\partial r}\right)^2 + k_z\left(\frac{\partial T}{\partial z}\right)^2 + k_{rz}\cdot\frac{\partial T}{\partial r}\cdot\frac{\partial T}{\partial z} + 2QT - 2\rho c\cdot\frac{\partial T}{\partial t}\cdot T \right] rdS - \int_{L_q} qTrdL + \int_{L_\alpha} \alpha\cdot\left(\frac{T}{2} - T_\infty\right) TrdL$$

where A denotes the magnetic vector potential, $\mu(H, T)$ the magnetic permeability depending on magnetic field strength H and temperature T, $\gamma(T)$ the electric conductivity, j_0 the external harmonic current density (within the inductor), A_∞ the value of the magnetic vector potential along the distant boundary Γ, α^* the "magnetic field transfer coefficient" to satisfy approximately the boundary conditions $A\big|_\Gamma = A_\infty$, t the time, $k_r(T)$, $k_z(T)$, $k_{rz}(T)$ the thermal conductivities, $\rho c(T)$ the volume specific heat, $Q(r, z, t)$ the specific internal heat sources (specific Joule losses), q the intensity of the heat flow through the boundary L_q, α and T_∞ the heat transfer coefficient and temperature of the medium along the boundary L_α.

To determine the stress-strain state the linearized Lagrange variational equation for increments is used

$$\iint_{S_0}\left(\Delta\sigma^{ij}\delta\Delta e_{ij} + \sigma^{ij}\delta\Delta\eta_{ij} - \Delta F^i\delta\Delta u_i\right)rdS - \int_{L_0}\Delta P^i\delta\Delta u_i rdL + \iint_{S_0}\left(\sigma^{ij}\delta\Delta e_{ij} - F^i\delta\Delta u_i\right)rdS - \int_{L_0} P^i\delta\Delta u_i rdL = 0$$

where S_0 and L_0 denote the surface and boundary of the meridian cross-section of the body in the initial non-deforming state, σ^{ij}, $\Delta\sigma^{ij}$ the components of the stress tensor and its increments, Δe_{ij}, $\Delta\eta_{ij}$ the increments of the linear and nonlinear parts of the strain tensor, Δu_i the increments of the displacements (Δu_r, Δu_z), F^i, ΔF^i the components of the volume load and its increments, and, finally, P^i, ΔP^i the components of the surface load and its increments.

Problems are solved using the time-stepping method with internal iterative processes for the parameters determination. The fact that the contact zone is unknown in advance does not allow setting conditions of interaction of bodies for the mechanical problem as well as for the thermal problem that determines their coupling.

When modeling the assembly and disassembly, the internal heat sources exist only during operation of the inductor. Redistribution of temperatures takes place as a result of thermal conductivity in the process of forced convective cooling. During the entry of the bodies in the contact or leaving from it the exchange of heat between them is realized through the time-varying contact zone (or zones) that must be determined iteratively. The contact thermal resistance is determined from empirical formula [1] and depends on the contact pressure, thermal conductivity of the bodies and medium in clearances between them, height of microroughness, etc. Conditions of the thermal and mechanical interaction are guaranteed by special thermocontact finite elements having no thickness. Contact interaction of the surface points are determined by inequalities $u_n^1 - u_n^2 - \delta_n \le 0$, $\sigma_n \le 0$ where u_n^1, u_n^2, δ_n are the displacements of the points

and gap (interference) in the direction of the common normal, σ_n the contact stress. For these points we introduce a sufficiently high stiffness to neglect the penetration of bodies.

As an example, numerical analysis of the process of assembly and disassembly of the joint "chuck-drill" of a drilling machine is carried out. The cross-section of the arrangement is depicted in Fig. 1. The drill is divided into 10 finite elements through the thickness while the chuck into 17 elements. The upper layer of the chuck with thickness of 1 mm containing heat sources is divided into 8 elements with mesh decreasing to the surface. Contact surfaces have a conic shape (conicity is 1:100). Their length is 40 mm (65 mm < z < 105 mm). To guarantee the uniform distribution of the contact pressure along the axis the varying interference is set (from 10 μm to 12.5 μm). Radius of the drill is 7 mm.

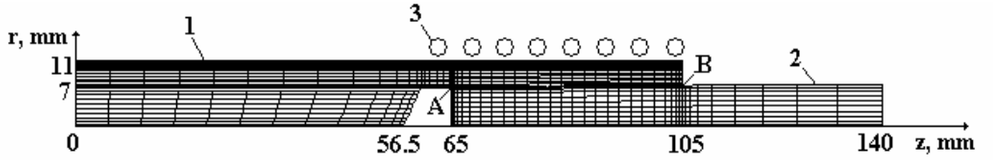


Fig. 1. Basic arrangement of the chuck (1) and drill (2), 3 denoting the inductor

Material of the chuck is a carbon steel with $k_r = k_z = k_{rz} = k = 16$ W/(m·K), $\rho c = 4 \cdot 10^6$ J/m^3, Young's modulus $E = 2 \cdot 10^5$ MPa, Poisson ratio $\nu = 0.3$, coefficient of the linear expansion $\alpha_T = 1.7 \cdot 10^{-5}$ K^{-1}. Material of the tool (hard alloy): k = 85 W/(m·K); $\rho c = 1.5 \cdot 10^6$ J/m^3, $E = 5.3 \cdot 10^5$ MPa; $\nu = 0.25$; $\alpha_T = 0.5 \cdot 10^{-5}$ K^{-1}. The total power of the internal heat sources is about 9.5 kW, frequency of current is 1 kHz. On the chuck face ($z = 0$) $\alpha = 10^4$ W/(m^2·K), $T_\infty = 20$ °C (heat removal along the chuck), on other free surfaces $\alpha = 2 \cdot 10^2$ W/(m^2·K), $T_\infty = 20$ °C (forced air cooling).

To realize the assembly, the chuck has to be heated about 3.5 s. Maximal temperature in it is 228 °C, maximal difference through the thickness is 86 °C. After 7.5 s of cooling (at $t = 11$ s) the chuck enters in contact with drill at point B (see Fig. 1) and at t =15 s along the whole surface. At the moment $t = 22$ s the temperature of the joint becomes practically uniform along the radius and contact pressures reach the values which guarantee the serviceability of the joint (the joint is able to transfer the real torque taking place during drilling [1]). Then, the contact pressure increases till the joint is cooled to 20 °C. This state is obtained by stationary thermomechanical problem solution ($t \to \infty$).

Part I of Tab. 1 presents the contact pressures at assembly for different times.

Tab. 1: Contact pressures (MPa) on cylindrical surface AB (Fig. 1) during assembly I and disassembly II

	t (s)	z (mm)								
		65.15	66.60	73.00	79.00	85.00	91.00	97.00	103.40	104.85
Assembly I	12	0	0	0	0	0	0	0	9,6	35.7
	14	0	0	0	0	7.7	13.8	37.3	56.7	147.8
	15	21.8	5.9	3.8	14.7	28.1	38.1	53.3	64.9	120.2
	22	192.4	71.9	50.6	58.0	63.0	70.0	77.0	82.5	111.2
	43	268.8	97.7	69.3	76.9	81.5	85.8	90.3	93.2	122.2
	∞	440.3	155.2	107.0	114.3	116.5	118.0	119.0	119.3	156.8
Disassembly II	2	227.4	56.7	32.7	39.9	43.0	45.8	37.8	50.8	251.2
	2.5	181.1	36.4	18.8	26.0	29.2	32.2	23.4	36.7	242.1
	3.5	80.4	0	0	0.5	4.8	5.6	0	0	172.9
	3.8	0.6	0	0	0	0.5	0	0	0	140.6
	4.0	0	0	0	0	0	0	0	0	0

Complete disassembly of the joint takes place in about 4 s after switching on the inductor. Maximal temperature in the chuck is now 231 °C (external edge of its face), in the drill (point A) - 85 °C. The distribution of the contact pressure during the disassembly of the joint is presented in part II of the table. Disassembly of the joint starts about 4 mm to the left from the point B at $t = 2.5$ s and at the maximal temperature in the chuck 181 °C. Then, the clearance appears in the region of the point A and the thin end of the drill gets free. The point B leaves from the contact later.

In order to obtain an interference of 10 μm along cylindrical contact surfaces [1], very high precision of the manufacture is necessary. For conic surfaces such a precision is not necessary because the interference will depend on the depth of penetration of the drill into the chuck that is determined by fixed temperature of the assembly at the selected point of the chuck. If the assembly will start at higher temperature, the appearance of small plastic strains does not lead to breakdown of serviceability of the joint later on.

References

[1] Shulzhenko M., Gontarowskiy P., Matyukhin Yu., Pantelyat M., Doležel I., Ulrych B.: Numerical analysis of induction heating-based assembly and disassembly of shrink fits. *Proc. of AMTEE' 03*, Czech Republic, Pilsen, A65-A73, 2003.

Dynamic characteristics and monitoring of rubbing surfaces quality

Musalimov V.M.,Ph.D.Prof,H.Research Worker;
Lisitsin Y.V.,D.Sc.,Sr.Research Worker;
Orlov S.V.,postgraduate

Institution of Problems of Mechanical Engineering,
Laboratory of Measurements

Abstract

This paper is devoted to identification of dynamics of cyclic wearing process. The experimental realization of the problem has been carried out with the use an original tribometrical of system "Tribal-2". The drive of the system allows to realize a reciprocating displacement of tested samples with a regulated speed of movement. Unpercussive normal loading is carried out with the help of feedback based on difference in phases of entrance and target signals. Signals' numbering is carried out with the use of computer technologies. "Tribal-2" is focused on a possibility of soft and rigid loading; on cyclic modes of preliminary displacement , and on slipping with friction wearing process. "Tribal-2" is equipped with a special set of thermographs and a number of applied programmes on MATLAB. All original components of the installation have been patented. The results of research of the circuit of contact interation coupling slipping under rigid loading have been obtained. In the offered method of data processing a process with one input and several outputs has been considered. The use of similar approaches allows to receive transfer functions of friction - wearing process. The theoretical substantiation of the method is based, firstly, on research of dynamics of levelling of the initial pressure epure during friction - wearing process; secondly, on the problem solution concerning fretting surfaces' form evolution. Thirdly , on the research of evolution's transient process. It has been established, that aperiodic element is in correspondence with an initial stage of wearing process , and the authors have taken that fact into consideration for description of wearing process' kinetics. As far as we know, that at the initial stage the quality of contacted surfaces is worse than at subsequent stages, the authors offer to use this dynamic characteristic as the bottom border of quality. As numerous experiments with metal and glass have shown, the final stage of surfaces' processing is in correspondence with oscillatory element without damping (doubling of amplitude) and this dynamic characteristic has been used as the top border of quality. An oscillatory element with damping is used for an operative estimation of processed surfaces' quality at intermediate stages. Practically, with the help of "Tribal-2" we

can have a reliable monitoring of rubbing surfaces' quality in a real time mode. Perhaps, it is the most important difference from other methods of surfaces' processing with the usage of programmed ways of frictional force and pressure distribution on different detail's zones with the help of elastic tool. The "Tribal-2" system allows us to investigate dynamics and kinetics of the third body. In conclusion , it has been shown, that dynamics' equation is in corresponndence with Bessel's equation and the first integral reflects its kinetics. Appropriate dissipative functions have been constructed and prophilogrammes have been measured at all stages of the investigation and laser scanning of surfaces' topography has been carried out. All data have been processed with the help of fast Fourier transformations and their wavelet analysis have been carried out too. The results of the analysis have been also submitted for consideration.

ELECTRIC-MECHANICAL BEAM-TO-BEAM CONTACT

Daniela P. Boso[*], Przemyslaw Litewka[**], Bernhard A. Schrefler[*], Peter Wriggers[***]
[*] *University of Padua, via Marzolo 9, I 35131 Padova, Italy*
[**] *Poznan University of Technology, Piotrowo 5, PL 60-965 Poznan, Poland*
[***] *University of Hanover, Appelstr. 9A, D 30167 Hanover, Germany*

Summary. In this paper the formulation of an electric-mechanical beam-to-beam contact element is presented. Beams with circular cross-sections are assumed to get in contact in a point-wise manner and with clean metallic surfaces. The voltage distribution is influenced by the contact mechanics, since the current flow is constricted through small contacting spots. Therefore the solution is governed by the contacting areas and hence by the contact forces. As a consequence the problem is semi-coupled with the mechanical field influencing the electric one. The electric-mechanical contact constraints are enforced with the penalty method within the Finite Element technique. The virtual work equations for the mechanical and electric fields are written and consistently linearized to achieve a good level of computational efficiency with the FE method. The equations set is solved with a monolithic approach.

INTRODUCTION

The pure mechanical beam-to-beam contact has been studied recently in [1] and [2]. In some advanced technology problems, such as nuclear and astronautics technology, electronic component mechanics, superconducting cables and coils, it is necessary to combine mechanical contact with other fields, such as the electric or thermal one. This paper is the first attempt to formulate a beam-to-beam contact element for the coupled electric-mechanical field. The electric part of the contact potential is taken in the same way as in [3], where it is described for the electric-mechanical contact between 2D continuum bodies using the node-to-segment approach. Concerning the contact area, taking into account the observations from [4] a long constriction is assumed, when considering a circular contact spot with a radius very small with respect to the beam radius. The contact area is calculated with Hertz contact theory for elastic bodies. In this way the problem is semi-coupled, the voltage distribution being affected by the mechanical contact areas. The virtual work equations for the mechanical and electric fields are written and consistently linearized to achieve a good level of computational efficiency with the FE method. The equations set is solved with a monolithic approach.

MECHANICAL CONTACT

For the clarity just two beams with circular cross-sections with radii r and $\bar{r}$ are considered. The extension to the case with more beams is straightforward. Beams are assumed to get in contact with clean metallic surfaces in a point-wise way. The key issue is to locate the closest points on the beams which are the potential candidates for the contact. To this end the orthogonality conditions are used involving the current position vectors of axis points for both beams: $\mathbf{x}$ and $\bar{\mathbf{x}}$ being the functions of respective local co-ordinates ξ and $\bar{\xi}$

$$\begin{cases} (\bar{\mathbf{x}} - \mathbf{x}) \cdot \mathbf{x}_{,\xi} = 0 \\ (\bar{\mathbf{x}} - \mathbf{x}) \cdot \bar{\mathbf{x}}_{,\bar{\xi}} = 0 \end{cases}$$

With the potential contact points known the normal gap is defined as

$$g_N = \|\bar{\mathbf{x}} - \mathbf{x}\|$$

and depending on its value the possible contact is determined with the geometrical check [1], [2].
In the frame of the penalty method the contact contribution to the virtual work for one active contact pair takes the form

$$\delta\Pi_m = \varepsilon_N \cdot g_N \cdot \delta_u g_N$$

where ε_N is the penalty parameter. Newton-Raphson method requires its linearization with respect to mechanical and electric unknowns

$$\Delta_u \delta_u \Pi_m = \varepsilon_N \cdot \delta_u g_N \cdot \Delta_u g_N + \varepsilon_N \cdot g_N \cdot \Delta_u \delta_u g_N \qquad \Delta_V \delta_u \Pi_m = 0$$

The first linearization represents the standard mechanical contact which will not be discussed here, see [1] or [2] for the details. The second one is zero since no dependence of the mechanical terms on the electric variables is considered.

ELECTRIC CONTACT

Having determined the location of the closest points their respective voltages V and $\bar{V}$ are computed linearly from the beam nodes voltages and are used to define the voltage gap

$$g_V = \bar{V} - V$$

With this in hand the electric contact contribution for one active pair takes the form

$$\delta\Pi_e = I \cdot \delta_V g_V$$

where I denotes the electric current intensity flowing through the contact area.

In our case of beam-to-beam contact it is assumed as a first approximation that the contacting area is circular with radius a much smaller than the radii r and $\bar{r}$ of the beams. In this way the conducting area is very small and with clean metallic surfaces the contact resistance is only the constriction resistance [4]

$$R = \frac{r}{2a}$$

where r denotes the material resistivity. Assuming an elastic behaviour of the contact area Hertz theory can be considered, and the contact radius is

$$a = \left(\frac{3\varepsilon_N g_N r^*}{4E^*} \right)^{\frac{1}{3}}$$

where the mean radius $r^* = \frac{r\bar{r}}{r+\bar{r}}$ and the mean Young's modulus $E^* = \frac{E\bar{E}}{\bar{E}\left(1-\nu^2\right)+E\left(1-\bar{\nu}^2\right)}$ have been introduced.

The linearization of the electric contact contribution with respect to all variables has the following form

$$\Delta_u \delta_V \Pi_e = \frac{\partial I}{\partial g_V} \cdot \Delta_u g_V \cdot \delta_V g_V + \frac{\partial I}{\partial g_N} \cdot \Delta_u g_N \cdot \delta_V g_V + I \cdot \Delta_u \delta_V g_V$$

$$\Delta_V \delta_V \Pi_e = \frac{\partial I}{\partial g_V} \cdot \Delta_V g_V \cdot \delta_V g_V$$

The first variation and the linearization of the kinematical and electric variables can be expressed as

$$\delta_u g_N = \mathbf{n}^T \left(\delta\bar{\mathbf{u}} - \delta\mathbf{u} \right)$$

$$\Delta_u g_V = \bar{V}_{,\bar{\xi}} \Delta\bar{\xi} - V_{,\xi} \Delta\xi \qquad \delta_V g_V = \delta\bar{V} - \delta V \qquad \Delta_u \delta_V g_V = \delta\bar{V}_{,\bar{\xi}} \Delta\bar{\xi} - \delta V_{,\xi} \Delta\xi$$

where the unit normal vector is defined as $\mathbf{n} = \frac{\bar{\mathbf{x}} - \mathbf{x}}{\left\| \bar{\mathbf{x}} - \mathbf{x} \right\|}$.

FE DISCRETISATION

The developed beam-to-beam electric-mechanical contact finite element corresponds to the following vector of nodal unknowns

$$\mathbf{q}_{(28\times1)} = \left\{ \bar{\mathbf{u}}_M{}^T, \mathbf{u}_M{}^T, \bar{\mathbf{V}}_M{}^T, \mathbf{V}_M{}^T \right\}$$

where vectors $\mathbf{u}_M$ and $\mathbf{V}_M$ represent the nodal displacements and nodal voltages, respectively of both beam elements within which the contact points lie

$$\mathbf{u}_M = \left\{ \mathbf{u}_1{}^T, \mathbf{u}_2{}^T \right\} = \left\{ u_{x1}, u_{y1}, u_{z1}, \varphi_{x1}, \varphi_{y1}, \varphi_{z1}, u_{x2}, u_{y2}, u_{z2}, \varphi_{x2}, \varphi_{y2}, \varphi_{z2} \right\}^T \qquad \mathbf{V}_M = \left\{ V_1, V_2 \right\}^T$$

The corresponding tangent stiffness matrix and residual vector have the following general form

$$\mathbf{K} = \begin{bmatrix} \mathbf{K}_{mm} & \mathbf{0} \\ \left(\mathbf{K}_{me1} + \mathbf{K}_{me2} + \mathbf{K}_{me3} \right) & \mathbf{K}_{ee} \end{bmatrix}_{(28\times28)} \qquad \mathbf{R} = \begin{bmatrix} \mathbf{R}_m \\ \mathbf{R}_e \end{bmatrix}_{(28\times1)}$$

where indices m and e represent the mechanical and electric terms, respectively.

CONCLUSIONS

The tangent stiffness matrix and residual vector for the electric-mechanical beam-to-beam contact finite element are presented. They are expressed in terms of the corresponding vector of nodal displacements and voltages. In this sense they are easy to be added to any FE package. The performance of the formulation will be confirmed by the numerical examples.

ACKNOWLEDGEMENTS

Support for this work was partially provided by EFDA Contract/02 – 660 FU05-CT-2002-00073, "Mechanical Modelling of ITER Superconducting Cable" and by The Polish Committee of Scientific Research, Grant DS-550/04. This support is gratefully acknowledged.

References

[1] Zavarise G., Wriggers P.: Contact with friction between beams in 3-D space, *Int. J. Num. Meth. Engng*. **49**, 977-1006, 2000.

[2] Litewka P., Wriggers P.: Frictional contact between 3D beams", *Comp. Mech*. **28**, 26-39, 2002.

[3] Boso D., Schrefler B.A., Zavarise G.: *A Coupled Electric - Mechanical Approach for Contact Problems*, Proceedings of the *Fifth World Congress on Computational Mechanics (WCCM V)*, July 7-12, 2002, Vienna, Austria, Editors: Mang, H.A.; Rammerstorfer, F.G.; Eberhardsteiner, J., http://wccm.tuwien.ac.at

[4] Holm R.: Electric Contacts Handbook. Springer-Verlag, Berlin Goettingen Heidelberg 1958.

CONTACT MECHANICAL ANALYSIS OF ELASTIC MULTIBODY STRUCTURES

Antero Miettinen, Herman Parland

Tampere University of Technology, Structural Mechanics, Po.Box 600, 33101 Tampere, Finland

Summary A theory of multibody structures of elastic blocks interconnected by plane dry joints with Coulomb friction is developed by basing the analysis on contact mechanics. A general theory of voussoir arches and segmental beams is developed.

This analysis is based on the contact mechanics of elastic blocks with approximately rectangular longitudinal section subjected at their end faces to normal force N, moment M and shear force Q with friction coefficient f at the plane joints. It is then possible to relate corresponding generalized deformations, translations v_x, v_z and rotations ω_y, linearly to N, Q and M. Based on these statical and kinematical concepts and their interrelations a mechanics of assemblages of elastic units in contact is developed and the effects of various structural factors are discussed.

If the blocks are rigid, the kinematics at collapse is determined by discontinuities at joints, mutual translations v_{xh}, v_{yh} and dito rotations ω_{yh}, which define linear gap deformations γ_x, γ_z with rotation axes being tangent to the cross section A or constant contact sliding γ_z over the whole of A. In both cases contact sliding $\gamma_z \neq 0$ requires

$$| q | = | Q/(fN) | = 1 \tag{1}$$

The corresponding load P_c can uniquely be determined only if friction coefficient $f = \tan\varphi = 0$ or ∞. In these cases the set of collapse loads P_c represent the lateral surface of uniquely determined convex cones $E_{\varphi=0}$ (shear stress $\tau = 0$) and $E_{\varphi=\pi/2}$ (slip $\gamma_z = 0$). In the intermediate range $0 < \varphi < \pi/2$ the corresponding $E(\varphi)$ cannot be uniquely determined. We introduce a combined friction $f = \tan(\rho+\beta)$, where β characterizes friction induced by the inclination $\tan\beta$ of the conical asperities on the contact plane and ρ represents the dissipative friction on the inclined slopes. At given $\varphi = \rho+\beta$ the cone $E(\rho,\varphi-\rho)$ represents a set of inclusions with extreme member $E(0,\varphi) \supset E(\rho,\varphi-\rho)$ and to every $E(\rho,\beta)$ corresponds its orthogonal polar cone $E^*(\rho,\beta) = \Xi(\beta)$ (Fig. 1b) that comprises the set of desintegrating velocities.

If the voussoirs are elastic we can separate the deformations of the blocks from those of the joints by linearization of the crack width to $\bar{\gamma}_{xh}(z) = v_{xh} + z\omega_{yh}$ and constant $\bar{\gamma}_{zh}$ over the entire surface A. This actually represents an extension to cracks of Reissner's linearizations in his plate theory. The modified stress energy enlarged with the slip work of the joints of the arch is thus

$$W''(\sigma) = \frac{1}{2}\int_L \left(\frac{N^2}{EA} + \frac{M^2}{EI} + \frac{\xi Q^2}{GA} \right) ds + \frac{1}{2}\sum_{i=1}^{n} \left(\frac{|N^i \bar{\gamma}^i_{xh}(e)|}{EA} + \frac{|Q^i \bar{\gamma}^i_{zh}|}{GA} \right) \tag{2}$$

Here $\bar{\gamma}^i_{xh}(e) = -v^i_{xh}(e)$ represents the interpenetration at the eccentricity e = km of force N (k is the kern point distance; for a rectangular cross section k = d/6) and $\bar{\gamma}^i_{zh}$ denotes the generalized shear deformation (Fig. 1a)

$$v^i_{zh} = \bar{\gamma}^i_{zh} = \int_A \frac{S_y \gamma_z}{I} dA \quad ; \quad \text{with rectangular cross section } A = bd: \ \bar{\gamma}^i_{zh} = \frac{3b}{2A}\int_d \left(1-(2z/d)^2\right)\gamma_z dz \tag{3}$$

where the integrals are extended over the area $A_\gamma = A - A_c + A_s$; A_c is the contact area and A_s denotes the area of contact sliding $A_s \subset A_c$. In order to make the v_{xh} independent of Q the joint plane must be a plane of symmetry with regard to the internal forces N and Q. This warrants that the contact area for combination (N,Q) doesn't differ from that for pure N and the nonelastic v_{zh} can be included in the elastic scheme. Thus we obtain

$$v^i_{xh} = \frac{|N^i|d}{EA}\eta_h(m^i); \quad \omega^i_{yh} = \frac{|N^i|d}{EAk}\alpha_h(m^i); \quad v^i_{zh} = \frac{Q^i d}{GA}\kappa_h(m^i, q^i); \quad |v^i_{xh}(e)| = \frac{|N^i|d}{EA}\delta_h(m^i) \tag{4}$$

where v_{xh}^i only depends on the crack volume $V_h^i = \int \gamma_x^i dA$ and (because of the impenetrability) stretches the centroid axis even if the crack doesn't extend to the centroid of the cross section. The quantity $q = Q/|fN|$ expresses the fullness of frictional contact at the joint $-1 \le q \le 1$ (Eqn. 1). Furthermore there applies

$$\delta_h = m\alpha_h - \beta_h \quad ; \quad \partial\delta_h / \partial m = 2\alpha_h \tag{5}$$

If the compressive force N acts at a point on the contour of the A with extreme value $| m |_{max}$ the values of α_h, β_h, δ_h and κ_h $\to \infty$. Similarly if $| q | \to 1$ then $\kappa_h \to \infty$ inducing unbounded translation γ_z on the entire contact area A_c of the joint. It

should be observed that the rotation axis of the end faces doesn't coincide with the zero-line of the σ_x stresses as in the corresponding rigid-plastic case, because the hinge is situated inside the compressed region (Fig. 1a).
The above results concerning symmetric joints of equal blocks can be extended also to curved voussoirs of varying length and depth and with unsymmetric joints by retaining equal plane contact faces A_c and equal normal forces N with the same point of action and equal shear forces at the joint. Thus for a joint of two ashlars (1) and (2) with rectangular cross sections $A_1 = bd_1$, $A_2 = bd_2$ the parameters of the joint are

$$\alpha_h \approx ½\,(\alpha_{h1}(m_1)+\alpha_{h2}(m_2))\,;\quad \beta_h \approx ½\,(\beta_{h1}(m_1)+\beta_{h2}(m_2))\,;\quad \kappa_h \approx ½\,(\kappa_{h1}(q_1,m_1)+\kappa_{h2}(q_2,m_2)) \qquad (6)$$

Corresponding approximation of of α_h , β_h and κ_h are determined for a collection of typical joints of beams, columns, plates and vaults.
Using formulae (2), (4) and (5) a solution of the redundant forces, thrust H, shear Y and moment Z at the elastic centroid of an arch with fixed supports is obtained by minimum condition of $W(\sigma)$ and an iterative solution process. Thus for the horizontal thrust we obtain the equation

$$H\int_L\left(\frac{z^2}{i^2}+\cos^2\vartheta+\frac{E}{G}\xi\sin^2\vartheta\right)\frac{ds}{EA}=\int_L\left(\frac{M^o z}{i^2}+N^o\cos\vartheta+\frac{E}{G}\xi Q\sin\vartheta\right)\frac{ds}{EA}+\sum_{i=1}^{n}\left(\frac{|N|d}{EA}(\eta_h\cos\vartheta+\frac{z}{k}\alpha_h)+\frac{Q}{GA}\bar{\gamma}_z\sin\vartheta\right) \qquad (7)$$

In the formulas (2) and (7) the integrals on the right hand side express the share of the monolithic arch, whereas the sums represent the share of the corresponding rigid body assemblage with dry joints.
A comprehensive representation provides the stiffness surface $F(\Delta)$ and the cone of load displacements Ξ (Fig. 1b). The effects of various factors (the number of blocks, the slenderness of the arch, the value of the friction coefficient) on the stiffness surface and the cone of load displacements of the structure are presented.
The voids γ_x developing at the joints may have a remarkable stabilizing effect at dynamic actions. The kinetic energy of an impact is mainly balanced by the increased potential energy of gravity induced by the vertical components of the crack volumes which many times exceeds the share of the strain energy (Fig. 1c).

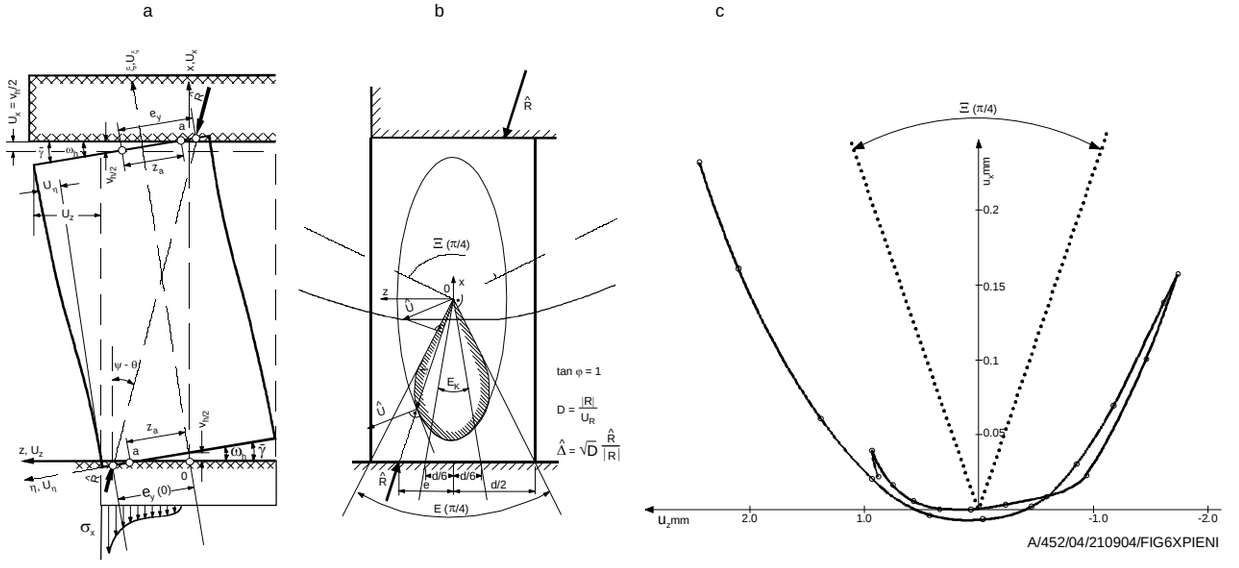


Fig. 1. a) Linearized deformation of a block between parallel rigid plates loaded by a force R. b) Stiffness ellipsoid and stiffness surface $F(\Delta)$ (shaded) of a block with the cone of monolithic kern E_k, the cone of stability $E(\pi/4)$ and the truncated cone of displacements Ξ. c) Staggering restitution u_x , u_z of the upper plate from imposed horizontal dislocation (test).

References

[1] Foce, F., Aita, D. : The masonry arch between "limit" and elastic analysis. Proc. 1st International Congress on Construction History, 2003.

[2] Miettinen A., Parland H. : On the stiffness characteristics of nonmonolithic elastic structures, Part II. Int. J. Solids and Structures 39 (2002), pp. 1701 – 1728.

EXISTENCE AND UNIQUENESS OF STEADY STATE SOLUTIONS IN THERMOELASTIC CONTACT WITH FRICTIONAL HEATING

L.-E. Andersson[1], A. Klarbring[2]
[1]*Department of Mathematics, University of Linköping, SE-581 83 Linköping, Sweden*
[2]*Department of Mechanical Engineering, University of Linköping, SE-581 83 Linköping, Sweden*

INTRODUCTION

It is well known that contact and friction in thermoelasticity result in mathematical problems which may lack solutions or may have multiple solutions. Previously, issues related to thermal contact and issues related to frictional heating have been discussed separately. In this work the two effects are coupled. Theorems of existence and uniqueness of solutions in two or three space dimensions are obtained, essentially extending, to frictional heating, results due to Duvaut, which were built on Barber's heat exchange conditions. Two qualitatively different existence results are given. The first one requires that the contact thermal resistance goes to zero at least as fast as the inverse of the contact pressure. The second existence theorem requires no such growth condition, but requires instead that the frictional heating, i.e., the sliding velocity times the friction coefficient, is small enough. Finally, it is shown that a solution is unique if the inverse of the contact thermal resistance is Lipschitz continues and the Lipschitz constant, as well as the frictional heating, is small enough.

VARIATIONAL FORMULATION

A thermoelastic body occupies a region Ω in R^d, $(d = 2, 3)$. The boundary of Ω contains three disjoint parts: Γ_0, Γ_1 and Γ_2. On Γ_0 the displacement vector u and the temperature T are prescribed to be zero. On Γ_1 the traction vector t and the heat flow q are prescribed. In the interior of Ω we have prescribed volume forces f and volume heat sources Q. Moreover, Γ_2 is the potential contact surface.
Now let us introduce function spaces V_1 and V_2 of displacements and temperatures, given by

$$V_1 = \{u \in (H^1(\Omega))^d : u = 0 \ \text{ on } \ \Gamma_0\},$$

$$V_2 = \{T \in H^1(\Omega) : T = 0 \ \text{ on } \ \Gamma_0\}$$

and the closed, convex subset

$$K_1 = \{u \in V_1 : u_N \leq 0 \ \text{ on } \ \Gamma_2\}.$$

then, using Green's formula in the usual way, we may reformulate the classical equations for equilibrium of forces and heat production into the following coupled variational problems
Find $(u, T) \in K_1 \times V_2$ such that

$$a_1(u, v-u) - \int_\Omega T s_{ij} \frac{\partial(v_i - u_i)}{\partial x_j}\, dx \geq \langle L_1, v-u\rangle \tag{1}$$

$$a_2(T, \varphi) + \int_{\partial\Omega} [k(p^*)(T - T_0) - \mu V p^*]\, \varphi\, dS = \langle L_2, \varphi\rangle \tag{2}$$

for all $(v, \varphi) \in K_1 \times V_2$.
Here $a_1(\cdot,\cdot)$ is the bilinear form of elastic energy, the second term in (1) represents the thermoelastic coupling and the linear functional L_1 in the right hand side represents the external volume and traction forces.
In equation (2), $a_2(\cdot,\cdot)$ is the bilinear form of heat flow. The contact pressure is $p = -\sigma_{ij} n_i n_j$, and since this may only be expected to be a positive measure in the function space $H^{-1/2}(\partial\Omega)$ we have introduced a regularization operator

$$H^{-1/2}(\partial\Omega) \ni p \mapsto p^* \in L^2(\partial\Omega) \quad \text{which is linear and bounded} \tag{3}$$

with norm C^* so that

$$\|p^*\|_{L^2(\partial\Omega)} \leq C^* \|p\|_{-1/2,\partial\Omega} \tag{4}$$

and that

$$p \geq 0 \Longrightarrow p^* \geq 0. \tag{5}$$

In addition we require that if p is a measure on $\partial\Omega$ then

$$p \geq 0 \Longrightarrow \|p^*\|_{L^\infty(\partial\Omega)} \leq c_0 \|p\|_{\mathcal{M}(\partial\Omega)} \tag{6}$$

where c_0 is independent of p and $\|\cdot\|_{\mathcal{M}(\partial\Omega)}$ denotes the total variation-norm on the space $\mathcal{M}(\partial\Omega)$ of bounded measures on $\partial\Omega$. The conditions (3)-(6) are certainly satisfied if for example the mapping * is given by a convolution (averaging) with a non-negative, piecewise C^1-function having compact support.
The heat balance of the contact interface is now represented by the second term in (2). Frictional heating produced on the boundary of the body, where μ is coefficient of friction and V is a given tangential velocity of the obstacle. The sum of these two heat flow contributions leaves into a perfectly conducting obstacle that has the temperature T_0. However, it then has to pass through a thermal resistance

$$R = 1/k(p^*),$$

where $k(p)$ is non-negative. The right hand side with the linear functional L_1 represents the external heat sources.

TWO THEOREMS OF EXISTENCE

In this section we will formulate two theorems of existence for the frictional thermoelastic problem. The first theorem deals with the case when the thermal conductance $k(p)$ is at least linearly increasing as the contact pressure p tends to infinity.

Theorem 1 *If $k(p) = 0$ for $p \leq 0$, if $mp \leq k(p)$ with $m > 0$ and if k is continuous, then the problem defined by (1) and (2) has at least one solution (u, T). Moreover, for this solution we have*

$$\|T\|_{H^1(\Omega)} \leq C(V\|\mu\|_{1/2,\partial\Omega}, 1/m)$$

with $C(\cdot,\cdot)$ an increasing function of both arguments.

The idea of the growth condition in this theorem came from the fact that if equality is assumed, i.e., $mp = k(p)$, one may define a modified temperature $T_1 = T_0 + \mu V/m \in H^1(\Omega)$, such that the integrand of the integral reads $k(p^*)(T - T_1)$. This means that our problem takes the form already considered by Duvaut (1979) for the case of no frictional heating and an existence result follows by analogy.
In the second theorem no growth condition is required for k. Instead there is a restriction on the size of μV *i.e.*, on the coefficient of friction and the velocity. On the other hand the regularity of μ is less restricted, only $\mu \in L^2(\partial\Omega)$ or $\mu \in L^\infty(\partial\Omega)$ is needed.

Theorem 2 *If $k(p) = 0$ for $p \leq 0$, if $k(p) \geq 0$ for $p \geq 0$, if k is continuous and if*

$$V\|\mu\|_{L^2(\partial\Omega)} < c_1c_2/c_0c_4C_1^2\|S\|\|\mathcal{E}\|^2 \tag{7}$$

or

$$V\|\mu\|_{L^\infty(\partial\Omega)} < c_1c_2/C^*c_4C_1\|S\|\|\mathcal{E}\| \tag{8}$$

then the problem defined by by (1) and (2) has at least one solution (u, T).

Here the constants c_1, c_2, C_1, C_2 are related to the bilinear forms $a_1(\cdot,\cdot)$ and $a_1(\cdot,\cdot)$, c_4 to a trace theorem and $\|\mathcal{E}\|$ is the norm of an extension operator from $H^{1/2}(\partial\Omega)$ to $H^1(\Omega)$.

UNIQUENESS

To prove a theorem on uniqueness of solutions we make the additional assumption that the function k is Lipschitz continuous.

Theorem 3 *The solutions proven to exist in Theorems 1 and 2 are unique if k is Lipschitz continuous with Lipschitz constant L, and if L and the sliding velocity V are small enough.*

References

[1] Barber, J.R. 1978 Contact problems involving a cooled punch. *J.Elasticity.* 8, 409–423.
[2] Duvaut, G. 1979 Free boundary problem connected with thermoelasticity and unilateral contact, In *Free boundary problems*, Vol 11, Pavia.

FE ANALYSIS OF BOND FOR SMOOTH FRP RODS EMBEDDED IN CONCRETE

Hamid R. Irannejad, Amir R. Khoei
Sharif University of Technology SUT, P.O.Box:11365-9313 Tehran, Iran

Summary The main objective of this paper is to propose a reliable method for numerical analysis of the bond interaction between FRP composites and concrete. The outline of research is based on a numerical simulation of an experiment, conducted in literature. Friction and chemical adhesion are the presumed factors supplying bond resistance. Contact parameters are evaluated and calibrated. Numerical graphs are compared with tentative results as a validation. Curves indicating changes in tangential and normal statue of the interface are shown.

Theory of bond of smooth rods with concrete

Application of the FRP reinforcement in modern concrete structures is increasing, in comparison with common techniques to inhibit or eliminate corrosion. Currently three types of fiber reinforcement are commonly used in polymer matrix composites; carbon, glass, and synthetic polymer fibers such as Kevlar [1]. It can be stated that whatever test procedure and mechanical properties are used, poor bond strength for smooth rebar with concrete will be obtained [2]. At early stages of loading, the bond shear force is dominated by chemical adhesion, which demolishes quickly and friction plays the main role in supplying bond resistance afterwards. The interface condition is affected by physical, chemical, and thermomechanical compatibility of the composite components with the outside environment [3].

FE modelling and the contact parameters

Figure 1 shows the configuration of the model simulated in this study. GFRP composite rod, which comprises E-Glass fibers and Vinylester matrix, was applied in the test. Appropriate thermal performance as well as excellent mechanical properties and toughness are the major causes for application of vinylester resins [4]. Modelling is performed in bar-scale mode. In this kind of simulation, the interface of rod with concrete is idealized by a cylindrical shape. Note that the proposed model is based on an FE simulation of a test carried out by Al-Zahrani et al. [5]. Non-linear spring and contact elements are employed to model the chemical adhesion and frictional behaviour between the concrete and rod respectively.

Contact parameters are: normal stiffness K_n, tangential stiffness K_s, coefficient of friction μ and initial interference δ. A consecutive procedure is used to obtain the true values of K_s and K_n parameters [6]. The initial interference which has been measured in test is 3.5~3.6 μm [5]. It is worth noting that the initial interference is normally a simulation of contact pressure along the interface, produced by a change in thermal situation due to cement hydratation. According to test, a 40°C decrease in the temperature of system results in an approximately 0.7 MPa reduction in average bond strength. The temperature of the analytical model is reduced in a similar way. Several consecutive analyses are carried out by increasing the coefficient of friction; μ, of the interface gradually, till a similar decrease of bond strength is gained numerically. It must be noted that the procedure of proposing the contact parameters involves three stages: Evaluation, Calibration and Validation. Finally, the values K_s=5.0E7; K_n=2.0E9; μ=0.21; δ=3.5 μm are proposed as evaluations of contact parameters. Authors calibrated the parameters by a comparison between numerical and experimental load-slip graphs [6] and concluded that the best coincidence is observed for μ=0.18. Note that a little change for any of the parameters at calibration stage is permitted.

Numerical Results

Al-Zahrani [5] carried out his experiment using three gages on the external surface of smooth rod at equal distances. To validate the proposed contact parameters, theoretical and tentative curves of bond stress-strain are compared in Figure 2. Figure 3 illustrates the mechanical behaviour of the interface. The linear branch (I) indicates the opening behaviour, however the uniform branch (II) implies the slipping statue. When more pull-out load is exerted, the mechanical interference will be opened. This will result in reduction of F_n, considering the fact that F_n is proportional to the value

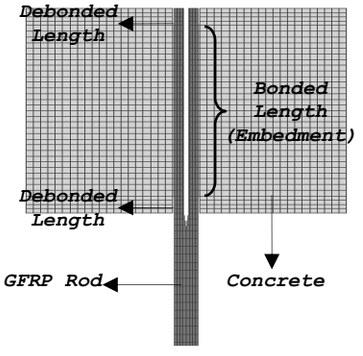


Figure 1- Typical shape of the axisymmetric FE model.

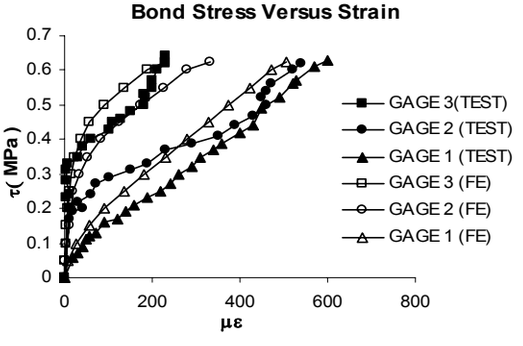


Figure 2- Bond stress vs. strain graph for different gages along the embedment.

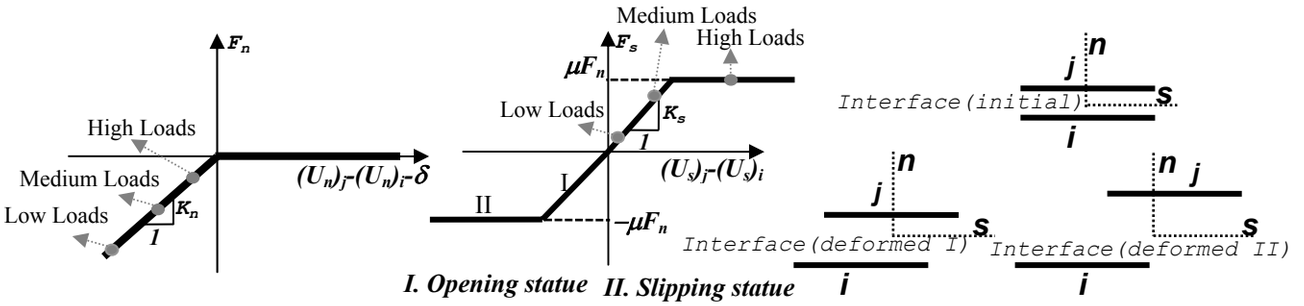


Figure 3- Normal and tangential mechanical behaviour along the boundary.

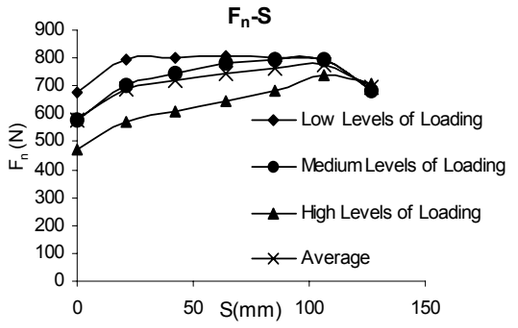


Figure 4- Variation of F_n along the embedment.

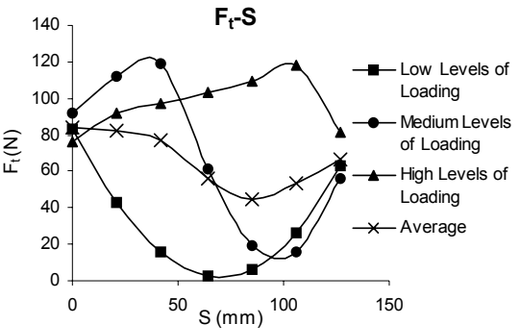


Figure 5- Variation of F_t along the embedment.

of interference while staying on part I of the graph. Decrease of F_n causes a subsequent reduction of the maximum bearable tangential force, which equals $\mu|F_n|$. Overall, it can be concluded that the contact elements throughout the boundary approach the slipping statue with an incremental rate by progress in loading. The maximum bond strength is obtained when all the contact elements along the boundary have either fallen into the slipping statue or the relevant mechanical interference has completely opened. Figure 4 shows the variation of interaction normal force along the contact embedment. At low and medium levels of loading, the minimum F_n takes place near the ends of the rod, which is mainly due to debonded lengths at both ends that result in stress concentration and decrease of resistance against radial dilation. At high levels of loading, the maximum value of F_n occurs nearly at the free end. This can be justified by the Poisson's rule, which states that the contraction of the rod in transverse direction decreases by reduction in the tensile force in longitudinal direction, while moving from the loaded-end part of the rod toward the free-end. Figure 5 illustrates the distribution of tangential force along the embedment. It is clear that the shear distribution is parabolic for low levels of loading. For high levels of loading, the distribution of shear force along the boundary is more uniform at and the maximum tangential shear can be measured at regions near the free-end of rod.

CONCLUSIONS

Contact and non-linear spring elements can be employed to simulate the frictional and adhesional function of the boundary of FRP and concrete respectively. Appropriate contact parameters were evaluated and calibrated, which are: K_n=2.0E9; K_s=5.0E7; μ=0.18; δ=3.5 μm. Cement hydratation of in-cast concrete results in a mechanical interference along the contact boundary, which opens gradually by progress in loading. Reduction in the temperature of reinforced system causes a consequent decrease of bond strength. Existence of debonded lengths culminates in low values of normal interaction between two materials at the ends of the rod, for average levels of loading. It was observed that the variation of bond tangential shear throughout the boundary becomes more complicated gradually by intensification of pull-out load. Finally, it has been concluded by comparison of numerical and experimental curves that the proposed model can be effectively used for simulation of bond behaviour between smooth FRP rods and concrete.

References

[1] Hyer M.W.: Stress Analysis of Fiber-Reinforced Composite Materials. Mc-Graw Hill, Boston, 1998.
[2] Cosenza E., Manfredi G. and Realfonzo R.: Behavior and Modelling of Bond of FRP Rebars to Concrete. *J. Compos Constr* **2**:40-51, 1997.
[3] Shalin R. E.: Polymer Matrix Composites. Chapman & Hall, London, 1995.
[4] ASM International Handbook Committee: Engineering Materials Handbook, OH 1993.
[5] Al-Zahrani M. M., Nanni A., Al-Dulaijan S.U. and Bakis C.E.: Bond of Fiber Reinforced Plastic (FRP) Rods to Concrete. *Proc. 51st Annual Conf Compos Inst*, pp.3A1-3A8, New York, 1996.
[6] Vafai A., Khoei A. R. and Irannejad H. R.: FE Analysis of Mechanical Interaction of Fiber Reinforced Polymer (FRP) with Concrete. *Proc. 6th Int Conf Civil Eng. (ICCE2003)*, pp.165-173, Isfahan, 2003.

MODELLING OF CONTACT OF STRUCTURED MATERIALS BASED ON DATA FROM SCANNING PROBE MICROSCOPY

Sergey A.Chizhik[*], Zygmunt Rymuza[**], Dmitri I. Shasholko[***]
[*] *Institute of Heat and Mass Transfer of the Academy of Sciences of Belarus, Minsk, Belarus*
[**] *Warsaw Uniersity of Technology Institute of Micromechanics and Photonics, Warsaw, Poland*
[***] *MicrotestMachines Co., Gomel, Belarus*

Summary Foundations of mechanical characterisation of structure and local elastic modulus for nanocomposites using scanning probe microscopy have been considered. Proposed were schemes to obtain input data for 3D modelling of contact of heterogeneous materials. They provide for imaging topography and mapping of structure and local micromechanical properties. Algorithms for computer modelling of contact of micro- and nanostructured composites have been described.

Introduction

Development of composites with fine micro- and nanostructure and their application in precision joints and microelectromechanical systems (MEMS) require an adequate description of the contact [1-4]. Difficulties in modelling of the contact of structured materials are conditioned by the necessity to consider heterogeneity of surface geometry (roughness, difference of film thickness) and physico-mechanical properties (elastic modulus, surface free energy) of the material surface layers.

New possibilities, however, appear with application of research methods employing scanning probe microscopy (SPM), particularly atomic force microscopy (AFM). Imaging in SPM is attributed by contact interaction between the probe tip and the sample material and results in static and dynamic phenomena in the probe cantilever [2, 3].

Input data preparation

AFM measuring system traces the probe cantilever movements and builds images based on these data. The measured data contain also information about the probe tip interaction with the tested sample surface. Heterogeneity of the material elastic properties caused by material structure and presence of different components can be mapped in contrast images. We analyzed micromechanical aspects of the AFM image formation and their relationships with local mechanical properties of materials. The analysis showed that the cantilever oscillation phase shift near the researched surface correlates with local elastic modulus of the material. That allows mapping of the physico-mechanical heterogeneity of surfaces. Proposed were the solutions of the contact problems that consider influence of surface forces and material layered structure (Fig. 1).

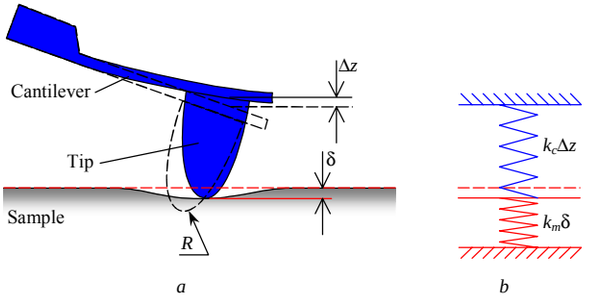


Fig. 1. Schematic diagram of the interaction between probe and sample surface (a) and mechanical model of the tip-sample interaction (b)

The experimental functions of interactions between the tip and the tested material were based on data obtained by analysis of force-vs-distance curves (static force spectroscopy) and dependencies of force gradient (oscillation amplitude) on tip-to-sample distance. We proposed algorithms for evaluation of the local elastic modulus and surface free energy and described the formation of the calibrated maps of the distribution of physico-mechanical properties over the surface. Result of the input data preparation is an equivalent topography image and map of reduced elastic modulus that are used then in the contact modelling. We discuss also the possibilities of surface nanotomography that is based on the phenomenon of non-uniform deformation of the surface layer by the tip with when harder inclusions are present in soft matrix. That allows obtaining information about heterogeneity of the material across its depth.

Contact zone modelling

As the result of the complex applications of the SPM methodology we propose to use the set of topography images, maps of the elastic modulus and surface free energy as input data for modelling contact of two rough surfaces.

We also tried to elaborate the spatial model of the real contact area for the structured materials with the application of the results of experimental studies.

In an elastic contact, the pressure and deformation of all surrounding points in the contact affect the displacement of a point under the load. The relationship is simplified in the Winkler surface model or elastic foundation model, where the contact surface is modelled as a set of elastic bars. The shear between them is neglected, so the contact pressure at a point is only dependent on the actual deformation at the point. The elements are considered as linear elastic bars of length h_d and with a spring constant or stiffness σ_j in z direction. Physical sense of h_d is the deformed layer depth. Resisting force against deformation for an elementary bar of material at point j is a function of approach δ_j (model of Winkler layer)

$$P_j = \sigma_j \Delta x \Delta y \delta_j. \tag{1}$$

Local effective stiffness σ_j is calculated at every data point from equivalent local elasticity modulus

$$E = [(1 - \nu_1^2)/E_1 + (1 - \nu_2^2)/E_2]^{-1}, \tag{2}$$

where ν_i, E_i (i=1,2) is the Poisson ratios and elastic moduli of the contacting materials respectively.
Molecular interaction between two surfaces is characterized by Lennard–Jones potential. The shape of the deformed surface is defined by the material compression dz_j in the areas of contact and non-contact tension beyond them [10]

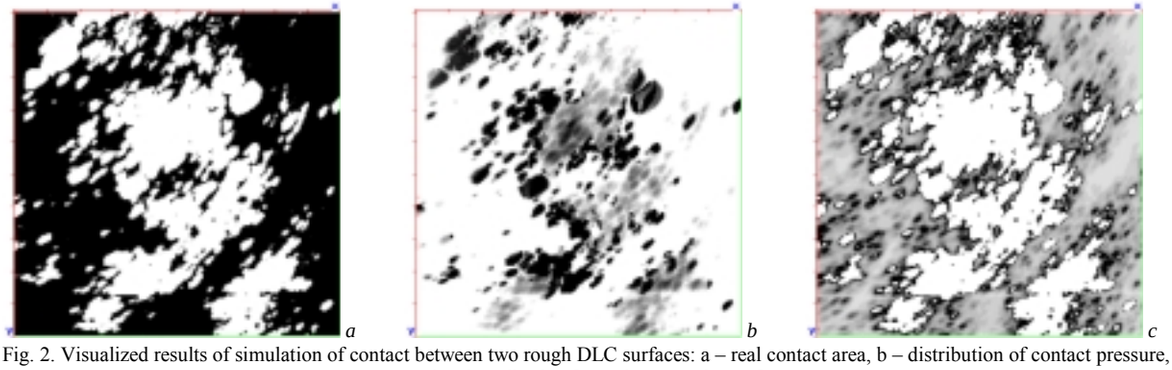
$$dz_j = \frac{8}{3}\Delta\gamma h_d \varepsilon^2 E_j^{-1} l_j^{-3} dz_j, \tag{3}$$

where l_j – is a local gap between the contacting surfaces.
The direction of the resultant force over elementary area $\Delta x \Delta y$ in the image was determined from the force balance. It enabled visualization of reflecting real contact area A_r.
For a new surface $z_j' = z_j + dz_j$, after summation over corresponding image nodes we calculated nominal contact load P and non-contact attractive molecular force between the surfaces F_s. They were found from corresponding deformation level h as

$$P(h) = -\Delta x \Delta y \sum_j \sigma_j \left(h - z'_j\right); \tag{4}$$

$$F_s(h) = \frac{8}{3}\varepsilon^2 \Delta x \Delta y \sum_j \Delta\gamma_j \left(h - z'_j\right)^{-3}, \tag{5}$$

where ε is an interatomic distance for the studied material; $\Delta\gamma$ is specific surface energy. The resultant force between contact and non-contact forces is not equal to zero for the considered surface site and depending on the sign that corresponds to either external compressive force or adhesion when the surfaces are separated.
Figure 2 shows results of the contact interaction simulation between two rough DLC surfaces.



a *b* *c*

Fig. 2. Visualized results of simulation of contact between two rough DLC surfaces: a – real contact area, b – distribution of contact pressure, c – molecular adhesive forces between the surfaces

Conclusions

A complex approach to characterization of the contacting surfaces with help of AFM and including measurement of topography, evaluation of heterogeneity of micromechanical properties and their quantitative characterization provides information for modelling the contact interaction of heterogeneous materials. Preparation of the input data and modelling of the precision contact can be realized using specialized atomic force microscope NT-206 and SPM processing software SurfaceView.

Partially supported by Fund Kasa Mianowskiego – Fundacja na Rzecz Nauki Polskiej, Warsaw, Poland.

References

[1] Burnham N. and Colton R.J.: Measuring the nanomechanical properties and surface forces of materials using an atomic force microscope. *J.Vac. Sci. Technol.* **A7**, 2906-13, 1989.

[2] Bhushan B., Fuchs H., Hosaka S. (eds). Applied Scanning Probe Methods. Springer, Berlin 2004

[3] Bhushan B. (ed). Springer Handbook of Nanotechnology. Springer Handbook of Nanotechnology. Springer, Berlin 2004

[4] Chizhik S.A., Gaiduk N.B., Myshkin N.K.: Computer simulation of precision contact with account of microgeometrical and mechanical heterogeneity of surfaces. *I.J.Mashine Tools & Manufacture*. **41**, 1909-1915, 2001.

A UNIVERSAL PROPERTY OF GEOMETRICAL HARDENING

Graham J. Weir*
*Industrial Research, Gracefield, PO Box 31310, Lower Hutt, New Zealand

Summary The main assumptions made in order to quantify geometrical hardening are that the impacts are collinear, and that torques can be ignored; the impact speeds are sufficiently slow so as to be quasi-static; the seismic wave energy losses are insignificant; and the materials are elasto-plastic. Repeated, identical impacts then increase Newton's coefficient of restitution in a universal manner, depending only on the initial coefficient of restitution, and the number of impacts.

INTRODUCTION

Hardening of elasto-plastic materials, due to repeated impacts, is a process made famous from the manufacture of samurai swords. In this process, the metal alters its grain boundary structure, which increases the yield strength of the metal, making it harder, and allowing a finer blade to be manufactured [1].

An analogous process occurs during repeated, identical impacts of elasto-plastic materials, called here "geometrical hardening". This occurs because the repeated, identical impacts increase the area of contact between the two bodies, which increases Newton's coefficient of restitution. Newton's coefficient of restitution is unity for impacts between two plane elasto-plastic bodies, and repeated impacts cause the impacting bodies to tend towards two plane bodies in the region of impact. This then resembles hardening of the metal. However, this is a wholly geometrical effect, and is not associated in any way with a change in the grain structure of the elasto-plastic material.

The aim of the rest of this paper is to detail the universal aspect of how Newton's coefficient increases during the process of geometrical hardening. The main assumptions made in order to derive the results below are that the impacts are collinear, and that torques can be ignored; the impact speeds are sufficiently slow so as to be quasi-static; the seismic wave energy losses are insignificant; and the materials are elasto-plastic.

THE UNIVERSAL CURVE FOR COLLINEAR IMPACTS

The sketch in Figure 1 shows the force-displacement curve for repeated, identical collinear impacts between two elasto-plastic bodies. The first impact occurs with initial and final relative speeds (always assumed collinear) of v (=v_1) and w_1. Subsequent impacts occur with the same initial relative speed of v, and separate with a relative speed of w_n. The speeds v_n are the initial relative speeds of approach needed to generate the same displacements as indicated by the points shown as v_n.

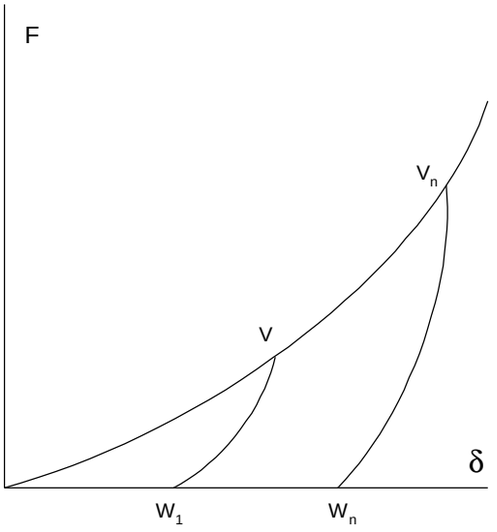


Figure 1. Sketch of the typical force-displacement curve for repeated, identical, quasi-static impacts between two elasto-plastic bodies. The steep path along the w entries is assumed to be wholly elastic, while the upper curve along the v entries is assumed to be essentially fully plastic.

Newton's coefficients of restitution are then C_n, where $C_n = -w_n/v$, and applying an energy balance to the curves in Figure 1 yields

$$C_{n+1}^{\frac{8}{3}} = C_n^{\frac{8}{3}} + C_1^{\frac{8}{3}}[1 - C_n^2] \qquad (1)$$

where we have assumed that the impacts are sufficiently energetic to be in the asymptotic "inverse one quarter" regime,

$$\frac{w_n}{v_n} = -\left(\frac{a}{v_n}\right)^{\frac{1}{4}} \qquad (2)$$

for some constant α [2].

From the recursion relationship in (1), it is clear that as n becomes large, C_n tends towards unity, and so after a great many impacts, the system behaves largely elastically. This is achieved by successively increasing deformations.

Equation (1) is completely independent of particle properties, apart from the appearance of C_1, Newton's coefficient of restitution for the first impact, and so is essentially a universal property of repeated, identical elasto-plastic impacts. The discrete solutions satisfying (1) are given in Figure 2. Given an initial coefficient of restitution on the ordinate, the subsequent increase in the coefficient of restitution is then fixed. Each discrete symbol in Figure 2 corresponds to the solution to the recurrence relationship in (1), with initial conditions running between 0.1 and 0.9 in steps of 0.1. The limiting case in Figure 1 is when w_n is essentially v, since then the impacts simply move the displacements elastically up and down the w lines.

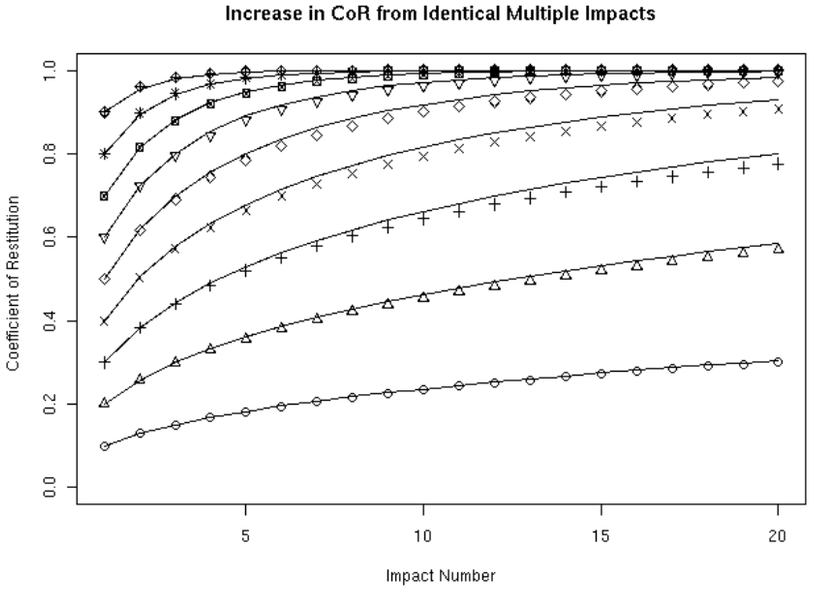


Figure 2. Discrete symbols denote the corresponding solutions to (1), for initial values C_1 between 0.1 and 0.9 in steps of 0.1, as a function of the number of impacts. The continuous lines in Figure 2 are the curves described by (3).

An approximate expression for C_n can be obtained from (1) by setting the term C_n^2 to $C_n^{8/3}$, and then replacing the resulting linear recurrence equation by the corresponding linear differential equation. The corresponding solution is

$$1-C_n^{\frac{8}{3}} \cong (1-C_1^{\frac{8}{3}})\exp[-(n-1)C_1^{\frac{8}{3}}] \qquad (3)$$

These continuous curves are plotted in Figure 2, for C_1 running from 0.1 to 0.9 in steps of 0.1. It is clear then that for very low values of C_1, many hundreds of repeated impacts are needed for C_n to approach unity, but for more typical values of C_1, say 0.7, then C_n approaches unity after about 10 or so impacts.

Finally, we note that it is problematical to attempt to quantify the increase in apparent hardening. The approach of Newton's coefficient of restitution to unity suggests the apparent hardening is increasing, whereas the increased displacements which occur suggest that the apparent hardening is reducing. This contradictory situation has developed because while the system is becoming, in practice, more elastic with time, the section of the upper curve in Figure 1 denotes behaviour which becomes more plastic with time.

CONCLUSIONS

The central result is contained in Figure 2, showing that the increase in Newton's coefficient of restitution follows universal curves, depending only on the starting coefficient of restitution, and the subsequent number of impacts. Experimental evidence supporting these universal curves is to appear [3]. In practice, seismic wave losses of a few percent, or so, mean that the universal curves above do not tend exactly to unity as shown, but to a few percent below unity, for quasi-static impacts. Before this happens, experimental difficulties can arise from failure to achieve perfect alignment of the impacting particles, which will cause the experimental measurements of the coefficients of restitution to lie somewhat below the universal curve in Figure 2. Before this happens, there are indications from experiment that the theory in this paper describes the early increases in the coefficient of restitution satisfactorily.

References

[1] Goldsmith, W.: Impact, Edward Arnold Ltd., London, 1960.
[2] Johnston, K.L.: Contact Mechanics, Cambridge Press, 1985.
[3] Weir, G. and Tallon, S.: The coefficient of restitution for normal incident, low velocity particle impacts, submitted to Chem. Eng. Sci, 2004.

CONTACT OPTIMIZATION PROBLEMS ASSOCIATED WITH THE WEAR PROCESS

István Páczelt[*], Zenon Mróz[**]
[*]*University of Miskolc, Department of Mechanics, H-3515 Miskolc-Egyetemváros,, Hungary*
[**]*Polish Academy of Sciences, IPPT PAN, Swietokrzyska 21, PL 00-049 Warszawa, Poland*

Summary The optimal shape design of contact surfaces has usually been aimed at controlling the contact pressure distribution. However, a much wider class of contact optimization problems can be formulated by maximizing contact force or displacement, torsional moment, or minimizing the rate of dissipation. A special class of optimization problems is considered, namely, the minimization of wear rate depending on both normal pressure and slip velocity. The specific modified Archard wear rule is assumed. The illustrative examples demonstrate the evolution of wear process toward their steady states. It is demonstrated that the wear dissipation power at the contact surface is minimal in the steady state of the wear process and in many cases corresponds to the uniform wear rate. The discretization of the contacting bodies was performed by the displacement based on *p*-version of finite elements assuring fast convergence of the numerical process and accurate specification of geometry for shape optimization, or by half space Boussinesq solution. It is assumed that the displacements and deformations are small, the material of the contacting bodies are elastic.

INTRODUCTION

In optimization problems the contact shape is usually determined in order to minimize the maximal pressure, thus achieving a uniform pressure over some contact portions. The book of Haslinger and Neittaanmaki [1] presents typical formulations of problems of optimal contact shape. An extensive survey of contact pressure optimization problems was presented by Hilding and Klarbring [2]. In Goryacheva's book [3] the contact problems of wearing process are investigated in analytical way. The papers by Páczelt [4] and Páczelt and Szabó [5] provide solutions for 2D and 3D problems in which the contact pressure distribution is partially controlled by minimizing the maximum contact pressure. The present work provides an analysis of evolution of contact surface shape and pressure due to wear process. It is supposed that the friction and wear is isotropic. The idea that wear depends on frictional dissipation was proposed by Mróz and Stupkiewicz [6] for the case of anisotropic friction and wear. It is believed that the optimal shape is achieved in this process when the wear rate becomes uniform within the contact domain. Such uniform wear rate criterion corresponds to the minimum of the dissipation power associated with the wear process. Without the restriction of generality, let us consider the contact problem of two elastic bodies B_α, $(\alpha = 1,2)$ with the usual boundary and loading conditions. The boundary portion $S_c^{(\alpha)}$ will be called the potential zone of contact. In this part of the bodies the shape may be modified. In the normal direction the Signorini contact conditions are valid [7]. The Coulomb dry friction models are investigated. In the analysis of wear problem, usually the elastic portion of relative tangent velocity is much smaller than the rigid body motion induced velocity, thus the effect of elastic component of tangent relative velocity can be neglected in the wear analysis. We shall use this fact in our numerical study of wear process. The temperature effects and heat generated at the frictional interface [7,8] in our investigation is out of consideration. The boundary value problem is solved by the variation principles using modified complementary energy, total potential energy with augmented Lagrangian technique [7]. The contact conditions are checked at the Gauss or Lobatto integration points of the contact elements during the solution process. The oscillations of contact pressure and displacements are minimized by using the node positioning and re-meshing technique described in [9].

Controlling of distribution of contact pressure. In optimization problems [4] we suppose that the bodies are in contact on the whole sub-domain Ω_c of the contact zone $S_c = \Omega$. The contact surface is modified in the way that the following function is held for the contact pressure $p(\mathbf{x}) = c(\mathbf{x})\, p_{\max}$, where the chosen control function must satisfy the condition $0 \le c(\mathbf{x}) \le 1$, and $p_{\max} = \max p(\mathbf{x})$, $\mathbf{x} = [s,t]$, where s and t are surface coordinates in the region Ω. In the sub-domain $\Omega_{nc}\,(\Omega = \Omega_c \bigcup \Omega_{nc})$ the satisfaction of the following inequality is required: $\chi(\mathbf{x}) = c(\mathbf{x})\, p_{\max} - p(\mathbf{x}) \ge 0$ $\mathbf{x} \in \Omega_{nc}$. Usually we use the control function $c(s)$ of class C^1 in the subregion Ω_c.

MINIMIZATION OF WEAR DISSIPATION POWER

Let us consider the wear problem of the punch B_1, translates or rotates with respect to the body B_2 which is constrained and does not undergo rigid body motion. In the case of translatory motion the relative sliding velocity at contact surface S_c v_r is constant, in the case of rotary motion, it is equal $v_r = r\,\omega$, where r denotes the distance of a point on S_c from the axis of rotation. Assume the isotropic wear rule in the form $\dot{w} = \beta\,(\mu\, p_n)^b\, v_r^a = \tilde{\beta}\; p_n{}^b\, v_r^a$, where a, b, β are

wear parameters, μ, p_n are coefficient friction and contact pressure, $\tilde{\beta} = \beta\,\mu^b$. The shearing stress in the contact surface denoting by τ_n and calculated from the contact pressure by the Coulomb dry friction law $\tau_n = \mu\, p_n$. The wear volume rate is calculated by the next formula $\dot{W} = \int_{S_c} \dot{w}\, dS = \int_{S_c} \tilde{\beta}\ \ p_n^{\ b}\, v_r^a\, dS$ and the wear dissipation power at the contact surface S_c equals $D_w = \int_{S_c} p_n \dot{w}\, dS = \int_{S_c} \tilde{\beta}\ \ p_n^{\ b+1}\, v_r^a\, dS$.

P.1 Consider first the stationary motion, $v_r = const.$ Assume the contact pressure $p_n(\mathbf{x})$ to satisfy the global equilibrium conditions, for body B_1, we have $\mathbf{f} = -\int_{S_c} \mathbf{n}_c\, p_n\, dS + \mathbf{f}_0 = \mathbf{0},\ \mathbf{m} = -\int_{S_c} \Delta\mathbf{r} \times \mathbf{n}_c\, p_n\, dS + \mathbf{m}_0 = \mathbf{0}$, where $\mathbf{n}_c$ is the contact normal direction vector, $\mathbf{f}_0$ and $\mathbf{m}_0$ are resultant force and moment of tractions acting on body B_1, $\Delta\mathbf{r}$ is the position vector. Introducing the Lagrange multipliers $\dot{\boldsymbol{\lambda}}_F$ and $\dot{\boldsymbol{\lambda}}_M$, consider the Lagrangian function $L_{D_w} = L_{D_w}\left(p_n, \dot{\boldsymbol{\lambda}}_F, \dot{\boldsymbol{\lambda}}_M\right) = \int_{S_c} \tilde{\beta}\ \ p_n^{\ b+1}\, v_r^a\, dS + \dot{\boldsymbol{\lambda}}_F \cdot \mathbf{f} + \dot{\boldsymbol{\lambda}}_M \cdot \mathbf{m}$. The stationary condition $\delta L_{D_w} = 0$ now provides the optimal contact pressures distribution and the equilibrium conditions thus $p_n = \left(\dfrac{\dot{\boldsymbol{\lambda}}_F \cdot \mathbf{n}_c + \left(\dot{\boldsymbol{\lambda}}_M \times \Delta\mathbf{r}\right) \cdot \mathbf{n}_c}{(b+1)\,\tilde{\beta}\, v_r^a} \right)^{\frac{1}{b}}$. For calculation of Lagrangian multipliers $\dot{\boldsymbol{\lambda}}_F, \dot{\boldsymbol{\lambda}}_M$ the equilibrium equations must be used. These nonlinear equations may be solved with Newton-Raphson technique.

P.2 Consider now the rotary motion of the punch B_1 with r_i internal and r_e external radius. Now we have $v_r = r\,\omega,\quad \dot{w} = \tilde{\beta}\ p_n^{\ b}\ (r\,\omega)^a$. Because the punch has rigid body translation in the direction of rotation axis, we consider only normal force constraint, that is, the Lagrange function takes the form $L_{D_w}^{rot}(p_n, \dot{\lambda}_F) = \int_{S_c} \tilde{\beta}\ p_n^{\ b+1}\ (r\,\omega)^a\, dS - \dot{\lambda}_F \left(\int_{S_c} p_n\, dS - F_0 \right)$. Introduce the integral $I_{D_w} = 2\,\pi \int_{r_i}^{r_e} r^{1-\frac{a}{b}}\, dr$, the Lagrangian multiplier equals $\dot{\lambda}_F = \left(\dfrac{F_0}{I_{D_w}}\right)^b (b+1)\,\tilde{\beta}\,\omega^a$ and contact pressure is $p_n = \dfrac{F_0}{I_{D_w}}\, r^{-\frac{a}{b}}$. In this case the wear rate is uniform $\dot{w} = \tilde{\beta}\,\omega^a \left(\dfrac{F_0}{I_{D_w}}\right)^b = const,$ and the wear volume rate can be calculated in a very easy way.

It is very important, that the optimal contact shape is attained when the wear dissipation power is minimal. This shape can be calculated "a priori" using the control technique with the optimal contact pressure which will be applied on the bodies at the surfaces $S_c^{(\alpha)}$ [4].

CONCLUSIONS

It is proved that minimum of the wear dissipation power at the contact surface provides the wear rate characterizing the steady wear process. The minimization of the total dissipation power gives different results dependent on form of rigid body motion and loading condition of contacting bodies. This optimal or steady state shape can be obtained through the optimization procedure based on required pressure distribution or through the modeling of wear process using the assumed wear rule.

Acknowledgement The present research was partially supported through the Polish Research Council (KBN) grant No 8T07A 02220, the Hungarian grant OTKA T05549 and Hungarian Academy of Sciences.

References

[1] Hilding D., Klarbring A., Petterson J.: Optimization of structures in unilateral contact, *ASME Appl. Mech. Rev.* **52**, No 4, 139-160, 1999.

[2] Haslinger J., Neittaanmaki P.: Finite element approximation for optimal shape design, John Wiley & Sons Ltd., London 1996.

[3] Goryacheva I.G., Dobichin M.H.: Contact problems in tribology (in Russian), Mashinostroenie, Moscow 1988.

[4] Páczelt I.: Iterative methods for solution of contact optimization problems, *Arch. Mech.* **52**, No. 4-5, 685-711, 2000.

[5] Páczelt I., Szabó T.: Solution of contact optimization problems of cylindrical bodies using the hp-FEM, *Int. J. Num. Meth. Eng.* **53**, 123-164, 2002.

[6] Mróz Z., Stupkiewicz S.: An anisotropic friction and wear model, *Int. J. Solids Structures* **31**, 1113-1131, 1994.

[7] Wriggers P.: Computational Contact Mechanics, J. Wiley & Sons, NY 2002.

[8] Strömberg, N., Johansson L., Klarbring, A.: Derivation and analysis of a generalized standard model for contact, friction and wear, *Int. J. Solids Structures* **33**, 1817-1836, 1996.

[9] Páczelt I., Baksa, A.: Examination of contact optimization and wearing problems, *Journal of Computational and Applied Mechanics* **3**, No.1, 61-84, 2002.

MOLECULAR ADHESIVE CONTACT FOR INDENTERS OF NON-IDEAL SHAPES

Feodor M. Borodich* and Boris A. Galanov**
* School of Engineering, Cardiff University, P.O. Box 925, Cardiff CF24 3AT, UK
** Institute for Problems in Materials Science (NASU), 3 Krzhyzhanovsky Street, 03142 Kiev, Ukraine

Summary The JKR and the DMT theories of adhesive contact are developed to describe contact between an indenter and an elastic sample, when the distances between the surfaces are described as monomial functions of arbitrary degrees. The results are applied to depth-sensing nanoindentation of soft and hard materials by indenters of non-ideal shapes.

Usually adhesion between contacting bodies has a negligible effect on surface interactions at the macro-scale, while it becomes significant as the contact size decreases, in particular adhesion becomes an important issue at nanoscale. Hence, adhesion of dry surfaces plays a key role in the development of various technologies, especially in such applications as nanoindentation, contact of clean surfaces, information storage devices and microelectromechanical systems (MEMS).

The mechanics of adhesion is well established for contact between homogeneous elastic solids having spherical surfaces [1]. Three theories of adhesion of elastic spheres are now in common use. They were introduced by Johnson, Kendall, and Roberts (JKR) in 1971, by Derjaguin, Muller, and Toporov (DMT) in 1975, and by Maugis (JKR-DMT transition) in 1992 [1]. However, solids in contact may often have more general shape, in particular the shape functions f can be monomial functions of radius ρ

$$f(\rho) = B_d \rho^d, \tag{1}$$

where B_d is a shape constant. For example, it was shown [2] that nanoindenters can be well approximated by monomial functions of degrees d in the range $1 < d < 2$. Here the JKR and the DMT theories of contact in the presence of surface forces are developed to describe contact between an indenter and an elastic sample, when the distances between the solids are described as monomial functions of arbitrary degrees.

It was assumed by Tabor and showed precisely by Muller [3] that the JKR and DMT theories apply to the opposite ends of the range of the non-dimensional parameter

$$\mu = \frac{32}{3\pi}\left(\frac{2w^2 R}{\pi (E^*)^2 z_0}\right)^{1/3}$$

where $w = 2\gamma$ is the work of adhesion, γ is the surface energy, z_0 is the equilibrium separation between surfaces, R is the radius of the sphere, and E^* is the reduced Young's modulus that can be obtained from the following formula $(E^*)^{-1} = (1-\nu_1^2)/E_1 + (1-\nu_2^2)/E_2$. Here E_i and ν_i $(i = 1, 2)$ are the Young's modulus and the Poisson ratio of the first and the second solid respectively. Roughly speaking, the DMT model is applicable to hard materials (μ is less than 0.1 say), while the JKR model should be used for soft materials (μ is greater than 5 say).

First we consider the JKR theory. Using Galin's solution [4], it was obtained by the authors (see, e.g. [5]) independently from each other that there is an exact formula giving relation between the load P and the radius of the contact region a

$$P = C(d) E^* B_d a^{d+1} - \sqrt{8\pi w E^* a^3}, \quad C(d) = \frac{d^2}{d+1} 2^{d-1} \frac{[\Gamma(d/2)]^2}{\Gamma(d)}. \tag{2}$$

Here $\Gamma(d)$ is the Euler gamma function. Evidently, (2) coincides with the classic JKR formula [1]

$$P = (4E^*/3R)a^3 - \sqrt{8\pi w E^* a^3}$$

in the case $d = 2$. When d is an even integer, (2) coincides with the solution obtained independently by Carpick *et al.* [6]. However, an exact solution for pressure within the contact region exists only in the Hertzian case $d = 2$. Hence, we use a numerical approach to obtain the pressure for monomial indentors.

Note that the DMT model shows a smooth change in contact radius a until the point contact, while it follows from the JKR model that the detachment of the spheres is accompanied by an abrupt change in the contact radius. Indeed, it follows from (2) that the radius a_0 of the contact region at $P = 0$ is

$$a_0 = [\sqrt{8\pi w/E^*}/(C(d)B_d)]^{2/(2d-1)}.$$

In general, one cannot obtain an analytic solution in the case of the DMT theory. Hence, an integral equation was derived. The integral equation the DMT theory is solved numerically. To perform the numerical simulations, we apply the method of non-linear boundary integral equations (NBIE) developed by Galanov (see, e.g. [7, 8]). To solve the Hertzian contact problem for indenters of non-ideal shapes, we consider not a traditional formulation of contact problem, but rather the following NBIE with an unknown function $v(\mathbf{x})$ [8]

$$\alpha v^-(\mathbf{x}) + \beta \int_\Omega K(\mathbf{x}, \mathbf{y}) v^+(\mathbf{y})\, d\mathbf{y} = g(\mathbf{x}), \quad \mathbf{x}, \mathbf{y} \in \Omega \tag{3}$$

where

$$v^+(\mathbf{x}) = \sup\{v(\mathbf{x}),\, 0\}, \qquad v^-(\mathbf{x}) = \inf\{v(\mathbf{x}),\, 0\},$$

α is an arbitrary positive fitting parameter, $\beta = (\pi E^*)^{-1}$, $g(\mathbf{x}, P) = h(p) - f(\mathbf{x})$, and K is the standard kernel (see for details [8]). Ω is an arbitrary bounded domain containing the closure of Ω_0, and $\Omega_0 \subset \mathbb{R}^2$ is a bounded domain such that

$$g(\mathbf{x}, P) > 0 \quad \text{for} \quad \mathbf{x} \in \Omega_0, \qquad g(\mathbf{x}, P) \le 0 \quad \text{for} \quad \mathbf{x} \notin \Omega_0 \tag{4}$$

The domain Ω_0 may be multiply connected or consist of non-connected sub-domains. Evidently, $G \subset \Omega_0$.

The mechanical meaning of the solution v to the NBIE (3) is the following

(i) for $\mathbf{x} \in G$, $v^+(\mathbf{x})$ is the contact pressure, i.e. $v^+(\mathbf{x}) = \sigma(\mathbf{x})$;

(ii) for $\mathbf{x} \in \Omega \backslash G$, the function $(-\alpha v^-(\mathbf{x}))$ defines the gap between the punch and the half-space after deformation.

To solve the adhesive contact problem for indenters of non-ideal shapes, we approximate Lennard-Jones potential F as

$$F(x) = Ax^{-m} - Bx^{-n}, \quad m > n > 0, \quad A > 0, \quad B > 0$$

and write the following integral equations for pressure σ

$$\sigma(\mathbf{x}) = F\left\{\left[g(\mathbf{x}) + 2\beta \int_\Omega K(\mathbf{x}, \mathbf{y})\sigma(\mathbf{y})d\mathbf{y}\right]^+ + c\right\}, \quad \mathbf{x}, \mathbf{y} \in \Omega \tag{5}$$

and for displacements

$$v(\mathbf{x}) = \left[g(\mathbf{x}) + 2\beta \int_\Omega K(\mathbf{x}, \mathbf{y}) F\left[v^+(\mathbf{y}) + c\right] d\mathbf{y}\right]^+, \quad \mathbf{x}, \mathbf{y} \in \Omega. \tag{6}$$

Solving (5), we obtain the pressure σ within the contact region, and solving (6), we obtain the function v and the vector of displacements.

For the Maugis theory, there are some exact results [9] obtained for $d = 2n$ where n is an integer. Evidently, the adhesive problem for arbitrary d for the Maugis theory can be solved numerically using the same approach.

The results are applied to depth-sensing nanoindentation of soft and hard materials by indenters of non-ideal shapes. Nanoindentation techniques are commonly used to obtain mechanical properties of materials of very small volumes [10]. The interpretation of nanoindentation tests is usually based on the main assumptions of the Hertz contact theory and formulae obtained for ideally shaped indenters. In particular, the elastic modulus of thin films is estimated using the following BASh formula for the slope S

$$S = \frac{dP}{dh} = \frac{2\sqrt{A}}{\sqrt{\pi}} E^*, \tag{7}$$

where A is the contact area ($A = \pi a^2$), and h is the indentation depth of the indenter tip. Although the formula is still valid for adhesive contact a flat punch (the Boussinesq-Kendall problem), molecular adhesion may affect the observed relations. For example, the above formula (7) is not valid for the JKR model because both P and a may decrease while h is constant.

Thus, both the adhesive molecular interaction and non-ideality of the shape may affect the results obtained using the standard Hertzian approach.

References

[1] Maugis D.: Contact, Adhesion and Rupture of Elastic Solids. Springer-Verlag, Berlin, 2000.

[2] Borodich F.M., Keer L.M., Korach C.S.: Analytical study of fundamental nanoindentation test relations for indenters of non-ideal shapes. *Nanotechnology*, **14**, 803-808, 2003.

[3] Muller V.M., Yushchenko V.S.: Influence of surface forces on deformation and adhesion of elastic particles to a rigid substrate or to each other. *Colloid J. USSR*, **42**, 411-419, 1980.

[4] Galin L.A.: Spatial contact problems of the theory of elasticity for punches of circular shape in planar projection. *J. Appl. Math. Mech. (PMM)*, **10**, 425–448, 1946.

[5] Galanov B.A., Grigor'ev O.N: Adhesion and wear of diamond. Part I. Modelling. *Technical Report. Institute Prob. Mat. Sci., Nat. Ac. Sci. Ukraine*, Kiev, 1-14, 1994.

[6] Carpick R.W., Agraït N., Ogletree D.F., Salmeron M. Measurement of interfacial shear (friction) with an ultrahigh vacuum atomic force microscope. *J. Vac. Sci. Technol. B*, **14**, 1289–1295, 1996.

[7] Galanov B.A.: On the nonlinear boundary equations of the mechanics of the contact of rough elastic bodies. *J. Appl. Math. and Mech.* , **50**, 357–361, 1986.

[8] Borodich F.M., Galanov B.A.: Self-similar problems of elastic contact for non-convex punches. *J. Mech. Phys. Solids* , **50**, 2441-2461, 2002.

[9] Goryacheva I.G., Makhovskaya Yu.Yu.: Adhesive interaction of elastic bodies. *J. Appl. Math. Mech.*, **65**, 273–282, 2001.

[10] Pethica J.B., Oliver W.C.: Tip surface interactions in STM and AFM. *Physica Scripta*, **T19**, 61–66, 1987.

XXI ICTAM, 15–21 August 2004, Warsaw, Poland

ADHESIVE COMPONENT OF THE ROLLING FRICTION FORCE

Irina Goryacheva*, Yulia Makhovskaya*
*Institute for Problems in Mechanics, Russian Academy of Sciences, Vernadskogo 101/1, Moscow, Russia

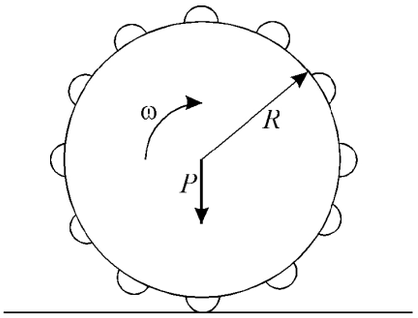
Summary A model is suggested for calculating the adhesive component of the friction force in rolling of a rigid rough cylinder on an elastic half-space. The rolling resistance arises due to the energy dissipation which occurs when an asperity approaches the half-space and then moves away from it. The cases of capillary adhesion of surfaces covered by fluid films and adhesion of dry surfaces are considered.

INTRODUCTION

Adhesive forces arise in the contact of bodies due to their surface energy and surface energy of fluid films covering the contacting surfaces. Contact problems for two elastic bodies taking into account adhesion were solved in [1-3] for various approximate forms of the potential of adhesive interaction. In [4,5], the interaction of two elastic bodies covered by films of fluid forming a meniscus in the gap between the bodies was investigated. The results show that when two elastic bodies possessing the surface energy cyclically approach each other and move away, the energy dissipation occurs. On the basis of this result, a model for calculating the adhesive rolling resistance is suggested.

NATURE OF ADHESIVE COMPONENT OF ROLLING FRICTION FORCE

Consider a simple scheme for a rough cylinder rolling on the boundary of an elastic half-space (Figure). The cylinder rolls with the angular velocity ω and it is acted on by the normal force P. There are N asperities of the same height h per unit area of the cylinder surface. The shape of an asperity is described by the function $f(r) = Ar^n$, where n is an integer.



When cylinder rolls, the distance between each asperity and the half-space decreases from d_∞, at which the asperity and the half-space experience no adhesive forces, to the minimum distance d_0 corresponding to the point of maximum contact pressure. Then the asperity moves away from the half-space surface up to the distance d_∞.

It is established [3] that if the value of d_0 does not exceed a critical value d_c then the energy dissipation takes place in an approach-separation cycle. The value of this energy dissipation is denoted by Δw. The energy dissipation per unit length of the cylinder in one revolution of the cylinder can be calculated as

$$\frac{w_0}{L} = 2\pi RN\Delta w \tag{1}$$

where L is the length of the cylinder. Assuming that the energy dissipation is equal to the work of adhesive friction force F_a done in a revolution of the cylinder, i.e., $w_0 = 2\pi RF_a$, we obtain the following relation for the friction force per unit length:

$$\frac{F_a}{L} = \Delta wN \tag{2}$$

Thus, to calculate the friction force, it is necessary to determine the energy dissipation Δw for one asperity in an approach-separation cycle.

ENERGY DISSIPATION IN AN APPROACH-SEPARATION CYCLE

Capillary adhesion

The interaction between a separate asperity and an elastic half-space is considered [5] taking into account a meniscus of fluid in the gap between the surfaces. A method is suggested to solve this problem both for contact between the surfaces and for the case where the surfaces are separated by the meniscus. As a result, the analytical relations for the contact pressure and shape of the boundary of the elastic half-space are obtained, which make it possible to calculate the dependence of normal force applied to the asperity versus distance between the bodies for various amount of fluid, its surface tension, shape of the asperity, and elastic properties of the bodies. It is shown that this dependence is nonmonotonic and ambiguous.

Adhesion of dry surfaces

The method developed for the problem of capillary adhesion is used for solving the problem of adhesion between an asperity and an elastic half-space possessing the surface energy [3]. It is shown that capillary adhesion and adhesion of dry surfaces lead to rather similar effects in contact of elastic bodies, in particular, to nonmonotonic and ambiguous character of the load-distance dependence.

Approach-separation cycle

The cyclic process in which an asperity approaches the elastic half-space and moves away from it is analyzed taking into account the adhesion of different nature [3]. The ambiguity of the load-distance dependence leads to an energy dissipation in this process. A method is developed for calculating the value of this energy dissipation. If the asperity tip has a spherical shape of raduis ρ which can be described by a parabolic function $f(r) = r^2/(2\rho)$, then the dimensionless energy dissipation

$$\Delta W = \Delta w \left(\frac{16E^{*2}}{9\pi^5\gamma^5\rho^4} \right)^{1/3} \tag{3}$$

where $E*$ is the reduced elastic modulus and γ is the surface energy (in the case of capillary adhesion, $\gamma = 2\sigma$, where σ is the surface tension of the fluid), can be expressed as a function of the only dimensionless parameter η for the case of capillary adhesion and the parameter λ for the adhesion of dry surfaces. These parameters are given by

$$\eta = \frac{\gamma^{4/3}\rho^{5/3}}{vE^{*4/3}}, \qquad \lambda = p_0 \left(\frac{9\rho}{2\pi\gamma E^{*2}} \right)^{1/3} \tag{4}$$

where v is the volume of fluid, p_0 is the adhesive pressure. The functions $\Delta W(\eta)$ and $\Delta W(\lambda)$ are determined numerically. For some particular cases, the function $\Delta W(\lambda)$ which describes the adhesion of dry surfaces is obtained in the closed form.

CALCULATION OF THE ROLLING RESISTANCE

Relation (2) and the method developed for the determination of Δw are used to calculate the adhesive component F_a of the rolling resistance. The value of this force is analyzed depending on the surface energy of the bodies, surface tension and volume of fluid, mechanical properties of the half-space, normal load applied to the cylinder, and shape of aspeirties. The results indicate that F_a increases as the surface energy increases and the volume of fluid in each meniscus decreases. This force is larger for softer materials (with smaller elastic modulus).

If asperities have spherical shape of radius ρ, then Eq. (2) can be represented in the form (see Eqs. (3) and (4)):

– for rolling of dry surfaces

$$\frac{F_a}{L} = N \left(\frac{16E^{*2}}{9\pi^5\gamma^5\rho^4} \right)^{-1/3} \Phi_1 \left(p_0 \left(\frac{9\rho}{2\pi\gamma E^{*2}} \right)^{1/3} \right) \tag{5}$$

– for rolling of lubricated surfaces

$$\frac{F_a}{L} = N \left(\frac{16E^{*2}}{9\pi^5\gamma^5\rho^4} \right)^{-1/3} \Phi_2 \left(\frac{(2\sigma)^{4/3}\rho^{5/3}}{vE^{*4/3}} \right) \tag{6}$$

where the functions $\Phi_1(t)$ and $\Phi_2(t)$ are calculated numerically.

Relations (5) and (6) are obtained by using the simplest model of rough body with asperities of the same height and they do not explicitly depend on the load P. The only condition on the value of P is the inequality $d_0 \le d_c$. Taking into account the height distribution of asperities in modelling roughness leads to substantial dependence of the number of asperities N_1 per unit area for which the energy dissipation takes place on the load P, cylinder radius R, and function $\varphi(h)$ of the height distribution of asperities, i.e., $N_1 = N_1(P, R, \varphi(h))$. In this case, we should set $N = N_1$ in Eq. (2).

References

[1] Maugis D.: Adhesion of spheres: The JKR–DMT transition using a Dugdale model. *J. Colloid Interface Sci.* **150**:243–269, 1991.

[2] Greenwood J.A., Johnson K.L.: An alternative to the Maugis model of adhesion between elastic spheres. *J. Phys. D: Appl. Phys.* V.31. **22**:3279–3290, 1998.

[3] Goryacheva I.G., Makhovskaya Yu.Yu.: Adhesive interaction of elastic bodies. *PMM [Applied Mathematics and Mechanics]* V.65. **2**, 2001.

[4] Maugis D., Gauthier-Manuel B.: JKR–DMT transition in the presence of a liquid meniscus. *J. Adhesion Sci. Technol.* V.8. **11**:1311–1322, 1994.

[5] Makhovskaya Yu.Yu., Goryacheva I.G.: The combined effect of capillarity and elasticity in contact interaction. *Tribology International* **32**:507–515, 1999.

FUNDAMENTAL RELATIONS FOR FRICTIONAL AND ADHESIVE NANOINDENTATION TESTS

Feodor M. Borodich* and Leon M. Keer**
* *School of Engineering, Cardiff University, P.O. Box 925, Cardiff CF24 3AT, UK*
** *Technological Institute, Northwestern University, Evanston, IL 60208-3109, USA*

Summary Fundamental relations for depth-sensing nanoindentation are derived for indenters of various shapes and for various boundary conditions within the contact region. In particular, it is shown that some uncertainties in nanoindentation measurements, which are sometimes attributed to properties of the material, can be explained and quantitatively described by properly accounting for geometric deviation of the indenter tip from its nominal geometry.

Indentation testing is widely used for analysis and estimations of mechanical properties of materials. Evidently, the load-displacement diagram at loading reflects both elastic and plastic deformations of the material, while the unloading is taking place elastically. The Bulychev-Alekhin-Shorshorov (BASh) equation for the stiffness S of the upper portion of the load-displacement curve at unloading is the following [4]:

$$S = \frac{dP}{dh} = \frac{2\sqrt{A}}{\sqrt{\pi}} E^*. \tag{1}$$

Here a is the radius of the contact region, A is the contact area ($A = \pi a^2$), P is the external load, h is the indentation depth of the indenter tip, and E^* is the reduced Young's modulus. Thus, nanoindentation techniques provide a unique opportunity to obtain mechanical properties of materials of very small volumes. The BASh relation is an example of fundamental relations which can be obtained from the analysis of frictionless contact problems.

The estimations of the thin film mechanical properties can be affected by various factors. It is widely accepted that the most significant source of uncertainty in nanoindentation measurement is the deviation of the indenter tip from nominal geometry. First, we consider the loading branch. It is assumed that the stress-strain behavior of materials can be described as a homogeneous (power-law) relation with the work-hardening exponent κ. It is argued that for shallow indentation where the tip bluntness is on the same order as the indentation depth, the indenter shapes can be well approximated by non-axisymmetric monomial functions of radius. However, if the stress-strain relation of the coating is $\sigma \sim \epsilon^\kappa$ and the indenter shape is described by a homogeneous function of degree d then the problem is self-similar. Let P_1, A_1, l_1 and h_1 be respectively some initial load, the corresponding contact area, the characteristic size of the contact region and the displacement. Using similarity rescaling formulae for 3D frictional contact problems [1], the fundamental relations are derived for depth of indentation, size of the contact region, load, hardness, and contact area, which are valid for both linear and non-linear, isotropic and anisotropic materials [2]:

$$\frac{l}{l_1} = \left(\frac{P}{P_1}\right)^{\frac{1}{2+\kappa(d-1)}}, \quad \frac{h}{h_1} = \left(\frac{P}{P_1}\right)^{\frac{d}{2+\kappa(d-1)}} \tag{2}$$

and the rescaling formula for the contact area is

$$\frac{A}{A_1} = \left(\frac{h}{h_1}\right)^{\frac{2}{d}}. \tag{3}$$

The formulae depend on the material hardening exponent κ and the degree of the monomial function of the shape d. However, it follows from (3) that $h \sim A^{d/2}$ independently of the work hardening exponent κ. Hence, one can calibrate the indenter tip from area-displacement curve. For example, one can obtain that the indenter shape used by Doerner and Nix [5] for $h \leq 90$nm can be described as a monomial function of degree $d = 1.44$. The formulae (2) and (3) are especially important for shallow indentation (usually less than 100 nm) where the tip bluntness is on the same order as the indentation depth. Further, the hardness (the average pressure) is the following function of the depth of indentation

$$\frac{H}{H_1} = \left(\frac{h}{h_1}\right)^{\frac{\kappa(d-1)}{d}}.$$

Hence, H is constant only for $d = 1$. Thus, the non-ideal indenter geometries can affect the interpretation of the experimental results, in particular the apparent hardness.

On the unloading branch, it is assumed that the materials are isotropic and linear elastic. The authors developed the Mossakovskii approach to the adhesive problem [7] and derived a relation that for evaluation of elastic modulus of materials by the slope of the unloading branch assuming adhesive (no-slip) contact [3]:

$$S = \frac{dP}{dh} = C\frac{2E}{1-\nu^2}\frac{\sqrt{A}}{\sqrt{\pi}}. \tag{4}$$

Thus, the BASh relation (1) should be corrected by the factor C in the case of frictional contact, where in the case of adhesive (no-slip) contact

$$C = \frac{(1-\nu)\ln(3-4\nu)}{1-2\nu}. \tag{5}$$

This factor decreases from $C = \ln 3 = 1.0986$ at $\nu = 0$ and takes its minimum $C = 1$ at $\nu = 0.5$. Taking into account that full adhesion preventing any slip within the contact region is not the case for real physical contact and there is some frictional slip at the edge of the contact region, one can conclude that the values of the correction factor C in (4) cannot exceed the upper bound (5). The relation is analogous to the BASh relation and similarly to the frictionless analysis [8], the obtained relation is independent of the geometry of the indenter.

Considering frictionless contact between an isotropic, linear elastic material and an arbitrary axisymmetric indenter of a monomial shape

$$f(\rho) = B_d \rho^d, \tag{6}$$

Galin [6] derived the following formulae

$$P = \frac{E}{1-\nu^2} B_d \frac{d^2}{d+1} 2^{d-1} \frac{[\Gamma(d/2)]^2}{\Gamma(d)} a^{d+1}, \quad h = B_d d 2^{d-2} \frac{[\Gamma(d/2)]^2}{\Gamma(d)} a^d. \tag{7}$$

Using (7), he established the following relation between the force P and the displacement h

$$P = \frac{E}{1-\nu^2} \left[B_d^{-\frac{1}{d}} 2^{2/d} d^{\frac{d-1}{d}} \frac{1}{d+1} [\Gamma(d/2)]^{-\frac{2}{d}} [\Gamma(d)]^{\frac{1}{d}} \right] h^{\frac{d+1}{d}}. \tag{8}$$

Developing the Mossakovskii approach [7], we obtained the following exact relations among the force P, the contact radius a and the displacement h:

$$P = \frac{E\ln(3-4\nu)}{(1+\nu)(1-2\nu)} B_d \frac{d}{d+1} 2^{d-1} \frac{[\Gamma(d/2)]^2}{\Gamma(d)} \frac{1}{I^*(d)} a^{d+1}, \quad h = B_d 2^{d-2} \frac{[\Gamma(d/2)]^2}{\Gamma(d)} \frac{1}{I^*(d)} a^d. \tag{9}$$

Using (9), one can establish the following relation between the force P and the displacement h for a monomial punch in the case of adhesive contact

$$P = \frac{E\ln(3-4\nu)}{(1+\nu)(1-2\nu)} \frac{d}{d+1} \left[\frac{4I^*(d)}{B_d} \frac{\Gamma(d)}{[\Gamma(d/2)]^2} \right]^{1/d} h^{\frac{d+1}{d}}, \quad \beta = \frac{1}{2\pi}\ln(3-4\nu), \quad I^*(d) = \int_0^1 t^{d-1} \cos\left(\beta \ln\frac{1-t}{1+t}\right) dt. \tag{10}$$

Here $\Gamma(d)$ is the Euler gamma function. In the case $\nu = 0.5$, the formulae (9) and (10) are identical with the corresponding formulae (7) and (8) obtained for frictionless contact. From (9) and (10), one can obtain the Mossakovskii solution [7] for a sphere ($d = 2$) and the Spence solution [9] for a cone ($d = 1$).

References

[1] Borodich F.M.: The Hertz frictional contact between nonlinear elastic anisotropic bodies (the similarity approach). *Int. J. Solids Structures*, **30**, 1513–1526, 1993.

[2] Borodich F.M., Keer L.M., Korach C.S.: Analytical study of fundamental nanoindentation test relations for indenters of non-ideal shapes. *Nanotechnology*, **14**, 803-808, 2003.

[3] Borodich F.M., Keer L.M.: Evaluation of elastic modulus of materials by adhesive (no-slip) nanoindentation *Proc. R. Soc. Ser. A*, (in press), 2003.

[4] Bulychev S.I., Alekhin V.P., Shorshorov M.Kh., Ternovskii A.P., Shnyrev, G.D.: Determination of Young's modulus according to the indentation diagram. *Industrial Lab.*, **41**, 1409–1412, 1975.

[5] Doerner M.F., Nix, W.D.: A method for interpreting the data from depth-sensing indentation instruments. *J. Mater. Res.*, **1**, 601–609, 1986.

[6] Galin L.A.: Spatial contact problems of the theory of elasticity for punches of circular shape in planar projection. *J. Appl. Math. Mech. (PMM)*, **10**, 425–448, 1946.

[7] Mossakovskii, V.I.: Compression of elastic bodies under conditions of adhesion (axisymmetric case). *J. Appl. Math. Mech.*, **27**, 630–643, 1963.

[8] Pharr G.M., Oliver W.C., Brotzen F.R.: On the generality of the relationship among contact stiffness, contact area, and elastic modulus during indentation. *J. Mater. Res.*, **7**, 613–617, 1992.

[9] Spence D.A.: Self similar solutions to adhesive contact problems with incremental loading. *Proc. R. Soc. London A*, **305**, 55–80, 1968.

HERTZ CONTACT AT FINITE FRICTION AND ARBITRARY PROFILES.

Bertil Storåkers and Denis Elaguine
Department of Solid Mechanics, Royal Institute of Technology, S-100 44 Stockholm, Sweden

Extended summary.
A consistent and robust method is described to solve normal axisymmetric contact problems at smooth and convex but otherwise arbitrary profiles. Special emphasis is put on the presence of finite friction causing partial slip between dissimilar solids. It is shown that at partial slip the evolving relative stick-slip contour is independent of any convex contact profile at monotonic loading. For flat and conical profiles with rounded edges and apes, relations between force, depth and contact contours are given together with surface stress distributions. For dissimilar solids, full field values were computed individually. The location and magnitude of critical stress measures are determined for a range of geometrical and material parameters.

The theory laid down by Hertz (1882) for normal frictionless contact between two nonconforming bodies of elliptical profiles stands as a landmark in linear elasticity. It would take almost a century until the corresponding problem was attacked for adhesive contact by Mossakovskii (1963) and Spence (1968) and for finite friction by Spence (1975a, 1975b). Already in the Hertz formulation based on linear kinematics, the problem is essentially nonlinear as a moving boundary is present. A further nonlinearity will evolve when finite friction prevails as stick-slip boundaries have to be determined when partial slip occurs. Substantial progress was made by Spence (1975a, 1975b), who showed that under monotonic loading a single stick-slip contour will appear being independent relatively to the contact profile provided it has a polynomial shape. More recently, c.f. e.g. Ciavarella and Hills (1999), Ciavarella (1999), contact of various non-standard profiles such as blunted cones and flat indenters with rounded edges, has been investigated. Besides more general contact law behaviour, the main intention has been to predict initiation of plastic flow or the occurrence of fracture and fatigue. The present effort follows in this spirit.

Mossakovskii (1963) seems to be the first to propose that normal contact problem at adhesive behavior may be attacked in two steps, by first solving the problem at an incremental advance and subsequently apply superposition. Emphasizing self-similarity for power law profiles, further progress was made by Spence (1968, 1975a, 1975b). Mossakovskii and Spence were mainly concerned with determination of surface tractions and displacements at contact. In case of axisymmetric and frictionless contact it was later shown by Hill and Storåkers (1990) that complete field values may readily be determined by a solution for incremental fields followed by cumulative superposition along radial paths. Numerically such a procedure is at advantage as only a stationary mesh is required when finite elements are to be used. The strategy was applied in full by Storåkers and Larsson (1994) for Norton creep by combining a finite element procedure with cumulative superposition, which for the case of linear viscosity corresponds to linear elasticity. In the present linear elastic case history dependence evolves through the presence of finite friction. It will be shown though that this issue is only fictitious as when partial slip arises, the stick-slip contour relative the external contact contour will be constant. This prevails for any contact profile provided that is smooth and convex and the loading is axisymmetric and monotonically increasing.

The problem to be analysed involves mutual impression of two isotropic elastic solids at normal contact. It is assumed that the two solids are homogeneous and have axisymmetric and convex though otherwise arbitrary smooth surface profiles. For simplicity and clarity, the problem is first posed for a rigid punch indented into an elastic half-space later to be generalized for the case of two dissimilar elastic solids.

Two axisymmetric punch shapes were investigated in particular, flat indenters with rounded corners and conical ones with rounded tips. The two profiles are described by

$$f(r) = \begin{cases} 0 \\ (r-b)^2/2R \end{cases}, \text{and} \qquad f(r) = \begin{cases} r^2/2R & r \le b \\ (2br-b^2)/2R & b \le r \le a \end{cases} \tag{1}$$

in obvious notation.

When finite Coulomb friction applies, μ, following Spence (1975a) for power law profiles, $f \sim r^p$, it is assumed *a priory* that only an interior stick region, $0 \le r \le c$, and an exterior slip region, $c \le r \le a$, evolve. It will be shown that this holds true for any profile, *f(r),* which is smooth and convex.

The problem so formulated involves a moving contact boundary, *a*, and a stick-slip contour, *c*, which have to be determined as part of the analysis. In a general situation when the contact profile, *f(r)*, is arbitrary the problem has to be treated incrementally and accordingly formulated in rate form.

Introducing reduced variables

$$a\tilde{x}_i = x_i, \qquad \dot{h}\tilde{u}_i(\tilde{x}_k) = \dot{u}_i(x_k, a) \tag{2}$$

where *h(a)* is the indentation depth, it may first be observed that at an incremental change, the reduced problem corresponds formally to that of flat punch of radius unity indented to a unit depth with an unknown relative stick-slip radius, c/a.

A finite element procedure, based upon the commercial code ABAQUS (2002), was developed to solve the intermediate flat die problem in reduced variables. The method adopted was essentially based on an earlier analysis of normal frictionless indentation as explained in detail by Storåkers et al. (1997) with the influence of finite friction subsequently taken into account by Carlsson et al. (2000). It should be observed in particular that the moving boundary is reduced to a stationary one.

Once the reduced problem has been solved, field values of the original problem may be found by simple cumulative superposition through integration along radial paths as proposed by Hill and Storåkers (1990). By quadrature of eq. (2), displacement fields follow as

$$u_i(x_k, a) = \int_0^a \tilde{u}_i(\tilde{r}) h'(s) ds \tag{3}$$

and stress fields alike.

The missing link between the physical depth of indentation, *h(a),* and contact profile, *f(r)*, is given by a Volterra integral equation

$$h(r) - \int_0^r \tilde{u}_z(\frac{r}{s}) \frac{dh}{ds} ds = f(r) \tag{4}$$

which is readily solved by standard methods.

The problem discussed so far has involved only contact between a rigid indenter and an elastic half-space. Accordingly, the interior fields to be determined, as by a finite element method, require solutions only for a half-space. When two dissimilar elastic solids are in contact, in general, solutions for interior fields are required in a full space. By a linear transformation, it has been shown explicitly by Mossakovskii (1963) and Spence (1968,1975a,1975b), that the resulting contact tractions may be directly determined by aid of a half-space solution for a tailored combination of material parameters. As a result, two uncoupled problems pertinent to dissimilar half-spaces with prescribed normal and tangential stresses are obtained and may be readily solved individually by the ABAQUS (2002) procedure.

Some selected results are illustrated for particular situations. The invariant relative stick-slip contour is shown in detail as a function of the friction coefficient, μ, and Poisson's ratio, ν, or alternatively the Dundurs parameter. For rounded conical and flat profiles, besides global contact laws, normal and tangential surface stresses are shown as functions of profile geometry, *b/a* cf. eq. (1), and μ. The location of maximum tensile stress is determined in order to predict Mode I fracture initiation. Interior fields are used to determine peak values of von Mises stress to predict initiation of plastic flow. The dissimilar case is analysed for different surface profiles, compliance values and friction coefficients. In particular it is shown where and when fracture and plastic flow is expected to occur.

References

1. Hertz, H. (1882), Über die Berührung fester elastischer Körper. *J. reine angewandte Matematik*, **92**, 156-171.
2. Mossakovskii, V. I. (1963), Compliance of elastic bodies under conditions of adhesion (axisymmetric case). *Prik. Mat. Mekh.*, **27**, 418-427.
3. Spence, D. A. (1968), Self similar solutions to adhesive contact problems with incremental loading. *Proc. Roy. Soc.*, **A305**, 55-80.
4. Spence, D. A. (1975a), The Hertz contact problem with finite friction. *J. Elasticity*, **5**, 297-319.
5. Spence, D. A. (1975b), Similarity considerations for contact between dissimilar elastic bodies. *Proc. IUTAM Symp. on Mech. of Contact,* Delft University Press, Delft, 1975.
6. Ciavarella, M. and Hills D., A. (1999), The influene of the indenter tip-radius on indentation testing of brittle materials. *J. of the European Ceramic Soc*., **19**, 239-245
7. Ciavarella, M. (1999), Indentation by nominally flat or conical indenters with rounded corners. *Int. J. Solids Struct.,* **36**, 4149-4181
8. Hill, R. and Storåkers, B. (1990), A concise treatment of axisymmetric indentation in elasticity. *Elasticity: Mathematical Methods and Applications* (eds G. Eason and R. W. Ogden), Ellis Horwood, Chichester, 199-210.
9. Storåkers, B. and Larsson, P.-L. (1994), On Brinell and Boussinesq indentation of creeping solids. *J. Mech. Phys. Solids,* **42**, 307-332.
10. ABAQUS (2002), (User's manual, Version 6.3) Hibbit, Karlsson and Sorensen, Providence, RI
11.Storåkers, B., Biwa, S. and Larsson, P.-L. (1997), Similarity analysis of inelastic contact. *Int. J. Solids Struct.*, **34**, 3061-3083
12. Carlsson, S., Biwa, S. and Larsson, P.-L. (2000), On frictional effects at inelastic contact between spherical bodies. *Int. J. Mech. Sci.,* **42**, 107-128.

FRICTIONAL CONTACT WITH WEAR DIFFUSION

Meir Shillor*, Mircea Sofonea†, J. Joachim Telega‡
* *Department of Mathematics and Statistics, Oakland University, Rochester, MI 48309, USA*
† *LTS, Université de Perpignan, 52 Avenue de Villeneuve, 66860 Perpignan, France*
‡*Polish Academy of Sciences IPPT PAN, Swietokrzyska 21, 00–049 Warsaw, Poland*

Summary A model for quasistatic frictional contact between a viscoelastic body and a moving foundation is described. The contact is modeled by the normal compliance and dry friction conditions and the wear of the contact surface is included. The novelty lies in allowing for the diffusion of the wear debris on the contact surface. Such phenomena arise in many settings, in particular in orthopedic biomechanics where they degrade the effectiveness of the joint prosthesis. A weak formulation of the problem is derived and, under a smallness assumption on the problem data, the existence of the unique weak solution for the model is stated.

THE MODEL

We model and analyze the processes when a viscoelastic body, which is acted upon by volume forces and surface tractions, is in frictional contact with a moving foundation and as a result a part of its surface may undergo wear. The wear particles or debris diffuse on the whole of the contact surface. Such situations arise, among others, in orthopedic biomechanics in the context of bone-implant interface. Since friction and the wear debris influence the quality and long term performance of artificial joints and implants, they need to be taken into account when modelling these processes, see, e.g., [1,2] and the references therein.
To describe the setting we denote by $\Omega \subset \mathbb{R}^3$ the domain occupied by the body and by Γ the boundary of Ω, which is assumed to be Lipschitz and is divided into three disjoint measurable parts Γ_D, Γ_N and Γ_C, such that $meas\,\Gamma_D > 0$. The body is clamped on Γ_D, prescribed surface tractions of density $\boldsymbol{f}_N$ act on Γ_N and volume forces of density $\boldsymbol{f}_0$ act in Ω. An initial gap g (≥ 0) exists between the potential contact surface Γ_C and the foundation, and is measured along the outward normal $\boldsymbol{\nu}$. To simplify the model we assume that the coordinate system is such that Γ_C occupies a regular domain in the plane $x_3 = 0$, the foundation is planar, and is moving with velocity $\boldsymbol{v}^*$ in the plane $x_3 = -g$. Furthermore, Γ_C is divided into two subdomains D_d and D_w by a smooth curve γ^*, and wear takes place only on the part D_w, while the diffusion of the wear particles takes place on the whole of Γ_C. The boundary $\gamma = \partial\Gamma_C$ of Γ_C is assumed Lipschitz and is composed of two parts γ_d and γ_w. Thus, $\partial D_w = \gamma_w \cup \gamma^*$ and $\partial D_d = \gamma_d \cup \gamma^*$. The setting is depicted in Fig 1.

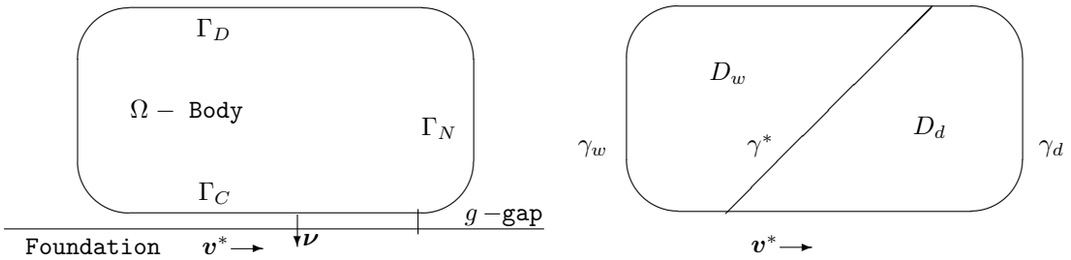


Fig. 1. The setting (left); contact surface Γ_C ; wear is produced in D_w (right).

We let $\mathbb{S}^3$ represent the space of second order symmetric tensors on $\mathbb{R}^3$ while "$\cdot$" and $\|\cdot\|$ denote the inner product and the Euclidean norm on $\mathbb{R}^3$ and $\mathbb{S}^3$, respectively. We let $\boldsymbol{u}$ be the displacement vector, $\boldsymbol{\sigma}$ the stress field and $\boldsymbol{\varepsilon}(\boldsymbol{u})$ the linearized strain tensor. Below u_ν and $\boldsymbol{u}_\tau$ represent the *normal* and *tangential* displacements, and σ_ν and $\boldsymbol{\sigma}_\tau$ represent the *normal* and *tangential* stresses, respectively, Also $[0,T]$ denotes the time interval of interest, for $T > 0$, and a dot above a variable denotes the time derivative.
We describe the wear of the surface in terms of the *wear function* $w = w(\boldsymbol{x}, t)$ which is defined on D_w, and the diffusion of the wear particles by the *wear particle surface density function* $\zeta = \zeta(\boldsymbol{x}, t)$ which is defined on Γ_C. Here, $\boldsymbol{x} = (x_1, x_2, 0)$, since Γ_C lies in the plane Ox_1x_2. The wear function w measures the volume density of material removed per unit surface area (see, e.g., [4] and references therein).
The classical formulation of the problem of *frictional contact of a viscoelastic body with wear diffusion* is as follows.

Problem P. *Find a displacement field* $\boldsymbol{u} : \Omega \times [0,T] \longrightarrow \mathbb{R}^3$, *a stress field* $\boldsymbol{\sigma} : \Omega \times [0,T] \longrightarrow \mathbb{S}^3$, *the wear function* $w : D_w \times [0,T] \longrightarrow \mathbb{R}$ *and a surface particle density field* $\zeta : \Gamma_C \times [0,T] \longrightarrow \mathbb{R}$, *such that*

$$\boldsymbol{\sigma} = \mathcal{A}(\boldsymbol{\varepsilon}(\dot{\boldsymbol{u}})) + \mathcal{G}(\boldsymbol{\varepsilon}(\boldsymbol{u})) \qquad \text{in} \quad \Omega \times (0,T), \tag{1}$$

$$\text{Div}\ \boldsymbol{\sigma} + \boldsymbol{f}_0 = \boldsymbol{0} \qquad \text{in} \quad \Omega \times (0,T), \tag{2}$$

$$\boldsymbol{u} = \boldsymbol{0} \qquad \text{on } \Gamma_D \times (0,T), \tag{3}$$

$$\boldsymbol{\sigma\nu} = \boldsymbol{f}_N \qquad \text{on } \Gamma_N \times (0,T), \tag{4}$$

$$-\sigma_\nu = p_\nu(u_\nu - w\chi_{_{[D_w]}} - g) \qquad \text{on}\Gamma_C \times (0,T), \tag{5}$$

$$\|\boldsymbol{\sigma}_\tau\| \le \mu|\sigma_\nu|; \qquad \boldsymbol{\sigma}_\tau = -\mu|\sigma_\nu|\frac{\dot{\boldsymbol{u}}_\tau - \boldsymbol{v}^*}{\|\dot{u}_\tau - \boldsymbol{v}^*\|} \quad \text{if } \dot{\boldsymbol{u}}_\tau \neq \boldsymbol{0} \qquad \text{on } \Gamma_C \times (0,T), \tag{6}$$

$$\dot{w} = \mu p_\nu R^*(\|\dot{\boldsymbol{u}}_\tau - \boldsymbol{v}^*\|) \qquad \text{on } D_w \times (0,T), \tag{7}$$

$$\dot{\zeta} - \operatorname{div}(k\,\nabla\zeta) = \kappa\mu p_\nu R^*(\|\dot{\boldsymbol{u}}_\tau - \boldsymbol{v}^*\|)\chi_{[D_w]} \qquad \text{on } \Gamma_C \times (0,T), \tag{8}$$

$$\zeta = 0 \qquad \text{on} \quad \gamma \times (0,T), \tag{9}$$

$$\boldsymbol{u}(0) = \boldsymbol{u}_0, \qquad \zeta(0) = \zeta_0 \qquad w(0) = w_0. \tag{10}$$

Here, (1) is the viscoelastic constitutive law of the material in which $\mathcal{A}$ and $\mathcal{G}$ are given nonlinear constitutive functions that may be nonhomogenuous; (2) are the equations of equilibrium, since the process is assumed quasistatic; (3) and (4) are the displacement and traction boundary conditions; (5) is the normal compliance contact condition, and (6) is the friction condition. The coefficient of friction $\mu = \mu(\zeta, \|\dot{\boldsymbol{u}}_\tau - \boldsymbol{v}^*\|)$ is assumed to depend on the density of the wear particles and on the slip rate. Equation (7) is the pointwise Archard type wear production rate in D_w, while (8) is the diffusion equation for the wear particles in which k denotes the wear particle diffusion coefficient, κ is the wear rate coefficient, and $R^* : \mathbb{R}_+ \to \mathbb{R}_+$ is the truncation operator: $R^*(r) = r$ if $r \le R$, $R^*(r) = R$ if $r > R$, R being a given positive constant. This operator is needed to avoid some mathematical difficulties, but from the applied point of view the use of R^* is not restrictive since, the slip velocity is bounded. We use $\chi_{[D_w]}$ on the right-hand side of (8) since the particles are produced only in D_w, and the rate of production is multiplied by β. An absorbing boundary condition (9) is used, since once a wear particle reaches the boundary $\gamma = \partial\Gamma_C$ it is removed from the system. Finally, the initial conditions are given in (10) in which $\boldsymbol{u}_0, \zeta_0$ and w_0 are prescribed.
A version of problem (1)–(10) in which it was assumed that $\zeta = \beta w$ in D_w, where β is a conversion factor from wear depth to wear particles surface density, was studied in [3]. This simplification allows to eliminate the wear function w. However, here we present the full problem, since the wear w may be nonzero even when most of the wear debris is gone so that ζ is virtually zero.

MAIN RESULTS

In [3] we established the existence of a weak solution for the simplified model. The assumptions on the problem data were provided, and by using Green's formula we obtained a variational formulation for the problem. It is in the form of a system coupling an evolutionary variational inequality for the displacement field $\boldsymbol{u}$, an ordinary differential equation for w and a parabolic evolution equation for the surface particle density field ζ. Under a smallness assumption on the data the existence was proved. The proof was carried out in several steps, by using arguments of evolutionary equations, time-dependent elliptic variational inequalities and fixed point. The full details can be found in [3].
Here we report on our progress in dealing with the full problem (1)–(10).

CONCLUSIONS

The mathematical problem is new and important in applications. These results extend some of our results for contact problems to include wear diffusion. The relaxing of the assumption that w and ζ are proportional has mathematical and applied merit. The topic is currently under investigation and we hope to deal with the mathematical and numerical aspects of various variants of the model in the very near future.

Acknowledgment. The work of the third author was partially supported by the State Comittee for Scientific Research (*KBN*, Poland) under the Grant No. 4 T11F 003 25.

References

[1] Rojek J., Telega J.J.: Contact problems with friction, adhesion and wear in orthopaedic biomechanics. I : General developments, *J. Theor. Appl. Mech.* **39**:655–677, 2001.
[2] Rojek J., Telega J.J., Stupkiewicz S.: Contact problems with friction, adhesion and wear in orthopaedic biomechanics. II : Numerical implementation and application to implanted knee joints, *J. Theor. Appl. Mech.* **39**:680–706, 2001.
[3] Shillor M., Sofonea M., Telega J.J.: Quasistatic viscoelastic contact with friction and wear diffusion, *Quart. Appl. Math.*, to appear.
[4] Strömberg, N., Johansson L., Klarbring, A.: Derivation and analysis of a generalized standard model for contact friction and wear, *Intl. J. Solids Structures,* **33**:1817–1836, 1996.

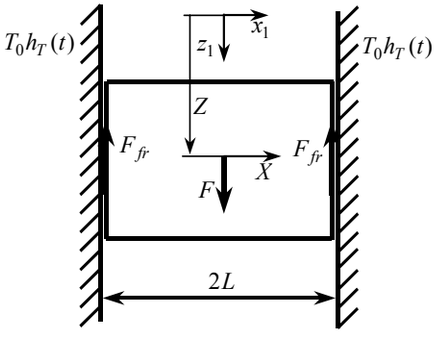
ON THE CONTACT THERMOELASTIC PROBLEM WITH FRICTIONAL HEATING, WEAR AND AUTO-VIBRATIONS

Jan Awrejcewicz, Yuriy Pyryev
Technical University of Lodz, Department of Automatics and Biomechanics,
Stefanowskiego 1/15, PL 90-924 Łódź, Poland

Summary The solution of a contact thermoelastic problem of a solid in the form of an elastic layer moving between two rigid walls with the heat generation and wear is presented. It is assumed that the friction coefficient depends on the relative velocity between the contacting bodies. A stability of the stationary solution is studied. Computation of contact parameters during heating of the bodies is performed.

PROBLEM FORMULATION

Friction, wear, heat generation, relative velocity and temperature deformation are complex processes which influence each other making up a sole diverse process of a friction unit work [1-4]. Consider contact and wear of one-dimensional model of the thermo-elastic contact of a body with a surrounding medium. Assume, that this body is represented by a rectangular plate (Fig.1). The vector components related to displacements as the plate temperature do not depend on Z, and the non-zero displacements $U(X,t), W(X,t)$ and temperature $T(X,t)$ components depended only on the co-ordinate X and time t. The plate has the mass M_1 subject to the force $F = F_* h_F(t)$ and moves vertically along walls in direction z_1 of the rectangular co-ordinates $0x_1y_1z_1$. The distance between walls is always equal to initial plate thickness $2L$. It is assumed also that according to Coulomb's law the friction force is proportional to normal part of reaction and kinematical friction coefficient f. The friction coefficient is assumed to be a nonlinear function of a relative velocity [2,3,5,6]. It is assumed that the heat conduction between the layer and the walls temperature is governed by the formula $T_0 h_T(t)$ ($h_T(t) \to 1, \ t \to \infty$). It causes a parallelepiped heat extension in the direction of $0x_1$, and the body starts to contact with walls. In the result of this process a frictional contact and wear on the parallelepiped sides $X = \pm L$ occurs. We assume Archard's law of wear [1], a speed of plate wear is proportional to the power of frictional force.



RESULTS AND DISCUSSION

From the mathematical viewpoint our problem is reduced to solution of the following dimensionless form of the non-linear system of integral and differential equations:

$$p(\tau) = Bi\int_0^\tau \dot{h}_T(\xi) G_p(\tau-\xi)d\xi + \gamma\int_0^\tau f(\dot{z})\dot{z}(\xi)p(\xi)\dot{G}_p(\tau-\xi)d\xi - u^w(\tau), \tag{1}$$

$$\dot{z}(\tau) = \varepsilon_1\left[m_0\int_0^\tau h_F(\xi)d\xi - \int_0^\tau f(\dot{z})p(\xi)d\xi\right], \quad \dot{u}^w(\tau) = k^w\dot{z}(\tau)p(\tau) \tag{2}$$

which yields the non-dimensional pressure $p(\tau)$ and velocity $\dot{z}(\tau)$. The temperature is defined through the following formula

$$\theta(x,\tau) = Bi\int_0^\tau \dot{h}_T(\xi) G_\theta(x,\tau-\xi)d\xi + \gamma\int_0^\tau f(\dot{z})\dot{z}(\xi)p(\xi)\dot{G}_\theta(x,\tau-\xi)d\xi, \tag{3}$$

$$\{G_p(\tau),\ G_\theta(1,\tau)\} = \frac{1}{Bi} - \sum_{m=1}^{\infty}\frac{\{2Bi,\ 2\mu_m^2\}}{\mu_m^2[Bi(Bi+1)+\mu_m^2]}e^{-\mu_m^2\tau}, \tag{4}$$

and μ_m are the roots of the following characteristic equation $\operatorname{tg}\mu_m = Bi/\mu_m$, $m = 1,2,...$

The numerical analysis of the problem is performed using the Runge-Kutta method.

In this case the steel made parallelepiped plate with $L = 0.01\,\mathrm{m}$, $T_0 = 5^\circ C$, $z^\circ = \dot{z}^\circ = 0$ and with non-constant friction coefficient is studied. In order to confirm the given conclusions, numerical analysis is carried out for $Bi = 5$ (critical value $\varepsilon_1 \approx \widetilde{\varepsilon} = 586.5$), and the computational results are carried out for a few values of the parameter $\varepsilon_1 = 400;\ 800$.

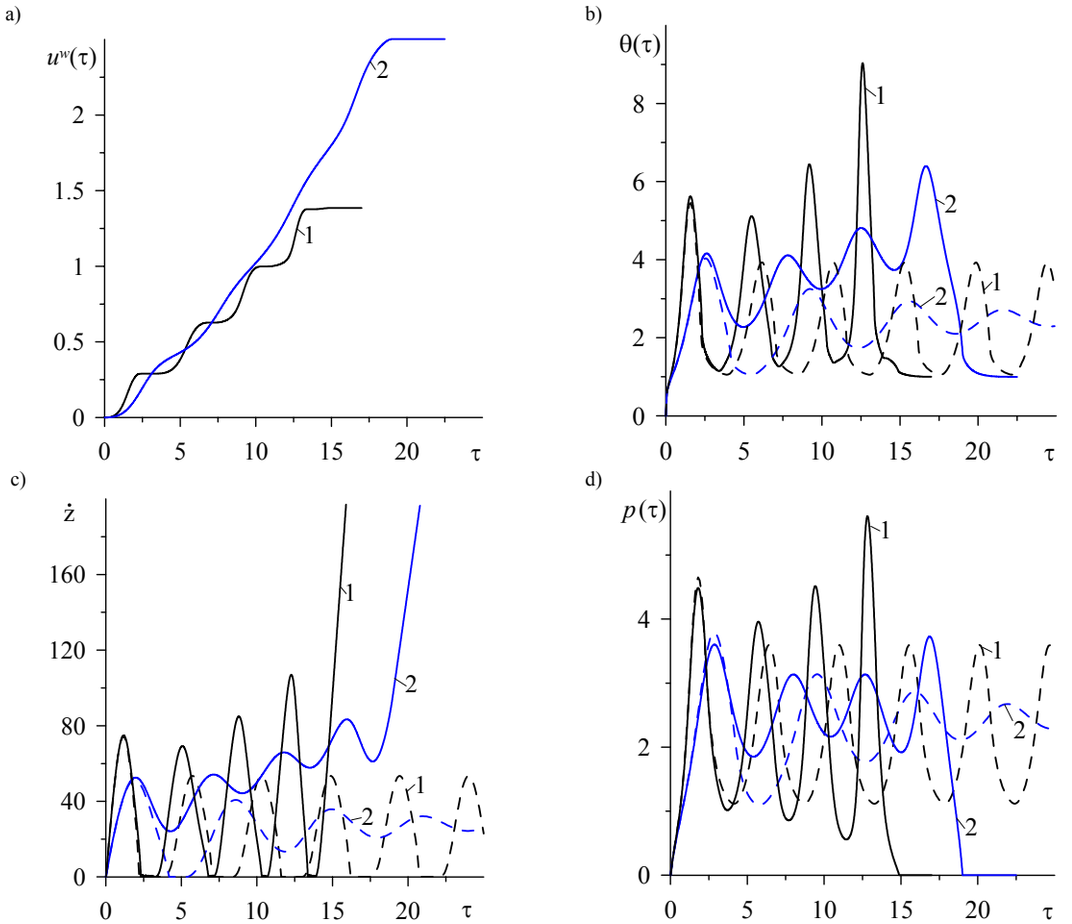


Figure 2 Time history of non-dimensional wear (a), contact temperature (b), body's velocity (c) and contact pressure (d) for various values of ε_1, solid curves $k^w = 0.001$, dashed curves $k^w = 0$ (curves 1: $\varepsilon_1 = 800$; curves 2: $\varepsilon_1 = 400$)

Dependence of non-dimensional wear $u^w(\tau)$, contact temperature $\theta(\tau) \equiv \theta(\pm 1, \tau)$, body velocity $\dot{z}(\tau)$ and contact pressure $p(\tau)$ on the non-dimensional time τ are also analysed. For $\varepsilon_1 = 800$, $k^w = 0$ a stationary solution is unstable, and a limiting stick-slip cycle appears with the expected period $T = 4.18$ (frictional auto-vibrations [5,6]). For $k^w = 0.001$ wear occurs and the sliding contact is lost.

CONCLUSIONS

In this work the results devoted to a novel problem of the mechanical system exhibiting frictional thermoelastic contact of a moving body subject to both non-constant friction coefficients and wear are presented and discussed. It is worth noticing that in the case of non-constant friction coefficient and heating, the self-excited vibration can appear in our system without an elastic part (stiffness). The last phenomenon is caused by body heating while accelerating, friction increase, and than braking and cooling of the system. Owing to wear auto-vibrations are damped, and the contact system state is bounded.

References

[1] Horyacheva I. H., Dobychin M.: Contact Problems in Tribology, Mashynostroyeniye, Moscow, 1988, in Russian.

[2] Awrejcewicz J, Pyryev Yu.: Thermoelastic contact of a rotating shaft with a rigid bush in conditions of bush wear and stick-slip movements. *International Journal of Engineering Sciences* **40**:1113-1130, 2002.

[3] Awrejcewicz J, Pyryev Yu.:Contact phenomena during breaking and acceleration of a bush-shaft system. *Journal of Thermal Stresses* (in press).

[4] Olesiak Z. S., Pyryev Yu. A.: A nonlinear, nonstationary problem of frictional contact with inertia and heat generation taken into account. *Acta Mechanica*, **143**:67-78, 2000.

[5] Kragelsky I.V., Hittis N.: Frictional Self-Oscillations. Nauka, Moscow, 1998, in Russian.

[6] Awrejcewicz J., Andrianov I.V., Manievich L.I.: Asymptotic Approaches in Nonlinear Dynamics: New Trends and Applications, Springer, Berlin, 1998.

THREE-DIMENSIONAL PROBLEM OF THE CONTACT BY DOUBLY CONNECTED DOMAIN TAKING INTO ACCOUNT ROUGHNESS AND FRICTION

Ganna Shyshkanova
Zaporozhzhia National Technical University, p/b 1018, 690104, Zaporizhzhia, Ukraine

Summary Expansion of simple fibre potential type integrals distributed on doubly-connected (and simply-connected) domain is received. The method of reduction to the sequence of problems for annular (and circular) contact domains is found out for three-dimensional contact problems with doubly-connected punch under nonlinear laws of friction, roughness of elastic half space.

Introduction

Different statements of contact problems taking into account roughness surfaces, friction and adhesion, for bodies with coating, etc. arose as a result of real-life characteristics consideration. Because of awkward mathematic difficulties in solving of specific real problems, there is a certain "distance" between theory and practical usage of the solutions.
Clear, effective, computational convenient methods are used in [1] for solving circular punch problem problems taking into account roughness surfaces, friction etc. [1,2].
Analogous methods for solving the problem about pressing of doubly-connected punch into elastic half-space under nonlinear friction and roughness laws are developed at present work.

Statement of the Problem

The problem about pressing of close to ring in plan punch into elastic half-space is in consideration. The problem reduced to the solution of the system of equilibrium equations and equation containing integrals with weak singularity.

$$\varphi(p(\rho_0,\theta_0)) + \iint_\Omega \lambda p(\rho,\theta)/r\, d\Omega + \iint_\Omega \cos\hat{r,x}\, \psi(p(\rho,\theta))/r\, d\Omega = f(\rho_0,\theta_0)\,, \qquad (1)$$

where $\varphi(p(\rho,\theta))$, $\psi(p(\rho,\theta))$, $p(\rho,\theta)$ - functions characterizing deformable properties of roughness, friction law and pressure distribution, correspondingly [1], $r^2 = \rho^2 + \rho_o^2 - 2\rho\rho_o\cos(\theta-\theta_o)$

Solution of the Problem for Annular Punch

Equation (1) is transformed to one-dimensional by the proposed in [3] method for the annular punch. Then direct method of successive iterations is used to solve the received equation of second kind. If we receive equation of first kind, regularization with parameter change is used.
Calculation method for the integral and norm of operator is used to specify parameter change interval, conditions of existence and unique solution. With help of potential expansion we assume that analytic in ring function, appropriated to desired pressure function, has singular point in zero relatively analytic extension of regular circular element of the function along any continuous curve through this point. Desired pressure function is presented in view of double series in terms of powers of $\ln\rho$, ρ. Infinite systems of linear algebraic equations are received by substitution of the double series at equation (1). The systems could be solved by method of successive iterations, reduction, exactly, etc.

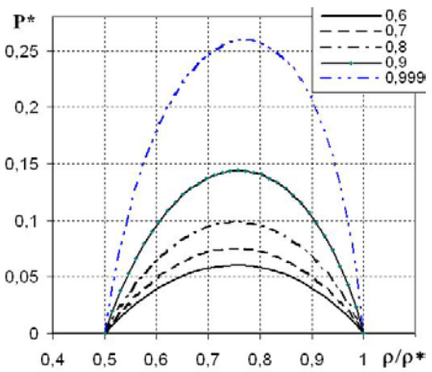


Figure 1

In case without friction and roughness, among the systems there are homogeneous with triangular matrixes, that have unique trivial zero solution. Only coefficients at plus even and minus odd powers of ρ are nonzero in the double series, they are exactly determined for any index.

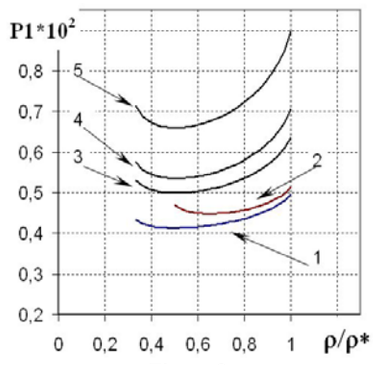


Figure 2

When in (1) $\psi(p(\rho,\theta)) = 0$, $\varphi(p(\rho,\theta)) = B_1 p(\rho,\theta)$ or $B_1 = (1-\alpha)$, fig. 1 shows curves of normal pressure distribution for non-plain parabolic annular punch, values of dimensionless parameters are $\alpha = 0.6, 0.7, 0.8, 0.9, 0.999$, $a/b = 0.5$, $D = 0.5$ - parameter, characterizing geometry of the punch. When α is close to 1 ($B_1 \approx 0$), we receive approximate pressure distribution under smooth punch without roughness of the elastic half-space [3].
We come to nonlinear Hammerstein integral equation in case of nonlinear law of roughness, in particular powers law $\varphi(p(\rho,\theta)) = B_1 p^k(\rho,\theta)$, when $\psi = 0$.
Graphs of contact pressure distribution under annular plain punch are presented on fig. 2 in case of nonlinear power dependence of micro asperity vertical displacement from normal pressure. Curve 1 has next values of parameters: $a/b = 1/3$, $\eta = 0.1$, $B_1 = 0.7$, $k = 0.4$. Next curves differ from curve 1: 2 - $a/b = 1/2$, 3 - $B_1 = 0{,}6$, 4 - $k = 0.45$, 5 - $\eta = 0.14$.

Solution of the Problem for Doubly-Connected Punch

The problem for doubly-connected punch is reduced to the sequence of problems for annular punch [4]. In every approximation, with use of expansion of potential with nonsymmetrical density [5], integral operators are transformed to operators with the same singularity and operators differentiable by Frechet. The problems are reduced to linear in every approximation besides zero approximation in case of nonlinear laws of roughness. Expansion of nonlinear integral operator by parameter is received upon continuous Frechet differentiability of abstract implicit function (Hammerstein operator), when the limits of integration depend from the parameter. Fig. 3 shows the surface of pressure distribution under doubly-connected plain punch close to rectangular ring in plan in case of linear dependence of roughness from pressure, taking into account two approximations, $\alpha = 0.6$, $a/b = 1/2$, $\varepsilon = 0.1406$.

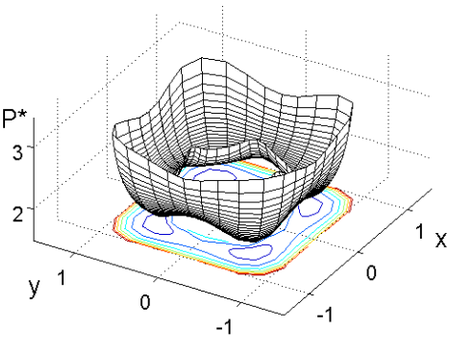


Figure 3

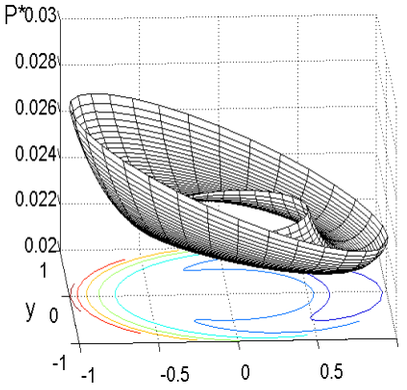


Figure 4

Solution of the Problem Taking into Account Friction

Equation (1) is reduced to one-dimensional with use of expansion of integral with weak singularity proposed in [6,7]. After the transformation of integral operators' kernels to Frechet differentiable, we define regions of parameter variation where the equation has unique solution. The solution could be found out by successive iterations method.

The surfaces of pressure distribution under annular (fig. 4) and circular (fig.5) plain punch are shown in case of nonlinear friction law and without rotation and horizontal diplacements of the punch. Here, condition of neglecting of vertical displacement of micro asperity, resulting from tangential force, takes place. The punch is loaded by vertical and horizontal forces; the last is balanced by friction force. Fig. 6 shows the surface of pressure distribution at the imbalance moment for plain circular punch (linear friction). When α is close to 1 ($B_1 \approx 0$) accounting friction, we receive approximate pressure distribution under the punch without roughness. Here, in case of linear friction the analytical solution is developed, which sensibly coincides with the solution by the method of successive iterations.

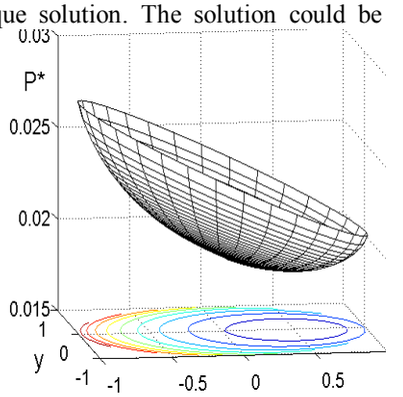


Figure 5

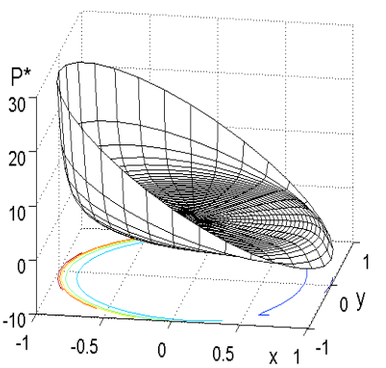


Figure 6

CONCLUSIONS

The method is developed for approximate and exact solutions of integral equations with weak singularity for contact problems with doubly-connected domains taking into account friction and roughness. The method gives possibility to reduce two-dimensional integral equations with weak singularity to one-dimensional. After proposed kernels transformations the reduced integral equations could be solved by approximate computational and analytical methods.

References

[1] Goryacheva I.G., Dobychin M.N.: Contact problems in tribology. Moscow: Mashinostroenie, 256 p., 1988.
[2] Goryacheva I.G.: Calculations of contact characteristics taking into account parameters of macro and micro geometry of the surfaces. *Friction and wear.* V.**20, #3,** p. 239-248
[3] Roytman A., Shyshkanova S.: Pressing of non plain annular punch into elastic half-space. *J.Applied Mech.*, v.**16**, №**4**, Kiev, p.35-41, 1980.
[4] Shyshkanova G.: To Use of Simple Fiber Potentials in Mathematical modeling in Technical systems. *J. Progressive Technologies and Systems in Industry.* iss. **22**. Donetsk. DonGTU, p.189-194, 2002
[5] Shyshkanova G.: To the Solution of Two Dimensional Integral Equation in the Problem of Annular Punch. - *Applied Problems on Mathematics & Mechanics*: Sebastopol: SevNTU, p.182-185, 2002
[6] Shyshkanova G.: Solution for the three-dimensional problem of punch motion taking into account forces of friction, adhesion. *Mechanika-2003*. Proceedings of the internation. conf. Kaunas: Technologija, p.311-317, 2003

EVOLUTIONS OF FRICTION ANISOTROPY AND HETEROGENEITY

Alfred Zmitrowicz
Institute of Fluid-Flow Machinery, ul. J. Fiszera 14, PL 80-952 Gdańsk, Poland

Summary Evolution and reorientation of microstructures take place in sliding surfaces of some polymers and layer-lattice materials. Advanced friction models describe evolutions of friction induced by a curvature of sliding trajectory. The sliding path curvature generates positive and negative additional friction and constraint forces normal to the sliding trajectory.

INTRODUCTION

During friction and sliding, besides surface roughness changes, material sliding surfaces may be subjected to evolution and reorientation of their microstructures. For instance, complex kinematics of sliding initiate microstructural and frictional changes in sliding surfaces of some polymers [1] and in layer-lattice materials as graphite [3] and molybdenum disulphide [2]. In these cases, microstructures of the sliding surfaces reorient themselves from randomly to highly oriented, and from one orientation to other (a self-organisation phenomenon). It may reduce (or increase) friction and wear. There are preferential sliding directions.
Advanced friction models can describe evolutions of frictional anisotropy and heterogeneity induced by the sliding kinematics. Due to this, first-, second- and higher-order descriptions of friction are developed with respect to powers of the sliding path curvature.

MODELS OF ANISOTROPIC AND HETEROGENEOUS FRICTION

Constitutive equations governing the phenomenon of anisotropic and heterogeneous friction are created in the frame of Amontons-Coulomb friction law. By the friction constitutive equation we mean a relation between a friction force vector **t** and a normal pressure N, a sliding velocity unit vector **v** and its derivative d**v**/ds with respect to a one-dimensional parameterization s of the sliding trajectory.

A first-order description

A first-order constitutive equation of the friction force has two independent variables, i.e. the sliding velocity unit vector **v** and its derivative d**v**/ds. It can be defined as a sum of two single-term polynomials as follows

$$\mathbf{t} = -N(\mathbf{C}_1\mathbf{v} + \mathbf{E}_1\mathbf{n}\frac{1}{\rho}), \tag{1}$$

where, according to the Frenet-Serret first formula d**v**/ds = **n**/ρ, **n** is a unit vector normal to the sliding path, ρ is a sliding path radius. Two second-order tensors $\mathbf{C}_1$ and $\mathbf{E}_1$ are equation coefficients (so called parametric tensors). For instance, the tensor $\mathbf{C}_1$ can define friction properties in the sliding surface which form (in geometrical terms): (a) concentric circles, (b) set of radii (i.e. rays emanating from the origin), see [4,5]. The tensor $\mathbf{E}_1$ describes constraints imposed on the motion in the directions tangent and normal to the sliding path. These constraints are functions of the first power of the sliding path curvature. The friction force (1) depends on the sliding direction and on a location of the contact point within the sliding area.

A second-order description

In the second-order formulation, the friction constitutive equation is a polynomial with respect to third-order tensors composed by **v** and **n**/ρ ; they are taken as the independent variables of the friction equation, i.e.

$$\mathbf{t} = -N\{\mathbf{C}_1\mathbf{v} + \mathbf{C}_2(\mathbf{v}^3) + \mathbf{E}_1\mathbf{n}\frac{1}{\rho} + \mathbf{E}_2[(\mathbf{v}^2,\mathbf{n})\frac{1}{\rho} + \ldots + (\mathbf{v},\mathbf{n}^2)\frac{1}{\rho^2} + \ldots + (\mathbf{n}^3)\frac{1}{\rho^3}]\}, \tag{2}$$

with the following notation of the third-order tensors

$$(\mathbf{v}^p,\mathbf{n}^q)\frac{1}{\rho^q} \equiv (\underbrace{\mathbf{v}\otimes\ldots\otimes\mathbf{v}}_{p-copies}\otimes\underbrace{\mathbf{n}\otimes\ldots\otimes\mathbf{n}}_{q-copies})\frac{1}{\rho^q}, \tag{3}$$

where, p = 0,1,2,3 q = 0,1,2,3 and (p + q) = 3. The equation coefficients $\mathbf{C}_2$ and $\mathbf{E}_2$ are tensors of the fourth-order; $\mathbf{C}_2$ defines other types of frictional anisotropy and heterogeneity (e.g. local tetragonal anisotropy), $\mathbf{E}_2$ describes additional friction and motion constraints which depend on first, second and third powers of the sliding path curvature.

Higher-order descriptions

Non-homogeneous friction described with the aid of other field singularities requires friction equations of higher order. Then, the polynomial form of the friction equation contains terms which are contractions of the friction tensors $\mathbf{C}_i, \mathbf{E}_i$, i = 1,2,...,n and the higher-order tensors composed by **v** and **n**/ρ. According to the objectivity axiom only odd order tensors composed by **v** and **n**/ρ may be included in the polynomial, i.e. first, third,...,2n-1. The independent variables are composed in accordance to the rule (3), where p = 0,1,...,2n-1, q = 0,1,...,2n-1 and $(p + q)$ = 3,5,...,2n-1. Tensors $\mathbf{C}_i$ define anisotropy and heterogeneity of friction. Tensors $\mathbf{E}_i$ define effects associated with the sliding motion. In this model, the friction force depends on an arbitrary power of the sliding path curvature.

COMPOSITIONS OF TWO FRICTION ANISOTROPIES AND HETEROGENEITIES

It is assumed that for a given normal pressure N the resultant friction force $\mathbf{t}_{AB}$ at the contact of two surfaces (A and (B) is equal to the product of a "composition coefficient" by the sum of the friction forces obtained for each surface taken separately, i.e.

$$\mathbf{t}_{AB} = \kappa(\overset{(A)}{\mathbf{t}} + \overset{(B)}{\mathbf{t}}), \tag{4}$$

where, κ is the experimental composition coefficient, $\overset{(A)}{\mathbf{t}}$ and $\overset{(B)}{\mathbf{t}}$ are friction forces which correspond to the friction when sliding a third body with isotropic homogeneous properties along the contacting surfaces (A) and (B). The friction forces for surfaces (A) and (B) can be represented by equations (1) and (2). The hypothesis (4) describes changes in friction anisotropy and non-homogeneity when two different sliding surfaces are composed together.

EXAMPLES

The friction constitutive equations proposed in this contribution are completed with illustrative examples. Sliding trajectories of a material point in the surface with complex tribological properties are investigated. Sliding motions are excited by initial velocities. Motion equations are given in the local basis defined by unit vectors tangent and normal to the sliding trajectory {**v**, **n**}. The friction force components in the basis {**v**, **n**} depend not only on the sliding direction but also on a shape of the sliding path. Different types of anisotropic and non-homogeneous friction properties are considered, e.g. the friction properties which form concentric circles in the surface. In this case, there are two types of privileged sliding directions: radial (along radii), concentric circular (along concentric circles). Essential changes of sliding trajectories of the material point are observed for various values of parameters of the friction tensors in the constitutive equations (1) and (2).

CONCLUSIONS

The sliding path curvature generates: (a) additional resistance to sliding (dissipative type forces), (b) constraint forces normal to the sliding path (gyroscopic type forces). It can induce positive and negative additional friction, and it can change essentially the sliding trajectory. Friction cones change cross-sectional shapes in dependence on the sliding trajectory curvature. Rectilinear and curved privileged sliding directions occur in this case.

As in the classical continuum mechanics and thermodynamics, mathematical restrictions on forms and parameters of the friction constitutive equations arise from the objectivity axiom and the Second Law of Thermodynamics (an entropy production inequality), see [4,5].

Acknowledgements

The financial support was provided by a grant from the State Committee for Scientific Research, No. 8T07A 03420.

References

[1] Briscoe B.J., Stolarski T.A.: The influence of contact zone kinematics on wear process of polymers. *Wear* **149**:233-240, 1991.
[2] Persson B.N.J.: Sliding Friction. Physical Principles and Applications. 2nd ed., Springer, Berlin 2000.
[3] Senouci A., Frene J., Zaidi H.: Wear mechanism in graphite-copper electrical sliding contact. *Wear* **225-229**:949-953, 1999.
[4] Zmitrowicz A.: An equation of anisotropic friction with sliding path curvature effects; Illustrative examples of anisotropic friction with sliding path curvature effects. *Int. J. Solids Structures* **36**:2825-2848, 2849-2863, 1999.
[5] Zmitrowicz A.: Glaciers and laws of friction and sliding. *Acta Mechanica* **166**:185-206, 2003.

INVERSE PROBLEMS OF THERMOELASTICITY FOR FRICTIONALLY INTERACTING LAYERS

Victor Shevchuk, Anatoliy Yasinskyi
Pidstryhach Institute for Applied Problems of Mechanics and Mathematics, National Academy of Sciences of Ukraine, 3b Naukova, 79060 Lviv, Ukraine

Summary New inverse thermoelasticity problems for frictionally interacting layers have been formulated, in which unknown thermal loading (temperature of boundary surface, intensity of frictional heat flux) is determined using additionally given vertical displacements of one of the outer boundary surfaces. The functional spaces, in which the problems are well-posed, have been found. The method for solving the problems has been suggested and numerically verified with the use of the solution of the direct problem.

INTRODUCTION

The thermal stressed state of frictionally interacting bodies under known initial-boundary thermal and mechanical conditions can be investigated with the use of well-known methods, such as, for example [1-3]. However, for the working friction couple, the information on thermal loading is often available only on the part of a surface as a result of the restriction of access possibility that makes an appropriate thermoelasticity problem ill-posed. To determine thermal regime and thermal stressed state of the friction couple in this case, it is possible to use additional information and to reduce the initial thermoelasticity problem to the inverse one [4, 5].
The problem of determining the friction coefficient of interacting bodies is also important. The friction coefficient is often considered in calculations as a constant value. In reality the friction coefficient changes in time and depends on many factors, such as normal loading, temperature of bodies, sliding velocity, etc., which are also changeable under the conditions of the non-stationary character of the process. It is shown in the paper that the problem of finding the unknown law of change in time of the layers friction coefficient under known boundary and initial conditions can be solved by using additionally measured vertical displacements of one of the outer boundary surfaces of the friction couple, that is by reducing it to the solution of the inverse problem.
Using the found change in time of the friction coefficient and known sliding velocity and contact pressure, it is possible to determine the change in time of the intensity of the frictional heat flux, which is important for adequate calculation of the friction couple and for the choice of rational regimes of its work.

STATEMENT OF PROBLEMS

Let us consider a one-dimensional model of the friction contact of two different layers. We assume that the lower surface of the first layer is elastically fixed, while the second layer is moving with variable speed over the first one and is pressed to it. As a result of friction on the contact surface, heat is formed. The intensity of the total frictional heat flux equals the specific power of friction forces. The mechanical contact of layers is assumed to be ideal, and the thermal contact is considered as non-ideal.
Within this assumed framework, the following problems are investigated:

- problem 1 consists in determining unknown thermal loading on the fixed surface of the friction couple by given temperature and vertical displacements of the other outer boundary surface;
- in problem 2, the change in time of the layers friction coefficient (intensity of frictional heat flux) is determined by additionally known vertical displacements of the outer loaded boundary surface of the friction couple under given initial and boundary thermal conditions.

The formulated problems are inverse thermoelasticity problems, in which the cause – thermal loading (temperature of the boundary surface) in problem 1 and the intensity of the frictional heat flux (friction coefficient) in problem 2 – is determined by the displacements of the boundary surface.

SOLUTION OF PROBLEMS

Using the well-known methods of solving equations of the appropriate contact problem of thermoelasticity for the layers under consideration [3], we represent vertical displacements of the second layer in the form of functional dependence upon the distribution of temperature of each layer. If we substitute into this dependence the temperatures of layers found with the help of the Laplace integral transformation in the form of functional dependences on loading thermal factors and take into account that the displacements of the outer boundary surface of the second layer are known, we will obtain the convolution type Volterra integral equations of the first kind

$$\int_0^t K_i(t-x)Q_i(x)dx = F_i(t), \qquad 0 \le x \le t, \qquad i = 1,2 \tag{1}$$

for determining at the time moment $t \in [0, t_*]$ the unknown function $Q_1(t)$ – the temperature of the boundary surface in problem 1 and $Q_2(t)$ – the intensity of the frictional heat flux (friction coefficient) in problem 2. In equations (1) F_i are known functions represented through the prescribed displacements and functions, which are given in the boundary and initial conditions, $K_i(t - x)$ are known kernels.

The investigation of the kernel $K_1(t - x)$ has shown that it is possible to find the unique continuous stable solution $Q_1(t) \in C[0, t_*]$ of problem 1 using the Laplace integral transformation, if input functions (displacements, temperature of the surface, intensity of the frictional heat flux) are twice continuously differentiable from space $C^2[0, t_*]$. This means that in the indicated functional spaces problem 1 is well-posed. Integral equation (1), which corresponds to problem 2, can be reduced to the Volterra integral equation of the second kind with the kernel with integrable singularity. The unique continuous stable solution $Q_2(t) \in C[0, t_*]$ of the obtained equation can be found by means of the method of averaged functional corrections [6]. Here the inverse problem is well-posed if input functions (displacements, temperatures of surfaces) are continuously differentiable from space $C^1[0, t_*]$.

The obtained solutions of the formulated problems allow us to investigate the change in time of functions $Q_i(t)$ during the whole period of bodies interaction as well as dependence of the friction coefficient on the determining parameters of the process (such as sliding velocity, contact pressure, temperature of contact surface).

NUMERICAL VERIFICATION

For the friction couple bronze-steel, the numerical verification of the suggested method for solving the formulated problems has been carried out. With this purpose, we prescribed boundary thermal conditions and determined the change in time of vertical displacements of the outer boundary surface of the second layer as a solution of the appropriate direct contact thermoelasticity problem. The found displacements were approximated by cubic spline with accuracy $d = 0.1\%$ and were used as given in inverse problems. Using the suggested here approach, we determined the solutions of inverse problems – temperature of the boundary surface (problem 1) and the friction coefficient (problem 2). Comparison of the found solutions with the functions given in direct problems has shown that maximal relative deviation of the solutions from appropriate known functions does not exceed $e = 0.8\%$ in problem 1 and $e = 1.4\%$ in problem 2 that provides evidence of satisfactory accuracy of obtained inverse problems solutions. It should be noted that the decrease of the error of displacements approximation d leads to the decrease of relative deviation e that numerically confirms stability of obtained solutions.

CONCLUSIONS

1. Within the framework of the one-dimensional model of frictional interaction of different layers, new inverse thermoelasticity problems have been formulated, in which unknown thermal loading (temperature of the outer boundary surface, frictional heat flux) is determined by the additionally known change in time of vertical displacements of one of the outer boundary surfaces.
2. The method for solving formulated problems has been suggested based on their reduction to the Volterra integral equations with further use of the Laplace integral transformation and of the method of averaged functional corrections.
3. On the basis of the analysis of the formulated problems, the functional spaces in which the problems are well-posed have been determined.
4. For the friction couple bronze-steel, the numerical verification of the suggested method for solving the formulated problems has been performed, which confirmed its efficiency.

References

[1] Barber J.R.: The Influence of Thermal Contact Resistance on the Heat Transfer Performance of Prestressed Duplex Tube. *Int. J. Heat Mass Transfer* **29**: 761–767, 1986.

[2] Goryacheva I.G., Dobychin M.N.: Contact Problems in Tribology. Mashinostroenie, Moscow 1988.

[3] Grylitskiy D.V., Pyryev V.A., Mandzyk Y.I.: Quasistatic Thermoelastic Contact Problem for Infinite Twolayer Circular Cylinder under Friction Heating. *J. Thermal Stresses* **20**:47-65, 1997.

[4] Yakhno V.G.: Inverse Problems for the Differential Equations of Elasticity. Nauka, Novosibirsk 1990.

[5] Yasinskyi A.V.: Reconstruction of Temperature Fields and Thermal Stresses for Given Displacements in the Case of Friction Contact of Layers. *Materials Science* **38**: 814 – 823, 2002.

[6] Luchka A.Yu.: Projective and Iterative Algorithms of the Solutions of Differential and Integral Equations. Naukova Dumka, Kiev 1980.

MULTIDIMENSIONAL MODEL OF COMBINED DRY FRICTION

Alexey A. Kireenkov*
*Institute for Problems in Mechanics of Russian Academy of Sciences
101-1 Prospekt Vernadskogo, 119526 Moscow, Russia

Summary. A new multidimensional model of combined dry friction is presented. This model is generalization of primary one-dimensional Coulomb model to the case when relative motion of rubbing solids is combination of sliding and spinning for arbitrary form of area of contact. The method of straight constricting of quadratic Pade approximation of components of friction force and momentum is developed for using of the proposed model in the task of solids dynamics

INTRODUCTION

Contensou in case of not point contact of the moving bodies had established the correlation between the friction of slide and the friction of spin [1]. Using the Hertz theory of contact, he had got the numeric function of the dry friction force from ration of the slide and rotation velocities, supposing that the both contiguous surfaces are local spheres. But Contensou had restricted the calculation by the friction force only and not considered the momentum of the friction forces.

Zhuravlev had significantly improved the Contensou theory [2]. He had got exact analytical functions of the dry friction force and momentum from ration of the slide and rotation velocities. To use these relations in the tasks of dynamics of rigid bodies, Zhuravlev had built the partial-linear Pade approximation of the dry friction force and momentum.

Kireenkov had applied Contensou - Zhuravlev theory to solve the task about motion with rotating of the flat disk on the plane [3]. He had got exact functions and Pade approximations of the dry friction force and momentum, supposed that area of contact is of the circle form, while distribution of the normal contact stress in the area of contact has form. Then Kireenkov has developed a direct method for constructing of partial-linear Pade approximation of friction force and momentum for area of contact having circle form as a function of ration of the slide and rotation velocities [4].

On the base of describing above investigations, Zhuravlev has built a two-dimensional model of combined dry friction [5]. He has developed a direct method for constructing partial-linear Pade approximations of friction force and momentum in term of velocities of sliding V and rotation ω for the case of the circle area of contact and arbitrary axial-symmetric distributions of contact stresses. Using partial-linear Pade approximations for force and momentum, Zhuravlev has constructed a “STANDSTIL” zone which is very convenient for qualitative describing the dynamics of solids when either friction force or momentum are tended to zero.

The suggested below multidimensional model of combined dry friction is logical generalization of two-dimensional Zhuravlev model on the case of arbitrary form of area of contact and arbitrary distributions of contact stresses.

MULTIDIMENSIONAL MODEL OF COMBINED DRY FRICTION

Under the words “model of dry friction” we understand the interrelations between forces, momentums and velocities. The physical nature of phenomena within the area of contact is not interested for us. It is supposed that the form of area of contact and distributions of contact stresses are known.

For the model constructing we used following basic suppositions:

- Arbitrary form of area of contact
- Arbitrary distributions of contact stresses
- Relative motion of friction solids is combination of sliding and spinning:

In suggestion of validity of the Coulomb low in local form for differential of the tangent friction force at any elementary square within the area of contact we have the following relations between force, momentum and velocities:

$$F_x(V,\omega) = -f_0 \iint \frac{(V-\omega y)\,\sigma(x,y)}{\sqrt{\omega^2(x^2+y^2)-2\omega V y+V^2}}\,dx\,dy$$

$$F_y(V,\omega) = -f_0 \iint \frac{\omega x\,\sigma(x,y)}{\sqrt{\omega^2(x^2+y^2)-2\omega V y+V^2}}\,dx\,dy$$

$$\mathrm{M}(V,\omega) = -f_0 \iint \frac{(\omega(x^2+y^2)-V y)\,\sigma(x,y)}{\sqrt{\omega^2(x^2+y^2)-2\omega V y+V^2}}\,dx\,dy$$

where $F_x(V,\omega)$ - component of the friction force in the direction of the vector of velocity of sliding V, $F_y(V,\omega)$ - component of friction force in perpendicular direction to the vector of velocity of sliding V, $M(V,\omega)$ - momentum of dry friction, $\sigma(x,y)$ - distribution of contact stresses, f_0 - coefficient of friction.

These expressions as function of V and ω are invariant with respect to similarity group. Consequently, any approximations for the friction force and momentum have to be invariant with respect to similarity group. To use these expression in the tasks of solids dynamics quadratic Pade approximations have constructed. Utilizing of quadratic Pade approximations is substantiated by the requirement simultaneously describing of the behavior of function at zero and infinity and insufficiency of partial-linear Pade approximations to approximate the component of force of friction in the perpendicular direction to the vector of velocity of sliding V. To calculate corresponded Pade approximations we choose the origin of coordinate systems from the conditions of conversion to zero the momentum of friction forces simultaneously with the velocity of spin ω: $M(V,0)=0$. This point is fixed in the area of contact and may be interpreted as the center of gravity of the contact spot in the supposition that the distribution of normal stresses is playing the role of density.

$$\iint_D x\sigma(x,y)dxdy = 0, \quad \iint_D y\sigma(x,y)dxdy = 0$$

Quadratic Pade approximations for force and momentum of dry friction

Quadratic Pade approximation, conserved the behaviour of the force and momentum and it's the first, the second and the third derivations in zero and infinity have form

$$F_{xp} = \frac{F_0(v^2 + a_1 v\omega)}{v^2 + a_1 v\omega + a_2\omega^2}, F_{yp} = \frac{b_1\omega^2}{b_2 v^2 + b_3 v\omega + \omega^2}, M = \frac{M_0(\omega^2 + m_1 v\omega)}{m_2 v^2 + m_1 v\omega + \omega^2}$$

where corresponded coefficients have been calculated.

In the case of axially symmetric areas of contact (circle, ellipse, rectangular) the force component F_y is zero. Consequently, the quadratic Pade approximations are significantly simplified, and have form

$$F_{xp} = \frac{F_0(v^2 + a_1 v\omega)}{v^2 + a_1 v\omega + a_2\omega^2}, M = \frac{M_0(\omega^2 + m_1 v\omega)}{m_2 v^2 + m_1 v\omega + \omega^2}$$

where coefficients are depend on the turn angle of the rotation solid respectively choosing system of coordinate.
Formulas defined the corresponded quadratic Pade approximations may be considered as the rheological model of combined dry friction.

CONCLUSIONS

- Quadratic Pade approximations are required to describe the appearance of component of dry friction force in perpendicular directions to vector velocity of sliding.
- Only quadratic terms contained in Quadratic Pade approximations.
- It is not needed to calculate the integrals, defining the coefficients of Pade approximation. The corresponded coefficients may be defined from experiments.

References

[1] Contensou P. Couplage entre frottement de glissement et frottement de pivotement dans la theorie de latoupie. Gyrodynamics. Symposium Celerina, August 20-23,1962, Springer, 1963.
[2] Zhuravlev V.F. About the model of dry friction in the tasks rolling motion of the solids.// Moscow, Nauka, Journal of Applied Mathematics and Mechanics 62(5), 705-710, 1998.
[3] Kireenkov A.A. Influence of the composed dry friction to the dynamics of the homogeneous rotating disk on a plane. 6th Conference on dynamical systems: theory and applications. Proceedings. Express Poligr. 61, 2001
[4] Kireenkov A.A. A Method of calculation of friction force and momentum in combined model of dry friction for circle area of contact Moscow, Nauka, Isvestiya RAN, Mechanica Tverdogo Tela 3, 2003, pp.51-56.
[5] Zhuravlev V.F. The regularities of friction at combination of sliding and spin. Moscow, Nauka, Isvestiya RAN, Mechanica Tverdogo Tela 4, 2003, pp.81-88.

NUMERICAL MODELING OF CONTACT FRACTURE OF ELASTO-PLASTIC CRACKED BODIES

Alexandr A. Bobylov, Yuriy A. Letser

Dniepropetrovsk National University, Department of Mechanics and Mathematics, pr. Naukovy 13, 49625, Dniepropetrovsk, Ukraine

Summary Based on the finite element method, the algorithm for numerical modelling is developed and analysis is carried out for processes of crack extension in elasto-plastic finite bodies under contact compression. It is clarified that both sliding mode and opening mode cracks can develop in an elasto-plastic body under contact compression.

PROBLEM DEFINITION

Different engineering devices are used in industrial production for fracture of elasto-plastic materials such as rock. Many of them use the mechanical principle of operation based on local indentation of the instrument into the destroyed body. Fracture occurs as a result of the crack extension in stress concentration zones near the contact area. Therefore, research of the crack extension processes in elasto-plastic finite bodies under a contact loading is important for further improvement of such devices.

Mathematical modelling of contact fracture is based on the solution of contact problems of elasto-plastic cracked finite bodies. Boundary conditions of unilateral contact with presence of the Coulomb friction are set on the surfaces of contact bodies and crack faces. Actual dimensions of contact areas of the bodies, contact areas of the crack faces and zones of engaging and slipping are unknown and are subject for definition.

Defining relation of the theory of plasticity were accepted in the generalized form

$$\dot{\sigma}_{ij} = A_{ijkl}\left(\chi_1, \chi_2, \ldots, \chi_r, \dot{\varepsilon}_{\xi\eta}\right)\dot{\varepsilon}_{kl},$$

where $\chi_1, \chi_2, \ldots, \chi_r$ are values of functionals of a deformation history. Coefficients $A_{ijkl}(\ldots)$ are homogeneous functions of a zero degree concerning components of $\dot{\varepsilon}_{\xi\eta}$ tensor. It is possible to write down the defining relation for practically all existing versions of a plasticity theory by selecting a particular kind of $A_{ijkl}(\ldots)$ coefficients.

METHODS

In the present work the variational method of contact problems solution for elasto-plastic cracked finite bodies is used. Quasivariational inequalities for definition of both velocities and displacement increments were built. Some versions of time coordinate semidiscretization are surveyed for quasivariational inequalities in velocities. Various iteration procedures were used to provide a usage of implicit integration schemes on a time for physical linearization of the problem.

In result, sequences of problems of minimization of functionals are obtained. The finite element method is used for their discretization with respect to space coordinates. Modifications of the successive overrelaxation method and the conjugate gradient method are developed for solution of the obtained finite-dimensional nonlinear programming problems.

Energy methods and path independent integrals [1, 2] were used for definition of fracture mechanics parameters. Prediction of a small crack length change and definition of its orientation was provided by a local fracture criterion. The location and orientation of the initial cracks were determined on the basis of the stress-strain analysis of a destroyed body with usage of phenomenological maximum shear stress criterion for sliding mode cracks and maximum normal criterion for opening mode cracks. The size of initial cracks was selected commensurable with the most typical defects of the material.

SOFTWARE

Developed computational algorithms are implemented as an application package for solution of elasto-plastic cracked finite bodies contact problems. The software package consists of three parts: the preprocessor of input data, the FEM processor and the graphics postprocessor. The preprocessor is intended for preparation and conversion of input data according to the interface of the FEM processor. The special attention is given to development of automatic grinding algorithms of FE grids in the area around apex of cracks. The FEM processor is intended for numerical solution of elasto-plastic cracked finite bodies contact problems by the finite element method utilizing described above computational algorithms. At the present time, the FEM processor is implemented for solution of two-dimensional problems. Triangular and quadrangular elements of the first and the second orders are used. The graphics postprocessor is intended for visualization and analysis of the calculated results.

RESULTS

The numerical modeling and analysis of crack extension in elasto-plastic finite bodies under indentation by instruments of different shapes and rigidity were obtained under conditions of a plane strain.
Dependencies of fracture mechanics parameters on sizes and positions of the cracks, which are located near to the contact area, are defined. Variations of crack extension paths with the selected local fracture criterion are investigated. Crack interaction effects are researched in case of a simultaneous extension in a body with several macrocracks.
Residual stresses in an elasto-plastic body after unloading are defined both in absence and in presence of cracks. Influence of residual stresses on behavior of cracks under a repeated local contact loading is researched.
Effect of friction force on contact surfaces of bodies and sliding mode crack faces on crack extension in elasto-plastic bodies is established.
Calculations were carried out based on various plasticity theories: the theory of small elasto-plastic deformations, the theory of plastic flow with isotropic, transmit and combined hardening. The comparative analysis of the results obtained for these plasticity theories is carried out.

CONCLUSIONS

Numerical modeling is an effective approach to research crack extension processes in elasto-plastic finite bodies under contact compression.
Based on the computational experiments, it is clarified that not only sliding mode cracks, but also opening mode cracks can develop in a body under contact compression. Regularities of residual stresses occurrence in elasto-plastic finite bodies under local compression and character of their influence on behavior of cracks under repeated contact compression are defined.
The further development of the offered approach should be directed on solution of three-dimensional elasto-plastic bodies' problems of fracture mechanics.

References

[1] Morozov Ye. M., Nikishkov G.P.: Finite Element Method in Fracture Mechanics. Nauka, Moskow, 1980. (in Russian)
[2] Computational Methods in the Mechanics of Fracture: Ed. by Atluri S.N. North-Holland, NY, 1986.

CRACK-LIKE AND PULSE-LIKE MODES OF FRICTIONAL SLIDING ALONG AN INTERFACE UNDER DYNAMIC SHEAR LOADING

Demirkan Coker*, Alan Needleman* and Ares J. Rosakis**
*Brown University, Division of Engineering, Providence, RI, 02912, USA
**California Institute of Technology, Division of Engineering and Applied Sciences, Pasadena, CA, 91125, USA

Summary Frictional sliding along an interface between elastic solids under impact shear loading conditions is analyzed numerically. The configuration analyzed consists of two plates of the same material connected along a planar interface. The plates are characterized as isotropic elastic materials and the interface is characterized by a rate- and state-dependent frictional law that also accounts for dependence on normal stress variations. Calculations are carried out for various characterizations of the frictional response and for various impact velocities. Two modes of sliding are observed: a pulse-like mode where the slipping at a point on the interface is of short duration and a crack-like mode where the duration of slipping is much longer. The dependence of these sliding modes on the initial compressive stress, the impact velocity and the friction parameters is explored. The convergence of the numerical results is also considered.

INTRODUCTION

Frictional sliding along an interface between two deformable solids is a basic problem of mechanics that arise in a variety of contexts including, for example, material processing, deformation and failure of fiber reinforced composites and earthquake dynamics. The classical Coulomb type of frictional relation relates the shear stress to the normal stress by a proportionaliy constant μ which can have a dependence on the relative sliding velocity. However, Adams [1] showed that the problem of frictional sliding along an interface between two elastic solids, with sliding governed by Coulomb friction, is unstable to perturbations and hence ill-posed for a significant range of values of μ. Rate- and state-dependent models of friction have been introduced [2-4] that phenomenologically characterize the surface evolution and provide a representation of the transition from static to dynamic friction at constant normal load. For varying normal stress, Prakash and Clifton [5] added an additional state variable to account for their observation of a delay in the change in shear traction following a sudden change in the normal traction. The use of these friction laws regularize the sliding friction problem of elastic bodies with changing normal stress and make it a well-posed problem. In this paper we report on the implementation of a modified form of the rate-state friction model in a finite-element code within a cohesive zone framework to simulate the frictional sliding behavior of two elastic surfaces under dynamic loading.

NUMERICAL BACKGROUND

Friction constitutive law used is a modified version of the Prakash-Clifton rate- and state-dependent law [6] characterized by the relation,

$$T_s = \mu(\theta_1, V_{slip})(\theta_2, \theta_3) \tag{1}$$

where V_{slip} is the relative sliding velocity of the interface, T_s is the shear traction at the interface, θ_i are the state variables characterizing the history of the interface. The evolution equations for the state variables also include a characteristic length and the parameters are chosen so that the shear traction decreases with sliding velocity (velocity-weakening).

A finite-strain finite element code with a cohesive surface formulation is used. The constitutive laws for the cohesive surface relates the traction rates to the displacement jumps and is given by the rate- and state-dependent friction laws. Computations are carried out for the specimen geometry shown in Fig. 1. Two Homalite plates of $L = 150$ mm height and $w = 100$ mm are subject to a uniform compressive stress of magnitude Σ_0. A Cartesian coordinate system $y^1 - y^2$ is used with the origin taken as shown in Fig. 1. At $t = 0$, the plate is subject to a prescribed normal velocity, $V_i(t)$, along a portion of the edge $y^1 = 0$. The duration of the impact velocity is taken to be 25 μs.

NUMERICAL RESULTS AND DISCUSSION

In the first simulation, the plates are subjected to a compressive stress $\Sigma_0 = 0.80$ MPa and the left side of the lower plate is subjected to an impact velocity of $V_{imp} = 40$ m/s. Figure 2a shows the variation of the slip rate at $t = 15$ and $25\mu s$. Initially there is a sharp increase in the slip velocity reaching a peak of 60 m/s followed by a slip velocity of $30 - 40$ m/s behind the propagating front. This represents the crack-like growth mode of the sliding surface where the interface continues to slide behind the initial rupture front. The amplitude of the initial peak does not vary significantly with distance. The rupture front propagates at the longitudinal wave speed of the material. Fig. 2(b) shows the total slip on the interface at different times. Total slip is monotonically increasing with time as expected for an expanding crack-like rupture front.

In the second simulation, the applied compressive load is increased to $\Sigma_0 = -8.0$ MPa MPa and the loading speed is decreased to $V_{imp} = 20$ m/s. Fig. 2c shows snapshots of the relative slip velocity along the interface at times of 30, 31,

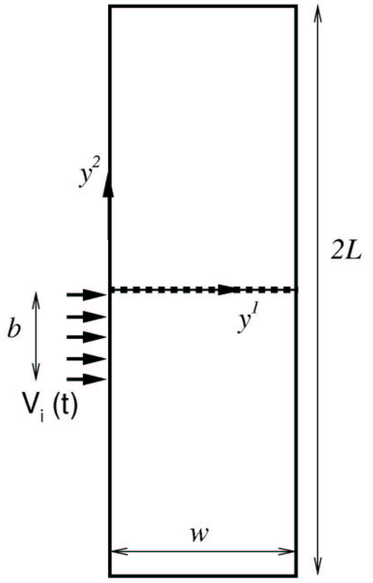


Figure 1.

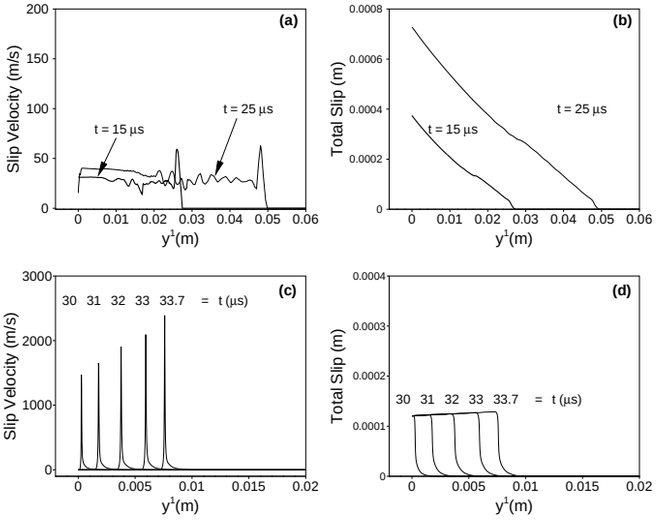


Figure 2.

32, 33, and 33.7 μs. At a fixed time the slip velocity increase drastically from zero to a peak value than drops down to zero again in a very short distance. This behavior represents a self-healing pulse and propagates at the longitudinal wave speed. The peak slip velocity increases with distance and time, and becomes an unstable slip pulse. Fig. 2(d) shows the total slip with time. In contrast to the crack-like mode, the total slip stays at a constant value after the initial jump in the slip distance showing that the sliding surfaces are locked together behind the rupture.

CONCLUSIONS

Computational simulations with a rate- and state-dependent friction constitutive relations for the interface showed the existence of self-healing slip pulses in the interface between two plates under dynamic shear loading conditions. Increasing impact speeds and increasing compressive load resulted in a transition from an enlargening crack-like frictional sliding to self-healing pulse-type frictional sliding. These slip pulses were unstable as the peak slip velocity value increased with distance.

References

[1] Adams, G. G.: Self-Excited Oscillations of Two Elastic Half-Spaces Sliding with a Constant Coefficient of Friction. *J. Appl. Mech.* **62**:867–872, 1995.

[2] Dieterich, J. H.: Modeling of Rock Friction 1. Experimental Results and Constitutive equations. *J. Geophys. Res.* **84**:2161–2168, 1979.

[3] Ruina, A. L.: Slip Instability and State Variable Friction Laws. *J. Geophys. Res.* :–, 1983.

[4] Rice, J. R. and Ruina, A. L.:Stability of Frictional Sliding. *J. Appl. Mech.* **50**:343–349, 1983.

[5] Prakash, V. and Clifton, R. J.: Pressure-Shear Plate Impact Measurement of Dynamic Friction for High-Speed Machining Applications. *Proc. 7th Int. Congress on Exp. Mech., SEM, Bethel, CT*: 556–564, 1993.

[6] Povirk, G. L. and Needleman, A.: Finite Element Simulations of Fiber Pull-Out. *J. Eng. Mat. Tech.* **115**:286–291, 1993.

EXPERIMENTAL AND NUMERICAL STUDY OF THE BRICK-MORTAR INTERFACE

Leila Abdou, Ramdane Ami Saada, Fékri Meftah, Ahmed Mébarki
LaM, Laboratoire de Mécanique, Université de Marne-La-Vallée, France

Summary The principal failure mode of the masonry walls is the shearing process in a brick-mortar bed interface. In order to understand this phenomenon, an experimental study was carried out. Loading/unloading shear tests have been performed using bricks with and without hollow. The influence of brick hole was in particularly studied. According to the obtained results, an interface model was proposed and then implemented in a finite element code.

EXPERIMENTAL STUDY

Many authors studied the shear bloc-mortar interface behaviour using several specimens (triplet or couplet) [1] and [2]. The Coulomb friction law using two material parameters (cohesion and friction angle), is generally assumed to represent the failure of masonry joints under coupled loading (shear and compression). The first objective of the experimental work presented here is the investigation of the shear mortar joint behaviour using loading/unloading shear tests. The second one is to study the influence of brick hole in the interface characteristics. A combination of both solid and hollow clay brick with one type of mortar has been used. The tensile and compressive strength of the employed mortar are respectively $4.14\,N/mm^2$ and $20\,N/mm^2$. The compressive strength of the brick was also determined in two directions: in the first one (parallel joint direction) the obtained values are $34\,N/mm^2$ and $20.31\,N/mm^2$ for solid and hollow brick. While in the perpendicular joint direction, the compressive strength values are respectively $42\,N/mm^2$ and $34\,N/mm^2$. The specimens were manufactured using only half brick glued by $10mm$ of mortar and stored for 28 days at constant temperature of $25\,C°$ and relative humidity of $90\,\%$.
The shear testing apparatus employed was designed at the Centre Scientifique et Technique du Bâtiment (CSTB – France). A vertical and horizontal jacks were used to apply normal and shear loads respectively. First the compressive normal stress is applied and then the shear stress is applied by imposing displacement with a velocity of $0.01mm/s$. The normal and shear stresses are recorded by mean of load cells. The relative displacement between the top and the bottom half brick was measured using two displacements transducer.

EXPERIMENTAL RESULTS

In order to avoid the rotation of the specimen while applying loading/unloading processes, a low compressive pre-stress is maintained at $0.3\,N/mm^2$. The shear stress versus the relative displacement curves are presented in figure1 for both combinations.

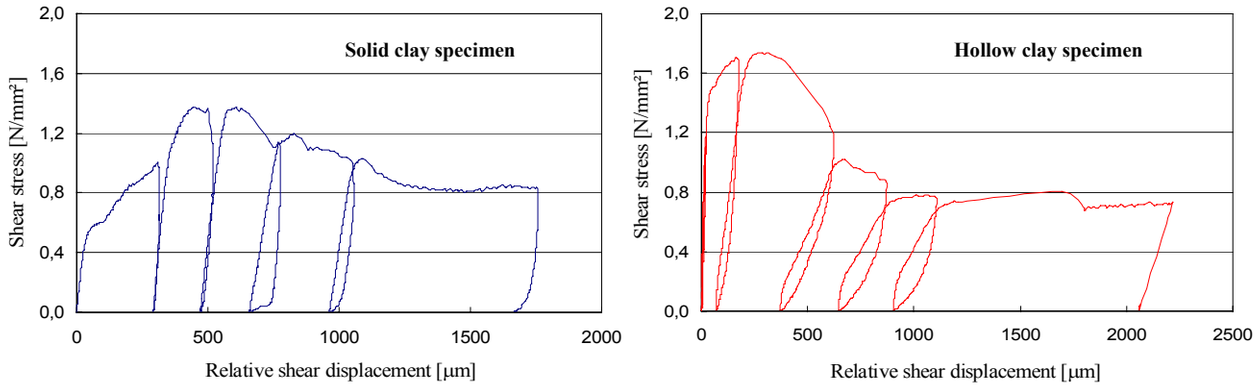


Figure1: Loading / unloading shear tests: shear stress versus relative displacement

The comparison between loading and unloading shear modulus indicates that no shear modulus degradation occurs. Furthermore, the interface shear behaviour can be considered to be elastoplastic. Irreversible displacements were registered when the stress exceeds 40% of shear strength.
In order to calculate the interface characteristics, tests were carried out using several normal compressive stresses, varied from -0.1 to $-1.5N/mm^2$. A linear relationship between shear bond strength τ_u and the applied normal compressive stress σ_n is experimentally observed for both solid and hollow brick. Therefore, the Coulomb friction law is applicable:

$$|\tau_u| = c + \sigma_n \cdot \tan\varphi \qquad (1)$$

where c and φ are respectively the cohesion and friction angle defined by linear regression. Likewise, the residual shear bond and the applied normal compressive stress relation determine the residual bond characteristics.
In literature, the tangent of the friction angle depends on the used material. These values range from $\tan\varphi = 0.7$ to $\tan\varphi = 1.2$ [3]. In our case, the internal friction angle φ is found to be equal to $45°$ $\left(\tan\varphi = 1.01\right)$ which remains within the interval of observed values. Further, this angle is the same for both solid and hollow bricks. However, the mortar penetrating into the brick holes increases the bond stiffness and the residual bond cohesion.

FAILURE MODES

For the solid clay, two failure modes were experimentally recorded: A brittle failure obtained for low pre-compression stress, and a quasi-brittle failure in the case of higher pre-compression. For the hollow brick, a quasi-brittle post-peak behaviour is often obtained whatever is the pre-stress. Moreover, the residual shear stress is about 50% of the shear strength (see figure1).
Figure2 shows the different failures modes obtained during the shear tests.

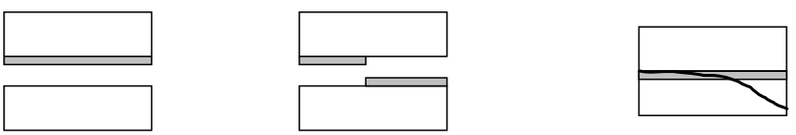


Figure2: Failure modes in shear tests

THEORETICAL CONSIDERATIONS

The experimental shear behaviour investigation helps us to propose an interface model accounting for tensile and shear behaviour. For the bond tensile behaviour, Pluijm R. van der is referred [2]. The yield criterion is given by a tensile yield function F_t and a shear yield function F_s:

$$\begin{cases} F_t = \sigma_n - \overline{\sigma}\left(\kappa_t\right) \\ F_s = \left|\tau\right| - \sigma_n \cdot \tan\varphi - c\left(\kappa_s\right) \end{cases} \tag{2}$$

Corresponding to the Rankine and the Mohr Coulomb failure criteria, respectively. σ_n and τ are respectively the normal and the tangential component of the stress vector. $\overline{\sigma}$ is the interface tensile strength, which is function of the tensile hardening parameter κ_t. The decrease of shear strength is represented by the cohesion variation, which is function of the shear hardening parameter κ_s. It is assumed that a configuration of joint without cohesion has a very small tensile strength, which is near 0. This model was implemented in finite element code CAST3M with which some simulations were performed.

CONCLUSIONS

The shear joint mortar behaviour was investigated using loading/unloading shear tests. According to the experimental results, the mortar joint behaviour can be considered to be elastoplastic. The brick hole influence was also studied with two combinations of bricks and mortar. This study shows that the friction angle is independent on the existing hole. The test results allow the development of an interface model. With this model, some numerical simulations were performed on, reproducing consequently non-linearity provoked by the material behaviour such as joint opening and sliding.

References

[1] Hamid A.A., Drysdale R.C.: The shear behaviour of brikwork bed joints, Proccedings of the Britich Ceramic Society , 30, pp. 101-109, 1982
[2] Pluijm R.van der: Shear behaviour of bed joints, The Sixth North American Masonry Conference, 6 & 9 June 1993, Philadelphia, Pennsylvania, p 125 – 136
[3] Lourenço P.B., Barros J.O., Oliveira J.T.: Shear testing of stack bonded masonry, Construction and Building Materials (Article in press)

EXPERIMENTAL AND ANALYTICAL INVESTIGATION OF RUBBER FRICTION

Markus Lindner[*], Matthias Kröger[*], Karl Popp[*], Holger Blume [**]
[*] *Institute of Mechanics, University of Hannover, Germany*
[**] *Hannover Center of Mechatronics, University of Hannover, Germany*

INTRODUCTION

The physical phenomenon of friction appears in many technical applications. One of the most interesting fields is friction of rubber that depends on different parameters e.g. velocity, roughness, normal pressure and temperature. It can cause acoustic problems like noise and squeal and also unwanted mechanical effects like wear. Therefore, friction affects the function of many products in technical applications, e.g. seals, belts and tires. Friction in the contact between a tire and the road is based on two physical effects. The roughness of the asphalt surface causes deformations in the viscoelastic tire material. The consequences are energy dissipation and friction. This effect is called hysteresis induced friction or hysteresis losses. Intermolecular bindings between the tire material and the road surface result in adhesion forces, that cause also energy dissipation and friction. This presentation is focused on the hysteresis and adhesion of rubber. Experiments performed under outdoor and indoor conditions are presented on real road surfaces and on more homogeneous surfaces like glass and safety walk as references.

MODELING

The hysteretic friction of rubber is caused by energy dissipation due to internal material damping during the process of deformation. The deformation itself occurs during the sliding of a rubber element across the asperities of a rough surface. The rubber element can be described by the Zener model also called standard linear viscoelastic solid, which is a linear spring-dashpot combination. A mechanical model of hysteretic friction has been developed using the following steps. In a first step a suitable model including relaxation and creeping properties of rubber material is developed. The behavior of a rubber element is simulated using frequency analysis and a special fit algorithm to obtain the system parameters. In a next step the model is validated by a harmonic excitation due to a sinusoidal surface. Finally, a simulation is performed that includes the material model and surface roughness based on real measurements. The advantage of the method described above is the approximation of the real physical hysteretic friction process and its description in time domain. The dependence of the friction coefficient on the velocity and the normal pressure is validated. The results have been compared with different theories that are mainly formulated in frequency domain, cp. [4]. The results show the same velocity dependence of the hysteretic friction coefficient.
Intermolecular bindings between the tire material and the road surface result in adhesion forces, that also cause energy dissipation and friction. Intermolecular bindings are based on Van-der-Waals or dipole forces. On a rolling wheel without sliding the intermolecular bindings are connected at the run-in and they are separated at the run-out. The forces at the run-in are negligible small in relation to the forces at the run-out. Roberts [9] shows that the forces and the energy dissipation at the run-out depend on the material properties and the separation velocity. Tests using a special adhesion pendulum confirm the velocity dependence of the dissipated energy by adhesion, cp. [5]. In a sliding contact the connection and disconnection of intermolecular bindings can occur frequently in dependence of the micro roughness of the contact partner, the viscoelastic properties of the rubber and the sliding velocity, see Achenbach [1]. The adhesion increases with the true contact area that depends on the macro roughness, on the viscoelasticity and on the sliding velocity and is described by the hysteresis effect. Tests show a strong sensitivity of the adhesion effect with respect to the surface conditions (wet or dry, lubricated or not) thus, in experiments the cleaning procedure of the surfaces is very important.

EXPERIMENTAL INVESTIGATION

The measurement of the kinetic friction coefficients μ between rubber compound and the road surface is limited because of the necessity for complex measuring systems, which are not available in the field. The integration of a measuring device into a mobile robot permits laboratory precision measurements on outdoor road surfaces, see [2] and [3]. To measure the kinetic friction coefficient, a rubber testing wheel that is adopted from the Grosch rubber wear test rig, is pressed onto the road surface by a predefined normal contact force in a closed loop force control. The rubber measuring wheel is driven providing constant macroscopic sliding velocity in the contact zone. By pressing the rotating rubber specimen onto the road surface, a friction force is generated. The kinetic friction coefficient is calculated as the ratio of the measured friction force and the actual normal contact force.



Figure 1: Outdoor measurement robot

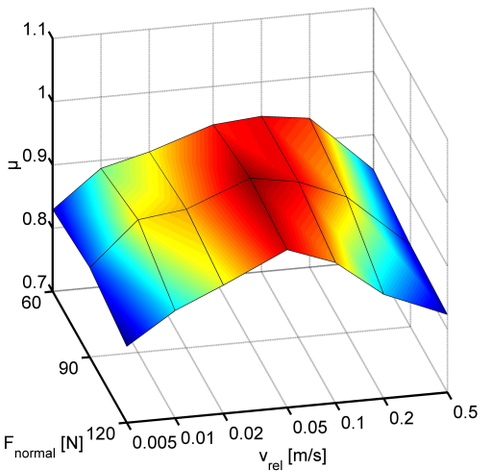


Figure 2: Friction coefficient field (wet road)

Laboratory measurements have been performed on a tribometer test rig. The rig consists of a pin on disc application, where the disc together with an exchangeable friction surface is driven with a predefined velocity and the pin consisting of a rubber specimen is pressed onto the disc in axial direction. Here, homogeneous surfaces like glass and safety walk (corundum like surface) are applied. The kinetic friction coefficient is also calculated as ratio of the measured forces. The measurements discussed below are based on stationary test conditions in which the test parameters remain on a constant level and are varied after every measurement. The kinetic friction coefficient of rubber on different surfaces depends on the relative velocity, the normal pressure in the contact zone as well as on contact temperature and wetness. The temperature in case of the outdoor measurements has been measured and the experiments have been performed in a limited temperature range. In **Figure 2** measurements of the stationary kinetic friction coefficient by the outdoor robot on a wet road surface are shown. Obviously, there is only a slight impact of the normal force but investigations on dry glass surfaces show a larger influence of the normal force, where the friction coefficient decreases with increasing normal force. The dependence on the relative velocity in this case is predicted in Persson [8]. As expected from theory, a maximum of the kinetic friction coefficient with velocity is observed. This effect is due to the hysteresis friction with varying excitation frequencies. On a wet road surface the maximum friction coefficient occurs at $v_{rel} \approx 0.1$ m/s. The theory also predicts a hysteresis based maximum at this velocity where the temperature influence is regarded by calculating an increasing contact temperature with increasing relative velocity. In **Figure 3** the variation of the normal force is shown for two different friction surfaces. The characteristic of the friction coefficient versus normal force is decreasing and steeper for glass than for safety walk. The graph of the friction force versus normal force, however, shows a linear increasing behavior starting at a constant value. Thus, we assume that the friction force can be divided into an almost linear and a constant part. By the observation of limit values the more or less decreasing behavior of the kinetic coefficient of friction versus normal force becomes clear. In the literature, for example [8], it is shown that the occurrence of hysteresis and adhesion causes friction forces proportional to the true contact area. On the glass surface the true contact area is larger than on safety walk where the area grows faster with increasing normal force. A large true contact area during small normal forces causes a large constant part of the friction force and, therefore, a strong decreasing behavior of the kinetic friction coefficient. Another topic of friction investigation is the unsteady behaviour of the friction contact, see [6] and [7], but this should not be discussed here.

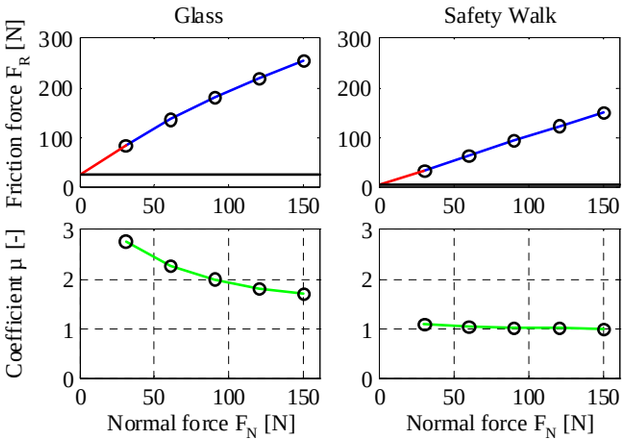


Figure 3: Friction force and friction coefficient versus normal force

CONCLUSIONS

Two effects of rubber friction have been investigated. The dependence of the kinetic friction coefficient on the relative velocity has been shown by measurements and has been predicted by a theoretical model. The dependence on the normal force has been explained and validated by measurements on different friction surfaces. The occurrence of these effects is well known, however, investigations of this type are necessary for the understanding of rubber friction.

References

[1] Achenbach M.; Frank E.: Reibung von Elastomeren. *Tribologie + Schmierungstechnik*, 48, 43-47, 2001.
[2] Blume H.; Heimann B.; Lindner M.; Volk H.: Friction Measurement on Road Surfaces, *Kautschuk Gummi Kunstoffe*, 56, 677-681, 12/2003.
[3] Blume H.; Heimann B.; Lindner M.: Design of an Outdoor Mobile Platform for Friction Measurement on Street Surfaces. *Proceedings of the International Colloquium on Autonomous and Mobile Systems*, pp. 65-68, Magdeburg, 2002.
[4] Klüppel M.; Heinrich G.: Rubber Friction on self-affine Road Tracks. *Rubber Chemistry and Technology*, 73, 578-606, 2000.
[5] Kröger M.; Popp K.; Kendziorra N.: Experimental and Analytical Investigation of Rubber Adhesion, *Maschine Dynamics Problems* (2003) (IP).
[6] Kröger M.; Lindner M.; Popp K.: Modellierung instationärer Reibkräfte, PAMM Proc. Appl. Math. Mech. 2 (2003), S. 140-141, 2003, (IP).
[7] Lindner M.; Kröger M.; Popp K.: Stick-Slip Vibrations of Pneumatic Seals, *Machine Dynamics Problems*, 25, 121-130, 2001.
[8] Persson B. N. J.: Sliding Friction – Physical Principles and Applications, Second Edition, Springer, Berlin, 2000.
[9] Roberts A. D.: Rubber Adhesion at High Rolling Speeds. *J. Nat. Rubber Res.*, 3(4), 239-260, 1988.

XXI ICTAM, 15–21 August 2004, Warsaw, Poland

PENALTY APPROXIMATION OF IMPACT WITH COULOMB FRICTION

Michelle Schatzman*
*Laboratoire de Mathématiques Appliquées de Lyon, CNRS et Université Claude Bernard Lyon 1, 69622 Villeurbanne Cedex, France

Summary Impact problems with Coulomb friction in a finite number of degrees of freedom are not yet completely understood from the mathematical point of view, and it is useful to possess a range of methods for the constuction of solutions. Moreau, Monteiro-Marques, Stewart used a time-stepping method in order to construct a solution. Here a penalty approximation is proposed; it is simpler than time-stepping, and it allows for more general friction cones and for more transparent mathematical proofs. The non interpenetration constraint is replaced by normal compliance approximation; it is not difficult to obtain estimates on the penalized equation. The passage to the limit on Coulomb's relation as the compliance tends to 0 seems to require the multiplication of Dirac masses by functions which are discontinuous at the coordinate of the Dirac masses. However, precise asymptotics of the approximating problem make it possible to find a relation in the limit between the tangential and normal components of the reaction.

INTRODUCTION

The mathematical understanding of impact with friction is not yet complete, even after the many contributions of Jean-Jacques Moreau, in particular [4] and [3], the work of Manuel Monteiro-Marques [2], [1] and David Stewart's paper of 1998 [6], which was the first to allow for generalized coordinates in this area.

These authors construct a solution through time-stepping; David Stewart needed linear complementarity problems for his analysis and this point of view forced him to approximate three dimensional round friction cones by pyramids.

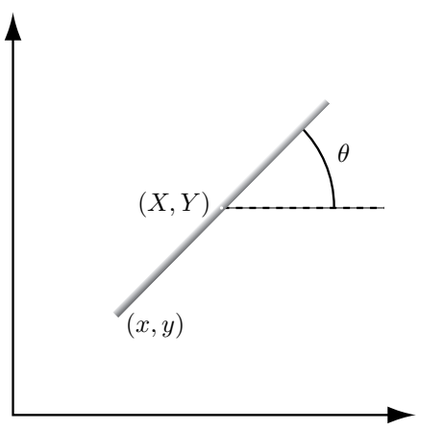
The purpose of the present paper is to give an alternative construction of solutions, which relies on a standard penalization technique, applied only to the impact part of the model.

The problems considered here use generalized coordinates, and the exact assumptions will be given in the presentation.

Energy estimates are applied in a classical way to obtain uniform bounds on the coordinates and the velocities. The variation of the generalized velocities can be estimated by ideas from convex analysis, though the set of constraints does not have to be convex.

The passage to the limit on the impact complementarity relation is not difficult; the real difficulty comes from the passage to the limit on Coulomb's relation. In this extended abstract, the principle of this passage to the limit will be described in a simple case, in order to make the ideas accessible. But the applicability of the methods goes well beyond the present case.

A SIMPLE MODEL



mass m, length 2ℓ

inertia $J = m\ell^2/3$

gravity g

tangential reaction force $\mathbf{R}_T$

normal reaction force $\mathbf{R}_N$

center of mass (X, Y)

$x = X - \ell\cos\theta, y = Y - \ell\sin\theta$

Figure 1. The mechanical set-up.

If we take into account the impact at only one end of the bar, the mathematical formulation of this problem is as follows,

$$\begin{aligned} m\ddot{X} &= \mathbf{R}_T, \\ m\ddot{Y} &= \mathbf{R}_N - mg, \\ J\ddot{\theta} &= -\ell\big(\mathbf{R}_N\cos\theta - \mathbf{R}_T\sin\theta\big); \end{aligned} \tag{1}$$

the non penetration condition is the complementarity condition

$$y \geq 0, \quad \mathbf{R}_N \geq 0, \quad \langle y, \mathbf{R}_N\rangle = 0, \tag{2}$$

and the Coulomb friction condition is

$$\mathbf{R}_T \in -\mu\,\mathrm{Sign}(\dot{x})\mathbf{R}_N, \quad \mathrm{Sign}(r) = \begin{cases} \{-1\} & \text{if } r < 0, \\ \{+1\} & \text{if } r > 0, \\ [-1,1] & \text{if } r = 0. \end{cases} \tag{3}$$

HOW TO PENALIZE

The penalization consists in replacing the interpenetration condition by a normal compliance law; if τ is a characteristic time which will tend to 0, we let

$$\mathbf{R}_{N,\tau} = m\max(-y_\tau, 0)/\tau^2. \tag{4}$$

Equations (1) and (3) are not changed and initial conditions are prescribed. The system can now be treated as an integrod-ifferential monotone problem, where the integral part can be seen as a perturbation of a standard class of equations.

CONVERGENCE

The easy estimates

The first easy estimate is an energy estimate: X_τ, Y_τ, θ_τ and their first derivatives are bounded uniformly in $\tau \in (0,1]$ and in $t \in [0,T]$. It is obtained by multiplying the first equation of (1) by $\dot{X}_\tau$, the second by $\dot{Y}_\tau$ and the third by $\dot{\theta}_\tau$, and by integrating and applying a Gronwall inequality.

The second easy estimate is an estimate on the integral over $[0,T]$ of $|\mathbf{R}_{N,\tau}|$, uniformly in τ as in [5]. This estimate implies another estimate on the integral of $|\mathbf{R}_{T,\tau}|$.

Therefore, one can extract subsequences, and the passage to the limit from (4) to (2) is standard; one should simply remark that the limiting $\mathbf{R}_N$ is a measure.

The difficult estimates

Passing to the limit on (3) is a more delicate problem, since $\mathbf{R}_T$ may have a Dirac mass precisely when $\dot{x}$ vanishes. It is possible to decompose the sequence of approximations $\mathbf{R}_{N,\tau}$ into the sum of two terms: one approximates the continuous part of $\mathbf{R}_N$ and one approximates the atomic part of this measure. On the continuous part, relation (3) passes to the limit. An equation of the form $\mathbf{R}_T^a \in -\mu S\mathbf{R}_N^a$ relates the atomic parts of the limiting measures, where S is a scalar function defined on the support of the atomic part $\mathbf{R}_N^a$ of $\mathbf{R}_N$. The value of S can be calculated from the knowledge of the generalized coordinates and the right and left limits of the velocities at each point supporting a Dirac mass.

CONCLUSION

What good are all these mathematics? First, the proof sketched above can be extended to much more general situations, and the extent of these generalizations will be described in the communication.

Second, the choice of a Coulomb friction model is a decision to simplify reality; how good this decision is can be evaluated by comparison to experiment and also by finding out whether the mathematics make sense or not. Having a range of mathematical methods to solve a problem means that the problem is tractable, and gives arguments in favor of this modelization. It also gives insight into the numerical approximation strategies, and is eventually helpful for understanding the mechanics of the problem.

References

[1] Markus Kunze and Manuel D. P. Monteiro Marques. An introduction to Moreau's sweeping process. In *Impacts in mechanical systems (Grenoble, 1999)*, volume 551 of *Lecture Notes in Phys.*, pages 1–60. Springer, Berlin, 2000.

[2] Manuel D. P. Monteiro Marques. *Differential inclusions in nonsmooth mechanical problems*. Birkhäuser Verlag, Basel, 1993. Shocks and dry friction.

[3] Jean-Jacques Moreau. Standard inelastic shocks and the dynamics of unilateral constraints. In G. del Piero and F. Maceri, editors, *Unilateral Problems in Structural Mechanics*, number 288 in C.I.S.M. Courses and Lectures, pages 173–221. Springer-Verlag, Vienna, New York.

[4] Jean-Jacques Moreau. Evolution problem associated with a moving convex set in a Hilbert space. *J. Differential Equations*, 26(3):347–374, 1977.

[5] Michelle Schatzman. A class of nonlinear differential equations of second order in time. *Nonlinear Anal., Theory, Methods and Applications*, 2:355–373, 1978.

[6] David E. Stewart. Convergence of a time-stepping scheme for rigid-body dynamics and resolution of Painlevé's problem. *Arch. Ration. Mech. Anal.*, 145(3):215–260, 1998.

CHAOTIC RESPONSE OF NON-REVERSIBLE DRY FRICTION OSCILLATOR

Andrzej Stefański[*], Jerzy Wojewoda[*], Marian Wiercigroch[**] and Tomasz Kapitaniak[*]
[*]*Division of Dynamics, Tech. University of Lodz, Stefanowskiego 1/15, 90-924 Lodz, Poland*
[**] *Centre for Applied Dynamics Research, University of Aberdeen, King's College, Fraser Noble Building, Aberdeen, AB24 8UE, Scotland, UK*

Summary In this short communication we investigate how the non-reversible dry friction characteristics will alter the non-linear responses of a simple mechanical oscillator. The presented approach is based on a certain mathematical description of the experimentally determined non-reversible dry friction characteristics, which causes chaotic and irregular motion of the studied system. A novelty of our idea is an introduction of the relative acceleration in description of the dry friction model.

INTRODUCTION

For many years the topic of dry friction has been actively researched with many attempts to identify the causes of unwanted behavior such as squeal of car brakes, extensive wear of the cutting tools, and others. A practical engineering approach, indebted to Coulomb simplifies the friction force to constant value directed opposite to the relative velocity of the contacting bodies. Such force can take two values with identical level but opposite sign only. Newer experiments show non-linear dependence on the contact velocity rather than the constant one. That was why most efforts were directed to built non-linear friction models and to determine differences in maximal values of the static and dynamic friction forces – see [3]. Another attempts to determine different types of friction characteristics showing dependencies on the relative acceleration on the contacting surface are so-called non-reversible friction characteristics [1,2,5]. However, from a viewpoint of the experiment, even such non-linear approaches well approximate real character of friction force only for periodic responses of the considered system. In case of irregular, non-periodic motion of a non-linear friction oscillator, friction characteristics generated from experiments, often have a form of area filling curves, in co-ordinates friction force versus relative velocity [4]. This fact cannot be explained by measurement errors and rises a need to formulate a more general, universal friction model taking under consideration also the irregular motion of the system with dry friction.

DRY FRICTION MODELLING

We will use the experimental data obtained from the dry friction oscillator, which allows to induce conditions where the relative velocity changes its sign. There is a good deal of flexibility in varying frequency and amplitude of excitation, and combination of frictional materials. In this study we will be using the cleanest data which comes from experiments steel on teflon. To avoid the double counting of viscous forces, in Figure 1, the viscous component in each dry friction force-relative velocity loop has been subtracted. The above described dependence between friction characteristic reconstructed experimentally and a kind of observed motion has been induced us to new approach to the problem of dry friction modelling. According to our intention such a developed model of dry friction should have a universal character e.g. it well approximates real relation between friction force and relative velocity in case of irregular motion of the system and it simplifies to a form similar to known friction characteristics when motion is regular. This condition is fulfilled by the example of dry friction model presented below which has been formulated on the basis of non-reversible friction model [5]. The proposed novel model has a symmetrical non-reversible characteristics (Eq.(1a)), with an auxiliary assumption that the parameter in the exponent is a function of the relative acceleration (Eq.(1b)) in contrast to primary model, where this coefficient is constant. Hence, the model is described with the following equations:

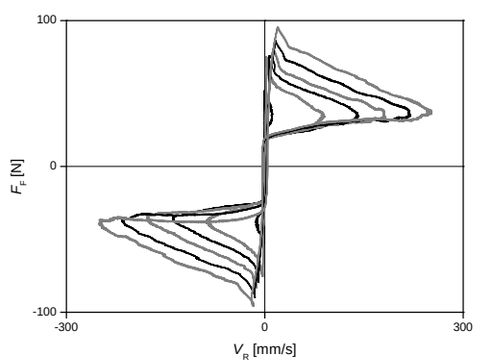


Figure 1. Family of dry friction characteristics

$$f = \begin{cases} f_u, & \operatorname{sgn}(\ddot{x}) > 0 \\ f_l, & \operatorname{sgn}(\ddot{x}) < 0 \end{cases} \quad \rightarrow \quad \begin{aligned} f_u &= f_d\left[1 + \frac{f_s - f_d}{f_d}\exp\left(-a(\ddot{x})|\dot{x}|\right)\right] \\ f_l &= f_d\left[1 - \frac{f_s - f_d}{f_d}\exp\left(-a(\ddot{x})|\dot{x}|\right)\right] \end{aligned} \tag{1a}$$

$$a(\ddot{x}) = \frac{a_1}{|\ddot{x}| + a_2} \tag{1b}$$

where a_1, a_2 >0 are constant parameters f_s, f_d – static and dynamic friction coefficient respectively.

To show universal character of the above presented model let us consider one-degree-of-freedom, mechanical oscillator to which a dry friction damper has been added where the model under consideration (Eqs(1a) and (1b)) has been applied in numerical simulations. The dynamics of this system can be described by a simple non-smooth first order differential equations

$$\begin{aligned} \dot{x}_1 &= x_2, \\ \dot{x}_2 &= q\cos(\omega t) - \alpha g(x_1) - 2hx_2 - \varepsilon f sign(x_2), \end{aligned} \tag{2}$$

Universal nature of proposed method of dry friction modelling is presented in Figs 2a and b, where friction characteristics for two different types of the oscillator under consideration and respective phase portraits of these systems are shown. It is clearly presented that for linear oscillator having periodic solution (Fig.2a, $g(x)=x$), friction model possesses a shape predicted in mathematical description of the classical non-reversible model and contains two lines representing relative the acceleration and deceleration phases respectively. In case of non-linear oscillator with chaotic attractor (Fig. 2b, $g(x)=x^3$) friction characteristic is an transformed image of this attractor according to the hypothesis presented above.

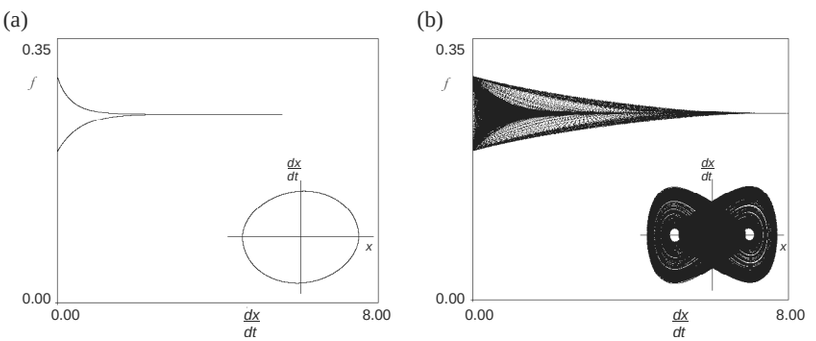


Figure 2. Friction characteristics for the novel friction model and the respective phase portraits of the oscillator applied in numerical experiment for two cases: a) linear friction oscillator– $g(x)=x$, α=1.00, h=0.05, q=0.50, η=1.00, ε=0.5, b) non-linear friction oscillator – $g(x)=x^3$, α=1.00, h=0.05, q=10.00, η=1.00, ε=0.5; parameters of the friction model (Eqs.1): f_s=0.30, f_d=0.25, a_1=12, a_2=0.10.

CONCLUSIONS

The presented model of dry friction only exemplifies the way of friction modelling and it is only the first step to formulate a novel model of dry friction for non-linear systems. Earlier numerical experiments carried out by authors have shown, that introduction of this model represented by Eqs(1), does not results in qualitative changes of motion character in comparison with another friction models. Hence, from a viewpoint of engineering applications, where the dynamics is simple, it is sufficient to apply classical Coulomb law. However, our recent experiments show that even for our oscillator where $g(x)$ is linear, the system can respond with an irregular stick-slip motion. Therefore there is a need for more comprehensive dry friction models, and this paper outlined one.

ACKNOWLEDGMENT

This study has been supported by the Polish Committee for Scientific Research (KBN) under project No. PB 0804/T07/2003/25

References

[1] Bell R., Burdekin M.: A study of stick-slip motion of machine tool feed drives, *Proc. Instn Mech. Engrs* (1970), **184**, 543-557..

[2] Fenny B., Moon F. C.: Chaos in a forced dry friction oscillator: experiment and numerical modelling, *Journal Sound & Vibration* (1994), **170**(3), 303-323.

[3] Popp K. & Stelter P.: Non-linear oscillations of structures induced by dry friction, in *Non-linear Dynamics in Engineering Systems* (1990), ed. W. Schiehlen, Springer, New York.

[4] Stefański A., Wojewoda J., Wiercigroch M. and Kapitaniak T.: Chaos Caused by Non-Reversible Dry Friction, *Chaos, Solitons & Fractals* (2003) **16**, 661-664.

[5] Wiercigroch M., Sin V. W. T., Liew Z. F. K.: Non-reversible dry friction oscillator: design and measurements, *Proc. Instn Mech. Engrs* (1999), **213**(C), 527-534.

XXI ICTAM, 15–21 August 2004, Warsaw, Poland

A DYNAMIC UNILATERAL CONTACT PROBLEM FOR A CRACKED BODY

Marius Cocou*, Eliane Bécache**, Patrick Joly**, Gilles Scarella**
*Laboratoire de Mécanique et d'Acoustique CNRS, 31, chemin Joseph Aiguier,
13402 Marseille Cedex 20, and Université de Provence, Marseille, France
**INRIA Rocquencourt, Domaine de Voluceau, B.P. 105, F-78153 Le Chesnay Cedex, France

Summary In this work we investigate a class of dynamic contact problems for cracked viscoelastic and elastic bodies, when Signorini's conditions between the two faces of the crack are considered. Firstly, using a penalty method we study a variational formulation of a unilateral contact problem with nonlocal friction for a cracked viscoelastic body. Several estimates on the penalized solutions are obtained which enable us to analyze the time and spatial discretizations of the problem. Then we consider the corresponding elastic problem, for which a fictitious domain formulation is proposed with Lagrange multipliers representing the normal jump of the displacements. Numerical examples, based on the fictitious domain method for solving the diffraction of elastic waves by cracks, are presented.

INTRODUCTION

In this paper we study some dynamic unilateral contact problems with friction for a cracked (visco)elastic body, see [5], [1], [10] and the references therein.
For the wave equation with unilateral boundary conditions, theoretical results were proved in the case of a half-space by G. Lebeau and M. Schatzman [8], in the case of a smooth bounded domain by J.U. Kim [7] and for a thermoelastic radially symmetric body by J. Muñoz-Rivera and R. Racke [9]. For a viscoelastic behaviour, J. Jarušek [6] was the first to obtain an existence result for the dynamic unilateral contact problem with given friction. In [4] dynamic contact problems with nonlocal friction were studied under boundedness hypotheses on velocity and acceleration and in [3] an existence result was proved for a dynamic Signorini's problem with nonlocal friction, without any additional assumptions.

ANALYSIS OF A VISCOELASTIC PROBLEM

In this section, using a penalty method we study the primal variational formulation of a unilateral contact problem with nonlocal friction for a cracked viscoelastic body of Kelvin-Voigt type.
We formulate a penalized contact problem with the solution verifying the same equations in the bulk and the same boundary conditions as in the initial problem, except for unilateral contact conditions. The penetration between the two faces of the crack is penalized.
An equivalent formulation using a decomposition of the domain is presented and time discretizations of the penalized problem are analyzed. Several estimates are obtained on the penalized solutions, which enable us to pass to the limit by using compactness results.

FICTITIOUS DOMAIN FORMULATION

We consider the corresponding elastic problem, for which a fictitious domain formulation is proposed with Lagrange multipliers representing the normal jump of the displacements, see [1].
Following a similar approach as in [2], where a free surface boundary condition was studied, we use a fictitious domain method for solving this problem. The main advantage of this method is to offer the efficiency of the finite difference method while taking into account the complex geometry of the crack, through the Lagrange multipliers defined on the crack. By this method the corresponding space discretization requires two meshes: a regular one of the bulk and another one of the crack.

NUMERICAL RESULTS

Numerical results are based on the fictitious domain method for solving the diffraction of elastic waves by cracks.
For example, in the case of radial symmetry for a circular crack unilateral contact condition is compared to free surface condition, for the same initial conditions and given forces, at the same time (see Figs. 1,2).
A second example concerns a vertical crack for which we compare, at the same time and for the same given conditions, unilateral contact solution to free surface solution (see Figs. 3,4).

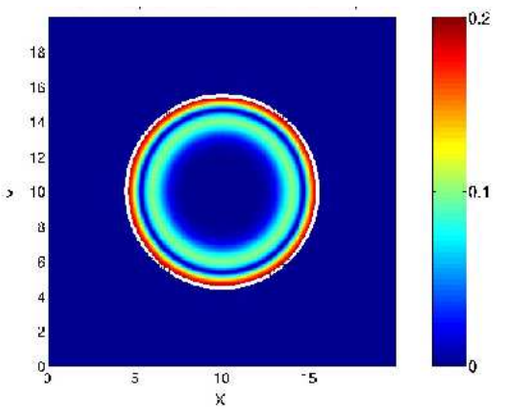


Figure 1. Circular crack, free surface. Norm of the displacement.

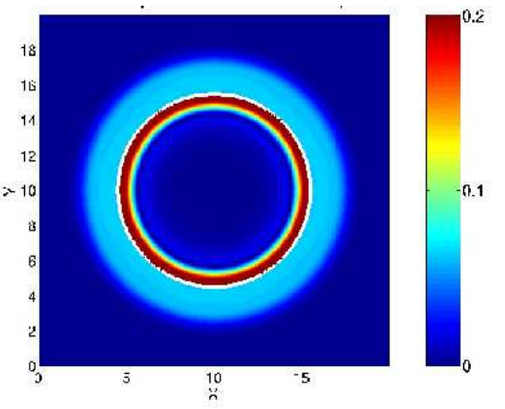


Figure 2. Circular crack, unilateral contact. Norm of the displacement.

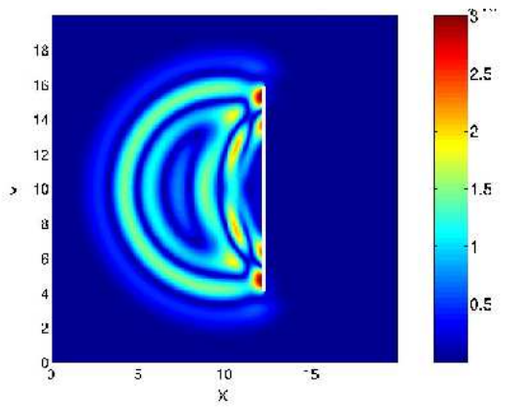


Figure 3. Vertical crack, free surface. Norm of the displacement.

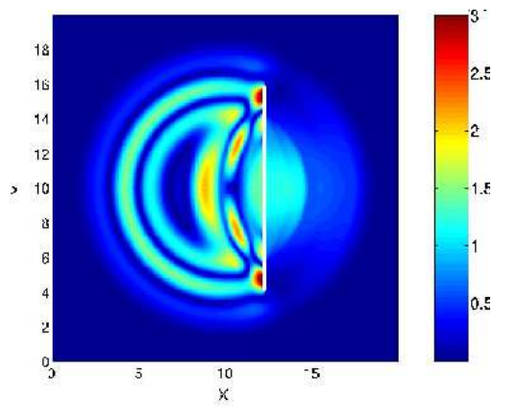


Figure 4. Vertical crack, unilateral contact. Norm of the displacement.

References

[1] Bécache E., Joly P., Scarella G.: A fictitious domain method for a unilateral contact problem. Mathematical and Numerical Aspects of Wave Propagation : Waves 2003, 431–436. Springer, Berlin 2003.

[2] Bécache E., Joly P., Tsogka C.: Fictitious domains, mixed finite elements and perfectly matched layers for 2D elastic wave propagation. *J. of Comp. Acoust.* **9**:1175–1203, 2001.

[3] Cocou M.: Existence of solutions of a dynamic Signorini's problem with nonlocal friction in viscoelasticity. *Zeitschrift für angewandte Mathematik und Physik (ZAMP)* **53**:1099–1109, 2002.

[4] Cocou M., Ricaud J.M.: Analysis of a class of implicit evolution inequalities associated to viscoelastic dynamic contact problems with friction. *Int. J. Engrg. Sci.* **38**:1535-1552, 2000.

[5] Cocou M., Scarella G.: Existence of a solution to a dynamic unilateral contact problem for a cracked viscoelastic body. *C. R. Acad. Sci. Paris, Ser. I*, **338**:341–346, 2004.

[6] Jarušek J.: Dynamic contact problems with given friction for viscoelastic bodies. *Czech. Math. J.* **46**:475–487, 1996.

[7] Kim J.U.: A boundary thin obstacle problem for a wave equation. *Commun. in Partial Differential Equations* **14**:1011-1026, 1989.

[8] Lebeau G., Schatzman M.: A wave problem in a half-space with a unilateral constraint at the boundary. *J. Diff. Eqs.* **53**:309-361, 1984.

[9] Muñoz-Rivera J., Racke R.: Multidimensional contact problems in thermoelasticity. *Siam J. Appl. Math.* **58**:1307-1337, 1998.

[10] Scarella G.: Etude théorique et numérique de la propagation d'ondes en présence de contact unilatéral dans un milieu fissuré. *PhD Thesis*, Université Paris Dauphine, 2004.

A SIMPLE MODEL TO ACCOUNT FOR THE LOCKING EFFECT BETWEEN TWO ROUGH SURFACES UNDER CYCLIC LOADING

Larissa Gorbatikh
Department of Mechanical Engineering, University of New Mexico, Albuquerque, NM 87131, USA

Summary A contact between two rough surfaces subjected to normal and shear loads is an unavoidable source of energy dissipation. It has been observed in experimental studies at Sandia National Laboratories that the loss of energy undergoes certain evolution when contact is subjected to cyclic loading. In the present work a simple model is developed that suggests a hypothesis that two rough surfaces brought into contact tend to lock up with a number of cycles resulting in a reduction of a total energy loss.

MOTIVATION

Proper modeling of energy dissipation caused by micro-slip is important for structural systems experiencing vibrations. Under favorable circumstances, the energy dissipated in damping can be significant when compared with the total strain energy stored in a structural element and the energy dissipated due to internal friction. As such proper use of an energy dissipation mechanism through friction may assist in reducing structural vibrations. Analysis of energy dissipation due to micro-slip may also give a valuable insight on phenomena taking place along contact regions. The present work is motivated by experimental studies conducted at Sandia National Laboratories to investigate physics of a micro-slip phenomenon and energy losses associated with it. For the detailed description of the experimental set-up and obtained data the reader is referred to work [1]. In brief, the energy dissipation is found to gradually decrease with cycling until it approaches an asymptotic value after thousands of cycles. Inspection of surface microstructure did not show any indication of wear or other changes in surface characteristics that could have held responsible for the observed effect. Moreover, the characteristic curve of damping is found to be fairly repeatable for the same test configuration after the surface contact is re-established. With this work we hope to explain the observed phenomenon by proposing a simple hypothesis that when two rough surfaces are pressed against each other and subjected to cyclic tangential loading a certain locking mechanism comes into play between them that causes less energy dissipation.

MULTIPLE-ASPERITY CONTACT

Our hypothesis suggests that the contact microstructure formed by two rough surfaces may change when it is subjected to cyclic loading as it tries to adapt itself to variations in the tangential load. By the change of the contact microstructure we do not mean the change of any surface characteristics (like roughness etc) but more the way two rough surfaces fit together. While the "surface microstructure" is made of asperity formations, the "contact microstructure" is attributed to multiple regions where asperities are in contact. The latter does depend on the system of applied loads. We assume that contacts are not necessarily normal but may be inclined to the mean plane (described by an angle of inclination θ). Under cyclic loading the normal contacts have a tendency to become inclined and those that are already inclined increase their inclination angles. The process of microstructure optimization eventually stops when asperities' freedom of locally adapt their positions is lost completely.

Analysis of the contact response formed by rough surfaces goes back to several decades [2-5]. In the sections to follow we present a contact model based on a multiple-asperity approach. We first analyze response of a normal contact and then introduce a theory of an inclined contact. The energy dissipation is estimated by calculating an area of the hysteresis loop that forms in T vs. Δ coordinates, where T is a shear load, Δ is a shear displacement.

When tangential load T is applied, multiple contacts between asperities of two rough surfaces may undergo gross or partial sliding (depending on the magnitude of the load and the height of the asperity). Partial sliding takes place if the asperity has a height exceeding the limit z^*. In this case, the total tangential load carried by all contact regions in the loading phase T_ℓ can then be calculated as follows:

$$T_\ell = \int_d^{z^*} \mu f_N(z-d)\Phi(z)dz + \int_{z^*}^{\infty} f_T(\Delta, z-d)\Phi(z)dz \qquad (1)$$

where μ is a coefficient of friction, f_N is a normal load carried by an individual asperity, f_T is a shear response of an individual asperity, $\Phi(z)$ is a distribution of asperity heights and d is a distance from the mean plane to the peak of the asperity. In the unloading phase we differentiate three types of the contact response: (1) gross sliding in the loading and unloading phases; (2) gross sliding in the loading phase and partial sliding in the unloading phase; (3) partial sliding in the loading and unloading phases. The total tangential force in the unloading phase T_u can be derived similarly to (1) just taking into account that the total displacement at an individual contact is a sum of the accumulated displacement in the loading phase and the displacement due to the reverse slip in the unloading phase.

The above formulas are valid only for the normal type contacts. With introduction of the inclination angle θ the local normal and shear displacements at the contact change according to the following rule:

$$\Delta_0 = \Delta\cos\theta\,, \qquad \delta_0 = (z-d)\cos\theta \tag{2}$$

where Δ_0 is a local shear displacement, δ_0 is a local normal displacement. Coupling between normal and shear responses in global and local coordinates is neglected. In the limiting case of $\theta = 0$ the contact becomes traditional normal with maximal loss of energy, and in the case of $\theta = \pi/2$ the contact is purely tangent with no energy loss. The total tangential load carried out by all asperities in the loading phase now becomes as follows:

$$T_\ell = \int_0^{\pi/2}\int_d^{z_1^*} \mu f_N\big((z-d)\cos\theta\big)\Phi(z)\Psi(\theta)dz\,d\theta + \int_0^{\pi/2}\int_{z^*}^{\infty} f_T\big(\Delta\cos\theta,(z-d)\cos\theta\big)\Phi(z)\Psi(\theta)dz\,d\theta \tag{3}$$

where $\Psi(\theta)$ is a function that describes distribution of inclination angles over all contacts. The total tangential forces in the unloading and reloading phases, T_u and T_r, respectively, can be found in a similar way.

As far as the local parameters are known as functions of θ the energy dissipation can be calculated choosing one of the existing contact models by calculating the area of the hysteresis loop formed in the T vs Δ coordinate system. For small θ energy dissipation reduces to the following simple relation:

$$D = D_0\left(1-\frac{1}{2}\left\langle\theta^2\right\rangle\right) \tag{4}$$

where $\left\langle\theta^2\right\rangle$ is a mean value over the angle distribution $\Psi(\theta)$ and D_0 is dissipation of energy in the case of a normal contact. Incorporation of angles always leads to the decrease of energy loss and as contact microstructure approaches its optimum, changes in global characteristics also tend to stabilize manifesting in the asymptotic behavior.

CASE STUDY

Now we demonstrate how the developed method works for the case of a generalized contact between two bodies with identical symmetric profiles Ar^α [6]. This profile covers a problem of two spheres when $\alpha = 2$ all the way to the flat punch when $\alpha \to \infty$. Functions introduced in (1) have the following forms:

$$f_N(z-d) = C_N(z-d)^{1+1/\alpha}\,, \qquad f_T(\Delta, z-d) = \mu\, f_N\left[1-\left(1-\frac{\Delta}{\mu\kappa(z-d)}\right)^{1+1/\alpha}\right] \tag{5}$$

where C_N is normal stiffness. Incorporation of angles can be done through (2) and the energy dissipation in this case reduces to the following simple integral:

$$D = D_0\int_0^{\pi/2}(\cos\theta)^{1+1/\alpha}\Psi(\theta)d\theta \tag{6}$$

We assume that the distribution of contact inclination angles changes during cycling according to the following law:

$$\Psi(\theta) = \frac{\cos^2\theta}{n} + \frac{n-1}{2n} \tag{7}$$

According to (7) the number of inclined contacts increases and the number of normal contacts decreases so that the distribution of angles tends to become uniform. The decrease of energy dissipation in this case is governed by the following relation:

$$D = D_0\frac{3n+1}{6n} \tag{8}$$

where n is related to a number of cycles the contact has undergone and it is to be determined from experimental data.

To conclude, we introduced a simple model to account for an interlocking effect between two rough surfaces that results in reduction of energy dissipation under cyclic loading. The model is simple in application and allows one to relate changes on the *micro*-level (inclination angles) with characteristics on the *macro*-level (energy dissipation) that can actually be measured.

References

[1] D. L. Gregory, D. O. Smallwood, R. G. Coleman, M. A. Nusser, " Experimental Studies to Investigate Damping In Frictional Shear Joints," Proceedings of the 70th Shock and Vibration Symposium, 1999

[2] Bjorklund S., A random model for microslip between nominally flat surfaces, J. of Tribology, Trans. of the ASME, Vol. 119, 726-731, 1997

[3] Tabor D, "The properties of diamond", ed. J. E. Field (London: Academic) ch 10, 1979

[4] Seal M, "The friction of diamond', Phil. Mag. A, 43, pp.587, 1981

[5] Ford I. J., Roughness effect on friction for multi-asperity contact between surfaces, J. of Physics D/: Applied Physics, 26, 2219-2225, 1993

[6] Jäger J., Uniaxial deformation of a random packing of particles, Applied of Archive Mechanics 69, 181-203, 1999

XXI ICTAM, 15–21 August 2004, Warsaw, Poland

BOUNDARY LAYERS INDUCED BY CONTACT OF ROUGH BODIES

Stanisław Stupkiewicz*

*Institute of Fundamental Technological Research, Świętokrzyska 21, 00–049 Warsaw, Poland

Summary A micromechanical framework is developed for the analysis of deformation inhomogeneities in the boundary layers that are induced by contact of rough bodies. The main idea is to average the inhomogeneous fields along the contact surface but preserve the dependence of the averages on the distance from the surface. Some properties of such averages are provided. As an example a boundary layer associated with ploughing by an array of periodic sine-shaped asperities is analyzed by the finite element method.

INTRODUCTION

In the case of contact of rough bodies, the characteristic lengths of the roughness are typically much smaller than those of the bodies. Thus two points of view can be adopted. At the *micro-level* the stress transfer is concentrated at small spots, so called real contacts, and the distribution of the contact pressure is highly inhomogeneous. These inhomogeneities govern the deformation of surface asperities and their interaction. At the *macro-level* it is the slowly-varying average (macroscopic) contact pressure that determines the overall deformation of the contacting bodies.

Friction laws are typically formulated in terms of the normal and tangential components of the contact traction vector $\boldsymbol{t} = \boldsymbol{\sigma} \cdot \boldsymbol{n}$, where $\boldsymbol{\sigma}$ is the stress tensor at the contact surface and $\boldsymbol{n}$ is the unit surface normal. Consequently, only the *exterior* part [1] of the stress tensor $\boldsymbol{\sigma}$ is involved in the description and the complete stress/strain state in the vicinity of the contact surface is typically not accounted for. However, in some situations, the *interior* (in-plane) parts of stress or strain significantly affect friction and other contact phenomena, particularly when the deformation in the sub-surface layer is inhomogeneous. This is for example the case of metal forming processes where the surface asperities are flattened more easily in the presence of bulk plastic deformation. This leads to high real contact area fractions [2, 3], even at moderate contact pressures. Depending on the lubrication regime this can result in an increased adhesive friction component or affect lubrication conditions. A closely related effect is also observed in hardness indentation testing, where the in-plane stresses affect the force-penetration response [4].

It seems that the effects associated with deformation inhomogeneities in the sub-surface contact layers and the interaction of these inhomogeneities with the macroscopic stresses and strains have not attracted sufficient attention in the literature yet. The aim of this work is thus to develop a micromechanical framework that would allow for consistent analysis of these effects and, in a broader perspective, would help to develop improved constitutive laws of contact phenomena.

BOUNDARY LAYERS: AVERAGING, COMPATIBILITY CONDITIONS AND PROPERTIES

Consider a homogeneous body occupying domain Ω with *micro-inhomogeneous* boundary conditions $\boldsymbol{t}^*$, the traction, and $\boldsymbol{u}^*$, the displacement, prescribed on the parts of boundary $\partial_t\Omega$ and $\partial_u\Omega$, respectively. By micro-inhomogeneity of $\boldsymbol{t}^*$ ($\boldsymbol{u}^*$) we understand that it consists of a slowly varying, average field $\bar{\boldsymbol{t}}^*$ ($\bar{\boldsymbol{u}}^*$) and its fluctuation $\tilde{\boldsymbol{t}}^*$ ($\tilde{\boldsymbol{u}}^*$). The wave-length of the fluctuation field is assumed small compared to the dimensions of Ω. It is also assumed that the inhomogeneity of deformation induced by the inhomogeneous boundary conditions is confined to a thin sub-surface layer, the *boundary layer*, along $\partial_t\Omega$ and $\partial_u\Omega$.

The equations of the boundary layer are obtained using the method of asymptotic expansions of the classical homogenization [5], under the assumption of periodicity of fluctuation fields $\tilde{\boldsymbol{t}}^*$ and $\tilde{\boldsymbol{u}}^*$. As a result, in addition to the *macroscopic* b.v.p. in Ω with *micro-homogeneous* boundary conditions $\bar{\boldsymbol{t}}^*(\boldsymbol{x})$ on $\partial_t\Omega$ and $\bar{\boldsymbol{u}}^*(\boldsymbol{x})$ on $\partial_u\Omega$, the *local* b.v.p. of the boundary layer is obtained for each point along the boundaries $\partial_t\Omega$ and $\partial_u\Omega$. The local b.v.p. of the boundary layer is a problem of a homogeneous half-space with a periodic traction or a periodic displacement prescribed along its boundary (the conditions of frictional contact can be treated accordingly). The displacement field in the boundary layer has the form

$$\boldsymbol{u}(\boldsymbol{x},\boldsymbol{y}) = \boldsymbol{u}_0(\boldsymbol{x}) + \boldsymbol{E}(\boldsymbol{x})\cdot\boldsymbol{y} + \boldsymbol{w}(\boldsymbol{y}), \qquad \boldsymbol{w}(\boldsymbol{y}^+) = \boldsymbol{w}(\boldsymbol{y}^-), \qquad \boldsymbol{w}(\boldsymbol{y}) \overset{y_3\to\infty}{\longrightarrow} \boldsymbol{0}, \tag{1}$$

where $\boldsymbol{y} = \boldsymbol{x}/\epsilon$, $\epsilon \ll 1$, is the local coordinate, $\boldsymbol{E}(\boldsymbol{x})$ is the macroscopic strain at point $\boldsymbol{x}$ on the boundary $\partial_t\Omega$ or $\partial_u\Omega$ and $\boldsymbol{w}$ is the unknown additional displacement field, which is periodic within the plane (S-periodic) and vanishes far from the plane (the local coordinate system is adopted such that the y_3-axis is normal to the surface).

The averaging operation is then defined. For a field $\varphi(\boldsymbol{y})$ its average $\bar{\varphi}$ at fixed y_3 is given by

$$\bar{\varphi}(y_3) = \langle\varphi\rangle \equiv \frac{1}{|S|}\int_S \varphi(\boldsymbol{y})\,\mathrm{d}y_1\mathrm{d}y_2, \qquad |S| = \int_S \mathrm{d}y_1\mathrm{d}y_2, \tag{2}$$

where S is the periodicity cell within the (y_1, y_2)-plane. The inhomogeneous field $\varphi(\boldsymbol{y})$ can now be decomposed into its average value $\bar{\varphi}(y_3)$ and fluctuation $\tilde{\varphi}(\boldsymbol{y})$, so that $\varphi(\boldsymbol{y}) = \bar{\varphi}(y_3) + \tilde{\varphi}(\boldsymbol{y})$ and $\langle\tilde{\varphi}\rangle = 0$.

Several properties of stress and strain averages can now be derived. The derivation is omitted here and three most important properties are provided below. First of all, the following compatibility conditions hold:

$$\Delta\bar{\boldsymbol{\sigma}}_A \equiv \bar{\boldsymbol{\sigma}}_A - \boldsymbol{\Sigma}_A = \boldsymbol{0}, \qquad \Delta\bar{\boldsymbol{\varepsilon}}_P \equiv \bar{\boldsymbol{\varepsilon}}_P - \boldsymbol{E}_P = \boldsymbol{0}, \tag{3}$$

where subscripts A and P denote, respectively, the exterior and the interior parts of a symmetric tensor [1], so that for example $\boldsymbol{\sigma} = \boldsymbol{\sigma}_A + \boldsymbol{\sigma}_P$ and $\boldsymbol{\sigma}_P \cdot \boldsymbol{n} = \mathbf{0}$. The macroscopic stress (i.e. the uniform stress far from the surface) is denoted by $\boldsymbol{\Sigma}$ and the macroscopic strain by $\boldsymbol{E}$.

Secondly, the (double) average total strain energy density is given by

$$\langle \boldsymbol{\sigma} : \boldsymbol{\varepsilon} \rangle = \bar{\boldsymbol{\sigma}} : \bar{\boldsymbol{\varepsilon}} + \frac{\mathrm{d}}{\mathrm{d}y_3} \langle \boldsymbol{n} \cdot \tilde{\boldsymbol{\sigma}} \cdot \tilde{\boldsymbol{w}} \rangle \,, \tag{4}$$

where $\boldsymbol{\sigma}$ is a statically admissible field, $\boldsymbol{\varepsilon}$ is the strain derived from a kinematically admissible displacement field of the form (1) with $\boldsymbol{w} = \bar{\boldsymbol{w}} + \tilde{\boldsymbol{w}}$. Note that the Hill's postulate of the classical micromechanics of heterogeneous materials (i.e. $\{\boldsymbol{\sigma} : \boldsymbol{\varepsilon}\} = \{\boldsymbol{\sigma}\} : \{\boldsymbol{\varepsilon}\}$, where $\{\cdot\}$ is the average over the representative volume) is not satisfied in the case of inhomogeneous boundary layers.

Consider now an elastic-plastic body. The local constitutive relation is $\boldsymbol{\sigma} = \boldsymbol{L} : (\boldsymbol{\varepsilon} - \boldsymbol{\varepsilon}^p)$ with a constant elastic moduli tensor $\boldsymbol{L}$ (the inelastic strain $\boldsymbol{\varepsilon}^p$ is, in general, inhomogeneous in the boundary layer). An analogous relation holds for the averages, $\bar{\boldsymbol{\sigma}} = \boldsymbol{L} : (\bar{\boldsymbol{\varepsilon}} - \bar{\boldsymbol{\varepsilon}}^p)$, while far from the surface we have $\boldsymbol{\Sigma} = \boldsymbol{L} : (\boldsymbol{E} - \boldsymbol{E}^p)$. In view of compatibility conditions (3) the average stress $\bar{\boldsymbol{\sigma}}(y_3)$ is fully determined if $\bar{\boldsymbol{\varepsilon}}^p(y_3)$ is known, namely

$$\Delta\bar{\boldsymbol{\sigma}}(y_3) = -\boldsymbol{Q}\Delta\bar{\boldsymbol{\varepsilon}}^p(y_3), \qquad \Delta\bar{\boldsymbol{\sigma}}(y_3) = \bar{\boldsymbol{\sigma}}(y_3) - \boldsymbol{\Sigma}, \qquad \Delta\bar{\boldsymbol{\varepsilon}}^p(y_3) = \bar{\boldsymbol{\varepsilon}}^p(y_3) - \boldsymbol{E}^p, \tag{5}$$

where the operator $\boldsymbol{Q}$ depends on $\boldsymbol{L}$ and $\boldsymbol{n}$. Similar relations hold also for the average strain $\bar{\boldsymbol{\varepsilon}}(y_3)$. Note that Eqn. $(5)_1$ is a special case of the interfacial relations that hold for local stress/strain jumps at regular discontinuities [1].

EXAMPLE: ASPERITY PLOUGHING

As an example consider a two-dimensional (plain strain) asperity ploughing problem. An array of rigid sine-shaped asperities ploughs through an elastic-plastic half-space which is subjected to macroscopic in-plane tensile or compressive strain $E_{11} = E_{11}^0$. After the sliding distance of $2l$ (l being the asperity spacing) the surfaces are separated and the macroscopic in-plane strain is released, $E_{11} = 0$. The finite element mesh of a periodic cell of boundary layer is shown in Fig. 1(a), where the distribution of plastic multiplier during relative sliding is also shown. It is seen that the plastic deformation is localized close to the real contact and thus inhomogeneous. The distribution of the average stress $\bar{\sigma}_{11}(y_3)$ normalized by the yield stress σ_y is shown in Fig. 1(b,c). The effect of the macroscopic in-plane strain E_{11}^0 on the residual stress $\bar{\sigma}_{11}$ in the boundary layer after separation and release of the in-plane strain is clearly visible in Fig. 1(c).

Note that it is only because of the inhomogeneity of deformation that plastic deformations appear in the sub-surface layer. Application of an equivalent (in terms of the average value) uniform normal and tangential traction would result in a purely elastic response (as it is the case far from the surface where the inhomogeneities vanish). Also note that the interior part of the average stress $\bar{\boldsymbol{\sigma}}_P$ (e.g. $\bar{\sigma}_{11}$) deviates from its macroscopic counterpart only in a part of the boundary layer adjacent to the surface, namely in the zone of non-zero plastic deformations, cf. Fig. 1(b,c), in agreement with relations (5).

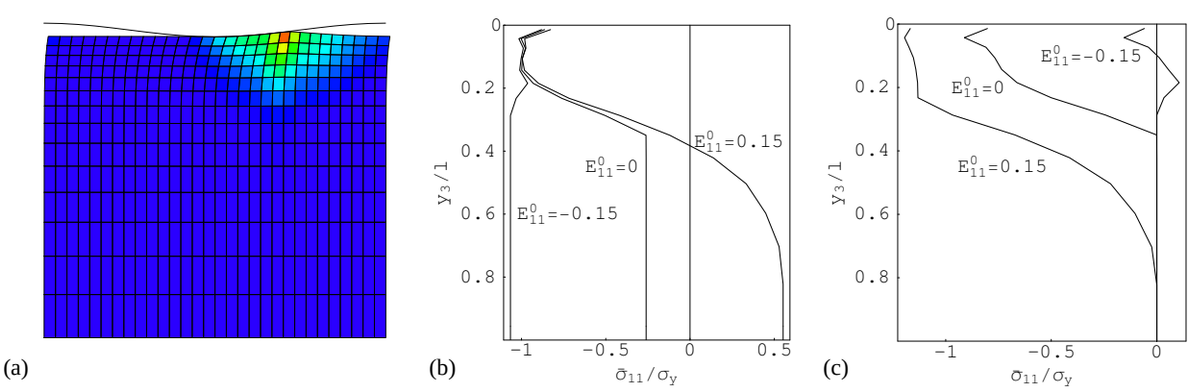


Figure 1. Asperity ploughing: (a) distribution of plastic multiplier; (b) distribution of the normalized average stress $\bar{\sigma}_{11}(y_3)/\sigma_y$, with applied in-plane strain $E_{11} = E_{11}^0$ and (c) after the in-plane strain is released, $E_{11} = 0$.

Acknowledgement. This work has been supported by the EC, ENLUB project, contract No. G1RD-CT-2002-00740.

References

[1] Hill R.: Interfacial operators in the mechanics of composite media. *J. Mech. Phys. Solids* **31**:347–357, 1983.
[2] Wilson W.R.D., Sheu S.: Real area of contact and boundary friction in metal forming. *Int. J. Mech. Sci.* **30**:475–489, 1988.
[3] Stupkiewicz S., Mróz Z.: Phenomenological model of real contact area evolution with account for bulk plastic deformation in metal forming. *Int. J. Plast.* **19**:323–344, 2003.
[4] Giannakopoulos A.E.: The influence of initial elastic surface stresses on instrumented sharp indentation. *ASME J. Appl. Mech.* **70**:638–643, 2003.
[5] Sanchez-Palencia. E.: Boundary layers and edge effects in composites. In E. Sanchez-Palencia and A. Zaoui, editors, *Homogenization Techniques for Composite Media*, *Lecture Notes in Physics* **272**:121–192, Springer, Berlin, 1987.

THE ACCOUNTING OF SURFACE ROUGHNESS IN CONTACT OF ARBITRARY SHAPED BODIES USING FEM

Alexandr A. Olshevsky, Alexei A. Olshevsky, Konstantin V. Shevchenko, Vladimir I. Sakalo
Bryansk State Technical University, Bulvar 50-letiya Oktyabrya 7, 241035 Bryansk, Russia

Summary The universal method of accounting the surface roughness in contact of arbitrary shaped bodies is developed. Procedure of computation of the contact stiffness and real contact area using finite element method are considered. Some results are presented.

INTRODUCTION

There are two principal approaches for modeling contact of rough bodies. The first one represents the rough surface of a body as a set of simple figures (columns, spheres, etc) with normally distributed heights. The analytical Hertzian solution of the contact problem for single asperity extends to all the asperities. In many cases it is assumed that there is no influence between neighboring contacts. This approach is detailed in, e.g. [1], [2], [3]. In the second approach the surfaces are considered as a set of finite elements and the shape of asperities is based on profilometric data of real surface and contact problem is solved numerically [4]. The last method is discussed in the paper. Methods using the first approach give good results when contact stiffness is investigated but they cannot be used in case of arbitrary shaped bodies or evaluation the stress-strain state for real asperities. Numerical methods are free of mentioned disadvantages. That is why there is the need for developing numerical methods for solving a contact problem for real rough bodies.

OBTAINING THE DISCRETE CONTACT PARAMETERS

General approach

The first approach for finite element modeling the contact of rough bodies is to build a FEM model of the whole bodies describing both the shape of each body and surface microgeometry. It is possible when contact areas are small and there are no heavy gradients of stresses. However, in some cases the contact area is comparable with size of bodies and the discrete pattern of contact caused by surface roughness requires fine finite element model so the dimension of a problem may be inadmissible large. Another way is to build a FEM model of a small part of rough surfaces of real machine elements in order to compute the contact stiffness parameters and then apply them to the contact problem for the whole bodies. A model of small parts of bodies also allows investigating the real contact area and stress-strain state of asperities. Numerical methods allow solving contact problem for rough surfaces with accounting of elastic-plastic deforming of material.

Finite element model forming

To obtain information about geometry of surface roughness a profilometer is used. Machine elements surfaces with Ra = 0.1-2.5 μm and Sm = 100 μm are typical. For surfaces with such parameters a model length 800-1000 μm containing 8-10 asperities and width 250-300 μm are appropriate. The typical size of finite element adjoining the contact surface equal to 5 μm provides enough accuracy of modeling. The height of the model providing the decay of stress peaks caused by contacts of asperities is 150 μm. The size of model is very small comparing with the size of bodies so the surfaces of models are assumed to be nominally flat. We consider a normal load of bodies only. Constraints are imposed normally to all lateral faced of a model. Ad hoc contact elements controlling mutual penetration and sliding of contact nodes are placed between nodes of upper and lower parts of model. Model contains 74532 elements (Figure 1).



model with loads and constraints | rough surface of the model | fragment of the lower part of the model

Figure 1. Finite element model of small parts of rough bodies in contact

Procedure of contact stiffness computation

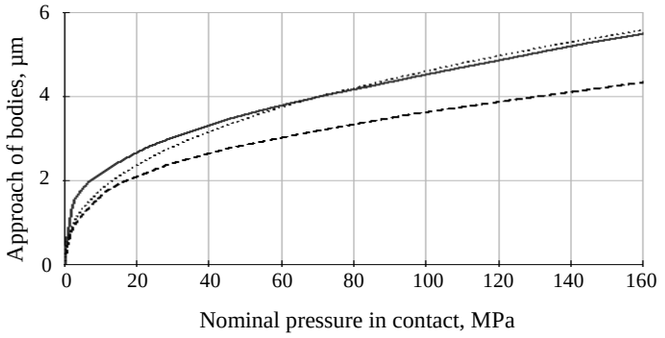
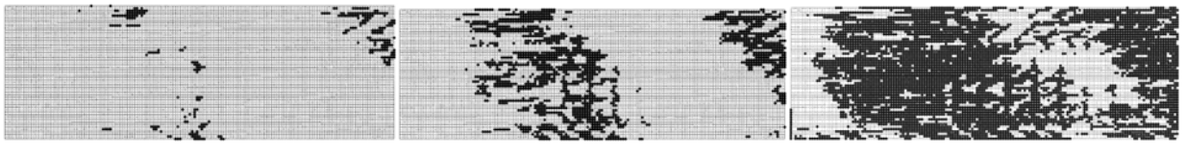


Figure 2. Approach of bodies with rough surfaces (Ra=0.41 μm, Sm=100.9 μm for both surfaces)

In order to realize kinematic load the upper face of a model is displaced down vertically. Step by step loading allows obtaining detailed information about bodies approach and changing the contact spots distribution during load increment. The accounting of elastic-plastic strain is based on yield theory with using plastic stress-strain matrix described in [5]. All of the computations were performed using a program package DSMFem (www.dsmsoft.ru) [6]. The main result of the contact problem solving is dependence of the bodies approach α on nominal pressure p_n at the contact surface, i.e. computation of the contact stiffness (Figure 2). The expression $p_n = c\alpha^x$ approximates the numerical result with average relative error 1%. Here c and x are parameters. The solid curve is the result of elastic-plastic solution of the contact problem, the dot one is its analytic approximation, and the dash one is the result of elastic solution shown for comparing. The analytic approximation is applied to solving the contact problem for arbitrary shaped real bodies further. In accomplish a behavior of contact areas during load increment was investigated (Figure 3). Each dark point is a node of a model where contact is occurred. The total number of nodes at the contact surface is 8965. Values of the nominal pressure and the real contact area A_r are given for 3 of 32 intermediate stages of load.



p_n =3.57 MPa, A_r =3.10% p_n =20.73 MPa, A_r =19.25% p_n =63.15 MPa, A_r =59.75%

Figure 3. Real contact area during load increment

APPLICATION

The curves describing the contact stiffness obtained for small parts of rough bodies can be applied to computing the contact parameters of arbitrary shaped bodies. It has been shown in [2] that the contact pressure distribution most depends on surface roughness in case of small load. The railway wheelset with differential rotation was chosen as an appropriate object, which has an extensive area of conformal contact between the wheel center and the bandage with typical value of nominal contact pressure 10-20 MPa [7]. A finite element model of the wheel was formed and the contact problem was solved for it. The obtained values of contact stiffness of rough layer were used in this computation as parameters. The accounting of surface roughness leads to 41-60% reducing of contact pressure in contact between the wheel center and bandage and 62-103% growth of nominal contact area for considered rough surfaces. Therefore, despite the displacements due to rough layer presence are small comparing to typical size of bodies, the value and distribution of the contact pressure can depend significantly on a surface roughness in some contact problems.

CONCLUSIONS

The universal method described in this paper allows accounting the surface roughness in contact of arbitrary shaped bodies using finite element method. They also allow investigation of the contact of rough surfaces.

References

[1] Greenwood J.A. The area of contact between rough surfaces and plate. – *ASME*, 1967,Ser. E, N 1.

[2] Greenwood J.A., Tripp J.H. The elastic contact of rough spheres. – *J. Applied mechanics*. March 1967, p.p. 153-159.

[3] Goryacheva I.G. Mechanics of frictional interaction. Moscow, 2001. – 478 p. (in Russian).

[4] Knothe K., Theiler A. Normal and tangential contact problem with rough surfaces. *Proc. of the 2nd mini conference on contact mechanics and wear of rail/way systems*, Budapest, 29-31 July, 1996, p. 34-43.

[5] Yamada Y., Yoshimura N., Sakurai T. Plastic stress-strain matrix and its application for the solution of elastic-plastic problems by the finite element method. – *International Journal of Mechanical Sciences*, 1968, v.10, N5, p. 343-354.

[6] Sakalo V., Olshevsky A., Shevchenko K. RSFEM Program Package for Contact Units Investigation/Consideration of Railway Transport Problems. *Proc. of the 4th International Conference on Railway Bogies and Running Gears*, Budapest, Hungary, 1998, pp. 162-164.

[7] Sakalo V.I., Vinnik L.V., Fridberg A.M., Olshevsky A.A., Shevchenko K.V. Wheelset with differential rotation of the wheels for decreasing wheel and rail wear. *Proc. of the 14th International Conference "Current problems in rail vehicles- PRORAIL "99"*, October 6-8, 1999, Zilina (Slovakia), p. 43-44.

XXI ICTAM, 15–21 August 2004, Warsaw, Poland

FRICTIONAL SLIDING OF A MULTISLIP SYSTEM

Thibaut Putelat*, John R. Willis**
*ITG / DAMTP, Centre for Mathematical Sciences, Wilberforce Road, Cambridge CB3 0WA, UK
**DAMTP, Centre for Mathematical Sciences, Wilberforce Road, Cambridge CB3 0WA, UK

Summary The brittle/ductile transition in rocks has an essential influence in determining the strain rate in lithospheric plates. With this motivation we attempt to study the micromechanics of an elastic medium with interfaces whose slip is governed by rate-and-state friction. As a preliminary analysis we study the stability of the steady-state slip of a finite number N of parallel interfaces caused by a constant velocity applied at one edge of the medium. We show that interfacial slip can occur with one or two different slip rates if the steady-state friction law displays a minimum as for dry friction. Our results suggest that, when active slip on all N interfaces is unstable, the medium will select a smaller number of interfaces which continue to slide, the others stopping.

INTRODUCTION

The mechanical behaviour of the earth's lithosphere is broadly described by the combination of a pressure-dependent brittle behaviour and a thermally activated viscoplastic one, called ductile. The brittle behaviour corresponds to the frictional sliding along preexisting faults and can roughly be modelled by a plastic material with a Drucker-Prager criterion. Concerning the mechanics of Plate tectonics, it has been shown that the brittle behaviour is essential because the brittle/ductile transition determines the strain rate of the lithospheric plate in relation to the forces equilibrium driving the plate [2]. This is why we are attempting to understand the micromechanics of such a brittle medium in order to propose homogenized constitutive models. As a preliminary approach, we study the linear stability of the steady sliding of N parallel frictional discontinuities in an elastic body.

THE PROBLEM

We consider a homogeneous elastic medium in mechanical equilibrium of thickness H, infinite in the horizontal direction x and divided by N horizontal interfaces along which friction phenomena occur. We consider rate-and-state friction laws defined by

$$\tau = F(\sigma, \dot{\delta u}, \psi) \quad \text{and} \quad \dot{\psi} = -G(\sigma, \dot{\delta u}, \psi). \tag{1}$$

Such friction laws relate the shear stress τ to the compressive normal stress σ and the rate of slip $\dot{\delta u}$ along the interface. The state of the asperity contacts is modelled by a single state variable ψ. It is supposed that $F_V > 0$, $F_\psi > 0$ and $G_\psi > 0$. The lower boundary is fixed and the upper one moves with a constant horizontal velocity V_H. A constant pressure P is applied on the upper boundary. Assuming the displacement such that $\boldsymbol{u} = u(y,t)\boldsymbol{e}_x$, it is found that the normal stress is homogeneous and equal to $-P$ and that the shear stress depends only on the time: $\tau(t)$. The boundary value problem, the stress continuity on each interface and the Hooke's law give a relation between the displacement $u(y,t)$ in the layer i ($0 \leqslant i \leqslant N$) and all the displacement jumps $\delta u_j(t)$ of each interface $0 \leqslant j \leqslant i$. For $y = H$, the time derivative of this relation leads to a differential equation for the shear stress

$$\dot{\tau} = k\left(V_H - \textstyle\sum_{i=1}^{N} \dot{\delta u}_i\right), \tag{2}$$

where $k = \mu/H$ is a stiffness parameter. Now, regarding the steady-state ($\dot{\tau} = 0$), the previous equation relates the N slip rates by

$$\textstyle\sum_{i=1}^{N} V_i = V_H. \tag{3}$$

We have denoted $V_i = \dot{\delta u}_i$ the steady-state slip rate on each interface. By the equation $(1)_2$ the state of each interface is a function of its corresponding slip rate $\psi_i^{ss} = \psi_i(V_i; P)$. Together with $(1)_1$, it leads to $N-1$ equations $\tau = F^{ss}(V_i; P)$ giving with (3) the nonlinear system to solve to find the steady-state slips V_i. Depending on the properties of the function F^{ss}, different cases can be envisaged. If F^{ss} is a monotonic function of V_i we expect a unique slip rate for the interfaces. If F^{ss} presents an extremum as observed in the case of dry friction [1], two slip rates V_1 and V_2 are expected. If there is a lubrication or a threshold at $V_i = 0$, the interfaces could slip with three different velocities.

MAIN RESULTS OF THE LINEAR STABILITY ANALYSIS

The stability of a steady-state solution is analysed by usual technique consisting of the linearization of the equations of perturbations around the steady state. It yields an eigenvalue problem defined by a matrix depending on a critical stiffness $k_c = F_\psi G_V - F_V G_\psi = -G_\psi \, \mathrm{d}F^{ss}/\mathrm{d}V$, the partial derivatives of F and G and parametrized by k and V_H. It is denoted $\mathsf{M}(k_c^{(l)}, F_V^{(l)}, F_\psi^{(l)}, G_V^{(l)}, G_\psi^{(l)}; k, V_H)$ where l denotes the number of distinct $V_i \neq 0$. Note that $k_c > 0$ corresponds to a velocity-weakening steady-state friction law. It has been shown that the velocity-weakening leads to an unstable sliding with stick-slip in the case of a single interface [4, 3]. We show that $k_c^{(i)}/F_V^{(i)}$ may be an eigenvalue of M whose algebraic multiplicity depends on the number of the interfaces which slip with the same slip rate.

Depending on the stability of the configuration of sliding, *i.e.* one, two or three slip rates, there is a selection of the number of the activated interfaces. We illustrate this result in the case of dry friction in the following.

One steady-state slip rate

When the steady-state friction law is monotonic, only one slip rate for all the interfaces is possible. Then $V_i = V_H/N \ \forall i$ because of (3). Hence, the determinantal equation is $(k_c/F_V - s)^{N-1}\left[s^2 - s\left(k_c - Nk\right)/F_V + NkG_\psi/F_V\right] = 0$. If $N > 1$, we show that if $k_c < 0$ the sliding is stable for all the interfaces. If $k_c > 0$, the biggest eigenvalue is k_c/F_V and the slip is unstable. It is important to note that, in this configuration, the most unstable mode is real and then the stick-slip instability as in the single-interface problem is not the most unstable mode. Looking at the associated eigenvector, it is remarkable that the presence of many interfaces allows the system to be unstable while the shear stress remains constant. The instability criterion of this configuration is then $k_c > 0$. That is, the slip rate V_H/N has to correspond to a velocity weakening behaviour of the friction law. About the evolution of an unstable system, the eigenvector associated to k_c/F_V suggests that $N-1$ of the interfaces have to slow down whereas one of them has to speed up. Using the Dieterich-Ruina law, this is confirmed by a direct numerical integration of the dynamical system (1)–(2) starting from an initial condition near the steady state. We then expect that an unstable system evolves from a configuration with N interfaces sliding at V_H/N towards a system which slips at V_H just on one interface. The slip is localised. Then, depending on the value of k this single-interface sliding can be unstable and present a Hopf bifurcation. A question then arises: because the shear stress has to increase, is this stick-slip instability able to promote a slip on another interface? It is impossible in the case of friction laws like the Dieterich-Ruina one because of its logarithmic singularity and the unbounded evolution of ψ.

Two steady-state slip rates

We consider a convex steady-state friction law with a minimum at $V = V_m$ so that two steady-state slip rates can exist: one in the creep regime, the other in the inertial one (cf. Fig. 1). By convention $V_1 < V_2$. Then, n interfaces slip at V_1 and m at V_2 such that $n+m = N$ and $nV_1 + mV_2 = V_H$ by (3). This relation, together with the steady-state condition $F^{ss}(V_1) = F^{ss}(V_2)$, has the obvious solution $V_1 = V_2 = V_H/N$ which is stable only if $V_H > NV_m$. A solution $V_1 \neq V_2$ can only exist if the curve $\tau^{ss}(V^{ss})$ is asymmetric around V_m. If the strengthening part of $\tau^{ss}(V^{ss})$ is steeper (resp. less steep) than the weakening part, a supercritical (resp. subcritical) pitchfork bifurcation is expected to occur at $V_H = NV_m$ (Fig. 2).

In fact, the linear stability analysis shows that the solution $V_1 \neq V_2$ is unstable when there is more than 1 slow interface ($n > 1$) and stable otherwise. Indeed, the roots of M are given by the polynomial $P_3(s)\left(s_1 - s\right)^{n-1}\left(s_2 - s\right)^{m-1} = 0$ where $P_3(s)$ is a cubic and $s_i = k_c^{(i)}/F_V^{(i)}$. Thus, 5 eigenvalues are expected. Using the Routh-Hurwitz criterion to study the location of the P_3's roots, we show that the mode s_1 is the most unstable for $k_c^{(1)} > 0$. Provided $n \neq 1$, this mode leaves the shear stress τ constant and suggests that $n-1$ interfaces stop and one of them speeds up. The total number of slipping interfaces changes. We then guess that such a multislip system should evolve towards a system with only one slow interface ($n = 1$) because s_1 is no longer a mode. It can be further shown that the solution $V_1 \neq V_2$ ($V_H < NV_m$) then is stable for any stiffness k, at least when V_H is close to NV_m.

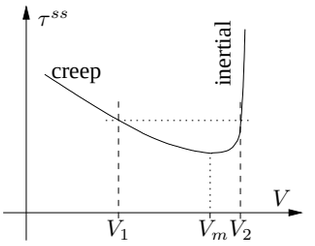


Figure 1. Dry friction law (cf. [1])

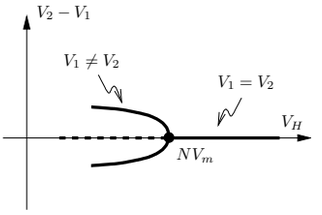


Figure 2. Bifurcation diagram of the two slip-rate solution

CONCLUSIONS

We show that the sliding of a heterogeneous medium holding a large number of dry frictional interfaces depends strongly on the nature of the steady-state rate-and-state friction law. A purely velocity-weakening law implies that the multislip is unstable and only one slipping interface is selected. On the other hand, if the steady-state law presents a minimum, there is a critical driving velocity $V_H^c = NV_m$ (*i.e.* a critical number of interfaces $N_c = \lfloor V_H/V_m \rfloor$) above which (*i.e.* such that $N \leq N_c$) the multislip system is stable, all interfaces sliding at V_H/N. Below V_H^c, a stable multislip system with 1 slow interface and $N-1$ faster ones could exist if the velocity-strengthening part of the friction law is steeper than the weakening part. Thus, for this multislip system, the nature of the instabilities is different from the stick-slip oscillations involved in the single interface problem and it could lead to interesting experimental investigations in order to constrain the friction law around its minimum and get a better understanding of what happens when $V \to 0$. Furthermore, the richness of behaviours of this system should give new insights concerning earthquake dynamics and the localisation of deformation in brittle media.

References

[1] F. Heslot, T. Baumberger, B. Perrin, B. Caroli, and C. Caroli. Creep, stick-slip, and dry-friction dynamics. *Phys. Rev. E*, 49:4973–4988, 1994.
[2] T. Putelat. *Quelques applications d'un modèle mécanique de la lithosphère*. PhD thesis, Université Claude Bernard — Lyon 1, 2002.
[3] J. R. Rice and A. L. Ruina. Stability of steady frictional slipping. *J. App. Mech.*, 50:343–349, 1983.

SECOND-ORDER CONE COMPLEMENTARITY FORMULATION FOR QUASI-STATIC INCREMENTAL FRICTIONAL CONTACT PROBLEM IN THREE-DIMENSIONAL SPACE

Y. Kanno*, A. Pinto da Costa**, J.A.C. Martins**
*Department of Architecture and Architectural Engineering, Kyoto University, Kyoto $606-8501$, Japan
**Instituto Superior Técnico, Departamento de Engenharia Civil e Arquitectura and ICIST, Av. Rovisco Pais, $1049-001$ Lisboa, Portugal

Summary The numerical solution of quasi-static incremental frictional contact problems involving discrete versions of two- and three-dimensional elastic solids or structures is sought with a Second Order Cone Linear Complementarity Problem (SOCLCP) formulation. The Coulomb friction cone is considered without any pyramidal approximation. Some illustrative numerical examples are given.

The SOCLP formulation

In this paper we deal with quasi-static problems in which finite-dimensional geometrically linear elastic structures may establish frictional contact with the surface of rigid obstacles. The nonlinearity of the three-dimensional Coulomb friction cone makes impossible the direct use of linear complementarity formulations to deal with three-dimensional frictional contact problems. In order to overcome this difficulty several formulations use pyramidal approximations of the friction cone. In this paper we consider the classical three-dimensional Coulomb friction cone without any pyramidal approximation. For a contact candidate node in the three-dimensional space, $(\Delta\mathbf{u}_{\mathrm{t}}, \Delta u_{\mathrm{n}}) \in \mathbb{R}^2 \times \mathbb{R}$ and $(\mathbf{r}_{\mathrm{t}}, r_{\mathrm{n}}) \in \mathbb{R}^2 \times \mathbb{R}$ denote the vector of incremental displacements and the vector of reactions, respectively. Here, the subscripts t and n denote the two tangential and the normal directions to the obstacle surface, respectively. Denoting the coefficient of friction by $\mu > 0$, Coulomb's friction law

$$\mu r_{\mathrm{n}} \geq \|\mathbf{r}_{\mathrm{t}}\|, \quad \mathbf{r}_{\mathrm{t}} \cdot \Delta\mathbf{u}_{\mathrm{t}} + \mu r_{\mathrm{n}} \|\Delta\mathbf{u}_{\mathrm{t}}\| = 0, \tag{1}$$

can be written as the following linear complementarity condition over two second-order cones [2]

$$(\lambda_{\mathrm{n}}, \Delta\mathbf{u}_{\mathrm{t}}) \cdot (\mu r_{\mathrm{n}}, \mathbf{r}_{\mathrm{t}}) = 0, \quad \lambda_{\mathrm{n}} \geq \|\Delta\mathbf{u}_{\mathrm{t}}\|, \quad \mu r_{\mathrm{n}} \geq \|\mathbf{r}_{\mathrm{t}}\|, \tag{2}$$

where $\lambda_{\mathrm{n}} \in \mathbb{R}$. The unilateral contact condition can be written as

$$\Delta u_{\mathrm{n}} - g \geq 0, \quad r_{\mathrm{n}} \geq 0, \quad (\Delta u_{\mathrm{n}} - g) r_{\mathrm{n}} = 0, \tag{3}$$

where g denotes the current distance to the obstacle. Let n^c denote the number of contact candidate nodes. The equilibrium equations after a condensation on the contact candidate nodes are

$$\mathbf{K}\Delta\mathbf{u} = \mathbf{r} + \mathbf{f}, \tag{4}$$

where $\mathbf{K} \in \mathbb{R}^{3n^c \times 3n^c}$ is the condensed stiffness matrix, $\Delta\mathbf{u} \in \mathbb{R}^{3n^c}$ and $\mathbf{r} \in \mathbb{R}^{3n^c}$ denote, respectively, the vector of incremental nodal displacements and the reactions at the contact candidate nodes and $\mathbf{f} \in \mathbb{R}^{3n^c}$ denotes the vector of independent terms that combines effects of applied forces, current gap and condensation process. Conditions (2) – (4), are equivalent to the following *second-order cone linear complementarity problem* (*SOCLCP*)

$$\begin{gathered} \text{find} \quad (\mathbf{x}, \mathbf{y}) \in \mathbb{R}^{4n^c} \times \mathbb{R}^{4n^c} \text{ such that} \\ \mathbf{y} = \mathbf{M}\mathbf{x} + \mathbf{q}, \quad \mathbf{x} \in \mathcal{K}_S, \quad \mathbf{y} \in \mathcal{K}_S, \quad \mathbf{x}^{\mathrm{T}}\mathbf{y} = 0, \end{gathered} \tag{5}$$

where $\mathbf{x} = (\lambda_{\mathrm{n}}, \Delta\mathbf{u}_{\mathrm{t}}, \Delta\mathbf{u}_{\mathrm{n}})$, $\mathbf{y} = (\mu\mathbf{r}_{\mathrm{n}}, \mathbf{r}_{\mathrm{t}}, \mathbf{r}_{\mathrm{n}})$, $\mathbf{M}$ and $\mathbf{q}$ are a matrix and a vector of dimension $4n^c$ and the second-order cone $\mathcal{K}_S = \mathcal{K}_1 \times \mathbb{R}^{n^c}_+ \subset \mathbb{R}^{3n^c}$ with $\mathcal{K}_1 = \{(\mathbf{s}_1, \mathbf{s}_2) \in \mathbb{R}^{n^c} \times \mathbb{R}^{2n^c} | s_{1i} \geq \|\mathbf{s}_{2i}\|\}$. Problem (5) can be solved efficiently by using the recently developed algorithm [1] that combines smoothing and regularization procedures, and is based on the Euclidean Jordan algebra on second-order cones.

Numerical examples

In this section we consider two numerical examples solved by the present formulation and algorithm. The first example is a double layer truss with 12×12 contact candidate nodes with an horizontal flat obstacle at $z = 0$ (Figure 1(b)). Figure 1(a) illustrates a 4×4 truss. The lengths of the members in the x- and y-directions are 2000.0 mm and 3000.0 mm, respectively, and the distance between the upper and lower layers is 2000.0 mm. The elastic modulus and the cross-sectional area for each member are 205.8 GPa and 10000.0 mm^2, respectively. The coefficient of friction is $\mu = 0.12$. The external loads applied to the nodes of the upper layer at load step k are $\gamma^{(k)}\hat{\mathbf{f}}$ for each interior node (denoted by $\circ$; see Figure 1 (a)), $\gamma^{(k)}\hat{\mathbf{f}}/2$ for each edge node (denoted by $\bullet$) and $\gamma^{(k)}\hat{\mathbf{f}}/4$ for each corner node (denoted by $\oplus$), where $\hat{\mathbf{f}} = (0, 0, -102.9)$ kN. The sequence of the load parameters $\gamma^{(k)}$ is 0, 5.00, 4.05, 3.1, 2.15, 1.20, 0.25 for $k = 0, \ldots, 6$; after an initial compression against the obstacle the downward forces are progressively alleviated. For $k = 6$ Figure 1(b) illustrates the configuration of the truss while Figure 1(c) shows the projection onto the xy-plane of the total displacements of the contact candidate nodes. The pattern of the residual tangential contact displacements is clearly observed in Figure 1(c) .

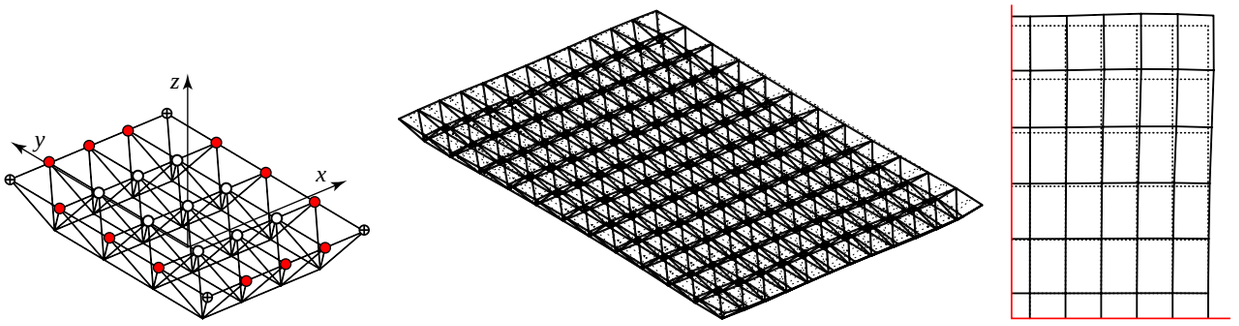


Figure 1. (a) A 4×4 double layer truss. At the end of the loading process (displacements amplified 1000 times): (b) perspective of the equilibrium configuration of the truss; (c) horizontal projection of one fourth of the contact candidate nodes (double symmetry).

The next example is a well known example in the literature. It consists of a linear elastic body (Young's modulus $E = 130\ \mathrm{GPa}$, Poisson's ratio $\nu = 0.2$) in a state of plane strain. One half of it occupies a $40\ \mathrm{mm} \times 40\ \mathrm{mm}$ square domain as illustrated in Figure 2 and is discretized in 512 bilinear (Q1) finite elements. The right boundary of that square belongs to an axis of symmetry, hence its points are constrained to move only in the vertical direction. The nodes of the bottom segment are submitted to frictional contact conditions ($\mu_i = 1,\ i = 1, \ldots, 33$). The left and top boundary segments are submitted to a monotonic proportional loading that consists of $100\ \mathrm{MPa}$ rightward and $50\ \mathrm{MPa}$ downward uniform stresses, respectively. The self-weight is neglected. The contact stresses are represented in Figure 2 and match the results presented in previous works; the tangential reaction stresses point to the right.

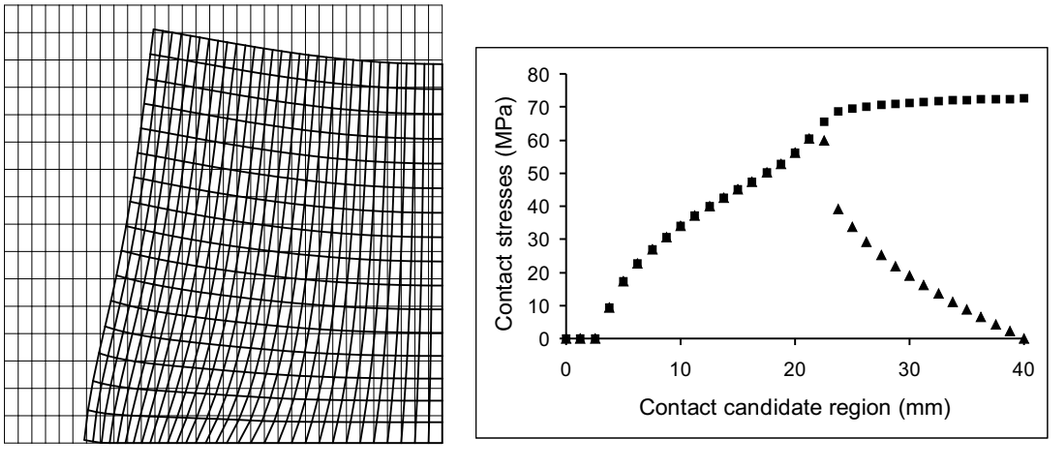


Figure 2. (a) Deformed configuration at an equilibrium state corresponding to a rightward pressure of $100\ \mathrm{MPa}$ on the left face and a downward pressure of $50\ \mathrm{MPa}$ on the upper face (displacements amplified 500 times); (b) Schematic representation of the normal contact stresses (■) and tangential contact stresses divided by μ (▲).

Conclusions

The equilibrium states of three- and two-dimensional structures and solids were computed by solving the incremental quasi-static frictional contact problem formulated as a SOCLCP. With this formulation no pyramidal approximation of the Coulomb friction cone is needed. The SOCLCP's were solved by a combined smoothing and regularization method.

References

[1] Hayashi S., Yamashita N., Fukushima M.: A combined smoothing and regularization method for monotone second-order cone complementarity problems. *Technical Report* **2003-002**, Department of Applied Mathematics and Physics, Kyoto University, Japan, 2003.

[2] Kanno Y., Ohsaki M.: Minimum principle of complementary energy of cable networks by using second-order cone programming. *Int. J. Solids Struct.* **40**: 4437–4460, 2003.

XXI ICTAM, 15–21 August 2004, Warsaw, Poland

A NOVEL CONTACT MODEL BASED ON VOLUMETRIC INFORMATION

Yves Gonthier*, John McPhee**, Christian Lange*, Jean-Claude Piedbœuf*
*Space Technologies, Canadian Space Agency, St-Hubert, Québec, Canada
**Systems Design Engineering, University of Waterloo, Ontario, Canada

Summary A novel contact model is presented which includes normal contact force and damping, rolling resistance torque and tangential friction force. It features a contact stiffness proportional to the contact area and leads automatically to the correct selection of the point of action of the force, which is shown to be proportional to the interpenetration volume. A numerical simulation of a sphere impacting on the inside surface of a cylinder is presented.

INTRODUCTION

Contact models often drastically simplify the interaction of complexly shaped bodies to simple cases, or even point contacts. The significance of the shapes of the colliding bodies on the resulting contact forces is generally not taken into account, or not modeled in a consistent manner for all components of the contact force, namely, normal and tangential force, rolling and spinning resistance torques.

The Hertzian contact model, which assumes an elastic half-space approximation, is often used to model contact phenomena. However, this approximation is not valid for bodies that have conforming surfaces. Strictly speaking, the Hertz theory should be used to model the contact mechanics only when the colliding body surfaces can be described by second order polynomials. However, in practice its application can be extended to bodies with smooth surfaces as long as the resulting contact area remains small with respect to the dimensions of the bodies. Even though the geometric boundary conditions may not be exactly fulfilled, the Hertz theory's assumption that the pressure distribution over the contact area is elliptical will still apply, or at least provide a good approximation, such that the theory still applies, but only for non-conforming geometries.

Johnson [1] suggests to use the Winkler elastic foundation as a simple approximation in complex situations where half-space theory would be very cumbersome. Hippmann [2] uses this approach to deal with complex, i.e., conforming, polygonal, geometries. The contact force is derived by numerically summing up the contribution of each polygon using a simple contact model.

In this paper, a model for distribution the pressure over the contact area will be presented. Using this model, it is shown how a complete contact model can be analytically derived by integrating the contact pressure over the area. This novel approach includes all forces and moments resulting from the contact mechanics effects between the colliding bodies, and in particular it includes the rolling resistance torque.

NORMAL AND TANGENTIAL FORCE MODEL

The Winkler elastic foundation model (Figure 1) predicts that the pressure $p(\underline{s})$ at any location $\underline{s}$ on the contact surface S is proportional to $h_s(\underline{s})$, the interpenetration depth between the two undeformed surfaces at point $\underline{s}$. However, it does not include any damping effect to dissipate energy during the contact process. The energy dissipation is best modeled using a hysteretic damping term a [3]. Therefore, a new pressure distribution model is proposed as

$$p(\underline{s}) = \frac{df_n(\underline{s})}{dS} = \frac{k_f}{h_f} h_s(\underline{s}) \left(1 + a\, v_n(\underline{s})\right) , \tag{1}$$

where k_f is the elastic modulus of the foundation, h_f is the depth of the foundation mattress, and v_n is the relative velocity component normal to S at $\underline{s}$. The volume V spanned by the intersection of the two undeformed geometries of the colliding bodies is labeled the *volume of interference*. By definition, the volume of interference contains the S. The volume of interference and its centroid $\underline{r}_c$ are given by

$$V = \int_S h_s(\underline{s})\, dS = \int_V dV \; ; \;\; \underline{r}_c = \frac{1}{V} \int_V \underline{r}\, dV , \tag{2}$$

where $\underline{r}$ is a point in the volume of interference. Integrating $df_n(\underline{s})$ over S and using Equations (2) the contact force results as

$$\underline{f}_n = \frac{k_f}{h_f} V \left(1 + a\, v_{cn}\right) \underline{n} , \tag{3}$$

where v_{cn} is the normal component of the relative velocity at $\underline{r}_c$. The tangential friction is computed as given in [3] using this new definition of $\underline{f}_n$ as given in Equation (3).

The interference volume, its centroid, and the contact surface normal, necessary to evaluate Equation (3), can be derived either analytically or numerically from geometric and kinematic information. This model features a contact stiffness proportional to the contact area and defines the location of the point of action of the contact force as $\underline{r}_c$. Contact models

based on penetration depth typically assume the point of action to be located at the point of maximum penetration. However this causes problems when the contact area is large and the surfaces of the colliding bodies are nearly parallel, i.e. instantenous change of point of action and of the moment arm of the contact force w.r.t. the colliding bodies.

ROLLING FRICTION MODEL

The shape of load distribution across the contact area gets distorted due to the presence of the hysteretic damping term. Hence, the centroid of the load distribution is not at the same location as the centroid of the interpenetration volume. If the point of application is selected as $\underline{r}_c$, an additional rolling resistance torque has to be applied.

The torque about $\underline{r}_c$ resulting from the contact force distribution over area of contact is computed by integrating the infinitesimal rolling friction torque $d\underline{\tau}_r(\underline{s}) = \underline{\rho}_s \times d\underline{f}_n(\underline{s})$ over S, where $\underline{\rho}_s = \underline{s} - \underline{r}_c$. It can be shown that

$$\underline{\tau}_r = \frac{k_f}{h_f} a\, \mathbf{J}_c \cdot \underline{\omega}_t \; ; \;\; \mathbf{J}_c = \int_S \left((\underline{\rho}_s \cdot \underline{\rho}_s)\, \mathbf{I} - \underline{\rho}_s\, \underline{\rho}_s \right) h_s(\underline{s})\, dS \;\; , \tag{4}$$

where $\underline{\omega}_t$ is the component of the relative angular velocity tangential to S. Since the interpenetration depth is typically small, $\mathbf{J}_c$ is closely approximated as the second moment of volume about the centroid of V.

When the bodies are rolling with respect to each other, then $\underline{\tau}_r$ is the resistance torque acting to prevent the rolling. Equation (4) shows that if the two bodies are not rolling with respect to each other ($\underline{\omega}_t = 0$), then the normal force is distributed symmetrically around the volume of interference centroid, so the net moment at the centroid is zero.

NUMERICAL EXAMPLE: BOUNCING SPHERE

The model described above was utilized to simulate a sphere bouncing inside a cylinder. Figure 2 shows the three-dimensional trajectory of the sphere center. Figure 3 shows the decays in both of the angular and translational velocities over time. Observe that the sphere eventually stops moving in y-direction. Clearly, the resistance torques act to prevent rotational motion, as we expected. The parameters used are give in [3].

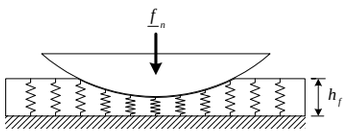


Figure 1. The Winkler elastic foundation model.

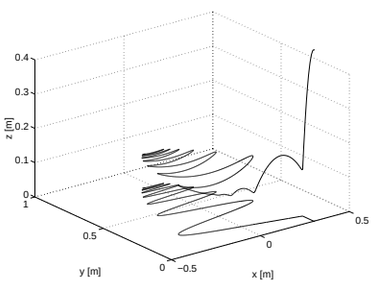


Figure 2. Trajectory of sphere center.

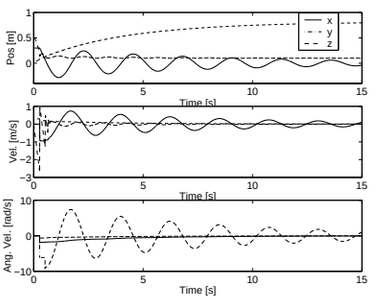


Figure 3. Position and velocity components versus time.

CONCLUSIONS

In this paper, a novel contact model was presented which includes normal contact force and damping, rolling resistance torque and tangential friction force. A modified Winkler elastic foundation model was introduced to obtain the pressure distribution across the contact area. The contact force is expressed analytically by integrating the pressure distribution over the contact area. The resulting model features a contact stiffness proportional to the contact area and leads automatically to the correct selection of the point of action of the force, which is shown to be proportional to the interpenetration volume. The proposed model is not restricted to contact situations where the bodies have non-conforming geometries, but can be used for any geometry with reasonably flat contact area. A numerical simulation example of a sphere colliding on the interior surface of a cylinder under the action of gravity was provided. The resulting dynamic behavior is physically realistic and satisfies the condition $|\underline{v}| = R|\underline{\omega}|$ and it is seen that the effect of the resistance torque is to dissipate rotational energy such that the sphere's motion is eventually stopped.

References

[1] K. L. Johnson, *Contact Mechanics*. London: Cambridge University Press, 1985.

[2] G. Hippmann, "An algorithm for compliant contact between complexly shaped surfaces in multibody dynamics," in *ECCOMAS Multibody Dynamics Conference*, Lisbon, Portugal, July 1–4 2003.

[3] Y. Gonthier, J. McPhee, C. Lange, and J.-C. Piedbœuf, "A regularized contact model with asymmetric damping and dwell-time dependent friction," *Multibody System Dynamics*, 2004, accepted for publication.

COUPLED OPTIMAL DESIGN OF BUILDING WITH TMD

Anupam S. Ahlawat*, Ananth Ramaswamy*
*Department of Civil Engineering, Indian Institute of Science, Bangalore-560 012, India

Summary A genetic algorithm based integrated approach to optimize the total cost of building and the associated control device has been proposed. Constraints for performance of the design include peak inter-story drift and peak absolute acceleration of the floors. Two examples, a three- and a nine-story building subjected to design seismic excitations have been studied. The control device considered is a tuned mass damper (TMD) installed at the roof of the building. The study concludes that for 3-story example problem, building alone without any TMD is an optimal solution while for 9-story, a building with a TMD is the best design.

INTRODUCTION

Stringent performance requirements to mitigate structural damage in the event of large environmental loads such as strong earthquake or wind gusts and occupant comfort during normal service of the structure have gained increased significance in recent years. These performance requirements can be met through the use of optimal design of the structure with constraints for dynamic response [1]. Alternatively, performance of the structures can be improved through the application of a passive, active or hybrid control system [2].

A substantial amount of research has been carried-out on structural optimization as well as on optimal control system design. However, deployment of an optimal control system in an optimal structure may not lead to an optimal design of combined structure-control system. Very little effort has been made in the direction of integrated structural-control system optimization and these were primarily focused on small aerospace structural components.

In the present paper, a coupled approach for an integrated optimization of seismically excited building structure with associated tuned mass damper (TMD) has been presented and demonstrated through example problems. Results indicate that proposed approach is robust and leads to superior designs not previously envisaged.

STRUCTURAL AND CONTROL SYSTEM

For the present study, idealized plane frame equivalent models of the 3-story and 9-story steel buildings have been considered. Building structure has been assumed to be linear elastic with Rayleigh damping. Mass of the building is lumped at floor levels. A TMD installed at roof of the building has been used as a passive vibration control device. Four actual earthquake records that are listed below have been used as design excitations.

- El Centro, May, 18, 1940: North-South (N-S) component recorded in El Centro, California, at the Imperial Valley Irrigation District substation with an absolute peak acceleration of 3.417 m/s^2.
- Hachinohe, May, 16, 1968: N-S component of the Tokachi-oki earthquake recorded in Hachinohe city, Japan with an absolute peak acceleration of 2.250 m/s^2.
- Northridge, January, 17, 1994: N-S component recorded in Sylmar, California, at the parking lot of the Sylmar County Hospital with an absolute peak acceleration of 8.2676 m/s^2.
- Kobe, January 17, 1995: N-S component recorded during the Hyogo-ken Nanbu earthquake at the Kobe Japanese Meteorological Agency (JMA) with an absolute peak acceleration of 8.1782 m/s^2.

FORMULATION OF OPTIMIZATION PROBLEM

The building consists of 3 or 9 storys of equal eights. For simplicity, all the columns for a story are considered to be of the same size and equi-spaced, however, the column size for different storys may be different. Cost associated with the mass of the floors do not change in the optimization process. Hence, the only variable component of the cost of the building depends on the column sizes. Cost of the TMD has been assumed to be directly proportional to its mass. Thus, the optimization problem can be defined as:

Design variables

Stiffness of the column K^i_{col} for all the storys, i.e., for $i = 1$ to N, (where N is total number of storys in the building), mass (m_{tmd}), stiffness (k_{tmd}) and damping (d_{tmd}) of the TMD have been considered as design variables. Here it should be noted that the column stiffness is a secondary design variable and is linked to the area of the column (A^i_{col} for standard column sections.

Objective function

$$f_{obj} = c_{col} N_{col} \sum_{i=1}^{N} A_{col}^{i} + c_{tmd}\, m_{tmd} \tag{1}$$

Where c_{col} is the unit cost of the column per unit area, N_{col} is the number of columns in each story, A_{col}^{i} is the area of a column of the i^{th} story, c_{tmd} and m_{tmd} are unit cost and mass of the TMD, respectively.

Constraints

Design constraints include structural strength related constraints (permissible stress, etc.), dynamic performance related constraints (peak inter-story drift, peak absolute acceleration at floor level) and control device related constraints (maximum limit on mass, stiffness and damping of TMD and maximum allowable displacement of the TMD relative to the roof).

Constant parameters

Material properties, mass of the floors, boundary conditions, modal damping coefficient for two predefined modes are the constant parameters and kept unchanged in the optimization process.

SOLUTION PROCEDURE

Idealized plane frame equivalent model of the building, and control device (TMD) have been simulated using SIMULINK [3] and MATLAB [4]. Genetic algorithm (GA) has been used to solve the optimization problem. Optimal design of the building with an optimal TMD has been introduced as a member in the randomly generated initial population. Boxed constraints for the design variables have been incorporated in coding of the chromosomes [2]. All the design variables have been represented by 8 bit long string. Thus total length of chromosome is $8\times$ Number of design variables.

ILLUSTRATIVE EXAMPLES

Two example problems namely, a 3-story and a 9-story building structures with TMD installed at the roof, have been considered to demonstrate the proposed coupled optimization approach. These example problems have been taken from the 3rd generation benchmarks on structural control [5]. These benchmark problems are for nonlinear analysis but for the present study, linear analysis has been carried-out. Story height for these buildings is 3.96m. Dimensions in plan are $36.58m \times 54.87m$ and $45.75m \times 45.75m$ for 3-story and 9-story building, respectively. Total mass is 2.95×10^{6}kg for 3-story and 9.00×10^{6}kg for 9-story building. The modal damping coefficients have been taken as 0.02 for first and third mode. Constraints for maximum mass of the TMD has been taken as 5% of the total mass of the structure. Constraint for maximum stiffness and damping of the TMD have been taken as 4000 kN/m and 1000 kN-s/m, respectively [6].

RESULTS

For 3-story building example problem optimal design is one without any TMD, i.e., the optimum mass of the TMD is zero. For the 9-story building, the best design is one with a TMD of 3.96×10^{5}kg. Constraint for maximum mass of the TMD is not active at the solution.

CONCLUSIONS

The proposed approach for coupled optimization of structural and control system leads to a superior design than the corresponding one obtained by plugging an optimal TMD in the optimal design of the building. It is clear from the design obtained for two example problems that the proposed method is robust and results in an optimal solution for both cases, one when the building alone is an optimal design and does not require any TMD and the other when building with a TMD is the optimal solution.

References

[1] Pantelides C.P., Tzan S.R.: Optimal Design of Dynamically Constrained Structures. *Computers & Structures* **62**:141–149, 1997.

[2] Ahlawat A.S., Ramaswamy A.: Multi-objective Optimal Design of FLC driven Hybrid Mass Damper for Seeismically Excited Structures. *Earthquake Engrg. and Struct. Dyn.* **31**:1459–1479, 2002.

[3] SIMULINK: version 4.0, The MathWorks, Inc.: Natick (USA), 2001.

[4] MATLAB: Version 6.1.0.450, The MathWorks, Inc.: Natick (USA), 2001.

[5] Ohtori Y., Christenson R.E., Spencer Jr. B.F., Dyke S.J.: "Benchmark control problems for seismically excited nonlinear buildings. web site http://www.nd.edu/~quake/benchmarks/bench3def, 2003

[6] Hadi M.N.S., Arfiadi Y.: Optimum design of absorber for MDOF structures. *J. Struct. Engrg.*, ASCE, **124**:1272–1280, 1998.

OPTIMAL VIBRATION CONTROL OF GUYED MASTS

Bartlomiej D. Blachowski*, Witold Gutkowski**
*IPPT PAN, Department of Computational Science, PL 00-049 Warszawa, Poland
**Polish Academy of Sciences, IPPT PAN, Swietokrzyska 21, PL 00-049 Warszawa, Poland

Summary Topics considered in this paper include: dynamic properites of the mast and nonlinearities present in the problem, linearized equations governing guyed mast motion, conditions of stability, contollability and observability. Control forces are exerted by an anchored mechanism in such a way, that they change tension in guy cables. A control algorithm ensuring robust optimal control is also proposed. Finally, the paper is verified by a numerical simulation of a vibration control process.

INTRODUCTION

Guyed masts belong to a class of vibration-prone structures. Their location in open spaces together with their height reaching even a few hundred meters, make them exposed to action of strong wind pressure. It often happens, that the time of the strongest windblasts coincides with that of the heaviest icing. For that reason, safety of the structure requires a robust control scheme, which can stabilize the mast under different load configurations. Dynamic analysis of a guyed mast is complex, because of nonlinear behaviour of guy cables [1]. During recent years many control methods have been developed, but their practical application to mast-like structures still remains limited. One of the recent approaches is presented by Preumont [2]. Using massless cables, he proposed integral force feedback controller to reduce vibration of a truss structure. Another control technique of cable structures, called Active Stiffness Control, was proposed by Fujino [3] and was applied to cable-stayed bridges. Recently, the problem of damping cable vibrations by semi-active control was investigated by Spencer [4]. The objective of this paper is a numerical simulation of an active vibration control of a mast, supported by guy cables.

MECHANICAL MODEL OF THE MAST

The guyed mast is discretized, following a three-dimensional finite element approach. The column of the mast is represented by a prismatic truss of a triangular cross section (Fig. 1). A single guy cable consists of a chain of tension-only elements. One cable end is attached to the mast, and the second one to an anchored mechanism, allowing control of tension in the cable. After assembling global stiffness and mass matrix, nonlinear analysis is performed, to find static equilibrium of such a composite structure. Next, for the purpose of dynamic analysis, small amplitudes of vibrations are assumed, to obtain linearized equations of motion including both the mast and guy cables. In practise, the assumption of small vibrations should be satisfied to ensure appropriate serviceability of the structure. Then, modal transformation is used in order to reduce the model of the structure and to retain the most dominant modes only. Mode shapes of the mast are divided into two groups. The first one includes dominant motions of guy cables (symmetrical and anti-symmetrical ones), and the second group includes vibrations of both mast and cables. By using the controllability index concept it is found, that symmetrical mode shapes are very poorly controllable by actuators located at anchor points.

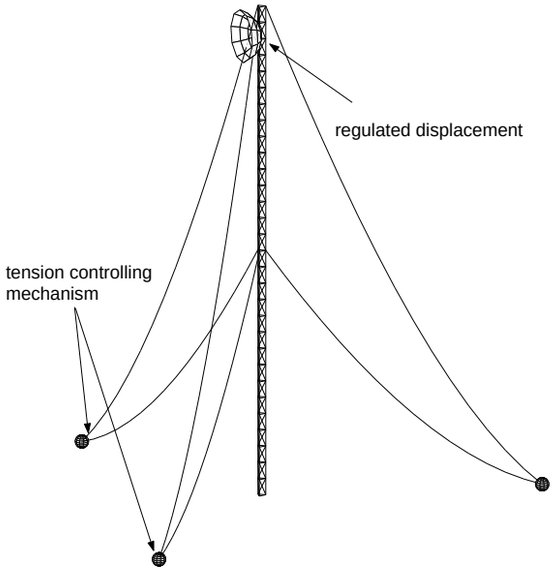


Figure 1. 3D finite element model of a guyed mast.

CONTROL SYSTEM

The designed control system of the mast is operating in varying environmental conditions. For that reason, a controller possessing dissipative properties in all possible weathers conditions is chosen. One of control algorithms satisfying this property is Direct Velocity Feedback introduced by Balas [5]. In the paper, the method is applied by measuring velocity of points, at which cables are attached to the mechanism, allowing adjustment of cable tension. A positive definite selection of control gain matrix for such a collocated system is ensuring both optimal performance and robust stability. Another issue is related to external loading. Classical optimal control methods assume, that the loading has the form of an impulse in a deterministic approach, or white noise in stochastic approach. In this study, a disturbing wind force with Davenport's power spectrum is taken into consideration. Finally, the aim of the closed-loop system is to suppress transverse dynamic displacement and slope of the top of the mast.

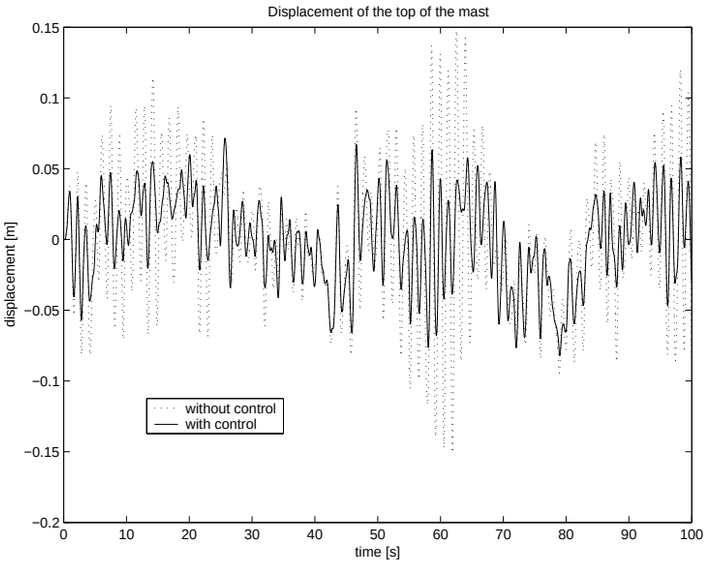


Figure 2. Dynamic response of the top of the guyed mast subjected to wind forces.

CONCLUSIONS

In the paper, a numerical investigation of the robust optimal control of vibrations of a guyed mast is presented. Results indicate, that active control system allowing adjustment of cable tension, can provide significant reduction of vibration amplitudes of the top of the mast (Fig. 2). However, it is recognized that amplitudes of guy cable vibrations are much less controllable than those of the mast.

ACKNOWLEDGEMENTS

The work described herein was carried out with the financial support provided by the State Committee for Scientific Research of Poland (KBN) under grant No. 5T7A 001 23 and this is gratefully acknowledged.

References

[1] McCaffrey R.J., Hartmann A.J.: Dynamics of guyed tower. *J. Structural Division Proceedings of the ASCE, vol. 98 no ST6*, June 1972.
[2] Preumont A.: Vibration control of active structures, An Introduction. 2nd edition, Kluwer, 2002
[3] Fujino Y., Warnitchai P., Pacheco B.M.: Active stiffness control of cable vibration. *ASME Journal of Applied Mechanics, vol 60*, December 1993.
[4] Spencer B.F.: Smart damping technology: Applications and opportunities. *34th Solid Mechanics Conference, SolMech 2002* Zakopane, September 2-7, 2002.
[5] Balas M.J.: Direct velocity feedback control of large space structures. *J. Guidance and Control, vol. 2 no 3*, 252–253, 1979.

TIME-OPTIMAL CONTROL OF HYDRAULIC MANIPULATORS

Witold Gutkowski [*], Pawel Holobut [**]
[*] *Polish Academy of Sciences, IPPT PAN, Swietokrzyska 21, PL 00-049 Warszawa, Poland*
[**] *IPPT PAN, Department of Computational Science, PL 00-049 Warszawa, Poland*

Summary The paper presents a control method, which makes a hydraulic arm robustly track a desired joint space path at high speed. Optimisation for speed is performed for the worst expected dynamic condition. The reference trajectory is given as a parametric function in a manipulator's joint space. Portions of the trajectory are online shrunk or stretched in time, to fully utilize capacity of the actuators.

INTRODUCTION

Many hydraulic manipulators work in unstructured surroundings at transporting loads, whose mass is not precisely known. In outdoor locations it is likely, that the desired path of the arm is input interactively by a human operator. The purpose of automatic control is then to follow the received trajectory closely, despite uncertainties in the arm's dynamics. Since, in many cases, high speed of tracking does not affect quality of performance, it is also desirable to speed up tracking to save time. Much work has been done into optimising for speed joint space trajectories of general manipulators. Examples include [1], where optimisation of open-loop tracking control is performed, or [2], where a learning algorithm is used to speed up execution of repetitive tasks of industrial manipulators. In this paper an algorithm is presented, intended for hydraulic manipulators performing non-repetitive tasks. It takes into account feedback effects of control, and uncertainties in the manipulator's equations of motion. An arbitrary reference trajectory is given, as a sequence of desired manipulator's configurations. The actual timing of the trajectory is then chosen such, that it fully utilizes the capacity of actuators, in the most disadvantageous dynamical case within uncertainty bounds.

EQUATIONS OF MOTION

Hydraulic manipulators are open chains of links, connected by prismatic or revolute joints. Each joint is actuated by a linear or rotary hydraulic motor. Assuming rigidity of links and joints and neglecting friction, dynamics of an arm, under the action of motor forces, is described by Lagrange equations of motion

$$\mathbf{D}\,\ddot{\mathbf{x}} + \mathbf{H} = \mathbf{F} \tag{1}$$

where $\mathbf{x}$ is a vector of generalized coordinates of the arm (chosen here as piston displacements to simplify notation), $\mathbf{D}(\mathbf{x})$ is a positive definite inertia matrix, $\mathbf{H}(\mathbf{x}, \dot{\mathbf{x}})$ is a vector of gravitation, Coriolis and centrifugal forces, and $\mathbf{F}$ is a vector of forces exerted by hydraulic motors. It is further assumed, that each motor acts independently (has its own hydraulic fluid supply). Fluid flow to and from hydraulic motors is governed by servovalves, whose spool displacements are the control inputs to the system. It is assumed, that flow intensities across valves can be accurately modelled by the square-root law $Q = C\sqrt{\Delta P}\,u$, where Q is the flow intensity, C is a valve dependent flow coefficient, ΔP is the pressure drop across the valve, and u is the spool displacement. The relation between piston forces and spool displacements is then given by

$$\dot{\mathbf{F}} = \mathbf{f}\,\mathbf{u} + \mathbf{g} \tag{2}$$

where $\mathbf{u}$ is the vector of all spool displacements, diagonal and positive definite matrix $\mathbf{f}(\mathbf{P_1}, \mathbf{P_2}, \mathbf{x})$ and vector $\mathbf{g}(\mathbf{P_1}, \mathbf{P_2}, \mathbf{x}, \dot{\mathbf{x}})$ represent properties of the hydraulic system, and $\mathbf{P_1}$, $\mathbf{P_2}$ are vectors of pressures in motor chambers. Differentiating equation (1) and substituting equation (2) yields

$$\dddot{\mathbf{x}} = \mathbf{D}^{-1}\mathbf{f}\,\mathbf{u} + \mathbf{R} \tag{3}$$

where $\mathbf{R}(\mathbf{P_1}, \mathbf{P_2}, \mathbf{x}, \dot{\mathbf{x}}, \ddot{\mathbf{x}})$ collects all remaining terms. Equation (3) is of third order, because of the inclusion of hydraulic system's dynamics. It forms the basis for further control study.

CONTROL OUTLINE

Problem formulation

The reference trajectory is given as a parametric curve $\mathbf{x_r}(s)$ in a manipulator's joint space, where s is an arbitrary parameter. For the purposes of control it is unimportant, what is the particular choice of parameter. However it is assumed, that $\mathbf{x_r}(s)$ is sufficiently smooth in s, and takes only physically feasible values. Equations of motion (3) are not exactly known in the sense, that $\mathbf{D}$, $\mathbf{f}$ and $\mathbf{R}$ might really differ from their nominal values. In particular, variations of $\mathbf{D}$ are mostly introduced by loads transported by the manipulator. However, all uncertainties are bounded, and values of the bounds are known. Also, variations in values of parameters do not change the general positive definiteness properties of the matrices. There are also bounds on admissible values of spool displacements $\underline{u}_i \le u_i \le \overline{u}_i$, and motor

chamber pressures cannot exceed pump and reservoir pressures. The purpose of control is to make the arm traverse $\mathbf{x_r}(s)$ at the highest possible speed, while guaranteeing robustness of motion to uncertainties. The problem can be decomposed into two stages: first choosing a robust tracking control, then optimising the reference trajectory for speed, with respect to the chosen tracking strategy.

Robust tracking control

Many techniques can be used to assure robust trajectory tracking. Here a discontinuous control technique, with a boundary layer to smooth the control signal, is adopted. By expanding equation (3) into the traditional first order state space form and using Lyapunov analysis, robust control can be derived of the general form

$$\mathbf{u} = -\alpha\, \bar{\mathbf{f}}^{-1}\overline{\mathbf{D}}\frac{\mathbf{v}}{\|\mathbf{v}\|} \quad for \quad \|\mathbf{v}\| \geq \varepsilon$$
$$\mathbf{u} = -\alpha\, \bar{\mathbf{f}}^{-1}\overline{\mathbf{D}}\frac{\mathbf{v}}{\varepsilon} \quad for \quad \|\mathbf{v}\| < \varepsilon \tag{4}$$

$$\alpha \geq \|\mathbf{v}\|\frac{\mathbf{v}^{\mathrm{T}}(\boldsymbol{\Omega} - \dddot{\mathbf{x}}_\mathbf{r})}{\mathbf{v}^{\mathrm{T}}\mathbf{D}^{-1}\mathbf{f}\,\bar{\mathbf{f}}^{-1}\overline{\mathbf{D}}\,\mathbf{v}} \tag{5}$$

where $\bar{\mathbf{f}}(\mathbf{P_1}, \mathbf{P_2}, \mathbf{x})$ and $\overline{\mathbf{D}}(\mathbf{x})$ are nominal values of $\mathbf{f}$ and $\mathbf{D}$ respectively, $\boldsymbol{\Omega}(\mathbf{P_1}, \mathbf{P_2}, \mathbf{x}, \dot{\mathbf{x}}, \ddot{\mathbf{x}}, \mathbf{x_r}, \dot{\mathbf{x}}_\mathbf{r}, \ddot{\mathbf{x}}_\mathbf{r})$ stands for all terms independent of $\dddot{\mathbf{x}}_\mathbf{r}$, $\mathbf{v}(\mathbf{x}, \dot{\mathbf{x}}, \ddot{\mathbf{x}}, \mathbf{x_r}, \dot{\mathbf{x}}_\mathbf{r}, \ddot{\mathbf{x}}_\mathbf{r})$ represents the position of the arm in state space with respect to chosen sliding surfaces, ε is the width of the boundary layer, and $\dot{\mathbf{x}}_\mathbf{r}$, $\ddot{\mathbf{x}}_\mathbf{r}$, $\dddot{\mathbf{x}}_\mathbf{r}$ denote derivatives with respect to time *t*. The value of α in (5) is calculated, using the most disadvantageous possible dynamical case. Control (4,5) is valid, if $\mathbf{D}^{-1}\mathbf{f}\,\bar{\mathbf{f}}^{-1}\overline{\mathbf{D}}$ can be guaranteed to be always positive definite. Also for the technique to work, $\mathbf{P_1}$, $\mathbf{P_2}$, $\mathbf{x}$, $\dot{\mathbf{x}}$ and $\ddot{\mathbf{x}}$ must be measured in real-time or estimated. Control (4,5) robustly tracks a time dependent reference trajectory to an accuracy, dictated by ε.

Trajectory optimisation

To speed up tracking $s(t)$ is chosen in such a way, that control (4,5) tracking $\mathbf{x_r}(s(t))$, fully utilizes the capacity of actuators. Since $\mathbf{x_r}(s)$ is given explicitly and is differentiable, its successive time derivatives are

$$\dot{\mathbf{x}}_\mathbf{r} = \frac{d\mathbf{x_r}}{ds}\dot{s} \qquad \ddot{\mathbf{x}}_\mathbf{r} = \frac{d^2\mathbf{x_r}}{ds^2}\dot{s}^2 + \frac{d\mathbf{x_r}}{ds}\ddot{s} \qquad \dddot{\mathbf{x}}_\mathbf{r} = \frac{d^3\mathbf{x_r}}{ds^3}\dot{s}^3 + 3\frac{d^2\mathbf{x_r}}{ds^2}\dot{s}\,\ddot{s} + \frac{d\mathbf{x_r}}{ds}\dddot{s} \tag{6}$$

If at any instant of time *s*, $\dot{s}$ and $\ddot{s}$ are given, values of $\mathbf{x_r}$, $\dot{\mathbf{x}}_\mathbf{r}$ and $\ddot{\mathbf{x}}_\mathbf{r}$ can be calculated from equations (6). On the basis of those, and the measured values of $\mathbf{P_1}$, $\mathbf{P_2}$, $\mathbf{x}$, $\dot{\mathbf{x}}$ and $\ddot{\mathbf{x}}$, vector $\bar{\mathbf{f}}^{-1}\overline{\mathbf{D}}\,\mathbf{v}$ in equation (4) can be calculated. Since it determines the direction of control vector **u,** the maximum permissible value of α can also be computed from equation (4). It is the value, which makes **u** reach control bounds in the direction of $\bar{\mathbf{f}}^{-1}\overline{\mathbf{D}}\,\mathbf{v}$. Using equations (6), $\dddot{s}$ can now be computed from equation (5), as the greatest value (if it exists) satisfying the inequality

$$\alpha_{\max} \geq \|\mathbf{v}\|\,\mathbf{v}^{\mathrm{T}}\left(\boldsymbol{\Omega} - \frac{d^3\mathbf{x_r}}{ds^3}\dot{s}^3 - 3\frac{d^2\mathbf{x_r}}{ds^2}\dot{s}\,\ddot{s} - \frac{d\mathbf{x_r}}{ds}\dddot{s}\right)\Big/\left(\mathbf{v}^{\mathrm{T}}\mathbf{D}^{-1}\mathbf{f}\,\bar{\mathbf{f}}^{-1}\overline{\mathbf{D}}\,\mathbf{v}\right) \tag{7}$$

for the most disadvantageous possible values of matrices. In summary, trajectory optimisation for speed is performed online. It is done by integrating in real-time *s*, $\dot{s}$ and $\ddot{s}$, and obtaining new values of $\dddot{s}$ from equation (7).

CONCLUSIONS

A control algorithm for hydraulic manipulators is presented, which robustly tracks a given reference trajectory, while fully utilizing the capacity of actuators to maximize speed. It is however computationally expensive, and requires real-time measurements of the full state of the system.

Acknowledgement

This work was supported by the State Committee for Scientific Research of Poland (KBN) under grant No. 5T07A 002 23 for the years 2002-2004.

References

[1] Lin C.S., Chang P.R., and Luh J.Y.S.: Formulation and Optimization of Cubic Polynomial Joint Trajectories for Industrial Robots. IEEE Trans. Automatic Control 28(12):1066-1074, 1983.

[2] Ma C.C.H., Qian T.W.T.: Rapid Tracking With Automatic Trajectory Optimization for Speed. ASME J. Dyn. Sys. Meas. and Control 121:697-702, 1999.

SURFACE ACCURACY OF INFLATABLE REFLECTOR COVERED WITH STRETCHED CABLE

Kazuo TANIZAWA*, Jun NISHIMURA** and Kazuo Yamamoto*
* *Department of Intelligent Systems, Kinki University, 930 Nishimitani, Uchida, Nagagun 649-6493, Japan*
** *The Institute of Space and Astronautical Science, JAXA, 3-1-1 Yoshinodai, Sagamihara 229-8510, Japan*

Summary We present here an idea of the inflatable reflector and the surface error evaluation of this reflector, which is segmented into N-regular polygonal facets by the uniformly stretched cable net to improve the reliability on surface accuracy. From this study, we made it clear the effects of design parameters on the surface accuracy, such as the internal pressure, the cable tension, the membrane tension, the facet size, and etc. We also derived simple approximate formulas to give the RMS surface accuracy within 5% error in the realistic design region, where the surface error was almost proportional to the ratio of the cable force to the membrane tension.

INTRODUCTION

Although the inflatable reflector has a long history of development, it has not yet been put to practical space use, and only few papers related to the design of accurate surface have been presented[1]. The inflatable reflector is largely behind to the competitive mesh reflector on the study and realization. In case of the inflatable reflectors there exist basic difficulties to form the accurate parabolic surface,because of deterioration of surface accuracy caused by inhomogeneity of material, folding lines in stowed configuration and the low performance of deployment repeatability. The surface accuracy of the conventional inflatables is highly sensitive to the non-uniformity of the material and internal pressure.

To achieve the accurate shape of surface, we propose the inflatable reflector which is covered by the inextensional N-regular polygonal supporting cable net, and show its practical structural validity using the detailed surface deformation analysis with the relevant surface error estimation. In this structure, the macroscopic configuration is determined by the stretched supporting cable net which is not so sensitive to the tension or the internal pressure and the smooth shape of each facet is formed by the flexible membrane. Since effects of the inhomogeneity of material and the change of the internal pressure on the surface accuracy are restricted within each facet, this type of structure is able to easily attain high and stable surface accuracy.

As the above results needs the complicated calculations, it is somewhat tedious to treat the problem in a practical sense. In this paper, we present a simple approximate treatment to estimate the surface error of this reflector. It is found that the surface error of the objective surface is approximately proportional to the ratio of the cable force to the membrane tension, and these approximate formulas give the results within an accuracy of 5% error in the realistic design region.

ANALYSIS

We consider the case that the additional tension of the membrane due to its deflection in the equilibrium state is negligibly small compared with the initial tension of the membrane. It is also assumed that the each facet portion of the parabolic surface is approximated by the spherical shape as shown in Fig.1. The N-regular polygonal facets with the side length L are stretched under uniform tension N_m on the sphere surface of the curvature ρ. Each facet is bounded by the supporting cables with the uniform tension T_s. The rectangular coordinates X, Y and Z is defined as shown in Fig.1. Here, one-2Nth part of the facet ($0 \leqq Y \leqq X\tan\phi$ and $0 \leqq X \leqq R\cos\phi$) is considered from the N-symmetric feature of the facet deformation.

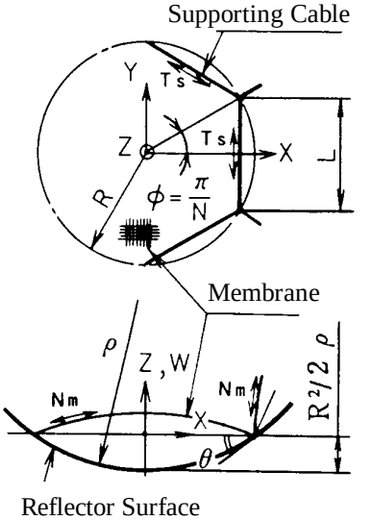


Fig.1 Analytical Model

When the displacement W in the Z direction is sufficiently small to the side length L, the equilibrium conditions in the facet membrane, on the cables (so called self-consistent equilibrium), and on the each lattice point are described as (for details see literature[2]),

$$\partial^2 W/\partial X^2 + \partial^2 W/\partial Y^2 = p/N_m \quad \text{in facet membrane} \qquad (1)$$

$$T_s\,\partial^2 W/\partial Y^2 = 2N_m(\partial W/\partial X - \theta) \text{ at } X = R\cos\phi \qquad (2)$$

$$\partial W/\partial Y = \partial W/\partial X = \theta\tan\phi \quad \text{at } (X,Y) = R(\cos\phi, \sin\phi) \qquad (3)$$

$$W = 0 \quad \text{at} \quad (X,Y) = R(\cos\phi, \sin\phi) \qquad (4)$$

Considering that the regular function of complex variable z(=x+jy; x=X/R, y=Y/R) satisfies the Laplace equation,and a special solution can be expressed by the quadratic expression of x and y, we get the general solution of the equation (1) expressed by the power series expansion of the complex variable as follows;

$$\frac{2\rho}{R^2} W = \mathrm{Re}\left(\sum_{i=0}^{\infty} A_i\, z^{N^* i}\right) - \left(\frac{pL}{4N_m\theta}\right)(1 - x^2 - y^2)\cot\phi \ , \qquad (5)$$

where the first term of the right side means a pillow deformation W_p, the second term means a particular solution of the equation (1) W_s, and the normalization factor $R^2/(2\rho)$ denotes the maximum distance to reflector surface from the facet surface. Putting the equation(5) into the equations(2) ~(4) and arranging the equations with the new parameters that are

the ratio of tension α (=$N_m L/T_s$) and a normalized pressure S_p(=$pL/(4N_m\theta)$), we obtain the following basic equations;

$$\sum_{i=0}^{\infty}(-1)^i A_i = 0 \quad (6) \qquad S_p = \tan\phi[1-(\frac{N}{2})\sum_{i=1}^{\infty}(-1)^i A_i] \quad (7)$$

$$\mathrm{Re}\sum_{i=1}^{\infty}[(\cos\phi+jy)^{N*i}-2(N*i-1)\tan\phi+(\cos\phi+jy)^{N*i-1}\alpha/\cos\phi]A_i = 2\alpha+2S_p(1-\alpha\cot\phi). \quad (8)$$

Since the equation (8) should be satisfied to arbitrary values of y, the equations to obtain the value of A_i are given by

$$\sum_{i=s}^{\infty}(N*i)!*(\cos\phi)^{N*i-2k}[\frac{\tan\phi}{(N*i-2k)!}+\frac{\alpha}{(N*i-2k+1)!}]A_i = 2\alpha+2S_p(1-\alpha\cot\phi) \ \text{ at } k=1, \ =0 \ \text{ at } k>1 \ , \quad (9)$$

where s means the minimum positive integer giving the positive number to the factorials of the equation. The equations (6),(7) and (9) are the final simultaneous equations to the deformation of the inflatable reflector.

NUMERICAL RESULTS

Best-fit Surface Error The best-fit surface error δ_{RMS} is defined by the following equation;

$$\frac{2\rho}{R^2}\delta_{RMS} = [\frac{1}{\Omega}\iint(W_1+W_2)^2 dXdY - \{\frac{1}{\Omega}\iint(W_1+W_2)dXdY\}^2]^{1/2} \ , \qquad (10)$$

where Ω, W_1 and W_2 are the area of facet, a membrane deflection(=W_p+W_s) and an objective parabolic surface given by W_2=[R^2-X^2-Y^2]/(2ρ) , respectively.

The numerical values of δ_{RMS} calculated from the equations (6),(7) and (9) with sufficient numbers of A_i ($i \leqq 20$) are shown on the logarithmic graph of Fig.2. Here, the data symbolized by ▲, ■ and ● mean the surface error δ_{RMS} of the triangular facet, the rectangular facet and the hexagonal facet, respectively. From this figure, it is found that δ_{RMS} is almost proportional to ($1/\alpha$).

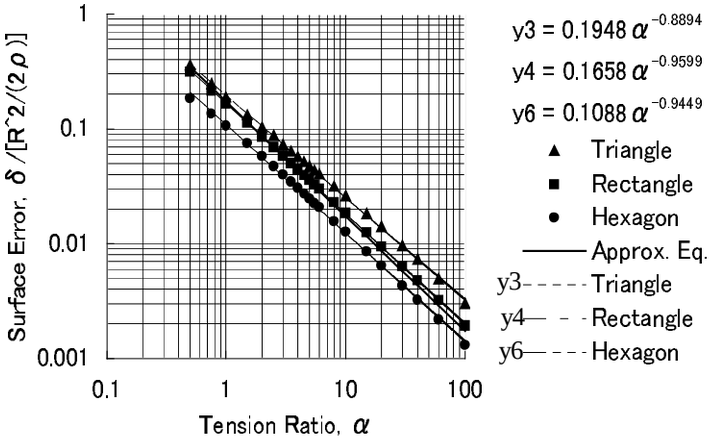


Fig.2 Effects of Tension Ratio α on Surface Error δ

Approximate design formula
Although the value of S_p should be determined rigorously from the force balance equation (7), it might be approximated well by the macroscopic force balance equation as follows;

$$S_p = \tan\varphi + (\tan^2\varphi)/\alpha \qquad (10)$$

Numerical results in Fig.3 show the validity of this approximation in the range of α>0.7. If we use the Eq.(11) instead of Eq.(7) and the approximate equation obtained in the mesh pillow deformation analysis[3),4)], we obtain the approximate design formulas on the surface error of the objective inflatable reflector which are shown as the broken lines in Fig.1.

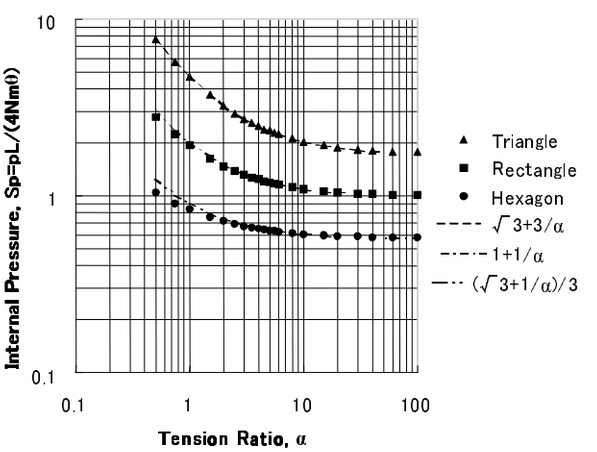


Fig.3 Relation between Tension Ratio α and Normalized Internal Pressure Sp

CONCLUSION

We proposed the inflatable reflector covered with the uniformly stretched cable net, and made clear the fundamental effects of design parameters on the surface error. We also presented the approximate formulas to evaluate the RMS surface error.

REFERENCES

[1] Freeland et al: Inflatable Deployable Space Structures Technology Summary, IAF-98-I.5.01,1998
[2] K.Tanizawa,J.Nishimura: Surface Accuracy of an Inflatable Reflector covered with Uniformly Stretched Cable, Transactions of Theoretical and Applied Mechanics, Vol.47,pp.41-46,1998
[3] K.Tanizawa,J.Nishimura: Pillow Deformation of a Mesh Reflector, JSASS,Vol.44,No.508.pp.291-297, 1996
[4] K.Miura,K.Tanizawa: Tension Truss Antenna-Concept, Reality and Future, 1st IUTAM/IASS Symposium,1998

H_∞ CONTROL FOR SMART MULTISTOREY BUILDING STRUCTURES

Daniela Marinova*, Georgios Stavroulakis**
*Technical University of Sofia, Kl. Ohridski Str. 8, 1756 Sofia, Bulgaria,
**University of Ioannina, GR-45510 Ioannina, Greece and Technical University of Braunschweig, D-38106 Braunschweig, Germany

Summary A dynamic model for multistorey buildings under external excitations is presented. Structured uncertainties are considered to reflect the errors between the model and the reality. $\mathbf{H}_\infty$ optimal control for the active control structure is implemented. The $\mathbf{H}_\infty$ norm of the transfer function from the disturbances to the errors is minimized. Numerical techniques, which have been done with the help of MATLAB routines, are applied to solve the arising structural control problem.

INTRODUCTION

The vibrations of flexible structures, like tall buildings, during the earthquake or gust wind may lead to damages and destructions of the structure systems. The control of the building's structural vibrations is an important goal for the structural engineer. Most of the active control systems built at present are mainly aimed at the response reduction to strong wind or quite moderate earthquake excitation. One of the important problems in achieving reliable active control systems that could ensure the safety for strong earthquake is their robustness. Robust control focuses on the issues of the performance and the stability in the presence of uncertainty, both in the parameters of the system and in exogenous inputs. $\mathbf{H}_\infty$ optimal robust control technique is used in this paper for vibration suppression of building structures.

PROBLEM STATEMENT

A dynamic model for multistorey building equipped with actuators under earthquake and wind excitations is presented in this paper. The structure is modeled by linear system using the finite element method. The equations of motion are

$$M\ddot{X}(t) + C\dot{X}(t) + KX(t) = Hu(t) + F(t) \tag{1}$$

where the vector $\boldsymbol{X(t)}$ describes the displacements, $\boldsymbol{u(t)}$ contains the control forces applied by the actuators and $\boldsymbol{F(t)}$ is the external loading vector. $\boldsymbol{M}$, $\boldsymbol{C}$ and $\boldsymbol{K}$ are mass, damping and stiffness matrices. $\boldsymbol{H}$ is a distribution matrix defining the locations of the actuators. All matrices with appropriate dimensions are constant and real.

As the quality of the model depends on how closely its responses match those of the true plant, structured uncertainties are considered to reflect the errors between the model and the reality. Suppose that the physical parameters $\boldsymbol{M}$, $\boldsymbol{C}$, and $\boldsymbol{K}$ are not known exactly. The nominal matrices $\boldsymbol{M^* = mI}$, $\boldsymbol{C^* = cI}$, $\boldsymbol{K^* = kI}$ are diagonal. The corresponding perturbations $\boldsymbol{\Delta_M}$, $\boldsymbol{\Delta_C}$, $\boldsymbol{\Delta_K}$ are unknown but restricted $\boldsymbol{\Delta_M = \delta_M I}$, $\boldsymbol{\Delta_C = \delta_C I}$, $\boldsymbol{\Delta_K = \delta_K I}$, $(-1 \le \boldsymbol{\delta_M}, \boldsymbol{\delta_C}, \boldsymbol{\delta_K} \le 1)$. The actual $\boldsymbol{M}$, $\boldsymbol{C}$, $\boldsymbol{K}$ are within $\boldsymbol{p_M}$, $\boldsymbol{p_C}$, and $\boldsymbol{p_K}$ percentages of the nominal $\boldsymbol{M^*}$, $\boldsymbol{C^*}$, $\boldsymbol{K^*}$

$$\begin{aligned} \boldsymbol{M} &= \boldsymbol{M^*}\,(\,\boldsymbol{I} + \boldsymbol{p_M}\,\boldsymbol{\Delta_M}\,) = \boldsymbol{m}\,(\,\mathbf{1} + \boldsymbol{p_M}\,\boldsymbol{\delta_M}\,)\,\boldsymbol{I} \\ \boldsymbol{C} &= \boldsymbol{C^*}\,(\,\boldsymbol{I} + \boldsymbol{p_C}\boldsymbol{\Delta_C}\,) = \boldsymbol{c}\,(\,\mathbf{1} + \boldsymbol{p_C}\,\boldsymbol{\delta_C}\,)\,\boldsymbol{I} \\ \boldsymbol{K} &= \boldsymbol{K^*}\,(\,\boldsymbol{I} + \boldsymbol{p_K}\boldsymbol{\Delta_K}\,) = \boldsymbol{k}\,(\,\mathbf{1} + \boldsymbol{p_K}\,\boldsymbol{\delta_K}\,)\,\boldsymbol{I} \end{aligned} \tag{2}$$

Let $\boldsymbol{X(t)}$, $\dot{X}\,\boldsymbol{(t)}$, and $\boldsymbol{F(t)}$ are the inputs of the system and $\boldsymbol{y = X(t)}$ is the output. To represent the model as linear fractional transformation (LFT) of the natural uncertainty parameters $\boldsymbol{\delta_M}$, $\boldsymbol{\delta_C}$, $\boldsymbol{\delta_K}$ we isolate the uncertainty perturbations $\boldsymbol{\Delta_M}$, $\boldsymbol{\Delta_C}$, $\boldsymbol{\Delta_K}$ and denote their inputs as $\boldsymbol{y_m}$, $\boldsymbol{y_k}$, $\boldsymbol{y_c}$ and their outputs as $\boldsymbol{u_m}$, $\boldsymbol{u_c}$, $\boldsymbol{u_k}$. Then the augment system's form is obtained as follows

$$[\,\dot{x}\;\boldsymbol{y_\Delta}\;\boldsymbol{y}\,]^{\mathbf{T}} = \boldsymbol{G_n}\,[\,\boldsymbol{x}\;\;\boldsymbol{u_\Delta}\;\boldsymbol{u}\,]^{\mathbf{T}}, \qquad \boldsymbol{u_\Delta = \Delta\, y_\Delta} \tag{3}$$

where $\boldsymbol{x} = [\,\boldsymbol{X}\;\dot{X}\,]^{\mathbf{T}}$, $\boldsymbol{y_\Delta} = [\,\boldsymbol{y_m}\;\boldsymbol{y_k}\;\boldsymbol{y_c}\,]^{\mathbf{T}}$, $\boldsymbol{u_\Delta} = [\,\boldsymbol{u_m}\;\boldsymbol{u_c}\;\boldsymbol{u_k}\,]^{\mathbf{T}}$. The plant transfer matrix $\boldsymbol{G_n}$ depends only on the nominal parameters of the system and is known. The uncertainty matrix $\boldsymbol{\Delta}$ is a block diagonal structural matrix and influences on input/output connection between $\boldsymbol{u}$ and $\boldsymbol{y}$ in a way that can be represented as feedback by upper LFT $\boldsymbol{y = L_U(G_n, \Delta)\,u}$.

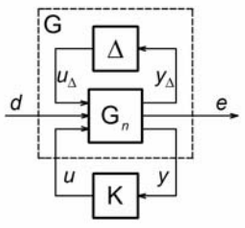


Figure 1.

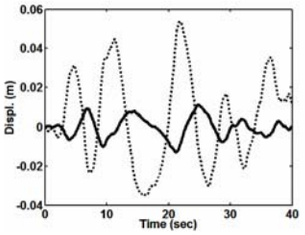


Figure 2.

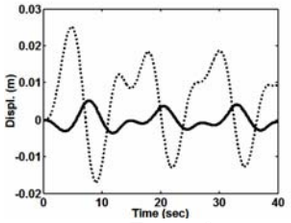


Figure 3.

The linear system (3) can be described with the structural scheme in Figure 1. The uncertainty block $\boldsymbol{\Delta}$ is supposed to be stable and norm bounded $\|\,\boldsymbol{\Delta}\,\|_\infty \le 1$. The block $\mathbf{K}$ is the controller. The nominal plant $\boldsymbol{G_n}$ has three sets of inputs: uncertainty inputs $\boldsymbol{u_\Delta}$, external disturbances $\boldsymbol{d}$ and control commands $\boldsymbol{u}$. Three sets of outputs are generated: uncertainty

outputs $\boldsymbol{y}_\Delta$, errors $\boldsymbol{e}$ and measurements $\boldsymbol{y}$. Let $\boldsymbol{w} = [\ \boldsymbol{u}_\Delta\ \boldsymbol{d}\ ]^{\mathbf{T}}$ are all external inputs coming to the system and $\boldsymbol{z} = [\ \boldsymbol{y}_\Delta\ \boldsymbol{e}\ ]^{\mathbf{T}}$ are all signals characterizing system's behavior. Than the system (3) is transformed in

$$[\ \boldsymbol{z}\ \boldsymbol{y}\ ]^{\mathbf{T}} = \boldsymbol{G}\ [\ \boldsymbol{w}\ \boldsymbol{u}\ ]^{\mathbf{T}}, \qquad \boldsymbol{u} = \boldsymbol{K}(\boldsymbol{s})\ \boldsymbol{y} \tag{4}$$

The transfer matrix $\boldsymbol{G}$ is obtained from the nominal model $\boldsymbol{G}_n$ and contains weights for the uncertainty, which depends on the control design. The closed loop system's transfer matrix from $\boldsymbol{w}$ to $\boldsymbol{z}$ is given by a lower LFT $\boldsymbol{z} = \boldsymbol{F}_{\mathbf{L}}(\boldsymbol{G}, \boldsymbol{K})\ \boldsymbol{w}$.
The problem of the control design consists in determination of a controller $\boldsymbol{K}$ that ensures internal stability of the system (4) keeping the transfer matrix $\boldsymbol{F}_{\mathbf{L}}(\boldsymbol{G}, \boldsymbol{K})$ between $\boldsymbol{w}$ and $\boldsymbol{z}$ minimal in the sense of $\mathbf{H}_\infty$ norm.

$$\| \boldsymbol{F}_{\mathbf{L}}(\boldsymbol{G}, \boldsymbol{K}) \|_\infty = \max_{\omega} \{ \bar{\sigma} (\boldsymbol{F}_{\mathbf{L}}(\boldsymbol{G}, \boldsymbol{K})(j\omega)) \} \quad \rightarrow \quad \min \tag{5}$$

In the frequency domain the minimization of the $\mathbf{H}_\infty$ norm minimizes the maximal value of the maximal singular value of $\boldsymbol{F}_{\mathbf{L}}(\boldsymbol{G}(j\omega), \boldsymbol{K}(j\omega))$. In the time domain minimizing this norm interpreted as the induced 2-norm gets the minimization of the worst case.

$$\min\| \boldsymbol{F}_{\mathbf{L}}(\boldsymbol{G}, \boldsymbol{K}) \|_\infty = \min \{ \max_{w(t)\neq 0} \frac{\|z(t)\|_2}{\|w(t)\|_2} \}\ , \text{ where } \|z(t)\|_2 = \sqrt{\int_0^\infty |z_i(t)|^2\, dt} \tag{6}$$

PERFORMANCE AND STABILITY

The robust performance and the robust stability for the closed loop system are of paramount importance. The parameter perturbations can amplify significantly the effect of the external influences. As a result the performance of the closed loop system can be deteriorated before loosing the stability. To arise a desirable performance it is necessary that

$$\| \boldsymbol{W}_p (\ \boldsymbol{I} + \boldsymbol{G}\boldsymbol{K}\ )^{-1} \|_\infty < \mathbf{1} \tag{7}$$

for all frequencies. The weight matrix $\boldsymbol{W}_p$, reflects the relative importance of different frequency ranges where the performance is requested.
For robust stability we are interested in finding the smallest perturbation $\boldsymbol{\Delta}$ ($\|\boldsymbol{\Delta}\|_\infty < 1$) in the sense of $\bar{\sigma}(\Delta)$ such that destabilizes the closed loop framework. The loop is well-posed and internally stable if and only if the structured singular value $\boldsymbol{\mu}_\Delta$ is less than one for all frequencies

$$\mu_\Delta = \frac{1}{\min \{ \bar{\sigma}(\Delta) : \|\Delta\|_\infty < 1 \}} < 1 \tag{8}$$

The quantity $(\max \boldsymbol{\mu}_\Delta)^{-1}$ is a stock of stability with respect to the structured uncertainty influenced the system.

NUMERICAL SIMULATIONS

Relevant numerical techniques, which have been done with the help of MATLAB routines, are applied to solve the arising structural control problem and to find the optimal controller. An upper and a lower bound of $\boldsymbol{\mu}_\Delta$ are calculated. The conclusions concerning the robust stability are made in terms of these bounds. The $\mathbf{H}_\infty$ norm of the closed loop system with $\mathbf{H}_\infty$ optimal controller $\boldsymbol{K}$ is obtained in request bounds. The respective transfer matrices are in norm less than one. Therefore, the closed loop system achieves nominal and robust performance. Numerical results show high robust performance.
For numerical simulations of the structure's behavior two types of dynamic loading are considered: random white noise modeling an earthquake ground motion and periodic sinusoidal pressure modeling a horizontal wind loading. The responses of the open-loop of the closed-loop systems are compared based on the reduction of the magnitude of the maximum horizontal displacement. Results for the tip of the uncontrolled (dot) and controlled (solid) building structure due to earthquake and wind loadings are presented in Figure 2 and Figure 3 respectively.

CONCLUSIONS

Robust control design of an uncertain multistorey building structure is considered. Structured uncertainties are introduced. The vector of active control forces subjected to $\mathbf{H}_\infty$ performance criterion and satisfying the system's dynamic equations such that to reduce the adverse earthquake and wind excitations is determined. High robust performance and robust stability are achieved. A two-dimensional finite element model is utilized for numerical experiments. Comparisons of the controlled and uncontrolled systems demonstrate the effectiveness of the proposed optimal control law.

References

[1] Zhou K.: *Essentials of Robust Control*. Printice-Hall, Upper Saddle River, NJ 1998.
[2] Schmitendorf W. E., Jabbari F., Yang, J. N.: Robust control techniques for buildings under earthquake excitation. *Earthquake Engineering and Structural Dynamics* **23**: 539-552, 1994.
[3] Marinova D. G, Stavroulakis G. E.: Robust Control Design of a Smart Building Structure. *Proc. 7-th Int Conference on Dynamical Systems: Theory and Applications*: 453-460, Łódź, Poland, 2003.

EXACT TRACKING CONTROL FOR NONLINEAR STRUCTURAL AND MECHANICAL SYSTEMS

Firdaus E. Udwadia
Department of Aerospace and Mechanical Engineering, Civil Engineering, and Mathematics,
University of Southern California, Los Angeles, California 90089-1453, USA fudwadia@usc.edu

Summary A new methodology for the *exact* tracking control of nonlinear structural and mechanical systems with holonomic and/or nonholonomic trajectory requirements is presented.

We consider in this paper an n degree-of-freedom structural or mechanical system described by Lagrange's equations [1] as

$$M(x,t)\ddot{x} = F(x,\dot{x},t)\,,\quad x(0)=x_0,\ \dot{x}(0)=\dot{x}_0\,. \tag{1}$$

Here, x is the *generalized* coordinate used in describing the configuration of the system. The n by n matrix M is positive definite and, in general, is a function of x and the time, t. We shall assume that the observation m-vector, $y(t)$, is related to the response $x(t)$ of the system by the observation equation

$$y(t) = Cx(t) \tag{2}$$

where C is the constant m by n measurement matrix. It is desired to control the system described by (1), and determine the control force vector $F^c(y,\dot{y},t)$ so that for the controlled system described by,

$$M(x,t)\ddot{x} = F(x,\dot{x},t) + F^c(y,\dot{y},t)\,, \tag{3}$$

the measurement $y(t)$ satisfies the s desired tracking relations

$$h(y,\dot{y},t) = 0\,, \tag{4}$$

where h is an s-vector. We assume that the functions $h_i(y,\dot{y},t)$ are C^1 and that (4) constitute a set of relations that are feasible for the system to satisfy. The set (4) may contain relations that are integrable and/or non-integrable. Also, the system's initial conditions $x(0)$ and $\dot{x}(0)$ are such as to satisfy equation (4). One can relax this assumption on the initial conditions [2]. Differentiating equation (4) with respect to time, one obtains

$$H(y,\dot{y},t)\ddot{y} = \frac{\partial h}{\partial \dot{y}}\ddot{y}(t) = -\frac{\P h}{\P y}\dot{y} - \frac{\P h}{\P t} \tag{5}$$

where we have denoted the s by m matrix $\frac{\P h}{\P \dot{y}}$ by H. In view of (2) this can be expressed as

$$B\ddot{x} = HC\ddot{x}(t) = b(y,\dot{y},t) = b(Cx,C\dot{x},t)\,, \tag{6}$$

where we have denoted the s by n matrix HC by B, and the s-vector b is given by

$$b(y,\dot{y},t) = -\frac{\P h}{\P y}\dot{y} - \frac{\P h}{\P t}\,. \tag{7}$$

We note that by using relations (2) and (4) on the right hand side of (7), the s-vector b may be thought of as a known function of x, $\dot{x}$ and t, as explicitly indicated in (6). From here on, we shall suppress the arguments of the various quantities unless required for clarification. We now state the following central result [2].

Main Result The class of control forces that minimize *at each instant of time* the quantity

$$J(t) = (F^c)^T N(x,t) F^c\,, \tag{8}$$

where the n by n matrix $N(x,t)$ is a given positive definite matrix at each instant of time t, while causing the controlled system (3) to satisfy relation (6), is given by

$$F^c = N^{-1/2} G^+ (b - BM^{-1}F) \tag{9}$$

where, G denotes the matrix $B(N^{1/2}M)^{-1}$, and G^+ denotes the Moore-Penrose generalized inverse of the matrix G.

Proof: For brevity, the proof will not be given here; it will be presented at the meeting. ❑

Example Consider a nonlinear mechanical system whose equation of motion is given by ($M = I$)

$$\ddot{x} = \begin{bmatrix} \ddot{x}_1 \\ \ddot{x}_2 \\ \ddot{x}_3 \end{bmatrix} = \begin{bmatrix} s\,(x_2 - x_1) - c_1\dot{x} \\ l x_1 - x_1 x_3 - x_2 - c_2\dot{x}_2 \\ F_3 = x_1 x_2 - b x_3 - c_3\dot{x}_3 \end{bmatrix} = F,\ x(0) = x_0,\ \dot{x}(0) = \dot{x}_0 . \tag{10}$$

We shall assume that the measurement m-vector, y, is given by the relation

$$y = Cx = \begin{bmatrix} 1 & 1 & 0 \\ 0 & 1 & -1 \\ 1 & -1 & 0 \end{bmatrix} x , \tag{11}$$

and the desired (and feasible), nonholonomic trajectory we want the system (10) to track is given to be

$$\dot{y}_2 = y_3 \dot{y}_1 . \tag{12}$$

We wish to apply a control force, F^c, so that in the presence of F, relation (12) is 'exactly' satisfied. For illustration, we take: $s = l = 1$, and $b = 2$; $c_1 = c_3 = 1/2$, and $c_2 = 0$; and, $x_1(0) = 0$, $x_2(0) = 1$, $x_3(0) = 1$, $\dot{x}_1(0) = \dot{x}_2(0) = \dot{x}_3(0) = 0$. Using numerical integration, Figure 1(a) shows the error in the satisfaction of this trajectory requirement, (12), without any control. Using the control force, F^c, that is explicitly given by equation (9), we see, from Figure 1(b), that this tracking error is reduced to within the numerical precision (10^{-8}) with which the equations of motion are integrated.

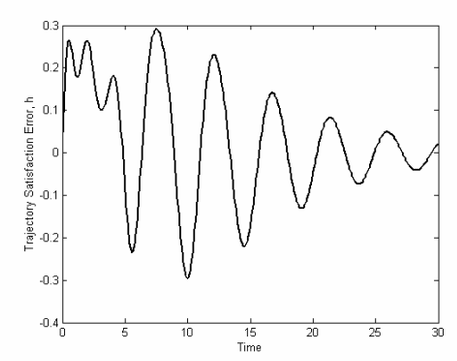


Figure 1(a)

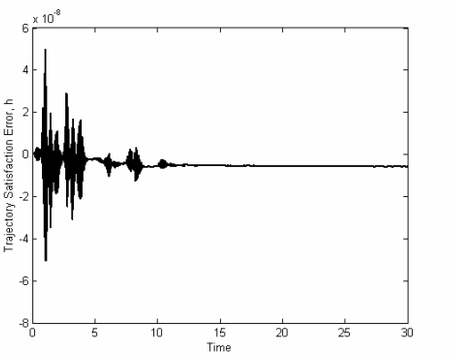


Figure 1(b)

Conclusions

This paper provides a powerful, new methodology for controlling nonlinear structural and mechanical systems. It has been inspired by recent results in analytical dynamics. The methodology has the following advantages: (1) the control force required to control the *nonlinear* system so that it satisfies the given nonholonomic and/or holonomic trajectory requirements is obtained *explicitly* in closed-form; (2) this control force, theoretically speaking, will cause the trajectory requirements to be 'exactly' satisfied by the nonlinear controlled system; (3) it allows the weighted norm of the control force to be minimized *at each instant of time*--most control methods minimize time integrals of such norms; (4) the computations required to determine the control force involve simple matrix multiplications and additions, making the method attractive for real-time, on-line control of nonlinear mechanical systems. An example of the control methodology is illustrated. It has also been successfully used for precision motion-control of multi-arm robots, for on-orbit formation-flight of satellites, and for controlling flexible, nonlinear vibrating systems.

References

[1] Udwadia F. E., Kalaba R. E.: What is the General Form of the Equation of Motion for Constrained Mechanical Systems? *Journal of Applied Mechanics* **69**:335-339, 2002.
[2] Udwadia F. E.: A New perspective on the Tracking Control of Nonlinear Structural and Mechanical Systems. *Proceedings of the Royal Society of London, Series A* **459**:1783-1800, 2003.

PRE-ACTING IMPACT ISOLATION SYSTEMS

Dmitry V. Balandin*, Nikolai N. Bolotnik**
* *Nizhny Novgorod State University, pr. Gagarina 23, 603950 Nizhny Novgorod, Russia*
** *Institute for Problems in Mechanics of RAS, pr. Verndskogo 101-1, 119526 Moscow, Russia*

Summary The pre-action control concept is considered as applied to impact isolation systems. The limiting performance analysis is performed for a single-degree-of-freedom system subject to an instantaneous impact. A substantial advantage of pre-acting isolators is established, as compared with isolators without pre-action. A pre-acting isolator based on a passive elastic element (spring) is suggested. The optimal parameters of this isolator are calculated.

INTRODUCTION

Impact isolators are normally start responding to an impact only after this impact has occurred. In fact, the impact itself serves as a signal for the isolation system to be engaged. In a number of cases, one can predict the initiation time of the impact and its characteristics. In this case, the isolation system can start operating ahead of time, before the impact has occurred. Such isolation systems can be referred to as *pre-acting isolation systems*. In the present paper, we analyze the limiting performance characteristics of pre-acting impact isolators as compared with those of isolators without pre-action. This analysis is performed for a single-degree-of-freedom model in the case of an instantaneous impact. Pre-acting isolators are shown to be able to considerably improve the isolation quality.

LIMITING PERFORMANCE PROBLEM

Consider a SDOF model of a shock/impact isolation system. The object to be protected is connected to the base by means of an impact isolator treated as a controller that generates a control force between the base and the object. The motion of the object relative to the base is governed by the differential equation

$$m\ddot{x} + u = mv, \quad v = -\ddot{z}, \tag{1}$$

where m is the mass of the object, x is the displacement of the object relative to the base, z is the displacement of the base relative to an inertial reference frame and u is the control force applied to the base (accordingly, $-u$ is the control force applied to the object). The variable v characterizes the disturbance of the base induced by an impact. Consider the optimization problem.

Problem. Let the motion of the object relative to the base be governed on the time interval $[-t_0, \infty)$, $t_0 \geq 0$, by Eq. (1), where $v = v(t)$ is a prescribed function of time, which is identically zero for $-t_0 < t < 0$. Let this system be subject to zero initial conditions

$$x(-t_0) = 0, \quad \dot{x}(-t_0) = 0. \tag{2}$$

It is necessary to find an optimal value t_0^* and a control $u_0(t)$ that is defined for $t \geq -t_0^*$, satisfies the constraint

$$|u_0(t)| \leq U, \tag{3}$$

where U is a prescribed positive constant, and minimizes the peak absolute value of the relative displacement of the object to be protected, i.e.,

$$J(u_0, t_0^*) = \min_{u, t_0} J(u, t_0), \qquad J(u, t_0) = \max_{t \in [-t_0, \infty)} |x(t; t_0, u)|. \tag{4}$$

The notation $x(t; t_0, u)$ stands for the solution of the initial value problem of Eqs. (1) and (2) for a specified control $u = u(t)$. The instant $t = 0$ is identified with the time at which the impact pulse starts acting and t_0 is the time before the impact since which the control is allowed to act (pre-action time), and U is the maximum magnitude of the force allowed to be transmitted to the object by the isolator.

This problem is frequently referred to as the *limiting performance problem*, since its solution yields the absolute minimum of the performance index that can be reached irrespective of the specific design configuration of the isolation system.

In what follows, we will consider an instantaneous impact for which $v(t) = v_0 \delta(t)$, where $\delta(t)$ is Dirac's delta function and v_0 is a positive number equal to the velocity increment imparted to the object by the impact. Then the solution of the limiting performance problem yields

$$J(u_0, t_0^*) = \frac{mv_0^2}{16U}, \quad t_0^* = \frac{mv_0}{U}. \tag{5}$$

In the case of the control without pre-action ($t_0 = 0$), the minimum value of the criterion J is 8 times that of Eq. (5).

PARAMETRIC SYNTHESIS OF A PASSIVE PRE-ACTING IMPACT ISOLATOR

A pre-acting impact isolator can be designed with a passive elastic element (spring). The pre-action operation of such an isolator can be provided by pre-straining (cocking) the spring and releasing it at an appropriate time instant before the impact. The preliminary strain and the time of its release are to be determined so as to provide the maximum effectiveness of the isolator. Let the spring have a power-law characteristic. In this case, $u = k|x|^n \operatorname{sign} x$ and the relative motion of the object is governed by the equation

$$m\ddot{x} + k|x|^n \operatorname{sign} x = 0, \quad n \geq 0, \tag{6}$$

where k is the stiffness coefficient of the spring. At the instant of the release of the spring, $t = -t_0$ (for t_0 time units before the impact), the object has been moved to the position $x = a$ (the spring has been cocked) as is in a state of rest. Accordingly, we have the initial condition

$$x(-t_0) = a, \quad x(-t_0) = 0. \tag{7}$$

At the impact instant $(t = 0)$, the relative velocity of the object jumps by v_0, which is expressed by the additional condition

$$\dot{x}(+0) = \dot{x}(-0) + v_0. \tag{8}$$

The optimal values of the parameters k, a, and t_0, chosen so as to minimize the peak magnitude of the relative displacement of the body under the constraint $|u| \leq U$, are

$$k = \left[\frac{8}{(n+1)mv_0^2}\right]^n U^{n+1}, \quad a = \frac{(n+1)mv_0^2}{8U}, \quad t_0 = \frac{mv_0}{4U} \mathrm{B}\left(\frac{1}{n+1}, \frac{1}{2}\right), \tag{9}$$

where $\mathrm{B}(\xi, \eta)$ is the beta-function (Euler's integral of the first kind). The corresponding minimum of the peak displacement of the object is $J = (n+1)mv_0^2/(8U)$. This value decreases as n decreases, and in the limit as $n \to 0$, we have $J = mv_0^2/(8U)$, which is by a factor of 4 less than the peak displacement corresponding to the limiting performance of isolators without pre-action and by a factor of 2 greater than the value of Eq. (5) characterizing the limiting performance of pre-acting isolators.

CONCLUSIONS

In the cases where one can predict the initiation time and the characteristics of the impact, it is reasonable to utilize pre-acting impact isolators that start responding to the impact before it has occurred. For a single-degree-of-freedom model subjected to an instantaneous impact, pre-acting isolators can provide a factor of 8 reduction in the peak absolute value of the displacement of the body to be protected, as compared with the limiting performance characteristics of isolators without pre-action. A factor of 4 reduction can be provided by a spring isolator, if one pre-stains the spring and then releases at an appropriate time instant before the impact. Pre-acing isolators can be effective in injury prevention systems on road and air transportation vehicles. This is the case, for example, for an aircraft ejection seat. The time history of the acceleration of the ejection seat after shooting (impact pulse) is known. One can introduce a small time delay between the instant of switching on the system and the instant of the beginning of the acceleration to enable the injury prevention system to get prepared to respond to the impact. Pre-acting isolators can be utilized on helicopter seats to reduce the severity of injuries in the case of hard vertical landing. By measuring the altitude and the descent velocity of the helicopter, one can calculate the instant and velocity of the impact ahead of time. Isolators of this type seem to be promising for utilizing in automobile safety systems.

CONTROL OF MULTIBODY SYSTEMS MOVING ALONG A PLANE

F .L. Chernousko
Institute for Problems in Mechanics of the Russian Academy of Sciences,
pr. Vernadskogo 101-1, 119526 Moscow, Russia

Summary The dynamics of multibody systems moving along a horizontal plane is investigated in the presence of dry friction acting between the system and the plane. Control algorithms are proposed for forces and/or torques created by actuators installed at the joints. The obtained results confirmed by experiments are related to mobile robots and the biomechanics of snake-like locomotion.

INTRODUCTION

Crawling motions of snakes and other limbless animals have always been of interest for mechanics and biomechanics [1]. Recently, these motions have been implemented in biologically-inspired snake-like robots [2].
In this paper (related to [3–6]) we study the dynamics of plane multibody systems consisting of several rigid bodies (connected by prismatic and/or revolute joints) and moving along the horizontal plane. Control forces and/or torques are created by actuators installed at the joints. Dry friction forces obeying Coulomb's law act between the system and the plane, the coefficient of friction is denoted by k. It is shown that two-member and three-member systems can perform various periodic motions by alternating slow and fast phases. For multilink systems, wavelike quasi-static locomotion is possible.

RECTILINEAR MOTION

Consider first multibody systems with prismatic joints moving along a straight horizontal line (Fig. 1). Control forces F act between each pair of neighboring masses. In the case of N equal masses m (Fig. 1a), wavelike regular progressive motion is possible, if $mgk < F < (N-1)mgk$. This condition does not hold for $N = 2$. Periodic motion of a two-mass system (Fig. 1b) is proposed and analyzed. This motion consists of a slow phase in which the smaller mass m approaches the bigger mass M which stays at rest, and a fast phase where the both masses move in the opposite directions. As a result, the whole system moves forward with an average speed $v = [g\eta km(M-m)/2]^{1/2}(M+m)^{-1}$. Here, η is the range within which the distance between masses can change. The maximum speed $v_{\max} = (g\eta k)^{1/2}/4$ is attained, if $m = M/3$.

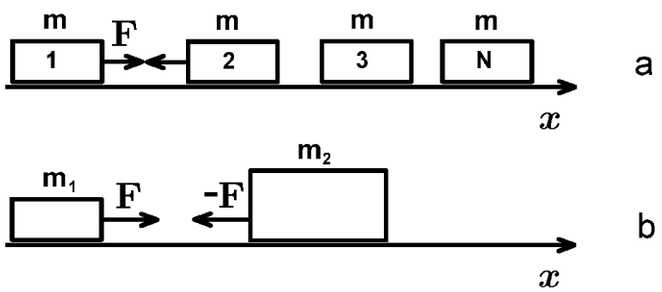


Fig. 1. Rectilinear motion

SNAKE-LIKE LOCOMOTION

Multilink systems with revolute joints can move along a horizontal plane by applying control torques at the joints connecting neighboring links (Figs. 2 and 3). Consider a two-link system with one active revolute joint where the control torque M is applied. Denote the masses and the lengths of the links by m_i, l_i, respectively, $i = 1, 2$. Here, the subscripts $i = 1, 2$ correspond to the longer and shorter links called the body and the tail, respectively. The mass of the joint is denoted by m_0.
The two-link system can perform the longitudinal motion with a period consisting of four slow and four fast phases (Fig. 2). In slow phases marked by even numbers in Fig. 2, the tail rotates by a certain angle while the body stays at rest. These phases are realizable, if $m_2 l_2 < m_1 l_1$ and $m_2(l_1 + l_2) < m_0 l_1$. In fast phases marked by odd numbers in Fig. 2, the control torque M should be much greater than the torques created by friction forces: $M \gg m^* gkl^*$, where $m^* = \max(m_0, m_1, m_2)$ and $l^* = \max(l_1, l_2)$.
Under the conditions given above, the two-link system can not only move forward (to the right in Fig. 2), but also follow any prescribed trajectory in the plane. Similar results are obtained also for the three-link system.

The nonlinear dynamics of snake-like motions is analyzed. Displacements and the average speed of the periodic motion for the two- and three-link systems are estimated. The dependence of the average speed on the geometrical and mechanical parameters of the system is analyzed, and the values of these parameters corresponding to the maximum speed are calculated. For the two-link system, we have $v_{\max} = c(gl_1k)^{1/2}$, $c \sim 0.05$. For the lengthwise and lateral motions of the three-link system, we have $c \sim 0.1$ and $c \sim 0.5$, respectively. It is natural that the three-link mechanism equipped with two actuators can move faster than the two-link system of the same size having only one actuator.

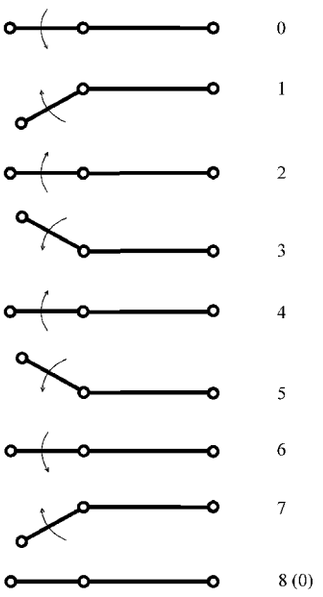


Fig.2. Motion of two-link system

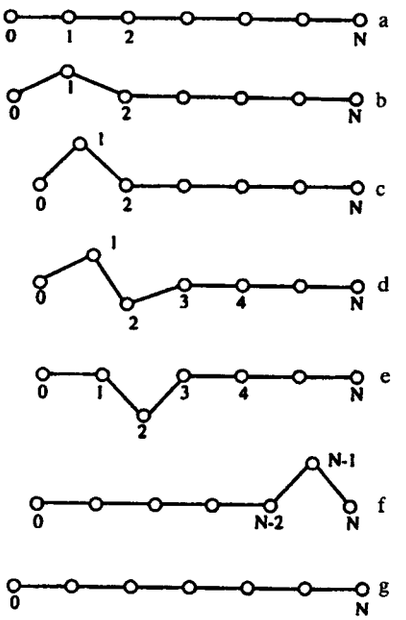


Fig. 3. Wavelike motion of multilink system

Multilink systems with more than four equal links can perform wavelike quasi-static motions (Fig.3). In these motions, only several links move at each time instant (for example, not more than three links in the motion shown in Fig. 3), while all other links stay at rest. The required control torques for the multilink mechanism are smaller than for two– and three-link systems: $M \leq 2mlk$. Here, m is the mass of the link, and l is its length.

CONCLUSION

The obtained results are confirmed by computer simulation and experimental data. The experiments were performed at the Institute for Problems in Mechanics of the Russian Academy of Sciences and at the Technical University of Munich. These results are related to the biomechanics of snake-like locomotion and may be of interest for mobile robots, especially for small ones, and for transportation systems.

References

[1] Gray J.: Animal Locomotion. Norton, NY 1968.

[2] Hirose S.: Biologically Inspired Robots: Snake-like Locomotors and Manipulators. Oxford University Press, Oxford 1993.

[3] Chernousko F.L.: The Wavelike Motion of a Multilink System on a Horizontal Plane. *J. Applied Math. and Mech.* **64**: 497–508, 2000.

[4] Chernousko F.L.: Controllable Motions of a Two-link Mechanism along a Horizontal Plane. *J. Applied Math. and Mech.* **65**: 565–577, 2001.

[5] Chernousko F.L.: The Optimum Rectilinear Motion of a Two-mass System. *J. Applied Math. and Mech.* **66**: 1–7, 2002.

[6] Chernousko F.L.: Snake-like Locomotions of Multilink Mechanisms. *J. Vibration Control* **9**: 235–256, 2003.

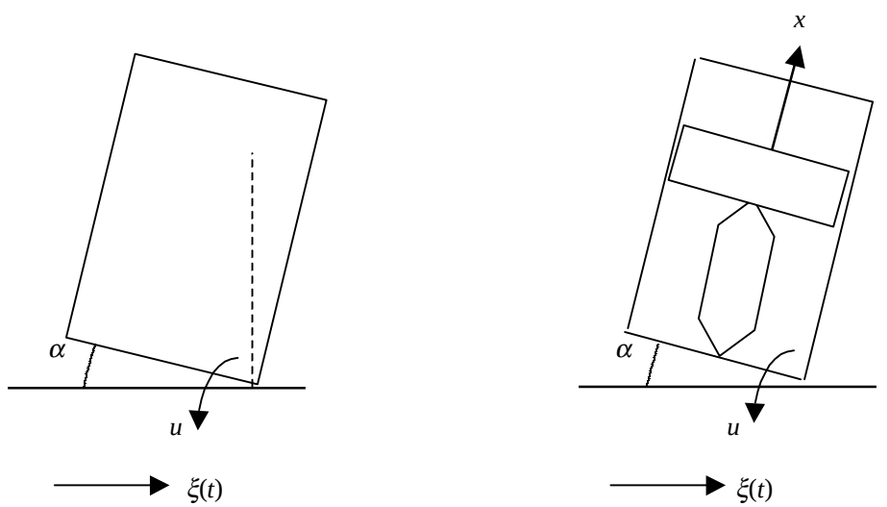
CONTROL OF RANDOM DYNAMICS OF A RIGID ROCKING BLOCK

Agnessa Kovaleva
Russian Academy of Sciences, Space Research Institute,
Profsoiuznaya 84/32, Moscow 117997 Russia

Summary. The problem of minimizing the toppling probability of a rocking block is considered as a control problem for a stochastic discontinuous oscillator. Formally, the control task is to minimize the probability of escape the system from the domain enclosed by the unperturbed separatrix. The problem is resolved by the dynamic programming method, with application of the stochastic averaging procedure.

PROBLEM FORMULATION

The paper studies controlled dynamics of a rigid block and a block structure. Rocking oscillations are excited due to random horizontal ground motion. Assuming rigid foundation, large friction to prevent sliding, and the Newton restitution law during the impact, the only possible response mechanism under ground excitation is the rocking about the corners of the block (Fig. 1 a, b). The control task is to minimize the toppling probability with due regard to control constraints.



(a) (b)

Fig.1. Rocking motion of a rigid block (a) and a block structure; α - inclination angle, u – control torque, x – mass displacement, $\xi(t)$ – ground acceleration

The response analysis of random rocking motion of a rigid block has been pursued for last decades; see [1] for the detailed review and discussion. The engineering approach for the toppling prevention lies in making use of the elastic tie-down rods or anchoring, see, e.g. [2], [3]. This paper considers the problem of the toppling prevention as a control problem.

ASYMPTOTIC ANALYSIS AND NEARLY OPTIMAL CONTROL

The first question addressed in the paper is the control problem for a rigid block. The equation of rocking motion corresponds to the equation of a quasiconservative nonlinear discontinuous oscillator. The phase plane of the conservative counterpart of the system is divided into two domains, the domain of bounded oscillations (librations) and the domain of unbounded motion (toppling), separated by the unperturbed separatrix. Escape through the separatrix is considered as a dangerous event to be avoided. The control task is thus to keep the system within the domain enclosed by the unperturbed separatrix.

The well-developed analysis and control procedure for systems with impact [4] cannot be directly applied to the strongly nonlinear system. We extend the averaging procedure to nonlinear discontinuous system. The equation of

motion is reduced to the standard form for the quasiconservative system, with the slow energy evolution and the associated fast phase. The Newton restitution law allows introduction of the impact dissipation in the equation of the slow variable. The coefficient takes the form of the periodic Dirac δ- function and allows averaging [4].
In order to simplify the system's structure and to reduce it to the form of the stochastic Ito equation, we employ the partial stochastic averaging approach [4]. At the first stage, the stochastic averaging reduces the perturbed system to the form of the stochastic Ito equation with slow and fast variables. At the second stage, the partial averaging of the deterministic coefficients, except for control, excludes fast components of the periodic coefficients and smoothes out the discontinuities in the equation of the slow motion.
The dynamic programming equation for the partially averaged system determines nearly optimal control. This equation is resolved asymptotically, by making use of the averaging in fast variable [4].
The second part of the paper centres on the effect of the secondary structure on the rocking dynamics (Fig. 1b). Motion can be presented as the superposition of the tracking rocking motion of the system as a whole and the relative oscillations of the secondary flexible structure. For a number of practical applications, the relative oscillations are small compared to the rigid motion. This allows simplification of the equations of motion and application of the asymptotic decomposition procedures to the analysis and control problems. The goal is to estimate the effect of the secondary structure to the statistical properties of motion and the probability distribution of the toppling time.

References

[1] Spanos P.D., Roussis P.C, Politis N.P.A. Dynamic Analysis of Stacked Rigid Blocks. *Soil Dynamics and Earthquake Engineering*. **21**: 559-579, 1995.
[2] Aslam M., Godden W., Scalise D. Earthquake Rocking Response of Rigid Bodies. *Journal of Structural Division of the ASCE.* **106**: 377-392, 1980.
[3] Markis N., Zhang J. Rocking Response of Anchored Blocks under Pulse Type Motion. *Journal of Engineering Dynamics.* **127**: 484-493, 2001
[4] Kovaleva A. Optimal Control of Mechanical Oscillations. Springer-Verlag. NY, 1999.

Suppression of train-induced vibrations of continuous truss bridge by hybrid TMDs

Jong-Dar YAU
Dept. of Architecture & Building Technology, Tamkang University, 10620 Taipei, Taiwan

Summary Steel truss bridges possess the advantages of light weight, high strength, and ease in construction, they therefore are often utilized in railways for crossing streams or chasms. However, because of the existence of clustered frequencies of vibration, there may occur multi resonant peaks in the impact response of continuous truss bridges subjected to high speed trains. To overcome this problem, a hybrid tuned mass damper (TMD) system will be employed to mitigate the train-induced vibrations of the continuous truss bridges. By modeling a continuous truss bridge as a combination of beam and truss elements and the train over it as a sequence of moving loads. The numerical results indicate that the proposed hybrid TMD system can effectively suppress the main resonant peaks of the continuous truss bridge due to the train loads moving at high speeds.

Extended Summary

This paper deals with the vibration suppression of railway bridges subjected to the passage of high-speed trains. In a practical design, the impact factor is used to evaluate the dynamic amplification effect of a bridge due to the action of vehicles moving over it. In this study, the impact factor I is defined as the ratio of the maximum dynamic to the maximum static responses of the beam under the action of the moving loads minus one. It has been indicated that for a bridge subjected to the moving action of a single truck with constant speed v, the impact factor may be linearly related to the speed parameter S, which represents the ratio of the driving frequency ($= \pi v/L$) implied by the moving loads to the fundamental frequency ω of the bridge (Yang et al. 1995).

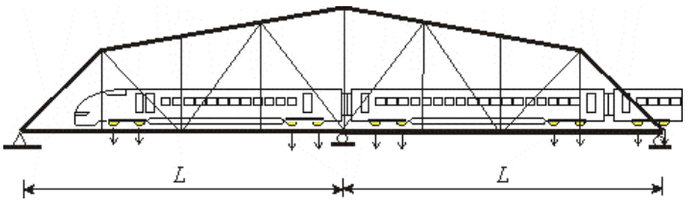


Fig. 1 Continuous truss bridges subjected to high speed trains

As shown in Fig. 1, a two-span continuous truss bridge with equal spans and simple supports subjected to a Shinkansen (*SKS*) train is considered. By modeling the truss bridge as a combination of beam-column and truss elements and the train moving over it as a series of moving loads, the *vehicle-bridge interaction* finite element program developed by the author (Yau, 1996) is employed to obtain the impact response of the truss bridge.

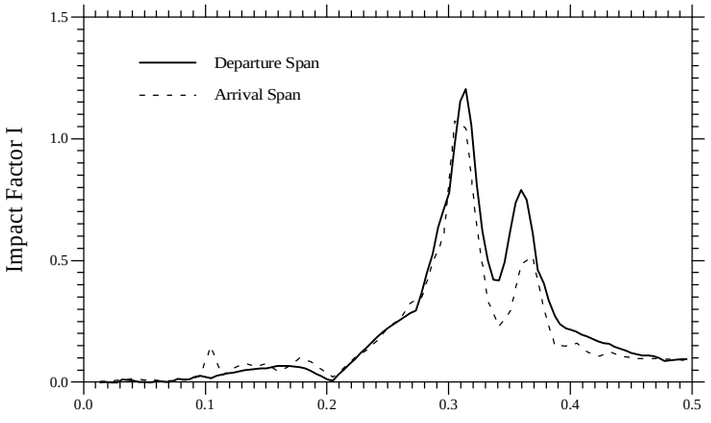


Fig. 2 Impact response of continuous truss bridge.

Fig. 2 shows that the displacement impact responses solved for the midpoint of each span of the truss bridge have been plotted against the speed parameter S. As can be seen, there exist two resonant peaks for the impact response curves of the arrival span and the departure span of the continuous truss bridge. This is mainly due to coincidence of some of the excitation frequencies implied by the moving wheel loads at different speeds with the fundamental or

higher frequencies of the truss bridge. Besides, it is observed that the impact factor for the departure span is larger than that of the arrival span. This can be attributed to the uplift action caused by the departure of the last moving load from the arrival span and entrance into the departure span. For this reason, only the impact response of the departure span will be considered in the illustrative example.

To effectively reduce both two resonant peaks of the continuous truss bridge due to vehicles moving at high speeds, a hybrid tuned mass damper (TMD) system is proposed for suppressing the train-induced responses of the truss bridge. Since the first two resonant peaks affect the departure span of the truss bridge, the hybrid TMD system is composed of *dual* TMD subsystems, namely, TMD-1 and TMD-2, as depicted in Fig. 3, each of which consists of a TMD tuned to one of the first two resonant frequencies of the truss bridge. Using the *minimum-maximum amplitude criterion* proposed by Randall et al. (1981) and enforcing the resonant peaks of interest to be equal to each other, one can determine the allocated mass and optimum parameters for the hybrid TMD system (Yau and Yang 2004). Because the response contribution of the first mode of the continuous truss bridge is greater than that of the second mode, the modal mass ratio with respect to the fundamental mode will be adopted for the hybrid TMD systems mounted on the truss bridge. On the other hand, an increase of the TMD mass ratio will result in a better control of the vibration of the main structure. However, the self-weight of the TMD will induce as well additional deformation on the main structure. Therefore, a small modal mass ratio 0.01 is adopted for the sum of the masses of all hybrid TMD systems attached to the continuous truss bridge in the example.

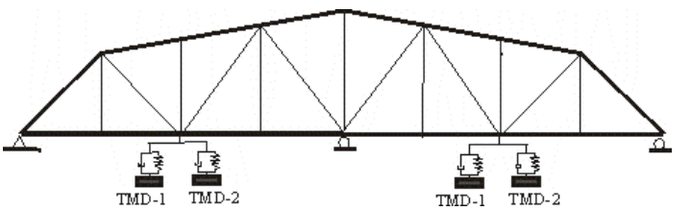


Fig. 3 Continuous truss bridge model with hybrid TMD systems

By mounting the proposed hybrid TMD systems on the midpoint of each span of the truss bridge, the impact response of the departure span for the truss bridge is depicted in Fig.4. As can be seen, the hybrid TMD system proposed considering only the contribution of the first and second modes is quite effective for suppressing the resonant responses of the continuous truss bridge subjected to high speed trains.

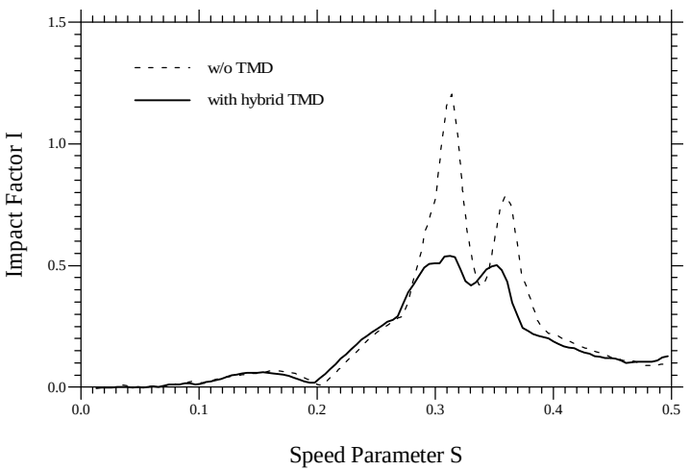


Fig. 4 Impact response of the departure span of the continuous truss bridge using hybrid TMD system.

References

[1] Yang YB, Liao SS, Lin BH. Impact formulas for vehicles moving over simple and continuous beams. ASCE J Struct Eng 1995;**121**(11): 1644-1650.

[2] Yau, JD, *Dynamic response of bridges traveled by trains) analytical and numerical approaches*, Ph.D. thesis, Dept. Civ. Eng., National Taiwan Univ., Taipei, Taiwan, R.O.C., 1996.

[3] Randall SE, Halsted DM, Taylor DL. Optimum vibration absorbers for linear damped systems. ASME J. Mechanical Design 1981;**103**: 908-913.

[4] Yau JD, Yang YB. Vibration reduction for cable-stayed bridges traveled by high-speed trains. Finite Elements in Analysis and Design, 2003, **40**: 341-359.

OPTIMIZATION OF ACTIVE CONTROL OF STRUCTURAL VIBRATION BY THE BEAM ANALOGY

W. Szyszkowski and M. Baweja
University of Saskatchewan, Dep. of Mech. Eng., Saskatoon, SK, Canada S7N 5A9

Summary: Optimal control of elastic vibrations by a set of actuators is determined using the finite element (FE) approach. The method combines two FE models, one standard model to represent the structure's dynamics and the second model consisting of fictitious static beams to solve the optimality equations for the problem.

The Problem and the Solution Methodology

Consider an elastic structure under the action of a set of discrete actuators. The structure is governed by the usual equation of motion in the form:

$$M\ddot{x}(t) + C\dot{x}(t) + Kx(t) = F(t) \qquad (1)$$

where M, C, and K are the symmetric mass, Rayleigh damping, and stiffness matrices respectively. It is assumed that a sufficiently accurate FE model with m degrees of freedom (DOF) is available to simulate the structure's dynamics. The actuators generate the control force vector $F_a(t)$ with the number of independent components equal to n_a, the number of actuators. The vector of nodal forces in equation (1) is $F = BF_a$ where the known placement matrix B has dimension $m \times n_a$. In general, the actuators are to move the structure in time t_f from an initial configuration $x(0) = x_0$, to a final configuration $x(t_f) = x_f$. The manoeuvre time t_f can be given, or may be treated as a variable of optimization. The objective is to determine the action of actuations that will minimize the performance index defined as:

$$J = 1/2 \int_0^{t_f} [x^T Q_d x + \dot{x}^T Q_v \dot{x} + F^T R F + G\,]dt \rightarrow \min \qquad (2)$$

where Q_d, Q_v, and R are symmetric positive definite weighting matrices, and Γ is a positive constant.

The above problem is usually handled by applying Pontryagin's Principle (PP) or by the parametric optimization approach. Both methodologies are computationally very intensive [1]. Typically, the PP's application leads to Riccati's coupled non-linear matrix equations the solution of which is *'the most time-consuming part of any optimal control problem'* ([1], p. 109), and the existing procedures *'do not universally guarantee stable and accurate computation'*([2], p. 248).

A different method, which appears to be numerically efficient, is presented here. For this particular problem the following optimality equations can be derived from the PP[3]:

$$MRM\dddot{x} + (2KRM - Q_v - CRC)\ddot{x} + (KRK + Q_d)x = 0 \qquad (3)$$

The initial conditions, x_0 and $\dot{x}_0$, represent the disturbed, and the final conditions $x_f = \dot{x}_f = 0$ the vibration-free structure. Equation (3) with these conditions constitutes the boundary value (BV) problem in the time domain that can formally be solved by using the FE methodology. This BV problem simplifies significantly if the weighing matrices are assumed to be linear combinations of the matrices M, C, and K, i.e.: $Q_d = a_1 M + a_2 K + a_3 C$, $Q_v = b_1 M + b_2 K + b_3 C$, and $R = [g_1 M + g_2 K + g_3 C]^{-1}$ where a_i, b_i, and g_i are non-negative *optimization constants* (Q_d, Q_v and R will always be positive definite). Next, substituting $x = Fh$, where F is the matrix of M-normalized eigenmodes and $h(t)$ is the vector of modal variables, the optimality equation (3) is transformed into the decoupled equations in the form:

$$\hat{R}_{ii}\dddot{h}_i + [2w_i^2(1-2x_i^2)\hat{R}_{ii} - \hat{Q}_{iiv}]\ddot{h}_i + (w_i^4\hat{R}_{ii} + \hat{Q}_{iid})h_i = 0\,, \qquad i=1...s \qquad (4)$$

where w_i are ordered eigenfrequencies (i.e. $0 \le w_1 \le w_2 ... \le w_s$) and x_i are modal damping ratios of the structure. The coefficients in equation (4) are known functions of the optimization parameters and w_i (for example, $\hat{R}_{ii}^{-1} = g_1 + g_2 w_i^2 + 2g_3 w_i x_i$). Equation (4) can be solved mode by mode for a certain number of s

initial modes (typically $s<<m$). Once it is solved, the optimal control force vector is determined from $F_a = (B^T \Phi \Phi^T B)^{-1} B^T \Phi U$, where s components of vector U are defined by $U_i = \ddot{h}_i + 2x_i w_i \dot{h}_i + w_i^2 h_i$.

A convenient method of solving equations (4) arises from analogy between these equation and the governing equations for a set of s fictitious independent static beam of length L resting on elastic foundation k_{fi}, and loaded by axial compressive force P_i. Each beam is governed by:

$$EI_i v_i'''' + P_i v_i'' + k_{fi} v_i = 0 \qquad i = 1..s \tag{5}$$

where $(.)' = \frac{\partial}{\partial y}$, and $0 \le y \le L$. Two geometrical boundary conditions can arbitrarily be imposed on each end of the beam. Equations (4) and (5) become analogous if the beam's bending stiffness is selected such that $EI_i \equiv \hat{R}_{ii}$ and if $P_i \equiv 2w_i^2 (1 - 2x_i^2)\hat{R}_{ii} - \hat{Q}_{iiv}$, and $k_{f_i} \equiv w_i^4 \hat{R}_{ii} + \hat{Q}_{iid}$. One can also assume that $L = t_f$ (where L is in meters and t_f is in seconds, for the SI unit system), then the variables of equation (4) relate to the variables of equation (5) as: $t \equiv y$ and $h_i(t) \equiv v_i(y)$. Consequently, for equivalent boundary conditions all the modal functions and their derivatives can be determined in terms of the deflection, slope, and bending moment the fictitious static beams (for example, $U_i = M_i / EI_i + 2w_i x_i q_i + w^2{}_i v_i$).

Besides the already mentioned structural FE model (any structural elements can be used in it), a second FE model, built of fictitious static 2-D beams, is needed to handle equations (5). The latter model can be solved using standard hermitian beam elements. Once the results of this model are known, the optimal actuator forces and the optimal response of the structure can be easily obtained. Note that for verification, the forces calculated from the analogy can be applied to the structural model to determine its 'true' transient dynamic response.

To illustrate the method active vibration control of an elastic aluminum fin modeled by two $2mm$ thick plates as shown in Figure 1 is presented. The dynamic model of the structure has about 2000 DOFs ($m \approx 2000$). If the fin's vibrations are to be attenuated by two actuators (placed at nodes 2 and 12, for example) then two fictitious beams ($s = n_a = 2$) are required to predict the optimal action of these actuators. Either the real disturbances can be considered for an open-loop control, or a somewhat arbitrarily initial configuration can be used to determine optimal gains for a close-loop control.

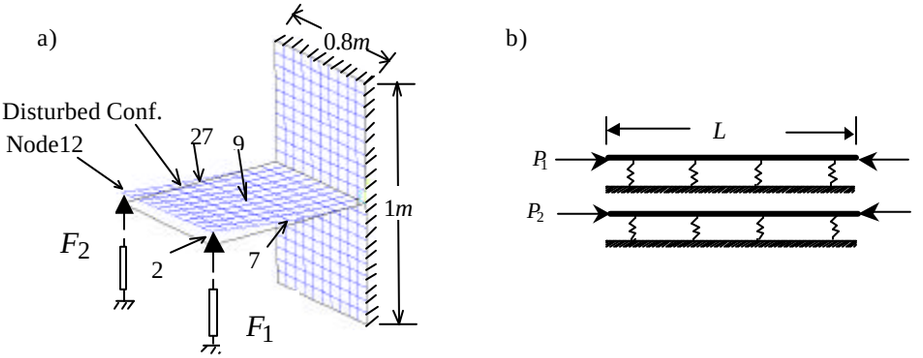


Figure 1. The structure controlled by two actuators (a), and the corresponding fictitious beams (b).

For example, the analysis indicates that the actuators capable of producing about $180N$ are required if $t_f \to \infty$ (for the time-invariant problem), and about $550N$ if the manoeuvre time is limited to $1s$.

References

[1] Saleh A, Adeli H. (1999) *"Control, optimization, and smart structures"*, J. Wiley&Sons, Inc, New York

[2] Junkins J L, Kim Y (1993) *"Introduction to Dynamics and Control of Flexible Structures"*. 2nd Edn. AIAA Education Series, Washington, DC

[3] Szyszkowski W, Grewal I S (2000) *"Beam Analogy for Optimal Control of Linear Dynamic Systems"*. Computational Mechanics, 25(5): 489-501.

CONTROL OF A NONLINEAR SLEWING FLEXIBLE BEAM

André Fenili, Luiz Carlos Gadelha de Souza
National Institute for Space Research – INPE (DMC), 12201-970 São José dos Campos, SP - Brazil

Summary The system under investigation here comprises a flexible beam connected to an actuator (dc motor) in such a way that the angular displacement of the motor axis and the beam deflection develops in the same plan perpendicular to the before quoted axis (this movement is named *slewing*). A control law is designed and tested for the linear and ideal (no influence of the structure dynamics over the energy source) and for the linear and nonideal (the structure dynamics interacts with the energy source dynamics) mathematical model. The beam curvature is considered linear and the only nonlinear term present here comes from centripetal effects. Although the gain of the controller is obtained using the linear model, its performance is tested also for the non-linear model with good results. Low and high velocities are investigated in order to verify the robustness of the proposed control law when dealing with the not initially considered term.

INTRODUCTION

Nowadays a great number of space missions involve Large Space Structure (LSS) using attitude control systems with high degree of pointing accuracy and at same time urging for quick time of response. Examples of mission with that requirement are the Hubble Space Telescope and the International Space Station. Other general examples are: lightweight robotic manipulators in industry or space applications and solar panels or antennas in satellites (to quote just a few).

In the modeling of flexible rotating structures, the interaction between the angular displacement, θ, and the deflection of a beam like structure, v (x,t) (or q(t) after discretization), can be very important, mainly when the maneuvers involve high angular velocities [1],[2]. Assuming linear curvature for the beam, this kind of interaction involves a nonlinear term in the governing equations. This term is of order three and is associated with centripetal stiffening. Figure 1 presents a schematic of the problem under considerations here. The elastic displacement of the beam, v(x,t), is excited by the angular motion θ (t) (and its derivatives).

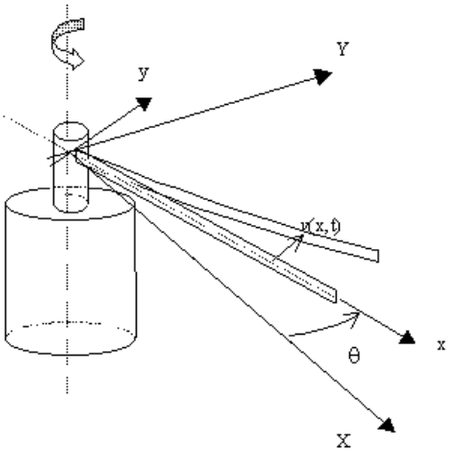


Figure 1 – The rotating flexible beam (XY is the inertial frame and xy is the rotating frame)

The actuator and energy source investigated here is a dc motor, which is also used for noncolocated control of the beam. Two different approaches used in this work to analyze the behaviour of the nonlinear system is related to the concepts of *ideal system* and *nonideal system*. When the dynamics of the driven system (the beam-like structure here) interacts with the dynamics of a limited energy source (the dc motor, for instance) it is very important to take into account the effects of this interaction (exchange of energy) in the control system design. The complete system is then said to be *nonideal.* For these systems, the excitation profile is not known previously (since it depends on the structure unknown response). Otherwise the system is said to be *ideal* [3]. The governing equations of motion for the system depicted in Figure 1 are derived in [4]. An investigation about the influences of the nonlinearties in the dynamical behavior of this system can be found in [5] and [6].

MATHEMATICAL MODELING AND RESULTS

The governing equations of motion for the flexible beam are derived through the lagrangian formalism [4]. For the system composed by the linear curvature beam together with a dc motor the governing equations are given by:

$$L_m\dot{i}_a + R_a i_a + K_b N_g \dot{\theta} = U \tag{1}$$

$$(I_{eixo} + I_{motor}N_g^2)\ddot{\theta} + (c_m N_g^2)\dot{\theta} - (N_g K_t) i_a - \beta\left(EI\sum_{i=1}^{n} q_j(t)\phi_j''(0)\right) = 0 \tag{2}$$

$$\ddot{q}_j + \mu\dot{q}_j + \mathbf{w}_j^2 q_j + \alpha_j\ddot{\theta} - \dot{\theta}^2 q_j = 0 \tag{3}$$

plus the boundary conditions: $\phi''(L,t)=0$, $\phi'''(L,t)=0$. In equation (2), if $\beta = 0$ the system is ideal and if $\beta = 1$ the system is nonideal.

The control used here is based on state feedback with pole placement. The idea is to control the beam vibrations after some specified value for the angle θ is reached. This angular displacement must be performed as fast as possible and the control signal (electric tension) is applied in the instant the slewing angle is equal to the desired final value.

The gains of the feedback control law are obtained applying the pole placement technique for the linear system (initially the nonlinear term is neglected). The nonlinear term considered depends on the square of the angular velocity of the slewing axis, which means that the greater this velocity the greater the influence of the nonlinear term. Despite the gain being calculated using a linear model, the control is evaluated considering the linear system and the nonlinear system (both ideal and nonideal).

Carrying out numerical simulations considering different values for the slewing velocity it is possible to evaluate the influence of the nonlinear term in the performance of the controller. As expected, the performance is degraded for high velocities in the nonlinear case. Increasing the angular (or slewing) velocity beyond some value it is noted that the control fails and the system is unstable. Though with this critical velocity the beam deflection is great enough for the linear curvature model adopted to be no more valid. Some numerical results are depicted in Figures 2 and 3. The nonlinear case (ideal and nonideal) is presented. The proposed control law was succesfully (numerically) tested.

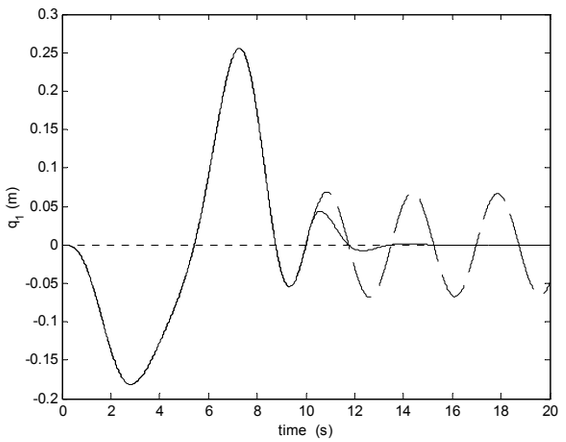


Figure 2 Nonlinear ideal system

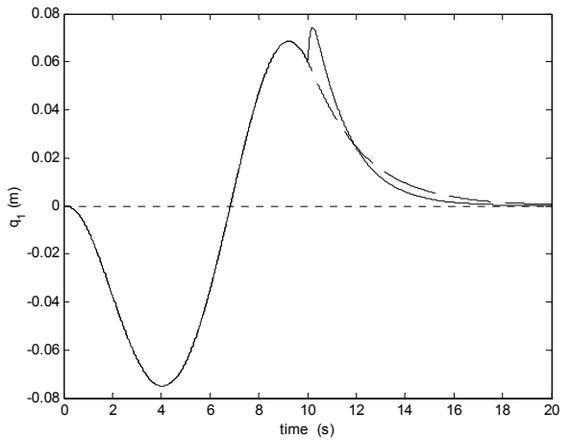


Figure 3 Nonlinear nonideal system

CONCLUSIONS

For a suitable range of beam deflections (associated with suitable angular velocities of the alewing axis), the proposed control law and gains derived based on the linear governing equations of motion works satisfactorily well, even in the presence of the nonlinear term. The beam vibrations in the ideal model is less damped than in the nonideal model and the control influence over the system response is more remarkable in the first case. The nonideal interaction between the beam and the actuator helps to eliminate the beam vibration, even though the control law is able to slightly improve this behaviour. Figures 2 and 3 shows that the linear control law works for both linear and nonlinear mathematical models.

References

[1] Low, K. H., "Vibration analysis of a tip-loaded beam attached to a rotating joint", Computers and Structures, vol. 52, no. 5, pp 955-968, 1994.

[2] Putter, S., Manor, H., "Natural frequencies of radial rotating beams", Journal of Sound and Vibrations", 56(2), pp 175-185, 1978.

[3] Kononenko, V. O., "Vibrating systems with a limited power supply", Iliffe Books Ltd., 1969.

[4] Fenili, A., "Mathematical modeling of nonlinear slewing structures and applications on mechanical engineering", PhD Thesis, Univ. Campinas, Campinas, São Paulo, Brazil, 2000.

[5] Fenili, A; Souza, L.C.G.; Góes, L.C.S.; Balthazar, J.M.; "On the Damping Effect of No ideal Interaction in Beam-Like Structures in Slewing Motion". In 6th Biennial Conference on Engineering Systems Design and Analysis – ESDA 2002. Istanbul, Turkey, July 8-11, 2002.

[6] Nayfeh, A. H., Mook, D. T., "Nonlinear oscillations", John Wiley and Sons, Inc., New York, 1979.

STABILITY AND CREEP DAMAGE OF QUASI-BRITTLE MATERIALS

Noël Challamel, Christophe Lanos and Charles Casandjian

LMSM, INSA de Rennes, 20 avenue des Buttes de Coësmes, 35043 Rennes, France

Summary A time-dependent damage model is developed for quasi-brittle materials like rock or concrete, in the framework of Continuum Damage Mechanics. Phenomena like relaxation, creep and rate-dependent loading are covered using a unified framework. Creep failure under high-sustained load is explained quite simply within stability theory. Kachanov's equation is commented within the new approach. Creep failure appears as the manifestation of a bifurcation phenomenon.

INTRODUCTION

Geomaterials, such as rock or concrete are often called quasi-brittle materials. Unlike perfectly brittle materials, there are significant zones of softening damage in front of the generated crack tip. Softening is a subject that has profited from a very rich literature for now two decades. It is now well admitted that local damage softening models (which do not exhibit internal length) suffer of a pathological mesh-dependence in finite-element computations. Techniques known as regularisation were developed to restore the well-posedness of the problem. An internal length is generally introduced and constrains the new regularised system towards a family of imposed solutions (non local damage models).
Moreover, the long term performance of concrete or rock structures is fundamentally affected by the behaviour of the material after cracking. In order to simulate realistic concrete or rock behaviour, time-dependence of fracture has to be also considered. Understanding the interaction between the two phenomena (time-dependence and softening) is important to design reliable civil engineering structures subjected to high level and long time loading. As most studies applied to time-dependent concrete modelling have considered viscoelasticity, very few time-dependent damage models are available in the literature. A time-dependent damage model is presented in this study applied to quasi-brittle materials like rock or concrete. This three-dimensional model is introduced in the framework of Continuum Damage Mechanics and is based on strong thermodynamical arguments. The model is a generalisation of the uniaxial model we have previously proposed to model creep failure in compression [1]. Broad range of loading paths can be covered with such model. The constitutive model incorporates different properties in tension and compression. One of the most features of the model is the aptitude to predict creep failure under high-sustained load.

DAMAGE EVOLUTION

For the considered visco-elastic damage process, internal variables are chosen as the strain tensor $\underline{\underline{\varepsilon}}$ and a scalar damage variable *D*. The fundamental equations of this time-dependent isotropic damage model are :

$$\dot{D} = \frac{1}{\eta}\left\langle \frac{\tilde{\varepsilon} - \left(\chi(D) + \tilde{\varepsilon}_D\right)}{\tilde{\varepsilon}_c} \right\rangle^m \; ; \quad \underline{\underline{\sigma}} = (1-D)\lambda_0 tr\underline{\underline{\varepsilon}}\,\underline{\underline{1}} + (1-D)2\mu_0\underline{\underline{\varepsilon}} \tag{1}$$

where $\tilde{\varepsilon}$ is the equivalent strain of the model proposed by Mazars. m is a dimensionless parameter and η is a time constant. $\tilde{\varepsilon}_c$ is a characteristic strain. χ is a definite positive function. $\underline{\underline{\sigma}}$ is the stress tensor. λ_0 and μ_0 are the Lamé's coefficients of the undamaged material. Such a mathematical system can be justified within thermodynamical arguments. $\tilde{\varepsilon}_D$ defines the size of the initial elastic strain domain. As for endochronic models, it is assumed that the model has no yield surface for the monotonic test ($\tilde{\varepsilon}_D = 0$). In cases of uniaxial compression or uniaxial tension tests, it can be shown with these assumptions that Eq. (1) can be converted into a dimensionless differential system (the dimensionless variables are noted by stars) :

$$\frac{dD}{dt^*} = \left\langle \varepsilon^* - \chi^*(D) \right\rangle^m ; \quad \sigma^* = (1-D)\varepsilon^* \tag{2}$$

EQUILIBRIUM CURVE

The differential equation (2) can also be written as :

$$\frac{d\sigma^*}{dt^*} = -\varepsilon^* \left\langle \varepsilon^* - \chi^*\left(1 - \frac{\sigma^*}{\varepsilon^*}\right) \right\rangle^m + \frac{\sigma^*}{\varepsilon^*}\frac{d\varepsilon^*}{dt^*} \quad \text{for } \varepsilon^* \neq 0 \tag{3}$$

This is a true non-linear differential equation which can not be written using Boltzmann's integral of linear viscoelasticity. Asymptotic solutions of constant strain rate tests are well documented in the literature for these non-linear systems. The stress-strain response for extremely slow loading is simply obtained when the term that does not involve strain or stress rate (term in bracket) vanishes in equation (3). This response is sometimes called "equilibrium curve". It turns out that for very slow motions, the stress-strain relation converges towards a time-independent damage model, chosen as :

$$\varepsilon^* = \chi^*(D) = 2D \tag{4}$$

An apparent elastic domain is identified for constant strain rate tests, which reveals the competition between the internal kinetics of damage and the strain rate imposed on the material.

CREEP DAMAGE MODELLING

Creep tests are now studied within this model. After a high rate loading test, the stress is assigned to a constant value during the creep test :

$$\sigma^*(t^*) = \bar{\sigma}^* \quad \forall\, t^* > 0 \tag{5}$$

The differential equations which govern the evolution of the state variable is now written as :

$$\varepsilon^* = \frac{\bar{\sigma}^*}{1-D}; \quad \frac{dD}{dt^*} = \left\langle \frac{\bar{\sigma}^*}{1-D} - \chi^*(D) \right\rangle^m \tag{6}$$

Formally, this equation is not so far to the specific creep Kachanov model, which expresses the rate of damage only according to the effective stress (Kachanov, 1958). Damage equilibrium solutions of Eq. (6) is investigated using Liapounov's stability theory. It is shown in [2] that the set of equilibrium solutions of this inelastic system is continuous. The smallest equilibrium solution (when it does exist) is stable for sufficiently small creep stress value. A bifurcation phenomenon appears for a critical stress ($\bar{\sigma}^* = 0.5$). Creep failure under high-sustained load (tertiary creep of figure 2) is explained as a bifurcation by loss of equilibrium (figure 1). m is equal to *1* for the simulations.

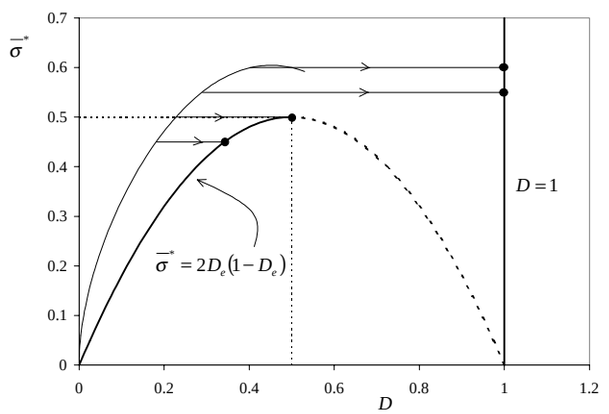


Fig. 1 – bifurcation diagram

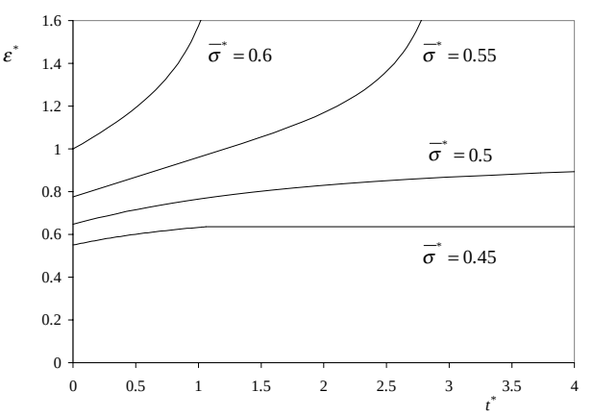


Fig. 2 – strain evolution for different creep stress

References

[1] Challamel N., Lanos C. and Casandjian C., Creep failure in concrete as a bifurcation phenomenon, *Int. J. Damage Mech.*, In Press, 2004.

[2] Challamel N. and Pijaudier-Cabot G., Stabilité et dynamique d'un oscillateur endommageable, *Revue Française de Génie Civil*, In Press, 2004.

MODELING OF THE DAMAGE EVOLUTION AT THE GRANULAR SCALE IN POLYCRYSTALS UNDER COMPLEX CYCLIC LOADINGS

A. ABDUL-LATIF, M. CHADLI
L3M, IUT de Tremblay, 93290 Tremblay-en-France, France

Summary A multi-scale model of damaged elasto-inelastic behavior is proposed to predict the plastic fatigue life for FCC metallic polycrystals under multiaxial loading paths. This model is expressed in the time dependent plasticity for a small strain theory. It is assumed that the damage variables initiate and then evolve at the grain level where the phenomenon of the localized plastic deformation occurs. The totally damaged polycrystal is defined by a probabilistic approach.

INTRODUCTION

A multi-scale model of the early fatigue damage initiation already proposed has been tested under different loading situations [1-3]. Based on the isotropic damage concept, this model assumed that the intragranular damage evolves when the accumulated slip reaches a given critical value (threshold). Its evolution is only governed by the inelastic energy at the slip system level. The multi-scale model has correctly predicted the fatigue life under different complex cyclic loadings. However, this developed approach has demonstrated some restrictions because it can only describe those materials like the Waspaloy [3] in which the damage initiation takes always place at the slip system level. It is obvious that the adopted assumptions make this approach quite limited in its application for a number of metals. Hence, to generalize such an approach and then increase its applicability, it is assumed now that the damage is modeled at the granular level using the rational framework of continuum damage mechanics. This allows to describe several types of defects in the granular level like the cavity and in levels lower than the granular (e.g., dislocations, lattice defects, etc.). A new damage criterion is also developed to faithfully describe the experimental results, notably those related to the effect of the loading path on the fatigue life. Furthermore, from the physical viewpoint, it is not possible to damage all the grains in the polycrystal to determine the fatigue life; the Weibull's law is thus used by which the overall fatigue life becomes function of the calculated probability.

THE MULTI-SCALE MODEL

It is assumed that the damage variables (d^g) initiate and then evolve at the well-plastified grains in the polycrystal. The associated generalized thermodynamic force (Y^g) is determined as a total granular energy being decomposed into elastic and inelastic part. The damage variable is coupled with elasto-inelastic constitutive equations of the multi-scale elasto-inelastic model used in [3]. It is well known that micro-crack initiation takes place at the end of stage I of fatigue. Then, the micro-cracks propagation can be observed during the stage II up to the final fracture of the fatigued specimen. An attempt is made here to model micro-crack initiation especially at the end of stage I of the fatigue. Despite the heterogeneous local damaged behavior on the granular level, the isotropic damaged behavior concept is adopted neglecting the anisotropy due to damage effect. The model is expressed in the self-consistent framework of time dependent plasticity for a small deformation theory. Based on slip theory, a granular damage scalar variable (d^g, Y^g) is introduced at the granular level for FCC crystalline structure. Its rate is supposed to be mainly characterized in term of energy and is defined by:

$$\dot{d}_g = \frac{\left(\overline{Y}^g\right)^{s_0^g}}{S_g} \frac{H\left(p_g - p_g^{th}\right)}{(1-d_g)^{m_g}} \sum_{s=1}^{N_{sys}} \dot{\lambda}_s \qquad (1) \qquad \text{with} \qquad p_g^{th} = \gamma_g^{th}\left(1 - \frac{N_{sp}}{N_{st}}\right)^n \qquad (2)$$

where p^g is the granular accumulated plastic strain, S^g, S_0^g and m_g are material constants characterizing the damage mechanism at the granular level. H is the classical Heaviside function. It is important to note that a recent work [4] shows that the fatigue damage initiation criterion ($p_g^{th} = \gamma_g^{th}$) gives some fatigue lives fairly far from the experimental observations notably under complex loadings. Therefore, a new damage criterion should be not only function of the granular accumulated strain, but also of the nature of the loading situation. Such a new criterion under which the fatigue damage cannot be nucleated is given in (2). γ_g^{th} represents a threshold of the granular accumulated plastic strain, N_{sp}: the number of the activated plastic slip, N_{st}: the total number of slip system in the polycrystal. In order to model the totally damaged polycrystal, it is assumed that this phenomenon is governed by a probability law. The later follows the Weibull's law. Thus, it is supposed that a polycrystal can be damaged, if its damaged energy (ψ) attains a critical value (ψ_u). The totally damaged polycrystal condition takes place when the probability is almost equal to one.

$$p_f = 1 - \exp\left[-\frac{1}{V_0}\int_V \left(\frac{\psi - \psi_u}{\psi_0}\right)^n dV\right] \qquad (3)$$

where V_o is the polycrystal's volume. ψ_o and n are material parameters.

APPLICATION OF THE MODEL

The main goal of this paragraph is to qualitatively describe the overall damaged-inelastic behavior of polycrystals in multiaxial low-cycle fatigue. All the numerical simulations are conducted by employing a polycrystal of 400 grains. Different cyclic loading paths are used in this investigation, namely: uniaxial tension-compression (TC) and biaxial tension-torsion with various out-of-phase angles: ϕ=0° (TT0), ϕ=30° (TT30), ϕ=45° (TT45), ϕ=60° (TT60) and ϕ=90° (TT90) and butterfly test. These tests are carried out under strain-controlled condition with the maximum von-Mises equivalent strain. The influence of the loading paths on the fatigue lives is obviously pointed out in Table 1. In fact, the obtained results show (Table 1 and figure 1) that the fatigue life decreases remarkably with increasing ϕ. Also, it reveals, in general, that d^g (for $d^g \geq 0.6$) decreases with the increasing of the applied loading complexity.

Type of loading	Nomber of plastifed systems/grain	Number of grains with dg=0.1	Number of grains with dg=0.3	Number of grains with dg=0.6	Number of grains with dg=0.95	Fatigue lives N_f (number of cycles)
TC	**2.14**	234	122	68	44	**802**
TT00	2.16	189	82	34	2	773
TT30	2.20	236	110	59	23	744
TT45	2.37	259	134	66	33	598
TT60	2.82	192	131	63	28	486
TT90	3.02	149	105	47	21	412
Butterfly	**4.16**	121	77	34	17	**215**

Table 1: Influence of the loading path on the fatigue lives

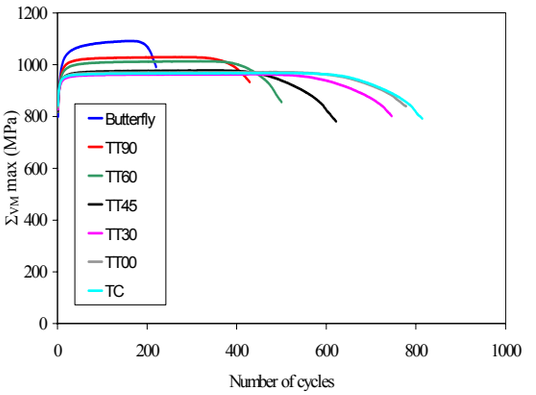


Figure 1: Predicted evolution of the overall maximum stress up to the final fracture of the polycrystal under different loading paths

As a typical example, figure 2 displays the maximum overall stress evolution during TT90 up to final damaging of the polycrystal when the probability (P_f) is near 1.

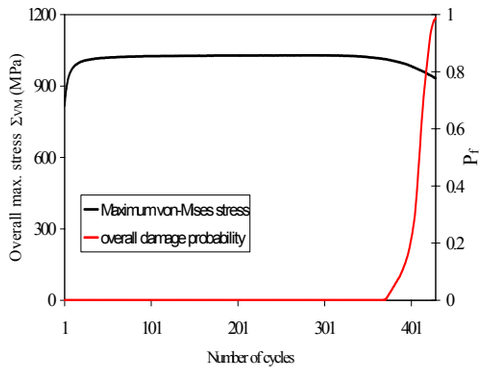


Figure 2: Predicted evolution of the maximum overall von-Mises stress and probability in TT90 up to final damaging of the polycrystal.

CONCLUSIONS

The proposed model reproduces successfully the inelastic fatigue behavior of polycrystals. It can naturally describe the overall cyclic stress-strain evolution using a local damaged constitutive equation. It gives a fairly well agreement with the experimental observations particularly for non-proportionality effect of the loading paths on the plastic fatigue life.

References

[1] Saanouni, K., and Abdul-Latif, A.: Micromechanical Modeling of Low Cyclic Fatigue under Complex Loadings-Part I. Applications. *Int. J. Plasticity* ***12***: 1111-1121, 1996.

[2] Abdul-Latif, A. and Saanouni, K.: Micromechanical Modeling of Low Cyclic Fatigue under Complex Loadings-Part II. Applications. *Int. J. Plasticity* ***12***: 1123-1149, 1996.

[3] Abdul-Latif, A., Ferney, V., and Saanouni, K.: Fatigue Damage of Waspaloy under Complex Loading. *J. Eng. Mat. Tech.* ***121***: 278-285, 1999.

[4] Chadli, M., and Abdul-Latif, A.: Heterogeneous Nature of the Meso-Damage in Polycrystals in Plastic Fatigue: 6th Mesomechanics 2004, May 31 – June 4, University of Patras, (Greece), 2004.

XXI ICTAM, 15–21 August 2004, Warsaw, Poland

CONTINUUM THERMODYNAMIC AND VARIATIONAL MODELING AND SIMULATION OF DUCTILE FAILURE AT LARGE DEFORMATION WITH APPLICATION TO ENGINEERING STRUCTURES

Bob Svendsen*, Frederik Reusch*, Dietmar Klingbeil**
*Chair of Mechanics, University of Dortmund, D–44227 Dortmund, Germany
**Laboratory V.3, Federal Institute for Materials Research and Testing, D-12220 Berlin, Germany

Summary
The purpose of this work is the extension of local Gurson-based ductile damage and failure modeling in engineering materials and structures to account for the non-local nature of void coalescence. In particular, the extension pursued here is based on the introduction of an non-local effective damage parameter ν analogous to that f^* of Needleman and Tvergaard which is modeled thermodynamically as a scalar-valued continuum microstructural field or generalized phase field via a recent thermodynamic approach. In the simplest case, the resulting field relation for ν is formally analogous to the inhomogeneous temperature equation. As such, analogous to temperature, ν represents an additional continuum degree-of-freedom here. And in the complete model, damage and deformation are coupled. Further, the field relation for ν contains a characteristic length determining the effective dimension of the process zone for void coelescence.

INTRODUCTION

The modeling of fracture in ductile metals due to damage is often based on the micromechanical model of [1] for the growth of a single void in an ideal elastoplastic matrix. In order to account for the effects of void nucleation and coalescence, and so obtain better agreement between the model, experimental results and numerical simulations for ductile failure and crack propagation, the original Gurson model, and in particular the Gurson yield function, was modified and extended into a semi-phenomenological form by [2], [3], and [4]. In the ensuing years, this modified approach has been extended yet further in a hypoelastic-based incremental fashion (*e.g.*, [5]) to account for isotropic and kinematic hardening, as well as for large inelastic deformation. In addition, a hyperelastic-based approach ([6], [7]) to such modeling has been used successfully to model ductile crack propagation in fracture mechanics specimens subject to more complex, and in particular to cyclic, loading histories. More recently, Gurson-based modeling has been extended to non-local form (*e.g.*, [8], [9]) in order to deal with mesh-dependence, and to model void coalescence as a non-local process ([10], [11]). In particular, the latter approach results in a delocalization of the model damage process and a minimization of mesh-dependence, such that ductile failure takes place in a region rather than at a point. In comparison to the local modeling, the proposed non-local extension involves a single additional material parameter, *i.e.*, that involving the characteristic lengthscale. The current extension reduces in fact to the existing local Gurson-based modeling as this lengthscale is reduced to zero.

EXTENDED GURSON-BASED DUCTILE DAMAGE MODELING

The non-local model formulation from [10] and [11] is based on the introduction of an effective continuum damage field ν (formally analogous to that f^* introduced by [3]) into the Gurson yield function. This damage parameter is itself modeled as a continuum microstructural field or generalized phase field via a recent thermodynamic approach ([12], [13]). The incorporation of this field into the existing Gurson-based framework is based on the assumption that the effect of ν on the yield behaviour due to ductile damage is the same as that of f^* on this behaviour in the local Gurson-based modeling of [3]. On this basis, ν is incorporated into the current model via the form

$$\phi = \frac{\sigma_{\rm V}^2(\boldsymbol{T})}{\sigma_{\rm M}^2} - 1 + 2\,q_1\,\nu\,\cosh\left(q_2\,\frac{\boldsymbol{I}\cdot\boldsymbol{T}}{2\,\sigma_{\rm M}}\right) - q_1^2\nu^2 \tag{1}$$

for the yield function ϕ formally analogous to the Gurson form. Here, $\sigma_{\rm V}(\boldsymbol{T})$ represent the von Mises stress as based on the Cauchy stress $\boldsymbol{T}$, $\sigma_{\rm M}$ the yield stress of the matrix material. Futher, q_1 and q_2 are constants. Again, note that this extension bears a formal resemblance to that formulated by [3] and embodied in their effective damage parameter f^*, which they introduced in order to account for the effect of void coalescence on the yield behaviour. Representing a quantity which characterises in an effective fashion the transition from the undamaged to the damage state, the field ν is modeled here as a continuum microstructural field or generalized phase field via a recent thermodynamic approach ([12], [13]) to the modeling of such structure. Specializing this general approach to the case of quasi-static conditions and a single scalar-valued microstructural field representing phenomenological damage, one derives in particular the basic evolution relation

$$\mathrm{div}(d_{,\nabla\dot\nu}) - \psi_{,\nu} - d_{,\dot\nu} = 0 \tag{2}$$

for the continuum damage field ν in terms of the forms

$$\begin{aligned} \psi &= \psi(\ln\boldsymbol{V}_{\rm E},\nu)\,, \\ d &= \alpha_{\rm D}\,(\dot\nu - \dot f^{*})^2 + \tfrac{1}{2}\,\alpha_{\rm D}\,\ell_{\rm D}^2\,\nabla\dot\nu\cdot\nabla\dot\nu\,, \end{aligned} \tag{3}$$

for the free energy density ψ and dissipation potential d, respectively. Here, $\ln \boldsymbol{V}_{\mathrm{E}}$ represents the elastic logarithmic left stretch tensor determining the Cauchy stress $\boldsymbol{T}$ via

$$\boldsymbol{T} = \det(\boldsymbol{F})^{-1} \psi_{,\ln \boldsymbol{V}_{\mathrm{E}}} \quad . \tag{4}$$

In addition, α_{D} represents a characteristic energy scale, ℓ_{D} a characteristic lengthscale, and τ_{D} a characteristic timescale, for the non-local damage process. Among other things, the con stitutive form for d is based on the idea that the nucleation, growth and coalescence of voids in the guise of $\dot{f}^*$ represents the source of continuum damage here.
Using the discretization of the weak field relations, the algor ithmic form of the model relations were implemented in the finite element programm ABAQUS/Standard using the user-inter face UEL. In addition, the local version of the model was implemented into ABAQUS/Standard using the user-interface UM AT.

MODELING AND SIMULATION OF DUCTILE CRACK PROPAGATION IN A C(T) SPECIMEN

In this section, the behaviour of the above gradient-type ex tension of Gurson-based ductile damage modeling is compared with the corresponding local modeling in the context of the si mulation of large mode 1 ductile crack growth in a C(T) specimen (Figure 1). Using material parameter values typica l for the ductile steel 10MnMoNi5-5 at room temperature, such crack growth was modeled using the local and non-local fo rmulations.

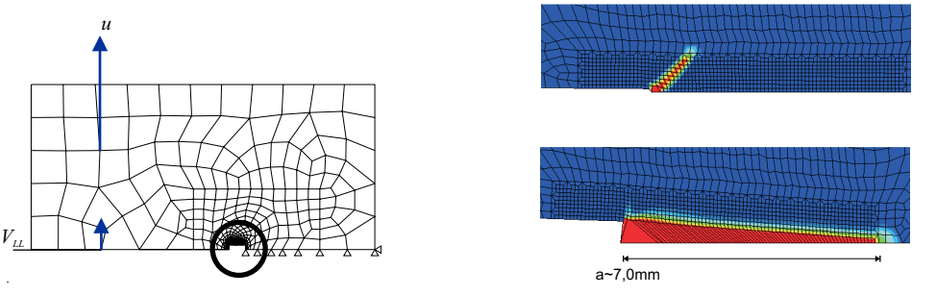


Figure 1. Simulation of mode 1 ductile crack propagation in a C(T) spec imen (left) using the local (upper right) and non-local (lower right) models.

Figure 1 (left) displays the finite element discretization o f the upper half the of the compact tension specimen. In parti cular, in the fracture zone, a regular element distribution with an e lement side length of 0.05 mm was used. Simulation results based on the local model (upper right) and non-local model ex tension (lower right) for the region around the crack tip (circled) are shown. As shown by the ellipticity and stability a nalyses of the local model, loss of ellipticity of the local model results in a bifurcation at crack initiation and an unr ealistic crack-path prediction that is extremely mesh-dep endent. On the other hand, the use of the non-local damage model predic ts stable mode 1 crack growth as observed in experiment.

References

[1] A. L. Gurson, *Continuum theory of ductile rupture by void nucleation and g rowth: Part I-yield criteria and flow rules for porous ductil e media*, J. Engng. Mat. Tech., 99, (1977), 2–15.
[2] C. C. Chu, A. Needleman, *Void nucleation effects in biaxially stretched sheets* , J. Engrg. Mat. Tech., 102, (1980), 249–256.
[3] A. Needleman, V. Tvergaard, *An analysis of ductile rupture in notched bars* , J. Mech. Phys. Solids, 32, (1984), 461–490.
[4] J. Koplic, A. Needleman, *Void growth and coalescence in porous plastic solids* , Int. J. Sol. Struct., 24, (1988), 835–853.
[5] R. Lammering, B. Percherski, E. Stein, *Theoretical and computational aspects of large plastic def ormations involving strain-induced anisotropy and developing voids*, Arch. Mech., 42, (1990). 347–375.
[6] S. Arndt, D. Klingbeil, B. Svendsen, *On the simulation of warm pre-stressing and ductile crack ext ension by constitutive modelling* , Proceedings of the 14th International Conference on Structural Mechani cs in Reactor Technology, V. 4, (1997), pp. 689–696.
[7] S. Arndt, *Modellierung der Warmvorbelastung mit einem Schädigungsm odell für kombinierte Verfestigung am Beispiel des Werksto ffes 10MnMoNi5-5*, Dissertation, Otto-von-Guericke Universität Magdeburg (20 00).
[8] V. Tvergaard, A. Needleman, *Effects of non-local damage in porous plastic solids* , Int. J. Sol. Struct., 32, (1995), 1063–1077.
[9] M. Feucht, *Ein gradientenabhängiges Gursonmodell zur Beschreibung d uktiler Schädigung mit Entfestigung* , Dissertation, Institut für Mechanik, Technische Universität Darmstadt (1998).
[10] F. Reusch, B. Svendsen, D. Klingbeil, *A non-local extension of Gurson-based ductile damage model ing*, Computational Material Science, 26, (2003a), 219–229.
[11] F. Reusch, B. Svendsen, D. Klingbeil, *Local and non-local Gur-son-based ductile damage and failu re modeling at large deformation* , European Journal of Mechanics A/Solids, 22, (2003b), 779-792.
[12] B. Svendsen, *On the thermodynamics of thermoelastic materials with addit ional scalar degrees of freedom* , Cont. Mech. Thermodyn., 4, (1999), 247–262.
[13] B. Svendsen, *Formulation of balance relations and configurational fields for materials with microstructure via invariance* , Int. J. Sol. Struct., 38, (2001a), 1183–1200.

MATERIAL MODELS FOR HOOKEAN MATERIALS WITH VOIDS OR CRACKS

Kari Santaoja, Anniina Kuistiala
Helsinki University of Technology, P.O.Box 4100, FIN-02015 HUT, Finland

Summary: Stress-strain relations for Hookean materials with spherical voids or penny-shaped microcracks are derived. The constitutive relation for voided material is based on the analytical expression by Eshelby whereas the theoretical work by Kachanov provided the foundation for the material model of microcracked material. The postulate of strain equivalence was shown to be incompatible with the analytical expression by Eshelby.

Damage description by the postulate of strain equivalence - the effective stress $\tilde{\boldsymbol{\sigma}}$ concept

By following the postulate of strain equivalence by Chaboche (1978, p. 19) the effective stress tensor $\tilde{\boldsymbol{\sigma}}$ and the constitutive tensor for the damaged material $\tilde{\mathbf{C}}$ can be obtained from

$$\tilde{\boldsymbol{\sigma}} := \mathbf{C}:\boldsymbol{\varepsilon}^{\mathrm{e}} \quad \text{and} \quad \boldsymbol{\sigma} := \tilde{\mathbf{C}}:\boldsymbol{\varepsilon}^{\mathrm{e}} \quad \text{which give} \quad \tilde{\boldsymbol{\sigma}} := \mathbf{C}:\tilde{\mathbf{S}}:\boldsymbol{\sigma}\,. \tag{1}$$

Equation $(1)_3$ utilises the definition of the compliance tensor for the damaged material $\tilde{\mathbf{S}}$. The definition is $\tilde{\mathbf{S}}:\tilde{\mathbf{C}} := \mathbf{I}$. The compliance tensor $\tilde{\mathbf{S}}$ is assumed to be separable as follows:

$$\tilde{\mathbf{S}} = \mathbf{S} + \mathbf{S}^{\mathrm{d}}, \tag{2}$$

where the superscript "d" refers to damage. Substitution of the Separation (2) into Equation $(1)_3$ yields

$$\tilde{\boldsymbol{\sigma}} = \mathbf{C}:\tilde{\mathbf{S}}:\boldsymbol{\sigma} = \mathbf{C}:[\mathbf{S} + \mathbf{S}^{\mathrm{d}}]:\boldsymbol{\sigma} = [\mathbf{I} + \mathbf{C}:\mathbf{S}^{\mathrm{d}}]:\boldsymbol{\sigma}\,. \tag{3}$$

The concept of the effective stress $\tilde{\sigma}$ by Rabotnov (1968, p. 344) can be extended for three-dimensional form as follows:

$$\tilde{\boldsymbol{\sigma}} = \frac{\boldsymbol{\sigma}}{1 - D}\,. \tag{4}$$

In order that Expressions $(1)_3$ and (4) would equal, the following should hold:

$$\mathbf{C}:\tilde{\mathbf{S}} = \mathbf{I}(1 - D)^{-1} \quad \text{which yields} \quad \tilde{\mathbf{S}} = (1 - D)^{-1}\mathbf{S}\,. \tag{5}$$

Separation (2) allows Equation $(5)_2$ to be written in the form

$$\mathbf{S} + \mathbf{S}^{\mathrm{d}} = (1 - D)^{-1}\mathbf{S}, \quad \text{which yields} \quad \mathbf{S}^{\mathrm{d}} = \frac{D}{1 - D}\,\mathbf{S}\,. \tag{6}$$

Porous material with linear elastic matrix

Eshelby (1957) studied the elastic field in a Hookean material containing an ellipsoidal inclusion. As a special case he determined the value for the complementary strain-energy density w^{c} of a material containing "a volume fraction f" of inhomogeneous spheres. For the purpose of this work the inhomogeneous spheres are "replaced" by spherical cavities. This is done by assuming that the values for the elastic constants for the cavities vanish. The complementary strain-energy density $w^{\mathrm{c}}(\boldsymbol{\sigma},f)$ takes the form (Eshelby, 1957, p. 390)

$$w^{\mathrm{c}}(\boldsymbol{\sigma},f) = \frac{1}{2}\left[\frac{1}{3(3\lambda + 2\mu)}(1 + Af)[\mathbf{1}:\boldsymbol{\sigma}]^2 + \frac{1}{2\mu}(1 + Bf)\,\mathbf{s}:\mathbf{s}\right], \tag{7}$$

where λ and μ are the Lamé elastic constants of the matrix material. The values for the parameters A and B for spherical cavities and the deviatoric stress $\mathbf{s}$ and are obtained from

$$A = \frac{6\mu + 3\lambda}{4\mu} \quad \text{and} \quad B = \frac{15(1 - \nu)}{7 - 5\nu} \quad \text{and} \quad \mathbf{s} := \mathbf{K}:\boldsymbol{\sigma} \quad \text{where} \quad \mathbf{K} := \mathbf{I} - \tfrac{1}{3}\mathbf{1}\,\mathbf{1}\,. \tag{8}$$

The notations $\mathbf{1}$ and $\mathbf{I}$ refer to the second-order and to the fourth-order identity tensor. Based on Expression (7) the elastic strain tensor $\boldsymbol{\varepsilon}^{\mathrm{e}}$ takes the following form:

$$\boldsymbol{\varepsilon}^{\mathrm{e}} = \frac{\partial w^{\mathrm{c}}(\boldsymbol{\sigma},f)}{\partial \boldsymbol{\varepsilon}^{\mathrm{e}}} = \frac{1}{3(3\lambda + 2\mu)}(1 + Af)\,\mathbf{1}\,\mathbf{1}:\boldsymbol{\sigma} + \frac{1}{2\mu}(1 + Bf)\,\mathbf{K}:\boldsymbol{\sigma}\,. \tag{9}$$

Expression (9) can be written in the form

$$\boldsymbol{\varepsilon}^{\mathrm{e}} = \left[\mathbf{S} + \mathbf{S}^{\mathrm{v}}(f)\right]:\boldsymbol{\sigma}, \tag{10}$$

where the compliance tensor for Hookean material $\mathbf{S}$ and the compliance tensor voids $\mathbf{S}^{\mathrm{v}}(f)$ are defined by

$$\mathbf{S} := \frac{1}{3(3\lambda + 2\mu)}\,\mathbf{1}\,\mathbf{1} + \frac{1}{2\mu}\,\mathbf{K} \quad \text{and} \quad \mathbf{S}^{\mathrm{v}}(f) := \frac{Af}{3(3\lambda + 2\mu)}\,\mathbf{1}\,\mathbf{1} + \frac{Bf}{2\mu}\,\mathbf{K}\,. \tag{11}$$

Equation $(6)_2$ shows that according to the postulate of strain equivalence the compliance tensors $\mathbf{S}$ and $\mathbf{S}^{\mathrm{d}}$ have a linear

relationship. Comparison of Definitions (11) hows that material parameters A and B have to equal in order the tensor $\mathbf{S}^{\mathrm{v}}(f)$ would be possible to express as a function of the tensor $\mathbf{S}$. If the Poisson's ratio took the value of $\nu = 0.2$. Therefore, for steels, for example, the postulate of strain equivalence does not give compatible results with the analytical expression.

Hookean material with micricracks

According to Kachanov (1980, p. 1045) the complementary strain-energy density w^{c} of a Hookean solid with non-interactive cracks is given by

$$w^{\mathrm{c}}(\boldsymbol{\sigma},\ldots) = \frac{1}{2}\left[\frac{1}{3\,(3\,\lambda + 2\,\mu)}\,[\mathbf{1}:\boldsymbol{\sigma}]^2 + \frac{1}{2\,\mu}\,\mathbf{s}:\mathbf{s}\right] + \frac{1}{\mathrm{V}^{\mathrm{b}}}\sum_{p=1}^{k}\frac{1}{2}\int_{A^p}(\vec{n}^{\,p}\cdot\boldsymbol{\sigma})\cdot\vec{b}^{\,p}\;\mathrm{d}A^p\,, \tag{12}$$

where V^{b} is the volume of the body in the initial crack free configuration and k is the number of cracks within the volume V^{b} (Vakulenko and Kachanov, 1971, p. 160 and 161). In Equation (12) the area of the p'th crack is denoted by A^p and the unit normal vector to the surface A^p is denoted by $\vec{n}^{\,p}$. The vector $\vec{b}^{\,p}$ describing the jump between the material points across the crack is, according to Kachanov [1980, Eq. (20a)], for penny-shaped cracks

$$\vec{b}^{\,\mathrm{pK}} = B_1\sqrt{(a^p)^2 - r^2}\left\{\boldsymbol{\sigma}\cdot\vec{n}^{\,p} - \frac{\nu}{2}\,\vec{n}^{\,p}\,(\vec{n}^{\,p}\cdot\boldsymbol{\sigma}\cdot\vec{n}^{\,p})\right\}, \qquad \text{where} \qquad B_1 = \frac{16\,(1-\nu^2)}{\pi\,E\,(2-\nu)}\,. \tag{13}$$

In Expression (13) a^p is the radius of the p'th microcrack, r is the radial coordinate of the microcrack. The superscript "K" in $\vec{b}^{\,\mathrm{pK}}$ refers to Kachanov. In Equation (13) a misprint is corrected i.e. the first term between the braces $\vec{n}^{\,p}\cdot\boldsymbol{\sigma}$ by Kachanov is replaced here by the term $\boldsymbol{\sigma}\cdot\vec{n}^{\,p}$. In this work Kachanov's Equation (13) [already corrected] is replaced by

$$\vec{b}^{\,p} = B_1\sqrt{(a^p)^2 - r^2}\left\{\boldsymbol{\sigma}\cdot\vec{n}^{\,p} - [1-H]\,\vec{n}^{\,p}\,(\vec{n}^{\,p}\cdot\boldsymbol{\sigma}\cdot\vec{n}^{\,p}) - \frac{\nu}{2}\,H\,\vec{n}^{\,p}\,(\vec{n}^{\,p}\cdot\boldsymbol{\sigma}\cdot\vec{n}^{\,p})\right\}, \quad \text{where} \quad H = H(\vec{n}^{\,p}\cdot\boldsymbol{\sigma}\cdot\vec{n}^{\,p})\,. \tag{14}$$

The Heaviside function $H(\boldsymbol{\sigma},\vec{n}^{\,p})$ guarantees that under compression the microcrack surfaces do not penetrate each other. Due to simplicity a uniaxial microcrack field is studied. The normals of the microcracks are assumed to be parallel to the x_1-axis. The stress-strain relation has the same form as for porous material, viz.

$$\boldsymbol{\varepsilon}^{\mathrm{e}} = \left[\mathbf{S} + \mathbf{S}^{\mathrm{c}}\right]:\boldsymbol{\sigma}\,. \tag{15}$$

If the number of parallel microcracks is denoted by ρ_{ij}, the non-zero components of the compliance tensor $\mathbf{S}^{\mathrm{c}}$ are

$$S^{\mathrm{c}}_{1111} = 4\,B\left(1 - \frac{\nu}{2}\right)\sum_{q=1}^{\rho_{ij}} A_q^{3/2}\,H(\sigma_{11})\,, \qquad \text{where} \qquad B = \frac{8\,(1-\nu^2)}{3\,\pi\sqrt{\pi}\;(2-\nu)\,E} \tag{16}$$

and

$$S^{\mathrm{c}}_{1212} = S^{\mathrm{c}}_{1221} = S^{\mathrm{c}}_{2112} = S^{\mathrm{c}}_{2121} = S^{\mathrm{c}}_{1313} = S^{\mathrm{c}}_{1331} = S^{\mathrm{c}}_{3113} = S^{\mathrm{c}}_{3131} = B\sum_{q=1}^{\rho_{ij}} A_q^{3/2}\,. \tag{17}$$

Discussion and conclusions

The above given stress-strain relations for Hookean material with spherical voids or penny-shaped microcracks play important role in damage mechanics, since they are based on analytical expressions. It is noteworthy that the results of the postulate of strain energy are in contradiction with the analytical stress-strain relation by Eshelby (1957). A keen reader on this topic may study the papers Santaoja (1989) and (2002).

References

Chaboche, J.-L. (1978). Description thermodynamique et phénoménologique de la viscoplasticité cyclique avec endommagement (Publication No. 1978-3). 92320 Chatillon, France: Office National d´Etudes et de Recherches Aérospatiales.

Eshelby, J. D. 1957. The determination of the elastic field of an ellipsoidal inclusion, and related problems. Proceedings of the Royal Society of London, A241, pp. 376-396.

Kachanov, M. 1980. Continuum model of medium with cracks. Journal of the Engineering Mechanics Division, vol. 106, no. EMS5, pp. 1039-1051.

Santaoja, K. 1989. Continuum damage mechanics approach to describe multidirectional microcracking of ice. In: N. K. Sinha, D. S. Sodhi & J. S. Chung (Eds.), Proceedings of the Eight International Conference on Offshore Mechanics and Arctic Engineering. The Hague, The Netherlands, March 19-23, 1989: The American Society of Mechanical Engineers. Vol. IV, pp. 55 - 65.

Santaoja, K. 2002. Evaluation of the Gurson-Tvergaard material model by using thermomechanics and damage mechanics. Proceedings of the Estonian Academy of Sciences; Engineering. Volume 8, No 4. Pp. 248-269.

Vakulenko, A. A. & Kachanov, M. L. 1971. Continuum model of medium with cracks. Mehanika Tverdogo Tela, no. 4, pp. 159-166. (In Russian)

Localized Necking Criterion Based on Acoustic Tensor for Materials with Anisotropic Damage

C.L.Chow and M.Jie
Department of Mechanical Engineering, University of Michigan – Dearborn, Dearborn, MI 48128, USA

Extended Summary

Criterion for localized necking in strain-softening materials is studied. The material is supposed to have anisotropic damage and anisotropic plasticity. The critical condition of damage evolution is of primary interest in this study. For localized necking as a consequence of plastic instability, the singularity of acoustic tensor is taken as the critical condition for localized necking in strain-softening materials.

A damage-coupled general criterion for localized necking based on acoustic tensor is proposed as

$$\det(\mathbf{n}\cdot\overline{\mathbf{C}}^{ep}\cdot\mathbf{n})=0 \tag{1}$$

where $\overline{\mathbf{C}}^{ep}$ is effective tangent modulus tensor and **n** the unit normal vector of localized band.

$$\dot{\boldsymbol{\sigma}} = \overline{\mathbf{C}}^{ep} : \dot{\boldsymbol{\varepsilon}} \tag{2}$$

Based on anisotropic damage theory, we have

$$\overline{\mathbf{C}}^{ep} = \mathbf{M}^{-1} : \mathbf{A}^{-1} : \mathbf{C}^{ep} : \mathbf{M}^{T,-1} \tag{3}$$

where **M** is damage effective tensor and $\mathbf{C}^{ep}$ the tangent modulus tensor.

$$\mathbf{M}(\mathbf{D})=\begin{bmatrix} \frac{1}{1-D_1} & 0 & 0 & 0 & 0 & 0 \\ 0 & \frac{1}{1-D_2} & 0 & 0 & 0 & 0 \\ 0 & 0 & \frac{1}{1-D_3} & 0 & 0 & 0 \\ 0 & 0 & 0 & \frac{1}{\sqrt{(1-D_2)(1-D_3)}} & 0 & 0 \\ 0 & 0 & 0 & 0 & \frac{1}{\sqrt{(1-D_3)(1-D_1)}} & 0 \\ 0 & 0 & 0 & 0 & 0 & \frac{1}{\sqrt{(1-D_1)(1-D_2)}} \end{bmatrix} \tag{4}$$

$$\mathbf{C}^{ep} = \mathbf{C}^{e} - \beta(\mathbf{C}^{e} : \frac{\partial F_p}{\partial \overline{\boldsymbol{\sigma}}}) : (\frac{\partial F_p}{\partial \overline{\boldsymbol{\sigma}}^T} : \mathbf{C}^{e}) \tag{5}$$

and

$$\mathbf{A} = \mathbf{I} + \alpha\{\frac{\partial \mathbf{M}}{\partial \mathbf{D}^T} : \frac{\partial F_d}{\partial(-\mathbf{Y})} : \mathbf{M}^{-1} + [\mathbf{C}^{ep} : \mathbf{M}^{-1} : (\frac{\partial \mathbf{M}}{\partial \mathbf{D}^T} : \frac{\partial F_d}{\partial(-\mathbf{Y})})^T] : \mathbf{C}^{e^{-1}}\} : \boldsymbol{\sigma}\frac{\partial F_d}{\partial \boldsymbol{\sigma}^T} \tag{6}$$

In eqns (5) and (6), F_p is plastic yield surface and F_d the damage surface.

$$F_p(\overline{\boldsymbol{\sigma}}, p) = \overline{\boldsymbol{\sigma}}_{eq} - [T_0 + T(p)] = 0 \tag{7}$$

and

$$F_d = Y_{eq} - [C_0 + C(Z)] = 0 \tag{8}$$

The damage evolution equations are

$$\dot{\mathbf{D}} = \dot{Z}\frac{\partial F_d}{\partial(-\mathbf{Y})} \tag{9}$$

and

$$\dot{Z} = \alpha\frac{\partial F_d}{\partial \boldsymbol{\sigma}^T} : \dot{\boldsymbol{\sigma}} \tag{10}$$

By deploying eqn (1), critical condition of localized necking for both negative and positive strain ratio can be obtained. For negative strain ratio, the localized necking criterion is

$$(\overline{C}_{12}^{ep}\overline{C}_{21}^{ep} + \overline{C}_{66}^{ep}\overline{C}_{21}^{ep} + \overline{C}_{66}^{ep}\overline{C}_{12}^{ep} - \overline{C}_{11}^{ep}\overline{C}_{22}^{ep}) - 2\overline{C}_{66}^{ep}\sqrt{\overline{C}_{11}^{ep}\overline{C}_{22}^{ep}} = 0 \tag{11}$$

while the inclination angle of localization band is

$$tg\theta = \pm(\frac{\overline{C}_{11}^{ep}}{\overline{C}_{22}^{ep}})^{\frac{1}{4}} \tag{12}$$

For positive strain ratio, the localized necking criterion is

$$\overline{C}_{11}^{ep} = 0 \tag{13}$$

In eqn (3), let

$$\mathbf{\Phi}=\mathbf{C}^{ep}:\mathbf{M}^{T^{-1}}=\begin{bmatrix}\Phi_{11} & \Phi_{12} & 0\\ \Phi_{21} & \Phi_{22} & 0\\ 0 & 0 & \Phi_{66}\end{bmatrix} \tag{14}$$

and

$$\mathbf{\Psi} = \mathbf{A} : \mathbf{M} = \begin{bmatrix}\Psi_{11} & \Psi_{12} & 0\\ \Psi_{21} & \Psi_{22} & 0\\ 0 & 0 & \Psi_{66}\end{bmatrix} \tag{15}$$

Then

$$\overline{\mathbf{C}}^{ep} = \mathbf{\Psi}^{-1} : \mathbf{\Phi} \tag{16}$$

Substitute eqns (14)-(16) into eqn (11). The localized necking criterion for negative strain ratio is revised as

$$\Psi_{66}(\Phi_{11}\Phi_{22}-\Phi_{12}\Phi_{21})+[\Psi_{21}\Phi_{11}-\Psi_{22}\Phi_{12}-\Psi_{11}\Phi_{21}+\Psi_{12}\Phi_{22}+2\sqrt{(\Psi_{12}\Phi_{21}-\Psi_{22}\Phi_{11})(\Psi_{21}\Phi_{12}-\Psi_{11}\Phi_{22})}]\Phi_{66}=0 \tag{17}$$

The inclination angle of localized band is

$$tg\,\theta = \pm\left(\frac{\Psi_{11}\Phi_{22}-\Psi_{12}\Phi_{21}}{\Psi_{22}\Phi_{11}-\Psi_{21}\Phi_{12}}\right)^{\frac{1}{4}} \tag{18}$$

Substitute eqns (14)- (16) into eqn (13). The localized necking criterion for positive strain ratio is

$$\Psi_{22}\Phi_{11}-\Psi_{21}\Phi_{12}=0 \tag{19}$$

In uniaxial loading condition, $\sigma_2=\sigma_6=0$ and $D_2=\eta D_1$.

$$\Phi=\begin{bmatrix}\dfrac{(1-D_1)e_0[4T'(p)+h^2e_0]}{4T'(p)(1-\nu^2)+(4+h^2-4h\nu)e_0} & \dfrac{2(1-\eta D_1)e_0[2T'(p)\nu+he_0]}{4T'(p)(1-\nu^2)+(4+h^2-4h\nu)e_0} & 0\\ \dfrac{2(1-D_1)e_0[2T'(p)\nu+he_0]}{4T'(p)(1-\nu^2)+(4+h^2-4h\nu)e_0} & \dfrac{4(1-\eta D_1)e_0[T'(p)+e_0]}{4T'(p)(1-\nu^2)+(4+h^2-4h\nu)e_0} & 0\\ 0 & 0 & \dfrac{\sqrt{(1-D_1)(1-\eta D_1)}e_0}{2(1+\nu)}\end{bmatrix} \tag{20}$$

and

$$\Psi_{11}=\frac{1}{1-D_1}+\frac{4T^2\{2T'(p)[2-(1+\eta)\nu^2]+[2+h^2-h(2+\eta)\nu]e_0-\eta D_1[4T'(p)(1-\nu^2)+(2+h^2-3h\nu)e_0]\}}{(1-\eta D_1)(1-D_1)[4T'(p)(1-\nu^2)+(4+h^2-4h\nu)e_0][3T^2-2C'(Z)e_0(1-D_1)^2]} \tag{21}$$

$$\Psi_{12}=\frac{2T^2\nu(1-D_1)(2\eta D_1-1-\eta)\{2T'(p)[2-(1+\eta)\nu^2]+[2+h^2-h(2+\eta)\nu]e_0-\eta D_1[4T'(p)(1-\nu^2)+(2+h^2-3h\nu)e_0]\}}{(1-\eta D_1)^4[4T'(p)(-1+\nu^2)-(4+h^2-4h\nu)e_0][3T^2-2C'(Z)e_0(1-D_1)^2]}$$

$$\Psi_{21}=\frac{4T^2[2T'(p)(-1+\eta)\nu-(h-2\eta\nu)e_0+\eta(h-2\nu)D_1e_0]}{(1-\eta D_1)(1-D_1)[4T'(p)(1-\nu^2)+(4+h^2-4h\nu)e_0][3T^2-2C'(Z)e_0(1-D_1)^2]}$$

$$\Psi_{22}=\frac{1}{1-\eta D_1}-\frac{2(1-D_1)T^2\nu(1+\eta-2\eta D_1)[2T'(p)(1-\eta)\nu+(h-2\eta\nu)e_0-\eta(h-2\nu)D_1e_0]}{(1-\eta D_1)^4[4T'(p)(-1+\nu^2)-(4+h^2-4h\nu)e_0][3T^2-2C'(Z)e_0(1-D_1)^2]}$$

$$\Psi_{66}=\frac{1}{\sqrt{(1-D_1)(1-\eta D_1)}}$$

Substituting eqns (20) and (21) into eqn (17), we can get an equation about D_1, i.e.

$$f(D_1, T, T'(p), C'(z)) = 0 \tag{22}$$

By solving eqn (22), we can get the critical damage value D_{1c} in terms of T, $T'(p)$ and $C'(z)$ for negative strain ratio.

For eqiaxial tension, $\sigma_1=\sigma_2$ and $D_1=D_2$. Similar equation as eqn (22) can be obtained for the solution of critical damage value D_{1c} at the positive strain-ratio region.

So far, the anisotropic damage model is coupled with the localized necking criterion based on acoustic tensor. Closed-form expressions for localized necking criteria for both positive and negative strain ratio are presented. Both of the criteria and the inclination angle are in relations with current stress and strain states as well as damage variables, which indicates that critical damage value for localized necking is not a constant. The proposed criterion is applicable to non-proportional loading condition involving multistage stamping processes. The closed-form expression of localized necking criterion has application potential in the analysis of failure in strain-softening materials such as hot metals, rocks, soil, solder, etc.

XXI ICTAM, 15–21 August 2004, Warsaw, Poland

AN ELASTO-VISCOPLASTIC MODEL COUPLED TO DAMAGE AND GRAIN GROWTH TO TAKE ACCOUNT OF MATERIAL VARIABILITY

Benoit Vereecke*, René Billardon**
*DEN/SAC/DM2S/SEMT/LM2S, CEA Saclay, 91191 Gif sur Yvette Cedex, France
**LMT Cachan, ENS-Cachan, Paris VI, CNRS, 61, Avenue du Président Wilson 94235 Cachan Cedex, France

INRODUCTION

The final objective of this study is the prediction of the failure of nuclear structures at very high temperatures in accidental conditions taking account of the material variability. Other studies on mini structures [1] have compared the failure behaviour of French and German steels for pressure vessels.
The material used to build French reactor pressure vessels 16MND5 steel, shows at high temperature different damage mechanisms according to its origin : transgranular by growth and coalescence of cavities or intergranular. We can see on figure 1 that this phenomenon can lead to very different failure times during creep tests.

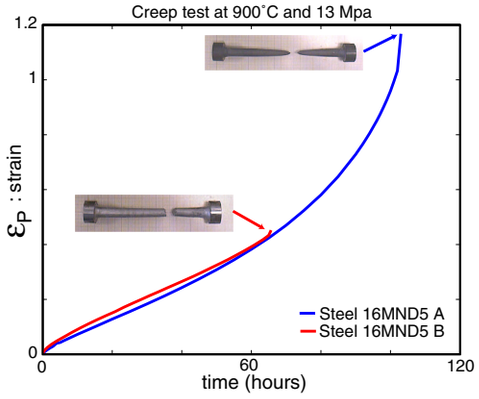


Figure 1. Failure time for 2 origins of 16MND5 steel with the same experimental conditions

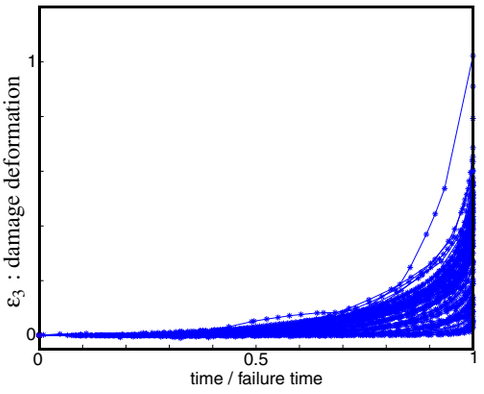


Figure 2. Random character of damage deformation

A statistical analysis of 61 creep tests [2], for 5 temperature levels (900 to 1300^{o}C) and 2 origins of 16MND5, showed that the damage threshold and damage evolution measured through the value of strain during tertiary creep (see figure 2), have a random character according to material origin and thermal history. The cause of these different damage evolutions has been seeked by metallurgical analyses. The metallurgical parameter that explains this random character has been identified and introduced in an elasto-viscoplastic constitutive law with isotropic hardening coupled to two damage evolution laws.

METALLURGICAL STUDY

Different heat treatments have been performed on 16MND5 of two different origins in order to reproduce the thermal history applied to creep specimens before the mechanical load is applied.



Figure 3. Austenitic grain of steel A after 10h at 1000^{o}C ($\simeq$ 100-150 μm in diameter)



Figure 4. Austenitic grain of steel A after 10h at 1000^{o}C ($\simeq$ 200-300 μm in diameter)

We have noticed that for long enough austenitisation the austenitic grain size is different from one steel to another.
For an austenitisation of 10 hours at 1000^{o}C (see figures 3 and 4), we observed after chemical attack that the austenitic grain size of steel A is about twice smaller than the austenitic grain size for steel B. We observed the same result for austenitisations of 0.5 hours and 5 hours at 1100^{o}C.
For austenitisation at lower temperatures or for shorter times, the austenitic grain is difficult to observe. However, for steel A, we have been able to observe the same austenitic grain size than M. Martinez [3].
To conclude, it appears that the austenitic grain size is the important metallurgical parameter to differentiate damage mechanisms in 16MND5 of different origins, intergranular damage becoming predominant for smaller austenitic grain sizes.

CONSTITUTIVE LAW

To describe these phenomena, we have chosen a macroscopic elasto-viscoplastic constitutive law with isotropic hardening coupled to two damage evolution laws [4] [5]. The limited complexity of such a macrocopic law is compatible with the cost of the numerical simulations of the ruin of industrial composants. However, we have taken account of the microstructural parameter viz. the austenitic grain size d_γ that controls the evolution of intergranular damage D_c. We supposed that the evolution of transgranular damage D_d is isotropic and not affected by this microstructural parameter. Conversely, we have considered that intergranular damage is anisotropic and dependent on austenitic grain size. Moreover, we have considered only one isotropic hardening R since we want to simulate only the failure for monotonic loadings. The partition of strain is as follows:

$$\varepsilon = \varepsilon^{elas} + \varepsilon^{vplas} + \varepsilon^{th} \tag{1}$$

where ε^{elas} stand for elastic strains, ε^{vplas} for viscoplastic strains and ε^{th} for strains due to thermal dilatation. We introduce both damages with damaged elasticity tensor as follows:

$$\varepsilon_{elas} = \tilde{E}^{-1}(D_c, D_d) : \sigma \quad \text{with} \quad \tilde{E}^{-1}(D_c, D_d) = \frac{1}{E(1-D_d)} \begin{bmatrix} \frac{1}{1-D_c} & -\nu & -\nu \\ -\nu & 1 & -\nu \\ -\nu & -\nu & 1 \end{bmatrix}_{\sigma_I, \sigma_{II}, \sigma_{III}} \tag{2}$$

where $\sigma_I \geq \sigma_{II} \geq \sigma_{III}$ stand for principal stresses, E for Young's modulus and ν for Poisson's ratio. The threshold of viscoplasticity is as follows:

$$f_{vp} = \tilde{\sigma}_{eq} - R - \sigma_Y(d_\gamma) - K\dot{p}^{\frac{1}{n}} \quad \text{with} \quad R = Q(d_\gamma)\left(1 - e^{-bp}\right) \tag{3}$$

where σ_Y, Q, b are material parameters that are dependent on temperature. The equivalent effective stress $\tilde{\sigma}_{eq}$ is obtained from the shear elastic energy. The law of normality and the generalized Norton's law are as follows:

$$\dot{\varepsilon}^{vplas} = \frac{3}{2}\dot{p}\frac{\partial\tilde{\sigma}_{eq}}{\partial\sigma} \quad \text{with} \quad \dot{p} = \left(\frac{\tilde{\sigma}_{eq} - R - \sigma_Y}{K}\right)^n \tag{4}$$

where K, n are temperature dependent parameters material. The evolution of transgranular damage is given by Lemaitre's ductile law [4] as follows:

$$\dot{D}_d = \left(\frac{Y}{S}\right)^s \dot{p} \tag{5}$$

where S, s are temperature dependent parameters material. The evolution of intergranular damage is defined by Kachanov's law as follows:

$$\dot{D}_c = \left(\frac{\sigma_I}{A(d_\gamma).(1-D_c)}\right)^r \tag{6}$$

where A, r are temperature dependent parameters material. These laws have been implemented in French finite element code CAST3M [6]. Experiments are under way to identify this law and the evolution of both damage mechanisms.

References

[1] H.-G. Willschütz and E. Altsadt and B.R. Sehgal and F.-P. Weiss: Simulation of creep tests with French or German RPV-steel and investigation of a RPV-support against failure. *Annals of NUCLEAR ENERGY* **1033**:1033–1063, 2003.
[2] B. Vereecke and R. Billardon: Analyse probabiliste du comportement en fluage du 16MND5. *Congrès Français de Mécanique Nice (France)* 2003.
[3] M. Martinez: Jonction 16MND5-Inconel-316LN par soudage diffusion, Elaboration et calcul des contraintes résiduelles de procédé. *Thèse de l'ENSMP 1999*
[4] J. Lemaitre and J.-L. Chaboche: Mechanics of solid materials. *Dunod 2nd edition* 2001.
[5] C. Petry: Caractérisation de l'endommagement du Narloy-Z en fluage *Rapport de stage de DEA S3M (Master degree), University Paris VI 2003*
[6] Cast3M: CEA finite element software, web site http://www-cast3m.cea.fr

DAMAGE AND FAILURE OF BRITTLE SOLIDS

Andrzej Litewka[*], Leszek Szojda[**]
[*]*Universidade da Beira Interior, Calçada Fonte do Lameiro, P 6200-358 Covilhã, Portugal*
[**]*Silesian University of Technology, Akademicka 5, PL 44-100 Gliwice, Poland*

Summary The aim of this paper is to study the process of the damage growth that results in material failure for rock-like cementitious brittle materials subjected to multi-axial state of stress. To this end the stress-strain curves and stress at failure were determined experimentally for cylindrical specimens of mortar under tri-axial state of stress. These experimental results were compared with the theoretical predictions obtained from the own theoretical model based on the methods of the damage mechanics.

INTRODUCTION

To formulate more precise theoretical models capable to describe the physical processes observed in materials subjected to complex loading the deeper theoretical and experimental studies of mechanical properties of materials are required. The results of such analyses available in the literature show that deformation of brittle rock-like materials and cementitious composites is accompanied by development of oriented cracks and that an amount and configuration of this internal damage are closely connected with the magnitude and directions of the principal stresses applied. That is why, some theoretical models based on the methods of the damage mechanics were formulated to describe the mechanical behaviour of concrete and rocks [1,2,3,4]. However, the realistic theoretical description of overall material response accounting for oriented damage growth and for development of damage induced anisotropy of such materials the extensive experimental studies are needed. The aim of this note is to supply new experimental data for brittle material subjected to tri-axial state of stress as well as presentation of the theoretical model capable to describe deformability and failure of initially isotropic brittle rock-like solids.

EXPERIMENTS

The experimental results presented in this note were obtained for 16 cylindrical specimens of mortar subjected to tri-axial compression. The tests were performed in testing machine ZD40 of 400 kN capacity combined with the hydraulic attachment necessary to apply a lateral compression. Longitudinal and lateral deformations of the specimen were measured by means of four electrical resistance strain gauges arranged in the form of two cruciform rosettes glued on the opposite sides of the cylinders. The programme of loading consisted of uni-axial compression (four specimens) and two cases of tri-axial loading referred to as tri-axial state of stress 1 (six specimens) and tri-axial state of stress 2 (six

Table 1. Experimental data and constants used in analysis of tri-axial state of stress of mortar

Constant	Unit	Mortar
E_0	MPa	8030
ν_0	-	0.175
f_c	MPa	-7.39
A	MPa^{-2}	2500×10^{-5}
B	MPa^{-2}	100.0×10^{-5}
C	MPa^{-1}	-1.000×10^{-5}
D	MPa^{-1}	2.188×10^{-5}
F	-	6.000

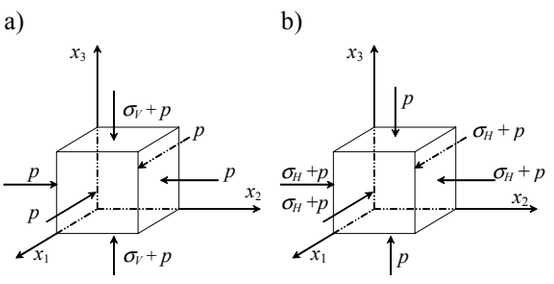


Fig. 1. Stress tensor components: a) tri-axial state of stress 1, b) tri-axial state of stress 2.

Table 2. Experimental and theoretical failure stress for mortar subjected to tri-axial state of stress 1

Specimen	Hydrostatic pressure p MPa	Failure stress σ_{33f} MPa	
		Experiment	Theory
ZC1	-1.05	-10.90	-11.48
ZD1	-1.05	-12.20	-11.48
ZC2	-2.05	-17.67	-15.65
ZD2	-2.05	-16.08	-15.65
ZC3	-3.05	-18.83	-19.60
ZD3	-3.05	-20.02	-19.60

Table 3. Experimental and theoretical failure stress for mortar subjected to tri-axial state of stress 2

Specimen	Hydrostatic pressure p MPa	Failure stress $\sigma_{11f} = \sigma_{22f}$ MPa	
		Experiment	Theory
ZA1	0	-7.19	-7.24
ZB1	-0.15	-9.40	-9.10
ZA2	-1.95	-15.89	-20.61
ZB2	-1.95	-16.83	-20.61
ZA3	-3.62	-23.55	-28.82
ZB3	-3.62	-24.87	-28.82

specimens). The configurations of the stress components in both tri-axial states of stress are shown in Fig. 1. The further details on equipment used and on experimental procedure adopted can be found in [5]. The objective of the test performed under uni-axial compression was to determine the initial Young modulus E_0 and Poisson ratio ν_0 as well as to measure the uni-axial compressive strength of the material f_c. The numerical values of these constant together with the other material parameters included in the theoretical model used in this note are shown in Table 1.
The loading paths for both tri-axial states of stress, shown in Fig. 1, were composed of two parts. The first stage of loading in both cases was the same and consisted in a monotonic increase of hydrostatic pressure up to prescribed value p. In the second stage of the tri-axial state of stress 1 (Fig.1a) the vertical normal stress σ_V was increased up to material failure. For tri-axial state of stress 2 shown in Fig. 1b the second stage of loading consist in simultaneous increase of two mutually perpendicular components σ_H up to material failure. The objective of the tests under tri-axial state of stress was to determine the respective stress-strain relations and to measure the failure load for each loading path. The numerical data concerning the prescribed values of the hydrostatic pressure p as well as maximum load sustained by the specimens are shown in Table 2 and 3.

BASIC EQUATIONS

Theoretical description of the experimental data presented here is based on own mathematical model developed and explained in [2,3]. The basic equation of this theoretical model is the stress strain relation

$$\varepsilon_{ij} = -\frac{\nu_0}{E_0}\delta_{ij}\sigma_{kk} + \frac{1+\nu_0}{E_0}\sigma_{ij} + C(\delta_{ij}D_{kl}\sigma_{kl} + D_{ij}\sigma_{kk}) + 2D(\sigma_{ik}D_{kj} + D_{ik}\sigma_{kj}) \tag{1}$$

which describes the anisotropic elastic response of the damaged material. Equation (1) contains the strain tensor ε_{ij}, the stress tensor σ_{ij}, the Kronecker delta δ_{ij}, the Young modulus E_0 and Poisson ratio ν_0 for an originally undamaged material, two constants C and D to be determined experimentally and the second order symmetric damage effect tensor D_{ij} responsible for the current state of internal structure of the material. Deterioration of the material structure due to applied load is described by the damage evolution equation expressed in the form of the tensor function

$$\Omega_{ij} = As_{kl}s_{kl}\left(1 + \frac{30\det\sigma_{pq}}{\left|\sigma_{ij}\sigma_{ik}\sigma_{kj}\right| + \left|\sigma_{II}^3\right|}\right)^F \delta_{ij} + B\sqrt{\sigma_{kl}\sigma_{kl}}\left(1 + \frac{30\det\sigma_{pq}}{\left|\sigma_{ij}\sigma_{ik}\sigma_{kj}\right| + \left|\sigma_{II}^3\right|}\right)^F \sigma_{ij} \tag{2}$$

where Ω_{ij} is a classical second order damage tensor, s_{kl} is the stress deviator and A, B, F are unknown material parameters to be determined experimentally. The equation

$$D_i = \frac{\Omega_i}{1-\Omega_i} \quad , \quad i = 1,2,3 \tag{3}$$

shows the relation between the principal components D_1, D_2 and D_3 of the damage effect tensor D_{ij} contained in Eqs. (1) and the principal values Ω_1, Ω_2 and Ω_3 of the damage tensor Ω_{ij} expressed by Eq. (2).
Equations (1), (2) and (3) and numerical data shown in Table 1 were used to construct the theoretical stress-strain curves and to determine the theoretically predicted maximum stress at material failure. The values of constants A, B, C, D and F seen in Table 1 and used in this analysis were determined experimentally according to the rules presented in [3]. The comparison of experimental and theoretical results obtained for the stresses at failure for various cases of tri-axial loading is shown in Table 2 and 3.

CONCLUSIONS

The study presented in this note makes it possible to conclude that theoretical stress-strain curves for tri-axial loading obtained from the relevant equations presented here show satisfactory agreement with experimental data determined for mortar subjected to various combinations of tri-axial compressions. Increasing compressive strength detected experimentally for specimens of mortar subjected to simultaneously applied hydrostatic pressure and uni-axial or bi-axial compression can also be explained theoretically within the mathematical model proposed.

References

[1] Halm D., Dragon A.: An Anisotropic Model of Damage and Frictional Sliding for Brittle Materials. *Eur. J. Mech. A/Solids* **17**: 439-460, 1998.
[2] Litewka A., Bogucka J., Debinski J.: Deformation Induced Anisotropy of Concrete. *Arch. Civil Eng.* **42**: 425-445, 1996.
[3] Litewka A., Debinski J.: Load-Induced Oriented Damage and Anisotropy of Rock-Like Materials. *Int. J. Plast*. **19**: 2171-2191, 2003.
[4] Murakami S, Kamiya K.: Constitutive and Damage Evolution Equations of Elastic-Brittle Materials Based on Irreversible Thermodynamics. *Int. J. Mech. Sci.* **39**: 473-486, 1977.
[5] Szojda L.: Analysis of Interaction of Masonry Structures and Deformable Foundation. *PhD Thesis*, Silesian University of Technology, Gliwice, 2001, (in Polish).

NUMERICAL ANALYSIS OF NONLOCAL ANISOTROPIC CONTINUUM DAMAGE

Sabine Ricci, Michael Brünig
Lehrstuhl für Baumechanik-Statik, Universität Dortmund, D-44221 Dortmund, Germany

Summary The present paper deals with the numerical analysis of large elastic-plastic deformation and localization behavior of anisotropically damaged ductile solids within the framework of nonlocal continuum mechanics. Estimates of the stress and strain histories are obtained from a numerical integration algorithm which employs an inelastic predictor followed by an elastic corrector step. Numerical simulations show the influence of several model parameters on the deformation and localization prediction.

INTRODUCTION

Large inelastic deformations of metals are usually accompanied by damage processes due to microdefects. Their proper understanding and their mechanical description are of importance in discussing the mechanical effects of the material deterioration on the macroscopic behavior of solids as well as in elucidating the mechanisms leading to final fracture. In this context, nonlocal effects seem to be important when deformation mechanisms governed by microscopic phenomena as well as scale effects are considered in order to explain and predict certain experimentally observed critical phenomena.

FUNDAMENTAL GOVERNING EQUATIONS

A nonlocal generalization of the framework presented by Brünig [1] is proposed to describe the inelastic deformation behavior of ductile metals. It is based on the introduction of respective Helmholtz free energy functions of fictitious undamaged and of current damaged configurations. In addition, to be able to minimize the analytical and numerical difficulties associated with general nonlocal formulations the nonlocal concept is applied only to those parameters which cause material softening while the elastic behavior is still assumed to be governed by a local formulation. Thus, the kinematic relations as well as the balance equations remain local, and the distribution of the stresses and displacements is still governed by the standard differential equations of equilibrium and the associated boundary conditions. Nonlocal effects, on the other hand, are described via additional length quantities which play the role of material parameters and are used to obtain weighted averages of the corresponding local plastic and damage variables over a material volume of the body. The effective specific free energy $\bar{\phi}$ of the undamaged matrix material is decomposed into an effective elastic and an effective plastic part

$$\bar{\phi} = \bar{\phi}^{el}\left(\bar{\mathbf{A}}^{el}\right) + \bar{\phi}^{pl}\left(\gamma, \hat{\gamma}\right), \tag{1}$$

where $\bar{\mathbf{A}}^{el}$ is the effective elastic strain tensor, γ and $\hat{\gamma}$ denote an internal plastic variable and its nonlocal counterpart, respectively. In addition, plastic yielding of the matrix material is described by the nonlocal yield condition

$$f^{pl}\left(\bar{I}_1, \bar{J}_2, c\right) = \left(1 - \frac{a}{c}\bar{I}\right)^{-1}\sqrt{\bar{J}_2} - c\left(\gamma, \hat{\gamma}\right) = 0 \ , \tag{2}$$

where $\bar{I}_1 = \mathrm{tr}\bar{\mathbf{T}}$ and $\bar{J}_2 = \frac{1}{2}\mathrm{dev}\bar{\mathbf{T}} \cdot \mathrm{dev}\bar{\mathbf{T}}$ are invariants of the effective stress tensor $\bar{\mathbf{T}}$, c denotes the strength coefficient of the matrix material and a represents the hydrostatic stress coefficient [2].
Moreover, the Helmholtz free energy function of the damaged material sample is assumed to consist of three parts:

$$\phi = \phi^{el}\left(\mathbf{A}^{el}, \mathbf{A}^{da}\right) + \phi^{pl}\left(\gamma, \hat{\gamma}\right) + \phi^{da}\left(\mu, \hat{\mu}\right) \quad . \tag{3}$$

Namely, the elastic free energy ϕ^{el}, which is an isotropic function of the elastic and damage strain tensors, $\mathbf{A}^{el}$ and $\mathbf{A}^{da}$, is used to describe the elastic response of the damaged material at the current state of deformation and material damage. Furthermore, the energies ϕ^{pl}, due to plastic hardening, and ϕ^{da}, due to damage strengthening, only take into account the respective internal state variables, γ and μ, as well as their nonlocal counterparts $\hat{\gamma}$ and $\hat{\mu}$ which are taken to be volume averages of γ and μ, respectively. In addition, evolution of damage is described by the nonlocal damage criterion

$$f^{da}\left(I_1, J_2, \tilde{\sigma}\right) = I_1 + \tilde{\beta}\sqrt{J_2} - \tilde{\sigma}\left(\mu, \hat{\mu}\right) = 0 \ , \tag{4}$$

where $\tilde{\beta}$ represents the influence of the deviatoric stress state on the damage condition and $\tilde{\sigma}$ denotes the equivalent damage stress measure.
On the numerical side a key factor in the numerical treatment of inelastic continuum models using the finite element method is the numerical integration of the nonlinear constitutive equations governing the flow and damage behavior as well as the evolution of internal state variables. Estimates of the irreversible strain histories are obtained via an extended

version of the inelastic predictor method. In the elastic corrector step the plastic and damage correctors, $\Delta_{er}\hat{\gamma}$ and $\Delta_{er}\hat{\mu}$, are expanded in respective Taylor series, e.g.

$$\Delta_{er}\hat{\gamma} = \Delta_{er}\gamma + d_{pl}\frac{\partial^2 \Delta_{er}\gamma}{\partial \mathbf{x}\cdot\partial \mathbf{x}} + \ldots = \Delta_{er}\gamma + d_{pl}\,\nabla^2\left(\Delta_{er}\gamma\right) + \ldots, \tag{5}$$

where only terms up to second order are retained and d_{pl} takes into account a plastic internal length scale [2]. This leads to the system of coupled elliptic partial differential equations for the estimates of the correctors of the equivalent plastic and damage strains

$$m_{pl}d_{pl}\frac{\partial c}{\partial \gamma}\nabla^2\left(\Delta_{er}\gamma\right) + \left[\sqrt{2}\,G_1 k_1 + \frac{\partial c}{\partial \gamma}\right]\Delta_{er}\gamma + \sqrt{2}\,G_1 k_2\,\Delta_{er}\mu = c_{pr} - c\left(t\right) \tag{6}$$

and

$$m_{da}d_{da}\frac{\partial \sigma}{\partial \mu}\nabla^2\left(\Delta_{er}\mu\right) + \left[\sqrt{2}\,G_2 k_4 + \frac{\partial \sigma}{\partial \mu}\right]\Delta_{er}\mu + \sqrt{2}\,G_2 k_3\,\Delta_{er}\gamma = \sigma_{pr} - \sigma\left(t\right). \tag{7}$$

where G_1 and G_2 as well as $k_1,\ldots,k_4$ represent modified material parameters and m_{pl} and m_{da} denote the relative weights of the nonlocal effects compared to the local ones. Equations (6) and (7) are solved via a standard finite difference method employing an overlay mesh defined by the Gaussian integration points of the underlying finite element mesh, whereas the global equilibrium equations are solved using standard displacement-based finite elements. At the end of each time step equivalent plastic and damage strain increments are computed simultaneously which then lead to the corresponding tensorial quantities employing an integration scheme with an exponential shift.

NUMERICAL EXAMPLES

The numerical simulations deal with the finite deformation and localization behavior of uniaxially loaded rectangular specimens with clamped ends. The corresponding load-deflection curves are shown in Fig. 1 based on a nonlocal elastic-plastic material model without damage, including isotropic damage and including anisotropic damage discussed above, respectively. In particular, Fig. 1 shows that with the onset of damage the numerical calculations including isotropic and anisotropic damage show rapid loss in load carrying capacity with increasing elongation of the specimen which agrees with experimental observations. Fig. 2 shows the evolution of the void volume fraction f with increasing equivalent plastic strain γ. The numerical calculation for the isotropic damage model shows an increase in void volume fraction after the onset of isotropic damage. The point where the two curves based on the isotropic and the anisotropic model separate characterizes the onset of anisotropic damage which leads to an even larger increase in void volume fraction with growing plastic strain.

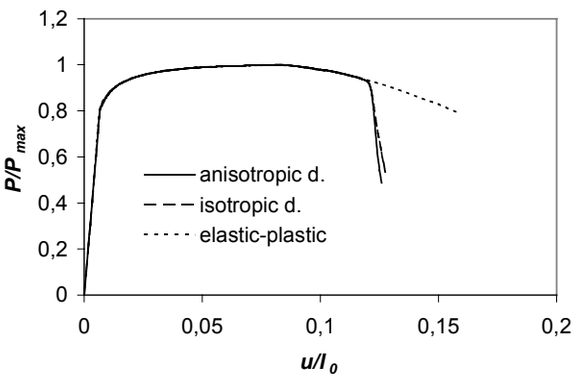


Fig. 1: Load-deflection curves

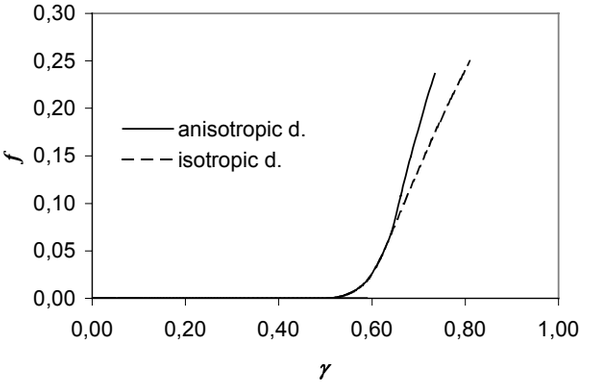


Fig. 2: Evolution of void volume fraction

CONCLUSIONS

The proposed large strain damage theory is a robust and efficient framework to develop structural models capable for providing practical solutions of general problems in engineering.

References

[1] Brünig, M.: Numerical analysis and elastic-plastic deformation behavior of anisotropically damaged solids. Int. J. Plasticity **18**, 1237-1270, 2002.

[2] Brünig, M., Ricci, S., Obrecht, H.: Nonlocal large deformation and localization behavior of metals, Comp. Struct. **79**, 2063-2074, 2001.

DISCRETE MODELS AND THEIR APPLICATION IN DAMAGE MECHANICS

Gian Antonio D'Addetta, Ekkehard Ramm
University of Stuttgart, Institute of Structural Mechanics, D 70550 Stuttgart

Summary We present different discrete element models for the simulation of two-dimensional problems in the context of damage mechanics. Target materials to be simulated are cohesive and non-cohesive geomaterials like concrete- or sand-type materials. The development of adequate homogenization methods supplements the definition of the discrete models.

DISCRETE ELEMENT MODELS

The failure mechanisms of geomaterials are characterized by complex failure modes and, furthermore, they show a highly anisotropic bias due to their inhomogeneous microstructure. Since localization phenomena like cracks or shear bands occur the material cannot be treated as continuous in the usual manner. If fracture and fragmentation of the solid occurs, the creation and continuous motion of the evolving crack surfaces apparently represent discontinuous phenomena and are difficult to handle. Therefore, most continuum models, and in particular those ones based on continuum damage mechanics, cannot account for the discrete nature of material failure in a natural way and need some extension. Alternatively, discrete particle models like discrete element methods (DEM) have been developed. As the name DEM suggests, a solid is replaced by a discontinuous particle composite which allows for a detachment of bonds between particles (if initially present) and a re-contact of open surfaces. In order to simulate and quantify the full range of geomaterials from non-cohesive ones like sand to cohesive ones like concrete, ceramics or rock, different types of discrete element models are presented. Starting from a basic polygonal two-dimensional DEM model for non-cohesive granular materials, more complex models for cohesive materials are obtained by inclusion of beam or interface elements between corresponding particles. The formulation of the standard DEM model is based on the work in [1] where individual particles are considered as unbreakable and undeformable rigid bodies. The local deformational behavior of the particles is approximated by an elastic repulsive force related to the overlapping area of contacting particles, i. e. the detailed representation of the contact is approximated. As initially presented in [2, 3], cohesive components are included by beams, allowing to model typical features in the failure of geomaterials like concrete or rock in a rather crude way. In order to enhance a quantification of the discrete model instead of beams, interfaces along the common particle edges have been introduced [4, 5, 6]. Thus, the complexity of the model is increased in that the representation of the bonds between particles is more detailed and physically coherent.

SIMULATION OF A VIRTUAL MICROSTRUCTURE

The last step in the series of increasing complexity is the realization of a microstructure-based simulation environment which utilizes the foregoing enhanced DEM models, confer [4]. In short, the microstructure is included, if different properties of the cohesive components (beam or interface) are assigned with respect to their position, i. e. inside the matrix, inside the aggregate and between aggregate and matrix. With the growing model complexity a wide variety of failure features of geomaterials can be represented, see [3, 4]. Furthermore, the inclusion of a real microstructure which regards for stiffer aggregates embedded in a less stiffer matrix enables a quantification of the model. If the softening of the interface elements (bond between the particles) is monitored, a detailed view of the microstructural softening process is obtained. Seven simulation series of a uniaxial compression test of a quadratic block have been carried out. The simplified picture of the composite structure of one of these simulation series in Fig. 1 (b) highlights the crack propagation through the specimen short after peak load. The dark grey color denotes the aggregate particles and light grey the surrounding matrix. Thereby, either the matrix as well as the aggregates are represented by a finite amount of individual particles. For this reason, the shape of the aggregates is irregular. The black lines in Fig. 1 (b) define those interfaces that have been

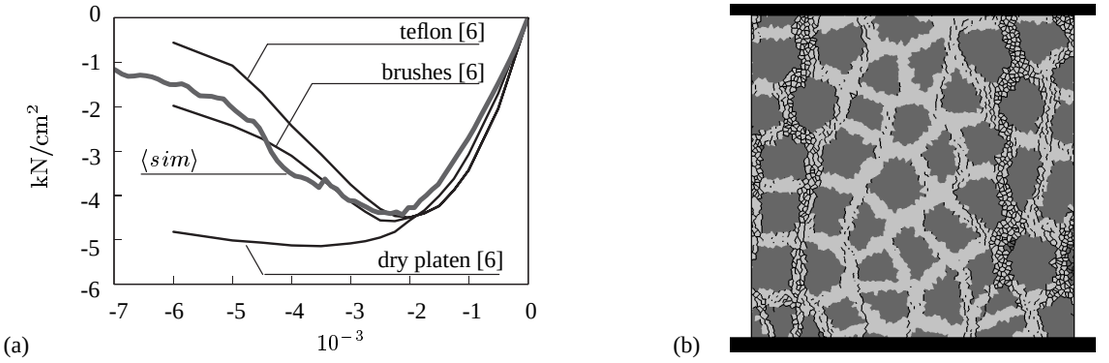


Figure 1. (a) Stress-strain diagram of simulations and experiments by [6] and (b) eliminated bonds.

eliminated in the course of the simulation. The average stress-strain curve of seven different (depending on the random generation of composition and position of aggregates) simulation series $\langle sim \rangle$ is plotted in Fig. 1 (a). The confrontation with experiments on concrete specimens with different boundary conditions [6] expresses the good agreement between simulations and experiments.

HOMOGENIZATION OF DISCRETE PARTICLE ASSEMBLIES

In parallel, homogenization techniques have been applied which allow us to relate microscopic quantities, like the contact forces and displacements, to corresponding macroscopic quantities, like stresses and strains, confer [4, 7, 8, 9]. Starting point of these homogenization approaches is the argument of scale separation. While the macroscopic problem is defined on a scale with characteristic length D, a representative or "averaging" volume is of size d, and, finally, individual particles are of characteristic diameter leading to the scale separation $D \quad d$. Utilizing these arguments the balance of linear and angular momentum provide simplified equilibrium conditions for a representative volume element (RVE) on the scale d. Application of usual averaging approaches on the RVE level yields average stress tensors in terms of contact forces. In a similar manner kinematic quantities like strains and velocity gradients as well as energetic quantities are obtained. The benchmark problem used for the validation of this homogenization procedure is a strain driven biaxial simulation of a cohesionless sample with rigid side walls, compare the setup in Fig. 2 (a) or the references [4, 7, 8, 9]. The target material to be simulated is of sand-type. Therefore, the material structure does not represent a two-phase microstructure as presented in the previous section, i. e. all particles possess the same stiffness and differ only in size. The rectangular sample consists of 2560 particles and is loaded in a strain driven format in vertical direction while a constant side pressure p_{const} is applied. The evaluation of the average vertical strain distribution $\langle \ _{22} \rangle$ leads to an interesting observation which is typically obtained in sand- and rock-type materials. The homogenization method provides the opportunity to study the pattern formation in combination with the self-organization of the granular body. Fig. 2 (b) pictures the formation of competing shear zones in the pre-localization regime of the simulation. After reaching the peak only one primary shear zone and reflections of it remain and drive the complete failure of the granular specimen, confer Fig. 2 (c). For clarity, in Figs. 2 (b) and (c) the color scales have been adapted to the maximum strain of the corresponding simulation stage.

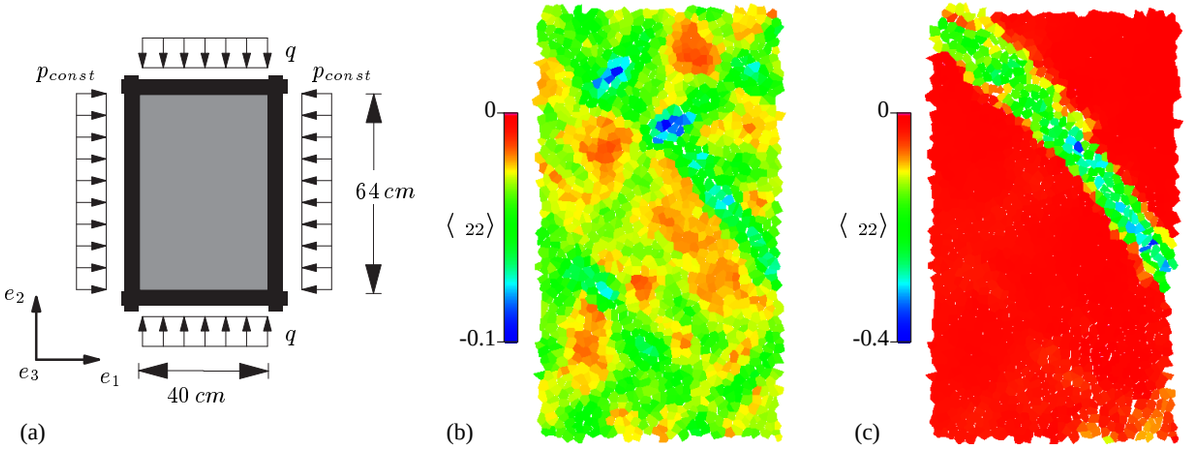


Figure 2. (a) Biaxial setup and geometry, vertical strains (b) before and (c) after localization.

References

[1] Tillemans, H.-J., Herrmann, H. J.: Simulating deformations of granular solids under shear. *Physica A* **217**:261–288, 1995.

[2] Kun, F., Herrmann, H. J.: A study of fragmentation processes using a discrete element method. *Comp. Meth. Appl. Mech. Engng.* **138**:3–18, 1996.

[3] D'Addetta, G. A., Kun, F., Ramm, E.: On the application of a discrete model to the fracture process of cohesive granular materials. *Granular Matter* **4**:77–90, 2002.

[4] D'Addetta, G. A.: Discrete models for cohesive frictional materials. *PhD Thesis*, Bericht Nr. 42, Institut für Baustatik, Universität Stuttgart, Germany, 2004.

[5] Ramm, E., D'Addetta, G. A., Leukart, M.: Interrelations between continuum and discontinuum models for geomaterials. In: Oñate, E. (ed.), *Proc. of the 7th Conf. on Computational Plasticity, Barcelona, Spain*, 2003.

[6] Vonk, R.: Softening of concrete loaded in compression. *PhD Thesis*, Technische Universiteit Eindhoven, The Netherlands, 1992.

[7] D'Addetta, G. A., Ramm, E., Diebels, S., Ehlers, W.: Homogenization for particle assemblies. In: Cook, B. K., Jensen, R. P. (eds.), *Discrete Element Methods - Numerical Modeling of Discontinua - Proc. 3rd Int. Conf. on DEM, Santa Fe, NM, USA*, Geotechnical Special Publication No. 117, ASCE, Reston, VI, USA, pp. 259–264, 2002.

[8] D'Addetta, G. A., Ramm, E., Diebels, S., Ehlers, W.: A particle center based homogenization strategy for particle assemblies. *Engng. Comp.* **21**:in press, 2004.

[9] Ehlers, W., Ramm, E., Diebels, S., D'Addetta, G. A.: From particle ensembles to Cosserat continua: Homogenization of contact forces towards stresses and couple stresses. *Int. J. Solids & Structures* **40**:6681–6702, 2003.

A NONLOCAL PLASTICITY-DAMAGE FORMULATION BASED ON THE MICROMECHANICS OF DEFECT GROWTH

R.H.J. Peerlings, R.A.B. Engelen, M.G.D. Geers

Department of Mechanical Engineering, Eindhoven University of Technology
PO Box 513, 5600 MB Eindhoven, The Netherlands

Summary: A large-strain plasticity formulation is coupled with a nonlocal damage influence in order to model damage development in ductile materials. Two damage variables are used: one which characterises the defect volume fraction and which is predominantly governed by hydrostatic stress and plastic dilatation, and one which describes the average defect shape and is particularly sensitive to shearing. Growth relations for these variables as well as the yield surface are determined from unit cell analyses of defect growth and defect extension.

INTRODUCTION

Industrial forming operations on ductile materials typically result in large plastic strains. Under the influence of these plastic strains, voids and microcracks are initiated, usually at second-phase particles or inclusions. Further straining results in growth and coalescence of the individual defects and may thus lead to a considerable degradation of the overall material strength and of the remaining ductility. In situations where the residual properties after forming are relevant – for instance in view of subsequent forming steps – or where the degradation is used to separate material (e.g. blanking), it is important to quantify the microstructural damage development and its influence on the material behaviour.

Accurate macroscopic models of ductile damage growth can only be developed based on a thorough understanding of the underlying microscopic processes. The formulation of a yield criterion on the basis of unit-cell analyses of void growth by Gurson [1] has been a landmark contribution in this respect. Ductile damage models based on this work are used widely, see for instance [2] for a review. However, although these models provide accurate predictions in cases where relatively high hydrostatic stresses exist, they are much less successful in shear-dominated situations. This limitation is due to the assumption of a spherical void which expands isotropically in deriving the yield criterion. For low triaxialities and large shear strains the defects are stretched and coalesce without much volume increase – an effect that cannot be described by the void volume fraction as used in the Gurson-based models.

A second limitation of existing ductile damage formulations originates in the fact that they are mostly based on local continuum mechanics. This means that when the damage growth leads to an overall softening material behaviour pathological localisation effects are observed and numerical results no longer converge upon refinement of the spatial discretisation. Post-peak results obtained with such formulations should therefore be used with extreme care. The lack of mesh-objectivity is related to the absence in the material model of a material length scale, which can set the width of damage bands and thus regularise the localisation of deformation.

NONLOCAL PLASTICITY-DAMAGE FRAMEWORK

In order to overcome the above limitations of existing ductile damage formulations, a new coupled large-strain plasticity-damage model has been developed, based on earlier work by Geers [3]. The model features two field variables which characterise the damage state of the material. One of them, denoted by f, represents the volume fraction which is occupied by defects. This variable plays a role which is similar to the void volume fraction in the Gurson-based models. An increase of this variable is accompanied by plastic dilatation and occurs mainly as a result of hydrostatic stress. The other damage variable, S, characterises the shape of the defects and can be compared to the aspect ratio used by Gologanu et al. [4]. The evolution of this variable is mainly governed by deviatoric straining, although large volumetric strains may also result in a decrease. As a result, it mainly comes into play in shear-dominated problems.

The influence of damage on the local material strength is reflected in the yield criterion, which depends on the two damage state variables: $\Phi(\boldsymbol{\tau}, \varepsilon_\mathrm{p}, f, S) \leq 0$; note in passing that, unlike standard von Mises plasticity, the yield criterion also depends on the hydrostatic part of the stress tensor. Generally speaking, an increase of damage results in a shrinking yield surface and thus in material softening. Care must therefore be taken to formulate the damage growth in such a way that pathological localisation of damage growth and deformation is avoided. For this purpose two additional kinematics-related variables are introduced: a nonlocal effective volumetric plastic strain $\bar{\varepsilon}_\mathrm{v}$ and a nonlocal effective deviatoric plastic strain $\bar{\varepsilon}_\mathrm{d}$. The evolution of the damage variables is described by evolution laws which related the damage rates $\dot{f}$ and $\dot{S}$ to the nonlocal deformation rates $\dot{\bar{\varepsilon}}_\mathrm{v}$ and $\dot{\bar{\varepsilon}}_\mathrm{d}$. The nonlocal field variables $\bar{\varepsilon}_\mathrm{v}$ and $\bar{\varepsilon}_\mathrm{d}$ are related to their local, standard counterparts ε_v and ε_d respectively by a partial differential equation which was first used in a plasticity context by Engelen et al. [5]. Together with an additional set of boundary conditions these partial differential equations form two boundary value problems which must be discretised and solved simultaneously with equilibrium. The additional differential equations provide spatial interactions at a length scale which appears in the differential operator and which may be related to the

average distance between defects. As a result, the localisation process is regularised and damage bands have a positive, finite width.

MICROMECHANICAL BASIS

Establishing the precise structure of the yield function and the evolution laws in the plasticity-damage framework is not trivial. Rather than assuming some phenomenological form for these relations, they are based on micromechanical analyses of defect growth and defect extension. Nucleation of voids or coalescence have not yet been considered. Plane strain finite element analyses have been carried out on unit cells containing elliptic voids of different sizes and shapes in an undamaged elastoplastic matrix. The unit cells have been subjected to a wide range of straining regimes, from purely deviatoric to equibiaxial. In these analyses, the evolution of the void volume fraction f and the shape parameter S, as well as overall stress measures, have been recorded. Examples are given in Figure 1, which shows the shape variable S versus strain as a dotted curve for different initial conditions (left) and different straining directions (right).

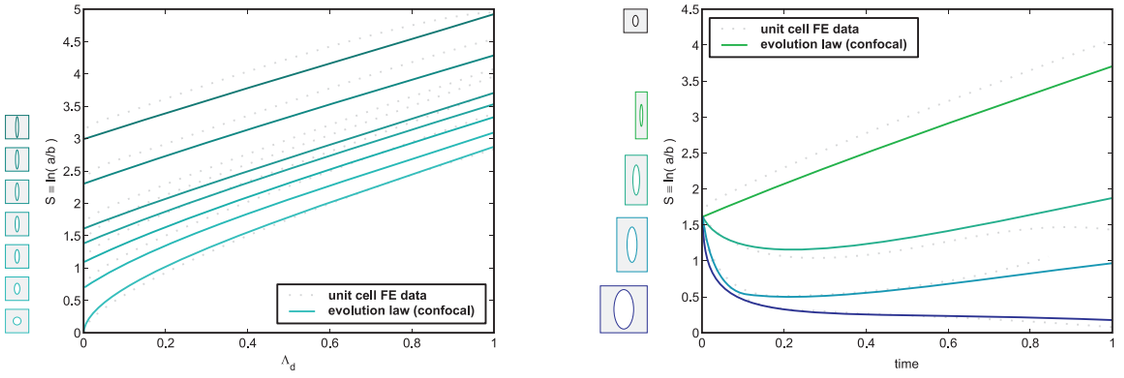


Figure 1: Evolution of the defect shape variables S for several initial shapes (left) and straining directions (right) as computed in the numerical unit cell analyses (dotted curves) and using the fitted evolution laws (solid curves).

Evolution laws for f and S in terms of the overall effective strain rates are formulated based on relatively simple mechanical approximations. In particular, it is assumed that the matrix material is incompressible and that the void and an approximate, elliptic unit cell remain confocal throughout the deformation process. The relations which can be derived from these assumptions pick up all relevant trends observed in the numerical unit-cell analyses. The quantitative agreement is subsequently improved by introducing a few parameters and fitting these to match the numerical results. The resulting fits have been plotted in Figure 1 as solid curves. The structure of the yield function is derived in a similar fashion from an approximation of the plastic work rate together with normality (cf. [1, 4]) and is subsequently adapted to fit the numerical experiments.

CONCLUDING REMARKS

The constitutive relations which result from the analyses as described above exhibit a response which is very similar to that of Gurson's theory in the regime in which this theory is known to perform well, i.e. for relatively high triaxialities. On the other hand, substantially different behaviour is obtained in shear, in which Gurson's theory predicts no damage growth at all. Particularly in the latter regime, however, the response of the model can still be improved by including coalescence effects. It is believed that the micromechanical modelling provides an excellent basis for introducing these effects in a realistic way.

References

[1] Gurson A.L.: Continuum theory of ductile rupture by void nucleation and growth: Part i – Yield criteria and flow rules for porous ductile media. *J. Eng. Mat. Technol.* **99**:2–15, 1977.

[2] Tvergaard V.: Material failure by void growth to coalescence. *Adv. Appl. Mech.* **27**:83–151, 1989.

[3] Geers M.G.D., Ubachs R.L.J.M., Engelen R.A.B.: Strongly nonlocal gradient-enhanced finite strain elastoplasticity. *Int. J. Num. Meth. Eng.* **56**:2039–2068, 2003.

[4] Gologanu M., Leblond J.B., Devaux J.: Approximate models for ductile metals containing non-spherical voids – case of axisymmetric prolate ellipsoidal cavities. *J. Mech. Phys. Solids* **41**:1723–1754, 1993.

[5] Engelen R.A.B., Geers M.G.D., Baaijens F.T.P.: Nonlocal implicit gradient-enhanced elasto-plasticity for the modelling of softening behaviour. *Int. J. Plast.* **19**:403–433, 2003.

PROPAGATION OF CRACKS IN TERMS OF CONTINUUM DAMAGE MECHANICS

Adam Bodnar, Marcin Chrzanowski
Institute of Structural Mechanics, Cracow University of Technology
ul. Warszawska 24, 31-155 Cracow, Poland

Summary The paper deals with numerical analysis of crack nucleation and propagation caused by time-dependent process of deterioration in creep conditions. Three distinctive stages of the damage growth in a rectangular plate subjected to uniform pressure load are considered: nucleation in a point, propagation through the plate thickness, and development of critical network of the cracks bringing a structure to the final collapse. With corresponding times denoted by t_1, t_2 , and t_3, their relationships had been evaluated to indicate the safety margins throughout the whole process. Spatial configuration of crack networks, including their profiles and branching, is shown as time-dependent process, which leads to the structure collapse caused by the loss of kinematical stability.

INTRODUCTION

Process of failure of structures caused by crack development is very complex one, but in general, three characteristic stages can be distinguished corresponding to the nucleation of first macro-crack, its propagation throughout structure's body, and to the formation of collapse mechanism. The corresponding times limiting these stages are denoted as t_1, t_2 , and t_3. The ratio of the values of these time instances can be viewed as safety margins set on structures' behaviour.
In the paper Continuum Damage Mechanics is used for analysis of damage growth in a metallic rectangular plate subjected to uniform pressure load. Some comparison between approach of Continuum Damage Mechanics and Fracture Mechanics to the problem of failure of structures solving is made.
The set of constitutive equations was chosen as simple as possible to facilitate numerical analysis, but yet complex enough – to reflect typical process of creep of metallic structures (non-stationary creep with steady-state and non-steady periods, stress redistribution, nonlinear dependency of strain rate on stress and coupling between deformation and deterioration):

$$\varepsilon_{ij}^{e} = D_{ijkl}^{-1}\,\sigma_{kl} \tag{1}$$

$$\frac{\partial \varepsilon_{ij}^{c}}{\partial t} = \gamma \left(\frac{\sigma_{eff}}{1-\omega} \right)^{n} \frac{\partial \sigma_{eff}}{\partial \sigma_{ij}} \tag{2}$$

$$\frac{\partial \omega}{\partial t} = A \left(\frac{\sigma_{eq}}{1-\omega} \right)^{m} \tag{3}$$

where: ε_{ij}^{e} - the elastic strain tensor, ε_{ij}^{c} - the creep strain tensor, σ_{ij} - the stress tensor, D_{ijkl} - the elastic constants tensor, ω - the scalar damage parameter, γ, n, A, m - creep and damage material constants, t - time.
The equivalent stress σ_{eq} in Eq. (3) is given by:

$$\sigma_{eq} = \alpha\, \sigma_{\max} + (1-\alpha)\sigma_{eff} \tag{4}$$

where: $\sigma_{\max}$ - the maximal principal tensile stress, σ_{eff} - the Huber – Mises effective stress, α - parameter $(0 \le \alpha \le 1)$ which characterises local failure mechanism mode.
The case of $\alpha = 0$ corresponds to ductile (transgranular) fracture controlled by the effective stress whereas for $\alpha = 1$ the brittle (intergranular) fracture governed by the maximal principal tensile stress occurs. The intermediate values of α correspond to mixed modes of failure.
The above constitutive equations completed together with equilibrium and compatibility equations form the set of problem governing equations that allow for effective solving of a problem of description the whole process of cracking structures.

NUMERICAL PROCEDURES

The set of problem governing equation has been integrated by means of numerical methods. The Finite Element Method for structure discretisation and Euler's procedure for time integration was used. In the computer code the layered isoparametric eight-node Serendipity shell elements with reduced integration were employed. Ten layers and two-point Gaussian quadrature for volume integration were adopted. The time t_1 is identified with $\omega = 1$ condition fulfilled in any layer and Gaussian point (that is numerical integration point). For time $t > t_1$ these numerical integration points were excluded from further integration. When critical condition for damage parameter is reached in all ten layers of a Gaussian points the time is referred to as t_2. Time of structure collapse t_3 were identified with critical values of damage parameter in a whole finite element, which in turn lead to instability in numerical calculations.

SOME NUMERICAL RESULTS

In Fig. 1 upper and lower surfaces of one of the analysed plate (clamped plate, $\alpha = 1$) are shown at time t_2. The networks of macrocracks is shown also, with indication of their onset marked by ○, and through-body proliferation at time t_2 marked by ◄. Though these cracks are seen as surface ones, in fact they penetrate the body of a structure. Profiles of the cracks along two cross sections (along clamped edge and through a mid-span of the plate) are shown in Fig.1 as well.

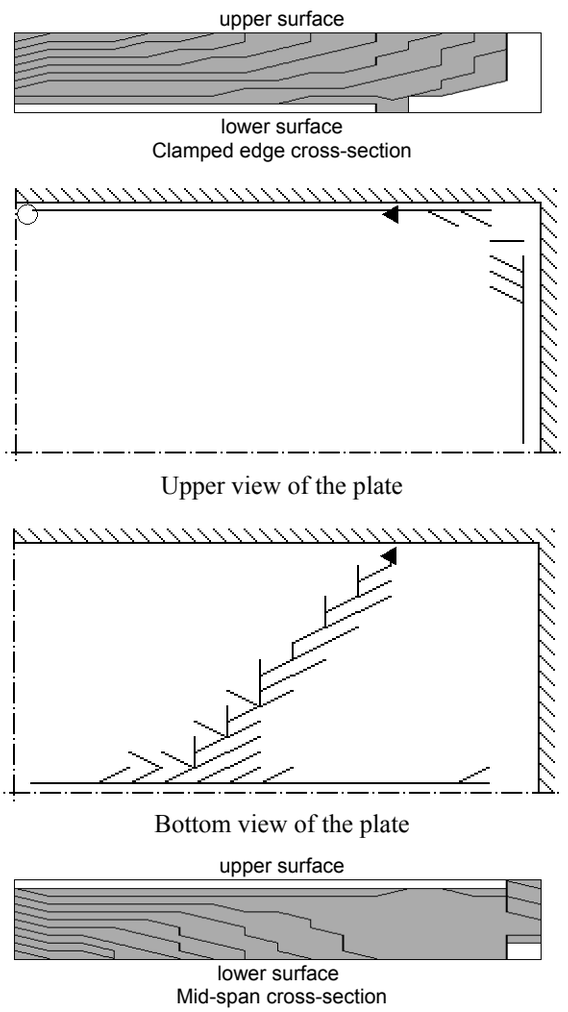


Figure 1: Cracking patterns at time t_2.

An advantage of Continuum Damage Mechanics' approach, fully exploited in the present analysis, is twofold: first, the location for a point at which a macrocrack initiates comes out as a result of analysis. No assumption of this location has to be made as unavoidable assumption prior to further analysis, which is a case when Fracture Mechanics is to be applied. Further, the direction of a macrocracks and their branching it comes out as the result of Continuum Damage Mechanics analysis. Finally, three-dimensional profiles of the cracks penetrating structure's body can be determined.

AN ASYMPTOTIC ANALYSIS OF MODE I CRACK IN CREEPING DAMAGED SOLIDS

Larisa V. Stepanova, Maria E. Phedina
Samara State University, Department of Continuum Mechanics, Akad. Pavlov 1, 443011 Samara, Russia

Summary To evaluate the mechanical behaviour around a Mode I crack tip the governing equations are formulated by light of Continuum Damage Mechanics. The asymptotic stress and continuity fields near the tip of a stationary crack are derived for non-linear viscous damaged materials, which deform according to the creep power constitutive law. The conventional Kachanov-Rabotnov creep-damage theory is utilized and the scalar continuity parameter is incorporated into the constitutive relations. Thus, the coupled system of damage mechanics – creep theory equations is considered. Based on the similarity variable a stress analysis is carried out for Mode I crack under plane stress and plane strain conditions assuming the existence of a totally damaged zone near the crack tip. It is found that the Hutchinson-Rice-Rosengren solution can't be used as the remote boundary condition and the actual far field stress is obtained. The shape of the totally damaged zone is given and analysed.

INTRODUCTION

Many works have been done to analyse the near crack tip fields coupled with elastic, elastic-plastic fatigue damage [1,2], creep damage [3,4] and elastic-plastic-viscoplastic damage. Some of the essential aspects of the considered set of problems and the results obtained can be highlighted. 1. The damage gives significant influence on the stress and strain (strain rate) fields near the crack tip. 2. The mathematical structure of governing equations is affected by the modelling of damage. 3. While the Hutchinson-Rice-Rosengren (HRR) - field of non-linear fracture mechanics always shows the stress singularity at the crack tip for any finite value of the stress exponent, the preceding material damage in front of the crack tip decreases the singularity, and may give non-singular stress field. 4. The totally damage and (or) active damage zone (process zone) need be modelled in the crack tip region.

In the present work the asymptotic stress, strain rate and continuity fields in the vicinity of the Mode I crack in damaged materials are obtained using the self-similar variable proposed by Riedel [5]. The form of the similarity solution has been introduced by Riedel. However, a general solution for the problem has not been constructed yet. The present contribution is an attempt to obtain the stress, strain rate and damage distribution near the crack tip as the dimensionless functions of the similarity variable under the assumption of the existence of a totally damaged zone near the crack tip. The shape and the characteristic length of the totally damaged zone are not known and should be found as a part of the solution. The asymptotic fields allow to find and to study the geometry of the totally damaged zone where the damage parameter reaches its critical value and all the stress tensor components are equal to zero.

FORMULATION OF THE PROBLEM AND BASIC EQUATIONS

Let us consider a semi-infinite crack in an infinite body in a material with constitutive equations formulated on the basis of the creep power law in the framework of Continuum Damage Mechanics.

$$\dot{\varepsilon}_{ij} = (3/2)B\left(\sigma_e/\psi\right)^{n-1} s_{ij}/\psi\,, \tag{1}$$

where ψ is the continuity (integrity) parameter, $\dot{\varepsilon}_{ij}$ is the strain rates, s_{ij} is the stress deviator, $\sigma_e = \sqrt{3s_{ij}s_{ij}/2}$ is the equivalent tensile stress, B is the creep coefficient and n is the creep exponent.

The cumulative damage evolution law can be described by the Kachanov – Rabotnov equation

$$\dot{\psi} = -A\left(\sigma_{eqv}/\psi\right)^m, \qquad \sigma_{eqv} = \alpha\sigma_I + \beta\sigma_e + (1-\alpha-\beta)\sigma\,, \tag{2}$$

where σ_I is the maximum principal stress, $\sigma = \sigma_{kk}$ is the hydrostatic stress, A, m are the material parameters.

Asymptotic remote boundary conditions are assumed to have the form

$$\sigma_{ij}(r\to\infty,\varphi,t) \to \tilde{C}r^s\bar{\sigma}_{ij}(\varphi,t)\,. \tag{3}$$

Note that if the far field stress is determined by the HRR-solution then $\tilde{C} = \left(C^*/(BI_n)\right)^{1/(n+1)}$ and $s = -1/(n+1)$. It implies that the stress field at infinity must approach the HRR-field. However it is shown that the remote boundary condition should be formulated in a more general form (3). The instantaneous response of a material characterized by equations (1) and (2) is non-linear viscous. The evolution of damage at short times after load application is concentrated in the vicinity of the crack tip and can be analysed under the remote boundary condition. If equation (3) represents the initial condition and the remote boundary condition, dimensional analysis shows that the damage mechanics equations must have similarity solution of the form

$$\sigma_{ij}(r,\varphi,t) = (At)^{-1/m}\Sigma_{ij}(R,\varphi), \quad \psi = \psi(R,\varphi), \quad R = r\tilde{C}^{1/s}(At)^{1/(sm)}\,. \tag{4}$$

The dimensionless functions Σ_{ij} and ψ are as yet unknown. The validity of these solutions has to be verified by insertion equations (4) into the governing equations (material law, compatibility and equilibrium equations) and boundary conditions.

ASYMPTOTIC SOLUTION

The asymptotic expansions of the effective stress (the stress referred to the surface that really transmits the internal forces) and the integrity parameter for large distances $(R \to \infty)$ from the crack tip are supposed to have the form

$$\Sigma_{ij} / \psi(R,\varphi) = R^{s} f_{ij}^{(0)}(\varphi) + R^{s_1} f_{ij}^{(1)}(\varphi) + \ldots \quad (s, s_1 < 0), \quad \psi(R,\varphi) = 1 - R^{\gamma} g^{(0)}(\varphi) - R^{\gamma_1} g^{(1)}(\varphi) + \ldots \quad (\gamma, \gamma_1 < 0). \tag{5}$$

Two-term asymptotic expansions for the effective stresses and integrity parameter (4) are sought outside of the totally damaged zone where the traditional Continuum Mechanics governing system of equations is not valid. The system of non-linear ordinary differential equations for the dimensionless functions $f_{ij}^{(k)}(\varphi), g^{(k)}(\varphi)$ is derived. The boundary value problem (the new eigenvalue problem for the eigenfunctions $f_{ij}^{(0)}(\varphi)$ and eigenvalue s) formulated is solved numerically using the Runge-Kutta-Fehlberg and a shooting method. Numerical results are presented in Table:

		Plane strain		Plane stress	
n	m	s	$f''(0)$	s	$f''(0)$
1	1	-1,5	-0,75	-1,5	-0,75
2	$0,7n$	-1,0	-0,5	-1,1540	-0,5686
3	$0,7n$	-0,7716	-0,4372	-1,0	-0,5
4	$0,7n$	-0,6684	-0,4092	-0,9133	-0,4658
5	$0,7n$	-0,6179	-0,3985	-0,8580	-0,4428
6	$0,7n$	-0,5901	-0,3950	-0,8197	-0,4261
7	$0,7n$	-0,5732	-0,3943	-0,7919	-0,4134
8	$0,7n$	-0,5621	-0,3948	-0,7708	-0,4035
9	$0,7n$	-0,5543	-0,3958	-0,7543	-0,3955

Here $f(\varphi)$ is the angular part of the Airy stress function $F(r,\varphi) = r^{s+2} f(\varphi)$ and $f''(0)$ is its second derivative on the line extending the crack. It is found that $s_1 = s + sm, \gamma = sm, \gamma_1 = 2sm$ and the geometry of the totally damaged zone is given by the equation $\psi(r,\varphi) = 1 - r^{\gamma} g^{(0)}(\varphi) - r^{\gamma_1} g^{(1)}(\varphi) = 0$.

CONCLUSIONS

It can be concluded that the HRR-field does not govern the geometry of the totally damaged zone. The new asymptotic stress field at infinity is found. It is shown that the configuration of the totally damaged zone is entirely determined by the far field stress obtained. The geometry of the totally damaged zone in the vicinity of the crack tip for $n = 3$ is given in Figure 1.

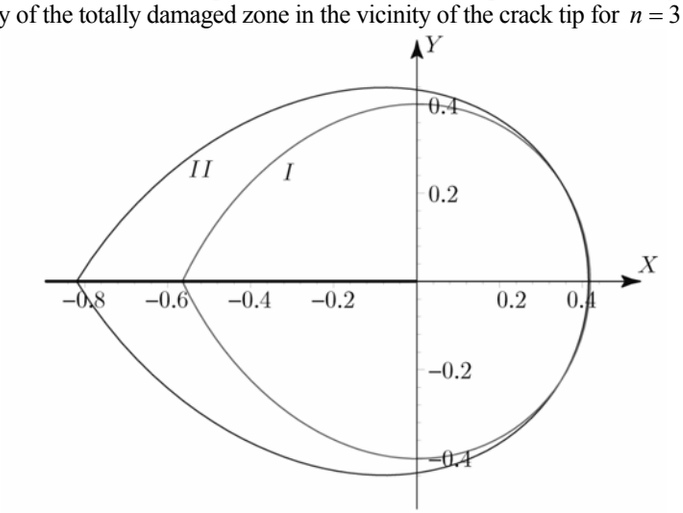


Figure 1. The geometry of the totally damaged zone in the crack tip region of a Mode I crack under plane strain conditions: I – the configuration given by the two-term asymptotic expansion of the continuity parameter, II - the configuration given by the three-term asymptotic expansion of the continuity parameter, $X = x\tilde{C}^{1/s}(At)^{1/(sm)}, Y = y\tilde{C}^{1/s}(At)^{1/(sm)}$.

References

[1] Zhao J., Zhang X.: The Asymptotic Study of Fatigue Crack Growth Based on Damage Mechanics. *Engn Fracture Mechanics* **50**:131-141, 1995.

[2] Zhao J., Zhang X.: On the Process Zone of a Quasi-Static Growing Tensile Crack With Power-Law Elastic-Plastic Damage. *In. J. of Fracture* **108**:383-395, 2001.

[3] Murakami S., Hirano T., Liu Y.: Asymptotic Fields of Stress and Damage of a Mode I Creep Crack in Steady-State Growth. *Int J. Solids Structures* **37**:6203-6220, 2000.

[4] Murakami S., Liu Y., Mizuno M.: Computational Methods for Creep Fracture Analysis by Damage Mechanics. *Comput Methods Appl Mech. Engrg* **183**:15-33, 2000.

[5] Riedel H.: Fracture at High Temperature. Springer, Berlin. 1987.

DAMAGE ACQUIRED ANISOTROPY IN ELASTIC-PLASTIC MATERIALS

Jacek J. Skrzypek, Halina Kuna-Ciskał, Jan Bielski*
*Institute of Applied Mechanics, Cracow University of Technology, Jana Pawła II 37, 31-864 Cracow, Poland

Summary Damage coupled model of elastic-moderate plastic material based on the concept by Hayakawa-Murakami is developed. Incremental matrix constitutive equations for plane stress conditions, that account for damage anisotropy and crack opening/closing effect, are explicitly derived and implemented to user subroutine of ABAQUS finite element code. Numerical examples illustrate consecutive stages of elastic-damage and plastic-damage as well as stiffness recovery on reverse loading.

A thermodynamically consistent framework for elasto-plasticity coupled with damage, based on existing state and dissipation coupling models, is discussed. Weak dissipation coupling, following a concept of existence of two dissipation potentials, plastic $F^{\mathrm{p}}(\boldsymbol{\sigma},R)$ and damage $F^{\mathrm{d}}(\mathbf{Y},B)$, expressed in the space of thermodynamic forces associated with the plasticity $(\boldsymbol{\varepsilon}^{\mathrm{p}},r)$ and damage $(\mathbf{D},\beta)$ variables, is focused. Crack opening/closing response to reverse loading cycles by the use of generalized projection operators that extends the Hansen and Schreyer [1] idea via the additional material constant $\zeta\in\langle 0,1\rangle$, $\overline{\mathbf{P}}_{\varepsilon/\sigma}=\mathbf{P}^{+}_{\varepsilon/\sigma}+\zeta\mathbf{P}^{-}_{\varepsilon/\sigma}$, is incorporated. This approach allows for effect of negative principal components of strain or stress tensor on damage evolution, as observed in brittle materials (cf. Murakami and Kamiya [2]).
The elastic-plastic-damage constitutive equations postulated in a total form and calibrated for spheroized graphite cast iron by Hayakawa and Murakami [3] are adopted. They are based on the assumption of the Gibbs state potential

$$\Gamma(\boldsymbol{\sigma},r,\mathbf{D},\beta)=\boldsymbol{\sigma}:\boldsymbol{\varepsilon}-\psi(\boldsymbol{\varepsilon}^{\mathrm{e}},r,\mathbf{D},\beta) \tag{1}$$

where ψ denotes the Helmholtz free energy per unit mass. based on the classical scheme the elastic strain and the conjugate forces are

$$\boldsymbol{\varepsilon}^{\mathrm{e}}=\frac{\partial\Gamma}{\partial\boldsymbol{\sigma}}={}^{\mathrm{s}}\mathbf{C}^{\mathrm{e}}(\mathbf{D}):\boldsymbol{\sigma},\ R=\frac{\partial\Gamma}{\partial r},\ \mathbf{Y}=\frac{\partial\Gamma}{\partial\mathbf{D}},\ B=\frac{\partial\Gamma}{\partial\beta} \tag{2}$$

where ${}^{\mathrm{s}}\mathbf{C}^{\mathrm{e}}(\mathbf{D})$ stands for the effective, secant elastic-damage compliance tensor.
The dissipation potential is composed of two coupled parts

$$F(X_m;r,\mathbf{D},\beta)=F^{\mathrm{p}}(\boldsymbol{\sigma},R;\mathbf{D})+F^{\mathrm{d}}(\mathbf{Y},B;\mathbf{D},r,\beta) \tag{3}$$

hence, when the extended normality rule is assumed both for plastic and damage surfaces, the plasticity and damage fluxes are controlled by two Lagrange multipliers $\dot{\lambda}^{\mathrm{p}}$ and $\dot{\lambda}^{\mathrm{d}}$

$$\dot{\boldsymbol{\varepsilon}}^{\mathrm{p}}=\dot{\lambda}^{\mathrm{p}}\frac{\partial F^{\mathrm{p}}}{\partial\boldsymbol{\sigma}},\ \dot{r}=\dot{\lambda}^{\mathrm{p}}\frac{\partial F^{\mathrm{p}}}{\partial(-R)},\ \dot{\mathbf{D}}=\dot{\lambda}^{\mathrm{d}}\frac{\partial F^{\mathrm{d}}}{\partial\mathbf{Y}},\ \dot{\beta}=\dot{\lambda}^{\mathrm{d}}\frac{\partial F^{\mathrm{d}}}{\partial(-B)} \tag{4}$$

The Khun-Tucker relations are used in order to specify loading/unloading conditions for plasticity and damage, respectively

$$\dot{\lambda}^{\mathrm{p/d}}\geq 0,\ F^{\mathrm{p/d}}=0,\ \dot{\lambda}^{\mathrm{p/d}}F^{\mathrm{p/d}}=0. \tag{5}$$

In order to derive elastic-damage equation in the incremental form

$$\{\dot{\boldsymbol{\varepsilon}}^{\mathrm{e}}\}=\mathbf{C}^{\mathrm{e}}(\boldsymbol{\sigma},\mathbf{D},\mathbf{Y})\{\dot{\boldsymbol{\sigma}}\} \tag{6}$$

we follow procedure described in Kuna-Ciskał and Skrzypek [4] where the effective, tangent elastic-damage stiffness matrix was determined based on the relevant model of elastic-damage materials [2]. The effective, tangent elastic-damage compliance tensor is determined according to the scheme

$$\mathbf{C}^{\mathrm{e}}(\boldsymbol{\sigma},\mathbf{D},\mathbf{Y})={}^{\mathrm{s}}\mathbf{C}^{\mathrm{e}}(\mathbf{D})+\frac{\partial{}^{\mathrm{s}}\mathbf{C}^{\mathrm{e}}(\mathbf{D})}{\partial\mathbf{D}}:\frac{\partial\mathbf{D}}{\partial\boldsymbol{\sigma}}:\boldsymbol{\sigma} \tag{7}$$

Plastic-damage strain increment is furnished as (cf. Bielski, Kuna-Ciskał and Skrzypek [5])

$$\{\dot{\boldsymbol{\varepsilon}}^{\mathrm{p}}\}=\mathbf{C}^{\mathrm{p}}(\boldsymbol{\sigma},\mathbf{D},\mathbf{Y},r)\{\dot{\boldsymbol{\sigma}}\} \tag{8}$$

Finally, in frame of small strain theory, we end-up with the general elastic-plastic-damage constitutive equation in the incremental form

$$\{\dot{\boldsymbol{\varepsilon}}\}=\mathbf{C}(\boldsymbol{\sigma},\mathbf{D},\mathbf{Y},r)\{\dot{\boldsymbol{\sigma}}\} \tag{9}$$

with the local compliance matrix $\mathbf{C}=\mathbf{C}^{\mathrm{e}}(\boldsymbol{\sigma},\mathbf{D},\mathbf{Y})+\mathbf{C}^{\mathrm{p}}(\boldsymbol{\sigma},\mathbf{D},\mathbf{Y},r)$ dependent on variables at the consecutive equilibrium point. When deriving equations (6), where unilateral damage effect is included by a concept of the modified stress

tensor $\overline{\sigma}_{ij} = B_{ijkl}\sigma_{kl}$ (cf. [3]), the main difficulty arises from the incremental transformation tensor $D_{ijkl} = \frac{\partial \overline{\sigma}_{ij}}{\partial \sigma_{kl}}$, the explicit application of which is somewhat cumbersome.

Hence, following [4], in the present paper we apply simplified formulae for the matrices $\mathbf{B}$ and $\mathbf{D}$, in order to derive explicit form of the compliance matrix $\mathbf{C}$ in plane stress $\sigma_{33} = 0$ conditions $\boldsymbol{\sigma} = \{\sigma_{11}, \sigma_{22}, \sigma_{12}\}$. In case of plane stress the plane rotation by the angle α of the stress tensor from a current system σ_{kl} to principal directions σ_I, modification to $\overline{\sigma}_I$ and backward transformation to the current system must be performed, such that, according to the procedure for complex function, the following holds

$$\frac{\partial \overline{\sigma}_{ij}}{\partial \sigma_{kl}} = B_{ijkl} + \frac{\partial B_{ijpq}}{\partial \alpha}\frac{\partial \alpha}{\partial \sigma_{kl}}\sigma_{pq} \tag{10}$$

Taking inverse of the matrix $\mathbf{C}$ the increments of stresses are calculated as

$$\{\dot{\boldsymbol{\sigma}}\} = \mathbf{C}^{-1}\{\dot{\boldsymbol{\varepsilon}}\} \tag{11}$$

where damage-coupled elastic-plastic stiffness $\mathbf{C}^{-1}$ is accepted as an approximation of the local Jacobian matrix of the constitutive model implemented to the ABAQUS finite element code. Effective algorithm for plastic and damage loading/unloading conditions based on the doubly-passive predictor-plastic/damage corrector approach is used. A more general, fully coupled return mapping computational algorithm, is due to Zhu and Cescotto [6].

Numerical examples illustrate capability of the model developed to simulate anisotropic damage effect on elastic and elastic-plastic response of simple structures under plane stress conditions. Partial stiffness recovery on reverse uniaxial loading cycles is also captured.

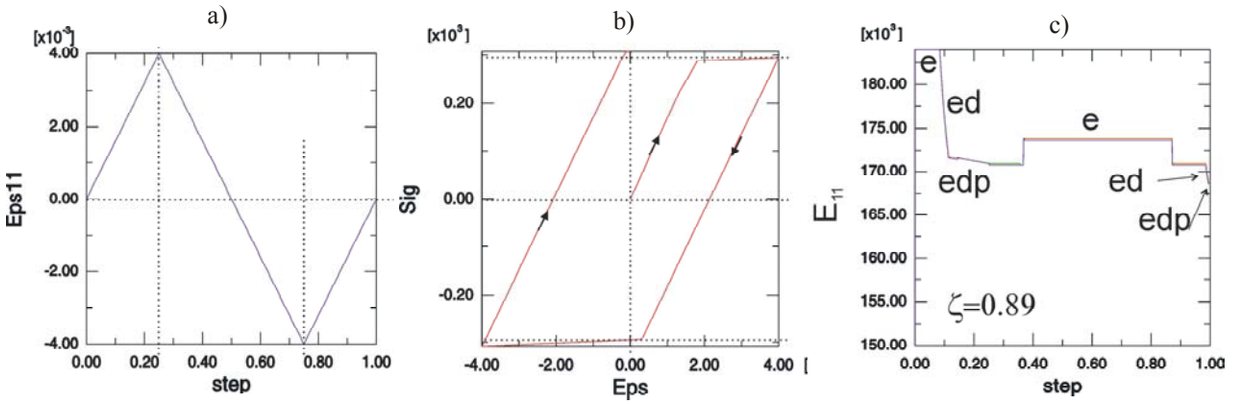


Fig.1.a) kinematic loading cycle; b) stress-strain hysteresis loop; c) elastic stiffness recovery

References

[1] Hansen N.R., Schreyer H.L.: A thermodynamically consistent framework for theories of elastoplasticity coupled with damage. *Int. J. Solids Struct., 31, 359-389, 1994.*

[2] Murakami S., Kamiya K.: Constitutive and damage evolution equations of elastic-brittle materials based on irreversible thermodynamics. *Int. J. Mech. Sci., 39,473-486, 1997.*

[3] Hayakawa K., Murakami S.: Thermodynamical modeling of elastic-plastic damage, an experimental validation of damage potential. *Int. J. Damage Mech., 6,333-363, 1997.*

[4] Kuna-Ciskał H., Skrzypek J.: CDM based modelling of damage and fracture mechanisms in concrete under tension and compression. *Eng. Fracture Mech., 71/4-6, 681-698, 2003.*

[5] Bielski J., Kuna-Ciskał H., Skrzypek J.: Numerical analysis of damage and fracture in elastic-plastic-damage materials. *Proc. Int. Symp. ABDM-2002, CD.*

[6] Zhu Y.Y., Cescotto S.: A fully coupled elasto-visco-plastic damage theory for anisotropic materials. *Int. J. Solids Struct., 32, 1609-1641, 1995.*

A CDM APPROACH OF DUCTILE DAMAGE WITH PLASTIC VOLUME CHANGES

J.L. Chaboche*, K. Saanouni**, M. Boudifa**
* Onera, Dept. MSE, 92322 Châtillon, France
** Univ. of Technology of Troyes, LASMIS, 10000 Troyes, France

Abstract Continuum Damage Mechanics appr oaches for ductile damage are revisited in order to incorporate plastic volume changes in conformation with micromechanics based approaches. The theory is still consistent with a general thermodynamic framework and allows the possibility for damage anisotropy as well as damage deactivation effects. Systematic comparisons are made for various multiaxial loading conditions and some applications are shown in the context of metal forming simulation.

GENERAL CONTEXT

Since a long time Continuum Damage Mechanics (CDM) concepts have been developed that obey a general thermodynamic framework. The theories proposed in the past by one of the authors, mainly for creep damage in metals and for the brittle and inelastic behaviour of composite systems, show several intere sting capabilities such as the damage anisotropy [1-2] (by second or fourth rank tensors) and the damage deactivation effects [3], both in terms of the actual mechanical behaviour of the damaged material and for the subsequent damage evolutions under compl ex non proportional loadings.

However, in the context of ductile damage of metals, the corresponding developments were not made inside the same modelling framework. The nearest approaches are made by Lemaître's school [4], mainly within isotropic damage variables. Similar theories based on the energy equivalence principle were also developed by Saanouni and co-workers, extensively applied for the simulation of metal forming processes [5]. Though expressed in a general thermodynamic framework, one of the lim itations of the above theories is to not consider properly the possibility for a volumetric plastic strain associated with the volumic damage development.

This is the main objective of the present paper to review some possibilities and to show how the stan dard thermodynamic framework can be extended in order to include such volumetric plastic strains that play important roles in the ductile fracture under high triaxialities, and are well incorporated into micromechanics based Gurson like approaches [6].

MODEL DEVELOPMENT

The concept of an effective stress based on a strain equivalence assumption is still used throughout the present theoretical development. It allows the consistent mechanical coupling between damage and both the elastic and plastic behaviours. Limiting here to the isothermal, small strain, rate independent framework, and to isotropic hardening and isotropic damage, we propose several coupled yield functions for the modelling of plastic flow. The two first ones are written in the context of a macroscopic CDM approach, incorporating the first stress invariant in various ways :

Parabolic model : $$f_p = \tilde{\sigma}_{eq} + \alpha^* D \frac{(Tr\tilde{\sigma})^2}{\tilde{R}+k} - \tilde{R} - k \le 0 \qquad (1)$$

Elliptic model : $$f_p = \sqrt{\tilde{\sigma}_{eq} + \alpha^* D (Tr\tilde{\sigma})^2} - \tilde{R} - k \le 0 \qquad (2)$$

In which $\tilde{\sigma}$ denotes the effective stress tensor, $\tilde{\sigma} = \sigma/(1-D)$ in the isotropic damage case, and $\tilde{R}$ is the corresponding isotropic hardening effect. K is the initial plastic threshold and $\alpha^* = \alpha + \beta\ Sgn(Tr\sigma)$ a material dependent parameter, depending on the sign of the first stress invariant, in order to adjust plastic volume changes under negative triaxialities. The damage growth obeys a pseudo standard format [2], with an independent dissipation potential that can be chosen Lemaître's form or any other.

A third model is developed in a micromechanics approach of polycrystals, through a scale change based on a self-consistent rule), in which the crystal plasticity is coupled to the slip damage evolutions through a Non Schmid la written at the level of each slip system.

SYSTEMATIC COMPARISONS

The developed models have been compared with classical ones, including the well known Gurson model, and the Rousselier model [7] (also incorporated in a consistent thermodynamic framework). Figure 1 illustrates the corresponding yield criteria at two stages of damage development (or volume fraction of cavities). The models have been implemented in the Z-Set platform (ZéBuLoN finite element code), and used systematically for convergence studies. In the case of the elliptic model (2), very near from Gurson's, figure 2 illustrates the evolutions of the

equivalent stress / hydrostatic stress, as well as the corresponding yield surfaces, during an elastoplastic -damage loading under strain control in which the total shear strain ε_{12} and the $Tr\varepsilon = \varepsilon_{11} + \varepsilon_{22} + \varepsilon_{33}$ are increasing proportionally. It has been shown that a limit point may exist, when changing the ratio between shear and hydrostatic strain controls, for which the damage cannot attain its critical value ($D=1$) and the stress cannot vanish continuously, even in the case of a representative volume element (the Gauss point level).

Compared to other approaches, the present one is thought to offer more capabilities and flexibilities. Thanks to previous works in other contexts, its generalization to the anisotropic damage evolutions, including non-proportional paths, seems to be straightforward, at least from a theoretical standpoint.

References

[1] Chaboche, J.L.: Anisotropic creep damage in the framework of Continuum Damag e Mechanics, "Nuclear Engng. and Design", 79:309 -319, 1984.

[2] Chaboche, J.L.: Thermodynamically founded CDM models for creep and other conditions, CISM Courses, "Creep and Damage in Materials and Structures", H. Altenbach and J.J. Skrzypek eds., Springer,.209-283, 1999.

[3] Chaboche, J.L., Maire, J.F.: A new micromechanics based CDM model and its application to CMC's, Aerospace Science and Technology, 6(2):131-145, 2002.

[4] Lemaître J.: "A course on Damage Mechanics", Springer-Verlag, 1992.

[5] Saanouni, K., Cherouat, A. and Hammi, Y: Numerical aspects of finite elastoplasticity with isotropic ductile damage for metal forming, Revue Européenne des Eléments Finis, 10(2-3-4):327-351, 2001.

[6] Tvergaard, V. and Needleman, A.:The modified Gurson model. In “H andbook of Materials Behavior Models”, J. Lemaître Ed, Academic Press, 2(6.5):430-435, 2001.

[7] Rousselier, G.: The Rousselier model for porous metal plasticity and ductile Fracture, In “Handbook of Materials Behavior Models”, J.Lemaître Ed, Academic Press, 2(6.6):436-445, 2001.

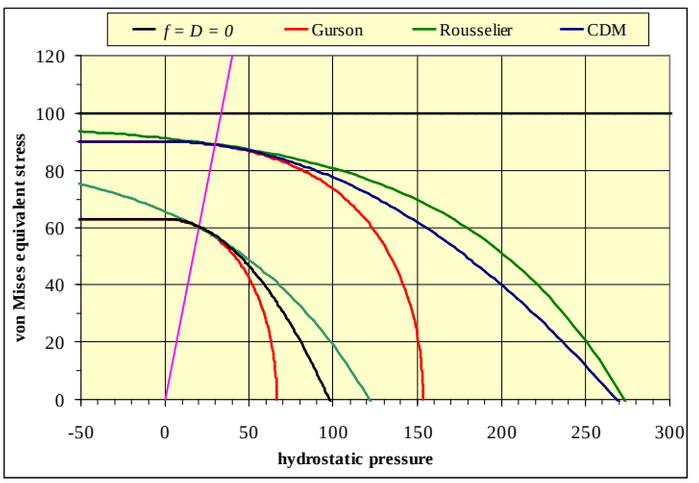


Fig. 1 : yield surfaces with the 3 models at two stages of damage development

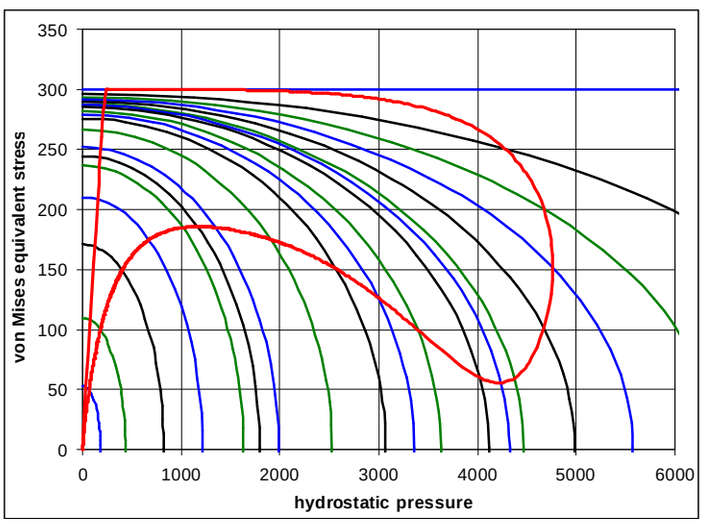


Fig. 2 : evolution of the yield surfaces with the CDM elliptical model for a proportional shear/hydrostatic stra in evolution

MICROMECHANICAL MODELLING OF THE DEFORMATION AND DAMAGE OF INELASTIC BRITTLE THREE-PHASE COMPOSITES: APPLICATION TO FIBER-REINFORCED CONCRETE

A. Ouaar*,**, I. Doghri*, J-Fr Thimus**, F. Hugé**
*CESAME/U.C.L, Bâtiment Euler, avenue Georges Lemaître, 4. 1348 L-L-N BELGIUM.
**Unité de Génie Civil et Environnemental/U.C.L, Bâtiment Vinci, Place du Levant, 1. 1348 L-L-N BELGIUM

Summary : This paper deals with some aspects of the modelling, simulation and experimentation of the deformation and damage of a class of non-linear three-phase brittle composite materials. To this end, Mori-Tanaka micromechanical model is used. The predictions obtained by our model are validated against finite element simulations and experimental results performed on Steel Fiber-Reinforced Concrete specimens.

Introduction

In the last decades, composite materials have occupied a great place in industrial applications. Consequently the study and the prediction of their mechanical behaviour have taken a crucial importance. In the present study, we have focused our work on some aspects of the modelling, simulations and experimentation of a class of inelastic brittle three-phase composite materials.

Micromechanical modelling

The aim of this section is to predict the mechanical response of an inelastic matrix containing perfectly bonded elastoplastic inclusions (spheres or ellipsoids) and cavities by means of the Mori-Tanaka homogenization scheme. To this end, we consider our three-phase composite as an aggregate made of two grains, one containing inclusions and matrix material, the other one containing cavities also embedded in the matrix phase. Next, each grain is homogenized using Mori-Tanaka model. Finally the set of the two homogenous grains is itself homogenized following Voigt scheme. After some algebraic developments we obtain the following expression of the homogenized non-linear tangent operator which relates the macro-strain to the macro-stress rates.

$\overline{C}(t) = C^{nl}_{ref}(t) + v_1[C^{nl}_1(t) - C^{nl}_{ref}(t)] : A_1 - v_2 C^{nl}_{ref}(t) : A_2$ where $A_{1,2}$ are the strain concentration tensors for each phase and C^{nl}_{ref} refers to the stiffness of a reference material which represents the matrix phase. We also assume that all non-linear operators are spatially uniform and vary with time.

Constitutive models

The damage in the matrix phase which occurs in the form of microcraks growth and coalescence, is accommodated with the help of Ju's model [2]. It is an energy-based damage model which the damage in the material is linked to the history of elastic plastic state variables. In our study, we only consider the case of elasticity coupled with damage. In summary, the model proposed by Ju gives the following expression of the damaged stiffness:

$$C^d_{t_{n+1}} = \begin{cases} C^d_{t_n} & \text{if } \tilde{G} - r \le 0 \\ C^d_{t_{n+1}} - \left(\xi_{t_{n+1}} - \xi_{t_n}\right) H_{t_{n+1}} P^+_{t_{n+1}} : C^0 : P^+_{t_{n+1}} & \text{if not} \end{cases}$$

One can see from this equation that the stiffness is governed by a competition between available energy "*G*"and suitable energy for damage "*r*". "*H*" represents the damage evolution function, ξ is a characteristic damage measure, C^0 is the elastic stiffness and P^+ is a positive projection tensor. This model also assumes a spectral decomposition of the strain tensor to take into account the anisotropic damage. Since the composite is assumed to be damaged only under tensile strains, the expression of ξ takes the following form:

$\xi = \frac{1}{2}\varepsilon^+ : C^0 : \varepsilon^+$. The elastoplastic behaviour of the reinforcement is described by the classical J_2 plasticity theory. To handle those constitutive models in our micromechanical modelling, we have developed a robust numerical algorithm for an incremental tangent formulation which enables us to predict and simulate within reasonable CPU time and memory the response of such composite materials. In this algorithmic part we have pointed out the crucial issue of the computation of the Eshelby tensor [1]. We have resolved this problem by extracting the isotropic part of the anisotropic non-linear operator of the matrix phase. From this isotropic part we compute the

instantaneous Poisson's coefficient which is needed for Eshelby's tensor computation. There are many ways to perform this extraction[1], in this work we use the following one:

$$C^{iso} = \frac{1}{3} C^{ani}_{lljj}\, I^{vol} + \frac{1}{5}\left(C^{ani}_{lljj} - \frac{1}{3} C^{ani}_{lljj}\right) I^{dev} \qquad \nu = \frac{C^{iso}_{1122}}{C^{iso}_{1111} + C^{iso}_{1122}}$$

We have seen that Ju's model is developed in a secant formulation and gives a secant damaged operator, to agree with our incremental formulation we have used the perturbation technique in order to compute the tangent damaged operator.

Experimental study

As an application, we have studied the mechanical behaviour of Steel Fiber Reinforced Concrete (SFRC). Several specimens of concrete and fiber-reinforced concrete with different volume fractions of fibers were manufactured. Those specimens were tested under four point bending. The tests on concrete specimens have allowed us to fit the parameters of Ju's model, the others were used in the validation step of our numerical code. The first results obtained seem to indicate that when fibers are added to concrete with a given volume fraction, the porosity increases and becomes significant. This lead us to consider our initially two-phase composite as a three phase one with cavities as the third phase. To make those experimental results useful, we also have developed a tangent formulation and it's corresponding numerical algorithm to allow us the construction of the stress-strain curve from the load-deflection one in the non-linear regime. The key idea of this formulation is to relate the increment of bending moment to the increment of the normal stress for a given cross section.

$M_i = B\left[\int_0^{H-C} \sigma_i\, y dy + \int_{-C}^{0} \sigma_i\, y\, dy\right]$ where B and H are the geometric characteristics of the section and C the position of the neutral axis and the stress at the i th increment is given by: $\sigma_i = \sigma_{i-1} + k_i\,(\varepsilon - \varepsilon_{i-1})$

Numerical simulations

The efficiency of our code is evaluated through numerical simulations compared against both 2D and 3D F.E simulations fig.1 and experimental results. Several discriminating tests were simulated, fig. 2 show an example.of FRC with 10% of volume fraction of fibers under cyclic tensile and compressive loading. We also validated our numerical predictions against our experimental results.

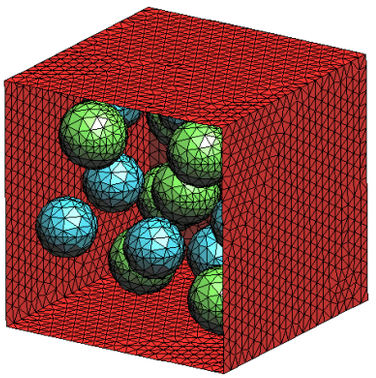


Fig. 1. 3D F.E simulations on a periodic cubic cell

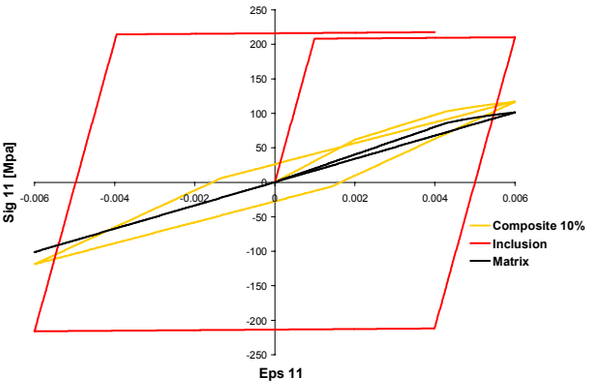


Fig. 2. Steel Fiber-Reinforced Concrete under cyclic loading

References

1. I. Doghri, A .Ouaar, Homogenization of two-phase elasto-plastic composite materials and structures. Study of tangent operators, cyclic plasticity and numerical algorithms. Int. J. Solids and Structures 40(2003) 1681-1712.
2. J.W.Ju, On energy-based coupled elastoplastic damage theories: Constitutive modeling and computational aspects. Int. J. Solids and Structures 25(1989) 803-833.

XXI ICTAM, 15–21 August 2004, Warsaw, Poland

DAMAGE FIELD IDENTIFICATION USING FULL-FIELD DISPLACEMENT MEASUREMENTS

Damien Claire, François Hild,* Stéphane Roux**
*LMT-Cachan, ENS de Cachan / CNRS-UMR 8535 / Université Paris 6
61 avenue du Président Wilson, F-94235 Cachan Cedex, France
**Laboratoire "Surface du Verre et Interfaces", UMR CNRS/Saint Gobain 125
39 quai Lucien Lefranc, F-93303 Aubervilliers Cedex, France

Summary It is proposed to determine damage parameters in two dimensions (surface of a material) or three dimensions (in the bulk of a solid) by using full-field displacement measurements. A finite-element approach is developed to evaluate piece-wise constant elastic parameters modeled by an isotropic damage variable. Two sets of examples are discussed. The first series deals with mechanical fields obtained by finite element simulations to assess the performance of the approach. The second series is concerned with displacement measurements performed during a biaxial test on a composite material.

INTRODUCTION

The current development of reliable displacement field measurement techniques enables one to better characterize the behavior of materials and the response of structures to external loadings. Homogeneous materials under complex load histories or heterogeneous microstructures induce kinematic fields that require full-field analyses to understand the interactions between the material microstructure and the external loading. Full-field measurements often need inversion techniques to determine the mechanical properties field of the materials. Updating techniques based upon the constitutive equation error [1, 2, 3] have been used in the analysis of vibrations [4], the determination of damage fields [5] or to study heterogeneous tests (*e.g.,* Brazilian test [6]). Similarly, the so-called virtual field method has been used to identify homogeneous properties of composites [7, 8] (*i.e.,* in anisotropic elasticity). Another procedure is based upon the reciprocity gap [9] that can also be used to determine the local elastic field or to detect cracks in elastic media [10]. An alternative method that only needs displacement field data is proposed. In the present case, the in-plane displacements are measured on surfaces of samples by digital image correlation. It therefore consists in identifying elastic property fields on the surface of a sample.

THE EQUILIBRIUM GAP METHOD

An identification formulation is derived in which the displacements $\boldsymbol{u}(\boldsymbol{x})$ are *known* and the elastic properties are unknown. This problem setting is unconventional in the sense that classical FE formulations assume known mechanical properties and try to determine the displacement field for different types of boundary conditions. The potential energy theorem allows for a weak formulation of the equilibrium equations, which is linearly dependent on the displacements *and* elastic properties. Quadratic square elements are considered for which each node corresponds to a measurement point. This hypothesis allows us to derive a specific formulation in which only middle nodes are considered. When the damage parameter D_e is constant for a given element e occupying a domain Ω_e, the elementary stiffness matrix can be written as

$$[\boldsymbol{K}_{me}](D_e) = (1 - D_e)[\boldsymbol{K}_{me0}] \tag{1}$$

where $[\boldsymbol{K}_{me0}]$ is the elementary stiffness matrix of an undamaged element. Similarly, the strain energy E_{me} can be written as

$$E_{me}(D_e, \{\boldsymbol{u}_e\}) = \frac{1 - D_e}{2}\{\boldsymbol{u}_e\}^t[\boldsymbol{K}_{me0}]\{\boldsymbol{u}_e\}, \tag{2}$$

where $\{\boldsymbol{u}_e\}$ is the nodal displacement column vector and ^{t} the matrix transposition. In the absence of external load on the considered nodes, a residual force $\boldsymbol{F}_r$ for each middle node '$\pm$' of two neighboring elements '$-$' and '$+$' arises when equilibrium is not satisfied

$$\boldsymbol{F}_r = \frac{\partial E_{m\pm}}{\partial \boldsymbol{u}_\pm}(D_e^-, D_e^+, \{\boldsymbol{u}_e^-\} = \{\boldsymbol{u}_m^-\}, \{\boldsymbol{u}_e^+\} = \{\boldsymbol{u}_m^+\}), \tag{3}$$

with $E_{m\pm}(D_e^-, D_e^+, \{\boldsymbol{u}_e^-\}, \{\boldsymbol{u}_e^+\}) = E_{me}(D_e^-, \{\boldsymbol{u}_e^-\}) + E_{me}(D_e^+, \{\boldsymbol{u}_e^+\})$, where $\boldsymbol{u}_\pm$ is the displacement vector of the considered middle node '$\pm$', D_e^-, D_e^+ are the damage variables in elements '$-$' and '$+$', respectively. In Eqn. (3), the nodal displacements $\{\boldsymbol{u}_e^-\}$ and $\{\boldsymbol{u}_e^+\}$ are equal to the corresponding measurements $\{\boldsymbol{u}_m^-\}$ and $\{\boldsymbol{u}_m^+\}$. The equilibrium gap method consists in minimizing a norm of the residuals $\boldsymbol{F}_r$ with respect to the unknowns D_e^- and D_e^+. By considering all the equilibrium equations, a global (over-determined) linear system is obtained [11]. Based upon the residuals, local error indicators are introduced. Of those, a whole family can be defined when the exact solution is unknown.

APPLICATIONS

A first series of computations considers a structure discretized with quadratic elements. Three edges are clamped and, in the middle of the fourth one, a point-force is applied. A uniform damage distribution is chosen and varies between 0 and 0.9. The first step consists in running a conventional FE analysis. The nodal displacements (*i.e.*, the “measurements") are stored and constitute the inputs to the damage identification procedure. The aim is to use the non-standard FE formulation to recover the damage field. Since the damage field is known, an RMS error between the prescribed and identified damage values can be used. For more than 2400 elements, a maximum error of 5.1% is observed for all the analyzed configurations [11].

Second, a vinylester matrix reinforced by E glass fibers is studied. A quasi-uniform distribution of orientations leads to an isotropic elastic behavior prior to matrix cracking and fiber breakage, which are the main damage mechanisms. A cross-shaped specimen is loaded in a multiaxial testing machine (Fig. 1-a). The experiment is performed in such a way that the forces applied along two perpendicular directions are identical. The displacement field of Fig. 1-b is measured by digital image correlation. Each “measurement point” corresponds to the center of an interrogation window of size 64×64 pixels, equivalent to a surface of about 8 mm^2. At this scale, the material is not homogeneous (see Fig. 1-a). The shift between two neighboring measurement points is 32 pixels. A sub-pixel algorithm is used. It enables for a displacement resolution of a few hundredths of one pixel for 8-bit pictures. To achieve a better robustness, an iterative and multi-scale version was used [12]. Figure 1-c shows the damage field computed from the measured displacement field. From the analysis of Fig. 1-b, a crack clearly appears on the top left corner for the last load level before failure. This crack can be observed by the three dark elements.

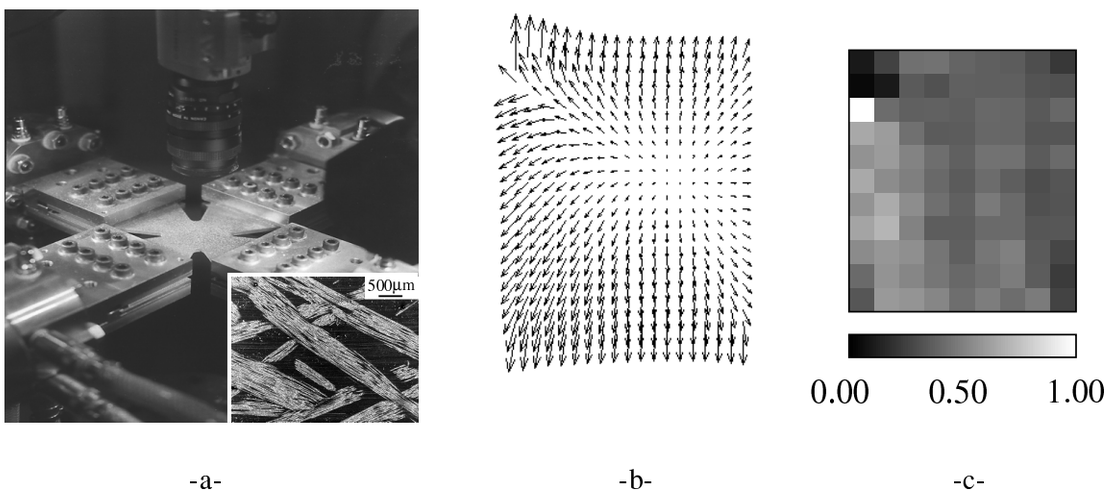


Figure 1. a-Sample in the testing machine ASTRÉE and microstructure of the studied composite. b-Displacement fields measured by digital image correlation for one load level close to failure. c-Corresponding damage field $(1 - D)$ identified with the proposed approach.

References

[1] Ladevèze P. Technical report Aérospatiale, les Mureaux (France), **33.11.01.4**, 1983.
[2] Kohn R.V., Lowe B.D. *Math. Mod. Num. Ana.* **22**: 119-158, 1988.
[3] Bui H.D., Constantinescu A. *Arch. Mech.* **52**: 511-522, 2000.
[4] Ladevèze P., Nedjar D., Reynier M. *AIAA* **32**: 1485-1491, 1994.
[5] Geymonat G., Hild F., Pagano S. *C. R. Mecanique* **330**: 403-408, 2002.
[6] Calloch S., Dureisseix D., Hild F. *Technologies et Formations* **100**: 36-41, 2002.
[7] Grédiac M. *C. R. Acad Sci. Paris* **309** [Série II]: 1-5, 1989.
[8] Grédiac M., Toussaint E., Pierron F. *C. R. Mecanique* **330**: 107-112, 2002.
[9] Bui H.D. *C. R. 2^e Colloque national de calcul des structures*. Hermès, Paris **1**: 25-35, 1995.
[10] Andrieux S., Ben Abda A., Bui H.D. *Inverse Problems* **15**: 59-65, 1999.
[11] Claire D., Hild F., Roux S. *C. R. Mecanique* **330**: 729-734, 2002.
[12] Hild F., Raka B., Baudequin M., Roux S., Cantelaube F. *Appl. Optics* **IP 41**: 6815-6828, 2002.

A NEW ENERGY-BASED ELASTOPLASTIC DAMAGE MODEL FOR CONCRETE

Jianying Wu*, Jie Li*
*Building Engineering Department, Tongji University, Shanghai, China

Summary In this paper, a new elastoplastic damage model is proposed, in which tensile damage variable and shear damage variable are adopted to describe the degradation of macro-mechanical properties of concrete. Within the framework of continuum damage mechanics, an elegant constitutive law which is the same as the effective stress concept is obtained. The plastic Helmholtz free energy is accounted for the damage growth, and the damage criteria are based on the elastoplastic damage energy release rates, which is consistent with thermodynamics theory. The evolutions of damage variables and plastic strains are established based on the normal rule and the effective stress space plasticity, respectively. Some pertinent computational aspects concerning the numerical algorithm are discussed. The model has been coded into a general finite element program which is capable of predicting the nonlinear behaviours of concrete under different stress states, whose predictive results demonstrate its adequate accuracy for the intended applications.

INTRODUCTION

Damage criteria are of significant importance to a damage model. In the current literatures, several different methods, including the equivalent strain-based, certain stress-based, and damage energy release rate-based, are adopted to define the damage criteria. Just as in classical plasticity most of yield criteria are functions of the invariants of stress tensor which is conjugated to plastic strain tensor, being the thermodynamic forces conjugated to damage variables, the damage energy release rate based damage criteria are more thermodynamically consistent[1],[2].However, the energy release rates based damage model of Mazars[1] and Ju[2] can predict neither the strength enhance in compression-compression stress states, nor the softening effect in the tension-compression stress states.
This paper attempts to present a novel rate-independent elastoplastic damage model for concrete, which not only is consistent with thermodynamics theory, but also fits the experimental results fairly well.

BASIC FORMULATIONS

Damage mechanisms

From the experimental phenomena observed, three types of mechanisms leading to the failure of concrete can be distinguished: tensile damage, shear damage, and compressive consolidation which results in the collapse of the micro-porous structure of the cement matrix under high hydrostatic compression and is not considered in present model.
Thus as generally accepted, there are two basic but distinct damage mechanisms that result in the degradation of macro-mechanical properties of concrete, which can be described by tensile damage variable d^+ and shear damage variable d^-, corresponding to pure tension and pure compression, respectively.

Elastoplastic Damage model

The classical effective stress is generally defined and can be decomposed as following[2],[3]:

$$\bar{\boldsymbol{\sigma}} = \mathbf{C}_0 : \left(\boldsymbol{\varepsilon} - \boldsymbol{\varepsilon}^p\right) = \bar{\boldsymbol{\sigma}}^+ + \bar{\boldsymbol{\sigma}}^-; \quad \bar{\boldsymbol{\sigma}}^+ = \mathbf{P}^+ : \bar{\boldsymbol{\sigma}}; \quad \bar{\boldsymbol{\sigma}}^- = \bar{\boldsymbol{\sigma}} - \bar{\boldsymbol{\sigma}}^+ = \mathbf{P}^- : \bar{\boldsymbol{\sigma}} \tag{1}$$

and the ratio of effective stress can also be similarly decomposed as:

$$\dot{\bar{\boldsymbol{\sigma}}} = \mathbf{C}_0 : \left(\dot{\boldsymbol{\varepsilon}} - \dot{\boldsymbol{\varepsilon}}^p\right) = \dot{\bar{\boldsymbol{\sigma}}}^+ + \dot{\bar{\boldsymbol{\sigma}}}^-; \quad \dot{\bar{\boldsymbol{\sigma}}}^+ = \mathbf{Q}^+ : \dot{\bar{\boldsymbol{\sigma}}}; \quad \dot{\bar{\boldsymbol{\sigma}}}^- = \dot{\bar{\boldsymbol{\sigma}}} - \dot{\bar{\boldsymbol{\sigma}}}^+ = \mathbf{Q}^- : \dot{\bar{\boldsymbol{\sigma}}} \tag{2}$$

where $\mathbf{C_0}$ denotes the usual fourth-order isotropic linear-elastic constitutive tensor; $\mathbf{P}^+$ and $\mathbf{P}^-$, $\mathbf{Q}^+$ and $\mathbf{Q}^-$ are all fourth-order symmetric tensor, introduced as the positive and negative projection tensors of $\bar{\boldsymbol{\sigma}}$ and $\dot{\bar{\boldsymbol{\sigma}}}$, respectively.
With elastic Helmholtz free energy defined as the degradation of initial free energy[2], relations can be derived as:

$$\boldsymbol{\sigma} = \left(\mathbf{I} - \mathbf{D}\right) : \bar{\boldsymbol{\sigma}}; \quad \mathbf{D} = d^+\mathbf{P}^+ + d^-\mathbf{P}^- \tag{3}$$

which is the same as the classical effective stress concept, and $\mathbf{D}$ is the fourth-order damage tensor.

Damage criteria

After the plastic free energy is considered, the following damage energy release rates can be obtained:

$$Y^+ = \sqrt{E_0\left(\bar{\boldsymbol{\sigma}}^+ : \boldsymbol{\Lambda}_0 : \bar{\boldsymbol{\sigma}}\right)}; \quad Y^- = \alpha\bar{I}_1 + \sqrt{3\bar{J}_2} \tag{4}$$

Then the damage criteria can be established as[2],[3]:

$$g^{\pm}(Y_n^{\pm}, r_n^{\pm}) = Y_n^{\pm} - r_n^{\pm} \le 0 \tag{5}$$

In eqn. (5), the thresholds of damage energy release rates $r_n^{\pm}$ are determined as:

$$r_n^{\pm} = \max\left\{r_0^{\pm}, \max_{\tau\in[0,n]} Y_\tau^{\pm}\right\} \tag{6}$$

where $r_0^{\pm}$ are the initial thresholds which can be expressed applying eqn.(4) under axial tension and axial compression.

Evolution laws of damage variables

Applying the normal rule, analogous to the plasticity, following evolution laws of damage variables are established:

$$\dot{d}^{\pm} = \dot{\lambda}^{d^{\pm}} h^{d^{\pm}}; \dot{\lambda}^{d^{\pm}} = \dot{r}_n^{\pm} = \dot{Y}_n^{\pm}; g^{\pm}\left(Y_n^{\pm}, r_n^{\pm}\right) \le 0, \dot{\lambda}^{d^{\pm}} \ge 0, \dot{\lambda}^{d^{\pm}} g^{\pm}\left(Y_n^{\pm}, r_n^{\pm}\right) \le 0 \tag{7}$$

Once proper expressions for the two damage variables are given, the above laws can be determined easily. In present model, for d^+ and d^-, the expressions of Oliver (1990) and Faria et al. [3] are adopted.

Plastic strains considerations

The plastic strains can be obtained based on the effective stress space plasticity:

$$\dot{\boldsymbol{\varepsilon}}^p = \dot{\lambda}^p \partial_{\bar{\boldsymbol{\sigma}}} G^p; \dot{\boldsymbol{\kappa}} = \dot{\lambda}^p \mathbf{h}^p; F^p(\bar{\boldsymbol{\sigma}}, \boldsymbol{\kappa}) \le 0, \dot{\lambda}^p \ge 0, \dot{\lambda}^p F^p(\bar{\boldsymbol{\sigma}}, \boldsymbol{\kappa}) \le 0 \tag{8}$$

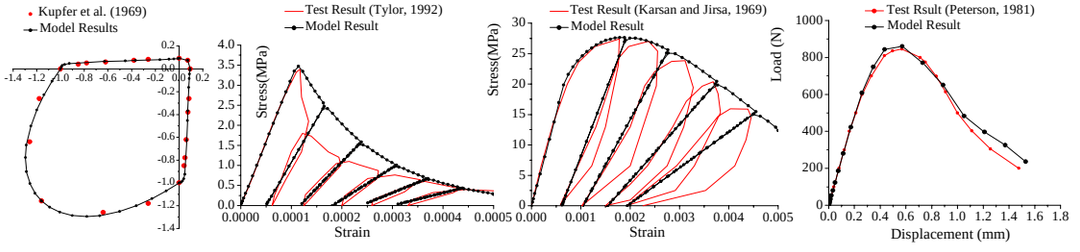
In present model, the plastic yield function of Lee and Fenvas[4] for F^p and the usual Drucker-Prager type function for G^p are adopted. The hardening parameters used here are referred to the equivalent plastic stains under tension and compression, respectively.

NUMERICAL ALGORITHM

In accordance with the operator-split method, the plastic flow and damage evolutions are decoupled, and three steps numerical system, i.e., the elastic-trial part, the plastic-corrector part and the damage-corrector part, are established. In the elastic-trial and the plastic corrector steps, for the yield function adopted, a new and uniform spectral-decomposition format of the classical return-mapping algorithm is developed and improved upon Lee and Fenvas[4], in which the principal vectors of the trial effective stress tensor remain unchanged in the plastic-corrector step, and the principal values can be easily determined based on the simple relation between the updated and the trial ones.

EXPERIMENTAL VERIFICATIONS

The present model and corresponding algorithm are coded into a finite element program, which is used to simulate the experimental results of concrete material and structures tests. Results presented following are the biaxial tests of Kupfer et al., cyclic tensile test of Tylor, cyclic compressive test of Karson and Jirsa, and the notched beam test of Peterson.



CONCLUSIONS

In this paper, to describe the degradation of macro-mechanical properties of concrete, tensile and shear damage variables are adopted, whose damage criteria are established based on the elastoplastic damage energy release rates upon considering the plastic free energy. The plastic strains are determined in accordance with the effective stress space plasticity. Thus an elegant elastoplastic damage model is derived, whose numerical algorithm is developed in the spectral-decomposition format of the classical return-mapping algorithm by decoupling the plastic flow and damage evolutions. Finally the model and its algorithm are applied to simulate several typical experimental tests, and the good agreements between predictive results and the test data verify their validity. Applying the present model to reinforced concrete structures will be forthcoming.

References

[1] Mazars, J. and Pijaudier-Cabot., Continuum damage theory: Application to concrete. Journal of Engineering Mechanics, ASCE, 115(2): 345-365 , 1989
[2] Ju, J. W., On energy-based coupled elastoplastic damage theories: Constitutive modelling and computational aspects. IJSS, 25(7): 803-833, 1989
[3] Faria, R. Oliver, J. and Cervera, M., A strain-based plastic viscous-damage model for massive concrete structures. IJSS, 35(14): 1533-1558, 1998
[4] Lee, J. and Fenvas, G. L., Plastic-damage model for cyclic loading of concrete structures. Journal of Engineering Mechanics, ASCE, 124: 892-900, 1998

XXI ICTAM, 15–21 August 2004, Warsaw, Poland

LIFETIME PREDICTION WITH A DAMAGE MODEL BASED ON MIXED-MODE MICROCRACK PROPAGATION

H. Schütte*
*Institute of Mechanics, Ruhr-University Bochum

Summary We will first present shortly a framework for brittle damage recently proposed by SCHÜTTE & BRUHNS (2002), where also a more detailed description can be found. The damage evolution equations are based on micro-mechanical considerations. The crack propagation in a unit cell containing a crack is based on a variational principle of an elastic body containing a crack in equilibrium (LE ET.AL., 1999). The thermodynamic equivalence of the micro- and macro-processes of crack growth and damage evolution is used to derive the damage evolution law. We will conclude with numerical examples, which show the possibilities of the proposed model for lifetime prediction.

MACROSCOPIC FRAMEWORK FOR FINITE ELASTODAMAGE

A finite framework for brittle damage is needed to consistently describe the damage process. For the underlying micromechanics see Figure 1.

A multiplicative decomposition of the total deformation can help to describe this process:

$$\mathbf{F} = \mathbf{F}^e \mathbf{F}^d. \tag{1}$$

Here $\mathbf{F}^e$ and $\mathbf{F}^d$ denote the elastic and damage parts of the deformation, respectively. The identification, however, of $\mathbf{F}^e$ and $\mathbf{F}^d$, is quite different from the approach chosen in finite elastoplasticity. $\mathbf{F}^e$ denotes that part of deformation, which leads to elastically recoverable energy and $\mathbf{F}^d$ the one, the energy of which is dissipated.

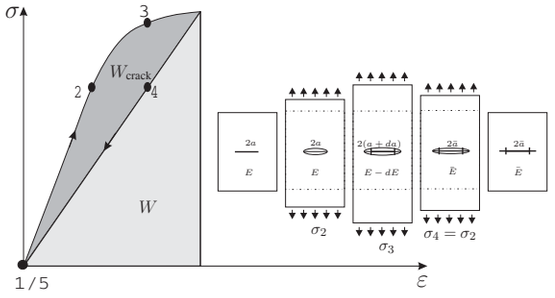


Fig. 1: The stress strain curve resulting from a growing (micro)-crack

Damaged tensor of elastic moduli

We want to show that the elastic properties can be represented in the proposed framework in a straight forward manner by the use of push- and pull operations. The free energy density can be stated as a quadratic form in the intermediate (damaged) configuration. The resulting stress-strain relation for the unloading process is then

$$\bar{\mathbf{s}} = \bar{\rho}\frac{\partial \bar{\psi}}{\partial \bar{\mathbf{e}}^e} = \bar{\mathbb{C}}^e : \bar{\mathbf{e}}; \quad (\mathbb{C}_0^e)^{ABCD} = \lambda\, G^{AB}G^{CD} + \mu\left(G^{AC}G^{BD} + G^{AD}G^{BC}\right)$$

where $\bar{\mathbf{e}}$ is the Almansi-strain of the intermediate configuration, G^{AB} means the components of the reference metric and we postulate isotropic undamaged material in the reference configuration. Damage can be represented by a push-forward with the damage mapping ($\bar{\mathbb{C}}^e = \mathbf{F}^d_{\triangleright}(\mathbb{C}_0^e)$.). The Finger-tensor of the damaged configuration $\bar{\mathbf{b}}^d$, works as an evolving structural tensor. So we get

$$(\bar{\mathbb{C}}^e)^{\alpha\beta\gamma\delta} = \lambda\,(\bar{b}^d)^{\alpha\beta}(\bar{b}^d)^{\gamma\delta} + \mu\left((\bar{b}^d)^{\alpha\gamma}(\bar{b}^d)^{\beta\delta} + (\bar{b}^d)^{\alpha\delta}(\bar{b}^d)^{\beta\gamma}\right), \quad \bar{\mathbf{b}}^d = \mathbf{F}^d_{\triangleright}\left(\mathbf{G}^{-1}\right)$$

which is pointwise orthotropic.

MICROSOPIC FRAMEWORK

2-D crack growth in a unit cell

The micro-mechanical framework is based on the mechanics of a growing crack in a unit cell. The equations for the threshold and direction of crack growth used in the subsequent derivations are based on LE & SCHÜTTE (1998) and LE ET. AL (1999). A crack subject to a mixed mode loading condition can kink at an angle ϕ when it grows. LE & SCHÜTTE (1998) have shown, that the driving force depending on the kinking angle ϕ can be expressed with the help of the SIFs at the kinked crack tip

$$G_\phi = \frac{1-\nu^2}{E}[(K_I^\star)^2 + (K_{II}^\star)^2 + \frac{1}{1-\nu}(K_{III}^\star)^2]. \tag{2}$$

So the crack will grow in the direction which maximizes $G_\phi 4$, if this exceeds certain threshold.

For the problem of an inclined crack in an infinite plate, we know the stress intensity factors prior to crack kinking (IRWIN, 1957) depending on the far-field stresses. The resulting kinking angle from the crack growth law is then

$$\phi_{max} = \text{sgn}(K_{II})[0.71\lambda^3 - 0.0977\sin^2(3.91\lambda) - 13.16\tanh(0.15\lambda)]; \quad \lambda = \frac{|K_{II}|}{K_I + |K_{II}|} \tag{3}$$

which is a curve fitting for the plane part of the solution presented in LE, SCHÜTTE & STUMPF (1999).
After each infinitesimal step of crack propagation, we replace the kinked crack by an equivalent straight crack to take advantage of the analytical equations. Equivalent crack means that it has the same rate of dissipation and amount of additional crack length. The resulting differential equation for the orientation angle is

$$\frac{d\hat{\beta}}{da} = 2\left(G^\star - \hat{J}_1\right) / \frac{\partial \hat{\psi}_{crack}}{\partial \hat{\beta}}, \hat{\psi}_{\text{crack}} = 2\int_0^{\hat{a}} \hat{J}_1 d\hat{a}; \quad \hat{J}_1 = \frac{1-\nu^2}{E}\left(\hat{K}_I^2 + \hat{K}_{II}^2\right), \tag{4}$$

Evolution law for the crack length

What is left up to specify now is an evolution equation for the crack length a. This relation shall be parametrized with the help of the number of cycles N. When the minimum load is such that $G^\star_{\text{min}}$ is smaller than the threshold value for crack propagation $G^\star_{\text{s}}$ the equation can be stated as (compare LEMAITRE & CHABOCHE (1990))

$$\frac{\mathrm{d}a}{\mathrm{d}N} = C\tilde{G}^{\star\,\eta/2}_{\text{max}}; \quad \tilde{G}^\star_{\text{max}} = \left\langle \sqrt{G^\star}_{\text{max}} - \sqrt{G^\star_{\text{s}}} \right\rangle^2 \tag{5}$$

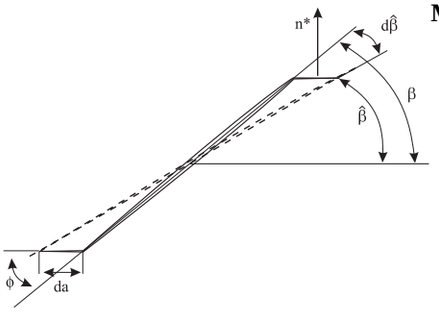


Fig. 2: The kinked and the replacement crack

MICRO-MACRO-TRANSITION

The transition is done by postulating the equivalence of the macroscopic damage dissipation rate and the microscopic change of the cracks potential

$$\mathcal{D}^d = \bar{\mathbf{k}}^d : \bar{\mathbf{d}}^d = \frac{\dot{\psi}_{\text{crack}}}{A} = \frac{2G^\star \dot{a}}{A}, \tag{6}$$

where A is the area of the unit cell, and t its thickness. This leads to the following damage evolution law

$$\bar{\mathbf{d}}^d = -\frac{\dot{a}}{t}(\mathbf{n}^\star \otimes \mathbf{n}^\star), \tag{7}$$

where $\mathbf{n}^\star$ is the normal vector onto the new developing crack surfaces.

NUMERICAL EXAMPLES

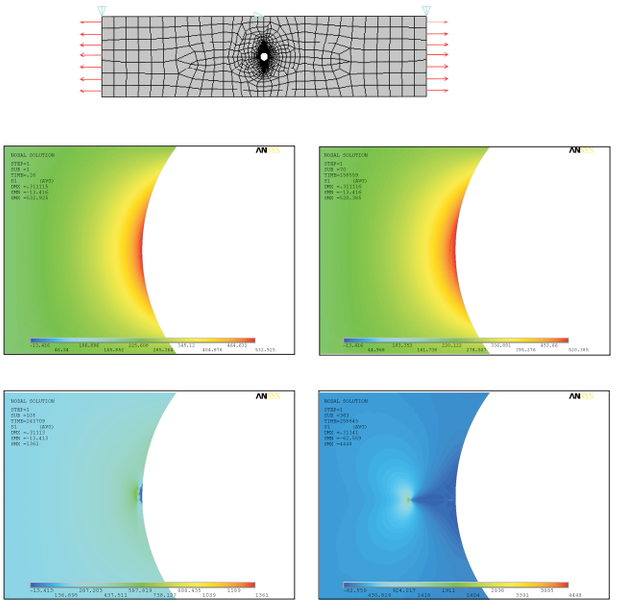


Fig. 4: The specimen and the evolution of stress state over lifetime

The example computed was a strip with a hole under a swelling unidirectional load. The constant maximum stress at the corner of the hole of approx. $533\,\text{MPa}$ is larger than the chosen fatigue limit of $\sigma_D = 500\,\text{MPa}$. The initial crack length of the microcracks is set to $a_0 = 0.001\,\text{mm}$. The parameters of the *Paris' law* have been chosen as $C = 0.001$ and $eta = 3.0$. In Figure 2 the stress in loading direction is given for the undamaged state, and three different numbers of cycles: $N = 158559,\ 243709,\ 258645$. At $N = 158559$ the stress field is maintained approximately in its undamaged form, but the stress at the corner is slightly reduced ($\approx 520\,\text{MPa}$), due to the distributed damage there. At $N = 243709$ one sees clearly that the damage heavily localizes, which results in a sharp crack emanating from the corner of the hole. This macro-crack grows fast and leads to the final failure of the specimen shortly after the stress state shown at $N = 258645$.

References

[1] Le K.C., Schütte H., Variational formulation of the crack problem with a virtual crack kinking, *In: Continuum Models and Discrete Systems (CMDS9), Proc. 9th Int. Symp.*, ed. Inan, E., K. Z. Markov, pp. 727–735, 1998.

[2] Le K.C., Schütte H., Stumpf H., Determination of the driving force acting on a kinked crack, *Arch. Appl. Mech.*, Vol. **69**, pp. 337-344, 1999.

[3] Lemaitre J., Chaboche J. L., *Mechanics of solid materials*, Cambride University Press, Cambridge, 1990.

[4] Schütte, H. Bruhns, O.T., 2002. On a geometrically nonlinear damage model based on a multiplicative decomposition of the deformation gradient and the propagation of microcracks, *J. Mech. Phys. Solids*, Vol. **50**, pp. 827–853, 2002.

XXI ICTAM, 15–21 August 2004, Warsaw, Poland

A MICROMECHANICALLY BASED NETWORK MODEL FOR RUBBERY POLYMERS INCORPORATING MULLINS–TYPE STRESS SOFTENING

Serdar Göktepe, Christian Miehe
Institute of Applied Mechanics (Civil Engineering), Chair I, University of Stuttgart, Pfaffenwaldring 7
D-70550 Stuttgart, Germany

Summary We present a new micromechanically based constitutive model for the description of the Mullins–type stress softening observed in rubbery polymers. The constitutive approach, embedded in the full network theory, has a basic two–step procedure: (i) The set up micromechanically based constitutive models for a *single chain orientation* and (ii) the definition of the macroscopic stress response of the network by a directly evaluated micro–to–macro transition for a *discrete orientation space* over the *micro sphere*. Due to the inherent structure of the model, one dimensional scalar variables govern the model and the deformation–induced anisotropy is achieved.

Description of Mullins' Effect

Rubbery polymers exhibit deformation–induced stress softening behavior, so–called Mullins' effect, in particular under cyclic loadings. Mullins' effect is more pronounced in the filled stock than in the pure gum one. Due to the this fact, molecular scenarios based on the breakdown of the stiffening due to the fillers have been proposed since 1960s. In our work we follow the molecular damage theory originally proposed by Bueche [1] and further developed by Govindjee and Simo [2]. In this theory, the softening is based on the breaking of bonds between the chains and the fillers. In Figure 1a, a schematic picture of the filled polymer network, composed of three chains with different contour lengths $L_C > L_B > L_A$, is shown. In a extension of the network in horizontal direction, first the chain A will reach its limiting extensibility and detach from a particle. Due to the loss of contribution of the chain A to the network stiffness upon retraction of the network, its response will be softer. In a further extension of the filled network from the totally unloaded state, stress–stretch curve will trace the unloading path but beyond the previous maximum extension the longer chains reach their limiting extensions. Therefore, chain B and chain C might debond from the particles and further softening is observed in the unloading response. Softening in the stress-stretch behavior of the material in a typical quasi–static cyclic tensile uniaxial experiment is depicted schematically in Figure1b. The curves in the stress–stretch diagram are labeled as a, b, c, which correspond to the loading intervals with the same labels.

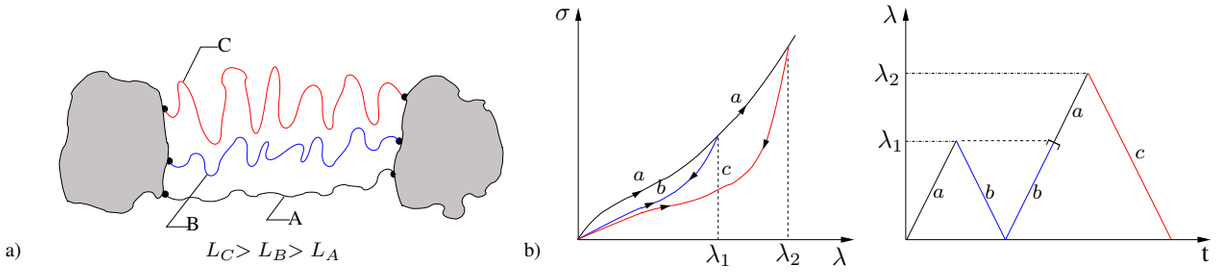


Figure 1. a) Schematic representation of the filled polymer network. Three chains, labeled as A, B and C, extending between two filler particles. Different contour lengths are assigned to each of them, $L_C > L_B > L_A$. b) Idealized description of Mullins' effect in a uniaxial cyclic tensile test. Stress–stretch response of the specimen is depicted along with corresponding loading function.

Constitutive Framework

During the addition of fillers in a sulfur vulcanization process of polymers, some of the chains constitute the network between fillers, so–called particle–to–particle (PP) network. Some of them, on the other hand, run between crosslinks so–called crosslink–to–crosslink (CC) network. Therefore, it is reasonable to decouple the total free energy into two parts, $\Psi = \Psi_{cc} + \Psi_{pp}$. Response of the CC network is described by the full network model recently proposed in Miehe et al. [4]. For the response of the PP network it is reasonable assume affine deformation due to the large size of the filler particles. Therefore, in the construction of constitutive model for PP network, we base the formulation on the affine version of the micro–sphere model. The free energy of the affine network Ψ_{af} is obtained by averaging of free energies of chains oriented in different directions over the unit sphere surface, see Figure2a,b.

$$\Psi_{af} = \langle n\psi(\bar{\lambda})\rangle := \frac{1}{|\mathcal{S}|}\int_{\mathcal{S}} n\psi(\bar{\lambda})dA \approx \sum_{i=1}^{np} n\psi_i(\bar{\lambda}_i)w_i \quad \text{where} \quad \bar{\lambda}_i = \sqrt{\boldsymbol{t}_i \cdot \boldsymbol{g}\boldsymbol{t}_i} \quad \text{and} \quad \boldsymbol{t}_i := \bar{\boldsymbol{F}}\boldsymbol{r}_i \tag{1}$$

In equation (1), continuous averaging integral over the continuous space directions is approximated by an effective discrete integration, see Figure2c. In (1), $\bar{\boldsymbol{F}}$ and $\boldsymbol{g}$ denote the isochoric part of the deformation gradient $\boldsymbol{F}$ and the current metric, respectively. Free energy in each direction has the celebrated Langevin form. Then Kirchhoff stresses read from Doyle–Ericksen formula $\bar{\boldsymbol{\tau}}_{af} = 2\partial_{\boldsymbol{g}}\Psi_{af} = \langle \beta\, \boldsymbol{t}\otimes\boldsymbol{t}\rangle = \sum_{i=1}^{np} w_i\beta_i\, \boldsymbol{t}_i\otimes\boldsymbol{t}_i$ with the micro stress components in each orientation $\beta_i := \mu(3N - \bar{\lambda}_i^2)/(N - \bar{\lambda}_i^2)$. In the stress expression, μ, N and w_i denote the shear modulus, the number of modules in a chain and the weighting factors, respectively. Following the observations reported in [2], Kirchhoff stresses contributed

by PP network, given in (2), is obtained by scaling the β_i with normalized stress function $\xi = \hat{\xi}(\bar{\psi}_i, d_i)$ where $\bar{\psi}_i$ and d_i stands for the normalized free energy computed in each direction i and the scalar damage parameter evolving in this orientation. The scaling function ξ has been found to be represented by family of curves each corresponding to the value of the damage d_i. Its explicit form is given by $\xi = \hat{\xi}(\bar{\psi}_i, d_i) = c_1(d_i)[\bar{\psi}_i - c_2(d_i)]^2 + c_3(d_i)$ with $c_m = k_m \exp((-1)^m \delta_m d_i)$ for $m \in \{1, 2, 3\}$. Here, k_m and δ_m are the additional material parameters.

$$\bar{\boldsymbol{\tau}}_{pp} = 2\partial_{\boldsymbol{g}} \Psi_{pp} = \langle \xi(\bar{\psi}, d)\beta \, \boldsymbol{t} \otimes \boldsymbol{t} \rangle = \sum_{i=1}^{np} w_i \xi(\bar{\psi}_i, d_i)\beta_i \, \boldsymbol{t_i} \otimes \boldsymbol{t_i} \, . \tag{2}$$

In order to complete the formulation, an evolution equation for the damage variable d_i is to be determined. The discontinuous evolution equation is canonically obtained in a thermodynamically consistent way by maximizing the dissipation in each direction with the constraint of a damage criterion function. The damage criterion function is assumed to have the form $\phi_i = \bar{\psi}_i - d_i \leq 0$, see Miehe and Göktepe [5] for the details of the algorithmic setting. It should be carefully noted that this type of damage formulations differ from the classical $(1 - d)$ theory in the sense that it is not possible to separate the damage parameters from the deformation. This feature of these models is essential for achieving correct shapes of hysteresis, see Göktepe [3] for the comparison of $(1 - d)$ theory with these type of models.

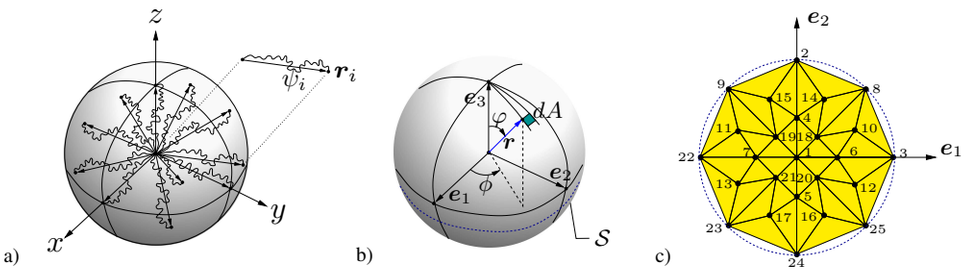


Figure 2. Unit sphere microstructure. a) Representation of network structure in the microsphere b) The orientation of unit vector $\boldsymbol{r}$ parameterized by spherical angles (ϕ, φ) c) Stereographic pole projection of the unit sphere. Numerical implementation uses $np = 21$ integration points for the discrete microstate evaluation on the sphere. The points 22–25 are introduced for plotting purposes.

Numerical Examples

The modeling capacity of the proposed constitutive approach is investigated with respect to the fitting of well known experimental data reported by Mullins and Tobin [6]. In Figure3a the performance of the proposed model is illustrated. It should be noted that set effect generally observed in the experiments at the zero stress level is obtained due to the inherent induced anisotropic feature of the model. In order to illustrate further the anisotropic feature of the model the simple shear test at a material point is performed. Deformation and corresponding deformation gradient is given in Figure3b. At the different stages of deformation, distribution of the softening is plotted on the pole figure, see also Figure2c. Evolution of the maximum damage orientation during the deformation is clearly depicted.

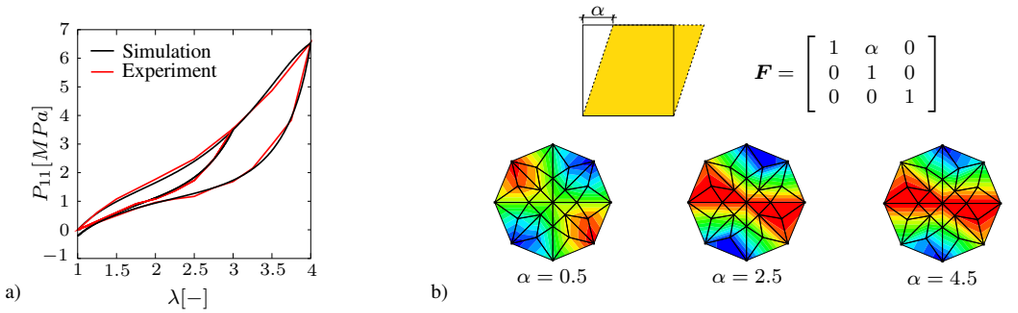


Figure 3. Numerical examples. a) Simulation of the test data reported by Mullins and Tobin [6] b) Distribution of damage over the microsphere in a simple shear test at different stages of loading. Damage is increasing from red zone to blue one.

References

[1] Bueche, F.: Molecular Basis for the Mullins Effect. *J. Appl. Poly. Sci*, **4**:107–114, 1960.

[2] Govindjee, S., Simo, J.: Transition from Micro-Mechanics to Computationally Efficient Phenomenology: Carbon Black-Filled Rubbers Incorporating Mullins' Effect. *J. Mech. Phys. Solids*, **40**:213–233, 1992.

[3] Göktepe, S.: A Micromechanically Based Constitutive Description of Elasticity and Damage in Rubberlike Materials. *MSc Thesis*, Report No. 02-I-02 of Institute of Applied Mechanics (Civil Engineering) Chair I, University of Stuttgart, 2002.

[4] Miehe, C., Göktepe, S., Lulei, F.: A Micro–Macro Approach to Rubber–Like Materials. Part I: The Non–Affine Micro–Sphere Model of Rubber Elasticity. *J. Mech. Phys. Solids*, in press, 2003.

[5] Miehe, C., Göktepe, S.: A Micro–Macro Approach to Rubber–Like Materials. Part III: The Micro–Sphere Model incorporating Mullins' Effect. To appear in *J. Mech. Phys. Solids*, 2004.

[6] Mullins, L., Tobin, N.R.: Theoretical Model for the Elastic Behavior of Filler Reinforced Vulcanized Rubbers. *Rubb. Chem. Technol.*, **30**:555–571, 1957.

XXI ICTAM, 15–21 August 2004, Warsaw, Poland

COMPUTATIONAL MICRO-MESO MODELING FOR LAMINATES UNDER THERMOMECHANICAL FATIGUE AND AN OXIDIZING ATMOSPHERE

Gilles Lubineau*, Pierre Ladevèze*
* *LMT-Cachan*
(E.N.S. de Cachan / Université Paris 6 / C.N.R.S.)
61 Avenue du Président Wilson, 94235 Cachan Cedex, France

Summary One computational approach for studying damage in laminated composites is the damage mesomodel for laminates, which has been developed for more than fifteen years, particularly at LMT-Cachan. Recently, we introduced micro-meso relations which prove that this mesomodel is compatible with classical micromechanical analysis and, therefore, can be viewed as a homogenization of classical theories on the microscale. Consequently, basic material quantities on the microscale can be easily interpreted on the mesoscale. Here, we propose to use these micro-meso relations as a tool for studying the degradation of laminates under fatigue in an oxidizing atmosphere. The reason why we are interested in this specific topic is that carbon-epoxy laminated composites are candidate materials for the construction of the future European civil supersonic aircraft. Our approach is rather simple: first, the influence of fatigue or oxidation on basic material characteristics is studied on the microscale; then, the equivalent damage evolution law on the mesoscale is obtained thanks to the micro-meso relations.

THE COMPUTATIONAL MICRO-MESO APPROACH FOR LAMINATES

The micro-meso relations for laminates

One of the computational approaches applicable to laminated composites is based on what we call a damage mesomodel for laminates, whose characteristic length is the thickness of the elementary ply ([1]). In such an approach, one assumes that the behavior of any laminated composite can be constructed using two elementary constituents which are continuous media: the ply and the interface ([3],[4]). The ply takes into account diffuse damage (quasi-homogeneous debonding of fiber/matrix interfaces), transverse microcracking, and local delamination (debonding of the interlaminar interface near the tip of each transverse microcrack). The interface is a surface entity which provides for the transfer of strains and stresses between plies.

Recent works ([7],[8]) using “virtual material testing" proved that the damage mesomodel can be viewed as a homogenized version of classical microdegradation schemes ([5], [2], ...). The guiding principle is that for each mesoconstituent the relations between micro quantities (e.g. microcracking rates, energy release rates, ...) and meso quantities (damage indicators and damage forces) are approximately independent of the stacking sequence in which the mesoconstituent is present. Consequently, there exist intrinsic operators (i.e. operators which depend only on the mesoconstituent being considered) which link the solutions on the two scales for any state of degradation.

Now it should be possible to design improved computational tools for damage analysis in two ways. First, thanks to that link, it is possible to build a damage mesomodel for laminates which relies extensively on micromechanics concepts. Quantities which have a strong meaning on the microscale (such as the critical energy release rate) can also be interpreted in the meso law of degradation. Consequently, this micro-meso link may be a way to introduce modifications of the properties due to mechanisms on the very fine scale into the calculation of the structure. Second, micro-meso relations can also be used as tools for interpreting the results of meso calculations in terms of the levels of microdegradation schemes. This provides a better physical understanding of the calculations.

Illustration under quasi-static and fatigue thermomechanical loading

Here this approach is first illustrated in the case of quasi-static and fatigue loading.

For quasi-static loading, we show that the basic mechanisms introduced on the microscale lead to consistent behavior on the mesoscale. First, the model is capable of predicting matrix microcracking for cross-ply laminates under tension. Second, thanks to the introduction of diffuse damage mechanisms on the microscale, the model is also capable of predicting the stiffness reduction under high shear loading, even though no microcracking occurs ([6]).

Concerning cyclic loading, our main assumption is that the diffuse damage mechanism alone is related to fatigue. We also assume that an increasing level of homogeneous diffuse damage leads to a progressive reduction of the ply’s toughness with respect to transverse microcracking ([9]). Consequently, if this toughness reduction becomes significant, transverse microcracking, for which the evolution law under quasi-static loading remains valid, develops. Contrary to classical micromechanical analysis, this approach still uses for fatigue microcracking the important concept of energy release rate, which leads to a consistent description of microcracking under quasi-static and cyclic loading. Thus, through the introduction of these micromechanical concepts, the micro-meso relations lead to an improved damage mesomodel for laminates.

INTRODUCTION OF THE EFFECT OF OXIDATION

Since this mesomodel can be interpreted as a homogenization of classical micromechanical models, basic quantities which have a strong material meaning on the microscale can now be interpreted directly on the mesoscale. Therefore, it is relatively simple to construct a computational tool on the mesoscale which takes into account oxidation. First, the effects of oxidation can be completely quantified on the microscale as modifications of the basic properties of the material. Then, these modified microquantities are used to get the equivalent damage law on the mesoscale, using the micro-meso relations. It appears that this approach could be used for any type of physical or chemical mechanism which modifies the material properties in an approximately homogeneous way throughout the thickness of the elementary ply (as long as it remains consistent with the basic hypothesis of the damage mesomodel).

In a very general way, transverse microcracking occurs when the energy release rate of the ply, depending on the loading (i.e. intralaminar stresses), on the level of damage (i.e., for example, the microcracking rate ρ) and on several basic properties of the ply (elastic modulus, thickness, etc.), reaches a certain critical energy release rate, which is a material quantity.

In the particular case of thermal oxidation, two major modifications appear on the microscale. First, the more oxidized the matrix, the more brittle it is. Thus, the critical energy release rate for microcracking must be considered to decrease with the amount of oxidation. Second, the increasing density of the matrix with oxidation ([10]) leads to shrinkage of the matrix between fibers and, therefore, to oxidation-induced intralaminar stresses.

Several simulations were performed on the mesoscale taking into account these considerations on the microscale. Comparisons are made with experimental observations on carbon-epoxy laminates under thermomechanical fatigue loading and an oxidizing atmosphere. We show that our approach is suitable for the description of the major aspects of damage behavior.

CONCLUSIONS

We presented an initial attempt to include on the mesoscale modifications of the material due to physical and chemical mechanisms on the very fine scale. This approach is based on the use of micro-meso relations developed at LMT-Cachan as a tool for transmitting information from the fine scale (the microscale) to the coarse scale (the mesoscale).

Acknowledgment: this study is part of a research program of the French Ministry of Research concerning the future European supersonic aircraft. This program is a joint effort of three laboratories: LMT-Cachan, LMPM (ENSMA Poitiers) and LTVP (ENSAM Paris). The authors thank the French Ministry of Research for its financial support.

References

[1] P. Ladevèze, *On damage mechanics of composite materials*, C.Bathias and D.Menkès", Proceedings of JNC5", Pluralis Publication, (1986), 667–683 (in french)

[2] N. Laws, G.J. Dvorak, *Progressive transverse cracking in composite laminates*, Jounal of Composite Materials, (1988), 22, 900–916.

[3] P. Ladevèze and E. LeDantec, *Damage modeling of the elementary ply for laminated composites*, Composite Science and Technology, (43), 3, (1992), 257–267

[4] O. Allix and P. Ladevèze, *Interlaminar interface modelling for the prediction of laminate delamination*, Composite Structures, (22), (1992), 235–242

[5] J. Nairn, S.H. Hu, *Matrix microcracking*, Damage Mechanics of Composite Materials, Taljera Ltd., (1994), 187–243.

[6] F. Lagattu, M. Lafarie-Frénot, *Variation of PEEK matrix crystallinity in APC-2 composite subjected to large shearing deformation*, Composite Science and Technology, 60,(2000), 605–612

[7] P. Ladevèze, G. Lubineau, *On a damage mesomodel for laminates: micro-meso relations, possibilities and limits*, Composite Science and Technology, 61, (2001), 2149–2158

[8] P. Ladevèze, G. Lubineau, *An enhanced mesomodel for laminates based on micromechanics.*, Composite Science and Technology, 62, (2002), 533–541

[9] P. Ladevèze and G. Lubineau, *A computational mesodamage model for laminate life prediction*, B. Harrys, Fatigue in Composite Materials: A Review of the Science and Technology of the Fatigue Response of Fibre-Reinforced Plastics" (2004).

[10] X. Colin, C. Marais and J. Verdu, *modelling and simulation of gravimetric curves: application to the oxidation of bismaleimide and epoxy resins* Polymer Degradation and Stability, 78(3), (2002), 545–553

A NON-ASSOCIATIVE ANISOTROPIC DAMAGE MODEL FOR BRITTLE MATERIALS

Luigi Gambarotta, Ilaria Monetto
DISEG, Department of Structural and Geotechnical Engineering, University of Genoa, Italy

Summary A friction-damage coupled model is derived from a micromechanically based description of the response of elastic matrices embedding statistically uniform distributions of crack-like defects. Symplifying assumptions on the mathematical representation of internal variables, governing the microscopic mechanisms responsible for the global inelastic response, permit a relatively simple formulation capable of describing the load-induced anisotropy of damage.

BACKGROUND

Inelastic behavior of materials responding in a predominantly brittle mode is the result of nucleation and propagation of crack-like microdefects, commonly referred to as damage, that may be accompanied by residual deformation due to possible frictional resistance to sliding of the internal crack surfaces. In the framework of thermodynamics with internal variables, convenient for dealing with the constitutive modeling of such dissipative materials, most literature has focused on modeling phenomenologically and micromechanically the progressive degradation of mechanical properties due to damage evolution rather than on the sliding-damage interaction [1]. Restricting the analysis to plane loading conditions, models for brittle solids under compression based on the sliding crack mechanism are a first step. As dual approach to the rigorous micromechanical model presented by Nemat-Nasser and Obata [2], Basista and Gross [3] in particular re-examined the sliding crack mechanism within the framework of thermodynamics with internal variables but deriving the potential functions from micromechanics.

CONSTITUTIVE MODEL

In order to analyze the different response of brittle and quasi-brittle materials in tension and compression, a non-associative anisotropic damage model incorporating the damage – frictional sliding interaction is derived in this paper. Brittle materials are modelled as elastic isotropic matrices embedding statistically uniform distributions of crack-like defects. The mean strain $\mathbf{E}$ may then be split into the elastic contribution due to the elastic matrix (having elastic compliance fourth-order tensor $\mathbb{K}$) and the inelastic contributions $\mathbf{E}_n$ and $\mathbf{E}_t$ due to microcrack opening and sliding, respectively:

$$\mathbf{E}=\mathbb{K}\mathbf{T}+\mathbf{E}_n+\mathbf{E}_t\,, \tag{1}$$

where $\mathbf{T}$ is the mean stress. Under the hypotheses of non-interacting and self-similarly propagating flat cracks, the analysis builds on that of Gambarotta and Lagomarsino [4] based on the concept of damage planes. The ensemble of microcracks is thought of as consisting of sets of identical equi-oriented flat cracks. The state of each set, identified by the orientation of the related crack plane, say $\mathbf{n}\in\Omega$ (the unit hemi-sphere in $\Re^3$ being denoted by Ω), can be defined by the characteristic size of the cracks, say $a(\mathbf{n})$, and by the vector of tangential contact tractions, say $\mathbf{f}(\mathbf{n})$; whereas, under the assumption of frictional sliding with no extension, normal contact tractions are given by compressive stresses. On the other hand, the introduction of such orientation fields as internal variables makes the model too cumbersome to have any practical appeal in a generic loading program.

The strategy applied in this paper for the reduction of the computational effort uses approximate representations of the orientation fields mentioned above in terms of appropriate series expansion of generalized spherical harmonics [5, 6], so allowing the forms:

$$a(\mathbf{n})\approx \mathbf{n}\bullet\mathbf{A}\mathbf{n}\,, \tag{2}$$

as previously assumed in [7], and, by analogy with the shearing stresses:

$$\mathbf{f}(\mathbf{n})\approx(\mathbf{I}-\mathbf{n}\otimes\mathbf{n})\mathbf{F}\mathbf{n}=(\mathbf{I}-\mathbf{n}\otimes\mathbf{n})\mathbf{F}'\mathbf{n}\,. \tag{3}$$

A more convenient description for damage and contact tractions in terms of two symmetric second-order tensors $\mathbf{A}$ and $\mathbf{F}$ (namely, the deviatoric component $\mathbf{F}''$ with $\mathrm{tr}\mathbf{F}'=0$ as the only significant component of $\mathbf{F}$) as new overall internal variables is then obtained. Note that at the undamaged state the damage tensor $\mathbf{A}=\mathbf{0}$, whereas during the damage process it is positive definite due to constraints provided by the irreversibility condition of damage. As for the internal friction tensor, $\mathbf{F}'=\mathbf{0}$ iff all the crack planes are subjected to tension. Using (2) and (3), the inelastic contributions to the mean strain shown in (1) can be specialized and the Gibbs free-energy function so derived from micromechanics permits one to associate $\mathbf{F}'$ and $\mathbf{A}$ with their thermodynamically conjugate variables: respectively, the sliding strain tensor $\mathbf{E}_t^-$ related to the closed cracks on compressive damage planes ($\mathbf{n}\in\Omega^-$, having defined $\Omega^-=\Omega-\Omega^+$ together with $\Omega^+=\{\mathbf{n}\in\Omega\,|\,\mathbf{n}\bullet\mathbf{T}\mathbf{n}\geq 0\}$) and the damage energy release rate tensor $\mathbf{Y}$. The latter in particular is a symmetric, positive definite second-order tensor.

The constitutive equation is finally complemented by limit conditions, governing potential activation of dissipation mechanisms, and equations of evolution for the associated internal variables, describing the way irreversible processes evolve. According to the simplified formulation based on overall (tensor-valued) variables, overall frictional sliding and crack growth criteria have been assumed.

RESULTS AND CONCLUSIONS

Because of nonlinearity and stress-path-dependence of the constitutive response, the model should be necessarily formulated in incremental form to predict the constitutive response to arbitrary stress applied to a brittle material at an arbitrary current state and requires, in general, numerical analyses to perform. Proportional loading, under which no crack changes its status is an exception and explicit solutions are possible as well. With reference to initiallly undamaged materials, biaxial and triaxial failure envelopes, together with some characteristic stress-strain curves, have been obtained and used for both identification and validation of the model.

As an example, figures 1, 2 and 3 show the biaxial limit strength domain and some related stress–strain curves, computed for some values of model parameters. Note that: (i) nonlinearity of the overall responses reflects damage evolution, which in the specific case of compression tests is accompanied by frictional sliding; (ii) if unloading is initiated, since damage evolution is locked, a linearly elastic tensile response is observed, whereas in compression the bilinear unloading branch reflects the occurence of backsliding. These results in general confirm the previous Brencich and Gambarotta [8] simulations but the use here of a second-order tensor rather than a single scalar variable permits a more convenient description for the load-induced anisotropy (namely, orthotropy) of damage.

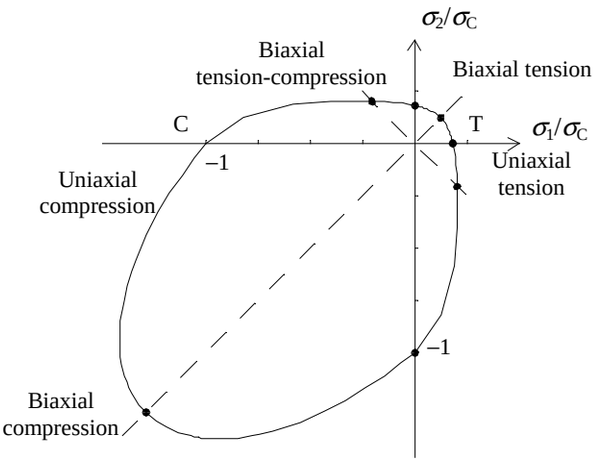


Figure 1. Biaxial limit domain.

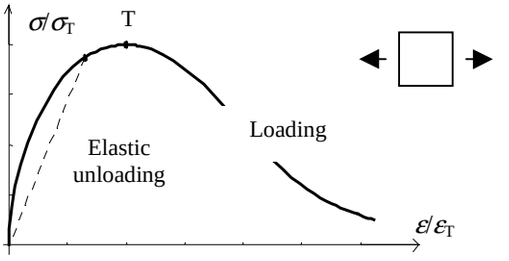


Figure 2. Model response to uniaxial tension.

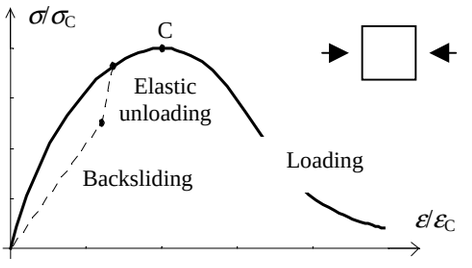


Figure 3. Model response to uniaxial compression.

It is straightforward that, because of the assumption of statistically uniformly distributed damage as an ensemble of non-interacting microcracks, the model is inherently incapable of predicting the onset of macroscopic failure occurring as damage localization into bands and coalescence of microdefects into a macrocrack. Practical application of the model is then restricted to the hardening phase of the mechanical response of brittle and quasi-brittle materials. Furthermore, due to the self-similar crack growth, the characteristic feature of dilatancy cannot be captured. On the other hand, with all of its limitations, in this model effects of anisotropic damage and sliding for prescribed (even complex) loading are combined in a relatively simple formulation which takes the physics of the problem into account.

References

[1] Krajcinovic D.: Damage mechanics: accomplishments, trends and needs. *Int J. Solids Struc* **37**: 267-277, 2000.
[2] Nemat-Nasser S., Obata M.: A microcrack model of dilatancy in brittle materials. *J. Applied Mech* **55**: 24-35, 1988.
[3] Basista M., Gross D.: The sliding crack model of brittle deformation:an internal variable approach. *Int J. Solids Struc* **35**: 487-509, 1998.
[4] Gambarotta L., Lagomarsino S.: A microcrack damage model for brittle materials. *Int J. Solids Struct* **30**: 177-198, 1993.
[5] Kanatani K.I.: Distribution of directional data and fabric tensors. *Int J. Engng Sci* **22**: 149-164, 1984.
[6] He Q.C., Curnier A.: A more fundamental approach to damaged elastic stress-strain relations. *Int J. Solids Struct* **32**: 1433-1457, 1995.
[7] Gambarotta L.: Friction-damage coupled model for brittle materials. *Eng Fracture Mech* **71**: 829-836, 2004.
[8] Brencich A., Gambarotta L.: Isotropic damage model with different tensile-compressive response for brittle materials. *Int J. Solids Struct* **38**: 5865-5892, 2001.

XXI ICTAM, 15–21 August 2004, Warsaw, Poland

ROBUST IDENTIFICATION OF AN AUGMENTED GURSON MODEL FOR ELASTO-PLASTIC POROUS MEDIA

Andrzej Stachurski*, Zdzislaw Nowak**
*Institute of Control and Computation Engineering, Warsaw University of Technology, Nowowiejska 15/19, PL 00-665 Warsaw, Poland
**Institute of Fundamental Technological Research, Polish Academy of Sciences, Swietokrzyska 21, PL 00-049 Warszawa, Poland

Summary In the paper we investigate robust identification approach to identify the material parameters in the augmented Gurson model for the elasto-plastic porous media. We consider the robust loss function given by Huber [3] and the loss function based on the L_1–norm. Our aim is to compare the results with our earlier standard least squares estimates.

PROBLEM FORMULATION

Our identification problem arises in modelling of the processes of nucleation and growth of voids in the elastic-plastic media. We consider the uniaxial test in the room temperature. At the neck there exists a complex state of stress and maximum deformations. Identification is carried out on the basis of Fisher's data [2] measured on the steel cylindrical specimens subjected to the uniaxial tension. We assumed that the effects of nucleation and growth of microvoids are summing up and we combined in one model, two models formulated separately for each of those two effects. Usually in literature material function g appearing in the model part responsible for the growth of microvoids is taken to be constant equal to 1 (no interaction of existing or nucleated new microvoids on the growth process is included). In our work we have assumed various shapes of g. Among others we have also studied the case with constant although unknown g function.

L_1–NORM MINIMIZATION

The L_1–norm minimization is an alternative approach to the standard least squares. In that case instead of the sum of the second powers of deviations we minimize

$$F_1(\Theta) = \sum_{i=1}^{M} |r_i(\Theta)|$$

with respect to the unknown parameters Θ. $r_i(\Theta)$ is the difference between the measured output and the output of the model for the particular values of the parameters Θ. The L_1–norm minimization decreases the influence of the large deviations compared to the least squares approach.

ROBUST IDENTIFICATION

Robust identification method (see Huber [3] or Seber and Wild [8]) is similar to the least squares. However, deviations larger then a given threshold value are rejected. Robust identification assumes minimization of the sum of the selected weighted differences between the measured and calculated from the model output values, i.e. we minimize loss function of the form

$$F_2(\Theta) = \sum_{i=1}^{M} \rho\left(\frac{r_i(\Theta)}{\chi}\right)$$

where

$$\rho(t) = \begin{cases} t^2, & |t| \le A, \\ 2A|t| - A^2, & |t| \ge A. \end{cases}$$

and χ is some measure of dispersion approximated by

$$\chi^a \approx \frac{1}{M} \sum_{i=1}^{M} |r_i(\Theta^a)|.$$

where Θ^a is an approximation to the estimate Θ.

The advantage of using a robust method which automatically rejects extreme observations is that it does not require a subjective decision on the part of the experimenter.

In the paper we investigate robust identification approach to identify the material parameters in the augmented Gurson model for the elasto-plastic porous media. The model describes processes of nucleation and growth of voids in the porous body subjected to inelastic deformation.

The identification problem is solved as in our earlier papers Nowak and Stachurski [5], [6] and [7] by means of the global optimization method of Boender at al. [1]. In the current version of our solver we permit the use of the Hooke-Jeeves [4] (see also Stachurski and Wierzbicki [9]) direct search method as the local minimizer that does not involve any derivatives. Our aim is to repeat identification of the material functions parameters using the robust identification and compare the results with our earlier standard least squares estimates.

CONCLUSIONS

Our earlier numerical experiments using the least squares method suggest that the nucleation of new voids can be modelled using the normal distribution material function. This choice was among the best in all cases tested by us. We have observed equally good results for the shifted hyperbolic tangent function. We have recommend the use of the normal distribution function because it is easier to interpret its parameters in mechanical terms. In view of our results we have found reasonable to use the porosity model with a constant value of the growth material function g, although with the constant not equal to 1. For the ductile steel this constant is probably near 0.86. It was somewhat unexpected by us and contrary to the common practice. We intend to verify those corollaries using other deviations measures. We expect that the results would be similar.

References

[1] Boender C.G., Rinnooy Kan A.H.G., Strougie L., Timmer G.T.: A Stochastic Method for Global Optimization, Mathematical Programming, 22, 125-140, 1982.

[2] Fisher J.R., Gurland J.: Void nucleation in spheroidized carbon steels. Part 1: Experimental. Metal Science, 15, No5, 185-192, 1981.

[3] Huber P.J.: Robust methods of estimation of regression coefficients, Math. Operationsforsch. Stat., Ser., Stat., 8, 141-153, 1977.

[4] Hooke R., Jeeves T.A.: Direct Search Solution of Numerical and Statistical Problems, J. Association Computer Machinery, 8, pp. 212-229, 1961.

[5] Nowak Z., Stachurski A.: Nonlinear regression problem of material functions identification for porous media plastic flow. Engineering Transactions, 49, 637-661, 2001.

[6] Nowak Z., Stachurski A.: Global optimization in material functions identification for voided plastic flow. Computer Assisted Mech. & Engng. Sciences, 9, 205-221, 2002.

[7] Nowak Z., Stachurski A.: Modelling and identification of voids nucleation and growth effects in porous media plastic flow. Control and Cybernetics, 32, No. 4, 2003 (to appear).

[8] Seber G.A.F., Wild C.J.: Nonlinear Regression. John Wiley & Sons, NY 1989.

[9] Stachurski A., Wierzbicki A.P.: Introduction to Optimization, (Podstawy Optymalizacji, in polish), second edition, Publishing House of the Warsaw University of Technology, Warsaw, 2001.

LOW CYCLE FATIGUE BASED ON UNILATERAL DAMAGE EVOLUTION

Artur Ganczarski
Cracow University of Technology, Institute of Applied Mechanics, PL 30-864 Kraków, Poland

Summary The present paper deals with a modelling of low cycle fatigue of AISI 316L stainless steel with aid of kinetic law of unilateral damage evolution. Results of numerical simulation are compared and verified in order to achieve the best agreement with the experimental data. Detailed quantitative and qualitative analysis of obtained solutions confirms necessity and correctness of an application of continuous microcrack closure/opening effect.

INRODUCTION

The most frequent approach to the low cycle fatigue, in case when a loading is periodic strain-controlled of constant amplitude, consists in taking into account the following assumptions: the material becomes perfectly plastic during first cycle, the variation of damage is neglected for the integration over one cycle and the stain-damage relations are identical both under tension and compression. These allow to simplify calculations of damage accumulation per one cycle and give linear dependency of damage with number of cycles, finally leading to the Manson-Coffin law of low cycle fatigue [4, 8, 9, 10, 11]. On the other hand, the more refined approaches to the low cycle fatigue presented in [1] and [7], based on the kinetic theory of damage evolution and the Gurson-Tvergaard-Needleman model of damage incorporated isotropic hardening, respectively, are able to predict some qualitative phenomena of damage accumulation, crack initiation and fracture only approximately since they do not account for the unilateral damage evolution.

GENERAL EQUATIONS

When a material is subjected to a cyclic loading at high values of stress or strain, damage develops together with cyclic plastic strain. If the material is strain loaded, the damage induces a drop of the stress amplitude and the decrease of the elasticity modulus. Damage evolution theory, suitable to the model such phenomenon is due to Lemaitre and Chaboche [7, 8]. The fundamental assumption is that, in case of low cycle fatigue, the damage is related to the accumulated plastic strain p. In the present formulation, as in the original one, the potential of dissipation is a sum of two parts, the first referring to Mises yield condition, where damage coupling acts only by the effective stress, and the other associated with the kinetic law of damage evolution. However, two separate damage mechanisms corresponding to isotropic transgranular microcracks growth and unilateral growth intergranular microcracks require application of two independent scalar damage variables. The first isotropic damage variable D_s acts on the deviatoric stress and the second unilateral damage variable D_v acts on the volumetric stress. Unilateral damage requires separate definitions of the effective stress, which allow to distinguish the case of tension (+), when microcracks remain open, and the case of compression (-), when they are partly closed, the effective stress takes final form valid for one dimension case

$$\tilde{\sigma}^{\pm} = \frac{\sigma}{3(1-D_\mathrm{s})} + \frac{2\sigma}{3(1-D_\mathrm{v}h)} \qquad h = \begin{cases} 1 & \text{for } \sigma > 0 \\ h_\mathrm{c} & \text{for } \sigma < 0 \end{cases} \tag{1}$$

where $h \in [h_\mathrm{c},1]$ stands for damage closure/opening parameter. Application of the classical formalism of associated plasticity to the potential of dissipation dependent of such defined effective stress Eq.(1) leads to the following form of the kinetic damage law written for one dimension case

$$\frac{\mathrm{d}D_\mathrm{s}}{\mathrm{d}p} = \frac{\sigma^2}{3ES_\mathrm{s}(1-D_\mathrm{s})^2}\exp(-ap) \qquad \frac{\mathrm{d}D_\mathrm{v}}{\mathrm{d}p} = \frac{\sigma^2(1-D_s)}{6ES_\mathrm{v}(1-D_\mathrm{v})^3}H(p-p_\mathrm{D}) \tag{2}$$

In order to obtain smooth transition of the strain-stress relation between the elastic range and the nonlinear plastic range the modified Ylinen approximation for loading cycles is applied

$$\frac{\mathrm{d}\sigma}{\mathrm{d}\varepsilon} = \tilde{E}^{\pm}\frac{\tilde{\sigma}_0^{\pm} - |\sigma|}{\tilde{\sigma}_0^{\pm} - c|\sigma|} \quad \text{for loading} \qquad \frac{\mathrm{d}\sigma}{\mathrm{d}\varepsilon} = \tilde{E}^{\pm} \quad \text{for unloading} \tag{3}$$

where the effective damage modulus of elasticity and the effective asymptotic yield stress of Ylinen's model become functions of damage

$$\frac{\tilde{E}^{\pm}}{E} = \frac{\tilde{\sigma}_0^{\pm}}{\sigma_0} = \frac{(1-D_\mathrm{s})(1-D_\mathrm{v}h)}{1-\frac{2}{3}D_\mathrm{v}h-\frac{1}{3}D_\mathrm{s}} \tag{4}$$

In case of unloading path, introduced definition of the effective stress Eq.(1), accounting for the crack closure/opening effect, leads to the linear relation between stress and strain that inclination is described by modulus $\tilde{E}(D)$. The defect of such a model is the switch from the part of path described by $\tilde{E}^{+}$ to the part of path characterised by the modulus of elasticity $\tilde{E}^{-}$. The real materials, however, do not exhibit such bilinear paths. Therefore, the more realistic model,

closer to real material behaviour, seems to be a proposal of curve-linear path, suggested in [5], inclination of which depends on percentage of microcrack closure. In the simplest case, the concept of continuous crack closure/opening consists in the replacement of parameter h by a function $h(\sigma)$ such that for one dimension state of stress is [3]

$$h(\sigma) = h_c + (1 - h_c)\langle\sigma\rangle / \sigma_b \tag{5}$$

Finally, simplified description of the neck mechanism, directly preceding failure, taking advantage of theory by Davidenkov-Spiridonova leads to the following 3D extensions of Ylinen's law

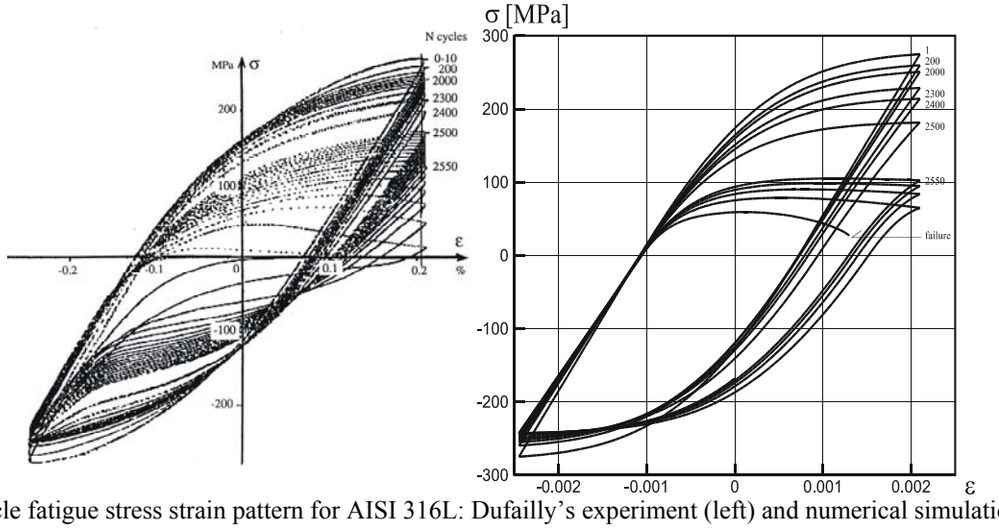
$$\frac{d\sigma}{d\varepsilon} = E^* \frac{\sigma_0^* - |\sigma|}{\sigma_0^* - c|\sigma|} \qquad \frac{E^*}{\widetilde{E}^{\pm}} = \frac{\sigma_0^*}{\widetilde{\sigma}_0^{\pm}} = \frac{1 + 0.25b\sqrt{\langle\varepsilon\rangle}}{1 + 0.5b\sqrt{\langle\varepsilon\rangle}} \tag{6}$$

and kinetic damage law

$$\frac{dD_s}{dp} = \frac{\sigma^2}{3\sqrt{2}ES_s(1-D_s)^2}\left(\frac{\exp(-ap)}{1 + 0.25b\sqrt{\langle\varepsilon\rangle}}\right) \quad \frac{dD_v}{dp} = \frac{\sigma^2(1-D_s)}{6\sqrt{2}ES_v(1-D_v)^3}\left(\frac{1 + 1.5b\sqrt{\langle\varepsilon\rangle}}{1 + 0.25b\sqrt{\langle\varepsilon\rangle}}\right)^2 H(p - p_D) \tag{7}$$

RESULTS

A systems of three ordinary differential equations Eqs (2, 3) or Eqs (6, 7) are numerically integrated using fourth-order Runge-Kutta technique with adaptive stepsize control. The numerical simulation with presented model of continuous crack closure/opening effect exhibits not only quantitative but also qualitative excellent correctness in comparison with experimental results. The smooth transition between tensile and compression as well as formation of the stress instability for tensile stress are observed.



Low cycle fatigue stress strain pattern for AISI 316L: Dufailly's experiment (left) and numerical simulation (right)

CONCLUSIONS

The model presented in this paper demonstrates necessity and correctness of the application of continuous microcrack closure/opening effect in kinetic law of damage evolution in order to model low cycle fatigue of AISI 316L stainless steel.

References

[1] Brocks W., Steglich D.: Damage models for cyclic plasticity. *Key Engineering Materials Vols.*: 389-398, 2003.

[2] Dufailly J., Lemaitre J.: Modeling of low cycle fatigue. *Int. J. Damage Mechanics*: **4**, 153-170, 1995.

[3] Foryś P., Ganczarski A.: Modelling of microcrack closure effect. Proc. *Int. Symp. Anisotropic Behaviour of Damaged Materials,* 1983 (on CD).

[4] Garion C., Skoczeń B.: Combined model of strain induced phase transformation and orthotropic damage in ductile materials at cryogenic temperatures. *Int. J. Damage Mech*., 2003 (in print).

[5] Hansen N.R., Schreyer H.L.: Damage deactivation, *Trans. ASME*: **62**, 450-458, 1995.

[6] Ladeveze P.: On an anisotropic damage theory. in *Failure criteria of structural media*, CNRS Int. Coll. No 351, Villard-de-Lans, ed. Boehler, Balkema, Rotterdam, 1983.

[7] Lemaitre J.: *A course on damage mechanics*, Springer-Verlag, 1992.

[8] Lemaitre J, Chaboche, J.-L.: *Mécanique des matériaux solides*, Bordas, Paris, 1985.

[9] Skoczeń B.: Generalisation of the Coffin equations with respect to the effect of large mean plastic strain, *ASME Journal of Eng. Mat. Techn*., 118, 1996.

[10] Skoczeń B.: *Material and structural stability issues at cryogenic temperatures*, Habilitation thesis, Cracow University of Technology, 88, 2002.

[11] Skrzypek J.J, Ganczarski A.: *Modeling of material damage and failure of structures*, Springer-Verlag Berlin Heidelberg, 1999.

COUPLED MESO-MACRO SIMULATION OF MASONRY CRACKING

T.J. Massart[1], R.H.J. Peerlings[2], M.G.D. Geers[2]
[1]*Continuum Mechanics Department, CP 194/5, Université Libre de Bruxelles, Brussels, Belgium*
[2]*Department of Mechanical Engineering, Eindhoven University of Technology, Eindhoven, The Netherlands*

Summary: A multi-scale framework is proposed for the representation of the complex non-linear behaviour of planar masonry structures. A standard continuum approach is used at the macroscale with embedded finite width localisation bands. A methodology to introduce homogenised material response snap-backs stemming from the finite size of the representative volume elements in the originally strain driven scale transition is proposed. Numerical examples are used to show the numerical robustness of the method.

INTRODUCTION

Ensuring the safety of historical buildings requires careful analysis of the residual strength of the (possibly damaged) structures and of the effect of repair operations. Finite element modelling of the failure process may be extremely useful in such analyses. Conventional finite element analyses require a constitutive model of the building material. For masonry, however, the formulation of closed-form constitutive relations which can accurately describe the aggregate degradation behaviour of bricks and mortar joints is a formidable challenge. Not only may both individual constituents and their bonding be degraded, these degradation processes also strongly influence each other, resulting in a range of possible failure mechanisms [1]. These failure modes and the mechanical responses associated with them are dominated by the mesostructure of the material, i.e. by the geometric arrangement of the bricks and mortar and by their individual properties. Most notably, cracks often follow the mortar joints and thus follow preferential directions which are set by the mesostructure. This results in the possible appearance of complex damage-induced anisotropy effects.

COUPLED MESO-MACRO MODELLING

Realistic predictions of strength and failure modes of masonry may be obtained from mesoscopic modelling, in which the geometry of the bricks and mortar joints is explicitly modelled, and homogeneous material behaviour is assumed for each of the phases [2]. Even if relatively simple constitutive relations are used for the brick and for the mortar materials, such models show a complex overall behaviour which agrees well with experimental observations. Furthermore, they allow to investigate the influence of brick shape, stacking mode, mortar strength, etc. on the overall response. Modelling the full mesostructure of entire walls or structures, however, may quickly become prohibitively expensive.
A compromise between computational cost and mesostructural detail can be obtained by using a coupled mesoscopic-macroscopic modelling approach. This means that walls are modelled using an homogenised continuum description, but the constitutive behaviour of the masonry material is determined on-line by mesoscopic analyses. In a finite element context, in each Gauss point of the macroscopic finite element discretisation a discretised sample of the mesostructure is used to determine this material response. For this purpose the local macroscopic strain is applied in an average sense to the mesostructure and the resulting mesostructural stresses are determined by a finite element analysis. The averaging of these mesostructural stresses and the condensation of the mesostructural tangent stiffness to the homogenised tangent stiffness then furnish the macroscopic material response associated with the Gauss point. This concept, which is also known as multilevel-FEM, FE^2 or computational homogenisation has been used before to model heterogeneous polymeric systems and other materials, see e.g. [3]. Its added value in the context of masonry resides in the fact that no complex closed form constitutive relation needs to be postulated for the representation of the overall material behaviour. The complexity associated with the damaging mesostructure of the material is naturally accounted for by scale transitions. Also, material identification issues are shifted to the level of mortar joints and brick constituents.

The definition of a multilevel-FEM scheme for masonry essentially requires the definition of four ingredients: (i) a mesoscopic constitutive setting for the brick and mortar materials, (ii) the definition of a representative mesostructural sample, (iii) the choice of a macroscopic continuum representation, and (iv) the set-up of scale transitions linking macroscopic and mesoscopic quantities. These features should carefully be selected in order to allow a proper incorporation of the localisation behaviour, both at the mesoscopic and macroscopic scales. Masonry constituents are quasi-brittle materials exhibiting low fracture energies and high sensitivities to tensile stresses. A scalar implicit gradient damage framework is therefore used at the mesoscopic scale. Based on the periodicity of the initial mesostructure of masonry, periodic homogenisation concepts are used in order to build scale transitions between the mesoscopic and macroscopic scales. In this contribution, the smallest periodic mesostructural sample is selected as the representative volume element in order to limit the computational effort at the mesoscopic scale. For running bond masonry, the smallest possible unit cell is represented in Figure 1. In order to deal with localisation at the macroscopic scale, embedded localisation bands surrounded by unloadin material are introduced in a standard first order continuum description. It is shown that a material bifurcation analysis based on the homogenised acoustic tensor as proposed in [4] allows to deduce band orientations which are consistent with the mesostructural damage patterns. The band width is deduced from this orientation and the initial periodicity of the mesostructure, as illustrated in Figure 1 for a staircase crack pattern. The resulting overall energy dissipation thus becomes

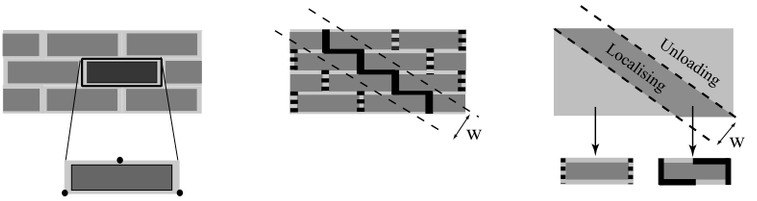


Figure 1: Identification of a mesostructural unit cell (left), and of a macroscopic localisation band (center and right)

sensitive to the ratio between mesostructural and structural sizes. Moreover, mesoscopic damage localisation in weaker zones of the order of a thin mortar joint may lead to snap-backs in the retrieved homogenised material response used at the macroscopic scale. Since the mesostructural problem is deformation-driven, an adaptation of the framework is introduced to handle such snap-backs. This enhancement consists in steering the mesostructural computation on the snap-back path. This is achieved where needed by forcing further mesoscopic energy dissipation through selected mesoscopic non-local strain unknowns which are transferred to the macroscopic solution procedure together with a non-local residual equation.

APPLICATION

The proposed multilevel scheme was implemented using parallel computing facilities. The capacities of the proposed approach are shown by means of structural computations. A typical structural application consists in a confined sheared wall as illustrated in Figure 2 with the associated mesoscopic damage patterns.

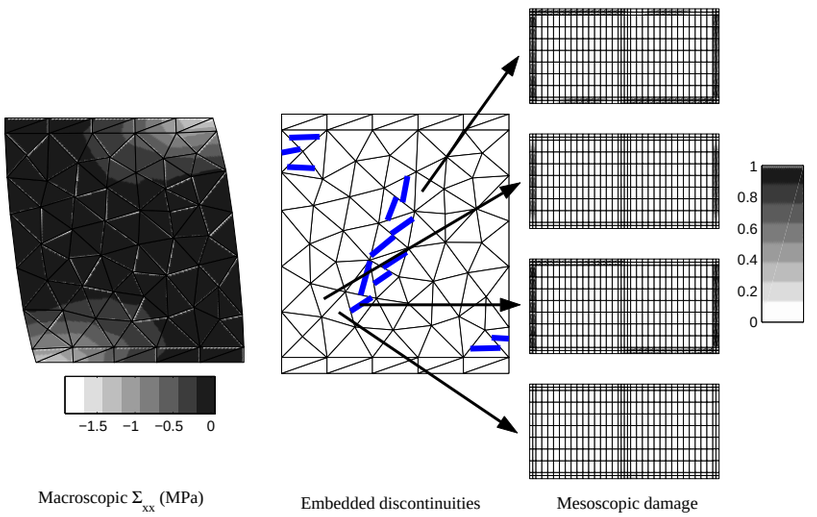


Figure 2: Application of the coupled meso-macro method to a masonry wall segment.

CLOSING REMARKS

FE^2 methodology proves to be a valuable tool for the investigation of masonry structures. In particular, it allows to account for the strong coupling between the structural response and the underlying mesostructural features of the material. In order to further exploit this methodology on large scale computations, it could still be improved in terms of performance. In this regard, improvement could be reached by the use of interface elements to represent mortar joints at the mesoscopic scale or by a restricting the use of mesoscopic on-line computations the damaging zones where degradation progresses.

References

[1] Dhanasekar M., Page A.W, Kleeman P.W.: The failure of brick masonry under biaxial stresses. *Proc. Instn Civ. Engrs., Part 2*:295–313, 1985.

[2] Massart T.J., Peerlings R.H.J., Geers M.G.D.: Mesoscopic modelling of damage-induced anisotropy in brick masonry. *Submitted to Eur. J. Mech.*, 2004.

[3] Smit R.J.M.: Toughness of heterogeneous polymeric systems. A modelling approach. *PhD Thesis*, Eindhoven University of Technology, The Netherlands, 1998.

[4] Rice J.R., Rudnicki J.W.: A note on some features of the theory of localisation of deformation. *Int. J. Sol. Struct.* **16**:597–605, 1980.

Coupling between progressive damage and permeability of concrete

George Chatzigeorgiou[1], Vincent Picandet[2], Abdelhafid Khelidj[3], Gilles Pijaudier-Cabot[4]

1. A.U.TH., Aristotle University of Thessaloniki, Dept. Of Civil Engineering, Division of Structures, University Campus, Gr – 54006 Thessaloniki, Greece
2. LG2M, Université de Bretagne Sud, Rue de Saint Maudé, BP 92116, 56321 Lorient Cedex, France
3. R&DO, GeM, I.U.T. de Saint Nazaire, dépt. Génie Civil, BP 420 Heinlex, 44600 Saint-Nazaire, France
4. R&DO, GeM, Ecole Centrale de Nantes, 1 rue de la Noë, BP 92101, 44321 Nantes cedex 3, France

Extended Summary

Quasi-brittle materials such as concrete very often fail during tension (or compression) due to localization. Micro-cracks, whose development at the beginning is almost homogeneous, start to concentrate in a region inside the material as the peak load is approached and the failure occurs with a sudden propagation of one or more macro-cracks. With the increase of diffuse cracking there is also a decrease in the stiffness of the material. In damage models this reduction of stiffness is expressed through a damage variable[1].

On the other hand, experimental results have shown that for low and intermediate stress levels, the permeability (water[2,3] or gas[4]) of concrete has significant change, and increases drastically when the load is very close to the ultimate strength of the material. From a microscopic point of view the width of the cracks is relatively small up to the peak load[5], but increases radically in the shoftening regime, causing a tremendous change in the permeability.

It is difficult to derive a proper relationship relating the variable of permeability of the material to mechanical quantity. Here we employ a lattice analysis for this purpose. The lattice which is described in this paper was used[6] in the past for the study of failure of quasi-brittle materials. It is a stiffness controlled model, where the mechanical problem is substituted by an electrical analogous, simplifying with this way the analysis by transforming it from vectorial to scalar and, as De Arcangelis et al.[7] have shown, this simplification is able to capture the most important physical aspects of the problem. The strain is substituted by the voltage, the stress by the current and the Young Modulus by the conductance.

The boundary conditions of the model are periodic in order to attain the creation of an infinite system and the partly avoidance of the boundary effects. They represent a homogeneous loading in the vertical direction: Periodicity is imposed along the boundaries parallel to vertical axis and a constant jump in voltage is applied along the two other boundaries. Every bond of the lattice behaves as a brittle material which has a conductance equal to 1 and when it reaches a threshold current it fails. This threshold differs from bond to bond following a uniform random distribution between 0 and 1 ensuring with this way the disorder of the model and, consequently, the heterogeneity of the material. For describing the state of the material at each step of damage we use the moments of the distribution of local stresses. The most important moments are these of order up to 4 because of their physical meaning: moments of order 0 represent the number of unbroken bonds in the lattice, of order 1 the average stress, of order 2 the average Young Modulus and of order 4 the dispersion of the Young Modulus.

In this article we start with the mechanical analysis and we recall the correlation between the mechanical properties: a) the average of the Young modulus, and not the number of broken bonds, is a lattice size independent parameter (i.e. the continuous variable which captures the evolution of damage in a continuum sense), b) the stress at the peak of the loading reduces with the increase of the lattice size and c) the post-peak area is strongly lattice-size dependent, a fact that was expected from experimental evidences.

The next step is to proceed to the hydraulic problem, trying to describe the relation between the permeability and the cracking mechanism. This time we use a lattice perpendicular to the mechanical one (figure 1), and solve for the hydraulic problem (assuming that when a bond fails in the mechanical problem, the bond that is perpendicular in the hydraulic problem increases its permeability). From the analysis of the corresponding moment distributions, we find first that the variable that is independent of the size of the lattice is the average permeability in the hydraulic problem. We find also that the average Young Modulus (M_{2m} in figure 2) is able to describe the hydraulic problem independently of the lattice size, which suggest that in a continuum model, the permeability should increase with damage. The permeability-stress ratio curve does not depend of the lattice size in the pre-peak area for one material and that the permeability-damage curve until the peak load is size independent and unique from experiments for different materials. This last result is consistent, from a qualitative point of view, with experimental curves obtained in Sugiyama et al.[4] and Picandet et al.[8]

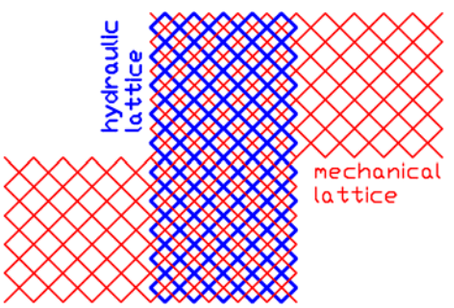


Figure 1: lattice model

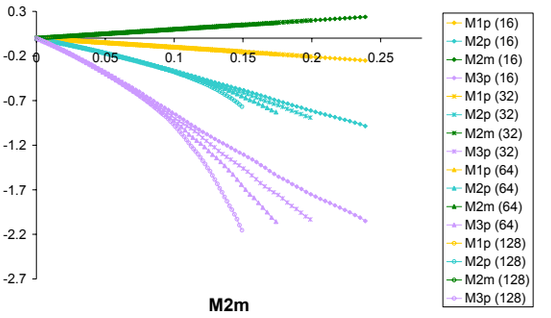


Figure 2: hydraulic moments vs. M_{2m} until the peak load

References

1. Pijaudier-Cabot G., Jason L. *Continuum damage modelling and some computational issues*. In Revue française de genie civil, volume 6 – n° 6, 2002, pp. 991-1017.
2. Kermani A. *Permeability of stressed concrete*. Building research and information, 1991, vol. 19, No. 6, pp. 360-366.
3. Hearn N. *Effect of Shrinkage and Load-Induced Cracking on Water Permeability of Concrete*. ACI Materials Journal, 1999, vol. 96, No. 2, pp. 234-241.
4. Sugiyama T., Bremner T. V., Holm T. A. *Effect of Stress on Gas Permeability in Concrete*. ACI Materials Journal, 1996, vol. 93, No. 5, pp. 443-450.
5. Wang K., Jansen D. C., Shah S. P., Karr A. F. *Permeability study of cracked concrete*. Cement and Concrete Research, 1997, vol. 27, No. 3, pp. 381-393.
6. Delaplace A., Pijaudier-Cabot G., Roux S. *Progressive damage in discrete models and consequences on continuum modeling*. Journal of Mechanics and Physics of Solids, 1996, vol. 44, No. 1, pp. 99-136.
7. De Arcangelis L., Herrmann H. J. *Scaling and Multiscaling Laws in Random Fuse Networks*. Physical Reviews B, 1989, vol. 39, No. 4, pp. 2678-2684.
8. Picandet V., Khelidj A., Bastian G. *Effect of axial compressive damage on gas permeability of ordinary and high-performance concrete"*. Cement and Concrete Research, 2001, vol. 31, pp. 1525-1532.

ANISOTROPIC DAMAGE MODEL FOR CONCRETE INCLUDING UNILATERAL EFFECTS

Godard V.[*,**], Leblond J.-B.[*], Badel P.-B.[**]
* LMM, Université Paris 6, 4 Place de Jussieu, 75005 Paris , France
** EDF R&D Département AMA, 1 avenue du général de Gaulle, 92141 Clamart, France

Summary

The complexity of microscopic mechanisms, which occur in concrete during the damage process, including notably the formation of cracks in tension and the closure of cracks in compression, with possible friction between the crack lips, seems to preclude any other approach than a phenomenological one. Furthermore, concrete exhibits an essentially elastic-brittle behaviour, which is the preferred domain of application of the damage theory, as initiated by Kachanov.

The aim of the present work is to propose a thermodynamically consistent model, which accounts for some anisotropy induced by damage, and which includes unilateral effects related to crack closure. Attention is paid to limiting the complexity of the model, and especially the number of parameters, in order to make the model a viable candidate for practical engineering computations.

The present work is an extension of the model developed by Badel [1] and Leblond. The model meets the 5 following features:

(i) It accounts for the anisotropy induced by damage.
(ii) It exhibits the asymmetry between tension and compression.
(iii) The stress varies continuously with respect to strain and damage in spite of the asymmetry between tension and compression.
(iv) A complete loss of stress-bearing capacity is possible for a totally damaged material.
(v) It fits within the framework of "generalized standard materials", as defined by Halphen and Nguyen [2].

Except for point (v), which is motivated by mathematical and numerical considerations, points (i) to (iv) are clearly desirable from a physical point of view. None of the models proposed up to now meets all 5 requirements. Many satisfy (i) and (ii) but fail to satisfy (iii), (iv) or (v).

The model in [1] satisfies all 5 requirements but fails to describe properly the mechanical behaviour of concrete in compression, and in particular shows no peak of stress. The main improvement of the present work is the introduction of a scalar damage variable representing the damage process that occurs in compression, in addition to the damage tensor representing the anisotropic damage (point (i)) induced by the formation of cracks perpendicularly to the direction of major tension already present in [1]. The use of two damage variables is motivated by the fact that the damage process seems to be different between tension and compression (see Mazars [3], Comi and Perego [4]). The evolution of both damage variables is coupled in only one criterion and one evolution law for physical and numerical reasons. Besides, unilateral effects (point (ii)) are taken into account by treating positive and negative principal strains (or eigenvalues of a combination of strain and damage) on a different footing in the thermodynamic potential. Moreover, the threshold in the criterion, formerly taken constant in [1], now depends on the confinement state, assimilated here to the negative part of the strain, in order to take into account the confinement effect (Kupfer et al. [5]). Point (iv) is adressed by using a free energy as the thermodynamic potential, instead of a free enthalpy; this leads to expressing the stress as a function of strain rather than vice versa. Finally, point (iii) and (v) are satisfied, thanks to the expressions of the free energy, the dissipation potential and the stress.

The model involves only 5 parameters (in addition to usual elastic moduli), what makes it very simple in comparison to other anisotropic models for concrete. The simplicity of the model and the demanding constraints placed on the model induce some defects, among which the absence of residual strains and of volumetric dilatancy in compression. However, numerical simulations show that in many situations, these defects should be acceptable, and that the model yields relatively good results. For instance, figure 1 shows the numerical simulation of a uniaxial tension followed by compression on one element:

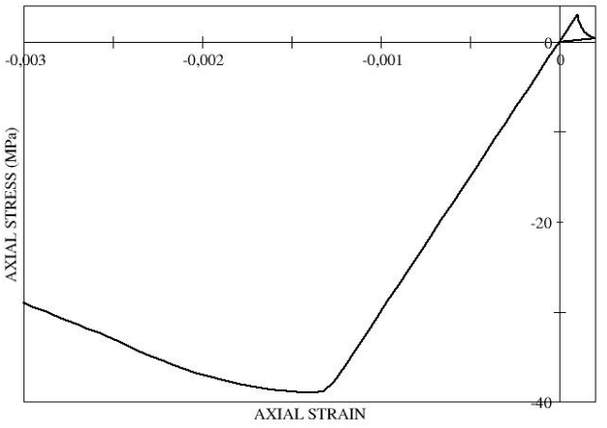


Figure-1: Axial stress/ axial strain for a uniaxial test of tension followed by compression

Finally, a non local model, based on the use of regularised deformations in the evolution equation of damage variables, which has been developed from the model proposed by Peerlings et al. [6], can be adapted to the present anisotropic damage model, in order to overcome the problem of mesh dependence induced by the softening regime.

References

1. Badel, P.-B., Contributions à la simulation numérique de structures en béton armé, *Thèse de doctorat de l'université Paris VI* , Paris, France, 2001.

2. Halphen, B., Nguyen, Q.S., Sur les matériaux standards généralisés, *J . de Mécanique*, **14**, pp 39-63, 1975.

3. Mazars, J., Application de la mécanique de l'endommagement au comportement non linéaire et à la rupture du béton de structure, *Thèse d'Etat* , UPMC, Paris, France, 1984.

4. Comi, C., Perego, U., Fracture energy based bi-dissipative damage model for concrete, *Int. J. Solids Struct.*, **38**, 6427-6454, 2001.

5. Kupfer, H.B., Hilsdorf, H.K., Rusch, H., Behaviour of concrete under biaxial stresses, *J. ACI 66 (8)*, 656-666, 1969.

6. Peerlings R.H.J., de Borst R., Brekelmans W.A.M., Geers M.G.D., Gradient-enhanced damage modelling of concrete fracture, *Mech. Cohesive-Frictional Mat.*, 3, 323-342, 1998.

BLAST RESISTANCE OF CLAMPED SANDWICH BEAMS

Vikram S. Deshpande*, Norman A. Fleck*
*Cambridge University, Department of Engineering, Trumpington Street, Cambridge CB2 1PZ, UK.

Summary A systematic design procedure has been developed for analysing the blast resistance of clamped sandwich beams. The structural response of the sandwich beam is split into 3 sequential steps: stage I is the 1D fluid-structure interaction problem during the blast loading event, and results in a uniform velocity of the outer face sheet; during stage II the core crushes and the velocities of the faces and core become equalised by momentum sharing; stage III is the retardation phase over which the beam is brought to rest by plastic bending and stretching. The 3-stage analytical procedure is used to obtain the dynamic response of a clamped sandwich beam to an imposed impulse. Performance charts for a wide range of sandwich core topologies are constructed for both air and water blast, with the monolithic beam taken as the reference case. These performance charts are used to determine the optimal geometry to maximise blast resistance for a given mass of sandwich beam. For the case of water blast, an order of magnitude improvement in blast resistance is achieved by employing sandwich construction, with the diamond-celled core providing the best blast performance. However, in air blast, sandwich construction gives only a moderate gain in blast resistance compared to monolithic construction.

AN ANALYTICAL MODEL FOR THE BLAST RESISTANCE OF SANDWICH BEAMS

Consider a clamped sandwich beam, with identical face sheets of thickness h and core thickness c. The core is modelled as a compressible material: in uniaxial compression the core is assumed to deform at a constant stress with no lateral expansion up to a densification strain; beyond densification no further deformation is assumed to occur. The response of the sandwich beam is split into three stages:

(i) Stage I - fluid-structure interaction phase.

(ii) Stage II - core compression phase,

(iii) Stage III - beam bending and stretching phase.

Stage I - The initial fluid-structure interaction phase

G.I.Taylor [1] developed the solution for a one-dimensional exponentially decaying wave (decay constant θ) impinging a free-standing plate and thus computed the momentum transmitted to the plate by the blast. We follow this approach and similarly compute the momentum transmitted to the sandwich beam by treating the outer face of the sandwich beam as a free-standing plate. When the blast wave (with maximum impulse I and wave speed c_w) strikes a free-standing plate of thickness h made from a material of density ρ_f, it sets the plate in motion and is partly reflected. At the instant the plate achieves its maximum velocity, the pressure at the interface between the plate and the fluid is zero and cavitation sets in shortly thereafter. The momentum per unit area $I_{\rm trans}$ transmitted into the structure is then given by

$$I_{\rm trans} = \psi^{\psi/(1-\psi)} I, \tag{1}$$

where $\psi \equiv \rho_w c_w \theta/(\rho_f h)$. Since ψ is much larger for the sandwich beam compared to a monolithic beam of the same mass, it is expected that a smaller impulse is transmitted into the sandwich beam compared to the monolithic beam.

Stage II - Core compression phase

The impulse $I_{\rm trans}$ per unit area imparts a velocity $v_o = I_{\rm trans}/(\rho_f h)$ to the outer face. The outer face compresses the core, decelerating the outer face while simultaneously accelerating the inner face. The final common velocity of the faces and the core is dictated by momentum conservation and thus also gives the loss in kinetic energy in this phase. Equating this loss in kinetic energy to the plastic dissipation in compressing gives the core compression strain. Typically, the core compression time is small compared to the structural response time, and thus the transverse deflection of the inner face of the sandwich beam in this stage can be neglected.

Stage III - Beam bending and stretching phase

At the end of Stage II, the sandwich beam has a uniform velocity except for a boundary layer near the supports. The beam is brought to rest by plastic bending and stretching. This problem has been investigated by a number of researchers and here an analyses valid for both small and large deflections was performed. The analyses gives the deflection w and response time T of the beam as a function of the beam geometry and impulse I.

The above analysis has been shown to compare well with 3D Finite Element calculations performed in a parallel study [2].

OPTIMAL DESIGN OF SANDWICH BEAMS FOR BLAST RESISTANCE

The analysis detailed above is used to investigate the relative response of monolithic and sandwich beams to blast loading. In a typical design scenario, the solid material and length of the structural element are dictated by design constraints such

as corrosion resistance and bulkhead spacing, thus leaving the sandwich panel geometry, viz. the face sheet and core thickness, and core relative density and topology, as the free design variables. Here we optimise with respect to these variables while keeping the span $2L$ of the beam fixed.

Water blast

The maximum blast impulse sustained by the sandwich beams with the five different topologies of the core subject to the constraint on the inner face deflection $w/L \leq 0.1$, are plotted in Fig. 1a as a function of the non-dimensional mass $\bar{M}$ of the beam. For comparison purposes, the blast impulse sustained by a monolithic beam subjected to the same constraints is also included in Fig. 1a. It is evident that sandwich beams all perform considerably better than the monolithic beam. This is mainly due to the fact that the sandwich beams have a thin outer face sheet which results in a small impulse transmitted into the structure whereas the relatively thick beams in monolithic design absorb a larger fraction of the blast impulse. A comparison of the various sandwich cores shows that sandwich beams with a metal foam and pyramidal core almost attain the performance of the hexagonal-honeycomb core. However, the diamond-celled core beams, which have high strength in both the through-thickness and longitudinal directions out-perform the other sandwich beams with a performance that approaches the "ideal" sandwich core limit.

Air blast

Due to the low acoustic impedance of air, the Taylor fluid-structure interaction parameter $\psi \approx 0$ for an air blast. The air blast performance of the optimised sandwich beams is compared to that of the monolithic beam in Fig. 1b. Specifically, the maximum sustainable impulse is plotted against the non-dimensional mass $\bar{M}$, with the deflection constraint $\bar{w} \leq 0.1$ imposed. In contrast to the case of water blast, the performance gain upon employing sandwich construction instead of monolithic beams is relatively small; at best the diamond-celled core sustains an impulse about 45 % greater than a monolithic beam of equal mass.

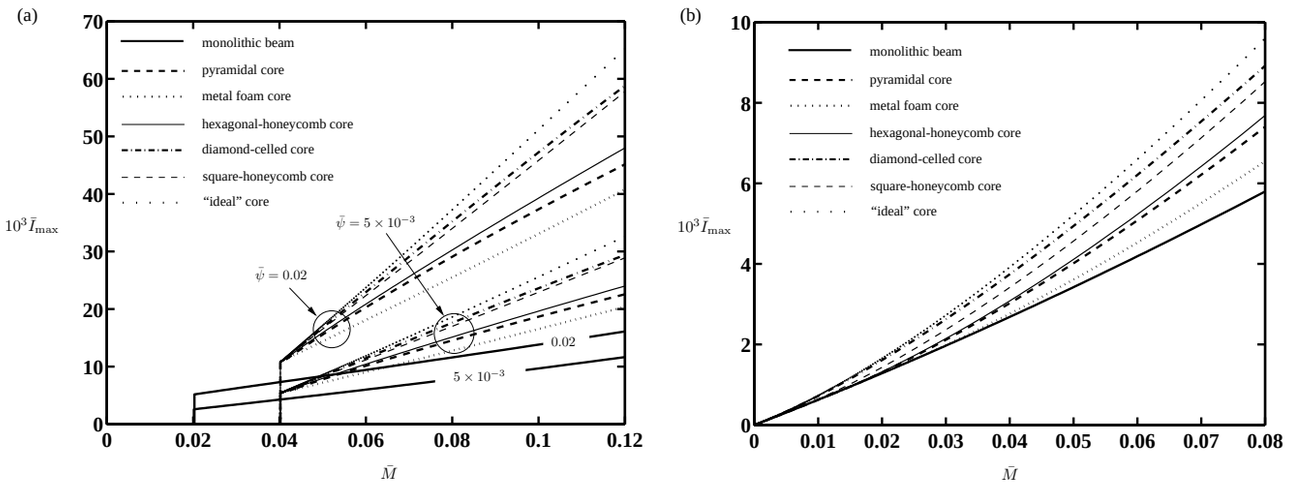


Figure 1. A comparison of the maximum blast impulse sustained by monolithic beams and by optimal designs of sandwich beams. (a) Water blast and (b) air blast.

CONCLUDING REMARKS

An analytical model has been developed to determine the response of both monolithic and sandwich beams subject to air and water borne blasts. For the case of water blast, an order of magnitude improvement in blast resistance is achieved by employing sandwich construction. This is mainly due to fluid-structure interaction: the reduced mass of the sandwich outer face leads to a reduction in the impulse transmitted to the structure from the water. In air, the impedance mismatch between air and the face sheet is comparable to that between air and a monolithic beam; consequently, the use of sandwich construction gives a more moderate gain in blast resistance compared to monolithic construction. For both air and water blast the diamond-celled core sandwich beam gives the best performance due to the longitudinal strength provided by the core.

References

[1] G I Taylor. *The scientific papers of G I Taylor, Vol III*, pages 287–303. Cambridge University Press, 1963, The pressure and impulse of submarine explosion waves on plates, 1941.

[2] Xue and J W Hutchinson. A comparative study of blast-resistant metal sandwich plates. To appear in *International Journal of Impact Engineering*, 2004.

Collision between Two Deformable Structures

T.X. Yu, H.H. Ruan
Dept. of Mech. Eng., Hong Kong University of Science & Technology (HKUST), Hong Kong

Summary This paper summarizes the complete solution, modal solution, local models and experiments on beam-on-beam collisions. The common features of structural collisions are explored through the analysis on the collision between mass-spring systems. These features are further exhibited in more complicated ring-on-beam collisions, based on the solutions obtained by the proposed MS-FD model.

INTRODUCTION

Over the last 50 years, the studies on dynamic plasticity of structures mainly concerned a single structure's response to prescribed impulsive/pulse loading or to the impact of a rigid projectile. However, the collision between two deformable structures (CBTDS) is a much more common incident in various engineering scenarios and is of practical interest. Hence, aiming to extend our knowledge to these more realistic problems and reveal some fundamental features of CBTDS, our group at HKUST has conducted a series of studies since 1998. A particular attention was paid to the energy partitioning between two colliding structures which actually reveals the structure's ability to absorb energy in a collision event and is exceptionally important for developing safety devices.

COMPLETE AND MODAL SOLUTIONS

The first compete solution of CBTDS was obtained by Yu *et al* [1,2] who analyzed a flying free-free beam impinging onto a cantilever beam. This solution considered the local rigid-plastic shear sliding, which actually defines a local rigid-plastic contact spring, as will be discussed later. After a shear-sliding phase, the stick assumption, which assumed the contact points remain attached to each other, was employed, so that the two-beam system was treated as a single T-shaped beam in the subsequent global flexural deformation.

The complete solution has to handle various combinations of various phases of the two beams. This complicity motivated us to examine simplified approaches, e.g. the modal approximation technique. However, difficulty was found in selecting an appropriate rigid, perfectly plastic mode based on the Lee's principal, since the latter always results in a fundamental mode, i.e. that with a single hinge in one of the colliding beams. As a new powerful tool, an elastic, perfectly plastic (E-PP) mode technique was proposed in Ref. [3], in which a potential plastic hinge is replaced by a natural hinge with an elastic-plastic rotational spring. In other words, the E-PP solution allows the structures to naturally select a proper mode. The E-PP modal solution was demonstrated to provide a good approximation to complete solutions, as shown in Fig. 1, which demonstrates the effect of beam thickness ratio on the energy partitioning between beams.

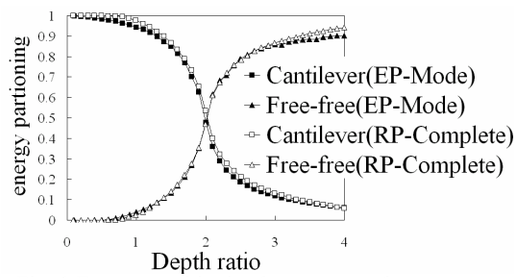
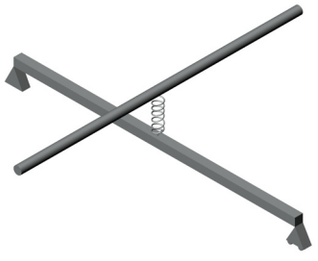


Fig. 1 Energy partitioning between two beams


Fig. 2 Beam-on-beam collision with a local contact spring

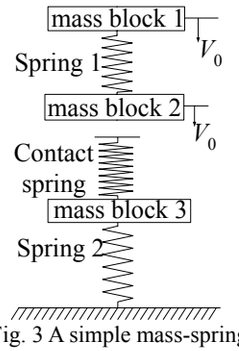


Fig. 3 A simple mass-spring collision system

LOCAL CONTACT MODEL

The local contact model between the two colliding structures is a vital issue in the structural collision, because it theoretically defines the interaction between the two colliding structures and provides a solution for the transmission of momentum and kinetic energy from the flying structure to the target one. Since the contact area is usually very small compared with the dimensions of the structures, the inertia of the locally deformed regions is negligible in the dynamic analysis, thus its behavior can be modeled by a massless non-linear contact spring. Thus, for a typical collision between a free-free cylindrical beam and a simply supported rectangular beam, the simplified model can be sketched as shown in Fig. 2. Due to the initial velocity discontinuity at the contact points (e.g. the mid points of a flying free-free beam and a target simply-supported beam), the relative displacement of these points exists and represents the magnitude of local contact deformation. Hence, if a contact model can relate the interaction force to the contact deformation, it defines the mechanical property of a (non-linear) contact spring. On the other hand, for each colliding structure, this contact force can be treated as an external force pulse, whilst the stick assumption is no longer necessary, so that the separation

between the colliding beams and multi-collision phenomena can be observed.
Several local contact models for beam-on-beam collisions have been proposed by Ruan and Yu [4]. Owing to the complexity of elastic-plastic contact problem, each contact model proposed in Ref. [4] assumes a particular deformation pattern and neglects some factors. For instance, the Elastic-Plastic (or Rigid-Plastic) Shear Deformation (EPS/RPS) model only accounts for the shear deformation in the contact region; the Blunt Indentation (BI) model assumes hydrostatic pressure applied to the material under the contact region and the deformation possesses radial symmetry; while the Uniaxial Compression (UC) model assumes a uniaxial compression along the direction of indentation and neglects the material's Poisson's effect and shear deformation.

ANALYSIS OF A MASS-SPRING SYSTEM

In order to reveal the fundamental features of structural impact/collisions with reduced complexity, one may utilize simple mass-spring systems, in which the complicated geometric analysis is no longer required whilst the two most essential factors for the structural dynamics – inertia and stiffness – are incorporated. A simple mass-spring colliding system (shown in Fig. 3) proposed in Ref. [5] was found equivalent to the E-PP modal solution of beam-on-beam collisions. Thus, the study of this mass-spring model is able to bear some physical meaning in real structures. Through this study, some common features of structural collision are elaborated. In general, a structural response to impact can be divided into two stages: a very brief collision stage, followed by a global structural deformation stage. The first stage starts with a severe velocity discontinuity in the contact region, and characterized by a local velocity change together with local contact dissipation. In the second stage, a restoring instant exists at which the stronger structure transfers from an energy dissipation state to a non-dissipation state, and the total energy dissipated by this structure is termed the restoring energy. The remaining kinetic energy after this restoring instant will be completely dissipated by the weaker structure, if the latter exhibits no deformation-hardening. For the structure with constant load-carrying capacity during its large plastic deformation, the initial velocity will not affect the energy partitioning; while the increase of the relative mass of the impinging structure will make the energy-partitioning pattern approaching an elementary static estimate; that is, the structure with lower strength will dissipate all the input energy. These features are further exhibited in a more complicated ring-on-beam collision based on the solutions obtained by the proposed MS-FD model [6].

EXPERIMENTS

In order to verify the above theoretical models, dynamic experiments were conducted on beam-on-beam collisions. The flying free-free beam was accelerated by a bullet fired from an air gun. In order to avoid a direct impact of the bullet onto the free-free beam before the beam-on-beam collision of the prime interest, an aluminum medial was employed to transform a part of kinetic energy from the bullet to the flying beam. The velocity that the free-free beam thus gained was up to 20m/s, which then generated notable plastic deformation in the two colliding beams. The flexural profiles of the beams after collision were scanned and fitted by piece-wise linear curves, which was then used to calculate the energy dissipated by each beam in its global flexural deformation. It is found that most of the curvature change was concentrated in the middle portions of the two beams, indicating that the most of plastic deformation occurred in their mid-spans. This fact verifies the modal solution which assumes that merely a single plastic hinge forms in each of the colliding beams at its mid-span while the two halves of the beam rotate about this hinge as rigid bodies. The energy dissipation ratio of the two beams obtained from the experimental results shows a good agreement with the theoretical predictions, verifying the theoretical models previously developed.

CONCLUSION

Our study indicates that the previous theoretical approaches for single structure's dynamic response are still applicable on the collision between two deformable structures. However, the local contact force-deformation behavior (e.g. as a massless contact spring) should be incorporated into the model to relate two structures' response. The E-PP modal solution technique was proposed as a powerful technique to replace the R-PP modal solution. In respect of energy partitioning, it was shown that the weaker structure always dissipates more energy. The energy-partitioning pattern mainly depends on the structures' mass and stiffness, rather than on the magnitude of initial velocity, especially when the structures display no deformation-hardening.

Acknowledgement – Support from Hong Kong RGC grant HKUST6035/99E to this study is gratefully acknowledged.

References

[1] Yu TX, Yang JL, Reid SR. Deformable body impact: dynamic plastic behavior of a moving free-free beam striking the tip of a cantilever beam. International Journal of Solids and Structures. 2001; 38: 261-287.
[2] Yu TX, Yang JL, Reid SR. Energy partitioning between two colliding beams. ICTAM2000, Chicago, USA, August 2000.
[3] Ruan HH, Yu TX, Hua YL. Plastic modal approximations in analyzing beam-on-beam collision. Int. J. Solids Struct. 2003; 40(12): 2937-2956.
[4] Ruan HH, Yu TX. Local deformation models in analyzing beam-on-beam collisions. Int. J. Mech. Sci. 2003; 45(3): 397-423.
[5] Ruan HH, Yu TX. Collision between mass-spring systems, Int. J. Impact Eng. (In press)
[6] Ruan HH, Yu TX. Collision between a ring and a beam, Int. J. Mech. Sci. (In press)

COUNTERINTUITIVE RESPONSE OF LONG CIRCULAR TUBES TO AXIAL IMPACT

D. Karagizova[*], Norman Jones[**]
[*]*Bulgarian Academy of Sciences, IMech, Acad. G.Bonchev St., Bl.4, Sofia 1113, Bulgaria*
[**] *The University of Liverpool, Brownlow Hill, L69 3GH Liverpool, UK*

Summary The dynamic transition from progressive buckling to global bending collapse of a long circular tube under an axial impact is studied in order to obtain the energy absorption characteristics. The developed theoretical modes are used to analyse the influence of various parameters on the buckling transition. The analysis reveals a specific impact velocity, which causes a counterintuitive response of a tube. An empirical criterion for the lower and upper bounds to the critical lengths for buckling transition is proposed.

INTRODUCTION

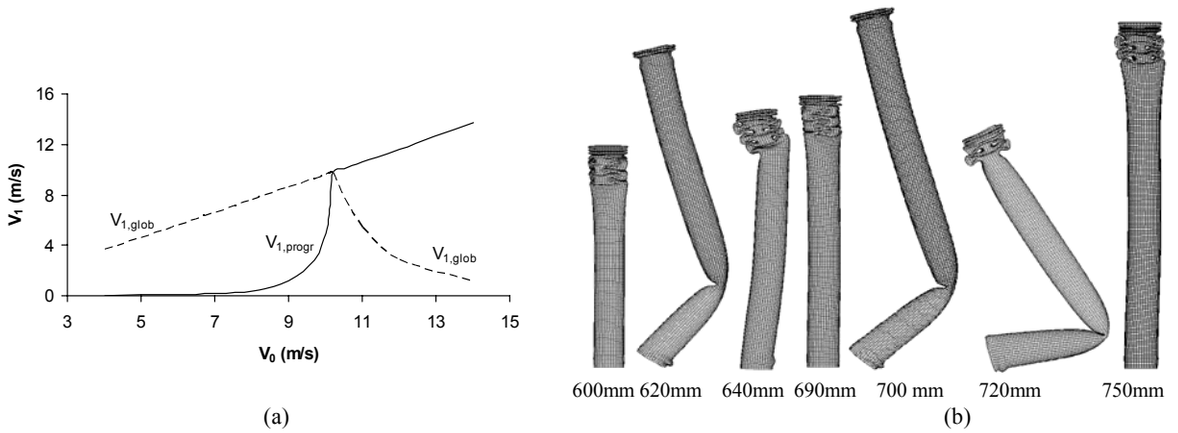
When tubes with various cross-sections are used as energy absorbing devices, the optimisation of these structures usually assumes that the particular geometry will promote a progressive buckling mechanism, which is maintained throughout the response [1]. The initiation of the desired buckling mode becomes rather complicated when long shell-like structures are to be used to absorb the impact energy as these structures can exhibit additional buckling modes leading to poor energy absorption. In particular, buckling modes similar to the Euler buckling mode characteristic for statically loaded rods or higher dynamic 'rod' modes can develop in long tubes (global bending) depending on the geometry, boundary conditions and material of the structure as reported in the experimental studies [2,3].
The mixed collapse modes - global bending with progressively developed wrinkles, which are observed experimentally and numerically [4,5], suggests that 'rod' and 'shell' buckling modes co-exist in long tubes and they can develop simultaneously during impact. It has been anticipated until recently that the increase of the impact velocity will lead to a stabilisation of the tube response due to the inertia effects. However, more comprehensive experimental studies [6] revealed that this increase is not monotonic and is accompanied by a counterintuitive response.
The purpose of this study is to bring an insight into the complex interaction between the two buckling modes and to analyse the predictability of the dynamic transition from progressive buckling to a global bending collapse.

THEORETICAL APPROACH

Two well distinguishing phases of deformation - initial compression and bending - characterise the response of shells that buckle in the plastic range and significant proportion of the initial kinetic energy can be absorbed during the first response phase of these structures, depending on how long the lateral inertia can support the unbuckled shape [4,5]. Thus, the compression phase can influence the initial conditions for the subsequent phase of deformation and in this way can affect the selection of the particular mode of collapse - global bending or progressive buckling (folding). This kind of response suggested to use a two-phase approach to estimate the speeds of the development of the two buckling modes during the initial compression and subsequent post-buckling response depending on the material properties and loading parameters. Due to the compressibility of the shells made from ductile materials, the initial displacements and velocities at the end of the compression phase at $t = t^*$ are functions not only of the loading parameters but also depend on the geometric and material properties of the shell. The numerical simulations show that bending deformations with small amplitudes associated with the global bending and progressive buckling modes start to develop during the compression phase. Therefore, different initial conditions can be set in the shell at the outset of the subsequent phase of deformation, which can be progressive buckling or global bending. These initial conditions determine the speeds of the development of the corresponding buckling mode and a relationship between the displacements and velocities at $t = t^*$ and the various parameters that characterise the dynamic buckling transition phenomenon exists.

RESULTS

The initial conditions for the development of the global bending mode and progressive buckling mode are obtained as functions of the loading parameters, geometrical and material characteristics of a shell when using separate structural models for the two deformation phases. The axial velocities $V_{glob}(t^*)$ and $V_{progr}(t^*)$ at $t = t^*$ for the initiation of the post-buckling development of global bending and a local wrinkle calculated according to the theoretical models are shown in Fig. 1(a) as functions of the initial impact velocity V_0 for a particular shell geometry. One can see that there is a specific impact velocity, $V_{0,cr}$, which causes equal speeds of the development of the two buckling modes ($V_{progr}(t^*) = V_{glob}(t^*)$). In this case, there is no obvious leading mode at $t = t^*$, which could determine the buckling pattern in a unique way causing its development during the bending phase. The axial velocities V_1 associated with the two buckling modes become incomparable away from the critical impact velocity $V_{0,cr}$ thus corresponding to the selected preferable mode associated with the higher speed. Impact velocities around the critical value cause a counter intuitive response as shown in Fig. 1(b) when identical impact loads are applied to shells with equal cross-section characteristics and made from the same materials but the shell length increases.



(a) (b)

Figure 1 (a) Velocities $V_1(t^*)$ at the end of the compressive phase: — progressive buckling mode, ---- global bending mode, L = 550 mm, h = 2.19 mm; (b) Buckling shapes of tubes made of an aluminium alloy ,V_0 = 10.4 m/s and G = 209 kg.

An empirical criterion for the lower and upper bounds to the critical lengths for buckling transition depending on the impact velocity and the striking mass is proposed in this study. This criterion is based on the absorbed energy during the development of a single wrinkle and the vertical velocities of the proximal end of a shell, which are associated with the two buckling modes.

The analysis of the buckling process of relatively long circular tubes suggests that an introduction of an appropriate trigger (either mechanical dent or altering locally the material properties) will improve the energy absorbing characteristics of the device by promoting the initiation of progressive buckling. However, in the case of large impact energy when a large number of wrinkles are necessary to absorb the initial kinetic energy, the buckling initiation into the desirable buckling mode will not promote entirely progressive buckling.

CONCLUSIONS

The present study reveals that, for practical purposes, it is advisable to analyse the response of relatively long tubes when subjected to the actual mass. The velocities causing comparable initial conditions for the buckling/bending phases and therefore counterintuitive deformation of the energy absorbers can be avoided by a variation of the cross-sectional characteristics of the tubes. If certain geometry is required, different materials can be selected to assure a predictable response of the energy absorber.

References

[1] Jones, N., 1989. Structural Impact. Cambridge University Press, Cambridge.
[2] Andrews, K.R.F., England, G.L., Ghani, E.: Classification of the axial collapse of circular tubes under quasi-static loading. *Int. J. Mech. Sci*., **25**, 687-696, 1983.
[3] Abramowicz, W., Jones, N.: Transition from initial global bending to progressive buckling of tubes loaded statically and dynamically. *Int. J. Impact Engng*, **19**, 415-437, 1997.
[4] Karagiozova, D., Alves, M.: Transition from progressive buckling to global bending of circular shells under axial impact - Part I: Experimental and numerical observations. *Int. J. Solids and Structures*, In Press, 2003.
[5] Karagiozova, D., Alves, M.: Transition from progressive buckling to global bending of circular shells under axial impact - Part II: Theoretical analysis. *Int. J. Solids and Structures*, In Press, 2003.
[6] Jensen, O., Langseth, M., Hopperstad, O.S.: Transition between progressive and global buckling of aluminium extrusions}. In: N. Jones and C. A. Brebbia and A. M. Rajandran, Editors. Structures Under Shock and Impact VII, pp. 269-277, W.I.T. Press, 2002.

SELF SIMILAR DYNAMIC EXPANSION OF A SPHERICAL CAVITY IN ELASTOPLASTIC MEDIA

Rami Masri and David Durban
Faculty of Aerospace Engineering, Technion-Israel Institute of Technology, Haifa 32000, Israel

Extended Summary

The dynamic Elastoplastic field induced by a pressurized spherical cavity expanding in an infinite medium is widely used in simulating penetration phenomena. The simplicity offered by the spherical symmetric pattern of the deforming material leads to fairly simple, yet accurate, expressions for key parameters like the resisting force and penetration depth. An extensive review of earlier work has been given by Hopkins [1] with emphasis on incompressible Mises elastic/perfectly-plastic models. Elastic compressibility in dynamic spherical cavity expansion has been considered by Forrestal and Luk [2] for an elastic/perfectly-plastic Tresca solid along with linear pressure-dilatation relation.

In the study lecture we attempt to present a unified treatment of dynamic spherical expansion in a pressure sensitive elastoplastic medium. Material response is modeled by the hypoelastic theory for the Drucker-Prager solid [3] with a non-associated flow rule. The theory accounts for both elastic and plastic compressibility and allows for arbitrary strain-hardening in the plastic range.

The lecture begins with a brief exposition of the governing dynamic field equations following the quasi-static spherical cavity expansion analysis in [3]. Assuming a self-similar expansion field we show that the governing system consists of four ordinary differential equations with two stress components, radial velocity and density as unknowns.

Next we examine the external elastic field, which is expected to develop at a distance from the cavity prior to plastic yielding. The governing system is reduced here to just two equations for the stresses, which can be further simplified, under the assumption of small elastic stresses, to the standard linear elastic model. A new observation that emerges from the elastic solution is the possible existence of a compressive elastic zone where yielding is prevented since the effective stress remains negative. A simple expression for the location of the inner boundary of that zone is derived along with a condition for its existence, which is due to plastic pressure sensitivity and Poisson's ratio.

The important case of a fully incompressible solid (where both elastic and plastic branches do not admit volume changes), which is also an extreme case of non-associativity, is discussed in some detail. The velocity profile behaves here as the inverse square of radial distance, with the deforming field extending to infinity. A quadrature type solution is given for the stresses with the elastic/perfectly-plastic characteristic. We have found that plastic pressure sensitivity causes an increase in the cavitation pressure but reduces the size of the plastic zone. These results are supported by a numerical solution for the stresses in a fully incompressible elastic/power-hardening material. In the absence of pressure sensitivity, we recover the closed form solution for the incompressible Mises material, which is valid for any hardening or softening characteristic.

Finally, we explore the material with an associated Drucker-Prager flow rule and show, with no further assumptions, that the exact field equations can be reduced to two equations for stresses. A few numerical solutions for both compressible and incompressible response reveal the coupled effect of plastic pressure sensitivity and material inertia in raising the level of cavitation pressure. By comparison, plastic compressibility appears to be much more important than elastic compressibility at low cavity expansion velocities. An elegant expansion in powers of Mach number, is derived for the cavitation pressure in a Mises solid, and shown to remain in close agreement with numerical solutions. Predictions of penetration depth, obtained from that expansion, compare favorably with available experimental data.

References

[1] Hopkins H.G.: Dynamic Expansion of Spherical Cavities in Metal. In: Sneddon, I.N., Hill, R. (Eds), Progress in Solid Mechanics **1**, North Holland, Amsterdam, 1960.

[2] Forrestal M.J., Luk V.K.: Dynamic Spherical Cavity-Expansion in a Compressible Elastic-Plastic Solid. *J. Appl. Mech* **55**, 275-279, 1988.

[3] Durban D., Fleck, N.A.: Spherical Cavity Expansion in a Drucker-Prager Solid. *J. Appl. Mech* **64**, 743-750, 1997.

XXI ICTAM, 15–21 August 2004, Warsaw, Poland

NUMERICAL INVESTIGATION OF DYNAMIC SHEAR BANDS IN INELASTIC SOLIDS AS A PROBLEM OF MESOMECHANICS

Adam Glema*, Tomasz Łodygowski*, Piotr Perzyna**
*Institute of Structural Engineering, Poznan University of Technology, Piotrowo 5, PL 60-965 Poznan, Poland
**Polish Academy of Sciences, IPPT PAN, Swietokrzyska 21, PL 00-049 Warszawa, Poland

The main objective of the present paper is the numerical investigation of dynamic shear bands in inelastic solids generated by impact–loaded adiabatic processes. Particular attention is focused on the proper description of a ductile mode propagating along the shear band for high impact velocities.

PROBLEM OF IMPACT-LOADED PRENOTCHED PLATE

An idea of this investigation has been inspired by recent experimental observations presented in [2,6]. These experimental works have been brought deep understanding of the initiation and propagation characteristic as well as the temperature field evolution of dynamic shear bands in C 300 maraging steel. Pre–fatigued single edge notched specimens were asymmetrically impacted on the edge under the notch to initiate adiabatic shear band. The advance of the shear band and its velocity as a function of time were presented and a sequence of thermal images revealing the development of the temperature field as a function of time were showed. A photograph of an arrested shear band in the specimen showed that the thickness of the band is about 40 μm (so it is mesoscale size range). A scanning electron microscope image of the specimen surface that failed by shear band propagation showed (presented) elongated voids, with shear edges that are characteristic of such a failure mode. The presence of voids reveals the development of triaxial tensile stresses that led to void growth and eventual a ductile fracture mode.

Numerical simulation of dynamic shear band propagation in an asymmetrically impact–loaded prenotched plate have been presented in [3,7]. However many problems at the moment are not clear and many are still open for investigation.

Applications of metals and polymers at mesoscale (a size scale that ranges from a fraction of micrometer to 100 μm) are recently multiplying rapidly. It is considerable experimental evidence that plastic flow and particularly fracture phenomena in crystalline solids are inherently size dependent over mesoscale range. However, conventional continuum mechanics models of inelastic deformation processes are size scale independent. The relatively large numbers of dislocations governing plastic deformation at the micron scale motivate the development of a continuum theory of plasticity incorporating size–dependence. The elastic viscoplastic theory can be developed for this purpose.

ELASTO–VISCOPLASTIC CONSTITUTIVE MODEL

A general constitutive model of elasto–viscoplastic damaged polycrystalline solids is developed within the thermodynamic framework of the rate type covariance structure with a finite set of internal state variables. The set of internal state variables consists of two scalars, namely equivalent plastic deformation and volume fraction porosity. The equivalent inelastic deformation can describe the dissipation effects generated by viscoplastic flow phenomena and the volume fraction porosity take into account the microdamage evolution effects, cf. [5].

The relaxation time is used as a regularization parameter. By assuming that the relaxation time tends to zero the thermo–elasto–plastic (rate independent) response of the damaged material can be obtained. Fracture criterion based on the evolution of microdamage is formulated.

It is noteworthy to stress that viscosity introduces implicitly a length–scale parameter into the dynamical initial–boundary value problem, i.e. $l = \alpha c T_m$, where T_m is the relaxation time for mechanical disturbances and is directly related to the viscosity of the material, c denotes the velocity of the propagation of the elastic waves in the material. The factor α depends on the particular initial–boundary value problem under consideration and may also depend on the microscopic properties of the material.

The thermo–elasto–viscoplastic theory developed takes account of (i) plastic non–normality; (ii) softening effects generated by microdamage mechanisms; (iii) thermomechanical couplings (thermal plastic softening and thermal expansion); (iv) influence of stress triaxiality on the evolution of microdamage; (v) rate sensitivity; (vi) dissipation and dispersion effects; (vii) synergetic effects generated by cooperative phenomena; (viii) length scale sensitivity; (ix) finite plastic deformation; (x) invariance with respect to diffeomorphism.

The identification procedure for the material functions and constants involved in the constitutive equations is developed basing on the experimental observations of adiabatic shear bands in HY–100 steel presented in [1]. We take here advantage of our previous numerical investigation presented in [4]. We consider dynamic shear band propagation in an asymmetrically impact–loaded prenotched plate (similar to that experimentally investigated in [2]).

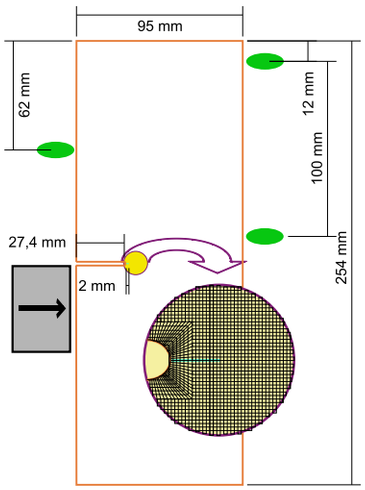


Figure 1. Specimen geometry, impact arrangement and finite discretization. Thickness of the specimen is 12 mm.

NUMERICAL EXPERIMENT

The plate is made of HY–100 steel. A notch (260 μm wide) is situated symmetrically on the edge, which is further extended by 2 mm as has been shown in Fig. 1. The specimen is supported at three points and is initially stationary. The constant velocity V_0 ($13 \div 39$ m/s) is imposed for projectile. The projectile comes into contact with the specimen over the width of 50 mm. The impact loading is simulated by a velocity boundary condition which are the results of dynamic contact problem. The velocity imposed in specimen in front of projectile increases from zero for the initiation of contact between the projectile and the specimen and increases during the process. The contact surface is assumed to be traction–free. The separation of the projectile from the specimen, resulting from wave reflections within the projectile and the specimen, occurs in the phenomenon. All surface areas have traction free boundary conditions except where the velocity boundary condition is applied. Utilizing the finite element method and ABAQUS system for regularized elasto–viscoplastic model the numerical investigation of dynamic shear band propagation in an asymmetrically impact–loaded prenotched plate is presented. We idealize the initial boundary value problem observed experimentally in [2] by assuming the velocity boundary condition and different material of the specimen.

FINAL REMARKS

The elaborated numerical algorithm satisfies the material objectivity principle with respect to diffeomerphism (any motion). The discretization parameters are assumed in such a way, cf. Fig. 1, to solve the problem of mesomechanics properly. The dimension of the accepted mesh is of order 20 μm. A thin shear band region of finite width which undergoes significant deformation and temperature rise has been determined. Its evolution until occurrence of final fracture has been simulated. Shear band advance, shear band velocity and the development of the temperature field as a function of time have been determined. Qualitative comparison of numerical results with experimental observation data has been presented. The numerical results obtained have proven the usefulness of the thermo–elasto–viscoplastic theory in the numerical investigation of dynamic shear band propagation.

References

[1] Cho K., Chi Y.C., Duffy, J.: Microscopic observations of adiabatic shear bands in three different steels, Brown University Report No. DAAL03–88–K–0015/3, September, 1988.

[2] Guduru P.R., Rosakis A.J., Ravichandran G.: Dynamic shear bands: an investigation using high speed optical and infrared diagnostic, *Mechanics of Materials*, **33**, 371–402, 2001.

[3] Li S., Liu W.–K., Qian D., Guduru P.R., Rosakis A.J.: Dynamic shear band propagation and micro–structure of adiabatic shear band, *Comput. Methods Appl. Mech. Engng.*, **191**, 73–92, 2001.

[4] Łodygowski T., Perzyna P.: Numerical modelling of localized fracture of inelastic solids in dynamic loading processes, *Int. J. Num. Meth. Engng.*, **40**, 4137–4158, 1997.

[5] Perzyna P.: Thermo–elasto–viscoplasticity and damage, in: *Handbook of Materials Behaviour Models* (Ed. J. Lemaitre), Academic Press, New York, pp. 821–834, 2001.

[6] Zhou M., Rosakis A.J., Ravichandran G.: Dynamically propagating shear bands in impact–loaded prenotched plates. I. Experimental investigations of temperature signatures and propagation speed, *J. Mech. Phys. Solids*, **44**, 981–1006, 1996.

[7] Zhou M., Ravivhandran G., Rosakis, A.J.: Dynamically propagating shear bands in impact–loaded prenotched plates. II. Numerical simulations, *J. Mech. Phys. Solids*, **44**, 1007–1032, 1996.

ON NON-AXISYMMETRIC COLLAPSE OF THIN TUBES

N. K. Gupta
Department of Applied Mechanics, Indian Institute of Technology, Delhi, Hauz Khas, New Delhi – 110016, India

Summary Occurrence of non-axisymmetric collapse modes in axial compression of thin tubes has been studied both experimentally and with the help of FE simulation. Variables considered are tube diameter to thickness ratio, annealing, variation in tube wall thickness, eccentricity, and boundary conditions. It is seen that amongst other factors, a certain combination of thickness eccentricity and unsymmetrical in plane end conditions favours formation of diamond mode.

INTRODUCTION

Progressively collapsing tubes in axisymmetric concertina, non-axisymmetric diamond or mixed mode are efficient kinetic energy absorbing structure elements and therefore mechanics of their collapse under axial loading conditions has received considerable attention in the past. Several experimental, analytical and numerical studies have appeared in recent years, which help in understanding of the plasto-mechanics of the collapse phenomenon. Experimental studies [1-3] have shown that tubes with D/t (diameter to thickness) ratio less than about 70-90 deform in axisymmetric mode while those with larger D/t values deform non-axisymmetrically. Analytical and numerical studies, however, have mostly been confined to axi-symmetric collapse mode, and not much is available in literature which deals with the analysis of the diamond mode of collapse or conditions under which this mode of collapse takes place. The present experiments were conducted on tubes of aluminium and mild steel in both as received and annealed conditions. Their D/t was varied from 10 to 40, and in this range these tubes were expected to collapse in axisymmetric concertina mode. Experiments however showed that many of these tubes collapsed in non-axisymmetric diamond or mixed mode. Detailed experimental and numerical studies were therefore undertaken to analyse the conditions under which the non-axisymmetric deformation would occur in a tube under axial compression. It is seen that the factors on which occurrence of non-axisymmetric collapse depends include tube diameter to thickness ratio, annealing, variation in tube wall thickness, eccentricity, and boundary conditions.

Experimental and Numerical Simulation

Transition of deformation mode shapes from axisymmetric concertina mode to non-axisymmetric diamond pattern have been studied with different configurations of tube wall thickness eccentricity, increasing levels of eccentricity in single lobe configuration, boundary conditions and tube shape deviations for round tubes of Aluminum with D/t ratio 27 and L/D = 2. The deformation process is modeled and simulated in the FE code ANSYS using a nonlinear implicit quasistatic analysis.

The wall thickness eccentricity was introduced around the circumference of a machined 50.8 mm diameter tube in a single lobe configuration through off center machining for the quasi static axial compression tests. The global geometric imperfection has been parameterized as a function of the specified eccentricity ‘e’ in the Finite Element model of the tube. The required reduction in the thickness around circumference is incorporated into the discretised domain by unchecking the FE mesh from the solid model. The nodal coordinates are updated as a half sine wave around half the tube circumference with amplitude ‘e’ as maximum reduction in thickness for the single lobe eccentricity. The collapse mode dependence on increasing level of wall thickness eccentricity (e/t ratio) in single lobe configuration has been studied with axisymmetric as well as non-axiaxisymmetric radial displacement tube end constraints (Fig. 1)

Different configurations investigated in addition to the single lobe eccentricity are 2, 3 and 4 lobe wall thickness eccentricity around the tube circumference; the wall thickness reduction around the tube circumference has been modeled as a full, one & half and double sine wave respectively around the tube circumference with an amplitude ‘e’. The sensitivity of collapse mode to varying wall thickness eccentricity configurations in 1 , 2 ,3 and 4 lobes has been studied numerically with axi symmetric as well as non-axiaxisymmetric radial displacement tube end constraints (Fig. 2). Validation and comparison of non-linear FE solution with experimental results based on quasi-static axial compression of Aluminum tubes of D/t = 29.19 and L/D = 1.4 in the single lobe eccentricity configuration has been carried out.

Collapse mode variations with tube shape deviations from circular cross section but with a uniform wall thickness have also been studied with variations in tube end conditions (inplane radial displacements). The tube radial coordinates at any point around the circumference is modeled by modifying the coordinates as a function of its polar coordinate ‘θ’ in 1,2,3 and 4 lobe configuration.

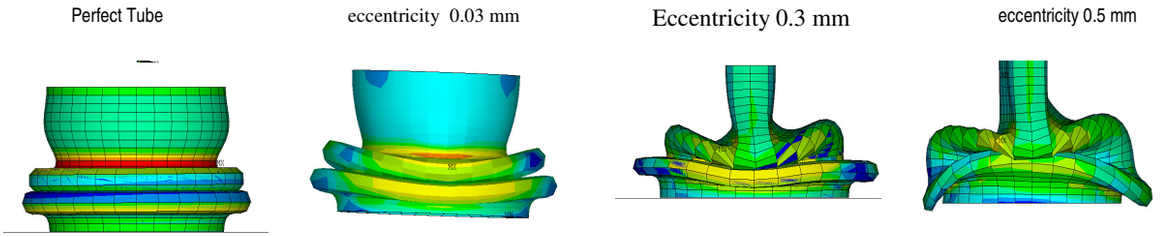


Fig 1 : FE simulation of collapse modes and deformation profiles with Perfect Tube, 0.03 mm , 0.3 mm, and 0.5 mm wall thickness eccentricity around circumference at 40 mm axial compression of the 50.8 mm diameter (D/t = 29.19) eccentric Al tube. The tube end conditions are perfect axisymmetric.

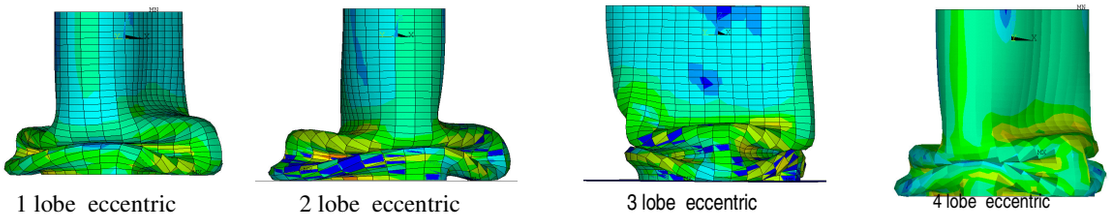


Fig 2 : FE simulation of collapse modes 1,2 , 3 and 4 lobe wall thickness eccentricity around circumference at 40 mm axial compression of the 50 mm diameter (D/t = 27) eccentric Al tube. The tube end conditions for inplane radial displacements are non axi symmetric (constrained over 180 degree sector only).

Results and Conclusions

Good correlation has been obtained between the experimental results and the numerical model for the load deformation response; energy absorbed and collapse mode shape. It has been established that there is a strong dependence of the collapse mode to the eccentricities in the tube end conditions. Deviations from axisymmetry in the inplane radial displacement constraints causes even a geometrically perfect tube to collapse in the diamond mode. It has also been demonstrated through numerical studies that diamond mode collapse tendency of Al tubes under quasi static axial compression increases with increasing tube wall thickness eccentricity around the circumference with axisymmetric tube end conditions. There is a linear decrease in Pi (First peak load) and Pm (Mean Load) with increasing level of tube wall thickness eccentricity in single lobe configuration.

For axisymmetric tube end conditions, it is seen that while the Al tubes with 1 and 2 lobe wall thickness eccentricity collapse in a mixed concertina and diamond mode, the models with 3 and 4 lobe eccentricity interestingly collapse in a concertina mode. In the latter case however, a non axisymmetric stress profile away from the plastic zone is observed. Collapse mode is found to be insensitive to minor tube shape deviations from circular cross section under axisymmetric tube end conditions. However, under non-axisymmetric inplane tube end conditions, the collapse mode is diamond for all the studied configurations of tube shape eccentricity.

It is seen that the diamond mode of collapse is more likely to occur when there is a combined effect of thickness eccentricity and unsymmetrical in plane end conditions.

References

[1] Gupta N.K., Gupta S.K.:Effect of annealing, size, and cutouts on axial collapse behavior of circular tubes, Int. j. Impact Eng., 27, 87-117, 1999
[2] Jones N., Abramowicz W., Static and dynamic axial crushing of circular and square tubes, Proc. Metal Forming and Impact Mech. Ppergoman Press, Oxford. 1985
[3] Andrews K.R.F, England G.L., Gani E., Classification of thin axial collapse of cylindrical tubes under quasistatic loading, Int. J. Mech. Sci., 25, 687-696, 1983

ON INVARIANTS OF THE ELASTICITY TENSOR FOR ORTHOTROPIC MATERIALS

Katarzyna Kowalczyk-Gajewska, Janina Ostrowska-Maciejewska
IPPT PAN, Department of Continuous Media, PL 00-049 Warszawa, Poland

Summary The fourth order elasticity tensor for linear elastic material of orthotropic symmetry is studied. The set of nine invariants of this tensor is proposed allowing uniquely specify the form of the tensor in any basis. The set of invariants is composed of six Kelvin moduli and three invariants of the selected orthogonal projectors. In order to derive the presented results spectral theorem for elasticity tensor as well as harmonic decomposition for the orthogonal projectors of the orthotropic stiffness tensor are used.

INTRODUCTION

Materials of new generation already during their projecting are supposed to be characterized by some prescribed properties. These properties can refer to their strength, way of deformation, resistance to external forces. Therefore, it is demanded to know appropriate criteria for the assessment of these properties. It requires profound theoretical knowledge and working-out new technological solutions. At the same time in many cases computer Finite Element Method simulations are conducted to determine elastic constants for the considered biological materials such as bones and other tissues or the current properties of damaged engineering materials. It is necessary to formulate the criteria for identification of symmetry type of the material.

The vast number of composites materials and textured metals exhibit at least orthotropic symmetry. Also for biological tissues as well as in damage analysis orthotropic approximation of elastic properties is considered to be admissible.

The form of stiffness tensor for orthotropic material and its spectral analysis is widely known [5] [2], [6]. As it was shown, such tensor is specified by nine independent parameters: six Kelvin moduli and three stiffness distributors defining three out of six eigen-states. However, definitions of three stiffness distributors with use of invariants of eigen-states was not yet proposed. Below, we derived such definitions that allow to specify uniquely elasticity tensor for any orthotropic material.

SPECTRAL THEOREM FOR ORTHOTROPIC SYMMETRY

Any orthotropic linear elastic material can be described by the fourth order tensor that in general has six mutually different positive eigenvalues called Kelvin moduli λ_K and six orthonormal eigen-states $\mathbf{w}_K$ among which three are pure shears with common direction of shearing for every pair among them. Let us number them subsequently by $I = 4, 5, 6$. Moreover, three direction of shearing obtained by these definition are mutually orthogonal and form the orthonormal basis of main orthotropy directions [1]. Remaining three eigen-states are coaxial and their eigenvectors are align along orthotropy directions. We may derive diads of orthotropy directions $\mathbf{m}_k \otimes \mathbf{m}_k$ where $k = 1, 2, 3$ (no summation) in following way

$$\mathbf{m}_1 \otimes \mathbf{m}_1 = \mathbf{I} - 2\mathbf{w}_4^2, \quad \mathbf{m}_2 \otimes \mathbf{m}_2 = \mathbf{I} - 2\mathbf{w}_5^2, \quad \mathbf{m}_3 \otimes \mathbf{m}_3 = \mathbf{I} - 2\mathbf{w}_6^2, \tag{1}$$

It should be noted that as far as ordering rule for $\mathbf{w}_I$, $i = 4, 5, 6$ has not been yet uniquely specified also *numbering* of orthotropy directions has not been established at this stage. We will introduce such rule later.

It was shown by use of spectral theorem that orthotropy can be described by 9 values independent on the basis selection that is six Kelvin moduli and three stiffness distributors specifying orientation of three orthonormal coaxial eigen-states in three dimensional space of the second order tensors with common eigenvectors. These three stiffness distributors may be defined with use of the polynomial invariants of considered eigen-states.

Six Kelvin moduli are derived from the characteristic equations for $\mathbf{C}$ where coefficients can be expressed by six invariants of powers of stiffness tensors $\mathbf{C}$, that is

$$\mathrm{Tr}\mathbf{C}, \quad \mathrm{Tr}\mathbf{C}^2, \quad \mathrm{Tr}\mathbf{C}^3, \quad \mathrm{Tr}\mathbf{C}^4, \quad \mathrm{Tr}\mathbf{C}^5, \quad \mathrm{Det}\mathbf{C} \tag{2}$$

where for $\mathbf{A}$ being the fourth order tensor with components A_{ijkl}, operation $\mathrm{Tr}\mathbf{A}$ gives A_{ijij}, $\mathrm{Det}\mathbf{A}$ denotes determinant of matrix with components $A_{KL} = \mathbf{a}_K : \mathbf{A} : \mathbf{a}_L$ where second order tensors $\mathbf{a}_K$ constitute orthonormal basis in the space of second order symmetric tensors.

STIFFNESS DISTRIBUTORS

Definition

First, let us order coaxial eigen-states according to the following rule

$$K > L \Longleftrightarrow (\mathrm{tr}\mathbf{w}_K)^2 > (\mathrm{tr}\mathbf{w}_L)^2 \quad K, L = 1, 2, 3 \tag{3}$$

If above squeres of traces are equal to each other we number the eigen-states by deacresing values of $(\det \mathbf{w}_K)^2$.

It can be prooved that the following set of three invariants allow uniquely specify diads of coaxial eigen-states called orthogonal projectors

$$\eta_1 = \mathrm{tr}\mathbf{h}_1^2, \quad \eta_2 = \frac{\det \mathbf{h}_1}{(\mathrm{tr}\mathbf{w}_1)^3} \tag{4}$$

where by $\mathbf{h}_K$ we denote deviator of $\mathbf{w}_K$. These two distributors one may expressed by following relations

$$\eta_1 = 1 - \frac{1}{3}(\mathrm{tr}\mathbf{w}_1)^2, \quad \eta_2 = \frac{1}{(\mathrm{tr}\mathbf{w}_1)^3}\left[\det \mathbf{w}_1 - \frac{5}{54}(\mathrm{tr}\mathbf{w}_1)^3 + \frac{1}{6}\mathrm{tr}\mathbf{w}_1\right] \tag{5}$$

Third distributor is defined in the general case as a following function of common invariants of $\mathbf{w}_1$ i $\mathbf{w}_2$

$$\eta_3 = \frac{\mathrm{tr}(\mathbf{w_1^2 w_2})}{\mathrm{tr}\mathbf{w}_2}. \tag{6}$$

The above definition must be modified in the case when $\eta_1 = 0$ or two eigenvalues of $\mathbf{w}_1$ are equal to each other correspondingly in the form

$$\eta_3^* = (\det \mathbf{h}_2)^2, \quad \eta_3^{**} = \frac{\det \mathbf{h}_2}{(\mathrm{tr}\mathbf{w}_2)^3}. \tag{7}$$

First two distributors allow to derive two sets of eigenvalues corresponding to $\mathbf{w}_1$ and $-\mathbf{w}_1$. According to the decreasing absolute value of these eigenvalues orthotropy axes are numbered. Let us underlined that the eigenstate $\mathbf{w}_3$ is specified within its sign by orthonormality conditions.

Let us note that $\eta_1 = 0$ implies immediately $\eta_2 = 0$ and specifies $\mathbf{w}_1$ as the normalized hydrostatic state $\frac{1}{\sqrt{3}}\mathbf{I}$. Remaining eigenstates are then deviatoric and orthotropy axes are numbered in view of decreasing absolute value of eigenvalues of $\pm\mathbf{w}_2$.

If two eigenvalues of $\mathbf{w}_1$ have the same absolute value then corresponding orthotropy axes are numbered in view of appropriate rule applied for $\pm\mathbf{w}_2$.

Finally, let us show that the invariants of eigenstates specified by equations (4) and (6) are also the invariants of the corresponding orthogonal projectors $\mathbf{P}_K = \mathbf{w}_K \otimes \mathbf{w}_K$ ($K = 1, 2, 3$, no summation). Let us apply for them invariant harmonic decomposition [3]: $\mathbf{P}_K \Leftrightarrow \{h_P^{(K)}, \quad h_D^{(K)}, \quad \mathbf{n}^{(K)}, \quad \mathbf{m}^{(K)}, \quad \mathbf{D}^{(K)}\}$. We find that

$$\eta_1 = 1 - h_P^{(1)}, \quad \eta_2 = \frac{\det \mathbf{m}^{(1)}}{(3h_P^{(1)})^3}, \quad \eta_3 = \frac{1}{3h_P^{(2)}}\left(\mathrm{tr}(\mathbf{m}^{(2)}\mathbf{n}^{(1)}) + h_P^{(2)}\right) \tag{8}$$

where $h_P^{(K)} = \frac{1}{3}\mathbf{I} : \mathbf{P}_K : \mathbf{I}$ and second order tensors $\mathbf{m}^{(K)}$ and $\mathbf{n}^{(K)}$ are deviators of the following tensors

$$\widetilde{\mathbf{m}}^{(K)} = \mathbf{P}_K : \mathbf{I}, \quad \widetilde{\mathbf{n}}^{(K)} = \mathrm{tr}_{2,5}\mathrm{tr}_{3,6}(\mathbf{P}_K \otimes \mathbf{I}). \tag{9}$$

Reduction for special cases of orthotropy

Let us now shortly discuss reduction of invariants for special cases of orthotropy such as volume-isotropic material, transversally isotropic material and material of cubic symmetry.

In the case of the volume-isotropic material the stiffness tensor is specified by six Kelvin moduli and one distributor $\eta_3^\star$. In this case $\mathbf{w}_I$ is hydrostatic and $\eta_1 = \eta_2 = 0$.

In the case of transversally isotropic material we have to do only with four essentially different Kelvin moduli. More details concerning spectral decomposition one may find in [4]. Furthermore it can be shown that out of three distributors only one is necessary to establish $\mathbf{w}_1$ and $\mathbf{w}_2$ that is η_2, so only five invariants uniquely define stiffness tensor for any transversally isotropic material.

For the material of cubic symmetry three Kelvin moduli are essentially different. For three pure shears $\mathbf{w}_K$, $K = 4, 5, 6$ we have one Kelvin modulus. For $\mathbf{w}_2$ and $\mathbf{w}_3$ we have the second Kelvin modulus and the third Kelvin modulus corresponds to $\mathbf{w}_1$ where $\eta_1 = \eta_2 = 0$. Distributor η_3 is then insignificant.

CONCLUSIONS

Nine invariants of the orthotropic elasticity tensor has been derived that allow uniquely specify this tensor independently on the basis selection. It allows to investigate apparent orthotropy of the material as well as to compare two orthotropic materials. It seems useful in projecting materials as well as in identifying material orthotropy for biological and damaged material. The proposed approach that is based on the spectral theorem can be applied for the stiffness tensors of lower symmetry.

References

[1] Blinowski A., Ostrowska-Maciejewska J.: On the elastic orthotropy. *Arch. Mech.* **48**:129–141, 1996.

[2] Cowin S.C., Mehrabadi M.M.: Eigentensors of linear anisotropic elastic materials *Q. J. Mech. Appl. Math.* **43**(5):16–44, 1990.

[3] Forte S., Vianello. M.:Symmetry classes for elasticity tensors. *J. Elasticity*, **43**:81–108, 1996.

[4] Kowalczyk K., Ostrowska-Maciejewska J.: Energy-based limit conditions for transversally isotropic solids. *Arch. Mech.* **54**:497–523, 2002.

[5] Rychlewski J.: On the Hooke's law [in Russian], *PPM* **48**, 420–435, 1984 [see translation *Prikl. Matem. Mekhan.*, **48**, 303–314, 1984].

[6] Sutcliffe. S.: Spectral decomposition of the elasticity tensor. *J. Appl. Mech.*, **59**(4):762–773, 1992.

MOTION AND STABILITY OF AN ELASTIC HEAVY TOP

Tsolo P. Ivanov*, Radijanka Savova**
* Sofia University St.Kl.Ohridski, FMI, blvd.J.Bourchier 5, 1164 Sofia, Bulgaria
** BAS, Institute of Mechanics, ul.Acad.G.Bontchev, bl.4, 1113 Sofia, Bulgaria

Abstract. Motion and stability of an elastic top with stress-free surface and a fixed point moving in a gravitational field is considered. The investigation is based on a direct approach in the energy momentum method split into two steps.Relative equilibrium states are determined and criteria for stability are proved.The obtained results are applied for the case of a sleeping heavy top when the top is an elastic circular cylinder.

DEFORMATION AND MOTION OF THE TOP

In this work we consider an elastic and asymmetric top with stress-free surface and a fixed point moving in a gravitational field. It is assumed that the elastic deformation of the top remains static during the motion. The literature on the problem when the top is rigid one is well known [1]. When the top is elastic one the problem becomes very complicated since the Hamiltonian system is infinite dimensional with respect to the elastic deformation whereas the motion of the deformed top as a rigid one is only determined by three independent variables. In order to solve this problem we split the solution into two steps. First we look for the static elastic deformation applying a direct approach in the energy momentum method with energy momentum functional which contains six independent variables at each point of the top. The next step is to rewrite the same Hamiltonian in such a way that the energy momentum function to contain only the independent variables that describe the motion of a rigid top. These two steps are connected each other by the angular velocity of rotation. When we consider the deformation of the top we assume that it depends not only on the gravitation but also on the rotation of the top with arbitrarily fixed angular velocity. In the next step we consider the deformed top as a rigid one. The deformation introduces the angular velocity via the components of the inertia tensor which we do not vary assuming now that the deformation is fixed but we vary the angular velocity when it enters in the Hamiltonian in connection with the rotation of the top as a rigid one. The result is that the position coordinate - the nutation and the cyclic velocity - the precession velocity are constants (there are no proper rotation) and therefore the motion is so called relative equilibrium. The existence of relative equilibria is connected with the fact that the top possesses a conserved quantity as consequence of a symmetry property.This conserved quantity has been included in the formulation of the energy momentum functional[2-4].

STABILITY OF THE TOP

We define that the state of the deformed elastic heavy top is stable at a relative equilibrium if it is in a stable state with respect to the internal(material) stability connected with the static deformation of the top and the external (rigid) stability due to the rotation of the top as a rigid one. Instead of the definition for formal stability adopted in Simo [2] the Koiter's definition for nonlinear stability with respect to the deformation [5] has been accepted. It is based on the Lyapunov ideas for stability developed for mechanics of continua. The advantage of this definition is in the properly chosen measures for the initial disturbance and the distance to the relative equilibrium state. The usual Lagrange definition for stability of the motion of the deformed top as a rigid one is adopted. On this basis necessary and sufficient conditions for internal and external nonlinear stability are proved for the determined relative equilibrium states. These stability conditions are more complicated than the corresponding one for a rigid top since they depend on the deformation of the top due to its rotation and the gravitation. Detailed consideration of this coupled problem is presented and discussed in this work.The obtained results are applied for the case of a sleeping heavy top when the top is an elastic circular cylinder.

References

[1] Lewis, D., T. Ratio, J. C. Simo, J. E. Marsden: The Heavy Top: a Geometric Treatment. *Nonlinearity*, **5**: 1-48, 1992.

[2] Simo J.,T. Posbergh, J. Marsden: Stability of Relative Equilibria Part. II: Application to Nonlinear Elasticity. Arch. Rat. Mech. Anal. **115**: 61-100, 1991.

[3] Ivanov, Ts. P.: Stability Analysis of Relative Equilibria. ZAMM, **76**: 221–222, 1996.

[4] Ivanov, Ts. P., R. Savova: Stability of Relative Equilibria of an Elastic Body. Eur. J. Mech., A/Solids, **16**: 823–832, 1997.

[5] Koiter, W.: The Energy Criterion for Stability of Continuous Elastic Bodies. Proc. Kon Ned. Ak. Wet, **68**: 178–202, 1965.

Stability of compressible elastic blocks

D. M. Haughton, Department of Mathematics, University of Glasgow, Glasgow G12 8QW, U.K.

Introduction

In recent work Chen and Haughton [1–4] have developed a method to study the full non–linear stability of inhomogeneous deformations based on the second variation of the energy. The method is quite general and ultimately involves the solution of a quadratically non–linear system of ordinary differential equations. For two dimensional problems, such as the one we consider here, we have a third order system. The corresponding bifurcation criterion for two dimensional problems involves the solutions of a linear fourth order system. Here we consider the simple problem of the equi-biaxial loading of a cube which is held fixed in the third direction. The simplicity of the problem allows us to make considerable analytic progress. The corresponding problem for incompressible materials has been considered by several authors. A review can be found in Ogden [5].

Basic Equations

We consider the biaxial plane strain deformation of a compressible elastic cube

$$0 \leq X \leq A, \quad 0 \leq Y \leq A, \quad 0 \leq Z \leq A, \tag{1}$$

where (X, Y, Z) are the material cartesian coordinates. The body is comprised of a homogeneous, isotropic, and compressible elastic material in the reference configuration. It is assumed to undergo the homogeneous deformation

$$x = \lambda_1 X, \; y = \lambda_2 Y, \; z = \lambda_3 Z, \tag{2}$$

where (x, y, z) are the spatial cartesian coordinates, and λ_i, $i = 1, 2, 3$ are the constant, positive, principal stretches. We suppose that the deformation is accomplished by equal loads T applied to the sides $X = 0, A$ and $Y = 0, A$ with the remaining sides $Z = 0, A$ held a fixed distance apart. The axial stretch λ_3 can then be regarded as a prescribed parameter for this problem. The equilibrium equations are automatically satisfied for this homogeneous deformation and the dead loading T is given by

$$T = W_1 = W_2, \tag{3}$$

where $W(\lambda_1, \lambda_2, \lambda_3)$ is the strain-energy function of the material and subscripts indicate partial differentiation, $W_i = \partial W / \partial \lambda_i$. The second equation in (3) gives either the trivial solution

$$\lambda_1 = \lambda_2, \tag{4}$$

or,

$$W_1 = W_2, \quad \lambda_1 \neq \lambda_2. \tag{5}$$

Taking the limit as $\lambda_2 \to \lambda_1 = \lambda$, say, in (5), we obtain the bifurcation point where the trivial and non-trivial solutions cross. This is given by

$$W_{11}(\lambda, \lambda, \lambda_3) = W_{12}(\lambda, \lambda, \lambda_3). \tag{6}$$

The non-trivial solution (5) can be regarded as an implicit equation for $\lambda_2(\lambda_1)$. Using this interpretation we can show that bifurcation points coincide with turning points of the load T.

Stability Analysis

For stability we require that the second variation of the energy is non negative. It is easily shown that

$$\ddot{E} = \int_\Omega \{\nabla \dot{\mathbf{x}} \cdot W_{\mathbf{FF}}[\nabla \dot{\mathbf{x}}]\} dV \; , \tag{7}$$

where $\dot{\mathbf{x}}$ is the variation in $\mathbf{x}$. We write $\nabla \dot{\mathbf{x}}$ as

$$\nabla \dot{\mathbf{x}} = \begin{pmatrix} u_X & u_Y & 0 \\ v_X & v_Y & 0 \\ 0 & 0 & 0 \end{pmatrix}, \tag{8}$$

where a subscript denotes the partial derivative. The non-zero components of $W_{\mathbf{FF}}$ are given by

$$(W_{\mathbf{FF}})_{iijj} = W_{ij} \, , \qquad i, j, \text{ no sum}, \tag{9}$$

$$(W_{\mathbf{FF}})_{ijij} = \frac{\lambda_i W_i - \lambda_j W_j}{\lambda_i^2 - \lambda_j^2}\,, \quad (W_{\mathbf{FF}})_{ijji} = \frac{\lambda_j W_i - \lambda_i W_j}{\lambda_i^2 - \lambda_j^2}\,, \quad i \neq j\,, \quad \lambda_i \neq \lambda_j\,, \text{ no sum.} \tag{10}$$

The integrand in (7) is then

$$\nabla\dot{\mathbf{x}} \cdot W_{\mathbf{FF}}[\nabla\dot{\mathbf{x}}] = W_{11}u_X^2 + W_{22}v_Y^2 + 2W_{12}u_X v_Y + W_{1212}(u_Y^2 + v_X^2) + 2W_{1221}u_Y v_X. \tag{11}$$

From this we deduce that the deformation is stable if and only if

$$W_{11} > 0\,, \quad W_{22} > 0\,, \quad W_{11}W_{22} - W_{12}^2 > 0\,, \quad W_{1212}^2 - W_{1221}^2 > 0\,, \tag{12}$$

since $W_{1212} > 0$ by the Baker–Ericksen inequalities.

Alternative Stability Analysis

The integrand in (7) involves two perturbation functions u and v. First we expand these functions into Fourier series in Y. We can show that we get

$$u(X,Y) = \sum_{n=1}^{\infty} f_n(X)\sin\frac{n\pi Y}{A} = \sum_{n=1}^{\infty} f_n(X)\sin\alpha Y, \quad v(X,Y) = \sum_{n=1}^{\infty} g_n(X)\cos\alpha Y. \tag{13}$$

Substituting (13) into (7), integrating with respect to Y and then applying the method outlined in [1–4] we have the alternative (but equivalent) stability criterion: First we solve the system of equations

$$\begin{aligned}
y_1' &= \frac{(W_{1212}^2 - W_{1221}^2)}{W_{1212}} - \frac{y_1^2}{W_{11}} + \frac{y_2(2\,W_{1221} - y_2)}{W_{1212}},\\
y_2' &= -\frac{y_1(W_{12} + y_2)}{W_{11}} + \frac{y_3(W_{1221} - y_2)}{W_{1212}},\\
y_3' &= \frac{W_{11}W_{22} - W_{12}^2}{W_{11}} - \frac{y_2(2\,W_{12} + y_2)}{W_{11}} + \frac{y_3^2}{W_{1212}}, \quad W_{11} \neq 0\,,
\end{aligned} \tag{14}$$

with

$$y_i(0) = 0, \quad i = 1,2,3. \tag{15}$$

For stability of the deformed body it is necessary and sufficient that

$$y_1(n\pi) > 0\,, \quad y_3(n\pi) > 0\,, \quad y_1(n\pi)y_3(n\pi) - y_2(n\pi)^2 > 0\,. \tag{16}$$

The problem of assessing the full non–linear stability of a body in a particular configuration then reduces to that of solving the initial value problem (14) with (15) and evaluating (16). We can determine any change in stability to within the accuracy of the numerical methods used. In particular we note that $y_i \equiv 0$ is a solution when

$$W_{1212}^2 - W_{1221}^2 = 0\,, \quad \text{and} \quad W_{11}W_{22} - W_{12}^2 = 0, \tag{17}$$

and this can be shown to be the case at the bifurcation point (6). We can make little analytic progress with (14) in general and so we mainly look at some specific examples to compare numerical results from (14–16) with the known results obtained in (12).

References

[1] Chen, Y. C. & Haughton, D. M. Stability and bifurcation of inflation of elastic cylinders. Proc. Roy. Soc. London, A459 (2003), 137.

[2] Haughton, D. M. & Kirkinis, E. A Comparison of Stability and Bifurcation Criteria for Inflated Spherical Elastic Shells. Math. Mech. Solids 8 (2003), 561.

[3] Chen, Y. C. Second variation condition and quadratic integral inequalities with higher order derivatives. J. Elast. 70 (2003) 111-127.

[4] Haughton, D. M. On non–linear stability in unconstrained non–linear elasticity. Int. J. Non–linear Mech. 39 (2004), 1181–1192.

[5] Ogden, R. W. 1997 *Non–Linear elastic deformations*. Dover Publications. New York.

XXI ICTAM, 15–21 August 2004, Warsaw, Poland

GENERALIZED STRESS CONCENTRATION FACTORS

Reuven Segev*
*Department of Mechanical Engineering, Ben-Gurion University, Beer-Sheva 84105, Israel

Summary While the traditional stress concentration factor for a given loading is the ratio between the maximal stress in a body and the stress evaluated using simplified geometry, we regard the stress concentration factor as the ratio between the maximum of a stress component over the body, and the maximum value of the applied force fields. Then, for the given loading, we consider an optimal stress distribution which is a stress tensor field together with additional volume force density that will equilibrate the external loading and will result in the smallest stress concentration factor. Finally, the generalized stress concentration factor K is defined as the maximum of all optimal stress concentration factors for all external loading fields. The generalized stress concentration factor is clearly a geometric property of the body. It is shown that K is equal to the norm of the mapping that extends Sobolev functions defined in the interior of the body to its closure.

BASIC DEFINITIONS

Traditional stress concentration factors (see for example Peterson [2]) specify the ratio between the maximal value of a stress component in a body and the maximum value of that component for simplified, idealized geometry. The stress concentration factors are evaluated using analytical, numerical and experimental methods for given loadings and material properties. It is noted that the nominal stress calculated for the simplified geometry may be regarded as the boundary traction at a large distance away from the nontrivial geometry. For example, for a finite plate containing a hole, the nominal stress may be regarded as the boundary traction on the edge of the plate. This suggests that the stress concentration factor be represented by the ratio

$$K_F = \frac{\sup_{x,i,k} \{|\sigma_{ik}(x)|\}}{\sup_{i,x,y} \{|b_i(x)|\,, |t_i(y)|\}}\,, \quad x \in \operatorname{Int} B,\ y \in \partial B,$$

where b_i and t_i are the body force and surface force distributions associated with the given loading F. Thus, the distribution of the body force is also considered in the comparison. It is assumed throughout that the body is a compact 3-dimensional submanifold of $\mathbb{R}^3$ having a differentiable boundary.

In the last expression, the maximum over i in the denominator (e.g., $\max_i\{|b_i(x)|\}$) and the maximum over i,k in the numerator serve as norms on $\mathbb{R}^3$ and on the space $L(\mathbb{R}^3, \mathbb{R}^3)$ of linear mappings defined on $\mathbb{R}^3$. These may be replaced by other norms and we will use $|b(x)|$ and $|t(x)|$ to denote the norms of the values at $x \in B$ of the body force vector field b and surface force vector field t associated with the given loading F. We denote by $|\sigma(x)|$ the norm of the the value of the stress at x. Thus, the stress concentration factor may be written as

$$K_F = \frac{\sup_{x} \{|\sigma(x)|\}}{\sup_{x,y} \{|b(x)|\,, |t(y)|\}}\,, \quad x \in \operatorname{Int} B,\ y \in \partial B.$$

Here and in the following, we ignore high values of the stresses and body forces if they are restricted to subsets of the body of zero volume. Similarly, we ignore high values of the surface force if it is restricted to subsets of the boundary of zero area. Thus, the suprema over x and y are in effect essential suprema.

The concept of stress concentration is developed below in a number of steps. Firstly, we consider for the given external loading F, the collection Σ_F of all stress fields that are in equilibrium with F. We denote by $K^{F,\text{optimal}}$ the smallest stress concentration factor. This may be conceived as a process of structural optimization. Thus,

$$K^{F,\text{optimal}} = \frac{\inf_{\sigma\in\Sigma_F} \left\{\sup_x \{|\sigma(x)|\}\right\}}{\sup_{x,y} \{|b(x)|\,, |t(y)|\}}\,.$$

In the abstract notation σ, we consider not just stress tensor fields σ_{ik} but include self forces—force volume densities σ_i. The self forces may be thought of as additional body forces that one may apply in order to reduce the stresses or as "3-dimensional elastic foundations". Thus, this generalized stress field σ has 12 components and the norm of its value at any point should be modified accordingly (e.g., $|\sigma(x)| = \sup_{i,k,l} \{|\sigma_i(x)|\,, |\sigma_{kl}(x)|\}$). With the self forces, the equations of equilibrium assume the form

$$\sigma_{ik,k} + b_i = \sigma_i\,, \quad \text{in Int } B.$$

Alternatively, the equivalent principle of virtual work is written as

$$\int_{\operatorname{Int} B} b_i w_i \mathrm{d}V + \int_{\partial B} t_i w_i \mathrm{d}A = \int_{\operatorname{Int} B} \sigma_i w_i \mathrm{d}V + \int_{\operatorname{Int} B} \sigma_{ik} w_{i,k} \mathrm{d}V.$$

Noting that one usually does not know the exact nature of the loading in advance, we allow the force distribution to vary and consider the worst case, i.e.,

$$K = \sup_F \left\{K^{F,\text{optimal}}\right\} = \sup_F \left\{\frac{\inf_{\sigma\in\Sigma_F} \left\{\sup_x \{|\sigma(x)|\}\right\}}{\sup_{x,y} \{|b(x)|\,, |t(y)|\}}\right\}.$$

We will refer to K as the *generalized stress concentration factor*. Clearly, the generalized stress concentration factor is a pure geometric property of the body.

THE RESULT: $K = \|\iota\|$

We prove that the generalized stress concentration factor K is equal to the norm of a mapping ι that takes a function defined in the interior $\operatorname{Int} B$ of the body and extends it to the closed body B (see [3]). Specifically, let $L^1_1(\operatorname{Int} B, \mathbb{R}^3)$ denote the Sobolev space of vector fields over the interior of the body with integrable components and integrable derivatives of the components. This space is equipped with the Sobolev norm

$$\|u\| = \int_{\operatorname{Int} B} |u| \, \mathrm{d}V + \int_{\operatorname{Int} B} |\nabla u| \, \mathrm{d}V.$$

Then, one of the basic properties of Sobolev functions (see [1]) implies that each Sobolev vector field $u \in L^1_1(\operatorname{Int} B, \mathbb{R}^3)$ may be extended to B in such a way that the restriction of the extension to the boundary, its trace $\hat{u}$, is integrable over the boundary. We use $L^{1,\mu}(B, \mathbb{R}^3)$ to denote the space of integrable vector fields over the body whose restrictions to the boundary are integrable over the boundary. For $w \in L^{1,\mu}(B, \mathbb{R}^3)$ we use the norm

$$\|w\|^{L^{1,\mu}} = \int_{\operatorname{Int} B} |w| \, \mathrm{d}V + \int_{\partial B} |w| \, \mathrm{d}A.$$

Thus, the norm of the extension mapping $\iota \colon L^1_1(\operatorname{Int} B, \mathbb{R}^3) \to L^{1,\mu}(B, \mathbb{R}^3)$ is given by

$$\|\iota\| = \sup_u \frac{\|\iota(u)\|}{\|u\|} = \sup_{u \in L^1_1(\operatorname{Int} B, \mathbb{R}^3)} \frac{\int_{\operatorname{Int} B} |u| \, \mathrm{d}V + \int_{\partial B} |\hat{u}| \, \mathrm{d}A}{\int_{\operatorname{Int} B} |u| \, \mathrm{d}V + \int_{\operatorname{Int} B} |\nabla u| \, \mathrm{d}V},$$

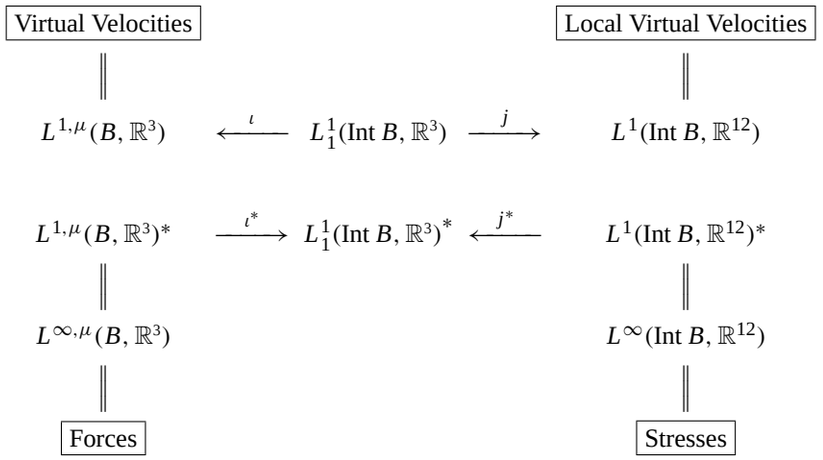
which is clearly a geometric property of the body.

OUTLINE OF THE PROOF

The proof (see [3] for the details) uses standard results of analysis. The various function spaces and mappings involved are presented in the diagram below. Specifically, one uses the duality of the L^1 and L^∞ spaces and the fact that $\|\iota\| = \|\iota^*\|$, where ι^* denotes the mapping dual to the extension ι. Referring to elements of $L^1(\operatorname{Int} B, \mathbb{R}^{12})$ as local virtual velocities, the mapping $j \colon L^1_1(\operatorname{Int} B, \mathbb{R}^3) \to L^1(\operatorname{Int} B, \mathbb{R}^{12})$ is defined by $j(u) = (u, \nabla u)$ and one can easily see that it is a norm-preserving injection. This implies that every element $S \in L^1_1(\operatorname{Int} B, \mathbb{R}^3)^*$ is of the form $S = j^*(\sigma)$ for some stress field σ. In addition, the dual norm of S may be calculated using

$$\|S\|^{L^1_1} = \inf_{S = j^*(\sigma)} \left\{ \|\sigma\|^{L^\infty} \right\}.$$

Finally, equilibrium or equivalently, the principle of virtual work, may be written as $\iota^*(F) = j^*(\sigma)$.



References

[1] Adams R.A.: Sobolev Spaces, Academic Press, New-York, 1975.
[2] Peterson R.E.: Stress Concentration Factors, Wiley, New-York, 1974.
[3] Segev R.: Generelized Stress Concentration Factors, submitted for publication.

ON ASYMPTOTIC METHOD OF STATIC AND DYNAMIC BOUNDARY PROBLEMS SOLUTION OF ELASTICITY THEORY FOR THIN BODIES

Lenser A. Aghalovyan*
*Institute of Mechanics of NAS of RA, Baghramyan 24b, 375019 Yerevan, Armenia

EXTENDED SUMMARY

Thinwalled bodies (bars, beams, plates, shells) own the very important property that one of their geometrical sizes essentially differs from the other two. By virtue of that, if in the corresponding equations of elasticity theory we pass to dimensionless coordinates, then the system of the transformed equations will have a small parameter and for the solution of the systems like that it is natural to use asymptotic methods. Meanwhile, the new system of the equations turned to be singularly perturbed and it is impossible to find its solution by a direct decomposition by small parameter. The solution of the corresponding boundary problem of elasticity theory consists of two qualitatively various types of solutions – solution of the inner problem and solution of the boundary layer. In the talk the ways of constructing these solutions and their conjunctions are described. Besides the classical boundary problem for thin bodies (on the facial surfaces the values of the stresses tensor components are given) nonclassical, from the position of plates and shells theories, boundary problems (on the facial surfaces the displacement vector or mixed conditions are given) are considered.

For the determination of solution Q of the inner problem the correct determination of asymptotic exponents of sought values is very important, since, as a rule not all the components of the stresses tensor and the displacement vector have the same contribution in the stress strain state. The solution of the inner problem is sought in the form of

$$Q(\xi,\zeta)=\varepsilon^{-q_a+s}Q^{(s)}(\xi,\zeta),\qquad s=\overline{0,N} \tag{1}$$

where Q is any of the stresses and displacements, q_a characterizes the asymptotic exponent of the given value. They are different for different values, their valuations react on the types of the boundary conditions on the facial surfaces. For example, in case of a plane problem for a rectangular area, if on the longitudinal borders of the rectangle, conditions of the first boundary problem of elasticity theory are given, we have

$$q=2 \text{ for } \sigma_{xx},u;\ q=1 \text{ for } \sigma_{xy};\ q=0 \text{ for } \sigma_{yy};\ q=3 \text{ for v} \tag{2}$$

and if on the longitudinal borders conditions of the second boundary problem (displacement vector) are given, then

$$q=1 \text{ for } \sigma_{xx},\sigma_{xy},\sigma_{yy};\ q=0 \text{ for } u,\mathrm{v}. \tag{3}$$

Substituting (1) into the transformed equations of elasticity theory and taking into account (2) or (3), a noncontradictory system for a consequent determination of decomposition $Q^{(s)}$ coefficients is obtained. Analogous (1)-(3) decompositions for plates and shells are found. The connection of the solution of the inner problem with the solutions on Bernoulli-Coulomb classical theory of beams, Kirchhoff-Love theory of plates and shells, with precise theories on the base of softened hypotheses is displaced. The denoted approach is applied as well for thin layered structures.

The solution for a boundary layer is constructed; it is shown that in case of the first boundary problem for a rectangle of boundary layer $\sigma_{xxb},\sigma_{xyb}$ stress along the rectangle hight are self-balanced. The connection of the boundary layer with Saint-Venant principle is found, it is proved that in case of the first boundary problem for a rectangle, Saint-Venant principle is fulfilled mathematically precisely.

In general case the procedure of conjugation of the inner problem solutions and the boundary layer is described.

The asymptotic method permits us to find solutions of new classes of boundary problems of elasticity theory for anisotropic plates and shells. The consideration of these problems for layered

structures made it possible to establish connection between the solutions on elasticity theory and on applied models of foundations and bases, to reduce the calculation formula of the bed coefficient for a layered base.
The method turned out to be especially effective for the solution of nonclassical dynamic boundary problems. Free and forced vibrations of thin bodies on the base of dynamics equations of elasticity theory are considered. Connections between the values of free vibrations frequencies and the propagation velocities of elastic shear and longitudinal waves are established.

References

[1] Aghalovyan L.A.: Asymptotic theory of anisotropic plates and shells. Moscow. Nauka. 1997. 414p.
[2] Aghalovyan L.A.: Asymptotics of solutions of classical and nonclassical boundary value problems of statics and dynamics of thin bodies. Int. Appl. Mech. (2002). V. 38. N 7. p. 3-24.

AXISYMMETRIC FORCE SOLUTION FOR A SEMI-INFINITE CUBIC SOLID

Charles Ruimy*, Marc Dahan**
*UHA, ERT Mécanique des Matériaux sous Grande Vitesse, F 68000 Mulhouse, France
**UFC, Laboratoire de Mécanique Appliquée, F 25000 Besançon, France

Summary An exact three-dimensionnal analysis is developped for an axisymmetric loading on the surface of a half-space composed by an anisotropic cubic medium. The general solution is given for a surface concentrated loading by exact integral expressions. Isovalue curves of stress permit easily to compare the anisotropic results with the isotropic ones.

BASIC EQUATIONS

We consider a homogeneous elastic half-space $z>0$, referred to a fixed rectangular Cartesian coordinate system $(Oxyz)$. We assume that the medium is characterized by cubic anisotropy, with the z-axis as elastic symmetriy axis. Let arbitrary axisymmetric normal stress be prescribed all over the boundary $z=0$. We need to find the complete field of stress and displacements in the half-space.

By using cylindrical coordinates (r,θ,z), we designate the components of the displacement field (u_r,u_θ,u_z), the components of the strain tensor $(\varepsilon_r,\varepsilon_\theta,\varepsilon_z,\varepsilon_{rz},\varepsilon_{r\theta})$ and the non-zero components of the stress tensor $(\sigma_{rr},\sigma_{\theta\theta},\sigma_{zz},\sigma_{rz})$.

We use some results obtained in [3], with the same notations, and we show that the introduction of a potential function permits to reduce to one the number of independant equations (compatibility and equilibrium). It is a differential equation of the 4th order which has the solution

$$\Phi(r,z) = \int_0^\infty (Ae^{s_1 mz} + Be^{s_2 mz} + Ce^{-s_1 mz} + De^{-s_2 mz}) J_0(mr)\, m\, dm$$

The coefficients A, B, C, D are determined by the boundary conditions and the regularity conditions at infinity. Then, the formulae for stresses take the form

$$\sigma_{zz}(r,\theta,z) = \int_0^\infty (Cs_1 g_1 e^{-s_1 mz} + Ds_2 g_2 e^{-s_2 mz}) m^4 J_0(mr)\, dm$$

$$\sigma_{rz}(r,\theta,z) = \int_0^\infty (Cp_1 e^{-s_1 mz} + Dp_2 e^{-s_2 mz}) m^4 J_1(mr)\, dm$$

RESOLUTION

We consider the case of a uniform normal pressure distribution p_0 on a circle (radius r_0) applied on the medium surface $z = 0$. The Hankel transformation of loading function is

$$p^H(m) = p_0 r_0 J_1(mr_0)$$

and we obtain successively $A = B = 0$,

$$C = \frac{k(m)p_2}{(p_2 s_1 g_1 - p_1 s_2 g_2)}$$

$$D = -\frac{k(m)p_1}{(p_2 s_1 g_1 - p_1 s_2 g_2)}$$

with

$$k(m) = -p_0 r_0 J_1(mr_0)/m^4$$

Thus, by integration of the expressions of σ_{zz} and σ_{rz}, it is possible to obtain the field of stress in the complete medium. The following curves present the results for two cubic materials (copper and molybdenum). The cupper has a behavior very different of the isotropic one (in dotted line). The molybdenum is similar. This is consistent with the values of the elastic coefficients of each material.

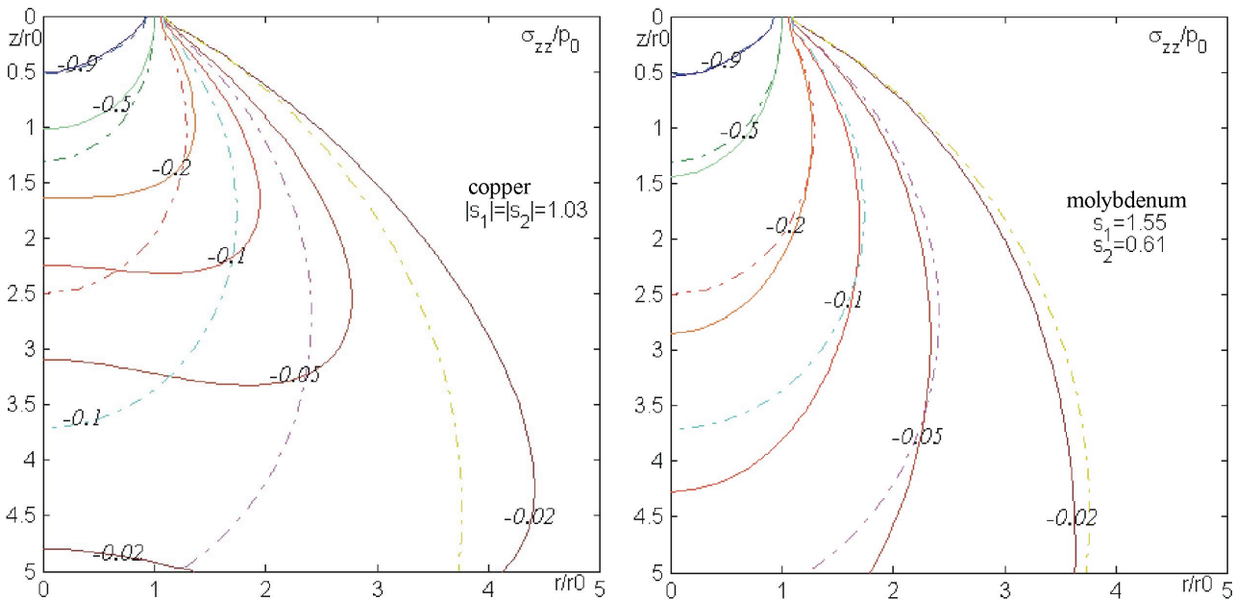
When the surface loading is reduced to a concentrated force P,

$$k(m) = -\frac{P}{2\pi m^3}$$

and thus we obtain explicit solutions for the stress and displacement in the half-space.

CONCLUSIONS

From fundamental equations of solid mechanics (equilibrium equations, compatibility conditions, generalized Hooke's law), we introduce a new potential function from the stresses and we are able to express the displacements only with this function. This method is usable for all axisymmetric loadings in the surface or in the interior of an infinite or semi-infinite cubic medium. It gives new solutions for contact elastic problems between anisotropic materials. Today, we have at our disposal only explicit solutions for isotropic materials [4] and transversely isotropic materials [1,2].



[1] Dahan M., Predeleanu M.: Solutions Fondamentales pour un Milieu Elastique à Isotropie Transverse. *ZAMP* **31**: 413-424, 1980.

[2] Fabrikant V.I. New Approach to Mixed-mixed Problems in Linear Elasticity. *Eur. J. Mech., A/Solids* **16** 595-618, 1997.

[3] Ruimy C. Chargements Axisymétriques sur un Milieu à Isotropie Tétragonale. *PhD Thesis*, University of Franche-Comté, Besançon, 2002.

[4] Ufliand Ia. The Contact Problem of the Theory of Elasticity for a Die, Circular in its Plane, in the Presence of Adhesion. *Prikladnaia Matematika i Mekhanika* **20** 578-587,1956.

An exactly solvable microgeometry in torsion

Tungyang Chen
Department of Civil Engineering, National Cheng Kung University
Tainan 70101, Taiwan (tchen@mail.ncku.edu.tw)

Summary Finding a geometric configuration that is amenable to an exact characterization of the torsional rigidity is a relatively new territory that has only recently begun to be explored. Here we present our latest finding of an exactly solvable microgeometry in torsion for cylindrical shafts with arbitrary cross sections.

Torsional rigidity is a crucial physical property in characterizing the twisting stiffness of a cylindrical object. This quantity, defined as the proportional ratio between the applied torque and the relative rotation of a cylindrical shaft, is generally understood as a structural property rather than a material property. Particularly, the rigidity depends not only on the microstructure of the cross section but also on its global geometry. Thus, the task of a general characterization of the torsional rigidity of a composite shaft, applicable for a variety of cross sections, has been hardly conceivable. A recent attempt [1] along this line was the finding of an exact torsional rigidity for a circular shaft that is filled with composite cylinder assemblage (CCA). The finding of the exact torsional rigidity of the CCA microgeometry in a circular cross section was striking in that it represents that the CCA microgeometry also permits an exact result under twisting loads. In this study, we make a further attempt by allowing that the cross section of the host shaft could be arbitrary in shape [2]. We show that, depending on the cross-sectional shape of the host shaft, an assemblage of multicoated cylinders is an exactly solvable microgeometry. To start with, we consider a circular multicoated cylinder, which is to be embedded inside the host shaft at a selected location. Under an applied torque at the ends of the cylindrical shaft, we ask what is the suitable shear modulus of the host shaft μ_0, or equivalently, what are the relationships between the phase moduli and area fractions of the multicoated inclusion, so that after the insertion of the multicoated cylinder inside the host shaft, the warping field and also shear traction in the shaft, remains unchanged as that of the unreinforced homogeneous shaft. Remarkably, we find that the framework of finding a neutral multicoated inclusion in a cylindrical shaft of arbitrary cross section in torsion is mathematically analogous to that of the conductivity problem but subject to boundary conditions of various orders. For instance, for a circular host shaft, it is equivalent to boundary conditions with positions of first order. For an elliptical host shaft, it corresponds to boundary conditions with positions of second order. When the cross section of the shaft becomes more irregular, e.g. rectangles, the order of boundary terms will become larger or even unbounded. For the present context in which the boundary condition contains various orders of positions, no relevant solutions were reported before. Nevertheless, we find that, depending on the presence of the orders of boundary terms, constraint conditions in the form of continued fraction can be established. For example, for a doubly coated cylinder (three-phase)

with boundary terms of order N, exactly N constraint conditions need to be fulfilled

$$\mu_0 = \mu_1 + \cfrac{2\left(1-\nu_1^{(m)}\right)\mu_1}{\nu_1^{(m)} - \cfrac{2\mu_1}{\mu_1-\mu_2 - \cfrac{2\nu_3^{(m)}\mu_2}{\nu_2^{(m)} - \cfrac{2\left(1-\nu_1^{(m)}\right)\mu_2}{\mu_2-\mu_3}}}}, \text{ with } m = 1, \cdots, N. \tag{1}$$

For a multicoated inclusion, we will demonstrate how to generate these continued fraction expressions of the constraint conditions without further derivations. Note that for an n-phase multicoated inclusion, we have $2n-1$ adjustable parameters for N constraint conditions. Conceptually, for a large N, one can generalize the multicoated inclusion as a functionally graded inclusion to have sufficient adjustable parameters to fit the constraint conditions. We mention that the constraint conditions are nonlinear algebraic equations. Finding exact analytical parameters that fulfill the constraint conditions may not be a simple task, but there is no difficulty to resolve the admissible sets of parameters numerically. Our next task is to investigate the torsional rigidity of a shaft containing a neutral multicoated inclusion. The torsional rigidity T of a cylindrical shaft with cross section Ω containing a neutral multicoated inclusion Σ is simply expressed by two parts T_Ω and T_i, one from the host shaft $\Omega \setminus \Sigma$ and the other from the multicoated inclusion Σ, given by

$$T\left(\Omega, \Sigma; \mu_0, \mu_1, \cdots, \mu_n\right) = T_\Omega + \frac{\pi}{2} R_1^4 \left[\sum_{k=1}^{n} \mu_k \left(r_{k-1}^4 - r_k^4\right) - \mu_0\right]. \tag{2}$$

In summary, neutral cylinders can serve as useful building bricks of an exactly solvable microgeometry for a host shaft under torsion. Depending on the cross-sectional shape of the host shaft, a neutral cylinder needs to be suitably multicoated. We have exactly identified the algebraic compatibility conditions between the shear rigidity of the host shaft, shear rigidities of the multicoated neutral inclusion and the constituent area fractions. In particular, we showed the key criterion to the neutrality can be expressed in terms of a continued fraction via a correspondence with the effective conductivity of multicoated composites. The exact torsional rigidity depends on the constituent shear rigidities, area fractions as well as the size distributions of constituent cylinders, but is independent of the assembly microstructure. This solution will serve as a benchmark for an analytical solution for the torsional rigidity of a cylindrical composite shaft. To our knowledge, this is the first microgeometry valid for arbitrary cross section of a cylindrical shaft that permits an exact determination of torsional rigidity.

References

[1] Chen, T., Benveniste, Y. & Chuang, P. C.: Exact solutions in torsion of composite bars: thickly coated neutral inhomogeneities and composite cylinder assemblages. *Proc. R. Soc. Lond.* A **458**: 1719-1759, 2002..

[2] Chen, T.: An exactly solvable microgeometry in torsion: assemblage of multicoated cylinders. *Proc. R. Soc. Lond.* A, in press, 2004.

A NEW NONLINEAR CONSTITUTIVE RELATION FOR MAGNETOSTRICTIVE MATERIAS

Xiao Jing Zheng **Xinen Liu**

Department of Mechanics, Lanzhou University, Lanzhou, P.R.China, 73000

SUMMARY A constitutive relation is suggested to describe the nonlinear and coupling features of magnetostrictive materials. It can effectively predict the magnetostrictive strains of the materials, the effect of the pre-stress on the maximum magnetostrictive strain and the magnetization, and the effect of the pre-stress and the magnetization on the Young's modulus. Its constitutive constants are material parameters and are easily measured in experiments.

INTRODUCTION

For magnetostrictive materials, many experiments have exhibited that their magneto-mechanical responses are nonlinear and coupled[1]. For example, for a Terfenol-D rod subjected to a compressive pre-stress, its the maximum value of the magnetostrictive strain is dependent on the pre-stress. Moreover, the Young's modulus of a Terfenol-D rod is not a constant, which is called as the ΔE effect. Many researchers have tried to establish the nonlinear constitutive relations for magnetostrictive materials, such as the SS Model[2], the HT Model and the DDS Model[3], and the D-H Model[4]. However, all of these models cannot exhibit good quantitative agreement with experimental data in the region of the high magnetic field, cannot simulate the experimental phenomenon that the maximum magnetostrictive strain of a Terfenol-D rod increases with the compressive pre-stresses, and cannot completely capture the main features of the ΔE effect in quality or in quantity. To overcome these deficiencies, a new nonlinear constitutive relation for magnetostrictive materials will be developed in this paper.

NEW CONSTITUTIVE RELATION

Several main steps are taken to derive the new constitutive relation given by Eq. (1). Firstly, the more high-order terms in the Taylor series expansion of Gibbs free energy function are reserved in the new relation than in the D-H Model so

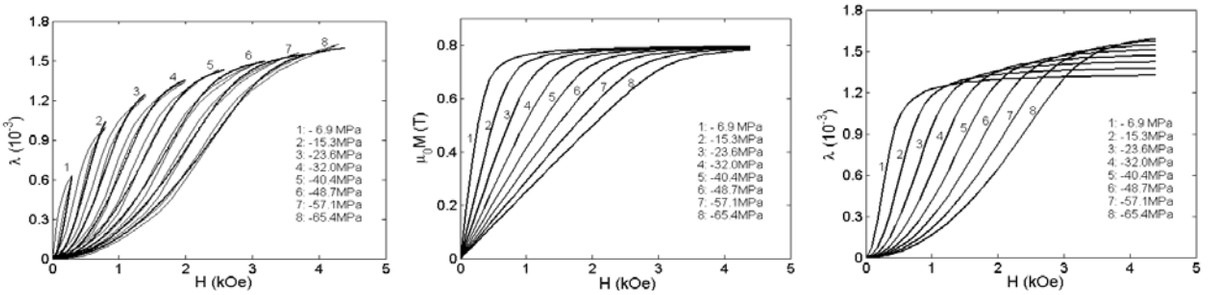
$$\varepsilon = \frac{\sigma}{E_s} + \begin{cases} \lambda_s \tanh(\frac{\sigma}{\sigma_s}) + [1 - \tanh(\frac{\sigma}{\sigma_s})]\frac{\lambda_s}{M_s^2} M^2 & \frac{\sigma}{\sigma_s} \geq 0 \\ \frac{\lambda_s}{2}\tanh(\frac{2\sigma}{\sigma_s}) + [1 - \frac{1}{2}\tanh(\frac{2\sigma}{\sigma_s})]\frac{\lambda_s}{M_s^2} M^2 & \frac{\sigma}{\sigma_s} < 0 \end{cases} \quad (1a)$$

$$H = \frac{1}{k} f^{-1}\left(\frac{M}{M_s}\right) - \begin{cases} 2\{\sigma - \sigma_s \ln[\cosh(\frac{\sigma}{\sigma_s})]\}\frac{\lambda_s}{\mu_0 M_s^2} M & \frac{\sigma}{\sigma_s} \geq 0 \\ 2\{\sigma - \frac{\sigma_s}{4}\ln[\cosh(\frac{2\sigma}{\sigma_s})]\}\frac{\lambda_s}{\mu_0 M_s^2} M & \frac{\sigma}{\sigma_s} < 0 \end{cases} \quad (1b)$$

that both the change of the Young's modulus with the stress in the case of $H = 0$ (or $M = 0$) and the effect of the pre-stresses on the maximum magnetostrictive strain may be described. Secondly, the nonlinear part of the elastic strain produced by the pre-stress is considered to be related to the rotation or movement of magnetic domains and can be approximated as a hyperbolic tangent function. Thirdly, according to magnetic domain analysis, the maximum magnetostrictive strain is expressed as the difference between the saturation magnetostrictive strain (or coefficient) and the nonlinear elastic strain produced by the pre-stress so that the new model can describe the change of the maximum magnetostrictive strain with the pre-stress.

QUANTITATIVE DISCUSSION AND CONCLUSIONS

The prediction values of magnetostrictive strain calculated by the new constitutive relation are plotted in Fig. 1. From Fig.1a, the calculated results are perfectly coincident with the Moffet et al's experimental data under the various compressive pre-stress levels not only in the region of the low and moderate magnetic fields but also in the region of the high field. From Fig. 1b, it can be found that the prediction values of the magnetization increase with the applied field under several pre-stress levels, and will reach a constant in the region of the high field. It means that the magnetization of the rod subjected to different pre-stresses will be saturated to the same level, i.e. the saturation magnetization. For a given magnetic field, the magnetization decreases with an increasing compressive pre-stress, which means that the axial compressive pre-stress makes the axial magnetization of the rod more difficult. When the applied magnetic field is in the high field region, or near the saturation field of the material, the predicted magnetostrictive strain of the rod, shown in Fig. 1c,will reach different saturation values for different pre-stresses. The larger the compressive pre-stress, the larger the maximum magnetostrictive strain. In the other words, the maximum magnetostrictive strain of the rod increases with the axial compressive pre-stress, which is obviously different from the characteristics in the region of the low and moderated fields. These predicted results are coincident with the observed experimental phenomena, and none of the previous constitutive relations (e.g. the SS Model, the HT Model, the DDS Model and the D-H Model) can capture all of them qualitatively or quantitatively. In addition, the predicted stress-strain relation is nonlinear and the calculated curves of Young's modulus versus compressive stress for some given magnetic bias fields are non-monotonic, which are very similar to those observed in experiments. Moreover, only one material parameter is added in the new relation by contrast with the D-H Model, and all the material parameters required by the new constitutive relation can easily be determined in experiments. So, the new constitutive relation suggested in this paper is convenient for engineering applications.



a:Comparison with the experimen tal data b: Prediction on Magnetization c: Prediction on Magnetostrictive strain

Fig. 1 Calculation values by the new constitutive equations (hysteresis loops: experimental;solid lines: theoretical)

Acknowledgements

This research was supported by a grant of the Key Fund of the National Natural Science Foundation of China (No. 10132010), and the Fund of Pre-Research for Key Basic Researches of the Ministry of Science and Technology of China. The authors gratefully acknowledge these supports.

References

[1] Moffet, M.B., Clark, A.E., Wun-Fogle, M., Linberg, J., Teter, J.P., McLaughlin, E.A., 1991. Characterization of Terfenol-D for magnetostrictive transducers. J. Acoust. Soc. Am. 89(3), 1448-1455.

[2] Carman, G.P., Mitrovic, M., 1995. Nonlinear constitutive relations for magnetostrictive materials with application to 1-D problems. J. Intell. Mater. Syst. Struct. 6, 673-683.

[3] Wan, Y.P., Fang, D.N., Hwang, K.C., 2003. Nonlinear constitutive relations for magnetostrictive materials. Inter. J. Nonlinear Mechanics 38(7), 1053-1065.

[4] Duenas, T., Hsu, L., Carman, G.P., 1996. Magnetostrictive composite material systems analytical/experimental (Invited paper). In: Advances in materials for smart systems—fundamental and applications, Materials Research Society Symposium, Boston.

XXI ICTAM, 15–21 August 2004, Warsaw, Poland

NONLINEAR RADIAL OSCILLATIONS OF ANISOTROPIC THIN-WALLED CYLINDRICAL TUBES

G. H-S Maluleke and D.P. Mason
Centre for Differential Equations, Continuum Mechanics and Applications, School of Computational and Applied Mathematics, University of the Witwatersrand, Johannesburg, South Africa

Summary Nonlinear radial oscillations of thin-walled cylindrical tubes with either radial, tangential or longitudinal isotropy are studied. Free oscillations are considered and the effect of the anisotropy is analysed. To investigate solutions with time dependent net applied pressures the Lie point symmetry structure of the differential equations is examined.

A hyperelastic material is said to prossess transverse isotropy with respect to a direction **h** if its strain-energy function W is invariant under rotations about **h** [1,2]. Nonlinear radial oscillations of a cylindrical tube with either radial, trangential or longitudinal transverse isotropy are considered [3,4].
Consider a thin-walled anisotropic cylindrical tube of incompressible elastic material of constant density ρ^*. The inner and outer radii of the undeformed tube are ρ_1 and ρ_2 and the inner radius of the deformed tube at time t is $r_1(t)$. Let

$$x(t) = \frac{r_1(t)}{\rho_1} \ . \tag{1}$$

Pressures $P_1(t)$ and $P_2(t)$ are applied to the inner and outer surfaces. The strain-energy function, W, is of the form

$$W = W(I_1, I_2,\ K_1, K_2), \tag{2}$$

where the principal invariants, I_1 and I_2, are given by

$$I_1 = I_2 = x^2 + \frac{1}{x^2} + 1 \tag{3}$$

and K_1 and K_2 for radial, tangential and longitudinal transverse isotropy are respectively,

$$K_1 = \frac{1}{x^2}\ ,\ K_2 = \frac{1}{x^4}\ ;\ K_1 = x^2,\ K_2 = x^4\ ;\ K_1 = K_2 = 1\ . \tag{4}$$

It is shown that for radial, tangential and longitudinal transverse isotropy,

$$\frac{d^2x}{dt^2} + \frac{dW_0}{dx} = x\,P(t)\ , \tag{5}$$

where

$$W_0 = \frac{1}{\rho^*\,\rho_1^2}\,W\ , \quad P(t) = \frac{2\Big(P_1(t) - P_2(t)\Big)}{\mu\rho^*\,\rho_1^2}\ ,\ \mu = \Big(\frac{\rho_2}{\rho_1}\Big)^2 - 1\ . \tag{6}$$

Equation (5) has the same form as that for radial oscillations of a thin-walled isotropic cylindrical tube.
The strain-energy function

$$W = C_1(I_1 - 3) + C_2(I_2 - 3) + C_3(K_1 - 1) + C_4(K_2 - 1), \tag{7}$$

where C_1, C_2, C_3 and C_4 are constants, is considered. The undeformed body is stress free provided $C_3 = -2C_4$. We will assume that $C_1 + C_2 + C_4 > 0$ to satisfy stability conditions. Then for radial, tangential and longitudinal transverse isotropy, equation (5) becomes, respectively,

$$\frac{d^2x}{dt^2} + \big(D_1 - P(t)\big)x = (D_1 - D_2)\,\frac{1}{x^3} + D_2\,\frac{1}{x^5}\ , \tag{8}$$

$$\frac{d^2x}{dt^2} + \big(D_1 - D_2 - P(t)\big)x = D_1\,\frac{1}{x^3} - D_2\,x^3\ , \tag{9}$$

$$\frac{d^2x}{dt^2} + \big(D_1 - P(t)\big)x = D_1\,\frac{1}{x^3}\ , \tag{10}$$

where

$$D_1 = \frac{2(C_1 + C_2)}{\rho^*\,\rho_1^2}\ , \quad D_2 = \frac{4C_4}{\rho^*\,\rho_1^2}\ . \tag{11}$$

When $P(t)$ is constant, equations (8), (9) and (10) can be integrated immediately and the solution reduced to a quadrature. Free oscillations with initial conditions

$$x(0) = x_0 \ , \quad \dot{x}(0) = 0 \ , \tag{12}$$

are considered. For both radial and tangential transverse isotropic materials the period of oscillation is less than that for isotropic materials. The range of oscillation is $x_0 \leq x \leq x_1$ if $x_0 < 1$ and $x_1 \leq x \leq x_0$ if $x_0 > 1$. For isotropic materials $x_0 x_1 = 1$. For radial transverse isotropy it is found that $x_0 x_1 > 1$ while for tangential transverse isotropy $x_0 x_1 < 1$.
The Lie point symmetries of (8), (9) and (10) are investigated to examine if the equations can be integrated when $P = P(t)$.
Equation (10) is the Ermakov-Pinney equation which also describes radial oscillations of an isotropic cylindrical tube. It has three Lie point symmetries which can be used to derive a nonlinear superposition principle, [5,6,].
Equation (8) has no Lie point symmetries when $P = P(t)$ if $D_1 \neq D_2$. However, if $D_1 = D_2$ then (8) has the Lie point symmetry

$$X = (t + A) \ \frac{\partial}{\partial t} + \frac{1}{3} \ x \ \frac{\partial}{\partial x} \ , \tag{13}$$

provided $P(t)$ is of the form

$$P(t) = D_1 - \frac{B}{(t + A)^2} \ , \tag{14}$$

where $A > 0$ and B are arbitrary constants. Using the Lie point symmetry (13), equation (8) can be transformed to the autonomous equation

$$\frac{d^2 x^*}{dt^{*2}} - \frac{1}{3} \ \frac{dx^*}{dt^*} + \Big(B - \frac{2}{9}\Big) x^* = \frac{D_1}{x^{*5}} \ , \tag{15}$$

where

$$x^* = \frac{x}{(t + A)^{1/3}} \ , \quad t^* = \ln \left(1 + \frac{t^*}{A}\right) \ . \tag{16}$$

Equation (9) has no Lie point symmetries when $P = P(t)$ if $D_1 \neq 0$ and $D_2 \neq 0$. For the extreme anisotropic case in which $D_1 = 0$, $D_2 \neq 0$, equation (9) has the Lie point symmetry

$$x = (t + A) \ \frac{\partial}{\partial t} - x \ \frac{\partial}{\partial x} \ , \tag{17}$$

provided $P(t)$ is of the form

$$P(t) = -D_2 - \frac{B}{(t + A)^2} \ , \tag{18}$$

where $A > 0$ and B are arbitrary constants. Using the Lie point symmetry (17), equation (9) can be transformed to the autonomous equation

$$\frac{d^2 x^*}{dt^{*2}} - 3 \ \frac{dx^*}{dt^*} + (2 + B) \ x^* = -D_2 x^{*3} \ . \tag{19}$$

Equations (15) and (19) are solved numerically using a 4th order Runge-Kutta method. The solutions are compared with radial oscillations of an isotropic thin-walled cylindrical tube with the same values of D_1, D_2 and $P(t)$.

References

[1] Green A.E. and Adkins J.E.: Large elastic deformations. Oxford, Ch.1, 1970.
[2] Ericksen J.L. and Rivlin R.S.: Large elastic deformations of homogeneous anisotropic materials. *J. Rat. Mech. Anal.***3**, 281-301, 1954.
[3] Huilgol R.R.: Finite amplitude oscillations in curvilinearly aelotropic elastic cylinders. *Quart. Appl. Math.* **25**, 293-298, 1967-68.
[4] Shahinpoor M.: Exact solution to finite amplitude oscillation of an anisotropic thin rubber tue. *J. Acoustic Soc. Am* **56**, 477-480, 1974.
[5] Shahinpoor M. and Nowinski J.L.: Exact solutions to the problem of forced large amplitude oscillations of a thin hyperelastic tube. *J. Non-Linear Mech.* **6**, 193-207, 1971.
[6] Mason D.P. and Roussos N.: Lie symmetry analysis and approximate solutions for non-linear radial oscillations of an incompressible Mooney-Rivlin cylindrical tube. *J. Math. Anal. and Applic.* **245**, 346-392, 2000.

NONLOCAL ESHELBY ENTITIES: A ONE-DIMENSIONAL EXAMPLE

Marcelo Epstein*, Les Sudak*
*Department of Mechanical and Manufacturing Engineering, University of Calgary, Calgary, Alberta, Canada

Summary The following paper describes a nonlocal formulation that differs from the global one in that one out of an infinite possible decompositions has been chosen to express the energy functional in two phases. The first phase indicates what the contribution of each material point (including the boundary) is and the second phase prescribes how all these contributions are to be added up to obtain the total energy of the material body. The formulation is then applied to a number of examples emphasizing the nonlocal effects

.

GLOBAL ELASTICITY

Configuration space

The material body $\boldsymbol{B}$ is by definition a one-dimensional manifold with boundary topologically equivalent to a closed interval of $\Re$. Physical space $\boldsymbol{S}$ is identified with $\Re$ itself. A configuration κ is a C^∞ - embedding of $\boldsymbol{B}$ onto $\Re$:

$$\kappa : B \to \Re \,. \tag{1}$$

The configuration space Q of the body $\boldsymbol{B}$ is the set of all such embeddings, namely:

$$Q = C^\infty(B, \Re). \tag{2}$$

This set has the natural structure of an infinite-dimensional differentiable manifold.

Global constitutive law

A global elastic constitutive law consists of the assignment of an internal force σ to every configuration κ. In other words, such a constitutive equation is simply a one-form on Q. A material body whose material response is completely characterized by such a one-form is said to be globally elastic. A globally elastic body $\boldsymbol{B}$ is globally hyperelastic if the one-form σ is exact, namely, if there exists a scalar function *W*:

$$W : Q \to \Re \tag{3}$$

such that

$$\sigma = dW \,. \tag{4}$$

The function *W*, if it exists, will be called the *stored-energy* function of the material body $\boldsymbol{B}$.

NONLOCAL ELASTICITY

An important feature for the representation of global constitutive laws for a material body is obtained by adopting the point of view that although the material may exhibit a completely general global behavior, there is still a physical meaning to be attached to the contribution of each material point to the total energy of the body. In other words, the state of the body, at a material point, is influenced by the state of all points in the body – the so-called *nonlocal effect*. This point of view has been adopted by one of the best established traditions of research in this area, namely that of A.C. Eringen and his collaborators, neatly summarized in a recent book by Eringen [1]. From our perspective, the nonlocal formulation differs from the global one in that one out of an infinite possible decompositions has been chosen to express the energy functional in two phases: the first phase indicates what the contribution of each material point (including the boundary) is, and the second phase describes how all these contributions are to be added up to obtain the total energy of the body.

Let us suppose that we assign to each material point $X \in \boldsymbol{B}$ a scalar function $w(.;X) : Q \to \Re$. For each fixed configuration κ this map can be regarded as a function $w(\kappa;.) \in C^\infty(B, \Re)$. In addition, let a particular function $f : C^\infty(B, \Re) \to \Re$ be specified. Then the composition

$$W = f \circ w(.\,;.) : Q \to \Re \tag{5}$$

is a legitimate global hyperelastic constitutive law. Note that this construction for the constitutive law is just an example; however, surprisingly enough, every global hyperelastic constitutive law can be expressed in this way, albeit not uniquely. Indeed, if we select a volume element in $\boldsymbol{B}$ (for example, the volume element *dV* induced by the Euclidean ambient of some reference configuration), then for any given hyperelastic constitutive law *W* we can define

$$w(\kappa; X) = \frac{W(\kappa)}{\int_B dV}, \tag{6}$$

and

$$f(\varphi) = \int_B \varphi dV\ . \tag{7}$$

Then it follows that $f(w(\kappa; X)) = W(\kappa), \forall\ \kappa$. As it can be seen, no generality or specificity has been gained by selecting a particular nonlocal representation except for the fact of a commitment to a particular expression of the constitutive law as a composition of two constitutive factors. This composition, therefore, must be justified in terms of some physical foundation. More specifically, we will apply it later to an example to allow certain forms of laws of material evolution on the grounds that these forms preserve in some way the constitutive identity of the material.
We now proceed to construct an example of the one-dimensional nonlocal Eshelby entities.

Example 1
Eringen's nonlocal elastic solid. Let

$$w(\kappa, X) = \int_B g(X, Y, F(X), F(Y))dV(Y), \tag{8}$$

where *g* is an ordinary smooth function of its arguments, *X* and *Y* are material points, *F*(*X*) is the deformation gradient evaluated at the point *X*, and so on. Let *f* be selected as per equation (7). Then, according to condition (5) and (6), the following expression for the Piola entity is calculated as follows:

$$<\sigma, \delta\kappa> = <dW, \delta\kappa> = \int_B \left\{ \int_B \left[\frac{\partial g(X,Y,F(X),F(Y))}{\partial F(X)} + \frac{\partial g(Y,X,F(Y),F(X))}{\partial F(X)} \right] dV(Y) \right\} : \delta F(X) dV(X)\ . \tag{9}$$

The expression in curly brackets is interpreted as in [1] as a nonlocal stress tensor Σ.
The corresponding Eshelby entity can be shown to have the following form:

$$< \varepsilon, \delta\beta > = \int_B (F^T \Sigma - GI) : \delta\nabla\beta(X) dV(X), \tag{10}$$

where *I* is the identity matrix and *G* is given by:

$$G = \int_B [g(X, Y, F(X), F(Y)) + g(Y, X, F(Y), F(X))] dV(Y). \tag{11}$$

Example 2
Let a reference configuration κ_o consist of an embedding of $\boldsymbol{B}$ onto the closed interval $I = [-1,1]$. Let $dV = \mu(X)dX$ be a fixed volume element in *I*, where *X* denotes the running variable and μ is some positive continuous real function. Let the expression of the constitutive contribution of the point *X* in the given reference configuration is given by:

$$w(\kappa, X) = \int_{-1}^{1} g(\kappa'(\xi), X)\mu(\xi)d\xi, \tag{12}$$

where *g* is defined as in the previous example and the prime denotes derivatives with respect to the variable ξ. An example of a possible choice of the of the function *g* at a point (say, $X = 0$) is:

$$g(\kappa', 0) = \frac{1}{2} E(\kappa' - 1)^2\ , \tag{13}$$

where *E* is a material constant. In a different reference configuration, the form ω(κ, ξ) is determined by an appropriate change of configuration represented by some diffeomorphism (for example the differomorphism λ: [a,b] → *I* where $a < b \in \Re$). Note that to complete this example, one still needs to specify the function *f* and the explicit dependence of ω on *X*. This point will be deferred to the presentation where the concepts of material uniformity and homogeneity will be discussed.

References

[1] Eringen, A.C., (2002), *Nonlocal continuum theories*, Springer-Verlag.

ANALYSIS OF TRABECULAR BONE AS A HIERARCHICAL MATERIAL

Iwona M. Jasiuk
The G.W.W. School of Mechanical Engineering, Georgia Institute of Technology, Atlanta, GA 30332-0405, U.S.A.

Summary We study trabecular bone as a hierarchical material with a highly complex and random structure. First, we characterize trabecular bone's structure at several structural levels: nanoscale (apatite crystals and collagen fibril level), sub-microscale (single lamella level), microscale (single trabecular pocket or single trabecula level), and mesoscale (porous trabecular network level) using atomic, scanning, and transmission electron microscopy, and x-ray microtomography. Then, we model trabecular bone at each structural level as a linear elastic solid employing either classical elasticity or higher order elastic theory (Cosserat theory). Modeling techniques include analytical micromechanics theories and numerical simulations involving finite element, spring network, and beam network approaches. We compare our theoretical results at different scales with our experimental measurements.

INTRODUCTION

In mechanical terms bone is a composite material, consisting of several phases [1]. The main two components are apatite crystals of calcium phosphate that are embedded in collagen fibrils. The apatite crystals are in the shape of irregular platelets, 20-50 nm in length and width and 1-3 nm in thickness. In trabecular bone, these crystals are located either within or around collagen fibrils. The fibrils reinforced with crystals are aligned and arranged in lamellar sheets (3-7 μm in thickness). These are stacked at different orientations and wind around to form randomly oriented cylindrical (or platelike) struts called trabeculae, which are about 0.1 mm in diameter and 1 mm long. This gives trabecular bone a porous appearance. Thus, the trabecular bone has a complex hierarchical structure in which different geometrical features occur on several length scales. These scales are classified as follows: a) nanoscale (single fibril and crystals), b) sub-microscale (single lamella level), c) microscale (trabecular pockets, single trabecula level), and d) mesoscale (random network of struts or plates). The next structural level, macroscale, represents the whole bone, which includes both trabecular (porous) and cortical (solid) bone types. These structural levels are illustrated in Fig. 1.

CHARACTERIZATION AND TESTING OF TRABECULAR BONE TISSUE

We study trabecular bone structure using bone samples from both normal and osteoporotic bones. Osteoporotic samples are selected based on a) known T score at sample site of at least –2.0 (a measure of bone density) or b) calcium ash weight < 0.75 g/cm^3. We also obtain measurements of bone density using DEXA (dual excitation absorptiometry). We study trabecular bone's structure at different structural levels using scanning electron microscopy (SEM), transmission electron microscopy (TEM), and atomic force microscopy (AFM). Photographs, representing a wide range of magnifications (10-50,000), are analyzed by image analysis techniques using Micromorph software. The data collected includes the area fraction and orientation of fibrils at the sub-microscale level, and the porosity, pore size distribution, connectivity of microstructure, and thickness of trabeculae at the microscale level. We also store digitized images of bone structures at each scale for use in numerical simulations. SEM, TEM, and AFM investigations provide us with two-dimensional data. Alternately, we use the x-ray microtomography (Micro-CT), a nondestructive technique, which gives three-dimensional details of bone structure.

Measurements of mechanical properties are done using MTS machine and nanoindentation apparatus. We use the MTS testing machine to determine the constitutive response of bone at mesoscale (5-10 mm samples). We employ the nanoindentation apparatus (Hysitron) to determine bone's mechanical properties at lower scales. Nanoindentation method involves pressing of a tip of nanoindentor into a specially prepared surface. The output is a load-deformation curve from which elastic modulus and hardness can be obtained.

MODELING OF TRABECULAR BONE AS A HIERARCHICAL MATERIAL

Following the characterization and testing of bone, the theoretical mechanics analysis of trabecular bone is conducted. Inputs reflecting structural features at different scales are rectified with our experimental observations obtained by methods described in the previous section. In the analysis, for simplicity, we model bone as a linear elastic solid material and we do not include solid-fluid interactions. We determine material responses, at each structural level defined in the Introduction, either analytically (using micromechanics theories) or numerically (using finite element, spring network, or beam network approaches). Bone's structure is analyzed in an "ascending" order by starting with the nanoscale level.

At the nanoscale level apatite crystals are represented as platelike or ellipsoidal inclusions, which are embedded in collagen fibrils (matrix). First we use micromechanics effective medium theories, for simplicity, and then conduct numerical simulations to account for a discrete (molecular) structure of bone at that structural level. At the next higher up scale (sub-microscale) a single lamella consisting of aligned collagen fibrils reinforced with apatite crystals is modeled using a finite element based beam network approach. At the microscale level, involving a lamellar structure of a single trabecula, we use laminate theory from mechanics of composite materials. The challenges at that scale include curved,

crescent like geometry of trabecular pockets which are made of several lamellar layers stacked at different orientations. Also, at that scale bone remodeling takes place and each trabecula undergoes a different stage of bone resorption and formation (remodeling). At the mesoscale level we have a random network of struts or plates in trabecular bone. The trabecular structure poses modeling challenges because of its complex and irregular geometry. Initially, we model this structure by assuming periodicity in the pores' arrangement and we represent this material as a micropolar one. This higher order theory allows us to account for microstructural features such as pore geometry via characteristic lengths. Then, we conduct large scale finite element computations accounting for random structural features of trabecular network. At this scale the inputs on geometry are taken from a Micro-CT digitized data of actual bone samples. Computational results are compared with experimental ones obtained by testing of digitized bone samples. Throughout this work we have studied the structure and properties of trabecular bone and we have focused on the differences between normal and osteoporotic bone at each scale of observation.

RESULTS

We found no distinct structural differences at the nanoscale, sub-microscale and microscale levels between normal and osteoporotic bone using AFM, SEM, and TEM, but observed a depleted trabecular network at the mesoscale level in trabecular bone. The latter observation is in agreement with the data reported in literature, while the information on bone's structure at lower levels is new [2].

In the numerical simulations we took properties of collagen fibrils as E = 1.5 GPa where E was elastic modulus, and ν = 0.3 where ν was a Poisson's ratio. Several models/approaches were used for each structural scale. Our computational prediction at mesoscale level (by bringing inputs from lower levels) was E = 600 MPa for a given osteoporotic trabecular bone sample (cylinder 5 mm in diameter and 5 mm high) while the experimental measurement gave E = 400 MPa.

CONCLUSIONS

We characterized, tested, and modelled trabecular bone as a hierarchical material. Good agreement was found between theoretical and experimental predictions, considering the complexity of bone's hierarchical structure and the idealizations used in modelling of each structural level. The approach taken presents a framework for studying other biological materials with complex hierarchical structures.

References

[1] Park, J.B. and Lakes, R.S., *Biomaterials: An Introduction*, 2nd ed., Plenum Press, NY, 1992.
[2] Rubin, M.A., I. Jasiuk, J. Taylor, J. Rubin, T. Ganey, R.P. Apkarian, *Bone* **33**:270-282, 2003

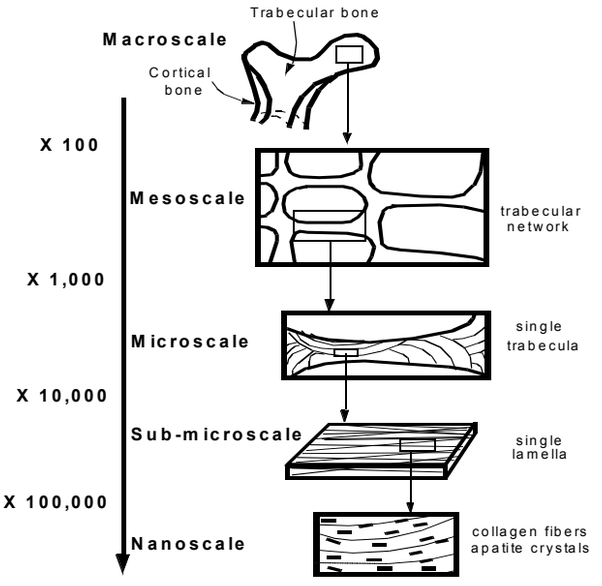


Fig.1 Schematic of a hierarchical structure of trabecular bone.

INVESTIGATION OF COUPLE-STRESS EFFECTS IN ELASTIC BODIES UNDER DEFORMATION

Valery P. Matveenko [*], Valery V. Korepanov[*] Michail A. Kulesh[*], Igor N. Shardakov[*]
[*]*Institute of Continuous Media Mechanics, Ural Branch of RAS, Perm, Russia*

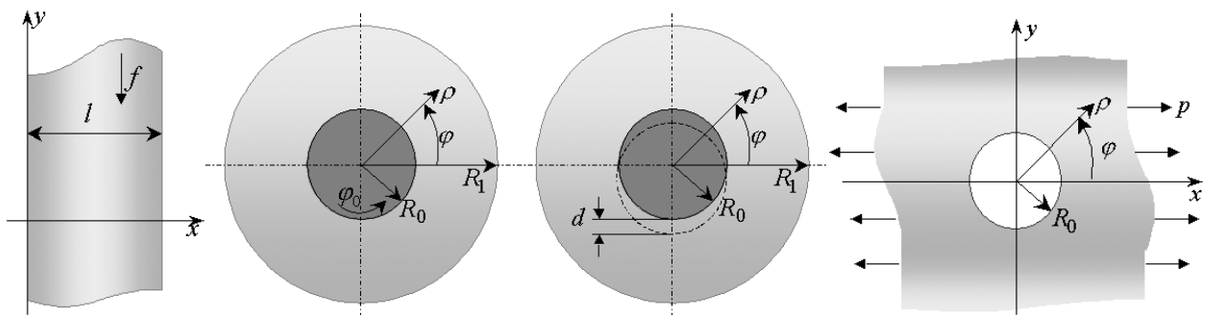
Summary The paper presents new analytical and numerical solutions to some problems of asymmetric elasticity theory. A comparison is made with the analytical solutions obtained in the framework of the classical elasticity theory. The results of experimental investigation of the couple-stress effects in materials under deformation are discussed.

INTRODUCTION

At present, in the framework of solid mechanics a number of models have been developed, in which the deformation of a medium is described not only in terms of the displacement vector but also in terms of the rotation vector. The classical works on the asymmetric elasticity theory state that the versions of this theory will be able to provide a better agreement with experiments, in which a material is subjected to essential gradient stresses. However, the engineering applications of these models are practically absent because there are no reliable data on the material constants of asymmetric elasticity theory. Moreover no experiments have been conducted to determine couple–stress effects in elastic solids under deformation.
One of the key factors that could provide an objective estimation of the usefulness of the asymmetric elasticity theory and offer considerable scope for experimental investigation is a sufficient amount of problems solved in the framework of this theory.

ANALYTICAL SOLUTIONS

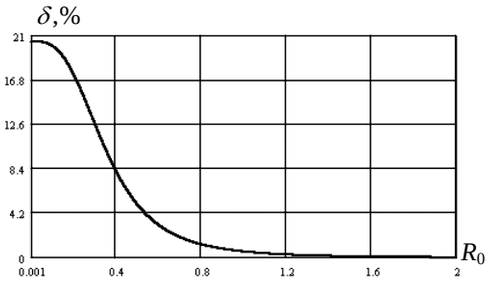
The work presents a number of new analytical solutions to the problems of asymmetric elasticity theory [1]: shear deformation of a plane infinite layer (plate) fixed at both edges under the action of gravitational force (Fig.1.a); torsion deformation of a ring rigidly fixed at the external contour due to rotation of the internal contour by a fixed angle (Fig.1.b); deformation of a ring with a rigidly fixed external contour due to displacement of the internal contour by a prescribed value (Fig.1.c); the Kirsh problem on the uniaxial tension of an infinite plate weakened by a central circular hole (Fig.1.d).



a b c d

Fig.1.

By comparing the dimensionless forms of the obtained solutions with their classical analogues we can draw a conclusion that solutions of the asymmetric elasticity theory are inhomogeneous functions of the characteristic geometrical dimension, whereas classical solutions are homogeneous functions. The obtained solutions have been analyzed with reference to macro-quantities that can be measured by experiment. For the first problem these are maximal axial displacements. For the second problem this is the torque moment at the internal contour, which is defined by the value of the internal contour stress. For the third problem this is the axial force of the internal contour response also defined by the value of stress on the internal contour. In the fourth problem the characteristic macro-parameter is the degree of distortion of the hole contour.
For the problems under consideration the above mentioned macro-quantities determined in terms of the asymmetric elasticity theory were compared with those obtained by the classical theory. The material used to obtain quantitative results was synthetic polyurethane, whose material constants are presented in work [2]. An example of such a comparison is given in Fig.2.



$$D = \left| \frac{u_\rho(R_0, 0)}{u_\rho(R_0, \pi/2)} \right|$$ – degree of distortion of a circular hole;

$$\delta = \left| \frac{D - D^*}{D^*} \right| \cdot 100\% \ ,$$

D – couple-stress solution

D^* – classical solution.

Fig.2.

NUMERICAL SOLUTIONS

To extend the scope of solvable problems we have developed an algorithm of the finite element method, which apply well to the problems of asymmetric elasticity theory. The finite element realization is based on the following variational equation of the asymmetric elasticity theory:

$$\int_V \left(\tilde{\sigma} \cdot\cdot \delta\tilde{\gamma} + \tilde{\mu} \cdot\cdot \delta\tilde{\chi} \right) dV - \int_V \left(\vec{X} \cdot \delta\vec{u} + \vec{Y} \cdot \delta\vec{\omega} \right) dV = \int_S \left(\vec{p} \cdot \delta\vec{u} + \vec{m} \cdot \delta\vec{\omega} \right) dS \qquad (1)$$

where: $\vec{u}$, $\vec{\omega}$ are the displacements and rotation vectors; $\tilde{\sigma}$, $\tilde{\mu}$ are tensors of force and couple stresses; $\tilde{\gamma}$, $\tilde{\chi}$ are the strain and bending-torsion tensors; $\vec{p}$, $\vec{m}$ are the vectors of forces and couple stresses prescribed on the boundary; $\vec{X}$, $\vec{Y}$ are the vectors of mass forces and mass moments.

The finite element used in calculations is a triangle with quadratic approximation of the displacement vector components and linear approximation of the rotation vector components. The developed finite-element algorithm has been used to obtain numerical solutions to a number of problems, in which couple-stress effects are more pronounced than in the problems for which the analytical solutions have been derived. For example, the problem of a plate weakened by several circular holes under tensile load.

EXPERIMENTAL INVESTIGATION

The experimental scheme of material deformation was developed in the context of the Kirsh problem. To define the appropriate dimensions of the plate we performed numerical calculations, which allowed us to eliminate the influence of the plate dimensions on the stress state in the vicinity of the central circular hole.

Two experimental schemes were realized. The first scheme was intended to measure the degree of distortion of the hole contour during extension of the plate. The second scheme involved measurements of the variations in the plate thickness along its contour. The surface profile was measured using the “New View-5000” microscope-interferometer. As a result of experiments the dimensions of the hole, at which the material under deformation exhibited couple-stress effects, were defined.

CONCLUSION

In this work, four new analytical solutions to the problems of asymmetric elasticity theory have been constructed. The obtained solutions allow us to identify the macroscopic parameters, which can be measured by available methods during experimental realization of the appropriate problems. To demonstrate the effects of couple-stress behavior of the material the obtained solutions have been compared with the corresponding solutions of the classical elasticity theory. The finite-element algorithm has been developed for solving two-dimensional problems of asymmetric elasticity theory. The algorithm enables us to extend the scope of the problems, which can be effectively used to analyze the couple-stress behavior of the materials. The experimental investigations have been performed to reveal situations, in which solids under deformation exhibit couple-stress effects.

This work was supported by Russian Foundation of Fundamental Research under project 03-01-00561 and in part by Award No. PE-009-0 of the U.S. Civilian Research & Development Foundation for the Independent States of the Former Soviet Union (CRDF).

References

[1] M.A. Kulesh, V. P. Matveenko, I. N. Shardakov. Parametric analysis of analytical solutions to one- and two-dimensional problems in couple-stress theory of elasticity // Z. Angew. Math. Mech, 83(4), P238-248, (2003).

[2] Lakes R. Cosserat micromechanics of structured media experimental methods. // Third technical conference "Proceedings of the American society for composites". September 25-29, Seatle, Washington. P.505-516.

XXI ICTAM, 15–21 August 2004, Warsaw, Poland

NEW ANALYTICAL APPROACH FOR INVESTIGATION OF NON-STATIONARY DYNAMICS OF MEDIA WITH MOVING INHOMOGENEITIES

Serge N. Gavrilov
Institute for Problems in Mechanical Engineering RAS, Bolshoy pr. V.O., 61, St. Petersburg, 199178, Russia

Summary Non-stationary processes in various elastic media with moving inclusions like material point bodies, phase boundaries, defects, are under investigation in this paper. The law of motion for an inclusion is considered to be unknown. Small strain approximation is used. The interaction of inhomogeneities with the continuum is described by configurational forces (internal and external). This statement leads to necessity to consider nonlinear (because configurational force is a quadratic quantity) non-stationary problems. A new asymptotical approach for problems of such kind is suggested. The solution of simplest model problem (a point mass moving along a string on an elastic foundation) is given and discussed.

CONFIGURATIONAL FORCES IN THE CASE OF INFINITESIMAL DEFORMATIONS

In frames of modern continuum mechanics the interaction of media with inhomogeneities like material point bodies, phase boundaries, defects can be described by means of configurational forces. The notion of configurational (material, thermodynamical) force appears as a generalization of notion of a force acting on a defect by Eshelby and crack-driving force (J-integral) by Rice. Configurational forces are quantities, which perform work on velocities of moving sources (defects, cracks, phase boundaries etc) in a continuum. They are useful to describe a dissipation (or, say better, energy exchange with environment) accompanying motion of sources. At the time being the theory of configurational forces is rapidly developing section of continuum mechanics. The state-of-the-art of the theory the reader can find in studies by Gurtin [1], Kienzler & Herrmann [2], Maugin [3]. Below we give a short summary of basic formulae of the theory of configurational forces for the case of infinitesimal deformations. Consider a pure mechanical non-polar medium. In the paper we use the notation of direct tensor calculus, following Lurie [4].

Let $\mathbf{U}$ be the displacement vector, $\mathbf{T}$ be the stress tensor, $\mathcal{U}$ be the strain energy per unit volume, $\mathbf{I}$ be the identity tensor, ρ be the mass density, $\mathbf{b}$ be the bulk external force. The equation for balance of momentum leads to the following relationship

$$\nabla\cdot\mathbf{C}+\mathbf{g}+\mathbf{e}+\mathbf{i}=\mathbf{0}, \tag{1}$$

where we call $\mathbf{C}=\mathcal{U}\mathbf{I}-\mathbf{T}\cdot\mathbf{U}\nabla$ the configurational stress (the Eshelby tensor), $\mathbf{g}=-\nabla\mathcal{U}+(\nabla\mathbf{U}\nabla)\cdot\cdot\mathbf{T}$ the bulk internal configurational force, $\mathbf{e}=-\nabla\mathbf{U}\cdot\mathbf{b}$ the bulk external configurational force, $\mathbf{i}=\rho\nabla\mathbf{U}\,\ddot{\mathbf{U}}$ the bulk inertial configurational force. Expression (1) can be transformed into different form

$$\nabla\cdot(\mathbf{C}-\mathcal{K}\mathbf{I})+\mathbf{g}+\dot{\mathbf{U}}^2\,\nabla\rho/2+\mathbf{e}=\dot{\mathfrak{p}}, \tag{2}$$

where $\mathfrak{p}=-\rho\nabla\mathbf{U}\cdot\dot{\mathbf{U}}$ is so-called pseudomomentum, $\mathcal{K}$ is the kinetic energy per unit volume. Quantities $\mathfrak{C}=\mathbf{C}-\mathcal{K}\mathbf{I}$, $\mathfrak{g}=\mathbf{g}+\frac{1}{2}\dot{\mathbf{U}}^2\,\nabla\rho$ are called sometimes the dynamic Eshelby tensor and the dynamic configurational force, respectively.

Introduce now a simple mechanical system, where configurational forces play an important role. This is a migrating control volume. The *migrating control volume* $\mathcal{P}_t$ is a set of $\mathbf{r}$ such as $\mathbf{r}\in\mathcal{P}_t$ if and only if $\mathbf{r}-\boldsymbol{\ell}(t)=\mathbf{x}\in\mathcal{P}$. Here $\mathcal{P}$ is an arbitrary domain fixed in reference configuration. Body $\mathcal{R}$ consists of different material points at different time instants. For an arbitrary field $\Phi(\mathbf{r},t)$ introduce the *time derivative of* Φ *following* $\mathcal{P}_t$: $\breve{\Phi}(\mathbf{r},t)=\partial\Phi(\mathbf{x}+\boldsymbol{\ell}(t),\tau)/\partial\tau\,\big|_{\tau=t}$. In fact, $\breve{(\cdot)}$ is the derivative with respect to time in co-moving with $\mathcal{P}_t$ co-ordinate system. One has $\breve{\Phi}=\dot{\Phi}+\mathbf{v}\cdot\nabla\Phi$, where $\mathbf{v}=\dot{\boldsymbol{\ell}}$. Let us formulate the energy balance equation for $\mathcal{P}_t$. One can obtain

$$\frac{d}{dt}\int_{\mathcal{P}_t}(\mathcal{K}+\mathcal{U})\,dV+\gamma=\int_{\partial\mathcal{P}_t}\mathbf{n}\cdot\mathbf{T}\cdot\breve{\mathbf{U}}\,dS+\int_{\mathcal{P}_t}\mathbf{b}\cdot\breve{\mathbf{U}}\,dV+\mathbf{v}\cdot\int_{\partial\mathcal{P}_t}\mathbf{n}\cdot\big(\mathcal{K}\mathbf{I}+\mathbf{C}\big)\,dS+\mathbf{v}\cdot\int_{\mathcal{P}_t}\mathbf{e}\,dV \tag{3}$$

Here $-\gamma$ is the rate of non-mechanical energy exchange with environment of control volume $\mathcal{P}_t$ (γ is the dissipation), $\mathbf{n}$ is the external normal to $\mathcal{P}_t$. Exactly this relationship allows us to introduce the notions of "force on an inhomogeneity", "force on a defect" etc. Utilizing the time derivative $\breve{(\cdot)}$ one can rewrite (2) into the form, which will be useful when considering dynamic problems concerning moving sources. Let us transform material derivatives in (2) in accordance with definition of $\breve{(\cdot)}$. After calculations one gets

$$\nabla\cdot\big(\mathbf{C}-\mathfrak{K}\big)+\mathfrak{g}+\mathbf{e}=\breve{\mathfrak{p}},\qquad \mathfrak{K}=\rho\big(\frac{1}{2}\breve{\mathbf{U}}^2\mathbf{I}+(\mathbf{v}\nabla\mathbf{U}\cdot\breve{\mathbf{U}}-\mathbf{v}\cdot\nabla\mathbf{U}\cdot\breve{\mathbf{U}}\,\mathbf{I})+(\frac{1}{2}\mathbf{v}\cdot\nabla\mathbf{U}\cdot\mathbf{U}\nabla\cdot\mathbf{v}\,\mathbf{I}-\mathbf{v}\nabla\mathbf{U}\cdot\mathbf{U}\nabla\cdot\mathbf{v})\big). \tag{4}$$

A MODEL PROBLEM AND ITS SOLUTION

Consider the classical problem concerning point body moving along the string on Winckler's foundation [5, 6]. We use the following notation: $u(x,t)\mathbf{e}_\perp$ is the transversal displacement of a point of the string with a position x at an instant of time t; T_0 is the string tension; ρ is the density of the string per unit length; $c=\sqrt{T_0/\rho}$ is the speed of sound (the critical

speed); $l(t)$ is the position of the point body; $k_0 = T_0 k > 0$ is the rigidity of foundation; $\mathbf{f}_0 = T_0(f_\parallel \mathbf{e}_\parallel + f_\perp \mathbf{e}_\perp)$ is the prescribed external force acting on the point body; $\mathbf{F}_0 = T_0(F_\parallel \mathbf{e}_\parallel + F_\perp \mathbf{e}_\perp)$ is the force acting on the string from the point body; $m_0 = T_0 m$ is the mass of the point body. The square and angle brackets denote the jump and mean value at $x = l(t)$, respectively. The governing equations are as follows

$$u'' - c^{-2}\,\ddot{u} - ku = -F_\perp\,\delta(x - l(t)), \qquad \frac{d^2}{dt^2}\,u(l(t),t) = f_\perp - F_\perp \tag{5}$$

The motion of the point body along the string is governed by the following law [5, 6]

$$m\ddot{l} = \mathcal{F} + f_\parallel \qquad \mathcal{F} = F_\perp\langle u'\rangle = -(1 - \dot{l}^2/c^2)[u'^2]/2. \tag{6}$$

Here $\mathcal{F}$ is so-called wave resistance force [5, 6]. The second equation in (6) can be obtained using energy balance equation in the form similar to Eq. (3) formulated for the control volume $[l(t) - R; l(t) + R]$ with sufficiently large R. Comparing the general definition of the external configurational force (see above) and the first representation for $\mathcal{F}$ from (6) one can show that $\mathcal{F}$ can be considered as external configurational force exerting on the string from the point body. The second representation of $\mathcal{F}$ follows from one-dimensional equation, which is analogous to Eq. (4). In fact the quantity $-(1 - \dot{l}^2/c^2)[u'^2]/2$ is exactly the jump of the one-dimensional analogue of tensor $\mathbf{C} - \mathfrak{K}$. For simplicity consider zero initial conditions for u. Thus we have non-stationary (because $\dot{l}$ is not a constant) nonlinear problem with unknown boundary $l(t)$. The nonlinearity is associated with quadratic law for $\mathcal{F}$. To investigate this problem we suggest a new analytical approach based on the work by Gavrilov & Indeitsev [7], where the motion of the point body with prescribed law $l(t)$ was considered. In our approach we utilize the stationary phase method and the method of multiple scales.
Main supposition: $\ddot{l}(t) = O(\epsilon^2)$, $t \to \infty$, $\dot{l} = O(1)$ — quasi-stationary asymptotics.

1. Suppose $l(t)$ to be a given function, $\dot{l} = \mathrm{const}$. For $t \to \infty$ select the set of pronounced frequencies in spectrum of $u(l(t), t)$.
2. For $\ddot{l}(t) = O(\epsilon^2)$ approximate $u(l(t), t)$ by a sum w of modes with slowly varying pronounced frequencies.
3. Describe the evolution in time of selected modes using the method of multiple scales.
4. Find out the near-field approximation of wave field in a vicinity of the source using the method of multiple scales.
5. Obtain w for given $l(t)$.
6. Find out $l(t)$ for given $f_\parallel$.

Application of this approach to the problem under consideration yields the following results. The law of motion for the point body is

$$(M\dot{l})^{\cdot} = f_\parallel, \qquad M = m\left(1 + \frac{\alpha}{(c^2 - \dot{l}^2)^{3/2}}\right), \qquad \alpha = \frac{c\,f_\perp^2}{4m\sqrt{k}}. \tag{7}$$

The "effective mass" M depends on the speed $\dot{l}$ and tends to infinity when $|\dot{l}| \to c$.

CONCLUSION

In this paper we demonstrated that the "wave pressure force", which is known from the beginning of XXth century, can be considered as a configurational force and can be calculated as jump (in the one-dimensional case) or flux of a quantity related to the Eshelby tensor. We guess that this is a quite important fact, since it leads to the similarity for mathematical statements of dynamical problems concerning phase boundaries propagation (in the theory of phase transformations of elastic bodies), moving dislocations etc on the one hand, and classical problems concerning moving loads on the other hand. Furthermore, we suppose that the analytical approach suggested, which works efficiently for moving inertial inclusions, can be applied also in frames of modern fields of mechanics mentioned above. In particular we expect that it can be used for the investigation of dynamical problems concerning phase transformation in one-dimensional elastic bodies (strings [8], beams [9]) and to obtain the equation for motion of dislocation [10] in more compact form.

References

[1] Gurtin M.E.: Configurational Forces as Basic Concepts of Continuum Physics. Springer-Verlag, NY 2000.
[2] Kienzler R., Herrmann G.: Mechanics in Material Space with Applications to Defect and Fracture Mechanics. Springer-Verlag, Berlin 2000.
[3] Maugin G.A.: Material Inhomogeneities in Elasticity. Chapman & Hall, London 1993.
[4] Lurie A.I.: Nonlinear Theory of Elasticity. Nauka, Moscow 1980.
[5] Nicolai E.L.: On a dynamical illustration of the pressure of radiation. *Phil. Mag. S6* **49**(289):171–177, 1925.
[6] Vesnitskiy A.I., Kaplan L.E., Utkin G.A.: Laws for balance of energy and momentum for one-dimensional systems with moving boundaries and loads Prikladnaya Matematika i Mekhanika **47**:863–866, 1983. (in Russian)
[7] Gavrilov S.N., Indeitsev D.A.: On the evolution of trapped mode of oscillation in system "string on an elastic foundation — moving inertial inclusion". *Prikladnaya Matematika i Mekhanika* **66**(5):864–873, 2002. (in Russian)
[8] Purohit P.K., Bhattacharya K: Dynamics of strings made of phase-transforming materials. *J. Mech. Phys. Solids* **51**:393–424. 2003.
[9] Purohit, P.K. and Bhattacharya, K: On beams made of a phase-transforming material *Int. J. Solids and Structures* **39**:3907–3929, 2002.
[10] Markenscoff, X.: On the equation of motion and the near-field of a nonuniformly moving dislocation *J. Elast.* **66**:99–108, 2002.

AGMON'S CONDITION FOR INCOMPRESSIBLE ELASTICITY: A VARIATIONAL FORMULATION

Gearoid P. Mac Sithigh
Department of Mechanical and Aerospace Engineering and Engineering Mechanics, University of Missouri-Rolla, Rolla, MO 65401-0249 USA.

Summary Agmon's condition for incompressible elasticity is recast in variational form. The main result obtained is the natural analog of one found for the compressible case by Mielke and Sprenger. The condition is applied to an assortment of illustrative cases.

Let $\mathbf{X_0}$ be a boundary point of an incompressible, elastic body, at which traction is prescribed. Let $-\mathbf{i_3}$ be the outer unit normal at $\mathbf{X_0}$, $\mathcal{G}_1^{(+)}$ a unit cube with base outer normal $-\mathbf{i_3}$. Let $W(\mathbf{F},\mathbf{X})$ be the stored energy function of the material, $\mathbf{F_0}$ the deformation gradient, and p the reaction pressure at $\mathbf{X_0}$. Then the local second variation condition at $\mathbf{X_0}$ is

$$\int_{\mathcal{G}_1^{(+)}} \mathbb{K}\big[\operatorname{grad}\mathbf{w}\big]\cdot(\operatorname{grad}\mathbf{w})\mathrm{dV} \geq 0. \tag{V2}$$

for all solenoidal vector fields $\mathbf{w}$ which vanish on $\partial_1\mathcal{G}_1^{(+)}$, the top and sides of $\mathcal{G}_1^{(+)}$. Here,

$$\mathbb{K}\big[\mathbf{G_1}\big]\cdot\mathbf{G_2} := W_{\mathbf{FF}}(\mathbf{F_0},\mathbf{X_0})[\mathbf{G_1F_0}]\cdot(\mathbf{G_2F_0}) + \mathrm{p}\,\mathrm{tr}\big(\mathbf{G_1G_2}\big). \tag{1}$$

For any tangent vector $\mathbf{s}$, define operators $\mathbf{M},\mathbf{N_s},\mathbf{P_s}$ by

$$\mathbf{Ma} := \mathbb{K}\left[\mathbf{a}\otimes\mathbf{i_3}\right]\mathbf{i_3}, \qquad \mathbf{N_s a} := -\,\mathbb{K}\left[\mathbf{a}\otimes\mathbf{s}\right]\mathbf{i_3}, \qquad \mathbf{P_s a} := \mathbb{K}\left[\mathbf{a}\otimes\mathbf{s}\right]\mathbf{s}, \tag{2}$$

and domains $\mathcal{H},\mathcal{D}_\mathbf{s}$ by

$$\mathcal{H} := \mathrm{W}^{1,2}\big([0,\infty)\big)\otimes\mathrm{W}^{1,2}\big([0,\infty)\big)\otimes\mathrm{W}^{2,2}\big([0,\infty)\big), \qquad \mathcal{D}_\mathbf{s} := \left\{\mathbf{z}(\cdot)\in\mathcal{H}\,\middle|\,\dot{\mathbf{z}}\cdot\mathbf{i_3} + i\mathbf{s}\cdot\mathbf{z} = 0\right\}.$$

Define a functional $\mathcal{J}_\mathbf{s}^\Lambda[\cdot]$ on $\mathcal{D}_\mathbf{s}$ by

$$\mathcal{J}_\mathbf{s}^\Lambda[\mathbf{z}] := \int_0^\infty \left\{\dot{\overline{\mathbf{z}}}\cdot\mathbf{M}\dot{\mathbf{z}} - 2\mathrm{Re}\big(i\,\dot{\overline{\mathbf{z}}}\cdot\mathbf{N_s z}\big) + \overline{\mathbf{z}}\cdot\big[\mathbf{P_s} + \Lambda^2\mathbf{1}\big]\mathbf{z}\right\}\mathrm{dt}. \tag{3}$$

Theorem 1 The inequality (V2) holds for all smooth complex-valued solenoidal vector-fields $\mathbf{w}$ which vanish on $\partial_1\mathcal{G}_1^{(+)}$ if and only if $\mathcal{J}_\mathbf{s}^\Lambda[\mathbf{z}]\geq 0$ for all $\mathbf{z}\in\mathcal{D}_\mathbf{s}$ and $\Lambda>0$.

Define quantities

$$2\Delta := \varepsilon_{\alpha\beta}\varepsilon_{\gamma\delta}\mathrm{M}_{\alpha\gamma}\mathrm{M}_{\beta\delta}, \qquad \Delta\mathrm{L}_{\alpha\beta} := \varepsilon_{\alpha\gamma}\varepsilon_{\beta\delta}\mathrm{M}_{\gamma\delta}, \qquad \mathbf{L} = \mathbf{L^T} := \mathrm{L}_{\alpha\beta}\mathbf{i}_\alpha\otimes\mathbf{i}_\beta := \mathbf{Q^2},$$

$$\mathbf{D} := \Big[\mathbf{N_s}^\mathbf{T} + \mathbf{s}\otimes\mathbf{M^{(i)}i_3}\Big]\mathbf{L} - \mathbf{s}\otimes\mathbf{i_3}, \qquad \mathbf{Z} := \mathbf{Q}\big[\mathbf{N_s} + \mathbf{Mi_3}\otimes\mathbf{s}\big],$$

$$\mathbf{Y} = \mathbf{Y^T} := \mathbf{P_s} - \mathbf{Z^T Z} + \mathbf{N_s^T i_3}\otimes\mathbf{s} + \mathbf{s}\otimes\mathbf{N_s^T i_3} + (\mathbf{i_3}\cdot\mathbf{Mi_3})\mathbf{s}\otimes\mathbf{s},$$

$$\mathbf{A} := \begin{pmatrix} 1 & 0 & 0 & 0 & 0\\ 0 & 1 & 0 & 0 & 0\\ 0 & 0 & -is_1 & -is_2 & 0\\ 0 & 0 & 1 & 0 & 0\\ 0 & 0 & 0 & 1 & 0\\ 0 & 0 & 0 & 0 & 1 \end{pmatrix}.$$

MAIN RESULT:- If $\Delta > 0$, following three conditions are equivalent:
(i) $\mathcal{J}^0_{\mathbf{s}}[\cdot]$ is nonnegative for all $\mathbf{s}$.

(ii) For each $\mathbf{s}$, there exists $\mathbf{H}$ positive-semidefinite, Hermitian such that if

$$\mathbf{E_H} := \begin{pmatrix} \mathbf{M} & -i\mathbf{N_s} + \mathbf{H} \\ i\mathbf{N_s^T} + \mathbf{H} & \mathbf{P_s} \end{pmatrix},$$

the 5×5 matrix

$$\tilde{\mathbf{E}}_{\mathbf{H}} := \mathbf{A}^\dagger \mathbf{E_H} \mathbf{A}$$

is positive-semidefinite .

(iii) For each $\mathbf{s}$, there exists $\tilde{\mathbf{H}}$ positive-semidefinite, Hermitian such that $\tilde{\mathbf{H}}$ solves the algebraic Riccati equation

$$\tilde{\mathbf{H}}\mathbf{L}\tilde{\mathbf{H}} - i\tilde{\mathbf{H}}\mathbf{D}^{\mathbf{T}} + i\mathbf{D}\tilde{\mathbf{H}} - \mathbf{Y} = \mathbf{0}. \qquad \text{(ARE)}$$

If $\Delta = 0$, conditions (i) and (ii) are equivalent.

This result has the same general form as the main result of [2]. Theorem 1 is proved in [1].

Thus, by Theorem 1, (ii), and if $\Delta > 0$, (iii) are each necessary and sufficient conditions for (V2), and the truth or falsity of (V2) may be determined by checking these conditions. This is done for the following examples:
(a) Equibiaxial stretch of a general isotropic material.
(b) General deformations of a neo-Hookean material.
(c) Some particular deformations of a special anisotropic material.

References

[1] G. P. Mac Sithigh. Necessary conditions at the boundary for minimizers in incompressible elasticity. In review.

[2] A. Mielke and P. Sprenger. Quasiconvexity at the boundary and a simple variational formulation of Agmon's condition. *J. Elasticity* **51** (1998) 23-41.

XXI ICTAM, 15–21 August 2004, Warsaw, Poland

MODELLING OF COMPLEX ELASTIC CRYSTALS BY MEANS OF MICROMORPHIC GYROCONTINUA

Elena F. Grekova*, Gérard A. Maugin**
*Institute for Problems in Mechanical Engineering of Russian Academy of Sciences, Bolshoy pr. V.O., 61, St. Petersburg, 199178, Russia; e-mail: elgreco@pdmi.ras.ru
**Laboratoire de Modélisation en Mécanique, Université P. et M. Curie, Paris, France

Summary We model elastic crystals with a complex deformable unit cell containing many gyroscopic subparticles. To obtain the equations of this medium we use two approaches, phenomenological and microstructural. The phenomenological approach is based on the fundamental laws of balance of mechanics. We introduce analogues for the stress and the couple tensor for this micromorphic gyroscopic continuum. For the microstructural consideration we model the interaction between subparticles as a potential interaction of general kind between rigid bodies both of force and torque nature. We sum the laws of the balance of linear and angular momentum over all subparticles of a cell. To pass from the discrete model to the continuum we expand these laws in space co-ordinates of different scale; one scale is concerned with the distance between subparticles, and another with the cell size. This theory may have applications for the description of magnetic crystals.

INTRODUCTION

The most interesting crystals from the point of view of magnetoacoustic interaction are ferrite crystals with a complicated structure, such as Yttrium-Iron Garnets (YIG). Each cell of such a crystal consists of many atoms, combined in clusters. Atoms of Fe are responsible for magnetic properties of the crystal. They interact with each other in a complicated way via the neighbouring atoms of oxygen and yttrium. The total number of atoms in the cell is more than 100. The interaction between neighbouring clusters is essential, but not the interaction between the clusters of the same cell if they are not neighbours. The magnetic moment of clusters is related to the angular momentum (including moment of momentum and spin). A cell contains several clusters possessing spin, and it is deformable. We suggest as an approximation to model such a cell as a deformable particle containing several interacting subparticles – infinitesimal rigid bodies possessing spin.

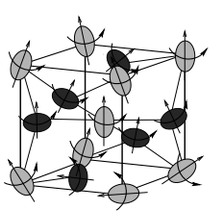


Figure 1. 1/8 of a cell of the Yttrium-Iron Garnet. Distribution of Fe.

PHENOMENOLOGICAL APPROACH

Let us first consider the medium as an inhomogeneous elastic Kelvin medium ([1]): each cluster corresponds to a point-body, which is an infinitesimal rigid point-body, able to perform rotations and translations of a general kind, and possessing rotational symmetry. Point-bodies interact with their neighbours. Suppose this interaction to be determined only by the geometrical configuration at the given moment in time. The rotations of a point-body around its axis do not induce stresses in the medium. In each point we write down the laws of balance of force and torque in Piola form:

$$\overset{\circ}{\nabla}\cdot\mathbf{T}+\rho_0\,\mathbf{Q}=\rho_0\,\ddot{\mathbf{u}},\qquad \overset{\circ}{\nabla}\cdot\mathbf{M}+(\mathbf{G}^{\top}\cdot\mathbf{T})_{\times}+\rho_0\,\mathbf{C}=\rho_0\,(\boldsymbol{\Theta}\cdot\boldsymbol{\omega})^{\cdot}, \tag{1}$$

where $\mathbf{T},\mathbf{M}$ are the first Piola-Kirchoff stress and couple stress tensors, $\mathbf{G}$ is the gradient of radius-vector, $\mathbf{Q},\mathbf{C}$ are external body force and torque, and in the right side of equations we have the inertial terms. We have two scales in space, one ("macro-scale") corresponds to the size of the cell, and another one ("micro-scale") to the distance between a point-body and its neighbours. The gradient $\overset{\circ}{\nabla}$ is the gradient in "micro-co-ordinates" in the reference configuration. The constitutive equations for this medium may be obtained from the law of balance of energy and objectivity requirements [1], so the system (1) is closed.

We pass to the homogeneous continuum, integrating over the initial volume V_0 of the cell equations (1), supposing that all the quantities are sufficiently smooth in the "macro-co-ordinates". Now a "point-body" of the medium is not any more a gyroscopic subparticle, but the cell itself. We obtain "macro"-analogues for the first Piola-Kirchhoff stress and couple stress tensors:

$$\partial_{\mathbf{s}}\cdot\overline{\mathbf{T}}+\frac{1}{V_0}\int_{V_0}\rho_0\mathbf{K}\,dV_0=\rho_0\ddot{\mathbf{S}}, \tag{2}$$

where $\partial_{\mathbf{s}}$ is the "macro-gradient" in the reference configuration, $\mathbf{S}$ is the centre of mass of the cell ("macro-co-ordinate"), $\overline{\mathbf{T}} = \mathbf{a}_i\mathbf{n}^i \cdot \frac{1}{V_0}\int_{\Sigma_{-i}} \mathbf{T}\, d\Sigma_{-i}$ is the "first Piola-Kirchhoff macro-stress tensor", $\mathbf{a}_i$ is a basic vector of the lattice, $\mathbf{n}^i$ is the normal to the surface of the cell Σ_i, and

$$\partial_{\mathbf{s}} \cdot \overline{\mathbf{M}} + [\partial_{\mathbf{s}}\mathbf{S}^\top \cdot \overline{\mathbf{T}}]_\times + \frac{1}{V_0}\mathbf{n}^i \cdot \int_{\Sigma_{-i}} \mathbf{T} \times ((\mathbf{l} + \mathbf{a}_i)\, d\Sigma_{-i}\mathbf{a}_i \cdot\cdot\, \partial_{\mathbf{s}}\partial_{\mathbf{s}}\mathbf{S}) + \frac{1}{V_0}\int_{V_0} \rho_0(\mathbf{L} \times \mathbf{Q} + \mathbf{C})\, dV_0 = \frac{1}{V_0}\int_{V_0} \rho_0(\mathbf{L} \times \dot{\mathbf{u}} + \boldsymbol{\Theta} \cdot \boldsymbol{\omega})\dot{}, \quad (3)$$

where $\overline{\mathbf{M}} = \mathbf{a}_i\mathbf{n}^i \cdot \frac{1}{V_0}\int_{\Sigma_{-i}} \mathbf{M}\, d\Sigma_{-i} - \frac{1}{V_0}\mathbf{a}_i\mathbf{n}^i \cdot \int_{\Sigma_{-i}} \mathbf{T} \times ((\mathbf{l} + \mathbf{a}_i)\, d\Sigma_{-i} \cdot \partial_{\mathbf{s}}\mathbf{S})$ is the "first Piola-Kirchhoff macro-couple stress tensor", $\mathbf{L}$ and $\mathbf{l}$ are the local co-ordinate of a subparticle within the cell in actual and reference configuration, respectively. In the law of balance of torque we see an additional term, which appears because the cell is deformable.

MICROSTRUCTURAL APPROACH

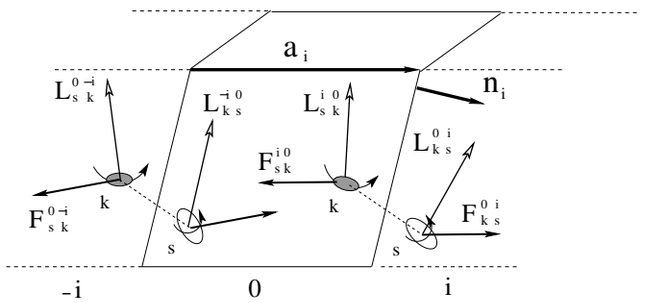


Figure 2. A cell of a crystal. Discrete model

Expansion in macro-co-ordinates

Let $\mathbf{F}_{s\ k}^{0\ -i}$ be a force acting from the subparticle s belonging to cell 0 (under consideration) upon a subparticle k belonging to cell $-i$ (obtained by translation of a cell 0 with the translation vector $-\mathbf{a}_i$), and $\mathbf{L}_{s\ k}^{0\ -i}$ be a corresponding torque, $\mathbf{R}_s^0$ be a radius-vector of a subparticle s from a cell 0 etc. (see Fig. 2). Using the periodicity of the crystal in the reference configuration, the assumption that forces and torques change smoothly with the change of a cell number, and the balance of forces and torques for a cell, we obtain, expanding in the "macro-co-ordinates",

$$\partial_{\mathbf{s}} \cdot \mathbf{a}_i \sum_{s,k} \mathbf{F}_{s\ k}^{0\ -i}/V_0 + \rho_0\mathbf{Q} = \rho_0\ddot{\mathbf{S}}, \quad (4)$$

(so we conclude that $\overline{\mathbf{T}} = \mathbf{a}_i \sum_{s,k} \mathbf{F}_{s\ k}^{0\ -i}/V_0$), and

$$\partial_{\mathbf{s}} \cdot \overline{\mathbf{M}} + [(\partial_{\mathbf{s}}\mathbf{S})^\top \cdot \overline{\mathbf{T}}]_\times - \frac{1}{V_0}\sum_{s,k} \mathbf{a}_i(\mathbf{r}_k^0 - \mathbf{r}_C) \cdot\cdot\, (\partial_{\mathbf{s}}\partial_{\mathbf{s}}\mathbf{S}) \times \mathbf{F}_{s\ k}^{0\ -i} + \rho_0\mathbf{C}^C = \frac{1}{V_0}\sum_{s\in\Omega}((\mathbf{R}_s^0 - \mathbf{S}) \times m_s\dot{\mathbf{R}}_s^0 + \boldsymbol{\Theta}_s \cdot \boldsymbol{\omega}_s)\dot{}. \quad (5)$$

where $\overline{\mathbf{M}} \stackrel{\text{def}}{=} \frac{1}{V_0}\sum_{s,k} \mathbf{a}_i(\mathbf{L}_{s\ k}^{0\ -i} + (\mathbf{R}_k^0 - \mathbf{S}) \times \mathbf{F}_{s\ k}^{0\ -i})$. Thus we have the expression for macro stress and couple stress tensors via forces and torques. This method is analogous to the one suggested in [3] for lattices with translational degrees of freedom of particles.

Expansion in micro-co-ordinates

To model forces and torques between subparticles we consider a sufficiently general law of interaction between two subparticles, based on the formula of the point-point interaction between two rigid bodies of general shape: [2]. Particular cases of this formula give, for example, electrostatic, gravitational, or the van der Waals interaction. We obtain the expressions for the force and torque between two sub-particles and expand them in the "micro-co-ordinates". We find out that strain tensors introduced in [4], participate in these complex expressions. Substitution of these expressions into equations (4), (5) completes the passage from the discrete to continuous model.

References

[1] E.F. Grekova and P.A. Zhilin. Basic equations of Kelvin's medium and analogy with ferromagnets. *Journal of Elasticity*, 64:29–70, 2001.
[2] E. Grekova. Moment interactions of rigid bodies. In *ZAMM Supplement 2*, volume 80, pages 347–348, 2000.
[3] A.M. Krivtsov. Constitutive equations of the nonlinear crystal lattice. *ZAMM*, 79(2):419–420, 1999.
[4] C.B. Kafadar and A.C. Eringen. Micropolar media. *Int. J. Engng. Sci.*, 9:271–305, 1971.

AXISYMMETRIC PROBLEM FOR AN ELASTIC MEDIUM WITH A SPHERICAL INCLUSION WHEN THERE IS A CRACK AT THE INTERFACE

Iryna V. Lebedyeva[*], Myhaylo A. Martynenko[**]
[*] *Kyiv Taras Shevchenko National University, Volodymyrs'ka 64, 01033 Kyiv, Ukraine*
[**] *Ukraine National University of Food technology, Volodymyrs'ka 68, 01033 Kyiv, Ukraine*

Summary A problem on the stressed state of an elastic medium with a spherical inclusion with a crack at the interface boundary is solved by exact methods of the linear theory of elasticity. At first the problem is reduced to an interrelated system of coupled integral equations with respect to the Legendre functions, and then to a system of singular integral equations with respect to two unknown functions. The behaviour of the equation solutions is studied near the interface circle of a spherical section. The case is examined when the cross-section surfaces are under normal internal pressure of constant intensity.

INTRODUCTION

As is well known in most cases the catastrophic destruction of constructions is caused by some hidden internal defects. The internal cracks, in the form of material solidity breaks have been examined by scientific literature for quite a long time. The problems on stress-strained state of elastic finite and infinite bodies with flat cracks of disk-shaped or elliptic forms, are among the best researched ones. More than a hundred publications deal with this issue. However, according to experimental analysis of the surfaces of damaged parts, the initial surfaces of the material breaks were of spherical or ellipsoidal shape, that is they were volumetrical, not flat. To evaluate the strength of material with internal cracks, one can start with the solution of a class of problems within the elasticity theory for three-dimensional bodies weakened by spatially-bent cracks. Such cracks could be modelled by cuts on a part of some surface of revolution with its non-zero curvature. In this case, there is a possibility to vary geometrical parameters of the surface and, by doing this, to bring them closer to the geometry of real cracks. The experimental study of composite materials emphasise the practical significance of this class of problems. Specifically, the heterogeneous media are being filled with the particles of spherical or ellipsoidal form (for example, wolfram-carbide matrix reinforced by diamond grains). Their mechanical characteristics depend, to a considerable degree, on the material solidity break, which appears, as a rule, on the interphase boundary and is located on the parts of the spherical or ellipsoidal surface. The theory of spatial cracks presents quite natural tendencies, when complicated geometry of cuts prompts the need to develop more complex mathematical methods and to increase significantly the number of mathematical operations needed for their analysis. This, obviously, provides an explanation to the fact that just a few publications deal with the studies of stress fields and the displacements of elastic bodies with volumetrical cuts, although the importance of such studies was repeatedly emphasised in research literature.The present paper examines the axisymmetric elastostatic problem for two-compound body with a crack on a part of spherical surface located on the boundary of the division of elastic characteristics of materials. This problem is linked to the study of stressed state of high-strength composite materials with low-percentage content of the spherical dispersed particles.

MATHEMATICAL FORMULATION

Throughout the paper we consider an elastic space (ν_2, G_2) containing a spherical inclusion (ν_1, G_1) and there is a spherical crack at their interface. Let r, θ, φ denote spherical coordinates. The crack is modeled by a mathematical cut along the part of spherical surface ($r=r_0$, $0\le\theta\le\theta_0$, $0\le\varphi\le 2\pi$). The surfaces are not at contact interact and the joint is ideal along another part of the phase boundary. To solve the problem one can apply a superposition principle: the stress field outside the cut is a sum of homogeneous stressed state for a space without crack and local stressed state of the crack surfaces under uniform load of opposite sign [1]. Under such assumption the boundary problem may be formulated as follows: to solve Lame's vector equation of equilibrium under the boundary conditions:

$$\sigma_r^{(1)}=\sigma_r^{(2)},\quad \tau_{r\theta}^{(1)}=\tau_{r\theta}^{(2)},\quad u_r^{(1)}=u_r^{(2)},\quad u_\theta^{(1)}=u_\theta^{(2)},\quad (r=r_0, 0<\theta\le\pi)$$

$$\sigma_r^{(1)}=\sigma_r^{(2)}=f_1(\theta),\quad \tau_{r\theta}^{(1)}=\tau_{r\theta}^{(2)}=f_2(\theta),\quad (r=r_0, 0<\theta\le\theta_0),$$

where $\sigma_r^{(i)}$, $\tau_{r\theta}^{(i)}$, $u_r^{(i)}$, $u_\theta^{(i)}$ – are the components of stress tensor and displacement vector for space (i=1) and spherical inclusion (i=2); $f_i(\theta)$ – are the known functions corresponding to loading on the infinity; ν_i are the Poisson's ratios, G_i are the shear modules of space (i=1) and inclusion (i=2) materials.

METHOD OF SOLUTION

The study of a problem on equilibrium of elastic bodies with cuts on surfaces of the second power is based on general solutions of the fundamental boundary problems of elasticity theory for bodies of revolution in curvilinear coordinates.

Mathematical tools applied to examine these class of tasks are very diverse. One of them is the method proposed by Love [2]. In Love's approach, the solution to the axisymmetric problem in classical elasticity may be represented in terms of a single strain function that satisfies the biharmonic equation. The method of eigenfunctions is another general one. The solutions of boundary problems for bodies of revolution in vector formulation with the help of complete vector eigenfunctions sets were given by Ulitko [1]. In the axisymmetric case the method of direct integration is the most simple and clear one for solving of Lame's equilibrium equation in the arbitrary curvilinear coordinates of revolution.
As assumed relationships the general solutions of elastic problems for a spherical inclusion and a space with a spherical cavity presented in the form of series expansions by Legendre functions were taken [3]. The problem is reduced to an interrelated system of coupled integral equations with respect to the Legendre functions, and then to a system of singular integral equations with respect to two unknown functions.
As the result the asymptotic expressions for stress components were obtained in the form [4]:

$$\sigma_{r\theta} + i\sigma_r \approx (K_2 + iK_1) r_0^{-0,5} \left(\sin\frac{\theta}{2} - \sin\frac{\theta_0}{2} \right)^{-\frac{1}{2}+i\lambda} \cdot \left(\sin\frac{\theta}{2} + \sin\frac{\theta_0}{2} \right)^{-\frac{1}{2}-i\lambda},$$

where the intensity factors of normal K_1 and tangential K_2 stress are determined by formula

$$K_2 + iK_1 = -4a_0\sqrt{1-4\gamma^2}\,\sqrt{r_0}\,L(\theta_0)\cdot\frac{\Gamma(1+i\lambda)\Gamma\left(\frac{1}{2}-\lambda\right)}{\Gamma(3/2)}.$$

SOME EXAMPLES

As an example let us examine the case when the cut surfaces are under normal internal pressure of intensity q. First of all note that the dependence of the stress intensity factors (SIF) on the Poisson's ratios that take values in the interval $0,2 \le \nu_1, \nu_2 \le 0,42$ is not significant. For example at $\nu_1=\nu_2=1/3$ and $\nu_1=1/3$, $\nu_2=1/4$ ($G_1=G_2$) SIF K_1 and K_2 are equal to 0,457 and 0,462, respectively. The behaviour of stress intensity factors in dependence on the ratio of inclusion and matrix shear modules $\beta=G_1/G_2$ for different angle θ_0 values of the cut is submitted in Figure 1. The results presented allows to compare stress intensity factors for a composite ($\beta>1$) and homogeneous ($\beta=1$) materials. It follows from Figure 1 that SIF increase with β increasing and exceed the corresponding values of SIF for homogeneous material. If one introduces parameters $S_1=K_1^{(k)} / K_1^{(0)}$, $S_2=K_2^{(k)} / K_2^{(0)}$, the superscripts (k) and (0) correspond to composite and homogeneous materials) they will vary in the interval $1<S_i<1,5$ (i=1,2) while $1<\beta<60$.

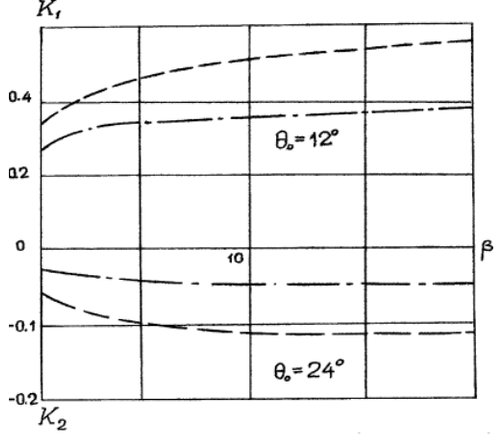


Figure 1. The dependence of stress intensity factors on the ratio of inclusion and matrix shear modules $\beta=G_1/G_2$ for different angle θ_0 values of the cut.

References

[1] Ulitko A. F.: Vector expansions in the three-dimensional theory of elasticity. Akademperiodica Press, Kyiv 2001 (in russian).
[2] Love A.E.H.: A Treatise on the Mathematical Theory of Elasticity. 4th edn. Cambridge University Press, Cambridge 1927.
[3] Lur'e A.I.: Three-Dimensional Problems of the Theory of Elasticity. Interscience Publishers, NY 1980.
[4] Martynenko M.A., Ulitko A.F. *J. Appl. Mech* **14**: 911-918, 1978.

XXI ICTAM, 15–21 August 2004, Warsaw, Poland

TRUNCATED ELASTIC WEDGE UNDER TORSIONAL LOAD

Vyacheslav V. Lyakh
Department of Theoretical & Applied Mechanics, Kiev National Taras Shevchenko University, 01033 Kiev, Ukraine

Summary This paper deals with an analytical solution of the boundary-value problem of plane elasticity for a truncated infinite wedge of an arbitrary opening angle 2α. The flanks of the wedge are free of traction. Its circular boundary is subjected to torsional load due to the given tangential displacements or the moment-replacement loading prescribed. The main goal of the paper is to verify whether the Carothers paradox is actual when the statement of the Carothers problem is modified and more rigorous. Two powerful methods, viz. the method of superposition and the method of homogeneous solutions, are introduced and compared. By means of them the boundary-value problem amounts to solving an infinite integro-algebraic system of equations and an infinite system of algebraic equations, respectively. Our numerical simulations with these systems provide graphical results. The distributions of stresses in some principal cases are presented. Numerical results turn out to be in a complete agreement with results by Neuber [1].

SHORT REFERENCES AND STATEMENT OF THE PROBLEM

A plane elastostatic problem for an elastic wedge loaded by a concentrated moment at its apex provides an example of violation of the Saint-Venant principle when the apex angle 2α of the wedge is over than the half-plane. This circumstance is due to Sternberg and Koiter [2]. They examined the non-degenerate modified problem, in which the couple is replaced by a statically equivalent continuous load distributed on the flanks close by the apex. As distinct from Sternberg and Koiter, Neuber [1] considered the problem for a truncated wedge. He showed the method of construction of an applicable solution for any apex angles in the range $\pi \leq 2\alpha \leq 2\pi$ despite the failure of the Saint-Venant principle. By all means further advancement in explanation of the Carothers paradox is possible provided that the wedge problem is modified in a certain manner and rigorously formulated (see Markenscoff [3]).

Therefore, this paper addresses two modified wedge problems. In the both cases we consider the truncated elastic wedge occupying the domain $\varepsilon \leq r < \infty$, $-\alpha \leq \vartheta \leq \alpha$ in the polar coordinates system (r, ϑ) with free surfaces $\vartheta = \pm\alpha$ (see Figure 1 and conditions (1)).

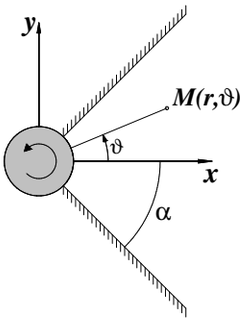


Figure 1. Truncated elastic wedge.

$$\sigma_\vartheta = 0, \quad \tau_{r\vartheta} = 0, \qquad \varepsilon \leq r < \infty, \quad \vartheta = \pm\alpha. \tag{1}$$

The difference lies in the boundary conditions on the circular surface.

Bonded contact with a rigid shaft (mixed problem)

Let us suppose that the truncated elastic wedge is bonded to a rigid shaft (cylinder) of radius ε (see Figure 1). The shaft is rigidly joined with the wedge across the contact zone $r = \varepsilon$, $-\alpha \leq \vartheta \leq \alpha$. A torsional moment M_0 is acting on the shaft which as consequence has rotated through a certain angle φ_0 counterclockwise. Therefore, the displacements in the contact zone are prescribed as

$$u_\vartheta = \varepsilon \cdot \varphi_0, \quad u_r = 0, \qquad r = \varepsilon, \quad -\alpha \leq \vartheta \leq \alpha, \tag{2}$$

As usually, the displacements are assumed vanishing at infinity $r \to \infty$.

This problem is natural in its technical aspect, and it agrees with the approach by Neuber [1]. The solution of the problem will be a function of the angle φ_0, and there is an one-to-one correspondence between φ_0 and the torsional moment M_0. Therefore, full qualitative agreement with Neuber [1] is expected.

On the other hand, if the Carothers paradox is actual then for the given φ_0 the moment M_0 transferred from the shaft to the truncated wedge is not a monotonous increasing function of the angular coordinate α. This matter is found out when solving the problem.

Moment-replacement loading

In contrast to Sternberg and Koiter [2], the replacement loading is applied on the surface $r = \varepsilon$. The normal σ_r and tangential $\tau_{r\vartheta}$ stresses are specified so that the resultant force of external tractions vanishes. Specifically, they are given as $\sigma_r = -X_n \cdot \cos\vartheta$, $\tau_{r\vartheta} = X_n \cdot \sin\vartheta$, where X_n is a given odd function. By replacing X_n with its Fourier series, the boundary conditions at $r = \varepsilon$ are written as

$$\sigma_r = \cos\vartheta \sum_{m=1}^{\infty} a_m \sin\Big(\frac{m\pi}{\alpha}\,\vartheta\Big), \quad \tau_{r\vartheta} = -\sin\vartheta \sum_{m=1}^{\infty} a_m \sin\Big(\frac{m\pi}{\alpha}\,\vartheta\Big), \qquad r = \varepsilon, \quad -\alpha \le \vartheta \le \alpha. \tag{3}$$

METHOD OF SOLUTION

The method of homogeneous solutions (see [4]) and the method of superposition (see [5]) are employed. They, respectively, allow to transform the boundary-value problem to an infinite system of algebraic equations and to an infinite integro-algebraic system of equations.

It is more convenient to apply the method of homogeneous solutions if the opening angle of the wedge 2α equals π or 2π. The last is important particular case when the truncated wedge degenerates into an elastic plane with a semi-infinite slit (see [6]). If 2α differs from π or 2π roots of characteristic equations are complex. In this connection natural difficulties were overcome.

RESULTS

Proceeding from the method of homogeneous solutions the mixed problem has been reduced to solving a singular infinite system of linear algebraic equations that can be brought to a regular form. An asymptotic analysis of singular system's equations and a regular system's solution has been carried out. On the basis of a numerical solution of the regular infinite system normal σ_r and shearing $\tau_{r\vartheta}$ stresses are plotted as a function of the angular coordinate ϑ on a joint area between the elastic wedge and the rigid shaft. Finally, the graphs display somewhat unexpected results: these relations are found in a complete qualitative agreement with Neuber's deductions (see Figure 2).

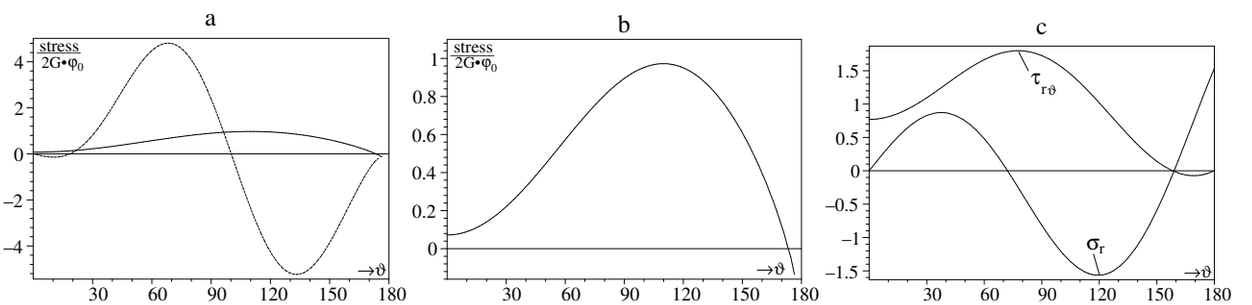


Figure 2. Stress distribution along the force transfer surface calculated for $\alpha = \pi$: (a) dashed and solid lines represent normal and shearing stresses respectively; (b) shearing stress scaled down; (c) according to Neuber [1].

As in a number of other problems, including bonded contact between elastic bodies and rigid boundaries, there is a certain inconsistency in the shear-stress behavior at the location $r = \varepsilon$, $\vartheta = \pm\alpha$. This character of the stress field is inevitable. Therefore, the points $r = \varepsilon$, $\vartheta = \pm\alpha$ are treated as singular, in which characteristics of the stress field are uncertain and fundamentally different in their close proximity.

References

[1] Neuber H.: Lösung des Carothers - Problems mittels Prinzipien der Kraftübertragung (Keil mit Moment an der Spitze). *Z. angew. Math. Mech.* 43 (1963) 211-228.

[2] Sternberg E., Koiter W. T.: The wedge under a concentrated couple: a paradox in the two-dimensional theory of elasticity. *Trans. ASME. J. Appl. Mech.* 25 (1958) 575-581.

[3] Markenscoff X.: Some remarks on the wedge paradox and Saint-Venant's principle. *Trans. ASME. J. Appl. Mech.* 61 (1994) 519-523.

[4] Lourje A. I., *Theory of Elasticity.* Moscow: Nauka (1970) 939pp. (in Russian).

[5] Grincenko V. T., *Equilibrium and Stady-State Oscillations of Elastic Bodies of Finite Dimensions.* Kiev: Naukova Dumka (1978) 264pp. (in Russian).

[6] Ulitko A. F., Lyakh V. V.:Torsional load transfer from a rigid shaft to an elastic plane with a slit. *J. Engng Math.* 46 (2003) 395-408.

Homogenization of triply periodic elastic media with random imperfections

V. A. Buryachenko
University of Dayton Research Institute, Dayton OH 45469-0168, USA

Summary. Triply periodic particulate matrix composites with imperfect unit cells are analyzed by three new different versions of the multiparticle effective field method (MEFM) proposed previously for the analysis of both the perfect periodic and random media. The general scheme and particular cases are presented which are based on the choice of a comparison medium coinciding with either the matrix or perfect periodic structure.

Micromechanical modeling and simulation of random structures are becoming more and more ambitious due to an advantage of modern computer software and hardware (see e.g. [1]). Triply periodic particulate matrix composites with random imperfect unit cells are analyzed in this paper by the multiparticle effective field method (MEFM). The MEFM is originally based on the homogeneity hypothesis **H1)** (see for details [2]) of effective field acting on the inclusions. In this way the pair interaction of different inclusions is taken directly into account by the use of analytical approximate solution. For the perfect periodic structures, the hypothesis **H1)** is enough for estimation of effective properties (see [3]). Imperfection of packing necessitates exploring an additional assumption called a closing hypothesis. The next imperfections were analyzed. A) The probability $\lambda^{(1)}$ of location of an inclusion in the center of a unit cell below one (missing inclusion). B) Some hard inclusions are randomly replaced by the porous (modeling the complete debonding) with the probability $\lambda^{(2)}$. The mentioned problems are solved by three methods. The first one is a generalization of the version of the MEFM proposed for the analysis of the perfect periodic particulate composites ($\boldsymbol{L}(\boldsymbol{x})=\boldsymbol{L}^{\rm per}(\boldsymbol{x})$) and based on the choice of a comparison medium coinciding with the matrix $\boldsymbol{L}^{\rm c}=\boldsymbol{L}^{(0)}$. The second one is a Monte Carlo simulation exploring an analytical approximate solution for the binary interacting inclusions obtained in the framework of the hypothesis H1). The third method uses a decomposition of the desired solution on the solution for the perfect periodic structure and on the perturbation produced by the imperfections in the perfect periodic structure.

In Fig. 1 the results of the first method obtained by the two-particle approximation are presented for the initially perfect packing of hard spheres $v^{(1)}$ ($\lambda^{(1)}=1$, $\lambda^{(2)}=0$) disordering by the random replacement of some hard spheres by the holes $v^{(2)}$. At the variation of the concentration of the hard inclusions $c^{(1)}(\lambda^{(1)})$ and the holes $c^{(2)}(\lambda^{(2)})$, their complete concentration is fixed $c^{(1)}(\lambda^{(1)}) + c^{(2)}(\lambda^{(2)})=0.3$. Effective elastic moduli presented in Fig. 1 are consistent with a continuous transition from the perfect packing of hard spheres ($\lambda^{(1)}=1$, $\lambda^{(2)}=0$) to the perfect packing of holes ($\lambda^{(1)}=0$, $\lambda^{(2)}=1$). The example in Fig. 1 can be considered as a simplified damage model where the broken inclusions are replaced by some microdiscontinuities, that is, the stiffness tensor of one broken inclusion is reduced to zero. More detailed analysis of damage models is beyond the scope of the present paper. It should be mentioned that the representation of effective properties in the second method was obtained by the average over the realization number $n^{\rm MC}$ of periodic structure with mesocell $\boldsymbol{\Omega}^{\rm meso}$ containing the random set of inclusions $X^{\rm meso}$. In the theory of periodic structures (see e.g. [4], [5]) this problem is usually solved on the mesocell $X^{\rm meso}$ with periodic boundary conditions. In the current approach, we analyzed all the inclusions from the whole space R^3 with the boundary conditions at infinity. However, due to the absolute convergence of the right-hand side of the obtained equation for the average strains in the inclusions, the real number of analyzed inclusions is limited by the inclusions belonging to the ellipsoidal domain $w^{\rm el}$ with linear size exceeding in a few times the linear size of $\boldsymbol{\Omega}^{\rm meso}$ (see for details [2]). Thus, although the periodic boundary conditions were not used in the obtained equation, nevertheless, the periodicity condition was explored for the solution $\boldsymbol{\varepsilon}(\boldsymbol{x})$, and, because of this, this equation contains only $N^{\rm meso}$ unknown strains associated with the inclusions contained in the mesocell $\boldsymbol{\Omega}^{\rm meso}$. As an example, we will considered an imperfect SC packing of identical hard spherical inclusions (the phase $v^{(1)}$) randomly replaced by the spherical voids of the same radius (the phase $v^{(2)}$). The statistical descriptors of the imperfect packing are fixed: $c^{(1)}(\lambda^{(1)}) + c^{(2)}(\lambda^{(2)})=0.4$, $\lambda^{(1)}=0.9$, $\lambda^{(2)}=0.1$. For instance, the values $\mu^{*}/\mu^{(0)}$ estimated for $400<n^{\rm MC}<500$ distinguish from their estimations for $n^{\rm MC}=2000$ and $n^{\rm MC}=600$ no more than 1.0% and 0.05% for $N^{\rm meso}=27$ and $N^{\rm meso}=343$, respectively. In so doing, the values $\mu^{*}/\mu^{(0)}$ estimated for $N^{\rm meso}=27$ and $N^{\rm meso}=343$ at $n^{\rm MC}=2000$ and $n^{\rm MC}=600$, respectively, can be distinguished by 0.35% (CPU times exploited for $n^{\rm MC}=1$ equal 5 sec. and 310 sec. for $N^{\rm meso}=27$ and $N^{\rm meso}=343$, respectively). The main idea of the fundamentally new third method is a decomposition of the desired solution on the known solution for the perfect periodic structure ($\boldsymbol{L}(\boldsymbol{x})=\boldsymbol{L}^{\rm per}(\boldsymbol{x})$), and on the perturbation produced by the imperfections in the perfect periodic structure. Analogously to the random structure matrix composites (RSMC), the effective moduli depend on three particular solutions: strain concentration factor $\boldsymbol{A}^{\rm per}(\boldsymbol{x})$ in the perfect periodic structure (analog of homogeneous strains in the RSMC without defects), strain concentration factor $\mathbf{A}_i^{imp}(\mathbf{x})$ in the infinite periodic medium with one imperfection (analog of Eshelby solution in the RSMC), strain concentration factor

$\mathbf{A}_{i,j}^{\mathrm{imp}}(\mathbf{x})$ in the infinite periodic medium with two arbitrary located imperfections (analog of the solution for two inclusions inside an infinite matrix, see [1]):

$$\mathbf{L}^{*} = \mathbf{L}^{(0)} + \sum_{i,j=2}^{N} \lambda^{(i)} \mathbf{R}^{(i)} \mathbf{D}_{ij} + \lambda^{(1)} \left\langle \mathbf{L}_2(\mathbf{x}) \mathbf{A}^{\mathrm{per}}(\mathbf{x}) \mathbf{D}_0(\mathbf{x}) \right\rangle_{(i)}^{\Omega} \qquad (1)$$

from which the effective elastic modulus for the perfect periodic structures $\mathbf{L}^{\mathrm{per}}*$ can be extracted. Here $\mathbf{L}_2(\boldsymbol{x})=\mathbf{L}^{\mathrm{per}}(\boldsymbol{x})-\mathbf{L}^{(0)}$, $\mathbf{L}_3(\boldsymbol{x})=\mathbf{L}^{\mathrm{imp}}(\boldsymbol{x})-\mathbf{L}^{\mathrm{per}}(\boldsymbol{x})$, $\mathbf{R}^{(i)}$ is obtained by the volume average over the unite cell $\left\langle (.) \right\rangle_{(i)}^{\Omega}$ with one imperfection: $\mathbf{R}^{(i)} = \left\langle \mathbf{L}_3(\mathbf{x})[\mathbf{A}_i^{\mathrm{imp}}(\mathbf{x}) + \mathbf{A}^{\mathrm{per}}(\mathbf{x})] \right\rangle_{(i)}^{\Omega}$, and the tensors $\mathbf{D}_{ij}$ and $\mathbf{D}_0(\boldsymbol{x})$ depend on all three solutions $\mathbf{A}^{\mathrm{per}}(\mathbf{x})$, $\mathbf{A}_i^{\mathrm{imp}}(\mathbf{x})$ and $\mathbf{A}_{i,j}^{\mathrm{imp}}(\mathbf{x})$. The method proposed is general, it is not limited by concrete numerical scheme, and can use particular known solutions for particular problems mentioned above (for example, the solutions for the perfect periodic structure $\mathbf{A}^{\mathrm{per}}(\mathbf{x})$ as well as the solution for one crack in doubly-periodic structure $\mathbf{A}_i^{\mathrm{imp}}(\mathbf{x})$, see [5]). The numerical results are obtained in the framework of the hypothesis **H1)**. All three methods proposed lead to close results in the considered example ($c^{(1)}(\lambda^{(1)}) + c^{(2)}(\lambda^{(2)})=0.4$, see Fig.3), however, the CPU time expended for the solution estimation by Monte Carlo simulation differ by a factor of 1000. Thus, we proposed general explicit analytical representation of effective moduli of periodic structures with the random field of imperfections (see for details [6]) depending on three tensors $\boldsymbol{A}^{\mathrm{per}}(\boldsymbol{x})$, $\mathbf{A}_i^{\mathrm{imp}}(\mathbf{x})$, $\mathbf{A}_{i,j}^{\mathrm{imp}}(\mathbf{x})$. No restrictions were assumed on both the concrete microstructure and method used for obtaining these solutions. It should be mentioned that the known numerical methods (such as e.g. finite element analysis and boundary element method) have a series of advantages and disadvantages (see for references [7]). However, their analysis is beyond the scope of the current paper where we considered the application of proposed scheme in the framework of the hypothesis **H1)** significantly simplifying the analytical representations of the tensors.

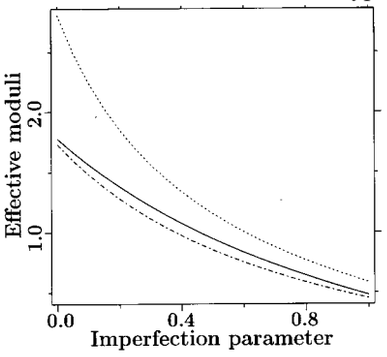


Fig. 1. Normalized effective moduli as the functions of $\lambda^{(2)}$: $\widetilde{\mu}^{*}/\mu^{(0)}$ (dotted line), $\mu^{*}/\mu^{(0)}$ (solid line), $k^{*}/k^{(0)}$ (dashed line).

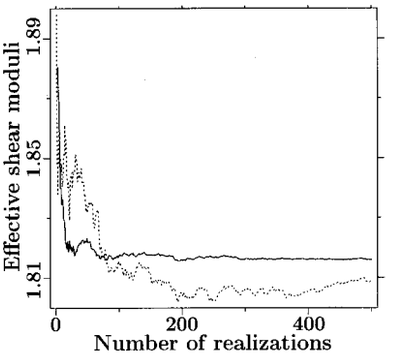


Fig. 2. Normalized effective elastic moduli $\mu^{*}/\mu^{(0)}$ as the functions of the number of Monte Carlo realizations n^{MC} for N^{meso}=343 (solid line), N^{meso}=27 (dotted line).

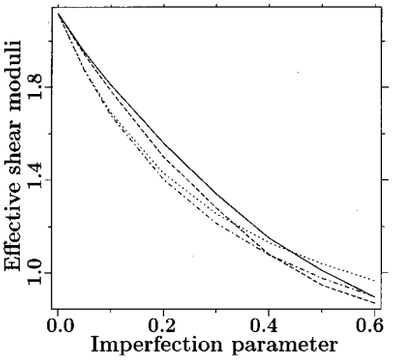


Fig. 3. $\mu^{*}/\mu^{(0)}$ vs $\lambda^{(2)}$: MC simulation (solid line), one point approximation ($\boldsymbol{L}^{\mathrm{c}}=\boldsymbol{L}^{(0)}$,dashed line), one-point approx. ($\boldsymbol{L}^{\mathrm{c}}(\boldsymbol{x})=\boldsymbol{L}^{\mathrm{per}}(\boldsymbol{x})$, dotted line), two-point approx. ($\boldsymbol{L}^{\mathrm{c}}(\boldsymbol{x})=\boldsymbol{L}^{\mathrm{per}}(\boldsymbol{x})$,dot-dashed line).

Acknowledgments: The work is supported by Air Force Research Laboratory, WPAFB, USA

References

[1] Buryachenko V. A. Editorial of the Special Issue Entitled *Recent Advances in Micromechanics of Composite Materials*. *J. Multiscale Computational Engineering* 2004, **2**(1). (In press).

[2] Buryachenko V.A. (2001) Multiparticle effective field and related methods in micromechanics of composite materials. *Appl. Mech. Review* **54**(1), 1-47.

[3] Buryachenko V. A. (1999) Triply periodic particulate matrix composites in varying external stress fields. *Int. J. Solids Structures* **36**, 3837-3859.

[4] Bensoussan A., Lions J. L. and Papanicolaou G. (1978) *Asymptotic Analysis for Periodic Structures.* North-Holland, Amsterdam, NY.

[5] Kalamkarov A. L. *Composite and Reinforced Elements of Construction.* John Wiley & Sons, Chichester, NY.

[6] Buryachenko V. A. (2004) Triply periodic particulate matrix composites with imperfect unit cells. (Submitted).

[7] Buryachenko V. A., Pagano N.J. (2004) Multiscale analysis of multiple interacting inclusions problem: Finite number of interacting inclusions. *Math. Mech. of Solids*., **9** (In press).

ON THE IMPACT LAW IN ELASTIC PLATE-LIKE BODIES

R. SBURLATI
Dipartimento di Ingegneria Strutturale e Geotecnica, Università di Genova, Italy, sburlati@diseg.unige.it

Summary. We study the problem of normal impact of a rigid sphere on a circular elastic plate whose thickness is not so small with respect to its diameter, so the Kirchhoff's theory cannot be applied. For plate-like bodies of this kind it is convenient to apply a theory proposed by Levinson (1985). To describe mathematically the pressure distribution and the extent of the contact area we adopt the Hertz's theory. By combining these theories we derive an impact law in elastic plate-like bodies.

In this paper we analyze the low velocity impact problem of a rigid sphere against a circular elastic plate. The solution of the equations of the three dimensional theory of the elastodynamic is obtained by using a semi-inverse method and a solving technique based on the method of the separation of variables [1].

We consider a circular isotropic plate-like body of thickness *2h* and radius *b* referred to a system of cylindrical coordinates such that its origin is placed at the center of the middle plane. We extent the Levinson's problem in a dynamical framework with axisymmetric load conditions; the displacement field assumes the following form

$$u(r,z,t) = -g(z)\,\frac{d}{dr}W(r)\,e^{iwt}\ , \qquad w(r,z,t) = f(z)\,W(r)\,e^{iwt}\ , \tag{1}$$

where the function *W(r)* is the deflection of the middle surface, and *g(z)* and *f(z)* are functions determining the variations in the displacements through the thickness of the plate [2].

We assume respectively the following conditions over the mantle and on the upper and lower faces

$$w(b,z,t) = 0\ ,\ s_{rz}(r,\pm h,t) = 0\ ,\ s_{zz}(r,-h,t) = 0 \quad \text{and} \quad s_{zz}(r,+h,t) = p(r,t)\ .$$

For the explicit expression of the function *p(r,t)* we adopt the periodic Hertz's normal pressure distribution

$$p(r) = \frac{3}{2}\frac{P\sqrt{a^2 - r^2}}{p\,a^3}\ , \qquad a = \left(\frac{3R(2m+l)}{16m(m+l)}\right)^{\frac{1}{3}} P^{\frac{1}{3}} \tag{2}$$

where *a* is the contact area radius, *R* the radium of the rigid sphere and *P* the resultant pressure [3].

The pressure *p(r)* is written as a Fourier Bessel expansion on the interval (0,b)

$$p(r) = \sum_{j=1}^{\infty} A_j J_0\left(f_j r\right)\ , \text{ with}$$

$$A_j = 3\frac{\sin\left(cP^{\frac{1}{3}}f_j\right) - cf_j P^{\frac{1}{3}}\cos\left(cP^{\frac{1}{3}}f_j\right)}{p\,b^2 c^3 f_j^3\left[J_1(bf_j)\right]^2}\ , \qquad c = \left(\frac{3R(2m+l)}{16m(m+l)}\right)^{\frac{1}{3}} \tag{3}$$

and $f_j = Z_j / b$ where Z_j are the *j*-th zeros of the *0*-order Bessel function of the first type. By substituting the displacement field in the linear elastodynamic equations for isotropic material, we obtain

$$\left(mg'' - (l+m)f'' - \frac{1}{r^2}(l+2m)g + rw^2 g\right)W' + (l+2m)\left(\frac{1}{r}W'' + W'''\right)g = 0\ , \tag{4}$$

$$\left((l+2m)f'' + rw^2 f\right)W + \left(mf - (l+m)g'\right)\left(\frac{1}{r}W' + W''\right) = 0\ , \tag{5}$$

with **r** the density and **l** and *m* the Lamé moduli.

The function *W(r)* can be written as

$$W(r) = BJ_0(kr) + DY_0(kr)\ ,$$

where $J_0(kr)$ and $Y_0(kr)$ are the 0-order Bessel functions of the first and second type respectively; since the second type Bessel function is unbounded in *r=0*, the coefficient *D* is zero. The condition on the mantle yields that *k* is f_j (*j*=1,2..), so we obtain the explicit solution of the (5), in the *j-th* term, as [4]

$$W_j(r) = J_0(f_j r)\,. \tag{6}$$

Now, by substituting the (6) in the (4) and, by differentiating it with respect to *z*, we get the solutions of the function *f(z)* and *g(z)* in the form

$$\begin{aligned} f_j(z) &= C_1^{(j)}\cosh(a_j z) + C_2^{(j)}\sinh(a_j z) + C_3^{(j)}\cosh(b_j z) + C_4^{(j)}\sinh(b_j z) \\ g_j(z) &= -\frac{a_j}{f_j^2}\left(C_1^{(j)}\sinh(a_j z) + C_2^{(j)}\cosh(a_j z)\right) - \frac{1}{b_j}\left(C_3^{(j)}\sinh(b_j z) + C_4^{(j)}\cosh(b_j z)\right). \end{aligned} \tag{7}$$

The coefficients $C_1^{(j)}, C_2^{(j)}, C_3^{(j)}$ and $C_4^{(j)}$ are uniquely determined by the conditions on the upper and lower faces of the body.

The displacement field is obtained by considering the sum on all value of *j*, so we have the following expansions

$$u(r,z,t) = -\sum_{j=1}^{\infty}\left(\frac{a_j}{f_j}\left(C_1^{(j)}\sinh(a_j z) + C_2^{(j)}\cosh(a_j z)\right) + \frac{f_j}{b_j}\left(C_3^{(j)}\sinh(b_j z) + C_4^{(j)}\cosh(b_j z)\right) \right) J_1(f_j r) e^{iwt} , \tag{8}$$

$$w(r,z,t) = \sum_{j=1}^{\infty}\left(C_1^{(j)}\cosh(a_j z) + C_2^{(j)}\sinh(a_j z) + C_3^{(j)}\cosh(b_j z) + C_4^{(j)}\sinh(b_j z) \right) J_0(f_j r)\, e^{iwt} . \tag{9}$$

where $a_j \equiv \sqrt{f_j^2 - \frac{r w^2}{m}}$ and $b_j \equiv \sqrt{f_j^2 - \frac{r w^2}{(l+2m)}}$.

By using (9) in $z=+h$ and $r=0$ we have the *impact law* in a circular thick elastic plate in the form

$$d^D = \sum_{j=1}^{\infty} K_j^D \left(\sin\left(cP^{\frac{1}{3}} f_j \right) - cP^{\frac{1}{3}} f_j \cos\left(cP^{\frac{1}{3}} f_j \right) \right) e^{iwt} , \tag{10}$$

with

$$K_j^D = \frac{8m(m+l) r w^2 b_j}{(2m+l) p\, R b^2 f_j^{\,3} \left(J_1(b f_j) \right)^2} \left(\frac{1}{D_1^{(j)}} \left(1+e^{2b_j h}\right)\left(1+e^{2a_j h}\right) - \frac{1}{D_2^{(j)}} \left(1-e^{2b_j h}\right)\left(1-e^{2a_j h}\right) \right) ,$$

$$D_1^{(j)} = \left(r^2 w^4 + 4 f_j^2 m \left(f_j^2 m - r w^2 \right) \right)\left(1+e^{2a_j h}\right)\left(1-e^{2b_j h}\right) - 4 f_j^2 m^2 a_j b_j \left(1-e^{2a_j h}\right)\left(1+e^{2b_j h}\right) ,$$

$$D_2^{(j)} = \left(-r^2 w^4 - 4 f_j^2 m \left(f_j^2 m - r w^2 \right) \right)\left(1-e^{2a_j h}\right)\left(1+e^{2b_j h}\right) + 4 f_j^2 m^2 a_j b_j \left(1+e^{2a_j h}\right)\left(1-e^{2b_j h}\right) .$$

In the static case we have the following *contact law*

$$d^S = \sum_{j=1}^{\infty} K_j^S \left(\sin\left(cP^{\frac{1}{3}} f_j \right) - cP^{\frac{1}{3}} f_j \cos\left(cP^{\frac{1}{3}} f_j \right) \right) , ,$$

with

$$K_j^S = \frac{8\left(1 - e^{8 f_j h} - 8 f_j h e^{4 f_j h}\right)}{p\, R b^2 f_j^{\,4} \left[J_1(b f_j) \right]^2 \left(-1 + e^{4 f_j h} + 4 f_j h e^{2 f_j h} \right)\left(1 - e^{4 f_j h} + 4 f_j h e^{2 f_j h} \right)} .$$

By using the analytical solution (10), in fig. 1 we show the impact law in the case of low frequencies for different ratios *h/b*. As expected, we remark the agreement with the hertzian law ($\mathbf{d}_{Hertz}$) for high values of the ratio *h/b*.

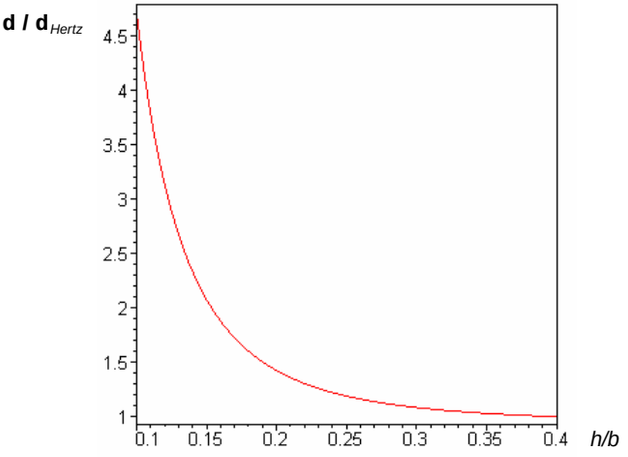


Fig. 1. Impact law for different ratios *h/b*.

References

[1] Sburlati R.: An exact solution for the impact law in thick elastic plates, *Int.J.Sol Stru*, in press 2004.

[2] Levinson M.: The simply supported rectangular plate: an exact three-dimensional linear elastic solution, *J.Elast* **7**:283-291, 1985.

[3] Stronge W.J., Impact Mechanics. Cambridge University Press, 2000.

[4] Sneddon I.N., Mixed Boundary Value Problems in Potential Theory; John Wiley &Sons Inc., 1966

AN OPTICAL STRAIN ROSETTE/RING-CORE METHOD APPLIED ON LASER WELD

Wei Ren, Keyu Li
Department of Mechanical Engineering, Oakland University, Rochester, MI 48309, U.S.A

Summary As a newly developed residual stress measurement method, the optical strain rosette/ring-core cutting method is introduced. Optical rosette has short gage length and noncontacting nature. Ring-core cutting involves almost complete relaxation of residual stresses. The principles of the method are presented and the test on the laser weld demonstrates its advantages over conventional measurement methods.

INTRODUCTION

Residual stresses exist in many industrial parts due to the inelastic strains induced in manufacturing processes. These stresses can largely affect the mechanical performances of the parts. The measured residual stress data can aid fatigue analysis, safety design and strength evaluation. Resistance strain rosette/hole-drilling method is a widely used method for residual stress measurement. During the drilling process, the resistance strain rosette detects the relieved strains. Numerical method is used to relate the relieved strains and the in-plane residual stresses. Therefore, the unknown residual stresses can be calculated. There are limitations for this method. The measuring grid with carrier of a resistance rosette has large size. The measured strains are the averaged values over the gage length. It is not suitable for the measurement on the small areas with high stress gradients.

An optical rosette called Interferometric Strain/Slope Rosette (ISSR) is developed with short gage length and noncontacting nature [1]. It can be used to measure displacements, strains and slopes. It was used in conjunction with the hole-drilling method to measure the residual stresses on the shot-peened titanium block [2]. One problem of hole-drilling method is that the sensitivity of the strain measurement is low due to the incomplete strain relief. To more fully relieve the residual stresses, the ring-core method is considered. The newly developed ISSR/ring-core method shows many advantages over the conventional methods. Since the ISSR is tiny (gage length is on the order of 100 micrometers), the central core can be cut small and it is suitable to be used on the small areas with high stress gradients.

BASIC PRINCIPLES

ISSR method and its measurement system

An ISSR consists of three micro-indentations and these indentations can form delta or rectangular shape. Indentations can have several types, such as four-faced, six-faced and eight-faced. Normally, the size of indentation is on the order of 10 micrometers (μm). Commonly used gage length is between 100μm and 250μm. An ISSR with delta configuration is shown in Fig. 1. If a normally incident laser illuminates the delta rosette, the six faces of each indentation reflect and diffract the light in six directions (60° apart). The diffraction patterns in the same direction interfere each other. So in every 60° direction, there exists an interferometric pattern. These fringe patterns would shift due to deformation or movement of the specimen. Considering that every two indentations constitute an optical gage, the in-plane strain and out-of-plane deflection of this gage can be determined using the following Eq. (1) [1].

$$\frac{\delta d}{d} = \frac{\lambda}{2d\sin\beta}(\delta m_1 + \delta m_2) \qquad \frac{\delta w}{d} = \frac{\lambda}{2d(1+\cos\beta)}(\delta m_1 - \delta m_2) \tag{1}$$

where λ is laser wavelength (0.6328μm for He-Ne laser in the test), d is gage length (250 μm in the test), β is the angle between the reflection beam and the normal of specimen surface, and δm_1 and δm_2 are the fringe shifts in the same gage direction. Three strains measured for the 60° ISSR are in 0°, 60° and 120° directions, respectively.

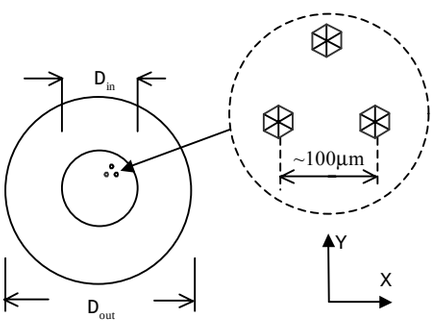


Fig.1 Schematic diagram of ring-core and ISSR

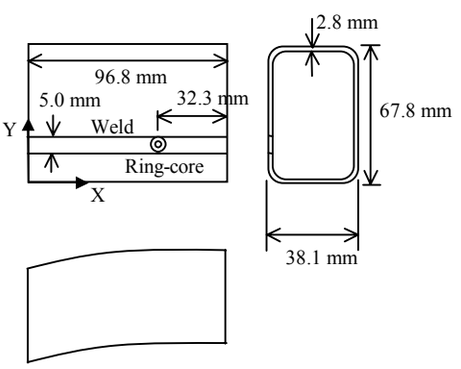


Fig. 2 Plan, elevation and side views of the hydroformed frame part

Ring-core cutting method

Ring-core cutting method is to mill an annular groove on the material surface. Ring-core cutting involves almost complete relaxation of residual stresses [3]. The ring-core method has higher sensitivity for strain measurement than the hole-drilling method. Small indentations of the ISSR are indented before ring-core cutting is performed. As shown in Fig. 1, the ISSR is located at the central core surface. The ring-core with smaller inner diameter could improve the measurement accuracy. To obtain the stress distribution with respect to the depth, layer-by-layer incremental ring-core cutting is carried out. Data acquisition is conducted before and after each step of cutting.

MEASUREMENT ON THE LASER WELD AND STRESS CALCULATION

A tubular member was cut from the truck frame as shown in Fig. 2. The seam was laser-welded and then the tube was hydroformed. Welding process induces highly concentrated residual stresses in the weld and the surrounding heat-affected zone (HAZ). So the fractures would most likely occur at weld and HAZ during the operation. Since the weld width is only 5mm, resistance strain rosette is too large to be applied on the weld.

The ISSR/ring-core method was conducted and five steps of incremental ring-core cutting were performed on the laser weld. A finite element model was built to simulate the cutting process. By applying the given loads to the inner and outer walls of the ring-core model, the stress-strain response relationship was established. The obtained coefficients were used to back-calculate the residual stresses and the integral method was adopted to correlate the residual stresses in different cutting layers. The core diameter D_{in} is 2.03mm and the outer diameter D_{out} is 4.76mm. As shown in Fig. 1, if $\vec{r}$ is defined as the vector from the core center to the ISSR center and θ is the angle from the x-axis to the vector $\vec{r}$ in CCW direction, norm of $\vec{r}$ is 0.25mm and θ is -84.07°.

RESULTS AND ANALYSIS

The measured strains for each incremental ring-core cutting and the calculated residual stresses are shown as marks in Fig. 3. The strains are fitted by the 3rd order polynomial and the fitted curves are used to calculate the residual stresses. The stress distributions are obtained by fitting the calculated residual stresses with the 4th order polynomial. The measured tensile stress in the hoop direction is caused by the stretching of the weld due to the spring-back tendency of the bent C-shape tube. This tensile stress in the hoop direction is the most concerned stress since it could be superposed upon the operation stress. The superposed resultant stress might cause the structure to fracture under the cyclic loadings. So the existence of this tensile stress could mainly reduce the frame fatigue life.

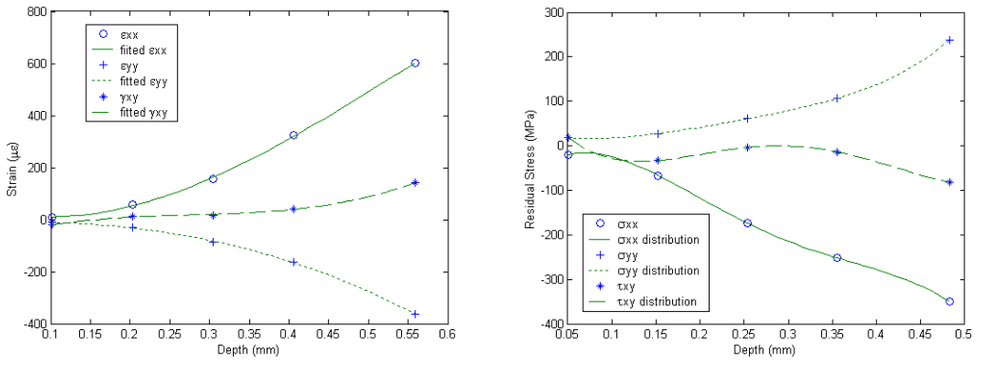


Fig. 3 Relieved strains and residual stresses on the laser weld

CONCLUSIONS

As a newly developed measurement method, the ISSR/ring-core method can be successfully applied to the residual stress measurement. Since the ISSR is tiny, the method is very suitable to the measurement on the small areas with high stress gradients. The experiment on the laser weld demonstrates its advantages over the conventional methods. The test results provide the valuable references for industrial applications. Micro ring-core cutting will be investigated to study the stress distribution across the laser weld.

References

[1] Li, K.: Out-of-plane Displacement Derivative Measurements Using Interferometric Strain/Slope Gage. *ASME J. App. Mech.*, **63**:1033-1038, 1996.

[2] Tjhung, T., Li, K.: Measurement of In-plane Residual Stresses Varying with Depth by the Interferometric Strain/Slope Rosette and Incremental Hole-Drilling. *ASME J. Eng. Mater. Technol.*, **125**:153-162, 2003.

[3] Lu, J.: Handbook of Measurement of Residual Stresses. The Fairmont Press, Lilburn, GA 1996.

Estimation of Principal Axes of Inertia

Masashi Sato* , Yasusuke Jinnouchi*

* *Kitakyushu College of Technology, 5-20-1 Shii, Kokuraminami, Kitakyushu, JAPAN*

Summary This paper presents a new experimental method to measure the principal axes of a rigid body without the principal axis transformation. A rigid body is suspended from a vertical axle by a slender rod. The axle rotates with a constant angular velocity. The experimental results for a cylinder and a rectangular prism agreed well with the theoretical results. And the principal axes of a golf club head were estimated experimentally.

INTRODUCTION

In the analysis of motion of a rigid body, it is necessary to know the inertia characteristics, that is, the moments and the products of inertia, the principal axes, the principal moments of inertia as well as the mass and the mass center of the rigid body. Although the estimation of the mass and the mass center is not difficult in general, the experimental measurement of the moments of inertia involves difficulties [1, 2].
Incidentally, it is well known that a rigid body under no moment can rotate about a fixed centroidal axis, if and only if that axis coincides with one of the principal axes of inertia of the body, and that the motion will be stable if the axis of rotation coincides with the major or minor axis of the Poinsot ellipsoid and unstable if it coincides with the intermediate axis [3]. We took note of this fact, and tried to estimate the principal axes of a rigid body without the principal axis transformation. Our goal is to propose a new experimental method to estimate the principal axes.

MOTION OF A SUSPENDED RIGID BODY SYSTEM

Motion of a rigid body

Figure 1 shows a system considered. A rigid body suspended by a slender rod rotates at a constant angular velocity ω about the z-axis fixed to space. $0-\xi\eta\zeta$ is the moving coordinate fixed to the rigid body, and 0 is the mass center of the body. the rod is attached to the body at point B on η-axis. Point A denotes the intersection of η-axis and z-axis. The angle α between η-axis and horizontal plane and the inclination θ are assumed to be constant. Air drag and friction are neglected.The equation of motion of the rigid body shown in Figure 1 is

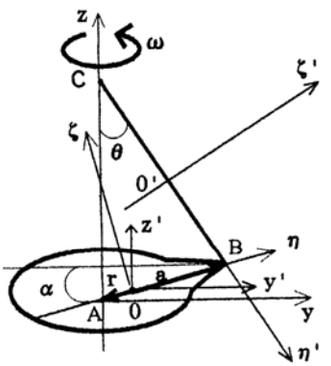


Fig.1 System considered

$$\frac{d^*\boldsymbol{L}}{dt}+\boldsymbol{\omega}\times\boldsymbol{L}=\boldsymbol{N} \tag{1}$$

where $\boldsymbol{L}$, $\boldsymbol{\omega}$, and $\boldsymbol{N}$ are the angular momentum, the angular velocity and the external moment respectively. They are presented in the form referred to the moving coordinate $0-\xi\eta\zeta$ as follows :

$$\boldsymbol{L}=(A_{\xi\eta}\,\omega\sin\alpha+A_{\zeta\xi}\,\omega\cos\alpha)\boldsymbol{e}_\xi+(A_{\eta\eta}\,\omega\sin\alpha+A_{\eta\zeta}\,\omega\cos\alpha)\boldsymbol{e}_\eta+(A_{\eta\zeta}\,\omega\sin\alpha+A_{\zeta\zeta}\,\omega\cos\alpha)\boldsymbol{e}_\zeta$$

$$\boldsymbol{\omega}=\omega\sin\alpha\,\boldsymbol{e}_\eta+\omega\cos\alpha\,\boldsymbol{e}_\zeta$$

$$\boldsymbol{N}=ma(g+r\omega^2\sin\alpha)\cos\alpha\,\boldsymbol{e}_\xi$$

where A_{ij} is the component of the inertia tensor, $\boldsymbol{e}_i$ is the unit vector of i-axis and g is the acceleration of gravity. In the present case α, θ and ω are constant. Hence the first term on the left hand side of Eq.(1) vanishes. Substituting $\boldsymbol{L}$, $\boldsymbol{\omega}$ and $\boldsymbol{N}$ into Eq.(1), the following three equations are obtained.

$$\omega^2\left\{\frac{1}{2}(A_{\zeta\zeta}-A_{\eta\eta})\sin 2\alpha-A_{\eta\zeta}\cos 2\alpha\right\}=mga\cos\alpha+mra\omega^2\sin\alpha\cos\alpha \tag{2}$$

$$\omega^2\cos\alpha\{A_{\xi\eta}\sin\alpha+A_{\zeta\xi}\cos\alpha\}=0 \tag{3}$$

$$-\omega^2\sin\alpha\{A_{\xi\eta}\sin\alpha+A_{\zeta\xi}\cos\alpha\}=0 \tag{4}$$

Then the products of inertia $A_{z'x'}$ and $A_{y'z'}$ are derived as follows.

$$A_{z'x'}=-\int z'x'dm=-\int(\eta\sin\alpha+\zeta\cos\alpha)\xi dm=A_{\xi\eta}\sin\alpha+A_{\zeta\xi}\cos\alpha \tag{5}$$

$$A_{y'z'} = -\int y'z'dm = A_{\eta\zeta}\cos 2\alpha - \frac{1}{2}(A_{\zeta\zeta} - A_{\eta\eta})\sin 2\alpha = -ma\cos\alpha(\frac{g}{\omega^2} + r\sin\alpha) \quad (6)$$

If the mass of the slender rod connected to the rigid body is negligible,

$$r = \frac{ag}{l\omega^2\cos\theta - g} \quad (7)$$

Finally, we may observe that $A_{z'x'}$ is equal to zero from Eq.(3) and that $A_{y'z'}$ also approaches zero if ω is sufficiently large. Then the z' axis becomes one of the principal axes and coincides with the z axis. In the successive experiment, if another stable rotation can be made, the principal axes will be obtained.

Motion of a slender rod BC

As the centroidal frame $0' - \xi'\eta'\zeta'$ of the slender rod BC (Fig.1) coincides the principal axes of inertia, the principal moments may be expressed as $I_{\xi'\xi'} = m'l^2/12$, $I_{\eta'\eta'} = 0$, $I_{\zeta'\zeta'} = m'l^2/12$, where m' is the mass and the l is the length of the rod. Substituting $\omega \times \boldsymbol{L}$ and $\boldsymbol{N}$ of the rod into Eq.(1), the equation of motion in ξ' direction may be written in the form

$$\left(\frac{r}{r+a} + \frac{1}{3}\frac{m'}{m}\right) = \frac{g}{l\omega^2\cos\theta}\left(1 + \frac{1}{2}\frac{m'}{m}\right) \quad (8)$$

In case the magnitude of m' cannot be disregarded, it is found that r does not become zero, even if ω becomes very large, and Eq.(8) reduces to

$$r = -\frac{1}{3}\frac{m'}{m}a \Big/ \left(1 + \frac{1}{3}\frac{m'}{m}\right) \quad (9)$$

In order that $A_{y'z'}$ may become zero, substituting Eq.(9) into Eq.(6), ω is obtained as

$$\omega^2 = \frac{3g}{2\mu}\left(\frac{1+\frac{\mu}{3}}{a\sin\alpha} + \frac{1+\frac{\mu}{2}}{l\cos\theta}\right)\left(1 \pm \sqrt{H}\right) \quad (10)$$

where

$$H = 1 - \frac{\frac{4\mu}{3}\left(1+\frac{\mu}{2}\right)(l\cos\theta)(a\sin\alpha)}{\left\{l\cos\theta\left(1+\frac{\mu}{3}\right) + a\sin\alpha\left(1+\frac{\mu}{2}\right)\right\}^2} \quad , \quad \mu = \frac{m'}{m} \quad (11)$$

If the magnitude of m' may be disregarded, Eq.(8) is led to Eq.(7).

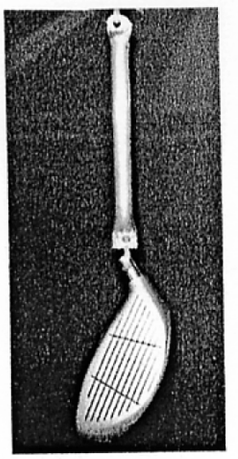


Fig.2 Photograph of the suspended rigid body



Fig.3 Photograph of the rotating rigid body

EXPERIMENTAL RESULTS AND CONCLUSIONS

Figure 2 shows that the suspended rigid body is at rest and Figure 3 shows it is rotating. The results indicate that this method is useful to estimate the principal axes.

References

[1] de Jong, R.C. and Mulder, J. A.:Accurate Estimation of Aircraft Inertia Characteristics from a Single Suspension Experiment, J. Aircraft, 24(1987), pp.363-370

[2] Ohta, H. and Nishimura, H.:Estimation of Aircraft Inertia Characteristics Using Maximum Likelihood Method, J. 42-481, (1994), pp.108-115 (in Japanese)

[3] For instance, Yamanouchi, T. et al.:Dynamics, Shokabo, (1957), p.261 (in Japanese)

THE WHOLE FIELD NON-DESTRUCTIVE OPTICAL SLICING METHOD IN THREE-DIMENSIONAL PHOTOELASTICITY

Michael N. Osipov, Vychislav K. Emelin

Samara State University, Department of Mechanics &Mathematics, Ac. Pavlov 1, 443011 Samara, Russia

Summary: The whole field non-destructive optical slicing method in three-dimensional photoelasticity based on the analysis of the scattered light field is presented. This method is based on the combination of the scattered light photoelasticity method, of the speckle photography method and the moiré technique. An analyses of the two-dimensional scattered light field from each plane sheets and theirs interference for the determination of the stress state in the thin optical slice is suggested.

INTRODUCTION

In a photoelastic medium a basic hypothesis consists in assuming that the medium must be slightly anisotropic, and that the secondary principal directions of the refractive indices tensor and of the stress tensor coincide. It follows that for a ray of light propagating along straight - line direction, the wave planes are orthogonal to this direction. In three-dimensional photoelasticity it is usually assumed that the directions of the secondary principal stresses and their values are constant through the thickness of a slice having its parallel faces. This assumption allows to consider this slice as a birefringent plate characterized by the two parameters - the difference of secondary principal stresses and the secondary principal directions.

It is known that optical techniques, such as holographic, speckle and moiré have been used for measurement of small displacements of objects. During the last decade increasing attention to speckle metrology and its applications in experimental mechanics has taken place. Moiré technique is also optical measurement method for strain analysis of materials and structures. These methods have been successfully applied to study of the static and dynamic problems.

The main disadvantage of optical methods in experimental mechanics is that they, in general, determine the displacement field or the difference of principal stresses, while the more important parameter is the strain and stress fields. Therefore the investigator dependents on the critical task of differentiation of the displacement field or he has to integrate the equilibrium equations using the finite difference calculus with known boundary conditions.

The purpose of this paper is to present a new optical technique for studying of the stress state in the three-dimensional photoelasticity. The method is based on the combination of the scattered light photoelasticity method, of the speckle photography method and the moiré technique.

BACKGROUND

The thin isolated optical slice of the photoelastic model is formed by two plane sheets [1] of light emitted from the same laser beam propagated in the direction of the axis **x** (Fig. 1). The polarization of the laser beam is linearly polarized along of the axis **y**. The two-dimensional scattered light field is analyzed in the direction of the axis **z** orthogonal to the plane of the two these illuminated plane sheets. The scattered light (according to Rayleigh's law) which is analyzed in the direction of the axis **z** is linearly polarized too and orthogonal to this axis. The two-dimensional scattered light field from the two plane sheets is analyzed by the analyzer **A**. An analyses of the two-dimensional scattered light field from each plane sheets and theirs interaction for the determination of the stress state in the thin optical slice is suggested.

Using combined method of the speckle photography with a ring aperture and moiré technique, have been received specklegrams for these two planes [2]. The pointwise filtering method is used for the analysis of double-exposure speckle photography. The scheme of the optical arrangement is shown in figure 2. The algorithm for the analysis of Young′s moiré fringe patterns for the optical system with the ring aperture is offered.

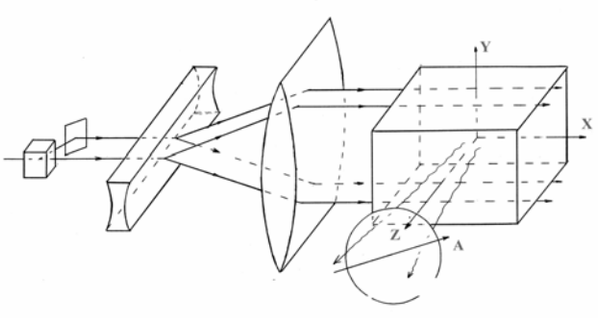


Fig.1. Schematic of optical slicing method.

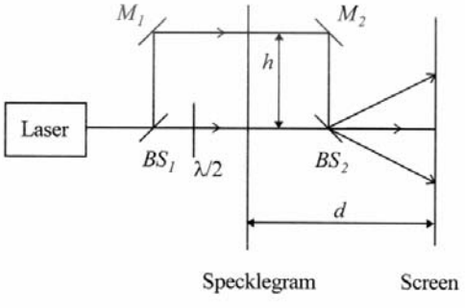
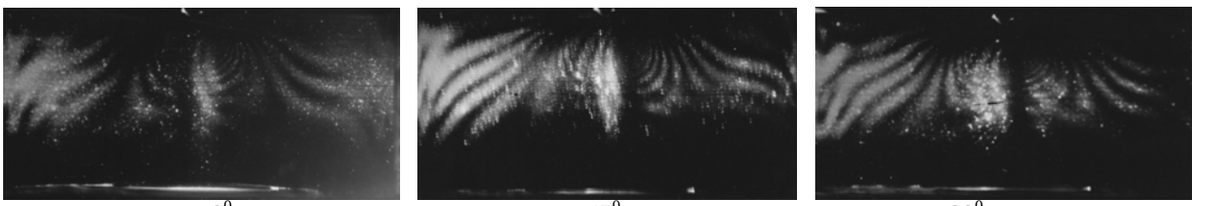


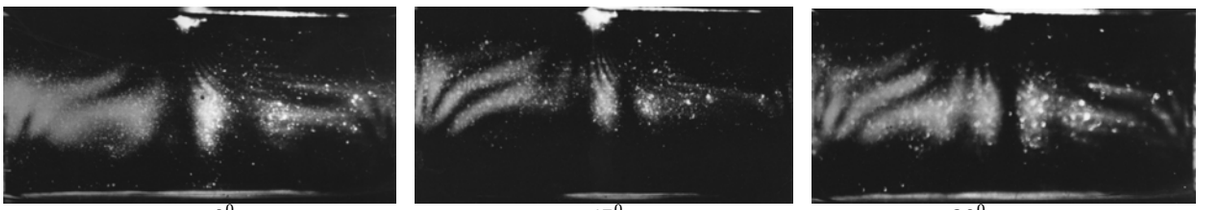
Fig.2. Schematic of the optical pointwise filtering method

This method is known as Young′s method. In the offered method the two narrow laser beams illuminate double-exposure speckle photography simultaneously. The distance between narrow laser beams can be changed. After passing through of the specklegram both laser beams are combined on the screen.
Figures 3, 4 and 5 shows an example of the experimental interference patterns that are observed for various directions of the analyzer **A**. Using Jones's method [1], the equations describing formations of the interference patterns have been received. These equations allow us to define the stress state in the thin optical slice.



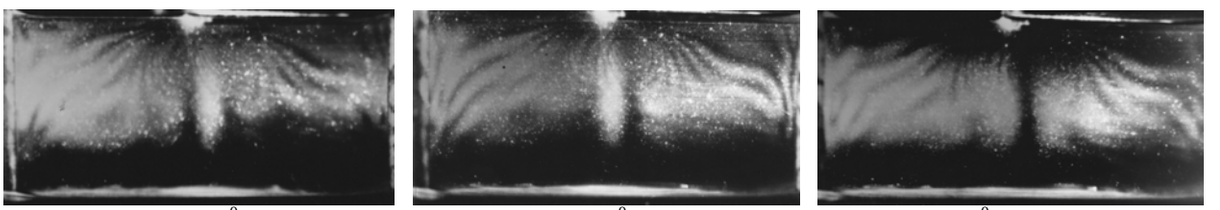
0^0 45^0 90^0

Fig.2. The interference patterns observable from the first plane sheet.



0^0 45^0 90^0

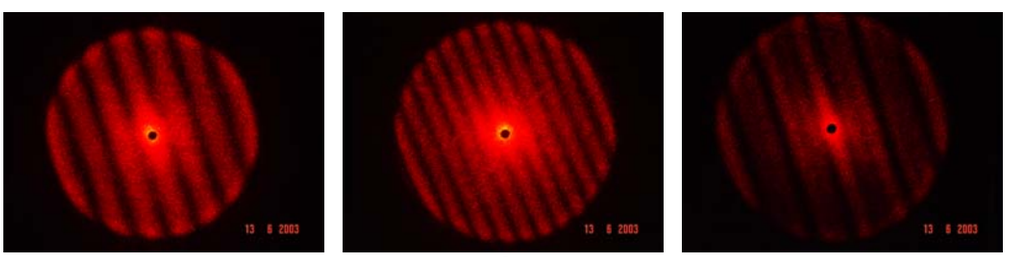
Fig.3. The interference patterns observable from the second plane sheet.



0^0 45^0 90^0

Fig.4. The interference patterns observable from interaction of two plane sheets.

Using combined method of the speckle photography with a ring aperture and moiré technique, have been received specklegrams for these two planes [2]. Photos on a figure 6, show an example of the experimental Young′s fringe patterns (a, b) for these two planes and moiré pattern (c) that is formed from their imposing. The equations for determination of a strain field from the moiré patterns are received.



a b c

Fig.6. Young′s fringe patterns (a, b) and moiré pattern (c).

CONCLUSIONS

The combination of the scattered light photoelasticity method, of the speckle photography method and the moiré technique allows to define the stress-strain state in the thin optical slice. Experimental optical arrangement with a C.C.D. camera is suggested to put this method in to practice. This work is fulfilled at support RFBR 02-01-00211.

References

[1] Lagarde A.: Progress in Photomechanics. *Proceeding of the 10th International Conference on Experimental Mechanics, Invited Lectures*, Lisbon, Portugal, 18-22 July, 1994.

[2] Osipov M.N., Shaposhnikov M.Y.: Strain measurements by combining of the speckle photography and moiré method. *Abstracts of the 20th International Congress of Theoretical and Applied Mechanics*, Chicago, USA, 27 Aug. - 2 Sept., 2000.

POROUS CERAMICS - EXPERIMENTAL RESEARCH AND MODELLING

Sylwester Samborski[*], Tomasz Sadowski [**]
[*]*Lublin University of Technology, Department of Applied Mechanics, PL 20-618 Lublin, Poland*
[**] *Lublin University of Technology, Department of Solid Mechanics, PL 20-618 Lublin, Poland*

Summary The paper presents the results of experimental research and modelling of porous ceramics under uniaxial compression. Alumina specimens with the porosity up to 30% were loaded axially, then unloaded and loaded again with a certain increase of the load. The loading-unloading process was stopped at the failure of the sample. The testing allowed to estimate approximately the influence of porosity on the initial elastic constants and further on change of elastic properties of ceramic material due to damage development. A scalar damage parameter evolution was also analysed.

INTRODUCTION

Nowadays ceramic materials are commonly used in many branches of industry: as lining in furnaces for steel and cement fabrication, in spacecraft, aircraft, nuclear engineering, automobile industry and others. One of the most important group of these materials is porous ceramics. They are often considered to be polyphase materials with a gas in pores as the second phase. They are applied for filters, thermal insulation, sound absorbers and furnace lining [5].
Up to now in research conducted in the world, ceramics was treated as a linear-elastic-brittle material. This approach is too much simplified, because real materials show physical non-linearity, i.e. their mechanical characteristics evolve during deformation [3].
Ceramic materials have good mechanical and thermal strength. However, for the cause of their brittleness it seems to be justified to search the new ways of describing the evolution of ceramics' properties. One of the basic ceramic polycrystalline materials is porous alumina. It is fabricated by sintering of Al_2O_3 powders at 1400 – 1900 °C. The final product is then built-up from grains of the mean diameter 20 – 30 microns. The solid matrix (with zero porosity) has high elasticity modulus (about 400 GPa [5]). In polycrystalline materials, especially those free sintered some microcavities occur. Their mean diameter is of an order of 1 – 4 microns. The global porosity may reach 30 % and more, what yields considerable loss of mechanical strength [2].

THEORETICAL BACKGROUND

As it is known the presence of pores in ceramics comes from fabrication process (sintering) and influences the total sample response to the applied load. As an example let us consider the effect of cavities on the Young modulus. Rice [6] gives a simple relation for cylindrical pores:

$$E_{\mathrm{M}}(p) = E_{\mathrm{M0}}(1-p) \tag{1}$$

where: E_M, E_{M0} are Young moduli of the pore-weakened and fully dense ceramic matrix, respectively; p is the volumetric porosity parameter.
Similar relations are given by others, for example [2]:

$$E_{\mathrm{M}}(p) = \frac{E_{\mathrm{M0}}}{1+3p} \tag{2}$$

or [5]:

$$E_{\mathrm{M}}(p,n) = E_{\mathrm{M0}}(1-p)^{n} \tag{3}$$

where n is material parameter.
In the paper we compared these theories with experimental outcomes. In case of equation (3) we assumed that n=5 for best compatibility with the real alumina behaviour.
The next question is the influence of the internal structure degradation of ceramic materials on it's strength. We use after Lemaitre [4] the following scalar damage parameter:

$$D(E_{\mathrm{M}}, E_{\mathrm{u}}) = 1 - \frac{E_{\mathrm{u}}}{E_{\mathrm{M}}(p)} \tag{4}$$

where: E_u stands for an actual elastic modulus of damaged material corresponding to unloading path.

EXPERIMENTS

Material description

For experiments samples of porous alumina were used. They were fabricated by sintering in Institute of Electronic Materials Technology, Warsaw. Porosity of the material was up to 30 % (p=0,30), while the sintering temperature was 1400 – 1730 °C and the time 1,5 hour. The samples were of cylindrical shape, 50 mm high and 14 mm in diameter. Young modulus of fully dense material was estimated to be 410 GPa.

Testing methods and equipment

There were four strain gages ("Vishay" EA-06-240LZ-120 and EA-06-240LZ-350) sticked on each specimen for the purpose of measuring axial and circumferential strains. Each gage worked in the Wheatstone quarter-bridge. Data acquisition was conducted with the "ESAM Traveller" system consisting of 8-channel bridge coupled with the PC and supervised by the adequate software. Samples were loaded by the universal testing machine "Zwick Z100". The loading process was the following: loading to a force P_1, unloading, reloading to a force $P_2=P_1+\Delta P$, unloading, reloading to a force $P_3=P_2+\Delta P$ and so on, until final failure of the specimen. The value of the force increment ΔP depended on sample's porosity: from 2 kN for p=0,30 to 10 kN for p=0,033. Straining velocity was kept at the level of 0,5 mm/min, so that the loading –unloading process was quasi-static. The results of experiments are presented below.

RESULTS AND DISCUSSION

The results indicate substantial influence of porosity on the mechanical properties of alumina (Fig. 1). It is visible, that experimental data fit well with theoretical background. The evolution of damage state seems to be similar for samples with various initial porosity (Fig. 2).

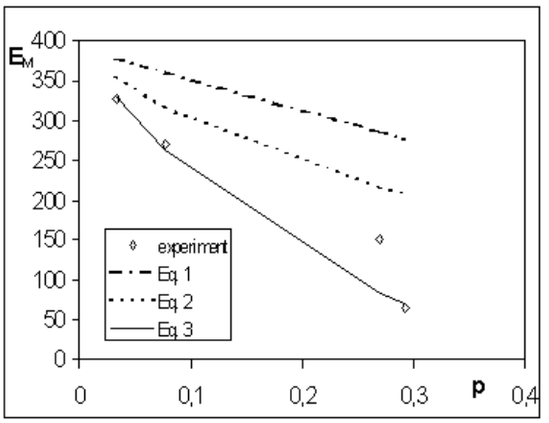


Fig. 1. Experimental values of elastic modulus vs. theory

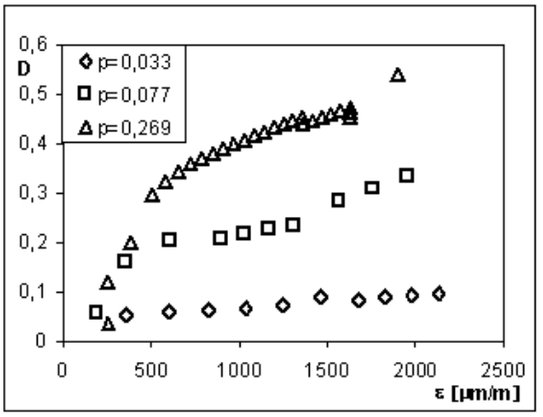


Fig. 2. Damage evolution of samples with various porosity as a function of axial strain

CONCLUSIONS

Experiments show good agreement of the ceramic material behaviour under compression with the theory. Damage evolution during loading-unloading process is connected with material structure degradation. Further research is essential. The prospective works will give detailed analysis of deformation process including material anisotropy (second order damage tensor).

References

[1] Davidge R.W.: Mechanical Behaviour of Ceramics. Cambridge University Press, London, 1979.
[2] Kachanov M.: On the Effective Moduli of Solids with Cavities and Cracks. *Int. J. Fracture* **59**:R17-R21, 1993.
[3] Krajcinovic D.: Damage Mechanics. Elsevier, Amsterdam 1996.
[4] Lemaitre J. (1996): A Course on Damage Mechanics. Springer, Berlin 1996.
[5] Munz D., Fett T. (1999): Ceramics. Mechanical Properties, Failure Behaviour, Materials Selection. Springer, Berlin 1999.
[6] Rice R.W. (1998): Porosity of Ceramics. Marcel Dekker, New York 1998.

CRITICAL SENSITIVITY IN ROCK EXPERIMENTS

Xianghong Xu, Mengfen Xia, Fujiu Ke and Yilong Bai
State Key Laboratory of Non-linear Mechanics, Institute of Mechanics, Chinese Academy of Sciences, Beijing 100080, PR. China

Summary This paper represents an experimental study on catastrophic rupture of a heterogeneous rock. Although rupture shows sample-specific behaviour, a universal sensitivity appears prior to catastrophic rupture. This critical sensitivity provides a valuable precursor for rupture prediction. Furthermore, we extend our previous theoretical model to explore the fluctuations in critical sensitivity in the rock tests.

Introduction

Rupture in heterogeneous brittle media, such as rock, displays catastrophe and sample-specificity [1-4]. Hence, the prediction of rupture is still questionable due to its complexity. Previous analytical works and numerical simulations suggested that critical sensitivity might be a possible common feature prior to catastrophe in these media [2,4,5].

To give the concept of critical sensitivity an experimental validation, a series of experiments has been conducted. 167 gabbro samples were compressed uniaxially and the damage process was observed with acoustic emission. The experimental results show that the response of the samples becomes significantly sensitive to minor variation of controlling variables as approaching the catastrophe. It is found that the results do support the concept of critical sensitivity reasonably.

In addition, we found that the sensitivity observed in experiments displays fluctuations, while the sensitivity obtained from a previous theoretical model [6,7] is monotonic and smooth curve. In order to reveal the mechanism governing the fluctuations in sensitivity, we extend the theoretical model. It is found that the discreteness of the distribution function of the mesoscopic unit's threshold might be a reason for the fluctuations shown in the critical sensitivity.

Experiments

In our tests, rectangular gabbro samples, $5\times5\times13\text{mm}^3$, were loaded uniaxially with a MTS810 testing machine. The loading mode is boundary-displacement control with velocity of 0.02mm/min. The displacement was measured by an extensometer with resolution of $3\mu\text{m}$ and an offset of load 1kN. Acoustic emission technique is an effective method to detect the statistical information of the microcracks in rock in real time [7,8]. In our experiment, two acoustic emission sensors were fixed on two sides of a sample with a specially designed clamp. The AE signals were recorded and processed by an AE21-C system produced by Institute of Computer Technology of Shenyang. The resonant frequency of the sensors is 140kHz and 250kHz, respectively.

Critical sensitivity in rock tests

Figure 1 shows the stress-strain curves for the gabbro samples. The catastrophe appears at the end of each curve. Clearly, it is hard to forecast when catastrophe will occur beforehand. In particular, the strength and the failure threshold show large diversity. This macroscopic uncertainty results in even great difficulty in rupture prediction. Now, we focus on whether critical sensitivity is a common precursor prior to eventual rupture or not. The critical sensitivity means that the response of a system to controlling variable may become significantly sensitive prior to catastrophe. The controlling variable in the present experiments is the boundary displacement denoted by U_b. Here we introduce a dimensionless controlling variable U,

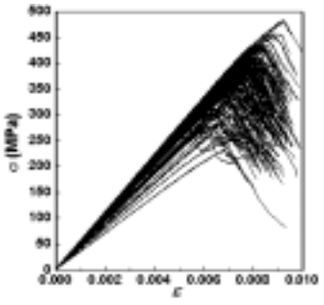


Fig.1 Stress-strain curves of tested gabbro samples

$$U = U_b / U_c , \tag{1}$$

where U_c is the boundary displacement at the catastrophic point of each sample. On the other hand, we adopt the energy release rate R resulting from mesoscopic damage as the response of the system. The definition of R is

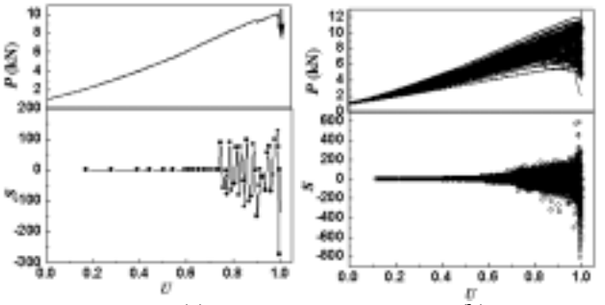
$$R = \Delta\Theta / \Delta t , \tag{2}$$

where $\Delta\Theta$ is the released energy received by acoustic emission sensors during the time interval Δt. Then, the sensitivity can be defined as

$$S = \frac{U}{R}\frac{\Delta R}{\Delta U} . \tag{3}$$

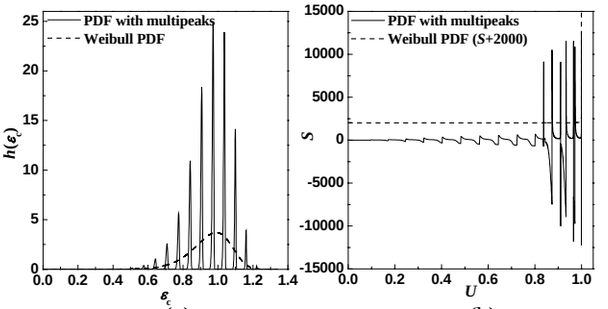
where ΔR is the increment of energy release rate corresponding to the increment of dimensionless boundary displacement ΔU. Figure 2(a) shows the sensitivity S calculated from the data of acoustic emission for a sample in the experiments. At the initial stage, S keeps in low level, which means that the system is in the state with low sensitivity. However, S increases significantly near the catastrophic transition point $U=1$. This implies that the system becomes highly sensitive

prior to catastrophe point. Figure 2(b) shows the sensitivity S for 131 samples. Noticeably, the series of S are different from sample to sample, but, more importantly, there is a common trend in S for all samples, namely S increases significantly near the catastrophe transition point. This is an experimental evidence of critical sensitivity prior to rupture in heterogeneous rock.



(a) (b)

Fig.2 Sensitivity observed in experiments
The arrows indicate the catastrophic rupture point.
(a) for a single sample, (b) for 131 samples



(a) (b)

Fig.3 (a) Threshold distribution function of mesoscopic units
(b) Sensitivity observed in theoretical models

Mechanism of the fluctuations of sensitivity in the experiments

However, the sensitivity shows fluctuations, and in particular, may become negative (Fig2), why? A theoretical model is proposed to explain the phenomenon. The rock sample and the MTS tester, be simplified as an elastic part, are in series and driven by boundary displacement U_b quasi-statically. The rock sample can be thought to be a driven, nonlinear threshold system [5,6], where the mesoscopic strain threshold ε_c follows a distribution function (PDF) $h(\varepsilon_c)$. Then, analytical expressions of the response of the system can be derived according to the mean field approximation.

In the case that $h(\varepsilon_c)$ is Weibull distribution function [9], the sensitivity is monotonic and smooth curve (Fig3 (b) dashed line). However, the distribution function of real materials may present complicated structure and can't be modeled by a continuous single-peak function. So we assume that it is a function with multi-peaks (Fig3 (a) solid line). If so, the sensitivity displays fluctuations (Fig3 (b) solid line), which is similar to the sensitivity in experiments (Fig2). So, the multi-peak structure of the distribution function might be the reason for the fluctuations shown in the critical sensitivity.

Discussions

Our experiments on gabbro indicate that critical sensitivity is a precursor prior to rupture. This highlights the essence of the rupture in heterogeneous media and can provide a clue to prediction of catastrophic rupture. The comparison between theoretical and experimental results shows that the multi-peak structure of the distribution function of mesoscopic strain threshold might be a reason for the fluctuations shown in the critical sensitivity.

Acknowledgements

This work is supported by the National Natural Science Foundation of China (Grant No. 10172084, 10232050, 10372012) and Major State Research Project "Nonlinear Science" G2000077305. The authors wish to thank Haisheng Yang for his assistance in experiments.

References

[1] Bai Y.L., Lu C.S., Ke F.J. and Xia M.F.: Evolution Induced Catastrophe. *Phys. Lett. A* 185:196-199, 1994.

[2] Xia M.F, Ke F.J. and Bai Y.L.: Threshold Diversity and Trans-scale Sensitivity in a Nonlinear Evolution Model, *Phys. Lett. A* 236: 60-64, 1997.

[3] Wei Y.J., Xia M.F., Ke F.J., Yin X.C. and Bai Y.L.: Evolution Induced Catastrophe and Its Predictability. *Pure Appl. Geophys* 157:1945-1957, 2000.

[4] M.F. Xia, Y.J. Wei, F.J. Ke and Y.L. Bai: Critical Sensitivity and Trans-scale Fluctuations in Catastrophe Rupture. *Pure Appl. Geophys.*159: 2491-2509, 2002.

[5] Zhang X.H., Xu X.H., Xia M.F. and Y.L. Bai: Critical Sensitivity in Driven Nonlinear Threshold Systems. *Pure Appl. Geophys.* 161, 2004 (accept).

[6] Zhang X.H., Rong F., Jia Z.K., Ke F.J., Xia M.F. and Bai Y.L.: Coupling Effects of Heterogeneity and Stress Fluctuation on Rupture. *Theor. Appl. Fract. Mech.*, 2004 (accept).

[7] Zietlow W.K. and Labuz J.F.: Measurement of the Intrinsic Process Zone in Rock Using Acoustic Emission. *Int. J. Rock Mech. Min. Sci.* 35: 291-299, 1998.

[8] Rudajev V., Vilhelm J. and Lokajíek T.: Laboratory Studies of Acoustic Emission prior to Uniaxial Compressive Rock Failure. *Int. J. Rock Mech. Min. Sci.* 37: 699-704, 2000.

[9] Weibull W.: A Statistical Distribution Function of Wide Applicability. *ASME Trans. J. Appl. Mech.* 18: 293-297, 1951.

PHASE TRANSITIONS AND MECHANICAL PROPERTIES OF TERNARY CHALCOGENIDES

Vladimir V. Shchennikov, Sergey V. Ovsyannikov, Natalya Yu. Frolova, Vsevolod V. Shchennikov*

Institute of Metal Physics of Russian Academy of Sciences, Urals Division, 18 S.Kovalevskaya Str, GSP-170, Yekaterinburg 620219, Russia, e-mail: sergey_v_o@imp.uran.ru

**Institute of Mathematics and Mechanics of Russian Academy of Sciences, Urals Division, GSP-384,16 S. Kovalevskaya Str, Yekaterinburg, Russia*

Summary In the present work the mechanical properties of mercury semiconductors in the vicinity of the phase transitions were studied. Under the high hydrostatic pressure treatment the macroscopic bending of samples was observed, that gave the evidence of high plasticity of these materials near the phase transition point. The influences of chemical substitutions in cation and anion sublattices on the properties of ternary chalcogenides were analysed.

INTRODUCTION

Pressure-induced phase transitions of chalcogenides are known to depend strongly on atom substitution in anion and cation sublattices [1-5]. For example, in ternary chalcogenides the replacement of cations or anions by analogous one shifts the beginning of phase transition from tetrahedral (sphalerite) into octahedral structures (rock salt, cinnabar) as well as corresponding abrupt jumps of resistivity in a wide pressure range [1-5]. In [6] the approach to the lattice stability for diamond-like and sphalerite crystals was suggested, based on the consideration of electron spectrum peculiarities. According to [6] the instability of lattice ought to arise when the indirect overlapping of forbidden gap takes place. The phase diagrams, obtained by using of this approach, gave a good accordance both with experimental data [6] and also with the results of current theoretical models [7]. The pressure shifts of electron bands at Γ, L and X-points of Brillouin zone as well as electron energy gaps for diamond-like and sphalerite compounds are indeed consistent with values of phase transition pressures P_t [8]. Value of P_t is connected also with elastic constants of these materials [9], so there has to be a correlation between electrical and mechanical properties at phase transformation, that makes above materials perspective for MEMS (micro-electro-mechanical systems) applications. In contrast to other tetrahedral bonded semiconductors Si, Ge, GaAs, the chalcogenides like HgCdTe possess a bad mechanical properties and so their handling in a technological device process is more difficult [14]. Thus, mechanical properties of ternary chalcogenides are of great interest. The most favourable technique for testing of mechanical properties being the microharness measurements [14].

EXPERIMENT

In the present work the influence of various kind of cation and anion substitution at electrical and mechanical properties (microhardness H before and after pressure treatment, plastic deformation) were investigated. For high pressure measurements a "piston-cylinder" chamber and diamond anvils cell (DAC) were used. Vickers' microhardness was measured before and after high pressure treatment of the samples by PMT–3 apparatus. A surface of the samples was investigated by photo method with assistance of microscope "Neofot". The content of elements in each sample was determined via X– ray spectra method by using of "Superprobe–JCXA–733" spectrometer. Lattice parameters were controlled by standard X–ray diffraction method. For high-pressure study the automated setup was used allowing to measure a several parameters of sample and environment simultaneously [10-13]. For investigations the single crystals of ternary chalcogenides $HgSe_{1-x}S_x$, $HgTe_{1-x}S_x$, Hg_{1-x} Cd_xSe, $Hg_{1-x}Mg_xTe$ have been taken. The analogous previously published data for other ternary compounds $HgTe_{1-x}Se_x$, $HgGa_2Se_3$, $HgIn_2Te_3$, $Hg_{1-x}Cd_xTe$, $Cd_{1-x}Zn_xTe$, $Hg_{1-x}Zn_xTe$, $Cd_{1-x}Mn_xTe$ etc. were also analysed.

RESULTS AND DISSCUSSION

The results obtained are: observation of macroscopic bending and plastic deformation of the samples undergone a high hydrostatic pressure treatment above the phase transition point P_t, microhardness dependencies on content of substitution atoms x, irreversible arising of $H(x)$ after reversible phase transition sphalerite ($B3$) $\rightarrow$ cinnabar ($B9$) controlled by resistivity measurements. The dependencies of $P_t(x)$ and $H(x)$ obtained were explained quantitatively by modern theoretical approaches [6-8,14] taking into account the recent neutron and synchrotron data of lattice transformation under variation of x and P [15-17].

The value of hardness is known to be inversely proportional to the compressibility β [18]:

$$H = \frac{M}{\rho \cdot q \cdot \beta} \qquad (1),$$

where M the molecular weight, ρ the density, q the number of atoms in a formula unit. Eq.1 was confirmed by experimental data for elemental solids and crystalline compounds. For ternary compounds H is also function of x [14]:

$$\frac{dH}{d(x)^{0.5}} = 0.48 \cdot G \cdot \left| \varepsilon_G - 6 \cdot \gamma \cdot \varepsilon_a \right| \qquad (2),$$

with $\varepsilon_G=(\mathrm{d}G/\mathrm{d}x)/G$, $\varepsilon_a=(\mathrm{d}a/\mathrm{d}x)/a$, G the bulk shear modulus, a the lattice constant, γ the Grûneisen constant. The contribution in H of stress field around solute atoms, caused by different size and modulus (elastic interaction) [14] has been taken into account in Eq. 2. The hardening effect is due to above elastical interaction between solute atoms and screw dislocations, being rate–controlling [14]. Using the HgTeS, HgSeS lattice parameters determined at structural testing to obtain e_a values the fitting of our $H(x)$ data have been performed. Grûneisen constant was supposed to be 0.5 [14]. The compressibility of HgSe and HgTe have been taken the paper [19]. Eq.2 described well the experimental data obtained in the present and previous work.

Theoretical models [6-7] predict the decreasing of $P_t(x)$ in $HgSe_{1-x}S_x$, $HgTe_{1-x}S_x$ compounds and increasing of it for $Hg_{1-x}Cd_xSe$ system, that in a good accordance with experimental data. The about two-fold increase of H established for samples undergone the phase transitions under hydrostatic P as well as the increase of electrical resistance after the pressure treatment may be explained by defects of crystal structure. The plastic bending of initially brittle samples suggested high plasticity arising in the vicinity of phase transformation which was accoplished by large hysteresis volumetric effect [1,2,15,16]. The previously studied electrical resistance $R(P)$, $P_t(x)$ and $H(x)$ data for ternary compounds $HgTe_{1-x}Se_x$, $HgGa_2Se_3$, $HgIn_2Te_3$, $Hg_{1-x}Cd_xTe$, $Cd_{1-x}Zn_xTe$, $Hg_{1-x}Zn_xTe$, $Cd_{1-x}Mn_xTe$ have the same features that indicates the overall tendency in their mechanical properties near phase transition point.



Fig. 1. The scheme of plastic bending of chalcogenides (HgSe, $Hg_{1-x}Cd_xSe$, $HgSe_{1-x}S_x$) samples investigated after applying of hydrostatic pressure.

CONCLUSION

A correlation between electronic and mechanical properties of ternary chalcogenides near the phase transition point has been revealed. High plasticity has been established of materials in the vicinity of phase transition under pressure. The mechanism of phase transitions from tetrahedral bonded to octahedral bonded lattice at Hg, Cd and Zn chalcogenides seems to be similar [14], so the behaviour of mechanical properties at phase transition may be the same for this family of ternary semiconductors [7].

The work was supported by the Russian Foundation for Basic Research (RFBR), Gr. No. 01-02-17203, US CRDF TGP-1125 and INTAS (Ref. Nr. 03-55-629).

References

[1] J.A. Kafalas et al. *J. Phys. Chem. Sol.* **23**:1541, 1962.
[2] A. Lacam et al. *Chem. Phys. Lett.* **18**:129, 1973.
[3] V.V. Shchennikov, et.al. *Fizika Tverdogo Tela* (St. Petersburg) **22**: 2868, 1980.
[4] V.V. Shchennikov, et.al. *Fizika Tverdogo Tela* (St. Petersburg) **37**: 2398, 1995.
[5] V.V. Shchennikov. *Fizika Tverdogo Tela* **37**:1015, 1995; **42**:626, 2000; **42**: 210, 2000.
[6] A.M. Altshuler et al. *phys. stat. sol.(b)* **90**:733, 1978.
[7] J.A. Majewski, P. Vogl. *Phys. Rev. Lett.* **57**:366, 1986.
[8] W. Paul, D. Warshawer. Solids under pressure. Moscow: Mir, 1966.
[9] P.J. Ford et al. *J. Phys. C: Solid State* **15**:657, 1982.
[10] VV. Shchennikov et al Proceedings of SPIE **3882**:247-254, 1999.
[11] V.V. Shchennikov, S.V. Ovsyannikov. *JETP Letters*, **74**:486-490, 2001.
[12] V.V. Shchennikov, S.V. Ovsyannikov. *Solid State Communications* **121**:323-327, 2002.
[13] S.V. Ovsyannikov, V.V. Shchennikov. *Proceedings of SPIE* **4692**:235-242, 2002.
[14] A. Fissel, M. Schenk. *Cryst. Res. Technol*. **24**:557-562, 1989; **25**:89-95, 1990.
[15] V.V. Shchennikov, et.al. *Fizika Tverdogo Tela* (St. Petersburg) **44**:1553, 2002.
[16] I.S. Bazhan et al. In Proc. of XIV Russian Conf. on Synchrotron radiation. July 15-19 2002, Novosibirsk, p. 151.
[17] Yu.S. Ponosov, V.V. Shchennikov et al. *phys. stat. sol. (b)* **223**:275, 2001.
[18] Yang at al *Phys. & Chem. of Minerals* **15**:191-195, 1987
[19] M.I. McMahon, R.D. Nelmes. *physica status solidi (b)* **198**:389-402, 1996.

SHPB TECHNIQUE FOR IDENTIFICATION OF COMPLEX MODULUS UNDER CONDITION OF NON-UNIFORM STRESS

S. Mousavi, U. Valdek, K. Welch and B. Lundberg
The Ångström Laboratory, Uppsala University, Box 534, SE-751 21 Uppsala, Sweden

Summary An SHPB procedure for non-parametric identification of the complex modulus was developed without assuming equilibrium or axial uniformity of the states of stress and strain. It was applied to testing of polypropylene with bars made of polymethyl methacrylate and aluminium, and it was compared with the classical SHPB 1-wave procedure.

INTRODUCTION

SHPB (Split Hopkinson Pressure Bar) testing is used extensively for study of the constitutive properties of materials at high strain rates. For testing of metals, it is common to use elastic high-impedance steel bars. Recently, there has been increased interest in testing soft materials, which has led to the use of viscoelastic low-impedance polymeric bars. Classical SHPB testing has been reviewed by Gray III [1], and a survey of SHPB testing of soft materials has been provided by Gray III and Blumenthal [2].

For an SHPB test to be considered valid, it is required that several conditions be fulfilled in an approximate sense. Some of them concerning the specimen are: (a) Equilibrium should prevail, (b) the states of stress and strain should be uniform, (c) the state of stress should be uni-axial, and (d) the effects of friction at the bar-specimen interfaces should be negligible. Some of these conditions are in conflict as (a) requires short specimens (low aspect ratios), whereas (c) and (d) require long specimens (high aspect ratios).

Equilibrium and axial uniformity of stress can be assessed by comparing the stresses at the bar-specimen interfaces. Significant stress differences may prevail due to the effects of inertia and wave propagation, especially at an early stage [3]. Because of the time and strain (often more than 1 percent) required to establish equilibrium, it has been considered that the modulus of elasticity cannot be estimated from a classical SHPB test [1]. In specimens made of polymeric materials, which at small strains are characterised by the complex modulus, it is particularly difficult to achieve equilibrium because of the low wave speeds. A parametric identification procedure [4] has been developed which does not require equilibrium or axial uniformity of stress and strain.

The aim of this study was to develop an SHPB procedure for non-parametric identification of the complex modulus without assuming equilibrium or axial uniformity of stress and strain, apply it to the testing of a polymeric material with use of polymeric as well as metallic pressure bars, and compare it with the classical SHPB 1-wave procedure. The procedure should be useful for testing materials which do not allow attachment of strain gauges and/or fabrication of relatively long specimens. Other wave propagation methods for identification of complex modulus commonly require measurements on specimens with lengths of the order of 1 m [5].

METHOD

The identification problem considered was as follows: Given the cross-sectional area A_b, the complex modulus E_b and the density r_b of the bars; the cross-sectional area A, the density r and the length a of the specimen; the distances b_1 and b_2 from the bar-specimen interfaces to the sections of measurement, and the Fourier transforms $F\{e_{RM}\}$ and $F\{e_{TM}\}$ of the measured strains associated with the waves reflected from and transmitted through the specimen; find the complex modulus of the material of the specimen.

An equation, exact in the context of 1D wave propagation, was derived which gives an estimation the complex modulus E in terms of the measured strains associated with the reflected and transmitted waves. For $b_1=b_2$ this equation takes the form $(1/2)(Z/Z_b-Z_b/Z)\sinh(\gamma a)= F\{e_{RM}\}/F\{e_{TM}\}$, where $g=\mathrm{i}w(r/E)^{1/2}$ is a wave propagation coefficient, $Z=A(Er)^{1/2}$ is the characteristic impedance of the specimen, and $Z_b=A_b(E_b r_b)^{1/2}$ is the characteristic impedance of the bars. An approximation E_0 of E, valid at low frequencies and low specimen-to-bar characteristic impedance ratios, was also derived. It corresponds to the classical SHPB 1-wave procedure. SHPB tests with pressure bars made of polymethyl methacrylate (PMMA) and aluminium (AL), and polypropylene (PP) specimens with diameter 20 mm and lengths 10, 20, 50 and 100 mm were carried out. The complex modulus of PP was estimated by E and E_0, and these estimations were compared with a result E_{ref} from [6] which was used as a reference.

RESULTS AND DISCUSSION

For the PMMA bars, there was a good general agreement between E and E_{ref} for the 10, 20 and 50 mm specimens. For the 100 mm specimen, the agreement was fair. The deviations were manifested mainly by oscillations in E. For the AL bars, there was a good agreement between E and E_{ref} for the 10 and 20 mm specimens. For the 50 mm specimen, there was a fair agreement, but with oscillations in E. For the 100 mm specimen, there were strong oscillations in E. For both bar materials, E_0 overestimates the magnitude of the complex modulus. This overestimation increases with frequency f, specimen length a and the magnitude $|Z/Z_b|$ of the specimen-to-bar characteristic impedance ratio (about 0.20 for PP/AL and 0.70 for PP/PMMA). The estimations E and E_0 for the complex modulus of PP versus frequency f obtained with PMMA and AL bars, and specimens of lengths 10 and 50 mm, are shown in Fig. 1.

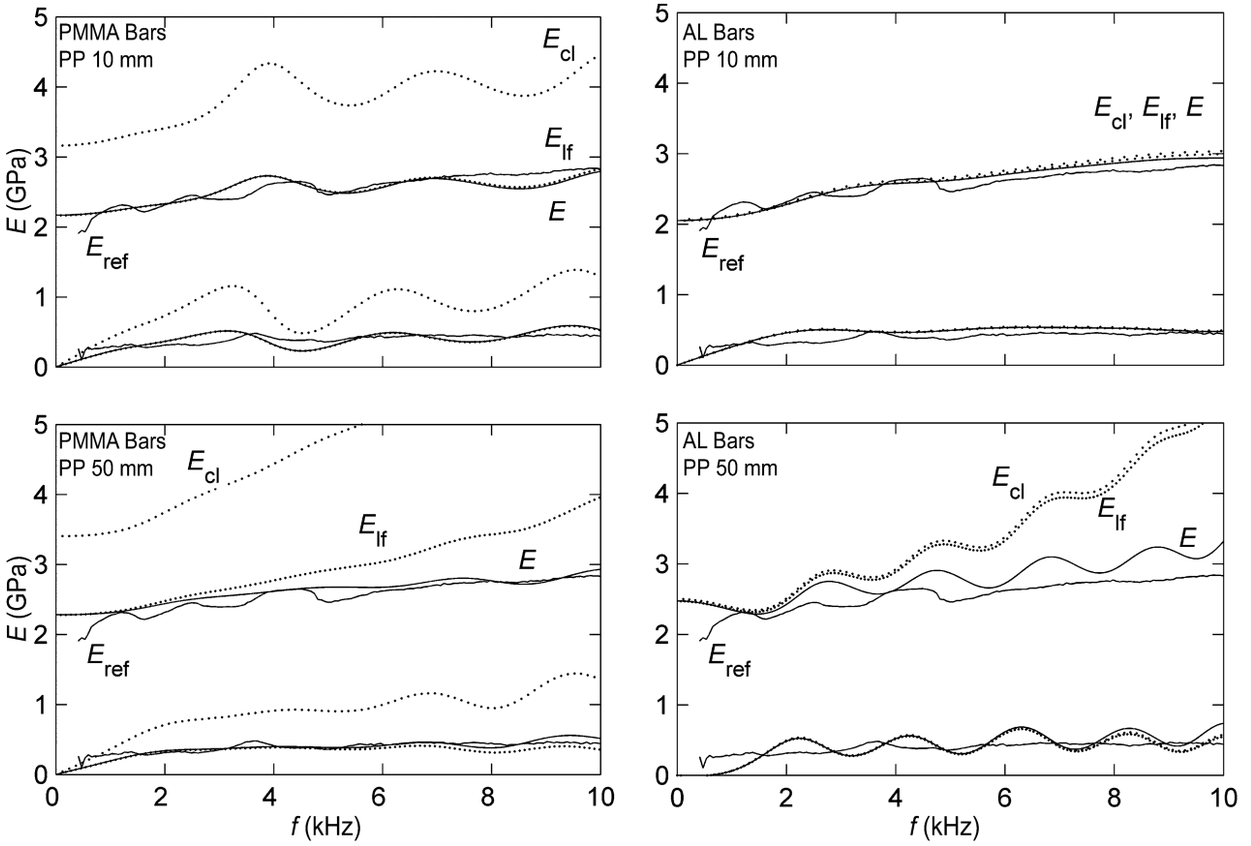


Fig. 1. Estimations E and E_0 of the complex modulus of PP versus frequency f obtained with PMMA and AL pressure bars, and specimens with diameter 20 mm and lengths 10 and 50 mm. The complex modulus E_{ref} of PP from [6] is shown as a reference. Real parts at top and imaginary parts at bottom of each diagram.

The oscillations in E were found to be sensitive to the time intervals chosen for isolation of the reflected and transmitted waves from other waves, which was done by cutting other waves and replacing them by zeroes. This indicates that the separation of the reflected and transmitted waves from other waves may not have been perfect as at very low signal levels it was not possible to distinguish contributions from the different waves, electrical disturbances and general noise. This explanation is supported by the circumstance that when AL bars were used, the oscillations in E increased with specimen length, i.e., with the lengths of the reflected and transmitted waves. For the PMMA bars, with shorter waves, the oscillations were relatively small and independent of specimen length. The oscillations were also found to be affected by the presence of even very weak bending waves in the pressure bars which may have disturbed the contact between the specimen and the pressure bars. Influence of 3D effects may also have had some effect on the oscillations.

ACKNOWLEDGEMENT

Funding from the Swedish Research Council for Engineering Sciences (TFR) under contract 2000-587 is gratefully acknowledged.

References

[1] Gray III GT: Classic Split Hopkinson Pressure Bar Testing. ASM Handbook Vol 8, Mechanical testing and evaluation. ASM. 462-476, 2000.
[2] Gray III GT, Blumenthal WR: Split Hopkinson Pressure Bar Testing of Soft Materials. ASM Handbook Vol 8, Mechanical testing and evaluation. ASM. 488-496, 2000.
[3] Wu XJ, Gorham DA: Stress Equilibrium in the Split Hopkinson Pressure Bar Test. *J Phys IV* Colloq C3 (Eurodymat 97) **7**:91-96, 1997.
[4] Zhao H, Gary G: On the Use of SPHB Techniques to Determine the Dynamic Behaviour of Materials in the Range of Small Strains. *Int J Solids Structures* **33**:3363-3375, 1996.
[5] Blanc RH: Transient Wave Propagation Methods for Determining the Viscoelastic Properties of Solids. *Journal of Applied Mechanics* **60**:763-768, 1993.
[6] Mousavi S, Nicolas DF, Lundberg B: Identification of Complex Moduli and Poisson's Ratio from Measured Strains on an Impacted Bar. *Journal of Sound and Vibration* (in press) 2004.

IN-SITU OBSERVATION OF FATIGUE CRACK GROWTH IN CARBON STEEL

Michal A. Miskiewicz [*], Zbigniew Pakiela [*], Krzysztof J. Kurzydlowski[*]
[*]*Warsaw University of Technology, Faculty of Material Science and Engineering, Woloska 141, PL 02-507 Warszawa, Poland*

Summary In this paper authors present results of their observation of crack development under cycling loading, using optical microscope. All measurements were made for ferritic/pearlitic carbon steel. This observation can help to clearly understand processes of cracking in multi-phases materials.

INTRODUCTION

One of the main features associated with small fatigue crack growth is that they frequently exhibit deceleration when they approach microstructural barriers such as grain boundaries. In-situ observation of crack propagation can give interesting information about crack development in multi-phases materials, especially when each phase has different mechanical and morphological properties [1,2].

MATERIAL AND EXPERIMENTAL PROCEDURE

For measurements it was chosen ferritic/pearlitic carbon steel (0.45% of carbon). Material had microstructure with higher volume fraction of pearlite (Fig. 2). Metallographic observation and stereological analyses confirmed that grains were rather equiaxial. Rectangle specimens of cross section 2.1mm thickness and 5.5mm width were used for testing. As optical observation device was used standard metallographic microscope, equipped with CCD camera connected to digital acquisition system. Digital acquisition was employed to precise measurement of crack length. Initial crack length was 1,2 mm. What is showed in Fig 1. Such prepared specimen was mounted into testing machine holders (Fig.4).

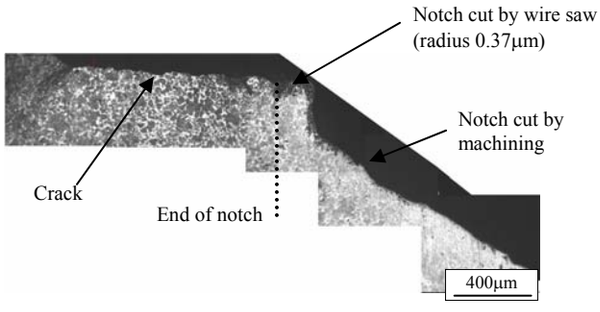


Fig. 1. Cross-section of specimen with notch and crack.

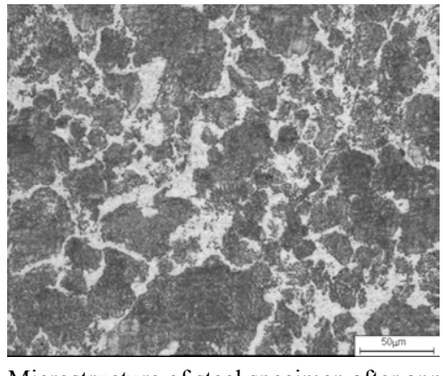


Fig. 2. Microstructure of steel specimen after annealing.

Cycling loads were forced by MTS hydraulic actuator connected to PC station which controlled force, displacement of actuator. It was also used as a data acquisition device. Whole frame was made in horizontal arrangement in order to easier mount standard metallographic microscope. As a feedback signal mini-extensometer was applied. It was attached to the specimen on notch side. Main experimental devices are presented in Fig. 3.

RESULTS AND DISCUSSION

For the material several crack inhibitory mechanisms were observed during experiments. Crack growth rate was slower when crack tip reached grains boundary as well as between pearlite-pearlite and ferrite-pearlite. In same cases cracks changed their direction because of crack- grain boundary interrelation (Fig. 5).
Main mechanism which caused limitation of crack propagation rate was plastic deformation on a crack tip. Process of plastic deformation was more intensive in ferrite grains than in pearlite. It is related to the lower yield strength of ferrite. After several hundreds of loading cycles as a result of strain haredning process in ferrite grains, crack started propagating farther. In figures below it is shown changing of crack propagation rate in areas of different phases in carbon steel specimens.

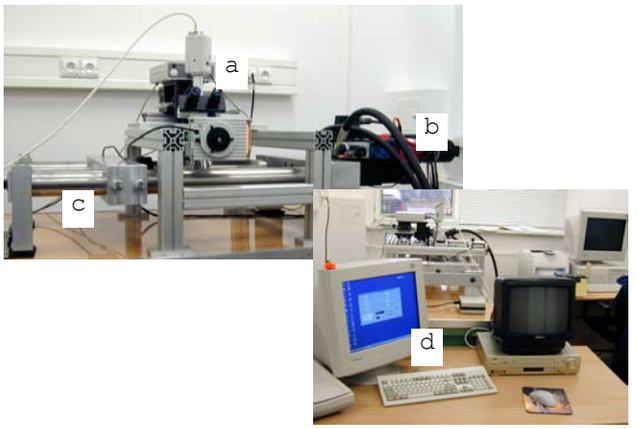


Fig .3. Experimental devices; a - microscope, b – actuator, c – frame, d – image acquisition system



Fig. 4. Specimen in holders during observation.

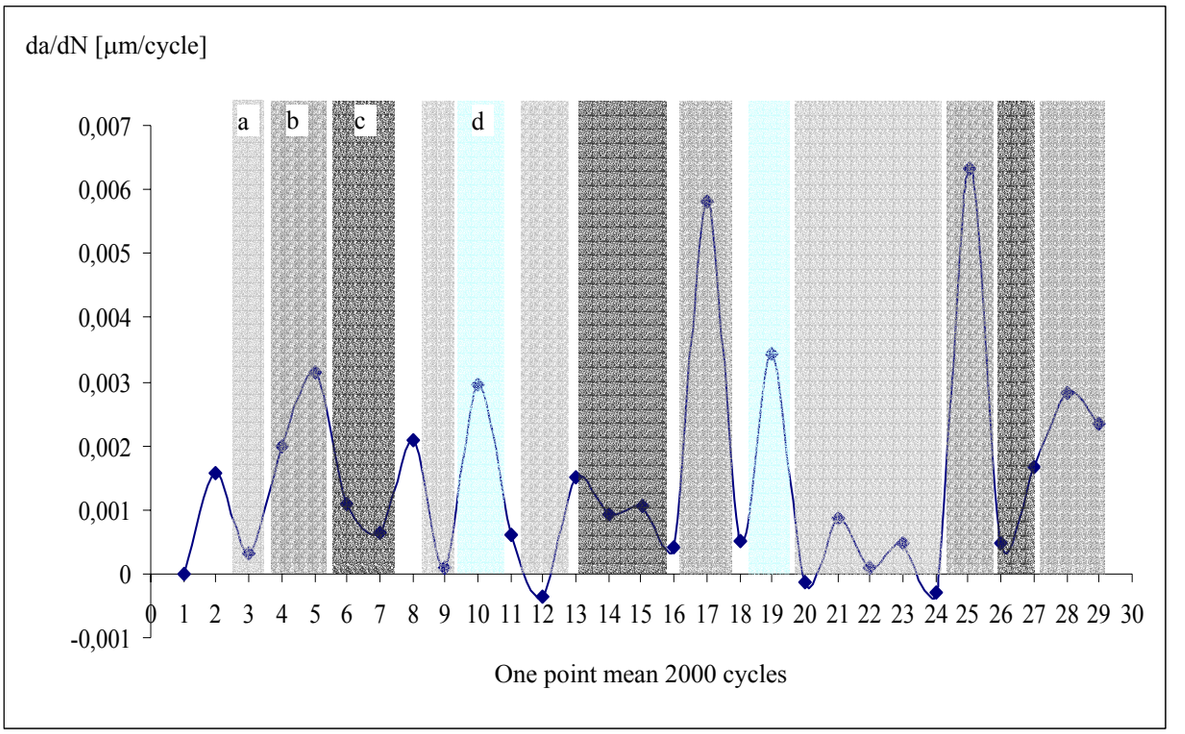


Fig. 5. Crack growth rate in different structure areas for short crack; a – area of ferrite, b – area of pearlite, c – area of grain boundaries perpendicular to crack line, d – areas of grain boundaries parallel to crack line.

CONCLUSION

Used technique gives opportunity to see closer mechanisms of crack propagation as a local process with relation to the materials structure.

ACKNOWLEDGEMENT

This work was supported by the Polish Committee of Scientific Research under grant 4T08A00322

REFERENCES

[1] Y.H.Zhang, L.Edwards, Mater.Sci. and Engn. A188 (1994)121-132
[2] L. Lawson , E.Y. Chen, M. Meshii International Journal of Fatigue 21 (1999) S15–S34

NEW SOLUTIONS IN EXPERIMENTAL MODAL ANALYSIS OF MECHANICAL STRUCTURES

T.Uhl, W.Lisowski, K. Mendrok, P.Kurowski
University of Science and Technology – AGH, Al. Mickiewicza 30, 30-059 Kraków, Poland

Summary The paper presents new solution of problems which are essential for modal analysis test engineers. The problems are related to automated modal analysis which is under development in many laboratories worldwide. The problems can be classified into two groups: selection of model structures and real time modal analysis. The first problem is important during experimental modal analysis in order to increase the analysis objectivity. The solution of second one helps to apply modal analysis for damage detection in mechanical structure. The algorithms, software implementation and case studies are presented.

INTRODUCTION

One of the most intensive investigates problem in modal analysis is automation of identification procedure. In the area two main problems can be distinguish:

- identification of modal properties of the mechanical systems if structure of model is not known (model order, location of excitation, predicted mode shapes, etc.)
- tracking of modal parameters during structure operation (real time modal analysis)

Both problems are under investigation at the University of Science and Technology – AGH from many years.
In the paper recent developments of experimental modal analysis procedures are presented.

AUTOMATION OF EXPERIMENTAL MODAL ANALYSIS PROCEDURES

During experimental modal analysis testing engineers and analysts are often forced to make decision about model structures, what constitutes one of the most important problems in automation of this analysis [1]. The idea of the proposed methodology is to formulate a set of algorithms that aid decision-making during modal analysis in order to increase the analysis objectivity. In the result the autonomous modal analysis procedure is formulated.

The modal analysis results depend on the modal experiment plan and execution as well as parameter estimation.

First, there are considered the modal experiment test planning algorithms aiming at selection of excitation points and response signal measuring points. These algorithms might use the preliminary modal experiment results, as numerical structural dynamics models are not too often available in the industrial practice.
Next, the modal experiment database architecture and implementation is investigated. This database should allow both easy data quality assessment and parameter estimation planning.
Finally, the autonomous parameter estimation procedure is formulated. The formulated parameter estimation planning procedure results in a definition of properties of a set of the estimation procedures which should allow obtaining of repeatable estimation results with use of various: subsets of modal experiment database, estimation algorithms and parameter values of estimation procedures. The formulated stabilization diagram processing algorithm uses fuzzy reasoning to select the most representative system poles. Usually analysis of the experimental database leads to a large amount of results. The modal model consolidation procedure aim is to aid determination of the final modal model which is the most representative for all the available estimation results.
The authors' experience showed that introduction of tools aiding the decision-making during modal analysis might considerably shorten the modal analysis time especially in case of investigation of complex structures.
Other type of decision which should be made by analysts during modal analysis is selection of model order. The solution based on neural network supported procedure is presented in the paper.
In presented procedure [2] a model order is selected with the use of a self-organizing neural network that classifies data contained in a stabilization diagram. to the desired length by the zero values.

The steps of a model order determining process are as follows:

- Determining a transfer function for an object of interest,
- Building stabilization diagrams with the use of the *Vioma* toolbox which is formulated by authors,
- Determining a vector of weight coefficients,
- Grouping the data contained in the vector of weight coefficients with the use of neural network,
- Counting the number of determined groups and displaying a number that unequivocally specifies a model order

.
There is also shown a comparison between results of model order selection obtained with the use of proposed neural network based approach and results obtained with the use of the classical stabilization diagrams method. The method of

model order selection with the use of a neural network aims at eliminating errors made during a model order visual assessment on the basis of a stabilization diagram.

REAL_TIME MODAL ANALYSIS AND ITS APPLICATION FOR DAMAGE DETECTION

The second group of newest problems in experimental modal analysis is related to on-line modal parameters estimation of mechanical structures during their operation [3]. The problem is formulated as follows: the model structure is assumed but during investigation parameters of structure are subjected to change, changes of modal parameters during operation should be monitored. This approach is very useful for control and diagnostics purposes of complex mechanical structures like airplanes, satellites, bridges, masts, etc. The following methods are applied for on-line modal analysis in the paper:

- a method based on measured signal segmentation
- a method based on parameters updating.

The methods are based on real-time identification of autoregressive model of acceleration signal measured during operation and employing relation between autoregressive models and modal model parameters. The schemes of both methods are shown in figure 1.

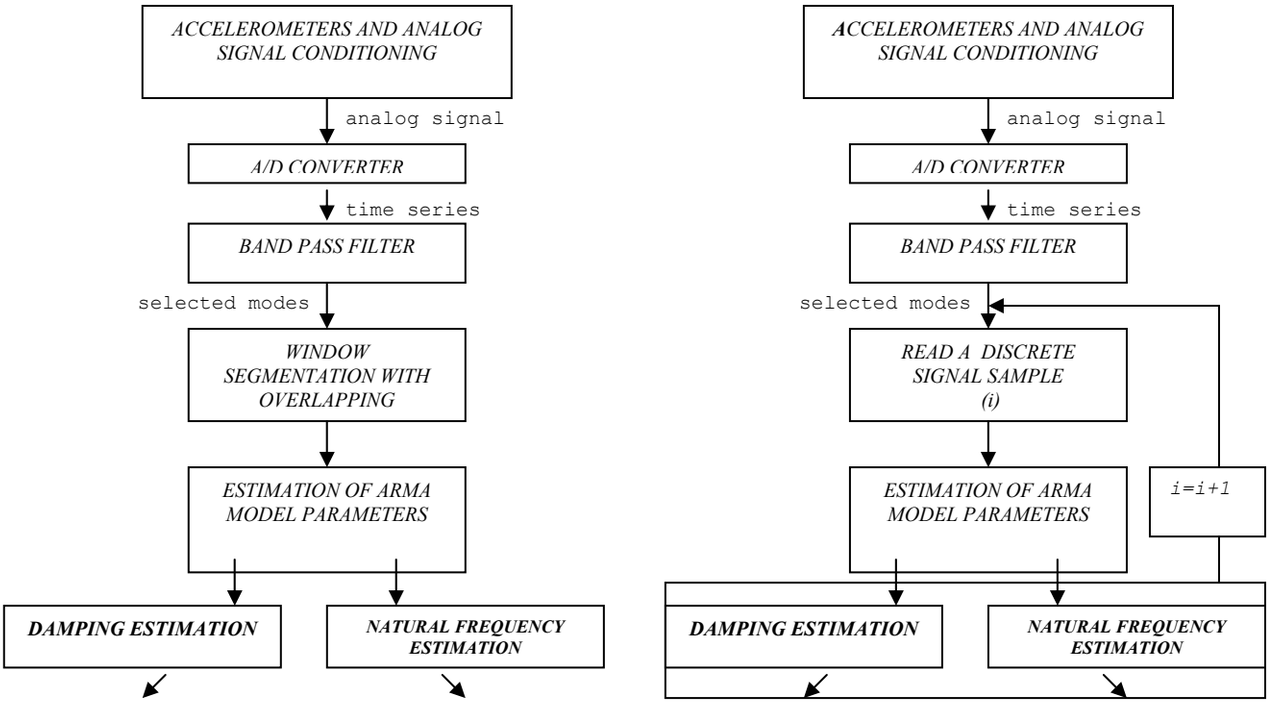


Figure 1. Schemes of formulated real time modal analysis a) signal segmentation based algorithm, b) model updating algorithm.

Simulation verification results of proposed procedure for two degrees of freedom system with varying damping parameters are discussed. The methods have been applied for identification of flutter region for trainer jet from in-flight vibration measurements. The electronic device based on DSP technology is designed and tested for on-line modal parameters monitoring during airplane flight. The results of this test are reported in the paper.

References

[1]Lisowski W., Assessment of applicability of an autonomous parameters estimation algorithm to monitoring of modal parameters of an airframe, ZEM vol.38, z.3 (135), 2003,pp. 19-38
[2] Uhl T., Góral G., Neural networks based identification of model order in modal analysis, Proc. Of ISMA2002, Leuven, 2002, pp.1643-1648
[3] Uhl T., Bogacz M., Real-time modal analysis and its application for flight flutter testing, 13 IFAC Symposium on System Identification, Rotterdam, 2003,pp. 707-712.

INFLUENCE OF CONTACT CONDITIONS ON FRETTING FATIGUE UNDER SPHERICAL CONTACT

Carlos Navarro*, Manolo Tur**, Javier Fuenmayor**, Jaime Domínguez*
*Dpto. de Ingeniería Mecánica y de los Materiales, Universidad de Sevilla, Spain
**Dpto. de Ingeniería Mecánica y de Materiales, Universidad Politécnica de Valencia, Spain

Summary This work analyzes the effect in fretting fatigue (stresses, stress intensity factor, eccentricity of the stick zone and estimated life) with spherical contact of several assumptions needed to calculate the stresses beneath the contact. These assumptions are: *i)* supposing plane stress or plane strain when introducing the bulk stress on the element; *ii)* taking or not taking into account the eccentricity of the stick zone due to the bulk stress.

INTRODUCTION

Fretting is a particular case of fatigue in which the stresses close to the contact surface are dominated by the contact between two solids that tend to slide. In addition to these local stress fields in the vicinity of contact, one or both of the solids may be subjected to a bulk stress caused by cyclic loads. This initiates many cracks in the process zone. These cracks may grow until final fracture occurs across one of the elements. In order to model this phenomenon correctly it is necessary that the stresses are calculated as accurate as possible. The stresses in the contact due to a normal constant load and a cyclic tangential load with spherical contact were deduced by Mindlin [1]. In this situation the contact zone has the shape of a circle and it has an inner, centered circle where no slip occurs between the surfaces (the stick zone) and an annulus around the stick zone where slip takes place. A bulk stress can be added to one of the elements in contact shifting the stick zone to one side [2]. Until not long ago the eccentricity of the stick zone was not taken into account when calculating the stresses but, obviously, that is an approximation. To solve this problem the deformation due to the bulk load is added, but a hypothesis has to be made, whether it behaves as plane strain or plane stress. These two points (plane stress/plane strain and eccentricity/no eccentricity) may vary the calculated stress field under the contact. The objective of the present work is to decide which option is the best and to determine the influence of it on the stresses, the stress intensity factor (SIF), the eccentricity of the stick zone and the estimated life.

STRESSES AND ECCENTRICITY

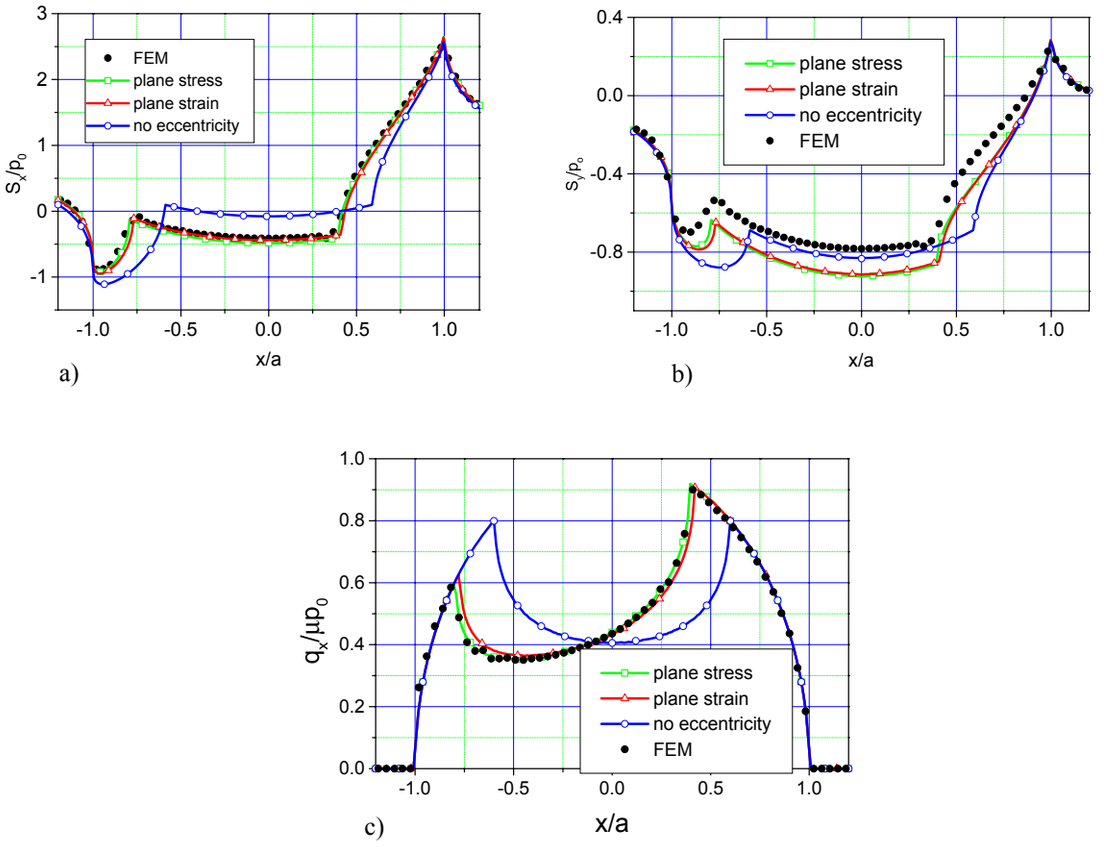


Fig. 1. Stress distribution on the surface on the line of symetry of the contact; a) normal stress in the loading axis; b) normal stress perpendicular to the loading axis; c) shear stress in the loading axis.

The stresses for the different conditions are obtained in a specific example, a 10x10mm cross section specimen of Al7075-T6 subjected to a normal load of 100N, a cyclic tangential load of 94.77N and a cyclic bulk stress of 110MPa. Figure 1 compares the analytical solutions for this problem with the Finite Element Method (FEM) solution. They show that the stress distribution for plane stress, plane strain and FEM are very similar but quite different for the case of no eccentricity. Nevertheless, the maximum normal stress in the direction of the loading axis and perpendicular to it has approximate the same value in the four curves, Fig. 1a and 1b. It can also be observed in the three figures, but more clearly in Fig. 1c, that the stress distribution and the value of the eccentricity of the stick zone is better represented by assuming plane stress.

STRESS INTENSITY FACTOR

The SIF is obtained analytically integrating, along the crack path, the stresses multiplied by a weight function. Figure 2 shows the analytical solution for the three possibilities (no eccentricity, plane stress and plane strain) for the example chosen. It can be seen that plane stress and plane strain give similar results. The SIF with no eccentricity is lower during initiation but very similar when the crack is long. The reason is that in the latter region the principal stress is due to the bulk stress which is the same for the three cases.

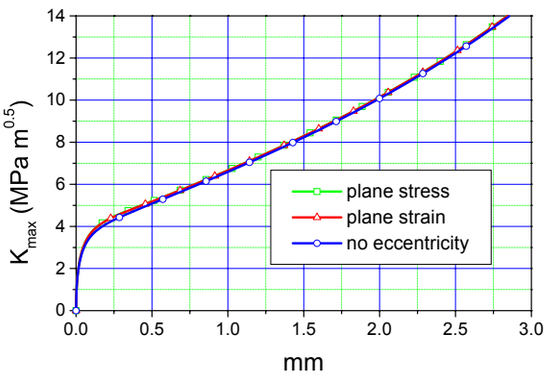


Fig 2a. SIF along the crack path.

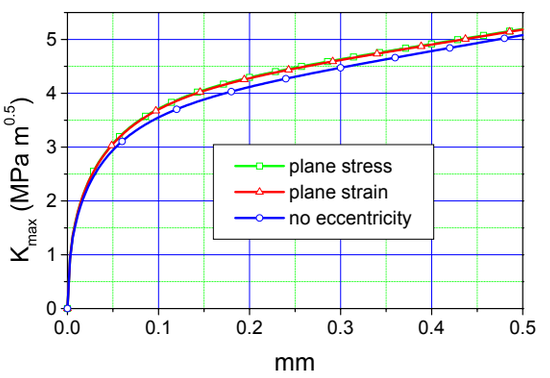


Fig2b. SIF along the crack path during initiation.

ESTIMATED LIFE

The influence on the estimated fretting fatigue life is studied using a model developed by the authors [3]. This model separates fatigue life into two phases, initiation and propagation, without fixing in any way beforehand the limit between initiation and propagation. The model uses a multiaxial fatigue criterion based on the calculated stresses to determine the initiation life and a crack propagation law together with the stress intensity factor to obtain the propagation life. The higher stresses in the case of plane stress produce shorter initiation and propagation lives, making the result more conservative, although quite similar to that of plane strain. Table I shows the estimated life for the three cases, the increment of the estimated life compared to that of plane stress, the maximum normal stress on the surface and the increment of this stress compared to that of plane stress. It can be observed that small variations of stresses produce large variations of the estimated life.

Table I. Results of the obtained estimated life.

	Life	Δ%	Max Stress (MPa)	Δ%
Plane stress	133078	-	387	-
Plane strain	134511	1.1	386.06	-0.24
No eccentricity	151086	13.5	375.6	-2.95

References

[1] Mindlin R. D.: Compliance of Elastic Bodies in Contact, *Journal of Applied Mechanics*, **16**:259–268, 1949.
[2] Navarro C, Domínguez J.: Contact conditions and stresses induced during fretting fatigue. Computational Methods In Contact Mechanics IV, L. Gaul y C. A. Brebbia, Eds. WIT Press/Computational Mechanics Publications, pp. 453-462, 1999.
[3] Navarro C, García M, Domínguez J, A procedure for estimating the total life in fretting fatigue, *Fatigue and Fracture of Engineering Materials and Structures*, **26**:459-468, 2003.

FATIGUE INVESTIGATIONS INTO A COMPOSITE GLIDER STRUCTURE

Miroslaw Rodzewicz, Krystyna Majorkowska-Knap
Warsaw University of Technology, Institute of Aeronautics and Applied Mechanics,
Nowowiejska 24, PL 00-665 Warszawa, Poland

Summary The authors present the results of fatigue investigations into the primary structure of composite glider undertaken at the Institute of Aeronautics and Applied Mechanics (IAAM) of WUT. The specimens representing the main joints of wings and fuselage, as well as the wing spar root were tested, since they form a most representative part of the glider primary structure. The integral fatigue tests of the wings-fuselage system were finally performed.

Introduction

Composite materials are primary candidates in the construction of the next generations of advanced aeronautical and aerospace vehicles. The design for primary and secondary structure of modern gliders will rely on FRPs to meet the structural weight criteria. Due to the economic and safety criteria, the structure of them must be durable over an expected life time at environmental conditions. From the survey of literature plenty of results are published in the field of fatigue of composite (e.g. recently published [1 ÷ 5]) and new smart [6] materials [7].

For several years the education and design program of light composite gliders has been developed at the IAAM, bringing about the "PW" family of six manufactured and tested glider prototypes, together with the widely known PW5 "Smyk" – the winner of FAI international technical competition for a new mono-type class - called the World Class glider. One of the main aims of the investigations undertaken after making successful tests of the PW-5 consisted in proving that its operation life was 9 000 hours, which was the level required for the World Class Glider. The investigations were conducted in the following three stages: 1st - fatigue tests of the main wing-fuselage joints, 2nd – fatigue tests of the root part of wing spar, and 3rd – integral fatigue tests of the wings-fuselage system. Before making the fatigue tests - the estimation the glider load spectrum was performed by means of calculations and in-flight load recording.

Fatigue tests of the main wings-fuselage joints

A special type of joints has been employed in the PW-5 and the following PW-gliders for the wings-fuselage fitting [8]. The work principle of such a joint consists in the introduction of a concentrated force into a composite multi-layer glass-epoxy (GFRP) shell by means of special metal sleeves and pins. The joints are located in the main fuselage frame and in the wing spars shear webs. The main feature revealed by those joints is the lack of adhesive connections between the metal parts of joints and composite shells, respectively, (i.e. the joint with a labyrinth fastener, patented under: PL 146658). These joints (Fig. 1a) have been tested in a low-cycle fatigue mode. The program of investigations comprises the following phases (Fig. 1b) a/ static tests of fresh - not-fatigued specimens (specimens No: K02, K04), b/ constant-amplitude cycle fatigue tests (specimens K03, K05, K06), c/ increasing amplitude cycle tests (specimens K08, K09), d/ residual strength tests (after 10 000 cycles). In the aforementioned cases the load lower limit was the force corresponding to **n = 1**, where **n** is a load factor (a multiplier of g = 9.81 m/sec $^{-2}$). The maximum load expected in glider service was exactly the same as in the case of specimen K03.

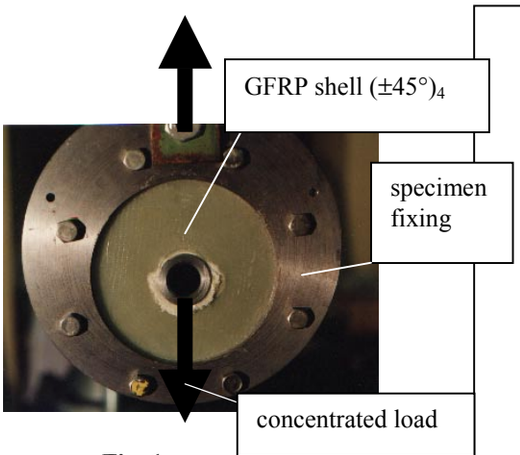


Fig. 1a

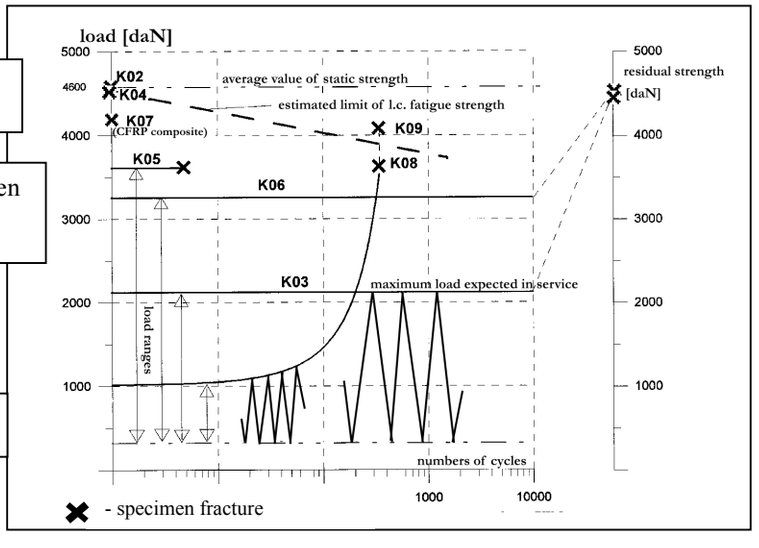


Fig. 1b

The rheological behaviour of specimens has been observed in the course of test procedures. A special attention was focused on the stagnation process of load-deformation hysteresis loops (Fig. 2a - the measured load deformation

hysteresis loops). Taking a general approach this process can be represented by a three-parameters phenomenological model [8, 9]. The bond-graphs and the results of numerical simulation of the specimen behaviour are shown in Fig.2b.

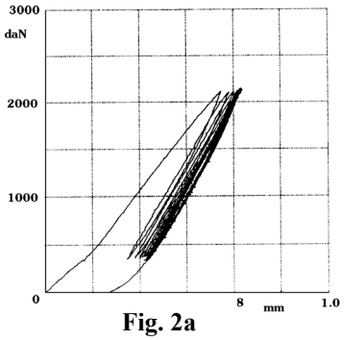
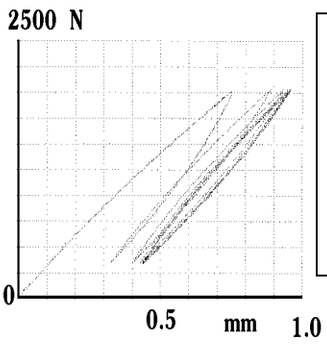


Fig. 2a



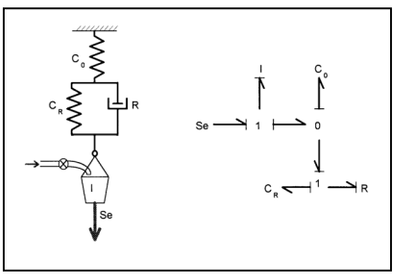


Fig. 2b

The fatigue and residual strength tests of the main wings-fuselage joints have proved that the fatigue loads not exceeding 70% of the fracture load exert only an insignificant influence on the residual strength.
This load level corresponds to the safety factor of 1.6 relative to the glider load limit. The number of 10 000 constant amplitude cycles at the design stress level was proposed as the proof covering fatigue of the glider FRP structure [10] .
The aforementioned type of joints was initially tested for the CFRP specimen (cf. K07 in the Fig. 1b).

Fatigue tests of the wing spar and the wings-fuselage system

The load spectrum as a basis for the fatigue tests – consisted of a number of constant amplitude load blocks [11]. Each load block is represented by an average value and amplitude of the load, and the number of cycles. For the PW-5 glider a cumulated sum of load cycles was about 900 000 per 1000 hours of the glider operation. Only a few percent of cycles reached the minimum and maximum limit load levels, and low amplitude oscillations around n = 1 dominated. In both the cases of fatigue test (wing-spar root and wings-fuselage system tests) the method for producing of the load was based on bending oscillation of specimens, excited a new, designed electrodynamic activator (patent PL 176320 B1).
The system used for fatigue test is shown in Fig. 3.

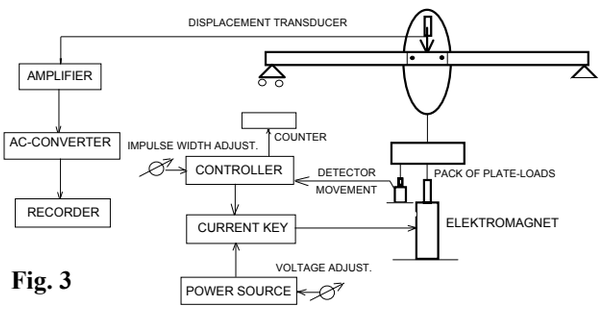


Fig. 3

During the tests there were simulated fatigue loads corresponding to 27 000 hours of flight for the wing spar, and 12 000 hours of flight for the wings-fuselage system. Basing on the results the aviation authorities have approved the service life of the glider.

References:

[1] R. Talreja, Fatigue of composite materials, Technomic Publ. AG., Basel, Swizerland 1986.
[2] Subramanian, S., Reifsnider, K. L. and Stinchcomb, W. W., A micromechanics model for the prediction of fatigue characteristics of off-axis unidirectional laminates, Applied Composite Materials, Vol. 1, No. 1, 1994, pp. 69-74.
[3] R. Talreja, A damage mechanics based methodology for life prediction of composite structures, 1999 ASME Mech. & Mater. Conf., (R.C. Batra & E.G. Henneke, eds) pp.123-124, June 27-30, 1999, Blacksburg, Virginia, USA.
[4] S.W. Case, Life prediction of composite materials: the MRLife approach, 1999 ASME Mech. & Mater. Conf., (R.C. Batra & E.G. Henneke, eds) p.141, June 27-30, 1999, Blacksburg, Virginia, USA.
[5] C. E. Harris, J.C.Newman, Jr., Fracture mechanics methodology to predict the onset of widespread fatigue damage in aircraft structure, 1999 ASME Mech. & Mater. Conf., p.72, June 27-30, 1999, Blacksburg, Virginia, USA.
[6] K. Majorkowska-Knap, On enhancement of microstructure in intelligent materials, 2001 ASME Mech. & Mater. Conf. (S. Nemat Nasser, ed.), p.210, June 27-29, 2001, San Diego, California, USA.
[7] P. Chaplya, G.P. Carman, Crack initiation between dissimilar oriented domains as a possible accelerated fatigue test, 1999 ASME Mech. & Mater. Conf., pp.159-160, June 27-30, 1999, Blacksburg, Virginia, USA.
[8] M. Rodzewicz, Problematyka modelowania w badaniach trwałości zmęczeniowej węzła kadłubowego połączenia skrzydła-kadłub szybowca PW-5, Konf. Mechanika w Lotnictwie, Warszawa 1995, 473 – 486.
[9] W. Nowacki, Teoria pełzania, Arkady, Warszawa 1963.
[10] G. Waibel, A. Schleicher, Safe life substantion for a FRP-sailplane, Technical Soaring, vol.26, No 2, 2002.
[11] M. Rodzewicz, A. Przekop, Experimental investigation of the load spectrum and fatigue tests of the PW-5 World Class glider, Technical Soaring, vol. 24, No 1, 2000, pp. 15-19.

A MICROSCOPIC MECHANICS MODEL OF CRACK GROWTH WITH FATIGUE-CREEP INTERACTION

Yi Sun*, Rei Zhang*, Jun Ma* and Jianmin Qu**
*Department of Astronautics and Mechanics, Harbin Institute of Technology, Harbin, China
**School of Mechanical Engineering, Georgia Institute of Technology, Atlanta, Georgia, USA

Summary An analytical micromechanics model is proposed to describe the influence and interaction of fatigue and creep. A recently proposed micromechanics model for fatigue crack growth is employed and further developed. The calculated dc/dN curves exhibit significant features of fatigue-creep interaction which is in general agreement with the experimental observation.

Many engineering components, such as steam turbine rotor systems, outer shell of nuclear reactors, or even solder connection in electronic packing, are prone to thermal fatigue under service condition. As their working temperatures are relative high, they may also endure creep damage. Up till now the most common way to treat the fatigue-creep problem is to make a simple linear superposition of the individual effects. However, the interaction between creep and fatigue is proved to be an important factor in engineering safety design[1]. It is also a very complex and difficult problem for researchers in the relative fields.

In the present work, an analytical micromechanics model is proposed to describe the influence and interaction of fatigue and creep. Here, a recently proposed fatigue crack growth model[2] is adopted which views the fatigue crack growth process as the intermissive elastic cleavage fracture of the dislocation free zone (DFZ). The effects of cyclic loading make the plastic zone hardening (or softening), thus raise the stress level in DFZ and bring it to fracture. The calculated dc/dN curves exhibit three different stages of fatigue crack growth which is in general agreement with the experimental observation.

In applying that model to thermal fatigue, we consider the following thermal loading condition (fig. 1). Here we suppose that, compared with the holding period at high temperature, the period of increasing and decreasing temperature is rather short, and the creep during that period may be neglected.

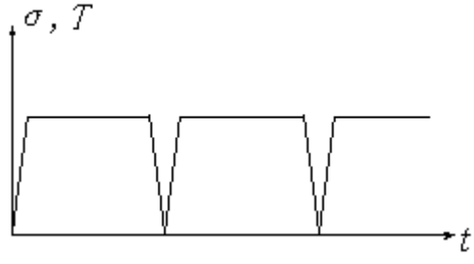


Figure 1 Schematic drawing of load spectrum

Thus at the period of increasing and decreasing temperature there is only the fatigue effect of thermal stress，while at the holding period there results the creep under the elevated stress caused by thermal loading.

The fatigue-creep interaction model is shown in Figure 2. Where the fatigue damage is

represented by the climbing dislocations and the creep damage is represented by the micro void ahead

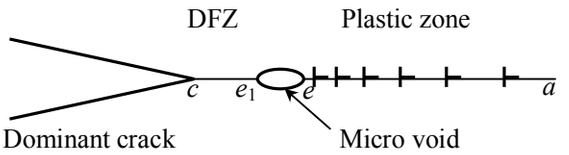
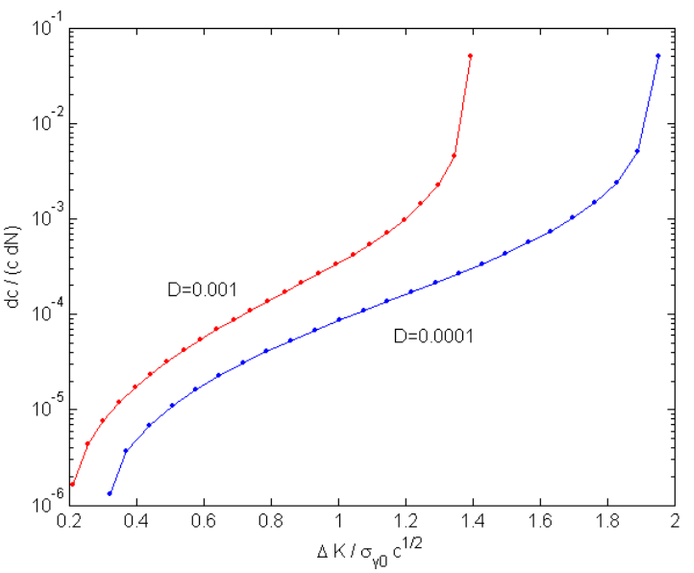


Figure .2 Schematic illustration of the coupling effect between fatigue and creep.

of the dislocation pile-up. The dislocation distribution function is determined by the integral equation of the equilibrium condition of dislocations [3]. For the tensile stress distribution in DFZ, we adopt the cohesive zone model. The bridging relation is taken of the form as nonlinear atomic action. When the bridging stress within DFZ increases up to the tensile strength, fracture takes place. If the cycle number is N, the DFZ size is Δ , then the fatigue crack growth rate becomes

$$\frac{da}{dN} = \frac{\Delta}{N}$$

Fig. 3 shows the effect of creep damage on fatigue crack growth behavior. From the figure we can see that the growth of the void enhances the stress concentration ahead of crack-tip, thus promote the growth rate of fatigue crack.



References

[1] Granacher, J, et al.: Creep fatigue crack growth behavior of two power plant steels, *Int. J. Pres. Ves. Piping,* **78**, 909-920, 2001

[2] Ma J., Sun Y.: A microscopic mechanism model and quantitative description of fatigue crack growth, Material Science and Engineering A, **355**, 14-17, 2003.

[3] Chang, S-J: Near threshold fatigue curve based on the dislocation free zone model of fracture. *Int. J. Eng. Sci.*, , **37**, 1289~1298, 1999

FATIGUE LIFE PREDICTION CONSIDERING RESIDUAL STRESS RELAXATION

Byeongchoon Goo*, Sungyong Yang*

*Rolling Stock Division, Korea Railroad Research Institute, 360-1, Woulamdong, Uiwangsi, Kyeonggido, Korea

Summary: It is necessary to take residual stress relaxation into account to predict fatigue lifetime more correctly. We developed a fatigue life prediction model based on a nominal stress approach considering residual stress relaxation. Finite element analysis of residual stress relaxation was carried out on an X-grooved butt weld specimen. The estimated fatigue lifetime was compared to experimental results.

INTRODUCTION

A lot of study on welding residual stress has been conducted in experimental and numerical areas but the effect of residual stresses on fatigue life has not been clearly explained until yet. Some results show the effect of welding residual stresses on fatigue life is significant. On the other hand, other results show specimens with tensile residual stresses have even longer fatigue life. These unclear conclusions seem to be mainly concerned with residual stress relaxation during fatigue tests and the metallurgical difference between weld metals and parent materials. In this study, we studied the effect of welding residual stress relaxation on the fatigue behavior of a material, JIS SM 490 A, with yielding strength of about 350 MPa and tensile strength of about 520 MPa. Fatigue tests of X-grooved butt weld plates under tensile loading and unloading at loading ratio, $R = 0.1$, were carried out to failure. The dimension of the specimens is 200×25×10 mm. The S-N curves are shown in Fig. 1 and 2. We can observe in the long life ($N > 2\times10^5$) the fatigue strength of AAY is higher than that of AAN, but in the short life, vice verse. These phenomena seem to be related mainly to residual stresses and structural changes due to post weld heat treatment. In the following section, a model considering residual stress relaxation and structural changes will be described.

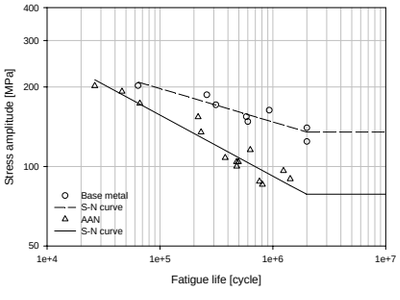


Fig. 1 S-N curves for base material and as-welded (AAN) specimens

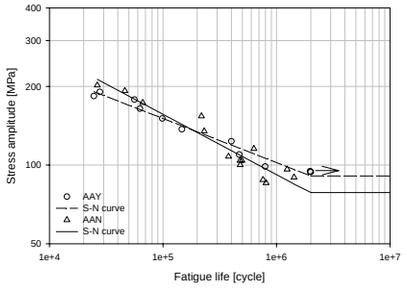


Fig. 2 S-N curves for annealed (AAY) and as-welded (AAN) specimens

FATIGUE LIFETIME PREDICTION CONSIDERING RESIDUAL STRESS RELAXATION

The effects of residual stresses and structural changes due to post weld heat treatment on fatigue behavior are presented schematically in Fig. 3. We consider a tensile loading-unloading constant amplitude fatigue test. The line A-E is the S-N curve for the base material. The line A-F is for a notched specimen without residual stresses. When the effect due to structural changes is added to the line A-F, the S-N curve A-F will move to a curve C-G, which may go upward or downward. When the effect due to residual stresses is added to the line A-F, the S-N curve would be a curve B-D-H. At point D the sum of applied stress and initial residual stress in the $S_{\max}$ direction, $(S_{\max} + \sigma_{r_{ini}})$, is equal to the yield

strength of the material, S_y. Notch root and nominal stresses are represented by σ and S respectively. When $(S_{\max}+\sigma_{r_{ini}})$ is greater than S_y, the initial residual stress is relaxed to σ_r. σ_r is assumed to be a function of applied load and loading cycles.

$$\sigma_r = \sigma_{r_{ini}}\left[1-k_1\ln(\frac{S_{\max}+\sigma_{r_{ini}}}{S_y})\right]e^{-k_2(N-1)} \quad \text{if} \quad (S_{\max}+\sigma_{r_{ini}}) \geq S_y \tag{1}$$

where k_1 and k_2 are constants. According to experimental results, the amount of relaxation through the first cycle is dominant. We consider only the first cycle.

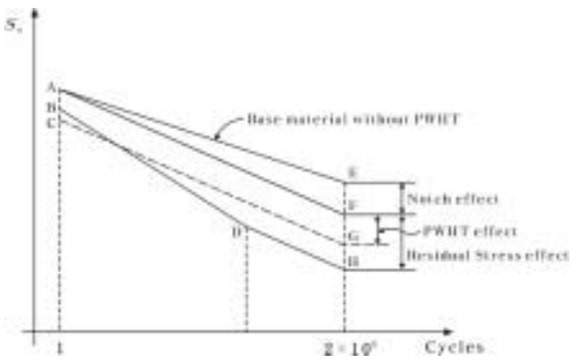


Fig. 3 Schematic diagram of S-N curves

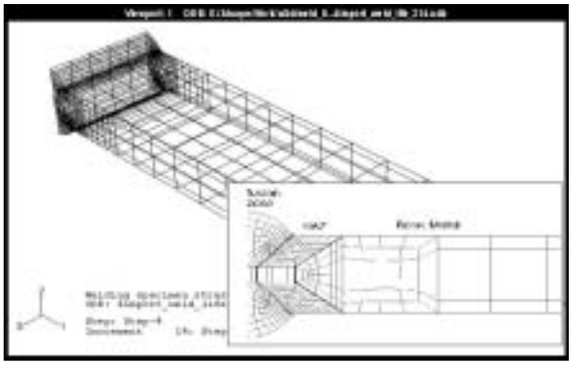


Fig. 4 3-D FE model for butt welded specimen

Fig. 4 shows the meshed geometry for an X-grooved butt weld specimen. A half of the specimen is considered. The initial residual stresses were obtained by thermal and elastoplastic analyses. Then, the relaxation of the initial residual stress was obtained by finite element analysis.

The S-N curve for the base metal is expressed by Basquin's equation:

$$S_a = AN^m \tag{2}$$

To predict the fatigue lifetime for a welded joint with residual stresses, the stress concentration factor by the applied load is obtained by finite element analysis and the fatigue notch factor, K_f, is calculated by Neuber's method. The fatigue strength for the notched part at 2 million cycles is given by S_f / K_f. The fatigue strength for the notched and smooth parts at one cycle is assumed to be the same. The S-N curve for the notched part, line A-F in Fig. 3, is written :

$$S_a = A_1 N^{m_1} \tag{3}$$

The residual stress after one cycle of loading, σ_r, is calculated by finite element analysis and Equ. 1. The residual stress σ_r is added to the mean stress term of the modified Goodman diagram :

$$\frac{S_a}{S_f}+\frac{(S_{mean}+\sigma_r)}{S_u}=1 \tag{4}$$

Inserting S_a obtained from Equ. 4 to Equ. 3, we can predict the fatigue lifetime of the welded member. The predicted lifetime is in good agreement with the experimental.

Acknowledgement

This work was supported by the National Research Laboratory (NRL) program of the Korea Ministry of Science and Technology. We are grateful for the support.

EFFECTS OF FREQUENCY, TEMPERATURE AND LOADING WAVEFORM ON FATIGUE CRACK GROWTH RATE IN STEEL 15Kh13MF

P. V. Yasniy, P. O. Maruschak

Department of Material Science, Ternopil Ivan Puluj State Technical University, Ternopil, Ukraine

The influences of frequency, loading cycle waveform and temperature on the crack growth resistance of steel 15Kh13MF, have been investigated. The data were analyzed using the linear and nonlinear fracture mechanic.

INTRODUCTION

Machines roll of billet continuous moulding are subjected to severe cyclic loads during service. Under these conditions fatigue creep are of major importance in determining the life of the components. Bimaterial 15Kh13MF/25Kh1M1F are widely used due to their superior high temperature properties; good fatigue and creep resistance in addition to resistance to corrosion and oxidation under severe operating conditions. Loading spectra during service includes combinations of fatigue cycles and hold times. Hence, in component life prediction knowledge of crack growth rates under frequencies ranging from 0.1 to 0.01 Hz and hold time at different temperatures is required.

MATERIAL

The tests were carried out on bimaterial single edge notch tension specimens made of steels 15Kh13MF/25Kh1M1F (Fig 1), and cut out from the machine roll of billet continuous moulding, produced by the centrifugal moulding. Specimens were tested under cyclic tension, the crack growth being perpendicular up to the bimaterial interface.

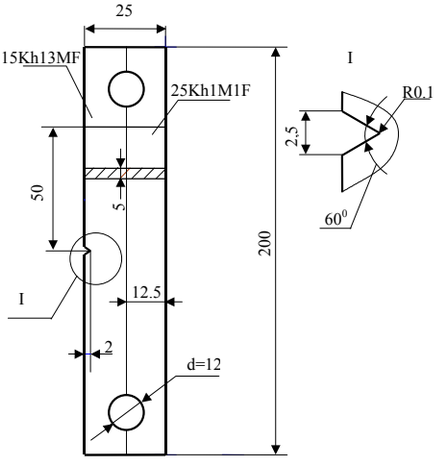


Fig. 1 Geometry and dimensions of test specimens (mm).

Table 1. Tensile properties of tested materials

Material	Temperature ^{0}C	Yield strength (MPa)	Ultimate strength (MPa)	Elongation %	Reduction of area %
15Kh13MF	20	338	456	6.0	4.80
	375	467	262	12.7	15.5
	600	242	334	24.2	56.6
25Kh1M1F	20	509	718	21.7	47.6
	375	431	582	21.5	48.5
	600	321	369	21.0	64.5

EXPERIMENT

The effects of frequency on fatigue crack growth (FCG) rate have been studied in steel 15Kh13MF. Fracture mode and FCG rate were studied at frequencies ranging from 0.1 to 0.01 Hz using a balanced triangular waveform. Fatigue testing was performed using a servo-hydraulic machine equipped with a micro-console and a data acquisition system. Tests were carried out under constant applied load, i.e. increasing ΔK as the crack growth, with and without hold-time, with a stress ratio R=0. An electric furnace chamber was used to achieve heating of the central part of the specimen at a uniform temperature of 375 and 600 ^{0}C. The temperature was controled by the Chromel-alumel thermocouple. A heat resistant glass window was designed to make possible video camera observations on the surface of the illuminated by a high intensity spotlight. Hold time of 10 s was performed at the maximum tensile stress giving trapezoidal waveform of frequency 0.1 Hz.

Crack lengths were monitored using optical microscope. Before commencement of high temperature testing, specimens were pre-cracked at room temperature using a 25 Hz triangular wave at an R = 0.1 to ensure subsequent crack growth during high temperature testing begins from a microscopically sharp crack away from any machining effects of the notch.

FCG rate in bimetal was described according to Paris equation:

$$\left(\frac{da}{dN}\right)_F = C\Delta K_{bi}{}^m \qquad (1)$$

here ΔK_{bi}- stress intensity factor (SIF) range [1];

FCG rate at high temperature was calculated using J – integral range ΔJ_f according to [2]

$$\frac{da}{dN} = C_1 \left(\Delta J_f\right)^n \tag{3}$$

Here C_1, n, C and m-material parameters depending on the mechanical properties – coefficient and index of the power correspondenly

The experimental procedure has been described in detail in a previous paper [2]. Only a brief description is given here.

RESULTS AND DISCUSSION

In Fig.2. dependencies of the FCG rate on the SIF range at different temperatures are built. Analysis of the dependencies shows that at +20 ^{0}C, +600 ^{0}C experimental points match well in scattering area. Decrease of fatigue crack growth rate was noticed at +375 ^{0}C, for ΔK_{bi}<28,6 MPa√m.

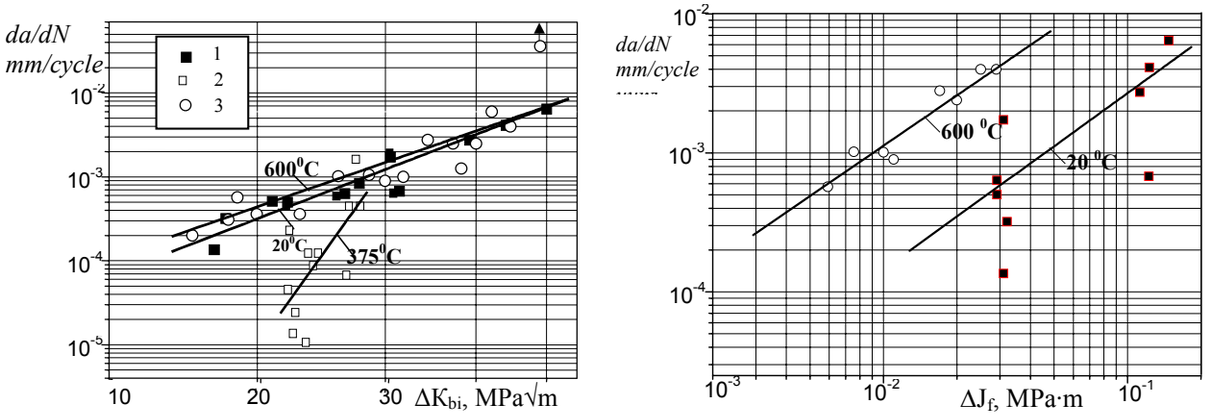


Fig.2 Dependence of the FCG rate in the bimetal specimen at +20 ^{0}C(1), +375^{0}C(2), +600 ^{0}C (3) on the SIF range (a) and the fatigue J_f-integral (b).

SIF range ΔK_{bi} is known to be used for the description of the FCG rate with the sufficient accuracy only when the size of the plastic zone at the crack tip is small.

That is why in order to describe FCG rate of non-linear fracture mechanics J_f- integral range was used. ΔJ_f- integral was calculated according to the technique [2] using the program “Fatigue”. Dependencies of the FCGR on the temperature in da/dN-ΔJ_f coordinates are presented in Fig. 2b.

According to the data presented in Fig. 2b, FCG rate increases in 6 times when the testing temperature increases from +20 ^{0}C till +600 ^{0}C.

Crack growth rate under trapezoidal cycle form at +375 ^{0}C increases, at +600 ^{0}C FCG rate increases in 2-3 times (Fig. 3a).

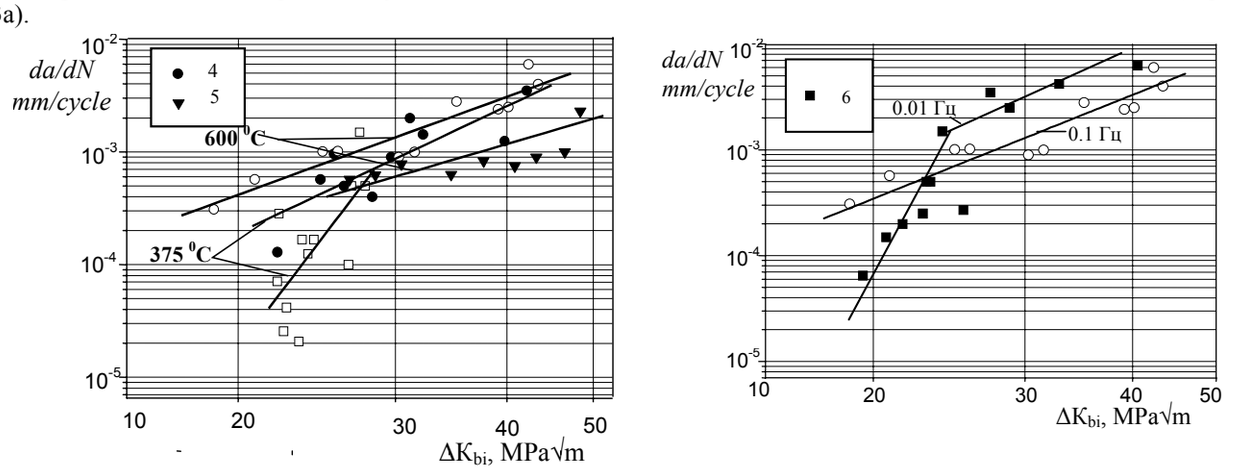


Fig. 3. Dependences of the FCGR on the SIF range ΔK_{bi}. under tempering 0 sec (1,2) and 10 sec (3,4); b) at frequency 0,1 Hz and 0,01 Hz (6)

The decrease of the loading frequency from 0,1 to 0,01 Hz causes the decrease of the FCG rate for ΔK_{bi}<26…28 MPa√m (Fig. 3).

When SIF range increases, the testing frequency influence decreases. The influence of the testing frequency at $\Delta K_{bi} \approx$ 26,6MPa√m is not available.

While testing the crack opening displacement as well as the photography of the crack at the bimaterial interface. were carried out.

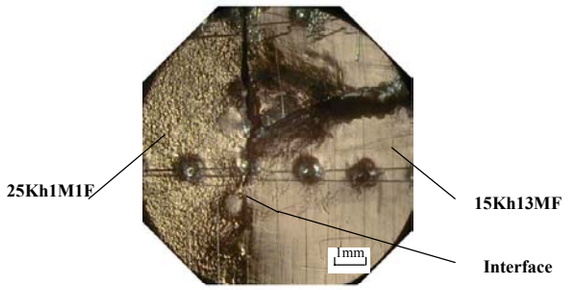


Fig. 4 Optical micrographs showing the bifurcation of the crack in steel 15Kh13MF, T=20 ^{0}C, ΔK_{bi}=55 MPa $\sqrt{m}$

For all experiments decrease of the crack growth rate before bimaterial interface was obtained. but it did not grow in steel 25Kh1M1F.

Table 2. Constant values used in formulae (1-2) for description of fatigue crack growth rate in 15Kh13MF steel.

Steel	t_h, s	T, ^{0}C	f, Hz	Fracture mechanics parameter			
				da/dN-ΔK_{bi} equat. (1)		da/dN-ΔJ_f equat. (3)	
				C, $\frac{mm/cycle}{(MPa\sqrt{m})^m}$	m	C_1, $\frac{mm/cycle}{(MPa\cdot m)^n}$	n
15Kh13MF	0	20	0.1	$2.67\cdot10^{-8}$	3.16	0.046	1.23
	0	600	0.1	$8.97\cdot10^{-8}$	2.84	0.36	1.25
	10	600		$4.93\cdot10^{-6}$	1.45		
	10	375		$2.64\cdot10^{-9}$	3.73	-	
	0	600	0.01	$5.08\cdot10^{-6}$	1.92	-	

SUMMARY AND CONCLUSIONS

Decrease of the loading frequency from 0,1 to 0,01 Hz leads to the decrease of the FCG rate at the SIF range ΔK_{bi}.<26 MPa$\sqrt{m}$.

In coordinates da/dN-ΔK_{bi} FCG rate in 15Kh13MF steel is not sensitive to the testing temperature (+20,+600^{0}C). But FCG rate increases in 5...7 times when the temperature raises from +20 ^{0}C to +600 ^{0}C depending on the crack tip opening range and the range of J-integral. Tempering causes the increase of crack growth rate at +375 ^{0}C, tempering at +600 ^{0}C causes the decrease creep-fatigue crack growth rate in 5-6 times as compared with the triangle form of loading cycle.

ACKNOWLEDGEMENTS

Scientific Fund of the Fundamental Researches of Ukraine (0101U006829) funded the project. Thanks to Dr. V. B. Hucajluk for his assistance in the experiments.

REFERENCES

1. P. V. Yasniy., P. O. Maruschak Procedure definition of stress intensity factor of prismatic bimetallic angle notched tension specimen // Visnyk ZhSTU. – 2004. Technical Science. (in press).

2. P. O. Maruschak Methodology research of a crack growth rate and description kinetic diagram of fracture in creep-fatigue conditions // Visnyk TSTU. No 2, Vol. 8, 2003, P. 23-28 (in Ukrainian).

XXI ICTAM, 15–21 August 2004, Warsaw, Poland

STRESS CONCENTRATIONS CAUSED BY DISLOCATIONS AT THE FREE SURFACE

Steffen Brinckmann, Erik Van der Giessen
Micromechanics Group, Department of Applied Physics, University of Groningen, Nijenborgh 4,9747AG Groningen, The Netherlands

Summary In this contribution discrete edge dislocation simulations (static and dynamic) are used to verify the analytical solution of Brown and Ogin (1984) for the stress state caused by the intersection of the persistent slip band with the free surface. Static and dynamic results show that, only in a rather unphysical limiting situation, the singular stress fields of the discrete dislocations lead to a logarithmic stress singularity at the free surface.

INTRODUCTION

In fatigue the key to predict and understand the nucleation of the crack lies in the stress concentrations at the free surface. Dislocations play an important role in the initiation of a crack through their long range stresses. During fatigue they cluster and form first the channel-vein and later the ladder-like structure found in persistent slip bands (PSBs). The PSB emerges at the free surface as an extrusion of material. The geometry of extrusions themselves can be the origin of stress concentrations, but the dislocations below the surface have long been recognized as potential sources for high stresses near the surface. Brown and Ogin [1] proposed an analytical model for PSB-induced stresses, which will be described in the following section. Subsequently, static and dynamic simulations are presented to verify the accuracy of this model.

BROWN'S ANALYTICAL MODEL

Dislocations in a persistent slip band are on primary slip planes. Areas of high dislocation density form walls which are separated by regions that are almost dislocation free. The Burgers vector of the dislocations in a single wall can be added up to form a 'super dislocation dipole' representing the wall. These super dislocation dipoles are then spaced uniformly along the PSB as shown in Figure 1.

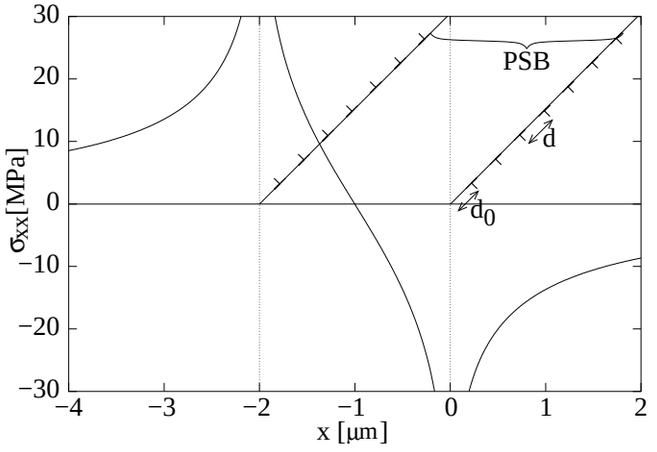


Figure 1. Idealized dislocation distribution in a PSB according to Brown and Ogin [1] and logarithmic singularity in the stress component σ_{xx} parallel to the surface at the root of the PSB.

The super dislocations are then 'smeared' out along the persistent slip band direction. The resulting stress field has been calculated analytically [1] and the resulting stress profile is shown in Figure 1. The stress profile reveals a logarithmic stress singularity at both sides of the PSB emerging at the free surface. The positive stress singularity supposedly leads to the initiation of a mode I crack along the interface between the PSB and the surrounding matrix.

STATIC DISLOCATION CALCULATIONS

To verify the above-mentioned results for a smeared dislocation distribution, discrete dislocation dipoles are placed at both ends of the wall in a PSB. Their stress profile fields are calculated as a function of the distance of the first dislocation to the surface, d_0, and the results are shown in Figure 2.
The stress σ_{xx} parallel to the surface has a maximum at $x \approx -2\mu m$ and a minimum close to $x = 0\mu m$. In this simulation with discrete dislocations the stresses remain finite. In addition, the stresses are not symmetric, i.e. the absolute value of the maxima is smaller than that of the minima and the position of the maxima is shifting with increasing spacing of the first dislocation to the surface.

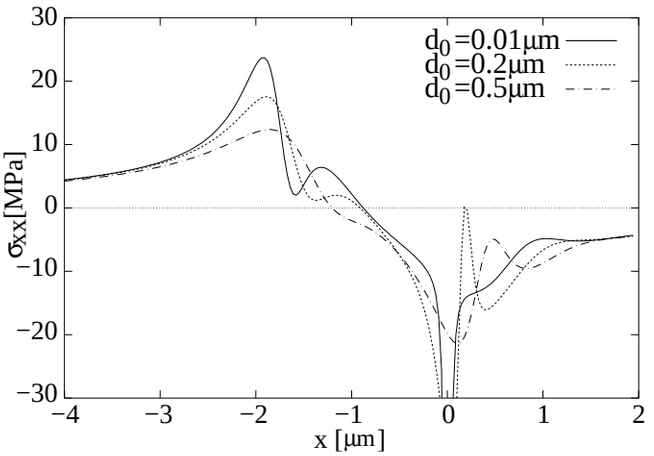


Figure 2. Stress profile at the free surface for different spacings of the first dislocation to the free surface.

DYNAMIC DISLOCATION CALCULATIONS

In addition to considering static dislocation structures, we also perform dynamic simulations where the dislocations can move along predefined slip planes in a single grain near the free surface [2]. This grain has three slip systems ($60°$ from each other) with the primary slip system oriented favorably at $45°$ to the applied load direction. Dislocations are generated from randomly placed two dimensional Frank-Read sources. Their movement is governed by a linear drag relation and they can annihilate with each other or move out at the free surface. Their movement is hindered by obstacles, representing forest dislocations or precipitates. The stress profile after 1897 cycles in a zig-zag fashion is shown in Figure 3.

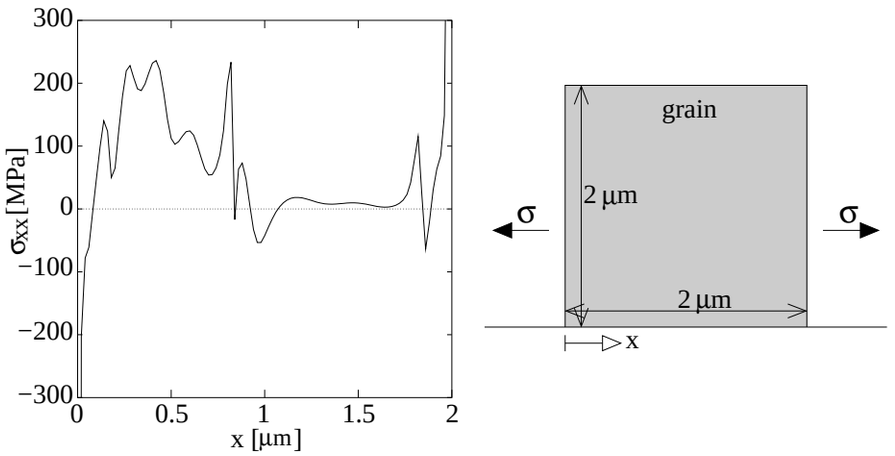


Figure 3. Stress profile at the free surface of a $2 \times 2\mu m$ grain after 1897 cycles.

DISCUSSION

Brown and Ogin [1] assume that the dislocations forming a wall can be smeared out along the persistent slip band. This leads to a dislocation with a Burgers' vector of b/d (d is the spacing of the dislocation dipoles, Figure 1) at the surface. A dislocation cannot stay at the free surface because of the image stress, pulling the dislocation out of the grain. Without a dislocation at the free surface the static dislocation calculations show no singular stress at the free surface. The dynamic simulations confirm the finite stresses at the free surface. The values of the stresses are expected to change with continuing load cycles.

References

[1] Brown, L. M. and Ogin, S. L.: Role of internal stresses in the nucleation of fatigue cracks. In: Bilby, Miller, Willis, *Fundamentals of deformation and fracture*, Eshelby memorial symposium, 501–528, 1984.

[2] Van der Giessen, E. and Needleman, A.: Discrete dislocation plasticity: a simple planar model. *Modelling and Simulation in Materials Science and Engineering*, **3**: 689-735, 1995.

A STUDY ON THE EFFECT OF RESIDUAL STRESS ON FATIGUE BEHAVIOR

Seung-Yong Yang*, Byeongchoon Goo*
*National Research Lab., Korea Railroad Research Institute, Uiwang-City, 437-050, Korea

Summary The effect of residual stress on fatigue crack growth was investigated in terms of finite element analysis. Simulations were performed on a CT specimen in plane strain. An interface-cohesive element that accounts for damage accumulation due to fatigue along the notch direction has been used. Numerical results show that fatigue crack growth rate slows down when compressive residual stress field exists in front of the crack tip.

INTRODUCTION

To extend the life time of metallic structures under fatigue loading, several methods have been tried, for example extending the time period of crack nucleation or repairing whole sections containing cracks fully penetrating through the thickness, etc. Song [1] has proposed to generate compressive residual stress around the crack tip by local heating to delay or stop the fatigue crack growth. Procedures using S-N and ε-N curves are widely being used as criteria for fatigue design.[2] In this paper, we directly simulate the fatigue crack growth by finite element method using a cohesive surface model. The effect of residual stress on delaying fatigue crack growth was investigated. Analyses were performed on a compact tension (CT) specimen in plane strain. The calculations are carried out on the commercial finite element code ABAQUS.

Several cohesive zone models have been suggested to simulate fatigue crack growth [3-4]. In [3], the traction-displacement behavior did not follow a predefined path, but cohesive properties were degraded as damage accumulates due to cyclic loading. In [4], an irreversible cohesive law with unloading-reloading hysteresis was used in finite element analysis to explain experimental observation. The same type of damage evolution law as in [3] was used in our work. The results showed fatigue crack growth slows down with compressive residual stress distribution around the crack tip.

RESIDUAL STRESS BY LOCAL HEATING

Before describing the constitutive laws of the cohesive zone model, we briefly summarize the generation of residual stress by local heating. Fig. 1 shows the plane strain finite element model used to simulate the heating procedure. The height of the model is 75mm, the distance between the notch and the right hand side boundary is 100mm, and symmetric boundary conditions were imposed on the AB line. Heat input of 368 MJ/m^{2}s is applied on the surface of the elements along the CD line moving downward with speed of 2.42 mm/s. The maximum temperature of the specimen increased up to 1500 ^{o}C. Thermo mechanical finite element calculation was performed to obtain the resultant residual stress.

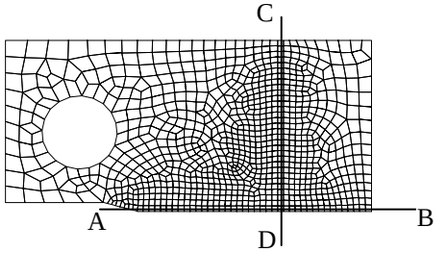


Fig. 1. Finite element mesh for CT specimen.

The cohesive surfaces are embedded along the line AB, and the surrounding volume undergoes elastic-plastic deformation. Changes of thermal and mechanical properties with temperature were considered in the analysis. The yielding strength at room temperature is 250MPa, and decreases to 0MPa at 1200 ^{o}C. Fig. 2(a) illustrates the distribution of vertical component σ_{yy} of the residual stress. One can observe that compressive stress distributes between the notch and the heating line. The maximum level of the tensile stress approaches to the yielding stress.

SIMULATION OF FATIGUE CRACK GROWTH

In this section, a brief description of the cohesive surface model is given, as the framework of the model is already well known by many researchers. The irreversible effective traction-displacement relation in [4] is used combined with the damage evolution equation given in [3] to account for the degradation of the cohesive strength due to fatigue. In this way, fatigue crack growth can be simulated directly without explicitly specifying crack growth criterion. Meanwhile, for normal contact compression, an effective displacement is defined only with the sliding component of the material separation, and the corresponding normal traction is assumed to behave as a linear spring with respect to the normal displacement. The initial cohesive strength was set to 1000MPa, the endurance limit was 150MPa, and the characteristic length parameter δ_c was 50 μm. Cyclic load of 5MN with period 2s is applied. Fig. 2(b) illustrates redistributed vertical residual stress after the crack tip propagates from the notch to the location marked by arrow after 100 cycles. The amount of stress relaxation is not severe since the stress is compressive on the crack face. In this simulation of crack growth, the mesh size Δx of the interface-cohesive element is the same as in Fig. 1 (Δx =2500 μm), but convergent

results were obtained compared with results from much finer model (Δx =200 μ m), and the mesh dependence of solution was not strong.

Fatigue crack growth rate vs. ΔK behaviour is drawn in Fig. 3 for the cases with and without the compressive residual stress. The stress intensity range ΔK was calculated from the specimen without residual stress, and the speed of crack growth was calculated from the simulation results in each case. We can observe that the crack growth rate slows down when compressive stress field exists in front of the crack tip. Meanwhile, the numerically predicted data without residual stress can be fitted to a Paris type power law $da/dN=C\Delta K^n$ with n=3.32.

Bye the way, the material parameters for the cohesive interface were presumed approximately, and they need to be calibrated by comparing with experimental works.

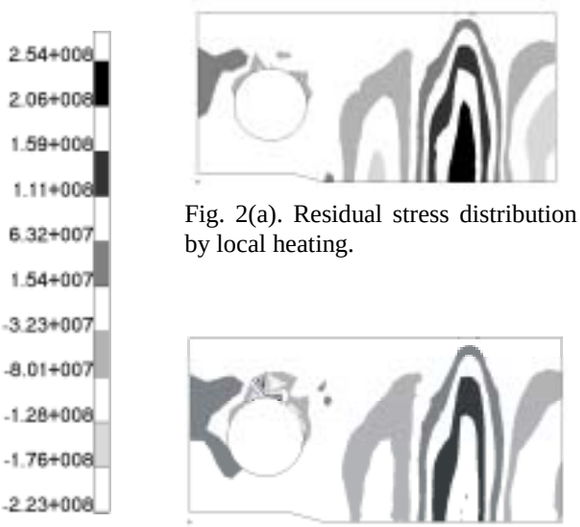


Fig. 2(a). Residual stress distribution by local heating.

Fig. 2(b). Residual stress distribution after cyclic loading. The current location of the crack tip is denoted by arrow.

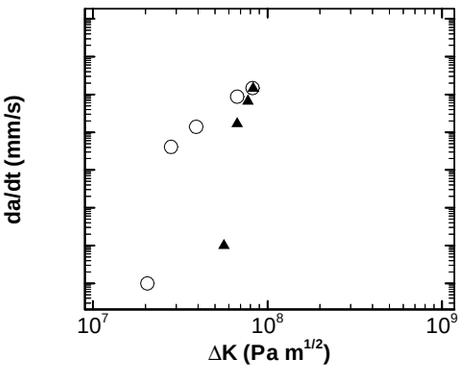


Fig. 3. Numerical fatigue crack growth rates with and without residual stress. Circles are results without residual stress, and triangles are results with residual stress.

CONCLUSIONS

The effect of residual stress on fatigue behaviour was investigated by finite element method incorporating a cohesive zone model with evolutionary damage law. Fatigue crack propagation was simulated for two-dimensional cases with and without compressive residual stress. The following conclusions can be made from the numerical study.

1. When compressive residual stress normal to the crack surface exists around the crack tip, the fatigue crack growth rate is reduced.
2. As the fatigue crack propagates, residual stress is redistributed.

Acknowledgement

This work was supported by the National Research Laboratory (NRL) program of the Korea Ministry of Science and Technology.

References

[1] Song, H.C.: Fatigue Life Extension of Steel Plates with a Through-the-Thickness Crack Using Local Heating. *PhD Thesis*, Seoul National University, 2001.

[2] Stephens, R., et al.: Metal Fatigue in Engineering. John Wiley & Sons, Inc., 2000.

[3] Roe, K.L. and Siegmund, T.: An Irreversible Cohesive Zone Model for Interface Fatigue Crack Growth. *Engineering Fracture Mech.* **70**:209-232, 2003.

[4] De-Andres, A. and Perez, J.L. and Ortiz, M.: Elastoplastic finite element analysis of three-dimensional fatigue crack growth in aluminum shafts subjected to axial loading. *Int. J. Solids & Structures* **36**:2231-2258, 1999.

PROBABILISTIC ANALYSIS OF FATIGUE CRACK GROWTH USING MOMENT METHOD

Ki-Seok Kim, Hyun Moo Koh, Hae Sung Lee
School of Civil, Urban and Geosystem Engineering, Seoul National University, Korea

Summary This paper presents an incremental approach to predict the path and probabilistic distribution of fatigue crack growth using the dual boundary element method. A new iterative scheme using a secant method is proposed to model curved crack growth. To predict the distribution and failure probability of fatigue crack, the second-order moment method using lognormal distribution is incorporated with the proposed incremental formulation.

INTRODUCTION

Fatigue crack growth is one of the most important factors in the design of the steel structures. Numerous experiment and researches have been performed for the prediction of fatigue crack growth [1]. This paper presents an incremental approach to predict the path and probabilistic distribution of the fatigue crack growth using a secant approach and moment method.

A fatigue crack usually does not grow in a straight line due to mixed-mode loadings or asymmetric geometry. Most numerical studies on crack growth adopt the incremental approach [2], in which the direction of crack growth is assumed as the tangent direction at the current crack tip without iterative modification. In this approach, the increment should be very small to describe the crack path because there is no correction. Some iterative scheme has been proposed to consider curved crack growth [3]. However, the increment of crack growth was considered as constant during the iterative modification. For each given increment of fatigue loading, the size of crack increment is evaluated in the integral of Paris-Erdogan equation along the crack path and should be modified according to the change of crack path. In this paper, a new iterative scheme is proposed considering the change of both the direction and growth rate.

Fatigue tests show great dispersion in the distribution of fatigue life due to many factors including imperfection of material [4]. Probabilistic approaches, such as the first-order reliability method (FORM) and the Monte-Carlo simulation (MCS), are devoted to estimate the failure probability. On the other hand, moment methods are adopted to estimate the moments of the response. Hong et al. [5] proposed a second-order third-moment method for the estimation of the failure probability. However, geometric changes according to crack growth were not considered because they used a very simplified form of Paris-Erdogan equation. In this paper, moment method is incorporated with the incremental formulation, in which geometric changes are taken into account.

FATIGUE CRACK GROWTH

The dual boundary element method (DBEM) [3] is employed for the analysis of two-dimensional plates with cracks. Paris-Erdogan law and maximum circumferential stress criterion are adopted for the crack growth rate and tangent direction, respectively. The mixed-mode stress intensity factors (SIF) are evaluated by J-integral. Crack growth is discretized by making incremental crack growths for a given increment of fatigue loading. In each loading step, both crack increments and growth path are updated iteratively. In the first iteration, the direction and size of crack increment are determined by using the SIF obtained at the current crack tip. In the later iterative modification, the SIF at the new crack tip is also utilized as well as the SIF at the previous one. For a given loading step, the size of increments is determined by evaluating iteratively the integral of Paris-Erdogan equation with trapezoidal rule. Each crack path is assumed as a parabola, but discretized as a straight line for the simplicity of integration in the DBEM. The parabola is modified iteratively utilizing the tangent direction determined at the new crack tip until the new direction converges to the tangent of the parabola assumed previously.

PROBABILISTIC ANALYSIS

Randomness in the initial crack, fatigue loading and material properties have an effect on the distribution of crack growth. The moment method gives an approximate solution to the problem of determining the behaviour of the dependent random variables. In the second-order moment method, response function is approximated by second-order Taylor expansion with respect to random variables. Approximations of the moments of the response function can be determined from those of the random variables. For simplicity, only the initial crack length is selected as a random variable. For each loading step, in the proposed incremental formulation, the moments of crack length are approximated by those of the previous loading step. The derivatives used in the approximations of moments are derived from the Paris-Erdogan equation. The first derivative is as follows:

$$\frac{\partial a_{n+1}}{\partial a_n} = \frac{K^m(a_{n+1})}{K^m(a_n)} \tag{1}$$

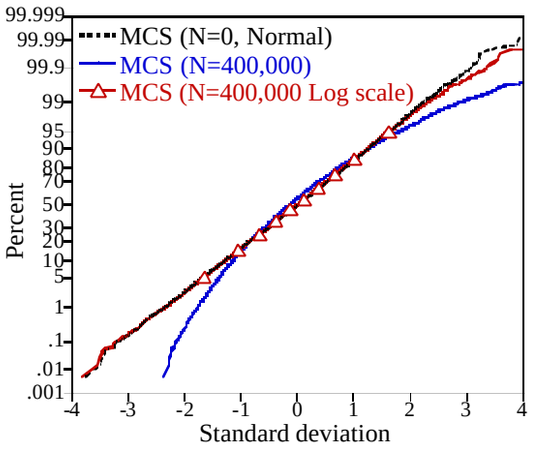


Fig. 1. Probabilistic paper of the crack distribution

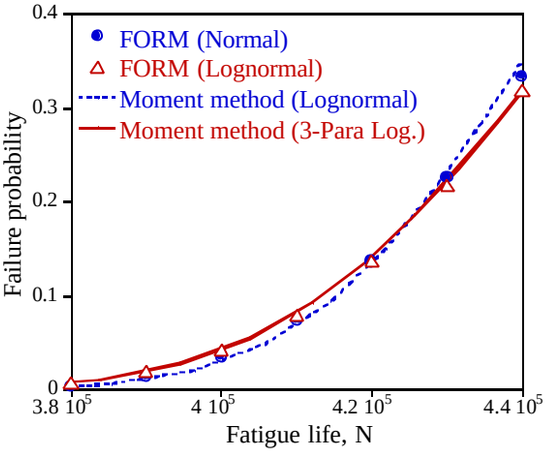


Fig. 2. Failure probability

Table 1. Crack distribution obtained from the proposed moment method and MCS

	Initial distribution (N=0)			Derived distribution (N=400,000)		
	Mean (cm)	SD (cm)	Skewness	Mean (cm)	SD (cm)	Skewness
Moment method	0.2000	0.0200	0.0000	1.3173	0.3764	0.8805
MCS (Size=10,000)	0.2001	0.0199	-0.0607	1.3170	0.3660	1.0140

where, a_n, K and m denote the crack length of n-th loading step, equivalent SIF and a coefficient used in Paris-Erdogan law, respectively. In this study, two- and three-parameter lognormal distribution is used to estimate the crack growth. In FORM, several crack-growth analyses for a given service life are required for the optimization to find the design point. On the other hand, in moment method, failure probability is directly predicted from the distribution derived at each loading step, and so only one crack-growth analysis is required. It is assumed that failure occurs when the fatigue crack reaches a critical length defined by the toughness of a material.

EXAMPLE

The proposed method is applied to 20cm× 40cm rectangular steel plate (E = 21,000 kN/cm^2, v = 0.3) with single edge-crack in the middle of the left side. This plate is subject to constant-amplitude loading which ranges from zero to 16.5 kN/cm^2. The coefficients of the Paris-Erdogan equation are $C = 1.886\times10^{-10}$ and m = 3.0. Mean and standard deviation (SD) of the initial crack length are 0.2cm and 0.02cm, respectively. Critical crack length is about 2.13cm. This plate is discretized by 293 nodes and 140 quadratic boundary elements.

Fig. 1 shows the initial and derived crack distribution obtained by MCS with 10,000 samples after 400,000 loading. In case initial distribution is normal, derived distribution approaches lognormal. Table 1 shows that the proposed moment method well approximates the mean and SD while there is 13% difference in skewness. It is believed that mean and SD is more important than skewness in most engineering problems. Also, the difference in skewness has a very little effect on the estimation of failure probability as shown in Fig 2. Failure probabilities obtained by the proposed method are compared with the results of FORM in Fig. 2. In FORM, 4 ~ 6 times of crack-growth analysis executed for a given service life. If failure probabilities are calculated for 10 service fatigue lives, around 50 times of crack-growth analysis should be executed. Two-parameter lognormal shows good fit for the initial normal distribution. In case of initial lognormal distribution, three-parameter lognormal is appropriate.

CONCLUSIONS AND FURTHER STUDY

Proposed moment method produces a good approximation of the crack distribution compared with the results of MCS. For the calculation of the failure probability, moment method needs much less computational cost than FORM. It is shown that lognormal is appropriate for the fatigue crack distribution. Additional researches on multivariable reliability problems should be performed.

References

[1] Kanninen M. F., Popelar C. H.: Advanced Fracture Mechanics. Oxford University Press, New York 1985.

[2] Lua Y. J., Liu W. K., Belytschko T.: Curvilinear Fatigue Crack Reliability Analysis by Stochastic Boundary Element Method. Int. J. Numer. Methods Eng. 36:3841-3854, 1993.

[3] Portela A., Aliabadi M. H., Rooke D. P.: Dual Boundary Element Incremental Analysis of Crack Propagation. Comput. Struct. 46:237-247, 1993.

[4] Kim J., Shim D.: The Variation in Fatigue Crack Growth due to the Thickness Effect. Int. J. Fatigue 22:611-618, 2000.

[5] Hong Y. J., Xing J., Wang J. B.: A Second-order Third-moment Method for Calculating the Reliability of Fatigue. Int. J. Pressure Vessels Piping 76:567-570, 1999.

ENERGY RELEASE RATE APPROACH FOR DELAMINATION IN A FATIGUE CRACK CONFIGURATION IN GLARE

René Alderliesten*
*Delft University of Technology, Faculty of Aerospace Engineering, Structures and Materials Laboratory, Kluyverweg 1, 2629HS Delft, The Netherlands

Summary Fatigue Crack growth in a Fibre Metal Laminate like Glare is accompanied by delamination growth at the interface between the aluminium and glass fibres. To incorporate this delamination growth in prediction methods the Energy Release Rate approach is applied. Tests were performed to determine the relationship between the 2D-delamination growth and the Energy Release Rate. The followed methodology and the experimental results are presented in this paper.

INTRODUCTION

Fibre Metal Laminates (FML's) were developed at Delft University of Technology as a family of hybrid materials that consist of bonded thin aluminium sheets and fibres embedded in epoxy. Two variants were successively developed for their excellent fatigue crack resistant behaviour: Arall, containing aramid fibres, and Glare, containing S2-glass fibres. The Glare variant will be applied in the upper fuselage of the wide-body aircraft Airbus A380, see figure 1.

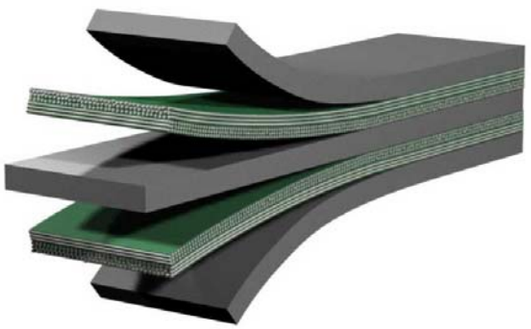


Figure 1. Glare will be applied in the Airbus A380

Besides the laminates with fibres oriented in one direction, denoted as uni-directional, the laminate concept provides the possibility to apply fibres in any direction. An illustration of a typical cross-ply lay-up is given in figure 2, where three aluminium layers are interspersed with two cross-ply fibre layers. This configuration with equal amount of fibres in both directions is for Glare generally denoted as a Glare3 grade with a 3/2 lay-up.

Fatigue crack propagation in Glare

Due to the presence of bridging fibres the crack growth retardation of Glare is excellent, showing very small and approximately constant crack growth rates. Since crack propagation in Glare occurs in the metal constituents only, the applied methodology utilises Linear Elastic Fracture Mechanics to describe the behaviour. This means that the effective Stress Intensity Factor (SIF) at the crack tips in the aluminium layers is divided in two components, one describing the crack opening effect due to the far field stress and one describing the restraining effect of the bridging fibres.


Figure 2. Typical cross-ply lay-up of a FML

To incorporate the effect of the bridging fibres in the expression for the effective SIF, the bridging stress at any location along the crack length should be known. The bridging stress at any location depends on the delamination shape and the crack opening shape along the crack length, which means that a delamination growth criterion should be determined. Whereas the crack opening in the aluminium is mainly a mode I fracture, the delamination at the interfaces is attributed mainly to the mode II fracture. The current investigation uses the Energy Release Rate (ERR) approach to determine the relation between the delamination growth and the mode II SIF at the delamination tip.

APPLIED METHODOLOGY

In early investigations it was assumed that the bridging stress was constant along a fatigue crack in Glare [1,2]. In accordance with the constant bridging stress the delamination shape was thought to be elliptical. However, recent investigations have clearly shown that the delamination shape is not elliptical and that the bridging stresses vary along the crack [3].

In order to model the delamination growth in a 3D fatigue crack configuration in Glare, as illustrated in figure 3 (a), and to verify it with experimental results, the configuration is simplified to a 2D delamination configuration as depicted in figure 3 (b). This configuration is only valid in case the crack length a in figure 3 (a) equals infinity. For the 2D configuration the entire axial load will be transferred through the fibre layer over the cracks in the aluminium layers. For this configuration the far field stresses in the individual layers and the fibre stresses in the delaminated layer can be calculated assuming constant stress distribution through the thickness. From these stresses the Energy Release Rate (ERR) can be calculated, which is related to the mode II SIF at the delamination tip.

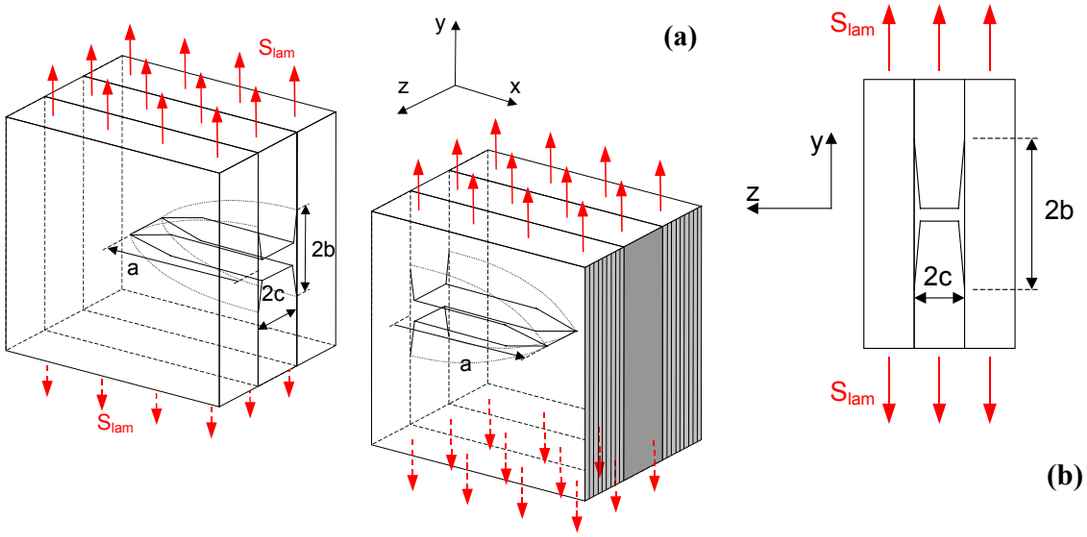


Figure 3. Fatigue crack configuration in Glare (a) and the 2D presentation of the delamination growth (b)

From experiments on 2D delamination specimens the relation between the ERR and the delamination growth can be obtained, from which a Paris type equation can be derived

$$\frac{db}{dN} = K\Delta G_d^m$$

where db/dN is the delamination growth rate and K and m are constants following from the test results. This relation can then be incorporated into the methods describing the 3D fatigue crack configuration in Glare.

EXPERIMENTS AND RESULTS

To incorporate the effect of the prepreg lay-up several Glare grades were tested: Glare 2 (uni-directional fibres layers) and Glare 4 (cross-ply fibre layers with 67% in rolling direction and 33% in transverse direction). The Glare delamination specimens were tested on a 100 kN servo-hydraulic, closed loop mechanical and computer controlled testing machine at a frequency of 10 Hz. The delamination length b was measured from both sides of the specimen as well as the crack opening in the aluminium layers.
Based on the fact that the ERR is not affected by the delamination length, each specimen was stepwise tested at several subsequent load levels with the same stress ratio. With this approach several sets of db/dN - ΔG_d could be obtained from one test specimen.
The ERR depends on the prepreg lay-up, however the db/dN - ΔG_d relation differs for the various prepreg lay-ups. Using a correction for the stress ratio, an effective ERR was determined to obtain the various curves for db/dN - $\Delta G_{d,eff}$. This relationship can be applied in the 3D configuration if the effective ERR along the delamination boundary is known.

CONCLUSIONS

From the current investigation it is concluded that the delamination behaviour under mode II loading can be related to the calculated effective ERR $G_{d,eff}$. The relation can be described by a Paris type relation, which is different for each Glare grade. This 2D relation must now be incorporated in the 3D fatigue crack configuration to determine the delamination criteria and to determine the delamination shape as result of the other parameters in this crack configuration.

References

[1] Marissen R.: Fatigue Crack Growth in ARALL, A hybrid Aluminium-Aramid Composite Material, crack growth mechanisms and quantitative predictions of the crack growth rate. *PhD Thesis,* TUDelft, Fac. of Aerospace Eng. Delft, 1988.

[2] Roebroeks G.: Towards GLARE - The Development of a Fatigue Insensitive and Damage Tolerant Aircrafts Material. *PhD Thesis,* TUDelft, Fac. of Aerospace Eng. Delft, 1991.

[3] Guo X.J., Wu X.R.: Bridging stress distribution in a center-cracked fiber reinforced metal laminates: modelling and experiment, *Eng Fract Mech* **63**:147-163, 1999.

MODELLING FATIGUE CRACK GROWTH WITH TIME-DERIVATIVE EQUATIONS.

Marion Risbet[*], Sylvie Pommier[**], Michel Clavel[*]
[*] *MSSMAT, Ecole Centrale Paris, Grande Voie des vignes, 92295 Chatenay Malabry, cedex, France.*
[**] *Laboratoire de Mécanique et de Technologie, ENS de Cachan, 61, avenue du Président Wilson, 94235, Cachan Cedex, France.*

Summary Fatigue crack growth is difficult to predict in case of complex loadings because of load history effects. A model based on a set of time-derivative equations has been developed within the framework of the thermodynamics of dissipative processes. It consists in a crack propagation law and a constitutive behaviour law for the cracked structure determined from finite elements analyses. Capabilities of the model to reproduce typical fatigue results have been tested and proved.

INTRODUCTION

Engineering models struggle with loads-load interaction effects in fatigue crack growth. Monotonic fatigue crack growth rates are usually successfully predicted using the Paris law. Under non-monotonic fatigue, damage accumulation rules are employed. The crack extension after a given lifetime is calculated by summing the contributions to the crack extent of each elementary fatigue cycle Ni, inside a non-monotonic loading sequence.

$$a(N+1) = a(N) + \left[\frac{da}{dN}\right]_{N_i} = a(N) + C.\left(\Delta K^i_{eff}\right)^m = a(N) + C.\left(K^i_{\max} - K^i_{op}(history)\right)^m$$

The crack opening stress intensity factor (K_{op}) can be introduced at this stage, in order to account for history effects inherited from crack tip plasticity [1]. Various methods are employed to determine the evolution of K_{op} with load history. It was shown previously that the sensitivity of K_{op} to load history is related to the sensitivity of the material itself to load history, which can be described using a constitutive behavior for the material including a kinematics and an isotropic hardening [2]. Provided that suitable constitutive equations are employed for the material, the finite element method is successful in predicting the evolution of K_{op} with load history and the evolution of the crack growth rate under a cyclic but non-monotonic fatigue loading.
However, at this stage there is no getting away from a fundamental difficulty of such approaches. As a matter of fact, the Paris law is a cycle-derivative equation. Therefore, before applying any damage accumulation rule, elementary cycles should be extracted from a loading sequence which may not be cyclic. For this purpose, counting methods are employed, such as, for instance, the "rainflow" method. With that method, small amplitude "cycles" are embedded inside high amplitude "cycles". However, in order to apply the damage accumulation rule, elementary cycles have to be applied consecutively, which imposes to make a choice. For any given portion of a complex signal, various combinations are always possible. The selection of the most conservative configuration is difficult because it depends on load history.
To sum up in a few words, because the Paris law is a cycle-derivative equation, cycles have to be extracted from real signals. However, because of load history effects this operation is questionable. Therefore, if we aim at taking into account load history effects, this operation should be avoided because it may modify significantly the load history. Therefore, a set of time-derivative equations was searched for fatigue crack growth, including load history effect inherited from crack tip plasticity.

BACKGROUND OF THE MODEL

The model was developed on the basis of the thermodynamics of dissipative processes. Three global variables are employed to characterize the velocity field at crack tip, the crack growth rate da/dt, the rate of plastic blunting dρ/dt and the rate of elastic crack opening. Thermodynamics counterparts are introduced for each velocity variable. Since crack tip residual stresses are well known to considerably influence fatigue crack growth under variable amplitude loading, the elastic energy stored inside the crack tip plastic zone is included in the energy balance equation. This equation leads to establish a yield criterion for the cracked structure. In this criterion, the energy stored within the crack tip plastic zone (residual stresses) leads to the appearance of a kinematics hardening term for the cracked structure. The second principle of thermodynamics provides an inequality between da/dt and dρ/dt, that the instantaneous cracking law employed in the model should observe. Finally, in the present model, the following crack propagation law was chosen, in agreement with the second law:

$$\frac{da}{dt} = \frac{\alpha}{2}\left\langle -\frac{d\rho}{dt}\right\rangle \quad with \begin{cases} \frac{d\rho}{dt} \geq 0 & \left\langle -\frac{d\rho}{dt}\right\rangle = 0 \\ \frac{d\rho}{dt} < 0 & \left\langle -\frac{d\rho}{dt}\right\rangle = -\frac{d\rho}{dt} \end{cases}$$

Once this propagation law is set, the crack growth rate is determined from the crack tip blunting rate. Therefore, the evolution law of crack tip blunting is still needed. The evolution of crack tip blunting during the loading sequence, is merely a mechanical problem and can be determined using the finite element method.

In this purpose, the conjugate force ϕ as opposed to crack tip blunting has been considered. When there is dissipation, this force is the sum of a conjugate force as opposed to plastic deformation within the crack tip plastic zone ϕ_{eff} and of a conjugate force as opposed to the storage of elastic energy within the crack tip plastic zone ϕ_X.

$$\phi = \phi^{eff} + \phi^{X}$$

This equality should always be observed when there is dissipation. Therefore this equation is a yield criterion for the cracked structure. The evolution equations of ϕ_{eff} and of ϕ_X with respect to an increase of the crack length or to a variation of crack tip blunting are still needed. These equations are the constitutive equations for the cyclic plasticity of the cracked structure.

From the finite elements calculations, it appeared that there are two distinct thresholds for the plasticity of the cracked structure. The first one corresponds to the plasticity within the cyclic plastic zone and the second one to the extent of the monotonic plastic zone. The "cyclic" threshold is reached first, and is let aside as soon as the "monotonic" threshold is activated. In such a case, four internal variables are now necessary :ϕ_m^{eff} and ϕ_c^{eff} respectively opposed to plastic deformation within the monotonic and the cyclic plastic zone, ϕ_m^{X} and ϕ_c^{X} respectively opposed to the storage of elastic energy within the monotonic and the cyclic plastic zone.

Various types of loading schemes were employed to determine the partial derivative of each of these four internal variables with respect to an increase of the crack length, and with respect to a variation of crack tip blunting. A set of 8 partial equations has been found with the involvement of 10 parameters. Except for the parameter α in the crack propagation law, the material parameter are determined using the finite element method and depend on the specific mechanical behaviour of the material.

The model was also implemented and tested. It reproduces successfully the Paris law under monotonic fatigue (fig.1). It allows also reproducing well known effects in non-monotonic fatigue, such as the stress ratio effect and the overload retardation effect.

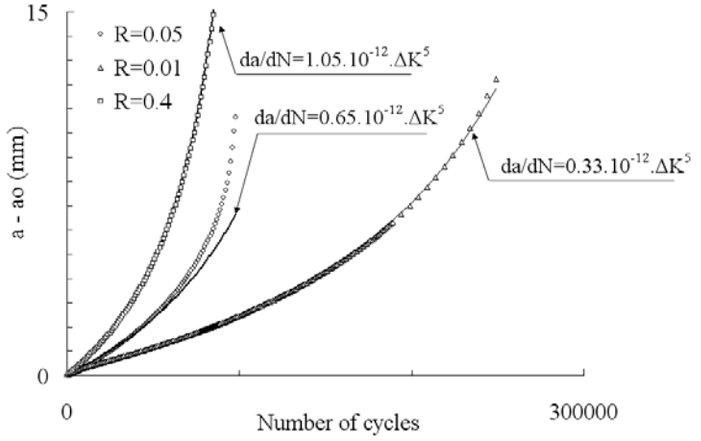


Fig. 1: Crack extent (a_o=10 mm) as predicted using the present model under a sinusoidal signal with a stress ratio equal to 0.01, 0.05 or 0.4.

CONCLUSION AND PERSPECTIVES

This approach appears to be promising to deal with the crack propagation previsions under variable amplitude loadings. It allows to free from the cycles extraction techniques by following directly the crack advance as a function of time. Moreover, it is expected to deal with the coupling of fatigue phenomena with time-dependent mechanisms such as oxidation and creep. The experimental validation of the model remains to be done by confronting numerical evolutions with crack propagation measurements. The extension of the model to multiaxial loadings is also planned.

References

[1] Skorupa M.: Load interaction effects during fatigue crack growth under variable amplitude loading – Part I : Empirical trends and Part II : Qualitative interpretation. *Fat. Fract. Eng. Mat. Struct.*. **21**:987-1006, 1999.

[2] Pommier S., Cyclic plasticity and variable amplitude fatigue *Int.. Jour. Fat.* **25**:983-997, 2003.

CHARACTERISTICS OF VERY-HIGH-CYCLE FATIGUE FOR A HIGH CARBON LOW ALLOY STEEL

Youshi HONG, Cheng-en ZHOU
LNM, Institute of Mechanics, Chinese Academy of Sciences, Beijing 100080, China

Summary This paper describes an experimental investigation on the behavior of very-high-cycle fatigue (VHCF) for a high carbon low alloy steel. The results shows that, fatigue failure may occur at relatively low loading capacity with the number of cycles larger than 10^7. At the regime of number of cycles to failure between 10^6 and 4×10^8, fatigue cracks almost initiated in the interior region of specimen. Fish-eye patterns were the main characteristics of VHCF.

INTRODUCTION

Very-High-Cycle Fatigue (VHCF) is the phenomenon of fatigue damage and failure of metallic materials or structures subjected to 10^8 cycles of fatigue loading or beyond. With the advancement of society and the development of technology, a variety of engineering structures and their components, such as air crafts, automobiles, ships, railway, bridges, etc., should be able to endure 10^8 loading cycles or more of safe performance. However, in the traditional fatigue study, research attention was only made on the fatigue process for up to 10^7 loading cycles. Whether a metallic material subjected to a relatively low loading force will suffer fatigue damage, when it is experienced 10^8 loading cycles, remains an unclear issue. This paper attempts to reveal the behavior and mechanism of VHCF for metallic materials. A high carbon low alloy steel was used, as an example, to investigate the behavior of VHCF for such a metallic material.

EXPERIMENTAL PROCEDURE

The test material was a high carbon low alloy steel with the main composition of C 1%, Cr 1.5% and Fe balance. The specimens were heated at 1108K then quenched in oil, followed by tempering at 453K for 2 hours. The yield stress of specimen was 1900MPa. The specimen for fatigue testing was hour-glass type with the minimum section diameter of 3mm as shown in Fig. 1. Fatigue testing was carried out in a rotating loading machine with a cyclic frequency of 52.5Hz. The test was at room temperature in normal laboratory environment.

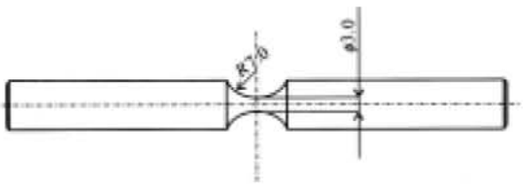


Fig.1 Schematic of specimen (dimensions in mm).

EXPERIMENTAL RESULTS

Figure 2 is the results of the fatigue tests showing the data of the applied maximum stress versus number of cycles to failure. Note that the nominal fatigue limit of this alloy is around 1250MPa. Most data in Fig.2 are below such limit indicating that fatigue failure occured at the loading capacity lower than the limit based on traditional concept. In such case, the initiation of fatigue crack was at the interior of specimen instead of on the surface. It is seen that, at the same maximum stress of loading, the life time of specimen with crack initiation at the interior is superior in comparison with the specimen with crack initiation at surface area. This suggests that

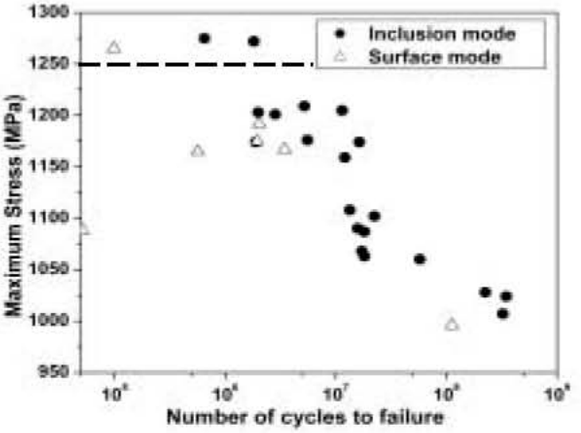


Fig.2 Results of fatigue testing.

the measures of strengthening surface state and the reduction of the probability for surface crack initiation may shift fatigue damage mode from surface to interior so that to improve the fatigue resistance.

FRACTOGRAPHY OBSERVATIONS

Scanning Electron Microscopy (SEM) was used to examine the fracture surface of fatigue failure specimen. The observations showed that, the inclusion near the surface is very likely the origin of fatigue crack. Figure 3 is an example of "fish-eye" pattern. We may see the morphology in different local regions labeled 1, 2 and 3. Local region 1 is the

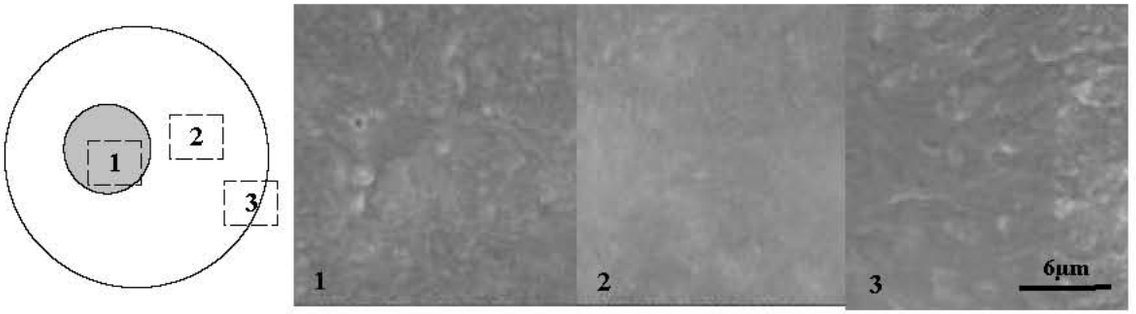


Fig.3 SEM photographs showing morphology of different local regions of a "fish-eye".

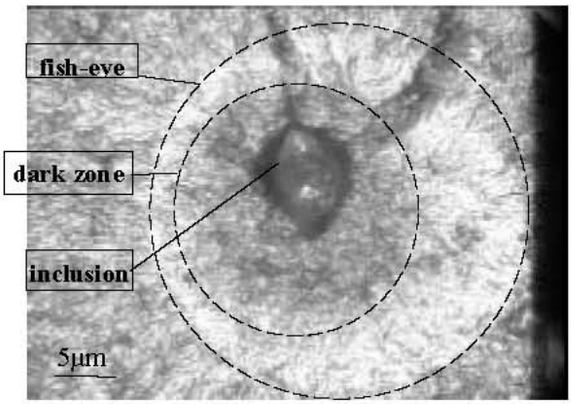


Fig.4 General view of a "fish-eye".

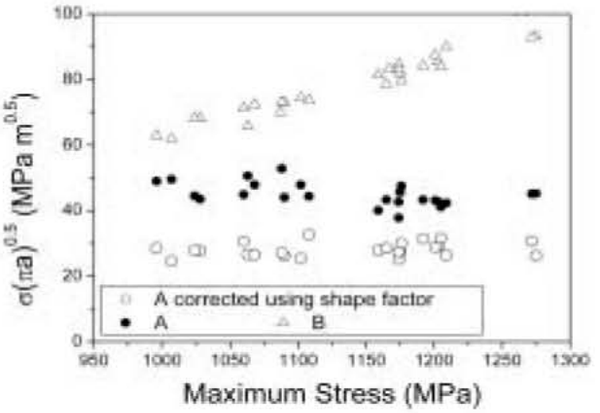


Fig.5 Estimation of fracture toughness vs max stress.

origin of the "fish-eye" i.e. the source of crack initiation. Figure 4 shows the entire morphology of a "fish-eye". The shape of the "eye" is almost circular. Therefore we measured the equivalent diameter of the "eye". Based on this measurements we are able to estimate the stress intensity factor and the results are given in Fig,5, where A is related to the inclusion area and B is related to dark zone area. The corrected value for A zone is about 30MPam$^{1/2}$, which is comparable to the fracture toughness of the test material. Further analysis obtained that the value of stress intensity factor for fatigue crack initiation is very close to the fatigue threshold of the material (about 6MPam$^{1/2}$).

CONCLUSIONS

Fatigue failure may occur below the traditional fatigue limit stress and the life time is larger than 10^7 cycles of loading. Such damage mostly initiates from the inclusion underneath the surface. The formation of "fish-eye" is the main characteristics of very-high-cycle fatigue and it is responsible for the majority of total fatigue life.

MODELLING OF SHORT FATIGUE CRACK GROWTH IN A METAL IN HCF RANGE

D. Kocańda
Military University of Technology, Depart. of Mechanical Engineering, Kaliskiego 2, 00-908 Warszawa, Poland

Su*mmary:* Modelling of short fatigue crack growth in a polycrystalline metal in high cycle fatigue range (HCF) is the subject of the paper. For this goal a fracture mechanics approach was adopted to predict stage-I and stage I-like crack growth. On the contrary, stage II crack growth is modelled using a probabilistic approach. Special attention is paid on the short crack behaviour under reversed cyclic torsion.

Description of the model

Short fatigue crack growth is analysed in three stages: as a small crack of a size comparable to the grain size (stage I), a microstructurally short crack (stage I-like) and a physically short crack (stage II). Stages I and I-like crack growth are strongly microstructurally depended and the crack advances under mode II. In the model the stage I crack growth is associated with one slip band and its growth is affected by a local elastic-plastic field resulted from a dislocation pile-up at the grain boundary. Assuming that a slip band of length L_{sb} and width h is approximated by a flattened elliptic crack of same length, the radius ρ of the crack tip and crack opening displacement (COD) δ_{II} $(h=\delta_{II}=2\rho)$ then the amplitude of a local effective shear stress $\tau_{a,eff}(r,\theta)$ ahead of crack-slip band gets the form in polar coordinates:

$$\tau_{a,eff}(r,\vartheta)=\frac{2\cdot\left(m\cdot\tau_{a,appl}-\tau_o\right)\sqrt{\pi L_{sb}}}{\sqrt{2\pi\left(c\delta_{II}+r\right)}}\cos(\theta/2)\left[1-3\sin^2(\theta/2)\right] \tag{1}$$

where: $\tau_{a,appl}$ is the amplitude of applied cyclic shear stress, τ_o is an intrinsic friction stress, m is the Taylor orientation factor, ρ is the radius of crack tip $\rho=c\delta_{II}$, r is a distance from the tip of crack-slip to a current point, c is constant geometric coefficient. The quantity θ is the angle between the slip band plane and the arrow to a current point.
The mechanism of stage I-like crack growth relies on repeated transfer of slip bands from grain to grain and crack nucleation on the slip band in the successive grains. Mikrocrack is blocked at the grain boundary until the shear stress at the crack tip achieves a relevant value allowing it to overcome the structural barrier and to spread slip band in the next grain on a slightly misoriented plane. Applying the Irwin's idea of modified crack length in the elastic-plastic fracture mechanics approach the local effective stress $\tau_{a,eff}(r)$ that acts at the tip of stage I-like crack in the plane of the crack is estimated as follows:

$$\tau_{a,eff}=\frac{K_{II\,eff}}{\sqrt{2\pi\left(c_e\delta_{II}+d^*\right)}}=\frac{1}{\sqrt{2\pi\left(c_e\delta_{II}+d^*\right)}}\left(m\cdot\tau_{a,appl}-\tau_{res}\right)\frac{\sqrt{\pi a}}{\sqrt{1-\frac{1}{2}\left(\frac{\tau_{a,appl}}{\tau_y}\right)^2}} \tag{2}$$

where: a denotes the length of a physical crack, r_{pl} is the radius of reversed plastic zone, τ_y is the yield stress, $d^*=r_{pl}$, c is a constant coefficient, τ_{res} is the resistance of material to dislocation motion [1,2,3]. The condition required for crack growth from grain to a grain is that $\tau_{a,eff}=\frac{K_{IIC}}{\sqrt{2\pi d}}$, where K_{IIC} means a critical stress intensity factor for mode-II cracking, d is an average size of the grain in a polycrystalline metal. Interaction with a successive grain boundary leads to decreasing of crack growth rate. This trend in the growth rate is simulated by crack propagation equation:

$$\frac{da}{dN}=B\left(\tau_{a,eff}\right)^n\left(L-a\right) \tag{3}$$

where: B and m are material constants, L means a characteristic dimension in the matrix structure like as length of ferrite band or transient length between stage I and stage II crack growth.
Crack growth in the stage II (physically short crack) exhibits smaller dependence or even independence on the microctructural barriers. Crack growth rate shows the oscillations with a decreasing amplitude as the crack becomes longer up to a transient length. In the paper stage II crack growth is modelled using probabilistic approach. Fatigue process in an elastic-plastic material is regarded as a set of random values of crack length a_i at the related time t_i. Main equation of a dynamics of crack growth is the Fokker-Planck partial differential equation (4):

$$\frac{\partial U(a,t)}{\partial t} = -\lambda(t)\cdot \Delta a \frac{\partial U(a,t)}{\partial a} + \frac{1}{2}\lambda(t)\cdot \Delta a^2 \frac{\partial^2 U(a,t)}{\partial a^2} \tag{4}$$

where $U(a,t)$ is a probability density function of that event that a crack of the length a was found in a time t, Δa means crack length increment, $\lambda(t)$ – frequency of cyclic load.
Constitutive equation is formulated in order to predict fatigue crack growth :

$$\frac{da}{dt} = C_{II}\,(CTOD)^n \tag{5}$$

where CTOD means crack tip opening displacement defined on the base of the Dugdale-Barenblatt model, C_{II} and n are material constants.
Equation (5) gives the rule for estimating the crack length increment Δa. After substitution it to the equation (4) and making the assumption of the Gaussian shape of the probability density function $U(a,t)$ one can derive the form for an average crack length and average crack growth rate at the time t.
Ability of the model proposed to predict the short crack growth has been verified using experimental data gathered for an hour glass shaped specimens of normalised 0.45% carbon steel fatigued under reversed torsion. Experimental curves that reflect the crack growth behaviour in the examined specimens indicated that the stage I and stage I-like crack growth cover the crack length range up to 130 μm. It relates to 20% of total life in each case of the tested specimens independently on the applied stress. Stage II crack growth comprises the crack length up to the threshold length =400 μm. It relates to 60-70% of total life in 0.45% carbon steel depending on the applied stress. Experimental and predicted plots of crack growth rate versus crack length and stress ratio N_i/N_f presents Fig. 1.

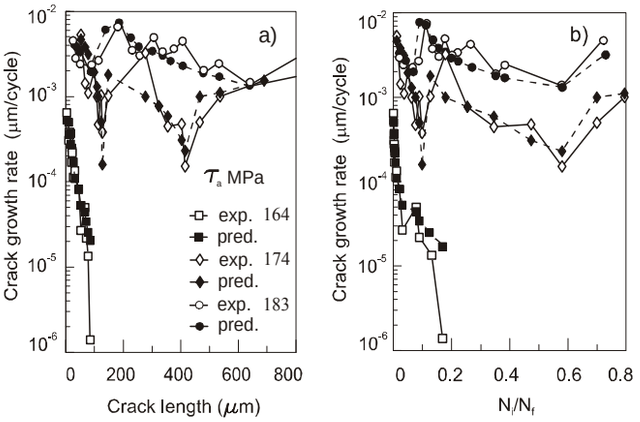


Fig. 1. Experimental and predicted plots of crack growth rate versus crack length and stress ratio Ni/Nf

CONCLUSION

The present model of short crack growth description carries significant modifications in the pre-existed models developed by authors [4, 5]. Taking into considerations the mechanism of crack growth in the stage I and stage II of short crack growth behaviour one can receive better prediction of crack growth as well as better estimation of fatigue life of a component. Experimental plots performed in the work indicate a long lasted period of short crack behaviour under reversed torsion in relation to the total life N_f.

References:

[1] G. P. Karzov, B. Z. Margolin, W. A Svecova: Physico-mechanical modelling of fatigue process, Polytechnika Press, 1993 (in Russian)
[2] A. Bochenek: Basis of fracture mechanics: Częstochowska Politechnika, 1999 (in Polish)
[3] S. Zuyu, E.De los Rios, K.J. Miller; Modelling of small fatigue cracks interacting with grain boundaries. J. Fatigue Fract. Engng Mater. Struct. **14**, 277-291, 1991
[4] D. Kocańda, S. Kocańda, H. Tomaszek: Probabilistic approach to the short and long crack growth description in a notched member. Proc. Seventh Int. Fatigue Congress, Fatigue'99, China, **4/5**, 2673-2678, 1999
[5] D. Kocańda, S. Kocańda, H. Tomaszek: Probabilistic description of fatigue crack growth in a titanium alloy under complex stress state, Proc. Eighth Int. Fatigue Congress, Fatigue 2002, Sweden, **2/5**, 1299-1306, 2002

A FRACTAL COHESIVE CRACK MODEL

by
Michael P. Wnuk
College of Engineering and Applied Science
University of Wisconsin - Milwaukee

1. MATHEMATICAL PRELIMINARIES

In order to investigate the size effects associated with imperfect materials weakened by voids and crack-like defects, we need to establish a characteristic length defined by the material microstructure and geometry of the defect. A certain length parameter, R, is embedded in all cohesive crack models. Equilibrium between the restraining tractions $S(X) = S_0 G(X)$ applied over the end zone itself, is determined by the finiteness condition

$$K_{tot}(\sigma, S) = K_I(\sigma) + K_{coh}(S) = 0 \tag{1.1}$$

With the pressure σ applied to the crack surface, $|X| \le a$, and the pressure $p = \sigma - S(X)$ applied over the end zones, $a \le |X| \le a + R$, equation (1.1) reads

$$\begin{aligned} &2\sqrt{\frac{a+R}{\pi}}\left\{\int_0^a \frac{\sigma\, dX}{\sqrt{a^2 - X^2}} + \int_a^{a+R} \frac{(\sigma - S(X))dX}{\sqrt{a^2 - X^2}}\right\} \\ &\qquad = 2\sqrt{\frac{a+R}{\pi}}\left\{\frac{\pi}{2}\sigma + \int_a^{a+R} \frac{-S(X)\, dX}{\sqrt{a^2 - X^2}}\right\} = 0 \end{aligned} \tag{1.2}$$

When the nondimensional loading parameter $\pi\sigma/2S_0$ is denoted by Q, the condition (1.2) can be re-written as

$$Q = \int_a^{a+R} \frac{\widetilde{G}(X)\, dX}{\sqrt{a^2 - X^2}} \tag{1.3}$$

Here, the cohesive stresses are given by the Wnuk-Legat distribution law, cf. [2],

$$\widetilde{G}(X) = \left(\frac{X-a}{R}\right)^n \exp\left[\omega\left(\frac{a-X}{R}\right)\right] \tag{1.4}$$

The material parameters n and ω are subject to experimental determination at the mesomechanical level. If the pertinent variables are nondimensionalized as follows,

$$\frac{a}{a+R} = m,\ \lambda = \frac{x}{R} = \frac{X-a}{R} = \frac{x-m}{1-m},\ x = \frac{X}{a+R} \tag{1.5}$$

Equation (1.5) reads

$$Q = \int_0^1 \frac{G(\lambda)(1-m)\,d\lambda}{\sqrt{1-\left[(1-m)\lambda + m\right]^2}} \tag{1.6}$$

In what follows we shall restrict the considerations to the case of R<<a, or $m \to 1$. This restriction is pertinent to the "small scale yielding" (ssy) condition frequently met in analyses of fracture in quasi-brittle solids. For this limiting case, when we consider (1-m) as a small quantity, the integral in Equation (1.6) can be simplified as follows

$$Q \cong \sqrt{\frac{1-m}{2}} \int_0^1 \frac{G(\lambda)}{\sqrt{1-\lambda}}\,d\lambda \tag{1.7}$$

Replacing (1-m) by R/a, we obtain

$$Q \cong \sqrt{\frac{R}{2a}} \int_0^1 \frac{G(\lambda)}{\sqrt{1-\lambda}}\,d\lambda \tag{1.8}$$

in which G(λ) results from G(X), when the appropriate transformation of variables, cf. Eq. (1.5), is completed. It reads

$$G(\lambda, n, \omega) = \lambda^n \exp\left[\alpha(1-\lambda)\right] \tag{1.9}$$

Multiplication of Q in (1.8) by the factor $2S_0\sqrt{a/\pi}$, where S_0 denotes the local value of the yield stress measured at the crack front, converts this expression to the so-called "cohesion modulus" (used in somewhat different form by Barenblatt [1]), namely

$$K_{coh} = \sqrt{\frac{2R}{\pi}} S_0 \int_0^1 \frac{G(\lambda, n, \omega)}{\sqrt{1-\lambda}}\,d\lambda \tag{1.10}$$

With the integral contained in (1.10) denoted by $W_0(n,\omega)$, it is customary to solve Equation (1.10) for the characteristic length

$$R = \frac{\pi}{2W_0^2}\left(\frac{K_{coh}}{S_0}\right)^2 \tag{1.11}$$

This value is considered to represent the characteristic length parameter reflecting the microstructural and mesomechanical properties of the material. The equations provided in this section are valid for a smooth crack.

2. A FRACTAL MODEL OF THE COHESIVE CRACK AND THE CHARACTERISTIC LENGTH

Recently proposed fractal model of Wnuk and Yavari [3] suggests a mathematical simplification based on associating a smooth crack to a stress field generated around a fractal crack. This is the so-called method of imaginary smooth crack. The approach provides a useful approximation to the problem at hand, including the cohesive aspects of a fractal crack. In the solutions now obtained a new variable enters: the fractal dimension of the crack. The fractal dimension, D, usually a non-integer, is a measure of how strongly a given entity diverges from its Euclidean counterpart. As a geometrical characteristic of the fracture surface, D enters as a new variable in most pertinent equations of the fractal fracture mechanics. Let us mention just one such relation – for a fractal version of the Griffith crack the familiar singularity of $r^{-1/2}$ is replaced by a somewhat weaker singularity for the near-tip stress, $r^{-\alpha}$, where for a self-similar crack α depends on the fractal dimension D, namely (see Yavari, et al. [4] and Yavari [5])

$$\alpha = \frac{2-D}{2}, \qquad 1 \le D \le 2 \tag{2.1}$$

The model allows one to generalize the formula for the cohesive modulus of a smooth crack (1.10), to the one representing a fractal crack, namely

$$K_{coh}^{f} = \frac{2}{\pi} S_0 \left(\frac{\pi R_f}{2} \right)^{\alpha} \int_0^1 \frac{G(\lambda, n, \omega)}{(1-\lambda)^{\alpha}} d\lambda \tag{2.2}$$

The inverse relation that relates the characteristic length R to the material properties such as S_0, n, ω, K^{f}_{coh}, and the fractal geometry represented by the order of singularity α, is given now as

$$R_f = \left(\frac{\pi}{2} \right)^{\frac{1-\alpha}{\alpha}} \left[K_{coh}^{f} / S_0 \right]^{\frac{1}{\alpha}} \left\{ \int_0^1 \frac{G(\lambda, n, \omega)}{(1-\lambda)^{\alpha}} \; d\lambda \right\}^{-\frac{1}{\alpha}} \tag{2.3}$$

Index and superscript “f” have been added to designate quantities pertinent to a fractal crack. It is readily seen that for the limiting case of $\alpha = ½$, the formulae (1.10) and (1.11), valid for a smooth crack, are recovered. With the notation

$$W(\alpha, n, \omega) = \int_0^1 \frac{G(\lambda, n, \omega)}{(1-\lambda)^{\alpha}} d\lambda, \qquad R_c^{f} = \left(K_{coh}^{f} / S_0 \right)^{\frac{1}{\alpha}} \tag{2.4}$$

equation (2.3) can be re-written in a nondimensional form

$$\frac{R_f}{R_c^f} = \frac{(\pi/2)^{\frac{1-\alpha}{\alpha}}}{W^{\frac{1}{\alpha}}(\alpha, n, \omega)} \tag{2.5}$$

Similarly, for a smooth crack, see Eqs, (1.10) and (1.11), we have

$$\frac{R}{R_c} = \frac{\pi}{2W_0^2}, \quad R_c = (K_{coh}/S_0)^2 \tag{2.6}$$

Dividing equations (2.5) and (2.6) side by side, one obtains a measure of the material characteristic length associated with a fractal crack

$$\Theta(\alpha) = \frac{R_f R_c}{R R_c^f} = \left(\frac{\pi}{2}\right)^{\frac{1-2\alpha}{\alpha}} \frac{W_0^2}{W^{\frac{1}{\alpha}}} \tag{2.7}$$

It is easy to verify that for the limiting case of $\alpha = ½$, when $W \rightarrow W_0$, the function $\Theta(\alpha)$ reduces to one, as expected. Fig. 1a shows the dependence of Θ on the fractal singularity exponent α, plotted for the range $\frac{1}{4} \le \alpha \le \frac{1}{2}$, while Fig. 1b shows a similar function, for which the fractal dimension D was chosen as an independent variable rather than α. As can be seen, the range $(\frac{1}{4}, \frac{1}{2})$ for α corresponds to the range $(1, \frac{3}{2})$ for D.

There is a problem with physical interpretation of a fractal crack behavior when D approaches 2. In this limiting case the crack resembles a 2D object spread over a plane (a plane filling curve). For this case, the stress intensity factor, cf. Wnuk and Yavari [3]

$$K_I^f = \frac{\sigma\sqrt{\pi a^{2\alpha}}}{\pi^{2\alpha}} \int_0^1 \frac{(1+s)^{2\alpha} + (1-s)^{2\alpha}}{(1-s^2)^{\alpha}} ds \tag{2.8}$$

attains the value $2\sqrt{\pi}\sigma$. Note that the crack length "a" is suppressed entirely, and the entity $2\sqrt{\pi}$ should thus be interpreted as Nueber's stress magnification factor (rather than a stress intensity factor) corresponding to a certain 2D void. Assuming the void to be in the shape of a blunted crack with a finite root radius ρ, and the crack front identified at $r = \rho/2$, cf. Wnuk and Kriz [6], the stress at the crack front may be evaluated as follows

$$\sigma_{\max} = \frac{2K_I}{(\pi\rho)^{\frac{1}{2}}} = \frac{2\sigma\sqrt{\pi a}}{(\pi\rho)^{\frac{1}{2}}} \tag{2.9}$$

Setting it equal to the value predicted by the fractal model

$$\sigma^{f}_{\max} = \left[\frac{\chi(\alpha)\sigma\sqrt{\pi a^{2\alpha}}}{(2\pi r)^{\alpha}} \right]_{r=\rho/2} = \frac{\chi(\alpha)\sigma\sqrt{\pi}\, a^{\alpha}}{(\pi\rho)^{\alpha}} \tag{2.10}$$

leads to an expression defining the root radius of the fractal crack when $D \to 2$, or $\alpha \to 0$, namely

$$\frac{\chi(\alpha) a^{\alpha-\frac{1}{2}}}{(\pi\rho)^{\alpha}} = \frac{2}{(\pi\rho)^{\frac{1}{2}}} \tag{2.11}$$

3. CONCLUSIONS

It has been demonstrated that a solid weakened by a fractal crack possesses a characteristic length, which is determined by the mesomechanical properties of the material, such as S_0, n, ω, K^{f}_{coh} and also by the fractal dimension of the crack, D. Two measures of this length have been suggested here for two intervals of the fractal dimension D. For the fractal dimension ranging from 1 (a smooth crack limit) to 1.846, the characteristic length R^{f}_{c} is used, and it varies between 1 for D = 1, and 201.8 for D = 1.846. It should be noted that the value of 201.8 is three to four orders of magnitude greater than the values of the characteristic length observed in ductile metals. This result is of significance when the size effects related to fracture in cementitious materials is interpreted. The value of D = 1.846 is used as a cut-off value for a fractal dimension. Beyond this limit a root radius of a hypothetical blunted crack (equivalent to a fractal when D approaches 2) is suggested as a measure of the characteristic material length. In the limit of D = 2, this root radius equals a/π, where "a" denotes the nominal crack length.

REFERENCES

1. G. I. Barenblatt, "The Mathematical Theory of Brittle cracks in Brittle Fracture", *Advances in Applied Mechanics* 1962, 7:55 – 129.
2. M. P. Wnuk and J. Legat, "Work of Fracture and Cohesive Stress Distribution Resulting from Triaxiality Dependent Cohesive Zone Model", *Int. Journal Fracture,* 2002, Vol. 114, pp. 29 – 46.
3. M. P. Wnuk and A. Yavari, "On Estimating Stress Intensity Factors and Modulus of Cohesion for Fractal Cracks", *Engineering Journal of Fracture,* 70 (2003), pp. 1659 – 1674.
4. A. Yavari, S. Sarkani, and E. T. Moyer, Jr., "The Mechanics of Self-similar and Self-affine Fractal Cracks", *International Journal of Fracture* **114**(1), 2002, pp. 1-27.
5. A. Yavari, "Generalization of Barenblatt's Cohesive Fracture Theory for Fractal Cracks", *Fractals* **10**(2), 2002, pp. 189-198.
6. M. P. Wnuk and D. Kriz, "CDM Model of Damage Accumulation in Laminated Composites", 1985, *Int. Journal Fract.,* Vol. 28, pp. 121 – 138.

INFLUENCE OF STRESS STATE ON CRACK-TIP DRIVING FORCE

Daniel Kujawski
Department of Mechanical and Aeronautical Engineering
Western Michigan University, Kalamazoo, MI, 49008-5343, USA

Summary In this paper, a two-parameter crack-tip driving force in terms of K_{max} and ΔK^+ has been developed to account for load interaction effects on fatigue crack growth behavior. The development is based on the premise that the load interaction effects depend upon the applied and residual stress state at the crack tip. Examples from the literature regarding crack growth behavior due to an overload application in air and vacuum are analyzed and discussed.

INTRODUCTION

The accurate modeling of load interaction effects associated with the application of an overload is a prerequisite for an accurate prediction of fatigue crack growth behavior under variable amplitude loading. The load interaction effects on fatigue crack growth behavior are commonly introduced through the modification of the crack-tip driving force. In the past, several mechanisms have been proposed to account for the crack-tip driving force modification namely, crack closure, residual stresses, crack-tip blunting or branching, strain hardening, and environmental influence. In the vast majority of investigations the Elber plasticity-induced crack closure concept [1], which operates behind the crack tip, has been adopted as the critical mechanism responsible for load interaction effects in metallic materials. In such approaches, an effective stress intensity factor range is defined as

$$\Delta K_{eff} = K_{max} - K_{op}, \tag{1}$$

where K_{max} and K_{op} are the stress intensity factors calculated for the maximum, P_{max}, and the crack opening load, P_{op}, respectively. This implies that only the load range between the opening load, P_{op}, and the maximum load, P_{max}, would affect the crack tip action during the load cycle. However, for most metallic materials, plasticity-induced phenomena are present not only in the crack wake but also in front of the propagating crack. In particular, when an elastic-plastic material is loaded, a plastic zone is developed, leaving compressive stresses at the crack tip after unloading. Therefore, not only crack closure behind the crack front, but also compressive stresses ahead of the crack front, would modify the actual crack-tip driving force. In other words, the load interaction effects depend upon the applied and residual stress state ahead of the crack tip and could significantly affect fatigue crack growth behavior depending on the environment [2-5]. This is in contrast with crack closure approach that explores the phenomena occurring behind the crack tip.

ASSUMPTIONS AND ANALYSIS

It is well known that for ductile materials the crack driving force is mostly affected by ΔK, whereas for brittle materials by K_{max}. Usually, the relative contribution of ΔK or K_{max} to crack driving force also depends on material's cyclic properties (hardening or softening), temperature, and environment. To account for these effects a two-parameter crack-tip driving force developed in Ref. 6 has been adopted

$$K^* = (K_{max})^{\alpha}(\Delta K^+)^{1-\alpha} \tag{2}$$

where ΔK^+ is the positive part of the stress intensity factor range and α is a parameter that characterizes the apparent sensitivity of the K* to the K_{max} value. In general, when α=1 the crack driving force is solely defined by K_{max} *(very brittle materials)*; however, when α=0 it is defined only by ΔK^+ *(ductile materials in vacuum).* The two-parameter crack-tip driving force is based on the following premises:

- The damage at the crack-tip process zone is an interplay of two damage processes, namely a monotonic damage due to K_{max} and a cyclic damage due to ΔK^+.
- The damage action at the crack-tip process zone is controlled by the elastic field around it.
- Existence of the tensile stresses in the process zone, $K_{max} = (K_{app} + K_{res}) > 0$, is a necessary condition for fatigue crack propagation, where K_{app} and K_{res} are the stress intensity factors calculated due to the applied load, P_{max}, and due to residuals stresses, respectively.
- The residual stress field induced by an overload is not relaxed significantly by subsequent fatigue crack extension. This assumption is based on the experimental evidence obtained using X-ray measurements [7].

It has been demonstrated that the two-parameter crack driving force, K*, unifies the overall crack prediction methodology regarding load ratio effects for both the long- and short-crack growth behavior [6]. In this paper, the K* driving force approach has been extended to account for crack growth retardation behavior by incorporating the effects of residual stress field due to an overload application.

Estimation of residual stress induced by an overload

In order to estimate residual stresses induced by an overload a simple analytical model was developed. The crack tip stress distribution obtained by Rice [8] for Mode III loading was modified for Mode I crack and the Ramberg-Osgood stress-strain relationship. This modified solution was used to estimate the stress distribution normal to the crack plane as a function of distance ahead of the crack tip. Applying Rice's superposition argument of the reversed flow during unloading, the residual stress after overload was evaluated. This simple modeling was compared with finite element analysis results and a reasonable agreement was found. Then, the weight function approach was utilized to calculate the resulting stress intensity factor, K_{res}, due to residual stress field versus crack extension and hence the $K_{max} = K_{app} + K_{res}$ at the crack-tip was obtained. Finally, the two-parameter driving force, K*, was determined and used to predict retardation behavior following an overload application.

COMPARISON WITH EXPERIMENTAL DATA

Taking examples from the literature, a crack growth transient behavior due to overload was analyzed in terms of the two-parameter driving force. Due to application of an overload, the crack first accelerates, then the crack slows down to a minimum growth rate, and finally the crack recovers to the pre-overload growth rate. The residual stress created by the overload affects both the maximum and the minimum crack-tip stress intensity factors [7]. As a result, at the crack-tip only the K_{max} is modified whereas the corresponding ΔK is unaffected. The minimum growth rate after overload is associated with a crack growth increment of about one-fourth to one-third the overload forward plastic zone size. It is shown that this corresponds to the minimum value of K_{max} at the crack-tip calculated from the applied load and residual stresses due to overload. As the crack advances near the boundary of the overload forward plastic zone both the crack-tip K_{max} and crack growth rate stabilize to the pre-overload values.

The proposed approach is then used for a comparative study of the fatigue crack growth behavior due to overload in air and vacuum environments. The results indicate that the transient behavior in the two environments is essentially the same. The observed quantitative variations are associated with the inherent differences in the fatigue crack growth behavior in air and vacuum. The apparent crack growth retardation behavior is coupled with the stress/environment interaction in the process zone ahead of the crack tip. In particular, the period when crack growth rate is recovering from the slowest transient growth rate to the post-overload stabilized value is sensitive to environment.

CONCLUSIONS

A new two-parameter crack driving force that takes into account the influence of residual stress state due to overload is proposed. The proposed parameter yields fairly good correlations between overload effects observed experimentally for a number of materials including steels, aluminium and titanium alloys compared in this study. The analysis shows explicitly the link between residual stresses induced by overload and the delayed crack growth retardation.

It unifies the load interaction prediction methodology regarding load ratio, overload, and environment on fatigue crack growth behavior and bridges the existing gap between them. Further studies are needed to examine the potential application of this new parameter for variable amplitude loading.

References

[1] Elber W.: The Significance of Fatigue Crack Closure. ASTM STP 468, 230-242, 1971.
[2] Ranganathan N., Petit J. and Bouchet B.: A Contribution to the Study of Fatigue Crack Retardation in Vacuum. Engng Frac. Mech, **11**: 775-789, 1979.
[3] Fleck N.: Influence of Stress State on Crack Growth Retardation. ASTM STP 924, 157-183, 1988.
[4] Vasudevan A.K., Sadanada K. and Louat N.: A Review of Crack Closure, Fatigue-Crack Threshold and Related Phenomena. Mater. Sci. Engng. **188**: 1-22, 1994.
[5] Sunder R., Porter W.J. and Ashbaugh N.E.: The Role of Air in Fatigue Load Interaction. Fatigue Fract Engng Mater Struct. **26**: 1-16, 2003.
[6] Kujawski D.: A Fatigue Crack Driving Force Parameter with Load Ratio Effects. Int. J. Fatigue, **23**: S239-S246, 2001.
[7] Allison J.E.: Measurement of Crack-Tip Stress Distribution by X-Ray Diffraction. ASTM STP 677, 550-562, 1979.
[8] Rice J.R.: Stress Due to a Sharp Notch in a Work-Hardening Elastic-Plastic Material Loaded by Longitudinal Shear. J. Appl. Mech. **34**: 387-298, 1967.

XXI ICTAM, 15–21 August 2004, Warsaw, Poland

BRANCHING INSTABILITY OF BRITTLE FRACTURE

M. Adda–Bedia*
*Laboratoire de Physique Statistique, Ecole Normale Supérieure
24 rue Lhomond, 75231 Paris Cedex 05, France

Summary A new method for determining the elastodynamic stress fields associated with the propagation of antiplane branched cracks is presented. The exact dependence of the stress intensity factor just after branching is given as a function of the stress intensity factor just before branching, the branching angle and the instantaneous velocity of the crack tip. The jump in the dynamic energy release rate due to the branching process is also computed. Applying a growth criterion for a branched crack, it is shown that the minimum speed of the initial single crack which allows branching is equal to $0.39c$, where c is the shear wave speed. At the branching threshold, the corresponding bifurcated cracks start their propagation at a vanishing speed with a branching angle of approximately 40 degrees. Using these exact results, the branching of a single propagating crack under mode I loading is also considered and the critical velocity for branching is computed.

INTRODUCTION

An issue of great interest in crack dynamics is the question of understanding the instabilities associated with the appearance and evolution of kinked or bifurcated cracks. We are particularly interested in this phenomenon in brittle materials, in which several experiments [1, 2, 3] have shown evidence of these instabilities. A main experimental distinction can be made between micro–branches and macro–branches. The fact is that over a crack velocity threshold, the so called micro–branching instability sets in : the broken surface left by the crack shows a dense array of micro–kinks that were incipient cracks that aborted quickly their inroad into the material. The angle that these micro–cracks make with the main crack direction depends on the scale at which these structures are observed. Also, there is the other experimental subset corresponding to macro–branches, that could occur at velocities of the crack of the order of $0.5 - 0.6c_R$ (the threshold for this instability is not precise) and that usually initiates the total rupture of the sample.

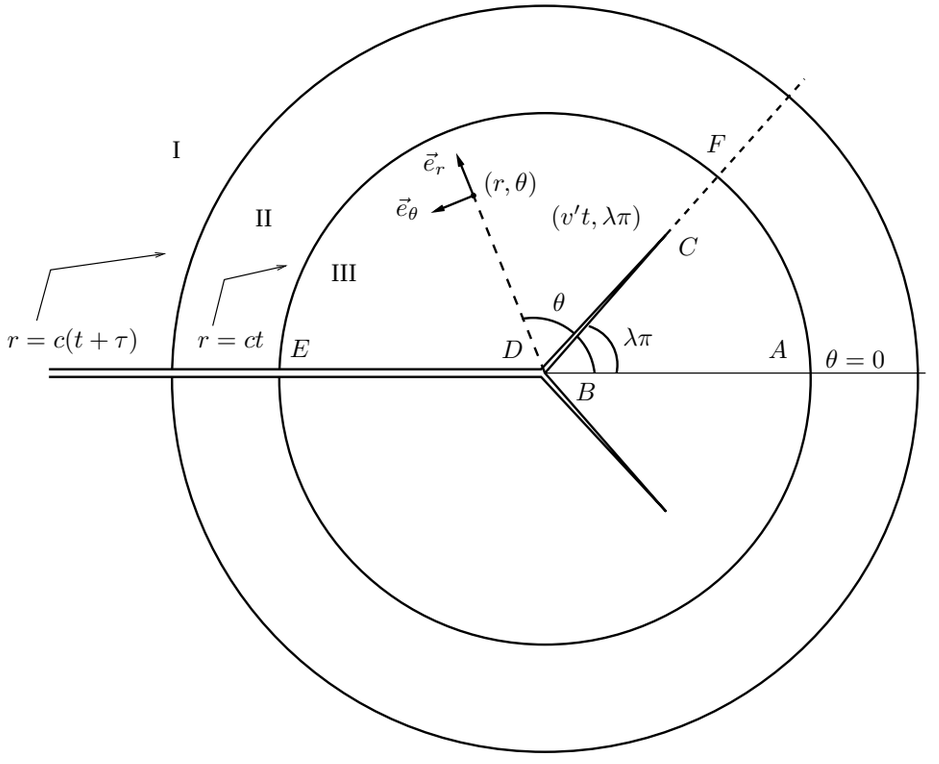


Figure 1. A half–plane crack that propagates at a speed v for $t < -\tau$ suddenly stops at $t = -\tau$. For $t > 0$, the new branches propagate straightly from the position $r = 0$ at a velocity v', following the directions $\pm\lambda\pi$. The orthonormal basis $(\vec{e}_r, \vec{e}_\theta, \vec{e}_z)$ corresponding to the cylindrical coordinate system (r, θ, z) is shown. The cylindrincal waves originated at the crack's arrest ($r = c(t+\tau)$) and at the start of branches propagation ($r = ct$) divide the material into three regions. In the region labelled I, the stress field comes only from the dynamical straight crack propagation, since the effects of the crack's arrest and the crack's branching are not experienced there. The region II is influenced by the crack arrest only, thus the stress field there is a static one [4, 6]. It is only the region III that is influenced by the crack's branching. Thus, one has to solve the branched crack problem only in this latter region.

Given this experimental phenomenology, a theoretical approach that has been suggested is to describe kinked or bifurcated

cracks in the framework of Linear Elastic Fracture Mechanics [4, 5], which has proven its validity for single straight crack dynamics in brittle materials [6, 7, 8]. The main goal of this approach is to obtain expressions for the stress intensity factors at the crack tips of the emergent bifurcated cracks. The idea is to compare their associated energy release rates with the unperturbed configuration, i.e. a crack from which no branches emanated. The dependence of these energy release rates in the crack kink angles, velocities, etc.. may elucidate the origin of the instability. This line of work involves solving a dynamic linear elasticity problem where the crack boundaries develop a kinked shape that makes the theoretical analysis quite involved. Our final goal is to solve the problem of determining the stress intensity factors of a kinked crack that starts at a given angle and velocity from a main crack whose velocity is also given. The present work is an intermediate step towards that final goal.

The aim of this presentation is to present a new method to calculate the dynamic stress intensity factors associated with the propagation of anti–plane kinked or branched cracks [9, 10]. This approach allows the exact calculation of the corresponding dynamic stress intensity factors. The latter are very important quantities in dynamic brittle fracture mechanics, since they determine the crack path and eventual branching instabilities. As an illustration, we consider the configuration depicted in Fig. 1 of an initially propagating antiplane crack that branches into two cracks that merge symmetrically. The explicit dependence of the stress intensity factor just after branching is given as a function of the stress intensity factor just before branching, the branching angle and the instantaneous velocity of the crack tip. The jump in the dynamic energy release rate due to the branching process is also computed. Similarly to the single crack case, a growth criterion for a branched crack is applied. It is based on the equality between the energy flux into each propagating tip and the surface energy which is added as a result of this propagation. It is shown that the minimum speed of the initial single crack which allows branching is equal to $0.39c$, where c is the shear wave speed. At the branching threshold, the corresponding bifurcated cracks start their propagation at a vanishing speed with a branching angle of approximately 40 degrees.

Using these exact results, the branching of a single propagating crack under mode I loading is also considered. It is shown that the formulation of the corresponding model problem is identical to the anti–plane case. The difficulty for solving completely the branching problem under plane loading configurations lies in the existence of two characteristic wave speeds and in the vectorial nature of the displacement field. However, this analogy allows the reasonable hypothesis that under plane loading configurations, the jump in the energy release rate due to branching is also maximized when the branches start to propagate quasi–statically. Using the Eshelby's approach, the branching of a single propagating crack under mode I loading is found to be energetically possible when its speed exceeds a threshold value. The critical branching parameters depend of the criterion applied for the selection of the paths followed by the bifurcated cracks. For instance, the maximum energy release rate criterion [11] or the principal of local symmetry [12]. It is found that the critical velocity for branching of the initial single crack is weakly sensitive to the applied criterion. However, the principal of local symmetry gives a larger branching angle, which is more consistent with experimental observations. Finally, it is shown that an increasing fracture energy with the velocity results in a decrease in the critical velocity at which branching is energetically possible.

References

[1] Ravi–Chandar, K., Knauss, W.G.: An experimental investigation into dynamic fracture–III. On steady–state crack propagation and crack branching. *Int. J. Fracture* **26**:141–154, 1984.

[2] Boudet, J.F., Ciliberto, S., Steinberg, V.: Dynamics of crack propagation in brittle materials. *J. Phys. II France* **6**:1493–1516, 1996.

[3] Sharon, E., Fineberg, J.: Microbranching instability and the dynamic fracture of brittle materials. *Phys. Rev. B* **54**:7128–7139, 1996.

[4] Eshelby, J.D.: Energy relations and the energy–momentum tensor in continuum mechanics. *Inelastic Behavior of Solids* (ed. Kanninen, M.F., Adler, W.F., Rosenfield, A.R. and Jaffee, R.I.), McGraw–Hill, New York, 77–115, 1970.

[5] Rice, J.R., Ben–Zion, Y., Kim, K.S.: Three–dimensional perturbation solution for a dynamic planar crack moving unsteadily in a model elastic solid. *J. Mech. Phys. Solids* **42**:813–843, 1994.

[6] Freund, L.B.: Dynamic Fracture Mechanics. Cambridge University Press, NY 1990.

[7] Sharon, E., Fineberg, J.: Confirming the continuum theory of dynamic brittle fracture for fast cracks. *Nature* **399**:333–335, 1999.

[8] Washabaugh, P.D., Knauss, W.G.: A reconciliation of dynamic crack velocity and Rayleigh wave speed in isotropic brittle solids. *Int. J. Fracture* **65**:97–114, 1994.

[9] Adda–Bedia, M., Arias, R.: Brittle fracture dynamics with arbitrary paths–I. Dynamic crack kinking under general antiplane loading. *J. Mech. Phys. Solids* **51**:1287–1304, 2003.

[10] Adda–Bedia, M.: Brittle fracture dynamics with arbitrary paths–II. Dynamic crack branching under general antiplane loading. *J. Mech. Phys. Solids* 2004.

[11] Erdogan, G., Sih, G.C.: On the crack extension in plates under plane loading and transverse shear. *J. Basic Engng.* **85**:519–527, 1963.

[12] Gol'dstein, R.V., Salganik, R.L.: Brittle fracture of solids with arbitrary cracks. *Int. J. Fracture* **10**:507–523, 1974.

SIZE EFFECT IN TENSILE FRACTURE OF CONCRETE - A STUDY BASED ON LATTICE MODEL APPLIED TO CT - SPECIMEN

R. Vidya Sagar
Civil Engineering Department
Indian Institute of Science
Bangalore 560 012, India

Summary: In this paper, a study on size effect in tensile fracture of concrete and simulation of strain softening of plain concrete using 2D lattice model is presented. A compact tension specimen (CT) is adopted and triangular lattice network is used to simulate the heterogeneous structure of concrete. A computer program is used to generate random variation of Young's modulus values for each individual element present in the lattice, which can represent a heterogeneous concrete medium. Load Vs. CMOD plots thus obtained show-softening behavior of concrete. A size effect curve in tensile strength of concrete has been plotted.

Introduction

The phenomenon of cracking is the most important feature of the concrete behavior. When the tensile strength of a material is reached in a structure, cracking will occur. The fracture mechanics studies deals with the conditions around and in front of a crack tip. The fracture of a heterogeneous solid subjected to external displacement is of great importance. Some materials, which are heterogeneous at the meso scale, exhibit strain softening behavior and fail progressively by damage-localization and fracture takes place in their components. Examples of these materials are mortar, concrete, ceramic composites, fibrous materials, rocks. There is similarity in the global behavior of these materials. One of the main characteristics of quasi-brittle materials like concrete and rock, composites are their high heterogeneity. Cracks generally propagate in a direction which is perpendicular to the maximum tensile stress. In heterogeneous materials cracks also follow the weakest links in the material. The crack patterns in this kind of material will therefore never be straight and continuous. Due to the heterogeneity of the material cracks are tortuous and there are overlaps or so called crack face bridges. Nowadays numerical simulation, coupled with theory and experiment, is considered to be an extremely important tool for further material development. In the concrete world, 'numerical concrete', developed by Wittmann and co-workers has already shown encouraging results. E.Schangen [4] *et al.* showed that by means of the generated material structure. Sadouki *et al.* investigated the possibility of analysis numerically to examine the mechanical behavior of concrete, using a particle model. Lattice models are one of the numerical methods developed by researchers for solving the classical problems. The concept of the lattice model is discretization of the continuum by line elements such as bar elements and beam elements, which can transfer forces and moments. Lattice with truss elements corresponds to the classical continuum, while lattice with beam elements corresponds to the micro polar continuum. The heterogeneity of the material can be incorporated in a lattice model, by assigning different strength and or stiffness values to the individual lattice members. By using these lattice model techniques it is possible to identify micro cracking, crack branching, crack tortuosity and bridging, which leads to the fracture process to be followed until complete failure. The concept of lattice analogy can be extended to two-dimensional continua. Essentially, lattice analogy replaces the continuous surface structure by an idealized discrete system, the elements of which are interconnected only at finite nodal or joint points. In such a substitute structure, having its size of subdivisions decreased, the state of stress approaches that of the corresponding continuum. The lattice analogy cannot be completely equivalent to the replaced continuum, an accuracy sufficient for most practical purposes, can be achieved. Over the last 45 years lattice models have been used for various applications. The earliest model was proposed by Hrennikoff [1], who introduced a regular triangular lattice of truss elements to solve classical problems in elasticity. Burt and Dougil *et al.* model a progressive failure in heterogeneous material. Theoretical physicists from the field of statistical mechanics Hans J. Herrman, Alex Hansen and Stephen Roux [2] simulated the brittle failure of disordered materials and the conductivity of the materials using a square lattice with beam elements. Schlangen and Van Mier [5] simulated the fracture in concrete materials with triangular lattice with beam elements. Schlangen *et al.* showed that local rotations at the nodes play an important role in the simulated fracture process. Schlangen and Van Mier *et al.* presented a report on experimental and numerical analysis of micro mechanisms of fracture of cement based composites and simulated a concrete plate with a notch using beam elements. Herrman *et al.* proposed a triangular lattice with elements of random length. In this paper the disorder of the medium is implemented by assigning randomly chosen material properties to the elements in the lattice and graphs related size effect in tensile fracture was obtained using bar element and beam element.

Lattice modeling of Concrete

Concrete is a porous composite material consisting of sand and coarse aggregates embedded in a cement paste matrix. The pores in the material play an essential role in strength, ductility and durability. Researchers in the field of fracture mechanics of concrete modeled concrete in three level approaches. These are micro, meso and macro levels. The meso - level considers the composite nature of concrete and distinguishes between hardened cement paste, aggregate, and a bond layer between cement paste and aggregate constituents. The stress-strain behavior under tensile loading of the aggregate, bond and matrix are assumed to be linear elastic. Disorder must be taken into account when a heterogeneous material like concrete is simulated. In this study a regular triangular lattice is adopted. All lattice member are ascribed

material properties of aggregate(gravel), matrix and bond following an order of matrix-bond-aggregate-bond-matrix-bond-aggregate….as shown in fig.2a. In fig.2b. "A" represents the aggregate phase, "M" the matrix and "B" the bond between matrix and aggregate. Material properties, which must be assigned for the three phases are the Young's moduli and tensile strengths. fig.2a shows a concrete plate with a notch at one of its sides idealized as a lattice with 317 members and 122 joints.

Material Constants

Phase	E (Mpa)	σ_t(Mpa)
Aggregate (A)	70000	10.00
Bond (B)	25000	5.00
Matrix (M)	25000	1.25

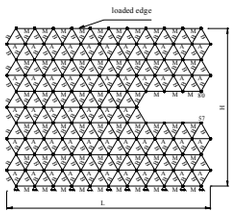


Fig. 2a. Lattice network of a concrete plate with a notch at one of its sides.

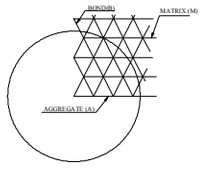


Fig. 2b. Triangular lattice and assigning different properties to the lattice elements

Method of analysis

Crack propagation in the structures is often simulated with finite element methods based on continuum. A standard Finite Element Method program for analysis of lattice structure has been developed. Fracture is simulated by performing a linear elastic analysis of the lattice and removing an element from the mesh that exceeds maximum tensile strength of the element. The displacement control method was adopted for loading the structure. In the present study analysis was carried on a model consisted of regular triangular lattice with bar type of elements. The lattice consists two node bar element which has two degrees of freedom at each node., i.e., U_x and U_y . For displacement simulation, the prescribed displacement 0.001 mm/step is imposed as a constraint. In each step of the fracture analysis the lattice mesh is loaded by external prescribed displacements. The displacement rate 0.001 mm/iteration is chosen which stipulate that the peak load in a displacement-controlled test. Gussian Elimination method which is a direct method is used for the solution of the simultaneous equations. A flow-chart of the implementation procedure is prepared. The x- direction displacements of the nodes located along the model's upper edge are kept at zero value and the all displacements at the nodes located along the lower edge were suppressed. The upper edge is subjected to a vertical displacement of 0.001mm in Y-direction. The analysis of concrete fracture process consists of a series of elastic steps. Each element stress is calculated and checked against the corresponding limiting stress. The aggregate, bond, and matrix truss elements, whose stresses have reached the limiting values are ascribed a negligible value of modulus of elasticity for corresponding element in the next increment of the load. The material constants and limiting tensile stress values for aggregate, bond and matrix are shown in the above table.

Failure Criteria for lattice members

When performing a fracture analysis on a lattice mesh, a failure criterion has to be chosen. Different criteria for fracture have been adopted and can be found in the literature[2]. A powerful, widely used approach in finite element analysis of concrete is the concept of smeared cracking, introduced by Rashid. According to this concept, the stress in a finite element is limited by the tensile strength of the material, $f_t^{'}$. After the limiting value of strength is reached, the stress in the lattice member decreases. The tensile strength of the three phases is used as fracture parameter. As mentioned introduction Herrmann et al[2]. simulated the fracture of metals using a square lattice and assumed that each individual elements in the lattice fail according to the following criterion motivated by Von Mises' failure criterion

$$p = \left(\frac{f}{t_f} \right)^2 + \frac{\max(|m_1|,|m_2|)}{t_m}$$

Where p is the limiting value that can be related to the probability of failure, f is the axial force in the element, m_1 and m_2 are the end moments and t_f and t_m are the corresponding threshold values, which depend on the given material. In this study whenever the axial stress in a member in lattice model with bar elements reaches limiting stress the modulus of elasticity of that member was reduced to negligible value for the next step. The limit stresses rather than the limit strains have been assumed

Size Effect

After Galilio, Licester *et al* seems to have been the first to investigate the effect of size on the strength of structures made of metals, timber and concrete. The effect of structural size on its normal strength has a long history . In order to illustrate the size dependence in a simple and dimensionless way, Hillerborg[2] introduced the concept of a characteristic length. As a unique material property, The characteristic length $l_{ch} = \frac{EG_f}{f_t^2}$ expresses the fracture of concrete and concrete-like materials, where l_{ch} value is proportional to f_t^2 . This means that brittleness increases with an increase in the strength of concrete, but it decreases with high fracture energy, according to fictitious crack model (F.C.M.). The brittle response of the concrete as a material can not be confused with the brittleness of a concrete structure. The brittleness of concrete structural elements depends on their size. In this way, for the same material, small elements fail with a ductile response, whereas large elements fail in a brittle manner. The variation of the structural response as the size of the structure changes is known as ductile-brittle transition. Bazant's size effect law [2] gives a measure of the brittleness of concrete members. According to this law, $\sigma_N = Bf_t(1+\beta)^{0.5}$ with $\beta = \frac{d}{d_0}$, σ_N = nominal strength, d= structural size, f_t =tensile strength of concrete, B and d_0 =constants. Both d_0 and B depend on the fracture properties of the material and on the geometry (shape) of the structure, but not on the structure size. The size effect is understood as the dependence of the structure strength on the structure size. The strength is conventionally defined as the value of the so called nominal stress is a load parameter defined to the proportional to the load divided by a typical cross sectional area.

Discussion of results

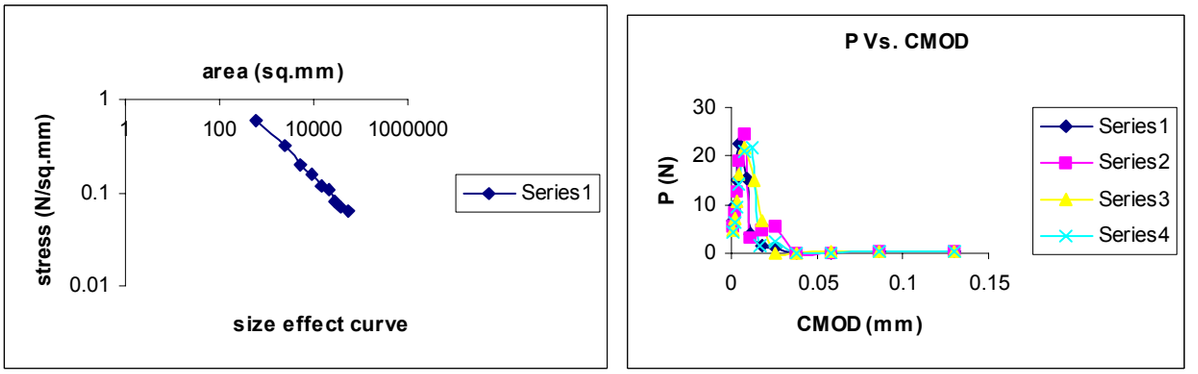


Fig.3

Conclusions

A lattice model at meso level, with a simple linear elastic purely brittle failure law in tension was used for simulating the fracture process of a notched concrete plate subjected to uniaxial tension. The results obtained from simulations with lattice models, depend on the fracture criterion used and the element selection for modeling the lattice. From the graph shown in fig.(3) one can observe that the peak stress in the graph of the applied stress against crack opening displacement of a loaded concrete plate with a notch decreases with increase in the size of the structure.

Acknowledgement

The author would like to thank Prof.B.K.Raghu prasad for his help during preparation of this paper.

References

1. Hrennikoff A. Solution of problems of elasticity by the frame work method, J. of Applied Mechanics (Transactions of the ASME), 8, 1941, pp. A169-A175.
2. Herrman.H.J,Hansen A, Roux S. Fracture of disorder elastic lattices in two dimensions. Phys Rev B 1989;39:637-648
3. Feng s., Thorpe, M.F., Garboczi, E.J., (1985) effective medium theory of percolation on central-force elastic networks. Phy. Rev. B., 31, 276-280.
4. E.Schangen , E.J.Garboczi, New method for simulating fracture using an elastically uniform random geometry lattice., Intl. J. Engng. Sci. 34, 10, 1131-1144, (1996).
5. Schlangen E. Van Mier J.G.M., Simple lattice model for numerical simulation of fracture of concrete materials, Material and structures, 1992, 25, 534-542.
6. Schlangen E, Garboczi.E.J., Fracture simulations of concrete using lattice models : computational aspects, Engineering fracture mechanics Vol. 57, No.2/3, pp.319-332, 1997.
18.Bazant, Z.P. Size effect in blunt fracture: concrete, rock, metal. J. of Engineering Mechanics (ASCE), 110(4), 1984, pp.518-535.

NUMERICAL AND EXPERIMENTAL STUDY OF THE PLASTIC ZONE IN THE VICINITY OF THE CRACK TIP BY THE OPTICAL CAUSTICS METHOD

Octavian Pop, Valéry Valle and Mario Cottron
Laboratoire de Mécanique des Solides – U.M.R. 6610 – Université de Poitiers
S.P. 2 M.I., Bd. M. et P. Curie, Téléport 2, B.P. 30179,
86962 Futuroscope Chasseneuil Cedex FRANCE
e-mail : Octavian.Pop@lms.univ-poitiers.fr

Summary In this paper we aim at demonstrating by numerical simulations, followed by experimental tests that for a ductile specimen SEN loaded in the mode I, the topological changes of the crack tip, due to plasticity, can be revealed by the optical caustics phenomenon.

INTRODUCTION

In industrial applications, knowing the morphology of the plastic region allows the prevention of crack propagation that may lead to serious crack extensions.
For real cracked structures, the topology of the field surrounding the crack tip is generally determined by the stresses and strains state [1]. In the case of fragile materials, the development of the plastic zone is ignored, but the same hypothesis does not apply to ductile materials. For these materials, when dealing with a stationary problem, we notice an important development of the plastic zone in the proximity of the crack tip, before reaching the rupture stress limit and before the crack begins to extend. We have to add that the plastic region keeps developping alongside with the crack extension. Assuming that the transition between the elastic zone and the plastic zone surrounding the crack tip implies a change in the displacements field configuration, we aim at approaching the influence of the plastic zone on the caustic shape by using the caustics method [2].

THE OPTICAL PHENOMENON OF CAUSTICS

Being associated to mathematical singularities, a caustic represents the image of a group of critical points, of lagrangian application, for which the rank of the derivative is inferior to its possible maximum value [3], [4]. In geometrical optics, the caustic curve stands for the envelope of a system of rays due to the deflection of an incidental light beam, which impinges on the outside boundary of the medium [5]. In our study, the outside boundary of the medium is reflective and in this case the only parameters influencing caustics are the residual strains field and the position of the image screen, determined in relation to the reflective boundary.
We know for a fact that in the case of elastic behaviour of the cracked medium, in the unloaded state, this one goes back to its initial state. Thus, the configuration area is reduced to a flat surface corresponding to the absence of caustics in the image screen (see, FIG. 1 (a)). According to this hypothesis, the appearance of a plastic zone in the proximity of the crack tip is accompanied by irreversible residual strains. When the depth of the configuration area is not zero, we have residual caustics due to residual strains.

NUMERICAL SIMULATION

In order to proceed to the numerical simulation, we have used finite elements modelling of a SEN ductile specimen with the size of 100x100x6 mm^3 and a length of the crack of 9.5 mm. The specimen is loaded in mode I beyond the initial elasticity limit. The behaviour model that we have associated to the discretized specimen is the von Mises model of kinematic linear hardening, while the mechanical characteristics of the material are experimentally determined for a polycarbonate known under the name of Makrolon [6]. Moreover, the kinematic boundary conditions imposed on the geometrical shape of the specimen require a plane stress state ($\sigma_{zz} = 0$).
In our paper, we assume that the plastic zone represents the node locus for which the stress state during the loading phase satisfies the plasticity criterion of von Mises [7].
The simulated caustics obtained in three image planes, for the unloaded state, are presented in FIG. 1 (b), (c) and (d).

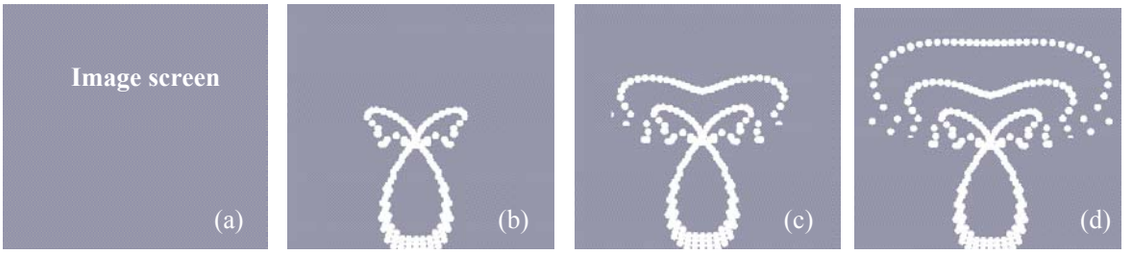


FIG. 1 - Simulated virtual caustics

EXPERIMENTAL TEST

The experimental test has been carried out for a SEN specimen of polycarbonate (Makrolon) having the same dimensions as the specimen used for numerical simulation. The loading of the specimen is done in the mode I beyond the initial elasticity limit. The reflective surface of the specimen is impinged on with a parallel beam by using a LASER source.
The acquisition of caustics is obtained through the reflexion of a CCD camera, in several measurement planes determined in relation to the reflective surface of the specimen. The depth variation in the measurement plane is obtained by moving the CCD camera in a perpendicular direction to the free surface of the specimen. Following the image acquisition stage and taking into account the magnification of the CCD camera, we can deduce the diameters of the caustics in mm.
We have showed in FIG. 2 the experimental caustics obtained in three image planes. These three image planes are situated at 0.25, 0.5 and 0.7 cm in relation to the reflective boundary of the specimen.

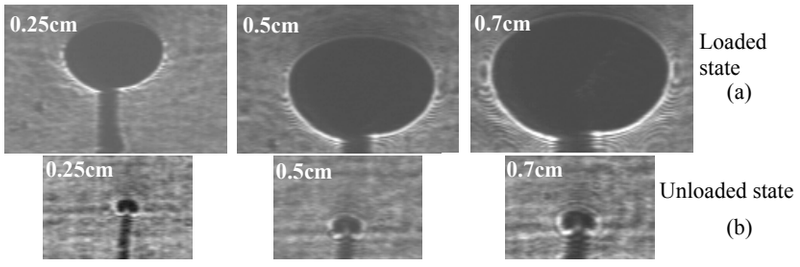


FIG. 2 - Experimental virtual caustics obtained for an image-plan situated at 0.25, 0.5 and 0.7 cm from the refractive boundary of specimen

DISCUSSION AND CONCLUSIONS

We have to specify that the caustics obtained through reflection and shown in FIG. 1 and 2 are virtual caustics [5].
Analysing FIG. 2 we can notice a difference in the shape of caustics observed in the loaded state of the specimen and those corresponding to the unloaded state. The caustics show in FIG. 2 (a) are generated by rays coming from the area of elastic behaviour of the specimen, whereas caustics in FIG. 2 (b) stand for the envelopes of rays reflected by the plasticity-affected area.
We can also note that in FIG. 1 and 2 the shape of caustics depends on the position of the image screen, that is to say on the topology of the residual displacement field.
In the case of the unloaded configuration of the specimen, FIG. 1 (b), (c), (d) and FIG. 2 (b) show that the residual strains, entailed by the plasticity phenomenon, can be revealed by residual caustics.
Attention should be drawn to the fact that visualised caustics for a residual strains field present standard singularities. In this context, the analysis of the caustics' shape allows us to find the locus of the critical points (i.e. reconstruct the residual displacements field) in order to determine the boundaries of the plastic zone.

References

[1] J. Lie, N. Recho, Rupture par fissuration des structures, Hermès, Paris, 1995.
[2] R.A. Tomlinson, E.A. Patterson, The effects of surface topography on the method of caustics, Experimental Mechanics, **39 (4)** 335-342, 1999.
[3] V. Arnold, A. Varchenko, S. Goussein-Zadé, Singularités des applications différentiables 1ère partie, Éditions Mir, Moscou, 1986.
[4] M. Born, E.Wolf, Principles of optics. Electromagnetic theory of propagation. Interference an diffraction of light, Pergamon Press, 1980.
[5] J.F. Kalthoff, Static and dynamic photoelasticity and caustic, in: A. Lagarde (ed.) CISM Courses and lectures 290, Springer, New-York, 1987.
[6] R. Tié Bie, J.C. Dupré, Optical techniques for the thermomechanic study og polymers, International workshop on video – Controlled materials testing 181-184, 2000.
[7] B. Haphen, J. Solençon, Elasto-plasticité, Presses de l'école nationale de ponts et chaussées, Paris, 1987.

THERMOELASTIC PROBLEMS FOR A BIMATERIAL WITH DEFECTS/SINGULARITIES

Vera E.Petrova
Voronezh State University of Architecture and Civil Engineering, 394006 Voronezh, Russia

Summary. The paper presents a method for the solution to 2D thermoelastic problems for a bimaterial with singularities/defects, like cracks, dislocations as well as a heat source. A number easy-to-use formulas, in particular, for the stress intensity factors evaluation is presented.

Bimaterial compounds are often used in different electronic devices, which are undergone to thermal loading. Interface fracture is commonly observed in such structures [1]. The interface crack problems have a long history many models have been developed up to now. The interaction problem of singularities, in particular, edge dislocations, with a bimaterial interface or an interface crack in isotropic and anisotropic materials were solved by Suo [2]. In the work by Petrova and Herrmann [3] the analogous relations have been obtained for the corresponding thermoconductivity and thermoelasticity problems. On the basis of these expressions for the complex potentials a solution is constructed for the problem of the system of internal cracks and an interface crack.

This paper presents a method for the solution to 2D thermoelastic problems for a bimaterial with internal singularities/defects, like cracks, dislocations. A bimaterial interface is either virgin or contains an interface crack. The bimaterial is subjected to thermal loading caused by a uniform heat flux, applied at infinity normal to the interface, or a heat source of intensity Q acts at a point z_0^s, as shown in Fig.1.

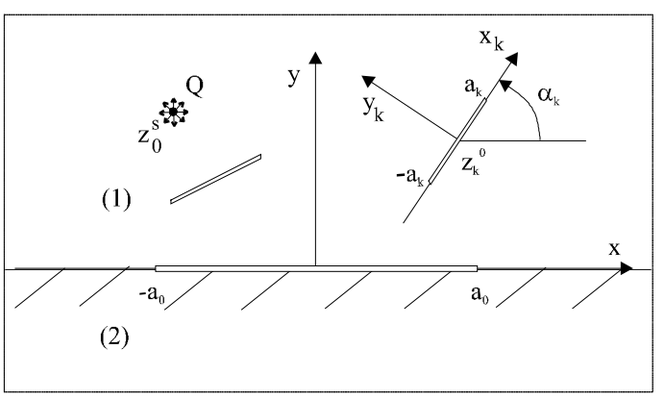


Fig.1. Cracks and a heat source in a bimaterial.

The geometry of the problem for defects-cracks is depicted in Fig.1. A bimaterial composes of two different isotropic semi-infinite media (1) and (2) with thermoelastic constants μ_i , α_{ti} , k_i , ν_i (i=1,2). The crack position is determined by an angle α_k to the x-axis and the defect midpoint coordinate z_k^0 $(k = 0,1,..., N)$.

In the previous studies by Petrova and Herrmann (see [3]) the thermoelastic fracture problems are considered for a bimaterial with perfectly bonded interface in exception of an interface crack. In this work the common method for the construction of the solution is presented and different types of interfaces are considered in accordance with boundary conditions on the interface line.

The uncoupled, quasi-static thermoelastic theory is applicable to this problem so that the solution consists of the determination of the temperature distribution, and the determination of the thermal stresses. The cracks are supposed to be thermal insulated and traction free, whereas, the interface is partially thermal conductive.

The method is based on
- the well-developed theory of complex potentials,
- analytical continuation theorem and
- superposition technique

and leads to singular integral equations for the problems in hand.

Due to the superposition principle the main temperature and thermoelastic problems decompose into a series of simple subproblems each of them contains either an internal crack or an interface crack. The general parts of the scheme of the solution are presented in the Table. The full temperature T* consists from the perturbation temperature T, caused by defects, and the temperature T^0 for the undamaged bimaterial. If a heat source is acts in a bimaterial then the solution is more complicated because of the heat source is a singularity and it causes stresses in the undamaged bimaterial (see the scheme II in the Table).

As examples of the effectiveness of this technique the solution of subproblems are presented and discussed. It should be noted that the well-known solutions for singularities in an infinite homogeneous medium are used for construction of these problems. These particular solutions also verify the validness of the method.

Table

FULL TEMPERATURE in a bimaterial with cracks $T^*=T+T^0$		
I	II	III
PERTURBATION TEMPERATURE PROBLEM (T) Determination of the temperature jumps on the crack lines	TEMPERATURE PROBLEM (T^0) for an undamaged bimaterial with a heat source	TEMPERATURE PROBLEM (T^0) for an undamaged bimaterial influenced by a heat flux. T^0 doesn't cause stresses in an undamaged bimaterial so that only perturbation solution (I) is needed
THERMOELASTIC PROBLEM for a bimaterial with cracks Determination of the stresses caused by the perturbation temperature	THERMOELASTIC PROBLEM for an undamaged bimaterial. Determination of the stresses on the crack lines ($\sigma_k - i\tau_k$)	
	ELASTIC PROBLEM for a bimaterial with cracks The edges of cracks are loaded by stresses with opposite signs, $-(\sigma_k - i\tau_k)$	

For internal cracks interacting with an interface crack the systems of singular integral equations are constructed for the temperature and thermoelastic problems, as well as antiplane problem. If the typical size of the internal cracks is much smaller then the size of the interface crack a small parameter method is used [4] for the solution. The small parameter is equal to the ratio of the length of the microcrack *2a* to the length of the interface macrocrack $2a_0$, i.e. $\lambda=a/a_0$. The solution of the problems is obtained up to λ^2 , which taking into account the interaction between the interface crack and each of microcracks. The closed form expressions for the temperature distribution in the bimaterial with cracks is obtained and then the stress intensity factors at the interface crack are derived. Further, the effect of the location of micro- defects as well as the influence of the material combination on the stress intensity factors at the interface macrocrack tip are investigated.

References

[1] Herrmann K.P.: Rissausbreitungsvorgänge in thermomechanisch belasteten Zweikomponenten-medien: Analysis und Experiment. *ZAMM* **77**: 163-188, 1997.

[2] Suo Z.: Singularities Interacting with Interfaces and Cracks. *Int. J. Solids Structures* **25**: 1133-1142, 1989.

[3] Petrova V., Herrmann K.: Thermal Crack Problems for a Bimaterial with an Interface Crack. *Proc.Int.Conf New Challenges in Mesomechanics*, Aalborg University, **2**: 591-597, 2002.

[4] Petrova V., Tamuzs V., and Romalis N.: A Survey of Macro-Microcrack Interaction Problems. *Appl. Mech. Rev*. **53**: 117-146, 2000.

DYNAMIC CRACK ANALYSIS UNDER THERMAL SHOCK

Parissa Hosseini-Tehrani , Alireza Hosseini-Godarzi
Automotive dept., Iran Univercity of science and tech., Tehran, Iran

Summary A boundary element method using Laplace transform in time domain is developed for the analysis of fracture mechanic considering transient coupled thermoelasticity problems with relaxation times in two dimensional finite domain. The dynamic thermoelastic model of Lord and Shulman are selected for showing finite thermal propagation speed. Thermal dynamic stress intensity factor for mode I is evaluated using different relaxation times.

Introduction

The classical theory of thermoelasticity assumes that the thermal disturbances propagate at infinite speeds. This prediction is a physically unacceptable situation. There is a class of problems dealing with impingement of a high intensity energy source on the surface of a structure that needs special consideration of the thermal wave model. The wave model in the heat transport process becomes even more important if some irreversibles physical processes, such as crack or void initiation and propagation in the solid, occur in the radiant duration. In these cases the orientation of crack initiation or crack propagation, for example, must be predicted according to the thermal wave model. In the classical study of thermoelastic crack problems, the theoretical solutions are available only for very few problems in which cracks are contained in infinite media under special thermal loading conditions. For example Lee and Sim [1] solved the problem of a surface cracked infinite strip under sudden conductive cooling and evaluated the mode-I thermal shock stress intensity factor (TSSIF) using Bueckner's weight function method. Katsareas et al. [2] used a boundary-only element method to compute shock stress intensity factors for a surface cracked infinite strip and a finite edge cracked plate. They considered uncoupled quasi-static thermoelasticity. Recently Hosseini-Tehrani et al. [3] present a boundary element formulation for the dynamic crack analysis Consider coupled theory of thermoelasticity. This paper presents a boundary element formulation for the crack analysis Considering the LS theory of thermoelasticity. In this work the body is exposed to a thermal shock on its boundary and the resulting thermal stress waves are investigated through the coupled thermoelastic equations. The discretized forms of the equations are obtained by the approximation of boundary variations by quadratic elements.

GOVERNING EQUATIONS

A homogeneous isotropic thermoelastic solid is considered. In the absence of body forces and heat generation, the governing equations for the dynamic coupled generalized thermoelasticity in time domain based on the LS theory are written as

$$(\lambda+\mu)u_{j,ij}+\mu u_{i,jj}-\gamma T_{,i}-\rho\ddot{u}_i=0 \qquad , \qquad kT_{,jj}-\rho c_e\dot{T}-\rho c_e t_0\ddot{T}-\gamma T_0(t_0\ddot{u}_{j,j}+\dot{u}_{j,j})=0 \qquad (1)$$

where a dot indicates time differentiation and the subscript *i* after a comma refers to partial differentiation with respect to x_i *(i=1,2)*, and λ, μ, u_i, ρ, T, T_0, k, , c_e, and t_0 are Lame's constant, the components of displacement vector, mass density, absolute temperature, reference temperature, thermal conductivity, stress-temperature modulus, specific heat at constant strain and, relaxation time proposed by LS theory respectively. Equations (1) can be rewritten in matrix from as

$$L_{ij}U_j=0 \qquad (2)$$

In order to drive the boundary integral problem, weak formulation of the differential equation set (2) for the fundamental solution tensor V_{ik}^* may be used

$$\int_\Omega (L_{ij}U_j)V_{ik}^*d\Omega=0 \qquad (3)$$

The detail mathematical formulations may be found in Hosseini-Tehrani et al. [3]. The stress intensity factor may be determined either from nodal traction or from the crack opening displacement (COD). To evaluate K_I, the quarter point singular element at the crack tip is used. If v_B at $r=l/4$ is considered (l is the length of the singular element at the crack tip) K_I, may computed as

$$K_I=\frac{\mu}{4-4\upsilon}\sqrt{\frac{2\pi}{l}}v_B \qquad (4)$$

RESULTS AND DISCUSSION

Structures covered with coatings and lining may be subjected to sever loading conditions. The load might be applied in the form of mechanical and/or thermal shocks. If the period of shock duration is small enough compared to the first natural frequency, then the dynamic thermoelasticity may be important. Considering an infinite strip shown in Fig. (1),

initially subjected to a uniform temperature T_0 with an edge crack perpendicular to its top surface. The strip is rapidly cooled by conduction at its upper surface $x_2=0$, whereas the bottom surface $x_2=W$ is insulated. This is a mode *I* crack opening problem. The crack edges assumed to be thermally insulated. Due to the symmetry about the x_2 axis, only half of the strip is discretized. The boundary element model is presented in Figure 1(b), for a crack depth of $a^*=0.05$ and $L/W=1$, where $a^*=a/W$. K_I^* is defined as the dimensionless TDSIF, which for plain strain condition is $K_I^* = K_I(1-v)/\left[E\sqrt{W}(T-T_0)\right]$ Where $t^*=Kt/(\rho c_e W^2)$ is the dimensionless time known as Fourier number. Validation of this method is shown in [3] for classical theory.

Figure (2) shows crack intensity factor variation versus dimensionless time t^*, while $t^*=1$ means *9.3E-12 sec*. In Fig. 2 comparison between conventional uncoupled and LS theory is done. In this figure curves are plotted for three different conditions. $C=0$ represent conventional uncoupled theory of thermoelasticity, in this case K_I^* is increased instantaneously after the application of the sudden cooling. At time $t^*=0.002$, the thermoelastic wave stress reaches the tip of the crack. This cold shock produces tensile stress in the x_2-direction and due to the effect of the Poisson's ratio, compressive stress is produced in the x_1-direction. This phenomena results into crack opening and thus K_I^* increases by time, as shown in Fig. (2). When $t_0 = 0.64$, the speed of propagation of the thermal wave is $C_t=1.25$ and the speed of the propagation of the stress wave is $Cs=1$ (dimensionless). In this condition at $t^*= 0.00175$ when cold wave reaches to the crack tip, crack opening begins. At $t^*=0.002$ when stress wave reaches to crack tip K_I^* variation takes place. For $t_0=1.5625$ the speed of propagation of thermal wave is $C_t=0.8$ and the speed of propagation of the stress wave is $Cs=1$ (dimensionless). In this condition at $t^*= 0.0025$ when cold wave reaches to the crack tip, crack opening begin, but stress wave that was already reached to crack tip has a decreasing effect on K_I^*.

CONCLUSIONS

A boundary element method and Laplace transform in time domain are developed for the analysis of fractured planar bodies subjected to thermal shock type loads. The important results of this study are: The appropriate time scale in which the effect of inertia term is observed is considered and the importance of inertia term is shown. In conventional theory of thermoelasticity, K_I^* has risen instantaneously after applying cold shock but in LS theory K_I^* rises when temperature or stress wave reaches to crack tip. The fracture analysis due to thermal shock using LS theory of thermoelasticity shows more fluctuation on K_I^* 's curve versus time.

Refrences

[1] Sih,G.: On the singular character of thermal stress near a crack tip. J.Appl. Mech, **29**,587-589,1962.
[2] Katsareas, D., Anifantis, N. K.: On the computation of mode I and II of thermal shock stress intensity factors using a boundary-only element method. Int. J. for Num. Meth. in Eng, **38**, 4157-4169,1995.
[3] Hosseini-Tehrani, P., Eslami, M., Daghyani H.:Dynamic crack analysis under coupled assumption. Trans. ASME J. of Appl. Mech., **38**, 584-588, 2001.

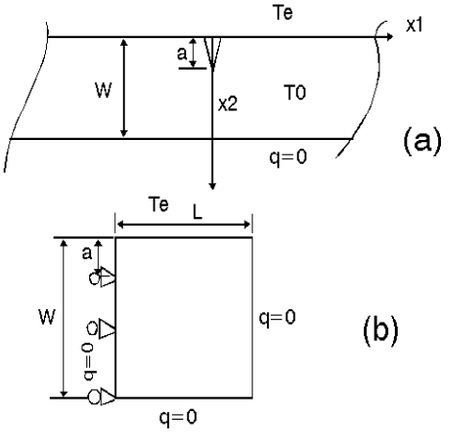


Fig. 1 (a) Cracked strip initially at T_0 under sudden cooling T_e , (b) boundary Condition.

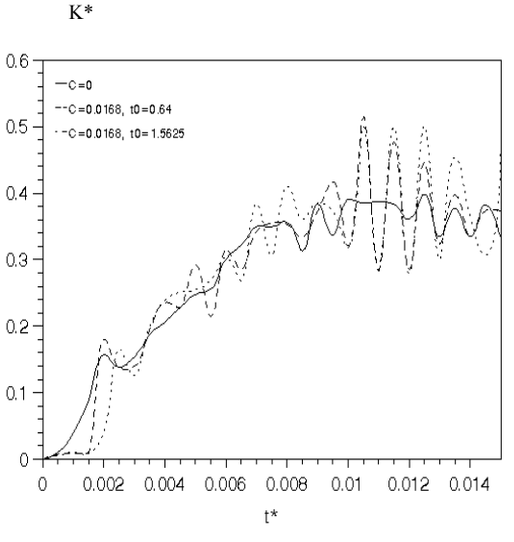


Fig. 2 Variation of the dimensionless thermal dynamic stress intensity factor versus dimensionless time for uncoupled and LS models.

EXPERIMENTAL INVESTIGATION ON CONCRETE SHEAR CRACK EXTENSION

Huijian Li Shengwang Hao
School of Civil Engineering and Engineering Mechanics, Yanshan University, Qinhuangdao, 066004.China P.R

Summary Most interests about concrete mode-Ⅱ fracture primarily focus on four-point specimens and Brazilian disk specimens, but there are many debates about printed results. This paper tries to present a detail investigation on these two specimens. The whole evolution process of crack initiation and propagation trajectory of two specimens are presented and discussed, and the fracture toughness is calculated.

Introduction

The four-point-shear geometry was first adopted by Arrea & Ingraffea [1] to investigat the concrete material. Banzant & Pfeiffer [2] proposed a double-edge-notched beam geometry. The same geometry was adopted by Melin [3]. Hao et al [4] give a combined experimental and numerical study on double-edge-notch concrete beams, this specimens also were studied by Ingraffea & Pathaki[4], Pietro Bocca et al[5], Enrico et al[6], A. Carpinteri et al[7], Geers et al[8,9]. The researchers' different conclusions contradict to each other. The Brazilian disk specimens also have been investigated by many researchers [10,11] with different materials.

To give a comprehensive analysis about the fracture mechanism of two kind concrete specimens, this paper provides the whole evolution process from crack initiation and propagation to catastrophe in both cases of concrete four-point-shear specimens and Brazilian disk specimens. Our interest focuses on trying to reveal the concrete mode-Ⅱ fracture mechanism according to a combined study on concrete four-point-shear specimens and Brazilian disk specimens. The values of fracture toughness of two kind specimens are calculated.

Description of test

Material: 525# silicate cement; river sand; limestone coarse aggregate (size is 5~10mm).

Cement: water: fine aggregate: coarse aggregate = 1:0.53:2.06:3.17

The specimens were cured in water bath for 7 days and then stored in laboratory conditions with temperature $+18\pm2°C$ and 90% relative humidity for 21 days. After 28 days, the strength and fracture characteristics were determined. The compressive strength is $39.8MPa$; internal friction angle is $23°$; tension strength is $3.06MPa$; Elastic modulus $E=29.7GPa$; Poisson ratio is 0.2; Mode-Ⅰ fracture toughness is $0.701MPa$. The geometries of experiments for four-point shear specimens and Brazilian disk specimens are respectively shown in fig.1 and fig.2. The loading rate applied was16.3N/s , and $s_2=2s_1$.

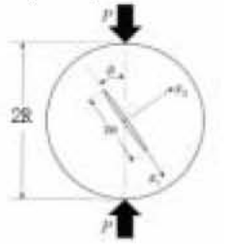


Fig.1 Brazilian disk specimens

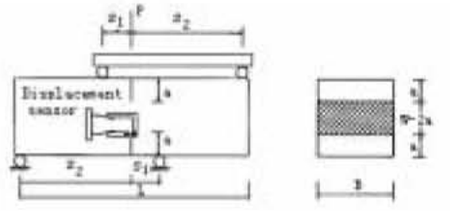


Fig.2 Four-point-shear specimens

Four-point shear specimens

In fig.3, a representative result of concrete four-point specimens is shown. The final main crack trajectory is that a crack at an angle with loading surface started at the under crack tip, then extend to the loading point. This result is agreed with other results of literatures.

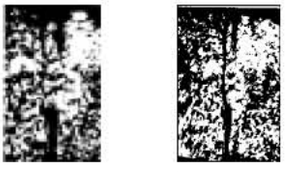


Fig.3 crack propagation trajectory of concrete four-point-shear specimens for $s_1=15mm$

Fig.4 shows the result when s_1 is $5mm$. In this case, a crack initiated at an angle with loading surface from the under crack tip, then it extend stably and turned to the direction paralleling to the loading surface, finally this initiation crack connected with the crack initiated from the up-crack tip and led to the specimen's failure. This fracture mode looks like shear fracture from macro-level, but the initiation direction did not parallel to the direction of loading or the direction of shear stress. The decreasing of the distance between loading point to crack surface did not change the fracture mode of specimens, it only decreased the crack propagation angle but did not obtain the pure mode-Ⅱ fracture. The critical stress intensity factors ratio K_{IIC}/K_{IC} is about 0.6~0.7 and agreed with the results of literatures.

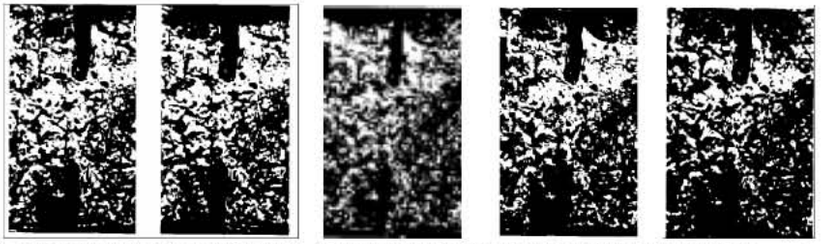


Fig.4 crack propagation trajectory of concrete four-point-shear specimens for $s_1 = 5$mm

Brazilian disk specimens

The radius R of specimen is $150mm$, the thickness B is 30mm. Because the $K_{\square}$ in the case of slope angle $\varphi = 15°$ increases most quickly than any other angle, and when the ratio of half crack length a with the radius R is 0.75, $K_{\square}$ almost equals to zero. So we significantly study this case.

The representative result is shown in Fig.6. A crack at an angle with crack surface initiated from two-crack tip. Then they continued to extend until they get to the load point. This result is agreed with that of other literatures[12]. Another interest result was also observed that when the initiation cracks from crack tips extended to some length, other two cracks from the boundary were induced. These two cracks should be resulted from the effect of boundary. Ratio $K_{\square C}/K_{\square C}$ is about 0.70~0.84 and larger than the results of four-point-shear specimens because of the pressure occurring near the tips of cracks.



Fig.6 crack propagation trajectory of Brazilian disk specimens

Discussions

In the case of concrete four-point-shear specimens, the orientation of crack extension is not at the direction of shear stress, and the fracture is resulted from the combined influence of mode-Ⅰbehaviours and mode-Ⅱbehaviours. The Ratio $K_{\square C}/K_{\square C}$ is agreed with the results of mixed mode of mode-Ⅰand mode-Ⅱ. It is difficult to achieve the mode-Ⅱ fracture with this specimen.

The crack propagation trajectory of concrete Brazilian disk specimens was agreed with other literature's[7] investigation with rock or other materials. In this case, the ratio of $K_{\square C}/K_{\square C}$ is larger than the results of four-point-shear specimens, but the crack initiation is not the true mode-Ⅱ fracture, it also includes the combined influence of mode-Ⅰand mode-Ⅱbehaviours.

To achieve the crack sliding initiation, there must be one measure to take to arrest the crack opening initiation in both cases of four-point-shear test and Brazilian disk test.

Reference

[1] Arrea & Ingraffea mixed mode crack propagation in mortar and concrete. Report, No.81-13, Department of Structural Engineering, School of Civil and Environmental Engineering, Cornell University. 1982

[2] Banzant & Pfeiffer. Shear fracture test of concrete. Material and Structure.1986, 110(119): 111-121.

[3] Hao et al. A combined experimental and numerical investigation of mode-Ⅱ fracture of compact four-point-shear concrete specimens. Engineering mechanics[J] (Chinese). 2003,020(002): 138-141

[4] Ingraffea & Pathaki. Analysis of Shear Fracture Tests of Concrete Beams, Finite Element Analysis of Reinforced Concrete Fracture. Asce, Tokyo. 1985:151-173

[5] Pietro Bocca, Alberto Carpinteri and Silvio Valente. Mixed mode fracture of concrete. International Journal of Solids and Structures. 1991, 27(9): 1139-1153

[6] Enrico Ballatore, Alberto Carpinteri, Gerardo Ferrara and Giorgio Melchiorri. Mixed mode fracture energy of concrete. Egineering Fracture Mechanics.1990,35(1-3):45-157

[7] A. Carpinteri, S. Valente, G. Ferrara and G. Melchiorrl. Is mode Ⅱ fracture energy a real material property. Computers & Structures. 1993,48(3)397-413

[8] M. G. D. Geers, R. de Borst and R. H. J. Peerlings. Damage and crack modeling in single-edge and double-edge notched concrete beams, Engineering Fracture Mechanics, 2000, 65(2-3) :247-261

[9] Geers, M.G.D.; de Borstc</cross-ref>, R.; Peerlingsa</cross-ref>, R.H.J. Damage and crack modeling in single-edge and double-edge notched concrete beams. Engineering Fracture Mechanics Volume. 2000,65(2-3):. 247-261

[10] .N. A. Al-Shayea, K. Khan and S. N. Abduljauwad. Effects of confining pressure and temperature on mixed-mode (I–II) fracture toughness of a limestone rock, International Journal of Rock Mechanics and Mining Sciences, 2000, 37(4): 629-643

[11] C. Liu, Y. Huang and M. G. Stout. Enhanced mode-Ⅱ fracture toughness of an epoxy resin due to shear banding. Acta Materialia, 1998,46(16):5647-5661

EFFECT OF INTER- AND INTRALAMINAR DAMAGE ON THE COMPRESSIVE FRACTURE OF HYPERELASTIC MATERIALS

Igor A. Guz*, Maria Kashtalyan*, Klaus P. Herrmann**
*College of Physical Sciences, University of Aberdeen,
Fraser Noble Building, King's College, Aberdeen AB24 3UE, Scotland, U.K
**Laboratory for Technical Mechanics, University of Paderborn,
Pohlweg 47-49, D-33098 Paderborn, Germany

Summary The present analysis investigates a mechanism of compressive fracture for heterogeneous non-linear materials undergoing large deformations under uniaxial or equi-biaxial loading. Special attention is given to accounting for the presence of both, inter- and intralaminar defects. The upper and the lower bounds for the critical load are examined. The analytical solution is found for different types of interlaminar boundary conditions.

In practical cases, the assumption of perfect bonding between neighbouring layers in composites does not correspond to reality. Various cases of interlaminar adhesion breakdown may occur in real layered materials during the fabrication process or in-service. If composites are compressed along layers and, therefore, along the mentioned interlaminar defects, the classical Griffith-Irwin criterion of fracture or its generalisations are inapplicable, since all stress intensity factors and crack opening displacements are equal to zero. This fact emphasises the importance and the necessity of a most careful (possibly exact) investigation of fracture due to specific mechanisms inherent to heterogeneous materials. The loss of stability in the heterogeneous structure of composites is one of such mechanisms; the moment of stability loss in the microstructure of the material – internal instability according to Biot – is associated with the onset of fracture.

The most accurate approach to studying the internal instability is based on the model of a piecewise-homogeneous medium, when the behaviour of each component of the material is described by the 3-D equations of solid mechanics provided certain boundary conditions are satisfied at the interfaces. It was used in numerous publications on the topic – see the reviews [2,5]. Along with the exact approach, there are also approximate models proposed by Rosen and later by many other authors. Detailed comparative analysis of different approaches was given in [1,2,5]. It was concluded [2,5,6] that the approximate methods are not accurate when compared to experimental measurements and observations.

However, all works mentioned above considered *perfectly bonded layers only*. Moreover, the approaches based on the Rosen model cannot be *altogether* applied in the case of *large* pre-critical (applied) deformations. The 3-D approach presented here allows us to take into account large deformations, geometrical and physical non-linearities and load biaxiality that the simplified methods cannot consider.

This paper investigates heterogeneous *non-linear* materials under *large* deformations. The composite consists of alternating layers with thicknesses $2h_r$ and $2h_m$ (Fig. 1), which are simulated by incompressible transversally isotropic solids with a general form of the constitutive equations. Henceforth all values referred to these layers will be labelled by indices *r* (reinforcement) and *m* (matrix). The analysis finds the bounds for critical compressive loads acting on the materials with imperfect interlaminar adhesion. As an example, a change in the nature of the interlaminar contact is studied, when an interaction of the layers is implemented so, that infinitesimal sliding is allowed, but still there are no gaps between the layers (e.g., molecular chains in some kinds of glue connection, Fig. 2). This kind of the cleavage-type delaminations is called *defects with connected edges* [3,6] or *perfectly lubricated interfaces*. For these defects, the continuity at the interface is retained for normal components only. For a layered material with an unidentified set of defects with connected edges, the following estimation can be suggested to find the lower bounds for the critical loads.

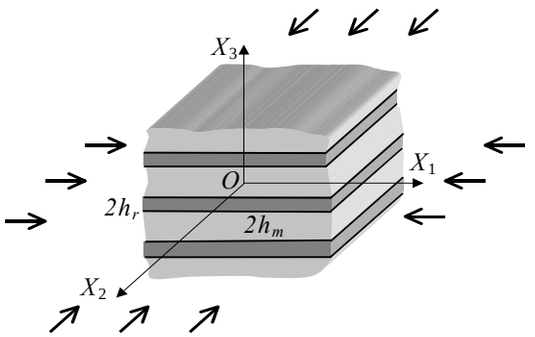


Fig. 1: The co-ordinate system and applied loads.

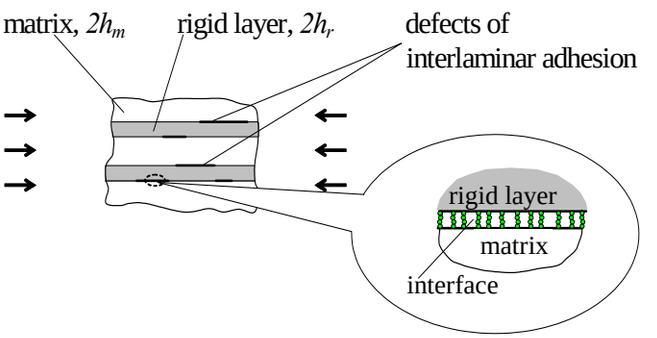


Fig. 2: An interface with a cleavage-type delamination.

Following [3], it can be said that the critical load for a material with the imperfections of interlaminar adhesion, e.g. containing the cleavage-type delaminations (P_{cr}^{imp}), must be smaller than for a material with the same internal structure with perfectly bonded layers (P_{cr}^{pb}); and must be larger than the critical load for a material with sliding layers (P_{cr}^{sl}). Hence, $P_{cr}^{pb} \geq P_{cr}^{imp} \geq P_{cr}^{sl}$, which, if written in the terms of shortening factors, λ_1, takes the form $\lambda_{cr}^{pb} \leq \lambda_{cr}^{imp} \leq \lambda_{cr}^{sl}$, since $u_i = (\lambda_i - 1)x_i$. This is true for an arbitrary set of defects with connected edges, i.e. for an arbitrary number, size and disposition of the defects. The substantiation of the bounds is based on a general principle of mechanics, which states that the release from a part of connections inside of the mechanical system cannot increase the value of the critical load.

In order to calculate the bounds, the non-axisymmetrical problem of the internal instability is considered within the model of a piecewise-homogeneous medium using the equations of the 3-D stability theory [2]. This allows us to eliminate the restrictions imposed by using the approximate theories as well as the inaccuracies they involve. The analytical solutions are found for different types of interlaminar boundary conditions, i.e. for perfectly bonded and sliding without friction layers. The characteristic determinants are derived for the first four modes, which are more commonly observed.

Of course, practical composite materials contain not only *interlaminar*, but also various sorts of *intralaminar* defects, cracks etc. The latter further complicate the problem. However, the developed method allows accounting for the presence of *intralaminar* damage by considering layers with reduced stiffness properties. The reduction in the axial material stiffness as well as in the Poisson's ratio due to matrix cracking was extensively investigated – see the review [4]. Based on the results [4,8], the effective properties of materials with intralaminar defects are calculated and incorporated into the analysis described above.

The effect of the different types of inter- and intralaminar damage, layer thickness and stiffness on the lower and the upper bounds is illustrated by several examples calculated for the particular non-linear models of materials. The obtained results show that the bounds present a good estimation. One of the examples is given below.

Let the composite (Fig. 1) consist of hyperelastic layers described by the simplified version of Mooney's potential, namely neo-Hookean potential, with the strain energy density function $\Phi = 2C_{10}I_1(\varepsilon_{ij}^0)$, where C_{10} is a material constant, and $I_1(\varepsilon)$ is the first algebraic invariant of Cauchy-Green strain tensor. This potential is also called Treloar's potential, after the author who obtained it from an analysis of model of rubber regarded as a system of long molecular interlinking chains [8]. The upper bound for critical shortening factors is found as a result of the following procedure.

Solving the characteristic equations derived for the case of sliding layers for different modes of stability loss, the shortening factors are obtained as functions $\lambda_1^{(N)}(\alpha_r)$ of the normalised wavelength, α, where N is the number of the mode ($N = 1, 2, 3, 4$). The critical value for the particular mode, $\lambda_{cr}^{(N)}$, can be found as a maximum of the corresponding function. The maximum of these N values will be the critical shortening factor of the internal instability for the considered layered material with sliding layers, λ_{cr}^{sl},

$$\lambda_{cr}^{sl} = \max_N \lambda_{cr}^{(N)} = \max_N \left(\max_{\alpha_r} \lambda_1^{(N)} \right)$$

which is also the upper bound for the critical shortening factor for composites with interlaminar defects with connected edges. The example of the upper bound is given in Fig. 3. It was calculated for the typical ratios of the material constants, C_{10}^r / C_{10}^m. The value of the critical shortening factor increases with increasing relative stiffness of the layers. The increase rate is much higher for smaller values of the relative stiffness of the layers, that means $C_{10}^r / C_{10}^m < 50$. At that, the increase is very sharp for $C_{10}^r / C_{10}^m < 20$.

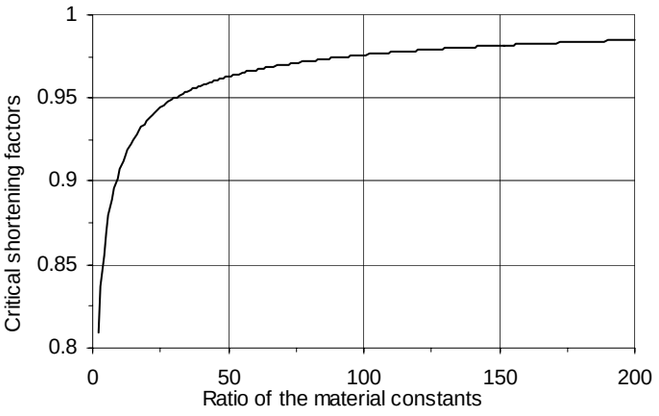


Fig. 3: The upper bound for λ_{cr} ; $h_r / h_m = 0.05$.

References

[1] Budiansky, B., Fleck, N.A., 1994. Compressive kinking of fibre composites: a topical review. Appl. Mech. Rev. 47(6), S246-S270.

[2] Guz, A.N., 1999. Fundamentals of the Three-Dimensional Theory of Stability of Deformable Bodies. Springer-Verlag, Berlin Heidelberg.

[3] Guz, I.A., 1998. Composites with interlaminar imperfections: substantiation of the bounds for failure parameters in compression. Compos. Part B 29(4), 343-350

[4] Kashtalyan, M., Soutis, C., 2002. Mechanisms of internal damage and their effect on the behavior and properties of cross-ply composite laminates. Int. Appl. Mech. 38(5), 641-657.

[5] Micromechanics of Composite Materials: Focus on Ukrainian Research (Guz, A.N., Ed.), 1992. Appl. Mech. Rev. 45(2), 15-101.

[6] Soutis, C., Guz, I.A., 2001. Predicting fracture of layered composites caused by internal instability. Compos. Part A. 32(9), 1243-1253

[7] Treloar, L.R.G., 1975. The Physics of Rubber Elasticity. Oxford University Press, England.

[8] Zhang, J., Herrmann, K.P., 1999. Stiffness degradation induced by multilayer intralaminar cracking in composite laminates. Compos. Part A 30(5), 683-706.

EXPERIMENTAL AND NUMERICAL CRACK GROWTH IN A SPECIAL GEOMETRY

Liviu Marsavina, Dan Mihai Constantinescu
Department of Strength of Materials, University "Politehnica" of Timisoara, Timisoara, Romania
Department of Strength of Materials, University "Politehnica" of Bucharest, Bucharest, Romania

Summary Experimental evidence on three-dimensional crack propagation is needed for a better understanding of the local mechanisms around the crack front in a motor grain geometry. The crack propagation and turning processes suggest that the role of the shear modes is important in the initial stages of growth and a two-dimensional plane strain finite element simulation is used to compare the SIF values as trying to assess the efficiency of such a simplified procedure.

INTRODUCTION

The desire to establish a three-dimensional framework for use in analyzing problems of stable mixed-mode crack propagation has received lately a considerable attention. The study of predicting crack paths under the most general possible hypotheses (three dimensions, arbitrary geometry of the body and of the crack, arbitrary loading) is an ambitious objective. Recently, Leblond [1] and Leblond, Lazarus and Mouchrif [2] established formulae which specify the general functional form of the successive terms of the expansions of the SIFs along the front of the extended crack and, as they underline, the formulation of the propagation criterion is an open problem only in the presence of mode III. Therefore, in a mode I+II situation, the widely accepted "principle of local symmetry" of Goldstein and Salganik [3] receives a general recognition. In fact, for the two-dimensional problem, Cotterell and Rice [4] presented an analysis for slightly curved or kinked cracks and accounted for the role of mode II in crack turning. Also Rubenstein [5], in analyzing test results, concluded that sharp kinks likely occur only in very brittle materials and that, more commonly, the change in direction during the crack growth is more of a gradual turning than a kink. In numerical experiments the FRANC3D code uses new concepts with a model that allows for the implementation of 3-D crack growth mechanics [6] with the support of both finite and boundary elements. Keeping in mind such beneficial developments, one should emphasize that for a specific geometry and loading we may obtain various experimental crack paths which are dependent on the local position of the initial crack, as any deviation from "symmetry" influences the future crack trajectory.
This study emphasizes some practical aspects which should be considered in the finite element modelling. One should analyze carefully results obtained from experimental observations, especially when a 3-D model is in view. A preliminary comparison with a FRANC2D/L analysis [7] gives higher numerical normalized SIFs than the experimental ones obtained at maximum depth penetration.

MODEL CONFIGURATION AND 3-D EXPERIMENTAL PROCEDURE

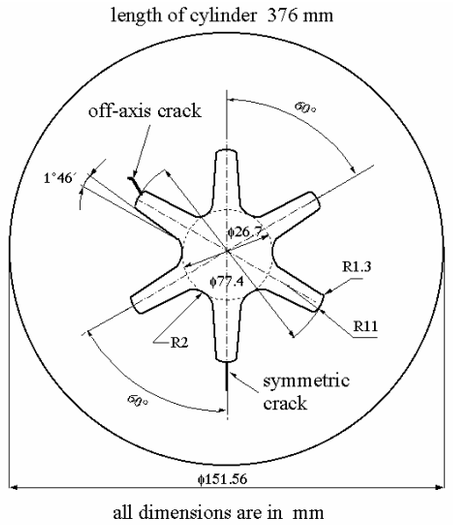


Fig. 1. Tested model geometry.

The geometry of the model studied here is shown in Fig. 1 and represents a motor grain configuration [8]. A model contained two starter cracks, a *symmetric* and an *off-axis* crack separated by an uncracked fin to avoid any interference. The *off-axis* crack (located at the coalescence of the two radii of 1,3 mm and 11 mm) can be inclined (as shown in Fig. 1) or straight-in – parallel with the fin axis. After inserting the starter cracks by striking a shaft with a blade at the end held normal to the inner fin surface, the models were capped with RTV rubber caps which were glued with PMC-1 adhesive and were subjected to the stress freezing cycle under internal pressure. The cracks were grown under internal pressure above critical temperature to desired size, after which the pressure was dropped to about 0,04-0,05 MPa and stress freezing was completed. After cooling, thin slices (around 1 mm thickness) were removed normal to the crack front and analyzed at maximum crack depth and in certain locations along the crack front, finally obtaining the values of the normalized stress intensity factors by using a two parameter algorithm valid within the linear elastic fracture mechanics (LEFM) constrains. Thus optical data (isochromatic fringes) can be converted into Mode I and Mode II SIFs, if the last one exists. All symmetric cracks remained in the plane of the axis of symmetry and grew as semi-elliptic cracks. If the cracks were off-axis straight-in parallel to the fin axis but (Fig. 1), a slight initial crack plane misalignment is possible due to the position of the blade or due to its bending after striking it, but the crack grows quickly by regaining its symmetry.
Studies of 11 tests on the motor grain geometry [8, 9] covered cracks of projected a/c values (crack depth/half length of crack in fin tip surface) of 0,5 to 0,9 and a/t values from 0,2 to 0,6 (t = 37,08 mm is the cylinder wall thickness at

fin tip). It appears that both SIF values and crack geometry during growth are quite variable due to shear modes for the off-axis inclined cracks. On the other hand, the symmetric cracks situated on the fin axis are quite predictable in their growth, as they tended to grow much more readily than the off-axis crack, always in the plane of the fin axis. It was found that the substantial delay in crack growth for the inclined cracks is also due to some initial misalignment of the blade with respect to the normal to the fin surface that is corrected by the turning of the crack as it grows and eliminates the shear modes.

NUMERICAL 2-D SIMULATIONS AND COMPARISON WITH EXPERIMENTAL RESULTS

A FRANC2D/L plane-strain finite element analysis was performed on half model using triangular 6-node elements. The mesh has 988 elements with 2153 nodes. A refined mesh was used around the notches. The material constants used in the analysis were the same as of the photoelastic material.
The initial numerical study was to find the SIFs versus crack length for three different configurations: symmetric crack, off-axis straight-in crack and off-axis inclined crack. The remeshing by delete and fill algorithm was used, which requires: to delete a group of elements in a region around the crack tip, then the crack is extended into this region, singular elements are placed around the crack tip, [4]. The stress intensity factors were obtained using the Modified Crack Closure Integral method. A study of crack propagation of off-axis cracks was carried on. The numerical prediction of the direction of crack trajectory was based on the maximum principal stress theory.

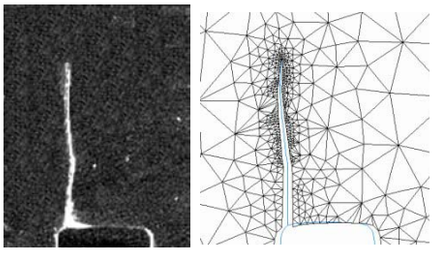


Fig. 2. Experimental off-axis straight-in crack and numerically simulated crack growth.

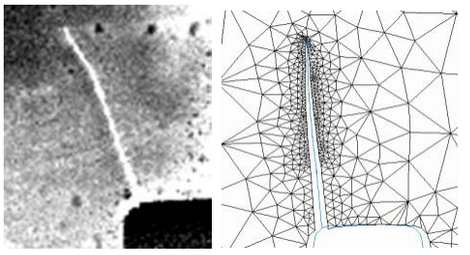


Fig. 3. Experimental off-axis inclined crack and numerically simulated crack growth in early stages.

The crack in Fig. 2 remains straight after some minor rearrangements, and Mode I is present. For the off-axis inclined crack, this one turns on a curved path (note path of mid-point at left of Fig. 3 in the experimental test), and after this limited amount of growth some Mode II as well as Mode I remained. Presumably, with further extension, the crack will straighten out and eliminate Mode II. The numerical simulation shows a rapid change of direction and presence of Mode I. At maximum depth all the experimental 3-D SIFs were smaller than the numerical 2-D corresponding values.

CONCLUSIONS

Off-axis cracks are retarded in growth by shear modes (II or II and III) and eventually gain their local and global symmetry. For three-dimensional numerical simulations mode III has to be considered. For two-dimensional simulations, one should remember that any local imperfections of crack location and loading will change at the beginning the crack trajectory, but later Mode I will be dominant.

Acknowledgements

The second author gratefully acknowledges the support of the experimental studies under P. 0. #RPO10230 with ERC Inc. through Air Force Research Laboratory and many useful discussions with Professor C.W. Smith.

References

[1] Leblond J.B.: Crack paths in three-dimensional elastic solids. I: two-term expansion of the stress intensity factors – application to crack path stability in hydraulic fracturing. *International Journal of Solids and Structures* **36**: 79-103, 1999.

[2] Leblond J.B., Lazarus V. and S. Mouchrif S.: Crack paths in three-dimensional elastic solids. I: three-term expansion of the stress intensity factors – applications and perspectives. *International Journal of Solids and Structures* **36**: 105-142, 1999.

[3] Goldstein R.V. and Salganik R.L.: Brittle fracture of solids with arbitrary cracks. *International Journal of Fracture* **10**: 507-523, 1974.

[4] Cotterell B. and Rice J.R.: Slightly curved or kinked cracks. *International Journal of Fracture* **16**: 155-169, 1980.

[5] Rubenstein A.: Mechanics of crack path formation. *International Journal of Fracture* **47**: 291-305, 1991.

[6] Carter B.J., P.A. Wawrzynek P.A. and Ingraffea A.R.: Automated 3-D crack growth simulation. *International Journal for Numerical Methods in Engineering* **47**: 229-253, 2000.

[7] Swenson D.V. and James M.A.: FRANC2D/L: A Crack Propagation Simulator for Plane Layered Structures, Version 1.4 User's Guide, Kansas State University, Manhattan, Kansas, 1996.

[8] Smith C.W., Constantinescu D.M. and Liu C.T.: Stress intensities and crack growth in photoelastic motor grain models. *Proceedings of the 2002 SEM Annual Conference& Exposition on Experimental and Applied Mechanics, Session 36, Experiments in Fatigue & Fracture*, Paper 3, June 10-13, Milwaukee, Wisconsin, 2002.

[9] Smith C.W., Constantinescu D.M. and Liu C.T.: Crack shapes and stress intensities in a motor grain geometry. *Proceedings of the 2002 International Conference on Computational Engineering & Sciences*, Chapter 7, Paper No. 5, Technical Science Press, Irvine, Ca., 2002.

ELASTODYNAMICS PROBLEMS IN DOMAINS WITH EDGES

S. I. MATIOUKEVITCH, N. F. MOROZOV, AND B. A. PLAMENEVSKII

DEPARTMENT OF MATHEMATICAL AND COMPUTATIONAL PHYSICS, ST. PETERSBURG UNIVERSITY, UL'YANOVSKAYA 1, ST.PETERSBURG 198504, RUSSIA

RESEARCH INSTITUTE OF MATHEMATICS AND MECHANICS (NIIMM), ST. PETERSBURG UNIVERSITY,ST. PETERSBURG, BIBLIOTECHNAJA SQ., 2, 198504, RUSSIA

DEPARTMENT OF MATHEMATICAL AND COMPUTATIONAL PHYSICS, ST. PETERSBURG UNIVERSITY, UL'YANOVSKAYA 1, ST.PETERSBURG 198504, RUSSIA

Summary. Basic initial-boundary value problems of elastodynamics are considered in a domain of general type with edges on the boundary, in particular, with cracks and conical points. The asymptotics of solutions near the singularities is obtained and justified.

Initial-boundary value problems of elastodynamics are considered in a domain of general type whose boundary may contain conical points and non-intersecting smooth edges. The Dirichlet and Neumann conditions (homogeneous and non-homogeneous) are imposed on the boundary. We study the behavior of solutions near the singularities of the boundary. To this end we investigate the solvability of the problems in a scale of weighted spaces, obtain and justify the asymptotics of solutions near the edges, derive explicit formulas for the coefficients in the asymptotics. We briefly describe the results for a domain G with conical point O. The principal part of the asymptotics of a solution near O is a linear combination $\sum c_j(t)\ u_j(x)$ of the functions u_j satisfying a homogeneous elliptic problem in the "tangent" cone; such a problem is the elliptic part of the initial hyperbolic problem. The hyperbolic character of the asymptotics manifests itself in the coefficients c_j that are functions in time. In the case of homogeneous boundary and initial conditions, the coefficients admit representation of the form

$$c_j(t) = \int\limits_G \int\limits_{\mathbb{R}} f(x, t-s)\overline{w_j(x,s)}dxds,$$

where f is a right-hand side of the problem and w_j is a solution to the corresponding homogeneous problem, singled out by its (growing) asymptotics near the conical point. For some model problems the functions w_j are calculated explicitly(for the wave equation in a cone, in a corner, in a plane with a half-infinite crack). Using these explicit formulas for w_j, we observe some phenomena in the coefficients c_j, for example, "the back front of singularities": the coefficients become smooth after the perturbation going from the singular support of an external load (i.e., from the singularities of the load) has left the vertex of cone. We also discuss the reaction of coefficients at the moment when a perturbation approaches the vertex. Part of the results was obtained jointly with A.Kokotov and P.Neittaanmaki.

3D MICROSTRUCTURAL EFFECTS ON PLANE STRAIN DUCTILE CRACK GROWTH

Alan Needleman*, Viggo Tvergaard**
*Division of Engineering, Brown University, Providence, RI 02912, USA
**Department of Mechanical Engineering, The Technical University of Denmark, 2800 Lyngby, Denmark

Summary Ductile crack growth under mode I, plane strain, small scale yielding conditions is analyzed. Overall plane strain loading is prescribed, but a full 3D analysis is carried out to resolve microstructural effects. An elastic-viscoplastic constitutive relation for a porous plastic solid is used to model the material. Two populations of second phase particles are represented, large inclusions with low strength, which result in large voids near the crack tip at an early stage, and small second phase particles, which require large strains before cavities nucleate. The larger inclusions are represented discretely and the effect of their 3D distribution on the crack path and on the overall crack growth rate is analyzed.

INTRODUCTION

In a wide variety of circumstances of practical interest, the stress and deformation fields near a crack tip in a structural metal, but outside the fracture process zone, are appropriately idealized as plane strain fields. However, the material microstructure in the process zone, which sets the plane strain crack growth resistance is inherently three dimensional. The main mechanism of ductile fracture in the process zone is void nucleation, growth and coalescence, and the spacing and distribution of void nucleating inclusions is the key microstructural feature for setting the crack growth resistance. Typically, for structural metals, the size of the void nucleating particles ranges from 0.1 μm to 100 μm, with volume fractions of a few percent. Quite commonly, the distribution of void nucleating particles can be idealized as involving two size scales; larger particles (e.g. MnS inclusions in steels) that nucleate voids at relatively small strains and smaller particles (e.g. carbides in steels) that nucleate voids at much larger strains. It is well appreciated that the distribution of inclusions plays a major role in setting the crack growth resistance in such materials, and while there have been a few 3D analyses of porosity induced ductile crack growth, e.g. Ruggieri *et al*. [1] and Hao and Brocks [2], full 3D analyses quantifying the role of inclusion distribution on crack growth behavior have not been carried out.

The analyses are carried out using a constitutive framework for progressively cavitating ductile solids stemming from the work of Gurson [3]. In this constitutive relation, the porosity is represented in terms of a single scalar parameter, the void volume fraction. The matrix material is modeled as an isotropic hardening viscoplastic solid. The large inclusions which nucleate voids at an early stage are modeled as a distribution of 'islands" of the amplitude of the void nucleation function. Thus, their size and spacing are directly specified in the analyses and introduce a characteristic length into the formulation. The smaller second-phase particles, which require large strains for nucleation, are uniformly distributed. This formulation has been used to carry out analyses of crack growth for 2D model microstructures, e.g. Tvergaard and Needleman [4], where the larger inclusions could only be represented as long cylinders, which is not geometrically realistic. It was shown in Needleman and Tvergaard [5] that in cases where the voids nucleated from the larger inclusions dominate the fracture process, the crack growth predictions exhibited practically no mesh sensitivity.

The same material model is used as in previous 2D studies, e.g. [4], but here 3D microstructures are analyzed. A slice of material with an initial crack is analyzed. Overall plane strain conditions are imposed and various distributions of larger spherical inclusions are specified. The calculations are for small scale yielding conditions with remote mode I loading, with a monotonically increasing stress intensity factor prescribed. The analyses account for finite deformations. For numerical efficiency, transient analyses are carried out, but the initial conditions and loading rate are chosen so that inertial effects are negligible. Although overall plane strain conditions are prescribed, the stress and deformation states that develop in the fracture process zone are fully three dimensional.

FORMULATION

A convected coordinate Lagrangian formulation is used with the dynamic principle of virtual work written as

$$\int_V \tau^{ij}\delta E_{ij}\, dV = \int_S T^i \delta u_i\, dS - \int_V \rho \frac{\partial^2 u^i}{\partial t^2}\delta u_i\, dV \tag{1}$$

where E_{ij} are the covaraiant Lagrangian strain components, τ^{ij} are the contravariant components of Kirchhoff stress on the deformed convected coordinate net, T^i are the contravariant components of nominal traction, ν_j and u_j are the covariant components of the reference surface normal and displacement vectors, respectively, ρ is the mass density, and V and S are the volume and surface of the body in the reference configuration.

With the origin of the coordinate system at the crack tip, the region analyzed is defined by $-W \le y^1 \le W$, $0 \le y^2 \le L$ and $0 \le y^3 \le H$ and the boundary conditions imposed are that $u_3 = 0$ on $y^3 = 0$ and $y^3 = H$ (giving overall plane strain); $u_2 = 0$ on $y^2 = 0$, $y^1 > 0$. The loading is prescribed through u_1 and u_2 on $y^1 = \pm W$ and $y^2 = L$ which are given by the plane strain mode I crack tip displacement fields. The mode I stress intensity factor, which is the amplitude of these displacements, is the prescribed quantity. The parts of the boundary where displacements are not prescribed, including of course the crack surface, are traction free. Also, the initial crack tip is taken to be a wedge-shaped notch.

The constitutive framework is the modified Gurson [3] flow potential given by

$$\Phi = \frac{\sigma_e^2}{\bar{\sigma}^2} + 2q_1 f^* \cosh\left(\frac{3q_2\sigma_h}{2\bar{\sigma}}\right) - 1 - (q_1 f^*)^2 = 0 \tag{2}$$

Here, σ_e is the effective stress, σ_h is the hydrostatic stress, $\bar{\sigma}$ is the matrix flow strength and the function f^* accounts for the effects of rapid void coalescence at failure

$$f^* = \begin{cases} f & f < f_c \\ f_c + (1/q_1 - f_c)(f - f_c)/(f_f - f_c) & f \geq f_c \end{cases} \tag{3}$$

where f is the void volume fraction. This constitutive relation and background on the basis for the choice of parameter values in it is discussed in Tvergaard [6].

The constitutive relation for the matrix material includes strain and strain rate hardening and thermal softening, with adiabatic conditions assumed. The crack growth mechanism analyzed involves two populations of void nucleating particles; large particles that nucleate voids at relatively small strains and smaller particles that nucleate voids at much larger strains. The small scale particles are taken to be uniformly distributed and nucleate by a plastic strain controlled mechanism. The large inclusions are modeled as constant amplitude spherical "islands" of stress-controlled void nucleation. The constitutive relation is such that the stress carrying capacity vanishes when f^* reaches a critical value. The initiation of crack growth as well as the subsequent rate and direction of crack growth are directly determined by the evolution of material failure.

Twenty node brick elements are used with eight point integration. The equations resulting from substituting the finite element discretization of the principle of virtual work (1) are integrated numerically by an explicit integration procedure. The mesh used has $71,424$ elements, $314,279$ nodal points and $942,837$ degrees of freedom.

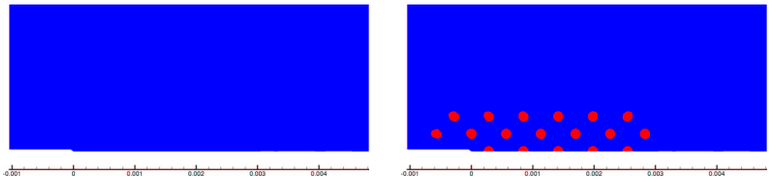


Figure 1. Contours of the amplitude of stress-controlled void nucleation in the near crack tip region showing the inclusion distribution for two slices of y^3 =constant.

RESULTS

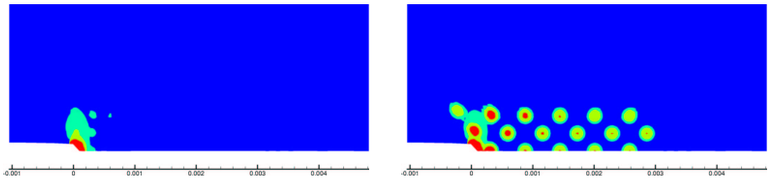


Figure 2. Contours of void volume fraction in the near crack tip region for the two slices of y^3 =constant in Fig. 1.

Calculations are carried out for various distributions of larger inclusions, with material parameter values representative of a structural steel. Figure 1 shows the distribution of the amplitude of stress-controlled void nucleation for one distribution. In one slice, corresponding to $y^3 = H/2$ no inclusions are present whereas a distribution of inclusions is seen in the slice at $y^3 = 0$, thus illustrating the three dimensional nature of the distribution. As a consequence of this inclusion distribution, crack growth does not occur in a uniform planar manner as seen from the contours of void volume fraction in Fig. 2 which shows a stage near the initiation of crack growth. The implications of the 3D inclusion distribution for the initiation of crack growth, for the evolution of the crack path and for the material's crack growth resistance are illustrated and discussed.

References

[1] Ruggieri T.L., Panontin T.L., Dodds R.H.: *Int. J. Fract.* **82**:67-95, 1996.
[2] Hao S., Brocks W.: *Comp. Mech.* **20**:34-40, 1997.
[3] Gurson A.L.: Plastic Flow and Fracture Behavior of Ductile Materials Incorporating Void Nucleation, Growth and Interaction. *PhD Thesis*, Brown University, 1975.
[4] Tvergaard V., Needleman A.: *J. Mech. Phys. Solids* **40**:447-471, 1992.
[5] Needleman A., Tvergaard, V.: *Engin. Fract. Mech.* **47**:75-91, 1994.
[6] Tvergaard, V.: *Adv. Appl. Mech.* **27**:83-151, 1990.

WEIGHT FUNCTIONS FOR CRACKS IN PIEZOELECTRICS

Andreas Ricoeur, Meinhard Kuna
TU Bergakademie Freiberg, Institute of Mechanics and Fluid Dynamics, 09596 Freiberg, Germany

Summary Two types of weight functions for cracks in piezoelectrics are derived yielding stress and electric displacement intensity factors for point loads/charges and local displacements/electric potentials, respectively. The weight functions are applied to calculate field intensity factors and displacement/electric potential fields in a cracked body under arbitrary electromechanical loading conditions. Further applications include the investigation of effects like bridging or small scale switching on the crack tip loading.

Fracture mechanics of piezoelectric and ferroelectric materials is of increasing interest for applicants of smart materials. The analytical framework of piezoelectric fracture mechanics has been established in the early 90s by researchers like Sosa [1], Pak [2] or Park and Sun [3] giving rise to an increasing interest of scientists in this field. Anyhow, the concept of crack weight functions, well known in fracture mechanics of classical materials since 1970 (Bueckner [4]) has only recently been extended to piezoelectric materials by Ma and Chen [5] as well as McMeeking and Ricoeur [6]. In [5] the derivation of the weight function is based on a work-conjugate integral following Bueckner, in [6] the derivation goes back on a procedure published by Rice [7] leading to a more transparent formulation.
The weight function in fracture mechanics relates the stress intensity factor at the tip of a crack in an elastic body to a point load at an arbitrary location. For a piezoelectric material, this definition is extended to include the effect of point charges and the presence of an electric displacement intensity factor at the crack tip. The weight function for cracks in piezoelectric materials is formulated from Maxwell relationships among the energy release rate with displacements and the electric potential as dependent variables and the applied loads and electric charges as independent variables. Applying the principle of linear superposition and Bettis theorem of reciprocity, one type of weight functions is derived for the different crack opening Modes from any known mixed-mode solution in terms of displacements and electric potentials of the cracked body under specific electromechanical loads. Fig. 1 shows all four field intensity factors for a Griffith crack in PZT-5H due to a near-tip unit line charge at an angle θ to the crack tip and at a distance r=1mm from the crack tip.

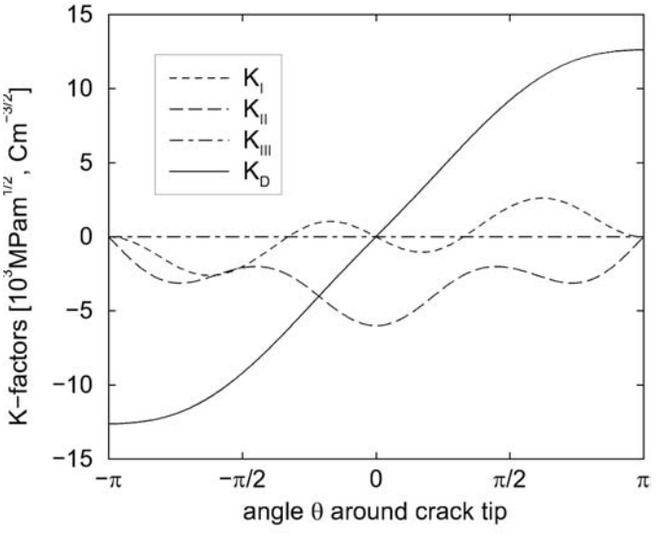


Fig. 1: Intensity factors for impermeable Griffith crack due to line charge at r=1mm and angle θ to crack tip (θ=0 on the ligament)

Another type of piezoelectric crack weight function yielding stress and electric displacement intensity factors due to local mechanical displacements and electric potentials can be derived following a similar principle. Here, the weight functions for the different crack opening modes are calculated from any mixed-mode solution in terms of stresses and electric charge densities. Having once derived both types of weight functions for a specific piezoelectric body containing a crack, field intensity factors can be calculated for arbitrary mixed – Dirichlet and Neumann – boundary conditions. Moreover it is possible to calculate mechanical displacement and electric potential fields in the cracked body knowing the weight functions for the different crack opening Modes and the stress and electric displacement intensity factors for the chosen electromechanical loading, which is demonstrated by examples.
Further results are presented for the Griffith crack taking into account different electric boundary conditions on the crack faces. From the piezoelectric asymptotic solution crack tip weight functions are derived. In connection with a process zone model for ferroelectrics (Ricoeur and Kuna [8]) they are applied to quantify the effect of small scale domain switching close to the crack tip showing a toughening effect if an external electric field is applied parallel to the

poling direction. Moreover, weight functions have been used to investigate the sensitivity of numerical errors occurring close to the crack tip on the calculation of the electric displacement intensity factor for electrically permeable cracks (Wippler *et al*. [9]). Finally, the effect of bridging tractions and charges on the field intensity factors is calculated by means of piezoelectric weight functions.

References

[1] Sosa, H.: Plane Problems in Piezoelectric Media with Defects. *Int. J. Solids Structures* **28**(4):491-505, 1991.

[2] Pak, Y.E.: Linear Electro-Elastic Fracture Mechanics of Piezoelectric Materials. *International Journal of Fracture* **54**:79-100, 1992.

[3] Park, S.B., Sun, C.T.: Effect of Electric Field on Fracture of Piezoelectric Ceramics. *International Journal of Fracture* **70**:203-216, 1995.

[4] Bueckner, H.F.: A Novel Principle for the Computation of Stress Intensity Factors. *Zeitschrift für Angewandte Mathematik und Mechanik* **50**:529-546, 1970.

[5] Ma, L.-F., Chen, Y.-H.: Weight Functions for Interface Cracks in Dissimilar Anisotropic Piezoelectric Materials. *International Journal of Fracture* **110**:263-279, 2001.

[6] McMeeking, R., Ricoeur, A.: The weight function for cracks in piezoelectrics. *Int. J. Solids Structures* **40**:6143-6162, 2003.

[7] Rice, J.R.: Some Remarks on Elastic Crack-Tip Stress Fields. *Int. J. Solids Structures* **8**:751-758, 1972.

[8] Ricoeur, A., Kuna, M.: A Micromechanical Model for the Fracture Process Zone in Ferroelectrics. *Computational Materials Science* **27**:235-249, 2003.

[9] Wippler, K., Ricoeur, A., Kuna, M.: Towards the Computation of Electrically Permeable Cracks in Piezoelectrics. *Engineering Fracture Mechanics*, accepted for publication.

THREE-DIMENSIONAL CORRECTION OF TWO-DIMENSIONAL FRACTURE CRITERIA USING A CONSTRAINT FACTOR

Rimantas Kačianauskas, Vladislav Žarnovskij, Eugeniuš Stupak
Vilnius Gediminas Technical University, Department of Strength of Materials, Sauletekio ave 11, LT–2040, Vilnius, Lithuania

Summary The three-dimensional (3D) stress state at the crack tip is transformed into quasi-two-dimensional one by introducing the effective elasticity constants governed by the stress or strain constraint factors (SCF). It is shown, that the variation of the deformation state and, as a consequence, of the fracture criteria along the crack front is predicted by the variation of the SCF, while 3D correction may be defined by integrating SCF along the crack front. The proposed approach is illustrated by an example of SENB specimen.

INTRODUCTION

For a long time most of the fracture analyses have been focussed on two-dimensional (2D) approach restricted by two limit cases, plane stress and plane strain, respectively. The deformation state in the vicinity of the crack tip is, however, of three-dimensional (3D) nature, therefore, a great amount of effort, recently, has been spent on the determination of three-dimensional effects [1]. Among the important issues to be clarified is the relationship between 2D and 3D fracture criteria.
In this report the thickness correction of the originally two-dimensional fracture criteria for cracked bodies of the finite thickness used in linear fracture mechanics is considered. The three-dimensional stress state at the crack tip is transformed into quasi-two-dimensional one by introducing the effective elasticity constants governed by the stress or/and strain constraint factors (SCF) [2]. The concept of effective elasticity characteristics suggested in [3] is employed.

CORRECTION CONCEPT

The stress and strain state in the vicinity of the crack tip is almost in the plane strain state, vanishing away from it and approaching the plane stress state. This 3D state is predefined by the dominant out-of-plane resultant. The 3D effect is regarded along the crack front co-ordinate z and may be characterised by stress constraint factor d [2] or modified strain constraint factor k [4], both of them depending on Poisson's ratio ν:

$$d(z)=\frac{1}{\nu}\frac{\sigma_{zz}(z)}{\sigma_{xx}(z)+\sigma_{yy}(z))}, \qquad k(z)=\frac{\nu-1}{\nu}\frac{\varepsilon_{zz}(z)}{\varepsilon_{xx}(z)+\varepsilon_{yy}(z)}. \tag{1}$$

Here, the limit value of d is zero, in case of plane stress, and unity, for plane strain, while the limit value of k is unity, in case of plane stress, and zero, for plane strain. It is necessary to note, that $k + d = 1$.
By applying the methodology used in the elasticity theory and a concept of the position-dependent effective elasticity constants, the 3D state may be transformed into quasi-two-dimensional one. The variation of the state variables along the crack front is, finally, governed by a single variable - constraint factor d or k (1). Originally, the effective elasticity modulus E is simply expressed by the factor d, while using first order Taylor's expansion by factor k, respectively:

$$E_{eff}(z)=E\frac{1}{1-\nu^2 d(z)}, \qquad E_{eff}(z)=E\frac{1}{1-\nu^2}\left(1-\nu^2 k(z)\right). \tag{2}$$

Similar expressions may be derived for Poisson's ratio or Lame constants.
On this basis it easy to show, that the crack front variation of the position-dependent 3D fracture criteria such as stress intensity factor $K(z)$ or energy release rate $G(z)$ is also predicted by the variation of the constraint factor. Assuming that the variation of fracture criteria may be presented as 2D value K_{2D} corresponding to plane strain and 3D correction $\Delta K_{3D}(z)$,

$$K(z)=K_{2D}+\Delta K_{3D}(z). \tag{3}$$

For the fixed front length t, the resultant value is

$$K_{3D}=K_{2D}+\Delta\overline{K}_{3D}\left(K_{2D}-K_{2Dc}\right), \tag{4}$$

where K_{2Dc} is 2D value corresponding to plane stress. The dimensionless correction factor is obtained taking into account the state variation predefined by (2) and by the integration along the crack front t

$$\Delta\overline{K}_{3D}=-\frac{1}{t}\int_t k(z)\mathrm{d}z. \tag{5}$$

Having obtained the variation of the constraint factor $k(z)$, (for example, numerically), the above expressions (3)-(5) may be applied to 3D evaluation and correction of the results of 2D analysis.

NUMERICAL RESULTS

The proposed approach has been applied to the simulation of fracture characteristics of the open-mode three-point bending SENB specimens having different thickness t. In order to recover the 3D fields required for the computation of SCF, the suitable 3D FE element model comprising h-adaptive in-plane and structured through thickness mesh [4] has been proposed. The obtained through the thickness variation of the strain constraint factor $k(\bar{z})$ at the tip of the notch for specimens with different relative thickness $\bar{t}$ is presented in Fig. 1, while the corresponding variation of the relative effective modulus $\overline{E} = E_{eff} / E$ is given in Fig. 2. The relative thickness $\bar{t} = t / h$ presents the ratio of specimen thickness t to its height h.

Finally, the theoretical results are compared to those obtained directly using 3D FE and displacement extrapolation technique. The through the thickness variation of numerically obtained stress intensity factor $\overline{K}(\bar{z}) = \overline{K}(\bar{z}) / K_{2D}$ is presented in Fig. 3. A comparison of the direct numerical simulation and theoretical model (4-5) for different thickness is presented in Fig. 4.

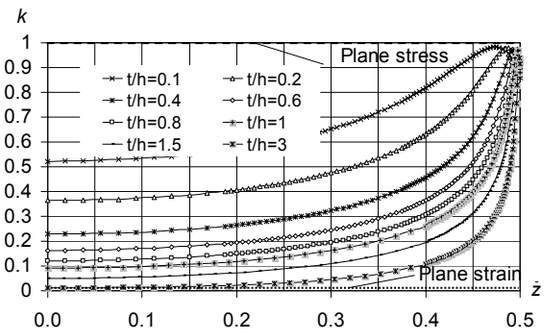


Fig. 1. Through the thickness variation of the strain constraint factor

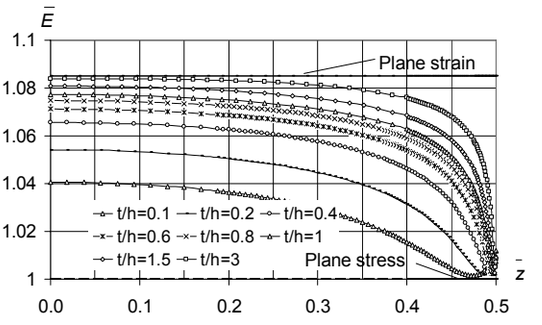


Fig. 2. Through the thickness variation of the relative effective modulus

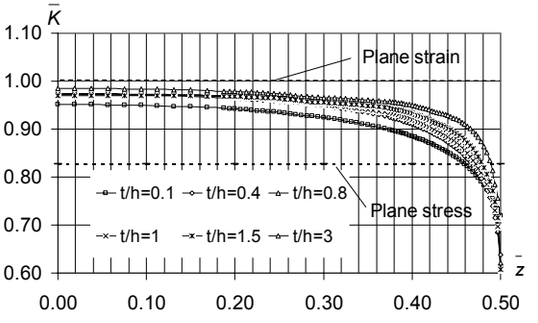


Fig. 3. Through the thickness variation of the relative stress intensity factor

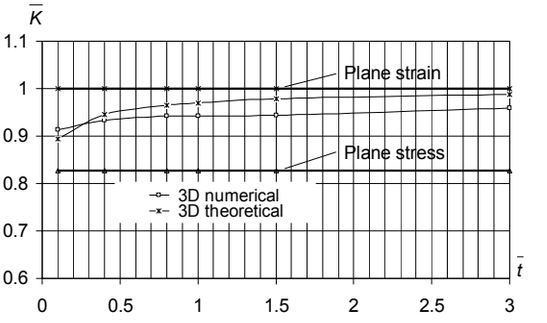


Fig. 4. Variation of the relative stress intensity factor for different thickness

CONCLUSIONS

It is shown, that the actual variation of the fracture criterion along the crack front is predicted by the variation of SCF, while 3D correction is described by the integrated values of SCF. The 2.5% differences occurring between the theoretical expression (5) and direct simulation may be explained by the inaccuracy of the 3D FE models, methodology of computation of fracture criteria and boundary effects on the free surface.

References

[1] Nikishkov, G.P., Alturi, S.N. Calculation of Fracture Mechanics Parameters for an Arbitrary Three-dimensional Crack by the Equivalent Domain Integral Method. *Int. J. of Num. Meth. Eng.* **24(9)**:1801-1821, 1987.

[2] Nakamura T., Parks D. M.: Antisymmetrical 3-D Stress Field Near the Crack Front of a Thin Elastic Plate. *Int. J. of Solids and Structures* **25**:1411–1426, 1989.

[3] Kwon S. W., Sun C. T.: Characteristics of Three-dimensional Stress Fields in Plates with a Through-the-thickness Crack. *Int. J. of Fracture* **104**:291–315, 2000.

[4] Žarnovskij V., Kačianauskas R.: The Finite Element Investigation of the Thickness Influence on 3D Stress and Strain Fields in the SENB Specimens. *Mechanika* **4(24)**:31–36, 2003.

XXI ICTAM, 15–21 August 2004, Warsaw, Poland

ELASTODYNAMIC CONTACT PROBLEM FOR TWO PENNY-SHAPED CRACKS

Oleksandr V. Menshykov*

*S.P. Timoshenko Institute of Mechanics, National Academy of Sciences, Nesterov str. 3, 03057 Kiev, Ukraine

Summary The contact interaction of the cracks' edges is considered for the case of two penny-shaped cracks located in the plane under normally incident harmonic tension-compression wave. The components of the stress-strain state are examined. The dependence of the mode I stress intensity factor on the wave number and mutual arrangement of cracks is studied. The solution is compared with the results obtained without allowance for the contact interaction.

Let a three-dimensional linearly elastic homogeneous isotropic space $\mathbb{R}^3$ contain two penny-shaped cracks located in the coordinate plane x_1Ox_2. The surfaces of cracks are defined by

$$\Omega_1 = \left\{x_1^2 + x_2^2 \le a^2,\ x_3 = 0\right\}, \quad \Omega_2 = \left\{(x_1 - c)^2 + x_2^2 \le b^2,\ x_3 = 0\right\}, \quad a + b < c.$$

A time-harmonic tension-compression wave with frequency $\omega = 2\pi/T$ and amplitude Φ_0 propagates normally to the cracks' surfaces. In the process of deformation the adjoining cracks' edges move (mutual displacements are exemplified by the displacement discontinuity vector $[\mathbf{u}(\mathbf{x},t)]$ and interact with formation of the time-dependent contact domains. The mentioned contact interaction implies the transformation of the stress-strain state and corresponding transformation of the stress intensity factors distribution.

The load vector on the cracks' edges has the form

$$\mathbf{p}(\mathbf{x},t) = \mathbf{p}^*(\mathbf{x},t) + \mathbf{q}(\mathbf{x},t), \quad \mathbf{x} \in \Omega_1 \bigcup \Omega_2, \quad t \in [0;T],$$

where $\mathbf{p}^*(\mathbf{x},t)$ is the load caused by the incident wave, $\mathbf{q}(\mathbf{x},t)$ is the contact forces vector originating on the cracks' surfaces.

In the absence of the tangential forces and displacements it is sufficient to determine only normal components of all mentioned vectors in order to solve the problem under consideration. According to [1], the following unilateral Signorini constraints must hold for the normal components of the displacement discontinuity and contact forces vectors

$$[u_3(\mathbf{x},t)] \ge 0, \quad q_3(\mathbf{x},t) \ge 0, \quad [u_3(\mathbf{x},t)]q_3(\mathbf{x},t) = 0, \quad \mathbf{x} \in \Omega_1 \bigcup \Omega_2, \quad t \in [0;T]. \tag{1}$$

Expand the normal components of the load vector and the displacement discontinuity vector into a Fourier series

$$p_3(\mathbf{x},t) = Re\left\{\sum_{k=-\infty}^{+\infty} p_3^k(\mathbf{x})e^{i\omega_k t}\right\}, \quad [u_3(\mathbf{x},t)] = Re\left\{\sum_{k=-\infty}^{+\infty} [u_3^k(\mathbf{x})]e^{i\omega_k t}\right\},$$

where $\omega_k = 2\pi k/T$ and

$$p_3^k(\mathbf{x}) = \frac{\omega}{2\pi}\int_0^T p_3(\mathbf{x},t)e^{-i\omega_k t}dt, \quad [u_3^k(\mathbf{x})] = \frac{\omega}{2\pi}\int_0^T [u_3(\mathbf{x},t)]e^{-i\omega_k t}dt. \tag{2}$$

The Fourier coefficients (2) are related by the following boundary integral system [1]:

$$p_3^k(\mathbf{x}) = -\int\limits_{\Omega_1 \bigcup \Omega_2} F_{33}(\mathbf{x},\mathbf{y},\omega_k)[u_3^k(\mathbf{x})]d\Omega, \quad \mathbf{x} \in \Omega_1 \bigcup \Omega_2, \quad k = \overline{-\infty,+\infty}. \tag{3}$$

Due to the presence of nonintegrable terms in the integral kernel $F_{33}(\mathbf{x},\mathbf{y},\omega_k)$, whose rank exceeds the dimension of the integration region, the hypersingular integrals included in the boundary integral systems (3) should be treated only in the sense of the Hadamard finite part [1, 4].

The present paper contains a great deal of numerical results and figures corresponding the distribution of the components of the stress-strain state and the mode I stress intensity factor versus frequency of the incident wave and geometrical parameters of considered problem (mutual arrangement of the cracks and ratio between the radii a and b).

The results obtained with allowance for contact interaction are compared with those neglecting the contact interaction [2, 3]. It is important to observe that the cracks' edges contact interaction changes the solution of the present problem essentially, both quantitatively and qualitatively.

The submitted solution is not symmetric, but with growth of the distance between the cracks, the interference of the cracks considerably decreases and the solution tends to the axisymmetric solution obtained for unique penny-shaped crack [1, 4, 5].

Information on the distribution of the normal components of the displacement discontinuity and contact forces on the central section $S = \{-a \leq x_1 \leq a, x_2 = 0, x_3 = 0\}$ of the crack Ω_1 versus time is presented in Figs. 1 and 2. The reduced wave number $k_2 a = 3.0$; $a/b = 1$; distance between cracks' centers $c = 2.1a$; elastic modulus $E = 200$ GPa, Poisson's ratio $\nu = 0.25$, density $\rho = 7800 kg/m^3$.

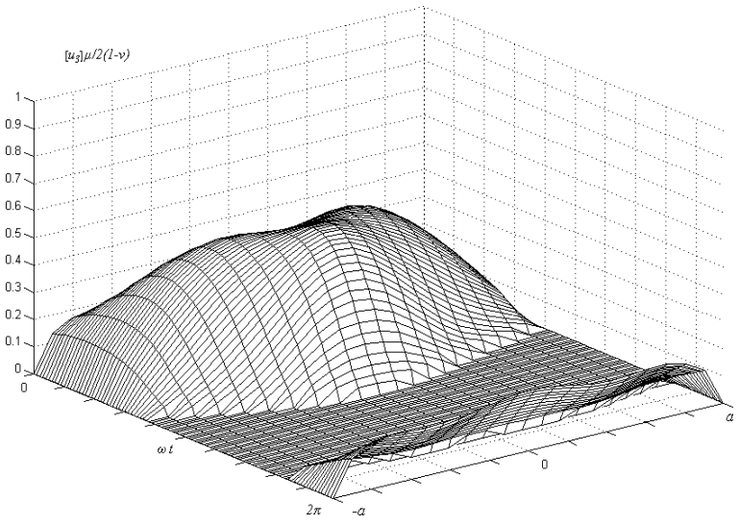


Figure 1. Normal components of the displacement discontinuity

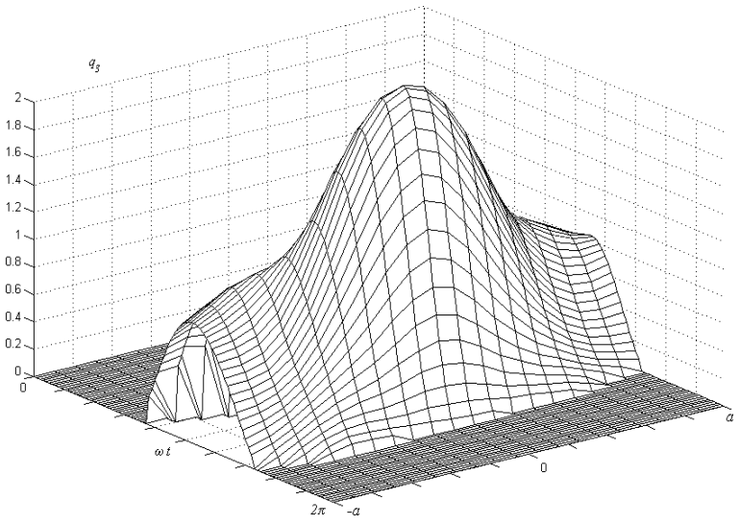


Figure 2. Normal components of the contact forces

The results presented here and in our previous publications indicate the necessity of the allowance for cracks' edges contact interaction in strength analyses of structures by methods of the fracture mechanics.

References

[1] Guz A.N., Zozulya V.V. Elastodynamic unilateral contact problems with friction for bodies with cracks. *International Applied Mechanics* 38(**8**): 895-932, 2002.
[2] Kassier M.K., Sih G.C.: Mechanics of fracture. Three-dimensional crack problems, Vol. 2, Netherlands Noordhoff Intern. Publ., Leyden, 1975.
[3] Zhang Ch., Gross D.: On wave propagation in elastic solids with cracks. Comp. Mech. Publ., Southampton, UK, Boston, USA, 1998.
[4] Zozulya V.V., Men'shikov A.V. On one contact problem in fracture mechanics for a normally incident tension-compression wave. *International Applied Mechanics* 38(**7**): 824-828, 2002.
[5] Zozulya V.V., Menshykov O.V. Use of the constrained optimization algorithms in some problems of fracture mechanics. *Optimization and Engineering*, **4**, 365-384, 2003.

NUMERICAL APPROACH FOR DYNAMIC FRACTURE IN PIEZOELECTRIC SOLIDS

José Domínguez[*], Andrés Sáez[*], Felipe García-Sánchez[**]
[*]*Continuum Mechanics Department, Univesidad de Sevilla, Camino de los Descubrimientos s/n, 41092-Sevilla, Spain*
[**]*Civil Engineering Department, Universidad de Málaga, Plaza de El Ejido s/n, 29013-Málaga, Spain*

Summary A mixed boundary element approach for two-dimensional dynamic piezoelectric fracture mechanics problems is presented. The numerical approach is based on displacement and traction integral equations for external and crack boundaries, respectively. Integral equations for time harmonic problems are considered. Transient problems are analyzed by means of the FFT. Curved and quarter-point elements are used. Stress and electric displacement intensity factors are evaluated from nodal values next to the crack tip. The present BE approach has allowed for solution of a variety of crack problems including curved cracks. Some of these problems had never been studied before.

PROBLEM STATEMENT

Piezoelectric materials are brittle and due to manufacturing process and complex electromechanical loads they are likely to develop cracks. The understanding and evaluation of the fracture process in piezoelectric materials is crucial to the advancement of modern intelligent material systems. Among the most significant publications on the field of piezoelectric materials fracture mechanics in terms of integral equations is the Ph. D. Thesis of Deeg [1].
In this paper, a general mixed BE formulation based on displacement and traction integral equations for 2-D cracked piezoelectric media under static and time harmonic load is presented. A new regularization procedure based on a simple change of variables is presented. All the strongly singular or hypersingular integrals are transformed into regular integrals and simple singular integrals with known analytical solution. The traction and normal electric displacement integral representations are written for the crack surface and the displacement and electric potential integral representation for the external boundaries. The basic variables are opening displacement and electric potential discontinuity along the crack, and displacement, electric potential, traction and normal electric displacement, on external boundaries. Quadratic quarter-point elements are used to represent the crack opening displacement (COD) and electric potential discontinuity near the crack tip. Standard curved or straight quadratic elements are used for the rest of the crack and external boundaries. Stress and electric displacement Intensity Factors (ESIF) are computed in a direct way from the COD and the electric potential discontinuity at a point extremely close to the tip.

NUMERICAL RESULTS

To show the use of the current procedure for curved crack geometries, the problem of a crack with circular arch shape in an unbounded domain is studied. The crack region is under a uniform static far field stress or electric displacement (Figure 1) along the material and crack axis of symmetry. The material is a PZT-4 ceramic. Cracks with different semi-angles θ are analysed. The BE mesh consists of eight curved quadratic elements and two very small (arch length/30) quarter-point straight elements at the tips (Figure 1). Computed values of K_I, K_{II} and K_{IV} when the load is a uniform electric displacement are shown in Figure 2, where the ratio between piezoelectric and dielectric parameters χ is used for normalization purposes. These results show the great influence that crack curvature has on ESIF. To the authors' knowledge, no solution for the curved crack problem in piezoelectric solids has been published up to the present.

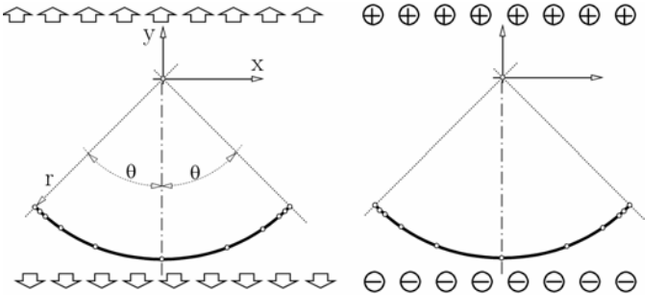


Figure 1. Geometry, mesh and loading conditions for a circular arch crack

A straight crack in an infinite piezoelectric plane under time harmonic waves impinging along the material axis of symmetry is studied next. Figure 3 shows the mode-I SIF versus dimensionless frequency. Results are in good agreement with those obtained by Shindo [2] for the same problem using a semi-analytical procedure. Time variation of K_I for a step load is shown in Figure 4, where time has been normalized as in Ref. [3]. Note that the peak in K_I is similar to that shown by the exact solution for elastic isotropic solids. Other numerical examples will be presented during the conference.

CONCLUSIONS

A general mixed boundary element formulation for static and dynamic crack problems in 2-D piezoelectric solids has been presented. The obtained results show the robustness, generality and simplicity of the procedure. The present results are in good agreement with solutions presented by other authors in the cases where those solutions exist.

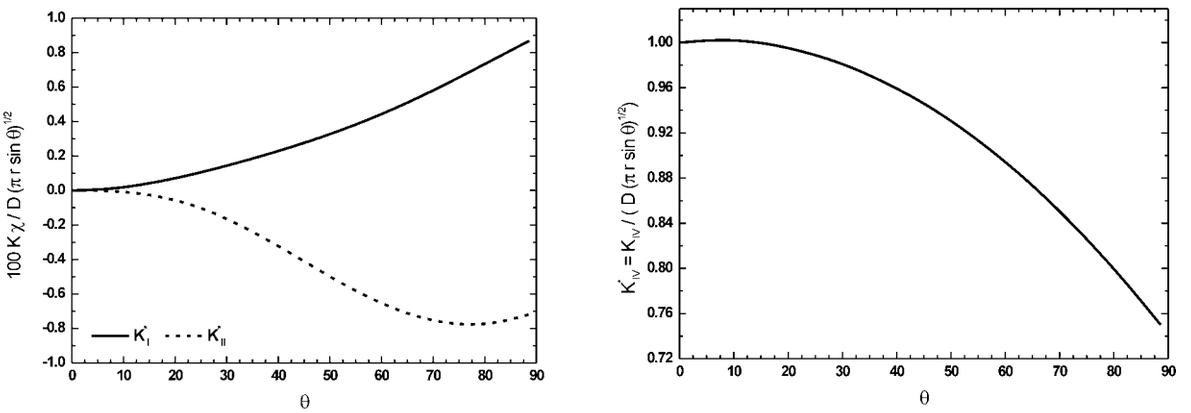


Figure 2. (i) Mode I and mode II SIF and (ii) Electric displacement intensity factor for circular crack in piezoelectric solid under uniform far field electric displacement

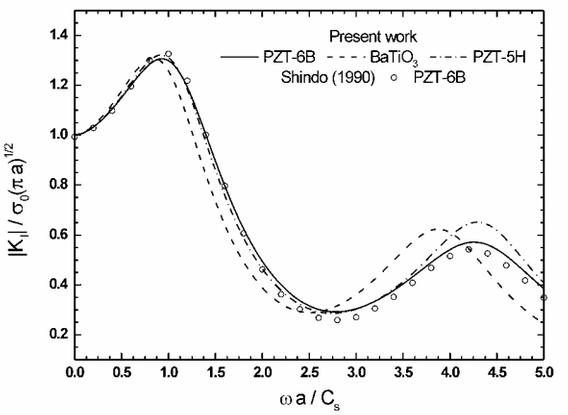


Figure 3. Mode I SIF versus dimensionless frequency for a Griffith crack under a plane harmonic wave

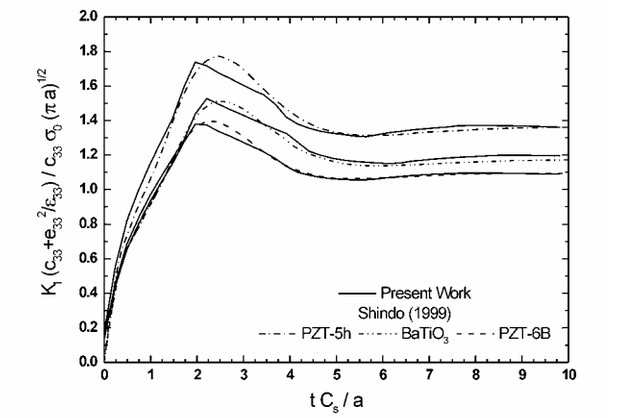


Figure 4. Mode I SIF versus dimensionless time for a Griffith crack under the action of normal impact loading

References

[1] Deeg W.F.: The analysis of dislocation, crack and inclusion problems in piezoelectric solids. *PhD Thesis*, Stanford University, 1980.

[2] Shindo Y., Ozawa E.: Dynamic analysis of a cracked piezoelectric material, in *Mechanical Modelling of New Electromagnetic Materials (Ed. R.K.T. Hsieh)*. Elsevier, 1990.

[3] Shindo Y., Narita F., Ozawa E.: Impact response of a finite crack in an orthotropic piezoelectric ceramic. *Acta Mechanica* **137**: 99-107, 1999.

FINITE ELEMENT ANALYSIS OF FRACTURE AND POLARIZATION SWITCHING BEHAVIOR IN MODIFIED SMALL PUNCH TESTING OF PIEZOELECTRIC CERAMICS

Yasuhide Shindo*, Fumio Narita, Yasuyo Magara and Masaru Karaiwa
* *Department of Materials Processing, Graduate School of Engineering,Tohoku University, Sendai 980-8579, Japan*

Summary The fracture behavior of piezoelectric ceramic was investigated under mechanical and electrical loads utilizing the modified small punch technique. A finite element model was developed to simulate the relation between MSP energy and applied electric field. The strain energy density was also computed. Measured fracture initiation loads and calculated maximum strain energy density are sensitive to the change in the applied electric field and polarization switching.

INTRODUCTION

PZT [$Pb(Zr, Ti)O_3$] is widely used in piezoelectric devices, e.g. transducers, filters, sensors, and actuators. The high mechanical stresses and intense electric fields in the PZT ceramic may cause microcracks to develop which eventually lead to failure of the device. The fracture behavior of PZT under mechanical and electrical loads has been the subject of recent studies [1,2]. Shindo et al. [3] performed the single-edge precracked beam tests on a commercial PZT ceramic, and simulated these tests numerically with the finite element method. Shindo et al. [4] also made indentation fracture tests on the PZT ceramics to estimate the fracture toughness, and employed a three-dimensional finite element analysis to calculate the energy release rate and stress intensity factor. On the other hand, the crack growth in a ferroelectric barium titanate ($BaTiO_3$) ceramic was investigated under applied electric fields up to 4 times the coercive field strength using the Vickers indentation technique. The change in crack length and fracture toughness was discussed in connection with the influence of polarization switching on the crack generating stresses.
In a series of articles, a model was developed to simulate the observed nonlinearities in material behavior [6,7]. The ceramics were considered as an aggregate of many grains which were modeled as single domain with switching. Hayashi et al. [8] investigated the displacement and polarization switching properties of piezoelectric laminated actuators theoretically, numerically, and experimentally. Shindo et al. [9] examined the effects of applied voltage and polarization switching on the electroelastic fields concentrations ahead of electrodes in multilayer piezoelectric actuators in a combined experimental and numerical investigation.
In the present paper fracture behavior of a piezoelectric ceramic under applied electric fields is discussed using the modified small punch (MSP) test technique. The purpose of the present paper is also to present a model for such MSP test. To carry out the analysis a polarization switching model is assumed for the specimen material.

EXPERIMENTAL PROCEDURE

Commercially supplied P-7 (Murata Manufacturing Co., Ltd., Japan) piezoelectric ceramic [3] was selected for the experiment. The coercive electric field E_c is 0.8 MV/m. At least 32 small, thin piezoceramic plate specimens of 10 by 10 by 0.5 mm used for MSP tests were sliced. Poling was done along the axis of the 0.5 mm dimension, and silver electrodes were coated on the two 10 mm$\times$10 mm surfaces.
Using a screw driven test machine, all MSP tests were conducted. To generate electric fields, a power supply for voltages up to 1.25 kV/D.C. was used to apply positive and negative electric fields of 0.2, 0.4, 0.8 and 1.0 MV/m. Loads which caused fracture were measured for each set of specimens for various electric fields. For 0, $\pm$0.4, $\pm$0.8, and $\pm$1.0 MV/m, four or five tests were performed.

FINITE ELEMENT ANALYSIS

We performed three dimensional finite element calculations to determine the MSP energy and maximum strain energy density for the PZT specimens. A rectangular Cartesian coordinate system (x,y,z) is used with the z-axis coinciding with the poling direction. The analytical model is shown in Fig. 1. A mechanical load was produced by the application of either a prescribed force P_0 or a prescribed displacement u_0 along the z-direction. For electrical loads, a negative or positive electric potential ϕ_0 was added on the surface, z=h. The surface z=0 is grounded. We use the commercial finite element code ANSYS. Eight-nodes 3-D space solid was used in the analysis. The contact between the specimen and the lower die was modeled using contact elements. Because of the double symmetry of the body and loading only one quarter of the body was modeled.
The polarization of each grain initially aligns as closely as possible with the z-direction. The polarization switching is defined for each element in a material. Boundary loads are applied, and the electroelastic fields of each element are computed from the finite element analysis. The switching criterion is checked for every element to see if switching will occur. After all possible polarization switches have occurred, the piezoelectricity tensor of each element is rotated to the new polarization direction. The electroelastic fields are re-calculated, and the process is repeated until the solution

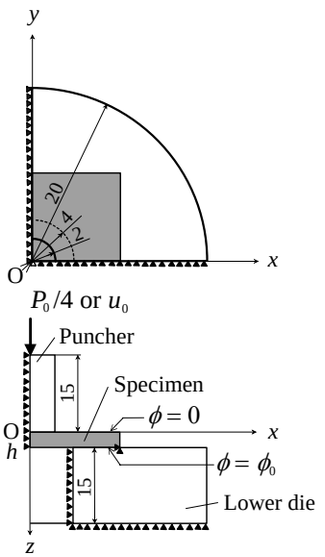


Table 1 Average fracture initiation loads and statistical deviations under electric fields for MSP specimen

E_0 (MV/m)	P_c (N)	
	Average	Standard Deviation
-1.0	17.7	5.0
-0.8	15.5	2.8
-0.4	13.9	1.6
-0.2	11.9	-
0.0	13.7	0.49
+0.2	15.0	-
+0.4	16.6	2.0
+0.8	17.5	0.35
+1.0	4.79	1.0

Fig. 1 Finite element model of the MSP test

converges. The macroscopic response of the material is determined by the finite element model, which is an aggregate of elements.

RESULTS AND DISCUSSION

Table 1 shows the average fracture initiation loads P_c and the statistically-determined standard deviations under different electric fields E_0 obtained from the experiment.

Fig. 2 presents the critical MSP energy E^c_{MSP} including 180^o and 90^o switching effects (open triangle) for various electric fields E_0. The load-displacement curves were drawn up to the average fracture initiation load P_c using finite element method, and the E^c_{MSP} was calculated from the area under the curve (energy to failure). A similar phenomenon was observed for the maximum energy density. Fig. 3 shows the MSP energy E_{MSP} of the finite element solutions without 90^o switching effect under an average fracture initiation load for zero electric field P_0 = 13.7 N and different electric fields E_0, where the result has been normalized by the MSP energy E_{MSP0} for E_0=0 MV/m. Also shown are the prediction with stress effect on polarization switching for the MSP specimen.

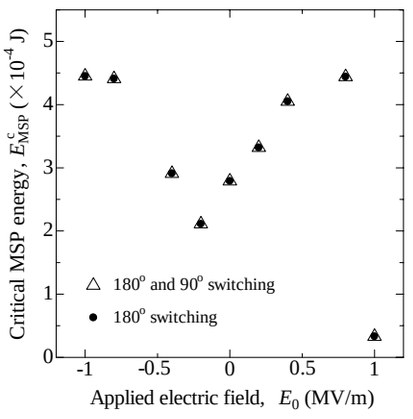


Fig.2 Critical MSP energy vs electric field

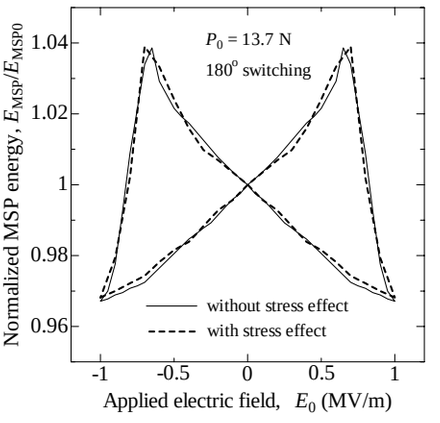


Fig.3 MSP energy vs electric field for applied force

References

[3] Shindo Y., Murakami H., Horiguchi K., Narita F.: Evaluation of electric fracture properties of piezoelectric ceramics using the finite element and single-edge precracked-beam methods. *J. Am. Ceram. Soc.* **85**: 1243-1248, 2002.

[4] Shindo Y., Oka M., Horiguchi K.: Analysis and testing of indentation fracture behavior of piezoelectric ceramics under an electric field. *ASME J. Eng. Mater. Tec.* **123**: 293-300, 2001.

XXI ICTAM, 15-21 August 2004, Warsaw, Poland

ON CRACK ASSESSMENT AT BIMATERIAL INTERFACES

Axel Müller*, Jörg Hohe**, Wilfried Becker***
*Universität Siegen, Institut für Mechanik, 57068 Siegen, Germany
**Fraunhofer-Institut für Werkstoffmechanik, IWM, 79108 Freiburg, Germany
***Technische Universität Darmstadt, Fachbereich Mechanik, 64289 Darmstadt, Germany

Summary Based on the knowledge of the singular fields at bimaterial wedges, the direction of crack nucleation can be determined using the novel and numerically highly efficient Boundary Finite Element Method. An essential question in the context of crack assessment is to find a criterion for crack nucleation. For that aim, the hypothesis of Leguillon is modified. Herein, the crack is assumed to be critical when and only when both the released energy and the local stress reach critical values along a hypothetical crack of finite length.

INTRODUCTION

The advantage of numerical simulation of the mechanical behaviour of complex systems is e. g. that potential initiation of failure may already be detected in an early state of development. Many modern multi-component structures require a number of joints and connections which consist frequently of at least two different materials. Thus, recent requirements for adhesive bonds place an increasing emphasis on the knowledge of the mechanisms responsible for fracture. As actual applications of the investigations presented here, ceramic thermal barrier coating systems or the sealings of high temperature fuel cells can be mentioned amongst others, like bonded joints of laminates for the use in aerospace, naval or automobile structures or soldered joints for electronics. For all these applications, particularly when they are under significant thermal loads, the regions in the vicinity of material and mostly additional geometrical discontinuities are considered to belong to the most critical locations of the whole component. In a first step, the local mechanical fields have to be analyzed. This can be done e. g. analytically by means of the complex potential method or by the semi-analytical Boundary Finite Element Method (BFEM) which is introduced as a novel approach by Wolf and Song [1]. At bimaterial wedges, these stress fields show a singular behaviour which differs from the crack tip singularity and depending on geometry and material combination, for real life situations it leads to non-separable singular fields in general.

DETERMINATION OF DIRECTIONS FOR CRACK INITIATION

At a general bimaterial wedge under arbitrary loading, a crack may be initiated not only at the interface but also at a certain angle φ_0 to the interface. The identification of these angles φ_0 can be based on the hypothesis of Erdogan and Sih [2], knowing that alternatively, there are several criteria which could be used for this aim, see [3]. According to this criterion, it can be assumed that a crack will grow in radial direction of the largest circumferential tensile stress perpendicular to the direction of $\sigma_{\varphi max}$, starting at its tip in radial direction.

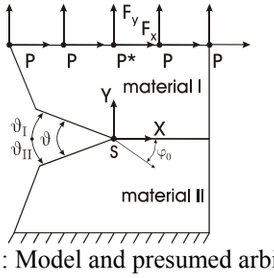


Figure 1: Model and presumed arbitrary mixed mode loading.

As shown in figure 1, a square respectively rectangular plane model with a notch like opening, and the centre of singularity S, has been analysed by the BFEM. The lower and the upper edge of the model have been kept straight and of equal length. No translations of the bottom boundary of the structure are allowed while the top edge nodes are tied to each other with a single master point $\mathbf{P}^*$ by multi-point constraints. The load components applied at that point are noted as $\mathbf{F}_x$ and $\mathbf{F}_y$. A load factor β characterizing situations of arbitrary mixed mode loading is introduced as: $\beta = \mathbf{F}_x / (\mathbf{F}_x + \mathbf{F}_y)$. In that sense, pure opening mode I corresponds to $\beta = 0$, and pure sliding mode II to $\beta = 1$. Thus, any value between -1 and +1 represents a mixed mode case of the applied loading.

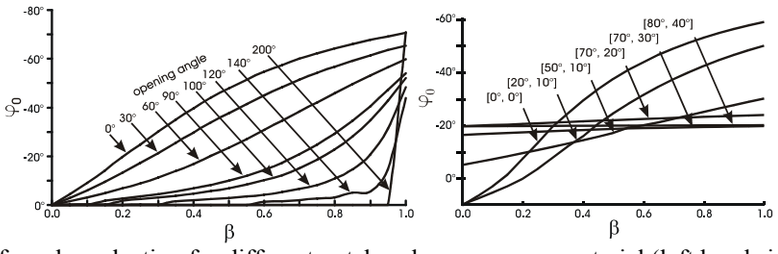


Figure 2: Directions of crack nucleation for different notches, homogeneous material (left hand side) and unsymmetric notch opening [ϑ_I, ϑ_{II}] in a bimaterial with $E_I/E_{II} = 0.4$ (right hand side).

The variation of predicted crack propagation directions under various mixed mode situations is depicted in figure 2. For the homogeneous wedge of linear-elastic material, one conclusion can be drawn directly, namely that under pure

mode I loading, crack initiation starts at the interface and under pure mode II loading the well-known characteristic angle $\varphi_0 = 70{,}5°$ is calculated. The graph on the right side illustrates the directions of crack initiation for unsymmetric bimaterial configurations.

INITIATION OF CRACK OF FINITE LENGTH

Apart from the more general example considered above, in this section a real geometry of a high temperature fuel cell stack is considered. For this case, the crack will grow along the interface, since the interface toughness is lower than the fracture toughness of the joined material. A composite part of thin ceramic layers is the membrane electrodes assembly (mea) which is embedded in a frame within the interconnect. In the first instance, a hypothetical crack growth along the interface between a thin glass ceramic sealing joint and an interconnector plate made of steel is assumed as given in the section sketch, figure 3. For this model, the energy release rate is calculated using the method of Rybicki and Kanninen [4] and integrated, so that the released energy E is known and can be compared to the critical value of the individual toughness of the joined materials and to that of the interface itself which is marked by $E_{crit.}$ in figure 4.

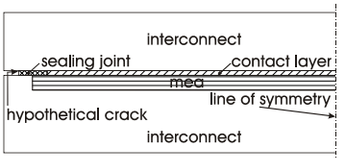


Figure 3: Sketch of the investigated geometry (not in scale), mea and sealing joint may be regarded as thin layers.

As a further necessary condition for crack initiation, in addition to a critical energy release sufficiently high stresses are required: Fracture occurs, if the material specific strength $\sigma_{crit.}$ as characteristic value of the tension σ_y is exceeded. According to Leguillon's hypthesis [5], both criteria together are necessary conditions of fracture.

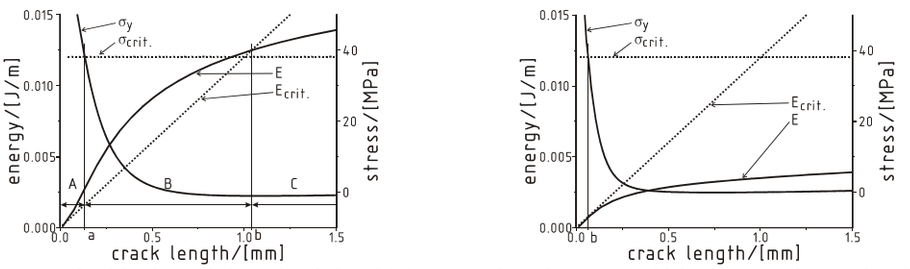


Figure 4: Assessment of critical crack lengths, joint thickness reduced to one half for the graphs on the right.

The graphs showing the released energy and the tensile stress on the left side of figure 4 are calculated for a virtual crack along the interface with a length of one half of the whole length of the interface (10 mm). In the illustration, the range is restricted to 15 %. Considering the released energy E, it is conspicuous that up to a crack length b of little more than 1 mm, corresponding to a section point between E and $E_{crit.}$, the amount of energy is sufficient for the creation of new crack surfaces. At the same time, the admissible tension exceeds the material respectively interface specific strength up to a crack length a, so that together both conditions for crack initiation are fulfilled within range A. This can be understood as a period of crack initiation. Range B corresponds to instable crack growth as here the necessary energy is available and the singular stress field moves with the crack tip and thus again violates the strength criterion. Since the energy E afterwards decreases below the critical value, the crack is assumed to stop at a length b, according to the hypothesis. For the case that no section point with a virtual crack length b between E and $E_{crit.}$ exists, no crack arrest will happen. The graph on the right side represents a geometry for which there is no crack initiation as the joint thickness is reduced to one half of the original thickness considered before.

CONCLUSIONS

The tendency to fracture may be appraised studying the energy available for crack growth, and at the same time comparing the local tensile stress to the specific interface strength. Together these two conditions allow the assessment of fracture. Using the criterion of maximal circumferential strength for the BFEM-calculation of the singular stress fields, a potential direction of crack propagation can be identified.

References

[1] Wolf J.P.: The scaled boundary finite element method. Wiley, Chichester 2003.

[2] Erdogan F., Sih G.C.: On the crack extension in plates under plane loading and transverse shear. *Journal of Basic Engineering* **85**: 519-527, 1963.

[3] Grenestedt J.L., Hallstrom S.: Crack initiation from homogeneous and bimaterial corners. *Journal of Applied Mechanics* **64**: 811-818, 1999.

[4] Rybicki E.F., Kanninen M.F.: A finite element calculation of stress intensity factors by a modified crack closure integral. *Engineering Fracture Mechanics* **9**: 931-938, 1977.

[5] Leguillon, D.: Strength or toughness? A criterion for crack onset at a notch. *European Journal of Mechanics A/Solids* **21**: 61-72, 2002.

ANALYSIS OF TENSILE TESTING OF A SOFT FERROMAGNETIC ELASTIC STRIP CONTAINING A CENTRAL CRACK UNDER A MAGNETCI FIELD

Daisuke Sekiya*, Yasuhide Shindo, Fumio Narita and Katsumi Horiguchi
* *Department of Materials Processing, Graduate School of Engineering,Tohoku University, Sendai 980-8579, Japan*

Summary The effect of magnetic fields on the fracture mechanics parameters is discussed by analyzing the plane problems of a soft ferromagnetic strip with a central crack under a uniform magnetic field. Tensile tests are also conducted on center-cracked soft magnetic plate with strain gage technique, and the numerical predictions are compared with the test results.

INTRODUCTION

With the increasing applications of ferromagnetic materials as fusion reactors, MHD devices, magnetically levitated vehicles, etc., the theme of magneto-elastic interactions has been addressed in the recent past. If a ferromagnetic material is used in a magnetic field, the combination of mechanical and magnetic forces could produce elevated stresses and strains. The ferromagnetic materials may be degraded in such a stress level. The strength of the ferromagnetic materials is also weakened by the presence of defects such as voids and cracks. It is therefore important to understand the degradation phenomena of the ferromagnetic materials. The fracture behavior of the ferromagnetic materials is thus of much recent interest. The influence of the magnetic field on the singular stress distributions near the crack tip in an infinite body was shown [1,2] based on a linear theory for the soft ferromagnetic elastic materials of multidomain structure [3]. Considered in [4] is the problem of determining the stress intensity factors in an infinitely long strip of a soft ferromagnetic elastic material with a crack parallel to the edges of the strip.
This paper applies a linear theory for the ferromagnetic elastic materials of multidomain structure [3] to the problem of determining the distribution of stress in a cracked soft ferromagnetic strip permeated by a uniform magnetostatic field normal to the crack surface. The plane problems are considered for the infinitely long strip containing a central crack normal to the edges of the strip. Tensile tests are also conducted on soft magnetic plate with a central crack to obtain the values of the fracture mechanics parameters, and the numerical results are compared with the experimental values.

ANALYSIS

Consider a soft ferromagnetic isotropic linear elastic strip of width $2h$ which contains a central crack of length $2a$ aligned with its plane normal to the free edges as shown in Fig. 1. A rectangular Cartesian coordinate system (x,y,z) is attached to be the center of the crack for reference purposes. The x-axis is directed along the line of the crack and y-axis along the direction of the perpendicular bisector of the crack. The edges of the soft ferromagnetic elastic strip are therefore the lines with equations $x=\pm h$, while the crack occupies the segment $-a < x < a$, $y=0$. We consider a uniform normal stress, $\sigma_{yy}=\sigma_0$, applied with a uniform magnetic field of magnetic induction $B_{0y}=B_0$. Only the first quadrant with appropriate boundary conditions needs to be analyzed owing to symmetry.

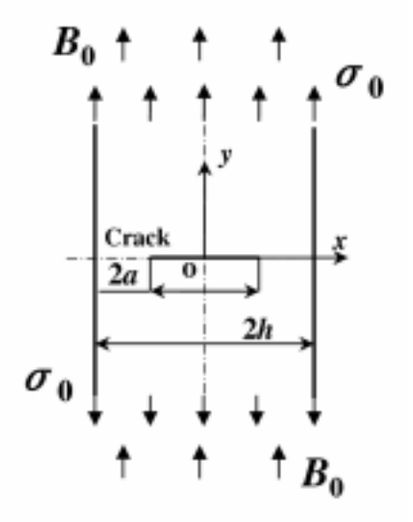


Fig. 1 A central crack in a soft ferromagnetic elastic strip

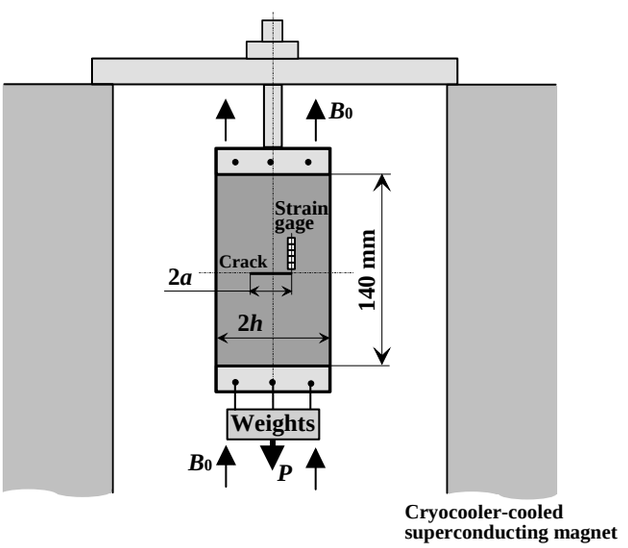


Fig. 2 Testing set-up

The method of solution involves the use of Fourier transforms to reduce the mixed boundary value problem to two simultaneous dual integral equations. The solution is then given in terms of a single Fredholm integral equation of the second kind.

The stress intensity factor k_{h1} is obtained as

$$k_{h1} = \lim_{x \to a^+} \{2\pi(x-a)\}^{1/2} \{t_{yy}(x,0) + t^M{}_{yy}(x,0)\}$$

where $t_{yy}(x,y)$ and $t^M{}_{yy}(x,y)$ are the components of magnetic and Maxwell stress tensors .

EXPERIMENTAL PROCEDURE

Tensile tests were conducted on nickel-iron soft magnetic materials with center-cracked plate specimen geometry in the 100 mm diameter bore of a 10 T (T: Tesla) cryocooler-cooled superconducting magnet at room temperature (Fig. 2). Three soft magnetic materials (TMC-V: Young's modulus E=182 GPa, Poisson's ratio ν=0.146, specific magnetic permeability μ_r=27900; TMH-B: E=203 GPa, ν=0.279, μ_r=10690; TMB: E=146 GPa, ν=0.228, μ_r=9030) developed by NEC/Tokin Co. Ltd. were selected. The specimens are 140 mm length and 1 mm thickness. The crack length was varied ($2a$= 10, 15, 20 mm) while keeping the specimen width fixed at $2h$=40 mm. Initial through-the-thickness notches were machined using electro-discharge machining. The specimens were fatigue precracked and then annealed to obtain the optimum magnetic properties. A simple strain gage method is very suitable to determine the magnetic stress intensity factor [5]. A five element strip gage (KFG-1-120-D19-16N10C2 from Kyowa Electronic Instruments Co., Ltd., Japan) was installed along the 90-deg line and the center point of the element closest to the crack tip was 2 mm. The strain sensors have an active length of 1 mm.

Tensile load and a magnetic field were simultaneous applied to center-cracked plate specimens. A superconducting magnet was used to create a static uniform magnetic field of magnetic induction B_0 normal to the crack surface. The specimens were loaded by P=29.4 N load that consisted of weights. For each specimen size five tests were performed. The strains were recorded as a function of magnetic field.

RESULTS AND DISCUSSION

Fig. 3 provides the normalized stress intensity factor $k_{h1}/\sigma_0 a^{1/2}$ as a function of h/a for ν=0.25, μ_r=10000 and the normalized magnetic field $b_c=(B_0{}^2/\mu_0\mu)^{1/2}$ = 0, 0.0032, 0.0047 (magnetic permeability of the vacuum $\mu_0=4\pi\times10^{-7}$N/A^2, shear modulus $\mu=E/2(1+\nu)$) obtained from the theoretical analysis. The dashed curve obtained for b_c=0 coincides with the purely elastic case. The normalized stress intensity factor tends to infinity as $h/a \to 1$, and decreases slowly as h/a increases and tends to the result of the infinite solid as $h/a \to \infty$. Applying the magnetic field increases the stress intensity factor. The calculated stress intensity factors $k_{h1}/\sigma_0 a^{1/2}$ of TMC-V, TMH-B and TMB for h/a=2 under various values of $b_c\times10^2$ are compared with the measured data in Fig. 4. The agreement between the two is good. A larger value of b_c tends to increase the stress intensity factor depending on the material.

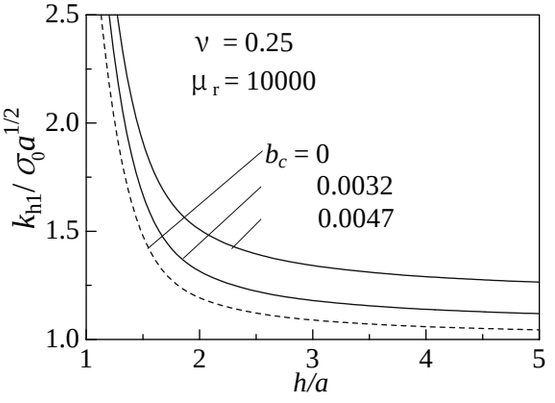


Fig.3 Stress intensity factor vs strip-width to crack-length ratio

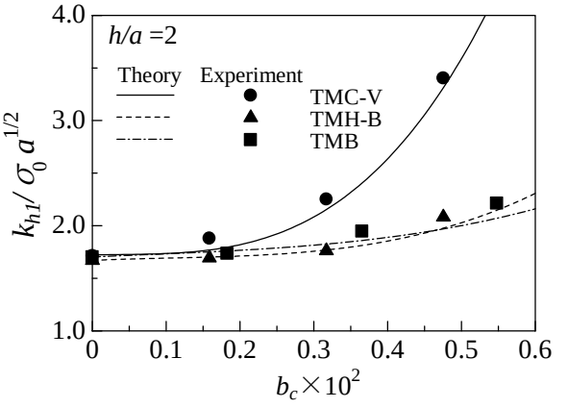


Fig.4 Stress intensity factor vs magnetic field

References

[1] Shindo Y.: The linear magnetoelastic problem for a soft ferromagnetic elastic solid with a finite crack. *ASME J. Appl. Mech.* **44**: 47-51, 1977.

[5] Yoshimura, K., Shindo Y., Horiguchi, K., and Narita, F.: Theoretical and experimental determination of magnetic stress intensity factors of a crack in a double cantilever beam specimen. *Fatigue & Fract. Eng. Mater. & Struct*, in press.

A QUASI-SPHERICAL COORDINATE SYSTEM AND ITS APPLICATION TO THE DETERMINATION OF VERTEX-TYPE SINGULARITIES

Hai-Tao Wang[*], K.Y. Sze[**]

[*]*Department of Civil Engineering, SCUT, Guangzhou City, P.R.China,510641*

[**]*Department of Mechanical Engineering, HKU, Hong Kong SAR, P.R. China*

Summary To avoid the inherent singularity of the spherical coordinates at their poles, a new quasi-spherical coordinate system is developed. In this coordinate system, a finite element procedure is proposed to determining the eigensolutions at three-dimensional vertices in which the field variables are proportional to the (λ+1)-th power of the distance from the vertices. The resulting global equation is a second order characteristic matrix equation. Several demonstrating problems are investigated. It can be seen that the formulation yield satisfactory results.

1. INTRODUCTION

Cracks, notches and multi-material joints are often found in modern engineering structures and materials. Thorough understanding of the singular stress fields around them is needed for the reliability prediction of these structures and materials during their service life. Many studies about singular asymptotic stress fields in linear elastic materials have been carried out in recent two decades. Most of the researches in this area have focused on two-dimensional geometry. Attention has also been given to three-dimensional conical configurations. The present concern is vertex-type singularity of the stress in the form of:

$$\rho^{\lambda}\mathbf{S}(\phi_z,\theta_z) \tag{1}$$

where (ρ,ϕ_z,θ_z) are the standard spherical coordinates with their origin at the vertex of the conical material domains.

Owing to the intrinsic mathematical complexity, vertex-type singularities were mostly identified by numerical methods [1]—[6]. These numerical methods are all developed in the standard ρ-ϕ_z-θ_z spherical coordinates and the concerned displacement is the one defined with respect to ρ, ϕ_z and θ_z. Moreover, the surface of the spherical domain is meshed uniformly in the ϕ_z-θ_z plane. Hence, the mesh in the physical space is densest and coarsest at the vicinity of the poles ($\phi_z = 0$ or π) and at the equator ($\phi_z = \pi/2$) respectively. All nodes at $\phi_z = 0$ (or $\phi_z = \pi$) in the ϕ_z-θ_z plane represent a single physical point which is the pole on the sphere. Interestingly, different values of displacement are yielded at different nodes at $\phi_z = 0$ (or $\phi_z = \pi$). This violates our physical awareness. Moreover, some strain components and thus the integrands in the weak form contain the $1/\sin\phi$ terms which are unbounded at the poles. Accurate numerical integration is difficult. Slow convergence was reported in Bazant [1] and Bazant & Estenssoro [2] by using finite difference and finite element methods. To yield accurate solutions, extrapolation was employed. Meanwhile, Pageau & Biggers [6] avoided the problem by excluding the small cones of material at the poles in their discretization. Nevertheless, their results are rather sensitive to the order of integration. The observation is probably due to the high strain energy density gradient at the vicinity of the poles due to the $1/\sin\phi$ terms. On the other hand, Ghahremani & Shih [4] overcame the problem by directly dividing the spherical surface into quadratic triangular element to reduce the nonuniformity arising from using uniform meshes in the ϕ_z-θ_z plane. To overcome the singularity at the poles, local spherical coordinates for each of the elements are defined in such a way that the element centre is close to the point wherein the local ϕ_z and θ_z are equal to $\pi/2$. Unfortunately, compatibility is not satisfied in the method.

In present study, in order to avoid the inherent singularity of the spherical coordinates at the poles, a three quasi-spherical coordinates system is employed to describe the three-dimensional space. A new finite element formulation for solving vertex-type singularities is developed in the frame of this new coordinates system. Moreover, the nodal d.o.f.s are the generalized displacement components along the global Cartesian coordinate axes. It will be seen that the formulation is compatible and insensitive to the order of numerical integration. Problems on quarter-infinite cracks as well as 1/8-1/8, 1/8-4/8 and 1/8-2/8 bi-material junctions are studied. The computed results are in closed agreement with those reported in the literature.

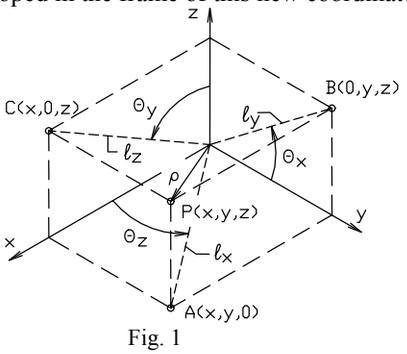


Fig. 1

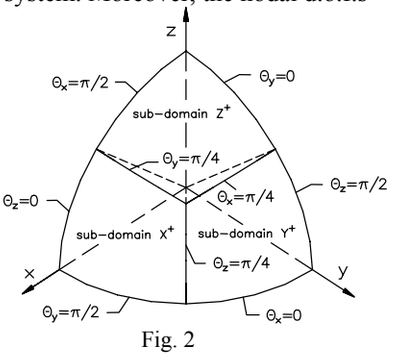


Fig. 2

2. A QUASI-SPHERICAL COORDINATE SYSTEM

In order to secure the mesh compatibility and the result insensitivity to the order of numerical integration, a complementary quasi-spherical coordinate system is here proposed. Besides the angular coordinate θ_z used in the standard spherical coordinates, θ_x and θ_y are introduced in this complementary quasi-spherical coordinate system (see Fig. 1). The three-dimensional space is divided into the following six sub-domains:

Domain $X^+ : 0 \le \rho \le \infty\,,\ \pi/4 \le \theta_y \le 3\pi/4\,,\ -\pi/4 \le \theta_z \le \pi/4$; Domain $X^- : 0 \le \rho \le \infty\,,\ -3\pi/4 \le \theta_y \le -\pi/4\,,\ 3\pi/4 \le \theta_z \le 5\pi/4$;

Domain $Y^+ : 0 \le \rho \le \infty\,,\ \pi/4 \le \theta_z \le 3\pi/4\,,\ -\pi/4 \le \theta_x \le \pi/4$;Domain $Y^- : 0 \le \rho \le \infty\,,\ -3\pi/4 \le \theta_z \le -\pi/4\,,\ 3\pi/4 \le \theta_x \le 5\pi/4$;

Domain $Z^+ : 0 \le \rho \le \infty\,,\ \pi/4 \le \theta_x \le 3\pi/4\,,\ -\pi/4 \le \theta_y \le \pi/4$;Domain $Z^- : 0 \le \rho \le \infty\,,\ -3\pi/4 \le \theta_x \le -\pi/4\,,\ 3\pi/4 \le \theta_y \le 5\pi/4$. (2)

Domain X's, Y's and Z's are described by the quasi-spherical coordinates (ρ, θ_y, θ_z), (ρ,θ_z, θ_x) and (ρ,θ_x, θ_y), respectively. Fig. 2 illustrates how a typical octant is partitioned.

3. FINITE ELEMENT FORMULATION IN THE QUASI-SPHERICAL COORDINATE SYSTEM

The weak form of the eigen problems with vertex-type singularities is ([1], [2]):

$$\int_V \delta\boldsymbol{\varepsilon}^T \boldsymbol{\sigma}\, dV - \int_S (\delta \mathbf{u}^T \mathbf{t})\Big|_{\rho=R} dS = 0 \tag{3}$$

in which δ is the virtual symbol, V denotes volume, S denotes the spherical surface at radius $\rho = R$, $\boldsymbol{\varepsilon}$ is the vector of strain components, $\boldsymbol{\sigma}$ is the vector of stress components, $\mathbf{u}$ is the displacement and t is the surface traction. Strain, stress and surface traction are all derived from the displacement. It should be noted that the above weak form is different from the virtual work statement wherein the surface traction is prescribed.

The displacement is assumed to be:

$$\mathbf{u} = \begin{Bmatrix} u \\ v \\ w \end{Bmatrix} = \mathbf{u}_o + \rho^{\lambda+1} \sum_{i=1}^{m} N_i \begin{Bmatrix} U \\ V \\ W \end{Bmatrix}_i \tag{4}$$

where the nodal d.o.f.s are the generalized Cartesian displacement components U, V and W which are interpolated inside each element to give the Cartesian displacement components u, v and w; $\mathbf{u}_o$ is the displacement at $\rho = 0$; N's are the interpolation functions defined in the new quasi-spherical coordinate system.

Following the standard procedures that used to formulate an assumed displacement isoparametric finite element, a second order characteristic matrix equation is obtained. It can be transformed into the standard first order characteristic matrix equation by introducing a dummy vector and the later can be solved by standard numerical subroutines.

5. CONCLUSIONS

With the asymptotic assumption of the displacement that leads to the vertex-type stress singularity, a two-dimensional finite element formulation is derived. Unlike the previously proposed formulations which suffer from either mesh incompatibility or the inherent singularity of the standard spherical coordinate system at its poles, the proposed formulation employs three quasi-spherical coordinate systems to describe different regions of the three-dimensional space. Moreover, the unknowns are the generalized displacement components along the Cartesian coordinates instead of the ones defined with respect to the standard or quasi- spherical coordinates. In this light, the shortcomings of the previous formulation are circumvented. The subsequent characteristic matrix equation is quadratic and can be transformed into a linear one by introducing a dummy vector of unknowns. Benchmark problems including quarter infinite crack in isotropic material (Fig.3), quarter infinite crack in orthotropic material, tri-material free edge and solutions, if any.

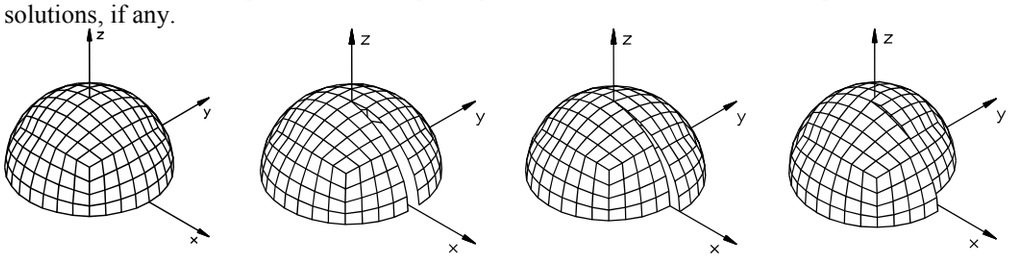


Fig. 3

References

[1] Bazant Z. P.: Three-Dimensional Harmonic Functions Near Termination or Intersection of Gradient Singular Lines: A General Numerical Method. *Inter.J.Engng.* **12**: 221-243,1974.

[2] Bazant Z. P. and Estenssoro L. F.: Surface Singularity and Crack Propagation. *Inter.J.Solids&Structures* **15**:405-426, 1979.

[3] Benthem J. P.: The Quarter-Infinite Crack in a Half-Space: Alternative and Additional Solutions. *Inter.J.Solids&Structures* **16**:119-130, 1980.

[4] Ghahremani F. and Shih C. F.: Corner Singularities of Three-Dimensional Planar Interface Cracks. *J.Appl.Mech.* **59**: 61-68, 1992.

[5] Picu C. R. and Gupta V.: Three-Dimensional Stress Singularities at the Tip of a Grain Triple Junction Line Intersection the Free Surface. *J.Mech.Phys.Solids* **45**: 1495-1520, 1997.

[6] Pageau S. S and Biggers S. B.: Finite Element Evaluation of Free-Edge Singular Stress Fields in Anisotropic Materials. *Inter.J.Numer.Methods Engrg.* **38**: 2225-2239, 1995.

FAILURE MODEL OF PROTECTIVE COATINGS

Asher A. Rubinstein and Yaliang Tang
Department of Mechanical Engineering, Tulane University
New Orleans, LA 70118, USA

Summary. The integrity and reliability of protective coatings under thermal and mechanical loadings are addressed. A rigorous analytical – computational model is presented. It relates the loading and the developing system of cracks through the coating and along the interface with associated crack driving parameters. The developed model serves as a guiding tool for service life predictions.

INTRODUCTION

The efficiency of aircraft engines can be improved significantly by increasing the temperature in the combustion chambers and the gas path temperatures in the high-pressure turbine sections. The temperatures in these areas of today's high thrust engines exceed the temperature capability of typical turbine metallic alloys. To combat this situation, ceramic thermal barrier coatings (TBCs) have been developed for application to turbine and diesel engine components. The ceramic layer is deposited on a metallic alloy substrate. In the course of fabrication, the formation of the surface of the coatings has a mud pie appearance with a system of small surface cracks serving as the boundaries. In a reasonably short service period, these initial cracks propagate through the thickness of the coating layer and reach the coating - substrate interface. These initial cracks through the coating layer form a network that in two-dimensional illustration may be presented as a periodical crack system. The formation and propagation of the interfacial cracks connecting the initial periodical system are essential steps of the developing failure in TBCs. The development of an analytical - computational model characterizing the failure process in TBCs in detail is the primary purpose of this project. The developed model is planned to be used as a tool for service life prediction of components with TBCs. In practical terms, one needs to determine the actual fracture mechanics parameters that initiate internal microcracks and promote their growth during specific thermo-mechanical service cycles.

THE MODELING CONCEPT

The initial surface cracks may be relatively short initially but, as was observed, they may reach the interface between the ceramic coating and the base metal in a relatively low number of service cycles. Typically, these cracks do not propagate through the interface into a substrate but rather deflect and continue to grow along or near the interface. Thus, the main safe service period of TBCs is primarily dependent on the time, or number of service cycles, required for these cracks to cross the link holding the individual "grains" attached to the substrate. The two dimensional schematic illustration of this process is given in Figure 1, which illustrates the model problem. The initial interface cracks are depicted as a periodically distributed net of cracks.

The modeling approach is based on the described observations. The practical goal is to determine the safe service time of the components with TBCs. Taking a conservative approach, the modeling effort concentrates on the time required for the cracks to bridge the interfacial link holding the coating layer. To make this determination, it is necessary to evaluate all crack growth driving parameters as they develop along the crack path. Determination of the stress intensity factors and the energy release rate as the crack progresses along the interface is a necessary step toward service life prediction. Establishing an analytical - computational relationship between these parameters and the thermomechanical loading parameters during the service cycle is the basis of the life prediction scheme for TBCs.

Although the process is three dimensional, a two dimensional problem could provide sufficient information regarding the nature of the process. The average "grain" size, that is, the parameter describing the initial spacing of the net of surface cracks, determines the size of periodic crack cells in a two-dimensional cross section. That is a period p, as illustrated in Figure 1. The initial spacing of the surface cracks depends on the fabrication process parameters and, possibly, can be controlled by the manufacturing process.

Model Problem

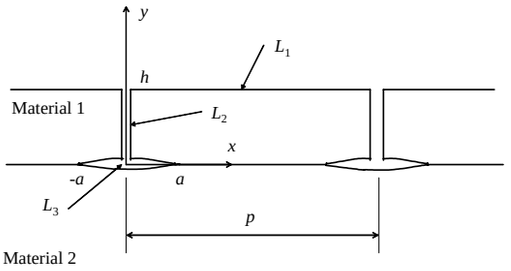


Figure 1. Initiation and growth of Interface cracks.

Possible Crack Path Trajectories

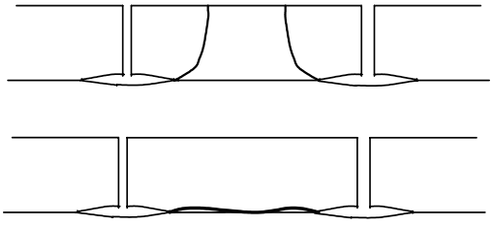


Figure 2. Illustration of possible crack path trajectories

Two alternative crack path directions are illustrated in Figure 2. Identification of a specific crack path option for a given TBS system is an important component of failure model development in this framework.

The numerical examples were computed using the data from experiments described by Zhu and Miller [1]. The definitions of the stress intensity factors and the energy release rate along the interface used in the computations are consistent with the definitions introduced by Rice and Sih [2].

The numerical examples represent the stress states developed under the thermal loads applied as a constant temperature at the surface and as a result of a cyclic temperature. Similarly, the heat flux boundary conditions were used.

CONCLUSIONS

Essential data leading toward an understanding of the interface crack driving force developed due to thermal loadings were established using a rigorous analysis of the corresponding thermoelastic problem. The present work is a basic development toward a service life prediction model for TBCs. This is an important technological step for potential commercial applications of the TBCs.

Acknowledgement. The work presented here was supported by NASA under Grant NAG3-2689.

References

[1] Zhu, D. and Miller, R. A. Influence of high cycle thermal loads on thermal fatigue behavior of thick thermal barrier coatings. NASA technical report, 3 – 10, NASA TP – 3676, 1998.

[2] Rice, J. R. and Sih, G. C.(1965) Plane problems of cracks in dissimilar media. *Journal of Applied Mechanics*. Vol.32, pp.418-423.

XXI ICTAM, 15-21 August 2004, Warsaw, Poland

MODELING OF ENVIRONMENT ASSISTED DELAMINATION
I. QUASISTATIC CASE

Alla V. Balueva
Spelman College, Department of Mathematics, 350 Spelman Lane SW, Atlanta, GA 30314, USA

Summary A theoretical model of quasistatic growth of delaminations of a protection covering of metal due to diffusion of dissolved in metal atomic hydrogen into the formed cavity is considered. For the case of a penny-shaped delamination the main equation describing its growth is derived.

INTRODUCTION

As is well known, in conditions of hydrogen embrittlement, hydrogen reduces the fracture resistance of many metals and steels. Hydrogen absorbed by a metal is usually dissolved in the lattice in the *proton* form (e.g., Turnbull, 1993; Vehoff, 1997). Some of the protons reach the surface of pre-existing cracks where they recombinate with electrons and form *molecular* hydrogen in the crack cavity, which leads to accumulation of gas hydrogen inside the crack. The appearing excessive pressure can be especially dangerous when the metal surface is coated by a protective material (e.g., Nayyar, 1992) that does not allow hydrogen diffusion. For example, in the case of pipelines for hydrocarbon transport, anti-corrosion, polymer coating sometimes results in more frequent appearance of small scale delaminations (Gapharov et al., 1998). In this paper, a model of a penny-shaped delamination controlled by a diffusion process is considered. Kinetic equations describing the delamination growth and resulting in the expressions for the crack size and velocity of growth are derived.

FORMULATION OF MODEL. DERIVING OF THE MAIN KINETICS EQUATION

Let a half-space (a substrate of the base metal) saturated by gas with a concentration c_∞ at infinity be covered by a thin infinite layer circular delamination of thickness, h, and initial radius, l_0, that appears in the plane of connection, $z=0$, at the moment of $t=0$ (Figure 1). The covering layer is assumed to be thin as compared to the half-space

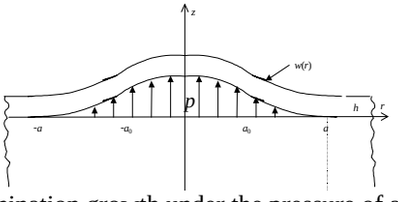


Figure 1. Delamination growth under the pressure of accumulated gas.

$D_0 = \frac{Eh^3}{12}$ is the plate flexural rigidity, h is the plate thickness.

Thus, if the typical size, l, of the delamination is smaller then its thickness, h, the major part of the strain energy is due to the deformation (bending) of the delaminated covering. Therefore, it is permissible to neglect the deformation of a substrate and to model it by the ideally rigid half-space from which a thin plate is delaminated (e.g. Balueva, 1999).

Once the gas is accumulated in the delamination, the critical condition is achieved on the crack contour and the delamination begins growing. The delamination crack is modeled by an ideal drain: we believe that the pressure inside the crack is sufficiently small so as not to achieve an equilibrum statement, and therefore, the molecular hydrogen accumulates inside the crack (see e.g. Goldstein, 1977). Then we can write the boundary value problem for finding of the concentration of atomic hydrogen, $c(r,z,t)$, at the moment of time, t, as the following:

$$\begin{aligned} &\Delta c = 0 \; z \le 0 \\ &c\big|_{z=0} = 0, r \le l(t) \\ &\partial c/\partial z\big|_{z=0} = 0, r > l(t) \\ &c\big|_{z=\infty} = c_\infty \end{aligned} \qquad (1)$$

from where the density q of diffusion flux into a crack can be obtained in the following form

$$q(r,t) = -D\partial c/\partial z\big|_{z=0} = \frac{2}{\pi}\frac{c_\infty D}{\sqrt{l^2 - r^2}}, r \le l(t) \qquad (2)$$

Then a full gas flux into the crack can be written as follows:

$$\partial n/\partial t = -2\pi D\int_0^l \partial c/\partial z\Big|_{z=0}(r,t)r\,dr = 4c_\infty Dl(t)\,, \tag{3}$$

where n is the amount of gas moles in the crack.
The opening of the delamination under applied load p can be determined under the approximation of thin plates in the form

$$w(r) = \frac{pl^4}{64D_0}\left[1-2\left(\frac{r}{l}\right)^2+\left(\frac{r}{l}\right)^4\right] \tag{4}$$

and the potential energy of a circular plate can be written as follows:

$$U = \frac{D_0}{2}\int_0^l\int_0^{2\pi}(\nabla^2 w)^2 r\,dr\,d\varphi \tag{5}$$

where

$$\nabla^2 w = \frac{d^2w}{dr^2}+\frac{1}{r}\frac{dw}{dr} = \frac{pl^2}{8D_0}\left(2\frac{r^2}{l^2}-1\right) \tag{6}$$

Substituting (6) into (5), we obtain the following expression for energy:

$$U = -\frac{\pi}{6\cdot 64}\frac{p^2l^6}{D_0} \tag{7}$$

The critical energy released rate can be written in the following form:

$$\gamma_{scc} = -\frac{1}{2\pi l}\frac{\partial U}{\partial l} = \frac{1}{2\cdot 64}\frac{p^2l^4}{D_0} \tag{8}$$

The molecular hydrogen state in a crack is assumed to be described by the equation for ideal gas and all processes are considered to be isothermal. We have the expression for the volume of a crack in the form

$$V = \int_0^l\int_0^{2\pi} w(r)r\,dr\,d\varphi = \frac{\pi}{6\cdot 32}\cdot\frac{pl^6}{D_0} \tag{9}$$

Taking into account (3), the equation of Mendeleev-Klaiperon can be written in the form

$$pV = 4c_\infty DRT\int_0^t l(t)dt \tag{10}$$

where R is the universal gas constant and T is the gas temperature.
Substituting expression (9) for volume into (10) and taking into account (8), we obtain the main equation for the analysis of quasistationary growth of a penny-shaped delamination:

$$\frac{2\pi}{3}l^2\gamma_{scc}^2 = 4c_\infty DRT\int_0^t l(t)dt \tag{11}$$

from where after differentiating with respect to t both parts of equation (11) the delamination growth velocity can be written in the form

$$\dot{l} = \theta c_\infty/2\gamma_{scc}\,, \qquad \theta = \frac{6}{\pi}RTD \tag{12}$$

The expression (12) reveals that the delamination under these conditions spreads with a constant velocity.
Author would like to thank Dr. Leonid Germanovich for inestimable help and support, and would hope that joint continuation of the paper, II. Transient Case, is going to appear in press soon.

References

Toribio, J. and Kharin, V. (1997). The Effect of History on Hydrogen Assisted Cracking: 1. Coupling of Hydrogenation and Crack Growth. Int. J. Fract. **88**, 233-245.
Turnbull, A. (1992). Test Methods for Environment Assisted Cracking. British Corrosion Journal **27**, 271-289.
Vehoff, H. (1997). Hydrogen Related Material Problems, *Hydrogen in Metals III, Properties and Applications*, Springer-Verlag, Berlin Heidelberg New York, 348.

XXI ICTAM, 15–21 August 2004, Warsaw, Poland

THE INFLUENCE OF REMOTE STRESSES ON THE NEAR CRACK TIP STRESS FIELD

Ewa Turska*, Krzysztof Wisniewski**
*IPPT PAN, Department of Theory of Continuous Media, Swietokrzyska 21, PL 00-049 Warszawa, Poland
**IPPT PAN, Department of Computational Science, Swietokrzyska 21, PL 00-049 Warszawa, Poland

Summary Two methods of finding the near crack tip field can be specified. While one consists of retaining only terms valid in the infinitesimal vicinity of the crack tip, the other is obtained by infinitely extending the whole crack. For one crack these approaches are equivalent. For interacting cracks or cracks with loads acting on their planes, we get a loss of uniqueness. This occurs for elastic and elastic-plastic materials. In the paper we present examples and a discussion which enables to distinguish the differences. From this point of view also the kinked crack tip is analyzed in the case of a small kink or small kink angle. Not to complicate the discussion only mode III cracks are studied.

Preliminaries

Let us assume a Cartesian coordinate system (x_1, x_2, x_3) with the origin at the crack tip and the negative part of x_1 axes aligned with the crack. In the case of mode III loading, the displacement vector $\mathbf{u}$ is of form

$$\mathbf{u} = [0, 0, w(x_1, x_2)], \tag{1}$$

where $w(x_1, x_2)$ is the displacement parallel to the x_3 axis. The displacement can be expressed as an imaginary part of a complex analytic function $f(z)$, i.e $w(x_1, x_2) = (1/\mu)Im[f(z)]$, where $z = x_1 + \imath x_2$. Thus, for the stresses in an elastic body we have

$$\sigma_{23} + \imath\sigma_{13} = f'(z), \tag{2}$$

In the perfectly plastic region at the crack tip [4] we obtain

$$\sigma_{23}(r, \theta) + \imath\sigma_{13}(r, \theta) = k\, e^{-\imath\theta}. \tag{3}$$

In an elastic body the asymptotic stresses at the crack tip are

$$\sigma_{23} + \imath\sigma_{13} \to \frac{K_{III}}{\sqrt{2\pi z}}. \tag{4}$$

The problem of an infinite crack in an infinite body with inverse square root singularity has the form eq.(4) (i.e. $f'(z) = K_{III}/\sqrt{2\pi z}$)

Load acting on crack plane

In the case of loads

$$\sigma_{23}(x_1, 0) = \frac{ka}{x_1 - a}, \tag{5}$$

acting on the crack plane, we obtain two stress distributions [1]

$$\sigma^0_{23} + \imath\sigma^0_{13} = k\frac{a}{\sqrt{z}(\sqrt{z} + \sqrt{a})} \tag{6}$$

and

$$\sigma_{23} + \imath\sigma_{13} = \frac{k\sqrt{a}}{\sqrt{z}}\left(\frac{\sqrt{a}}{\sqrt{z} + \sqrt{a}} + 1\right), \tag{7}$$

which differ only by the asymptotic decay ratio in infinity. It is the same on the crack plane because both solutions satisfy the same BVP on the crack, also on the 'infinite' end of the crack.

Two parallel cracks

Let two parallel infinite cracks be at distance $2h$ from each other and the stresses on the outside of the cracks vanish in infinity such as $z^{1/2}$. The inverse stress function is given by [2]

$$f'(z) = \sigma_{23} + \imath\sigma_{13} = \frac{K_{III}}{\sqrt{h}}\ \frac{\sqrt{z_1 - 1}}{z_1} \tag{8}$$

for

$$z = \frac{h}{\pi}(z_1 + \ln(1 - z_1)) \tag{9}$$

The above result can be added to any loaded case to obtain a different stress distribution satisfying the same BVP.

Kinked crack

The exact solution for a mode III crack was given by [3], where the conformal mapping was obtained using the Schwarz-Christoffel formula. Quite often the main most cumbersome problem in the use of this formula is the determination of the unknown constants. There they were chosen for the sake of simplifying the integration. In conformal mappings there are three arbitrary constants. Luckily, in this case of an infinite crack, they can be analytically obtained to satisfy the condition that the two cases: of a vanishing kink and a vanishing kink angle result in the same BVP of one straight crack. For a kink angle β :

$$f'(z_1) = \frac{\imath}{1+\phi h\beta}(z_1+h\beta)^{\beta}(z_1-h\beta)^{-\beta} \tag{10}$$

where

$$z = -(z_1-h\phi)^{1+\beta}(z_1+h\phi)^{1-\beta}, \qquad \phi = (1+\beta)^{-(1+\beta)/2}(1-\beta)^{-(1-\beta)/2} \tag{11}$$

Small scale yielding

In the case of small scale yielding for one crack we can obtain different stress distributions (they both have vanishing remote stress but of different order)[1]:

$$F_1(\omega) = A_1(\frac{1}{\omega^2}+1) + \imath A_2(\frac{1}{\omega^3}-\omega), \qquad F_1(\omega) = A_1(\frac{1}{\omega^2}+1) + A_3(\frac{1}{\omega^4}+\omega^2). \tag{12}$$

where

$$F_1(\omega) = f'^{-1}(\omega), \qquad \omega = \sigma_{23} - \imath\sigma_{13} \tag{13}$$

For two parallel cracks different solutions can be obtained even with the same order in infinity [2]:

$$\begin{aligned} \omega(\varphi)\, F(\omega(\varphi)) &= -\frac{h}{\pi}\sqrt{P(\varphi)}\left(\frac{\sqrt{1/4-b^2}}{\sqrt{1/4-\varphi^2}}\ln\frac{4(\varphi\sqrt{1/4-b^2}-b\sqrt{1/4-\varphi^2})^2}{\varphi^2-b^2} - \ln\frac{\varphi-b}{\varphi+b}\right) \\ &+ C\sqrt{P(\varphi)}, \qquad \varphi(\omega) = \frac{\sqrt{(1-S'^2\omega^2)(S'^2-\omega^2)}}{(1-S'^2\omega^2)+(S'^2-\omega^2)}. \end{aligned} \tag{14}$$

CONCLUSIONS

To ensure uniqueness of either asymptotic crack tip stresses or an infinite crack problems it is suffices to demand finite displacements at the crack tip and attenuation of stresses in infinity. In other cases it is not enough and can lead to multiple solutions of the same problem. Multiple in the sense that the same BVP can have two solutions, which in the limit, at the crack tip, give different Stress Intensity Factors (see eq.(6, 7)). Or, in the case of a kinked crack, a vanishing kink is not consistent with vanishing kink angle. Thus, there is a need to impose some additional condition (eg. rate and order) relevant to the considered physical problem.

Acknowledgement This research was partially supported by the Polish Committee for Scientific Research (KBN) Grant 7T11F01921.

References

[1] Turska E., Wisniewski K.: On Semi-infinite Crack Problems in Elastic-Plastic Bodies; Uniqueness and Examples. *International Journal of Engineering Science* **41**:1767 - 1783, 2003.

[2] Turska E., Wisniewski K.: Elastic-Plastic and Elastic Anti-plane Shear of Two Parallel Cracks. *Theoretical and Applied Fracture Mechanics* **38**:301-310, 2002.

[3] Sih G.C.: Stress Distribution Near crack Tips for Longitudinal Shear Problems. *Journal of Applied Mechanics* **32**:51-58, 1965

[4] Broberg, K.B.: Cracks and Fracture. Academic Press, San Diego, 1999.

THE ELASTO-PLASTIC THIN FILM/SUBSTRATE VIA BUCKLE-DRIVEN DELAMINATION AND CRACK GROWTH

Yu Shouwen* Li Qunyang
(*Department of Engineering Mechanics, Tsinghua University, Beijing 100084, China*)

Summary: Thin films have a wide range of applications in microelectronics and magnetic recording industries where properties are needed to insure performance and reliability. In general, these applications are tied directly to interface structure and composition, i.e. the films must remain adhered to be of use. While many of these tests are semi-quantitatively measurements and are useful for functional or comparative purposes, there are some applicable to be direct quantitative assessment and indentation technique is a representative one of them for its simplicity, reproducibility and the ease of interpretation of the results. It is very interesting for this problem by using a combined approach between the elastic-plastic fracture mechanics and interfacial mechanics of buckling driven delamination. For brittle, weakly bonded films, indentation can be used to delaminate the films from the substrates, thus measuring the thin film interfacial strength. During this process. This indentation technique is mainly based on the pioneer works of Marshall & Evans[1] and Evans & Hutchinson[2] which gave the theoretical analysis for the conical indentation-induced thin film delamination.

Consider an indentation-induced interface crack in a residually stressed film. The film has a thickness t on a semi-infinite substrate, loaded by a hard angular indenter which leaves a permanent impression, and the residual stress is assumed to be σ_R. The strain energy release rate is obtained as follows by considering a few hypothetical operations with a combination of Linear Elastic Fracture Mechanics (LEFM) and simplified post-buckling theory [1,2]

$$G = t(1-\nu)\left\{(1-\alpha)\sigma_R{}^2 + \sigma_0{}^2\left[(1+\nu)/2 - (1-\alpha)(1-\sigma_c/\sigma_0)^2\right]\right\}/E \qquad (1)$$

where $\alpha = 1$ for $\sigma_0 + \sigma_R < \sigma_c$ (no buckling) or $\alpha = \left(1+1.207(1+\nu)\right)^{-1}$ for $\sigma_0 + \sigma_R > \sigma_c$ (buckling),.The subscripts o, *R*, c denote characteristic stress, residual stress and critical buckling stress respectively. After measuring the strain energy release rate G or J integral, the interfacial adhesion between the thin film and substrate can be calculated, which needs the knowledge of the fracture of interface and the phase angle to interpret the results correctly. However it must be noted that the applicability of indentation technique to measure thin film adhesion has been limited because several complex fracture processes are involved and the results are not yet well understood, for example the equation (1) is only valid for initial stage of post-buckling, especially for the single buckling case, and Euler plate buckling assumption is taken without considering the plasticity of thin films. Most of the discussion in the references are based on the assumption of elastic deformation. But because of the large deformation during the post-buckling stage, it may be very helpful if we take the plasticity of the film into consideration to investigate its influence, especially for the film with low value of yield stress σ_y . The schematic of the model is similar as [2], but the thin film is modified as an elasto-plastic material which obeys the power hardening law.

In many indentation tests, if the indenter is driven deep enough, so that the crack reaches its critical buckling length, the film often double buckles during indentation with the plastic indentation volume V_0. But as what is mentioned above, the full analysis of double-buckling has not yet been

done, which is essential for the indentation technique. Experiment of Kriese et al.[3] found that during indentation the interfacial fracture toughness was reproducibility high for shallow indents, $8-10\ \mathrm{J/m^2}$, but dropped to a fairly steady $0.7-1.2\ \mathrm{J/m^2}$ for deeper indents. It is hard to explain these experimental data via conventional analysis. As we know, the plasticity of materials will greatly affect the buckling process; can it be a reason for this phenomenon?

In this paper, we will also emphasize on some aspects of thin film bucking and their influences to the indentation test. An investigation on the post-buckling of thin film is carried out by FEM calculation. Some of the important factors, which are often omitted before, such as the double-buckling phenomenon and material plasticity, are discussed. The results show that for the case of $\sigma < 3\sigma_c$, the asymptotical solution is satisfactory with a relative error less than 10% for the elastic film/substrate system. For the double-buckling cases, the critical stress and initial slope parameter are obtained, and the comparison of the energy release rate with the single-buckling case shows that the different is obvious and need to be treated properly. Then we calculate the case of $\sigma_y / E = 2\times 10^{-3}$, i.e. $\sigma_c / \sigma_y \approx 1.7$. The post-buckling responses for different values of hardening exponent n are plotted under deformation plasticity. the non-dimensional critical stress decreases significantly when considering the film plasticity. For the perfect plastic case, the J integral or energy release rate decreases to one half of the linear elastic one when $\sigma \approx \sigma_c$, to 20% when $\sigma \approx 2\sigma_c$.

The plasticity has significant influence on the post-buckling responses and should be considered in interpreting the indentation test results. The greater the value of ratio of critical buckling stress to yielding stress σ_c / σ_y, the more contributions of the plasticity. The quantitative influences of plasticity on the energy release rate are shown by figures. the influence of the film plasticity will be a dominant factor for shallow indent, so it must be included to interpreter the results correctly. This might be one of the reasons for the discrepancy between shallow and deeper indent.

The results are shown that the plasticity is a significant factor for those films with low yield stress and must be taken in account in adhesion measurement. The abnormal experimental results of Kriese [3] can be explained by this calculation.

References

[1] Marshall D B and Evans AG, *J.Appl.Phys*,1984, 56(10):2632-2638.

[2] Evans AG and Hutchinson J, *Int J. Struct. and Solids*,1984,20(5):455-466.

[3] Kriese MD et al, *Engng Fract.Mech.*,1998,61:1-20.

Acknowledgement: This project is supported by NSFC (10172050, 10320120167) and SRFDP-306416 in China

---

*Correspondence author: E-mail: yusw@mail.tsinghua.edu.cn

For-21st ICTAM-pre-nominated session SM9: Fracture and Crack Mechanics.

ON 3-D THERMOELASTIC PROBLEMS OF INTERFACIAL CRACKS IN A PERIODIC STRATIFIED SPACE

Andrzej Kaczynski [*] , Stanislaw J. Matysiak [**]
[*] *Warsaw University of Technology, Faculty of Mathematics and Information Science, Plac Politechniki 1, PL 00-661 Warszawa, Poland*
[**] *Bialystok University of Technology, Faculty of Mechanical Engineering, Wiejska 45C, PL 15-351 Bialystok, Poland*

Summary The methods of solutions to three-dimensional stationary thermoelastic problems involving a two-layered microperiodic space containing an interface crack of arbitrary smooth profile. An approximate analysis is performed within the framework of linear stationary thermoelasticity with microlocal parameters. The resulting boundary-value problems are reduced to the corresponding ordinary crack problems with mechanical loading in homogeneous isothermal elasticity.

INTRODUCTION

The rapidly increasing use of new composite materials with a large number of dissimilar layers in advanced engineering structures requires the study of different aspects of their fracture behavior. A great deal attention has been drawn to interfacial cracking. It is well known that many conventional solutions for interfacial cracks have oscillatory singularities, which causes the overlapping of crack faces. To eliminate these unsatisfactory features, several interfacial zone models have been proposed and discussed (see e.g. a review in [1]).
In this paper, an approximate theory called the linear stationary thermoelasticity with microlocal parameters, devised in [2,3], is used to analyze three-dimensional problems with a crack of arbitrary shape lying on an interface in a periodic two-layered elastic space. The advantage of this approach is a relatively simple form of the governing equations appearing similar to the thermoelasticity for transverse isotropy, which makes it possible to construct the appropriate potentials and establish an analogy between the thermal crack problems and their mechanical counterparts. Thus, the typical inverse square root crack-border stress singularities, characterized by the stress intensity factors, are obtained.

PROBLEM FORMULATION AND GOVERNING RELATIONS

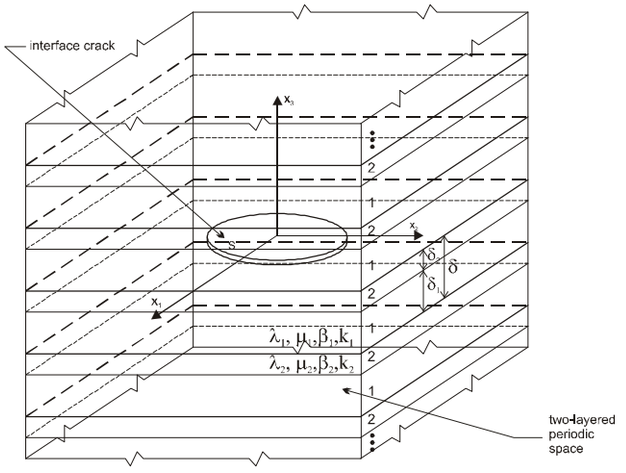


Fig. Two-layered periodic space with an interface crack

Consider a bimaterial-laminated space as shown in Figure. A repeated fundamental layer of thickness δ is composed of two homogeneous sublayers, denoted by $l = 1$ and $l = 2$, with thicknesses δ_1 and δ_2, and characterized by different thermo-mechanical properties. Let λ_l, μ_l be the Lamé constants, k_l the thermal conductivities, $\beta_l / \left(\lambda_l + \frac{2}{3}\mu_l\right)$ the coefficients of the volume expansion, $l = 1,2$.
To determine the temperature-stress fields in this laminated body, the linear stationary thermoelasticity with microlocal parameters ([2], [3]) is applied to seek an approximate solution. Without going into details we recall below only the final governing equations and constitutive relations of the macro-homogeneous homogenized model of the treated body (see [4] for the details of the derivation; summation over repeated subscript $\gamma = 1,2$ is taken for granted):

– the equation of heat conduction for a macro-temperature ϑ (in the absence of heat sources)

$$\vartheta_{,11} + \vartheta_{,22} + k_0^{-2}\vartheta_{,33} = 0 \tag{1}$$

– the equations for macro-displacements w_i (in the absence of the body forces)

$$\begin{aligned} &0,5\left(c_{11}+c_{12}\right)w_{\gamma,\gamma\alpha} + 0,5\left(c_{11}-c_{12}\right)w_{\alpha,\gamma\gamma} + \\ &+ c_{44}w_{\alpha,33} + \left(c_{13}+c_{44}\right)w_{3,3\alpha} = K_1\vartheta_{,\alpha}, \quad \alpha = 1,2, \\ &\left(c_{13}+c_{44}\right)w_{\gamma,\gamma 3} + c_{44}\,w_{3,\gamma\gamma} + c_{33}\,w_{3,33} = K_3\vartheta_{,3} \end{aligned} \tag{2}$$

– the constitutive relations for the fluxes $q_i^{(l)}$ and the stresses $\sigma_{ij}^{(l)}$ in the layer of the l th kind

$$\begin{aligned} &q_\alpha^{(l)} = -k_l\vartheta_{,\alpha}, \quad \alpha = 1,2, \qquad q_3^{(l)} = -K\vartheta_{,3}, \\ &\sigma_{\alpha 3}^{(l)} = c_{44}\left(w_{\alpha,3} + w_{3,\alpha}\right), \quad \alpha = 1,2, \\ &\sigma_{33}^{(l)} = c_{13}\left(w_{1,1} + w_{2,2}\right) + c_{33}\,w_{3,3} - K_3\vartheta, \\ &\sigma_{12}^{(l)} = \mu_l\left(w_{1,2} + w_{2,1}\right), \\ &\sigma_{11}^{(l)} = d_{11}^{(l)}\,w_{1,1} + d_{12}^{(l)}\,w_{2,2} + d_{13}^{(l)}\,w_{3,3} - K_2^{(l)}\vartheta, \\ &\sigma_{22}^{(l)} = d_{12}^{(l)}\,w_{1,1} + d_{11}^{(l)}\,w_{2,2} + d_{13}^{(l)}\,w_{3,3} - K_2^{(l)}\vartheta. \end{aligned} \tag{3}$$

Positive constants appearing in the above equations, describing material and geometrical characteristics of the composite constituents are given in the sited paper [4]. Observe that the condition of a perfect bond between the layers is satisfied, and setting $\mu_1 = \mu_2 \equiv \mu,\ \lambda_1 = \lambda_2 \equiv \lambda$ and $\beta_1 = \beta_2 \equiv \beta,\ k_1 = k_2 \equiv k$ we get $c_{11} = c_{33} = \lambda + 2\mu$, $c_{12} = c_{13} = \lambda,\ c_{44} = \mu$, $K_1 = K_3 = \beta,\ K = k,\ k_0 = 1$, passing directly to the well-known equations of stationary thermoelasticity for a homogeneous isotropic body.

The solution of the governing equations (2) is dependent on the material constants of the sublayers. In the general case $\mu_1 \neq \mu_2$, $t_\alpha \neq k_0$ (the other cases are detailed in [4]; all constants appearing are given in [4]) it is expressed in terms of three harmonic potentials $\phi_i(x_1, x_2, z_i),\ z_i = t_i x_3,\ i = 1,2,3$ and the temperature harmonic potential $\omega(x_1, x_2, z_0)$, $z_0 = k_0 x_3$, related to the solution of (1) such that $\vartheta(x_1, x_2, x_3) = -\dfrac{\partial^2 \omega(x_1, x_2, z_0)}{\partial^2 z_0}$, as follows

$$
\begin{aligned}
w_1 &= \left(\phi_1 + \phi_2 + c_1\,\omega\right)_{,1} - \phi_{3,2}\,, \\
w_2 &= \left(\phi_1 + \phi_2 + c_1\,\omega\right)_{,2} + \phi_{3,1}\,, \\
w_3 &= \sum_{\alpha=1}^{2} m_\alpha\, t_\alpha \frac{\partial \phi_\alpha}{\partial z_\alpha} - c_2\, k_0 \frac{\partial \omega}{\partial z_0}\,,
\end{aligned}
\qquad
\begin{aligned}
\sigma_{31} &= c_{44}\left[\sum_{\alpha=1}^{2}(1+m_\alpha)\, t_\alpha \frac{\partial \phi_\alpha}{\partial z_\alpha} + (c_1 - c_2)\, k_0 \frac{\partial \omega}{\partial z_0}\right]_{,1} - t_3 \frac{\partial^2 \phi_3}{\partial z_3 \partial x_2}\,, \\
\sigma_{32} &= c_{44}\left[\sum_{\alpha=1}^{2}(1+m_\alpha)\, t_\alpha \frac{\partial \phi_\alpha}{\partial z_\alpha} + (c_1 - c_2)\, k_0 \frac{\partial \omega}{\partial z_0}\right]_{,2} + t_3 \frac{\partial^2 \phi_3}{\partial z_3 \partial x_1}\,, \\
\sigma_{33} &= c_{44}\left[\sum_{\alpha=1}^{2}(1+m_\alpha) \frac{\partial \phi_\alpha}{\partial z_\alpha} + \alpha_0 \frac{\partial^2 \omega}{\partial z_0^2}\right].
\end{aligned}
\tag{4}
$$

SOLUTIONS TO THERMALLY LOADED INTERFACE CRACKS

Of interest are two general problems (symmetric, denoted by 1 and skew-symmetric, denoted by 2) related to the half-plane $x_3 \geq 0$ when the boundary plane $x_3 = 0$ is subjected to the following general thermal-stress conditions:

Problem 1:
$$
\begin{aligned}
&\vartheta\left(x_1, x_2, 0^+\right) = -T_0(x_1, x_2),\ (x_1, x_2) \in S \\
&\vartheta_{,3}\left(x_1, x_2, 0^+\right) = 0,\quad (x_1, x_2) \in Z - S, \\
&\sigma_{31}\left(x_1, x_2, 0^+\right) = \sigma_{32}\left(x_1, x_2, 0^+\right) = 0,\quad (x_1, x_2) \in Z, \\
&\sigma_{33}\left(x_1, x_2, 0^+\right) = 0,\quad (x_1, x_2) \in S, \\
&w_3\left(x_1, x_2, 0^+\right) = 0,\quad (x_1, x_2) \in Z - S,
\end{aligned}
$$

Problem 2:
$$
\begin{aligned}
&\vartheta_{,3}\left(x_1, x_2, 0^+\right) = -\frac{q_0(x_1, x_2)}{K},\ (x_1, x_2) \in S, \\
&\vartheta\left(x_1, x_2, 0^+\right) = 0,\quad (x_1, x_2) \in Z - S, \\
&\sigma_{33}\left(x_1, x_2, 0^+\right) = 0,\quad (x_1, x_2) \in Z, \\
&\sigma_{31}\left(x_1, x_2, 0^+\right) = \sigma_{32}\left(x_1, x_2, 0^+\right) = 0,\quad (x_1, x_2) \in S, \\
&w_1\left(x_1, x_2, 0^+\right) = w_2\left(x_1, x_2, 0^+\right) = 0,\quad (x_1, x_2) \in Z - S,
\end{aligned}
$$

where Z denotes the entire $x_1 x_2$-plane. In addition, the usual requirements at infinity, namely, vanishing of the temperature and displacements in Problem 1 and heat fluxes and stresses in Problem 2 are assumed.

It is shown how these problems are reduced to the classical mixed problems of potential theory. A general formulation in terms of singular two-dimensional integral and integro-differential equations is also presented.

Problem 1 is reduced to the mechanical counterpart in isothermal elasticity, involving the crack S under symmetrical normal loading (Mode I of crack deformation). It should be mentioned here that this problem does not require the evaluation of the temperature distribution ϑ.

Problem 2 (more involved) is reduced to its mechanical skew-symmetrical problem (Mode II and III of crack deformation).

It follows that the thermoelastic fields and stress intensity factors of the problems under consideration can be obtained from their mechanical counterparts provided that the corresponding solutions for the isotropic elastic materials are available.

Paper [5] demonstrates how to implement this method for the solution to the problem of an interface insulated plane crack obstructing a uniform heat flux in a two-layered microperiodic space.

References

[1] Erdogan F.: Fracture Mechanics of Interfaces. Proceedings of the First International Conference on Damage and Failure of Interfaces (ed. H-P Rossmanith), A.A. Balkema / Rotterdam / Brookfield, 3-36, 1997.

[2] Wozniak C.: A Nonstandard Method of Modelling of Thermoelastic Periodic Composites. *Int. J. Engng Sci.* **25**: 483-499, 1987.

[3] Matysiak S.J., Wozniak C.: On the Microlocal Modelling of Thermoelastic Periodic Composites. *J. Tech. Phys.* **29**: 85-97,1988.

[4] Kaczynski A.: Three-Dimensional Thermoelastic Problems of Interface Cracks in Periodic Two-Layered Composites. *Engng Fract. Mech.* **48**: 783-800, 1994.

[5] Kaczynski A., Matysiak S.J.: On the Three-Dimensional Problem of an Interface Crack Under Uniform Heat Flow in a Bimaterial Periodically Layered Space, *Int. J. Fract.* **123**: 127-138, 2003

AUTOMATIC 3D CRACK GROWTH SIMULATION BASED ON BOUNDARY ELEMENTS

Karsten Kolk, Günther Kuhn
Institute of Applied Mechanics, University of Erlangen–Nuremberg, Egerlandstr.5, 91058 Erlangen, Germany

Summary An automatic 3D crack growth algorithm for fatigue crack propagation of arbitrary three dimensional problems with linear-elastic material behavior is presented. The stress analysis is based on the 3D Dual–BEM. An optimized evaluation of very accurate SIF's and T–stresses and the knowledge of 3D corner singularities are the basis of the proposed 3D crack growth criterion. Finally, the high level of automatization is accomplished by a sophisticated re–meshing algorithm for the update of the numerical model.

INTRODUCTION

A 3D simulation of crack growth is presented to determine the shape of 3D crack fronts as they occur during stable fatigue crack propagation as realistic as possible. It is embedded in an automatic incremental crack growth algorithm for arbitrary three dimensional problems with linear-elastic material behavior. Due to the non–linearity of crack growth, the incremental procedure mainly includes the numerical solution of the current boundary value problem and an algorithm controlling the 3D crack growth automatically.

The boundary value problem of cracked bodies is solved by a powerful tool for stress concentration problems – the boundary element method (BEM). Furthermore, the boundary–only formulation offers the advantage of an easy update of the numerical model compared to volume oriented methods.

The 3D crack growth algorithm contains the determination of an optimized new crack geometry based on a suitable 3D crack growth criterion: a predictor–corrector procedure ensuring a bounded energy release rate along the whole crack front. Finally, the numerical model has to be updated for the next increment. In case of surface breaking cracks the outer boundary needs also to be re–meshed. Therefore, an automatic local re–meshing algorithm capable of handling arbitrary smooth surfaces, which are discretized by quadrilaterals, is presented.

STRESS ANALYSIS

The boundary value problem as shown in Fig. 1 is solved by a special formulation of the BEM – the 3D Dual Discontinuity Method (DDM) – which is used in case of cracked specimens [3].

The domain $\Omega \in \mathbb{R}^3$ is homogeneous and isotropic with linear elastic material behavior. Ω is bounded by the normal boundary Γ^n and the coincident crack surfaces Γ^c and $\Gamma^{\bar{c}}$. Neumann $(\bar{\boldsymbol{t}}(\boldsymbol{x}))$ and Dirichlet $(\bar{\boldsymbol{u}}(\boldsymbol{x}))$ boundary conditions are prescribed along the boundary Γ.

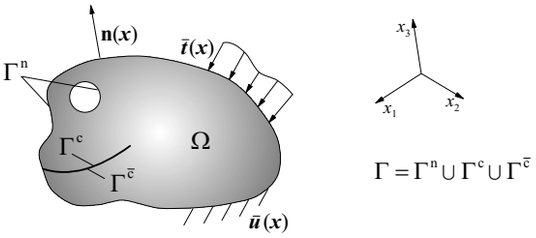


Figure 1. Sketch of the boundary value problem

The relevant displacement boundary integral equations (BIE) are evaluated in the framework of a collocation method on Γ^n and only on one crack surface. To separate the coincident crack surfaces, the hypersingular traction BIE is additionally applied on the remaining crack surface. Finally, the introduction of displacement and traction discontinuities along the crack as new variables leads to the DDM. The advantage of this formulation is a substantially reduced system of equations, due to the elimination of one crack surface.

A special advantage of this procedure in case of the simulation of 3D crack growth is, that it can be used within a single subregion. Especially in the area of high stress concentrations - ahead of the crack front - no discretization is needed.

3D CRACK GROWTH ALGORITHM

The three steps of the crack growth algorithm are indicated in Fig. 2. Firstly, the stress intensity factors (SIF's) and the T-stresses are evaluated very precisely along the crack front by an extrapolation method via a regression analysis [2] from the numerical crack near-field. For every crack front node a new position is determined by the evaluation of a suitable crack growth criterion. It includes the determination of the kink angle and the crack extension. With these two quantities the shape and position of the new crack front can be defined. Then, the gap between the old and new crack front has to be closed during the update of the numerical model. There are two options for this closing procedure. Depending on the amount of crack extension a new row of elements can be inserted or the old crack front nodes are moved towards the new crack front as shown in Fig. 2. However, special attention is needed in case of surface breaking cracks, as the normal boundary Γ^n has also to be considered. To ensure an optimized mesh an automatic local re-meshing procedure is needed. Subsequently, the numerical model for the next increment is generated in a fully automatic way.

Crack growth criterion

A predictor–corrector procedure concerning the crack extension with an implicit correction of the kink angle will be presented.

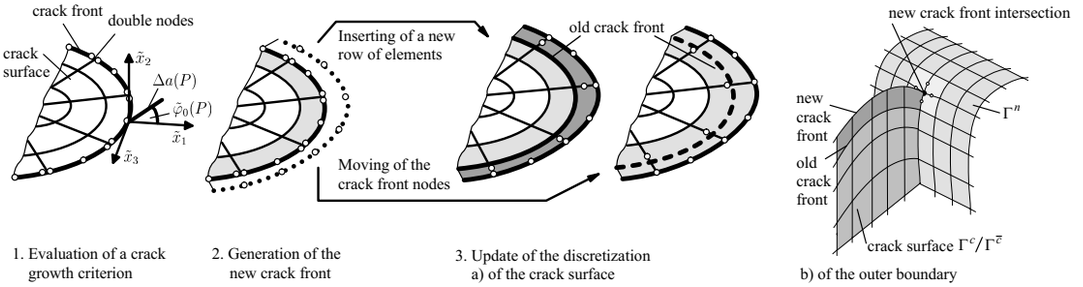


Figure 2. Basic principle of the crack growth algorithm

The kink angle is predicted by the MTS–criterion providing an angle of a differential crack extension as a function of K_{I} and K_{II}. Thus, the tangent to the deflecting crack path related to the current crack front is described. Depending on the finite incremental crack extension an error occurs. Therefore, the MTS–criterion is extended by including the T-stress T_{I} to correct the kink angle. Then, the kink angle additionally depends on T_{I} and on the finite crack extension. Moreover, this concept is expanded following the idea, that the crack growth angle is perpendicular to the maximum principal stress on an imaginary cylindrical sphere around the crack front [1]. It leads to a kink angle dependent on all three SIF's, even K_{III}. In this case, the introduction of all T-stresses leads to a kink angle which additionally depends on the Poisson's ratio and on the crack extension.

For the prediction of the crack extension a user–defined incremental length Δa_0 is specified. This length is assigned either to the maximum or average value of an appropriate fracture mechanics parameter (e.g. the energy release rate G) and is distributed linearly along the crack front. Alternatively, an exponential distribution based on the Paris Law is performed.

The shape of the crack front and therefore the resulting crack path depends on Δa_0. Thus, a corrector step is introduced to improve the shape of the crack front. It is assumed that the energy release rate controls the crack growth and the crack front will propagate in a way that G is constantly distributed along the crack front. Moreover, a valid square-root singularity is assumed along the whole crack front, especially in the vicinity of the crack front intersection with the free surface. This is ensured by an analysis of 3D corner singularities in this vicinity followed by an appropriate adjustment of the crack front angle.

Local re-meshing on Γ^n

During the update process of the discretization, the free surface must also be considered in case of surface breaking cracks. An automatic local re-meshing procedure incorporating the requirements – inserting the new crack front intersection at an arbitrary point and guaranteeing an optimal mesh quality – is designed. This procedure is based on the current discretization and consists of the steps: 1) identification of the local re-meshing patch, 2) triangulation, 3) insertion of the new crack front intersection, 4) optimization of the triangulation, 5) generation of quadrilateral elements and 6) smoothing of the new discretization.

Primarily, the local area in which the discretization needs to be optimized, has to be identified. This area (patch) is meshed generally with quadrilaterals and triangles. Therefore, a complete triangulation is performed to have a common basis for all forthcoming mesh modifications. Afterwards, the new crack increment will be inserted into the triangulation. As the triangulation is the basis for the final generation of quadrilaterals, the triangular mesh has to be optimized. Finally, the newly created quadrilaterals are smoothed.

NUMERICAL EXAMPLE

The efficiency and capability of the proposed procedure will be shown by a complex example. It is a three point bending specimen with a slanted crack. Due to the orientation of the initial crack a complex stress state including all fracture modes is caused. Consequently, the crack is twisting towards the center plane. The geometrical situation at the crack front intersection influencing the 3D singularities is changing permanently. Finally, the curved crack path is a real challenge concerning the re–meshing of Γ^n.

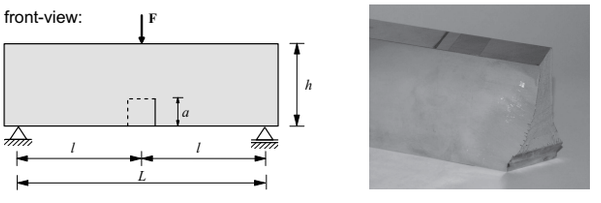


Figure 3. Three point bending specimen with a slanted crack

References

[1] Fulland, M., Schöllmann, M. and Richard, H.A., Simulation of fatigue crack propagation processes in arbitrary three-dimensional structures with the program system ADAPCRACK3D, *Advances in Fracture Research, Proceedings of the* 10^{th} *International Conference on Fracture*, Ravi-Chandar, K., Karihaloo, B.L., Kishi, T., Ritchie, R.O., Yokobori, A.T. and Yokobori, T. Eds, CD, ICF10, Honolulu, 2001.

[2] Kolk, K. and Kuhn, G., 3D crack growth simulation, *Solids, Structures and Coupled Problems in Engineering, Proceedings of the Second European Conference on Computational Mechanics*, Waszczyszyn, Z. and Pamin, J. Eds, CD, ECCM, Cracow, 2001.

[3] Partheymüller, P., Haas, M. and Kuhn, G., Comparison of the basic and the discontinuity formulation of the 3D-Dual boundary element method, *Eng. Anal. Boundary Elements*, 24, pp. 777-788, 2000.

XXI ICTAM, 15–21 August 2004, Warsaw, Poland

MASSIVELY PARALLEL SIMULATIONS OF DYNAMIC FRACTURE AND FRAGMENTATION OF BRITTLE SOLIDS

Irene Arias*, Jaroslaw Knap*, Anna Pandolfi**, Michael Ortiz*
*Graduate Aeronautical Laboratories, California Institute of Technology, Pasadena CA 91125, USA
**Dipartimento di Ingegneria Strutturale, Politecnico di Milano, 20133 Milano Italy

Summary Massively parallel finite element simulations of dynamic fracture and fragmentation of brittle solids are presented. Fracture is introduced by the adaptive insertion of cohesive elements. The model is validated against specially designed experiments and the crack branching instability is investigated. Mesh sensitivity issues are addressed through the renormalization of the cohesive law.

INTRODUCTION

We present the results of massively parallel numerical simulations of dynamic fracture and fragmentation in brittle solids. Our approach is based on the use of cohesive models to describe processes of separation leading to the formation of new free surface. Within the framework of the conventional finite element analysis, the cohesive fracture models are introduced through *cohesive elements* embedded in the bulk discretizations. These cohesive elements bridge nascent surfaces and govern their separation in accordance with a cohesive law [1]. In this work we assess the validity of the cohesive models and the computational algorithms. We present careful quantitative validation against experiments designed specifically for this purpose by A. J. Rosakis *et al*. Moreover, the branching instability is investigated numerically. Finally, in relation to the mesh dependency observed for under-resolved meshes, we explore the concept of renormalization of cohesive laws.

VALIDATION

Xu *et al*. [2] have experimentally investigated the deflection of dynamic mode I cracks at inclined interfaces. Using similar methodology, A. J. Rosakis *et al*. have recently designed a set of well-controlled experiments with the specific goal of testing the fidelity of cohesive fracture models under dynamic conditions. The details of the experimental and selected preliminary results are presented in Fig. 1.

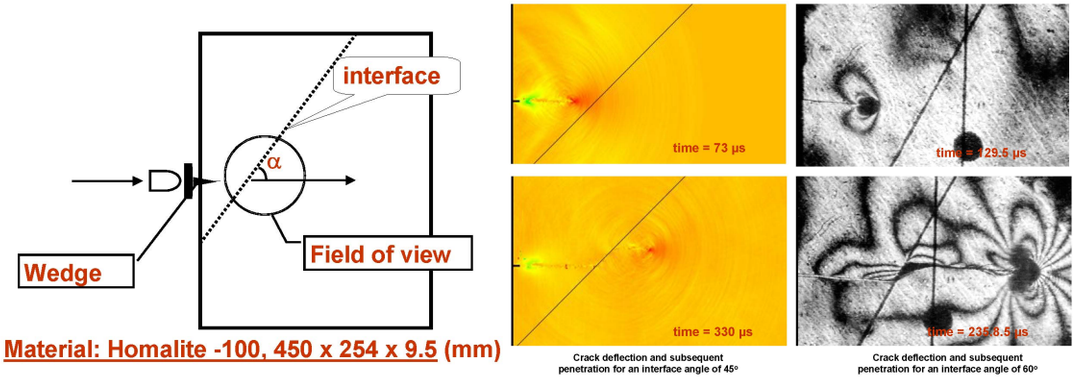


Figure 1. Sketch of the experimental set up (left): a pre-notched homalite plate with an inclined interface under a dynamic wedge-loading mechanism, and qualitative comparison of simulation and experiment (right).

BRANCHING INSTABILITY

Over the last decade, Fineberg and Sharon [3] have conducted a series of well-controlled experiments designed to investigate the dynamic crack propagation in brittle amorphous materials. They have observed that the experimental measurements are in good agreement with the classical continuum theory [4] for low crack velocities. However, the highest crack velocity, they have recorded, is considerably smaller than the predicted asymptotic value c_R, i. e., the Rayleigh wave speed of the material. Indeed, the crack behavior goes through a transition when the speed of the advancing crack exceeds the critical velocity $v_c \approx 0.4\ c_R$. Namely, beyond v_c, the main crack issues small microscopic side branches. This is a dynamic instability which has a pronounced effect on the structure of the fracture surface. Fineberg and Sharon [3] have made a number of important observations and suggested some universal features of the crack branching instability. We have performed 2D calculations in an attempt to simulate their experiments. A square pre-notched PMMA plate is subjected to an initial uniform strain rate in the vertical direction. Fig. 2 shows three snapshots of the fracture process, in which crack instability, followed by branching and fragmentation are well captured. The main features of the phenomenon pointed out by Fineberg and Sharon (onset of branching, branching patterns), are investigated.

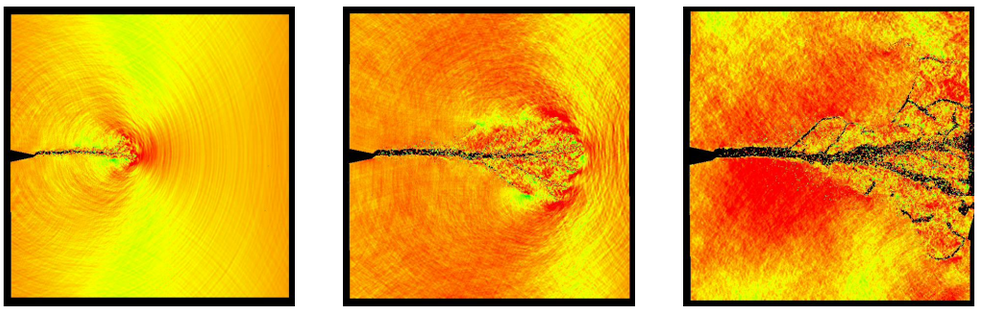


Figure 2. Snapshots (increasing times to the right) of the fracture process of a square pre-notched PMMA plate is subjected to an initial uniform strain rate in the vertical direction.

RENORMALIZATION

As previously noted, simulations concerned with materials possessing as small characteristic length scale may require a large number of elements in the finite element discretization. By way of example, simulations of the Rosakis *et al*. experiment may require as many as 50 million elements. This level of resolution is often prohibitively expensive even when advanced distributed computing environments are available. An alternative approach is to compensate for the lack of resolution by a suitable renormalization of the cohesive law. Specifically, we apply the scaling proposed by Nguyen and Ortiz [5], which relates the effective cohesive energy of a material layer to the interplanar potential under the assumption of nearest-neighbor interactions. A generalization of this renormalization which accounts for arbitrary interactions and surface relaxation has been proposed by Hayes *et al.* [6]. A rigorous mathematical proof of the universality of the renormalized cohesive law has been given by Braides *et al.* [7].

We assess the feasibility of this approach numerically in a double-cantilever-beam test configuration [4] and present preliminary results. Specifically, we endow the cohesive elements with a cohesive law scaled according to the mesh size. Thus, the cohesive strength scales as $1/\sqrt{h}$ and the critical opening displacement scales as $\sqrt{h}$, where h is the characteristic mesh size. The resulting renormalized cohesive law represents the effective behavior of a layer of material of thickness h, and has the property that the corresponding cohesive length is automatically resolved by the mesh. In addition, the fracture energy remains invariant under the renormalization. Fig. 3(a) shows the position of the crack tip as a function of time for several under-resolved meshes. The strong mesh sensitivity is apparent in this figure. However, the solutions for these meshes nearly collapse into one curve when renormalized cohesive laws are used, as shown in Fig. 3(b).

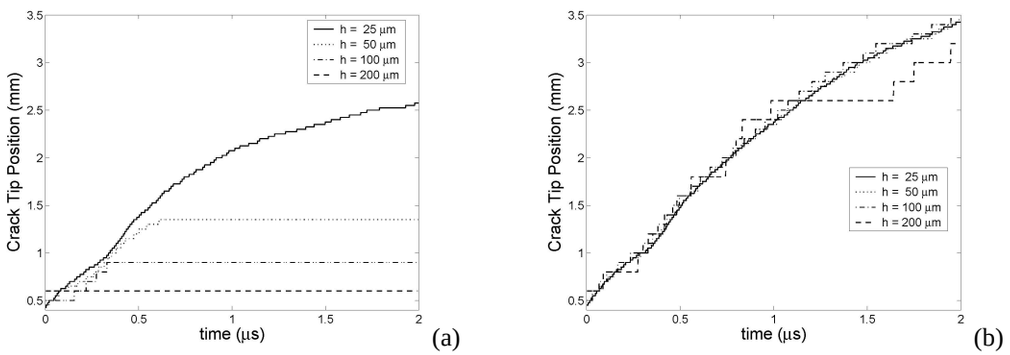


Figure 3. Double-cantilever beam test: solutions for under-resolved meshes with actual (a) and renormalized (b) cohesive parameters.

References

[1] Camacho G.T., Ortiz M.: Computational modeling of impact damage in brittle materials. *Int. J. Solids Struct.* **33**:2899–2938, 1996.

[2] Xu L.R., Huang Y.Y., Rosakis A.J.: Dynamic crack deflection and penetration at interfaces in homogeneous materials: experimental studies and model predictions. *J. Mech. Phys. Solids* **51**:461–486, 2003.

[3] Sharon E., Fineberg J.:Confirming the continuum theory of dynamic brittle fracture for fast cracks. *Nature* **397**:333–335, 1999.

[4] Freund L.B.: Dynamic Fracture Mechanics. Cambridge Univ. Press, NY 1990.

[5] Nguyen O., Ortiz M.: Coarse-Graining and Renormalization of Atomistic Binding Relations and Universal Macroscopic Cohesive Behavior. *J. Mech. Phys. Solids* **50**:1727–1741, 2002.

[6] Hayes R.L., Ortiz M., Carter E.A.: Universal Binding Energy Relation for Crystals, 2004 (submitted for publication).

[7] Braides A., Lew A. J., Ortiz M.: Effective cohesive behavior of layers of interatomic planes, 2004 (in preparation).

The shield effect of phase transformation stress field at crack tip

* Ping Wang [1] Zhengguo Tian [1] Zhiren Wang [1]
Lijuan Zheng [2] Xiangzhong Bai [2]

[1] School of Civil Engineering and Mechanics, Yanshan University, Qinhuangdao City, Hebei Province, China, Postcode 066004

[2] State Key Laboratory of Nonlinear Mechanics, Institute of Mechanics, Chinese Academy of Sciences, Beijing, 100086 China

* Presenter, Email: wangpin0721@vip.sina.com

1. Introduction

Metal always be used as main materials of advanced industry. Thus, fracture or crack propagation problem is difficult to avoid. If the problem could be solved, the metal equipment's service life would be extended and the disaster due to the brake of crack propagation could be prevented. From the above, we know the technique of crack arresting is strongly needed in practice.

Experimental observation presented that: heat concentration can be formed by electric current flowed around crack tip when the current direction is not parallel with crack direction in a current conductor and small welded joints also can be formed by the melting of metal as a result of heat concentration effect at crack tip. It can be observed that the structure around the crack tip has been refined; means the phase transformation has been occurred. Around the crack tip, a white-bright layer is formed after discharging. It is the new phase transformation structure to prevent the crack propagation. The technique of arresting crack propagation by electromagnetic heat effect could be used in practice someday.

2. Compressive stress field of phase transformation at crack tip

The thermal compressive stresses around crack tip increase instantly in a very short time. It is the thermal compressive stress to help preventing the crack propagation at the moment of discharging. After cooling, a white-bright layer around will be formed, and high compressive stresses field of phase transformation will be there to prevent crack propagation.

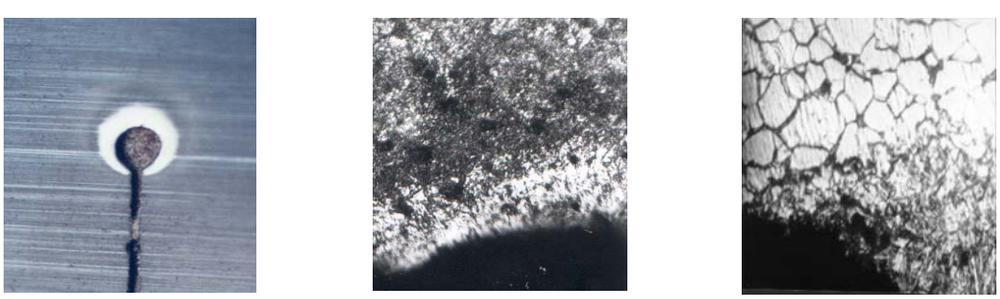


Fig1. White-bright layer macroscopical appearance and microstructure around crack tip

3. Measurement of phase transformation volume expansion

The measurement of phase transformation volume expansion is done by using equipment made in the US.



Fig2. The specimen and the state around crack tip after discharging

4. Mechanical Property Test Under Nanometer Scale by SPM

The mechanical properties tests under nanometer scale have finished by using SPM (Scanning Probe Microscopy). The conclusion shows that the micro-hardness and Young's modulus under nanometer scale have been promoted greatly after discharging. This test provided the experimental supporting of the technique of arresting crack propagation by pulse current discharging in engineering application.

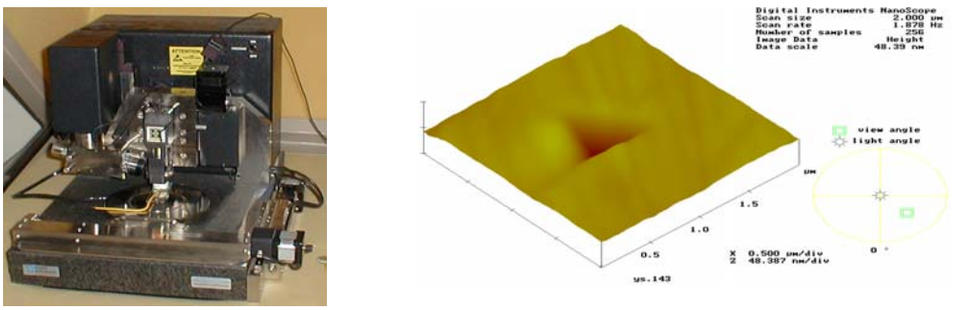


Fig3. The equipment of SPM and the pressure mark

5. Calculation and analysis of the shield effect of the compressive stress field

The following phenomena can be observed at the crack tip: heat concentrate effect, area of melting and tiny welded joints, the sharp crack tip turning into a blunt ball shape, and the radius of curvature increasing instantly etc. The microstructure around the crack tip after discharging is shown in Fig.2. It is clear that the structure around the crack tip is obviously refined, the content of pearlite is greatly increased, and lathy martensite also appears. The material of the white-bright layer is made up of super fine martensite and carbon particles. It is the new phase transformation structure to prevent the crack propagation.

6. Conclusion

After stop crack propagation by using electromagnetic effect, the microstructure around the crack tip is refined. The white-bright layer is the fundamental reason to stop crack propagation. It is the new phase transformation structure to prevent the crack propagation. All these provide the references for engineering practice.

References

[1]Finkelj. V. M, Golovin Iu. I, Sletkov A. A. Destroy The Crack Tip Using A strong Electromagnetic Field, Reports of Academy of Sciences, CCCP, 1977

[2] Xiangzhong Bai. Theory and Application of Magnetic-Elasticity and Thermo-Magnetic-Elasticity, Chinese J. Advanced Mech. 1996. Vol. 26. No. 3:389-406

[3] Xiangzhong Bai, etc. Development of Stopping Crack Propagation By Using Electromagnetic Heat Effect, Chinese J. Advanced Mech. 2000, Vol. 30. No. 4: 546-557

[4] Xiangzhong Bai, etc. Experimental Research on Stopping Crack Propagation By Using Electromagnetic Heat Effect. Chinese J. Experimental Mechanics, 2000, Vol. 15. No. 3:354-360

CONTACT ZONE APPROACH TO THE ANALYSIS OF INTERFACE CRACKS IN THERMOMECHANICALLY LOADED PIEZOELECTRIC BIMATERIALS

Klaus P. Herrmann[*], Volodymyr V. Loboda[**]
[*] Dept.of Mechanical Engineering, LTM, Paderborn University,
Pohlweg 47-49, D-33098 Paderborn, Germany
[**] Dept. of Theoretical and Appl. Mech., National University,
Nauchny Str. 13, Dniepropetrovsk 49050, Ukraine

Summary An interface crack with a mechanically frictionless contact zone in a piezoelectric bimaterial under the action of a remote mixed mode mechanical loading as well as of thermal and electrical fields is considered. Electrically permeable and electrically insulated conditions at the open part of the crack are taken into consideration. The influence of the mechanical loading as well as of the thermal and electrical fluxes upon the electromechanical values is studied.

The interface crack investigation in a piezoelectric bimaterial, because of its importance, attracts an essential attention during the last years. The most investigations on this subject are performed by means of the "open" crack model possessing an oscillating singularity at the crack tips (Shen and Kuang [1], Gao and Wang [2]). Only in the paper by Qin and Mai [3] a thermopiezoelectric bimaterial with an electrically impermeable interface crack under the assumption of a contact zone model has been investigated by means of the method of singular integral equations, and moreover, electro-mechanically loaded electrically permeable and impermeable interface cracks having a contact zone in a piezoelectric bimaterial have been analytically studied by Herrmann and Loboda [4] and Herrmann et al. [5], respectively.

But the problem of the correct choose of the electrical conditions at the interface crack faces remains still insufficiently clear, and therefore, many investigations are concerned with an electrically permeable interface crack whilst in another group of investigations an electrically impermeable interface crack is considered.

In this study due to an exact analytical investigation of an interface crack with a contact zone in a piezoelectric bimaterial space the influence of the mechanical, thermal and electrical fields upon the fracture mechanical characteristics is analyzed for different electrical conditions at the crack faces.

Consider a crack situated in the region $c \le x_1 \le b$, $x_3=0$ between two semi-infinite spaces ($x_3 > 0$, material 1 and $x_3 < 0$, material 2) which are loaded at infinity with uniform stresses $\sigma_{33}^{(m)} = \sigma$, $\sigma_{13}^{(m)} = \tau$ and $\sigma_{11}^{(m)} = \sigma_{xm}^{\infty}$ as well as with uniform electric fluxes $D_3^{(m)} = d$, $D_1^{(m)} = D_{xm}^{\infty}$ satisfying the continuity conditions at the interface. Besides, a uniform temperature flux q_0 in the x_3-direction is imposed at infinity. It is assumed that the crack surfaces are traction-free for $x_1 \in (c,a)$ whilst they are in frictionless contact for $x_1 \in (a,b)$, and the position of the point $a<b$ is arbitrarily chosen for the time being. It means that the interface conditions for the thermally perturbed state have the following form

$$x_1 \notin (c,b):,\ [\mathbf{V}(x_1,0)] = 0, [\mathbf{t}(x_1,0)] = 0, \tag{1}$$

$$x_1 \in (c,a):\ q_3^{\pm} = -q_0,\ \sigma_{13}^{(m)}(x_1,0) = 0, \sigma_{33}^{(m)}(x_1,0) = 0,\ [D_3(x_1,0)] = 0,\ [\varphi(x_1,0)] = 0 \tag{2}$$

-for an electrically permeable crack,

$$q_3^{\pm} = -q_0,\ \mathbf{t}^{(m)}(x_1,0) = 0 \text{ - for an electrically impermeable crack,} \tag{3}$$

$$x_1 \in (a,b):\ [T] = 0,\quad [q_3] = 0,\ [u_3(x_1,0)] = 0,\ \sigma_{13}^{(m)}(x_1,0) = 0, [\sigma_{33}(x_1,0)] = 0,$$
$$[D_3(x_1,0)] = 0,\ [\varphi(x_1,0)] = 0. \tag{4}$$

where $[\mathbf{V}'(x_1,0)] = \mathbf{V}'^{(1)}(x_1,0) - \mathbf{V}'^{(2)}(x_1,0)$, $\mathbf{V} = [u_1, u_2, u_3, \varphi]^T$, $\mathbf{t} = [\sigma_{13}, \sigma_{23}, \sigma_{33}, D_3]^T$.

Assuming all fields are independent on the coordinate x_2 for the solution of the formulated problem the expressions of the temperature jump $[T(x_1)]$ across the material interface, the temperature flux q_3 as well as the vectors $[\mathbf{V}']$ and $\boldsymbol{t}$ via the sectionally-holomorphic functions are constructed similarly to the presentations of Shen and Kuang [1]. Due to these presentations the thermal problem can be reduced to a relatively simple Hilbert problem and solved exactly both for an electrically permeable and an electrically impermeable interface crack. Moreover, the satisfaction of the electromechanical boundary conditions (1)-(4) leads for an electrically permeable interface crack to the following inhomogeneous combined Dirichlet-Riemann problem for a sectionally-holomorphic function *F(z)*

$$F^+(x_1) + \gamma F^-(x_1) = \Psi_1(x_1) \quad for \quad x_1 \in (c,a) \tag{5}$$

$$\mathrm{Im}\, F^{\pm}(x_1) = \Psi_2(x_1) \quad for \quad x_1 \in (a,b), \tag{6}$$

where the functions $\Psi_1(x_1)$ and $\Psi_2(x_1)$ are defined by the thermal solution obtained above. It is important that the solution of the problem of the linear relationship (5), (6) has been presented in a closed form similarly to those given by Herrmann and Loboda [6].

For an electrically impermeable interface crack a Hilbert problem appears in addition to the problem (5), (6), but nevertheless the analytical solutions of all obtained problems are found and all necessary thermal, mechanical and electrical characteristics at the interface are presented in a closed form. Moreover, the closed analytical formulas for the stress intensity factors (SIFs)

$$k_1 = \lim_{x_1 \to a+0} \sqrt{2\pi(x_1 - a)}\,\sigma_{33}^{(1)}(x_1,0),\quad k_2 = \lim_{x_1 \to b+0} \sqrt{2\pi(x_1 - b)}\,\sigma_{13}^{(1)}(x_1,0)$$

as well as the electrical displacement intensity factor $k_4 = \lim_{x_1 \to a+0} \sqrt{2\pi(x_1 - a)}\,D_3^{(1)}(x_1,0)$ have been obtained for an arbitrary value of the relative contact zone length $\lambda = \dfrac{b-a}{b-c}$.

Further, the real contact zone length could be obtained. For this purpose additional conditions $\sigma_{33}^{(1)}(x_1,0) \le 0$ *for* $x_1 \in (a,b)$, $[u_3(x,0)] \ge 0$ *for* $x_1 \in (c,a)$ should be satisfied. For an electrically permeable crack the satisfaction of these inequalities gives a transcendental equation with respect to the relative contact zone length λ. The largest root λ_0 of this equation from the interval (0, 1) defines the required real contact zone length. This root can be found numerically, but for a small λ_0 an analytical formula has been obtained as well.

The numerical results were obtained for a bimaterial composed of piezoelectric Cadmium Selenium (Ashida and Taushert [7]) (the upper material) and glass (the lower one). The variation of the relative contact zone length λ_0 and the correspondent SIF k_2 with respect to the intensity of the thermal flux q_0 and the coefficients of the normal-shear loading $k = \tau/\sigma$ are studied. It is worth to note that for an electrically permeable interface crack neither the contact zone length nor the intensity factors depend on the intensity of the electrical flux *d*.

A more complicated situation concerning the determination of the real contact zone length takes place for an electrically impermeable interface crack. In this case the inequalities mentioned above hold true if *a* is taken from the segment $[a_1, a_2]$ providing $a_1 \le a_2$ holds true, where $a = b - \lambda l$, $a_1 = b - \lambda_1 l$, $a_2 = b - \lambda_2 l$ and λ_1 is the maximum root from the interval (0,1) of the equation $k_1 = 0$ and λ_2 is the similar root of the equation $\lim_{x_1 \to a-0} \sqrt{a - x_1}\,[u_3'(x_1,0)] = 0$. The required roots of the mentioned equations can be found numerically or analytically (for small λ_1 and λ_2, respectively), and the segment $[a_1, a_2]$ can be obtained. An additional analysis based upon the theorem of the minimum potential energy shows that the real position of the point *a* coincides with a_1 providing $a_1 \le a_2$ holds true. If the last inequality is not valid then the inequalities from above cannot be satisfied and other thermal and electrical interface conditions should be introduced.

The numerical analysis showed that for the electrical flux *d=0* the contact zone lengths correspondent to an electrically insulated or an electrically permeable crack are practically the same. However, a nonzero electrical flux changes the real contact zone length and the associated fracture mechanical parameters for an electrically impermeable interface crack. The essential dependencies of these values on *d* appear for rather large intensities of the electrical flux only. This is particularly demonstrated by the Table 1 where the values of the relative contact zone length λ_1 are shown with respect to the intensity of the electrical flux $d^* = c_{33}^{(1)} d / (e_{33}^{(1)} \sigma)$ for $q_0=0$, k=0 and for the same bimaterial as earlier.

Table 1

d^*	10^3	10^4	2×10^4
λ_1	6.38×10^{-13}	6.62×10^{-4}	*0.0177*

References

[1] Shen S, Kuang Z.B. Interface crack in bi-piezothermoelastic media and the interaction with a point heat source. *Int. J. Solids Structures* **35**: 3899-3915, 1998.

[2] Gao C.F., Wang M.Z. A permeable interface crack between dissimilar thermopiezoelectric media. *Acta Mechanica* **149**: 85-95, 2001.

[3] Qin Q.H., Mai Y.W. A closed crack tip model for interface cracks in thermopiezoelectric materials. *Int. J. Solids Structures* 36: 2463-2479, 1999.

[4] Herrmann K.P., Loboda V.V. Fracture mechanical assessment of electrically permeable interface cracks in piezoelectric bimaterials by consideration of various contact zone models. *Arch. Appl. Mech.* **70**: 127-143, 2000.

[5] Herrmann K.P., Loboda V.V., Govorukha V.B. On contact zone models for an electrically impermeable interface crack in a piezoelectric bimaterial. *Int. J. Fract.* **111**: 203-227, 2001.

[6] Herrmann K.P., Loboda V.V. Contact zone models for an interface crack in a thermomechanically loaded anisotropic bimaterial. *J. Thermal Stresses.* **24:** 479-506, 2001.

[7] Ashida F., Tauchert T.R. Temperature determination for a contacting body based on an inverse piezothermoelastic problem. *Int. J. Solids Structures* **34**: 2549-2561, 1997.

INTERACTION OF PROPAGTING CRACKS AND SHEAR WAVES

Daniel Bonamy* and Krishnaswamy Ravi-Chandar**
* *Commissariat l'Energie Atomique DSM/DRECAM/SPCSI, Centre de Saclay, 91191 Gif sur Yvette Cedex, France*
** *Department of Aerospace Eng and Engineering Mechanics, University of Texas, Austin, TX 78712-0235, USA*

Summary: Shear waves generated from an ultrasonic transducer are used to twist dynamically growing crack fronts; the response of crack front to such external perturbations is examined in order to investigate the primary cause of surface roughening in brittle materials. The response to random perturbations, introduced by localized material inhomogeneities at the free surface, is also discussed.

INTRODUCTION

Fluctuations in the crack tip structure should result in the release of elastic waves that propagate both into the bulk as well as along the surface. Ramanathan and Fisher (1997), and Morrisey and Rice (1998) examined such wave interactions in a series of increasingly sophisticated models. The possibility that in-plane and out-of-plane perturbations could persist along the crack surface, resulting in new kind of waves - crack front waves and corrugation waves - was discovered by these authors. Such waves were suggested to be the possible sources of crack surface roughening, even in brittle materials. Sharon *et al*., (2001) generated dynamically growing cracks in soda lime glass plate specimens; perturbations were introduced by scribing one face of the plate with a 100 - 1000 μm deep groove. Post-mortem examination of the crack surface indicated surface undulations that emanated from the location of the crack front perturbation, traveled across the width of the specimen, reflected off the opposite specimen surface and bounced back and forth for a distance many times the width of the perturbation. Based on their observations, Sharon *et al*., (2001) suggested that such undulations were indeed evidence of crack front waves. Here we report on an experimental investigation aimed at examining the interaction between propagating cracks and shear waves (Bonamy and Ravi-Chandar, 2003a, b).

CRACK RESPONSE TO A LOCALIZED MODE III PERTURBATION

Soda-lime glass is chosen as representative of brittle materials. Parallelipedic specimen of size 51 x 51 x 13 mm in the x (propagation), y (loading) and z (sample thickness) are loaded in mode I by pushing a triangular wedge into a cut out on one of the two 51 x 13 mm (y-z) surfaces. An initial seed crack (5-10 mm long) is introduced at the tip of the wedge cut. The precise value of the crack speed is measured during the experiment using the potential drop technique. Three different transducers (0.5 MHz, 5 MHz and 20 MHz) are used to generate a short pulse (2.0 μs, 0.2 μs and 0.05 μs) of a plane shear wave. The speed C_s and decay rate of shear waves in our specimen were measured to be 3444 m/s and 0.1 dB/mm respectively. The wavelengths λ of the induced disturbances are thus expected to be 6.9 mm, 690 μm and 172 μm respectively. The location of the point where this pulse interacts with the crack can be timed precisely by a trigger signal generated when the crack cuts through a thin conducting line ahead of the seed crack.

The transducer is oriented such that the pulse polarized in the y-direction propagates in the z-direction. The interaction of this shear wave with the crack growing along the x direction in the x-z plane, perturbs the crack front and generates tracks running along the crack surface that are readily visible to the unaided eye. These tracks are rendered visible when photographed in a shadowgraphic arrangement – a slight defocusing of the specimen enables better visualization (Fig. 1). The interaction between the shear wave and the crack front is observed to persist for quite a long time, and to continue upon sequential reflections of the shear wave from the opposite sides of the specimen. The profile of the surface perturbations is measured in an interference microscope. From these measurements, it was apparent that along the trace of the interaction of the shear wave with the crack front the crack surface undulates out of the x-z plane. From measurements of the peak amplitude as a function of the distance traveled by the shear wave, it was seen that the amplitude decay matched the 0.1 dB/mm decay rate of the shear wave. Qualitatively similar features were observed in repeated experiments with ultrasonic modulation at 0.5 MHz and 20 MHz. These results indicate that the amplitude and wavelength of the surface undulation depend on the perturbing shear wave as well as the crack speed.

The spatio-temporal domain over which the shear wave and the crack front interact is indicated schematically in Fig. 2a. Consider the crack propagating along the x direction at a constant speed v; in the thick specimens used in our experiments, the crack front is usually curved - typically of parabolic shape - and at any point the front makes an angle θ with respect to the propagation direction as indicated in the figure. The line of the common space-time interaction between the crack tip and the shear wave is indicated by the dark line in Fig. 2a. From Fig. 2b it can be recognized that the perturbation provided by the ultrasonic shear wave generates a mode III loading on the crack. In response, the crack front twists about the x axis with a corresponding warping of the crack surface. This twist in the crack front is carried along the moving crack front by the shear wave. Thus, the crack plane does not tilt about the z axis to produce the undulation as one might have guessed from post-mortem examination of the fracture surface, but does a twist about the x axis. The wavelength of the crack surface perturbation can now be related quantitatively to the wavelength of the shear wave. In the time $\tau = \lambda/C_s$, the shear wave travels through a length λ in the z direction and the crack moves through a length

$\lambda v/C_s$ in the x direction. From Fig. 2a it is clear that the shear wave interacts with the crack front over a length $\lambda_{cf} = \lambda [\sec\theta + v/C_s]$. When the undulation is measured along the x-direction the corresponding wavelength is $\lambda_x = \lambda v/C_s$. The measured undulation wavelengths λ_x of the crack surface for (f = 5 MHz, v = 480 m/s), f = 5 MHz, v = 867 m/s) and f = 20 MHz, v = 895 m/s) are 76 μm, 176 μm and 57 μm respectively, in agreement with the theoretical values 96 μm, 174 μm, and 45 μm obtained from the preceding equation. It is worth to mention that these tracks are similar to the ones observed by Wallner, (1939) on fracture surfaces of glass *without any external source of shear waves*, and identified by him as interactions of the crack front with shear disturbances generated by random sources on the glass specimen.

DISCUSSION

The experiments reported in this paper explore the interaction of shear waves with propagating crack fronts and evaluate the persistence of crack front perturbations. Three main conclusions are evident: (i) shear waves introduced from the plate surfaces induce a mode III loading on the crack front, and in response the crack front twists; (ii) the interaction is linear, with the amplitude, frequency, and decay of the crack surface perturbations matching the underlying shear wave that transmits the perturbations to the crack front, and (iii) there is no persistence of the perturbations on the crack front. These conclusions enable a discussion of crack front waves and surface roughening. The similarities between the perturbations driven by the plane shear waves and the perturbations generated by a scratched groove suggest that surface undulation markings found on fracture surfaces are indeed Wallner lines and not crack front waves. In contrast to the observations of Sharon et al., (2001), we find that the surface undulations continue to decay to levels that are below the limit of measurement resolution 10 nm. The lack of persistence of the surface undulations when the shear wave is removed from the crack plane suggests that if crack front waves were to exist, they are below the threshold of measurability; such small undulations cannot lead to roughening. We must point out, however, that there remains the question of large amplitude perturbations. In all of our experiments, crack growth was driven primarily by an opening mode loading introduced by the wedge and the ultrasonic waves merely provided a small amplitude perturbation. Sommer's experiments (1969) make it clear that under larger mode III perturbations, the crack front must fragment. The physical origin and the length and time scales of such fragmentation still require careful study.

D. Bonamy and K. Ravi-Chandar, (2003a), *Phy Rev. Lett.*, **91**, 235502.
D. Bonamy and K. Ravi-Chandar, (2003b), *Int. J Fracture*, submitted 2003.
J.W. Morrissey and J.R. Rice, (1998), *J. Mech. Phys. Solids,* **46**, 467.
S. Ramanathan and D.S. Fisher, (1997), *Phys. Rev. Lett*. **79**, 877.
K. Ravi-Chandar and W. G. Knauss, (1984), *Int. J. Fracture*, **25**, 141; **25**, 247; **26**, 65; **26**, 189.
J.R. Rice Y. Ben Zion and K.S. Kim, (1994), *J. Mech. Phys. Solids*, **42**, 813.
E. Sharon, G. Cohen and J. Fineberg, (2001), *Nature*, **410**, 68.
E. Sommer, (1969), *Eng. Fracture. Mech*., **1**, 539.
H. Wallner, (1939), *Z. Physik,* **114**, 368.

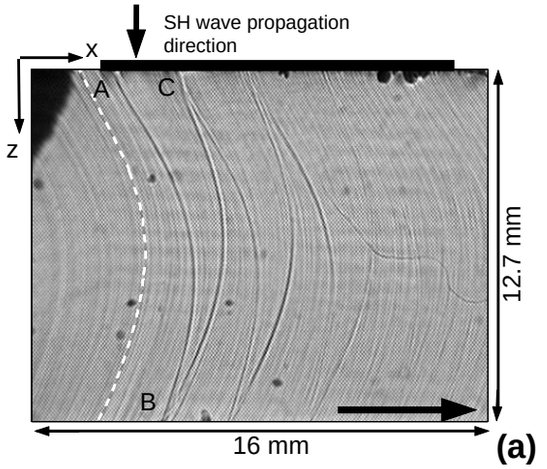


Figure 1. Shadowgraph of the fracture surface in glass indicating the line of interaction between the crack propagating from left and right (f = 5 MHz, v = 480 m/s) and the shear wave propagating in the z direction. The dashed white line indicates the instantaneous crack front. The continuous line from A to B to C represents the interaction between the shear wave and the crack front.

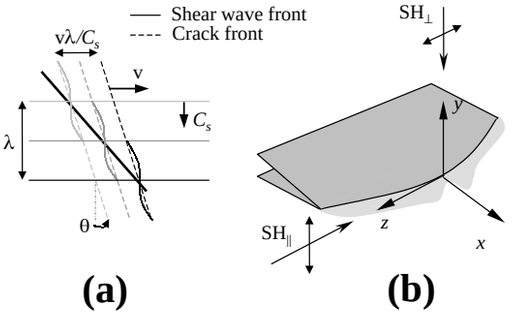


Figure 2. (a): Sketch of the interaction of the shear wave and the crack front at three successive time steps. (b): Schematic diagram of the interaction of shear waves with crack fronts.

Paper 12393

DISORDER OF THE FRONT OF A TENSILE TUNNEL-CRACK PROPAGATING IN SOME INHOMOGENEOUS MEDIUM

Jean-Baptiste Leblond

**Laboratoire de Modélisation en Mécanique,
Université Pierre et Marie Curie, Paris, France**

A number of theoretical, numerical and experimental works have recently been devoted to the study of geometrical disorder of the front of planar cracks propagating in inhomogeneous solids, with applications to propagation of cracks in composites, and geological faults during earthquakes. Prominent contributions in this field are notably due to Rice and coworkers, who considered the case of a semi-infinite crack propagating dynamically in an infinite brittle material with random toughness. They showed that the "degree of disorder" of the crack front, as measured by the autocorrelation function of the distance from the actual front to some "reference" straight front, increases in time without bound.

No characteristic lengthscale was included in the geometry considered by Rice and coworkers. The aim of this paper is to introduce this feature in such theoretical studies. This is done by considering the simplest model crack geometry involving some characteristic length, namely some tunnel-crack of finite width in some infinite medium.

Although the geometry considered is still very simple, the problem becomes notably more involved and it reveals impossible to treat it with the same hypotheses as Rice and coworkers; simplifications are compulsory. These simplifications are two-fold : dynamic effects are disregarded and the Griffith crack propagation law, appropriate for brittle solids, is replaced by some Paris law. This law involves 2 material parameters, some constant C and some exponent N ; it is adequate for fatigue or subcritical crack growth and "simulates" Griffith's law in some sense in the limit of very large Paris exponent N . Also, to simplify the treatment, it is assumed that the crack is loaded in pure mode I, that its front remains symmetrical with respect to its middle line at all instants, and that the sole Paris constant C fluctuates within the material, the exponent N being uniform.

The treatment uses a first-order perturbative approach which assumes that the perturbation $\delta a(z)$, that is the local distance (at position z) from the actual crack front to some "reference" straight front, remains small as compared to the mean half-width a of the crack at all instants. A formula providing the variation of the stress intensity factor along the crack front in terms of its perturbation $\delta a(z)$ was derived a few years ago by Leblond, Mouchrif and Perrin. Using this formula, a Fourier transform of the perturbation in the direction z of the crack front, and the propagation law, one derives evolution equations for all Fourier components of the perturbation. Since the analysis is performed within a linearized context, the evolutions of the various Fourier

components are found to be independent of each other. The evolution equations can be integrated in time explicitly so as to yield the expression of each Fourier component at any instant in terms of its initial value, thus opening the way to study of the development of geometrical disorder of the front.

This disorder is evaluated via the autocorrelation function of the perturbation $\delta a(z)$. This autocorrelation function can be expressed, at all instants, in terms of the autocorrelation function of the Paris constant C. The formula obtained allows for study of the asymptotic expression, for large times, of various quantities related to the autocorrelation function (power spectrum of the perturbation, root mean square deviation of the front from a straight line, etc.).

It is found that the disorder of the front increases without bound for large times, at a considerable rate; for instance, the root mean square deviation from a straight line increases proportionally to $(a/a_0)^{(N-1)/2}$ where a_0 denotes the initial value of the mean half-width a of the crack. However, this conclusion is mitigated by the fact that the "correlation distance" of the crack front, that is the characteristic distance over which the advance at some point "influences" the advance at other points, also increases, proportionally to a. This suggests that the crack front tends to "straighten" in time in some sense.

The growth rate of disorder found in this work is much larger than that found by Rice and coworkers. This is necessarily due to one of the differences between the hypotheses adopted in their works and here, namely consideration, in the present work, of a crack with finite width, neglect of dynamic effects, and use of Paris's propagation law instead of Griffith's. But it can be shown that the last 2 differences can only generate a lower growth rate of disorder in the present work. Therefore the higher growth rate actually found can only arise from the first difference, that is existence of some characteristic length in the problem envisaged here.

The "destabilizing" effect of the finite geometry considered can be qualitatively explained as follows. The theoretical analysis reveals that perturbations with wavelength greater than some critical value grow in time, whereas those with wavelength smaller than it decay; the "critical wavelength" is proportional to the mean half-width of the crack. Thus the finite crack geometry envisaged is intrinsically "unstable" versus perturbations of large wavelength. This effect disappears for a semi-infinite crack, because the critical wavelength is infinite for such a geometry, so that perturbations of all wavelengths decay.

Although dynamic effects could not be included for technical reasons in the present work, it seems reasonable to infer from it that existence of some characteristic length should also enhance the growth rate of disorder of the front of a crack propagating dynamically. The implication for the study of propagation of geological faults during earthquakes is that it would be highly desirable to consider finite cracks rather than semi-infinite ones in future studies, in spite of the technical difficulties implied.

CREEP DEFORMATION IN THERMAL BARRIER COATINGS DUE TO THE EFFECT OF THERMAL GROWTH OXIDATION AND TEMPERATURE GRADIENT

Y. C. Zhou, D. Wu
Institute of Fundamental Mechanics and Materials Engineering, Xiangtan University,Hunan, 411105, China

Summary In the paper, the creep deformation in thermal barrier coatings due to the effect of thermal growth oxidation and temperature gradient were theoretically and experimentally studied. In the theoretical investigation, the residual stress in the thermal barrier coating were analytically obtained for a plane rectangle sample. It was found that the temperature gradient and TGO have great effect on the residual stress. In the experiment, the samples were heated in high temperature furnace at different temperature and with different time. The oxidized and non-oxidized samples were again heated by a laser beam and in this case there was a high temperature gradient along the thickness direction of TBCs. It was found that the failure modes would be surface crack or interface crack for different thickness TGO and different temperature gradient. The experimental results were good agreement with the theoretical results.

INRODUCTION

Thermal barrier coatings (TBCs) have been utilized in order to increase the turbine inlet temperature and hence increase the efficiency of turbine engines. A TBCs system consists typically of an oxidation-resistant metallic bond coat on a superalloy substrate and a heat-insulating ceramic top coat attached on the bond coat. An yttria-stabilised zirconia (6-8wt.% Y_2O_3 stabilized ZrO_2) is usually employed as the top material. Due to the fact that the TBCs system was working at high temperature, a thermal growth oxidation(TGO) would form at the interface of top ceramic coating and bond coat and the deformation of the TBCs system would be creep. The creep deformation and TGO, especially their nonlinear effect would induce the failure of the TBCs. In the paper, the creep deformation in thermal barrier coatings due to the effect of thermal growth oxidation and temperature gradient were theoretically and experimentally studied.

THEORETICAL MODEL

In the theoretical investigation, the stresses fields in the thermal barrier coating due to the effect of creep deformation and thermal growth oxidation at the condition of temperature gradient along the thickness direction of TBCs were first studied for a plane rectangle sample as shown in Fig.1. The histories of temperature cycles in thermal barrier ceramic coatings system is sketched Fig.2. T_1 and T_0 are the steady state heating temperature and room temperature in the coating. The deformation of ceramic coating, bond coat and substrate are regarded as creep and that of TGO is regarded as elastic.

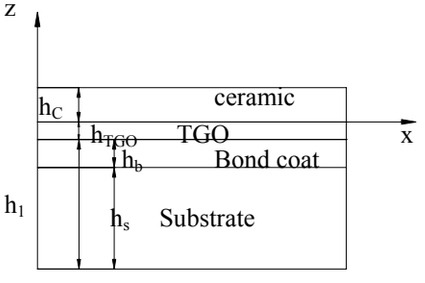


Fig.1 Crossing-section of thermal barrier ceramic coating system

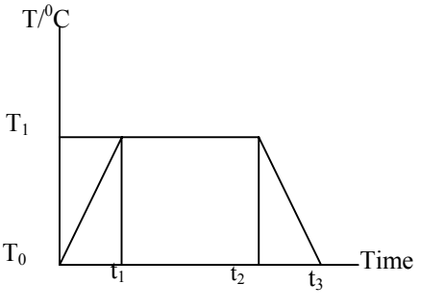


Fig.2 The histories of temperature in the TBCs

The temperature histories and temperature gradient along coating thickness direction could be expressed as in the following,

$$T(z,t)=\begin{cases}\dfrac{T_1(z)-T_0}{t_1}\times t+T_0 & (0\le t\le t_1)\\ T_1(z) & (t_1\le t\le t_2)\\ T_1(z)-\dfrac{T_1(z)-T_0}{t_3-t_2}\times(t-t_2) & (t_2\le t\le t_3)\end{cases} \qquad T_1(z)=\begin{cases}\dfrac{T_s-T_i}{h_c}\times(z-h_1)+T_i & 0\le z\le h_c\\ T_i & -h_1-h_{TGO}\le z\le 0\end{cases} \tag{1}$$

The residual stress in the thermal barrier coating at the end of every cycle were analytically obtained as,

$$\sigma_c^{residual}=\sigma_c(z,t)+\sigma_c^{elastic}(z,t) \tag{2}$$

In the above expression, the first one on the right side is due to the contribution of thermal stress at the end of loading, the second one is the contribution of the elastic unloading.

Fig.3 illustrates the characterization of stress as a function of interface temperature, surface temperature and position. Above the curved surface, the thermal stress in ceramic was compressive, while below the curved surface, the stress

was tensile. The numerical results for thermal stresses and residual stresses illustrated that the temperature gradient and TGO have great effect on the residual stress. In some cases, the residual stresses in ceramic coating are compressive, but in other cases the residual stress are tensile. As we know, the failure mode is very different for different residual stresses. For compressive residual stresses, the ceramic coating would fail due to the buckling of the ceramic coating, however, for tensile residual stresses, the ceramic coating would fail due to the surface crack in the ceramic coating. In the paper, we obtained the failure map in the general space of ceramic surface temperature, the substrate surface temperature and heating time.

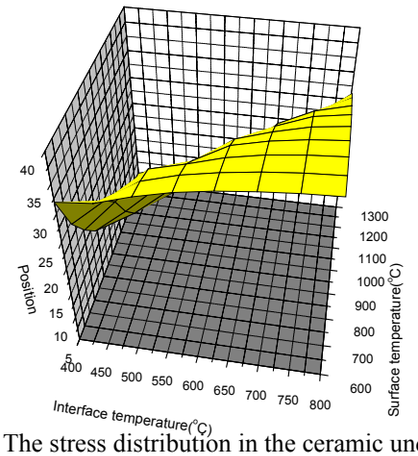


Fig.3 The stress distribution in the ceramic under different temperature gradient.

EXPERIMENT

In the experiment, the samples were heated in high temperature furnace at different temperature and with different time. In this case, the uniform high temperature in TBCs induced the formation of thermal growth oxidation at the interface of top ceramic coating and bond coat and the thickness was measured by two methods, such as scanning electron microscopy (SEM), impedance spectroscopy. The oxidized and non-oxidized samples were again heated by a laser beam and in this case there was a high temperature gradient along the thickness direction of TBCs and the schematic of the experimental setup for CO_2 laser heating method is shown in Fig.4.

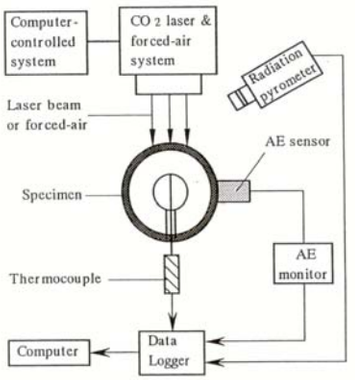


Fig.4 Schematic of the experimental setup for CO_2 laser heating method

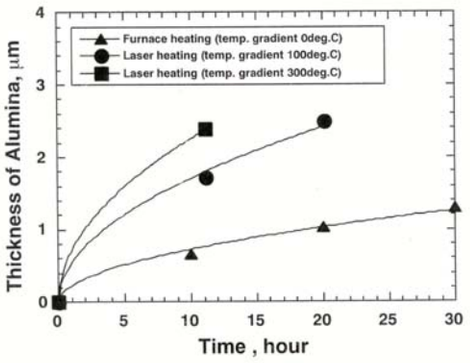


Fig.5 The effect of temperature gradient on the thickness of thermal growth oxidation, i.e., alumina

The effect of temperature gradient on the thickness of thermal growth oxidation, i.e., alumina is shown in Fig.5, where the temperature at interface was same. As the result, in spite of equal YSZ/NCrAlY interface temperature between the non-uniform heated specimen and uniform heated one, the alumina thickness are markedly different. The alumina is thicker for non-uniform heated case than that for uniform heated case. Namely, larger temperature gradient forms thicker alumina than smaller temperature gradient. The reason of the phenomenon is that the diffusion of oxygen through the YSZ accelerates in order to being high temperature concerning YSZ surface in case of laser heating as local heat. Moreover, due to the fact that the laser heated specimen has many porosity accompanied by formation of microcracks by virtue of larger thermal stress, oxygen rapidly penetrates interface through microcracks. Accordingly, laser heating which has temperature gradient is more effective condition to evaluate oxidation behavior of real plants. In our experiment, it was also found that the failure modes would be surface crack or interface crack for different thickness TGO and different temperature gradient. The experimental results were good agreement with the theoretical results.

References

[1] Zhou Y.C., Hashida T.: Coupled Effects of Temperature Gradient and Oxidation on Thermal Stress in Thermal Barrier Coating System, *Int. J. Solids and Structures*, **38**: 4235-4264,2001.

[2] Freborg A.M., et al.:, Modeling Oxidation Induced Stresses in Thermal Barrier Coatings, Mater. Sci. Eng. , **A245**: 182-190, 1998.

NUMERICAL ANALYSIS OF STRAIN HARDENING AND PRESSURE SENSITIVITY EFFECTS ON *J*-INTEGRAL

A. Al-Abduljabbar
Riyadh College of Technology, Riyadh, Saudi Arabia

Summary *J*-integral is investigated for compact tension specimen for a strain-hardening pressure-sensitive material. Alower-bound plastic limit-load analysis is used with linear hardening assumed for the material. Pressure sensitivity, is accounted for by using the Drucker-Prager yield criterion. FE analysis was conduted using ABAQUS, with strain hardening modelled for typical hardening materials. Numerical and theoretical results are compared; *J* increases with increasing strain hardening and decreasing pressure sensitivity.

INTRODUCTION

While linear elastic fracture mechanics (LEFM) theory is utilized for estimation of fracture behaviour of materials in the elastic range, it is not adequate for large scale inelastic behaviour is encountered. To characterize the elastic-plastic fracture behaviour, Rice [1, 2] introduced the path-independent *J*-Integral around the tip of fracture notch. Considering a rigid perfectly-plastic material, Merkle and Corten [3] presented *J* estimation for compact tension specimens using a limit load analysis by considering the effects of the combined loading of axial force and bending moment applied to the remaining ligament of the specimens. Recently, Al-Abduljabbar and Pan [4] considered the effect of pressure sensitivity on the evaluated values of η and *J* for compact tension specimens with the same assumption of rigid perfectly-plastic material behaviour. Using finite element analysis, Kirk and Dodds [5] considered different equations used for estimating the η-factor, and highlighted the η dependency on strain hardening, which is not taken into account in the relevant standard (ASTM E 1290). In this work, we derive analytical expressions for factors of the *J*-Integral for a material with strain hardening by assuming a simple linear hardening model for the material. Moreover FE analysis is used to model the specimen with pressure sensitivity is accounted for by using the Drucker-Prager yield criterion for solid materials. The strain hardening behaviour is modelled for typical hardening materials as well as that of the simplified model using linear hardening curve which was used in the theoretical work. The effect of different hardening behaviours is also considered.

PLASTIC LIMIT ANALYSIS

Effects of the axial force and the bending moment acting on the upper half of the compact tension specimen are analysed by the use of a lower-bound approach whereby a single parameter can be identified to express the effect of the axial force. First, the material hardening behaviour is expressed according to Ludwik's expression,

$$\sigma = \sigma_0 + H\varepsilon^n , \tag{1}$$

where *H* and *n* are the hardening constants. Consider a compact tension specimen of perfectly plastic material as shown in Figure 1, loaded up to fully-plastic limit load P_0. Stress distribution in remaining ligament of the specimen is assumed as shown. The dimensionless parameter, α, is used as an indicator of the deviation of stress reversal point from the centre of the remaining ligament *b*. Another parameter, β, is used to account for the hardening effect. The slope of the linear hardening curve on the stress diagram is $\beta\,\sigma_0 / c$, and stresses σ_A and σ_B are determined as

$$\sigma_A = [1+\beta(1-\alpha)]\sigma_0 ; \tag{2}$$

$$\sigma_B = [1+\beta(1+\alpha)]\sigma_0 . \tag{3}$$

The force and moment balance around stress reversal point are enforced, from which an expression for α is obtained:

$$\alpha = \left[(1+\beta)^2 \left(\frac{a}{c} + 1 \right)^2 + \left(1 + \frac{2}{3}\beta \right) \right]^{1/2} - (1+\beta)\left(\frac{a}{c} + 1 \right). \tag{4}$$

An expression for the *J*-Integral is determined by namely two parts: the real work and complimentary work done on the specimen due to the applied load, as follows,

$$J = \int_0^{\Delta} \frac{1}{2P_0} \frac{\partial P_0}{\partial c} P d\Delta + \int_0^{\Delta} \frac{1}{2} \frac{\partial \theta}{\partial c} \left[\frac{\partial \theta}{\partial \Delta} \right]^{-1} dP ; \tag{5}$$

where θ is the angle of rotation defined from the relation between applied displacement Δ and crack-tip opening displacement δ. The coefficients of the first and second terms in Equation (5) are assigned to η and $\eta*$ respectively. From the relations of α to geometry and *J* definition, the parameter η is derived as

$$\eta = 2\frac{\phi + (1+\beta)\phi}{\phi + \alpha^2} , \tag{6}$$

where ϕ=1+2 β/3. For perfectly-plastic materials, β=0; so Eq. (7) reduces to perfectly-plastic material solution.

Discussion

The finite element code ABAQUS is used to model the specimen of a pressure-sensitive strain-hardening material. Pressure sensitivity is modeled by using the Drucker-Prager yield criterion wherein the generalized equivalent stress is represented as a combination of the equivalent stress and the hydrostatic stress by the means of a pressure sensitivity factor. Strain hardening behavior is modeled for typical hardening materials as well as that of the simplified model using linear hardening curve which was used in the theoretical work. Plain-strain reduced-integration elements CPER8 are used for the model. The specimen dimensions are according to standard test specimen dimensions from ASTM E 1290. Consider the change of η with respect to the strain-hardening coefficient β for different cases of normalized crack length as depicted in Figure 2. It shows that for specimens with shallow cracks, an increase in the hardening factor β results in considerable change in η.

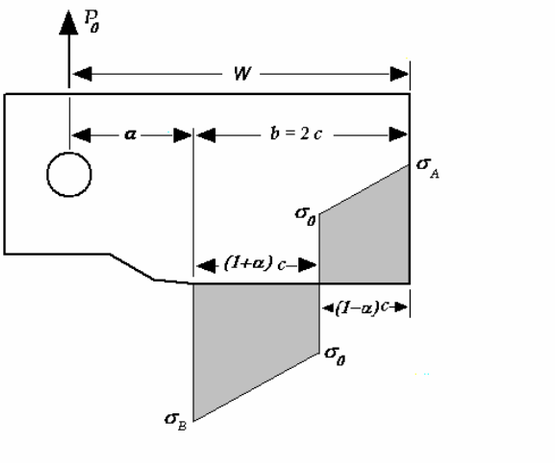


Figure1: CT specimen and stress distribution in remaining portion.

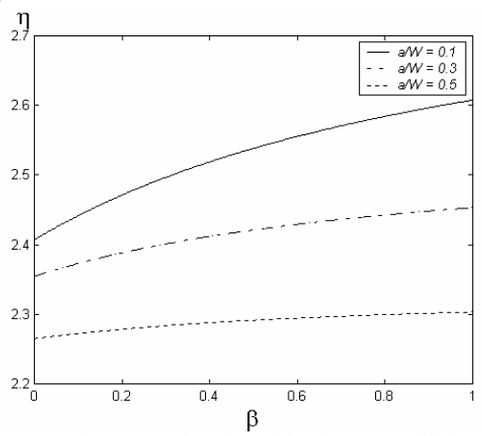


Figure2: η factor as a function of hardening coefficient β.

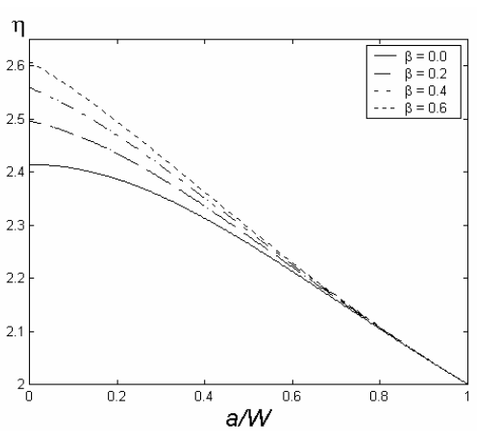


Figure3: η as a function of normalized crack length a/W.

Figure 3 shows the η factor as a function of the normalized crack length a/W. We can see from the plot that the effect of hardening decreases as the crack gets deeper and η converges to the value of 2 because for deeply cracked specimens, η approaches 2 regardless of the material constitutive behavior [6].

CONCLUSION

Results obtained from numerical and theoretical work show that as the material strain hardening increases, the J-Integral increases especially at low values of crack length. The effect of pressure sensitivity, on the other hand, tends to reduce the value of J. These results are relevant to ductile hardening solids with pressure-sensitive yielding such as nodular and malleable cast irons and even some steels. The forgoing analysis permits an improved estimation of the fracture parameter η for a material with strain hardening over the results reported for rigid perfectly plastic materials. Since most metals exhibit strain-hardening behavior, it is most suited to investigate the change in the fracture parameters due to the material hardening under further loading beyond the yield limit.

References

[1] Rice, J. R., "A Path independent integral and the approximate analysis of strain concentration by notches and cracks," J. Appl. Mech., 35 (1968) pp. 379-386.

[2] Rice, J. R., "Mathematical analysis in mechanics of fracture," in "Fracture II," edited by H. Liebowitz (Academic Press, 1969) pp. 191-311.

[3] Merkle, J. G. and H. T. Corten, "A J-Integral analysis for the compact specimen, considering axial force as well as bending effect," J. Press. Vess. Tech., Trans. ASME, (1974) pp. 286-292.

[4] Al-Abduljabbar, A. and J. Pan, "Effects of pressure sensitivity on the η-factor and J-Integral estimation for compact tension specimens," J. Mat. Sci. (1999) pp. 1-8.

[5] Kirk, M. T, and R. H Jr. Dodds, "J and CTOD estimation equations for shallow cracks in single edge notch bend specimens," J. Testing Eval., Vol. 21, No 4, (Jul 1993) pp. 228-238.

Incremental minimization principles in fracture and damage Mechanics

G. Francfort J.-J. Marigo

January 17, 2004

The formulation of crack evolution or damage evolution in a body from a principle of minimization of the total energy of the body is an alternative to usual appoaches. It offers as main advantage to be free of any *a priori* assumption on the evolution of the defects in space and in time. On the other hand it is more difficult to introduce into the model the irreversibility condition requiring that the defects can only grow in space with time. A discretization of the loading process and therefore of the evolution is first needed. That leads to the notion of incremental evolution problems. This discrete formulation is sometimes sufficient to obtain accurate information on the damaging process. It is the case when numerical computations are considered. However this bypass is not satisfactory from a theoretical point of view and one has to pass to the limit when the discretization step goes to zero to obtain the so-called "time-continuous evolution problem". From a mathematical point of view this passage to the limit can lead to very technical difficulties. The goal of the conference is to illustrate these different points from several examples chosen in Damage Mechanics, in Griffith Fracture Mechanics and in Barenblatt Fracture Mechanics.

Brittle damage We consider a brittle material the rigidity of which can fail from A_0 to A_1 when a criterion based on the elastic energy release is satisfied: $(A_0 - A_1)\varepsilon \cdot \varepsilon = 2\kappa$, ε denoting the strain tensor and κ is the "toughness" parameter of the material. Considering a body Ω made of this material and submitted to a loading process f_t, the problem consists in finding the characteristic function χ_t of the damaged zone and the displacement field u_t at each instant t. If no irreversibility condition is introduced for the damage evolution (χ_t can return to the value 0 even if it took the value 1 in the past), the evolution problem consists simply in the following minimization:

$$(\chi_t, u_t) = Argmin_{\chi,v} \int_\Omega \Big(\frac{1}{2}((1-\chi)A_0 + \chi A_1)\varepsilon(v) \cdot \varepsilon(v) + \kappa\chi\Big)dx - f_t(v).$$

Because of the loss of lower semicontinuity this problem must be relaxed; there does not exist in general a classical minimizer because the optimum consists in mixing locally the sound and the damaged material to obtain an intermediary effective material the effective elasticity of which is less than the average value of the elasticity of the mixture. The relaxed problem reads then

$$(\alpha_t, u_t) = Argmin_{\alpha,v} \int_\Omega \Big(\frac{1}{2}(A_\alpha)\varepsilon(v) \cdot \varepsilon(v) + \kappa\alpha\Big)dx - f_t(v),$$

where α takes now its value in the whole interval $[0,1]$ and represents the local volume fraction of the damaged material whereas A_α is the optimal homogenized elasticity tensor corresponding to this fraction.

If now we intoduce the irreversibility condition, χ_t must increase with t and the evolution problem is first formulated as the following incremental one: $\chi_0 = 0$ and for $i \geq 1$

$$(\chi_i, u_i) = Argmin_{\chi \geq \chi_{i-1}, v} \int_\Omega \Big(\frac{1}{2}((1-\chi)A_0 + \chi A_1)\varepsilon(v) \cdot \varepsilon(v) + \kappa\chi \Big) dx - f_i(v).$$

Always for the same reasons, this problem must be relaxed. For the first step, the relaxation remains unchanged, but for the next steps one encounters a real difficulty. It is in general not sufficient to consider increasing volume fraction α_t with t, the growth of the minimizing sequences must also be considered.

Griffith Fracture Mechanics The elastic body can now contain growing cracks view as surfaces of discontinuity $S(u)$ of the displacement field u. If we adopt Griffith assumption for the surface energy, denoting by G_c the toughness of the material, the incremental problem reads as : $u_0 = 0$ and for $i \geq 1$

$$u_i = Argmin_{v \in \mathcal{C}_i : S(v) \supset S(u_{i-1})} \int_\Omega \frac{1}{2} A\varepsilon(v) \cdot \varepsilon(v) dx + G_c \mathcal{H}^2(S(v))$$

where $\mathcal{C}_i$ denotes the set of admissible displacements at step i. To obtain the time continuous evolution problem we must pass to the limit when the discretization step goes to zero. This task can be achieved for a scalar problem (like in antiplane elasticity) but, at the present time, not in the general context of threedimensional elasticity for technical reasons. In the limited context where the proof works, the limit problem consists always in a minimization of the energy with respect to "admissible" larger surfaces of discontinuities plus a condition of continuity of the real energy with respect to time.

Barenblatt Fracture Mechanics If the Griffith surface energy is replaced by a Barenblatt surface energy by introducing a continuous increasing function of the jump of the displacements, $\phi([\![u]\!])$, increasing from 0 to G_c and if we do not consider irreversibility of the cracking, the evolution problem reads simply as

$$u_t = Argmin_{v \in \mathcal{C}_t} \int_\Omega \frac{1}{2} A\varepsilon(v) \cdot \varepsilon(v) dx + \int_{S(v)} \phi([\![v]\!]) d\mathcal{H}^2(x).$$

To take into account irreversibility, we introduce an internal variable δ on the surface of discontinuity $S(u)$, called the cumulated opening of the crack, which can only increase with time. The incremental problem traducing the evolution of the cracks is then : $u_0 = 0$ anf for $i \geq 1$

$$u_i = Argmin_{v \in \mathcal{C}_i} \int_\Omega \frac{1}{2} A\varepsilon(v) \cdot \varepsilon(v) dx + \int_{S(v)} \phi(\delta_{i-1} + [\![v - u_{i-1}]\!]^+) d\mathcal{H}^2(x),$$

and $\delta_i = \delta_{i-1} + [\![v - u_{i-1}]\!]^+$, x^+ denoting the positive part of x. It appears that this incremental problem is able to render account for fatigue phenomenon, that is for growth of cracks under cyclic loading.

DYNAMIC STABILITY OF FUNCTIONALLY GRADED PLATE UNDER IN-PLANE COMPRESSION

Andrzej Tylikowski
Warsaw University of Technology, Institute of Machine Design Fundamentals
PL 00-661 Warszawa, Poland

Summary Parametric vibrations of functionally graded plates subjected to in-plane time-dependent forces destabilizing the equilibrium state are analyzed. Nonlinear moderately large deflection equations taking into account a coupling of in-plane and transverse motions are used. Material properties are graded in the thickness direction of the plate according to volume fraction power law distribution. The asymptotic stability criteria are derived using Liapunov's direct method.

PROBLEM FORMULATION

Functionally graded materials have gained considerable attention in the high temperature applications. Functionally graded materials are composite materials, which are microscopically inhomogeneous, and the mechanical properties vary smoothly or continuously from one surface to the other. It is this continuous change that results in gradient properties in functionally graded materials (FGM). Many studies have examined FGM as thermal barriers. With the increased usage of these materials it is also important to understand the dynamics of FGM structures. A few studies have addressed this. Transient thermal stresses in a plate made of functionally gradient material were examined by Obata and Noda (1993).Vibration analysis of functionally graded cylindrical shells was performed by Loy, Lam and Reddy (1999). Recently, Lam, Liew, and Reddy (2001) presented dynamic stability analysis of functionally graded cylindrical shells under periodic axial loading. Consider the thin functionally graded rectangular plate with in-plane dimensions a and b, and thickness h. In-plane and transverse displacements are denoted by u, v, and w, respectively. Moderately large deflection equations taking into account a coupling of in-plane and transverse motions are used. Due to a small thickness rotary inertia terms are neglected. An oscillating temperature causes generation of in-plane time-dependent forces destabilizing plane state of the plate equilibrium. Material properties are graded in the thickness direction of the plate according to volume friction power law distribution. The viscous model of external damping with a constant coefficient ß is assumed. Taking into account the Kirchhoff hypothesis on non-deformable normal element and the Karman-type geometric nonlinearity the plate dynamics is described by partial differential equations system in the domain $O \bullet (0,a)\times(0,b)$. The membrane forces are stochastic with means equal to zero and known probability distributions. The processes are physically realizable and sufficiently smooth in order the solution of dynamics equations exists. We use the extensional, coupling and bending stiffnesses A_{ij} , B_{ij} , and D_{ij} , (i,j)=1,2,6) in the form

$$\left(A_{ij},B_{ij},D_{ij}\right)=\int_{-h/2}^{h/2} Q_{ij}(z)\left(1,z,z^2\right)dz$$

where Q_{ij} are the reduced stiffnesses for plane isotropic materials. Relationships between in-plane forces (N_x, N_y, N_{xy}) and moments (M_x, M_y, M_{xy}) and the middle plane strains ($u_{,x}+1/2\ w_{,x}^2$, $v_{,y}+1/2\ w_{,y}^2$, $u_{,y}+v_{,x}+w_{,x}\ w_{,y}$) and curvatures ($w_{,xx}$, $w_{,yy}$, $2w_{,xy}$) are described by the known constitutive equations. The effective elastic modulus, effective Poisson's ratio, and mass density ? of the functionally graded plate are denoted by E_{ef} , $?_{ef}$, and $?_{ef}$, respectively. In order to model the material properties of functionally graded materials, the properties must be both temperature and position dependent. This is achieved by using a rule of mixtures for the mechanical parameters E, ?, ?. The volume fraction is a spatial function and the properties of the constituents are functions of the temperature. The combination of these functions gives the effective material properties of functionally graded materials F_{ef} in terms of the appropriate properties of the ceramic and the metal, respectively, and V is the volume fraction of the ceramic constituent of the functionally graded material. A simple power law exponent of the volume fractions is used to describe the amount of ceramic and metal in the functionally graded material

$$V(z)=\left((2z+h)/2h\right)^q$$

where q is the power law exponent. The plate is assumed to be simply supported along each edge. The conditions imposed on displacements and internal forces and moments, called according to Almroth's (1966) classifications S2. The transverse motion of the plate is described by the nonlinear uniform equations with the trivial solution $w = w_{,t} = 0$ corresponding to the plane (undisturbed) state. In the paper a stochastic extension of Liapunov stability called the almost sure asymptotically stability of the trivial solution is analyzed. The crucial point of the method is a

construction of a suitable Liapunov functional, which is positive for any motion of the analyzed system. The measure of distance between disturbed solutions and equilibrium state is chosen as the square root of Liapunov functional.

STABILITY ANALYSIS

The energy-like Liapunov functional has the form of a sum of modified kinetic energy and potential energy

$$V_n = T + \frac{1}{2}\int_O \Big[-M_x w_{,xx} - M_y w_{,yy} - 2M_{xy} w_{,xy} + N_x\left(u_{,x} + 0.5w_{,x}^2\right) + N_y\left(v_{,y} + 0.5w_{,y}^2\right) + N_{xy}\left(u_{,y} + v_{,x} + w_{,x}w_{,y}\right) +$$

$$+ \overline{N}_x w_{,xx} + \overline{N}_y w_{,yy}\Big] dO \qquad T = \frac{1}{2}\int_O \left[w_{,t}^2 + 2\beta w w_{,t} + 2\beta^2 w^2\right] dO$$

It may be observed that contrary to the linear or linearized case is the fourth order functional. It is assumed that the in-plane forces are periodic or stochastic non-white stationary and sufficiently smooth ergodic process. Therefore, it is legitimate to use the classical differentation rule. Upon differentiation with respect to time, substituting dynamic equations and using the boundary conditions we obtain the time derivative of Liapunov functional

$$\frac{dV_n}{dt} = -2\beta V_n + 2U_n$$

where the auxiliary functional U is given. Therefore, the stability analysis of the nonlinear system depends on the construction of the bound $U_n = ?V_n$. The associate Euler equations are nonlinear in the case of the fourth-order functionals. It complicates a stability analysis and in order to obtain the analytical form of function we have to modify the variational problem. Therefore, our object is to find such second order functionals V* and U* that the inequality $U^* = ?V^*$ will imply the inequality for the nonlinear problem. In order to do this we express functional in the form where V is the second order Liapunov functional for a linearized problem. Omitting in considerations the fourth order terms we obtain the lower estimation of V_n and the upper estimation of U_n. Solving the associated Euler equations for the modified linearized problem we find the function ?. If the in-plane processes are ergodic with the known probability distribution, the sufficient condition of the almost sure asymptotic stability is written as follows $\beta \le E\lambda$, where E denotes the mathematical expectation. The stability region of the plate made of steel and zirconia for a zero-mean Gaussian force acting in x direction with the variance σ^2 is shown in Fig. 1.

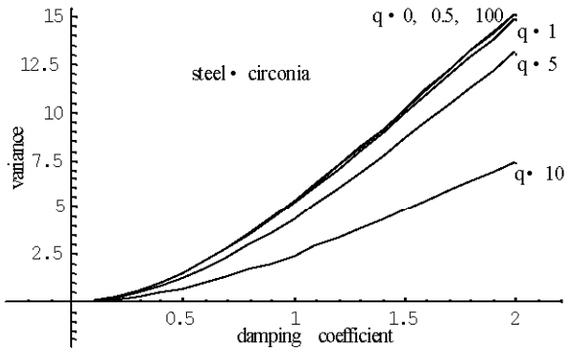


Fig. 1 Stability domains of quadratic plate unidirectionally loaded by in-plane time-dependent Gaussian force for the different power law exponents

CONCLUSIONS

The applicability of the direct Liapunov method has been extended to geometrically nonlinear functionally graded plates subjected to time-dependent, in-plane forces. The major conclusion is that the linearized problem should be modified to ensure the stability of nonlinear problem. The critical value of stability domains for intermediate values of power law exponent is substantially decreased.

References

[1] Almroth B.O.: Influence of edge conditions on the stability of axially compressed shells, *AIAA J.* **4**, 134-140, 1966.

[2] Loy C.T., et al.: Vibration of functionally graded cylindrical shells, *Int.J Mech. Sci.* **41**, 309-324, 1999.

[3] Ng T.Y., et al.: Dynamic stability analysis of functionally graded cylindrical shells under periodic axial loading, *Int. J. Sol. Str.* **38**, 1295-1309, 2001.
[4] Obata Y, and Noda N.: Transient thermal stresses in a plate of functionally gradient material, *Ceramic Transactions* **34**, 403-410, 1993.

MICROMECHANICS-BASED ELASTIC MODEL FOR FUNCTIONALLY GRADED MATERIALS WITH PARTICLE INTERACTIONS

Lizhi Sun*, Huiming Yin*, Glaucio H. Paulino**
*Dept. of Civil & Environmental Engineering, The University of Iowa, Iowa City, IA 52242, USA
**Dept. of Civil & Environmental Engineering, University of Illinois, Urbana, IL 61801, USA

Summary A micromechanical framework is proposed to investigate effective elastic behavior of functionally graded materials (FGMs). Microstructurally, particles are randomly dispersed in the matrix with gradual transitions. The effect of pair-wise interactions between particles is taken into account for the local stress and strain fields by using the modified Green's function method. Homogenization of the local field renders relations between the averaged strain, strain gradient and external loading.

INTRODUCTION

Functionally graded materials (FGMs) are characterized for spatially varying microstructures created by non-uniform distributions of the reinforcement phase, as well as by interchanging the role of the reinforcement and matrix in a continuous manner [1,2]. They are typically manufactured by two phases of materials with different properties. Experimental observations show that the typical microstructure of FGMs contains a particle-matrix zone with discrete particles filled in continuous matrix, followed by a skeletal transition zone in which the particle and matrix phases cannot be well defined because the two phases are interpenetrated into each other as a connected network.

While FGMs have been designed and fabricated by diverse methods to achieve unique microstructures, very limited analytical investigations are available to tackle the spatial variation of microstructure. Conventional composite models such as the Mori-Tanaka method and the self-consistent method are directly applied to estimate the effective elastic responses of FGMs [1-4]. Because they were originally developed for homogeneous mixtures, those models are not able to capture the material gradient nature of FGMs. Furthermore, since no direct local interactions between particles are taken into consideration, they could not take into account the graded particle distribution for FGMs.

In this paper a micromechanical framework is proposed to investigate the effective elastic behavior of FGMs. Based on the Eshelby's equivalent inclusion method, the pair-wise particle interaction is collected for any two particles embedded in the matrix medium. Given a uniform loading on the upper and lower boundaries of FGMs, averaged strains in particles are derived by integrating pair-wise interaction contributions of all particles. In the course of derivation, the microscopic representative volume element (RVE) is constructed to reflect the microstructure of FGMs. A transition function is adopted in the skeletal transition zone. From the effective stress and strain fields distributed in the gradation direction of FGMs, the effective elasticity distribution is solved as a function of gradation direction.

MICROMECHANICAL ANALYSIS OF FGMS

Consider a typical FGM microstructure in Fig. 1 containing two phases A and B with isotropic elastic stiffness $\mathbf{C}^A$ and $\mathbf{C}^B$, respectively. The overall grading thickness of the FGM is t. In each graded layer, micro-particles are uniformly distributed with a two-dimensionally random setting so that the material layer is statistically homogeneous. While these micro-particles cannot be observed in the macroscopic scale, the volume fraction of phase A or B (for convenience, we use ϕ to denote the volume fraction of phase A) is gradually changed in the gradation direction X_3. The transition zone boundaries d_1 and d_2 are generally determined by the FGM fabrication process directly related to $\phi(X_3)$. To calculate the effective FGM elastic stiffness $\bar{\mathbf{C}}(X_3)$, a uniform far-field stress tensor $\boldsymbol{\sigma}^0$ is applied on the FGM X_3 boundary. Based on the equilibrium condition, the averaged stress should be equal to the far-field stress as

$$\boldsymbol{\sigma}^0 = \phi(X_3)\mathbf{C}^A : \langle\boldsymbol{\varepsilon}\rangle^A(X_3) + \left[1-\phi(X_3)\right]\mathbf{C}^B : \langle\boldsymbol{\varepsilon}\rangle^B(X_3) \tag{1}$$

For any material point $\mathbf{X}^0$ in the range of $0 \le X_3 \le d_1$, the corresponding microstructural RVE contains a number of micro-particles of the phase A embedded in a continuous matrix of the phase B so that the overall volume fraction of particle phase A and the its gradient should be consistent with the macroscopic counterparts $\phi(X_3^0)$ and $d\phi/dX_3|_{X_3=X_3^0}$.

The volume-averaged particle strains are collected based on the local strain fields in particles located at various graded layers. Specifically, particle's averaged strain in the center of RVE can be written in two parts: the elastic-mismatch interaction between the central particle and the matrix and the pair-wise interaction between the central particle and other particles. The first part can be solved by Eshelby's theory and the second part can be obtained by Mura's solution for two particles embedded in the infinite domain. Because all particles are statistically distributed in a random way, the probability of particle distribution can be introduced to statistically demonstrate the particle interaction effect. By applying Taylor series expansion of $\langle\boldsymbol{\varepsilon}\rangle^B(x_3)$ up to linear term in terms of x_3 and transferring the local coordinate of RVE to global coordinate of FGMs, we can integrate the particle interaction tensor and finally obtain particle's averaged

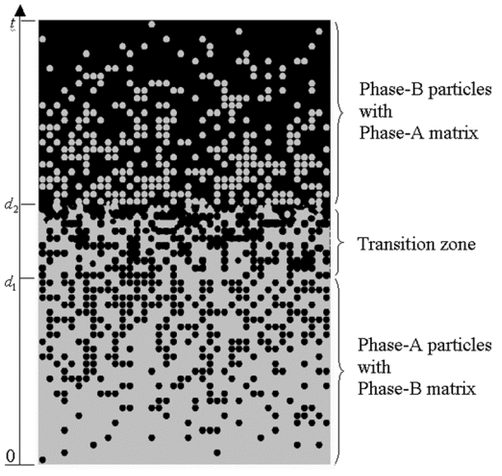


Fig. 1 Schematic illustration of a two-phase FGM sample

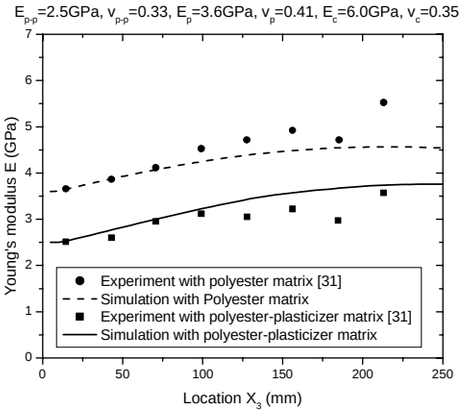


Fig. 2 Comparisons with experimental data [5]

strain along the gradation direction as:

$$\langle \boldsymbol{\varepsilon} \rangle^A (X_3) = (\mathbf{I} - \mathbf{P}_0 \cdot \Delta\mathbf{C})^{-1} : \langle \boldsymbol{\varepsilon} \rangle^B (X_3) + \phi(X_3) \Delta\mathbf{C}^{-1} \cdot \mathbf{D}(X_3) : \langle \boldsymbol{\varepsilon} \rangle^B (X_3) + \phi_{,3}(X_3) \Delta\mathbf{C}^{-1} \cdot \mathbf{F}(X_3) : \langle \boldsymbol{\varepsilon} \rangle^B_{,3} (X_3) \qquad (2)$$

With the combination of Eqs. (1) and (2), the averaged particle strain tensor $\langle \boldsymbol{\varepsilon} \rangle^A (X_3)$ and the averaged matrix strain tensor $\langle \boldsymbol{\varepsilon} \rangle^B (X_3)$ in the FGM gradation direction X_3 can be solved in terms of the far-field stress $\boldsymbol{\sigma}^0$. Since Eq. (2) is an ordinary differential equation, we also need the appropriate boundary conditions. In the particle-matrix zone with $0 \le X_3 \le d_1$, the boundary at $X_3 = 0$ corresponds to the 100% matrix material, so the corresponding boundary conditions can be proposed as $\langle \boldsymbol{\varepsilon} \rangle^B (0) = \mathbf{C}^{B^{-1}} : \boldsymbol{\sigma}^0$. Thus the averaged strain tensors in both phases can be solved.

Similarly, in the other particle-matrix with the range of $d_2 \le X_3 \le t$, we can also calculate the averaged strain fields by the switch of matrix and particle phases. For the transition zone, a transition function is introduced so that the averaged strain of each phase (A or B) can be approximated as a cubic Hermite function appropriately contributed by the averaged strain of the same phase (A or B) from two particle-matrix zones. Thus the overall averaged strain tensor at each layer in the transition zone can be further obtained. From the relations of averaged stress and strain, we can easily derive Young's modulus and Poisson's ratio. It is noted that the proposed transition function satisfies the requirement that the effective FGM elastic fields and corresponding moduli should be bounded, continuous, and differentiable.

RESULTS AND CONCLUSIONS

From the above procedures, we can find that the proposed model considers direct interactions between particles and capture the material gradient nature of FGMs. In the particle-matrix zone, if the particle interaction terms are dropped, the proposed model is reduced to the Mori-Tanaka's model. To demonstrate the validity of the micromechanics-based particle interaction model, in Fig. 2 we compare the proposed model with the experimental data [5] for two types of FGM fabrications: cenospheres in the polyester matrix and cenospheres in the polyester-plasticizer matrix with volume fraction distributions $\phi = -0.4731 + 4.226\times10^{-3} X_3 - 8.666\times10^{-6} X_3^2$ and $\phi = -0.3729 + 4.561\times10^{-3} X_3 - 1.06\times10^{-5} X_3^2$, respectively. The thickness of the two FGMs is 250mm ($0 \le X_3 \le 250mm$). The phase Young's moduli and Poisson's ratios are given as: $E_p = 3.6GPa$, $v_p = 0.41$, $E_{p-p} = 2.5GPa$, $v_{p-p} = 0.33$ with the subscript p denoting the polyester matrix and $p-p$ representing the polyester-plasticizer matrix. Cenosphere particles are the hollow spheres made of aluminum silicates with the mean diameter of $127\mu m$ and wall thickness of $12.7\mu m$. During the simulation process, the hollow spheres are replaced by solid particles with the estimated Young's modulus and Poisson's ratio as $E_c = 6.0GPa$ and $v_c = 0.35$. With these parameters as input data, the effective Young's moduli of the FGMs are simulated and shown in Fig. 2 as a function of location. The proposed model compares well with the experimental results.

References

[1] Suresh S, Mortensen A.: Fundamentals of Functionally Graded Materials. IOM Communications Ltd, 1998.

[2] Miyamoto Y, et al.: Functionally Graded Materials: Design, Processing and Applications. Kluwer Academic Publishers, 1999.

[3] Vel SS, Batra RC.: AIAA J **40**:1421, 2002.

[4] Kim JH, Paulino GH.: Inter J Num Meth Eng: **58**:1457, 2003.

[5] Parameswaran V, Shukla A. J Mater Sci : **35**:21, 2000.

A STATE SPACE FORMALISM FOR PIEZOTHERMOELASTICITY OF FUNCTIONALLY GRADED MATERIALS

Jiann-Quo Tarn, Hsi-Hung Chang
Department of Civil Engineering, National Cheng Kung University, Tainan 70101, Taiwan

Summary A state space formalism for electromechanical analysis of functionally graded materials (FGM) with rectilinear anisotropy and cylindrical anisotropy is presented. On the basis of the formalism, the piezothermoelastic solution to a problem may be determined analogously through its elastic counterpart. Viable schemes for solving the non-uniform state equation are proposed. Problems of electromechanical analysis of FGM can be treated in an elegant way.

STATE SPACE FORMULATION

The conventional approach to anisotropic elasticity is the Lekhnitskii or Stroh formalism. For piezothermoelasticity the usual approach is to extend the Stroh formalism to include the piezoelectric effects. Extension of the Stroh formalism to piezothermoelasticity of FGM is unwieldy in formulation and restrictive in application. Herein we present a general formalism and solution approach for electromechanical analysis of FGM. The piezoelectric materials considered possess rectilinear anisotropy or cylindrical anisotropy of the most general kind. The novelty of the formalism lies in that the 3D equations of piezothermoelasticity are represented in full by a state equation and an output equation in which only a displacement vector, a stress vector, and six sub-matrices that characterize the material properties appear. This is achieved through grouping the field variables and selecting the state vector judiciously. In addition, the equations of piezothermoelasticity in the state space bear a remarkable resemblance to their elastic counterparts. As such, the piezothermoelastic solution to a problem may be obtained in an analogous manner through the corresponding elastic solution. The formalism brings in matrix algebra in the solution. When dealing with FGM, the material inhomogeneity renders the system non-uniform; it is very difficult to obtain an analytic solution to the state equation in general. Viable schemes for solving the non-uniform state equation are suggested. The schemes are useful for problems both in Cartesian coordinates and in cylindrical coordinates.

FGM with Rectilinear Anisotropy

The fundamental equations of piezothermoelasticity are given in [1]. To avoid dealing with individual field variables and many of the material constants, we make judicious grouping of the field variables and partitioning of the constitutive matrices. On the basis of the derivation in [2-4] for homogeneous anisotropic elastic and piezoelectric materials, the basic 3D equations in Cartesian coordinates can be reformulated into a state equation and an output equation as follows:

$$\frac{\partial}{\partial x_2}\begin{bmatrix}\mathbf{u}\\ \boldsymbol{\tau}_2\end{bmatrix}=\begin{bmatrix}\mathbf{D}_{11} & \mathbf{D}_{12}\\ \mathbf{D}_{21} & \mathbf{D}_{11}^{\mathrm{T}}\end{bmatrix}\begin{bmatrix}\mathbf{u}\\ \boldsymbol{\tau}_2\end{bmatrix}+\begin{bmatrix}\mathbf{b}_1\\ \mathbf{b}_2\end{bmatrix}\mathrm{T}-\begin{bmatrix}\mathbf{0}\\ \mathbf{F}\end{bmatrix}+\frac{\partial^2}{\partial t^2}\begin{bmatrix}\mathbf{0}\\ \mathbf{Ku}\end{bmatrix} \tag{1}$$

$$\boldsymbol{\tau}_2=\begin{bmatrix}\mathbf{L}_1 & \mathbf{L}_2\end{bmatrix}\begin{bmatrix}\mathbf{u}\\ \boldsymbol{\tau}_2\end{bmatrix}-\mathbf{b}_3\mathrm{T} \tag{2}$$

The notations similar to those in [2-4] are used. x_2 is considered to be a distinct axis; the state vector consists of $\mathbf{u}=[u_1\ u_2\ u_3\ \varphi]^{\mathrm{T}}$ and $\boldsymbol{\tau}_2=[\sigma_{12}\ \sigma_{12}\ \sigma_{12}\ D_2]^{\mathrm{T}}$, the vector $\boldsymbol{\tau}_1$ contains the remaining stress components and electrical displacements; $\mathbf{D}_{ij}$ are linear differential operators of x_1, x_3 and the material constants. For FGM the system matrix in (1) is spatial dependent and the state equation is non-uniform with variable coefficients.

FGM with Cylindrical Anisotropy

The state equation and output equation in cylindrical coordinates take the form

$$\frac{\partial}{\partial \mathrm{r}}\begin{bmatrix}\mathbf{u}\\ \mathrm{r}\boldsymbol{\tau}_\mathrm{r}\end{bmatrix}=\begin{bmatrix}\mathbf{L}_{11} & \mathbf{L}_{12}\\ \mathbf{L}_{21} & \mathbf{L}_{22}\end{bmatrix}\begin{bmatrix}\mathbf{u}\\ \mathrm{r}\boldsymbol{\tau}_\mathrm{r}\end{bmatrix}+\begin{bmatrix}\mathbf{a}_1\\ \mathbf{a}_2\end{bmatrix}\mathrm{T}-\begin{bmatrix}\mathbf{0}\\ \mathbf{F}\end{bmatrix}+\frac{\partial^2}{\partial t^2}\begin{bmatrix}\mathbf{0}\\ \mathbf{Hu}\end{bmatrix} \tag{3}$$

$$\mathrm{r}\boldsymbol{\tau}_\mathrm{s}=\begin{bmatrix}\mathbf{L}_1 & \mathbf{L}_2\end{bmatrix}\begin{bmatrix}\mathbf{u}\\ \mathrm{r}\boldsymbol{\tau}_\mathrm{r}\end{bmatrix}-\mathbf{a}_3\mathrm{T} \tag{4}$$

where r is considered to be a distinct axis; $\mathbf{u}=[u_r\ u_\theta\ u_z\ \varphi]^{\mathrm{T}}$, $\boldsymbol{\tau}_\mathrm{r}=[\sigma_\mathrm{r}\ \sigma_{\mathrm{r}\theta}\ \sigma_{\mathrm{rz}}\ D_r]^{\mathrm{T}}$, $\boldsymbol{\tau}_\mathrm{s}$ contains the remaining components of the field variables; $\mathbf{L}_{ij}$ are linear differential operators of θ, z and the material constants.

Equations (1) to (4) bear a remarkable resemblance not only in themselves but also to their elastic counterparts [2, 3]. As a result, the piezothermoelastic solution of a problem may be determined from the corresponding elastic solution by analogy and correspondence. A proper replacement of the corresponding matrices in the elastic solution produces the piezothermoelastic solution. When the formalism is applied to plane problems of homogeneous materials, the solution of the homogeneous equations leads naturally to the eigenrelation and the octet equation based on the Stroh formalism [4].

Equations (1) and (3) are not easy to solve in general except for special classes of FGM, such as a power-law distribution of the inhomogeneity. A formal solution may be obtained by using successive integration. Yet it is difficult to carry out the integration and assess the convergence. Herein we propose two solution schemes.

Piecewise-Constant Approximation

The basic idea is to approximate the inhomogeneity of the FGM by piecewise-constant functions so that the state equation in the sub-regions becomes uniform and solvable analytically. Continuity conditions at the jumps introduced by the piecewise-constant approximation are satisfied by means of the transfer matrix. In the case of a FGM plate (or a radially inhomogeneous FGM cylinder), the scheme amounts to approximating the FGM body by a system composed of homogeneous layers (or coaxial homogeneous cylinders). It applies to a laminated system in an obvious way. The scheme has been applied to problems of circular cylinders and tubes of FGM and laminated composites [5].

Power Series Approximation

The scheme is well suited when the inhomogeneity of the FGM is describable by polynomials. For illustration, let us consider FGM with radial inhomogeneity. Suppose, upon expressing the dependence of θ and z in some way (such as Fourier series representation), that (3) reduces to

$$\frac{\mathrm{d}}{\mathrm{d}\,\mathrm{r}}\mathbf{X}(\mathrm{r})=\mathbf{A}(\mathrm{r})\mathbf{X}(\mathrm{r})+\mathbf{P}(\mathrm{r}) \tag{5}$$

The dependence of the material property on r renders the system matrix $\mathbf{A}(\mathrm{r})$ a polynomial given by

$$\mathbf{A}(\mathrm{r})=\mathbf{A}_0+\mathbf{A}_1\,\mathrm{r}+\mathbf{A}_2\,\mathrm{r}^2+\mathbf{A}_3\,\mathrm{r}^3 \tag{6}$$

where $\mathbf{A}_i$ are known constant matrices.

The homogeneous solution of (5) can be determined by assuming a power series representation of $\mathbf{X}(\mathrm{r})$:

$$\mathbf{X}(\mathrm{r})=\sum_{n=0}^{\infty}\mathbf{X}_n\,\mathrm{r}^n \tag{7}$$

where $\mathbf{X}_n$ are unknown vectors. A substitution of (7) in (5) leads to the following recursive relation

$$(n+1)\mathbf{X}_{n+1}=\mathbf{A}_0\mathbf{X}_n+\mathbf{A}_1\mathbf{X}_{n-1}+\mathbf{A}_2\mathbf{X}_{n-2}+\mathbf{A}_3\mathbf{X}_{n-3},\quad \mathbf{X}_{-1}=\mathbf{X}_{-2}=\mathbf{X}_{-3}=0,\quad n=0,1,2,\cdots \tag{8}$$

The relation allows one to express the higher-order terms of $\mathbf{X}_n$ in terms of the lower-order terms, and $\mathbf{X}(r)$ in turn can be expressed in terms of $\mathbf{X}_0$ as

$$\mathbf{X}(\mathrm{r})=\sum_{n=0}^{\infty}\mathbf{X}_n\,\mathrm{r}^n=\mathbf{M}(\mathrm{r})\mathbf{X}_0 \tag{9}$$

Now $\mathbf{M}(\mathrm{r})$ plays the role of the transfer matrix. With the homogeneous solution so determined, the particular solution of (5) can be easily found using a standard method of matrix algebra. The unknown in $\mathbf{X}_0$ can be determined from the boundary conditions on the cylindrical surfaces $r = constant$ for a specific problem.

SOME REMARKS

The state space formalism is elegant in formulation and systematic in operation. It has been used for treating the generalized plane strain and generalized torsion of an elastic body [6] and a piezoelectric body [7], where focuses were on formulations and solutions of specific problems. A number of exact solutions have been obtained with relative ease using the approach. For more general problems Hamiltonian characteristics of the system may be used to advantage. For piezothermoelasticity of FGM the material inhomogeneity, in addition to electromechanical coupling and material anisotropy, leads to a challenging mathematical problem. The state space formalism makes treatment of the problem less formidable. It appears that the electromechanical analysis of FGM is best viewed and treated in the state space setting.

References

[1] Nowacki W.: Dynamic Problems of Thermoelasticity. PWN-Polish Scientific Publishers, Warszawa, 1975.
[2] Tarn J.Q.: A State Space Formalism for Anisotropic Elasticity Part I: Rectilinear Anisotropy, *Int. J. Solids. Struct*. **39**: 5143-5155, 2002.
[3] Tarn J.Q.: A State Space Formalism for Anisotropic Elasticity Part II: Cylindrical Anisotropy, *Int. J. Solids. Struct.* **39**: 5157-5172, 2002.
[4] Tarn J.Q.: A State Space Formalism for Piezothermoelasticity, *Int. J. Solids. Struct.* **39**: 5173-5184, 2002.
[5] Tarn J.Q., Wang Y.M.: Heat conduction in a cylindrically anisotropic tube of a functionally graded material, *Chinese J. Mech.* **19**: 365-372, 2003.
[6] Tarn J.Q.: Exact solutions for functionally graded anisotropic cylinders subjected to thermal and mechanical loads, *Int. J. Solids. Struct.* **38**: 8189-8206, 2001.
[7] Tarn J.Q.: Exact Solutions of a Piezoelectric Circular Tube or Bar under Extension, Torsion, Pressuring, Shearing, Uniform Electric Loadings and Temperature Change, *Proc. R. Soc. Lond.* A**458**: 2349-2367, 2002.

CONSERVATION LAWS OF FUNCTIONALLY GRADED MATERIALS IN ELASTODYNAMICS

Shi Weichen
Department of Mechanical Engineering, Shanghai Maritime University
Pudong Avenue 1550, Shanghai 200135, China

Summary A special version of Noether's theorem for the sake of absolute invariance on invariant variational principles is applied to the Lagrangian density function for obtaining conservation laws of functionally graded materials. It is found that the mass density and Lamé's coefficients have to satisfy a set of first-order linear partial differential equations. Under the consideration of varying the volume fraction of the constituent materials, the effective mass density and Lamé's coefficients, satisfying those partial differential equations, are obtained. Four conservation laws in material space are presented. A path-independent integral, which is directly related to the dynamic energy release rate, in the moving coordinate reference attached at the tip of crack is given.

CONSERVATION LAWS IN MATERIAL SPACE

Conservation laws constitute a basic tool in the analysis of properties of solutions to any given system of partial differential equations and provide valuable information on the physical quantities pertaining to the problem under investigation, so that the conservation laws of functionally graded materials (FGMs) should be inquired.
The Lagrangian density function L and the constitutive equations of FGM are

$$L=\frac{1}{2}\rho\dot{u}_i\dot{u}_i-W(x_i,\varepsilon_{ij})=\frac{1}{2}\rho\dot{u}_i\dot{u}_i-\frac{1}{2}C_{ijkl}\varepsilon_{ij}\varepsilon_{kl},\qquad \sigma_{ij}=\frac{\partial W}{\partial\varepsilon_{ij}}=C_{ijkl}u_{k,l},\qquad C_{ijkl}=\delta_{ij}\delta_{kl}\lambda+(\delta_{ik}\delta_{jl}+\delta_{il}\delta_{jk})\mu \quad (1)$$

where W is the elastic potential; u_i, ε_{ij} and σ_{ij} are the components of displacement, strain and stress, respectively; ρ, λ and μ stand for the mass density and Lamé's coefficients, which are functions of space x_i for FGMs. By applying Lie's infinitesimal criterion on the invariance to the Lagrangian (Olver, [1]), it follows that

$$\tau=bt+\beta,\qquad \zeta_i=Bx_i+e_{ijk}\Omega_j x_k+C_i,\qquad U_i=Au_i+e_{ijk}\Omega_j u_k+e_{ijk}\omega_j x_k+\gamma_i \quad (2)$$

where β, ω_j and γ_i are arbitrary constants. Values of the constants b, B, Ω_j, C_i and A depend on satisfaction of the following equations

$$\zeta_m\frac{\partial\rho}{\partial x_m}+(2A+3B-b)\rho=0,\qquad \zeta_m\frac{\partial\lambda}{\partial x_m}+(2A+B+b)\lambda=0,\qquad \zeta_m\frac{\partial\mu}{\partial x_m}+(2A+B+b)\mu=0 \quad (3)$$

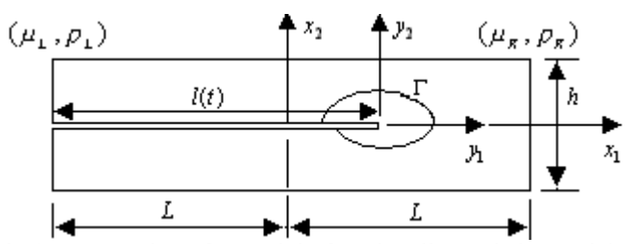


Fig.1. Propagation of a crack in functionally graded material.

FGMs are composite, microscopically non-homogenous materials, in which the material coefficients vary smoothly and continuously from one surface to the other as shown in Fig.1. This is achieved by gradually varying the volume fraction of the constituent materials. In such a way, the effective shear modulus μ may be expressed as

$$\mu=\mu_L V_L(x_1)+\mu_R V_R(x_1) \quad (4)$$

where μ_L and μ_R are the shear moduli on the left-hand and right-hand surfaces, respectively; $V_L(x_1)$ and $V_R(x_1)$ denote the volume fractions and related by

$$V_L(x_1)+V_R(x_1)=1 \quad (5)$$

Similarly, the effective mass density ρ can be expressed in terms of volume fractions as shown above. As discussed in many other papers, Poisson's ratio ν depends weakly on position, so that it is assumed to be a constant. Under the consideration of (4) and (5), the effective shear modulus and mass density are obtained by solving equations in (3) as follows

$$\mu=\tilde{\mu}[1+Rx_1]^N,\qquad \rho=\tilde{\rho}[1+Rx_1]^M \quad (6)$$

where $$\tilde{\mu}=[(\mu_L^{\frac{1}{N}}+\mu_R^{\frac{1}{N}})/2]^N,\qquad \tilde{\rho}=[(\rho_L^{\frac{1}{M}}+\rho_R^{\frac{1}{M}})/2]^M,\qquad M=N[\ln(\rho_R/\rho_L)/\ln(\mu_R/\mu_L)] \quad (7)$$

$$B=RC_1,\qquad b=(M-N+2)RC_1/2,\qquad A=-(M+N+4)RC_1/4,\qquad R=[(\mu_R^{\frac{1}{N}}-\mu_L^{\frac{1}{N}})/(\mu_R^{\frac{1}{N}}+\mu_L^{\frac{1}{N}})]/L$$

and N is an arbitrary constant. Here, owing to V_L and V_R being functions of x_1 only, constants Ω_2 and Ω_3 within ζ_1 have been set equal to zero. The normalized values μ/μ_L and ρ/ρ_L are given in Fig.2, in which $\mu_L = 25.94$ (GPa) and $\rho_L = 2700$ (kg/m^3) for aluminum Al 6061-TO, and $\mu_R = 200.00$ (GPa) and $\rho_R = 4920\,(kg/m^3)$ for ceramic TiC. They are numerically well and would not be unrealistic for various FGMs under the consideration of varying the volume fraction.

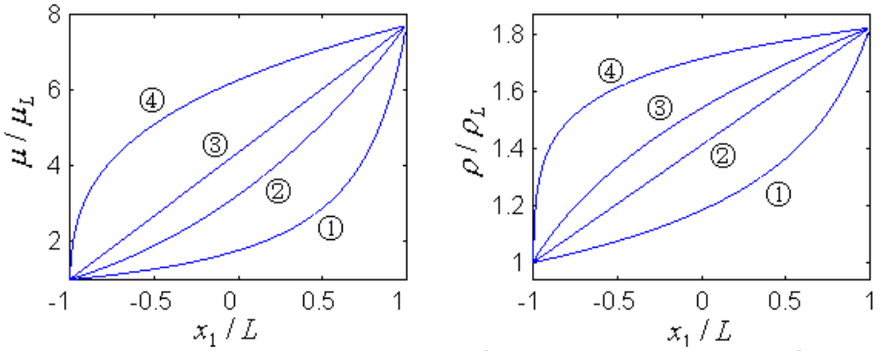


Fig.2. Effective shear modulus and mass density; ①: $N=-1$, $M=-0.2938$; ②: $N=3.4308$, $M=1$; ③: $N=1$, $M=0.2938$; ④: $N=0.3$, $M=0.0881$.

Noether's theorem [1,2] asserts the existence of conservation laws, namely

$$D_t(\tau H - \zeta_k \Sigma_k - U_k Q_k) + D_i(-\tau \dot{u}_k \sigma_{ik} + \zeta_k S_{ik} + U_k \sigma_{ik}) = 0 \tag{8}$$

where $H = W + \frac{1}{2}\rho \dot{u}_i \dot{u}_i$ is the Hamiltonian density, $\Sigma_k = -\rho \dot{u}_i u_{i,k}$ the pseudomomentum, $Q_k = \rho \dot{u}_k$ the linear momentum and $S_{ik} = (W - \frac{1}{2}\rho \dot{u}_j \dot{u}_j)\delta_{ik} - \sigma_{ji} u_{j,k}$ a dynamic version of Eshelby's energy-momentum tensor. Substituting expressions (2) into equation (8), considering the independence of C_i and Ω_1, and neglecting independent constants β, ω_j and γ_i for conservation laws in physical space, we obtain the following conservation laws in material space

(1) $C_1 \neq 0$: $\quad D_i P_i = D_t P_t$ (9)

where

$$P_i = S_{i1} + R x_k S_{ik} - [1 + (1 + \frac{\ln(\rho_R/\rho_L)}{\ln(\mu_R/\mu_L)})\frac{N}{4}] R u_k \sigma_{ik} - [1 - (1 - \frac{\ln(\rho_R/\rho_L)}{\ln(\mu_R/\mu_L)})\frac{N}{2}] R t \dot{u}_k \sigma_{ik} \tag{10}$$

$$P_t = \Sigma_1 + R x_k \Sigma_k - [1 + (1 + \frac{\ln(\rho_R/\rho_L)}{\ln(\mu_R/\mu_L)})\frac{N}{4}] R u_k Q_k - [1 - (1 - \frac{\ln(\rho_R/\rho_L)}{\ln(\mu_R/\mu_L)})\frac{N}{2}] R t H$$

(2) $C_2 \neq 0$: $\quad D_i S_{i2} = D_t \Sigma_2$ (11)

(3) $C_3 \neq 0$: $\quad D_i S_{i3} = D_t \Sigma_3$ (12)

(4) $\Omega_1 \neq 0$: $\quad D_i(x_3 S_{i2} - x_2 S_{i3} + u_3 \sigma_{i2} - u_2 \sigma_{i3}) = D_t(x_3 \Sigma_2 - x_2 \Sigma_3 + u_3 Q_2 - u_2 Q_3)$ (13)

It should be emphasized that these conservation laws under the consideration of absolute invariance of the Lagrangian are non-trivial.

THE PART-INDEPENDENT INTEGRAL

By using the effective shear modulus and mass density given in (6), it can be reaffirmed that the dominant terms in the crack tip stress field are identical to those of a homogeneous material having the material properties of the FGM crack tip vicinity. It is also known that near the tip of an extending crack, field quantities obey the "transport assumption", that is, $\partial(\,)/\partial t = -\dot{l}\,\partial(\,)/\partial x_1$. Therefore, as shown in Fig.1, the path-independent integral emanating from the conservation law (9) in the moving coordinate reference (y_1, y_2) attached at the tip of crack can be calculated as

$$J = \lim_{\Gamma \to 0} \int_{\Gamma} [(P_1 + \dot{l} P_t) n_1 + P_2 n_2] d\Gamma = \{1 + Rl - [1 - \frac{N}{2}(1 - \frac{\ln(\rho_R/\rho_L)}{\ln(\mu_R/\mu_L)}) R\dot{l}]\} G \tag{14}$$

where G is the dynamic energy release rate (Freund, [3]).

References

[1] Olver, P. J.: Applications of Lie Groups to Differential Equations. Springer-Verlag, NY 1993.

[2] Noether, E.: Invariant variational problems. *Klg-Ges. Wiss. Nach. Göttingen, Math. Physik*, **Kl.2**, 235-253, 1918. English Translation: Transport Theory and Statistical Physics **1**: 183-207, 1971.

[3] Freund, L. B.: Dynamic Fracture Mechanics. Cambridge University Press, NY 1990.

XXI ICTAM, 15–21 August 2004, Warsaw, Poland

TRANSIENT DYNAMIC CRACK ANALYSIS IN FGMS UNDER IMPACT LOADING

Chuanzeng Zhang*, Jan Sladek**, Vladimir Sladek**
*Department of Civil Engineering, University of Applied Sciences Zittau/Görlitz, D-02763 Zittau, Germany
**Institute of Construction and Architecture, Slovak Academy of Sciences, 84503 Bratislava, Slovakia

Summary Transient elastodynamic analysis of a two-dimensional (2-D) in-plane crack in functionally graded materials (FGMs) is performed by a time-domain boundary integral equation method (BIEM). An exponential law is applied to describe the material gradients of the FGMs. The crack is subjected to an impact crack-face loading. Special attention is devoted to explore the effects of the material gradients and the crack orientation on the dynamic stress intensity factors (DSIFs) and their overshoot over static values.

PROBLEM STATEMENT AND BOUNDARY INTEGRAL EQUATIONS

Transient elastodynamic crack analysis in FGMs is of particular interest to fracture mechanics and ultrasonic quantitative non-destructive evaluation of FGMs, which received in last years more and more attention in material sciences and engineering applications due to their superior thermal and mechanical properties. Due to the mathematical complexity arising in such an analysis, most of the previous works on crack analysis in FGMs have been limited to very special crack orientation and loading conditions. In this paper, we present a transient elastodynamic crack analysis in unidirectional or bidirectional FGMs subjected to an impact crack-face loading.
We consider an infinite, isotropic, continuously non-homogeneous, and linear elastic solid containing a finite crack of length $2a$ as shown in Fig. 1.

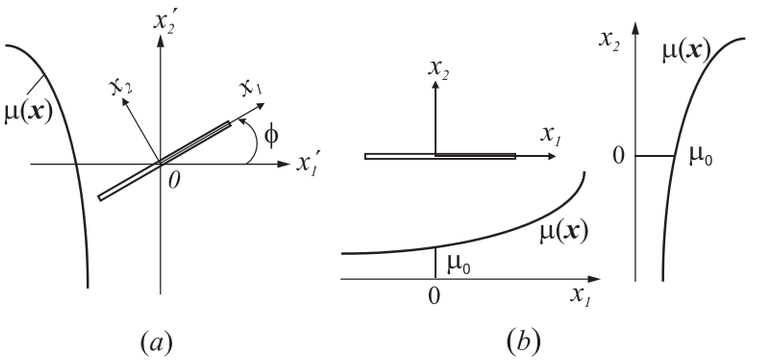


Figure 1. A finite crack in FGMs with (a) unidirectional gradation and (b) bidirectional gradation

The crack is subjected to an impact crack-face loading, and the deformation of the solid is in plane strain or plane stress. In the absence of body forces, the cracked FGMs satisfy the equations of motion

$$\sigma_{\alpha\beta,\beta} = \rho(\mathbf{x})\ddot{u}_\alpha \,, \tag{1}$$

the Hooke's law

$$\sigma_{\alpha\beta} = \mu(\mathbf{x}) E^0_{\alpha\beta\delta\gamma} u_{\delta,\gamma} \,, \tag{2}$$

the initial conditions

$$u_\alpha(\mathbf{x},t) = \dot{u}_\alpha(\mathbf{x},t) = 0 \,, \qquad \text{for} \quad t = 0 \,, \tag{3}$$

and the boundary conditions on the crack-faces

$$f_\alpha(\mathbf{x},t) = \sigma_{\alpha\beta}(\mathbf{x},t) n_\beta(\mathbf{x}) = f^*_\alpha(\mathbf{x},t) \,, \qquad \mathbf{x} \in \Gamma_c \,. \tag{4}$$

In Eqs. (1)-(4), $\rho(\mathbf{x})$ is the mass density, $\mu(\mathbf{x})$ is the shear modulus, $\Gamma_c = \Gamma_c^+ + \Gamma_c^-$ are the crack-faces, n_β is the unit normal vector, $f^*_\alpha(\mathbf{x},t)$ is a pre-scribed crack-face loading, and

$$E^0_{\alpha\beta\delta\gamma} = \frac{3-\kappa}{\kappa-1}\delta_{\alpha\beta}\delta_{\delta\gamma} + \delta_{\alpha\delta}\delta_{\beta\gamma} + \delta_{\alpha\gamma}\delta_{\beta\delta} \,. \tag{5}$$

Here, $\kappa = 3 - 4\nu$ for plane strain, $\kappa = (3-\nu)/(1+\nu)$ for plane stress, ν is Poisson's ratio which is assumed to be constant in this analysis, and $\delta_{\alpha\beta}$ is the Dirac-delta. The spatial variations of the shear modulus and the mass density are described by the following exponential laws

$$\mu(\mathbf{x}) = \mu_0 e^{\alpha x_1 + \beta x_2} \,; \qquad \rho(\mathbf{x}) = \rho_0 e^{\alpha x_1 + \beta x_2} \,, \tag{6}$$

where α and β are gradient parameters of the FGMs. The exponential law (6) enables us to describe crack problems in both unidirectional and bidirectional FGMs as shown in Fig. 1.
The initial-boundary value problem governed by Eqs. (1)-(4) can be formulated as a set of time-domain traction BIEs as

$$n_\beta(\mathbf{x}) \int\limits_{\Gamma_c^+} T^G_{\gamma\alpha\beta}(\mathbf{x},\mathbf{y};t,\tau) * \Delta u_\gamma(\mathbf{y},\tau) ds = f^*_\alpha(\mathbf{x},t)\,, \qquad \mathbf{x} \in \Gamma_c^+\,, \tag{7}$$

where $T^G_{\gamma\alpha\beta}$ are the time-dependent traction Green's functions, Δu_α represent the unknown crack-opening-displacements (CODs), and an asterisk denotes Riemann convolution. Note here that the time-domain traction BIEs (7) are hypersingular. The hypersingular integral in (7) has to be understood in the sense of Hadamard finite-part integral.

NUMERICAL SOLUTION PROCEDURE

A time-stepping scheme is developed for solving the hypersingular time-domain BIEs (7). The scheme uses the convolution quadrature formula of Lubich [1] for computing the temporal convolution integral and a Galerkin-method for the spatial approximation of the unknown CODs. The unknown CODs are approximated by

$$\Delta u_\gamma(y_1,\tau) = \sqrt{a^2-y_1^2} \sum_{k=1}^{K} c_{\gamma;k}(\tau) U_{k-1}\left(\frac{y_1}{a}\right)\,, \tag{8}$$

where K is the number of series, $c_{\gamma;k}(\tau)$ are the unknown time-dependent expansion coefficients, and $U_{k-1}(y_1/a)$ are the Chebyshev-polynomials of second kind. Substituting Eq. (8) into Eq. (7), multiplying both sides by $\sqrt{a^2-x_1^2}U_{l-1}(x_1/a)$, integrating them with respect to x_1 from $-a$ to $+a$, and applying the convolution quadrature formula of Lubich [1] lead to a system of linear algebraic equations for the expansion coefficients

$$\sum_{j=0}^{n-1} \mathbf{A}^{n-j}\mathbf{d}^j = \mathbf{t}^n\,, \qquad n = 1,2,...,N\,, \tag{9}$$

where $\mathbf{d}^j = \{\mathbf{c}_1^j, \mathbf{c}_2^j\}^T$ and $\mathbf{t}^n = \{\mathbf{f}_1^n, \mathbf{f}_2^n\}^T$, with $\mathbf{c}_\gamma^j = \{c_{\gamma;k}^j\}$ and $\mathbf{f}_\gamma^n = \{f_{\gamma;l}^n\}$. Here, the time variable t is divided into N equal time-steps Δt and the upper indices stand for the time-steps. The system matrix and the right-hand side of Eq. (9) can be obtained by using

$$\mathbf{A}^n = \frac{r^{-n}}{N} \sum_{m=0}^{N-1} \hat{\mathbf{A}}(p_m) e^{-2\pi i \cdot nm/N}\,, \tag{10}$$

$$f_{\alpha;l}^n = (-1)^{l+1} \int\limits_{-a}^{+a} f_\alpha^*(x_1, n\Delta t)\sqrt{a^2-x_1^2}U_{l-1}\left(\frac{x_1}{a}\right) dx_1\,. \tag{11}$$

In Eq. (10), $p_m = \delta(\zeta_m)/\Delta t$, $\delta(\zeta_m) = \sum_{j=1}^{2}(1-\zeta_m)^j/j$, $\zeta_m = re^{2\pi i\cdot m/N}$, and $r^N = \sqrt{\epsilon}$ with ϵ being the numerical error arising in the computation of the Laplace-domain system matrix $\hat{\mathbf{A}}(p_m)$. An essential feature of the present time-domain method is that it uses the Laplace-domain instead of the time-domain Green's functions, which are yet not available in literature for FGMs. An explicit expression of the time-domain Green's functions $T^G_{\gamma\alpha\beta}$ is not required in the present method. The Laplace-domain Green's functions $\hat{T}^G_{\gamma\alpha\beta}$ are expressed as Fourier-integrals. The computation of Eq. (10) can be performed very efficiently by using the Fast-Fourier-Transform (FFT). The system of linear algebraic equations (9) can be solved time-step by time-step to obtain the expansion coefficients $c_{\gamma;k}^j$. The DSIFs can be computed immediately in a simple manner.

NUMERICAL RESULTS AND CONCLUSIONS

Numerical results obtained by the present time-domain BIEM show that the method is highly accurate, efficient and stable. Several numerical examples will be presented, to analyze the effects of the material gradients and the crack orientation with respect to the material gradation on the DSIFs and their dynamic overshoot over the corresponding static values.
To the authors knowledge, the results presented in this paper are completely new and they cannot be found elsewhere in literature. The corresponding anti-plane crack problem has been investigated in [2], while a 2-D elastostatic crack analysis in FGMs has been performed in [3] by the authors .

References

[1] Lubich, C.: Convolution Quadrature and Discretized Operational Calculus. I. *Numerische Mathematik* **52**: 129–145, 1988.
[2] Zhang, Ch., Sladek, J., Sladek, V.: Effects of Material Gradients on Transient Dynamic Mode-III Stress Intensity Factors. *Int. J. Solids Struct.* **40**:5251–5270, 2003.
[3] Zhang, Ch., Sladek, J., Sladek, V.: Numerical Analysis of Cracked Functionally Graded Materials. *Key Eng. Mater.* **251-252**:463-471, 2003.

ASYMPTOTIC ANALYSIS OF A STATIONARY CRACK IN A DUCTILE FUNCTIONALLY GRADED MATERIAL

Dhirendra V. Kubair*, Philippe H. Geubelle**, John Lambros**
* *Department of Aerospace Engineering, Indian Institute of Science, Bangalore 560012, India*
** *Department of Aerospace Engineering, University of Illinois at Urbana-Champaign, Illinois 61801, USA*

Summary The dominant and higher-order asymptotic stress and displacement fields surrounding a stationary crack in a ductile functionally graded material subjected to anti-plane shear loading are derived. It is shown that the leading (most singular) term in the asymptotic expansion is the same in the graded material as in the homogeneous one. The second term in series may differ from that of the homogeneous case depending on the particular material property variation.

INTRODUCTION

Many naturally occurring engineering materials have properties that vary continuously and smoothly with position. Examples include animal bones, teeth and wood. Engineering materials with inhomogeneous material properties are used in order to design efficient structures. For the purpose of this article, a *functionally graded material* is one, in which the material properties such as Young's modulus, density or yield stress are a function of spatial position and the functional form of the variations are known. Functionally graded materials have a broad range of applications as in thermal barrier coatings in gas turbines, artificial dental implants, bearing surfaces in MEMS devices and ballistic impact resistant structures. Functionally graded materials can be formed in a variety of ways, for example a thermal barrier coating is formed by depositing a porous ceramic coating on a metallic substrate (bond coat). The material properties of such a a graded system varies from that of a pure metal on one side to that of a ceramic on the other and hence will have the advantages of both a metal and ceramic at the same time. Fracture behavior of graded materials is not fully understood which limits their usage. Static (Eischen, 1987) and dynamic (Parameswaran and Shukla, 1999) analysis of cracks in inhomogeneous materials do exist in the literature, but they all ignore the effect of inelastic deformations even when the material is ductile. In this paper, we focus our attention on the asymptotic solution of a stationary crack in a ductile, inhomogeneous material subjected to an anti-plane shear loading. The analysis is developed in the lines of the HRR solution (Hutchinson, 1968; Rice and Rosengren, 1968) and the elastic deformations are assumed to be negligibly small compared to the plastic ones. A variable separable solution is assumed to exist near the crack tip, even when the material properties vary with spatial position. As in the elastic case (Eischen, 1987; Parameswaran and Shukla, 1999), we see that the first-term (the most singular term) of the asymptotic solution remains unaffected by the material inhomogeneity even in the plastic case. In this article we explore whether the second-term is affected by the material property variation.

FORMULATION

A semi-infinite stationary crack embedded in a functionally graded material subjected to a far field mode 3 loading is considered. The analysis is performed in the polar coordinates choosing the crack tip as the origin. The material is assumed to follow the infinitesimal J_2-deformation theory along-with the Ramberg-Osgood power law hardening model. The shear stresses in the anti-plane case can be written as

$$\sigma_{\gamma z} = G\left(r,\theta\right)\left[2\epsilon_{\beta z}\epsilon_{\beta z}/3\right]^{\frac{1}{n}-1}\epsilon_{\gamma z},\ \gamma = r,\theta, \tag{1}$$

with $G = 2\sigma_o\left[\alpha\epsilon_o\right]^{-1/n}/3$, where σ_o and ϵ_o are the stress and strain at initial yield respectively and α is a non-dimensional parameter. For mathematical simplicity we restrict the hardening index n to be a constant, while allowing the other material properties in the above equation to vary with position. Traction free boundary condition is enforced on the crack faces in order to obtain a solution ($\sigma_{\theta z}(r,\pm\pi) = 0$).

LEADING ORDER TERM

The leading order solution is obtained by assuming a variable separable one-term expansion for the out of plane displacement as

$$\frac{w\left(r,\theta\right)}{r_P} \approx A\left(\frac{r}{r_P}\right)^{p+1} f\left(\theta\right) \text{ as } r \to 0, \tag{2}$$

where r_P is the radius of the plastic zone, A is a non-dimensional amplification factor and p is the strain singularity, which must be greater than -1 to ensure a bounded displacement field. The governing non-linear ordinary differential equation for $f(\theta)$ is obtained by using the strain-displacement, stress-strain and stress equilibrium equations, which can be written as

$$G\phi_1 + \frac{r_P}{r_F}\frac{r}{r_P}\left[\frac{\partial G}{\partial r}\phi_{2r} + \frac{\partial G}{\partial \theta}\phi_{2\theta}\right] = 0, \tag{3}$$

here r_F denotes the intrinsic material length scale associated with the material gradient. In the above equation ϕ_1, ϕ_{2r} and $\phi_{2\theta}$ are functions of the angular function f and its derivatives. When the material gradient is absent the above system of equations reduce to $\phi_1 = 0$ and the solution for the homogeneous material is recovered. The material property G is required to be finite and strictly positive at the crack tip and hence the solution to the leading order term in the case of a graded material is identical to that of a homogeneous material. This result is expected and follows the trend observed in elastic analyses of graded materials (Eischen, 1987).

HIGHER ORDER TERM

As seen in the previous section, the material property gradient does not affect the solution to the leading order term. Here, we explore the possibility whether the second (less singular) term is affected by the material gradient.

Homogeneous case

Now the displacement is assumed to be given by a two term expansion as

$$\frac{w(r,\theta)}{r_P} \approx A\left(\frac{r}{r_P}\right)^{p+1} f(\theta) + B\left(\frac{r}{r_P}\right)^{q+1} g(\theta), \tag{4}$$

where A and B are non-dimensional amplitude factors, p and q are the exponents for the leading and second terms, respectively (with $q > p$). A set of governing non-linear ordinary differential equations are obtained for f and g as

$$Ar^{3p-1}\phi_1 = 0, Br^{2p+q+1}\phi_3 = 0 \text{ and } \left.\frac{df}{d\theta}\right|_{\pm\pi} = \left.\frac{dg}{d\theta}\right|_{\pm\pi} = 0. \tag{5}$$

In the above equation ϕ_3 is a function of both the angular functions f and g and their derivatives. The solution to the first of the above equations is identical to the solution obtained earlier for the leading order term. With the knowledge of p and f a solution for q (eigen value) and g (eigen vector) can be obtained by solving $\phi_3 = 0$. The amplitude factor B is left undetermined by this asymptotic analysis. The exponent q obtained for the homogeneous material is denoted as q_h and forms as the upper bound for the second term exponent of a graded material as shown in the next section.

Graded material

A two term expansion for the out of plane displacement described in the previous section is used even in the case of the graded material. In the homogeneous case the material property G was independent of the spatial position. In the graded material we assume the material property to be

$$G(r,\theta) = G_o + \left[\frac{r}{r_F}\Gamma(\theta)\right]^c G_1. \tag{6}$$

The above type of power-law material property variation is most generic and can describe any functional form of property variation, such as linear, exponential etc., by setting $c = 1$ (Taylor series expansion). By choosing an appropriate trigonometric function for $\Gamma(\theta)$ the material property can be described along radial lines, on the crack line and perpendicular to the crack plane. The boundary value problem for the higher order term for a graded material is now given by

$$\phi_1 = 0, \phi_3 + \left(\frac{r}{r_P}\right)^{(c+p)-q} \underbrace{c\left(\frac{G_1}{G_o}\right)\left(\frac{r_P}{r_F}\right)^c \frac{A}{B}}_{m}\left[\phi_{2r} + \frac{1}{\Gamma}\frac{d\Gamma}{d\theta}\phi_{2\theta}\right] = 0, \text{ and } \left.\frac{df}{d\theta}\right|_{\pm\pi} = \left.\frac{dg}{d\theta}\right|_{\pm\pi} = 0. \tag{7}$$

It can be seen from the above equation that the higher order term will or not be affected by the material property variation depending on the value of $(c + p) - q$. When $q > c + p$ the first term which is the most singular term is the only possible solution. When $q < c + p$ the asymptotic solution for a graded material is identical to that of a homogeneous material upto and including the second term. The material property gradient is going to alter the asymptotic solution only when $q = c + p$. In this case the exponent of the second term is completely determined and the multiplying factor in (7) $m = c(G_1G_o)(r_P/r_F)^c(A/B)$ becomes the eigen value of the boundary value problem. It is interesting to note that the amplification factor B which was left undetermined by the asymptotic analysis in the homogeneous case is now fully determined. Our analysis has shown that a variable separable solution is not possible when $q \geq q_h$, which specifies an upper bound for the material exponent as $c_{max}(n) = q_h - p$.

References

[1] Hutchinson J. W.: Singular behavior at the end of a tensile crack in a hardening material. *Journal of the Mechanics of Solids* **16**:13–31, 1968.

[2] Rice J. R. and Rosengren G. F.: Plane strain deformation near a crack tip in a power-law hardening material. *Journal of the Mechanics and Physics of Solids* **16**:1-12, 1968.

[3] Eischen J. W.: Fracture of non-homogeneous materials. *International Journal of Fracture* **34**: 3-22, 1987.

[4] Parameswaran V. and Shukla A.: Crack-tip fields for dynamic fracture in functionally graded materials. *Mechanics of materials* **31**: 579-596, 1999.

THE PLANE CRACK IN A FUNCTIONALLY GRADED ORTHOTROPIC STRIP

Linzhi Wu, Licheng Guo and Li Ma

(*Center for Composite Materials, Harbin Institute of Technology, Harbin 150001, P.R. China*)

Summary The plane crack problem of a functionally graded orthotropic strip under concentrated loads is studied. The edge crack is perpendicular to the boundary and the elastic property of materials is assumed to vary continuously along the thickness direction. By using integral transform method, the present problem can be reduced to a singular integral equation. The influences of geometric and material's parameters on stress intensity factors are analyzed.

FORMULATION OF PROBLEM

Though there are a lot of papers related to the crack problem of FGMs, very few papers on the plane crack problem of a functionally graded strip with a crack perpendicular to the boundary are published. It is very significant to investigate this kind of crack problems since the model can be used as an approximation to a number of structural components and laboratory specimens.

Consider the plane crack problem of a functionally graded orthotropic strip with properties varying along the x-axis (see Fig.1). The strip is infinite along the y-axis and has a thickness *h* along the x-axis. The edge crack is perpendicular to the boundaries. The material properties are defined as

$$c_{11}(x)=c_{110}e^{\delta x},\quad c_{12}(x)=c_{120}e^{\delta x},\quad c_{22}(x)=c_{220}e^{\delta x},\quad c_{66}(x)=c_{660}e^{\delta x} \tag{1}$$

where $c_{110}, c_{120}, c_{220}, c_{660}$ and δ are constants.

Substituting the constitutive equation into the equilibrium equation and using Fourier's transform technique, we can obtain the corresponding displacement field and stress field. Introducing the auxiliary function and according to boundary conditions, after some manipulation, we can obtain the following integral equation for the edge crack

$$\int_0^b [h_1(u,x)+h_2(u,x)]g(u)du=-e^{-\delta x}[\sigma(x)+\frac{2}{\pi}\int_0^\infty X_3X_1^{-1}X_2ds],\qquad 0\le x<b \tag{2}$$

where the right hand of equation (2) is the known function, and

$$h_1(u,x)=\lim_{y\to 0}\frac{1}{2\pi}\int_{-\infty}^{+\infty}K_1(y,s)e^{is(x-u)}ds,\quad h_2(u,x)=\lim_{y\to 0}\frac{2}{\pi}\int_0^{+\infty}K_2(u,x,s)\cos(sy)ds \tag{3}$$

To derive the singular integral equation, an asymptotic analysis is needed. When $y\to 0$ and $s\to\infty$, the asymptotic form of $K_1(y,s)$ can be expressed as

$$K_{1\infty}(0,s)=w_{11}+w_{12}/s \tag{4}$$

where w_{11} and w_{12} are known constants related to the material constants.

RESULTS AND DISCUSSIONS

Let's consider the edge crack of a functionally graded orthotropic strip as shown in Fig.1. In numerical calculations, two kinds of orthotropic materials given by Chen et al.[1] are chosen. The constants $\mathbf{C}_{110}$, $\mathbf{C}_{120}$, $\mathbf{C}_{220}$ and $\mathbf{C}_{660}$ are taken as 1.048×10^{10}, 3.248×10^{9}, 1.578×10^{10} and 7.07×10^{9}, respectively.

Fig.2 shows the variations of normalized stress intensity factors with the crack length $a_0=b/2h$ when the nonhomogeneity constant δh takes different values. It can be found that $k_1(b)/k_0$ increases with the increasing of the crack length. However, $k_1(b)/k_0$ decreases with the increasing of the nonhomogeneity constant δh. Therefore, the normalized SIFs are greater when the edge crack lies in the stiffer side of the strip. To investigate the

influence of loading conditions on SIFs, we take $r_0 = 3.0$. From Fig.3, it is found that normalized SIFs increase with the increasing of $a_0 = b/h$ for the same nonhomogeneity constant δh. By further observation, it can be found that $k_1(b)/k_0$ increases with the increasing of δh. Here, $\delta h < 0$ implies that the crack side is stiffer than the other side, while $\delta h > 0$ means the crack side is softer than the other side of the strip. Therefore, it can be concluded that the normalized SIFs are greater when the edge crack lies in the stiffer side of the strip. By comparing Fig.2 with Fig.3, we see that the applied loads have important effects on the distribution of stress intensity factors near the crack tip. Similarly, the present works can be expanded to investigate the internal crack problem of FGMs.

CONCLUSIONS

For the edge crack problem, to our knowledge, it is the first time to provide the asymptotic expression in the singular integral equation. The stress intensity factors for the mode I problem are solved under two different loading conditions, namely crack surface pressure and fixed-grip loading. The effects of material constants and geometry parameters on stress intensity factors are studied. It is found that the effect of the material nonhomogeneity constant on stress intensity factors is very significant. For the uniform crack surface pressure, normalized SIFs near the stiffer crack tip of the strip are greater. For the fixed-grip loading, normalized SIFs near crack tips increase with the increasing of δh.

References

[1] Chen J, Liu Z.X., Zou Z.Z. Transient internal crack problem for a nonhomogeneous orthotropic strip (Mode I). Int J Eng Sci, 40: 1761-1774, 2002.

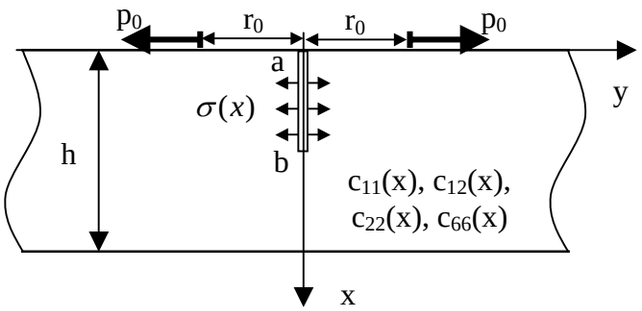


Fig.1 The schematic of the orthotropic functionally graded strip with an edge crack

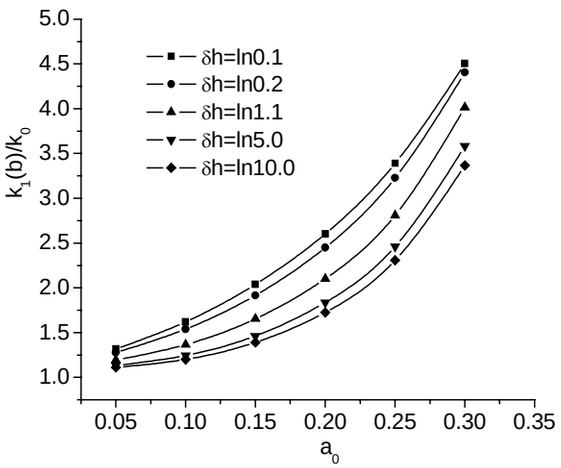


Fig.2 Normalized SIFs of the edge crack under uniform crack surface pressure

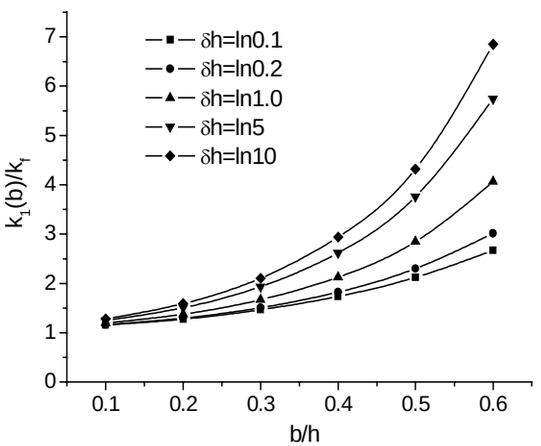


Fig.3 Normalized SIFs of the edge crack under the fixed-grip loading

FRICTIONAL SLIP BETWEEN A GRADIENT NON-HOMOGENEOUS LAYER AND A HALF-SPACE IN ANTI-PLANE ELASTIC WAVE FIELD

GAI BING-ZHENG

Department of Astronautics and Mechanics, P.O.Box .344,

Harbin Institute of Technology, Harbin 150001, People's Republic of China

EXTENDED SUMMARY

The problem to treat here is shown As in Fig.1. An elastic layer with thickness H is pressed a elastic half-space by an applied pressure p°. Both the layer and half-space are composed of the gradient non-homogeneous medium, and suppose that there is the Coulomb friction with static and kinetic friction coefficients f_s and f_k at the interface between them The anti-plane motions in the layer and half-space will be aroused under the action of SH parabolic pulse incidence wave, as shown in Fig.2. When the shear elastic modulus $m(m^*)$ and the density $r(r^*)$ of medium vary by the laws of the second power in the gradient direction of medium, the analytical solution of the problem is found as

$$w=\int_{-\infty}^{+\infty}[A(k)(1+ay)^{\frac{1}{2}}H_{\frac{1}{2}}^{(1)}(p\frac{k}{a}(1+ay)) + B(k)(1+ay)^{-\frac{1}{2}}H_{\frac{1}{2}}^{(2)}(p\frac{k}{a}(1+ay))]e^{ikx}\,dk \tag{1}$$

$$w^*=\int_{-\infty}^{+\infty}[A^*(k)(1+a^*y)^{\frac{1}{2}}H_{\frac{1}{2}}^{(1)}(p^*\frac{k}{a^*}(1+a^*y)) + B^*(k)(1+a^*y)^{-\frac{1}{2}}H_{\frac{1}{2}}^{(2)}(p^*\frac{k}{a^*}(1+a^*y))]e^{ikx}\,dk \tag{2}$$

$w(w^*)$ is the anti-plane displacement; a, a^* are two known gradient constants of media; $p=\sqrt{\left(\frac{c}{c_s(c_s^{\bullet})}\right)^2-1}$; c is the apparent velocity of elastic wave along the interface $c_s(c_s^{\bullet})$ $c_s(c_s^{\bullet})$ is shear wave speed of medium; A, B,A^*,B^* are known functions of k; asterisk * refers to the quantities of the layer; $H_{\frac{1}{2}}^{(1))}$, $H_{\frac{1}{2}}^{(2)}$ are Hankel function of 1,2 kind of 1/2 order. From these, he distribution of dimensionless shearing traction

$t(h)$ and that of dimensionless relative slip $d(h)$ are obtained as

$$t(h) = \mathrm{Re}\int_{-\infty}^{+\infty}(H_{\frac{3}{2}}^{(2)}(p\frac{k}{a}) + \frac{A(k)}{A^i(k)}H_{\frac{3}{2}}^{(1)}(p\frac{k}{a})) \times \frac{2p(\frac{h}{l})}{pkH_{\frac{1}{2}}^{(2)}(p\frac{k}{a})}(\frac{\sin kl}{kl} - \cos kl)e^{ikx}dk \tag{3}$$

$$d(h) = \mathrm{Re}\int_{-\infty}^{+\infty}(H_{\frac{1}{2}}^{(2)}(p\frac{k}{a}) + \frac{A(k)}{A^i(k)}H_{\frac{1}{2}}^{(1)}(p\frac{k}{a})) + \frac{A^*(k)}{A^i(k)}H_{\frac{1}{2}}^{(1)}(p^*\frac{k}{a^*}) + \frac{B^*(k)}{A^i(k)}H_{\frac{1}{2}}^{(2)}(p^*\frac{k}{a^*})] \times \frac{2(\frac{h}{l})}{pkH_{\frac{1}{2}}^{(2)}(p\frac{k}{a})}(\frac{\sin kl}{kl} - \cos kl)e^{ikx}dk \tag{4}$$

Take $al = a^*l = 0.2$; $f_0 = f_k / f_s = 0.8$; $m^*/m = 1.5$; $ph/2l = 1$; $c^*/c = 1.2$; $q_0 = \sin^{-1}(c_s/c) = p/6$; $H/l = 50$; $x = (x - ct)/l$. $A^i(k)$ incident wave amplitude; Fig.3 shows the variation of $t(h)$ with h (real line) and the extent and location of the stick and slip zone for given parameters. It can be seen from the figure that the state of the interface reveals periodicity. The periodic length is 50. There are 3 slip zones (2 in right direction and 1 in inverse direction) in a periodic length, and on which put a number (1), (2) or (3), respectively. As the dimensionless external pressure s increase, the number of the slip zone will increase, its extent become larger. Fig.4 shows the distribution of the dimensionless shear traction $t(h)$ and dimensionless relative slip $d(h)$ in the slip zone (1)-(3) and neighborhoods of them. It can be seen from the figures that the shear traction $t(h)$ at the leading edge of the slip zone has a jump, but is continuous at the training edge, which is caused by the difference between the static and kinetic friction. Besides, there is a rigid displacement between the leading edge and the training edge. In order to reveal the effect of the interface thickness, we calculate the variations of the dimensionless shear traction t (33) and the dimensionless relative slip $d(33)$ with the dimensionless layer thickness H/l, as shown in Fig.5. From the figures we see that the change the dimensionless layer thickness H/l will make the state of the interface change, but the change is not monotonous.

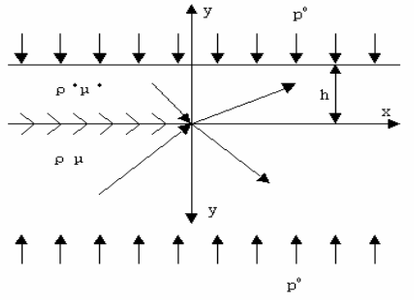


Fig.1 Anti-plane wave field in a half-space with a layer

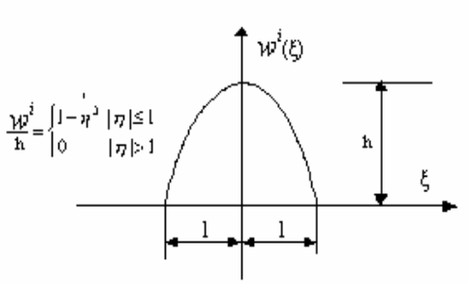


Fig.2 Incident parabolic pulse

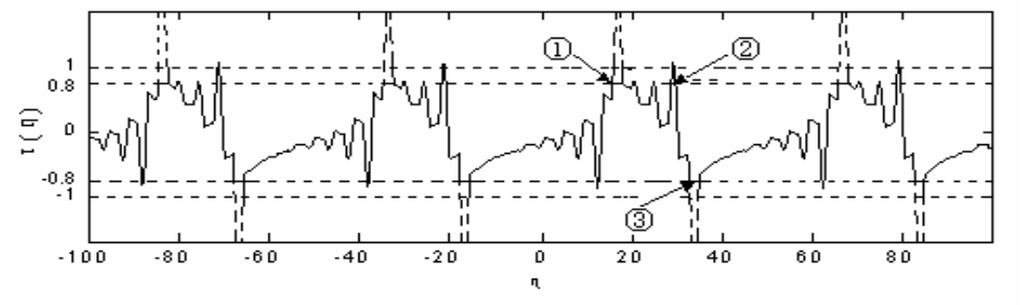


Fig.3 The stick and slip zones and distribution of shearing traction $\tau(\eta)$ at the interface

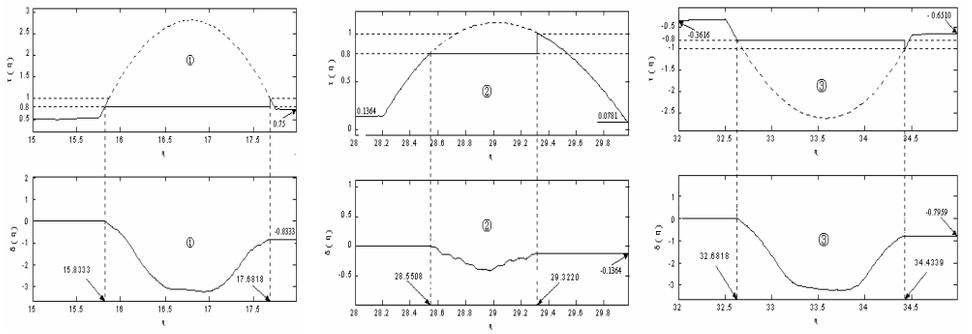


Fig. 4 Distribution of shearing tractions $t(h)$ and relative slip $d(h)$ at ① ② ③ point and its neighborhood

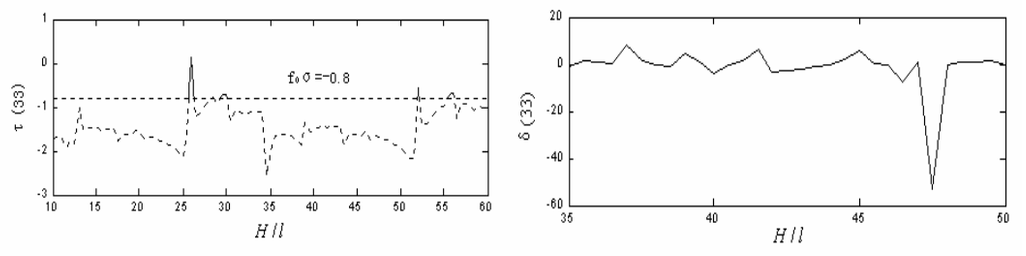


Fig.5 Variations of shearing traction $t(33)$ and relative slip $d(33)$ with dimensionless layer thickness H/l (real linear)

1. BaBaei R., Lukasiewicz S. A., 1998. Dynamic response of a crack in a functionally graded material between two dissimilar half planes under anti-plane shear impact load. Engineering Fracture Mechanics 60, 479-487.
2. BaBaei R., Lukasiewicz S. A., 1998. Fracture in functionally gradient material subjected to the time-dependent anti-plane shear load. ZAMM, 78, 383-390.
3. Comninou M. and Dundurs J., 1977.Reflection and refraction of elastic waves in presence of separation. Proceeding of Royal Society of London Series A356,509-528.
4. Comninou M. and Dundurs J., 1978.Elastic interface waves and sliding between two solids. Journal of Applied Mechanics 45,325-330
5. Comninou M. and Dundurs J., 1979.Interaction of elastic waves with a unilateral interface. Proceeding of Royal Society of London Series A368,1451-154.
6. Comninou M. and Dundurs J.,1980. Interface slip caused by an SH pulse. International Journal of Solids and Structure 16,283-289.
7. Comninou M. Barbe J.R.and Dundurs J.,1982. Disturbance at a frictional interface caused by a plane elastic pulse. Journal of Applied Mechanics 49,361-365.
8. Gai B.Z.,2000.Interaction of elastic waves with the unilateral interface between alayer and a half- space. International Journal of Solids and Structure 37,5233-5245.
9. Gai B.Z. and Chen C.C.,2001. BEM-analysis of interaction of elastic wave with unilateral interface crack. Communication in Numerical Methods In Engineering 17,137-147..
10. Liu. J.B., Wang. D., Yao. L., 1993. A contact force model in the dynamic analysis of contactable crack. Acta Mechanics Solida 4, 439-502. (in Chinese).
11. Li C. Y., Wang, G. J., 2001. Dynamic stress intensity factor of a cylindrical interface crack with a functionally graded interlayer. Mechanics of Materials 33, 325-333
12. Meguid S. A., Wang X. D., Jiang, L.Y., 2002. On the dynamic propagation of a finite crack in functionally graded materials, Engineering Fracture Mechanics 69, 1753-1768
13. Miller R.K.1977.Anapproximate method of analysis of the transmission of elastic waves through a friction. Journal of Applied Mechanics 44,625-656
14. Miller R.K.1978.The effects of boundary friction on the propagation of elastic waves. Bulletin of the Seismology Society of America 68,987-998.
15. Miller R.K. and Tan H.T.,1979. Reflection, refraction and absorption of elastic waves at a frictional interface: SH motion. Journal of Applied Mechanics 46,625-630
16. Miller R.K. and Tan H.T.,1981, Reflection refraction and absorption of elastic waves at a frictional interface :P and SV motion. Journal of Applied Mechanics 48,155-160.
17. Parameswaran. V. and Shukla A., 1999. Crack-tip stress fields for dynamic fracture in functionally gradient materials. Mechanics of Materials 31, 579-596.
18. Parameswaran. V. and Shukla A., 1998. Dynamic fracture of a functionally gradient material having discrete property variation. Journal of Materials Science 33, 3303-3311.
19. Shul C.W. and Lee K. Y., 2002. A subsurface eccentric crack in a functionally graded coating layer on the layered half-space under antiplane shear impact load. International Journal of Solids and Structure 39, 2019-2029..
20. Wang B.L., Han J. C and. Du S. Y., 2000. Crack problems in non-homogeneous composites subjected to dynamic loading, International Journal of Solids and Structure 37, 1251-1274
21. Wang Y.S. Yu G.L. and Gai B.Z., .1997.Slip with friction between an elastic layer and a substrate caused by an SH pulse. International Journal of Solids and Structure 35,2001-2021.
22. Wang Y.S. Yu G.L. and Gai ,B.Z.,1998.In-plane motion induced by an SH pulse at a frictional contact interface .Mechanic Research Communications25,203-210

WAVE PROPAGATION IN FUNCTIONALLY GRADED MATERIALS

Arkadi Berezovski[*], Jüri Engelbrecht[*], Gérard A. Maugin[**]
[*] *Institute of Cybernetics at Tallinn Technical University, Centre for Nonlinear Studies, Akadeemia tee 21, 12618 Tallinn, Estonia*
[**] *Université Pierre et Marie Curie, Laboratoire de Modélisation en Mécanique, UMR 7607, Tour 66, 4 Place Jussieu, Case 162, 75252, Paris Cédex 05, France*

Summary The propagation of two-dimensional stress waves in functionally graded materials (FGMs) is studied numerically. Two distinct models of FGMs are considered: i) a multilayered metal-ceramic composite with averaged properties within layers; ii) randomly embedded ceramic particles in a metal matrix with prescribed volume fraction. The numerical simulation demonstrates the applicability of the composite wave-propagation algorithm to the modelling of FGMs without any averaging procedure. The analysis based on simulation shows significant differences in the stress wave characteristics for the distinct models that can be used for optimizing the response of such structures to impact loading.

BACKGROUND

Studies of the evolution of stresses and displacements in FGMs subjected to quasistatic loading [1] show that the utilization of structures and geometry of a graded interface between two dissimilar layers can reduce stresses significantly. Such an effect is also important in case of dynamical loading where energy-absorbing applications are of special interest.

A two-dimensional problem of the impulsive loading of a plate of thickness h and length L >> h is considered. The load is applied transversally at the central region of the plate upper surface of length a (a < L). The material of the plate is assumed to be compositionally graded along the thickness direction. The gradation is described in terms of the volume fraction of a ceramic reinforcing phase within a metal matrix. Both metal and ceramics are assumed to behave as linear isotropic elastic media.

We focus our attention on the case of dynamic loading of a plate where the wavelength of stress pulse is comparable with the plate thickness. This means that the wavelength is much larger than the size of inclusions and the distance of wave travel is relatively small. In addition, the rise time of applied stress pulse (0.75 μs) is much larger than the ratio of the reinforcement dimension to the fastest wave speed in the reinforcing material.

For the comparison of the two distinct models of FGMs, it is sufficient to employ the linear rule of mixtures for the Young's modulus and Poisson's ratio of the graded layer in the multilayered model of metal-ceramic composite with averaged properties within layers. The same individual material properties without any averaging are used in the model of the composite with randomly embedded ceramic particles in a metal matrix.

The idea of direct numerical simulation of FGMs by means of regular [2] or random [3] particle distribution is not a new one: it allows us to analyze the influence of shape and aspect ratio of particles on the FGM behavior [4]. Our goal is simply to show the differences in dynamical behavior of FGMs by using distinct models. The main aim of the paper is to compare the time evolution of the field quantities as a result of wave propagation and interaction with interfaces and gradients in these two models and clarify the significance of the choice of gradation on impact applications.

NUMERICAL SIMULATION

We applied the composite wave-propagation algorithm [5-6] to compare the models of discrete layers with averaging the material properties and of randomly embedded ceramic particles in a metal matrix. Numerical difficulties concerning rapidly-varying properties of the medium are overcome by using the composite wave-propagation algorithm, because every discontinuity in the parameters is taken into account by solving the Riemann problem at each interface between discrete elements. The reflection and transmission of waves at each interface are handled automatically.

Here these studies are extensively enlarged. Several possible forms of the ceramic reinforcement volume fraction along the thickness are considered. First, the cases examined in [7] for the axisymmetric case are studied: uniform, layered and graded with two different distributions of volume fraction. Second, more complicated cases are analysed: multi-layer coated, partly layered medium with uniform and randomly distributed layering. The influence of the thickness of graded layers on dispersion of waves is clarified.

Typical examples of contour plots showing the full displacement fields are presented in Fig. 1 for the same density distribution in different models. Computations performed under the same conditions for distinct models of the same FGM: L=49 mm, h=24.5 mm, a=12.25 mm, maximal amplitude of loading was equal to 125 MPa. The difference in the propagation speed of stress wave is clearly seen whereas the particle volume fraction was distributed similarly in both models. In addition, we have the distortion of the symmetrical shape of the wavefronts in the model with randomly embedded particles due to random particle distribution.

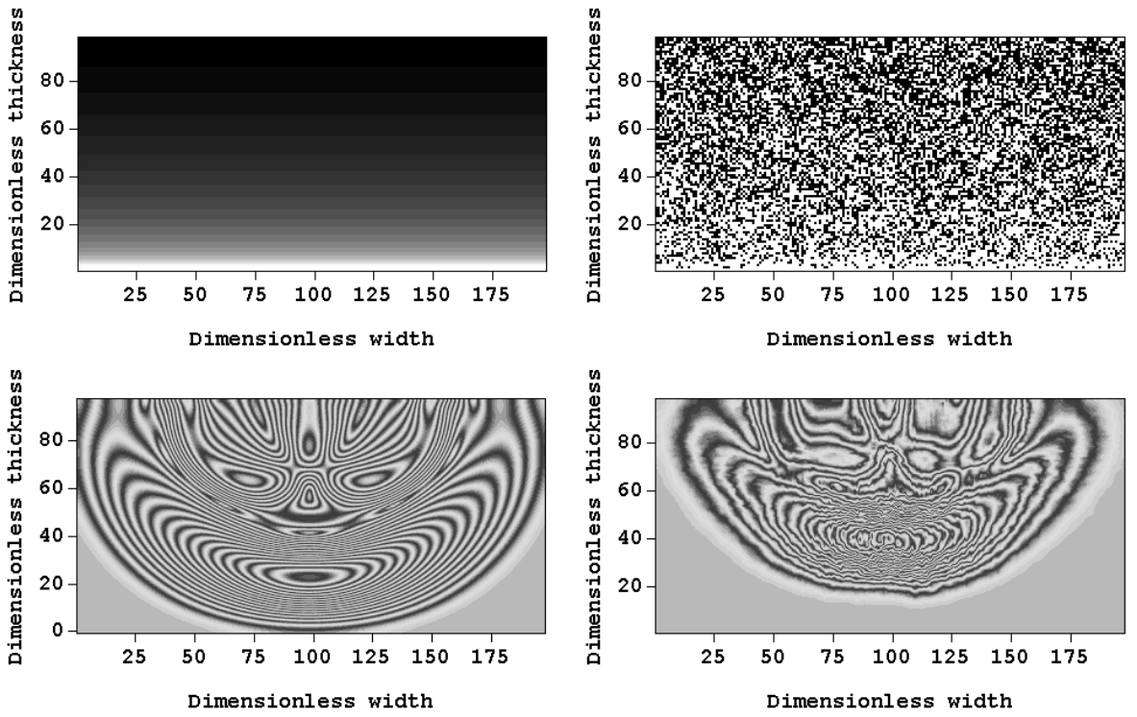


Fig.1. Density distributions and wavefronts in metal-ceramic composite for different models.

CONCLUSIONS

Theoretical prediction of dynamic behaviour of FGMs depends on how well their properties are modelled in computer simulations. While many averaging models of the properties of FGMs are widely accepted, a more natural model of a matrix with randomly embedded particles is seldom used because of numerical difficulties in the case of rapidly-varying properties of the medium. In this paper, we applied the composite wave-propagation algorithm to compare the models of discrete layers with averaging the material properties and of randomly embedded ceramic particles in a metal matrix.

The results of performed numerical simulations of stress wave propagation in FGMs show a significant difference between characteristics of wave fields in the distinct models. This means that a model of FGM without averaging of material properties can give more detailed information about the dynamic behaviour of a chosen structure. In addition, using this information for the nondestructive evaluation (NDE) of material properties is proposed; these studies are in progress.

References

[1] Suresh, S., Mortensen, A.: Fundamentals of Functionally Graded Materials. The Institute of Materials, London, 1998.

[2] Banks-Sills, S., Elasi, R., Berlin, Y.: Modeling of functionally graded materials in dynamic analyses. *Composites: Part B* **33**: 7-15, 2002.

[3] Leggoe, J. W., Mammoli, A. A., Bush, M. B., Hu, X. Z.: Finite element modelling of deformation in particulate reinforced metal matrix composites with random local microstructure variation. *Acta mater*. **46**: 6075-6088, 1998

[4] Li, Y., Ramesh, K. T.: Influence of particle volume fraction, shape, and aspect ratio on the behavior of particle-reinforced metal-matrix composites at high rates of strain. *Acta mater*. 4**6**: 5633-5646, 1998.

[5] Berezovski, A., Maugin, G.A.: Simulation of thermoelastic wave propagation by means of a composite wave-propagation algorithm. *J. Comp. Physics* **168**: 249-264, 2001.

[6] Berezovski, A., Engelbrecht, J., Maugin, G.A.: Numerical simulation of two-dimensional wave propagation in functionally graded materials. *Eur. J. Mech. Solids* **22**: 257-265, 2003.

[7] Li, Y., Ramesh, K.T., Chin, E.S.C.: Dynamic characterization of layered and graded structures under impulsive loading. *Int. J. Solids Struct.* **38**: 6045-6061, 2001.

XXI ICTAM, 15–21 August 2004, Warsaw, Poland

ADAPTIVE MODELLING OF MICROSCOPIC HETEROGENEOUS MEDIUM UNDERGOING LARGE DEFORMATION

Eduard Rohan*, Vladimír Lukeš*
*New Technologies Research Centre and Department of Mechanics, University of West Bohemia, Univerzitní 22, 306 14 Plzeň, Czech Republic

Summary In this paper we propose an algorithm for numerical modelling of the hyperelastic heterogeneous medium. Its microstructure changes with increasing deformation, depending on the spatial position in terms of the macroscopic deformation. The homogenized stiffness coefficients and the averaged stresses associated with the updated Lagrangian formulation are approximated over the macroscopic domain according to the local deformation. A concept of the so-called macroelements is introduced, each macroelement is related to a subdomain. Problems of the modelling error and of the adaptive approximation refinement are discussed. Numerical examples for materials with incompressible, or rigid inclusions are introduced to demonstrate performance of the method.

INTRODUCTION

The problem of computing large deformation in heterogeneous media is characterized by macroscopically non-uniform change of microstructure, thereby depending on the spatial position. Starting with perfect periodic distribution of inhomogeneities (e.g. inclusions) in the reference state, due to nonuniform deformation the material becomes functionally graded. This phenomenon tightly couples the sequence of the macroscopic and the local microscopic problems, that result from the two-scale homogenization method applied to the incremental formulation. This difficulty has been addressed in [4], where the microscopic cell problems are solved for each macroscopic element using parallel computational tools. Another approach, cited therein, is based on creating the database of pre-computed homogenized coefficients. In [3] an approximation scheme for the homogenized coefficients is proposed which allows for significant reduction of computational cost related to the local cell problems. Here we extend the approach by adaptive refinement of the approximation, which is controlled by the "modelling error" indicator, cf. [1].

HOMOGENIZED PROBLEM AND LOCAL CELL PROBLEMS

The two-scale homogenization procedure is applied to the finite deformation problem linearized using the updated Lagrangian formulation. We consider microstructures formed by hyperelastic incompressible matrix and incompressible inclusions. Such material yields the decomposition of the microscopic representative cell $Y \in \mathbb{R}^d$, $Y = \overline{Y_m \cup Y_c}$, where Y_c is the inclusion. The following local cell problems are solved to compute the corrector functions $\chi_i^{kl} \in H^1_{\#}(Y_m)^d$ for displacements and $\tilde{\pi}^{kl} \in L^2(Y_m)$ for the pressure nonuniformity (the difference between the pressure in Y_m and the uniform pressure in Y_c)

$$\tilde{a}_{Y_m}(\chi^{kl} - \Pi^{kl}, v) - (\tilde{\pi}^{kl}, \mathrm{div}_y v)_{Y_m} = 0 \quad \forall v \in H^1_{\#}(Y_m)^d \,, \tag{1}$$

$$(q, \mathrm{div}_y \chi^{kl} - \mathrm{div}_y \Pi^{kl})_{Y_m} = 0 \quad \forall q \in L_2(Y_m) \,, \tag{2}$$

where $\Pi_i^{kl} = \delta_{ik} y_l$, the bilinear form $\tilde{a}_{Y_m}(u,v) = \int_{Y_m} \left(D^{\mathrm{eff}}_{ijkl} + \tau^{\mathrm{eff}}_{lj} \delta_{ki} + J\tilde{p}\, \delta_{il}\delta_{jk} \right) \partial^y_l u_k \, \partial^y_j v_i \, J^{-1} dy$ is defined in terms of the tangent modulus, the Kirchhoff stress and the pressure nonuniformity, $\tilde{p}(y) = p(y) - \bar{p}$ for $y \in Y_m$ and $\bar{p}$ is the pressure in Y_c. The correctors determine the homogenized stiffness coefficients $Q_{ijkl} = |Y|^{-1}\, \tilde{a}_{Y_m}(\chi^{kl} - \Pi^{kl}, \chi^{ij} - \Pi^{ij}) + \bar{p}\delta_{il}\delta_{jk}$, which constitute the bilinear form of the macroscopic subproblem: given the external load functional $L(v)$, the temporary averaged stress functional $\mathcal{S}(v)$ and the out-of-incompressibility functional $Z(q)$, find the displacement and pressure incremental fields $\delta u \in V(\Omega)$ and $\delta\bar{p} \in L^2(\Omega)$, respectively, for which

$$\mathcal{B}(\delta u, v) - (\delta\bar{p}, \mathrm{div}_x v)_\Omega = L(v) - \mathcal{S}(v) \,, \quad \forall v \in V(\Omega) \tag{3}$$

$$(q, \mathrm{div}_x \delta u)_\Omega = Z(q) \,, \quad \forall q \in L^2(\Omega) \tag{4}$$

where $\mathcal{B}(\delta u, v) = \int_\Omega Q_{ijkl} \partial^x_l \delta u_k \, \partial^x_j v_i \, dx$, and $\mathcal{S}(v) = \int_\Omega |Y|^{-1} \int_Y \tau_{ij} J^{-1} \, dy \, \partial^x_j v_i \, dx$. In order to recover the homogenized coefficients in Ω, we use the approximation scheme, as briefly introduced below.

ALGORITHM FOR SOLVING THE 2-SCALE NONLINEAR PROBLEM

Given the temporary (deformed) reference macroscopic configuration Ω, the approximation scheme $\mathbb{F}$ for the homogenized coefficients and a new load represented by $L(v)$ in (3), the following 2 step algorithm applies:

1. Using the macroscopic deformation update $\mathbb{F}$, if necessary, then compute the approximation of Q_{ijkl} and that of the averaged stresses for each macroscopic (integration) point of Ω;
2. Solve (3)–(4) for $\delta u(x)$ and $\delta\bar{p}(x)$; update Ω and the macroscopic deformation gradients; if the "convergence"is not achieved, return to step 1.

Approximation of the homogenized coefficients

We now explain the step 1. The approximation scheme $\mathbb{F}$ is represented by the so-called "macroelements" M_k defined in the deformation space, each one associated with (disconnected) subdomain $\Omega_k \subset \Omega$. For 2D problems M_k is a box with vertices $\boldsymbol{f}_i$, $i = 1, \ldots, m(= 8)$ and one "central" point ${}^*\boldsymbol{F}$, which characterizes the deformation in Ω_k:

$$M_k({}^*\boldsymbol{F}, \{\boldsymbol{f}_j\}_{j=0}^m) = \{\boldsymbol{F} \mid \exists \boldsymbol{f} \in \mathrm{conv}\{\boldsymbol{f}_j\}_{j=0}^m \ : \ \boldsymbol{F} = \boldsymbol{f}\ {}^*\boldsymbol{F}\}\ , \tag{5}$$

so that the deformation gradients $\boldsymbol{F}(x) \in M_k$, $x \in \Omega_k$, up to the rigid body rotation. Each $\boldsymbol{f}_j\ {}^*\boldsymbol{F}$ determines a fictitious microstructural configuration (Y, p), for which (1)–(2) must be solved and which alternatively should be updated using macroscopic strains and the corrector functions. Using the sensitivity analysis of homogenized coefficients and stresses w.r.t. the macroscopic deformation, cf. [2], an interpolation scheme is defined over any simplex S_k^I, $I \subset \{1, \ldots, m\}$ embedded in M_k; this is the tool for constructing the approximation scheme $\mathbb{F}\{M_k\}$.

Adaptive approximation refinement strategy

Obviously, the quality of the solutions to (3)–(4) depends on the approximation scheme outlined above, which introduces the modelling error. We suggest a concept of adaptive refinement of $\mathbb{F}$ to use as few computations of the microscopic cell problems as possible. Given the set $\{M_k\}_{k=1}^N$, consider two different schemes $\mathbb{F}^i\{M_k\}_{k=1}^N$, $i = 0, 1$. For these we obtain the corresponding functionals $\mathcal{B}^i(u, v)$ and $\mathcal{S}^i(v)$. The macroscopic solution δu^0, $\delta \bar{p}^0$ is known only for $i = 0$. The upper and lower bounds of difference in the solution $\|\delta u^1 - \delta u^0\|_{\mathcal{B}^1}$ can be computed using the residual function, cf. [1], $\mathcal{R}_{\delta u^0}(u) \equiv -\Delta\mathcal{B}(\delta u^0, u) - \Delta\mathcal{S}(u)$, defined by subtracting $\mathcal{B}^1 - \mathcal{B}^0$ and $\mathcal{S}^1 - \mathcal{S}^0$. The error evaluated over Ω_k serves as the indicator for refinement of the macroelement M_k. In the paper we discuss also the influence of the macroscopic modelling error on the microscopic responses. In Fig. 1 we illustrate the adaptive algorithm: finite extension of the clamped strip considered, material with incompressible inclusions; subdomains for 2 and 4 macroelements, respectively, displayed with different colours. The maxima of norms for variation of deformation within the subdomains are: 0.185 for 1 subdomain, 0.159 for 2 subdomains and 0.083 for 4 subdomains.

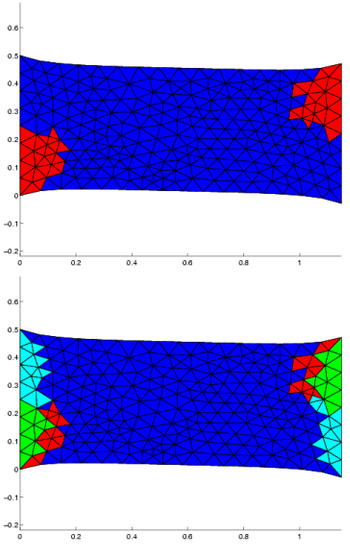


Fig. 1: Macroscopic subdomains for 2 and 4 macroelements.

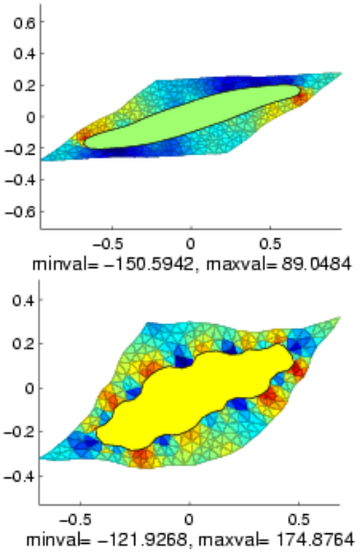


Fig. 2: Microstructures for smooth muscle modelling.

CONCLUSIONS

The adaptive approximation scheme for homogenized coefficients was employed in the large deformation analysis of hyperelastic heterogeneous materials. The strategy for modelling refinement is based on error indication associated with two different approximations of stiffnesses and stresses. For enhancement of the computational speed parallel computing tools can be used. Further modifications of the approach for functionally graded materials are possible, which may allow for applications e.g. in muscle tissue modelling, see Fig. 2. (The research has been supported by the project LN00B084 of The New Technologies Research Centre, UWB, Plzeň.)

References

[1] Oden, J.T., Vemaganti, K.: Adaptive modeling of composite structures: Modeling error estimation, part 1. *Jour. of Computational Physics*, **164**:22–47, 2000.

[2] Rohan, E.: Sensitivity strategies in modelling heterogeneous media undergoing finite deformation. *Math. and Computers in Simul.*, **61**:261–270, 2003.

[3] Rohan, E: Mathematical modelling of soft tissues. *Habilitation thesis*, University of West Bohemia, Dept. of Mechanics, Plzeň, 2002.

[4] Takano, N., Ohnishi, Y., Zako, M., Nishiyabu, K.: The formulation of homogenization method applied to large deformation problem for composite materials. *Int. J. Solids Struct.* **37**:6517–6535, 2000.

ACTUATOR AND SENSOR MODELLING FOR LAMINATED PIEZOELECTRIC PLATES

Amâncio Fernandes[(a)], Joël Pouget[(b)]
(a) Laboratoire de Modélisation en Mécanique (UMR 7607) Université Pierre et Marie Curie, Paris, France
(b) Laboratoire d'Etudes Mécaniques des Assemblages (FRE 2481) Université de Versailles, Versailles, France

Summary. We propose an accurate and efficient approach to laminated piezoelectric plates based on a refinement of elastic displacement and electric potential through the plate thickness. Different situations are investigated among them (i) bimorph and (ii) sandwich structures for two kinds of electromechanical loads and are compared to the finite element computations. The prediction of the modal frequencies of vibration of the piezoelectric plate is presented as well.

INTRODUCTION

Due to the successful applications of piezoelectric actuators and sensors, piezoelectric components made of laminated plates have received a particular attention in recent years. The main idea is that certain kinds of structure enable to adapt to or correct for changing operating conditions (geometry, behaviour, etc.) according to electromechanical loads in order to extend the optimum behaviour of the structure in which they are hosted, making them very attractive for innovative technological application. The high performance of piezoelectric composites are used for *multi-purpose devices* or *smart materials* and numerous applications have been proposed, running from aerospace structures (shape control of large space antennas, control of vibrations) to miniature devices due to the possibility of their integration on active electronic circuits (medical apparatus, micro-pump, micro-robots, etc.) [1]
The main objective of the present work attempts to present a consistent and efficient approach to piezoelectric composites made of laminated plate with active piezoelectric layers. Although a number of consistent and accurate approaches to piezoelectric laminated plates have been proposed [2], most of these models are able to accuratly predict the global responses of laminated plates, but they cannot provide excellent estimates of the local responses such as the through-the-thickness variations of the electromechanical quantities and the frequencies of the higher modes of vibration. Here, we propose an alternative approach which combines an *equivalent single-layer representation* for the mechanical displacement with a *layerwise-type approximation* for the electric potential. This approach becomes an interesting feature because multilayered piezoelectric structures are appropriate to accommodate multiple voltage actuator inputs and sensor outputs. Various situations are considered such as bimorph and sandwich structures undergoing two different electromechanical loads (i) surface density of force and (ii) electric potential applied to the piezoelectric layers. In order to show the *quality of predictions* of the present approach, the results are compared to *finite element computations* performed on the 3D problem. In particular, the *global structural response* (deflection, elongation, electric potential or charges, the frequencies of the mode vibrations), as well as the *local response* or the variation of the electromechanical states through the plate thickness are obtained and discussed.

APPROXIMATION OF THE ELECTROMECHANICAL FIELDS

We consider an expansion of the displacements and electric potential as a function of the thickness coordinate as follows

$$\left\{\begin{array}{lcl} u_\alpha & = & U_\alpha - z w_{,\alpha} + f(z)\gamma_\alpha, \qquad \alpha \in \{1,2\}\,, \\ u_3 & = & w\,, \\ \phi^{(\ell)} & = & \phi_0^{(\ell)} + z_\ell \phi_1^{(\ell)} + P_\ell(z_\ell)\phi_2^{(\ell)} + g(z)\phi_3^{(\ell)}\,. \end{array}\right.$$

With $\ell \in \{1, \cdots, N\}$ is the layer number, z_ℓ is the thickness coordinate with respect to the mid-plane of the ℓth layer, U_α is the *middle plane displacement component*, w is the *deflection* and γ_α represents the *shearing function*. The functions of the thickness coordinate are choosen as follows

$$P_\ell(z_\ell) = z_\ell^2 - \left(\frac{h_\ell}{2}\right)^2, \qquad f(z) = \frac{h}{\pi}\sin\left(\frac{\pi z}{h}\right), \qquad g(z) = \frac{h}{\pi}\cos\left(\frac{\pi z}{h}\right),$$

where h is the plate thickness and h_ℓ is the thickness of the ℓth layer and $z_\ell \in [-h_\ell/2, h_\ell/2]$.
However, the continuity of the electric potential as well as the normal component of the electric induction must be satisfied at $z = z_I^{(\ell)}$ ($\ell \in \{1, ..., N-1\}$). The conditions are $\mathcal{A}_\ell = \phi^{(\ell+1)}(x, y, -h_{\ell+1}/2) - \phi^{(\ell)}(x, y, +h_\ell/2) = 0$ and $\mathcal{B}_\ell = D_3^{(\ell+1)}(x, y, -h_{\ell+1}/2) - D_3^{(\ell)}(x, y, +h_\ell/2) = 0$, where the normal component of the electric induction of the ℓth layer is calculated from the constitutive equations. The second condition must be satisfied if no electric potential is applied at $z = z_I^{(\ell)}$, otherwise the condition of continuity is not considered and it is replaced by the jump condition $[\![D_3]\!]_{z=z_I^{(\ell)}} = Q_\ell$ where Q_ℓ is the output surface density of electric charge at the interface $z = z_I^{(\ell)}$. In order to account for the additional conditions, Lagrange multipliers are introduced in the variational formulation [3].

NUMERICAL RESULTS

A collection of benchmark tests is proposed for the piezoelectric bimorph and sandwich structures for plates simply supported under cylindrical bending. Two kinds of electromechanical loads are considered (i) *sensor function* with a surface force density applied to the top face and (ii) *actuator function* with an electric potential applied to the top and bottom faces of the plate and eventually at the layer interfaces [3,4].
In order to illustrate the effectiveness of the proposed approach, we consider, as an example, a laminated plate made of composite material (graphite fibers in an epoxy matrix) for the central layer sandwiched with two piezoelectric PZT layers. The sandwich plate is then subject to a surface density of force normal to the top face. The profile of the induced electric potential at $x = L/2$ within the piezoeletric layers is depicted in Fig.1. For an Applied electric potential the through-the-thickness distribution of the deflection at the plate center is plotted in Fig.2. All these results demonstrate the effectiveness of the present modelling.

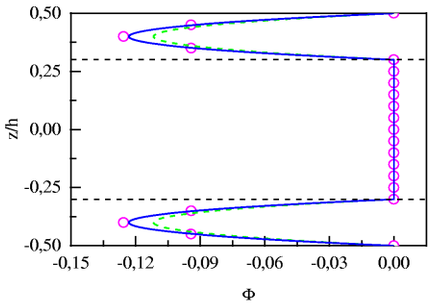


Figure 1. *Sensor function*

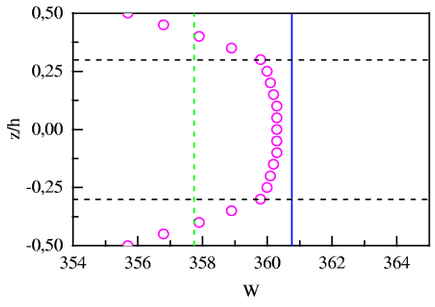


Figure 2. *Actuator function*

We propose the prediction of modal frequencies of piezoelectric plates. Table 1 gives the computational results and comparison to finite element simulations and to simplified model for which no shear correction has been included. The prediction of the modal frequencies for the present approach remains within 5 % for the first seven flexural modes while the simplified model based on the Love-Kirchhoff kinematics plate theory overcomes 20 %. Such an investigation of modal frequencies of vibration is a first step in controlling vibration of elastic structures.

Table 1. *Modal frequencies for piezoelectric sandwich plate (L/h=10).*

Frequencies (Hz) - L/h=10					
MODES	FE	Present Model	Error	Simplified Model	Error
Flex. $n = 1$	29530	29570	0.1 %	29869	1.1 %
Flex. $n = 2$	112624	113295	0.6 %	117537	4.2 %
Flex. $n = 3$	236707	239584	1.2 %	257639	8.1 %
Flex. $n = 4$	388585	396150	1.9 %	442512	12.2 %
Flex. $n = 5$	557423	573241	2.7 %	663571	16 %
Flex. $n = 6$	734569	764062	3.9 %	912474	19.5 %
Flex. $n = 7$	912254	964119	5.4 %	1181874	22.8 %
Axial $n = 1$	324061	324220	0.05 %	324220	0.05 %

CONCLUSIONS

The present study proposes an accurate and efficient approximation for the elastic displacement including a shear function and a layerwise modelling for the electric potential. Such an approach can incorporate the local electromechanical response of the individual layer and becomes a necessity when an electric potential is applied to metallized interfaces between layers. The numerical results and comparisons to FE simulations demonstrate the efficiency of the present model and its capability to accuratly predict the local (field distributions) and global responses.

References

[1] Tani J., Takagi T., Qiu J.: Intelligent material systems : Application of functional material. *Appl. Mech. Rev.* **52**: 505-521, 1998.
[2] Saravanos D.A., Heyliger P.R.: Mechanics and computational models for laminated piezoelectric beams, plates and shell. *Appl. Mech. Rev.* **52**: 305-320, 1999.
[3] Fernandes A., Pouget J.: An accurate modelling of piezoelectric multi-layer plates. *Eur. J. Mech. A/Solids* **21**: 629-651, 2002.
[4] Fernandes A., J. Pouget J.: Analytical and numerical approaches to piezoelectric bimorph. *Int. J. Solids and Structures* **40**: 4331-4352, 2003.

COMPLEX -VARIABLE METHODS APPLIED TO FUNCTIONALLY-GRADED ELASTIC PLATE PROBLEMS

A.H. England, A.J.M. Spencer
School of Mathematical Sciences, University of Nottingham, Nottingham NG7 2RD, UK

Summary. Exact solutions are obtained to the equations of linear elasticity in a thick elastic plate of inhomogeneous material in which the elastic moduli are specified functions of the coordinate normal to the plane of the plate. These solutions are expressed in terms of four complex potentials that are analytic functions of an in-plane complex coordinate. The solutions admit the specification of the standard resultant force and moment conditions or averaged displacement conditions at the edges of the plate. As illustrations we consider an infinite plate containing a cylindrical hole or through-thickness crack.

There has been a considerable interest in materials that have been deliberately constructed to be inhomogeneous on the macroscopic scale. Such materials may have discontinuous mechanical properties, such as occur in a laminated material, or continuously varying properties as occur in a functionally-graded material. In a series of papers (several of which are summarized and referenced in [1]), Rogers, Spencer and others have developed and applied a procedure for deriving exact solutions of the equations of elasticity for material that are isotropic but whose elastic moduli are general functions of a single space variable. The origins of the method can be found in classical solutions by Michell for moderately thick plates in a state of plane stress. Kaprielian, Rogers and Spencer [2] reformulated and generalized Michell's equations so as to derive exact solutions of the three-dimensional elasticity equations for a material whose elastic constants are any specified functions of a single space coordinate z, which is here taken to be in the direction normal to the surface of a thick flat plate. The dependence of the elastic moduli on z is subject to the usual positive definiteness requirements on the strain energy, but otherwise the Lamé constants λ and μ (or equivalently, Young's modulus and Poisson's ratio) may be any specified functions of z. The dependence of λ and μ on z need not be continuous, so that the case of a laminated material, in which λ and μ are piecewise constant functions of z, is included as a special case. In this formulation any solution of the equations of the plane elastic problem for homogeneous material generates a corresponding *exact* solution of the equations of three-dimensional elasticity for material with the specified inhomogeneity.

A limitation of the method is that, although it generates exact solutions of the field equations in plates which have uniform thickness with traction-free upper and lower surfaces, these solutions are not sufficiently general to match the standard boundary conditions at each point on the edge of a thick plate. However they may be used to satisfy the usual resultant force and moment conditions or averaged displacement conditions at the edge of the plate. Hence these solutions should be regarded as interior solutions in a plate and, for completeness, need to be supplemented by edge boundary-layer solutions.

In plane problems in elasticity, the complex variable methods developed by Muskhelishvili [3] and many others have been used to generate complete solutions of the field equations and have proved very effective in solving boundary-value problems. England and Spencer [4] have applied complex-variable theory to the inhomogeneous thick plate problems outlined above and have shown that it provides a concise and elegant formulation of the problem, and a convenient basis for the solution of a variety of problems. The intention in this presentation is firstly to describe the formulae obtained in [4] and then to describe some illustrative applications to boundary-value problems.

We employ a system of rectangular Cartesian coordinates (x, y, z).in which displacement components are denoted by u, v and w, and the components of the stress tensor σ by $\sigma_{xx}, \sigma_{xy}, ...$

We consider a thick plate or slab of linearly elastic material, bounded by the planes $z = \pm h$. The material is isotropic, but may be inhomogeneous in the z direction, so that, in general, λ and μ are specified functions (not necessarily continuous) of z. We also introduce the complex variable $\zeta = x + iy$ and its complex conjugate $\overline{\zeta}$.

Then it was shown in [4] that the three-dimensional displacement field

$$\begin{aligned} u(x,y,z) + iv(x,y,z) &= \frac{\kappa_1+1}{\kappa_1-1}\phi(\zeta) - \zeta\overline{\phi\prime(\zeta)} - \overline{\psi(\zeta)} - 2\left(\frac{\kappa_2}{\kappa_1}+z\right)\{\beta(\zeta)+\zeta\overline{\beta\prime(\zeta)}\} - 2z\overline{\alpha\prime(\zeta)} \\ &\quad + \frac{4}{\kappa_1-1}F(z)\phi\prime\prime(\zeta) - 8\left(\frac{\kappa_2}{\kappa_1}F(z) - B(z)\right)\overline{\beta\prime\prime(\zeta)}, \\ w(x,y,z) &= \alpha(\zeta) + \overline{\alpha(\zeta)} + \overline{\zeta}\beta(\zeta) + \zeta\overline{\beta(\zeta)} \\ &\quad + \frac{2}{\kappa_1-1}G(z)\left(\phi\prime(\zeta) + \overline{\phi\prime(\zeta)}\right) - 4\left\{\frac{\kappa_2}{\kappa_1}G(z) - C(z)\right\}\left(\beta\prime(\zeta) + \overline{\beta\prime(\zeta)}\right), \end{aligned}$$

exactly satisfies the equations of elastostatics in three dimensions for the plate, with zero tractions on the lateral surfaces $z = \pm h$. In these equations, $\phi(\zeta), \psi(\zeta), \alpha(\zeta)$ and $\beta(\zeta)$ are complex potentials and analytical functions of ζ. The coefficients $B(z), C(z), F(z)$ and $G(z)$ are functions of z that depend on the Lamé constants $\lambda(z)$ and $\mu(z)$ and can be evaluated by quadratures when $\lambda(z)$ and $\mu(z)$ are specified. The constants κ_1 and κ_2 can also be evaluated by quadratures when $\lambda(z)$ and $\mu(z)$ are specified.

In general terms the potentials $\phi(\zeta)$ and $\psi(\zeta)$ represent stretching deformations of the plate, and $\alpha(\zeta)$ and $\beta(\zeta)$ are associated with bending deformations. In general these deformation modes are coupled. An exception is the case of a symmetric plate in which $\lambda(z)$ and $\mu(z)$ are even functions of z. In this case $F(z)$ and $C(z)$ become even functions of z and $G(z)$ and $B(z)$ are odd functions of z, and $\kappa_2 = 0$. Then the stretching deformations represented by $\phi(\zeta)$ and $\psi(\zeta)$ uncouple from the bending deformations represented by $\alpha(\zeta)$ and $\beta(\zeta)$, and the two deformation modes can be treated separately.
The stress components associated with the deformation are

$$\begin{aligned}
\sigma_{xx}+\sigma_{yy} &= \frac{4\mu(3\lambda+2\mu)}{\lambda+2\mu}\{\frac{1}{\kappa_1-1}\left(\phi\prime(\zeta)+\overline{\phi\prime(\zeta)}\right)-2\left(\frac{\kappa_2}{\kappa_1}+z\right)\left(\beta\prime(\zeta)+\overline{\beta\prime(\zeta)}\right)\},\\
\sigma_{xx}-\sigma_{yy}+2i\sigma_{xy} &= 4\mu\{-\zeta\overline{\phi\prime\prime(\zeta)}-\overline{\psi\prime(\zeta)}-2\left(\frac{\kappa_2}{\kappa_1}+z\right)\zeta\overline{\beta\prime\prime(\zeta)}-2z\overline{\alpha\prime\prime(\zeta)}\\
&\quad+\frac{4}{\kappa_1-1}F(z)\overline{\phi\prime\prime\prime(\zeta)}-8\left(\frac{\kappa_2}{\kappa_1}F(z)-B(z)\right)\overline{\beta\prime\prime(\zeta)}\},\\
\sigma_{xz}+i\sigma_{yz} &= 4\mu\{\frac{1}{\kappa_1-1}\left(\frac{dF}{dz}+G\right)\overline{\phi\prime\prime(\zeta)}-2\left[\frac{\kappa_2}{\kappa_1}\left(\frac{dF}{dz}+G\right)-\left(\frac{dB}{dz}+C\right)\right]\overline{\beta\prime\prime(\zeta)}\},\\
\sigma_{zz} &= 0.
\end{aligned}$$

From these it is straightforward to evaluate the stress resultants and the moments

$$(N_{xx},N_{yy},N_{xy})=\int_{-h}^{h}(\sigma_{xx},\sigma_{yy},\sigma_{xy})dz,\quad (M_{xx},M_{yy},M_{xy})=\int_{-h}^{h}z(\sigma_{xx},\sigma_{yy},\sigma_{xy})dz$$

in terms of the complex potentials.
Hence we may also calculate the forces and moments that act on a surface generated by an arc C in the ζ-plane in terms of the complex potentials; for example the components (X,Y,Z) of the force on an arc connecting $\zeta=t_0$ to $\zeta=t$ are

$$\begin{aligned}
X+iY &= \frac{4h}{i}[\mu_1\left(\phi(\zeta)+\zeta\overline{\phi\prime(\zeta)}+\overline{\psi(\zeta)}\right)+2\left(\mu_1\frac{\kappa_2}{\kappa_1}+\mu_2\right)\left(\beta(\zeta)+\zeta\overline{\beta\prime(\zeta)}\right)+2\mu_2\overline{\alpha\prime(\zeta)}\\
&\quad-\frac{2}{h(\kappa_1-1)}\int_{-h}^{h}\mu F(z)dz\,\overline{\phi\prime\prime(\zeta)}+\frac{4}{h}\left(\frac{\kappa_2}{\kappa_1}\int_{-h}^{h}\mu F(z)dz-\int_{-h}^{h}\mu B(z)dz\right)\overline{\beta\prime\prime(\zeta)}]_{t_0}^{t},\\
Z &= [-\frac{2i}{\kappa_1-1}\int_{-h}^{h}\mu\left(\frac{dF}{dz}+G\right)dz\left(\phi\prime(\zeta)-\overline{\phi\prime(\zeta)}\right)\\
&\quad+4i\left\{\frac{\kappa_2}{\kappa_1}\int_{-h}^{h}\mu\left(\frac{dF}{dz}+G\right)dz-\int_{-h}^{h}\mu\left(\frac{dB}{dz}+C\right)dz\right\}\left(\beta\prime(\zeta)-\overline{\beta\prime(\zeta)}\right)]_{t_0}^{t}
\end{aligned}$$

where $2h\mu_1=\int_{-h}^{h}\mu(z)dz,\ 2h\mu_2=\int_{-h}^{h}\mu(z)zdz$.
Clearly the solution of boundary-value problems reduces to the determination of the complex potentials $\phi(\zeta),\psi(\zeta),\alpha(\zeta)$ and $\beta(\zeta)$. In many simple, but non-trivial, cases, the form of these can be deduced by inspection and use of experience of solving related problems in plane elasticity. For more complicated problems the techniques of complex analysis that have been developed for use in plane elasticity may be applied to determine the complex potentials that are appropriate for specific boundary conditions on the stress resultants, moments and averaged displacements.
To illustrate the theory, we apply the formulae obtained in [4] to investigate the elastic field in a plate containing a cylindrical hole or a line crack through its thickness under a uniform force field at infinity. As might be expected, the elastic field near the cylindrical hole is quite similar to that found in the corresponding plane strain problem, but in the case of a crack the singularity in the stress field near the crack tip is found to be much more extreme than that found in the plane-strain case (see England [5]).
The extension of the theory to include the case of surface loading of the lateral surfaces of the plate is discussed briefly.

References

[1] Mian, M.A., Spencer, A.J.M., *Journal of the Mechanics and Physics of Solids* 46, 2283-2295, 1998
[2] Kaprielian, P., Rogers,T.G., Spencer, A.J.M., *Phil. Trans. Roy. Soc. Lond.* A324, 565-594, 1988
[3] Muskhelishvili, N.I.: Some basic problems of the mathematical theory of elasticity, transl. by J.R.M. Radok, P. Noordhoff, Groningen, 1953
[4] England, A.H., Spencer, A.J.M., *Mathematics and Mechanics of Solids* (to appear)
[5] England, A.H., *Mathematics and Mechanics of Solids* (to appear)

STUDY OF TWO-DIMENSIONAL ELASTICITY ON FGM

Takemasa Seto*, Prof. Tetsu Nishimura *
* *Nihon University, Department of Mechanical Engineering, College of Science & Technology, Tokyo, Japan*

Summary Functionally Graded Materials (FGMs) are future composite materials, which have non-uniform elastic property over the body. However, the classical theory of elasticity [1] cannot apply to the FGMs because their elastic coefficients are not uniform. Hence, two-dimensional problem for the body of non-uniform elastic modulus will be discussed in this paper. And it is mention that the edge bonded dissimilar materials problem is resolved by the suggested method.

INTRODUCTION

Functionally Graded Materials (FGMs) are developing as future composite materials. This new progressive materials realize the required property of strength or flexibility and a chemical resistance according to the actual applications by changing the property over the body. However, there is no theory to calculate the stress distribution of the structure composed of FGM which has a non-uniform elastic modulus. The classical theory of elasticity is only applicable for the ordinary materials with constant elastic modulus. Hence, the new theory applicable for the body with a non-uniform elastic modulus is demanded.

TWO-DIMENSIONAL PROBLEM

In the classical theory, the differential equation of equilibriums, the compatibility equation and the Hooke's law must be satisfied together with the boundary conditions to determine the stress distribution of two-dimensional problems. Using the stress function ϕ, the compatibility equation, that is the government equation, can be expressed as follows.

$$\frac{\partial^4\phi}{\partial x^4}+2\frac{\partial^4\phi}{\partial x\partial y}+\frac{\partial^4\phi}{\partial^4 y}=0 \tag{1}$$

Thus the solution of stress distribution of two-dimensional problem reduces to finding the solution of Eq.(1).

COMPATIBILITY EQUATION FOR FGM

In the case of FGMs, although the equations of equilibrium and the compatibility equation are the same with classical theory, the Hooke's law includes the Young's modulus represented by the function of x and y, because the Young's modulus varies over the body. Therefore, using the same procedure as the classical theory, the compatibility equation can be derived as follows.

$$\begin{aligned} &a\left(\frac{\partial^4\phi}{\partial x^4}+2\frac{\partial^4\phi}{\partial x^2\partial y^2}+\frac{\partial^4\phi}{\partial y^4}\right)+2\frac{\partial a}{\partial x}\left(\frac{\partial^3\phi}{\partial x^3}+\frac{\partial^3\phi}{\partial x\partial y^2}\right)+2\frac{\partial a}{\partial y}\left(\frac{\partial^3\phi}{\partial y^3}+\frac{\partial^3\phi}{\partial x^2\partial y}\right)\\ &\quad+\frac{\partial^2 a}{\partial x^2}\left(\frac{\partial^2\phi}{\partial x^2}-\nu\frac{\partial^2\phi}{\partial y^2}\right)+\frac{\partial^2 a}{\partial y^2}\left(\frac{\partial^2\phi}{\partial y^2}-\nu\frac{\partial^2\phi}{\partial x^2}\right)+2(1+\nu)\frac{\partial^2 a}{\partial x\partial y}\frac{\partial^2\phi}{\partial x\partial y}=0 \end{aligned} \tag{2}$$

Where $a(x)=1/E(x,y)$ and assuming the Poisson's ratio ν is constant. Therefore the solution of stress state of two-dimensional problem with non-uniform elastic modulus is reduced to find this stress function in Eq.(2). It is clear from Eq.(2), the stress distribution is affected by inverse function of the elastic modulus. However, the compatibility equation of non-uniform elastic modulus is too difficult to solve theoretically.

UNI-AXIAL TENSION PROBLEM OF RECTANGULAR PLATE

It is difficult to solve Eq.(2). Here, the uni-axial tension problem of rectangular plate which has the Young's modulus varies only along the x direction (Fig.1) will be considered. Then, Eq.(2) is reduced to the next equation.

$$a\left(\frac{\partial^4\phi}{\partial x^4}+2\frac{\partial^4\phi}{\partial x^2\partial y^2}+\frac{\partial^4\phi}{\partial y^4}\right)+2\frac{\partial a}{\partial x}\left(\frac{\partial^3\phi}{\partial x^3}+\frac{\partial^3\phi}{\partial x\partial y}\right)+\frac{\partial^2 a}{\partial x^2}\left(\frac{\partial^2\phi}{\partial x^2}-\nu\frac{\partial^2\phi}{\partial y^2}\right)=0 \tag{3}$$

Here, because of difficulty of solving theoretically, the finite difference method is used in order to calculate this equation in this study. In the numerical calculation, assuming the distribution of Young's modulus is $E(x)=100x+10$. So the value of Young's modulus changes 10 to 110 from end to end. The external forces $P=200$ are applied to both ends. And the length $L=1$ and width $W=0.25$ are used in this numerical calculation.

From the calculated result (Fig.2), it can be seen that the large stress disturbance appears at the limited portion where the Young's modulus is smaller. While, the stress disturbance approaches to uniform around the lager Young's modulus. The second derivative of $a(x)$ takes maximum values at $x=0$, and decrease abruptly with increasing of x in this calculated condition. So it is concluded that the stress disturbance is strongly affected by the second derivative of $a(x)$.



Fig.1 RECTANGULAR PLATE

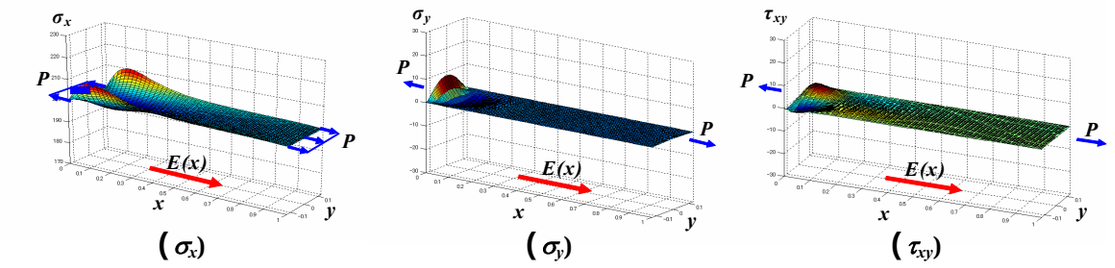


Fig.2 CALCULATED RESULT

APPLICATION TO THE EDGE BONDED DISSIMILAR MATERIALS PROBLEM

The compatibility Equation of non-uniform elastic modulus is also applicable to the edge-bonded dissimilar materials problem when the function of distribution of Young's modulus takes the step function. But it is impossible to use the step function in this calculation because of discontinuous function. Hence, to solve this problem, the sigmoid function Eq.(4) is adopted instead of the step function. The sigmoid function is able to explain the step function when the parameter λ takes to infinity (Fig.3).

$$a(x) = \frac{1}{E(x)} = a_A - \frac{a_A - a_B}{1 + \exp(-\lambda x)} \tag{4}$$

Where, a_A and a_B are inverse of the Young's modulus of material *A* and *B*. Fig.4 shows the calculated result in case of λ=30. Here this calculation is assumed that the length *L*=2 and width *W*=0.5. The young's modulus of material *A* and *B* are 200 and 400 respectively. The external forces *P*=200 are applied both ends of the plate. The tensile stress σ_x around the joint portion at the free sides takes maximum value in the material *A* with smaller Young's modulus, and minimum value in the material *B* with larger Young's modulus. Fig.5 shows the calculated result of difference between maximum and minimum stresses value and divided by external force *P*. This figure explains the stress disturbance rate of the tensile and lateral stresses. It is clear from this figure that these stress disturbances seems to converge to the certain values for the large number of parameter λ in the sigmoid function. Fig.6 shows difference of the maximum and minimum stress value positions on the x-axis. The stress of σ_x converges to the constant value with increasing λ. Consequently, it can be concluded that the stress distribution of σ_x continues across the bonded portion of the plate.

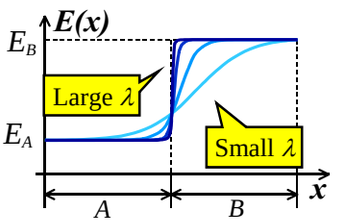


Fig.3 SIGMOID FUNCTION

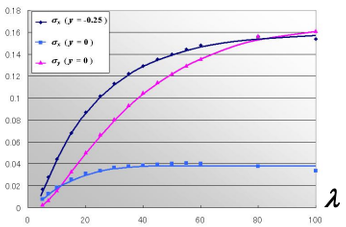


Fig.5 STRESS DISTURBANCE RATE

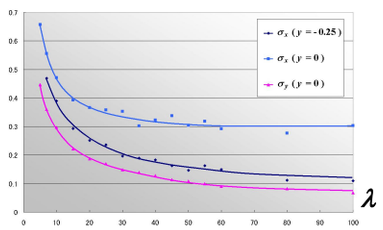


Fig.6 EXTREME VALUE POSITION

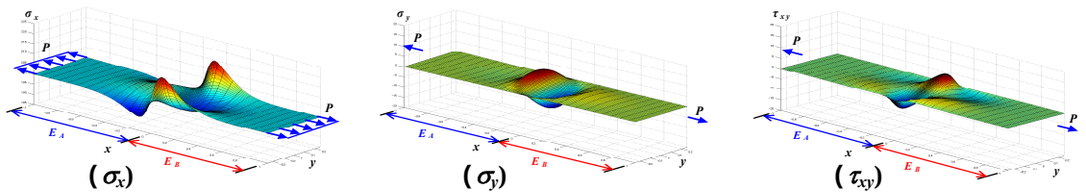


Fig.4 CALCULATED RESULT

CONCLUSIONS

Stress distribution of two-dimensional elastic problem applicable for the non-uniform elastic modulus was analysed by the numerical calculation in this study. And the edge bonded dissimilar materials problem is also applicable to this compatibility equation when the Young's modulus is expressed by the sigmoid function. It is indicated that the limited value of stress exists and the normal stress continuously distributes over the bonded portion.

References

[1] Timoshenko, S. & Goodier, J.N.: Theory of Elasticity (second edition). McGraw Hill, 1951.
[2] Kuranishi, M. : Applied elasticity. Kyoritsu-zensho, 1980.
[3] Omori, M. et al : Proceedings of the 3rd International Symposium on structural and Functionally Gradient Materials, 1994.

THREE-DIMENSIONAL TRANSIENT THERMOELASTIC ANALYSIS OF ORTHOTROPIC FUNCTIONALLY GRADED RECTANGULAR PLATE

Yoshihiro Ootao, Yoshinobu Tanigawa
Department of Mechanical Systems Engineering, Graduate School of Engineering,
Osaka Prefecture University, 1-1 Gakuen-cho, Sakai, 599-8531 JAPAN

Summary This paper is concerned with the transient thermoelastic analysis of an orthotropic functionally graded rectangular plate due to nonuniform heat supply. The material constants of the orthotropic rectangular plate are assumed to vary exponentially in the thickness direction. We obtain the exact solution for the three-dimensional temperature change in a transient state, and three-dimensional thermal stresses of a simple supported rectangular plate.

INTRODUCTION

Functionally graded materials (FGM) have been developed as a new material that is adaptable for a super-high-temperature environment. It is well-known that thermal stress distributions in a transient state can show large values compared with the one in a steady state. Therefore, the transient thermoelastic problems become important. On the other hand, the exact treatments for thermoelastic problems of FGM have been done thus circumventing the laminate theory approximation. The reports concerned with the three-dimensional transient thermoelastic problems of FGM are few. Recently, Vel and Batra [1] treated a simply supported functionally graded rectangular plate, which material properties are represented by a Taylor series expansion.

In the present paper, we analyzed exactly the three-dimensional transient problem of thermoelasticity involving an orthotropic functionally graded rectangular plate due to nonuniform heat supply. The material properties of the orthotropic rectangular plate are assumed to vary exponentially in the thickness direction.

ANALYSIS

We consider an orthotropic functionally graded rectangular plate that has nonhomogeneous thermal and mechanical properties in the thickness direction. The thickness and the lengths of the sides of it are represented by B, $2L_x$ and $2L_y$, respectively. We assume that the rectangular plate is initially at zero temperature and is suddenly heated from the lower and upper surfaces by surrounding media with relative heat transfer coefficients h_a and h_b. We denote the temperatures of the surrounding media by the functions $T_a f_a(x) g_a(y)$ and $T_b f_b(x) g_b(y)$ and assume its end surfaces are held zero temperature. The transient heat conduction equation is taken in the following form:

$$\frac{\partial}{\partial x}\left\{\lambda_x(z)\frac{\partial T}{\partial x}\right\}+\frac{\partial}{\partial y}\left\{\lambda_y(z)\frac{\partial T}{\partial y}\right\}+\frac{\partial}{\partial z}\left\{\lambda_z(z)\frac{\partial T}{\partial z}\right\}=c\rho\frac{\partial T}{\partial t} \tag{1}$$

The thermal conductivities is assumed to take the following forms:

$$\lambda_i(z)=\lambda_{i0}\,exp(az/B),\quad i=x,y,z \tag{2}$$

while the specific heat c and density ρ are constant. In Eq.(2), a is an arbitrary constant which is not zero. Substituting the Eq.(2) into the Eq.(1), the transient heat conduction equation in dimensionless form is

$$\bar{\lambda}_{x0}\frac{\partial^2\bar{T}}{\partial\bar{x}^2}+\bar{\lambda}_{y0}\frac{\partial^2\bar{T}}{\partial\bar{y}^2}+a\frac{\partial\bar{T}}{\partial\bar{z}}+\frac{\partial^2\bar{T}}{\partial\bar{z}^2}=e^{-a\bar{z}}\frac{\partial\bar{T}}{\partial\tau} \tag{3}$$

For the sake of brevity, we introduce that the temperature functions $f_a(x)$, $f_b(x)$, $g_a(y)$ and $g_b(y)$ are distributed symmetrically in x and y axes. Introducing the finite cosine transformations with respect to the variable $\bar{x}$ and $\bar{y}$ and Laplace transformation with respect to the variable τ, the solution of Eq.(3) can be obtained as follows:

$$\bar{T}=\sum_{k=1}^{\infty}\sum_{m=1}^{\infty}\bar{T}_{km}(\bar{z},\tau)\cos q_k\bar{x}\cos s_m\bar{y} \tag{4}$$

where

$$\bar{T}_{km}(\bar{z},\tau)=\frac{4}{\bar{L}_x\bar{L}_y}\left[\frac{1}{F}\left\{\bar{A}'exp\left[-\frac{a}{2}(1-\gamma)\bar{z}\right]+\bar{B}'exp\left[-\frac{a}{2}(1+\gamma)\bar{z}\right]\right\}\right.$$

$$\left.-\sum_{j=1}^{\infty}\frac{2\,exp(-\frac{a}{2}\bar{z}-\frac{a^2\mu_j^2}{4}\tau)}{\mu_j\Delta'(\mu_j)}\left\{\bar{A}J_\gamma\left[\mu_j\,exp(-\frac{a}{2}\bar{z})\right]+\bar{B}Y_\gamma\left[\mu_j\,exp(-\frac{a}{2}\bar{z})\right]\right\}\right] \tag{5}$$

In Eqs.(4) and (5), q_k, s_m and γ are

$$q_k = \frac{(2k-1)\pi}{2\bar{L}_x}, \quad s_m = \frac{(2m-1)\pi}{2\bar{L}_y}, \quad \gamma = \sqrt{1+\frac{4}{a^2}(q_k^2\bar{\lambda}_{x0} + s_m^2\bar{\lambda}_{y0})} \tag{6}$$

We now analyze the transient thermoelasticity of an orthotropic functionally graded rectangular plate with simply supported edges as a three-dimensional problem. The elastic stiffness constant C_{ij} and the coefficient of linear thermal expansion α_i are assumed to take the following forms:

$$\bar{C}_{ij}(\bar{z}) = \bar{C}_{ij}^0 \, exp(l\bar{z}), \quad \bar{\alpha}_i(\bar{z}) = \bar{\alpha}_{i0} \, exp(b\bar{z}) \tag{7}$$

where l and b are arbitrary constants. Substituting the displacement-strain relations, the stress-strain relations and Eq.(7) into the equilibrium equations, the displacement equations of equilibrium are written as

$$\bar{C}_{11}^0\bar{u}_{,\bar{x}\bar{x}} + \bar{C}_{66}^0\bar{u}_{,\bar{y}\bar{y}} + \bar{C}_{55}^0\bar{u}_{,\bar{z}\bar{z}} + l\bar{C}_{55}^0\bar{u}_{,\bar{z}} + (\bar{C}_{12}^0 + \bar{C}_{66}^0)\bar{v}_{,\bar{x}\bar{y}} + (\bar{C}_{13}^0 + \bar{C}_{55}^0)\bar{w}_{,\bar{x}\bar{z}} + l\bar{C}_{55}^0\bar{w}_{,\bar{x}} = \bar{\beta}_x^0 \, exp(b\bar{z})\bar{T}_{,\bar{x}} \tag{8}$$

$$(\bar{C}_{12}^0 + \bar{C}_{66}^0)\bar{u}_{,\bar{x}\bar{y}} + \bar{C}_{66}^0\bar{v}_{,\bar{x}\bar{x}} + \bar{C}_{22}^0\bar{v}_{,\bar{y}\bar{y}} + \bar{C}_{44}^0\bar{v}_{,\bar{z}\bar{z}} + l\bar{C}_{44}^0\bar{v}_{,\bar{z}} + (\bar{C}_{23}^0 + \bar{C}_{44}^0)\bar{w}_{,\bar{y}\bar{z}} + l\bar{C}_{44}^0\bar{w}_{,\bar{y}} = \bar{\beta}_y^0 \, exp(b\bar{z})\bar{T}_{,\bar{y}} \tag{9}$$

$$(\bar{C}_{13}^0 + \bar{C}_{55}^0)\bar{u}_{,\bar{x}\bar{z}} + l\bar{C}_{13}^0\bar{u}_{,\bar{x}} + (\bar{C}_{23}^0 + \bar{C}_{44}^0)\bar{v}_{,\bar{y}\bar{z}} + l\bar{C}_{23}^0\bar{v}_{,\bar{y}} + \bar{C}_{55}^0\bar{w}_{,\bar{x}\bar{x}} + \bar{C}_{44}^0\bar{w}_{,\bar{y}\bar{y}} + \bar{C}_{33}^0\bar{w}_{,\bar{z}\bar{z}} + l\bar{C}_{33}^0\bar{w}_{,\bar{z}}$$
$$= \bar{\beta}_z^0 \, exp(b\bar{z})[(l+b)\bar{T} + \bar{T}_{,\bar{z}}] \tag{10}$$

If the lower and upper surfaces are traction free, the boundary conditions of lower and upper surfaces can be represented as follows:

$$\bar{z} = 0, \; 1; \quad \bar{\sigma}_{zz} = 0, \quad \bar{\sigma}_{yz} = 0, \quad \bar{\sigma}_{zx} = 0 \tag{11}$$

We now consider the case of a simply supported rectangular plate.

$$\bar{x} = \pm\bar{L}_x; \quad \bar{\sigma}_{xx} = 0, \quad \bar{v} = 0, \quad \bar{w} = 0 \tag{12}$$

$$\bar{y} = \pm\bar{L}_y; \quad \bar{\sigma}_{yy} = 0, \quad \bar{u} = 0, \quad \bar{w} = 0 \tag{13}$$

We assume the solutions of Eqs.(8)- (10) in order to satisfy Eqs.(12) and (13) in the following form.

$$\bar{u} = \sum_{k=1}^{\infty}\sum_{m=1}^{\infty}\left[U_{ckm}(\bar{z}) + U_{pkm}(\bar{z})\right] sin\, q_k\bar{x}\, cos\, s_m\bar{y}, \quad \bar{v} = \sum_{k=1}^{\infty}\sum_{m=1}^{\infty}\left[V_{ckm}(\bar{z}) + V_{pkm}(\bar{z})\right] cos\, q_k\bar{x}\, sin\, s_m\bar{y},$$

$$\bar{w} = \sum_{k=1}^{\infty}\sum_{m=1}^{\infty}\left[W_{ckm}(\bar{z}) + W_{pkm}(\bar{z})\right] cos\, q_k\bar{x}\, cos\, s_m\bar{y} \tag{14}$$

In expressions (14), the first term on the right side gives the homogeneous solution and the second term of right side gives the particular solution. In order to obtain the homogeneous solution, we assume that

$$\left[U_{ckm}(\bar{z}), V_{ckm}(\bar{z}), W_{ckm}(\bar{z})\right] = (U_{ckm}^0, V_{ckm}^0, W_{ckm}^0)\, exp(\lambda\bar{z}) \tag{15}$$

The details of the homogeneous solution are omitted here for the sake of brevity. In order to obtain the particular solution, we use the series expansions of the Bessel functions. Since the order γ of the Bessel function in Eq.(5) is not integer in general, Eq.(5) can be written as the following expression.

$$\bar{T}_{km}(\bar{z},\tau) = \sum_{n=0}^{\infty}\left\{a_{n1}(\tau)\, exp\left[-\frac{a}{2}(2n+1+\gamma)\bar{z}\right] + a_{n2}(\tau)\, exp\left[-\frac{a}{2}(2n+1-\gamma)\bar{z}\right]\right\} \tag{16}$$

$U_{pkm}(\bar{z})$, $V_{pkm}(\bar{z})$ and $W_{pkm}(\bar{z})$ of the particular solution are obtained as the function system like Eq.(16).

In expressions (3)-(16), we have introduced the following dimensionless values:

$$\bar{T} = T/T_0, \quad (\bar{x},\bar{y},\bar{z},\bar{L}_x,\bar{L}_y) = (x,y,z,L_x,L_y)/\mathrm{B}, \quad (\bar{\lambda}_{x0},\bar{\lambda}_{y0}) = (\lambda_{x0},\lambda_{y0})/\lambda_{z0}, \tau = \kappa_{z0}t/B^2,$$
$$\kappa_{z0} = \lambda_{z0}/(c\rho), \quad \bar{C}_{ij} = C_{ij}/E_0, \quad \bar{\alpha}_i = \alpha_i/\alpha_0, \quad \bar{\sigma}_{ij} = \sigma_{ij}/(\alpha_0 E_0 T_0), \quad (\bar{u},\bar{v},\bar{w}) = (u,v,w)/(\alpha_0 T_0 B) \tag{17}$$

NUMERICAL CALCULATION

To illustrate the foregoing analysis, numerical parameters of heat conduction and shape are presented as follows:

$$H_a(=h_aB) = H_b(=h_bB) = 1.0, \quad \bar{T}_a = 1, \quad \bar{T}_b = 0, \quad \bar{L}_x = \bar{L}_y = 3.0,$$
$$f_a(\bar{x}) = (1-\bar{x}^2/\bar{x}_0^2)H(\bar{x}_0 - |\bar{x}|), \; g_a(\bar{x}) = (1-\bar{y}^2/\bar{y}_0^2)H(\bar{y}_0 - |\bar{y}|), \; \bar{x}_0 = 1.0, \quad \bar{y}_0 = 1.0 \tag{18}$$

where $H(x)$ is Heaviside's function. We assume that the plate is heated partially from the lower surface by surrounding media. The effects of the nonhomogeneity and orthotropy of the material on the temperature change, the displacement and the stress distributions are investigated.

We conclude that we can evaluate all stresses of the orthotropic functionally graded rectangular plate in a transient state.

Reference

[1] Vel S.S., Batra R.C., International Journal of Solids and Structures 40, 7181-7196, 2003.

The initiation and propagation of adiabatic shear bands (ASBs) in functionally graded materials (FGMs) deformed at high strain rates in plane strain tension have been studied by the finite element (FE) method. An ASB is a narrow region, usually a few microns wide, of intense plastic deformation that forms after softening of the material due to heating and damage evolution has overcome its hardening due to strain- and strain-rate effects. ASBs usually precede ductile fracture. The volume fraction of each phase varies continuously in a cross-section. Each constituent and the composite are modeled as isotropic, microporous, strain- and strain-rate hardening, and thermally softening materials with effective properties of the composite derived either by the rule of mixtures or from studying deformations of a representative volume element. Each phase and the homogenized composite obey the Johnson-Cook thermoviscoplastic relation, Gurson's type flow potential, the associated flow rule, and a hyperbolic heat equation. Thermoelastic material parameters of the composite are assumed to degrade with the evolution of the porosity which is taken to represent the damage. No initial defect is introduced.

Results have been computed for tungsten (W) particles interspread in a NiFe matrix with the volume fraction of NiFe given by one of the following two expressions:

Type I

$$v_{f,NiFe} = \begin{cases} c\dfrac{r}{H}, & r < H \\ c, & r \geq H \end{cases}$$

Type II

$$v_{f,NiFe} = \begin{cases} c\left(1-\dfrac{r}{H}\right), & r < H \\ 0, & r \geq H \end{cases}$$

Here r is the radial distance from the specimen centroid, and 2H equals the length of a side of the square cross-section. In both type-I and type-II FGMs, material properties in the region r > H are constants. In type-I FGMs, the volume fraction of NiFe varies from zero at the specimen centroid to c at r = H, and in type-II FGMs, it varies from c at the specimen centroid to zero at r = H.

The developed code has been verified by comparing computed results with those available in the literature. Results presented below are with a uniform FE mesh of 1600 4-node quadrilateral elements. Results computed with a finer mesh of 6400 elements changed the ASB initiation time by less than 1%. For reference and to delineate the effect of the initial porosity distribution, Table 1 lists the ASB initiation times for five materials. It is clear that an ASB initiates considerably sooner in initially porous materials than in those with zero initial porosity. Also, tungsten is most susceptible to shear banding and Armco iron the least.

Table 1. Axial strain at ASB initiation in five homogeneous materials

Material	Axial strain at ASB initiation in plane strain tension	
	nonuniform initial porosity	zero initial porosity
Tungsten (W)	0.137	0.386
4340 steel	0.315	0.615
Nickel iron	--	0.944
OFHC copper	0.391	1.045
Armco iron	0.433	1.095

Numerical experiments on type-I and type-II FGMs yielded interesting results summarized in Table 2. In the first subset of tests on type-I FGMs, the maximum volume fraction,c, of NiFe was varied from 0.1 to 0.5. In each case, an ASB initiated at the specimen centroid and propagated along a line inclined at 45º to the horizontal axis in the present configuration. However, the axial strain at the instant of ASB initiation decreased monotonically with an increase in the maximum volume fraction of NiFe at the centroid. Contours of the effective plastic strain in a type-I FGM are depicted in Fig. 1. The effective plastic strain within the ASB exceeds 1 with a peak value of 1.4 at some points. For type-II FGMs with the maximum volume fraction of NiFe at the centroid, an ASB initiated from a point on the top surface and propagated inwards along the two directions of the maximum shear stress. As shown in Fig.2, there are several narrow regions of intense plastic deformation. The point where an ASB initiated on the top surface varied with the compositional profile. Results for numerical experiments on other type-I FGMs containing different matrix material are also summarized in Table 2. Of the FGMs studied, the type-I with NiFe matrix delays most the onset of an ASB and that with copper matrix the least. Composites comprised of tungsten in the region

r <5 and NiFe elsewhere or vice-a-versa were also analyzed. In these an ASB initiated from different points on the top surface and propagated inwards in two directions.
The numerical tests reveal that the addition to pure tungsten of a material less susceptible to shear banding than tungsten delays the initiation of an ASB in the composite. The analysis can be used to optimize the compositional profile to either delay or to enhance the onset of an ASB.

Table 2. Axial strain and the point of initiation of ASBs in FGMs

Specimen type and constituents	Max. v_f of NiFe	Axial strain at ASB initiation	Point of ASB initiation (ref. config) X	Y
W/NiFe Type I	0.1	0.371	0.000	0.000
	0.2	0.339	0.000	0.000
	0.3	0.327	0.000	0.000
	0.4	0.325	0.000	0.000
	0.5	0.331	0.000	0.000
W/NiFe Type II	0.1	0.340	1.125	5.000
	0.2	0.314	1.250	5.000
	0.3	0.304	1.375	5.000
	0.4	0.298	4.750	2.875
	0.5	0.292	4.875	2.875
W/4340 Type I	0.3	0.364	1.125	5.000
W/NiFe Type I	0.3	0.327	0.000	0.000
W/Cu Type I	0.3	0.218	0.625	5.000
W/Fe Type I	0.3	0.268	1.000	5.000

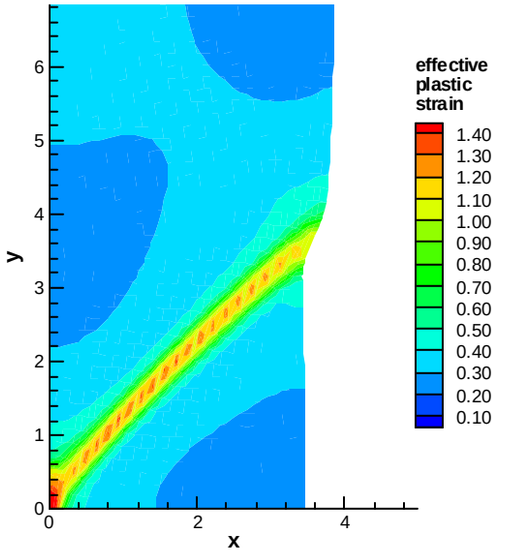


Figure 1. Contours of effective plastic strain for a type-I W/NiFe FGM with c = 0.3 at an axial strain of 0.40.

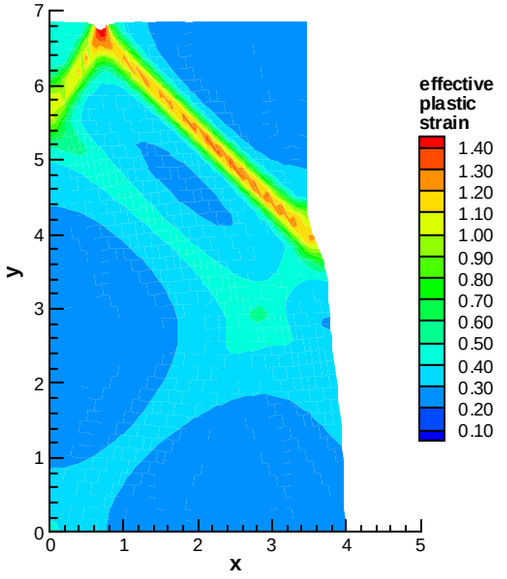


Figure 2. Contours of effective plastic strain for type-II W/NiFe FGM with c = 0.3 at an axial strain of 0.3725.

Nonlocal effects in micromechanics of functionally graded composites of random structure

G. Schoeppner*, V. A. Buryachenko**
*Air Force Research Laboratory, AFRL/WPAFB, OH 45433-7750, USA
**University of Dayton Research Institute, Dayton, OH 45469-0168, USA

Summary. The general non-local integral equation involving the statistical averages of stresses in the composite and inclusions of random structure functionally graded composite is obtained and solved by three different methods: the quadrature method, the iteration method, and the Fourier transform method with subsequent comparative analysis. The different nonlocal effects are detected, some of them are fundamentally new.

For *statistically inhomogeneous* composites [or functionally graded materials (FGM)], the ergodicity fails and ensemble and volume averages do not coincide. The degenerate case of these materials is a random matrix composite for which the inclusions are located in a region bounded in some directions, although unrestrictedness of the domain of inclusion locations does not preclude statistical inhomogeneity. For example, any laminated composite materials with randomly reinforced by aligned fibers in each ply, are the statistically inhomogeneous material. The concept of clusters is similar to that of fractal structures, and the role of statistical descriptor can be treated by such parameters as cluster size, the fractal dimension, and the radius of gyration. The informative characteristics of the random configurations use statistical second-order quantities which examine the association fillers relative to other particle in an immediate local neighborhood of the reference filler. We will analyze so-called ideal cluster materials where the concentration of particles is a piecewise and homogeneous one within the areas of ellipsoidal clouds and composed matrix. In particular, in this paper we will consider a single particle cloud with the shape of a thick ply located in an infinite matrix with zero concentration of particles. For FGM where the concentration of the inclusions is a function of the coordinates ($\varphi(\mathbf{x}_i)\neq$const.), the micromechanical approach is based on the generalization of the multiparticle effective field method, previously proposed for statistically homogeneous (SH) random structure composites (see for references and details [1]). The nonlocal integral effective operator of elastic effective properties is estimated. The nonlocal dependencies of the effective elastic moduli as well as of conditional averages of the strains in the components on the concentration of the inclusions in a certain neighborhood of a considered point are detected.

The trivial generalization of the approach for statistically homogeneous composites [1] leads to the estimation of statistical average of strains inside the inclusions

$$\langle\boldsymbol{\sigma}\rangle_i(\boldsymbol{x})=\mathbf{Y}(\boldsymbol{x})\langle\boldsymbol{\sigma}\rangle(\boldsymbol{x})+\boldsymbol{K}(\boldsymbol{x})\langle\boldsymbol{\sigma}\rangle_i, \quad \boldsymbol{K}(\boldsymbol{x})\langle\boldsymbol{\sigma}\rangle_i=\int\mathbf{K}(\boldsymbol{x},\boldsymbol{y})[\langle\boldsymbol{\sigma}\rangle_i(\boldsymbol{y})-\langle\boldsymbol{\sigma}\rangle_i(\boldsymbol{x})]d\boldsymbol{y} \tag{1}$$

as well as effective properties. One obtains the explicit representations of tensors $\mathbf{Y}(\boldsymbol{x})$ and $\mathbf{K}(\boldsymbol{x},\boldsymbol{y})$ as the function of conditional probability density of inclusion locations $\varphi(\mathbf{x}_j|;\mathbf{x}_i)$ and their mechanical properties. The particular cases of the nonlocal integral Eq. (1) was solved by three different methods: the quadrature method, the iteration method, and the Fourier transform method with subsequent comparative analysis. For the SH media ($\varphi(\mathbf{x}_i)=$ const., $\langle\boldsymbol{\sigma}\rangle(\boldsymbol{x})\neq$const), the standard scheme of iteration and Fourier transform methods permit one to obtain the explicit representations for the nonlocal integral and differential operators, respectively, of any order describing overall effective properties as well as the stress concentration factor in the components. It is shown that the integral operator reduces to the differential one for sufficiently smooth statistical average stress fields and demonstrated the advantage of the iteration method over the Fourier transform method. For the FGM, an applicability of the Fourier transform method is questionable (in contrast with the iteration method). Only at first glance, the relation (1) is equivalent to the corresponding one obtained for the global effective properties in the framework of zero order approximation ($\mathbf{K}(\boldsymbol{x},\boldsymbol{y})=\mathbf{0}$). The main difference is that $\mathbf{Y}(\boldsymbol{x})$ and, therefore, $\boldsymbol{L}^*(\boldsymbol{x})$ depends on the parameters of the inclusion distribution not only at the point $\boldsymbol{x}$, but also in a certain neighborhood of that point leading to a so-called *nonlocal effect*, though, of course, the effective parameter $\boldsymbol{L}^*(\boldsymbol{x})$ are the local ones in the sense of nonlocal elasticity theory. The diameter of this region mentioned above is estimated as three times the characteristic dimension of the inclusions. As a result, a statistically inhomogeneous composite medium behaves like a macroscopically inhomogeneous medium with local effective modulus $\boldsymbol{L}^*(\boldsymbol{x})$ determined for a nonlocal distribution of the inclusions in a certain neighborhood of the point considered. Let us consider a strip model of ideal fiber cluster with probability densities $\varphi_1(\boldsymbol{x})=n$ and $\varphi_2(\boldsymbol{x}_1|\boldsymbol{x}_2)=ng(|\boldsymbol{x}_1-\boldsymbol{x}_2|)$ inside the thick ply $|\boldsymbol{x}|<a_w=16a$ (a=1 is the inclusion radius) and *0* otherwise. We will consider the volume fiber fraction inside the ply c=0.65, and two radial distribution functions $g(r)$ (step and nonstop functions, see [1]). The neglect of the binary interaction of inclusions for statistically homogeneous medium $n(\boldsymbol{x})$=const. reduces the formula for the effective elastic moduli to the analogous relation obtained by the Mori-Tanaka method which is invariant to the $g(r)$. Assume the matrix is epoxy resin which

contains identical circular glass fibers. As can be seen from Fig. 1 the use of the approach based on the quasicrystalline approximation (also called Mori-Tanaka (MT) approach) leads to an underestimate of the effective moduli L^*_{2222} compared to the more exact approximation of the MEFM which provides a good comparison with experimental data for statistically homogeneous media (see [2]). The stress concentrator factors found at the previous local evaluations permits one to estimate the stresses in the inclusions $<\sigma>_i(x_2)$ (see Fig. 2). For the SH media, we will consider inhomogeneous

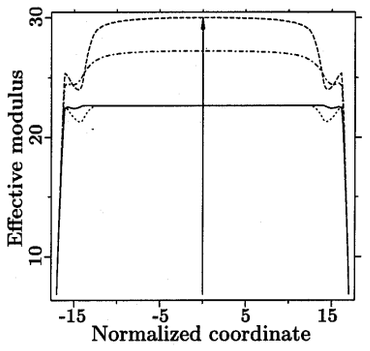


Fig. 1. L^*_{2222} vs x_2 estimated by: MEFM and nonstep $g(r)$ (dashed line), MEFM and step $g(r)$ (dot-dashed line), MT and nonstep $g(r)$ (dotted line), MT and step $g(r)$ (dotted line).

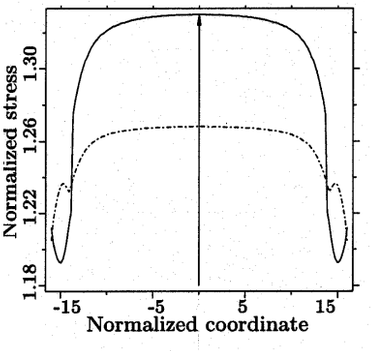


Fig. 2. $<\sigma_{22}>_i(x_2)$ (solid line) and $<\sigma_{12}>_i(x_2)$ (dot-dashed line) for the external loading at the infinity $\sigma^{\infty}_{ij}=\delta_{i2}\delta_{j2}$ and $\sigma_{ij}{}^{\infty}=\delta_{i1}\delta_{j2}$, respectively, and a step function g.

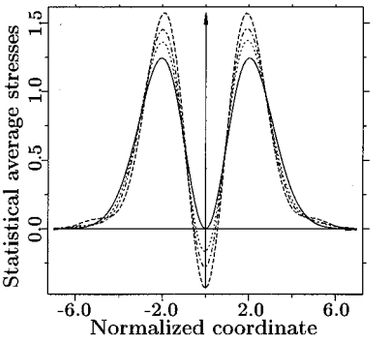


Fig. 3. $<\sigma_{22}>_i(x_2)$ vs x_2 estimated for nonstep $g(r)$ by the MEFM. Zero order (solid line), first order (dotted line), second order (dot-dashed line), sevens order (dashed line) approximations.

loading $<\sigma_{ij}>(x)=\delta_{i2}\delta_{j2}f(x_2)$ with the $f(x_2) = 0.6584\ |\ x_2\ |^{1.999}\ e^{-0.2422\ x_2^2}$. The function $f(x_2)$ is not twice differentiable that makes the use of the Fourier transform method questionable. However, exploring of the iteration method for the solution of Eq. (1) presents no difficulties and provides fast convergence of the obtained iterations (see Fig. 3. and [3], [4]). It is noted that the estimation of the effective elastic moduli is a linear problem with respect to the local stress distribution analyzed which is less sensitive than nonlinear micromechanical problems of elastoplastic deformation, fracture, and fatigue of composite materials. However, the method also allows one to estimate the second moment of stresses in the constituents as well as at each point on the interface between the matrix and fibers. The dispersion of these interface stresses, defined only by stress fluctuations, will is used for the prediction of the effective envelope for failure initiation. The dependence of effective failure envelope on the elastic, geometrical, and failure parameters of the constituents and the interphase matrix/fibers are analyzed (see for details [5]). The nonelliptical shape of the effective failure envelopes (EFE) using the proposed method of integral equations is demonstrated in Fig. 4 ($X=<\sigma_{11}>$, $Y=<\sigma_{12}>$).

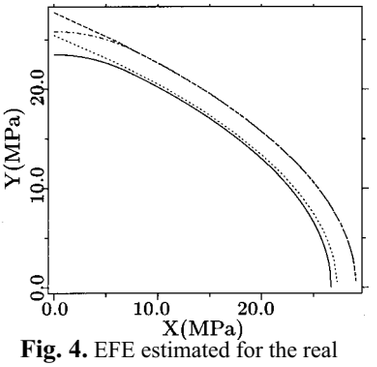


Fig. 4. EFE estimated for the real failure parameters for nonstep and step $g(r)$ (solid and dot-dashed curves) as well as for the assumed neglecting of shearing failure (dotted and dashed curves).

Acknowledgments: The work is supported by AFRL/WPAFB, USA

References

[1] Buryachenko, V.A. (2001) Multiparticle effective field and related methods in micromechanics of composite materials. *Appl. Mech. Review* **54**(1), 1-47.

[2] Buryachenko, V. A., Rammerstorfer, F. G. (2001) Local effective thermoelastic properties of graded random structure composites. *Arch. Appl. Mech.*, **71**, 249-272.

[3] Buryachenko, V. A., Pagano, N. J. (2003) Nonlocal models of stress concentrations and effective thermoelastic properties of random structure composites. *Math. Mech. of Solids,* 2003, **8**, 403-433.

[4] Buryachenko, V. A. (2004) Multiscalar mechanics of nonlocal effects in heterogeneous materials. *J.Multiscale Computational Engineering*, **2**(1). (In press).

[5] Buryachenko, V.A., Schoeppner, G. (2003) Influence of reinforcement random distribution on effective elastic and failure properties of fiber aligned composites. (Submitted).

TOPOLOGY OPTIMIZATION APPLIED TO THE DESIGN OF FUNCTIONALLY GRADED MATERIAL (FGM) STRUCTURES

Emílio Carlos Nelli Silva[*], Glaucio H. Paulino[**]
[*]*Department of Mechatronics and Mechanical Systems Engineering, Escola Politécnica da Universidade de São Paulo, São Paulo – SP, Brazil*
[**]*Department of Civil and Environmental Engineering, University of Illinois at Urbana-Champaign, Newmark Laboratory, Urbana - IL, USA*

Summary Functionally Graded Materials (FGMs) possess continuously graded properties with gradual change in microstructure. The concept of FGM is closely related to the topology optimization concept which essentially consists in a design method that seeks a continuum optimum material distribution in a design domain. This suggests that FGM structures can be designed by using topology optimization method. Thus, in this work topology optimization method is applied to design FGM structures considering a minimum compliance design problem. The topology optimization formulation considers the so-called continuous topology optimization formulation where a continuous change of the material properties is considered inside the design. As example, a new design was obtained where the problem is considered in an FGM domain, that is, a domain where the properties change in a certain direction in according to a specified law, leading to a structure with asymmetric stiffness properties.

INTRODUCTION

Functionally Graded Materials (FGMs) possess continuously graded material properties and are characterized by spatially varied microstructures created by nonuniform distributions of the reinforcement phase as well as by interchanging the role of reinforcement and matrix (base) materials in a continuous manner. The smooth variation of properties offer advantages such as reduction of stress concentration and increased bonding strength [1]. In this paper, FGMs are studied in conjunction with the concept of topology optimization design [2]. The design of FGM structures considering topology optimization has been considered in previous works [3,4] focusing mainly on thermal and thermomechanical applications, including transient problems, by defining the design variable in a piecewise manner in the discretized domain. The objective of the present work is to design FGM structures by using the concept of *continuum topology optimization* [5]. In this method, a continuum distribution of the design variable inside of the finite element domain is considered leading to a fully continuous FGM during the design problem. As objective function, the traditional formulation for stiffness design problem is considered initially where the objective is to find the material distribution that minimizes the mean compliance. A new design of structure is obtained by considering the distribution the FGM material itself in the design domain which leads to a structure with asymmetric stiffness properties.

THEORETICAL FORMULATION

Topology Optimization Concept

The objective of topology optimization is to determine holes and connectivities of the structure by adding and removing material in the extended domain which is a large fixed domain that must contain the whole structure to be determined. A main question in topology optimization is how to change the material in a binary form (e.g. from zero to one). The use of a discrete approach would present difficulties in the numerical treatment of the problem due to multiple local minimum. Thus, a material model must be defined to allow the material to assume intermediate property values by defining a function of a continuous parameter (design variable) that determines a mixture of two materials throughout the domain. This provides enough relaxation for the design problem. In this work, the topology optimization implementation considers material models based on the so-called density methods or artificial power law approaches, which will be employed together with a filtering technique to control the mesh dependency [2].

FGM-SIMP material model

The traditional SIMP (Solid Isotropic Material with Penalization) model [2] states that in each point of the domain, the material property is given by $E^H = \rho^p E_0$, where E^H and E_0 are the Young modulus of the homogenized material and basic material that will be distributed in the domain, respectively, ρ is a pseudo-density describing the amount of material in each point of the domain which can assume values between 0 and 1, and p is a penalization factor to recover the discrete design. For ρ equal to 0 the material is equal to void and for ρ equal to 1 the material is equal to solid material. Considering the objective of designing a structure in an FGM domain where the properties change in a certain direction in according to a specified law, the property E_0 above will depend on the position **x**, e.g. defining an exponentially graded material. Thus, the new material model can be written in the following form:

$$E^H = \rho^p E_0 e^{\alpha x + \beta y} \qquad (1)$$

where α and β are coefficients that define the change of material property in the domain, and x and y are the position Cartesian coordinates. This is a common situation when dealing with FGM materials [1], which is expected to result in a non-symmetric design. The domain is discretized into finite elements and the pseudo-density is defined for each node and interpolated inside the finite element [1,5].

Design Problem Formulation

The traditional formulation for stiffness design problem is considered where the objective is to find the material distribution that minimizes the mean compliance ($C_{mean}=\boldsymbol{U}^t\boldsymbol{F}$) considering a volume constraint ($\sum_{I=1}^{N}\rho_I \le V_{des}$) and equilibrium equation ($\boldsymbol{KU}=\boldsymbol{F}$) [2], where $\boldsymbol{K}$ is the stiffness matrix, $\boldsymbol{U}$ denotes displacements, and $\boldsymbol{F}$ denotes the force vector. The design variables are the pseudo-density ρ_I, which can assume different values in each finite element node [1,5].

RESULTS

The algorithm was implemented using C language. Four node bilinear elements considering plane stress formulation are used in the finite element formulation. Since the traditional stiffness design problem is considered, the optimality criteria method [2] was applied to solve the optimization problem since it is very efficient. A graded structural design is presented in an FGM domain, that is, a domain where the properties of the basic material change in a certain direction according to equation (1). The idea is to obtain a structure with asymmetric stiffness properties. The normalized Young`s modulus E_0 is equal to 10. The design domain considered and corresponding applied distributed load is shown in Figure 1a. A volume material constraint of 30% and a filter with radius equal to 1.5 was considered. Figures 1b and 1c illustrate the designs obtained considering the material variation in the x ($\beta=0$) direction. Notice the significant change of the resulting topology as a function of the material gradient.



a) b) c) d)

Figure 1: a) Initial design domain (50 x 50 mesh); b) Topology obtained using the traditional SIMP material model; c) Same using FGM-SIMP material model in the x direction with α=0.04, and filter (radius equal to 1.5); d) same with α=0.06.

CONCLUSIONS

Continuum topology optimization [5] was successfully applied to design FGM structures in which the material properties change within the design domain in a continuous manner. New designs were obtained where the distribution of the FGM itself is considered in the design domain, resulting in a structure with asymmetric stiffness properties. Thus, novel structural types are obtained by exploring the functionally graded materials idea. As future work, the design of composite unit cells made of FGMs will be considered using continuum topology optimization concepts.

ACKNOWLEDGMENTS

We acknowledge the USA NSF through the project “Inter-Americas Collaboration in Materials Research and Education” (PI, Prof. W. Soboyejo, Princeton University). We also thank Ms. Mariana Silva for her help with the numerical results.

References

[1] Kim, J-H. and Paulino, G. H.: Isoparametric graded finite elements for nonhomogeneous isotropic and orthotropic materials. ASME Journal of Applied Mechanics, 69:502-514, 2002.

[2] Bendsøe, M. P., Sigmund, O.: Topology Optimization. Theory, Methods and Applications. Springer-Verlag, Berlin, 2003.

[3] Turteltaub, S.:Optimal Material Properties for Transient Problems. *Structural Multidisciplinary Optimization*, 22: 157-166, 2001.

[4] Turteltaub, S.: Functionally Graded Materials for Prescribed Field Evolution. *Computer Methods in Applied Mechanics and Engineering*, 191: 2283-2296, 2002.

[5] Matsui, K. and Terada, K., (2003), “Continuous Approximation of Material Distribution for Topology Optimization”, *International Journal for Numerical Methods in Engineering*, in press.

FIRST PRINCIPLES-BASED EQUATIONS OF STATE FOR FUNCTIONALLY GRADED MATERIALS

S. Hanagud, Xia Lu
School of Aerospace Engineering, Georgia Institute of technology, Atlanta, Georgia 30332-0150

SUMMARY: Equations of state for mixture of solids are obtained from abinitio techniques or quantum mechanical method and compared with the available experimental data.

INTRODUCTION

Many kinetic energy projectiles are designed to penetrate through granular materials like concrete targets before the initiation of the reaction of energetic materials housed in the projectile. Critical loading conditions for the design of such projectiles are not the aerodynamic forces but the loading environment during penetration through granular materials. At high striking velocities, in the range of 1200 – 1500 m/sec, sharp noses of steel projectiles are subjected to a severe shock environment and nose tips are blunted while the pay load in the shank of the projectile are subjected to shock loads. The material is eroded from the nose of the projectile. In the case of the steel projectiles, melted and refrozen steel are observed on the shank of the projectile. Sections of the steel projectiles, recovered following penetration tests through concrete have displayed heat-affected zones, evidence of phase transformation including melting. Undesirable effects of the nose erosion are the deviation of the trajectory through the concrete from the intended trajectory and performance of the projectile including the penetration depth. The trajectory deviations are attributed to nose shape changes, compressive loads on the projectile and the asymmetric formation of micro cracks in the targets. The effective compressive loads and micro crack formation are also functions of the change of nose shape.

To minimize the nose erosion while the payloads, housed in the projectile, are protected from shock loads resulting from impact at high striking velocities, one choice is to design the projectiles by the use of functionally graded materials. The functionally graded materials can consist of mixtures that are excellent heat resistant materials at the nose tip to shock resistant energetic materials like the mixture of inter-metallic materials in the shank of the projectile. From the point of view of mechanics, the challenge is to formulate constitutive equations for the mixture of materials to evaluate their performance during impact. The constitutive equations are assumed to be represented by a combination of equations of state and the behavior of the contribution of the stress deviators. The mixture can contain varying ratios of different materials and thus it is very expensive to conduct a series of gas or powder gun tests for each representative mixture.

ABINITIO TECHNIQUES FOR EQOATION OF STATE FOR MIXTURES

Thus, in this paper, thermodynamically complete equations of state (EOS), which characterizes the material thermo-mechanical behavior under hydrostatic pressure and is expressed as the dependence of pressure on the specific volume and temperature, are predicted by using quantum mechanical methods. EOS is a part of the constitutive relations used in shock analysis. Traditionally, EOS has to be obtained by experimental measurement. The complete EOS requires a large amount of measurements at different state points. However, the extreme difficulty of the temperature measurement in shocked systems unavoidably leads to an incomplete EOS. Especially at the design stage of new materials, the measuring of EOS involves a tremendous effort at high cost. Therefore, using first principles calculations to obtain EOS of new materials seems very appealing. It saves not only the time of synthesizing materials but also the high cost for measurement. The most important is that it can provide the thermodynamically complete EOS.
There exist some literature on the use of the first principles to calculate EOS of solids including semiconductor material silicon and some metals. For the energetic intermetallic mixture like the Al-Ni mixture (payload) and refractory mixture at the nose tip, we use the following procedure to obtain the EOS of the mixture by ab initio quantum mechanical calculations. First, the EOS is obtained for each individual component from first-principle calculations. Ab initio methods are based on the psuedopotential plane-wave methods. The generalized gradient approximations and the ultrasoft psuedopotential are utilized. The prediction of the EOS consists of two parts: the static-lattice EOS and thermal effects. The range of the

pressure and the temperature of consideration is up to 300 GPa and 1000K. As known, the melting temperatures of aluminum and nickel at the ambient pressures are about 933 K and 1728 K, respectively. Also aluminum was theoretically predicted to undergo the pressure-induced crystallographic phase sequence from fcc→hcp→bcc, at predicted phase transition pressures; 205±20GPa and 565±60 GPa. In this work, the possible polymorphic phase transitions are not considered. The single-phase EOS agrees well with the experimental shock Hugoniot. The EOS of the mixture is approximated using appropriate mixture theories, namely homobaric mixture theory and uniformly blended mixture theory.

RESULTS

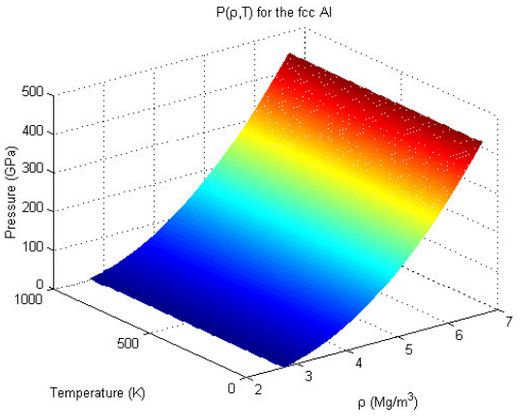
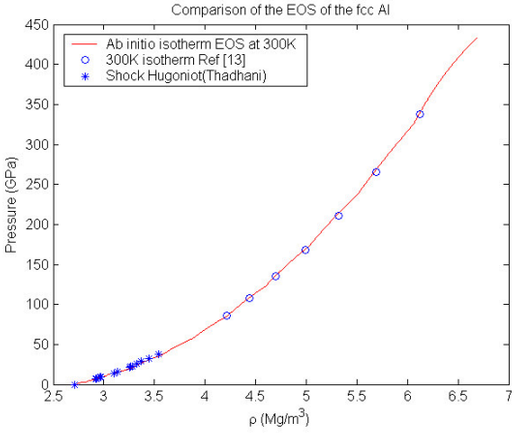
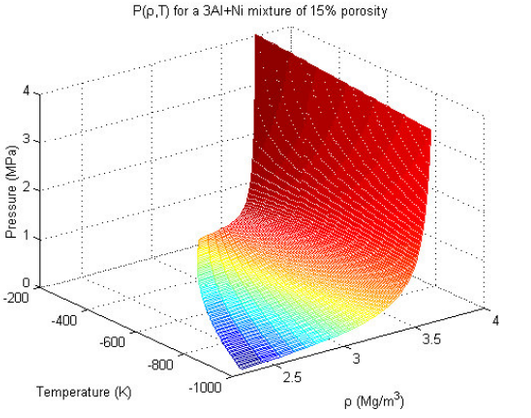


Figure 1 The thermodynamically complete equation of state of Al.





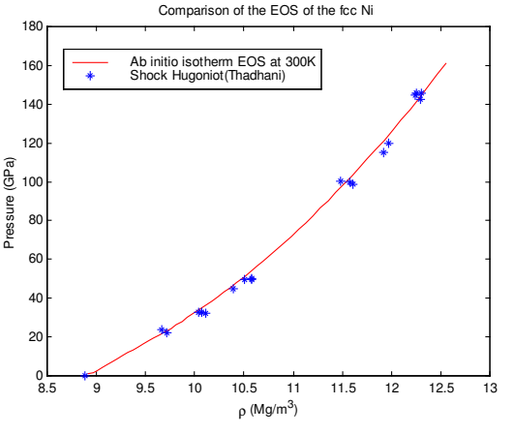


Fig.2-4: Comparison of EOS for Al & Ni with available Exptl. Data; EOS for the Mixture

DESIGN OF FGM BIMORPH PIEZO-ACTUATORS

Minoru Taya, Professor and Director
Center for Intelligent Materials and Systems
Department of Mechanical Engineering
University of Washington, Box 352600
Seattle, WA 98195-2600
USA
Email:tayam@u.washington.edu

Fig. 1(a) and (b) are mono-morph and bimorph actuators, respectively. Despite large bending displacement, the bimorph piezo-actuator is known to suffer from large induced stress at the interface region. To overcome this, we designed two types of piezo-actuators, one-sided (Rainbow type) actuator with functionally graded microstructure (FGM), Fig. 1(c) where the electroelastic properties are graded smoothly along the thickness direction [3] and FGM bimorph actuator [1,2,4] where the top and bottom piezoelectric plates are composed of multilayers where the electroelastic properties are graded smoothly across the plate thickness, Fig. 1(d).

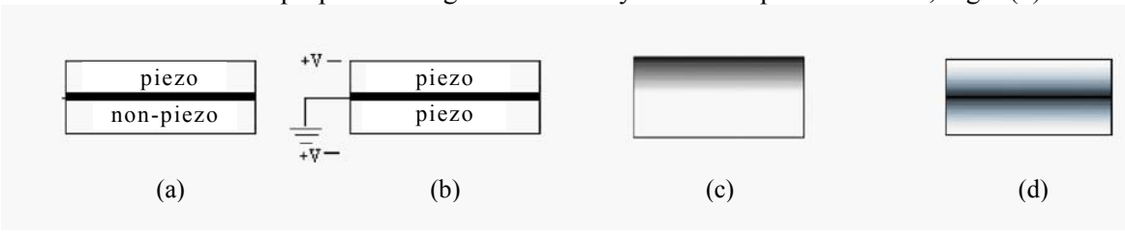


Fig. 1 Different types of piezoactuators, (a) monomorph, (b) bimorph, (c) one-sided FGM, and (d) FGM bimorph.

In this talk, I will introduce two types of FGM piezo-actuator designs, one is one-sided FGM, Fig. 1(c), the second is FGM bimorph, Fig. 1(d). Fig. 2 shows the cross section of one sided FGM piezo-actuator [3] and the results of curvature of the piezo actuator beam and applied electric field are shown in Fig. 3 indicating a good agreement between our model and the experimental data.

.

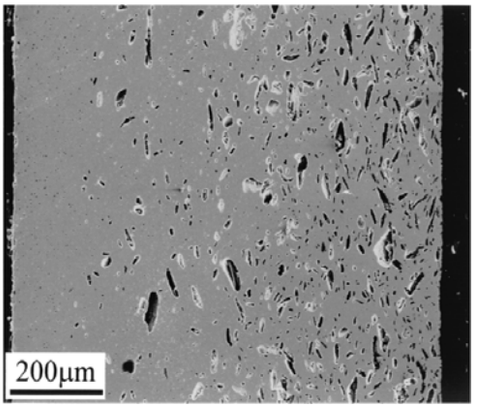


Fig. 2 SEM micrograph of the fabricated PZT sample with a linear porosity gradient.

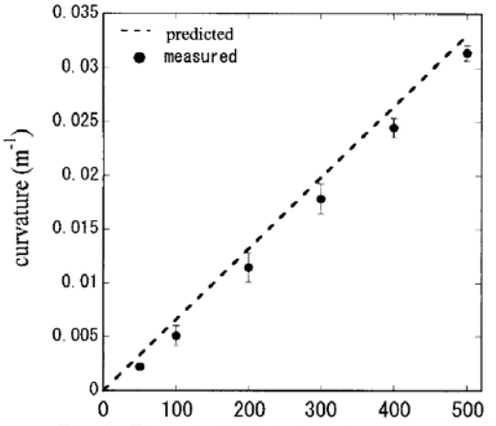


Fig. 3 Electric-field-induced curvature of the porosity-graded PZT beam-shaped as a function of applied voltage.

The requirements of bending actuators are large displacement and minimum stress induced in piezo-layers. In this respect, the Rainbow type piezo-actuators satisfy the second requirement, but not the first. In order to satisfy both requirements, we designed a set of FGM bimorph piezo-

actuators, Fig. 1(d). The distribution of mechanical and piezoelectric properties are assumed to vary throughout the FGM plate thickness in a step wise manner as shown in Fig. 4 where two cases of stepwise linear distributions are considered, type A and type B. For each type, six layers of FGM are considered.



Fig. 4. Electroelastic properties distribution in FGM-bimorph

Bimorph System		Maximum Bending Displacement (μm)	σ_x Max. (MPa)	τ_{xz} Max. (MPa)
Standard Bimorph	Experimental	49.6	----	----
	CLT	47.5	3.08	----
	2D elasticity	47.8	3.07	1.48
	FEM	47.6	3.17	1.56
FGM Bimorph type-A	Experimental	43.8	----	----
	CLT	43.6	1.48	----
	2D elasticity	44.9	1.63	0.59
	FEM	44.8	1.65	0.63
FGM Bimorph type-B	Experimental	30.4	----	----
	CLT	29.2	3.38	----
	2D elasticity	29.5	3.69	1.82
	FEM	29.4	3.75	1.9

Table 1 Comparison of ANSYS FEM results with the analytical values for piezoactuators, standard bimoph EGM bimoph tapes A and B

We have processed two different types of FGM actuators (type A and B) and also standard bimorph[4]. A comparision between the experimental data and predictions by our models(classical lamination theory(CLT), 2D elasticity model and FEM) are summarized in Table 1. It is clear from Table 1 that the FGM bimorph type A exhibits the best performance, i.e large bending displacement, slightly less that that of the standard bimorph, while the induced stresses(σ_x and τ_{xy}) are smaller than those of the standard bimorph and the FGM bimorph type B. It is also noted in Table 1 that the 2D elasticity model[2] predicts reasonably accurate shear stress which could not be possible by CLT.

References

[1] Almajid, A.Taya, M and Hudnut, S., "Analysis of out-of-plane displacement and stress field in a piezoelectric composite with functionally graded microstructure", *Intl. J. Solids Struct.*, 38, 3377-3391, 2001.

[2] Almajid, A. and Taya, M. "2D-analysis of FGM piezo-laminate under cylindrical bending", *Intell. Mater. Sys. & Struct.* , 12, 342-351,2001

[3] Li, J.F., Takagi, K., Ono, M., Pan, W., Watanabe, R., Almajid, A. and Taya, M., "Fabrication and evaluation of porous piezoelectric ceramics and porosity-graded piezoelectric actuators", *J. Amer. Ceram. Soc*., 86, 1094-1098, 2003.

[4] Taya, M., Almajid, A.,Dunn, M., Takahashi, H., "Design of bimorph piezo-composite actuators with functionally graded microstructure", *Sensors and Actuators*, A107, 248-260,2003.

THERMOELASTIC ANALYSIS OF FUNCTIONALLY GRADED MATERIALS SUBMITTED TO SHOCKS

Carlos. A. V. Carneiro, Fernando A. Rochinha, Lavínia S. A. Borges
Federal University of Rio de Janeiro, Mechanical Engineering Department C.P. 68503,Rio de Janeiro,Brazil

Summary In this present work, it presents a model to solve the strongly coupled thermomechanical problem submitted to thermodynamic solicitations. Traditional staggered algorithm without upsetting the unconditional stability property characteristic of fully implicit schemes is used. Numerical simulations are presented for a bar with materials FGM submitted to thermal loadings and analysis is accomplished for cases of thermal shocks.

Introduction

Layered composite materials due to their thermal and mechanical merits compared to single-composed materials, have been widely used on a variety of engineering applications. However, the interfaces might represent regions of stress concentration and, due to that, risk of presenting failure mechanisms like lost of cohesion. For instance, linear elastic materials present stress singularities at the interfaces or at the free edges. In recent years, nonhomogeneous materials have been developed to attenuate the interfacial stresses under a new concept: functionally graded materials (FGMs). FGMs are composites whose mechanical properties vary smoothly or continuously along its domain. They have been used in thermal protection systems due to their high temperature resistance in order to decrease thermal stresses distribution and to increase the effect of protection from heat. It is possible by controlling the volume fractions of these materials to obtain very different thermomechanical responses. The utilization of FGMs in the attenuation of stress wave propagation[1] can be very useful in important engineering applications like, for instance, the re-entry motion of space vehicles, in which a rapidly changing temperature can lead to a dramatic failure scenario. In this type of situations the dynamic thermoelastic response should be considered. Dynamic thermoelastic problems have been studied, since several decades, in different structures[2, 3]. Transient response prediction of thermodynamical loaded structures without mechanical coupling[4] considering FGMs have been studied. The present work presents a numerical formulation to solve the strongly coupled thermomechanical problem submitted to thermal shock like solicitations. A staggered algorithm without upsetting the unconditional stability property characteristic of fully implicit schemes is used. The proposed scheme is a fractional step method associated with a two phases operator split of the linearized thermoelasticity system into an adiabatic elastodynamics phase, followed by a heat conduction phase. Numerical simulations are presented for an FGM bar submitted to an abrupt variation of external temperature representing thermal shocks.

Numerical Modeling of the coupled FGM thermomechanical problem

Here, a FGM material is considered as binary composite in which a power-law distribution governs the composition of the basic material volume fraction. Based on microstructures theory, this volume fraction determines the effective mechanical properties of the composite. Particularly, the rule of mixture was employed. The coupled thermomechanical stems from the balance equations of momentum and energy and from constitutive equations that use the effective thermomecanical properties. Among then, the parameter that is responsible for thermomechanical coupling. This parameter has a direct relation with the thermal dilatation coefficient and the Bulk modulus, and it is very important to verify this thermomechanical effect and defines the strategy for the solution of this kind of problem.

The proposed strategy for the solution of this linear coupled first order system of partial differential equations of mixed hyperbolic parabolic type in this thermoelastic problem is a staggered scheme in which partitions this linear differential operator in two distinct phases. It consists in one adiabatic elastodynamic phase, in which the entropy of the system is held constant, followed by a heat conduction phase at fixed configuration[5]. This method of solution for this problem obtains, as a consequence, no dissipation within the mechanical phase, since the total entropy is remained constant, while the dissipation in the subsequent thermal phase is the total dissipation generated by heat conduction. Initially one solves the adiabatic elastodynamic phase with spatial discretization by the Finite Element Method (FEM) combined with the time discretization provide by the Crank Nicholson scheme, well known to be second order accurate and unconditionally stable. Using the values obtained in the mechanical phase, the final temperature field by applying an unconditionally B-stable scheme to heat conduction is computed. A rigorous stability analysis of this specific split of the evolution thermoelastic problem by the staggered algorithm is achieved making use by Von Neumann stability and via the energy method analysis[5].

Numerical Results

To assess the thermoelastodynamical response in FGM structures, a simulation involving a one-dimensional composite bar with two dissimilar materials of uniform thickness with transversal area 3.10^{-4} m^2 and length total 310mm is presented. The bar is divided into two different regions, the first one of 10mm corresponds to the thermal protection while the second region represents the basic structure .The metal and ceramics layers selected are SUS304 steel and PSZ ceramic. In order to understand the role played by different composites obtained by using different distributions of the components, two situations are analyzed. In the first case the composite presents two homogenous regions, therefore not constituting an FGM and presenting an interface. In the second one, a typical smooth transition is

provided by an FGM with the same volume fraction of the components. In the first case, the thermal shield is constituted of pure ceramic and in the second situation a FGM composite is adopted. These materials are submitted to external abrupt temperature variation in the left corner and the bar's initial temperature is 300K. In both cases, the bar is clamped at the ends and thermically isolated at 300K in the right border. A pulse de temperature is applied to these materials to estimate the stress wave propagation by thermal shock conditions.

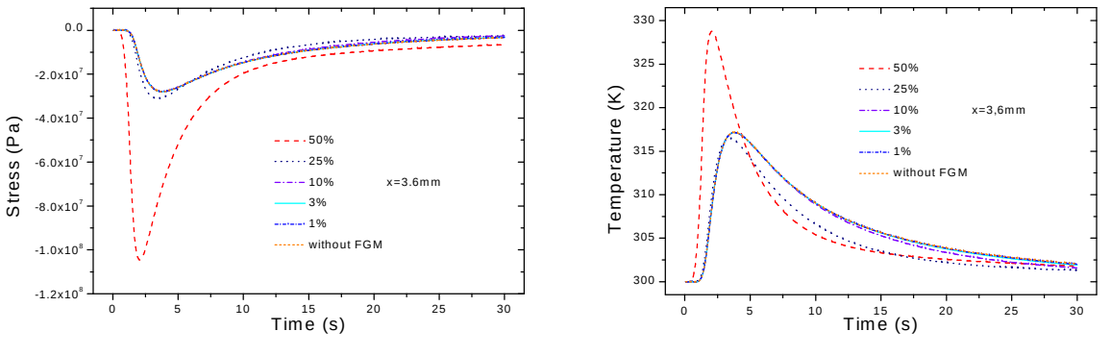


Figure1- Stress and temperature distributions at 3.6mm of PSZ/steel FGM bar submitted to temperature pulse 1000K with variation of material composition.

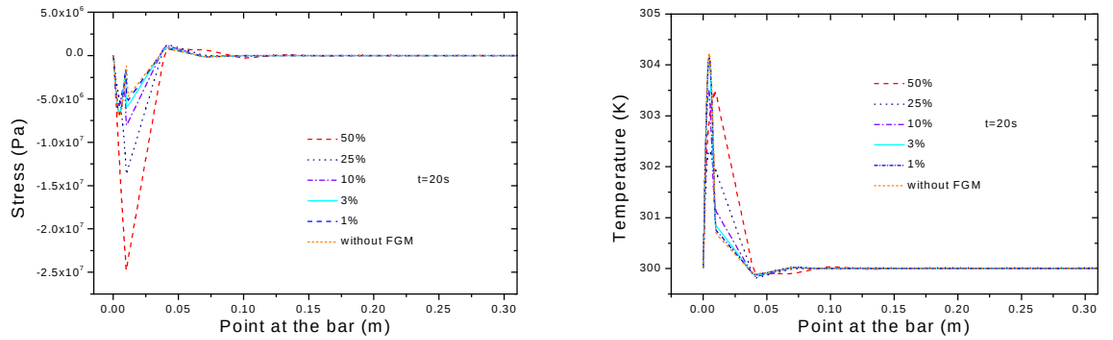


Figure2- Stress and temperature distributions in the domain of PSZ/steel FGM bar at the time 20s after submitted to temperature pulse 1000K with variation of material composition.

The numerical solution involves a spatial discretization consisting of 20 linear finite elements, 10 in each dissimilar material. Initially, two numerical simulations are considered, corresponding to application of temperature submitted to different materials. The figure1 shows the stress in time at 3.6mm of the first corner of the bar. One can observe that the bar experiments tension in the beginning, immediately followed by compression. This fact occurs because the bar is clamped in both ends. The compositional variation in the FGM bar, given by volumetric percentual, breeds new stress and temperature fields as observed. One can verify that when decreasing the volumetric percentual material, which means that a greater quantity of PSZ ceramic is used in the FGM, the amplitude of stress and temperature decrease. Furthermore, in the first case, where the FGM solution is not applied, the initial portion of the bar corresponding to the thermal shield, present the lower peak stress. Nonetheless two important aspects must be considered. The peak stress obtained with FGM's shield are in compression, which seems no to represent an important danger, as ceramics are fragile materials and do not resist to traction. The second, and most important, aspect is related to the fact that the stress distribution obtained when FGM shows a significant better behavior in what concerns the interface between the thermal protection and the structure as it is presented in Figure2.

Conclusions

A numerical formulation based on a staggered approach is used to understand the role of FGM materials for enhancing the quality of thermal protection systems. The variation of the composition is analyzed by comparing the thermomechanical of the different resulting systems.

References

[1] Jin Z.-H., Paulino G.H.: Transient thermal stress analysis of cracked functionally graded materials, *Ceramic Transactions* **114**: 747-754, 2001.

[2] Cho H., Kardomateas G.A.:Thermal shock stresses due to heat convection at a bounding surface in a thick orthotropic cylindrical shell. *Int J. Solids Struct* **38**: 2769-2788, 2001.

[3] Praveen G.N., Reddy J.N.:Nonlinear transient thermoelastic analysis of functionally graded ceramic-metal plates. *Int J. Solids Struct* **35**: 4457-4476, 1998.

[4] Turteltaub S.: Optimal control and optimization of functionally graded materials for thermomechanical processes. *Int J. Solids Struct* **39**:3175-3197, 2002.

[5] Armero F., Simo J.C.: A new unconditionally stable fractional step method for non-linear coupled thermomechanical problems. *Int J. Num Met in Eng* **35**: 737-766, 1992.

SURFACE WAVES ON AN IMPERMEABLE BOUNDARY OF A POROELASTIC MEDIUM

Bettina Albers
Weierstrass Institute for Applied Analysis and Stochastics, Mohrenstr. 39, D 10117 Berlin, Germany

Summary The dispersion relation for surface waves on an impermeable boundary of a fully saturated poroelastic medium is investigated numerically in the whole range of frequencies. To this aim a linear simplified model of a two-component poroelastic medium is used. Similarly to the classical Biot's model, it is a continuum mechanical model but it is much simpler due to the lack of coupling of stresses. In the whole range of frequencies there exist two modes of surface waves corresponding to the classical Rayleigh and Stoneley waves. The numerical results for velocities and attenuations of these waves are shown for different values of the bulk permeability coefficient in different ranges of frequencies. In particular, we expose the low and high frequency limits, demonstrate the existence of the Stoneley wave in the whole range of frequencies as well as the leaky character of the Rayleigh wave.

PROCEDURE

The purpose of this work is to investigate the dispersion relation for surface waves on an impermeable boundary of a fully saturated poroelastic medium in the whole range of frequencies. Therefore we present the linear form of the model for a two-component poroelastic saturated medium. We show the governing equations and the construction of the solution for a semiinfinite medium with an impermeable boundary. One part is devoted to the presentation of the boundary conditions on such an interface between a porous medium and a vacuum. Afterwards we show the general dispersion relation and summarize results of an earlier work [4] for the high and low frequency approximations. The main part of the presentation concerns numerical aspects: first we indicate the applied numerical procedure and then we illustrate the numerical results for the normalized velocities and attenuations of the Rayleigh and Stoneley waves. It is known that surface modes of propagation in linear models result from the combination of bulk modes. Physically, this means that at any point of the boundary classical longitudinal and shear waves combine into the Rayleigh wave which must be slower than both bulk waves. The presence of the second longitudinal bulk wave P2 yields the existence of the second surface mode - the Stoneley wave which should be slower than the P2-wave - the slowest of bulk waves. Both quantities, velocities and attenuations, are shown for different values of the bulk permeability coefficient, π, in different ranges of frequencies. A decay of the Rayleigh wave velocity, mentioned in the book [1] has been confirmed in the range of small frequencies in spite of the lack of static coupling between components. Moreover we compare the behaviour of the two types of surface waves with the behaviour of two bulk waves: P1, and P2.

In this summary we only show a part of the presentation, namely the governing equations, the boundary conditions, and the numerical results for a chosen value of the permeability coefficient: $\pi = 10^7 \ \frac{\mathrm{kg}}{\mathrm{m^3 s}}$.

MODEL

Within the linear model of a two-component poroelastic saturated medium the process is described by the macroscopic fields $\rho^F(\mathbf{x},t)$ - partial mass density of the fluid, $\mathbf{v}^F(\mathbf{x},t)$ - velocity of the fluid, $\mathbf{v}^S(\mathbf{x},t)$ - velocity of the skeleton, $\mathbf{e}^S(\mathbf{x},t)$ - symmetric tensor of small deformations of the skeleton and the porosity n. These fields satisfy the following set of linear equations

$$\begin{aligned}
&\frac{\partial \rho^F}{\partial t} + \rho_0^F \operatorname{div} \mathbf{v}^F = 0, \quad \left|\frac{\rho^F - \rho_0^F}{\rho_0^F}\right| << 1, \quad \rho_0^F \frac{\partial \mathbf{v}^F}{\partial t} + \kappa \operatorname{grad} \rho^F + \beta \operatorname{grad}(n - n_E) + \hat{\mathbf{p}} = 0, \quad \hat{\mathbf{p}} := \pi(\mathbf{v}^F - \mathbf{v}^S), \\
&\rho_0^S \frac{\partial \mathbf{v}^S}{\partial t} - \operatorname{div}\left[\lambda^S (\operatorname{tr} \mathbf{e}^S)\,\mathbf{1} + 2\mu^S \mathbf{e}^S + \beta(n - n_E)\mathbf{1}\right] - \hat{\mathbf{p}} = 0, \quad \frac{\partial \mathbf{e}^S}{\partial t} = \operatorname{sym} \operatorname{grad} \mathbf{v}^S, \quad \left\|\mathbf{e}^S\right\| << 1, \quad n_E := n_0(1 + \delta \operatorname{tr} \mathbf{e}^S), \qquad (1) \\
&\frac{\partial (n - n_E)}{\partial t} + \Phi \operatorname{div}(\mathbf{v}^F - \mathbf{v}^S) + \frac{n - n_E}{\tau} = 0, \quad \left|\frac{n - n_0}{n_0}\right| << 1.
\end{aligned}$$

Here ρ_0^F, ρ_0^S, n_0 denote constant reference values of partial mass densities, and porosity, respectively, and κ, λ^S, μ^S, β, π, τ, δ, Φ are constant material parameters. The first one describes the macroscopic compressibility of the fluid component, the next two are macroscopic elastic constants of the skeleton, β is the coupling constant, π is the coefficient of bulk permeability, τ is the relaxation time and δ, Φ describe equilibrium and nonequilibrium changes of porosity, respectively. For the purpose of this work we assume β=0.

BOUNDARY CONDITIONS

In order to determine surface waves in a saturated poroelastic medium we need conditions for $z=0$. In the general case of a boundary between a saturated porous material and a fluid the boundary conditions were formulated by Deresiewicz & Skalak. We quote them here in a slightly modified form and for an impermeable boundary

$$T_{13}\big|_{z=0} \equiv T_{13}^{S}\big|_{z=0} = \mu^{S}\left(\frac{\partial u_1^{S}}{\partial z}+\frac{\partial u_3^{S}}{\partial x}\right)\Bigg|_{z=0} = 0, \qquad \frac{\partial}{\partial t}\left(u_3^{F}-u_3^{S}\right)\Big|_{z=0} = 0,$$

$$T_{33}\big|_{z=0} \equiv \left(T_{33}^{S}-p^{F}\right)\Big|_{z=0} = c_{P1}^{2}\rho_0^{S}\left(\frac{\partial u_1^{S}}{\partial x}+\frac{\partial u_3^{S}}{\partial z}\right)-2c_S^{2}\rho_0^{S}\,\frac{\partial u_1^{S}}{\partial x}-\kappa\left(\rho^{F}-\rho_0^{F}\right)\Big|_{z=0} = 0,$$

where u_1^{S}, u_3^{S} are x-, and z-components of the displacement $\mathbf{u}^{S}$, respectively, and u_3^{F} the z-component of the displacement $\mathbf{u}^{F}$.

RESULTS FOR VELOCITIES AND ATTENUATIONS

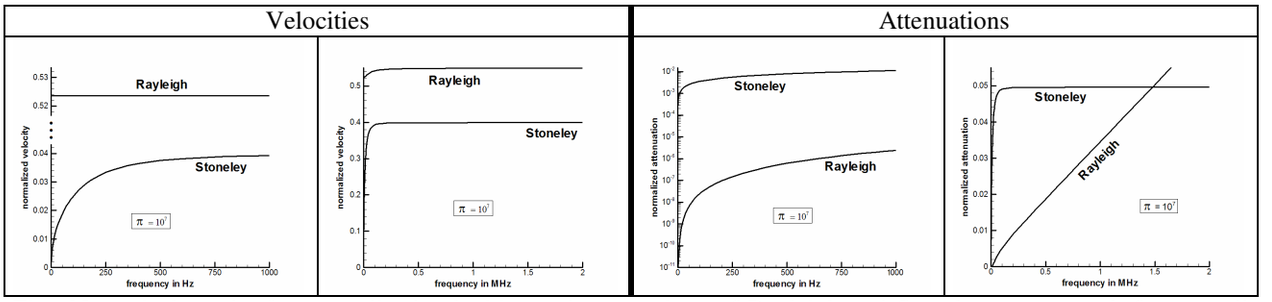


Fig.: Numerical results for normalized velocities and attenuations of Rayleigh and Stoneley waves, each for a small frequency range (left) and a large frequency range (right) for the permeability coefficient: $\pi = 10^{7}\ \frac{\mathrm{kg}}{\mathrm{m^3 s}}$.

CONCLUSIONS

Rayleigh

- the velocity of propagation of this wave lies in the interval determined by the limits $\omega\to 0$ and $\omega\to\infty$. The high frequency limit is app. 4.7% higher than the low frequency limit. The wave is always slower than the S-wave. As a function of ω it possesses an inflection point and it is slightly nonmonotonous,
- this nonmonotonicity appears in the range of small frequencies. The velocity possesses in this range a minimum whose size is very small. Interestingly, the minimum value remains constant for the different values of π. This means that the decay is not driven by the diffusion. Such a behaviour is also observed within Biot's model;
- the attenuation of this wave grows from zero for $\omega=0$ to infinity as $\omega\to\infty$. In the range of large frequencies it is linear (a constant positive quality factor). This means that it is a leaky wave.

Stoneley

- the velocity of this wave grows monotonically from the zero value for $\omega=0$ to a finite limit which is slightly smaller than the velocity of the P2-wave. The growth of the velocity of this wave in the range of low frequencies is much steeper than this of Rayleigh waves similarly to the growth of the P2-velocity;
- both the velocity and attenuation of the Stoneley wave approach zero as $\sqrt{\omega}$,
- the attenuation of the Stoneley wave grows monotonically to a finite limit for $\omega\to\infty$ (zero quality factor). It is slightly smaller than the attenuation of P2-waves. Consequently, in contrast to the claims in the literature, the Stoneley wave is attenuated.

References

[1] Bourbie T., Coussy O., Zinszner B.: Acoustics of porous media, Editions Technip, Paris 1987.
[2] Deresiewicz H., Skalak R.: On uniqueness in dynamic poroelasticity. *Bull. Seismol. Soc. Am.* **53**:783-788, 1963.
[3] Wilmanski K.: Waves in porous and granular materials, in: Kinetic and Continuum Theories of Granular and Porous Media, K. Hutter, K. Wilmanski (eds.), 131-186, CISM Courses and Lectures No. 400, Springer Wien New York 1999.
[4] Wilmanski K., Albers B.: Acoustic waves in porous solid-fluid mixtures, in: Dynamic Response of Granular and Porous Materials under Large and Catastrophic Deformations, K. Hutter, N. Kirchner (eds.), 285-314, Lecture Notes in Applied and Computational Mechanics, Vol.11, Springer, Berlin 2003.

BULK SOLITONS DO NOT DECAY IN ELASTIC WAVE GUIDES

Alexander M. Samsonov*, Galina V. Dreiden*, Irina V. Semenova*
*The A.F.Ioffe Physico-technical Institute of the Russian Academy of Sciences, 194021 St.Petersburg, Russia

Summary Theoretical and experimental research has been performed to prove the existence of long bulk strain solitary waves produced by a laser-induced impact in nonlinearly elastic isotropic wave guides. In experiments with short wave guides (up to 30 length scale), we were not able to prove a lossless propagation of observed bulk solitons. *New experiments* on bulk soliton propagation in much longer wave guides (up to 150 length scale) allow to confirm that the solitons do not reveal any amplitude decay and shape transformation, while *any* linear or shock wave completely disappear at much shorter distance. It allows to propose a new NDT approach and a method to determine the 3d order elastic moduli of non-crystalline materials based on bulk elastic solitary waves propagation theory.

THEORY AND EXPERIMENTAL SETUP DESCRIPTION

Our aim is to prove the possibility of energy transfer by means of bulk solitary waves for very long distances without significant losses in 1D and 2D elastic wave guides. These wave guides have strong dispersion and made of materials with remarkable linear dissipation, that leads to disappearance any of linear or shock waves in short distances. Long nonlinear solitary strain waves (solitons) may be of considerable importance to study the time evolution of strains, the impact loading of materials with radiation and/or wear resistance, the nonlinear elastic parameters of materials etc. Nonlinear elastic features of these materials result in generation of strain solitons even under short-run and reversible (elastic) loading. Mathematical theory of long nonlinear waves in elastic wave guides is well developed in order to initiate the successful experiments in generation of strain solitons in solids. The nonlinear doubly dispersive equation (DDE in [1]) describes propagation of the long nonlinear wave of strain component $u(x,t)$ in a rod of radius R,

$$u_{tt} - c_0^2 u_{xx} = (1/2)\left[\beta\, u^2/\rho + \nu R^2\left(c_0^2 u_{xx} - (1-\nu)u_{tt}\right)\right]_{xx}. \qquad (1)$$

where c_0 is the 'rod' sound velocity, $\beta = \beta(E,\nu;l,m,n)$ is a nonlinearity coefficient, (l,m,n) are the 3d order elastic moduli, ρ, ν are the specific density and the Poisson ratio, subscripts x,t denote derivatives in space and time, and u, β, ν may be of *any* sign. General travelling wave (TW) solution to (1), depending on $z = x \pm Vt$, is obtained in terms of the Weierstrass elliptic function $\wp$ as $u = u_0 + \wp(z + z_0; g_2; g_3)$, As appropriate limit it has also a particular solitary wave solution with velocity V and width Λ:

$$u = A\cosh^{-2}\frac{x \pm t\sqrt{c_0^2 + A\beta/(3\rho)}}{\Lambda}; \quad V^2 = c_0^2 + \frac{A\beta}{3\rho} > 0; \quad \Lambda^2 = 2(\nu R)^2\left[-\frac{1-\nu}{\nu} + \frac{3E}{A\beta}\right] > 0 \qquad (2)$$

In conventional solids with $0 < \nu < 1/2$ the soliton velocity lies in the interval: $c_0^2 < V^2 < c_0^2/(1-\nu) \equiv c_{\lim}^2$, and is limited from above, while no subsonic ($V < c_0$) solitary compression wave exists. Moreover, the value of V depends on nonlinearity of material and may be equal or *even greater* than the longitudinal sound wave velocity $c_l = \sqrt{(\lambda+2\mu)/\rho}$ in the medium: $\nu \le 1/3 \Rightarrow c_{\lim} \ge c_l$.

Two main applications were proposed for bulk solitons in mechanics: a new introscopy (NDT) method suitable for lengthy structures and a method to determine the 3d order elastic moduli of isotropic materials. Both are to be based on elastic energy transfer in a wave guide, and the main problem to be solved is for how long may a bulk solitary wave propagate without decay? In theory an ideal solitary wave is powerful and lossless, contrary to the 'common experience' with most of bulk longitudinal waves in mechanics of real solids.

We have performed numerous experiments on the generation and propagation of bulk strain solitary waves in polystyrene and plexiglas wave guides. The materials were selected due to unique combination of non-linear elasticity and optical properties allowing the translucent recording of wave patterns. The first generation of solitary nonlinear longitudinal strain wave (the soliton) was made in various 1D and 2D elastic wave guides by means of laser driven shock wave, the observation of waves was based on holographic interferometry. The experimental technique used for generation and observation of strain solitary waves in different wave guides was described, e.g., in [2], and is based on the laser generation and optical recording of the waves under study. The apparatus (see Fig.1) consists of a channel to produce the strain wave in a solid from a weak shock wave, which is induced by laser pulse evaporation of a metallic target placed nearby an entrance of the wave guide; a synchronizer; a holographic interferometer. This setup allows to record a wave pattern in and outside the transparent wave guide due to the wave induced density variations, which lead to the shifts of the carrier fringes on the resulting holographic interferogram. The relationship between the measured fringe shift ΔK on the interferogram inside the rod and soliton amplitude A was derived (see [1-2]):

$$A = -\lambda_1\,\Delta K\,/[2h[(n_1-1)(1-2\nu) + \nu(n_1-n_0)]]$$

where λ_1 is the recording light wave length, n_1 , n_0 are refractive indices of solids and water, h is the rod thickness along the recording light path. We have demonstrated the successful generation and subsequent propagation of strain solitons in different rods and plates, observed the soliton amplification in a tapered wave guide, the soliton reflection

from free or clamped ends of the rod, and soliton propagation in a wave guide embedded into another elastic medium. In numerical simulation the phase shift of the wave, its amplitude growth and the increase of a number of separate solitons were observed as distinctive characteristics suitable for introscopy of a wave guide.

RESULTS AND DISCUSSION

We certified the observed wave as a genuine strain solitary wave. It keeps the shape permanent, has no long wave of opposite sign behind, and its amplitude and width are proportional to the wave speed. In experiments with polystyrene and plexiglas we found that $\Lambda > 7R$.

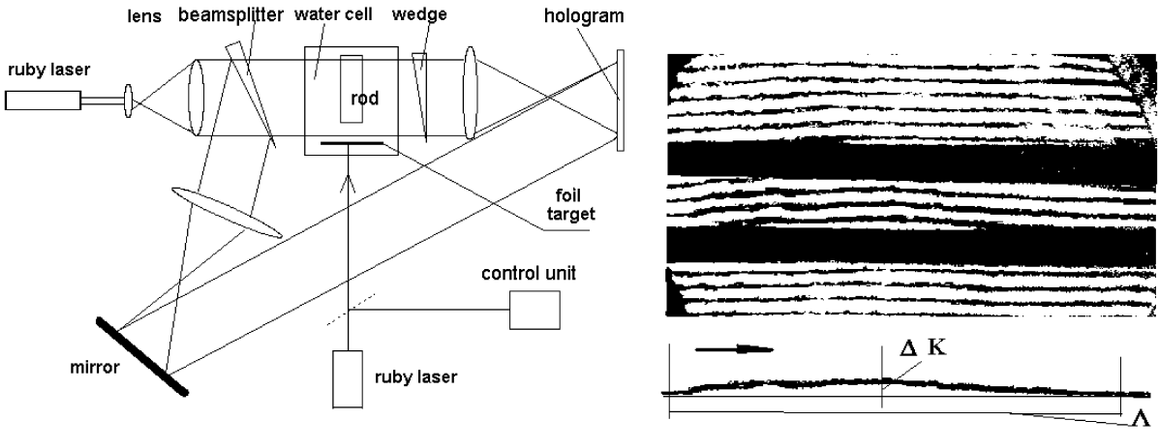


Figure 1. *Left*: Setup; *Right*: Interferogram of the soliton in the plexiglas rod. One of the fringes in the rod is extracted from the interferogram and shown below for convenience. Wave shape and amplitude both remain permanent at long distances.

Table. Parameters of solitons observed in polystyrene and plexiglas bars

Material	Amplitude,A	Width,Λ, mm	V, m/s	c_0,m/s	c_l,m/s
Polystyrene	$2.82 \cdot 10^{-4}$	32.5	≈ 2280	1870	2310
Plexiglas	$4.3 \cdot 10^{-4}$	32	≈ 2530	2060	2570

However, up to now we were limited by relatively short wave guides (up to 150 mm long, i.e., 30 scale units equal to R), that provoked some doubts in that the observed waves are genuine non-decaying solitary waves.

Now we demonstrate new experimental results on soliton behavior in lengthy polymeric wave guides (700 mm and longer). We prove that even *at very long distances* bulk solitons do not show any decrease of amplitude or shape transformation when propagating in an isotropic wave guide. On the contrary any of linear or shock waves in these materials disappear completely at much shorter distances. Numerical simulations were made also to demonstrate the advantages of the strain solitons usage for development of a new NDT method.

The measurements of (l, m, n) require to derive 3 independent algebraic relations, see [3]. In addition to (2) the coupled equations for the soliton propagation in the 2D wave guides (plates) and exact TW solutions to them were obtained in closed form in [1], providing an algebraic relation to the 3d order elastic moduli. The third independent relationship for nonlinear elasticity of solids was found as a solution to the solitary wave propagation problem in a wave guide made of the material under study embedded into another given elastic medium. The set of these three equations allows to calculate the values of the 3d order elastic moduli using our experimental data.

CONCLUSIONS

We proved for the first time in experiments an abnormally small decay rate (almost lossless propagation) of bulk longitudinal solitary deformation waves in solid wave guides in true consistency with the theory.

References

[1] Samsonov, Alexander M.: Strain Solitons in Solids and How to Construct Them. Chapman & Hall/CRC, London et al, 2001.

[2] Dreiden, G.V. et al.: Experiments in the propagation of longitudinal strain solitons in a nonlinearly elastic rod. *Techn.Phys.Lett.* **21**, 415-417, 1995.

[3] Semenova, I.V et al.: A novel approach to determination of the 3d order elastic moduli of isotropic materials. *Proc. SPIE*, **5144**, 521-532, 2003.

STRESS-FOCUSING EFFECT IN A SPHERICAL ZIRCONIA INCLUSION WITH DYNAMICALLY TRANSFORMING STRAINS

Toshiaki Hata*
*Faculty of Education, Shizuoka University, Shizuoka, 422-8529, Japan

Summary Some composite materials, such as Zirconia toughened ceramics, are remarkable material, which has a high strength, a high elastic modulus, and an improved toughness, etc. These good qualities are made possible through the stress-induced phase transformation of composite particles, which is accompanied by a volumetric expansion. When a spherical inclusion in infinite elastic domain is suddenly subjected to an instantaneous phase transformation, stress waves occur at the surface of spherical inclusion the moment instantaneous transformation strains are applied. The wave may accumulate at the center of the inclusion and show the stress-focusing effects, even though the initial stress should be relatively small.
This paper analyzes the stress-focusing effect caused by the instantaneous phase transformation in the spherical Zirconia inclusion. By using the ray theory, the numerical results give a clear indication of the mechanism of stress-focusing effect in an inclusion embedded in the infinite elastic me.

INTRODUCTION

Recently, the transformation toughening of ceramics has attracted considerable attention in several works such as Mikata and Nemat-Nasser[1]. The mechanism in the toughening of ceramics is the stress-induced phase transformation of a Zirconia particle as shown in the work by Garvie *et al.*[2], which is accompanied by volumetric expansion. Due to this expansion, the composite material consisting of Zirconia particles within a brittle matrix becomes more resistant to the thermal fracture. While in the dynamic state the mechanism in the toughening of ceramics is not well understood.
In the paper a phenomenological model is proposed to describe the situation, which involves the dynamic inhomogeneity with a stress-induced martensitic transformation in a spherical particle of Zirconia embedded in an infinite elastic matrix.
When an infinite elastic medium with a spherical inclusion of Zirconia is suddenly subjected to a uniform phase transformation, stress waves occur at the interface of a spherical inclusion the moment a phase transformational impact is applied. The stress wave in an inclusion proceeds radially inward to the center of the inclusion. The wave may accumulate at the center and show the stress-focusing effects in the work of Hata[3].
As for the study of the stress-focusing effects, Hata[4] solved, in an exact manner, the thermal stress-focusing effect in a spherical inclusion embedded in an infinite medium by using the ray integrals. In this paper, following the ray methods, we clarify the stress-focusing effect caused by the instantaneous phase transformation in a spherical inclusion of Zirconia. It should be noted that the mechanism in the toughening of ceramics in the steady state does not hold in the dynamic state.

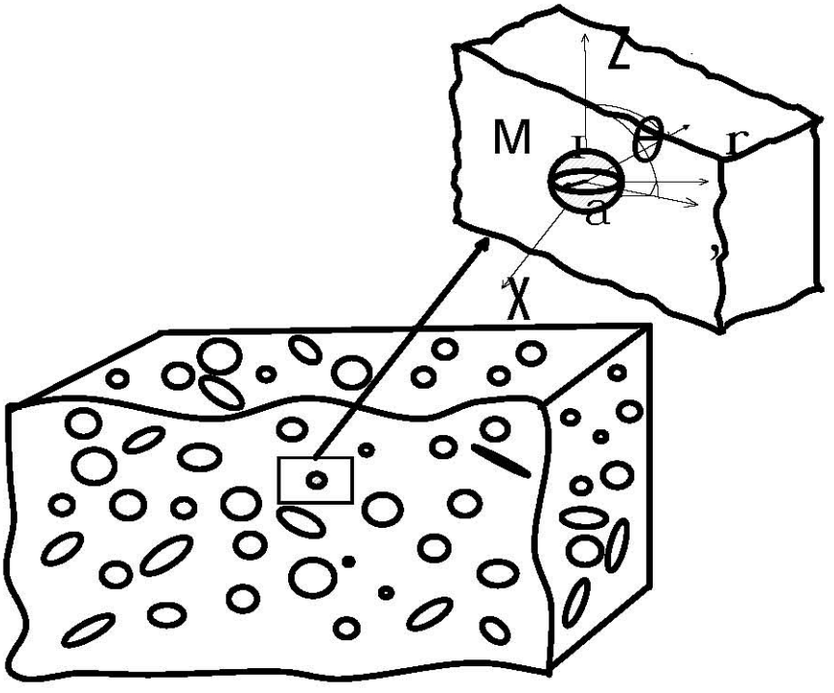


Fig.1 Coordinate system of a spherical Inclusion embedded in the infinite elastic medium

Formulation of Problem

The geometry of the problem is shown in Fig.1. The medium and the inhomogeneity are denoted M and I, respectively. Consider an infinite isotropic elastic medium of M containing a spherical Inclusion of I with an eigenstrain (or transformation strain) $e^*_{ij}(\in \Omega)(i,j=1,2,3)$. The governing equations for an inclusion are given by Mura[5] as

$$\sigma^I_{ij,j} = \rho_{0I}\ddot{u}^I_i, \quad \sigma^I_{ij} = C^I_{ijkl}(e^I_{kl} - e^*_{kl}), \quad e^I_{kl} = (u^I_{k,l} + u^I_{l,k})/2, \tag{1}$$

where ρ_{0I} is the mass density and C^I_{ijkl} is the elastic tensor of the inclusion as follows;

$$C^I_{ijkl} = \mu_I(\delta_{ik}\delta_{jl} + \delta_{il}\delta_{jk}) + \lambda_I\delta_{ij}\delta_{kl} \tag{2}$$

For the medium with a spherical inclusion, the boundary conditions on the interface of $r = a$ are

$$\sigma^I_r = \sigma^M_r, \qquad u^I_r = u^M_r. \tag{3}$$

The additional condition is that the displacement of an infinite medium at infinity is $u^M_r = 0$. The medium with a spherical inclusion is at rest prior to time $t = 0$ and the initial conditions of displacement are

$$u^I_r(r,t) = u^I_r(r,t)_{,t} = 0, \qquad u^M_r(r,t) = u^M_r(r,t)_{,t} = 0. \tag{4}$$

In the analysis the eigen strains of phase transformation are given by

$$\begin{aligned} &e^*_r = \epsilon_0 f(t) \quad e^*_\theta = e^*_\varphi = \epsilon_0 f(t) \qquad (0 < r \le r_0) \\ &e^*_r = e^*_\theta = e^*_\varphi = 0 \qquad (r_0 < r \le a) \end{aligned} \tag{5}$$

Under the action of phase transformation, the eigen strains expand along its radial direction self-similarly with a constant velocity V. Therefore, the function $f(t)$ is given by

$$f(t) = H[t - \frac{r}{V}] \tag{6}$$

In order to analyse the wave propagation we introduce the equation of motion with the time-dependent eigen stains. Applying Laplace transform, we can easily obtain the Laplace transformed solution. Since it is difficult to get the inverse Laplace transformed solution, we introduce the ray theory. By using the theory, the Laplace transformed solutions of stress waves in a spherical inclusion and in the infinite medium are sorted out into rays according to the ray path of multiply reflected waves. The inverse Laplace transform of each ray leads to the exact solution of the transient response up to the arrival time of the next ray. Following the ray methods, we clarify the stress-focusing effect in a spherical Zirconia inclusion caused by the moving phase transformation and carried out the numerical calculation concerned with the strength of the Zirconia composite[6].

CONCLUSIONS

The major accomplishment of this study has been in gaining a better understanding of the stress-focusing effect in a spherical Zirconia inclusion with the instantaneous phase transformation embedded in an infinite ceramics matrix. The stress-focusing effects in a spherical inclusion occur when stress waves reflect from the spherical surface of the inclusion and accumulate radially inward to the center. It should be important to note that the singular behavior of both stresses and displacement can be observed at the center of an inclusion for the focusing time in the case of instantaneous phase transformation.
Following the ray methods, we clarify that the stress-focusing effects in a spherical inclusion play an important role. Therefore it should be noted that the stress-induced mechanism of phase transformation in the toughening of the Aluminum Oxide ceramics with a Zirconia inclusion in the steady state does not hold in the dynamic state.

References

[1] Mikata, Y.and Nemat-Nasser, S.: Elastic Field Due to a Dynamically Transforming Spherical Inclusion, J. *Applied Mechanics*, **57:** 845-849,1990
[2] Garvie, R.C., Hannink,R.H. and Pascoe,R.T. Ceramic Steel, *Nature*, **258:**703-704,1975
[3] Hata, T.: Thermal Stress-Focusing Effect Following Rapid Uniform Heating of Spheres and Long Cylindrical Rods, *Journal of Thermal Stresses*, **20:** 819-852,1997
[4] Hata, T.: Analysis of the Thermal Stress-Focusing Effect in a Spherical Inclusion Embedded in an Infinite Elastic Medium, *JSME International Journal*,**42:** 176-182,1999
[5] Mura, T.: Micromechanics of defects in solids, Mura, Martinus Nijhoff Publishers, Dordrecht, The Netherlands, second edition,1987
[6] Lange, F.F.: Transformation toughening Part 4 Fabrication, fracture toughness and strength of Al_2O_3-ZrO_2,*J. Materials Science*,**17:** 247-254,1982

SIMULTANEOUS SIMULATION OF DISPERSION CURVES AND H/V SPECTRA

Toshiro Maeda*

**Dept. of Architecture, Waseda Univ.,3-4-1 Okubo, Shinjuku-ku, 169-8555 Tokyo, Japan*

Summary Subsurface modelling beneath an earthquake observation station is necessary to study incident waves from observed earthquake records. By a case study, we will show an advantage of simultaneous simulation of surface wave dispersion curves and H/V spectra obtained by micro-tremor measurement for subsurface modelling; shallower part of the subsurface model can be evaluated by stable surface wave dispersion curves and deeper part of the model can be constrained by less informative peak and trough frequencies of H/V spectra.

INTRODUCTION

Once strong earthquake ground motion is captured, incident waves at bedrock raise interest for a study of earthquake characteristics and future structural design. We need a subsurface model to decompose earthquake ground motion on the ground into incident waves. Unless there situates a vertical array, we will deduce it from micro-tremor measurement on the ground at the cheapest. We can deduce surface wave dispersion curves by micro-tremor array observation and simulate them for subsurface models and also we can use H/V spectrum to obtain rough image of subsurface model such as base rock depth; however, simultaneous use of them has been scarcely reported. With a case study, we will demonstrate an advantage of simultaneous simulation where array size is only valid for higher frequencies; shallower part of the subsurface model is evaluated by stable surface wave dispersion curves and deeper part of the model is constrained by less informative peak and trough frequencies of H/V spectra.

RAYLEIGH WAVE DISPERSION CURVES AND H/V SPECTRA

A test site is selected at one of the Kik-net [1] observation stations in the western part of Japan, where a vertical array up to the depth of 100m is situated and PS logging data is available, so that we can study a subsurface model deduced by micro-tremor measurement referencing to the PS data and will be able to verify it with transfer function of horizontal components. We constructed regular-triangular shaped micro-tremor array of three different circumscribed radii of 3m, 10m, and 20m, with a three-component portable seismograph at each array point, which enables us to evaluate H/V spectrum at the same time. Micro-tremor was measured for 20 minutes with 200Hz sampling in acceleration, low pass filtered at 50Hz.

The SPAC method [2] is used on vertical components of array data to evaluate Rayleigh wave phase velocity dispersion curves shown in Fig. 1a. Symbols representing different array radii lie successively on a line, which can be assumed as Rayleigh wave fundamental mode dispersion curve. H/V spectrum [3] is evaluated by Hv type transfer function algorithm for stationary signal shown in Eq. 1, which is considered optimal for noise contaminated input and output, in this case vertical component as input and horizontal component as output,

$$\begin{bmatrix} G_{AA} & G_{AB} \\ G_{BA} & G_{BB} \end{bmatrix} \begin{Bmatrix} -H_V \\ 1 \end{Bmatrix} = \varepsilon \begin{Bmatrix} -H_V \\ 1 \end{Bmatrix} \quad (1),$$

where G_{AA} and G_{BB} are auto power spectrum densities, G_{AB} and G_{BA} are cross power spectrum densities, and H_v the transfer function is the one for the smallest eigenvalue of ε. In Fig. 2a, averaged H/V spectrum over azimuth with 5 degree interval is shown with $H_1 = G_{AB} / G_{AA}$ and $H_2 = G_{BB} / G_{BA}$ exhibiting clear peaks compared to H_1.

SIMULTANEOUS SIMULATION FOR SUBSURFACE MODEL

The generalized transfer and reflection matrix method [4] is used to simulate Rayleigh wave dispersion curves and H/V spectra by H/V ratio of Rayleigh wave trajectory. We have formulated a transcendental equation to obtain Rayleigh poles by imposing a wave existence condition without an internal source. PS logging data and a former proposed subsurface model by Higashi and Abe [5] are compared in Fig. 3a, the latter has base rock below 84m referencing to reflection survey around the station. A comparison of dispersion curves and H/V spectra for these models supports the idea of base rock underneath; however, the velocity structure of Higashi-Abe model looks stiffer between 4Hz and 10Hz. The Higashi-Abe model can produce a peak of H/V ratio of Rayleigh wave trajectory around 2Hz, which is similar property seen in H/V spectrum though with some anbiguity.

In order to simulate the dispersion curves based on the Higashi-Abe model, shear wave velocities should be lowered. With trial and error basis, we have lowered shear wave velocities of the third and forth layers by about 30% (model A) to simulate the dispersion curves shown in Fig. 1b; however, a peak frequency of H/V ratio is also lowered and separated from the H/V spectrum as shown in Fig. 2b. Since we found the dispersion curve between 3Hz and 10Hz was controlled by the upper four layers, we tried to simulate H/V peak frequency by increasing shear wave velocity of the fifth layer as shown by model B in Fig. 3b; nonetheless, any higher shear wave velocities cannot bring the peak

frequency higher. Then we tried to get the interface between the forth and fifth layers shallower (model C) and succeeded to simulate both of the dispersion curves and a peak frequency of the H/V spectrum at the same time. This case study shows that unless we can situate a large size micro-tremor array, the surface wave dispersion curves can provide information for shallower part of the subsurface model only, even if the data is good and stable. H/V spectra can supplement the dispersion curves with peak and trough frequencies, though the data is less informative.

CONCLUSIONS

We have shown an advantage of simultaneous simulation of Rayleigh wave dispersion curves and H/V spectra for subsurface modelling with detailed shallower part and rough estimate of the deeper part, which can be done as the cheapest unless we have a vertical array data. The subsurface model will be verified by the vertical array transfer function.

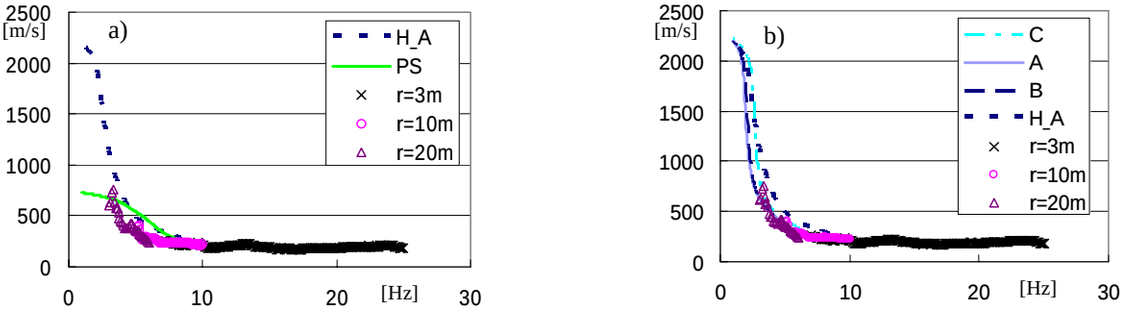


Fig.1 Dispersion curves by micro tremor and Ralyeigh wave velocity of various models

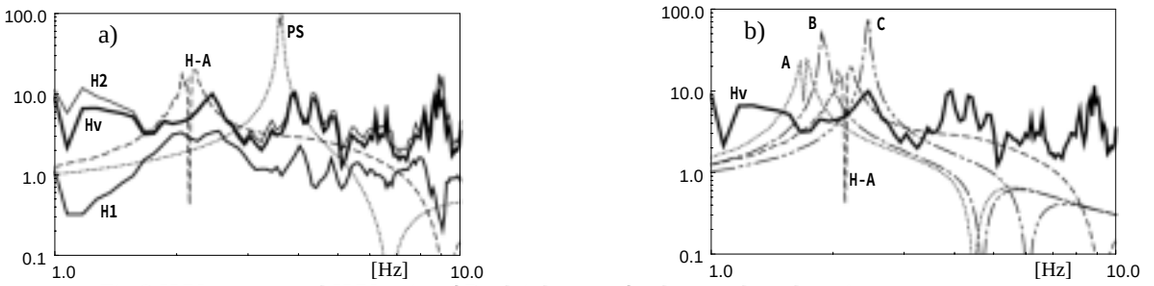


Fig.2 H/V spectra and H/V ratio of Rayleigh wave fundamental mode trajectory

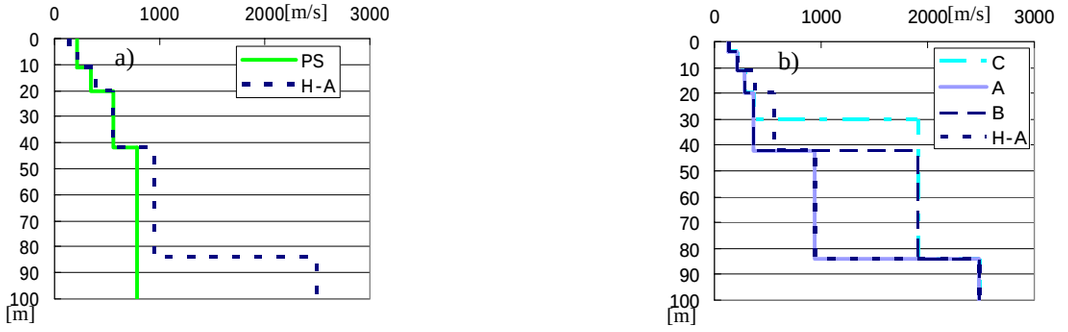


Fig.3 Shear wave velocity structure of subsurface models

References

[1] http://www.k-net.bosai.go.jp/.

[2] Aki, K.: Space and Time Spectra of Stationary Stochastic Waves, with Special Reference to Microtremors, *Bulletin of the Earthquake Research Institute*, **35**: 415–457, 1957.

[3] Nakamura, Y.: A Method for Dynamic Characteristics Estimation of Subsurface Using Micro Tremor on the Ground Surface, *QR Railway Tech. Res. Inst.*, **30**:25–33, 1989.

[4] Luco, J. E., Apsel, R. J.: On the Green's Functions for a Layered Half-space. Part 1, *Bulletin of the Seismological Society of America*, **73(4)**:909–929, 1983.

[5] Higashi, S., Abe, S.: Estimation of Bedrock motions at Kik-net Hino site during the 2000 Tottori-ken Seibu Earthquake Based on the Results of Seismic Reflection Survey, *Proceedings of the 11th Japan Earthquake Engineering Symposium*, 461-464, 2002.

NONLINEAR WAVES IN SHOCK-LOADED SOLIDS

Nikolai N. Myagkov
Institute of Applied Mechanics, Russian Academy of Sciences, 32a Lenin av., Moscow 119991, Russia

Summary Nonlinear wave processes in shock-loaded elastic-plastic solids are modeled on the basis of the approximate equations proposed. It is shown that the equations correctly describe the stress-distribution evolution in both the elastic-flow and plastic-flow regions and can be used to solve 1D and 2D problems of pulsed deformation and fracture of elastoplastic solids.

THE APPROXIMATE EQUATIONS DESCRIBING PROPAGATION OF NONLINEAR LONGITUDINAL WAVES IN ELASTOPLASTIC SOLID

Studying the evolution of nonlinear waves generated by a shock loading of solids is of scientific and practical interest. Experiments of this kind are usually performed under conditions corresponding to the stress range from several gigapascals to tens of gigapascals. In these cases, the stress amplitude is small in comparison with the bulk modulus but exceeds considerably the elastic limit for most metals. Therefore, a set of small parameters can be defined and the asymptotic methods known in the general theory of nonlinear waves may be extended to these problems.
As a result a system of approximate independent nonlinear equations belonging to different directions of longitudinal characteristics is obtained. The equations have the form [1, 2]

$$\lambda_i \frac{\partial V_i}{\partial z} - \frac{1}{4}(\alpha+2)V_i \frac{\partial V_i}{\partial \xi_i} - 3\nu \frac{\partial \psi_i}{\partial \xi_i} - \frac{1}{2}\mu \frac{\partial^2 V_i}{\partial \xi_i^{\,2}} - \frac{1}{2}\varepsilon_\Delta \int_{-\infty}^{\xi_i} \Delta_\perp V_i \, d\xi_i' = 0 \tag{1}$$

Here $V_i = -\sigma_{11}' + \lambda_i u_1' = O(\varepsilon)$, $\lambda_{1,2} = \pm 1$, $\xi_i = t' - \lambda_i^{-1} x_1'$, $z = x_1'(1+O(\varepsilon))$, $\Delta_\perp = \partial^2/\partial r'^2 + \partial/r'\partial r'$ $(r' = \sqrt{x_2^2 + x_3^2}/r_0)$, $t' = t/t_0$, $x_1' = x_1/C_0 t_0$; $\sigma_{11}' = \sigma_{11}/K$ and $u_1' = u_1/C_0$ are the components of the stress tensor and velocity vector (K is the bulk modulus, $C_0 = \sqrt{K/\rho_0}$); ψ makes sense of the dimensionless shear stress; t_0 is the characteristic load duration; r_0 is the characteristic size of the loading area. The parameter α is determined from an equation of state. Set of small parameters includes the following: $\varepsilon = P_{max}/K$, $\varepsilon_\Delta = (C_0 t_0 / r_0)^2$ characterizing the transverse divergence of the wave, μ characterizing the internal-friction viscosity and thermal conductivity, $\nu = 2G/K$ (G is the shear modulus) meaning that the stress-deviator components are assumed to be quantities of a higher order of smallness compared to the average stress. Indeed for stresses that occur in typical shock-wave tests for metals $\varepsilon \sim 0.1$ while for the dimensionless components of stress deviator an estimate gives $|s_{ij}'| = \nu \cdot 3|s_{ij}| / (2G) \le \nu \cdot Y/G \sim 0.01 \div 0.001$, where Y is the yield stress.
The equations (1) are closed by a constitutive equation taking into account the elastic-plastic deformation kinetics of solid. For example, the constitutive equation corresponding to the elastoplastic medium of the Prandtle-Reuss type with the Mises yield criterion has the form

$$\frac{\partial \psi_i}{\partial \xi_i} = \frac{1}{3}\frac{\partial V_i}{\partial \xi_i} \text{ for } |\psi_i| \le \frac{Y}{3G} \text{ and } \psi_i = \frac{Y}{3G}\operatorname{sgn}(\psi_i) \text{ for } |\psi_i| > \frac{Y}{3G}. \tag{2}$$

One can see that the nonlinear waves belonging to different directions of longitudinal characteristics are governed separately by systems consisting of the transport equation (1) and the constitutive equation of solid. The interaction of these (oppositely facing) waves can be described implicitly by nonuniform deformation of the phase variables in the solution constructed without regard to the interaction. To describe the interaction, the corrections of order ε and ν are introduced into the phase variables

$$\xi_i = t' - \lambda_i^{-1}(x_1' + \varepsilon\Phi_i(x_1', t') + \nu\theta_i(x_1', t')), \; i = 1,2. \tag{3}$$

Equations for phase functions Φ_i and θ_i taking into account a change of a phase velocity caused by the square-law nonlinearity and the elastoplasticity can be written in the form

$$\frac{\partial(\varepsilon\Phi_i + \nu\theta_i)}{\partial z} = -\frac{\left(C_\sigma^2\right)_{V_1+V_2} - \left(C_\sigma^2\right)_{V_i}}{2C_0^2}, \tag{4}$$

where $C_\sigma = (dz/dt')_V$ is the Lagrangian phase velocity associated with the stress profile of longitudinal wave. This quantity has clear physical sense and can be measured in experiment (see, for example, [3]).

The equations (1)-(4) are used to solve one- and two-dimensional problems of propagation and interaction of shock waves.

PROBLEMS OF PROPAGATION AND INTERACTION OF SHOCK WAVES

Reflection of shock wave from a free surface of plate. Simulation of the Taylor and Rice experimental data [4, p. 29] for 50.8 mm armco-iron plate loaded by 170 m/s direct impact is conducted using Eqs. (1), (3), (4) and Gilman's constitutive model.

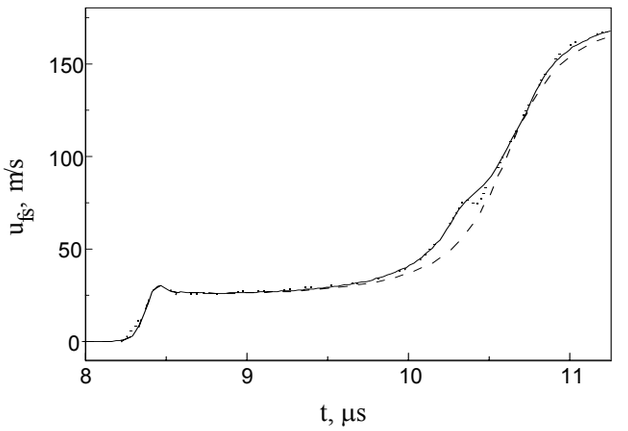


Fig 1. Velocity of the free surface versus time: the solid curve refers to the numerical solution taking into account interaction between the incident and reflected waves, dashed curve refers to the numerical solution ignoring this interaction, and the dotted curve refers to the experimental data. One can see that the solution that takes into account the interaction agrees well with the experimental data.

Propagation of a two-dimensional shock wave in an elastoplastic half-space. A shock pulse is produced by detonation of a cylindrical tablet of explosive located on the half-space. The ratio of thickness of the tablet to its diameter is equal to 0,2. Material of the half-space is the steel.

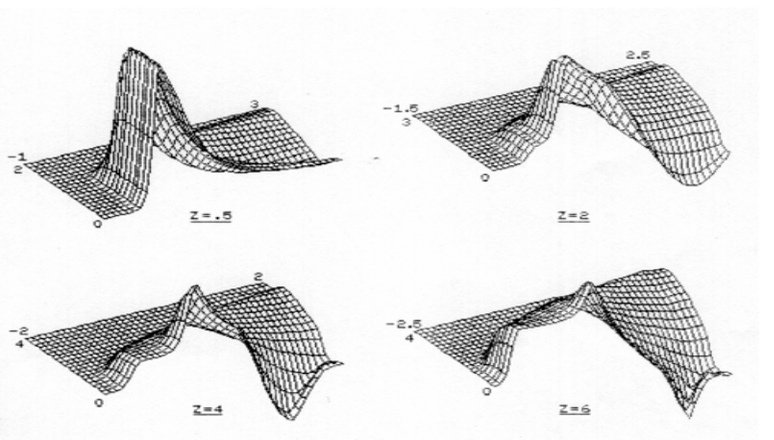


Fig. 2 shows snapshots of the wave (the numerical solution) at different distances from surface. The elastic precursor and elastic unloading are clearly visible. In general one can see that the approximate equations correctly describe both the plastic flow and elastic flow regions.

Simulation of a two-dimensional damage of a plane plate. Using Eqs. (1) and (2), we solve numerically the problem of the normal-impact damage of a plane plate, produced by a cylindrical impactor with a velocity of 185 m/sec. Material of the plates is aluminum. The impactor thickness is l=1.14 mm and target thickness is L=2.8·l. The radius of the impactor is r_0= 6·l. Equations governing the evolution of the material damage are taken the same as in [5].

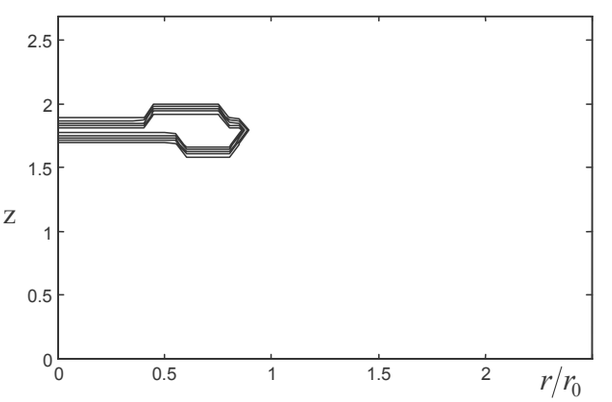


Fig. 3 shows snapshot of the right-hand half of the plate cross-section for t=0.856 μsec (the impact is performed along the lower surface). Contour lines correspond to the specific volume of voids greater than 0,01. The central region enclosed by the lines corresponds to the failed material. One can see that the impact failure forms a disc-like crack.

References

[1] Myagkov N.N.: Nonlinear waves in shock-loaded condensed matter. *J. Phys. D: Appl. Phys.* **27:** 1678-1686, 1994.
[2] Myagkov N.N.: Asymptotic modeling of nonlinear wave processes in shock-loaded elastic-plastic solids. *J. Appl. Mech. Techn. Phys*. **44**: 249-254, 2003.
[3] Asay J.R.,.Chhabildas L.C., Dandekar D.P.: Shear strength of shock-loaded polycrystalline tungsten. *J. Appl. Phys.* **51**: 4774-4783, 1980.
[4] Morris C.E.(ed): Los Alamos Shock Wave Profile Data. University of California, Berkeley 1982.
[5] Seaman L., Curran D.R., Shockey D.: Computational models for ductile and brittle fracture. *J. Appl. Phys*. **47:** 4814-4826, 1976.

CRITICAL TIME FOR ACOUSTIC WAVES IN WEAKLY NONLINEAR POROELASTIC MATERIALS

Krzysztof Wilmanski

Weierstrass Institute for Applied Analysis and Stochastics, Mohrenstr. 39, D 10117 Berlin, Germany

Summary The final time of existence (critical time) of acoustic waves is a characteristic feature of nonlinear hyperbolic models. We consider such a problem for poroelastic saturated materials whose material properties are described by Signorini-type constitutive relations for stresses in the skeleton and whose material parameters depend on the current porosity. In the one-dimensional case under considerations the governing set of equations describes changes of an extension of the skeleton, a mass density of the fluid, partial velocities of the skeleton and of the fluid, and a porosity. We rely on a second order approximation. Relations of the critical time to an initial porosity and to an initial amplitude are discussed.

MODEL

The problem of time of existence of weak discontinuity waves has been investigated for a two-component poroelastic model with a nonlinear constitutive relation for fluids [1]. It has been shown that such a model yields a finite time of existence of these waves and, consequently, a possibility of creation of shock waves if the fluid component is gaseous. In a series of subsequent papers (e.g. [2]) it has been shown by means of an asymptotic analysis that a dependence of material parameters of such a model on nonequilibrium changes of porosity yields for porosity soliton-like solutions of the Riemann problem. As changes of porosity were assumed to be given by a function of the fraction of partial mass densities ρ^F/ρ^S considerations were limited solely to a very rigid skeleton characteristic for rocks.

The present work is devoted to a one-dimensional wave analysis of a weakly nonlinear model of poroelastic materials in which material parameters depend on the current porosity. We limit the attention to granular materials for which Gassmann relations [3] can be applied. The model is based on three simplifying assumptions: 1) the relaxation of porosity is ignored, i.e. $\tau\to\infty$, where τ denotes the relaxation time in the porosity balance equation, 2) couplings between partial stresses are negligible, i.e. Q=0, where Q is the Biot's coupling parameter, and β=0, where β is the constant describing an explicit influence of nonequilibrium porosity changes on stresses, 3) the parameter c^S of the Signorini model is zero. Then partial stress tensors satisfy the following constitutive relations [4]

$$\mathbf{T}^S = \mathbf{T}_0^S + \left[\lambda^S(n)e + \tfrac{1}{2}\left(\lambda^S(n)+\mu^S(n)\right)e^2\right]\mathbf{1} + 2\left[\mu^S(n) - \left(\lambda^S(n)+\mu^S(n)\right)e\right]\mathbf{e}^S,$$

$$\mathbf{T}^F = -p^F\mathbf{1}, \quad p^F = p_0^F - \rho_0^F\kappa(n)\varepsilon, \quad e := tr\,\mathbf{e}^S, \quad \varepsilon := \frac{\rho_0^F - \rho^F}{\rho_0^F},$$

where $\mathbf{e}^S$ is the Almansi-Hamel deformation tensor of the skeleton, ρ^F is the current mass density of the fluid, $\rho^F{}_0$ – its constant initial mass density, n – porosity.

We assume deformations of the skeleton $\mathbf{e}^S$ and mass changes of the fluid ε to be sufficiently small for neglecting contributions of the order higher than two.

GOVERNING EQUATIONS

We consider a one-dimensional problem of plain deformations described by the fields

- e – deformation of the skeleton with $\mathbf{e}^S = e\,\mathbf{e}_x\otimes\mathbf{e}_x$, $\mathbf{e}_x$ - unit vector along x-axis,
- ρ^F – current mass density of the fluid component, or, equivalently, $\varepsilon = \left(\rho_0^F - \rho^F\right)/\rho_0^F$,
- v^S – velocity of the skeleton in the x-direction,
- v^F – velocity of the fluid in the x-direction,
- n – porosity.

Field equations for these fields result from the partial mass conservation laws, momentum balance equations, and the balance equation of porosity. Under assumptions presented in the first Section they have the form

$$\frac{\partial e}{\partial t} + v^S\frac{\partial e}{\partial x} - (1-2e)\frac{\partial v^S}{\partial x} = 0, \qquad \rho_0^S\sqrt{1-2e}\left(\frac{\partial v^S}{\partial t} + v^S\frac{\partial v^S}{\partial x}\right) - \frac{\partial}{\partial x}\left[E^S e - \tfrac{3}{2}\left(E^S-\mu^S\right)e^2\right] - n_E\pi_0\left(v^F - v^S\right) = 0,$$

$$\frac{\partial \varepsilon}{\partial t} + v^F\frac{\partial \varepsilon}{\partial x} - (1-\varepsilon)\frac{\partial v^F}{\partial x} = 0, \qquad \rho_0^F(1-\varepsilon)\left(\frac{\partial v^F}{\partial t} + v^F\frac{\partial v^F}{\partial x}\right) - \rho_0^F\frac{\partial}{\partial x}[\kappa\varepsilon] + n_E\pi_0\left(v^F - v^S\right) = 0,$$

$$\frac{\partial \Delta_n}{\partial t} + v^S\frac{\partial \Delta_n}{\partial x} + n_0\gamma\frac{\partial}{\partial x}\left(v^F - v^S\right) = 0, \qquad \Delta_n := n - n_E, \qquad n_E = n_0(1+\delta e),$$

where $\delta, \gamma, \pi_0 n_0$ are constants, $E^S := \lambda^S + 2\mu^S$, and a dependence of remaining material parameters on *n* is such that (compare [3]) $E_n^S := \partial E^S / \partial n < 0, \quad \mu_n^S := \partial \mu^S / \partial n < 0, \quad \kappa_n := \partial \kappa / \partial n > 0.$

CRITICAL TIME

Let us note that the solution of the porosity balance equation can be written in the form

$$n = n_0[1 + \delta e + \gamma(e - \varepsilon)] + O\left(\min\left\{|e|^2, |\varepsilon|^2\right\}\right)$$

As we consider contributions up to the second order, material parameters depend solely on the linear contribution in the above relation. Simultaneously, it was shown in [3] that γ is at least one order of magnitude smaller than δ. Consequently, we have to account solely for the equilibrium porosity $n_E = n_0(1 + \delta e)$ in relations for material parameters, i.e. E_n^S, μ_n^S, κ_n are constant and $E^S = E_0^S + E_n^S \delta e, \quad \mu^S = \mu_0^S + \mu_n^S \delta e, \quad \kappa = \kappa_0 + \kappa_n \delta e,$ where E_0^S, μ_0^S, κ_0 are constant. The balance equation of porosity separates from the remaining equations and it does not have any influence on critical times.

The time of existence (critical time) of acoustic waves as solutions for weak discontinuities of the above set of field equations is given, as usual, through the Bernoulli equation whose coefficients are determined by the solution of the corresponding eigenvalue problem. The derivation of the equation for evolution of amplitude is standard for hyperbolic systems (e.g. [6]). In our case the eigenvalue problem has the form

$$\frac{\partial u_A}{\partial t} + A^{AB} \frac{\partial u_B}{\partial x} = B^A, \quad i.e. \quad \left(A^{AB} - \lambda \delta^{AB}\right) r_B = 0, \qquad u_1 := e, \quad u_2 := \varepsilon, \quad u_3 := v^S, \quad u_4 := v^F,$$

where

$$\left(A^{1B}\right) = (u_3, 0, -(1 - 2u_1), 0), \quad \left(A^{2B}\right) = \left(0, \frac{1}{\rho_0^F} u_4, 0, 1 - u_2\right), \quad \left(A^{3B}\right) = \left(-\frac{E_0^S}{\rho_0^S} + \frac{2E_0^S - 3\mu_0^S - 2E_n^S \delta}{\rho_0^S} u_1, 0, u_3, 0\right),$$

$$\left(A^{4B}\right) = (\delta \kappa_n u_2, -\kappa_0 - \kappa_n \delta u_1 - \kappa_0 u_2, 0, u_4),$$

and λ denotes the eigenvalue corresponding to the right eigenvector r_B. The critical time follows from the equation for the amplitude Π

$$\frac{d\Pi}{dt} + \alpha_1 \Pi - \alpha_2 \Pi^2 = 0, \quad \left[\left[\frac{\partial \mathbf{u}}{\partial x}\right]\right] = \Pi \mathbf{r},$$

where the double bracket denotes the difference of limits on the front of the wave and

$$\alpha_1 = l_A \frac{\partial B^A}{\partial u_B} r_B \frac{1}{\mathbf{r} \cdot \mathbf{l}}, \quad \alpha_2 = l_A \frac{\partial A^{AB}}{\partial u_C} r_B r_C \frac{1}{\mathbf{r} \cdot \mathbf{l}},$$

$$\left(B^A\right) = \left(0, 0, \frac{n_0 \pi_0}{\rho_0^S}[(1 + (1 + \delta) u_1)(u_3 - u_4)], -\frac{n_0 \pi_0}{\rho_0^F}[(1 + \delta u_1 - u_2)(u_3 - u_4)]\right),$$

provided a wave enters an undisturbed region. $\mathbf{l}$ denotes the left eigenvector.

We prove the existence of a finite critical time t_C for which $\Pi \to \infty$ in dependence on the initial porosity n_0. As an inverse problem, it indicates an existence of a critical porosity for a given time of existence of acoustic waves. This complements the analysis of critical values of porosity for flows in granular materials (the onset of fluidization, e.g. see: [7]) and of critical values of porosity in a static analysis of rocks (comp. [8]).

References

[1] K. Wilmanski; On the time of existence of weak discontinuity waves in poroelastic materials, *Arch. Mech.*, **50**, 3, 657-669, 1998..

[2] E. Radkevich, K. Wilmanski; On dispersion in the mathematical model of poroelastic materials with the balance equation for porosity, *Jour. Math. Sci.*, **114**, 4, 1431-1449, 2003.

[3] K. Wilmanski; On a micro-macro transition for poroelastic Biot's model and corresponding Gassman-type relations, WIAS-Preprint #868, 2003; submitted for publication to *Geotechnique.*

[4] B. Albers, K. Wilmanski K.; An axisymmetric steady-state flow through a poroelastic medium under large deformations, *Archive of Applied Mechanics*, **69**, 121-132, 1999.

[5] B. Albers, K. Wilmanski K.; On modeling acoustic waves in saturated poroelastic media, WIAS-Preprint #874, 2003; submitted for publication to *Jour. Engn. Mechanics.*

[6] K. Wilmanski; Thermomechanics of continua, Springer, Berlin, 1998.

[7] T. Wilhelm, K. Wilmanski; On the onset of flow instabilities in granular media due to porosity inhomogeneities, *Int. Jour. Multiphase Flow*, **28**, 1929-1944, 2002.

[8] A. Nur, G. Mavko, J. Dvorkin, D. Galmudi; Critical porosity: a key to relating physical properties to porosity in rocks, *The Leading Edge*, **17,** 357-362, 1998.

RAYLEIGH-LIKE SURFACE WAVES ON A NONLINEAR LAYERED ELASTIC HALF SPACE

Semra Ahmetolan*, Mevlut Teymur**
Istanbul Technical University, Department of Mathematics, 34469, Maslak Istanbul, Turkey

Summary Nonlinear modulation of Rayleigh-like Surface Waves on a layered half space is examined by employing an asymptotic perturbation method. It is shown that the first order slowly varying amplitude of the wave modulation is governed by a nonlinear Schrödinger (NLS) equation. Then the effects of material nonlinearities on the existence of bright (envelope) and dark (hole) surface solitons are discussed for both hypothetical and real material models.

FORMULATION OF THE PROBLEM

Recently, the propagation of nonlinear Rayleigh-like surface waves on a layered elastic half space has been the subject of several investigations [1,2,3]. In these works mainly the propagation of long nonlinear waves are considered and Benjamin-Ono (BO)-like evaluation equations are derived to describe the wave field asymptotically. Then the existence of nonlinear periodic and solitary wave solutions are discussed via BO-like equations. These examinations are restricted effectively to the small wave number, low frequency region since the layer is assumed to be thin and in some works also is assumed to be linear [2.3]. In this work, the problem is investigated for a finite nonlinear layer.
In a rectangular frame (X,Y,Z), it is assumed that the layer occupies the region between the planes Y=h and Y=0 and the half space lies in the region Y<0, where h>0 represents the thickness of the layer. Then the Rayleigh waves are supposed to propagate along the positive X-axis and their displacements lie in the (X,Y)-plane, the saggital plane. Thus the equation

$$x = X + u_1^{(\nu)}(X,Y,t)\ ,\ \ y = Y + u_2^{(\nu)}(X,Y,t)\ ,\ \ z = Z \tag{1}$$

represent the wave motion, where $u_1^{(\nu)}$ and $u_2^{(\nu)}$ are the displacement components in X and Y directions, (x,y,z) are the spatial rectangular coordinates and t is the time. Here and henceforth superscript value ν=1 refers to the layer and ν=2 to the half space. The constituent materials are assumed to be homogenous, isotropic and compressible elastic, and the stress constitutive relations are taken in the following quadratic nonlinear form;

$$\begin{aligned} T_{Kk} = &\big[\lambda(tr\widetilde{\mathbf{E}}) + \tfrac{\lambda}{2}u_{p,M}u_{p,M} + \tfrac{1}{2}(6l+3m+n)(tr\widetilde{\mathbf{E}})^2 - \tfrac{1}{2}(m+n)(tr\widetilde{\mathbf{E}}^2)\big]\delta_{Kk} + \big[2\mu - (m+n)\\ &(tr\widetilde{\mathbf{E}})\big]\widetilde{E}_{KL}\delta_{Lk} + \big[\lambda(tr\widetilde{\mathbf{E}})\big]u_{k,K} + 2\mu\widetilde{E}_{KL}u_{k,L} + \mu u_{p,K}u_{p,L}\delta_{Lk} + n\widetilde{E}_{KN}\widetilde{E}_{NL}\delta_{Lk} \end{aligned} \tag{2}$$

where T_{Kk} is the first Piola-Kirchoff stress tensor, E_{KL} is the linear Lagrangian deformation tensor and λ, μ are the Làme and l,m,n are Murnaghan constants. In the absence of body forces, the equations of motion in the reference state are

$$T_{\beta 1,\beta}^{(\nu)} = \rho_0 \ddot{u}_1^{(\nu)}\ ,\ T_{\beta 2,\beta}^{(\nu)} = \rho_0 \ddot{u}_2^{(\nu)} \quad \nu = 1,2 \tag{3}$$

where the subscripts preceded by comma indicate partial differentiation with respect to X or Y and an over-dot represents the partial differentiation with respect to t. The free boundary Y=h of the layered half space is assumed to be traction free and stresses and displacements are continuous at the interface Y=0 and the displacements tend to zero as the depth increases. Hence the following boundary conditions are written;

$$\begin{aligned} &T_{21}^{(1)} = 0\ ,\ T_{22}^{(1)} = 0 \ \text{ on } \ Y = h \ \text{ and } \ u_1^{(2)}, u_2^{(2)} \to 0 \ \text{ as } \ Y \to -\infty \\ &u_1^{(1)} = u_1^{(2)},\ u_2^{(1)} = u_2^{(2)} \ \text{ and } \ T_{21}^{(1)} = T_{21}^{(2)},\ T_{22}^{(1)} = T_{22}^{(2)} \ \text{ on } \ Y = 0\ . \end{aligned} \tag{4}$$

THE NONLINEAR MODULATION OF RAYLEIGH-LIKE WAVES

To investigate how the slowly varying amplitude of a weakly nonlinear Rayleigh-like wave is modulated by nonlinear self interaction, the method of multiple scales is employed. For this purpose, the new independent variables

$$x_i = \epsilon^i X\ ,\ \ y_i = \epsilon^i Y\ ,\ \ t_i = \epsilon^i t \quad i = 0,1,2, \tag{5}$$

are introduced where $\epsilon > 0$ is a small parameter representing the weakness of the nonlinearity. $\{x_0, y_0, t_0\}$ are fast variables describing the fast variations in the problem while $\{x_1, x_2, y_1, y_2, t_1, t_2\}$ are slow variables to describe the slow variation. The displacements $u_1^{(\nu)}$ and $u_2^{(\nu)}$ are assumed to be functions of these new variables and they are expanded in the following asymptotic power series in ϵ [4];

$$u_1^{(\nu)} = \sum_{n=1}^{\infty} \epsilon^n u_{1n}^{(\nu)}\ ,\ \ u_2^{(\nu)} = \sum_{n=1}^{\infty} \epsilon^n u_{2n}^{(\nu)}. \tag{6}$$

Then following the usual procedure of an asymptotic analysis a hierarchy of problems to determine $u_{1n}^{(\nu)}$ and $u_{2n}^{(\nu)}$ are obtained. These problems, at each step, are linear and the first order problem is simply the classical linear wave problem

in a layered linear elastic half space [5]. This first order problem is solved by assuming that the phase velocity c of the waves satisfies the inequality $c_{1_T} < c_{1_L} < c < c_{2_T} < c_{2_L}$ where c_{ν_L} and c_{ν_T} denote linear longitudinal and shear wave velocities in the layered half space. Under these assumptions and since also the harmonic resonance phenomena is excluded in the analysis the solutions are found as

$$\begin{aligned}
u_{11}^{(1)} &= A_1\big[R_1 e^{ikp_L y_0} + R_2 e^{-ikp_L y_0} - p_T R_3 e^{ikp_T y_0} + p_T R_4 e^{-ikp_T y_0}\big] e^{i\phi} + c.c. \\
u_{21}^{(1)} &= A_1\big[p_L R_1 e^{ikp_L y_0} - p_L R_2 e^{-ikp_L y_0} + R_3 e^{ikp_T y_0} + R_4 e^{-ikp_T y_0}\big] e^{i\phi} + c.c. \\
u_{11}^{(2)} &= A_1\big[R_5 e^{kv_L y_0} + iv_T R_6 e^{kv_T y_0}\big] e^{i\phi} + c.c. \\
u_{21}^{(2)} &= A_1\big[-iv_L R_5 e^{kv_L y_0} + R_6 e^{kv_T y_0}\big] e^{i\phi} + c.c.
\end{aligned} \tag{7}$$

where a "$c.c.$" symbol denotes the complex conjugate of the preceding terms and $\mathcal{A}_1$ is the complex function of the slow variables $\{x_1, x_2, t_1, t_2\}$ representing the first-order slowly varying amplitude of the wave modulation. Also, $\phi = kx_0 - \omega t_0$, $p_\alpha = (c^2/c_{1_\alpha}^2 - 1)^{1/2}$, $v_\alpha = (1 - c^2/c_{2_\alpha}^2)^{1/2}$, ($\alpha = L, T$), and R_i's are some constants. Obviously, to complete the first order solutions $\mathcal{A}_1$ has to be determined. This can be achieved by examining the higher order perturbation problems. A compatibility condition in the second order perturbation problem related with the fundamental mode yields that

$$\mathcal{A}_1 = \mathcal{A}_1(x_1 - V_g t_1, x_2, t_2) \tag{8}$$

i.e., $\mathcal{A}_1$ remains constant in a frame of reference moving with the group velocity V_g of the waves. And then a compatibility condition in the third order problem related with the fundamental mode yields the following equation for $\mathcal{A} = k\mathcal{A}_1$;

$$i\frac{\partial \mathcal{A}}{\partial \tau} + \Gamma \frac{\partial^2 \mathcal{A}}{\partial \xi^2} + \Delta |\mathcal{A}|^2 \mathcal{A} = 0 \, . \tag{9}$$

where $\tau = \omega t_2$, $\xi = k(x_1 - V_g t_1)$, $\Gamma = \frac{k^2}{2\omega}\frac{d^2\omega}{dk^2}$ and the coefficient Δ depends on nonlinear material parameters. The equation (9) is a NLS equation and it is derived in various branches of science and engineering to describe the nonlinear self modulation of waves asymptotically.

CONCLUSIONS

It is known that the stability of the solutions of the NLS equation describing the asymptotic wave field and the existence of various types of soliton solutions depend on the sign of the product of the coefficients of the dispersion term, Γ, and the coefficient of the nonlinear term, Δ. Therefore to investigate the dependence of the sign of $\Gamma\Delta$ on the nonlinearity of the constituent materials, the numerical evaluation of this product with respect to the wave number is performed by fixing the linear material constants. The behavior of Γ and Δ are also analyzed in the limit as $h \to 0$ and for fixed k, i.e. in the thin layer limit. It has been observed that, in this limit the behavior of Δ is dominated by the nonlinear properties of the half space, but as h increases (or kh grows) the effects of the nonlinear properties of the layer on Δ begin to increase. It has been also observed that, depending on the linear properties of the layered half space, in the neighbourhood of the critical wave number k_c satisfying the second harmonic resonance condition, $|\Delta|$ grows without bound, i.e., $|\Delta|$ goes to infinity as $k \to k_c$. Also, in the thin layer limit $|\Delta|$ grows without bound for the layered half-space models whose half space made of a nonlinear material. But, if the half space is linear then Δ goes to zero in this limit. These results also indicate that in the thin layer limit, the nonlinear properties of the half space dominates the nonlinear wave modulation.

References

[1] Porubov A.V., Samsonov A.M.: Long non-linear strain wave in layered elastic half-space. *Int. J. Non-Linear Mech* **30**:861-877, 1995.

[2] Eckl C., Mayer A.P., Kovalev, A.S.: Do surface solitons exist?. *Phys. Rev. Lett.* **81**:983-986, 1998.

[3] Eckl C., Schöllmann J., Mayer A.P., Kovalev A.S., Maugin G.A.: On the stability of surface acoustic pulse trains in coated elastic media. *Wave Motion***34**:35-49, 2001.

[4] Jeffrey A., Kawahara T.: Asymptotic Methods in Nonlinear Wave Theory. Pitman, London, 1982.

[5] Teymur,M.: Nonlinear modulation of Love waves in a compressible hyperelastic layered half space. *Int. J. Engng Sci.***26**:907-927, 1988.

Non-destructive testing of wood by wave propagation

István A. Veres, Mahir B. Sayir
Swiss Federal Institute of Technology, IMES - Center of Mechanics, ETH Zentrum, CH-8092 Zurich, Switzerland

Summary In this paper the determination of the material properties of a rectangular wooden bar is presented and the detection of defects in the bar is discussed. The material properties of the bar are evaluated by theoretical and measured dispersion curves using parametric model fitting. A numerical finite difference model with second- and fourth-order approaches is developed. To detect a defect a numerical time-reversal experiment using this model is discussed.

INTRODUCTION

Non-destructive testing of wood is challenging because of its anisotropy and inhomogeneity. It can be tested by ultrasonic waves in high (>1 MHz) [1] or in deep (< 100 kHz) frequency range. In high frequency range the waves are not dispersive but wood has a high damping. A simple “time-of-flight“ method can be used on a small cube but it is difficult to test a few meters long bar. Furthermore in this frequency range the wavelength and the natural inhomogeneities, like annual rings, are in the same range, thus they can disturb the measurement.
In low frequency range the damping is weaker and the wavelength is longer but the waves become to be dispersive. A larger bar can be tested and the inhomogeneities do not disturb the measurement but the “time-of-flight“ method can not be used. The velocity change caused by dispersion has to be considered for the testing.

PROBLEM STATEMENT

Let us consider a wooden bar with rectangular cross-section. Wood will be modeled as an orthotropic material and the main directions of the orthotropy are parallel to the sides of the bar. The dimensions of the bar are 2700x20x25 mm.
In the first case we are interested in the material properties of the bar. Theoretical and experimental dispersion curves of the bar will be determined and the material properties will be evaluated by parametric model fitting. In the second case we are interested in detecting a defect in the bar. A numerical finite difference model with second- and fourth-order approaches is developed and a numerical time-reversal experiment using this model is discussed [5].

DETERMINATION OF THE MATERIAL PROPERTIES

Theoretical dispersion curves of the bar

A semi-analytical finite element method [2] is applied to determine the dispersion curves of the bar. The cross-section of the bar is discretized by two-dimensional finite elements and in the longitudinal direction harmonic functions were applied. The following displacement functions were used:

$$u(x, y, z, t) = N(x, y)\cos(\omega t + kz)$$
$$v(x, y, z, t) = N(x, y)\cos(\omega t + kz)$$
$$w(x, y, z, t) = N(x, y)\sin(\omega t + kz)$$

where u, v and w are the displacements in x-, y- and z-directions, $N(x,y)$ denotes the biquadratic approximation function, ω the angular frequency, k the wave number and t the time. This leads to an eigenvalue problem:

$$(\mathbf{K}(k_i) - \omega\mathbf{M}(k_i))\mathbf{v} = \mathbf{0}$$

in which $\mathbf{K}$ denotes the stiffnes-, $\mathbf{M}$ the mass matrix, and $\mathbf{v}$ the displacements of the nodes. The eigenvalues of this equation system are the quadrates of the eigenfrequencies ω for the wave number k_i. Solving this eigenvalue problem for different wave numbers k_i results in a dispersion diagram.

Evaluation of the dispersion curves from measurements

The measurement setup on Fig. 1. was used to detect the displacements of the bar. The measurement processes are repeated in few hundred points along the longitudinal axis. Using the linear prediction method [4] the dispersion curves of the bar were evaluated from the measurements (black points on Fig. 2).

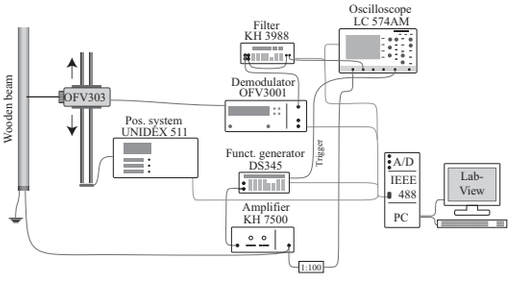


Figure 1. Measurement setup.

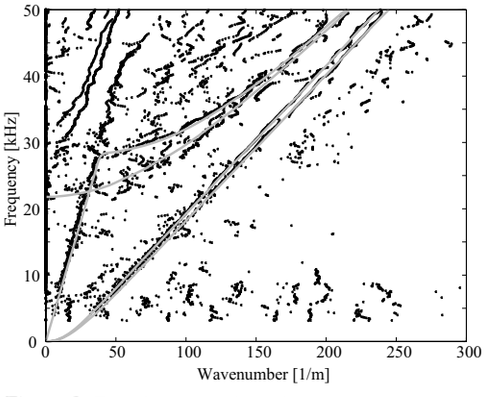


Figure 2. Experimental dispersion curves compared to the theoretical curves evaluated with the determined material properties: C_{22}=1505 N/mm^2, C_{33}=15073 N/mm^2, C_{44}=480 N/mm^2, C_{55}=1350 N/mm^2, C_{66}=1410 N/mm^2.

Parametric model fitting

The total least squares method [1] was applied to evaluate the material properties. The dispersion relation is the relationship between material parameters (Θ) and measurement data $\mathbf{z}(\omega, k)$, in implicit form: $\mathbf{f}(\Theta,\mathbf{z})=0$. In our case there is no analytical relationship, a numerical one was used: $\mathbf{f}(\Theta,\mathbf{z})=\omega_{eig}-\omega_m$, the difference between the calculated (eigenvalue problem) and the measured frequencies. The problem was linearized and solved by the Lagrangian multiplier method [1]. To distinguish between the points of the different wave modes and the points which do not represent a wave mode a statistical test [1] was applied to classify the points into inlier and outlier. The results are presented on Fig. 2.

SIMULATION OF THE WAVE PROPAGATION BY FINITE DIFFERENCES

The applied governing equations are the equations of motion, the orthotropic material's law and the kinematic relations:

$$\sigma_{ij,j} = \rho u_{i,tt}, \qquad \sigma_{ij} = C_{ijkl}\varepsilon_{kl}, \qquad \varepsilon_{ij} = \frac{1}{2}(u_{i,j} + u_{j,i}).$$

The equations are discretized in space and time domain by second- and fourth-order finite differences on a staggered grid [5]. The second-order finite difference approach of the first derivative of u_x with respect to x and second derivative of it with respect to t are:

$$\frac{\partial u_x}{\partial x} \cong \frac{-{}_{i-1,j,k}u_x^n + {}_{i,j,k}u_x^n}{\Delta x}, \qquad \frac{\partial^2 u_x}{\partial t^2} \cong \frac{{}_{i,j,k}u_x^{n-1} - 2\,{}_{i,j,k}u_x^n + {}_{i,j,k}u_x^{n+1}}{\Delta t^2},$$

where i, j and k denote the indices of the cell on the grid. The derivatives of u_y and u_z with respect to x, y, z, respectively can be calculated in a similar way. A fourth-order approach was applied in space for the first derivative:

$$\frac{\partial u_x}{\partial x} \cong \frac{{}_{i-2,j,k}u_x^n - 27\,{}_{i-1,j,k}u_x^n + 27\,{}_{i,j,k}u_x^n - {}_{i+1,j,k}u_x^n}{24\Delta x}.$$

The model was verified by the dispersion curves. In a virtual measurement the displacements of the bar in the simulation were detected. The dispersion curves of the bar were determined by the linear prediction method and compared to the theoretical curves (Fig. 3.).

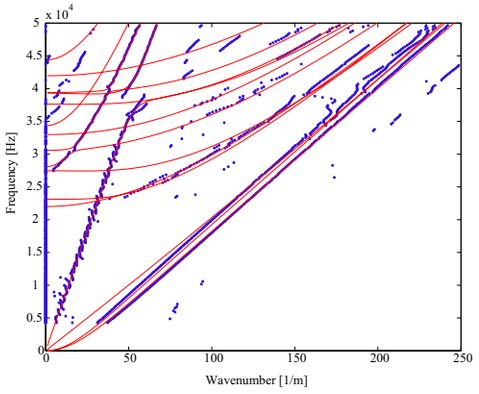


Figure 3. Theoretical dispersion curves determined by the semi-analytical finite element method and experimental ones by simulation (orthotropic bar, second-order approach).

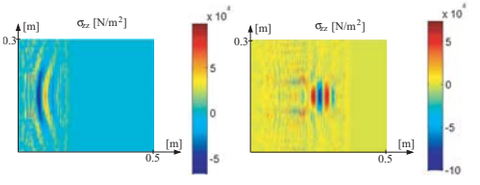


Figure 4. Playing back and focusing of the waves (isotropic plate, second-order approach).

The finite difference model can be applied in a numerical time-reversal experiment [5] to detect a defect in a structure. By this method structural waves in the bar are excited in an experiment and the displacements are recorded in several points. The recorded signals including the reflections from the defect are played back in the numerical model of the structure, and the waves interfere just at the position of the defect.

A numerical example of this technique is presented in Fig. 4. A notch is implemented in the finite difference model in the middle of an isotropic plate. Longitudinal waves are excited. Waves are detected in a virtual measurement at the end of the plate and than reversed in the time domain and played back in the numerical model without notch (Fig. 4). Limitations of this method should still examined especially the influence of the orthotropy and of the frequency content compared to the geometrical dimensions (slenderness) of the bar.

CONCLUSION

Experimental and theoretical determination of the dispersion curves are presented. It is shown that the material properties of a wooden bar could be determined using the dispersion curves and parametric model fitting. The wave propagation phenomenon was simulated by second- and fourth-order finite differences. A notch was implemented in the model and a numerical time-reversal experiment is considered in the isotropic case.

References

[1] Danuser G., Stricker M.: Parametric Model Fitting: From Inlier Characterization to Outlier Detection. *IEEE Transactions on pattern analysis and machine intelligence* 20(2) (1998) 263-280.

[2] Mazúch T.: Wave Dispersion Modelling in Anisotropic Shells and Rods by the Finite Element Method. *Journal of Sound and Vibration* 198(4) (1996) 429-438.

[3] Bucur V.: Acoustics of Wood. CRC Publication Boca Raton 1995.

[4] Tufts D. W., Kumaresan R.: Estimation of Frequencies of Multiple Sinusoids: Making Linear Prediction Perform Like Maximum Likelihood. *Proceedings of the IEEE* 70(9) (1982) 975-989.

[5] Leutenegger T.: Detection of defects in cylindrical structures using a time reverse numerical simulation method. *PhD Thesis*, ETH Zurich 2002.

A TWO-DIMENSIONAL ANALYSIS OF SURFACE ACOUSTIC WAVES IN FINITE ANISOTROPIC SOLIDS WITH ELECTRODES

Ji Wang and Jingbo Lin
Department of Engineering Mechanics and Material Science, School of Engineering, Ningbo University, 1211 Zhenning Xilu Road, Ningbo, Zhejiang 315211, CHINA
E-mail: {wangji, linjingbo}@nbu.edu.cn

Summary A two-dimensional theory based on the expansion of displacements in exact solutions from semi-infinite solids offers complete equations and boundary conditions for surface acoustic waves in finite elastic solids similar to well-known plate theories for high frequency vibration applications. By considering the electrode layer and discontinuous electrodes on an elastic substrate, the mass effect is evaluated through the integration of displacements along the thickness direction with simplified equations.

INTRODUCTION

The analysis of surface waves in elastic solids has been clearly demonstrated with semi-infinite solids by assuming displacements decay exponentially along the thickness coordinate, and solutions including the velocity are obtained by applying the traction-free boundary conditions [1]. While surface waves found in some occasions like in earthquakes can be treated like travelling in infinite media, in other applications such as electronic devices utilizing surface acoustic waves (SAW) for frequency control have to be considered as in bounded elastic or piezoelectric solids requiring precise evaluation of complication factors like the periodic electrodes known as interdigital transducers.

It is known that the wave propagation in bounded elastic solids is difficult to analyze because of the reflections in the boundaries produce many modes and their overtones, making both deformation and vibration frequency have many strong couplings. One typical method for the analysis of bulk acoustic waves in bounded solids is Mindlin plate theory [2], which uses series expansion of the displacements to reduce the three-dimensional elasticity equations. Mindlin plate theory and its variations like Lee plate theory [3] have been widely used in the high frequency vibration analysis of quartz crystal plates for their applications in piezoelectric resonators [4], and subsequent applications include the finite element method which enhanced their practical capabilities for complicated structures [5, 6, 7]. For surface acoustic waves in bounded solids, a similar two-dimensional theory is proposed by Wang and Hashimoto [8] with the displacements expanded exponentially with exact surface acoustic wave solutions. It is found that the two-dimensional theory has only two terms for isotropic material and three for anisotropic materials, different from the plate theories that require a truncation procedure to improve the accuracy with limited terms, or the order of the plate theory.

In this study, the periodic electrodes are considered for their mass effect on the SAW velocity, and continuity conditions of displacements are applied so the periodicity can be accounted for. The solutions with finite number of electrodes are obtained from a set of successive boundary conditions and extended to very large number of equations for the limiting case there are infinite number of electrodes. With the periodic solutions for a SAW resonator structure, the effect of the finite sizes of the structure, including the thickness, length, and width of both substrate and electrodes, can be precisely predicted. For demonstration purpose, we analysed a simple device problem with straight-crested waves.

TWO-DIMENSIONAL THEORY FOR SURFACE ACOUSTIC WAVES

It is known that the displacements of surface acoustic waves travelling in x_1 direction in a semi-infinite solid are

$$(u_1, u_2) = (A, B) e^{k\beta x_2} e^{ik(x_1 - ct)}, \tag{1}$$

where $u_1, u_2, A, B, k, \beta, c, t$ are displacement of x_1 direction, displacement of x_2 direction, amplitude of x_1 direction displacement, amplitude of x_2 direction displacement, wavenumber, decaying index, velocity, time, respectively [1]. For a given material, we can find two pairs of real β from the equations of motion. To ensure the exponential decaying of the displacements with negative x_2 in our coordinate system, we must choose positive β_1 and β_2 in (1). Applying traction-free boundary conditions on the surface where $x_2 = 0$, we can find the velocity c with the corresponding β_1 and β_2. Now for a finite solid, we consider the displacements as

$$u_j(x_1, x_2, x_3, t) = \left[u_j^{(1)}(x_1, x_3, t) e^{k\beta_1 x_2} + u_j^{(2)}(x_1, x_3, t) e^{k\beta_2 x_2} \right] e^{ik(x_1 - ct)}, \; j = 1,2, \tag{2}$$

where β_1 and β_2 are known and $u_j^{(n)} (j = 1,2; n = 1,2)$ are to be determined. This assumption is natural because we can expect that the solutions of solids with finite thickness or depth can be accurately represented from the semi-infinite solutions. Following the procedure of higher-order plate theory by Mindlin [1], we apply the variational equation

$$\int_{-h}^{0} dx_2 \int_A (T_{ij,i} - \rho \ddot{u}_j) \delta u_j \, dA = 0, \tag{3}$$

where $T_{ij}^{(n)}, \rho, h, A$ are stress, density, thickness, and faces, respectively. By integrating (3) with known displacement patterns in (2) over the thickness coordinate, we can write out the equations of motion as

$$\sum_{n=1}^{2}\int_{A}\left(T_{ij,i}^{(n)} - k\beta_n T_{3j}^{(n)} + F_j^{(n)} - \rho\sum_{m=1}^{2} A_{mn}\ddot{u}_j^{(m)}\right)\delta u_j^{(n)} dA = 0. \tag{4}$$

The two-dimensional quantities in (4), $T_{ij}^{(n)}, F_j^{(n)}, A_{mn}$, are defined by the two-dimensional variables in (2) and details are in [8] along with the corresponding boundary conditions. Obviously, (4) can be treated like the plate equations of Mindlin and others for the bulk acoustic wave analysis. Equation (4) represents a set of four two-dimensional equations in terms of displacement components given in (2). The equations and the solution procedure associated with (4) are validated through the precise agreement of results from present two-dimensional theory and three-dimensional equations.

MASS EFFECT OF ELECTRODES AND THEIR PERIODIC STRUCTURE

For a thin electrode layer on top of elastic solids, by neglecting the stiffness of the thin layer, which is much smaller in comparison to the substrate, we have (4) revised as

$$\sum_{n=1}^{2}\int_{A}\left[T_{ij,i}^{(n)} - k\beta_n T_{3j}^{(n)} + F_j^{(n)} - \rho\sum_{m=1}^{2} A_{mn}(1+R)\ddot{u}_j^{(m)}\right]\delta u_j^{(n)} dA = 0, \tag{5}$$

with the mass ratio of the electrode defined as

$$R = \frac{\bar{\rho}\bar{h}}{\rho h}, \tag{6}$$

where $\bar{\rho}, \bar{h}$ are density and thickness of the electrode, respectively. With (5), fully electroded elastic solids can be studied for the effect on the displacements and SAW velocity.

For an elastic solid with periodic electrodes, we can use (4) and (5) alternatively for unelectroded and electroded regions with separated displacement solutions. By applying the continuity conditions to ensure the displacements and stresses are continuous and the boundary conditions are satisfied at the ends, we shall have a set of equations for the periodic structure for displacements and velocity. It is expected that there will be a velocity equation with large number of variables and corresponding matrix, enabling us to evaluate them for both numerical and analytical solutions.

CONCLUSIONS

Utilizing the two-dimensional surface acoustic wave theory, a thin metal layer on top of elastic solids is considered for the mass effect on the displacements and velocity. For a periodic structure with discontinuous electrodes, the equations are alternated between the unelectroded and electroded regions with the continuity boundary conditions, resulting a set of equations for precise consideration. By solving the boundary condition equation numerically and analytically, we have the displacement and velocity solutions of a finite periodic structure along with the mass effect of electrodes.

ACKNOWLEDGMENT

This study is supported by *Qian* River Fellow Fund established jointly by Zhejiang Province and Ningbo University and administered by Ningbo University.

References

[1] Achenbach, J.D.: *Wave Propagation in Elastic Solids*, North-Holland/American Elsevier, 1987.
[2] Mindlin, R.D.: High-frequency vibrations of piezoelectric crystal plates, *Intl. J. Solids Struct.*, **8**: 891-906, 1972.
[3] Lee, P.C.Y., S. Syngellakis, and J.P. Hou: "A two-dimensional theory plate equations for high-frequency vibrations of piezoelectric crystal plates", *J. Appl. Phys.*, **61**(4): 1249-1262, 1987.
[4] Wang, J. and J.S. Yang: "Higher-order theories of piezoelectric plates and applications", *Applied Mechanics Review*, **53**(4): 87-99, 2000.
[5] Wang, J., J.-D. Yu, Y.-K. Yong, T. Imai: "A new theory for electroded piezoelectric plates and its finite element application for the forced vibrations of quartz crystal resonators", *Intl. J. Solids Struct.*, **37**: 5653-5673, 2000.
[6] Wang, J., Y.-K. Yong, T. Imai: "Finite element analysis of the piezoelectric vibrations of quartz plate resonators with higher-order plate theory", *Intl. J. Solids Struct.*, **36**(15): 2303-2319, 1999.
[7] Peach, R.C.: "A normal mode expansion for the piezoelectric plates and certain of its applications", *IEEE Trans. UFFC*, 35(5): 593-611, 1988.
[8] Wang, J. and K.-Y. Hashimoto: "A two-dimensional theory for the analysis of surface acoustic waves in anisotropic elastic solids", *Proceedings of 2003 IEEE International Ultrasonics Symposium*, Honolulu, Hawaii, Oct 5-8, 2003.

NONLINEAR WAVE PROCESSES IN A BI-LAYER

Karima R. Khusnutdinova*, Roger H. J. Grimshaw

Department of Mathematical Sciences, Loughborough University, Loughborough LE11 3TU, UK

e-mails: K.Khusnutdinova@lboro.ac.uk, R.H.J.Grimshaw@lboro.ac.uk

Summary Combinations of two materials are commonly used to obtain a structure with the properties better than that of the parent constituents. Coupled nonlinear Klein-Gordon equations can be used to study the properties of wave propagation in a bi-layer. Applying exact analytical methods, asymptotic analysis and numerical simulations we show that heterogeneity leads to a number of interesting nonlinear wave processes in bi-layers.

MODEL OF A BI-LAYER

We study the one-dimensional nonlinear dynamics of a bi-layer using the model of coupled chains of particles [1], i.e. two one-dimensional periodic chains with linear links between elements and nonlinear interaction between the chains. This can be considered as a natural generalization of the Frenkel-Kontorova model [2]. The long-wave dynamics of this system is described in dimensionless variables by coupled nonlinear Klein-Gordon equations

$$u_{tt} - u_{xx} = f_u(u, w), \quad w_{tt} - c^2 w_{xx} = f_w(u, w), \tag{1}$$

where c is the ratio of characteristic speeds of non-interacting components. The function $f(u, w)$ describes interaction between the chains, and should be found experimentally.

Similar two-component models were proposed to describe dynamics of hydrogen-bonded chains, molecular crystals and polymer chains, etc. (see review [3]), and also in connection with the crack propagation in solids (e.g., [4], [5], [6]). It's also worth noting that similar equations describe some processes in the DNA double helix (see [7] and the references there).

When the potential function is $f(u, w) = \cos(\delta u - w) - 1$, system (1) reduces to coupled sine–Gordon equations:

$$u_{tt} - u_{xx} = -\delta^2 \sin(u - w), \quad w_{tt} - c^2 w_{xx} = \sin(u - w), \tag{2}$$

where the variable u replaces δu, compared to system (1).

NONLINEAR WAVE PROCESSES

The travelling wave solutions of (1) (in particular, solitary waves) can be found analytically. If the characteristic speeds of the non-interacting chains are different ($c^2 \neq 1$), a gap appears in the velocity spectrum of the solitary waves, i.e. the system acts as a filter for solitary waves. Here the relative displacement ("upper" particles relative to the "lower" ones) remains the same as in the FK model (per period of the chain), but the absolute displacement depends on the velocity of the wave [1]. The influence of a delamination zone on kink propagation is studied numerically in [8].

Another essential feature of the considered system is the possibility of energy exchange between its physical components (layers) [9], in particular, in the situation when one component is initially excited (say, u) with another component (w) being initially at rest. Periodic and quasi-periodic processes in the wave system (2) are analogous to the energy exchange in a system of coupled pendulums in classical mechanics.

The energy exchange between the two components u and w of the system (2) takes place since different branches of the dispersion curve coexist for the same wavenumber k, which is typical for bi-layers.

We consider the structure and stability of solutions involving two waves or two pairs of counter-propagating waves and describing periodic energy exchange between the layers. The exact two-wave solution of system (2) for the periodic energy exchange is found for $c = 1$ (Fig. 1). In the general case, it is possible to construct weakly nonlinear two- and four-wave solutions describing the energy exchange between two components u and w. Using both the theoretical predictions following from the asymptotic analysis and numerical simulations of the original unapproximated equations we show that these solutions may be modulationally unstable. These instabilities may lead to the formation of localized structures, and to a modification of the energy exchange between the components [10], [11] (Fig. 2).

*On leave from: Institute of Mechanics, Ufa Branch of the Russian Academy of Sciences, Karl Marx Str. 6, Ufa, 450000, Russia

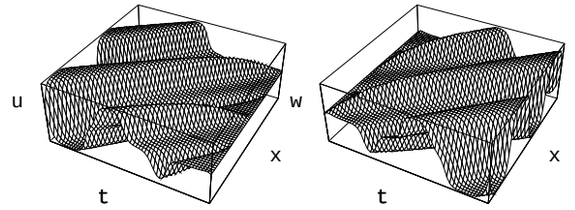


Figure 1: Energy exchange in exact two-wave solution.

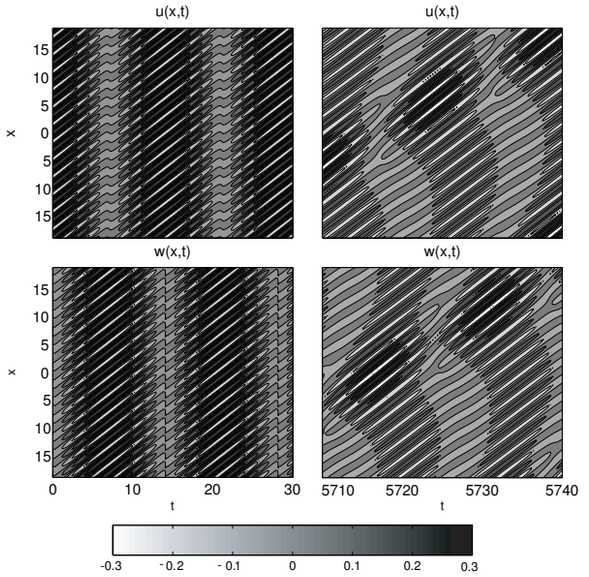


Figure 2: Energy exchange under the influence of modulational instability.

CONCLUSIONS

A major difficulty in the application of lattice models to real physical or biological processes is in the derivation of the interaction potentials and parameters of the model. In the case of bi-layers, this should (and can) be done experimentally. Here, we consider a simple model situation close to the Frenkel-Kontorova model to study the peculiarities of nonlinear wave processes in bi-layers.

References

[1] Akhatov I.Sh., Baikov V.A., and Khusnutdinova K.R.: Non-linear dynamics of coupled chains of particles. *J. Appl. Maths Mechs* **59**: 353-361, 1995.
[2] Kontorova T.A. and Frenkel Ya.I.: On the theory of plastic deformation and twinning I. *JETP* **8**: 89-95, 1340-1348, 1938.
[3] Braun O.M. and Kivshar Yu.S.: Nonlinear dynamics of the Frenkel-Kontorova model. *Phys. Rep.* **306**: 1-108, 1998.
[4] Slepyan L.I.: Models and Phenomena in Fracture Mechanics. Springer, Berlin 2002.
[5] Smith E.: The effect of the discretness of the atomic structure on cleavage crack extension: Use of a simple one-dimensional model.II. *Mater. Sci. & Engng* **30**: 15-22, 1977.
[6] Ginzburg V.V. and Manevitch L.I.: The extended Frenkel-Kontorova model and its application to the problems of brittle fracture and adhesive failure. *Int. J. of Fracture* **64**: 93-99, 1993.
[7] Yakushevich L.V.: Nonlinear Physics of DNA. Wiley, Chichester 1998.
[8] Khusnutdinova K.R. and Silberschmidt V.V.: Lattice modelling of nonlinear waves in a bi-layer with delamination. *Proc. Estonian Acad. Sci. Phys. Math.* **52**: 63-75, 2003.
[9] Khusnutdinova K.R. and Pelinovsky D.E.: On the exchange of energy in coupled Klein-Gordon equations. *Wave Motion* **38**: 1-10, 2003.
[10] Griffiths S.D., Grimshaw R.H.J. and Khusnutdinova K.R.: The influence of modulational instability on energy exchange in coupled sine-Gordon equations, *Theor. Math. Phys.* **137**: 1446-1456, 2003.
[11] Griffiths S.D., Grimshaw R.H.J. and Khusnutdinova K.R.: Nonlinear dynamics of two pairs of counter-propagating waves in two component media, *in preparation.*

Shock-induced surface waves in porous reservoirs

G. Chao*, D.M.J. Smeulders * and M.E.H. van Dongen**

* Delft University of Technology, dept. of Applied Earth Sciences, P.O. Box 5028, 2600 GA, Delft, The Netherlands
** Eindhoven University of Technology, dept. of Applied Physics, P.O. Box 513, 5600 MB, Eindhoven, The Netherlands

Summary The frequency-dependent characteristics of the surface waves that propagate along boreholes in fully saturated porous formations are studied in a broad band of frequencies (100 Hz-200 kHz). Numerical results are presented for the dispersion relation, pore pressure and displacements. Experimental data regarding speed and attenuation are reported. The experiments were performed using a shock tube technique in natural and synthetic porous materials.

INTRODUCTION

A detailed knowledge of the relation between the material properties and the propagation of surface waves in liquid-saturated porous media is important in order to obtain an accurate characterization of water and hydrocarbon reservoirs. The frequency-dependent phase velocities and damping coefficients can be inverted in order to obtain the porosity and the elastic properties of the surrounding formation. There are also theoretical and some experimental indications that the speed and attenuation of the surface waves are strongly influenced by the permeability[1][2]. Therefore, accurate acoustic measurements could be used to infer permeability information from the waveform recordings. However, the analysis are basically restricted to the fundamental surface wave usually called tube wave. Furthermore, laboratory data for surface waves along boreholes in porous formations are scarce[2].

In this work we study the frequency-dependent properties of the different surface modes that propagate in a cylindrical interface between a fluid and a fully saturated porous medium. Numerical calculations based on Biot's theory are presented for the dispersion relation, pore pressure and displacements of the different waves. Experimentally, we use shock waves to generate surface waves in a borehole in porous cylinders. Synthetic and natural samples with permeability values ranging from 360 mD to 10.8 mD were used to study the permeability effects in the broad band of frequencies (1-60 kHz) involved in the experiments. The experiments were performed in a shock tube setup[3]. The influence of the confinement due to the shock tube wall is also studied.

PERMEABILITY EFFECTS ON THE PSEUDO-STONELEY WAVE

Figs. 1 show the phase velocities and damping coefficients as a function of frequency for different permeability values for a natural rock sample of Berea sandstone. The results correspond to the pseudo-Stoneley wave. We generally assumed laterally infinite media, except for the case $k_0 = 360$ mD where also the shock tube wall is considered (confined reservoir).

The contribution of the slow wave in comparison with the other bulk modes has been calculated for the averaged radial displacement induced by the pseudo-Stoneley wave. The outcome of these calculations explains the strong permeability dependence for low frequencies, where the slow wave contribution is one order of magnitude larger than the fast compressional and shear waves in the porous reservoir.

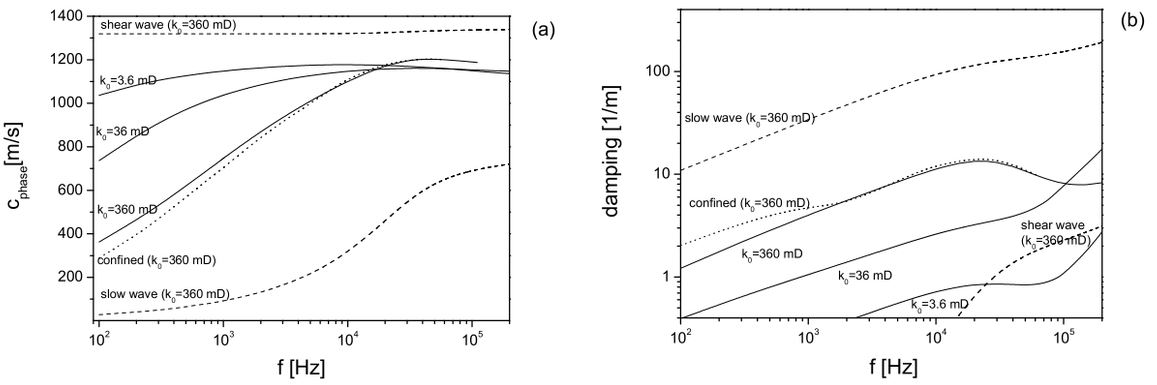


Figure 1: *Frequency-dependent phase velocities (a) and damping coefficients (b) for the pseudo-Stoneley wave for different permeability values. The solid lines correspond to the infinite reservoir configuration. The results for the confined reservoir for $k_0 = 360$ mD are shown in dotted line. The slow wave and shear wave velocities and damping are also dislayed for this case ($k_0 = 360$ mD).*

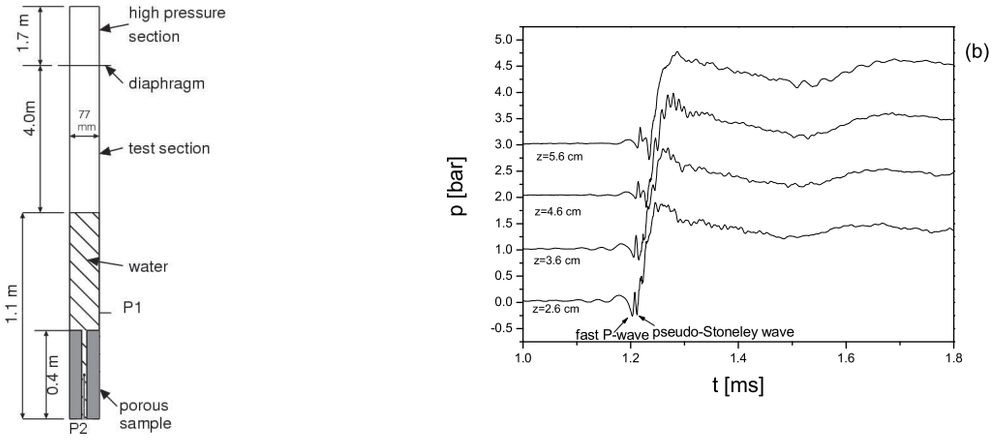


Figure 2: *Vertical shock tube setup (a) and typical pressure recordings at different depths (b).*

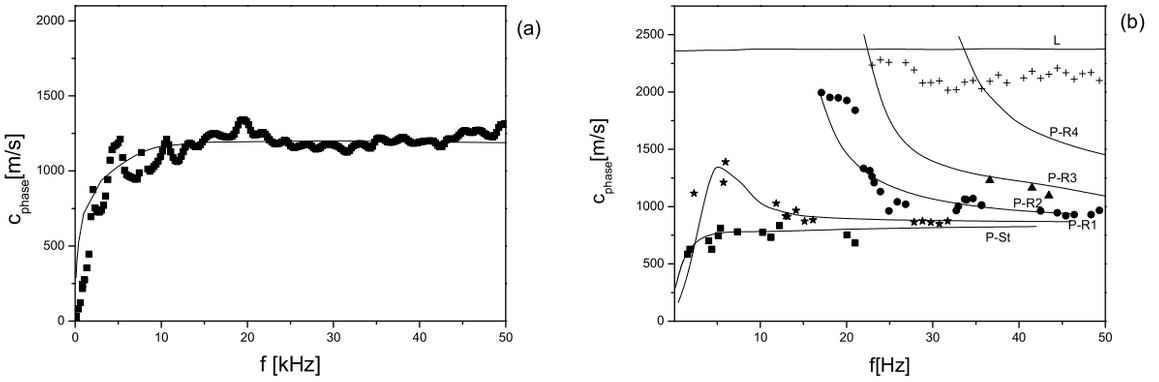


Figure 3: *Comparison between experiments and theory(solid lines) for the phase velocities of the surface waves in a Berea sandstone sample ($k_0 = 360$ mD) (a) and a synthetic sample (b) ($k_0 = 10.8$ D).*

EXPERIMENTAL RESULTS

The experiments were performed in water-saturated porous cylinders with a concentric borehole placed in the test section of a shock tube (Fig 2-a).
A miniature pressure transducer is mounted in a mobile probe that can be displaced along the axial direction of the borehole axis. In this way pressure measurements are performed at different positions along the borehole. Fig. 2-b shows a representative series of signals for a Berea sandstone material. The measurements are processed using a FFT-Prony method to obtain the frequency-dependent phase velocities and damping. The results for the phase velocityies for two different samples are shown in Figs. 3. A good resolution of the pseudo-Stoneley wave is observed in both the time and frequency domain for the Berea sandstone sample (Fig. 3-a). In the synthetic sample, multiple surface waves (pseudo-Stoneley wave and pseudo-Rayleigh waves) as well as the compressional wave in the porous material are excited (Fig. 3-b). Mode transition are observed between the different surface modes.

References

[1] Andrew N. Norris. Stoneley-wave attenuation in permeable formations. *Geophysics*, 54(3):330–341, 1989.

[2] K.W. Winkler, H-S Liu, and D.L. Johnson. Permeability and borehole stoneley waves: Comparison between experiment and theory. *Geophysics*, 54:66–75, 1989.

[3] C.J. Wisse, D.M.J. Smeulders, M.E.H. van Dongen, and G. Chao. Guided wave modes in porous cylinders: Experimental results. *J. Acous. Soc. Am.*, 112(3):890–895, 2002.

TRAPPING OF PLASTIC WAVES BY ADIABATIC DEFORMATION

Janusz R. Klepaczko
Metz University, Laboratory of Physics and Mechanics of Materials, UMR-CNRS 7554, Ile du Saulcy, F-57045 Metz, France

Summary The adiabatic heating due to conversion of plastic work into thermal energy substantially changes the boundary value problem of plastic wave propagation. The thermal coupling in plastic wave propagation leading to adiabatic wave trapping is the main subject of this study. Two cases are analysed, the adiabatic wave trapping in tension and also in shear. The case of shear is relatively new. Theory, experiments and numerical analyses of the Critical Impact Velocity (CIV) in shear is the main part of this contribution. A review of author's recent publications on CIV in tension and shear is presented.

INTRODUCTION

In the late forties of the last century von Kàrman [1-3] and others developed a theory for propagation of one-dimensional plastic waves in a slender bar. It was demonstrated that if a long bar is loaded in tension by a sufficiently high impact velocity , plastic deformation is concentrated near the impact end of the bar. The theory was limited to rate-independent and isothermal case. However, plastic deformation of materials is rate and temperature dependent. The adiabatic heating causes usually a material softening leading to adiabatic wave trapping. Localization of plastic deformation in adiabatic conditions superimposed on inertia effects (waves) causes that the plastic wave speed reaches zero and the Critical Impact Velocity (CIV) appears. It is shown that the CIV can occur in both tension and shear. The case of shear has been found and analysed more recently [5-10].

CRITICAL IMPACT VELOCITIES IN TENSION AND SHEAR

The Critical Impact Velocity in tension

In the previous analysis of the CIV in tension the adiabatic heating was neglected. A more complete and closer to the reality of fast plastic deformation is assumption of the adiabatic deformation. The equation of heat conduction with internal sources applicable to dynamic plasticity is given by

$$\rho C_p \frac{\partial T}{\partial t} = \beta \sigma(\varepsilon_p, \dot{\varepsilon}, T) \frac{\partial \varepsilon_p}{\partial t} - \lambda \frac{\partial^2 T}{\partial x_1^2} \tag{1}$$

where ρ , C_p , β and λ are respectively the density, specific heat, Taylor-Quinney coefficient and thermal conductivity, ε_p and σ are respectively the plastic strain and true stress, the direction of the heat conduction is x_1 . In fast processes of plastic deformation it can be assumed that the conductivity is zero, then one yields

$$\frac{dT}{d\varepsilon_p} = \frac{\beta}{\rho C_p} \sigma(\varepsilon_p, \dot{\varepsilon}, T) \quad \text{and after integration} \quad \Delta T_A \approx \frac{\beta}{\rho C_p} \int_0^{\varepsilon_{pm}} \sigma\left[\varepsilon_p, T(\varepsilon_p)_{\dot{\varepsilon}}\right] d\varepsilon_p \tag{2}$$

where $\Delta T_A = T - T_0$, T_0 is the initial temperature. Here is assumed that the strain rate is a parameter. The standard wave equation is given by

$$\frac{\partial^2 U_1}{\partial t^2} = C^2(\varepsilon) \frac{\partial^2 U_1}{\partial x_1^2} \quad \text{in the elastic range } C_0 = \left(\frac{E}{\rho}\right)^{1/2} \text{ and in the plastic range } C_p(\varepsilon_p) = \left(\frac{1}{\rho}\frac{d\sigma}{d\varepsilon_p}\right)^{1/2} \tag{3}$$

where C_0 is the slender-bar elastic wave speed in the x_1 direction, E is the Young's modulus. In the adiabatic conditions the tangent modulus $(d\sigma/d\varepsilon_p)_A$ versus plastic strain for most of metals and alloys is lower than the isothermal. Therefore, the speed of plastic waves in the adiabatic conditions is lower than in the isothermal case. A simple evaluation of the adiabatic tangent modulus was given in [4]. If constitutive relation $\sigma(\varepsilon_p, T)_{\dot{\varepsilon}}$ is explicitly known the adiabatic tangent modulus is given by

$$\left(\frac{d\sigma}{d\varepsilon_p}\right)_A = \frac{d}{d\varepsilon_p}\left[\sigma(\varepsilon_p, (T_0 + \Delta T_A(\varepsilon_p))_{\dot{\varepsilon}})\right] \quad \text{and} \quad C_p(\varepsilon_p)_A = \left[\frac{1}{\rho}\left(\frac{d\sigma}{d\varepsilon_p}\right)_A\right]^{1/2} \tag{4}$$

The critical impact velocity in tension can be found by applying the method of characteristics [3,5]. The CIV in adiabatic conditions is therefore obtained in the following form

$$V_{CR} = \int_0^{\varepsilon_m} \left[\frac{1}{\rho}\left(\frac{d\sigma}{d\varepsilon}\right)_A\right]_{\dot{\varepsilon}}^{1/2} d\varepsilon \quad \text{if} \quad \varepsilon = \varepsilon_m \quad \text{then} \quad \left(\frac{d\sigma}{d\varepsilon_p}\right)_A = 0 \quad \text{and} \quad C(\varepsilon_m)_A = 0 \tag{5}$$

It is clear that ε_m is the instability point of the adiabatic stress vs. total strain curve at predefined value of strain rate $\dot{\varepsilon}$. Theoretical values of CIV in tension are close to that found from experiments, for example [3,5]. Values of this material

constant (CIV) vary in the following limits 60 m/s < V_{CR} < 200 m/s. In single crystals of Al : 30 m/s < V_{CR} < 90 m/s depending on orientation, [5].

The Critical Impact Velocity in shear

Localization of plastic deformation during fast shearing by Adiabatic Shear Bands (ASB) is a common failure mode in many materials. If the rate of shearing is sufficiently high the adiabatic process of deformation is superimposed on propagation of plastic waves in shear and it leads to failure near the area of impact. In that case the plastic waves propagate in x_2 direction and displacement is in x_1 direction. The wave equation is given by

$$\frac{\partial U_1}{\partial t^2}=C_2^2(\Gamma)\frac{\partial U_1}{\partial x_2} \quad \text{in the elastic range} \quad C_2=\left(\frac{\mu}{\rho}\right)^{1/2} \quad \text{and in the plastic range} \quad C_{2p}(\Gamma_p)=\left[\frac{1}{\rho}\left(\frac{d\tau}{d\Gamma_p}\right)\right]^{1/2} \tag{6}$$

where C_2 is the elastic wave speed in shear, C_{2p} is the plastic wave speed, and τ and Γ_p are respectively the shear stress and plastic shear strain. It should be noted that in this case there is no change of the current surface where the shear stress is imposed and the instability and localization are triggered exclusively by adiabatic softening. The CIV in shear is relatively a new subject of research and was introduced and discussed in [6] and [7]. An analytical model has been developed in [6] and [7], according to that analysis the CIV in shear is given by

$$V_{CR}=C_2\,\Gamma_e+\int_{\Gamma_e}^{\Gamma_m}C_{2p}(\Gamma_p)\,d\Gamma_p \tag{7}$$

where Γ_e is the elastic shear strain at the yield limit and Γ_m is the localisation strain in the *adiabatic* conditions of deformation. It must be remembered that all derivations are for a constant strain rate, characteristic for the process range, that is 5.10^2 1/s < $\dot{\Gamma}$ < 10^3 1/s. Experiments performed at LPMM with the direct impact Modified Double Shear (MDS) technique, [8], confirmed existence of the CIV in shear for many metals and alloys. Numerical analyses by FE code with complete wave propagation scheme and thermal coupling also confirmed existence of CIV in shear for VAR 4340 steel and Ti-6Al-4V alloy, [9,10]. Values of CIV for those alloys determined by FE analyses are respectively 103 m/s and 121 m/s.

CONCLUSIONS

Existence of the Critical Impact Velocities in tension and shear has been confirmed by theoretical, experimental and numerical means. The analysis of CIV in tension has been improved by introduction of thermal coupling in the form of adiabatic heating. The phenomenon of CIV in shear is relatively new. A complete analysis of the CIV in shear with thermal coupling (adiabatic process of deformation) has been performed in [11]. It was found that an unique superposition of plastic shear waves and adiabatic softening triggers this phenomenon. Both, CIV in tension and shear can be assumed as specific material constants.

References

[1] Kàrman T.: On the propagation of plastic strains in solids, Reports NDRC A-29, OSRD 365, Feb. 1942.
[2] Duwez P.E., Clark D.S.: An experimental study of the propagation of plastic deformation under conditions of longitudinal impact, Proc. ASTM **47**: 502-532, 1947.
[3] Kàrman T., Duwez P.E.: The propagation of plastic deformation in solids, J. Appl. Phys., **21**: 987-994, 1950.
[4] Klepaczko J.R.: Strain rate history effects in Body-Center-Cubic metals, ASTM-STP 765, 251-267, 1982.
[5] Klepaczko J.R.: Generalized conditions for stability in tension test, Int. J. Mech. Sci., **10**: 297-313, 1968.
[6] Klepaczko J.R.: Plastic shearing at high and very high strain rates, Proc. Conf. Eurodymat, J. Phys. **IV-4**: C8-C35, 1994.
[7] Klepaczko J.R.: On the critical impact velocity in plastic shearing, EXPLOMET'95, Proc. Int. Conf. on Metallurgical and Materials Application of Shock-Wave and High-Strain-Rate Phenomena, Elsevier Science, Amsterdam, 413-419, 1995.
[8] Klepaczko J.R.: An experimental technique for shear testing at high and very high strain rates, the case of mild steel, Int. J. Impact Engng, **15**: 29-39, 1994.
[9] Klepaczko J.R., Klosak M.: Numerical study of the critical impact velocity in shear, Eur. J. Mech. A/Solids, **18**: 93-113, 1999.
[10] Bonnet-Lebouvier A.S., Klepaczko J.R.: Numerical study of shear deformation in Ti-6AL-4V at medium and high strain rates, Int. J. Impact Engng, **27:** (2002), 755-769.
[11] Klepaczko J.R., On critical impact velocities in tension and shear; Int. J. Impact Engeng, **29**: (2005), in print.

MODELING OF SOLITARY IMPULSES IN A COMPOSITE MATERIAL USING WAVELET ANALYSIS

Kateryna V. Terletska
S.P. Timoshenko Institute of Mechanics, Nesterov str. 3, 03680 Kyiv, Ukraine

Summary An original method for description of the solitary wave evolution in a material with the microstructure (a composite) is presented. A peculiarity of the proposed technique consists in using wavelet-analysis on the base of "Mexican hat" wavelets (MH-wavelets). Elastic wavelets based solution permits to reveal the microstructure effects, namely the essential dependence of the distance, on which evolution is visible, on the characteristic size of microstructure, and to extend the class of investigated pulses.

INTRODUCTION AND PROBLEM STATEMENT

We study plane solitary waves that propagate in a material with the microstructure. The material is considered within the framework of the microstructure theory of two-phase mixture. Solitary wave propagating in a mixture is considered to be plane, so in the concerned problem of the wave motion two independent variables only are presented – spatial coordinate x and time coordinate t.

One assumes that solitary wave is produced by the action of an impulse to the composite material, and this impulse propagates in the material as the solitary wave, that initially coincides by shape with the initial one. Modeling process consists of many stages. The initial stages include: the material model choice, choice of the appropriate impulse type, mathematical formulation of the wave motion problem and the choice of the analyzing way of the problem. Together they form theoretical part of the modeling.

The next part is linked with the wavelet-analysis application as the up-to-date tool of the computational mechanics. Elastic wavelets were suggested in [5], and were first applied for the solitary wave evolution study in [4]. In contrast to the prior studies when the initial pulses had to satisfy rather strict conditions, it is shown that initial impulse shape can be an arbitrary form (it should only admit wavelet representation and be solitary one). It is correct, however, under the condition that the profile can be approximated by MH-wavelets that possess the main property of elastic wavelets – they are solutions of the wave equation system of the considered problem. The certain class of solitary waves that correspond to known in classical experimental mechanics impulses [1] is studied in the work. These impulses were observed in classical experiments with short-time loadings.

ANALYSIS OF THE SOLITARY WAVE PROBLEM USING MH-WAVELET

The concrete dispersive medium, namely, microstructure mixture of two linearly elastically deformed components is considered. The basic system of equations for plane waves in such a medium is [4-6]

$$\rho_{\alpha\alpha}u_{1,tt}^{(\alpha)} - a_\alpha u_{1,xx}^{(\alpha)} - a_3 u_{1,xx}^{(\delta)} - \beta\left(u_1^{(\alpha)} - u_1^{(\delta)}\right) = 0. \tag{1}$$

Next step consists in MH-wavelets family using.

MH-wavelets were first used in computer vision to detect multiscale edges. It was noted earlier [4,5] that MH-wavelet, under some restrictions, is one of the solutions of system (1). This wavelet and its Fourier transform can be written analytically as [2,3]

$$\psi(x) = \frac{2}{\sqrt[4]{\pi}\sqrt{3\sigma}}\left(\frac{x^2}{\sigma^2} - 1\right)e^{-\frac{x^2}{2\sigma^2}}, \qquad \hat{\psi}(\omega) = -\frac{2\sqrt{2\sigma^5}\sqrt[4]{\pi}}{\sqrt{3}}\omega^2 e^{-\frac{\sigma^2\omega^2}{2}}. \tag{2}$$

Approximation of the initial impulse using MH-wavelets.

Let us choose the impulse that follows impulse obtained in [1] (see Fig.1.) Since MH-wavelets family form the tight frame [3] then the approximation, has the form

$$f_\varepsilon(x) \approx \frac{1}{A}\sum_{j=-2}^{9}\sum_{k=-14}^{14} d_{j,k}\psi_{j,k}(x), \tag{3}$$

where $A \approx 3.409$ is a frame bound and only coefficients $|d_{j,k}| > 10^{-4}$ are used.

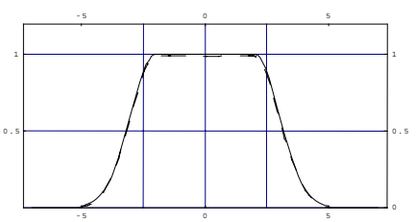


Fig.1

The idea of MH-wavelet application in the solitary wave evolution study lies in the representation of the initial profile using these wavelets and the assumption of the profile slow change during its propagation through weakly dispersive medium. Wavelet coefficients $d_{j,k}$ are supposed to be constant, and profile changes are results of nonlinear changes of phase velocities that are included in MH-wavelet arguments $v_{ph}^{(\alpha)}$. The idea of possibility of profile evolution descriptions by means of the phase variable only at the permanent functional profile representation lies in the basis of the simple wave theory [7]. Let us assume that the solution can be represented in the

form of two displacements corresponding to two mixture phases and looking like initial impulse (3) with the wave phase in the argument

$$u^{(\alpha)}(x,t) = \frac{1}{A}\sum_{j=-2}^{9}\sum_{k=-14}^{14} d_{j,k}\psi_{j,k}\left(x - v^{ph}t\right).$$

This finite wavelet sum is the solution of wave equations (1) in the same meaning as MH-wavelets are solutions of (1) i.e. under some restrictions. The phase velocity, however, will depend on scaling level j.

Finally, impulse propagating in the mixture can be represented as

$$u^{(\alpha)}(x,t) = \frac{1}{A}\sum_{j=-2}^{9}\sum_{k=-14}^{14}\left(B^{(\alpha)}\tilde{f}_{(\alpha,l)} + p\left(z^{(\delta,j)}/l\right)B^{(\delta)}\tilde{f}_{(\delta,l)}\right), \qquad (4)$$

$$\tilde{f}_{(\alpha,l)} = d_{j,k}\,2^{j/2}\psi\left(2^{j}\left(z^{(\alpha,j)}/l\right) - k\right), \qquad z^{(\alpha,j)} = x - v_{ph}^{(\alpha,j)}t\,.$$

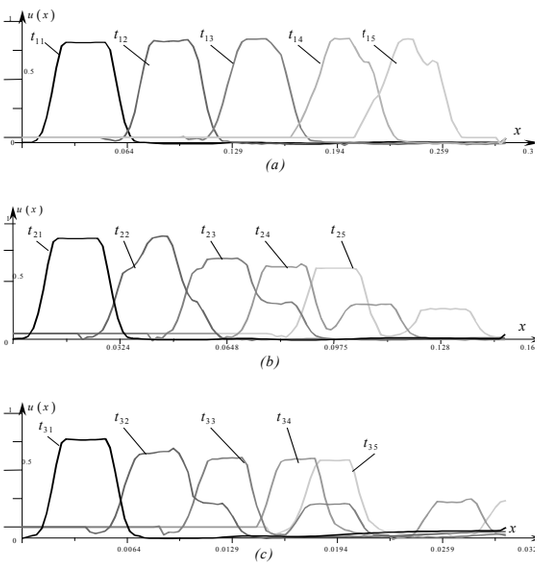


Fig. 2

Modeling of the solitary impulse evolution.

Composite materials "aluminum matrix - tungsten fibers" is chosen for the modeling. The volume fraction of tungsten fibers is $\xi_1 = 0,022$ [6]. Characteristic size of the microstructure is equal to $a^I = 0,648\cdot 10^{-3} m$. Waves with the length that exceeds the characteristic size of microstructure in 100, 50 and 10 times are examined. That is, the lengths of the wave bottoms are equal, respectively, to $0.648\cdot 10^{-1}, 0.324\cdot 10^{-1}, 0.648\cdot 10^{-2} m$. Amplitude coefficients are assumed to be $B^{(\alpha)} = B^{(\delta)} = 10^{-4}$. Profile evolution plots are built using analytical expression (4) and computation algorithms. Profiles are built for the first phase of composite material and for five sequential moments of time (in microseconds) $t_{11} = 25$, $t_{12} = 51$, $t_{13} = 76$, $t_{14} = 100$, $t_{15} = 120$, $t_{21} = 12,5$, $t_{22} = 25$, $t_{23} = 37,5$, $t_{24} = 50$, $t_{25} = 62,5$, $t_{31} = 2.5$, $t_{32} = 5.1$, $t_{33} = 7.6$, $t_{34} = 10$, $t_{35} = 12$. Two main microstructural effects are well apparent. The first effect: is the breaking down the solitary wave into two modes that propagate with different velocities and simultaneous propagation of both modes in two composite components. As well, the second effect that concerns a microstructure is shown up. This effect consists in the essential dependence of the distance, on which evolution is observed, from the characteristic size of microstructure. So, the advantage of this method consists in the possibility of representation of wave impulses that haven't analytic representations using elastic wavelets, which have analytic representation and are the solutions of the basic system of equations of plane waves in a composite material. It extends sufficiently the class of investigated impulses.

CONCLUSIONS

To solve the problem of solitary wave evolution during propagation through a material with the microstructure (a composite) the wavelet-analysis was applied. The main result consists, above all, in the ability of the proposed technique to study arbitrary wave shapes without any limitation on the initial profile. Also it permits to reveal the microstructure effects, and to extend the class of investigated initial pulses.

References

[1] Bell. J. F.: An experimental diffraction grating study of the split Hopkinson bar experiment. *J. Mech. Phys. Solids* **14**: 309-321, 1966.

[2] Geranin V.O., Pisarenko L.D., Rushchitsky J.J.: Wavelet Theory with the Elements of Fractal Analysis. Tutorial with 32 lectures. VPF Ukr INTEI, K 2002.

[3] Mallat S. A.: Wavelet Tour of Signal Processing. Academic Press, SD-NY-L 1999.

[4] Rushchitsky J.J., Cattani C., Terletska E.V.: Evolution of solitary wave in material with microstructure – experience of wavelet-analysis application. *Int. Appl. Mech* **40**, 2004.

[5] Rushchitsky J.J., Cattani C.: Solitary elastic waves and elastic wavelets. *Int. Appl. Mech* **39**: 741-752, 2003.

[6] Rushchitsky J.J.: Elements of Mixture Theory. Naukova Dumka, K 1991.

[7] Zaslavsky G.M., Sagdeev R.Z.: Introduction to Nonlinear Physics: From Pendulum to Turbulence and Chaos. Nauka, M 1988.

SOME DEGENERATED AND EXTENDED WAVE MODELS OF ELASTO- AND HYDRODYNAMICS WITH FINITE VELOCITY DISTURBANCE PROPAGATION

Igor Selezov
Department of Wave Processes, Institute of Hydromechanics, NASU,
8/4, Sheliabov Str., Kiev 03680, Ukraine

Summary Hyperbolic degeneration of the problems for wave guide type systems with respect to transverse coordinate is considered. Some models are presented when parabolic models singularly degenerate into hyperbolic ones and, controversly, when hyperbolic models can be obtained by the extension of parabolic operator up to hyperbolic ones.

The problem of finite velocity disturbance propagation as a condition of the correctness of the statement of initial boundary value (IBV) problem for hyperbolic equations and its solvability have been considered by Hersh [1] presented some cases of nonexistence of the solutions of IBV problem with finite velocities. Correctly stated IBV problems for hyperbolic equations were investigated and the conditions guaranteeing a finite velocity were established. Later on the considerations of such a kind were developed in [2, 3, 4].

In general, degeneration of an original model in small parameter β leads to some simplified models of different kind. The necessary condition of finite velocity disturbance propagation is the hyperbolity of model, i. e. it should by governed by the hyperbolic system of partial differential equations. It should be noted that asymptotic degeneration can change the type of equations. That is why, only limiting hyperbolic models are of our interest from above point of view. For example, parabolic model degenerates into hyperbolic ones, hyperbolic elastodynamic model for layer degenerates into hyperbolic ones but not into classical parabolic model predicting infinite velocity of disturbance propagation.

We consider degeneration of the original IBV problem in R^n for a finite hyperbolic system of arbitrary order partial differential equations with respect to the transverse coordinate x^s of a hyperlayer $\Omega \subset R^n$ whose thickness is assumed to be much lesser than the others. It allows to construct power series expansions of desired functions and to reduce consequently the problem dimensionality. At that, the infinite system can be truncated by different manners allowing to obtain different approximations. In this connection three cases are possible: degeneration to models of hyperbolic, parabolic or mixed type. The question is what is correct ? From the point of view of finite velocity disturbance propagation only the case of hyperbolic to hyperbolic is correct and having the physical sense. However, it is reached by the price of degeneration of the original problem spectrum.

Our aim is to derive hyperbolic approximations degenerated with respect to coordinate x^s, i.e. to construct a mapping $R^n \to R^{n-1}$ satisfying the condition of limiting correctness to be of hyperbolic type [2]. Necessary and sufficient conditions are established to such a hyperbolic degeneration. The necessary condition is to obtain a closed system to determine new unknown functions. The close is necessary but not sufficient condition because a lot of closed systems can be obtained depending on the selection criteria but not all of them will be of hyperbolic type. The sufficient condition is announced for obtaining hyperbolic approximations: to keep in infinite systems all space-time differential operators up to given order. This is proved for the case R^3 considering the elastodynamic problem for the layer. As a result, 3-D problem for the layer is reduced to the extended 6 order hyperbolic operator for bending waves in plate which includes as particular cases the known Timoshenko-Mindlin (4 order) and Kirchhoff models.

Expanding field functions in power series with respect to a middle hyperlayer surface

$$u_i\left(t, x^2, ..., x^{n-1}, x^n\right) = \sum_{k=1}^{\infty} u_{ik}\left(t, x^2, ..., x^{s-1}, x^{s+1}, ..., x^n\right)\left(x^s\right)^k. \tag{1}$$

yields the degenerated problem to determine the series coefficients depending now only on n-1 coordinates..

Let us consider the elastodynamic problem for an infinite layer of the thickness $2h$ occupied the region $\Omega = \left\{(x_1,\ x_2,\ x_3) \in R^3 : x_1,\ x_2 \in (-\infty, \infty),\quad x_3 \in \left[-\xi/2,\ \xi/2\right]\right\}$ in a Cartesian coordinate system $(x_1,\ x_2,\ x_3)$. The corresponding IBV-problem for the displacement vector (u_1, u_2, $u_3 = w$) is presented as follows: to find the functions $u_k = u_k(x_1,\ x_2,\ x_3,\ t)$ as the solutions of the hyperbolic equations

$$\nabla^2 u_k + (1 + \lambda/G)\,\partial_k\,(\vec{\nabla}\cdot\vec{u}) = \partial_{tt}\,u_k, \quad k = 1, 2, 3 \qquad \text{in} \quad \Omega \times [0,\ T],\ \ T > 0 \tag{2}$$

satisfying the boundary conditions for the stress-tensor components

$$\sigma_{33}\Big|_{x_3 = \pm\xi/2} = q^{\pm}(x_1,\ x_2,\ t),\ \ \sigma_{3i}\Big|_{x_3 = \pm\xi/2} = p_i{}^{\pm}(x_1,\ x_2,\ t), \qquad i = 1,\ 2 \tag{3}$$

and the initial conditions

$$u_k\Big|_{t=0} = 0,\ \ \partial_t u_k\Big|_{t=0} = 0, \qquad k = 1, 2, 3. \tag{4}$$

It is assumed that $2h/l = \xi << 1$ (l is a horizontal length scale), λ and $G = const$.

The functions u_k are presented according to (1) in the form of power series in x_3

$$u_k\ (x_1, x_2, x_3, t) = \sum_{\nu=0}^{\infty} u_{k\nu}\ (x_1,\ x_2, t)\ x_3^{\nu}, \qquad k = 1, 2, 3\ . \tag{5}$$

In the case of symmetric deformation with respect to the middle surface we obtain from equations (2)-(4) (when $q_1,\ q_2 = 0$), as the second approximation – the new more exact two-mode hyperbolic equation for $e_0 = (u_0)_{i,\,i}$

$$\left(-\xi a_1' \nabla^2 + \xi a_2' \frac{\partial^2}{\partial t^2} + \xi^3 b_1' \nabla^2\nabla^2 - \xi^3 b_2' \nabla^2 \frac{\partial^2}{\partial t^2} + \xi^3 b_3' \frac{\partial^4}{\partial t^4}\right) e_0 =$$

$$= \left\{d_1' + \xi^2 d_2' \nabla^2 + \xi^2 d_3' \frac{\partial^2}{\partial t^2}\right\} \left(\frac{\partial}{\partial x_2}\frac{p_1 - p_2}{2} + \frac{\partial}{\partial x_1}\frac{p_3 - p_4}{2}\right). \tag{6}$$

The equation (6) includes as a particular case the one-mode hyperbolic approximation (generalized stress state): two the first terms in the left hand side and the first term in the right hand side.

In the case of asymmetric deformation, keeping all the operators up to seventh order inclusively, we obtain from (6)-(8) (when $p_1, p_2, p_3, p_4 = 0$) the new three-mode hyperbolic approximation which can be reduced to the following generalized resolving hyperbolic equation

$$\left\{\left[\left(\xi \frac{\partial^2}{\partial t^2} + \xi^2 a_1 \nabla^2\nabla^2\right)_K - \xi^3 a_2 \frac{\partial^2}{\partial t^2}\nabla^2 + \xi^3 a_3 \frac{\partial^4}{\partial t^4}\right]_{TM} -\right.$$

$$-\xi^5 b_1 \nabla^2\nabla^2\nabla^2 + \xi^5 b_2 \frac{\partial^2}{\partial t^2}\nabla^2\nabla^2 - \xi^5 b_3 \frac{\partial^4}{\partial t^4}\nabla^2 +$$

$$\left. + \xi^5 b_4 \frac{\partial^6}{\partial t^6}\right\}_{TMS} \qquad w_0 = \left\{\left[1 - \xi^2 d_1 \nabla^2 + \xi^2 d_2 \frac{\partial^2}{\partial t^2}\right]_{TM} + \xi^4 d_3 \nabla^2\nabla^2 -\right.$$

$$\left. - \xi^4 d_4 \frac{\partial^2}{\partial t^2}\nabla^2 + \xi^4 d_5 \frac{\partial^4}{\partial t^4}\right\}_{TMS} \left(q^+ - q^-\right) \tag{7}$$

In (7) the sixth order hyperbolic operator TMS includes the fourth order Timoshenko-Mindlin hyperbolic operator TM and the Kirchhoff parabolic operator K.

It can be noted that unlike phenomenologocal approaches, for realization of the purely analytical approach presented in this paper it is not necessary to attract some physical prerequisities to construct the hyperbolic models.

Another problem is considered on the basis of the algorithm above presented allowing to construct extended degenerated close to hyperbolic model for nonlinear water wave propagation in the fluid of variable depth. Starting from a fully nonlinear statement asymptotic approximations are developed when the dispertion parameter β is assumed to be small while there is no limitations on the value of the nonlinear parameter α unlike previous works. As a result, the extended nonlinear-dispersive evolution equations for solitary waves are derived which include all known models as particular cases. The evolution of soliton running-up to slope is investigated showing the soliton distortion and appearing oscillating trails.

In addition the singular degeneration in parameter of parabolic model into hyperbolic ones takes place in the cases when operator include as a kernel the hyperbolic operator of lower order. For example, Navier-Stokes equations, Burgers equation, equations of magnetoelasticity and magnetohydrodynamics when the magnetic Reynolds number tends to zero, and others.

Alternatively, some examples are presented when hyperbolic models can be obtained by the extension of parabolic operator up to hyperbolic once: kinetic theory of gases (Maxwell, 1876), diffusion equation (Davydov, 1935), Smoluchowski equation (Davies, 1954), relativistic body (Bento, 1985), sediment evolution (Selezov, 1985).

References

[1] Hersh R.: Boundary Conditions for Equations of Evolution. Arch. Ration. Mech and Analysis **16**: 243-264, 1964.

[2] Selezov I.T.: Conception of Hyperbolity in the Theory of Control Dynamical Systems (In Russian). In: Cybernetics and Computing Engineering. Naukova Dumka, Kiev **1** : 131-137, 1969.

[3] Mizokhata S. The Theory of Partial Differential Equations (Russian translation from Japanese). Mir, Moscow 1977.

[4] Selezov I. Some Hyperbolic Models for Wave Propagation. In: Hyperbolic Problems: Theory, Numerics, Applications. Int. Series of Numerical Mathematics. Eds. M. Fey and R. Jeltsch,Basel / Switzerland: Birkhauser Verlag,**130**: 833-842, 1999.

UNIQUENESS RESULTS FOR THE REFLECTION-TRANSMISSION PROBLEM

Angelo Morro
University of Genova, DIBE, Via Opera Pia 11a, 16145 Genova, Italy

Summary Reflection and transmission of mechanical waves are investigated for a viscoelastic layer sandwiched between homogeneous elastic half-spaces. On the basis of appropriate boundary conditions for the layer, uniqueness is established for C^2 solutions to the initial/boundary-value problem in the space-time domain.

INTRODUCTION

This paper investigates the reflection and transmission of waves, in the time domain, generated by a viscoelastic (anisotropic) layer sandwiched between homogeneous elastic half-spaces. The problem is regarded as a initial/boundary-value problem for the layer. At least on a interface, both the incident and the reflected/transmitted waves occur simultaneously and hence we cannot pick part of the boundary where the solution is known. This explains why ordinarily existence and/or uniqueness results are lacking in reflection-transmission problems.
The approach presented in this paper follows an energy method and is based on two main steps. First, the boundary conditions for the layer are written in a form which accounts directly for the outgoing character of the (unknown) reflected and transmitted waves. Second, an energy functional is considered for the viscoelastic layer which is a potential for the traction. As a result, uniqueness is established for C^2 solutions in the space-time domain.

Notation and assumptions

Consider a layer of thickness L sandwiched between two half spaces. Let z be the Cartesian coordinate such that $z \in (0, L)$ is the layer and $z < 0$ and $z > L$ are the half spaces. Let $\mathbf{u}(\mathbf{x}, t)$ on $\mathbb{R}^3 \times \mathbb{R}$ be the displacement. We disregard body forces and write the equation of motion as

$$\rho \partial_t^2 \mathbf{u} = \nabla \cdot \mathbf{T}$$

where ρ is the mass density, $\mathbf{T}$ is the symmetric Cauchy stress tensor and ∂_t denotes (partial) time differentiation. To account for viscoelasticity we let $\mathbf{T}$ be given by the gradient of displacement, $\nabla \mathbf{u}$, in the form

$$\mathbf{T}(\mathbf{x}, t) = \mathbf{G}_0(\mathbf{x}) \nabla \mathbf{u}(\mathbf{x}, t) + \int_0^\infty \mathbf{G}'(\mathbf{x}, \eta) \nabla \mathbf{u}(\mathbf{x}, t - \eta) d\eta$$

where the values of $\mathbf{G}_0$ and $\mathbf{G}'$ are fourth-order tensors and $\mathbf{G}'(\mathbf{x}, \cdot) \in L^1(\mathbb{R}^+)$. We also assume that $\nabla \mathbf{u}(\mathbf{x}, \cdot)$, $\partial_t \mathbf{u}(\mathbf{x}, \cdot)$, $\partial_t^2 \mathbf{u}(\mathbf{x}, \cdot) \in L^1(\mathbb{R})$. Both $\mathbf{G}_0$ and $\mathbf{G}'$ are required to satisfy the minor and major symmetries. The traction, at the planes $z =$ constant, is denoted by $\boldsymbol{\tau} = \mathbf{T}\mathbf{e}_3$, $\mathbf{e}_3$ being the unit vector of z. In the elastic half-spaces $z < 0$ and $z > L$ it is $\mathbf{G}' = 0$. In the layer $z \in (0, L)$ both $\mathbf{G}_0$ and $\mathbf{G}'$ are allowed to depend on $\mathbf{x}$ only through z (axial inhomogeneity). Thermodynamics requires that $\mathbf{G}_0$ be positive definite. We also assume that $\mathbf{G}'$ is negative semidefinite.
For isotropic solids the governing equations decouple [1]. The present approach for anisotropic solids leads again to decoupled equations, in the elastic homogeneous half-spaces, by using the eigenvectors of the acoustic tensor.

EQUATIONS FOR ANISOTROPIC SOLIDS AND NORMAL INCIDENCE

Assume that ρ and $\mathbf{G}_0, \mathbf{G}'$ depend on $\mathbf{x}$ through z and $\mathbf{u} = \mathbf{u}(z, t)$, which is the case if the incident wave is normal. Hence the equation of motion becomes

$$\rho \partial_t^2 \mathbf{u} = \partial_z [(\mathbf{Q}_0 + \mathbf{Q}' *) \partial_z \mathbf{u}], \qquad z \in (-\infty, 0) \cup (0, L) \cup (L, \infty),$$

where $*$ means convolution in $\mathbb{R}^+$ and $\mathbf{Q}_0 = \mathbf{e}_3 \mathbf{G}_0 \mathbf{e}_3$ and likewise for $\mathbf{Q}'$; in suffix notation $Q'_{ik} = G'_{i33k}$. As the half-spaces are elastic and homogeneous we can write $\mathbf{Q}' = 0$ and $\mathbf{Q}_0 =$ constant as $z \in (-\infty, 0) \cup (L, \infty)$.
Letting $\mathbf{a}_1, \mathbf{a}_2, \mathbf{a}_3$ be the eigenvectors of $\mathbf{Q}_0$ we find that

$$\mathbf{u}(z, t) = \sum_{r=1}^{3} [u_r^f(z, t) + u_r^b(z, t)] \mathbf{a}_r, \qquad z \in (-\infty, 0) \cup (L, \infty)$$

where the superscripts f and b are reminders for forward- and backward-propagating d'Alembert's solutions [2]. Now, for any function $h(z \pm ct)$ we have $\partial_z h \, \partial_t h = \pm c (\partial_z h)^2$. Hence for any component u_r^f and u_r^b we have

$$\partial_z u_r^f \, \partial_t u_r^f \leq 0, \qquad \partial_z u_r^b \, \partial_t u_r^b \geq 0.$$

For definiteness we let the incident wave come from $z<0$ and then the reflected and transmitted waves take the general form

$$\mathbf{u}^R(z,t)=\sum_{r=1}^{3}u_r^b(z,t)\mathbf{a}_r,\qquad z<0,\qquad \mathbf{u}^T(z,t)=\sum_{r=1}^{3}u_r^f(z,t)\mathbf{a}_r,\qquad z>L.$$

Hence, because $\boldsymbol{\tau}=\mathbf{Q}_0\partial_z\mathbf{u}$ we find that the power $\boldsymbol{\tau}\cdot\partial_t\mathbf{u}$ for the reflected and the transmitted waves satisfies the inequalities

$$\boldsymbol{\tau}^R\cdot\partial_t\mathbf{u}^R=\sum_{r=1}^{3}q_r\partial_z u_r^b\,\partial_t u_r^b\geq 0,\qquad \boldsymbol{\tau}^T\cdot\partial_t\mathbf{u}^T=\sum_{r=1}^{3}q_r\partial_z u_r^f\,\partial_t u_r^f\leq 0$$

where q_1,q_2,q_3 are the positive eigenvalues of $\mathbf{Q}_0$, in the pertinent half-space.

Energy functional

Let $\mathbf{u}\in C^2((-\infty,0)\cup(0,L)\cup(L,\infty)\times\mathbb{R}^+)$. For any point $\mathbf{x}$ of the layer, $z\in(0,L)$, and time t, consider the functional

$$\Psi(\partial_z\mathbf{u}(t),\partial_z\mathbf{u}^t)=\frac{1}{2}\partial_z\mathbf{u}(t)\cdot\mathbf{Q}_\infty\partial_z\mathbf{u}(t)-\frac{1}{2}\int_0^\infty[\partial_z\mathbf{u}(t-\xi)-\partial_z\mathbf{u}(t)]\cdot\mathbf{Q}'[\partial_z\mathbf{u}(t-\xi)-\partial_z\mathbf{u}(t)]d\xi$$

the dependence on $\mathbf{x}$ being understood and not written. A direct calculation shows that Ψ is the potential for the traction,

$$\frac{\partial\Psi}{\partial[\partial_z\mathbf{u}^t]}=\mathbf{Q}_0\partial_z\mathbf{u}(t)+\int_0^\infty\mathbf{Q}'(\xi)\partial_z\mathbf{u}(t-\xi)d\xi=\boldsymbol{\tau}(t).$$

Consider the energy $E(t)$ for the layer in the form

$$E(t)=\int_0^L\Big\{\frac{1}{2}\rho[\partial_t\mathbf{u}(t)]^2+\Psi(\partial_z\mathbf{u}(t),\partial_z\mathbf{u}^t)\Big\}dz.$$

The assumption that $(\mathbf{Q}')'$ be positive semidefinite, integrations by parts and use of the symmetry of $\mathbf{Q}_0,\mathbf{Q}'$ allow us to find that the time derivative $\dot{E}$ is bounded by

$$\dot{E}(t)\leq\boldsymbol{\tau}(L_-,t)\cdot\partial_t\mathbf{u}(L_-,t)-\boldsymbol{\tau}(0_+,t)\cdot\partial_t\mathbf{u}(0_+,t).$$

UNIQUENESS FOR THE REFLECTION-TRANSMISSION PROBLEM

The reflection-transmission problem P consists in finding a function $\mathbf{u}(z,t)\in C^2((-\infty,0)\cup(0,L)\cup(L,\infty)\times\mathbb{R}^+)$ such that $\mathbf{u}(z,t)=0, z\in\mathbb{R}, t\leq 0$ whereas $\mathbf{u},\boldsymbol{\tau}$ are continuous everywhere and the incident wave $\mathbf{u}^I$ is known so that $\mathbf{u}^I(0_-,t)=\mathbf{w}(t)$, $t\geq 0$. Uniqueness is proved first for the layer $z\in(0,L)$ and next for the half-spaces $z<0$, $z>L$.

Theorem 1 (Layer) *The restriction to $z\in(0,L)$ of the solution $\mathbf{u}$ to* P *is unique in $C^2((0,L)\times\mathbb{R}^+)$.*

Proof. Let $\mathbf{u}_1,\mathbf{u}_2$ be two solutions to P and $\boldsymbol{\tau}_1,\boldsymbol{\tau}_2$ the associated tractions. The differences $\mathbf{v}=\mathbf{u}_1-\mathbf{u}_2$ and $\boldsymbol{\sigma}=\boldsymbol{\tau}_1-\boldsymbol{\tau}_2$ satisfy the equation $\partial_z\boldsymbol{\sigma}=\rho\partial_t^2\mathbf{v}$ as $z\in(0,L)$, $t>0$, the initial condition $\mathbf{v}(z,0)=0$, $z\in[0,L]$ and the inequalities $\boldsymbol{\sigma}\cdot\partial_t\mathbf{v}\geq 0$ as $z=0_+$ and $\boldsymbol{\sigma}\cdot\partial_t\mathbf{v}\leq 0$ as $z=L_-$. The energy of the layer $E(t)$ associated with $\mathbf{v}$ is shown to satisfy $E(t)\geq 0$, $E(0)=0$, and $\dot{E}\leq 0$. This implies the vanishing of E in $\mathbb{R}^+$ and hence the vanishing of $\mathbf{v}$ in $[0,L]\times\mathbb{R}^+$. This in turn implies uniqueness. □

Because $\mathbf{u}$ is unique as $z\in[0,L]$ and $\mathbf{u}$ is continuous then $\mathbf{u}(0_-,t)$ and $\mathbf{u}(L_+,t)$ are unique.

Theorem 2 (Half-spaces) *For every finite $T>0$ the solution $\mathbf{u}$ to* P *subject to $\mathbf{u}(0_-,t)=\boldsymbol{\psi}(t)$, $\mathbf{u}(L_+,t)=\boldsymbol{\zeta}(t)$, $t\leq 0$ and $\mathbf{u}(z,0)=\mathbf{l}(z)$, $z\in(-\infty,0]\cup[L,\infty)$, whereas $\mathbf{u}(z,t)$ has compact support as $t\leq T$, is unique in $C^2((-\infty,0)\cup(L,\infty)\times[0,T])$.*

Proof. The difference $\mathbf{v}$ of two solutions has compact support and is subject to $\mathbf{v}(0_-,t)=0$, $\mathbf{v}(L_+,t)=0$, $t\geq 0$, $\mathbf{v}(z,0)=0$, $z\in(-\infty,0_-)\cup(L_+,\infty)$. Consider the energy of the half-space $z<0$, $E_-(t)$, associated with $\mathbf{v}$. We find that $\dot{E}_-(t)=\boldsymbol{\sigma}(0_-,t)\cdot\partial_t\mathbf{v}(0_-,t)=0$. Because $E_-(t)\geq 0$ and $E_-(0)=0$ it follows that $E_-(t)=0$, $t\in[0,T]$. Hence we conclude that $\mathbf{u}$ is unique as $z\in(-\infty,0]$. Likewise we establish uniqueness for $z\in[L,\infty)$. □

Uniqueness is shown to hold also if the half-space $z>L$ is replaced by a fixed boundary, $\mathbf{u}(L,t)=0$, or a free boundary, $\boldsymbol{\tau}(L,t)=0$.

References

[1] Morro A.: Uniqueness results for reflection and transmission in a solid layer, Math. Mech. Solids, in print.
[2] Caviglia G., Morro A.: Reflection and transmission of transient waves in anisotropic elastic multilayers, Quart. Jl Mech. Appl. Math., in print.

XXI ICTAM, 15–21 August 2004, Warsaw, Poland

WAVE INTERACTION RESONANCES IN INHOMOGENEOUS ELASTIC MATERIALS

Andres Braunbrück*, Arvi Ravasoo*
*Institute of Cybernetics at TTU, Department of Mechanics and Applied Mathematics, Akadeemia 21, 12618 Tallinn, Estonia

Summary Weakly inhomogeneous nonlinear elastic material is considered. Nonlinear interaction of two counter-propagating longitudinal waves is studied theoretically. An analytical solution is derived. Oscillations on the material boundaries are investigated and wave interaction resonances are clarified. This resonance is sensitive to the properties of the material and to the excitation frequency. This phenomenon is proposed to used for qualitative and quantitative nondestructive characterization of the material.

INTRODUCTION

Wave-wave and wave-material interaction is under investigation due to promising applications in nondestructive testing (NDT) of materials[1, 2]. Utilization of nonlinear effects of wave motion extends the possibilities of NDT [3, 4].
In this paper counter-propagation of two sine waves in weakly inhomogeneous nonlinear elastic material is studied theoretically. An analytical solution is derived for the initial stage of nonlinear wave interaction process. On the basis of this cumbersome solution numerical computations are carried out. Oscillations on the material boundaries are investigated. Wave interaction resonances are clarified. It cleared up that the value of the resonance is sensitive to the properties of the material and to the excitation frequency. Resonance data may be used for qualitative and quantitative nondestructive characterization of inhomogeneous nonlinear elastic material. The last conclusion is supported by the results of numerical experiments.

PROBLEM FORMULATION

A nonlinear elastic material with weak physical inhomogeneity is considered. Deformations of the material are described by the five coefficient nonlinear theory of elasticity [5]. In the one dimensional case the wave process is governed by the equation of motion [6]

$$[\,1 + k_1(X)\,U_{,X}(\,X,t)\,]\;U_{,XX}(\,X,t) + k_2(X)\,U_{,X}(\,X,t) + \;k_3(X)\,[U_{,X}(\,X,t)]^2 - k_4(X)\,U_{,tt}(\,X,t) = 0\,, \qquad (1)$$

where U denotes displacement, X the Lagrangian space coordinate and t the time. The commas and the variables in the indices indicate partial derivations with respect to corresponding variables. The coefficients $k_i(X)$, $i = 1 \ldots 4$ are functions of variable properties of the material: density $\rho(X)$, second order elastic coefficients $\lambda(X)$ and $\mu(X)$ and the third order elastic coefficients $\nu_1(X)$, $\nu_2(X)$ and $\nu_3(X)$. In the one dimensional case elastic coefficients are grouped. The coefficient $\alpha(X) = \lambda(X) + 2\,\mu(X)$ characterizes linear elastic properties of the material and the coefficient $\beta(X) = 2\,[\nu_1(X) + \nu_2(X) + \nu_3(X)]$ the nonlinear elastic properties. Inhomogeneous material properties ($\gamma = \rho,\, \alpha,\, \beta,\; \varepsilon \ll 1$)

$$\gamma(X) = \gamma^{(1)} + \varepsilon\,\gamma^{(2)}(X),\; \gamma^{(2)}(X) = \gamma_{1\xi}X + \gamma_{2\xi}X^2 + \gamma_{3\xi}X^3,\; \xi = \rho,\, \alpha,\, \beta \qquad (2)$$

have a polynomial functionality.

WAVE INTERACTION

Simultaneous propagation of two waves with arbitrary smooth initial profiles $\varphi(t)$ and $\psi(t)$ are excited on parallel surfaces of the material under initial and boundary conditions $U(X,0) = U_{,t}(X,0) = 0\,,\; U_{,t}(0,t) = \varepsilon\,a_0\,\varphi(t)\,H(t)\,,\; U_{,t}(L,t) = \varepsilon\;a_L\;\psi(t)\;H(t)\,$, where $H(t)$ is a Heaviside function and constants εa_0 and εa_L depict the initial wave amplitudes.
Eq. (1) with Eq. (2) is solved following the perturbation procedure. The solution is sought in the form of series

$$U(X,t) = \sum_{n=1}^{\infty} \varepsilon^n\,U^{(n)}(X,t)\,, \quad 0 < \varepsilon \ll 1. \qquad (3)$$

The first three terms in solution (3) are derived making use of the software package *Maple*. The first term is the solution to the linear wave equation and it consists of four constituents

$$\begin{aligned} &U^{(1)}_{,t}(X,t) = a_0 H(\chi)\varphi(\chi) + a_L H(\eta)\psi(\eta) - a_0 H(\theta)\varphi(\theta) - a_L H(\zeta)\psi(\zeta)\,, \\ &\chi = t - X/c,\;\; \eta = t - (L-X)/c,\;\; \theta = t - (2L-X)/c,\;\; \zeta = t - (X+L)/c\,. \end{aligned} \qquad (4)$$

Second and subsequent terms are solutions to the PDEs with known r.h.s. Expressions for these terms are too cumbersome to be presented here. They correct the linear solution and take the nonlinear effects of wave motion and material inhomogeneity into account.
The derived solution is valid in the interval $0 \le t\,c/L < 2$, where c is the phase velocity.

WAVE INTERACTION RESONANCES FOR MATERIAL CHARACTERIZATION

For applications, the excited wave profiles are specified by sine functions $\varphi(t) = \psi(t) = \sin(\omega\, t)$, where ω is the radial frequency, i.e., simultaneous propagation, reflection and interaction of harmonic waves is considered. The corresponding cumbersome solution is derived and analyzed numerically. The material is assumed to be duralumin with constant part of the density $\rho^{(1)} = 3000$ kg/m^3, the elastic coefficients $\alpha^{(1)} = 100$ GPa and $\beta^{(1)} = -750$ GPa. Material has two parallel boundaries and the thickness $L = 0.1$ m. The following notation for the parameters of inhomogeneity is used:

$$\gamma(X) = \gamma^{(1)}\,(1 + \delta_{i\xi}(X)), \quad \delta_{i\xi}(X) = \varepsilon\gamma_{i\xi}X^i/\gamma^{(1)}, \quad \delta_{i\xi}(L) \equiv \delta_{i\xi}, \quad i = 1,2,3, \quad \gamma,\xi = \rho,\alpha,\beta. \tag{5}$$

Wave processes is excited in the range of the values of excitation amplitudes $-1.30\,c \le a_0 \le -0.35\,c$, $a_L = -a_0$ m/s and $\varepsilon = 10^{-4}$. Some of the computed twenty values of the boundary oscillation amplitudes $A_{li},\ i = 1\ldots 20$ are plotted in Fig 1 for the linear case. The maximum (resonant) amplitude in the interaction interval $1 < t\,c/L < 2$ occurs always at the same frequency $\omega_l = 2\,\pi\,c\,n/L$ where n is an integer.

Results of the numerical simulation of the resonance in the interaction interval on the basis of the whole nonlinear solution are presented in Fig.2. Amplitudes A and frequencies ω are computed in Fig. 2 for the first oscillation peak by $n = 4$. It becomes clear that the wave interaction resonance is essentially sensitive to the values of material properties and to the inhomogeneity in density and linear elastic properties. The weak inhomogeneity in nonlinear elastic coefficient $\beta(X)$ practically does not affect on the value of the resonance. Results of the numerical simulation compose cascades in different regions in Fig. 2. These cascades form different *corridors* for linear, quadratic and cubic inhomogeneities in material properties. This is illustrated for $\alpha(X)$ in Fig. 2. Important is that inhomogeneity in density has essentially different effect on wave interaction resonance than other material properties (see Fig. 2). This makes it possible to use the obtained results in ultrasonic nondestructive evaluation of the properties of inhomogeneous materials.

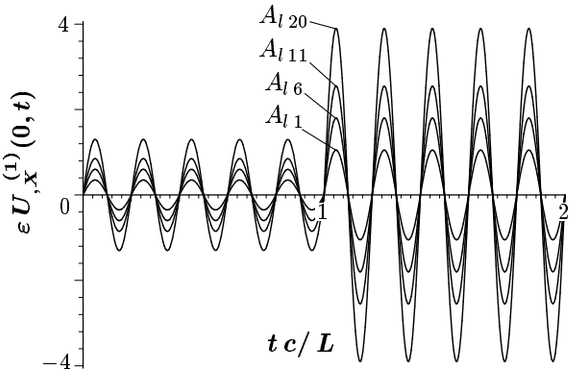


Figure 1. Variation of the boundary oscillation amplitude for the linear case ($n = 5$).

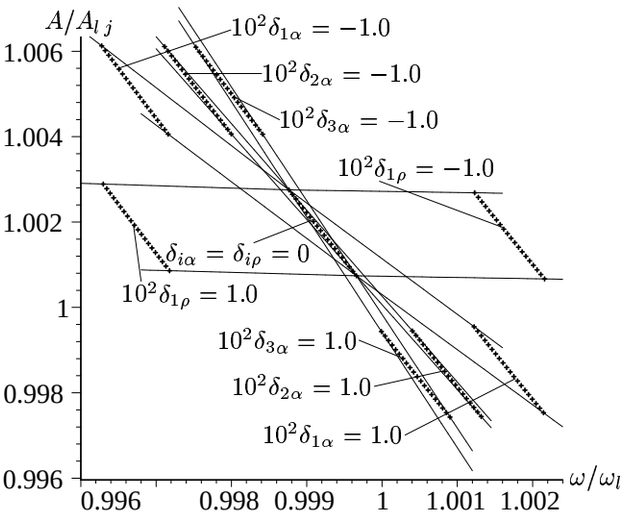


Figure 2. Nonlinear resonance as a function of the frequency and material properties ($j = 1\ldots 20,\ i = 1,2,3$).

CONCLUSIONS

Two wave interaction resonance in the inhomogeneous elastic material is studied theoretically. This resonance is sensitive to the inhomogeneous material properties and it may be used in NDT. The work is supported by ESF through NATEMIS program and by Estonian SF through grant no. 4706.

References

[1] Donskoy D., Sutin A., Ekimov A.: Nonlinear acoustic interaction on contact interfaces and its use for nondestructive testing. *NDT&E Int.* **34**:231–238, 2001.

[2] Gusev V., Bailliet H., Lotton P., Bruneau M.: Interaction of counterpropagating waves in media with nonlinear dissipation and in hysteretic media. *Wave Motion* **29**:211–221, 1999.

[3] Guyer R. A., Johnson P. A.: Nonlinear mesoscopic elasticity: evidence for a new class of materials. *Physics Today* **april**:30–36, 1999.

[4] TenCate J. A., Smith E., Byers L. W., Michel A. S.: Nonlinear resonant ultrasound for damage detection. *Review of Progress in QNE*:1387–1392, 2000.

[5] Bland D. R.: Nonlinear Dynamic Elasticity. Waltham, Massachusetts, 1959.

[6] Ravasoo A., Braunbrück A.: Wave interaction for characterization of nonlinear elastic material. *Proc. Estonian Acad. Sci. Eng.* **6/3**:171–185, 2000.

ACCELERATION WAVEFRONTS IN RANDOM MEDIA

Martin Ostoja-Starzewski[*], Jerzy Trebicki [**]

[*]*Department of Mechanical Engineering, McGill University, Montreal, Que. H3A 2K6, Canada*

[**]*Polish Academy of Sciences, IPPT PAN, Swietokrzyska 21, PL 00-049 Warszawa, Poland*

Summary In contradsitinction to deterministic continuum mechanics, we consider wavefronts whose thickness is smaller than the Representative Volume Element (RVE) size. As a result, the wavefront is an object more appropriately analyzed as a Statistical Volume Element (SVE) rather than an RVE, and therefore to be treated via a stochastic, rather than a deterministic, dynamical system.

INTRODUCTION

In conventional deterministic continuum mechanics, wavefronts are commonly modeled as singularity surfaces traveling in homogeneous media. Although a wavefront's thickness is very thin - mathematically infinitesimal, indeed - the ensuing analyses assume that the Representative Volume Element (RVE) size is even smaller (!) and no consideration of material spatial randomness is made. Whereby a typical grains' size $\langle d \rangle$ is supposed to tend to zero relative to the wavefront's thickness L. In contradistinction to that classical approach, just like in our previous studies [1, 2] we consider the wavefront as an object much more appropriately analyzed as a Statistical Volume Element (SVE). Our focus is primarily on acceleration wavefronts, and there are two entirely new aspects considered in the present study. One is the explicit consideration of spatial randomness and various cross-correlations of the instantaneous modulus, the dissipation coefficient, the instantaneous second-order tangent modulus, and the reference state mass density. The second new facet is the coupling of these four random fields to the wavefront amplitude: as the amplitude grows, the wavefront gets thinner tending to a shock, and thus the material heterogeneity shows up as an ever `stronger' random field.

BACKGROUND

Acceleration waves are generally governed by the Bernoulli equation [e.g. 3]

$$\frac{d\alpha}{dx} = -\mu\alpha + \beta\alpha^2 \tag{1}$$

Here x is position, α is jump in particle acceleration, while the coefficients μ and β represent, respectively, two effects: dissipation and elastic non-linearity. The most interesting aspect of acceleration waves uncovered through this equation is that, due to the competition between these two effects, there is a possibility of blow-up, and hence, of shock formation in a finite distance x_∞, providing the initial amplitude α_0 exceeds a *critical amplitude* α_c; x_∞ is called the *distance to blow-up*.

The explicit formulas for the dissipation coefficient, the nonlinear amplification coefficient, and the velocity of acceleration wave are [3]

$$\mu = -\frac{G_0^{'}}{2G_0}\ , \quad \beta = -\frac{\widetilde{E}_0}{2G_0}\sqrt{\frac{\rho_R}{G_0}}\ , \quad c = \sqrt{\frac{G_0}{\rho_R}} \tag{2}$$

where G_0 is called the instantaneous modulus, $G_0^{'}$ is the coefficient responsible for dissipation, is $\widetilde{E}_0$ the instantaneous second-order tangent modulus, and ρ_R is the mass density in the reference state. The dynamical system (1) is driven by these four basic material coefficients, and, given their randomness, both α_c and x_∞ are random processes.

BERNOULI EQUATION PERTURBED BY VECTOR RANDOM PROCESS

Wavefront evolution is governed by a stochastic differential equation

$$\frac{d\alpha}{dx} = \frac{G_0^{'}}{2G_0}\alpha - \frac{\widetilde{E}_0}{2G_0}\sqrt{\frac{\rho_R}{G_0}}\alpha^2 \tag{3}$$

driven by a four-component random process $\Theta_x = [G_0, G_0^{'}, \widetilde{E}_0, \rho_R]$ with

$$\begin{aligned} &G_0 = \langle G_0 \rangle + S_1 X_1(x,\omega) > 0\ , \quad G_0^{'} = \langle G_0^{'} \rangle + S_2 X_2(x,\omega) \le 0 \\ &\widetilde{E}_0 = \langle \widetilde{E}_0 \rangle + S_3 X_3(x,\omega) \le 0\ , \quad \rho_R = \langle \rho_R \rangle + S_4 X_4(x,\omega) > 0 \end{aligned} \tag{4}$$

where $\langle \cdot \rangle$ denotes the mean value, $\mathbf{X}(x,\omega) = [X_i(x,\omega)]_{i=1}^4$ is a standard Gaussian vector random process with zero mean value $\langle \mathbf{X}(x,\omega) \rangle = 0$ ($\langle X_i(x,\omega) \rangle = 0$), variances $\operatorname{var} X_i = 1$, and positive defined correlation matrix $K_{ij}(\Delta x) = \langle X_i(x,\omega) X_j(x+\Delta x,\omega) \rangle$, $\omega \in \Omega$ where Ω is an element of the probability space $\{\Omega, F, P\}$. We assume that parameters S_i satisfy condition $S_i << 1.0$. Upon transformations, we may write:

$$\mu(x,\omega) = -\frac{\left\langle G_0^{'}\right\rangle + S_2 X_2(x,\omega)}{2[\left\langle G_0\right\rangle + S_1 X_1(x,\omega)]} \quad , \quad \beta(x,\omega) = -\frac{[\left\langle \tilde{E}_0\right\rangle + S_3 X_3(x,\omega)]\sqrt{\left\langle \rho_R\right\rangle + S_4 X_4(x,\omega)}}{2[\left\langle G_0\right\rangle + S_1 X_1(x,\omega)]^{3/2}} \tag{5}$$

so that the 1-*D* statistics of $\mu(x,\omega)$ and $\beta(x,\omega)$, and of α_c and x_∞, may be determined from $[X_i(x,\omega)]_{i=1}^4$. The first case which we investigate in depth is that of all $X_i(x)$'s being a stationary Ornstein-Uhlenbeck (O-U) process $U(x,\omega)$ with a correlation function $K_U(\Delta x) = \sigma_U^2 \exp(-a\,|\,\Delta x\,|)$ where $\sigma_U^2 = 1$, whereby the dynamical system is

$$\frac{d\alpha}{dx} = -\mu\big(U(x,\omega)\big)\alpha + \beta\big(U(x,\omega)\big)\alpha^2 \quad , \quad dU = -aUdx + \sqrt{2a}\,dW_x(\omega) \tag{6}$$

with $W_x(\omega)$ being the standard Wiener process; $\alpha(x=0) = \alpha_0$. As an example, Fig. 1 shows the probability densities of x_∞ at various values of parameter *a*, all obtained via the method of Winterstein (e.g. [1]) for first four statistical moments of x_∞ obtained as result of Monte Carlo simulations of equations (6) where O-U process starts from its stationary state. The cases when processes $[X_i(x,\omega)]_{i=1}^4$ are independent or slightly correlated will be also reported during the presentation.

COUPLING OF THE AMPLITUDE OF AN ACCELERATION WAVE WITH MEDIUM'S SPATIAL RANDOMNESS

We now modify the original Bernoulli equation (6) by introducing the coupling between the processes $\alpha(x,\omega)$ and $\mu(x,\omega)$, $\beta(x,\omega)$ in the following way

$$\begin{aligned} &\frac{d\alpha}{dx} = -\mu\big(U\big)\alpha + \beta\big(U\big)\alpha^2 \quad , \quad dU = -a(\alpha)Udx + \sigma_U(\alpha)\sqrt{2a(\alpha)}\,dW_x(\omega) \\ &\frac{d\sigma_U}{dx} = C_1\alpha^{m_1} \quad , \quad \frac{da}{dx} = C_2\alpha^{m_2} \quad , \quad \sigma_U(x_0) = 1 \ , \ a(x_0) = a_0 \ , \ C_1, C_2, m_1, m_2 > 0 \end{aligned} \tag{7}$$

Thus, as α grows, so does the variance of the driving random fields μ and β, and decreases their correlation length. Of course, in the particular case of the Ornstein-Uhlenbeck process, r=1/a. Figure 2 shows comparison of distribution functions of x_∞ (for small probabilities) when there is no coupling vis-à-vis when there is coupling as modelled here. It is seen that the introduction of coupling causes growth of the probability of blow-up by up to factor two for the considered values of parameters. Related effects on α_c will also be reported orally. Our presentation will end with an extension of the concept of SVE to shock waves in random media and with the setup of a corresponding stochastic dynamical system governing their evolution.

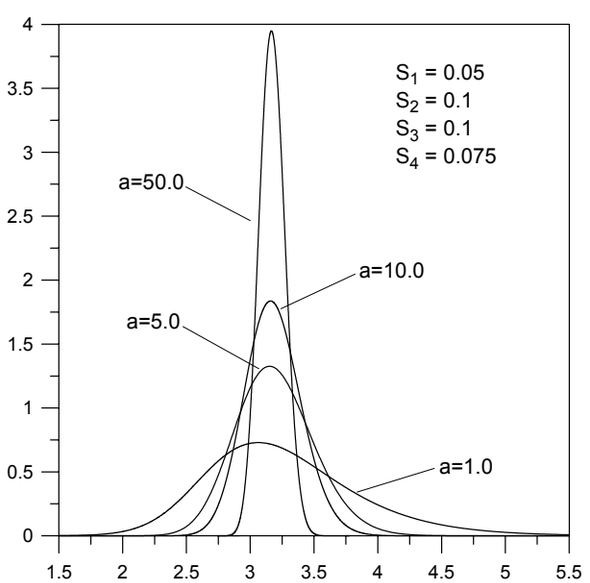


Figure 1. Probability densities of x_∞ for different values of parameter *a* in uncoupled model (6).

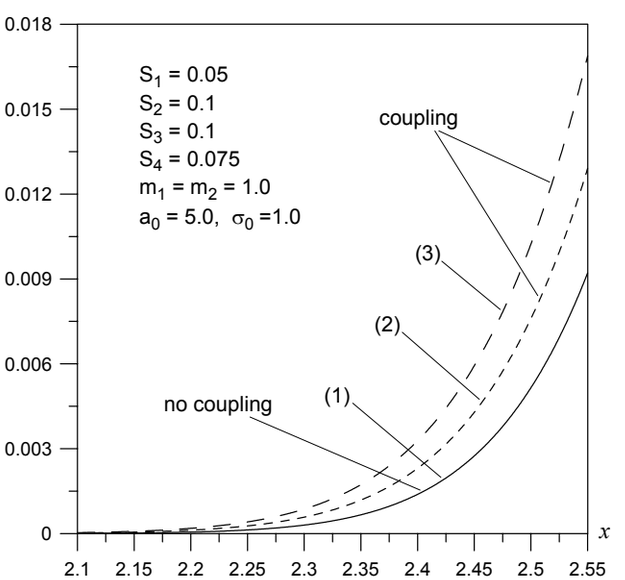


Figure 2. Distribution function of x_∞ for uncoupled model (6) (curve (1)) and coupled model (7) (for curve (2): $C_1 = C_2 = 0.05$, and for curve (3): $C_1 = C_2 = 0.1$)

References

[1] Ostoja-Starzewski M., Trebicki J., On the growth and decay of acceleration waves in random media, *Proc. R. Soc. Lond. A 455*: 2577-2614, 1999

[2] Ostoja-Starzewski M., Trebicki J., On the distance to blow-up of acceleration waves in random media, *Cont. Mech. Thermodyn*. 15, 21-32, 2003

[3] Chen P.J., Growth and Decay of Acceleration Waves in Solids, *Encyclopedia of Physics VI a/3 (S. Flügge and C. Truesdell, eds.),* Springer-Verlag, Berlin, 1973

XXI ICTAM, 15–21 August 2004, Warsaw, Poland

INHOMOGENEOUS CIRCULARLY POLARIZED WAVES IN ORTHORHOMBIC CRYSTALS

Philippe Boulanger*, Michael Hayes**
*Université Libre de Bruxelles, Dpt. de Mathématique, Campus Plaine CP218/1, 1050 Bruxelles, Belgium
**University College Dublin, Department of Mechanical Engineering, Belfield, Dublin 4, Ireland

Summary For elastic homogeneous plane waves in crystals, Fedorov § Fedorov introduced a decomposition of the acoustical tensor, valid for all orthorhombic, tetragonal, hexagonal and cubic crystals. Here, in considering the propagation of inhomogeneous waves in orthorhombic crystals, we generalize the Fedorov § Fedorov concept of "pseudo-transverse" and "pseudo-longitudinal" waves to elliptically polarized inhomogeneous waves, and determine the corresponding possibilities for circularly polarized waves.

BASIC EQUATIONS

Within the context of linearized elasticity theory, the equations of motion governing the displacement u_i of an anisotropic elastic body of material density ρ are

$$d_{ijkl}\partial^2 u_k/\partial x_j \partial x_l = \rho \partial^2 u_i/\partial t^2, \tag{1}$$

where d_{ijkl} are the elastic stiffnesses, assumed constant, with the symmetries $d_{ijkl} = d_{jikl} = d_{ijlk} = d_{klij}$. For orthorhombic crystals, using Voigt's notation, the only non-zero elastic stiffnesses are $d_{11}, d_{22}, d_{33}, d_{44}, d_{55}, d_{66}, d_{12}, d_{13}, d_{23}$. The propagation of time-harmonic inhomogeneous plane waves with complex slowness $\mathbf{S} = N\mathbf{C}$ and complex amplitude $\mathbf{A}$ is governed by the propagation condition

$$\mathbf{Q}(\mathbf{C})\mathbf{A} = w\mathbf{A}\ , \quad Q_{ik}(\mathbf{C}) = d_{ijkl}C_j C_l\ , \quad \text{with } w = \rho N^{-2}. \tag{2}$$

The tensor $\mathbf{Q}(\mathbf{C})$ is called the "complex acoustical tensor". For each chosen bivector $\mathbf{C}$, the eigenvalue problem $(2)_1$ for w and $\mathbf{A}$ has to be solved. This procedure is called the "directional-ellipse method", or "DE-method"[4].

FEDOROV § FEDOROV DECOMPOSITION

For crystals of orthorhombic, tetragonal, hexagonal or cubic symmetry, Fedorov & Fedorov[1] introduced a decomposition of the acoustical tensor. Generalizing this decomposition to the case of inhomogeneous waves, the complex acoustical tensor $\mathbf{Q}(\mathbf{C})$ may be written as

$$\mathbf{Q} = \mathbf{D} + \mathbf{N} \otimes \mathbf{N}\ , \tag{3}$$

where $\mathbf{D}$ is a complex diagonal tensor and $\mathbf{N}$ a bivector, given by

$$\mathbf{D} = \text{diag}[D_1,\ D_2\ , D_3]\ , \qquad \mathbf{N} = (\beta_1 C_1, \beta_2 C_2, \beta_3 C_3)\ . \tag{4}$$

For orthorhombic crystals, we have

$$\begin{gathered} D_1 = (d_{11} - \beta_1^2)C_1^2 + d_{66}C_2^2 + d_{55}C_3^2\ , \quad D_2 = d_{66}C_1^2 + (d_{22} - \beta_2^2)C_2^2 + d_{44}C_3^2\ , \\ D_3 = d_{55}C_1^2 + d_{44}C_2^2 + (d_{33} - \beta_3^2)C_3^2\ , \end{gathered} \tag{5}$$

and

$$\beta_1^2 = \frac{(d_{12} + d_{66})(d_{13} + d_{55})}{(d_{23} + d_{44})}\ ,\ \beta_2^2 = \frac{(d_{23} + d_{44})(d_{12} + d_{66})}{(d_{13} + d_{55})}\ ,\ \beta_3^2 = \frac{(d_{13} + d_{55})(d_{23} + d_{44})}{(d_{12} + d_{66})}\ . \tag{6}$$

With the Fedorov & Fedorov decomposition (3), the secular equation, $\det\{\mathbf{Q}(\mathbf{C}) - w\mathbf{1}\} = 0$, reads

$$(w - D_1)(w - D_2)(w - D_3) - N_1^2(w - D_2)(w - D_3) - N_2^2(w - D_3)(w - D_1) - N_3^2(w - D_1)(w - D_2) = 0. \tag{7}$$

In considering the decomposition (3) of the acoustical tensor for homogeneous waves, Fedorov & Fedorov[1] introduced "pseudo-longitudinal" and "pseudo-transverse" waves. "Pseudo-longitudinal" waves are those waves whose amplitude $\mathbf{A}$ is along $\mathbf{N}$, whilst "pseudo-transverse" waves are those waves whose amplitude $\mathbf{A}$ is orthogonal to $\mathbf{N}$. Here, we consider "pseudo-longitudinal" and "pseudo-transverse" *inhomogeneous* waves, and analyze the possibility of circularly polarized waves. Circularly polarized waves are possible if and only if the secular equation (7) has a double root.

PSEUDO-LONGITUDINAL WAVES

Pseudo-longitudinal waves ($\mathbf{N} \times \mathbf{A} = \mathbf{0}$) are only possible when $\mathbf{N}$ satisfies the condition[1] $\mathbf{N} \times \mathbf{QN} = \mathbf{0}$. This is a condition on the bivector $\mathbf{C}$. From (3), it is easily seen that this reduces to $\mathbf{N} \times \mathbf{DN} = \mathbf{0}$, which means that $\mathbf{DN}$ has to be parallel to $\mathbf{N}$, and thus

$$(D_1 N_1)/N_1 = (D_2 N_2)/N_2 = (D_3 N_3)/N_3\ . \tag{8}$$

Because one or two of the components of $\mathbf{N}$ may be zero, three possibilities have to be considered. Here we consider only the general case general when $N_1N_2N_3 \neq 0$ for which circularly polarized waves are possible. In this case, the conditions (8) reduces to $D_1 = D_2 = D_3$. These are two equations for the ratios C_2/C_1 , C_3/C_1. The real solutions yield acoustic axes of the crystal[3], along which circularly polarized homogeneous waves may propagate. However, depending on the elastic stiffnesses, complex solutions are also possible. These yield bivectors $\mathbf{C}$ for which the secular equation has a double root. The corresponding solutions are given by

$$w_1 = D_1 + \mathbf{N}\cdot\mathbf{N}\ , \quad \mathbf{A}_1 = \mathbf{N}\ ; \qquad w_2 = w_3 = D_1\ , \quad \mathbf{N}\cdot\mathbf{A} = 0\ . \tag{9}$$

The solution $(w_1,\ \mathbf{A}_1)$ represents a pseudo-longitudinal wave, whilst the solution $(w_2,\ \mathbf{A})$ represents a pseudo-transverse wave with an arbitrary amplitude $\mathbf{A}$ orthogonal to $\mathbf{N}$. In particular, for this wave, $\mathbf{A}$ may be chosen to be isotropic, $\mathbf{A}\cdot\mathbf{A} = 0$ and then, the wave is circularly polarized.

PSEUDO-TRANSVERSE WAVES

Pseudo-transverse waves ($\mathbf{N}\cdot\mathbf{A} = 0$) are only possible when $\mathbf{N}$ satisfies the condition[1] $(\mathbf{N}\times\mathbf{QN})\cdot\mathbf{Q}^2\mathbf{N} = 0$, which means that $\mathbf{N}$, $\mathbf{QN}$, $\mathbf{Q}^2\mathbf{N}$ are linearly dependent. From (3), it is easily seen that this reduces to $(\mathbf{N}\times\mathbf{DN})\cdot\mathbf{D}^2\mathbf{N} = 0$, which may be written explicitly as[1]

$$N_1N_2N_3(D_1 - D_2)(D_2 - D_3)(D_3 - D_1) = 0. \tag{10}$$

Two possibilities have to be considered, namely when one of the N_i is zero, or when two of the D_i are equal. As an example, we here present results for the case $D_1 = D_2$. In this case the secular equation (7) is factored so that we have the solution

$$w_1 = D_1 \quad , \qquad \mathbf{A}_1 = (-N_2, N_1, 0)\ , \tag{11}$$

whilst the two other roots $w = w_2, w_3$ of (7) are the roots of the quadratic

$$(w - D_3)(w - D_1 - \mathbf{N}\cdot\mathbf{N}) + N_3^2(D_1 - D_3) = 0\ . \tag{12}$$

Clearly, (11) represents a pseudo-transverse wave ($\mathbf{N}\cdot\mathbf{A} = 0$). The two roots of (12) yield two other wave solutions. Circularly polarized waves are possible either (a) when w_1 given by (11) is also a root of of the quadratic (12), or (b) when the quadratic (12) has a double root.

Case (a) The root $w_1 = D_1$ is also a root of (12) when

$$(D_1 - D_3)(N_1^2 + N_2^2) = 0\ . \tag{13}$$

We note that for inhomogeneous waves, (13) may be satisfied by choosing $N_2 = \pm iN_1$. In this case, there is a simple infinity of isotropic eigenbivectors corresponding to the double root w_1 of the secular equation (7). We have

$$w_1 = D_1 \quad , \qquad \mathbf{A}_1 = (\pm i, -1, 0)\ . \tag{14}$$

This solution represents an inhomogeneous plane wave which is circularly polarized in the x_1x_2-plane.

Case (b) The quadratic (12) has a double root when

$$(D_1 - D_3 + N_1^2 + N_2^2 - N_3^2)^2 + 4(N_1^2 + N_2^2)N_3^2 = 0\ . \tag{15}$$

For inhomogeneous waves, this condition may be satisfied by requiring that

$$D_1 - D_3 + N_1^2 + N_2^2 - N_3^2 = \pm 2i(N_1^2 + N_2^2)^{1/2}N_3\ . \tag{16}$$

We here assume $N_1N_2N_3 \neq 0$. Then, when (16) is satisfied, the secular equation (7) has a double root w, and corresponding to this double root there is a simple infinity of isotropic eigenbivectors $\mathbf{A}$. These are given by

$$w = \frac{1}{2}(D_1 + D_3 + \mathbf{N}\cdot\mathbf{N}) \quad , \qquad \mathbf{A} = (iN_1, iN_2, \pm(N_1^2 + N_2^2)^{1/2})\ . \tag{17}$$

This solution represents a circularly polarized inhomogeneous plane wave. Using (5) and (6), the results may be explicited in terms of the elastic stiffnesses.

References

[1] Fedorov, F. I. & Fedorov, A. F.: On the structure of the Green-Christoffel tensor. *J. Phys. A: Math. Gen.* **24**:71–78, 1991.
[2] Boulanger, Ph. & Hayes, M.: Bounds on elastic wave-speeds in crystals: Theory and applications. *Proc. Roy. Soc. A* **454**:2298-2322, 1998.
[3] Boulanger, Ph. & Hayes, M.: Acoustic axes for elastic waves in crystals: Theory and applications. *Proc. Roy. Soc. A* **454**:2323-2346, 1998.
[4] Boulanger, Ph. & Hayes, M.: Bivectors and waves in mechanics and optics. Chapman & Hall, London 1993.

XXI ICTAM, 15–21 August 2004, Warsaw, Poland

HIDDEN AND DRIVEN SOLITONS IN MICROSTRUCTURED MEDIA

Andrus Salupere, Jüri Engelbrecht
Centre for Nonlinear Studies, Institute of Cybernetics at Tallinn Technical University, Akadeemia tee 21, 12618 Tallinn, Estonia

Summary Wave propagation in microstructured materials is studied by making use of the Korteweg–de Vries type model equations. Model equation are solved numerically under harmonic initial and periodic boundary conditions. Existence of hidden solitons in conservative cases and emergence of driven solitons in nonconservative cases are demonstrated.

INTRODUCTION

Over the recent decade, the attention to microstructured materials has been arisen enormously. This concerns granular materials, polycrystalline solids, ceramic composites, functionally graded materials, alloys, etc. These advanced materials have found wide application in mechanical, electrical and computational engineering. In the present paper Korteweg–de Vries (KdV) type nonlinear evolution equations

$$u_t + [P(u)]_x + \delta_3 u_{3x} + \delta_5 u_{5x} = \alpha F(u), \quad P(u) = \gamma_2 u^2 + \gamma_4 u^4 \tag{1}$$

are used for modelling the 1D longitudinal wave propagation in nonlinear microstructured media. Here γ_2 is the second- and γ_4 the fourth-order nonlinear parameter while δ_3 is the third- and δ_5 the fifth-order dispersion parameter, x and t are space and time coordinates, respectively. The function $F(u)$ represents the influence of amplitude dependent external body force field. The most important point in this context is the possibility of emerging of solitons, i.e., solitary waves propagating without changing their shape and speed due to the balance of all physical effects (here between dispersion and nonlinearity). This important physical phenomenon was at first found in shallow water waves but nowadays is also found in solids, circuits, plasma, optical fibres, etc.

Our cases of interest are $\gamma_2 \neq 0$, $\gamma_4 \neq 0$, $\alpha = 0$ and $\gamma_2 \neq 0$, $\gamma_4 = 0$, $\alpha \neq 0$. The first case corresponds to alloy-type microstructured materials [1, 2], the second case — to a microstructured layer with energy influx like seismic waves in lithosphere [3]. With special scaling the examples studied below are $\gamma_2 = -0.5$, $\gamma_4 = 0.25$, $\alpha = 0$ and $\gamma_2 = -0.5$, $\gamma_4 = 0$, $\alpha \neq 0$, respectively. Both cases are analysed in order to cast light over the mechanism of possible emerging the solitary waves which bear the constant energy. The basic feature in both models is the existence of hidden solitons which can be amplified in the second case. Although our studies are confined to dynamics of solids, such mechanisms are of wider importance in solitonics.

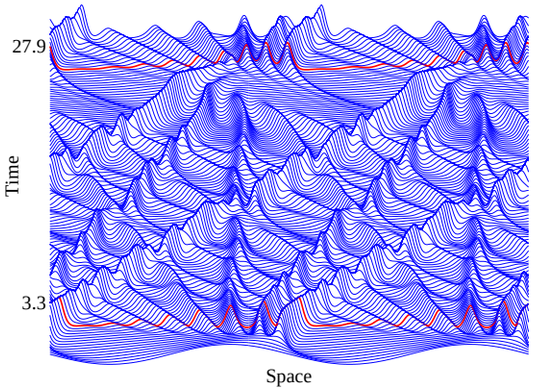


Figure 1. Interaction of KdV solitons: time slice plot over two 2π space periods ($d = 10^{-2.2}$).

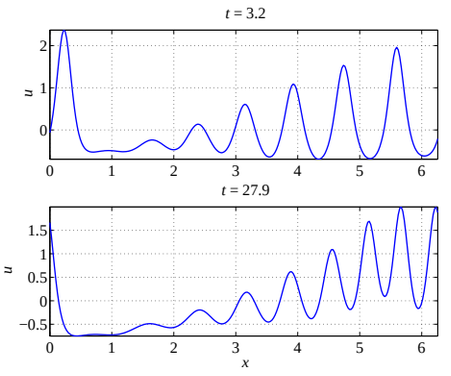


Figure 2. Initial train of 8 solitons at $t = 3.2$ and train of 9 solitons at $t = 27.9$.

HIDDEN SOLITONS

It is well known, that in systems governed by the KdV-type evolution equations the interaction of solitons causes phase shifts in soliton trajectories and simultaneous specific changes in their amplitudes (as a rule the amplitude of the higher soliton decreases during the interaction). If only single solitons are propagating in the media then the number of solitons is known and one can predict the location of a certain soliton at a certain time moment. However, in the case of arbitrary initial and periodic boundary conditions (harmonic, for example) a train of interacting solitons emerges. In this case the number of solitons taking part in the subsequent interaction process is usually higher than the number of solitons that can be determined making use of the initial train of equally spaced solitons. The solitons detectable from the initial train are called *visible*. In addition to these, some solitons can be hidden in the initial soliton train but they take part in the interaction process causing "additional" phase shifts and minima in trajectories and amplitude curves of visible solitons. Furthermore, when a certain number of interactions have taken place one can see in waveprofiles more solitons than

initially during a short time interval. We call these small amplitude solitons *hidden*. Such a phenomenon can be found in the case of the KdV equation [4] as well as for our first case [5]. In Figs. 1 and 2 the existence of hidden solitons is demonstrated in the case of KdV equation. At time moment $t = 3.2$ the initial train of eight solitons (per one 2π period) is formed. However, at $t = 27.9$ one can observe a train of nine solitons.

In order to understand the essence of physical processes the actual number of solitons (including hidden ones) is of importance. The concept of hidden solitons is: (i) hidden solitons can emerge from arbitrary periodic initial excitation and they have small energy and amplitude; (ii) they cause changes, specific for soliton type interaction, in amplitudes and velocities of other solitons interacting with them; (iii) they can be detected in wave profiles for a short time interval only when several soliton interactions have been taken place and the equilibrium state is fluctuated, if ever; (iv) the physical essence of visible and hidden soliton is the same.

DRIVEN SOLITONS

In [6] the force field is given in by the cubic polynomial, i.e. $F(u) = \alpha u(u - \beta_1 u)(u - \beta_2)$, and the forced KdV equation is solved numerically under harmonic initial conditions. If $\alpha < 1$, then the influence of the field is weak which suppers some solitons in the KdV soliton train (including the influence of hidden ones). However for higher values of α the force field results in stationary solutions in the form of solitary- or cnoidal waves and no soliton interactions can be detected.

In the present paper the influence of periodic driving field $F(u) = \alpha \sin \beta u$ is discussed. Compared with the cubic field the influence of the periodic one is more complex. Now due to the driven field the KdV solitons can be suppressed or amplified to three different amplitude-levels. Solitons, amplified to different levels, have different velocities and therefore they interact (Figs. 3 and 4). The elastic character of these interactions shows their solitonic behaviour. In Fig. 3 the total number of amplified solitons (per one 2π period) is five: two solitons (amplified to the first level) are propagating to the left, two second level solitons and one third level soliton two the right. Other KdV solitons (including hidden ones) are suppressed (cf. Fig. 1). In Fig. 4 the total number of solitons is twelve: one first level soliton is going to the left and a group of eleven second level solitons to the right. Here the strength of the driven field is so high, that it introduces additional nonlinearity and dispersion to the system. Therefore the total number of amplified solitons is higher then in the corresponding KdV (conservative) case.

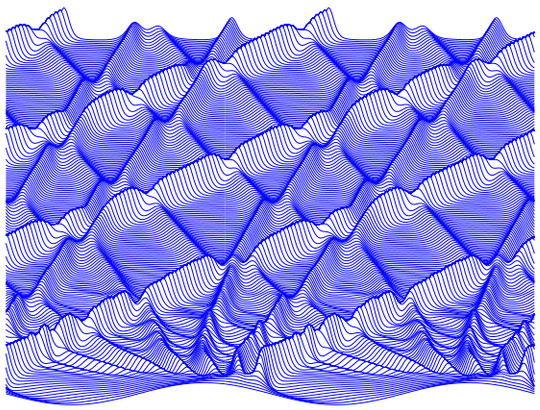


Figure 3. Emerging of driven solitons: time slice plot over two 2π space periods ($\alpha = 0.1$, $\beta = 7$, $d = 10^{-2.2}$)

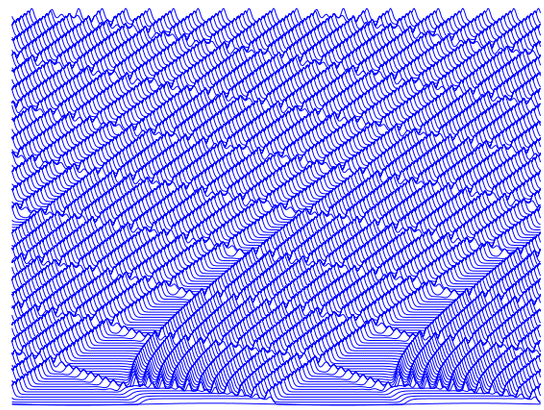


Figure 4. Emerging of driven solitons: time slice plot over two 2π space periods ($\alpha = 50$, $\beta = 1$, $d = 10^{-2.2}$)

CONCLUSIONS

In the conservative case the hidden solitons play a role in causing additional phase shifts in interaction processes, but do not play any significant role in energy sharing within the train of solitons. Their existence, however shows "possible energy pockets". In the nonconservative case those hidden solitons may be amplified under certain resonance conditions between driving field and the train of solitons. Such a phenomenon may open new possibilities for generating wave fields with designed properties. Energy conservation in such fields may be used in nondestructive testing of materials.

References

[1] Maugin, G.A.: Material Inhomogeneities in Elasticity. Chapman & Hall, London et al., 1993.

[2] Salupere, A., Engelbrecht, J., Maugin, G.A.: Solitonic structures in KdV-based higher order systems. *Wave Motion*, **34**: 51–61, 2001.

[3] Engelbrecht J. and Peipman T.: Nonlinear waves in a layer with energy influx. *Wave Motion*, **16**: 173–181, 1992.

[4] Salupere A., Maugin G.A., Engelbrecht J., Kalda J.: On the KdV soliton formation and discrete spectral analysis. *Wave Motion*, **23**: 49–66, 1996.

[5] Ilison O., Salupere A.: On formation of solitons in media with higher order dispersive effects. *Proc. Estonian Acad. Sci. Phys. Math.*, **52**: 125–134, 2003.

[6] Peterson P., Salupere A.: Solitons in a perturbed Korteweg-de Vries system. *Proc. Estonian Acad. Sci. Phys. Math.*, **46**: 102–110, 1997.

XXI ICTAM, 15–21 August 2004, Warsaw, Poland

THERMO-MECHANICAL WAVE PROPAGATION IN MATERIALS WITH INTERNAL STATE VARIABLES

Kurt Frischmuth * Witold Kosiński **
*Fachbereich Mathematik, Universität Rostock, D–18051 Rostock, Germany
kurt.frischmuth@mathematik.uni-rostock.de
**Research Center, Polish–Japanese Institute of Information Technology
ul. Koszykowa 86, 02-008 Warszawa
wkos@pjwstk.edu.pl

in memoriam Prof. Henryk Zorski

Summary Conditions imposed on the initial data by the assumption that an acceleration wave may propagate in a termo-visco-plastic material and its amplitude blow-up to infinity in finite time are discussed. Full termomechanical coupling in 3D case is considered. Constitutive model is derived from a free energy function taking into account the non-negativity of entropy production. Thermal properties are characterized by the dependence of the heat flux on the gradient of a new thermal variable called the semi–empirical temperature scale. The theory leads to a modified model of thermo-elasto-viscoplasticity with an extra thermal stress effect and wave-type heat conduction. In the case of plane waves the solution is constructed numerically even beyond the point where Lipschitz continuity is lost and a shock with finite amplitude arises. Conditions under which a pure mechanical disturbance generates thermal one and the both may lead to blow up are established. Such a situation can model the ultimate state of a viscoplastic material in the vicinity of the dynamically propagating crac tip.

We study the propagation of thermo-mechanical waves in a nonlinear material with internal state variables. The general framework of such material models was proposed by Valanis[9], Coleman and Gurtin [1]. It was further developed by Perzyna, and Kosiński [6], who were the first to study wave propagation in this context. The results of those derivations were applied to 3D thermoelasticity in [8]. Further generalization for more complex materials was done in [10]) and then partially reported in the monograph [5]. The theory of thermal waves at low temperatures was developed in co-operation with V. A. Cimmelli and K. Frischmuth [2]. For this case material functions were identified and numerical solutions obtained. In co-operation with K. Saxton analytical results on weak singularities (acceleration waves) were developed, ordinary differential equations for the amplitude of acceleration waves were discussed and the possibility of blow up shown [7]. Next, the developed thermal models were imbedded into models of deformable bodies, first thermoelastic, then thermo-visocoplastic ones, [4, 3].

The presented constitutive models were derived from a free energy function taking into account the non-negativity of entropy production. In this way a representation of material functions is facilitated even in a full 3D setting. In a recent paper, [3], the mechanical part is governed by Perzyna's *overstress* function. The thermal properties are characterized by the dependence of the heat flux on the gradient of a new thermal variable called the *semi–empirical temperature scale* as studied before in the case of rigid and elastic heat conductors.

The theory leads to a modified model of thermo-elasto-viscoplasticity with an *extra thermal stress effect* and wave–type heat conduction. This contribution can have a substantial meaning in describing thermo-mechanical coupling phenomena in viscoplastic materials, especially in the context of fracture and damage phenomena under very high strain rates [11]. Moreover, even for isotropic material extra thermal stress introduces anisotropy due to its dependence on the heat flux vector.

When introduced into the general system of balance equations for mass, momentum and energy, the material functions and kinetic equations lead to a system of quasi–linear hyperbolic equations.

For such systems acceleration waves as well as shock waves and rarefaction fans are of interest. Following our previous papers[4, 3], the coupled system of field and constitutive equations modelling 3D thermo-mechanics at finite inelastic strain is derived and analyzed in the case of solutions with weak discontinuities.

Let us notice that in 3D case we have a system of four homogeneous equations for two amplitudes: the vector–valued mechanical amplitude $\mathbf{s}$ and the scalar thermal one v. To get a nontrivial solution, the determinant of the system has to vanish. This gives us the so-called characteristic (or dispersion) relation for the normal speed U of the wave front in terms of the unit normal to the wave front $\mathbf{n}$ and values of state variables at the front. In general thermomechanical wave propagation is not symmetric like in the other models, cf.[6, 8, 10]. Amplitudes of those discontinuities satisfy ordinary differential equations of Bernoulli type, [7].
In the present paper, we discuss the conditions imposed on the initial data by the assumption that an acceleration wave may propagate and its amplitude blow-up to infinity in finite time. Full termomechanical coupling is considered; which leads to non-zero amplitudes of the both types. Furthermore, we analyze such situations numerically. In the case of plane waves this enables us to construct the solution approximately even beyond the point where Lipschitz continuity is lost and a shock with finite amplitude arises. Conditions under which a pure mechanical disturbance generates thermal one and the both may lead to blow up are established. Such a situation can model the ultimate state of a viscoplastic material in the vicinity of the dynamically propagating crac tip [11].

References

[1] B. D. Coleman, M. E. Gurtin, Thermodynamics with internal state variables, *J. Chem. Phys.* **47**, 597–613 (1967)
[2] K. Frischmuth, V. A. Cimmelli, Numerical reconstruction of heat pulse experiments, *Int. J. Engng. Sci.* **33** (2), 209–215 (1995)
[3] K. Frischmuth, W. Kosiński, Thermomechanical coupled waves in a viscoplastic medium, *Arch. Mech.* **54** (5-6), 439–457 (2003)
[4] K. Frischmuth, W. Kosiński, Thermomechanical coupled waves in a nonlinear medium, *Wave Motion*, **34** (1), 131–141 (2001)
[5] KOSIŃSKI W.: Field Singularities and Wave Analysis in Continuum Mechanics, Ellis Horwood Series: Mathematics and Its Applications, Ellis Horwood Ltd., Chichester, *Halsted Press: a Division of John Wiley & Sons*, New York Chichester Brisbane Toronto, PWN – Polish Scientific Publishers, Warsaw, 1986.
[6] W. Kosiński, P. Perzyna, Analysis of acceleration waves in materials with internal parameters, *Arch. Mech.* **24** (4), 629–643 (1972)
[7] W. Kosiński, K. Saxton, The effect on finite time breakdown due to modified Fourier laws, *Quarterly of Applied Mathematics*, **LI** (1), 55–68 (1993)
[8] Mihailescu M., Suliciu I., Finite and symmetric thermomechanical waves in materials with internal state variables, *Int. J. Solids Struct.* **12**, 559-575 (1976)
[9] K. C. Valanis, Unified theory of thermomechanical behavior of viscoplastic materials, in *Symp. Mech. Behav. Mater. Dyn. Loads, San Antonio 1967*, Springer, New York, pp. 343–364 (1968)
[10] WOŁOSZYŃSKA K.: On coupling acceleration and shock waves in a thermoviscoplastic medium, Part I. Symmetry and hyperbolicity conditions, Part II. One-dimensional waves, *Arch. Mech.* **33**, 261-272, 451-468 (1981)
[11] ZEHNDER A.T., ROSAKIS A.J.: On the temperature distribution at the vicinity of dynamically propagating cracks in 4340 steel, *J. Mech. Phys. Solids* **39** (3), 385 (1991).

SELF-CONSISTENT METHODS IN THE PROBLEM OF ELASTIC WAVE PROPAGATION THROUGH MATRIX COMPOSITE MATRIALS

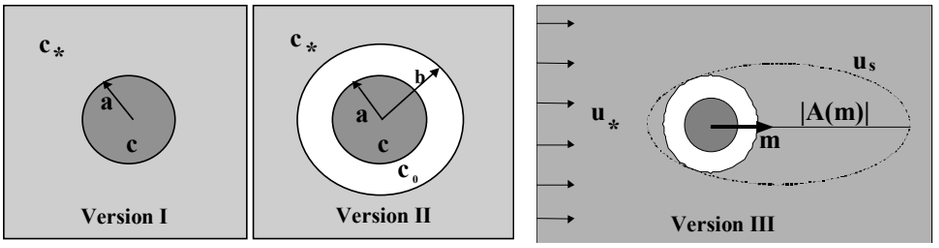
Sergey K. Kanaun*, Valery M. Levin**
*ITESM-CEM, Apdo Postal 3-6, Edo de México, 52926 México; kanaoun@itesm.mx
**Instituto Mexicano del Petróleo, Eje Central Lázaro Cárdenas 152, México; vlevine@imp.mx

Summary The mathematical structures of two main self-consistent schemes used for the solution of the homogenization problem in the mechanics of heterogeneous media are analyzed and discussed. The dispersion equations for the wave numbers of the mean wave field that correspond to every of these schemes are developed for the composite medium with spherical particles and with unidirected cylindrical fibers. These equations serve for all frequencies of the monochromatic incident field and arbitrary properties and volume concentrations of inclusions. The results of the predictions of both methods are analyzed and compared.

THE MAIN HYPOTHETHIS OF SELF-CONSISTENT METHODS

Self-consistent methods are widely used for the solution of the problem of monochromatic wave propagation through inhomogeneous media. In the case of the medium with random sets of isolated inclusions this problem cannot be solved exactly, and only approximate solutions are available. Among various approximations self-consistent methods have many important advantages. These methods are based on simple and physically clear hypotheses that reduce the problem of interactions between many inclusions in the composite to a diffraction problem for one inclusions. These hypothesis may be changed and corrected in order to improve the predictions of the methods. As a rule it is difficult to evaluate the area of application of these hypotheses, although in many cases self-consistent solutions are in a good agreement with experimental data. It is possible to point out two main self-consistent schemes: the effective field and effective medium methods. Let us consider the basic hypotheses of every of these methods.

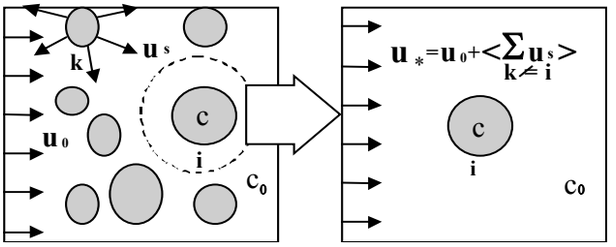
Effective medium method (EMM). The effective medium method is in fact a group of methods based in a common hypothesis that for the evaluation of the wave field inside a typical inclusion the composite material outside some vicinity of this inclusion may be changed for a homogeneous medium with effective properties of all the composite. Let as consider a composite medium that consists of a matrix phase with the tensor of elastic properties C_0 and density ρ_0 and spherical inclusions with properties C and ρ. In the simplest version of the method (version I) for the calculation of the wave field inside an arbitrary inclusion it is assumed that this inclusion is embedded into a homogeneous medium with overall properties of all the composite C*. This hypothesis (H1) reduces the problem of interaction between many inclusions in the composite to the one particle problem. The second hypothesis (H2) is the assumption that the mean wave field in the composite coincides with the wave field in the effective medium (condition of self-consistency).
One can point out a more complex version of the method when the behavior of every inclusion is supposed to be coincided with the kernel of a layered inclusion embedded into the matrix with effective properties. The properties of the layer coincides with the properties of the matrix, and the size of the layer depends on the volume concentration p of inclusions $(a/b)^3 = p$ (version II). The condition of self-consistency in this case coincides with the hypothesis H2 of version I of the method.
Another version of the method (version III) is based on hypothesis H1 of version II but condition of self-consistency is formulated as follows. The properties of the effective medium is to be chosen in order to eliminate the forward amplitude **A(m)** of the field $\mathbf{u}_s$ scattered on the layered inclusion embedded into the effective medium, **m** is the wave normal of the mean wave field.



Analyses of this three versions of the EMM in the case of electromagnetic waves propagating through particulate composites is presented in [1] and for elastic waves propagation through fiber and particulate composites in [2,3,4].

Effetive field method (EFM). Another self-consistent method is based on the hypothesis that every inclusion on the composite behaves as an isolated one in the original matrix, and the presence of the surrounding inclusions is taken into account through the local external field (effective field) that acts on this inclusions. The main hypothesis of the EFM concern the structure of this field. The simplest ones assumes that the effective field is a plane wave that is the same for

all the inclusions (quasicrystalline approximation). This hypothesis allows to write an integral equation for the effective field which kernel depends on a pair correlation function of the random field of inclusions. Thus, unlike the EMM, the predictions of the EFM depend on the spatial distribution of inclusions through the mentioned correlation function. The details of the application of this method are presented in [1] for electromagnetic waves and in [3] for elastic waves in fiber composites.



DISPERSION EQUATION FOR THE EFFECTIVE WAVE NUMBER

The hypothesis of the methods allow to develop dispersion equation for the effective wave vector **k*** of the mean wave field in the composite medium. This equation may be written in the following canonical form

$$\det[k_i^* C_{ijkl}^*(k^*) k_l^* - \rho_*(k^*)\omega^2 \delta_{jk}] = 0.$$

For the EMM the effective dynamic elastic moduli tensor C* and effective dynamic density ρ^* have the following structure

$$C^*(k^*) = C_0 + p(C - C_0) H_C(k^*), \quad \rho_* = \rho_0 + p(\rho - \rho_1) H_\rho(k^*).$$

Here functions H_C and H_ρ are known from the solution of the one particle problem. For the EFM the functions H_C and H_ρ have more complex structure and depend on the following integrals

$$\int G(x)\Phi(x) e^{ik_* x} dx, \quad \int \nabla G(x)\Phi(x) e^{ik_* x} dx, \quad \int \nabla\nabla G(x)\Phi(x) e^{ik_* x} dx.$$

Here G(x) is the Green function of the homogeneous medium with the properties of the matrix, $\Phi(x)$ is a specific two point correlation function of the random field of inclusions.

LONG WAVE AND SHORT WAVE ASYMPTOTIC SOLUTIONS OF THE DISPERSION EQUATIONS

Asymptotic solutions of the dispersion equations of the EMM and EFM in the region of long (k*a<<1) and short (k*a>>1) may be obtained in analytical forms. In the long wave limit the dispersion equations give equations for the effective elastic properties of composite materials and the attenuation factors of the Rayleigh wave scattering (see[1-4]). In the short wave limit the methods predict that the phase velocity of the mean wave field coincides with the wave velocity in the matrix, and the attenuation factor γ does not depends on the properties of the inclusions and the matrix and γa=3p/4 for the EMM. For the EFM γa=f(p), where function f(p) depends on the pair correlation function Φ(x) and coincides with 3p/4 only for small volume concentrations of inclusions. The discussion of these properties of short wave asymptotics of the solutions of the dispersion equations see in[1-4].

CONCLUSION

The dispersion equations for the effective wave vector of the EMM and EFM are obtained and analyzed. Long and short wave solutions of these equations obtained in analytical forms. Numerical solutions of these equations are constructed in the wide region of frequencies of the incident field that covers the long middle and short regions. The main discrepancies and the sources of possible errors in the predictions of the methods are indicated, and the ways of corrections of these errors are discussed. It is shown that the EFM has some advantages in comparison with the EMM. The EFM allows to describe the influence of spatial distribution of inclusion on the mean wave field in composite, e.g., to evaluate the positions of photonic gaps in the frequency region for periodic composites. The latter result is impossible to obtain in the framework of the EMM.

References

[1] S.K. Kanaun, Self-consistent methods in the problem of wave propagation through heterogeneous media, In: K. Markov and L. Preziosi (Eds.), Heterogeneous Media. Micromechanics Modeling, Methods and Simulations, Birkhauser, Boston, Basel, Berlin, 241-319, 2000.

[2] S.K. Kanaun and V.M. Levin, Effective medium method in the problem of axial elastic shear wave propagation through fiber composites, Int. J. Solids and Structure, **40**, 4859-4878, 2003.

[3] S.K. Kanaun and V.M. Levin, Self-consistent methods in the problem of elastic shear wave propagation through fiber composites". Archive of Applied Mechanics, **73**, 105-130, 2003.

[4] S.K. Kanaun, V.M. Levin, F.J. Sabina, Propagation of elastic waves in composites with random set of spherical inclusions (effective medium

WAVES OF DEFORMATION PROPAGATION IN NONLINEAR VISCOUSLY ELASTIC POROUS MATERIAL

Vladimir I. Erofeyev, Anton G. Pegushin

Wave Dynamics dept., IMASH RAN, Nizhny Novgorod, Russia

Summary A mathematical model of an isotropic viscously elastic porous medium is studied in this paper. Cavities are spherical and are quasi-equally spaced in the medium. Distance between cavities is a lot larger than the average radius of cavities and in turn is a lot smaller than the length of the wave that propagates in the medium. Dependencies of velocity and damping of the wave on the parameters of porosity of the material have been established and the analysis carried out. The phenomenon of non-linear stationary wave of deformation propagation has been studied for the material also and the dependencies of it's parameters on porosity have been established.

PRELIMINARY ASSUMPTIONS

A mathematical model of dynamics of porous medium has been proposed in [1]. The following assumptions were made. Studied medium is firm isotropic and viscously elastic; pores are spherical and equally spaced. Propagating wave has finite amplitude, which means that geometrical, physical and porous nonlinearities are taken into account. Distance between cavities L is a lot larger than radius of a cavity R_0 $(L >> R_0)$ and in turn is a lot smaller than the length of a wave Λ $(L << \Lambda)$, so there can be no interaction between the cavities. We consider, that the propagating wave is quasi-longitudinal, so we can state that pressure on a cavity is caused by longitudinal stress $\sigma_{33} = (\lambda + 2\mu)\dfrac{\partial u_3}{\partial x_3} - (\lambda + 2\mu)z$. In this expression $z = NV$, where N is a number of cavities in the volume, V is a volume of a cavity, besides that $V = V_0 + V'$, where V_0 is a starting volume of a cavity, V' is a volume of a cavity indignant by a wave, λ and μ are Lame coefficients, considering $\mu < \lambda$. Pressure in cavities is neglected.

DISPERSIVE PROPERTIES

Longitudinal wave propagation in porous medium lengthways the x_3 axis can be described using the following combined nonlinear equations (since one-dimensional problem is studied in this paper, the x_3 coordinate can be denoted by x, and longitudinal constituent of the displacement vector u_3 is denoted by u):

$$\begin{cases} \rho_0 \dfrac{\partial^2 u}{\partial t^2} = (\lambda + 2\mu)\dfrac{\partial^2 u}{\partial x^2} - N(\lambda + 2\mu)\dfrac{\partial v}{\partial x} + b\dfrac{\partial^3 u}{\partial t\,\partial x^2} + \dfrac{P}{2}\dfrac{\partial}{\partial x}\left(\dfrac{\partial u}{\partial x}\right)^2 \\ \ddot{v} + \omega_0^2 v - \dfrac{R_0}{c_l}\dddot{v} - Gv^2 - \beta_1\left(2v\ddot{v} + \dot{v}^2\right) = (\lambda + 2\mu)\dfrac{4\pi R_0}{\rho_0}\left(\dfrac{\partial u}{\partial x} - Nv\right) \end{cases} \tag{1}$$

The first equation describes propagation of a plane longitudinal wave in medium with pores taking into account that each pore volume is changing. The second one describes oscillatory process of cavity volume changing caused by the material deformation.

In these equations ρ_0 is a starting density of the material, $\omega_0^2 = 4\mu / \rho_0 R_0^2$ is a square of resonant frequency of cavity volume oscillations and $c_l^2 = (\lambda + 2\mu)/\rho_0$ is a square of longitudinal velocity. The following are some additional notations:

$G = 11\omega_0^2 / 16\pi R_0^3$, $\beta_1 = 1/8\pi R_0^3$ and $P = (4\mu + 3\lambda + 2A + 6B + 2C)$, where P is a coefficient, caused by geometrical and physical nonlinearities, A, B, C are Landau constants of third order.

From these joint equations (1) it can be seen, that the consequences of the existence of cavities are the dispersion of a wave (frequency-dependent wave propagation velocity) and an additional nonlinear effect (so-called cavitary nonlinearity). These factors manifest in different regimes.

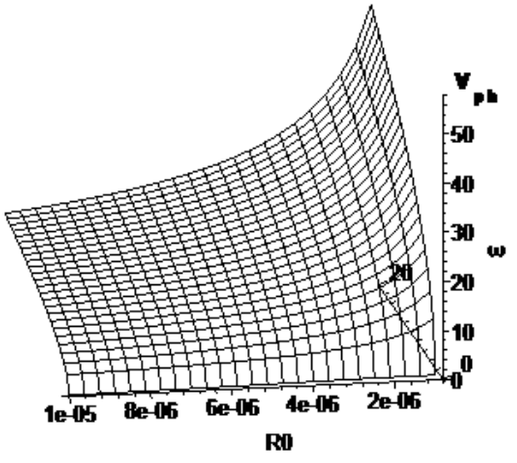


Fig. 1. Phase velocity dependence on porosity

Expressions for phase velocity and coefficient of damping for the propagating wave were obtained and are given graphically on figures 1 and 2 respectively.
During the analysis we came to the conclusion, that taking both viscosity of the material and dissipation of the wave due to porosity into account causes an additional dispersive component to appear. Also analysis was carried out separately for the case of viscosity present with no dissipation from the cavities and vice versa to compare their contributions.

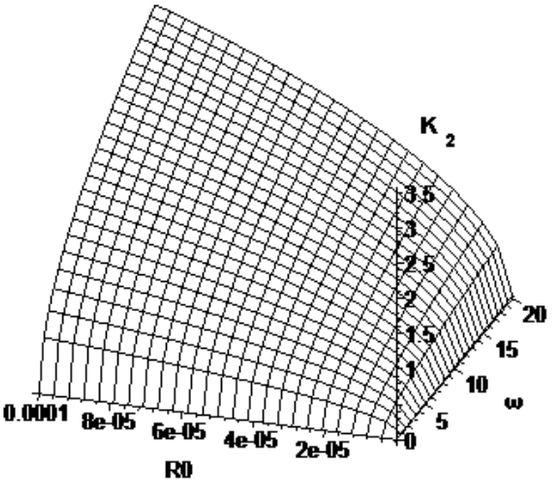


Fig. 2. Coefficient of damping dependence on porosity

SOLITON OF DEFORMATION

From (1) it follows that the propagating wave, in terms of this model, is influenced by both dispersion and nonlinearity. Non-linearity causes generation of additional harmonics to which the energy is being swapped, which mainly causes drops in the profile of the wave, while dispersion causes smoothing of the drops because of the difference in wave velocities. The combined effect of these two factors can be a reason for forming nonlinear stationary waves. These are the waves that propagate with constant velocity without changing its form.
We seek for a solution of (1) in the form of stationary wave of deformation $W(\xi = x - Vt) = U$, propagation of which is described by the following equation $\frac{\partial^2 W}{\partial \xi^2} + aW + bW^2 = 0$, where V is the velocity of the stationary wave and ξ is a new coordinate.
Physically realizable are only the cases when the wave form does not have any constant constituent. In this particular case it is possible only if wave velocity changes in the ranges $\sqrt{\frac{\omega_0^2}{4\pi R_0 c_l^2 N + \omega_0^2}} < V < 1$, which is that $a < 0, b > 0$. Expressions for amplitude of the soliton and width of the soliton were obtained and analyzed. Figures 3 and 4 respectively represent amplitude and width dependence on the porosity.

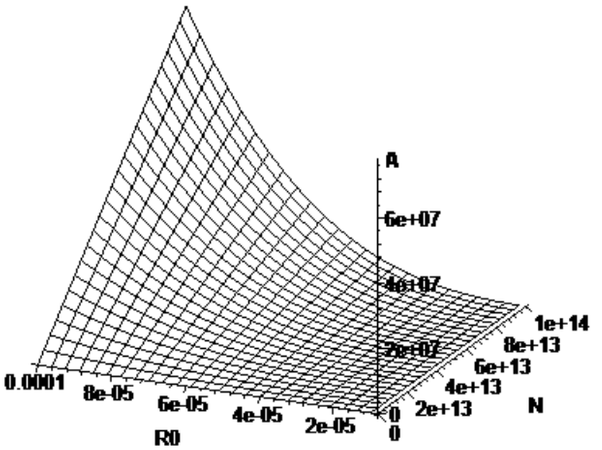


Fig. 3. Soliton amplitude dependence on porosity

CONCLUSIONS

Dependencies of velocity of the wave on the parameters of porosity of viscously elastic material have been established and the analysis carried out.
The phenomenon of non-linear stationary wave of deformation propagation has been studied for the material also and the dependencies of basic parameters of the soliton on porosity have been established.

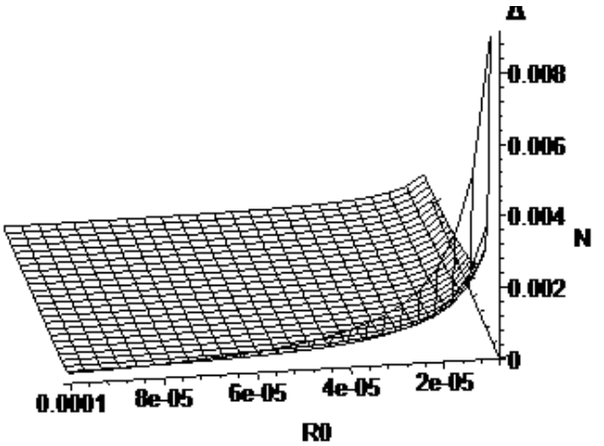


Fig. 4. Soliton width dependence on porosity

References

[1] Bagdoev, A. G. and Shekhoyan, A. V., *Nonlinear waves in the solid viscous medium with pores*, Acoust. Physics, 2 (1999) 149-156.

XXI ICTAM, 15–21 August 2004, Warsaw, Poland

ELASTOPLASTICITY OF GRAVEL PROTECTING ROCKFALL-ENDANGERED STEEL PIPELINES

Bernhard Pichler*, Christian Hellmich*, and Herbert A. Mang*
*Institute for Strength of Materials, Vienna University of Technology, Karlsplatz 13, A-1040 Vienna, Austria

Summary This contribution deals with the development of a numerical model providing reliable estimates of the loading of a gravel-buried steel pipe subjected to rockfall. The reliability test is based on two physically and statistically independent sets of experiments. The first set is related to elastoplastic material modeling and the second set to structural model verification. Since model verification can be accomplished successfully, the developed model is well suited to provide prognoses of the loading of a gravel-buried steel pipe for rockfall scenarios that were not investigated experimentally.

INTRODUCTION

The rapid climate change in recent years leads to thawing of former permafrost regions in Alpine regions. A consequence of this evolution is the increased rockfall activity. This motivates a closer study of protection systems for transalpine infrastructure such as roads, railways, and pipelines.

Herein a gravel-buried steel pipe is considered. If a downfalling rock boulder impacts onto the overburden of the pipe, the kinetic energy of the rock boulder is transformed into other types of energy. Most of the impact energy is transformed such that inelastic deformations of the overburden are produced, i. e., an impact crater is formed. Other parts of the impact energy are transmitted through the gravel via elastoplastic waves to the buried pipe, which represents a rather stiff component of the statically overdetermined load-carrying system. Accordingly, the gravel acts as an energy-absorbing and load-distributing system.

This contribution deals with the development of an analysis tool that permits reliable predictions of the loading of a gravel-buried steel pipeline subjected to rockfall. The reliability test is based on two physically and statistically independent sets of experiments. Set ① is related to elastoplastic material modeling concerning the mechanical behavior of gravel and set ② to structural model verifi cation.

ELASTOPLASTIC BEHAVIOR OF GRAVEL

Experimental set ① follows from the evaluation of a testing series for the elasticity of gravel as well as from the wealth of data on (triaxial) gravel strength published in the open literature. This data set is used for the identifi cation of material parameters for gravel, i. e., of physical quantities attached to a "representative volume element" with a characteristic length scale of one to several decimeters. This identifi cation is possible because the related experiments are characterized by homogeneous conditions, i. e., by the absence of spatial gradients of material parameters and loading conditions in the aforementioned length scales. Thus, the identifi ed parameters are independent of structure-specifi c boundary conditions: they are valid for virtually all structures made of the investigated types of gravel.

Modeling of the material behavior of gravel

The elastoplastic Cap Model [1] suitably represents the rather complex material behavior of gravel, whereby the elastic domain follows the isotropic generalized Hooke's law. In the principal stress space, the elastic domain is bounded by three surfaces: (i) a tension cut-off, accounting for tensile failure, (ii) a Drucker-Prager surface, defi ning shear failure under pronounced deviatoric stress states, and (iii) an ellipsoidal cap, representing the hardening of the material associated with compaction. The direction of plastic flow is given by an associated flow rule. Consequently, loading in the cap mode leads to compaction whereas loading in the failure-surface mode or in the tension cut-off mode results in plastic volume dilatation. The material model involves nine material parameters: two referring to gravel elasticity, one to the failure of gravel under tensile loading, two corresponding to shear failure of gravel, two governing the hardening law for description of compaction of gravel, and two referring to the initial size and shape of the cap.

Identification of gravel elasticity

For identifi cation of material parameters referring to gravel elasticity, dynamic tests were performed. Signals were produced by hitting the bucket of a dredger vertically onto the surface of wide-range-grained gravel. This led to propagation of both longitudinal and shear waves through the gravel. Their velocities were determined by means of accelerometer measurements. In the framework of the theory of wave propagation in elastoplastic solids, wave velocities obtained in repeated experiments allow for the calculation of a set of values of the two independent coeffi cients C_{1111} and C_{1212} of the isotropic fourth-order elasticity tensor $\mathbf{C}$. Assuming a scatter of the elastic properties of gravel according to a lognormal distribution, a statistical analysis yields estimates for the most probable elasticity parameters and respective 95%-confi dence bounds.

Identification of the inelastic behavior of gravel

Identification of the parameters referring to shear failure of gravel is based on triaxial compression tests carried out on cylindrical specimens [3]. Remarkably, one set of material parameters characterizes shear failure of gravels of different grain shape, size, and distribution, mineral hardness, void ratio, and hydrostatic precompression satisfactorily (r^2 = 0.995).

Identification of material parameters describing compaction of gravel is again based on the tests reported in [3]. Apparently, grain shape, size, and distribution, mineral hardness, void ratio, and hydrostatic precompression do have a non-negligible influence on the compaction of gravel. However, rather small confinement pressures are of interest herein. This allows for unique identification of material parameters characterizing compaction of gravel.

The initial size and the shape of the cap are determined from constant volume tests, see [2]. The material parameter referring to tensile failure of gravel is set equal to a very small positive value in the numerical analysis.

Identification of the indentation resistance of gravel and loading assumptions for rockfall onto gravel

To model a gravel-buried pipeline subjected to rockfall, estimates of the penetration depth and the maximum impact-force of rock boulders are required as functions of the rock boulder mass, the height of fall, and the strength-like indentation resistance of the gravel. Therefore, impact tests were performed comprising heights of fall from 2 m to 19 m, and rock boulder masses from 4380 kg to 18260 kg.

The test results were evaluated by means of dimensionless formulae for the penetration depth of non-deformable projectiles onto concrete and soil targets. This analysis together with statistical methods allow for the determination of the most probable value, the 5 %-quantile, and the 95 %-quantile of the indentation resistance of gravel.

Finally, a model of the impact kinematics was deduced from experimental acceleration measurements. It allows for the estimation of the maximum impact-force arising from rockfall onto gravel. Given the wide range of dimensionless parameters for which the aforementioned dimensionless formulae were validated, extrapolations to rockfall events with heights of fall up to 100 m become possible.

DEVELOPMENT AND VERIFICATION OF A STRUCTURAL MODEL

The identified material parameters are used to simulate the structural behavior of a gravel-buried steel pipe subjected to rockfall. Thereby, the almost entirely inelastic indentation process of the rock boulder is not modeled in detail. Instead, the impact loads are considered in a simplified manner: the maximum impact force is applied to the surface of the Finite Element (FE) model, the overburden of which is reduced – with respect to the real overburden – by the indentation depth of the rock boulder at which the maximum impact force occurs. A quasi-static analysis is performed.

For verification of these simulations, an experiment on a real-scale gravel-buried steel pipe was designed, performed, and evaluated: A pipeline with an outer diameter d = 1016 mm and a wall thickness s = 11.13 mm, resting on a 40 cm thick layer of sand, was buried by wide-range-grained gravel in the middle of a trench of 3 m width such that the height of overburden was equal to 2 m. At selected positions of the pipe, the loading of the pipe steel was measured during the impact of a rock boulder with a mass of 18260 kg, dropped from a height of 18.85 m, by means of strain-gauges. The obtained data are collected into experimental set ②.

Simulation results obtained from the structural FE model based on the material parameters identified from experimental set ① are compared to the results of measurements from experimental set ②. In this way, experimental set ② allows for validation (i) whether the degree of sophistication of the material description based on the experimental set ① is sufficient for the assessment of the loading of a gravel-buried steel pipe subjected to rockfall, and (ii) whether the developed FE model is adequate. Since the simulation results compare well to independent experimental measurements, the developed model is well suited to provide prognoses of the loading of a gravel-buried steel pipe for rockfall scenarios that were not investigated experimentally.

It is shown that gravel may effectively serve as an energy-absorbing and load-distributing protection system for steel pipes subjected to moderate rockfall scenarios. However, it is not effective for rockfall events characterized by heavy rock boulders (such as investigated herein, e. g, m = 18260 kg) and heights of fall up to 100 m or even more. In order to provide a highly effective rockfall-protection system for a pipeline, the two tasks “damping of the impact” and “load distribution and carriage” must be performed by two separate structural elements. Such a system could consist, e. g., of (i) gravel acting as an energy-absorbing and, hence, impact-damping system, and (ii) additionally buried construction elements, made, e. g., of reinforced concrete acting as a structural component allowing for the distribution and for carrying of the impact load.

References

[1] F.L. DiMaggio and I.S. Sandler. Material models for granular soils. *Journal of Engineering Mechanics (ASCE)*, **97**:935–950, 1971.
[2] Ch. Kropik and H.A. Mang. Computational mechanics of the excavation of tunnels. *Engineering Computations*, **13**:49–69, 1996.
[3] D. Penumadu and R. Zhao. Triaxial compression behavior of sand and gravel using artificial neural networks (ANN). *Computers & Geotechnics*, **24**:207–230, 1999.

FLAW IDENTIFICATION BY ANGLE BEAM ELECTROMAGNETIC ACOUSTIC TRANSDUCERS

Shumpei Hanada, Toshihiko Sugiura
Department of Mechanical Engineering, Faculty of Science and Technology, Keio University, Yokohama, 223-8522, Japan

Summary This research deals with quantitative nondestructive evaluation by angle beam electromagnetic acoustic transducers (EMATs) through inverse analysis based on elastodynamics and electromagnetics. FEM-BEM simulations, agreeing well with experimental results, show us some relation between the receiver signal's peaks and the size of a flaw. With initial guess based on this relation obtained numerically, flaw size was successfully identified from measured receiver signals through parameter optimization.

INTRODUCTION

Electromagnetic acoustic transducers (EMATs) can transmit and detect ultrasonic waves in a conductive specimen without any contact. This process can be given theoretical modeling and formulation based on elastodynamics and electromagnetics [1]. It suggests some possibility of quantitative nondestructive evaluation using EMATs. This research deals with angle beam EMATs which can transmit ultrasonic waves in oblique directions as plane waves. FEM-BEM simulations of this inspection system show us some relation between the receiver signal's peaks and propagation of ultrasonic waves, and also explain effects of a flaw. Numerical results of receiver signals were compared with experimental ones for verifying our mathematical modeling of the inspection process. Flaw identification is formulated as a problem of parameter optimization. The initial guesses of the parameter were evaluated from the computed relationship between the flaw parameter and the peak's area of the receiver signal. Identification of flaw size was tried from receiver signals obtained in experiments.

MEASURED AND COMPUTED SIGNALS OF RECEIVER EMAT

Figure 1 shows the system in this research: both the transmitter and receiver EMATs are arranged above the same surface of an aluminum specimen. The EMATs and the specimen are supposed to be long enough in the z direction for electromagnetics and elastodynamics to be considered as two-dimensional. Coil pitch P of the EMATs is 2.47mm and the oblique angle θ = 40 deg. A cylindrical cavity of diameter d is located as an artificial flaw inside the specimen. Experiments were carried out for several specimens, each of which has a flaw of different diameter *d*, by supplying 3-pulse 4 App sinusoidal current of frequency 1MHz to the transmitter coil. Experimental results of receiver coil voltage are shown in Fig.2.

Two-dimensional numerical analysis has also been carried out. For the region of the specimen, Maxwell's equations and equations of motion of an elastic body are converted into discrete form by the Galerkin finite element method. The boundary element method is used for the electromagnetic field in the air region. The Newmark β method is adopted for time history analysis. Computed receiver signals, also shown in Fig.2 agree well with the above experimental ones, which validates our numerical analysis.

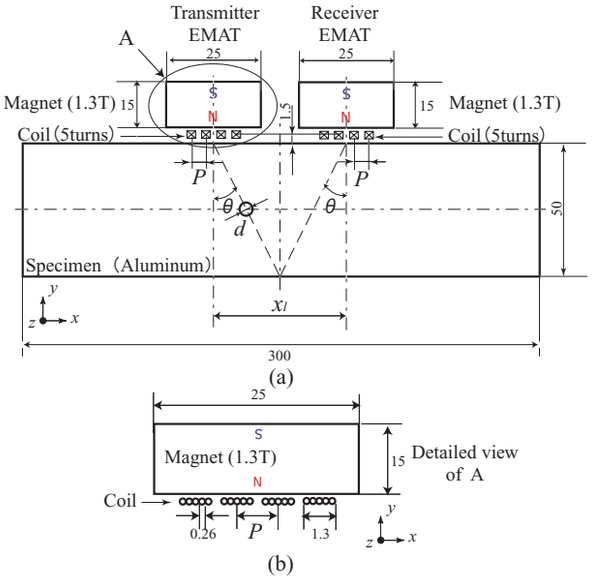


Figure 1. System of angle beam EMATs

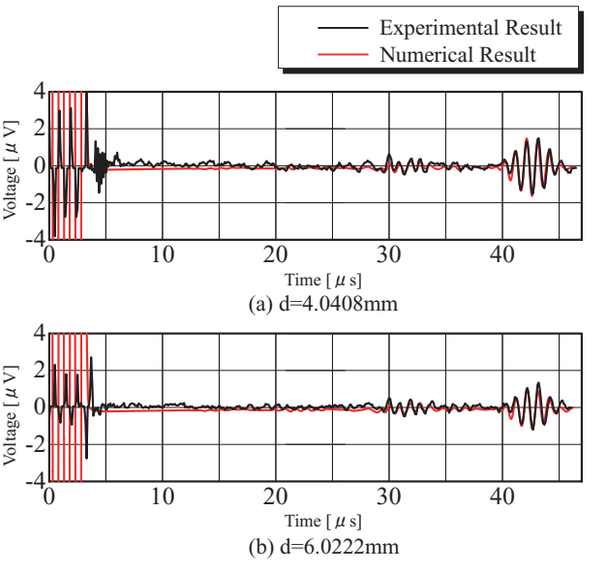


Figure 2. Time histories of receiver coil voltage

EFFECTS OF A FLAW ON RECEIVER SIGNALS

The size of a flaw gives distinct change to the value of the peak appearing in the receiver signals at $t = 40\mu s$, as shown in Fig.2. This signal peak, hereafter denoted by [SS], corresponds with the arrival of the S wave reflected at the opposite surface without mode conversion. Effects of the flaw on the propagation of this wave can be understood in more detail from the numerical results. Figure 3 shows the gray scales of the divergence and rotation of computed displacement of the specimen, which thus visualize the propagation of the P and S waves, respectively. As shown in Fig.3, the ultrasonic waves propagating in the oblique direction are in part reflected at the surface of the flaw and cannot reach the receiver. Therefore the peaks[SS] are lower for a bigger flaw.

FLAW IDENTIFICATION BY INVERSE ANALYSIS

Flaw identification is formulated as a problem of parameter optimization. Here the diameter d of a cylindrical cavity as a flaw is an unknown parameter to be identified from a measured receiver signal v_m. We define a cost function $R(d)$ as

$$R(d) = \int_{T_1}^{T_2} (v_m(t) - v_c(d;t))^2 dt,$$

where $v_c(d;t)$ denotes a computed receiver signal for a flaw of diameter d. The optimized parameter d, minimizing this cost function R, can be found by iterative computation with Brent's method. To avoid being trapped in a local optimum, the initial guess d_i was successfully evaluated, as shown in Fig.4, by using the numerically obtained relationship between the area of peak [SS] and the diameter d mentioned in the above section. Figure 5 shows examples of good optimization, verifying the method of flaw identification presented here.

CONCLUSIONS

Numerically predicted receiver signals of angle beam EMATs agree well with the experimental ones, which validates our analysis. The peak [SS] of receiver signals is well influenced by the size of the flaw. By using this relation, initial guesses were successfully evaluated. Flaw size was identified well through optimization from measured receiver signals, which verified the method of flaw identification presented here.

References

[1] R.Ludwig, Z.You and R.Palanisamy: Numerical Simulations of an Electromagnetic Acoustic Transducer-Receiver System for NDT Applications. *IEEE Trans. Magn.* **29-3**:2081–2089, 1993.

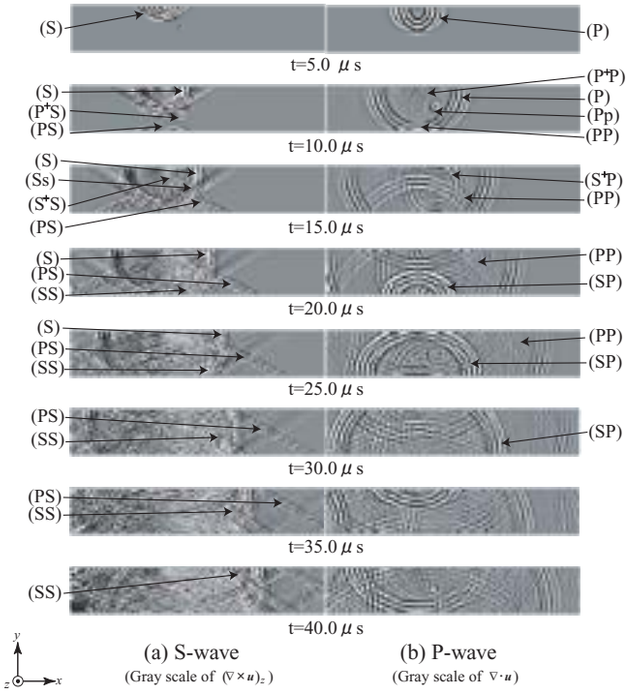


Figure 3. Propagation of *P* and *S* Waves

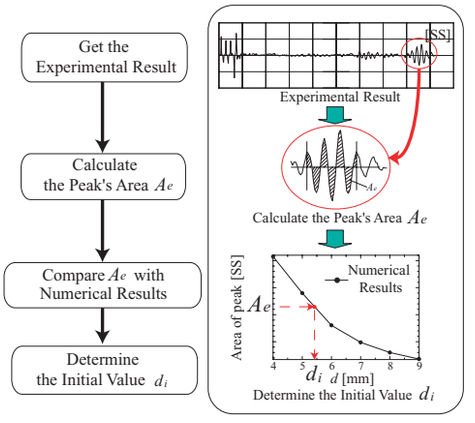


Figure 4. Method of initial guess for flaw size

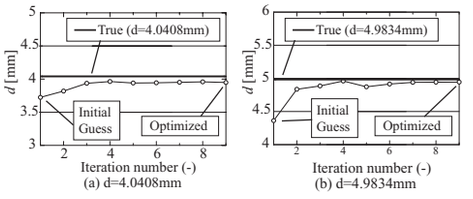


Figure 5. Flaw identification by optimization

XXI ICTAM, 15–21 August 2004, Warsaw, Poland

IMPACT FRACTURE OF ROCK MATERIALS DUE TO PERCUSSIVE DRILLING ACTION

Anton M. Krivtsov*, Ekaterina E. Pavlovskaia**, Marian Wiercigroch**
*St. Petersburg State Polytechnical University, Dep. of Theoretical Mechanics, 195251 St. Petersburg, Russia
**Centre for Applied Dynamics Research, Aberdeen University, AB24 3UE Aberdeen, UK

Summary A theoretical model describing impact fracture of rocks caused by percussive drilling is presented. The process is modeled using particle dynamics (molecular dynamics) approach where a special interaction law for brittle materials is formulated. Relations between the microscopic quantities of the model and the macroscopic mechanical properties have been established. The material fracture and cracks formation under the periodic set of inserts are investigated.

INTRODUCTION

Percussive drilling is proved to be superior when compared to a convention rotary drilling especially in the case of hard and brittle rock materials [1]. The impacts generated by the percussive drilling action produce fracture in the brittle material, which allows increasing drastically the penetration rate. Rotation of the tool for the percussive drilling is mostly responsible for the debris removal, while the main progression is caused by the impact fracture. That is why to predict and optimize the behavior of the drilling tool it is essential to study thoroughly the impact interaction between the tool and the processed material. In the previous work the low-dimensional models where developed, allowing to describe the specifics of the percussive drilling, in particular the optimum ratio between the static and dynamic components of the load were predicted [2, 3]. However, these models describing the material behavior are crude, limiting its properties to only several effective parameters. To understand better the fracture processes accompanying the percussive drilling more detailed study of the fracture scenario is needed. This investigation can be based on the particle dynamics model, which gives advantages comparing to the continuum approaches when the assumption of the material continuity fails [4, 5].

MODELLING THE IMPACT FRACTURE

Let us assume that the drillbit surface is covered by a set of inserts, which interact with the material surface. The interaction of the insert with the rock half-space is depicted in Fig.1 a, where the model state just after the impact is shown. The upper rectangle simulates the insert, the lower one — the rock material. In the horizontal direction periodic boundary conditions are used to mimic the periodic set of inserts. Initially the rock has zero velocity, the tool has constant velocity directed towards the rock. For the parameters estimation this problem can be reduced to 1D continuum model, which shows that the main dimensionless parameters to take into account are

$$\tilde{v} \stackrel{\text{def}}{=} \frac{v_1}{v_2}\,, \qquad \tilde{\rho} \stackrel{\text{def}}{=} \frac{\rho_1}{\rho_2}\,; \qquad v_2^2 \stackrel{\text{def}}{=} \frac{C_{1111}}{\rho_2} = \frac{1-\nu}{(1+\nu)(1-2\nu)}\,\frac{E}{\rho_2}\,; \tag{1}$$

where v_1 is the tool velocity, v_2 is the velocity of longitudinal waves in the rock material, ρ_1 is the tool density, ρ_2 is the material density; C_{1111} is the longitudinal stiffness, E is the Young modulus, and ν is the Poisson ratio of the rock material. Then the shock wave propagation can be described by the equation (below H is the Heaviside step function)

$$\varepsilon(\tau,\tilde{x}) = -\tilde{v}e^{-(\tau-\tilde{x})/\tilde{\rho}}H(\tau-\tilde{x})\,; \qquad \tau \stackrel{\text{def}}{=} \frac{t}{w/v_2}\,, \qquad \tilde{x} \stackrel{\text{def}}{=} \frac{x}{w}\,; \tag{2}$$

where ε is the longitudinal deformation, x is the longitudinal coordinate, w is the average distance between the inserts.

Particle dynamics technique

The impact dynamics is simulated on the base of conventual molecular-dynamics technique [6], where the both materials (the insert and the rock) are formed by close-packed crystal lattices of particles. The motion of the particles is obtained through integration of the Newtonian equations of motions with the prescribed interaction forces:

$$F_1(r) = \left[\begin{array}{ll} F(r)\,, & 0<r\le b\,; \\ k(r)\,F(r)\,, & b<r\le a_{\text{cut}}\,; \end{array}\right. \qquad F(r) = \frac{12D}{a}\left[\left(\frac{a}{r}\right)^{13} - \left(\frac{a}{r}\right)^{7}\right], \qquad b \stackrel{\text{def}}{=} \sqrt[6]{\frac{13}{7}}\,a \approx 1.11a\,; \tag{3}$$

where $F(r)$ is the force corresponding to the Lennard-Jones potential with the equilibrium distance a and bond energy D; quantity b is the brake distance for the Lennard-Jones interaction, $k(r)$ is the shape function

$$k_1(r) \stackrel{\text{def}}{=} (1+\alpha)\left(1-\left(1+\sqrt{\frac{\alpha}{1+\alpha}}\right)\left(\frac{r^2-b^2}{a_{\text{cut}}^2-b^2}\right)^2\right)^2 - \alpha\,, \tag{4}$$

where α is a positive parameter, defining brittleness of the material, $a_{\text{cut}} > b$ is the cut-off distance for the interaction. Increase of α results in the repulsion appearing in the vicinity of the cut-off distance. This produces potential barrier for joining two particles, which where separated due to the impact fracture.

The stiffness of the interparticle force is given by the expression $C \stackrel{\text{def}}{=} -F'(a) = 72D/a^2$. If we consider triangular lattice in 2D, then the elastic moduli of the corresponding material are $E_2 = 2C/\sqrt{3}$, $\nu_2 = 1/3$, where E_2 stands for the 2D Young modulus, ν_2 for the Poisson ratio. The elastic moduli E and ν for the corresponding 3D material (using the 2D strain assumption), can be expressed as

$$E = \frac{15\sqrt{2}}{16}\frac{C}{a} = \frac{135\sqrt{2}}{2}\frac{D}{a^3}, \qquad \nu = \frac{1}{4}; \qquad a = \sqrt{\frac{2S}{\sqrt{3}NS_0}}; \tag{5}$$

where S is considered cross-section area of the entire specimen, S_0 is the area occupied by a single particle, N is number of particles in the model. Formulae (5) allow obtaining potential parameters D and a from the macroscopic parameters of the system. The obtained value for the Poisson ratio is about the upper limit of the Poisson value for the dense rocks. In the frames of the current model the Poisson ratio can not be adjusted, but this is unlikely to produce big errors in computations, considering that the experimental data for the rocks is very irregular. In the current simulation the computational parameters are taken to obtain the computational rock material properties close to crystalline quartz, the indenter material is chosen to be 5 times harder then the rock material.

Simulation results

The sequential stages of the impact process are shown in Fig.1a–d, where propagation of the shock wave can be observed ($T \stackrel{\text{def}}{=} w/v_2$). Colors show distribution of the stress intensity $\sigma \stackrel{\text{def}}{=} \sqrt{\frac{1}{2}(\sigma_1 - \sigma_2)^2 + 2\tau_{12}^2}$, where σ_1 and σ_2 are normal stresses in the horizontal and vertical directions, τ_{12} is the corresponding shear stress. The color scale from blue to red corresponds to the stress scale from zero to the maximum value obtained in the experiment. Fig.1e shows the final stage of the impact fracture formation in the vicinity of the inserts. The simulation takes advantage of the model periodicity and this picture shows three periods in the horizontal direction. Cracks formed due to the impacts are well visible.

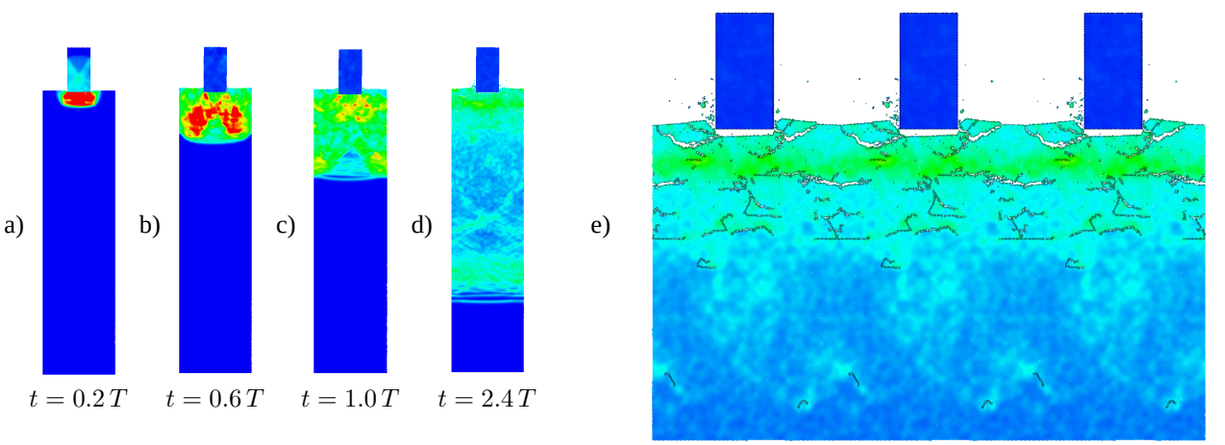


Fig.1. Simulation results: a)–d) shock wave propagation (10^4 particles); e) impact fracture in the specimen ($2 \cdot 10^5$ particles).

CONCLUSIONS

The study shows that the impact fracture locates mainly in the areas under inserts and between them, which is due to the shock wave interactions. A comparison between 2D particle dynamics and 1D continuum models shows a good agreement at the distances from the impact area, which are greater than the average distance between inserts. The cracks distribution and their orientation differ significantly from the quasistatic computations [7] and correlate well with the known experimental impact tests [8], and this confirms the dynamic nature of the considered process.

This work is supported by EPSRC Grant GR/R85556/01.

References

[1] Wiercigroch M., Krivtsov A. M., Wojewoda J. Dynamics of Ultrasonic Drilling of Hard materials. In Wiercigroch M. and de Kraker A. eds. *Applied Non-linear Dynamics and Chaos of Mechanical Systems with Discontinuities.* World Scientific. 403–444. 2000.
[2] Krivtsov A. M., Wiercigroch M. Penetration Rate Prediction for Percussive Drilling. *Chaos, Solitons & Fractals.* **11**(15): 2479–2485. 2000.
[3] E. Pavlovskaia, M. Wiercigroch. Periodic solution finder for an impact oscillator with a drift. *Journal of Sound and Vibration* **267**: 893-911. 2003.
[4] Krivtsov A. M. Relation between Spall Strength and Mesoparticle Velocity Dispersion. *International Journal of Impact Engineering.* **23**(1): 466–476. 1999.
[5] Krivtsov A. M. Molecular dynamics simulation of impact fracture in polycrystalline materials. *Meccanica.* 2003, **38**(1): 61-70. 2003.
[6] Hockney R. W. and Eastwood J. W. *Computer simulation using particles*. IOP Publishing. 1988.
[7] Liu H.Y., Kou S.Q., Lindqvist P.A., Tang C.A. Numerical simulation of the rock fragmentation process induced by indenters. *Int. J. Rock Mech. Min. Sci.* **39**:491–505. 2002.
[8] Mishnaevsky L. Jr. Rock fragmentation and optimization of drilling tools. In: *Fracture of Rock.* Chapter 6. Ed. M.H. Aliabadi. Computational Mechanics Publications. 167–203. 1998.

DISPERSION AND STABILITY ANALYSIS OF WAVES IN PRE-STRESSED IMPERFECTLY BONDED LAYERED COMPOSITES

Anil C. Wijeyewickrema, Sasikorn Leungvichcharoen
Department of Civil Engineering, Tokyo Institute of Technology, O-okayama, Meguro-ku, Tokyo 152-8552, Japan

Summary The dispersive behaviour and stability issues of time-harmonic waves propagating in an imperfectly bonded pre-stressed symmetric layered composite, which consists of incompressible isotropic elastic materials is considered. The shear spring type resistance model is employed to simulate the imperfect interface. Dispersion relations for both flexural and extensional waves are obtained. The stability criteria are discussed and the neutral curves are plotted.

BACKGROUND AND FORMULATION OF THE PROBLEM

Wave propagation in pre-stressed layered composites has been studied in [1, 2] for the perfectly bonded case. In the present paper, recent work done by the authors on the more general case of imperfectly bonded composite [3, 4] is discussed.

The bimaterial pre-stressed symmetric layered composite consists of an inner layer (thickness $2d$) and two identical outer layers (thickness h) of isotropic incompressible elastic materials, where the principle axes of strain in each layer are coincident. The Cartesian coordinate system is chosen such that the origin O is at the mid-plane of the composite, x_1 and x_2-axes are also coincident with the principal axes, the x_2-direction is normal to the free surface of the layered composite and time harmonic wave propagation is in x_1-direction. The outer layers and inner layer are homogeneous with material parameters and mass density α, β, γ, ρ and α^*, β^*, γ^*, ρ^*, respectively. In the remainder of this paper, all quantities with an asterisk refer to variables and parameters of the inner layer.

Harmonic wave propagating in the outer layer are expressed as $(u_1,u_2,p)=(A_1,A_2,kP)e^{qkx_2}e^{ik(x_1-vt)}$, where u_i is the displacement increment in x_i-direction, p is pressure increment, k is wavenumber, v is phase speed, t is time, A_i, P are arbitrary constants and q is calculated from $q^4+(\xi-2\overline{\beta})q^2+(\overline{\alpha}-\xi)=0$, where $\overline{\beta}=\beta/\gamma$, $\overline{\alpha}=\alpha/\gamma$ and $\xi=\rho v^2/\gamma$ [3]. The corresponding solution for the inner layer will yield $q^{*4}+(\xi^*-2\overline{\beta}^*)q^{*2}+(\overline{\alpha}^*-\xi^*)=0$, where $\xi^*=a\xi$ and $a=r\rho^*/\rho,\ r=\gamma/\gamma^*$.

Due to the symmetric geometry of the composite, only the upper half of the composite needs to be considered. The incremental traction free surface conditions are $s_{021}(x_1,d+h,t)=s_{022}(x_1,d+h,t)=0$ where s_{02i} are the nominal stress increment components. The mid-plane conditions for flexural waves are $u_1^*(x_1,0,t)=s_{022}^*(x_1,0,t)=0$, and for extensional waves are $u_2^*(x_1,0,t)=s_{021}^*(x_1,0,t)=0$. At the interface, the continuity conditions are $s_{021}^*(x_1,d,t)=s_{021}(x_1,d,t)$, $s_{022}^*(x_1,d,t)=s_{022}(x_1,d,t)$, $u_2^*(x_1,d,t)=u_2(x_1,d,t)$ and the incremental nominal shear stress is $s_{021}^*(x_1,d,t)=k_x(\gamma/h)[u_1(x_1,d,t)-u_1^*(x_1,d,t)]$, where k_x is the non-dimensional shear spring parameter.

DISPERSION RELATIONS AND STABILITY CONSIDERATIONS

For flexural waves the dispersion relation is obtained as

$$\begin{aligned}&q_1^*S_1^*C_2^*\left[f^*(q_2^*)^2\hat{\Delta}_1+f^*(q_2^*)\hat{\Delta}_2+\hat{\Delta}_3\right]-q_2^*C_1^*S_2^*\left[f^*(q_1^*)^2\hat{\Delta}_1+f^*(q_1^*)\hat{\Delta}_2+\hat{\Delta}_3\right]-\left[f^*(q_1^*)-f^*(q_2^*)\right]\left[q_1^*q_2^*S_1^*S_2^*\hat{\Delta}_4+C_1^*C_2^*\hat{\Delta}_5\right]\\&+\left(\frac{kh}{rk_x}\right)\left\{\left[f^*(q_1^*)-f^*(q_2^*)\right]C_1^*C_2^*\hat{\Delta}_3+\left[q_1^*f^*(q_2^*)^2S_1^*C_2^*-q_2^*f^*(q_1^*)^2C_1^*S_2^*\right]\hat{\Delta}_4\right\}=0,\end{aligned}\tag{1}$$

where

$$\begin{aligned}&\hat{\Delta}_1=2q_1q_2f(q_1)f(q_2)-q_1q_2\left[f(q_1)^2+f(q_2)^2\right]C_1C_2+\left[q_1^2f(q_2)^2+q_2^2f(q_1)^2\right]S_1S_2,\\&\hat{\Delta}_2=2r\left\{q_1q_2f(q_1)f(q_2)\left[f(q_1)+f(q_2)\right](C_1C_2-1)-\left[q_1^2f(q_2)^3+q_2^2f(q_1)^3\right]S_1S_2\right\},\\&\hat{\Delta}_3=r^2\left\{-2q_1q_2f(q_1)^2f(q_2)^2(C_1C_2-1)+\left[q_1^2f(q_2)^4+q_2^2f(q_1)^4\right]S_1S_2\right\},\\&\hat{\Delta}_4=r\left[f(q_1)-f(q_2)\right]\left[q_1f(q_2)^2C_1S_2-q_2f(q_1)^2S_1C_2\right],\quad\hat{\Delta}_5=rq_1q_2\left[f(q_1)-f(q_2)\right]\left[q_1f(q_2)^2S_1C_2-q_2f(q_1)^2C_1S_2\right],\\&C_m=\cosh(q_mkh),\quad S_m=\sinh(q_mkh),\quad C_m^*=\cosh(q_m^*Dkh),\quad S_m^*=\sinh(q_m^*Dkh)\quad(m=1,2),\\&f(q_m)=1+q_m^2-\sigma,\quad f^*(q_m^*)=1+q_m^{*2}-r\sigma,\quad\sigma=\sigma_2/\gamma,\quad D=d/h.\end{aligned}$$

Equation (1) reduces to the dispersion relation of the perfectly bonded case [1] when $k_x\to\infty$, while it reduces to the fully slipping interface case when $k_x=0$. The dispersion relation for extensional waves is obtained from Eq. (1) by replacing C_m^* by S_m^* and S_m^* by C_m^* ($m=1,2$).

For a particular mode when $\xi < 0,$ the phase speed v is pure imaginary and instead of harmonic wave propagation in x_1-direction, standing waves with amplitudes that grow exponentially with time are produced i.e., an *unstable* state. On the other hand, harmonic waves travelling in x_1-direction will be *stable* for a particular mode when $\xi > 0$ while $\xi = 0$ corresponds to the *neutral* state. By setting $\xi = 0,$ Eq. (1) yields the bifurcation equation, which is a quartic equation of σ i.e.,

$$\Phi_4^{(\mathrm{F})}\sigma^4 + \Phi_3^{(\mathrm{F})}\sigma^3 + \Phi_2^{(\mathrm{F})}\sigma^2 + \Phi_1^{(\mathrm{F})}\sigma + \Phi_0^{(\mathrm{F})} = 0, \tag{2}$$

where the coefficients $\Phi_i^{(\mathrm{F})}$ $(i = 1,...,4)$ are functions of kh, k_x, $\overline{\alpha}$, $\overline{\beta}$, $\overline{\alpha}^*$, $\overline{\beta}^*$, r, a and D. The neutral curves, used to separate the stable and unstable region can be obtained from Eq. (2). This equation will reduce to a quadratic equation of σ when $k_x \to \infty,$ while it remains as a quartic equation when $k_x = 0.$ Hence, in general four branches of neutral curves are expected for an imperfect interface and fully slipping cases while a maximum of only two branches could occur for perfectly bonded case. Similar equations for extensional waves are discussed in [4].

NUMERICAL RESULTS

One of the Examples considered in [3, 4] will be briefly discussed here. The outer and inner layers are Mooney-Rivlin and Varga materials and the primary deformation of both layers are plane strain with principle stretches $\lambda_1 = \lambda_2^{-1} = 1.25$ and $\lambda_1^* = \lambda_2^{*-1} = 2.25$ in which yields $\overline{\alpha} = 2.441,$ $\overline{\beta} = 1.721,$ $\overline{\alpha}^* = 25.629,$ and $\overline{\beta}^* = 5.063.$ The other prescribed parameters are $r = 2.5,$ $a = 20,$ $\sigma = 0$ and $D = 1$. The dispersion curves and neutral curves are shown in Figs. 2 and 3 where the limiting values as $kh \to 0$ and $kh \to \infty$ are given in [4].

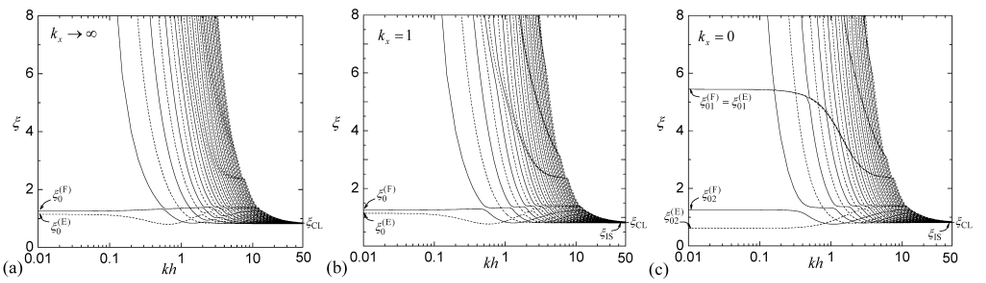


Fig. 2. Non-dimensional squared phase speed ξ ; solid lines - flexural waves and dashed lines - extensional waves.

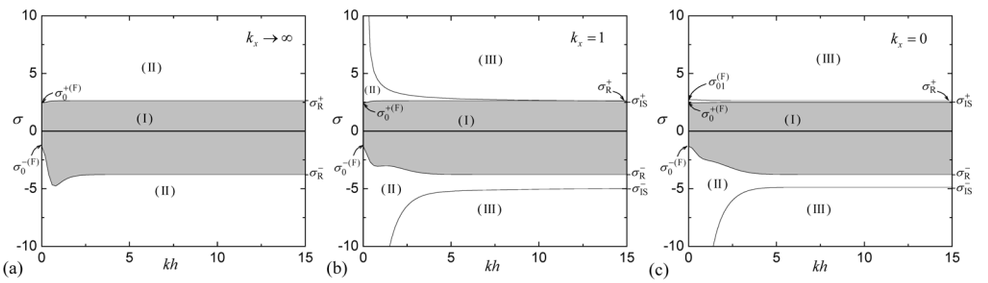


Fig. 3. Neutral curves for flexural waves; shaded area is the region (I) where all modes are stable, region (II) is where the fundamental mode is unstable and region (III) is where the fundamental and the next lowest modes are unstable.

CONCLUSIONS

The dispersive behaviour, for flexural and extensional waves are similar at low and high wavenumber limits. For each type of wave at low wavenumber limit, for $k_x > 0$ only one finite limiting squared phase speed ($\xi_0^{(\mathrm{F})}$ or $\xi_0^{(\mathrm{E})}$) exists while for $k_x = 0$ two finite limiting squared phase speeds ($\xi_{01}^{(\mathrm{F})}, \xi_{02}^{(\mathrm{F})}$ or $\xi_{01}^{(\mathrm{E})}, \xi_{02}^{(\mathrm{E})}$) are found. At high wavenumber limit, both flexural and extensional waves tend to the same limits, which may be squared phase speeds of surface waves (ξ_R), interfacial waves (ξ_{IS} or ξ_{IP}), and limiting phase speed of the composite (ξ_{CL}). The same stable ranges of σ are found for perfectly bonded and imperfect interface cases at the low wave number limit, while at the high wavenumber limit the stable range is the same for imperfect interface and fully slipping interface cases.

References

[1] Rogerson G. A., Sandiford K. J.: Flexural waves in incompressible pre-stressed elastic composites, *Q. J. Mech. Appl. Math.* **50**:597-624, 1997.

[2] Rogerson G. A, Sandiford K. J.: The effect of finite primary deformations on harmonic waves in layered elastic media, *Int. J. Solids Struct*. **37**: 2059-2087, 2000.

[3] Leungvichcharoen S., Wijeyewickrema A. C.: Dispersion effects of extensional waves in pre-stressed imperfectly bonded incompressible elastic layered composites. *Wave Motion* **38**:311-325, 2003.

[4] Leungvichcharoen S., Wijeyewickrema A. C., Yamamoto T.: Flexural waves in pre-stressed imperfectly bonded incompressible elastic layered composites. *Int. J. Solids Struct*. (under review).

XXI ICTAM, 15–21 August 2004, Warsaw, Poland

ON THE PROPAGATION OF SOLITARY WAVES IN MICROSTRUCTURED SOLIDS

Olari Ilison, Andrus Salupere
Centre for Nonlinear Studies, Institute of Cybernetics at Tallinn Technical University, Akadeemia tee 21, 12618 Tallinn, Estonia

Summary In the present paper a Korteweg–de Vries (KdV) type evolution equation, including the third- and fifth order dispersion and the fourth order nonlinearity is used for modelling the wave propagation in microstructured solids. The model equation is solved numerically under localised initial conditions. Possible solution types are introduced and discussed.

INTRODUCTION

Wave propagation in microstructured media is essentially influenced by nonlinear and dispersive effects. The simplest model governing these two effects results in the celebrated KdV equation $u_t + uu_x + du_{3x} = 0$. However, studies of microstructured materials have shown that higher-order dispersive effects together with higher-order nonlinear effects can give rise to dramatic changes in the behaviour of emerging waves. In the present paper a KdV type evolution equation, including the third- and the fifth order dispersive and the fourth order nonlinear terms,

$$u_t + [P(u)]_x + du_{3x} + bu_{5x} = 0, \qquad P(u) = -0.5u^2 + u^4, \tag{1}$$

is used for modelling the 1D longitudinal wave propagation in microstructured solids. Here u is the excitation, t the time coordinate, x the space coordinate, d and b the third- and the fifth-order dispersion parameters, respectively and elastic potential $P(u)$ introduces the quartic nonlinearity. Logarithmic dispersion parameters $d_l = \log d$ and $b_l = \log |b|$ are used instead of d and b for analysis herein after. The sources of higher order effects can be dislocations in the crystal structure of martensitic-austenitic shape-memory alloys [1, 2].
The character of dispersion depends on the signs of parameters d and b: for $db < 0$ one has normal dispersion, however for $db > 0$ the dispersion is normal for some wavenumbers and anomalous for others [3]. In the present paper the case $d > 0$ and $b < 0$ is considered.

THE PROBLEM AND GOALS.

In [3, 4] we have shown that in the case of harmonic initial conditions the equation (1) admits soliton type solutions without reference to the character of dispersion (normal or anomalous). In the present paper the model equation (1) is solved numerically under localised initial conditions

$$u(x,0) = A \ \mathrm{sech}^2 \frac{x}{\Delta}, \qquad \Delta = \sqrt{12d/A}. \tag{2}$$

The initial solitary wave (2) corresponds to the analytical solution of the KdV equation. Therefore in systems governed by the KdV equation such solitary waves are called solitons , i.e., they propagate with constant speed and amplitude and interact elastically (they restore their amplitude and speed after the interaction).
Our main goal here is to answer the following questions: (i) whether or not solitary waves (2) can propagate in media described by the equation (1) with constant speed and amplitude and (ii) how do such solitary waves interact in such a media. In the other words, do the solitary waves (2) behave like solitons in media where the higher order effects, governed by the equation (1), are of importance.

RESULTS AND DISCUSSION

Numerical solutions are found in the domain of logarithmic dispersion parameters $0.8 \le d_l \le 2.4$ and $1.2 \le b_l \le 4.8$. For numerical integration the discrete Fourier transform (DFT) based pseudospectral method [5] and periodic initial conditions

$$u(x,t) = u(x + 4n\pi), \ n = \pm 1, \pm 2, \ldots \tag{3}$$

are used. The length of the space period is chosen 4π in order to separate the initial localised waves.

Solution types

Making use of the numerical results three solution types can be detected. The type of solution depends essentially on the value of the amplitude A of the initial localised wave (2).
First type. Small amplitude initial localised waves decay to a chaotic wave-train (Fig. 1).
Second type. If the amplitude A exceeds a certain value $A_1(d_l, b_l)$ then a wave-train, having regular behaviour in time, forms (Fig. 2). In this case one can discuss about the solitonic character of the solution, recurrence and superrecurrence phenomena.

Third type. If the amplitude has values over a certain critical value $A^*(d_l, b_l)$ then the initial excitation propagates with minimal disturbances, i.e., its speed and amplitude changes by a small extent only during the propagation. The higher the amplitude A, the faster the solitary wave propagating to the right (Figs. 3 and 4). Unfortunately there does not exist such a direct relation between the amplitude and speed like in the KdV case. From the other hand, the higher the amplitude, the more distinctive the left-going small amplitude radiation (Fig. 4).

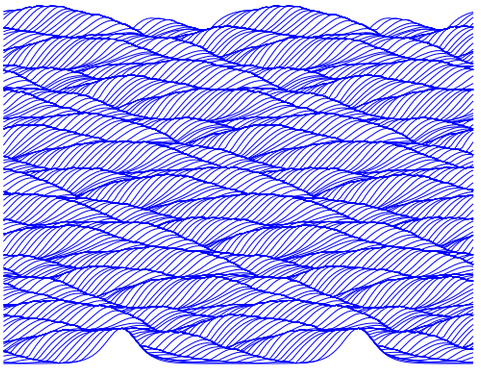


Figure 1. First solution type: time slice plot over two space periods ($d_l = 0.8$, $b_l = 2.0$, $A = 1.5$, $0 \leq t \leq 300$)

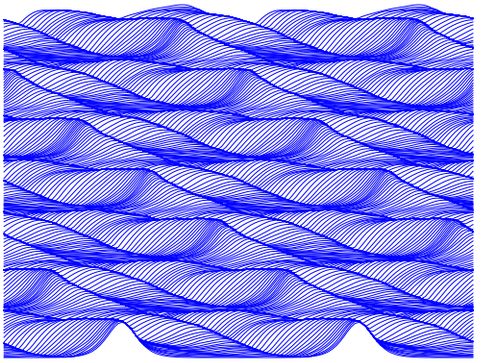


Figure 2. Second solution type: time slice plot over two space periods ($d_l = 0.8$, $b_l = 2.0$, $A = 1.75$, $0 \leq t \leq 300$)

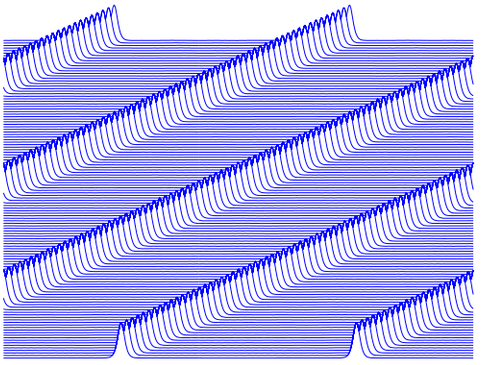


Figure 3. Third solution type: time slice plot over two space periods ($d_l = 2.0$, $b_l = 4.0$, $A = 2.1$, $0 \leq t \leq 100$)

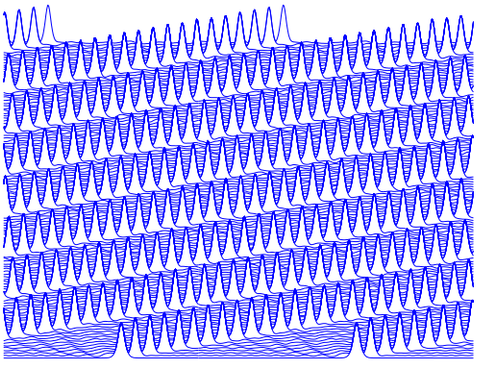


Figure 4. Third solution type: time slice plot over two space periods ($d_l = 2.0$, $b_l = 4.0$, $A = 2.3$, $0 \leq t \leq 100$)

In the subdomain $-0.8 < b_l - 2d_l < 1.6$ one can say that neither the third- nor the fifth order dispersive effects are dominating. In the other words, in this subdomain both dispersive terms (du_{3x} and bu_{5x}) play essential role. In this subdomain the critical amplitude $1.7 \leq A^* \leq 3.41$. Furthermore, the second solution type was detected only in this subdomain for $d_l \leq 1.2$. For $b_l < 2d_l - 0.8$ the fifth order dispersive effects dominate over that of the third order and the value of A^* increases rapidly. For $b_l > 2d_l 1.6$, vice versa, the third order dispersive effects are dominating and the value of the critical amplitude decreases slowly having the limit value $1.67 < A^* < 1.68$.

CONCLUSIONS

In the present paper it is shown that if the amplitude $A > A^*$ then the solitary wave (2) can travel with a constant speed and without significant changes in its amplitude. However, numerical experiments with solitary waves having different amplitudes (and therefore different speeds) demonstrate that they do not interact like solitons — there exist a certain transformation of energy and/or mass between interacting solitons. This phenomenon causes the slower solitary wave move more slowly and the faster one even faster. The results are important for the nondestructive evaluation of material properties of microstructured solids.

References

[1] Maugin, G.A.: Material Inhomogeneities in Elasticity. Chapman & Hall, London et al., 1993.

[2] Maugin G.A., Christov C.: Nonlinear duality between elastic waves and quasi-particles in microstructured solids. *Proc. Estonian Acad. Sci. Phys. Math.*, **46**: 78–84, 1997.

[3] Salupere, A., Engelbrecht, J., Maugin, G.A.: Solitonic structures in KdV-based higher order systems. *Wave Motion*, **34**: 51–61, 2001.

[4] Ilison O., Salupere A.: On formation of solitons in media with higher order dispersive effects. *Proc. Estonian Acad. Sci. Phys. Math.*, **52**:125–134, 2003.

[5] Fornberg, B.A.: Practical Guide to Pseudospectral Methods. Cambridge University Press, Cambridge, 1998.

LEVEL-SETS AND MIXED APPROACHES FOR DYNAMIC CONTACT PROBLEMS

Hachmi Ben Dhia*, Chokri Zammali*
*Ecole Centrale Paris, Labo. MSS-Mat, 92295 Châtenay-Malabry, France

Summary The Signorini-Moreau contact conditions are set as equations by using unknown *Level-Set* fields. From this, a mixed weak-strong formulation of dynamic contact problems is derived; the *Level-Set* fields being the intrinsic contact unknown fields. The problem is then discretized by time, space and collocation schemes and some numerical experimentations are carried out, showing the effectiveness of our global approach. The paper is ended with a prospective use of the local multiscale *Arlequin* method [1].

INTRODUCTION

Impact problems are nonlinear in essence, but also irregular and multiscales in space and time. Theses evidences are shown by analytical investigations giving explicit solutions of simple model impact problems (see e.g. Gloldsmith [2]). General industrial impact problems have however to be approximated by means of numerical tools. Hughes et al. [3], have designed special numerical schemes since the late seventies and increasing efforts have been since furnished by the computational contact community to address this numerical issue (see e.g. [4] and the sampling references therein). Very important advances have this way been done and some of the most pertinent schemes are now capitalized in commercial codes. But to our best knowledge and due to the aforementioned intrinsic difficulties of the impact problems (strong nonlinearities and both space and time irregularities and multiscale intrinsic characters), none of the available numerical schemes is yet sufficiently robust, efficient and accurate to address for instance dynamic contact problems such as those involved by vibrating structures under impact. The present work is a contribution to this wide and complex theme.

Using the "*viability lemma*" of J.J. Moreau [5], the unilateral contact laws are written in a first part as equations by using two unknown possibly multivoque *Level-Set* type fields standing for i) a location of the position of contact surfaces with respect to each other and ii) the *Signe* of the normal velocity jump on the interface. A weak-strong formulation of dynamic unilateral contact conditions is then derived in a straightforward manner. In a second part, an original continuous weak-strong mixed formulation of a dynamic 3-D contact problem is carried out. The associated discrete nonlinear systems are then derived by using a θ-scheme time discretization, a Galerkin method and a collocation one. The numerical solution strategy used to solve this problem is briefly commented and numerical tests are carried out in a third part. It is particularly shown that the numerical solutions do not exhibit pathologies (due to shocks) such as spurious oscillations of the numerical mechanical fields. The paper is ended with a prospective use of the local multiscale *Arlequin* method [1] to superpose to the global (coarse) model local refined ones just in the neighbourhood of impacted zones in order to save human and machine resources. First promising numerical results exemplifying this approach are given.

A DYNAMIC CONTACT MODEL

Let us consider two solids (elastic, for simplicity) which may come into (frictionless, for clarity) contact/impact during their evolution. The classical Signorini contact laws can then be set as flollowing (with rather classical notations) :

$$d_n \le 0,\ \lambda \le 0 \ \text{ and } \ \lambda\, d_n = 0, \ \text{ on } \Gamma_c \times I \tag{1}$$

where Γ_c, I, d_n and λ are the potential "slave" contact surface, the time interval, the so-called signed distance and the normal contact pression, respectively.

By using the "viability lemma" of J.J. Moreau [5], and by assuming that at the initial time, the conditions (1) are satisfied, these conditions can then be written in an equivalent manner in terms of placements and velocities as follows.

If $d_n < 0$ then a free boundary condition is imposed

$[[v_n]] \le 0$, $\lambda_v \le 0$ and $\lambda_v\,[[v_n]] = 0$, otherwise, with $[[v_n]]$ standing for the normal velocities-jump

By using the *Signe* function introduced in [6], these Signorini-Moreau inequalities can be transformed to equalities:

$$\lambda_v = \mathbf{S}_d \mathbf{S}_v\left(\lambda_v - h[[v_n]]\right), \text{ on } \Gamma_c \times I \tag{2}$$

$$\mathbf{S}_d = 1_{\mathrm{IR}^-}(-d_n),\ \mathbf{S}_v = 1_{\mathrm{IR}^-}\left(\lambda_v - \rho[[v_n]]\right), \text{ on } \Gamma_c \times I \tag{3}$$

with $h \neq 0$, $\rho > 0$ and 1_{IR^-} the characteristic function of the semi-negative axis.

This new setting of Signorini-Moreau contact conditions is interesting from a numerical point of view since it leads itself "naturally" to a weak formulation, well-suited to numerical approximations.

WEAK-STRONG FORMULATIONS OF THE DYNAMIC CONTACT PROBLEM

By using the Virtual Power Principle *VPP* (in which a behaviour law is used to express the First Piola-Khirchhoff stress $\mathbf{\Pi}^i$) and a weak formulation of equation (2), keeping equations (3) as local strong ones, the following (original, to our knowledge) weak-strong mixed formulation of the dynamic contact problem is obtained:

Find ($\mathbf{u}^i$, $\mathbf{v}^i$, λ_v, $\mathbf{S}_d$, $\mathbf{S}_v$) such as for all admissible $\mathbf{w}^i$ and λ^* and for t in I,

$$\left.\begin{array}{l} \sum_{i=1}^{2}\int_{\Omega_0^i}\rho_0^i\dot{\mathbf{v}}^i.\mathbf{w}^i d\Omega+\sum_{i=1}^{2}\int_{\Omega_0^i}\mathbf{\Pi}^i:\nabla(\mathbf{w}^i)d\Omega-\int_{\Gamma_c}\mathbf{S}_d\mathbf{S}_v\lambda_v[[w_n]]d\Gamma=0 \\ -\frac{1}{h}\int_{\Gamma_c}\left[\lambda_v-\mathbf{S}_d\mathbf{S}_v\left(\lambda_v-h[[v_n]]\right)\right]\lambda^* d\Gamma=0 \end{array}\right\| \left.\begin{array}{l} \mathbf{u}^i(t)=\mathbf{u}^i(t_0)+\int_{t_0}^{t}\mathbf{v}^i(\tau)d\tau \\ \mathbf{S}_d=1_{\mathrm{IR}^-}(-d_n),\quad \mathbf{S}_v=1_{\mathrm{IR}^-}\left(\lambda_v-\rho[[v_n]]\right)\ \text{on}\ \Gamma_c \end{array}\right. \tag{4}$$

where $\mathbf{u}^i$, $\mathbf{v}^i$ stand for the displacement and velocity fields.

We notice that since the velocity fields may be locally discontinuous with respect to time, the time derivative in the *VPP* is to be understood in an appropriate sense. We notice also that although the above formulation may recall available lagrangian formulations of frictionless contact problems, it is original to our best knowledge: it is a non augmented, non constrained lagrangian formulation of dynamic contact problems.
To be solved, this problem is discretized by means of three numerical tools. A low-order finite time difference scheme of Euler type is used to approximate partial time derivatives. A Galerkin space discretisation method (of the finite element type, or spectral one) is used to approximate the continuous fields $\mathbf{u}^i$, $\mathbf{v}^i$ and λ_v, *w*hile respecting the compatibility condition (see [7], in the quasistatic case). The *Level-Set* like fields $\mathbf{S}_d$, $\mathbf{S}_v$ are approximated by means of a collocation method, related intimately in practice to numerical contact integration points. The nonlinear discrete systems will be detailed during the conference.

NUMERICAL SOLUTION STRATEGY AND RESULTS

Our non linear systems are solved, at each time step, by a fixed point strategy on the *Level-Set* fields $\mathbf{S}_d$ and $\mathbf{S}_v$ (actually on their values on the selected finite collocation contact points, for the discrete systems), coupled with classical numerical methods for the solution of the others nonlinearities of the problem.
Let us now give a numerical illustration. We consider the very well-known shock of two bars of identical mechanical characteristics and represent the interface mechanical fields obtained by using: i) the Signorini contact conditions (1) and a Newmark scheme, with numerical damping and ii) the suggested approach (figure 1). Other results showing the effectiveness of our global approach of dynamic contact problems, (taking also into account friction phenomena), will be given during the conference.

A PROSPECTIVE USE OF THE ARLEQUIN FRAMEWORK

Our work is ended by showing the use of the local multiscale Arlequin method [1] to introduce, with great flexibility while saving machine resources, a mechanical and numerical refinement of impact problems in critical zones. The Taylor bar test, treated in the Arlequin framework by superposing a local elastoplastic refined model to a global elastic one, is shown in figure 2.

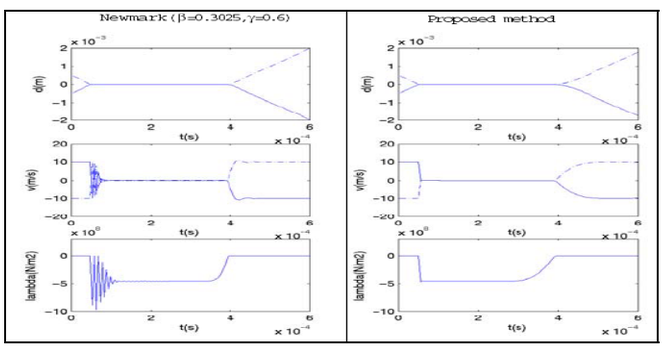


Figure1

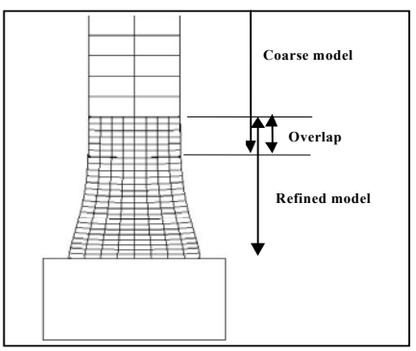


Figure 2

References

[1] Ben Dhia H.: Problèmes mécaniques multi-échelles: La méthode Arlequin. *CRAS* **236**, *série IIb*; 899-904, 1998.
[2] Goldsmith W.: Impact problems, London 1960.
[3] Hughes T.J.R. et al.: A finite element method for a class of contact-impact problems. *Comp. Methods App. Mech. Eng.* **8**; 249-276, 1976.
[4] Love G.R., Laursen T.A.: Improved implicit integrators for transient impact problems, *Comp. Methods App. Mech. Eng.* **192**; 2223-2248, 2003.
[5] Moreau J-J.: In Unilateral Problems in Structural Analysis. *CISM courses and lectures*, 173-221. Springer-Verlag. NY 1985.
[6] Ben Dhia H.: Modelling and solution by penalty duality method of unilateral contact problems. *Cacul des Structures et Int. Art.* **2**; 1-18, 1988.
[7] Ben Dhia H., Zarroug M.: Hybrid frictional contact particles-in elements. *Revue Europeenne des Elements Finis* **9**; 417-430, 2002.

ANALYSIS AND DESIGN OF DISPERSIVE MATERIALS AND STRUCTURES

Mahmoud I. Hussein, Gregory M. Hulbert and Richard A. Scott

Department of Mechanical Engineering, University of Michigan, Ann Arbor, MI 48109, U.S.A.

Summary First, a multiscale assumed strain variational formulation is developed for the prediction of frequency spectra of periodic materials. This approach facilitates the generation of reduced order models using mode projections, hence practically providing up to an order of magnitude decrease in computational problem size compared to direct analysis. Second, computed frequency band structures are tailored to yield synthesized composite materials with desired dynamic characteristics. The designed materials are then used to form structures, at a larger length scale, for a variety of purposes. The generated composite structures are significantly more amenable to manufacturing compared to those generated via traditional topology optimization. Applications include high-frequency vibration isolators and structural waveguides.

FREQUENCY RESPONSE OF PERIODIC MATERIALS

Within periodically heterogeneous media, wave scattering and dispersion take place across constituent material interfaces in such a way that an overall wave attenuation effect arises at certain frequency ranges known as *stop bands*. This phenomenon, which is attributed to a mechanism of destructive interference among the scattered wave field, can be utilized in designing composite materials and structures with tailored frequency-dependent dynamic characteristics. A necessary tool for this design process is an accurate and efficient analysis technique for computing band diagrams (dispersion curves) for periodic materials.

Multiscale assumed strain variational formulation

A local (unit cell) domain Y is considered as part of a global periodic bounded structure Ω, where the ratio ε between the length scales of the domains is assumed to be large (i.e., ε is a small number). Based on this multiscale construct, the following two-field variational problem is defined:

Problem 1: *Find* $\mathbf{u} \in S_{\Omega\times Y}$ and $\boldsymbol{\varepsilon} \in E_{\Omega\times Y}$ *such that*

$$\int_\Omega \langle (\nabla_{\mathbf{x}}\mathbf{w} + \frac{1}{\varepsilon}\nabla_{\mathbf{y}}\mathbf{w}) : \mathbf{C} : \boldsymbol{\varepsilon} \rangle d\Omega + \int_\Omega \langle \rho \mathbf{w} \cdot \frac{\partial^2 \mathbf{u}}{\partial t^2} \rangle d\Omega - \langle G_{\text{ext}}(\mathbf{w}) \rangle + \int_\Omega \langle \boldsymbol{\gamma} : \mathbf{C} : (\nabla_{\mathbf{x}}\mathbf{u} + \frac{1}{\varepsilon}\nabla_{\mathbf{y}}\mathbf{u} - \boldsymbol{\varepsilon}) \rangle d\Omega = 0, \qquad (1)$$

where $\mathbf{u}$ and $\boldsymbol{\varepsilon}$ denote displacement and strain, respectively, and $\mathbf{w}$ and $\boldsymbol{\gamma}$ are the weighting functions associated to each, and ρ, $\mathbf{C}$ and G_{ext} denote density, elasticity tensor and virtual work done by external forces, respectively. Based on McDevitt *et al.*[1], the displacement and strain fields are assumed to take the following forms:

$$\mathbf{u}(\mathbf{x},\mathbf{y},t) = \bar{\mathbf{u}}(\mathbf{x},t) + \varepsilon \mathbf{P}(\mathbf{y}) \cdot \boldsymbol{\phi}(\mathbf{x},t), \qquad (2)$$

$$\boldsymbol{\varepsilon}(\mathbf{x},\mathbf{y},t) = (\nabla_{\mathbf{x}}\bar{\mathbf{u}} + \nabla_{\mathbf{y}}(\mathbf{P}\cdot\boldsymbol{\psi}))^S, \qquad (3)$$

where $\bar{\mathbf{u}}$ represents an averaged macroscale displacement, $\boldsymbol{\phi}$ and $\boldsymbol{\psi}$ are macroscale vectors of generalized coordinates, and $\mathbf{P}$ is a 'projection matrix'. Substituting (2)-(3) into (1) yields a set of Euler-Lagrange equations. Subsequently, assuming a Floquet-Bloch solution results in the following dispersion relation eigenvalue problem:

$$\mathbf{K}^*(\mathbf{k})\{\bar{\mathbf{U}}^{\mathbf{T}} \quad \boldsymbol{\Phi}^{\mathbf{T}} \quad \boldsymbol{\Psi}^{\mathbf{T}}\}^{\mathbf{T}} - \omega^2 \mathbf{M}^*\{\bar{\mathbf{U}}^{\mathbf{T}} \quad \boldsymbol{\Phi}^{\mathbf{T}} \quad \boldsymbol{\Psi}^{\mathbf{T}}\}^{\mathbf{T}} = \mathbf{0} \qquad (4)$$

The central development in the present work is the choice of functions (vectors) for projection matrix $\mathbf{P}$. A selected set of Floquet-Bloch eigenvectors based on an assessment of the modal contribution of the eigenvectors in both the temporal and spatial frequency domains is used to form $\mathbf{P}$.

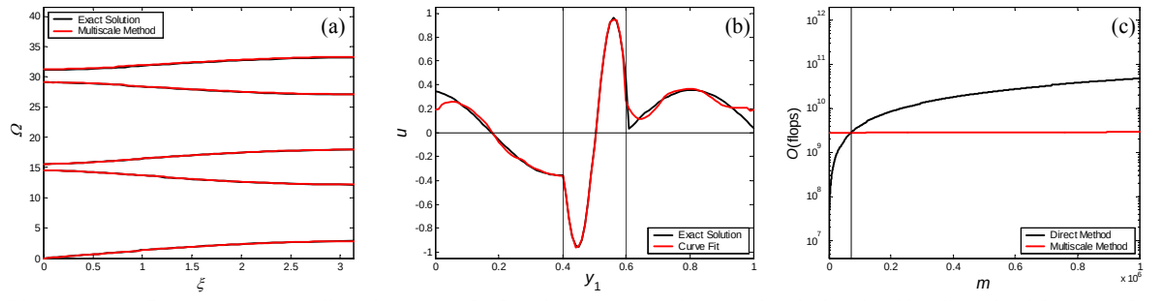


Figure 1. (a) Frequency spectrum (dispersion curves) for *P*-mode wave propagation normal to the layering. Non-dimensional frequency Ω and wavenumber ξ define the ordinate and abscissa, respectively. Insert: schematic of unit cell, where black color represents stiff material and white color represents compliant material. (b) Least square fit of a particular exact mode shape onto projection subspace $\mathbf{P}$. (c) Computational effort (order of operation count) for multiscale and direct methods (m denotes the size of the matrix problem, which in turn is dependent on the resolution of the finite element mesh). The vertical line identifies the break-even point among the two methods.

Accuracy and efficiency considerations

To test the accuracy and efficiency of the developed multiscale method, several analyses were conducted on a simple 1D bi-material layered material whose exact solution is readily available. Fig. 1a shows an excellent agreement of computed dispersion curves with the exact solution. Fig. 1b demonstrates the richness of the chosen projection space through curve fitting a particular mode shape. Finally, in Fig 1c, the efficiency of the multiscale reduced order method is compared to that of a direct method, indicating significant reduction in *flops* for large systems.

DESIGN METHODOLOGY

The technique mentioned above is employed as an analysis tool for designing periodic materials and structures with desired dynamic characteristics. The design methodology (see ref. (2) for 1D problems) also has a multiscale character.

Design of fine-scale unit cell

The unit cell constitutes a "building block" from which the global structure is to be formed. It is designed in such a way as to have stop bands located in predetermined locations in the frequency domain. These locations are selected in accordance to the desired function of the cell within the bounded structure. Figure 2 illustrates a designed 2D unit cell and shows a stability diagram that is used for material selection. The resulting frequency spectra (for *SH* and *P-SV* wave motion) of the designed periodic material are also shown.

Design of coarse-scale structure

The designed unit is used to form a bounded composite structure. As an example, a waveguiding structure (which can employed as a vibration isolator) is designed using the proposed methodology. The aim is to have the structure steer mechanical waves along a prescribed path at a particular frequency. The unit cell from which the guide "wall" is built is designed to have this frequency lie within its first stop band. Figure 3 shows the wave field conforming to the guide as desired. Compared to structures designed by traditional topology optimization, this structure has the advantage that its material layout geometric features are simple and hence amenable to manufacturing.

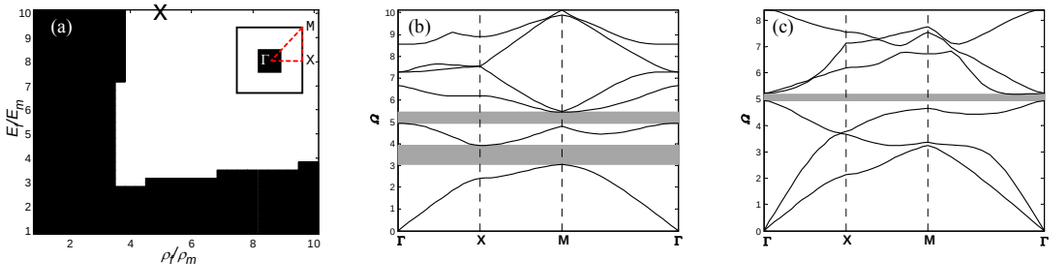


Figure 2. (a) Contrasting material properties stability map for the designed unit cell (for *SH* wave motion). E and ρ denote Young's modulus and density, respectively. $(\cdot)_f$ and $(\cdot)_m$ refer to stiff (fiber) and compliant (matrix) materials, respectively. The black zone corresponds to a pass band and the white zone corresponds to a stop band. "x" mark indicates choice of ratios of material properties. Insert: Designed unit cell material layout. Simple square configuration is chosen for ease of manufacture. The irreducible Brillouin zone is shown in dashed lines. Points marked Γ, X and M correspond to the following wave vectors: $\mathbf{k} = [0, 0]$ at Γ, $\mathbf{k} = [\pi/d, 0]$ at X, and $\mathbf{k} = [\pi/d, \pi/d]$ at M, where d is the unit cell side length. Frequency spectrum for chosen design is shown for (b) out-of-plane *SH*, and (c) in-plane coupled *P-SV*, wave propagation. In (b)-(c), the abscissa is defined by the magnitude of the wave vector whose end point sweeps the paths Γ>X, X>M, and M>Γ, respectively. Stop bands are shaded in grey.

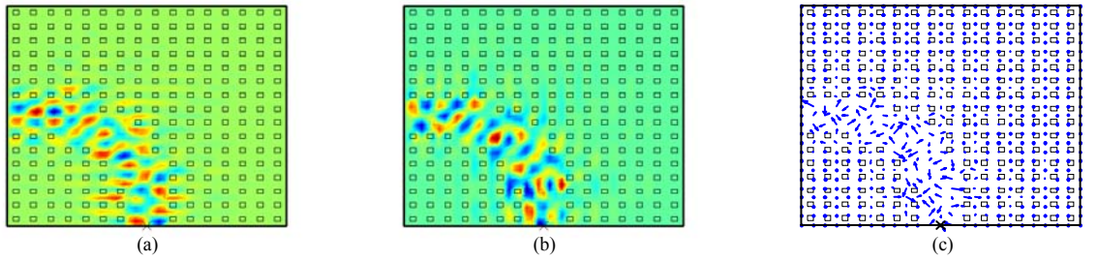


Figure 3. Dynamic response due to excitation at point "x". The forcing load is in-plane and perpendicular to the edge of the structure. (a) x-component, and (b) y-component, of displacement wave field. (c) Resultant displacement vector field indicating "vorticial-type" wave motion. Excitation frequency lies at the center of the first stop band corresponding to the designed unit cell for in-plane wave motion (see Fig. 2c). Note, that this unit cell is used to form the "wall" of the waveguide.

References

[1] McDevitt, T.W., Hulbert, G.M., and Kikuchi, N.: An Assumed Strain Method for the Dispersive Global-Local Modeling of Periodic Structures. *Computer Methods in Applied Mechanics and Engineering*, **190**:6425-6440, 2001.

[2] Hussein, M.I., Hulbert, G.M., and Scott, R.A.: Tailoring of Wave Propagation Characteristics in Periodic Structures with Multilayer Unit Cells," *17th American Society of Composites Technical Conference* [CD-ROM], West Lafayette, Indiana, October 2002.

XXI ICTAM, 15–21 August 2004, Warsaw, Poland

MATERIAL INSTABILITIES IN THERMO-MECHANICAL PROCESSES

Ahmed Benallal*, Davide Bigoni **
*LMT-Cachan, ENS de Cachan/CNRS/Université Paris 6 , Cachan, France
**Dipartimento di Ingegneria Meccanica e Strutturale, Università di Trento, Trento, Italy

Summary The paper investigates the roles of thermal effects and thermo-mechanical couplings in the development of material instabilities and strain localisation. The main result is that during a thermo-mechanical process, two conditions are shown to play the essential roles and correspond to the singularity of the isothermal and the adiabatic acoustic tensors.

INTRODUCTION

Thermal effects have important consequences on behaviour of materials and are fully accessible to measurements. For instance, experimental results relative to polymers demonstrate that fracture initiation and growth may be influenced by temperature variations ahead of the crack tip . Thermal loading strongly affects the plastic deformation of soils and rocks and consequently strain localization in these materials . In structural steel, the important effect of heating on nucleation and growth of shear bands has been observed. These experimental evidences suggest that thermal phenomena can play an important role in promoting or inhibiting global and local instabilities in materials. The objective of this work is to fully include these thermal effects and thermo-mechanical couplings in the analysis of material instabilities.The main result r evidences that adiabatic analyses may be not sufficient to understand the development of material instabilities and strain localization phenomena.
Different thermal effects and thermo-mechanical couplings affect the mechanical behaviour of solids. In particular, while it is known that all mechanical properties are usually temperature dependent and constitute concurrent causes of thermal softening, other less recognized phenomena such as thermal expansion, heat conduction, mechanical dissipation and phase transformations need to be considered.

THERMOINELASTIC CONSTITUTIVE EQUATIONS

The analysis is carried out for a broad class of *rate-independent*, coupled thermo-irreversible constitutive equations including thermoplasticity and thermodamage. The presentation here is restricted to small strain for simplicity. In the framework of continuum thermodynamics of irreversible processes, the behaviour of the material is described by:

- The Helmholtz free energy per unit mass $\Psi = \Psi(\boldsymbol{\epsilon}, \boldsymbol{\alpha}, T), \quad \Psi = e - Ts$ where $\boldsymbol{\epsilon}$ is the (small) strain tensor, T the absolute temperature and $\boldsymbol{\alpha}$ is a generic collection of internal variables of various tensorial nature (scalars, vectors or second-order tensors) describing different physical mechanisms governing inelastic deformation. Moreover, e and s are the specific internal energy and the specific entropy, respectively.

- The reversibility domain, defining the range in which inelastic processes are excluded, is defined through the yield (or damage) function $f(\mathbf{A}, \boldsymbol{\alpha}, T) \leq 0$ where $\mathbf{A}$ are the thermodynamical forces associated to the internal variables $\boldsymbol{\alpha}$. Inelastic deformations are therefore possible only if $f = 0$, and during plastic flow the evolution of the internal variables must satisfy Prager's consistency $\dot{f} = 0$.

- The evolution of internal variables given by $\dot{\boldsymbol{\alpha}} = \dot{\lambda}\mathbf{P}, \quad \mathbf{P} = \frac{\partial F}{\partial \mathbf{A}}$ where the potential function $F = F(\mathbf{A}, \boldsymbol{\alpha}, T)$ is a function of the state variables and $\dot{\lambda}$ satisfies the Kuhn-Tucker conditions $\dot{\lambda} \geq 0, \quad f \leq 0, \quad \dot{\lambda} f = 0$

- Local conservation of energy or the First Law of Thermodynamics is $\rho\dot{e} = \boldsymbol{\sigma} \cdot \dot{\boldsymbol{\epsilon}} - div\mathbf{q} + r$ where r is the heat supply per unit volume generated by internal sources, $\mathbf{q}$ is the heat flux, taken to obey a generalized Fourier law of heat conduction $\mathbf{q} = -\mathbf{K}\nabla T$ in which tensor $\mathbf{K} = \mathbf{K}(\mathbf{A}, \boldsymbol{\alpha}, T)$ is assumed positive definite.

Two constitutive properties are important in the analysis of material instabilities. These are the isothermal tangent modulus $\mathbf{H}^i$ and the adiabatic tangent modulus $\mathbf{H}^a$. The isothermal modulus relates the stress rate to the strain rate *under isothermal conditions* ($\dot{T} = 0$) while the adiabatic modulus relates the stress rate to the strain rate under *local adiabatic conditions* ($r = \div bq = 0$). These moduli are easily obtained when the the free energy Ψ, the yield function f and the potential F are given.

RESULTS

Within the above constitutive framework , strain localization under quasi-static conditions is addressed, using the classical shear band analysis restricted to the loading branch of the constitutive operator (Hill, 1962, Rice, 1976), though now extended to include thermal effects and thermomechanical couplings. This extension is performed by employing, additionally to the usual discontinuity conditions on mechanical variables, the jump conditions associated to the thermal variables, essentially, the temperature rate and the heat flux. This is done under general thermo-mechanical conditions in

contrast to Raniecki (1976) who considered only the adiabatic situation. Localization is shown to first occur when either of the thresholds corresponding to singularity of the isothermal or adiabatic acoustic tensor is reached. The mechanical interpretation of such a condition involves the formation of a discontinuity of the heat flux divergence across a band in the former case or of the temperature rate in the latter case.

Plastic acceleration waves are also considered to show that propagation velocity is related to the eigenvalues of the isothermal acoustic tensor, while the adiabatic acoustic tensor does not play a role. A consequence of this is that, while strain localization corresponds to stationarity of acceleration waves in the isothermal case, when thermal effects are considered, localization may occur in adiabatic conditions, with still propagating acceleration waves.

The above analysis is completed by a perturbation analysis where at a certain stage of a homogeneous deformation of an infinite body, an infinitely small perturbation is applied and the resulting perturbed motion studied. Assuming a linearized response around the homogeneous state, the conditions for unbounded growth of perturbation are derived. When inertia is neglected, the perturbation analysis corresponds to a bifurcation analysis in a sense much similar to the internal instabilities defined by Biot (1965). The growth condition is found to be (when the rate of growth η is large enough, i.e. when $|\eta| \to \infty$)

$$\eta N \det\left[\mathbf{n}\cdot\mathbf{H}^{a}\cdot\mathbf{n}\right] + k\xi^{2}\det\left[\mathbf{n}\cdot\mathbf{H}^{i}\cdot\mathbf{n}\right] = 0 \tag{1}$$

where N is a material positive constant and k the coefficient heat conduction(isotropic heat conduction was considered here so that $\mathbf{K} = k\mathbf{1}$ with $\mathbf{1}$ the second order unit tensor). Note that to obtain (1) perturbations were taken in the form $\delta\mathbf{X} = \tilde{\mathbf{X}} exp[i\xi\mathbf{n}\cdot\mathbf{x} + \eta t]$ with ξ the wavenumber and η the rate of growth of the perturbation. $\tilde{\mathbf{X}}$ is the amplitude of the perturbation. It is therefore shown that for a quasi-static path —which in general is neither isothermal nor adiabatic— internal instability corresponds either to the singularity of the isothermal acoustic tensor (localization in the incrementally isothermal conditions) or to the singularity of the adiabatic acoustic tensor (localization in the incrementally adiabatic conditions) and is associated to the full range of wavelengths. Under dynamic conditions, unbounded growth is associated only to the short wavelength regime and to divergence growth or flutter phenomena governed by the *isothermal* acoustic tensor.

COMMENTS

The analyses performed in the present paper share analogies with those relative to deformation of porous, fluid-saturated inelastic materials, where pore pressure plays a role similar to heat conduction. Isothermal and adiabatic conditions are replaced in that context by drained and undrained conditions. However, differently from the porous plastic problem, the adiabatic constitutive tangent operator is not symmetric for thermoplasticity, even in the relevant case of associative flow rule. An important consequence of this is that a hierarchy between instability in incrementally isothermal and adiabatic conditions does not exist, so that the latter may be critical for stability.

The analysis was limited in the present study to a homogeneous and infinite solid. A current analysis shows that many of the results contained in this paper remain valid when one considers heterogeneous situations and includes boundary conditions. These boundary conditions however bring new features.

It may be also important to mention, in closure, that the obtained results may be of interest in the numerical treatment of coupled problems, with emphasis on the consequences of material instabilities on numerical analyses. When perturbations may grow unboundedly, the initial boundary-value problem becomes ill-posed and one should expect mesh and *time step* dependency of the results. Classical algorithms are seen to be not consistent as no convergence is obtained as the time step $\Delta t \to 0$.

References

[1] Biot, M.A.: Mechanics of incremental deformations, J. Wiley and Sons, New York 1965.

[2] Hill, R.: Acceleration waves in solids, *J. Mech. Phys. Solids*, **10**:1-16, 1962.

[3] Raniecki, B.: Ordinary waves in inviscid plastic media. In Mechanical Waves in Solids ", (Edited by Mandel, J. and Brun, L.) CISM Courses and Lectures n. 222, Springer-Verlag, Wien, (1976).

[4] Rice, J. R.: The localization of plastic deformation, In *Theoretical and Applied Mechanics*, (Edited by Koiter, W.T.) North-Holland, Amsterdam, 207-220, 1976.

DYNAMICAL SYSTEMS THEORY IN MATERIAL INSTABILITIES

Peter B. Béda
HAS-BUTE Research Group on Dynamics of Machines and Vehicles, Budapest University of Technology and Economics, Bertalan L. 2. H-1111 Budapest, Hungary

Summary The paper aims to present a unified method to deal with various material instability problems. As mathematical background the theory of dynamical systems is used, especially Lyapunov's stability definitions and elementary bifurcation theory. We follow continuum mechanics and its basic set of equations in describing solid bodies. By applying our methodology a few material instability phenomena are studied like strain localization or flutter, and a kind of mathematical interpretation can be obtained. There is also a possibility to explain the origin of mesh dependence in numerical studies of post-localization and the role of internal length in this context.

INTRODUCTION: BACKGROUND AND MOTIVATION

The definitions of material instability

The study of instability in elasto-plastic solid continua can be traced back to Drucker [1] and Hill [2] in the late fifties and has re-appeared in the famous work of Rice [3] on shear bands.

Since then there are a lot of papers pubished and several stability definitions are applied. These can be originated in either energy concepts [4] or kinematic conditions. The way of stability analysis is more or less determined by such definitions. For energy approaches the stability is defined as Lyapunov stability and the investigation performed is similar to the so called Lyapunov's direct method. In works based on kinematic conditions the study concentrates on wave speeds and the acoustic tensor. The sate of the solid body is considered to be stable, if all the eigenvalues c_i^2 (i.e. the squares of the wave speeds c_i) are strictly positive. Rice [3] introduces a classification for the loss of stability, which may be caused by the increase of loading. Firstly, the appearance of a zero eigenvalue is an instability being interpreted as the onset of localization (or divergence). Secondly, the material gets unstable, if the acoustic tensor has complex eigenvalues, which is called the flutter.

Dynamical systems, stability and bifurcation

In the theory of dynamical systems a system of autonomous differential equations

$$\dot{x} = g\left(x\right). \tag{1}$$

Assume that $x = 0$ is a solution of (1). Then the stability investigation of solution $x = 0$ can be performed by using Lyapunov's second method. Now a small perturbation is substituted $x = 0 + \Delta x$ into (1) and the linearized part Lx of $g\left(x\right)$ is studied.

The eigenvalues λ_i of operator L determine stability:

- if for all of them Re$\lambda_i < 0$, the solution is stable;
- if for at lest one of them Re$\lambda_i > 0$, the solution is unstable.

For the critical index k the stability boundary is Re$\lambda_k = 0$. There are two basic ways of loss of stability:

- if Im$\lambda_k = 0$, there is a static bifurcation;
- if Im$\lambda_k \neq 0$, there is a dynamic bifurcation.

In this paper the Lyapunov stability definition is used, but we do not use energy functionals. Instead a set of partial differential equations is derived from the fundamental field equations of the classical continuum mechanics. These are interpreted as an infinite dimensional dynamical system for basic functions satisfying the boudary conditions. The Lyapunov's indirect method is applied for that generalized dynamical system.

DYNAMICAL SYSTEMS THEORY IN MATERIAL INSTABILITIES

Assume that state S^0 of the solid body can be described by the values v^0, σ^0, ε^0 etc. and the stability of S^0 is studied. To explain the main steps of our investigation the study may be simplified to small deformation theory. Then the set of fundamental equations consists of the Cauchy equation of motion for the symmetric stress tensor σ

$$\rho\ddot{u} = \sigma\nabla, \tag{2}$$

the kinematic equation

$$\varepsilon = \frac{1}{2}\left(u \circ \nabla + \nabla \circ u\right), \tag{3}$$

and assume that the constitutive equation has the general form

$$0 = F\left(\varepsilon, \dot{\varepsilon}, \nabla^2\varepsilon, \nabla\varepsilon, \dot{\sigma}, \sigma\right). \tag{4}$$

After proper rearrangements and under some general conditions the set of equations (2), (3), (4) can be transformed into the field of the perturbation velocities

$$\Delta v = v - v^0.$$

Then a linear operator L is defined, which acts on the perturbation velocity field satisfying homogeneous boundary conditions. Note that L is a differential operator (represented by a set of partial differential equations). Now the investigations concentrates on the eigenvalues of that operator. The stability – instability conditions are the same as for dynamical systems (see the previous section). The main difficulty at this point is that the determination of the eigenvalues requires to solve a system of partial differential equations. This is almost impossible in a general case by analytic methods. Two approximate methods are applied instead. The one is a restriction into uniaxial case, the other is the use a specific set of perturbation functions, which are generally harmonic functions.

The first approach keeps the exact mathematics of the treatment, but in some cases leads to an over-simplification of the mechanical problem. The benefit is that we have a clear insight into what happens at the loss of stability. We could analyze the spectrum of the operator, its changes at the variation of the load and we may even look at the critical eigenspace of the critical eigenvalue. This point is closely related to the mesh sensitivity, mesh dependence appearing in numerical post-localization [5].

When a specific set of perturbation functions is applied we may consider more complicated mechanical problems, like nonlinear cases for example. Both material and geometrical nonlinearities (finite displacements) can be encountered.

APPLICATIONS, MAIN RESULTS

By using the method outlined above, we could obtain a few interesting observation on material instability phenomena. From the uniaxial investigations we find that the static or dynamic bifurcation seems to be a better classification of the loss of stability. Both divergence and flutter can be considered as special cases of one of them.

Our method enables us to study the role of the forms of the constitutive equations in the way of the loss of stability. We could show, how the inclusion of rate and first or second gradient dependence acts on the critical spectrum and eigenspace, and we are able to give a mathematical interpretation of the problematic behavior in numerical studies.

Especially, for the rate and second strain gradient dependent material we could show the origin of the nice post-localization behavior and the role of internal length. We can perform an analytical post-localization investigation for such material, and including material nonlinearity a so-called transcritical bifurcation can be found.

For large displacements we apply our method for the small pertubations of a state obtained by the equations of the large displacement theory. These perturbations are treated as in the linearized continuum mechanics. When a second order constitutive equation (a generalization of the second gadient dependent material) is used for large deformations, we get back a similar behavior as in small deformation case.

CONCLUSIONS

The theory of dynamical systems and Lyapunov's stability are useful mathematical tools for studying material instability problems. The benefits are quite obvious on the stability bondary when the way of the loss of stability is under consideration.

References

[1] Drucker, D.C.: On uniqueness in the theory of plasticity. *Quart. Appl. Math.* **14**:35–42, 1956.

[2] Hill, R.: A general theory of uniqueness and stability in elastic-plastic solids. *J. Mech. Phys. of Solids* **6**:236–249, 1958.

[3] Rice, J.R.: The localization of plastic deformation. In: Theoretical and Applied Mechanics, (Ed.: W.T. Koiter), North-Holland Publ. Amsterdam, pp. 207–220, 1976.

[4] Petryk, H.: A consistent energy approach to defining stability of plastic deformation processes. In: Stability in the Mechanics of Continua, Proceeding of the IUTAM Symposium. Numbrecht 1981, (Ed.: F.H. Schroeder), Springer, Berlin, Heidelberg, pp. 262–272, 1982.

[5] De Borst, R., Sluys, L.J., Mühlhaus, H.-B., Pamin, J.: Fundamental issues in finite element analyses of localization of deformation. *Engineering Computations* **10**:99–121, 1993.

An idea and theory of hypothetical device for investigating the localization phenomena

Eugene I. Ryzhak

Inst. of Physics of the Earth, RAS, B. Gruzinskaya, 10, 123995, Moscow, Russia

Summary Suggested and supported by the stability analysis is an idea of the lamination shear device with a domain of deformation of rather arbitrary shape. The device is intended to clarify the relation between the localization pattern and the shape of solid deformed.

The localization phenomena considered as a mechanism of incipiency of discontinuities in solids, are of great interest for a number of theoretical and applied disciplines. Systems of discontinuities that arise from the zones of localized deformation, inherit the geometry of corresponding localization patterns. The ralation between the localization pattern, that arises as a pecular mode of instability of a uniform or quasiuniform deformation, and the shape of doma in of deformation, attracts attention of the researchers for a long period, still remaining unclear.

For experimental study of the relation pointed out the devices are needed that would provide the following: (1) uniformity of the basic deformation process; (2) the possibility to set different (ideally, arbitrary) shapes of the deformation domain; (3) stability of the uniform deformation up to violation of strong ellipticity, which stipulates the onset of localized instability.

In this work an essential scheme of such a device is suggested and it is proved theoretically that the properties listed above do take place.

The device itself is a pile of thin laminae (fig.) in which a cavity of certain shape is cut. The lamination forms a parallelepiped confined from two opposite sides by two rigid and smooth flat walls (not represented on the figure), parallel to each other; corresponding side faces of the lamination can slide over inner surface of the walls. The cavity reaches one or both walls which close its side openings. It is filled by a homogeneous material tested (bulk or soft plastic one), which forms the body subsequently called the “specimen”. The lamination undergoes prescribed quasistatic simple shearing in the plane paralled to the walls. Then a possible deformation of the specimen is the same uniform simple shearing, which is considered as the basic deformation process (note that certain part of the specimen boundary contacts the walls, with sliding being assumed there). If the basic process is stable, it is unique and hence its uniformity will be preserved up to the onset of instability.

Let us show that under rather loose assumptions regarding the material tested, the specimen stability is preserved as long as the incremental constitutive relation remains strongly elliptic. We suppose that the material is initially specularly symmetric with respect to the plane of shearing (parallel to the smooth walls); in particular, it can be initially isotropic or orthotropic. In that case it can be proved readily that during the uniform shearing not only homogeneity of the material is preserved, but additionally the plane of its specular symmetry, which remains parallel to the planes of boundary sliding. Disturbing infinitesimal displacements (additional to those of the basic process) vanish over the part of the specimen boundary that lies inside the lamination and are tangential over its flat parts contacting the smooth side walls and sliding over them. Thus, the material symmetry of the specimen and its kimematical perturbation boundary conditions correspond to the hypothesis of a modification (one of those proved by the author [1, 2]) of the well–known Van Hove’s theorem [3], which enables to prove stability of the basic process up to violation of strong ellipticity. Taking into account, that the stability criterion (going back to studies by D. Drucker and R. Hill) is nowadays standard and commonly known, we state only the abovementioned Modified Van Hove’s theorem, making use of which is crucial for the proof of stability.

Modified Van Hove’s theorem. Let B be a regular subregion of the plane layer with a boundary $\partial B = \partial B_1 \cup \partial B_2$, ∂B_1 lying inside the layer and ∂B_2 lying on its boundary planes; let a constant fourth-order tensor $\mathbf{C}$ be strongly elliptic and specularly symmetric with respect to the plane parallel to boundary planes of the layer; let vector field $\mathbf{u}(\mathbf{r})$ be continuous, piecewise-smooth, vanishing on ∂B_1, and tangential on ∂B_2. Then the functional $\int_B \nabla \otimes \mathbf{u} : \mathbf{C} : \nabla \otimes \mathbf{u} dV$ is definitely positive.

Since the stability criterion is just definite positiveness of the functional of such a type, we conclude that asserted stability up to the bound stated is proved. Thus, instability of the uniform deformation arises as a re-

sult of violation of strong ellipticity and hence is localized. As for the experiments with different shapes of the cavity, they can help to reveal the influence of the shape on geometry of the localization pattern.
Note that the lamination shear device with definite (the parallelepipedal) shape of cavity was described (without any kind of stability analysis) in [4].
This work was supported by the Russian Foundation for Basic Research.

References

[1] *Ryzhak E.I.* On stable deformation of "unstable" materials in a rigid triaxial testing machine. J. Mech. Phys. Solids **41**: 1245-1256, 1993.
[2] *Ryzhak E.I.* On stability of homogeneous elastic bodies under boundary conditions weaker than displacement conditions. Q.J. Mech. Appl. Math. **47**: 663-672, 1994.
[3] *Van Hove L.* Sur l'extension de la condition de Legendre du calcul des variations aux integrales multiples a plusieurs functions inconnues. Proc. Kön. Ned. Akad. Wet. **50**: 18-23, 1947.
[4] *Revuzhenko A.F. et al.* On the mechanism of deformation of a bulk material at large shears. Soviet Mining Science **N 3**: 130-133, 1974.

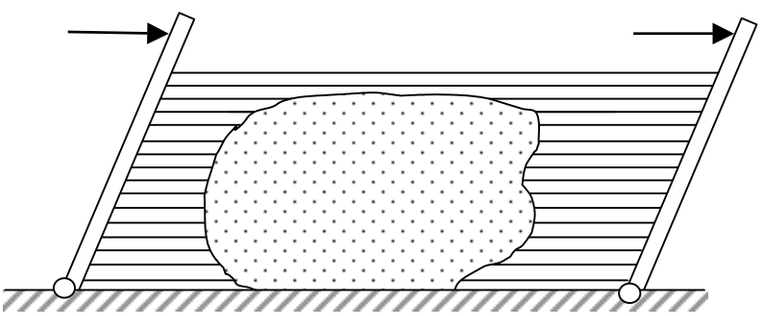


Fig. A plane scheme of the device. The figure plane is parallel to the plane of shearing and to the planes of two smooth side walls (not represented), the latter closing side openings of the cavity

XXI ICTAM, 15–21 August 2004, Warsaw, Poland

INCREMENTAL ENERGY MINIMIZATION IN MATERIAL INSTABILITY PROBLEMS

Henryk Petryk*, Klaus Thermann**
*Institute of Fundamental Technological Research, Polish Academy of Sciences, 00-049 Warsaw, Poland
**Department of Mechanical Engineering, Dortmund University, 44221 Dortmund, Germany

Summary Recent theoretical developments of the incremental energy minimization and its novel applications to material instability problems in time-independent inelastic solids are presented. Necessity of imposing a symmetry restriction on the constitutive law is discussed. The approach yields a natural criterion of selection of the post-critical deformation pattern and provides a computational method for determining deformation paths with automatic branch switching.

INTRODUCTION

The idea of determining the response of an inelastic body to slowly varying loading by minimizing *incrementally* the energy supply to the examined system received recently a wider attention. The concept was originally developed in relation to stability of solution paths in time-independent plasticity at finite deformation, cf. the first author's sectional lecture at IUTAM Congress in Kyoto, 1996 [1]. The theory provided a basis for the computational method that employs non-convex minimization of the incremental energy functional defined on a set of kinematically admissible fields. This method has found applications in calculations of microstructure formation in incrementally nonlinear materials and in crossing multiple bifurcation points with automatic selection of the post-critical deformation path [2].

The aim of this lecture is to provide recent theoretical developments of the incremental energy minimization and its novel applications to material instability problems in inelastic solids.

THEORETICAL DEVELOPMENTS

In outline, the incremental energy minimization in isothermal quasi-static deformation is characterized as follows

$$\Delta E \to \min \qquad \text{subject to kinematical constraints,} \qquad \Delta E = \Delta W + \Delta\Omega\,, \tag{1}$$

where a prefix Δ denotes a virtual increment corresponding to a non-zero increment of a loading parameter λ, ΔW is the total work increment supplied to the deforming body, and $\Delta\Omega$ is an increment in potential energy of the loading device (assumed conservative). It has been shown that an exact incremental solution represented by a velocity field $\widetilde{\mathbf{v}}$ is found by the minimization (1) applied to the part $\Delta_2 E$ that contains only the *second-order* terms with respect to a time increment Δt, reduced to

$$\int_B U(\dot{\mathbf{F}})\,dV \;+\ldots\to \min \qquad U=\tfrac{1}{2}\dot{\mathbf{S}}\cdot\dot{\mathbf{F}}\,, \qquad \dot{\mathbf{S}}=\partial U/\partial\dot{\mathbf{F}}\,, \qquad \dot{\mathbf{F}}=\operatorname{Grad}\mathbf{v}\,, \qquad \widetilde{\mathbf{v}}\in\mathcal{V}\,, \tag{2}$$

where U is the constitutive potential for determining the nominal stress rate $\dot{\mathbf{S}}^T$ from the forward rate $\dot{\mathbf{F}}$ of deformation-gradient $\mathbf{F}$, and $\mathcal{V}$ is a set of kinematically admissible velocity fields on a reference domain B. In (2), only the leading term (corresponding to $\Delta_2 W$) is displayed, while the second-order terms corresponding to $\Delta_2\Omega$ are indicated by dots. Existence of a potential U is required for a rigorous justification of the second-order minimization approach. The essence of (2) is that it represents *non-convex* minimization. In result, the modern *relaxation methods* (quasi-convexification and rank-one-convexification) developed in the context of elastic energy minimization are extended in a natural way to material instabilities in a class of inelastic solids. On using the approximation $\Delta\mathbf{F}=\operatorname{Grad}\mathbf{v}\,\Delta t+...$ and homogeneity of degree two of U, (2) can be used to generate finite increments as in some recent papers by other authors, e.g. [3]. However, finite time-step solutions are merely approximate unless further constitutive assumptions are introduced.

In a thermodynamic framework with internal variables $\boldsymbol{\alpha}$, the incremental response of the material can be determined from the following minimization problem derived from (1)

$$J(\dot{\boldsymbol{\alpha}})=\tfrac{1}{2}\dot{\boldsymbol{\alpha}}\cdot\phi_{,\boldsymbol{\alpha}\boldsymbol{\alpha}}\cdot\dot{\boldsymbol{\alpha}}+\tfrac{1}{2}D_1(\dot{\boldsymbol{\alpha}},\dot{\boldsymbol{\alpha}})+\dot{\mathbf{F}}\cdot\phi_{,\mathbf{F}\boldsymbol{\alpha}}\cdot\dot{\boldsymbol{\alpha}}\to\min\,, \qquad D_1(\dot{\boldsymbol{\alpha}},\hat{\boldsymbol{\alpha}})=\hat{\boldsymbol{\alpha}}\cdot D_{,\boldsymbol{\alpha}}(\dot{\boldsymbol{\alpha}},\boldsymbol{\alpha}) \tag{3}$$

where ϕ is the Helmholtz free energy density, $D=D(\dot{\boldsymbol{\alpha}},\boldsymbol{\alpha})$ is the dissipation function, and $\dot{\boldsymbol{\alpha}}$ lies within the cone $\mathcal{L}=\{\dot{\boldsymbol{\alpha}}:\ D(\dot{\boldsymbol{\alpha}},\boldsymbol{\alpha})=-\phi_{,\boldsymbol{\alpha}}\cdot\dot{\boldsymbol{\alpha}}\}$. As in (2), the essence of (3) lies in non-convex minimization. It has recently been shown [4] that the symmetry restriction $D_1(\dot{\boldsymbol{\alpha}},\dot{\boldsymbol{\alpha}}+\delta\dot{\boldsymbol{\alpha}})=D_1(\dot{\boldsymbol{\alpha}}+\delta\dot{\boldsymbol{\alpha}},\dot{\boldsymbol{\alpha}})$ for $\dot{\boldsymbol{\alpha}}\pm\delta\dot{\boldsymbol{\alpha}}\in\mathcal{L}$ must be imposed on the dissipation function as a condition necessary for the intrinsic consistency between the first- and second-order minimization in (1). Under this symmetry restriction and in the internal-variable formulation of multi-mode inelasticity, in the present paper theorems are formulated and proven that provide a novel justification of the second-order version of (1) as the energy condition necessary for stability of a solution path.

NOVEL APPLICATIONS

Three examples of application of (1), not published so far, are presented and discussed.

Of special interest is the case when instability of a uniform deformation path leads to the formation of a microstructure in an initially homogeneous material. This is illustrated by simulation of the formation of initially one and later two families of shear bands, cf. Fig 1, in an incrementally nonlinear elastoplastic material subjected to non-proportional straining. The results to be presented in the lecture provide an extension of those in [2] by incorporating the effect of an angular path of deformation. A particular feature of the obtained deformation pattern is that its formation is accompanied by multiple bifurcations. The step-by-step use of non-convex minimization makes it possible to follow the complex deformation path with automatic selection of the post-bifurcation solutions.

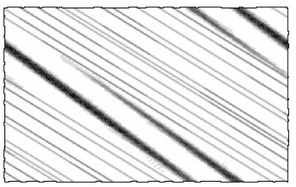


Fig. 1. Two intersecting families of shear bands in an incrementally nonlinear material, initially homogeneous.

The second example is concerned with rapid formation of shear bands that carry large plastic strains. While in the example mentioned above the shear bands develop gradually, in this example a single band forms instantaneously in the time scale of a loading program ($\lambda(t)$). It is shown how the incremental energy minimization (1) can be used to predict the onset of formation of such bands as well as their orientation.

In another example, bifurcation of the layered pattern of martensitic phase transformation in a shape memory alloy is analyzed. The upper pattern (I) sketched (not to scale) in Fig. 2 corresponds to macroscopically uniform distribution of internally twinned martensite plates, while in an alternative solution (II) the martensite plates first appear within a certain volume fraction only, forming an evolving rank-three laminated microstructure. Performed calculations have shown that the pattern (II) is energetically preferable initially, in the sense of the minimization rule (1).

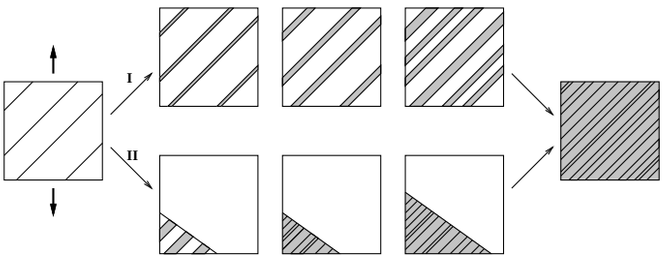


Fig. 2. Bifurcation of the layered transformation pattern: the transformation can proceed quasi-uniformly (upper pattern I) or be completed first within some volume fraction of the material (lower pattern II). [5]

CONCLUSIONS

The non-convex minimization of incremental energy

– is applicable to a broad class of time-independent inelastic solids, but requires a *symmetry assumption*,

– yields a natural *criterion of selection* of the material response or deformation pattern,

– provides a *computational method* for determining deformation paths with automatic branch switching.

References

[1] Petryk H.: Instability of plastic deformation processes. *Theoretical and Applied Mechanics 1996, Proc. XIXth IUTAM Congress, Kyoto*, 497-516. Elsevier, Amsterdam 1997.

[2] Petryk H., Thermann K.: Post-critical plastic deformation in incrementally nonlinear materials. *J. Mech. Phys. Solids* **50**: 925-954, 2002.

[3] Ortiz M., Repetto E.A.: Nonconvex energy minimization and dislocation structures in ductile single crystals. *J. Mech. Phys. Solids* **36**: 286-351, 1999.

[4] Petryk H.: Incremental energy minimization in dissipative solids, *C.R. Mecanique* **331**: 469-474, 2003.

[5] Petryk H., Stupkiewicz S.: Multi-scale micromechanical modeling of stress-induced martensitic transformation. *Proc. NATO-ARW: New Trends in Phase Transformations and Their Applications to Smart Structures* (to appear).

DYNAMICS OF PERTURBATIONS AND SHEAR BAND INSTABILITIES

Davide Bigoni[*] **Domenico Capuani**[**]
[*]*Dipartimento di Ingegneria Meccanica e Strutturale, Università di Trento,*
Via Mesiano 77 – 38050 Povo, Trento, Italia. Email bigoni@ing.unitn.it.
[**] *Dipartimento di Ingegneria, Università di Ferrara,*
Via Saragat 1– 44100 Ferrara, Italia. Email cpd@dns.unife.it

Summary The dynamic Green's function is obtained for an infinite nonlinear-elastic, incompressible solid homogeneously deformed and subject to time-harmonic incremental perturbations. The formulation is employed to investigate the effects of perturbations on the dynamic behaviour of solids near the shear band formation threshold. Results shed light on the problem of interaction between dynamics and shear band formation.

THE GREEN'S FUNCTION

Superimposed small disturbances are considered under dynamic (time-harmonic) conditions upon an elastic, incompressible, infinite body described by the Biot (1965) incremental equations and subject to plane, homogeneous –but arbitrary– deformation. Following Willis (1991), the dynamic, infinite body Green's function (or fundamental solution) is found for this problem. This solution –which paves the way for integral methods in incremental elastodynamics, generalizing previous findings by Brun et al. (2003)– is employed to analyze shear band formation following a perturbative approach.

THE PERTURBATIVE APPROACH

The perturbative approach is a generalization of that developed by Bigoni and Capuani (2002) for quasi-static deformation [see also the related results by Radi et al. (2002)] and consists in the analysis of the incremental displacement maps produced by a dipole formed by two unit, opposite forces. In the quasi-static case, it has been shown that a perturbation close enough to the elliptic boundary may induce localization patterns that are formally excluded in terms of the usual bifurcation approach (e.g. Rice, 1977). For instance, a localized pattern is clearly visible in Fig. 1 pertaining to a Mooney-Rivlin material, pre-deformed up to a stretch level close to the value 3, at which shear bands are formally excluded in the framework of the bifurcation approach (see Bigoni and Capuani, 2002, for details).

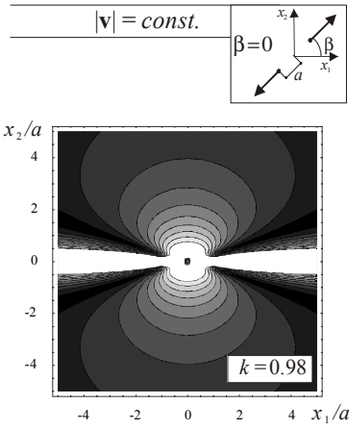


Fig. 1- Level sets of the modulus of incremental displacement vector for Mooney-Rivlin material for a dipole of width a, aligned along the x_1 axis (i.e. $\beta = 0$). Pre-stress parameter $k = 0.98$ corresponds to a stretch λ close to 3.

In this work, maps of incremental displacement produced in an infinite body by a harmonically pulsating dipole are analyzed with the aim of investigating the response to dynamic perturbations of a solid near the boundary of

shear band formation. The solution now depends on the frequency of the applied perturbation, which turns out to represent an important parameter in the analysis.

References

[1] Bigoni, D., Capuani, D., 2002. Green's function for incremental nonlinear elasticity: shear bands and boundary integral formulation. J. Mech. Phys. Solids 50, 471-500.
[2] Biot, M.A., 1965. Mechanics of Incremental Deformations. J. Wiley and Sons, New York.
[3] Brun, M., Capuani, D., Bigoni, D. A boundary element technique for incremental, nonlinear elasticity. Part. I: Formulation and Part. II: Bifurcation and shear bands. *Comp. Meth. Appl. Mech. Eng.* 192 (22-24), 2003, 2461-2479.
[4] Radi, E., Bigoni, D., Capuani, D. 2002 Effects of pre-stress on crack-tip fields in elastic, incompressible solids. *Int. J. Solids Structures*, 39, 3971-3996.
[5] Rice, J. R., 1977. The localization of plastic deformation. In: Theoretical and Applied Mechanics (ed. W.T. Koiter), pp. 207-220. North-Holland, Amsterdam.
[6] Willis, J.R., 1991. Inclusions and cracks in constrained anisotropic media. In: Wu, J.J., Ting, T.C.T. and Barnett, D.M. (Eds.), Modern Theory of Anisotropic Elasticity and Applications. SIAM, Philadelphia, pp. 87-102.

XXI ICTAM, 15–21 August 2004, Warsaw, Poland

ON CONVEXITY CONDITIONS IN SPATIAL AND MATERIAL SETTINGS OF HYPERELASTICITY

Paul Steinmann*, Ellen Kuhl*, Harm Askes**
*Mechanical Engineering, University of Kaiserslautern, D-67653 Kaiserslautern, Germany
**Civil Engineering and Geosciences, Delft University of Technology, NL-2600 Delft, Netherlands

Summary In this contribution convexity conditions for the spatial and material motion problem are investigated.
Whereas the spatial motion problem corresponds to the usual equilibrium equations, the material motion problem is driven by the inverse deformation gradient, thus it deals with material or configurational forces that are energetically conjugated to material variations, i.e. variations at fixed spatial positions.
The duality between the two problems is elaborated in terms of balance laws, their linearisations including the consistent tangent operators and in particular the so-called acoustic tensors.
Issues of convexity and in particular of rank-one-convexity are discussed in both settings. As a remarkable result it turns out, that if the rank-one-convexity condition is violated, the loss of well-posedness of the governing equations occurs simultaneously in the spatial and in the material motion problem.
Thus, the inclusion of the material motion problem does not lead to additional requirements to maintain rank-one-convexity or ellipticity.
The results are developed for the hyperelastic case in general and highlighted analytically and numerically for a material of Neo-Hookean type.

EXTENDED ABSTRACT

The motion of a continuous medium can be described via a Lagrangian or an Eulerian parametrisation. In the former, material particles are followed in space, whereas in the latter, material flow along fixed spatial positions is tracked. This is closely related to spatial and material settings of continuum mechanics, see e.g. [1, 3, 5]. In the spatial setting, spatial or physical forces are dealt with that are energetically conjugated to spatial variations of fixed material points. This is the viewpoint of classical mechanics involving forces in the sense of Newton. Conversely, in the material setting, material or configurational forces are encountered that are energetically conjugated to material variations at fixed spatial positions. This is the viewpoint of configurational mechanics involving forces in the sense of Eshelby.

The material setting of continuum mechanics has received considerable attention in recent years due to its theoretical as well as its numerical implications, see e.g. [2, 6, 8, 11, 13], whereby in particular the duality between the spatial and material setting has been elucidated for various cases and applications, see e.g. [4, 7, 12]. The related contributions of this group [1-13], which contain also the relevant references, are listed in the attached bibliography.

Material force residuals arise as a result of inhomogeneities and/or heterogeneities. Thus, the study of the material motion problem is relevant for problems involving propagating defects e.g. such as cracks, interfaces, voids and inclusions.

However, (spurious) material force residuals may also appear as a consequence of non-optimal finite element discretisations, which can be considered as numerical or algorithmic (as opposed to physical) inhomogeneities. Indeed, by moving nodes opposite to the (spurious) material force residual additional energy is released and vanishing (spurious) material force residuals can be obtained.

This has inspired the idea to consider in addition to the spatial motion problem the material motion problem whereby both the spatial coordinates and the material coordinates are taken as simultaneous degrees of freedom. Thus, an Arbitrary Lagrangian-Eulerian (ALE) parametrisation is obtained in a natural manner, see [9, 10]. It has been shown in [9, 10] that the meshes obtained via this dual equilibrium problem are optimal in the sense that the potential energy is the lowest possible for the given element connectivity. Thus the material motion problem can be used as a mesh optimisation method.

A relevant issue in the above methodology is the analysis of convexity of the spatial and the material motion problem. In the infinitesimal context, the convexity condition is strongly related to the classical criterion of uniqueness in terms of the positive definiteness of the second order work. The general convexity condition, however, is typically too restrictive from a physical point of view and, moreover, too difficult to evaluate from a mathematical point of view.

A weaker condition, yet having a well-established mathematical status is the condition of rank-one-convexity. In the infinitesimal sense, rank-one-convexity corresponds to the classical Legendre-Hadamard condition which dates back to the early work of Hadamard on the propagation of waves. For the class of non-transient problems considered herein, the loss of rank-one-convexity is one-to-one related to the loss of ellipticity which is typically accompanied by the loss of well-posedness of the governing equations. The elaboration of the rank-one-convexity condition is thus of fundamental relevance, not only for the spatial but also for the material motion problem.

Although the notions of convexity, uniqueness, monotony, stability, rank-one-convexity, ellipticity and well-posedness are well-established in the spatial motion context, the appropriate classification of the material motion problem turns out to be rather cumbersome. Nevertheless, in particular a difference between the two settings in this respect would be significant, for instance if the material motion problem would lose rank-one-convexity or rather ellipticity at an earlier stage of loading than the spatial motion problem, or vice versa.

After reiterating the governing equations in both settings, the convexity conditions of the two problems are discussed. To this end, relevant tangent operators are derived through a consistent linearisation of the corresponding problem. Next we elaborate the issue of rank-one-convexity which can be expressed in terms of the acoustic tensors. It turns out that their relation is of remarkable simplicity: the acoustic tensor of the one setting can be obtained from the acoustic tensor of the other setting by a double push forward / pull back and a scaling in terms of the applied stretch!

As a consequence, a loss of ellipticity occurs simultaneously in both settings. This implies that the material motion problem offers no additional difficulties compared to the spatial motion problem, as regards the loss of well posedness.

For illustration purposes, the corresponding analyses are exemplified for a Neo-Hookean material, whereby the eigenvalues of both acoustic tensors are investigated.

References

[1] Steinmann P., [2000]
Application of Material Forces to Hyperelastostatic Fracture Mechanics.
Part I: Continuum Mechanical Setting
Int. J. Solids Structures, Vol. 37, pp. 7371-7391

[2] Steinmann P., D. Ackermann & F.J. Barth, [2001]
Application of Material Forces to Hyperelastostatic Fracture Mechanics.
Part II: Computational Setting
Int. J. Solids Structures, Vol. 38, pp. 5509-5526

[3] Steinmann P., [2002]
On Spatial and Material Settings of Hyperelastodynamics
Acta Mechanica, Vol. 156, pp. 193-218

[4] Steinmann P., [2002]
On Spatial and Material Settings of Hyperelastostatic Crystal Defects
J. Mech. Phys. Solids, Vol. 50, pp. 1743-1766

[5] Steinmann P., [2002]
On Spatial and Material Settings of Thermo-Hyperelastodynamics
J. Elasticity, Vol. 66, pp. 109-157

[6] Liebe T., R. Denzer & P. Steinmann, [2003]
Application of the Material Force Method to Isotropic Continuum Damage
Comp. Mech., Vol. 30, pp. 171-184

[7] Kuhl E. & P. Steinmann, [2003]
On Spatial and Material Settings of Thermo-Hyperelastodynamics for Open Systems
Acta Mechanica, Vol. 160, pp. 179-217

[8] Denzer R., F.J. Barth & P. Steinmann, [2003]
Studies in Elastic Fracture Mechanics Based on the Material Force Method
Int. J. Num. Meth. Engrg., Vol. 58, pp. 1817-1835

[9] Kuhl E., H. Askes & P. Steinmann, [2003]
An ALE Formulation Based on Spatial and Material Settings of Continuum Mechanics
Part 1: Generic Hyperelastic Formulation
Comp. Meth. Appl. Mech. Engrg., accepted

[10] Askes H., E. Kuhl & P. Steinmann, [2003]
An ALE Formulation Based on Spatial and Material Settings of Continuum Mechanics
Part 2: Classification and Applications
Comp. Meth. Appl. Mech. Engrg., accepted

[11] Kuhl E., R. Denzer, F.J. Barth & P. Steinmann, [2003]
Application of the Material Force Method to Thermo-Hyperelasticity
Comp. Meth. Appl. Mech. Engrg., accepted

[12] Kuhl E. & P. Steinmann, [2003]
Material Forces in Open System Mechanics
Comp. Meth. Appl. Mech. Engrg., accepted

[13] Menzel A., R. Denzer, & P. Steinmann, [2003]
On the Comparison of Two Approaches to Compute Material Forces for Inelastic Materials.
Application to Single-Slip Crystal-Plasticity
Comp. Meth. Appl. Mech. Engrg., accepted

XXI ICTAM, 15–21 August 2004, Warsaw, Poland

COMPUTATIONAL CHARACTERIZATION OF MICRO- TO MACROSCOPIC MECHANICAL BEHAVIOR OF CARBON BLACK-FILLED RUBBER

Yoshihiro Tomita, Wei Lu, Yasuhiro Furutani
Graduate School of Science and Technology, Kobe University, Kobe, 657-8501, Japan

INTRODUCTION

It is well known that the blending of particulate fillers such as carbon black induce an increase in ultimate properties such as tear and tensile strength and abrasion resistance [1]. Fillers also increase the moludus of elasticity. The hysteresis loss, i.e., Mullins effect [2], during loading and unloading processes for carbon black-filled rubber is marked as compared with that of unfilled rubber, which is strongly related to the ultimate properties of filled rubber [2]. Here, we focus our attention on the computational evaluation of the enhancement of deformation resistance and hysteresis loss, caused by filling carbon black to rubber.

The constitutive equation for rubber is established by employing a nonaffine molecular-chain network model [3], which may account for the change of the entanglement situation during the deformation processes. Meanwhile, the carbon black is assumed to be sufficiently hard compared with rubber and the deformation behavior is governed by the linear elastic constitutive equation. The computational simulations employing these constitutive equations and unit cell models of rubber containing carbon black clarify the mechanisms of enhancement of deformation resistance and hysteresis loss, and the effect of volume fraction and distribution patterns of carbon black on these characteristics. The computationally predicted results and experimental results are compared to evaluate the adequacy of the present simulation.

CONSTITUTIVE EQUATION AND COMPUTATIONAL MODEL

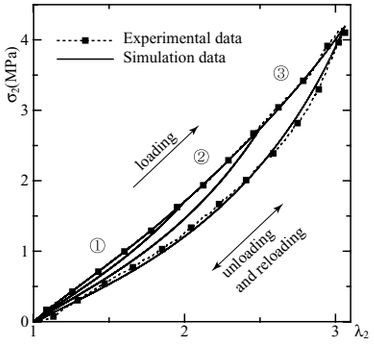


Figure 1. Hysteresis of unfilled rubber under cyclic loading.

It has been suggested that a network is formed by linking polymer chains together, and this linkage may be either physical or chemical. The physical links are, in general, not permanent and may change depending on deformation and temperature change. On the other hand, chemical links are permanent and preserve the entangled situation. The physical links play a very important role in the manifestation of the hysteresis of cyclic deformation behavior of rubber [4]. The decrease in the number of entangled points due to deformation causes the increase of the average number of segments in a single chain, enhanced extensibility, and the reduction of the stiffness of the material, i.e., softening. Here, we employ the nonaffine molecular-chain network model [3] to accommodate the change in the average number of segments N depending on stretch λ_c, as $N(\lambda_c) = N_0 + f(\lambda_c)$, where N_0 is the initial average number of segments in a single chain, $f(\lambda_c)$ is a polynomial which suitably expresses the experimental results, and we employ the quartic expression of λ_c.

Figure 1 indicates the true stress-stretch relationship for unfilled rubber under cyclic loading. The dotted lines represent the experimental results. To reproduce the experimental results, we identify the concrete form of $N(\lambda_c)$, by the least mean squares method, for the loading process of the first cycle and it is preserved during the unloading process. Furthermore, the number of segments N is preserved until stretch λ_c due to subsequent loading reaches the maximum value of previous loading processes. The corresponding stress-stretch relationships shown in Fig.1 by solid lines approximately reproduce the experimentally obtained results.

The mechanical characteristics of carbon black-filled rubber are strongly dependent on the volume fraction and distribution patterns of carbon black. Although the distribution of carbon black is somewhat random to aggregated, here, we assume that it is periodic and evaluate the detailed characteristics of microscopic deformation and clarify their effect on the macroscopic mechanical characteristics of carbon black-filled rubber. The discussions are focused on the essential feature of the effect of volume fraction and distribution patterns on the mechanical characteristics of carbon black-filled rubber.

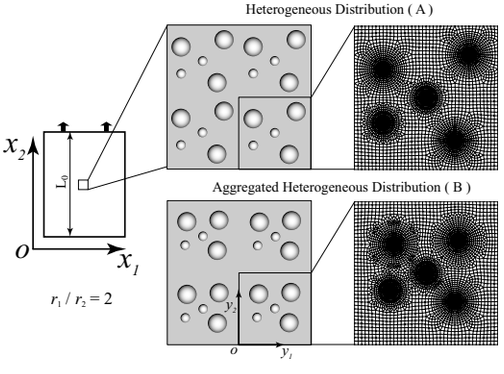


Figure 2. Simulation models of carbon black-filled rubber with volume fraction 20%.

Figure 2 shows the computational model in which heterogeneous carbon black is assumed to be distributed periodically. As indicated in Fig.2, in the present investigation, the heterogeneous carbon black is assumed to comprise circular cylinders of radii of curvature r_1 and r_2 contained in a square unit cell. Case A corresponds to carbon black distributed throughout the unit cell, and Case B is the somewhat aggregated case. The homogenization method [5] has been employed to correlate the micro- to macroscopic deformation behavior.

For a typical unit cell, which is the microscopic element of carbon black-filled rubber, a macroscopically homogeneous strain is applied. The material parameters for the rubber employed are $N_0 = 4.5$, $N_a = 4.36 \times 10^{26}$, $C_0^R = n_0 k_B T =$

0.394, $n_0 = N_a/N_0$, and $T = 296K$ [6]. For carbon black, elasticity modulus and Poisson's ratio are $E_c = 100\mathrm{MPa}$ and $\nu_c = 0.3$ respectively. To suppress the onset of numerical instability caused by the extreme difference between the stiffnesses of carbon black and rubber, rather low stiffness for carbon black is introduced. It has, however, been verified that this value provides suitable results.

RESULTS AND DISCUSSION

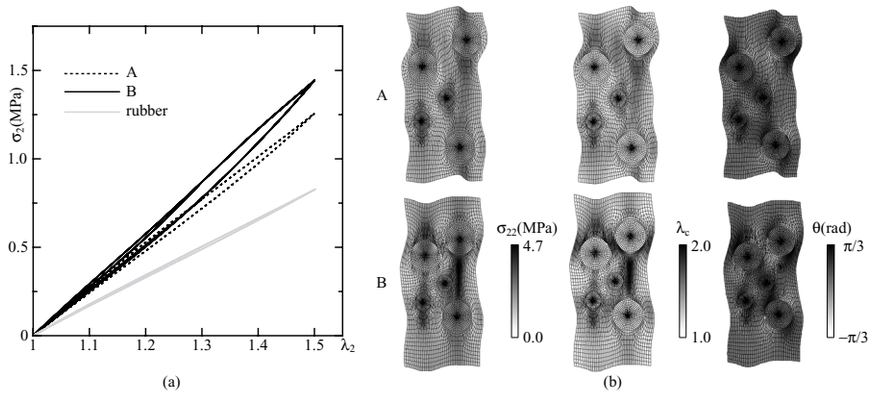


Figure 3. Deformation behavior of carbon black-filled rubber with $f_0 = 20\%$. (a) True stress-stretch relationships. (b) Distribution of stress, stretch and rotation for cases A and B at deformation stage $\lambda_2 = 1.5$.

Three cyclic deformations up to maximum average stretches of 1.1, 1.3 and 1.5 for 1st, 2nd and 3rd cycles, respectively, are simulated. Figure 3(a) shows the typical true stress-stretch relationships for unfilled rubber and carbon black-filled rubber for cases A and B in Fig.2. Carbon black-filled rubber exhibits markedly high deformation resistance as compared with unfilled rubber. The aggregated distribution of carbon black, case B, contributes to the further increase of deformation resistance. The resistance to deformation rises with an increase of the volume fraction of carbon black f_0.

As indicated in Fig.3(b), the concentrated deformation connecting the carbon black causes high stretching accompanied by locally large rotation in the surrounding area of highstretch. The orientation hardening of rubber develops in the highly stretched area where the resistance to deformation rises and the stress attains a high value. On the other hand, in the highly rotated area, deformation is mainly absorbed by rotation and orientation hardening is suppressed, which limits the stress to a rather low value. The localized deformation connecting large particles is much stronger, therefore, in addition to the distance between the particles, heterogeneity of the particles also affects the deformation resistance. The increase of the volume fraction of carbon black reduces the particle spacing, which facilitates the emergence of localized deformation connecting the particles and high resistance to deformation. Thus an additional increase in deformation resistance is expected upon filling the rubber with carbon black.

Furthermore, as indicated above, the higher concentration of the deformation causes locally high stretch in rubber, which promotes the change of the average number of segments. As a result, this contributes to the manifestation of hysteresis loss, i.e., Mullins effect, in the cyclic stress-stretch relationships.Figure 4 indicates the hysteresis loss for 1st, 2nd and 3rd cycles for unfilled rubber and carbon black-filled rubber with patterns A and B. The hysteresis loss $\Delta\phi$ is defined by the difference in the areas under the stress-stretch curves for a loading cycle followed by an unloading cycle. Hysteresis loss $\Delta\phi$ increases with the increases of average stretch and aggregation of carbon black. Furthermore, the effect of the volume fraction of carbon black on hysteresis loss is substantial and is amplified with the increase in the number of cycles, in other words, the increase in the amount of stretch in the present loading processes. These are attributable to the softening caused by the change in the average number of segments due to the increase in the amount of stretch.

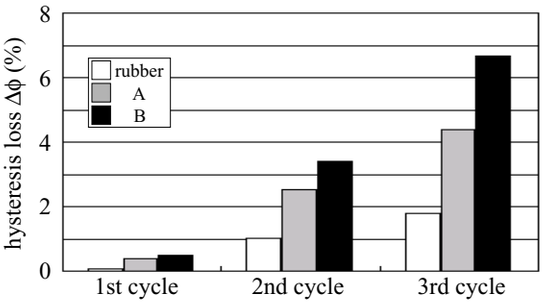


Figure 4. Hysteresis loss for different distribution patterns.

The results obtained partially clarified the essential physical enhancement mechanisms of deformation resistance and hysteresis loss, i.e., Mullins effect, for rubber filled with carbon black with different distribution patterns and volume fractions.

References

[1] Medalla, A.I., Kraus, G.: Reinforcement of Elastomers by Particulate Fillers. *Scence and Technology of Rubber*:387–418. Second Edition, Academic Press, 1994.

[2] Mullins, L.: Effect of Stretching on the Properties of Rubber. *Rubber Chem. Technol.***21**:281–300, 1948.

[3] Tomita, Y., Adachi, T., Tanaka, S.: Modelling and Application of Constitutive Equation for Glassy Polymer Based on Nonaffine Network Theory. *Eur. J. Mech. A/Solids***16**:745–755, 1997.

[4] Marckmann, G., Verron, E., Gornet, L., Chagnon, G., Charrier, P., Fort, P.: A Theory of Network Alteration for the Mullins Effect. *J. Mech. Phys. Solids***50**:2011–2028, 2002.

[5] Higa, Y., Tomita, Y.: Computational Prediction of Mechanical Properties of Nickel-based Superalloy with Gamma Prime Phase Precipitates. *Advance Materials and Modeling of Mechanical Behavior* **III**:1095–1099. Fleming Printing Ltd., 1999.

[6] Furutani, Y., Lu, W., Uchida, M., Naito, M., Tomita, Y.: Simulation of Deformation Behavior of Carbon Filled Rubber with Heterogeneous Chain Structures. *CMD2003*:399–400, 2003, (in Japanese).

MATERIAL INSTABILITIES OF FIBER-REINFORCED NONLINEARLY ELASTIC SOLIDS

J. Merodio [*], R. W. Ogden [**]
[*] *Department of Structural and Mechanical Engineering, E.T.S. Ing. Industriales y Tel., University of Cantabria, 39005, Santander, Spain*
[**] *Department of Mathematics, University of Glasgow, Glasgow G12 8QW, UK*

Summary Fiber kinking, fiber splitting, fiber de-bonding and matrix failure are addressed within the context of nonlinear elasticity for fiber-reinforced materials under plane deformation. Fiber failure is given by loss of ellipticity of the governing differential equations.

EXTENDED SUMMARY

A continuum mechanical model designed to predict fiber instabilities in fiber reinforced composite materials is proposed in the context on nonlinear elasticity theory and examined under plane deformation extending the analysis given recently by Merodio and Ogden [1,2]. The (material) instabilities under consideration include fiber kinking, fiber de-bonding, fiber splitting and matrix failure of fiber-reinforced composite materials. In particular, the material models examined are isotropic nonlinearly elastic models augmented with a function that accounts for the existence of a unidirectional reinforcing. This function endows the material with its anisotropic character and is called a *reinforcing model*. The onset of failure is associated with the incipient loss of elliptcity of the governing differential equations (or, equivalently, of the material model). Previous work has dealt with the analysis of specific reinforcing models (see [1] and [2] for references), in particular the so-called *standard reinforcing model*. It was established that the loss of ellipticity for these augmented isotropic materials requires contraction in the reinforcing direction. The loss of ellipticity was related to fiber kinking. Here we generalize these results and establish sufficient conditions to guarantee the ellipticity of the governing equations of equilibrium for more general reinforcing models. Both compressible and incompressible materials are considered. The incipient loss of ellipticity is interpreted in terms of fiber kinking, fiber de-bonding, fiber splitting and matrix failure in fiber-reinforced composite materials.

The loss of ellipticity condition provides the deformation associated with the existence of surfaces of weak discontinuity as well as the directions of the normals to such surfaces for any particular strain-energy function. Surfaces of weak discontinuity (or weak surfaces) are surfaces across which the second derivative of the displacement field is discontinuous (a strong surface of discontinuity, across which the first derivative is discontinuous, is necessarily also a weak surface). In the present analysis, we relate the angle between the weak surface and the fiber reinforcement direction to a particular failure mechanism for a given material model. The onset of fiber kinking is associated with weak surfaces close to the normal of the fiber-reinforcement direction under fiber contraction [3]. Hence, if the loss of ellipticity analysis gives a weak surface perpendicular to the fiber under fiber contraction, the associated fiber failure may be identified as fiber kinking. On the other hand, the angle between the weak surface and the fiber reinforcement is close to zero for fiber debonding [4]. For fiber kinking with fiber splitting, the simultaneous existence of weak surfaces close to and normal to the fiber direction is required [5]. Matrix failure is associated with weak surfaces perpendicular to the fiber reinforcement under fiber extension [6].

In three dimensions, two invariants are sufficient to characterize the anisotropic nature of a transversly isotropic material model. These invariants are deformation measures. One of these two invariants is related only to the fiber stretch of the fiber reinforcement. It is denoted by I_4. The standard reinforcing model is a quadratic function that depends only on this invariant. The other invariant, denoted I_5, is also related to the fiber stretch but introduces an additional effect that influences directly the behavior of the reinforcement under shear deformations. For plane deformation containing the fiber direction these invariants are not independent. Hence, the ellipticity analysis for a general strain-energy function depends on at most one transversly anisotropic invariant. Nevertheless, both invariants are considered since each invariant adds a distinct anisotropic character to the isotropic base material.

First, the ellipticity status of general reinforcing models depending on I_4 is established. The result is the same for both compressible and incompressible materials. It is shown that fiber failure is expected in fiber compression. Under compressive loading in the fiber direction the incipient loss of ellipticity is related to fiber kinking. Fiber failure can also involve fiber extension if the reinforcing model loses convexity, in which case fiber debonding is the expected failure mode. The ellipticity analysis and its relation to fiber failure for reinforcing models depending on the invariant I_5 is also established. In this case the results for compressible and incompressible materials are quite different for fiber extension but similar for fiber contraction. Under compressive loading in the fiber direction, fiber kinking and fiber splitting are the expected failure modes for either compressible or incompressible materials. On the other hand, matrix failure is the expected failure mode under tensile loading in the fiber direction for compressible materials. For incompressible materials, it is shown that the expected failure mode is a weak surface neither perpendicular nor parallel to the fiber direction. This is a failure mode often associated with isotropic materials and corresponds to the initiation of

shear bands. Finally, it is shown that convex reinforcing models can fail under fiber extension regardless of the specific form of the model.

References

[1] Merodio J., Ogden R.W.: Material Instabilities in fiber-reinforced nonlinearly elastic solids under plane deformation, *Archives of Mechanics* **54** 525-552, 2002.

[2] Merodio J., Ogden R.W.: Instabilities and loss of ellipticity in fiber-reinforced compressible non-linearly elastic solids under plane deformation, *International Journal of Solids and Structures* **40** 4707-4727, 2003.

[3] Budiansky B., Fleck N.A.: Compressive failure of fiber composites, *Journal of the Mechanics and Physics of Solids* **41** 183-211, 1993.

[4] Piggott M.R.: Why interface testing by single-fibre methods can be misleading, *Composites Science and Technology* **57** 965-974,1997.

[5] Lee S.H., Yerramalli C.S., Waas A.M.: Compressive splitting response of glass-fiber reinforced unidirectional composites, *Composites Science and Technology* **60** 2957-2966, 2000.

[6] Liao K., Reifsnider K.L.: A Tensile Model for Unidirectional Fiber-Reinforced Brittle Matrix Composite, *International Journal of Fracture* **106** 95-115, 2000.

ULTRASTIFF ELASTIC COMPOSITES VIA NEGATIVE STIFFNESS INCLUSIONS, AND MATERIAL STABILITY IMPLICATIONS

Walter J. Drugan
University of Wisconsin-Madison, Department of Engineering Physics,
1500 Engineering Drive, Madison, WI, 53706, USA

Summary Composite materials of extremely high stiffness, far higher than that of either phase and exceeding all standard bounds, can be produced by using negative stiffness inclusions. We show this via several exact solutions within linearized and also fully nonlinear elasticity, and via the overall modulus estimate of a variational principle shown to be valid in this case. Negative-stiffness materials are unstable alone, but these composites can be stable under appropriate conditions.

INTRODUCTION

We consider elastic two-phase composite materials comprised of isotropic phases. For such materials, the Voigt bound provides an upper limit on the elastic stiffness of the composite material. If the composite material is macroscopically isotropic, the Hashin-Shtrikman bound provides a tighter (lower) upper bound on the composite elastic stiffness. These bounds are based on the assumption that the elastic materials comprising the composite's phases are both positive-definite. Lakes and Drugan [1] showed that if this assumption is relaxed, composite materials having elastic stiffnesses far higher than these bounds, and than that of either phase, can be produced. For the case of matrix-inclusion composites in which the matrix material is positive-definite, this will occur if the inclusions, which may have a very small volume fraction, have a specifically-tuned negative stiffness. We show this by several exact solutions within linearized and also fully nonlinear elasticity, and also via the overall modulus estimate of a variational principle that we show to be valid in this case of negative stiffness inclusions. Negative-stiffness materials are not stable by themselves, but we present arguments and preliminary results showing that a composite material of the type just described can have overall stability under the appropriate conditions.

EXACT SOLUTIONS AND VARIATIONAL ESTIMATES SHOWING ULTRAHIGH STIFFNESS

We demonstrate that a composite material can have an extremely high stiffness via several exact solutions within linearized and fully nonlinear elasticity. A brief summary of some results is given here; detailed derivations are in [1]. The simplest problem analysed is that of a spherical body containing a concentric spherical inclusion, because of the complete clarity of the results. It is shown in [1] that the overall bulk modulus $\overline{B}$ of the composite sphere is

$$\overline{B} = \frac{B_1(1+2c_1) + 2B_2(1-c_1)(1-2\nu_2)/(1+\nu_2)}{(1-c_1)B_1/B_2 + 2(1-2\nu_2)/(1+\nu_2) + c_1}\ , \tag{1}$$

so that the overall bulk modulus has an extremely high positive value when the (negative) inclusion bulk modulus is just slightly below the critical value

$$B_1 = -\frac{1}{1-c_1}\left[\frac{2(1-2\nu_2)}{1+\nu_2} + c_1\right]B_2. \tag{2}$$

In these results, B is bulk modulus, ν is Poisson's ratio, c is phase volume fraction, and subscripts 1 and 2 refer to the inclusion and matrix phases, respectively. We will also describe the finite elasticity analysis of this problem.

Another exact solution to a more complex microstructure is that of Hashin [2], who derived the composite bulk modulus of a hierarchical microstructure of coated spheres of different sizes in which the outer layer (phase 2) radius and core (phase 1) radius have a specified ratio for all inclusions. The composite is made by adding inclusions of progressively smaller size until the space is filled. The solution remains valid if the core phase has a negative stiffness. This solution turns out to be identical to (1), so that again the overall bulk modulus of this hierarchical composite has an extremely high positive value when the inclusion bulk modulus is just slightly below the critical value (2).

A more novel, general and practically important result showing that an extremely high composite stiffness results from the appropriate choice of negative inclusion stiffness comes from the following demonstration that an existing variational principle is valid in this case. For simplicity, let us consider an infinite linear elastic composite body consisting of firmly-bonded phases that is loaded only by a body force distribution $\boldsymbol{f}(\mathbf{x})$. Following Hashin and Shtrikman, Willis [3] showed that the governing equations of linear elasticity for the stress and infinitesimal strain tensor fields $\boldsymbol{\sigma}$, $\boldsymbol{\varepsilon}$, and the displacement vector field $\mathbf{u}$, can be recast as follows: One introduces a *homogeneous* "comparison" body with fourth-rank modulus tensor (independent of position $\mathbf{x}$) $\mathbf{L}_0$ [and having solutions $\boldsymbol{\sigma}_0(\mathbf{x})$, $\boldsymbol{\varepsilon}_0(\mathbf{x})$, to the same applied $\boldsymbol{f}(\mathbf{x})$], so that, in terms of the actual material's position-dependent modulus tensor $\mathbf{L}(\mathbf{x})$,

$$\boldsymbol{\sigma}(\mathbf{x}) = \mathbf{L}_0\boldsymbol{\varepsilon}(\mathbf{x}) + \boldsymbol{\tau}(\mathbf{x}), \qquad \boldsymbol{\tau}(\mathbf{x}) \equiv [\mathbf{L}(\mathbf{x}) - \mathbf{L}_0]\boldsymbol{\varepsilon}(\mathbf{x}), \tag{3}$$

where the second equation defines the "stress polarization" tensor field $\boldsymbol{\tau}(\mathbf{x})$. The solution to the elasticity field equations can then be shown to involve solution of the following integral equation for $\boldsymbol{\tau}(\mathbf{x})$:

$$\left(\mathbf{L}(\mathbf{x})-\mathbf{L}_0\right)^{-1}\boldsymbol{\tau}(\mathbf{x})+\int \boldsymbol{\Gamma}_0(\mathbf{x}-\mathbf{x}')\boldsymbol{\tau}(\mathbf{x}')\mathrm{d}\mathbf{x}' \;=\; \boldsymbol{\varepsilon}_0(\mathbf{x}), \tag{4}$$

where $\boldsymbol{\Gamma}_0(\mathbf{x})$ is a fourth-rank tensor field that is two spatial derivatives of the infinite-homogeneous-body (i.e., comparison body) Green's function.

The important fact for present purposes is that Willis [3] proved that self-adjointness of (4) arises solely from the usual index symmetries of the actual elastic modulus tensor $\mathbf{L}(\mathbf{x})$ and the comparison modulus tensor $\mathbf{L}_0$, and that this self-adjointness immediately implies from (4) the Hashin-Shtrikman (stationary) variational principle

$$\delta\left\{\int\left[\boldsymbol{\tau}(\mathbf{x})\left(\mathbf{L}(\mathbf{x})-\mathbf{L}_0\right)^{-1}\boldsymbol{\tau}(\mathbf{x})+\boldsymbol{\tau}(\mathbf{x})\int \boldsymbol{\Gamma}_0(\mathbf{x}-\mathbf{x}')\boldsymbol{\tau}(\mathbf{x}')\mathrm{d}\mathbf{x}' - 2\boldsymbol{\tau}(\mathbf{x})\boldsymbol{\varepsilon}_0(\mathbf{x})\right]\mathrm{d}\mathbf{x}\right\}=0. \tag{5}$$

Therefore, this variational principle is valid even when one of the phases of the composite has negative stiffnesses, so long as the actual and comparison elastic modulus tensors have the usual index symmetries, and provided that the comparison modulus tensor is chosen such that a Green's function exists for the body.

Willis [4] showed how to apply (5) to random composite materials. Retaining up through two-point statistical information, and assuming statistical uniformity and ergodicity of the composite, he deduced the stochastic form of (5). Making for simplicity the further assumption of isotropic *distribution* of the phases, the stochastic form of (5) gives the following estimate for the effective modulus tensor of the random composite material having n phases each with modulus tensor $\mathbf{L}_r$:

$$\overline{\mathbf{L}}=\left\{\sum_{r=1}^{n} c_r\left[\mathbf{I}+\left(\mathbf{L}_r-\mathbf{L}_0\right)\mathbf{P}\right]^{-1}\right\}^{-1}\sum_{s=1}^{n} c_s\left[\mathbf{I}+\left(\mathbf{L}_s-\mathbf{L}_0\right)\mathbf{P}\right]^{-1}\mathbf{L}_s, \quad \text{where} \quad \mathbf{P}\equiv\frac{1}{4\pi}\int_{|\boldsymbol{\xi}|=1}\tilde{\boldsymbol{\Gamma}}_0(\boldsymbol{\xi})\mathrm{d}S\ . \tag{6}$$

Here, $\mathbf{I}$ is the fourth-rank identity tensor and the constant fourth-rank tensor $\mathbf{P}$ is given in terms of the Fourier transform of $\boldsymbol{\Gamma}_0(\mathbf{x})$.

Result (6) is thus a variational estimate valid for composites having a negative stiffness phase. To be completely explicit, we now consider two-phase composites consisting of an isotropic matrix containing a random distribution of isotropic inclusions (of arbitrary shape). In this case, (6) simplifies to give the following variational estimates for the overall bulk and shear moduli of the composite, where subscripts 1, 2 indicate inclusion and matrix, respectively, and the unsubscripted quantities are the comparison moduli

$$\overline{B}=\frac{4G\left(c_1B_1+c_2B_2\right)+3B_1B_2}{4G+3\left(c_1B_2+c_2B_1\right)}, \qquad \overline{G}=\frac{G\left(9B+8G\right)\left(c_1G_1+c_2G_2\right)+6\left(B+2G\right)G_1G_2}{G\left(9B+8G\right)+6\left(B+2G\right)\left(c_1G_2+c_2G_1\right)}. \tag{7}$$

Let us consider specifically a composite consisting of a positive-definite matrix phase containing inclusions of negative stiffness. A permissible and sensible choice for the comparison moduli is that they equal the matrix moduli. Then (7) show that the variational estimates of the bulk and shear moduli can be made to be arbitrarily large and positive by suitable (negative) choice of the inclusion moduli, namely just slightly below the following critical values

$$B_1=-\frac{4G_2+3c_1B_2}{3c_2}, \qquad G_1=-G_2\,\frac{3\left(3+2c_1\right)B_2+4\left(2+3c_1\right)G_2}{6c_2\left(B_2+2G_2\right)}. \tag{8}$$

STABILITY ISSUES

The above results demonstrate that a composite material having inclusions with appropriately-tuned negative stiffnesses can exhibit composite stiffnesses far greater than those of either component and of existing bounds. For such a composite material to be useful in structural components, it must be stable. As noted above, materials with negative stiffness are unstable by themselves, but negative stiffness inclusions in a positive-definite matrix can yield a composite material that is stable under appropriate conditions. We will review the known results on stability of elastic materials and composites and discuss how it applies in the present context. We will also present the latest results of our theoretical efforts, currently underway, to prove precisely the conditions under which such composite materials are stable.

References

[1] Lakes, R. S. and Drugan, W. J.: Dramatically Stiffer Elastic Composite Materials Due to a Negative Stiffness Phase? *J. Mech. Phys. Solids* **50**:979-1009, 2002.

[2] Hashin, Z.: The Elastic Moduli of Heterogeneous Materials. *J. Appl. Mech.* **29**:143-150, 1962.

[3] Willis, J. R.: Bounds and Self-Consistent Estimates for the Overall Properties of Anisotropic Composites. *J. Mech. Phys. Solids* **25**:185-202, 1977.

[4] Willis, J. R.: Elasticity Theory of Composites. In: Hopkins, H. G. and Sewell, M. J. (Eds.), Mechanics of Solids: The R. Hill 60th Anniversary Volume. Pergamon Press, Oxford, pp. 653-686, 1982.

STABILITY OF IDEAL INFINITE CRYSTAL UNDER FINITE UNIFORM DEFORMATION

Pavel V. Tkachev
Institute for Problems in Mechanical Engineering Russian Academy of Sciences, Molecular and Particle Dynamics Simulation Group , Bolshoy pr. V. O., 61, 199178 St. Petersburg, Russia
St. Petersburg State Polytechnical University, Dep. of Theoretical Mechanics, 195251 St. Petersburg, Russia

Summary. Strong deformation and fracture are very difficult to describe using macroscopic continuum methods. Lack of a material continuousness makes description of such processes to be a serious challenge. In the presented paper the onset of the material fracture is studied from both micro- and macroscopic points of view. First an ideal infinite crystal lattice is considered. Transfer from microstructure to continuum mechanics is made using long-wave approximation. This allows obtaining nonlinear continuum equations of the infinite crystal under finite uniform deformation. These equations are found without limitation to the space dimension. For the stability verification a small deformation is superposed to a finite deformation of the crystal lattice being described by the obtained nonlinear macroscopic equations. Criterions of the material stability and their relevance to the crystal structure are obtained.

INTRODUCTION

A lot of facts give evidence about crucial role of the internal structure in the processes which attend deformation. That is why an influence of the material structure to its mechanical behavior requires a serious attention. Most of classic continuum methods have serious problems describing strong deformation and fracture, because the material is not really continuous in this case.
Generally the microstructure can be considered by the following three ways. The first way is to analyze microstructure and obtain stability criterion for the crystal cell [1] using microscopic equations for the atoms motion. The second way is to compute deformation and fracture processes using molecular dynamics method [2, 3, 4, 5, 6]. The third way is to consider the microstructure in the classic continuum mechanics equations, in other words make transfer from the microstructure to continuum mechanics [7, 8, 9]. In the presented paper we will follow the third way and then use the continuum mechanics methods to analyze stability of the material under finite deformation.

METHODS AND ANALYSIS

The material is represented as an infinite crystal. The dynamics of the particles (atoms) forming the crystal is described by Newtonian equations of motion, where each particle is interacting with the other particles via prescribed potential interaction forces. Transfer from microstructure to continuum mechanics is made using long-wave approximation [7, 10]. This allows obtaining nonlinear continuum equations of the infinite crystal in the Piola [11] form

$$\rho \ddot{\underline{u}} - \overset{\circ}{\nabla} \cdot \underline{\underline{P}} = 0, \tag{1}$$

where ρ is the material density in the reference configuration, $\underline{u}$ is the displacement vector, $\overset{\circ}{\nabla}$ is the vector differential operator in the reference configuration, $\underline{\underline{P}}$ is the Piola stress tensor, which can be expressed in the terms of the microscopic parameters as following [7]

$$\underline{\underline{P}} \equiv \frac{1}{2v_*} \sum_{\alpha} \Phi\left(A_\alpha^2\right) \underline{a}_\alpha \underline{A}_\alpha \ ; \tag{2}$$

where v_* is the volume of the elementary crystal cell in the reference configuration; $\underline{a}_\alpha$ is the vector from the current particle to the particle number α in the reference configuration; $\underline{A}_\alpha$ is the vector $\underline{a}_\alpha$ in the actual configuration;

$$\Phi\left(A_\alpha^2\right) = -\frac{\Pi'\left(A_\alpha\right)}{A_\alpha}, \tag{3}$$

where $\Pi\left(r\right)$ is the pair potential of interaction between the particles, which is a function of the distance between the particles. These equations are valid for both 2D and 3D considerations.

For the stability verification a small deformation is superposed to a finite deformation of the crystal lattice being described by the obtained nonlinear macroscopic equations. As a result the system of equations in variations can be obtained. Criterions of the material stability and their relevance to the crystal structure are obtained and will be presented in the lecture. Instability is considered as non-oscillation motion of the crystal lattice.

CONCLUSIONS

Using long-wave approximation it is possible to consider interaction only within a limited vicinity of the current particle. However, using the presented method it is possible to take into account not only the nearest neighbors, but as many coordination shells as needed. Thereby this method can describe materials for which the interaction between the particles decreases relatively slowly with respect to the distance between them.
The material is represented as an infinite crystal. Consequently in the paper the influence of the boundary effects and material imperfections is neglected. But in spite of these rude assumptions the method allows describing the important feature of all materials — stability loss under strong deformations in correlation with the material microstructure, which is difficult to describe using purely continuum considerations.

ACKNOWLEDGEMENTS

This work was supported by Russian Foundation for Basic Research, grant No 02-01-00514. The author is grateful to A. M. Krivtsov for the statement of the problem and D. A. Indeitsev, P. A. Zhilin for the discussions.

References

[1] Tkachev P. V.: Stability of particle triangle under compression. Proceedings of the XXX Summer School "Advanced Problems in Mechanics", St.–Petersburg, 2002, p. 593-595.
[2] Allen M. P. and Tildesley A. K. Computer Simulation of Liquids. – Oxford: Clarendon Press. 1987.
[3] Gilabert F. A., Krivtsov A. M., Castellanos A. Computer simulation of mechanical properties for powder particles using Molecular Dynamics. Proc. of XXX Summer School "Advanced Problems in Mechanics", St. Petersburg, Russia, 230-239.
[4] Hockney R.W. and Eastwood J.W. Computer simulation using particles – IOP Publishing. 1988.
[5] Krivtsov A. M., Wiercigroch M. Molecular dynamic simulation of mechanical properties for polycrystal materials. Materials Physics and Mechanics, 2001, 3(1), 45-51.
[6] Tkachev P. V., Krivtsov A. M.: Computer simulation of 2d dynamic fracture. Book of abstracts of the XXXI Summer School "Advanced Problems in Mechanics", St. Petersburg, 2003, p. 91.
[7] Krivtsov A.M. Constitutive Equations of the Nonlinear Crystal Lattice. ZAMM Z. angew. Math. Mech. 1999. 79(S2). 419-420.
[8] Krivtsov A.M. Relation between Spall Strength and Mesoparticle Velocity Dispersion // International Journal of Impact Engineering. 1999, 23, 477-487.
[9] Krivtsov A. M. From nonlinear oscillations to equation of state in simple discrete systems. Chaos, Solitons & Fractals, 2002, 17(1), 79-87.
[10] Born, M. and Huang, K. Dynamical Theory of Crystal Lattices. Oxford, England: Clarendon Press, 1954.
[11] Lurie, A. I: Nonlinear theory of elasticity. North-Holland Series in Applied Mathematics and Mechanics. 1990.

XXI ICTAM, 15–21 August 2004, Warsaw, Poland

EXPLOSIVE INSTABILITIES IN A CLASS OF HYPERELASTIC MATERIALS WITH HIGHER-ORDER GRADIENTS

Igor Dobovšek
University of Ljubljana, Faculty of Mathematics & Physics
Jadranska 19, 1000 Ljubljana, Slovenia
e-mail:igor.dobovsek@fmf.uni-lj.si

Summary We establish a continuum mechanics framework for three–dimensional analysis for the onset of material instability in second–gradient hyperelasticity based on a linear stability analysis of governing field equations. Critical conditions for the formation of two qualitatively different types of instability are discussed. We analyze necessary conditions for the occurrence of exponential growth of infinitesimal disturbances describing a relative motion with respect to the intermediate state of homogeneous deformation. Thus the instability may be considered as a consequence of a singular behavior of constitutive relations and equations of balance.

INTRODUCTION

The essence of the method presented in the paper is to consider an evolution of exponential disturbances and their growth or decay from homogeneous states which are defined by a set of relations describing isothermal hyperelastic behavior of the material with the second–gradient type of deformation. If the material in the elastic range exhibits a certain amount of non–local interaction with surroundings, the velocity dependence of propagating waves through such a medium depends on the wavelength and it is non–trivial.

Instability develops as a result of explosive growth of imposed disturbance of governing field equations. Special attention must be given to detection of critical conditions leading to the standard and the symmetry breaking bifurcation. We display a derivation of a general dispersion relation of the expanded stability equation and also discuss some particular issues regarding critical conditions leading to the spatial heterogeneity in the evolution of fluctuation.

The question on which we focus is the possibility of existence of a real value of the wave number of imposed perturbation where one or more bifurcation parameters of the characteristic bifurcation set attain extreme. If there exists only a trivial solution with the value of the wave number equal to zero, which implies that the characteristic wavelength goes to infinity, this obviously corresponds to a space–independent situation. Consequently, the dominant mode in the vicinity of the first critical point will induce a homogeneous transition. If the extreme occurs at a non–trivial value of the wave number at a well–defined characteristic wavelength, the resulting dominant mode in the close vicinity of the critical point will be spatially non–homogeneous. So when the system is on the threshold of instability, the disturbance will evolve in time with the specific critical wavelength. The first unstable mode that will be excited is space dependent. Thus the instability will evolve from a spatially homogeneous initial mode into a spatially heterogeneous mode characterized by an intrinsic space scale; the situation also known as space symmetry breaking.

FOUNDATIONS

Let $\mathbf{x} = \chi(\mathbf{X}, t)$ designate a smooth motion of the material between its natural reference configuration $\mathcal{K}_R$ equipped with the set of Lagrangian coordinates $\mathbf{X} = \{X_K, K = 1, 2, 3\}$ and the actual configuration $\mathcal{K}_t$ at time t with the coordinate set $\mathbf{x} = \{x_k, k = 1, 2, 3\}$. The deformation mapping $\mathbf{F} : \mathcal{K}_R \mapsto \mathcal{K}_t$ is defined by $\mathbf{F} = \chi\nabla_{\mathrm{R}} = \partial\chi/\partial\mathbf{X}$ and has components $F_{iK} = \partial\chi_i\partial X_K$, while $\mathbf{C} = \mathbf{F}^T \cdot \mathbf{F}$ is the right Cauchy–Green tensor. The second order gradient is defined as

$$\boldsymbol{\kappa} = \mathbf{F}\nabla_{\mathrm{R}}, \quad \{\kappa_{iJK} = \partial^2\chi_i/\partial X_J\partial X_K\}\,.$$

We postulate the existence of strain energy function with smooth dependence on both two–point tensor fields. In the sequel $W(F, \boldsymbol{\kappa})$ represents the strain energy density per unit volume in reference configuration. The strain energy density is assumed to admit an additive decomposition $W = \Psi(\mathbf{C}) + \Phi(\mathbf{C}, \boldsymbol{\kappa})$ so that

$$\mathbf{P} = \left(\frac{\partial W}{\partial \mathbf{F}}\right)^T = 2\frac{\partial W}{\partial \mathbf{C}} \cdot \mathbf{F}^T, \quad \{P_{Ik} = 2\frac{\partial W}{\partial C_{IJ}}F_{Jk}\}, \quad \boldsymbol{\Pi} = \frac{\partial W}{\partial \boldsymbol{\kappa}}, \quad \{\Pi_{iJK} = \frac{\partial W}{\partial \kappa_{iJK}}\}\,,$$

where $\mathbf{P}$ is the first Piolla–Kirchhoff stress, and $\boldsymbol{\Pi}$ is a new internal stress intensity that may be perceived as the Piolla–Kirchhoff hyperstress.

FIELD EQUATIONS

To derive the proper form and the structure of governing equations we can basically use the standard approach as developed for example in the classical field theory where one through the proper choice of fundamental field variables in Lagrangian of the system derives the corresponding field equations. The Lagrangian density of the second-gradient field theory of elasticity reads

$$\mathcal{L} = \mathcal{L}(\mathbf{v}, \mathbf{F}, \mathbf{F}\nabla_{\mathrm{R}}) = \mathcal{L}\left(\frac{\partial \chi}{\partial t}, \frac{\partial \chi}{\partial \mathbf{X}}, \frac{\partial^2 \chi}{\partial \mathbf{X}\partial \mathbf{X}}\right) = \frac{1}{2}\rho_{\mathrm{R}}(\mathbf{X})\mathbf{v}^2 - W(\mathbf{F}, \boldsymbol{\kappa})\,.$$

The structure of kinetic energy density remains simple since we do not consider the local influence of microstructure on effects of long–range interaction and dispersion. In this model such effects are induced by second gradients only. Consequently, the corresponding momentum balance in absence of body forces is given as

$$\nabla_{\mathrm{R}} \cdot \mathbf{P} - \boldsymbol{\Pi} \cdot \cdot \nabla_{\mathrm{R}}\nabla_{\mathrm{R}} = \rho_{\mathrm{R}}\dot{\mathbf{v}}\,.$$

Perturbation kinematics

By instability we mean instability with respect to small or linear perturbations that can take the shape of a wave. A perturbation of velocity with respect to the current configuration $\mathbf{x}$ as reference is defined as a relative motion of a body $\boldsymbol{\xi} = \boldsymbol{\chi}_t(\mathbf{x}, \tau)$, which designates the position $\boldsymbol{\xi}$ occupied at time τ relative to the spatial position $\mathbf{x}$ at time t so that $\mathbf{F}_t(\mathbf{x}, \tau) = \boldsymbol{\chi}_t\nabla_{\mathbf{x}}$. The perturbation is characterized by a function $\Delta\mathbf{v}(\mathbf{x}, t)$ such that

$$\mathcal{K}_t \overset{\mathbf{F}_t(\tau)}{\longmapsto} \mathcal{K}_\tau : \quad \mathbf{v}(\boldsymbol{\xi}, \tau) = \mathbf{v} + \Delta\mathbf{v}(\mathbf{x}, t), \quad \Delta\mathbf{v} = \hat{\mathbf{V}}\exp(\omega_R t + i\varphi)\,,$$

where $\hat{\mathbf{V}}$ is small ($\|\hat{\mathbf{V}}\| \ll 1$) constant amplitude, $\varphi = k(ct + \mathbf{n}\cdot\mathbf{x})$ is the phase, $\omega_R = \Re[\omega]$ is the growth rate, $\omega_I = \Im[\omega]$ is the wave frequency, $c = \omega_I/k$ is the wave (phase) speed, $k = 2\pi/\lambda$ is the wave number, and $\mathbf{k} = k\mathbf{n}$ the wave vector. We seek solutions of the system in terms of normal modes, keeping in mind that the stability analysis is purely local, assuming that the boundaries are far away. In this way we exclude the effects of geometrical and structural instabilities that may emerge from the influence of boundary conditions and close boundaries. Consequently, if $\Re[\omega] < 0$ then $\Delta\mathbf{v}$ is exponentially decreasing function with or without oscillatory modulation according to whether $\Im[\omega]$ is non–vanishing or vanishing. Hence, the basic solution is asymptotically stable. If on the other hand $\Re[\omega] > 0$, disturbances tend to grow exponentially and the reference solution is unstable. The regime which separates the two classes of states, stable from unstable, defines the state of marginal stability. By this definition, the marginal state is the state of neutral stability and $\Re[\omega] = 0$ determines the threshold of instability of the reference state. Two qualitatively different states can be distinguished here. In most cases it is postulated that beside $\Re[\omega] = 0$ one also has $\Im[\omega] = 0$. The eigenvalue ω changes its sign by passing through zero. Some authors refer to this type of critical point as a divergence point. Another possibility is the case of Hopf bifurcation where in addition to $\Re[\omega] = 0$ one also has $\Im[\omega] \neq 0$. Consequently, we get a bifurcation into a time–periodic flow. By assuming homogeneous conditions at the reference configuration, by using relations describing incremental kinematics, the linearization of momentum balance and constitutive equations yields

$$i\mathbf{k}\cdot\Delta\mathbf{P} + \Delta\boldsymbol{\Pi}\cdot\cdot\,\mathbf{k}\otimes\mathbf{k} = \rho_{\mathrm{R}}\omega\hat{\mathbf{V}}\,, \quad \Delta\mathbf{P} = i\mathcal{A}\colon\hat{\mathbf{V}}\otimes\mathbf{k} - \mathcal{B}\dddot{\colon}\hat{\mathbf{V}}\otimes\mathbf{k}\otimes\mathbf{k}\,, \quad \Delta\boldsymbol{\Pi} = i\mathcal{C}\colon\hat{\mathbf{V}}\otimes\mathbf{k} - \mathcal{D}\dddot{\colon}\hat{\mathbf{V}}\otimes\mathbf{k}\otimes\mathbf{k}\otimes\mathbf{k}\,,$$

where the two–point tensor fields $\mathcal{A}$, $\mathcal{B}$, $\mathcal{C}$, and $\mathcal{D}$ are of the 4-th, 5-th, 5-th, and 6-th order, respectively, as a result of mixed partial differentiation with respect to deformation fields $\mathbf{C}$ and $\boldsymbol{\kappa}$. By choosing current placement as reference $\mathcal{A}$, $\mathcal{B}$, $\mathcal{C}$, and $\mathcal{D}$ represent instantaneous or tangent moduli. Expressing the incremental momentum balance in terms of corresponding increments of stress and hyperstress yields the homogeneous system of equations

$$(\mathbf{Q}_R + i\mathbf{Q}_I + \rho_{\mathrm{R}}\omega\mathbf{I})\cdot\hat{\mathbf{V}} = \mathbf{0}\,,$$

where $\mathbf{Q}_R$ is the real part of the acoustic tensor of perturbation and $\mathbf{Q}_I$ is the imaginary part which may vanish under certain symmetry conditions. Due to the complexity of expressions involved both tensors are not given here. A condition for the nontrivial solution of the system yields the characteristic equation which has the major role in stability analysis of the problem. The characteristic equation is given in the form of determinant

$$\mathcal{D}(\omega, \mathbf{k}) = \det\left[\mathbf{Q}_R + i\mathbf{Q}_I + \rho_{\mathrm{R}}\omega\mathbf{I}\right] = 0\,,$$

which in expanded form yields the dispersion relation $\mathcal{D}(\omega, \mathbf{k}) = 0$ from where we can determine the relationship $\omega = \omega(\mathbf{k})$. This relationship is not trivial for majority of second gradient hyperelasticity models and should be carefully examined in connection with the given stability criteria.

References

[1] Dobovšek I.: Adiabatic material instabilities in rate–dependent solids. *Arch. Mech.* **46**:893–936, 1994.
[2] Glansdorff P., Prigogine I.: Thermodynamic Theory of Structure, Stability and Fluctuations. Wiley–Interscience, London, 1971.
[3] Leon de M., Epstein M.: The geometry of uniformity in second–grade elasticity. *Acta Mech.* **114**:217–224, 1996.
[4] Mindlin R. D.: Second gradient of strain and surface tension in linear elasticity. *Int. J. Solids Structures* **1**:417–438, 1965.
[5] Ogden R. W.: Non-Linear Elastic Deformations. Ellis Horwood Ltd., 1984.
[6] Petryk H. (Ed.): Material Instabilities in Elastic and Plastic Solids. *CISM*:**414** Springer–Vien, 2000.
[7] Ru C. Q., Aifantis E. C.: A simple approach to solve boundary–value problems in gradient elasticity. *Acta Mech.* **101**:59–68, 1993.
[8] Triantafyllidis N., Aifantis E. C.: A gradient approach to localization of deformation. *J. Elasticity* **16**:225–237, 1986.

ON THE CONCEPT OF "DYNAMIC (IN)STABILITY OF QUASI-STATIC PATHS"

J.A.C. Martins [*], F.M.F. Simões[*], A. Pinto da Costa[*] and Isabel Coelho[**]
[*] *Instituto Sup. Técnico, Dep. Eng. Civil and ICIST, Av. Rovisco Pais, 1049-001 Lisboa, Portugal*
[**] *CMAF-UL, Avenida Prof. Gama Pinto, 2, 1649-003 Lisboa, Portugal*

Summary In this paper, a concept of "dynamic stability of quasi-static paths" is discussed that takes into account the existence of fast (dynamic) and slow (quasi-static) time scales. It is essentially a continuity property with respect to the smallness of the initial perturbations (as in Lyapunov stability) and to the smallness of the quasi-static loading rate (that plays the role of the small parameter in singular perturbation problems). Three mechanical examples are presented that illustrate the similarities, the differences and the relations between this concept of "dynamic stability of quasi-static paths" and the one of Lyapunov stability of some related equilibrium configurations or dynamic trajectories.

INTRODUCTION

Force equals mass times acceleration is the classical balance law that governs the motion of mechanical systems. Yet a common and useful approximation for the equations that govern the slow evolution of mechanical systems is to neglect inertia effects and take the balance equations simply as force equals zero. Slow evolutions calculated with the above approximation are called quasi-static evolutions.

The relationship of this issue with the theory of singular perturbations has been established in [3], where the existence of fast (dynamic) and slow (quasi-static) time scales is recognized: a change of variables is performed that replaces the (fast) physical time t by a (slow) loading parameter λ whose rate of change with respect to time, $\varepsilon = d\lambda/dt$, is eventually decreased to zero. This change of variables, done preferably after appropriate non-dimensionalizations are performed, leads to a system of dynamic (ordinary or partial) differential equations that defines (in finite or infinite dimensions) a singular perturbation problem, i.e. a problem that is governed by a system of equations where at least the highest order derivative with respect to λ appears multiplied by a small parameter ε.

An issue that is relevant in the study of quasi-static trajectories is their "stability". The concept of Lyapunov stability has been used for long to study the stability of dynamic trajectories of mechanical systems, namely the zero acceleration trajectories of the equilibrium configurations under constant applied loads. But the application of that concept to quasi-static paths with slowly varying loads faces the difficulty that such paths are not, in general, true dynamic solutions [3]: the supposedly negligible quasi-static accelerations are not null in general.

Energetic or thermodynamic considerations have been used to propose stability criteria for quasi-static paths [1, 4, 5] but such energetic character restricts their application to the case of symmetric stiffness operators and, also, their relationship with dynamics is not always clear. Linearization techniques have also been used to discuss stability of quasi-static paths, but in some cases the non-autonomous character of the linearized equations has been neglected (freezed) [2] and/or it has not been recognized that the quasi-static paths in general do not solve the dynamic equations [4].

The definition of "dynamic stability of a quasi-static path" that we propose in this paper takes inertia into account, recognizes the distinction between the quasi-static and the dynamic governing equations and time scales, and selects the quasi-static paths close to which the dynamic evolutions will remain when:

- the dynamic evolutions initiate sufficiently close to the quasi-static path,
- and the load is applied sufficiently slowly.

DYNAMIC STABILITY OF A QUASI-STATIC PATH AT SOME EQUILIBRIUM POINT

The proposed mathematical definition of dynamic stability of a quasi-static path at an equilibrium state is presented in the context of the following finite-dimensional (dynamic) system of differential inclusions and initial conditions:

$$\begin{cases} \varepsilon\, \mathbf{y}'(\lambda) \in \psi\,(\mathbf{x}(\lambda), \mathbf{y}(\lambda), \lambda, \varepsilon) \\ \mathbf{x}'(\lambda) \in \phi\,(\mathbf{x}(\lambda), \mathbf{y}(\lambda), \lambda, \varepsilon) \end{cases} \qquad \begin{Bmatrix} \mathbf{y}(\lambda) \\ \mathbf{x}(\lambda) \end{Bmatrix} \in \mathcal{D} \qquad \begin{Bmatrix} \mathbf{y}(\lambda_0) \\ \mathbf{x}(\lambda_0) \end{Bmatrix} = \begin{Bmatrix} \mathbf{y}_0 \\ \mathbf{x}_0 \end{Bmatrix} \in \mathcal{D}. \tag{1}$$

Here $\mathcal{D}$ is the domain of admissibility for (some of) the variables in presence, the notation $(\,)' = d(\,)/d\lambda$ is adopted, and, recalling that $\varepsilon = d\lambda/dt$, the derivatives with respect to the physical time t are related to the derivatives with respect to the load parameter λ by $d(\,)/dt = \varepsilon\, d(\,)/d\lambda = \varepsilon\, (\,)'$. In a (finite-dimensional, rate independent) elastic-plastic problem (like the Shanley column [6]), the vector $\mathbf{y}$ is composed of the N generalized displacements of the system, $\mathbf{u}$, plus their corresponding time rates of change, $\mathbf{v}$ (velocities), while the vector $\mathbf{x}$ contains the internal variables $\boldsymbol{\alpha}$ of the system, namely the generalized plastic strains. In that case, the relevant restriction in the domain $\mathcal{D}$ corresponds to requiring that the generalized forces $\mathbf{A}(\mathbf{u}, \boldsymbol{\alpha})$ associated to the internal variables $\boldsymbol{\alpha}$, which depend on $\mathbf{u}$ and $\boldsymbol{\alpha}$, remain in some convex set C. In that case, ψ is not multivalued, and the $\mathbf{y}'$ differential inclusion in (1) is actually a system of $2N$ first order differential equations, the first N of which are the kinematic relations between the displacements $\mathbf{u}$ and the velocities $\mathbf{v}$, while the second N are the governing equations of Dynamics; on the other hand, ϕ may be multivalued and, actually, it is the normal cone to the set C at the generalized forces $\mathbf{A}(\mathbf{u}, \boldsymbol{\alpha})$, $N_C[\mathbf{A}(\mathbf{u}, \boldsymbol{\alpha})]$, so that the $\mathbf{x}'$ differential inclusion is nothing but the flow rule.

$$\mathbf{y}(\lambda) = \begin{Bmatrix}\mathbf{u}(\lambda)\\ \mathbf{v}(\lambda)\end{Bmatrix}, \quad \psi\left(\alpha, \begin{Bmatrix}\mathbf{u}\\ \mathbf{v}\end{Bmatrix}, \lambda, \varepsilon\right) = \begin{Bmatrix}\mathbf{v}\\ \mathbf{m}^{-1}[\mathbf{f}^{\text{ext}}(\mathbf{u}, \lambda) + \mathbf{f}^{\text{int}}(\mathbf{u}, \alpha)]\end{Bmatrix}, \quad \phi\left(\alpha, \begin{Bmatrix}\mathbf{u}\\ \mathbf{v}\end{Bmatrix}, \lambda, \varepsilon\right) = N_C[\mathbf{A}(\mathbf{u}, \alpha)], \tag{2}$$

where $\mathbf{m}$ is the mass matrix of the system, and $\mathbf{f}^{\text{ext}}(\mathbf{u}, \lambda)$ and $\mathbf{f}^{\text{int}}(\mathbf{u}, \alpha)$ denote the vectors of generalized external and internal forces, respectively. The corresponding reduced (quasi-static) system is obtained by letting $\varepsilon = 0$ in (1),

$$\mathbf{0} \in \psi(\mathbf{x}^0(\lambda), \mathbf{y}^0(\lambda), \lambda, 0), \qquad \mathbf{x}^{0\prime}(\lambda) \in \phi(\mathbf{x}^0(\lambda), \mathbf{y}^0(\lambda), \lambda, 0), \tag{3}$$

or, in the quasi-static elastic-plastic case, the rate of change of the displacements with respect to the physical time can be considered null, $\mathbf{v}^0(\lambda) = \mathbf{0}$, while the equilibrium equations and the flow rule are:

$$\mathbf{f}^{\text{ext}}(\mathbf{u}^0(\lambda), \lambda) + \mathbf{f}^{\text{int}}(\mathbf{u}^0(\lambda), \alpha^0(\lambda)) = \mathbf{0}, \qquad (\alpha^0)'(\lambda) \in N_C[\mathbf{A}(\mathbf{u}^0(\lambda), \alpha^0(\lambda))]. \tag{4}$$

In this context, we say that *the quasi-static path* $(\mathbf{y}^0(\lambda), \mathbf{x}^0(\lambda))$, $\lambda \in I = [\lambda_0, \lambda_1[$ that solves the quasi-static system (3) in I *is dynamically stable at the equilibrium state* $(\mathbf{y}^0(\lambda_0), \mathbf{x}^0(\lambda_0))$ *if there exists* $0 < \Delta\lambda < \lambda_1 - \lambda_0$, *such that, for all* $\delta > 0$, *there exist* $\bar{\rho} > 0$ *and* $\bar{\varepsilon} > 0$ *such that for all initial conditions* $(\mathbf{y}_0, \mathbf{x}_0) \in \mathcal{D}$, *all parameters* $\varepsilon > 0$ *and all load parameters* λ *such that* $\|\mathbf{y}_0 - \mathbf{y}^0(\lambda_0)\| + \|\mathbf{x}_0 - \mathbf{x}^0(\lambda_0)\| < \bar{\rho}$, $\varepsilon < \bar{\varepsilon}$, *and* $\lambda \in [\lambda_0, \lambda_0 + \Delta\lambda]$, *the solutions* $(\mathbf{y}(\lambda), \mathbf{x}(\lambda))$ *of the dynamic problem* (1) *with the value* ε *of the perturbation parameter and the initial conditions in* (1) *satisfy* $\|\mathbf{y}(\lambda) - \mathbf{y}^0(\lambda)\| + \|\mathbf{x}(\lambda) - \mathbf{x}^0(\lambda)\| < \delta$.

This definition is essentially a continuity property of the solutions of (1) with respect to *both* the size of the initial perturbations (as in Lyapunov stability theory) and the value of the small parameter ε (as in singular perturbation theory). In this context we remark that, contrary to the singular perturbation theory, the reduction of ε to zero, *alone*, does not always guarantee the convergence of the dynamic solution to the quasi-static one, even in the case of stable quasi-static paths: the reduction of the initial perturbations may be also needed, namely, in the case of undamped mechanical systems. It may look strange that (unlike the definition of Lyapunov stability) a finite interval of the independent variable λ is considered in the proposed definition, and also that the defined property is termed stability. But it is important to observe that the qualitative behavior of the dynamic evolutions in the neighborhood of different portions of the same quasi-static path may be quite distinct. And it should be kept in mind that finite intervals of the (slow) load parameter correspond to infinitely large intervals of the (fast) physical time *t*, as the loading rate $\varepsilon = d\lambda/dt$ becomes negligibly small.

THREE EXAMPLES OF DYNAMIC (IN)STABILITY OF QUASI-STATIC PATHS

Three simple mechanical examples are used to illustrate and interpret the differences and the relations between this concept of "dynamic stability of quasi-static paths" and the one of Lyapunov stability. Indeed, there may exist:

- quasi-static trajectories that (in the vanishing load rate limit) may be considered as unstable, and that have all their equilibrium points also unstable (for constant loads); the well-known *Ziegler column* [7] illustrates this situation: not surprisingly, the resulting flutter oscillations for slowly varying loads have amplitudes that vary with the load parameter in the same manner as the amplitudes of the corresponding limit cycles obtained at constant load.
- quasi-static trajectories that are made of stable equilibrium points (for constant loads) but that may be considered as unstable (in the vanishing load rate limit); the well-known *Shanley column* [6] illustrates this situation: the dynamic solutions initiating close to the stable (for constant load) equilibrium positions of a portion of the fundamental path from which quasi-static solutions bifurcate with increasing load, do not necessarily remain close to that fundamental quasi-static path.
- and quasi-static trajectories that (in the vanishing load rate limit) may be considered stable, although they coincide with dynamic trajectories that are Lyapunov unstable for any non-vanishing load rate; a *pin-on-flat friction apparatus* discussed here has some features in common with a more complex problem [3] in non-associative elasto-plasticity: the amplitude of the limit cycle oscillations due to the expected flutter instability depends on the load rate ε and becomes vanishingly small as ε is decreased to zero.

References

[1] Bazant, Z., Cedolin, L. (1991). *Stability of Structures*. Oxford University.

[2] Dudzinski, D., Molinari, A. (1990). Perturbation analysis of thermoviscoplastic instabilities in biaxial loading, *Int. J. Solids and Structures*, 27, 601-628.

[3] Loret, B., Simões, F.M.F., Martins, J.A.C. (2000). Flutter instability and ill-posednes in solids and fluid-saturated porous media, in *Material Instabilities in Elastic and Plastic Solids*, H. Petryk, ed., International Centre for Mechanical Sciences, Courses and Lectures Nº 414, Springer-Verlag, Wien, New York.

[4] Nguyen, Q.-S. (2000). *Stabilité et mécanique non linéaire*, HERMES Science Publications, Paris.

[5] Petryk, H. (1993). *General theory of bifurcation and stability in time-independent plasticity*, *Bifurcation and Stability of Dissipative Systems*, Q.S. Nguyen, ed., International Centre for Mechanical Sciences, Courses and Lectures, **327**, Springer-Verlag, Wien, New York.

[6] Shanley, F.R. (1947). Inelastic column theory. *Journal of the Aeronautical Sciences*, **14**, 5, 261-267

[7] Ziegler, H. (1952). Die Stabiltätskriterien der elastomechanik. *Inginieur-Archiv*, **20**, 49-56.

STRAIN LOCALIZATION AT THE BRITTLE-DUCTILE TRANSITION OF THE EARTH'S CONTINENTAL CRUST

Yves M. Leroy*, Frédéric Gueydan**,Laurent Jolivet***
* *Laboratoire de Mécanique des Solides, CNRS UMR 7649, Ecole polytechnique, Palaiseau, France*
** *Géosciences Rennes, Université de Rennes 1, UMR CNRS 6118, Rennes, France*
*** *Laboratoire de Tectonique, Université Pierre et Marie Curie, UMR CNRS 7072, Paris, France*

Summary The main objective of this presentation is to show that the shear zones that ultimately lead to the formation of detachment planes at mid-crustal depths during post-orogenic extension are the results of strain localization. The destabilizing factor is the transformation of feldspar grain into weaker white mica. The prerequisite to that transformation is the fracturing of the feldspar grain. A constitutive model which capture those features is presented and constrained from field data before being applied to obtain the numerical solution of the localization problem.

INTRODUCTION

The two objectives of this presentation are first to study the origin of low-angle extensional shear zones at the brittle ductile transition of the extending continental crust and, second, to reconcile, tentatively, the apparent contradiction between their observed sub-horizontal orientation with the approximately +/- 45^o predicted by classical failure criteria for frictionless materials. Regional studies have shown with little ambiguity that normal faulting can occur indeed with a low original dip as in the Basin and Range province, the Woodlark Basin or the Aegean region. This normal faulting nevertheless contradicts Andersonian mechanics and question the overall mechanical behaviour of the continental crust and its state of stress. To explain the rotation of the principal stress directions at mid-crustal depth, Melosh [1] considered the crust to be ductile and sustaining a combined simple shear and extension. The linear viscosity model used for that construction, however, cannot explain the trend towards failure which is assumed here to be initiated by localization.

Low-angle shear zones at the brittle-ductile transition are also evidenced by seismic profiles and micro-seismicity recorded in active regions. In the northern Aegean Sea, seismic profiles show shallow dipping reflectors in the downward prolongation of major normal faults [2]. The shallow-dipping detachment of the southern margin of the Gulf of Corinth proposed by Sorel [3] could root at depth in a seismically active decollement at the brittle-ductile transition. The destabilizing factor responsible for strain localization at mid-crustal depths and the low dip angle of these shear zones are two prerequisite questions to be addressed before discussing this micro-seismicity, as it will be done in this presentation.

MODEL PROBLEM AND MAIN RESULTS

At mid-crustal depths, reaction-softening due mostly to feldspar to mica reaction, is the major destabilizing factor responsible for strain localization. This phase transformation required feldspar fracturing which is detected with the Mohr-Coulomb criterion. Gueydan et al. [4] have incorporated these features in a rheological model, which will be first discussed, for a mixture of three phases, feldspar, quartz and mica, undergoing dislocation creep at a common strain rate. The proposed constitutive material parameters are constrained by comparing the results of the 1D simple shear analysis of the lower crust with data obtained in the East Tenda Shear Zone, Alpine Corsica, France. It is shown that the formation of a horizontal shear zone at the brittle-ductile transition occurs after less than half a million years. Strain localization occurs only if the shearing velocity Vs is increased by at least a factor of five from the steady state value so that the equivalent shear stress becomes sufficiently large to permit the feldspar grain fracturing. The depth of the shear zone is mostly governed by the Mohr-Coulomb criterion used to detect this fracturing and by the time lapse during which the shearing velocity Vs is increased. The time required for the shear band to form depends on the reaction kinetics. Timing and depth are consistent with Pressure-Temperature constraints obtained in the field for the East Tenda Shear Zone.

The second part of this talk deals with the prototype of the extending continental crust which consists of ductile layers sustaining a flow which combines stretch and shear by applying appropriately the velocities Ve and Vs, respectively, at the boundaries. Starting from a simple shear steady state, the velocities are first increased with time and then kept constant defining a transient regime during which localization can develop. The 1-D and 2-D solutions of this thermo-mechanical boundary value problem are found by numerical means using the finite-element method implemented in the code SARPP [5]. A Lagrangian description of the deformation is adopted and the incompressibility constraint imposed by penalty so that the nodal unknowns are the displacement and the temperature. Note that the periodic boundary conditions are also enforced by penalty. The upper crust and the upper lithospheric mantle are discretized by two sets of 40x5 nine-noded Lagrangian elements for the 2-D analysis. The lower crust is partitioned into 40x 30 elements of the same type. This discretization, as well as the element type selected, was found to be sufficient to capture strain localization. The heat equation is solved throughout the whole structure with radiogenic heat production and shear heating contribution in the ductile crust corresponding to the conversion of mechanical work into heat. The boundary conditions for the thermal problem are the flux from the mantle set to 30 mW/m2, and the surface temperature kept to 300 K. Mechanical equilibrium and the heat equation are enforced in a staggered manner. Further information on the numerical scheme is found in [6].

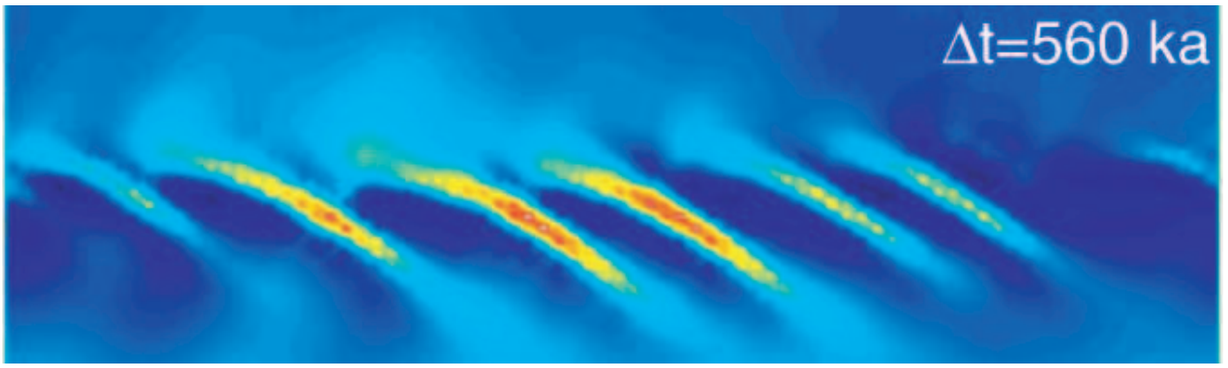


Figure 1. Isocontours of equivalent strain rate (over one order of magnitude) over a length of 20 km and the depth ranging from 10 to 15 km [7]. Note that the dip of the shear bands is consistent with the combined extension and shear loading but are found in a horizontal shear zone where the feldspar to mica reaction took place and has weakened the rock.

The 1D finite element solutions of this combined flow, for which the localization has to remain in a flat region, show a depth partitioning in deformation mode between the mid-crust, mostly dominated by pure shear, and the deep crust, sustaining simple shearing. The velocities ratio Ve/Vs has to be as low as 0.001 for localization to take place at the depth of approximately 13 km which is the base of the reaction zone below which the feldspar-to-mica reaction is not activated. Strain localization does not propagate to greater depths because feldspar fracturing is not possible but can propagate laterally, leading to the formation of a periodic system of synthetic shear bands within half a million years, as it is revealed by the 2D solution, Figure 1. These results could explain the presence of a flat weakened zone at the brittle-ductile transition of the extending continental crust without contradicting classical local failure criteria. Indeed, these criteria predictions are found to be consistent with the orientation of the shear bands which define the internal structure of the flat weakened zone. Finally, the stress state within the weakened zone is examined in details to shed light on potential micro-earthquakes and local fluids migration.

References

[1] Melosh, H.J., Mechanical basis for low-angle normal faulting in the Basin and Range province, Nature, 343, 331-335, 1990.
[2] Laigle, M., A. Hirn, M. Sachpazi, and N. Roussos, North Aegean crustal deformation: an active fault imaged to 10 km depth by reflection seismic data, Geology, 28, 71-74, 2000.
[3] Sorel, D., A Pleistocene and still-active detachment fault and the origin of the Corinth-Patras rift, Greece, Geology, 28, 83-86, 2000.
[4] Gueydan, F., Y.M. Leroy, L. Jolivet, and P. Agard, Analysis of continental midcrustal strain localization induced by microfracturing and reaction-softening, J. Geophys.Res., 108, B2, 2064, doi:10.1029/2001JB000611, 2003.
[5] SARPP, Structural Analysis and Rock Physics Program, LMS, Ecole polytechnique, Palaiseau, France, 2003.
[6] Gueydan, F., La transition fragile-ductile de la croûte continentale en extension. Du terrain à la modelisation. Thèse de doctorat, Université Pierre et Marie Curie, Paris, 2001.
[7] Gueydan, F., Y.M. Leroy, L. Jolivet, Mechanics of low-angle extensional shear zones at the brittle-ductile transition, submitted for publication.

NUMERICAL EVALUATION OF MIXED MODE DELAMINATION IN A U-GLASS/EPOXY COMPOSITE IN 2D AND 3D STATES

M.R. Khoshravan[*], Arash Yourdkhani[**]
[*]*University of Tabriz, Faculty of Mechanical Engineering, 51664, Tabriz, Iran*
[**]*Mechanic Group, East Azarbaijan Jahad Research Center, 51745-346, Tabriz, Iran*

Summary In this paper the delamination phenomena in the mixed mode I+II that is one of the important causes of failure in multilayer composites, is studied. Finite element analysis is used to evaluate fracture mechanic parameters of the composite. 2D (2 Dimension), and 3D (3 Dimension) analysis are carried out. Then the obtained numerical results are compared with the existing experimental and discussed.

INTRODUCTION

The composite is a glass fiber reinforced plastic and is studied under static monotonic loading. Using Irwin-Kies criteria, usual laws of elasticity and VCCT (Virtual Crack Closure Technique), based on finite element method, the SERR (Strain Energy Release Rate) in mode I, mode II, and four ratio modes (G_I/G_{II}) is evaluated. The finite element analysis of test bars is carried out using ANSYS5.5 software in two dimensions, and boundary conditions are chosen to bring the analysis in the vicinity of reality. Our numerical results are compared with existing experimental ones and with application of the local effects, such as 3D effect in the width of the test bar with the shape of MMB (Mixed Mode Bending)[1] specimen, the scattering between experimental and numerical results is evaluated and discussed. For the 3D effect, the variation of the stress components in the plan of delamination versus the width of specimen is obtained. Then the variation of strain energy release rate in the different ratio modes, in the width of test bars is calculated.

Table 1: Mechanical properties and geometry of the test bar

Specimen Dimension	Mechanical Property
L = 65 mm	E_{11} = 25.7 GPa (±8%)
2h = 5 mm	E_{22} = 6.5 GPa (±8%)
b = 20 mm	G_{12} = 2.5 GPa (±8%)
L_T = 150 mm	υ_{12} = 0.32 (±8%)
a_0 = 35 mm	ν_{fibre} = 35.4% (±1%)
	ν_{void} = 4.2% (±1%)

FINITE ELEMENT METHOD

In this section, VCCT method is used and the components of strain energy release rate are obtained with the following relations:

$$G_I = \lim_{\Delta a \to 0} \frac{1}{2b\Delta a} p_y^0 (v_1 - v_2)$$

$$G_{II} = \lim_{\Delta a \to 0} \frac{1}{2b\Delta a} P_x^0 (u_1 - u_2)$$

u and v are the relative displacement between nodes 1 and 2. Da is the length of crack which should close virtually. P_x^0 and P_y^0 are the loading components, which are used for the closure of the crack.

FINITE ELEMENT MODEL OF MMB SPECIMEN

For 2D modeling, we have used eight noded solid elements and singularity elements with quarter point nodes at crack tip. As the width of specimen is higher than his thickness, the problem is studied in plane strain state. As the stress concentration zone is smaller relative to the dimensions of the specimen, only a small zone in crack tip is mesh generated with high density. The type of elements leads to the singularity of stresses and strains at the end of the crack.
In 3D finite element model, we have used twenty noded solid elements. The goal of 3D modeling is analyzing the stress and strain energy in the width of specimen [2]. The elements are refined regularly at the width of the crack. The coordinated system is situated at the end of the crack and z-axis is on the direction of the width of specimen. As the boundary conditions and dimensions of 3D specimen are symmetrical relative to xy plane, only the half of specimen is modeled.
Because of the sliding of the faces on each other, in 2D and 3D models, contact elements are used.

RUPTURES IN THE END OF THE CRACK

In the studying of delamination, identification of the beginning of the crack propagation is a discussible case. In this paper, with using the finite element analysis of specimen, different stresses in the end of the crack are calculated. Using rupture criteria in composite materials and calculated stresses in the end of the crack, we analyze the delamination. From the mechanical point of view, the composite materials with epoxy resin matrix operate as the brittle materials. So the plastic zone in the end of the crack is very small and in the theoretical analyses and in the finite element model, the rupture in the end of the crack is considered only elastic.

EXPERIMENTAL CRITERIA OF RUPTURE

The point of the initiation of crack in an experimental specimen is obtained using three methods. In the first method, the crack growth leads to a deviation of the curve of load-displacement from the linear state. The point of deviation is called NL, which is not always easily distinguishable [3]. In the second method a line with a slope less than 5% of the initial slope of the curve of load-displacement is considered [4]. The intersection of this line with the curve of load-displacement is the beginning point of crack propagation. In the third method, point AE (Acoustic Emission), which corresponds to the registration of the first signal during the test, is defined as the beginning of the crack growth.

2D RESULTS

Numerical analyses of the specimen are carried out as per experimental in pure mode I, pure mode II, and four ratios of mode (G_{II}/G_I) 0.25, 0.50, 0.75 and 0.89 with a precrack of a=35mm. The stress distribution σ_x has the same shape for all of the mode ratios and it has not a significant influence in the crack growth because of the high strength of the composite specimen in the x-axis direction. The σ_y distribution for the mode ratios, for which mode I exists, has the shape of two tangent circles (Bean Shape). The maximum stress in y direction has the highest distribution and is the principal cause of crack growth in mode I. The lowest distribution is in x direction. The τ_{xy} distribution for the mode ratios in which mode II exist has a spindle shape. The maximum stress in x direction has the highest distribution and is the principal cause of crack growth in mode II. The lowest distribution is observed in y direction. The maximum stress σ_y in pure loading of mode II and τ_{xy} in pure loading of mode I happens in a zone farther than crack tip and it can deviate the crack from it's principal route.

3D RESULTS

Results explain the variation of stress in the width of specimen and 3D effects. In all of the cases, pick of the curve is situated at crack tip. The highest value of σ_x and σ_y is on the middle of specimen width and decreases in the margins. On the mode ratios which mode II loading exists, the transversal strains of the upper and lower layers of crack plane are in opposite direction on z-axis. This phenomenon leads to slide these layers on each other, maximize τ_{xz} in the margins and use a part of the strain energy for the mode III. The τ_{xy} stress distribution is a composition of above-mentioned cases.

For all ratios in which mode II is associated, we observe a local increasing of G_{III} in the margins. The G_{total} variation in the different ratio of modes is influenced by G_I, G_{II} and G_{III} behavior.

CONCLUSION

2D model and plane strain conditions cannot explain completely the stress distribution in crack width and regarding above behaviors, the fracture toughness of the 3D model is lower than the 2D model. In pure mode II loading, sliding of layers has an important influence in the increasing of the fracture toughness of 3D relative to 2D model. 3D effects of model are applied as a percentage of error to the results of fracture toughness of 2D model. Experimental results of NL and AE have a better agreement with together, for the ratios of G_{II}/G_T, from 0 until 89%. The fracture toughness of 3D model G_{3D} has decreased in maximum 39% relative to the fracture toughness of 2D model G_{2D} and for the pure mode II loading has increased 35%. In all the cases with increasing of mode II loading component, the fracture toughness increases.

References:

[1] JR. Reeder and J.H. Crews, “Nonlinear analysis and redesign of the mixed mode bending delamination test”, NASA TECHNICAL MEMORANDUM 102777.

[2] Krueger, R. and O’Brien, T.K, “A shell/3D modeling technique for the analysis of delaminated composite laminates.” Composite, Part A: applied science and manufacturing, vol.32, no.1, 2001,pp.25-44.

[3] Davies, P., Round robin, “Analysis of G_{IC} interlaminar fracture test.”, Applied composite materials,1996.

[4] ASTM standard E399-81, “Standard test method for plane strain fracture toughness of metallic materials”.

INTERFACIAL PROPERTIES OF NANOWIRE-POLYMER COMPOSITES

Ryszard Pyrz
Institute of Mechanical Engineering, Aalborg University, Pontoppidanstraede 101
9220 Aalborg East, Denmark

Summary The mechanical performance of composite materials is critically controlled by the interfacial characteristics of the reinforcing phase and the matrix material. Her we report a study on the interfacial properties of a silicon nanowire-reinforced polystyrene nanocomposite system through molecular mechanics simulations. Results of a nanowire pullout simulation suggest that the interfacial shear transfer stress of this novel system is significantly higher than for many traditional fiber reinforced composite systems.

INTRODUCTION

Nanocomposites are a new class of composites, that are particle-filled polymers for which at least one dimension of the dispersed particles is in the nanometer range. Three types of nanocomposites can be distinguished, depending on how many dimensions of the dispersed phase are in the nanometer scale. When the three dimensions are in the order of nanometers, we are dealing with isodimensional nanoparticles such as spherical silica and aluminium nanoparticles or semiconductor nanoclusters. When two dimensions are in the nanometer scale and the third is larger, forming an elongated structure, we speak about nanotubes or nanowires. Finally, the third type of nanocomposites is characterized by only one dimension in the nanometer range. In this case the filler is present in the form of sheets of a few nanometers thickness and up to one micrometer long. This family of nanocomposites, known as polymer-layered crystal nanocomposites, is almost exclusively obtained by the intercalation of the polymer inside the galleries of layered host crystals. There exist a wide variety of both synthetic and natural crystalline fillers, which are able, under specific conditions, to intercalate a polymer. Polymer-layered crystal nanocomposites are now commercially available and have been throughout investigated in a large amount of publications during last ten years.
Nanocomposites with elongated structural fillers have recently attracted many investigations. A focus is exclusively on nanocomposites with carbon nanotubes due to carbon nanotubes unique physical properties, including mechanical, thermal, optical and electrical. However, after nearly a decade of research, their potential as reinforcement for polymers has not been fully realized; the mechanical properties of derived composites have fallen short of expectations. Yet, given the magnitude of the carbon nanotubes mechanical properties, strength as high as 200 GPa and elastic moduli close to 1 TPa range, significant improvement on current composites should be possible provided means to harness the nanotubes unique attributes exhibited at nanoscale can be transferred to the macroscale. Since these excellent mechanical properties of carbon nanotubes cannot as yet to be utilized to a full extent (not mentioning their high price), seeking an alternative seems to be well motivated. Nanowires, having a diameter comparable to carbon nanotubes, aspect ratio close or above 10^3 and a few hundred times more surface area per volume than a classical fiber reinforcement, may be considered as a new family of a reinforcing phase for nanocomposites, and their study will constitute the main object of this contribution.

Silicon-based nanotubes and nanowires

Carbon nanotubes have been providing increasing challenges for silicon in the field of nanotechnology. Since silicon-based materials have been the focus of extensive research due to their technological importance, new forms of stable silicon nano-structures are required to sustain the current silicon-based technology and as a by-product it might bring benefits to the field of structural nanocomposites. Unlike carbon nanotubes, no silicon nanotube has been yet observed experimentally. However, an intensive theoretical work has been done, exploring the possibility of the existence of silicon nanotubes and similarities with carbon nanotubes regarding their structural and electronic properties have been found. It is well known that carbon and silicon posses different bonding capabilities, despite the fact that they belong to the same group of the periodic table. Nevertheless, the partial substitution of carbon with silicon atoms was achieved and the first experimental synthesis of hetero-nanotubes was performed in 2001 resulting in 50% silicon-50% carbon nanotubes.
As opposite to hypothetically possible silicon nanotubes, the knowledge and technology of silicon nanowires is well advanced. Silicon has long been synonymous with semiconductor technology. This role is due largely to the remarkable properties of the silicon-silicon dioxide interface, which covers bulk crystalline core of the nanowires. The technology is also available to remove the silicon-dioxide shield to obtain pure silicon nanowires. The fabrication of silicon nanowires with diameters ranged from 1.3 to 190 nm, growing rate up to the order of 8 micrometers per minute and length of a few micrometers is now well established.

NANOWIRE-POLYMER INTERFACE

A number of micromechanical calculations have been performed to predict behaviour of composite interfaces, showing that the detailed behaviour of the material at these interfaces frequently dominates the behaviour of the composite as a

whole. In order to calculate mechanical properties of specific interfaces an atomistic model is necessary. We choose to study the behaviour of an interface in a silicon nanowire/polystyrene matrix nanocomposite. Adhesion strength between two phases was studied using a molecular mechanics model shown in Fig. 1. The polystyrene chain has been pulled away from the silicon-silicon dioxide sheet, and the energy of the system at specified distances between the two was cal-

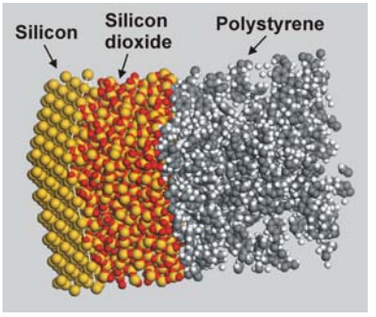


Figure 1

culated. The adhesion energy is calculated as the difference between the minimum energy and the energy at infinite separation. It has been shown that the adhesion energy depends on the length of polystyrene chains. The nature of this adhesion energy comes from electrostatic and van der Waal`s forces. For the nanowire totally embedded in the polymer matrix an additional interaction is present due to constrained deformation of the nanowire.

A single nanowire composite model was constructed with either a pure silicon core or a wire having also the silicon dioxide shield. A former case is depicted in Fig. 2, where a front view (a) and configuration before a pullout (b) are illustrated. Nanowire pullout simulations were performed after carrying out optimisation procedures for energy minimization of the system and pulling out the nanowire with predetermined displacement intervals, Fig. 2c. The energy

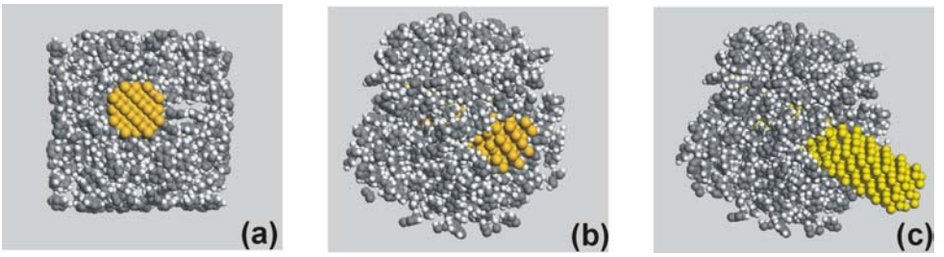


Figure 2

difference between the fully embedded nanowire and the complete pullout configuration is the work required for nanowire pullout. Inclusion-matrix interfacial shear stress is a critical parameter controlling the efficiency of stress transfer and hence important properties of composites. The interfacial shear stress is derived from the total work done during pulling the nanowire from the polymer matrix and is about 150 MPa, which is about one order of magnitude higher than many fiber reinforced composites. The calculated interfacial shear stress is based on an average shear stress assumption. Determination of the shear stress distribution would necessitate a detailed analysis of individual chain displacements during pullout in a vicinity of the nanowire, which is computationally very demanding task.

CONCLUSION

A novel silicon nanowire-polystyrene nanocomposite has been investigated using molecular mechanics simulations with respect to interfacial characteristics of the system. The adhesion energy and the interfacial shear stress has been determined indicating significant bonding quality as compared with traditional fiber reinforced composite systems. Further improvement of the shear stress transfer could be achieved with functionalization of silicon nanowires with coupling agents.

An extended molecular simulation study should consider influence of nanowire geometry such as critical aspect ratio and diameter on interfacial stress distribution, both of which are shown to affect stress transfer behaviour. Furthermore, an immobilization of polymer chains in a vicinity of nanowires should be investigated in order to determine an effective domain of reinforcement of the polymeric matrix. All these factors may serve as an input for micromechanical modelling of nanocomposites at micrometer length scale and subsequently at a continuum level for the determination of effective bulk properties.

PLANE HARMONIC WAVES IN A MICROPERIODIC LAYERED THERMOELASTIC SOLID REVISITED

Józef Ignaczak
Polish Academy of Sciences IPPT PAN, Swietokrzyska 21, PL 00-049 Warszawa, Poland

Summary A one-dimensional dynamic coupled thermoelastic refined averaged theory for a microperiodic composite is used to study plane harmonic waves in a layered infinite solid. In such a theory an eight-order in time partial differential equation involving a high intrinsic mechanical frequency Ω_M and a high intrinsic thermal frequency Ω_T is a central one. It is shown that if Ω_M and Ω_T are finite, there are two harmonic thermoelastic waves of a given frequency ω that propagate in a positive direction normal to the layering. Numerical results illustrating propagation of the two waves in a nanoperiod composite are included.

INTRODUCTION

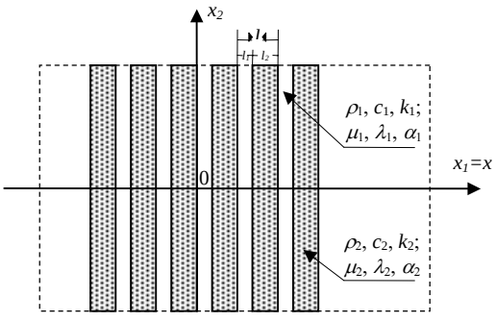


Fig. 1 A microperiodic layered infinite thermoelastic solid

Consider a layered infinite thermoelastic solid which is composed of an infinite number of identical thin subunits that form a spatially periodic pattern with a period l as shown in Fig. 1. Each subunit consists of two layers that, in general, have different dimensions and are made of different homogeneous isotropic thermoelastic materials. Let $l_i, \rho_i, c_i, k_i, \mu_i, \lambda_i$, and α_i (i=1,2), respectively, denote the thickness, density, specific heat, thermal conductivity, shear modulus, Lame modulus, and thermal expansion of the *i*th layer in a subunit. Also, assume that an external thermomechanical load is uniformly distributed over a plane parallel to the layering for every time $t > 0$. Then a thermoelastic process corresponding to the load is one-dimensional, and can be described by the dimensionless partial differential equations (see [1]-[2])

$$\left\{\left(\frac{\partial^2}{\partial\tau^2}+\kappa_1^2\right)\left[\left(\frac{\partial^2}{\partial\xi^2}-\frac{\partial}{\partial\tau}\right)\left(\frac{\partial}{\partial\tau}+\alpha\right)-(\alpha-\beta)\frac{\partial^2}{\partial\xi^2}\right]+\varepsilon_1\left(\frac{\partial}{\partial\tau}+\alpha\right)\frac{\partial^3}{\partial\tau^3}\right\}$$
$$\times\left[\left(\frac{\partial^2}{\partial\tau^2}+\kappa_1^2\right)\left(\frac{\partial^2}{\partial\xi^2}-\frac{\partial^2}{\partial\tau^2}\right)-\kappa_2^2\frac{\partial^2}{\partial\tau^2}\right]S-\varepsilon_2\left(\frac{\partial^2}{\partial\tau^2}+\kappa_3^2\right)^2\left(\frac{\partial}{\partial\tau}+\alpha\right)\frac{\partial^3}{\partial\tau^3}S=0 \tag{1a}$$

$$\left(\frac{\partial^2}{\partial\tau^2}+\kappa_3^2\right)\frac{\partial^2}{\partial\tau^2}\theta-\left[\left(\frac{\partial^2}{\partial\tau^2}+\kappa_1^2\right)\left(\frac{\partial^2}{\partial\xi^2}-\frac{\partial^2}{\partial\tau^2}\right)-\kappa_2^2\frac{\partial^2}{\partial\tau^2}\right]S=0 \tag{1b}$$

where $S=S(\xi,\tau)$ and $\theta=\theta(\xi,\tau)$ denote the stress and temperature fields, respectively; the parameters κ_1, κ_2, and κ_3 represent the frequencies proportional to an intrinsic mechanical frequency Ω_M while ε_1 and ε_2 stand for the thermoelastic coupling parameters; and α and β represent the frequencies proportional to an intrinsic thermal frequency Ω_T.

Equation (1a) is an eight-order in time partial differential equation that plays a central role in the theory. Once a solution $S=S(\xi,\tau)$ to Eq. (1a) is found, the temperature $\theta=\theta(\xi,\tau)$ is obtained by integrating Eq. (1b) with respect to time.

The existence of two time-periodic solutions (S,θ) to Eqs. (1) that represent waves propagating in a positive direction normal to the layering was established in [1]-[2] when $\Omega_M\to\infty$ and $\Omega_T<\infty$ or $\Omega_M<\infty$ and $\Omega_T\to\infty$. In the present paper the existence of two harmonic thermoelastic waves is proved when $\Omega_M<\infty$ and $\Omega_T<\infty$. In the next section an existence theorem on two harmonic thermoelastic waves is formulated, and a numerical analysis of the two waves for a particular composite is presented. Finally, results and conclusions are summarized.

PLANE HARMONIC WAVES IN A MICROPERIODIC LAYERED THERMOELASTIC SOLID WHEN $\Omega_M<\infty$ AND $\Omega_T<\infty$

We look for a solution to Eq. (1a) in the form

$$S(\xi,\tau)=\hat{S}\exp[i(\omega\,\tau-\eta\xi)],\quad i^2=-1,\quad |\xi|<\infty,\quad 0\le\tau<\infty \tag{2}$$

where $\hat{S}$ is a constant, ω is an assigned frequency $(\omega > 0)$ and η is the wave number to be selected from the condition that $S = S(\xi, \tau)$ be a nontrivial solution to Eq. (1a). A function S given by Eq. (2) represents a plane harmonic stress wave propagating in the ξ-direction with a velocity c and with an attenuation q if

$$\eta = \omega / c - i\, q, \quad c > 0, \quad q > 0 \tag{3}$$

Substituting $S = S(\xi, \tau)$ from Eq. (2) into Eq. (1a) a fourth-degree algebraic equation for η is obtained. A root analysis of this equation leads to the Theorem: If $0 < \omega < \kappa_3(l) < \kappa_1(l)$ and $0 < \varepsilon_2 < 0.5$ then there are two wave numbers of the form

$$\eta_k = \omega / c_k - i\, q_k, \quad c_k > 0, \quad q_k > 0, \quad (k = 1, 2) \tag{4}$$

The associated thermoelastic waves are then represented by the formulas

$$S_k(\xi, \tau) = \mathrm{Re}\,\{\hat{S}_k \exp[i(\omega\, \tau - \eta_k \xi)]\} \tag{5}$$

$$\theta_k(\xi, \tau) = \mathrm{Re}\,\{\hat{S}_k \omega^{-2} (\kappa_3^2 - \omega^2)^{-1} [(\eta_k^2 - \omega^2)(\kappa_1^2 - \omega^2) - \kappa_2^2 \omega^2] \exp[i(\omega\, \tau - \eta_k \xi)]\} \tag{6}$$

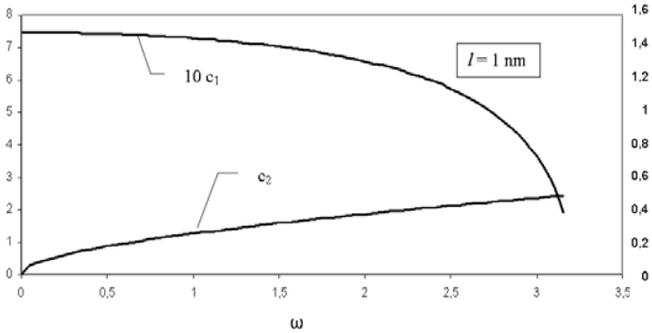


Fig. 2 The velocities c_1 & c_2 treated as functions of ω for a nanocomposite.

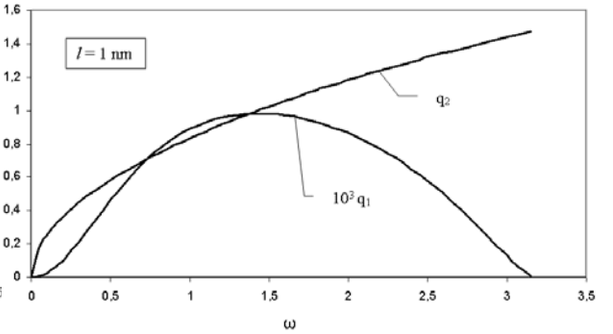


Fig. 3 The attenuation coefficients q_1 & q_2 treated as functions of ω for a nanocomposite

where $\hat{S}_k$ stands for a constant and $\mathrm{Re}\,\{\cdot\}$ denotes the real part of $\{\cdot\}$. To illustrate numerically the solution (4)-(6) we assume that each subunit is made of a zirconium oxide and a titanium alloy layers (see [3]). Figures 2 and 3, respectively, show the pairs (c_1, c_2) and (q_1, q_2) treated as functions of ω for l = 1nm. It follows from Figures 2 and 3 that a thermoelastic wave propagating with the smaller velocity is almost dispersionless and of a small damping, while that of the greater velocity reveals a high dispersion and a large damping. An analysis of the wave profiles S_1, θ_1, S_2 and θ_2 propagating along the positive ξ-axis indicates that the pair (S_1, θ_1) is represented by an isothermal elastic wave with a small damping $(\theta_1 \approx 0)$ while (S_2, θ_2) is represented by a thermoelastic wave with a fast decay on the ξ-axis.

CONCLUSIONS

- A one-dimensional averaged theory of thermoelastic waves in a microperiodic layered infinite solid is revisited in which an eight-order in time PDE involving a high intrinsic mechanical frequency Ω_M and a high intrinsic thermal frequency Ω_T is a central one. It is shown that if Ω_M and Ω_T are finite, there are two harmonic thermoelastic waves of a given frequency ω that propagate in a positive direction normal to the layering.
- The numerical analysis of the two waves for a zirconium oxide-titanium alloy composite with a period l = 1nm indicates that a wave propagating with the smaller velocity is almost dispersionless and isothermal in nature while that of the greater velocity reveals a high dispersion and a large damping.
- The two harmonic thermoelastic waves may be useful in a study of harmonic waves in a microperiodic layered semi-infinite thermoelastic body.

References

[1] J. Ignaczak, Plane harmonic waves in a microperiodic layered infinite thermoelastic solid, *Proceedings of The Fifth Int. Congress on Thermal Stresses;TS2003,* June 8-11, 2003, Blacksburg, VA, USA, pp. TM-1-1-1 to TM-1-1-4.

[2] J. Ignaczak, Plane harmonic waves in a microperiodic layered infinite thermoelastic solid, *J. Thermal Stresses*, vol. 26, pp.1033-1054, November-December 2003.

[3] Y. Ootao, R. Kawamura, Y. Tanigawa, and R. Imamura, Optimization of material composition of nonhomogeneous hollow circular cylinder for thermal stress relaxation making use of neural network, *J. Thermal Stresses*, vol. 22, pp. 1-22, 1999.

DAMAGE PROGRESSION BY THE ELEMENT-FAILURE METHOD (EFM) AND STRAIN INVARIANT FAILURE THEORY (SIFT)

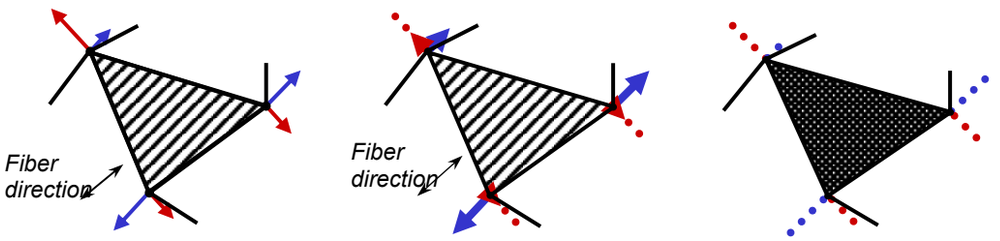
T.E. Tay, V.B.C. Tan and S.H.N. Tan
Dept of Mech Engng, National University of Singapore, 10 Kent Ridge Cres, Singapore 119260

Summary The element-failure method (EFM) is a novel finite element-based method for the modelling of damage, fracture and delamination in fibre-reinforced composite laminates. The nature of damage in composite laminates is generally diffused and complex, characterized by multiple matrix cracks, fibre pullout, fibre breakage and delaminations. It is usually not possible to model or identify crack tips in the conventional fashion of fracture mechanics. The central idea of the EFM, on the other hand, is to model the damaged portions with partially failed elements, whose nodal forces have been modified to take into account the local damage modes. This has the additional benefit of unconditional computational stability compared to other methods such as material property degradation (MPD) models. Here, we present the application of EFM with a recently-proposed failure criterion called the Strain Invariant Failure Theory (SIFT) in the prediction of damage progression in a composite laminated structure, and show that the damage patterns are in very good agreement with experiments. It is also shown that the EFM is more versatile and general than the MPD method.

ELEMENT-FAILURE METHOD (EFM) FOR COMPOSITES

The central concept of the EFM for fiber-reinforced polymeric composites is that the effects of damage on the mechanical behaviour can be essentially described by the effective nodal forces of a finite element (FE). The manner by which these effects of damage translate to the effective nodal forces will in general depend upon the damage evolution law appropriate to the local mode of damage experienced by the composite material, as well as the FE formulation. For the purpose of illustration, consider an FE of a virgin (undamaged) composite material (Fig.1 (a)), experiencing a set of nodal forces. Suppose damage in the form of transverse matrix microcracks are formed (which may or may not be uniformly distributed within the FE), the load-carrying capacity of the FE will be compromised, very likely in a directionally and spatially dependent manner (Fig.1 (b)).

Fig.1 The element-failure or force modification method



(a) FE of undamaged material and nodal force components

(b) Partially failed FE with damage and modified nodal forces

(c) Completely failed FE with extensive damage and zeroed nett nodal forces from adjacent elements

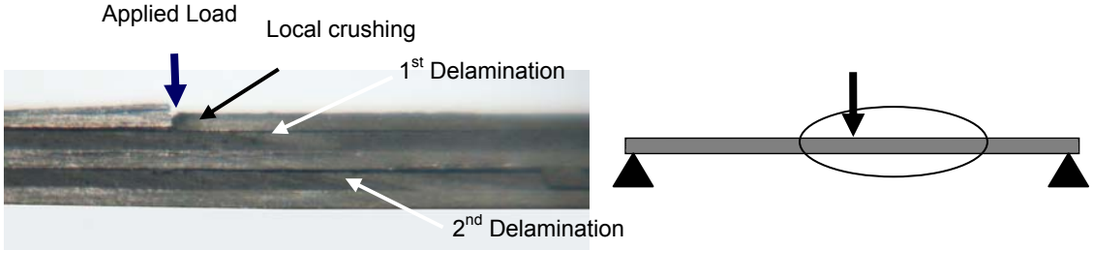
In conventional material degradation models, this reduction in load-carrying capacity is achieved by reducing or zeroing certain pertinent material stiffness properties of the damaged finite element. In the EFM however, the reduction is effected by applying a set of *external* nodal forces such that the *nett internal* nodal forces of elements adjacent to the damaged element are reduced or zeroed (the latter if complete failure or fracture is implied (Fig.1 (c)). The decision whether to fail an element is guided by a suitable failure theory and in each step, only one or two elements are failed at a time. The "correct" or required set of applied nodal forces to achieve the reduction within each step is determined by successive iterations until the nett internal nodal forces (residuals) of the adjacent elements converge to the desired values. Typically, less than 20 iterations are required and convergence is guaranteed. Note that it is not the internal nodal forces of the damaged element that is zeroed (for the case of complete failure (Fig.1 (c)), but the nett internal nodal forces of adjacent elements. Thus the "stresses" within the failed element no longer have physical meaning although compatibility may be preserved. This process leaves the

original (undamaged) material stiffness properties unchanged, and is thus computationally efficient as every step and iteration is simply an analysis with the updated set of loading conditions at the nodes. In contrast to the MPD method, computational stability is always guaranteed, as the stiffness matrices are untouched.

DAMAGE PROGRESSION IN A THREE-POINT BEND SPECIMEN

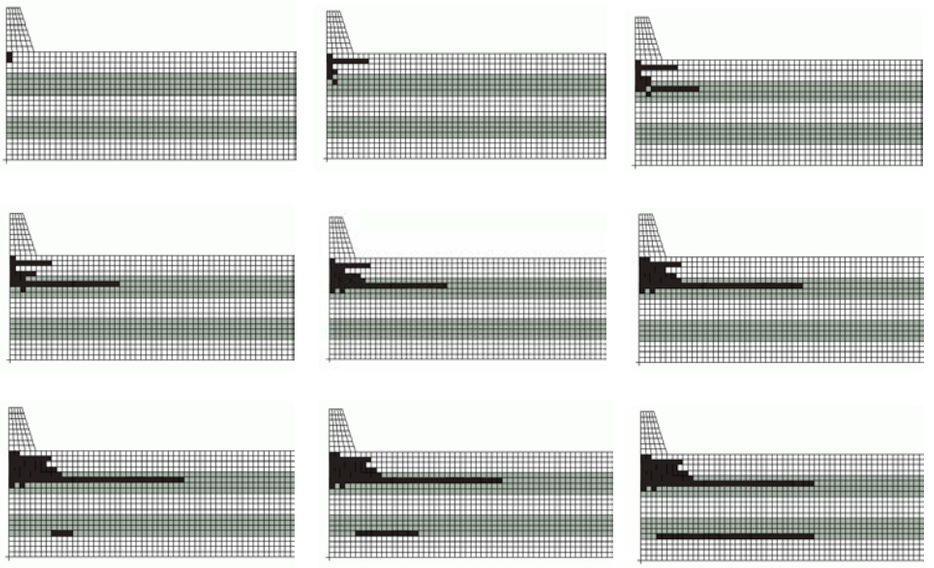
The EFM is used to analyze a $[0_3/90_3/0_3/90_3/0_3]$ graphite-epoxy laminate under three-point bend test until failure (Fig.2). Shortly after the maximum load is attained, damage propagated rapidly, resulting in final failure. The first sign of damage occurred in the form of local crushing of the first 0º plys near the point of application of load and the growth of the first delamination at the interface between the first (0º) and second (90º) layers. This is rapidly followed by the initiation and growth of the second delamination at the interface between the third (0º) and fourth (90º) layers. Here, the layers are referred to consecutively from the top surface; each layer consists of 3 plys of unidirectional tape. After the second delamination has propagated some distance to the right, it kinks into the fourth (90º) layer and continued along the interface with the fifth (0º) layer.

Fig.2 The three-point bend test and damage in specimen



The predicted progressive damage pattern is shown in Fig. 3. The qualitative agreement with the observed experimental damage pattern of Fig. 2 is remarkable. It is seen that the EFM coupled with the new micromechanics-based failure theory SIFT, is able to predict the local crushing in the top 0º layer, as well as the first delamination near the interface of the first and second layers. It is also able to predict the onset of the second delamination, although the position at the interface of the fourth and fifth layers is not quite correct.

Fig.3 Predicted damage pattern by EFM and SIFT



Effective Properties of Solids Containing Randomly Distributed Multi-Phase Spherical Particles

Hossein.M. Shodja, Farshid Roumi
Department of Civil Engineering, Sharif University of Technology, P.O. Box 11365-9313, Tehran, Iran

With the ever growing demands for the manufacturing of various innovative particle reinforced composite materials, each tailored for a specific purpose, development of an accurate and unified method for estimations of the effective properties of such materials is inevitable. In this paper, the micromechanical method of homogenization is used to estimate the overall mechanical behaviour of solids containing high concentration of heterogeneous spherical particles. The previous treatments in the literature have failed to account for the long and short range interactions of thickly coated particles rigorously. Based on the extension of Eshelby's equivalent inclusion method (EIM) [1] to multi-inhomogeneities [2], the overall behaviour of solids with periodic distribution of multi-phase interacting particles has been estimated by Shodja and Roumi [3], which involved the Fourier series expansions of the eigenstrains. The present theory is applicable to random distribution of multi-phase particles, where there exist variable thickness interfacial transition zones between the matrix and the core inhomogeneities. To account for the randomness of the reinforcement particles the methodology departs from those presented in [3]. Note that, the interactions between different phases of an isolated multi-inhomogeneity system are inherent in the disturbance strains, [2]. The present paper addresses the complex interaction of many interacting multi-inhomogeneities, a scenario encountered when dealing with non-dilute concentration of multiple coated fiber reinforced composites. For the latter situation, the disturbance strain $\boldsymbol{\varepsilon}^{d(\Omega^{\alpha,\beta})}(\mathbf{x})$ in $\Omega^{\alpha,\beta}$ is given by

$$\boldsymbol{\varepsilon}^{d(\Omega^{\alpha,\beta})}(\mathbf{x}) = \sum_{\gamma \ |\mathbf{x}_{o\gamma}-\mathbf{x}_{o\alpha}|<r}^{NI} \Big\{ \boldsymbol{\varepsilon}^{(\Omega^{\alpha,\beta})}\left(\mathbf{x};\boldsymbol{\varepsilon}^{*(\Omega^{\gamma,1},\Sigma^{\gamma,1})}\right) + \sum_{j=2}^{NL} \boldsymbol{\varepsilon}^{(\Omega^{\alpha,\beta})}\left(\mathbf{x};\boldsymbol{\varepsilon}^{*(\Omega^{\gamma,j},\Sigma^{\gamma,j})}\right) - \varepsilon^{(\Omega^{\alpha,\beta})}\left(x;\varepsilon^{*(\Omega^{\gamma,j},\Sigma^{\gamma,j-1})}\right)\Big\}$$

$$\mathbf{x} \in \Omega^{\alpha,\beta}, \qquad \alpha = 1,2,...,\mathrm{NI}, \quad \beta = 1,2,...,NL$$

where $\mathbf{x}_{o\gamma}$ and $\mathbf{x}_{o\alpha}$ are the coordinates of the centers of the γ-*th* and α-*th* interacting multi-inhomogeneities, respectively. In the above relation, r denotes the radius of the interaction zone for the α-*th* particle, NI stands for the number of inhomogeneities, whose centers fall within the interaction zone, i.e., $\left|\mathbf{x}_{o\gamma} - \mathbf{x}_{o\alpha}\right| < r$, and NL is the number of layers surrounding the γ-*th* inhomogeneity. $\Omega^{i,j}$, $i = 1,2,...,\mathrm{NI}$, $j = 1,2,...,NL$, refers to the j-*th* coating layer of the i-*th* core inhomogeneity, $\Omega^{i,1}$. The region $\Omega^{i,1} = \Sigma^{i,1}$, and $\Sigma^{i,j} = \Omega^{i,j} \bigcup \Sigma^{i,j-1}$, Fig. 1.

Results

For verification the experiment of Amdouni et al. [4] on composites containing spherical particles with very thin coatings is reexamined by the present analysis. The material properties are: $E^m = 2.9\,GPa$, $\nu^m = 0.4$; $E^f = 73\,GPa$, $\nu^f = 0.2$; $E^c = 10\,GPa$, $\nu^c = 0.49$ for matrix, fiber, and coating, respectively. It is seen that the theoretical result accords the experiment, Table 1. Next example considers a composite containing spherical particles with thick coatings, for which $\mu^f / \mu^m = 25$, $\mu^c / \mu^m = 5$, and $\nu = 0.3$ for all phases. In this example the volume fractions of particles and coatings are f_{fiber}=10%, $f_{coating}$ =20%, respectively, Table 2. Note that in Tables 1 and 2, n indicates the total number of particles in the representative volume element (RVE).

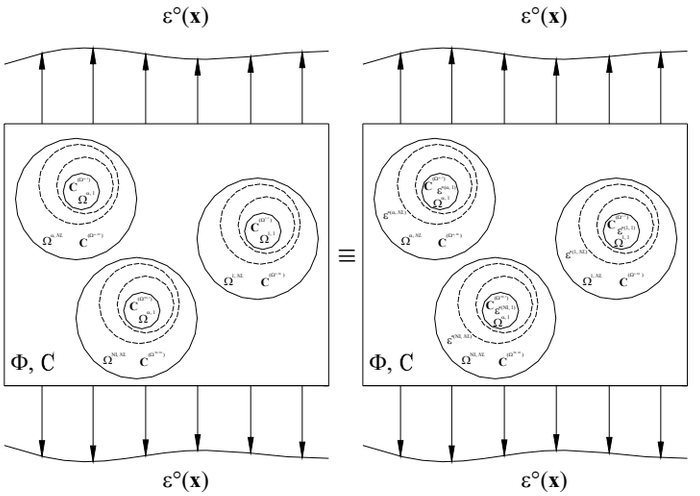


Figure 1. Homogenization scheme for a solid containing non-dilute distribution of multi-phase spherical particles.

n	f_{fiber}	$f_{coating}$	C^*/C_{1212}	C^*/C_{1122}	C^*/C_{1111}	Ps. E*	Exp. E*
25000	10%	1.3%	1.195	1.003	1.063	3.4	3.5
			1.139	1.253	1.219		
			1.205	0.958	1.031		
			1.267	2.014	1.729		

Table 1. Comparison of the elastic moduli: present study (Ps. E*) vs. experiment of Amdouni et, al. [4] (Exp. E*).

n	f_{fiber}	$f_{coating}$	C^*/C_{1212}	k*/k	C^*/C_{1122}	C^*/C_{1111}
1000	10%	20%	1.216	1.151	1.136	1.165
			1.001	1.320	1.284	1.350
5000			1.216	1.156	1.132	1.178
			1.217	1.155	1.132	1.175
10000			1.278	1.147	1.134	1.158
			1.253	1.148	1.132	1.162

Table 2. Elastic moduli of a composite containing thick coated spherical particles via present theory.

References:

[1] Eshelby, J.D., 1957. The determination of the elastic field of an ellipsoidal inclusion and related problems. *Proc. Roy. Soc*. A241, 376-396.

[2] Shodja, H.M., Sarvestani, A.S., 2001. Elastic fields in double inhomogeneity by the equivalent inclusion method. *J. Appl. Mech*. 68, 3-10.

[3] Shodja, H.M., Roumi, F., 2003. Overall behavior of composites with periodic multi-inhomogeneities. To appear in *Mechanics of Materials*, Special Issue on Micromechanics.

[4] Amdouni, N., Sautereau, H., Gerard, J.F., 1992. Epoxy composites based on glass beads, II. Mechanical properties. *J. Appl. Polym. Sci.* 46, 1723-1735.

POROUS ANISOTROPIC COMPOSITES UNDER MICROFRACTURE

Lidiya Nazarenko

Institute of Hydromechanics of NAS of Ukraine, Zhelyabova 8/4, 03680 Kiev, Ukraine

Summary The aim of the present paper is to study the behavior of the matrix composite materials of stochastic structure weakened by randomly distributed microcraks. It is considered the case of transversally-isotropic components. It is assumed that the matrix is porous and the loading processes leads to the microdestruction and the accumulation of damage in it. As basic relations the stochastic equations of elasticity theory and porosity balance equation are taken.

MECHANICAL MODEL

Let's consider a representative volume of composite of stochastic structure with transversally-isotropic components and porous matrix at given macrodeformations and suppose, that the pores shape is quasispherical. The effective deformative properties and the strain-stress state of material are determined on the basis of stochastic equations of the elasticity theory, allowing for an accidental character of microdestructions, by a method of conditional moment functions. Then Hook's low will connect the macroscopic stresses and strains fields of such material by the following equation:

$$\left\langle \sigma_{ij} \right\rangle = \lambda^{*}_{ij\alpha\beta} \left\langle \varepsilon_{\alpha\beta} \right\rangle . \tag{1}$$

Here $\lambda^{*}_{ij\alpha\beta}$ - tensor of effective elastic constants. The effective elastic constants are the functions of the elastic moduli tensors of composite components $\lambda^{[1]}_{ij\alpha\beta}$ and $\lambda^{[2]}_{ij\alpha\beta}$, their volume concentrations c_1, c_2, porosity p_2 of matrix and parameter *t* characterizing the shape of inclusions. Indexes *1* and *2* denote inclusions and matrix respectively:

$$\lambda^{*}_{ij\alpha\beta} = \lambda^{*}_{ij\alpha\beta}\left(\lambda^{[1]}_{ij\alpha\beta}, \lambda^{[2]}_{ij\alpha\beta}, c_1, p_2, t\right). \tag{2}$$

If macrodeformations of composite and effective elastic moduli tensor are known we can define the matrix stresses:

$$\left\langle \sigma_{ij} \middle|_2 \right\rangle = \lambda^{[2]}_{ij\alpha\beta}\left(I_{\alpha\beta\,kl} + c_2 \left(\left\langle \lambda_{\alpha\beta\,kl} \right\rangle - \lambda^{*}_{\alpha\beta\,kl} \right) \lambda^{[3]\ -1}_{kl\gamma\rho} \right) \left\langle \varepsilon_{\gamma\rho} \right\rangle \ ; \tag{3}$$

here,

$$\left\langle \lambda_{\alpha\beta kl} \right\rangle = c_1 \lambda^{[1]}_{\alpha\beta kl} + c_2 \lambda^{[2]}_{\alpha\beta kl} \ ; \ \lambda^{[3]}_{kl\gamma\rho} = \lambda^{[1]}_{kl\gamma\rho} - \lambda^{[2]}_{kl\gamma\rho} . \tag{4}$$

Stresses averaged over matrix skeleton are connected with stresses in porous matrix $\left\langle \sigma_{ij} \middle|_2 \right\rangle$ by equations:

$$\left\langle \sigma^{2}_{ij} \right\rangle = \left\langle \sigma_{ij} \middle|_2 \right\rangle \Big/ (1 - p_2) . \tag{5}$$

According to formulas (3) – (5) the stresses $\left\langle \sigma^{2}_{ij} \right\rangle$ averaged over the matrix skeleton are connected with macrodeformations as follows:

$$\left\langle \sigma^{2}_{\alpha\beta} \right\rangle = \lambda^{[2]}_{\alpha\beta mn}\left(I_{mnkl} + c_2 \left(\left\langle \lambda_{mnkl} \right\rangle - \lambda^{*}_{mnkl} \right) \lambda^{[3]\ -1}_{kl\gamma\rho} \right) \left\langle \varepsilon_{\gamma\rho} \right\rangle \Big/ (1 - p_2) . \tag{6}$$

For an anisotropic material, the simplest structural model of microdamageability is constructed on the basis of the strength criterion for a macrovolume as the limiting value of the second invariant of the deviator of the average-stress tensor for the undamaged part of the material, i.e., the Huber-Mises criterion. In the considered case (a transversally isotropic material with isotropy plane $x_1 x_2$), we proceed from a generalization of the Huber-Mises criterion in the form:

$$\bar{J}^{2}_{\sigma} = \sqrt{\left\langle \sigma^{2}_{ij} \right\rangle' \left\langle \sigma^{2}_{ij} \right\rangle' + a_1 \left\langle \sigma^{2}_{33} \right\rangle'^{2} + a_2 \left(\left\langle \sigma^{2}_{11} \right\rangle' + \left\langle \sigma^{2}_{22} \right\rangle' \right) \left\langle \sigma^{2}_{33} \right\rangle' + a_3 \left(\left\langle \sigma^{2}_{13} \right\rangle'^{2} + \left\langle \sigma^{2}_{23} \right\rangle'^{2} \right)} = k_2 , \tag{7}$$

where parameters a_1, a_2, a_3 are dimensionless constants characterizing the transverse-isotropy of the strength properties of the matrix skeleton and k_2 is the limiting significance of the corresponding expression, which is a random function of coordinates. For $a_1 = a_2 = a_3 = 0$, the Huber-Mises criterion follows from (7).

The single-point distribution function *F (k)* of parameter can be represented by the exponential-power distribution function in a semi-infinite domain, i.e., the Weibull distribution:

$$F(k_2) = \begin{cases} 0 & , k_2 < k_0 \\ 1 - \exp\left(- n (k_2 - k_0)^{\alpha} \right) & , k_2 \geq k_0 \end{cases} . \tag{8}$$

Here k_0 is the lower limit value of the intensity of the average tangential stresses over matrix skeleton, from which the destruction begins, n and α - the parameters selected from the condition of the most approximation of strength spread. They are determined by experimentally for the concrete material.

If the stresses of matrix skeleton $\langle \sigma_{ij}^2 \rangle$ are known, then formulas (7), (8) determine the relative content $F(k_2)$ of destroyed microvolumes in matrix. If the pores are modeled by the destroyed microvolumes, we can write the porosity balance equation:

$$p = p_2 + F(k_2)(1 - p_2) \ . \tag{9}$$

The matrix skeleton stresses $\langle \sigma_{ij}^2 \rangle$ can be defined by the composite macrostrains $\langle \varepsilon_{\alpha\beta} \rangle$ in accordance with given above formulas (2) – (6). These relations allow to determine the dependence of the current porosity of matrix p, caused by microdestruction, at the given macrostrains. Then, substituting p instead of p_2 into equations (2) – (6), we can obtain the nonlinear dependence of the macrostresses on the macrostrains, caused by microdestruction. These relations take into account the strength spread of material.

The relations (2) – (9) at the given functions of distribution (8) represent the nonlinear equations for determination of porosity at given macrodeformations $\langle \varepsilon_{ij} \rangle$. Their solution can be constructed by iterative methods.

BIAXIAL EXTENSION OF TRANSVERSALLY-ISOTROPIC COMPOSITE

Using described above methods and obtained equations of a porosity balance, as an example, the nonlinear diagrams of macrodeformation are constructed and the behaviour of a transversally-isotropic porous material for biaxial expansion is researched:

$$\left(\langle \varepsilon_{11} \rangle \neq 0, \quad \langle \varepsilon_{22} \rangle = 0.002\right),$$

for given elastic moduli of inclusions and matrix:

$$\lambda_{11}^{[1]} = 118.4\ GPa,\ \lambda_{33}^{[1]} = 107\ GPa,\ \lambda_{13}^{[1]} = 32\ GPa,\ \lambda_{12}^{[1]} = 19\ GPa,\ \lambda_{44}^{[1]} = 35\ GPa,$$
$$\lambda^{[2]} = 3.7\ GPa,\ \mu^{[2]} = 1.1\ GPa, \tag{19}$$

the volume concentration of inclusions and pores in matrix and the shape of inclusions:

$$c_1 = 0.4\,, \qquad p_2 = 0; 0.2; 0.4\,, \qquad t = 2\,, \tag{20}$$

without allowance for strength spread and at given parameters of the strength distribution function of matrix material:

$$\alpha = 2\,, \quad n = 10^3; 2\times 10^3\,, \quad k_0 = 0.015\ Gpa. \tag{21}$$

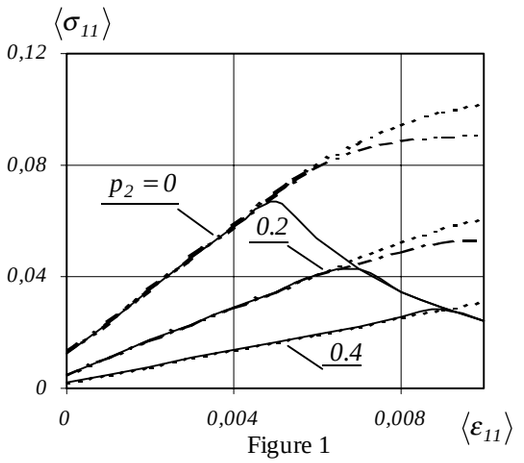


Figure 1

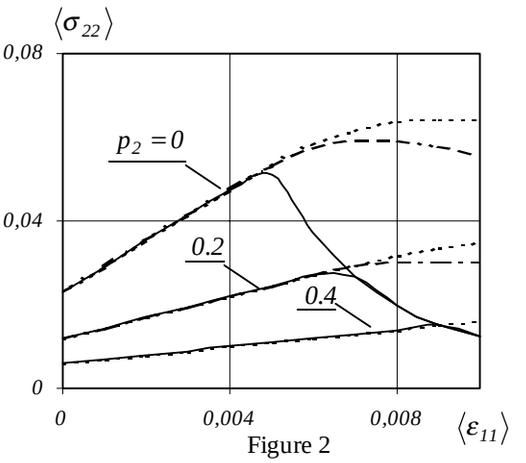


Figure 2

References

[1] Khoroshun L.: Principles of the micromechanics of material damage.1.Short-term damage. *Int. Appl. Mech.*, **34**, 120-127, 1998.

[2] Nazarenko L.: The influence of the microdestruction on the deformative properties of anisotropic materials. *Dopovidy NAS of Ukraine*, **10**, 63-67, 1999.

[3] Khoroshun L, Nazarenko L.: Model of Short-term Damaging of Transversally Isotropic Materials. *Int. Appl. Mech.*, **37**, 74-83, 2001.

REISSNER-MINDLIN-VON KÁRMÁN TYPE PLATE MODEL FOR POSTBUCKLING ANALYSIS OF LAMINATED COMPOSITE STRUCTURES

Petri Kere[*1] and Mikko Lyly[**]
[*] *Tampere University of Technology, Institute of Applied Mechanics and Optimization*
P.O. Box 589, FIN - 33101 Tampere, Finland
[**] *Center for Scientific Computing, P.O. Box 405, FIN - 02101 Espoo, Finland*

Summary Postbuckling behaviour of laminated composite structures using Reissner-Mindlin-Von Kármán type plate model is considered. The potential energy functional where the linearized strain tensor has been replaced by nonlinear Von Kármán model for large deformation is formulated. The stabilized MITC-technique is used to discretize the problem by finite elements. Load-displacement behaviour of the structure as well as the failure prediction and the identification of the critical areas of the model are illustrated with numerical examples.

REISSNER-MINDLIN-VON KÁRMÁN MODEL FOR PLATE BENDING

Due to their unique strength and stiffness properties, and their dimensional stability under hygrothermal loads, fiber-reinforced composites are widely used in many weight-critical industries like aerospace, automotive, and marine industry. In practical engineering problems, the buckling load often becomes a critical design criterion because of the thin-walled nature of the strength-optimized structure. Composite materials usually do not exhibit large yielding deformations before failure and therefore do not allow stresses to be redistributed in the postbuckling region [5]. Hence, a more detailed analysis of the postbuckling region is needed to fully predict the behaviour of composite structures.

In this work, we consider nonlinear analysis of laminated composite structures subjected to large deflections. The model is based on a facet approximation of the midsurface and a Reissner-Mindlin-Von Kármán type plate equations. We formulate the potential energy functional where the linearized strain tensor has been replaced by nonlinear functions, i.e., the Von Kármán model for large deformation. The fourth-order tensors connecting membrane stress resultants and bending moment resultants to membrane strains and curvatures, respectively, and the coupling one for in-plane and flexural behaviour as well as the second-order tensor connecting transverse shear forces to transverse shear strains are defined according to the Classical Lamination Theory.

In the FE-implementation we use linear triangular elements [3]. The transverse shear strains are discretized by the stabilized MITC-technique of Brezzi, Fortin, and Stenberg [2]. The normal rotation ("drilling rotation") is introduced as an auxiliary function and discretized by the stabilized method of Hughes and Brezzi [4]. The material principal orientation is defined by three rotations for each element.

Table 1 AS4/3501-6 carbon-epoxy ply mechanical properties.

E_1 [GPa]	E_2 [GPa]	G_{12} [GPa]	G_{31} [GPa]	ν_{12}	ν_{23}
139.3	11.1	6.0	6.0	0.3	0.4

X_t [MPa]	X_c [MPa]	Y_t [MPa]	Y_c [MPa]	S [MPa]
1950.0	1480.0	48.0	200.0	79.0

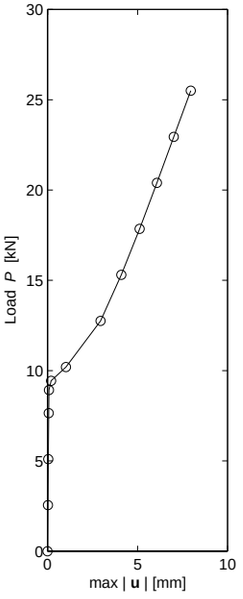


Figure 1 Compressive load-displacement behavior of the [2(0)/2(+45)/0]SE plate.

[1] Currently at Center for Scientific Computing.

In the laminate First Ply Failure (FPF) analysis, we employ a generalized method for solving the laminate failure margin with an iterative solver. Failure criteria are handled as black boxes whose internal formulation has no effect on the solution procedure.

NUMERICAL EXAMPLE

The shell model has been recently implemented in the ELMER software package [1] developed at CSC for solving PDEs by FEM. In the numerical example shown here we consider a rectangular plate of 255×255 mm composed of layers having the nominal ply properties of Hercules AS4/3501-6 carbon-epoxy [5] indicated in Table 1. The laminate lay-up is [2(0)/2(+45)/0]SE with $N = 10$ layers and the plate is subjected to compressive load at one end of the plate. The boundary conditions are considered to be clamped on all four sides of the plate. The element mesh contains 3200 linear triangular elements. In computation we have used the stabilation factor $\alpha = 0.2$.

The results show the minimum energy solution corresponding to the first buckling mode of plate. The critical linear buckling load is $P = 9425$ N. In Figure 1 the compressive load-displacement behavior of the plate in terms of max $|\mathbf{u}|$ is represented. Figure 2 illustrates the reserve factor value as a function of compressive load for maximum strain and Tsai-Wu failure criteria with logarithmic scales. The failure analysis results can also be visualized by using the inverse reserve factor to identify the critical areas of the FE model.

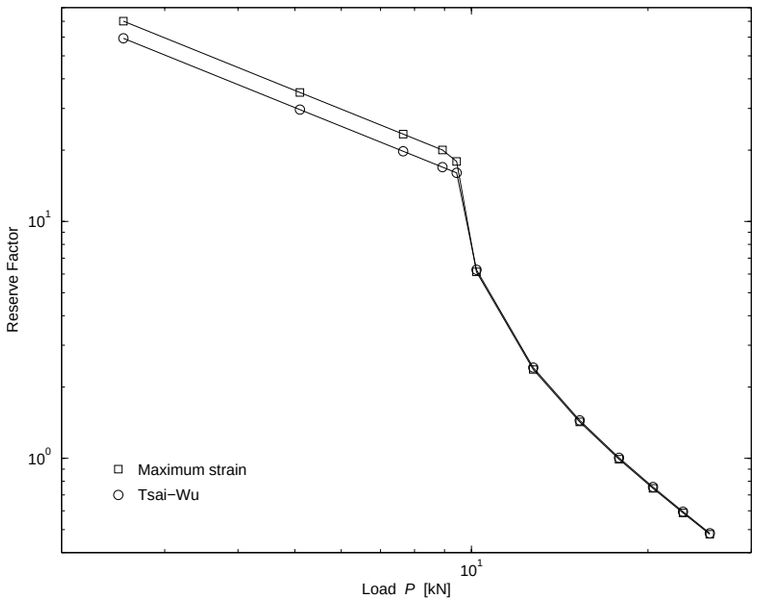


Figure 2 Reserve factor value as a function of compressive load with logarithmic scales.

Acknowledgement

The work of the first author was funded by the Academy of Finland postdoctoral researcher appropriation, Grant 202283.

References

[1] ELMER web site at www.csc.fi/elmer.
[2] Brezzi F., Fortin M., and Stenberg R.: Error analysis of mixed-interpolated elements for Reissner-Mindlin plates. *Math. Models Methods Appl. Sci.* **1**: 125-151, 1991.
[3] Lyly M.: On the connection between some linear triangular Reissner-Mindlin plate bending elements. *Numer. Math.* **85**: 77-107, 2000.
[4] Hughes T. J. R. and Brezzi F.: On drilling degrees of freedom. *Computer Methods in Applied Mechanics and Engineering* **72**: 105-121, 1989.
[5] Minguet P. J., Dugundji J., and Lagace P.: Postbuckling Behavior of Laminated Plates Using a Direct Energy-Minimization Technique. *AIAA Journal* **27**: 1785-1792, 1989.

http://ictam04.ippt.gov.pl
ictam04@zm8pc.ippt.gov.pl

Three-Dimensional Transmission in Plane Layered Elastic Composites

K. ADEROGBA

Department of Mathematics, University of Lagos, Nigeria.

Extended Summary

We already have a complete theory of three-dimensional elastic images in the case of two linearly elastic isotropic media (Aderogba, 1977) separated by a flat surface. Whatever be the distribution of elastic singularities in the first medium, the elastic field induced in the two media can instantly be calculated by routine differentiation and integration, without going through the rigour of solving the equilibrium equations and satisfying the necessary interface continuity conditions.

Specifically, if u_i is the displacement field induced by any distribution of singularities in an unbounded isotropic elastic solid, then the specification of the same distribution of singularities in an elastic upper half-space $z > 0$ which is perfectly bonded to a dissimilar elastic lower half-space $z < 0$ yields the displacement fields

$$u_i^{(1)} = u_i(x, y, z) + L_{ij}^{(1)} \; u_j(x, y, -z)$$

for $z > 0$, $i, j = 1, 2, 3$, and

$$u_i^{(2)} = L_{ij}^{(2)} \; u_j(x, y, z)$$

for $z < 0$, where $L_{ij}^{(k)}$ are suitably defined integro-differential operators which contain combinations of the elastic moduli of the two isotropic half- spaces. The effect of a single flat surface of material discontinuity thus appears like an ordinary translation and rotation of rectangular Cartesian coordinate system.

It therefore seems logical to predict that a similar complete theory of elastic images is possible in the generalized case of three media separated by two parallel plane surfaces. This prediction is actually inspired by Maxwell's (1873) magnificient compact solution of the corresponding electrostatic problem of electrical conduction through a thick plate separating two other dissimilar dielectric media. We may also refer to another inspiration, again by Maxwell (1873) who provides an instructive image treatment to the problem of a point charge arbitrarily placed between two conducting grounded non-intersecting spherical surfaces.

The present investigation is therefore concerned with the determination and characterization of the three-dimensional image system produce by an arbitrary elastic singularity which is operative in or near a thick layer which separates two other dissimilar isotropic semi-infinite solids. This determination naturally hinges on a systematic stepwise application of the aforementioned complete theory of images in the case of two media, resulting in an infinite series representation which does not involve the introduction of any special function. From the series, general interesting asymptotic values can be extracted.

References

Aderogba K. 1977 **On Eigenstresses in Dissimilar Media.** Philosophical Magazine, Vol. **35**, No.2, 281 – 292.

Aderogba K., 2000 **Axisymmetric Transmission Through An Interface Layer.** Math. Proc. Camb. Phil. Soc., **129**, 179.

Aderogba K., 2000 **Plane Elastostatic Transmission Through An Interface Layer.** Math. Proc. Camb. Phil. Soc. **129**, 371.

Aderogba K., 2003 **An Image treatment of Elastostatic Transmission From An Interface Layer.** Journal of the Mechanics and Physics of Solids., **51,** 267 – 279.

Maxwell, J.C., 1873 **A Treatise on Electricity and Magnetism,** Vol. **1**.p 443, 266. Dover Publication Inc., New York, USA.

Mindlin. R.D. 1936 **Force at a Point in the Interior of A Semi-Infinite Solid.** Physics Volume **7**., 195 – 202.

Michell. J.H. 1899 **The Transmission of Stress across a Plane of Discontinuity in an Isotropic Elastic Solid, and the Potential Solutions for a Plane Boundary.** Proc. Lond. Math. Soc., **31**, 183 – 192.

Aspects of the mechanical response of randomly reinforced, chopped fiber strand, polymeric composites

Y.J. Weitsman*and A. Ioniţă

The University of Tennessee
Knoxville, TN 37996, USA

Urethane resin composites, randomly reinforced by chopped carbon-fiber strands are candidate materials for automotive structural applications. A dry preform of such a composite is shown in Fig. 1.

Extensive stiffness and failure data, collected by 1 inch long extensometer, resulted in significant scatter as shown by the bar diagrams in Figs. 2. It was also noted that data scatter depended on the length of the measuring device, increasing substantially with diminishing device length.

The random layup shown in Fig.1 was simulated numerically, where the random geometry is depicted by the "moving" window shown in Fig. 3. The simulation employed a random selection of strand central locations and orientations, and can also select random strand lengths and widths. The number of strands N in the single randomly oriented "layer" shown in Fig. 3 is determined by the requirement that the of the projected areas A_i of all strands covers the area A of the "window", i.e. $\sum_{i=1}^{N} A_i = A$. ($A_i = w_i l_i$, where l_i abd w_i denote strand length and width respectively. (w_i is not shown in Fig. 3).

The in-plane stiffness of a single layer is obtained by a concept akin to laminate theory. Accordingly, let $\overline{Q}_{pq}^{(i)}$ of the $i^{\underline{th}}$ strand be its stiffnesses oriented into the common coordinates of the coupon, and $\mu_i = A_i/A$ the projected area fraction, then $\overline{Q}_{pq}$ of the entire layer is given by $\overline{Q}_{pq} = \sum_{i=1}^{N} \mu_i \overline{Q}_{pq}^{(i)}$.

The corresponding overall stiffnesses of the layered lay-up, A_{ij}, B_{ij} and D_{ij} are obtainable from $\overline{Q}$ by a straightforward application of laminate theory. Since the presumed common thickness h of the strands is known the number of layers k is obtained from the total coupon thickness H.

In this manner it is possible to generate values of the stiffness E (and Poisson's ratio ν) by simulating a large number of random geometries shown in Fig. 3, for various window dimensions. A typical simulation, shown in Fig. 4, illustrates the dependence of scatter on window size, i.e. length measuring device. Though not shown here, data scatter for 1 inch long window resemble the data shown in Fig. 2.

The simulation also enables to evaluate departures from isotropy and homogeneity. While departure from isotropy resembles essentially the trends exhibited in Fig. 4, departure from homogeneity reflects the extent of strand continuity between adjacent windows. It turns out that strands straddling neighboring "windows" tend to reduce the inhomogeneity when the distances between window centers is less than about twice the strand length, beyond which material inhomogeneity becomes random, i.e. uncorelated.

The foregoing observations have important ramifications regarding modeling and computations of the mechanics of random, chopped reinforcement. For instance, since size of RVE -if such exists- should exceed the strands length by at least of one order of magnitude, it assumes a structural dimension. Also, in view of the aforementioned strand overlap phenomenon, it would be erroneous to employ, say, a stochastic finite element method that does not account for an appropriate degree of continuity between neighboring elements.

A simulation of failure stresses was performed by means of a strand discount approach, akin to the ply discount method in laminate failure analysis. Though this approach resulted in failure levels that departed from recorded data, it predicted scatter resonably well.

*Also, Metals and Ceramics Division, Oak Ridge National Laboratory, Oak Ridge, TN, USA.



Figure 1: A photograph of a dry preform of a chopped strand mat.

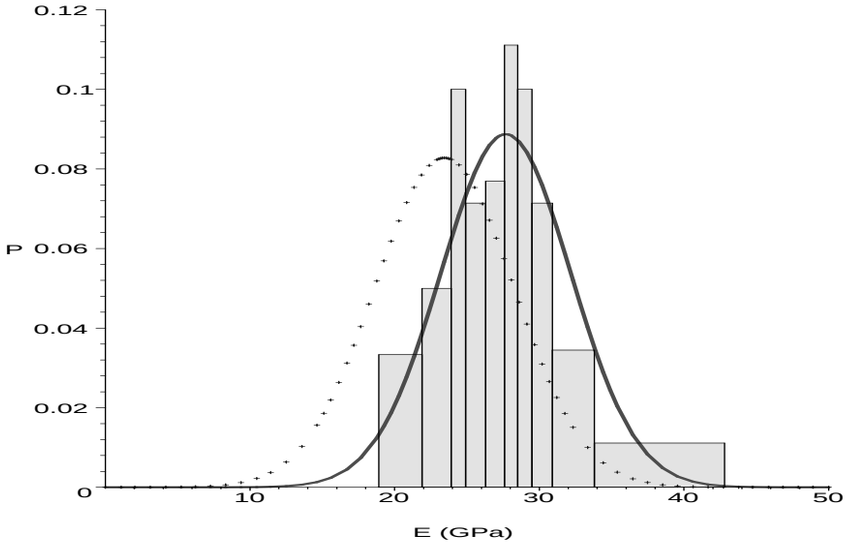


Figure 2: Distribution of longitudinal modulus E as recorded by a 25.4 mm (one inch) long extensometer. Samples thickness $H = 3$ mm. Bar diagrams and "best" Gaussian distribution fit with $\overline{E} = 27.68$ GPa. Dotted line corresponds to $H = 1.5$ mm

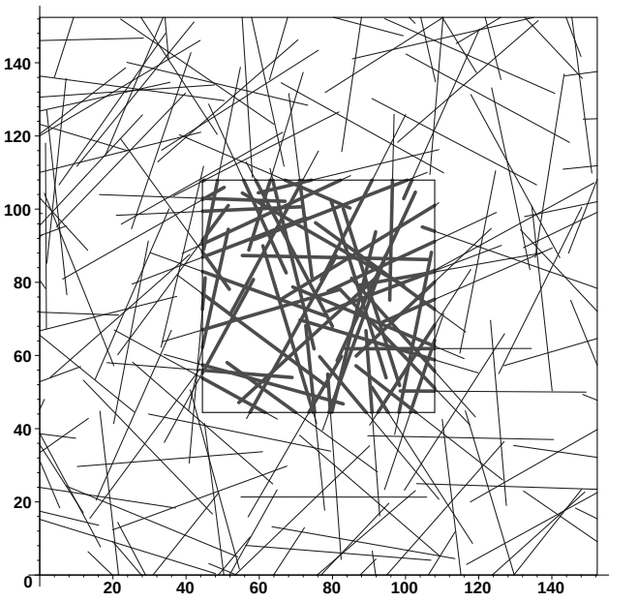


Figure 3: Random generation of strands of $L = 50.8$ mm. A typical "moving window" used for strands selection. Only the strands, or the portions of strands, inside the window are selected.

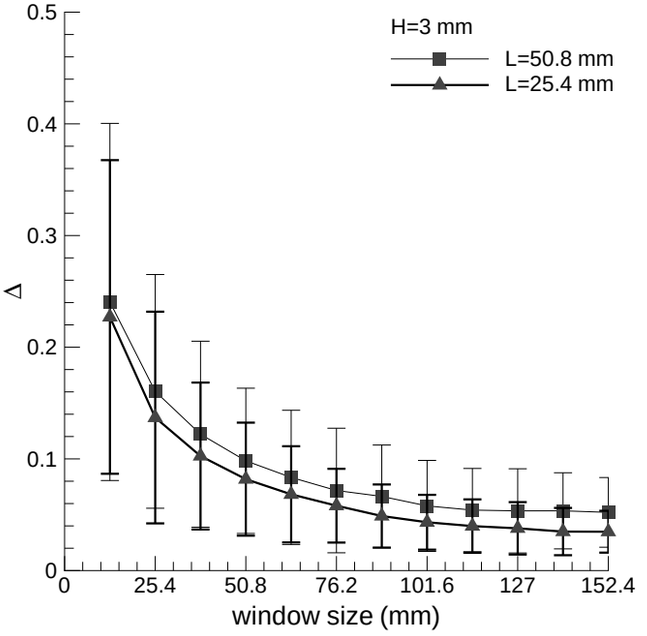


Figure 4: Departure from isotropy, as measured by the parameter Δ, vs. window size for two strand lengths and sample thickness of $H = 3$ mm, (i.e. 13 strand "layers").

COMPUTATIONAL MODELING OF DEFORMATION AND DAMAGE IN PARTICLE-REINFORCED COMPOSITES

Javier Segurado and Javier LLorca
Department of Materials Science. Polytechnic University of Madrid.
E. T. S. de Ingenieros de Caminos. 28040 - Madrid, Spain

Summary The micromechanisms of deformation and fracture in particle-reinforced composites are studied through the finite element simulation of 3D multiparticle cubic cells. The simulations provided new insights on the role played by reinforcement clustering and damage (particle fracture, interface decohesion, ductile matrix failure) on the overall composite tensile response as well as on the micromechanisms of damage nucleation and growth.

INTRODUCTION

The optimization of composite properties requires the use of sophisticated simulation tools to understand the relationship between the microstructural factors and the overall properties. This has been achieved by the development of micromechanical models, which initially considered only the matrix and reinforcement properties and their respective volume fractions. It was soon evident that this information was not sufficient for accurate prediction of many properties, and more refined models, which included the effect of particle shape, size and orientation, were elaborated. There is, however, unmistakable experimental evidence that the spatial distribution of particles and the onset of damage in regions with high local volume fraction of reinforcements determine critical important mechanical properties such as the yield strength, the ductility, the fracture toughness, etc. but the current micromechanics tools are not able to handle properly both problems. On the one hand, homogenization techniques deal with random and homogeneous descriptions of the microstructure and cannot take into account the presence of reinforcement clusters. Moreover, damage is triggered by the extremal values of stresses and strains while homogenization techniques deal with volume-average quantities. On the other hand, periodic descriptions of the composite based in a simple unit cells (FCC, BCC, etc.) cannot include the strain localization which takes place after the onset of damage. These limitations are overcome with a new analysis technique based on the three-dimensional finite element simulation of multiparticle cells. This technique provides unique information on the effect of reinforcement spatial distribution on the nucleation and growth of damage in composites as well as on the effect of damage on the overall composite properties.

SIMULATION STRATEGY

The composite mechanical behavior was studied from the finite element simulation of a three-dimensional cubic cell representative of the microstructure. The size of the cubic cell and the computer time to solve the problem increased with the number of particles in the cubic cell, and the actual figure (30 to 50, depending on the problem) was dictated by a compromise between the two factors. Moreover, the accuracy of the solution was improved by averaging the results obtained with different cells.

New algorithms were developed to generate composites with homogeneous and inhomogeneous (clustered) particle distributions, and the statistical parameters which characterize the reinforcement spatial distribution (radial distribution function, average nearest-neighbor distance, etc.) were determined. Representative volume elements of the microstructures were discretized and analyzed by the finite element method. Particles were assumed to behave as linear elastic solids, while the matrix was modeled as an elasto-plastic solid with isotropic hardening. The simulations took into account the various damage mechanisms experimentally observed. Damage in the matrix was introduced by the modified Gurson model while reinforcement fracture and interface decohesion at the matrix/reinforcement interface were included using three-dimensional interface elements especially developed to this purpose, the interface and/or particle strength and toughness being given by the constitutive equation of the cohesive crack. The new interface element, made up of two triangular surfaces compatible with the faces of the ten-node tetrahedra, was developed using a large displacement formulation, necessary to account for the large voids formed at the interface and within the particles during fracture. In addition, a new control technique was presented to obtain the whole load-displacement response in a simulation at a reasonable computational cost because the nucleation of damage in the microstructure often leads to numerical instabilities, which delay (or even impede) the convergence.

RESULTS AND CONCLUSIONS

The numerical results provided the macroscopic composite response as a function of the reinforcement volume fraction and spatial distribution, and showed how the details of the local particle arrangement controlled the nucleation and growth of

damage in the composite throughout the three-dimensional microstructure. In particular, the simulations were aimed at elucidating the role of the spatial particle distribution on the composite response with and without damage. Cubic cells representative of homogeneous and highly clustered composites were generated (Fig. 1) and the composite behavior in tension was obtained by the finite element method. It was found that the overall composite response was weakly influenced by the reinforcement particle distribution in the absence of damage, although the maximum principal stresses in the particles at the local level were significantly higher in the clustered microstructures. This difference did influence the composite behavior when damage (as particle fracture, interface decohesion or ductile matrix failure) was included in the simulations. This is shown in the tensile stress-strain curve of a composite containing 15 vol. % of spherical particles embedded in an elasto-plastic matrix presented in Fig. 2. Four curves corresponding to two different microstructures (homogeneous and clustered) with two particle/matrix interfaces (perfect bonding or interfacial decohesion) are plotted. They show the synergistic contribution of an inhomogeneous particle distribution and interfacial fracture to the composite strain hardening capacity, and the results were more marked when other damage mechanisms were included. As a conclusion of the simulations, the influence of the statistical parameters which describe the microstructure on the mechanical properties was obtained as a function of the dominant damage mechanism.

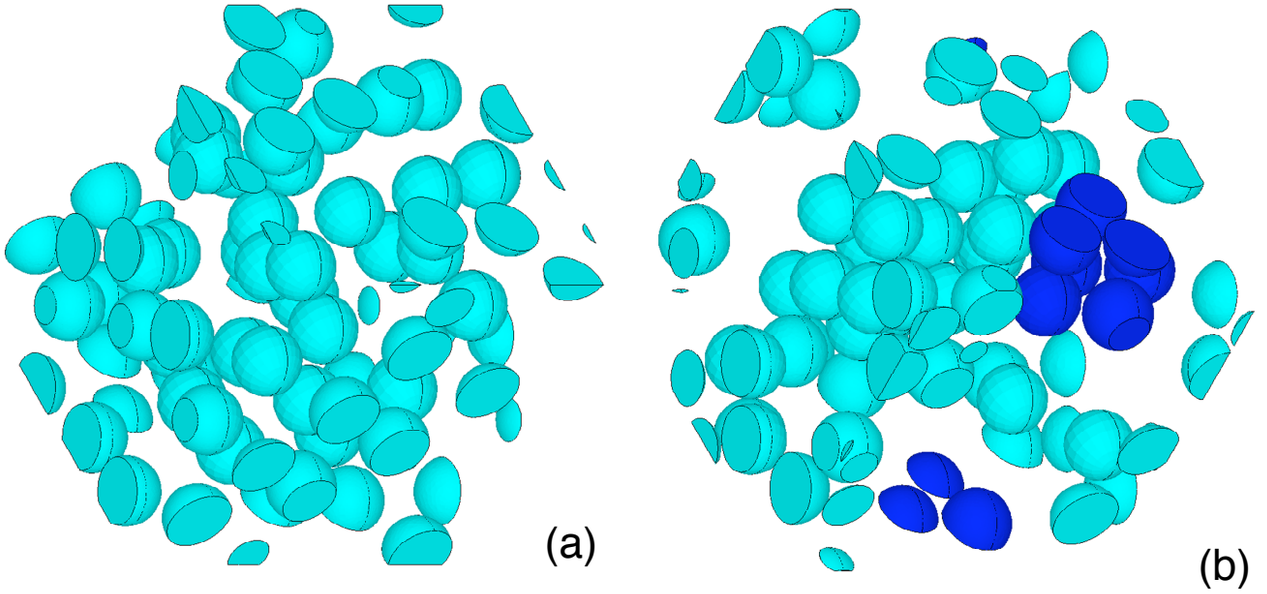


Figure 1. Particle distribution within the cubic cell. (a) Homogeneous. (b) Clustered.

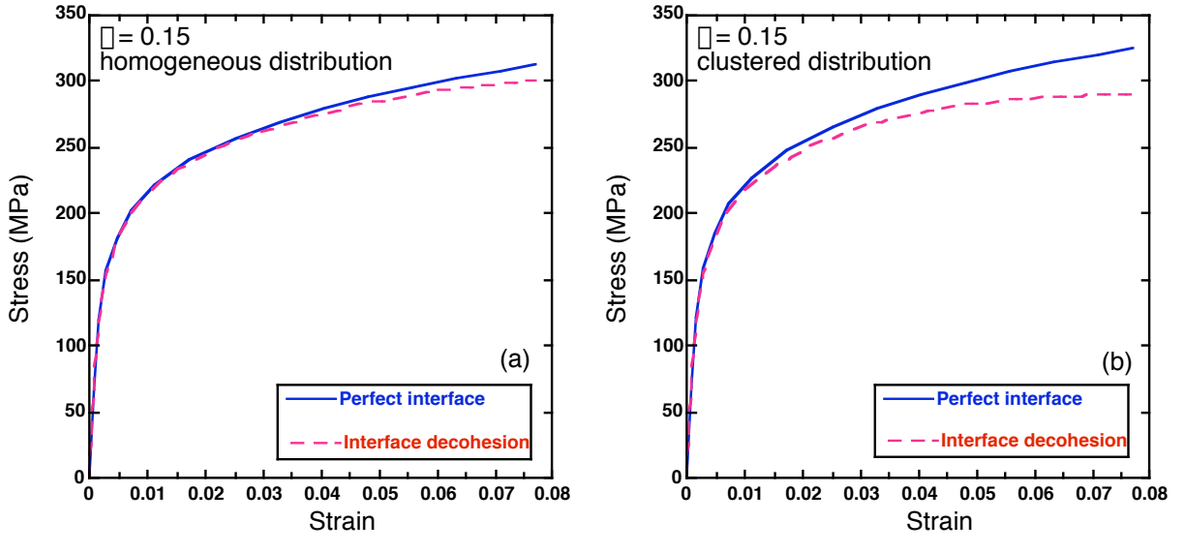


Figure 2. Tensile stress-strain curve of the composite. (a) Homogeneous. (b) Clustered microstructure.

XXI ICTAM, 15-21 August 2004, Warsaw, Poland

Elastic Interaction of Multiple Delaminations in Laminated Structures

Martin G. Andrews[*], Roberta Massabò[**], Brian N. Cox[***]

[*]*Northwestern University, Department of Civil and Environmental Engineering, IL, USA*
[**]*University of Genova, Department of Structural and Geotechnical Engineering, Genova, Italy*
[***]*Rockwell Scientific, California, USA*

Summary The elastic interaction of multiple delaminations in laminated structures subject to out of plane loading has been investigated. This has been done by utilizing beam theory approximations of elasticity. Shielding and amplification of the energy release rate of the cracks has been quantified for the case of a cantilever beam. Results show important short and long range interactions between these cracks, depending mostly on their transverse spacing. The results have some similarity to those found by other investigators for the interaction of cracks in infinite bodies, but with strong modification of certain characteristics by mode ratio and thickness effects. The shielding and amplification effects strongly influence the propagation of the system of cracks leading to local instabilities, local strain hardening and crack arrest. The results are being validated using finite element solutions.

INTRODUCTION

Laminated structures are found in many man-made systems, such as aeronautical, aerospace and civil structures. They are also found in natural systems, such as seashells and insect cuticles. During manufacture (or growth) or under service conditions, these systems may develop delaminations that have the potential to reduce the stiffness and structural capacity of the system or to grow and cause premature and often catastrophic failures. Depending on the internal structure and loading conditions, the delaminations may tend to localize into a single crack or to spread into a diffuse region of multiple cracks leading to different macrostructural responses. The problem of quasi-static and dynamic delamination of structures in the presence of one single crack has been studied extensively, accounting also for cohesive and bridging mechanisms (see for instance [3,4] for some work of the authors). This paper deals with the problem of multiple delamination fracture.

An important phenomenon in delamination failure of laminated structures is the interaction between the cracks. An example is the interaction of a single crack with a field of micro-cracks, which can simulate damage in materials such as concrete or rock (see for instance [1-2]). This type of problem has introduced the concept of crack tip shielding and amplification, referring to the tendency of the cracks to either decrease or increase the stress intensification at the tips of the other cracks in the system. The problem of the interaction of multiple delaminations in structures subject to static, dynamic and impact loading has not yet been solved. In these structures, shielding and amplification phenomena are strongly controlled by structural effects that may alter the results previously obtained for other material systems.

DISCUSSION

The problem under consideration is a beam or plate, with n multiple through-width cracks of arbitrary length and transverse spacing. The material is assumed to be homogeneous, isotropic, and linear elastic. Figure 1 shows an example cantilever beam with multiple edge cracks, subjected to a static, concentrated force P at its end. The system is divided up into beam segments and Euler-Bernoulli beam theory is applied to determine the solution.

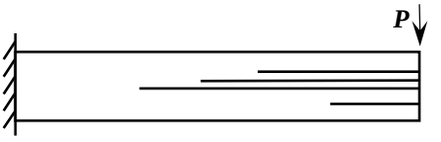


Figure 1 – Cantilever beam with multiple delaminations

The simplest configuration is when all of the cracks in the system are of the same length a and are assumed to propagate simultaneously. In this configuration the energy release rate for the extension of one of the cracks, $\mathcal{G}_i$, is easily determined from the total potential energy of the system. Equations (1) show $\mathcal{G}_i$ corresponding to n equally spaced cracks (1.a) and to n arbitrarily spaced cracks (1.b):

$$\text{(a)} \quad \mathcal{G}_i = \frac{6P^2a^2}{Eh^3}(n+2) \qquad \text{(b)} \quad \mathcal{G}_i = \frac{1}{2n}\frac{P^2a^2}{EI_0}\left(I_0 \Big/ \sum_{n+1} I_k - 1\right) \tag{1}$$

where E is the Young's modulus, h is the height of the beam, I_k (k=1,..n+1) is the moment of inertia of the beams in the cracked region and I_0 is the moment of inertia of the intact beam. Results show that as the number of equally spaced, equal length cracks increases so does $\mathcal{G}_i$ (diffuse damage), whereas, if the cracks are concentrated into a small layer (localized damage) then as the number of cracks increases, $\mathcal{G}_i$ decreases.

In order to analyze general crack configurations, the assumptions of equal length cracks and simultaneous propagation have been relaxed and the system of two cracks shown in Fig. 2 has been considered. Two solutions have been derived, the first valid when the upper crack is longer than the lower crack, $a_U > a_L$ and the second valid when $a_L > a_U$.

When the upper crack is longer, $a_U > a_L$, contact arises between beam segments 3 and 4. This contact has been

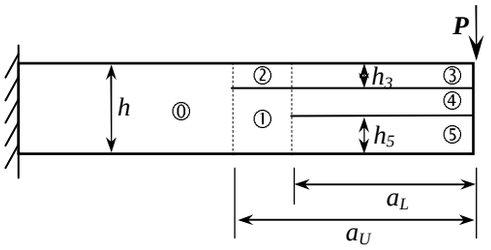


Figure 2 – Beam with two cracks

accounted for in three ways. The first, *A*, is to allow the beams to interpenetrate. The second, *B*, is to assume that the deflections of the beams in the cracked region are the same, thus preventing interpenetration (constrained model). The third, *C*, is to approximate contact with distributed linear springs that resist interpenetration. The stiffness of the springs depends on the transverse elasticity and heights of the two beam segments. This is considered the *exact* solution in the realm of beam theory. Contact between beams 3 and 4 also causes contact between beams 4 and 5, which is approximated similarly. The sizes of the contact regions are unknown *a priori*; therefore the problem is non-linear. When the lower crack is longer, $a_L > a_U$, there is opening between beam segments 4 and 5. In this case no additional assumptions are required.

The energy release rates for the upper, $\mathcal{G}_U$, and the lower, $\mathcal{G}_L$, cracks are calculated using the J-integral around paths surrounding each crack tip. Figure 3.a shows $\mathcal{G}_L$ normalized by the energy release rate for the same crack in the absence of the upper crack, $\mathcal{G}_{Lo}$, for one set of parameters. When the upper crack is longer (left side of the diagram), solutions *A* and *B* are upper and lower bounds of the exact solution *C*. When the upper crack is shorter (right side), all solutions coincide. For this set of parameters, $\mathcal{G}_L$ is always amplified. This amplification is strong when the lower crack is shorter. Also visible is a jump in $\mathcal{G}_L$ when the cracks are of equal length. This jump is similar to what was observed in [1] for the interaction of a semi-infinite main crack with a pair of micro-cracks in an infinite medium.

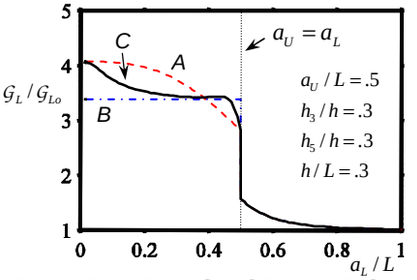


Figure 3a - Normalized Energy Release Rate of Lower Crack

Figure 3b shows contours of regions of amplification and shielding as a function of the transverse positions of the two cracks. If the positions fall in the lower left regions, e.g., point (a), then $\mathcal{G}_L$ will always be amplified (Fig. 3a). If they fall in the shaded region, point (b), then there will be a mixture of amplification and shielding depending on the relative length of the two cracks. Finally, if the positions fall in the upper region, point (c), then $\mathcal{G}_L$ will always be shielded.

When the cracks have similar lengths, beam segment 1 becomes stocky and the validity of Euler-Bernoulli beam theory is questionable. The importance of shear deformation has been investigating by using Timoshenko beam theory. The results show that for sufficiently long cracks the shear deformations of beam segment 1 have no effect on the macrostructural response and $\mathcal{G}_i$.

A study of the quasi-static propagation of the two-crack system has yielded contour maps that highlight different crack propagation mechanisms controlled by the crack configuration. It has also revealed many interesting effects. For instance, for certain crack geometries, there is a local strain hardening behavior due to the shielding effect. For other geometries, there is crack pull-along, in which one crack will begin to propagate, and then some distance later the second crack will begin to propagate as well. The jumps in the energy release rate (Fig. 3) can also be seen in the quasi-static load deflection curve as local snap-back instabilities.

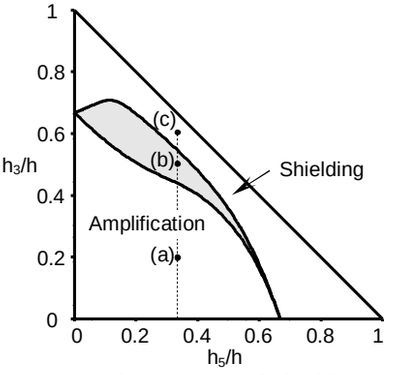


Figure 3b –Regions of Shielding and Amplification

CONCLUSIONS

The study has shown that there are significant short and long range interaction effects between cracks in a structure with multiple delaminations. These interaction effects can be shielding or amplification of the energy release rate of a crack and strongly depend on the geometry of the system. The results are currently being validated using finite element solutions. Additional effects, such as friction in the regions of crack face contact and the effect of cohesive and bridging mechanisms acting along the cracks are under investigation.

Acknowledgments

MGA and RM supported by Northwestern University, BNC supported by ARO Research Contract DAAD19-01-C-0083.

References

[1] Brencich, A. and Carpinteri, A., (1996), Interaction of a Main Crack with Ordered Distributions of Microcracks: A Numerical Technique by Displacement Discontinuity Boundary Elements, *Int. J. Fracture*, **76**, 373-389.

[2] Kachanov , M. (1985), On Crack - Microcrack Interactions , *Int. J. Fracture*, **30**(4), 65-72.

[3] Massabò, R., and Cox, B.N., (1999), Concepts for Bridged Mode II Delamination Cracks, *J. Mech.Phys.Solids*, **47**(6), 1265-1300.

[4] Sridhar, N., Massabò, R., Cox, B.N., and Beyerlein, I., (2002), Delamination Dynamics in Through-Thickness Reinforced Laminates with Application to DCB Specimen, *Int. J. Fracture* **118**, 119-144.

OVERALL PROPERTIES OF PERIODIC BIOCOMPOSITES

Lucia Doval-Montes*, Eduardo López-López**,***, Federico J. Sabina***,
Julián Bravo-Castillero****, Raúl Guinovart-Díaz***,****, Reinaldo Rodríguez-Ramos****
*Plantel Azcapozalco Melchor Ocampo, Rosario s/n, esq. Hidalgo, 02205 México, D.F., México
**Posgrado en Ciencias Matemáticas
***Instituto de Investigaciones en Matemáticas Aplicadas y en Sistemas, Universidad Nacional Autónoma de México, Apartado Postal 20-726, 01000 México, D.F., México
****Facultad de Matemática y Computación, Universidad de La Habana, San Lázaro y L, Vedado, La Habana 4, CP-10400, Cuba

Summary Electroelastic properties of two-phase circular cylindrical fibre-reinforced biocomposites are calculated for square and hexagonal periodical arrays using the asymptotic homogenization method. The materials of the composite belong to the hexagonal system, classes 622 and 6. Easy to compute closed-form formulae are obtained. Numerical results are shown for several biomaterials, e.g., collagen and collagen-hydroxyapatite composite and others.

INTRODUCTION

Composites, whether natural or man-made, span a wide variety of geometries (particulates, fibers, laminates, etc.). Composition is guided, and even tailored, by the application at hand. In medical applications the constituents must fulfill a number of prerequisites to be of any use [1]. At present there are a number of biomaterials, as they are called, under study for, say, bone regeneration, implants, replacement scaffolds, etc. [2]. Electroelastic properties of two of them, collagen and collagen-hydroxyapatite, have been measured lately [3]. Their anisotropy belongs to the hexagonal system, class 622. Other related biomaterials (bone, tendon, etc.) have the symmetry 6. It is of interest to find the effective properties of composites with these elements. Recently, the overall properties of two-phase fiber-reinforced periodic composites, i.e., long parallel circular cylindrical fibers of one material embedded into another one, have been found in closed-form for square [4] and hexagonal [5] arrays and materials with the 6mm symmetry. These were found using the asymptotic homogenization method. Here it is proposed to use that method as to include the classes 622 and 6. For the purpose of brevity, only one such problem (hexagonal array and 622 symmetry) is explicitly addressed here.

STATEMENT OF THE PROBLEM

Figure 1 shows the unit cell. As a consequence of the geometrical axial symmetry, the initial set of equations uncouple into two independent systems. For brevity, the simpler problem is described here, since it typifies the method and some of the results. This corresponds to the case of out-of-plane mechanical displacement/in-plane electric field. The governing equations are

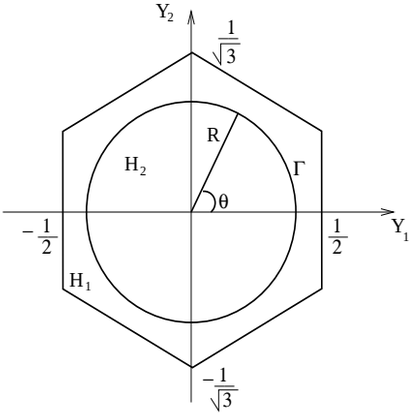


Figure 1: Hexagonal Unit Cell

$$\text{div}\,(\sigma_{13}^{(\epsilon)}, \sigma_{23}^{(\epsilon)}) = 0 = \text{ div}\,(D_1^{(\epsilon)}, D_2^{(\epsilon)}) \text{ in } R^2, \tag{1}$$

where $\sigma_{13}^{(\epsilon)}, \sigma_{23}^{(\epsilon)}$ are the stress components; $D_1^{(\epsilon)}, D_2^{(\epsilon)}$ those of the electric displacement and $\epsilon \ll 1$. The constitutive relations for the class 622 are

$$\sigma_{23} = 2p\epsilon_{23} - s'E_1,\ \sigma_{13} = 2p\epsilon_{13} + s'E_2, \tag{2}$$

$$D_1 = 2s'\epsilon_{23} + tE_1,\ D_2 = -2s'\epsilon_{13} + tE_2, \tag{3}$$

where p, s' and t are the composite's axial shear modulus, stress piezoelectric constant and axial permittivity, respectively. The same notation is used for the properties of the phases except that an index 1 (2) is used for the matrix (fiber). The components of the strain are $\epsilon_{13}, \epsilon_{23}$ and those of the electric field E_1, E_2.

Asymptotic homogenization method

The method proceeds as usual [6]. The focus here is on the effective properties p, s' and t. They are given by

$$p = p_v + \langle pM_{,1} - s'N_{,2}\rangle,\ s' = s'_v + \langle s'M_{,1} + tN_{,2}\rangle, \tag{4}$$

where the comma notation denotes differentiation with respect to y_1 or y_2, the index v indicates the Voigt (arithmetic) mean, e.g., $p_v = (1 - V_2)p_1 + V_2 p_2$, where V_2 is the area fraction occupied by the fiber and $|H|\langle F(y)\rangle = \int_H F(\mathbf{y})da, H = H_1 \cup H_2$ is the unit cell (Fig. 1). As for t, it is obtained from the universal relation derived using the Milgrom-Shtrikman compatibility equation, since it connects p, s' and t. The functions $M^{(\gamma)}$ and $N^{(\gamma)}, \gamma = 1, 2$, are the solution of the following unit cell problem, the so-called local problem:

$$\Delta M^{(\gamma)} = \Delta N^{(\gamma)} = 0 \text{ in } H = H_1 \cup H_2, \parallel M^{(\gamma)} \parallel = \parallel N^{(\gamma)} \parallel = 0 \text{ on } \Gamma, \tag{5}$$

$$\parallel (p_\gamma M^{(\gamma)}_{,2} - t_\gamma N^{(\gamma)}_{,1})n_1 + (p_\gamma M^{(\gamma)}_{,2} + s'_\gamma N^{(\gamma)}_{,1})n_2 \parallel = - \parallel p_\gamma \parallel n_1, \text{ on } \Gamma, \tag{6}$$

$$\parallel (s'_\gamma M^{(\gamma)}_{,2} - t_\gamma N^{(\gamma)}_{,1})n_1 - (s'_\gamma M^{(\gamma)}_{,1} + t_\gamma N^{(\gamma)}_{,2})n_2 \parallel = \parallel s'_\gamma \parallel n_2, \text{ on } \Gamma, \tag{7}$$

$$\langle M \rangle = \langle N \rangle = 0, \tag{8}$$

where the contrast to p across Γ is $\parallel p_\gamma \parallel = p_1 - p_2$, etc., (n_1, n_2) is the unit normal to Γ. Potential methods are used to find $M^{(\gamma)}$ and $N^{(\gamma)}$ using doubly periodic harmonic functions of periods $1, \exp(i\pi/3)$ (the quasi-periodic Weierstrass zeta function and its derivatives of order k). The application of Green's theorem to (4), yields

$$p = p_1(1 - 2\pi a_1), s' = s'_1 + 2\pi t_1 b_1, \tag{9}$$

where a_1, b_1, are the residues at the origin of the functions $M^{(1)}$ and $N^{(1)}$, respectively. They can be found after solving an infinite system of algebraic equations that converge very quickly. Its truncation to a sequence of finite systems leads to the sought coefficients a_1, b_1 and the overall properties (4). The numerical scheme ends when enough accuracy is achieved.

NUMERICAL EXAMPLES

The material properties for the calculations that follow were taken from [3]. After some minor calculations, the data used is: for collagen, taken as the matrix medium $p_1 = 1.4\ GPa, t_1/\varepsilon_0 = 2.825 (\varepsilon_0 = 8.854 \times 10^{-12} C^2/Nm^2$, permittivity of free space), $d_1 = 6.2.10^{-14} C/N$; the fiber material is a collagen-hydroxyapatite (HA) composite, whose properties are $p_2 = 2.697\ GPa, t_2/\varepsilon_0 = 2.509, d_2 = 4.1. \times 10^{-14} C/N$. The results are shown in Fig. 2, which displays a plot of the overall properties $p, t/\epsilon_0$ and d as a function of the fiber volume fraction V_2, up to the percolation limit (i.e., when the fibers get in contact). The three properties show a monotonic behaviour as a function of the fiber volume fraction. Note that $d = s'/p$ is the strain piezoelectric coefficient.

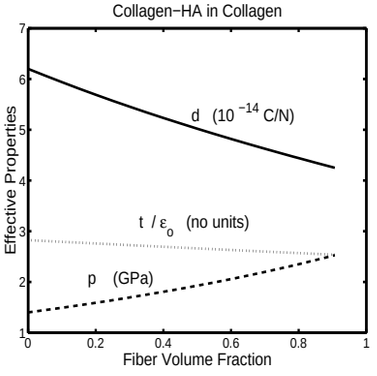


Figure 2: Overall Properties

CONCLUSIONS

Closed-form formulae for the overall properties of fiber-reinforced composites, whose electroelastic characteristics belong to the hexagonal system, classes 622 and 6, are obtained for square and hexagonal arrays. An example using newly measured properties of collagen and a collagen-hydroxyapatite composite is shown here. Other examples will be shown.

References

[1] Thompson I., Hench L.L.: Medical Applications of Composites. In: Kelly A., Zweben C., eds., Comprehensive Composite Materials. Elsevier, Amsterdam 2000.

[2] Hollister S.A., Chu T.G., Halloran J.W., Feinbert A.E.: Design and Manufacture of Bone Replacement Scaffolds, In: Cowin S.C., ed., Bone Mechanics Handbook, 2nd ed., Chapter 36, 14 pp; CRC Press, Boca Raton 2001.

[3] Silva C.C., Thomazini D., Pinheiro A.G., Aranha N., Figueiró S.D., Góes J.C., Sombra A.S.B.: Collagen-Hydroxyapatite Films: Piezoelectric Properties. *Mat Sci Engng* **B86**:210–218 2001.

[4] Bravo-Castillero J., Guinovart-Díaz R., Sabina F.J., Rodríguez-Ramos R.: Closed-Form Expressions for the Effective Coefficients of Fibre-Reinforced Composite with Transversely Isotropic Constituents. II: Piezoelectric and Square Symmetry. *Mech Mat* **33**:237–248 2001.

[5] Sabina F.J., Rodríguez-Ramos R., Bravo-Castillero J., Guinovart-Díaz R.: Closed-Form Expressions for the Effective Coefficients of Fibre-Reinforced Composite with Transversely Isotropic Constituents. II: Piezoelectric and Hexagonal Symmetry. *J Mech Phys Solids* **49**:1463–1479 2001.

[6] Bensoussan A., Lions J.L., Papanicolau G: Asymptotic Analysis for Periodic Composites. North-Holland, Amsterdam 1978.

DAMAGE TOLERANCE OF COMPOSITE STRUCTURES WITH THERMAL SHIELD

Christophe Bouvet[*], Sandrine Petit[**], Alain Bergerot[***], Jean-Jacques Barrau[*]
[*]*LGMT, Université Paul Sabatier, Toulouse, France*
[**]*LMS, IPPT PAN, École Nationale Supérieure de l'Aéronautique et de l'Espace, Toulouse, France*
[***]*EADS, Space Transportation, Saint Médard en Jalles, France*

Summary The aim of this paper is to present a study on the influence of the cork thermal shield on composite panels during a low velocity impact. The results show the good mechanical behaviour of the thermal shield during the impact. Indeed, the thermal protection acts like a mechanical protection during the impact and reveals it before having damage in the laminate.

STUDY OBJECTIVES

Composite materials have been increasingly introduced in airframe and spatial applications in the last decade because of their interesting characteristics. Nevertheless, damage induced in these materials by impacts by foreign objects during the life of the structure can cause drastic reductions in the strength of the structure and, for this reason, the problem of impact on laminated structures has been a subject of intense research efforts [1]. Aeronautical and spatial structures are often subjected to accidental damages. Consequently, it is essential to define a damage tolerance demonstration as soon as a new project begins.
Damage tolerance was introduced at the end of 1978 for aircraft structures [2]. It is intended to ensure that, with serious fatigue, corrosion, or accidental damage occurring within the operational life of the airplane, the remaining structure can withstand reasonable loads without failure or excessive structural deformation until the damage is detected. In the military and spatial launchers fields, the damage tolerance concept only begins to appear.
This study focuses on the influence during low velocity impact of the cork thermal shield [3] used for civil and military launchers' fairing.
The purposes are to complete the characterisation works performed on laminates used for the launchers' fairing considering damage tolerance demonstration. Damage phenomena will have to be examined on cork shielded composite panels, induced by a low velocity impact.

EXPERIMENTAL STUDY

Two composite materials, with carbon fibres and epoxy matrix, are used in this investigation : a high modulus unidirectional composite M46J/M18 with 18 plies $(0°/60°/0°/-60°/0°/60°/90°/-60°/0°)_S$ of 3.78 mm-thickness and a high strength unidirectional composite T300/914 with 28 plies $(0°/60°/0°/-60°/0°/60°/90°/90/-60°/0°/-60°/0°/60°/0°)_S$ of 3.64 mm-thickness. Experiments are carried out on shielded and unshielded panels to analyse the thermal protection influence on impacted damaged monolithic and sandwich panels. The detectability criterion and the delaminated areas are determined. Post-Impact Compression Loading tests are being conducted in order to define the residual strength and the allowable damages for impacted composite structures.

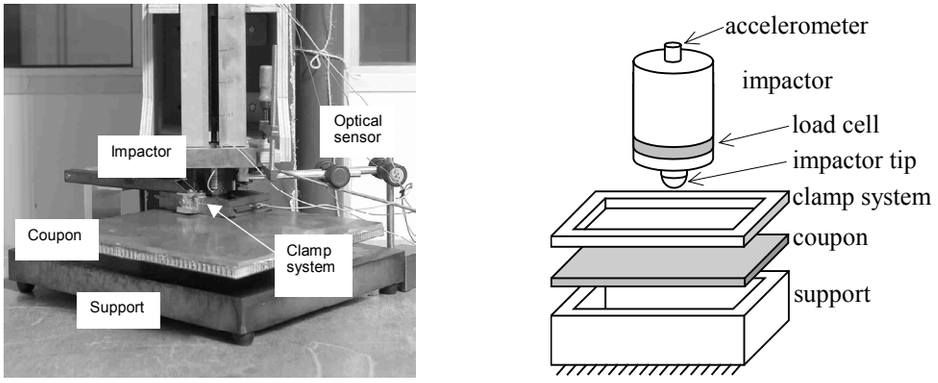


Figure 1 : Impact apparatus

The apparatus used to impact the composite coupons is shown in Figure 1. It consists in dropping an impactor, equipped with a load cell and an accelerometer, on a laminate panel, clamped by a 125 x 75 mm² window. The velocity is measured owing to an optical sensor. Ultrasonic waves analyses are then realised on the impacted coupons to evaluate the delaminated area.

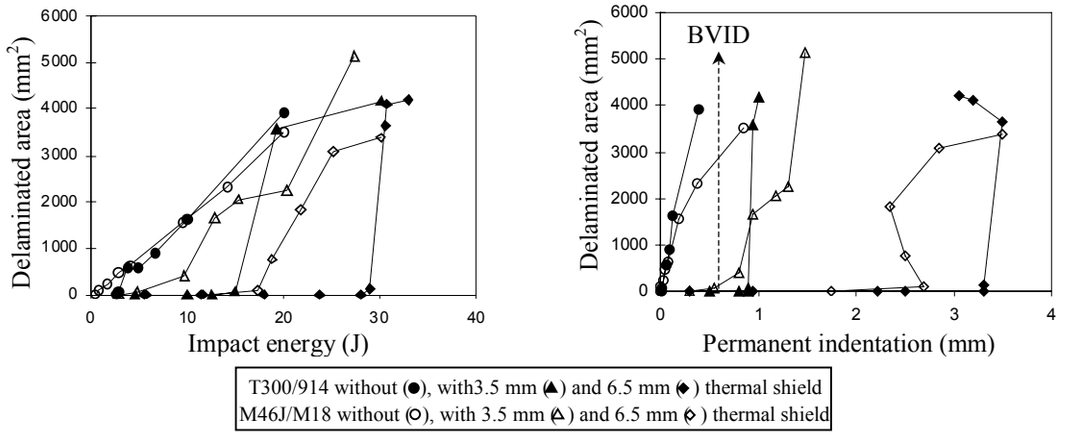


Figure 2 : Delaminated area versus impact energy (a) and permanent indentation (b)

RESULTS

The delaminated area evolution versus the impact energy of the projectile is drawn in figure 2a for laminate panels without thermal shield and with cork thermal shield of 3.5 and 6.5 mm-thickness, for the two studied materials. This figure shows that, for shielded panels, delamination appears at higher impact energy, in particular for low delaminated area. So the thermal protection acts like a mechanical protection during an impact. This result is valid for the two materials, even if the M46J/M18 material is more brittle than the T300/914, without or with thermal shield.
In figure 2b, the delaminated area is reported versus the permanent indentation measured after the impact. This figure shows that permanent indentation for shielded panels is much more important than for the unshielded panels for the same delaminated area. Besides, damage threshold appears at a higher permanent indentation than the BVID (Barely Visible Impact Damage) [4] aeronautic threshold of 0.6 mm. Thus, the thermal protection, in addition of having a mechanical protection function, reveals impact before having damage in the laminate.

CONCLUSIONS AND PERSPECTIVES

Impact tests have been conducted in order to define the behaviour laws of shielded composite structures used for launchers fairing versus impact damages. This preliminary study allows to demonstrate the beneficial effect of thermal shield to the damage tolerance concept. The thermal shield has a mechanical protection function on the composite structures and reveals the impact before the damage appears in the structure.
Post-impact compression loading tests are being performed and will allow to study the thermal shield influence on the residual strength.
Numerical analyses are equally in progress. The purpose is to be able to foresee a damage on an impacted shielded structure without having to realise costly experimental tests. Finally, from simple numerical models of impacted shielded laminate coupons, the engineer should be able to comprehend the damage phenomena on a more complex impacted structure (a launcher fairing for example).

References

[1] Abrate S.: Impact on composite structures, Ed. Cambridge university press, 1998.
[2] Rouchon J.: Certification of large airplane composite structures, recent progress and new trends in compliance philosophy, 7th ICAS congress, Stockholm, 1990.
[3] Davis J.B., Morgan P.E.D., Oka K.S., Barney A.O., Hogenson P.A.: Damage-Tolerant thermal protection systems, AIAA Space Conferences & Expositions, 2000
[4] Rouchon J.: Fatigue and damage tolerance aspects for composite aircraft structures, Delft, 1995.

Can it be made?

Predicting the Formability of Textile Composite Components

M. J. Clifford, P. Harrison, A. C. Long

School of Mechanical, Materials, Manufacturing Engineering and Management,
The University of Nottingham, University Park, Nottingham NG7 2RD, U.K.

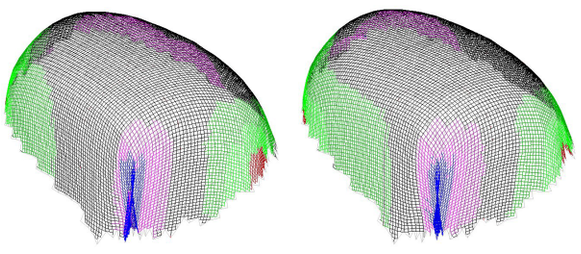
email: mike.clifford@nottingham.ac.uk
tel: 00 44 (0) 115 8466134

Extended Summary

There are many ways of forming components from composite materials. These include injection moulding, hand lay-up, diaphragm forming, stamping, pultrusion, resin transfer moulding, filament winding, and vacuum forming [1]. In recent years, attention has been focused on optimising the structural properties of composite components by using continuous fibres. Producing materials that can be formed with minimum force to produce high quality components is a challenging task.

In order for a textile composite material to form a given shape, various deformation mechanisms may occur. The most important and widely studied of these is intra-ply shear. One simple approach to predict the formability of components - kinematic draping - is to idealise a textile as a pin-jointed net, and to compute deformed fibre paths via a geometric algorithm [2]. The algorithm has been implemented commercially (e.g. MSC Laminate Modeler) and can provide a rapid solution. The kinematic approach can be used by designers to optimise the shape of components to minimise shear deformation and to predict mechanical properties, but since the algorithm takes no account of material properties, it cannot provide material manufacturers with any assistance in designing conformable textiles or recommend one material over another for production. In many cases, designers do not have the luxury of reshaping parts, and so compromises have to be made such as inserting cuts or splits into the fabric. Inevitably, these modifications reduce performance (strength, stiffness).

It has been shown that many shapes cannot be formed without inserting cuts into an idealised woven textile composite. One simple example is the cube [3]. Rapid changes in curvature also produce difficulties. Figure 1 shows a car wing mirror holder being draped by a 0/90 woven textile. Whatever initial fibre orientation is chosen, the algorithm fails to completely cover the surface without fibres crossing over each other, forming folds and wrinkles.



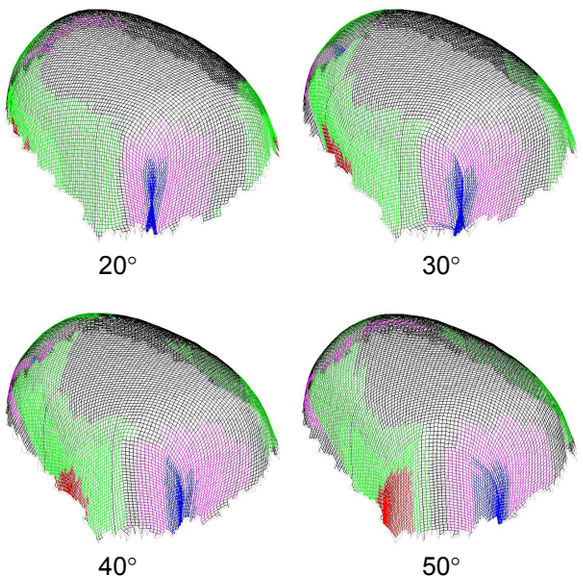


Figure 1: Drape simulations for car wing mirror holder at various initial fibre orientations.

Fortunately for manufacturers, textile composites can deform by modes other than shear. These include inter-tow slip and fibre extension or uncrimping [4]. Figure 2 shows a car wing mirror holder produced from Twintex (a glass/polypropylene woven thermoplastic composite) via vacuum forming. Before the component was formed, a grid was marked on the material to indicate the fibre directions. In the region where the kinematic algorithm predicted a fold, there is considerable shear deformation, but the component is formable due to other deformation modes coming into play.



Figure 2: Car wing mirror holder formed from Twintex.

More sophisticated algorithms have been devised that take into account material properties and additional deformation modes such as fibre extension and un-crimping. Explicit finite element codes (eg. ESI PAM-FORM) can represent material behaviour and processing conditions, but take much longer to compute and require significant material property data [5]. An alternative has been developed by the authors, based on the kinematic model described above implemented within an iterative scheme. In this approach, the appropriate mapping of fibres onto the surface is chosen to minimise shear strain energy. This can utilise data either from experimental shear testing or from constitutive modelling, thus enabling the effects of material construction to be considered [6].

For manufacturing processes that require textile composites to be shaped to a component's surface by hand, an additional limitation on forming is the energy required to deform the material. Various experimental test methods such as the bias extension and picture frame shear tests can be used for existing materials, but a large number of costly tests are required to fully characterise each material at a range of forming conditions (rate, temperature, etc). However, a constitutive model for intra- and inter-ply shear behaviour, based on constituent properties (fibre architecture, matrix rheology) has been developed and validated for both thermoset and thermoplastic prepregs over a range of processing conditions [7]. The model is entirely predictive, and requires a small set of input data including matrix rheology characterisation, fibre volume fraction, and tow properties, all of which should be relatively easy to obtain from manufacturers' data sheets or from a small number of additional tests. The advantage of the constitutive modelling approach is that the sensitivity of materials to changes in matrix viscosity or other variables can be assessed, providing material manufacturers with design information, which can be used to manufacture more conformable textile composites.

A forming limit diagram can be constructed by considering the energy required to form a given component from a woven textile composite material. Figure 3 shows such a diagram. The graph was constructed by computing the energy required to form the helmet from a fibre reinforced composite with a range of fibre volume fractions at various forming temperatures via the energy draping algorithm. It is assumed that the operators can apply a given amount of energy. When the energy is exceeded, the component is unformable.

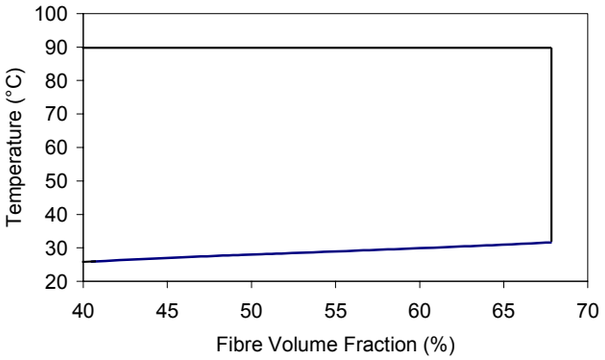


Figure 3: Forming limit diagram for a helicopter pilot helmet.

References

1. Hull, D. An introduction to composite materials. Cambridge University Press, 1996.

2. Long A.C. and Rudd C.D., A simulation of reinforcement deformation during the production of preforms for liquid moulding processes. Proc Inst Mech Engrs 208 (1994), pp. 269–277.

3. Robertson RE, Chu T-J, Gerard RJ, Kim J-H, Peterson RC. Three-dimensional fiber reinforcement shapes obtainable from flat, bidirectional fabrics without wrinkling or cutting. 1. A single four-sided pyramid. Compos, Pt A, Appl Sci Manufact 2000;21:703–715.

4. Potter, K. D. (1979), The Influence of Accurate Stretch Data for Reinforcements on the Production of Complex Structural Mouldings, Composites, pp. 161-173.

5. De Luca P., et al., Development validation and first industrial numerical results of a finite element code to simulate the thermoforming process, in: Proceedings of the Fourth International Conference on Automated Composites (ICAC'95), Nottingham, UK, 1995.FEA.

6. De Luca, P., Lefebure, P., Pickett, A.K. Numerical and experimental investigation of some press forming parameters of two fibre reinforced thermoplastics: APC2-AS4 and PEI-CETEX. Composites Part A, 29A, 101-110, 1998.

7. Harrison, P., Clifford, M.J., Long, A.C. and Rudd, C.D. A constitutive model for pre-impregnated viscous textile composites. Composites Part A (in press), 2004

ELECTROELASTIC FIELDS CONCENTRATIONS AND POLARIZATION SWITCHING BY CIRCULAR ELECTRODES IN PIEZOELECTRIC DISK COMPOSITES

Fumio Narita*, Yasuhide Shindo and Masaru Karaiwa

* *Department of Materials Processing, Graduate School of Engineering,Tohoku University, Sendai 980-8579, Japan*

Summary The linear axisymmetric electroelastic problem for a piezoelectric composite with an electrode was analyzed theoretically. A numerical and experimental investigation of a piezoelectric disk composite with circular electrodes was also conducted. It is found that high values of electroelastic fields arise in the neighborhood of the circular electrode tip. These values are sufficiently high to produce polarization switching, electromechanical failure and dielectric breakdown.

INTRODUCTION

Piezoelectric ceramics play a significant role as active electronic components in many areas of science and technology, such as new biomaterials, smart structures and MEMS. Stress and electric field concentrations in the neighborhood of a crack tip or an electrode tip in piezoelectric ceramics can result in mechanical and electrical degradation. It is therefore important to understand the electroelastic fields in the vicinity of the crack or the electrode in piezoelectric ceramics and to improve the device's design and performance. Work on piezoelectric fracture mechanics has been reported by several research groups [1-4]. Recently, Shindo et al. have performed the indentation fracture [5], single-edge precracked-beam [6], and modified small punch [7] tests, and corresponding finite element analyses on piezoelectric ceramics.

Several theoretical investigations of piezoelectrics with electrodes have been presented. Shindo et al. [8] considered the behavior of the elastic and electric variables in the vicinity of a surface electrode attached to a piezoelectric ceramic, and found that high values of electroelastic fields arise in the neighborhood of the electrode tips. Ye and He [9] analyzed the distribution of the displacement and electric potential near the edges of parallel electrodes in piezoelectric ceramics. Some designs are in existence for piezoelectric MEMS devices with circular electrodes [10,11]. Bonded piezoelectric and elastic disks with a circular electrode embedded at the interface are also used as sounders. The purpose of this paper is to report a theoretical, numerical and experimental evaluation of electroelastic fields in the neighborhood of a circular electrode in a piezoelectric disk composite. A nonlinear finite element model incorporating the polarization switching mechanism is used to predict electroelastic fields concentrations ahead of circular electrodes in piezoelectric disk composites.

A SEMI-INFINITE PIEZOELECTRIC COMPOSITE WITH A CIRCULAR ELECTRODE

The electroelastic response of two-dissimilar piezoelectric half-spaces with an electrode is analyzed based on the linear theory of piezoelectricity. Hankel transforms are employed to reduce the electroelastic problem to the solution of a pair of dual integral equations. Then the closed form solutions of these dual integral equations are obtained.

A PIEZOELECTRIC DISK COMPOSITE WITH CIRCULAR ELECTRODES

Consider the piezoelectric disk I with radius b^{I} and thickness h^{I} as shown in Fig. 1. The piezoelectric disk is bonded to the upper surface of the piezoelectric disk II with radius b^{II} and thickness h^{II}. The origin of the coordinates (r, θ, z) coincides with the center of the interface considered as z=0, $0 \le r \le b^{\mathrm{I}}$. Three parallel circular electrodes of radius a lie in the planes z=-h^{II}, 0, h^{I}. Let the voltage applied to the internal electrode surface be denoted by V_0. The surface electrodes are grounded.

The enhanced electroelastic fields level at the electrode tips results in localized domain switching. When the electrical and mechanical work exceeds a critical value, polarization switching occurs [12]. The model is used to predict the

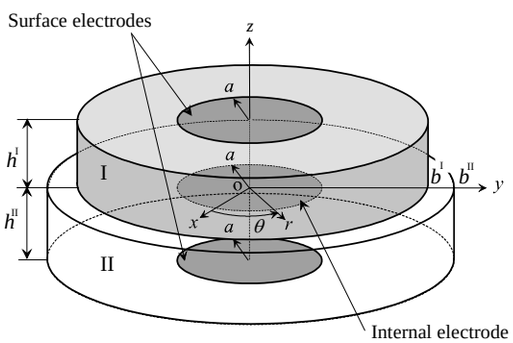


Fig. 1 Piezoelectric disk composite with circular electrodes

macroscopic nonlinear response involving 180° and 90° polarization switching.
The axisymmetric models were generated using the commercial finite element method (FEM) software package ANSYS. The surface electrode layers were not incorporated into the model. Four-node elements PLANE 13 were used in the model.

EXPERIMENTAL PROCEDURE

Strain measurements were performed on soft PZT piezoelectric ceramic disks (h^{II}=0 mm), C-91 (Fuji Ceramics Co., Ltd., Japan).The coercive field was approximately E_c = 0.35 MV/m. Disk-shaped specimens of dimensions 30 mm diameter by 5.0 or 1.0 mm thickness were prepared, and nickel-based electrodes with 20 mm diameter were deposited onto the top and bottom faces. The high-voltage amplifier used for the study was limited to 1.25 kV so that a 1.25 MV/m field corresponded to a sample thickness of 1.0 mm. Six strain gauges (KFL-02-120-C1-16 from Kyowa Electronic Instruments Co., Ltd., Japan) were placed at 60° increments around the circular electrode tip region. The centers of the strain gages were at approximately 0.05, 0.1, 1.5, 2.5, 3.0 and 4.0 from the electrode tip. The sensors have an active length of 0.2 mm.

RESULTS AND DISCUSSION

Semi-infinite piezoelectric composite

Consider the problem of an infinite piezoelectric composite ($h^{I} \to \infty$, $h^{II} \to \infty$, $b^{I} \to \infty$, $b^{II} \to \infty$). It is found that high values of electroelastic fields arise in the neighborhood of the circular electrode tip.

Circular piezoelectric disk composite

For the purpose of comparing the numerical simulations directly with measured strain, the radial strains ε_{rr} of nodes placed at 0.05, 0.1, 1.5, 2.5, 3.0 and 4.0 mm from the electrode-tip (corresponding to the strain gage location) in the finite element model are extracted. The computed strains on the lower surface of the specimen of h^{I}=5 mm (h^{II}=0 mm) under various values of electric field $E_0=V_0 / h^{I}$ are compared with the measured data in Fig. 2.
Fig. 3 displays the computed radial strain ε_{rr} on the interface of bonded C-91 and brass [13] disk of a=10 mm against the electric field E_0 for r-a=1.5 mm and variaus values of h^{II}, while letting b^{I}=15 mm, b^{II} =25 mm and h^{I}=1 mm. The experimental data for C-91 disk (h^{II}=0 mm) are also plotted. The increase of the negative electric field causes the polarization switching, and the strain vs. electric field curves show the nonlinear behavior. The results for two bonded C-91 composite disk are also obtained.

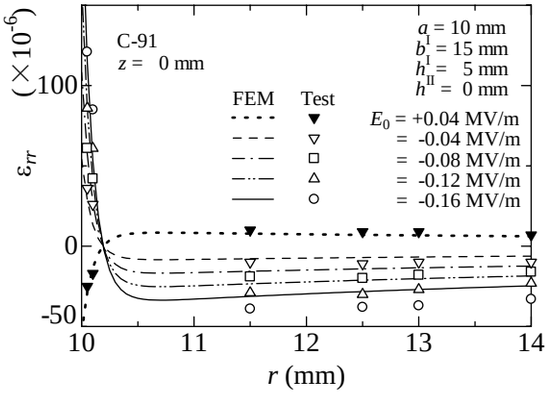


Fig.2 Radial strain ε_{rr} vs r: h^{I}=5mm, h^{II}=0mm

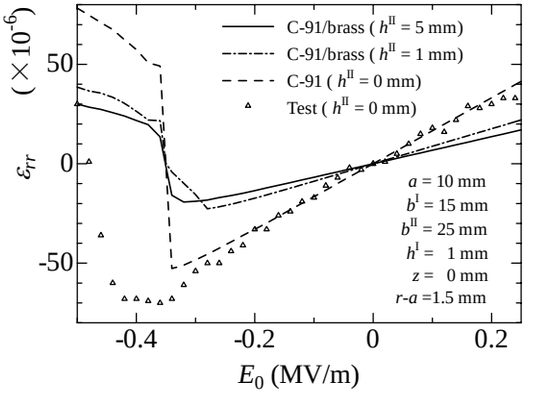


Fig.3 Radial strain ε_{rr} vs electric field E_0

References

[5] Shindo Y., Oka M., Horiguchi K.: Analysis and testing of indentation fracture behavior of piezoelectric ceramics under an electric field. *ASME J. Eng. Mater. Tec.* **123**: 293-300, 2001.
[6] Shindo Y., Murakami H., Horiguchi K., Narita F.: Evaluation of electric fracture properties of piezoelectric ceramics using the finite element and single-edge precracked-beam methods. *J. Am. Ceram. Soc.* **85**: 1243-1248, 2002.
[7] Shindo Y., Narita F., Horiguchi K., Magara, Y., Yoshida, M.: Electric fracture and polarization switching properties of piezoelectric ceramic PZT studied by the modified small punch test. *Acta mater*. **51**: 4773-4782, 2003.
[8] Shindo Y., Narita F., Sosa H.: Electroelastic analysis of piezoelectric ceramics with surface electrodes. *Int. J. Eng. Sci.* **36**: 1001-1009, 1998.

Fuzzy Set Approach to Modelling Composite Mechanical Properties

Aleksander Muc
Institute of Machine Design, Cracow University of Technology, Kraków, Poland

Introduction

The field of composites mechanics, engineering and technology is relatively young, and the test methods and measurements techniques are not yet fully developed. The modelling of their mechanical properties is even further behind the experimental investigations. The study and application of composite materials is a truly interdisciplinary endeavour since their properties are strongly dependant on the physical and chemical bonding between three constituents: a reinforcement, a matrix and an interface layer being in fact a new material. Therefore, the origin and source of imprecision (or uncertainty) lies mainly in the lack of information dealing with their microstructure, mechanical properties of constituents, behaviour and the number of factors responsible for gradual degradation of their properties and final failure. Commonly, the theoretical (deterministic) analysis of composites is based on homogenisation theories that may include an increasing number of different parameters. However, it is unknown in advance what number of parameters is sufficient to describe satisfactorily the problem considered. On the other hand, the material parameters are evaluated in the experimental way being the source of randomness in the traditional (deterministic) analysis or impreciseness or vagueness in the fuzzy set approach. The imprecise, vague, qualitative, linguistic or incomplete information may be present in geometry, material properties, degradation of properties, applied loads or boundary conditions.

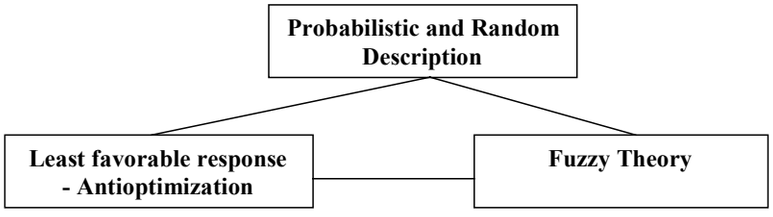


Fig.1 Approaches to modelling uncertainty

In the analysis of engineering problems three different approaches are used depending on the nature and extent of uncertainty by the introduction of the uncertainty triangle (Muc [1]) – see Fig. 1. If we know the probability distributions of the system variables and the covariance matrices the performance of the system may be considered with the use of probability theory. If only the fragmentary information on the uncertainty quantity is available an upper bound on the maximum response may be evaluated using the anti-optimisation approach. Between the above models lies the third approach – the fuzzy set theory that can be implemented to predict the structural response in the sense of evaluation of its upper and lower bounds, respectively.

In the paper we intend to present qualitative and quantitative differences of results (understood in the sense of composite mechanical properties) comparing two models: a deterministic and the second, which is based on the fuzzy, set approach. They are used in the description of two types of composite materials – a unidirectional and a textile (a twisted yarn composite). In both cases considered herein the fuzziness of variables is expressed by the triangular membership function. The variability (understood as the fuzziness) of material and geometrical parameters is taken to be equal to ±10 %, whereas the nominal (average) values correspond to α=1 and are equivalent to the deterministic description. The vertex method associated with the α-cuts representation of the membership functions is used to derive the upper and lower bounds of fuzzy output variables [1].

Micromechanics model of unidirectional composites

The Aboudi micromechanics model [2] is applied to study the effects of micromechanics constituent properties as fuzzy variables. In the model the unidirectional composite is represented by fibres, which are aligned in the x_1–direction and distributed regularly in the matrix and finally the components form a doubly periodic array in the x_2 and x_3 directions. The fibres have a rectangular cross-section (h_1, l_1) and are arranged at distances h_2, l_2 apart. The cell is further divided into four subcells, each of them with a local coordinate system. At the micromechanics level, the transversely isotropic material is expressed in terms of the five engineering constants. They are functions of the material variables, i.e. of the fibre and the matrix properties: $E_{f11}, E_{f22}, G_{f12}, \nu_{f12}, \nu_{f13}, E_m, \nu_m, V_f$, where V_f is the fibre volume ratio, f denotes fibre property, and m–a matrix property. Let us assume that the above variables characterising the fibre and matrix properties, the fibre volume fraction and the representative cell geometry are fuzzy variables. Using the procedure proposed above for a given α -cut one can evaluate the upper (the right end point) and lower bounds (the left end point) of the effective transverse Young modulus. The numerical results are evaluated for

the glass/epoxy resin, i.e. the identical material as discussed in Ref. [3]. The lower and upper bounds plotted in Fig. 2 (denoted by the superscripts L and R) are not symmetrical with respect to the nominal curve (α =1).

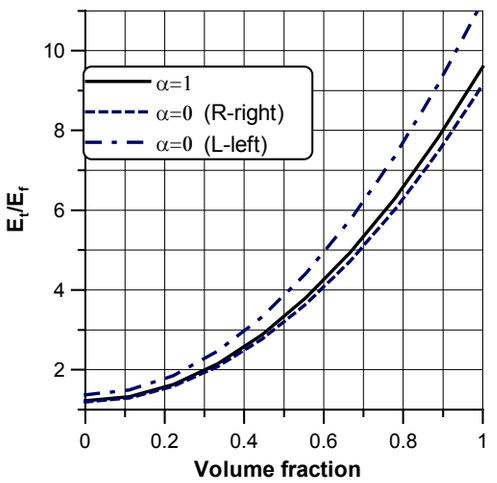


Fig.2 Distributions of the effective transverse Young modulus at α = 0 and 1 for unidirectional composites

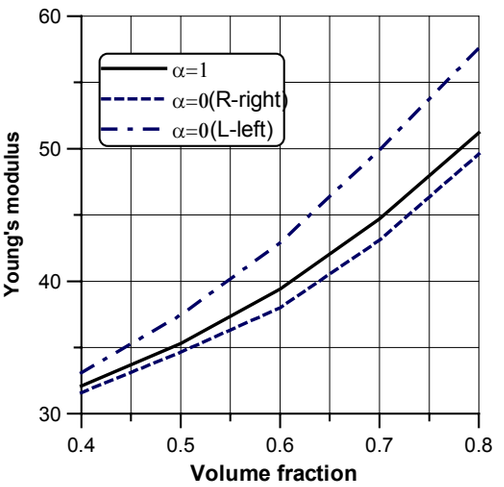


Fig.3 Variations of Young's modulus with fibre volume fraction for twisted yarns

Fuzziness in textile composites

The development of innovative fibre architecture and textile manufacturing technology has significantly expanded the potential of fibre reinforced composites. An emerging area is textile composites reinforced with 3-D preforms such as woven, braided and knitted fabrics. The integrated fibre network provides stiffness and strength in the thickness direction thus reducing the potential for the interlaminar failure. To demonstrate the impreciseness in the modelling the elastic constants of twisted yarn composites are predicted based upon the unit cell structure and volume averaging of elastic constants of constituent materials – see Ref. [4]. Similarly as previously the composite material is assumed to have transversely isotropic properties.

The geometry of twisted yarns is characterised by the twist angle θ and the number of yarns twisted expressed by a parameter λ – linear density of a twisted yarn. Geometrical parameters θ, λ and Young's moduli of fibres and matrix have been treated as the fuzzy parameters. However, the fibre volume fraction is assumed to be constant as the geometrical parameters of the twisted yarn vary. The nominal properties, both material and geometrical, are identical to those prescribed in Ref. [4]. The results of computations are plotted in Fig.3. As it may be seen, again there is no symmetry with respect to the nominal curve denoted by the value α =1 (the solid line).

Concluding Remarks

The effectiveness of the proposed method can be estimated by the comparison with experimental results. Therefore, it is interesting to note that the presented in Ref. [5] comparison of the theoretical and experimental data shows that the experimental values are located rather above the nominal curve (the solid line in Fig.2) what directly corresponds to the obtained fuzzy results. For textile composites similarly as in the case of the unidirectional fibres the experimental data lie above the nominal curve corresponding to the theoretical deterministic predictions – Ref [4].

At the end of this section it is worth mentioning that the presented method allows one to build the appropriate membership functions for the evaluated values of the Young moduli taking into account various (not only triangular) normalised to 1 probabilistic distributions of mechanical properties of constituents and their geometrical ratios. In this way it is possible also to take into consideration the interface layer having variable, unknown in advance, mechanical and geometrical properties.

References

[1] Muc A., Kędziora P., Application of Fuzzy Set Theory in Mechanics of Composite Materials, *Soft Computing in Textile Sciences* (L.M.Sztandera, Ch.Pastore edits), Physica-Verlag, Heidelberg, New York 2003, pp.16-50.
[2] Aboudi, J., *International Journal Engineering Science*, **20**,1982, pp.605-621.
[3] Aboudi J. (1987), *International Journal Engineering Science*, **25**, no. 9, pp. 1229-1240.
[4] Byun J.H. and Chou T.W. (1995), Effect of yarn twist on the elastic property of composites, *Proc. ICCM/10*, Whistler, B. C., Canada, 4, pp. 293-299.
[5] Aboudi, J., (1989), *Appl. Mech. Rev.,* **42**, pp. 193-221.

XXI ICTAM, 15–21 August 2004, Warsaw, Poland

EVALUATION OF LINEARIZATION PROCEDURES SUSTAINING NONLINEAR HOMOGENISATION THEORIES

Amna REKIK, Michel BORNERT, André ZAOUI, François AUSLENDER*
*Laboratoire de Mécanique des Solides, École Polytechnique, 91128 Palaiseau Cedex

Summary A systematic methodology for the evaluation of various existing linearisation procedures sustaining mean field theories for nonlinear composite materials is proposed and applied to the 'modified secant' and various 'affine' formulations. It relies on the analysis of a composite for which an exact treatment of both the nonlinear homogenisation problem and the linear homogenisation of the 'linear comparison material' with identical microstructure is possible; the effects of the sole linearization method can then be evaluated.

Introduction

The present study aims at defining a methodology and a numerical tool which could be used for a systematic evaluation of the various existing homogenization methods for nonlinear heterogeneous materials and composites. These methods classically rely on two separate procedures:
- first, they propose a way to approximate the actual nonlinear behavior by linear constitutive equations, through a specific linearization procedure, so as to define a heterogeneous linear comparison material ('LCM');
- an appropriate linear homogenization model is then chosen to predict the overall as well as the local responses of this fictitious LCM.

A number of such nonlinear homogenization schemes have been proposed recently which deserve systematic comparisons both at the global and the local levels in order to select the most efficient ones or to propose improved new ones. When doing so, two main difficulties have to be overcome: first the two above-mentioned procedures (i.e., linearization and linear homogenization) should preferably be evaluated separately in order to focus attention on the most critical step of defining the LCM and dealing with the intra-phase heterogeneity; second, the comparison would be more conclusive if an exact and complete (i.e. providing both global response and local fields) solution of the studied problem was available.

Proposed methodology

These statements have led to the choice of a periodic microstructure so as to make possible an exact (numerical) resolution of the nonlinear problem and, after application of various linearization approaches, to be left with a linear homogenization problem to be addressed with the same (periodic) microstructure, which can also be solved exactly. Thus, attention can be focused only on the specific effects of the choice of such or such linearization procedure through the comparison of the associated predicted overall properties and local stress and strain fields with the exact solution. Such a methodology improves on more classical approaches, in which predictions of mean field theories for nonlinear random microstructures are often compared to numerical simulations for periodic composites, the effects of the linearisation procedures and the approximate treatment of the homogenisation of the LCM being then combined.

As a first step, constitutive behavior deriving from one single potential only is considered. For the sake of simplicity, the studied material reduces to a (periodic) two-phase composite with a nonlinear matrix (constitutive relation $\sigma = f(\epsilon)$ and aligned identical elastic spheroidal inclusions. The periodic unit cell is subjected to periodic conditions and an axial loading. The nonlinear solution is obtained thanks to a finite element computation under code Cast3M, whereas the linearization procedures (incremental, classical and modified secant methods, classical affine, with its full formulation as well as several simplified formulations, are considered) are implemented in C++ routines. The effective properties and the local responses of the LCM are derived exactly by means of an additional FEM Cast3M computation, which is interfaced with the C++ code.

Application

An illustrative example of preliminary results already obtained this way is described below. It is first devoted to the evaluation of the so-called 'modified secant formulation' proposed by Suquet [1], in close connection with Ponte Castañeda's variational procedure [2], through the quantitative comparison of its global and local (not shown here) predictions with the exact ones. According to this formulation the local behavior of the constitutive phases of the LCM is isotropic and defined by $\sigma(x) = L^{sct}(\langle\epsilon \otimes \epsilon\rangle) : \epsilon(x)$ with $L^{sct} = 3kJ + 2\mu^{sct}(\langle\epsilon \otimes \epsilon\rangle)K$, where μ^{sct} is the secant moduli. The second-order moment of the local strain in the matrix $\langle\epsilon \otimes \epsilon\rangle$ can be evalutated by direct integration of the numerical solution, or by means of a partial derivative of the overall axial response with respect to the local shear moduli. Only one axisymmetric FEM calculation is required for the LCM even though its overall linear behavior is anisotropic. The same analysis has also been applied to the classical 'affine' linearisation procedure [3, 5] for which constitutive equations of the matrix in the LCM read $\sigma(x) = L^{tgt}(\langle\epsilon\rangle) : \epsilon(x) + \tau^0(x)$, with use of the anisotropic tangent moduli $L^{tgt} = \frac{df}{d\epsilon}(\langle\epsilon\rangle)$ and the eigenstress $\tau^0 = f(\langle\epsilon\rangle) - L^{tgt}(\langle\epsilon\rangle) : \langle\epsilon\rangle)$. In the case of uniaxial load, the local elastic behavior in the LCM exhibits transverse isotropy : $L^{tgt} = 3kJ + 2\mu^{sct}(\langle\epsilon\rangle)F + 2\mu^{tgt}(\langle\epsilon\rangle)E$ - notations of [4], and so does its overall linear behavior. The 'full anisotropic implementation' of the affine formulation requires the computation of all the components of the effective tensor of moduli and that is why transverse and longitudinal shearing modes must be considered through a Fourier analysis in

be simplified first by considering an isotropic matrix with moduli given either as $L^m = 3kJ + 2{\mu_m}^{tgt}(\langle\epsilon\rangle)K$ (simplified affine-1), or $L^m = 3k_mJ + 2{\mu_m}^{iso}(\langle\epsilon\rangle)K$ where ${\mu_m}^{iso} = \frac{4{\mu_m}^{sct}+{\mu_m}^{tgt}}{5}$ (simplified affine-2), but still computing exactly the anisotropic behavior of the LCM. An additional simplification is provided when, in addition, one assumes the overall behavior isotropic and identifies its moduli through its response to tension ('full isotropic' affine formulation).
All the corresponding results are shown in Figure 1.

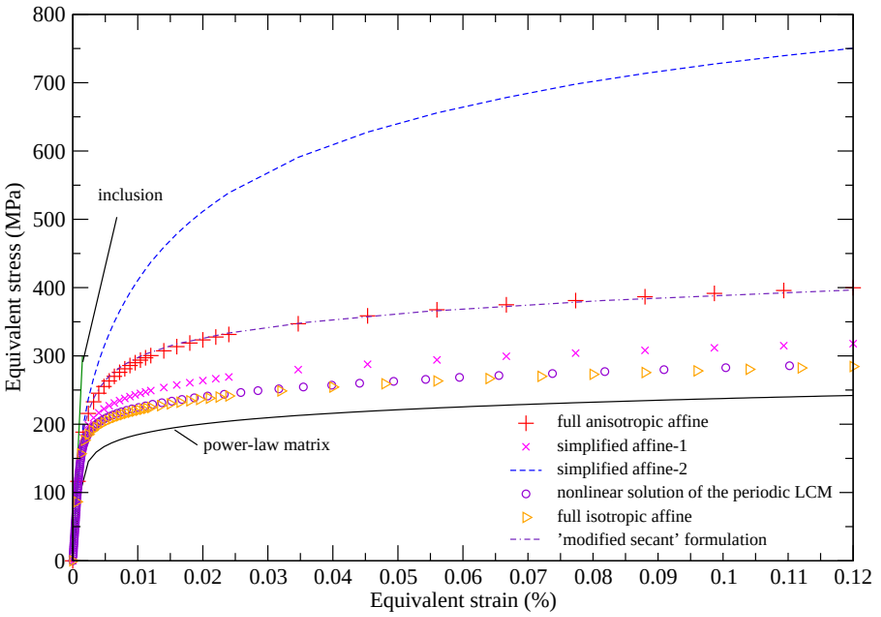


Figure 1. Effects of the choice of a linearization method (modified secant and various affine versions) on the tensile stress-strain curve of a two-phase composite. Inclusion volume fraction : 30%; Inclusion elastic properties : $E^I = 400$ GPa and $\nu^I = 0.3$. Power-law matrix properties: $E^m = 75$ GPa, $\nu^m = 0.2$, $n = 10$, $\epsilon_0 = 1\%$ and $\sigma_0 = 300$ MPa.

Conclusions

As a preliminary conclusion, one can notice that the 'full isotropic' affine linearization treatment yields the softest global response, and is very close to the exact nonlinear solution. This apparently good prediction of this very approximate procedure is probably the consequence of two opposite trends: the 'classical' formulation of the affine procedure, which does not account for intra-phase heterogeneities in the definition of the LCM, is known to yield somewhat too hard predictions and this is compensated by the recourse to a very soft simplification of the tensor of tangent moduli (${\mu_m}^{tgt} << {\mu_m}^{sct}$). The deeper analysis of this comparison, in particular in terms of local strain and stress fields, but also local density of potential energy, is under progress and should provide more insight. The evaluation of the recently proposed 'second-order' linearization procedure [4], closely related to the affine one [5], but taking into account to some extent the intra-phase heterogeneity, is also planed and might lead to other conclusions regarding the pertinence of the recourse to a simplified isotropic tensor of tangent moduli. More generally, it is expected to propose from such comparisons some optimized linearization treatment, with respect to some criteria, still to be defined. In the long term, the application of such a methodology to two-potential behavior might also be investigated.

References

[1] P.Suquet: Overall propreties of nonllinear composites: a modified secant moduli theory and its link with Ponte Castañeda's nonlinear variational procedure. *C.R.Acad.Sc. Paris, 320, Série IIb, 563-571*, 1995.

[2] P.Ponte Castañeda: New variational principles in plasticity and their application to composite materials. *Journal of the Mechanics and Physics of Solids 40, 1757-1788*, 1992.

[3] A.Zaoui & R.Masson: Micromechanics-based modeling of plastic polycrystals: an affine formulation. *Materials Science and Engineering A285, 418-424*, 2000.

[4] P.Ponte Castañeda: Exact second-order estimates for the effective mechanical propreties of nonlinear composite materials. *Journal of the Mechanics and Physics of Solids 44(6), 827-862*, 1996.

[5] R.Masson, M.Bornert, P.Suquet, A.Zaoui: An affine formulation for the prediction of the effective propreties of nonlinear composites and polycrystals. *Journal of the Mechanics and Physics of Solids 48, 1203-1227*, 2000.

THREE-DIMENSIONAL THERMOELASTIC ANALYSIS OF PLAIN WEAVE GLASS/EPOXY COMPOSITES WITH CRACKS AT CRYOGENIC TEMPERATURES

Tomo Takeda*, Yasuhide Shindo, and Fumio Narita

* *Department of Materials Processing, Graduate School of Engineering, Tohoku University, Sendai 980-8579, Japan*

Summary This study presents a numerical investigation of the thermo-mechanical behavior of G-11 woven glass/epoxy laminates with cracks subjected to tensile loading at cryogenic temperatures. Three-dimensional finite elements are employed to model the architecture of the two-layer woven laminates. Numerical results for the Young's modulus, Poisson's ratio, and stress distributions and concentrations are obtained and discussed in detail.

INTRODUCTION

Composite materials have received increased attention for applications in cryogenic environment because of their unique and highly tailorable properties [1]. In recent years, carbon-fiber/epoxy-resin composites have been evaluated for cryogenic tankage in RLV (reusable launch vehicle) [2]. Woven-fabric glass/epoxy laminates are used as thermal insulation, electrical insulation, structural support and permeability barrier in superconducting magnets which are essential components of most current and planned fusion devices [3]. Residual thermal stresses develop in these materials when they are exposed to cryogenic temperatures. These stresses are the result of a difference in the CTEs (coefficients of thermal expansion) between the reinforcement and the matrix. The non-zero state of residual thermal stresses at cryogenic temperatures is the underlying cause of microcracking in composites and the microcracks could have an important influence on their performance [4]. To secure the structural integrity of superconducting magnets, understanding of the thermo-mechanical behavior of cracked woven-fabric glass/epoxy laminates at cryogenic temperatures is of great importance.

Recently, Takeda et al. have studied the influence of residual thermal stresses and cracks on the mechanical behavior of two-layer [5] or multi-layer [6] G-11 woven glass/epoxy laminates under tension at cryogenic temperatures by a finite element method. The approximation for two-dimensional finite element model appears to be a serious oversimplification, which models only a portion of the woven structure. It is necessary, therefore, to develop a complete three-dimesional model which leads to more accurate predictions. In this paper, the thermo-mechanical behavior of G-11 woven glass/epoxy laminates with cracks under tension at cryogenic temperatures is investigated using three-dimensional finite element analysis.

STATEMENT OF THE PROBLEM

Consider a two-layer woven laminate with the out-of-phase stacking configuration, which implies the mirror symmetry about the middle plane, and cracks, as shown in Fig. 1. A rectangular Cartesian coordinate system (x, y, z) is used with the x-axis coinciding with the direction of mechanical load. The two-layer woven laminate of thickness $2H$ occupying the region ($|x| < \infty$, $|y| < \infty$, $|z| \leq H$) consists of two sets of interlaced fiber bundles and pure resin matrix. The fiber bundles which run in the x-direction are the warp fiber bundles. The fiber bundles running perpendicular to these are the fill fiber bundles. Based on the experimental observations of Kriz and Muster [7], it is assumed that the cracks of length a lie in the fill fiber bundles. The crack fronts are situated at equal distances away from the boundaries of the fill fiber

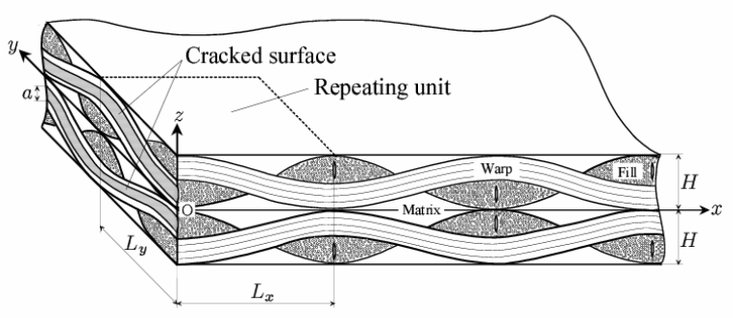


Fig. 1 Two-layer woven laminate with cracks

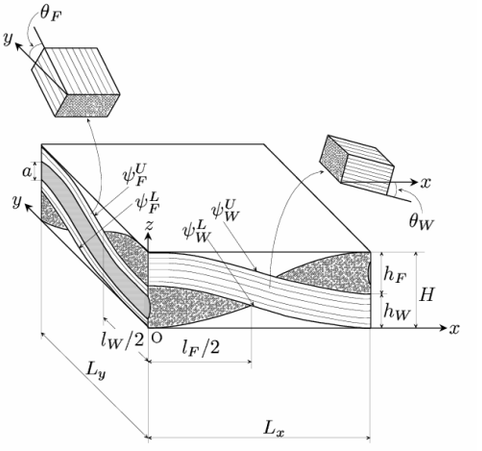


Fig. 2 Repeating unit

bundles. We will consider two cases: two-layer woven laminate with cracks located in $x = \pm 2nL_x$ (n = 0, 1, 2, …) planes of the fill fiber bundles (Case 1) and woven laminate with cracks in all fill fiber bundles (Case 2). Then, from symmetry and periodicity only the repeating unit illustrated in Fig. 2, which is also identified in Fig. 1 using dashed lines, needs to be analyzed. The undulation of fiber bundles is assumed to be sinusoidal functions $\psi_W^L, \psi_F^L, \psi_W^U$ and ψ_F^U. As depicted in this figure, L_x and L_y stand for the length of the repeating unit in the x- and y-directions, l_W and l_F denote the width of the warp and fill fiber bundles, h_W and h_F represent the thickness of the warp and fill fiber bundles, θ_W is the local angle between the warp fiber bundle and the x-axis of the global coordinate system, and θ_F is the local angle between the fill fiber bundle and the global y-axis.

Suppose that the woven laminate is subjected to the thermal load of $\Phi - \Phi_s$ and the mechanical mean stress σ^*_{xx} in the x-direction, where Φ is the temperature of the woven laminate and Φ_s is the stress-free temperature, often assumed to be the cure temperature. The mechanical mean stress σ^*_{xx} induces the uniform displacement in the x-direction at $x = L_x$ plane of the repeating unit.

THREE-DIMENSIONAL FINITE ELEMENT ANALYSIS

We use a commercial finite element package ANSYS to perform the analysis. The finite element model uses four-noded, three-dimensional, linear, tetrahedral elements. A typical finite element mesh utilizes a total of 49859 elements which lead to a total of 10834 nodes.

RESULTS AND DISCUSSION

The geometrical parameters of G-11 woven glass/epoxy laminates used in the present investigation are the actual dimensions measured with a SEM (scanning electron microscope) [8] and listed in Table 1. The fiber volume fraction in the fiber bundles is taken to have the value of 0.75, corresponding to that of actual G-11 woven laminates. The cure temperature of the thermal strain free state Φ_s is assumed to be 395 K.

Table 1 Geometrical parameters of G-11 woven glass/epoxy laminates

L_x (mm)	L_y (mm)	H (mm)	l_W (mm)	l_F (mm)	h_W (mm)	h_F (mm)
0.81	0.63	0.19	0.63	0.65	0.11	0.08

Table 2 shows a comparison of the Young's moduli (E_x^0, E_x^c) at Φ = 293, 77, 4 K from the three-dimensional finite element analysis (3-D FEA) with those from the micromechanics model [8] by Hahn and Pandey [9] and experiments [8]. Also shown are the results for the Poisson's ratio (ν_{xy}^0, ν_{xy}^c). Figure 3 provides the stresses σ_{xxW} in the warp fiber bundle at $x = 0$ and $y = 0$ as a function of the distance from the crack front $(z - h_F)/h_W$ for Φ = 293, 77, 4 K. For this figure, solid and dashed lines indicate the three-dimensional finite element results with and without thermal effects, respectively.

Table 2 Elastic properties of two-layer G-11 woven glass/epoxy laminates

			293 K	77 K	4 K
Young's moduli					
E_x^0 (GPa)	3-D FEA		26.75	33.10	36.04
	Micromechanics model		26.66	32.98	35.94
	Experimental		27.9	32.7	36.9
E_x^c (GPa)	3-D FEA	Case 1	25.88	31.89	34.69
		Case 2	25.51	31.23	33.89
Poisson's ratios			293 K	77 K	4 K
ν_{xy}^0	3-D FEA		0.140	0.193	0.214
	Micromechanics model		0.13	0.19	0.21
	Experimental		0.17	0.19	0.23
ν_{xy}^c	3-D FEA	Case 1	0.137	0.188	0.209
		Case 2	0.132	0.182	0.202

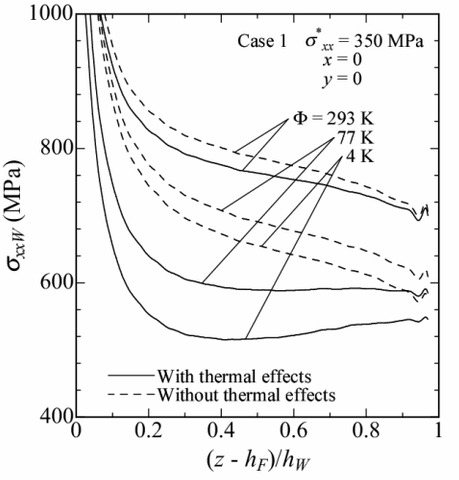


Fig.3 Variation of stresses σ_{xxW} at x=0 and y=0 (Case 1)

References

[5] Takeda T., Shindo Y., Kumagai S., Narita F., Horiguchi K.: Thermal-mechanical response of cracked woven glass/epoxy laminates in a tension field at low temperature. *Physical Mesomechanics* **4**: 97-104, 2001.

[6] Takeda T., Shindo Y., Narita F., Kumagai S.: Thermoelastic analysis of cracked woven GFRP laminates at cryogenic temperatures. *Cryogenics* **42**: 451-462, 2002.

ADVANCED BEAM MODEL FOR FIBER-BRIDGING IN UNIDIRECTIONAL COMPOSITE DOUBLE-CANTILEVER BEAM SPECIMENS

András Szekrényes[*], József Uj[**]

[*]*Department of Applied Mechanics, Budapest University of Technology and Economics, PoB 11, H-1521 Budapest, Hungary, Phone: +36 1 463 1170, e-mail: szeki@mm.bme.hu*

[**]*Department of Applied Mechanics, Budapest University of Technology and Economics, PoB 11, H-1521 Budapest, Hungary, Phone: +36 1 463 2228, e-mail: uj@mm.bme.hu*

Summary In the present work we develop a model based on linear beam theory incorporating elastic foundation and bridging effects in composite DCB specimens. The model is applicable for fiber-bridging [1] modeling in the case of optional number of bridgings. Traditional DCB test on unidirectional glass/polyester specimens was carried out providing input data for the analysis. The model is suitable to predict the nonlinear bridging law, the total force exerted by the bridgings and the total number of bridging fibers.

ANALYSIS OF THE BRIDGED DCB SPECIMEN

We provide closed-form expressions for the compliance of unidirectional composite DCB specimens. The model incorporates the Winkler-type foundation [2] (classical solution of Williams) and the effect of fiber-bridging. The foundation stiffness can be related to the through-the-thickness moduli of the specimen. The bridgings were represented by elastic beams, described by their tensional stiffness and initial length. Fig.1 shows the model of the DCB specimen including one bridging. Based on the present model the following equation can be derived for the specimen compliance:

$$C_{DCB}=\frac{8a^3}{bh^3E_{11}}[1+1.92\left(\frac{h}{a}\right)\left(\frac{E_{11}}{E_{33}}\right)^{\frac{1}{4}}+1.22\left(\frac{h}{a}\right)^2\left(\frac{E_{11}}{E_{33}}\right)^{\frac{1}{2}}+0.39\left(\frac{h}{a}\right)^3\left(\frac{E_{11}}{E_{33}}\right)^{\frac{3}{4}}]+$$
$$-\frac{P_1}{P}\frac{[(3a(L_1^2+L2^2)-(L_1^3+L_2^3))\lambda^3+6a(L_1+L_2)\lambda^2+3\lambda(L_1+L_2+2a)+6]}{6\lambda^3 I_y E_{11}}=C^0_{DCB}-C^{FB}_{DCB} \quad ,(1)$$

where the term C^0_{DCB} is the specimen compliance based on the Winkler foundation model [3]. The term C^{FB}_{DCB} accounts for fiber-bridging in the delaminated region. The fracture toughness can be obtained by differentiating Eq.(1). We must differentiate all the quantities which are dependent on the crack length in Eq.(1). This is a quite complex problem, and cannot be solved analytically. However the location of bridgings $L_1(a)$ and $L_2(a)$ are linear functions of the crack length a, the force $P_1(a)$ as the function of crack length is difficult to obtain. Hence the term resulting from the derivative of the second term C^{FB}_{DCB} in Eq.(2) is denoted symbolically by G_I^{FB}, thus the fracture energy:

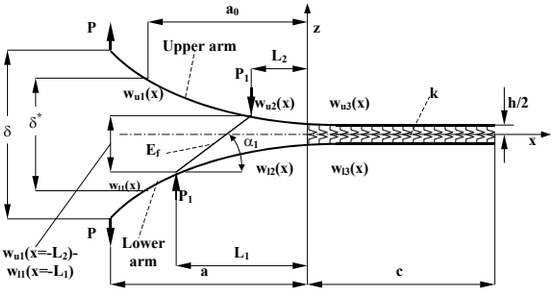


Fig.1.
For the analysis of the fiber-bridging in the DCB specimen

$$G_I=\frac{12Pa^3}{b^2h^3E_{11}}[1+1.28\left(\frac{h}{a}\right)\left(\frac{E_{11}}{E_{33}}\right)^{\frac{1}{4}}+0.41\left(\frac{h}{a}\right)^2\left(\frac{E_{11}}{E_{33}}\right)^{\frac{1}{2}}]-G_I^{FB}. \quad (2)$$

Eq.(1) can be generalized for optional number of bridgings. According to our analysis the compliance of the bridged DCB specimen has the following from:

$$C_{DCB}=\sum_i^n\{\lambda^3[4Pa^3+P_i(L_{2i}^2(L_{2i}-3a)+L_{2i-1}^2(L_{2i-1}-3a))]+6\lambda^2[a(2Pa-P_i(L_{2i}+L_{2i-1}))]+$$
$$+3\lambda[4Pa-P_i(L_{2i}+L_{2i-1}+2a)]+6(P-P_i)\}/(6P\lambda^3 I_y E_{11}) \quad , \quad (3)$$

where n is the number of bridgings, L_{2i}, L_{2i-1} are the location of bridgings at the upper and lower arms, P_i are the forces exerted by the bridgings.

EXPERIMENTAL

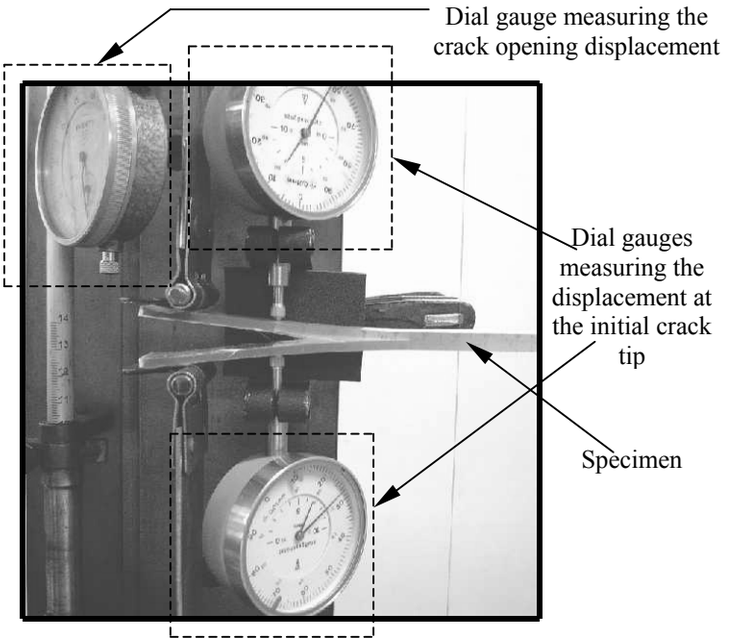


Fig.2.
Experimental setup for DCB testing

The DCB test was performed on glass/polyester specimens as shown by Fig.2. The results of the experiments are shown in Fig.3. Initiation and propagation tests were carried out. Initiation tests proved the accuracy of the Winkler model. On the other hand the Winkler foundation model gives misleading result if the fiber-bridging during propagation is not taken into account for. This model significantly overpredicts the experimental compliance and fracture energy, as shown by Fig.3.

CONCLUSIONS

The overpredictions were attributed to the fiber-bridgings. The experimental data was analysed using the present beam equations. The developed model is suitable to predict the total force exerted by the bridgings and the total number of bridging fibers. Both quantities have a peak value after crack initiation and a steady-state value during crack propagation. Furthermore the present model can used to determine the nonlinear bridging law approximately.

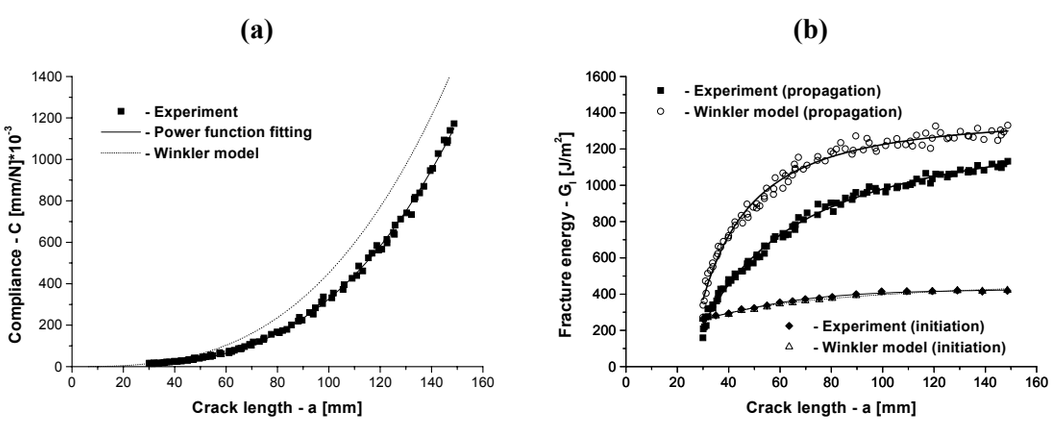


Fig.3.
Compliance from experiment and analysis (propagation) **(a)**. Initiation and propagation R-curves, comparison between experiment and analysis **(b)**

References

[1] Tamuzs V., Tarasovs S., Vilks U. Progressive delamination and fiber bridging modelling in double cantilever beam composite specimen. *Engineering Fracture Mechanics* **2001**;68;513-525

[2] Ozdil F., Carlsson L.A. Beam analysis of angle-ply laminate DCB specimens. *Composites Science and Technology* **1999**;59;305-315

[3] Olsson R. A simplified improved beam analysis of the DCB specimen. *Composites Science and Technology* **1992**;43;329-338

INTERFACIAL JUMP CONDITIONS IN STRAIN-GRADIENT PLASTICITY AND RELATIONS OF HALL-PETCH TYPE

K. Aifantis and J.R. Willis
Department of Applied Mathematics and Theoretical Physics
Centre for Mathematical Sciences, Wilberforce Road, Cambridge CB3 0WA, U.K.

EXTENDED ABSTRACT

Strain-gradient plasticity requires boundary conditions, and jump conditions across interfaces, additional to those required in ordinary plasticity. In recent work, Fleck and Willis [1] demonstrated an effect of the scale of the microstructure on the effective flow stress of a composite. The effective flow stress had a definite upper limit, equal to the "Taylor upper bound", for very fine microstructure; this was because plastic strain-gradients were obliged to tend to zero as the scale of the microstructure reduced giving, in the limit, the Taylor "uniform plastic strain" approximation. However, Fleck and Willis adopted the simplest assumption, that both plastic strain and higher-order traction were continuous across interfaces. This need not be so. For instance, a dislocation crossing an interface will leave a ledge on the interface and so add to its energy. In the work to be described, we retain the assumption that plastic strain is continuous across an interface but penalise dislocations crossing the interface by admitting an interfacial potential that is a function of the plastic strain; this induces a jump in the higher-order traction, which is analogous to allowing dislocations to pile up. The theory is illustrated by a number of simple one-dimensional examples, both linear and nonlinear. The microstructure is taken to be periodic and the "homogenised", or "effective", response is studied by taking the total strain to be periodic with prescribed mean value; the plastic strain is likewise periodic but its mean value is obtained from the solution. A pronounced scale-dependence of effective flow stress -- a kind of Hall-Petch relation -- is obtained in every case. It is due entirely to the presence of the interfacial potential: the original Fleck-Willis analysis would yield no scale-dependence in the one-dimensional cases that are considered.

One-dimensional problems with periodically distributed interfaces require only the solution of ordinary differential equations. It is also possible to evaluate the utility of an approximation scheme, of wider applicability, for solving nonlinear problems, by applying it in the nonlinear periodic setting. The scheme employs a linear “comparison problem”, in which the parameters are chosen to reproduce, as closely as possible, the field in the original nonlinear problem, in the way introduced for non-strain-gradient composites by Ponte Castaneda [2] and also employed by Fleck and Willis [1] in the strain-gradient context. Work in progress includes allowance for randomly-distributed interfaces, using this scheme of approximation.

Implementation of the present model in two or three dimensions is planned; it is likely to predict the attainment of effective flow stresses larger than the Taylor upper bound.

References

[1] N.A. Fleck and J.R. Willis, “Bounds and estimates for the effect of strain gradients upon the effective plastic properties of an isotropic two phase composite”. J. Mech. Phys. Solids (to appear).
[2] P. Ponte Castaneda, “The effective mechanical properties of nonlinear isotropic composites”, J. Mech. Phys. Solids **39,** 45-71, 1991.

XXI ICTAM, 15–21 August 2004, Warsaw, Poland

A STUDY OF PARTICLE DEBONDING WITH ANISOTROPY

Brian Nyvang Legarth
Department of Mechanical Engineering, Solid Mechanics, Technical University of Denmark

Summary Failure arising from debonding of rigid inclusions embedded in an elastic-viscoplastic matrix, modeled with plastic anisotropy, is investigated numerically using a plane strain biaxially loaded unit cell. Periodical boundary conditions are used to represent cases where the principal axes of anisotropy are inclined relative to the tensile direction. The average stress-strain response of the cell is evaluated and debonding is observed as a sudden stress drop. Depending on the initial orientation of the principal axes of plastic anisotropy, debonding in the present material is significantly delayed due to a reduction of the yield stress.

INTRODUCTION

Material properties like the Young modulus, the yield stress, the ductility and the fracture toughness are strongly affected by adding second phase particle to an otherwise pure material. Commonly, the fracture toughness is reduced due to void nucleation and growth along the particle-matrix interface. An early study of inclusion debonding was carried out in Ref. [1]. Besides the presence of inclusions, many parameters have a crucial impact on the strength of the composite, in particular the constitutive conditions of the matrix material and the inclusions, the bonding at the particle-matrix interface and the geometrical configuration of the composite.

PROBLEM FORMULATION AND MATERIAL DESCRIPTION

Here, focus is given to debonding of rigid inclusions of elliptical cross sections embedded in a plastically anisotropic matrix material using a unit cell model subjected to periodical boundary conditions. This allows for arbitrary initial orientation of the principal axes of plastic anisotropy. The periodical boundary conditions ensure compatibility as well as force equilibrium across any cell edge. The constitutive modeling of the matrix material is based on an multiplicative decomposition of the deformation gradients taking full account of small elastic and finite viscoplastic strains. The plastic strain increments are evaluated on the basis of a yield function, $J(\hat{\sigma}_{ij})$, where $\hat{\sigma}_{ij}$ are true stress components. In addition to the isotropic von Mises yield surface, this work considers two anisotropic yield criteria, namely Hill[2] and the proposal by Barlat *et al.*[3], subsequently referred as Hill-48 and Barlat-91. The hardening is isotropic. On compact form Hill-48 can be expressed as

$$J = \sqrt{\frac{3}{2(F+G+H)}\left[F(\hat{\sigma}_{22}-\hat{\sigma}_{33})^2 + G(\hat{\sigma}_{33}-\hat{\sigma}_{11})^2 + H(\hat{\sigma}_{11}-\hat{\sigma}_{22})^2 + 2N\hat{\sigma}_{12}^2 + 2L\hat{\sigma}_{23}^2 + 2M\hat{\sigma}_{13}^2\right]} \quad (1)$$

For $F = G = H = 1$ and $N = L = M = 3$ this yield function simplifies to the isotropic von Mises yield criterion. Barlat-91 can be expressed as

$$J = \left(\frac{\Phi}{2}\right)^{1/d} \quad \text{with} \quad \Phi = [S_1 - S_2]^d + [S_2 - S_3]^d + [S_1 - S_3]^d \quad (2)$$

where S_i are the principal values of a modified stress deviator, which includes six coefficients of anisotropy. The exponent d depends on the crystal structure, and is here taken to be eight corresponding to FCC-structures.
Debonding is modeled by the phenomenological cohesive zone model proposed by Tvergaard[4]. For increasing interfacial separation, the traction across the interface reaches a maximum, then decreases and eventually vanishes.

RESULTS AND DISCUSSION

The numerical results are obtained incrementally by applying a finite element method based on the principle of virtual work in an updated Lagrangian formulation using constant strain quadrilaterals elements. Due to highly unstable solution regimes and the periodical boundary conditions the combined finite element and Rayleigh-Ritz procedure developed by Tvergaard[5] is adopted. The results presented here are limited to circular inclusions in quadratic cells (volume fraction of 3%) loaded such that the average stress in the main tensile direction is haft the average stress in the transverse direction. Fig. 1 shows the calculated true stress versus logarithmic strain in the main tensile direction for plastically isotropic matrix material as well as plastically anisotropic matrix material using Barlat-91 for different values of the initial orientation of plastic anisotropy, θ_0. The sudden stress drop indicates the point of debonding initiation. The yield stress in plane strain tension for Hill-48 and Barlat-91 can be shown to vary periodically for any set of the coefficients of anisotropy, and has the same values at any of the four orientations $\pm\theta_0$ and $\pm(90^o - \theta_0)$. Minimum and maximum values are obtain for $\theta_0 = 45^o + 90^o z$ and $\theta_0 = 90^o z$ with $z = [..-1, 0, 1..]$, respectively. This observation is recognized in Fig. 1 since the results for $\theta_0 = 0^o$ and $\theta_0 = 22.5^o$ coincide with the results for $\theta_0 = 90^o$ and $\theta_0 = 67.5^o$, respectively. For a high yield stress a large fraction of the critical interfacial stress will be generated in the elastic range and debonding will occur after a relatively small amount of deformation, as shown in Fig. 1 for $\theta_0 = 0^o$ and $\theta_0 = 90^o$. As the yield stress decreased, larger overall deformation is required in order to generate stresses near the inclusion that are high enough to initiate debonding. This effect is seen in Fig. 1 for $\theta_0 = 22.5^o, \theta_0 = 67.5^o$ and $\theta_0 = 45^o$.

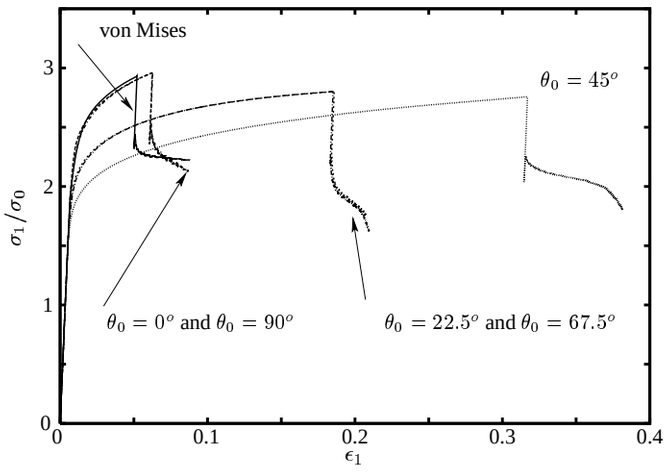


Figure 1: Stress strain responses for Barlat-91. The sudden stress drop indicates the point of debonding initiation.

For selected overall strains, ϵ_1, contours of constant effective plastic strain, ϵ^{p}, are shown in the deformed configuration in Fig. 2 using Hill-48 and Barlat-91 with $\theta_0 = 22.5^o$. For the configurations where debonding has occurred, $\epsilon_1 = 0.1$ or $\epsilon_1 = 0.2$, the contours illustrate intensive plastic deformation in the region near the void. Especially at the tip of the void where the inclusion is still bonded, high gradients of the effective plastic strain are found, indicating progressive void growth due to further debonding. Wavy deformation of the initially straight cell edges is observed due to development of non-symmetric shear stress across the cell boundaries.

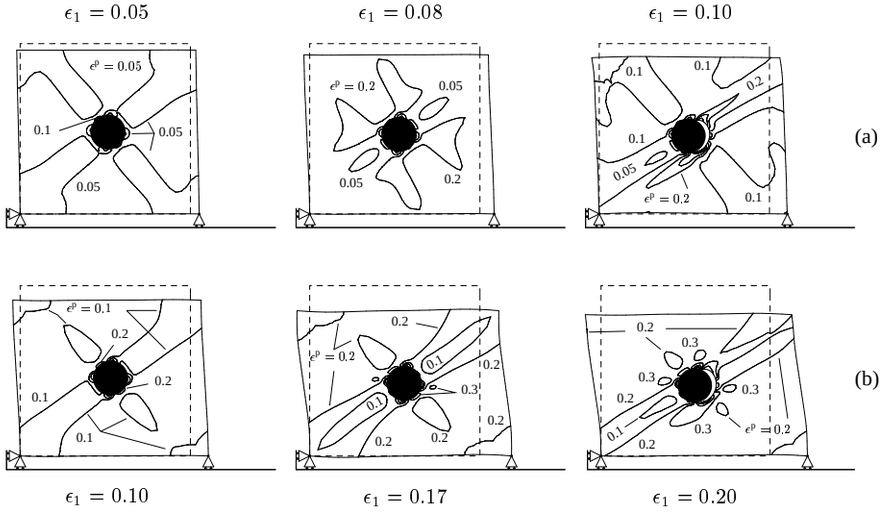


Figure 2: Deformed configurations for $\theta_0 = 22.5^o$ at different overall strains. The undeformed geometry is shown by the dashed line. (a) Hill-48 (b) Barlat-91.

For elliptical cross sections of the inclusion or for non-quadratic cells anisotropy due to the geometry is induced in addition to the plastic anisotropy. Results based on combinations of these two types of anisotropy will be shown as well.

ACKNOWLEDGMENT

This work is supported by The Danish Technical Research Council under the Materials Research Programme.

References

[1] Needleman, A.: A continuum model for void nucleation by inclusion debonding, *J. App. Mech.* **54**:525-531, 1987.
[2] Hill, R.: A theory of the yielding and plastic flow of anisotropic metals, *Proc. Royal Soc. Lond.* **A193**:281-297, 1948.
[3] Barlat, F., Lege, D. J., Brem, J. C.: A six-component yield function for anisotropic materials, *Int. J. Plast.* **7**:693-712, 1991.
[4] Tvergaard, V.: Effect of fibre debonding in a whisker-reinforced metal, *Mat. Sci. & Eng.* **A125**:203-213, 1990.
[5] Tvergaard, V.: Effect of thickness inhomogeneities in internally pressurized elastic-plastic spherical shells, *J. Mech. Phys. S.* **24**:291-304, 1976.

XXI ICTAM, 15–21 August 2004, Warsaw, Poland

NONLINEAR AFFINE EXTENSION OF THE THREE-PHASE SPHERE MODEL

Emmanuelle Chabert*, Michel Bornert*, André Zaoui*
*LMS École Polytechnique, CNRS, 91128 Palaiseau cedex, France

Summary To model the nonlinear behaviour of particulate composites, the classical procedure of transforming, at a given strain, a nonlinear problem into a linear one has been used. The chosen linearisation method is the recently proposed affine formulation [1, 2] which has been coupled to the three phase self-consistent estimate [3] of the linearised overall properties, in the case of uniaxial loading. This modelling has been applied to two-phase composites with nonlinear elastic behaviours described by power-law stress-strain relationships, but the same developments are still valid for viscous materials.

AFFINE PROCEDURE

According to the affine procedure, the nonlinear behaviour of each phase r ($\sigma = f_r(\varepsilon)$) is approximated, at a given reference strain ε_r^0 which is set equal to the average local strain in the phase, by a thermoelastic linear behaviour defined by the tangent moduli L_r and the pre-stress τ_r^0, both being taken constant per phase:

$$\langle\sigma\rangle_r = L_r : \langle\varepsilon\rangle_r + \tau_r^0 \quad , \quad L_r = \frac{df_r}{d\varepsilon}(\varepsilon_r^0) \quad , \quad \tau_r^0 = f_r(\varepsilon_r^0) - L_r : \varepsilon_r^0 \tag{1}$$

Such a linearisation procedure leads to the definition of a Linear-thermoelastic Comparison heterogeneous Medium (LCM) whose effective moduli $\tilde{L}$ have to be estimated by a linear homogenisation scheme. An appropriate choice for a matrix-inclusion morphology is the three-phase self-consistent model, which needs recourse to a numerical resolution because of the anisotropic tangent behaviour. After numerical computation of $\tilde{L}$, the average local strains $\langle\varepsilon\rangle_r$ are given, for two-phase thermoelastic composites, by Levin's relation [4]:

$$\langle\varepsilon\rangle_r = A_r : E - (A_r - I) : (L_1 - L_2)^{-1} : (\tau_1^0 - \tau_2^0) \tag{2}$$

where E is the prescribed macroscopic strain and A_r the averaged linear localisation tensors for each phase r, i. e.:

$$A_1 = \frac{1}{c_1}(\tilde{L} - L_2) : (L_1 - L_2)^{-1} \quad , \quad A_2 = \frac{1}{c_2}(I - c_1 A_1) \tag{3}$$

where c_1 and c_2 are the concentrations of phase 1 and 2 and I is the fourth-order unit tensor.
The two steps of linearisation and estimation of the effective properties of the LCM are repeated until, as prescribed by the affine method, the reference strains ε_r^0 are equal to the average strains in the corresponding linearised phase $\varepsilon_r^0 = \langle\varepsilon\rangle_r$. After convergence, the overall stress of the composite is given by:

$$\Sigma = \tilde{L} : E + \Sigma^0 \quad , \quad \tilde{L} = \langle L : A\rangle \quad , \quad \Sigma^0 = \langle {}^tA : \tau^0\rangle \tag{4}$$

NUMERICAL 3-PHASE SELF-CONSISTENT ESTIMATE FOR TRANSVERSELY ISOTROPIC PHASES

Due to the anisotropic tangent behaviour, the linear three-phase self-consistent estimate (or generalised self consistent estimate) for the effective properties of the LCM has to be computed numerically. The 3-phase sphere model, initially proposed by Christensen and Lo [3], is devoted to composites constituted by a continuous matrix in which inclusions are isotropically distributed. It refers to Hashin's assemblage of homothetic composite spherical inclusions mapping the whole representative volume element: the inclusions are constituted of a sphere of filler phase, coated by a concentric shell of matrix phase with the same volume fractions as the whole composite. The resolution of the three-phase model requires to determine the linear mechanical response of the composite inclusion embedded in an infinite reference medium with elastic moduli L^0 and subjected to the homogeneous displacement field $E^0 x$ at infinity. The overall elastic tensor $\tilde{L}_{HS}(L^0)$ verifying $\langle\sigma\rangle = \tilde{L}_{HS}(L^0)\langle\varepsilon\rangle$, is the so-called generalised Hashin-Shtrikman estimate, which, depending on the choice of the reference medium, corresponds to bounds or estimates [5]. The self-consistent estimate is generated when the reference medium has the properties of the homogenised equivalent medium itself, i. e., $L^0 = \tilde{L}_{HS}(L^0)$.
This problem has been addressed by the Finite Elements method by means of the FEM code Cast3M in the case of uniaxial loadings of unit vector n, leading to transversely isotropic tangent stiffness tensors, noted in the form [6]:

$$L_r = \alpha E_L + \beta J_T + \gamma F + \gamma'^T F + \delta K_T + \delta' K_L \tag{5}$$

where $E_L = n \otimes n \otimes n \otimes n$ is the projector on uniaxial tensors, $J_T = \frac{1}{2} i_T \otimes i_T$ is the projector on the identity in the transverse plane ($i_T = i - n \otimes n$, with i the second-order unit tensor), $K_L = K - K_T - K_E$ (with $K_E = \frac{1}{6}(2n \otimes n - i_T) \otimes (2n \otimes n - i_T)$) is the projector on longitudinal shears, $K_T = I_T - J_T$ (I_T being the fourth-order identity tensor in the transverse plane) is the projector on transverse shears and $F = \frac{1}{\sqrt{2}} i_T \otimes n \otimes n$ is related to Poisson's effect.

Five independent constants have to be found for each phase (eq. 5): α, β, γ and γ', characterizing the response to axisymmetric loadings, and δ and δ', defining the shear behaviour. These components are obtained by the computation of the average stress and strain tensors in the composite inclusion for four applied strain conditions (uniaxial load, plane compression, longitudinal shear and transverse shear). Using axisymmetric and Fourier modes, these calculations have been conducted on two-dimensional axisymmetric cells (fig. 1 (a)). To get the self-consistent estimate we used an iterative procedure: starting from an initial reference medium L^0, we compute an estimate $\tilde{L}_{HS}$ which is then used as a new reference medium; this procedure is repeated until the self-consistent condition is achieved within a given convergence criterium.

APPLICATIONS

This treatment has been applied to particulate composite made of isotropic power-law phases with the local constitutive equations: $\varepsilon^{eq} = \sigma^{eq}/3\mu + \varepsilon_0(\sigma^{eq}/\sigma_0)^n$ where μ is the shear modulus, ε^{eq} and σ^{eq} are the equivalent Von Mises strain and stress, ε_0 is a reference strain and σ_0 characterises the stiffness of the phase. Fig. 1 (b) shows the effective behaviour of a composite with 30% inclusions obtained for a contrast of 5 between phases: $\sigma_0^{(2)} = 5\sigma_0^{(1)}$ and, for each phase, $n = 5$, $\varepsilon_0 = 1$, $\sigma_0/E = 10^{-3}$, $\nu = 0.3$. One can observe that the affine three-phase self-consistent estimate does not violate the upper bound for such nonlinear composite with a particulate microstructure obtained by the combination of the variational procedure for nonlinear behaviour of Ponte Castañeda [7] and a linear upper bound due to Hervé, Stolz and Zaoui [8]. This new model predicts a stiffer behaviour than the modified secant three-phase self-consistent scheme, which is however limited to nonlinear elasticity and viscoplasticity, which is not the case of the affine procedure. Moreover, the comparison with preliminary experimental data obtained for a silica-filled polymer has shown a great agreement [9].

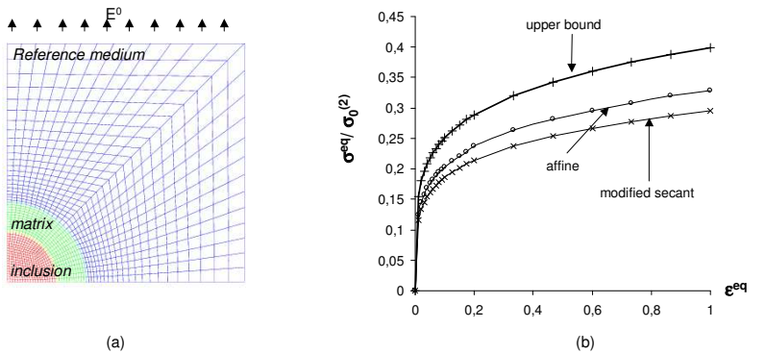


Figure 1. (a) Example of 2D mesh used. (b) Effective behaviour of a two-phase, power-law type, particulate composite with 30% inclusions and a contrast of 5.

CONCLUSION

The modelling of nonlinear composites with a matrix-inclusion microstructure has been achieved by the combination of the affine procedure with the three-phase sphere self-consistent estimate, in the framework of nonlinear elasticity and for uniaxial loads. Such a linearisation procedure presents also the advantage, with respect to other linearisation schemes, to be able to deal with hereditary behaviours, such as elastoviscoplasticity. Further work is under program to extend the present procedure to such behaviours.

References

[1] Masson R., Bornert M., Suquet P., Zaoui A.: An affine formulation for the prediction of the effective properties of nonlinear composites and polycrystals. *J. Mech. Phys. Solids* **48**:1203–1227, 2000.
[2] Zaoui A., Masson R.: Micromechanics-based modeling of plastic polycrystals: an affine formulation. *Mater. Sci. Eng. A* **285**:418–424, 2000.
[3] Christensen R. M., Lo K. H.: Solutions for effective shear properties in three phase sphere and cylinder models. *J. Mech. Phys. Solids* **27**:315–330, 1979.
[4] Levin V. M.: Thermal expansion coefficients of heterogeneous materials. *Mekh. Tver. Tela* **2**:83–94, 1967.
[5] Bornert M., Stolz C., Zaoui A.: Morphologically representative pattern-based bounding in elasticity. *J. Mech. Phys. Solids* **44**:307–331, 1996.
[6] Bornert M., P. Suquet: Rappels de calcul tensoriel et d'élasticité. In: Homogénéisation en Physique et Mécanique des Matériaux, tome 2. Bornert, Bretheau and Gilormini Eds. Hermes Science, Paris, 2001.
[7] Ponte Castañeda P.: Exact second-order estimates for the effective mechanical properties of nonlinear composite materials. *J. Mech. Phys. Solids* **44**:827–862, 1996.
[8] Hervé E., Stolz C., Zaoui A.: A propos de l'assemblage des sphères composites de Hashin. *C. R. A. S. série II* **313**:857–862, 1991.
[9] Chabert E., Bornert M., Cavaillé J.-Y., Dendievel R., Gauthier C., Zaoui A.: Micro-mechanical modelling of small and large strain behaviour of particulate nanocomposites. In: Deformation, Yield and Fracture of Polymers. IOM Communications Ltd Eds. 75–78, 2003.

H-CONVERGENCE AND MULTILAYERING IN PIEZOCOMPOSITES

Antoni Gałka, Barbara Gambin, Józef J. Telega, Stanisław Tokarzewski
Polish Academy of Sciences, IPPT PAN, Swietokrzyska 21, PL 00-049 Warszawa, Poland

Summary The aim of this paper is to solve the following problems related to piezocomposite: 1) to extend the notion of H-convergence 2) to derive the formula for the effective moduli of multilaminated composite. The obtained formula for the lamination is used to optimal design for minimum compliance.

EXTENSION OF H-CONVERGENCE TO PIEZOELECTRICITY

Microstructure of piezoelectric material is characterized by a small parameter ε, say $\varepsilon = 1/n$, where $n \in \mathrm{N}$; N stands for the set of natural numbers. Homogenization means passing with ε to 0. Physically such a passage denotes smearing out microinhomogeneities. The considered piezoelectric body occupies $\Omega \subset \mathbb{R}^3$ a bounded, sufficiently regular domain, $\Gamma = \partial\Omega$, $\Gamma = \overline{\Gamma}_0 \cup \overline{\Gamma}_1$, $\Gamma_0 \cap \Gamma_1 = \emptyset$, $\Gamma = \overline{\Gamma}_2 \cup \overline{\Gamma}_3$, $\Gamma_2 \cap \Gamma_3 = \emptyset$. Let U^ε denote the internal energy for fixed $\varepsilon > 0$. It has the following form: $U^\varepsilon(\mathbf{e},\mathbf{D}) = \frac{1}{2} a^\varepsilon_{ijkl} e_{ij} e_{kl} - h^\varepsilon_{ijk} D_i e_{jk} + \frac{1}{2} \kappa^\varepsilon_{ij} D_i D_j$

where the strain $e \in M^s_3$ and electric induction $\mathbf{D} \in \mathbb{R}^3$. By M^s_3 we denote the set of symmetric 3 x 3 matrices. The electric enthalpy $H^\varepsilon(\mathbf{e},\mathbf{E})$ is calculated as partial concave conjugate of $U^\varepsilon(\mathbf{e},\mathbf{D})$,

$$H^\varepsilon(\mathbf{e},\mathbf{E}) = \inf\left\{-\mathbf{E}\cdot\mathbf{D} + U^\varepsilon(\mathbf{e},\mathbf{D}) \,|\, \mathbf{D} \in R^3\right\} = \frac{1}{2} c^\varepsilon_{ijkl} e_{ij} e_{kl} - g^\varepsilon_{ijk} E_i e_{jk} - \frac{1}{2} \in^\varepsilon_{ij} E_i E_j ,$$

where $\mathbf{E}$ = -grad φ; φ is the electric potential, $c^\varepsilon_{ijkl} = a^\varepsilon_{ijkl} - g^\varepsilon_{mij} h^\varepsilon_{mkl}$, $\in^\varepsilon = (\kappa^\varepsilon)^{-1}$, $g^\varepsilon_{mij} = \in^\varepsilon_{ml} h^\varepsilon_{lij}$.

We observe that under physically plausible assumptions the internal energy U^ε is convex whilst H^ε is concave in $\mathbf{E}$. We assume the material moduli are essentially bounded, i.e., they belong to $L^\infty(\Omega)$. We set

$$\mathbf{A}^\varepsilon = \begin{bmatrix} \mathbf{c}^\varepsilon & -\mathbf{g}^\varepsilon \\ \mathbf{g}^\varepsilon & \in^\varepsilon \end{bmatrix}, \qquad \mathbf{B}^\varepsilon = \begin{bmatrix} \mathbf{a}^\varepsilon & -\mathbf{h}^\varepsilon \\ -\mathbf{h}^\varepsilon & \boldsymbol{\kappa}^\varepsilon \end{bmatrix},$$

The constitutive relationship takes the following form:

$$\sigma^\varepsilon_{ij} = \frac{\partial H^\varepsilon}{\partial e^\varepsilon_{ij}} = c^\varepsilon_{ijkl} e^\varepsilon_{kl} - g^\varepsilon_{kij} E^\varepsilon_k \qquad \sigma^\varepsilon_{ij} = \frac{\partial U^\varepsilon}{\partial e^\varepsilon_{ij}} = a^\varepsilon_{ijkl} e^\varepsilon_{kl} - h^\varepsilon_{kij} D^\varepsilon_k$$

or equivalently

$$D^\varepsilon_i = -\frac{\partial H^\varepsilon}{\partial E^\varepsilon_i} = g^\varepsilon_{ikl} e^\varepsilon_{kl} + \in^\varepsilon_{ik} E^\varepsilon_k \qquad E^\varepsilon_i = \frac{\partial U^\varepsilon}{\partial D^\varepsilon_i} = -h^\varepsilon_{ikl} e^\varepsilon_{kl} + \kappa^\varepsilon_{ik} D^\varepsilon_k .$$

Let $\{\mathbf{B}^\varepsilon(\mathbf{x})\}_{\varepsilon>0}$, $\mathbf{x} \in \Omega$, be a sequence of matrices such that $\mathbf{B}^\varepsilon \in L^\infty(\Omega; M_{\alpha,\beta})$, where $\beta \geq \alpha > 0$ denote constants and

$$M_{\alpha,\beta} = \{\mathbf{B} \mid a_{ijk} \in L^\infty(\Omega), h_{ijk} \in L^\infty(\Omega), \kappa_{ij} \in L^\infty(\Omega),\ \mathbf{B}(\mathbf{x})\phi\cdot\phi \geq \alpha(|\phi_1|^2 + |\phi_2|^2),$$

$\mathbf{B}^{-1}(\mathbf{x})\phi\cdot\phi \geq \beta(|\phi_1|^2 + |\phi_2|^2)$, $\forall \phi_1 \in M^s_3, \phi_2 \in R^3$, for almost every $\mathbf{x} \in \Omega\}$. It is clear that piezoelectric layered materials are covered by the definition of $M_{\alpha,\beta}$.

A sequence of matrices $\mathbf{B}^\varepsilon(\mathbf{x}) \in L^\infty(\Omega; M_{\alpha,\beta})$ is **H-convergent** to $\mathbf{B}^h \in L^\infty(\Omega; M_{\alpha,\beta})$ if for arbitrary $b_i \in H^{-1}(\Omega)$, $f_i \in H^{-1/2}(\Gamma_1)$, $d \in H^{-1/2}(\Gamma_3)$, $\varphi_0 \in H^{1/2}(\Gamma_2)$, the sequence $(\mathbf{u}^\varepsilon, \mathbf{D}^\varepsilon)_{\varepsilon>0}$ of solutions to the equations

$$-[a^\varepsilon_{ijkl} e^\varepsilon_{kl}(\mathbf{u}^\varepsilon) - h^\varepsilon_{kij} D^\varepsilon_k]_{,j} = b_i, \quad \text{in } \Omega \qquad D^\varepsilon_{i,i} = 0, \quad \varepsilon_{\lim}[h^\varepsilon_{ijk} e_{jk}(\mathbf{u}^\varepsilon) + \kappa^\varepsilon_{ij} D^\varepsilon_j]_{,m} = 0 \quad \text{in } \Omega$$

with the boundary conditions $u^\varepsilon_i = 0$ on Γ_0, $\sigma^\varepsilon_{ij} n_j = f_i$ on Γ_1, $\varphi^\varepsilon = \varphi_0$ on Γ_2, $D^\varepsilon_i n_i = d$ on Γ_3.

is such that $\mathbf{u}^\varepsilon \rightharpoonup \mathbf{u}$ weakly in V, $\mathbf{D}^\varepsilon \rightharpoonup \mathbf{D}$ weakly in $L^2(\Omega)^3$, $a^\varepsilon_{ijkl} e^\varepsilon_{kl}(\mathbf{u}^\varepsilon) - h^\varepsilon_{kij} D^\varepsilon_k \rightharpoonup a^h_{ijkl} e_{kl}(\mathbf{u}) - h^h_{kij} D_k$ weakly in V^*, $-h^\varepsilon_{ijk} e_{jk}(\mathbf{u}^\varepsilon) + \kappa^\varepsilon_{ij} D^\varepsilon_j \rightharpoonup -h^h_{ijk} e_{jk}(\mathbf{u}) + \kappa^h_{ij} D_j$ weakly in $L^2(\Omega)$ where $(\mathbf{u},\mathbf{D})$ is a solution to the homogenized system

$[a^h_{ijkl} e_{kl}(\mathbf{u}) - h^h_{kij} D_k]_{,j} = b_i$, in Ω, $D_{i,i} = 0$, $\varepsilon_{\lim}[h^h_{ijk} e_{jk}(\mathbf{u}) + \kappa^h_{ij} D^h_j]_{,m} = 0$ in Ω,

$u_i = 0$ on Γ_0, $\sigma_{ij} n_j = f_i$ on Γ_1, $\varphi = \varphi_0$ on Γ_2, $D_i n_i = d$ on Γ_3.

Here $V = \left\{v \in H^1(\Omega)^3 \,\middle|\, v = 0 \text{ on } \Gamma_0\right\}$ and V^* is the dual space of V; moreover $\sigma^h_{ij} = a^h_{ijkl} e_{kl} - h^h_{kij} D_k$,

$E^h_i = h^h_{ijk} e_{jk}(\mathbf{u}) + \kappa^h_{ij} D^h_j$.

MULTILAYERING

The constitutive relationship for piezocomposite can be written as follows

$$\boldsymbol{\Sigma}^{\varepsilon} = \mathbf{A}^{\varepsilon}\mathcal{E}^{\varepsilon}, \text{ where } \quad \boldsymbol{\Sigma}^{\varepsilon} = \begin{bmatrix} \boldsymbol{\sigma}^{\varepsilon} \\ \mathbf{D}^{\varepsilon} \end{bmatrix}, \quad \mathbf{A}^{\varepsilon} = \begin{bmatrix} \mathbf{c}^{\varepsilon} & -\mathbf{g}^{\varepsilon} \\ \mathbf{g}^{\varepsilon} & \in^{\varepsilon} \end{bmatrix}, \quad \mathcal{E}^{\varepsilon} = \begin{bmatrix} \mathbf{e}^{\varepsilon} \\ \mathbf{E}^{\varepsilon} \end{bmatrix}, \quad \mathbf{E}^{\varepsilon} = -\text{grad}\varphi^{\varepsilon}.$$

Let us now assume that the moduli depend only on one variable in the direction of unit vector $\mathbf{n}_1$, e.g. $\mathbf{n}_1$ denotes the unit vector of axis x_1: $\mathbf{A}^{\varepsilon} = \chi^{\varepsilon}(x_1)\overset{(1)}{\mathbf{A}} + (1-\chi^{\varepsilon}(x_1))\overset{(2)}{\mathbf{A}}$, where $\overset{(1)}{\mathbf{A}}$, $\overset{(2)}{\mathbf{A}}$ are the matrices of materials (1) and (2), respectively. Here $\chi^{\varepsilon}(x_1)$ is the characteristic function equal 1 in the domain occupied by the material (1) and equal zero otherwise.

Performing homogenization (H-convergence), i.e., letting ε tend to zero we get the macroscopic constitutive relationship in the form:

$$\boldsymbol{\Sigma} = \mathbf{A}^{h}\ \mathcal{E}, \quad \text{where} \quad \boldsymbol{\Sigma} = \begin{bmatrix} \boldsymbol{\sigma} \\ \mathbf{D} \end{bmatrix}, \quad \mathbf{A}^{h} = \begin{bmatrix} \mathbf{c}^{h} & -\mathbf{g}^{h} \\ \mathbf{g}^{h} & \in^{h} \end{bmatrix}, \quad \mathcal{E} = \begin{bmatrix} \mathbf{e} \\ \mathbf{E} \end{bmatrix},$$

We denote by θ the weak-* limit of the sequence of the characteristic functions $\{\chi^{\varepsilon}\}$, i.e.,
$\chi^{\varepsilon} \rightharpoonup \theta$ in $L^{\infty}(\Omega)$ as ε tends to zero.
The following implicit formula for the effective piezoelectric moduli of layered composite:

$$\theta(\mathbf{A}^{h} - \overset{(2)}{\mathbf{A}})^{-1}\boldsymbol{\eta} = (\overset{(1)}{\mathbf{A}} - \overset{(2)}{\mathbf{A}})^{-1}\boldsymbol{\eta} + (1-\theta)(\mathbf{q}_{(2)}(\mathbf{n}_1)(\boldsymbol{\eta}\mathbf{n}_1)) \oplus \mathbf{n}_1$$

where $\mathbf{q}^{-1}_{(2)}(\mathbf{n}_1)$ is a symmetric 4x4 matrix given by $\mathbf{q}^{-1}_{(2)}(\mathbf{n}_1) = \begin{bmatrix} \overset{(2)}{c}_{ijkl}\, n_{1j}n_{1l} & -\overset{(2)}{g}_{ijk}\, n_{1j}n_{1k} \\ \overset{(2)}{g}_{jkl}\, n_{1l}n_{1j} & \overset{(2)}{\in}_{ij} n_{1i}n_{1j} \end{bmatrix}$.

The relationship for the pth-order lamination, performed as follows. In the first step we find the homogenized matrix $\mathbf{A}^{h}_1$ for a piezoelectric layered two-phase material characterized by $\overset{(1)}{\mathbf{A}}, \overset{(2)}{\mathbf{A}}$, the volume fraction θ_1 and lamination direction $\mathbf{n}_1$. In the second step of lamination we find the homogenized matrix $\mathbf{A}^{h}_2$ for a layered two-phase piezoelectric material characterized by $\mathbf{A}^{h}_1$, $\overset{(2)}{\mathbf{A}}$, the volume fraction θ_2 and lamination direction $\mathbf{n}_2$, etc. Finally at the p-th step we get

$$\prod_{i=1}^{p}\theta_i(\mathbf{A}^{h}_{p} - \overset{(2)}{\mathbf{A}})^{-1}\boldsymbol{\eta} = (\overset{(1)}{\mathbf{A}} - \overset{(2)}{\mathbf{A}})^{-1}\boldsymbol{\eta} + \sum_{i=1}^{p}(1-\theta_i)\left[(\mathbf{q}_{(2)}(\mathbf{n}_i)(\boldsymbol{\eta}\mathbf{n}_i)) \oplus \mathbf{n}_i\right]\prod_{k=1}^{i-1}\theta_k$$

FINAL REMARKS

We conclude that the derived formula for the lamination is convenient for a control of parameters involved in it. For instance, changing angles of lamination and preserving the volume fractions of successive steps of the lamination we can generate composites with various properties. Similarly, preserving directions and choosing optimal, from prescribed point of view partial volume fractions we have wide possibilities of control of macroscopic properties of composites.

An essential role in the study of optimal design for minimum compliance is played by homogenization and relaxation of relevant compliance functional. More precisely, it has been shown that a two-phase composite with minimum compliance (maximum stiffness) is realized by laminates of suitable order. This deep result has been proved only for composites made of two isotropic elastic materials with order bulk and shear moduli, see [1,2].

The compliance functional is assumed in the following form

$$J(\chi) = \int_{\Omega} b_i u_i dx + \int_{\Gamma_1} f_i u_i d\Gamma + \int_{\Gamma_2} D_i n_i \varphi_0 d\Gamma + \int_{\Gamma_3} \bar{d}\varphi d\Gamma.$$

The minimum compliance problem means evaluating

$$\inf\{ J(\chi) | \chi \in L^{\infty}(\Omega;\{0,1\}), \quad \int_{\Omega}\chi(\mathbf{x})d\mathbf{x} = V_1, \text{ equilibrium and boundary conditions are satisfied}\}.$$

Similarly to the elastic case one can consider optimal shape design for minimum compliance, cf. [1,2]. Formally, it suffices to assume that the moduli of weaker material disappear. However, it is worth noting that a piezocomposite with optimal shape may consists of three regions; the first region is made of material (1) (the stronger one), the second region contains voids whilst the third region is a composite obtained by mixing (in homogenization sense) of the material (1) and microvoids.

Acknowledgements. The authors were supported by the State Committee for Scientific Research (KBN, Poland) through the grant No 8 T07A 052 21 .

References

[1] Allaire G.: Shape Optimisation by the Homogenisation Method. Springer, New York, 2002.

[2] Lewiński T., Telega J.J.: Plates, Laminates and Shells: Asymptotic Analysis and Homogenisation. World Scientific, Singapore, 2000.

ON THE ROLE OF INTER-GRANULAR LAYERS IN POLYCRYSTALLINE CERAMICS

T.Sadowski*, Stephen Hardy**, E. Postek**,

* *Lublin University of Technology , Department of Solid Mechanics, PL 20-618 Lublin, Poland*

** *School of Engineering, University of Wales Swansea Singleton Park, Swansea, SA8P, Wales, United Kingdom*

Summary Ceramic polycrystalline materials show a non-linear and complex response to applied loads due to their internal structure. The inter-granular layers significantly change the macro-response of the material.. The aim of the paper is to present a new constitutive model for the case of uniaxial tension of the polycrystalline materials, including the inter-granular metallic layers that create its internal structure. The quasi-static deformation process of this material include description of: elastic deformation of brittle grains, elasto-plastic deformation of inter-granular layers and deformation due to micro-porosity development in layers.

INTRODUCTION

Ceramic polycrystalline materials show a non-linear and complex response to applied loads due to their internal structure, [1], [2]. Experimental observations show that the important element of the internal structure is the thin layer between grains. The size of these layers is relatively small in comparison to the grain diameter. The inter-granular layers significantly change the macro-response of the material. This is particularly evident when the two phases are made of different materials. For example, the grains may be brittle but the thin layers exhibit properties of a metallic material, so the softening effect due to porosity development should be taken into account.

The aim of the paper is to present a new constitutive model for the case of uniaxial tension of the polycrystalline materials, including the inter-granular metallic layers that create its internal structure. The quasi-static deformation process of this material include description of: elastic deformation of brittle grains, elasto-plastic deformation of inter-granular layers and deformation due to micro-porosity development in layers.

The effective continuum model has been applied to obtain constitutive relations. A Representative Volume Element (RVE) was analysed taking into consideration an initial internal structure of the material obtained from SME photographs. Owing to the high complexity of the internal structure of the composite material, the FEM technique was used to obtain macroscopic stress-strain correlations. They include gradual changes of the internal structure of the material due to defects development under quasi-static tension.

THEORETICAL BACKGROUND

According to [3] and [4] the total strain rate can be split into elastic strain rate and viscoplastic strain rate

$$\dot{\boldsymbol{e}} = \dot{\boldsymbol{e}}^{e} + \dot{\boldsymbol{e}}^{vp}$$

The onset of viscoplastic behaviour of the material is governed by a scalar yield condition

$$F(\boldsymbol{s}, \boldsymbol{e}^{vp}) = F_0$$

where F_0 corresponds to uniaxial yield stress. Then the viscoplastic flow rule can be expressed as follows

$$\dot{\boldsymbol{e}}^{vp} = g\left\langle \exp[M(F - F_0)/F_0] - 1 \right\rangle \frac{\partial F}{\partial \boldsymbol{s}}$$

where g is viscosity parameter.

The total visco-plastic strain increment (applying implicit time stepping scheme) for the time while $t^{(n)}$ is equal to

$$\Delta \boldsymbol{e}^{vp(n)} = \dot{\boldsymbol{e}}^{vp(n)} \Delta t^{(n)}$$

whereas the stress increment $\Delta \boldsymbol{s}$ and displacement increment $\Delta \boldsymbol{d}$ are equal to

$$\Delta \boldsymbol{s}^{(n)} = \boldsymbol{D} : \Delta \boldsymbol{e}_e^{(n)} = \boldsymbol{D} : (\Delta \boldsymbol{e}^{(n)} - \Delta \boldsymbol{e}^{vp(n)})$$

$$\Delta \boldsymbol{d}^{(n)} = [\boldsymbol{K}_T^{(n)}]^{-1} : \Delta \boldsymbol{V}^{(n)}$$

where $\Delta t^{(n)}$ is the time increment, $\boldsymbol{D}$ is the elasticity matrix, $\boldsymbol{K}_T^{(n)}$ is the tangential stiffness matrix, $\Delta \boldsymbol{V}^{(n)}$ is the incremental pseudo-load.

Having calculated stress increment and displacement increment it is easy to estimate current values of stress, strain and displacements.

NUMERICAL EXAMPLE

The FEM mesh of the representative element is shown in Fig. 1, whereas loading and supporting conditions are presented in Fig. 2. AL_2O_3 grains of the polycrystal have Young modulus equal to 4,1 $(10)^{11}$ MPa and Poisson coefficient equal to 0,25. Interfaces are viscoplastic with Young modulus equal to 2,1 $(10)^{11}$ MPa and Poisson coefficient equal to 0,235.

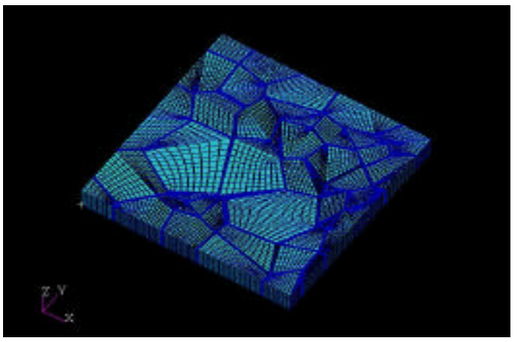


Fig. 1. FEM mesh

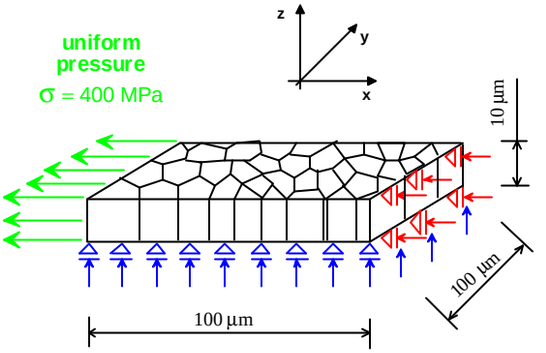


Fig. 2. Loading and supporting conditions

RESULTS AND DISCUSSION

Fig. 3 presents the distribution of equivalent viscoplastic strains in representative element. The influence of the viscosity parameter on the maximum value of equivalent viscoplastic strains is shown in Fig.4.

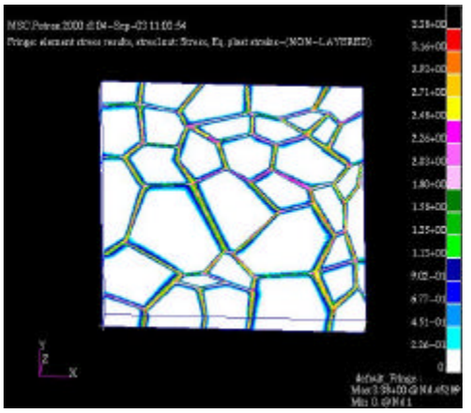


Fig. 3. Equivalent visco-plastic strains

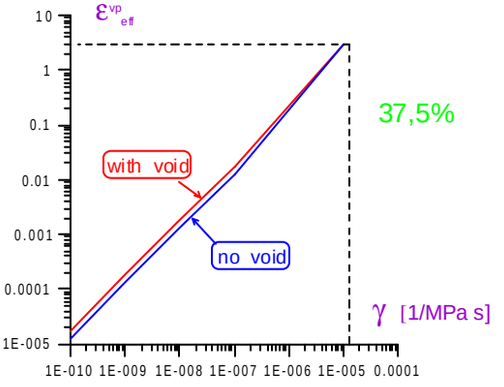


Fig. 4. Maximum visco-plastic strains vs viscosity parameter

CONCLUSIONS

- Introduction of interfaces made of different material (viscoplastic) radically changes the internal stress distribution inside the polycrystalline structure.
- Microvoid placed inside the viscoplastic interface leads to stress concentration equal to 1,58.
- Equivalent plastic strain at the void boundary is higher 37% in comparison to the interface without void.

References

[1] Davidge R.W.: Mechanical Behaviour of Ceramics. Cambridge University Press, London, 1979.
[2] Sadowski T., Samborski S.: Modeling of Porous Ceramic Response to Compressive Loading. J. Am. Ceram. Soc. **86**:2218-2221, 2003
[3] Owen D.R.J., Hinton E.: Finite Elements in Plasticity, Theory and Practice. Pineridge Press Ltd. Swansea, UK, 1980
[4] Perzyna P.: Thermodynamic Teory of Viscoplaticity, in Advances in Applied Mechanics, Academic Press, New York, **11**, 1971.

XXI ICTAM, 15–21 August 2004, Warsaw, Poland

A HOMOGENIZATION BASED LAMINATED BEAM THEORY

Jorn S. Hansen*, Sérgio F. M. de Almeida **
*University of Toronto, Institute for Aerospace Studies, Toronto, Ontario, Canada
**Instituto Tecnológico de Aeronáutica, Mechanical Engineering, São José dos Campos - SP , Brasil

Summary The analysis of laminated and sandwich structures is very significant as may be appreciated by the extensive literature devoted to both the development of enhanced beam, plate and shell theories as well as the application of these theories in the design of laminated composite and sandwich structure. There are essentially two aspects of these problems which have driven the theoretical development. First, it is desirable to obtain accurate displacement solutions; second, accurate and complete through-thickness stress/strain distributions are crucial in the prediction of failure/delamination. In both cases a minimal computational effort should be involved. The challenge is that the through-thickness character of the stress, strain and displacement fields are in general non-differentiable and may also be discontinuous; thus modelling the through-thickness response using low-order polynomials will in general lead to poor approximations. The literature dealing with this subject is vast; the reader is referred to [1] which presents a review as well as the complete details of the present work. The de facto standard method of analyzing laminated beams, plates or shells is to use a Timoshenko or Reissner-Mindlin formulation, the so called first-order shear deformation theory, with appropriate shear correction factors and then complete a post-processing calculation in which the in-plane stresses are used in the full equilibrium equations to determine approximations for the transverse shear stresses. The difficulty with this approach is the definition of the shear correction factor and the fact that the post-processing calculation is inconsistent with the beam/plate assumptions used in the analysis. The present work adopts a very different point of view which is completely internally consistent and, as will be shown, leads to an extremely accurate modelling capability.

The present work provides a straight-forward yet extremely accurate approach by which a sequence of beam models is developed; both laminated and sandwich beams are modelled with equal fidelity. This development is based on the assumption that beam response characteristics can be represented in terms of far-field stress and strain solutions corresponding to constant, linear, quadratic, ... , nth degree bending states; such solutions are referred to as Fundamental Solutions, can be determined uniquely and are independent of boundary conditions. Based on the Fundamental Solutions, through-thickness moments of stress and strain are used to obtain definitions of homogenized flexural and shear stiffness, homogenized transverse Poisson's ratio as well as a unique definition of a shear-strain-moment correction. The homogenized flexural stiffness is defined as the ratio of the first moments of σ_x and ϵ_x for a state of pure bending. That is

$$E_x \triangleq \frac{{}_1s_x^1}{{}_1e_x^1} \tag{1}$$

This stiffness does is not reduce to the conventional definition of flexural stiffness. For a single layer material, E_x reduces to Young's modulus. The homogenized transverse shear stiffness is defined as the ratio of the zeroth moments of σ_{xz} and γ_{xz} for a state of linearly varying bending; that is constant transverse shear stress.

$$G_{xz} \triangleq \frac{{}_2s_{xz}^0}{{}_2e_{xz}^0} \tag{2}$$

In the above, the exact shear stress and strain distributions are used to evaluate G_{xz}; therefore no shear correction factor is required. Furthermore, for a single layer material, G_{xz} is identical to the exact transverse shear stiffness, independent of the stress and/or strain distribution. The use of through-thickness stress and strain moments eliminates difficulties commonly associated with discontinuous or non-differentiable solution fields and also means model complexity is independent of the number or type of layers in the beam. A hierarchical sequence of models results from this approach depending on the number of Fundamental States included in a particular model. All models adopt a form similar to that of Classical Timoshenko Beam Theory with the addition of *correction* terms which account for the effects of surface tractions. In addition, the system displacement approximations of the present and the Timoshenko model have different meanings. Finally, a simple, well-defined post-processing step allows determination of complete and precise stress and strain fields based on the Fundamental Solution stress and strain fields used in the model development. The theory is internally self-consistent and the post-processing calculations are based on precisely the same approximations involved in developing the theory

Comparisons between the present approach and a full two-dimensional finite element analysis are completed using the commercial finite element code ANSYS. A sequence of cantilever sandwich-beams subjected to either an end shear load or a uniform lateral pressure is considered; the beam is 100mm long by 10mm thick and the face sheets are 0.5mm thick. The face sheets are assumed to be aluminum; a sequence of core stiffnesses are modelled as degraded aluminum with modulii taking values of 1.0, 0.1, 0.01 times the modulus of aluminum. The ANSYS calculation uses 200x40 bi-quadratic elements. Three examples of typical results are presented in Figures 1, 2 and 3 for the case of a normal surface traction of 0.5 MPa applied on both the upper and lower beam surface. As can be seen there is excellent agreement between the current beam theory and the finite element calculations for the shear stress σ_{xz}, shear strain γ_{xz} and the transverse normal stress σ_z. Complete results show that at the beam mid-length the finite element and beam theory predictions are numerically identical for all stress and strain components. At a distance of 1/2 a beam thickness from the cantilever root the maximum worst case error in the shear stress is approximately 11%; this error be attributed to three-dimensional boundary effects. The through-thickness displacement moments have a maximum worst case error of approximately 1% over the length of the beam .

The present approach provides insights and extensions to existing beam theories including Classical Euler-Bernoulli and Timoshenko beam theory.

References

[1] Hansen, J.S., de Almeida, S.F.M.: A Theory for Laminated Composite Beams. *Final Report* submitted April 2001, FAPES Grant No. 00/06183-0, São Paulo, Brasil.

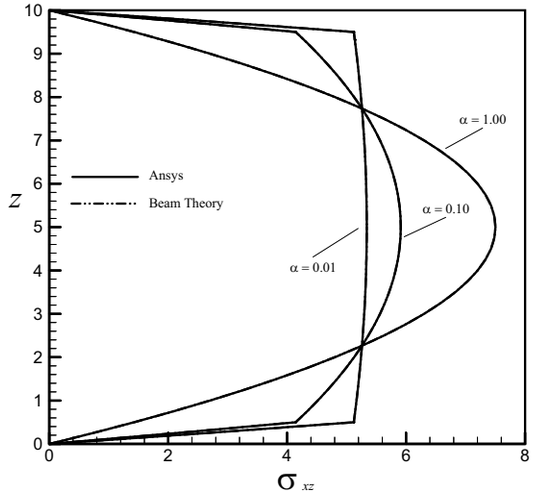


Figure 1. Transverse shear stress σ_{xz} (MPa) through thickness at beam mid-length.

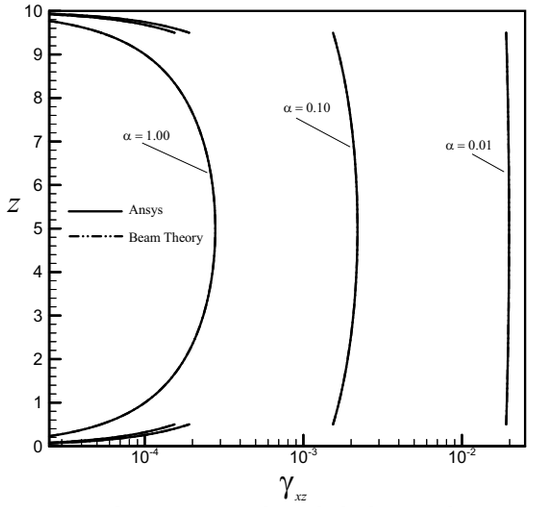


Figure 2. Transverse shear strain γ_{xz} through thickness at beam mid-length.

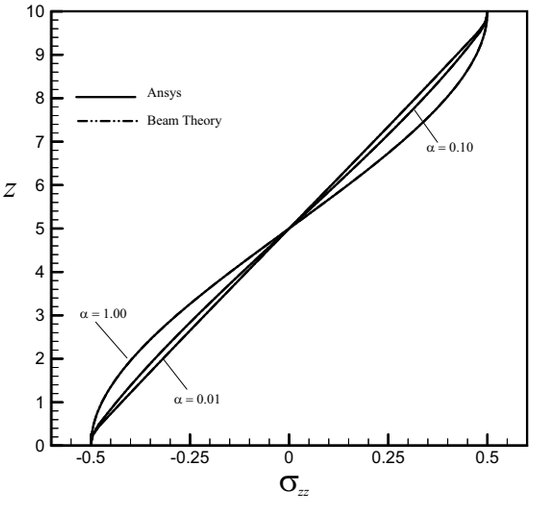


Figure 3. Transverse normal stress σ_{zz} (MPa) through thickness at beam mid-length.

XXI ICTAM, 15–21 August 2004, Warsaw, Poland

COMPRESSIVE STRENGTH OF FIBER COMPOSITE WITH POROSITY

Ulrik Borg*
*Department of Mechanical Engineering, Solid Mechanics, Technical University of Denmark, Kgs. Lyngby, Denmark

Summary The compression strength of fiber composites is analysed using a finite element model which includes finite strain plasticity. A separate discretization of fiber and matrix is performed using plane strain elements. The sensitivity of the compression strength to the geometric imperfection parameters given by fiber misalignment and kink band angle is investigated. Porosities are included in the model as material imperfections and it is shown that they only have a limited effect on the compressive strength of the composite.

INTRODUCTION

It has been a well known fact for many years that the compressive strength of fiber composites is significantly less than the tensile strength. An explanation for this difference is that a fiber composite in tension normally fails by fiber fracture while compressive stresses can lead to a number of different failure mechanisms. The dominating failure mechanism in polymer matrix fiber composites in compression is failure by fiber kinking [1].
It has been observed that in most fiber composites there are small volumes of air included in the matrix. During manufacturing the amount of porosities is being minimized but it is difficult to totally avoid the presence of them. The influence of these porosities on the compression strength has not been investigated in the litterature.

ANALYSIS

In this work the compression strength of fiber composites is analysed using a finite element model. The composite is modeled with a separate discretization of fiber and matrix using plane strain elements. The fiber material is carbon and the fibers are assumed to be linearly elastic. A polymer material named PEEK is used as matrix and its nonlinear behavior is modeled with a finite strain version of J_2 flow theory as made for shear bands in [2]. The reason for using the finite strain version is the large shear strains in the region around the kink band.
To initiate the development of a kink band an imperfection given by a cosine function is made as a band transverse to the fibers. The boundary conditions are shown in figure 1 where the grey areas are fibers. The initial fiber misalignment angle ϕ_0 can be approximated by $\phi_0 \approx h/L_{kb}$ and the kink band angle is given by β. The width of the specimen is determined by fiber width, fiber volume fraction and number of fibers. To apply the compressive load the end displacement U is prescribed.

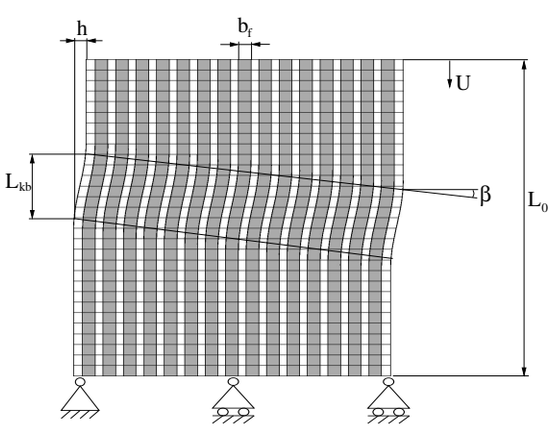


Figure 1: Specimen with 15 fibers showing the boundary conditions and the geometric imperfection.

RESULTS

The sensitivity of the compression strength to the imperfection parameters given by fiber misalignment and kink band angle has been investigated. It has been found that the fiber misalignment angle has a great influence on the compression strength. Furthermore, it was observed that the critical kink band angle changes with fiber misalignment angle, as was also observed by Jensen and Christoffersen [3].

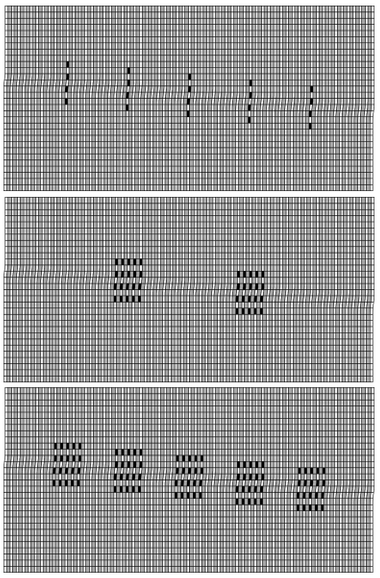


Figure 2: 3 specimens with porosities. From top an d down refered to as 5x1, 2x5 and 5x5.

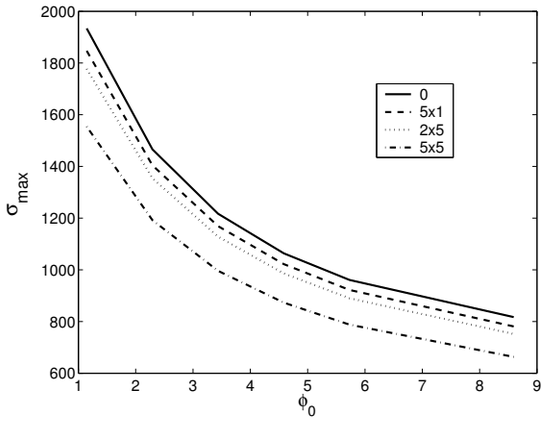


Figure 3: The compressive strength in MPa as a function of the initial fiber misalignment angle.

The behavior of the kink band in the post peak region has also been investigated. After the limit load was reached the average axial stress decreased toward a constant value. During the steady state loading the misalignment angle only changed sligthly and a band broadening was observed. The method used here is somewhat similar to the work of Kyriakides et al. [4] and the results in the absence of porosity show the same tendency.

The main focus here is to investigate how air inclusions in the composite influence the compressive strength. In figure 2 black areas indicate how the porosities are included in the model of a specimen consisting of 60 fibers. As shown, the porosities are placed around the imperfection band in either a single band or in small clusters in the matrix.

The compressive strength is plotted as a function of the initial fiber misalignment angle in figure 3. The solid line represents a specimen without porosities. It is seen that the introduction of porosities reduces the compressive strength as expected. Introducing five single bands of porosities, named 5x1 in figure 3, reduces the compressive strength by 3-5% while the specimen with 2 clusters, named 2x5, reduces the compressive strength by 6-8%. When implementing five clusters in the model, named 5x5, a significantly reduction of 15-20% is seen in the compressive strength. However this high concentration of porosities is not very realistic for fiber composites manufactured with modern manufacturing facilities. Hence the numerical analysis indicates that a limited amount of porosities only has a small influence on the compressive strength of the composites. In addition it is seen from figure 3 that the amount of porosities only has a minor effect on the sensitivity of the compression strength to the misalignment angle.

CONCLUSIONS

The analyses performed show that the fiber misalignment angle has a dominant influence on the compressive strength of the composite and that the critical kink band angle is depending on the initial fiber misalignment angle, as also found in [3] and [4].

The investigation of the influence of porosities on the compressive strength shows a reduction of the compressive strength by up to 15-20% for the porosities considered. Realistic levels of porosity are expected to be smaller.

References

[1] Fleck N.A.: Compressive Failure of Fiber Composites. *Advances in Applied Mechanics* **33**: 43-117, 1996

[2] Hutchinson J.W., Tvergaard V.: Shear Band Formation in Plane Strain. *Int. J. Solids Structures* **17**:451-470, 1981

[3] Jensen H.M., Christoffersen J.: Kink Band Formation in Fiber Reinforced Materials. *J. Mech. Phys. Solids* **45**:1121-1136, 1997

[4] Kyriakides S., Arseculeratne R., Perry E.J., Liechti K.M.: On the Compressive Failure of Fiber Reinforced Composites. *Int. J. Solids Structures* **32**:689-738, 1995.

THERMAL RESIDUAL STRESS IN Al_2O_3/SiC_{nano} CERAMIC COMPOSITES MEASURED BY NANOINDENTER*

Zhong LING

LNM, Institute of Mechanics, Chinese Academy of Sciences, Beijing 100080, P.R China

Summary Thermal residual stresses in Al_2O_3 ceramics containing SiC_{nano} particles were measured by nanoindentation instrument. Pure Al_2O_3 ceramics was selected as a reference without thermal residual stress. Considered the contact stiffness would vary due to local heterogeneities of microstructure in current composites, data on the surface sensitivity of a series of samples probed at different peak depths were collected. The experimental results on the residual stress of two composites were obtained in local region probed by indenter tip. Also the influence of volume fraction of SiC particles to magnitude of thermal residual stress and the external work and deformation energy during indentation under a fixed applied load, 250mN, were investigated.

Key words: nano-ceramic composite, thermal residual stress, nanoindentaion experiment

INTRODUCTION

Nano-ceramic matrix composites are ceramics containing nanosized-ceramic particles of 1-5% volume fractions. The nanosize-particles dispersed in the grains of matrix would lead to a change in the fracture modes, from predominantly inter-granular to predominantly trans-granular fractures. This would also lead to enhanced fracture toughness of the composite. Among the toughening mechanisms of such particulate ceramic composites, a primary one is residual stress (strain) in the matrix grains due to a mismatch between the coefficients of thermal expansion (CTEs) of the ceramic matrix and nano-sized particles. Obviously, the estimation of thermal residual stress is an important issue in these nano- ceramic composites.

In the past decades, a number of experimental work had been reported on the averaged residual stresses in matrix composites determined by X-ray and neutron diffraction [1]. More recently, however, with the rapid development of nano-instruments, the nanoindentation technique has been applied to probe quantitatively the residual stresses at a very tiny volume [2,3].

Motivated by the above research and the need to better understand how the thermal residual stress quantitatively distributed in the ceramic composites, we preformed nanoindentation experiments for typical nano-ceramic composites, Al_2O_3/SiC_{nano}. The thermal residual stress developed in the matrix of the composites was also probed.

MATERIALS AND EXPERIMENTAL RESULTS

Materials and experiments

The testing materials for the present study were sintered aluminum and its composites containing SiC particles (Al_2O_3/SiC). The volume fractions of SiC particles were 5% and 10%. The SiC particle size was ~60-100 nm (d_{SiC} = 60-100 nm). Because the SiC particles existed as a second phase in the current composite, the microstructure of the composite have involved a number of scales over the entire indentation process. The distance between two nearest SiC particles, δ_{SiC}, is an intrinsic scale of particulate reinforced composite, which is related with particle size and its volume fraction. Microstructure scales in current materials were list in Table I. Nanoindentation tests were carried out under fixed applied indentation loads, 3-250mN, with a constant load rate over load, $\dot{F}/F = 2$. The typical loading curves of current materials are presented in Figure 1.

Table I. Microstructure coefficients in current materials

Al_2O_3/SiC_p	Ratio	Size	δ_{SiC}
Al_2O_3	balance	~5μm	—
Al_2O_3/SiC_p	f_v=0.05	60-100nm	145-242nm
Al_2O_3/SiC_p	f_v=0.10	60-100nm	88-147nm

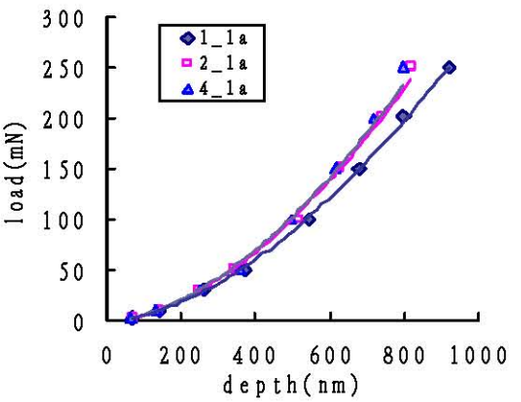


Figure 1. Loading-depth curves for three materials, 1-1:Al_2O_3; 2-1: Al_2O_3/SiC(5%); 4-1: Al_2O_3/SiC(10%)

Experimental results and analysis

Usually, the recorded indentation curves could actually be evaluated with respect to their curvatures and preliminarily pooled as apparently 捞oft" and 揾arder" locations on the microstructure of the contact surface. Also the contact stiffness, S, would vary due to local heterogeneities of the material. Considering the matrix and SiC particles in the current composites, data on the contact stiffness of a series of samples probed at different peak depths were collected and analyzed. Figure 2 showed relations between contact stiffness and depth for three test materials. At

depth less 200nm, contact stiffness of three materials does not change significantly (Figure 2). Notice the distance between two nearest SiC particles, δ_{SiC}, not over 200nm for Al_2O_3/SiC (10%), and δ_{SiC}~150-240nm for Al_2O_3/SiC (5%). So present samples were almost all initially local to aluminum phase between two nearest SiC particles of the current materials. In the other word, information on thermal residual stress in matrix of current composites could be probed by indenter tip at depth<200nm.

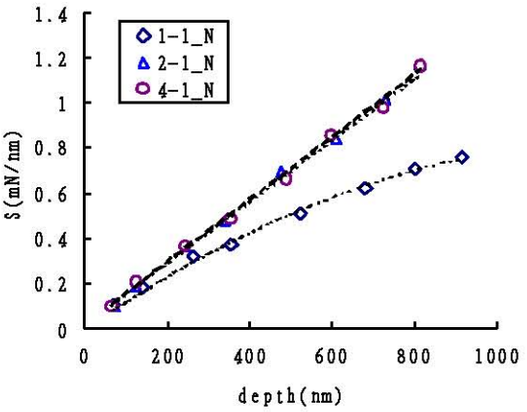


Figure 2 Contact stiffness obtained at different peak load of current materials:
◇Al_2O_3,△- Al_2O_3/SiC(5%),○- Al_2O_3/SiC(10%)

According to the method described in [3], the residual stress state in the local region could be estimated in the loading curves. As a reference material, Al_2O_3 should be in a non-residual stress state compared with both composites during loading. For another two composites, compressive residual stress seems to have been probed. In Figure 1, at fixed applied indentation loads, 3-250mN, indentation depths of two composites were smaller than that of Al_2O_3. This should be a contribution of compressive residual stress in matrix of two composites. The compressive residual stress would make the effective indentation loads smaller and consequently arise apparently the indentation stiffness. Obviously, magnitudes of the residual stress varied slightly with volume fractions of SiC particles in the composites.

Additionally, external work done by the load, elastic (recoverable) and plastic (permanent) deformation energy during indentation were investigated. Let $\eta_e=W_e/W_t$ and $\eta_p=W_p/W_t$ as normalized elastic and plastic deformation energy, respectively. Where W_t is external work, W_e elastic deformation energy and W_p plastic deformation energy. Experimental results presented that, under maximum peak load, 250mN, $\eta_{e1}=W_{e1}/W_{t1}$, normalized elastic deformation energy of Al_2O_3 material is greater than that of both composites. And the normalized elastic deformation energy of Al_2O_3/SiC(5%) is greater than that of Al_2O_3/SiC(10%). That is, $\eta_{e1}>\eta_{e2}=W_{e2}/W_{t2}>\eta_{e4}=W_{e4}/W_{t4}$. The normalized plastic deformation energy of these materials, however is, another way around, $\eta_{p1}<\eta_{p2}<\eta_{p4}$. As stated above, compressive residual stress developed by SiC particles in composites raised apparently the indentation stiffness therefore the percent of recoverable deformation energy in total work would be lower under a fixed applied load. As for the permanent deformation energy of these materials, it is probably related to other factors, such as plastic deformation in the matrix, surface roughness and interface between particles and the matrix as well.

CONCLUSSIONS

Considering microstructure scales in current composites, data on the contact stiffness of a series of samples probed at different peak depths were collected. At indentation depth less 200nm, recorded contact stiffness of three materials did not change significantly. So present samples were almost all initially local to aluminum phase between two nearest SiC particles of the current materials.

Compressive residual stresses in two composites were obtained from loading-depth curves referenced to that of matrix material, Al_2O_3; The compressive residual stress would make the effective indentation loads smaller and consequently arise apparently the indentation stiffness and their magnitudes depended on volume fractions of SiC particles of the composite;

Under the fixed applied indentation load, 250mN, the normalized elastic deformation energy, η_e, of three materials followed as $\eta_{e1}>\eta_{e2}>\eta_{e4}$; but normalized plastic deformation energy of these materials followed as $\eta_{p1}<\eta_{p2}<\eta_{p4}$.

References

[1] I. Levin, et al, Residual Stresses in Alumina-SiC Nanocomposites, *Acta Metall. Mater*. **42:**1147-1154, 1993

[2] W.C. Oliver and G.M.Pharr, An Improved Technique for Determining Hardness and Elastic Modulus using Load and Displacement Sensing Indentation, *J.Mater. Res*. **7:**1564-1583, 1992

[3] S.Suresh and A.E. Giannakopoulos, A New Method for Estimating Residual Stress by Instrumented Sharp Indentation, *Acta. Mater*. **46:**5755-5767, 1998

*This work is financially supported by National Natural Science Foundation of China (Grant No.50172053) and the Chinese Academy of Sciences (Grant No. KJCX-SW-L2)

COMPOSITES WITH PLANAR RANDOM FIBER ARRANGEMENTS

Dominik Duschlbauer, Helmut J. Böhm, Heinz E. Pettermann
Institute of Lightweight Design and Structural Biomechanics,
Vienna University of Technology, A–1040 Vienna, Austria

Summary A short fiber reinforced composite material with particular fiber arrangement is investigated by means of a numerical unit cell approach as well as by an analytical mean field type approach. Homogenization and localization is performed for Carbon fiber reinforced Copper with respect to the linear thermoelastic and thermal expansion properties. Simulation results are compared and their applicability is assessed.

INTRODUCTION

Tailorable materials are desired for high performance applications. The properties of fiber composites can be modified within a wide range by changing the composition and the microgeometry such as fiber length, fiber orientations, etc. Frequently, transversally isotropic material symmetry is required which can be obtained by a fiber orientation distribution of the planar random type. As an example the linear behavior with respect to elasticity, thermal expansion, and thermal conductivity is investigated.

MICROMECHANICAL APPROACHES

Numerical Method — Periodic Microfield Approach

Short fibers of aspect ratio 10 are modeled in a planar random type orientation arrangement. A minimum distance between neighboring fibers is maintained in all cases. Agglomerations of parallel fibers within clusters are excluded. Two different unit cells with some fifty fibers and a fiber content slightly higher than 20%vol are generated [1]. Starting from a dilute fiber arrangement, compaction to the final topology is modeled by *PALMYRA (Materials Simulations GmbH, Zürich, Switzerland)*. The final topology is transferred to the finite element program *ANSYS (ANSYS Inc., Canonsburg, PA)*, meshed (Fig. 1), and solved. Homogenization is done by standard approaches giving rise to the overall properties. Localization is performed in terms of field variables within individual fibers by means of statistics [2].

Analytical Method — Mori–Tanaka Type Mean Field Approach

The analytical simulations are based on a multi-inclusion Mori–Tanaka formulation [3]. The orientation distributions are given both by smooth continuous probability functions and by discrete orientations corresponding to those in the unit cells. The fibers are modeled as spheroids (typical for standard methods) and as cylinders. For the latter a numerical evaluation of averaged concentrations tensors is performed. Localization is based on averaged fields within individual fibers.

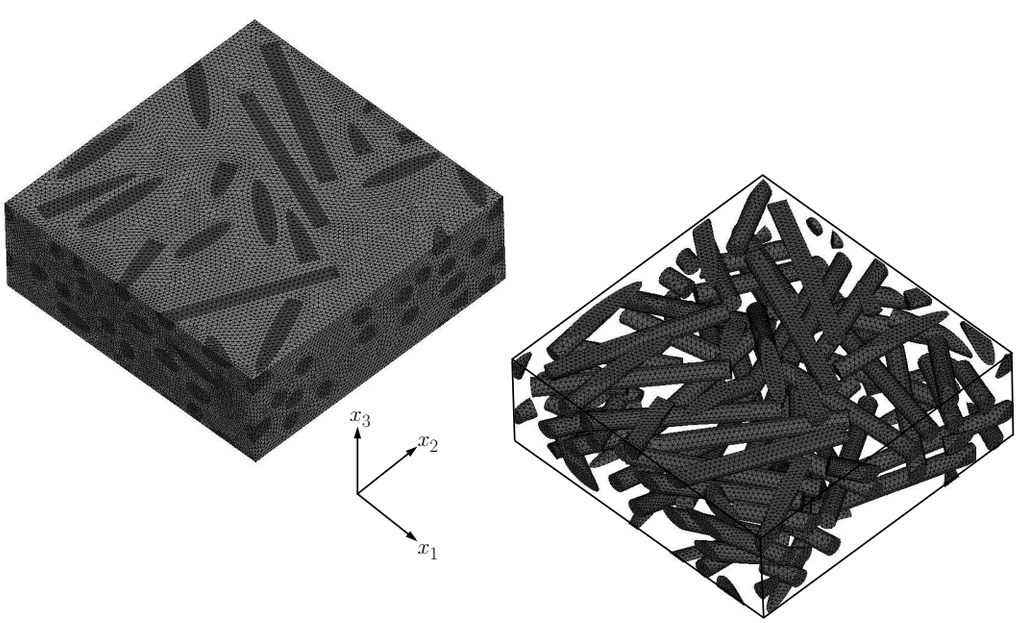


Figure 1: Finite element model of one unit cell; fibers and matrix (left) and fibers only (right).

Table 1: Material data for isotropic Copper matrix and transversally isotropic Carbon fibers.

	E_1 [GPa]	$E_2 = E_3$ [GPa]	$\nu_{12} = \nu_{13}$	$G_{12} = G_{13}$ [GPa]	G_{23} [GPa]	α_{11} [10^{-6}/K]	$\alpha_{22} = \alpha_{33}$ [10^{-6}/K]	K_{11} [W/mK]	$K_{22} = K_{33}$ [W/mK]
Cu	125	125	0.35	46.3	46.3	16	16	360	360
C	220	15	0.2	10	5	−0.5	10	1000	100

EXAMPLE AND RESULTS

As example Copper reinforced by Carbon short fibers is investigated. Material data is given in Table 1. A perfect interface is assumed throughout the present work; detailed studies on the effect of imperfect thermal interfaces are given in [1,4].

Homogenization

Both methods allow for the prediction of the complete set of overall material parameters, i.e. the extraction of the entire tensors. The predicted overall thermal conductivity, $\boldsymbol{k}$, the overall coefficient of thermal expansion, $\boldsymbol{\alpha}$, and the overall elasticity tensor, $\boldsymbol{E}$, are given for one unit cell.

$$\boldsymbol{k} = \begin{pmatrix} 378.9 & 0.2 & -1.4 \\ 0.2 & 370.8 & 1.4 \\ -1.4 & 1.4 & 289.8 \end{pmatrix} \quad [\mathrm{W/mK}] \qquad \boldsymbol{\alpha} = \begin{pmatrix} 13.8 & -0.08 & -.16 \\ -0.08 & 13.8 & 0.10 \\ -.16 & 0.10 & 17.3 \end{pmatrix} \quad [10^{-6}/\mathrm{K}]$$

$$\boldsymbol{E} = \begin{pmatrix} 140.97 & 64.22 & 60.00 & -0.38 & 0.12 & -0.37 \\ 64.23 & 145.69 & 60.73 & 0.53 & 0.12 & 0.19 \\ 59.99 & 60.71 & 123.14 & -0.02 & 0.02 & -0.21 \\ -0.38 & 0.53 & -0.02 & 40.56 & -0.40 & 0.21 \\ 0.12 & 0.12 & 0.02 & -0.40 & 33.23 & 0.07 \\ -0.37 & 0.19 & -0.21 & 0.21 & 0.07 & 33.51 \end{pmatrix} \quad [\mathrm{GPa}]$$

The variation of the predicted properties from the second cell is less than 2%. The tensor elements by the Mori–Tanaka computations differ from the unit cell predictions by a few percent only. Results based on the probability funcitons are transversally isotropic.

Localization

Localization is performed by both approaches. Here, as example, the fields in individual fibers as response to an overall temperature rise of 1K are given. The maximum principal stresses evaluated from both unit cells is of Gaussian type distribution with a minimum of 2.39 and a maximum of 2.93MPa. The analytical approach yields 3.14–3.21MPa and 3.00–3.06MPa for spheroidal and cylindrical fibers, respectively.

CONCLUSIONS

The unit cells are sufficiently large for practical predictions of the composite's behavior, which is indicated by the overall tensors as being nearly transversally isotropic. The analytical approach is shown to be sufficiently accurate for homogenization as well as localization for the studied material system and properties.

References

[1] Duschlbauer D.: Computational simulation of the thermal conductivity of MMCs under consideration of the inclusion–matrix interface. *PhD Thesis*, Vienna University of Technology, Vienna, Austria, 2003.

[2] Böhm H.J., Eckschlager A., Han W.: Multi–inclusion unit cell models for metal matrix composites with randomly oriented discontinuous reinforcements. *Comput.Mater.Sci.* **25**: 42-53, 2001.

[3] Duschlbauer D., Pettermann H.E., Böhm H.J.: Mori–Tanaka based evaluation of inclusion stresses in composites with nonaligned reinforcements. *Scripta Mater.* **48**: 223-228, 2002.

[4] Duschlbauer D., Pettermann H.E., Böhm H.J.: Heat conduction of a spheroidal inhomogeneity with imperfectly bonded interface. *J.Appl.Phys.* **94**: 1539-1549, 2003.

Acknowledgements

The financial support by the Austrian Science Fund (grant P14532-N02) and by the Hochschuljubiläumsstiftung der Stadt Wien (grant H-1048/2002) is gratefully acknowledged.

XXI ICTAM, 15–21 August 2004, Warsaw, Poland

INCLUSION DISPERSION: EFFECTS ON STRESS AND EFFECTIVE PROPERTIES

Jan Schjødt-Thomsen, Ryszard Pyrz
Aalborg University, Inst. of Mechanical Engineering, DK-9220 Aalborg East, Denmark

Summary A 3D stress analysis method based on Mura's eigenstrains and Eshelby's equivalency principle is proposed. Multiple inclusion interaction is considered, and thus the eigenstrains in each inclusion are no longer uniform. The multiple inclusion problem is solved from the governing elasticity equations to give a set of coupled singular integral equations in the unknown eigenstrains of each inclusion. The set of coupled singular integral equations are rewritten using numerical integration, to give a set of algebraic equations in the unknown eigenstrains. For illustrative purposes the inclusions are dispersed in a cubic arrangement of 3 by 3 by 3 inclusions, thus involving 27 inclusions. 4 different inclusion separation distances are considered and in each of the 4 situations 3 different inclusion stiffnesses are considered.
The obtained stresses from the analysis are seen to be highly influenced by inclusion separation. It is found that the "center" inclusion is shielded by the other inclusions and this shielding effect displays a local minimum as the separation distance changes.

INTRODUCTION

Interaction between heterogeneities such as cracks, flaws, reinforcing fibres or particles has been the subject of research for some years and various methods have been proposed. Influence of heterogeneities on the effective properties of the material have been the subject of intensive study and a vast amount of litterature covers this subject, [1-3]. Especially, the determination of local or effective properties of materials with non-dilute volume fractions of heterogeneities calls for solutions which describes interaction adequately. Since, for 3D problems, no closed form solution of the governing equations exist for more than one inclusion, approximations of some kind are needed. The methods of [4] and [5] are somewhat similar to the present approach, however, in this paper no assumptions are made concerning the distribution of eigenstrains in the inclusions. The present paper solves the system of coupled singular integral equations using numerical integration. The theory presented is general, meaning that the composite may be hybrid, i.e. contain different types of inclusions such as pores and/or particles of different stiffness, but results presented are from spherical inclusions with identical stiffness.
The advantage of the present method is that once the eigenstrains have been obtained it is possible to calculate both local stress/strain fields and obtain informations on the overall effective properties of the considered composite. Furthermore, no assumptions regarding the inclusion dispersion is needed, thus the present theory can be used to quantitatively and qualitatively evaluate various statistical dispersions in terms of e.g. extreme values of stress or overall stiffness.

GOVERNING EQUATIONS

The governing equations for the multi inclusion problem is based on Eshelby's equivalency principle. For inclusion I, the equivalency condition is

$$C^I_{ijkl}(\epsilon^\infty_{kl} + \epsilon^I_{kl}) = C_{ijkl}(\epsilon^\infty_{kl} + \epsilon^I_{kl} - \epsilon^{I*}_{kl}) \tag{1}$$

where C^I_{ijkl} and C_{ijkl} are the stiffness tensor of the inclusions and the matrix, respectively. ϵ^∞_{ij} is the applied strain, ϵ^I_{ij} is the induced strain field due to the presence of inclusion I and ϵ^{I*}_{ij} is the equivalent eigenstrain in inclusion I. The induced strain field, ϵ^I_{ij}, is obtained as the sum of the induced strain field from the inclusion itself and the contributions from all the other inclusions present in the representative volume element, (RVE), as

$$\epsilon^I_{ij} = \int_{V^I} K_{ijkl}(\mathbf{x}, \mathbf{x}')\epsilon^{I*}_{kl}(\mathbf{x}')\mathrm{d}\mathbf{x}' + \sum_{R\neq I}^{N} \int_{V^R} K_{ijkl}(\mathbf{x}, \mathbf{x}')\epsilon^{R*}_{kl}(\mathbf{x}')\mathrm{d}\mathbf{x}' \tag{2}$$

where V^I and V^R are the volumes of inclusions I and R, respectively. N is the number of inclusions in the RVE, and $\mathrm{d}\mathbf{x}'$ is an infinitesimal volume element centered at $\mathbf{x}'$. The kernel in the integrals, $K_{ijkl}(\mathbf{x}, \mathbf{x}')$, contains second order derivatives of Green's function $G_{ij}(\mathbf{x}, \mathbf{x}')$ as

$$K_{ijkl}(\mathbf{x}, \mathbf{x}') = -\frac{1}{2}C_{pqkl}[G_{ip,qj}(\mathbf{x}, \mathbf{x}') + G_{jp,qi}(\mathbf{x}, \mathbf{x}')] \tag{3}$$

with

$$G_{ij}(\mathbf{x}, \mathbf{x}') = \frac{1}{16\pi\mu(1-\nu)}\left[\frac{(3-4\nu)\delta_{ij}}{|\mathbf{x}-\mathbf{x}'|} + \frac{(x_i - x'_i)(x_j - x'_j)}{|\mathbf{x}-\mathbf{x}'|^3}\right] \tag{4}$$

where μ and ν are the shear modulus and Poisson's ratio of the matrix material.

The above four tensor equations form a system of $6N$ by $6N$ coupled singular integral equations in the unknown eigenstrains. The first integral in Eq. (2) contain a singularity at $\mathbf{x} = \mathbf{x}'$, which must be removed. This is done by rewriting the

integral as

$$\int_{V^I} K_{ijkl}(\mathbf{x},\mathbf{x}')\epsilon^{I*}_{kl}(\mathbf{x}')\mathrm{d}\mathbf{x}' = \int_{V^I} K_{ijkl}(\mathbf{x},\mathbf{x}')(\epsilon^{I*}_{kl}(\mathbf{x}') - \epsilon^{I*}_{kl}(\mathbf{x}))\mathrm{d}\mathbf{x}' + \left(\int_{V^I} \mathbf{K}(\mathbf{x},\mathbf{x}')\mathrm{d}\mathbf{x}'\right)\epsilon^{I*}_{kl}(\mathbf{x}) \qquad (5)$$

now the first integral on the rigth hand side becomes zero when $\mathbf{x} = \mathbf{x}'$ and the second integral is simply the Eshelby tensor, S_{ijkl}.
Now applying a numerical integration procedure decouples the singular integral equations to a set of algebraic equations in the unknown eigenstrains.

RESULTS AND DISCUSSION

The 3 inclusion stifnesses, E_f, considered are: $E_f = 5E_m$, $10E_m$ and glass particles with $E_f = 73000$ MPa. The Poissons ratios are, $\nu_m = 0.32$ and $\nu_f = 0.3$ and $E_m = 1500$ MPa. The inclusion separation is given in terms of inclusion radius, r, (r =0.01 mm) and the edge-to-edge separation δ, see Fig. 1A. δ in the 4 cases are: $\delta = \frac{r}{10}$, $\frac{r}{5}$, $\frac{r}{2}$ and r. The RVE was applied to the 6 different load cases $\sigma^{\infty}_{ij} = 1$ MPa. In each situation the volume averaged stresses for each inclusion, $\langle\sigma^{(I)}_{ij}\rangle$ is calculated. The volume averaged stress for the "center" inclusion, $\langle\sigma^{(14)}_{11}\rangle$ in the situation of $\sigma^{\infty}_{11} = 1$ MPa is shown in Fig. 1B. The figure shows that inclusion separation has a pronounced effect on the volume averaged stress,

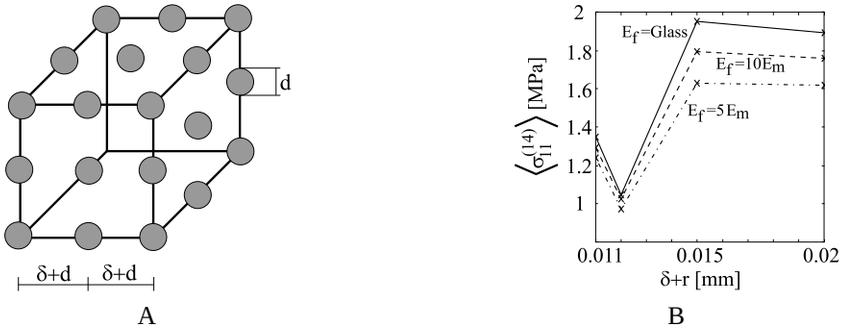


Figure 1. *A) The RVE and B)* $\langle\sigma^{(14)}_{11}\rangle$ *as a function of inclusion separation,* $\delta + r$.

which is what should be expected. However, the interesting feature displayed by Fig. 1B is that at intermediate inclusion separations there is a minimum of average inclusion stress which suggest that for this type of RVE there is an optimal volume fraction of inclusions, at which the inclusions, in an average sense, do not introduce severe stress concentrations. This may be beneficial for designing composites which are less sensitive to failure. The reason for the behaviour of the graph of $\langle\sigma^{(14)}_{11}\rangle$ is due to shielding effects. At small inclusion separations the center inclusion is situated in an area which shields the inclusion, however, the shielding effect becomes more pronounced for slight increases in separation distance, leading to a decrease in stress. Finally, further increase of the inclusion separation diminish the shielding effect and the average stress increases.

CONCLUSIONS

A 3D stress analysis method based on the theory of eigenstrains and Eshelby's equivalency principle has been shown. Multiple inclusion interaction is considered, leading to non-uniform eigenstrains in the inclusions. Volume averaged quantities are readily obtained and the method may be used for calculating both local field quantities and effective properties. An interesting feature displayed by the volume averaged stress,$\langle\sigma^{(I)}_{ij}\rangle$, of the "center" inclusion of the RVE is that at intermediate inclusion separations there is a minimum of inclusion stress which suggest that for this type of RVE there is an optimal volume fraction of inclusions, at which the inclusions, in an average sense, do not lead to severe stress concentrations. This may be beneficial for designing composites which are less sensitive to failure.

References

[1] Nemat-Nasser S., Hori M.: Micromechanics: Overall properties of heterogeneous materials, North-Holland series in applied mathematics and mechanics, 1993.
[2] Suquet P., (Ed.): Continuum Micromechanics, CISM Courses and Lectures No. 377, International Centre for Mechanical Sciences, Springer, 1997.
[3] Mura T.: Micromechanics of Defects in Solids, 2nd. Rev. Ed. Kluwer Academic Publishers, 1993.
[4] Rodin G. J.: The overall elastic response of materials containing spherical inhomogeneities. *Int. J. Solids Structures* **30**:1849-1863, 1993.
[5] Moschovidis, Z.A., Mura, T.: Two ellipsoidal inhomogeneities by the equivalent inclusion method. *J. Appl. Mech.* **42**:847-852, 1975.

THERMAL FATIGUE OF MMC INDUCED BY LASER HEATING

S. G. Long, Y. C. Zhou
Institute of Fundamental Mechanics and Materials Engineering,
Xiangtan University, 411105, Hunan, China

Summary The thermal fatigue of particle reinforced metal matrix composites (MMC) induced by laser heating and applied mechanical load was experimentally and numerically studied. It was found that the initial fatigue damage took place near the edge of laser-irradiated region. The initial damage was the form of the void nucleation, growth and subsequent coalescence in the matrix or the interface separation. The fatigue damage parameters were determined by ultrasonic method. The plane of mechanical load with the times of pulsed laser heating could be divided into three regions, i.e. non-damage region, damage region and failure region. The damage processing was numerically investigated by finite element method. The fields of temperature, macroscopical stress and microscopical stress induced by the laser heating and tensile load were numerically obtained. The simulative results were good agreement with the experimental results.

INTRODUCTION

MMC are excellent candidates for structural components in the aerospace and automotive industries due to their high specific modulus, strength, and thermal stability [1]. The structural components applied for those industries are often subjected to thermal and mechanical loads simultaneously [2]. The thermal and mechanical loads are usually cycled. Thermal load will lead to intense thermal stress concentration in the components of MMC because of the mismatch of thermal and mechanical properties between the metal matrix and ceramic reinforced particle. Such a concentration of thermal stress around defects often results in catastrophic failure of components. Therefore, it is necessary to study the properties of MMC subjected to the combined loads with thermal and mechanical cycled loads.
Generally, the thermal fatigue is produced by quenching method. Here, a new method of multi-pulsed laser beam heating the specimen was used to produce thermal fatigue. In the new method, the rate of temperature rise, i.e. the thermal fatigue intensity, could be easily controlled by adjusting the laser intensity and laser heating region.

EXPERIMENTAL PROCEDURE

SiC particle/6061 aluminum alloy composites was chosen as a model MMC system for this study. The composite with 15-vol. pct SiC was fabricated by melt casting route, and as-cast ingots of the composite were subsequently extruded. The average size of the reinforced particle is $10\mu m$. Fig.1 is the schematic of the specimen configuration. In the figure, the geometrical parameter, a, is the radius of the multi-pulsed laser irradiation region. When the multi-pulsed laser irradiated on the specimen, the mechanical load, i.e. the applied tensile mechanical stress, σ, was applied on the two end of the specimen simultaneously. The frequency, f, of the laser is $10Hz$. The full width, FW, of one pulse laser was $4ms$. The spatial distribution of the laser intensity was non-Gaussian, which was roughly uniform within the laser-irradiated region and declined very sharply toward the edge where the laser spot terminated. The total energy, E, of one pulsed laser is $20J$.

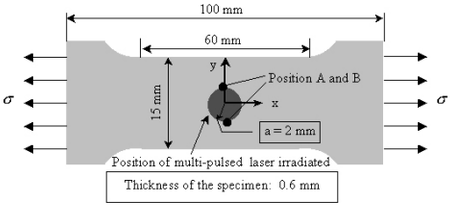


Fig. 1 The schematic of the specimen configuration and loads model

In order to study the evolution of the damage on the surface of the specimen, when the pulsed laser heating times were up to the designed times, the pulsed laser heating was paused. Then the surface of the specimen was observed by SEM and the time of an ultrasonic traveled in the specimen was measured to determine the damage of the specimen. After that, the specimen was again heated and loaded. The surface of the specimen was again observed and the damage was again measured. In this case, the damage evolution of the specimen due to the pulsed laser thermal fatigue and mechanical load could be understood.

EXPERIMENTAL RESULTS

For the thermal load induced by the laser with above parameters and the mechanical load of $\sigma = 100MPa$, after 600 times laser heated, Fig.2(a) shows the microstructure on the surface of the specimen at position A, where the position A is near the edge of laser-heating region as shown in Fig.1. One could find that the damage had taken place and the damage form was the voids in matrix and the debonding of interface. There was no fractured particles. Through much observations, we could have the conclusions that the damage initially took place at the positions A and B as shown in Fig.1, wherein, the initial damage was induced by void nucleation, growth and subsequent coalescence in the matrix or separation of interface. Fig.2(b) shows the microstructure on the surface of the specimen at position A after 1200 times laser heated. One could find that the damage forms were the voids in matrix, the debonding at interface as well as the fracture of particles.

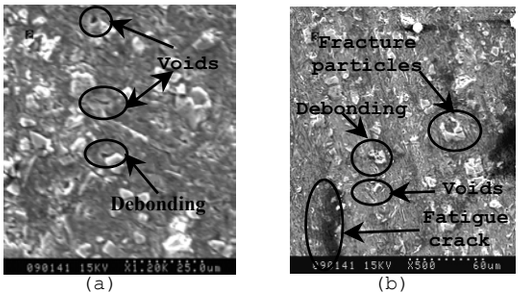


Fig.2 The microstructure on the surface at position A, (a) 600 times laser heating, (b) 1200 times laser heating

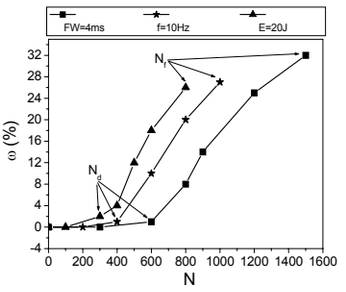


Fig.3 The fatigue damage parameters determined by ultrasonic method

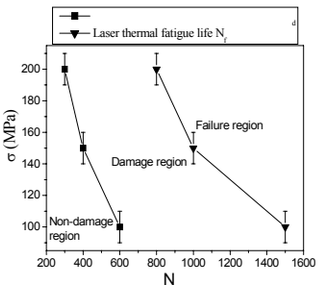


Fig.4 The plane of mechanical load and times of pulsed laser heating

The fatigue damage parameters, ω, were determined by ultrasonic method as shown in Fig.3. It was found that the varied level of the damage parameters was very different for different fatigue stage. According to the fatigue damage curves, the parameters of laser thermal fatigue damage threshold, N_d, and laser thermal fatigue life, N_f, were defined as shown in Fig.3. The plane of mechanical load and times of pulsed laser heating could be divided into three regions, i.e. non-damage region, damage region and failure region as shown in Fig.4.

FINITE ELEMENT SIMULATION

In the simulation, it was assumed that the particle was elastic and the matrix was elastic-plastic. The stress-strain relationships of MMC were dependent on the temperature. Fig.5 shows the stress fields, σ_{xx}, on the laser heating surface at the time of $3ms$. The figure shows that the maximum tensile stress occurred at positions A and B(as shown in Fig.1). Therefore, the damage would initially take place at position A and B. The results are good agreement with the experimental results.

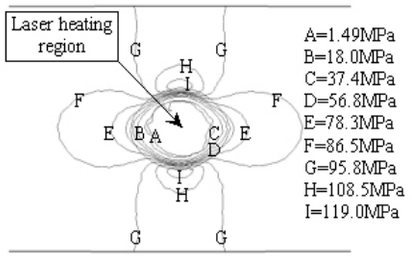


Fig.5 The stress field, σ_{xx}, on the laser heating surface

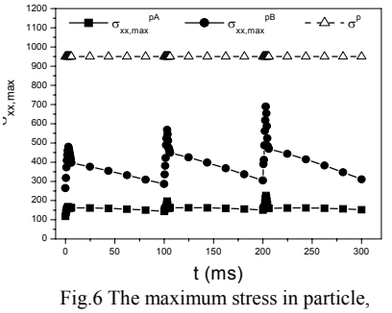


Fig.6 The maximum stress in particle, $\sigma^{p}_{xx,\max}$, and particle strength, σ^{p}

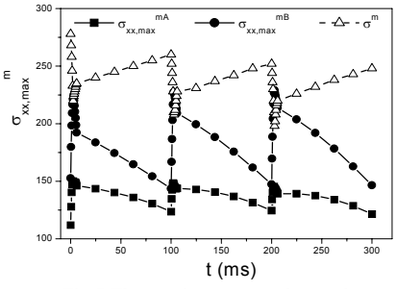


Fig.7 The maximum stress in matrix, $\sigma^{m}_{xx,\max}$ and matrix strength, σ^{m}

Fig.6 is the histories of the maximum stress, $\sigma^{pA}_{xx,\max}$, in the round particle and $\sigma^{pB}_{xx,\max}$, in the square particle as well as the particle strength, σ^{p}. Fig.7 is the histories of the maximum stress, $\sigma^{mA}_{xx,\max}$, in the matrix for round particle model and $\sigma^{mB}_{xx,\max}$, in the matrix for the square particle model as well as the matrix strength, σ^{m}. The figures show that the matrix is more easily damage than particles induced by thermal fatigue and mechanical load and the square particle is more easily fractured than round particle.

CONCLUSIONS

The thermal fatigue of MMC induced by laser heating and applied mechanical load was experimentally and numerically studied. The initial fatigue damage position and form were found. The fatigue damage parameters were determined by ultrasonic method. The plane of mechanical load with the times of pulsed laser heating could be divided into three regions, i.e. non-damage region, damage region and failure region. The damage processing was numerically investigated by finite element method. The simulative results were good agreement with the experimental results.

References

[1] Llorca J.: Fatigue of particle and whisker-reinforced metal matrix composites. Progress Mater Sci 47: 283-353, 2002

[2] Long S. G.: Determination of damage parameter in particle reinforced metal matrix composite by ultrasonic method. J. Mater Sci Lett 22: 911-913, 2003

THERMO-MECHANICAL STABILITY AND VIBRATION ANALYSIS OF COMPOSITE SHELLS

J. Girish and L.S.Ramachandra

Department of Civil Engineering, Indian Institute of Technology, Kharagpur–721302, India.
E-mail: lsr@civil.iitkgp.ernet.in

The postbuckling and postbuckled vibration analysis of curved panels subjected to thermo-mechanical loading is presented here. The formulation is based on the modified Sanders' theory incorporating the geometric nonlinearities. The multi-term Galerkin's technique is used to obtain the true postbuckled shape of curved panels, postbuckled frequencies and associated mode shapes.

The buckling and postbuckling behavior of laminated curved panels (spherical and cylindrical) are investigated extensively and reported in the literature. However, relatively less work has been done in the area of postbuckled free vibration analysis of laminated curved panels under thermo-mechanical loading. Librescu et al. [1-3] presented the analytical results of simply supported single-layer and three-layer flat and curved panels made from transversely isotropic materials. The authors solved the nonlinear boundary-value problem using Airy's stress function and one-term Galerkin's approximation. Most of the analytical results presented in the literature are based on the Donnell approximation. The main advantage of the Donnell approach is the possibility of using Airy stress function F, where the number of unknown functions is reduced from three (u, v, w) to two (w, F). The validity of the w-F formulation vis-à-vis its u-v-w counterpart has been investigated by Sheinman and Goldfeld [4] and showed that the w-F fails to bring out the lowest buckling load accurately.

The postbuckling and postbuckled vibration results of curved panels subjected to thermo-mechanical loading are presented here. The formulation is based on the modified Sanders' theory incorporating the geometric nonlinearities. The higher-order shear deformation displacement field used in the present study is that of Reddy and Liu [5], which accounts for parabolic distribution of the transverse shear strains through thickness of the shell and tangential stress-free boundary conditions on the boundary surfaces of the shell.

Adopting Galerkin's procedure, the governing nonlinear partial differential equations are converted into a set of nonlinear algebraic equations in the case of postbuckling analysis and nonlinear ordinary differential equations in the case of free vibration analysis. The critical buckling temperature is obtained from the solution of linear eigenvalue problem. The postbuckled equilibrium paths are obtained by solving the nonlinear algebraic equations, using the Newton-Raphson iterative procedure. In the case of free vibration analysis of buckled panel, the solution of differential equations is assumed to be the sum of time dependent solution (vibration amplitude) and time independent solution (postbuckling deflection). The vibration amplitude is considered small compared to the postbuckled deflection and hence higher order time dependent terms are neglected. The free vibration frequencies of a postbuckled shell panel about the static equilibrium state are obtained by solving the eigenvalue problem for different postbuckled deflections. Numerical results are presented for curved composite panels with and without initial geometric imperfections. The modal participation of each mode in the postbuckling deflection is obtained using multi-term Galerkin's procedure. The results show the thermo-mechanical load interaction on buckling, limiting points and snap-through buckling. Apart from the fundamental mode, higher vibration modes of curved panels about the prebuckling and postbuckling equilibrium states subjected to thermo-mechanical loading are presented.

Response of doubly curved shell panels subjected to thermo-mechanical loads: The nonlinear equilibrium paths of doubly curved symmetric [*0/90/0*] cross-ply shell panels under combined uniform temperature distribution (T in ^{o}C) and sinusoidal distributed lateral load are presented in Fig 1. The simply supported immovable edge boundary conditions are considered at all edges. The curves are plotted showing the variation of nondimensional load parameter q^* with nondimensional central deflection (w/h). Fig. 2 shows the fundamental frequencies of a doubly curved shell corresponding to the static equilibrium paths shown in the Fig 1 where, ω_o represents the fundamental frequency of unloaded shell. The imaginary frequencies below the abscissa shown in the figure 2 correspond to unstable equilibrium paths shown in the Fig.1.

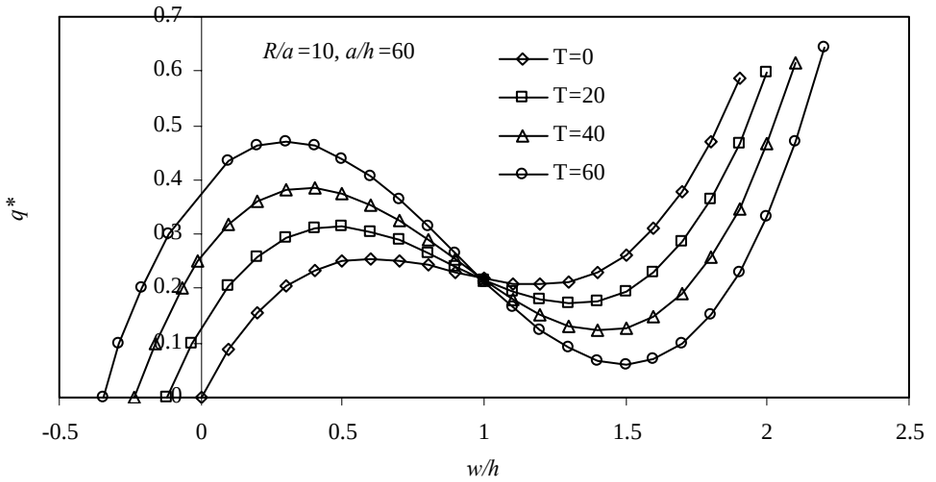


Figure 1: Response of doubly curved shell panel [*0/90/0*] subjected to thermo mechanical loads. (a/b = 1, $R_1 = R_2 = R$, $q^* = q_0 R_2/E_2 h^2$, $E_1 = 25E_2$, $G_{12} = G_{13} = 0.5E_2$, $G_{23} = 0.2E_2$, $\nu_{12} = 0.25$, $\alpha_2/\alpha_1 = 3$)

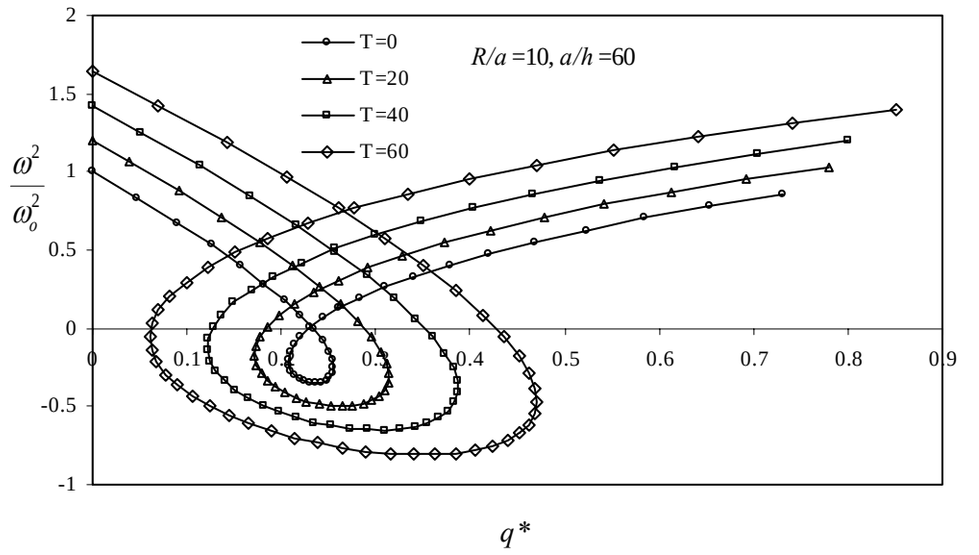


Figure 2: The influence of uniform temperature distribution on the fundamental frequencies of symmetric cross-ply spherical shell panel under sinusoidal distributed load.

References:

[1] Librescu, L., Lin, W., Nemeth, M. P., and Starnes, J. H., "Vibration of Geometrically Imperfect Panels Subjected to Thermal and mechanical Loads", *Journal of Spacecraft and Rockets*, vol. 33, No. 2, 1996, pp. 285-291.

[2] Librescu, L., Lin, W., Nemeth, M. P., and Starnes, J. H., "Frequency-Load Interaction of Geometrically Imperfect Curved Panels Subjected to Heating", *AIAA Journal*, vol. 34, No. 1, 1996, pp. 166-177.

[3] Librescu, L., and Lin, W., "Vibration of Thermomechanically Loaded Flat and curved Panels Taking into Account Geometric Imperfections and tangential Edge Restraints", *Int. J. of Solids Structures*, vol. 34, No. 17, 1997, pp. 2161-2181.

[4] Sheinman, I., and Goldfeld, Y., "Buckling of Laminated Cylindrical Shells In Terms of Different Theories and Formulations", *AIAA Journal*, vol. 39, No. 9, 2001, pp. 1773-1781.

[5] Reddy, J.N., and Liu, C. F., "A Higher-Order Shear Deformation Theory of Laminated Elastic Shells", *Int. J. Engng Sci*, vol. 23, No. 3, pp. 319-330.

New Trends in Optimal Design of Composite Materials

Aleksander Muc, Marcin Trzebicki
Institute of Machine Design, Cracow University of Technology, Kraków, Poland

Introduction

The current trends in machine design demonstrate evidently that a centre of gravity is continuously moved/shifted from a structural design towards a material design mainly due to an increasing number of new materials (e.g. micro- and nano-composites, functionally graded materials etc.) and a development of new technologies enabling us to produce better and quicker required machines. On the other hand, the material design is mainly directed to the design of a strictly limited group of structures subjected to prescribed boundary and loading conditions and of course such a design should be in advance planned as an optimal one. However, it is worth to emphasise that the optimal material design should take into account not only the required functional properties of designed machines but also the availability and limitations of technological processes and their influence on the final mechanical properties of products.

The aim of the paper is two-fold: (1) to show the possibility of optimisation of technological processes in order to eliminate or to enhance the effects of induced internal stresses/strains during production of multilayered composite structures and (2) using homogenisation approach to periodic structures to discuss the problem of a fibre shape optimisation in order to obtain the required composite material properties. Both problems are analysed in the elastic range only using variational formulations with Lagrange coefficients.

The influence of technological processes

The automated technological processes such as e.g. the resin injection moulding (RIM) or the resin transfer moulding (RTM) introduce internal stresses/strains due to different thermal and chemical shrinkage of fibres and matrices – see Refs [1,2]. The chemical and physical properties of fibres and matrices do not allow to eliminate those effects completely, however, it is possible to reduce them taking into consideration various technological factors – an external pressure is one of them. Using a general formulation for 3-D orthotropic bodies with internal stresses λ_i the stress-strain relations takes the following form:

$$\Omega = \Omega_f \cup \Omega_m \tag{1}$$

The above relation is used to build the functional of total potential energy Π:

$$\Pi = \tfrac{1}{2}\int_{\Omega} \sigma[u(\lambda)]C^{-1}\sigma[u(\lambda)]d\Omega - \int_{\Gamma} pu(\lambda)d\Gamma - \sum_{i=1}^{n} \omega_i A_i\left(\sigma_i^{ad} - \sigma_i - s_i\right) \tag{2}$$

where Ω denotes the space occupied by the body having the boundary Γ, p is an external pressure applied to bond together individual composite plies, ω_i are Lagrange's multipliers, A_i means the area of individual plies and $\left(\sigma_i^{ad} - \sigma_i - s_i\right)$ is a condition of an interlaminar bonding and it has one uknown paramter s_i. The optimisation problem is formulated in the following way:

To find:

$$Min\Pi \tag{3}$$

subjected to constraints:

$$\lambda \le \lambda_0 \tag{4}$$

The constraint condition (4) may be valid for all layers in the laminate or for individual layer.

Using the above formulation the minimisation problem (3) have been solved for multilayered orthotropic plates and cylinders. In mathematical terms the problem is reduced to a system of non-linear algebraic equations. The results demonstrate evidently the possibility (or even necessity) of equalization of internal stresses or possible redistribution of them between layers. Having an information about the required internal stress distribution in the laminate and knowing the functional relation between internal stresses/strains and the parameters of the technological process one can find the optimal set of parameters. The latter problem have been illustrated on the example of the optimal choice of the external pressure distribution.

Shape optimisation of a fibre bundle

In unidirectional composites fibres are not made individual fibres but they constitute in fact a bundle of fibres that is embedded in a matrix material. Using a homogenisation theory for periodic structures a shape of a bundle in each of subcells is assumed/prescribed a priori and it depends on the assumed homogenisation method, i.e. the bundle boundary $\Gamma=\partial\Omega_f$ can be described by a circle, a square, a rectangle or other curve. For our purposes the Suquet homogenisation theory [3] is applied herein. In general, it is based on the introduction of the tensor A. For a given subcell ($\Omega = \Omega_f \cup \Omega_m$)the functional of the total potential energy can be expressed as follows:

$$\Pi = \tfrac{1}{2}\left[C^m_{ijkl} + \left(C^f_{ijkl} - C^m_{ijkl}\right)\left\langle A_{kl\alpha\beta}\right\rangle\right]\varepsilon_{\alpha\beta}\varepsilon_{ij} + \omega\left(\int_{\Omega_f} d\Omega - V_f\right) \tag{5}$$

where the superscripts (or subscripts) f, m corresponds to fibre and matrix, respectively, and V_f means the fibre volume fraction. The optimization problem is formulated in the following way:
For the given displacement field minimize the functional (5) subject to the constraint in the form of the constant fibre volume fraction.
In this way it is possible to control the shape of the bundle of fibres, however, it should be mentioned that the above problem requires additional constraints that refer mainly to the method of composite material production. The bundle of fibres is filled (penetrated) by a matrix material (a resin) and cannot be too thin. Therefore, we propose to introduce the additional condition dealing with the convexity of the boundary Γ. The problem has been formulated in 2-D space. The initial shape of the bundle is assumed in the form of a circle – see Fig.1. The differences in the optimal solutions for two formulations (convex and non-convex boundary) are shown in Fig. 1. The problem has been solved with the use of the FE package NISA II. The bundle boundary is modelled with the help of Bezier's splines. The optimisation method is analogous to that described in Ref. [4]. As it may be seen the additional constraint drastically changes the optimal solutions. However, in order to be closer to practical situations, it is necessary to take also into account the interface layer surrounding fibres. It may have a great influence on a possible failure of composites but its mechanical properties and size are uknown in advance.

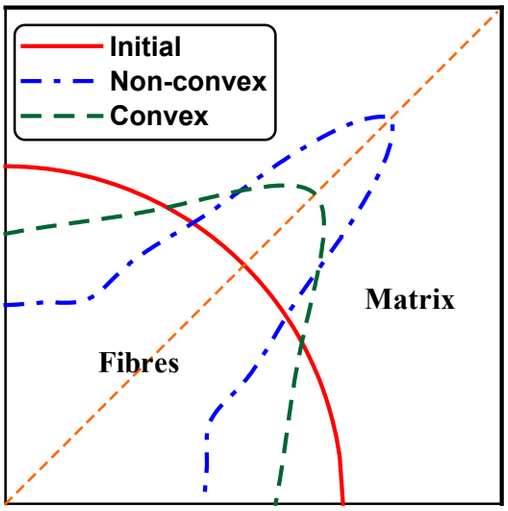


Fig.1 Optimal distributions of fibres in an elementary subcell (a quarter).

References

1. A. Muc, P. Saj, *Structural Optimization*, **25**, 2003, pp.1-10 (in print).
2. A. Muc, *Proc. ICCM/14*, San Diego 2003.
3. P. M. Suquet, *Lecture Notes in Physics*, **272**, 1987.
4. A. Muc, W. Gurba, Composite Structures, **54**, 2001, pp. 275-281.

AN ANISOTROPIC DAMAGE MODEL FOR THE PREDICTION OF THE DEGRADATION BEHAVIOUR OF NOVEL TEXTILE REINFORCED COMPOSITES

Werner Hufenbach, Robert Boehm, Albert Langkamp
Technische Universitaet Dresden, Institut für Leichtbau und Kunststofftechnik (ILK), D-01062 Dresden, Germany

Summary Novel textile reinforced composites are very suitable for applications in lightweight structures, since they can resist high mechanical and thermal load. In this paper a phenomenological damage-mechanics-based model for these composites is presented. Damage variables are introduced to describe the evolution of the damage state and as a subsequence the degradation of the material stiffness. Special emphasis is given to the interaction between fibre failure due to fibre stress and matrix failure due to transverse and shear stress. The predictive capability of the presented model is evaluated by carrying out a series of tensile tests using acoustic emission techniques to detect the strength and the failure behaviour of CF/PEEK, GF/RP and CF/RP. The performance of the model strongly depends on the correct determination of the material parameters. Thus, model parameters may be determined either by experimental measurement, by micromechanical models or by crack density studies.

INTRODUCTION

The optimum utilisation of special multi-axial textile reinforcement, in particular, could make a significant contribution to developments of highly innovative lightweight structures, which will be of great interest not only from a scientific-technical, but also from an economic point of view. The component optimisation requires adapted analytical and numerical simulation techniques as well as suitable realistic failure criteria which take into account the occurring damage mechanisms. Composite failure conditions have to cover the full failure behaviour, fracture conditions and the non-linear analysis of the degradation behaviour within the composite. Though, in recent years first investigation has been undertaken to determine the damage mechanisms and the degradation behaviour of textile reinforced composites. MATZENMILLER et al. [1] proposed a model, based on continuum damage mechanics, for the non-linear analysis of fiber composites. LANGKAMP [2] proposed a method that enables the use of physically based failure criteria for the description of the initial fracture of textile-reinforced composites. The phenomenological failure model [2] and the degradation model [1] are combined to describe the degradation behaviour of braided composites, of glass-fibre reinforced multi-layered composites and of multi-layered carbon fibre reinforced PEEK [3]. However, the performance of all these models strongly depends on the correct determination of the introduced damage parameters. On this account, special emphasis in this work is given to the experimental observation of stiffness loss and crack initiation.

PHENOMENOLOGICAL ASPECTS OF DAMAGE IN TEXTILE COMPOSITES

In recent years, novel textile reinforcements, composed of multi-axial reinforcing layers have been developed (Fig. 1). The reinforcing yarn systems provide a high composite strength and stiffness as well as a very good impact behaviour of the composite material.

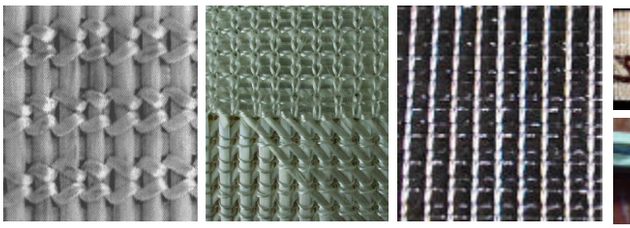


Fig. 1: Different textile preforms for composite applications

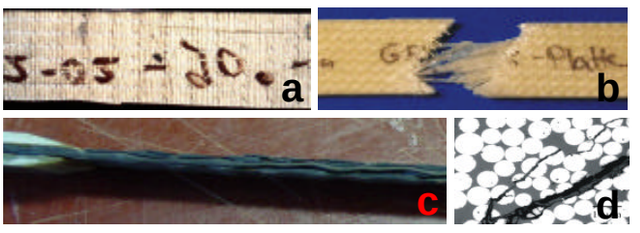


Fig. 2: Experimentally observed failure modes in textile reinforced composites

Due to the complexity of the geometry and the fracture mechanisms of these heterogeneous textile reinforced composites, a convenient structural failure analysis causes extensive difficulties, since the micro-structural configuration is of vital importance for the description of the degradation behaviour. It becomes apparent that a successful damage analysis initially requires a phenomenological determination of all occurring damage mechanisms. Although matrix micro-cracking (Fig. 2a) is normally not the most important failure mode of a textile composite structure, it can trigger fibre failure (Fig. 2b), delamination (Fig. 2c) or compressive failure (Fig. 2d), which is far more important in practical cases.

FAILURE CRITERIA

In order to formulate physically based fracture conditions, different fracture modes, namely „fibre failure“ (FF) and „inter-fibre failure“ (IFF), have to be distinguished. On the basis of the assumption that fracture is determined by the stresses of the fracture plane, the proposed criterion records the failure modes FF and IFF by different failure conditions, which take into account only the acting stresses in the fracture plane. It is assumed that FF is solely initiated by the fibre-parallel stress $s_1^{\pm}$ and remains unaffected by other stresses that occur:

$$\left(\frac{s_1}{g_{\parallel}^{(\pm)} R_{\parallel}^{(\pm)}} \right)^2 = 1.$$

The fracture conditions for IFF are, in comparison to the FF criterion, clearly more complex as different types of failure such as adhesive failure of the fibre-matrix interface or cohesive failure of the matrix as well as different failure modes such as tension, longitudinal shear and cross-sectional shear failure need to be realistically described. The failure initially occurs parallel to the fibres in a plane variable with the fracture angle q_B. The associated failure criterion then results in the following general formulation

$$\max_q F(s_n, t_{nt}, t_{n1}) = 1.$$

DAMAGE MECHANICS MODEL

The stress-strain response of textile reinforced composites is known to be non-linear especially for shearing. However, linear elasticity is assumed to hold if the damage state does not change. All non-linear effects are attributed to damage. The microscopic damage phenomena are represented by internal damage variables (D_{11}, D_{22}, D_s) which describe the effects of these microdefects on the macroscopic or mesoscopic scale. The unknown damage variables are treated as phenomenological variables, since they have no direct relation to the micromechanical phenomena. In this case, plane stress conditions (CLT) are assumed adequate to model the stress-strain behaviour of the textile composite:

$$\tilde{\boldsymbol{C}}(\boldsymbol{D}) = \begin{bmatrix} \tilde{C}_{11} & \tilde{C}_{12} & 0 \\ \tilde{C}_{21} & \tilde{C}_{22} & 0 \\ 0 & 0 & \tilde{C}_{66} \end{bmatrix} = \frac{1}{d} \begin{bmatrix} (1-D_{11})E_{\parallel} & (1-D_{11})(1-D_{22})n_{21}E_{\perp} & 0 \\ (1-D_{11})(1-D_{22})n_{12}E_{\parallel} & (1-D_{22})E_{\perp} & 0 \\ 0 & 0 & d(1-D_s)G \end{bmatrix}$$

The proposed failure criteria act as damage threshold for the damage mechanics model. Since the different physical nature of the degradation parameters is clear (D_{11} as degradation parameter due to fibre damage, D_{22} as degradation parameter due to matrix cracking and D_s as the shear degradation parameter), it is possible to determine the damage evolutions laws experimentally.

EXPERIMENTAL INVESTIGATION AND RESULTS

The phenomenological method consists of measuring the internal structural changes by their effects on the mechanical response. Since direct measurement of damage in textile composites is not feasible, an adapted acoustic emission (AE) technique is used to classify and qualitatively analyse the occurring damage mechanisms. The capability of acoustic emission analysis to determine matrix micro-cracking, fibre failure and fibre-matrix debonding will be shown. Additionally, the change of the effective elastic constants has been measured using long-range strain-twist extensometers. The experimentally measured curves have been approximated by the stress-strain curve resulting from the failure calculation. Examples of the predictions of the proposed model will be given.

CONCLUSIONS

The demand for a high degree of lightweight design is, for scientific and technical interests, increasingly becoming the focus of design efforts in the development of a new generation of textile reinforced structural components. Currently, in the sense of developing practical composite failure conditions, endeavours have not only focused on a realistic description of the initial failure but also on the non-linear analysis of novel textile reinforced composites. The proposed results are of the greatest practical significance for innovative developments in high-performance lightweight applications.

References

[1] MATZENMILLER, A.; LUBLINER, J.; TAYLOR, R.L.: *A constitutive model for anisotropic damage in fiber-composites*. Mech. Mater., Vol. 20, 1995, No. 2, p. 125-152.

[2] LANGKAMP, A.: *Bruchmodebezogene Versagensmodelle von faser- und textilverstärten Verbundwerkstoffen mit polymeren, keramischen sowie metallischen Matrices.* Dissertation, TU Dresden, 2002

[3] HUFENBACH, W.; LANGKAMP, A.; KROLL, L.; BÖHM, R.: *Experimental investigation and modeling of failure and damage behaviour of multi-layered carbon fibre reinforced PEEK* 14th. International Conference on Composite Materials (ICCM 14), San Diego, July 14th–18th 2003, published on CD-ROM

ASYMPTOTIC STUDY OF IMPERFECT INTERFACIAL BONDING IN PERIODIC COMPOSITE MATERIALS

Igor V. Andrianov [*], Vladyslav V. Danishevs'kyy [**], Dieter Weichert [*]
[*] *Institute of General Mechanics RWTH, Templergraben 64, Aachen 52062, Germany*
[**] *Prydniprovska State Academy of Civil Engineering and Architecture, 24-a Chernyshevskogo St., Dnipropetrovsk 49600, Ukraine*

Summary An asymptotic approach for analytical study of the mechanical behaviour of composite materials is proposed. We start with the asymptotic homogenization method. The cell problem is solved by means of a boundary perturbation technique. In order to simulate the phenomenon of the imperfect interfacial bonding we introduce an artificial layer between the components and tend its thickness to zero. As the results effective moduli and local stresses are evaluated for all values of the components' volume fractions and properties.

INTRODUCTION

Effects of imperfect bonding between components play a crucial role in the functionality and reliability of composite materials. It is evident that partially debonded composites are characterized by weaker effective moduli than perfectly bonded ones. Moreover, low strength of the interface between inclusions and a matrix can also significantly change the behaviour of the structure on micro level. In most cases a weak interface response leads to the development of dislocations and voids, which dramatically decreases the strength of the whole material.

Simulation of the imperfect bonding attract considerable attention of many authors. Important results are obtained for prediction of the debonding evolution from initial decohesion through complete separation with a subsequent voids' growth. For this aim Needleman [1] has proposed a specific potential function governing the mechanical response of the interface depending on the displacements' jump across it. Needleman's model has received further development in number of papers of other authors. This interface's description is a phenomenological one, and for its practical implementation it is necessary to know a number of input parameters: the maximal interfacial traction, characteristic lengths of the interfacial displacements and the interface's shear-to-normal strength ratio, which are expected to be determined in experimental way.

In the present paper a new asymptotic approach for simulation of the imperfect interfacial bonding is proposed. We introduce between the components an artificial intermediate layer and tend its thickness to zero. In the asymptotic limit varying the elastic properties of this layer we are able to simulate different types of the interface response. The basic idea of our interface model is in certain sense similar to the approaches proposed by Benveniste & Miloh [2] and Hashin [3], who also considered a thin coating layer between the components for a description of imperfect bonding. However, in contrast to the previous investigations, an advantage of our work is the possibility to develop analytical solutions valid for all degrees of the debonding and for all values of the components' volume fraction and stiffness.

COMPOSITE MATERIALS UNDER CONSIDERATION

As an illustrative example we consider a longitudinal shear deformation of composites consisting of isotropic matrixes and regular square and hexagonal arrays of circular fibres. This stress-strain state may correspond to torsion of the fibre-reinforced bar about the longitudinal axis. In order to simulate the phenomena of imperfect interfacial bonding an artificial intermediate layer of a volume fraction c_0 and a non-dimensional rigidity λ_0 is introduced between the components. We derive a solution for such three-component structure and finally tend $c_0, \lambda_0 \to 0$. Then in the asymptotic limit the intermediate layer disappears and depending on the ratio λ_0/c_0 we can simulate different types of the interface response and describe different rates of debonding. The non-dimensional debonding parameter is $\alpha = (1+\lambda_0/c_0)^{-1}$. Here $\alpha = 0$ corresponds to the perfect interfacial bonding, $\alpha = 1$ corresponds to the complete separation of the matrix and inclusions, any value of α between zero and one represents imperfect bonding. From the mechanical point of view the proposed asymptotic model corresponds to the equality of stresses across the interface (the equilibrium condition of the medium is satisfied) and to a jump of displacements (the continuity condition is not satisfied so that a certain sliding occurs).

THE ASYMPTOTIC PROCEDURE

We start with the asymptotic homogenization method [4, 5], which allows to separate *slow* and *fast* components of the solution. *Slow* components describe the behaviour of the composite on macro level, within the whole sample of the material. *Fast* ones represent local oscillations of stresses and displacements on the scale of heterogeneities and correspond to the micromechanical response of the inhomogeneous medium. *Fast* components should be determined from a so called cell boundary value problem, which is considered within one distinguished periodically repeatable unit cell of the composite structure. We derive an approximate analytical solution of the cell problem by means of the

boundary perturbation method [6]. Knowing the local stresses we can predict the appearance of plastic domains and evaluate the effective elastic moduli.

The developed analytical solutions are valid for all values of the inclusions' volume fraction and properties. In particular, they work well in cases when rapid oscillations of stresses occur on micro level (e.g., in the case of perfectly rigid nearly touching fibres, in the case of inclusions with considerably thin coating etc.), when FEM simulation may face principal difficulties.

NUMERICAL RESULTS

At Fig. 1 we present numerical results for the effective longitudinal shear modulus $\langle G \rangle$ (normalized to the shear modulus of the matrix G_1) for the square array of circular fibres (fibres' volume fraction c_2 varies from 0 to $\pi/4$). Data for different values of the debonding parameter α are displayed. In the case of perfect bonding ($\alpha = 0$) the present solution (solid curves) is compared with the results of Perrins et al. [7] (boxes). In the case of complete debonding ($\alpha = 1$) inclusions do not take part in the longitudinal shear deformation, so the solution shows a good agreement with the results for fibrous holes ($G_2/G_1 = 0$, G_2 is the shear modulus of the fibres) [7].

The distribution of the interfacial stress τ_0 (normalized to the homogenized stress $\langle \tau \rangle$) with respect to the polar angle θ is shown in Fig. 2. The data for only a quarter of the unit cell ($\theta = -\pi/4 ... \pi/4$) are displayed, for other values of θ the interfacial stress τ_0 continues periodically. It can be easily seen that for a perfectly bonded composite with rigid fibres ($G_2/G_1 > 1$) τ_0 reaches maximum in the points $\theta = \pi n/2$, $n = 0, 1, 2...$, where the distance between neighbouring fibres is minimal (i.e., interaction between the fibres is maximal). These results allow us to predict the appearance of plastic areas and to calculate the effective initial yield limit, which corresponds to the beginning of the plastification in the composite medium.

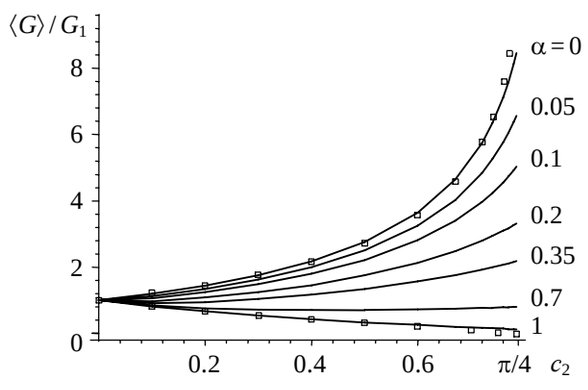


Fig. 1. Effective shear modulus $\langle G \rangle$; $G_2/G_1 = 20$.

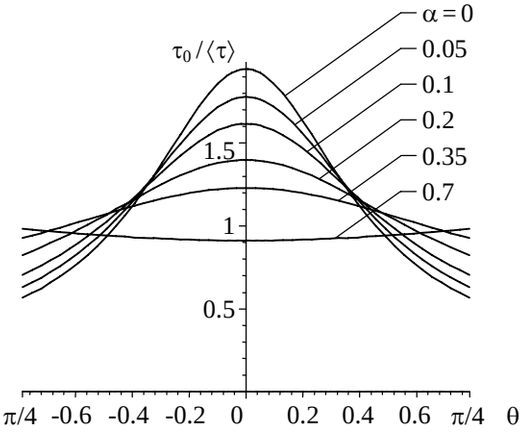


Fig. 2. Interfacial stresses τ_0; $G_2/G_1 = 20$, $c_2 = 0.72$.

CONCLUSIONS

An asymptotic approach for analytical study of the mechanical behaviour of composite materials is proposed. We start with the asymptotic homogenization method. The cell problem is solved by means of a boundary perturbation technique. In order to simulate the phenomenon of the imperfect interfacial bonding we introduce an artificial layer between the components and tend its thickness to zero. As the results effective moduli and local stresses are evaluated in the whole range of the components' volume fractions and properties. The developed approach may be extended to study of different stress-strain states of various periodically inhomogeneous media.

References

[1] Needleman A.: A continuum model for void nucleation by inclusion debonding. *J. Appl. Mech.* **54**: 525-531, 1987.

[2] Benveniste Y., Miloh T.: Imperfect soft and stiff interfaces in two-dimensional elasticity. *Mech. Mater.* **33**: 309-324, 2001.

[3] Hashin Z.: Thin interface / imperfect interface in elasticity with application to coated fibre composites. *J. Mech. Phys. Solids* **50**: 2509-2537, 2002.

[4] Andrianov I.V., Danishevs'kyy V.V., Weichert, D.: Asymptotic determination of effective elastic properties of composite materials with fibrous square-shaped inclusions. *Eur. J. Mech. Solids* **21**: 1019-1036, 2002.

[5] Manevitch L.I., Andrianov I.V., Oshmyan V.G.: Mechanics of Periodically Heterogeneous Structures. Springer, Berlin 2002.

[6] Guz A.S., Nemish Yu.N.: Method of Boundary Perturbations in Mechanics of Solids. Vyscha Shkola, Kyiv 1989. (in Russian)

[7] Perrins W.T., McKenzie D.R., McPhedran R.C.: Transport properties of regular arrays of cylinders. *Proc. R. Soc. Lond. A* **369**: 207-225, 1979.

T-INCLUSION REGIONS FOR THE EFFECTIVE TRANSPORT COEFFICIENTS OF TWO–PHASE MEDIA

S. Tokarzewski, A. Gałka, B. Gambin, J.J. Telega.
Polish Academy of Sciences IPPT PAN, Świętokrzyska 21, 00–049 Warsaw, Poland

Summary By starting from power series expanded at a number of real points and infinity we derive the fundamental inclusion relations for the special T-inclusion regions estimating in the complex domain the effective transport coefficients of two-phase media. The T- inclusion regions derived are new and the best over the entire class of rational functions and the given input data. For a particular cases they reduce to the classical complex bounds derived by Bergman [1] and Milton [2], and rederived in a different manner by Tokarzewski and Telega [4]. Nontrivial numerical examples illustrating the results obtained are also provided..

FORMULATION OF THE MATCHING PROBLEM

A macroscopic modelling of microinhomogeneous media and composites requires the evaluation of effective moduli. However their exact values are available only in specific cases; for instance in the one-dimensional periodic homogenization. In the relevant literature many papers deal with estimating of the effective coefficients of two-phase media, such as dielectric constants, magnetic permeabilities, thermal and electrical conductivities.

Assume that the macroscopic response $q_{ef}(z)/q_1,\ z=h-1,\ h=q_2/q_1$ of two-phase composite is isotropic, where q_1 and q_2 characterize the mechanical properties of two materials the composite is made of. The following problem arises: how to determine the best bounds on $q_{ef}(z)/q_1$ in terms of its power expansions at finite number of real points $x_1, x_2,\ ...,\ x_N<\infty$ and at infinity?

It is well known that the effective transport coefficient of a two-phase medium with macroscopically isotropic symmetry has a Stieltjes integral representation given by

$$f_1(z)=\frac{Q(z)-1}{z}=\int_0^1\frac{d\gamma_1(u)}{1+zu},\ d\gamma_1(u)>0,\ z=h-1,\ h=\frac{q_2}{q_1},\ Q(z)=\frac{q_{ef}(z)}{q_1};\ f_1(-1)\le 1. \tag{1}$$

Let the truncated power expansions of $f_1(z)$ at $x_1,\ x_2, ...,\ x_N,\ \infty,\ -1$

$$f_1(z)=\sum_{i=0}^{p_j-1}c_{ij}(z-x_j)^i+O((z-x_j)^{p_j}),\ j=1,2,...,N;\quad f_1(z)=\frac{1}{z}\sum_{i=0}^{p_{N+1}-1}c_{i(N+1)}\left(\frac{1}{z}\right)^i+O\left(\frac{1}{z}\right)^{p_{N+1}}$$
$$f_1(z)=f_1(-1)+O(z+1);\ f_1(-1)\le 1 \tag{2}$$

be given, where $-1<x_j,\ j=1,2,...,N+1$. We use the following notation

$$f_1(z)=f_1|_{\boldsymbol{x}}^{\boldsymbol{p}}(z-\boldsymbol{x})+O(z-\boldsymbol{x})^{\boldsymbol{p}},\ \boldsymbol{x}=[x_1,x_2,...,\infty,-1],\ \boldsymbol{p}=[p_1,p_2,...,p_\infty,1],\ f_1(-1)\le 1. \tag{3}$$

Problem *By starting from the power expansions (3), construct in a complex plane the general T-inclusion regions estimating both the Stieltjes function $f_1(z)$ and via (1_1) the effective coefficient $Q(z)$ of the two-phase composite.*

T-INCLUSION REGIONS

In the first step the inequality $f_1(-1)\le 1$ is replaced by the equality $f_1(-1)=1$, cf. (3). The input data (3) transform to

$$f_1(z)=f_1|_{x_1,...,\infty,1}^{p_1,...,p_\infty,1}(z-\boldsymbol{x})+O(z-\boldsymbol{x})^{\boldsymbol{p}},\quad f_1(-1)=1. \tag{4}$$

Next by introducing $P_0=0,\ P_j=\sum_{i=1}^j p_i,\ j=1,2,...,N;\quad P=2P_N+1$ and using linear fractional transformation of type T we expand the given Stieltjes function $f_1(z)$ to the new Stieltjes one $f_{P_\cdot}(z)$:

$$\begin{aligned}
&f_{P_0+1}(z)=\frac{f_{P_0+1}(x_1)}{1+(z-x_1)f_{P_0+2}(z)},\ =\frac{f_{P_0+1}(x_1)}{1+(z-x_1)G_{P_0+2}+(z-x_1)f_{P_0+3}(z)},\ ...,f_{P_1-1}(z)=\frac{f_{P_1-1}(x_1)}{1+(z-x_1)G_{P_1}+(z-x_1)f_{P_1+1}(z)},\\
&f_{P_1+1}(z)=\frac{f_{P_1+1}(x_2)}{1+(z-x_2)f_{P_1+2}(z)},\ =\frac{f_{P_1+1}(x_2)}{1+(z-x_2)G_{P_1+1}+(z-x_2)f_{P_1+2}(z)},\ ...,\ f_{P_2-2}(z)=\frac{f_{P_2-1}(x_2)}{1+(z-x_2)G_{P_2}+(z-x_2)f_{P_2+1}(z)},\\
&\cdots\cdots\cdots

$\Phi_P(z)$ should incorporate all admissible values of the Stieltjes functions $f_1(z)$ matching the input data (3). Hence we have

$$f_1(z) \in \Phi_P(z) = \{F_P(z,u);\ 0 \le v \le 1,\ -1 \le u \le 1\}\,,$$
$$F_P(z,u) = f_{1\,x_1,\ldots,\infty\,,1}^{\,p_1,\ldots,p_\infty,1}(z, vw_pF_0(z,u)),\ F_0(z,u) = (1+u \text{ if } -1 \le u \le \text{ and } \tfrac{1-u}{1+zu} \text{ if } 0 \le u \le 1). \tag{7}$$

Here $F_0(z,u)$ is called the elementary bounding function. It consists of two lines, the straight line $1+u$ if $-1 \le u \le 0$ and the arc of the circle $(1-u)/(1+zu)$ if $0 \le u \le 1$, see (7_2).

FUNDAMENTAL RELATIONS FOR T-INCLUSION REGIONS

Now we are prepared to formulate the main result of this contribution reading by the following theorem:.
Theorem 1. *Let the truncated power expansions of Stieltjes function* $f_1(z)$

$$f_1(z) = f_1|_{\boldsymbol{x}}^{\boldsymbol{p}(k)}(z-\boldsymbol{x}) + O(z-\boldsymbol{x})^{\boldsymbol{p}(k)},\ \ \boldsymbol{x} = [x_1, x_2, ..., x_N, \infty, -1]\,,\ \boldsymbol{p}(k) = [p_1(k), p_2(k), ..., p_\infty(k), 1] \tag{8}$$

be given, where $k = \sum_{j=1}^{N} p_j + p_\infty + 1$. *Then T-inclusion regions* $\Phi_{p(k)}(z)$ *generated by the truncated series (8) satisfy the following fundamental relations*

$$f_1(z) \in \Phi_{P(k)}(z) \subset \Phi_{P(k-1)}(z),\ k = 2, 3, \ldots\,,. \tag{9}$$

provided $p(k) \le p(k+1),\ k = 1, 2, ...,$ *i.e.* $p_j(k+1) - p_j(k) \ge 0,\ j = 1, 2, ...$ *These inclusion relations imply that the best* $\Phi_{P(k)}(z)$ *estimate of* $f_1(z)$ *is obtained using only the given number of power series coefficients (*k *is fixed) and that the use of additional coefficients (higher* k*) improves the estimate* $\Phi_{P(k)}(z)$.

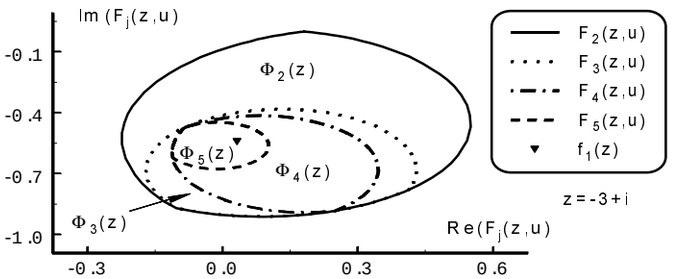


Fig. 1: Monotonic sequence of T-inclusion regions generated by the power series $f_1|_{\boldsymbol{x}}^{\boldsymbol{p}}(z-\boldsymbol{x}) + O(z-\boldsymbol{x})^{\boldsymbol{p}(k)}$, $\boldsymbol{x}= [0, 3, \infty, -1]$ $\boldsymbol{p}(2) = [1, 0, 0, 1]$, $\boldsymbol{p}(3) = [1, 0, 1, 1]$, $\boldsymbol{p}(4) = [1, 1, 1, 1]$, $\boldsymbol{p}(5) = [1, 1, 2, 1]$ representing the Stieltjes function $f_1(z) = \dfrac{1}{z}\left(1 + \frac{2.5}{z} \ln \frac{1.2+0.1z}{2+0.5z}\right)$, cf. (9)

For $p_\infty = 0$ we have $G_{2i} = 0,\ i = 1, 2, ...,\ p_\infty$, see (3) and (5). For such a case the T-continued fraction expansion of $f_1(z)$ transforms to the S-continued fraction one reported in mathematical literature. Moreover, the substitution $p_1 = 1, p_2 = 1, ..., p_\infty = 0$ reduces the matching problem (3) to the fitting one investigated by Bergman [1] and Milton [2], see also Tokarzewski *et al* [3.4].

FINAL REMARKS

By starting from the several truncated power series we derive, using special T-multipoint continued fraction technique, the general T-inclusion regions estimating in a complex domain the effective transport coefficients $Q(z)$ of two-phase media such as dielectric or diffusion constants, thermal or electrical conductivities, magnetic permeabilities. The T-inclusion regions obtained are new and furnish the best estimates of $Q(z)$. In special cases they reduce to the known complex bounds. Numerical examples exhibiting the usefulness of the results obtained are also provided.

Acknowledgment The authors were also supported by the State Committee for Scientific Research (KBN, Poland) through the Grant No 8 T07A 052 21 and No 3 P04D 007 25

References

[1] D.J. Bergman, Hierarchies of Stieltjes functions and their application to the calculation of bounds for the dielectric constant of a two-components composite medium, SIAM J. Appl. Math., **53**:915–930, 1993.

[2] G.W. Milton, Bounds on the complex permittivity of two-component composite materials, J. Appl. Phys.,**52**:5286–5293, 1981.

[3] S. Tokarzewski, J.J. Telega, S- Continued fraction method for the investigation of a complex dielectric constant of two- components composite, Acta Applicandae Mathematicae, **49**: 55-83, 1997.

[4] S. Tokarzewski, J.J. Telega, M. Pindor, J. Gilewicz, A note on total bounds on complex transport moduli of parametric two-phase media, Z. angew. Math. Phys., **54**: 713-726, 2003.

XXI ICTAM, 15–21 August 2004, Warsaw, Poland

CRACK TUNNELING IN LAMINATES

Akke S.J. Suiker*, Norman A. Fleck**
*Delft University of Technology, Faculty of Aerospace Engineering, P.O. Box 5058, NL 2600 GB, Delft, The Netherlands
**Cambridge University, Department of Engineering, Trumpington Street, Cambridge, CB2 1PZ, United Kingdom

Summary Steady-state tunneling and plane-strain delamination of an H-shape crack are examined for elastic, isotropic multi-layers. Both tunneling and delamination are analysed by employing linear elastic fracture mechanics within a 2D finite element framework. Failure maps are produced to reveal the sensitivity of cracking path to the relative toughness of layer and interface, and to the stiffness mismatch of layers. A comparison with experimental values taken from the literature shows that the model results are useful in the determination of the residual strength and the fatigue crack growth rate in elastic multilayers.

FAILURE MECHANISMS

The current study considers possible crack propagation paths for alternating layers of two dissimilar but isotropic elastic, brittle solids, designated as materials '1' and '2' in Figure 1. The initiation/nucleation phase of cracking is neglected, and it is assumed that the crack has grown from a large pre-existing flaw in the mid-layer (material 1) and is driven by a *remote tensile stress*. The competition is addressed for: (i) tunneling of a mode I crack in the mid-layer with delamination absent (*mechanism 1*), (ii) tunneling of an H-shape crack with constant delamination length (*mechanism 2*), and (iii) unstable delamination in all directions (*mechanism 3*). It is assumed that the penetration toughness of the layers of material 2 is

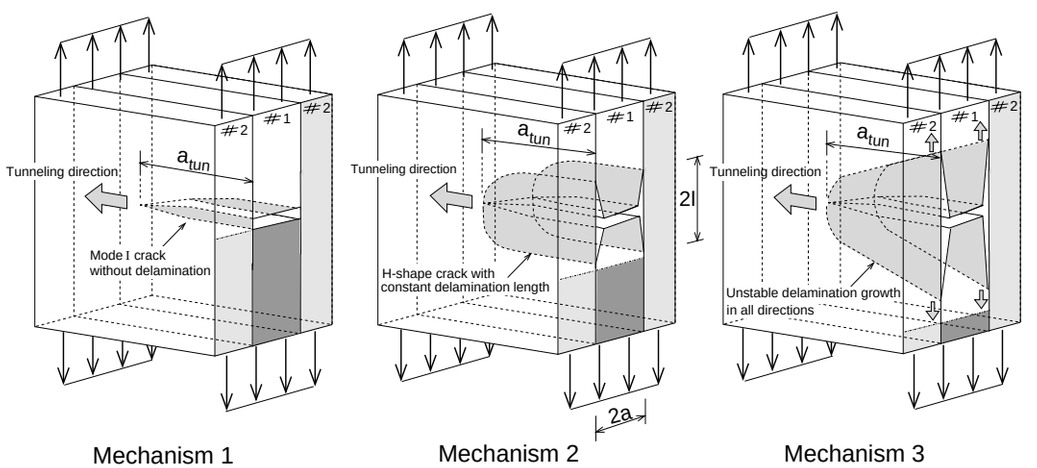


Figure 1. Three possible failure mechanisms for a laminate of two dissimilar, isotropic materials. *Mechanism 1* : Tunneling of a mode I crack without delamination. *Mechanism 2* : Tunneling of an H-shape crack with constant delamination length. *Mechanism 3* : Unstable delamination growth in all directions.

sufficiently high for the initial mode I crack in the material 1 layer not to penetrate them; this is commonly the case for the fibre-metal laminates such as ARALL and GLARE (aluminium sheets alternately stacked with aramid fibre layers and glass fibre layers, respectively). The assumption of elastic isotropy may be an acceptable simplification for multi-directional fibrous laminates when the elastic mismatch between fibres and matrix is moderate.

Both plane-strain delamination of an H-shape crack and steady state tunneling of an H-shape crack are investigated by 2D finite element analyses. Although tunneling is a 3D phenomenon, the remote stress for steady-state tunneling can be computed from a plane-strain elasticity solution for an H-shape crack: the difference in strain energy upstream and downstream of the tunneling crack front is equated to the delamination work and, for simplicity, the delamination toughness is taken to be independent of the mode-mix, see Hutchinson and Suo (1992).

RESULTS

One of the cracked configurations analysed is a 5/4 lay-up (5 layers of material 1 alternately stacked with 4 layers of material 2) where the specific fracture scenarios plotted in Figure 1 occur in the mid-layer. The numerical results have been reduced to failure mechanism maps, such as Figure 2a, in which the minimum remote tunneling stress in the layer of material 1, $\sigma_{tun,min}$ is plotted against the toughness ratio G_{dc}/G_{Ic} for selected stiffness mismatches $\bar{E}_2/\bar{E}_1$. Here, G_{dc} is the delamination toughness, G_{Ic} is the toughness related to mode I cracking in the layer of material 1 and $\bar{E}_i$ is the plane-strain Youngs modulus in layer $i \in \{1, 2\}$. The three failure modes plotted in Figure 1 are displayed with

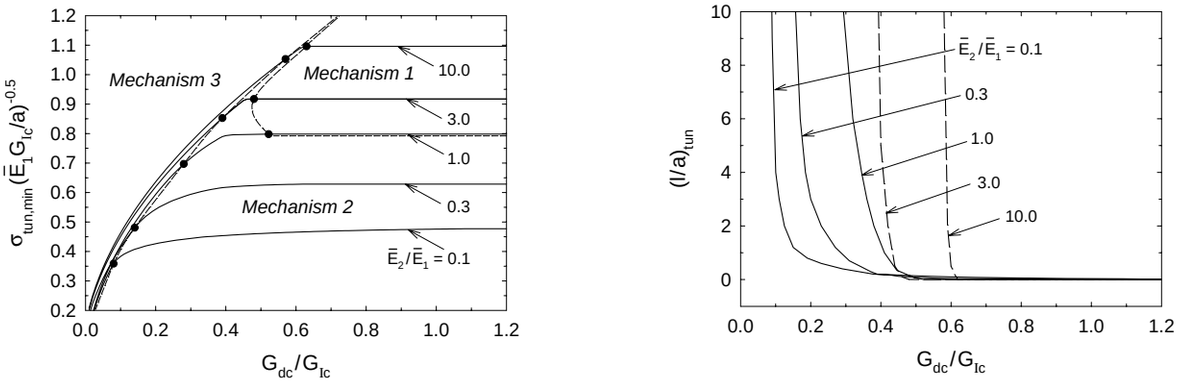


Figure 2. Cracking in the centre layer of the 5/4 lay-up. *LEFT:* Minimum tunneling stress $\sigma_{tun,min}$ versus fracture toughness ratio G_{dc}/G_{Ic}. Dashed lines indicate the zones corresponding to the three failure mechanisms in Figure 1. *RIGHT:* Delamination length $(l/a)_{tun}$ versus fracture toughness ratio G_{dc}/G_{Ic}.

the location of their boundaries indicated by dashed lines. For each curve of tunneling stress versus toughness ratio the transition from one mechanism to another is indicated by a black dot. The corresponding values for the delamination length at tunneling are depicted in Figure 2b, where l and a are the semi-length and the semi-width of the H-shape crack (*Mechanism 2*) depicted in Figure 1. Figure 2 can be used to estimate the (critical) tunneling stress $\sigma_{tun,min}$ and the delamination l/a for assumed values of G_{dc}/G_{Ic} and $\bar{E}_2/\bar{E}_1$. More details about the model, as well as the results for other cracked configurations, can be found in Suiker and Fleck (2004a).

A comparison with experimental results taken from the literature shows that the present study provides a useful tool for the prediction of the residual strength of laminates (Suiker and Fleck, 2004a). Also, combining the results with Paris law provides excellent predictions for the steady-state fatigue crack growth rate in ARALL and GLARE laminates (Suiker and Fleck, 2004b), see Figure 3.

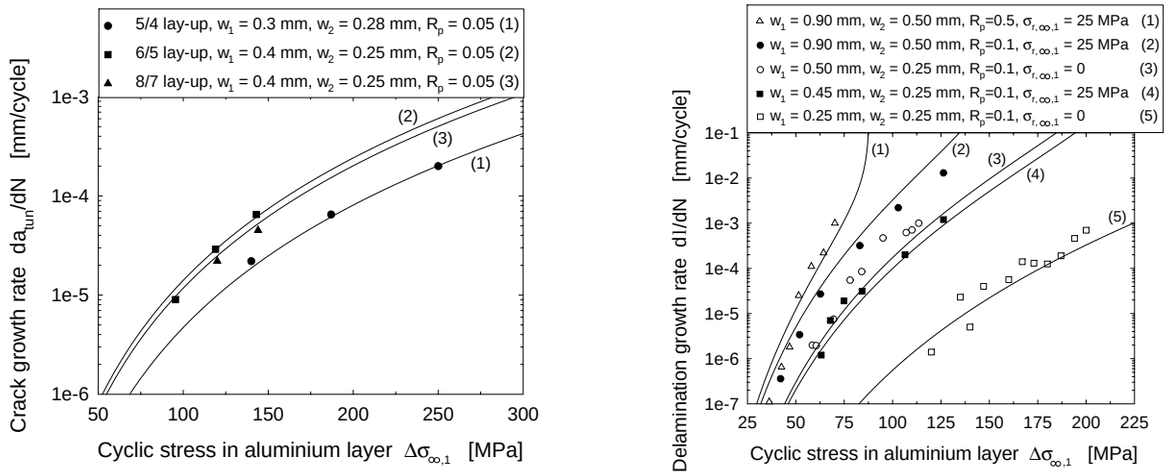


Figure 3. Fatigue crack growth rate in laminates, model (*solid lines*) and experiments (*symbols*). *LEFT:* Tunneling crack growth rate da_{tun}/dN versus remote cyclic stress in aluminium layer $\Delta\sigma_{\infty,1}$ (material 1 layer) for various centre cracked GLARE specimens. *RIGHT:* Delamination growth rate dl/dN versus versus remote cyclic stress in aluminium layer $\Delta\sigma_{\infty,1}$ (material 1 layer) for ARALL 2/1 lay-ups under various conditions. The parameters w_1 and w_2 are widths of the material 1 and 2 layers, respectively, R_p is the load ratio and $\sigma_{r,\infty,1}$ is the remote residual stress in the aluminium layer (material 1 layer). The experimental values for ARALL have been taken from Marissen (1988), and for GLARE have been taken from Takamatsu *et al.* (1999) and Shim *et al.* (2003).

References

[1] Hutchinson J.W., Suo, Z.: Mixed mode cracking in layered materials. *Adv. Appl. Mech.* **29**:63–191, 1992.

[2] Suiker A.S.J., Fleck, N.A.: Crack tunneling and plane-strain delamination in layered solids. *Int. J. Frac.* (to appear), 2004a.

[3] Suiker A.S.J., Fleck, N.A.: Modelling of steady-state fatigue crack growth in laminates. (in preparation), 2004b.

[4] Marissen R.: *Fatigue crack growth in ARALL. A hybrid aluminium-aramid composite material.* Dissertation, TU Delft, 1988.

[5] Takamatsu T., Matsumura T., Ogura N., Shimokawa T., Kakatu Y.: Fatigue crack growth properties of a GLARE3-5/4 fiber/ metal laminate. *Eng. Frac. Mech.* **63**:253-272, 1999.

[6] Shim D.J., Alderliesten R.C., Spearing S.M., Burianek D.A.: Fatigue crack growth prediction in GLARE hybrid laminates: *Comp. Sci. Tech.* **63**:1759-1767, 2003.

MACROSCOPIC RELATIONS FOR THERMODIFFUSION IN HETEROGENEOUS ELASTIC MEDIUM

Antoni A. Gałka, Józef J. Telega, Ryszard Wojnar
Polish Academy of Sciences IPPT PAN, Swietokrzyska 21, 00–049 Warsaw, Poland

Summary We consider heterogeneous thermoelastic body with periodic microstructure in which diffusion takes place. Using homogenisation methods we derive macroscopic coefficients describing thermodiffusion in a nonlinear elastic composite. In the case of layered composites, exact analytical formulae for the overall coefficients have been obtained.

INTRODUCTION

Temperature gradients lead to thermal stresses and influence diffusion in solids. The effect of large thermal gradients on the mass transport in gold and nonlinearity of hydrogen diffusion in nickel is is well known, [1-3]. Overall properties of elastic composites with coefficients independent of temperature in which thermodiffusion takes place were investigated by homogenisation method in several papers where the temperature-displacement and entropy-displacement formulations of thermoelastic solid were used, cf. [4]. Also in [4] the procedure of homogenisation of quasi-linear heat equation was performed. Here we extend this procedure to thermodiffusive processes in solids.

ASYMPTOTIC METHOD

We consider an elastic body occupying a volume $\Omega \subset \mathbb{R}^3$ and exhibiting a microperiodic structure characterized by the cell ϵY. The physical properties of the body change in microperiodic manner. The relation of the characteristic dimension of the cell ℓ to the characteristic dimension of the body L is taken as a small parameter $\epsilon = \ell/L$. The following balance laws are to be satisfied:
(*i*) *The equation of motion*

$$\rho \ddot{u}_i = \frac{\partial}{\partial x_j}\sigma_{ij} \tag{1}$$

with σ_{ij} given by

$$\sigma_{ij} = c_{ijmn}\varepsilon_{mn} - g^T_{ij}(T - T_0) - g^c_{ij}c \tag{2}$$

where the deformation ε_{ij} and displacement u_i are related by the linear expression $\varepsilon_{ij} = \frac{1}{2}(u_{i,j} + u_{j,i})$, T and T_0 denote the absolute and reference temperatures, while c_{ijmn}, g^T_{ij} and g^c_{ij} are the elasticity, stress-temperature and stress-diffusion coefficients, respectively. The coefficients may depend on the position $\mathbf{x}$, temperature T and concentration c in a given manner.
(*ii*) *The conservation of mass and heat*

$$\frac{\partial c}{\partial t} = -\frac{\partial}{\partial x_i}j_i + r^c \quad \text{and} \quad c_p\frac{\partial T}{\partial t} = -\frac{\partial}{\partial x_i}q_i + r^T \tag{3}$$

with c_p - the specific heat at constant pressure, r^c and r^T - the mass and heat sources depending on ε_{ij} and T. The mass and heat currents j_i and q_i are given by

$$j_i = -D\frac{\partial}{\partial x_i}c + M\frac{\partial}{\partial x_i}T \quad \text{and} \quad q_i = -N\frac{\partial}{\partial x_i}c + \lambda_T\frac{\partial}{\partial x_i}T \tag{4}$$

where D, M, N and λ_T are the coefficients of diffusion, thermodiffusion (direct and reciprocal) and heat conduction, which can depend also on $\mathbf{x}$, T and c.
In composite with a periodic microstructure all material coefficients are ϵY-periodic functions, where Y is the basic cell. For instance,

$$c^\epsilon_{ijmn} = c^\epsilon_{ijmn}(\mathbf{x}, T) = c_{ijmn}(\frac{\mathbf{x}}{\epsilon}, T), \quad g^{T\epsilon}_{ij} = g^{T\epsilon}_{ij}(\mathbf{x}, T) = g^T_{ij}(\frac{\mathbf{x}}{\epsilon}, T) \qquad x \in \Omega$$

and so on. For any fixed $\epsilon > 0$ both the displacement, concentration and the temperature fields are denoted by $\mathbf{u}^\epsilon, c^\epsilon$ and T^ϵ and have the ϵ - expansions. For instance,

$$u^\epsilon_i(\mathbf{x}) = \overset{0}{u}_i(\mathbf{x}) + \epsilon\ \overset{1}{u}_i(\mathbf{x}, \mathbf{y}) + \epsilon^2\ \overset{2}{u}_i(\mathbf{x}, \mathbf{y}) + \cdots$$

$$T^\epsilon(\mathbf{x}) = \overset{0}{T}(\mathbf{x}) + \epsilon\ \overset{1}{T}(\mathbf{x}, \mathbf{y}) + \epsilon^2\ \overset{2}{T}(\mathbf{x}, \mathbf{y}) + \cdots$$

where $\mathbf{y} = \mathbf{x}/a$. Also, the material coefficients are to be expanded, e.g.

$$c^{\epsilon}_{ijmn} = \overset{0}{c}_{ijmn} + \epsilon^1 \overset{1}{c}_{ijmn} + \epsilon^2 \overset{2}{c}_{ijmn} + \cdots$$

After lengthy calculations the field equations are obtained. For instance,

$$\rho^{\epsilon}\ddot{u}^{\epsilon}_i = \left(\frac{\partial}{\partial x_j} + \frac{1}{\epsilon}\frac{\partial}{\partial y_j}\right)\left[c^{\epsilon}_{ijmn}\left(\frac{\partial}{\partial x_n} + \frac{1}{\epsilon}\frac{\partial}{\partial y_n}\right)u^{\epsilon}_m - g^{T\epsilon}_{ij}(T^{\epsilon} - T_0) - g^{c\epsilon}_{ij}(T^{\epsilon} - T_0)\right].$$

Homogenization means passing with ϵ to zero and yields the macroscopic field equations involving homogenized (overall) coefficients. For instance,

$$\begin{aligned} c^h_{ijpq} &= <\overset{0}{c}_{ijpq}(\mathbf{y}) + \overset{0}{c}_{ijmn}\frac{\partial \chi_{mpq}(\mathbf{y})}{\partial y_n}>, \\ g^{Th}_{ij} &= <\overset{0}{g}^{T}_{ij}(\mathbf{y}) - \overset{0}{c}_{ijmn}\frac{\partial \Gamma_m(\mathbf{y})}{\partial y_n}>, \\ \lambda^T_{ik} &= <\overset{0}{\lambda}_T(\mathbf{y})\delta_{ik} + \overset{0}{\lambda}_T(\mathbf{y})\delta_{ij}\frac{\partial \theta_k(\mathbf{y})}{\partial y_j}>. \end{aligned} \tag{5}$$

Here χ_{mpq}, Γ_m and θ_k denote Y-periodic local functions. The superscript h stands for the homogenized quantities; $\chi_{mpq}, \Gamma_m, \theta_k$ are the functions obtained from solution of local problems, and $< \cdots >$ denotes the averaging over Y.

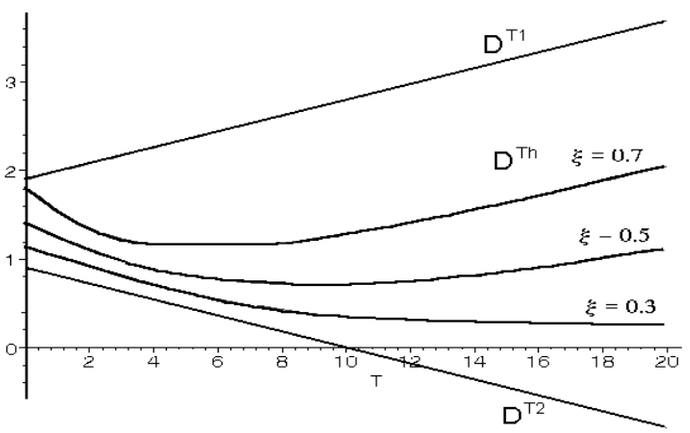


Figure: Effective direct thermodiffusion coefficient versus temperature for different volume fraction of components for: $D_1 = 1 + 0.1T$, $D_1^T = 0.9 - 0.09T$, $\lambda_1^D = 0.5 + 0.05T$, $\lambda_1 = 0.4 + 0.04T$, $D_2 = 5 + 0.1T$, $D_2^T = 1.9 - 0.09T$, $\lambda_2^D = 1.5 + 0.05T$, $\lambda_2 = 1.4 + 0.04T$.

CONCLUSIONS

The equations of nonlinear thermodiffusion in elastic solids with periodic microstructure have been analysed. By using homogenisation methods the macroscopic equations have been derived. To illustrate these general results, the microperiodic layered composite has been studied in which the coefficients depend on T and c. As an example, see Figure.

Acknowledgment. The authors were supported by the Ministry of Science and Information Technology through the grant No 8 T07A 052 21.

References

[1] Mock W.: Thermomigration of Au^{195} and Sb^{125} in gold. Mathematical description of the diffusion in a temperature field and measuring the heat of transport. *Physical Review* **179**(3): 663–75, 1969.
[2] Dudek D., Baranowski B.: Diffusion coefficients of hydrogen during absorption and desorption of hydrogen in Pd_{81}/Pt_{19} membrane. I. Time-lag method. *Zeitschrift für Physikalische Chemie* **206**(1-2): 21–9, 1998.
[3] Rudakov V.I., Ovcharov V.V.: Mathematical description of the diffusion in a temperature field and measuring the heat of transport. *International Journal of Heat and Mass Transfer* **45**(4): 743–53, 2002.
[4] Gałka A., Telega J.J., Tokarzewski S.: Heat equation with temperature-dependent conductivity coefficients and macroscopic properties of microheterogeneous media. *Mathematical & Computer Modelling* **33**(8-9): 927–42, 2001.

STUDY OF THE USABILITY OF VARIOUS CRUCIFORM GEOMETRIES FOR BIAXIAL TESTING OF FIBER REINFORCED COMPOSITES

Smits A.*, Van Hemelrijck D.*, Philippidis T.**, van Wingerde A.M.***, Cardon A.*

** Department of Mechanics of Materials and Constructions (MeMC), Vrije Universiteit Brussel (VUB), Pleinlaan 2, 1050 Brussels, Belgium*
*** Department of Mechanical Engineering & Aeronautics, University of Patras, P.O. Box 1401, Patras 265 00, Greece*
**** Wind turbine Materials and Constructions, Knowledge Centre WMC, P.O. Box 43, 1770 AA Wieringerwerf, The Netherlands*

Summary To investigate the behaviour of fibre reinforced composites as much as possible approximating real life, a biaxially loaded planar cruciform specimen was developed by performing finite element simulations in combination with experiments on different geometries of cruciform specimens.

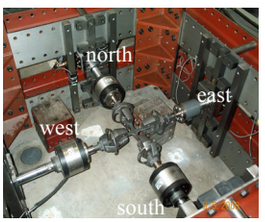
INTRODUCTION

Experimental investigation of fibre reinforced composites was predominantly performed using uniaxially loaded specimens. However, in real applications fibre reinforced composites are hardly ever loaded in one direction. Consequently, experimental investigation of these materials should approximate real life behaviour as much as possible. In an attempt to achieve this goal biaxial tests can be considered [1]. However, these tests are using mainly tubular specimens subjected to torsion in combination with tension or compression [2, 3]. Unfortunately, these highly curved tubular specimens behave different from most fibre reinforced composite components which are often flat or gently curved [4]. For this reason a biaxial testing facility for planar cruciform test specimens was developed at the department of Mechanics of Materials and Constructions of the Free University of Brussels (Figure 1). The design of a suitable cruciform specimen is the subject of this paper.

BIAXIAL TEST BENCH AND CRUCIFORM SPECIMEN REQUIREMENTS

The planar biaxial test bench has a loading capacity of 100kN. In order to fix the central point of the specimen during testing, the force P has to be equal and co-linear to P', F equal and co-linear to F' and the forces P & P' need to be perpendicular to F & F' (Figure 2). To fulfil these requirements four servo-hydraulic cylinders were used. As no cylinders with hydrostatic bearings were used, the test frame is limited to tensile loading. Failure or slip in one arm of the specimen would result in sudden radial forces, which could seriously damage the servo-hydraulic cylinders and load cells. To prevent this, hinges were used to connect the specimen to the cylinders and the cylinders to the test frame.

Figure 1: Biaxial test bench for flat cruciform specimens



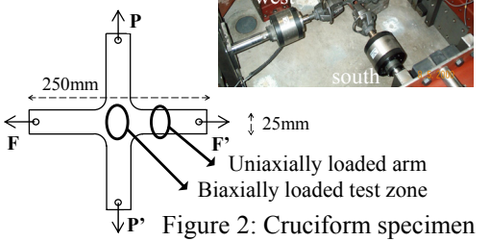


Figure 2: Cruciform specimen

A valid biaxial test avoids premature failure in the uniaxially loaded arms, gives a large region of uniform strain in the biaxially loaded test zone and avoids strain concentrations at the intersection of two perpendicular arms. These conditions are not easily obtained simultaneously. To investigate the influence of parameters like (i) the rounding radius at the intersection of two arms, (ii) the thickness of the biaxial loaded test zone in relation to the thickness of the arms and (iii) the geometry of the test zone on the above mentioned requirements, finite element simulations were performed. Afterwards, these numerical results were compared with experimental results obtained from biaxial tests on selected cruciform geometries.

FINITE ELEMENT SIMULATIONS OF CRUCIFORM GEOMETRIES

Figure 4 shows the finite element results of the first principal strains for three different geometries A, B and C. Due to symmetry, only one quarter is shown. The load ratio between the directions x and y was chosen equal to the strength ratio of both arms (i.e. 3.85/1). The material tested was glass fibre reinforced epoxy with a $[(+45° \ -45° \ 0°)_4(+45°\text{-}45°)]$-lay-up (zone 2 on Figure 4 with lay-up 2 on Figure 3). In the middle of the specimens one layer of (0° +45° -45°) was milled away at each side of the specimen resulting in a$[(45° \ -45° \ 0°)_2(+45°\text{-}45°)]$-lay-up (zone 3) for geometries B and C. End-taps were glued on the specimens (zone 1). The applied load was F_x/F_y = 46.2kN/12kN.

For geometry A, strains in the x-direction just after the end taps are higher than in the end-taps, but are less in the direction to the centre of the specimen. This is due to the enlargement of the area taking the load in this region. Consequently, failure of the specimen will occur close to the end taps. In order to increase the strains and the possibility to cause failure in the biaxial loaded zone, a reduction of thickness and/or changing the rounding radius is necessary. In geometry B the first suggestion is shown. The strain results are improved and for this kind of geometry failure can occur at the middle of the specimen. If we use a combination of both suggestions, as shown in geometry C, even higher strains are obtained in the biaxial loaded zone.

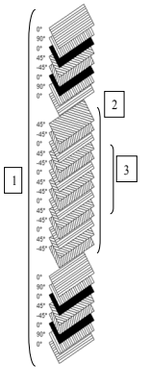


Figure 3: Lay-up of specimens.

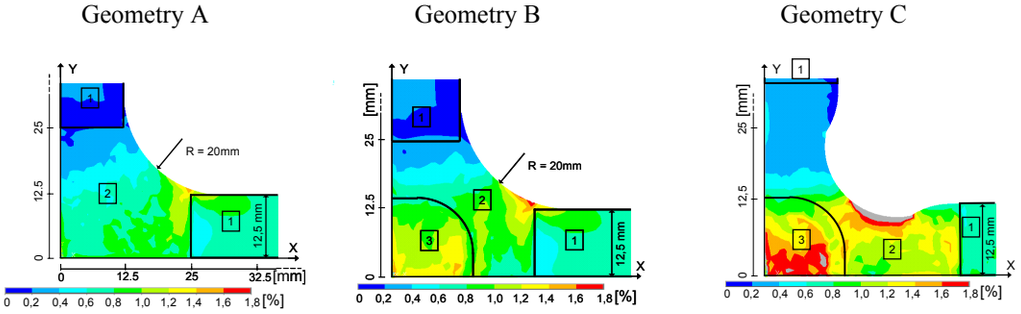


Figure 4: Finite element results for three cruciform geometries. First principal strains are shown.

TENSION TESTS ON CRUCIFORM GEOMETRIES

The experimental results for the three tested geometries A, B and C are shown in Table 1. Each value is an average of at least three experiments. Strain measurements are obtained in x- and y- direction by using strain gauges glued in the centre of each specimen. The failure loads and failure strains are measured in both directions. The failure stresses were calculated using the experimentally obtained failure strains and the stiffness moduli and Poisson's ratios from uniaxially loaded specimens. The highest failure strains are obtained for geometry C, indicating this geometry is the most promising one. For geometry A, failure of the specimen didn't occur in the biaxial loaded test zone, in contrast to geometries B and C (Figure 5). These results confirm the results of the finite element simulations. The high strains at the rounding between the two arms in geometry C do not cause early failure of the specimen as can be seen in the experimental results.

	[kN]		[%]		[MPa]	
	F_x	F_y	ε_x	ε_y	σ_x	σ_y
geometry A	63,2	16,5	1,35	-0,56	395	14
geometry B	60,5	15,8	1,52	-0,66	442	13
geometry C	47,9	12,4	1,68	-0,79	516	56

Table 1: Experimental results on three cruciform geometries.



Figure 5: Failure of cruciform specimen geometry C at 48.2kN. Failure occurs in the biaxial loaded zone.

CONCLUSIONS

The performed finite element simulations in combination with the experiments on three different geometries of cruciform specimens, led to the selection of a suitable geometry for biaxial testing of composite materials. This geometry has a reduced thickness in the central region of the specimen in combination with a rounding radius between two arms inside the material. In that way failure occurs in the biaxially loaded test zone.

References

[1] Soden P. D., Hinton M. J., Kaddour A. S., *A comparison of the predictive capabilities of current failure theories for composite laminates*, Composites Science and Technology, Volume 58/7, pg. 1225-1254, 1998.
[2] J. S. Welsh and D. F. Adams, *An experimental investigation of the biaxial strength of IM6/3501-6 carbon/epoxy cross-ply laminates using cruciform specimens*, Composites Part A: Applied Science and Manufacturing, Volume 33/6, pg. 829-839, 2002.
[3] Smith E. W. and Pascoe K. J., *Biaxial fatigue of a glass-fibre reinforced composite. Part 2: Failure Criteria for Fatigue and Fracture*, Mechanical Engineering Publications, London, Appendix 1.
[4] D. S. Dawicke and W. D. Pollock, *Biaxial testing of 2219-T87 aluminium alloy using cruciform specimens*, NASA Contractor Report 4782, Langley Research Center, Hampton, Virginia, 1997.

INCREMENTAL EFFECTIVE CONSTITUTIVE LAW FOR COMPOSITE MATERIAL IN THE FORM OF ARTIFICIAL NEURAL NETWORK

Marek Lefik
Technical University of Łódź, Chair of Geotechnical Engineering and Engineering Structures, 93-590 Łódź, Poland

Summary Description of effective behaviour of composites in the form of a suitably trained Artificial Neural Network is presented in this paper. We assume an incremental form of constitutive relationship approximated by ANN. We propose three methods of acquisition of data for training the ANN. The first one furnishes the pairs: average stress - average strains and their increments - resulting from the solution of boundary value problem defined over a representative volume, with given mean strain imposed. The second and the third methods base on sampling of global behaviour of the composite material. The presented approach is fully numerical. The corresponding algorithm seems to be applicable for a large class of composites. The representation of the constitutive law by ANN can be included as a subroutine into any FE code. Example shows the application of the method for Neo-Hookean material.

INTRODUCTION

For a non-linear composite an adequate description of effective behaviour is usually very difficult to obtain. The classical, symbolic constitutive law is usually theoretically deduced from known properties of a representative volume, basing on a suitable version of homogenisation theory. In this paper we use an Artificial Neural Network (ANN) trained with pairs: mean stress – average strain (or respective increments) has been used as a numerical representation of the effective constitutive law. Different strategies of collecting the training data are possible. Three of them are analysed in the paper.

FORMULATION OF THE PROBLEM

Let $\mathbf{u}^0$, σ^0 be the solution of the "homogenised" problem i.e. a classical BV problem of mechanics in which the variable material coefficients ***a(y)*** in:

$$\sigma_{ij}^{\varepsilon}(\mathbf{u}^{\varepsilon})(\mathbf{x},\mathbf{y}) = a_{ijkl}(\mathbf{y})e_{kl}(\mathbf{u}^{\varepsilon}(\mathbf{x},\mathbf{y})) \quad \text{(and} \quad \sigma_{ij}^{\varepsilon} \in P(\mathbf{y}) \text{ where is an admissible subset of of the stress space)}$$

are replaced with some unknown constant values $\boldsymbol{a}^{\boldsymbol{h}}$. We suppose that the periodicity of material characteristics imposes an analogous periodical perturbation on the quantities describing the mechanical behaviour of the body. Hence, for displacements we have:

$$\mathbf{u}^{\varepsilon}(\mathbf{x}) \equiv \mathbf{u}^0(\mathbf{x}) + \varepsilon\,\mathbf{u}^1(\mathbf{x},\mathbf{y}) \;,\; \mathbf{u}^1 \text{ Y-periodic}$$

For $\boldsymbol{a}^{\boldsymbol{h}}$ uniquely defined via classical homogenisation procedure $\mathbf{u}^{\varepsilon}$ converges weakly to $\mathbf{u}^0$ as ε tends to zero. In this case the tensor $\boldsymbol{a}^{\boldsymbol{h}}$ defines an effective constitutive relationship between $\mathbf{e}(\mathbf{u}^0)$ and σ^0 (a new admissible set in the stress space P^{h} makes a part of this effective constitutive description). In this paper, instead of looking for $\boldsymbol{a}^{\boldsymbol{h}}$ and P^{h} we are going to use a numerical representation of the effective constitutive law by a suitably trained ANN N. The input-output vector of N contains components of strains $\mathbf{e}(\mathbf{u}^0)$ and stress tensor σ^0 (in the vector-like notation):

$$\boldsymbol{\sigma}^0 = N@\mathbf{e}(\mathbf{u}^0): \quad \sigma_i = \sum_m w^2_{q(i)} f_{(q)}\left(e_p w^1_{p(q)} + \theta^1_{(q)}\right) + \theta^2_{(i)}$$

Weights, biases and transfer functions are respectively $\mathbf{w}$, θ and f in (4). The finite element code with N included as a material description subroutine can be used to solve for $\mathbf{u}^0$ the problem:

$$\text{find } u_i^0 \in V \text{ and } \sigma_{ij}^0 \in L^2 \text{ be such that: } \forall\; v_i(\mathbf{x}) \in V$$

$$\int_{\Omega h} \sigma^0_{kl}(\mathbf{u}) v_{k,l}\, d\Omega = \int_{S_f} F_i v_i\, dS_f \qquad \boldsymbol{\sigma}^0 = N^h @ \mathbf{e}(\mathbf{u}^0)$$

The correct, effective constitutive law in the above, represented by the ANN called N^{h} assures the following requirement:

$$\forall \mathbf{F}: \left\| \mathbf{u}^{\varepsilon} - \mathbf{u}^0 \right\|_{L^2(\Omega)} \le \tau \qquad \tau \le \varepsilon \left\| \mathbf{u}^1 \right\|_{L^2(Y)} \quad \text{as } \varepsilon \text{ tends to } 0$$

The above expression defines a correspondence between the heterogeneous and the homogeneous (homogenised) fictitious body in the manner suitable for our purpose. In the numerical practice the comparison of the effective solution with the exact one is checked only in few strategic points. The above equivalence condition formulated for any $\mathbf{F}$ is verifiable in practice only for a finite number of prescribed loads. In the example below the only one case of load is reported. In what concerns the convergence to zero with cell's diameter: as it is shown in many papers, a relatively small trying portion of the composite is sufficient to predict the overall behaviour of the non-homogeneous material.

THREE STRATEGIES

The most natural method of data acquisition assumes that ANN is trained with pairs: mean stress – average strain (or respective increments). The averaging is done over a cell of periodicity or a representative volume of the composite. The second method of data acquisition uses a composed neural network (CNN). Inside the CNN a Hopfield-Tank sub-network specialises in construction of a variety of statically admissible fields for a fictitious, "homogenised" body. An ANN with hidden layer associates the generated, statically admissible stresses with strains computed from the displacements, known from a numerical experiment. The third method we use in the training process is a so called "self-learning" finite element procedure, developed recently by Shin and Pande. Hybrid, FE-ANN code generates some trial solutions obtained for an initial approximation of the constitutive law. These trial solutions are then corrected after a comparison with known behaviour of the studied composite. According to the "self-learning" method displacements are compared and the difference (error) is then used – via FE solution of the new BV problem - to improve the initial guess. In the second and third methods the data are collected from many points of the sample. The composition: CNN and ANN with hidden layers - can be used for elaboration of results of the experiment in which homogeneous state of stress is not needed. Because of this a large class of data resulting from observations of real structures can be used as a source of knowledge about the structural constitutive behaviour. Representation of a Constitutive Law by ANN with Hidden Layers is crucial for the proposed modelling procedure. In the paper, We discuss the structure of the network, its approximation abilities. The networks automatic generalisation capability enables us to predict the material behaviour i.e. to produce the graph stress-strain for an arbitrary sequence of stress or strain values, never presented to the ANN before.

EXAMPLES

We show two examples: regular, perpendicular mesh of elastic-plastic inclusions in elastic-plastic matrix and the second – hiper-elastic material with a regular array of circular holes. The first example was studied by analysis of 20 cells of periodicity, the second – by a single, repetitive cell.

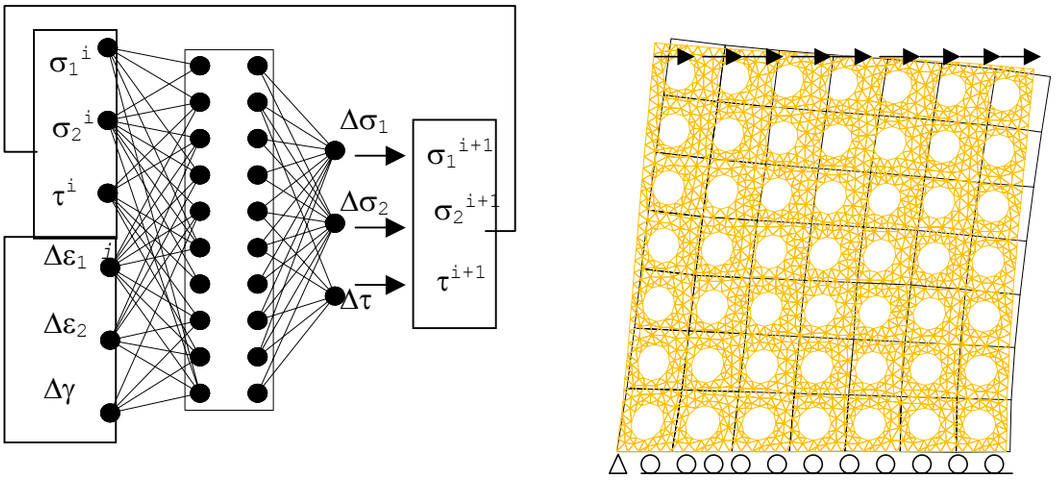


Figure 1.a Scheme of the ANN for approximation of a constitutive operator and autonomous networks activity in computing σ along a given path in space of strains. 1.b. Comparison of displacements: FE model with hyperelastic material (light lines), FE code with ANN defining the homogeneous material (coarse rectangular mesh scale of the displacements is 1:1). This case of loading has never been presented to the network in training

CONCLUSIONS

The ANN representation of any constitutive law is a flexible tool for identification of the global (effective) behavior of materials with complex internal structure. This representation is derivable from both possible sources of knowledge about the material: real experiment and numerical simulation. ANN representation is very suitable for analysis of composites since it is "automatic" in the sense that it does not require any "a priori" choice or adaptation of the existing constitutive theory for the description of the observed material behavior. We show that it is possible to incorporate the ANN constitutive description into a Finite Element code. A realistic FE model can be thus constructed for a material described by ANN. The examples show that the model is possible even in the case of complicated non-linear behaviour. Convergence of the third method is surprisingly fast. Three or four steps are enough to obtain a qualitatively good model.

ANALYSIS OF THICK LAMINATED PANEL WITH PIEZOELECTRIC SENSORS BASED ON THREE-DIMENSIONAL THEORY OF ELASTICITY

Daneshmehr A. R. *, Shakeri M. **, Alibiglu A.***

* *Scientific Board Member, Islamic Azad University (IAU), central Tehran Branch, Tehran / Iran*
Email: alidaneshmehr@yahoo.com
** *Professor, Dept. of Mechanical Engineering, Amirkabir univ. of Tech. , Tehran / Iran*
*** *Assistant Professor, Bu Ali Sina university, Hamedan / Iran*

Summary A study on the elasticity solution of shell panel with piezoelectric sensors is presented. In this paper, the structure is simply-supported, orthotropic and under pressure excitation on outer surface. Three-dimensional equations of equilibrium, which are coupled partial differential equations, are reduced to ordinary differential equations with variable coefficients by means of Fourier series expansion in circumferential and axial directions. The resulting ordinary differential equations are solved by Galerkin finite element method. Numerical results are presented for [0/90/P] lamination.

INTRODUCTION

In recent years, smart structures with piezoelectric sensors and actuators have attracted serious attention for they can sense and alter the mechanical response during in-service operation. On the other hand, light-weight shell and panel structures may be one of the most popularly used structures in space vehicles. For these reasons, shell-type smart structures have become the subject of focus for many researchers. Tzou and his co-workers published a series of papers on finite element and analytical analysis of piezoelectric shell-type continua (Tzou , 1993 and Tzou et al., 1994). In addition to the aforementioned approximate analysis, exact studies of piezoelectric circular cylindrical shells (Chen et al., 1996) and piezothermoelastic shells (Chen and Shen, 1996a) were also performed. The theories of plates and shells coupled with piezoelectricity theory were applied to piezoelectric sensor and actuator design (Lee 1996). The piezoelastic solutions to long cylindrical panel and shell structures were also presented (Kapuria 1997) . Elastic solution of orthotropic thick laminated cylindrical panels subjected to dynamic loading was obtained by author (Shakeri 2002).

The objective of the present study is to investigate the elastic solution of cross-ply laminated panels with piezoelectric layer using three-dimensional theory of elasticity.

GOVERNING DIFFERENTIAL EQUATIONS

The equations of equilibrium in the absence of body force and the charge equation of equilibrium of electrostatics in cylindrical coordinates are:

$$\begin{aligned}
&\frac{\partial \sigma_r}{\partial r}+\frac{\sigma_r-\sigma_\theta}{r}+\frac{1}{r}\frac{\partial \tau_{r\theta}}{\partial \theta}+\frac{\partial \tau_{zr}}{\partial z}=0\\
&\frac{\partial \tau_{r\theta}}{\partial r}+\frac{1}{r}\frac{\partial \sigma_\theta}{\partial \theta}+\frac{\partial \tau_{z\theta}}{\partial z}+2\frac{\tau_{r\theta}}{r}=0\\
&\frac{\partial \tau_{rz}}{\partial r}+\frac{\partial \tau_{z\theta}}{r\partial \theta}+\frac{\partial \sigma_z}{\partial}+\frac{1}{r}\tau_{rz}=0\\
&\frac{\partial D_r}{\partial r}+\frac{D_r}{r}+\frac{\partial D_\theta}{r\partial \theta}+\frac{\partial D_z}{\partial z}=0
\end{aligned} \qquad (1)$$

SOLUTION OF GOVERNING DIFFERENTIAL EQUATIONS

The solution satisfying the boundary conditions maybe assumed as:

$$u_r=\sum_{m=1}^{\infty}\sum_{n=1}^{\infty}\phi_r(r)\sin(b_m\theta)\sin(b_n z) \qquad u_\theta=\sum_{m=1}^{\infty}\sum_{n=1}^{\infty}\phi_\theta(r)\cos(b_m\theta)\sin(b_n z)$$

$$u_z = \sum_{m=1}^{\infty}\sum_{n=1}^{\infty}\phi_z(r)\sin(b_m\theta)\cos(b_n z) \qquad \psi = \sum_{m=1}^{\infty}\sum_{n=1}^{\infty}\psi(r)\sin(b_m\theta)\sin(b_n z) \tag{2}$$

NUMERICAL RESULTS AND DISCUSION

A sensor consisting of a three-layered cross-ply panel which its sequence lay-up is (0/90/P) composed of graphite-epoxy and piezoelectric is considered. The in-plane shear stress and radial normal stresses across the thickness are as the figures 1 and 2.

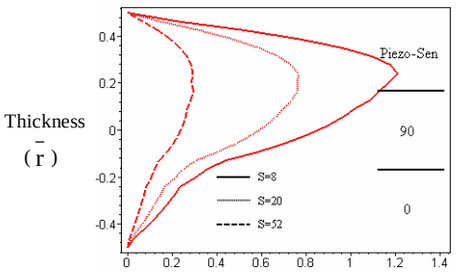


Fig.1 In plane shearing stress ($\tau_{r\theta} / P_0$)

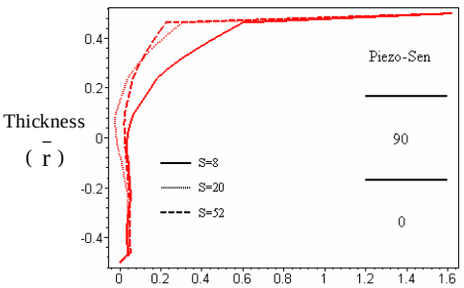


Fig.2 Radial stress (σ_r / P_0)

CONCLUSION

A study on the three-dimensional elasticity solution of shell panel piezoelectric sensors is presented. In this paper, the structure is simply-supported, orthotropic and under pressure excitation. The present study has shown that the Fourier series expansion method is suitable for the mechanical displacement and electric potential analysis in panel-type sensors.
The piezoelectric effect in the piezoelectric layer subjected to outer pressure is investigated in detail. In analytical investigation of the piezoelectric structures, it is always assumed that the electric potential in the piezoelectric layers varies linearly and the displacements change in the form of prescribed functions across its thickness [10]. However, it has been shown that the distributions of the mechanical displacements and electric potential of piezoelectric response are very complicated and cannot be treated as pure elastic structures or piezoelectric structures. Therefore, three-dimensional analysis of piezoelastic behavior of structures is recommended even for thick and thin laminated structures. Since a comprehensive and exact study of active piezoelectric structures is still unavailable, the present work provides an enhanced insight to the mechanical and electric behaviors of this type of smart structure.

References

[1] Tzou H.S. , Zhong J.P.: Electro mechanics and vibrations of piezoelectric shell distributed systems. *J Dyn syst. Meas control* 115(3), 506-517,1993.

[2] Tzou HS , Zhong JP: Linear theory of piezoelectric shell vibrations. *Jsound Vib*. 175(1), 77-88, 1994.

[3] Chen C-Q, Shen Y-P and Wang X-M :Exact solution for orthotropic cylindrical shell with piezoelectric layers under cylindrical bending. *Int. J. Solids struct.* 33(30), 4481-4494, 1996.

[4] Lee P.C.Y. , Yu J.D. : Governing equations of piezoelectric plates with graded properties across the thickness. *Proc. Annual IEEE Int. freq. control symp.* , 623-631, 1996.

[5] Kapuria S., Sengupta S., and Dumir P.C.: Three-dimensional solution for simply-supported piezoelectric cylindrical shell for axisymmetric load. *Compu. Methods in Appl. Mech. Eng.* 140(1-2), 139-155, 1997.

[6] Shakeri M., Alibiglu A. and Eslami M.R.: Elastisity solution for thick laminated anisotropic cylindrical panels under dynamic load. *J. Mech. Eng. Sci. Vol. 216 Part C, I Mech E* , 2002 .

[7] Chen C. Q , Shen Y. P. : Piezothermoelasticity analysis for a cylindrical shell under the state of axisymmetric deformation. *Int. J. Engng Sci.* Vol. 34, No 14, pp. 1585-1600, 1996.

TEMPERATURE AND STRAIN RATE EFFECTS ON TRIP SHEET STEEL. MEAUSREMENT OF TEMPERATURE BY INFRARED THERMOGRAPH

W.K. Nowacki*, A. Rusinek, J.R. Klepaczko , P. Gadaj*

Laboratory of Physics and Mechanics of Materials, UMR CNRS 75-54, Université de Metz, Ile du Saulcy, 57045 Metz cedex, France
Institute of Fundamental Technological Research, Polish Academy of Sciences, Swietokrzyska 21, 00-049 Warsaw, Poland

Summary More frequently, new sheet steels are applied to assure a high energy level absorption, for example DP steel or TRIP steel. The high energy level absorption of this materials is due to high stress level combined with large ductility. However some problems appear to define precisely analytical behavior of TRIP steel since the behavior is strongly dependent on the phase transformation which occurs during plastic deformation. To obtain a complete knowledge of the behavior affected by phase transformation, a series of experiments has been performed in the form of tensile test and shear test at different strain rates and temperatures. During those tests, a thermographic set-up has been used to measure the temperature increase with plastic deformation. This complementary information may be useful to explain and understand the phase transformation in TRIP steel during plastic deformation. Preliminary analysis of the temperature gradients in specimen has been performed via relaxation tests.

EXPERIMENTAL SET-UP

To analyse the thermoviscoplastic behavior of TRIP 800 a special arrangement has been used with an infrared thermographic camera. The range of strain rate applied during experimental tests was from $10^{-3}\,s^{-1} \le \dot{\varepsilon} \le 100\,s^{-1}$. Several temperatures have applied for TRIP 800 steel to study the effect of temperature on the phase transformation during plastic deformation. The test temperature varied in the following limits $213\,K \le T \le 373\,K$. The temperature affects strongly the plastic behavior as it is shown, Fig. 1-a-b.

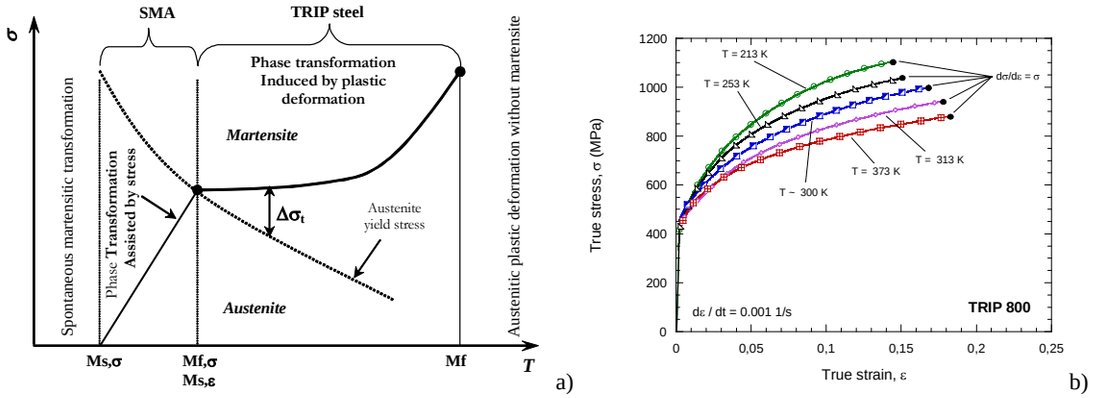
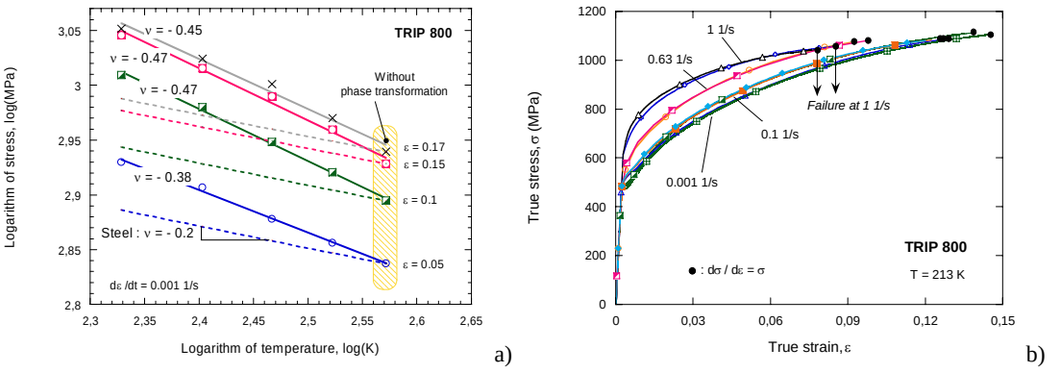


Fig.1. a - Schematic representation of the kinetic phase transformation with the initial temperature, b – Effect of the initial temperature on the plastic behavior in quasi-static tension

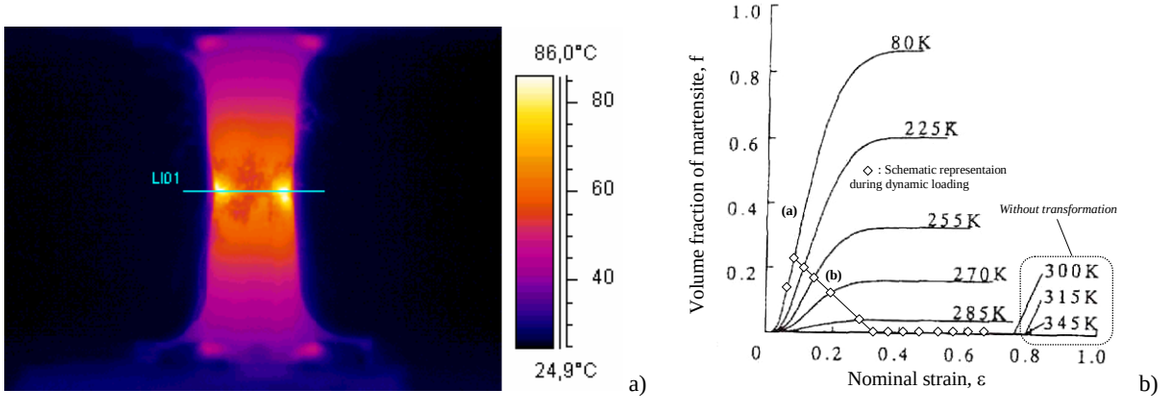
In Fig. 1-a substantial increase of strain hardening is observed when the initial temperature decreases. In fact, at low temperature ($T = 213\,K$), Fig. 1-a, the phase transformation austenite-martensite appears without plastic deformation in comparison to other temperatures inducing an instantaneous increase of stress level, Fig. 1-b. To approximate of the correctly the behavior of TRIP steel the temperature must be introduced in the kinetic description of transformation. In fact, the TRIP steels are strongly affected by the temperature sensitivity in comparison to mild steel, Fig. 2-a. Concerning the strain rate sensitivity it is essential to take into account this variable to take into account correctly the viscoplastic effect and the coupling strain rate-temperature, Fig. 2-b. The temperature increase has been measured to complete analysis of the mechanical behavior of TRIP 800 sheet steel. We observe on the following curves maximum temperature in the necking zone, Fig. 3-a, equal to $\Delta T = 86\,K$. The substantial temperature increase in TRIP steel is due to high failure stress level and high ductility with $\varepsilon_{max} \ge 0.2$ induces a high temperature increase. This phenomenon is a negative factor on the phase transformation as is shown on Fig. 3-b since the phase transformation is reduced by temperature increase. In fact, an approach which takes into account a constant temperature in the volume (specimen) will induce an overestimation of the martensite volume faction. In fact the phase transformation is not uniform (path (a)), Fig. 3-b, and it is closed to path (b) defined by (◊), Fig. 3-b. A complete analysis on the temperature increase is given in [3] in quais-static and dynamic loading.



a) b)

Fig.2. a – Temperature sensitivity in quasi-static loading, b – Strain rate sensitivity at low temperature, $T = 213\,K$

Moreover, with the complete experimental analyse a correlation has been found between the temperature sensitivity $\nu(\varepsilon) = \partial \log \sigma / \partial \log T\big|_{\dot{\varepsilon},T}$ and the velocity of the volume fraction of transformed martensite $\dot{f}(\varepsilon)$, [1]. The experimental analysis has also permitted to verify that at high strain rate, or in adiabatic conditions, the latent heat generation due to phase transformation is very reduced.



a) b)

Fig.3. a – Temperature measurement during quasi-static tensile loading, $\dot{\varepsilon} = 10^{-2}\ s^{-1}$ and $t = 27.4\,s$, b - Kinetics of phase transformation versus strain for different initial temperatures [2]

The observation of the previous curves, Fig. 1-a and Fig. 3 a-b, allows to show that the temperature and the strain rate increase have a negative effect on the rate of phase transformation, $\dot{f} \to 0$. Analysis has been performed on temperature increase in TRIP 800 steel at different strain rates. At $\dot{\varepsilon} = 10\,s^{-1}$ the ΔT is equal to 150 K for maximum strain equal to $\varepsilon_{max} = 0.2$ in the necking zone. A more general comparison has been made between several kinds of sheet steels in [3].

CONCLUSIONS

Application of standard experimental techniques coupled with infrared thermograph a complementary information on the local temperature during transformation is obtained. The temperature is essential to define correctly the phase transformation during plastic deformation. The effect of temperature must be added to the viscous effect notably at low temperatures since temperature effect on the phase transformation is very reduce at high temperature. Thus, a description of thermoviscoplastic behavior for TRIP steel without these effects does not allow a correct description transformation kinetics. A constitutive description with a semi-physical approach as in [4] coupled with strain rate and temperature to define the phase transformation seem to be a good way in comparison to micro-macro approach where the strain rate and temperature sensitivity are rarely considered.

References

[1] Rusinek, A., Gadaj, P., Klpeaczko, J.R., Nowacki, W.K., Thermographic analysis of temperature increase during plastic deformation of sheet steel TRIP 800, Revue Material & Technique (2004), pp. 1-11 (accepted)
[2] Tomita, Y., Iwamoto, T., Constitutive modeling of TRIP steel and its application to the improvement of mechanical properties, Int. J. Mech. Sci., **37** (1995), pp. 1295-1305
[3] Rusinek, A., Klepaczko, J.R., Gadaj, P., Nowacki, W.K., Behavior of Dual-Phase and TRIP steel sheets during fast shear and tensile tests – Constitutive relations and temperature measurements by thermovision, European Journal of Mechanics (2004), pp. 1-30 (submitted)
[4] Klepaczko, J.R., Modelling of structural evolution at medium and high strain rates, FCC and BCC structures, in : Constitutive Relations and Their Physical Basis, Risö Math. Lal. Roskilde, Denmark (1987), 387

A NUMERICAL APPROACH TO MARTENSITIC PHASE TRANSFORMATIONS

Thomas Antretter[*], Franz D. Fischer[*], Georges Cailletaud[**]
[*]*Institute of Mechanics, Montanuniversität Leoben, A-8700 Leoben, Austria*
[**]*Centre des Matériaux, Ecole des Mines, B.P.87, F-91003 Evry Cedex, France*

Summary Martensitic phase transformations triggered either thermally or mechanically entail a series of peculiar effects on the macro-scale. A thermodynamic criterion deciding upon the formation of a new martensite variant is interpreted as transformation surface bounded by planes, which can be adapted for use as a material subroutine in a finite element program. In combination with flow-plasticity such a concept enables to explain the overall mechanical consequences of transformation induced plasticity.

INTRODUCTION

The present study investigates the peculiarities of MarvalX12, a maraging steel entirely transforming from the austenitic phase into martensite at temperatures low enough to facilitate the experimental verification of the phenomena of interest without having to cope with side effects coming into play in the high temperature regime such as creep. This paper lays out a concept on how to make the thermo-mechanical behavior of materials undergoing a martensitic phase transformation during loading in combination with classical plasticity accessible to a numerical treatment. The relevant equations associated with the phenomenon of transformation induced plasticity have already been derived and presented in [1]. According to this work the issue of transformation is essentially decided by the competition of mechanical and chemical driving forces being a function of the mechanical and thermal state competing with dragging forces represented by the energies required to accommodate the newly created phase.

MODEL

Under certain simplifying circumstances the transformation condition in the notation of [1] can be rewritten in terms of specific quantities as

$$\underline{\sigma} : \underline{\varepsilon}_i^* + \rho\Delta\varphi_{chem}(T) = R_i(\xi_i, \xi_j) . \tag{1}$$

If the equality is satisfied a portion of the parent phase transforms into martensite. The mechanical driving force is defined by the double contraction of the stress state at the start of transformation, denoted by $\underline{\sigma}$ with one of 24 distinct transformation eigenstrains $\underline{\varepsilon}_i^*$ corresponding to each variant known in advance from a crystallographic theory. The chemical driving force $\rho\Delta\varphi_{chem}$ can very well be approximated as a linear function of the temperature *T*. The right hand side of equation (1) comprises a variety of different mechanisms inhibiting transformation, e.g. a barrier that needs to be overcome in order to rearrange the atoms, a surface energy term and the additional elastic and plastic energies necessary to accommodate the newly created phase. These effects that can be summarized as the dragging forces of martensitic phase transformation are hard to quantify. They essentially depend on the fraction and combination of the martensite variants already present and blocking the space for fitting in a new lath or plate. In this work the symbol ξ_i will be used for the local volume fraction of the *i*-th variant. $R_i(\xi_i, \xi_j)$ represents the function that subsumes the dragging forces. Experimental results involving non-monotonic temperature paths ([2]) give some indication on the shape of this function, and a reasonable fit can be found.

In analogy to the yield locus concept in plasticity martensitic transformation can formally be treated in stress space where the transformation conditions span a surface defining the transformation loci. Each of the 24 equations (1) represents a six-dimensional hyperplane intersecting the neighboring planes, all parameterized by the temperature. Using the terminology of standard plasticity the dragging forces will alternatively be referred to as hardening terms. A small strain setting is assumed for all further relationships. For realistic deformations the resulting error will be small. Then the total strain $\underline{\varepsilon}$ can be decomposed into its various components:

$$\underline{\varepsilon} = \underline{\varepsilon}^{el} + \underline{\varepsilon}^{pl} + \underline{\varepsilon}^{th} + \underline{\varepsilon}^{*}, \quad \underline{\varepsilon}^{*} = \sum_{i=1}^{24} \xi_i \underline{\varepsilon}_i^* \tag{2}$$

with $\underline{\varepsilon}^{el}, \underline{\varepsilon}^{pl}, \underline{\varepsilon}^{th}$ being the elastic, plastic and thermal strain in vector notation. The total transformation strain is obtained by adding up the discrete transformation eigenstrains $\underline{\varepsilon}_i^*$ weighted by their respective volume fractions ξ_i. The plastic strain is calculated based on the laws of Mises plasticity, i.e. a yield condition

$$\sqrt{\tfrac{3}{2}\underline{S} : \underline{S}} \le \sigma_y(p) , \tag{3}$$

where $\underline{S}$ denotes the deviator of $\underline{\sigma}$, and $\sigma_y(p)$ is the flow stress as a function of the accumulated plastic strain *p* thus defining the plastic hardening behavior of the material. For the time being isotropic hardening is assumed. Realistically, only the austenite phase shows non-negligible plastification so the flow rule will be formulated for the austenite only, and the total plastic strain of the composite follows from a rule of mixture, i.e.

$$\dot{\underline{\varepsilon}}_{\gamma}^{pl} = \dot{p}\underline{n}, \qquad \underline{\varepsilon}^{pl} = (1 - \sum_{i=1}^{24} \xi_i)\underline{\varepsilon}_{\gamma}^{pl} \tag{4}$$

with $\underline{n}$ being the normal to the yield surface, which can be derived from the flow potential. For the sake of simplicity the influence of the thermal strain will not be discussed here.
For the numerical implementation the relevant equations have to be formulated in an incremental notation. Due to the resulting discretization error the linear strain decomposition, the yield condition and finally the transformation condition are generally violated, so that a vector of residual values $\underline{\mathfrak{R}}_e$, $\mathfrak{R}_p$ and $\mathfrak{R}_t^i$ remains:

$$\underline{\mathfrak{R}}_e = \Delta\underline{\varepsilon}^{el} + (1 - \sum_{i=1}^{24} \xi_i)\Delta p\underline{n} - \sum_{i=1}^{24} \Delta\xi_i \underline{\varepsilon}_{\gamma}^{p} + \sum_{i=1}^{24} \Delta\xi_i \underline{\varepsilon}_i^{*} - \Delta\underline{\varepsilon} \tag{5}$$

$$\mathfrak{R}_p = \sqrt{\tfrac{3}{2}(\underline{S} + \Delta\underline{S}) : (\underline{S} + \Delta\underline{S})} - \sigma_y(p + \Delta p) \tag{6}$$

$$\mathfrak{R}_t^i = (\underline{\sigma} + \Delta\underline{\sigma}) : \underline{\varepsilon}_i^{*} + k(T - T_{ref}) - R(\xi_i + \Delta\xi_i, \xi_j + \Delta\xi_j), \; i, j = 1,...,24 \tag{7}$$

Note that here an implicit formulation has been chosen for the equations (5), (6) and (7) where all state variables are evaluated at the end of the current time increment. Obviously the parameters have to be determined such that the residuals disappear. Then the equations represent a set of 31 non-linear functions of altogether 31 solution variables $\Delta\underline{\varepsilon}^{el}$, Δp and $\Delta\xi_i$. Numerically, this can be accomplished using a root finding algorithm such as the standard Newton-Raphson technique. Note that several constraints on the volume fractions of the variants have to be observed, e.g. the increment of the fraction of each variant must always be positive while the total volume fraction must not exceed 1.

RESULTS

The calculations have been performed at one single material point, subjected to an external stress state. Two different load cases have been investigated with the main focus on the orientation effect, i.e. the issue which set of variants is selected by a given stress field. Figure 1b shows the evolution of the volume fractions of the active variants for the case of uniaxial tension of 50 MPa as the temperature is decreased below martensite start. It turns out that for this load level only two variants are activated by the selection mechanism which, in turn, favors those variants that create the highest mechanical driving force. In contrast, if the load is reduced to 20 MPa, two additional variants (number 1 and 12) appear, see Figure 1a. Variant 10 is still dominating, but its fraction reaches only about 50%, which is far less than in the case of the higher load. The algorithm yields qualitatively reasonable results in the sense that the number of active variants increases as the load level decreases.

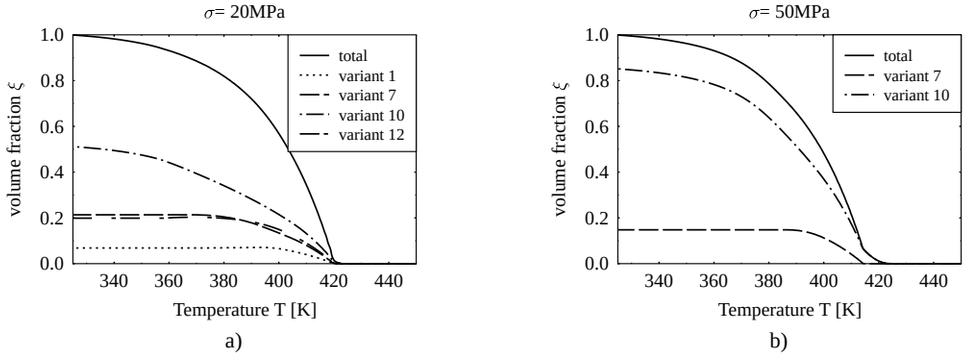


Figure 3: Variant evolution for two different load levels: a) 20 MPa, b) 50MPa.

CONCLUSIONS

An equivalent formalism as for classical flow plasticity establishes the theoretical foundation of the numerical scheme presented towards the end of this paper. The presented concept is based on the underlying idea of a transformation surface. The relevant equations for transformation induced plasticity, essentially the strain decomposition, the yield condition and the transformation condition are formulated in an incremental notation and resolved by means of an implicit integration method. Even for uniaxial stress states constant in time, the algorithm finds sets of martensitic variants whose number varies depending on the stress level. For higher loads one of the active variants prevails accounting for a significant orientation effect in terms of the overall elongation of the specimen.

References

[1] Fischer, F.D., Reisner, G.: *Acta mater.* **46**:2095-2102, 1998.
[2] Tanaka, K., Terasaki, T., Goto, S., Antretter, T., Fischer, F.D., Cailletaud, G.: *Mater. Sci. Eng.* **A341**:189-196, 2002.

MACRO-, MESO- AND MICRO-SCOPIC METALLO-THERMO-MECHANICS
--- Theories and applications –-

Tatsuo INOUE

Department of Mechanical Systems Engineering, Fukuyama University
Gakuen-cho 1-Sanzo, Fukuyama 729-0292, Hiroshima, Japan
Phone;+81-84-936-2112(Ext.4942), Fax: +81-84-936-2023
E-mail; inoue@fume.fukuyama-u.ac.jp, inoue-tat@nifty.com

Coupling among metallic structures including molten state, temperature, and stress and/or strain occurring in processes accompanied by phase transformation sometimes affects predominant influence in determining such fields in industrial processes as quenching, welding, casting and so on. Outer triangle in figure 1 represents the schematic representation of the effect of *metallo-thermo-mechanical coupling* with the induced phenomena. When the temperature distribution in a material varies, *thermal stress* is caused in the body, and the induced phase transformation affects the structural distribution, which is well known during melting or solidification in solid-liquid transition and austenite-pearlite or -martensite transformation in solid phase. Local dilatation due to structural changes in the body bring out the *transformation stress* and interrupts the stress or strain field in the body, and effect of transformation plasticity on the stress/strain constitutive equation is not also negligible.

In contrast to these phenomena, which are well known in ordinal analysis, arrows in the opposite direction indicate coupling in the following manner. Part of the *mechanical work* done by the existing stress in the material is converted into heat, which may be predominant in the case of inelastic deformation, thus disturbing the temperature distribution. The acceleration of phase transformation by stress or strain, which is called *stress- or strain-induced transformation*, has been treated by metallurgists as one of leading parameters of transformation kinetics. The opposite arrow corresponds to the *latent heat* due to phase transformation, which is essential in determining the temperature. When no coupling among the fields, independent analyses of heat conduction, stress and transformation kinetics are possible to be carried out. However, in such case of coupled issue, global formulation based on continuum thermodynamics is needed.

Formulation of the fundamental coupled equations for stress-strain relationships, heat conduction and transformation kinetics based on continuum thermodynamics will be made in the first part of this paper, and the finite element implementation is carried out, which is termed as ***macroscopic metallo-****thermo-mechanics* (or, in general, *materio-thermo-mechanics*).

However, if we treat the motion of atoms or molecules consisting of the continuum, all three fields are identified by solving Newton equations of motion for each atom, since the structural change depends on the *configuration*, temperature is the *vibration* itself and stress/strain is related to the *interatomic distance* as is shown by the inner illustration in the figure. *Molecular dynamics method* is one of the most promising techniques to emit a light especially to such kind of coupled metallo-thermo-mechanical problems. The way to solve the problem is here called ***microscopic, or nanoscopic metallo-thermo-mechanical approach.***

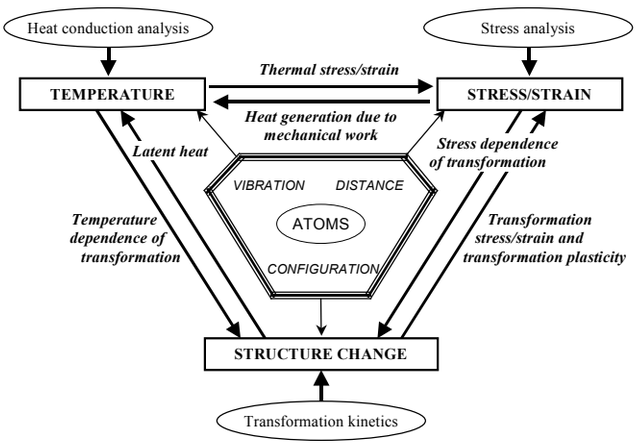


Figure 1. Macro- and micro-scopic representation of *metallo-thermo-mechanics.*

In such a situation of the restriction of so small domain and so short time period to be treated by the molecular dynamics simulation, the *phase field method* has been developed as a promising technique to solve the fields of phase change associated with temperature, and some successful results are obtained for initiation and growth of solidifying crystal from liquid state, and in-solid phase transformation. However, few papers for the phase field method treat the mechanical field of stress and strain.

In the first half of this paper, thermodynamic consideration will be presented to derive the series of fundamental equations governing the coupled mechanical, thermal and phase fields, which the author calls as a ***mesoscopic metallo-thermo-mechanics***.

A parameter ψ termed as *transformation parameter* representing the structural change due to in-solid or solid-liquid transformation is introduced, which will be reduced to a volume fraction ξ in the former case and a phase field parameter ϕ in the latter case. Based on the continuum thermodynamics, the evolution equation of the parameter is obtained from the restriction of continuum thermodynamics ;

$$\tau\dot{\psi} = TK(\psi) - \frac{\partial G}{\partial \psi}$$

with a positive constant τ, and free energy function G as well as the coupled heat conduction equation and stress-strain constitutive equation.

$$\rho c\dot{T} = \sigma_{ij}\dot{\varepsilon}_{ij} - \frac{\partial}{\partial x_i}\left(k\frac{\partial T}{\partial x_i}\right) + \rho\gamma + K_u(\psi)\dot{\psi}$$

$$\varepsilon_{ij}^{\mathrm{e}} = \left(\Sigma\frac{1+\nu_I}{E_I}\xi_I\right)\sigma_{ij} - \left(\Sigma\frac{\nu_I}{E_I}\xi_I\right)\delta_{ij}\sigma_{kk} + \delta_{ij}\int_{T_0}^{T}\Sigma\alpha_I\xi_I dT + \delta_{ij}\Sigma\beta_I(\xi_I - \xi_{I0})$$

Applications of the derived equations are now introduced to solve some engineering processes incorporating phase transformation, such as quenching of a gear wheel and a sword by the finite element method as the macroscopic application and dendrite growth coupled with mechanical field by the phase field method as mesoscopic viewpoint. Some results on melting and /or solidification depending on stress by the molecular dynamics method are also presented as example of microscopic simulation.

XXI ICTAM, 15–21 August 2004, Warsaw, Poland

MULTISCALE MODELING OF STEELS ASSISTED BY TRANSFORMATION-INDUCED PLASTICITY.

S. Turteltaub and A.S.J. Suiker
Faculty of Aerospace Engineering, Delft University of Technology, Kluyverweg 1, 2629 HS Delft, The Netherlands

Summary We develop a multiscale thermomechanical model for retained austenite in carbon steels where the effects of fine-scale substructures, within an austenitic grain, is accounted for via a homogenization procedure and the mesoscale interaction with neighboring phases is modelled numerically via a three-dimensional analysis of a representative mesostructure.

INTRODUCTION

The favorable combination of strength and ductility in carbon steels whose mechanical response is enhanced by a transformation induced plastic behavior (known as TRIP steels) has been attributed to the presence of islands of retained austenite in the initial microstructure. Austenite is a solid phase that usually is unstable at room temperature and zero stress. Nonetheless, with the addition of certain elements (e.g., Si, Al) and under a controlled thermal processing route, it is possible to have regions where austenite is metastable at room temperature. Several models have been proposed to study the contribution of retained austenite; however, there are still many open issues regarding the role of retained austenite on the overall material response of TRIP steels (see, e.g., [2]). In view of this, we develop a multiscale model and focus attention on representative inclusions of retained austenite. We study in detail their contribution to the macroscopic material response under mechanical loads. Additionally, we take into account the effect of other phases in the microstructure and analyze their contribution as well.

MULTISCALE MODEL

The mesoscopic response of TRIP steels depends upon the interaction of several phases present in the mesoscale structure, i.e., ferrite, bainite and retained austenite. The evolution of retained austenite depends on smaller scale phenomena, particularly its transformation into different types of twinned martensite (referred to as "transformation systems", numbered $\alpha = 1, \ldots, 24$). These systems have their own internal structure, formed by body-centered tetragonal variants of martensite. The different scales and structures of interest are shown in Figure 1. We divide the scales of observation into a lattice, lower microscale, upper microscale and finally a mesoscale. To study the behavior of retained austenite in a ferrite-based

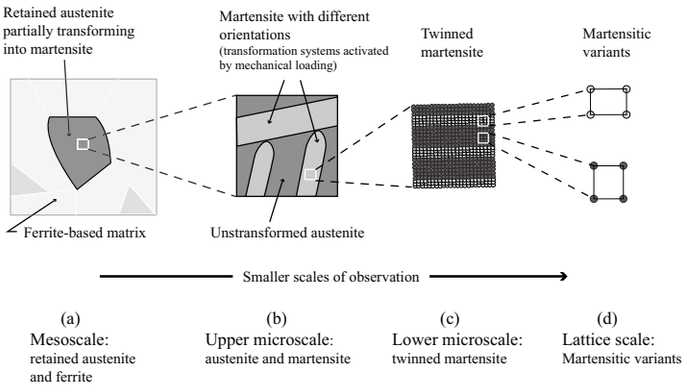


Figure 1. Scales of observation.

matrix at the mesoscale, we first develop a multiscale model that takes into account the thermomechanical response at the various scales of observation as sketched in Figure 1. Subsequently, we perform a numerical simulation of a representative austenite inclusion in a ferrite-based matrix. The model is developed within a three-dimensional, geometrically nonlinear framework. The different configurations and scales are shown in Figure 2a.

MESOSCALE THERMOMECHANICS

The variables used to describe the thermomechanical response of retained austenite at a mesoscopic level are the deformation gradient $\boldsymbol{F}$, the entropy η and a set of internal variables $\xi^{(\alpha)}$ that correspond to the volume fractions of the transformation systems. We use information from the nonlinear theory of martensitic transformations at the lattice and the microscales [1] and irreversible thermodynamics, together with a homogenization procedure to determine the mesoscopic form of the transformation deformation gradient $\boldsymbol{F}_{tr}$ and the transformation entropy η_{tr}. The influence of local

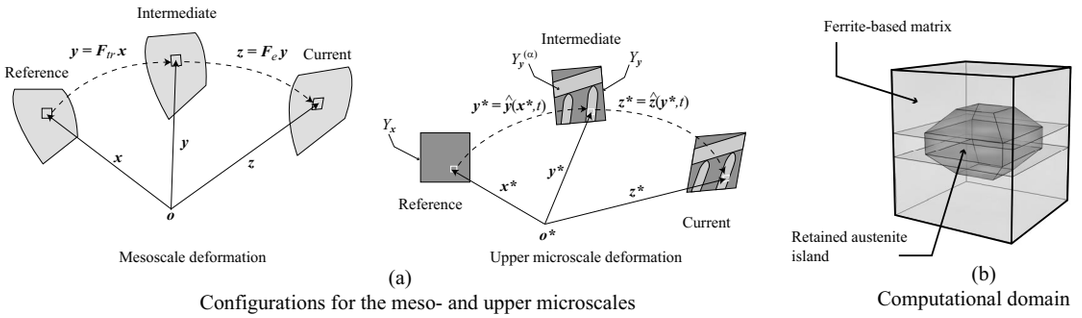


Figure 2. (a) Reference, intermediate and current configurations at the upper microscale and mesoscale levels. (b) Typical island of retained austenite in a ferrite-based matrix for FEM analysis.

carbon concentration in the retained austenite is also included in the transformation deformation gradient. The plasticity induced in the soft ferrite-based matrix surrounding the retained austenite is incorporated in our model via an elastoplastic formulation for large deformations. Since most of the plastic deformation occurs in the matrix, the austenite is assumed not to deform plastically. Consequently, the deformation gradient and the entropy in the austenite are decomposed as

$$\boldsymbol{F} = \boldsymbol{F}_e \boldsymbol{F}_{tr} \ , \qquad \eta = \eta_e + \eta_{tr} \ , \tag{1}$$

where $\boldsymbol{F}_e$ represents the elastic deformation gradient and η_e is the conservative part of the entropy. Through a multiscale analysis we estimate the effective thermomechanical response at a mesoscopic level. We provide constitutive expressions for the second Piola-Kirchhoff stress $\boldsymbol{S}$ in the intermediate configuration and for the temperature θ in terms of the elastic Green-Lagrange strain $\boldsymbol{E}_e = \frac{1}{2}(\boldsymbol{F}_e^T \boldsymbol{F}_e - \boldsymbol{I})$ and the entropy η_e, respectively, as well as the internal variables. The effective stiffness can be expressed in terms of the stiffness $\mathbb{C}^A$ of the austenite, the stiffness $\mathbb{C}^{(\alpha)}$ of each transformation system and the internal variables that measure the evolution of the transformation. We develop a similar formula for the effective specific heat in terms of the specific heats h^A and h^M of austenite and martensite respectively. The surface energy is included by means of an expression that depends on the martensitic volume fractions. All this information is used to construct a Helmholtz potential that characterizes the material behavior. The evolution of the distinct phases is described by a kinetic law. A key ingredient in the model is the expression for the transformation driving force. With the decomposition for the entropy given by (1), one can obtain thermal analogues for the mechanical terms of the transformation driving force for each transformation system α (twinned martensite). The driving force for each α has been derived as [3]

$$\begin{aligned} f^{(\alpha)} = \det(\boldsymbol{F}_{tr}) \boldsymbol{F}_e^T \boldsymbol{F}_e \boldsymbol{S} \boldsymbol{F}_{tr}^{-T} \cdot \boldsymbol{\gamma}^{(\alpha)} + \tfrac{1}{2} \left(\mathbb{C}^A - (1 + \operatorname{tr} \boldsymbol{\gamma}^{(\alpha)}) \mathbb{C}^{(\alpha)} \right) \boldsymbol{E}_e \cdot \boldsymbol{E}_e \\ - \frac{\chi}{l_0} \left(1 - 2\xi^{(\alpha)} \right) + \rho_0 \theta \frac{\lambda_T^{(\alpha)}}{\theta_T} + \rho_0 (h^M - h^A) \left(\theta \ln \frac{\theta}{\theta_T} - (\theta - \theta_T) \right) \ , \qquad \alpha = 1, \ldots, 24, \end{aligned} \tag{2}$$

where $\boldsymbol{\gamma}^{(\alpha)}$ is the shape strain of system α, χ is the surface energy of an austenite-twinned martensite interface, l_0 is a characteristic length of platelets of twinned martensite, ρ_0 is the mass density in the reference configuration, $\lambda_T^{(\alpha)}$ is the latent heat for system α and θ_T is the transformation temperature. Additional details of the model can be found in [3].

SIMULATIONS

We perform three-dimensional numerical simulations of a domain, shown in Figure 2b, formed by a ferrite-based matrix and an island of retained austenite. Details of the numerical implementation can be found in [4]. We explore the transformation of retained austenite into martensite as a function of lattice orientation and we quantify the plastic deformation induced by this transformation. The detailed analysis of the TRIP effect at the mesoscale will be used to determine optimal microstructures for the next generation of high-strength, high-ductility steels.

References

[1] Ball J.M., James R.D.: Fine phase mixtures as minimizers of energy, *Arch Ration Mech An* **100** (1): 13-52, 1987
[2] Fischer F.D., Reisner G., Werner E., Tanaka K., Cailletaud G., Antretter T.: A new view on transformation induced plasticity (TRIP) *Int J. Plast* **16** (7-8): 723-748, 2000
[3] Turteltaub S., Suiker, A.S.J.: Multiscale model of martensitic transformations in carbon steels. In preparation.
[4] Suiker, A.S.J., Turteltaub S.: Computational modelling of plasticity induced by martensitic phase transformations. In preparation.

XXI ICTAM, 15–21 August 2004, Warsaw, Poland

THE NATURE OF STRESS AND STRAIN FIELDS IN SHAPE MEMORY POLYCRYSTALS

Isaac Chenchiah*, Kaushik Bhattacharya
California Institute of Technology, Pasadena, CA 91125, USA
* *Currently at, Max Planck Institute for Mathematics in the Sciences, Inselstr. 22, 04103 Leipzig, Germany*

Summary A central open problem in the study of shape memory polycrystals is the prediction of their recoverable strains. Solving this problem requires an understanding of the possible stress and strain fields that arise in such polycrystals. For polycrystals made of materials undergoing cubic-tetragonal transformations, we show that the strains fields associated with macroscopic recoverable strains are related to the solutions of hyperbolic partial differential equations. We explore consequences of this relationship and connections to previous conjectures characterizing polycrystals with non-trivial recoverable strains. We also show that stress fields in shape memory polycrystals could be concentrated on lower-dimensional surfaces (planes and lines). We do this by proving a dual variational characterization of recoverable strains and presenting several examples. Implications of this characterization for effective properties and the development of numerical methods are discussed.

THE SHAPE MEMORY EFFECT IN POLYCRYSTALS

Shape memory (SM) effect is the ability of a solid to recover on heating apparently plastic deformation sustained below a critical temperature. Many alloys (e.g. NiAl, FeNiC) exhibit good SM behavior as single crystals but little or none as polycrystals while others (e.g. CuAlNi, NiTi) are good SM materials both as single crystals and as polycrystals. Since the utility of SM alloys critically depends on their polycrystalline behavior, this issue is of both scientific interest and technological importance. Thus we desire (a) to know the reason for this difference in the behavior of SM polycrystals; (b) to predict which materials generically exhibit good polycrystalline SM behavior; and (c) to characterize, for a given material, those polycrystals which exhibit good SM behavior.

This paper provides insight into these difficult problems by presenting results on the nature of stress and strain fields that arise in shape memory polycrystals.

STRAIN FIELDS IN CUBIC-TETRAGONAL POLYCRYSTALS

A model for the SM effect in single crystals and polycrystals [2, §1]

A SM single crystal has a multi-well microscopic energy, each well corresponding to a variant of Martensite. An undeformed single crystal consists of self accommodated mixtures of Martensitic variants. A deformation is recoverable precisely when the variants can accommodate it by reorganizing themselves: the recoverable strains of a single crystal are precisely those that lie in the zero-set of its mesoscopic energy. Likewise, the recoverable strains of a polycrystal are the macroscopic averages of strain fields which locally lie in the zero-set of the mesoscopic energy of each grain.

Connections with hyperbolic partial differential equations

For a material that undergoes the cubic-tetragonal transformation, the zero-set of the mesoscopic energy of an unoriented crystal is contained in the subspace

$$\left\{\epsilon \in \mathbb{R}^{3\times 3}_{\text{sym}} \mid \epsilon_{12} = \epsilon_{13} = \epsilon_{23} = 0\right\}.$$

Using the strain compatibility equation, we deduce that strain fields constrained to lie in this subspace are of the form

$$\begin{aligned}
\epsilon_{11} &= f_2(x_1, x_3) - f_3(x_1, x_2) + c_1,\\
\epsilon_{22} &= f_3(x_1, x_2) - f_1(x_2, x_3) + c_2,\\
\epsilon_{33} &= f_1(x_2, x_3) - f_2(x_1, x_3) + c_3,
\end{aligned}$$

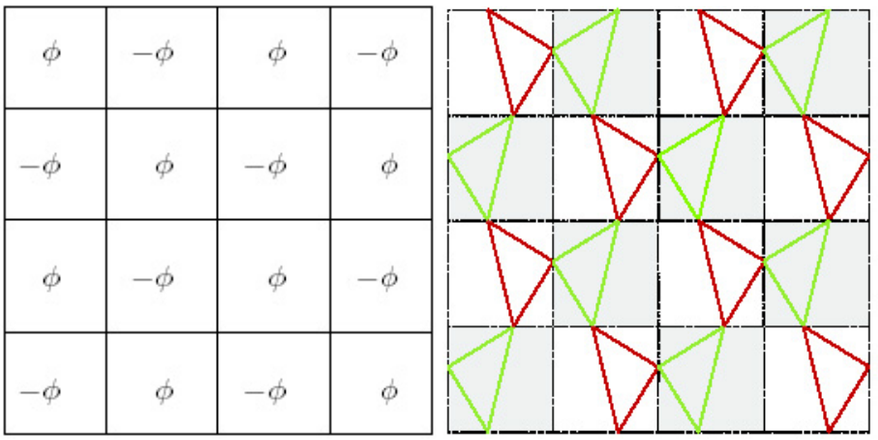
where $f_1, f_2, f_3 \in L^\infty(\mathbb{R}^2, \mathbb{R})$ satisfy

$$\begin{aligned}
\left(\frac{\partial^2}{\partial x_2^2} - \frac{\partial^2}{\partial x_3^2}\right) f_1(x_2, x_3) = 0,\\
\left(\frac{\partial^2}{\partial x_3^2} - \frac{\partial^2}{\partial x_1^2}\right) f_2(x_1, x_3) = 0,\\
\left(\frac{\partial^2}{\partial x_1^2} - \frac{\partial^2}{\partial x_2^2}\right) f_3(x_1, x_2) = 0.
\end{aligned}$$

Associated with these three hyperbolic partial differential equations are three pairs of characteristic planes.

Implication: characterizing polycrytals with non-trivial recoverable strain

Thus associated with each grain are three pairs of characteristic planes. Imposing strain compatibility at the grain bound-



(a) A checkerboard with grains oriented at ϕ and $-\phi$. Four periodic cells are shown.

(b) A stress field in this checkerboard as a response to loading (beyond a threashold) in the $\left(\begin{smallmatrix} 0 & 1 \\ 1 & 0 \end{smallmatrix}\right)$ direction.

to percolation theory observed earlier in such problems [2, 3]. Polycrystals that exhibit good SM behavior are precisely those whose texture is such that at least some characteristics percolate.

The preceeding analysis is strong evidence in support of the conjecture [1, 2] that cubic-tetragonal SM polycrystals are essentially those polycrystals whose texture is either (a) a rank-I laminate or (b) bamboo like—i.e. the orientation of all grains share the same axis of rotation. It is hoped that this and similar methods will lead to the characterization of the recoverable strains of polycrystals.

STRESS FIELDS

Dual variational characterization of recoverable strains

Let $\widehat{\mathcal{S}} \subset \mathbb{R}^{n\times n}_{\text{sym}}$ be the zero-set of the mesoscopic energy of an unoriented crystal. Then $\overline{\mathcal{S}} \subset \mathbb{R}^{n\times n}_{\text{sym}}$, the zero-set of the macroscopic energy of a polycrystal has the characterization

$$\delta_{\overline{\mathcal{S}}}(\bar{\epsilon}) = \sup_{\sigma\in\mathcal{S}_{\text{ad}}} \frac{1}{|\Omega|}\int_\Omega \sigma(x)\cdot\bar{\epsilon} - \delta^\star_{\widehat{\mathcal{S}}}(R^T(x)\sigma(x)R(x))\,\mathrm{d}x.$$

Here $\delta_{(\cdot)}\colon \mathbb{R}^{n\times n}_{\text{sym}} \to \{0,\infty\}$ and $\delta^\star_{(\cdot)}\colon \mathbb{R}^{n\times n}_{\text{sym}} \to \mathbb{R}$ are the indicator and support functions of the set $\cdot$ respectively; $R\colon \Omega \to SO(n)$ is the texture of the polycrystal; and $\mathcal{S}_{\text{ad}}$ is the set of all signed radon measures with finite mass.

Implication: stress localization

This implies, in particular, that stress fields could localize to lower dimensional surfaces (plane and lines in three-dimensions). As an example, consider the two-dimensional checkerboard polycrystal shown in Figure (a). A stress field corresponding to a macroscopic strain of the form $s\left(\begin{smallmatrix} 0 & 1 \\ 1 & 0 \end{smallmatrix}\right)$, $|s| > \tan\phi$, is shown in Figure (b). The stress localizes to the diagonal lines shown (everywhere else the polycrystal is unstressed).

This behavior is analogous and dual to the appearance of strain localization (slip planes and lines) in rigid perfectly-plastic materials. Prager in 1957 raised the question of the existance of such materials [5, 6]; our work provides an affirmative answer.

It follows that any attempt to compute the recoverable strains of a polycrystal numerically will, in general, fail unless the numerical method is able to handle stress localization. Since most current algorithms cannot do so, this calls for the development of new numerical methods.

References

[1] Kaushik Bhattacharya and Robert V. Kohn. Symmetry, texture and the recoverable strains of shape-memory polycrystals. *Acta Materialia*, 44(2):529–542, 1996.

[2] Kaushik Bhattacharya and Robert V. Kohn. Elastic energy minimization and the recoverable strains of polycrystalline shape-memory materials. *Archive for Rational Mechanics and Analysis*, 139:99–180, 1997.

[3] Kaushik Bhattacharya, Robert V. Kohn, and S. Kozlov. Some examples of nonlinear homogenization involving nearly degenerate energies. *Proceedings of the Royal Society of London. Series A - Mathematical Physical and Engineering Sciences*, 455:567–583, 1999.

[4] Isaac Chenchiah. *Energy-minimizing microstructures in multiphase elastic solids*. PhD thesis, California Institute of Technology, 2004.

[5] William Prager. On ideal locking materials. *Transactions of the Society of Rheology*, 1(1):169–175, 1957.

[6] William Prager. Elastic solids of limited incompressibility. In *Proceedings of the 9th International Congress on Applied Mechanics*, volume 5,

SHAPE MEMORY ALLOY UNDER STRAIN- AND STRESS-CONTROLLED CONDITIONS – THERMOMECHANICAL ASPECTS OF THE MARTENSITE AND REVERSE TRANSFORMATIONS

Wojciech K. Nowacki, Elzbieta A. Pieczyska, Stefan P. Gadaj,
Hisaaki Tobushi[#], Makoto Takagi[#]

Polish Academy of Sciences, IPPT PAN, Swietokrzyska 21, PL 00-049 Warszawa, Poland
[#]AICHI Inst. of Technology, 1247, Yachigusa, Yagusa-cho, Toyota-city, Aichi, 470-03, Japan

Summary Thermomechanical aspects of martensite and reverse transformations in TiNi shape-memory alloy subjected to strain and stress control were investigated. The temperature distributions on the specimen's surface were determined by using an infrared camera. The results differ in mechanical behavior, however at both approaches, heterogeneous temperature distributions, related to the nucleation and development of the new phase, were observed. The similar heterogeneous effects were observed during unloading, while the reverse transformation took place, accompanied by significant temperature decrease.

Shape memory alloys (SMAs) are interesting group of modern materials with the feature to remember a shape after a significant deformation, up to 8%, recovered by an increase in temperature (shape memory effect) or large nonlinear elastic range (pseudoelasticity). These characteristics as well as significant internal damping and high yield stress enable them using in advanced and smart structures [1, 2]. Most popular and widely applied to practical use is TiNi SMA, due to its superior memory, structure properties and excellent corrosion resistance. The objective of our work is to provide accurate experimental data of a TiNi shape memory alloy in order to study of thermomechanics of nucleation and further development of stress induced martensite transformation. To this end, stress and strain controlled tensile tests were performed with various rates of deformation. A thermovision camera was used in order to register the distribution of infrared radiation and calculate the temperature changes of the TiNi specimens subjected to loading. The infrared camera is very useful in such research, since it enables to identify the area of higher or lower temperature, related to occurrence of the new material phase. The obtained temperature images were stored for further analysis; such approach enabled to observe, register and analyze the kinetics and thermodynamics of the phase transitions.
The sheet specimens of 160 x 10 x 0.4 were cut off from the band of SMA. Each specimen was covered by carbon powder in order to obtain a higher and homogeneous emissivity. The specimens were subjected to the strain controlled tensile test with the strain rates 5 x $10^{-3}s^{-1}$, $10^{-2}s^{-1}$, 5 x $10^{-2}s^{-1}$, and the stress controlled tensile test with the stress rates 12.5 MPa s^{-1}, 25 MPa s^{-1}, 50 MPa s^{-1}, 75 MPa s^{-1}. The temperature changes were calculated as an average from the specimen area ≈ 400 mm^2. The examples of obtained characteristics are shown in Fig.1a and Fig.1b. Taking advantages from the infrared camera, it was observed that just after the uniform temperature distribution registered in the elastic range, the temperature slightly increased in the central area of the sample which was followed by the sudden occurrence of the first inclined line of significantly higher temperature (Fig.2a), probably related to the nucleation of the new, martensite phase. After a while, a few such lines parallel to each other occurred and moved towards the sample borders, as well as the next "family" of them, developing in the perpendicular direction (Fig.2b). At higher strain, the regions of higher temperature became less clearly defined (Fig.2c), most likely because of the further martensite phase development in the whole material volume and the heat flow. When the martensitic transformation was completed, the temperature of the specimen surface became almost homogeneous again. The heterogeneous field of temperature distribution has been observed also during unloading of the TiNi, when the reverse transformation took place (Fig.2d), although it was surprising in comparison to the previously obtained results for slightly different kind of TiNi SMA [3].

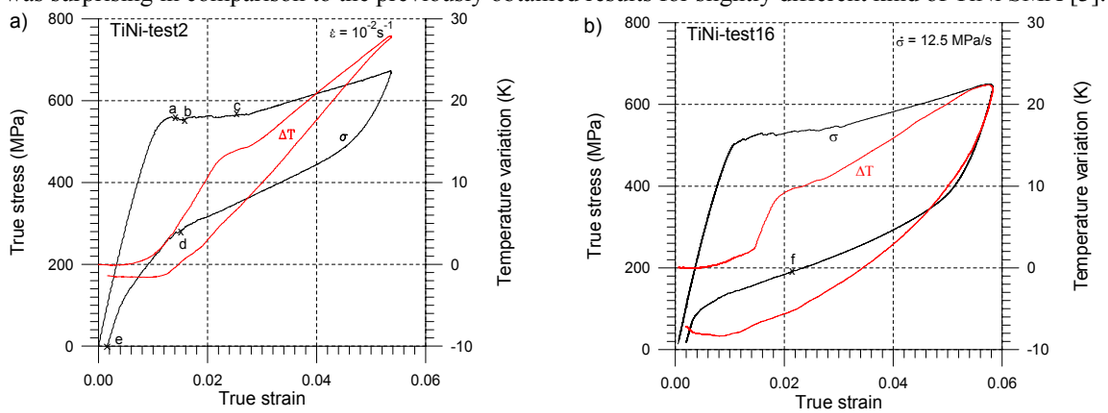


Fig. 1. Stress-strain curve and temperature changes under a) strain- and b) stress- controlled conditions of TiNi SMA

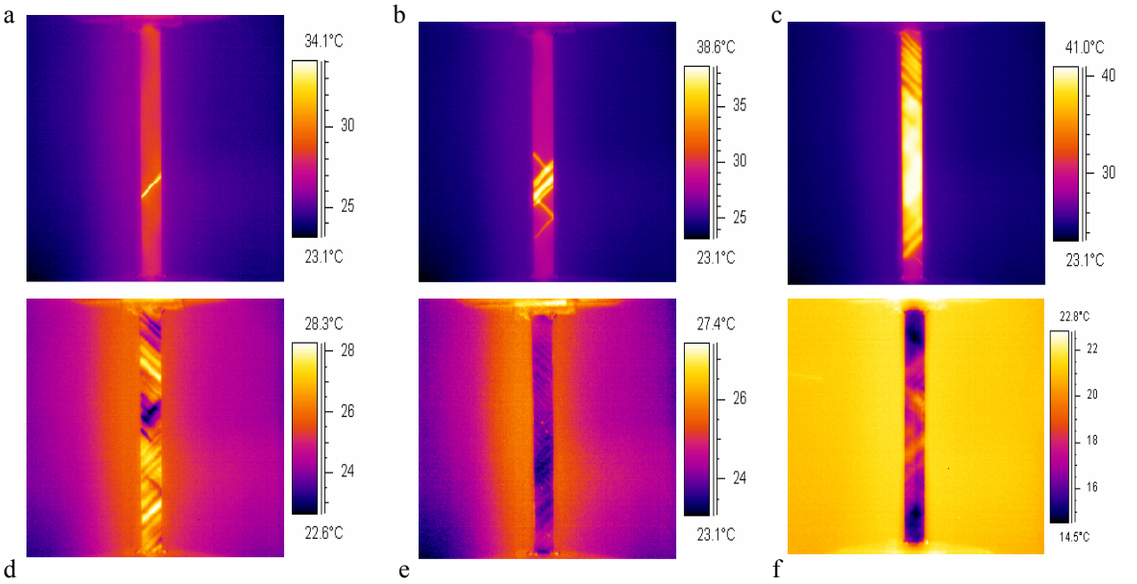


Fig. 2. Temperature distribution of TiNi subjected to uniaxial tensile test at room temperature: The letters correspond to the proper points of the stress-strain curves shown in Fig.1: a, b, c – during martensite transformation, d – during reverse transformation, e – after unloading; f – final part of the stress controlled tensile test.

CONCLUSIONS

The thermomechanical behavior of SMA reflects the exothermic character of the austenite into martensite transformation and endothermic character of the reverse one. The higher the strain rate, the higher the stress of the martensite transformation due to the significant temperature increase and the higher decrease of the transformation stress, caused by the larger decrease in temperature [1]. The sufficiently high rates of deformation applied caused significant temperature changes, which influence on the mechanical characteristics. Such effects of the thermomechanical couplings are noticed in Figs.1a and 1b. The maximal increase in temperature, related to martensitic transformation, was quite significant, up to 30 K in some area: the higher temperature was measured at the cross-section of the interphase bands (Fig.2b). During the unloading, when the reverse transformation (martensite into austenite) took place, the temperature of the specimen in some area falls down with the drop up to 10 K: the lower temperature was measured at the cross-section of the interphase bands (Fig.2d). Particularly interesting were the results obtained after unloading of the strain-controlled test. Namely, after 3.26 s of the unloading to null, the temperature distribution remained still heterogeneous (Fig.2e). It can be explained like this. After unloading, some residual martensite remains. That is, though the reverse transformation completes macroscopically, it does not microscopically complete. Based on this residual martensite, there appears residual or internal stress after unloading. Therefore, some local microscopic reverse transformation still occurs in the elastic region of unloading after the macroscopic finish point of the reverse transformation. Due to this effect, the heterogeneous temperature distribution may appear after unloading. It will be cleared up in research related to cycling tests. The similar effects of heterogeneity accompanied the stress-controlled tests. It means that after a nucleation, the mechanism of the phase transition is the same and does not depend on the stress level. However, the development of the both martensite and austenite transitions took place not exactly the same way. Namely, the temperature distributions observed during the stress-controlled test were more uniform and the changes were smoother. Furthermore, at the end of the stress-controlled test (Fig.1b), significant temperature decrease has been observed, particularly in the grips area (Fig.2f).

Acknowledgments:

This research has been carried out with the partial support of the Polish Ministry of Scientific Research and Information Technology under Grants No. 8 TO7A 046 20, 4 T08A 060 24, 4T08E 051 24 and of the Japan Society for the Promotion of Sciences under Grant No. 13650104 of Scientific Research (C).

References

[1] Tobushi, K. Okumara, M. Endo and K. Tanaka, Deformation behavior of TiNi shape memory alloy under strain or stress-controlled conditions, Arch. Mech., v. 54, 1, (1999).
[2] John A. Shaw, Simulation of localized thermo-mechanical behavior in NiTi shape memory alloy, Plasticity, Vol. 16, (2000).
[3] S.P.Gadaj, W.K. Nowacki, E.A. Pieczyska, Temperature evolution in deformed shape memory alloy, Infrared Physics & Tech, 43 (2002).

HIGH PRESSURE MECHANOCHEMISTRY: CONCEPTUAL MULTISCALE THEORY AND INTERPRETATION OF EXPERIMENTS

Valery I. Levitas
Texas Tech University, Center for Mechanochemistry and Synthesis of New Materials,
Department of Mechanical Engineering, Lubbock, TX 79409, USA

Summary A simple multiscale (nano-, micro- and macro-) continuum thermodynamic theory for strain-induced phase transitions (PTs) and chemical reactions (CRs), as well as closed form solutions were developed which explain a number of mechanochemical phenomena. The results enabled the development of new methods for control of PTs and CRs under plastic deformation, some of which have experimental confirmations.

Experimental Phenomena

Mechanochemistry studies the plastic strain-induced structural changes (SCs) that include PTs and CRs. After compression of the materials in Bridgman or diamond anvils, a very high pressure is produced in the center of the specimen, which leads to a number of PTs and CRs. It is known, from numerous experiments (Bridgman, Vereschagin, Blank, Zharov, Enikolopyan) summarized in [1] that the addition of plastic shear leads to findings that have both fundamental and applied importance. In particular, superposition of plastic shear, due to the rotation of an anvil, and high pressure in rotational diamond anvil cell (RDAC) leads to

(a) a significant (by a factor of 3-5) reduction of SC pressure and pressure hysteresis,
(b) an appearance of new phases, which were not obtained without additional shear,
(c) a substitution of a reversible SC by an irreversible SC,
(d) strain-controlled kinetics,
(e) nanostructured phases, and
(f) pressure self-multiplication effect, i.e. pressure growth in the transforming region under a fixed compressive force (despite the volume decrease due to SC). Despite the basic and applied importance, there has not been any theory describing thermodynamic and kinetic coupling between plasticity and SCs and any one of the above experimental effects. In this paper, a first multiscale continuum thermodynamic theory was developed which explains the above phenomena. Thus enabling the development of new characterization methods of SCs under plastic deformation as well as methods for controlling SCs.

The developed theory consists of: (a) thermodynamic criterion for SC, (b) extremum principle for determination of geometry of transformed region (in the case of nucleation) and other unknown parameters (e.g. volume fraction of martensitic variants and orientation of interface between them) and (c) a kinetic equation for transformation time (in the case of nucleation) or interface velocity [1,2]. Finite strains and rotations were taken into account. This theory was applied at nano- and microscales.

Nanoscale approach

At the nanoscale, the primary reason for the above phenomena is related to the generation of new defects during plastic flow, which produce strong stress concentration and serve as new nucleation sites. A model of nucleation at the tip of dislocation pile-up was developed. Geometric parameters and orientation of nucleus were determined. It was further demonstrated that shear stress can lead to substitution of thermally activated nucleation with barrierless nucleation and significantly reduce SC pressure for direct SC, as well as increase SC pressure for reverse SC. Barrierless nucleation explains the strain-controlled rather than time-controlled kinetics. Indeed, the prescribed strain increment generates defects with barrierless, i.e. very fast, nucleation and growth of the product phase up to the size where stress concentration is reduced and cannot drive the interface further. For the observation time of 1 s, this looks like instantaneous SC. As straining stops, no new defects and nuclei appear, and the growth of the existing nuclei is thermodynamically impossible. This explains also a nanosize of grains. As the contribution of the stress concentration to the driving force for SC is finite, there exists a lowest possible pressure below which strain-induced SC is impossible. Dislocation pile-ups generate both compressive and tensile pressure, which are of the same magnitude. Consequently, they simultaneously promote both direct and reverse SC in different regions. All of these results were conceptually incorporated into the microscale model. For the thermally activated regime, it was obtained that shear strain does not change significantly SC pressure, but accelerate SC kinetics, in accordance with experimental observations.

Strain-controlled kinetic equation

At the microscale, a new strain-controlled kinetic equation is derived from our thermodynamic SC criterion. It considers the possibility of direct and reverse PT and the difference in plastic strain in each phase due to the different yield stress of the phases. A stationary solution of this equation is found and analyzed. Stationary solution explains zero pressure hysteresis observed experimentally as well as the appearance of new phases, especially strong phases, which were not obtained without shear. However, zero hysteresis can be obtained at any pressure in some range and has nothing to do with phase equilibrium pressure. Phase equilibrium pressure does not appear in any equation and cannot

be obtained from experiment on strain-induced SC. Also an explanation was obtained why a nonreacting matrix with a yield stress higher (lower) than that for reagents significantly accelerates (slows down) the reactions.

Macroscale approach

At the macroscale, mechanics of plastic flow and SC in rotating diamond anvils is modeled. A strain-controlled kinetic equation derived at the microscale was used. Sliding of an anvil with respect to material is determined. Promotion of the SC due to the rotation of the anvil is related to reduction in radial component of shear stress. This leads to the possibility of additional axial displacement, which compensates a volume decrease due to SC, increases plastic strain and pressure. If new phase has larger yield strength, pressure grows in transforming regions; this explains and quantifies a pressure self-multiplication effect observed experimentally. It was also obtained that the rotation of an anvil can lead to new phases, especially hard phases, which were not only but cannot be obtained without the rotation of the anvil. Possible reasons for appearance of small steps (regions with almost homogeneous pressure) on very heterogeneous pressure distribution are found. One of which is related to reduction of contact shear stresses due to transformation-induced plasticity for PTs or reaction-induced plasticity for CRs. However, this constant pressure is not related to any basic properties of SCs and therefore cannot be used for their characterization.

Methods of control of structural changes

The results obtained enabled the development of new methods of control of PT and CR under plastic deformation, even without rotation of the anvils. Some of them have experimental confirmations. One of the most impressive confirmations consists of the following. For rhombohedral rBN single crystals, deforming by slip on the basal plane only, the theoretical compressive yield strength varies from infinity, for compression along the C-axis, to the minimum value when the basal plane and slip direction are at 45^0 to the compression direction. If a single crystal is compressed in a diamond anvil, in the C-direction with a small disorientation, the rotation of the C-axis will occur during plastic flow. Consequently, this rotation will lead to a reduction of the yield stress in the direction of compression (rotational softening and instability), and to a reduction of disk thickness at constant force. Indeed, the following extraordinary experimental results were obtained [3]. A highly textured rBN was compressed along the C-axis $\pm 3^0$. An abrupt irreversible martensitic rBN$\rightarrow$cubic cBN PT was recorded at the sample center at a pressure 5.6 GPa before the PT. The thickness of the disc in different tests decreased from 0.175-0.450 mm to 0.020-0.050 mm. In comparison, under hydrostatic loading the irreversible PT rBN$\rightarrow$cBN occurs at 55 GPa (Ueno et al. 92). Thus a reduction of PT pressure, by one order of magnitude has been achieved. Note that cBN is an important superhard material with hardness second to a diamond. It was concluded that a new phenomenon, namely PT induced by rotational plastic instability takes place.

Concluding remarks

The obtained results predict the unique potential of plastic straining to produce high-strength nanostructured phases. They also suggest a new approach for characterization of strain-induced SCs. In most cases, even without the rotation of an anvil, when a high pressure experiment is performed without hydrostatic media, the specimen undergoes large plastic deformations. This is the case in experiments under megabar pressure, in particular, with solid hydrogen. PT conditions for such a case are characterized by the pressure only (like for pressure-induced SC) and are compared with or led by atomistic calculations of phase equilibrium pressure. We believe that this is conceptually wrong, and even the term "pressure-induced PT or CR" is misleading in such a situation. This is even more true for the case with rotation of an anvil. The usual way of characterization (SC pressure at prescribed rotation or shear) is not complete. Strain-induced SCs under high pressure can be completely characterized by a strain-controlled kinetic equation only.
Some recent experiments in RDAC performed at the Center for Mechanochemistry will be reported [4, 5].

References

1. Levitas V.I. Continuum Mechanical Fundamentals of Mechanochemistry. In *High Pressure Surface Science and Engineering*. Section 3. Institute of Physics, Bristol and Philadelphia, Eds. Y. Gogotsi and V. Domnich, 2004, pp. 159-292.
2. Levitas V.I. Structural Changes without Stable Intermediate State in Inelastic Material. Part I and II. *Int. J. Plasticity*, **16**, 805-892, 2000.
3. Levitas V.I. and Shvedov, L.K. Low Pressure Phase Transformation from Rhombohedral to Cubic BN: Experiment and Theory. *Physical Review B*, **65**, 104109(1-6), 2002.
4. Levitas, V. I., Hashemi, J., Mathis, W., Holtz, M., and Ma, Y. Synthesis of Superhard Phases of Boron Nitride in a Rotation Diamond Anvil Cell. *Brookhaven National Laboratory Year Book*, 2002.
5. Y. Ma, V. Levitas, J. Hashemi, W. Mathis, and M. Holtz. X-Ray Diffraction Study of Superhard BN Phases Synthesized in a Rotational Diamond Anvil Cell. *Brookhaven National Laboratory Year Book*, 2002.

STRESS-INDUCED MARTENSITIC PHASE TRANSITION FRONT PROPAGATION

Arkadi Berezovski[*], Gérard A. Maugin[**]
[*] *Institute of Cybernetics at Tallinn Technical University, Centre for Nonlinear Studies, Akadeemia tee 21, 12618 Tallinn, Estonia*
[**] *Université Pierre et Marie Curie, Laboratoire de Modélisation en Mécanique, UMR 7607, Tour 66, 4 Place Jussieu, Case 162, 75252, Paris Cédex 05, France*

Summary A non-equilibrium description of states of computational elements and their interaction is proposed for the numerical simulation of stress-induced martensitic phase transition front propagation in thermoelastic solids. This description is based on the generalization of the thermodynamics of discrete systems to the thermoelastic case. A finite-volume numerical scheme is then constructed by means of corresponding contact quantities. Additional constitutive information is introduced by means of certain assumptions about the entropy production at the phase boundary. Results of numerical simulations capture experimental observations.

BACKGROUND

The propagation of phase interfaces in shape-memory alloys under applied stress is an experimentally observed phenomenon. At the macroscopic level of description, the diffusionless stress-induced martensitic phase-transition front propagation can be viewed as an example of moving discontinuities in thermoelastic solids. From the mathematical point of view, such a problem is considered as a non-classical shock problem for conservation laws.

There are two distinct approaches to the macroscopic description of the stress-induced martensitic phase-transition front propagation. The first one stems from Ericksen's analysis of the non-monotone behavior of stress-strain relation in an elastic bar. The second one represents the generalization of the constitutive modelling of shape-memory alloys behavior for the dynamic case.

Energy minimization [1] naturally leads to distinct material regions with continuous strain, that are separated from each other by strain discontinuity interfaces so as to avoid unstable branches. Placing the distinct stable branches of the strain-stress curve into correspondence with distinct material phases provides the connection to stress-induced phase transformation. Standard boundary value problems do not have a unique solution when phase boundaries are present. The crucial assumption in the model is the application of a kinetic law relating the front propagation speed and the driving force. Additionally, a nucleation criterion is also introduced. Theoretical prediction of possible forms of the kinetic law can be extracted from more refined theories in which the phase boundaries are regarded as transition zones exhibiting additional physical effects [2].

The problem of stress-induced phase transformation was also considered on the basis of a constitutive model of the shape memory effect and pseudoelasticity of polycrystalline shape-memory alloy [3]. The key feature of this approach is to introduce one or more internal variables describing the internal structure of the material. Several models fitting into this basic framework have been proposed although sometimes employing quite different formalisms [4]. They involve a constitutive information prescribed via state equations and kinetic equations for the internal variables. Macroscopic free energy function is decomposed into elastic and inelastic parts. The first part represents the energy storage in consequence of elastic deformations and temperature. The second part represents the energy storage due to internal stress fields (internal variables). Differences involve the choice and interpretation of the internal variables and the form of kinetic equations.

The above mentioned approaches represent the best we can obtain both from the point of view of energy minimization (without introduction of internal variables) and from the point of view of the constitutive modelling of SMA behavior based on the martensitic volume fraction as an internal variable in the framework of the thermomechanics of continua.

In spite of the differences between the above mentioned approaches, one assumption is common: both of them exploit the local equilibrium approximation. However, to perform simulations of practical examples we need to move to numerical approximation. In this case we meet with a non-equilibrium behavior of finite-size discrete elements or computational cells accompanied by entropy production at the moving phase boundary. The local equilibrium approximation is not sufficient to describe such a behavior.

NON-EQUILIBRIUM DESCRIPTION AND NUMERICAL APPROXIMATION

A consistent non-equilibrium description of the process means that we need to have both the non-equilibrium description of states of computational elements and their interactions. The best possibility is provided by the thermodynamics of discrete systems [5]. In this theory, in addition to usual local equilibrium quantities, so-called contact quantities are introduced which provide the description of interaction between the systems. The constitutive modelling in some sense is in between above mentioned approaches: we suppose different free energy functions for austenitic and martensitic phases (like in [1]) but the free energy is decomposed into a local equilibrium and an excess part (like in [3]). The state equations for the contact quantities (related to the excess of free energy) are established in

the same way as the state equations for the local equilibrium quantities based on the local equilibrium part of free energy. A finite-volume numerical scheme is then constructed by means of corresponding contact quantities.
The next step is to establish the non-equilibrium jump conditions at the phase interface. Each model of the stress-induced martensitic phase-transition front propagation uses its own jump relations. All of them one way or another differ from the classical equilibrium jump relations, which consist in the case of thermoelastic solids in the continuity of temperature and chemical potential and the continuity of the normal Cauchy traction at the phase boundary. We apply the *non-equilibrium jump relations* [6], which should be fulfilled for each pair of adjacent discrete elements. Additional constitutive information is introduced by means of certain assumptions about the entropy production at the phase boundary. It is shown [7] that the final rules for the determination of the averaged quantities following from the non-equilibrium jump relation and kinematic condition fully coincide with those obtained from the solution of the Riemann problems at the interfaces between cells in the wave propagation algorithm in the absence of phase transformation.

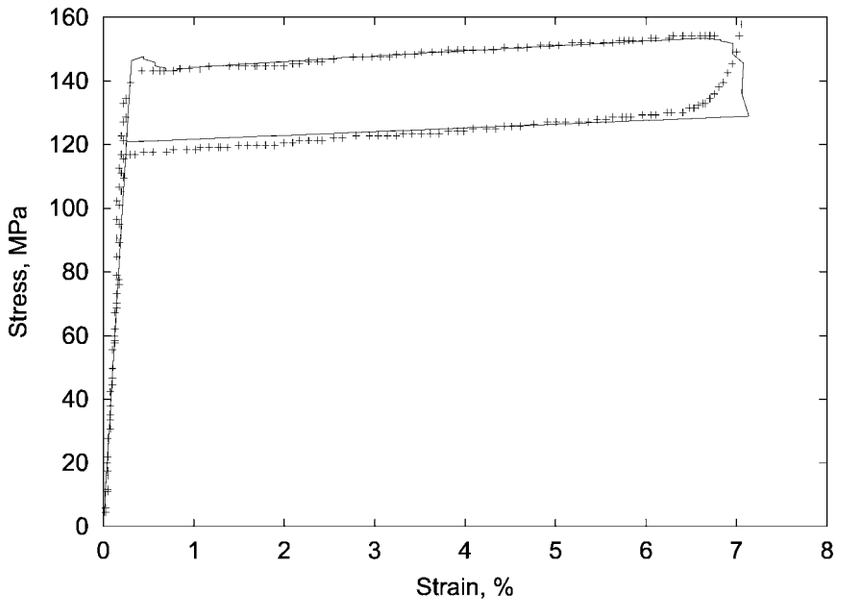


Fig.1. Stress-strain relation at the phase boundary: comparison with experimental data.

NUMERICAL RESULTS

To show the capability of the algorithm, we compare the results of computation for the stress-strain relation in single crystalline CuZnAl shape-memory alloy with the experimental data [8]. The comparison of the stress-strain relation in the case of the full recovering of austenite after unloading is shown in Fig. 1. Here the solid line corresponds to computations, and crosses denote the experimental data.

References

[1] Abeyaratne, R., Bhattacharya, K., Knowles, J.K.: Strain-energy functions with local minima: Modeling phase transformations using finite thermoelasticity. In: Fu, Y., Ogden, R.W. (Eds.), Nonlinear Elasticity: Theory and Application. Cambridge University Press, 2001, pp. 433-490.
[2] Ngan, S.-C., Truskinovsky, L.: Thermo-elastic aspects of dynamic nucleation. *J. Mech. Phys. Solids* **50**: 1193-1229, 2002.
[3] Lagoudas, D.C., Ravi-Chandar, K., Sarh, K., Popov, P.: Dynamic loading of polycrystalline shape memory alloy rods. *Mech. Mater.* **35**: 689-716, 2003.
[4] Bernardini, D., Pence, T.J.: Shape memory materials, modeling. In: Schwartz, M. (Ed.), Encyclopedia of Smart Materials, Wiley, New York, 2002, pp. 964-980
[5] Muschik, W.: Fundamentals of non-equilibrium thermodynamics. In: Muschik, W. (Ed.), Non-Equilibrium Thermodynamics with Application to Solids. Springer, Wien, 1993, pp. 1-63.
[6] Berezovski, A., Maugin, G.A.: On the thermodynamic conditions at moving phase-transition fronts in thermoelastic solids. *J. Non-Equilib. Thermodyn.* (to be published)
[7] Berezovski, A., Maugin, G.A.: Thermoelastic wave and front propagation. *J. Thermal Stresses* **25**: 719-743, 2002.
[8] Goo, B.C., Lexcellent, C.: Micromechanics-based modeling of two-way memory effect of a single-cristalline shape-memory alloy. *Acta Mater.* **45**: 727-737, 1997.

XXI ICTAM, 15–21 August 2004, Warsaw, Poland

MODELING MARTENSITIC TRANSFORMATION IN THE ELASTO-PLASTIC MATERIAL AT FINITE STRAIN

S.P. Chen*, V. Kouznetsova*, M.G.D. Geers**
*Netherlands Institute for Metals Research, Rotterdamseweg 137, 2628AL Delft, The Netherlands
**Department of Mechanical Engineering, Eindhoven University of Technology, P.O. Box 513, 5600 MB Eindhoven, The Netherlands

Summary In this paper, a model of martensitic transformation in TRIP steel was established in the framework of the continuous mechanics and thermodynamics at a large strain. The model is based on the concept of a laminated microstructure composed of the martensitic plate and austenite layer. The internal structure of the martensite and austenite composite is variable and changes with moving interface. The model includes the essential features of the deformation induced martensitic transformation and provides a local kinetics description of martensite growth. A distinctive feature of the current model is that each phase is characterized by its own material constitutive model, and therefore, the evolution of the stress in both phases as the martensite transformation proceeds under a given deformation gradient can be properly predicted.

INTRODUCTION

The aim is to develop a physically-based, multi-scale model to predict the structure-property relations in low alloyed multi-component TRIP steel. It is suggested that a unique combination of high ductility and high toughness in this steel come from both TRansformation Induced Plasticity (TRIP) and the synergy between the properties of multicomponents [1]. Therefore, the model should include the martensitic transformation, the plastic flow of the matrix phases, the plastic flow of the parent phase and the interaction between the transformed region and its surroundings. A general scheme of the multi-scale model is demonstrated in Figure 1. As a first step, this paper presents a model for deformation-induced martensitic transformation at the micro-level in the framework of the continuous mechanics and thermodynamics.

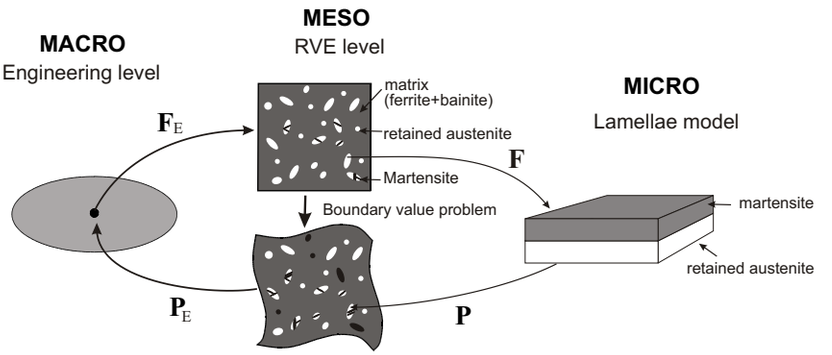


Figure 1. A general scheme of the multi-scale model for multi-component low alloyed TRIP steel.

KINEMATICS OF MARTENSITIC TRANSFORMATION AND DEFORMATION

A major feature of the martensitic transformation is its shape deformation, which can be observed as a surface relief effect and has the characteristics of an invariant-plain strain. According to the phenomenological theory of the martensite crystallography [2], the shape deformation, represented by total transformation deformation gradient, $\mathbf{F_{tr}}$, can be described by:

$$\mathbf{F_{tr}} = \mathbf{I} + \vec{M} \otimes \vec{N} \tag{1}$$

where $\vec{N}$ is the habit plane unit normal and $\vec{M}$ is the shape deformation vector, $\mathbf{I}$ is the second order unit tensor.

Let the motion of a material point in a process of martensitic transformation be described by the deformation gradient tensor $\mathbf{F}$. We assume that the deformation gradient in the austenite can be multiplicatively decomposed into an elastic part, $\mathbf{F^e_A}$, and a plastic part, $\mathbf{F^p_A}$. After martensite transformation it is possible to decompose the total deformation gradient into a plastic deformation gradient $\mathbf{F^p_A}$ in austenitic phase, a transformational $\mathbf{F_{tr}}$ and an elastic and a plastic deformation gradients, $\mathbf{F^e_M}$ and $\mathbf{F^p_M}$ in martensitic phase. Therefore,

$$\mathbf{F_A} = \mathbf{F^e_A} \cdot \mathbf{F^p_A} \qquad \mathbf{F_M} = \mathbf{F^e_M} \cdot \mathbf{F^p_M} \cdot \mathbf{F_t} \cdot \mathbf{F^p_A} \tag{2}$$

THE MARTENSITIC TRANSFORMATION CRITERION

The local transformation criterion proposed by Fischer and Reisner [3] and Levitas [4] is applied as:

$$G = [\phi] - \rho_0^{-1} \cdot \langle \mathbf{P} \rangle^{\mathbf{T}} : [\mathbf{F}] \geq G_c \tag{3}$$

where $\langle \mathbf{P} \rangle = (\mathbf{P_A} + \mathbf{P_M})/2$ with $\mathbf{P_A}$ and $\mathbf{P_M}$ being the first Piola-Kirchhoff stress tensors in the austenite and martensite phases, respectively, $[\mathbf{F}] = \mathbf{F_A} - \mathbf{F_M}$ is the jump of the deformation gradient across the moving interface, $[\phi]$ is the jump of the Helmholtz free energy across the interface, ρ_0 is the mass density of the austenite. G is the effective driving force including both chemical and mechanical terms, acting at the material points on the moving interface, which can be obtained by applying the jump condition across the interface. G_c is the threshold value of the transformation barrier, which includes the contributions from both phase transformation and plastic dissipation. It depends on not only the shape deformation strain but also the history of the stress and strain variation during the transformation process. In this research we assume that G_c is a material constant.

MODEL FOR DEFORMATION-INDUCED MARTENSITE TRANSFORMATION

The total deformation gradient tensor $\mathbf{F}$ at a transforming region is assumed to be known. As soon as the martensite forms, this microregion can be treated to consist of austenite containing parallel layers of martensite plate. The parallel interface separating the two constituents are characterized by the habit plane normal $\vec{N}$ in the reference configuration. As martensitic transformation is an invariant plane strain deformation, therefore,

$$\mathbf{F_A} \cdot (\mathbf{I} - \vec{N} \otimes \vec{N}) = \mathbf{F_M} \cdot (\mathbf{I} - \vec{N} \otimes \vec{N}) \tag{4}$$

Assuming a quasi-static equilibrium state, the balance of linear momentum on the interface requires that:

$$\mathbf{P_A} \cdot \vec{N} - \mathbf{P_M} \cdot \vec{N} = 0 \tag{5}$$

The deformation and stress fields within each phase (layer) are assumed to be homogeneous. The given deformation $\mathbf{F}$ and the first Piola-Kirchhoff stress $\mathbf{P}$ at the transforming region is assumed to be distributed between the phases according to the rule of mixtures

$$\mathbf{F} = (1-\xi)\mathbf{F_A} + \xi \mathbf{F_M} \qquad \mathbf{P} = (1-\xi)\mathbf{P_A} + \xi \mathbf{P_M} \tag{6}$$

Where ξ is the volume fraction of the martensite. Each phase is characterized by its own constitutive relations. A finite strain logarithmic elasto-plastic constitutive relations [5] is assumed for austenite while elastic behavior is taken for martensite

$$\boldsymbol{\tau_A} = f(\mathbf{C_A}, \ln \mathbf{B_A^e}, \triangle\gamma) \qquad \boldsymbol{\tau_M} = \frac{1}{2}\mathbf{C_M} : \ln \mathbf{B_M^e} \tag{7}$$

Where $\mathbf{B_A^e}$ and $\mathbf{B_M^e}$ are the elastic left Cauchy-Green deformation tensors in austenite and martensite, respectively; $\boldsymbol{\tau_A}$ and $\boldsymbol{\tau_M}$ are the Kirchhoff stress tensors in austenite and martensite, respectively. $\mathbf{C_A}$ and $\mathbf{C_M}$ are the fourth-order tensors of material constants; $\triangle\gamma$ is the increment of plastic flow in austenite. The standard J_2 plasticity model restricted to isotropic hardening is applied to the austenite phase.

By solving system of equations constructed by (2)-(7), the martensite volume fraction and the stress evolution in each phase during martensite growth can be obtained. The increment of the martensite appeared ($\Delta\xi$) is calculated in such a way that $G = 0$ (where G is calculated with the updated values of the variables, e.g.$\mathbf{P}$, $\mathbf{F}$ etc.). If the calculated fraction $\Delta\xi$ is less than zero, no transformation occurs during this increment, otherwise, if $\Delta\xi > 0$, the transformation takes place. This algorithm is analogous to the return-mapping algorithm in plasticity.

CONCLUSIONS

A model of deformation-induced martensitic transformation in TRIP steel was established in the framework of the continuous mechanics and thermodynamics at a large strain. The model provides a local kinetics description of martensite growth and the evolution of the stress in both phases as the martensite transformation proceeds.

References

[1] Fischer, F.D.; Sun, Q.-P.; Tanaka, K.: Transformation-induced plasticity (TRIP). *Appl. Mech. Rev.* **49**:317–364, 1996.

[2] Wayman, C.M.: Introduction to the Crystallography of Martensitic Transformation. Macmillan, New York 1964.

[3] Fischer, F.D.; Reisner, G.: A criterion for the martensitic transformation of a microregion in an elastic-plastic material. *Acta mater.* **46**:2095–2102, 1998.

[4] Levitas, V.I.: Thermomechanical theory of martensitic phase transformations in inelastic materials. *Int. J. Solids Structures* **35**:889–940, 1998.

[5] Geers, M.G.D.: Finite strain logarithmic hyperelasto-plasticity with softening: a strongly nonlocal implicit gradient framwork. *Comput. Meth. Appl. Mech. Engrg.* **193**:3377–3401, 2004.

XXI ICTAM, 15–21 August 2004, Warsaw, Poland

MODELING OF THE MICROSTRUCTURAL EVOLUTION IN CR-MO STEELS DURING TEMPERING AND HYDROGEN EXPOSURE

Sabine M. Schlögl
Fraunhofer Institute for Mechanics of Materials, D-79108 Freiburg, Germany

Summary
Hydrogen attack is a dangerous material degradation process that occurs in steels subjected to high pressures of hydrogen at elevated temperatures. A detailed study of the coupled processes responsible for hydrogen attack requires a combination of continuum mechanics with solid solution thermodynamics, kinetics and chemistry. This paper is concerned with the development of numerical models that combine these ingredients.

INTRODUCTION

Cr-Mo steels consisting of a ferritic matrix and alloy carbides can suffer from hydrogen attack when they are in contact with a hydrogen containing atmosphere. It is the combination of high hydrogen pressure and high temperatures which leads to the nucleation of cavitities at the grain boundaries and the formation of methane. The methane-filled cavities grow, which finally can result in intergranular failure. The objective is to develop models which incorporate several processes involved in hydrogen attack such as substitutional and interstitial diffusion in the ferrite, the chemical reaction at the cavity–ferrite interface, the movement of the carbide-ferrite interfaces due to the dissolution of carbides as well as the creep and diffusional deformation. First, a relatively simple one-dimensional model is presented which takes into account these processes within the framework of a multi-component, multi-phase continuum description. Secondly, the first steps in the development of a finite element code for a more sophisticated microstructural model is addressed where the spatial arrangement of the carbides is taken into account. These two models are applied to predict the evolution of the carbides in a Cr-Mo steel during tempering and their outcome are compared to find out whether the simple model is sufficient.

ONE-DIMENSIONAL MODEL

The one-dimensional (1D) model presented in [1] consists of three parts. Submodel 1 describes the dissolution of carbides as well as the diffusion of the substitutional elements and of C in the ferrite away from the carbide. Submodel 2 takes care of the chemical reaction that takes place inside the cavity once diffused carbon atoms meet hydrogen. Finally, submodel 3 handles the growth of the cavity due to the methane pressure built up during the chemical reaction.
The microstructure is represented by means of a spherical unit cell of radius r_{o}. A total of N carbides with radius ρ^j are embedded in the ferritic matrix (α-Fe) of the unit cell. The spatial arrangement of the carbides is neglected: each carbide is considered to be located at the center of the unit cell. Furthermore, it is assumed that all elements remain homogeneously distributed in the ferritic matrix. Besides carbides, the unit cell contains one already nucleated cavity of radius a. Inside this cavity, the hydrogen pressure corresponds to the hydrogen pressure in the gas atmosphere to which the material is subjected (inside the reactor or autoclave). In this model the chemical reaction of carbon with hydrogen is assumed to occur rapidly so that the diffusion of the carbon atoms towards the cavity controls the kinetics of the methane formation.
As a result, the three submodels of the 1D model provide at each instant the change of the sizes of the carbides, the growth rate of the cavity and the number of newly formed methane molecules per unit of time. These rates allow us to update the composition of the ferrite and the methane pressure at each new time increment via an explicit time integration scheme.

MICROSTRUCTURAL MODEL

A second microstructural model is under development where, in contrast to the one-dimensional model, i) variations in spatial concentration can occur, ii) the spatial positions of the carbides are resolved and iii) methane formation is not per definiton purely diffusion controlled. The concept of this modelling is based on the variational methodology developed by Cocks and Gill [2] using the finite element technique. In its present state the microstructural model can handle interstitial (carbon) and substitutional (metal) diffusion in the ferritic finite elements and the chemical reaction to methane with the help of special surface reaction elements. The derivation of the governing equations and their discretization via shape functions is given in [3, 4]. The movements of carbide-ferrite interfaces can also be treated within the variational methodology. However, a simpler approach is used in the present code to incorporate the effect of carbides which allows to avoid higher computer times (for details see [4]). The outcome of the microstructural model are the distribution of the alloying elements, the sizes of the carbides and the methane pressure in a cavity of fixed size in dependance of the exposure time.

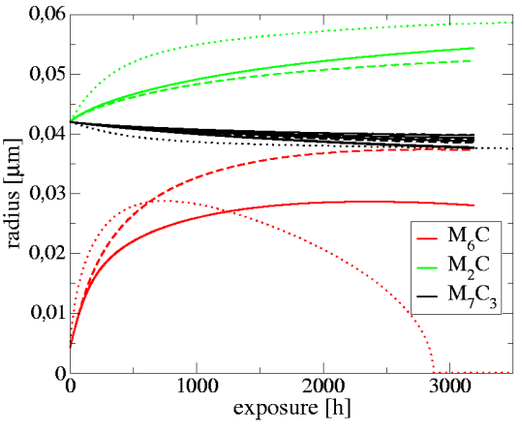


Figure 1. Carbide evolution of different carbides (black: 7 M_7C_3 carbides, red: 1 M_6C and green: 1 M_2C) during tempering at 570°C. Solid and dashed lines are the results of the microstructural model for two arrangements and the dotted lines refer to the results of the one-dimensional model.

RESULTS

In this paper the 1D model and the microstructural model are applied to simulate the microstructural evolution of the 2.25Cr1Mo steel during air exposure at 570°C. To limit the calculation time of the second model a relatively small two-dimensional sample is chosen. Nine carbides are distributed randomly in a ferrite: 7 M_7C_3 and 1 M_2C and a smaller M_6C carbide. Two different arrangements are investigated where the main difference lies in the distance between the Mo carbides M_2C and M_6C. In arrangement 1 they are nearer to each other than in arrangement 2. The predicted evolution curves of the carbide radii are potted in Fig. 1 as solid lines for arrangement 1 and as dashed lines for arrangement 2. Fig. 1 shows that M_2C grows while the M_7C_3 carbides shrink a bit. In arrangement 2 the M_6C carbide reaches a bigger size because, due to the larger distance, there is less interference between the Mo carbides. It holds for both carbide types that their driving force for growth increases with the Mo content of the ferrite. Consequently, these two carbide types compete for the Mo of the ferrite.

Additionally, the microstructural evolution obtained by the 1D model are shown as dotted lines (see Fig. 1). As the spatial arrangement is not taken into account in this simpler model and the ferrite composition is taken to be homogeneous, one just obtains a single curve per carbid type. The 1D model gives the same trend as the more sophisticated model, but the kinetics differ significantly. According to the 1D model M_2C grows faster because the impoverishment of Mo around the growing carbide is not resolved. The dissolution of the M_7C_3 carbides also goes slightly quicker in the 1D model. First the M_6C carbide grows but from 700h on its size shrinks while in the microstructural model it grows slowlier but reaches a larger size before shrinkage starts. As in the 1D model there is no spatial variation of the Mo-concentration, M_6C is directly affected by the M_2C carbide and vice versa. In the microstructural model the spatial variation of the alloying elements in the ferrite is resolved. Then, the substitutional diffusion determines the time until the carbides feel each other via the Mo concentration while the interaction between the carbides via the ferritic carbon concentration is present in both models from the beginning on.

Further results are available from the simulation of exposure tests in hydrogen.

CONCLUSIONS

In this paper two models are presented and applied to describe the microstructural evolution of carbides during tempering and exposure to hydrogen: i) a simple one-dimensional model and ii) a sophisticated microstructural model. Both are a multi-component, multi-phase continuum description of several processes involved in hydrogen attack.

References

[1] Schlögl S.M., Svoboda J., Van der Giessen E.: Evolution of the methane pressure in a standard 2.25Cr-1Mo steel during hydrogen attack, *Acta Mat.* **49**: 2227–2238, 2001.

[2] Cocks A.C.F., Gill S.P.A.: Modeling microstructural in engineering materials, *Adv. Appl. Mechanics* **36**, 81-162, 1999.

[3] Schlögl S.M., Van der Giessen E.: Computational model for carbon diffusion and methane formation in a ferritic steel during hydrogen attack, *Scripta Mat.* **46**: 431–437, 2002.

[4] Schlögl S.M., Van der Giessen E.: Numerical treatment of substitutional and interstitial diffusion for methane formation in low alloy Cr-Mo steels during hydrogen attack, *Advances in Science and Technology* **36**: 67–74, 2003.

EQUILIBRIUM AND STABILITY OF TWO-PHASE DEFORMATIONS WITHIN THE FRAMEWORK OF PHASE TRANSITION ZONES

Alexander B. Freidin*, Yibin Fu**
*Institute of Mechanical Engineering Problems, Russian Academy of Sciences,
Bolshoi pr. 61, V.O., St. Petersburg 199178, Russia
**Department of Mathematics, Keele University, Staffordshire ST5 5BG, UK

Summary Stress-induced phase transitions in nonlinear elastic materials are analyzed within the framework of phase transition zones. A procedure to examine the stability of piece-wise homogeneous two-phase deformation is developed. Spherically symmetric two-phase deformation are studied in detail to demonstrate efficiency of the approaches developed.

INTRODUCTION

If phase transitions take place in some parts of a deformable body, interfaces which bound new phase areas can be considered as surfaces across which the deformation gradient $\mathbf{F}$ is discontinuous at continuous displacements. Phase boundaries of this kind appear in the case of martensite transformations. Related phenomena are shape memory effects, localized orientation transformations in polymers (crazes, shear bands). On the whole, studies in this field direct toward the development of the theoretical basis for using and creating smart materials and structures.

The analysis of the conditions on the equilibrium interface [1, 2, 3] leads to the concept of phase transition zones (PTZ)[4]. The PTZ is formed in strain-space by all deformations which can exist on the equilibrium interface. Since the equilibrium two-phase deformations can be supported by a nonlinear elastic material only if ellipticity fails at some deformations [5], the PTZ is crossed by the non-ellipticity sub-zone. The PTZ boundary acts as a phase diagram or yield surface in strain-space. With the aid of the PTZ construction, what kind of phase boundaries will appear and when they can appear are determined entirely by properties of the strain energy function and the deformation path.

Since the PTZ results from the analysis of the local equilibrium conditions, every point of the PTZ corresponds to some equilibrium piecewise-homogeneous two-phase deformation. That is why we develop a procedure to examine the stability of such deformations. The other important reason follows from the fact that if a two-phase deformation in a non-linear elastic body is a local energy minimizer, then given any point $\mathbf{p}_0$ of the interface, the piece-wise homogeneous deformation corresponding to the two values $\mathbf{F}^{\pm}(\mathbf{p}_0)$ is a global energy minimizer [3]. Thus, instability of the latter state would imply instability of the former state.

In this paper the stability of the piece-wise homogeneous deformation is investigated with the aid of two test criteria. One is a kinetic stability criterion developed for the case of small strains in [7]: the two-phase state is unstable if superimposed perturbations grow. Our analysis draws upon recent results obtained in [8] for the half-space problem. The other criterium is the energy criterion. We compare the total energies corresponding to the two-phase piece-wise homogeneous deformation and to the perturbed inhomogeneous deformation.

Then we study some aspects of boundary value problems for bodies undergoing phase transformations. Usually the equilibrium two-phase solution is non-unique and can be meta-stable or unstable, and global minimizers of the total energy are not the only ones that are of interest from the physical point of view. Locally stable solutions can also be met in physical reality. Then the choice of the solution in a static approach can be made on the base of the stability analysis and estimations of energy changes due to phase transformations.

To discuss the problems we consider the equilibrium spherically symmetric two-phase deformation of a nonlinear elastic isotropic material. We develop a general procedure to construct the solution for a material with an arbitrary strain energy function. Then we study phase transformations in a sphere made of the Hadamard material. We describe characteristic features of the deformation fields in the equilibrium two-phase sphere for the obtained solutions in the context of the PTZ. We show that the number of solutions can be predicted if the PTZ is constructed. Then we examine the stability. Finally, we compare these results with the results obtained earlier by a small strain approach [7].

CONDITIONS ON THE EQUILIBRIUM PHASE BOUNDARY AND PHASE TRANSITION ZONES

The conditions on the equilibrium interface include the kinematic condition, traction continuity condition, and thermodynamic condition [1, 2, 3]. The last two conditions can be rewritten as

$$(\mathbf{S}(\mathbf{F}+\mathbf{f}\otimes\mathbf{m})-\mathbf{S}(\mathbf{F}))\mathbf{m}=0,\quad W(\mathbf{F}+\mathbf{f}\otimes\mathbf{m})-W(\mathbf{F})=\mathbf{f}\cdot\mathbf{S}(\mathbf{F})\mathbf{m} \tag{1}$$

where $\mathbf{F}$ is the deformation gradient on one side of the interface, $\mathbf{S}$ is the Piola stress tensor, W is the strain energy function, $\mathbf{m}$ is a unit normal to the interface. Given $\mathbf{F}$, the above equations can be considered as a system of four equations for five unknowns: $\mathbf{f}$ and $\mathbf{m}$. Those $\mathbf{F}$ for which this system of equations can be solved form the *phase transition zone* [4]. In the case of isotropic materials the PTZ can be constructed in the space of principal stretches $\lambda_i,\ i=1,2,3$ [4, 6].

If the interface is perturbed and the thermodynamic equilibrium fails then in a quasi-static approach we replace $(1)_2$ by

$$\frac{\partial\Gamma}{\partial t}=-k([W]-\mathbf{f}\cdot\mathbf{S}\widetilde{\mathbf{m}}),\quad k>0, \tag{2}$$

where $\partial\Gamma/\partial t$ is the normal speed of the interface, and $\widetilde{\mathbf{m}}$ is a normal to the perturbed interface. The evolution equation (2) is motivated by the fact that the rate of energy dissipated as the interface traverses the material must be positive [9].

STABILITY AND BIFURCATION OF PIECEWISE-HOMOGENEOUS DEFORMATIONS

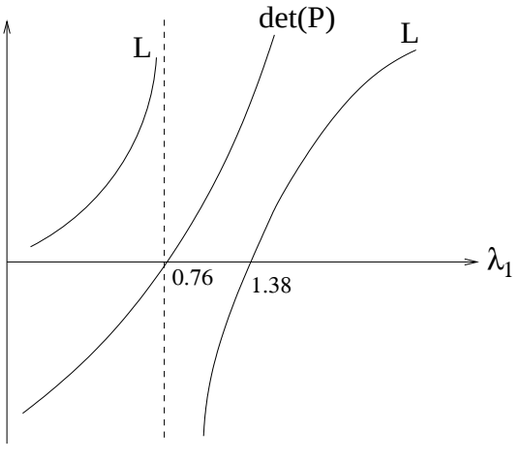


Figure 1.

The interface is given in the reference configuration by a parametric form $\mathbf{X} = \mathbf{Y}(s)$ $(-\infty < s < \infty)$. The perturbed interface is given by $\mathbf{X} = \mathbf{Y}(s) + \boldsymbol{\xi}(s,t)$. In a normal mode approach the perturbation is of the form

$$\Gamma(s,t) = \gamma \mathrm{e}^{i\mathbf{K}\cdot\mathbf{X}} = \gamma(t)\mathrm{e}^{is} \quad (\Gamma \equiv \boldsymbol{\xi}\cdot\mathbf{m},\ \mathbf{K}\perp\mathbf{m},\ |\boldsymbol{\xi}| \ll 1). \quad (3)$$

The incremental displacement is sinusoidal along the interface and decays away from the interface. Linearizing the right hand side of (2), we obtain a linear differential equation of the form

$$-\frac{1}{k}\frac{d\gamma}{dt} = L\gamma, \quad (4)$$

By the kinetic stability criterion, the two-phase deformation is unstable if $L < 0$. Analogously to [8], linearizing the traction continuity condition we obtain the expression for the interfacial impedance tensor P. As a result it is found that two types of bifurcations are possible, with bifurcation conditions given by $\det P = 0$ and $\det P \neq 0$ but $L = 0$. It becomes clear the necessary and sufficient conditions for the energy increment to be positive definite: (i) P is positive definite, and (ii) $L > 0$. Fig.1 shows the signs of $\det P$ and L in the case of the specified Hadamard material. The normal to the primary interface is directed as the second eigenvalue of the strain tensor. Then λ_1 is continuous across the interface. The stability conditions are satisfied only for $\lambda_1 > 1.38$, which is only a subset of the λ_1 values (namely $\lambda_1 > 0.76$) over which the pairwise homogeneous deformation is stable when viewed as joint-body problem.

EQUILIBRIUM SPHERICALLY-SYMMETRIC TWO-PHASE DEFORMATIONS

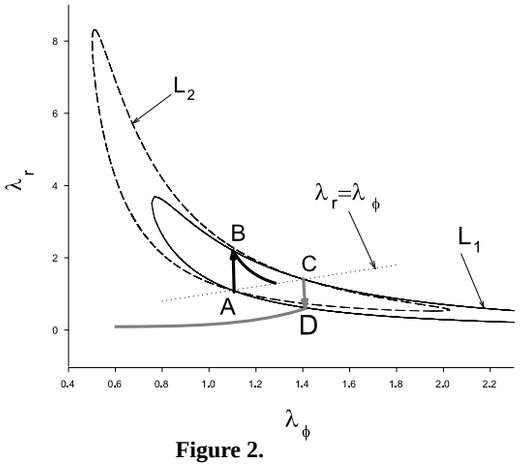


Figure 2.

Applying the general procedure to the sphere made of the Hadamard material we demonstrate that two different equilibrium two-phase states as well as a uniform one-phase state can be found. Fig. 2 shows the PTZ cross-section by the plane $\lambda_1 = \lambda_2 \equiv \lambda_\Phi$. The lines L_1 and L_2 are the PTZ-boundaries. The points A, B and C, D represent the jumps in deformations across the spherical interfaces for two solutions. The thick lines characterize strains along the radius of the sphere. We find the radius of the interface depending on the predicted external radius of the sphere, construct pressure–volume diagrams, study energy changes and analyze how the stable and unstable solutions in the cases of the Hadamard material and small strains relate with the PTZ.

Acknowledgement. This research is supported by a Royal Society Joint Project Grant.

References

[1] Grinfeld M.A.: On conditions of thermodynamic equilibrium of the phases of a nonlinear elastic material. *Dokl. Acad. Nauk SSSR* **251**:824–827, 1980.
[2] James R.D.: Finite deformation by mechanical twinning. *Arch. Rat. Mech. Anal.* **77**:143–177, 1981.
[3] Gurtin M.E.: Two–phase deformations of elastic solids. *Arch. Rat. Mech. Anal.* **84**:1–29, 1983.
[4] Freidin A.B., Chiskis A.M.: Phase transition zones for nonlinear elastic isotropic materials. *Mechanics of Solids* (Translated from *Izvestia RAN, MTT*) **29**, No. 4: 91–109, No. 5: 46–58, 1994.
[5] Knowles J.K., Sternberg E.: On the failure of ellipticity and the emergence of discontinuous deformation gradients in plane finite elastostatics. *J. Elasticity* **8**:329–379, 1978.
[6] Freidin A.B., Vilchevskaya E.N., Sharipova L.L: Two-phase deformations within the framework of phase transition zones. *Theoretical and Apllied Mechanics* **28-29**:149–172, 2002.
[7] Eremeev V. A., Freidin A. B., Sharipova L. L.: Nonuniqueness and stability in problems of equilibrium of elastic two-phase bodies. *Doklady Physics* **48** (7):359–363, 2003. (Translated from *Doklady Akademii Nauk* **391** (2):189–193, 2003.
[8] Fu Y.B., Mielke A.: A new identity for the surface-impedance matrix and its application to the determination of surface-wave speeds. *Proc. Roy. Soc. Lond.* A**458**: 2523-2543, 2002.
[9] Knowles J.K.: On the dissipation associated with equilibrium shocks in finite elasticity. *J. Elasticity* **9**:131–158, 1979.

ON MODELING THE LONGITUDINAL IMPACT OF TWO SHAPE MEMORY BARS

Cristian Făciu* and Alain Molinari**
* *Institute of Mathematics of the Romanian Academy, P.O. Box 1-764, RO-70700 Bucharest, Romania.*
** *Laboratoire de Physique et Mécanique des Matériaux, Université de Metz, U.M.R. - C.N.R.S. 7554, Ile du Saulcy, F-57045 Metz, France.*

Summary We study the propagation of phase transformation fronts induced by the longitudinal impact of two shape memory bars. The corresponding wave structure is investigated by using the non-monotone elastic model versus a Maxwell's rate-type model containing a rate sensitivity parameter and a time of relaxation of kinetic origin. Laboratory measurements are suggested.

Experiments with longitudinal impact of SMA bars are an effective mean for understanding the kinetics of phase transformation. We investigate here this problem in an one-dimensional and isothermal setting since this study provides an important insight into the wave structure. In a future work we extend the analysis to account for thermal effects.
The balance laws of momentum and mass in a 1-D Lagrangian description are

$$\varrho\frac{\partial v}{\partial t}-\frac{\partial \sigma}{\partial X}=0, \qquad \frac{\partial \varepsilon}{\partial t}-\frac{\partial v}{\partial X}=0, \tag{1}$$

where v, σ, ε and ϱ are the particle velocity, the stress, the strain and mass density, respectively.
The theory of elasticity with non-monotonic stress-strain relation $\sigma=\sigma_{eq}(\varepsilon)$, has been frequently used to describe the main features of phase transformations in solids. For a three-phase elastic material the simplest non-monotonic stress-strain relation is given in Fig.1. This constitutive relation is viewed as corresponding to a material which can exist in an *austenite phase* and in two *variants of martensite*. E_1 =const.>0 is called the elastic modulus of the austenite phase, while E_3 =const.>0 is the elastic modulus of the martensite variants. $-E_2$ =const.<0 is called the softening modulus and it corresponds to the unstable phases of the material.

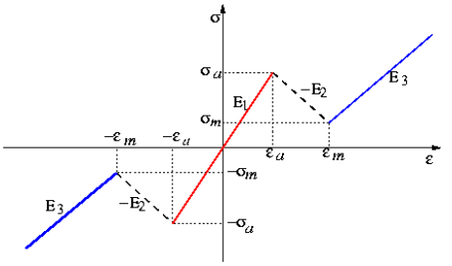


Figure 1: The three phase elastic material - equilibrium curve $\sigma=\sigma_{eq}(\varepsilon)$.

It is known that initial-boundary value problems for the non-monotone elastic system (1)+($\sigma=\sigma_{eq}(\varepsilon)$) can be ill-posed. This situation reflects in fact a constitutive insufficiency of the model. One way to remedy it is to embed the elastic bar theory as a special case of a broader theory which can describe the way the body may deviate from the equilibrium. We adopt in this paper the following Maxwellian rate-type constitutive equation

$$\frac{\partial \sigma}{\partial t}-E\frac{\partial \varepsilon}{\partial t}=-\frac{E}{\mu}|\sigma-\sigma_{eq}(\varepsilon)|^{\lambda-1}(\sigma-\sigma_{eq}(\varepsilon)), \tag{2}$$

where $\sigma_{eq}(\varepsilon)$ is a non-monotone stress-strain relation as in Fig.1 . E =const.>0 is the *dynamic Young modulus*. μ =const.>0 is a *Newtonian viscosity coefficient*, $\frac{\mu}{E}$ is a *relaxation time* of the model. λ =const.>0 is a *rate sensitivity parameter*. When $\mu\to 0$ this rate-type constitutive equation can be seen as a viscoelastic approach of the elastic model in a $L^{\lambda+1}$ sense.
From mathematical point of view, the rate-type system (1)+(2) has the advantage that it is always *hyperbolic semilinear*. The initial-boundary value problems are now well-posed even in the unstable phases. It was shown in [3], for the case $\lambda=1$, that this system incorporates some physical instabilities due to the shape of the equilibrium curve and it is able to describe general issues pertaining to phase transition phenomena. The rate-type constitutive relation (2) has the capacity to describe the nucleation of phases. The new parameters μ, λ and E influence in fact the kinetics of the growth of phases and should be connected with the time of growth or time of nucleation of microscopic theories of phase transitions.
This work is organized as follows. First we investigate analytically the wave structure corresponding to the rate-type system (1)+(2). By following [1], we analyze the behavior of the waves near the source and far from

the source of a perturbation. Thus we determine which set of waves are the most important and will be really observed. By using a method of multiple scales we establish that near the source the waves propagate with the speeds $\pm\sqrt{E/\varrho}$ (*instantaneous waves*) being immediately exponentially damped. On the other hand, in the unstable phases any inhomogeneity in the strain field leads to the nucleation and, consequently to the formation of a *stationary phase boundary*. Far from the source, the main part of the disturbance moves with the speeds $\pm\sqrt{E_0/\varrho}$ (*delayed waves*), where E_0 is the elastic modulus of the austenite phase (E_1) or of the martensite variants (E_3). The disturbance decreases like $1/\sqrt{at}$, which is typical for diffusion and spreads out like $\sqrt{at}$ where $a = 2(E - E_0)\mu/\varrho E$. In order to determine the speed of propagation of phase boundaries we investigate *traveling wave solutions* for the Maxwell's type model. We establish an admissibility criterion to identify those moving phase boundaries within the elastic theory. This is just the well known *chord criterion*. The viscosity parameter μ, the rate sensitivity parameter λ and the dynamic Young modulus E will only influence the smooth transition layer which approximate a sharp interface.

The main goal of this work is to investigate the longitudinal impact of two phase transforming bars. Thus we consider at the initial moment a bar called "target" impacted at one end by another bar called "flyer" which is moving with a known initial velocity V. After impact the two bars remain in contact and move together until a time t_S called *time of separation*. This time corresponds to the moment when the first tensile wave arrives at the point of contact $X = 0$.

Exact solution - First we construct an exact solution of this problem using the elastic model and the chord criterion. The building blocks in solving this problem are the simplest initial-boundary value problems for the elastic system, i.e., the Goursat and Riemann problems which are thoroughly investigated. If the impact velocity V is larger than $V_{ph} \equiv 2\sigma_a/\sqrt{\varrho E_1}$ then a phase transformation is induced. Interactions of the unloading elastic wave reflected at the free end of the target with the propagating phase boundary are explored. Critical values of the impact velocity are determined such that this phase boundary propagates backward, remains stationary or propagates forward.

Numerical solution - We determine numerically the evolution in time of the stress, strain and particle velocity in the " flyer" and "target" bar predicted by the rate-type system (see Fig. 2). Increasing the impact velocity, the transforming region increases and the separation time changes. Inside the transforming region longitudinal waves propagate reflecting at the phase boundaries and also being transmitted across them. Velocity time profiles obtained at the rear end of the target provides additional information for understanding the forward and reverse transformation kinetics. We focus on the numerical results which can be compared with experimental data: the time of separation (optical methods), the velocity at the end of the target bar (interferometry), the stress at the impacted end (piezoelectric wafers), the variation in time of the strain at various cross-sections (diffraction gratings). Some connections with experimental results in which the transformation was obtained by pressure-shear plate experiments (see [2]) are discussed.

The numerical experiments for the Maxwell's rate-type system illustrate the potentiality of the adopted model to describe specific phenomena accompanying stress-induced phase transformations during impact tests.

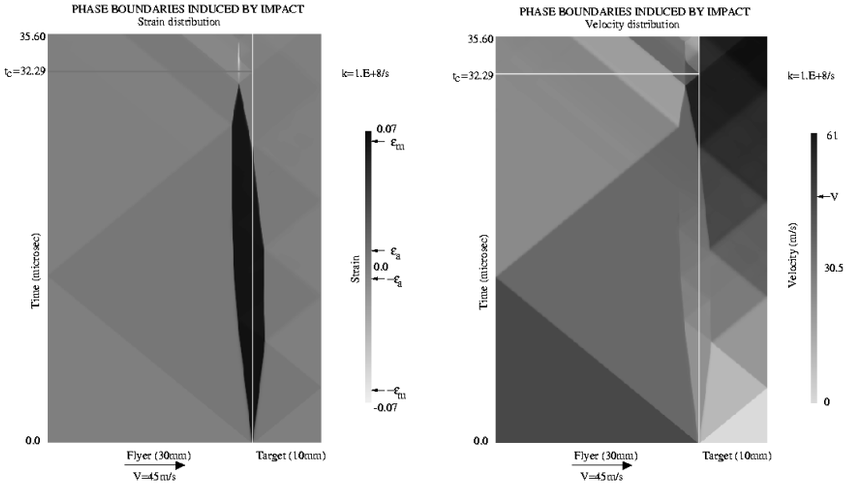


Figure 2:

References

[1] Brun, L., Molinari, A.,: Transient linear and weakly non-linear viscoelastic waves, in Wave Propagation in Viscoelastic Media (Ed. F. Mainardi), Research Notes in Mathematics, No. 52, Pitman (1982).

[2] Escobar, J.C., Clifton, R.J.,: Stress-wave induced martensitic phase transformations, *Metallurgical and Materials Applications of Shock-Wave and High-Strain-Rate Phenomena*, Eds. L.E. Murr, K.P. Staudhammer, M.A. Meyers, 451-462, Elsevier Science B.V. (1995).

[3] Făciu, C., Suliciu I.,; A Maxwellian model for pseudoelastic materials, *Scripta Metall. et Mat.*, **31**, 1399-1404, (1994).

XXI ICTAM, 15–21 August 2004, Warsaw, Poland

A MICROMECHANICAL MODEL FOR SINGLE-CRYSTAL SHAPE-MEMORY-ALLOYS

Thorsten Bartel*, Klaus Hackl*
*University of Bochum, Institute of Mechanics, D-44780 Bochum, Germany

Summary This work is dealing with solid to solid phase transformations in shape-memory-alloys and the simulation of the characteristic phenomena, e.g. pseudoelasticity and the shape-memory-effect. In particular it focuses on the micromechanical behaviour of the material like the appearance of microstructures.

The mechanical model is based on the idea of combining energy densities of several martensite and one austenite phase to an averaged energy density of the mixture within a representative volume element (RVE). Let us assume that we want to simulate the behaviour of shape-memory-alloys like Indium-Thallium (InTl), which undergo a cubic to tetragonal transformation. According to [1] we have to take 3 martensite variants in account.
The averaged energy density of the representative volume element can be written as

$$\bar{\psi} = \left(1 - \sum_{i=1}^{3} \beta_i\right) W_A(\boldsymbol{\varepsilon}) + \sum_{i=1}^{3} \beta_i \, W_{M_i}(\boldsymbol{\varepsilon}) \tag{1}$$

where W_A is the free energy of the austenite phase and W_{M_i} is the free energy of the martensite variant i. The phase-energies are adopted from a thermomechanical approach by Frémond [3] and consist only of physically well defined properties, e.g. the fourth-order isotropic material tensor or the heat-expansion-coefficient. The symbols β_i represent the volume fraction of the martensite variant i and can be treated as internal variables from the mechanical point of view.
Regarding all β_i as minimizers of the energy functional will lead us to a non-quasiconvex problem as shown in [4]. This can be avoided by the assumption of an inhomogenous distribution of the strain $\boldsymbol{\varepsilon}$ which constitutes a microstructure. We assume a certain microstructure which is inspired by those found in micrographs [2] as shown in fig.1(left). It consists of

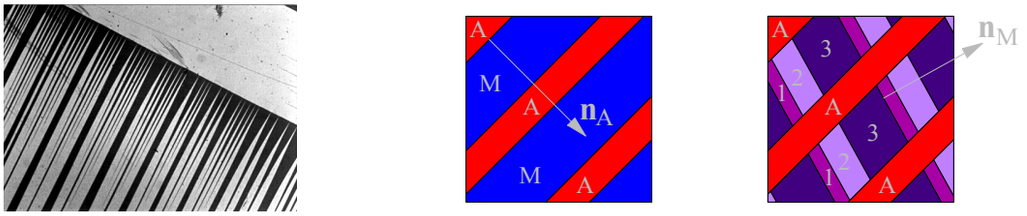


Figure 1. micrograph of martensite twins (left) and assumed microstructure (right)

alternating regions of austenite and martensite, which are repeated periodically. These regions, which are called laminates, are orientated along a direction $\mathbf{n}_A$. The martensite-laminate itself consists of the three different variants, which are supposed to be arranged in laminates too and orientated along a different direction n_M (see fig.1,right). We assume deformation-states in the different laminates, which are compatible at the interfacial boundaries and, integrated over the whole RVE, equivalent to the homogenous macroscopic deformations, as follows:

$$\boldsymbol{\varepsilon}_A \;:=\; \boldsymbol{\varepsilon} - \left(\sum_{i=1}^{3} \beta_i\right) (\mathbf{u}_A \otimes_s \mathbf{n}_A) \tag{2}$$

$$\boldsymbol{\varepsilon}_i \;:=\; \begin{cases} \boldsymbol{\varepsilon} + \left(1 - \sum\limits_{i=1}^{3} \beta_i\right) (\mathbf{u}_A \otimes_s \mathbf{n}_A) + \beta_3 \, (\mathbf{u}_i \otimes_s \mathbf{n}_M)\,, & \text{if } i = 1 \ldots 2 \\ \boldsymbol{\varepsilon} + \left(1 - \sum\limits_{i=1}^{3} \beta_i\right) (\mathbf{u}_A \otimes_s \mathbf{n}_A) - \sum\limits_{j=1}^{2} \beta_j \, (\mathbf{u}_j \otimes_s \mathbf{n}_M) & , \text{ if } i = 3 \end{cases} \tag{3}$$

with $\mathbf{u}_A \otimes_s \mathbf{n}_A := \mathbf{u}_A \otimes \mathbf{n}_A + \mathbf{n}_A \otimes \mathbf{u}_A$. The averaged energy density can now be written as

$$\bar{\psi} = \left(1 - \sum_{i=1}^{3} \beta_i\right) W_A(\boldsymbol{\varepsilon}_A) + \sum_{i=1}^{3} \beta_i \, W_{M_i}(\boldsymbol{\varepsilon}_i) \qquad . \tag{4}$$

The variables $\mathbf{u}_A$,$\mathbf{u}_1$,$\mathbf{u}_2$ are considered as minimizers of the averaged energy density. This minimization process yields the relaxed energy functional

$$\psi R_1 = W_A(\boldsymbol{\varepsilon}) + \sum_{i=1}^{3} \beta_i \, c - \alpha \, \bar{\boldsymbol{\tau}} : \boldsymbol{\varepsilon} + \mathcal{G}_{R_1}\left(\boldsymbol{\beta}, \mathbf{n}_A, \mathbf{n}_M\right) \tag{5}$$

with

$$\mathcal{G}_{R_1}\left(\boldsymbol{\beta}, \mathbf{n}_A, \mathbf{n}_M\right) = -\alpha \left[\left(1 - \sum_i \beta_i\right) \mathbf{u}_A \cdot \bar{\boldsymbol{\tau}} \cdot \mathbf{n}_A + \beta_1 \, \beta_3 \, \mathbf{u}_1 \cdot (\boldsymbol{\tau}_1 - \boldsymbol{\tau}_3) \cdot \mathbf{n}_M + \beta_2 \, \beta_3 \, \mathbf{u}_2 \cdot (\boldsymbol{\tau}_2 - \boldsymbol{\tau}_3) \cdot \mathbf{n}_M \right] \tag{6}$$

The remaining variables are related to dissipative energy terms. We can derive evolution equations from a given dissipation functional $\Delta(\dot{\mathbf{P}})$, where the vector $\mathbf{P}$ contains all remaining variables. The minimization of the total power expended in the material leads us to the condition

$$\dot{\mathbf{P}} \in \frac{\partial J(\mathbf{Q})}{\partial \mathbf{Q}} \tag{7}$$

with the Legendre-transform of $\Delta(\dot{\mathbf{P}})$

$$J\left(\mathbf{Q}\right) := \max\left\{\mathbf{Q} \cdot \dot{\mathbf{P}} - \Delta; \dot{\mathbf{P}}\right\} \tag{8}$$

and

$$Q_i := -\frac{\partial \psi R_1}{\partial P_i} \quad , i = 1 \ldots 9 \qquad . \tag{9}$$

We are now able to simulate the characteristic hysteretic behaviour of shape-memory-alloys. Fig.2 shows the results of a homogenous uni-axial tension-test.

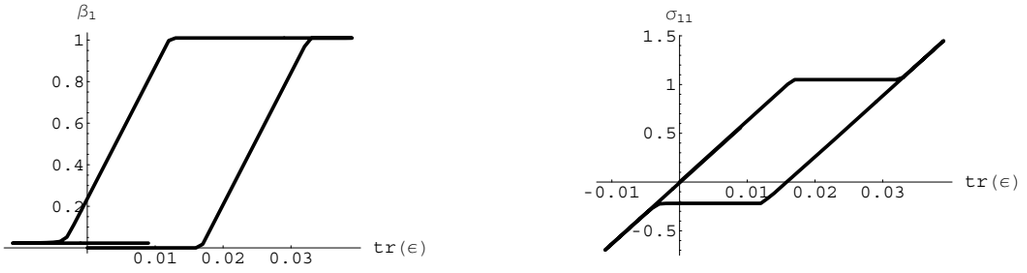


Figure 2. results for the volume fraction β_1 and the stress component σ_{11}

For the analysis of structures we can apply the introduced algorithm to the FEM, where the local computation mentioned above is done at every Gauss-Point. Fig.3 shows the results of a bending test of a 2D-structure.

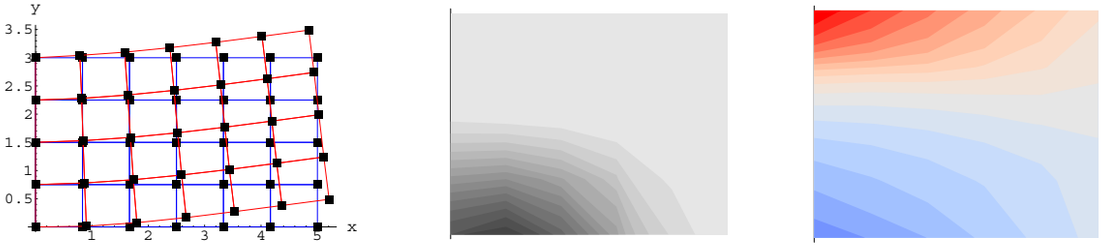


Figure 3. results for the volume fraction β_1 and the stress component σ_{11}

References

[1] Bhattacharya, K.: Theory of martensitic microstructure and the shape-memory effect.
[2] Chunhwa Chu, Ph.D Thesis, University of Minnesota, 1993
[3] Frémond, M.: Materiaux a memoire de forme, C. R. Acad. Sci.,34(2),239-244,1987
[4] Pagano, S.; Alart, P.; Maisonneuve, O.: Solid-solid phase transition modelling. Local and global minimizations of non-convex and relaxed potentials. Isothermal case for shape memory alloys. Int. J. Sol. Struct.,36,1143-1172,1998

XXI ICTAM, 15–21 August 2004, Warsaw, Poland

SIMULATION OF DISCONTINUITY MOVEMENT BY BOUNDARY ELEMENTS

Claus Oberste-Brandenburg
Institute of Mechanics, Ruhr-University Bochum, 44780 Bochum, Germany

Summary A numerical scheme which describes the movement of a discontinuity in a continuum is presented. The local behavior governing the propagation of the discontinuity as well as the behavior of the bulk material is considered. The same discretization is used for the description of the interface propagation and the bulk behavior by employing a moving finite element scheme ([1]) and the boundary element method. Results obtained using a three dimensional implementation of the scheme described above for a phase transformation problem are presented.

INTRODUCTION

For problems involving the movement of a discontinuity in a continuum, the explicit knowledge of its position is often of vital importance for the numerical simulation of the material response. The movement of this discontinuity can usually be expressed in terms of the state in its direct vicinity. However, the local state at the discontinuity may be heavily influenced by the behavior of the bulk material. Thus, for an accurate description of the material response, both aspects may have to be taken into account.

MATERIAL BEHAVIOR

The procedure leading to the identification of the driving force for the movement of the discontinuity is described by numerous authors (see e.g. [3]). In the following, a jump at the discontinuity is denoted by $[\bullet]$. The term

$$T\dot{s}_\Lambda = \rho\dot{l}\ \boldsymbol{n}\cdot[\boldsymbol{\mu}]\cdot\boldsymbol{n}\ \geq 0 \tag{1}$$

is identified as the term describing the local dissipation $\dot{s}_\Lambda$ due to the movement of the discontinuity. $\boldsymbol{n}$ denotes the normal vector to the discontinuity, ρ the mass-density, and $\dot{l}$ the normal velocity of the propagating interface, all terms in the referential description. T denotes the absolute temperature. Furthermore,

$$\boldsymbol{\mu} := \varphi\,\mathbf{1} - \frac{1}{\rho}\,\mathbf{C}\cdot\mathbf{S} \tag{2}$$

has been introduced. φ denotes the specific free Helmholtz energy, $\mathbf{1}$ the second-order unit-tensor in the referential description, $\mathbf{C}$ the right Cauchy-Green tensor, and $\mathbf{S}$ the second Piola-Kirchhoff stress. It is noteworthy that the transpose of $\boldsymbol{\mu}$ is often denoted "Eshelby-Tensor". As this tensor is always used in conjunction with a projection in direction of the normal $\boldsymbol{n}$ (i.e. $\boldsymbol{n}\cdot\boldsymbol{\mu}\cdot\boldsymbol{n}$), the asymmetric part of $\boldsymbol{\mu}$ does not influence this problem and the difference of the descriptions is not of importance. Heidug and Lehner have shown in [3] that the condition $\boldsymbol{n}\cdot[\boldsymbol{\mu}]\cdot\boldsymbol{n} = 0$ is a necessary condition for unconstrained thermodynamic equilibrium, i.e. for the absence of movement of the discontinuity. Thus, the projection of the tensor $\boldsymbol{\mu}$ can be interpreteded as the thermodynamic force for the local movement of the discontinuity and may be used in a concept which describes locally the movement of the discontinuity. A linear relation between the thermodynamic driving force and the movement of the interface $\dot{l}$ is used here (cf. [5]), i.e.

$$\dot{l} - c\,\boldsymbol{n}\cdot[\boldsymbol{\mu}]\cdot\boldsymbol{n} = 0 \tag{3}$$

with the constant parameter $c > 0$. This ensures the validity of equation (1). For the bulk, a linear elastic isotropic behavior is assumed.

NUMERICAL REALIZATION

For simplicity, the behavior of the bulk material and the interface movement are treated independently for the current time step. For the time t, the BEM-solution delivers the terms to calculate the vector F_I, which is derived later. The interface-evolution step is performed advancing the solution by the time step Δt, leading to a new position of the interface. Then again, the BEM-procedure is used and so on. Furthermore, it is assumed that small strain procedures are sufficient.

Description of the Interface Movement

The position vector of a point on the interface is denoted by $\boldsymbol{r}$. In the current implementation, only the movement of the interface normal to itself is considered, hence

$$\dot{\boldsymbol{r}} = \boldsymbol{n}\,\dot{l}. \tag{4}$$

An additional term $\boldsymbol{n}^*\,l^*$ with $\boldsymbol{n}^*\cdot\boldsymbol{n} = 0$ may be added later to avoid a degeneration of the mesh. The weak form of equation (3) can be derived by introducing a trial function $\boldsymbol{r}^*$, reading

$$\int_\Lambda \boldsymbol{r}^*\cdot\dot{\boldsymbol{r}}\,\mathrm{d}A = \int_\Lambda c\,(\boldsymbol{r}^*\cdot\boldsymbol{n})\,(\boldsymbol{n}\cdot[\boldsymbol{\mu}]\cdot\boldsymbol{n})\ \mathrm{d}A \tag{5}$$

where $\int_\Lambda \bullet \, \mathrm{d}A$ denotes the integration over the interface. Using the approximations

$$\boldsymbol{r}(\boldsymbol{x},t) = \sum_I \mathbf{N}_I(\boldsymbol{x})\, r_I(t) \quad \text{and} \quad \boldsymbol{r}^*(\boldsymbol{x},t) = \sum_I \mathbf{N}_I(\boldsymbol{x})\, r_I^*(t) \tag{6}$$

with the shape functions $\mathbf{N}_I(\boldsymbol{x})$ provided by the boundary element method ($\boldsymbol{x}$ may be interpreted as the initial position of the point considered, i.e. $\boldsymbol{x} = \boldsymbol{r}(\boldsymbol{x},0)$) leads to

$$\sum_I \sum_J r_I^* \int_\Lambda \mathbf{N}_I \cdot \mathbf{N}_J \, \mathrm{d}A \, \dot{r}_J = \sum_I r_I^* \int_\Lambda c \, (\mathbf{N}_I \cdot \boldsymbol{n}) \, (\boldsymbol{n} \cdot [\boldsymbol{\mu}] \cdot \boldsymbol{n}) \, \mathrm{d}A. \tag{7}$$

As equation (7) holds for arbitrary $\boldsymbol{r}^*$, it can be expressed as

$$\sum_J D_{IJ} \, \dot{r}_J = F_I \tag{8}$$

using the abbreviations

$$D_{IJ} = \int_\Lambda \mathbf{N}_I \cdot \mathbf{N}_J \, \mathrm{d}A \quad \text{and} \quad F_I = \int_\Lambda c \, (\mathbf{N}_I \cdot \boldsymbol{n}) \, (\boldsymbol{n} \cdot [\boldsymbol{\mu}] \cdot \boldsymbol{n}) \, \mathrm{d}A. \tag{9}$$

Explicit and implicit integration schemes (cf. [6]) are used to integrate equation (8).

Description of the Bulk Material

The boundary element description used to approximate the behavior of the bulk material is based on the code described in [7]. The code is extended to handle a spatially varying additional deformation following the initial strain approach (cf. [2]). For each domain of the material, a discretization of its boundary is used. Consequently, usual boundary element matrices can be formulated and combined to solve the overall mechanical problem.

EXAMPLES

The influence of the choice of the time step Δt on stability and computational cost is studied by some simple examples for the explicit and implicit integration schemes.

As a more illustrative example, the propagation of phase transformation front in a NiTi single crystal is considered. The crystallographic theory of martensite ([4]) is followed to determine the active martensite variants in the transformation layer. For a Ti-rich alloy, the influence of a Ti-inclusion on the overall transformation behavior during a differential scanning calometry test is investigated.

References

[1] Miller, K.: Alternate Modes to Control the Nodes in the Moving Finite Element Method, in Adaptive Computational Methods for Partial Differential Equations, SIAM, Philadelphia, 165–182, 1983.

[2] Brebbia, C. A., Telles, J. C. F., Wrobel, L. C.: Boundary element techniques. Springer Verlag Berlin, Heidelberg, 1984.

[3] Heidug, W., Lehner, F.:Thermodynamics of coherent phase transformations in nonhydrostatically stressed solids. Pure Appl. Geophys. 123, 91–98, 1985.

[4] Ball, J. M., James, R. D.: Fine phase mixtures and minimizers of energy. Arch. Rat. Mech. Anal 100, 13–52, 1987.

[5] Gurtin, M. E.: Thermomechanics of evolving phase boundaries in the plane. Clarendon Press, Oxford, 1993.

[6] Carlson, N. N., Miller, K.: Design and Application of a Gradient-Weighted Moving Finite Element Code II: In two Dimensions. SIAM J. Sci. Comput. 19(3), 766–798, 1998.

[7] Beer, G.: Programming the boundary Element Method, Wiley, Chichester, 2001.

DETERMINATION OF PHASE TRANSFORMATION YIELD SURFACE OF ANISOTROPIC SHAPE MEMORY ALLOYS

Karine TAILLARD**, Sylvain CALLOCH**, Christophe BOUVET***
and Christian LEXCELLENT*

* Laboratoire de Mécanique Appliquée R. Chaléat
Université de Franche-Comté
25030 BESANCON CEDEX - FRANCE

** Laboratoire de Mécanique et Technologie
61, Avenue du Président WILSON
94235 CACHAN CEDEX - FRANCE

*** Laboratoire de Génie Mécanique de Toulouse
Université Paul Sabatier
118, route de Narbonne - 31062 TOULOUSE CEDEX 04 - FRANCE

INTRODUCTION

The superelastic behavior of Shape Memory Alloys (SMA) is useful for several industrial applications. To determine the behavior of SMA structures, the development of specified phenomenological constitutive models is necessary. In particular, the definition of the criterion in order to detect the elastic behavior from the non-linear one related to the martensitic transformation is required. Recently, a macroscopic model, based on the concept of two transformation surfaces (a first surface drives the forward transformation and the second drives the reverse transformation) has been proposed and validated on a large data base of experimental results under uniaxial and multiaxial loadings [1-2]. This model, in its initial version, is only valid for the pseudoelastic behavior of isotropic polycrystalline SMA. However, it is well-known that the initial crystallographic texture is an important parameter in the behavior of SMA and in particular in the shape of the transformation yield surface [3-4]. The aim of this paper is to present some results concerning, on the one hand, the determination and the modeling of the transformation surface of polycrystalline textured SMA and, on the other hand, the relation between the volumic fraction of martensite and the macroscopic transformation strain.

EXPERIMENTAL CHARACTERIZATION OF TRANSFORMATION YIELD SURFACE OF SMA

The material studied, in this part, is a Cu-Al-Be shape memory alloy. The Cu-Al-Be alloy has a weight composition of 87.75 % of Copper, 11.33 % of Aluminum, 0.49 % of Beryllium and balance trace elements including iron and silicon. After machining from wiredrawn bars, all Cu-Al-Be specimens were treated at 650°C for 20 minutes in atmospheric air and quenched in boiling water at 100°C for 1 hour. The four transformation temperatures at stress free state have been determined by using electrical resistance measurements, (the austenite start temperature, A_s^0=19°C, the austenite finish temperature, A_f^0=32°C, the martensite start temperature, M_s^0=21°C, and the martensite finish temperature, M_f^0=-7°C).
A series of tests under tension (compression)–internal pressure and tension (compression)-torsion on tubular specimen and under bi-axial compression on cubic specimen has been performed to determine the initial surface of phase transformation of Cu-Al-Be SMAs in the principal stress plane (σ_1,σ_2) and in the axial-shear stress plane (σ, $\sqrt{3}\tau$). Figures 1 and 2 show the experimental results.

MACROSCOPIC CRITERION OF ONSET TRANSFORMATION FOR ANISOTROPIC SMA

This part is concerned with a proposition of a generalized macroscopic criterion of transformation onset based on the experimental results presented herein. The main objective of this macroscopic criterion is the description of the boundary of the domain, in the stress space, in which one the martensite phase transformation is not activated. This macroscopic criterion has the same role as the yield domain in the case of elasto-plastic materials. One can assume that the martensite transformation of SMAs is volume-invariant. Therefore the criterion for transformation onset, f, can be supposed to be independent of the first stress invariant, $\overline{P}$. Then, the following choice is made:

$$f\left(\overline{\sigma^H}, y_\sigma, \sigma_0\right) = \overline{\sigma^H}\, g\left(y_\sigma\right) - \sigma_0 = 0 \quad \text{with} \quad g\left(y_\sigma\right) = \cos\left[\frac{\cos^{-1}\left(1 - a\left(1 - y_\sigma\right)\right)}{3}\right]$$

where $\bar{\sigma}^H = \sqrt{H\,\mathrm{dev}(\sigma):\mathrm{dev}(\sigma)}$ is the Hill's equivalent stress, σ_0 is the tension yield stress and y_σ is the third stress invariant. H and y_σ are defined by the following relations:

$$H = \frac{3}{2}\begin{bmatrix} c & 0 & 0 & 0 & 0 & 0 \\ 0 & d & 0 & 0 & 0 & 0 \\ 0 & 0 & d & 0 & 0 & 0 \\ 0 & 0 & 0 & 1 & 0 & 0 \\ 0 & 0 & 0 & 0 & 1 & 0 \\ 0 & 0 & 0 & 0 & 0 & 1 \end{bmatrix} \quad \text{and} \quad y_\sigma = \frac{27}{2}\frac{\det(\mathrm{dev}(\sigma))}{\left(\sqrt{\frac{3}{2}\mathrm{dev}(\sigma):\mathrm{dev}(\sigma)}\right)^3}$$

The values of the material parameters have been identified with the experimental results. Figures 1 and 2 show the comparison between the experimental results and the macroscopic criterion. The macroscopic criterion is in good agreement with the experimental observations. Moreover, Figure 1 shows that the initial transformation strain rate is normal to the initial surface of martensite transformation.

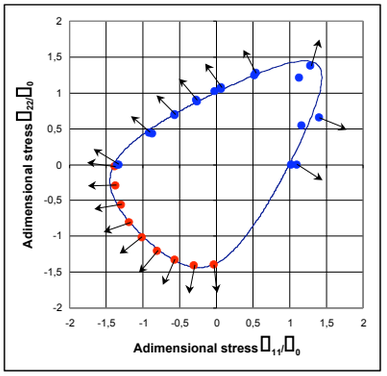


Figure 1. Critical stresses at the onset of phase transformation in (σ_1,σ_2) for polycrystalline Cu-Al-Be

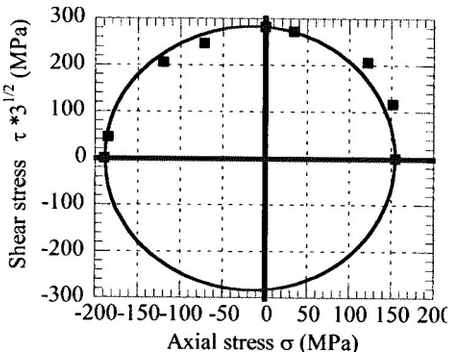


Figure 2. Critical stresses at the onset of phase transformation in $(\sigma, \sqrt{3}\tau)$ for polycrystalline Cu-Al-Be

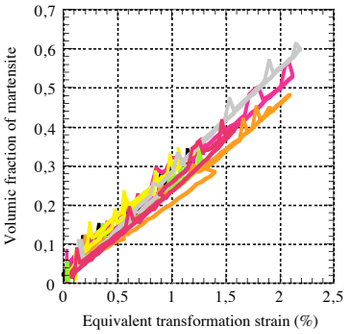


Figure 3. Volumic fraction of martensite versus equivalent transformation strain for different prop. tension-torsion loadings

RELATION between MARTENSITE VOLUMIC FRACTION and TRANSFORMATION STRAIN

A great number of authors has proposed a linear empirical relation between the martensite volumic fraction, f, and the transformation strain, ε^t. This relation has been identified only under uniaxial tension-compression loading [5]. We propose in this section a generalization of this relation for any multiaxial proportional loadings. One can show that a general equivalent strain, ε^t_{eq}, can be built and given by the following relation:

$$\varepsilon^t_{eq} = \frac{\bar{\varepsilon}^{t\,H}}{\sqrt{G\left(y_\sigma, a, H\right)}}$$

where G is a function, $\bar{\varepsilon}^{t\,H}$ is the Hill equivalent transformation strain and y_σ is the third strain invariant.
A series of tests under tension (compression)-torsion on tubular specimen has been performed to determine the relation between the volumic fraction of martensite and the equivalent transformation strain. During the tests, the volumic fraction of martensite has been determined by using electrical resistance measurements and the equivalent transformation strain has been calculated with the strain gauges measurements. Figure 3 shows the experimental results for different loading paths on a Cu-Al-Be SMA. We can see that the linear relation between volumic fraction of martensite, f, and the equivalent transformation strain, ε^t_{eq}, is validated.

References

[1] Bouvet C., Calloch S., Lexcellent C.: Mechanical Behavior of a Cu-Al-Be SMA under Multiaxial Proportional and Nonproportional Loadings. J. Eng. Mat. Techn **124**:112-124, 2002.
[2] Bouvet C., Calloch S., Lexcellent C.: A Phenomenological Model for Pseudoelasticity of SMA under Multiaxial Proportional and Nonproportional Loadings. Eur. J. Mech. accepted, 2004.
[3] Bhattacharya K., Kohn R.V. Acta mater. **44**:529-542, 1996.
[4] Gall K., Sehitoglu H.: The role of texture in tension–compression asymmetry in polycrystalline NiTi. Int. J. Plast. **15**:69-92, 1999.
[5] Vacher P., Lexcellent C.: Study of pseudoelastic behavior of polycrystalline SMA by resistivity measurements and acoustic emission. Proc. of ICM VI, **6**:231-236, 1991.

NUMERICAL DETERMINATION OF DIFFUSIONAL TRANSFORMATION INDUCED PLASTICITY FROM COMPUTATIONS OF RANDOM MICROSTRUCTURES

F. Barbe, R. Quey, L. Taleb
LMR, INSA de Rouen, F-76801 Saint Etienne Du Rouvray, France

Summary This work presents a finite elements approach for the modeling of diffusional transformation induced plasticity in a macro-homogeneous volume containing randomly-positioned nucleates. Assuming ergodicity, the effective TRIP is determined through ensemble averages over sub-domains extracted randomly from the bulk material.

INTRODUCTION

Solid-solid phase transformations of metals under applied stress can lead to permanent strains of the medium being transformed. They occur even though the loading stress is well below the yield stresses of all constituents. For this reason this phenomenon is usually refered to as TRansformation Induced Plasticity and requires improvements of classical plasticity formulations for its modeling. This has been achieved with good quantitative agreements with experimental results by Leblond, Fischer, and, Taleb and Sidoroff [1–3]. Yet, as explained in [4], calling upon particular loading history of the transformed material, one may evidence the fact that predictions of TRIP from modeling and experimental measurements are opposite in signs: if, previously to the transformation, the material has been strained permanently in the direction of the tensile stress imposed during transformation and then unloaded, the modeled TRIP is tensile whereas the experimental TRIP is compressive. Numerical modeling can provide elements of comprehension of the mechanisms involved in the development of TRIP and thus contribute to improvements in theoretical modeling. With finite elements, one is able to simulate the transformation of a volume element by taking into account the main mechanical effects of phase transformation: a change in the volumic density and in the elastoplastic properties of the finite elements being transformed. By opposition to martensitic transformations where plates with particular orientations form quasi-instantaneously, the diffusional transformation considered in this study is supposed to be progressing from a nucleate with an isotropic continuous growth. The question as to how the computed TRIP may be affected by the spatial distribution of nucleates, the number of elements in the mesh, the number of nucleates in the mesh and other parameters has been addressed in a previous study [5] and is still in the process of completion; it is the object of the first part of this summary. Then we present a method to compute the effective TRIP in a macro-homogeneous volume with a given density of randomly positioned nucleates.

NUMERICAL MODELING AND RESULTS

Spherical transformation from a single nucleate

The direct computation of a volume representative of a macro-homogeneous medium –necessarily consisted of a large number of nucleates since they are positioned randomly– would require a mesh so huge that a single parallel computing can hardly be envisaged, as emphasized in [5]. This difficulty can be circumvented by considering that, rather than randomly positioned, the nucleates are distributed along a regular cubic array thus forming a periodic composite material made of austenite matrix and bainitic growing particulates. By further assuming that all nucleates appear at a same instant and grow at a same rate, one can restrict the volume of computation to a cubic cell with a single central nucleate. This is an approach proposed by Ganghoffer *et al* [6], which we have adopted to validate our computations with the finite element code ZeBuLoN and to make firsts comparisons to our experimental results about bainitic transformation [7]. The cubic region of study with a central nucleate is reduced to a eighth as the symmetries in geometry and loading allow it. The first element to be transformed is accordingly located at a corner of the cubic mesh. This latter is discretised into $n \times n \times n$ cubic 8-node elements. The diffusional transformation is proceeded through the transformation of the successive layers of elements surrounding the product phase region. Meanwhile, a constant tensile stress well below the yield stresses of austenite and bainite is imposed to one of the faces of the cube. Some results (voided symbols) are given in fig. 1a with TRIP as function of the volumic fraction of product phase. They are in good qualitative agreement with experimental results, but it is not so true when comparing quantitatively, and there remains a mesh size effect even for the largest sizes of mesh.

Ensemble averaging over random realisations

In order to respect the randomness in the positions of the nucleates, one can simply perform computations where there are several nucleation elements randomly positioned in the mesh, as has been presented in [6] with few computations. It has been demonstrated in [5] that such computations are strongly sensitive to mesh size, number of nucleates and, above all, spatial distribution of the nucleates. Fig. 1b illustrates this last point: 100 TRIP curves obtained from microstructures differing only in the positions of the nucleates (number of nucleates is fixed to 4) have been plotted. They display so large a dispersion that only by calling upon several tenth of realisations would one obtain an ensemble average over individual curves that is unsensitive to the number of

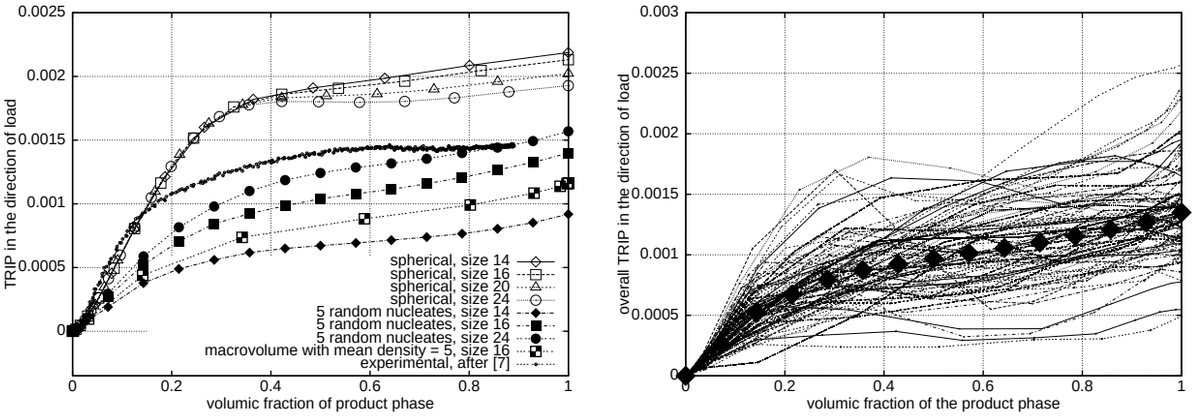


Figure 1: (a) TRIP obtained in different configurations of computations and experimentally. (b) TRIP computed in 100 microstructures with 4 randomly-positioned nucleates and the corresponding ensemble average result (◇)

realisations. It is further noticed on fig. 1a that the response computed by ensemble averaging (symbols filled in black) is dependent on the mesh size and, as shown in [5], on the number of nucleates: *(i)* the bigger the mesh the larger the TRIP, *(ii)* the larger the number of nucleates, the smaller the TRIP. Fortunately, the experimental curve is bounded by the responses provided by the computations on cells with single central nucleates (upper) and the responses determined by ensemble averaging (lower). Moreover, the bigger the mesh, the narrower the bounds. These considerations confirm that mesh size should be as large as possible and that, dealing with random distribution of nucleates, one gets a better quantitative agreement with experimental results. The slight increase in TRIP observed at the end of a transformation with random nucleates is partly due to the fact that, as compared to single nucleate cells, the probability of an austenitic element to be surrounded by bainite is much more important. Bainite having the highest yield stress, it can hold elastic stresses that would strain austenite plastically, all the more if austenite is embedded in bainite.

With the aim to perform random computations on a realistic macro-homogeneous medium, we have taken into account the fact that a sub-domain extracted randomly from the bulk material contains a number of nucleates that might vary with the position of the sub-domain. As nucleates positions are defined by a Poisson process, the probability of finding such or such number of nucleates in a sub-domain with a given size is known. The resulting set of probabilities (of finding 0 nucleate, 1, 2...) corresponds to the volumic fractions of all types of sub-domains encountered in the macro-volume. The effective response of the macro-volume is then obtained through an ensemble average over the responses in all types of sub-domain, balanced by their respective volumic fraction. The possibility for a sub-domain to be transformed partly or completely with the product phase growing from an external nucleate has also been implemented. An example of the results provided by the complete method is given in fig. 1a (symbol: half filled square): about 800 sub-domains of size $16 \times 16 \times 16$ have been extracted randomly from a quasi-infinite macro-volume; the density evolves from 0 to 7 nucleates per sub-domain and has a mean value equal to 5. This leads to an amount of TRIP significantly inferior to the one obtained with sub-domains of the same size containing strictly 5 nucleates (symbol: filled square), a difference that indicates that the full character of position-randomness in the macro-volume should be respected.

CONCLUSION

A classic method of the mechanics of disordered media have been adapted for problems of diffusional transformation. It is based on FE computations over meshes representing microstructures with nucleates varying randomly in their position and number. The effective TRIP is the result of a ensemble averaging balanced by the probabilities of finding such or such number of nucleates in a microstructure. Forthcoming improvements concern the optimisation of the number of computations required to get a result within a given interval of confidence.

References

[1] J. Leblond, Mathematical modelling of transformation plasticity in steels II: coupling with strain hardening phenomena, Int J Plasticity 5 (1989) 573–591.

[2] F. Fischer, A micromechanical model for transformation plasticity in steels, Acta Metall Mater 38 (1990) 1536–1546.

[3] L. Taleb, F. Sidoroff, A micromechanical modeling of Greenwood-Johnson mechanism in transformation induced plasticity, Int J Plasticity 19 (10) (2003) 1821–1842.

[4] L. Taleb, S. Petit-Grostabussiat, Elastoplasticity and phase transformations in ferrous alloys: some discrepancies between experiments and modeling, J Phys IV 12 (2002) Pr11–187–194.

[5] F. Barbe, L. Taleb, Numerical investigations on diffusional transformation induced plasticity. Submitted for publication in Comput Mat Sc.

[6] J. Ganghoffer, S. Denis, E. Gautier, A. Simon, S. Sjöström, Finite element calculation of the micromechanics of a diffusional transformation, Eur J Mech, A/Solids 12 (1) (1993) 21–32.

[7] S. Petit-Grostabussiat, L. Taleb, J. Jullien, Experimental results on classical plasticity of steels subjected to structural transformations, Int J Plasticity to be published.

NUMERICAL ANALYSES OF THE INTERACTION CLASSICAL PLASTICITY - TRIP

Salem Meftah [*], Fabrice Barbe [*], Lakhdar Taleb [*] and François Sidoroff [**]

[*]INSA/LMR, 08 avenue de l'université, 76801 St Etienne du Rouvray Cedex, France.
[*]ECL/LTDS, UMR 5513, 136 avenue Guy de Collongue, BP 163, 69131 Ecully Cedex, France.

Summary The effect of classical plasticity on TRIP is analyzed considering martensitic transformation of ferritic steel. It is experimentally shown that TRIP is influenced by the previous strain hardening of the parent phase. As the obtained results are not easily explainable in the light of the existing models in the literature, the objective of this paper is to contribute to a better understanding of the mechanisms at the origin of the observed discrepancies.

TRansformation Induced Plasticity (TRIP) is one of the mechanical consequences of structural transformations at the solid state in steels. It can be defined as the anomalous plastic strain observed when metallurgical transformation occurs under 'moderate' external stress [1], [2], [3]. More generally a similar phenomenon may also result from some kind of internal stresses within the material and this has been advocated by Videau et al. [4] some years ago (studying martensitic transformation of a Fe-20Ni-0.5C) to explain the influence of an initial pre-deformation of the parent phase on the transformation and the resulting deformation. Two mechanisms are considered to explain the TRIP phenomenon: Magee and Greenwood-Johnson mechanisms. The relative importance of these two mechanisms depends on the steel and the transformation under consideration. It is generally admitted that Magee mechanism is present in martensitic transformation (diffusionless) whereas Greenwood-Johnson mechanism is dominant in diffusional transformations.
In this paper, TRIP is analyzed considering martensitic transformation of a 16MND5 steel (AFNOR norm). Different kinds of coupling may exist between the martensitic transformation and the classical plasticity in both phases. We shall focus here on the effect of classical plasticity on TRIP: the TRIP evolution generally depends on the mechanical characteristics and internal state of the parent and product phases. These may be influenced by the mechanical history of the parent phase and in particular by previous strain hardening. From an experimental point of view, this influence has been shown [5] through the comparison of the evolution of strain in free dilatometric test and in a test consisting in a significant strain hardening of the austenitic phase during cooling and before the metallurgical transformation occurs followed by the transformation without external applied load (Figure 1).

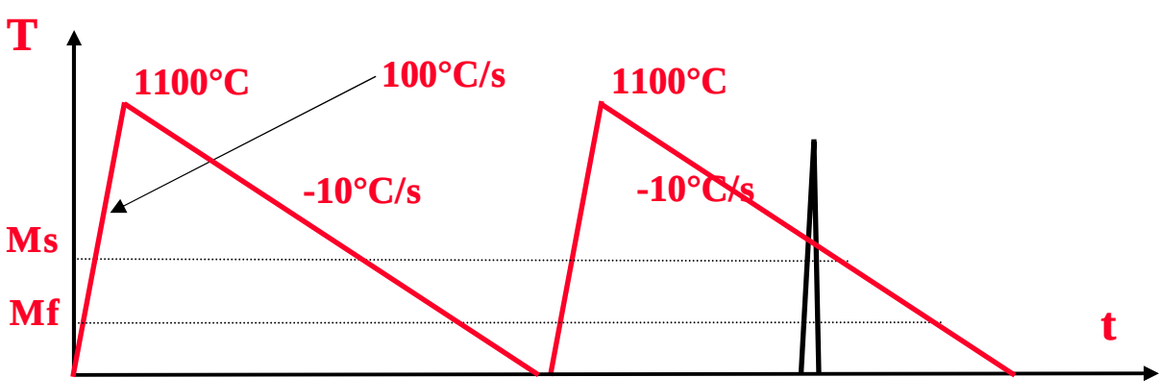


Figure 1: Free dilatometric test followed by predeformation test with a loading-unloading cycle applied before the starting of the martensitic transformation (M_s). The applied stress largely exceeds the yield limit of the austenitic phase.

These test results have been compared to the predictions of Leblond's model [6] that enables to take into account the interaction classical plasticity - TRIP. As it can be remarked in figure 2, the predictions are not at all in agreement with experiments: when experiment exhibits positive TRIP (after positive pre-deformation), the model predicts negative TRIP and vice-versa after negative pre-deformation. The objective of this paper is to contribute to a better understanding of the mechanisms at the origin of the observed discrepancies. For that, we consider in a first stage a classical finite element micromechanical approach already used (see for instance [7]). The mesh (2D) being loaded by a constant uniaxial stress, an arbitrary set of elements constituting a plate is first transformed (changing the material properties of the plate that is subjected to a strain corresponding to the transformation strain). Then the driving force is measured in each element of the mesh in order to select the following elements to be transformed. Figure 3 gives the results of two numerical FE simulations of TRIP following such procedure: it appears that the obtained TRIP depends on the first selected element to be transformed. Furthermore, it can be remarked that TRIP is negative under tensile applied stress which is not consistent regarding experiments. Before simulating the pre-deformation tests, other

conditions enabling the selection of the transformed elements are now under consideration: the simulations are in progress and the results will be presented during the conference.

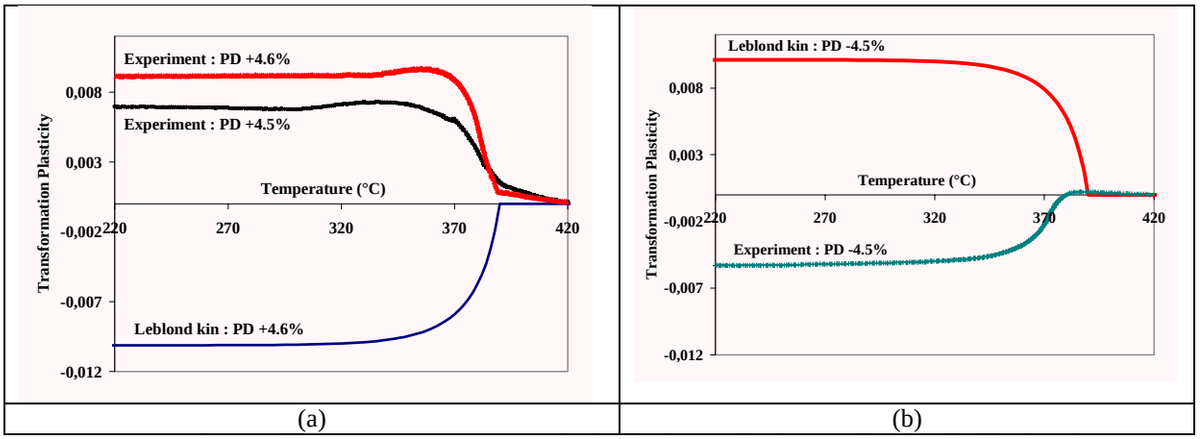


Figure 2: TRIP after pre-deformation (PD) test in which a loading-unloading cycle is applied before the starting of the martensitic transformation (M_s). The applied stress largely exceeds the yield limit of the austenitic phase. Comparison between experimental results and the predictions of Leblond's model: (a) Response after positive pre-deformation; (b) Response after negative pre-deformation.

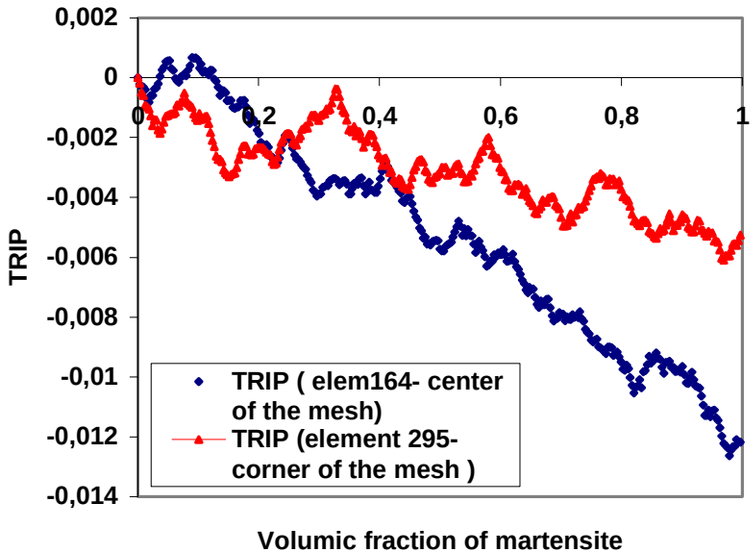


Figure 3: Numerical FE simulation of TRIP under constant applied stress. The result strongly depends on the choice of the first transformed element.

References

[1] Fischer, F. D., Sun, Q-P., Tanaka, K., 1996. Transformation Induced Plasticity (TRIP). Appl. Mech. Rev. **49**, 317-364.
[2] Taleb, L., Cavallo, N., Waeckel, F., 2001. Experimental Analysis of Transformation Plasticity. Int. J. Plasticity, **17**, 1-20.
[3] Taleb, L., Sidoroff, F., 2003. A Micromechanical Modeling of the Greenwood-Johnson Mechanism in Transformation Induced Plasticity. Int. J. Plasticity 19, 1821-1842
[4] Videau, J.Ch., Cailletaud, G., Pineau, A., 1995. Experimental study of the transformation induced plasticity in a Cr-Ni-Mo-Al-Ti steel. International seminar MECAMAT'95 : Mechanisms and mechanics of solid phase transformations, la Bresse, France, 16-19 may
[5] Grostabussiat, S., Taleb, L., Jullien, J. F., Sidoroff, F., 2001. Transformation Induced Plasticity in Martensitic Transformation of Ferrous Alloys. J. Phys. IV, **11**, 173-180.
[6] Leblond, J.B., 1989. Mathematical modelling of transformation plasticity in steels- II. Coupling with strain hardening phenomena. Int. J. Plasticity, **5**, 573-591.
[7] Ganghoffer, J. F., Simonson, K. A micromechanical Model of The Martensitic Transformation. Mechanics of Materials, 1998, pages 125-144.

NUCLEATION AND MOTION OF PHASE BOUNDARY IN SHAPE MEMORY ALLOY MICROTUBES

Qingping Sun
Department of Mechanical Engineering, Hong Kong University of Science and Technology, Hong Kong, P. R. China.

Summary Helical-type martensite band nucleation and propagation in superelastic NiTi SMA microtube under tensile and torsional mechanical loadings are investigated. Using constitutive relation with intrinsic strain softening, 3D FEM simulation of the tube is performed to reproduce the observed phase boundary motion and deformation patterns. The results demonstrated the roles of material instabilities and the competition between bulk and surface energy in the observed martensite band morphology.

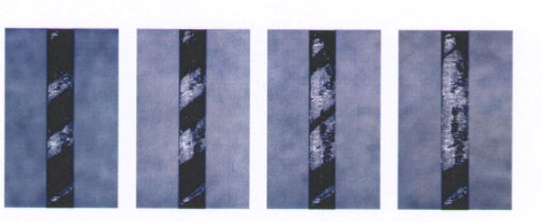
Helical-type martensite band nucleation and propagation in superelastic NiTi SMA microtube under uniaxial tension was observed recently as shown in the figure. This paper investigates this phenomenon from continuum mechanics point of view. Major results of the investigation on such pattern-forming deformation instability process during stress-induced phase transformation are summarized as follows. (1) Based on detailed experimental observation and possible deformation mechanism, a simple trilinear stress-strain relation with intrinsic strain softening is proposed to approximate the material constitutive behavior during stress-induced transformation. (2) Three-dimensional finite deformation simulation of the tube under loading was performed to model the detailed band nucleation and growth process. A combined analytical-experimental approach is used to extract the constitutive parameters of the material from the experimental measurement. The observed phase boundary motion and deformation patterns are successfully reproduced in the simulation by the identified trilinear constitutive law. The results demonstrated that only geometry instability due to finite deformation is not sufficient to quantify the experimental observation, both material and geometric instabilities, as well as the competition between bulk and surface energy play important roles in the observed martensite band morphology and its evolution. (3) Compared with the previous investigations based on a similar local constitutive theory, the issue of mesh sensitivity in the nucleation process of the martensite is addressed and demonstrated in the present simulation via the tube geometry. This important issue indicated that interfacial energy must be taken into consideration, which needs to be quantified by a non-local constitutive theory in the future investigation.

Acknowledgements — This work has been supported by the Research Grants Council of the Hong Kong Special Administrative Region, China (Project No. HKUST 6074/00E and HKUST 6234/01E) and the Hong Kong University of Sci. & Tech. (Project No. HIA01/02.EG18).

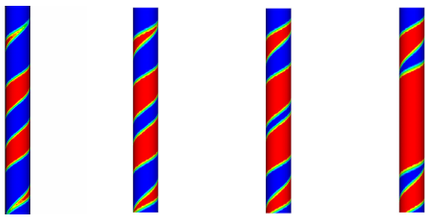
Key references

1. Li, Z. Q. and Q. P. Sun, 2002, *Int. J. of Plasticity*, 18 (11), 1481-1498.
2. Sun, Q. P. and Li, Z. Q., 2002, *Int. J. Solids and Structure,* 39 (13-14), 3797-3809
3. Sun, Q. P. and K. C. Hwang, 1993, *J. Mech. Phys. Solids,* 41, 1-33.
4. Shaw, J.A. and Kyriakides, S., 1995, *J. Mech. Phys. Solids*, 43, 1243-1281.
7. Abeyaratne, R. and J. K. Knowles, 1990, *J. Mech. Phys. Solids*, 38, 345-360.
8. Abeyaratne, R. and J. K. Knowles, 1993, *J. Mech. Phys. Solids*, 41, 541-571.

Helicity of martensite Band Morphology —— Experiment



Martensite helicoid —— FEM Simulation



BIODEGRADATION IN POROUS LANDFILL BODIES

Tim Ricken*, Reint de Boer*, Veronika Ustohalova**, Renatus Widmann**
*Institute of Mechanics, University of Duisburg-Essen, Campus Essen, 45117 Essen, Germany
**Institute of Waste Management, University of Duisburg-Essen, Campus Essen, 45117 Essen, Germany

Summary In this contribution a constitutive model based on the macromechanical Theory of Porous Media (TPM) for a saturated thermo elastic porous body has been developed. The body under investigation consists of an organic and inorganic moisturized phases and a gas phase. Based on a consistent thermomechanical treatment the governing equations and constitutive equations will be given. Thus, we obtain a mathematical concept describing the motion of the solid phase, the pressure of the gas phase, the temperature of the mixture and the biodegradation of organic material into a gas mixture of methane and carbon dioxide produced by bacterial decomposition during stable methane fermentation (biogas).

INTRODUCTION

The Earth's average surface temperature rose by around 0.6 °C during the 20th century. It seems to be evidence that most of the global warming is caused by emissions of carbon dioxide (CO_2), methane (CH_4) and other greenhouse effect gases. Landfilling belongs to an important global sources of greenhouse gases. In this case, the time scale belongs to hundreds of years. Therefore, development of a numerical model describing the effect of solid phase composition (consisting of organic and inorganic materials) and the pore structure of the landfill body on the conversion phenomena and multi-component gas transport is of great importance. This has been done based on the well established Theory of Porous Media for which basic relations will be summarized in the following section.

MODELING

The Theory of Porous Media is the mixture theory restricted by the concept of volume fractions. Hereby, we consider a continuum which consists of several constituents. As aforementioned, the investigated porous body consists of φ^{S} (solid), φ^{O} (organic) and φ^{G} (gas). A porous medium occupying the control space of the porous solid $\mathrm{B_S}$, with the boundary $\partial \mathrm{B_S}$, consists of constituents φ^α ($\alpha = \mathrm{S,O,G}$) with real volumes v^α. The boundary $\partial \mathrm{B_S}$ is a material surface for the solid phase and a non-material surface for the liquid and gas phases. The volume fractions $\mathrm{n}^\alpha(\mathbf{x},\mathrm{t}) = \mathrm{dv}^\alpha/\mathrm{dv}$ refer the volume elements dv^α of each individual constituents φ^α to the bulk volume element dv. The main statement of the volume fraction concept can be founded by the saturation condition $\sum_\alpha^{\mathrm{SOG}} \mathrm{n}^\alpha(\mathbf{x},\mathrm{t}) = \sum_\alpha^{\mathrm{SOG}} \rho^\alpha/\rho^{\alpha\mathrm{R}} = 1$, see [1], wherein $\mathbf{x}$ is the position vector of the spatial point x in the actual placement and t is the time. Moreover, the partial density of the constituent φ^α, namely ρ^α, is related to the real density of the materials $\rho^{\alpha\mathrm{R}}$ involved via the volume fractions n^α. The concept of volume fractions is an important part of the theory following in the next sections. Due to the volume fraction concept, all geometric and physical quantities, such as motion, deformation and stress, are defined in the total control space. Thus, they can be interpreted as the statistical average values of the real quantities.

Field equations

The local statements of the balance equations of mass and of of momentum are given for the constituents φ^α by

$$(\rho^\alpha)'_\alpha + \rho^\alpha \operatorname{div} \mathbf{x}'_\alpha = \hat{\rho}^\alpha, \qquad \operatorname{div} \mathbf{T}^\alpha + \rho^\alpha(\mathbf{b} - \mathbf{x}''_\alpha) + \hat{\mathbf{p}}^\alpha - \hat{\rho}^\alpha \mathbf{x}'_\alpha = \mathbf{0}\,. \tag{1}$$

In (1), "div" denotes the divergence operator, $\hat{\rho}^\alpha$ represents the mass supply between the phases which has to conform to $\hat{\rho}^{\mathrm{S}} + \hat{\rho}^{\mathrm{O}} + \hat{\rho}^{\mathrm{G}} = 0$, $\mathbf{T}^\alpha$ is the partial CAUCHY stress tensor, $\rho^\alpha\,\mathbf{b}$ specifies the volume force and $\hat{\mathbf{p}}^\alpha$ describes the interactions of the constituents φ^α which are restricted to $\hat{\mathbf{p}}^{\mathrm{S}} + \hat{\mathbf{p}}^{\mathrm{O}} + \hat{\mathbf{p}}^{\mathrm{G}} = \mathbf{0}$. Additionally, the balance of energy concerning the whole mixture body must be taken into account:

$$\begin{aligned}\textstyle\sum_\alpha^{\mathrm{S,O,G}}\big(\,\rho^\alpha\,[\underbrace{(\psi^\alpha)'_\alpha + (\theta^\alpha)'_\alpha\,\eta^\alpha + \theta^\alpha\,(\eta^\alpha)'_\alpha}_{(\varepsilon^\alpha)'_\alpha}] - \mathbf{T}^\alpha \cdot \mathbf{D}_\alpha - \rho^\alpha\,\mathrm{r}^\alpha\,\big) = \\ = \textstyle\sum_\alpha^{\mathrm{S,O,G}}\big(-\operatorname{div}\mathbf{q}^\alpha + \hat{\mathrm{e}}^\alpha - \hat{\mathbf{p}}^\alpha\,\mathbf{x}'_\alpha - \hat{\rho}^\alpha(\underbrace{\psi^\alpha + \theta^\alpha\,\eta^\alpha}_{\varepsilon^\alpha} - \frac{1}{2}\,\mathbf{x}'_\alpha \cdot \mathbf{x}'_\alpha)\,\big).\end{aligned} \tag{2}$$

Herein, $(\psi^\alpha)'_\alpha$ and $(\varepsilon^\alpha)'_\alpha$ represent the material time derivation of the free HELMHOLTZ energy ψ^α and of the internal energy ε^α, respectively, θ^α is the temperature, η^α specifies the specific entropy, $\mathbf{D}_\alpha$ is the symmetric part of the spacial velocity gradient, r^α denotes the local external heat supply and $\mathbf{q}^\alpha$ is the heat influx vector. The local energy supply term $\hat{\mathrm{e}}^\alpha$ must satisfy the constrain condition $\hat{\mathrm{e}}^{\mathrm{S}} + \hat{\mathrm{e}}^{\mathrm{O}} + \hat{\mathrm{e}}^{\mathrm{G}} = 0$. At least, in order to close the set of equation, the saturation condition has to be taken into consideration.

Assumptions

The system is investigated under the condition of a compressible gas phase but an incompressible solid and organic phase and we imbibe that the immobile phases have the same motion: $(\rho^{\mathrm{SR}})'_{\mathrm{S}} = 0$, $(\rho^{\mathrm{OR}})'_{\mathrm{S}} = 0$, $\mathbf{x}'_{\mathrm{S}} = \mathbf{x}'_{\mathrm{O}}$. The liquid is

assumed to be an integral part of organic and solid phase. Moreover, we assume the solid to be not involved in the mass transition: $\hat{\rho}^{\mathrm{S}} = 0$. In addition, the organic phase is neglected in respect to the interaction forces: $\hat{\mathbf{p}}^{\mathrm{O}} = \mathbf{0}$. In order to keep the numerical complexity in a manageable scope, we have made restrictions for all phases of small deformations, excluding accelerations and a unique temperature of all phases at the same place: $\mathbf{x}''_{\alpha} = \mathbf{0}$, $\theta^{\mathrm{S}} = \theta^{\mathrm{O}} = \theta^{\mathrm{G}} = \theta$.

Constitutive equations

From the evaluation of the entropy inequality of the the liquid and/or gas saturated porous body considering saturation condition as a constraint, see [1], we obtain the constitutive relations for $\mathbf{T}^{\beta}$ ($\beta = \mathrm{S}, \mathrm{O}$) and the mobile phase $\mathbf{T}^{\mathrm{G}}$:

$$\mathbf{T}^{\beta} = -\,\mathrm{n}^{\beta}\,\mathrm{p}^{\mathrm{GR}}\,\mathbf{I} + 2\,\rho^{\beta}\,\mathbf{F}_{\mathrm{S}}\frac{\partial \psi^{\beta}}{\partial \mathbf{C}_{\mathrm{S}}}\,\mathbf{F}_{\mathrm{S}}^{\mathrm{T}}, \qquad \mathbf{T}^{\mathrm{G}} = -\,\mathrm{n}^{\mathrm{G}}\,\mathrm{p}^{\mathrm{GR}}\,\mathbf{I}\,, \tag{3}$$

with the realistic gas pressure p^{GR}, the tensor of identity $\mathbf{I}$, the deformation gradient $\mathbf{F}_{\mathrm{S}}$ and the right Cauchy-Green tensors $\mathbf{C}_{\mathrm{S}}$ according to the solid. For the compressible gas phase, p^{GR} is related to the real density ρ^{GR} with the nonlinear expression: $\mathrm{p}^{\mathrm{GR}} = \mathrm{c}_{\mathrm{p}}^{\mathrm{G}}\ln(\rho_0^{\mathrm{GR}}/\rho^{\mathrm{GR}})$ wherein $\mathrm{c}_{\mathrm{p}}^{\mathrm{G}} = \rho_0^{\mathrm{GR}}\,\theta\,\mathrm{R}_{\mathrm{G}}$ denotes a parameter concerning the reference density ρ_0^{GR} and the specific gas constant R_{G}. From the evolution of the entropy inequality, see [2], we gain restrictions concerning the interaction force $\hat{\mathbf{p}}^{\mathrm{G}}$ and the heat flux $\mathbf{q}^{\mathrm{SOG}}$ with $\mathbf{q}^{\mathrm{SOG}} = \sum_{\alpha}^{\mathrm{S,O,G}}\mathbf{q}^{\alpha}$:

$$\hat{\mathbf{p}}^{\mathrm{G}} = \mathrm{p}^{\mathrm{GR}}\,\mathrm{grad}\,\mathrm{n}^{\mathrm{G}} + \theta\,\alpha^{\mathrm{G}}_{\mathbf{w}_{\mathrm{GS}}}\,\mathrm{grad}\,\theta - \theta\,\mathrm{S}_{\mathrm{G}}\,\mathbf{w}_{\mathrm{GS}}, \qquad \mathbf{q}^{\mathrm{SOG}} = -\,\alpha_{\theta}\,(\theta)^2\,\mathrm{grad}\,\theta - \alpha^{\mathrm{G}}_{\mathbf{w}_{\mathrm{GS}}}\,(\theta)^2\,\mathbf{w}_{\mathrm{GS}}. \tag{4}$$

Herein, "grad" denotes the gradient operator, $\alpha^{\mathrm{G}}_{\mathbf{w}_{\mathrm{GS}}}$ represents a value concerning the dependency between the heat flux and interaction forces and α_{θ} is the heat conductivity. Moisture content is an important influencing factor concerning heat conductivity. Moreover, S_{G} describes the interaction between the gas phase and the remaining constituents in connection with the seepage velocity $\mathbf{w}_{\mathrm{GS}}$ with $\mathbf{w}_{\mathrm{GS}} = \mathbf{x}'_{\mathrm{G}} - \mathbf{x}'_{\mathrm{S}}$. The material parameter function S_{G} is postulated in dependence of the volume fraction n^{L}, see [3]. The Ansätze concerning to the free Helmholz energy functions ψ^{α} have been taken over by [2]. However, an intensive investigation on ψ^{α} has to be exerted. The mass supply reads

$$\hat{\rho}^{\mathrm{O}} = -\,\delta^{\mathrm{O}}_{\psi^{\mathrm{OG}}}\,\frac{1}{\theta}(\Psi^{\mathrm{O}} - \Psi^{\mathrm{G}}) = -\,\delta^{\mathrm{O}}_{\psi^{\mathrm{OG}}}\,\mathrm{K}_{\mathrm{B}}\,(\frac{\theta - \theta_{0\mathrm{S}}}{\theta_{0\mathrm{S}}})\,\rho^{\mathrm{O}}, \tag{5}$$

wherein $\delta^{\mathrm{O}}_{\psi^{\mathrm{OG}}}$ defines a positiv constant for the chemical potential functions Ψ^{O} and Ψ^{G} , see [2], K_{B} denotes a parameter associated with active biomass and $\theta_{0\mathrm{S}}$ is the reference temperature. The organic mass supply expresses the changes in organic phase due to bacterial activity, by which degradable organic matter is degraded. The more organic waste presents in a landfill, the more landfill gas is produced by the bacteria during decomposition. Organic mass supply depends on substrate concentration, expressed as density of organic matter, active biomass and temperature.

Numerical Treatment

Within the framework of a standard GALERKIN procedure, weak formulations are formed. Under consideration of the assumptions as well as the constitutive equations we receive the set $\Re$ of unknown quantities $\Re = \Re(\mathbf{x}, \mathrm{t}) = \{\mathbf{u}_{\mathrm{S}}, \mathbf{w}_{\mathrm{GS}}, \mathrm{n}^{\mathrm{S}}, \mathrm{n}^{\mathrm{O}}, \mathrm{n}^{\mathrm{G}}, \mathrm{p}^{\mathrm{GR}}, \theta\}$ wherein $\mathbf{u}_{\mathrm{S}}$ denotes the displacement of the solid phase. In order to develop an effective calculation concept, we insert the saturation condition, the integral statement of the balance of mass concerning the solid phase: $\mathrm{n}^{\mathrm{S}} = \mathrm{n}^{\mathrm{S}}_{0\mathrm{S}}\ \det\mathbf{F}_{\mathrm{S}}^{-1} = \mathrm{n}^{\mathrm{S}}_{0\mathrm{S}}\,\mathrm{J}_{\mathrm{S}}^{-1}$, into the set of equations. Therein $\mathrm{n}^{\mathrm{S}}_{0\mathrm{S}}$ denotes the reference volume fraction of the solid phase. Moreover, the seepage velocity concerning the gas phases $\mathbf{w}_{\mathrm{GS}}$ will be calculated using the balance of momentum in the DARCY formulation, see [3]. Finally, the set of unknown quantities $\Re$ can be reduced to $\Re = \Re(\mathbf{x}, \mathrm{t}) = \{\mathbf{u}_{\mathrm{S}}, \mathrm{n}^{\mathrm{O}}, \mathrm{p}^{\mathrm{GR}}, \theta\}$.

CONCLUSION

A closed calculation concept for the simulation of thermal mass transition in porous media has been developed. An essential contribution is given by implementation of the thermal mass transfer on the basis of an thermodynamical and physical motivated investigation. To this subject, there have been many empirical approaches published but only a limited number of continuum mechanical treatments are known. The presented contribution in the framework of a "smeared" continua has led to reasonable field equations, and in particular, to proper constitutive equations for the stresses, interaction volume forces, heat flux and mass supply. Nevertheless, further investigations are necessary to fit the presented calculation concept in respect of landfill bodies.

References

[1] DE BOER, R. [2000], "Theory of Porous Media: highlights in the historical development and current state.", Springer-Verlag Berlin • Heidelberg • New York.

[2] BLUHM, J. [2002], "Modelling of saturated thermo-elastic porous solids with different phase temperatures.", in Porous Media : Theory, Experiments and Numerical Applications / W. Ehlers; J. Bluhm (ed.), Springer-Verlag Berlin • Heidelberg • New York.

[3] RICKEN, T., DE BOER, R. [2003] "Multiphase flow in a capillary porous medium.", *Computational Materials Science*, **28**, Issues 3-4, pp. 704-713.

MANDEL & CRYER PROBLEMS FOR FLUID-SATURATED FOAMS WITH NEGATIVE POISSON'S RATIO

Michio Kurashige, Keiichi Sato and Kazuwo Imai
Iwate University, Department of Mechanical Engineering, Morioka, Iwate 020-8551, Japan

Summary The advent of various foams with negative Poisson's ratio has interested us in how these foams will behave when they are saturated with fluid. To explore this behavior, we have solved 2D and 3D versions of the Mandel and Cryer problems in a unified manner. The results show that much more remarkable Mandel-Cryer effect and additional interactions between the elastic deformation and pore fluid diffusion are observed for the negative Poisson's ratio than for the conventional one.

INTRODUCTION

It has been well known that the value of Poisson's ratio thermodynamically ranges from -1.0 to 0.5 for isotropic linear elastic materials, although the negative ratios are counterintuitive and real conventional isotropic materials have the positive ratios. In 1987, Lakes [1] created polymer and metal foams having negative Poisson's ratios and, following this creation, he and his coworkers have explored various characteristics of such materials and discussed their microstructures and their real and possible applications.
This advent of foamed polymers and metals with negative Poisson's ratios have stirred our interest and imagination in how these unconventional foams will behave and what phenomena their negativeness will bring when they are fully saturated with fluid. To explore these behavior and phenomena, we picked up the four problems: the original Mandel problem [2] and a corresponding axisymmetric problem, and the original Cryer problem and a corresponding plane strain problem. We call these four problem "2D and 3D, Mandel and Cryer problems." We selected these four problems among many other problems because we expected that they manifest most remarkable interactions between the elastic deformation of sample skeletons and pore fluid flow. We analytically solved these problems in the Laplace transform space in a unified manner and numerically inverted the solutions into the real time space.

FOUR PROBLEMS TO SOLVE

To describe the problems, we introduce the Cartesian, cylindrical polar and spherical polar coordinate systems: (x,z) (r,θ,z) and (r,φ,θ). The four problems are presented in Fig.1 together with their boundary conditions, where only the statically equivalent, lower halves of a circular cylinder and a sphere in the Cryer problems are shown to make it more convenient to discuss the results of solutions. For all problems, the initial conditions are that all variables are zero at time $t = 0$ and the loading is a step-like one; in addition, the basic equations applicable for an irrotational displacement field are used. In the figure, $\sigma_0 = P_0/(\pi a^2)$, which means the average axial compressive stress for the Mandel problem and pressure loading on the surface for the Cryer problem.

SOLUTIONS IN LAPLACE TRANSFORM SPACE

Only the solutions for the 2D Cryer problem are presented here, for the economy of space and because they have not seen in literature.

$$\bar{p}(r,s) = \left(\frac{\sigma_0}{s}\right)\frac{\nu_u-\nu}{\eta}\left\{1-\frac{I_0(\sqrt{s/c}r)}{I_0(\sqrt{s/c}a)}\right\}/F(s), \tag{1}$$

$$\bar{\sigma}_r(r,s) = \left(-\frac{\sigma_0}{s}\right)\left[1+2(\nu_u-\nu)\left\{\frac{I_1(\sqrt{s/c}a)}{(\sqrt{s/c}a)I_0(\sqrt{s/c}a)}-\frac{I_1(\sqrt{s/c}r)}{(\sqrt{s/c}r)I_0(\sqrt{s/c}a)}\right\}/F(s)\right], \tag{2}$$

$$\bar{\sigma}_\theta(r,s) = \left(-\frac{\sigma_0}{s}\right)\left[1+2(\nu_u-\nu)\left\{\frac{I_1(\sqrt{s/c}a)}{(\sqrt{s/c}a)I_0(\sqrt{s/c}a)}+\frac{I_1(\sqrt{s/c}r)}{(\sqrt{s/c}r)I_0(\sqrt{s/c}a)}-\frac{I_0(\sqrt{s/c}r)}{I_0(\sqrt{s/c}a)}\right\}/F(s)\right], \tag{3}$$

with

$$F(s) = (1-\nu)-2(\nu_u-\nu)\frac{I_1(\sqrt{s/c}a)}{(\sqrt{s/c}a)I_0(\sqrt{s/c}a)}, \quad \eta = \frac{\alpha(1-2\nu)}{2(1-\nu)}, \quad \alpha = \frac{3(\nu_u-\nu)}{B(1-2\nu)(1+\nu_u)}, \tag{4}$$

where ν and ν_u are Poisson's ratios in the drained and undrained states; B denotes Skempton's coefficient and c the coefficient of pore fluid diffusion. The bar over variables means the Laplace transform with its parameter s. With all other notations, see Fig.1.

RESULTS AND DISCUSSIONS

Numerical calculations have been carried out only for the incompressible constituents model ($\nu_u = 0.5$, $B = 1.0$), because the bulk modulus of drained foams is much smaller than that of pore fluid (e.g., water) and skeleton material (e.g., polyester and cupper). In all figures, $\rho = r/a$ and $\tau = t/(a^2/c)$ are the nondimensional radial coordinate and time.

The Mandel-Cryer effect for the four problems is shown in the case of $\nu = -0.8$ in Fig.2. We can see from it that the effect is very remarkable for this negative Poisson's ratio and that the peak pressure is higher for the Cryer problems than for the Mandel ones and for the 3D problems than for the 2D ones. The analysis shows that the Mandel-Cryer effect is more remarkable for decreasing Poisson's ratio. It is also shown that the peak pressures in the limit $\nu = -1$ for the Cryer and Mandel problems are 2.5 and 2.0 times those immediately after loading, respectively. In what follows, we will focus on the 3D Mandel problem, because it corresponds to usual compression tests of a circular cylinder. Fig.3 shows variation with time of circumferential stress component $-\sigma_\theta$ for various radius positions. At very deep positions, that stress starts from zero, goes up to the peak, and then decreases and vanishes, as corresponds to the variation of pore fluid pressure. In contrast, at the shallow positions it has the minimum value at some time after loading. It must be noted that its initial value is zero for $\rho < 1$ while $-\sigma_\theta / \sigma_0 = (\nu_u - \nu)/(1-\nu)(1+\nu_u)$ at $\rho = 1$, which is not zero; there exists a discontinuity at the cylinder surface. The same things appear in axial stress $-\sigma_z$. Similar behavior is also seen for the Cryer problem, as may be understood from the halved disc and sphere in Fig.1.

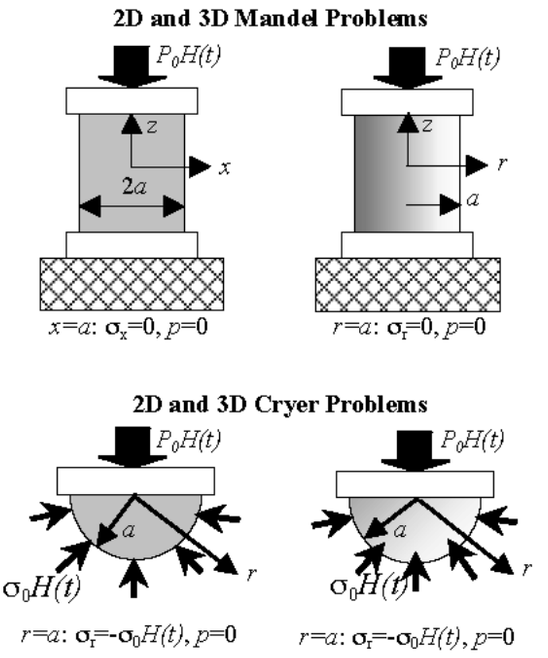


Figure 1 Four problems to solve

Figure 4 depicts time variation of radial displacement u_r at the cylinder surface for various Poisson's ratios. It is found that the cylinder of negative Poisson's ratio under abrupt compression expands just after loading, gradually shrinks, and finally becomes slenderer than the original one, as is interesting and intuitively well understandable. It should be added that this displacement is normalized by using Young's modulus, which are reported to decrease with decreasing Poisson's ratio but its decrease is not so big.

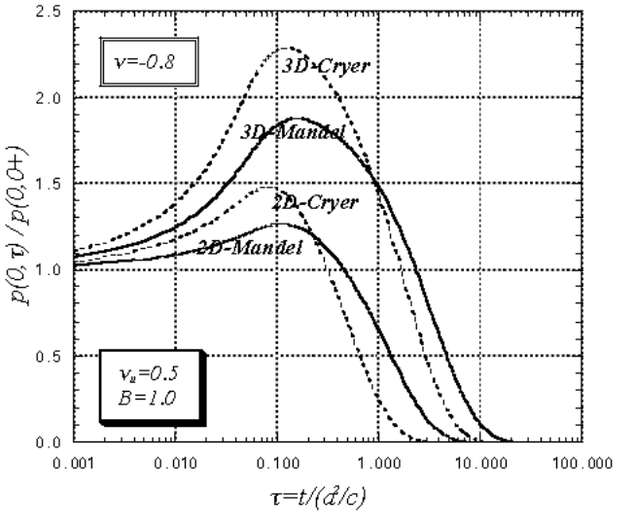


Figure 2 Mandel-Cryer effect for four problems

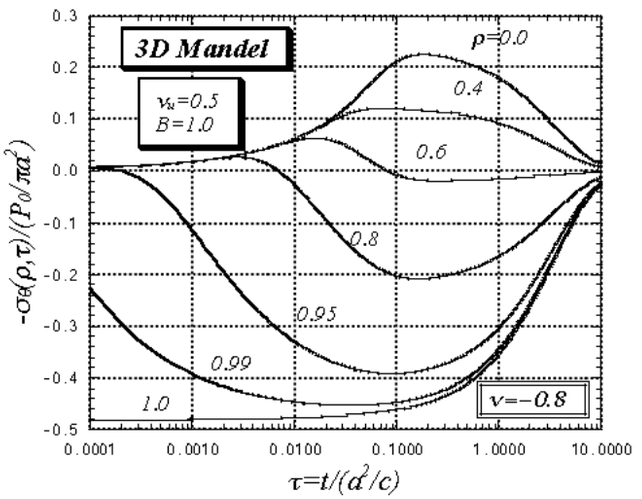


Figure 3 Hoop stress for various positions

CONCLUSIONS

We have demonstrated various interesting behaviors of fluid-filled poroelastic samples with negative Poisson's ratio.

References

[1] Lakes, R., Science, 237, 1038-1040 (1987).
[2] Mandel, J., Geotechnique, 3, 287-299 (1953).

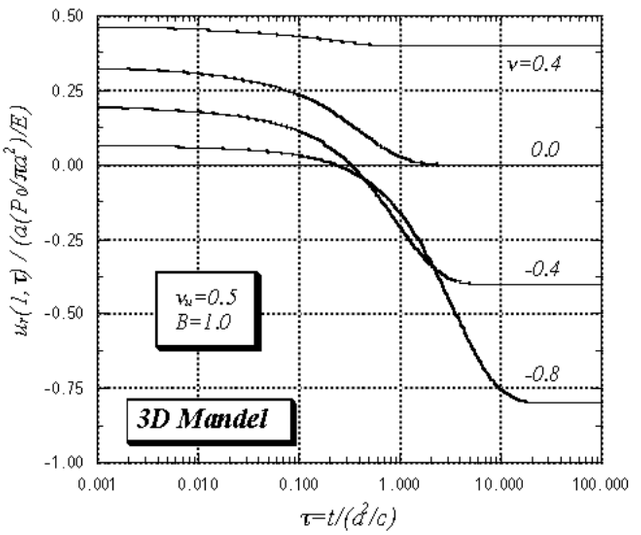


Figure 4 Radial displacement at the cylinder surface

LOCALIZATION AND STABILITY OF UNSATURATED SOIL

Wolfgang Ehlers, Martin Ammann, Tobias Graf
Institute of Applied Mechanics (CE)
University of Stuttgart, 70550 Stuttgart, Germany
http://www.mechbau.uni-stuttgart.de/ls2

Summary Unsaturated soil plays a dominant role in geotechnical engineering, e. g., when the draining of embankments or embankment deformation and stability problems are concerned. Based on the well-founded Theory of Porous Media, the contribution describes unsaturated soil as a triphasic continuum of solid, fluid and gas and exhibits the numerical implementation together with the demonstration of various initial boundary-value problems including the localization and stability behaviour of embankment problems.

INTRODUCTION

In the framework of continuum mechanics, the Theory of Porous Media (TPM) provides an excellent basis for the description of a variety of volumetrically coupled solid-fluid problems. In the present contribution, the focus lies on the investigation of unsaturated soil modelled as a triphasic continuum consisting of a porous solid skeleton (the soil), a pore-liquid (water) and a pore-gas (air), thus including saturated soil (solid matrix and pore-water) and empty soil (solid matrix and pore-gas) as special cases. Proceeding from a triphasic material, realistic problems in soil mechanics can be computed, as there are, on the one hand, the general problem of draining and, on the other hand, those phenomena combining the effects of draining with the deformation and localization behaviour of the soil skeleton. All these issues are of great importance in geotechnical engineering and occur, for example, when localization and stability problems of embankment structures have to be investigated.

UNSATURATED SOIL AS A TRIPHASIC CONTINUUM

Based on a triphasic continuum embedded in the TPM, the model is assumed to consist of a materially incompressible, elasto-viscoplastic soil skeleton saturated by an immiscible mixture of two viscous fluid components, a materially incompressible liquid and a materially compressible gas. In particular, the viscoplastic formulation of the soil is based on the single-surface yield criterion by Ehlers [1] together with the overstress concept of Perzyna type [2, 3], where an elasto-plastic model is included as a special case. In addition, the liquid and the gas phases are governed by Darcy-like relations together with an extended van Genuchten model for the description of the capillary pressure and the relative permeability functions [4].

NUMERICAL TOOLS

Based on a weak formulation of the overall continuum problem, a volumetrically coupled set of equations has to be solved. Proceeding from quasi-static situations, the computations are governed by the overall momentum balance tested by the solid displacement function together with the liquid volume and the gas mass balances tested by the effective liquid and gas pressures. As a result of the liquid incompressibility, the liquid pressure acts as a Lagrangean, while the gas pressure is obtained as a function of the effective gas density. The governing set of equations is incorporated into the FE tool PANDAS [5, 6], which has been particularly designed for the solution of volumetrically coupled solid-fluid problems. Apart from standard displacement-pressure formulations, PANDAS has been extended towards time- and space-adaptive methods, thus offering the possibility to produce proper and reliable numerical results. In case that localization phenomena occur, which, usually, lead to mathematically ill-posed problems, several regularization procedures can be used to overcome this problem, where, in the present contribution, use is made of the solid viscoplasticity concept.

NUMERICAL RESULTS

Proceeding from a two-pressures-displacement formulation for the numerical description of unsaturated soil, embankment localization and stability problems can be solved for arbitrary embankment geometries and structures. Apart from the general draining problem following, e. g., the Liakopoulos test [7], the present contribution concentrates on embankment problems, cf. Figures 1 and 2, where the coupled draining-deformation behaviour has been investigated. Considering a standard embankment structure with a filter unit at the air side, Figure 1 exhibits the stationary state, where the pore-water is draining through the embankment towards the filter. As a result of the embankment design governed by the filter unit together with the moderate angle of both embankment slopes, there is no water leaking through the air side of the structure. As a consequence, no localization of plastic strains can be observed, and the structure can be concluded to be save with respect to the given height of the water table at the left slope. On the other hand, if an embankment with the

same water table would have been designed, however, without a filter unit at the air side, where, furthermore, a steeper slope had been chosen, cf. Figure 2, it is immediately seen that the construction runs into problems. In particular, water is leaking from the embankment through the slope at the air side, thus leading to a typical situation that can be observed after natural hazards, such as heavy rainfall, etc. Furthermore, as a result of the leakage, the soil body is under buoyancy,

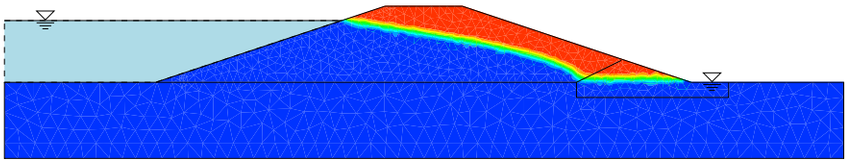


Figure 1: Pore-liquid distribution in an embankment.

thus losing strength obtained from gravitational forces. As a consequence, plastic strains are localizing forming a shear band with the onset at the kink between the slope and the ground level. If the water table does not rapidly decrease, this shear band is running up to the top of the embankment and will lead to a destruction of the complete structure. Following this, steps have to be taken to prevent the embankment from destruction, e. g., by loading the air side of the structure by additional weights as is usually done by sandbags.

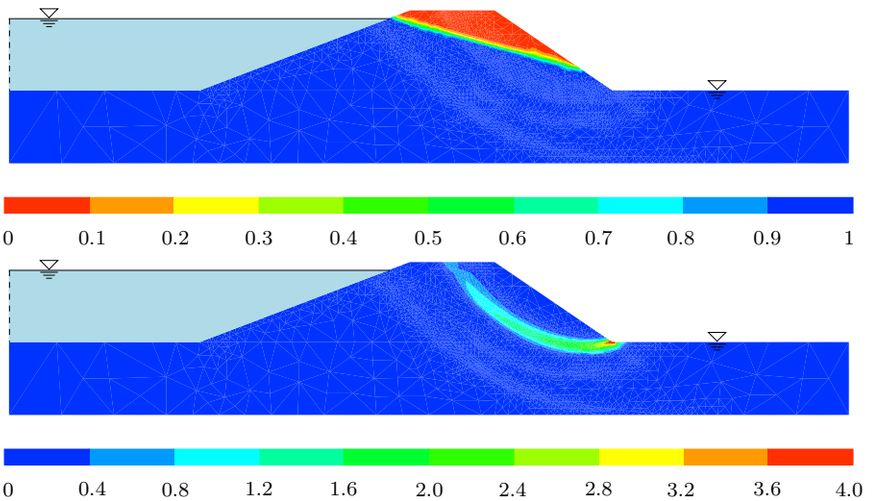


Figure 2: Pore-liquid distribution (top) and localization of the accumulated plastic strains $[10^{-1}]$ (bottom).

CONCLUSION

Based on a triphasic material, unsaturated soil has been investigated within the framework of the well-founded TPM [3]. Proceeding from an elasto-viscoplastic soil skeleton saturated by an immiscible mixture of two viscous and mobile pore-fluids, water and air, the numerical examples reveal the volumetrically coupled solid-fluid behaviour from draining to the onset and the development of shear bands. Apart from the 2-dimensional examples presented above, the oral presentation will furthermore include 3-dimensional examples computed by both single-processor and multi-processor (parallel) techniques.

References

[1] EHLERS, W.: Constitutive equations for granular materials in geomechanical context. In Hutter, K. (ed.): *Continuum Mechanics in Environmental Sciences and Geophysics*, CISM Courses and Lectures No. 337, Springer-Verlag, Wien 1993, pp. 313–402.

[2] PERZYNA, P.: Fundamental problems in viscoplasticity. *Advances in Applied Mechanics* **9** (1966), 243–377.

[3] EHLERS, W.: Foundations of multiphasic and porous materials. In Ehlers, W. & Bluhm, J. (eds.): *Porous Media: Theory, Experiments and Numerical Applications*, Springer-Verlag, Berlin 2002, pp. 3–86.

[4] EHLERS, W.; GRAF, T. & AMMANN, M.: Deformation and localization analysis in partially saturated soil. *Computer Methods in Applied Mechanics and Engineering*, accepted 2003.

[5] EHLERS, W. & ELLSIEPEN, P.: PANDAS: Ein FE-System zur Simulation von Sonderproblemen der Bodenmechanik. In Wriggers, P.; Meißner, U.; Stein, E. & Wunderlich, W. (eds.): *Finite Elemente in der Baupraxis: Modellierung, Berechnung und Konstruktion*, Ernst & Sohn, Berlin 1998, pp. 391–400.

[6] `www.get-pandas.com`.

[7] LIAKOPOULOS, A.: *Transient flow through unsaturated porous media*. Ph. D. thesis, University of California at Berkeley, 1964.

XXI ICTAM, 15–21 August 2004, Warsaw, Poland

CONVOLUTION QUADRATURE BASED BOUNDARY ELEMENT METHOD FOR QUASI-STATIC POROELASTICITY

Martin Schanz*, Thomas Rüberg*
*Institute of Applied Mechanics, Technical University Braunschweig,
P.O. Box 3329, D-38023 Braunschweig, Germany

Summary Applying the usual spatial discretization on the poroelastic quasi-static integral equations and using the Convolution Quadrature Method for the temporal discretization yields a boundary element time-stepping procedure. The proposed methodology is tested with an example for consolidation processes in a poroelastic half space. The algorithm shows no stability problems and behaves well over a broad range of time step sizes.

INTRODUCTION

Convolution Quadrature Method (CQM)-based Boundary Element formulations are up to now used only in dynamic formulations [3]. The main difference to usual time-stepping BE formulations is the way to solve the convolution integral appearing in most time-dependent integral equations. In the CQM formulation, this convolution integral is approximated by a quadrature rule whose weights are determined by the Laplace transformed fundamental solutions and a multi-step method.

For quasi-static problems in poroelasticity there is no need to apply the CQM because time-dependent fundamental solutions are available. However, these fundamental solutions are highly complicated yielding to very sensitive algorithms. Therefore, it is promising to apply the CQM also on the quasi-static integral equations in poroelasticity (details see [4]).

GOVERNING EQUATIONS

Following Biot's approach [1] to model the behavior of porous media, the governing set of differential equations for the unknowns solid displacement u_i and pore pressure p reads

$$G u_{i,jj} + \left(K + \frac{1}{3}G\right) u_{j,ij} - \alpha p_{,i} = -F_i \qquad \kappa p_{,ii} - \frac{1}{M}\frac{\partial}{\partial t} p - \alpha \frac{\partial}{\partial t} u_{i,i} = -a \,, \tag{1}$$

with the assumption of a linear elastic skeleton and the fluid flow modeled by Darcy's law. The permeability is denoted by κ and the porosity by ϕ. The bulk material is defined by the shear modulus G and the compression modulus K known from elasticity. Biot's effective stress coefficient α and M complete the set of material parameters. The load vector consists of the bulk body forces F_i and a source in the interstitial fluid a.

The respective integral equation necessary to establish a BE formulation is achieved by formulating the weighted residual statement of the governing differential equations (1) with the matrix of fundamental solutions as weights. The usual procedure, i.e., two integrations by part with respect to the spatial variable $\mathbf{x}$ and one with respect to the time variable t, results in a boundary integral equation. Fortunately, the strong singular behavior of the fundamental solutions T^s_{ij} and Q^f is equal to the elastostatic or acoustic fundamental solutions, respectively. All other fundamental solutions are weakly singular or regular. Hence, the limit to the boundary Γ yields

$$\begin{bmatrix} c_{ij}(\mathbf{y}) & 0 \\ 0 & c(\mathbf{y}) \end{bmatrix} \begin{bmatrix} u_i(t,\mathbf{y}) \\ p(t,\mathbf{y}) \end{bmatrix} = \int_\Gamma \begin{bmatrix} U^s_{ij}(t,\mathbf{y},\mathbf{x}) & -P^s_j(t,\mathbf{y},\mathbf{x}) \\ U^f_i(t,\mathbf{y},\mathbf{x}) & -P^f(t,\mathbf{y},\mathbf{x}) \end{bmatrix} * \begin{bmatrix} t_i(t,\mathbf{x}) \\ q(t,\mathbf{x}) \end{bmatrix} \mathrm{d}\Gamma - \cancel{\int_\Gamma} \begin{bmatrix} T^s_{ij}(t,\mathbf{y},\mathbf{x}) & Q^s_j(t,\mathbf{y},\mathbf{x}) \\ T^f_i(t,\mathbf{y},\mathbf{x}) & Q^f(t,\mathbf{y},\mathbf{x}) \end{bmatrix} * \begin{bmatrix} u_i(t,\mathbf{x}) \\ p(t,\mathbf{x}) \end{bmatrix} \mathrm{d}\Gamma \,, \tag{2}$$

where the integral free terms c_{ij} and c are those known from elastostatics and acoustics, respectively. The time convolution defined in (3) is denoted by $*$ and all capital letters denote fundamental solutions.

Next, the boundary surface Γ is discretized by E iso-parametric elements Γ_e where F polynomial shape functions $N^f_e(\mathbf{x})$ are defined, i.e., ansatz functions are used to approximate the spatial behavior of the boundary states. Further, a time discretization has to be introduced. Instead of using the time-dependent fundamental solutions, here, the convolution quadrature method proposed by Lubich [2]

$$f * g = \int_0^t f(t-\tau)\, g(\tau)\, \mathrm{d}\tau \approx \sum_{k=0}^{n} \omega_{n-k}\left(\hat{f}, \Delta t\right) g(k\Delta t) \quad \text{with } \omega_n\left(\hat{f}, \Delta t\right) = \frac{\mathscr{R}^{-n}}{L} \sum_{\ell=0}^{L-1} \hat{f}\left(\frac{\gamma\left(\mathscr{R} e^{i\ell\frac{2\pi}{L}}\right)}{\Delta t}\right) e^{-in\ell\frac{2\pi}{L}} \tag{3}$$

is used as a promising alternative. In eq. (3), $\hat{f}$ denotes the Laplace transformed function of f and the underlying multi-step method is characterized by the quotient of the generating polynomials $\gamma(z)$.

Hence, after dividing time period t in N time steps of equal duration Δt, so that $t = N\Delta t$, the convolution integrals between

the quadrature formula (3) is applied to the integral equation (2). This results in the following boundary element time stepping procedure ($n = 0, 1, \ldots, N$)

$$\begin{bmatrix} c_{ij}(\mathbf{y}) & 0 \\ 0 & c(\mathbf{y}) \end{bmatrix} \begin{bmatrix} u_i(\mathbf{y}, n\Delta t) \\ p(\mathbf{y}, n\Delta t) \end{bmatrix} = \sum_{e=1}^{E} \sum_{f=1}^{F} \sum_{k=0}^{n} \left\{ \begin{bmatrix} \omega_{n-k}^{ef}\left(\hat{U}_{ij}^{s}, \mathbf{y}, \Delta t\right) & -\omega_{n-k}^{ef}\left(\hat{P}_{j}^{s}, \mathbf{y}, \Delta t\right) \\ \omega_{n-k}^{ef}\left(\hat{U}_{i}^{f}, \mathbf{y}, \Delta t\right) & -\omega_{n-k}^{ef}\left(\hat{P}^{f}, \mathbf{y}, \Delta t\right) \end{bmatrix} \begin{bmatrix} t_i^{ef}(k\Delta t) \\ q^{ef}(k\Delta t) \end{bmatrix} - \begin{bmatrix} \omega_{n-k}^{ef}\left(\hat{T}_{ij}^{s}, \mathbf{y}, \Delta t\right) & \omega_{n-k}^{ef}\left(\hat{Q}_{j}^{s}, \mathbf{y}, \Delta t\right) \\ \omega_{n-k}^{ef}\left(\hat{T}_{i}^{f}, \mathbf{y}, \Delta t\right) & \omega_{n-k}^{ef}\left(\hat{Q}^{f}, \mathbf{y}, \Delta t\right) \end{bmatrix} \begin{bmatrix} u_i^{ef}(k\Delta t) \\ p^{ef}(k\Delta t) \end{bmatrix} \right\} \tag{4}$$

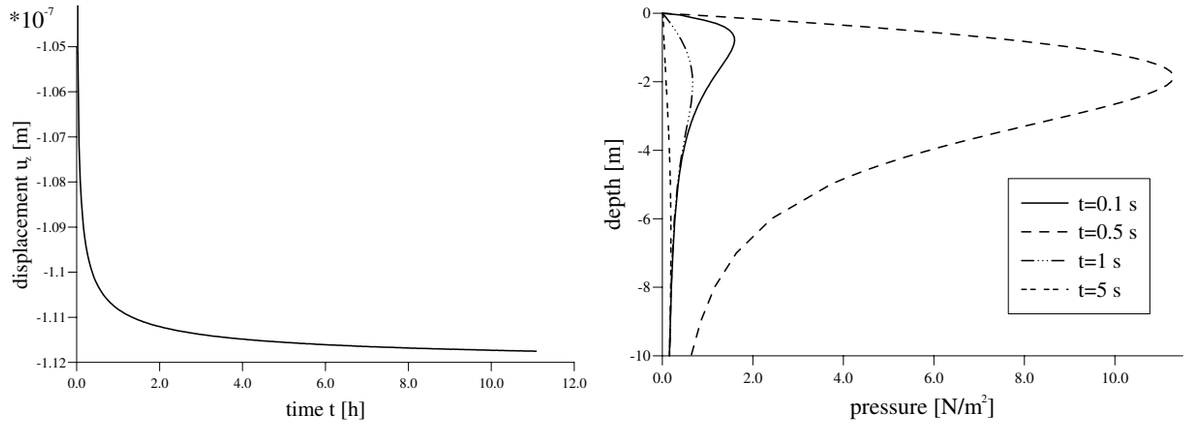
with the integration weights corresponding to (3), e.g.,

$$\omega_n^{ef}\left(\hat{U}_{ij}^{s}, \mathbf{y}, \Delta t\right) = \frac{\mathscr{R}^{-n}}{L} \sum_{\ell=0}^{L-1} \int_{\Gamma_e} \hat{U}_{ij}^{s}\left(\mathbf{x}, \mathbf{y}, \frac{\gamma\left(\mathscr{R} e^{i\ell\frac{2\pi}{L}}\right)}{\Delta t}\right) N_e^f(\mathbf{x})\, \mathrm{d}\Gamma\, e^{-in\ell\frac{2\pi}{L}} . \tag{5}$$

Note, the calculation of the integration weights is only based on the Laplace transformed fundamental solutions known from literature. After performing the numerical integrations a system of algebraic equations is obtained by the collocation method. Finally, a direct equation solver is applied.

CONSOLIDATION PROCESS IN A POROELASTIC HALF SPACE

In quasi-static poroelasticity, the main interest is in calculating the consolidation of the poroelastic material. To simulate this behavior, a poroelastic half space is loaded perpendicular to the surface by the total stress vector $t_z = -1000\,\mathrm{N/m^2} H(t)$, i.e., it is kept constant over time. The remaining surface is traction free and permeable, i.e., the pore pressure is assumed to be zero at the surface. The mesh is truncated outside an area of $6\,\mathrm{m} \times 15\,\mathrm{m}$ and the material data are those of soil ($K = 2.1 \cdot 10^8\,\frac{\mathrm{N}}{\mathrm{m}^2}, G = 9.8 \cdot 10^7\,\frac{\mathrm{N}}{\mathrm{m}^2}, \phi = 0.48, \alpha = 0.98, M = 5.24 \cdot 10^9\,\frac{\mathrm{N}}{\mathrm{m}^2}, \kappa = 3.55 \cdot 10^{-9}\,\frac{\mathrm{m}^4}{\mathrm{Ns}}$).
In Fig. 1, the displacement at the surface in a point in 10 m distance to the load is depicted versus time. The consolidation process is obviously observed. Additionally to the settlement, the pore pressure distribution below the surface is given in Fig. 1 versus depth for four different times, i.e., at $t = 0.1\,\mathrm{s}, t = 0.5\,\mathrm{s}, t = 1\,\mathrm{s}$, and $t = 5\,\mathrm{s}$. As expected, the pore pressure



(a) Vertical surface displacement versus time

(b) Pressure below the surface versus depth

Figure 1. Numerical results for the half space

rises very fast from zero (the boundary condition at the surface) to its maximum value and tends afterwards to a constant value. For later times this maximum value is smaller and shifted to larger depth.
It should be remarked that the proposed algorithm is not sensitive to the time step size or shows any instabilities [4]. Further, not only for 3-d examples as above, also for 2-d the algorithm performs well.

References

[1] Biot M.A.: General theory of three-dimensional consolidation. *Journal of Applied Physics* **12**:155–164, 1941.
[2] Lubich C.: Convolution quadrature and discretized operational calculus. I., II. *Numerische Mathematik*, **52**:129–145, 413–425, 1988.
[3] Schanz M.: Wave Propagation in Viscoelastic and Poroelastic Continua: A Boundary Element Approach. Lecture Notes in Applied Mechanics. Springer-Verlag, Berlin, Heidelberg, New York, 2001.
[4] Schanz M., Antes H., Rüberg T.: Convolution Quadrature Boundary Element Method for quasi-static visco- and poroelastic continua. *Computer*

THEORY AND NUMERICS OF MULTICOMPONENT MIXTURE MODELS FOR SOFT BIOLOGICAL TISSUES

B. Markert, W. Ehlers, A. Acartürk & N. Karajan
Institute of Applied Mechanics (CE)
University of Stuttgart, 70550 Stuttgart, Germany
http://www.mechbau.uni-stuttgart.de/ls2

Summary One natural category of porous materials is represented by biological soft tissues, such as cartilage, lung or skin. The challenge of describing these materials lies in their complex inhomogeneous microstructure consisting of mostly ionized water and collagen fibers embedded in an extracellular meshwork of charged protein compounds. In order to describe the physiological behaviour of soft tissues on the macroscale, the electro-chemomechanical couplings between the constituents as well as the viscoelastic and anisotropic properties of the extracellular matrix must be considered. In order to meet these requirements, the well-founded Theory of Porous Media (TPM) is applied, which consistently allows for the description of multiphasic continua with internal interactions. For the efficient numerical treatment within the FEM, the governing set of multi-field equations is rewritten in weak form including physically meaningful boundary terms. The overall applicability of the multicomponent mixture approach is finally shown by representative numerical examples.

INTRODUCTION

Currently, most models that describe the electro-chemomechanical behaviour of soft biological tissues are restricted either to small strains or to finite but purely elastic skeleton deformations. Moreover, anisotropic and inhomogeneous properties are, in general, not considered. In fact, these types of naturally grown materials undergo large viscoelastic deformations, where the extracellular matrix exhibits so-called intrinsic viscoelastic properties [2]. These flow-independent viscoelastic effects are strongly coupled with the dissipative phenomena resulting from the interstitial fluid flow and the electrochemical (osmotic and electrostatic) swelling mechanisms [5, 6]. Furthermore, their inner structure and thus, the associated physical properties are inhomogeneously distributed over the 3-d anatomic shape of the tissue. In addition, anisotropic properties may occur due to embedded collagen fibers and orientation-dependent hydraulic and electrolytic conductivities.

The goal of this contribution is to present a consistent theoretical framework based on the Theory of Porous Media (TPM), where the constitutive assumptions, necessary to cover all relevant tissue properties, are merged in a modular manner. This actually allows for a concise representation of the resulting system of coupled partial differential equations, which can be efficiently treated within the finite element method (FEM) and thus, enables the numerical solution of even large 3-d problems at suitable computational costs.

MULTICOMPONENT MIXTURE MODEL

The TPM is a macroscopic continuum theory, which is based on the theory of mixtures extended by the concept of volume fractions [1]. Proceeding from a binary mixture consisting of solid and fluid constituents φ^α denoted by $\alpha = \{S, F\}$, the solid phase is extended by incorporating the volume free fixed charges φ^{fc}. Furthermore, the interstitial fluid φ^F is assumed to be composed of three components φ^β, namely the liquid solvent, the cations and the anions, indicated by $\beta = \{L, +, -\}$ (figure 1). Assuming materially incompressible constituents, the volume fractions $n^\alpha = \mathrm{d}v^\alpha/\mathrm{d}v$ (partial volume v^α per bulk volume v) serve as describing physical quantities consistent with the saturation constraint $\sum_\alpha n^\alpha = 1$. In addition, the molar concentrations $c^\beta_m = \mathrm{d}n^\beta_m/\mathrm{d}v^F$ (moles n^β_m per fluid volume v^F) are introduced as the describing quantities of the ionic components. Note that the chemical potentials can be used, alternatively [4].

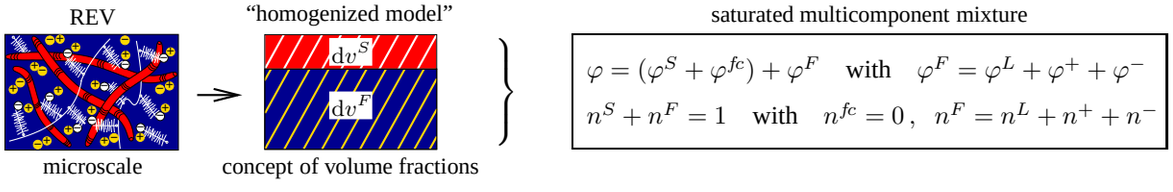


Figure 1: *Multicomponent TPM model of charged hydrated tissue*

Following the idea of superimposed continua [1], each component follows its individual motion $\mathbf{x} = \boldsymbol{\chi}_\alpha(\mathbf{X}_\alpha, t)$ and has its own velocity field $\overset{\prime}{\mathbf{x}}_\alpha = \mathrm{d}\boldsymbol{\chi}_\alpha(\mathbf{X}_\alpha, t)/\mathrm{d}t$ with respect to different reference positions $\mathbf{X}_\alpha$. Therein, $(\,\cdot\,)'_\alpha$ denotes the material time derivative following the motion of φ^α. Thus, the model under consideration incorporates seven independent fields, namely the solid displacement $\mathbf{u}_S = \mathbf{x} - \mathbf{X}_S$, the seepage velocity $\mathbf{w}_F = \overset{\prime}{\mathbf{x}}_F - \overset{\prime}{\mathbf{x}}_S$, the relative ion velocities

$\mathbf{w}_\gamma = \dot{\mathbf{x}}_\gamma - \dot{\mathbf{x}}_S$, the effective interstitial fluid pressure p, and the molar ion concentrations c_m^γ, where $\gamma = +, -$ indicates only the mobile ions. Note that the fixed charges are directly coupled to the solid displacement and thus, represent no independent field. Moreover, for the liquid solvent, it is assumed that $\dot{\mathbf{x}}_L \approx \dot{\mathbf{x}}_F$, i. e. $\mathbf{w}_L \approx \mathbf{w}_F$.

GOVERNING EQUATIONS

For the numerical treatment within the FEM, weak forms of the governing multi-field equations are required. Therefore, the seepage velocity and the cation diffusion are eliminated by use of the extended *Darcy* filter law and the extended *Nernst-Planck* equation. Together with the electroneutrality condition, this yields a concise representation of the governing balance relations by means of the primary variables $\mathbf{u}_S$, p, and c_m^+. Subsequently, weighted by independent test functions and integrated over the spatial domain Ω with the surface $\partial\Omega$, one finds the respective weak form of the mixture volume (MV), the cation concentration (CC), and the mixture momentum (MM) balances:

$$\mathcal{G}_{\mathrm{MV}} \equiv \int_\Omega \delta p \,\mathrm{div}\,(\mathbf{u}_S)'_S \,\mathrm{d}v - \int_\Omega \mathrm{grad}\,\delta p \cdot n^F \mathbf{w}_F \,\mathrm{d}v + \int_{\partial\Omega} \delta p\, \bar{q}\,\mathrm{d}a = 0\,,$$

$$\mathcal{G}_{\mathrm{CC}} \equiv \int_\Omega \delta c_m^+ \left[\, n^F (c_m^+)'_S + c_m^+ \,\mathrm{div}\,(\mathbf{u}_S)'_S \,\right] \mathrm{d}v - \int_\Omega \mathrm{grad}\,\delta c_m^+ \cdot n^F c_m\, \mathbf{w}_+ \,\mathrm{d}v + \int_{\partial\Omega} \delta c_m^+\, \bar{\jmath}\,\mathrm{d}a = 0\,,$$

$$\mathcal{G}_{\mathrm{MM}} \equiv \int_\Omega \mathrm{grad}\,\delta\mathbf{u}_S \cdot (\mathbf{T}^S_{E\,\mathrm{mech.}} - p\,\mathbf{I}\,)\,\mathrm{d}v - \int_{\partial\Omega} \delta\mathbf{u}_S \cdot \bar{\mathbf{t}}\,\mathrm{d}a = 0\,.$$

Therein, $\delta\mathbf{u}_S$, δp, and δc_m^+ are the corresponding test functions, $\bar{q}$ denotes the efflux of the interstitial fluid over the surface $\partial\Omega$, $\bar{\jmath}$ is the anion diffusion over $\partial\Omega$, and $\bar{\mathbf{t}}$ is the external load vector acting on the entire mixture. Moreover, $\mathbf{T}^S_{E\,\mathrm{mech.}} = \mathbf{T}^S_{EQ} + \mathbf{T}^S_{NEQ} + \mathbf{T}^S_{ANISO}$ represents the purely mechanical *Cauchy* extra stress tensor, which is constitutively decomposed into isotropic elastic (equilibrium) and viscoelastic (non-equilibrium) parts $\mathbf{T}^S_{EQ}$ and $\mathbf{T}^S_{NEQ}$, as well as an anisotropic term $\mathbf{T}^S_{ANISO}$. Note that the hydraulic and osmotic stress contributions are completely included in the entire fluid pressure p.

NUMERICAL EXAMPLES

The efficiency of the presented model is shown by two fully coupled 3-d simulations using the FE tool PANDAS. By incorporating appropriate constitutive equations for the description of the osmotic and electrostatic phenomena [3], it is possible to simulate free swelling behaviour. For the example depicted in the left hand side of figure 2, the external ion concentration was lowered on the yellow surrounding surface to initiate swelling. Furthermore, the model can be applied for the description of intervertebral disc (IVD) tissue, whenever the implemented constitutive law for $\mathbf{T}^S_{ANISO}$ is suitable for the macroscopic simulation of the collagen fiber-bundles within the anulus fibrosus. First physically sound results are achieved on an idealized 3-d geometry of a motion segment of the lumbar spine subjected to an axial compressive load yielding a finite deformation response of the IVD (figure 2 right).

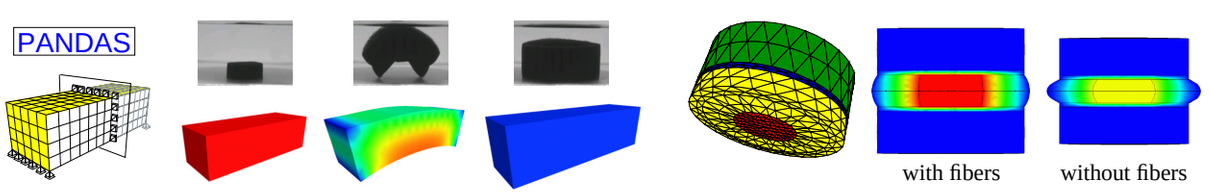


Figure 2: *Free swelling of a hydrogel block (left) and idealized model of the IVD with nucleus pulposus and anulus fibrosus (right)*

References

[1] EHLERS, W.: Foundations of multiphasic and porous materials. In Ehlers, W. & Bluhm, J. (eds.): *Porous Media: Theory, Experiments and Numerical Applications*, Springer-Verlag, Berlin, 2002, pp. 3–86.

[2] EHLERS, W. & MARKERT, B.: A linear viscoelastic biphasic model for soft tissues based on the Theory of Porous Media. *ASME J. Biomech. Eng.* **123** (2001), 418–424.

[3] EHLERS, W.; MARKERT, B. & ACARTÜRK, A.: Large strain viscoelastic swelling of charged hydrated porous media. In Auriault, J.-L. et al. (eds.): *Poromechanics II*, Balkema, Lisse, The Netherlands, 2002, pp. 185–191.

[4] HUYGHE, J. M. & JANSSEN, J. D.: Quadriphasic mechanics of swelling incompressible porous media. *Int. J. Engng Sci.* **35** (1997), 793–802.

[5] LAI, W. M.; HOU, J. S. & MOW, V. C.: A triphasic theory for the swelling and deformation behaviors of articular cartilage. *ASME J. Biomech. Eng.* **113** (1991), 245–258.

[6] MOW, V. C.; ATESHIAN, G. A.; LAI, W. M. & GU, W. Y.: Effects of fixed charges on the stress-relaxation behavior of hydrated soft tissues in a confined compression problem. *Int. J. Solids Structures* **35** (1998), 4945–4962.

XXI ICTAM, 15-21 August 2004, Warsaw, Poland

PROBABILISTIC HOMOGENIZATION OF HYPERELASTIC SOLID FOAMS

Jörg Hohe[*], Wilfried Becker[**]
[*]*Fraunhofer Institut für Werkstoffmechanik (IWM), Wöhlerstr.11, 79108 Freiburg/Brsg., Germany*
[**]*Technische Universität Darmstadt, Inst. f. Mechanik, Hochschulstr. 1, 64289 Darmstadt, Germany*

Summary The present study is concerned with a probabilistic homogenization scheme for amorphous hyperelastic solid foams. The scheme is based on the multiple analysis of a small-scale representative volume with a randomized microstructure. The macroscopic stress-strain characteristics are determined by means of a strain energy based homogenization procedure. The results are evaluated stochastically in terms of the stress mean values and the corresponding standard deviations describing the scatter band width.

INTRODUCTION

Solid foams are important materials in modern lightweight construction. Their main advantage is their low specific weight and their good strength-to-weight ratio (Gibson and Ashby [2]). For reasons of numerical efficiency, components consisting of foamed materials are analyzed in terms of effective properties rather than by a detailed model of the given microstructure. The determination of the effective stress-strain-response can be performed either by experimental or by analytical methods. Although solid foams are amorphous assemblies of pores with different shapes and sizes, most studies in literature use regular, perfectly periodic models for the homogenization analysis. Only few studies of random foams are available which are usually based on large-scale representative volume elements containing a microstructure with a large number of pores obtained by means of a Voronoi technique. It has been shown by Fortes and Ashby [1] that this approach might yield inappropriate results. Instead, direct probabilistic approaches are proposed.

PROBABILISTIC HOMOGENIZATION

The present study is concerned with a probabilistic approach to the determination of the effective properties of solid foams. The scheme is based on the analysis of a periodic reference microstructure with a prescribed topology. An example together with an appropriate representative volume element (RVE) is presented in Fig. 1. Prior to the analysis, the geometry of the microstructuer is randomized by a probabilistic determination of the spatial positions of the cell wall intersections within prescribed areas of dimension $2\Delta x_i$ (see Fig. 2) using a random number generator. The randomization and subsequent homogenization analysis is performed multiple times in n numerical experiments. The results are evaluated stochastically in terms of the mean stress field and the corresponding standard deviation

$$\bar{\tau}_{ij}^{a} = \frac{1}{n}\sum_{k=1}^{n}\bar{\tau}_{ij}^{(k)} \qquad \text{and} \qquad \bar{\tau}_{ij}^{s} = \frac{1}{n-1}\left(\sum_{k=1}^{n}\left(\bar{\tau}_{ij}^{a} - \bar{\tau}_{ij}^{(k)}\right)^{2}\right)^{1/2} \tag{1}$$

where τ_{ij} are the components of the second Piola-Kirchhoff stress tensor. Advantage of this method compared to the standard probabilistic approaches based on a single analysis of a large scale representative volume element is the numerical efficiency due to the small mechanical model to be analyzed and the fact that the scatter of the effective stresses can be assessed in terms of the standard deviation.
For the determination of the effective stresses in the individual numerical experiments, a strain energy based homogenization procedure is utilized which has been proposed earlier by the present authors for a finite strain analysis of strictly periodic cellular solids (Hohe and Becker [3]). Within this scheme, the mechanical response of a representative volume element for the given microstructure and a similar volume element consisting of the effective medium is defined to be macroscopically equivalent, if the average the strain energy density in both elements is equal provided that both volume elements are subjected to deformation states where the volume average of the deformation gradient is equal:

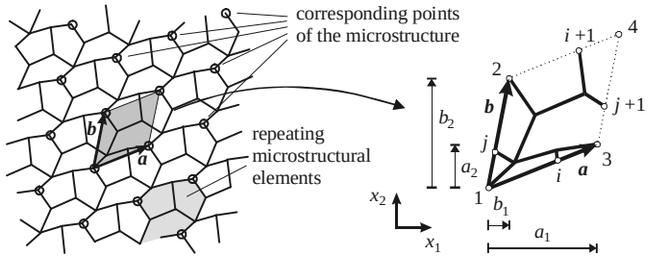


Fig. 1: RVE for general periodic 2D microstructures

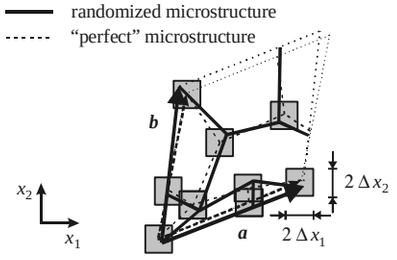


Fig. 2: Randomized RVE

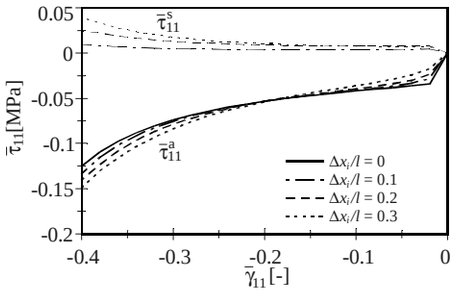


Fig. 3: Stress-strain response under uniaxial compression

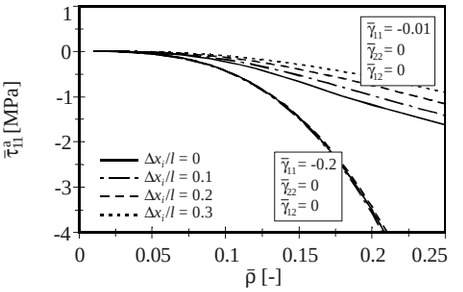


Fig. 4: Effect of the relative density (uniaxial compression)

$$\overline{w} = \frac{1}{V^{RVE}} \int_{\Omega^{RVE}} w\, dV = \frac{1}{V^{RVE*}} \int_{\Omega^{RVE}} w^*\, dV = \overline{w}^* \qquad \text{if:} \qquad \overline{F}_{ij} = \frac{1}{V^{RVE}} \int_{\Omega^{RVE}} F_{ij}\, dV = \frac{1}{V^{RVE*}} \int_{\Omega^{RVE}} F^*_{ij}\, dV = \overline{F}^*_{ij} \qquad (2)$$

The determination of the strain energy is performed numerically by means of a finite element model with periodic boundary conditions.

RESULTS

The probabilistic homogenization scheme defined in the previous section is applied to the analysis of a two-dimensional model foam. As a periodic reference material, a regular hexagonal structure is used. Three different degrees $\Delta x_i / l$ of microstructural disorder are considered where l is the nominal cell wall length for the periodic reference material. On the cell wall level, an Ogden-type hyperelastic constitutive model is employed. In a study of convergence a number of $n = 50$ numerical experiments proves to be sufficient.

The macroscopic stress-strain response in terms of the second Piola-Kirchhoff stress tensor as a function of the Green-Lagrange strain tensor is presented in Fig. 3. The considered example is a model foam with a relative density of $\rho = 5\%$ under uniaxial compressive deformation. For comparison, results obtained by means of a perfectly periodic model without any microstructural disorder are included as a solid line. Distinct effects of the microstructural disorder are observed for small effective strains where a kink in the stress-strain curve for the perfectly ordered microstructure indicates a bifurcation. No instabilities in the Eulerian sense occur for the geometrically imperfect disordered foams. At large effective strain levels, an increasing disorder results in increasing effective stresses. Throughout the considered effective strain range, increasing degrees of microstructural disorder yield increasing standard deviations indicating increasing scatter band widths, especially at large levels of the effective compressive strain.

In Fig. 4, the effect of the relative density is studied. Two different effective strain states are considered for which the relative density is varied from small values up to $\rho = 25\%$. For the large effective stress level ($\gamma_{11} = -0.2$), an approximately cubic dependence of the effective stresses on the relative density is obtained. In this case, the microstructure is in a postbuckling state where the microstructural mode of deformation is distributed bending of the entire cell walls in the model. Since the bending stiffness increases cubically with the cell wall thickness and therefore with the relative density, the observed cubic dependence of the effective stresses on the relative density is obtained. A similar behavior is observed for the small effective strain level at small relative densities. For large relative densities, the microstructure is in a prebuckling state due to the larger cell wall thicknesses. In this case the underlying microstructural mode of deformation changes from overall bending to longitudinal compression of the cell walls. Especially in this range, strong effects of the microstructural disorder are observed.

CONCLUSION

Subject of the present study is a probabilistic homogenization scheme for hyperelastic cellular solids. Advantage of the direct probabilistic approach compared to previous studies is the possibility to address the scatter to be expected in the effective stresses and its numerical efficiency due to the employment of small-scale representative volume elements. It is observed that the microstructural disorder has distinct effects on the macroscopic stress-strain response of cellular solids. Therefore, classical deterministic approaches based on strictly periodic models might yield inaccurate results.

References

[1] Fortes, M.A., Ashby, M.F.: The effect of non-uniformity on the in-plane modulus of honeycombs. *Acta Mater.* **47**: 3469-3473, 1999.

[2] Gibson, L.J., Ashby, M.F.: Cellular Solids – Structure and Properties. Cambridge University Press, London 1997.

[3] Hohe, J., Becker, W.: Effective mechanical behavior of hyperelastic honeycombs and two-dimensional model foams at finite strain. *Int. J. Mech. Sci.* **45**: 891-913, 2003.

XXI ICTAM, 15–21 August 2004, Warsaw, Poland

COUPLING BETWEEN PERMEABILITY AND DAMAGE : A MICROMECHANICAL APPROACH

Luc Dormieux*, Djimedo Kondo**
*LMSGC, CNRS UMR 113, Ecole Nationale des Ponts et Chaussées, France
**LML, CNRS URA 1441, Université des Sciences et Technologies de Lille, France

Summary A self-consistent scheme is used in order to determine the permeability of a cracked porous medium. For weak values of the permeability of the uncracked porous matrix, the order of magnitude of the permeability increases beyond a critical threshold of the crack density parameter. The micromechanical model also shows that both the evolution of crack opening and the crack propagation are controlled by Terzaghi's effective stress which therefore captures the coupling between permeability and mechanical loading.

a self-consistent estimate of the macroscopic permeability

Experimental evidences show a very strong coupling between damage and permeability. This paper proposes to model this phenomenon within a micromechanical framework that also allows to quantify the influence of a mechanical loading on permeability.

The starting point is a classical idea in rock physics ([1]) which consists in approximating the real fluid flow within a crack by the Poiseuille flow which takes place between two parallel planes (half-distance c). This leads to introduce a fictitious porous medium with permeability $\boldsymbol{k}_c$, equivalent to the real crack as regards the relation between flow and pressure gradient. Denoting the unit normal to the crack by $\underline{n}$ and the second order identity tensor by $\mathbf{1}$, $\boldsymbol{k}_c$ reads :

$$\boldsymbol{k}_c = k_c\mathbf{1} + (k_p - k_c)\underline{n}\otimes\underline{n} \quad \text{with} \quad k_c = \frac{c^2}{3} \tag{1}$$

where k_p denotes the isotropic permeability of the uncracked porous medium. We now look for the effective intrinsic permeability tensor $\boldsymbol{K}$ of a representative elementary volume (r.e.v.) Ω made up of the porous material with permeability k_p and of a set of cracks. $\boldsymbol{K}$ relates the macroscopic filtration vector $\underline{Q}$ to the macroscopic pressure gradient $\underline{\nabla P}$:

$$\underline{Q} = -\frac{\boldsymbol{K}}{\mu}\cdot\underline{\nabla P} \tag{2}$$

where μ is the fluid viscosity. Replacing the cracks by the fictitious porous material with permeability $\boldsymbol{k}_c$ introduced in (1), the r.e.v. considered at the microscopic scale appears as a heterogeneous Darcy material : the local permeability is $\boldsymbol{k}(\underline{z}) = k_p\mathbf{1}$ in the uncracked phase and $\boldsymbol{k}(\underline{z}) = \boldsymbol{k}_c$ in the cracks. Note that $\boldsymbol{k}_c$ depend on the crack orientation and opening through $\underline{n}$ and c.

Let $\underline{q}(\underline{z})$ and $\underline{\mathrm{grad}}_z\, p\,(\underline{z})$ denote the filtration vector field and the pressure gradient field within the r.e.v., i.e. at the microscopic scale. They are related by the heterogeneous Darcy Law (3b). The macroscopic filtration vector is related to the microscopic field $\underline{q}(\underline{z})$ by the average rule $\underline{Q} = <\underline{q}>$. In turn, the microscopic pressure field $p(\underline{z})$ is subjected to the standard Hashin boundary conditions (3c) associated with the macroscopic pressure gradient $\underline{\nabla P}$

$$(\Omega) :\ \mathrm{div}\,\underline{q} = 0 \quad (a) \quad ; \quad (\Omega) :\ \underline{q} = -\boldsymbol{k}(\underline{z})\cdot\underline{\mathrm{grad}}_z\, p \quad (b) \quad ; \quad (\partial\Omega) :\ p = \underline{\nabla P}\cdot\underline{z} \quad (c) \tag{3}$$

where (3a) expresses the fluid mass balance equation. The linearity of the solution $(p, \underline{q})$ to (3) with respect to $\underline{\nabla P}$ is classically expressed through the concept of localization tensor $\boldsymbol{A}(\underline{z})$ which relates the local and the macroscopic pressure gradients :

$$\underline{\mathrm{grad}}_z\, p\,(\underline{z}) = \boldsymbol{A}(\underline{z})\cdot\underline{\nabla P} \tag{4}$$

Combining (3b) and (4) with (2) yields a general micromechanical interpretation of the macroscopic permeability :

$$\boldsymbol{K} = <\boldsymbol{k}\cdot\boldsymbol{A}> = f_p k_p\mathbf{1}\cdot <\boldsymbol{A}>_p + \sum_j f_j\boldsymbol{k}_c^j\cdot <\boldsymbol{A}>_j \tag{5}$$

where f_p (resp. f_j) denotes the volume fraction of the uncracked phase (resp. of crack $\mathcal{C}^j$) and $<>$ (resp. $<>_\alpha$) is the average over Ω (resp. over the α-phase). The various homogenization schemes aim at estimating the phase averages of $\boldsymbol{A}$, depending on the morphological properties. The self-consistent scheme is selected here since it seems reasonable to expect that it is able to take into account the existence of a hydraulic connexion between cracks beyond a certain damage threshold. In order to take advantage of the analytical estimates based on Eshelby's problem, we adopt an ellipsoidal modelling of the fictitious porous inclusion associated with a given crack. The orientation of the ellipsoid is that of the crack, it is symmetric around the normal to the crack and has the same half-opening c and radius a as the crack itself. Its aspect ratio is $X = c/a \ll 1$. The self consistent estimate $\boldsymbol{k}^{SC}$ of the macroscopic permeability is the solution to :

$$\boldsymbol{k}^{SC} = <\boldsymbol{k}\cdot(\mathbf{1} + \boldsymbol{P}^{SC}\cdot(\boldsymbol{k} - \boldsymbol{k}^{SC}))^{-1}>\cdot <(\mathbf{1} + \boldsymbol{P}^{SC}\cdot(\boldsymbol{k} - \boldsymbol{k}^{SC}))^{-1}>^{-1} \tag{6}$$

where the tensor $\boldsymbol{P}^{SC}(\underline{z})$ is related to the Eshelby tensor $\boldsymbol{S}^{SC}(\underline{z})$ by $\boldsymbol{P}^{SC} = \boldsymbol{S}^{SC}\cdot\boldsymbol{k}^{SC\,-1}$. The first order expansion of $\boldsymbol{S}^{SC}$ with respect to X reads :

$$(z\in\mathcal{C}^j) \quad \boldsymbol{S}^{SC} = \frac{1}{4}\pi X\mathbf{1} + (1 - \frac{3}{4}\pi X)\underline{n}^j\otimes\underline{n}^j \quad ; \quad (z\in\Omega^s) \quad \boldsymbol{S}^{SC} = \frac{1}{3}\mathbf{1} \tag{7}$$

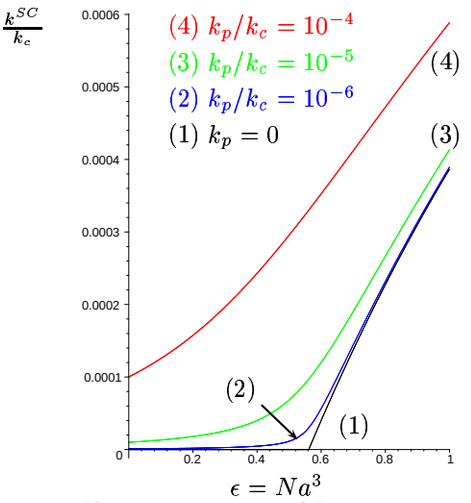


Figure 1. self-consistent estimate of the macroscopic permeability

We now consider the case of an isotropic distribution of crack orientations. $\boldsymbol{k}^{SC}$ is therefore isotropic : $\boldsymbol{k}^{SC} = k^{SC}\mathbf{1}$. In addition, the crack opening is taken uniform. Let N denote the crack density. The ratio k^{SC}/k_c determined from (6)-(7) is a function of the ratio k_p/k_c and of two geometrical characteristics, namely the "damage parameter" $\epsilon = Na^3$ and the aspect ratio X. For a constant value of X, the variations of k^{SC}/k_c versus ϵ for different values of k_p/k_c are plotted at figure 1. In the limit case $k_p = 0$, k^{SC} remains equal to 0 until a critical value $\epsilon^* = 9/16$. Beyond this threshold, the existence of a macroscopic permeability is the hydraulic counterpart for the appearance of a connected crack network. Hence, the self-consistent scheme is able to capture the concept of percolation threshold.
For $k_p \neq 0$, the variations of k^{SC} as a function of ϵ strongly depends on k_p/k_c. For higher values of this ratio, damage increases the macroscopic permeability without changing its order of magnitude. In contrast, figure 1 shows that k^{SC} can increase by several orders of magnitude when ϵ goes beyond ϵ^*, depending on the value of k_p/k_c, if this ratio is small enough. In this case, the variations of k^{SC} for $\epsilon < \epsilon^*$ are negligible ($k^{SC} \approx k_p$). For $\epsilon > \epsilon^*$, k^{SC} can be reasonably approximated by the estimate obtained for $k_p = 0$, for which an analytical expression is available :

$$k_p = 0 \;\Rightarrow\; k^{SC} = 3\pi k_c X \frac{16\epsilon - 9}{64\epsilon + 108} \tag{8}$$

Recalling that $k_c = c^2/3$, the above expression shows that $k^{SC} = \mathcal{O}(a^2X^3)$. This result reveals the two contributions to the coupling between permeability and mechanical loading. On the one hand, the latter affects the crack opening and aspect ratio. On the other hand, it may induce crack propagation, i.e. an increase of a. Both phenomena can be addressed within a micromechanical framework. We hereafter briefly mention some results concerning crack propagation.

a micromechanical modelling of damage

For simplicity, we consider an isotropic crack propagation process in an elastic brittle solid (bulk modulus k^s, Poisson coefficient ν^s) induced by an isotropic loading (macroscopic stress $\boldsymbol{\Sigma} = \Sigma\mathbf{1}$ and strain $\boldsymbol{E} = E\mathbf{1}$). The pore space is made up of an isotropic distribution of cracks, connected and saturated by a fluid at pressure P. Let $\psi^*(E, P, \epsilon)$ denote the macroscopic potential energy of the cracked solid ([2],[3]). The thermodynamic force $\mathcal{F}$ associated with the damage parameter ϵ is shown to be equal to the derivative $-\partial\psi^*/\partial\epsilon$ ([4]). This means that the dissipation associated with the rates $\dot{E}$, $\dot{P}$ and $\dot{\epsilon}$ is equal to $-\dot{\epsilon}\,\partial\psi^*/\partial\epsilon$. We then adopt a Griffith type propagation criterion of the form $\mathcal{F} \leq \mathcal{F}_o$:

$$\mathcal{F} = k^s(E + \frac{p}{3k^s})^2\mathcal{G}(\epsilon) \leq \mathcal{F}_o \quad \text{avec} \quad \mathcal{G}(\epsilon) = 648\frac{(1-\nu^2)(1-2\nu)}{(16\epsilon(1-\nu^2) + 9(1-2\nu))^2} \tag{9}$$

Once the propagation is initiated, the equality holds in (9). The evolution of ϵ can therefore be determined as a function of E and P. It is also found that the propagation is associated with a threshold of Terzaghi's effective stress :

$$\frac{8}{9k^s}\frac{1-\nu^2}{1-2\nu}(\Sigma + p)^2 \leq \mathcal{F}_o \tag{10}$$

References

[1] Guéguen Y., Palciauskas V. : Introduction to physics of rocks. Princeton University Press, 1994.
[2] Dormieux L., Molinari A., Kondo D. : Micromechanical approach to the behavior of poroelastic materials. J. Mech. Phys. Solids, 50, 2002.
[3] Pensée V., Dormieux L., Kondo D. et Deudé V. (2002). Poroélasticité d'un milieu mésofi ssuré. C. R. Acad. Sci. Paris, t. 330, série IIb, 147-152.
[4] Pensée V., Kondo D., Dormieux L. : Micromechanical analysis of anisotropic damage in brittle materials. J. Eng. Mech., 128(8), 2002.

THERMO-HYDRO-CHEMICAL-MECHANICAL ANALYSIS OF CONCRETE AT HIGH TEMPERATURES

S. Dal Pont[*] [**], B.A. Schrefler[**], A. Ehrlacher[*]
[*]*ENPC-LAMI, 6 et 8, Av. B.Pascal, Cité Descartes, 77455 Marne La Vallée Cedex 2, France*
[**]*Dipartimento di Costruzioni e Trasporti, Universitá di Padova, via Marzolo 9, 35131 Padova, Italy*

Summary This paper presents an experimental and numerical analysis of a hollow cylinder submitted to high temperatures. The evaluation of heat and mass transfers, evolution of the phases constituting the porous medium, mechanical performances of concrete are taken into account in a full three phases coupled analysis. A hollow cylinder has been heated up to $523.15K$ ($250^{\circ}C$) at a $5K/h$ velocity on the internal side and submitted to gas pressure/temperature measurements. A numerical simulation of the cylinder has been performed, showing a good correlation with the experimental observations.

INTRODUCTION

The problem of a porous medium (i.e.concrete) subjected to high temperatures is of great interest in civil engineering. The porous structure of concrete is subjected to strong alterations when exposed to high temperatures i.e. a fully coupled model is necessary. Chemical decomposition of the cement paste (i.e. dehydration) introduces in concrete pores free liquid water and modifies microstructure geometry and transport properties. During the dehydration process, considerable amounts of heat are consumed. The sorption isotherms of concrete are strongly temperature dependent, influencing the hygro-thermal behaviour of concrete. Permeability has a sharp increase above $378.15K$ i.e. when dehydration is considered to begin. Moreover physical properties of fluids (i.e. liquid water and air) change with temperature. Concrete is an hygroscopic material with a considerable portion of the pores belonging to the lower range of meso pores, meaning that during air/vapour diffusion, Knudsen effects must be considered. Physical properties of fluids (liquid water and moist air) saturating the medium are also strongly temperature dependent. For what the solid phase is concerned, isotropic damage effects, together with thermo-chemical damage, are taken into account. The present model, deriving from the coupled formulation presented in [1],[2],[3], [4] takes into account all the mentioned phenomena.

THE MATHEMATICAL MODEL

Concrete is a porous multiphase material where the voids are filled with liquid and gas. The liquid phase consists of bound water (or adsorbed water) which is present in the whole range of the medium, and capillary water. The gas phase is a mixture of dry air and water vapour (condensable) and is assumed to behave like an ideal gas. The mathematical model consists of a series of balance equations: mass of solid skeleton, mass of dry air, mass of the water species (in liquid and in gaseous state, taking into consideration phase changes i.e. evaporation-condensation, adsorption-desorption, hydration-dehydration process), enthalpy of the whole medium (latent heat of phase changes, heat effects of hydration-dehydration) and linear momentum. These balance equations are completed by an appropriate set of constitutive and state equations and some thermodynamic relationship. The governing equations of the model are given in terms of the chosen state variables. This choice is of particular importance: from a practical point of view, the chosen quantities should be easy to measure during experiments. From a theoretical point of view they must describe in a unique way the medium thermodynamic condition. State variables have been determined in the number of five: gas pressure p_g, capillary pressure p_c, temperature T and displacement vector of the solid matrix $\mathbf{u}(u_x, u_y)$.

Conservation equations are obtained by means of the hybrid mixture theory in the formulation proposed by Lewis and Schrefler [1]. The full development of the model equations starting from the local microscopic balance equations with successive volume averaging is presented in [1], [3]. In the pores, water is usually present as a condensed liquid which, thanks to the surface tension, is separated from its vapour by a concave meniscus (capillary water). The equilibrium equation between liquid water and gas is given by means of the well-known Laplace equation. Due to the curvature, the equilibrium vapour water pressure differs from the liquid water pressure and the relationship can be obtained by means of the Kelvin equation. The law describing moisture transport is Darcy's law in association with Fick's law. Darcy law is applied as constitutive equation. $\mathbf{K}$ is the intrinsic permeability, K_{rw} and K_{rg} are relative permeabilities of the liquid and the gaseous phase. Intrinsic permeability is a material characteristic depending only on concrete microstructure. During heating of concrete at high temperature complex physical and chemical processes take place, leading to inner structure changes and intrinsic permeability augmentation. Permeability is strongly dependent on damage. For the bound water flow a generalized Fick's law is applied (see [3] for further details details). For the description of the diffusion of the binary gas species mixture (dry air and vapour) Fick's law is applied.

Tensile stresses as well as pore fluid pressure are assumed as positive. The effective stress is given in the usual manner as a function of the total stress tensor, pressure and the Biot's coefficient.The constitutive relationship for the solid skeleton is classically obtained by means of the tangent matrix $\mathbf{K}_T$ as a function of strain. Mechanical damage effect is taken into consideration following the Mazars scalar isotropic model. During heating concrete is subjected to many changes in its inner structure with strong alterations of material properties. This degradation is not only due to mechanical damage, but

must lead also to thermally induced material deterioration. This kind of damage has been called thermo-chemical damage V. Full details of thermo-chemical damage in association with classical mechanical damage are given in [3] (see fig.1).

RESULTS AND DISCUSSION

The experiment has been performed on a hollow cylinder heated from the internal side, equipped with temperature and pressure sensors for the monitoring of the behaviour of concrete. The cylinder is 1.5m in height with an internal radius of 0.25m and an external of 0.55m. Microcracks (due to heating) on the external face had to be limited for avoiding moisture escape. For this reason the cylinder has been encircled by a steel layer. The concrete used in the analysis is an ultra high strength concrete of M100 type whose general characteristics at reference state are presented in [4]. Concerning temperature measurements a standard thermocouple of type K has been used. For what concerns the monitoring of gas pressures, a cylindrical sensor type of 3cm in height and 1.5 cm in diameter has been adopted. Only three pressure sensors have been used.The hollow cylinder has been discretized using the finite element method by means of 150 eight-node serendipity elements (501 nodes).Initial, boundary conditions and concrete characteristics are fully presented in [4]. Computations for the first 60 hours of the experimental analysis, using time steps of 4s. Temperature and gas pressure profiles show a good correlation with experimental results (fig.2 and 3).

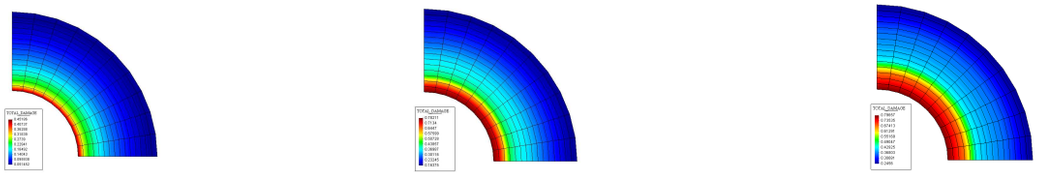


Figure 1. Total damage at t=20h, 40h, 60h

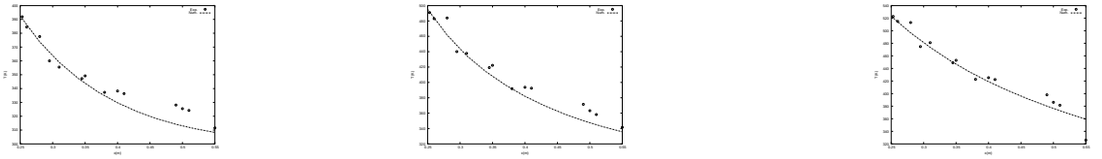


Figure 2. Numerical and experimental temperature vs radius at t=20h, 40h, 60h

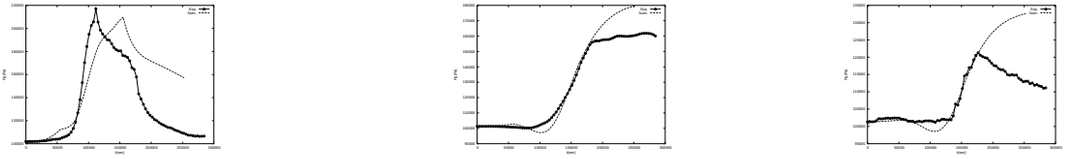


Figure 3. Numerical and experimental gas pressure vs time on sensor 1 (3cm), 3 (16cm) and 4 (25cm)

CONCLUSION

High temperatures effects have been considered through temperature/pressure dependance of many parameters by means of phenomenological expressions widely validated. An experimental set-up has been presented together with the related temperature and pore pressure measurements. The subsequent numerical analysis has shown qualitatively acceptable results, comparable to the observed data, allowing a deeper understanding of concrete at high temperatures.

References

[1] R. Lewis, B. Schrefler, The Finite Element Method in the static and dynamic deformation and consolidation of porous media, J.Wiley&Sons, 1998.

[2] D. Gawin, B. Schrefler, F. Pesavento, Modelling of hygro-thermal behavior and damage of concrete at temperature above the critical point of water, Int.J.Numer.Anal.Meth.Geomech (26) (2002) 537–562.

[3] D. Gawin, F. Pesavento, S. B.A., Modelling of hygro-thermal behaviour of concrete at high temperature with thermo-chemical and mechanical material degradation, Comput.Methods Appl.Mech.Engrg (192) (2003) 1731–1771.

[4] S. Dal Pont, B. Schrefler, A. Ehrlacher, Experimental and finite element analysis of a hollow cylinder submitted to high temperatures, sub. Mat. and struct. .

[5] S. Dal Pont, A. Ehrlacher, Numerical and experimental analysis of chemical dehydration, heat and mass transfer in a concrete hollow cylinder submitted to high temperatures, Int.J.Heat and Mass transfer 1 (47) (2004) 135–147.

FE-INVESTIGATIONS ON SHEAR LOCALIZATIONS IN GRANULAR BODIES WITHIN HYPOPLASTICITY

Jacek Tejchman

Gdańsk University of Technology, PL 80-952 Gdańsk, Poland

Summary A spontaneous shear localization in granular bodies is investigated with a finite element method based on a hypoplastic constitutive model. To simulate properly the formation of shear zones, a hypoplastic model was extended by polar, non-local and gradient terms to take into account a characteristic length of the microstructure. Two different rate boundary value problems were numerically analyzed with an extended model.

INTRODUCTION

Localization of deformation in the form of narrow zones of intense shearing is a fundamental phenomenon in granular materials. It can develop in granular bodies during processes of flow or shift of objects with sharp edges against granular materials. It can occur spontaneously inside of granular materials or can be induced along walls of stiff structures at granular bodies. An understanding of the mechanism of the formation of shear zones is important since they act as a precursor to ultimate soils failure.

Classical FE-analyses of shear zones are not able to describe properly both the thickness of localization zones and distances between them since they suffer from a spurious mesh sensitivity (its size and alignment). The rate boundary value problem becomes ill-posed, i.e. the governing differential equations of motion change the type by losing ellipticity for static and hiperbolicity for dynamic problems. Thus, the localization is reduced to zero-volume zones. To overcome this drawback, classical constitutive models require an extension in the form of a characteristic length to regularize the rate boundary value problem and to take into account microscopic inhomogeneities triggering shear localization (e.g. size and spacing of microdefects, grain size, fiber spacing). Different strategies can be used to include a characteristic length and to capture properly the post-failure regime (in quasi-static problems): polar models, non-local models, strain gradient models, and models with an artificial viscosity.

In this paper, a spontaneous shear localization in granular bodies was investigated with a finite element method based on a hypoplastic constitutive law extended by polar, non-local and gradient terms. The FE-analysis was performed with enhanced hypoplastic models for a specimen of dry sand for two different rate boundary value problems: vertical compression under constant lateral pressure and earth pressure of a retaining wall in conditions of plane strain. The numerical results were compared to corresponding laboratory tests carried out at the Karlsruhe, Cambridge and Tokyo University.

HYPOPLASTICITY

Hypoplastic constitutive models [1], [2] are an alternative to elasto-plastic ones for continuum modelling of granular materials. In contrast to elasto-plastic models, a decomposition of deformation components into elastic and plastic parts, yield surface, plastic potential, flow rule and hardening rule are not needed. The hypoplastic models describe the behaviour of so-called simple grain skeletons assuming that the macroscopic state can be sufficiently characterised by mean values of stress and void ratio. They describe the evolution of effective stress components with the evolution of strain components by a differential equation including isotropic linear and non-linear tensorial functions. The hypoplastic laws include also barotropy (dependence on pressure level), pycnotropy (dependence on density), dependence on the direction of deformation rate, dilatancy and contractancy during shearing with constant pressure, increase and release of pressure during shearing with constant volume, and material softening during shearing of a dense material. The feature of the model is a simple formulation and procedure for determination of material parameters with standard laboratory experiments [3]. The parameters are related to granulometric properties encompassing grain size distribution curve, shape, angularity and hardness of grains. Owing to that one set of material parameters is valid within a large range of pressures and densities. To simulate properly the formation of shear zones, a hypoplastic model was extended by polar, non-local and gradient terms to take into account a characteristic length of the microstructure.

EXTENDED HYPOPLASTICITY

The polar terms were introduced in a hypoplastic law with the aid of a polar (Cosserat) continuum. A Cosserat continuum takes into account two linked levels of deformation: micro-deformation at the particle level and macro-deformation at the structural level. Each material point has for the case of plane strain three degrees of freedom: two translational degrees of freedom and one independent rotational degree of freedom. The gradients of the rotation are connected to curvatures which are associated with couple stresses. It leads to a non-symmetry of the stress tensor and a presence of a characteristic length in the form of a mean grain size. The capability of a polar hypoplastic model has already been demonstrated in solving boundary value problems involving localization such as biaxial test, shearing of a narrow granular layer, silo filling and silo flow, furnace flow, footings and sand anchors [4]-[7]. A close agreement between

calculations and experiments was achieved. A polar model has good physical grounds since it takes into account rotations and couple stresses which are observed during shearing but remain negligible during homogeneous deformation. A characteristic length is directly related to a mean grain diameter.
A non-local approach is based on spatial averaging of tensor or scalar state variables in a certain neighborhood of a given point (i.e. material response at a point depends both on the state of its neighborhood and the state of the point itself). To obtain a full regularization effect according to both the mesh size and mesh inclination, it is sufficient to treat non-locally only one internal constitutive variable (e.g. equivalent plastic strain in an elasto-plastic formulation or modulus of the deformation rate in a hypoplastic approach [8]) whereas the others can retain their local definitions. The FE-calculations were carried separately with a non-local modulus of the deformation rate and non-local density factor (stresses, strains and other variables remained local). The error density function (normal Gaussian distribution function) was chosen as a weighting function.
The gradient approach is based on the introduction of a characteristic length by incorporating higher order gradients of strain or state variables into the constitutive law. In the calculations, the first and second gradient of the modulus of the deformation rate or density factor were used. To evaluate the gradient terms, instead of additional shape functions, a standard central difference scheme was employed.

FE-IMPLEMENTATION

The FE-calculations of plane strain compression tests were performed with a sand specimen which was 100 mm high and 20 mm wide. Only quadrilateral finite elements composed of four diagonally crossed triangles were applied to avoid volumetric locking due to dilatancy effects. A quasi-static deformation in sand was initiated through a constant vertical displacement increment prescribed at nodes along the upper edge of the specimen. The boundary conditions of the sand specimen were no shear stress at the top and bottom. To preserve the stability of the specimen against the sliding along the bottom boundary, the node in the middle of the bottom was kept fixed. To numerically obtain a shear zone inside of the specimen, a weaker element with a high initial void ratio was inserted in the middle of the left side of the specimen.
The calculations of a earth pressure problem were performed with a sand body of a height of 200 mm and length of 400 mm. The calculations were carried out with large deformations and curvatures (updated Lagrange formulation). Two sides and the bottom of the sand specimen were assumed to be very rough. The top of the sand specimen was traction and moment free. The retaining wall was assumed to be stiff and very rough. Three different wall modes were assumed in passive and active tests: uniform horizontal translation, rotation around the wall bottom and rotation around the wall top. The calculations were carried out only with a uniform, random and stochastic (with an exponential frequency function) distribution of the initial void ratio.

CONCLUSIONS

The results with a conventional hypoplastic constitutive model suffer from a mesh-dependency. The thickness of shear zones inside of a specimen and load-displacement diagrams are severely mesh-dependent.
A polar, non-local and gradient hypoplastic model provide a full regularization of the boundary value problem during plane strain compression and earth pressure of a retaining wall. Numerical solutions converge to a finite size of the localization zone upon mesh refinement.
The thickness of the localized shear zone and bearing capacity of granular specimens increase with increasing characteristic length.
The distribution of the initial void ratio influences the geometry of shear zones in the granular specimen (passive and active rotation of the retaining wall around the bottom).
The characteristic length within a non-local and gradient theory can be directly related to the mean grain diameter of the granular body.

References

[1] Gudehus, G.: Comprehensive equation of state of granular materials. *Soils and Foundations* **36** (1):1-12, 1996.
[2] Bauer, E.: Calibration of a comprehensive hypoplastic model for granular materials. *Soils and Foundations* **36** (1):13-26, 1996.
[3] Herle, I., Gudehus, G.: Determination of parameters of a hypoplastic constitutive model from properties of grain assemblies. *Mechanics of Cohesive-Frictional Materials* **4**:461-486, 1999.
[4] Tejchman, J., Herle, I., Wehr, J.: FE-studies on the influence of initial density, pressure level and mean grain diameter on shear localisation. *Inter. J. Num. Anal. Meth. in Geomechanics*, **23**: 2045-2074,1999.
[5] Tejchman, J., Gudehus, G.: Shearing of a narrow granular strip with polar quantities. *Inter. J. Num. and Anal. Meth. in Geomechanics*, **25**: 1-28, 2001.
[6] Tejchman, J.: Patterns of shear zones in granular bodies within a polar hypoplastic continuum. *Acta Mechanica*, **155** (1-2): 71-95, 2002.
[7] Tejchman, J.: Bauer, E. Effect of cyclic shearing on shear localisation in granular bodies. *Granular Matter*, 2004 (in print).
[8] Tejchman, J.: Comparative FE-studies of shear localizations in granular bodies within a polar and non-local hypoplasticity. *Mechanics Research Communications*, 2004 (in print).

MODELLING OF COMPOSITES PROCESSING USING A TWO-PHASE POROUS MEDIA THEORY

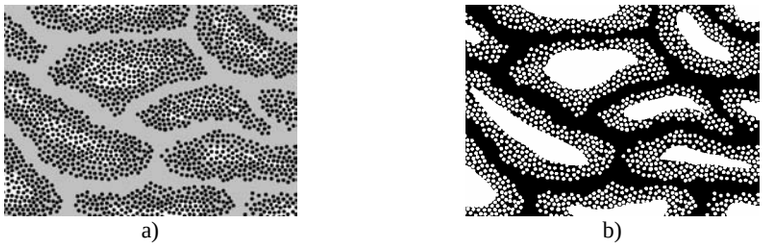
Maciej Wysocki*, Ragnar Larsson**, and Staffan Toll**
*IFP Sicomp AB, Division of Composite Materials, S-431 22 Mölndal, Box 104, Sweden
**Chalmers University of Technology, Department of Applied Mechanics, S-412 96 Göteborg, Sweden

Summary In the present contribution we propose a framework for the modelling of various forming processes for biphasic fiber composites. The class of processes considered involves deformation of a fiber bundle network, wetting by penetration of resin into fiber bundles, and resin flow through the fiber bundle network. The wetting process is considered as an irreversible dissipative mechanism that leads to the compaction of solid phase due to the exclusion of voids and "elastic" packing of the fibers. In the present contribution, we use a micro-mechanically motivated viscous flow rule for the evolution of the wetting. In addition, anisotropic macroscopic Darcian flow of the resin is accounted for. In the numerical example, a finite element analysis creep test representing the press-forming processing of a polymeric composite material is demonstrated.

INTRODUCTION

In the processing of fibre composite materials, three basic tasks must be performed: wetting of fibres by the resin, forming into shape and, when applicable, macroscopic drainage of resin. There is a variety of new, high speed manufacturing processes for fibre composites, which perform all these tasks in a single operation. Simulation of such process will require a series of sub-models describing the various mechanisms. But it will also require an appropriate continuum mechanical formulation to handle all the sub-models simultaneously while ensuring positive energy dissipation and balance of mass, momentum and energy.
In parallel with the increasing computer capacity, the porous media theory has been extensively developed and exploited. As an example, we may mention the development of the continuum theory of porous media formulated by Bowen [1]. In recent years the thermodynamic basis and the constitutive equations in the finite strain regime, along with the description of the various dissipative mechanisms have been further exploited, cf. Ehlers and Diebels [2], Armero [3] and Larsson and Larsson [4]. A few researchers, e.g. Pillai et al. [5], have proposed formulations to model the processing of fibre composites using porous media theory, a concept that is further developed in the present contribution.

CONSTITUENTS AND DEFORMATION PROCESSES



a) b)

Figure 1. Schematic of a) the considered microstructure consisting of matrix (grey), intra-bundle voids (white) and particles i.e. fibres (black) and b) the assumed phases, consisting of a solid phase (white) and a fluid phase (black)

Consider the coupling between the micro- and macro-scales in terms of a mixture consisting of three different micro-scale constituents, as depicted in Fig. 1a. To address the wetting process, the fiber bundles are subdivided into a wet portion (already penetrated by fluid) and a dry portion. It is emphasized that the void constituent is considered to be embedded within the fiber bundles. Consequently, the fibres and the voids are assumed to move in a synchronous fashion. A two-phase continuum model thus describes the three-constituent system, as depicted in Fig. 1b.
During processing of such a material system, four primary mechanisms can be identified: The two first mechanisms concern the deformation of the fiber-network and the "macroscopic" Darcian flow, i.e. drainage of matrix between the bundles. The other two mechanisms relate to wetting of individual fiber bundles, i.e. micro-scale infiltration with matrix, and the densification of the bundles.

A TWO-PHASE CONTINUUM MODEL AND CONSTITUTIVE EQUATIONS

As alluded to in the previous section, the problem of three constituents is reduced to a two-phase problem, which is resolved using the two-phase theory of porous media. We therefore assume that each spatial point $\mathbf{x}$ of the mixture is simultaneously occupied by the material particles $\mathbf{X}^s$ and $\mathbf{X}^f$, as shown in Fig. 2. Note that the two phases relate to different reference configurations.

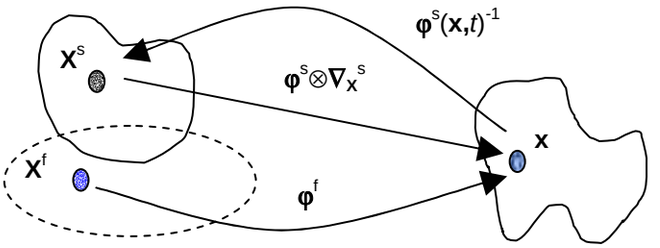


Figure 1. Deformation of a two-phase continuum body

Following the developments in [5], the momentum balance, the conservation of mass, the energy balance are combined in the entropy inequality. The constitutive equations can now be established, by distinguishing three different types of dissipative mechanism, from the total dissipation $\mathcal{D}$ defined as

$$\mathcal{D} = \underbrace{\boldsymbol{\sigma} : \mathbf{l} - n^s \rho^s \dot{\psi}^1}_{\mathcal{D}_1} - \underbrace{n^s p \dot{\varepsilon} - n^s \rho^s \dot{\psi}^2}_{\mathcal{D}_2} - \underbrace{\boldsymbol{h} \cdot \boldsymbol{v}^d}_{\mathcal{D}_3} \geq 0 \qquad (1)$$

where $\boldsymbol{\sigma}$ is the effective Terzaghi stress, $\mathbf{l}$ is the spatial velocity gradient, n^s is the solid volume fraction, ρ^s is intrinsic solid density, ψ^1 and ψ^2 are the Helmholtz free energies relating to the macro- and micro-scale processes, respectively, p is the fluid pressure, ε is a logarithmic compaction strain relating the initial and current solid densities, $\mathbf{h}$ is the effective drag force acting on the fluid phase and $\mathbf{v}^d$ is the Darcian velocity. The three dissipative mechanisms are: $\mathcal{D}_1$, the response due to effective stress, $\mathcal{D}_2$, the response due to fluid pressure, and $\mathcal{D}_3$, the response due to fluid-solid interaction owing to macroscopic Darcy flow. Note that these mechanisms correspond to the material responses of 1) elastic interaction between bundles, 2) wetting and compressing of fibre bundles by the liquid resin and 3) matrix flow between bundles, i.e. macroscopic drainage.

RESULTS AND CONCLUSIONS

In the presented examples, for the effective stress response, a hyper-elastic model based on isochoric-volumetric split is proposed. The isochoric response is described using a Neo-Hooke model, whereas the volumetric response is derived on the basis of a fibre packing law originally proposed by Toll [6]. As to the compaction of the bundles, the same fiber packing law was used in combination with specific infiltration model. The macroscopic drainage, is modeled based on anisotropic Darcian flow.

We emphasize in the present contribution, a developed framework for the modelling of a family of manufacturing processes of fiber composites using two-phase porous media theory. We have shown that a system involving three constituents may be described as a two-phase continuum, where the solid phase includes the voids as well as the fibers in the reinforcing fiber bundles. In this development, elimination of voids by penetration of liquid into a fiber bundle accompanied by an elastic compression of the bundle is manifested as an intrinsic compaction of the solid phase. The intrinsic compressibility of a fiber bundle was described by an established packing law. The same type of packing law was used at the fiber network level as well as at the fiber bundle level.

References

[1] Bowen, R.M., Compressible porous media models by the use of the theory of mixtures, Int. J. Eng. Sci. 20, 697-735, 1982

[2] Diebels, S., and Ehlers, W., Dynamic analysis of a fully saturated porous medium accounting for geometrical and material non-linearities, Int. J. Num. Meth. Engrg. 39, 81-97, 1996

[3] Armero, F., Formulation and finite implementation of a multiplicative model of coupled poro-plasticity at finite strains under fully saturated conditions, Comput. Methods Appl. Mech. Engrg. 171, 205-241, 1999

[4] Larsson, J., and Larsson, R., Non-linear analysis of nearly saturated porous media - Theoretical and numerical formulation, Comp. Meth. Appl. Mech. Engng. 191, 3885-3907, 2002

[5] Pillai, K.M., Tucker, C.L., and Phelan, F N, Numerical Simulation of Injection/Compression Liquid Composite Moulding. Part 2: Preform Compression, Composites: Part A 32, 207-220, 2001

[6] Toll, S., Packing Mechanics of Fibre Reinforcement, Polymer Engineering and Science, 38, 1337-1350, 1998

XXI ICTAM, 15–21 August 2004, Warsaw, Poland

WAVE PROPAGATION IN HIGH POROSITY BONES - A CELLULAR MODEL

Michal Pakula, Jozef Kubik, Mariusz Kaczmarek
Bydgoszcz University, Institute of Environmental Mechanics and Applied Computer Science, PL 85-064 Bydgoszcz, Poland

Summary Experimental ultrasonic studies for high porosity cancellous bone give the results which can not be properly described in the wide frequency range (especially for high frequencies) using two phase macrocontinual models (Biot's or Schoenberg model). Hence, a cellular model for propagation of ultrasonic waves in such media is proposed. The sensivity analysis of frequency dependent phase velocities and attenuations of both longitudinal ultrasonic waves is presented in order to extract physical properties and structural parameters of the cellular model which mostly influence wave parameters. The parameters calculated from the proposed model are compared with the data obtained from Biot's theory. It was shown that only for the long wave range (low frequencies) the predictions of both considered models are close to each other and that the results obtained from cellular model are in good qualitative agreement with the experimental data received from ultrasonic studies.

INTRODUCTION

Ultrasonic methods are currently well known and useful tools for non-destructive and non-invasive studies of properties of porous materials, both saturated or dry. An essential component of such studies applied for the complex materials is a mathematical model, which needs to be used for description of wave propagation in the materials and for extracting their mechanical and structural properties from wave parameters (phase velocity, attenuation coefficient and backscattering coefficient). While the macroscopic Biot's model is well verified for many lower porosity materials, in the case of higher porosity materials such as cancellous bones (porosity of cancellous bone is 80 - 90% or even higher) the model is less appropriate. Ultrasonic studies for cancellous bone, [4, 5, 7, 8, 9], show existence of two longitudinal modes, but the properties of the measured waves do not fit the data derived from the existing two phase macroscopic models (e.g. positive dispersion of phase velocity and higher attenuation of the slow wave than attenuation of the fast wave) when the wavelength is comparable with the characteristic pore size [8, 9]. One of the possible sources of the divergence between the model and experimental observations is the fact that the validity of the macroscopic model requires much longer waves than the size of inhomogeneity.
As the result appropriate for studies of short ultrasonic waves (when the averaged wavelength is comparable with or shorter than the pore size) model is needed. This paper develops cellular model of material for propagation of ultrasonic waves in cancellous bones propagating in the main direction of trabecular network.

MODELLING

The model of cellular material as composition of periodic system of two cells along with the exact solution for propagation of plane harmonic waves in each cell, [1, 6], (tube filled with fluid and layered cell composed of solid and fluid) is used. It is assumed that the solid material is elastic and isotropic while fluid is treated as the newtonian. Periodicity of the model allows to limit our analysis to a single cell, [1]. Considering propagation of plane harmonic wave independently for fluid (layer or channel filled with fluid) and solid (layer or tube) the displacements and stresses in the fluid and solid (solutions) are found. In order to receive the characteristic equation the boundary and matching conditions for the cell, outer boundary and interface between the fluid and solid, need to be satisfied. The matching conditions are: the equality of the normal and tangential stresses in the solid and fluid and the continuity of particle velocities normal and tangential to the interface. The outer cell boundary conditions are: the vanishing tangential stresses and normal displacement in the solid, [9]. The received characteristic equation is nonlinear complex algebraic equation for unknown wave number k_z which is solved numerically in order to find the propagation velocity ($V(f)$) and attenuation coefficient ($\alpha(f)$) of the plane harmonic waves as a functions of frequency (f) according to the equations:

$$V(f) = \frac{2\pi f}{Re(k_z)}, \quad \alpha(f) = Im(k_z)\ . \tag{1}$$

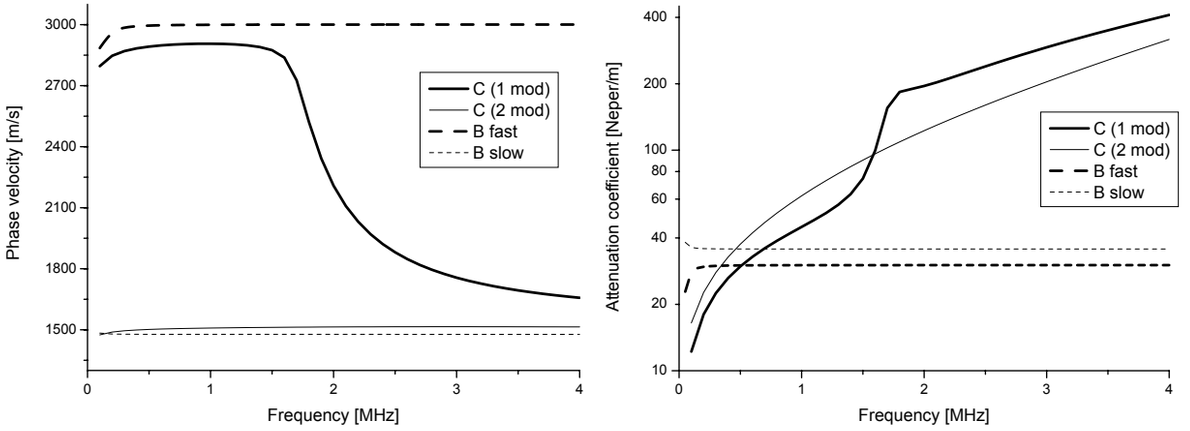
In order to evaluate the role of physical properties of phases and structural parameters of the model the sensivity analysis of frequency dependence of phase velocities and attenuations of both longitudinal US waves was performed. It was shown the wave parameters are practically insensitive to changes of porosity for long waves and the phase densities for the whole frequency range, while the other parameters: fluid viscosity, speed of sound in fluid, shear and longitudinal wave velocity in solid phase and characteristic size of inhomogeneity strongly influence both the phase velocity and attenuation.

It is also interesting to notice that the cellular model predicts infinite number of wave modes, but only two of them exist in the whole frequency range. Additional modes appear at some characteristic frequencies f_n, which satisfy the relation:

$$f_n = \frac{nc_f\pi}{l_f}\sqrt{\frac{c_{fn}^2}{c_{fn}^2 - c_f^2}}\ , \tag{2}$$

where c_f is speed of sound in fluid, c_{fn} - phase velocity at frequency f_n, n- integer number which correspond to consecutive wave modes and l_f is the characteristic size of inhomogeneity in the model (thickness of the layer or channel diameter). Since each frequency f_n is related to the size of channel or cell, the formula (2) can be used in the evaluation of averaged characteristic size of inhomogeneity and its changes during some processes (in the case of cancellous bone - during osteoporosis).

In Fig. 1 the theoretical predictions obtained from the cellular model are compared with results from the macrocontinual (Biot's) model (see Fig.1). It is worth noticing that both considered models predict more than one longitudinal wave modes. The results from the cellular model show strong negative dispersion of the phase velocity of fast wave, while the velocity of slow wave is almost constant for the whole considered frequency range (see Fig. 1_a). In the case of Biot's model velocities of both wave modes (fast and slow) change insignificantly with frequency. For the long waves



(a) (b)

Figure 1. Comparison of phase velocity (a) and attenuation coefficient (b) from the macrocontinual Biot's (B) and cellular model (C) - numerical calculations

(low frequency) wave velocities derived from the cellular model are close to that obtained from Biot's theory. When the frequency increases (for shorter wavelengths) the discrepancy between two models rises, particularly when the fast wave is considered.

Attenuation coefficients (see Fig.1_b) derived from of both models show essentially different qualitative and quantitative behaviour. In particular attenuations from the Biot's model for the whole frequency range have almost constant values. The parameter from cellular model strongly increases as a function of frequency. It is also interesting to stress that accordingly to the cellular model, from some characteristic frequency (~ 1.7MHz), independently of the porosity, attenuation of the slow wave is lower than that for the fast one, while in terms of Biot's model such behaviour is observed only for high porosities (over 85%).

References

[1] Achenbach, J. D. and Sun, C. T. and Herrmann, G.: On the vibrations of a laminated body, *J. Appl. Mech.*, **35**:689-699, 1968.
[2] Biot, M.A.: Theory of Propagation of Elastic Waves in a Fluid-Saturated Porous Solid, *J. Acoust. Soc. Am.*, **28**:168-191, 1956.
[3] Brekhovskikh, L.M.: Waves in layered media, Academic Press, New York, 1980.
[4] Chaffai, S. and Padilla, F. and Berger, G. and Laugier, P.: In vitro measurement of the frequency-dependent attenuation in cancellous bone between 0.2 and 2 MHz, *J. Acoust. Soc. Am.*, **108**(3):1281-1289, 2000.
[5] Cowin, S.C.: Bone poroelasticity, *J. of Biomechanics*, **32**:217-238, 1999.
[6] Del Grosso, V. A.: Analysis of Multimode Acoustic propagation in Liquid Cylinders with Realistic ... , *Acoustica*, **24**:299-311, 1971.
[7] Hughes, E.R. and Leighton, T.G. and Peteley, G.W. and White, P.R.: Ultrasonic propagation in cancellous bone: A new stratified model, *Ultrasound in Med. & Biol.*, **25**(5):1-5, 1999.
[8] Kubik, J. and Kaczmarek, M. and Pakula, M.: Multiphase nature and structure of biomaterials studied by ultrasound, *Ultrasonics*, **38**:703-707, 2000.
[9] Kubik, J. and Kaczmarek, M. and Pakula, M.: Short ultrasonic waves in cancellous bone, *Ultrasonics*, **40**(1-8):95-100, 2002.
[10] Schonberg, M.: Wave propagation in alternating solid and fluid layers, *Wave Motion*, **6**:303-320, 1984.

SOFT POROUS MEDIA MODEL OF MAGNETIC FLUID

Mariusz Kaczmarek*, Tomasz Hornowski**
*Bydgoszcz University, Inst. Env. Mech. Appl. Comp. Sci, Chodkiewicza30, 85-064 Bydgoszcz, Poland
**A. Mickiewicz University, Institute of Acoustics, Umułtowska 85, 61-614 Poznań, Poland

Summary Mechanical behaviour of magnetic fluids is influenced by magnetic field. In particular ultrasonic tests show anisotropy and dependence of wave parameters on strength of the field. Adopting the physical model of magnetic fluid as a composition chains of clusters (skeleton) in carrier liquid the soft porous media model of the material is considered. The model takes into account mutual interaction of clusters constituting soft skeleton and interaction of clusters with the carrier liquid. The description is used to determine attenuation and phase velocity of mechanical waves for transversally isotropic model of the fluid in constant magnetic field. The results are compared with experimental data for different intensity of magnetic field.

INTRODUCTION

An interesting class of intelligent materials are magnetic fluids which without magnetic field are homogeneous colloidal suspensions of ferromagnetic particles coated with surface-active dispersive medium (typical diameters of particles range from 5 to 10 nm) in a carrier liquids (water, oils, etc.). Under influence of magnetic field certain amount of colloidal particles forms aggregates (clusters) which are joined into chains. The presence of chains induces certain small stiffness and anisotropy of mechanical properties of the materials. In order to describe the above features and incorporate interactions between clusters and surrounding liquid which contribute to the dissipation of energy, [1, 2], a model of soft porous media is considered. It is assumed that the two phases of the medium are: the soft skeleton made of interacting chains of clusters and the liquid composed of carrier liquid with free colloidal particles (particles not gathered into clusters). The mutual interactions of clusters are represented through non-vanishing components of stress tensor for the solid phase. The interactions of clusters with liquid are expressed as the sum of viscous, inertial drag and Basset force. Given the assumed symmetry of the medium (transversal isotropy) induced by DC magnetic field the possible harmonic wave modes predicted by the model in infinite medium are specified. Quantitative results obtained from the model for dependence of wave parameters on strength of magnetic field, angle between directions of magnetic field and wave, and on frequency are compared with experimental data.

EXPERIMENTAL DATA

The techniques which were used to study mechanical (acoustic) properties of magnetic liquids both with and without magnetic field are pulse and continuous wave methods. The methodology can be applied to observe anisotropy of mechanical properties of the liquids in variable strength of magnetic or electric field, study frequency dependence of wave parameters and test the materials in wide range of temperatures. They can be also useful to assess the role of carrier fluids, history of magnetic or electric loads etc. In the reported studies the measuring chamber with magnetic fluid was placed in constant magnetic field with maximum strength 1 T. The Figures 1 and 2 present results for ultrasonic attenuation and phase velocity versus magnetic field obtained from testing of liquid EMG-605 (Ferrofluidics) performed for pulse waves generated by transducer with frequency 1.18 MHz, parallel to the magnetic field. The results show that the attenuation is approaching a maximum value at certain strength of magnetic field and velocity increases monotonically with the field.

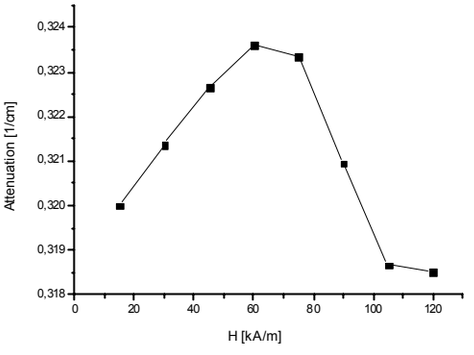


Fig. 1

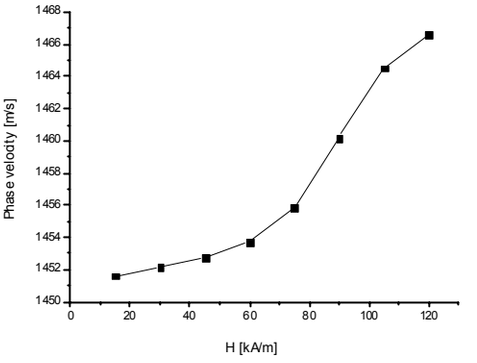


Fig. 2

MODELLING

Formulation of dynamic two-phase model of magnetic liquid is based on equations of balance of linear momentum for solid and fluid phase

$$\rho^s \frac{\partial \mathbf{v}^s}{\partial t} - \Delta \cdot \mathbf{T}^s - \mathbf{R}^s = \mathbf{0} \ , \quad \rho^f \frac{\partial \mathbf{v}^f}{\partial t} - \Delta \cdot \mathbf{T}^f - \mathbf{R}^f = \mathbf{0} \ ,$$

where ρ^s and ρ^f stand for the average mass densities of solid and fluid phase, $\mathbf{v}^s$ and $\mathbf{v}^f$ are macroscopic velocities, $\mathbf{T}^s$ and $\mathbf{T}^f$ denote stress tensors, and $\mathbf{R}^s$ and $\mathbf{R}^f$ are interaction forces between the phases.
Assuming magnetically induced transversal isotropy and field directed along axis z the following set of components of constitutive relationships is proposed (see [3])

$$T_{ij}^f = -\beta p \, \delta_{ij} + \pi_{ij} \ ,$$

$$\pi_{xx} = 2\mu \, d_{xx} + \alpha(d_{xx} + d_{yy} + d_{zz}) \ , \quad \pi_{yy} = 2\mu \, d_{yy} + \alpha(d_{xx} + d_{yy} + d_{zz}) \ , \quad \pi_{zz} = \gamma \, d_{zz} + \beta(d_{xx} + d_{yy} + d_{zz})$$

$$\pi_{xz} = \pi_{zx} = 2\delta \, d_{xz} \ , \quad \pi_{yz} = \pi_{zy} = 2\delta \, d_{yz} \ , \quad \pi_{xy} = \pi_{yx} = 2\mu \, d_{xy} \ ,$$

$$\beta p = -M(e_{xx} + e_{yy}) + Q \, e_{zz} + R\varepsilon$$

$$T_{xx}^s = 2N \, e_{xx} + A(e_{xx} + e_{yy}) + F e_{zz} + M\varepsilon \ , \quad T_{yy}^s = 2N \, e_{yy} + A(e_{xx} + e_{yy}) + F e_{zz} + M\varepsilon \ , \quad T_{zz}^2 = C \, e_{zz} + F(e_{xx} + e_{yy}) + Q\varepsilon$$

$$T_{xz}^s = T_{yx}^s = 2L \, e_{xz} \ , \quad T_{yz}^s = T_{zy}^s = 2L \, e_{yz} \ , \quad T_{xy}^s = T_{yx}^s = 2N \, e_{xy} \ .$$

$$R_x^{sf} = -b_T(\upsilon_x^f - \upsilon_x^s) - c_T \frac{\partial(\upsilon_x^f - \upsilon_x^s)}{\partial t} \ , \quad R_y^{sf} = -b_T(\upsilon_y^f - \upsilon_y^s) - c_T \frac{\partial(\upsilon_y^f - \upsilon_y^s)}{\partial t} \ , \quad R_z^{sf} = -b_z(\upsilon_z^f - \upsilon_z^s) - c_z \frac{\partial(\upsilon_z^f - \upsilon_z^s)}{\partial t} \ ,$$

where p is fluid pressure, β denotes volume fraction of carrier liquid, and $\boldsymbol{d}$ and $\boldsymbol{\varepsilon}$ are rate of deformation of fluid and strain of solid phase. The other parameters are coefficients representing elastic properties (*A, C, F, L, M, N, Q, R*), viscosities (α, β, δ, γ, μ) and interface interactions (b_T, b_z, c_T, c_z). Combining the above equations and considering plane harmonic waves in infinite medium one obtains dispersion relationships predicting velocities and coefficients of attenuation of four types of waves which are related to disturbances in plane x, z. Two of them are quasi-longitudinal waves (for which motion of particles of fluid and solid phase take place in or out of phase). The remaining waves are the shear like waves resulting from the existence of the stiffness of solid phase and viscosity of carrier liquid.
The numerical results for wave velocity which qualitatively agree with the experimental data can be derived from the model assuming linear dependence of volume fraction of clusters (solid phase) on strength of magnetic filed and evolution of elasticity parameters as functions of magnetic field according to the logistic equation. The analysis of attenuation shows that for appropriately selected values of parameters of the model the experimental data can be also well fitted but the attenuation is very sensitive to viscosity of liquid phase and terms representing viscous interaction (drag) between solid and fluid phase. As the results further theoretical studies including microscopic considerations of properties of phases and experimental works are necessary to find reliable evolution functions for macroscopic parameters.

CONCLUSIONS

The predicted by porous media model values of attenuation and velocity of fast quasi-longitudinal wave in magnetic fluid can describe some basic ultrasonic data. It justifies assumption that the growth and interaction of clusters, represented by changes of volume fraction and elasticity modulus, may serve as an explanation of the observed evolution of wave propagation parameters with changing magnetic field. The best qualitative prediction can be obtained for the maximum value of bulk modulus about 50 kN/mm^2. It should be noted that the model predicts also the existence of slow quasi-longitudinal wave. Its velocity is about ten times lower, and attenuation over thousand times higher as compared with the parameters of the fast wave. With the currently available measuring methods it is impossible to detect this wave experimentally. The analysis of other predictions of the proposed model, e.g. the effects of anisotropy of the material and the frequency dependence of wave propagation parameters has been undertaken. Directions of further development of the model such as frequency dependence of interactions between phases and possible non-linear effects, e.g. due to magnetic couplings and saturation are discussed.

References

[1] Taketomi S.: The anisotropy of the sound attenuation in magnetic fluid under an external magnetic field, *J. Phys. Soc. Jpn.*, **55**, 838-844, 1986.
[2] Gogosov V.V., Martyniv S. I., Curikov S.N., Saposnikova G.A.: Rasprostranienije ultrazwuka w magnitnoj żidkosti, *Magn. Gidrodin*, 19-27, 1987.
[3] Sharma M. D., Gogna M.L.: Wave propagation in anisotropic liquid-saturated porous media, *J. Accoust. Soc. Am.*, **90**, 1068–1073, 1991.

MECHANICS OF SATURATED HIGH POROSITY/SOFT MATERIALS

Józef Kubik, Mariusz Kaczmarek, Michał Pakuła
Bydgoszcz University, Inst. Env. Mech. Appl. Comp. Sci, Chodkiewicza30, 85-064 Bydgoszcz, Poland

Summary Dynamical properties and macroscopic modelling of fluid saturated high porosity and/or soft materials are considered. The properties are obtained form ultrasonic tests and discussed in light of results for low and medium porosity materials. The effective medium approximations are applied in order to evaluate elasticity parameters and microscopic considerations with averaging to find interaction forces of the two-phase model. Results for wave propagation parameters as functions of porosity, frequency and parameters of structure of solid skeleton which contribute to dissipation are analysed and compared with available data.

INTRODUCTION

There is a quite large number of natural (biological) or artificial (absorbing) porous materials with high porosity. Porosity of trabecular bones, particularly in diseased – osteoporotic state may reach 95%. Soft porous materials such as foams, gels or structured liquids (e. g. magnetic liquids) may have even higher porosity and additionally very low stiffness of their solid frame. The high porosity and/or low stiffness result in specific properties of the materials as compared with materials having low or average porosity. The particular role may be played then by transfer of loads or energy in fluid, viscous dissipation in fluid due to its deformation rate (term usually neglected in modelling of lower porosity materials), interactions between phases represented by couplings in stress tensors and drag or dynamic couplings, as well as the history dependence of the interactions. In experimental studies of waves in such materials one observes for example extremely high dispersion of fast longitudinal wave and attenuation of fast wave higher than that for slow wave in some range of frequencies. Another specific property of the materials comprises in presence of maximum of attenuation for certain range of high porosities. While the theoretical studies of porous materials belong to strongly developing field of mechanics, relatively little attention is devoted to modelling of high porosity materials. As the result the knowledge of specific constitutive functions, boundary conditions, and material parameters as well as the usefulness of predictions of the classical porous media model (for lower porosity materials) are not well established.
The purpose of this paper is to consider predictions and applicability of the macroscopic model of porous media for high porosity materials. Experimental results for trabecular bones are used to illustrate the peculiarities of the materials and few theoretical aspects of the macroscopic modelling such as problems of effective elasticity parameters, role of viscous dissipation in fluid and solid materials, history dependence of interaction force and their meaning for wave characteristics are considered.

DATA FROM STUDIES OF HIGH POROSITY TRABECULAR BONES

Experiments for bovine trabecular bones saturated with marrow, alcohol and water have been performed by using pulse transmission method and the immersion technique. Three unfocused pairs of broadband ultrasonic transducers (Panametrics 2.25, 1.00 and 0.50 MHz) were applied with the ultrasonic pulser-receiver (Panametrics 5058). The received signals have been digitized by oscilloscope (TDS420A) and transferred to PC. The phase velocity and attenuation coefficient were obtained as functions of frequency based on FFT of signals transmitted through samples of different thickness. Figure 1 shows time records for waves transmitted in the same sample of water saturated bone at different frequencies of transducers.

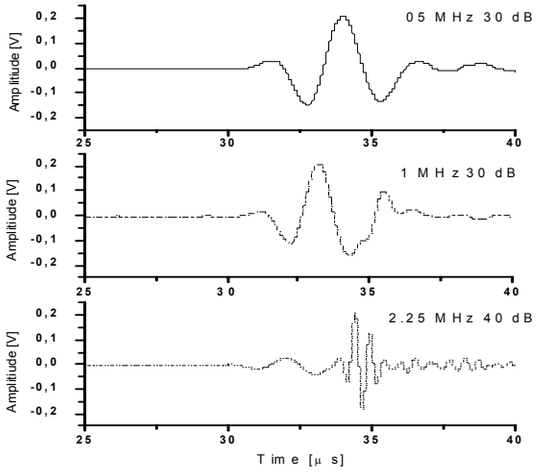


Fig.1

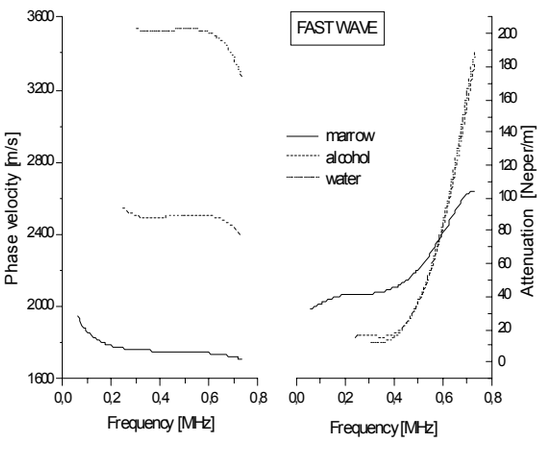


Fig. 2

Strong frequency dependence of the waves is visible. For the highest frequency (2.25 MHz) separated longitudinal wave modes can be identified and the amplitude of the fast wave becomes significantly smaller than that for the slow one. Such behaviour is not observed for other types of liquid saturated porous materials and does not agree with results known from the Biot's theory applied for lower porosity materials. In Fig. 2 the frequency dependence of phase velocity and attenuation of the fast wave measured with transducers 0.5 MHz for materials saturated with marrow, alcohol and water are compared. The results show significant negative dispersion, and strong frequency dependence of attenuation.

MACROSCOPIC MODELLING OF HIGH POROSITY MATERIALS

The macroscopic approach which can be applied as a starting point to model dynamical behaviour of saturated high porosity materials is the Biot's theory [1, 2]. The model takes into account mechanical interaction of phases due to their equipresence in elementary volumes (macroscopic particle) and interaction being result of relative motion of phases. The elastic characteristics of isotropic material within the Biot's theory define four constants. Besides the experimental techniques which for the high porosity materials were not well developed a way to determine elasticity constants is to use theoretical relations between elastic properties of materials of phases and porosity, derived by so called effective medium approximations. The methods were mostly elaborated for low or medium porosity materials and some are not useful above certain critical value of porosity. It is also worth noticing that the effective medium theories can be applied for determination of moduli of porous materials for drained or undrained conditions. The predictions to be consistent should satisfy Gassmann relation. Within the performed studies number of effective medium models were applied to evaluate macroscopic elastic parameters of high porosity materials. In Fig. 3 and 4 results for bulk drained moduli and shear moduli refered to the corresponding parameters of solid materials are compared using Differential Medium (DM), Gauss Open Cell (OC) and Two Cut (TC) models as well as giving identical results Mori-Tanaka and Kuster-Toksoz model (MT/KT). One should notice that the two Gaussian models were established [3] particularly for high porosity materials by computer simulation methods.

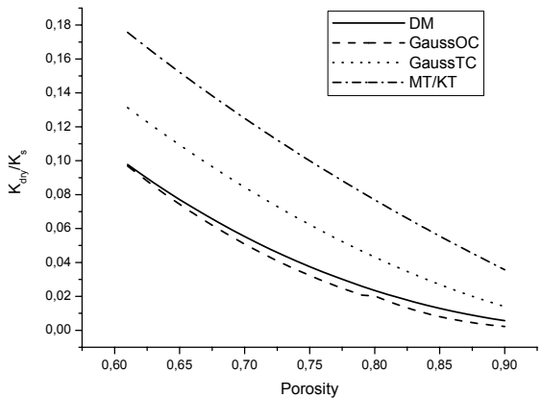


Fig. 3

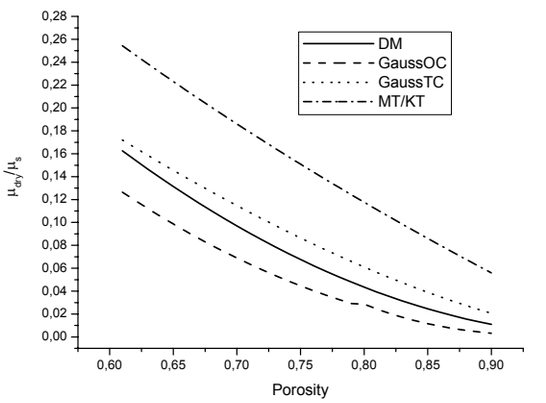


Fig. 4

The macroscopic elasticity constants derived from effective medium models were used to determine wave parameters as functions of porosity and good approximation of experimentally observed wave velocities could be obtained. The studies have also shown that due to the low stiffness of the skeleton the results for fast longitudinal wave derived with help of bulk moduli of high porosity materials are close to the results obtained for suspension model of the materials. Analysis for attenuation shows much more sensitivity of the parameter to micro-geometry (structural parameters) and the fact that the solid component constitutes continuous phase has a crucial meaning.

References

[1] Biot, M.A.: Theory of Propagation of Elastic Waves in a Fluid-Saturated Porous Solid, J.Acoust.Soc.Am **28**,168-191, 1956.

[2] Kaczmarek M.,Kubik J., Pakula M.: Multiphase nature and structure of biomaterials studied by ultrasound, Ultrasonics, **38**, 703-707,2000.

[3] Robersts A. P., Garboczi E. J.: Computation of the linear elastic properties of random porous materials with a wide variety of microstructure, Proc. R. Soc. Lond. A **458**, 10033-1054, 2002.

XXI ICTAM, 15–21 August 2004, Warsaw, Poland

A THREE LAYER POROUS MEDIA MODEL OF CUTANEOUS CIRCULATION WITH APPLICATION TO MECHANICAL SKIN IRRITATION

Daniela Bauer*, Reinhard Grebe*, Alain Ehrlacher**
*Univérsité de Technologie de Compiegne, Laboratoire de Biomécanique, UMR 6600, 60529 Compiègne, France
**Ecole Nationale des Ponts et Chaussées, Laboratoire d'Analyse des Matériaux et Idenification, 77455 Marne la vallée Cedex 2, France

Summary Scratching skin induces vasodilatation on the line of stroke and in the surrounding tissue. Vascular network has been described using a model consisting of three layers. First and last layer presenting irrigation and drainage of the system, are described as horizontal bidimensional porous media. Intermediate layer, described by means of compartments, does not allow horizontal fluxes. Mechanical skin irritation is modelized by changing compliance of vessels situated at the entrance of microcirculation.

INTRODUCTION

Already in 1927 Lewis [4] described skin reaction to scratch. He distinguished three different reactions. The first one, local reaction, describes vasodilatation on the line of stroke, its onset taking place after a very short delay. The second reaction considers spreading of the zone of vasodilatation in the neighboring area after a delay of $20s$ to $30s$. Scratching skin leads to mast cell compression and pain receptor stimulation. Mast cell compression induces histamine release on the line of stroke. Stimulated pain receptors induce nervous signals which induces neuropeptide release in a region situated around the zone of scratching. Histamine and neuropeptides are vasodilatators.

Blood circulation has been described by different types of models. Muscle circulation has been studied by Braakman et al. [2] using compartment models (lumped parameter model). Here, mechanical behavior of each type of vessel is described by the resistance and compliance of one compartment. Huyghe et al. [3] propose to describe vascular networks using porous media. Vankan et al. [5, 6] describe muscle circulation by a model consisting of five layers. Each layer is defined by laws of porous media permitting horizontal fluxes. Exchange fluxes inbetween two layers are allowed taking in account correct physiological direction. Cutaneous vascular network and irritation has already been described using discrete model by Bauer et al. [1]. The model proposed here is inspired by the models of Braakman, Huyghe and Vankan. It shows description of vascular network as continous media. It will permit to study whether widening of the zone of vasodilatation is only due to nervous signals or whether a diffusion process, leading blood from the zone of stimulation into the neighboring areas, takes place.

THE MODEL

Vascular network has been described by a model consisting of three layers. First and last layer presenting irrigation and drainage of the system, are described as horizontal two-dimensional porous media. Intermediate layer, described by means of lumped parameter method, does not permit horizontal fluxes, taking in account the fact that cutaneous capillaries show only very few connections between themselves. Hierarchical fluxes are directed from first to second layer and then towards drainage layer considering physiological flow direction.

The model is based on a surface representation of skin while fixing constant value for depth. Consider a surface element $dS = (dx, dy)$ in which vascular network is situated. Blood flow in this element is defined by geometry of vascular network and pressure gradient between irrigation layer and system of drainage.

Formulation of volume balances for the point (x, y) of each layer, considering blood as incompressible, we obtain the following equations (ϕ_I: volume of irrigation layer , ϕ_M: volume of microcirculation layer, ϕ_D: volume of drainage layer)

$$\dot{\phi}_I = -div\vec{I} - \Psi_{I\to M} \tag{1}$$

$$\dot{\phi}_M = \Psi_{I\to M} - \Psi_{M\to D} \tag{2}$$

$$\dot{\phi}_D = -div\vec{D} + \Psi_{M\to D} \tag{3}$$

where $\vec{I}$ and $\vec{D}$ are spatial volume flow fields of the first and last layer. $\Psi_{I\to M}$ describes hierarchical volume flow between first and second layer. $\Psi_{M\to D}$ illustrates hierarchical volume flow between second and third layer. Volume flow fields $\vec{I}$ and $\vec{D}$ are described by Darcy's law using two-dimensional permeability tensors. Hierarchical fluxes $\Psi_{I\to M}$ and $\Psi_{M\to D}$ are given by Poiseuille's law applied to pressure difference between first and second layer and difference between second and third layer. Volume is supposed to be proportional to pressure by means of compliance. All permeabilities depend on volume. Irritation is simulated by changing compliances of vessels situated at the entrance of microcirculation. The model can be applied at macroscopic scale considering the system arteries, microcirculation and veins and at microscopic scale describing the behavior of arterioles, capillaries and veinules. All data for model parameters is given by Vankan et al. [5, 6] and Braakman et al. [2].

RESULTS

Fig.1 shows time dependency of volumes of stimulated points. Fig.2 shows difference between first and second equilibrium state of the somme of volumes of three layers. White zone corresponds to area of stimulation. Results are given for both scales. All results are normalized by volumes of first equilibrium state. One can note that change in volume in neighboring area is very small in comparison to increase in volume in stimulated points.

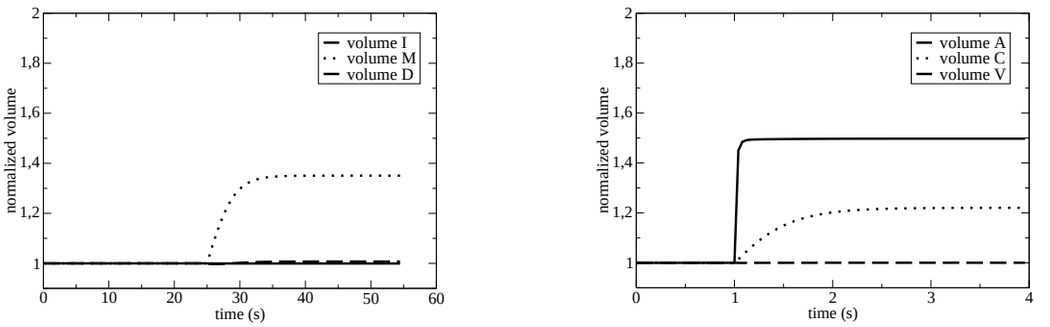


Figure 1. Time evolution of volumes of stimulated point (right: macroscopic scale, left: microscopic scale)

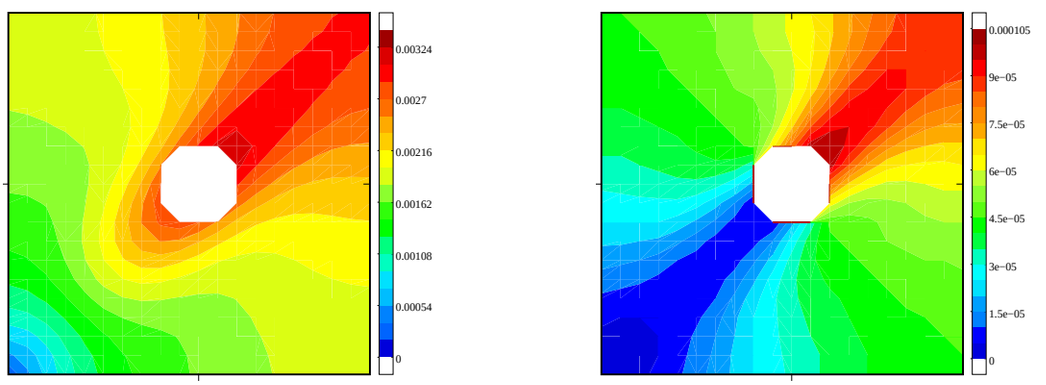


Figure 2. Difference in volume in neighboring area (right: macroscopic scale, left: microscopic scale)

CONCLUSION

Combining a two layer porous media model with compartment model permits to describe spatial and hierarchical fluxes in continuous media without the necessity to have information on geometric data. As the model can be used at different scales, it permits to investigate influence of irritation on microcirculation and total circulation. Vasodilatation taking place in the zone of stimulation corresponds to first reaction described by Lewis. Although volume does increase in the sourrounding zone, increase is not sufficiently high to explain vasodilatation due to nervous reflex. Thus the model is in accordance with Lewis theory. We can conclude, if widening of the zone of vasodilatation should be simulated, nervous reflex has to be modeled.

References

[1] Bauer, D., Grebe, R. & Ehrlacher, A.: Change in Microcirculation due to Mechanical Skin Irritation - Discrete Model *XXVIIIème Congrès de la Société de Biomécanique* Poitiers, Septembre 2003

[2] Braakman, R., Sipkema, P. & Westerhof, N.: A Dynamic Non-linear Lumped Parameter Model for Skeletal Muscle Circulation. *Ann Biomed Eng* **17**, 593–616, 1989.

[3] Huyghe, J., Oomens, C., Van Campen, D. & Heethaar, R.: Low Reynolds Number Steady State Flow through a Branching Network of Rigid Vessels: I. A Mixture Model. *Biorheology* **26**,73–84, 1989.

[4] Lewis, T.: The Blood Vessels of the Human Skin and their Responses. London, 1927.

[5] Van Donkelaar, C., Huyghe, J., Vankan, W., & Drost, M.: Finite Element Simulation of Blood Perfusion in Muscle Tissue during Compression and Sustained Contraction. *Am J Phys* **273**, H1587–H1594, 1997.

[6] Vankan, W., Huyghe, J., Janssen, J., & Huson, A.: Poroelasticity of Satured Solids with an Application to Blood Perfusion . *Int J Engng Sci* **34**, 1019–1031, 1996.

XXI ICTAM, 15–21 August 2004, Warsaw, Poland

IDENTIFICATION OF SOME CHEMOPOROELASTIC PARAMETERS OF A REACTIVE SHALE FROM EXPERIMENTAL DATA

Joël Sarout*, Emmanuel Detournay*
*University of Minnesota, Department of Civil Engineering, MN 55455 Minneapolis, USA

Summary This paper is concerned with the experimental identification of some chemoporoelastic parameters of a chemically reactive shale from data obtained in pore pressure transmission-chemical potential tests. The parameter identification is carried out by matching the observed pressure response with a theoretical solution of the experiment. This solution is obtained within the framework of Biot theory of poroelasticity, extended to include physico-chemical interactions.

EXPERIMENTAL ISSUES

The so-called pore pressure transmission-chemical potential test is used in the petroleum industry to evaluate the osmotic membrane efficiency of a shale in contact with a drilling fluid [10, 8]. It is motivated by the need to assess the capacity of improving the stability of a borehole in a chemically active shale by increasing the salt concentration of the drilling fluid [4, 5, 9]. In this test, a saturated cylindrical sample of shale is subjected sequentially to a hydraulic and a chemical loading at the upstream end of the sample ($z = 0$), with the downstream end ($z = L$) connected to a closed reservoir. The hydraulic loading consists of applying a pressure p_m at $z = 0$ with the solution used during the saturation phase. In the chemical loading the upstream end is placed in contact with a solution of a different salt concentration but at the same hydraulic pressure p_m.
This experimental program was conducted with a two-fold objective: (i) check the relevance of the theory by its ability to be consistent with the observations; (ii) provide data to allow identification of the parameters of the model.

Experimental Setup

A series of experiments on Pierre II shale (a shale from the Rocky Mountains in Colorado) has been carried out with the Membrane Efficiency Screening Equipment (MESE) in the laboratory of CSIRO Petroleum, Australia [11]. This apparatus consists of six test cells with a confining pressure and pore pressure capacity of 35 MPa and 20 MPa, respectively. There is a fluid cylinder for each test cell. Up to six different solutions can be tested at any one time and the test on each cell may be started and terminated independently from the others. Six different samples of 25.4 mm diameter and length up to 25 mm can be tested at the same time in this device. For each cell, both upstream and downstream pressures are recorded with the help of a computerized data acquisition system using a dedicated program built in the Labview environment. This program also controls the loading and confining pumps.

Specific Test Conditions

Six samples of Pierre II shale were tested in the six cells of the MESE; four of them were 13 mm long and two were 25 mm long samples. The applied confining pressure was $p_c = 20$ MPa. The saturation stage was conducted under a pressure $p_s = 10$ MPa applied at the bottom end (upstream) of the sample using a simulated Pierre II shale pore fluid [6]. The pressure transmission stage (hydraulic loading) was conducted under a pressure $p_m = 15$ MPa applied at the bottom end of the sample using the same solution as previously. Eventually, the chemical potential stage (chemical loading) was conducted under the same pressure p_m but with a highly concentrated solution of either potassium or sodium chloride.

PARAMETERS IDENTIFICATION

The aim is now to identify the unknown chemoporoelastic parameters, characterizing a shale-drilling fluid system, involved in the theoretical solution of the problem. In other words, we want to identify the parameters $\mathbf{c}$ of the model from experimental measurements $\mathbf{y}$ for given loadings $\mathbf{F}$. This process may be performed by using only a few characteristics of the system response curves such as extrema and position of these extrema, or by applying an iterative minimization procedure, using the whole set of experimental data [3].

Minimization Procedure

The identification of parameters from experimental data is a typical inverse problem. Generally, the direct problem is solved under the form

$$\mathcal{L}\left(\mathbf{u}\left(\mathbf{c}\right),\mathbf{c}\right)=\mathbf{F} \tag{1}$$

where $\mathcal{L}$ is a partial differential operator and $\mathbf{u}$ is the solution of the direct problem, the experimental measurements $\mathbf{y}$ being, in a sense, a discrete sampling of $\mathbf{u}$. Note that the parameters in (1) appear implicitly in the formulation of the direct problem. There is an explicit way to link the parameters of the direct problem $\mathbf{c}$ to the experimental measurements

$\mathbf{y}$ through a matrix operator $\mathbf{A}$ as follows

$$\begin{aligned} \mathbf{A} \quad : \quad & \mathcal{C}_{ad} \rightarrow \mathcal{Y} \\ & \mathbf{c} \rightarrow \mathbf{y} = \mathbf{A}(\mathbf{c}) \end{aligned} \tag{2}$$

where $\mathcal{C}_{ad}$ is the space of admissible parameters (corresponding to the unknowns of the inverse problem); $\mathcal{Y}$ denotes the space of measurements. The inverse problem may then be formulated as

$$\text{knowing } \; y \in \mathcal{Y}, \; \text{find } \mathbf{c} \in \mathcal{C}_{ad} \; \text{ such that } \; \mathbf{A}(\mathbf{c}) = \mathbf{y} \tag{3}$$

In this problem, $\mathbf{A}$ is known explicitly and is non-linear with respect to the parameters $\mathbf{c}$. Typically, when $\mathbf{A}$ is non-linear, the problem of identification becomes a problem of iterative minimization of a cost functional $\mathcal{J}(\mathbf{c})$ quantifying the distance between the measurements $\mathbf{y}$ and the predictions $\mathbf{A}(\mathbf{c})$ [1, 2]

$$\begin{aligned} & \min_{\mathbf{c} \in \mathcal{C}_{ad}} \mathcal{J}(\mathbf{c}) \\ \mathcal{J}(\mathbf{c}) \quad = \quad & \|\mathbf{A}(\mathbf{c}) - \mathbf{y}\| \end{aligned} \tag{4}$$

The form of the functional is a matter of choice; however, most of the time a least square procedure is used, i.e.,

$$\mathcal{J}(\mathbf{c}) = \|\mathbf{A}(\mathbf{c}) - \mathbf{y}\|^2 \tag{5}$$

Moreover, the functional form chosen may not be convex with respect to the parameters $\mathbf{c}$. Actually, the convexity and the geometry of the functional is partly related to the unicity of the inverse problem solution (ill-posedness. of the inverse problem).

Sensitivity Analysis

An analysis of the sensitivity of the theoretical solution to the parameters is carried out along with this iterative minimization procedure. A mathematical way to quantify the sensitivity of a solution $\mathbf{u}$ to a given parameter c_i is

$$\delta_{c_i} \mathbf{u} = c_i \frac{\mathrm{d}\mathbf{u}}{\mathrm{d}c_i} \tag{6}$$

The critical parameters are then brought out among all the parameters of the solution, i.e., the transport parameters which are the hydraulic diffusivity D_h, the apparent chemical diffusivity D_c and, above all, the chemical reflection coefficient $\mathcal{R}$ (membrane efficiency) [7]. The robustness of the algorithm is also estimated through several numerical tests on simulated data.

Eventually, a more pragmatic approach is deduced from this analysis, e.g., the chemical reflection coefficient is directly correlated with the pressure drop during the chemical loading. Coherence of the results obtained with both methods is shown.

References

[1] J. V. Beck and K. Woodbury. Inverse problems and parameter estimation: Integration of measurements and analysis. *Meas. Sci. Technol.* **9**, 839–847 (1998).

[2] M. Bonnet. Problèmes inverses. Course of Dynamique des Structures et Couplages in DEA. (2000).

[3] B. Lecampion. "Sur l'Identification Des Paramètres Des Lois de Comportement Des Roches Argileuses". PhD thesis, Ecole Polytechnique (Sept. 2002).

[4] F. K. Mody and A. H. Hale. A borehole stability model to couple the mechanics and chemistry of drilling fluid shale interaction. *J. Pet. Tech.* **1093** (Nov. 1993).

[5] E. V. Oort, A. H. Hale, and F. K. Mody. Manipulation of coupled osmotic flows for stabilization of shales exposed to water-based drilling fluids. SPE Annual Technical Conference and Exhibition, Dallas TX, USA, 1995 (1995).

[6] G. W. Schmidt. Interstitial water composition and geochemistry of deep gulf coast shales and sandstones. *Am. Ass. Pet. Geol. Bull.* **57**(2), 321–337 (Feb. 1973).

[7] A. J. Staverman. The theory of measurement of osmotic pressure. *Rec. Trav. Chim* **70**, 344–352 (1951).

[8] C. Tan, S. S. Rahman, B. G. Richards, and F. K. Mody. Integrated rock mechanics and drilling fluid design approach to manage shale instability. SPE/ISRM Eurock'98 (1998).

[9] C. P. Tan, C. J. Drummond, F. K. Mody, and U. A. Tare. High membrane efficiency water-based drilling fluids: Alternatives to invert emulsion fluids for drilling troublesome shale formations. SPE Asia Pacific Oil and Gas Conference and Exhibition, Melbourne, Australia, October 2002 (2002).

[10] C. P. Tan, B. G. Richards, and S. S. Rahman. Managing physico-chemical wellbore instability in shales with the chemical potential mechanism. SPE Asia Pacific Oil and Gas Conference and Exhibition, Adelaide, Australia, 1996 (1996).

[11] C. P. Tan, E. M. Zeynaly-Andabily, and S. S. Rahman. A novel method of screening drilling muds against mud pressure penetration for effective borehole wall support. IADC/SPE Asia Pacific Drilling Technology Conference, Kuala Lumpur, Malaysia, 1996 (1996).

MESOSCALE PREDICTIONS FOR THE THERMOMECHANICS OF GRANULAR ENERGETIC COMPOSITES[1]

Michael W. Crochet[2] and Keith A. Gonthier[3]
Mechanical Engineering Department, Louisiana State University, Baton Rouge, LA, USA 70803

Summary A finite-element analysis is performed to characterize the impact induced multiscale thermomechanical response of explosively coated aluminum microspheres. Emphasis is placed on accurately describing the dependence of bulk uniaxial stress wave structure, including local stress and temperature fluctuations occurring near intergranular and material contact surfaces, on explosive mass fraction and impact speed. The time-dependent bulk wave structure is obtained by averaging the mesoscale response over representative elementary volumes. This analysis is a preliminary step in assessing the impact sensitivity of energetic composites.

Extended Summary

Energetic composites consisting of small explosively coated metal grains (diameter < 50 μm) can potentially provide higher energy release rates than conventional explosives by combining the high exothermicity of metal-oxides ($q_{rxn} \approx$ 14 MJ/kg) with the rapid combustion of high-explosives ($\dot{M}_b \approx 5 \times 10^9$ kg/m^3/s). An important unresolved problem is determining conditions for which the metal and explosive energy release rates can be suitably coupled for maximum power generation. In addition to combustion rate coupling, it is equally important to fundamentally understand their thermomechanical response (i.e., sensitivity) to impact if they are to find use in practice. Experiments and modeling have long demonstrated that confined granular explosives can be detonated by low amplitude shocks due to the formation and interaction of reactive hot-spots at the grain scale [1, 2]. Hot-spots are regions of intense localized heating induced by plastic deformation, intergranular friction, and fracture. In this study, we perform a numerical analysis on large grain ensembles to characterize both the grain and bulk scale response of explosively coated aluminum grains to constant speed piston impact. The high-explosive modeled in this work is RDX ($C_3H_6N_6O_6$). We are particularly interested in identifying the effect of RDX mass fraction, grain size, interface adhesion strength, and piston impact speed on bulk uniaxial stress wave structure and hot-spot formation within the material. Combustion is ignored for simplicity.

The simulations are performed on a 2.0 GHz Pentium IV Windows Workstation using the finite-element package ABAQUS/Explicit. The explicit algorithm incorporates an adaptive grid technique for increased accuracy and utilizes numerical damping to mitigate dispersive oscillations in the neighborhood of shocks; thus, it is well-suited for impact analysis. For tractability and computational expediency, we perform a 2-D stress analysis for the planar impact of a constant speed piston with a composite material consisting of a large number of identifiable grains ($50 \leq N \leq 500$). As shown in Fig. 1(a), each grain initially has an outer radius R_o and an inner radius R_i, the latter being the dimension of the Al core. An important parameter in this analysis is the nondimensional RDX thickness defined by $\eta \equiv (R_o - R_i)/R_o$, where $0 \leq \eta \leq 1$ (here, $\eta = 1$ corresponds to pure RDX). The RDX mass fraction is related to η by

$$\lambda(\eta) \equiv \frac{m_{RDX}}{m_{RDX} + m_{Al}} = \frac{(1-\eta)^2}{(1-\eta)^2(\frac{\rho_{Al}}{\rho_{RDX}} - 1) - 1},$$

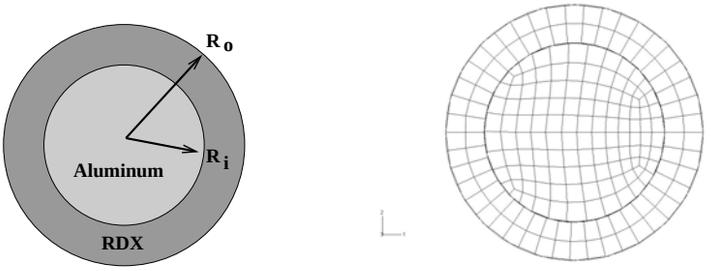
where ρ_{Al} and ρ_{RDX} are the mass densities of aluminum and RDX, respectively. A random grain packing arrangement is numerically generated by an iterative 2-D Monte Carlo algorithm that minimizes the gravitational potential energy of the granular system [3]. We use simple constitutive theories to facilitate interpretation of the results. The material models describe isotropic, elastic-perfectly plastic behavior. Other material properties used for aluminum and RDX are taken from Refs. [4, 5, 6].

Representative predictions for the grain scale temperature field are shown in Fig. 2 at time $t = 0.7$ μs for (a) adiabatic plastic heating of the grains and (b) plastic heating with thermal energy transport by conduction. All grains were initially at an ambient temperature of 300 K. Only fifty grains were used in this simulation; for each grain $R_o = 25$ μm and $\eta = 0.3$. The computational grid within a single grain is shown in Fig. 1(b); it consists of approximately 56 quadrilateral elements within the RDX layer and 120 elements within the aluminum core. Here, the piston impacted the grains from above at a constant speed of 150 m/s. The dispersed waves within the granular material generated by the impact have just reached the rear boundary at the time shown. A comparison of the two cases indicates that lower peak temperatures are predicted within the RDX layer near intergranular contact surfaces for the simulation that includes thermal energy transport; a peak temperature of 398 K is predicted for case (a) whereas a value of 373 K is predicted for case (b). These temperature predictions, while well below that needed for RDX ignition ($T_{ig} \approx 550$ K), suggest that thermal conduction may have a significant effect on the evolution of grain-scale temperature for low impact speeds. Higher temperatures are

[1]This research is sponsored by the U.S. Air Force Research Laboratory, MNME, Eglin Air Force Base, FL, under agreement number F08630-02-1-0002. The contract monitor is Mr. Chad Rumchik.

[2]Graduate Research Assistant. Email: *mcroch2@lsu.edu*

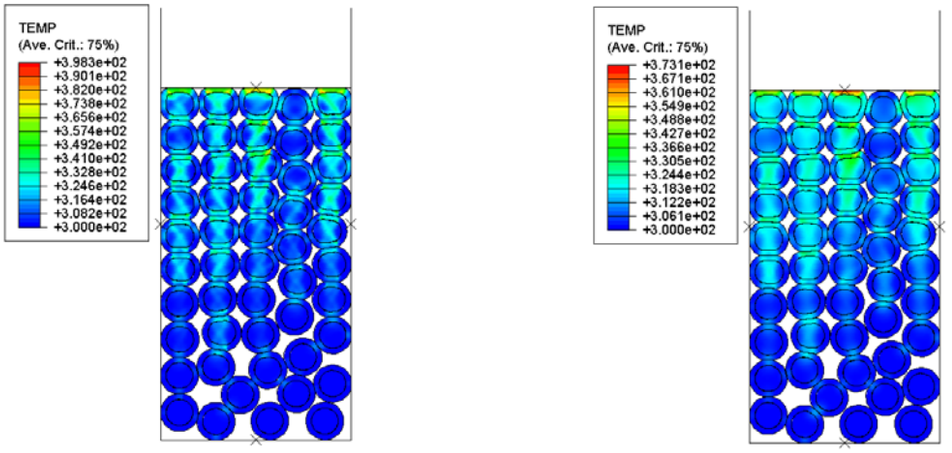
[3]Assistant Professor. Corresponding author. Email: *gonthier@me.lsu.edu*



(a) (b)

Figure 1: Schematic of (a) an explosively coated aluminum grain and (b) the computational grid within a grain used for the representative simulation.

expected for larger grain ensembles having more internal degrees of freedom due to significant stress chain formation. As piston speed increases, plastic heating will become more pronounced resulting in higher peak temperatures. There likely exists a critical piston speed beyond which thermal diffusion is inconsequential. A key objective of this work, that will be explored in depth, is to determine if the cool aluminum core can suppress hot-spot formation in large grain ensembles due to its comparatively high thermal conductivity. As such, these composites may exhibit significantly lower impact sensitivity than conventional explosives.



(a) (b)

Figure 2: Predicted temperature field for explosively coated aluminum grains for a piston speed of 150 m/s: (a) without thermal conduction and (b) with thermal conduction.

References

[1] McAfee J. M., Asay B. W., Campbell W., and Ramsay J. B.: Deflagration to Detonation Transition in Granular HMX, Proceedings of the Ninth (International) Detonation Symposium, 265-278, 1989.
[2] Gonthier, K. A.: Modeling and Analysis for Reactive Compaction of Granular Energetic Solids, *Comb. Science Tech.*, **175**:1679-1709, 2003.
[3] Lin C. L., and Miller J. D.: Pore Structure and Network Analysis of Filter Cake. *Chem. Eng. J.* **80**:221-231, 2000.
[4] Callister W. D., Jr.: Materials Science and Engineering: An Introduction, 6th Edition. Wiley, NY 2000.
[5] Gibbs T. R., and Popolato A.: LASL Explosive Property Data, University of California Press, CA 1980.
[6] Armstrong R. W., Ammon H. L., Elban W. L., Tsai D. H.: Investigation of Hot Spot Characteristics in a Energetic Crystals. *Thermochimica Acta* **384**:303-313, 2002.

THE STRUCTURE OF CONSTITUTIVE LAWS FOR POWDER METALLURGICAL COMPONENTS

Alan Cocks[*], Csaba Sinka[**] and Ludwig Schneider[*]
[*]Department of Engineering, University of Leicester, Leicester LE1 7RH UK
[**] Merck Sharp and Dohme Ltd., Hoddesdon, Hertfordshire, EN11 9BUUK

Summary Deformation and incremental theory models of the deformation of particulate materials are presented. A potential surface can be constructed for the deformation theory by determining the complementary work done along extremal paths in stress space. Yield surfaces for the incremental model nest inside these surfaces.

INTRODUCTION

In this paper we examine the structure of constitutive laws for the compaction response of particulate materials, where deformation results from the plastic deformation of the individual particles. Micromechanical modelling suggests a number of different structures for the constitutive laws. A deformation theory model is described which is based on the construction of surfaces of constant complementary work density in Kirchhoff stress space. Alternatively, an incremental anisotropic constitutive law can be constructed based on the existence of a yield surface, whose size and shape evolves as the powder compact is deformed plastically. It is demonstrated that the yield surfaces nest inside surfaces of constant complementary work density. The models can be calibrated using data generated in a triaxial cell. The nesting character of the different types of surface is demonstrated for a commercial steel powder.

THEORETICAL CONSIDERATIONS

Ponter and Martin [1] examined the relationship between incremental and deformation theories of plasticity and identified a set of extremum theorems which allow an appropriate deformation theory to be developed for a given assumed incremental theory. They demonstrate that fora given incremental plasticity model that there is exists a path, or paths, in stress space which maximises the complementary work $\overline{\omega}(\sigma_{ij})$, ie

$$\overline{\omega}_e(\sigma_{ij}) \geq \overline{\omega}(\sigma_{ij}) \tag{1}$$

The strain accumulated along the extremal path is then given by

$$\varepsilon_{ij} = \frac{\partial \overline{\omega}_e}{\partial \sigma_{ij}} \tag{2}$$

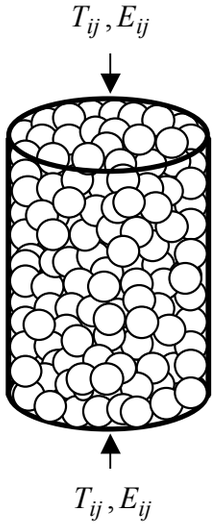


Figure 1 Random arrangement of spherical particles

The extremal paths effectively define a stable hyperelastic material which is less stiff than the inelastic material used to define it. Now consider a porous or particulate body which is made of the hyperelastic material, as shown in Figure 1, where T_{ij} represents the Kirchhoff stress and E_{ij} the true strain. It can be shown that

$$E_{ij} = \frac{\partial \overline{\Omega}_e}{\partial T_{ij}} \tag{3}$$

where $\overline{\Omega}_e = \frac{1}{V}\int_V \overline{\omega}_e dV$. It is possible to determine lower bounds to the potential $\overline{\Omega}_e$ in terms of any assumed internal starin field that is compatible with the macroscopic strain E_{ij} [2]. It can be further shown that if the incremental plasticity material is rigid-perfectly plastic, that the macroscopic yield surfaces for states generated from macroscopic extremal paths nest inside the surface of constant $\overline{\Omega}_e$. This is illustrated in Figure 2, where the yield surfaces and the surface of constant $\overline{\Omega}_e$ were constructed using the same material and geometric assumptions as Fleck [3].

EXPERIMENTAL STUDIES

Experimental studies have been constructed on a range of metal powders with particles of different size, shape and composition using a computer controlled triaxial cell [4] in which cylindrical samples are subjected to axial and radial stresses. Specimens have been loaded along either radial loading paths in stress or strain space to a prescribed level of complementary work per unit current volume (ie constant $\overline{\Omega}_e$). The specimens were then unloaded and the yield surface corresponding to the state created from each of the initial radial loading paths was determined by a probing technique in which the specimen was reloaded along a series of different paths until plastic strain was detected (further details are given in [4]). Figure 3 shows a surface of constant $\overline{\Omega}_e$ determined during the initial loading (the dashed curve) and the yield surfaces corresponding to a series of different initial loading paths (coloured solid curves) for a commercial steel powder. The yield surfaces nest inside the surface of constant $\overline{\Omega}_e$. Also the strain corresponding to a given loading path is normal to the surface of constant $\overline{\Omega}_e$, in agreement with eqn (3) [5]. As the ratio of deviatoric to mean stress increases the yield surface becomes more elongated in the direction of loading, in agreement with the micromechanical model. Experimentally, however, these surfaces can be approximated as ellipses. As the compact is deformed further to higher levels of stress and strain the elliptic yield surfaces grow and their aspect ratio decreases, until at high relative densities they virtually fill the surface of constant $\overline{\Omega}_e$, ie the yield surface is not very sensitive to the detailed loading path. Schneider [4] has described a constitutive model for the evolving yield surface which describes the evolution of the size, aspect ratio and orientation in terms of the accumulated plastic strain.

The deformation theory model uses the initial dense random packed state of the particles as the reference configuration, which is macroscopically isotropic, thus the constitutive response can be expressed in terms of the stress and strain invariants. An incremental model which follows the evolving yield surface must take into account the anisotropic nature of the evolving microstructure. This results in a more complex structure of the constitutive model. In many practical powder metallurgical manufacturing procedures elements of material see smoothly changing monotonically increasing stress states, allowing the use of a simple deformation theory model.

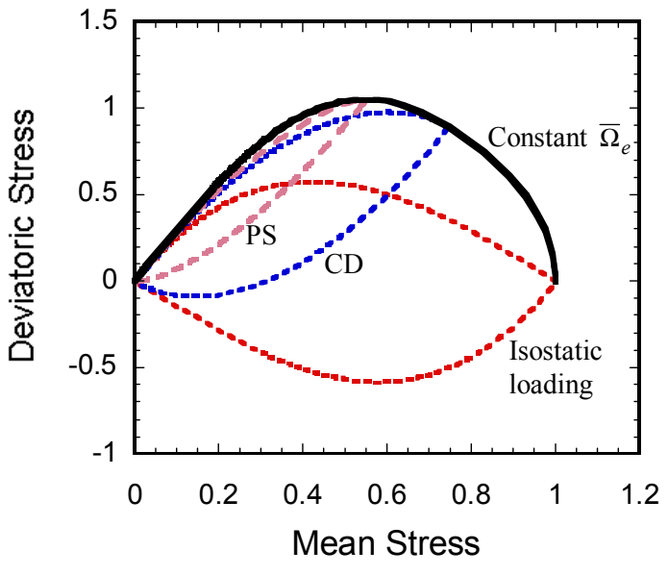


Figure 2 Yield surfaces for the particulate material of Figure 1generated under isostatic, pure shear (PS) and simulated closed die compaction (CD) which nest inside the surface of constant $\overline{\Omega}_e$.

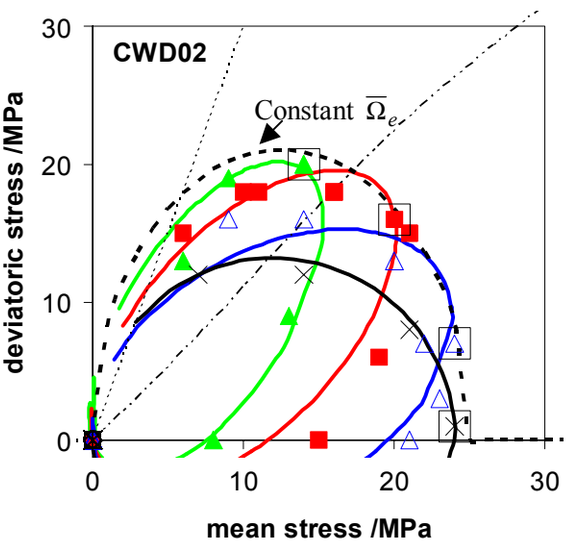


Figure 3 Experimental yield surfaces and a surface of constant $\overline{\Omega}_e$ for a commercial steel powder during the early stages of compaction.

References

[1] Ponter, A.R.S. and Martin, J.B., *J. Mech Phys. Solids*, 1972, **20**, 281.
[2] Cocks, A.C.F. and Sinka, I.C., to appear
[3] Fleck, N.A., *J. Mech Phys. Solids*, 1995, **43**, 1409.
[4] Schneider, L.C.R. PhD thesis, University of Leicester, 2003
[5] Sinka, I.C. and Cocks, A.C.F., to appear

EXPERIMENTAL CHARACTERISATION AND NUMERICAL MODELLING OF DENSITY DISTRIBUTION IN TABLETS

I.C. Sinka*, J.C. Cunningham** and A. Zavaliangos***
*Merck, Sharp and Dohme Ltd., Hertford Road, Hoddesdon, Hertfordshire EN11 9BU, UK
**Merck and Co., Inc., West Point, PA 19486, USA
*** Department of Materials Engineering, Drexel University, Philadelphia, PA19104, USA

INTRODUCTION

Density gradients in pharmaceutical tablets are important for they affect the local properties of the material which in turn influence the mechanical response of the tablet during post-compaction operations, such as coating, packaging, transport, storage or use.
Experimental density maps obtained using techniques such as indentation hardness and X-ray computed tomography (CT) are presented.
Constitutive models have been developed to describe the compaction behaviour of the powder and the friction interaction between powder and die wall. The models were calibrated for microcrystalline cellulose using data from a compaction simulator and a die instrumented with radial stress sensors. The results are implemented in the finite element program ABAQUS/Standard. The predictions of the model for a selection of tablet images and given die wall lubrication conditions are compared with the experimental density maps generated for various stages during compaction.
The agreement between the experimental data and simulation results gives confidence in the predictive capabilities of the model. The applicability of the technique to formulation design, process development, tablet image and tool design is discussed.
The experimental and numerical methodologies presented are applicable for any powder system in general.

EXPERIMENTAL METHODS

Indentation tests

Indentation hardness tests were carried out on cross-sections of tablets manufactured under controlled die wall lubrication conditions. Density distribution maps were obtained using an empirical relationship [1] between indentation hardness and density.

X-ray CT

For a given material the X-ray attenuation energy is approximately proportional to the density. X-ray CT density maps obtained using a 250 kV X-ray cabinet (X-Tek Systems) with TOMOHAWK CT [2] (AEA Technology) are presented for two capsule shaped tablets having different curvatures, break-line and embossing.

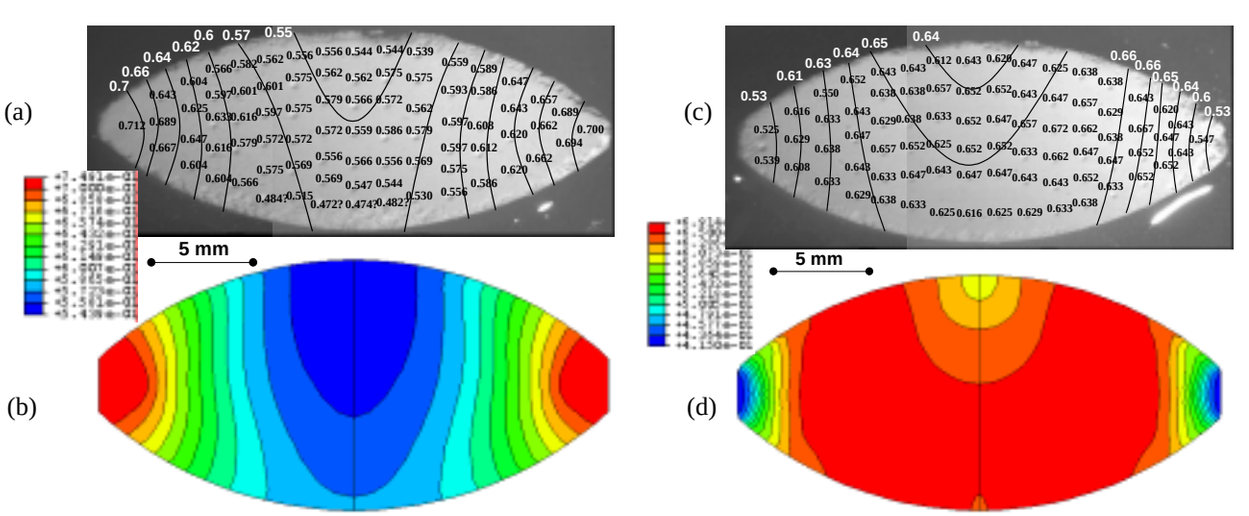


Figure 1 Indentation hardness density maps for tablets compacted in unlubricated (a) and lubricated (c) die, respectively and the corresponding numerical predictions (b) and (d), respectively.

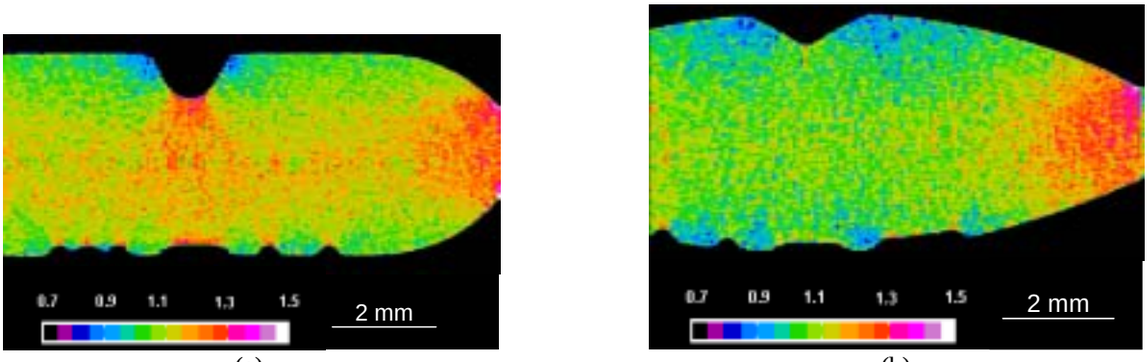
RESULTS AND DISCUSSION

Indentation hardness

Experimental and numerical results presented in Figure 1 indicate that by manipulating the die wall friction conditions opposite density distribution trends are induced.

X-ray CT

X-ray CT for capsule shape tablets with different curvatures and break-line geometry (Figure 2) indicate the importance of the details of the tablet geometry.
Quantitative and qualitative results from friability, abrasion and disintegration tests indicate that the low density zones around the lettering (at the bottom of the tablets) or close to the break-line are prone to erosion.



(a) (b)

Figure 2 X-ray CT density images

FACTORS INFLUENCING TABLET COMPACTION

Numerical analysis of tablet compaction [3] require detailed knowledge of:

- Constitutive behaviour of powder
- Friction between powder and die wall
- Geometry of die and punches
- Sequence of punch motions
- Initial conditions from die fill

CONCLUSIONS

The factors influencing tablet compaction were characterised experimentally and numerical analysis was carried out. The model predictions are in good agreement with the experimental data.
It is shown that different die wall lubrication conditions induce opposite density distribution trends in identical tablets (weight, height and material) and this affects the break force, failure mode and friability: it is then demonstrated that for a given average tablet density the break force and failure mode are not unique [4]. Also, tablet regions having lower density locally have higher propensity for damage.
The application of numerical analysis for optimising tablet formulation, process development and tablet image is discussed.

References

[1] Sinka, I.C., Cunningham, J.C. and Zavaliangos, A.: The effect of wall friction in the compaction of pharmaceutical tablets with curved faces: A validation study of the Drucker-Prager Cap model. *Powder Technology*, **133**: 33-43, 2003.
[2] Sinka I.C., Burch S.F., Tweed J.H. and Cunningham J.C.: Measurement of density variations in tablets using X-ray computed tomography; *International Journal of Pharmaceutics*, In press, available online 14 January 2004.
[3] Cunningham, J.C., Sinka, I.C. and Zavaliangos, A.: Analysis of tablet compaction. Part 1 – Characterisation of mechanical behaviour of powder and powder/tooling friction. *Journal of Pharmaceutical Sciences*. To appear.
[4] Sinka, I.C., Cunningham, J.C. and Zavaliangos, A.: Analysis of tablet compaction. Part 2 – Finite element analysis of density distribution in convex tablets. *Journal of Pharmaceutical Sciences*. To appear.

Stresses and Fractures in Capillary-Porous Materials under Drying

Stefan Jan Kowalski and **Jacek Banaszak**
Poznań University of Technology, Institute of Technology and Chemical Engineering
Pl. Marii Skłodowskiej-Curie 2, 60-965 Poznań, Poland

Extended Summary

Introduction. Fracture of materials during drying processes is a well-known phenomenon in industry drying, as for example, in ceramics industry, wood industry, etc. Efforts are made to minimize this negative effect. This paper is a contribution to this issue. Main aim of this paper is a theoretical and experimental analysis of fracture risk in saturated capillary-porous materials under drying. In particular, we want to show that the acoustic emission method (AE) may serve for identification of fracture intensity accruing in such materials and in this way to prevent the material against its destruction.

The reason for fracture is the shrinkage phenomenon and the drying induced stresses. In this paper, the drying induced stresses are detected theoretically on the basis of mechanistic model of drying. The boundary-value problem for cylindrically shaped kaolin sample is solved under the assumption that the saturated kaolin is viscoelastic and obeys Maxwell model. The distribution of the stresses in the cross-section of the cylindrical sample and the time evolution of the stresses on the cylinder surface (maximal) are presented for different temperatures of the drying medium (air).

The cylindrical kaolin sample of the same dimensions as that analyzed theoretically was dried convectively in different temperatures in the chamber drier. The AE set-up installed in the drier was used for measurement *on line* of the number of AE events rate (the number of AE occurrences per 30 s time intervals) as well as the energy of the individual occurrences and the total energy emitted by the material under drying. Parallel, the so-called drying curves illustrating the time-change of moisture content in the sample were appointed by making use of the electronic balance and software, which registered and drawn the curves automatically. The drying curves allowed us to identify at which periods of the drying the fracture phenomenon became the most intensive.

Comparing the history of AE energy emitted from the material during drying with the theoretically appointed curves of stress evolution allowed to state that the most intensive fracture of the material occurred at those moments at which the stresses reached maximal values. As the most amount of energy is released due to micro- and macro cracking of the material structure, it denotes an immediate correlation between the growth of stresses and the intensification of fracture phenomena.

Mechanistic model of drying. The thermomechanical model of drying used for analysis of the drying induced stresses was developed on the basis of mechanics of continua (Kowalski, 2003). The differential equation describing the alteration of moisture content in dried body follows from the mass balance and the rate equation of mass transport for moisture. The latter relates the moisture flux with the gradient of moisture potential $\mu(T, \varepsilon, \theta)$, which is a function of temperature T, the body volume deformation ε, and the moisture content θ (mass of water referred to mass of dry body).

The distribution and evolution of temperature in the body under drying follows from balance of energy, The energy equation reduces to the balance of entropy $s(T, \varepsilon, \theta)$ after application of Gibbs identity. The heat flux supplied to the body consists of two parts: conductive and convective. The later expresses the transport of heat by moisture flux. In our considerations concerning kaolin, however, we applied the empirical observation that the most shrinkage of this material and the maximal stresses occur during the so called constant drying rate period, during which the temperature of the body is constant in natural way. Therefore, we have confined our theoretical analysis to this period and assumed constant but different in various drying processes temperature of the body.

The stresses $\sigma_{ij}(T, \varepsilon, \theta)$ in the body under drying are determined from the condition of mechanical equilibrium of internal forces, $\sigma_{ij,j} = 0$, and the Maxwell physical relation

$$\dot{\sigma}_{ij} + \frac{M}{\eta}\sigma_{ij} = 2M\dot{\varepsilon}_{ij} + \left(\frac{A}{K}\dot{\sigma} + \frac{\xi}{\chi}\frac{M}{\eta}\sigma\right) - \frac{2}{3}M\dot{\varepsilon}^{TX}\delta_{ij}, \qquad \text{where} \qquad \varepsilon^{TX} = 3\left(\alpha_T\vartheta + \alpha_X\theta\right),$$

with $\vartheta = T - T_r$ and $\theta = X - X_r$ denote the relative temperature and the moisture content. The former is assumed constant in this paper and the latter is determined from the differential equation mentioned above. In the Maxwell relation ε_{ij} denotes the total strain tensor and ε^{TX} is the volumetric strain caused by the temperature and moisture content alterations, α_T and α_X are the coefficients of thermal and humid expansion, $K = 2M/3 + A$,

$\chi = 2\eta/3 + \xi$, and M and A are the elastic and η and ξ the viscous counterparts of Lame constants for dried material.

The moisture content distribution in the cylindrical sample and its time evolution were calculated by making use of the finite difference method (Crank-Nicholson scheme) with taking into account the initial and boundary conditions. The stresses in viscoelastic cylinder were determined analytically due to correspondence principle between elastic end viscoelastic behavior of materials, and by making use of the Laplace transforms and the Borel's convolution formula. The stresses in elastic cylinder were determined by the assumption that the cylindrical sample is long enough (problem of axial symmetry).

Experimental studies. In order to test the stress generation in kaolin under drying, the drying processes were carried out in five temperatures of the drying medium: 120°C, 100°C, 85°C, 75°C and 45°C and of the relative humidity 3.9%, 4.2%, 4.6%, 4.9% and 7.9% respectively. The samples were made of the composite consisting of kaolin (70%) and sand (30%), and were molded into cylinders of external radius 0.025 m and height 0.09 m (Fig. 1). The samples were dried convectively in the chamber drier, in which the acoustic emission transducer, the balance, the temperature and humidity sensors were installed. The kaolin sample placed in the drier constituted the generator of AE signals during drying. These signals were transported as elastic waves to the boundary of the sample where they were detected by the piezoelectric transducer. The transducer transformed the AE signals into electric impulses, which after suitable filtration and amplifying were registered by the computer thanks to software compatible with the canvassing card GPIB, and observed and the oscilloscope as well. The balance registered the moisture removal in prescribed time periods with accuracy of 0.01 g.

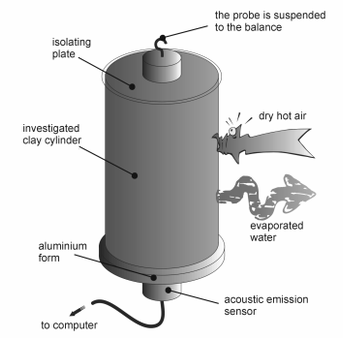


Fig. 1. The clay sample

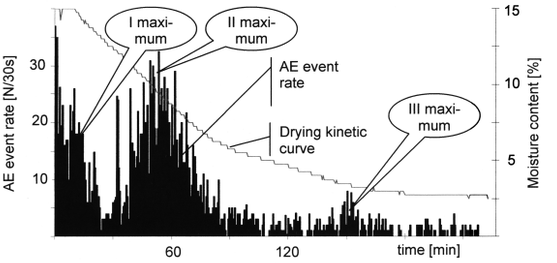


Fig. 2. AE signals and the curve of drying

Fig. 2 presents the registered AE signals and the removal of moisture content in time for drying at temperature 100 °C and 4.2% humidity of the air.

Fig.3a presents the rate of AE events and Fig.3b the evolution of circumferential stresses at the cylinder surface for drying in different temperatures

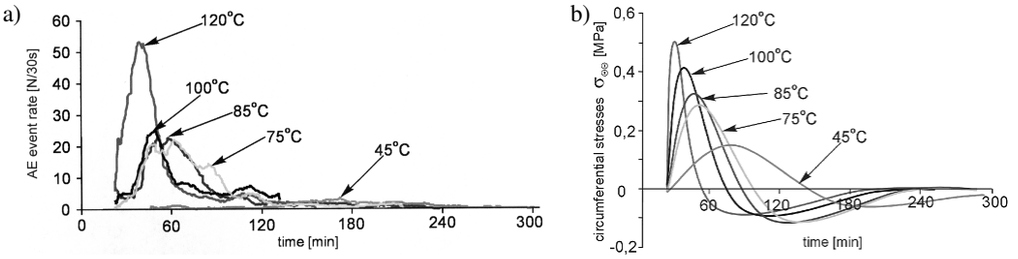


Fig. 3.Drying of clay cylinders in different temperatures a) the rate of AE events during drying b) evolution of circumferential stresses at the cylinder surface

Conclusions. The AE event rate descriptor illustrates the evolution of the drying induced stresses. The maximal values of the AE event rates depend on the drying temperature and coincide with the maximal stresses. Their peaks are greater and appear quicker in time for higher temperatures.

The AE energy descriptor can be used for the statement whether or not the dried product suffer the fracture. In those moments when the macrocracks occur, sometimes visible with the naked eye, the total AE energy curves manifest a rapid increase. The macrocracks were observed, particularly on the cylinder surface, when the drying conditions were very hard.

References

Kowalski S.J., Thermomechanics of drying processes, Springer Verlag, 2003;

Kowalski S.J., Banaszak J., Rajewska K., Acoustic emission in materials under drying, Inżyniria i Aparatura Chemiczna, **42**(34), 2003, (in Polish);

STABILITY ANALYSES OF ELECTROSTATIC TORSIONAL RF MEMS SWITCH

Ya-Pu Zhao[1], Jian-Gang Guo
State Key Laboratory of Nonlinear Mechanics (LNM), Institute of Mechanics, Chinese Academy of Sciences, Beijing 100080, People's Republic of China

Summary The stability analyses of the electrostatic torsional RF MEMS (radio frequency micro-electro-mechanical-systems) Switch are presented in the paper with the consideration of van der Waals (vdW) force. The critical applied voltage and tilting angle are calculated by static equilibrium equations. Furthermore, the dynamic behavior of RF MEMS switch is studied by the qualitative analysis of nonlinear equation of motion.

INTRODUCTION

Pull-in phenomenon is an important characteristic in the RF MEMS or NEMS switches. The actuating forces inducing pull-in include electrostatic force, vdW force, Casimir force and other surface forces. The analyses of pull-in phenomenon on torsional microactuators have been reported in some literatures [2-5], and the analytical models have been derived for the calculation of the pull-in voltage and tilting angle. The torsional NEMS actuator driven by Casimir force in experiments is introduced [1]. However, those researches did not consider vdW force. VdW force can be approximately neglected in MEMS, but play important roles in NEMS. Lin and Zhao [6] studied the dynamics behavior of nanoscale electrostatic parallel-plate RF switches, considering vdW force.

The SEM (Scanning Electron Microscope) image and 1 Degree of Freedom schematic of the torsional RF Switch [4] are shown in Fig.1. The angle of torsion φ is the only degree of freedom. When a voltage between one of the actuator electrodes and the movable plate is applied, the electrostatic force between them will produce an electrostatic torsion $M_{electr.}$ [4], simultaneously, vdW force between two parallel plates will produce vdW torsion M_{vdW}. When the plate rotates, the torsional beam will produce the mechanical restoring torque $M_{restoring}$ [4]. In addition, due to inertia and damping, there exists damping and inertia torque $M_{damping}$ and $M_{inertia}$ [4].

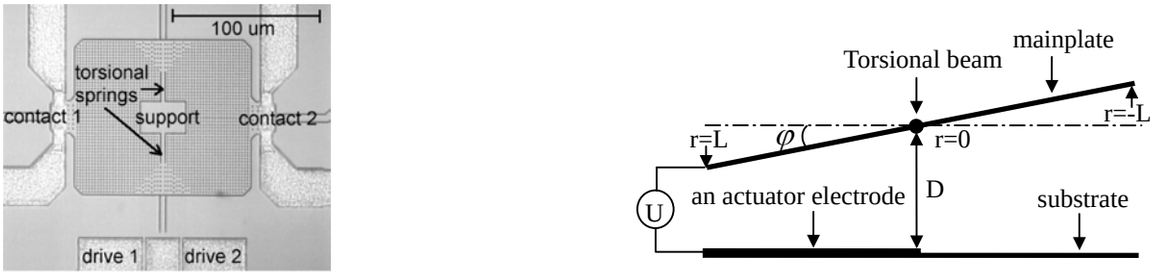


Fig.1. Topview micrograph and the schematic side view of the MEMS RF Switch

THEORICAL ANALYSIS OF STABILITY

Static equilibrium

In the static equilibrium, the equation with vdW torsion can be derived by

$$M_{electr.} + M_{vdW} = M_{restoring} \tag{1}$$

[1] To whom all correspondence should be addressed. Phone: +86 10 6265 8008; Fax: +86 10 6256 1284;
E-mail: yzhao@lnm.imech.ac.cn (Ya-Pu Zhao).

The relation of applied voltage and tilting angle can be obtained by Eq.(1), furthermore, the critical voltage and tilting angle can be calculated. The critical tilting angle is not independent on the sizes of structures as shown in [4], but varies with the scales of structures, especially in nano-scale. Simultaneously, the error of critical voltage is large for the cases with and without the consideration of vdW torsion. It is because that vdW force plays an important role when the scale of device is sufficient small. When the gap between two plates gets further small and reaches critical value, the pull-in occurs even without the applied voltage.

Qualitative analysis of equations of motion

The dimensionless nonlinear equation of motion including vdW torsion can be obtained by

$$M_{electr.} + M_{vdW} = M_{restoring} + M_{damping} + M_{inertia} \tag{2}$$

The qualitative analysis of autonomous system of Eq.(2) shows that there are two equilibrium points when applied voltage exists, and three equilibrium points when applied voltage doesn't exist. For the first case, two equilibrium points are respectively a stable center point or focus point, and an unstable saddle point. The phase portraits connecting two equilibrium points on the phase plane show periodic, heteroclinic and homoclinic orbits (as shown Fig.2a and 2b). It can be concluded that the movable plate makes periodic oscillation or convergent oscillation near the stable equilibrium point and snaps down the substrate beyond the saddle point. For the second case, three equilibrium points are respectively a stable center point or focus point, and two unstable saddle points. The phase portraits connecting three equilibrium points on the phase plane show periodic, heteroclinic and homoclinic orbits (as shown Fig.2c and 2d).

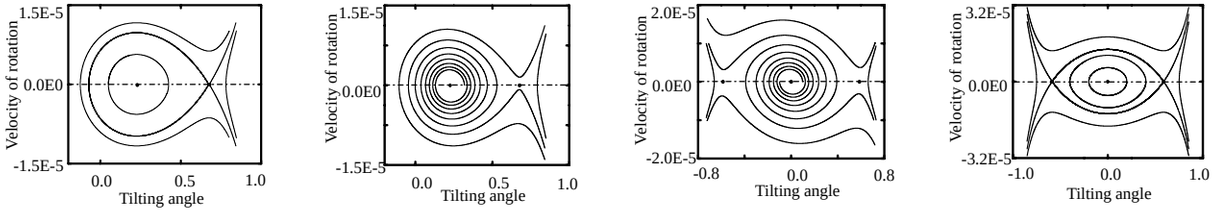


Fig.2 The phase portraits of the torsional RF MEMS switch with vdW torsion: (a) with voltage and without damping; (b) with voltage and damping; (c) without voltage and with damping; (d) without voltage and damping.

CONCLUSION

When the scales of structures are sufficient small, vdW force should be considered at the design of MEMS/NEMS actuator. Analysis shows that the inherent instability of the RF switch is dependent on the scales of structures. The critical tilting angle varies with the sizes of devices. The critical pull-in voltage has large relative error for sufficiently small scale if vdW torsion is neglected. Moreover, the pull-in can still happen without the driving voltage when the critical gap is reached. Furthermore, the qualitative analysis of the equation of motion shows that the equilibrium points of the corresponding autonomous system include stable focus point and center point, as well as unstable saddle point. The phase portraits show the periodic, heteroclinic and homoclinic orbits.

References

[1] H.B. Chan, V.A. Aksyuk, R.N. Kleiman, D.J. Bishop, F. Capasso: *Science*, vol. 291: 194-197, Mar. 2001.

[2] Y. Nemirovsky, O. Degani: *J. Microelectromech. Syst.*, vol. 10: 601-615, 2001.

[3] O. Degani, Y. Nemirovsky: *J. Microelectromech. Syst.*, vol. 11: 20-26, 2002.

[4] R. Satter, F. Plötz, G. Fattinger, G. Wachutka: *Sens. Actuators A*, vol. 97-98: 337-346, 2002.

[5] F. Plötz, S. Michaelis, R. Aigner, H.-J. Timme, J. Binder, R. Noé: *Sens. Actuators A*, vol. 92, no. 1-3: 312-317, 2001.

[6] W.H. Lin, Y.P. Zhao: *Chinese Physics Letters*, vol. 20, no.11: 2070-2073, 2003.

IMPROVEMENT OF POSITIONING ACCURACY OF DELTA PARALLEL ROBOT

Dominique Deblaise, Cédric Baradat, Patrick Maurine and Vigen Arakelian
Laboratoire de Mécanique Appliquée, Automatique et Géomécanique, EA3218
Institut National des Sciences Appliquées (INSA)
20, Avenues des buttes de Coësmes, CS 14315, 35043 Rennes Cedex, France

Introduction

Parallel manipulators show better stiffness, positioning accuracy and load-carrying capacity than serial manipulators [1]. They can operate at a higher velocity and acceleration. In recent years, more attention has been paid to the increasing number of possible industrial applications, such as manipulation, packing, assembly processes, motion simulation and milling machines [2]. Now there are many other promising applications in medical robotics and the machine-tool industry, which require high positional accuracy. In other words, more precise reproduction of predetermined end-effector positions, which is strictly related to a higher manufacturing accuracy. For this purpose, in the present study, a new method of geometrical calibration is developed, which takes into account the elasticity of links.

Problem statement

The aim of the geometrical calibration is to identify the real values of the parameters of a geometrical model which allows the improvement of the positioning accuracy of the robot [3,4]. The positioning errors of the end-effector have two principal origins:

- Lack of knowledge of the real robot geometry due to the manufacture tolerances and assembly errors of all its components.
- Some physical aspects such as the elasticity of links, the clearance in the joints and the temperature variations.

At the first, the robot structure is considered a rigid-body system. The end-effector location is calculated by the forward kinematic (FK) model. The initial calibration process consists of the determination of the vector **K** of the geometrical parameters which minimizes the difference: $Z_r - Z_m(\mathbf{K})$, where Z_r is the real moving plate altitude measured by an external device and $Z_m(\mathbf{K})$ is the nominal altitude calculated by the forward kinematic model. Such a calibration is a nonlinear optimization problem which is solved for $k=3p$ number of measurement points, where p is the number of the identified parameters of the examined structure. Then, the errors produced by the elasticity of links are used in the geometrical calibration process and final correction is achieved by taking into account these errors.
Let us examine the efficiency of such a solution for the Delta parallel robot.

Modeling of the Delta robot

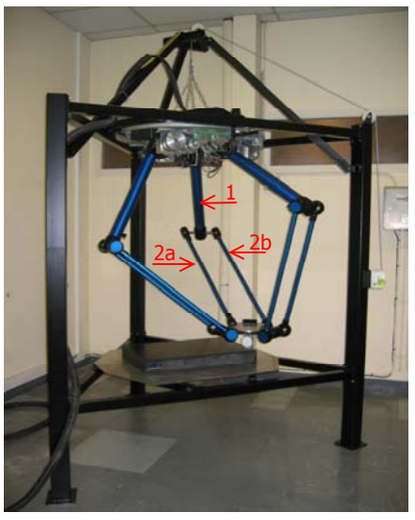


Fig.1. Delta robot (LMA2G, INSA Rennes)

The displacement of the end-effector of the Delta robot is the result of the movement of the three articulated arms mounted on the base, each of which are connected to a pair of parallel rods [5,6] (Fig.1,2). The three orientations are eliminated by joining the rods in a common termination and the three parallelograms ensure the stability of the end-effector.

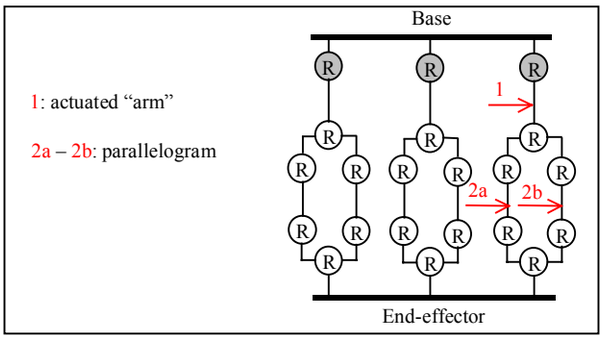


Fig.2. Joint-and-loop graph of the Delta robot.

This configuration of the robot has three degrees of freedom. The plate end-effector stays constantly parallel to a reference plane (base) and cannot rotate about the axis perpendicular to this plane. To simplify the model of the robot let us consider that the parallelograms are perfect which allows us to describe the structure with a complete and independent model having 18 geometrical parameters (7 parameters which describe the link length errors and 11 parameters which describe the orientation errors) [7].

STEP 1. Calibration of the Delta robot: rigid body model

First, we carried out a geometrical calibration with 82 measurement points, uniformly distributed in the restricted area of the robot workspace (700x500x400 mm). In this case, the calibration was realized without taking into account the elasticity of links. A comparative analysis was accomplished for the end-effector positions along the Z axis. The measurements after calibration were compared with the forward kinematic model, which was calculated for the nominal and corrected parameters. The obtained results show a significant improvement in the robot accuracy (Table 1, see Step 1). The comparative analysis of these results also showed that the difference between the identified and real values is important (see Table 2) . It is obvious that such an important difference cannot be due only to the geometrical effects, so we decided to get to the root of this problem and take into account the elasticity of links.

Table 1

Before calibration (Not corrected FK)	Geometric calibration (Step 1)	Corrected calibration (Step 2)
1060 µm	13,8 µm	12,6 µm

Table 2

Arms length	L1 (mm)	L2 (mm)	L3 (mm)
Nominal values in mm	950	950	950
Geometric calibration (Step 1)	953,58	955,21	953,12
Corrected calibration (Step 2)	952,32	954,11	952,31
Identification improvement	35%	21%	26%

STEP 2. Corrected calibration of the Delta robot: flexible model

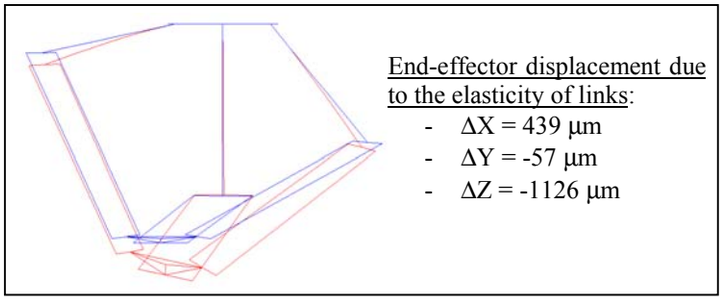


Fig.3. Rigid-body and flexible models.

In this case, we introduced the flexibility of links in the calibration process. For this purpose, the displacements of the end-effector were calculated by taking into account the elasticity of links (see Fig.3). A finite element model developed on the Castem software, allowed us to calculate the deviation of the end-effector positions along the Z axis with great precision. This deviation represents the errors due to the elasticity of links. The geometrical model of the robot was then studied, which took into account this deviation and allowed us to improve the calibration process. Such a modification shows, that for the second step, the vector **K** of estimated parameters better corresponds to the structure image.

Thus, by compensating for elastic deformations, the positioning accuracy is improved by 9% (Table 2). Also, the difference between identified and real parameters is significantly reduced, meaning that the obtained robot model is more realistic.

Conclusions

This paper deals with a solution to the problem of improving the positioning accuracy of the Delta robot. The suggested approach is based on the geometrical calibration, which is carried out by the integration of the elastic deformations structure in the calibration process. Such a solution allows us to obtain a more exact geometrical model and consequently, to improve the positioning accuracy of the robot. We hope that this new solution will find a broad application in high-accuracy robotics.

References

[1] Merlet J.P.: Les Robots Parralèles. Hermes, Paris 1997.
[2] Neugebauer R. Development Methods and Application Experience of Parallel Kinematics. Verlag Wissenschaftliche Scripten, Zwickau (Germany) 2002.
[3] Khalil W., Dombre E.: Modélisation identification et commande des robots, Collection Robotique, Hermes, Paris 1999.
[4] Visher P., Clavel R.: Kinematic Calibration of the Parallel Delta Robot. *J Robotica*, 16:207-218, 1998.
[5] Clavel R.: Conception d'un robot parallèle rapide à 4 degrés de liberté. *PhD-thesis* N° 925, EPFL, 1991
[6] Clavel R.: Device for displacing and positioning an element in space. Patent EP0250470 B1, 07.01.1988.
[7] Baradat C. and all. : Artefact Based Calibration of Parallel Kinematics Machines. The 35th International Symposium on Robotics (ISR-2004), March 23-26, Paris (to be published).

TECHNISCHE UNIVERSITÄT MÜNCHEN

Angewandte Mechanik

Univ. Prof. Dr.- Ing. Friedrich Pfeiffer i.R.

Dynamics and Control of a hydraulically driven Boring Plant

Friedrich Pfeiffer
Lehrstuhl für Angewandte Mechanik, TU-München
Boltzmannstrasse 15, D-85748 GARCHING
Tel. 0049-89-28915200
Fax 0049-89-28915213
e-mail: pfeiffer@amm.mw.tum.de

In civil and underground engineering very large boring plants are used for drilling holes into the ground having a size of up to 30 m in depth and .5 m in diameter. Today such machines possess hydraulically driven cable winches, which control both, the lifting and the lowering of the heavy drilling tools (Fig. 1).One problem of controlling the machine consists in an interaction of the hydraulic control and the mechanical system dynamics generating sometimes self-excited oscillations with large amplitudes. Another problem is connected with the groundwater contact when the drilling tool comes down rather fast. Both phenomena may lead to slack cables, which must be avoided at all costs.

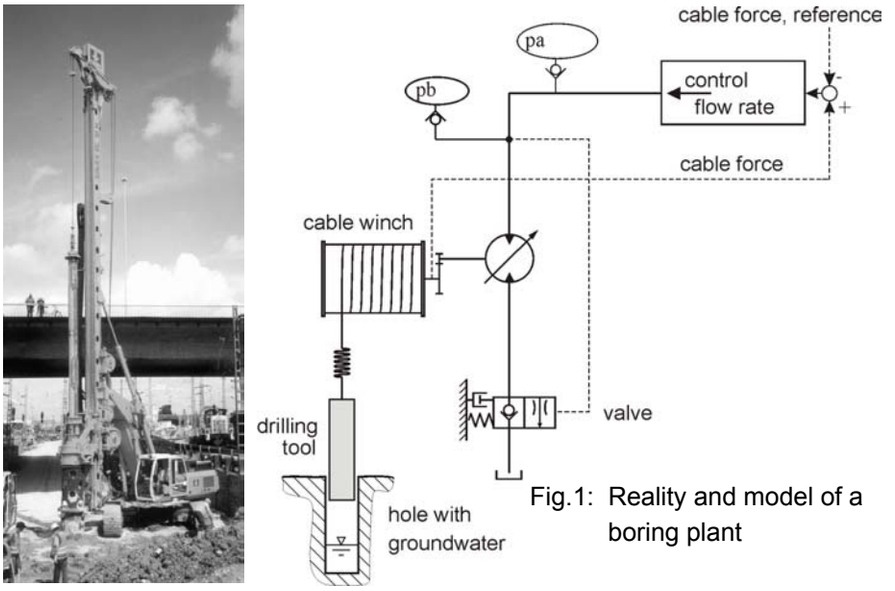


Fig.1: Reality and model of a boring plant

The first step for solving these problems consisted in considering the hydraulic and mechanical model of Fig. 1 and in deriving the corresponding equations of motion /1,2/. For this we must take into account the hydraulic and the mechanical degrees of freedom together with the appropriate bilateral and unilateral constraints as given by the configuration itself as well as by hydraulic or mechanical non-smooth features. We come out with a typical set of equations of motion for non-smooth systems containing the differential equations, some equality constraints, for example Kirchhoff´s equations, and some set-valued force-laws in the form of complementarity conditions /3/. On the numerical side we use the one-step-method Runge-Kutta-3/4 in combination with a solver of the complementarity problem (LCP) according to Lemke /1/. All non-smooth events are interpolated and then the integration started anew. A solution of these equations

demonstrates the problems as discussed above, namely large amplitude nonlinear vibrations and the impact of the drilling tool with the groundwater /1/.

The requirements with respect to a control system solving these problems are the following:

- Stability of the tool moving in the air or in the groundwater, which means significant reduction of all types of possible vibrations.
- Very fast control reactions with respect to impacts on the surface of the groundwater or on the ground itself.
- Large tool velocities for all phases of operation.

The basic structure of the control is PID, but with the control matrices adapted to the three phases, motion in the air, impact on the water surface, motion in the water /4/. All problems as discussed above could be removed. Figure 2 stands for quite a lot of simulations and experiments, which all confirm the taken measures. It depicts the effectiveness of an adaptive control structure for all phases of the motion: large cable forces in the air and small ones in the groundwater, an impact at the water surface and excellent control in the adaptive case, bad control with a controller possessing constant coefficients. The new control system has been implemented into the process control unit of the boring plant, existing machines have been modified correspondingly, all newly produced machines (by a Bavarian company) have it as standard. Since then problems of the above type did not occur any further.

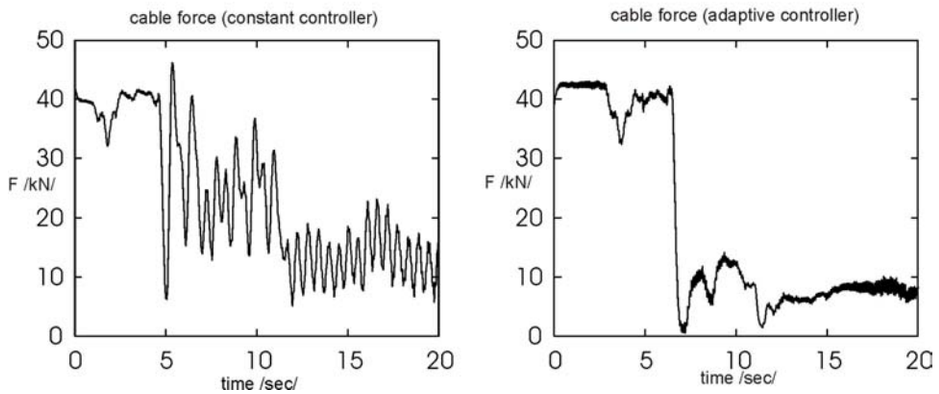


Fig. 2: Measurements without and with adaptive control

Literature

/1/ Borchsenius, F.: Simulation ölhydraulischer Systeme, Fortschritt-Berichte VDI, Reihe 8, Nr. 1005, VDI-Verlag Düsseldorf 2003

/2/ Borchsenius, F., Pfeiffer, F.: Modellierung hydraulischer Steuersysteme, 2. Internationales Fluidtechnisches Kolloquium, Dresden 2000, pp. 467-480

/3/ Pfeiffer, F., Glocker, Chr.: *Multibody Dynamics with Unilateral Contacts*, John Wiley & Sons, New York, 1996

/4/ Slotine, J., Li, W.: *Applied Nonlinear Control*, Prentice Hall, Eaglewood Cliffs, 1991

INVESTIGATION OF POWERFULL AND HIGH PRECISION PIEZOELECTRIC ACTUATOR FOR TWO-DIMENSIONAL POSITIONING

Piotr Vasiljev*, Dalius Mazeika**, Genadijus Kulvietis**
*Vilnius Pedagogical University, Department of Technical Subjects, LT-2004 Vilnius, Lithuania
**Vilnius Gediminas Technical University, Sauletekio av. 11, LT-2040 Vilnius, Lithuania

Summary The investigation of novel design high precision piezoelectric actuator for the object positioning in two-dimensional space is presented. Piezoelectric actuator has main advantages of large driving force, high dynamic resolution and short response time. Optimization analysis of piezoelectric actuator and numerical investigation using finite element method were done. Results of numerical and experimental research were compared.

INTRODUCTION

A lot of devices based on the different techniques are used for the object positioning in two-dimensional space. Piezoelectric actuators are advanced in this field of machinery [1]. Usually piezoelectric actuator moves slider or turns rotor in one dimensional space while multidimensional movement of the positioning object is achieving by using complex mechanical systems. Most of the high precision piezoelectric actuators have small-scale driving force, so its not applicable for weighty objects positioning. Novel design for high precision piezoelectric actuator is investigated in this paper. This actuator achieves driving force till 10N and has positioning accuracy till 10 nm. Due to the special design of the actuator object positioning in two-dimensional space is achieved.

CONCEPT OF TWO-DIMENSIONAL POSITIONING

Principle of elliptic moving trajectory of the actuator contact core is based on exciting the ends of the beam *ab* (Fig. 1) by two harmonic loads that have the same frequency, but different phases by π/2. With the given loads flexural

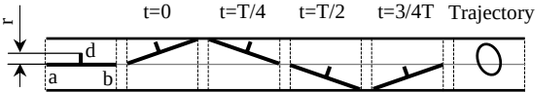


Fig.1 The position of the beams through every quarter the oscillations period

oscillations of the beam are excited. So moving trajectory of contact point *d* (Fig.1) can be written as follows:

$$\zeta(t,x)=r\left(\frac{\partial\xi(x)}{\partial x}+\frac{\xi(l)}{l}\right)sin(\omega t+\varphi)\qquad \delta(t,x)=\xi(x,t)+r\left(1-\left(\frac{\partial\xi(x)}{\partial x}+\frac{\xi(l)}{l}\right)sin(\omega t+\varphi)\right) \tag{1}$$

where $\zeta(t,x)$ and $\delta(t,x)$ are displacements of the contact core in horizontal and vertical directions accordingly, $\xi(x,t)$ is flexural oscillations of the beam, ω is the oscillation frequency, *r* is the length of contact core, *l* is length of the beam, *t* is the time and φ is the phase. Second modal shape of the beam must be exited in order to achieve driving force maximum of the piezoelectric motor. Special actuator for body positioning in the plane was developed concatenating two oscillating beams perpendicularly. Depending on excitation control actuator can position object in two perpendicular directions and achieve linear, curvilinear and rotational motion of the positioning object.

FEM MODELLING OF THE ACTUATOR

Basic dynamic equation of the piezostack-based actuator can be written as follows [2]:

$$\left.\begin{aligned}[M]\{\ddot{u}\}+[C]\{\dot{u}\}+[K]\{u\}+[T_1]\{\phi_1\}+[T_2]\{\phi_2\}&=\{F\}\\ [T_1]^T\{u\}-[S_{11}]\{\phi_1\}-[S_{12}]\{\phi_2\}&=\{Q_1\}\\ [T_2]^T\{u\}-[S_{12}]^T\{\phi_1\}-[S_{22}]\{\phi_2\}&=\{0\}\end{aligned}\right\} \tag{2}$$

where [*M*], [*K*], [*T*], [*S*], [*C*] are accordingly matrices of mass, stiffness, electroelasticity, capacity, damping, $\{u\}, \{\phi\}, \{F\}, \{Q\}$ are accordingly vectors of nodes displacements, potentials, external mechanical forces and charges coupled on the electrodes. Referring to Eq. 2, vector of external mechanical forces can be calculated as follows:

$$\{F\}=\left([T_2][S_{22}]^{-1}[T_2]^T-[T_1]\right)\{U\}sin\,\omega_k t \tag{3}$$

where $\{U\}$ is the vector of voltage amplitude. Modal analysis of the piezoelectric actuator was done in order to find out proper natural frequency and modal shape (Fig.2a) for the contact point elliptic trajectory formation. A full

harmonic response analysis was performed to give an adequate response curve of the contact point (Fig.2b) and to calculate parameters of elliptic trajectory (Fig. 2c) at the resonance frequency.

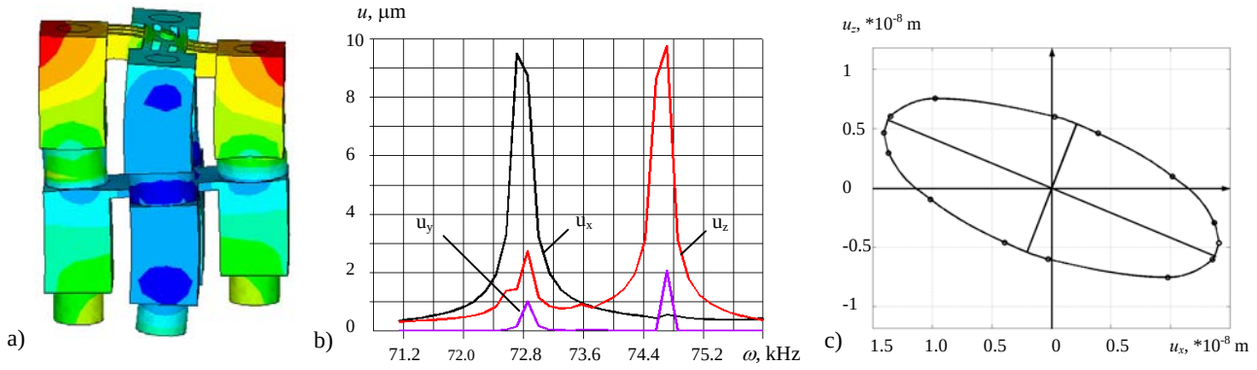


Fig.2 Results of actuator numerical investigation: a) modal shape at 73.59 kHz, b) amplitude versus frequency display, c) trajectory of contact points at 73.3 kHz

OPTIMIZATION OF THE ACTUATOR

Trajectory of the contact point strongly depends on geometrical parameters of the actuator, so optimization of actuator must be performed. Actuator (Fig. 2a) is analysed as frame of vertical and horizontal beams. Length of the beams is chosen as optimization parameters. Difference between first natural frequency longitudinal oscillation of the vertical beams and second natural frequency of flexural oscillation of the horizontal beams is chosen as optimization criteria. It allows achieving the best trajectory of the contact point. Optimization problem can be written as follows.

$$\begin{cases} \omega_{l1} - \omega_{f2} \Rightarrow max \\ l_h < l_{h_cr} \\ l_v < l_{v_cr} \end{cases} \tag{4}$$

where ω_{l1} is first natural frequency of longitudinal oscillation of the vertical beam, ω_{f2} is second natural frequency of flexural oscillation of the horizontal beams, l is the length of the beams.

EXPERIMENTAL RESEARCH

Experimental research was carried out in order to find distribution of the oscillations amplitudes on the surfaces of actuator, trajectories of the contact core movement and driving force characteristics (Fig.3). Experimental investigation also must sustain theoretical prerequisites of the object positioning in the plane using this type of actuator.

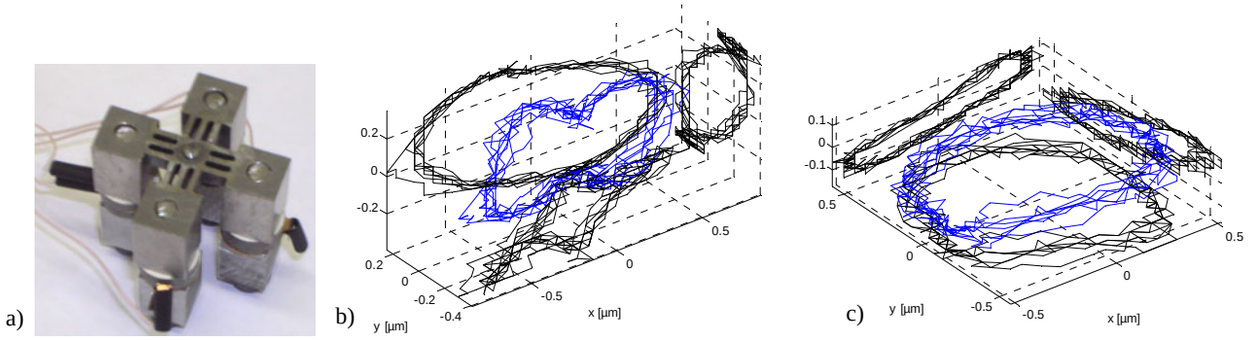


Fig. 3 Experimental model of the piezoelectric actuator (a), three dimensional trajectory of the actuator contact point when exciting two opposite shoulders (b) and all four shoulders of the actuator (c)

CONCLUSIONS

High precision piezoelectric actuator of the novel design was developed for the object positioning in the plane. Results of numerical and experimental investigation confirmed the possibility to use this type of piezoelectric actuator for two-dimensional positioning.

References

[1] Kenji Uchino.: Piezoelectric Actuators and Ultrasonic Motors. Kluwer Academic Publishers, Boston/Dordrech /London, 1997.

[2] Bansevicius R., Barauskas R., Kulvietis G., Ragulskis K.: Vibromotors for Precision Microrobots.Hemisphere Publishing Corp., USA, 1988.

GAIN-SCHEDULING CONTROL OF MACHINE TOOLS WITH VARYING STRUCTURAL FLEXIBILITIES

Wim Symens, Hendrik Van Brussel, Jan Swevers
PMA, Mechanical Engineering Department, Katholieke Universiteit Leuven, Celestijnenlaan 300B, 3001 Heverlee, Belgium

Summary In this paper an experimental set-up, consisting of one axis of an industrial pick-and-place machine, driven by a linear motor, is controlled based on the gain-scheduling approach. The set-up contains a flexible arm of which the stiffness depends on its length. Next to an ad-hoc scheduled H∞ controller, analytically scheduled controllers are designed using a global linear time varying (LTV) model of the set-up. Experiments show that scheduling is necessary if high-performance controllers are demanded.

INTRODUCTION

The growing competition on the international markets pushes manufacturers towards faster machine tools while preserving or improving final accuracy. High accelerations of the fast machines excite the machine structure up to high frequencies thereby exciting the structure's modes of vibration. These structural vibrations need to be damped if accurate positioning or trajectory tracking is required.
An additional problem is that the dynamical behaviour of the machine tool depends on the position of the work tool as a consequence of the varying machine configuration during machining. Such time-varying behaviour cannot be controlled by classical linear control methods as these methods require a linear time invariant (LTI) model of the system. One solution to this problem is to ensure that the designed LTI-controller makes the system behaviour robustly stable against the varying dynamics of the machine tool. The performance of the closed loop behaviour however could be improved if the variations could be included in the controller by making the controller also dependent on the instantaneous configuration of the machine tool by *gain-scheduling*. In classical gain-scheduling, LTI controllers are designed for several fixed positions of the machine, and these controllers are scheduled ad-hoc. More recent design methods for gain-scheduling controllers start from a linear parameter varying (LPV) description of the model [1]. Using this kind of models, criteria for robustness can be derived analytically. The most up-to-date and generalised framework for LPV-based control design is given in [3].

DESCRIPTION OF THE SET-UP

In this paper, the control of the X-Z axis of a Philips 4-axis pick-and-place machine (FlexCell) is considered (Fig. 1). The position of the X-motor and the length of the vertical arm are measured with an optical encoder. An accelerometer measures the acceleration of the end point of the arm. The objective is to move the end point of the arm accurate and fast along a prescribed trajectory in the X-Z plane. Fast movements of the linear motor will excite the eigenfrequencies of the flexible arm.

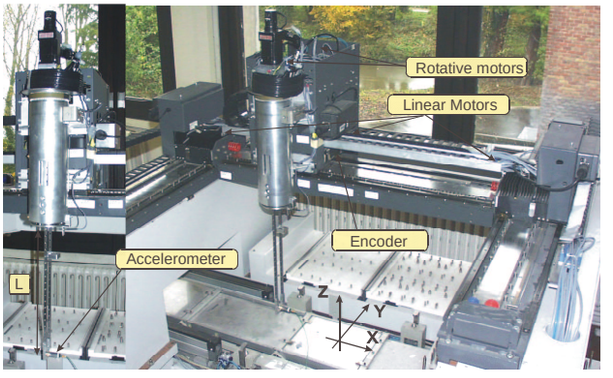


Fig. 1: Set-up: pick-and-place machine.

EXPERIMENTAL IDENTIFICATION OF THE SET-UP

Fig. 2 shows frequency response functions (FRFs) from the linear motor force excitation to end point acceleration, for different lengths of the arm. This figure clearly shows the dependency of the first two eigenfrequencies of the arm on the length of the arm. The FRFs from the motor force to the motor displacement and from the rotative motor input torque to the Z-position of the tool tip do not depend on the length of the beam and are omitted for reasons of brevity.

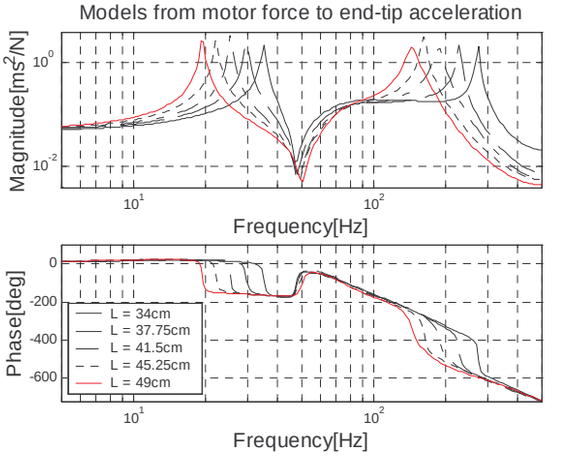


Fig. 2:FRFs from linear motor force excitation (N) to end point acceleration (m/s^2).

CONTROL DESIGN

The objective of the control design is to move the end point of the arm as accurate and fast as possible using the actuators that are present on the machine tool. For the set-up the motion controller is designed with a vibration controller in a HAC-LAC structure [2] (Fig. 3). The position of the motor is used for the

position control of the end point of the arm and the acceleration of the arm tip is used to damp the vibrations.

VIBRATION CONTROLLER

In this section, vibration controllers aimed at damping the first eigenfrequency of the flexible arm are presented.

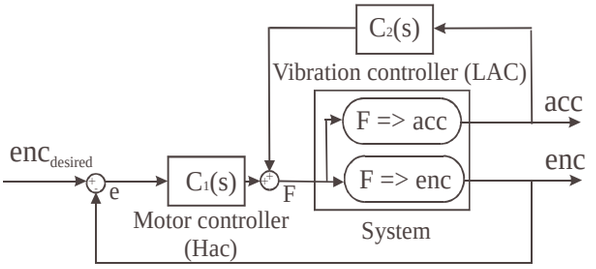


Fig. 3: Control scheme.

Ad-hoc scheduled H∞ controller

H∞ controllers [4] are designed for constant arm lengths to suppress both disturbances entering at the motor input and at the end point of the arm. These controllers are linearly scheduled based on the arm length and result in a controller with high performance as will be shown in the next section.

Analytically scheduled LPV controller

The robustness of the ad-hoc scheduled H∞ controller is not guaranteed theoretically. To guarantee this stability a model is needed that depends on the length of the arm. Such a model is called a linear parameter varying (LPV) model.
The most general framework for LPV-control design is presented in [3] and writes the design problem as a linear matrix inequality (LMI) that needs to be solved to obtain the controller. An LPV model of the set-up is identified and used to design an LPV controller. The performance of this controller is very low compared to the scheduled H∞ controller. The inherent conservatism of the used LPV-design method and bad numerical conditioning of the resulting LMI design problem explain this low performance.
As the synthesis of LPV controllers proved to be conservative and the analysis tools for LPV systems are less conservative, an LPV model is identified for the ad-hoc scheduled H∞ controller and the resulting closed-loop system is analysed for stability and performance. Even the state-of-the-art analysis tools are however not able to predict the correct stability region of this closed loop LPV system as they are still conservative to an extended degree.

EXPERIMENTAL RESULTS

To validate the different controllers a reference trajectory is applied to the set-up. Fig. 5 shows the acceleration signal for this trajectory with and without vibration control for the scheduled H∞ controller. The figure clearly shows the damping effect of the controller. For reasons of brevity the (poor) results of the analytically scheduled controller is not shown in the paper.

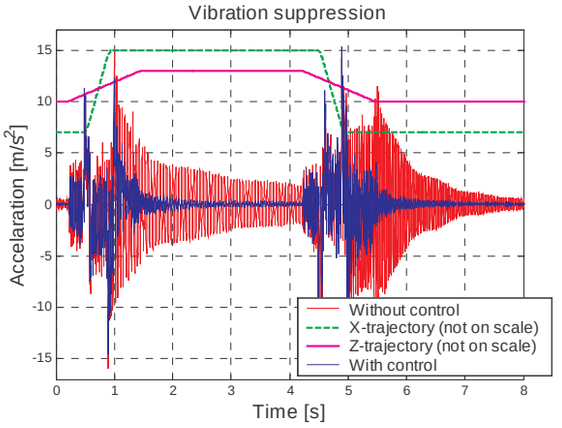


Fig. 5: Response with and without the scheduled H∞ controller.

CONCLUSIONS

In this paper ad-hoc scheduled H∞ controllers and analytically scheduled LPV vibration controllers are designed for a machine tool with varying dynamic stiffness. The performance of the analytically scheduled controller is much lower than this of the ad-hoc scheduled controller. This can be explained by the extended degree of conservatism that is introduced in the LPV design methods and numerical limitations of present day LMI solvers.
This study shows that further development of the LPV-tools is necessary to be able to design high-performance analytically scheduled LPV controllers for motion and vibration control systems for machine tools.

Acknowledgments

This research is sponsored by the Belgian program of Interuniversity Poles of Attraction by the Belgian State, Prime Minister's Office, Science Policy Programming (IUAP). W. Symens was a Research Assistant of the Fund for Scientific Research - Flanders (Belgium) (F.W.O.) in the period that this research was performed (1999-2003).
The authors would like to thank Carsten Scherer for providing a draft version of the LPV-synthesis toolbox.

References

[1] Apkarian P., Gahinet P.: A convex characterization of parameter dependent H∞ controllers. *IEEE Transactions on Automatic Control* **40**(5):853-864, 1995.
[2] Preumont, A.: Vibration control of active structures. Kluwer Academic Publishers, Dordrecht 1997.
[3] Scherer C.: LPV control and full block multipliers. *Automatic* **37**:361-375, 2001.
[4] Skogestad S., Postlethwaite I.: Multivariable feedback control: Analysis and Design. John Wiley & Sons, 1996.

XXI ICTAM, 15–21 August 2004, Warsaw, Poland

A SYSTEMATIC LOAD IDENTIFICATION PROCEDURE FOR PARALLEL ROBOT MANIPULATORS

Horst Schulte*, Patrick Gerland*
*Department of Mechanical Engineering, Division of Control Eng. and System Dynamics, University Kassel, D-34109 Kassel, Mönchebergstr.7, Germany, Email: schulte@ieee.org

Summary This paper presents a systematic load identification procedure for a class of parallel robot manipulators. It is considered as a regular dynamic robot identification problem since the load is rigidly fixed on the robot-platform. The challenge is that the estimation must be based only on the measurements obtained through sensors in the robot actuators. The load identification procedure is exemplified by experimental studies with a calibrated test load using periodic robot excitation.

INTRODUCTION

Advanced control techniques for robot manipulators demand the knowledge of the values of dynamic parameters of the manipulator model. At this the rigidly fixed load can be regarded as a structural modification of the manipulator. Computing such parameters on the basis of the geometry and material coefficients of the components (e.g. links, actuators) and the payload via CAD modeling techniques is inaccurate due to unmodeled dynamics and simplifications. In addition the payload geometry and material coefficients are mostly unknown in practice. Identification techniques are used in order to achieve more accurate values. In the case of serial robot manipulators, the load modifies the dynamic parameters of the last link or end effector. Due to the open kinematic chain the load parameters can be identified by a single motion of the last link. Several systematic procedures for experimental identification of serial robot manipulators exist, e.a. [2] and [4]. They estimate the parameters based on direct measurements of motion and actuator torque data during robot movements along optimized trajectories. Exploiting the simplification by a single motion of the last link is obviously not applicable to parallel robot systems with closed kinematic chains. Because the end-effector of a n-DOF parallel mechanism is connected to the base by at least n independent kinematic chains.
In this paper, we discuss a novel experimental load identification procedure for parallel robot manipulators. The estimation scheme uses the fact that the equations of motion are linear with respect to the inertia parameters and the gravity term. At first, the identification equations of the estimator are derived using the equation of motion of a rigid body written with respect to an arbitrary reference point P [1]. The experimental design is presented in the last section. We discuss a data preprocessing method, which removes the influence of the time variable Coulomb friction in the actuators, and apply a weighting matrix to compensate the unmodelled dynamics in the force measurements.

IDENTIFICATION PROCEDURE

The robot load identification procedure in this paper based on two weighted least-squares estimators. They are derived from the equations of motion of a unconstrained rigid body written with respect to an arbitrary reference point P

$$\hat{\boldsymbol{\theta}}_k = [\boldsymbol{\Phi}_k^T \boldsymbol{W}_k \boldsymbol{\Phi}_k]^{-1} \boldsymbol{\Phi}_k^T \boldsymbol{W}_k \boldsymbol{Y}_k \ , \qquad k = 1, 2 \ , \qquad \boldsymbol{Y}_k = \left[\begin{array}{ccc} \boldsymbol{y}_k^T(1) & \dots & \boldsymbol{y}_k^T(N) \end{array} \right]^T \in \mathbb{R}^{3N} \tag{1}$$

with $\boldsymbol{W}_k \in \mathbb{R}^{3N \times 3N}$ as a weighting matrix, $\boldsymbol{\Phi}_1 \in \mathbb{R}^{3N \times 4}$ and $\boldsymbol{\Phi}_2 \in \mathbb{R}^{3N \times 6}$ as matrices of regressors, which contain N data samples of the actuator forces represented in an inertial reference frame R, the orientations, angular velocities and angular accelerations of the robot-platform (see Fig. 1). The unknown inertia parameters are the load mass, the center of gravity and the inertia matrix of the load. In the *first step* the estimator (1) with index $k = 1$ is used to calculate the unknown mass of the load and common center of gravity of the load and the robot platform. The parameter vector $\boldsymbol{\theta}_1$ is defined as

$$\boldsymbol{\theta}_1 = \left[\begin{array}{cc} 1/m & \boldsymbol{r}_{Cp}^L \end{array} \right]^T \in \mathbb{R}^4 \ , \qquad m = m_l + m_r \ , \qquad \boldsymbol{r}_{CP}^L = \left[\begin{array}{ccc} x_{CP}^L & y_{CP}^L & z_{CP}^L \end{array} \right]^T \tag{2}$$

with the load mass m_l and the robot-platform mass m_r. The center of gravity $\boldsymbol{r}_{CP}^L$ with respect to the body-fixed frame L of the robot-platform refers to a reference point P, that is, in this case, located at the surface of the platform. The $3N \times 1$ column vector $\boldsymbol{Y}_k, k = 1$ in (1) consists of the translational acceleration of the platform with respect to frame R where $\boldsymbol{y}_1(i)$ is defined as

$$\boldsymbol{y}_1(i) = \left[\begin{array}{cccc} 0 & 0 & g \end{array} \right]^T - \left[\begin{array}{ccc} \ddot{x}_P^R(i) & \ddot{y}_P^R(i) & \ddot{z}_P^R(i) \end{array} \right]^T \qquad \text{for} \qquad i = 1, \dots, N \ . \tag{3}$$

These translational accelerations are not necessarily measured directly. We exploit the Jacobian inverse solution for nonredudant parallel manipulators [3] to calculate the motion of the platform based only on standard sensors integrated in the actuators (see the following section). The matrix of the regressors $\boldsymbol{\Phi}_1$ is written as

$$\boldsymbol{\Phi}_1 = \left[\sum_{j=1}^{n_A} \boldsymbol{F}_j^R \qquad \boldsymbol{A}^{RL} \tilde{\boldsymbol{\omega}}_{LR}^L \, \tilde{\boldsymbol{\omega}}_{LR}^L + \boldsymbol{A}^{RL} \dot{\tilde{\boldsymbol{\omega}}}_{LR}^L \right] \in \mathbb{R}^{3N \times 4} \tag{4}$$

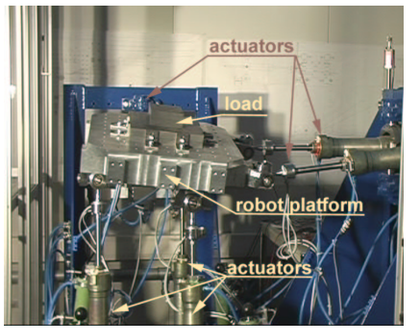


Figure 1. Experimental setup: Parallel robot manipulator powered by six pneumatic actuators with a calibrated load ($m_l = 22.26$ kg).

with $n_A = 6$ as the number of actuators of the parallel mechanism (see Fig. 1) and $\boldsymbol{A}^{RL}$ as the orientation matrix of the robot-platform with respect to an inertial frame R. The external force vector $\boldsymbol{F}_j^R,\ j = 1, \ldots, n_A$ in (4) can be calculated by the measured actuator forces and direct kinematic equations, which transform the body-fixed frame of each actuators in the inertial frame. The matrix elements of $\tilde{\boldsymbol{\omega}}_{LR}^L \in \mathbb{R}^{3\times3}$ and $\dot{\tilde{\boldsymbol{\omega}}}_{LR}^L \in \mathbb{R}^{3\times3}$ consist of the vector components of the angular velocities and angular accelerations of the robot-platform with $\boldsymbol{\omega}_{LR}^L = [p^L\ q^L\ r^L]^T$ and $\dot{\boldsymbol{\omega}}_{LR}^L = [\dot{p}^L\ \dot{q}^L\ \dot{r}^L]^T$ with respect to frame R represented in L. As before the translational accelerations in (3), the determination of this is based only on the measured actuator positions, velocities and accelerations using the Jacobian inverse solution. In the *second step* of the identification process the estimator (1) for $k = 2$ is used to calculate the unknown common inertia tensor of the robot-platform with the rigidly fixed load. Here, the parameter vector is defined as $\boldsymbol{\theta}_2 = \left[\ J_{Cx}^L\ J_{Cy}^L\ J_{Cz}^L\ J_{Cxy}^L\ J_{Cyz}^L\ J_{Cxz}^L\ \right]^T \in \mathbb{R}^6$ with three moments of inertia and three products of inertia represented in body-fixed frame. The vector $\boldsymbol{Y}_2 \in R^{3N}$ in (1) consists of the external torques, calculated by the actuator forces using the manipulator kinematic equations, the estimated mass $\hat{m}$, and the center of gravity defined by $\hat{\boldsymbol{r}}_{CP}^L$, which are estimated before. The elements of this vector and the matrix $\boldsymbol{\Phi}_2 \in \mathbb{R}^{3N\times6}$ are described in detail in [1]. The *last step* of the procedure regards the fact that the estimated parameter vectors $\boldsymbol{\theta}_1$ and $\boldsymbol{\theta}_2$, obtained from the least-squares formulation (1) using (3) and (4), are a combination of the inertial parameter of the platform *and* the load. For this, we apply the parallel axis theorems for moments and products of inertia to seperate known robot manipulator parameters (e.g. as a result of an estimation process without a load) from the desired parameters of the load.

EXPERIMENT DESIGN

The design of the identification experiment includes the planning of the robot trajectory and the choices, which measured signal should be used to obtain the regressors in (1). We use a sinusoidal trajectory to excite the three orientation angles of the robot-platform during one experiment. As mentioned before the estimation is based only on signals that are readily available through sensors integrated into the actuators. The piston positions, piston velocities, and piston accelerations of the pneumatic actuators are measured. In addition, the chamber pressure measurements $p_{I,II_j}(i)$ with $i = 1, \ldots, N$ for $j = 1, \ldots, n_A$ are recorded to calculate the actuator forces. Yet another important point is that the unmodeled robot dynamics such as friction must be compensated in the data recording. First, a goal-oriented data-preprocessing method is used to reduce the influence of the friction in the actuators using a combination of Coulomb and viscous friction models. The second scheme takes into account the influence of unmodeled stick-slip motion in low-velocity regimes caused by Stribeck friction on the calculation of the actuator forces. For this purpose the following weighting matrix in (1) is chosen: $\boldsymbol{W}_k = \text{diag}\,[w_k(\bar{v}(1)), w_k(\bar{v}(1)), w_k(\bar{v}(1)),\ \ldots, w_k(\bar{v}(N)), w_k(\bar{v}(N)), w_k(\bar{v}(N))] \in \mathbb{R}^{3N\times3N}$ for $k = 1, 2$ with a time-dependent average value $\bar{v}(i)$ of the measured piston velocities $v_j(i)$ for $j = 1, \ldots, n_A$ and a weighting function w_k, that goes to zero at low-velocity regimes.

CONCLUSION

In this paper a systematic load identification procedure has been presented and applied to a parallel robot manipulator using only measurements from sensors integrated in the actuators of the robot. Furthermore, it is of interest to consider the quality of a recursive weighted least-squares algorithm for the purpose of adaptive control.

References

[1] Hahn H., Niebergall M.: Development of a Measurement Robot for Identifying all Inertia Parameters of a Rigid Body in a Single Experiment. *IEEE Transaction on Control Systems Technology*, **9**(2):416–423, 2001.
[2] Kozlowski K., Modelling and Identification in Robotics, Springer Verlag, New York, 1998.
[3] Merlet J.-P.: Parallel Robots. Kluwer Academic Publishers, 2002.
[4] Swevers J., Verdonck W., Naumer B., Pieters S., Biber E.: An experimental robot load identification method for industrial application. *The International Journal of Robotics Research*, **21**(8):701–712, 2002.

DEVELOPMENT OF POSITIONING OF MECHANISMS WITH PIEZOELECTRIC ENGINES

Alfredas Busilas* and Romualdas Naumavičius **
*Vilnius Gediminas Technical University, Vilnius, Lithuania
**Sutota Ltd, Kaunas, Lithuania

Summary. Positioning mechanisms with carts moving in a horizontal plane and with piezoelectric vibroengines analyzed in the article form a group of mechanisms, having elastic and dissipative links and carts moving between deflectors, which interact with the engine without intermediate transference links. Positioning mechanism piezoelectric vibroengine of original construction has been developed, which eliminates looseness, energy losses and acoustic noises.

Introduction. Mechanisms with moving carts are one of the main parts of majority of devices and machines. They differ and often precondition technical progress in various technical areas. However, precision, stability and speed of many such mechanisms depend on input links interconnected by elastic and dissipative elements. Moreover, while increasing precision and sensitivity of mechanisms, undesirable effect of foundation vibrations also increases. Therefore, such control algorithms of moving links must be developed, which would not excite undesirable vibrations in mechanisms [1, 3].

The analyzed positioning mechanisms with moving carts along a horizontal plane and with piezoelectric engines make a mechanisms group, having elastic and dissipative links as well as moving carts between deflectors, which interact with the engine without intermediate transition links. Such equipment of different construction is characterized by common regularities of dynamic processes. Synthesis of designed mechanisms practically means that the cart movement law is set and, pursuant to it, control of a power mechanism is determined [2, 4].

The main requirements of precision positioning mechanisms are as follows: high positioning sensitivity and precision, reaching micron segments in accordance with linear displacements and second segments in accordance with angular displacements; wide range of linear speeds (0 – 100 mm/s); wide range of linear speeds (10 mm – 6 m); multi-regime control; reliability and durability; wide range of cart masses (5 – 200 kg). This requires a high tightness of power mechanism connection with a cart; there should be no intermediate transition links, the cart should move pursuant to several coordinates, control system should be simple.

Control of one degree-of-freedom positioning mechanism. Control system of such mechanisms is developed in a way it could realize the whole of algorithms, which would force elastically and dissipatively interconnected carts to move following the set paths. Moreover, it is required that the set path should have certain marginal conditions in its beginning and the end. For example, when the cart is in transition from a still status to a determined point, it often requires to make a movement when the speed and acceleration levels in the environment of determined points are close to zero. Mathematical content of control task of such positioning mechanisms is such that it requires determining the values of control forces, which would move the cart in accordance with a set path. To solve control task under mathematical attitude is to develop calculation algorithm of control variables (forces), which would realize a determined movement or position of elastically and dissipatevely interconnected carts. Technical solution of control task requires realization of values of control forces with executive gears. In other words, executive gears must move the object to a preset position at any moment of time.

It is known [1, 2, 3] that in order to move the cart without transitional processes, speed and acceleration laws must conform to the following conditions: 1. Maximum speed value must be reached in the middle of the path, i.e. $X'\big|_{t = T/2} = X'_{max}$, $X'\big|_{t = 0} = X'\big|_{t = T} = 0$. 2. Maximum acceleration value must be reached at the moment of time t = T/4, and minimum – at the moment of time t = 3T/4, i.e. $X''\big|_{t = T/4} = X''_{max}$, $X''\big|_{t = 3T/4} = X''_{min}$, $X''\big|_{t = T/2} = X''\big|_{t = T} = 0$.

The second condition is best implemented under the following acceleration law:

$$X'' = \begin{cases} 0, & \text{when } t \le 0, \\ X''_0 \sin(2\pi/T)\, t, & \text{when } 0 \le t < T, \\ 0, & \text{when } t \ge T. \end{cases} \quad (1)$$

After integration (1) and considering that in the marked time interval $X''\big|_{t = 0} = 0$, we get the following movement speed law of the cart:

$$X' = \begin{cases} 0, & \text{when } t \le 0, \\ -X''_0 (T/2\pi) \cos(2\pi/T)\, t + X''_0 (T/2\pi), & \text{when } 0 \le t < T, \\ 0, & \text{when } t \ge T. \end{cases} \quad (2)$$

After integration (2) and considering that in the marked time interval $X'\big|_{t = 0} = 0$, we get displacement law of a stably moving cart:

$$X = \begin{cases} 0, & \text{when } t \le 0, \\ -X''_0 (T/2\pi)^2 \sin(2\pi / T)\, t + X''_0 (T/2\pi)\, t, & \text{when } 0 \le t < T, \\ X_T, & \text{when } t \ge T. \end{cases} \quad (3)$$

here X'', X', X - acceleration, speed and displacement moment time components of the cart, X''_0 –maximum acceleration value, T – duration of cart shift, X_T – set displacement size of the cart.

Positioning mechanisms with piezoelectric engines. In order to develop precision positioning mechanisms, it is required to develop their element base first. Therefore, the authors developed new technical solutions of the engines, their control systems and new mechanism constructions. Widely used piezoelectric engines, operating principle of which is that high frequency mechanical vibrations are transformed into linear or angular movement of the cart. The scheme of piezoelectric engines is as follows. Operating part of the engine is pressed to a moving part of the cart. Due to a friction contact of the moving part with a vibrating element, movement moment is created. By canceling electrical high frequency signal, and when piezoelectric element halts its vibrations, the cart is forced to stop. This happens because the same piezoelectric element firmly connected to the frame, is pressed by a friction gear to the moving part. Therefore, these piezoelectric engines may be successfully used to implement different regimes of the mechanisms.
Piezoelectric vibroengine of a linear movement has been developed. One electrode of a piezoelectric plate of the device is divided into four symmetric parts, and the other electrode is left undivided. In the ends of plate between electrodes rectangular vibration concentrations are glued. Besides, plate is pressed through concentrators to cart. Pressing mechanism is "П"-shaped holder with a cut in the middle where plate is installed. One end of holder is firmly assembled to foundation by bolt, another end with a cut leans to an adjustable bolt through elastic spacer and spring. Moreover, parts of the divided electrode are correspondingly glued at the junction to four electrodes with terminals, and the other non-divided electrode is glued at the center to electrode also with a terminal. All electrodes are firmly intercollected into a package by isolators. Positioning device with a cart moving along one coordinate, piezoelectric engine of which determines the optimal cart speed has been developed. Positioning device where the optimal control law of the cart movement is used has been developed. Device for information accumulation positioning in the plane has been developed, which has been used in optical information recording and reading systems. Here information accumulation planes are shifted by lines in automatic continuous regime. It may be also used for positioning of various objects along the plane. The device contains two coordinate positioning mechanisms with piezoelectric vibroengine and photoelectric raster displacement transducers as well as a control unit. Technical characteristics of this device are as follows: minimum positioning plane – 90 x 90 mm.; distance between lines – 6 μm; speed of movement along the line – 90 mm/s; positioning error – 1 μm. Positioning mechanisms with a control system having piezoelectric vibroengines and feedback circuits under displacements has been developed. Construction of positioning mechanism is such that the cart independently moves along perpendicular directions in the plane and two identical control systems register position of the cart on the plane at any point of positioning field at a maximum speed and without slipping. The suggested device considerably increases evenness of movement speed and precision of position registering when the cart stops or when it moves under the unknown program. Moreover, stabilization of cart speed enables to decrease positioning pace. Precision high-speed two-coordinate positioning mechanism controlled under the program has been developed and analyzed, which has been used for mechanical processing and correction of resistor schemes. This device has control unit connected to computer. Movement speed increase zone of the cart reaches 60 μm. Stopping zone of the cart moving at speed of 40 mm/s reaches 100 μm. Unevenness of movement speed of the cart is 1 %, and slipping size after halt does not exceed 0,5 μm. In addition, technical characteristics of the mechanism are as follows: positioning plane 90x90 mm; stabilized speed 2 – 40 mm/s; displacement pace 1 μm.

Conclusions Suggested algorithm of positioning mechanism cart discrete shift without transition processes and formulated control task enabled to determine law dependencies of controllable forces effecting elastically and dissipatively interconnected carts on system parameters. Developed control devices of positioning mechanisms with piezoelectric vibroengines, which form the optimal control law of cart shift, considerably increase mechanism precision and movement speed as well as significantly decrease displacement pace, as they eliminate cart slipping during "start – stop" regimes and maintain a constant acceleration, independently from the length of the path. An original precision positioning device with displacement transducer, vibroengine and controllable feeding voltage formation scheme, which considerably increases speed evenness and precision of cart position registration while shifting the cart under a freely chosen program, has been developed. Minimum displacement pace has reached 1 μm at movement speed of 40 mm/s. Speed growth zone has made 0 μm, and stopping zone – 100 μm. Speed unevenness has reached 1 %, and slipping size after halt does not exceed 0,5 μm. Developed positioning mechanisms piezoelectric vibroengine of original construction considerably increases precision, useful effect ratio and reliability, as looseness, energy losses and acoustic noises are being eliminated.

References

[1] Higuchi K: A piezoelectric linear motor driven by superposing standing waves with phase difference. Structures, structural dynamics & materials conf., 1995.
[2] Helmsel T., Wallaschek J.:.Piezoelectric linear motor. Actuator 2000, 7th International Conference on New Actuators, 2000.
[3] Ueha S., Tomikawa Y. Ultrasonic Motors Theory and Applications.Oxford, 1993.
[4] Kurosawa M., Higuchi T. Surface acoustic wave linear motor. Mechatronics and Advanced Motion Control, 3rd International Heinz Nixdorf Symposium, 1999.

Hierarchical Tracking Control of Wheeled Mobil Robot

Pu-Sheng Tsai[1], Li-Sheng Wang[2], Fan-Ren Chang[1], Yih-Hsing Pao[2]

[1] Department of Electrical Engineering, National Taiwan University, Taipei, Taiwan, ROC
[2] Institute of Applied Mechanics, National Taiwan University, Taipei, Taiwan, ROC

Summary : Tracking control for autonomous vehicles or mobile robots plays an essential role in the exploration of hazardous areas or planets, such as Mars. If the motion is realized through no-sliding wheels, the problem associated with nonholonomic constraints naturally arise. Based on Jourdain's variational equation, it is possible to formulate the dynamics of such system in terms of the privileged coordinates. Given the desired trajectory, the corresponding reduced Appell's equation can be used to design the control law for the privileged coordinates. On the other hand, to track the non-privileged coordinates, the conditions of constraints are re-structured from which the compensations for the desired values of privileged coordinates are computed. From the simulation results, it is shown that such hierarchical tracking control strategy which simultaneously takes kinematics and dynamics into consideration indeed gives rise to an effective algorithm for tracking problem.

Problem Description

The non-integrability of the nonholonomic constraints makes the problem of tracking control of mobile robot with rolling-without-sliding wheels very difficult to be managed. In the literature, cf. [1], some approaches are based on the kinematic equations and the dynamical equations of the system are not taken into consideration. Such methods ignore the mass and the moment of inertia of the system and thus the designs are deemed impractical. Some of the other methods combine both sets of kinematic and dynamic equations together and consider either enlarged or reduced set of equations to find the control law. However, the former case raises the complexity of the design, while the latter may be subject to under-actuated problem. It is then desired to develop a feasible and practical methodology of controller design which appropriately accommodates the dynamics and the kinematic constraints. The hierarchical tracking control algorithm proposed in this paper suits such need.

The practical problem to be solved in this paper is the tracking of a desired trajectory for a three-wheeled mobile robot, cf. [3], whose configuration is depicted in Figure 1, moving on a horizontal plane. The system may be modeled by a rigid body interconnected with two rolling-without-sliding wheels, cf. Figure 2. The castor wheel is ignored due to its negligible effects on the dynamics of the system. The motion of the wheels may be described by $(x_j, y_j, \psi_j, \theta_j)$, $j = 1, 2$, where (x_j, y_j) denote the coordinates of the center of mass and ψ_j, θ_j are the rotation angle and the orientation angle of the wheels, respectively. The body may be characterized by (x_3, y_3, θ_3), where θ_3 denotes the heading angle of the vehicle. There are total of 11 variables which are subject to five holonomic constraints: (1) $\theta_1 = \theta_2 \equiv \theta$, (2) $\theta_2 = \theta_3 \equiv \theta$, (3) $y_3 = y_1 - b\cos\theta + d\sin\theta$, (4) $x_3 = x_1 + b\sin\theta + d\cos\theta$, (5) $r\dot{\varphi}_2 = r\dot{\varphi}_1 + 2b\dot{\theta}$; and four nonholonomic constraints: (6) $\dot{x}_1 = r\dot{\varphi}_1\cos\theta$, (7) $\dot{y}_1 = r\dot{\varphi}_1\sin\theta$, (8) $\dot{x}_2 = r\dot{\varphi}_2\cos\theta$, (9) $\dot{y}_2 = r\dot{\varphi}_2\sin\theta$. It is assumed further that the two wheels are rotated by motors which generate torques τ_1, τ_2, respectively. The objective of the design is to obtain a controller which enables the system to track a reference trajectory $(x_{jr}(t), y_{jr}(t), \psi_{jr}(t), \theta_{jr}(t), j = 1, 2, x_{3r}(t), y_{3r}(t), \theta_{3r}(t))$ which satisfies the above-mentioned geometric and kinematic constraints.

The Methodology

Based on Jourdain's variational equation and Appell's approach, cf. [2], one may choose ψ_1, θ as privileged coordinates, and derive the reduced Appell's equations of motion as follows:

$$\begin{cases} (m_c + 2m_w + 2m')r^2\ddot{\varphi}_1 + (m_c + 2m_w + 2m')br\ddot{\theta} - m_c dr\dot{\theta}^2 = \tau_1 + \tau_2, \\ (m_c + 2m_w + 2m')br\ddot{\varphi}_1 + [m_c(d^2 + b^2) + \frac{1}{3}m_c'(w^2 + \ell^2) + m'(r^2 + 4b^2) + 4m_w b^2]\ddot{\theta} + m_c dr\dot{\varphi}_1\dot{\theta} = \frac{2b}{r}\tau_2, \end{cases}$$

where m_c, m_w, m' denotes the masses of the components of the system. It is noted that these two equations are decoupled from the non-privileged coordinates, and the controller can be designed independently to track $(\psi_1(t), \theta(t))$. Various methods can be applied to obtain such a controller. Here, the adaptive sliding mode controller is adopted due to its capability of dealing with parameter uncertainties.

While the privileged coordinates can be drived to the desired values without too much effort, the non-privileged coordinates may deviate from the reference values significantly if the initial conditions are not set appropriately or there are some disturbances during the motion. To solve this problem, it is noted from the practical experience of driving that we may change the reference values of the privileged coordinates to steer the non-privileged coordinates. The compensated values for the privileged coordinates may be computed from the kinematic equations: (6), (7), (8') $\dot{x}_2 = r\dot{\varphi}_1 \cos\theta + 2b\dot{\theta}\cos\theta$, (9') $\dot{y}_2 = r\dot{\varphi}_1 \sin\theta + 2b\dot{\theta}\sin\theta$, and those for the reference trajectory. Let $\mathbf{z}_2 = (x_1, y_2)$, $\mathbf{z}_2^e = (x_{1r} - x_1, y_{2r} - y_2)$, $\mathbf{v}_r = (\dot{\varphi}_{1r}, \dot{\theta}_r)$, $\mathbf{y} = (\varphi_1, \theta)$, $\mathbf{y}_r = (\varphi_{1r}, \theta_r)$, and

$$\mathbf{B}_2(\mathbf{y}) = \begin{bmatrix} r\cos\theta & 0 \\ r\sin\theta & 2b\sin\theta \end{bmatrix}, \quad \mathbf{B}_2^r(\mathbf{y}_r) = \begin{bmatrix} r\cos\theta_r & 0 \\ r\sin\theta_r & 2b\sin\theta_r \end{bmatrix}, \quad \boldsymbol{\lambda} = \begin{bmatrix} 10 & 0 \\ 0 & 10 \end{bmatrix}.$$

It is found that the corresponding compensation is $(\delta\varphi_1, \delta\theta)^T = (\mathbf{B}_2^{-1}(\mathbf{y})(\mathbf{B}_2^r(\mathbf{y}_r)\mathbf{v}_r + \boldsymbol{\lambda}\mathbf{z}_2^e) - \mathbf{v}_r)\Delta t$, where $\boldsymbol{\lambda}$ is used to specify the rate of convergence. From these data, a new set of reference values for the privileged coordinates is computed. The adaptive sliding mode controller mentioned above is then invoked to track the new reference, which in turn drives the non-privileged coordinates to the desired values. It can be shown that with such hierarchical design, all the variables can be steered to the desired value asymptotically.

Simulation Result

Consider the wheeled mobile robot with the following parameters: m_w = 1, m_c = 20, b = 0.5, d = 0.25, r = 0.1. Simulations are conducted to evaluate the performance of the proposed methodology. As shown in Figure 3 and 4, the motion of the wheeled mobile robot can track the desired trajectory (including the heading) successfully, even if the initial configuration is away from the desired configuration. The results demonstrate the effectiveness of the proposed hierarchical control scheme which may be extended to general reducible mechanical systems.

References

[1] Kolmanovsky, I., N.H. McClamroch, "Developments in Nonholonomic Control Problems", IEEE Control Systems, 1995, pp.20-36.

[2] Wang, L.-S., Y.-H. Pao, 2003, "Jourdain's Variational Equation and Appell's Equation of Motion for Nonholonomic Dynamical Systems," *American Journal of Physics*, Vol. 73, No. 1, pp.72-82.

[3] Tsai, Pu-Sheng, Li-Sheng Wang, Fan-Ren Chang and Ter-Feng Wu, "Point Stabilization Control of Car-Like Mobile Robot in Hierarchical Skew Symmetry Chained Form", IEEE International Conference on Networking, Sensing and Control, Taipei, 2004.

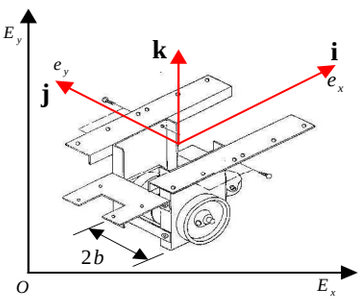


Figure 1

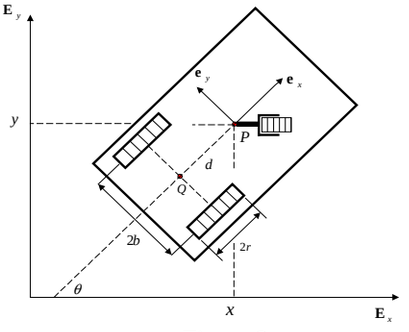


Figure 2

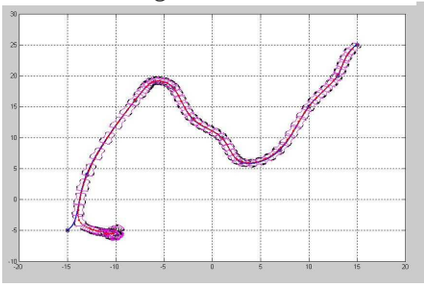


Figure 3

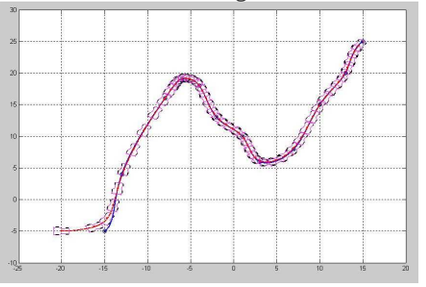


Figure 4

XXI ICTAM, 15–21 August 2004, Warsaw, Poland

RAPID PROTOTYPING OF MODEL BASED CONTROL ALGORITHMS FOR DIESEL-ENGINES WITH TURBOCHARGER

Matthias Weber*,Rolf Isermann *
*Darmstadt University of Technology, Institute of Automatic Control
Phone: +49/6151-162114, Fax: +49/6151-293445

Summary A Control Prototyping system for the design of electronic control unit (ECU) functions for truck Diesel engines is presented. By this way the different steps of the control development can be optimized. As an application example, the design of a control algorithm for the charging pressure of a variable geometry turbocharger is described. The modeling process for the required dynamic nonlinear turbocharger model with variable turbine geometry (VTG) an the resulting control performance is shown in detail.

INTRODUCTION

Without appropriate tools for the design, implementation, and test of new engine control algorithms, the tight schedules in the development process of engine control systems can not be met anymore. Especially in the automotive industry, the concurrent design of engine, body and electronics requires efficient development methods. In this context the model based control design increasingly plays an important role in all steps of the development process. The Control Prototyping is used to test the new control function together with the real already existing control unit and the simulated or the real process. In contrast to the Software-in-the-Loop simulation, only a selected subset of the ECU functions is realized as a software model. Only these interesting parts are calculated on a real-time computer system in a bypass mode to the real ECU. The presented real time system for the design of engine control functions was developed in cooperation with the DaimlerChrysler AG. The presented application demonstrates as one example an efficient way to design a control algorithm for the turbine inlet guide vanes of a variable geometry turbocharger.

TURBOCHARGER MODEL

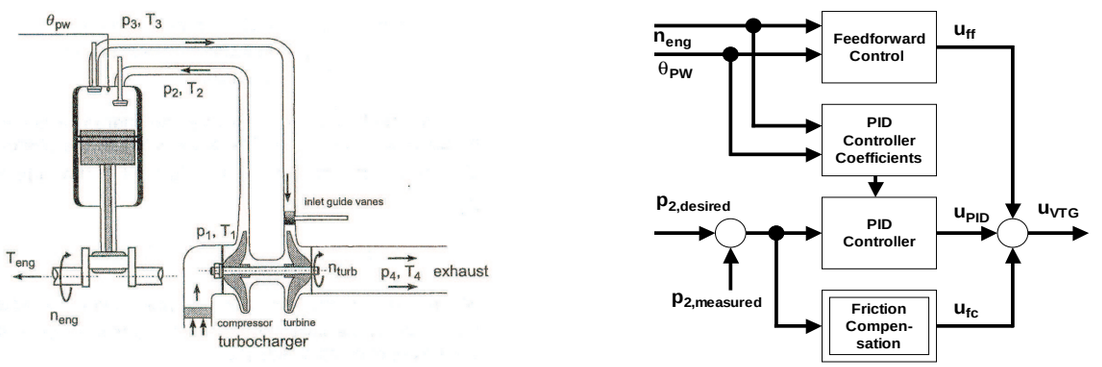


Figure 1. Basic structure of a Diesel engine with a variable turbine geometry turbocharger (VTG) and VTG controller with friction compensation

Figure 1 schematically represents the exhaust turbocharger with variable turbine geometry (VTG) (Heywood, 1988).For the charging pressure control the position of the turbine inlet guide vanes u_{VTG} is the input and the charge pressure p_2 is the output variable. The charging process has a nonlinear static input/output behavior as well as a strong dependency on the dynamics on the operating point. There are several ways to build a model of a turbocharger: (Isermann *et al.*, 1998)(Kessel *et al.*, 1998). In general, the static behavior of the turbocharger may be sufficiently described by characteristic maps (Look-up tables) of the compressor and turbine. However, if the dynamics of the turbocharger need to be considered, basic mechanical and thermodynamical modelling is required. Practical applications have shown that theoretical models are capable of reproducing the characteristic dynamic behavior of the turbocharger. The model quality, however, essentially depends on the accurate knowledge of several process parameters, which have to be laboriously derived or estimated, in most cases by analogy considerations. A further disadvantage is the considerable computational effort due to the complexity of these models. For these reasons, simple and easy identifiable input/output models suitable for real-time simulation are required for typical control engineering applications such as controller design, fault diagnosis and hardware-in-the-loop-simulations. Therefore, realtime capable Neural Networks (LOLIMOT (Nelles, 1999)) are chosen. The pulse width of injection θ_{pw} , the engine speed n_{eng} , and the control signal for the turbine inlet guide vanes u_{pwm} are chosen as inputs while the charge-air pressure p_2 is the output. The sampling time is $T_0 = 0.1s$.

CONTROL PROTOTYPING SYSTEM

In this section, the development system for the design of truck Diesel engine management systems is presented. The Control Prototyping is used to test new ECU functions together with the simulated or real process in a bypass mode to the real ECU. To fulfill the necessary real-time constraints, a powerful computer hardware is required. The used real time computer system is based on a dSPACE-system equipped with digital signal processors and a DEC Alpha processor. This system has the advantage of a high computing power and the possibility to download models realized in MATLAB/SIMULINK to the real-time hardware in an automated way. If the Control Prototyping system is used together with the real engine, the necessary sensor signal inputs for the investigated ECU-functions can be accessed via an A/D converter and a CAN-interface. Different types of Control Signals (e.g. PWM-signals, continuous signals) can be generated by the dSPACE I/O-Boards. Signal conditioning is done by a voltage level converter.

APPLICATION EXAMPLE

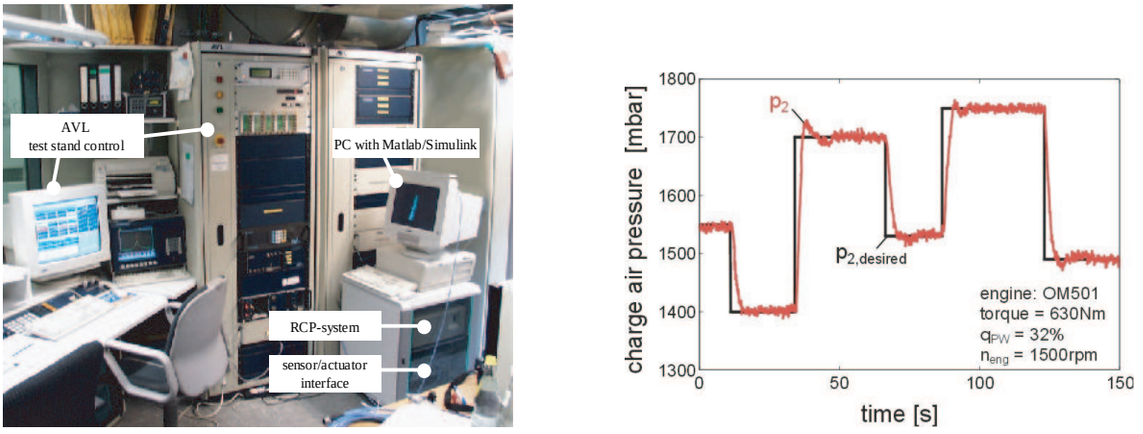


Figure 2. Dynamic engine test stand with Control Prototyping System and measured controlled charge air pressure for setpoint changes

As an application example, the development of a control algorithm for the turbine inlet guide vanes of a variable geometry turbocharger is presented. For this application, a PID controller with adaptive proportional and integral action factors and feed forward control was investigated (Figure 1). During the off-line simulation, MATLAB scripts may be used to perform a comprehensive set of automated simulation runs. The controller structure can be tested and an initial optimization of the parameters, based on the turbocharger model of section , can be done. MATLAB supports the optimization process with different tools and algorithms. After a promising controller structure is found, the Control Prototyping can be used to test the new control algorithm together with the real turbocharger and Diesel engine. Therefore a dynamic engine test stand, (Figure 2), or a real truck can be used. The VTG control algorithm is computed on the real-time hardware in a bypass mode to the already existing ECU. Important input signals of the controller, as the engine speed or the actual boost pressure can be transmitted via CAN bus. Additional sensor signals can be accessed via an A/D converter board. Figure 2 shows the charge air pressure set point ($p_{2,desired}$) and the measured charge air pressure (p_2) of an heavy truck diesel engine at the test bed. The controller output is generated by the dSPACE system, amplified and connected to the actuator for positioning the turbine inlet guide vanes. With the method of Control Prototyping this new control algorithm could be tested together with the real process in real-time, before the function was implemented in the production ECU.

CONCLUSION

Modern techniques like model based control and Control Prototyping are increasingly employed in the automotive industry to reduced the development time and cost. It has been shown, that this method can optimize the development process of ECU control functions substantially. As an application example for model based control prototyping, the development of a PID control algorithm for the turbine inlet guide vanes of a variable geometry turbocharger was demonstrated.

References

Heywood, J.B. (1988). *Internal Combustion Engine Fundamentals*. McGraw-HiII series in mechanical engineering. McGraw-Hill.

Isermann, R., S. Sinsel and J. Schaffnit (1998). Modeling and real-time simulation of diesel engines for control design. number Paper 980706 In: *SAE International Congress & Exposition*. SAE. Detroit, USA.

Kessel, J.A., J. Schaffnit and M. Schmidt (1998). Modeling and real-time simulation of a turbocharger with variable turbine geometry (vtg). number Paper 980770 In: *SAE International Congress & Exposition*. SAE. Detroit, USA.

Nelles, O. (1999). Nonlinear System Identification with Local Linear Neuro-Fuzzy Models. PhD thesis. Darmstadt, Technische Universität.

DEVELOPMENT OF HIGH-PERFORMANCE MOTION SIMULATOR FOR VIRTUAL REALITY SYSTEMS

Dzmitry O. Tsetserukou*, Alena V. Neviarouskaya**
*Department of vibroprotection of machines, Institute of Mechanics and Reliability of Machines of the National Academy of Sciences of Belarus (IMRM of NAS of Belarus), Minsk, Belarus
**Department of Marketing, Invention and International Contacts of IMRM of NAS of Belarus
Akademicheskaya 12, 220072 Minsk, Belarus

Summary: the paper is concerned with development of the high-performance and simple system of the motion effect simulation on the operator. These mechanisms are widely applied in virtual reality systems: trainers for truck drivers and aircraft pilots; entertainment; medical research application. The new construction of the spherical motion platform on the basis of four-bar linkage has been developed with simple structure, sufficient fidelity of motion and small energy consumption. In the paper the force analysis of spherical motion platform has been presented. The three-dimensional model of developed motion simulator has been given.

The purpose of the motion simulator is to give perception of continuous dynamic motion inside a vehicle or robot to the human nervous system. It is accomplished by a combination of realistic audio and visual presentation. In driving simulators, the driver interacts with a virtual vehicle model reproducing the behavior of a real vehicle under given environmental conditions and under given driven commands. Motion perception is obtained by means of the simulator cabin movement generated by a computer model. The cab is moved by platform ideally reproducing the motion of a seat of the vehicle driver. There are two main types of platform used in motion simulator: Gough-Stewart platform; spherical platform based on arc guiding rails. Gough-Stewart platform (Fig.1) - six-degree of freedom (DOF) parallel mechanism with six identical kinematic chains, composed of a universal joint, a prismatic actuator, and a spherical joint. Gough V.E. [1] devised a six-linear jack system for use as a universal tire testing machine. Stewart D.A. [2] developed a six-degree of freedom platform manipulator for use as an aircraft flight simulator. Spherical motion platform using arc guiding rails (Fig.2) was developed during project SIMUSYS: "*Innovative high-performance motion simulation system for entertainment, research and training applications*" in the university of Saragossa. The SIMUSYS driving simulator is formed by 4-DOF spherical motion platform providing 3 rotation motion and 1 translation motion. The basic spherical surface is created by means of curved sliding guides. This paper is concentrated on development of the rational variants of the movable platform in order to create simulator with more simple structure in comparison with above-mentioned types, sufficient fidelity of motion and small energy consumption under following initial data: position restriction area of the movable platform – 1700X1700 mm; distance from platform center up to the operator head center h – 1220 mm; sphere radius of permissible positions of operator cochlea center r – 100 mm.



Fig.1



Fig.2

Trajectory of the motion of the spherical platform center in projections on plain represents symmetrical arc relatively vertical axis Z. In order to create this trajectory to make the most efficient use of the four-bar linkage with equal length of input and output crank. To simplify design the scheme with usage of one four-bar linkage mounted on the platform making rotational motion relative to the vertical axis Z is developed. Thus the spherical motion is realized by combination of tilting motion created by the four-bar linkage and rotational motion of the supporting platform. Operator tilting simulation in the plane orthogonally to the four-bar linkage position is created by Coriolis force acting on the operator head. Thus platform having only two-DOF gives excellent fidelity of motion. One stage of force analysis has been presented below. The balance equation of forces acting on the dyad 2-3 (Fig.3) in projections on the axis Y is:

$$\sum Y = 0 \Rightarrow \; R_B^{\tau y} + R_B^{ny} + R_D^{ny} + (G + F_y) = 0$$

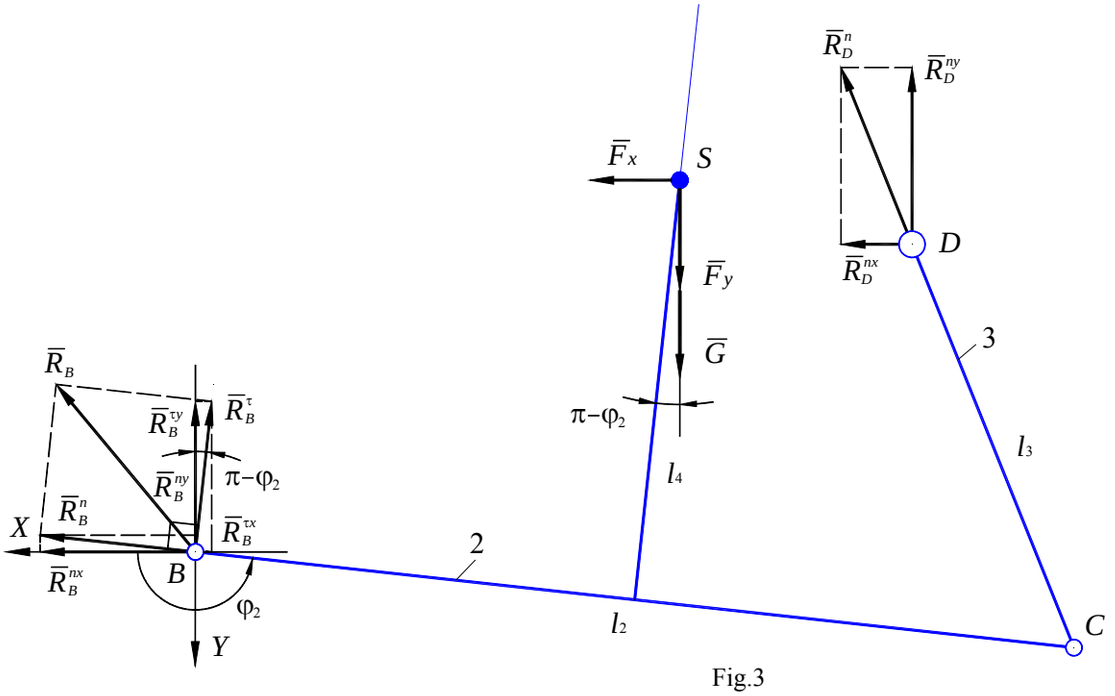


Fig.3

The value of R_D^n can be expressed after mathematical transformation:

$$R_D^n = R_D = \frac{R_B^{\tau} \cdot (\sin(\pi - \varphi_2) \cdot tg(\pi - \varphi_2) - \cos(\pi - \varphi_2)) + F_x \cdot tg(\pi - \varphi_2) - F_y - G}{\cos(\varphi_3 - \pi/2) - \sin(\varphi_3 - \pi/2) \cdot tg(\pi - \varphi_2)}$$

Generalized motion force F_d can be written as:

$$F_d = -R_B^y \cdot \cos\varphi_1 - R_B^x \cdot \sin\varphi_1$$

Motor power without account friction losses is defined:

$$N_{F_d} = F_d \cdot \omega_1 \cdot l_1$$

CONCLUSIONS

Developed construction of the spherical motion platform permits under simplicity of the main detail manufacturing and low system cost allows to diminish the overall dimensions of structure in 1,8 times and reduce the required motor power in 1,4 times in comparison with analogs. In addition the required restrictions about sphere of permissible positions of operator cochlea center and angle of chair tilting for extreme positions are secured. Presented results have been obtained during joint research in frame of contract between Institute of mechanics and reliability of machines of the National academy of sciences of Belarus (IMRM of NAS of Belarus) and Centre Robotique Integre en Ile de France (CRIIF).

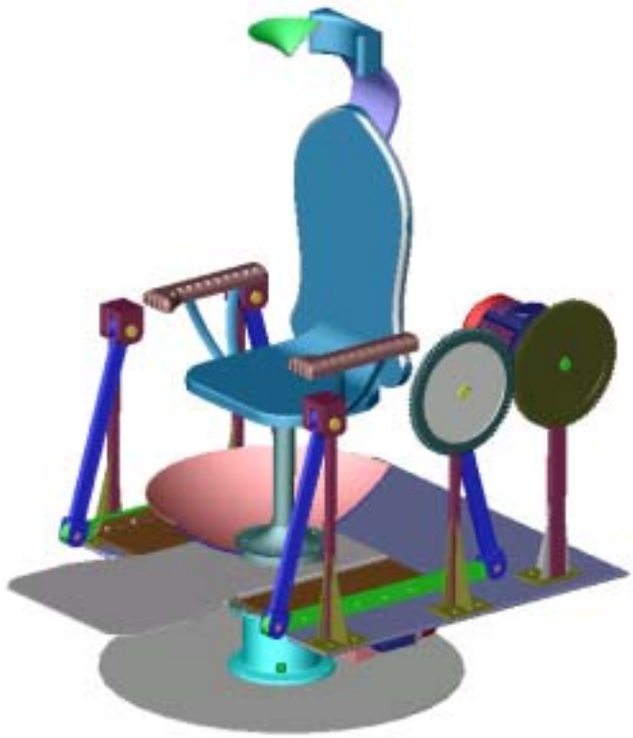


Fig.4

References

[1] Gough V.E., Whitehall S.G. Universal Tire Test Machine. *Proceedings 9th International Technical Congress*, F.I.S.I.T.A., 1962.
[2] Stewart D.A. Platform with Six Degrees of Freedom. *Proceedings Institution of Mechanical Engineers*, London, England, 1965.
[3] Maza M., Fontaine J-G. Motion Transmission in VR Systems: The Spherical Platform Concept. *Topical Workshop on Virtual Reality and Advanced Human-Robot Systems*, ISMCR'99, 15 IMEKO, Tokyo, Japan, 1999.
[4] Tsetserukou D.O. Synthesis of the mechanism of the spherical motion simulation on the basis of the four-bar system. *Proceedings of the Republican conference of young scientists of the National academy of sciences of Belarus "Youth in a science"*, Minsk, 2003.

A GEOMETRICAL FRAMEWORK FOR MODELING AND SIMULATION OF NONHOLONOMIC MECHANICAL SYSTEMS

Wojciech Blajer
Technical University of Radom, Institute of Applied Mechanics, ul. Krasickiego 54, 26-600 Radom, Poland

Summary. A systematic geometrical framework for effective modeling and simulation of nonholonomic systems is presented. Using this powerful means of analysis, different types of equations of motion in dependent and independent variables are obtained in compact matrix forms. Some other relevant aspects – the constraint violation problem, the involvement of independent velocities and their initial values, and the determination of constraint reactions – are also addressed. Some examples are reported.

INTRODUCTION

Many textbooks and even modern studies on analytical dynamics, and especially those devoted to the analysis of nonholonomic (NH) systems, are strongly influenced by various historical approaches and the mathematical description which are rather arduous in practical/computer applications. A large variety of formulations for NH systems [1-3] may sometimes be furthermore misleading – one can never shake off the feeling that some of them had been introduced only to solve a specific problem, and one may sometimes have difficulty in choosing the proper/best method when solving his own problem. A frequent belief is also that disparate approaches to H and NH should be used. This proves truth only in one way – the original formalism of Euler and Lagrange developed for H systems had indeed been found inapplicable to solving NH system problems [1]. The methodologies developed for NH systems are however valid for H systems as well [4-6], and a unified treatment of systems subject to H and/or NH is possible. A legitimate means of presenting these problems in a systematic way is to illustrate them geometrically [6,7].
The aim of this contribution is to present a systematic geometrical framework for effective modeling and simulation of NH systems. Different types of equations of motion in dependent and independent variables are obtained in compact matrix forms. Some other relevant aspects – the constraint violation problem, the involvement of independent velocities and their initial values, and the determination of constraint reactions – are also addressed. Some classical examples of NH systems serve as an illustration of the considerations.

MODELLING OF NONHOLONOMIC SYSTEMS

The starting point is an n-degree-of-freedom system defined in generalized coordinates $\mathbf{p}=[p_1 \dots p_n]^T$ and velocities $\mathbf{v}=[v_1 \dots v_n]^T$, whose kinematical and motion equations are $\dot{\mathbf{p}}=\mathbf{A}(\mathbf{p})\mathbf{v}$ and $\mathbf{M}(\mathbf{p})\dot{\mathbf{v}}+\mathbf{d}(\mathbf{p},\mathbf{v})=\mathbf{f}(\mathbf{p},\mathbf{v},t)$. The system can be viewed as a generalized particle on an n-dimensional manifold $\mathcal{N}$. The n-dimensional tangent space $E^n=T_p(\mathcal{N})$ to $\mathcal{N}$ at $\mathbf{p}\in\mathcal{N}$ is an Euklidean (linear vector) space, and $\mathbf{M}$ is the metric tensor matrix of the basis referred to $\mathbf{v}$ in E^n. By imposing m H and l NH constraints (bilateral and scleronomic for simplicity) on the system, $\mathbf{\Phi}(\mathbf{q})=\mathbf{0}$ and $\mathbf{C}_{nh}(\mathbf{p})\mathbf{v}=\mathbf{0}$, respectively, the attainable configuration is confined to a k-dimensional ($k=n-m$) manifold $\mathcal{K}$, while the degrees of freedom reduce to $r=n-(m+l)=k-l$. A set of independent generalized coordinates $\mathbf{q}=[q_1 \dots q_k]^T$ can then be introduced to define the system position as $\mathbf{q}\in\mathcal{K}$. The k-dimensional tangent space to $\mathcal{K}$ at $\mathbf{q}\in\mathcal{K}$ is then $\overline{E}^k=T_q(\mathcal{K})$, and the metric tensor of the basis referred to $\dot{\mathbf{q}}$ in $\overline{E}^k$ is $\overline{\mathbf{M}}=\mathbf{D}^T\mathbf{M}\mathbf{D}$, arising in k dynamic equations $\overline{\mathbf{M}}(\mathbf{q})\ddot{\mathbf{q}}+\overline{\mathbf{d}}(\mathbf{q},\dot{\mathbf{q}})=\overline{\mathbf{f}}(\mathbf{q},\dot{\mathbf{q}},t)$ obtained using the explicit forms of H constraint equations: $\mathbf{p}=\mathbf{g}(\mathbf{q}) \Rightarrow \mathbf{v}=\mathbf{D}(\mathbf{q})\dot{\mathbf{q}} \Rightarrow \dot{\mathbf{v}}=\mathbf{D}(\mathbf{q})\ddot{\mathbf{q}}+\boldsymbol{\gamma}(\mathbf{q},\dot{\mathbf{q}})$ [6]. Due to NH constraints, $\overline{E}^k$ splits into an r-dimensional subspace $\overline{U}^r$ of admissible velocities and an l-dimensional subspace $\overline{V}^l$ where the system velocity vanishes. Introduced a set of independent velocities $\mathbf{u}=[u_1 \dots u_r]^T$ and the explicit forms of NH constraint equations: $\dot{\mathbf{q}}=\overline{\mathbf{D}}(\mathbf{q})\mathbf{u} \Rightarrow \ddot{\mathbf{q}}=\overline{\mathbf{D}}(\mathbf{q})\dot{\mathbf{u}}+\overline{\boldsymbol{\gamma}}(\mathbf{q},\mathbf{u})$, the minimal-form governing equations of a NH system arise as $k+r$ ordinary differential equations (ODEs) $\dot{\mathbf{q}}=\overline{\mathbf{D}}(\mathbf{q})\mathbf{u}$ and $\widehat{\mathbf{M}}(\mathbf{q})\dot{\mathbf{u}}+\widehat{\mathbf{d}}(\mathbf{q},\mathbf{u})=\widehat{\mathbf{f}}(\mathbf{q},\mathbf{u},t)$, where $\widehat{\mathbf{M}}=\overline{\mathbf{D}}^T\overline{\mathbf{M}}\,\overline{\mathbf{D}}$ is the metric tensor matrix of the basis referred to $\mathbf{u}$ in $\overline{U}^r$.
The above concepts from differential geometry and the associated matrix formulation constitute a useful projective approach [6] to the modelling of NH systems. By applying this geometrical framework, different types of motion equations can be obtained, which, depending on the state variables used, can be grouped as follows.

① When using the dependent states $\mathbf{p}$ and $\mathbf{v}$, the motion equations $\dot{\mathbf{p}}=\mathbf{A}\mathbf{v}$ and $\mathbf{M}\dot{\mathbf{v}}+\mathbf{d}=\mathbf{f}-\mathbf{C}^T\boldsymbol{\lambda}$ are supplemented by the constraint equations either in the original or time-differentiated forms. The obtained differential-algebraic equations (DAEs) can either be solved directly by using the DAE solvers or, after explicit/implicit elimination of Lagrange multipliers $\boldsymbol{\lambda}$, by using the standard ODE integrators.

② Another possibility is to exclude H constraints/reactions from evidence and formulate the motion equations in independent coordinates $\mathbf{q}$ (the velocities $\dot{\mathbf{q}}$ are dependent). The reduced motion equations $\overline{\mathbf{M}}\ddot{\mathbf{q}}+\overline{\mathbf{d}}=\overline{\mathbf{f}}-\overline{\mathbf{C}}_{nh}^T\boldsymbol{\lambda}_{nh}$ are now supplemented by only NH constraints with equations rewritten to $\overline{\mathbf{C}}_{nh}(\mathbf{q})\dot{\mathbf{q}}=\mathbf{0}$. Again, the arising DAEs can be solved directly by using the DAE solvers or integrated indirectly with ODE methods.

③ The final possibility is to use the independent state variables $\mathbf{q}$ and $\mathbf{u}$ as defined above. The obtained minimal-form equations of motion $\dot{\mathbf{q}}=\overline{\mathbf{D}}\mathbf{u}$ and $\widehat{\mathbf{M}}\dot{\mathbf{u}}+\widehat{\mathbf{d}}=\widehat{\mathbf{f}}$ are pure ODEs in the same number of state variables $\mathbf{q}$ and $\mathbf{u}$.

The details of these formulations and their advantages/shortcomings will be the matter of the planned presentation.

OTHER RELEVANT ASPECTS

There are at least four important aspects relevant the modeling and simulation of NH systems in practical applications.

- The constraint violation problem relates to those formulations of group ① and ② in which the constraint equations are involved in the time-differentiated forms. The problem can conveniently be solved by using the geometrical schemes developed in [8], which consist in appropriate corrections of the dependent state variables so that to eliminate the constraint violations after each step of integration or a sequence of steps.
- In formulation ③ independent velocities $\mathbf{u}$ are involved. The way they are defined, and the way the explicit forms $\dot{\mathbf{q}} = \overline{\mathbf{D}}(\mathbf{q})\mathbf{u}$ and $\ddot{\mathbf{q}} = \overline{\mathbf{D}}(\mathbf{q})\dot{\mathbf{u}} + \overline{\boldsymbol{\gamma}}(\mathbf{q},\mathbf{u})$ of NH constraints are obtained will be explained in the presentation. The other related problem is the determination of proper initial values of $\mathbf{u}$ as these may be kinematical parameters of no physical relevance.
- In the reduction procedures leading to formulations ② and ③, respectively the H and both H and NH constraint reactions are excluded from evidence. A novel method for determination of the constraint reactions, naturally associated with the reduction procedures, will be presented. The arising codes are simple and the constraint reactions are obtained in a "resolved" forms, convenient in both symbolic manipulations and computer applications.
- A closely connected problem is "physical" formulation of constraint equations so that the associated Lagrange multipliers appearing in mathematical modelling be forces and moments in physical sense. Each constraint equation must also precisely express/describe a specified vanishing translation/velocity.

ILLUSTRATIVE EXAMPLES

Two classical examples of nonholonomic systems [1] will be reported as illustration. In the first one (Fig. 1), a sharp-edged homogeneous disc that rolls without sliding on the horizontal plane is considered. The disk is subject to one H and two NH constraints. As distinct from many standard formulations, the thickness of the disc can be included to model it as a coin, and the rolling resistance can be considered which makes the H constraint nonideal. The other example is motion of a sphere on the inside of a rough vertical cylinder (Fig. 2). Again, one H and two NH constraints are imposed on the sphere. One of the observations deduced analytically in [1] are the following features of the motion. Looking on the motion "from above" (along *z* axis), the sphere center moves on a circle with a constant angular speed. However, the "side-view" is so that the mass center describes a sinusoid path on the side cylinder surface. The motion corresponds to a paradoxical behavior of a basketball which, when rolling on the basket ring, often goes up and falls out of the basket. This character of the sphere motion will be approved by numerical simulation.

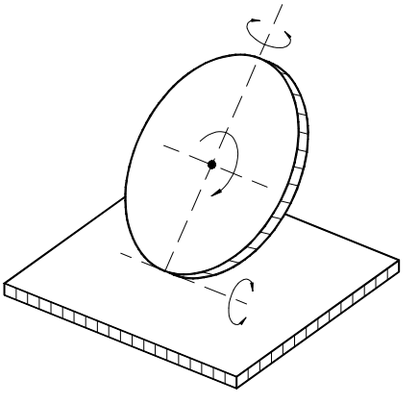


Fig. 1. The rolling disc.

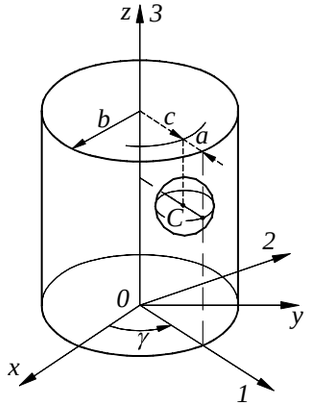


Fig. 2. A sphere moving inside a rough cylinder.

References

[1] Neimark, J.I., Fufaev, N.A.: Dynamics of Nonholonomic Systems (in Russian). Moscow University Publishers, Moscow (1967).

[2] Papastavridis J.G.: A panoramic overview of the principles and equations of motion of advanced engineering dynamics. *Appl Mech Rev* **51**: 239-265, 1998.

[3] Ostovskaya S., Angeles J., Nonholonomic systems revisited within the framework of analytical mechanics. *Appl Mech Rev* **51**: 415-433, 1998.

[4] Kane T.R., Levinson D.A.: Dynamics: theory and applications. McGraw-Hill, New York 1985.

[5] Kurdila A., Papastavridis J.G., Kamat M.P.: Role of Maggi's equations in computational methods for constrained multibody systems. *J Guidance* **13**: 113-120, 1990.

[6] Blajer W.: A geometrical interpretation and uniform matrix formulation of multibody system dynamics. *ZAMM* **81**, 247-259, 2001.

[7] Kielau G., Maißer P.: Nonholonomic multibody dynamics. *Multibody Sys Dyn* **9**: 213-236, 2003.

[8] Blajer W.: Elimination of constraint violation and accuracy aspects in numerical simulation of multibody systems, *Multibody Sys Dyn* **7**: 265-284, 2002.

RESEARCH OF MOVEMENT OF THE MECHANISM SUFFICIENT WITH ELASTIC PART.

Gakhip Ualiyev [*], Zair G. Ualiyev [**]
[*] *Institute of mechanics and machine sciences, Akademgorodok 60, Almaty, Kazakhstan*
[**] *Kazakh national university, Masanchi 39, Almaty, Kazakhstan*

Summary In the given work some principles of drawing up of mathematical models of transfer and executive mechanisms of independent movement with elastic parts are resulted. The system of the equations describing the movement of 2-rocker mechanism with elastic connecting-rod.

The mathematical modeling of complex mechanical systems, especially of multi-mass torsional oscillatory systems with concentrated and distributed masses, in which we have many settlement circuits of technological machines and automatic transfer lines, is connected with constructions of general dynamic models and local models of the executive or transfer cam-lever mechanisms with nonlinear state functions.
In mechanisms with considerable elastic parts the complete cycle of their movement is supposed to be considered as separate periods. In the various periods of movement the elastic parts are represented both as communication, and as source of movement, i.e. movement is carried out at the expense of the potential energies of elastic parts [1].
The movement of a link of reduction of the executive and transfer mechanism can be described by elastic parts with one degree of freedom by such an equation:

$$J_n(\varphi)\ddot{\varphi}(t) + 0{,}5J_n'(\varphi)\dot{\varphi}^2(t) \equiv M_{\Pi}(\varphi), \tag{1}$$

In the period of accumulating, i.e. in process of compression of springs or rotating of the elastic shaft the given moment of forces is represented as the sum of driving M_q and moment of resistance to elastic deformation M_c. The latters depend on the statement of a link of reduction. Inertial parameters - the given moment of inertia of the mechanism $J_n(\varphi)$ is always a positive function.
The return task of dynamics of mechanisms with considerable elastic parts is formulated. The law of movement of the executive mechanism in the period of accumulation is determined by the speed of rotation of the main shaft, which is possibly approximately to consider as constant
α (t) = const. In such case the equation (1) can be written down concerning the given moment of inertia, as the linear differential equation of the first order.

$$\dot{\varphi}^2(t)J_n'(\varphi) + 2\ddot{\varphi}(t)J_n(\varphi) = K\varphi(t), \tag{2}$$

Where $\dot{\varphi}(t)$, $\ddot{\varphi}(t)$ - are angular speeds and acceleration of entrance link of the executive mechanism.
These transfer functions can be determined through functions of the situation between the main shaft of machines — of automatic devices and entrance part of the executive mechanism.

From the equation (2) at $\dot{\varphi}(t) \neq 0, J_{n0} = J_n(\varphi_0)$ the analytical expression of the given moment of inertia is defined $J_n = A(\varphi, \dot{\varphi})$

The decisions of a return task allows to construct mathematical model of the executive mechanism, and by the decision of the equation (1) the law of movement of the mechanism with elastic parts in process of re -accumulating is defined, i.e. in the period of re- twisting of the elastic shaft or release of springs.
The mechanisms of making of duck thread of weaver's machine tools such as STB [2], such as the dashing mechanism, 4-color and 6-color mechanisms of change of duck, the mechanisms of braking construction represent cam-lever mechanisms with elastic parts and connections. And movement in these mechanisms is carried out at the expense of potential energy of twirled torso platen or compressed cylindrical springs. In connection with research of movements of such mechanisms there is a necessity to account final elastic movements of its parts.
In flat 4-part mechanism (fig. 1) the elastic connecting-rod can be considered as well as non-stationary connection. The mathematical expression of deformation of an elastic link allows to unit in one system equations of movement of firm bodies located till both parties of an elastic link. We got differential equation for defining the movement of elastic connecting-rod as following:

$$\frac{d\lambda}{d\varphi_1} - a_1\lambda^2 - b_1\lambda = F(\varphi_1, \dot{\varphi}_2), \tag{3}$$

where $\lambda = l_2 - l_2^0$ change of length of connecting-rod .

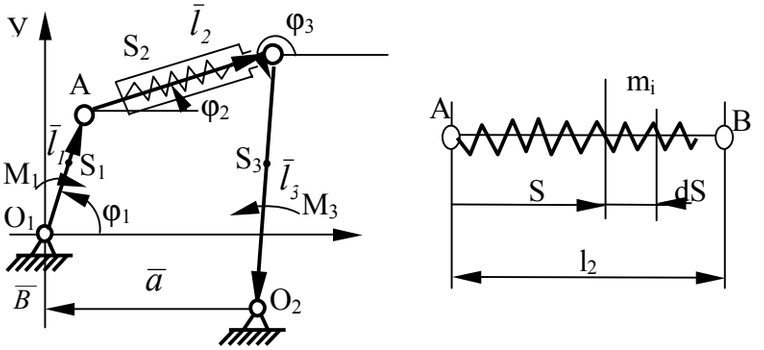


Fig. 1 The mechanism of 4-part machine with elastic connecting-rod.

From the equation (3), as the special case, the well-known expression for small elastic movements will be got [3].
The system of the equations describing the movement of 2-rocker mechanism with elastic connecting-rod is received:

$$\left.\begin{aligned} I_1\ddot{q}_1 + (I_3\ddot{q}_2 + I_3\ddot{q}_3)\Pi' = M_1 - M_3\Pi' \\ I_3\ddot{q}_2 + I_3\ddot{q}_3 + c^* q_2 = -M_3 \end{aligned}\right\}, \tag{4}$$

where $q_1 = \varphi_1, q_2 = \Delta\varphi_3 = \left(\frac{d\Pi}{dl_2}\right)^0 \lambda, q_3 = \Pi(q_1),$

«0» is a statement at $\Delta l_2 = \lambda = l_2 - l_2^0 = 0$

$I_1, I_3 \quad M_1, M_3$ - moments of inertia and moments of forces.

It is shown, that kinetic energy of elastic connecting-rod is defined from the expression

$$2T = m_2\left(l_1^2\dot{\varphi}_1^2 + \dot{\lambda}^2 + 2l_1^2\dot{\varphi}_1\dot{\lambda}\cos\beta\right) + I_2(\varphi_1)\dot{\varphi}_2^2, \tag{5}$$

where $\dot{\lambda} = V_{S_2A}$ - is a component of relative speed of a point S_2 along the connecting-rod;

β - angle between vectors and

I_2 - variable moment of inertia of connecting-rod.

The system of the equations describing movement of the flat 4-part mechanism in view of weight of elastic connecting-rod is received as following:

$$\begin{aligned} I_{11}\ddot{\varphi}_1 + I_{13}\ddot{\varphi}_3 + c\frac{l_1 l_2}{2l_2^2}\cos(\varphi_3 - \varphi_1)\frac{\partial\phi}{\partial\varphi_3} = M_1, \\ I_{31}\ddot{\varphi}_1 + I_{33}\ddot{\varphi}_3 + c\frac{\varphi_3 l_3}{2l_2^2}\cdot\frac{\partial\phi}{\partial\varphi_3}\left(\varphi_3\frac{\partial^2\phi}{\partial\varphi_3^2} + \frac{\partial\phi}{\partial\varphi_3}\right) = M_3, \end{aligned} \tag{6}$$

where $\phi(\varphi_3, l_2)$ - the equation of connection.

The decision of systems of equations (4) defines the laws of movement of 2-rocker mechanism at known deformation of a center of gravity of an elastic part determined from the equation (3). The specified laws of movement for the periods of compression and re-accumulating are defined from systems of equations (6) in view of weight of elastic connecting-rod.

References

[1] Ualiev G.U.: Dynamics of mechanisms and machines. Almaty, 2001.
[2] Djoldasbekov U.A., Ualiev G.U.: Perfection of mechanisms of weaver's machine tools STB. M., Legpromisdat, 1986.
[3] Bat I.: The equation of movement of flat 4-part mechanism with an elastic intermediate link. *Works of a seminar on TMM*, №3, 1957.

HOMOCLINIC ORBITS LAYERING IN THE COUPLED ROTOR NONLINEAR DYNAMICS AND CHAOTIC CLOCK MODELS: A PARADIGM FOR VIBRATIONS AND NOISE IN MACHINES

Katica (Stevanović) HEDRIH
Faculty of Mechanical Engineering University of Niš, Ul. Vojvode Tankosića 3/22, Yu-18 000 - Niš,
Telefax: +381 18 41-663, Mobitel: 063 8 75 75 99, e-mail: katica@masfak.ni.ac.yu; khedrih@eunet.yu

Summary: For examining natural clocks of reductor (power transmission), as well as source of nonlinear vibrations and noise in its dynamics, it is necessary to investigate properties of nonlinear dynamics, and phase portraits, as well as structures of homoclinic orbits, layering and sensitivity of this layering of homoclinic orbits and bifurcation of homoclinic points. In the paper, the natural clocks of nonlinear dynamics of coupled rotors are studied.

Key words: *Homoclinic orbits and points, separatrice layering, trigger, coupled singularities, bifurcation, vector method, mass moment vectors, phase plane and portrait, couple triggers, the form of number eight or it multiplicand, Chaotic Clock Models.*

INTRODUCTION

Dynamics of coupled rotors (see Fig. 1) and of gyrorotors are very old engineering problems with many different search results and discoveries of new nonlinear phenomena, and of stationary and nonstationary vibrations regimes with different kinetic parameters of the dynamical system (see Refs. [2] – [7]). However, even nowadays many researchers pay attention to this problem again.
Chaotic clock models, as well as original ideas on a paradigm for noise in machines were presented by F. Moon (see ref. [11]): "*All machines exhibit a greater or lesser amount of noise. The question arises as to whether a certain level of noise is natural or inevitable in a complex assembly of mechanical or electromechanical devices*? " In the cited paper, the nature of noise or chaos in a specific class of complex multi-body machines, namely the clock was examined.
For examining natural clocks of reductors (power transmission), as well as source of nonlinear vibrations and noise in its dynamics, it is necessary to investigate properties of nonlinear dynamics, and phase portraits, as well as structures of homoclinic orbits, layering and sensitivity of this layering of homoclinic orbits and bifurcation of homoclinic points.
In the paper mass moment vectors introduced by author (see Refs. [2], [5] and [10]), are used to present a vector method for the analysis of kinetic parameter dynamics of coupled rigid rotors with deviational properties of mass changeable distribution and with coupled rotations.
Following up the idea of Mossera that the distance between trajectories be measured maintaining different time scales or "clock" with which time is measured along each motion, Leela (see Ref. [12]) defines the new concepts of orbital stability in term of given topology of the function space. Leela's paper pointed out the different kind of clock. Perfect clock corresponds to stable system dynamics, entire clocks space corresponds to the chaotic topology and chaoticlike dynamics of the system.

Forced Nonlinear Dynamics Differential Equation of Heavy Coupled Rotors in the Field of Turbulent Damping

Our attention is focused on the motion of the representative point on the phase trajectory in the phase plane of forced and free nonlinear dynamics of multi-step coupled heavy rigid rotor dynamics in the field with and without turbulent damping (see Fig. 1. a*). The corresponding differential equation is in the following form (see Ref. [:

$$\ddot{\varphi}_1 + 2\delta_{1M}\dot{\varphi}_1|\dot{\varphi}_1| + \Omega_{1M}^2\left\{\sin\varphi_1 + \left[\sum_{i=2}^{i=M}\frac{\prod_{j=1}^{j=i} i_{j,(j+1)}}{\prod_{j=1}^{j=i}\lambda_{j,(j+1)}}\nu_{1i}^2\sin\left(\prod_{j=1}^{j=i} i_{j,(j+1)}\varphi_1\right)\right]\right\} = h_{1M}\cos\omega t \qquad (1)$$

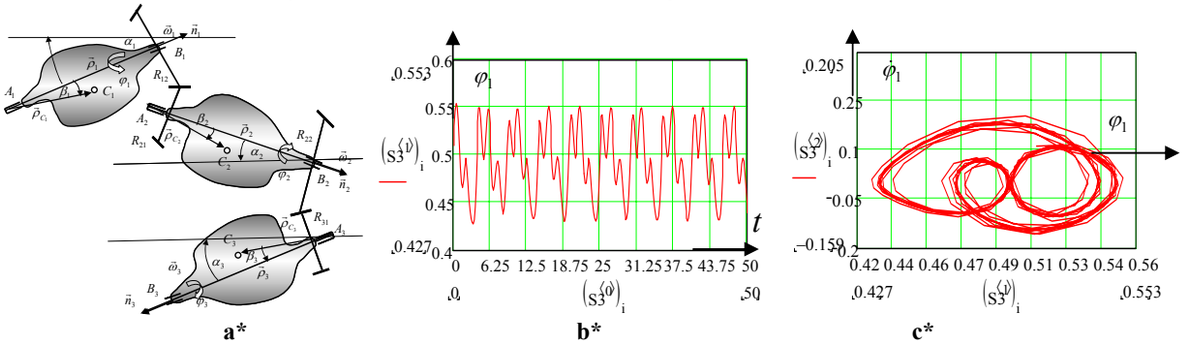


Figure 1. Three-step coupled heavy rotors (a*) forced nonlinear dynamics vizualizations.(reductor and multipliers) . b* Time-history curves; and c* Phase trajectory portraits of the forced nonlinear dynamics.

where φ_1 is generalized coordinate, Ω_{1M} , $\lambda_{j,k}$, $i_{j,k}$ kinetic parameters of the system, h_{1M} , ω and δ_{1M} parameters of external excitations, forced and damping.

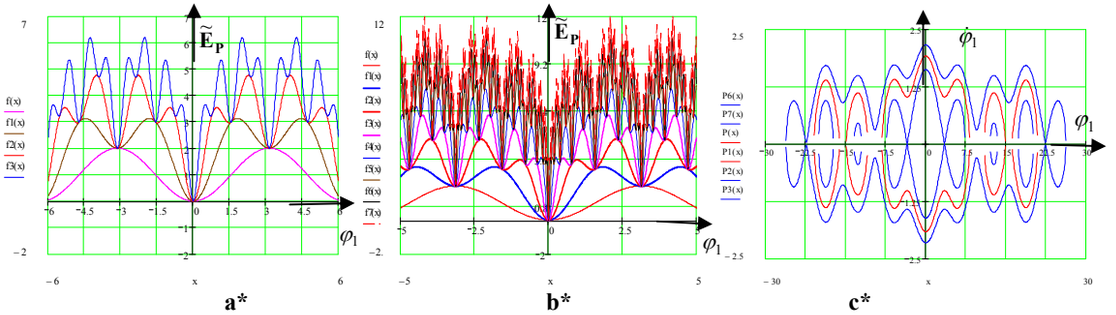


Figure 2. Multistep-coupled heavy rotors free nonlinear dynamics vizualizations (Multipliers).a* and b* Potential energy curves families. c* Phase homoclinic trajectories potraits (constante energy curves). Homoclinic orbits layering for conservative system.

Concluding Remarks

A numerical experiment with the use of derived analytical expressions and of MathCAD program was used to create a visualization of phase portraits of nonlinear dynamics of coupled rotors and the layering of homoclinic orbits with respect to the system parameters change.

The phenomenon of layering of homoclinic orbits with an increased number of coupled rotors is determined, so that in two coupled rotors in the earth's gravity field phase portrait a closed homoclinical orbit in the form of number eight and a trigger of coupled singularities composed of three singular points, one unstable saddle type homoclinic points and two stable centre type points appears. When the number of coupled rotors is greater then two, a greater number of homoclinic orbits layers and triggers of coupled singularities appear in series ordered a* 3, 7, 11, 15, 19....(4i-1) or b* 5, 9, 13, 17, 21,.. (4i+1); i=1, 2, 3, 4, 5,..., N. During that process in the first line (set) of coupled singularities, an odd number of unstable saddle type homoclinic points appears N(2i-1) and an odd number of stable centre type points S(2i) appears, while in the other line of coupled singularities an even number of homoclinic unstable saddle N(2i) type and an odd number of stable center type points S(2i+1) appears. With them, an appropriate number of corresponding closed homoclinic orbits that pass through homoclinic points of unstable saddle type that cut themselves, during which those with higher number of singularities envelop those with smaller number of coupled singularities.

This paper shows, on an example of coupled rotors, the correctness of the trigger of coupled singularities theorem and the existence and nonexistence of homoclinic orbits in the form of number eight theorem formulated by the author in his paper (see Ref. [10]). A theorem of layering of homoclinic orbits and of properties of those orbtis is also formulated.

The existence of the trigger of coupled singularities and closed homoclinic orbits and that their layering with respect to change of kinetic parameters of the system is the cause for the appearance of chaotic and stochasticlike system behaviour under the influence of purely periodical system excitation, as well as the appearance of sensitivity of system dynamics on small changes of starting initial conditions in the area of homoclinic points and oribits, was shown. *Than we conclude that model of reductor has set of natural clocks depending of initial conditions in free and also in forced regimes. We can point out that in this system in the forced regimes of nonlinear motion we have sensitive dependence of the initial conditions, and in this case many possible chaoticlike and stochastic lake processes appear. Than we point out direct coupling between vibrations regime, noise and clock of the system.*

Acknowledgment

Parts of this research were supported by the Ministry of Sciences, Technologies and Development of Republic Serbia trough Mathematical Institute SANU Belgrade Grants No. 1616 Real Problems on Mechanics and Faculty of Mechanical Engineering University of Niš Grant No. 1828 Dynamics and Control of Active Structures.

References

[1] Andronov, A.A., Vitt, A.A., Haykin, S.E., (1981), *Teoriya kolebaniy,* Nauka, Moskva., pp. 568

[2] Hedrih (Stevanović), K. (2001), *The Vector Method of the Heavy Rotor Kinetic Parameter Analysis and Nonlinear Dynamics*, Monograph, University of Niš, 2001, pp. 252., YU ISBN 86-7181-046-1.

[3] Hedrih (Stevanović), K., *Nonlinear Dynamics of a Gyrorotor, and Sensitive Dependence on initial Conditions of a Heavy Gyrorotor Forced Vibration/Rotation Motion*, Semi-Plenary Invited Lecture, Proceednings: 2nd Int. Conf. - Control of Oscilations and Chaos - COC 2000, Edited by F.L. Chernousko and A.I. Fradkov, IUTAM, IEEE, CSS, SPICS, Inst.Probl.Mech.Eng.RAS, St. Pet. 2000., Vol. 2 of 3, pp. 259-266.

[4] Hedrih (Stevanović), K..(1998), *Vectorial method of the kinetic parameters analysis of the rotor with many axes and nonlinear dynamics*, Parallel General Lecture, Third International Conference on Nonlinear Mechanics - ICNM III, August 17-20, 1998, Shanghai, China, pp. .42-47.

[5] Hedrih (Stevanović), K., (1999), *Vectorial Method, Mass Moments Vectors and Rotator Vectors in Nonlinear Heavy Gyrorotor Dynamics*, Abstracts, EUROMECH 3rd ENOC, Copenhagen 1999, 3C, http:// www.imm.dtu.dk/documents/user /mps/ENOC/proceeedings/, 4A, pp. 1-35..

[6] Hedrih (Stevanović) K., Homokliničke orbite nelinearne dinamike višestepenog Reduktora (Homoclinic Orbits of Nonlinear Dynamics of Multi-step Reductor), Nauka Tehnika Bezbednost – NTB, Godina XII, No. 1(2002) 45-65., UDC 531.3.YU ISSN 0353-5517, UDC 62+66:54(05).

[7] Hedrih (Stevanović) K., *Fascinating Nonlinear Dynamics of a Heavy Material Particle(s) Along Circle(s) with Coupled Rotations,* Booklet of Abstaracts, IUTAM Symposium on Chaotic Dynamics and Control of Systems and Processes in Mechanics, Dipartimento di Ingegneria Strutturale e Geotecnica, *Università di Roma "La Sapienza", Roma, Italy, 2003, pp. 85-86.*

[8] Hedrih (Stevanović) K., *A Trigger of Coupled Singularities*, MECCANICA, Vol.38, No. 6, 2003., pp. 623-642. International Journal of the Italian Association of Theoretical and Applied mechanics, CODEN MECC B9, ISSN 025-6455, Kluwer Academic Publisher.

[9] Katica (Stevanović) Hedrih, *On Rheonomic Systems with Equaivalent Holonomic Conservative System,* Forth Int. Conf. Nonlinear Mechanics (ICNM-IV), ed. by Wei Zang Chien and All, 2002, Shanghai, pp. 1046-1054. ISBN 7-81058-077-9/0-007.

[10] Hedrih (Stevanović), K., (1992), *On some interpretations of the rigid bodies kinetic parameters,* XVIIIth ICTAM HAIFA, Apstracts, pp. 73-74.

[11] Moon F,C.: Chaotic Clock Models: A Paradigm for Noise in Machines, Booklet of Abstaracts, IUTAM Symposium on Chaotic Dynamics and Control of Systems and Processes in Mechanics, Dipartimento di Ingegneria Strutturale e Geotecnica, *Università di Roma "La Sapienza", Roma, Italy, 2003, pp. 41-44.*

[12] Leela S.: *A new Unified Concept of Stability,* Facta Universitatis Series Mechanics, Automatic Control and Robotics, Vol. 3, No.16, 2004.

DESIGN OF THE REAR CARRIAGE STABILIZER OF A LOW-FLOOR ARTICULATED TROLLEYBUS

Pavel Polach*
*ŠKODA RESEARCH Ltd., Tylova 57, CZ 316 00 Pilsen, Czech Republic

Summary During test drives with a low-floor articulated trolleybus focused on the vehicle driving stability considerable rolling of the rear carriage appeared during all the driving manoeuvres. Using a stabilizer in the rear carriage is a suitable constructional solution. Verification of the suitability of its constructional solution from the point of view of the required effect on the driving stability was performed using the computer simulations with the trolleybus multibody models.

INTRODUCTION

Computer simulations are irreplaceable in solving concrete problems of technical practice especially when experimental measurements on a real product cannot be carried out. Computer programs meant for the kinematic and dynamic analysis of mechanical systems are an important instrument in developing and improving vehicles´ properties and in improving comfort and passive safety of a driver and passengers [1].
ŠKODA RESEARCH Ltd. has been cooperating with the producer of road vehicles of municipal public transport ŠKODA OSTROV Ltd. [2] for a long time. The ŠKODA 22 Tr low-floor articulated trolleybus has been produced in ŠKODA OSTROV Ltd. since 1996. In the course of trolleybus modernization in 2002 other type of the articulation and driving axles was used in construction among others. During test drives with the modernized trolleybus focused on the vehicle driving stability considerable rolling of the rear carriage appeared during all the driving manoeuvres. Using a stabilizer in the rear carriage is a suitable constructional solution. Verification of the suitability of its constructional solution from the point of view of the required effect on the driving stability was performed using the computer simulation with the trolleybus multibody models. Multibody models of the ŠKODA 22 Tr low-floor articulated trolleybus with the HÜBNER articulation, the RÁBA driving axles and the rear carriage stabilizer [3] are created in the **alaska** software [4].

MULTIBODY MODELS OF THE ARTICULATED TROLLEYBUS

Multibody models of the both empty and loaded ŠKODA 22 Tr low-floor articulated trolleybus with the HÜBNER articulation, the RÁBA driving axles and the rear carriage stabilizer [3] were created on the basis of the data and technical documentation provided by the producer. They are formed by 47 rigid bodies, which are mutually coupled by 57 kinematic joints. The degree of freedom of the multibody models is 157. Air springs, shock absorbers and silentblocks are modelled by connecting the corresponding bodies by the force spring-damper elements. Pacejka formulae are used to describe the tires´ directional properties [4].
The proposed constructional solution considered the rear carriage stabilizer made of a steel bar of the circle cross section, the optimum diameter of which was to be determined on the basis of the computer simulations´ results. In the trolleybus multibody models the rear carriage stabilizer is not considered to be the individual rigid body, its activity is modelled by acting the external forces on the rear carriage chassis and the rear axle and their magnitude is dependent on the rear carriage roll angle.

SIMULATIONS OF TEST DRIVES

Simulations of test drives according to the experimental measurements documented in [5] were performed with the multibody models of the both empty and loaded ŠKODA 22 Tr trolleybus. Measurements were performed in the chosen sections of the trolleybus lines in Ústí nad Labem (Czech Republic) in March 2002. Originally the measurements should have been only verifying, the necessity of using the stabilizer and the application of computer simulations were not considered at that time. Time histories of steering wheel angle, speed and vehicle mass were the input data for the test drives simulations.
Simulations were performed with multibody models both without the stabilizer and with the stabilizer of the rear carriage. The monitored quantities were, like in case of experimental measurements, time histories and extreme values of the angle of mutual position of the trolleybus front and rear carriages, rear carriage roll angle and lateral acceleration of the rear carriage above the rear axle. In addition in the course of simulations with multibody models the extreme values of time histories of torsional deformations of articulated joint and relative deflections of the rear axle were monitored. Further in the course of simulations with the trolleybus multibody models with the rear carriage stabilizer the extreme values of time histories of the stabilizer vertical deformation and of forces acting between the stabilizer and the rear axle and between the stabilizer and the rear carriage chassis were monitored.
Results of the simulations were used for the evaluation of the effect of the proposed stabilizer constructional solution on the trolleybus driving stability improvements (especially on decreasing the rear carriage roll angle) and for the

determination of the cause of the considerable local extremes in the time histories of the measured quantities during the test drives with he real trolleybus (it was not obvious if they were caused by exceeding the limited torsional deformation of the articulation or by rear carriage bottoming on the rear axle bump stops).

RESULTS

Comparison of the results of the simulations and the test drives with the real trolleybus without a stabilizer

Time histories and extreme values of the monitored quantities found out in the course of experimental measurements on the real trolleybus and in the course of simulations with multibody models are not fully identical. Differences are caused on the one hand by the ignorance of all the conditions of the test drives with the real trolleybus needed for more precise simulations (initial conditions when recording the experimental measurements were not fully known – distances of the rear carriage and rear axle bump stops are not known as well as the time histories of the real trolleybus speed – keeping constant speed for all the duration of the driving manoeuvre is improbable) and on the other hand by the character itself of the computer models (virtual model is always the simplification of the real construction). But in any case those facts do not affect the information abilities of simulations.

Simulations confirmed, that the cause of considerable local extremes in the time histories of the measured quantities during the test drives with the real trolleybus is in rear carriage bottoming on the rear axle bump stops. Maximum elastic torsional deformation of the HÜBNER articulation, which is 3°, was not achieved during the simulation of any test drive. Rear carriage bottoming on the rear axle bump stops was found out during the simulations of the same drives like during the experimental measurements. Extreme values of the time histories of lateral acceleration of the rear carriage above the rear axle found out in the course of the test drives with the real trolleybus and in the course of simulations with multibody models are approximately identical. Extreme values of the time histories of the angle of mutual position of the front and rear carriages of the empty trolleybus determined during the simulation are smaller and those of the loaded trolleybus are greater. Extreme values of the time histories of the rear carriage roll angle found out during the simulation are smaller. Differences are less considerable than with the angle of mutual position of the front and rear carriages.

Results of the trolleybus with the rear carriage stabilizer simulations

Simulations of test drives with the multibody models of the ŠKODA 22 Tr trolleybus with the rear carriage stabilizer were performed for various diameters of the steel rod of the circle cross section, which the stabilizer was to be made of. Time histories and extreme values of the angle of mutual position of the front and rear carriages and lateral acceleration of the rear carriage above the rear axle does not almost differ from time histories and extreme values found out during the simulations with the multibody models of the trolleybus without the stabilizer for all the verified rod diameters. Extreme values of time histories of the rear carriage roll angle and thus also extreme values of other related quantities – relative deflections of the rear axle suspension and torsional deformations of the articulated joint – decreased significantly.

CONCLUSIONS

On the basis of the results of the test drives simulations the optimum diameter of the steel rod used for the stabilizer production (0.04m) was proposed and the suitability of the complete constructional solution of the rear carriage stabilizer of the ŠKODA 22 Tr low-floor articulated trolleybus with the HÜBNER articulation and the RÁBA driving axles for improving its driving stability was confirmed. In the course of simulated drives the rear carriage roll angles decreased by 20 % to 30 % considering the original state owing to the use of the proposed stabilizer. During the simulation of any test drive with the multibody models with the rear carriage stabilizer neither the maximum permitted stabilizer deformation nor the maximum permitted forces acting on the stabilizer were exceeded.

References

[1] Polach P.: Multibody Simulations of a Low-Floor Trolleybus Model with a Driver and Passengers. *CD-ROM Proc. of ECCOMAS Thematic Conference on Advances in Computational Multibody Dynamics 2003*, Lisbon, 2003.
[2] Kepka M., Hejman M., Polach P., Václavík J.: Using the Computer Simulations at Trolleybus Development: Strength, Dynamic and Fatigue. *CD-ROM Proc. European Conference on Computational Mechanics '99*, Munich, 1999.
[3] Polach P.: Multibody Models of the ŠKODA 22 Tr Low-Floor Articulated Trolleybus - Modification with the HÜBNER Articulation, the RÁBA Driving Axles and the Rear Carriage Stabilizer. *Research Report ŠKODA RESEARCH Ltd.* VYZ 0569/2002, Pilsen, 2003. (in Czech)
[4] ***alaska**, User Manual, Version 2.3*. Institute of Mechatronics Chemnitz, 1998.
[5] Report No. 40103-02. L16 Laboratory of Maneuverability and Driving Comfort, Institute for the Research of Motor Vehicles, Prague, 2002. (in Czech)

STABILIZATION BY ROTATING RIGID BODIES FOR UNSTABLE ROTATION OF A RIGID BODY WITH CAVITIES CONTAINING A FLUID

Kononov Y. N., Khom'yak T. V.

On XII International congress on theoretical and applied mechanics (ICTAM 1972) A. Y. Ishlinsky [1] has set the problem about definition of conditions for stability of uniform rotations of system in two heavy gyroscopes of Lagrange. The interesting effect of stabilization in unbalanced gyroscope of Lagrange by the second rotating [2, 3] has been found in the works of Donetsk school on mechanics under supervision of P.V.Kharlamov. In S. L. Sobolev's known work [4] it is shown that the Lagrange gyroscope if contains the perfect fluid is rather unstable. Therefore, the problem on the possibility of stabilization in unstable rotation of the gyroscope in question by one or two rotating rigid bodies has been put out.

The possibility for stabilization by rotating rigid bodies in unstable rotation of the Lagrange gyroscope containing a perfect fluid is shown in our study. The case of free motion and the case when the Lagrange gyroscope with fluid rotates about a fixed point are considered. The equations of the works [5, 6] are foundations of the conclusion on the motion equations for the considered mechanical system.

1. Free system of the connected rigid bodies with fluid (SCRBF).

Consider free motion of the rotating Lagrange gyroscope with a cavity containing a perfect fluid. Let the considered gyroscope (body S_2) have the common points O_2 and O_3 with rotating rigid bodies S_1^0 and S_3^0 accordingly (fig. 1). The body S_2 consists of a rigid body S_2^0 with a cavity entirely filled with a perfect fluid of the density ρ and is connected with rigid bodies S_1^0 and S_3^0 in points O_2 and O_3 by elastic restoring spherical hinges k_1 and k_2 accordingly ($k_1 > 0, k_2 > 0$). Rigid bodies are rotating with angular velocities ω_{0i} about the common axis of symmetry (i=1, 2, 3). We set the problem on the possibility for stabilization by rotating rigid bodies S_1^0 and S_3^0 for unstable free motion of rotating body S_2. The characteristic equation of motion of the system above is as follows [6]:

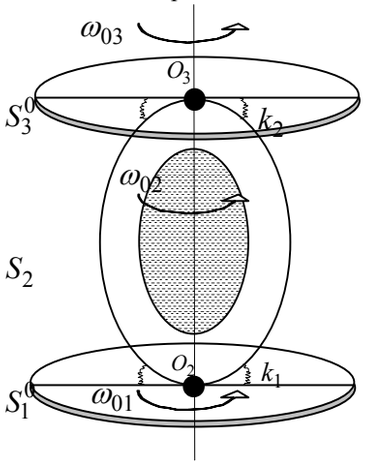


Fig. 1.

$$\begin{vmatrix} F_1 & \mu_1 + \dfrac{k_1}{\lambda^2} & \mu_2 \\ \mu_1 + \dfrac{k_1}{\lambda^2} & F_2 & \mu_3 + \dfrac{k_2}{\lambda^2} \\ \mu_2 & \mu_3 + \dfrac{k_2}{\lambda^2} & F_3 \end{vmatrix} = 0 \qquad (1)$$

Here

$$F_i = A_i' + \frac{C_i\omega_{0i}}{\lambda} - \frac{k_{i-1} + k_i}{\lambda^2},\ (i = 1,3),\ k_0 = k_3 = 0,$$

$$F_2 = A_2' + \frac{C_2\omega_{02}}{\lambda} - \frac{k_1 + k_2}{\lambda^2} - (\lambda + \omega_{02})\sum_{n=1}^{\infty}\frac{E_n}{\lambda + \omega_{02}\lambda_n^*},$$

$$A_1' = A_1 + \frac{m_1 m_{23}}{m}c_1^2,\ A_2' = A_2 + \frac{1}{m}(m_2 m_{31}c_2^2 - 2m_2 m_3 c_2 s_2 + m_3 m_{12}s_2^2),\ A_3' = A_3 + \frac{m_3 m_{12}}{m}c_3^2,$$

$$\mu_1 = \frac{m_1 c_1}{m}(m_2 c_2 + m_3 s_2),\ \mu_2 = \frac{m_1 m_3}{m}c_1 c_3,\ \mu_3 = \frac{m_3 c_3}{m}[m_1 s_2 + m_2(s_2 - c_2)],$$

$$m = m_1 + m_2 + m_3,\ m_{ij} = m_i + m_j,\ \lambda_n^* = 1 - \tilde{\lambda}_n,\ \tilde{\lambda}_n = \lambda_n/\omega_{02},\ c_i = C_i O_i,\ s_2 = O_2 O_3,$$

A_i, C_i - equatorial and axial inertia moments of the bodies S_1^0, S_2 and S_3^0 as to their centers of weights. The definition of other variables is given in the work [6].

The necessary condition fort stability of uniform rotation in the considered system is the following: all roots of the characteristic equation (1) are real.

2. Not free system of the connected rigid bodies with fluid (SCRBF).

Let point O_2 be fixed (Fig. 1). In this case the characteristic equation is the following [5]:

$$\begin{vmatrix} F_1 & s_1a_2+\dfrac{k_1}{\lambda^2} & s_1a_3 \\ s_1a_2+\dfrac{k_1}{\lambda^2} & F_2 & s_2a_3+\dfrac{k_2}{\lambda^2} \\ s_1a_3 & s_2a_3+\dfrac{k_2}{\lambda^2} & F_3 \end{vmatrix} = 0. \qquad (2)$$

Here

$$F_i = A_i' + \frac{C_i\omega_{0i}}{\lambda} + \frac{a_ig - k_{i-1} - k_i}{\lambda^2},\ (i=1,3),\ k_0 = k_3 = 0,$$

$$F_2 = A_2' + \frac{C_2\omega_{02}}{\lambda} + \frac{a_ig - k_1 - k_2}{\lambda^2} - (\lambda+\omega_{02})\sum_{n=1}^{\infty}\frac{E_n}{\lambda+\omega_{02}\lambda_n^*},$$

$$A_1' = A_1 + m_{23}s_1^2,\ A_2' = A_2 + m_3s_2^2,\ A_3' = A_3,\ m_{ij} = m_i + m_j,$$

$$a_1 = m_1c_1 + s_1m_{23},\ a_2 = m_2c_2 + s_2m_3,\ a_3 = m_3c_3,$$

$$\lambda_n^* = 1 - \widetilde{\lambda}_n,\ \widetilde{\lambda}_n = \lambda_n/\omega_{02},\ c_i = C_iO_i,\ s_1 = O_1O_2,\ s_2 = O_2O_3.$$

From a kind of the characteristic equations (1) and (2) it follows that if one elastic restoring moment (ki=0) is absent and the center of weights of a rigid body S_i^0 is a common point, each and every of the equations (1) and (2) will be divided into two independent equations, and the rotation of a rigid body S_i^0 will not effect the conditions of stability (i=1, 2). If the both of elastic restoring moments (k_1=k_2=0) are absent and the centers of weights of bodies S_1^0 and S_3^0 are points O_2 and O_3 accordingly, each and every of the equations (1) and (2) will be divided into three independent equations, and, in this case, the stabilization effect for unstable rotation of a body S_2 by rotating rigid bodies S_1^0 and S_3^0 will be absent.

Numerical studies of the characteristic equations (1), (2) have been carried out for ellipsoidal and cylindrical cavities, as well as for rigid bodies S_1^0 and S_3^0 as flat, convex and concave circular disks for constant weight of a fluid.

Following analytical and numerical researches the conclusions are made:

1) To stabilize for unstable rotation of a rigid body with cavities containing a fluid is possible by virtue of one or two rotating rigid bodies.
2) If elastic restoring moments are absent and the centers of weights of rotating rigid bodies are common points SCRBF, stabilization will be impossible.
3) For the counterbalanced rotating rigid bodies (c_1<0, c_2<0) the effect of stabilization increases in comparison with unbalanced rigid bodies (c_1=0, c_2=0).

The literature:

1. Ishlinsky A. Yu. On the dynamics of a system of rigid bodies // Theor. and Appl. Mech. - Berlin etc, 1973. - P. 141-149.
2. Savchenko A. J. Stability for stationary motion of mechanical systems. Kiev, 1977. - 160 p.
3. Savchenko A. J., Bolgrabskaja I. A., Kononyhin G. A. Stability for motion of systems connected rigid bodies. - Kiev, - 1991. - 168 p.
4. Sobolev S. L. On the motion of a symmetric top with a cavity filled a fluid // Appl. Math. Tech.phiz, 1960. - №3. - P. 20-55.
5. Kononov Y. N. On the motion of system two rigid bodies with cavities containing a fluid // Mech. rigid body. – 1997, 29. – P. 76-85.
6. Kononov Y. N. On the motion of system connected rigid bodies with cavities containing a fluid // Mech. rigid body. - 2000, 30. - P. 207-216.

SIMULATION OF CONSTRAINED RIGID AND ELASTIC BODIES WITHOUT CONSTRAINT EQUATIONS

Oleg N. Dmitrochenko, Dmitry Yu. Pogorelov
Bryansk State Technical University
B. 50 let Oktyabrya 7, 241035 Bryansk, Russia
{don,pogorelov}@tu-bryansk.ru

Su-Jin Park, Wan-Suk Yoo
Pusan National University, Busan, Korea
Kumjung-Ku, Busan 609-735, Korea
{psjjk,wsyoo}@pusan.ac.kr

Summary Mechanical systems of both rigid and elastic bodies are considered. Differential-algebraic equations (DAE) of their motion and a technique of elimination of the algebraic part to obtain ordinary differential equations (ODE) are discussed.

INTRODUCTION

The most common case of coupling rigid and elastic bodies 1 and 2 assumes employing DAE like these:

$$\begin{aligned}&\mathbf{M}_1\ddot{\mathbf{x}}_1 = \mathbf{f}_1 + (\mathbf{G}_1^{\mathrm{T}}\boldsymbol{\lambda})\\ &\mathbf{M}_2\ddot{\mathbf{x}}_2 = \mathbf{f}_2 + (\mathbf{G}_2^{\mathrm{T}}\boldsymbol{\lambda})\\ &(\mathbf{g}(\mathbf{x}_1,\mathbf{x}_2) = \mathbf{0})\end{aligned} \qquad (1)$$

with mass matrices $\mathbf{M}_i$, generalized forces $\mathbf{f}_i$ and coordinates $\mathbf{x}_i$ of the two bodies. Constraints $\mathbf{g}$ result in reaction forces $\mathbf{G}_i^{\mathrm{T}}\boldsymbol{\lambda}$ with Jacobian matrices $\mathbf{G}_i = \partial\mathbf{g}/\partial\mathbf{x}_i^{\mathrm{T}}$ and undefined Lagrangian multipliers $\boldsymbol{\lambda}$: dim $\boldsymbol{\lambda}$ = dim $\mathbf{g}$. DAE introduce additional difficulties into numerical investigations such as problems of constraint violations. They can be successfully solved using special methods, e.g. [5]. However in many cases it is possible to avoid DAE, for example, in the finite element method (FEM).

THE ASSEMBLING PROCEDURE IN FEM

Let us consider two finite elements shown as beams in Fig. 1. Let 1st FE's nodal coordinates are divided on two parts $\mathbf{x}_1$ and $\mathbf{x}_2$, while those for 2nd one are $\mathbf{x}_3$ and $\mathbf{x}_4$, so that $\mathbf{x}_2$ and $\mathbf{x}_3$ are compatible (the elements can be linked in these variables).

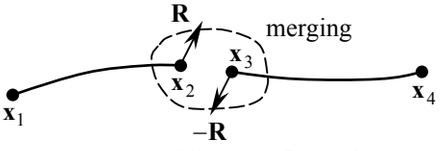


Figure 1. Assembling two finite elements

Equations of motion of the two elements are:

$$\begin{cases}\mathbf{M}_{11}\ddot{\mathbf{x}}_1 + \mathbf{M}_{12}\ddot{\mathbf{x}}_2 = \mathbf{f}_1\\ \mathbf{M}_{21}\ddot{\mathbf{x}}_1 + \mathbf{M}_{22}\ddot{\mathbf{x}}_2 = \mathbf{f}_2 + (\mathbf{R})\end{cases}$$

$$\begin{cases}\mathbf{M}_{33}\ddot{\mathbf{x}}_3 + \mathbf{M}_{34}\ddot{\mathbf{x}}_4 = \mathbf{f}_3 - (\mathbf{R})\\ \mathbf{M}_{43}\ddot{\mathbf{x}}_3 + \mathbf{M}_{44}\ddot{\mathbf{x}}_4 = \mathbf{f}_4\end{cases}$$

$$(\mathbf{x}_2 \equiv \mathbf{x}_3 = \mathbf{x}_*)$$

with mass matrices $\mathbf{M}_{ij}$, generalized forces $\mathbf{f}_i$ and reaction forces $\mathbf{R}$. Terms in brackets appear when the elements are joined as shown in Fig. 1. The equations have DAE form (1) but the constraints are trivial. Eliminating $\mathbf{R}$ from the second and third equations and accounting the fifth one leads to ODE

$$\left[\begin{array}{c|c|cc} \mathbf{M}_{11} & \mathbf{M}_{12} & & \mathbf{O} \\ \hline \mathbf{M}_{21} & \mathbf{M}_{22} + \mathbf{M}_{33} & \mathbf{M}_{34} & \\ \hline \mathbf{O} & & \mathbf{M}_{43} & \mathbf{M}_{44} \end{array}\right] \left\{\begin{array}{c}\ddot{\mathbf{x}}_1\\ \ddot{\mathbf{x}}_*\\ \ddot{\mathbf{x}}_4\end{array}\right\} = \left\{\begin{array}{c}\mathbf{f}_1\\ \mathbf{f}_2 + \mathbf{f}_3\\ \mathbf{f}_4\end{array}\right\}$$

where the whole system mass matrix and generalized forces are composed of that for separated elements. Further we will use this idea to assemble rigid and elastic bodies to each other.

Compatible coordinates of rigid and elastic bodies

The possibility of eliminating constraint equations depends on compatibility of coordinates of rigid and elastic bodies ($\mathbf{x}_2$ and $\mathbf{x}_3$ above). Rigid bodies usually have rotation angles as generalized coordinates: e.g. φ in 2D case or any triplet α, β, γ in 3D case.

We consider large displacement finite-element formulations for simulation of elastic bodies. One of them is the *large rotation vector formulation* [3], which employs absolute rotation angles. For example, plane beam elements in Fig. 1 have the following structure of generalized coordinates: $\mathbf{x}_i = \{x_i, y_i, \varphi_i\}^{\mathrm{T}}$, where x_i and y_i are absolute Cartesian coordinates of i-th node while φ_i is the absolute rotation angle of the beam cross section. 3D beam and plate elements in this formulation [2] have nodal coordinates like these: $\mathbf{x}_i = \{x_i, y_i, z_i, \alpha_i, \beta_i, \gamma_i\}^{\mathrm{T}}$. Obviously, these finite elements can be easily assembled with rigid bodies due to coordinate compatibility.

FEM formulations with incompatible coordinates

Another large displacement finite-element approach is the *absolute nodal coordinate formulation* (ANCF). The structure of nodal coordinates for beam elements in this method is as follows (cf. Fig. 1 and 2): $\mathbf{x}_i = \{\mathbf{r}_i^{\mathrm{T}}, \boldsymbol{\tau}_i^{\mathrm{T}}\}^{\mathrm{T}}$, where $\mathbf{r}_i$ and $\boldsymbol{\tau}_i$ are the absolute radius vectors and the slope vectors. This approach leads to a constant mass matrix and zero centrifugal and Coriolis inertia forces, in contrast to other large displacement formulations [6]. It is clear that attaching a 2D rigid body to such an

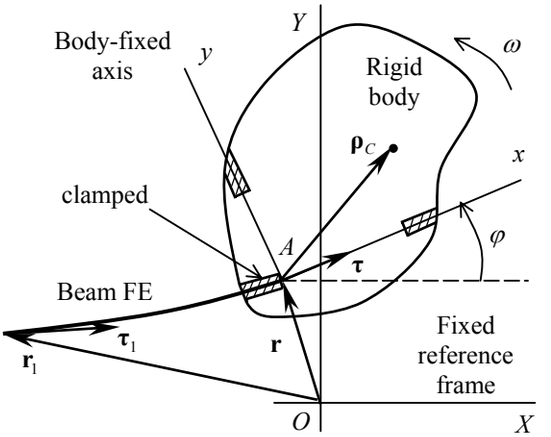


Figure 2. Rigid body attached to a beam element

ANCF beam element [7] leads to the constraint equation

$$\varphi = \arctan(\tau_Y / \tau_X) \qquad (2)$$

and, therefore, to differential-algebraic equations (1).

To eliminate the constraints we must make the rigid body coordinates compatible to that for beam element:

$$\mathbf{x} = \{\mathbf{r}^{\mathrm{T}}, \boldsymbol{\tau}^{\mathrm{T}}\}^{\mathrm{T}}. \qquad (3)$$

We introduce four scalar coordinates for planar rigid body and must redevelop its equations of motion [7].

Angular velocity of the body is derived from (2):

$$\omega = \dot{\varphi} = \frac{\dot{\boldsymbol{\tau}}^{\mathrm{T}} \widetilde{\mathbf{I}} \boldsymbol{\tau}}{\tau^2}, \text{ where } \widetilde{\mathbf{I}} = \begin{bmatrix} 0 & -1 \\ +1 & 0 \end{bmatrix}, \ \tau^2 = \tau_X^2 + \tau_Y^2 .$$

Velocity vector of an arbitrary point $\boldsymbol{\rho}$ of the body is

$$\mathbf{v} = \dot{\mathbf{r}} + \widetilde{\boldsymbol{\omega}}\boldsymbol{\rho} = \boldsymbol{\Phi}\dot{\mathbf{x}},$$

where the velocity transformation Jacobian matrix $\boldsymbol{\Phi} = \begin{bmatrix} \mathbf{I} & \widetilde{\mathbf{I}}\boldsymbol{\rho}\boldsymbol{\omega}_{\boldsymbol{\tau}}^{\mathrm{T}} \end{bmatrix}$ is introduced, $\boldsymbol{\omega}_{\dot{\boldsymbol{\tau}}} = \partial\omega / \partial\dot{\boldsymbol{\tau}} = \widetilde{\mathbf{I}}\boldsymbol{\tau} / \tau^2$.

Then, we use the principle of virtual work

$$\int_V \delta\mathbf{r}^{\mathrm{T}} \mu(\mathbf{a} - \mathbf{g}) \mathrm{d}V = 0 \qquad (4)$$

with virtual displacement $\delta\mathbf{r} = \boldsymbol{\Phi}\delta\mathbf{x}$ and acceleration $\mathbf{a} = \dot{\mathbf{v}} = \boldsymbol{\Phi}\ddot{\mathbf{x}} + \dot{\boldsymbol{\Phi}}\dot{\mathbf{x}}$ of a body point $\boldsymbol{\rho}$. Integration in the body volume V is assumed. μ is the body mass density while $\mathbf{g}$ is the gravity acceleration.

Equations of motion (4) take the matrix form

$$\mathbf{M}\ddot{\mathbf{x}} + \mathbf{f}^{\mathrm{inert}} = \mathbf{f}^{\mathrm{grav}}, \qquad (5)$$

$$\mathbf{M}(\mathbf{x}) = \int_V \mu \boldsymbol{\Phi}^{\mathrm{T}} \boldsymbol{\Phi} \mathrm{d}V = \begin{bmatrix} m\mathbf{I} & m\widetilde{\mathbf{I}}\boldsymbol{\rho}_C \boldsymbol{\omega}_{\dot{\boldsymbol{\tau}}}^{\mathrm{T}} \\ m\boldsymbol{\omega}_{\dot{\boldsymbol{\tau}}}(\widetilde{\mathbf{I}}\boldsymbol{\rho}_C)^{\mathrm{T}} & I_A \boldsymbol{\omega}_{\dot{\boldsymbol{\tau}}} \boldsymbol{\omega}_{\dot{\boldsymbol{\tau}}}^{\mathrm{T}} \end{bmatrix},$$

$$\mathbf{f}^{\mathrm{inert}}(\mathbf{x}, \dot{\mathbf{x}}) = \int_V \mu \boldsymbol{\Phi}^{\mathrm{T}} \dot{\boldsymbol{\Phi}} \mathrm{d}V \, \dot{\mathbf{x}} = -\mathbf{M} \begin{Bmatrix} \omega^2 \boldsymbol{\rho}_C \\ 2\tau^{-2}(\boldsymbol{\tau}^{\mathrm{T}}\dot{\boldsymbol{\tau}})\dot{\boldsymbol{\tau}} \end{Bmatrix},$$

$$\mathbf{f}^{\mathrm{grav}}(\mathbf{x}) = \int_V \mu \boldsymbol{\Phi}^{\mathrm{T}} \mathrm{d}V \, \mathbf{g} = \begin{Bmatrix} m\mathbf{g} \\ \boldsymbol{\omega}_{\dot{\boldsymbol{\tau}}} m \mathbf{g}^{\mathrm{T}} \widetilde{\mathbf{I}} \boldsymbol{\rho}_C \end{Bmatrix}.$$

Here m is the body mass, $\boldsymbol{\rho}_C$ is the position of the body mass center in axes XY and I_A is the body mass inertia moment (both with respect to the attachment point A).

Attaching a rigid body to ANCF plate element

There are implementations of plate elements in ANCF proposed by various authors [4], [1]. All of them use, similarly to 2D beam elements, absolute nodal radius vectors and slopes as generalized coordinates (Fig. 3):

$$\mathbf{x} = \{\mathbf{r}^{\mathrm{T}}, \boldsymbol{\tau}_1^{\mathrm{T}}, \boldsymbol{\tau}_2^{\mathrm{T}}\}^{\mathrm{T}}. \qquad (6)$$

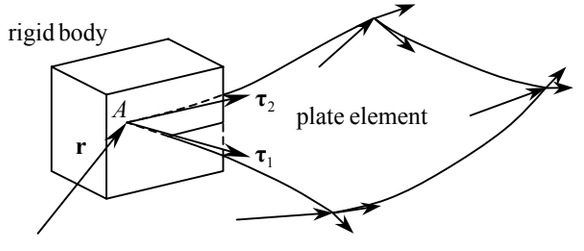


Figure 3. Rigid body attached to a plate element

In paper [8], coupling rigid body and plate was simulated using DAE technique (1). This work first handles this problem as a constraint-free one.

We use the approximate matrix of directing cosines composed of the almost orthonormal vectors: $\mathbf{A} \approx \begin{bmatrix} \boldsymbol{\tau}_1 & \boldsymbol{\tau}_2 & \boldsymbol{\tau}_3 \end{bmatrix}$, where $\boldsymbol{\tau}_3 = \widetilde{\boldsymbol{\tau}}_1 \boldsymbol{\tau}_2$ is the normal vector. The skew-symmetric tensor of angular velocity $\widetilde{\boldsymbol{\omega}} = \dot{\mathbf{A}}\mathbf{A}^{\mathrm{T}} = \dot{\boldsymbol{\tau}}_1\boldsymbol{\tau}_1^{\mathrm{T}} + \dot{\boldsymbol{\tau}}_2\boldsymbol{\tau}_2^{\mathrm{T}} + (\widetilde{\boldsymbol{\tau}}_1\dot{\boldsymbol{\tau}}_2 - \widetilde{\boldsymbol{\tau}}_2\dot{\boldsymbol{\tau}}_3)\boldsymbol{\tau}_3^{\mathrm{T}}$ and the matrix $\boldsymbol{\Phi} = \begin{bmatrix} \mathbf{I} & \rho_1^*\mathbf{I} - \rho_3^*\widetilde{\boldsymbol{\tau}}_2 & \rho_2^*\mathbf{I} + \rho_3^*\widetilde{\boldsymbol{\tau}}_1 \end{bmatrix}$ are found after that. The values $\rho_k^* = \boldsymbol{\tau}_k^{\mathrm{T}}\boldsymbol{\rho}$ correspond to local components of the radius vector $\boldsymbol{\rho}$ of a point of the body.

After some cumbrous calculations we obtain equations of motion of the body in the form (5) with

$$\mathbf{M} = \begin{bmatrix} m\mathbf{I} & & \text{symm.} \\ m(\rho_1\mathbf{I} + \rho_3\widetilde{\boldsymbol{\tau}}_2) & I_{11}\mathbf{I} - I_{33}\widetilde{\boldsymbol{\tau}}_2\widetilde{\boldsymbol{\tau}}_2 & \\ m(\rho_2\mathbf{I} - \rho_3\widetilde{\boldsymbol{\tau}}_1) & I_{12}\mathbf{I} - I_{13}\widetilde{\boldsymbol{\tau}}_1 - I_{23}\widetilde{\boldsymbol{\tau}}_2 + I_{33}\widetilde{\boldsymbol{\tau}}_1\widetilde{\boldsymbol{\tau}}_2 & I_{22}\mathbf{I} - I_{33}\widetilde{\boldsymbol{\tau}}_1\widetilde{\boldsymbol{\tau}}_1 \end{bmatrix}$$

$$\mathbf{f}^{\mathrm{inert}} = 2\begin{bmatrix} m\rho_3\mathbf{I} \\ I_{13}\mathbf{I} + I_{33}\widetilde{\boldsymbol{\tau}}_2 \\ I_{23}\mathbf{I} - I_{33}\widetilde{\boldsymbol{\tau}}_1 \end{bmatrix}\dot{\widetilde{\boldsymbol{\tau}}}_1\dot{\boldsymbol{\tau}}_2, \quad \mathbf{f}^{\mathrm{grav}} = \begin{bmatrix} \mathbf{I} \\ \rho_1\mathbf{I} + \rho_3\widetilde{\boldsymbol{\tau}}_2 \\ \rho_2\mathbf{I} - \rho_3\widetilde{\boldsymbol{\tau}}_1 \end{bmatrix} m\mathbf{g}.$$

Here ρ_k are components of the radius vector of the body mass center while I_{ij} are components of the body inertia tensor in the coordinate system with orts $\boldsymbol{\tau}_1$, $\boldsymbol{\tau}_2$, $\boldsymbol{\tau}_3$.

CONCLUSIONS

Simulation of coupled rigid and elastic bodies can be handled as a constraint-free problem. This was shown in this paper by giving examples of beam and plate elements attached to a rigid body without relative degrees of freedom. However this technique can be generalized to any kind of joints between the bodies.

The authors thank the Ministry of Science and Technology of Korea for its financial support (grant (M1-0203-00-0017) under the National Research Laboratory project research. The research was also supported by RFBR (02-01-00364-A) and by the scientific program “Universities of Russia” (UR.04.01.046).

References

[1] Dmitrochenko O.N., Pogorelov D.Yu.: Generalization of plate finite elements for absolute nodal coordinate formulation. *Multibody System Dynamics* 10, No.1, Special issue ‘Virtual Nonlinear Multibody Systems’, Kluwer, Dordrecht, 2003, 17-43.

[2] Dmitrotchenko O.N.: Efficient simulation of rigid-flexible multibody dynamics: Some implementations and results. *Preprints of NATO ASI on Virtual Nonlinear Multibody Systems*, Vol. 1, W. Schielen and M. Valášek (eds.). – Czech Technical University in Prague, Prague, 2002, 51-56.

[3] Geradin M., Cardona A., Doan D.B., Duysens J.: Finite element modeling concepts in multibody dynamics. *Computer-Aided Analysis of Rigid and Flexible Mechanical Systems*, M.S. Pereira and J.A.C. Ambrosio (eds.), Kluwer, Dordrecht, 1994, 233-284.

[4] Mikkola A.M., Shabana A.A.: A new plate element based on the absolute nodal coordinate formulation. *Proceedings of ASME 2001 DETC*, Pittsburgh, 2001.

[5] Pogorelov D.: Differential-algebraic equations in multibody system modeling. *Num. Alg.* 19, Baltzer, 1998, 183-194.

[6] Shabana A.A.: Flexible multibody dynamics: Review of past and recent developments. *Multibody System Dyn.* 1, 1997, 189-222.

[7] Yoo W.-S., Lee J.-H., Park S.-J., Sohn J.-H., Dmitrochenko O., Pogorelov D.: Large oscillations of a thin cantilever beam: Physical experiments and simulation using absolute nodal coordinate formulation. *Journal of Nonlinear Dynamics*, Vol. 34, Issue 1, Oct 2003, 2003, 3-29.

[8] Yoo W.-S., Lee J.-H., Park S.-J., Sohn J.-H., Pogorelov D.Yu., Dmitrochenko O.N.: Large Deflection Analysis of a Thin Plate: Computer Simulations and Experiments. *Multibody System Dynamics* **11**, No.2, 2003, 185-208.

XXI ICTAM, 15–21 August 2004, Warsaw, Poland

ANALYSIS OF GRAZING BIFURCATIONS IN IMPACT MICROACTUATORS

Xiaopeng Zhao, Harry Dankowicz
Department of Engineering Science and Mechanics,
Virginia Polytechnic Institute and State University, Blacksburg, VA 24060, USA

Summary Impact microactuators rely on repeated collisions to generate gross displacements of a microelectromechanical machine element without the need for large applied forces. Their design and control rely on an understanding of the critical transition between non-impacting and impacting long-term system dynamics and the associated changes in system behavior, known as grazing bifurcations. In this paper, we present three characteristically distinct transition scenarios associated with grazing conditions for a periodic response of an impact microactuator: a discontinuous jump to an impacting periodic response (associated with parameter hysteresis), a continuous transition to an impacting chaotic attractor, and a discontinuous jump to an impacting chaotic attractor. A theoretical normal-form analysis is presented that predicts the character of each transition from a set of conditions that are computable in terms of system properties at grazing. This analysis is validated against results from numerical simulations of a model impact microactuator.

MICROACTUATORS

Precise displacement control and manipulation is required in microscopes, optical devices, nanoscale data storage and during micro surgery. Microdevices are ideal for micropositioning due to their small sizes. Microactuators used to produce small displacements would need large actuation forces and a long driving distance. Actuators based on impulsive forces provide a solution to this problem, as repeated impacts can be used to generate relatively large motion from the accumulation of many small displacements [1]. Recently, impact microactuators have attracted a lot of attention due to ease of fabrication, capability of batch processing, robustness to environment, high accuracy and high power [2, 3, 4, 5]. A schematic of the microactuator studied by Mita *et al* [5] is shown in Figure 1 below. Here, excitation through an applied voltage between the movable block m_2 and electrodes rigidly attached to the frame m_1 results in repeated impacts between the block and the frame (through the stoppers) and resultant brief episodes of sliding motion of the frame. Although each such sliding event contributes only on the order of hundreths of microns of displacement, periodic excitation may be used to generate controlled gross sliding.

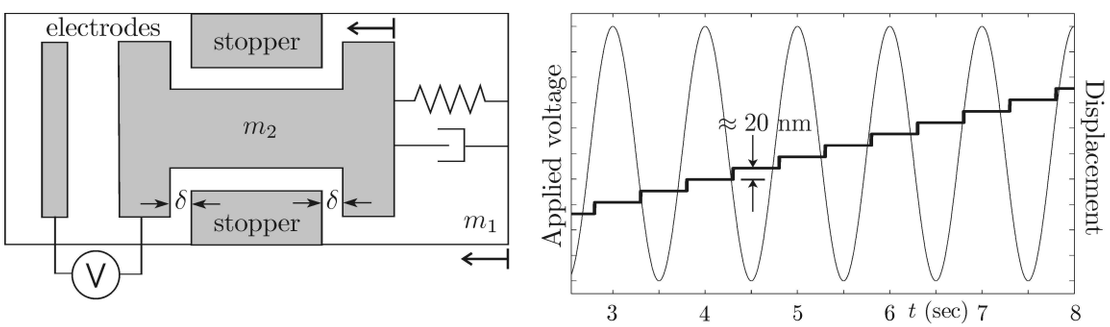


Figure 1. Schematic of microactuator (left panel) and displacement pattern resulting from a periodic voltage excitation (right panel).

Analysis and design of proper function of an impact microactuator relies on an understanding of the possibly dramatic changes in system response that originate at the onset of impacting motions as a system parameter μ (for example, the amplitude or frequency of the driving voltage) is varied. Specifically, we are concerned with bifurcations in the long-term system response that occur as μ increases past some critical value μ_{grazing}, at which value there exists a periodic non-impacting oscillation of m_2 that achieves zero-relative-velocity contact with the stoppers. In a state-space description of the dynamics of the microactuator, such zero-relative-velocity contact corresponds to a *grazing contact* between a state-space trajectory and a discontinuity surface, here representing the sudden change in velocity of m_1 and m_2 that results from an impact. In contrast to periodic trajectories in smooth systems, the local description in the vicinity of a grazing trajectory is well-known to be non-differentiable with dramatic implications to the stability of the grazing trajectory and its persistence under further parameter variations. Indeed, as there is no advance warning of this instability, any local description must account for the nonsmooth character of the flow near the grazing trajectory.

TRANSITION SCENARIOS

Three different transition scenarios are observed in simulations of a periodically forced two-degree-of-freedom model of the impact actuator as shown in Figure 2 below. We note, in particular, that Types I and III are associated with parameter hysteresis as the asymptotic dynamics jump discontinuously between impacting and non-impacting attractors, where the former involve appreciable impulses. In contrast, in Type II, although the previously stable non-impacting periodic trajectory loses stability at grazing, the post-grazing attractor is still local in state space and impacts occur with small relative velocity.

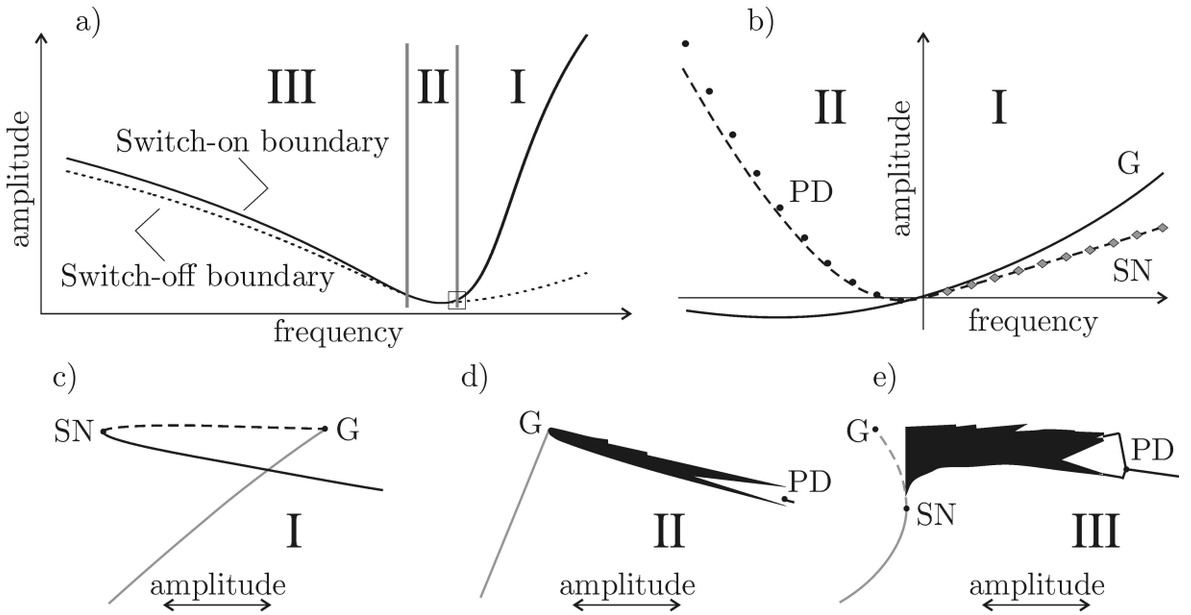


Figure 2. Transition scenarios between non-impacting to impacting asymptotic dynamics under variations in driving amplitude and frequency (G=grazing contact, SN=saddle-node bifurcation, PD=period-doubling bifurcation). In a), the solid line corresponds to the onset of impacting motion under increases in amplitude, while the dashed line corresponds to the termination of impacting motions under decreases in amplitude. Panel b) shows a blow-up of the rectangular region in a) at the boundary between Type I and Type II transitions illustrating the close agreement between the analytical theory (curves) using discontinuity mappings and numerical data (circles and squares). Panels c), d), and e) exhibit the bifurcation scenarios associated with the switching between impacting motions (black) and non-impacting motions (gray) that occurs under variations in driving amplitude. Here, solid curves correspond to stable periodic motions and dashed curves to unstable periodic motions. The black regions correspond to impacting chaotic attractors.

DISCONTINUITY MAPPINGS

The local dynamics in the vicinity of a grazing trajctory for parameter values near the critical parameter values can be analyzed through the introduction of a discontinuity mapping that i) captures the local dynamics in the vicinity of the grazing contact including variations in time-of-flight to the discontinuity and the impact mapping; ii) can be entirely characterized by conditions at the grazing contact; iii) is nonsmooth in the deviation from the point of grazing contact; and iv) can be studied to arbitrary order of accuracy [6]. In this paper, we formulate local mappings in the vicinity of the grazing trajectory for each of the three transition scenarios. We also show how it is necessary to include higher-order terms in the local mapping to accurately capture the bifurcations that occur in an open neighborhood of the co-dimension-two points at the boundaries between the different transition scenarios. As an example, Figure 2b) shows the prediction of the local mapping on the form of the bifurcation curves in the vicinity of a grazing trajectory at the boundary between the Type I and Type II scenarios.

ACKNOWLEDGEMENTS

The authors gratefully acknowledge support for this work from the National Science Foundation, Division of Civil and Mechanical Systems, grant number 0237370.

References

[1] Ragulsikis, K., Bansevicus, Barausleas, R., and Kulvietis, G., *Vibromotors for Precision Microrobots*, New York: Hemisphere, pp. 289-295, 1988.
[2] Lee, A.P., Nikkel, D.J. Jr., and Pisano, A.P., "Polysilicon Linear Microvibromotors", in *Proc. 7th Int. Conf. Solid-State Sensors and Actuators*, Vol. 1(2), pp. 46-49, 1993.
[3] Daneman, M.J., Tien, N.C., Solgaard, O., Pisano, A.P., Lau, K.Y., and Muller, R.S., "Linear Microvibromotor for Positioning Optical Components", *IEEE Journal of Microelectromechanical Systems*, Vol. 5(3), pp. 159-165, 1996.
[4] Saitou, K., Wang, D.A., and Wou, S.J., "Externally Resonated Linear Microvibromotor for Microassembly", *IEEE Journal of Microelectromechanical Systems*, Vol. 9(3), pp.336-346, 2000.
[5] Mita, M., Arai, M., Tensaka, S., Kobayashi, D., and Fujita, H., "A micromachined impact microactuator driven by electrostatic force", *IEEE Journal of Microelectromechanical Systems*, Vol. 12(1), pp. 37-41, 2003.
[6] Nordmark, A.B., "Non-Periodic Motion Caused by Grazing Incidence in an Impact Oscillator," *J Sound Vibration* Vol. 145(2), pp. 279-297, 1991.

LOW ENERGY CONTROL OF PERIODIC MOTIONS IN MANUFACTURING

Nils Guse, Werner Schiehlen
Institute B of Mechanics, University of Stuttgart,
Pfaffenwaldring 9, 70569 Stuttgart, Germany

Summary This paper presents two methods for designing linear and nonlinear springs as local energy storage devices to improve the efficiency of nonlinear rheonomic systems such as assembly robots. Firstly, the shooting method is applied to find parameters of a mechanical system resulting in a conservative limit cycle close to the desired trajectory. The second method describes an alternative approach to design a system with low energy consumption by fitting the characteristics of a spring to an optimal force function calculated by inverse dynamics. With both methods, the fine tuning of the prescribed trajectory is achieved by some additional low energy control.

INTRODUCTION

Manufacturing processes require periodic motions which may be realized by an active robot. A well established robot control principle is inverse dynamics which is used to overcome high nonlinearities typical for mechanical systems undergoing large displacement motion. Based on an accurate model of the system under consideration, all the nonlinearities are compensated firstly by control action and then, the remaining double integrator is controlled by linear feedback. This approach is very attractive to control engineers since a broad variety of established tools can be applied successfully. However, this principle results in high energy demand, see e.g. WALDRON [1].

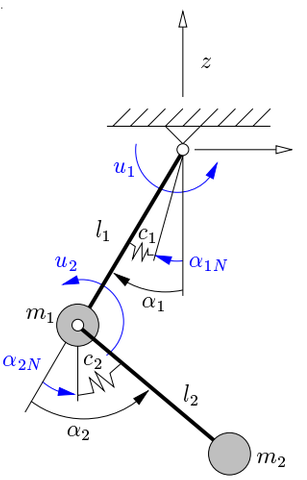


Figure 1: 2 DOF Robot

To improve the efficiency it is proposed to design the mechanical system in such a way that the desired trajectory is approximated by a passive limit cycle of a nonlinear conservative system and some additional low energy control, see SCHIEHLEN [2]. The design parameters case are the stiffness of linear springs or the characteristics of nonlinear springs, respectively, both of which serve as local energy storage.

Since, the parameters for the limit cycle of a system may be hard to find, it is proposed, too, to minimize the consumed energy by fitting the stiffness and characteristics of the springs to a force function resulting from inverse dynamics. In this case, the position/force function for meeting a certain trajectory has to be computed first.

These two methods are applied to a two degree of freedom assembly robot modelled as double pendulum as shown in Figure 1. The angles α_1 and α_2 are the degrees of freedom, u_1 and u_2 are the torques of two motor drives. The springs have the coefficients c_1 and c_2, their zero position can be adjusted using the spring mounts α_{1N} and α_{2N}.

ENERGY OPTIMAL DESIGN USING LIMIT CYCLES

In this section, a properly designed nonlinear conservative oscillator is proposed to generate the required motion coarsely without energy dissipation and to adjust the motion finely by linear control with strongly reduced energy consumption. Thus, periodic trajectories are adapted as closely as possible to the limit cycle of the underlying mechanical system. The fundamentals of energy consumption and energy storage of mechanical systems with rheonomic constraints have been analyzed for a linear harmonic oscillator, see SCHIEHLEN [3]. It is shown how spring characteristics have to be chosen to reduce the energy consumption for arbitrary periodic trajectories of a robot arm.

The desired trajectory of the system, e.g. a sinusoidal straight motion as shown in Figure 2, defines the boundary conditions for the state of the motion. These conditions are the positions α_i and the velocities $\dot{\alpha}_i$ at the beginning and at the end of the motion, respectively. In particular, for a periodic motion, the state has to be the same after a full cycle. Thus, the boundary conditions read as

$$\left.\begin{aligned} F_i(s) &= \alpha_i(t_{end}, s) - \alpha_{i0} = 0\,, \\ F_i(s) &= \dot{\alpha}_i(t_{end}, s) - \dot{\alpha}_{i0} = 0\,, \end{aligned}\right\} i = 1, 2.$$

The goal is to design the mechanical system to meet the boundary conditions by adjusting its parameters. Therefore, the standard shooting method which is a helpful tool to solve boundary value problems is modified to obtain all these parameters. For the assembly robot the shooting parameters are the stiffness coefficients c_i and the spring fastening α_{Ni}.

Using a set of starting parameters, values for stiffness and spring fastening can be found by iteration, such that the boundary conditions for finding a limit cycle are met. Figure 3 shows the trajectory of the system for some chosen starting parameters (dashed line) and the limit cycle using the starting parameters calculated by the shooting method (solid line). The limit cycle motion with two additional linear springs reduces the energy consumption by 52%.Other trajectories, e.g. a sinusoidal motion in z-direction, offer savings of up to 94%.

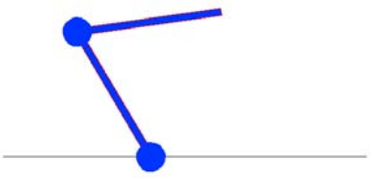


Figure 2: Desired trajectory.

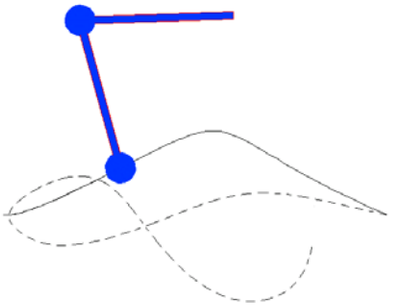


Figure 3: Trajectory using starting parameters (dashed line) and the limit cycle (solid line). Both motions are conservative.

ENERGY OPTIMAL DESIGN USING CURVE FITTING

A more engineering approach is to compute the required controlling force or torque as function of the position of the robot arm, and then to use a linear or cubic polynomial to fit this curve. The area between the linear or cubic fit and the required force represents the work that has to be applied by a secondary PD-control such that the robot trajectory meets its desired path, see also ACKERMANN et. al. [4].

Starting from the trajectory prescribed by the manufacturing process the required control signal, here the torque of the motor drive, is computed using inverse dynamics. Then, this torque is converted to a function of the position, as shown in Figure 4. The solid line shows the control force u_1 calculated by inverse dynamics with respect to angle α_1 for the time $t_0 < t < t_{end}$. A linear function is used as a curve fit (dashed line) representing a linear spring where the spring coefficient is the slope of this curve fit and the axis intercept being the spring fastening.

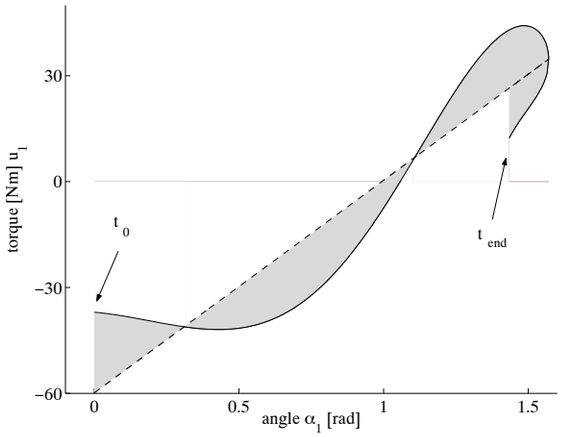


Figure 4: Torque u_1 calculated by inverse dynamics (solid line) and the fitting function, i.e. torque of a linear rotational spring.

The area between the required force function and the curve fit (grey area in figure 4) is equal to the work that has to be applied by the PD-controller to force the system on the desired trajectory. Therefore, this area has to be minimized by curve fitting. The amount of energy that can be saved is approximately the same as for the springs designed using a limit cycle. Savings of more than 50% were obtained for a linear rotational spring. For nonlinear springs, e.g. cubic progressive or cubic degressive springs, the stiffness and characteristics of can be found very easily, too. Same procedure has been successfully applied to the second robot arm.

CONCLUSIONS

Two methods were shown to design system parameters for reducing the energy consumption of rheonomic nonlinear mechanical systems. The first method uses that a limit cycle of a system generate a periodic motion close to the desired motion without energy dissipation. The second method reduces the work that has to be applied by fitting a spring characteristics to a position/force curve computed by inverse dynamics. For both methods only low energy control is needed to force the system on its desired trajectory. They both deliver approximately the same parameter values and the same amount of energy savings of easily more than 50%.

References

[1] Waldron, K. J.: Some Thoughts on the Design of Power Systems for Legged Vehicles. Advances in Multibody Systems and Mechatronics. Gerhard-Mercator-Universität, Duisburg, 1999, pp. 389-394.

[2] Schiehlen, W.; Guse, N.: Control of Limit Cycle Oscillation, Proc. IUTAM Symposium on Chaotic Dynamics and Control of Systems and Processes in Mechanics, to appear with KLUWER, 2003.

[3] Schiehlen, W. O.:Power Demand of Actively Controlled Multibody Systems. ASME Proceedings of DETC2001, ASME Design Engineering Conference, DETC2001/VIB-21343, Pittsburgh, Pennsylvania, USA, 2001.

[4] Ackermann, M.; Lakrad, F.; Guse, N.: Improving Efficiency of Controlled Rheonomic Systems by Curve Fitting, Zwischenbericht ZB-136. Stuttgart: Universität Stuttgart, Institut B für Mechanik, 2003.

SELECTED PROBLEMS OF DISCRETE-CONTINUOUS MECHANICAL SYSTEMS WITH LOCAL NONLINEARITIES

Amalia Pielorz
Kielce University of Technology, Faculty of Management and Computer Modelling, Al. 1000-lecia Panstwa Polskiego 7, PL 25-314 Kielce, Poland

Summary In the paper nonlinear discrete-continuous systems torsionally, longitudinally and transversally deformed with local nonlinearities having softening characteristics are considered. Two sets of functions are proposed for the description of nonlinearities. In the discussion a wave approach leading to solving differential equations with a retarded argument is applied. Detailed considerations and numerical results are presented for a multi-mass torsional system and for a single gear transmission.

INTRODUCTION

The considerations concentrate on the dynamic analysis of nonlinear discrete-continuous models of various elements and machines. Such models consist of rigid bodies connected by means of elastic elements. To these models also belong those where the motion of elastic elements can be described by the classical wave equation. The use of this equation gives some limitations for the group of the systems under considerations; on the other hand, it enables to apply the solution of the d'Alembert type leading to equations with a retarded argument. Such an approach allows to consider the systems torsionally, longitudinally or transversally deformed. Some examples of such systems one can find in [1-4].
In the discrete-continuous systems local nonlinearities can be incorporated. The variety of nonlinear problems is wide. It may include weak and strong nonlinearities, hardening and softening characteristics. The presence of local nonlinearities in the discrete-continuous models of mechanical systems is justified by engineering solutions and it can have important consequences for their overall dynamic behaviour.
In the paper it is assumed that local nonlinearities have softening characteristics and they are described by two sets of nonlinear functions.
The external loading can be described by an arbitrary function, periodic or nonperiodic. Damping is taken into account by means of an equivalent internal and external damping.

NONLINEAR FORCES AND GOVERNING EQUATIONS

Consider the nonlinear discrete-continuous systems consisting of an arbitrary number of elastic elements connected by rigid bodies. The cross-sections of the elastic elements are constant and they can be torsionally, longitudinally or transversally deformed. In the considered discrete-continuous models a single local nonlinearity by means of a nonlinear spring is taken into account and it represents mechanical properties of various elements having a nonlinear characteristics. It is assumed that these characteristics are of a soft type.
The forces in the nonlinear spring can be described by various nonlinear functions. In the case of hard characteristics the polynomial of the third degree satisfactory describes such forces, as it is shown in [3] for a discrete-continuous torsional system. In the case of nonlinearities having softening characteristics, two sets of nonlinear functions are proposed in the dynamic analysis of appropriate discrete-continuous systems.
The first set of nonlinear functions consists of the polynomial of the third degree with negative coefficients standing by the nonlinear term, and of the sinusoidal function, the hyperbolic tangent function and the exponential function. The parameters in these functions are chosen in such a way that all the functions give the same linear case, the polynomial function is the extension of the sinusoidal function and all functions have similar maximum values. The proposed functions are assumed in the following form

$$1)\ F(X) = K_1 X + K_3 X^3,$$

$$2)\ F(X) = A\sin(BX), \qquad 3)\ F(X) = A\tanh(BX),$$

$$4)\ F(X) = A(-1+\exp(BX)) \ \text{ for } \ X \le 0 \ \text{ and } \ F(X) = A(1-\exp(-BX)) \ \text{ for } \ X \ge 0,$$

and the parameters of the above functions satisfy the relations $AB = K_1$, $AB^3 = -6K_3$, where X is a displacement connected with the location of the local nonlinearity.
The second set of nonlinear functions consists of the irrational functions, the hyperbolic tangent function and the exponential function. The irrational functions are assumed in the following form

$$5)\ F(X) = K_1 X - K_w(-X)^w \ \text{ for } \ X \le 0 \ \text{ and } \ F(X) = K_1 X + K_w X^w \ \text{ for } \ X \ge 0,$$

and the relations $AB = K_1$, $A = K_1 X_m + K_w (X_m)^w$, $X_m = (-K_1 / wK_w)^{1/(w-1)}$ are satisfied now by the parameters of the proposed functions. We are interested in the characteristics of a soft type, so the coefficient standing by the nonlinear term has negative values, and according to the satisfied relations all three functions give the same linear case and have the same maximum values.

The determination of the displacements in the cross-sections of the elastic elements in the considered discrete-continuous systems is reduced to solving several classical wave equations with appropriate initial and nonlinear boundary conditions. Seeking the wave solutions for equations of motion and substituting them into the boundary conditions, the nonlinear differential equations with a retarded argument are obtained. For each discrete-continuous model these equations have a slightly different form, however generally they can be solved numerically by means of the Runge-Kutta method.

NUMERICAL RESULTS

In numerical calculations the external loading as a harmonic function is assumed and the solution is sought in steady states. The detailed results are obtained for two discrete-continuous systems: for a multi-mass torsional system and for a single gear transmission. It is found that the polynomial function, the sinusoidal function and the irrational functions have some restrictions for their application. Namely, for certain parameters describing the considered systems the escape phenomena can be observed. That means that there exist intervals of the frequency of the external loading for which the solutions diverge to infinity. Some such cases are shown in Fig. 1 for amplitudes P_A of nonlinear forces in a single gear transmission when using irrational functions with several values of the exponent w.

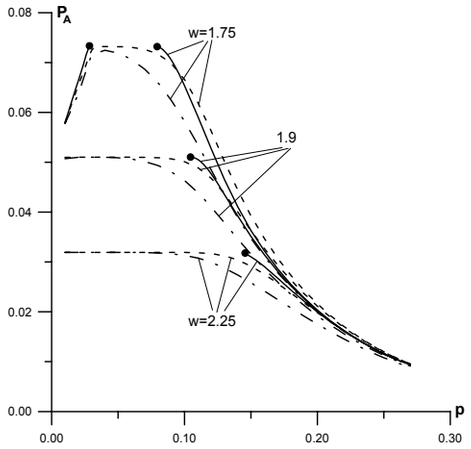


Fig. 1. Amplitude-frequency curves for nonlinear forces in a single gear transmission.

CONCLUSIONS

In the paper it is shown that local nonlinearities can be incorporated in the dynamic analysis of discrete-continuous systems being torsionally, longitudinally or transversally deformed. Though various nonlinear functions can be used for the description of these nonlinearity, some of them have restrictions for their application. It concerns the polynomial function, the sinusoidal function and the irrational functions. The application ranges indicate when the above functions have to be replaced by the remaining nonlinear functions. Two sets of functions are proposed for the description of the local nonlinearity. The first set is suggested for strong nonlinearity and the second one for weaker local nonlinearities.
In the case of local nonlinearities having a hardening characteristic the polynomial function of the third degree can be used. In this case no restrictions were noticed, [3].

References

[1] Nadolski W., Pielorz A.: Theoretical investigations of nonlinear loads on gear teeth in single gear transmission. *Int. J. Mech. Sci.* **43**:299-311, 2001.
[2] Pielorz A.: Vibrations of discrete-continuous models of low structures with a nonlinear spring. *J. Theor. Appl. Mech.* **39**:153-174, 2001.
[3] Pielorz A.: Vibration problems in selected torsional mechanical systems. *Meccanica* **38**:731-738, 2003.
[4] Pielorz A.: The investigation of the influence of a local elastic nonlinearity on vibration of plane truss members. *Eng. Trans.* **51**:3-24, 2003.

MODELLING BALLAST BEHAVIOUR USING A THREE-DIMENSIONAL POLYHEDRAL DISCRETE ELEMENT METHOD.

Gilles Saussine*, Catherine Cholet*, Pierre Etienne Gautier *, Frédéric Dubois **, Claude Bohatier **, Jean-Jacques Moreau**

* *SNCF, Research and Technology Department, 45 rue de Londres, 75379 Paris Cedex 08, France*
** *LMGC, UM2, cc048, Place Eugène Bataillon, 34095 Montpellier Cedex 05, France*

Summary The deterioration of the railway track under a large number of train runnings, in particular the settlement mechanism of the ballast layer or the lateral buckling of track, remains insufficiently known. In order to study the behaviour of ballast layer a three-dimensional Discrete Element Method (DEM), based on the Non Smooth Contact Dynamic (NSCD) approach has been developed.

INTRODUCTION

Since the beginning of the railways, ballasted tracks have been widely employed because of their flexibility from the point of view of the construction and the maintenance but also, because they fulfill well the mechanical requirements imposed by the transport of heavy loads at long distance. The ballast is one of the elements that support the track. The ballast bed consists of a layer of coarse grained material and ensures several functions such as the transmission of the static and dynamic loads to the railway platform and the transversal and longitudinal anchoring of the track.

The track modelling deals with various time and size scale ranges. Ballast is often modelled as a continuous medium. Such a modelling should be relevant when considering the whole track system but this is not necessary the case when studying a small part of the ballast, since the thickness of the ballast layer is only about ten grains under the sleepers. We developed an approach, at the grain scale, resulting from research on the granular medium, referred to as discrete element method.

The three dimensional approach is a new model developed in order to introduce a more realistic physical model. It is much more develop to conceive an experimental set up to validate, with a sufficient accuracy, the three-dimensional approach but some instructive applications like lateral resistance of the track can be performed.

THREE-DIMENSIONAL DISCRET ELEMENT APPROACH

Discrete element method (DEM) present an interesting alternative to the continuous model or discrete/continuous approach [5] for a better understanding of mechanisms occurring in railway track. It makes possible to model geometrical discontinuities of material and to take into account the grains rearrangements. The Research and Technology Department of the SNCF, supported by RFF [1], undertook, in collaboration with the LMGC, the development of a discrete element software for ballast modelling.

Several computational techniques are currently available in the simulation of collections of rigid bodies. The most popular ones, commonly called Distinct Element or Discrete Element Methods, derive from the work of P.A. Cundall [2]. They consist in approximating the mechanical constraint of non inter-penetrability of each body pair by some close-range steep repulsion law.

A different approach is used in this lecture, characterized by the absence of smoothing approximation. This approach is called (Non Smooth) Contact Dynamics Method [3]. For each rigid body we can write the motion equation with Newton-Euler equation :

$$\begin{aligned} M\ddot{x} &= P(t) + r \\ I\dot{\omega} + \omega \wedge \omega(I.\omega) &= M_P(t) + M_r \end{aligned} \tag{1}$$

where x denotes the position of the center of mass, ω the angular velocity, $P(t)$ and $M_P(t)$ the resultant and the moment of the external forces, r and M_r the resultant and the moment of the contact efforts, M the mass matrix and I the inertia matrix. The second equation of this system is possibly nonlinear because of the second term of the left hand side expression.

The "contact" contribution r comes from interaction between bodies. These laws are written in term of relative algebraic distance (g) and velocity (U) between the two bodies. If we consider a contact α, it comes from classical kinematic analysis that $U^\alpha = H^{\star\alpha}(q)(\dot{q})$, and from duality considerations (conservation of the power expressed with either local variables or global variables) that the contribution r^α due to the local reaction R^α satisfy the relation $r^\alpha = H^\alpha(q)R^\alpha$.

To identify these interactions we need geometrical information about the contact, an algorithm to investigate geometrical intersection between convex polyhedrons has been developed [4]. In fact r is the sum of all these contributions. The mapping $H^{\star\alpha}(q)$, $H^\alpha(q)$ are linear and transposed one from the other.

We use the local form which require a condensation of the global dynamical equations in term of local unknown variables (relative velocities).

[1] Réseau Ferré de France

Considering a contact α, we can rewrite the equation (1) in the following manner with nc the total number of "contacts":

$$U^\alpha = U^\alpha_{free} + W^{\alpha\alpha} hR^\alpha + \sum_{\beta=1,\ \beta\neq\alpha}^{nc} W^{\alpha\beta} hR^\beta \tag{2}$$

We can observe that if we "freeze" contact contribution for $\beta \neq \alpha$ this equation express a linear relation between U^α and R^α. The solution (U^α, R^α) which verify this equation, velocity Signorini condition and the Coulomb's friction law can be obtain with an iterative Newton solver [1]. Then the global solution is very simple, we will solve these couples of equations (dynamical and interaction) for each contact considering the other one's as "frozen". We will consider that the method has converged once the solution for each contact does not change. This is something like a nonlinear block Gauss-Seidel algorithm.

LATERAL RESISTANCE EXPERIMENTS

The evaluation of the influence of vehicle induced forces on the lateral stability of the track has been a major research concern for several decades. The load capacity of the track or its "lateral strength" to handle these loads is a key requirement for track alignment retention, hence to safe train operation. The growing tendency toward higher speeds and heavier axle loads tends to make the issue of track lateral stability more critical.

A numerical experiment to study lateral resistance implies the preparation of a sample representative of a portion of railway track. We decided to take into account the ballast granulometry (25-50 mm) and a sleeper of the type 'VAX U41' usually used on high speed tracks. The sample composed of 25000 digitized ballast grains is prepared by deposition under gravity (fig. 1).

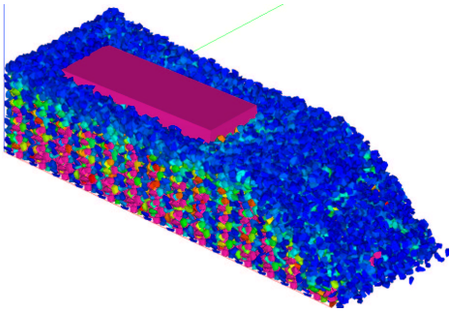


Figure 1. A numerical sample.

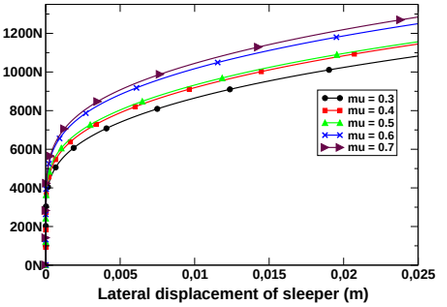


Figure 2. Results from numerical experiment.

On this kind of sample it is possible to undertake specific studies for example to analyse the influence of the shape of the sleeper on the efforts distribution or the influence of the granulometry of the ballast on lateral resistance. Initially we studied the influence of friction coefficient between the grains and the sleeper on lateral resistance. We applied an incremental lateral force on the sleeper with different friction coefficients, and we record its displacement.

The curves force-displacement (fig. 2) show that the friction coefficient has not a very significant role on the threshold of release of the phenomenon of shifting but has an influence on the amplitude of displacement following the shifting.

CONCLUSION

The model proposed is an alternative to the finite elements methods to study ballast behaviour. In spite of the numerical difficulties, contact detection between polyhedron, local problem of contact and friction, the model allows us to study a large collection of rigid bodies with a polyhedral shape. The use of discrete element method for a better understanding of the buckling phenomenon of track show the accuracy of this approach to simulate a real behaviour of ballast. It is possible to study micromechanics quantities not easily measurable by experiments like stress or influence of friction coefficient.

References

[1] Alart P., Curnier A. : A mixed formulation for frictional contact problems prone to newton like methods, *Computer Methods in Applied Mechanics and Engineering*, **92(3)**,353-375,1991.

[2] Cundall P., O. Strack: A discrete numerical model for granular assemblies. *Geotechnique* **29(1)**,47-65,1979.

[3] Moreau J.J. : Unilateral contact and dry friction in finite freedom dynmics, In J. Moreau and P. Panagiotopoulos (Eds), *Non Smooth Mechanics and Applications*,Springer-Verlag,**302**:1-82 1988.

[4] Saussine G. : Etude du comportement dynamique du ballast par une approche éléments discrets 3D, *Ph.D. Thesis*, Université des Sciences et Techniques du Languedoc, in progress.

[5] Suiker A., A. Metrikine, R. De Borst : Dynamic behaviour of layer of discrete particles, part1: analysis of body waves and eigenmodes. *J. of sound and vibration* **240**:1-18, 2000.

EFFICIENT GENERALIZED SPEEDS IN A RECURSIVE FORMULATION OF FLEXIBLE MULTIBODY DYNAMICS

ARUN BANERJEE and MARK LEMAK
LOCKHEED MARTIN ADVANCED TECHNOLOGY CENTER
PALO ALTO, CA 94304, USA

Summary
A recursive formulation of the dynamical equations of an articulated multibody system with flexible components is given in terms of efficient motion variables for elastic motion and hinge rotation about revolute, Hooke and spherical joints. We treat motion under external forces, as well as prescribed motion with internal loads calculation, and show computational efficiency of the formulation with examples.

Introduction

Simulations of large overall motion of a hinge-connected multibody system with elastic components tend to be computationally intensive. Recently, Banerjee [1] reviewed methods of reducing computer time that include defining new motion variables and using recursive or parallel algorithms. Mitiguy and Kane [2] had given a choice of generalized speeds that reduce simulation time for a system of rigid bodies with rotation in revolute, Hooke, and revolute joints. D'Eleuterio and Barfoot [3] proposed a variable for describing elastic motion that yields a constant mass matrix for a single flexible body in large overall motion. This paper uses these motion variables to modify the recursive formulation of Ref. [4] for a system of hinge-connected flexible bodies. The formulation is also extended to situations where some or all of the degrees of freedom at a joint are prescribed, as when determining internal loads. Examples demonstrate the computational efficiency of the formulation.

Single Flexible Body in Large Overall Motion

Using generalized speeds u_i representing orthogonal components of angular velocity of a reference frame and the velocity of a point fixed in that frame, with vibration mode variables of Ref. [3], the velocity of a material point and the kinematical equations for n modal coordinates can be shown to be

$$\mathbf{v} = \sum u_i \mathbf{b}_i + \sum u_{3+i} \mathbf{b}_i \times \mathbf{p} + \sum \boldsymbol{\varphi}_i u_{6+i} \tag{1}$$

$$\sum \int \boldsymbol{\varphi}_i \bullet \boldsymbol{\varphi}_j \, dm \, (u_{6+j} - \dot{q}_j) = \sum u_{3+i} \mathbf{b}_i \bullet \sum \int \boldsymbol{\varphi}_j \times \boldsymbol{\varphi}_i \, dm \, q_j, \quad (i, j = 1,\ldots,n) \tag{2}$$

Kane's dynamical equations [5] for a body with potential energy P and dissipation function D are

$$\int \frac{d\mathbf{v}}{dt} \bullet \frac{\partial \mathbf{v}}{\partial u_i} dm = -\sum \left[\frac{\partial P}{\partial q_j} + \frac{\partial D}{\partial \dot{q}_j} \right] \frac{\partial \dot{q}_j}{\partial u_i}, \qquad (i = 1,\ldots,6+n) \tag{3}$$

Eqs. (3) lead to the same equations as those obtained in Ref. [3] by using Hamilton's principle with quasicoordinates. Eqs. (1) and (3) reveal that the mass matrix in Eqs. (3) is time-invariant. Rotation-deformation coupling in Eqs. (2) produces contributions to generalized active force due to elasticity, geometric stiffening, and dissipation in Eqs. (3) for rotational as well as modal generalized speeds.

Kinematics of Hinge Motion in Flexible Multibody Systems

Angular velocity $\boldsymbol{\omega}^j$ of the reference frame of body j connected to inboard flexible body c(j) is written after accounting for elastic rotation rate at the hinge of body c(j) in its reference frame. Following Ref. [2] for a Hooke's joint, with generalized speeds u_1 and u_2, hinge vectors $\mathbf{h}_1$and $\mathbf{h}_2$, and unity dyadic $\mathbf{U}$, this yields

$$\boldsymbol{\omega}^j = [\, \boldsymbol{\omega}^{c(j)} + \sum \varphi_i^{c(j)} \dot{q}_i^{c(j)} \,] \bullet [\, \mathbf{U} - \mathbf{h}_1\mathbf{h}_1 - \mathbf{h}_2\mathbf{h}_2 \,] + u_1 \mathbf{h}_1 + u_2 \mathbf{h}_2 \tag{4}$$

Revolute joint kinematics is a reduction of Eq. (4). Generalized speeds for a spherical joint are body components of angular velocity and those for slider joints are relative translational rates. These generalized speeds require modifying the kinematics in the algorithm of Ref. [4], with the dynamical equations generated in a sequence of forward, backward, and forward passes. When a generalized speed at a hinge is prescribed, the associated internal load is obtained by dot-multiplying the augmented inertia and active torques and forces by the partial angular velocity or partial velocity [5] for the prescribed joint motion.

Simulation Results

Large angle slewing of a single flexible body, a solar sail spacecraft with 44 elastic modes, is simulated by the above formulation and compared to Standard Kane and recursive methods using customary generalized speeds (time derivatives of translational, rotational and modal generalized coordinates). Identical results as in Figs. 1 and 2 are obtained for this 50 degrees of freedom (dof) system for a 300 sec simulation.

Method:	**Standard Kane**	**Recursive (Customary Variables)**	**Recursive (Efficient Variables)**
CPU Times:	**699 sec**	**667 sec**	**140 sec**

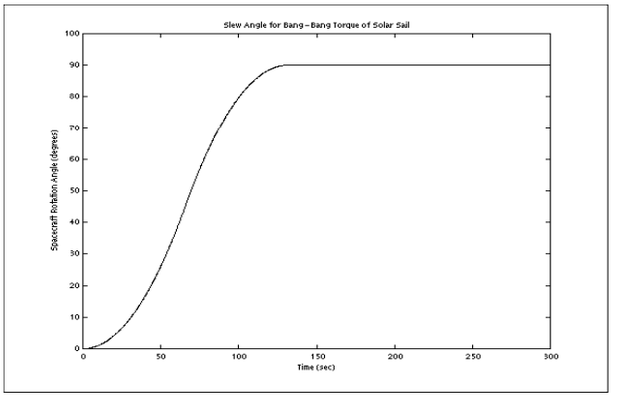


Fig. 1 Solar sail large angle slewing

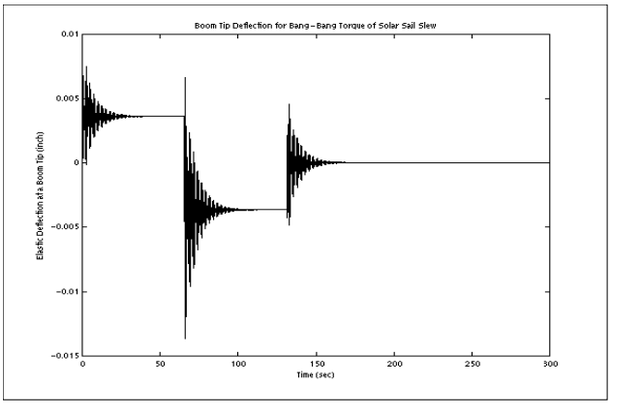


Fig. 2 Sail boom tip deflection with bang-bang torque

Figures 3 shows four flexible bodies connected by three types of rotational joints, and Figure 4 overlays plots of an internal load computed by the three methods. A 10 sec simulation of this articulated 52 dof system requires the following computation times.

Method:	**Standard Kane**	**Recursive (Customary Variables)**	**Recursive (Efficient Variables)**
CPU Times:	**10.2 sec**	**7.6 sec**	**5.2 sec**

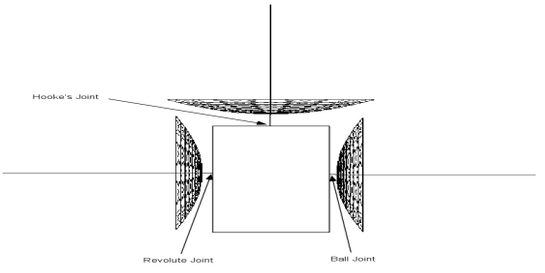


Fig. 3 Four flexible bodies with revolute, Hooke, and ball joints

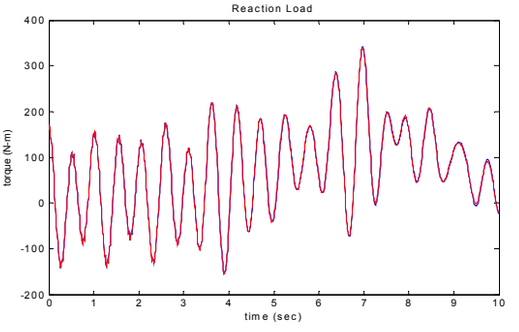


Fig. 4 Load for a prescribed rotation

References

1. Banerjee, A.K., “Contributions of Multibody Dynamics to Space Flight: A Brief Review”, Journal of Guidance, Control, and Dynamics, vol. 26, no. 3, 2003, pp. 385-394.

2. Mitiguy, P.C., and Kane, T.R., “Motion Variables Leading to Efficient Equations of Motion”, International Journal of Robotics Research, vol. 15, no. 5, 1996, pp. 522-532.

3. D’Eleuterio, G.M.T. & Barfoot, T.D., “Just a Second, We’d Like to Go First: A First Order Discretized Formulation for Elastic Multibody Dynamics”, Proc. of 4th Intl. Conf. on Dynamics and Control of Structures in Space, Ed. by C.L. Kirk & R. Vignjevic, Cranfield University, U.K., May 24-28, 1999.

4. Banerjee, A.K., “Block-Diagonal Equations for Multibody Elastodynamics with Geometric Stiffness and Constraints”, Journal of Guidance, Control, and Dynamics, 1993, vol. 16, no. 6, pp. 1092-1100.

5. Kane, T.R. and Levinson, D.A., Dynamics: Theory and Applications, McGraw-Hill, 1983.

ON APPROXIMATE JACOBIAN MATRICES IN SIMULATION OF MULTIBODY SYSTEMS

Dmitry Pogorelov
Bryansk State Technical University, Department of Applied Mechanics,
b. 50 let Oktyabrya 7, 241035 Bryansk, Russia

Summary Different forms of approximate Jacobian matrices of equations of motion for stiff multibody systems are under consideration.

INTRODUCTION

It is well known that equations of motion of many multibody models of technical systems are stiff. Solving the corresponding differential or differential-algebraic equations with implicit methods requires evaluations of Jacobian matrix (JM), which is often strong nonlinear in coordinates and velocities. Usually the JM is computed by finite differences, and this process increases several times the CPU expenses for evaluation of the equations [1]. Moreover, use of the JM often increases the profile of the system matrix and makes impossible the application of some effective algorithms such as articulated body method. Evaluation of the JM could be accelerated if analytic expressions for its elements are used [2]. Approximate JM of different types allows further reducing the computational expenses.

EQUATIONS OF MOTION

To simplify the expressions, consider holonomic scleronomic multibody system without closed loops. Let q be coordinates of the system, $q = \left(q_1^T \quad \cdot\cdot \quad q_n^T\right)^T$, where q_j is the $n_j \times 1$ matrix of local coordinates in joint j, which define the position of body j relative to the previous body i. Consider recursive kinematic relations for 6×1 vectors V of linear and angular velocities of adjusted bodies

$$V_j = C_{ij}V_i + S_j\dot{q}_j,\ V_j = \left(v_j^T \quad \omega_j^T\right)^T,\ C_{ij} = \begin{pmatrix} I_3 & -\tilde{r}_{ij} \\ 0 & I_3 \end{pmatrix}.$$

Here I_3 is the 3×3 identity matrix, r_{ij} is the vector connecting origins of body-fixed frames i, j. The recursive relations yield the explicit expressions for velocities

$$V_j = \Phi_j(q)\dot{q},\ \Phi_j = C_{0j}\sum_{k\in J(j)}\hat{S}_k^*,\ \hat{S}_k^* = \left(0 \quad \cdot\cdot \quad 0 \quad C_{0k}^{-1}S_k \quad 0 \quad \cdot\cdot \quad 0\right),$$

where $J(k)$ is the set of indices of joints included in the path from body k to body 0. Similar expressions are valid for 6×1 vectors of accelerations $W_j = \Phi_j\ddot{q} + W_j'(q,\dot{q})$.

Equations of motion are derived with the help of the Newton-Euler formalism.

$$f(\ddot{q},\dot{q},q,t) = \sum_{j=1}^{n}\Phi_j^T\left(M_j(q)\ddot{q} + M_j(q)W_j'(q,\dot{q}) + k_j(q,\dot{q}) - f_j(q,\dot{q},t)\right) = 0,\qquad M_j = \begin{pmatrix} m_jI_3 & 0 \\ 0 & J_j \end{pmatrix},\ k_j = \begin{pmatrix} 0 \\ \tilde{\omega}_jJ_j\omega_j \end{pmatrix}.$$

Here m_j is the mass and J_j is the inertia tensor of body j, the 6×1 matrix f_j contains applied forces and moments reduced to the center of mass. Origins of the body-fixed frames are located in the corresponding centers of mass.

Variation of equations with respect to q and $\dot{q}$ produces the Jacobian matrices

$$\delta f = J^q\delta q + J^v\delta\dot{q}.$$

Taking into account the structure of the equations of motion, the JM can be presented by the following parts:

$$J^q = \frac{\partial M\ddot{q}}{\partial q^T} + \frac{\partial k}{\partial q^T} - \frac{\partial Q}{\partial q^T} = J_M^q + J_k^q + J_Q^q,\quad J^v = \frac{\partial k}{\partial\dot{q}^T} - \frac{\partial Q}{\partial\dot{q}^T} = J_k^v + J_Q^v,$$

where the mass matrix M and vectors of the generalized inertia forces k and the applied forces Q are introduced,

$$M = \sum_{j=1}^{n}\Phi_j^TM_j\Phi_j,\quad k = \sum_{j=1}^{n}\Phi_j^T\left(M_jW_j' + k_j\right),\quad Q = \sum_{j=1}^{n}\Phi_j^Tf_j.$$

APPROXIMATE JACOBIAN MATICES

The main condition for the approximation of JM consists in assumption that the stiffness of the equations is caused by the applied forces,

$$\left\| J_Q^q \right\| >> \left\| J_M^q \right\|, \left\| J_Q^q \right\| >> \left\| J_k^q \right\|, \left\| J_Q^v \right\| >> \left\| J_k^v \right\| ,$$

or $J^q \approx J_Q^q$, $J^v \approx J_Q^v$.

This assumption is valid if coordinates *q* change slowly. In particular, partial derivatives of matrices Φ_j are neglected, and variations of velocities and generalized forces are approximately as follows:

$$\delta V_j = \delta\Phi_j \dot{q} + \Phi_j \delta\dot{q} \approx \Phi_j \delta\dot{q}, \tag{1}$$

$$\delta Q = \sum_{j=1}^{n} \delta\Phi_j^T f_j + \Phi_j^T \delta f_j \approx \sum_{j=1}^{n} \Phi_j^T \delta f_j$$

Let $f_j = \sum f_{jk}$, where the force f_{jk} depends on positions and velocities of interacting bodies *j*, *k*,

$$f_{jk} = f_{ij}\left(r_j, r_k, A_{0j}, A_{0k}, v_j, v_k, \omega_j, \omega_k\right).$$

Taking into account assumption (1), the variation δf_{jk} looks like

$$\delta f_{jk} \approx \left(G_{jk1}^r \Phi_j + G_{jk2}^r \Phi_k\right)\delta q + \left(G_{jk1}^v \Phi_j + G_{jk2}^v \Phi_k\right)\delta\dot{q} .$$

The (6×6) *local Jacobian matrices* (LJM) $G_{jk1}^r, G_{jk2}^r, G_{jk1}^v, G_{jk2}^v$ should be computed for every stiff force element. After that the approximate JM of equation of motion can be obtained from the following expressions:

$$\begin{aligned} J^q &\approx -\sum_{j=1}^{n} \Phi_j^T \left(\left(\sum_k G_{jk1}^r \right) \Phi_j + \sum_k G_{jk1}^r \Phi_k \right) = -\sum_{j=1}^{n} \Phi_j^T \left(G_j^r \Phi_j + \sum_k G_{jk1}^r \Phi_k \right), \\ J^v &\approx -\sum_{j=1}^{n} \Phi_j^T \left(\left(\sum_k G_{jk1}^v \right) \Phi_j + \sum_k G_{jk1}^v \Phi_k \right) = -\sum_{j=1}^{n} \Phi_j^T \left(G_j^v \Phi_j + \sum_k G_{jk1}^v \Phi_k \right), \end{aligned} \tag{2}$$

Evaluation of these matrices is similar to that for the mass matrix.

Some reduction of computational expenses is achieved by simplification of expression for LJM. In fact, the following important relations are often valid for simplified LJM:

$$G_{jk1}^{r*} = G_{jk1}^{v*} = -G_{jk2}^{r*} = -G_{jk2}^{v*} = G_{kj1}^{r*} = G_{kj1}^{v*} = -G_{kj2}^{r*} = -G_{kj2}^{v*} = G_{ji}^{*}, \quad G_{jk1}^{v*} = C_{0j}^T G_{jk1}^v C_{0j} \ldots$$

Moreover, the simplified JM are often symmetric.

BLOCK–DIAGONAL JACOBIAN MATRICES

Expressions for JM obtained in the previous section allow their fast evaluating. Nevertheless, widening of the system matrix profile makes their usage impossible in some cases. For example, consider a system of 1000 bodies interacting due to contact forces. Such system can be used for analyses of a track ballast properties. Mass matrix of the system is block-diagonal whereas the system matrix, which is the sum of the mass matrix and weighted JM, has usually a wide profile so that solving the corresponding equation requires too much CPU time. Numeric experiments show that a very easy and effective solving of this problem consists in the usage of block–diagonal JM, i.e. the non-diagonal blocks G_{jk2}^r, G_{jk2}^v are removed from the expressions (2). The JM assume the form

$$J^q \approx \sum_{j=1}^{n} \Phi_j^T G_j^r \Phi_j, \quad J^v \approx \sum_{j=1}^{n} \Phi_j^T G_j^v \Phi_j .$$

For constraint multibody systems the LJM G_j^r, G_j^v are added to the corresponding local mass matrix M_j. It is not required a separate evaluation both the global mass matrix *M* and the JM. Consequently, the system matrix can be computed with the help of the composite rigid body algorithm. No widening of the profile is expected because the system matrix obtains the same profile as the mass matrix. Finally, articulated body algorithms can be used as well.

ACKNOWLAGEMENT

The work was supported by Russian Foundation for Basic Research under grant 02-01-00364 and by scientific program “Universities of Russia – Basic Research” (UR.04.01.046)/

References

[1] Andrzejewski, T, Bock, H. G., Eich, E. and von Schwerin, R. Recent advances in the numerical integration of multibody systems, in W. Schiehlen (ed.), *Advanced Multibody System Dynamics – Simulation and Software Tools*, Kluwer Academic Publishers, Dordrecht, 127-151, 1993.

[2] Pogorelov D. Yu: On Calculation of Jacobian Matrices in Simulation of Multibody Systems, in W. Shiehlen, M.Valasek (eds), Virtual Nonlinear Multibody Systems, NATO Advanced Study Institute, **1**, 159-164, 2002.

Intrinsic Formulation of Dynamics of Curvilinear Systems

Jean LERBET
Institut Navier, Lami, Ecole Nationale des Ponts et Chaussées
6 et 8 avenue Blaise Pascal, Cité Descartes Champs-sur-Marne
77455 MARNE-LA-VALLEE Cedex 2, France.
e-mail: lerbet@univ-tours.fr

Introduction

In a lot of mechanical systems different models of curvilinear elements are used: string, beam, cable, rods,.... The formation of the general equations of such systems (large strains and displacements: translatory motions and rotations) remains a difficult problem which has been studied for a long time ([6], [2], [7] for example) We shall use the intrinsic differential calculation in a Lie group which has already been used in another cases (see [4] for example for an use in mechanics of systems of rigid bodies) to write the general and coordinate-free equations of any curvilinear system. The advantages are for example: the hexa-dimensional aspect, the generality of the calculations (without hypothesis of smallness of displacements or strains), the possibility of intrinsic limited expansion (linearisation for example), the possibility to point out precisely the difficulties (non linearities,...), the automatic generation of scalar equations.

1 Mathematic tools

$\mathcal{E}$ is the affine space of three dimensions of ordinary Euclidean geometry and E the associated vector space. $\mathbf{D}$ is the group of affine mappings A such that the linear part $\mathbf{A}$ is an element of the special orthogonal group $SO(E)$. $\mathcal{D}$ is the vector space of six dimensions of skew symmetric vector fields $X : \mathcal{E} \to E$ such that there exists $\boldsymbol{\omega}_X$ in E with the well-known following property: $\forall a, b \in \mathcal{E} \quad X(a) = X(b) + \boldsymbol{\omega}_X \wedge \overrightarrow{ba}$ and $\mathcal{D}$ shall be identified with the set of screws.
The Lie bracket is defined in $\mathcal{D}$ by $[X, Y](a) = \boldsymbol{\omega}_X \wedge Y(a) - \boldsymbol{\omega}_Y \wedge X(a)$ for all a in $\mathcal{E}$. Thus $\mathcal{D}$ is a Lie algebra which is isomorphic (and identified with) to the classical Lie algebra of $\mathbf{D}$.

2 Kinematics, Kinetics, Dynamics

The system is described as following. The reference configuration is similar to a distribution $\sigma \mapsto r(\sigma) = (A(\sigma); \vec{i}_1(\sigma), \vec{j}_1(\sigma), \vec{k}_1(\sigma))$ of affine frames where σ is the curvilinear abscissa of the curve $\sigma \mapsto A(\sigma)$. $A(\sigma)$ is **for example** the inertia center of the section of abscissa σ and $\vec{i}_1(\sigma), \vec{j}_1(\sigma), \vec{k}_1(\sigma)$ is a basis connected to the rigid section of abscissa σ (one may choose **for example** the Frenet frame of the curve $\sigma \mapsto A(\sigma)$).
In the following, each rigid section and its associated frame shall be identified.
On each section $r(\sigma)$ and at each time t, is acting an unknowwn displacement $D(\sigma, t)$ such that $r(\sigma) \to s(\sigma, t) = D(\sigma, t) \bullet r(\sigma)$ where $s(\sigma, t) = (a(\sigma, t); \vec{i}_2(\sigma, t), \vec{j}_2(\sigma, t), \vec{k}_2(\sigma, t))$. Notice that no hypothesis of perpendicularity of the section with the curve $(\sigma, t) \mapsto a(\sigma, t)$ is made and $\bullet$ is the natural action of $\mathbf{D}$ on the set of affine frames (in mathematical terms it is a structure of fibered bundle).

The kinematics of the system is described by the following fields: the velocity $(\sigma, t) \mapsto v^c(\sigma, t) = \mathbf{D}(\sigma, t)^{-1} \circ \frac{\partial D(\sigma,t)}{\partial t}$ and the strain $(\sigma, t) \mapsto e^c(\sigma, t) = \mathbf{D}(\sigma, t)^{-1} \circ \frac{\partial D(\sigma,t)}{\partial \sigma}$ ($\sigma \mapsto e^c(\sigma, t)$ is unchanged by superposition of a rigid motion).
According to the chosen model, it is supposed that at each time t and on each section $r(\sigma)$ there are:

a distribution $(\sigma,t) \mapsto \mathcal{T}(\sigma,t)$ describing the massic external actions, a distribution $(\sigma,t) \mapsto \Theta(\sigma,t)$ describing the internal actions , action of the right-side on the left one (according to the abscissa σ), two concentrated massic strengths at the ends $\mathcal{T}_0(t), \mathcal{T}_l(t)$ (in some cases, one could consider a family $\mathcal{T}_k(t)$ at σ_k for $k = 1, \ldots, n$ which introduce a discontinuity of $\sigma \mapsto \Theta(\sigma,t)$ and we should use what follows on each $[\sigma_k, \sigma_{k+1}]$), a distribution $\sigma \mapsto H_r(\sigma)$ of operators of $\mathcal{D}$ describing the inertia strengths.

3 The equations

The equations of the system (Σ) are in a lagrangian expression (the functions of σ and of t are omitted):

$$\begin{aligned} \mathcal{T}^c &= \rho H_r(\dot{v}^c) + [v^c, \rho H_r(v^c)] - [e^c, \Theta^c] - \frac{\partial \Theta^c}{\partial \sigma} \\ \mathcal{T}_0^c = \Theta^c(0) \quad &, \quad \mathcal{T}_l^c = -\Theta^c(l) \end{aligned}$$

If some restrictions are done on the field $(\sigma,t) \mapsto D(\sigma,t)$ (planar motion, small displacement, perpendicularity of the section to the curve $(\sigma,t) \mapsto A(\sigma,t)$ (Kirchoff-love hypothesis) and so on), one comes back to the classical equations of beams, strings, cables and so on.
Moreover, choosing a basis in the Lie algebra $\mathcal{D}$ which may be canonically asociated with a choice of an affine frame in the affine space, intrinsic relations become scalar ones. Linear operators become matrices, vectors become columns and the most part of the operations can be automatically done (with MAPLE for example). The main steps of a programm allowing to do it shall be presented in the fulle text and one of the expanded equation shall be given, its complexity justifying the intrinsic approach. The questions of constitutive laws and of linearized equations preserving the same intrinsic approach shall constitute future works and shall be suggested.

References

[1] S.AHMED A.SHABANA *Transient analysis of flexible multibody systems, Part1. Dynamics of flexible bodies* CMAME 54 (1986)

[2] A. CARDINA M. GERADIN *A Beam Finite Element Non-linear Theory with Finite Rotations* Int. Journal for Nal Methods in Eng., vol. 26, pp. 2403-2438 (1988)

[3] D.P.CHEVALLIER *Lie Algebras, Modules, Dual Quaternions and Algebraic Methods in Kinematics* Mech. Mach. Theory Vol. 26, No. 6, pp.613-627 (1991)

[4] J.LERBET *Analytic Geometry and singularities of mechanisms* ZAMM 78,10, pp 687-694 (1998)

[5] J.PICHON *Groupes de Lie. Représentations linéaires et applications* Coll. Méthodes, Hermann (1973)

[6] J.C. SIMO *A Finite Strain Beam Formulation. The Three-dimensional Dynamic Problem. Part I* Comp. Methods in Applied Mechanics and Eng. 49, pp. 55-70 (1985)

[7] F. SCHURICHT, H. Von der MOSEL *Euler-lagrange Equations for Nonlinearly Elastic Rods with Self-Contact* Arch. Rationnal Mech. Anal. 168, pp.35-82 (2003)

SIMULATION OF TRACK BALLAST

Dmitry Agapov[*], Dmitry Pogorelov[*], Aleksandr Bidulya[**]
[*]*Bryansk State Technical University, Bulvar 50-letiya Oktyabrya 7, 241035 Bryansk, Russia*
[**]*All-Russian Research and Design Institute, ul. Oktyabrskoy Revolutsii 410, 140402 Kolomna, Russia*

Summary Algorithms for simulation railway track ballast are considered. Mathematical model of ballast, collision detection algorithms and features of numerical methods are discussed. Some simulation results are presented.

INTRODUCTION

There are two principal approaches for simulation of granular system dynamics. The first one represents the system as a continuum media. In the second approach, such systems are considered as a set of interacting rigid bodies (particles). The last method is discussed in the paper. Its main lack is increased requirement to computational resources. However, the first method does not allow accounting the real geometry of interacting particles. Therefore there is the need for improving numerical methods for solving equations of motion of system with great number of degrees of freedom.

MATHEMATICAL MODEL DESCRIPTION

All bodies of the system are considered as planar both convex and non-convex polygons. Each of the particles has three degrees of freedom corresponding to plane motion. A contact interaction between each pair of bodies is implemented by contact forces. They appear when the shapes of bodies overlap and disappear when the shapes are going away from each other.

Contact force model

We consider the contact between two polygons. Since the interception of the polygons is small, we suppose that the vertices of the first polygon are penetrating through the edges of the second one and vice versa. That is why we discuss a model of the vertex-edge contact as a special case of the point-plane contact described in [1]. When the vertex penetrates into the inner side of the edge, the contact forces appear. In a simplest case the contact force consists of a linear viscous-elastic normal force and a dry friction force. The dry friction has two modes: sliding and sticking ones.

Collision detection

The collision detection consists of two levels. The first one is so-called far collision level, which checks interlacing simple hulls of particle shapes. The linked linear list method is used in this work [2]. All the bodies are surrounded with square hulls and ordered lists of the hull bounds for each axis are created. All the pairs of the bodies having far contact are placed to a collision heap. Additional use of circle hulls could reduce the collision heap length. Then the second level of collision detection is carried out for the pairs from the collision heap. The sensitivity cell method is used for this level. The sensitivity cell for an edge of a polygon is a region bounded with the same edge, straight line parallel to the edge and shifted to a distance d from the edge inside the polygon and two inner bisectors of the neighbor angles. The parameter d is called the depth of sensitivity. A vertex of another polygon lies inside the sensitivity cell if several conditions are satisfied. These conditions require calculation of oriented distances form the vertex to the straight lines bounding the sensitivity cell (Figure 1). The oriented distances are calculated as

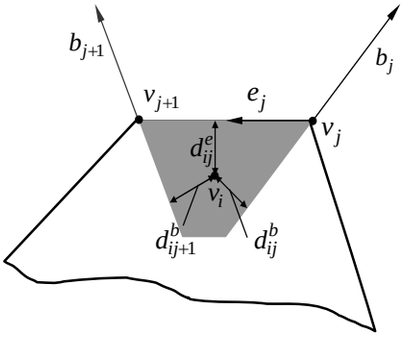


Figure 1. Sensitivity area of j-th edge of the first polygon with i-th point of the second polygon.

$$d_{ij}^e = (\vec{e}_j \times (\vec{r}_{vi} - \vec{r}_{vj}))_z;$$
$$d_{ij}^b = (\vec{b}_j \times (\vec{r}_{vi} - \vec{r}_{vj}))_z;$$
$$d_{i,j+1}^b = -(\vec{b}_{j+1} \times (\vec{r}_{vi} - \vec{r}_{v\ j+1}))_z,$$

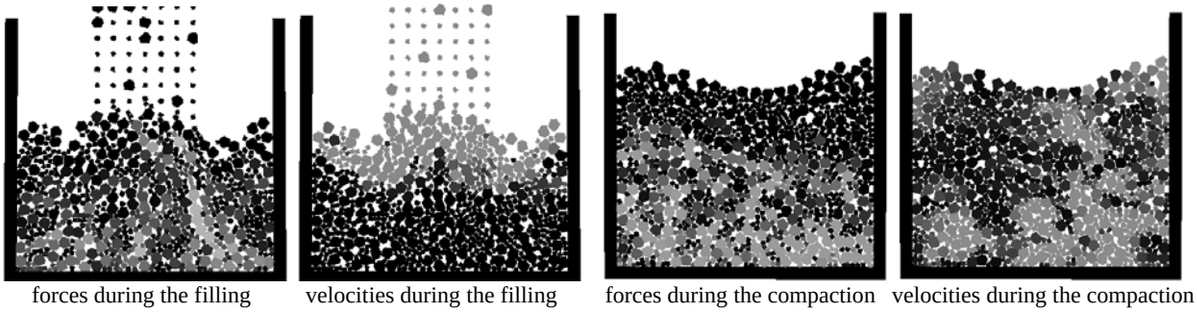
here $\vec{e}_j$ is the unit vector along j-th edge, $\vec{b}_j, \vec{b}_{j+1}$ are the bisectors of j-th and $(j+1)$-th angles, $\vec{r}_{vj}, \vec{r}_{vj+1}$ are the radius-vectors of j-th and $(j+1)$-th vertices, $\vec{r}_{vi}$ is the radius-vector of point v_i. If the vertex of the body is in the polygon of other body, the corresponding contact force appears. Thus the collision detection algorithm is as follows: 1) the loop over all the bodies is preformed with creating linked linear lists for the neighbor collision level; 2) far collision level is checked; 3) neighbor collision level is performed for the pairs of the bodies, which satisfy the far collision level. If the pair of bodies passes the neighbor collision level test, the corresponding contact force element is added; 4) the contact force element is destroyed if the contact is broken; 5) integration step is executed; 6) if simulation is not over go to item 2.

Simplification of the Jacobian matrices of contact forces

The implicit Park's method with calculation of simplified Jacobian matrices is used for numerical integration of equation of motion [4], [5]. However, the use of this method increases the width of the system matrix profile and decelerates the simulation process in the case of ballast model consisting of thousands of bodies [6]. Therefore, a method of block-diagonal Jacobian matrices was developed. To clarify the method, consider force $F_{ij}^c(q_i, q_j, \dot{q}_i, \dot{q}_j)$, which acts on the *i*-th body. The Jacobian matrix includes derivatives $\partial F_{ij}^c / \partial q_i$, $\partial F_{ij}^c / \partial \dot{q}_i$ and does not include $\partial F_{ij}^c / \partial q_j$, $\partial F_{ij}^c / \partial \dot{q}_j$. Single integration step expenditure is about 10-20 percents as large as that without Jacobian matrix. However the integration step increases and the computational expenses are reduced. The convergence of this method is improved as well.

REALIZATION AND IMPLEMENTATION

The methods described above were realized for railway track ballast simulation as a module of the program package Universal Mechanism (www.umlab.ru). This module has ability of input the statistics of particle geometry, two methods for filling a work area by particles, horizontal, vertical and combined types of vibrocompactions in the rigid box (work area), compaction by sleepers. The output date is global and local porosity, kinematics of the system and each particle and so on. There exists ability to colouring the particles depending on their velocity or contact power factor (Figure 2). The system of thousand particles is presented in this figure. All the bodies are convex polygons. The amplitude of the vertical vibration is 7 mm and the frequency is 45 Hz.



forces during the filling | velocities during the filling | forces during the compaction | velocities during the compaction

Figure 2. Distribution of velocities and forces in cases of filling and compaction

CONCLUSIONS

The algorithms described in this paper allow simulating dynamics of two-dimensional ballast models including up to several thousands bodies of arbitrary shape. The realized module solves such tasks as ballast packing and compaction. It is supposed to generalize the methods to the three-dimensional case.

ACKNOWLEDGEMENTS

The research war supported by Russian Foundation for Basic Research under the grant 02-01-00364-A as well as by the scientific program "Universities of Russia – Basic Research" (UR.04.01.046).

References

[1] Pogorelov D.Yu., Pavlyukov A.E., Yudakova T.A., Kotov S.V.: Contact Interactions Simulation in System Dynamics Tasks. *Sel. Dynamics, strength and reliability of transport machines.* Bryansk 2001,p.11-23.

[2] Beate Muth, Peter Eberhard and Stefan Luding: Contact Simulation for Many Particles Considering Adhesion. *J. Mechanics of Structures and Machines* 2002. p.1-28.

[3] Mirtich B.V.: Impulse-based Dynamic Simulation of Rigid Body Systems. *PhD Thesis*, Graduate Division of the University of California at Berkeley, 1996.

[4] Garg V.K., Dukkipati R.V.: Vehicle Dynamics. Translated. 1988. 391 p.

[5] Pogorelov D.Yu.: Differential-algebraic equation in multibody system modeling. *J. Numerical algorithms* 1998.

[6] Pogorelov D.Yu.: On Calculation of Jacobian Matrices in Simulation of Multibody Systems. *Preprints of NATO ASI on Virtual Nonlinear Multibody Systems*: Prague 2002.-V.II.p.159-164.

Configuration Control and Dynamic Analysis of Redundant Link-type Manipulators

Kazuo YAMAMOTO*, Masashi OKADA** and Kazuo TANIZAWA*
* *Department of Intelligent Systems, Kinki University, 930 Nishimitani, Uchita, Nagagun 649-6493, Japan*
** *Graduate School of Kinki University*

Summary We present numerical simulations for configuration control and dynamic behavior of redundant link-type manipulators which are boarded on the spacecraft and are operated avoiding obstacles in the work space. Simulations consist of determination of orbit and configuration, and dynamic analysis with/without the elasticity of links. Numerical works have made clear that configuration control using artificial potentials of obstacles is possible and the elasticity of links influences avoidance and final positioning of the manipulators.

INTRODUCTION

Space manipulators are characterized by their lightweight and redundancy because of a quite low load level in the orbit. Utilizing this redundancy of the dynamical system, we can add various functions to the manipulators. Another feature of them is expressed by having no point constrained to the inertial space. If a manipulator changes its configuration in operation, the spacecraft changes its attitude due to the counter force. In this work avoiding obstacles is examined utilizing this dynamical redundancy of the link system which is floating in the non-gravitational space. First, a method for determining the orbit and the configuration of redundant manipulators is studied by point-to-point control approach [1] using the artificial potentials which make possible for the links to avoid obstacles. Second, this configuration change is solved as a dynamical problem of the rigid link system introducing the concept of time. Finally, motion of an actual link system, which has elastic deformation, is discussed focusing on the capability of avoiding obstacles and final positioning as a manipulator.

MODEL AND ANALYSIS

Analytical Model A simulation model, which is in two-dimensional space, consists of a spacecraft main body, a redundant multi-link manipulator, obstacles with the array of line and a target as shown in Fig.1. Configuration and motion of the manipulator system (including a spacecraft main body) are expressed by variables which consist of the translational coordinates and the attitude angle at the center of gravity of each link. The redundant degree of freedom is constrained by geometrical relations among the variables.

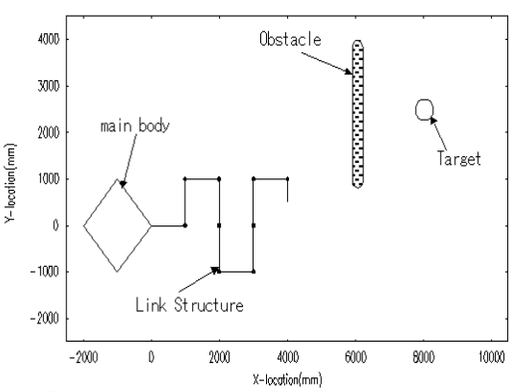


Fig.1 Analitical model of the system

Determination of Orbit In order to start from the initial position, avoid obstacles and converge to the target, artificial potentials are formed in the objective function. The steepest descent method is used to minimize the objective function and obtain the orbit of end effecter. The orbit is divided into finite segments by some points (called orbital points).

Determination of Link Configuration The objective function is formed by artificial potentials in order for all links to avoid obstacles and the sum of change in attitude angle between the adjacent orbital points. Moreover, constraint conditions for constant momentum and angular momentum are given to the variables depending on the free-free condition in the orbit. The configuration of the link is obtained by solving the nonlinear equations which are based upon the stationary condition of the objective function.

Dynamics of Rigid System Rigid multi-body dynamics is adopted to solve the equations of motion for the link system. A series of link configurations corresponding the orbital points is assumed as the time change of hinge angle (difference of attitude angle between the adjacent links), and enforced acceleration functions are given as the polynomial of time.

Dynamics of Flexible System The elasticity and inertia property of flexible links are modeled by using the finite elements for the beam which represent the large bending deformation.[2][3] Nonlinear equations of motion for rigid and flexible link systems are solved by Newmark's iterative time integration scheme .

NUMERICAL RESULTS

Link Configuration A series of link configurations from the initial position toward the target is shown in Fig.2. Not only the orbit of end effecter but also all links of the manipulator can successfully avoid the obstacle. By appropriate choosing the weighting parameter of the objective function, it is possible to find a link configuration by which the end effecter and all links of the manipulator avoid the obstacles. In dynamic analysis for rigid links it was confirmed to obtain the same configuration at each time as the configuration analysis though the figure is not shown here.

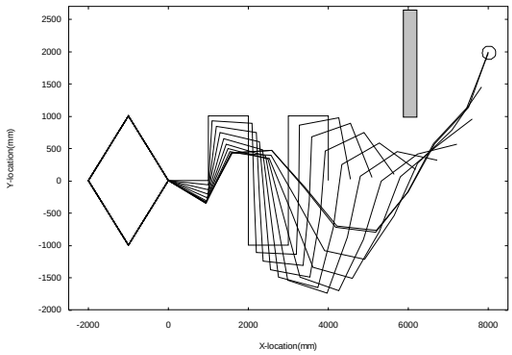


Fig.2 A series of link configuration

Influence of Elasticity When considering the elastic deformation of the link, we can do nothing but change the above conclusion. Influence of the link elasticity appears in two directions; capability of obstacle avoidance and final positioning of the end effecter. As shown in Fig.3, the orbit of end effecter differs between for the rigid and flexible link formulations. This can easily lead to the risk of collision between the link and the obstacles under manipulation. When the elasticity of the link is considerably low, vibration is generated over the manipulator and the final positioning of end effecter becomes quite difficult after stop of manipulation. If the elasticity of the link is properly designed, these can be predicted and easily avoided.

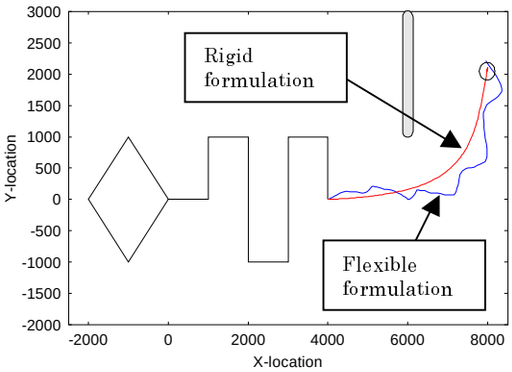


Fig.3 Difference of orbit between rigid and flexible links

CONCLUSION

As results of simulations, end effecter orbits and link configurations were obtained which can avoid the obstacles, and influence of the link elasticity were clarified for the avoidance of obstacles and the final positioning.

REFERENCES

[1] Fenton,R.G. ,Benhabib,B. and Goldenberg,A.A., Optimal point-to-point Motion Control of Robots with Redundant Degrees of Freedom. Trans. ASME, J. of Engineering for Industry, Vol.108, May 1986, pp.120-126.

[2] Yamamoto,K., Parameter Estimation of Deployable Flexible Structures for Space Application Using Large Deformation Analysis. Theoretical and Applied Mechanics Japan, Vol.49, November 2000, pp.153-161.

[3] Langhaar,H.L., Energy Methods in Applied Mechanics, John Wiley & Sons, 1962.

A STUDY ON THE BRUSH NOISE REDUCTION OF A DC MOTOR USING MULTI-BODY DYNAMICS

Tae-Won Park*, Il-Ho Jung**, Jong-Hwi Seo**
*Division of Mechanical Engineering, Ajou University, 5 Wonchun-dong, Yeongtong-gu, Suwon-city, Gyeonggi-do, 443-749, Rep. of Korea
**Graduate School of Mechanical Engineering, Ajou University, 5 Wonchun-dong, Yeongtong-gu, Suwon-city, Gyeonggi-do, 443-749, Rep. of Korea

Summary The DC Motor of a vehicle can cause noise and vibration due to high-speed revolution, which can make a driver feel uncomfortable. There have been various studies that attempted to solve these problems, focusing mostly on the causes of noise and vibration and the means of preventing them. The CAE methodology is more efficient than a real test for the purpose of looking for various design parameters to reduce the noise and vibration of the DC motor. In this study, a design process for reducing brush noise is presented with the use of a computer model which is made by using multi-body dynamics program (DADS). The design parameters to reduce the brush noise and vibration were proposed using a computer model. They were used to reduce the noise and vibration of a DC motor and verified using the test results of a fan DC motor in a vehicle. This method may be applicable to various DC motors.

INTRODUCTION

The DC motor of a fan motor (hereinafter called the DC motor) is widely used as a control motor because of its excellent features: it has a simple structure, it is easy to operate, its revolution is easy to control, and it has an affordable price. However, the DC motor revolves at a high speed, so it can cause noise/vibration during operation of the system. In particular, the DC motor used in the actuators of automobiles and home appliances can give discomfort to users due to noise/vibration. It is necessary to solve this problem.

A survey of previous studies shows that the main cause of noise/vibration in DC motors is the dynamic interaction between the brush and the commutator. Due to the structure of a DC motor, there is the contact between the brush and the commutator, which causes friction. This friction is the main cause of noise/vibration in DC motors, which is generally known as brush noise. Other than this, noise/vibration can also be caused by nonparallel armature and the interaction between the armature shaft and bearing.[1,2] In this study, the multi-body dynamics model of the whole DC motor system was organized to analyze the dynamics features of the DC motor. Based on the result of the dynamics analysis, the characteristics of reaction force between the parts of the DC motor were observed and a study was done on the relevance of reaction force and noise/vibration of the DC motor. An improved design that can reduce brush noise was also presented, and the improved design was finally validated through tests.

MAIN SUBJECT

Dynamics model and Analysis

The target for analysis is a DC brush motor used in the radiator fan of an automobile, which is in the initial stage of development. The parts of the DC motor were modeled with a 3D geometry modeller for dynamics model data, as shown in Fig. 1. The DC motor was modeled with a multi-body dynamics program (DADS) for dynamics analysis, as shown in Table 1. The dynamics model was modeled based on the real data. A case study was carried out about design parameter, as shown Table 2.

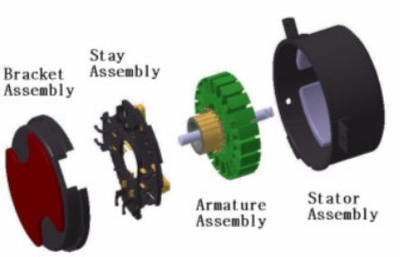


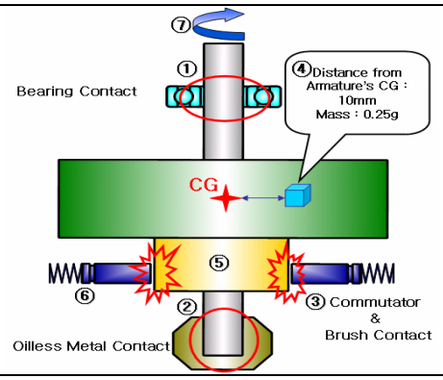
Fig. 1 3D CAD Model of DC motor

Results of dynamics analysis

Among the results of dynamics analysis, bearing reaction forces and reaction forces between brushes and a commutator were observed, as shown Fig. 1 3D CAD Model of DC motor in Table 2. The former was related to the structural vibration of the DC motor and the latter was related to the brush noise. From the results of Table 2, it can be seen that the smaller the design parameters, the lower the noise and vibration level of the DC motor. However, the upper design parameters are very small. Considering the quality cost, lowering the upper design parameters is not a good option for reducing the noise and vibration. Finally it is certain that the roundness of the commutator is the most important design parameter, because the roundness of the commutator was the only variable parameter during the durability test. Referring to Fig. 2, the critical point of the roundness was 0.11 mm. A durability test was carried out to verify the analysis result. After analyzing the result (Table 3) of the durability test, it could be seen that the element that has the biggest influence is the roundness of the commutator. According to the test data, the roundness deteriorated as the DC motor ran and this increased the brush noise. Therefore, the roundness of the commutator needs to be maintained in order to maintain the brush noise under a certain level throughout the durability life span of the DC motor. When compared with the current

DC Motor (#1 ~ 4 in Table 3), in the case of the commutator including lubricating oil (#5, 6 in Table 3), it is obvious that the roundness was maintained below the critical point and the brush noise was reduced after the durability test.

Table 1 Summary of the multi-body dynamics model of the DC motor



- ▶ Clearance and contact using contact element
  - ① Ball bearing
  - ② Metal bearing
  - ③ Between brush (4EA) & commutator
- ▶ Armature unbalance using dummy mass
  - ④ Fixation between armature and dummy
- ▶ ⑤ Roundness of commutator using random number
- ▶ ⑥ Brush Motion using translational joint & Spring
- ▶ ⑦ 2180 RPM revolution using control element

Table 2 Result of dynamics analysis

Design Parameter	Specification	Result	Comment
Commutator Roundness	Max 0.003 mm	Critical Point : 0.1 ~ 0.11 mm	Change during durability test (refer to Table 3) ➔ The most important design parameter to reduce the brush noise
Armature Unbalance	Max 0.25gfcm	The smaller unbalance, the lower vibration	No Change during durability test Unbalance is small enough
Spring Stiffness	10.3 g/mm	The smaller stiffness, the lower vibration	No Change during durability test Stiffness is small enough
Bearing Clearance	Ball : 0.008 ~ 0.013 mm Metal : 0.0045 ~ 0.013 mm	The smaller clearance, the lower vibration	No Change during durability test Clearance is small enough

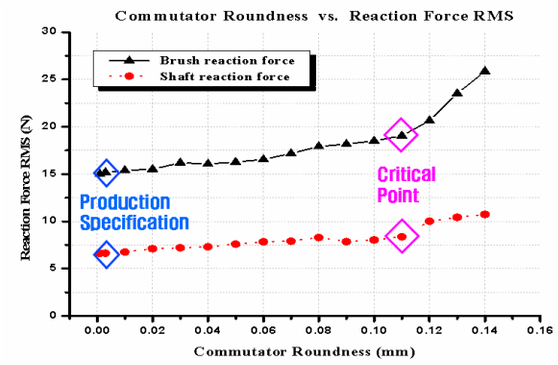


Fig. 2 Graph of Commutator roundness vs. Reaction force

Table 3 Table 1 Relation of roundness and noise before/after durability test

No.	Before		After	
	Roundness [mm]	Noise [dB(A)]	Roundness [mm]	Noise [dB(A)]
#1	Max. 3	61.4	0.146	78.8
#2	Max. 3	58.8	0.140	78.6
#3	Max. 3	60.3	0.137	78.9
#4	Max. 3	59.0	0.148	79.5
#5	Max. 3	60.3	0.078	76.5
#6	Max. 3	56.8	0.042	71.1

CONCLUSIONS

1. Using multi-body dynamics, we can see the dynamics features of the DC motor for a vehicle
2. The smaller each design parameter, the lower the noise and vibration level of the DC motor.
   ➔ Considering the quality cost, the lowering of the upper design parameters has little benefit.
3. After analyzing the result of the dynamics analysis and the durability test, it is obvious that the roundness of the commutator is the most important design parameter to reduce the brush noise of the DC motor.
   ➔ The roundness of the commutator needs to be maintained in order to maintain the brush noise under a certain level throughout the durability life span of the DC motor.
   ➔ Commutator including lubricating oil can reduce brush noise after durability test.

References

[1] H. Kang: The Study of DC Motor Noise and Vibration, SAE 951350, p. 2461, 1995.
[2] K. W. Kim and T. K. Ahn: A Study on the Vibration Reduction of Small DC Motor, Proceeding of the KSNVE Autumn Annual Meeting, p. 88, 2000.
[3] J. S. Kim: A Study on the Active Balancing System for High-Speed Rotating Machinery, Ph.D. Dissertation, Ajou University, 2003.

XXI ICTAM, 15–21 August 2004, Warsaw, Poland

THE ABSOLUTE COORDINATE FORMULATION WITH REDUCED STRAIN AND STIFFENING

Johannes Gerstmayr, Hans Irschik
Institute for Technical Mechanics, Johannes Kepler University of Linz, Altenbergerstr. 69, 4040 Linz, Austria

Summary The present work contributes to the field of multibody systems with respect to the absolute coordinate formulation (ACF) with a reduced expression of the strain energy. The ACF is known to be advantageous with respect to the description of constraint equations and the constant mass matrix. Absolute coordinates are used as unknowns, similar to nonlinear finite element methods. In the present work, a consistent linearization of the equations of motion with respect to small deformations but large rigid-body motions is performed. This formulation leads to a constant mass matrix while the nonlinear stiffness matrix is composed of the constant small strain stiffness matrix rotated by the underlying rigid body rotation. The equations of motion are derived for the case of a constrained multibody system and geometrical stiffening terms are introduced.

INTRODUCTION

The computation of stress and vibration in heavily loaded machine elements is necessary in order to design such parts for a specific lifetime. Since the beginning of multibody system dynamics, several computational strategies emerged, see e.g. Shabana[6]. The methodologies can be separated into ones that use absolute coordinates and a nonlinear strain-displacement relation and others that use relative coordinates with respect to a co-moving frame and a linear strain-displacement relation, also known as floating frame of reference formulation (FFRF), which leads to a constant stiffness matrix but highly nonlinear mass matrix. Absolute coordinates, which can be e.g. displacements or displacement gradients, have been utilized according to standard finite element formulations or specific beam, plate or shell models have been derived, see e.g. Mikkola and Shabana[5]. Recently, the ACF, which is basically equivalent to a geometrically nonlinear finite element formulation with specific generalized coordinates, has been extended with respect to a reduced strain formulation, see Gerstmayr[3]. The idea of the reduced strain formulation is to linearize the geometrically nonlinear Green strain tensor with respect to a virtual co-moving frame similar to the FFRF. The linearization is based on the rotation of the co-moving frame and leads to a constant mass matrix, but nonlinear stiffness matrix. The method has already been tested with for 3D solid multibody systems with constraints, see Gerstmayr and Schöberl[3], and extended with respect to elasto-plasticity, see Gerstmayr[2]. The method turned out to be computationally very efficient in the case of implicit Runge Kutta time integration schemes, see Gerstmayr and Schöberl[4]. As a specific feature of the method, the mass matrix is constant, the stiffness matrix is consisting of the transformed (rotated) constant stiffness matrix and some additional small nonlinear terms.

ABSOLUTE COORDINATE FORMULATION WITH A REDUCED STRAIN TENSOR

The derivation of the equations of motion starts with the weak form of the equations of motion without any simplifications regarding deformation or displacements,

$$\int_{V_0} \rho \ddot{\mathbf{u}} \cdot \delta\mathbf{u}\, dV_0 + \int_{V_0} \mathbf{S} : \delta\mathbf{E}\, dV_0 - \int_{V_0} \mathbf{f}_0 \cdot \delta\mathbf{u}\, dV_0 = 0 \tag{1}$$

The Lagrangian formulation is used throughout, $\mathbf{S}$ denotes the 2^{nd} Piola-Kirchhoff stress tensor and $\mathbf{E}$ is the Green strain tensor. External forces are denoted by $\mathbf{f}_0$, $\mathbf{u}$ are the unknown displacements, V_0 is the initial Volume and ρ is the material density. The goal of the present formulation is to neglect some terms in the virtual work of internal forces according to the widely used assumptions in multibody systems, such that the deformations are small and that displacements are small with respect to an underlying rigid body motion. According to Figure 1, the displacement of a point $\mathbf{X}$ is split into a rigid part $\mathbf{u}_r$ and a flexible part $\mathbf{u}_s$ defined by

$$\mathbf{u} = \mathbf{u}_0 + (\mathbf{R} - \mathbf{I})\mathbf{X} + \mathbf{u}_s = \mathbf{u}_r + \mathbf{u}_s. \tag{2}$$

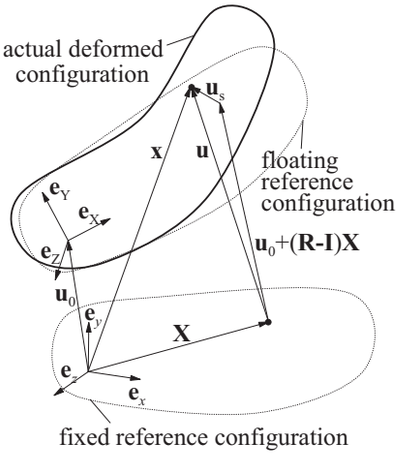


Figure 1: Kinematical relations, small deformation $\mathbf{u}_s$ and large rotation $\mathbf{R}$.

The unknowns are $\mathbf{u}$ and Eq. (2) is used to compute the flexible part $\mathbf{u}_s$ as function of $\mathbf{u}$. This kind of decomposition is a priori non-unique. The rotation matrix $\mathbf{R}$ and the displacement of the reference point $\mathbf{u}_0$ depend either on the whole displacement field $\{\mathbf{u}(\mathbf{X}), \mathbf{X} \in V_0\}$ or on some parts of it. Examplarily, we can use three specific points such as

$$\mathbf{R} = \mathbf{R}(\mathbf{u}(\mathbf{X}_1), \mathbf{u}(\mathbf{X}_2), \mathbf{u}(\mathbf{X}_3)) \quad \text{and} \quad \mathbf{u}_0 = \mathbf{u}_0(\mathbf{u}(\mathbf{X}_1)). \tag{3}$$

The dependence onto the three displacements might be highly nonlinear, and a certain orthogonalization rule has to be

chord or tangential frames in the FFRF. Alternatively, weighted integrals can be used for the definition of mean axis frames, see Gerstmayr and Schöberl[3]. The flexible part of displacements $\mathbf{u}_s$ can be written as function of $\mathbf{u}$

$$\mathbf{u}_s = \mathbf{u} - \mathbf{u}_0 - (\mathbf{R} - \mathbf{I})\mathbf{X}. \tag{4}$$

The fully nonlinear Green strain tensor is defined by

$$\mathbf{E} = \frac{1}{2}\left(\nabla\mathbf{u} + \nabla\mathbf{u}^T + \nabla\mathbf{u}^T\nabla\mathbf{u}\right) = \frac{1}{2}\left(\nabla\mathbf{u}_s^T\mathbf{R} + \mathbf{R}^T\nabla\mathbf{u}_s + \nabla\mathbf{u}_s^T\nabla\mathbf{u}_s\right). \tag{5}$$

In the FFRF deformations are frequently assumed to be small, the linearized strain tensor is utilized and therefore the stiffness matrix is constant. It can be shown that this assumption is equivalent to $||(\nabla\mathbf{u}_s)|| \ll 1$ in the proposed ACF. Thus, a reduced Green strain tensor $\widetilde{\mathbf{E}}$ is introduced, where the quadratic part $\widetilde{\mathbf{E}}_{nl} = \frac{1}{2}\nabla\mathbf{u}_s^T\nabla\mathbf{u}_s$ is assumed to be negligible, $||\widetilde{\mathbf{E}}_{nl}|| \ll 1$,

$$\widetilde{\mathbf{E}} = \mathrm{Sym}(\mathbf{R}^T\nabla\mathbf{u}_s) = \mathrm{Sym}(\mathbf{R}^T(\nabla\mathbf{u} + \mathbf{I}) - \mathbf{I}). \tag{6}$$

The variation of this tensor is $\delta\widetilde{\mathbf{E}} = \mathrm{Sym}(\delta\mathbf{R}^T\nabla\mathbf{u}_s + \mathbf{R}^T\delta\nabla\mathbf{u}_s)$ and contains the cumbersome variation of the rotation matrix $\mathbf{R}$. The reduced Green strain tensor of Eq. (6) is inserted into Eq. (1). A weak formulation for $\mathbf{u}$ is derived by means of a linear elastic constitutive law, $\mathbf{S} = \lambda\mathrm{tr}(\widetilde{\mathbf{E}})\mathbf{I} + 2\mu\widetilde{\mathbf{E}} = \widetilde{\mathbf{E}} : {}^4\mathbf{D}$, with the Lamé coefficients μ and λ and the identity matrix $\mathbf{I}$. According to Eq. (1), the ACF with the reduced Green strain tensor reads for the linear elastic case

$$\int_{V_0} \rho\ddot{\mathbf{u}} \cdot \delta\mathbf{u}\, dV_0 + \int_{V_0} \widetilde{\mathbf{E}} : {}^4\mathbf{D} : \delta\widetilde{\mathbf{E}}\, dV_0 = \int_{V_0} \mathbf{f}_0 \cdot \delta\mathbf{u}\, dV_0. \tag{7}$$

According to Zienkiewicz and Taylor[7], the geometrical stiffening could be represented by means of additional terms in the virtual work of internal forces, such as $\int_{V_0}\mathbf{S}_0 : \delta\widetilde{\mathbf{E}}_{nl}\, dV_0$, where $\mathbf{S}_0$ is represents an appropriate approximation of stresses within the body of interest. In multibody systems, it can be sufficient to approximate these terms by means of centrifugal forces due to high angular velocities of the underlying rigid body motion. The final weak form of equations of motion reads

$$\int_{V_0} \rho\ddot{\mathbf{u}} \cdot \delta\mathbf{u}\, dV_0 + \int_{V_0} \widetilde{\mathbf{E}} : {}^4\mathbf{D} : \delta\widetilde{\mathbf{E}}\, dV_0 + \int_{V_0} \mathbf{S}_0 : \delta\widetilde{\mathbf{E}}_{nl}\, dV_0 = \int_{V_0} \mathbf{f}_0 \cdot \delta\mathbf{u}\, dV_0. \tag{8}$$

The discretized equations follow from a particular finite element discretization, see e.g. Zienkiewicz and Taylor[7]. According to standard constraint formulations in multibody system dynamics based on Lagrange multipliers we write

$$\begin{aligned} \mathbf{M}\ddot{\mathbf{q}} + {}^h\mathbf{R}\mathbf{K}\,{}^h\mathbf{R}^T(\mathbf{q} - \mathbf{q}_r) + \mathbf{f}_{\mathrm{nl}}(\mathbf{q}) + \mathbf{f}_{\mathrm{stiff}}(\mathbf{q}) + \left(\frac{\partial\mathbf{C}}{\partial\mathbf{q}}\right)^T\lambda &= \mathbf{f}_{ext} \\ \mathbf{C}(\mathbf{q}) &= 0 \end{aligned} \tag{9}$$

The kinetic energy leads to a constant mass matrix where $\mathbf{q}$ are the discretized displacements, $\mathbf{q}_r$ is the rigid body part of discretized displacements, $\mathbf{M}$ is the constant mass matrix, $\mathbf{K}$ is the constant small strain stiffness matrix of the body in the reference configuration, $\mathbf{f}_{ext}$ are the external forces, $\mathbf{f}_{nl}$ is a nonlinear function of $\mathbf{q}$ which is of the order $\mathbf{q}_s^2$ and $\mathbf{f}_{\mathrm{stiff}}$ is the part due to stiffening. The matrix ${}^h\mathbf{R}$ consists of sub-matrices $\mathbf{R}$ in the diagonal. In previous investigations it turned out that Eq. (9) can be solved efficiently, see Gerstmayr and Schöberl[4]. Due to special properties of the mass and the stiffness and rotation matrices, only a nonlinear system of the size of the constraint forces λ has to be solved during each time step of an implicit time integration method, assuming the nonlinear parts to be solved in the fixed point iteration. In the case of small deformations, the nonlinear part and the part due to stiffening are computed by means of an additional fixed point iteration, which converges within a few iterations. Therefore, no large system of nonlinear equations has to be solved, and no large Jacobian or stiffness matrix of a large nonlinear system has to be assembled during every time step.

References

[1] J. Gerstmayr. Comparison of the absolute nodal coordinate and the floating frame of reference formulation by means of a simplified strain formulation. In *Proceedings of DETC'03 2003 ASME Design Engineering Technical Conferences*, Paper Number VIB-48306, ASME, New York, 2003.

[2] J. Gerstmayr. The absolute nodal coordinate formulation with elasto-plastic deformations. In *Proceedings of the Multibody Dynamics 2003 conference*, J.A.C. Ambrósio (Ed.), IDMEC/IST, Lisbon, Portugal, 2003.

[3] J. Gerstmayr and J. Schöberl. A 3D finite element approach to flexible multibody systems. In Eberhardsteiner Mang, Rammerstorfer, editor, *Proceedings of the Fifth World Congress on Computational Mechanics (WCCM V)*, Vienna University of Technology, Austria, 2002.

[4] J. Gerstmayr and J. Schöberl. A 3D Finite Element Solver for Multibody Systems Based on Implicit Runge-Kutta Schemes. PAMM, Volume 3, Issue 1, 2003, pp. 154-155.

[5] A.A. Shabana, A.M. Mikkola. Use of the finite element absolute nodal coordinate formulation in modeling slope discontinuity. Transactions of the ASME, Volume 125, 2003, pp. 342-350.

[6] A.A. Shabana. *Dynamics of Multibody Systems*. Cambridge University Press, 2^{nd} edition, 1998.

[7] O.C. Zienkiewicz and R.L. Taylor. *Volume 2 – solid mechanics*. Butterworth Heinemann, London, 2000.

STABILITY ANALYSIS OF A TETHERED SYSTEM

J. Valverde, J.L. Escalona and J. Domínguez
Dept. of Mechanical and Materials Engineering, University of Seville, Spain

Summary The SET is an electrodynamic tether (thin rod) that is subjected to a continuous rotation about the longitudinal axis. The system is similar to an umbalanced rotor. The linear rotordynamics theory predicts instability above a critical velocity. However, it has been probed that the geometric non-linearities can stabilize the system under certain operating conditions.

Space-tethers are very slender and flexible structures that are deployed in outer space. In recent times space-tethers have been the subject of numerous studies in the field of astronautics. The material presented here continues the work carried out by Valverde et al. [1] on a prototype of the European Space Agency called SET (Short Electrodynamic Tether). The SET comprises a central module or main satellite from which two tethers extend. The tethers are about 100 m long and have a tiny cross-section of about $4 \cdot 10^{-6}$ m^2 (thin rod), see Fig. 1. The tethers are electric conductors so the SET interacts with Earth's magnetic field. A plasma contactor (modelled as a disk) is placed at the end of each tether. Due to the Faraday effect [2], a thrust or drag force can be created without spending chemical fuel. Hence, the satellite can be maneuvered without cost.

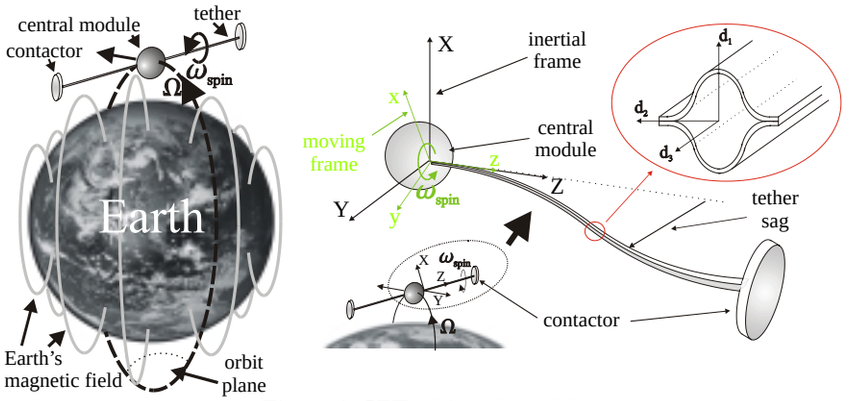


Figure 1. SET orbit and model.

Typically, electrodynamic tethers orbit in the natural position of a free body in space, that is to say, with the axis of smallest moment of inertia pointing towards the centre of the Earth. In this position (vertical tether), it is structurally stable due to the gravity gradient [2]. At high ionosphere altitudes (low orbits, 50-100 *km*), the usual vertical tethers are highly inefficient due to the shape of the Earth's magnetic field. In this case, the axis of the smallest moment of inertia needs to be perpendicular (normal position) to the orbit plane in order to interact in a convenient way with the magnetic field lines, see Fig. 1. Due to the gravity gradient, the system, however, has a tendency to migrate so that it is pointing towards the centre of the Earth. In order to avoid this, a spin velocity (ω_{spin}) is applied about the axis of smallest moment of inertia and the gyroscopic pairs maintain the system in the desired operating position. However, the presence of a gravity gradient does not guarantee the structural stability of the tethers in this normal position.

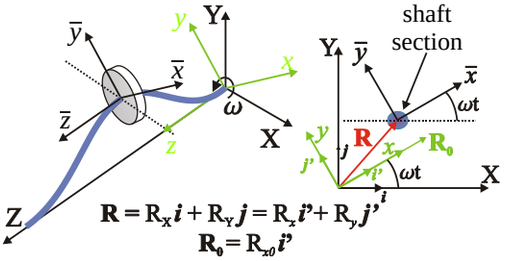


Figure 2. Jeffcott model.

The tethers are stored rolled up in drums prior to extension. The storage and deployment of the tethers from the central module produces an initial deviation from the straight configuration, or sag, when extended into their operating position, i.e., the tether is intrinsically curved when it is deployed, see Fig. 1. As can be seen in Fig. 1, the tether cross-section is orthotropic. The aim of this work is to study the dynamics of the system and to analyze the conditions (values of ω_{spin} , etc.) for which the described operating position is stable. As the spin velocity of the SET is much higher than the rotational velocity about the Earth Ω , a coordinate frame {X,Y,Z} located at the central module can be considered inertial, see Fig. 1. In order to understand the problems related to the structural stability of the SET, a simple low-degree-of-freedom unbalanced rotor-system analogy can be used. Fig. 2 shows the Jeffcott model which has been successfully used in rotordynamics to characterize the different problems that arise in rotating devices such as engine rotors,

turbomachinery, etc. The main feature is that this easy-to-manage system is suitable for the study of different phenomena such as the bearing clearances in rotor supports, external damping, etc. The Jeffcott model is a three degrees of freedom system which contains the main dynamic properties of a rotor system. If only one of the tether-contactor systems is taken into account (assume symmetry with respect to the orbit plane, see Fig. 1), the tether is analogous to the shaft and the contactor is analogous to the rotor [3]. If the motion of the shaft-disk model is asynchronous, alternative stresses arise in the shaft and internal damping forces appear in the system due to the hysteretic dissipative process. In this situation, for spin velocities above the first bending natural frequency of the system (critical velocity), the linear rotordynamics theory predicts structural instability in the shaft. Since the motion of the tether-contactor system is asynchronous due to the torsion in the tether and the spin velocity of the SET is higher than the critical velocity, it seems that the SET would be structurally unstable. The tether sag would increase without bound and the SET would not work conveniently.

Previous works on rotordynamics [3] suggest that a rotor system with internal damping forces is stable due to the effect of geometric non-linear elastic and internal damping forces. In order to probe the previous assertion, the authors studied [1] the fully non-linear system by means of multibody dynamic simulations. These dynamic simulations show that the tether sag could remain bounded under certain operating conditions. It would be useful to know under which values of the spin velocity, initial deviation, etc. the SET behaves as a structurally stable system.

In this work, a stability analysis of a non-linear simplified system has been carried out. In particular, equilibrium or periodic solutions of the rotating system are sought under different conditions. Once the steady-state conditions of the system are obtained as a function of a set of parameters, namely ω_{spin}, length, initial deviation, etc., the stability of these solutions is studied. Therefore, a general map regarding the dynamics of the SET can be outlined and the behaviour of the system can be finally understood. It is important to take into account that the non-linearity of the system plays an essential role in the behaviour of the SET. The geometric non-linear terms completely change the dynamic behaviour (topology) of the system, in a way that a linear model of the SET is structurally unstable above the critical velocity but a non-linear model has been probed to be stable under certain operating conditions [1]. A modified Jeffcott model with geometric non-linear elastic and damping forces is simple enough to develop the stability analysis analytically. An equivalent viscous damping model has been used to describe the internal hysteretic damping of the material. The power dissipated by the damping forces is obtained and used as a Rayleigh dissipation function. The shaft has been discretized by means of Rayleigh-Ritz method. One shape function has been used in each transversal direction (x, y). The system is studied in moving frames $\{x,y,z\}$ instead of inertial frames because the expected periodic solutions are equilibrium points in moving frames, easier to manage. Two different cases have been studied: isotropic case (circular cross section shaft) and orthotropic case (real tether cross section). The initial deviation is assumed to appear in the direction of minimum second moment of area of the section, R_{x0}. For subcritical velocities, the system is stable as the linear rotordynamics theory predicts. On the other hand, for supercritical velocities (operating conditions of the SET) different features arise. In both cases, a branch of equilibrium solutions in the initial deviation x-plane appear ($R_y = 0$). These solutions are given by the following cubic equation ("in-plane solutions"):

$$y = (R_x - R_{x0}) \quad \therefore \quad y^3 + (1-\overline{\omega}^2)y = \overline{\omega}^2 R_{x0} \;\Rightarrow\; f(y,\overline{\omega}) = \lambda\left(R_{x0},\overline{\omega}\right) \;\Rightarrow\; \overline{R}_x \; equilibrium$$

where $\overline{\omega}$ is the dimensionless angular velocity. The stability of these solutions is shown in Fig. 3. Depending on the value of the parameters, there can be 1, 2 or 3 equilibria. In the orthotropic case, there is also a branch of solutions ("out-of-plane solutions") out of the initial deviation plane ($R_y \neq 0$). In any case, there is always one stable equilibrium (periodic in inertial frames) to which the system finally tends.

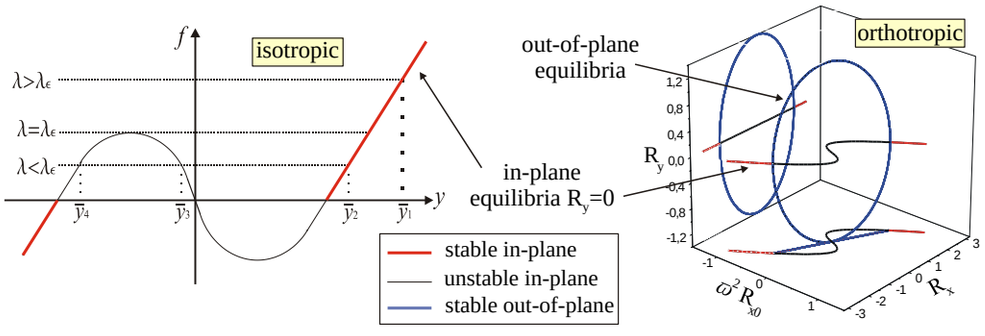


Figure 3. Jeffcott model equilibria. Isotropic and orthotropic cases.

Qualitatively, this stability analysis supports the results obtained from the dynamic simulations [1].

References

[1] Valverde, J., Escalona, J.L., Mayo, J. and Domínguez, J., "Dynamic analysis of a light structure in outer space: Short Electrodynamic Tether", *Multibody System Dynamics* **10**(1) 125-146, 2003.

[2] Cosmo, M.L. and Lorenzini, E.C., *Tethers in space handbook*, Third Edition, Smithsonian Astrophysical Observatory (NASA), 1997.

[3] Childs, D.W., *Turbomachinery Rotordynamics*, Wiley Interscience, New York, 1993.

SIMULATION OF CONTACTING SPATIAL POLYHEDRAL PARTICLES

Beate Muth[*], Peter Eberhard[*], Stefan Luding [**]
[*]*Institute B of Mechanics, University of Stuttgart, Pfaffenwaldring 9, 70569 Stuttgart, Germany*
[**]*Delft ChemTech, Particle Technology Group, Julianalaan 136, 2628 BL Delft, The Netherlands*

Summary In the following, the collective dynamical behaviour of many convex and non-convex polyhedral bodies in space is described. To be able to simulate a high number of bodies, methods from Molecular Dynamics (MD) are frequently used. Here these methods are combined with collision detection methods and contact formulations adopted from Multibody Systems (MBS). The used methods are presented briefly and some simulation results are given.

MOLECULAR DYNAMICS

Originally in MD molecules are considered and it is the goal to describe their interactions and their collective behaviour. These interactions depend on macroscopic measurable properties of the materials, e.g. viscosity or elasticity. In such systems, where the dynamical behaviour is calculated on the scale of the molecules, a very high number of particles is investigated. In order to simulate such a high number of bodies, in MD the molecules are often modelled by rigid spheres, [1]. The material behaviour is then represented by the forces that are acting between the bodies. In MD such forces can be attractive forces like Van der Waals forces, but they can also be contact forces that are applied to a colliding molecule pair. To calculate the forces effectively, overlaps between the particles are accepted, and the value of the force depends on the distance between the colliding bodies. Such methods for the calculation of contact forces are also called constitutive methods, [7]. The constitutive laws from MD are here applied to three dimensional solid bodies of different shape. Another idea that is used in MD is the neighbourhood search. As the motion of a body depends on other bodies of the system, it is possible to search for close body pairs in advance and to evaluate the necessary force only between such body pairs. Different neighbourhood search methods have been developed, [1], and we compared some of the main methods, [2]. Here we want to use only the most efficient one for our applications, where the influence between the bodies is restricted to contacts only, [5], the Linked Linear List Method (LLL). In this method, neighbouring body pairs are determined before real collision detection is performed. Without such a neighbourhood search method, in the worst case, the number of necessary body pairs that have to be tested for collision is of $O(n^2)$. In order to check, whether bodies are close to each other, their positions are projected onto the system axes separately.
By means of LLL neighbouring body pairs are found by creating an overlap list for each axis. For each body the beginning and the ending of its projection are compared, and the order of these beginnings and endings is stored in the list. An overlap of two bodies along an axis is given, if there is a beginning or an ending of a body between the beginning and the ending of another body. In the next time step this list does not have to be created again. A linear behaviour of the simulation can be obtained, by investigating the almost sorted list of the old time step for changes in the order. Body pairs which are overlapping along all system axes are stored and these pairs then have to be checked for collision.

MULTIBODY SYSTEM DYNAMICS

Simulations of granular material or bulk solids are based on free bodies in space. In the space a free body has six degrees of freedom. Then, the equations of motion can be obtained easily taking into account three elementary rotations for example the Kardan-angles and three translational degrees of freedom, summarised in the vector $\mathbf{y}_i$, for every body *i*.

$$m_i \mathbf{H}_{Ti} \cdot \ddot{\mathbf{y}}_i = \mathbf{f}_i ,$$

$$\mathbf{I}_i \cdot \mathbf{H}_{Ri} \cdot \ddot{\mathbf{y}}_i + \mathbf{I}_i \cdot \dot{\mathbf{H}}_{Ri} \cdot \dot{\mathbf{y}}_i + \tilde{\boldsymbol{\omega}}_i \cdot \mathbf{I}_i \cdot \boldsymbol{\omega}_i = \mathbf{l}_i .$$

Here, $\mathbf{H}_{Ti}$ and $\mathbf{H}_{Ri}$ are the Jacobian matrices of translation and rotation of body *i*, respectively, m_i and $\mathbf{I}_i$ are the mass and the inertia tensor, $\boldsymbol{\omega}_i$ is the vector of angular velocity and $\mathbf{f}_i$ and $\mathbf{l}_i$ are the forces and moments acting on the body due to collision or other forces, [4]. After neighbouring body pairs have been found the time consuming collision detection for polygonal convex or non-convex bodies can be accomplished. In order to check, whether there is a collision between two neighbouring body pairs, it has to be checked, whether there is a vertex of one body inside the other body. We consider point P as a vertex of a body, which we want to check for collision with the star-shaped test body, compare Figure 1.

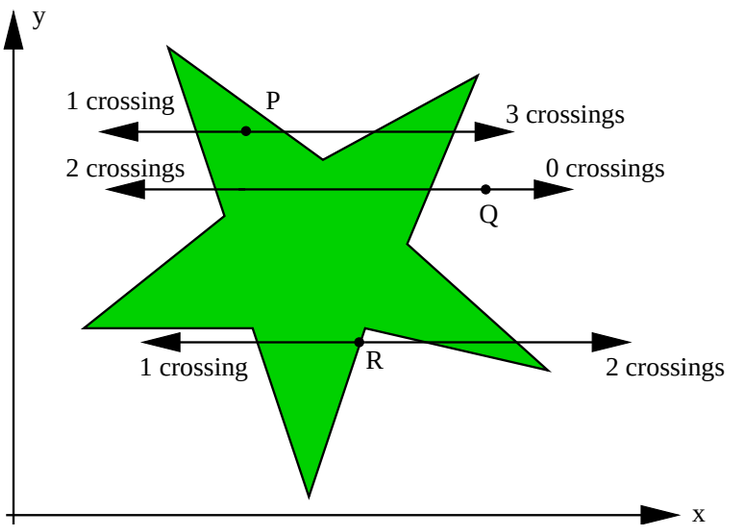


Figure 1: Collision Detection

Therefore, we define a ray from the observed point and another ray 180° rotated to it and count the intersections with the test body, [3]. In the planar case, point P is inside the other body, if the number of intersections with the surface of the other body is odd for the arbitrary ray, to both sides of the point. Also it can be said, that the point, e.g. point Q, is outside the other body, if the number of intersections is even for both rays (where we consider 0 to be an even number), and the point is positioned on the surface of the other body, e.g. point R, if the number of intersections is odd for on one side of the ray and even on its other side. For the spatial case the basic idea is the same but some more considerations have to be taken into account [3,6], and will be addressed in the talk. For the colliding bodies contact forces have to be computed. To apply the contact force to the bodies, the contact geometry has to be detected. For spherical bodies, the normal contact force simply acts in radial direction to the surface of the body. Here, more complex geometries are considered and the relevant surface part has to be found out. In the talk we want to line out, how we detect the contact geometry and how we compute the contact forces. The resulting forces and moments acting on each body must then be incorporated into the equations of motion given above.

RESULTS

The combination of MD and MBS makes it possible to simulate the dynamical behaviour of large systems of granular media consisting of arbitrary shaped bodies, as e.g. carriage systems. In the left part of Figure 2 a screw can be seen, where some bodies are moving down the winding. The right hand side of Figure 2 shows results of a different system that consists of spheres. In the figure a simulated system consisting of about 65000 bodies in space is shown. It can be seen, that it is possible to calculate quite large systems by combining both methods.

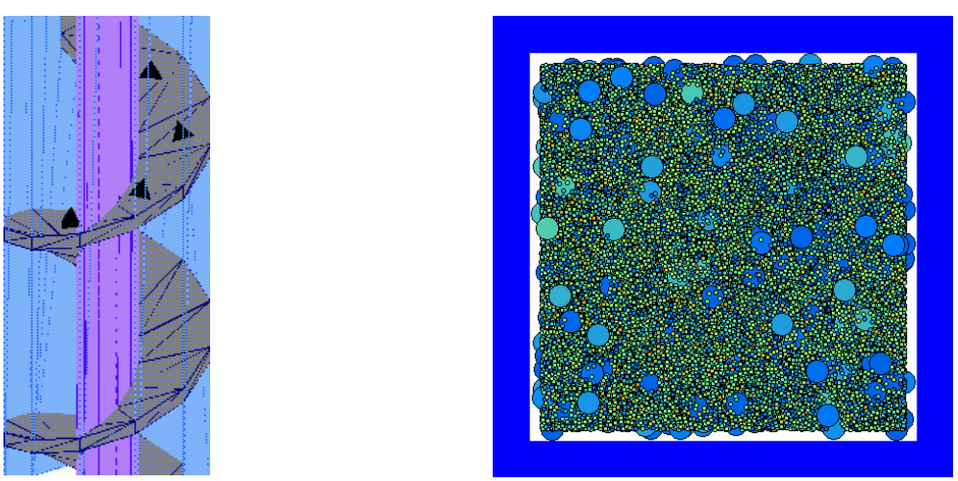


Figure 2: Results for polygonal and spherical bodies

References

[1] Allen M. P., Tildesley D. J.: Computer Simulation of Liquids. Clarendon Press Oxford, 1987.

[2] Muth, B., Eberhard, P., Luding, S.: Contact Simulation of Many Particles Considering Adhesion. *Mechanics Based Design of Structures and Machines* **31**:433-457, 2003.

[3] O'Rourke J.: Computational Geometry in C. University Press, Cambridge, 1998.

[4] Schiehlen, W.: Technische Dynamik. Teubner, Stuttgart, 1986.

[5] Schinner, A.: Fast Algorithms for the Simulation of Polygonal Particles. *Granular Matter* **2**:35-43, 1999.

[6] Wessel, W.: Kontakterkennung räumlicher polyhedraler Körper mit Hilfe von Methoden der Molekulardynamik. *Student-Thesis,* Institute B of Mechanics, University of Stuttgart, 2004.

[7] Wriggers, P.: Computational Contact Mechanics. Wiley, Chichester, 2002.

PLASTIC DEFORMATION BY IMPACTS IN MULTIBODY SYSTEMS

Robert Seifried, Werner Schiehlen
Institute B of Mechanics, University of Stuttgart, 70569 Stuttgart, Germany

Summary In multibody system dynamics the coefficient of restitution is used to describe the energy loss during impact. A numerical method is presented to evaluate the coefficient of restitution considering plastic deformation in the contact region and wave propagation in the bodies. The longitudinal impact of a steel sphere on different aluminum rods is used as testing example for the presented approach and the results are compared with measurements.

INTRODUCTION

In machine dynamics, the multibody system approach proves to be most efficient for the dynamical analysis of the overall motion. Collisions in multibody systems might result in impacts between the system's bodies. During impact kinetic energy is lost, described macro-mechanically by the coefficient of restitution [1]. The loss of kinetic energy is due to local plastic deformation resulting from high forces in the contact region and the initiation of elastic waves in the bodies. After separation of the bodies the waves die away due to material damping. For impacts of compact bodies, e.g. the impact of two spheres, the main source of kinetic energy loss is plastic deformation of the contact region, whereas for impacts involving slender bodies, such as rods, beams, plates or shells a significant amount of the initial kinetic energy is transformed into waves. The coefficient of restitution cannot be computed within the multibody system approach, but it has to be measured experimentally, estimated from experience or evaluated numerically by additional simulations on a fast time scale, resulting in a multi-time-scale simulation [2], respectively.

SIMULATION ON THE FAST TIME SCALE

For an accurate numerical evaluation of the coefficient of restitution the simulation models on the fast time scale must be capable to represent the high-frequency phenomena of wave propagation as well as the local plastic deformation in the contact region. For impacts of simple shaped bodies, such as the impact of a sphere on a rod, the equation of motion for elastodynamics can be introduced and solved by D'Alembert's approach for wave propagation combined with the Hertzian contact law [3]. However, the Hertzian contact law is restricted to elastic contact with spherical contact geometry. For the impact of more complex shaped bodies and more complex contact conditions the Finite-Element-Method can be used [4]. The contact regions of the discretized bodies are connected by contact elements, which are often based on a penalty formulation. Material nonlinearities, such as plasticity can be included in the simulation, too. However, due to the high frequency phenomena resulting from the collision a globally small element length and a small integration time step size are required to catch the wave propagation correctly. This results in a high computation time.
Using a modal approach for the colliding bodies, the elastodynamic behavior can be simulated more efficiently. Using the Finite-Element-Method for the computation of the mode shapes, complex shaped bodies can be simulated, too. The contact can be described by a compliance law such as the Hertzian contact law. For the inclusion of plasticity in the contact region a hysteretic force-indentation law might be used, see e.g. [5], however, these laws require parameters which cannot be computed from the yield stress and, thus, have to be measured experimentally.
In this paper a combination of the modal approach, describing the global elastodynamic behavior of the bodies and a Finite-Element simulation of the contact region is presented, using the longitudinal impact of a steel sphere on an aluminum rod as testing example. The sphere is modeled as a rigid body whereas the rod is represented by the modal approach. The rods eigenfrequencies and mode shapes are computed by a FE-model of the rod. Using the modal approach the displacement of a point of the discretized rod is given by the sum of the rod's rigid body motion $x_1(t)$ and the first n eigenmodes given by the previously computed mode shapes $\boldsymbol{\phi}_i$ and the corresponding modal coordinates q_i,

$$u_p(t) = x_1(t) + \sum_{i=1}^{n} \phi_{ip}\, q_i(t), \qquad p = 1,2,...$$

where the index p identifies the nodes of the rod's FE model. For the modeling of impacts frequencies up to 100kHz are taken into account. The investigated rod is suspended like a pendulum, thus the equations of motion of the rod reads as

$$m\ddot{x}_1 + m\frac{g}{l}x_1 = F(t)$$

$$\ddot{q}_i + \omega_i^2 q_i = f_i, \qquad i = 1(1)n,$$

where m is the rod's mass, g the gravity, l the length of the pendulum, F the contact force and ω_i the angular frequency of the ith eigenmode. The modal contact force is given by $f_i = F\phi_{ic}$ where $p=c$ denotes the node at the point of the contact of the modal model. The contact force F is computed in parallel by a FE-simulation of the contact region using ANSYS including plastic material properties. The modal model and the FE-model of the contact region are connected in each integration time step by exchanging displacements of the boundary of the contact region and the contact force as shown schematically in Figure 1.

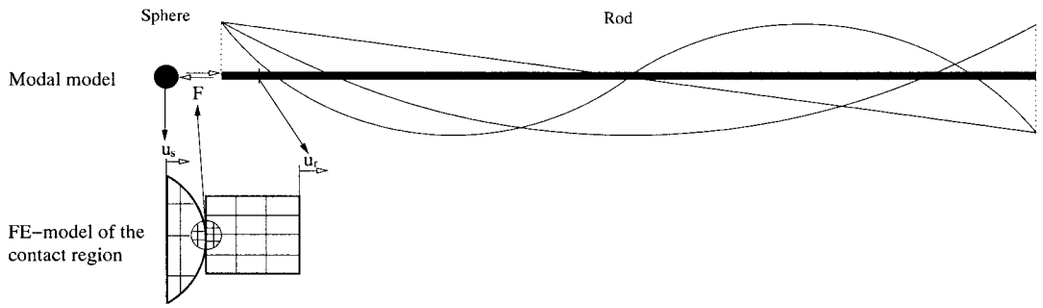


Figure 1: Schematic presentation of the combined simulation procedure

Comparisons of the combined simulation procedure with plain FE-simulations show good consistency, however, especially for larger models the computation time is reduced significantly. By removing the FE-model of the contact region after impact the post impact behavior, i.e. the vibration of the solid bodies, can be simulated even more efficiently.

COEFFICIENT OF RESTITUTION

From the impact force computed on the fast time scale the coefficient is determined [3] and then fed back to the multibody system simulation. In Figure 2 the computed coefficients of restitution for the impact of a steel sphere of radius 15mm on two different aluminum rods are presented for a velocity range from 0.025m/s to lm/s. Both rods have a radius of 10mm and a length of 1m, however rod 1 has a yield stress of 575Mpa whereas the yield stress of rod 2 is 204Mpa. In both plots the results of purely elastic and elastic-plastic simulations are presented. Rod 1 shows for a wide range elastic material behavior, i.e. the energy loss are mostly due to wave propagation; rod 2 shows already for very low velocities plastic deformations. The presented combined model is also modified to compute multiple impacts of the same bodies including the deformation history of the contact region. It is shown that in a series of successive impacts on a body the contact region gets plastically deformed by the first few impacts until a configuration is reached where no additional plastic deformation occurs, in these examples after maximal 10 impacts. In this phase the remaining energy loss is due completely to wave propagation. Therefore, the coefficient of restitution changes with the number of impacts until a stationary value is reached. In Figure 2 measured values using Laser-Doppler-Vibrometers [3] are indicated, too. They show good agreement with the plastic simulation results. Also the increase of the coefficient with the number of impacts can be observed. Due to slight variations of the contact point during the experiments the stationery value for coefficient of restitution is reached after a larger number of impacts than predicted in the simulations.

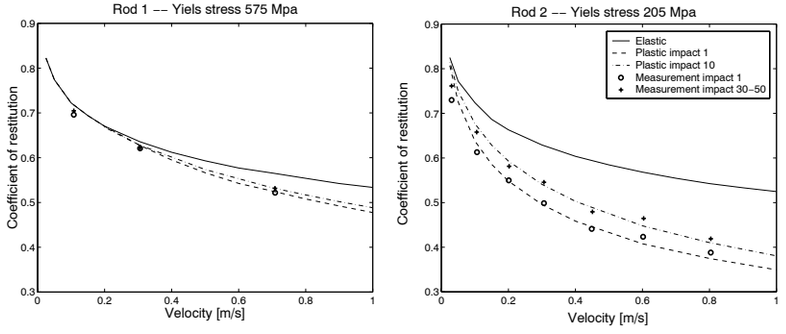


Figure 2: Computed and measured coefficients of restitution

CONCLUSIONS

A simulation technique for the evaluation of the coefficient of restitution is presented using a model combing the modal approach for the elastodynamic behavior of the bodies and a FE-model including plastic material behavior for the contact region. Also multiple impacts of the same bodies including the deformation history are analyzed. Longitudinal impacts of a sphere on rods are used as testing example and compared with experiments. It is shown that a substantial amount of kinetic energy is lost into wave propagation and in plastic deformation, depending on the material's yield stress. With the number of impacts the coefficient of restitution is increasing due to hardening phenomena.

References

[1] Pfeiffer F., Glocker C.: Multibody Dynamics with Unilateral Contacts. Wiley, New York , 1996.

[2] Schiehlen W., Seifried, R.: Multiscale impact models: Interaction between multibody dynamics and wave propagation. In: *Proceeding of the IUTAM Symposium on Nonlinear Stochastic Dynamics*. Kluwer, Dordrecht, 353-362, 2003.

[3] Hu B., Eberhard P., Schiehlen, W.: Comparison of analytical and experimental results for longitudinal impacts on elastic rods. *Journal of Vibration and Control*, 9, 157-174, 2003.

[4] Seifried R., Hu B., Eberhard P.: Numerical and experimental investigation of radial impacts on a half-circular plate. *Multibody Systems Dynamics*, 9, 265-281, 2003.

[5] Lankarani H.M., Nikravesh P.E.: Continuous Force Models for impact analysis in multibody systems. *Nonlinear Dynamics*, 5,193-207, 1994.

XXI ICTAM, 15–21 August 2004, Warsaw, Poland

A SYSTEMATIC MODEL REDUCTION METHOD FOR THE CONTROL OF FLEXIBLE MULTIBODY SYSTEMS

Olivier Brüls*, Pierre Duysinx**, Jean-Claude Golinval*
*University of Liège, Department of Aerospace, Mechanical and Materials Engineering Sciences (ASMA), Chemin des Chevreuils 1, B 4000 Liège, Belgium
**University of Liège, Department of Production Management, Mechanics and Thermodynamics (PROMETHE), Chemin des Chevreuils 1, B 4000 Liège, Belgium

Summary This paper presents a method to build closed-form dynamic equations for flexible multibody systems with a minimal kinematic description. Relying on the Finite Element formalism, the method is able to tackle complex topologies with closed-loops in a systematic way. Thus, it will be of great use in the framework of model based control of flexible mechanisms. The reduction procedure is based on an interpolation strategy: a Finite Element model is built and reduced for a number of selected points in the configuration space, and then, a piecewise polynomial model is adjusted to match the collected data. A few applications of the reduction method are considered: a serial pick-and-place machine, a flexible four bar mechanism, and a parallel kinematic manipulator.

STATE OF THE ART

The development of parallel kinematic mechanisms is a major advance in the field of high-speed machine-tools and manipulators: the motorized joints can be located on the base so that the moving mass is reduced, and faster motions are possible. However, the extended bandwidth of the actuators may excite the natural vibration modes of the system so that the deformations have a significant influence on the performances.

Flexible mechanisms with parallel architecture exhibit a complex kinematic and dynamic behaviour which requires powerful control algorithms, usually based on the input-output feedback linearization of the dynamic equations. This technique is performed with an inverse dynamic model, which outputs the required joint actions given a set of joint values, rates and accelerations. In fact, this algebraic relationship is directly connected to the Ordinary Differential Equations (ODEs) of the underlying state-space model. Thus, the design of the control algorithm requires a high-quality mechanical model in terms of accuracy, efficiency, and conciseness.

Modeling methods in flexible multibody dynamics may be grouped into two classes. On the one hand, assumed modes based methods, such as the recursive Lagrangian formulation presented by Book [1] and the symbolic non-recursive method introduced by Cetinkunt and Book [3], are able to provide compact closed-form descriptions of open kinematic chains, which are very useful for control. But their extension to more complex topologies is less attractive, since closed-loops introduce algebraic constraints between redundant variables. The system is then described by Differential Algebraic Equations (DAEs), and a numerical constraint elimination technique is necessary to construct an underlying set of ODEs. On the other hand, numerical Finite Element (FE) methods [5] are systematic and general in nature, and they are able to handle complex topologies and highly flexible components. However, the generated DAEs contain many redundant variables and the constraint elimination involves expensive computations. Thus, none of these methods meets the requirements for model based control of flexible mechanisms with complex parallel architecture.

SUMMARY OF THE REDUCTION TECHNIQUE

In this work, a systematic and general methodology has been developed to provide closed-form ODEs for such flexible mechanisms with complex topology. The method relies on two ingredients: a numerical reduction procedure and an interpolation strategy. The authors have already demonstrated the relevance of this philosophy for rigid mechanisms [2]. This paper proposes a generalization to flexible multibody systems.

Starting from a FE model, a component mode synthesis is applied to build the reduced set of ODEs in any given configuration. Then, an explicit description of the reduced model is obtained by interpolation in the whole configuration space. Selecting the number of component modes and the interpolation precision level, the user is able to balance accuracy against efficiency and conciseness. The procedure, illustrated in figure 1, is performed offline, so that the closed-form dynamic equations are almost directly available online for the control algorithm.

Numerical reduction

In structural dynamics, the well-established Craig-Bampton and Mc-Neal/Rubin component mode methods [4, 7] allow to reduce the order of a linear model. They have been extended in the framework of flexible multibody dynamics (see [5]), so that a substructure with a linear elastic behaviour within a local frame can be represented by a low-order modal model.

In this research, we exploit those substructuring techniques to build the linearized reduced-order model of a full mechanism in a given configuration. As we are concerned by control, the actuated and sensed degrees of freedom represent a natural choice for the boundary degrees of freedom that should be kept in the reduced model. In general, the remaining internal vibration modes associated with this local model depend on the configuration. This means that the system is described by a time-varying modal basis, and that the physical interpretation of the modal amplitudes also changes during

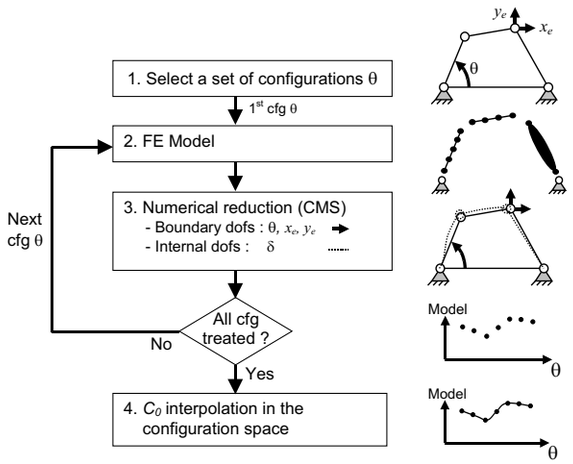


Figure 1. Basic principle of the reduction method. Illustration: a flexible four bar system, where the effector motion (x_e, y_e) is controlled at the joint angle θ. The configuration space is 1-dimensional.

the motion. To guarantee the continuity of the model, a modal tracking strategy is elaborated on the basis of the Modal Assurance Criterion (MAC value) defined in structural identification.

Interpolation

All the coefficients of the linearized reduced model may be collected in a vector f, which is a function of the configuration variables θ. As in response surface optimization methods [6], the construction of an explicit model $f(\theta)$ from sampled data ($f_i(\theta_i),\ i = 1...r$) can be achieved with an efficient interpolation strategy in the n-dimensional configuration space.
Among interpolation strategies, we can distinguish the global ones, based on a high-order interpolation function (neural networks, rational approximations, kriging...) and the local ones, based on a collection of simple interpolation functions defined on a tesselation of the configuration space.
The computational efficiency being a major issue for real-time control, the second family is retained in this research. In general, those local piecewise methods suffer from discontinuous transitions. But some interpolation functions, such as the Lagrange polynoms, yield a global C_0 description. In this paper, several polynomial functions are compared from the point of view of accuracy, continuity, computational load and memory size required to store the model.

CONCLUSIONS

A model reduction method has been developed for flexible multibody systems, which allows to build suitable models for control from Finite Element models. The user is able to adjust the trade-off between accuracy, efficiency and conciseness. The relevance of the method is demonstrated with three examples: a serial pick-and-place machine, a flexible four bar mechanism, and a parallel kinematic manipulator.

ACKNOWLEDGMENTS

M. Brüls is supported by a grant from the Belgian National Fund for Scientific Research (FNRS) which is gratefully acknowledged. This work also presents research results of the Belgian programme on Inter-University Poles of Attraction initiated by the Belgian state, Prime Minister's office, Science Policy Programming. The scientific responsibility is assumed by its authors.

References

[1] Book W.J.: Recursive Lagrangian Dynamics of Flexible Manipulator Arms, *Int. Jnl. of Robotics Research* **3**:87–101, 1984.
[2] Brüls O., Duysinx P., Golinval J.C.: A model reduction method for the control of rigid mechanisms, *Proc. of the ECCOMAS Conf. on Advances in Computational Multibody Systems (Lisbon, Portugal)*, July 2003.
[3] Cetinkunt S., Book W.J.: Symbolic modeling and dynamic simulation of robotic manipulators with compliant links and joints, *Robotics and Computer Integrated Manufacturing* **5**:301–310, 1989.
[4] Craig R., Bampton M.: Coupling of substructures for dynamic analysis, *AIAA Jnl.* **6**:1313–1319, 1968.
[5] Géradin M., Cardona A.: Flexible multibody dynamics: A Finite Element approach, John Wiley & Sons, New York, 2001.
[6] Myers R.H., Montgomery D.C.: Response surface methodology, Wiley Series in Probability and Statistics, 1995.
[7] Rubin S.: Improved component mode representation for structural dynamics analysis, *AIAA Jnl.* **13**:995–1006, 1975.

EXPRESSION ON THE DEFLECTION OF A FLEXIBLE THIN ROD AND IT'S MEASUREMENT

Kohichi Miura*, Tetsu Nishimura*
* *Nihon University, Department of Mechanical Engineering, College of Science & Technology, Tokyo, Japan*

Summary A purpose of this investigation is to discuss the suitable expression of motion of flexible body for experimental observation. The authors have intended to establish an expression of motion of flexible body system which consists of interconnected rigid and deformable components. In this paper, a deformable body element which is very long in comparison with its width and have a uniform circular cross section, such as a flexible rod, flexible beam, or cable element, are investigated specifically.

INTRODUCTION

Many mechanical systems which consist of interconnected components, so called a multibody system, are able to perform variable and large transformational and rotational displacements. The motion of component also is kinematically restricted because of different types of connecting joints. Hence each subsystem included in the system behaves according to the specific nature of the transformational and rotational displacements. The procedures on a dynamic analysis of multibody system are mainly developed for many mechanical systems such as robots, vehicles, aircraft, space structures and machine mechanisms. The expression of motion on kinematics is established in this field with the intention to control the mechanical systems. However these approaches are not suitable for grasping a broad view of motion for a flexible body, because the rotation of the whole system is difficult to define especially.

It is necessary to discuss the suitable expression of motion of flexible body for experimental observation. As an example, a deformable body element, which is very long in comparison with its width and have a uniform circular cross section, such as a flexible rod, flexible beam, or cable element, are investigated. Many mechanical systems such as industrial robots, automated production systems, and crane systems which containing cable elements, power cable, a distributing cable and cable carrier are able to perform variable and large transformation and rotational displacements.

Along with a high speed or performances on these mechanical systems, these cable elements occasionally meet with the severe condition. In these cases, cable elements are strained by bending deformation accompanied with a torsional deformation. Here, the bending and torsional deformation within the element is discussed. It is assumed that the cross section normal to its longitudinal axis remains plane after deformation, and axial tension is disregarded. In this case, the problem what to measure the position of centroid of body element arises as mentioned before. Since it is difficult to estimate directly the torsion and the curvature of deformable cable elements, to obtain a broad view of the motion is an effective measurement.

MEASUREMENT METHOD

In this study, useful methods are investigated for the kinematical measurement of torsion and curvature of a circular cable element, which is observed by two high-speed video cameras. (See Fig.1) In order to investigate a motion analysis of a deformable circular cable element, a family of compact formulation of bending and twisting for a deformable circular cable element is introduced. The measurement of cable element, suggested here, may be available for a motion analysis of cable structures. If the mass distribution is variable, measurement of the centroid is exceedingly complicated furthermore. However, the centroid of deformable body moves whenever the element deformation occurs, it is very difficult to measure the centroid of deformable body element.

To measure the deformation of thin rod element, the circumferential marking lines are graduated in equal distance along longitudinal direction. In order to express the bending with sole curvature, the longitudinal distance is properly selected as L, which depends on its diameter and stiffness. Moreover, the longitudinal marking lines are positioned equally around the circumference. Then, intersections of circumference and longitudinal lines are the target points to measure. If the positions of three points on the circumference of the rod element are measured, the position of center of cross section and normal direction on the measuring cross section are obtained from a geometrical consideration. For the purpose of obtaining the three-dimensional position data, it is necessary to observe the rod element from two directions. Considering a blind spot, eight or more points are required along the circumference line in order to obtain the three position data on the measuring cross section.

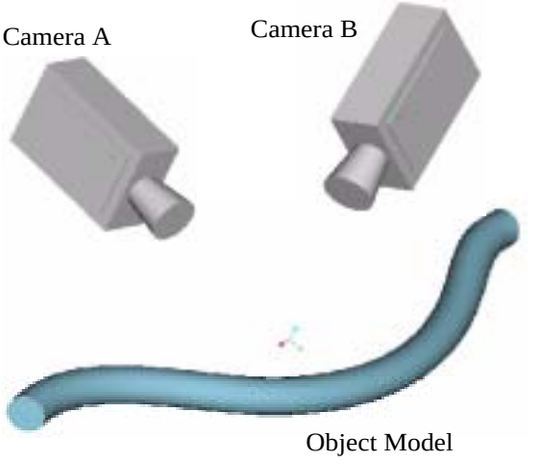


Fig.1 MEASURING IMAGE

One end plane of component, that is the unit element, is the

base plane, and another plane is rotational plane (See Fig.2). Searching the relation of transformation between the body-coordinates on the base plane and the rotational plane, the deformation is resolved. By measuring the position and the direction on both end planes of the component, the curvature of deformed rod component is determined geometrically. And, the profile of the deformed rod component is approximated by an arc with the obtained curvature. As a necessary consequence, the position of the centroid and the inertia tensor of the rod component are able to determine by the arc profile. Finally, the position of the centroid and the inertia tensor of whole rod element are obtained. From the measurement of deformation and the measurement of motion, the angular motion of flexible body system containing deformable elements becomes clear. The authors have intended to establish an expression of motion of flexible body system which consists of interconnected rigid and deformable components. A family of compact generalized formulations of rotational motion for a flexible body or multibody has been derived by adopting an instantaneous rotational axis of the whole body.[1]

For general deformable elements which have a few constraints on the deformation, it is difficult to determine the deformed profile; its analysis requires a special technique.

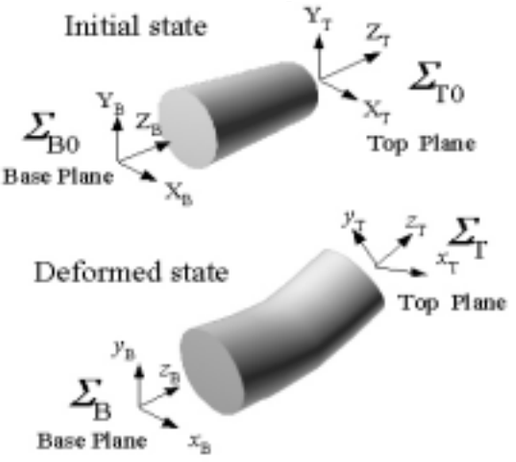


Fig.2 MEASURING MODEL

EXPRESSION ON THE DEFLECTION

In the actual methods for the dynamic analysis of multibody system, the expression of angle variables are required in order to define the orientation of the multiple body. Some of the most commonly used parameters for expressing the angle variables are Euler angles, Euler parameters, navigation angles and the direction cosines. These variables are used to consider the physical meaning of angular parameter set which correspond to the degree of freedom at each joint or motion of the system. However these expressions are not suitable for grasping a broad view of motion and deformation for cable, because it is difficult to estimate directly the torsion and the curvature of deformable cable elements.

To consider a deflection of the element, the local coordinate system Σ_T located on the top plane is observed in the fixed coordinate systemΣ_{B0} located on the base plane (See Fig.2). In initial state, the local coordinate system Σ_T coincide with the fixed coordinate systemΣ_{B0}. After deformation, the coordinate system located on the top plane is denoted Σ_{BT}. At first, the coordinate system Σ_{BT} is swiveled through ω about Z_B axis. Next, Σ_{BT} is swiveled through θ about the axis which is turned Y_B axis round the Z_B axis by an angle ϕ. Obtained coordinate system is rewritten by an expression in the fixed coordinate system. Using the coordinate transform matrix, Σ_{BT} is expressed by the following equation.

$$\Sigma_{BT} = \mathbf{R}_{\Phi}\mathbf{R}_{\Theta}\mathbf{R}_{\Phi}{}^{T}\mathbf{R}_{\Omega} \tag{1}$$

A noteworthy finding is that ω is the angle of twist of element and the physical meaning of θ is considered to be the normal curvature. Furthermore, ϕ define the binormal vector of element.[2] Using the set of angular parameter introduced here, the transformation matrix can be multiplicatively decomposed into the product of a matrix due to bending deformation and a matrix due to twisting deformation. This expression is possible to draw a clear distinction between bending and twisting for experimental operation.

CONCLUSIONS

The expression on the deflection of a cable element and its measurement, suggested here, may be available for a dynamic analysis of cable structures or many mechanical systems which containing cable elements. These approaches are effective in supplementary experiment to the main experiment with electric measurement.

References

[1] K.Miura, T.Yamada, K.Kawamura & T.Nishimura: Expression of Angular Rotation of a Multibody System -Application to a rotational expression of a flexible body-. 6th International Conference on Motion and Vibration Control, Vol.1, pp520- 525

[2] A.E.H.LOVE.: A Treatise on The Mathematical Theory of Elasticity (fourth edition). Dover Publications, 1927.

DYNAMIC ANALYSIS AND VIBRATION CONTROL OF THE PLANAR BEAMS MOVING ALONG THE AXIAL DIRECTION

Naoki Sugano*, Etsujiro Imanishi*
**Mechanical Engineering Research Laboratory, KOBE STEEL, LTD. Kobe, Hyogo, 651-2271, JAPAN*

Summary In this paper, a dynamic simulation method and vibration control technique are proposed for a flexible body moving along the axial direction, such as the plates or the wire rods in the mill. At first, a dynamic simulation model of the planar beams moving along the axial direction using FEM formulation is proposed. Next, a vibration control method using optimal damper-spring support system is proposed and the effect of this control is investigated by this simulation.

INTRODUCTION

Recently, for the purpose of investigating the vibration problem of wire or plate in a mill, dynamic analysis of flexible materials moving along the axial direction is required.

In the former studies, the strict solution of the moving beams under the fixed-fixed boundary condition was investigated[1][2]. Moreover, Stylianou[3] proposed the linear FEM method of moving beams. However, the beams are treated as a linear model in this study, so it has the problem of linearizing error or neglecting the stiffness change by the tension. Sugiyama[4] proposed a method in which the beam is treated as the connection of many small rigid bodies and springs. However, it has a problem in that the number of small bodies must be large to obtain the precise result.

Therefore, the nonlinear FEM method is adapted to the analysis of beams moving along the axial direction in this study. The flexible materials are treated as planar beams and the effect of movement along the axial direction and the effect of geometric nonlinearity are taken into account. The precision of the analysis is investigated by comparing this method and the strict solution. This calculation result indicates that the unstable phenomenon by divergence occurs when the moving velocity becomes large.

Next, a vibration control method is proposed for this vibration phenomenon. Stability of the system is examined for the damper-spring property at the beam support point, and the optimal damper-spring properties for stabilizing the system are obtained. Furthermore, it is shown that the outstanding vibration reduction effect is obtained by conducting the dynamic simulation proposed above.

DYNAMIC ANALYSIS OF THE PLANAR BEAMS MOVING ALONG THE AXIAL DIRCTION USING FINITE ELEMENT FORMULATION

This research examines the vibration of a flexible body moving along the axial direciton by modeling as a 2-dimensional beam moving along the axial direction using a finite element method shown in fig.1. In this method, the displacement vectors of the arbitrary point along the element are obtained in the local coordinates and transformed into the global coordinates. By differentiating this displacement vectors, the velocity vectors in the global coordinates are obtained, considering the effect of the movement along the axial direciton. Next, substituting this velocity vectors into the Lagrange's equation of motion, the equation of motion is obtained.

The calculation result shows that the cantilever beams are pulled into the fixed area with vibration and the cycle of vibration becomes shorter as the time increases, as shown in fig.2. For the purpose of investigating the accuracy of the analysis, the calculation result is compared with the result using the large displacement beam element in the former study. This result shows that this method can analyze the vibration problem of the beam pulled into the fixed area accurately and more effectively than the method of former study.

VIBRATION CONTROL METHOD FOR THE MOVING BEAM

Relation between the damper-spring property at the support point and the system stability

The vibration control technique for the cantilever beam moving along the axial direction is examined in this section.

In order to examine the effect of vibration control by the damper-spring at the support point of the cantilever beam, the system stability evaluation is carried out by the complex eigenvalue analysis. The non-dimensional parameters are employed to express the damper-spring property at the support point. The eigenvalue analyses are conducted using these parameters under the condition that the length of the cantilever beam is changed. The optimal parameters which make the damping ratios maximum are obtained from these analyses.

Evaluation of the vibration control method by using the finite element model

In this section the vibration control method for the cantilever moving beam is examined considering the results obtained in the previous section. The proposed vibration control system is shown in fig.3. From the examination in the previous section, the vibration control method proposed for the system to be stable requires that the damper- spring

property at the support point is varied in proportion to the cantilever beam length.The vibration control effect is verified by using the finite element model proposed above. It is shown that the vibration control is conducted fairly and the beam is drawn without the vibration because the vibration energy is absorbed by the damper at the support point shown in fig.4.

CONCLUSION

In this paper, dynamic simulation method and vibration control technique are proposed for flexible body moving along the axial direction, such as the plates and the wire rods in the mill. In consequence the following conclusions are obtained.

(1) An FEM beam model that takes account of the movement of the axial direction and geometric nonlinearity is proposed.
(2) The optimal damper-spring property for controlling the cantilever beam vibration is obtained by examining the relation between damper-spring property at the support point and the system stability.
(3) A vibration control method is proposed and the effect of the control is verified by numerical simulation using the finite element model. Finally, it is verified that the vibration of the beam is reduced by the proposed vibration control method.

References

[1] Simpson,A., J.Mech.Eng.Science, 15-3(1973), 149-164.
[2] Wickert,J.A. and Mote,C.D., J.Applied Mech., 57(1990), 738-744.
[3] Stylianou, M. and Tabarrok, B. J. Sound and Vib., 178(1994),433-533.
[4] Sugiyama, H. and Kobayashi, N., Trans. JSME, 65-631,C(1999),910-915.

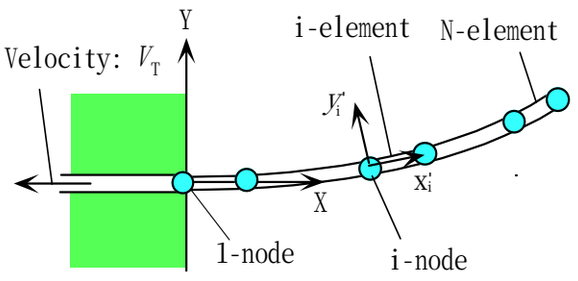


Fig.1 Plannar beam model moving along the axial direction using FEM formulation

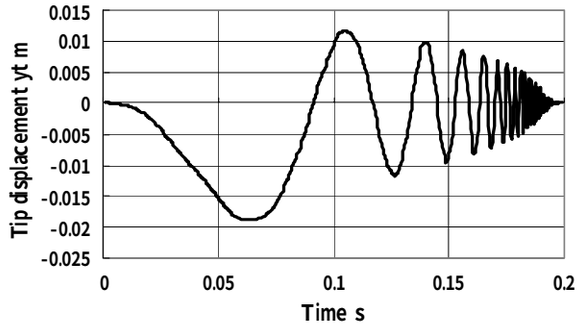


Fig.2 The tip displacement response of the moving beam

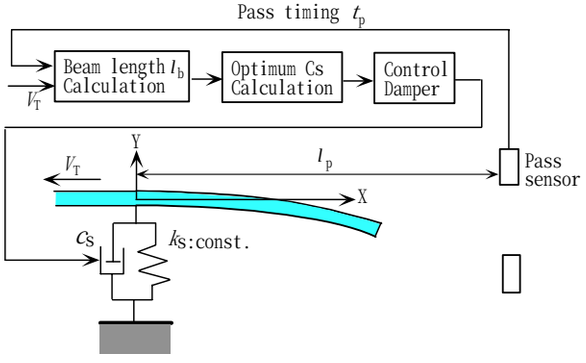


Fig.3 Vibration control system of the moving beam

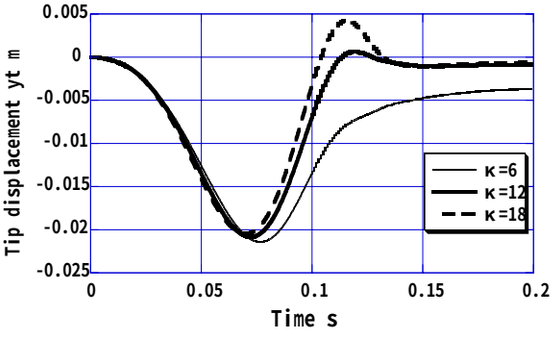


Fig.4 The tip displacement response of the moving beam with the vibration control

GENERATING OPTIMAL MOTIONS OF CONSTRAINED MULTIBODY SYSTEMS

Guy Bessonnet, Pascal Seguin
LMS, UMR6610, University of Poitiers, SP2MI, BP 30179, 86962 Futuroscope Chasseneuil, France

Summary A general approach to optimal motion synthesis of constrained multibody systems is presented. It applies to controlled mechanical systems such as industrial manipulators and legged-locomotion systems. An optimal control problem is stated. A parametric optimization technique based on approximating joint motion coordinates using spline functions of class C^3 is developed to recast this primary problem into an optimization problem of mathematical programming. The latter is solved using SQP algorithms.

INTRODUCTION

Fully actuated multibody systems such as robotic manipulators and walking machines present kinematic redundancies which require organizing their movements appropriately. Furthermore, we are especially interested with motion phases during which the mechanical system may present kinematic loops. In that case, over-actuation must be solved suitably in order to avoid undesirable stress in the closed kinematic chains, together with antagonistic forces which could result in sudden break of contact, or sliding when one-sided contacts are at stake. In any case, there is the need for generating well coordinated movements, dynamically efficient and few energy consuming. A general approach consists in setting and solving an optimization problem that minimizes a dynamic performance criterion. In this way, a constrained optimal control problem is stated. It can be solved using two main computational techniques. In [1], Pontryagin's Maximum Principle was implemented to generate a variety of optimal motions. In this presentation, we are interested in more widespread techniques based on parametric optimization as in [2-4]. Such an approach helps to cope with the computational complexity of dynamic models of multibody systems. Moreover, the optimization problem can be solved in that case using sequential quadratic programming algorithms which are computationally quite efficient.

AN OPTIMAL CONTROL PROBLEM

Dynamic modeling

We consider any rooted multibody systems with tree-like topology and having possibly kinematic loops when moving. All joints are assumed to be actuated. The common approach used for modeling the constrained dynamics of such systems consists in considering closed loops as cut at appropriate joints or contacts, while accounting for relevant closure conditions which restore the original kinematics. Then, introducing a full set of configuration coordinates put together in the n_q-vector $\mathbf{q}$, a Lagrangian dynamic model can be formulated as the differential-algebraic set of equations

$$t \in [0,T],\ \begin{cases} \mathbf{M}(\mathbf{q}(t))\,\ddot{\mathbf{q}}(t) + \mathbf{C}(\mathbf{q}(t),\dot{\mathbf{q}}(t)) + \mathbf{G}(\mathbf{q}(t)) = \mathbf{A}_\tau(\mathbf{q}(t))\,\boldsymbol{\tau}(t) + \boldsymbol{\Phi}^T(\mathbf{q}(t))\,\boldsymbol{\lambda}(t) & (1) \\ \mathbf{C}_c(\mathbf{q}(t)) = 0 & (2) \end{cases}$$

The n_c-order vector-function $\mathbf{C}_c$ represents a set of closure constraints. Its Jacobian matrix is $\boldsymbol{\Phi}(\mathbf{q}) \equiv \partial \mathbf{C}_c / \partial \mathbf{q}$. In (1), $\mathbf{M}$ stands for the mass-matrix, the vector function $\mathbf{C}$ contains centrifugal and Coriolis inertia terms, and $\mathbf{G}$ represents gravity terms. The n_τ-vector $\boldsymbol{\tau}$ stands for actuating joint torques, and $\boldsymbol{\lambda}$ is the n_c-vector of Lagrange's multipliers associated with closure constraints $\mathbf{C}_c$ **.** $\mathbf{A}_\tau$ is a $(n_\tau \times n_q)$- matrix depending on the choice of generalized coordinates.

Constraints defining feasible movements

Some boundary conditions must be accounted for as initial and final equality constraints:

$$\mathbf{C}_0(\mathbf{q}(0),\dot{\mathbf{q}}(0)) = \mathbf{0} \in \Re^{n_0}, n_0 \le n_q\ ;\ \mathbf{C}_T(\mathbf{q}(T),\dot{\mathbf{q}}(T)) = \mathbf{0} \in \Re^{n_T},\ n_T \le n_q \quad (3)$$

Joint motion and velocity limitations, actuating torques limitations, obstacle avoidance, and one-sided contact conditions, result in constraints we represent formally as the set of inequalities:

$$t \in [0,T],\ k \le n_h\ ,\ h_k(\mathbf{q}(t),\dot{\mathbf{q}}(t),\boldsymbol{\tau}(t),\boldsymbol{\lambda}(t)) \le 0 \quad (4)$$

Some h_k in (4) do not depend explicitly on all variables introduced in (4).

Performance criterion

The performance criterion we want to minimize is basically the integral amount of quadratic joint actuating torques. However, as $\boldsymbol{\lambda}$ in (1) represents a set of forces to be applied in order to hold the tips of cut kinematic chains in their prescribed positions defined by the closure constraints (2), we consider such efforts as additional active forces. In this way, we add a quadratic function in $\boldsymbol{\lambda}$ to the Lagrangian of a quadratic functional in $\boldsymbol{\tau}$ to be minimized, namely:

$$\text{Minimize } J,\ J(\boldsymbol{\tau},\boldsymbol{\lambda}) = \tfrac{1}{2}\int_0^T [\boldsymbol{\tau}(t)^T\boldsymbol{\tau}(t) + \boldsymbol{\lambda}(t)^T\boldsymbol{\lambda}(t)]\,dt \quad (5)$$

Then, the problem to be solved consists in computing a triple-vector time-function $t \to (\mathbf{q}(t),\boldsymbol{\tau}(t),\boldsymbol{\lambda}(t))$ minimizing the criterion J in (5) while satisfying the conditions (1) to (4). Let us underline that the minimization of $\boldsymbol{\lambda}$ through J, plays a key role in our approach for succeeding in generating optimal motions of constrained multibody systems

STATING A PARAMETRIC OPTIMIZATION PROBLEM

A key point in dealing with parametric optimization applied to motion synthesis lies in the representation of time functions such as generalized coordinates, using a finite set of discrete parameters. In [2-3], coefficients of polynomial functions are dealt with as optimization parameters for approximating generalized coordinates. A more accurate approach consists in fitting spline-functions at knots uniformly distributed along the motion time. In [4], splines of class C^2 were used for optimizing gait cycles of a planar biped. However, it appeared that optimal actuating torques could have jerky variations at knots. This situation may be overcome using splines of class C^3 ensuring the differentiability of joint accelerations at knots. We define such functions as the concatenation of 4-order polynomials as follows:

$$\{t_1(=0),\, t_2,...,\, t_k,...,t_N\,(=T)\};\, \forall k \le N-1,\;\; t_{k+1}-t_k=\alpha>0,\; t\in[t_k,t_{k+1}],\begin{cases}\tau=(t-t_k)/(t_{k+1}-t_k)\\ q_i(t)\cong \varphi^*_{ik}(\tau)=\sum_{j=0}^{4} c_{ikj}\,\tau^j\end{cases} \tag{6}$$

Connecting polynomials φ^*_{ik}'s at knots up to their third derivative yields spline functions of class C^3. Then considering x_i's in

$$\mathbf{x}=(x_1,...,x_{n_x})^T \equiv (q_1(t_1),...,q_1(t_N),...,q_{n_q}(t_1),...,q_{n_q}(t_N);\; \dot{q}_i(0),\dot{q}_i(T),\; i\le n_q)^T$$

as a set of optimization parameters, the connecting conditions of φ^*_{ik}'s result in the linear system: $\mathbf{M}_c\,\mathbf{c}=\mathbf{M}_x\,\mathbf{x}$ in which $\mathbf{c}$ stands for a column-vector of coefficients c_{ijk}'s, and $\mathbf{M}_c$ is a sparse, hexadiagonal matrix. Assuming that $\mathbf{M}_c$ is invertible, the vector $\mathbf{c}$ can be expressed as the linear function of $\mathbf{x}$: $\mathbf{c}=\mathbf{M}_c^{-1}\mathbf{M}_x\mathbf{x}$. Thus, generalized coordinates q_i's in (8) can be written as functions of $\mathbf{x}$ and t, namely

$$\mathbf{x}\in\Re^{n_x},\; i\le n_q,\; q_i(t)\cong\varphi_i(\mathbf{x},t) \tag{7}$$

Then, the next step consists in expressing $\boldsymbol{\tau}$ and $\boldsymbol{\lambda}$ as functions of ($\mathbf{x}$, t) through (7) and (1). Defining the matrix $\mathbf{A}=(\mathbf{A}_\tau,\boldsymbol{\Phi}^T)$ and the vector $\mathbf{u}^T=(\boldsymbol{\tau}^T,\boldsymbol{\lambda}^T)$, equation (1) may be rewritten using (7), as the vector equation linear in $\mathbf{u}$:

$$t\in[0,T],\; \mathbf{A}(\mathbf{x},t)\,\mathbf{u}(t)=\mathbf{b}(\mathbf{x},t) \tag{8}$$

If $\boldsymbol{\lambda}\neq\mathbf{0}$, $\mathbf{A}$ is not invertible, and equation (8) is underdetermined in $\mathbf{u}$. However, $\mathbf{A}$ is a full rank matrix. Thus for any given ($\mathbf{x}$, t), it is possible to extract a minimum norm solution using the right pseudo-inverse matrix $\mathbf{A}^+$ of $\mathbf{A}$, namely

$$\mathbf{u}(t)\;\equiv\;\mathbf{u}^*(\mathbf{x},t)\;\equiv\;(\boldsymbol{\tau}^*(\mathbf{x},t)^T,\;\boldsymbol{\lambda}^*(\mathbf{x},t)^T)^T\;=\;\mathbf{A}^+(\mathbf{x},t)\,\mathbf{b}(\mathbf{x},t) \tag{9}$$

Using this new expression for $\mathbf{u}$, the criterion (5) is changed into the real function of $\mathbf{x}$

$$F(\mathbf{x})=\tfrac{1}{2}\int_0^T[\,\boldsymbol{\tau}^*(\mathbf{x},t)^T\boldsymbol{\tau}^*(\mathbf{x},t)+\boldsymbol{\lambda}^*(\mathbf{x},t)^T\boldsymbol{\lambda}^*(\mathbf{x},t)\,]\,dt \tag{10}$$

Now, through (7) and (9), we account for closure constraints (2), boundary conditions (3), and constraints (4) as the double set of equality and inequality constraints defined at every knots t_k :

$$k\le N,\begin{cases}j\le N^e,\; C^e_j(\mathbf{x},t_k)=0\\ j\le N^i,\; C^i_j(\mathbf{x},t_k)\le 0\end{cases} \tag{11}$$

The initial optimal control problem defined by the statements (1) to (5) is then restated through (10) and (11) as a constrained, non-linear minimization problem of mathematical programming. It can be efficiently solved using computing codes available in numerical software libraries.

CURRENTLY AVAILABLE SIMULATIONS and CONCLUSIONS

The above approach was implemented to generate optimized cyclic steps of a human-like seven-link planar biped. The only data required to create a gait pattern is the walking velocity. Step length, postural configurations at transitions between single-support and double-support phases, and transition times between successive phases are optimized as well. It was possible to generate smooth gait cycles for any walking speed between 0.4m/s and 1.3m/s. Quite restrictive constraints such as unilaterality of ground-foot contacts and non-sliding conditions are perfectly satisfied.
The method presented yields suboptimal solutions having smooth properties: no undesirable oscillations for the q_i's, and no jerks for the τ_i's. It does not require a great number of control points. It could be easily developed for industrial and space manipulators, as well as to simulate human movements.

References

[1] Bessonnet G., Sardain P., Chessé S.: Optimal Motion Synthesis – Dynamic Modelling and Numerical Solving Aspects. *Multibody System Dynamics* **8** : 257-278, 2002.

[2] Channon, P. H., Hopkins, S. H., Pham, D. T.: Derivation of optimal walking motions for bipedal walking robot. *Robotica* **10:** 165-172, 1992.

[3] Muraro, A., Chevallereau, C., Aoustin, Y.: Optimal trajectories for a quadruped robot with *Trot, Amble and Curvet* gait for two energetic criteria. *Multibody System Dynamics* **9**: 39-62, 2003.

[4] Saidouni, T., Bessonnet, G.: Generating globally optimised sagittal gait cycles of a biped robot. *Robotica* **21**: 199-210, 2003.

XXI ICTAM, 15–21 August 2004, Warsaw, Poland

CONTACT PROBLEMS IN ROLLER CHAIN DRIVE SYSTEMS

Sine Leergaard Pedersen
Department of Mechanical Engineering, Solid Mechanics, Technical University of Denmark, Nils Koppels Allè, Building 404, DK-2800 Kgs.Lyngby, Denmark

Summary A model of a roller chain drive is developed and applied to the simulation and analysis of roller chain drives of large marine diesel engines. The model includes the impact with guide-bars that are the motion delimiter components on the chain strands between the sprockets. The main components of the model of the roller chain drive include the sprockets with different sizes and the chain made of rollers and links, which are represented by rigid bodies, mass particles and spring-damper assemblies respectively. The guide-bars are modeled as rigid bodies and their contact with the rollers are represented by a continuous force. The models proposed effectively represent the polygonal effect, always present in this type of drives, and therefore, all vibration dynamics associated to it.

INTRODUCTION

The presented work is a further development of the methods used in [1]. The dynamics of the roller chain drives are characterized by a complex behavior with impacts between the chain links and sprockets and by discontinuities in the system components velocities giving raise to transversal and longitudinal vibrations of the spans of the chain. These events are the responsible factors for part of the noise presented by mechanical devices that use roller chains and ultimately by the wear of the roller chain drives. Though roller chains have been used for a long time as a reliable mechanical component to transmit power and to handle materials mechanically, only in the last decades their dynamical behavior started to be studied [2]. The main reason for this situation is that their dynamics is very complex, making it impossible to find general analytical procedures able to describe thoroughly the problem. With the development of fast computers some recent efforts have been put forward in order to better understand different aspects of these mechanical components [3]. In a review of the state-of-art Wang and Liu [2] identify many of the investigations that have been carried out and state that integrated models describing the full dynamics of the system are necessary.
In this study an integrated model describing the complex dynamics of the roller chain drive including chain guides and moving sprockets is proposed. The roller chain drive model, based on a multibody dynamics formulation, has one driving sprocket and one or more driven sprockets. The complete chain is modeled by lumped masses connected by spring-damper uniaxial elements. The methodology proposed for the roller-sprocket contacts is penalty forces, which use the continuous force model proposed by Lankarani and Nikravesh [4]. Through the application of this, it is shown that the full dynamics of the roller-chain drive is captured and the contact problem is fully characterized.

THE MODEL OF THE ROLLER CHAIN DRIVE

A typical roller-chain drive is composed of one chain that wraps around two or more sprockets. The roller chain is made of alternating inner and outer links assembled in pivots by bearing pins and bushes. For the purposes of the study presented here, the mass of the chain is assumed to be lumped at the roller locations. Springs and dampers with constant stiffness and damping coefficients model the links. In this model the clearances between pin and bushing are neglected as well as the rotational inertia of the rollers about their center of gravity.
Even if the velocity of the driving sprocket is constant the driven sprocket velocity will fluctuate. This is known as the polygonal effect and it is the responsible for the transverse and longitudinal vibrations that develop in the chain. The excitation resulting from the impact of the roller when it seats on the sprocket and the polygonal effect are the responsible parts for the noise and vibration of the roller-chain drive. In order to have a correct model of the vibration behavior of the chain and the tension fluctuation special attention must be paid to the correct engagement and disengagement description. In the model that is developed here both the driving side and the slack side of the chain are represented. No assumption is made that limits the number of sprockets in the drive, the minimum number of teeth engaged at a certain time or the variance of the angular velocity of the driving sprocket. Moreover the location of the center of the sprockets can be fixed or be time dependent. This allows the introduction of active tensioners in the roller-chain drive. Let the roller-chain be modeled as a system of particles connected by translational springs and dampers. The rollers that are not seated in the sprockets constitute a particle system free in space. The equations of motion of the rollers are

$$m_r \mathbf{I} \ddot{\mathbf{q}}_r = \mathbf{f}_r \tag{1}$$

where $\mathbf{I}$ is the identity matrix, m_r is the mass of a link and $\ddot{\mathbf{q}}_r$ is the translational accelerations of the rollers. The right hand side $\mathbf{f}_r$ is the vector with the forces acting on the individual chain links due to the flexibility of the links. For the rollers in contact with a sprocket or a guide-bar it also includes the contact force between the rollers and either the sprockets or guide-bars. For a sprocket having an external applied force $\mathbf{f}_s$ made up from the forces with which the chain affect the sprocket and from optional directly applied forces the equations of motions are

$$\mathbf{M}_s \ddot{\mathbf{q}}_s = \mathbf{f}_s \tag{2}$$

where matrix $\mathbf{M}_s$ contains the mass and mass moment of inertia of the sprocket, the vector $\ddot{\mathbf{q}}_s$ contains the acceleration of the sprocket in the x- and y-direction and the angular acceleration, thus rotational inertia for the sprocket is taken into account.

THE CONTACT MODELS

A procedure to describe the capture of the roller by a sprocket is to use a non-linear force contact model that can take into account the impact that occurs during engagement.
Based on the Hertzian contact theory [5] several models have been proposed which take into account the energy dissipation due to heat, noise, vibrations or localized deformations. Lankarani and Nikravesh [4] proposed an impact-contact model that besides providing an accurate description of the physical phenomena is numerically stable, leading to an efficient computer performance. The contact model proposed here to describe the roller-sprocket engagement is based on the model by Lankarani and Nikravesh and it takes into account the specifics of the roller-chain dynamics. The contact force is given by

$$\mathbf{f}_c = K_g \delta^n \left[1 + \frac{3(1-e^2)v}{4v^{(-)}} \right] \mathbf{n} \tag{3}$$

where K_g is the generalized coefficient of stiffness, δ is the indentation, the power n is 1.5 for metallic surfaces, e is the coefficient of restitution, v is the relative velocity and $\mathbf{n}$ is the normal vector to the contact surface. The contact model is

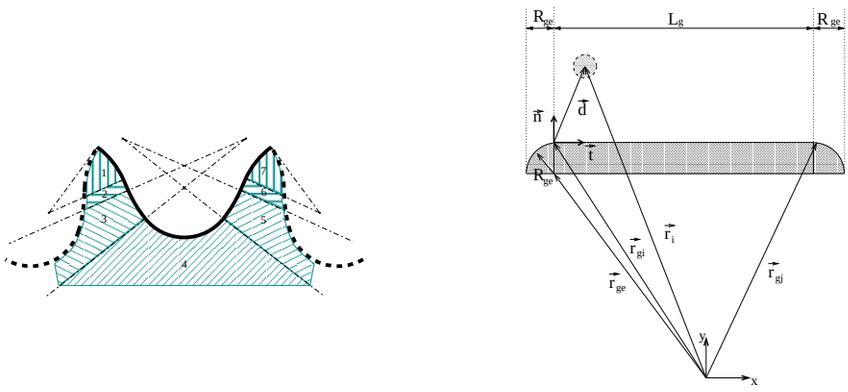


Figure 1. The tooth profile and the shape of a guide-bar

applied to contact between the roller and the surface of the real profile of the teeth, as an extension to earlier work [1], where a circular profile was used. Figure 1 shows the shape of the real tooth profile and the shape of the guide-bars.

NUMERICAL EXAMPLE

The methodology is applied to the simulation of a two stroke diesel marine engine roller-chain drive. The drive is standard in the engines that have between 4 and 12 cylinders for a power range of 1760 to 78000 KW. The roller-chain drive, composed by four sprockets and a chain made of 122 links. The sprocket in the top of the chain drive is part of the pre-tensioning system and it is located 0.372 m to the right of the crankshaft and 3.127 m above it during normal operating conditions. Each link of the chain, with a pitch of 0.0889 m and a mass of 3.01 Kg, is modeled as a flexible element with a stiffness of 815 MN/m, according to the experimental data obtained from the manufacturer.
The application to the roller-chain drive of a large marine engine demonstrates the level of modeling that is possible to achieve with the purposed formulation.

References

[1] Pedersen, S. L., Hansen, J. M. and Ambrósio, J. A. C.: A Roller Chain Drive Model Including Contact with Guide-bars. *Multibody Dynamics 2003 - ECCOMAS Conference*:16 pages on cd,2003
[2] Wang, K. W., and Liu, S. P.: On the Noise and Vibration of Chain Drive Systems. *The Shock and Vibration Digest*, **23(4)**: 8–13, 1991
[3] Veikos, N., and Freudenstein, F.: On the Dynamic Analysis of Roller Chain Drivers, Part I - Theory. *Mechanical Design and Synthesis, ASME*,**DE-Vol.46**: 431–439, 1992
[4] Lankarani, H. M., and Nikravesh, P. E.: Continuous Contact Force Models for Impact Analysis in Multibody Systems. *Nonlinear Dynamics*, **5**: 193–207, 1994
[5] Hertz, H.: Gesammelte Werke Vol.1. *Leipzig, Germany*, 1895

MOTION AND VIBRATION CONTROL OF THE LIFT MECHANISM OF A LADDER TRUCK

Katsuhisa Fujita*,Yasuhiro Shiono*,Mitihiro Itihara**,Takuro Koseki**
*Osaka Pref.Univ. 1-1 Gakuen-cho, Sakai, Osaka, Japan
** Morita Co. Ltd,Japan

Summary A ladder truck with lift mechanism has played an important role in life-saving and fire-fighting. Although the safer and quicker operation mechanism is requested to be developed due to these demands, the lift operation generates a lot of vibration at the time of the lift operation. A coupled equation of a ladder model is derived using the differential algebraic equation. The dynamic behavior under the operation is discussed by the parameter studies.

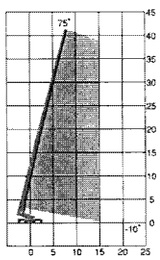
INTRODUCTION

A ladder truck with lift mechanism has played an important role in life-saving and fire-fighting for the increase of complex urban-space and high-rise building. Especially, the recent demands for the specification of a ladder truck, which are the larger load capacity of the basket at a ladder tip, the elongation of the total length and the light-weighting of a ladder itself, have been increased. However, accompanying with these trend, the lift operation generates vibrations much more and suppressing vibrations become more important problem for the quicker and safer operation mechanism.

In this paper, though an actual ladder truck is composed of four or five sections, as shown in Fig. 1, a two-sections ladder model is investigated to make the physical understanding on the dynamic behavior of a flexible ladder easier. A coupled equation of motion for the two-sections ladder model is derived using the differential algebraic equation (DAE). Performing the numerical simulation studies taking the dimensions of the two-sections flexible ladder model as parameters, how the dimensions of a ladder affect on the occurrence of vibrations is made to be clear. And the vibration control is investigated on the modification of the input driving motion of a ladder. Moreover, the optimal control method for minimizing the vibration and the required moving time of a ladder simultaneously is discussed.



(a) Photograph of an actual ladder truck



(b) Working area of the ladder

Fig. 1: Example of an actual ladder truck for the object of simulation analysis

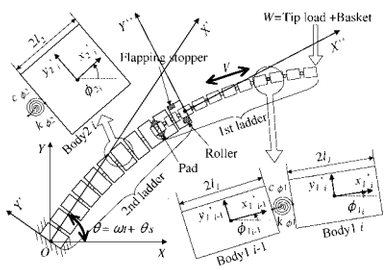


Fig. 2: Mechanical model of the 2 sections ladder

ANALYSIS METHOD

Figure 2 shows the mechanical model of the two-sections ladder. The 1st and 2nd ladder-sections are divided into n equivalent rigid bodies respectively (hereafter called "body"). The rotational springs which are equivalent to their flexual rigidity and structural damping are installed at each joint between bodies (hereafter called "hinge"). Therefore, the 1st and 2nd ladder-sections are composed of a combination of bodies, rotational springs and dampers.

The local coordinate $X'-Y'$ is defined at the bottom point of the 2nd ladder-section which can rotate with an angular velocity around the fixed point O at the bottom of the 2nd ladder-section. Furthermore, the local coordinate $X''-Y''$ is defined at the tip point of the 2nd ladder-section. The ascending and descending motions and the turning motion can rotate around Z-axis and Y-axis respectively. The extending and retracting motions can move with a velocity V along the X''-axis.

The kinematic constraint equation $\mathbf{\Phi}^{\mathsf{K}}_{2(\mathsf{i}-1),\mathsf{i}}$ between the $(i-1)$th body and ith body of the 2nd ladder-section can be obtained in the following equation:

$$\mathbf{\Phi}^{\mathsf{K}}_{2(\mathsf{i}-1),\mathsf{i}} = \left\{ \begin{array}{c} x_{2_\mathsf{i}} - x_{2_{\mathsf{i}-1}} - l_2\cos\phi_{2_\mathsf{i}} - l_2\cos\phi_{2_{\mathsf{i}-1}} \\ y_{2_\mathsf{i}} - y_{2_{\mathsf{i}-1}} - l_2\sin\phi_{2_\mathsf{i}} - l_2\sin\phi_{2_{\mathsf{i}-1}} \end{array} \right\} = \mathbf{0} \tag{1}$$

When the 2nd ladder-section is subjected to the ascending and descending motions rotating with an angular velocity ω around Z'-axis at the fixed point O, the driving constraint equation $\mathbf{\Phi}^{\mathsf{D}}_{2,\mathsf{AD}}$ is given as follows:

$$\mathbf{\Phi}^{\mathsf{D}}_{2,\mathsf{AD}} = \left\{ \begin{array}{c} x_{2_1} - l_2\cos(\omega t + \theta_\mathsf{s}) \\ y_{2_1} - l_2\sin(\omega t + \theta_\mathsf{s}) \\ \phi_{2_1} - (\omega t + \theta_\mathsf{s}) \end{array} \right\} = \mathbf{0} \tag{2}$$

Similarly, the diving constraint equation $\mathbf{\Phi}^{\mathsf{D}}_{2,\mathsf{T}}$ under the turning motion is also obtained. Moreover, when the two-sections ladder is extending or retracting with a velocity V, the driving constraint equation $\mathbf{\Phi}^{\mathsf{D}}_{1}$ can be defined.

The equation of motion using the differential algebraic equation(DAE) as for the two-sections flexible ladder model is described as follows:

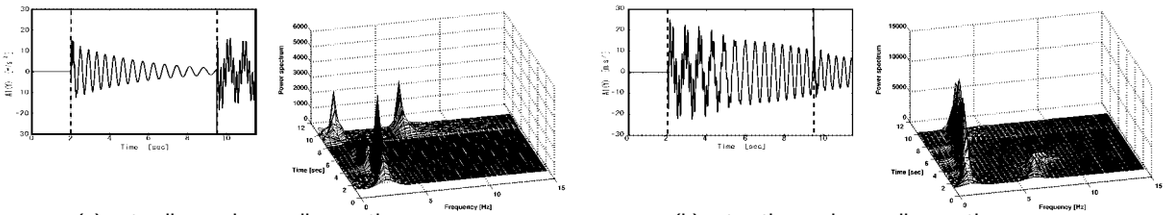
$$\begin{bmatrix} \boldsymbol{M} & \boldsymbol{\Phi}_{\mathrm{q}}{}^{\mathsf{T}} \\ \boldsymbol{\Phi}_{\mathrm{q}} & \boldsymbol{0} \end{bmatrix} \begin{Bmatrix} \ddot{\boldsymbol{q}} \\ \boldsymbol{\lambda} \end{Bmatrix} = \begin{Bmatrix} \boldsymbol{Q} \\ \boldsymbol{\gamma} \end{Bmatrix}, \tag{3}$$

where $\boldsymbol{q}$ is the total generalized coordinate, $\boldsymbol{M}$ the total mass matrix, $\boldsymbol{\Phi}$ the total constraint equation, $\boldsymbol{Q}$ the total generalized equation, λ the Lagrange multipliers and $\boldsymbol{\gamma}$ the function of $\boldsymbol{\Phi}$ and $\boldsymbol{q}$.

NUMERICAL SIMULATION

Extending and ascending motions simultaneously and retracting and ascending motions simultaneously

These simultaneous motions are carried out with an extending and retracting velocity $V = 1[m/s]$ and an ascending angular velocity $\omega = 0.07[rad/s]$. And, the profile of the input driving motion is an impulse-type shape as aftermentioned. Figure 3 shows the time history waves and the power spectrum.



(a) extending and ascending motions (b) retracting and ascending motions

Fig. 3: Time history waves and power spectrum of tip acceleration

Control of input driving motion of a ladder

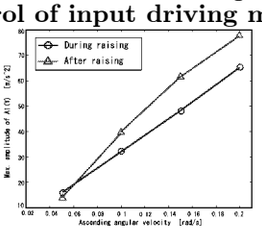
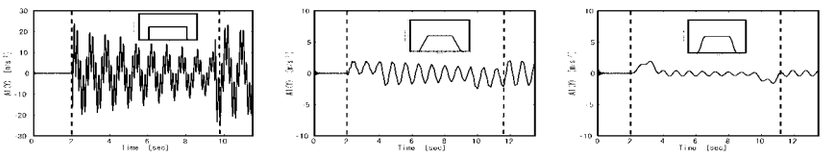


Fig. 4 Influence of ascending angular velocity on tip acceleration



(a) Impulse-type input (b) Trapezoid-type input (c) Secondary function-type input

Fig. 5: Tip acceleration under ascending motion

Figure 4 shows the influence of the angular velocity at the ascending motion. To control the motion and vibration of an actual ladder truck, let us regulate the profile of the input driving motion of a ladder in advance as feed-forward control. Figure 5 shows the time history waves under the ascending motion when the profile of the input driving motion is adjusted to the three kinds of types, impulse-type, trapezoid-type and secondary function-type.

DISCUSSION

The vibration of a ladder is found to be suppressed for the combination of the extending and other rotating motions. On the contrary, it is found to be amplified for the combination of the retracting and other rotating motions. This dynamic behavior is considered to be due to the phenomena which is called as "spaghetti problem", and to be affected much by the Coriolis' force.

Moreover, the control of the input driving motion of a ladder can be said to be important for reducing the vibration under the lift operation. The optimal control for minimizing the vibration and the required moving time is thought to be necessary for developing the ladder truck with the safer and quicker lift mechanism.

CONCLUSIONS

The following is concluded from the above-mentioned considerations and discussions;

- The proposed analysis method is proved to be useful for simulating the dynamic behavior of the two-sections ladder under the extending and retracting motions, the ascending and descending motions, and the turning motion.
- The extending motion is found to suppress the vibration generated by the rotating motions such as the ascending, descending and turning. On the contrary, the retracting motion to amplify the vibration.
- The control of the input driving motion of a ladder is clarified to have much influence on minimizing the vibration of a ladder.

References

[1] E. J. Haug.:Computer-Aided Kinematics and Dynamics of Mechanical Systems Basic Methods. Allyn and Bacon, pp.181-215, 1989.

[2] J. W. Baumgarte.:A New Method of Stabilization for Holonomic Constraints. Trans. of ASME, Journal of Applied Mechanics, 50, pp.869-870, 1983.

[3] K.Fujita, K.Koike, Y.Shiono and T.Koseki.:Multibody Dynamics of the 2 Sections Flexible Ladder Model Extending and Retracting Each Other. Proc. of The 2003 ASME International Design Engineering Technical Conferences & Computers and Information in Engineering Conference, DETC2003/VIB-48367 in CD-ROM.

METAL FORMING PROCESSES CONDITIONED BY CYCLIC LOADING. A NEW CHALLENGE FOR THE THEORY OF PLASTICITY

Zenon Mróz[*], Ryszard B. Pęcherski[**]
[*] *Polish Academy of Sciences, IPPT PAN, Swietokrzyska 21, Pl 00-049 Warszawa, Poland*
[**] *IPPT PAN, Department of Mechanics of Materials and Biomechanics/ Cracow University of Technology, Institute of Structural Mechanics, Warszawska 24, PL 31-155 Kraków, Poland*

Summary Since early works of cyclic plasticity, it was observed that stress-strain cycles of large amplitude imposed on the cold-worked specimens of metallic materials produce cyclic softening. Korbel and Bochniak proposed the improvement of a method for plastic forming operations conditioned by cyclic loading. The experimental investigations led to the identification of shear banding as the basic mechanism responsible for plastic softening. A new approach to the theory of plasticity describing the discussed above phenomena is proposed and an example illustrating its predictive power is presented. In particular, the parameters controlling cyclic loading under torsion: the amplitude of the cycle and its frequency are related with the microscopic model of shear banding.

Since early works of cyclic plasticity, it was observed that stress-strain cycles of large amplitude imposed on the cold-worked specimens of copper, steel, and aluminum alloy produce cyclic softening [1]. It was also reported that the length of the specimen increases during cyclic loading while subjected to combined tension and torsion, with the axial load maintained constant and with the alternating torque [2]. One of first attempts of the theoretical description of this phenomenon, called recently ratchetting, was proposed in [3]. Due to the importance of the latter phenomenon for the prediction of the risk of failure of structures subjected to repeated loads the cyclic plasticity theory was developed. On the other hand, the search for the applications of controlled cyclic torsion [2] for the reduction in load during the processes of drawing of copper and extrusion of lead was reported [4]. It transpired, however, that the problem is far to be solved and that the understanding of the process with cyclic strain path change requires further experimental and analytical study.

The effects of the change of strain path on the reduction of load in elementary tests of tension or compression as well as in the processes of drawing, extrusion, rolling and forging have been studied for two decades by Korbel and Bochniak [5, 6, 7]. The systematic experimental investigations, related with microstructural analysis and physical interpretation of the phenomenon, led to the identification of patterned distribution of shear banding as the basic mechanism responsible for plastic softening. Due to this observation, the search for the new energy-saving plastic forming processes of metallic materials resulted in several patents for the improvement of method for plastic forming operations conditioned by cyclic loading, called KOBO Type Forming [7]. In order to make the new operations more efficient and suitable for industrial implementations, one needs to optimize the considered forming process. This requires modelling and simulating numerically the process. The key point, which is necessary to execute this task, is the knowledge of constitutive description of material behaviour during forming operation with the cyclic change of loading scheme. The plastic flow law accounting for the effects of shear banding with the application of Armstrong-Frederick model of non-linear kinematic hardening for the approximation of the generic micro-shear banding surface was presented in [8]. However, proper understanding of the phenomenon of material softening during plastic flow, conditioned by cyclic loading with a particular amplitude and frequency, remains an unsolved and challenging problem in the recent theory of plasticity.

Our aim is to study this problem from the point of view of cyclic plasticity accounting for multiscale description of shear banding. A new approach to the theory of plasticity describing the phenomena discussed above is proposed and an example illustrating its predictive power is presented. In particular, the parameters controlling cyclic loading under torsion: the amplitude of the cycle and its frequency are related with the microscopic model of shear banding. Our task is to predict and give an assessment of the optimal ranges of these parameters from the point of view of required plastic softening.

The available results of metallographic observations reveal that in heavily deformed metals, or even at small strains if they are preceded by a change of deformation path, a multiscale pattern of shear localization modes progressively replaces the crystallographic multiple slip or twinning. Different terminology is used depending on the level of observation. The term micro-shear band is understood as a long and very thin (of order 0.1 μm) sheet-like region of concentrated plastic shear crossing grain boundaries without deviation and forming a definite pattern in relation to the principal directions of strain. It bears very large shear strains and lies in a "non-crystallographic" position. It means that micro-shear bands are usually not parallel to a particular densely packed crystallographic plane, of conventionally possible active slip system, in the crystallites they intersect. This change of deformation mode produces plastic softening. The experimental observations reveal the time and spatial organisation of dislocations and the resulting hierarchy of plastic slip processes: from coplanar

dislocation groups moving collectively along active slip systems, through slip bands to coarse slip bands, which may further transform into transgranular micro-shear bands and form clusters (packets) of micro-shear bands of the thickness of order (10÷100) μm. At this level of observation, the clusters can be considered as elementary carriers of plastic strain, cf. Fig.1. It appears that the successive generations of active micro-shear bands competing with the mechanism of multiple crystallographic slips are responsible for the process of advanced plastic flow. Basing on this observation, a new description of shear banding contribution to plastic flow is proposed. The developed microscopic model of shear banding is implemented into the macroscopic model of cyclic plasticity [9]. The "lifetime" $\Delta\tau$ of the cluster of active micro-shear bands is related with the frequency of cyclic loading and the amplitude of the cycle is estimated, in terms of accumulated energy, by means of plastic shakedown theorems and the analysis of the transition from plastic shakedown to ratchetting. The nonlinear hardening rule implicitly introduces the second limit surface corresponding to the saturation of micro-stresses, which is correlated in our study with massive formation of micro-shear bands.

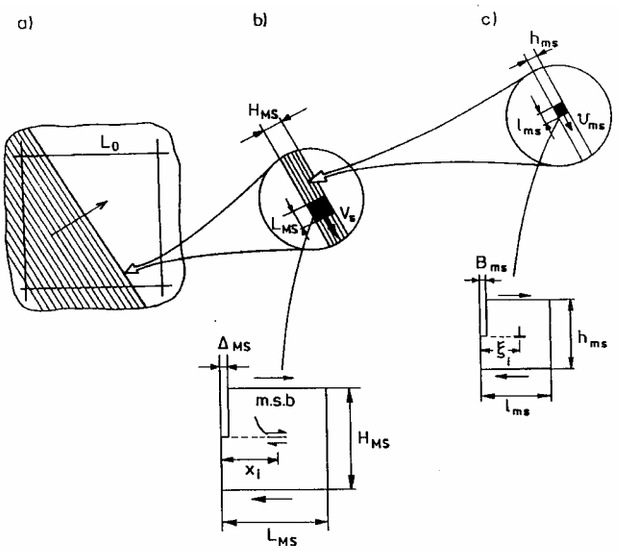


Fig. 1. Schematic view of the multiscale system of shear banding: a) The RVE of the dimension of $L_0 \approx 1$ *mm* traversed by the region of shear banding progressing in the direction pointed by the arrow. b) The cluster of active micro-shear bands with the active zone of the thickness $H_{MS} \approx (10 \div 100)$ μm and the width L_{MS} being of the same order. Beneath, the fundamental mechanism of plastic shear strain generated by the active micro-shear bands operating within the active zone during their "lifetime" $\Delta\tau$, and producing the total displacement Δ_{MS} is depicted. c) The active zone of a single micro-shear band of the thickness $h_{ms} \approx 0.1$ μm and the width l_{ms} of the same order with the picture of an elementary dislocation model of plastic shear in the active zone.

Particular examples were calculated, for the case of cyclic torsion superposed upon steady tension or compression, to illustrate the relation of the parameters of micro-shear banding model with the frequency of cyclic loading and the amplitude of the cycle. The optimal ranges of these parameters from the point of view of required plastic softening were estimated. Our analysis shows that such phenomena as ratchetting and plastic softening, which can appear dangerous in cyclically loaded structures, do play beneficial role in suitably designed manufacturing processes.

References

[1] D.S. Dugdale, Stress-strain cycles of large amplitude, J. Mech. Phys. Solids, **7**, 135-142, 1959.
[2] L.F. Coffin, Jr.: The stability of metals under cyclic plastic strain, J. Basic Eng., **82 D**, 671-682, 1960.
[3] Z. Mróz, An attempt to describe the behavior of metals under cyclic loads using a more general workhardening model, Acta Mech., **7**, 199-212, 1969.
[4] L.X. Kong, L. Lin, P.D. Hodgson, Material properties under drawing and extrusion with cyclic torsion, Matl. Sci. Engng., **A308**, 209-215, 2001.
[5] J.D. Embury, A. Korbel, V.S. Raghunathan, J. Rys. Shear band formation in cold rolled Cu-6% Al single crystals, Acta Metall., **32**, 1883-1894, 1984.
[6] A. Korbel, W. Bochniak, The structure based design of metal forming operations, J. Matl. Proces. Technology, **53**, 229-236, 1995.
[7] A. Korbel, W. Bochniak, KOBO Type Forming: forging of metals under complex conditions of the process, J. Matl. Proces. Technology, **134**, 120-134, 2003.
[8] R.B. Pęcherski, Macroscopic effects of micro-shear banding in plasticity of metals, Acta Mech., **131**, 203-224, 1998.
[9] Z. Mróz, H.P. Shrivastava, R.N. Dubey, A non-linear hardening model and its application to cyclic loading, Acta Mech., **25**, 51-61, 1976.

ON SLIGHTLY DISORDERED QUASI RATE-INDEPENDENT VISCOPLASTIC FCC-POLYCRYSTALS

Milan V Micunovic*
*Faculty of Mechanical Engineering, UNIVERSITY OF KRAGUJEVAC, Sestre Janjica 6a, 34000 Kragujevac, Serbia

Summary Geometry and kinematics of intragranular as well as intergranular plastic deformation of polycrystals are discussed. Elastic strain is covered by the effective medium homogenization method inside a representative volume element (RVE). Evolution equation formed by tensor representation is derived from very simple micro-evolution equation. It has incremental form obtained by Vakulenko's concept of thermodynamic time. The rate dependence takes place by means of stress rate dependent value of the initial yield stress. Following [3] strain geometry is based on constrained micro and free macro rotations in intermediate reference configuration. This leads to the fact that evolution equation for plastic spin of RVE is an outcome of evolution equation for plastic stretching. The theory is applied to slightly disordered fcc-polycrystals. For some characteristic given stress histories (with low, medium and high strain rates) the micro-meso transition is tested and number of active slip systems grains are found and compared with so-called J2-approach.

INTRODUCTION

Background

a1) *Rabotnov's delay*. An incremental evolution equation accounts for diverse process speeds by means of dependence of initial yield stress on stress rate. Here the notion of Rabotnov's plastic strain initiation delay is employed.

a2) *Incrementality* is based on almost exact experimentally observed proportionality of equivalent stress rate and equivalent plastic strain rate. It is given by an universal material constant constituting most important part of hereditary Rabotnov's kernel. The constant holds for diverse multiaxial stress histories and a wide range of strain rates - as it has been found in [1].

a3) *Non-associate flow rule.* The equation is not necessarily of associate type i.e. plastic stretching could be not perpendicular to loading surface. However, if it is of associate type, then only four material constants suffice for very high correlation coefficient when calibrating it for processes mentioned in a2-property.

a4) *Tensor function representation* has been extensively used in [1,4,5,6,7] for its development along the line developed by Sawczuk, Murakami and Boehler in the field of inelasticity. Such an approach makes question of induced anisotropy logical and easy.

a5) *Thermodynamic background* fits into the Vakulenko's concept of thermodynamic time [2]. However, it has been necessary to extend his concept of steady aging introducing either accelerated or decelerated aging in order to cover creep-plasticity interaction. Most specifically the Langevin ageing function is shown to describe all three known regimes of creep behavior.

a6) *Plastic spin issue*. The controversial issue of plastic spin has been solved in the mentioned papers by the concept of fixing of orientations of intermediate reference configurations [3]. Thus we have not needed any new material constants apart those already appearing in the evolution equation for plastic stretching [4].

Problems treated previously

b1) *Localized instability of stainless steel sheets.* Nonproportional dynamic stress histories at wide range of plastic strain rates have been analyzed in [5]. The a1-a6 model has shown considerable stability at very large strains and gave smooth transition to localization commence. However, the J2-based associate flow rule with the so-called universal flow curve has been shown to be too stiff for a reliable prediction of advanced strains particularly for localization onset giving rise to unrealistically low failure strains and forming limit diagrams with vertical asymptotes.

b2) *Thermo-ratchetting with 3D viscoplastic strain.* A rectangular block made of AISI 316H austenitic stainless steel with one of its sides is loaded by constant normal stress whereas two lateral side surfaces are acted upon by harmonically variable shear stress [6]. It is known from experiments that such temporal variation induces progressive but saturated increase of axial strain in the direction of tension stress components. The strain rate is of the order of $[0.001, 1000]\ s^{-1}$. The model with 6 material constants (plastic stretching is second order polynomial in stress and linear in plastic strain) is compared with extended Perzyna-Chaboche's model (with 8 material constants) having incorporated evolution equations for back stress and equivalent flow stress. Comparison with experiments has shown better agreement of a1-a6 model.

b3) *The Hopkinson bar apparatus* consisted of two elastic long bars enclosing much smaller specimen [7]. Unlike traditional viscoplasticity where only elastic wave speeds are met, the quasi rate-independent model permitted visco-plastic wave speeds in the obtained hyperbolic wave equation. The numerical analysis gives experimentally observed homogeneous stress as well as inelastic strain up to 50%-strains.

EVOLUTION AND CONSTITUTIVE EQUATIONS

Geometric preliminaries

The total deformation tensor of an representative volume element (RVE) consists (according to Kroener's rule) of two incompatible constituents – plastic and elastic distortion tensors. It is essential that according to [3] plastic rotation of natural state reference configuration elements is arbitrary. On the other hand, RVE is composed of N monocrystal

grains, such that each grain has N slip systems (for instance, for fcc crystals N=12). Comparing a RVE in natural state initial and current configurations we may write Kroener's formula for micro-distortions. However, there is an essential difference – micro-plastic (and accordingly micro-elastic) rotations of individual grains are constrained. Since arbitrary plastic meso-rotation is assumed to be unity. This has two important consequences: 1. an improved Taylor's procedure in numerical treatment of polycrystals and 2. abundance of new material constants in evolution equation for plastic spin.

Hooke's Law By Homogenization Approach

For treating elastic meso and micro-strains the effective medium variant of the self-consistent method [8] is applied with an assumption that for monocrystals residual microstrains they are negligible. Moreover for considered fcc-polycrystals slight disorder is assumed such that all the grains are almost aligned giving rise to anisotropy. Then the effective Hooke's tensor has the approximate simplified form:

$$D_{\Lambda}^{eff} = D_M \left\{1 + D_{\Lambda}\left(1 + \langle S \rangle D_{\Lambda} - \langle SD \rangle\right)\right\} \tag{1}$$

where D is stiffnes tensor (subscript M stands for the imagined matrix – average of grains and Λ for a grain) and S is the Eshelby tensor. Angular parentesses denote spatial averaging like in [8]. It is worth noting that the simplest linear approximation for the effective grain stiffnesses is worthless since it does not include Eshelby tensor at all.

Evolution equation – micro to meso transition

A special attention is paid to associativity of flow rule based on loading function and derived by Rice. The experimental evidence (cf. [1]) has shown that real time has to be replaced by a thermodynamic Vakulenko's time ζ [2]. If such a time is the same for all the grains then normality could hold. In such a case the meso evolution equation reads (**T** is the stress, $\mathbf{e}_P$ – plastic strain and $\mathbf{M}_\Sigma$ – Spenser-Boehler's tensor describing anisotropy type):

$$\mathbf{D}_P = \partial_T \Omega\left(\mathbf{T}, \mathbf{e}_P, \mathbf{M}_\Sigma\right) D\zeta / Dt \ . \tag{2}$$

In the sequel a special type of tensor representation described in [1] is used. When thermodynamic time is a nonlinear function of plastic power (i.e. non-steady aging happens) the above equation covers creep-plasticity interaction as well.

Some numerical experiments

In order to explore whether a simple micro-evolution equation leads to tensor representation such an equation is integrated for some characteristic strain histories and calibration of an assumed meso-evolution equation is performed. Meso-micro transition is used for computer simulation in two cases of a RVE composed of N=1000 as well as N=125 fcc-grains with slightly disordered crystal orientations and 12 potential slip systems.Residual stresses and number of active slip systems are found. The RVE was loaded by slow and fast stresses with three typical stress states: uniaxial tension, uniaxial shear (with one principal stress vanishing and the other two being opposite) and equibiaxial shear. In all cases smooth increase of active slip systems has been remarked during stress growth.A comparison with J_2-theory is given.

CONCLUSIONS

a) Meso-evolution equation is derived from simple micro-evolution equation. Conditions of associativity of flow rule are derived and connected to concept of thermodynamic time.
b) Plastic spin isue is discussed and clarified.
c) Vakulenko's thermodynamic time must be extended to include non-steady ageing property if we want to describe coupled inelastic processes like plasticity-creep interaction.
d) The constitutive model proposed here has shown much smaller number of active slip systems than J_2-model. Moreover J_2-model was unable to distinguish among fast and slow processes being in such a way rate independent by its very nature.

References

[1] Micunovic M, Albertini C, Montagnani M: High strain rate viscoplasticity of AISI 316H stainless steel from tension and shear experiments. [In:] SOLID MECHANICS, P. Miljanic [Ed.], SerbianAcad.Sci.-Sci. Meetings, Vol. LXXXVII, Dept.Techn.Sci. Book **3**: 97--106, 1997.

[2] Vakulenko A. A.: Superposition in Continuum Rheology (in Russian), Izv. AN SSSR Mekhanika Tverdogo Tela **1**: 69--74, 1970.

[3] Zorawski M.: private communication, 1974.

[4] Micunovic M.: Some issues in polycrystal viscoplasticity of steels, Kroener's Symposium on Structured Media, Poznan 2001

[5] Micunovic M., Kudrjavceva L.: Localized Instability of AISI 316H Stainless Steel Sheets At Nonproportional Dynamic Stress Histories, YUCTAM' 97, Vrnjacka Banja , Yugoslavia, 1997.

[6] Micunovic M., Veljkovic D.: Ratchetting phenomenon at low strain rates for AISI 316H stainless steel, Facta Univ. **2-7/2:** 503-511, 1997.

[7] Micunovic M., Baltov A.: Plastic wave propagation in Hopkinson bar - revisited, Arch. Mech. Stosow. **54/5-6**: 577-602, 2002.

[8] Levin V. M., On Thermoelastic Stresses in Composite Media (in Russian), Appl. Math. Mech. PMM, 1982, Vol. 46, No. 3, p. 502-506.

[9] Micunovic M.: Low order inelastic micromorphic polycrystals, Theoret. Appl. Mech. **28-29**: 235-259, 2002.

PHYSICALLY BASED THERMOMECHANICAL MODELING OF METALS OVER A WIDE RANGE OF STRAIN RATES AND TEMPERATURES

George Z. Voyiadjis*, and Farid H. Abed*
*Department of Civil and Environmental Engineering, Louisiana State University, LA 70803, USA

Summary Microstructural physical based constitutive models are developed in this work in order to characterize the thermomechanical response of different types of metals subjected to low and high strain rates and temperatures. The concept of thermal activation energy as well as the dislocations interaction mechanisms is used in the derivation procedure taking into consideration the effect of the mobile dislocation production as well as the dislocation speed on the flow stress of the deformed material. The model is verified using different sets of experimental data for the same material parameters obtained from other independent tests. Good correlation is observed between the model predictions and the experimental observations. The plastic flow is considered in the range of temperatures and strain rates where diffusion and creep are not dominant.

INTRODUCTION

Developing plastic flow models which are physically based, widely applicable and capable of accounting for complex paths of deformation, temperature and strain rate is considered the main desirable goal in constitutive modeling of metals. The understanding of high-strain-rate behavior of metals at elevated temperatures is essential for the modeling and analysis of large deformation problems such as high-speed machining, impact, penetration and shear localization. Deforming a metal beyond the elastic limit activates and moves its dislocations through the crystal. In turn, two types of obstacles that try to prevent dislocation movements through the lattice are encountered; long range and short-range barriers. The long-range barriers are due to the structure of the material and cannot be overcome thus introducing thermal energy through the crystal. On the other hand, the short-range barriers can be overcome by thermal energy activation. Body centered cubic (bcc) and face centered cubic (fcc) metals as well as different types of steel are considered in the present model.

MODEL THEORY AND FORMULATION

In relating the plastic strain rate tensor $\dot{\varepsilon}_{ij}^{p}$ at the macroscale to the plastic shear strain rate $\dot{\gamma}^{p}$ at the microscale (which is related to dislocation density ρ_m, dislocation distance *l*, and Burgers vector *b*), an average form of the Schmidt tensor M_{ij} is assumed since plasticity at the macroscale incorporates a number of differently oriented grains into each continuum point [1]:

$$\dot{\varepsilon}_{ij}^{p} = \dot{\gamma}^{p} M_{ij} \quad \text{where} \quad M_{ij} = (n_i \otimes v_j + v_i \otimes n_j)/2 \quad \text{and} \quad \dot{\gamma}_p = (\partial \gamma^p / \partial \rho_m)\dot{\rho}_m + (\partial \gamma^p / \partial l) v \tag{1}$$

where $\hat{n}$ denotes the unit normal on the slip plane and $\hat{v}$ denotes the unit vector in the slip direction. In a conservative glide, the plastic flow rate defined in Eq.(1) clearly depends on both dislocation production $\dot{\rho}$ and dislocation speed v. Recently, great efforts were made in order to obtain an evolution equation for the dislocation densities in terms of strain rate and temperature. The following equation that describes the mobile dislocation density evolution is proposed [2]:

$$\dot{\rho}_m = (\lambda_1 / b^2 - \lambda_2 \rho_m - \lambda_3 \sqrt{\rho_f} / b)\dot{\varepsilon}_p \tag{2}$$

where ρ_f represents the forest dislocation density and the constant coefficients λ_i are related to the multiplication of mobile dislocations (λ_1), their mutual annihilation and trapping (λ_2), and their immobilization through interaction with forest dislocations (λ_3). The average dislocation velocity *v* can be determined through thermal activation by overcoming local obstacles to dislocation motion. Many authors have introduced velocity expressions for thermally activated dislocation glides. However, the following general expression is postulated [1].

$$v = v_o \exp(-G/kT) \tag{3}$$

where $v_o = d / t_w$ is the reference dislocation velocity, t_w is the time that a dislocation waits at an obstacle, *d* is the average distance the dislocation moves between the obstacles, *G* is the shear stress-dependent free energy of activation which may depend not only on stress but also on temperature and the internal structure, *k* is Boltzmann's constant, and *T* is the absolute temperature. Many authors using different forms have related the activation energy *G* to the thermal flow stress σ_{th}; for example, Kocks et al. [3] suggested the following definition:

$$G = G_o \left(1 - \left(\sigma_{th} / \hat{\sigma}\right)^p\right)^q \tag{4}$$

where G_o is the reference Gibbs energy at T=0, $\hat{\sigma}$ is the threshold stress at which the dislocations can overcome the barriers without the assistance of thermal activation, and *p* and *q* are constants defining the shape of the short-range barrier. The typical values of the constants *q* and *p* are 1.5 and 0.5 respectively [3].

Body cubic centred (bcc) and face cubic centred (fcc) models

The behavior of bcc metals shows a strong dependence of the thermal yield stress on the strain rate and temperature. The thermal stress is attributed to the resistance of the dislocation motion by the Peierls barriers (short-range barriers) provided by the lattice itself. On the other hand, the emergence and evolution of a heterogeneous microstructure of dislocations as well as the long-range intersections between dislocations dominates and controls the mechanisms of thermal activation analysis in fcc metals. Thus, the thermal activation is strongly dependent on the plastic strain. Utilizing Eqs.1 to 4 and using the additive decomposition of the thermal and athermal stresses, the equivalent flow stress in terms of the equivalent plastic strain, equivalent plastic strain rate and temperatures is given as follows:

for bcc metals $$\sigma = \hat{Y}(1-(\beta_1 T - \beta_2 T \ln \dot{\varepsilon}_p)^{1/q})^{1/p} + B\varepsilon_p^n + Y_a \quad (5)$$

for fcc metals $$\sigma = B\varepsilon_p^n(1-(\beta_1 T - \beta_2 T \ln \dot{\varepsilon}_p)^{1/q})^{1/p} + Y_a \quad (6)$$

The parameters β_s are related to the microstructure quantities as follows:

$$\beta_1 = \frac{k}{G_o}\ln\left(\frac{\tilde{m}b\rho_m v_o}{1-\tilde{m}l(\lambda_1/b-\lambda_2 b\rho_m-\lambda_3\rho_f^{0.5})}\right) \quad \text{and} \quad \beta_2 = \frac{k}{G_o} \quad \text{where} \quad \tilde{m} = (2M_{ij}M_{ij}/3)^{1/2} \quad (7)$$

RESULTS & CONCLUSIONS

The effectiveness of the foregoing models is tested using independent experimental data obtained in the literature [4, 5] for different bcc and fcc metals (e.g. Vanadium, Molybdenum, Niobium, Tantalum and OFHC Copper) over a wide range of strain rates and temperatures. The comparison of the theoretical isothermal and adiabatic flow stress show very good correlations with the experimental results (see Figs.1 and 2 for example). A combination of the above two models is used in modeling the thermo-mechanical response of different types of steel (e.g. AL-6XN stainless steel and DH-36 structural steel) which is a combination of bcc and fcc crystal components. The agreement between the experimental results and those obtained using the present model was found excellent (see Fig.3 for example). It's found that the contribution of the generation of the mobile dislocation density during the plastic deformation in the proposed model shows considerable effect on the prediction of the flow stress particularly in the case of high strain rates and temperatures. On the other hand, ignoring the mobile dislocation density rate from the present formulation causes additional hardening that overpredicts the experimental data. The parameter β_1 plays an important task in determining the temperature and strain rate behavior of the proposed model during the plastic deformation since it contains the effects of dislocation densities as well as the dislocation distance which represents crucial aspects in controlling the scale effect of the internal deformation behavior. In the case of bcc metals, the physical quantities that define the proposed model parameters, are related to their initial values while, the thermal hardening behavior of fcc metals shows strong coupling between the plastic deformation and the effects of strain rates and temperatures, thus, the mobile dislocation densities are accumulated up to their saturated values as the plastic hardening evolves.

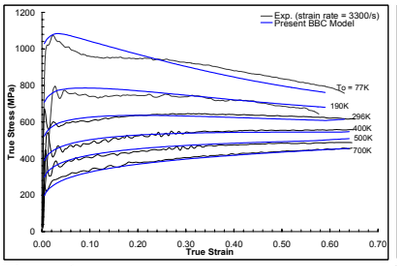


Figure 1 Adiabatic stress-strain curves for the proposed bcc model, for Niobium (Nb), and compared to the experimental results at 3300s^{-1} strain rate and for different initial temperatures.

$$\sigma = 1350(1-(0.00193T - 0.0000937T\ln\dot{\varepsilon}_p)^{2/3})^2 + 440\varepsilon_p^{0.25} + 60$$

$$T = T_o + 0.44\int \sigma d\varepsilon_p$$

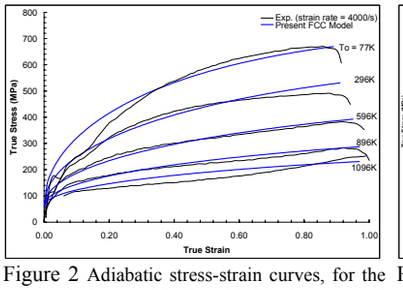


Figure 2 Adiabatic stress-strain curves, for the proposed fcc model, for OFHC Copper, and compared to the experimental results at 4000s^{-1} strain rate and for different initial temperatures.

$$\sigma = 950\varepsilon_p^{0.47}(1-(0.0006739T - 0.0000355T\ln\dot{\varepsilon}_p)^{2/3})^2 + 60$$

$$T = T_o + 0.262\int \sigma d\varepsilon_p$$

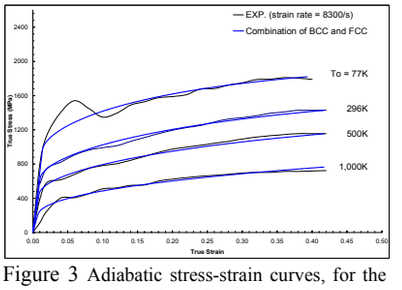


Figure 3 Adiabatic stress-strain curves, for the proposed models, for AL-6XN stainless steel, compared to the experimental results at 8300 s^{-1} strain rate and for different initial temperatures.

$$\sigma = 139 + 800\varepsilon_p^{0.45} + 1100\left(1-\left(0.00121T - 0.0000618T\ln\dot{\varepsilon}_p\right)^{2/3}\right)^2 + 2190\varepsilon_p^{0.71}\left(1-\left(0.001137T - 0.000051T\ln\dot{\varepsilon}_p\right)^{2/3}\right)^2$$

$$T = T_o + 0.252\int \sigma d\varepsilon_p$$

References

[1] Bammann, D.J., Aifantis, E.C.: A Model for Finite-Deformation Plasticity. *Acta Mech.* **69**:97-117, 1987.

[2] Kubin, L.P., Estrin, Y.: Evolution for Dislocation Densities and the Critical Conditions for the Portevin-le Chatelier Effect. *Acta Metall. Mater.* **38**: 697-708, 1990.

[3] Kocks, U.F., Argon, A.S., Ashby, M.F.: Thermodynamics and Kinetics of Slip. *Prog. Mater. Sci.* **19**, Pergamon, Oxford, 1975.

[4] Nemat-Nasser, S., Li, Y.: Flow Stress of F.C.C. Polycrystals with Application to OFHC Cu. *Acta Mater.* 46: 565-577, 1998.

[5] Nemat-Nasser, S., Guo, W., Kihl, D.: Thermomechanical Response of AL-6XN Stainless Steel Over a Wide Range of Strain Rates and Temperatures. *J. Mech. Physics Solids.* **49**: 1823-1846, 2001.

PLASTIC PROPERTIES IDENTIFICATION WITH PLURAL SHARP INDENTERS

Norimasa Chiba, Nagahisa Ogasawara
National Defense Academy, Yokosuka, Kanagawa 239-8686, Japan

Summary An identification method for elastic-plastic material constants that obey the power-law hardening rule, from a couple of instrumented sharp micro-indentation tests, is proposed. This method utilizes plural triangular pyramid indenters with different apex angles, and is based on a similarity function that is determined from the 3D-FE calculation. A physical explanation of the similarity function expression is given. An experimental validation for this method with actual metal is also shown.

SIMILARITY RELATION FOR POWER-LAW HARDENING MATERIAL

Indentation load, P, when indented into a half infinite solid, can be expressed as $P=Ch^2$, known as Kick's law, where h and C are the indented depth and the loading curvature, respectively. We assume the indented material is elastic power-law hardening plastic (Fig. 1), with Young's modulus E, yield strength σ_Y, and hardening exponent n. Then, the loading curvature C can be expressed in Eq. (1), using a dimensionless function Π and an arbitrary stress measure σ_r[1,2]. In Eq. 1, E^* means reduced Young's modulus, which is the only elastic property determined from indentation, and θ half angle of the apex of the conical indenter. The reduced Young's modulus E^* is expressed by $1/E^*=(1-\nu^2)/E$, if we assume the indenter to be rigid. In the actual micro-indentation test, a triangular pyramid indenter is used. However, analytical results used in this paper have been obtained on the basis of 2D axisymmetricity. Therefore, we use an equivalent cone that has the same h-A relation with the triangular pyramid (Fig. 2). Dao, et al. showed from their extensive FE calculation that if we choose an appropriate value of σ_r, then the relation, shown in Eq. 2, holds for a fixed cone angle θ of the indenter [2]. This means that the value of Π for the appropriate σ_r is independent of the hardening exponent n. We also verified that Eq. (2) holds for 3 angles of cones from 3D FE calculation. These results are described later in this paper.

$$\frac{P}{\sigma_r h^2}=\frac{C}{\sigma_r}=\Pi\left(\frac{E^*}{\sigma_r},n,\theta\right) \quad (1) \qquad \frac{P}{\sigma_r h^2}=\frac{C}{\sigma_r}=\Pi\left(\frac{E^*}{\sigma_r},\theta\right) \quad (2)$$

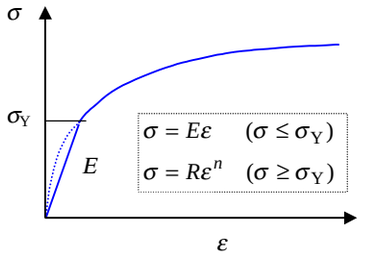
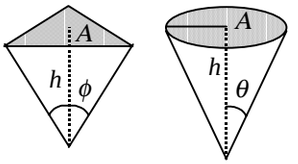


Fig. 1 Power-law hardening stress-strain relation



(a) Triangular pyramid (b) Cone

ϕ (deg)	θ (deg)	A/h^2
111	63.34	12.25
115	70.06	24.5
117.5	75.88	49.0

(c) Three angles chosen in the analysis

Fig. 2 Triangular pyramid and equivalent cone

EXPRESSION OF Π AS AN INTERPOLATION BETWEEN TWO EXTREMES

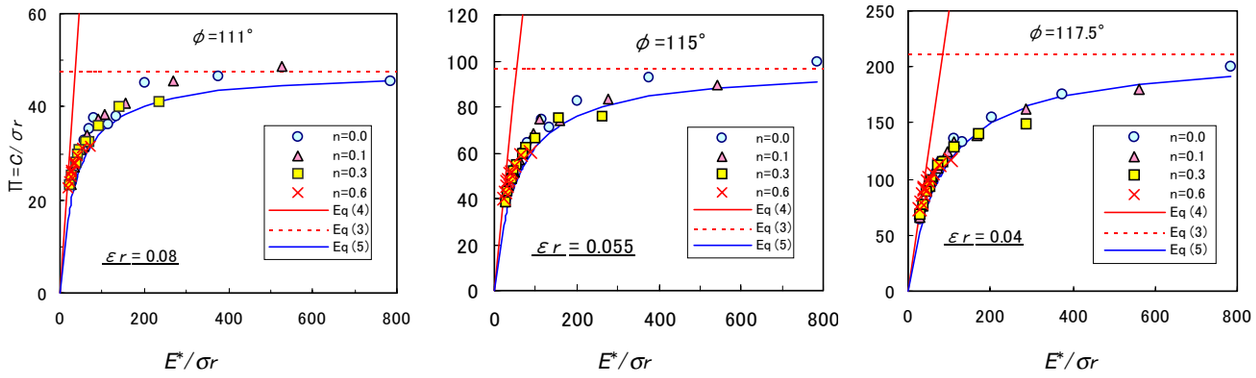
If we plot the relation of Eq. (2) in the form of C/σ_r versus E^*/σ_r, then we may consider that the relation has two extremes: one is the rigid/perfectly plastic solution, where E^* tends to be infinite, and σ_r represents a finite value of yield strength σ_Y. The other extreme is the elastic solution, where E^* has a finite value, and $\sigma_r = \sigma_Y$ tends to be infinite. Lockett obtained an axisymmetric slip-line field solution indented by a rigid cone [3]. The solution assumed smooth contact between the indenter and the solid, and the solution method has been extended to take account of the friction effect [4]. Using Lockett's solution, the dimensionless function Π for the rigid/perfectly plastic extreme is expressed in Eq. (3), where k and $f(r_C)$ stand for the yield strength in shear mode, and the piling-up height, respectively. Using elastic solution [5], the function Π for the elastic extreme is expressed in Eq. (4). Then, we may write the function Π for elastic plastic region as Eq. (5), which is a simple interpolation between the two extremes.

$$\Pi=\frac{P}{\sigma_Y h^2}=\left(\frac{P}{k\pi}\right)\frac{\pi}{2(\cot\theta-f(r_C))^2}\equiv a_p \quad (3) \qquad \Pi=\frac{P}{\sigma_r h^2}=\left(\frac{2}{\pi}\tan\theta\right)\frac{E^*}{\sigma_r}\equiv a_e\frac{E^*}{\sigma_r} \quad (4)$$

$$\frac{1}{\Pi\left(\frac{E^*}{\sigma_r},\theta\right)}=\frac{1}{a_e(\theta)\times\left(\frac{E^*}{\sigma_r}\right)}+\frac{1}{a_p(\theta)} \quad (5)$$

DIMENSIONLESS FUNCTION Π DETERMINED FROM FINITE ELEMENT CALCULATION

We carried out 3D FE calculation for three angles ϕ of pyramid indenters, shown in Fig. 2(c). The material parameters chosen for each apex angle ϕ are: E ranging from 10 to 210 GPa, σ_Y from 30 to 3000 MPa, and n from 0.0 to 0.6. We confirmed that Eq. (2) holds if the appropriate value of representative strain ε_r is chosen for each indenter angle ϕ. This is shown in Fig. 3. The representative stress σ_r was determined from representative strain ε_r on the corresponding σ-ε curve. The three values of representative strain determined from the calculation for each indenter angle are shown in Fig. 4.



(a) ϕ =111°(θ = 63.34°) (b) ϕ = 115°(θ = 70.06°) (c) ϕ =117.5°(θ = 75.88°)

Fig. 3 Dimensionless function Π constructed from FE calculation for three indenter angles

EXPERIMENTAL VALIDATION

We carried out indentation tests with the three different indenters on two types of copper polycrystal specimens, work hardened and annealed. Fig. 5 shows the result. The symbols on the σ-ε curve represent the results determined from our plural indenter method. The lines show the tensile test results obtained from bulk material. It can be concluded that our method provides a satisfactory result.

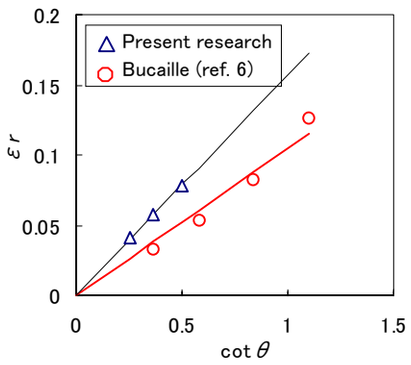


Fig. 4 Representative strains for different indenter angles

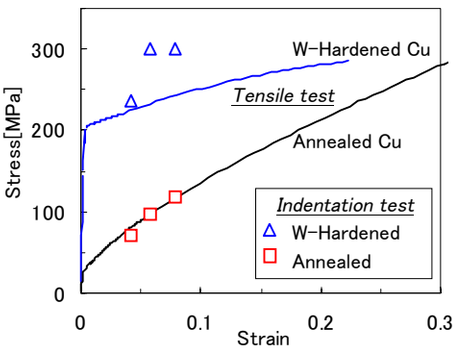


Fig. 5 Points determined from indentation

References

[1] Cheng, Y-T. , et al., *J. Appl. Phys.* **84**: 1284-1291, 1998.
[2] Dao, M., et al., *Acta Mater.* **49**: 3899-3918, 2001.
[3] Lockett, F. J., *J. Mech. Phys. Solids* **11**: 345-355, 1963.
[4] Chitkara, N. R., et al., *Int. J. Mech. Sci.* **34**: 849-862, 1992.
[5] Sneddon, I. N., *Proc. Cambridge Phil. Soc.* **44**: 492-507, 1948.
[6] Bucaille, J. L., et al., *Acta Mater.* **51**: 1663-1678, 2003.

A viscoplastic model for thermoplastic polymers under uniaxial monotonic and cyclic straining

Elhem Ghorbel

LM^{2}S UMR CNRS N°7143 – Univ. Cergy Pontoise-Univ. Paris 6
Université de Cergy Pontoise
Rue d'Eragny – Neuville sur Oise
95 000 Cergy Pontoise Cedex

Elhem.ghorbel@iutc.u-cergy.fr

ABSTRACT: The thermodynamic approach of the continuous medium and the local state method is used for the study of the mechanical behavior of thermoplastic polymers under uniaxial monotonic and cyclic staining. Viscoplastic constitutive equations are proposed into the restrictive framework of standard generalized materials and the field of the small deformations. A yield criterion is established. A non-linear kinematic hardening rule is proposed to describe cyclic softening that several polymers exhibit under strain controlled cyclic tests.

INTRODUCTION: The increase in using polymers for several industrial applications leads to a strong need of developments of constitutive models. These models are based on either phenomenological or microscopic aspects. The purpose of this paper is to use the general principles of thermodynamics with internal variables for standard generalized materials to predict the thermo-mechanical behavior of polymers. This formalism offers a good framework to introduce viscoplastic constitutive equations. It has widely used for modeling inelastic behavior of polycristalline metals and their alloys. In this case, the assumption of incompressibility and isotropy implies the dependence of the viscoplastic potential only on the second invariant of the stress deviator. This potential is often expressed in the form of a power, exponential or hyperbolic sine yield function. The aim of the present work is to extend the use of this approach to polymeric materials, to propose a generalized yield function, to discuss the various possibilities to express the form of the viscoplastic potential and to discuss the possibilities for the equations governing hardening variables. Assumptions as initial isotropy, homogeneity and normality are checked then adopted.

MATERIALS: Amorphous as well as crystalline thermoplastic polymers are considered in this work: polyethylene terephthalate "PET", polycarbonate "PC", polyoxymethylene "POM" and polyamide 12 "PA12". These polymers are presented in plate shape obtained by extrusion. X-ray measurements and texture analyses were performed on as-received polymers by Siemens diffractometer using Cu-kα x-radiation. The main results corroborated the DSC results show that PET is amorphous on the contrary for other polymers (POM and PA12) crystalline phases have been detected. For texture analyses, POM pole figures of the (110) and (115) reflections show no anisotropy due to its manufacturing. The homogeneity and isotropy of the as received polymers are verified using ultrasonic characterization tests. They were led in immersion and using two transducers of 2.25 MHz.

YIELD FUNCTION: Viscoplastic models formulated into the framework of thermodynamics with internal variables require the definition of a yield function from which is derived the viscoplastic potential. A considerable amount of experimental works dealing with macroscopic yielding of polymers has been done over the last 40 years. It has been established that hydrostatic pressure affects significantly the mechanical behavior of polymers. Therefore, several criteria based on classical plasticity theory involving the hydrostatic component of the stress tensor "I_1" were proposed. Bowden and all [1972] proposed a modified form of the Tresca and the Von Mises criterion. The basic idea they suggested consists to relate linearly the equivalent stress to hydrostatic one. They tested several polymers and concluded that either of both criteria, according to the considered polymer, provides a good description of yielding. This result was highlighted more recently by other authors (Escaig [1997]; Quinson and al. [1997]; Lesser and al. [1997]) who studied yielding of glassy polymers. Raghava and all [1973] have proposed a single yield criterion that is another modification of the Von Mises' one. The results they obtained were in good agreement with prediction. The review of these studies shows that there is no consensus concerning the choice of the most appropriate criterion. To propose a unique yield criterion, we have used experimental results provided from papers mentioned above. For the purpose of this study, experimental data at yield are plotted in the meridional plane (I_1/σ_{st}, J_2/σ_{st}) where σ_{st} is the tensile yield stress. The results that we obtain are:

- Eqn. (1) describes the most suitable criterion that represents the yield behavior.
- The parameter "m" does not depend on strain rate, temperature and molecular weight M_c. Hence, strain rate and temperature effects are introduced in the tensile yield stress σ_{st}.. σ_{sc} is the compressive yield stress.
- For semi-crystalline polymers (PET) a lower von Mises equivalent stress level for pure shear compared to uniaxial tensile at the same hydrostatic pressure.

$$f = \frac{3 \cdot J_2}{\sigma_{st}^2} + (m-1) \cdot \left(\frac{I_1}{\sigma_{st}} \right) - m \quad \text{where} \quad m = \frac{\sigma_{sc}}{\sigma_{st}} \geq 1, \; I_1 = \mathrm{tr}(\underline{\underline{\sigma}}) \quad \text{and} \quad J_2 = \frac{1}{2} \cdot tr(\underline{\underline{S}}^2) \tag{1}$$

In order to study the effects of the cristallinity content "X_c" on the polymers yielding and to verify the stress-state behavior dependency, an experimental procedure is developed. Uniaxial as well as biaxial tests are performed at room temperature. The polymers used in the experiments are thermoplastics at the amorphous and semi crystalline state (PA12, PC, POM, amorphous and heat-treated PET). To measure the stress level at which yielding occurs, a conventional value of inelastic strain equal to 0.3% is used. Experimental results show that " X_c " has a negligible influence in the parameter "m". In addition, it appears that the yield function described by Eqn (1) overestimates the shear yielding. To delineate the experimentally observed stress state effects we propose to modify Eqn.(1) by introducing the third invariant of the stress deviator J_3. The expression of the yield function, given by Eqn.**Erreur ! Source du renvoi introuvable.**, where τ_o is the shear yield stress , verifies the convexity conditions. Despite the improvements provided by modifying the yield function, the shear stress at yielding remains overpredicted.

$$f = \frac{3J_2}{\sigma_{st}^2} \Psi(J_2, J_3) + (m-1)\left(1 - \frac{\kappa}{8}\right)\frac{I_1}{\sigma_{st}} - (1 - \frac{\kappa}{8})m \quad \text{with} \quad \begin{cases} \Psi(J_2, J_3) = \left(1 - \frac{27}{32} \cdot \kappa \cdot \frac{J_3^2}{J_2^3}\right), \; J_3 = \frac{1}{3} \cdot tr\left(\underline{\underline{S}}^3\right) \\ \kappa = \left(1 - \frac{3 \cdot r^2}{m}\right) = g(X_c) \text{ and } r = \frac{\tau_o}{\sigma_{st}} \end{cases} \tag{2}$$

VISCOPLASTIC CONSTITUTIVE EQUATIONS: Strain controlled cyclic tests conducted on several polymers (PA12, PC and PET) in tension-compression show that only non-linear kinematic hardening can be considered to describe hardening that the back stress $\underline{\underline{X}}$ represents. Moreover, before reaching the stabilized cycle cyclic softening is observed leading to consider an evolution of law for $\underline{\underline{X}}$ governed by Eqn. (6) initially proposed for metallic materials. However, as the overall behavior of polymeric materials depends on hydrostatic pressure and considering the assumption of generalized normality, the back stress $\underline{\underline{X}}$ is necessary a non deviatoric tensor. Tow formulations are considered. In the first, recovery effects are neglected so that only the viscoplastic potential is used while for second the dissipation potential is the sum of a viscoplastic potential and a recovery one. The proposed constitutive equations are expressed as follows:

Strain partition :
$$\underline{\underline{\varepsilon}} = \underline{\underline{\varepsilon}}^e + \underline{\underline{\varepsilon}}^{in} \quad \text{where} \quad \underline{\underline{\varepsilon}}^e = \underline{\underline{\underline{S}}} : \underline{\underline{\sigma}} \tag{2}$$

Viscoplastic potential :
$$\Omega_{vp} = \frac{K}{n+1} \cdot \left\langle \frac{\Gamma}{K} \right\rangle^{n+1} \quad \text{where} \quad \Gamma = F - \frac{\gamma(p) \cdot b(T)}{2} \underline{\underline{\alpha}} : \underline{\underline{\alpha}} \tag{4}$$

$$F = f(\underline{\underline{S}} - \underline{\underline{X}}') + \frac{\gamma(p)}{2 \cdot b(T)} \cdot \underline{\underline{X}} : \underline{\underline{X}} \quad , \; \underline{\underline{X}}' : \text{deviator of } \underline{\underline{X}} \tag{5}$$

Kinematic hardening rule:
$$\begin{cases} \underline{\underline{X}} = b(T) \cdot \underline{\underline{\alpha}} \text{ and } \dot{\underline{\underline{\alpha}}} = \dot{\underline{\underline{\varepsilon}}}_{in} - \gamma(p) \cdot \underline{\underline{\alpha}} \cdot \dot{p} \\ \gamma(p) = \gamma_o + \zeta \cdot \left[1 - \exp(-\omega \cdot p)\right] \end{cases} \tag{6}$$

In order to simulate the behavior of the considered polymers numerical implementation of these equations using Runge-Kutta's method is done. It appears that the proposed model allows a good prediction of cyclic behavior. The introduction of recovery potential improves the prediction of relaxation but has a negligible influence in the other loading conditions.

REFERENCES:

Bowden, P. B. and Jukes, J. A. 1972, " The plastic flow of isotropic polymers" in J. of Mat. Sc. 7, 52-63.

Raghava, R.; Caddell R. M. and Y. Yeeh, G. S. 1973, " The macroscopic yield behaviour of polymers" in J. of Materials Science, 8, 225-232.

Escaig, B. 1997, "A physical model of the pressure dependence and biaxial mechanical properties of solid polymers" in Poly. Eng. and Sc. , october, Vol. 37, No. 10, 1641-1654.

Quinson, R. ; Perez, J. ; Rink, M. and Pavan, A. 1997, "Yield criteria for amorphous glassy polymers" in J. of Mat. Sc. 32, 1371-1379

Lesser, A. J. and Kody, R. S. 1997, " A generalized model for the yield behavior of epoxy networks in multiaxial stress states" in J. Polym. Sci. B/ Polym. Phys. 35, 1611-1619.

ADVANCED THERMO-VISCO-PLASTIC CONSTITUTIVE RELATIONS FOR DIRECT APPLICATIONS IN NUMERICAL ANALYSES

Alexis Rusinek, Ramon Zaera*, Janusz R. Klepaczko

Laboratory of Physics and Mechanics of Materials, UMR CNRS 75-54, Université de Metz, Ile du Saulcy, 57045 Metz cedex, France
** Department of Continuum Mechanics and Structural Analysis, University Carlos III of Madrid, Avda. de la Universidad 30, 28911 Leganés, Madrid, Spain*

Summary In this contribution thermo-visco-plastic constitutive relations are proposed and analyzed. This phenomenological approach is partly based on theory of dislocations and processes of thermal activation. The main advantages of such constitutive relation are reduction of number of material constants in comparison with the complete approach based on materials science (theory of dislocations). This constitutive relation has been used so far many times in finite element codes to simulate dynamic processes of impact loading. An original algorithm using J_2 plasticity theory proposed by Zaera et al. [4] has been recently applied in this study.

CONSTITUTIVE RELATIONS

The original constitutive relation proposed in this paper is based on the formalism proposed by Klepaczko [1] which applies theory of dislocations. In the original approach, the evolution of microstructure is taken into account by internal variables S_j.

$$\sigma = g\left[\varepsilon, \dot{\varepsilon}, T, S_j(\varepsilon, \dot{\varepsilon}, T)\right] \tag{1}$$

However, this complete model is complicated to be implemented into a Finite Element Code due to the complexity of each equation coupled with the great number of physical constants in comparison with phenomenological approach. To reduce the number of constant and to facilitate the utilization in a FE codes, a semi phenomenological approach has been proposed by Rusinek and Klepaczko [2] to simplify modelling by physical intuition. Thus, the plastic flow stress is defined as follow :

$$\sigma(\varepsilon, \dot{\varepsilon}, T) = \frac{E(T)}{E_0}\left[\sigma_\mu(\varepsilon, \dot{\varepsilon}, T) + \sigma^*(\dot{\varepsilon}, T)\right] \quad \text{with} \quad E(T) = E_0\left\{1 - \frac{T}{T_m}\exp\left[\theta^*\left(1 - \frac{T_m}{T}\right)\right]\right\} \tag{2}$$

where $E(T)$ is the temperature-dependent Young's modulus with the characteristic homologous temperature θ^*, E_0 is the Young's modulus at $T = 0\,K$, T_m is the melting temperature.

The explicit form proposed to define the two stress components are inspired by the physical approach [1] and the theory of thermal activation [3]. Thus

$$\sigma_\mu = B(\dot{\varepsilon}, T)(\varepsilon_0 + \varepsilon)^{n(\dot{\varepsilon}, T)}, \quad \sigma^* = \sigma_0^*\left[1 - D_1\left(\frac{T}{T_m}\right)\log\left(\frac{\dot{\varepsilon}_{max}}{\dot{\varepsilon}}\right)\right]^{m^*} \quad \text{with} \quad \dot{\varepsilon} \neq 0 \quad \text{and} \quad \sigma^* \geq 0 \tag{3}$$

Best way to define correctly the effect of temperature is to assume that temperature effect on plastic deformation is taken into account by two expressions.

$$n(\dot{\varepsilon}, T) = n_0\left[1 - D_2\left(\frac{T}{T_m}\right)\log\left(\frac{\dot{\varepsilon}}{\dot{\varepsilon}_{min}}\right)\right] \quad \text{with} \quad n \geq 0 \qquad B(\dot{\varepsilon}, T) = B_0\left[\frac{T}{T_m}\log\left(\frac{\dot{\varepsilon}_{max}}{\dot{\varepsilon}}\right)\right]^{-\nu} \tag{4}$$

where n_0 is the strain hardening exponent at $T = 0\,K$, D_2 is a constant, $\dot{\varepsilon}_{min}$ is the minimal strain rate assumed in the model, B_0 is a constant, $\dot{\varepsilon}_{max}$ is the maximal strain rate assumed in the model and ν is the temperature sensitivity.

Reduced number of constant is eight and it allows to approximate the same tendencies as predicted by the physical approach. A complete optimization algorithm has been written to determine the unique optimal set of constants for each material [2]. In order to apply the set of constitutive relations a integration scheme must be applied. Such original integration scheme has been proposed by Zaera et al. [4].

IMPLICIT INTEGRATION ALGORITHM

The yield stress σ_y is defined by Eq. 2, $(\sigma_y = \sigma)$, which takes into account strain hardening, strain rate sensitivity and temperature effect. Thus in general loading conditions, the yield surface is defined as follows:

$$f\left(\sigma_{ij}, \bar{\varepsilon}^p, \dot{\bar{\varepsilon}}^p, T\right) = \bar{\sigma} - \sigma_y\left(\bar{\varepsilon}^p, \dot{\bar{\varepsilon}}^p, T\right) = 0 \quad \text{with} \quad \bar{\sigma} = \sqrt{\frac{3}{2} s_{ij} : s_{ij}} \tag{5}$$

where $\bar{\sigma}$ is the equivalent stress, $\bar{\varepsilon}^p$ is the equivalent plastic strain, $\dot{\bar{\varepsilon}}^p$ is the equivalent plastic strain rate and s_{ij} is the deviatoric part of the stress tensor σ_{ij}

In this approach, the total strain tensor ε_{ij} is a sum of the elastic strain tensor ε_{ij}^e, the plastic strain tensor ε_{ij}^p and the thermal strain ε_{ij}^θ. To define the plastic flow, the normality rule is used allowing to relate plastic strain rate $\dot{\varepsilon}_{ij}^p$ to the stress. The last is defined as follows:

$$\dot{\varepsilon}_{ij}^p = \dot{\lambda}\frac{\partial f}{\partial \sigma_{ij}} \quad \text{with} \quad \dot{\lambda} > 0\,; \quad \dot{\bar{\varepsilon}}^p = \sqrt{\frac{2}{3}\dot{\varepsilon}_{ij}^p : \dot{\varepsilon}_{ij}^p} \quad \text{and} \quad \bar{\varepsilon}^p = \int \dot{\bar{\varepsilon}}^p \, dt \tag{6}$$

where $\dot{\lambda}$ is the plastic multiplier. In classical overstress models [5], the consistency condition is not used and excursions of stress outside the yield surface are allowed. Several authors have proposed the so called "consistency viscoplasticity models" to include rate effects in the consistency condition, Eq. 7. Following the work of Winnicki et al. [6], who used the approach $\dot{\bar{\varepsilon}}^p = \Delta\bar{\varepsilon}^p / \Delta t$ to include viscoplastic effects in the consistency condition for the yield surface, the present algorithm is developed for J_2 plasticity including thermal effects

$$\dot{f}\left(\sigma_{ij}, \bar{\varepsilon}^p, \dot{\bar{\varepsilon}}^p, T\right) = \frac{\partial f}{\partial \sigma_{ij}}\dot{\sigma}_{ij} + \frac{\partial f}{\partial \bar{\varepsilon}}\dot{\bar{\varepsilon}}^p + \frac{\partial f}{\partial \dot{\bar{\varepsilon}}^p}\ddot{\bar{\varepsilon}}^p + \frac{\partial f}{\partial T}\dot{T} = 0 \quad \text{with} \quad \dot{T} = \frac{\beta}{\rho C_p}\sigma_{ij} : \dot{\varepsilon}_{ij}^p \tag{7}$$

where $\ddot{\bar{\varepsilon}}^p$ is the equivalent plastic acceleration, ρ is the density of material, β is the Quinney-Taylor coefficient and C_p is the specific heat at constant pressure assumed constant during numerical simulations.

The linearization of the consistency equation, Eq. (7), leads to Eq. (8) where k is an iterative index [4].

$$f_{k+1} \approx f_k + \left.\frac{\partial f}{\partial \sigma_{ij}}\right|_k : \left(-\delta\Delta\bar{\varepsilon}_k^p 2G \left.\frac{\partial f}{\partial \sigma_{ij}}\right|_k\right) + \left.\frac{\partial f}{\partial \bar{\varepsilon}^p}\right|_k \delta\Delta\bar{\varepsilon}_k^p + \left.\frac{\partial f}{\partial \dot{\bar{\varepsilon}}^p}\right|_k \frac{\delta\Delta\bar{\varepsilon}_k^p}{\Delta t} + \left.\frac{\partial f}{\partial T}\right|_k \frac{\beta}{\rho C_p}\left(\delta\Delta\bar{\varepsilon}_k^p \bar{\sigma}_{n+1}^{\text{trial}} - 6G\delta\Delta\bar{\varepsilon}_k^p \delta\Delta\bar{\varepsilon}_k^p\right) = 0 \tag{8}$$

This leads to an iterative Newton-Raphson scheme, which is stopped when the residual f_{k+1} is small enough. One advantage of this algorithm is its similarity to those previously employed in the rate independent and temperature independent plasticity. The complete characterization of the algorithm is given in [4]. Concerning the unloading conditions, the Hooke's law is programmed causing an instantaneous unloading.

CONCLUSIONS

The combination of the thermoviscoplastic model and a new integration scheme taking into account the strain hardening, strain rate sensitivity and temperature effects, allows to simulate and study variety of processes of dynamic loading and impact. Up to now, the constitutive relations have been used without the new algorithm in [4] to analyze impact behavior for several kinds of sheet steel as mild steel or DP steel. The numerical analyses were also applied to study the problem of elastic-plastic wave propagation in sheet metals[7].

References

[1] Klepaczko, J.R., Modelling of structural evolution at medium and high strain rates, FCC and BCC metals, in : Impact : Effects of fast transient loading, A.A. Balkema, Rotterdam-Brookfield, Denmark (1988), pp. 3-35
[2] Rusinek, A., Klepaczko, J.R., Shear testing of a sheet steel at wide range of strain rates and a constitutive relation with strain-rate and temperature dependence of the flow stress. Int. J. of Plasticity, **17** (2000), pp. 87-115
[3] Kocks, U.F., Argon, A.S. and Ashby, M.F., Thermodynamics and Kinetics of Slip, Oxford, Pergamon Press (1975)
[4] Zaera, R. Fernández-Sáez, J., Navarro, C., A consistent algorithm for the integration of thermoviscoplastic constitutive equations in adiabatic conditions, Int. J. Mechanical Sciences (to be submitted 2004)
[5] Perzyna P., The Constitutive Equations for Rate-Sensitive Plastic Materials. *Q. Appl. Math.*, **20** (1963), pp. 321-332
[6] Winnicki, A., Pearce, C.J., Bicanic, N., Viscoplastic Hoffman consistency model for concrete, Computers & Structures, **79** (2001), pp. 7-19
[7] Rusinek, A., Klepaczko, J.R., Effect of adiabatic heating in some processes of plastic deformation, Impact Engineering and Application, Akira Chiba, Shinji Tanimura and Kazuyuki Hokamoto (Eds), Elsevier Science Ltd, **2** (2001), pp. 541-546

CALIBRATION OF ANISOTROPIC ELASTIC- PLASTIC MODELS FOR THIN LAYERS AND FOILS IN MICROTECHNOLOGIES: TWO NOVEL TECHNIQUES

Massimiliano Bocciarelli, Gabriella Bolzon, Giulio Maier
Politecnico di Milano, Department of Structural Engineering, I 20133 Milano, Italy

Summary The methods presented in this paper for the identification of material parameters in anisotropic elastoplasticity at the microscale exhibit the following new features in their experimental stage: data gathered from both indentation curves and imprint mapping in the former technique, which is intended for the mechanical characterisation of thin layers on substrate; in the latter, a device which pressurises a free foil specimen and measures the geometry of the inflated membrane by a laser profilometer. At the computational stage, traditional least-square techniques are employed for the inverse analysis based on finite-element large-strain simulations, which are used also for sensitivity analyses.

INTRODUCTION

Anisotropy in elastic and inelastic mechanical behavior of materials is often a consequence of fabrication processes. In particular thin foils produced by laminations usually exhibit significantly different stiffness and strength properties in the "machine direction" and in the "cross direction".
Current research motivated by real-life industrial problems has led to the two model calibration methods presented herein, both centered on the integration of new experimental procedures and traditional inverse analysis techniques. In both engineering situations considered the material behavior is assumed to be elastic-plastic, ductile, orthotropic and realistically described by the classical constitutive model proposed by Hill in 1974 [1]. In both cases the computer simulation of the experimental tests are performed by a commercial finite element code in finite strains [2] and the identification of parameters is carried out by means of a deterministic batch approach; see, e.g., [3, 4]. The proposed methods are validated by means of "pseudo-experimental data", namely by using measurable quantities computed on the basis of assigned parameters which must be recovered through the inverse analysis.

INTEGRATED INDENTATION TEST OF THIN LAYERS

The first method considered is intended for thin layers which may adhere on a substrate. The experimental stage consists of a conventional micro-indentation test performed by an axi-symmetric indenter followed by the mapping of the residual imprint, the geometry of which is defined through a number of measurements by means of suitable instruments; specifically, in the present study, an atomic force microscope (AFM) is considered. The gathered experimental information, namely "indentation curves" (force versus penetration depth) and imprint mapping, see Figure 1, are input into the inverse analysis stage, namely: a norm of the discrepancy between the available experimental data and their computed counterparts is minimized with respect to the parameters to identify, which are contained in the material model adopted and implemented for the computer simulation of the test.
In this study comparative assessment of merit are presented of various identification strategies and algorithms and of sensitivity computations as guidelines for the experiment design. The main novelty of the proposed methodology (at present motivated primarily by the industrial production of MEMS) rests on the combined use of indentation, imprint mapping and inverse analysis: this combination permits the quantitative characterization of local inelastic anisotropy at the micro and nanoscale, which is not recoverable from indentation curves only; see, e.g., [5, 6].

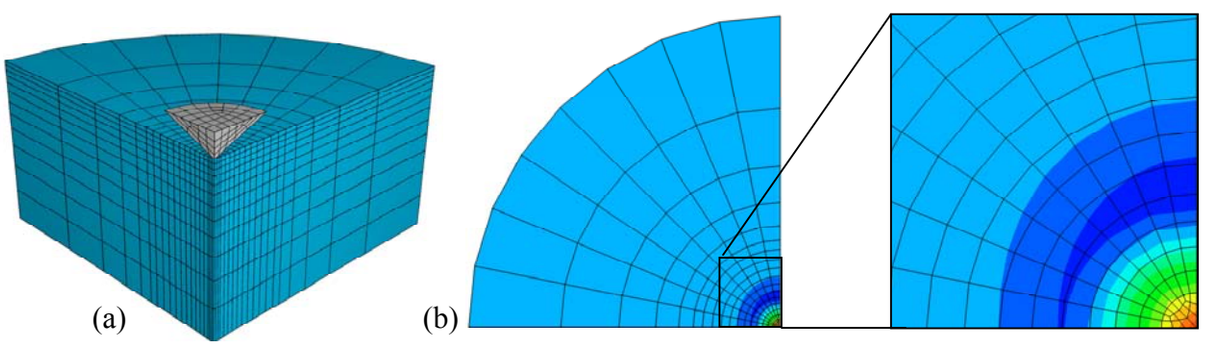


Figure 1: Finite element model of indentation test (a) and contours of the imprint mapping (b).

MEMBRANOMETER TEST ON FREE FOILS

The second method presented herein concerns free anisotropic foils, e.g. those produced by the paper industry and the ones of aluminum and polyethylene employed in laminates for food containers. A new experimental instrumentation, called "membranometer", is proposed, see Figure 2: the foil to be mechanically characterized is placed over a circular window and is inflated by a pressurized fluid; for each pressure level the deformation process of the inflated sheet is monitored by a "profilometer" placed above the foil specimen and simulated by a finite element technique; the discrepancy between the measured and computed displacements under given pressures is minimized with respect to the parameters in the material model adopted for the finite element simulation; the estimates of these parameters are provided by the computer post-processor.
The inverse and the sensitivity analyses are performed by the same approach previously outlined; various techniques comparatively discussed in this study validated the proposed methodology. A prototype of the novel experimental equipment is being designed and constructed by colleagues in the Mechanical Engineering Department for a preliminary validation of the proposed experimental technique.

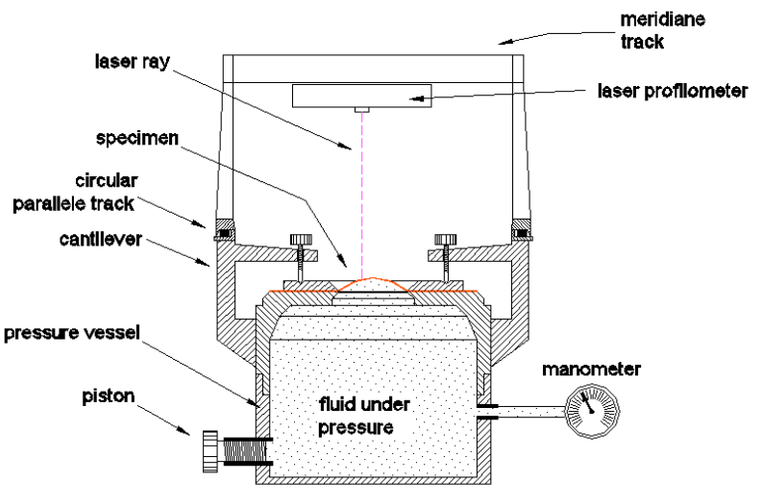


Figure 2: Schematic representation of the membranometer.

CONCLUSIONS

The two methods proposed for the calibration of inelastic material models in thin layers and foils exhibit the following novelties: imprint mapping as supplement of indentation curves in the former; mapping of the inflated membrane in the latter. The inverse analysis stages are based on rather traditional least-square approach; however, stochastic approaches like extended Kalman filters are envisaged for the sequel of this study. Both proposed methods turn out to be promising in terms of cost-effective, fast and routine use in industrial environments.

References

[1] Hill, R.: A Theory of the Yielding and Plastic Flow of Anisotropic Materials, *Proceedings of the Royal Society A* **193**: 281-297, 1947.
[2] ABAQUS/Standard: Theory and User's Manuals, release 6.2-1, Hibbitt, Karlsson and Sorensen Inc., Pawtucket, RI, USA, 1998.
[3] Bui H. D.: Inverse Problems in the Mechanics of Materials: an Introduction. CRC Press, Boca Raton, FL, 1993.
[4] Stavroulakis G., Bolzon G., Waszczyszyn Z., Ziemianski L.: Inverse Analysis. In: Comprehensive Structural Integrity, B. Karihaloo, R.O. Ritchie, I. Milne eds, Vol. 3, Chapter 13, Elsevier Science Ldt, Kidlington (Oxfordshire), UK, 2003.
[5] Bolzon G., Maier G., Panico M.: Material Model Calibration by Indentation, Imprint Mapping and Inverse Analysis. *Int. J. Solids and Structures*, accepted for publication, 2003.
[6] Tunvisut K., Busso E.P., O'Dowd N.P., Brantner, H.P.: Determination of the Mechanical Properties of Metallic Thin Films and Substrates from Indentation Tests. *Philosophical Magazine A* **82**:2013-2023, 2002.

SIMULATION OF DYNAMIC POLYCRYSTALLINE THERMOELASTOVISCOPLASTICITY AND FRACTURE

John D. Clayton*

*Impact Physics, U.S. Army Research Laboratory, Aberdeen Proving Ground, MD, USA, 21005-5069

Summary Presented is a framework for modeling the dynamic response of multi-phase polycrystalline microstructures, accounting for finite deformations, rate dependence of flow stress, thermal softening, thermal expansion, heat conduction, and thermoelastic coupling. Fracture is simulated via the cohesive zone approach. Aspects associated with constitutive modeling of anisotropic damage in the homogenized material system are discussed in light of the results.

INTRODUCTION

Tungsten Heavy Alloys (WHAs) are attractive candidates for use as kinetic energy penetrators because of their relatively large mass density, high melting point, and high strength at elevated rates of loading. The material studied here consists of relatively stiff and brittle pure tungsten grains (BCC), most often nearly equi-axed in shape, embedded in a relatively compliant and ductile matrix (FCC) consisting of nickel, iron, and tungsten. Experimental [1] and numerical [2] methods have demonstrated a clear correlation between lattice orientation of W single crystals and the performance of such crystals as kinetic energy penetrators. The potential exists for development of more descriptive constitutive models accounting for local crystallographic orientation effects, models which would simultaneously engender more accuracy to ballistic simulations and support design of microstructures tailored for enhanced thermomechanical properties. The present work employs single crystalline plasticity models for the constituent phases of the WHA. Models for both materials are embedded within a general thermodynamic framework applicable for describing any thermoelastic-viscoplastically-deforming single crystal. Previous investigations [3, 4] reveal a variety of failure modes exhibited by WHAs strained at high rates, including brittle fracture at W-W grain boundaries, transgranular cleavage of W grains, matrix-grain decohesion, ductile matrix rupture, and adiabatic shear banding. Recent high rate experiments of Weerasooriya [4] indicate that tensile failure of WHA specimens often initiates via local fracture at W-W (i.e., grain-grain) interfaces and less often at interfaces between W grains and the matrix phase. In our framework, we model interface fracture by invoking the cohesive zone approach [5].

CONSTITUTIVE THEORY

A multiplicative decomposition of the local deformation gradient $\mathbf{f}$ is assumed as follows:

$$\mathbf{f} = \partial \mathbf{x} / \partial \mathbf{X} = \mathbf{f}^{\mathbf{e}}\mathbf{f}^{\boldsymbol{\theta}}\mathbf{f}^{\mathbf{p}}, \tag{1}$$

with spatial coordinates $\mathbf{x} = \mathbf{x}(\mathbf{X},t)$, $\mathbf{f}^{\mathbf{e}}$ the elastic deformation, $\mathbf{f}^{\boldsymbol{\theta}}$ the stress-free thermal deformation, and $\mathbf{f}^{\mathbf{p}}$ the plastic deformation due to dislocation glide. Time rates of thermal and plastic deformation gradients are described by

$$\dot{\mathbf{f}}^{\boldsymbol{\theta}}\mathbf{f}^{\boldsymbol{\theta}-1} = \alpha\dot{\theta}\mathbf{1}, \qquad \dot{\mathbf{f}}^{\mathbf{p}}\mathbf{f}^{\mathbf{p}-1} = \sum_{\alpha=1}^{n}\dot{\gamma}^{(\alpha)}\mathbf{s}_0^{(\alpha)} \otimes \mathbf{m}_0^{(\alpha)}, \tag{2}$$

where $\dot{\gamma}^{(\alpha)}$, $\mathbf{s}_0^{(\alpha)}$, and $\mathbf{m}_0^{(\alpha)}$ are slip system shearing rates, referential slip directors, and referential slip plane normals, respectively. Also, θ is the absolute temperature, and α is the coefficient of (isotropic) thermal expansion. The Helmholtz free energy per unit mass, ψ, has the following functional form:

$$\tilde{\rho}\psi = \tilde{\rho}\psi\left(\mathbf{e}^{\mathbf{e}},\theta,\xi\right) = \underbrace{\frac{1}{2}\mathbf{e}^{\mathbf{e}} : \mathbf{c}(\theta,\xi) : \mathbf{e}^{\mathbf{e}}}_{\text{hyperelasticity}} + \underbrace{\frac{1}{2}\kappa\mu(\theta,\xi)\xi^2}_{\text{lattice defects}} + \underbrace{y(\theta)}_{\substack{\text{heat}\\ \text{energy}}}, \tag{3}$$

with $\tilde{\rho}$ the mass density in the relaxed intermediate configuration, $2\mathbf{e}^{\mathbf{e}} \equiv \mathbf{f}^{\mathbf{e}T}\mathbf{f}^{\mathbf{e}} - \mathbf{1}$ an elastic strain, $\mathbf{c}$ the elastic modulus, $\xi \equiv b\sqrt{\rho_T}$ a dimensionless internal variable associated with the total dislocation density ρ_T and burgers vector b, κ a material parameter, and μ an elastic shear modulus. The localized spatial energy balance becomes

$$\underbrace{\rho c_p \dot{\theta}}_{\substack{\text{temperature}\\ \text{change}}} = \underbrace{\sum_{\alpha=1}^{n}\tau^{(\alpha)}\dot{\gamma}^{(\alpha)}}_{\substack{\text{plastic}\\ \text{dissipation}}} - \underbrace{\rho\left(\left(\partial_{\xi}\psi\right) - \theta\left(\partial_{\theta\xi}\psi\right)\right)\dot{\xi}}_{\substack{\text{energy of}\\ \text{lattice defects}}} + \underbrace{\rho\theta\partial_{\theta\mathbf{e}^{\mathbf{e}}}\psi : \dot{\mathbf{e}}^{\mathbf{e}}}_{\text{thermoelastic coupling}} + \underbrace{div\left(k\nabla_{\mathbf{x}}\theta\right)}_{\substack{\text{heat}\\ \text{conduction}}}, \tag{4}$$

where ρ is the current mass density, c_p is the specific heat capacity, $\tau^{(\alpha)}$ is the resolved Cauchy stress on system α, and k is the thermal conductivity. Evolution of the plastic deformation is specified by a viscoplastic flow rule

$$\dot{\gamma}^{(\alpha)} = \dot{\gamma}_0 \left\{ \tilde{\tau}^{(\alpha)} \left(\theta_0 / \theta\right)^p / g_0^{(\alpha)} \right\}^m \operatorname{sgn}\left(\tilde{\tau}^{(\alpha)}\right), \tag{5}$$

where $\tilde{\tau}^{(\alpha)}$ is a resolved Kirchhoff stress, $g_0^{(\alpha)}$ a slip resistance under isothermal conditions, p a thermal softening exponent, m the strain rate sensitivity, and $\dot{\gamma}_0$ and θ_0 material parameters. The dislocation density ρ_T evolves in conjunction with changes in the average strength of all slip systems. Intergranular fracture events at interfaces between W grains and at grain-matrix interfaces are captured by cohesive models in which the interfacial load decreases linearly with separation distance (i.e., crack opening displacement) upon attainment of a critical stress level at the interface [5].

NUMERICAL SIMULATIONS AND RESULTS

The above constitutive model was implemented within the EPIC dynamic wave propagation finite element code [6]. Meshes of triangular elements were generated using the PPM2OOF software package [7], readily enabling meshing of digital images with refinement along material interfaces (i.e., mesh refinement along potential cohesive fracture surfaces). Figure 1 shows the deformed grid from a representative 2D calculation: a large crack has developed along the interface shared by three W crystals, and two smaller cracks have opened at the lateral boundaries. Results from parametric studies show the effects of initial crystallographic texture and relative failure strengths of the interface types upon the net flow stress and crack initiation and propagation within the volume element.

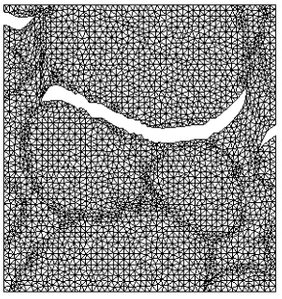


Figure 1. Deformed mesh.

MACROSCOPIC DAMAGE MODEL

An important objective of the present work is support of the construction of physically realistic macroscopic models of the kinematics, thermodynamics, and kinetics of fully anisotropic damage for subsequent implementation in design codes. Addressing the kinematics, the homogenized deformation gradient $\mathbf{F}$ for a damaged material element containing k internal surfaces can be decomposed as [8]

$$\mathbf{F} \equiv \frac{1}{V}\int_S \mathbf{x} \otimes \mathbf{n} dS = \frac{1}{V}\int_V \mathbf{f} dV + \frac{1}{V}\sum_k \int_{S^{(k)}} \mathbf{x} \otimes \mathbf{n} dS^{(k)} = \mathbf{F}^{\mathbf{m}} + \mathbf{F}^{\mathbf{d}}, \tag{6}$$

where S is the external surface of the volume element of referential volume V, with unit surface normal vector $\mathbf{n}$. In Eq. (6), $\mathbf{F}^{\mathbf{m}}$ is the deformation gradient contribution from the intact material, and $\mathbf{F}^{\mathbf{d}}$ is the contribution from internal surface discontinuities associated with damage (e.g., cracks, voids, and shear bands). For the tensile-type fracture modes observed in experiments [4] and our numerical calculations, we propose the following simplified evolution laws:

$$\mathbf{F}^{\mathbf{d}} = \Lambda\left(\mathbf{F}^{\mathbf{m}} - \mathbf{1}\right), \qquad \dot{\Lambda} = \dot{\Lambda}\left(\mathbf{T}, t\right), \qquad \mathbf{F}^{\mathbf{d}}\left(t=0\right) = \mathbf{0}, \tag{7}$$

with $\mathbf{T}$ the net first Piola-Kirchhoff stress for the volume element and Λ a stress state dependent history variable—nonzero upon attainment of a critical nucleation criterion—scaling the rate of deformation accommodation from damage. For a given imposed total deformation gradient $\mathbf{F}$, the greater the magnitude of $\mathbf{F}^{\mathbf{d}}$, the less strain remaining to be accommodated by the net elastic part of $\mathbf{F}^{\mathbf{m}}$, resulting in a reduction in magnitude of the net stress.

References

[1] Bruchey, W.J., Herring, R.A., Kingman, P.W., Horwath, E.J.: Deformation mechanisms in tungsten single crystals in ballistic impact experiments. In: *High Strain Rate Behavior of Refractory Metals and Alloys*, Eds. R. Asfahnai et al., Warrendale, PA, TMS, 1992.

[2] Schoenfeld, S.E., Benson, D.J.: Modeling penetration mechanisms and ballistic performance in high aspect ratio tungsten single-crystal rods: a crystal plasticity model suitable for impact calculations. In: *Advances in Computational Engineering Science*, Eds. S.N. Atluri and G. Yagawa, Tech Science Press, pp. 1116-1121, 1997.

[3] Zhou, M., Clifton, R.J.: Dynamic constitutive and failure behavior of a two-phase tungsten composite. *J. Appl. Mech.* **64**: 487-494, 1997.

[4] Weerasooriya, T.: Deformation and failure behavior of a tungsten heavy alloy under tensile loading at different strain rates. Presented at SEM Annual Conference on Experimental Mechanics, Charlotte, NC, USA, June 2-4, 2003.

[5] Camacho, G.T., Ortiz, M.: Computational modelling of impact damage in brittle materials. *Int. J. Solids Structures* **33**: 2899-2938, 1996.

[6] Johnson, G.R., Stryk, R.A., Beissel, S.R.: *User instructions for the 2001 version of the EPIC code*. Alliant Techsystems Inc., Hopkins, MN, 2001. Distribution authorized to U.S. government agencies and their contractors.

[7] Langer, S., Reid, A., Carter, C., Fuller, E., Roosen, A.: *PPM2OOF v1.1*, 2003, website http://www.ctcms.nist.gov/

[8] Clayton, J.D. and McDowell, D.L.: Finite polycrystalline elastoplasticity and damage: multiscale kinematics. *Int. J. Solids Structures* **40**: 5669-5688, 2003.

XXI ICTAM, 15–21 August 2004, Warsaw, Poland

ASSESSING DIFFERENT SELF-CONSISTENT APPROXIMATIONS BY COMPARISON WITH FULL-FIELD SIMULATIONS IN VISCOPLASTIC POLYCRYSTALS

Ricardo A. Lebensohn*, Yi Liu**, Pedro Ponte Castañeda**
*MST Division, Los Alamos National Laboratory, MS G755, Los Alamos, NM, 87544, USA
**Department of Mechanical Engineering and Applied Mechanics,University of Pennsylvania, Philadelphia, PA 19104-6315, USA

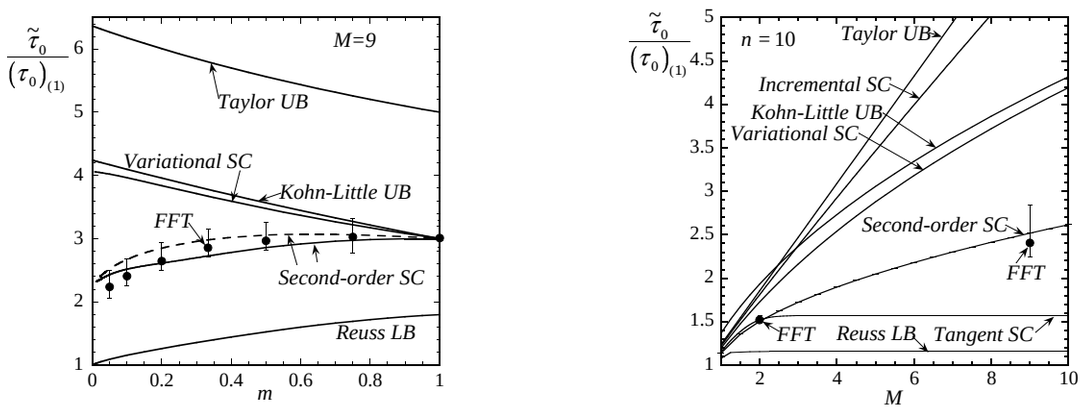
Summary In this work we compare full-field numerical simulations for the effective behavior and the statistical field fluctuations in 2-D and 3-D viscoplastic polycrystals with various estimates of the self-consistent (SC) type. For linear systems, the above comparison demonstrates the accuracy of the standard SC approximation. On the other hand, of the various non-linear self-consistent formulations, the recent 'second-order' method, based on a linearization that takes into account the second-order moments of the mechanical fields, gives the best overall agreement with the full-field simulations.

INTRODUCTION

Because most metals and minerals appear in polycrystalline form, the computation of the *effective* response of polycrystalline aggregates starting from the *properties* of their constituent single-crystal grains and the polycrystal's *microstructure* is a fundamental problem in materials science. For non-linear materials, several self-consistent (SC) models, such as the 'incremental' method of Hill [1], the 'tangent' procedure of Molinari *et al.* [2] and the 'affine' method of Masson *et al.* [3] are available. While these various approximations generally provide improvements on the Taylor and Reuss bounds, and reduce to the linear self-consistent estimate for linearly viscous behavior, they give widely diverging predictions for low rate-sensitivity materials. Alternative extensions of the SC estimates for viscoplastic polycrystals have been proposed recently making use of rigorous nonlinear homogenization methods. More specifically, these novel SC estimates are based on the use of 'variational' *linear comparison* methods, which express the effective potential of the nonlinear viscoplastic polycrystal in terms of that of a *linearly viscous* polycrystal [4] with properties that are determined from suitably designed variational principles. The most recent of these variational formulations is the 'second-order' method [5], which makes use of the SC approximation for a linear *thermoelastic* polycrystal to generate more accurate SC estimates for viscoplastic polycrystals that take into account the second order moments of the mechanical fields inside the constituent grains. On the other hand, the dramatic increases in computational power of recent years have begun to make possible full-field simulations of polycrystalline samples. Recently, a technique based on the use of Fast Fourier Transform (FFT) has been introduced by Moulinec and Suquet [6] and applications of the method have been given recently for polycrystals [7]. The aforementioned uncertainties associated with the various self-consistent schemes and the availability of powerful full-field numerical simulations suggest the computation of *ensemble averages* [8] of the later to verify the accuracy of the former.

RESULTS

2-D polycrystals



(a) (b)

Figure 1. Comparison of the 'second-order' SC estimates with the FFT simulation results, and the Taylor, Kohn-Little and Reuss bounds for the effective viscosity $\tilde{\tau}_0$: (a) as functions of the strain-rate sensitivity m for $M = (\tau_0)_{(2)}/(\tau_0)_{(1)} = 9$; ($b$) as functions of the grain anisotropy M for $n = 1/m = 10$. Also shown in (a) and (b) are the 'variational' SC estimates, and in (b) the 'incremental' and 'tangent' SC estimates.

We show here results for a special class of model polycrystals, consisting of columnar orthorhombic grains with random in-plane orientations. When such polycrystals are loaded in antiplane strain, only two slip systems (with flow stresses $(\tau_0)_{(1)}$ and $(\tau_0)_{(2)}$, respectively) can be activated and a 2-D boundary value problem is thus defined. This special class of 2-D polycrystals has received considerable attention in the literature in recent years, due to the fact that the effective stress is known to have an exact solution, $\tilde{\tau}_0 = \sqrt{(\tau_0)_{(1)}(\tau_0)_{(2)}}$, when the behavior of the single-crystals is linear. For more general power-law polycrystals, the exact result is not known, but an upper bound that is sharper than the classical Taylor bound is available [9]. In Fig. 1, different SC estimates for the effective viscosity $\tilde{\tau}_0$ are shown and compared with the FFT simulation results. Note that the 'error' bars for the FFT results correspond to the maximum and minimum values of $\tilde{\tau}_0$ over all the configurations in the ensemble. Figure 1(a) shows results for $\tilde{\tau}_0$ plotted as functions of the strain-rate sensitivity $m = 1/n$, for a fixed value of the grain anisotropy ($M = (\tau_0)_{(2)}/(\tau_0)_{(1)} = 9$). Figure 1($b$) shows results for $\tilde{\tau}_0$ as functions of the grain anisotropy M, for a fixed value of the nonlinearity ($n = 1/m = 10$). The results shown include the Taylor, Reuss and Kohn-Little bounds, the 'incremental' [1], 'tangent' [2] and 'variational' [4] SC estimates, as well as two slightly different versions of the 'second-order' [5] estimates (continuous and dashed lines). The main observations from these figures are: (i) all the various types of SC estimates satisfy the bounds, except the 'incremental' which violates the Kohn-Little bound, and (ii) the 'second-order' estimate appears to be the *only one* that is consistent with the FFT simulations, for values of $m = 1/n$ different from 1 (the linear case).

FCC polycrystals

Table 1 shows bounds, SC and FFT estimates for the effective flow stress and suitably normalized measures of the *overall standard deviation (SD)* associated with the stress and strain-rate fields (see [10] for details), for a random, non-linear ($n = 10$) FCC polycrystal deformed in uniaxial tension. As for the 2-D case, the 'second-order' SC estimates appear to give the best overall agreement with the FFT results.

model	$\widetilde{\sigma}_0/\tau_0$	$\mathrm{SD}(\sigma_e)/\overline{\sigma}_e$	$\mathrm{SD}(\epsilon_e)/\overline{\epsilon}_e$
Taylor	2.905	0.568	0.
Reuss	2.201	0.	0.825
incremental	2.880	0.752	0.185
affine	2.741	0.576	0.752
tangent	2.617	0.349	0.947
variational	2.811	0.696	0.188
second-order	2.540	0.413	0.878
FFT	2.614	0.480	0.586

Table 1. Taylor, Reuss, different self-consistent, and FFT estimates of the effective flow stress and the overall field SD's for a non-linear, isotropic FCC polycrystal ($n = 10$).

CONCLUSIONS

Among the various nonlinear extensions of the self-consistent approximation, the 'second-order' variational method, gives the best overall agreement with the effective properties and field fluctuations obtained by means of FFT full-field simulations, for 2-D and 3-D polycrystals.

References

[1] Hill R.: Continuum micro-mechanics of elastoplastic polycrystals. *J. Mech. Phys. Solids* **13**, 89–101, 1965.

[2] Molinari A., Canova G.R., Ahzi S.: A self-consistent approach of the large deformation polycrystal viscoplasticity. *Acta Metall. Mater.* **35**, 2983–2994, 1987.

[3] Masson R., Bornert M., Suquet P., Zaoui A.: An affine formulation for the prediction of the effective properties of nonlinear composites and polycrystals. *J. Mech. Phys. Solids* **48**, 1203–1227, 2000.

[4] Ponte Castañeda P.: The effective mechanical properties of nonlinear isotropic composites. *J. Mech. Phys. Solids* **39**, 45–71, 2001.

[5] Ponte Castañeda P.: Second-order homogenization estimates for nonlinear composites incorporating field fluctuations. I—Theory, *J. Mech. Phys. Solids* **50**, 737–757, 2002.

[6] Moulinec H., Suquet P.: A numerical method for computing the overall response of nonlinear composites with complex microstructure. *Comp. Meth. Appl. Mech. Engng.* **157**, 69–94, 1998.

[7] Lebensohn R.A.: N-site modelling of a 3D viscoplastic polycrystal using the Fast Fourier Transform. *Acta. Mater.* **49**, 2723–2737, 2001.

[8] Lebensohn R.A., Liu Y, Ponte Castañeda P.: Macroscopic properties and field fluctuations in model power-law polycrystals: full-field solutions versus self-consistent estimates *Proc R Soc Lond A*, in press, 2004.

[9] Kohn R.V., Little T.D.: Some model problems of polycrystal plasticity with deficient basic crystals. *SIAM J. Appl. Math.* **59**, 172–197, 1998.

[10] Lebensohn R.A., Liu Y, Ponte Castañeda P.: On the accuracy of the self-consistent approximation for polycrystals: comparison with full-field numerical simulations. *Acta Mater.*, submitted.

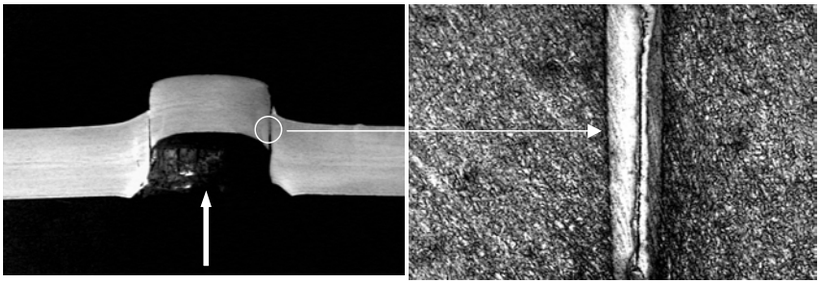
THREE-DIMENSIONAL MODELLING OF THERMO-ELASTO/VISCOPLASTIC SOLIDS CONTAINING ADIABATIC SHEAR BANDS

Patrice Longère[*], André Dragon[*], Hervé Trumel[***], Thibaut de Rességuier[**], Xavier Deprince[****]
[*] *LMPM-ENSMA, UMR CNRS n°6617, 86962 FUTUROSCOPE-CHASSENEUIL Cedex, France*
[**] *LCD-ENSMA, UPR CNRS n°9028, 86962 FUTUROSCOPE-CHASSENEUIL Cedex, France*
[***] *CEA/DAM, 37260 MONTS, France*
[****] *GIAT Industries, 18023 BOURGES Cedex, France*

Summary The aim of the present contribution is to embrace salient features of the adiabatic shear banding (ASB) within the framework of three-dimensional finite strain modelling regarding viscoplastic flow coupled with ASB-related microdamage process. The ASB damage-induced anisotropy is being accounted for. An application of the model is given for the hat shape structure under impact loading.

INTRODUCTION

The main objective of the work presented is the numerical prediction of the adiabatic shear banding (ASB) induced degradation of a structural material under dynamic loading, including target/penetrator interaction. This phenomenon which occurs in particular in thermo/viscoplastic metals as the result of a thermal instability – bringing about discontinuity in the local velocity gradient and temperature - is actually known to lead to the ultimate fracture of the structure (see Fig.1).



a) Steel plate after impact b) Micrograph showing ASB and crack

Fig.1 : Impact of a flat end projectile onto a hard steel target (from GIAT Industries)

Though extensive investigation (metallurgical and mechanical, experimental and theoretical) has been devoted to the matter from the mid 20th century on, see f.ex. the references given in Longere et al.[1], only a few tentatives have been made to incorporate ASB phenomena into three-dimensional rigorous modelling involving viscoplastic flow coupled with specific ASB microdamage evolution, see Perzyna [2].

CONSTITUTIVE MODEL

In this work adiabatic shear banding is treated as an anisotropic damage process within the irreversible thermodynamics framework. In the approach proposed, the (system of) band(s) is incorporated in the representative volume element (RVE). With this viewpoint, informations relative to the variables characterizing the state of the band material (temperature, isotropic hardening, metallurgical transformation, …) together with geometric parameters related to the band itself (width and orientation) are all included in a single 2nd order tensorial internal variable $\mathbf{D}=d.\mathbf{N}$ whose norm d accounts for the intensity of adiabatic shearing (evolution of the variables mentioned before) and whose direction $\mathbf{N}=\mathbf{n}\otimes\mathbf{n}$ is collinear to the normal of the band plane $\mathbf{n}$. While the 'damage' variable $\mathbf{D}$ governs the anisotropic degradation of the material (RVE), kinematic consequences of the presence of the bands, viewed as those of an idealised super dislocation, are dealt with by using the coresponding part of the velocity gradient – intervening in addition to the genuinely plastic part. A large deformation anisotropic plasticity and damage formulation based on the multiplicative decomposition of the deformation gradient is developed involving objective rates needed to ensure material frame indifference.
Constitutive equations integrating ASB-damage are derived from thermodynamic potentials namely the free energy and dissipative potentials in the general framework of the internal state variable formulation.
The reversible part of the free energy includes the initial isotropic linear thermo-elasticity of the sound material and damage induced anisotropic (orthotropic) elasticity for the ASB-degraded material. The form of the stored energy reflects the competition that takes place in the material between hardening and softening. Hardening is a consequence

of the micromechanisms of plasticity in the material outside the band, while softening is due to heating on the one hand and to current ASB-related damage on the other one. During their evolution (formation and propagation), adiabatic shear bands modify the state of internal stresses. In this sense, one can assume that damage acts much like temperature to release stored energy.
Shear banding being in itself a singular viscoplasticity-like process, it is natural to consider it as rate dependent. Consequently, the existence of two dissipative potentials, which refer respectively to the homogeneous viscoplasticity and to the viscous damage, is supposed. The hypothesis of a single yield function has been put to describe the chronology of the dissipative viscous mechanisms mentioned and to account for the strong coupling between plasticity and damage.
An auxiliary indicator needed to determine the conditions for shear bands initiation and orientation has been obtained from a simplified analysis based on the linear theory of perturbations. This damage process incipience indicator is integrated within the constitutive model.

NUMERICAL SIMULATION AND COMPARISON WITH EXPERIMENT

The above constitutive model, including finite anisotropic elasto-plastic strains, rate sensitivity, strain hardening, thermal softening and anisotropic damage (by adiabatic shear banding), has been implemented as 'user-material' in the finite element code LS-DYNA. The numerical integration algorithm of the evolution equations is purely explicit combined with an adaptive time step procedure which controls the stability of the response. In addition, viscosity of the dissipative mechanisms – plasticity and damage – at stake favours regularization of the boundary value problem in the softening regime. A complementary mesh size dependence analysis is put forward ; it confirms much restrained sensitivity of the numerical results to the discretization, i.e. fair efficiency of the regularizing procedure involving finite difference scheme, see also Dornowski and Perzyna [3].
3D numerical simulations of adiabatic shear banding induced degradation in structural steels are performed considering the hat-shape structure dynamic test employing a direct Hopkinson pressure bar device (see Fig.2). The geometry of the hat-shape structure has been defined to localize deformation in a well-controlled area in which pressure remains quasi constant and uniform[4]. This test is used to study the sensitivity of metals to adiabatic shear banding.



Fig.2 : Dynamic hat-shape structure test employing a direct Hopkinson pressure bar device

CONCLUSION

A model coupling 3D viscoplastic response and damage evolution related to ASB process is put forward. Its numerical implementation and application allow to account for the ASB-induced degradation for the prediction of the post-localization response of the structure under dynamic loading. In the structural application shown for the hat shape structure one can see the propagation and/or the arrest of ASB-related damage bands being simulated with success. Numerical results show the evolution of the band tip velocity during the process. Numerical damage maps inside the hat shape structure and the load transmitted to the output bar are in good agreement with experimental evidence.

References

[1] Longère P., Dragon A., Trumel H., de Rességuier T., Deprince X., Petitpas E.: Modelling adiabatic shear banding via damage mechanics approach. *Arch. Mech* **55**:3-38, 2003.

[2] Perzyna P.: Influence of anisotropic effects on the micro-damage process in dissipative solids in *Yielding, Damage and Failure of Anisotropic Solids*, Boehler J.-P. (Ed.), Mech. Engng. Publ., 483-507, 1990.

[3] Dornowski W., Perzyna P.: Constitutive modeling of inelastic solids for plastic flow processes under cyclic dynamic loadings. *J. Engng. Mater. Techn. (Proc. ASME)* **121**:210-220, 1999.

[4] Couque H.: A hydrodynamic hat specimen to investigate pressure and strain rate dependence on adiabatic shear band formation. *J. Phys. IV* **110**:423-428, 2003.

ENERGY STORAGE RATE IN NON-HOMOGENEOUS DEFORMATION

Wiera Oliferuk, Michał Maj

Institute of Fundamental Technological Research, Polish Academy of Sciences, Świętokrzyska 21, 00-049 Warsaw, Poland

When a material deforms plastically, a part of mechanical energy w_p expended in the plastic deformation is converted into heat q_d while the remainder e_s is stored in the material. Thus

$$e_s = w_p - q_d . \quad (1)$$

The stored energy is an essential feature of the cold-worked state and represents the change in internal energy of the material. The measure of energy conversion at each instant of the deformation process is the rate of energy storage $\frac{de_s}{dw_p}$.

Deformation processes modify the temperature field of the strained specimen. At the first stage of plastic deformation the temperature distribution on the specimen surface is uniform what is usually used as an indicator of homogeneous deformation, on the macroscopic scale [1]. With the increase in strain the temperature distribution on the specimen surface becomes non-uniform what corresponds to non-homogeneous deformation. It is well known that before the fracture the strain hardening rate $\frac{d\sigma}{d\varepsilon}$ (σ is the yield stress and $\varepsilon = \ln(l/l_0)$ where l is the instantaneous length of gauge part of the specimen, and l_0 the initial length) rapidly decreases with strain because of damage mechanisms appearance [2]. The energy storage rate seems to be influenced by these mechanisms as well. As far as the authors are aware, there is no systematic work done to confront the strain hardening with the energy storage rate in the non-homogeneous deformation range. A mention to this problem is included in paper by Chrysochoos [3]. Some attempts have been made in present work to investigate a change in $\frac{de_s}{dw_p}$ with a change in $\frac{d\sigma}{d\varepsilon}$ during uniaxial tensile deformation of austenitic steels and to confront one with another.

Two groups of specimens made from austenitic steels 316L and 304L were strained by using the MTS-810 testing machine at the constant deformation rate $\dot{\varepsilon} = 4.3 \cdot 10^{-3}\ s^{-1}$. The steels were initially annealed at 1100 °C and water quenched. The dimensions of gauge part of specimens were 25 mm x 10 mm x 1.5 mm. In the course of deformation process, the tensile force, elongation and temperature distribution on the sample surface as functions of time were measured and recorded. The temperature distribution on the specimen surface was determined by IR camera. On the basis of the mechanical and thermo-mechanical characteristics, the strain hardening rate and the stored energy as the function of the plastic work were obtained.

For the homogeneous deformation range the experimental method of stored energy determination, proposed in previous works by Oliferuk et al. [1, 4] was employed. The energy w_p was found from the load versus elongation curve. The heat q_d was determined by simulating the process of specimen heating during deformation using a controlled electrical power supply in such a way that the temperature increase with time during the simulation was identical with that measured during tensile testing. The energy storage rate $\frac{de_s}{dw_p}$ was obtained by differentiating e_s as a function of w_p. The method makes possible to measure *in situ* the energy balance only under condition of homogeneous deformation**.**

The estimation of the energy storage rate $\frac{\Delta e_s}{\Delta w_p}$ during non-homogeneous deformation is based on comparison of the average temperature increment of deformed sample related to the given increment of the expanded energy (for example equal to 1 J) during a homogeneous deformation and during non-homogeneous one [5]. It has been shown in paper [5] that such approach allows us to estimate the highest value of the energy storage rate. The real rate of energy storage can not exceed this maximal value.

The results for both groups of specimens are shown in Fig. 1. It is seen that before the fracture the energy storage rate $\frac{\Delta e_s}{\Delta w_p}$ rapidly decreases with strain and then becomes negative for both groups of the tested specimens. This means that a part of energy stored during previous deformation begins to release. The energy storage rate $\frac{\Delta e_s}{\Delta w_p} = 0$ at

$\varepsilon = 0.36$ for the 316L steel and at $\varepsilon = 0.46$ for the 304L steel. It is easy to notice that the $\frac{\Delta e_s}{\Delta w_p} = 0$ nearly corresponds to the point on the stress-strain curve at which the Considère stability criterion $\frac{d\sigma}{d\varepsilon} = \sigma$ is satisfied at $\varepsilon = 0.35$ for the 316L steel and at $\varepsilon = 0.43$ for the 304L steel. Taking into account that the real rate of energy storage can not exceed the estimated maximal value the discrepancy between the point corresponding to Considère criterion and the point $\frac{\Delta e_s}{\Delta w_p} = 0$ can be even smaller. This result provides the physical confirmation of Considère criterion. The release of stored energy may be connected with evolution of damage mechanisms.

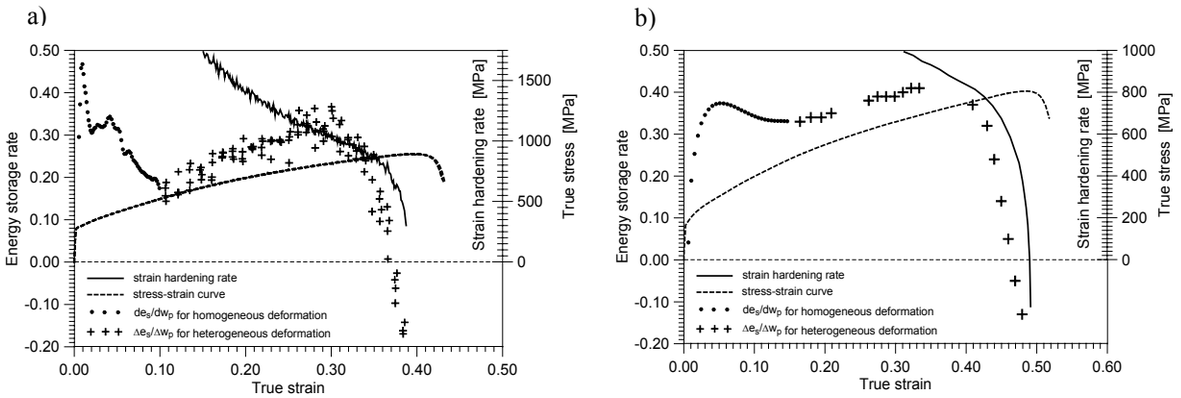


Fig. 1. The stress-strain curve, the energy storage rate and the strain hardening rate as a function of true strain for: a) the 316L austenitic steel (4 specimens), b) the 304L austenitic steel (1 specimen).

The amount of the energy storage rate $\frac{\Delta e_s}{\Delta w_p} = 0$ could be used as an indicator to describe the progressive predominance of damage leading to the fracture of a material.

[1] W. Oliferuk, S. P. Gadaj, W. M. Grabski, Mater. Sci. Eng. 70 (1985) 131.
[2] Z. S. Basinski, M. S. Szczerba, J, D, Embury, Phil. Mag. A 76 (1997) 743.
[3] A. Chrysochoos, J. M. Murracciole, B. Wattrisse, Continuous damage and fracture, Ed.: A. Benallal (2000) 41.
[4] W. Oliferuk, W. A. Świątnicki, M. W. Grabski, Mater. Sci. Eng. A161 (1993) 55.
[5] W. Oliferuk, A. Korbel, W. Bochniak, Mater. Sci. Eng. A319-321 (2001) 250.

DYNAMIC BEHAVIOR OF MANY-DISLOCATION SYSTEMS IN SILICON

Kazuwo Imai, Shigeru Fujinuma and Michio Kurashige

Department of Mechanical Engineering, Iwate University, Morioka, Iwate 020-8551, Japan

Summary Dynamic behavior of dislocations in silicon crystals deformed at constant strain rates is simulated using a two-dimensional discrete-dislocation model. The model consists of infinitely repeated cells, each of which contains the same number of positive and negative mobile dislocations. Calculated results indicate that the experimentally observed *steady state of deformation* corresponds to the dislocated state that maximizes the mean internal stress on moving dislocations.

INTRODUCTION

Semiconductor is a rare kind of material where both the mobility of individual dislocations under stress and the state of collective dislocation motion during its macroscopic deformation have been obtained experimentally by highly reliable methods. Mechanical behavior of a silicon crystal deformed at a constant strain rate has several noticeable features [1]. Among them, the appearance of a *Steady State of Deformation* (SSD) is particularly remarkable. The SSD appears shortly after the lower yield point and continues at least throughout stage I of the stress-strain curve. In this state the value of effective stress, which corresponds to the mean of the stresses acting on all the moving dislocations in the crystal, remains constant irrespective of increase in strain and in dislocation density. The steady value of the effective stress depends on deformation condition (strain rate and temperature), but not on the initial density of dislocations nor on deformation history of the crystal before the SSD begins.

Although it has been a long time since the SSDs were discovered first in germanium crystals and later in silicon and other semiconductor crystals [1][2], the fundamental problems of why and how the states appear and are determined by deformation condition have not been solved completely yet. There have been studies [3]-[5] on the problems in terms of mean field quantities of stresses and dislocation densities, but no attempt was made on the basis of interactions between many discrete dislocations.

As a step toward physical understanding and solution of the problems, the present study simulates dynamic behavior of discrete dislocations in silicon crystals under constant strain rates, using a two-dimensional model of many-dislocation systems.

MODEL

The model crystal consists of infinitely repeated rectangular cells, each of which has a length L in X-direction and a height H in Y-direction and contains N ($N/2$ positive and $N/2$ negative) mobile straight dislocations having the same Burgers vector, with N being an even number (Fig.1). The dislocations are parallel to Z-axis and glide on slip planes parallel to X-Z plane. Configuration of N dislocations within each cell is the same. Under an *applied stress* τ_a or a uniform external shear stress acting on the slip planes and in the slip direction (parallel to the Burgers vector), the dislocations move in positive or negative X-direction. In order to focus on how the interaction between mobile dislocations affects dynamic behavior of many-dislocation systems, multiplication and annihilation of dislocations are not considered.

In the present study, a constant total shear strain rate $\dot{\gamma}$ with respect to the slip system is imposed at and after time $t = 0$ as a deformation condition; temperature is kept constant at 800 degrees centigrade. A density of dislocations ρ in the crystal is given as a material condition. If these conditions, the cell size, and an initial configuration of dislocations in a cell are given, we can obtain dynamic behavior of the N dislocation system by solving a system of differential equations in $N+1$ unknown functions of t, *i.e.*, in τ_a and N x-values of dislocations in a cell.

The cell size was chosen to be $L = 40\,[\mu\mathrm{m}]$ and $H = N/(L\rho)$. Four kinds of cell (P, Q, R, and S) were prepared, whose H values were given by this relation from four experimental values [2] of moving dislocation density in the SSDs at imposed strain rates $\dot{\gamma}_P = 2.4\times10^{-5}[\mathrm{s}^{-1}]$, $\dot{\gamma}_Q = 1.2\times10^{-4}[\mathrm{s}^{-1}]$, $\dot{\gamma}_R = 2.4\times10^{-4}[\mathrm{s}^{-1}]$, and $\dot{\gamma}_S = 6.0\times10^{-4}[\mathrm{s}^{-1}]$. Configuration of N dislocations ($N = 30$) in a cell at $t = 0$ was obtained by using uniform pseudorandom numbers. M initial configurations ($M = 7$) were considered for each of four kinds of cell. Dislocations were assumed to have screw character, because motion of screw dislocations is rate controlling in plasticity of silicon crystals [1].

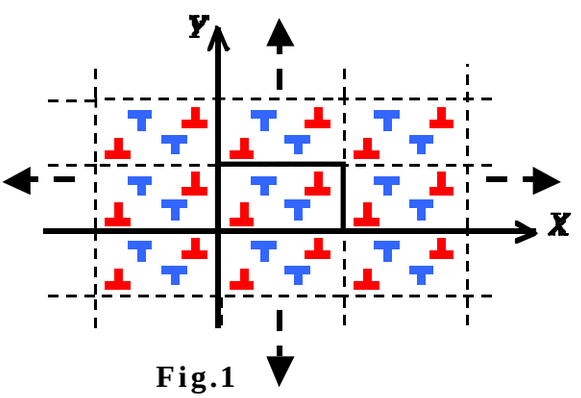


Fig.1

RESULTS AND DISCUSSION

A *dislocation average* of effective stress, $<\tau_{eff}>$, is defined by the mean of effective stresses acting on N dislocations in a cell of a dislocation system at time t. Fig.2 shows an example of the changes in τ_a and $<\tau_{eff}>$ with time in cell Q starting from a certain initial configuration of dislocations and deformed at strain rate $\dot{\gamma}_Q$. Several seconds after the start of deformation, $<\tau_{eff}>$ comes to fluctuate around a constant value of stress. Two horizontal lines in the figure indicate time averages of τ_a and $<\tau_{eff}>$ over the time interval 40 to 100[s], which are called *T-averages* and denoted by τ_{aT} and $<\tau_{eff}>_T$ respectively. *Configuration averages* (C-averages) $<\tau_{aT}>$ and $<<\tau_{eff}>_T>$ are defined as the mean of τ_{aT} and $<\tau_{eff}>_T$ respectively over M many-dislocation systems with different initial configurations.

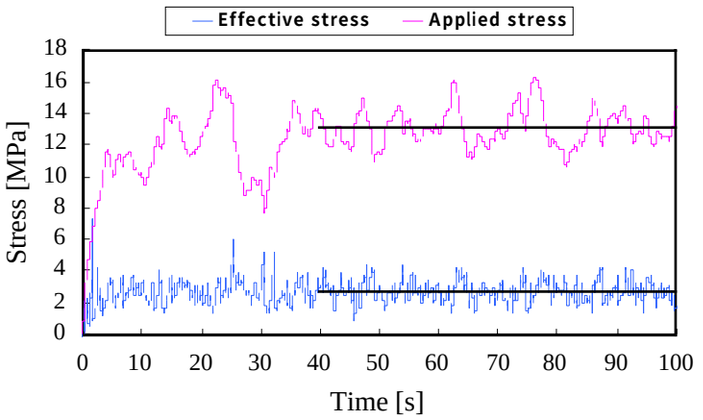


Fig.2

Fig.3 shows strain rate dependence of $<<\tau_{eff}>_T>$ in cells P, Q, R, and S. The calculated mean effective stress at each of four circled points in the figure equals the experimental value of effective stress in the SSD at each strain rate. Strain rate dependence of the experimental effective stress in the SSD is significantly different from that of calculated one in any of the cells. The discrepancy should come from the fact that moving dislocation density ρ_{mov} changes autonomously in deformation of Si crystals, while in the simulation such change does not occur and instead the density of mobile dislocations in each cell is fixed.

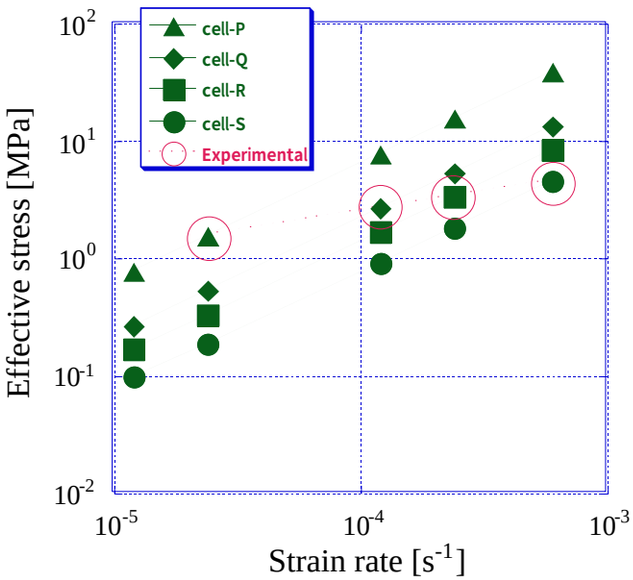


Fig.3

In Fig.4, C-averages of internal stress (applied stress minus effective stress) acting on moving dislocations in cells P, Q, R, and S are plotted against strain rate. As in Fig.3, the strain rate at each of the four points circled corresponds to the deformation condition when each cell was prepared.

What is most striking here is that each circled point lies at the maximum of the strain rate dependence curve for each cell. This indicates that the SSDs found in experiment correspond to the dislocated states that maximize the mean internal stresses on moving dislocations.

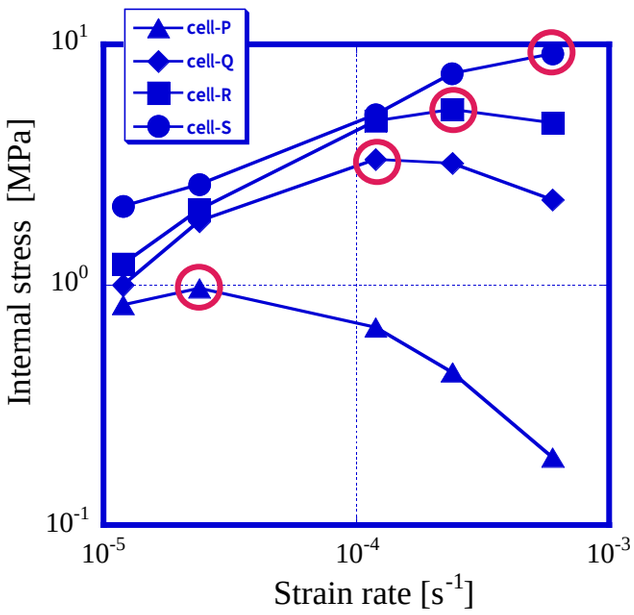


Fig.4

References

[1] K. Sumino: *Handbook on Semiconductors*, Vol.3, ed. S. Mahajan, (North-Holland, 1994), 73.

[2] I. Yonenaga and K. Sumino: *Phys. Stat. Sol.* (a), **50** (1978), 685.

[3] K. Sumino: *Mater. Sci. Engng.*, **13** (1974), 269.

[4] K. Imai, T. Arasawa, and M. Kurashige: *Jap. Soc. Mech. Eng.* (A), **57 (**1991), 1155.

[5] K. Imai et al.: to be published; ICTAM 2000, Chicago, USA.

THE ESHELBY PROBLEM FOR ELASTIC VISCOPLASTIC MATERIALS

Sébastien Mercier, Alain Molinari, Nicolas Jacques
LPMM, University de Metz, Ile du Saulcy, 57045 Metz, FRANCE

Summary Micro-macro schemes contain two important steps. First, the localization process must link the fields inside the inclusion to those applied in the infinite matrix. Secondly, an averaging process is used to derive the macroscopic behavior. For elastic viscoplastic materials, there is no exact solution for the first step. In this work, we adopt the interaction law proposed in [2]. By comparison with Finite element calculations, it is shown that the localization step is well described by the proposed interaction law.

THEORY

To account for intergranular heterogeneities during deformation of elastic-viscoplastic polycrystals, one has to face complicated problems due to the constitutive behavior of the phases. The global elastic viscoplastic behavior is characterized by a long memory effect. Attempts have been proposed recently, based on the extension of interaction laws developed for elastic-plastic materials. These approaches overestimated the internal stresses. In other approaches, the elastic-viscoplastic behavior is linearized at each step of the deformation and this linear problem is solved with Laplace transform. These techniques are complex and time consuming. A different way has been proposed by Kouddane et al in [1] and extended by Molinari [2].
In this work, the Eshelby problem is considered, where an ellipsoidal inclusion is embedded in an infinite homogeneous matrix. Homogeneous strain rate is applied at the remote boundary of the matrix. A small deformation theory is adopted so that the total strain rate is the sum of the elastic and viscoplastic strain rates :

$$\underline{d} = \underline{d}^{e} + \underline{d}^{vp}$$

Both phases (inclusion and matrix) have non linear elastic-viscoplastic behaviors. The rate of the Cauchy stress $\underline{\dot{\sigma}}$ is linked to the elastic strain rate as follows :

$$\underline{\dot{\sigma}} = \underline{\underline{a}}^{e} : \underline{d}^{e}$$

The viscoplastic response is described by a powerlaw but with no restriction, other type of constitutive responses can be analysed. The viscoplastic strain rate is linked to the deviatoric Cauchy stress $\underline{s}$ by :

$$\underline{d}^{vp} = \frac{3}{2}\frac{\sigma^{eff}}{d^{eff}}\underline{s} \qquad \text{with} \qquad \sigma^{eff} = k(d^{eff})^{m}$$

σ^{eff} and d^{eff} are the effective stress and strain rate. m denotes the strain rate sensitivity, k the hardness.
The proposed interaction law [2] is :

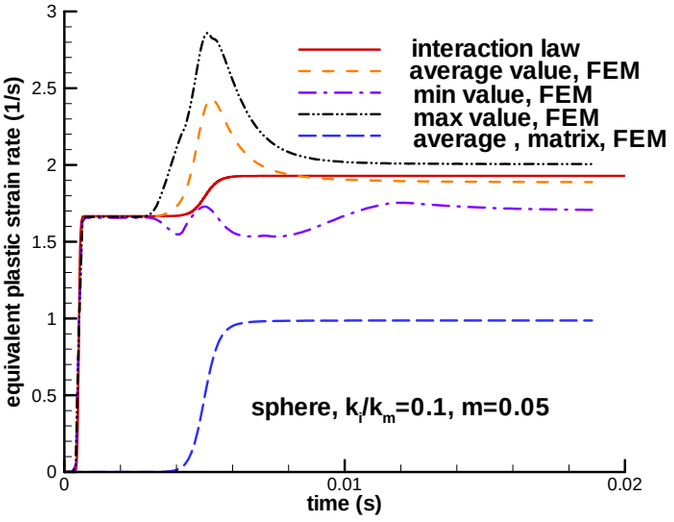
$$\underline{d}^{i} - \underline{D} = (\underline{\underline{A}}^{tg} - \underline{\underline{P}}^{tg^{-1}})^{-1} : (\underline{s}^{i} - \underline{S}) + (\underline{\underline{A}}^{e} - \underline{\underline{P}}^{e^{-1}})^{-1} : (\underline{\dot{\sigma}}^{i} - \underline{\dot{\Sigma}})$$

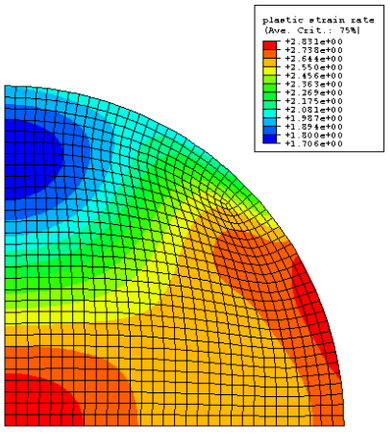
$\underline{d}^{i}, \underline{\sigma}^{i}, \underline{s}^{i}$ correspond to the average values in the inclusion. $\underline{D}, \underline{\Sigma}, \underline{S}$ are the strain rate and stress fields prescribed in the matrix far from the inclusion. $\underline{\underline{A}}^{tg}$ and $\underline{\underline{A}}^{e}$ are the viscoplastic tangent moduli (depending on the strain rate $\underline{D}$) and the elastic moduli of the matrix. $\underline{\underline{P}}^{tg}$ (resp. $\underline{\underline{P}}^{e}$) is a fourth order tensor calculated with use of Green functions related to $\underline{\underline{A}}^{tg}$ (resp. $\underline{\underline{A}}^{e}$).

RESULTS

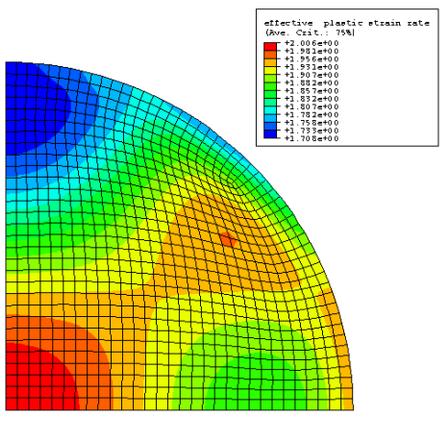
A comparison between predictions of the interaction law and finite element calculations performed with ABAQUS software is carried out. The goal of this study is to demonstrate the capability of the interaction law to capture the elastic-viscoplastic coupling.
The applied loading prescribed at the remote boundary is the following $D_{11} = 1s^{-1}, D_{22} = -0.5s^{-1}, D_{33} = -0.5s^{-1}$.
For incompressible (elastic and viscoplastic) and linear behavior ($m = 1$), the time evolving solution for the strain rate field in the inclusion can be found analytically using Laplace transform. The prediction of the interaction law coincides with the analytical solutions. For non linear elastic-viscoplastic bahavior, no exact solution exists. Numerous F.E. calculations have been performed for different shape of inclusion (sphere , prolate or oblate ellipsoids), hardness ratio, strain rate sensitivity and elastic properties. It can be observed that in all cases (compressible or incompressible elasticity) the average value of the strain rate field inside the inclusion is in close agreement with the average value obtained with use of ABAQUS. As can be seen on the figure, the elastic response at the beginning of the loading is accurately captured. Latter in the deformation process, the elastic contribution vanishes and the fully viscoplastic solution is retrieved. The validity of the interaction law in viscoplasticity (with no elastic deformation) has been demonstrated in [3]. Therefore the proposed interaction law is able to capture accurately the instantaneous elastic

response as well as the asymptotic viscoplastic state. For intermediate time, where the elastic-viscoplastic coupling occurs, the results derived from the interaction law follows the trends obtained with ABAQUS. Note the heterogeneity inside the inclusion occuring during the loading is clearly observed with the F.E. The proposed interaction law can only provide information concerning the average value.





t=5.2e-3 s



t=1.8e-2 s

Figure : Comparison between prediction of the interaction law and F.E. calculations. The inclusion has a spherical shape. The hardness ratio is k_i / k_m =0.1. The matrix and the inclusion have the same strain rate sensitivity m=0.05 and the same incompressible elastic behavior ($\mu_i = \mu_m = 66.6$). On the left, the plastic strain rate heterogeneity in the inside the inclusion is shown (results obtained with ABAQUS).

Note that comparisons have been performed also for lower remote strain rate $D_{11} = 10^{-4}\ s^{-1}$ and for cyclic loading. It is observed that the interaction law is able to describe correctly the elastic-viscoplastic coupling.
Using a self consistent scheme together with the interaction law, which is now validated, the macroscopic behavior of a two phases material has been described. When the two phases have linear incompressible behavior, an analytical solution exists. Good predictions are obtained by the proposed model.

CONCLUSIONS

The localization step for elastic-viscoplastic behavior is well captured by the interaction law proposed in [2]. Finally, this interaction law is used with an averaging scheme to obtain the macroscopic behavior of multiphase elastic viscoplastic materials.

References

[1] Kouddane R, Molinari A, Canova G R : Self-consistent modelling of heterogeneous viscoelastic and elastic-viscoplastic materials In Teodosiu, T. et al. (Eds), Large plastic Deformations, Fundamentals and Applications of Metal Forming. P 121. 1993

[2] Molinari A : Averaging Models for Heterogeneous viscoplastic and elastic viscoplastic materials, J. Engng Mat. *Tech.,Trans. of ASME* **124:**62-70, 2002

[3] Molinari A., El Houdaigui F., Tóth L.S. : Validation of the tangent formulation for the solution of the non-linear Eshelby inclusion problem, Int. J. Plasticity; **20**:291-307,2004

MULTISCALE MODELING OF THE STRUCTURE–PROPERTY RELATIONSHIP FOR SEMICRYSTALLINE MATERIALS

J. A. W. van Dommelen, W. A. M. Brekelmans, and F. P. T. Baaijens
Dutch Polymer Institute, Eindhoven University of Technology,
Department of Mechanical Engineering,
PO Box 513, 5600 MB Eindhoven, The Netherlands

Summary A multiscale numerical model is developed to describe the structure–property relationship for semicrystalline polymers. A polycrystalline model is used to represent the mechanical behavior of the semicrystalline microstructure. The basic element in this model is a layered two-phase composite inclusion, comprising both a crystalline and an amorphous domain. An aggregate of composite inclusions is used in macroscopic finite element models of unfilled and particle-modified semicrystalline materials.

INTRODUCTION

The mechanical performance of semicrystalline polymers is strongly dependent on the underlying microstructure, consisting of crystallographic lamellae and amorphous layers. In this work, a micromechanically-based numerical model for the elasto-viscoplastic deformation and texture evolution of semicrystalline materials is presented.

METHODS

A distinction between three different scales is made, as is schematically depicted in figure 1. The constitutive properties of the material are identified at the microscopic scale for the individual crystallographic and amorphous components. At the mesoscopic scale, an aggregate of individual phases is formed, with either a random or a preferential orientation distribution. To bridge between those scales, an elasto-viscoplastic two-phase composite inclusion model is formulated [1–3]. Each composite inclusion consists of a crystalline lamella which is assumed to plastically deform by rate dependent crystallographic slip, and an amorphous layer which is modeled as elasto-viscoplastic with strain hardening resulting from molecular orientation. The local inclusion-averaged deformation and stress fields are related to the mesoscopic fields of the aggregate by a hybrid interaction law, which compromises between local compatibility and local equilibrium. A full micro-meso-macrolevel bridge is obtained by using an aggregate of composite inclusions in each integration point of a macroscopic finite element (FE) model.

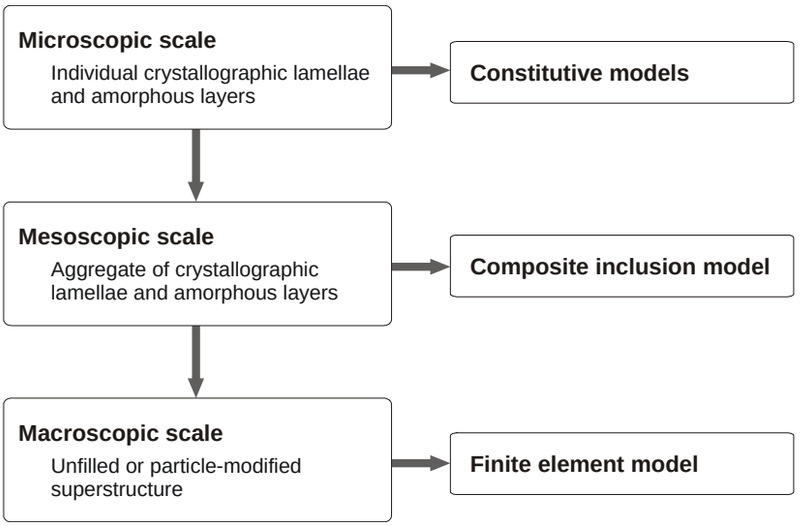


Figure 1: Different scales which can be identified in particle-modified semicrystalline polymeric systems.

APPLICATIONS

The multiscale model is employed to study the mechanics of intraspherulitic deformation for unfilled polyethylene [4]. The spherulitic macrostructure is described by FE models of representative volume elements (RVE). The macroscopic stress-strain response resembles that of a random polycrystalline model; however, the RVE model includes the geometrical effect of the anisotropic structure within a spherulite, causing strain concentrations in the centers. The deformations are linked to microstructural processes as interlamellar deformation and intralamellar crystallographic slip.

The stacked lamellar morphology commonly observed in extruded semicrystalline materials gives rise to a strong influence of the direction of flow with respect to the loading direction on the stability and localization phenomena in tensile experiments. The multiscale numerical model is used to simulate the effect of a stacked lamellar microstructure on the macroscopic behavior [5]. The selection of orientations is based on WAXS experiments on extruded material. The averaged fields of an aggregate, having preferential orientations, constitute the mechanical behavior of extruded material. A macroscopic tensile bar is described by a finite element model. The microstructure-induced deformation hardening in the extrusion direction is found to stabilize the macrostructure, when loaded in the flow direction, whereas when loaded perpendicular to the extrusion direction, a neck is formed.

To enhance the toughness of semicrystalline polymeric materials, it is common practice to blend these materials with rubber particles. The present-day notion of the toughening-mechanism in semicrystalline polymers is expressed in a criterion, which states that toughened material behavior occurs when the average interparticle matrix ligament thickness is smaller than a critical value [6], which is attributed to thin layers of transcrystallized material appearing in the microstructural morphology [7–9]. Multiscale calculations are performed on particle-modified HDPE [10, 11]. The effect of a transcrystallized structure of matrix material versus randomly oriented material is examined. A limited effect of dispersed shear yielding for transcrystallized orientations is observed. Moreover, a relocation of maximum triaxial stresses in the polar area is found. Further improved properties in a specific loading direction are obtained for a hypothesized, partly flow-induced, microstructure.

CONCLUSIONS

A multiscale model has been developed to investigate the micromechanically-induced behavior of unfilled and filled semicrystalline material. The macrostructure is described by RVE models. In each integration point of the finite element models, an aggregate of composite inclusions is used as a representative structural element that provides the constitutive behavior of the material at the mesoscopic level. Material properties are assigned at the microstructural level to both the amorphous and the crystalline phase. Besides these properties, the mesoscopic constitutive behavior is formed by the crystallographic and lamellar orientations of the composite inclusions. The multiscale model is employed to study the mechanics of intraspherulitic deformation for polyethylene and the behavior of material with a lamellar row structure. Finally, multiscale calculations are performed on particle-modified HDPE. The effect of a transcrystallized structure of matrix material versus randomly oriented material is examined. A limited effect of the preferential orientations is observed. Further improved properties in a specific loading direction are obtained for a hypothesized, partly flow-induced, microstructure.

ACKNOWLEDGEMENTS

The authors gratefully acknowledge Prof. D. M. Parks and Prof. M. C. Boyce of the Massachusetts Institute of Technology for their stimulating and helpful discussions concerning the modeling of particle-modified semicrystalline material.

References

[1] Lee B. J., Parks D. M., Ahzi S.: Micromechanical modeling of large plastic deformation and texture evolution in semicrystalline polymers. *J. Mech. Phys. Solids* **41:**1651–1687, 1993.

[2] Lee B. J., Argon A. S., Parks D. M., Ahzi S., Bartczak Z.: Simulation of large strain plastic deformation and texture evolution in high density polyethylene. *Polymer* **34**:3555–3575, 1993.

[3] Van Dommelen J. A. W., Parks D. M., Boyce M. C., Brekelmans W. A. M., Baaijens F. P. T.: Micromechanical modeling of the elasto-viscoplastic behavior of semi-crystalline polymers. *J. Mech. Phys. Solids* **51:**519–541, 2003.

[4] Van Dommelen J. A. W., Parks D. M., Boyce M. C., Brekelmans W. A. M., Baaijens F. P. T.: Micromechanical modeling of intraspherulitic deformation of semicrystalline polymers. *Polymer* **44**:6079-6101, 2003.

[5] Van Dommelen, J. A. W., Schrauwen, B. A. G., Van Breemen, L. C. A., Govaert, L. E.: Micromechanical modeling of the tensile behavior of oriented polyethylene, *J. Polym. Sci.*, submitted.

[6] Wu S.: Phase structure and adhesion in polymer blends: a criterion for rubber toughening. *Polymer* **26**:1855–1863, 1985.

[7] Muratoglu O. K., Argon A. S., Cohen R. E.: Crystalline morphology of polyamide-6 near planar surfaces. *Polymer* **36**:2143–2152, 1995.

[8] Muratoglu O. K., Argon A. S., Cohen R. E.: Toughening mechanism of rubber-modified polyamides. *Polymer* **36**:921–930, 1995.

[9] Bartczak Z., Argon A. S., Cohen R. E., Kowalewski T.: The morphology and orientation of polyethylene in films of sub-micron thickness crystallized in contact with calcite and rubber substrates. *Polymer* **40**:2367–2380, 1999.

[10] Van Dommelen J. A. W., Brekelmans W. A. M., Baaijens F. P. T.: Micromechanical modeling of particle-toughening of polymers by locally induced anisotropy. *Mech. Mater.* **35**:845–863, 2003.

[11] Van Dommelen J. A. W., Brekelmans W. A. M., Baaijens F. P. T.: Multiscale modeling of particle-modified polyethylene, *J. Mater. Sci.* **38**: 4393–4405, 2003.

MODELING OF VISCOPLASTIC CONSTITUTIVE EQUATION FOR POLYMERS BY TAKING INTO ACCOUNT STRAIN RECOVERY

Mamoru Mizuno [*], Yukio Sanomura [**]
[*] *Akita Prefectural University, Tsuchiya, Honjo, Akita 015-0055, Japan*
[**] *Tamagawa University, Tamagawa Gakuen, Machida, Tokyo 194-8610, Japan*

Summary A viscoplastic constitutive equation for inelastic deformation of polymers is formulated by combining the kinematic hardening creep theory of Malinin and Khadjinsky with the nonlinear kinematic hardening rule of Armstrong and Frederick. The nonlinear kinematic hardening rule is modified in order to describe peculiar strain recovery of polymers during unloading in particular. Experimental results for polyethylene are simulated by the constitutive equation and the validity of the modification is verified.

INTRODUCTION

Polymers reveal significant viscoplastic deformation at the room temperature. Peculiar strain recovery is shown during unloading in particular, and it is quite different from what is shown in metals. Such deformation during unlading in polymers has been clarified experimentally [1] and theoretical formulation of the deformation has been attempted [2].
The authors have employed a viscoplastic constitutive equation which was formulated by Murakami et al. [3] by combining the kinematic hardening creep theory of Malinin and Khadjinsky [4] with the nonlinear kinematic hardening rule of Armstrong and Frederick [5]. Then the authors have attempted to modify the nonlinear kinematic hardening rule in order to describe the strain recovery of polymers during unloading so far.
In the present study, a loading surface will be defined in a viscoplastic strain space, and a criterion of loading-unloading will be defined by using the loading surface. Moreover, a parameter will be defined by using the loading surface, and the nonlinear kinematic hardening rule will be modified by using the parameter in order to describe the peculiar deformation of polymers during unloading.

VISCOPLASTIC CONSTITUTIVE EQUATION

A Small deformation is assumed for simplification here. The total strain ε_{ij} is assumed to be the sum of an elastic strain ε_{ij}^{e} and a viscoplastic strain ε_{ij}^{vp}: i.e., $\varepsilon_{ij} = \varepsilon_{ij}^{e} + \varepsilon_{ij}^{vp}$. The elastic deformation is subjected to the Hooke's law.

The viscoplastic strain rate $\dot{\varepsilon}_{ij}^{vp}$, on the other hand, is derived from the kinematic hardening creep theory of Malinin and Khadjinsky [4]. The viscoplastic deformation is assumed to be incompressibility and independence on the hydrostatic stress, and a viscoplastic potential g is given by an effective stress $\xi_{ij} = s_{ij} - a_{ij}$ as $g = (1/2)\xi_{ij}\xi_{ij}$ where s_{ij} is a deviator of the stress σ_{ij} and a_{ij} is that of a back stress α_{ij} which is the center of the viscoplastic potential surface in the deviatoric stress space. Then the viscoplastic strain rate $\dot{\varepsilon}_{ij}^{vp}$ is derived as $\dot{\varepsilon}_{ij}^{vp} = \Lambda(\partial g / \partial \sigma_{ij}) = \Lambda\xi_{ij}$ where Λ is a positive scalar function depending on a stress and a stress path.
An equivalent effective stress $\bar{\xi}$ and an equivalent viscoplastic strain rate $\dot{\bar{\varepsilon}}^{vp}$ are defined as $\bar{\xi} = [(3/2)\xi_{ij}\xi_{ij}]^{1/2}$ and $\dot{\bar{\varepsilon}}^{vp} = [(2/3)\dot{\varepsilon}_{ij}^{vp}\dot{\varepsilon}_{ij}^{vp}]^{1/2}$. Then the viscoplastic strain rate $\dot{\varepsilon}_{ij}^{vp}$ is derived as $\dot{\varepsilon}_{ij}^{vp} = (3/2)(\dot{\bar{\varepsilon}}^{vp} / \bar{\xi})\xi_{ij}$. In this equation, the relation between the equivalent effective stress $\bar{\xi}$ and the equivalent viscoplastic strain rate $\dot{\bar{\varepsilon}}^{vp}$ is necessary. In the present study, the Sorderberg's rule, $\dot{\bar{\varepsilon}}^{vp} = n[\exp(\bar{\xi} / K) - 1]$, is adopted where n and K are material constants.
Finally, the back stress α_{ij} is represented by the sum of a linear term $\alpha_{ij}^{(1)}$ and a nonlinear term $\alpha_{ij}^{(2)}$: i.e., $\dot{\alpha}_{ij} = \dot{\alpha}_{ij}^{(1)} + \dot{\alpha}_{ij}^{(2)}$. The linear term $\alpha_{ij}^{(1)}$ is given by the Prager's rule as $\dot{\alpha}_{ij}^{(1)} = A\dot{\varepsilon}_{ij}^{vp}$ and the nonlinear term $\alpha_{ij}^{(2)}$ is given by the nonlinear kinematic hardening rule of Armstrong and Frederick [5] as $\dot{\alpha}_{ij}^{(2)} = b(C\dot{\varepsilon}_{ij}^{vp} - \alpha_{ij}^{(2)}\dot{\bar{\varepsilon}}^{vp})$ (AF model) where A, b and C are material constants.

MODIFICATION OF EVOLUTION EQUATION OF BACK STRESS

A loading surface $f = 0$ is defined in a viscoplastic strain space as $f = (2/3)\varepsilon_{ij}^{vp}\varepsilon_{ij}^{vp} - \rho^2$ where ρ represents a radius of the loading surface $f = 0$ which is depicted as a hypersphere. Development of the loading surface and a criterion of loading-unloading are prescribed as follows:

$$\dot{\rho} = \begin{cases} \dot{\bar{\varepsilon}}^{vp} & f = 0 \text{ and } n_{ij}\dot{\varepsilon}_{ij}^{vp} \geq 0 \quad \text{loading} \\ 0 & f < 0 \text{ or } n_{ij}\dot{\varepsilon}_{ij}^{vp} < 0 \quad \text{unloading} \end{cases}, \qquad n_{ij} = \frac{\partial f / \partial \varepsilon_{ij}^{vp}}{\left[\left(\partial f / \partial \varepsilon_{mn}^{vp}\right)\left(\partial f / \partial \varepsilon_{mn}^{vp}\right)\right]^{1/2}},$$

where $\dot{\bar{\varepsilon}}^{vp}$ is a rate of change in the equivalent viscoplastic strain $\bar{\varepsilon}^{vp}$ with respect to time t.

Then a parameter Ψ is introduced [3]. The parameter Ψ is defined by the relation between the loading surface and the present state of a viscoplastic strain as $\Psi = [\rho - \bar{\varepsilon}^{vp}\,\mathrm{sgn}(\dot{\bar{\varepsilon}}^{vp})]/2\rho$. The parameter Ψ is always 0 during loading. On the other hand, the parameter Ψ has some value depending on the relation between the loading surface and the present state of a viscoplastic strain only during unloading.

In the present study, the nonlinear kinematic hardening rule of Armstrong and Frederick is modified by using the parameter Ψ in order to describe significant strain recovery during unloading. Following two models are discussed.

$$\underline{\text{Model 1}}: \ \dot{\alpha}_{ij}^{(2)} = b(C_1\dot{\varepsilon}_{ij}^{vp} - C_2\Psi^m\dot{\varepsilon}_{ij}^{vp} - \alpha_{ij}^{(2)}\dot{\bar{\varepsilon}}^{vp}), \qquad \underline{\text{Model 2}}: \ \dot{\alpha}_{ij}^{(2)} = b(1-\lambda\Psi)(C\dot{\varepsilon}_{ij}^{vp} - \alpha_{ij}^{(2)}\dot{\bar{\varepsilon}}^{vp}),$$

where C_1, C_2, m and λ are material constants.

In the Model 1, the transient recovery term [3] is introduced into the AF model, and the term works only during unloading. In the Model 2, on the other hand, a rate of evolution in the nonlinear term of a back stress changes depending on the value of the parameter Ψ during unloading.

RESULTS OF SIMULATION

Experimental results for polyethylene [6, 7] are simulated by using the viscoplastic constitutive equation and two modified models where the Model 1 or the Model 2 is used instead of the AF model in the constitutive equation.

Figure 1 shows stress-strain relations under monotonic compression at constant total strain rates. Figure 2, on the other hand, shows creep curves under constant compressive stresses. In the figures, each symbol represents the experimental result [6] and each line is a result of the simulation. There is no difference among three models, and viscoplastic deformation of polyethylene can be described by the viscoplastic constitutive equation proposed in the present study.

Figure 3 shows a stress-strain relation in shear deformation at a constant strain rate in which the loading direction is reversed at γ =0.13. Significant strain recovery appears immediately after the reverse of the direction, and the AF model can not describe the behavior adequately. The modified models, on the other hand, can describe the strain recovery, and prediction by the Model 2 is closer to the experimental result [7] than that by the Model 1.

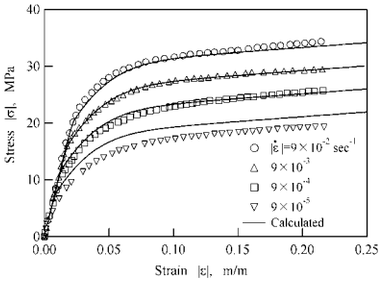


Fig.1 Monotonic compression.

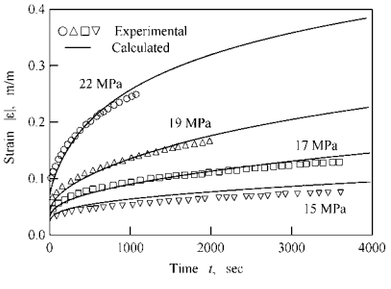


Fig.2 Creep curves.

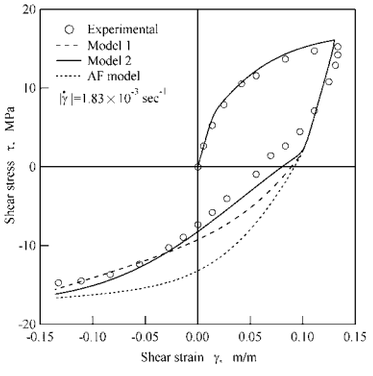


Fig.3 Strain recovery during unloading.

References

[1] Kitagawa, M, Zhou, D and Qiu, J, Stress-Strain Curves for Solid Polymers, *Polymer Eng. Sci.*, **35**:1725-1732, 1995.

[2] Krempl, E and Ho, K., An Overstress Model for Solid Polymer Deformation Behavior Applied to Nylon 66, *ASTM STP*, **1357**:118-137, 2000.

[3] Ishii, T., Mizobe, T, Mizuno, M. and Murakami, S., Inelastic Constitutive Equation of Polymer-Matrix Composites by Taking into Account Transient Recovery Surface, *J. Soc. Mater. Sci. Jpn.*, **50**:973-979, 2001, (in Japanese).

[4] Malinin, N. N. and Khadjinsky, G. M., Theory of Creep with Anisotropic Hardening, *Int. J. Mech. Sci.*, **14**:235-246, 1972.

[5] Chaboche, J. L., Time-Independent Constitutive Theories for Cyclic Plasticity, *I. J. Plasticity*, **2**:149-188, 1986.

[6] Kitagawa, M. and Matsutani, T., Stress-Strain Curve in Polyethylene, *J. Soc. Mater. Sci. Jpn.*, **37**:1391-1396, 1988, (in Japanese).

[7] Kitagawa, M., Yoneyama, T., Qui, J. and Nishida, K, Cyclic Torsional Test of Polymers under High Pressure, *Trans. Jpn. Soc. Mech. Eng.*, **57**:1680-1685, 1991, (in Japanese).

THICKNESS DEPENDENT YIELD STRENGTH OF THIN FILMS

Peter Gudmundson, Per Fredriksson
KTH Solid Mechanics, Royal Institute of Technology, SE 100 44 Stockholm, Sweden

Summary Biaxial and shear loading of a thin film on an elastic substrate are modelled by a strain gradient plasticity theory. The governing equations are implemented in a finite element programme. Simulations are presented for varying ratios between the film thickness and a microstructural length scale parameter. It is showed that both yield strength and hardening are influenced by the film thickness for sufficiently small thicknesses. This is in contrast to alternative theories, which only show an influence on the hardening.

INTRODUCTION

Thin films are applied in a range of applications. Examples are microelectronic devices and surface coatings. Experiments have showed that the yield strength and hardening behaviour depend on the thickness of the film if the thickness is sufficiently small. This thickness dependence cannot be explained by standard local plasticity or viscoplasticity theories. Microstructural length scales must be taken into account. There are several ways to incorporate microstructural length scales. A number of continuum-based theories have been presented in the literature [1, 2]. Gudmundson [3] has presented a framework similar to Gurtin [4] that covers some of the other theories as special cases. A particular feature of this theory is that the structural dimension influences both the elastic range and the hardening. This is in contrast to alternative theories, which only show an influence on the hardening. The theory will be demonstrated by application to two thin film problems. A thin film on a thick elastic substrate is considered. Firstly, the film is subjected to a pure shear stress. Secondly, a prescribed biaxial strain of the film-substrate is considered. The results are compared to experiments and alternative models.

THEORETICAL MODEL

Here, only the equations for shear of a thin film on a thick elastic substrate are presented. The reader should refer to [3] for a detailed derivation of the equations for a general case. The variational principle for pure shear reads,

$$\int_0^t \left[\tau\delta\left(\frac{du}{dz}\right) + (q-\tau)\delta\gamma_p + m\delta\left(\frac{d\gamma_p}{dz}\right)\right] dz = \tau\delta u\big|_{z=t} \tag{1}$$

where τ denotes the shear stress, u the displacement in x- direction, γ_p the plastic shear, q a micro stress and m a moment stress which is conjugate to the plastic shear gradient. The film is perpendicular to the z- axis and $z = 0$ corresponds to the film-substrate interface. The displacement and the plastic shear are assumed to vanish at the interface. If instead a plastically compliant interface is considered, the constraint of vanishing plastic shear at the interface is relaxed and an additional contribution to the variational principle results [3]. It is furthermore assumed that the moment stress m vanishes at the free surface. The constitutive law is defined by,

$$\dot\gamma_p = \dot\gamma_0\left(\frac{\Sigma}{\tau_f}\right)^n \frac{q}{\Sigma}, \qquad \frac{d\dot\gamma_p}{dz} = \frac{\dot\gamma_0}{\ell^2}\left(\frac{\Sigma}{\tau_f}\right)^n \frac{m}{\Sigma}, \qquad \tau = G\left(\frac{du}{dz} - \gamma_p\right) \tag{2}$$

where

$$\Sigma^2 = q^2 + \frac{m^2}{\ell^2}, \quad \dot E^2 = \dot\gamma_p^2 + \ell^2\left(\frac{d\dot\gamma_p}{dz}\right)^2, \quad \tau_f = \tau_s + HE \tag{3}$$

The microstructural length scale is captured by ℓ. An effective stress Σ and effective strain E are introduced. Only linear hardening, described by the hardening modulus H, is here considered. The material parameters are described by $\dot\gamma_0, n$, the shear modulus G and the yield stress τ_s. It is observed that the constitutive law reduces to a local viscoplastic law for vanishing plastic shear gradients. If the exponent n tends to infinity, a rate-independent plastic solution is approached. A finite element formulation of the equations (1-3) has been formulated. Simulations are presented for $n = 30$ which should correspond to almost rate-independent plasticity. The hardening modulus H is set to $G/20$.

RESULTS

In Figure 1, the shear stress is presented as a function of the total average shear for varying ratios between the microstructural length scale ℓ and the film thickness *t*. A yield strength and hardening can be identified for each ratio. The yield strength can be defined from the shear stress where the linear elastic slope crosses the linear hardening slope. In Figure 2, the yield strength is presented as a function of ℓ/t. It is observed that the yield strength is inversely proportional to the film thickness for large thicknesses. The results are in qualitative agreement with alternative strain gradient plasticity theories and dislocation dynamics simulations [5, 6].

The governing equations for biaxial strain have a similar structure as (1-3). The external loading is in this case defined by the biaxial strain ε_0, which gives an additional contribution to the integral term in (1). The right hand side of the variational principle (1) vanishes in this case, because of the free surface. Simulations have been performed for a range of thicknesses *t*. The results are similar to those for pure shear and they are in qualitative agreement with experiments [7, 8] and dislocation dynamics simulations [9].

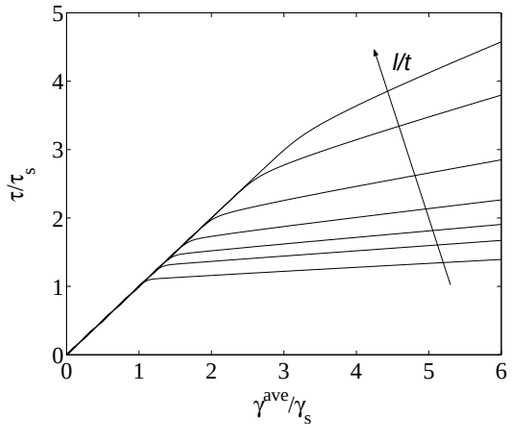


Figure 1. Normalized shear stress versus normalized average shear for varying ratios ℓ/t between microstructural length scale ℓ and film thickness *t*, ℓ/t = 0.082, 0.29, 0.41, 0.57, 0.82, 1.22, 1.63.

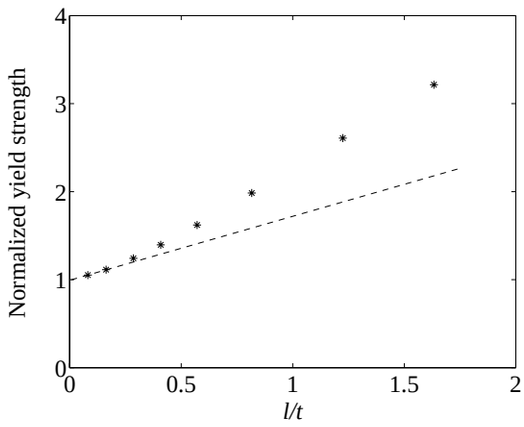


Figure 2. Normalized yield strength versus the ratio ℓ/t between microstructural length scale ℓ and film thickness *t*.

DISCUSSION

It has been demonstrated that the effect of increasing elastic range with decreasing structural dimension can be captured by the theory. Most of the alternative continuum based gradient plasticity models only influence the hardening behaviour. It should be noted that the present results have been obtained for a model of a plastically stiff interface. If a plastically compliant interface is considered, it turns out that small plastic deformations appear after the local yield stress criterion is satisfied. Numerical results will be presented also for this condition.

References

[1] Hutchinson, J.W.: Plasticity at the micron scale. *Int. J. Solids Struct*. **37**:225-238, 2000.

[2] Needleman, A.: Computational mechanics at the mesoscale. *Acta mater*. **48**:105-124, 2000.

[3] Gudmundson, P.: A unified treatment of strain gradient plasticity. *J. Mech. Phys. Solids* to appear.

[4] Gurtin, M.E.: On a framework for small-deformation viscoplasticity: free energy, microforces, strain gradients. *Int. J. Plasticity* **19**:47-90, 2003.

[5] Fleck, N.A., Hutchinson, J.W.: A reformulation of strain gradient plasticity. *J. Mech. Phys. Solids.* **49**:2245-2271, 2001.

[6] Shu, J.Y., Fleck, N.A., van der Giessen, E., Needleman, A.: Boundary layers in constrained plastic flow: comparison of nonlocal and discrete dislocation plasticity. *J. Mech. Phys. Solids* **49**:1361-1395, 2001.

[7] Venkatraman, R., Bravman, J.C.: Separation of film thickness and grain boundary strengthening effects in Al thin films on Si. *J. Mater. Res.* **7**:2040-2048, 1992.

[8] Yu, D.Y.W, Spaepen, F.: The yield strength of thin copper films on Kapton. Submitted to *J. Appl. Phys.*, 2003.

[9] Nicola, L., van der Giessen, E., Needleman, A.: Discrete dislocation analysis of size effects in thin films. *J. Appl. Phys.* **93**:5920-5928, 2003.

YIELD SURFACES USING AN EXTENSION OF THE "REGULARIZED" SCHMID LAW TO POLYCRYSTALLINE MATERIALS

Stéphane Berbenni †, Patrick Franciosi
G.E.M.P.P.M., UMR CNRS 5510, INSA, 69621 Villeurbanne Cedex, France.
†Present address: *Dept. Mech. Engng., Northwestern University, Evanston, IL. 60208-3111, USA.*

Summary A new micromechanical model based on an extension of a "regularized" Schmid law to polycrystalline materials is presented. The homogenization procedure is based on the Transformation Field Analysis method (TFA). Yield surfaces for FCC metals are generated .

INTRODUCTION

On the mechanical ground, crystal plasticity obeys a non linear and anisotropic flow law, which has been differently described according to the chosen assumption of rate-independent or rate-dependent plasticity. In the former case, the Schmid flow criterion is used, while in the latter, power law descriptions are widely called for. More recently, a "regularized" Schmid flow rule has been proposed [1,2] to eliminate the singularities of the classical Schmid yield surface for single crystals. In this work, the "regularized" Schmid flow law is considered to account for a heterogeneous plasticity in a FCC polycrystal. Being so treated as an aggregate of plastically flowing grains, the effective polycrystal behavior, and the stresses in each grain, can be estimated by using the Transformation Field Analysis (TFA), which is an elastic "affine" homogenization procedure [3]. The paper is organized as follows. The first part introduces the micromechanical model in the framework of a "regularized" Schmid law and details the homogenization step. The second part gives numerical results and particularly yield surfaces obtained for isotropic FCC polycrystals. Concluding remarks are given in the last part.

MICROMECHANICAL MODEL

Regularized Schmid law and crystallographic approach

The yield criterion proposed is an extension to an aggregate of the "regularized" Schmid law proposed initially by Gambin [1] and Arminjon [2] for single crystals. In this work, the plastic flow criterion reads:

$$F = \left(\sum_{I} f^{(I)} \sum_{g(I)} \left(\frac{\left| \tau^{g(I)} \right|}{\tau_c^{g(I)}} \right)^n \right)^{\frac{1}{n}} - 1 = 0 , \qquad (1)$$

where n is an exponent which has to be correctly chosen. $\tau_c^{g(I)}$ deals with the strain-hardening state and $\tau^{g(I)}$ is the resolved shear stress on each slip system g(I) for the set of grains I with volume fraction $f^{(I)}$. For each grain, a homogeneous multiple (anisotropic) slip description is used and the set of slip systems {111} <110> is considered. By calculating the differential form of F and accounting for the whole microstructure of the polycrystal, the equation $dF = 0$ is solved and leads to the definition of a new plastic multiplier $d\lambda$. Then, the plastic slip increment is defined by:

$$d\gamma^{g(I)} = d\lambda \frac{\partial F}{\partial \tau^{g(I)}} . \qquad (2)$$

The form of (1) is convenient with most of the FEM codes and includes in the elastic-plastic moduli the crystallographic nature of the material, in particular its textural anisotropy and its intra crystalline strain-hardening.

Homogenization procedure

The framework of the so called "affine formulation" [4] has been used and more specifically the TFA procedure proposed by Dvorak [3] which implies only concentration stress and strain tensors calculated in elasticity. This elastic nature within the TFA method gives a useful simplicity to model strongly non linear behaviors like elastic-plastic polycrystals. Thus, the resolved shear stress takes the following form:

$$\tau^{g(I)} = R^{g(I)} : \sigma^{(I)} = R^{g(I)} : \left(B^{(I)} : \Sigma + \sigma_0^{(I)} \right), \text{ and:} \qquad (3)$$

$$\sigma_0^{(I)} = \sum_{J} G^{(IJ)} \varepsilon^{p(J)} , \qquad (4)$$

where $R^{g(I)}$ is the orientation tensor, $\sigma^{(I)}$ is the local stress tensor and $G^{(IJ)}$ is a related to the elastic stress concentration tensor $B^{(I)}$, the elastic properties and the volume fraction of each grain J; $B^{(I)}$ is calculated using the

self-consistent scheme in elasticity. The effective plastic strain of the Representative Volume Element (RVE) is given by:

$$E^{Pe} = \sum_{I} f^{(I)}\ {}^{t}B^{(I)} : \varepsilon^{p(I)} . \qquad (5)$$

Results are provided considering a RVE of spherical grains characterized by their Euler angles and their volume fraction.

NUMERICAL RESULTS

Single crystal

Following the work of Franciosi et al. [5] for FCC metals, the hardening matrix is composed of 2 terms. The first term corresponding to self-hardening is H1=μ/250 (slope of stage II for a tensile test on FCC single crystal [4] where μ is the shear modulus); the second term corresponding to latent hardening is H2=qH1 with q=1.4. Tensile curves for different grain orientations capture the marked orientation dependence for FCC single crystals. Yield surfaces (obtained with $f^{(I)}$=1 and 1 grain) for different orientations are in agreement with previous works [1,2]. Elastic constants for Al are used in the simulations and $\tau_0 = 2$MPa for each slip systems.

Yield surfaces for polycrystals

Macroscopic tensile curves denote a linear stage consistent with a slope of E/100 (E: Young modulus) characterizing FCC polycrystalline metals. Yield surfaces have been successfully generated for isotropic (Fig. 1) and textured polycrystals. For n>100, the shape of the initial yield surface is in agreement with the one obtained by the classical Schmid law. For n=2, yield surfaces are similar to Hill's 1948 and Von Mises quadratic criterions respectively for anisotropic and isotropic aggregates.

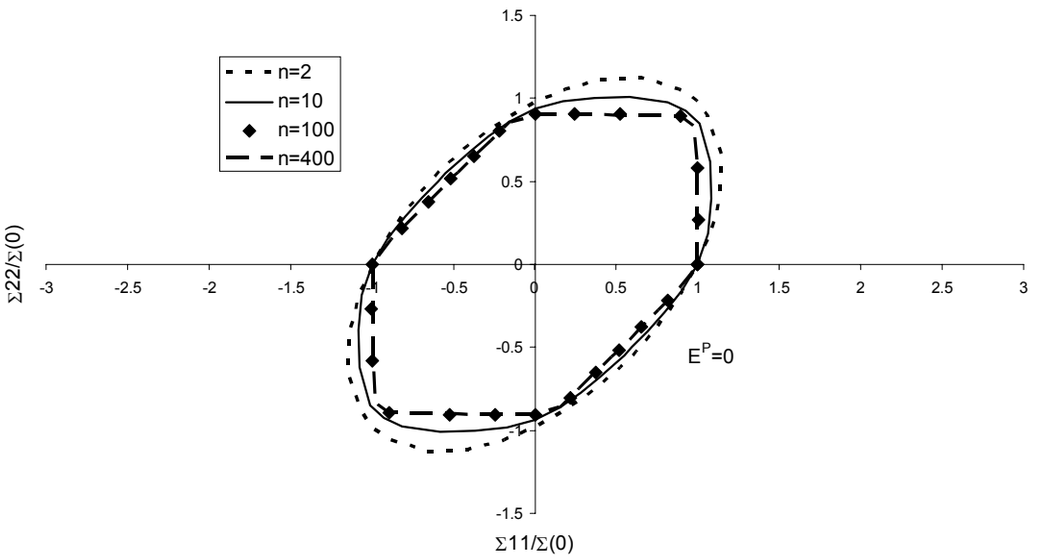


Fig.1. Normalized (initial) yield surfaces of an isotropic aggregate (2016 orientations) for several values of n.

CONCLUSIONS

The present model based on a "regularized" plastic flow rule and the TFA approach avoids the ambiguity problem for the selection of active slip systems within elastic-plastic polycrystals. Yield surfaces are in good agreement with the ones obtained using the classical Schmid law. At this step, a hypothesis of "average" plastic strain per crystal is used. We propose to subdivide each crystal into a N-laminate structure, according to the N slip planes of the considered lattice type, such that the plastic strain fields are piecewise uniform. That allows to use the TFA method at the micro level to better describe the intra granular deformation mechanisms and to estimate more accurately the overall behavior of polycrystals.

References

[1] Gambin W.: Refined analysis of elastic-plastic crystals. *Int. J. Solids Structures* 29, 2013, 1992.

[2] Arminjon M.: A regular form of the Schmid law - Application to the ambiguity problem. *Textures and Microstructures* 14-18, 1121, 1991.

[3] Dvorak G.J.: Transformation Field Analysis of inelastic composite materials. *Proc. R. Soc. Lond.* A 437, 311, 1992.

[4] Masson R., Bornert M., Suquet P., Zaoui A.: An affine formulation for the prediction of the effective properties of non linear composites and polycrystals. *J. Mech. Phys. Solids* 48, 1203, 2000.

[5] Franciosi P., Berveiller M., Zaoui A.: Latent hardening in copper and aluminium single crystals. *Acta Metall.* 28, 273, 1980.

XXI ICTAM, 15–21 August 2004, Warsaw, Poland

SIZE-EFFECTS IN VOID GROWTH

Christian F. Niordson
Department of Mechanical Engineering, Technical University of Denmark, 2800 Kgs. Lyngby, Denmark

Summary A recent finite strain generalization of a higher order strain gradient plasticity theory is used to study how void growth is influenced by the material length parameters on the micron scale. The analyzes are based on a unit cell model considering either a plane strain model with cylindrical voids or an axisymmetric model with more realistic arrays of spherical voids. It is shown that gradient contributions to the material hardening suppress void growth significantly when voids are small.

INTRODUCTION

Recent experimental and numerical work (e.g. [1]) have shown that void growth on the micron scale exhibit significant size-effects. These findings are supported by theoretical arguments based on the concept of geometrically necessary dislocations from dislocation mechanics. Such size effects cannot be modeled by conventional continuum theories, since they use no material length parameters. In recent years several gradient theories have been proposed, which can model size effects by using material length parameters. Some of these theories are of higher order nature, using higher order stresses as work conjugates to higher order strains and higher order boundary conditions, while others are of lower order nature, in that they retain the structure of conventional boundary value problems in solid mechanics.
While some studies of void growth are based on growth of a single void in an infinite medium [2], the present work studies size effects for void growth in elastic-plastic materials with periodic distributions of cylindrical or spherical voids. Since the focus is on size-effects, a recent higher order strain gradient plasticity theory proposed in [3] is used to model the matrix material. The problem of void growth inherently involves large plastic deformations, which means that a finite strain model is needed. Hence, a recent finite strain generalization proposed in [4] is implemented into a finite element program and used to study the problem numerically.
The results presented in the present work focus on the effect of material length parameters on the overall properties of metals containing voids. Results are presented which highlight the strength of the materials containing different size voids, and which illustrate the growth in void volume vs. overall deformation at different ratios of the void radius to the material length scales.

FINITE STRAIN GRADIENT PLASTICITY MODEL

The finite strain generalization [4] of the strain gradient plasticity theory proposed in [3] is based on the following form of the principle of virtual work in the current configuration

$$\int_V \left(\sigma_{ij}\delta\dot{\epsilon}_{ij} + \left(Q-\sigma_{(e)}\right)\delta\dot{\epsilon}^P + \tau_i\delta\dot{\epsilon}^P_{,i}\right)dV = \int_S \left(T_i\delta\dot{u}_i + t\delta\dot{\epsilon}^P\right)dS \tag{1}$$

Here, σ_{ij} is the conventional Cauchy stress tensor, $\dot{\epsilon}_{ij}$ is the strain rate, $\sigma_{(e)}$ is von Mises's effective stress, Q is a generalized effective stress, and $\dot{\epsilon}^P = \sqrt{\frac{2}{3}\dot{\epsilon}^P_{ij}\dot{\epsilon}^P_{ij}}$ is the effective plastic strain rate, with $\dot{\epsilon}^P_{ij}$ denoting the plastic strain rate. The higher order stress, which is work conjugate to the gradient of the effective plastic strain, is denoted τ_i. With N_i denoting the unit surface normal, the right hand side of the principle of virtual work consists of contributions from the traction $T_i = \sigma_{ij}N_j$ which works against the displacements u_i, as well as from the higher order traction $t = \tau_i N_i$, which work against the effective plastic strain.
Letting J denote the material dilatation, Kirchhoff stress measures are defined as

$$\varsigma_{ij} = J\sigma_{ij}, \qquad \sigma^{\varsigma}_{(e)} = J\sigma_{(e)}, \qquad \rho_i = J\tau_i, \qquad q = JQ \tag{2}$$

With an updated Lagrangian formulation in mind, these Kirchhoff stresses can be used to rewrite the incremental principle of virtual work as follows

$$\int_V \left(\overset{\triangledown}{\varsigma}_{ij}\,\delta\dot{\epsilon}_{ij} - \sigma_{ij}\left(2\dot{\epsilon}_{ik}\delta\dot{\epsilon}_{kj} - \dot{e}_{kj}\delta\dot{e}_{ki}\right) + \left(\dot{q}-\dot{\sigma}^{\varsigma}_{(e)}\right)\delta\dot{\epsilon}^P + \overset{\vee}{\rho}_i\,\delta\dot{\epsilon}^P_{0,i}\right)dV = \int_S \left(\dot{T}_{0i}\delta\dot{u}_i + \dot{t}_0\delta\dot{\epsilon}^P\right)dS \tag{3}$$

Here, derivatives are evaluated in the reference configuration, and the right hand side is based on nominal tractions. The constitutive relation for the Jaumann rate of the Kirchhoff stress is taken to be

$$\overset{\triangledown}{\varsigma}_{ij} = \mathcal{R}_{ijkl}(\dot{\epsilon}_{kl} - \dot{\epsilon}^P_{kl}) \tag{4}$$

where $\mathcal{R}_{ijkl}$ is the isotropic elastic stiffness tensor. Denoting the hardening modulus by h, and defining gradient tensors A_{ij}, B_i, and C, as in [3], the constitutive relation for the generalized effective stress can be expressed as

$$\dot{q} = h\left(\dot{\epsilon}^P + \frac{1}{2}B_i\dot{\epsilon}^P_{,i} + C\dot{\epsilon}^P\right) \tag{5}$$

and the constitutive equation for the convected derivative of the higher order Kirchhoff stress as

$$\overset{\vee}{\rho}_i = h(A_{ij}\dot{\epsilon}^P_{,j} + \frac{1}{2}B_i\dot{\epsilon}^P) \tag{6}$$

NUMERICAL RESULTS AND DISCUSSION

The finite strain gradient plasticity model has been incorporated in an updated Lagrangian finite element program, using 8-noded isoparametric elements. Due to the higher order nature of the theory, the discretized equations are based on plastic strain degrees of freedom on equal footing with displacement degrees of freedom.
Figure 1 shows overall results for a simple cubic distribution of cylindrical voids under plane strain deformation. Figure 1a shows the nominal stress, σ_n, as a function of the linear strain, ϵ_l, while Figure 1b shows the ratio of current void volume to initial void volume, V/V_0. Each family of curves corresponds to a certain ratio of void radius to half the void distance, $\frac{R_0}{a_0}$, with varying values of the internal material length parameter l_*. The solid curve shows results for a material without voids, the dashed curves show results for a material with $\frac{R_0}{a_0} = 0.25$, and the dotted curves show results for a material with $\frac{R_0}{a_0} = 0.5$. The markings on the curves in Figure 1a show the maximum load point. The figure illustrates how the strength decreases with increasing void volume fraction, but more interestingly it shows how the strength increases with increasing material length parameter. From Figure 1b it is seen how the increase in strength with the material length parameter is linked to the suppression of void growth, which is due to the gradient hardening.

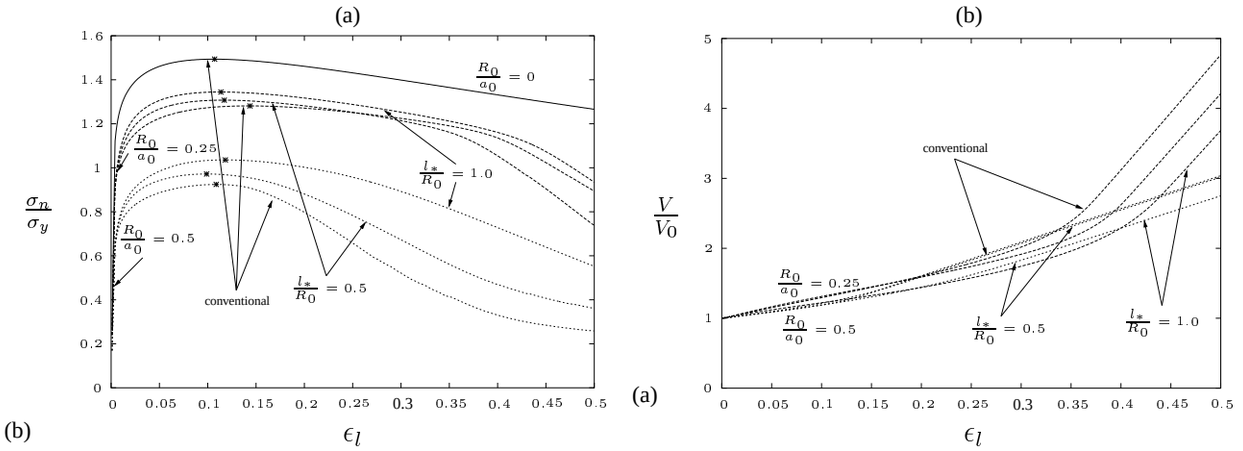


Figure 1. The figures show overall results for materials with different size voids and different internal material length parameters. Figure (a) shows the nominal stress as a function of the overall linear strain, and figure (b) shows the void volume normalized with the initial void volume as a function of the overall linear strain.

Thus the work shows how a strain gradient plasticity theory can be used to model the fact that small voids grow less than larger voids. Due to the lack of length parameters in conventional theories they cannot capture such size-effects. It is illustrated how gradient hardening increases the strength of an elastic-plastic material with voids and suppresses void growth when compared to conventional predictions. The results in Figure 1 are based on plane strain analyzes of cylindrical voids, but the work also includes axisymmetric analyzes for the growth of initially spherical voids in elastic-plastic solids. The results also highlight the effect of triaxial loading which has a significant effect on void growth.

References

[1] Schlüter, N., Grimpe, F., Bleck, W., Dahl, W.: Modelling of the damage in ductile steels. *Computational Materials Science* **17**:27-33, 1996.
[2] Liu, B., Qiu, X., Huang, Y., Hwang, K.C., Li, M., Liu, C.: The size effect on void growth in ductile materials. *J. Mech. Phys. Solids* **51**:1171-1187, 2003.
[3] Fleck, N.A., Hutchinson, J.W.: A reformulation of strain gradient plasticity. *J. Mech. Phys. Solids* **49**:2245-2271, 2001.
[4] Niordson, C.F., Redanz, P.: Size-effects in sheet-necking. *Technical report*, Technical University of Denmark, Department of Mechanical Engineering, Solid Mechanics, 2003.

ON THE ACCOUNTING OF DISLOCATION INTERNAL STRESS IN CONTINUUM PLASTICITY

Amit Acharya, Anish Roy
Carnegie Mellon University, Pittsburgh, PA 15213, USA

Summary We discuss existing gradient plasticity proposals that are intended to represent internal stress effects of dislocation distributions, and show by a common and simple example that all such proposals overestimate the strain energy or stress of a dislocated medium by the introduced phenomenology. Based on the above observation, we propose a model of crystal plasticity of unrestricted nonlinearity, both in material response and kinematics, that does not have the above defect. The model phenomenologically accounts for short-range interactions through the usual strength-based hardening assumptions of conventional crystal plasticity and calculates the long-range stress and evolution of so-called geometrically necessary dislocation distributions, at the desired scale of resolution, in a mechanically rigorous manner. We present computational results for a simplified version of the model. The development of microstructure is a natural consequence of the model.

The analysis of metal plasticity based on a (physically) rigorous connection to its origins in the mechanics of defects in elastic solids is a complex matter. The primary source of complexity arises in achieving an adequate theory that can describe the dynamics of crystal defects, namely dislocation distributions, as it arises from the interaction of the stress fields of these defects as well as applied loads. Also, simply calculating the stress field of a dislocation distribution in a body undergoing finite deformations and whose crystal elastic response is non-convex is not a trivial matter. Moreover, even if such a theory could be developed, its physical resolution would have to be in the nanometer scale, whereas the effects of the physical mechanisms described above are manifest in plasticity even at the micron scale and above. Consequently, a coarse-graining technique for nonlinear evolutionary systems becomes essential, once a fine-scale theory of plasticity/dislocation mechanics has been constructed.

It is fair to say that there are no modeling approaches available presently that can rigorously deal with all of the aspects mentioned above. Gradient plasticity approaches (Aifantis, 1987; Fleck and Hutchinson, 1997; Gao et al. 1999; Acharya and Bassani, 2000; Busso et al. 2000; Menzel and Steinmann, 2000; Gurtin, 2002) are being developed to deal with such challenges. The approaches amongst these that address single crystal plasticity are based on modifications of conventional single crystal plasticity theory (Rice, 1971; Asaro, 1983; Bassani, 1994) that add the prediction of size dependent response to the list of capabilities of the conventional theory. The description of short-range interactions of dislocations leading to work hardening is phenomenological in these approaches, but is calibrated robustly for practical and scientific applications so as to yield good predictive capability with respect to the various other features of single crystal response apart from work-hardening. It should also be mentioned that work-hardening is the most complex feature of plastic response and, as of now, there are no fundamental treatments of the problem that may be called a theory.

As to the issue of handling the evolving stress field in the body that provides the driving force for its inelasticity, conventional as well as gradient approaches utilizes the same technique whose conceptual connection to the actual stress field of the dislocation distribution in the body is not so clear.

As a perceived improvement of this situation, some gradient plasticity theories have been proposed where the incompatibility of the plastic distortion, a continuum measure of so-called geometrically necessary dislocations (GND), is included in the list of dependencies of the free energy of the solid along with the elastic distortion. The incompatibility being a measure of dislocation density, under the *assumption* that the conventional theory is unable to represent the strain energy and internal stress contribution of the GND distribution, such a device may be expected to be a better reflection of the strain energy and stress content of the body.

However, we show that the internal stress, and consequent strain energy, of a dislocation distribution that is represented by the incompatibility of the constitutively specified plastic distortion is automatically taken into account by the conventional theory employing an elasto-plastic constitutive assumption in which the strain energy and stress depend only on the elastic distortion. Consequently, an added contribution to the strain energy due to the incompatibility is unnecessary, and can be shown to be strictly erroneous in many situations.

However, it remains a fact that conventional plasticity fails to represent strain energy and stress effects of dislocation distributions in a realistic manner. Combining this observation with the conclusion of the previous paragraph, this failure may only be attributed to an inadequate prescription of the plastic distortion in the conventional theory. A theory of nonequilibrium dislocation mechanics that addresses the issues of calculating the stress field of a dislocation density distribution in a nonlinear material under finite deformations and the evolution of such a density giving rise to plasticity has recently been proposed (Acharya, 2001; 2003; 2004). While its complete range of predictive capability still remains to be explored, initial results seem to be promising. This theory, however, is for plasticity at the smallest scales. Apart from its intrinsic value for the analysis of inelasticity at scales of a tenth of microns to a tenth of a nanometer, it is envisioned that it will serve as the fine theory for coarse-graining to achieve a proper theory of macroscopic plasticity, when such a coarse-graining technique for nonlinear evolutionary equations becomes available in the scientific literature.

As a practical expedient, in this work we adopt the ideas of field dislocation mechanics pertaining to calculating the stress field and evolution of GND distributions and append them to the gradient plasticity approach of Acharya and Beaudoin (2000). The rationale behind this approach is that the gradient plasticity approach is thought to be adequate for the modeling of short-range interactions of unresolved dislocation distributions (statistically stored dislocations, SSD), and the long-range stress field and kinetic effects of the dislocation distribution at scales that are resolved by the calculation (so-called geometrically-necessary dislocations, GND) are fundamentally accounted for by the additional dislocation mechanics component of the theory. The ‘combined’ model does not suffer from the inconsistency mentioned earlier with respect to accounting of strain energy of dislocation distributions.

We describe this finite deformation ‘combined’ model of single crystal plasticity, and show computational results for a simplified version that includes all the important conceptual details of the model.

References

[1] Acharya A. : *J. Mech. Phys. Solids* **52**, 301-316, 2004.
[2] Acharya A.: *Proc.R. Soc. Lond. A* **459**, 1343-1363, 2003.
[3] Acharya A.: *J. Mech. Phys. Solids* **49**, 761-785, 2001.
[4] Acharya A., Bassani J. L.: *J. Mech. Phys. Solids* **48**, 1565-1595, 2000.
[5] Acharya A., Beaudoin A. J.: *J. Mech. Phys. Solids* **48**, 2213-2230, 2000.
[6] Aifantis E. C.: *Int. J. Plasticity* **3**, 211-247, 1987.
[7] Asaro R. J.: *Adv. Appl. Mech.* **23**, 2-115, 1983.
[8] Bassani J. L.: *Adv. Appl. Mech.* **30**, 191-258, 1994.
[9] Busso E. P., Meisonnier F. T., O’Dowd N. P.: *J. Mech. Phys. Solids* **48**, 2333-2361, 2000.
[10] Fleck N. A., Hutchinson J. W.: *Adv. Appl. Mech.* **33**, 295-361, 1997.
[11] Gao H., Huang Y., Nix, W. D., Hutchinson J. W.: *J. Mech. Phys. Solids* **47**, 1239-1263, 1999.
[12] Gurtin M. E.: *J. Mech. Phys. Solids* **50**, 5-32, 2002.
[13] Menzel A., Steinmann P. : *J. Mech. Phys. Solids* **48**, 1777-1796, 2000.
[14] Rice J. R.: *J. Mech. Phys. Solids* **19**, 433-455, 1971.

STEADY-FLOW OF A NON-HOMOGENEOUS BINGHAM MATERIAL OVER A WEDGE

Oana Cazacu[*], N.D. Cristescu[**]
[*]*University of Florida/GERC, Department of Mechanical &Aerospace Engineering, Shalimar,FL,USA*
[**] *University of Florida, Department of Mechanical &Aerospace Engineering,Gainesville,FL,USA*

Summary A model for describing steady flow of a cementitious target over a wedge shaped penetrator is proposed. The target medium is described by a rate dependent constitutive equation that accounts for combined effects of strain rateand compaction on yielding. The influence of characteristics of the penetrator/target interface, impact velocity, target mechanical properties and nose geometry on the resistance to penetration is investigated.

Kinetic energy penetration phenomena are of interest in a variety of applications ranging from terminal ballistics to protection of spacecraft due to meteoroid impact, containment of high mass or high velocity debris due to accidents or high rate energy release, design of hardened protective facilities, erosion and fracture of solids due to impact, *etc*. The occurrence of multiple phenomena in the impacted material such as localization, plasticity, slip dependent friction, anisotropic damage, fragmentation pushes the limits of existing modeling and computational capabilities for description of the target response.
In this paper, a model for describing the flow of a cementitious material over a penetrator is proposed. The cementitious medium is described by a non-homogeneous Bingham with locked hydrostat (see [1],[2]). The rationale for adopting such a model is that it can account for both rate dependency and compaction effects on yielding, which are key properties of concrete or any other geologic material. The projectile is wedge-shaped
The extent of the domain affected by the impact event is considered to be 2 (F+1) R, where R is the shank radius, and F is an integer number estimated from tests. In the domain D_o, in front of the projectile, and in the domain D_f behind it, the target medium is moving as a rigid body with the striking velocity V, while in domain D_{visco} the material undergoes viscoplastic deformation. To reduce the complexity of the problem, we further suppose that in the viscoplastic domain D_{visco}, the flow lines are centered at a certain pole O.

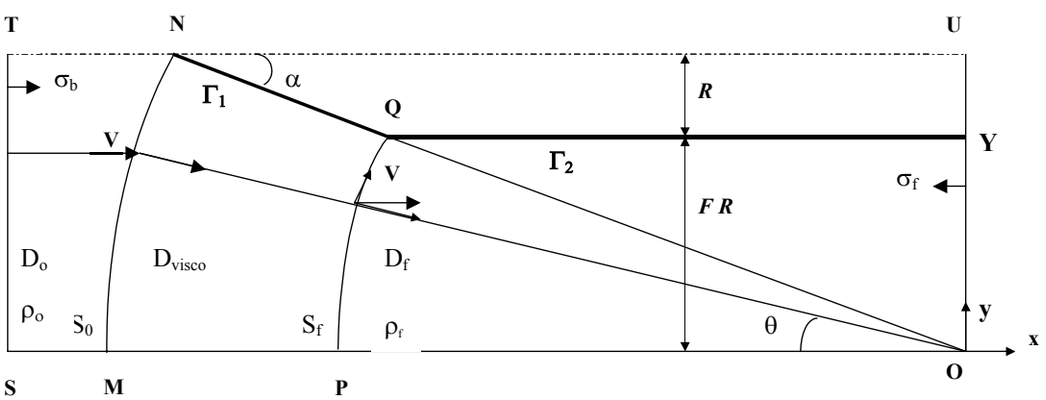


Figure 1: Schematic of the flow

The viscoplastic domain D_{visco} is bounded by the nose surface, Γ_1, MP, and the two surfaces S_0 and S_f. We assume that there exist velocity discontinuities tangent to the surfaces S_0 and S_f while the components of velocity normal to these surfaces are continuous. It follows that in the viscoplastic domain D_{visco}, the only non-zero velocity component is the radial component. From the continuity equation in D_{visco}, we obtain that the density in the viscoplastic domain is directly proportional to the inverse of the radius. Using the work-hardening law in conjunction with the radial compaction law for the material, the stress distribution in the viscoplastic domain is calculated. It is assumed that Coulomb friction law applies along the surface area of contact between the nose of the rigid projectile and the target. Along the surface area of contact between the compacted target material and the shank a slip-dependent friction law is considered. The resistance to penetration is calculated using the theorem of power expanded. Based on this analysis optimization of the wedge angle is performed. To illustrate the predictive capabilities of the model, its application to mortar is presented. The data available on mortar consists of laboratory quasi-static unconfined and confined compression tests for confining pressures in the range 50- 450 MPa under a strain rate of 10^{-6}/s and both confined and unconfined Split-Hopkinson bar data at strain rates of 60/s to 160/s. The theoretical resistance to penetration σ_b normalized by the locking pressure p^* as a function of the projectile semi-angle α for different striking velocities V is shown in Figure 2. For any given impact velocity, the minimum of each of the resistance to penetration vs. semi-angle curves corresponds to an optimum semi-angle nose. The plot of the optimal nose half-angles vs. the corresponding

impact velocities is presented in Figure 3. Analysis of the effect of interface conditions shows that for the same impact velocity, at lower friction on the nose, the optimum nose angle is smaller. As expected, for the same impact velocity, at lower friction between the nose and target, a sharper nose projectile encounters less resistance to penetration.

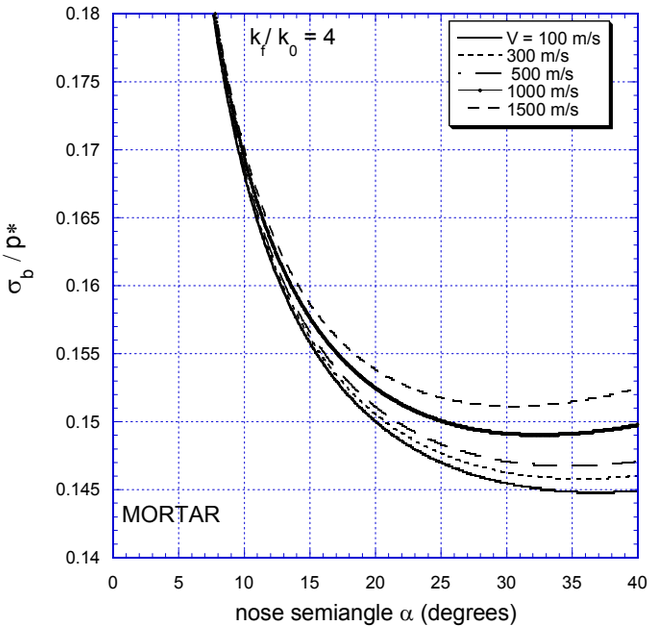


Figure 2: Resistance to penetration σ_b normalized by the locking pressure p^* for different striking velocities.

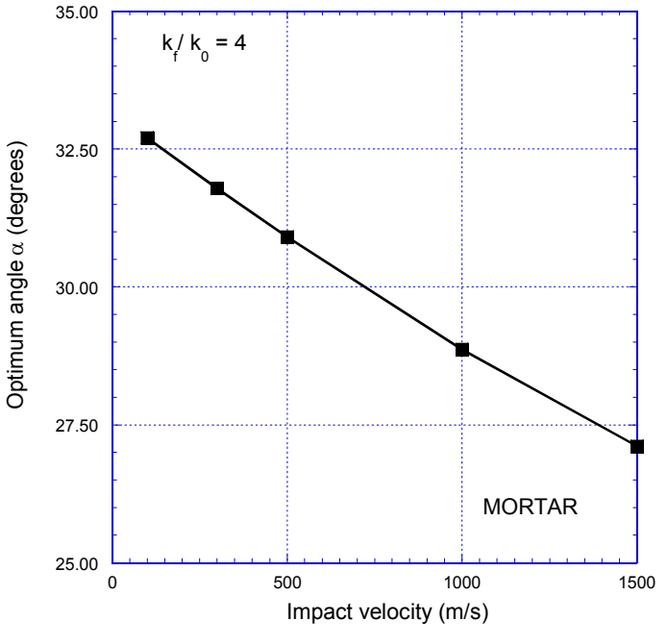


Figure 3: Optimum projectile semi-angle vs. impact velocity.

References

[1] Cazacu, O. and Cristescu, N. D. *Italian Geotechnical Journal*, **34**, (3), 44-54, 2000.

[2] Cristescu, N. D., Cazacu, O.,and Cristescu, C. A Model for Landslides, *Canadian Geotechnical Journal*, **39**, 924-937, 2002.

MODELLING OF ELASTIC-PLASTIC OR VISCOPLASTIC MATERIALS SENSITIVE TO THE TYPE OF THE PROCESES – DIFFERENT APPROACHES

Anguel I. Baltov[*], Georgi B. Stoychev[**]
[*]*Bulgarian Academy of Sciences, Institute of Mechanics, BG 1113 Sofia, Bulgaria*
[**]*Technical University Sofia, BG 1000 Sofia, Bulgaria*

Summary Modelling of the nonelastic materials sensitive to the type of the processes are presented. Two different approaches are given. Some experimental verifications and model parameter identifications are demonstrated for different characteristic models.

Introduction

Sensitivity to the type of the process is universal property well known in many practical cases. The presentation of this property is like different behavior of the nonelastic material during fore example: extension or compression; loading or unloading; hardening or softening; plastic deformation with athermal or thermofluctuational micromechanismes; relaxation or creep; etc. The principle of the modeling of this type of material behavior is based on the introducing models with different material constants according to the type of process in consideration.

In this paper we will give two approaches:

(1) First: It is more or less classical approach, using nonsymmetric yield surfaces in the stress space;

(2) Second: It is on the base of extended strain space, introducing the process type indicators

and incremental constitutive relations with different material functions for different process types.

First approach

Grey cast iron, some steels, light alloys, ceramics, polymers, composites, rocks and soils etc., show in tests different plastic behavior and strength in tension and compression, volumetric plastic deformation and other nonclassical effects. A nonclassical effect for this material is the volumetric dilatation in tension, compression and torsion. The classical theory of plasticity which is based on the Huber-von Mises-Henckly or the Tresca conditions in the case of significant nonclassical effects is unworkable. In the case of different behavior in tension and compression we propose extension of the classical yield conditions formulated on the base of the modified plastic work as a hardening parameter.

We propose the yield function

$$f = \sqrt{J_2} + \varphi(\chi)\sigma_1 - \psi(\chi) = 0\,,$$

where J_2 is the second invariant of the stress deviator, σ_1 is the maximum principal stress, χ is the hardening parameter, $\varphi(\chi)$ and $\psi(\chi)$ are material functions determined by uniaxial tests

$$\varphi(\chi) = \frac{\sigma_C(\chi) - \sigma_T(\chi)}{\sqrt{3}\sigma_T(\chi)}\,,\quad \psi(\chi) = \frac{\sigma_C(\chi)}{\sqrt{3}}\ .$$

The functions $\sigma_T(\chi)$ and $\sigma_C(\chi)$ can be obtained as a current yield stresses in uniaxial tension and compression respectively.

The hardening parameter taking in account the pressure sensitivity of the grey cast iron can be defined as

$$\chi = \int \frac{1}{\omega(\sigma_m,\theta)}\sigma_{ij}d\varepsilon_{ij}^p\,,\ \text{with}\ \omega(\sigma_m,\theta) = \frac{b_1 - b_2}{1 + \exp\left(\dfrac{\sigma_m - b_3}{b_4}\right) + b_2}$$

where σ_{ij} is the stress tensor and $d\varepsilon_{ij}^p$ is the increment of the plastic strain tensor, $\sigma_m = I_1/3$ is the mean stress and b_1, b_2, b_3, b_4 are material parameters depending on the loading type. These parameters can be identified by simple tests in tension, compression and torsion.

Since the experimental results indicate plastic volume dilatation in tension, compression and pure torsion calculation of transverse strain using associated flow rule gives unrealistic values independent of the choice of the yield function. More accurate modeling of the volume change in the elastoplastic region can be obtained using non-associated flow rule. The plastic potential is proposed in the following form

$$g = J_2 + \gamma(\chi)I_1 + \vartheta(\chi)I_1^2\,,$$

where $\gamma(\chi)$ and $\vartheta(\chi)$ are functions of the hardening parameter and can be identified using experimental data from uniaxial tests in tension and compression. The increment of the volumetric plastic deformation can be determined from the

flow rule $d\varepsilon_V^p = d\lambda\delta_{ij}\dfrac{\partial g}{\partial\sigma_{ij}}$, where $d\lambda$ is plastic multiplier. The stress increment can be computed via the elastic stress-strain relations $d\sigma_{ij} = D_{ijkl}d\varepsilon_{kl}$ with $d\varepsilon_{ij}^e = d\varepsilon_{ij} - d\varepsilon_{ij}^p$ since the total strain increment can be divided to an elastic and plastic part. Based on the plastic consistency condition the plastic multiplier can be expressed in the form

$$d\lambda = \omega(\sigma_m,\theta)\frac{\dfrac{\partial f}{\partial\sigma_{kl}}D_{klmn}d\varepsilon_{mn}}{-\dfrac{\partial f}{\partial\chi}\sigma_{rs}\dfrac{\partial g}{\partial\sigma_{rs}}+\dfrac{\partial f}{\partial\sigma_{kl}}D_{klmn}\dfrac{\partial g}{\partial\sigma_{mn}}},$$

where D_{klmn} is fourth order tensor of elastic material constants and $d\varepsilon_{mn}$ is the tensor of total strains.
The verification of the model was realized using experimental data for grey cast iron. Experimental tensile stress-strain relation $(\sigma_1 - \varepsilon_1)$ was used to obtain the function $\sigma_T(\chi)$. There is a good agreement between the computed values and the experimental data from uniaxial and biaxial tests with tubular specimens.

Second approach

For modeling the material's sensitivity to the type of the process we introduce: (1) six dimensional strain vector $\in_\alpha$, (α=1, 2… 6) on the base of the strain tensor; (2) Back stress vector $\sum_\alpha^\times$ on the base of the back stress tensor, (3) Damage vector D_α on the base of the damage tensor; (4) Temperature T; (5) internal time τ. We build a linear seven dimensional vector space $L=Y_6 \times I_T \times I_T^+$, where Y_6 is the six dimensional vector space, I_T is the one dimensional axis for T and I_T^+ is the one dimensional positive axis for τ.

The process measures in the fixed point (x_i) and the time t are $\Lambda_t \equiv \{\in_\alpha, \Sigma_\alpha^a, D_\alpha, T, \tau\}$, with $\Sigma_\alpha^a = \Sigma_\alpha - \Sigma_\alpha^\times$, $\in_\alpha = \in_\alpha^{(rev)} + \in_\alpha^{(irrev)}$.

The process duration is from t_o to t_f e.g. $t \in [t_o, t_f]$. At the fixed time $t=t_h$ we assume to know the state measures $\Lambda_h \equiv \{\in_{\alpha(h)}, \Sigma_{\alpha(h)}^a, D_{\alpha(h)}, T_h, \tau_h\}$. This state is reached from the process in previous time interval Δt with the type according to the values of the indicator manifold $\Lambda_c \equiv \{g, d, q\}$. All indicators take the values: (-1) – for the small quantities: (0) – for the moderate quantities and (+) – for the big quantities. g is for the strain-rate range; d is for the damage range; q is for temperature range.
We examine the process evolution during the actual process time interval $\Delta t_h = t_a - t_h$, where t_a is the actual process time. All process measures change $\Delta\Lambda_h \equiv \{\Delta\in_\alpha, \Delta\Sigma_\alpha^a, \Delta D_\alpha, \Delta T, \Delta\tau\}$. The type of the process during this small evaluation is identify using the fallowing indicator manifold $\Lambda_d \equiv \{\lambda_E, \lambda_D, \theta, \upsilon\}$. λ_E gives the type of the deformational process development; λ_D gives the type of the damage process development;

$$\theta = \frac{\Delta T}{|\Delta T|} = \begin{cases} +1 \text{ for war min g;} \\ 0 \text{ for isotehermal process change;} \\ -1 \text{ for cooling.} \end{cases}$$

$$\upsilon = \frac{\Delta\tau}{|\Delta\tau|} = \begin{cases} 0 \text{ for reversibal process change;} \\ +1 \text{ for irreversible process change.} \end{cases}$$

(-1) is impossible according to thetthermodynamical restrictions.
The constitutive equations are in incremental form:

$$\Delta\Sigma_\alpha = E_{\alpha\beta}\Delta\in_\beta^{(rev)} + N_{\alpha\beta}\Delta\in_\beta^{(irrev)};$$
$$\Delta\Sigma_\alpha^\times = R_{\alpha\beta}\Delta\in_\beta^{(irrev)};$$
$$\Delta D_\alpha = Q_{\alpha\beta}\Delta\in_\beta^{(irrev)},$$

where the matrixes ($E_{\alpha\beta}$), ($N_{\alpha\beta}$), ($R_{\alpha\beta}$) and ($Q_{\alpha\beta}$) depend on the state Λ_h at the moment t_h and on the two indicator groups: Λ_c and Λ_d. It is possible to define the internal time in connection with the dissipation energy e.g.

$$\tau = \int_{t_0}^{t_h} \Sigma_\alpha^a.\Delta\in_\alpha^{(irrev)}\,dt\,.$$

We give, like examples, some models for different particular cases (deformational type sensitive material; sensitive to type of rheological process; sensitive to the type of loading etc). We give also some experimental verifications and model parameter identifications for various materials – some composites, metals, woods etc.

STRAIN GRADIENT CRYSTAL PLASTICITY INCORPORATING GRAIN BOUNDARY EFFECTS

Marc G.D. Geers, L.P. Evers**, W.A.M. Brekelmans*
*Eindhoven University of Technology, Department of Mechanical Engineering, P.O. Box 513, 5600 MB Eindhoven, The Netherlands
**Netherlands Institute for Metals Research, Rotterdamseweg 137, 2628 AL Delft, , The Netherlands

Summary This paper focuses on the micromechanical description of the mechanical response of an FCC multi-crystal microstructure on the basis of geometrical details (grains, orientations, internal/external boundaries) and the physics of the underlying plastic deformation (dislocation driven crystal plasticity). A strain gradient dependent crystal plasticity approach is presented to model the constitutive behavior of polycrystal FCC metals under large plastic deformations. The model is applied to predict the non-homogeneous deformation of a polycrystalline sample including grain boundary effects. The resulting response naturally leads to grain size effects and strengthening of the Hall-Petch type.

INTRODUCTION

Conventional single and polycrystal plasticity models do not explicitly incorporate the influence of inter– and intragranular inhomogeneities in the constitutive description, whereas it is the basic origin of scale dependent behaviour and associated size effects. In general, such inhomogeneities at the microscale can be caused by externally applied macroscopic gradients of plastic deformation, by the presence of grain boundaries locally obstructing the plastic deformation, or by a combination of both. The occurring non-uniform plastic deformations give rise to the development of geometrically-necessary dislocation (GND) densities (preserving crystallographic lattice compatibility) and statistically-stored dislocation (SSD) densities (carrying the crystallographic slip), which physically differ in their role only.
In this paper, a strain gradient enhanced crystal plasticity framework is outlined, based on an extended slip law incorporating a slip resistance and a back-stress, that emerge from the evolution of the SSD, GND, and "grain boundary dislocation" (GBD) densities. Particularly the latter contribution is original, since it has not been addressed in related frameworks like e.g. [1, 2, 4]. The framework is next applied to an example that emphasizes the role of the grain size and grain boundaries in developing hardening effects in plasticity.

STRAIN GRADIENT CRYSTAL PLASTICITY

A non-local crystal plasticity framework has been developed, which incorporates the distinct interactions of various types of dislocation densities. This has been accomplished by including a phenomenological flow rule at the slip system level, which depends on an effective resolved shear stress (τ^{α}_{eff}) and a slip resistance term (s^{α}) [3]. The first one is composed

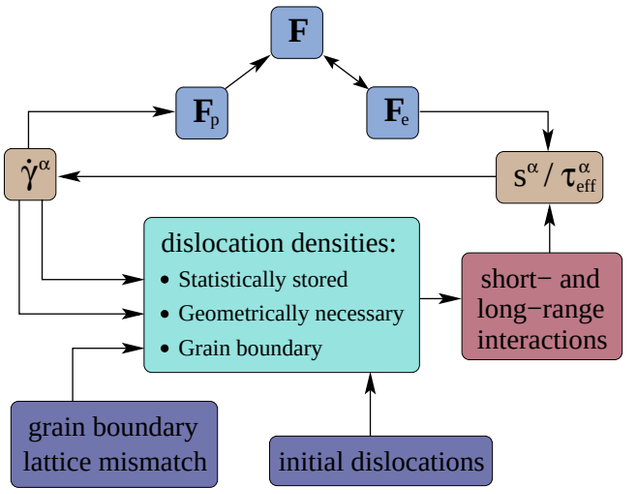


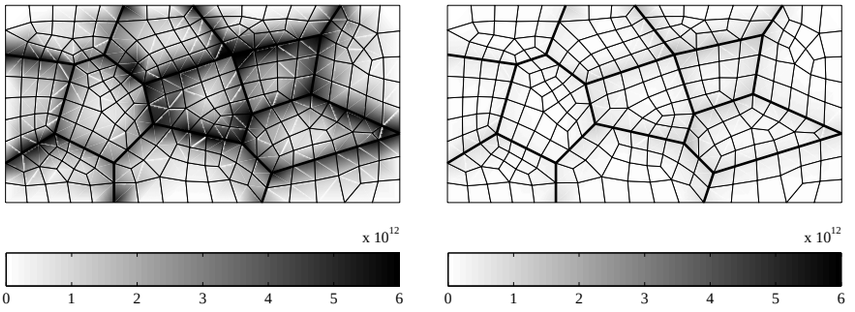
Figure 1. Sketch of the dislocation density based crystal plasticity framework

of the ordinary Schmid stress, yet in this case "corrected" by a newly developed back-stress measure, which represents the long-range interactions that are characteristic of GND density fields, because of their specific dislocation sign and relatively large range of influence. It naturally incorporates a kinematic hardening contribution and includes dependencies between various slip systems based on their spatial orientation. The second term –the slip resistance– depends on the short-range interactions between all dislocations on all slip systems present in the material. Whereas the SSD densities are controlled by a "generation-annihilation" evolution equation adopted from literature, the GND densities follow directly

from the spatial gradients of crystallographic slip (γ^α). Finally, grain boundary dislocation densities (GBD's) have been determined as well, based on the crystallographic lattice mismatch at the grain boundaries. These GBD densities constitute an initial GND density field at the grain boundaries. The dislocation density based crystal plasticity model is outlined schematically in figure 1. Next to the slip resistance as caused by the (short-range) interactions of all SSD's and GND's, any heterogeneity in the GND density field also causes a long-range influence on crystallographic slip, namely through the resulting back-stress contribution. This second influence of the GND densities is caused by the fact that, at a length scale of several orders of magnitude larger than the individual dislocation size, the net effect of the GND densities does not vanish (in contrast to the SSD densities).
The implementation of the entire SSD/GND/GBD density based crystal plasticity framework has been established by means of a weak formulation, consistent linearization and discretization of the governing equations, i.e. the ordinary stress equilibrium condition completed with the GND evolution expression, resulting in a global system of equations to be solved iteratively. Extra nodal degrees of freedom are introduced – i.e. the GND densities– that allow for the specification of various additional boundary conditions which closely approach reality, i.e. dislocation free outer surfaces, strongly obstructed plastic deformation between grains, and an initial GND density field near the grain boundaries.

DEFORMATION OF A POLYCRYSTALLINE SAMPLE, INCLUDING GRAIN BOUNDARY EFFECTS

The mechanical response of a polycrystal sample under plane stress conditions has been simulated for various sample sizes, preserving the grain morphology and the crystallographic orientations. An assembly of grains is therefore considered, in which each grain is discretized in finite elements in order to be able to describe the intragranular inhomogeneities. Obstructing plastic slip at grain boundaries within a plane stress simulation on a polycrystalline sample leads to a grain size dependent flow curve, consistent with a Hall-Petch behaviour. Furthermore, at the grain boundaries, a grain boundary dislocation (GBD) density has been inserted as well, which causes the initial yield stress to be grain size dependent as well. As an example, a plane stress analysis of a polycrystal aluminum sample is presented, for which the geometrical and material parameters are given in [3]. The distribution of the GND's for two different sizes are depicted in figure 2. The SSD density field appears to be nearly size independent, where the largest SSD densities are found in the crystal



(a) $L = 1.0$ mm. **(b)** $L = 10$ mm.

Figure 2. Distribution of the characteristic GND density for two sample lengths at an equivalent strain of 1%.

core, related to the unhindered crystallographic slip in that region. The GND field appears to be strongly size dependent (figure 2), as the plastic inhomogeneities between the grain boundaries and the cores have to be accommodated by the GND field within a varying distance for the different sample sizes. This leads to the observed strengthening.

CONCLUSIONS

A strain gradient enhanced crystal plasticity model that incorporates the intrinsic role of dislocations in their various roles (SSD, GND, GBD) provides meaningful micromechanical predictions of inter- and intragranular deformations and associated size or strengthening effects.

References

[1] A. Acharya, J.L. Bassani, and A. Beaudoin. Geometrically necessary dislocations, hardening, and a simple gradient theory of crystal plasticity. *Scripta Materialia*, 48(2):167–172, 2003.
[2] P. Cermelli and M. E. Gurtin. Geometrically necessary dislocations in viscoplastic single crystals and bicrystals undergoing small deformations. *International Journal of Solids and Structures*, 39:6281–6309, 2002.
[3] L.P. Evers. *Strain gradient crystal plasticity based on dislocation densities.* PhD thesis, Eindhoven University of Technology, 2003.
[4] M. E. Gurtin. A gradient theory of single-crystal viscoplasticity that accounts for geometrically necessary dislocations. *Journal of the Mechanics and Physics of Solids*, 50:5–32, 2002.

METAL FORMING AND TEXTURE EVOLUTION MODELLING

Wiktor L. Gambin
Warsaw University of Technology, Division of Applied Mechanics PL 02-525 Warszawa, Poland
and IPPT PAN, Department of Theoretical Mechanics, PL 00-049 Warszawa, Poland

Summary A description of plastic anisotropy evolution due to texture development during metal forming processes is presented. It bases on the model of single crystal with the regularized Schmid law. The single crystal model is used to description of polycrystal behaviour basing on the Taylor assumption. The approach makes possible to predict a texture development in plastically deformed elements during the metal forming processes. The associated evolution of plastic anisotropy in drawing wires, rolled or sheared sheets is discussed.

INTRODUCTION

In the metal forming processes, the crystals of deformed elements are seldom oriented completely at random. At first, during the casting process, due to solidification, grains are formed along a specific crystallographic direction. Next, through subsequent plastic deformations, the crystals rotate to certain stable orientations. Finally, upon the recrystallization process, new crystals are formed. All these processes lead to the development of non-random grain orientations, known as textures. It is commonly known, that many of the physical, mechanical and chemical properties of single crystals vary with the crystallographic directions and planes. Thus, a textured polycrystalline material usually exhibits anisotropic properties. Depending on the texture and the use of the material, the property of anisotropy may or may not be a desirable feature from the practical point of view. This is the reason that much research on the texture development and the principles governing such development has been conducted recently. Below, it is presented a model of polycrystal plastic behaviour observed during metal forming processes. It is a generalization of the model of a single crystal behaviour proposed in the papers [1-3] and described in the book [4].

SINGLE CRYSTAL BEHAVIOUR

At first, recall the model of single crystal behaviour introduced independently by Arminjon [1] and by Gambin [2]. Consider a single metallic grain with M slip systems $\{\boldsymbol{m}^{(r)}, \boldsymbol{n}^{(r)}\}$, for $r = 1,..., M$, where $\boldsymbol{m}^{(r)}$ is the unit vector of slip direction, and $\boldsymbol{n}^{(r)}$ — the unit vector orthogonal to the slip plane of the r-th slip system. The orientation of crystallographic lattice is described by 3 Euler angles $(\varphi_1, \Phi, \varphi_2)$. For a given stress tensor $\boldsymbol{\sigma}$, one can introduce the resolved shear stress $\tau^{(r)} = \boldsymbol{m}^{(r)} \boldsymbol{\sigma}\, \boldsymbol{n}^{(r)}$ on the slip plane prescribed by the unite vector $\boldsymbol{n}^{(r)}$ and in the slip direction given by the unite vector $\boldsymbol{m}^{(r)}$. A glide of the on the r-th slip system appears when $\tau^{(r)}$ reaches its critical value $\tau_{cr}^{(r)}$. As the yield condition for single metallic grain, the following $2n$-th order polynomial is assumed:

$$\sum_{r=1}^{M} \left(\frac{\tau^{(r)}}{\tau_{cr}^{(r)}} \right)^{2n} - m = 0 , \tag{1}$$

where $m > 0$ and $1 \leq n \leq 20$ are non-dimensional material constants of the considered grain. The above polynomial describes a smooth, but strongly non-linear yield surface with rounded-off corners [2]. Denote by $\boldsymbol{D}^p$ the strain rate tensor, and by $\boldsymbol{\Omega}^p$, the plastic spin tensor. The assumed smooth yield condition generates the conjugate flow rule and the plastic spin rule, respectively:

$$\boldsymbol{D}^p = \frac{1}{2} \lambda \sum_{r=1}^{M} \frac{1}{\tau_{cr}^{(r)}} \left(\frac{\tau^{(r)}}{\tau_{cr}^{(r)}} \right)^{2n-1} \left(\boldsymbol{m}^{(r)} \boldsymbol{n}^{(r)} + \boldsymbol{n}^{(r)} \boldsymbol{m}^{(r)} \right), \quad \boldsymbol{\Omega}^p = \frac{1}{2} \lambda \sum_{r=1}^{M} \frac{1}{\tau_{cr}^{(r)}} \left(\frac{\tau^{(r)}}{\tau_{cr}^{(r)}} \right)^{2n-1} \left(\boldsymbol{m}^{(r)} \boldsymbol{n}^{(r)} - \boldsymbol{n}^{(r)} \boldsymbol{m}^{(r)} \right) \tag{2}$$

where the coefficient $\lambda > 0$ is the same for all slip systems. The above relations may be used to formulation of rigid-plastic [2] or elastic-plastic [3] model of single crystal behaviour. In both cases, for a given stress given stress $\boldsymbol{\sigma}$ acting on the crystal, one can find an adequate velocity field $\boldsymbol{v}$ and the total spin of the crystal $\boldsymbol{\Omega}$. On the other hand, the lattice spin of the crystal is given by the rule $\boldsymbol{\Omega}^* = \boldsymbol{\Omega} - \boldsymbol{\Omega}^p$. Because, the lattice spin $\boldsymbol{\Omega}^*$ is described by time derivatives of the Euler angles $(\dot{\varphi}_1, \dot{\Phi}, \dot{\varphi}_2)$, one can determine the increments $(\Delta\varphi_1, \Delta\Phi, \Delta\varphi_2)$ uniquely describing grain reorientations at each step of the considered deformation process [4].

MODEL OF CRYSTAL AGGREGATE

Assume that polycrystalline element contains grains with the same kind of the crystallographic lattice. Let the element consists of N groups of grains with the same lattice orientation. Denote by $\kappa^{(g)}$ the volume ratio of grains with the orientation g (g = 1,…, N) to all grains of the element. For each group of grains the material constants $m^{(g)}$ in Eq. 1 are prescribed. If a stress tensor $\boldsymbol{\sigma}$ is applied to the element, we have the same resolved shear stress $\tau^{(r,g)}$ and the critical shear stress $\tau_{cr}^{(r,g)}$ in all grains of the g-th group. It is convenient to introduce the reference critical shear stress τ_{cr}, which is the critical shear stress for a fixed group of grains and a fixed slip system. Denote by $\bar{\tau}^{(r,g)}$ the ratio $\tau^{(r,g)}/\tau_{cr}$. Then the yield surface for polycrystalline element will be described by the following $(2\bar{n})$-th order polynomial [5]:

$$\sum_{g=1}^{N} \kappa^{(g)} \frac{1}{m^{(g)}} \sum_{r=1}^{M} \left(\frac{\tau^{(r,g)}}{\bar{\tau}_{cr}^{(r,g)}} \right)^{2\bar{n}} = \tau_{cr}^{2\bar{n}}, \tag{3}$$

where exponent $\bar{n}$ belongs to the interval $1 < \bar{n} < 8$. Then, the plastic corners of polycrystalline yield surface are more rounded than the yield surface of single crystal ($0 < n < 20$). The plastic flow rule (2) and the plastic spin rule (3) for single crystals are conjugated with the polycrystalline yield surface (4). Consider a polycrystalline element under a plastic deformation. Assuming the Taylor model of polycrystal behaviour, that the plastic strain rate $\boldsymbol{D}^p$ in each of the grains is the same, one can calculate lattice reorientations caused by the given deformation. The above reorientations will change the directions of vectors $\boldsymbol{m}^{(r,g)}$ and $\boldsymbol{n}^{(r,g)}$, and then the quantity $\tau^{(r,g)} = \boldsymbol{m}^{(r,g)} \boldsymbol{\sigma} \boldsymbol{n}^{(r,g)}$. We may observe the *texture development* caused by plastic deformation of the polycrystalline element. On the other hand, we have to do with change of a shape of the yield surface. It leads to generation of plastic anisotropy in the element.

TEXTURE DEVELOPMENT SIMULATION

To describe the texture development, changes of pole figures for drawing of wires with diameter diminishing 2, 5 and 10 times are shown. The same results are given for rolling of sheets with thickness diminishing 2, 5, and 10 times and for pure shear of a metal sheet. Next, the associated evolution of plastic anisotropy in the drawn wires, the rolled sheets and the sheets under pure shear, are analysed. To do it, changes of shape of the plastic yield surfaces are discussed. On the above surfaces, we may observe a shift of plastic corners causing a change of plastic flow direction. Independently, an influence of texture development in the rolled sheets on variations of the Lankford coefficient is shown. Its distribution on the sheet plane, that enables to predict a form and place of strain localization, is discussed in details.

CONCLUSIONS

The presented models of single grain and polycrystalline element based on the concept of yield surfaces with rounded corners are good tools for prediction of texture development in plastically deformed metals. Within the rate-independent plasticity, the single grain model overcomes the problem of non-uniqueness in the choice of active slip systems. Although this problem may be solved with the help of rate-dependent approach, the proposed formulation eliminates influence of viscous effects. It allows the use of standard FEM procedures in numerical analysis of polycrystals.

Acknowledgement
The State Committee for Scientific Research of Poland (KBN) supported this work within framework of the research project KBN 5 T07A 031 22

References

[1] M. Arminjon, A regular form of the Schmid law, *Textures and Microstructures* **14-18**, 1121-1128, 1991 (referred to the 9th ICOTOM meeting, Avignon, September 1990).

[2] W. Gambin, Crystal plasticity based on yield surfaces with rounded-off corners, *ZAMM* **71**, 4, T 265-T 268, 1991 (referred to the GAMM Conference, April, 1990).

[3] W. Gambin, Refined analysis of elastic-plastic crystals, *Int. J. Solids Structures* **29**, 16, 2013- 2021, 1992.

[4] W. Gambin, *Plasticity and Textures*, Kluwer Academic Publishers, Dordrecht 2001.

[5] K. Kowalczyk and W. Gambin, Model of plastic anisotropy evolution with texture dependent yield surface, *Int. J. Plasticity* **20,** 19-54, 2004.

LIMIT AND SHAKEDOWN ANALYSIS WITH DECOHESIVE EFFECTS

Dieter Weichert* , Abdelkader Hachemi
Institute of General Mechanics, RWTH, Templergraben 64, D-52056 Aachen, Germany
** at present: INSA-Rouen, Place Emile Blondel, F-76131 Mont-Saint-Aignan, France*

Summary A methodology to predict failure of composite materials is proposed. It is based on local shakedown analysis on the microscopic level of the composite and the use of homogenisation technique to determine the influence of each component (matrix, fiber and interface) on the macroscopic response of such composite.

INTRODUCTION

Local failure under variable loading can be considered as being caused by repeated, dissipative events occurring on the micro-structural level of materials. In this paper, the scale chosen for observation of these effects will be called "meso-scale", small compared to the scale for measuring the macroscopic dimensions of a mechanical structural element and large compared to the atomistic scale. We suppose that on this mesoscopic level the laws and methods of classical continuum-mechanics are applicable, but that the different components of the material can be recognised, forming a mechanical structure by itself on this level of observation. The interaction between these components determines the local response of the material, in particular the mechanisms leading to local damage and overall failure. Therefore, the study of these mechanisms on the meso-level of specific materials under complex loads can be helpful to better understand the causes of failure and methods developed for this purpose can be used in a constructive manner for the design of materials [1].
A particularly interesting class of materials for this kind of studies are composite materials. Their heterogeneity causes in general large gradients of the mechanical field quantities, initiating local damage and overall failure by the interaction of different local effects, which depend upon the mechanical and geometrical properties of the individual components of the composite. For certain types of composites realistic modelling should take into account not only inelastic behaviour of the matrix material but also debonding of the interfaces between matrix and reinforcements. Special attention has to be paid to the realistic reproduction of the mechanical behaviour of interfaces between matrix and reinforcements, observed in experiments [2]. It is important not only to understand and to model the mechanical effects for this type of materials on the meso-structural level but to link them to the characteristic macroscopic material properties. Here, averaging techniques such as the homogenisation technique [3] are proposed to bridge the gap between local (mesoscopic) and global (macroscopic) properties.
It is shown in this paper, how direct methods, namely limit and shakedown analysis, can help to assess composites which exhibit plastic deformations on the meso-scale and how this theory can be used in a constructive manner for the design of materials. In this contribution, the debonding process is modelled within the framework of interface damage mechanics, where the displacement discontinuities created by the progressive decohesion are related to constitutive equations extended by an anisotropic damage model [4].

DEFINITIONS AND BASIC ASSUMPTIONS

We consider in particular the problem of materials reinforced by straight fibres. The macroscopic behaviour of this heterogeneous material is observed on the scale **x** and the mesoscopic behaviour on the scale **y**. A significant characteristic of fibre-reinforced composites is the limited strength of the interface between fibres and matrix. The micromechanical representative element of total surface Ω presented herein includes the fibre phase, the matrix phase occupying the domains Ω_+ and Ω_-, respectively and the cohesive zone represented by the band-shaped domain Ω_δ of width $\delta << 1$ ($\Omega = \Omega_- \cup \Omega_+ \cup \Omega_\delta$), defined by

$$\Omega_\delta = \left\{ \mathbf{y} = \mathbf{y}_0 + \epsilon \mathbf{n} \;\middle|\; \forall \mathbf{y}_0 \in \Gamma, -\frac{\delta}{2} \le \epsilon \le \frac{\delta}{2} \right\}. \tag{1}$$

The strain field corresponding to the displacement field is derived as

$$\boldsymbol{\varepsilon} = \nabla_s \underline{\mathbf{u}} + (\llbracket \mathbf{u} \rrbracket \otimes_s \mathbf{n} \delta_R), \quad \forall \mathbf{y} \in \Omega, \tag{2}$$

where $\underline{\mathbf{u}}$ is the continuous displacement field and $\llbracket \mathbf{u} \rrbracket$ is the displacement jump vector, i.e. $\llbracket \mathbf{u} \rrbracket = \mathbf{u}^+ - \mathbf{u}^-$. Here, $\mathbf{u}^+$ and $\mathbf{u}^-$ are the displacement vectors at the interior and the exterior borders of the interface zone. $\mathbf{n}$ is the unit vector and δ_R is the Dirac-delta function. For the considered representative volume element (RVE) Ω, we adopt the usual homogenisation assumption for the local displacement field $\mathbf{u}$ at position $\mathbf{y}$

$$\mathbf{u} = \mathbf{E}.\mathbf{y} + \mathbf{u}^{per} \tag{3}$$

where $\mathbf{E}$ is the macroscopic strain tensor and $\mathbf{u}^{\text{per}}$ is a displacement field satisfying the periodicity conditions. Then, the Hill relationship [5] holds

$$\boldsymbol{\Sigma}(\mathbf{x}) = <\boldsymbol{\sigma}(\mathbf{y})> = \frac{1}{|\Omega|}\int_{\Omega} \boldsymbol{\sigma}(\mathbf{y})\, \mathrm{d}\Omega \text{ and } \mathbf{E}(\mathbf{x}) = <\boldsymbol{\varepsilon}(\mathbf{y})> = \frac{1}{|\Omega|}\int_{\partial\Omega} (\mathbf{u} \otimes_{\mathrm{s}} \mathbf{n})\, \mathrm{d}S. \tag{4}$$

Here, $\boldsymbol{\sigma}$ and $\boldsymbol{\varepsilon}$ are mesoscopic stresses and strains also satisfying the periodicity condition. Within the unit cell, $\boldsymbol{\varepsilon}$ and $\boldsymbol{\sigma}$ fulfil compatibility and equilibrium conditions, respectively.

FORMULATION OF LIMIT AND SHAKEDOWN PROBLEM

Adopting these definitions and hypotheses, the statical shakedown theorems can be stated as follows [6]:
If there exist a real number $\alpha > 1$, a time-independent field of periodic residual stresses $\boldsymbol{\sigma}^{(\mathrm{r})}$, a time-independent vector of traction forces $\boldsymbol{\tau}^{(\mathrm{r})}$ at the interface and an admissible domain P of macroscopic states of stress $\boldsymbol{\Sigma}$:

$$\mathrm{P} = \{\boldsymbol{\Sigma} \mid \exists\boldsymbol{\sigma}^{(\mathrm{s})}, \exists\boldsymbol{\tau}^{(\mathrm{s})};\ \boldsymbol{\sigma}^{(\mathrm{s})}(\mathbf{y}) \in \mathrm{F}(\mathbf{y}),\ \boldsymbol{\tau}^{(\mathrm{s})}(\mathbf{y}) \in \mathrm{G}(\mathbf{y})\} \tag{5}$$

then the fibre-reinforced composite material shakes down to the given domain of loading. Safe states of stresses $\boldsymbol{\sigma}^{(\mathrm{s})}$ and traction forces $\boldsymbol{\tau}^{(\mathrm{s})}$ are defined, resp., by

$$\boldsymbol{\sigma}^{(\mathrm{s})} = \alpha\,\boldsymbol{\sigma}^{(\mathrm{c})} + \boldsymbol{\sigma}^{(\mathrm{r})},\ \ \boldsymbol{\tau}^{(\mathrm{s})} = \alpha\,\boldsymbol{\tau}^{(\mathrm{c})} + \boldsymbol{\tau}^{(\mathrm{r})} \tag{6}$$

such that

$$\mathrm{F}(\mathbf{y}) = \left\{\boldsymbol{\sigma}^{(\mathrm{s})} \mid f(\boldsymbol{\sigma}^{(\mathrm{s})}, \mathbf{y}) < 0,\ \forall\mathbf{y} \in \Omega_{-} \cup \Omega_{+}\right\} \text{ and } \mathrm{G}(\mathbf{y}) = \left\{\boldsymbol{\tau}^{(\mathrm{s})} \mid g(\boldsymbol{\tau}^{(\mathrm{s})}, \mathbf{d}, \mathbf{y}) \le 0,\ \forall\mathbf{y} \in \Omega_{\delta}\right\} \tag{7}$$

Here, $\boldsymbol{\sigma}^{(\mathrm{c})}$ and $\boldsymbol{\tau}^{(\mathrm{c})}$ are respectively, the stress field and the traction forces in a purely elastic representative volume element under the same boundary conditions as for the RVE of the original problem, $\boldsymbol{\sigma}^{(\mathrm{r})}$ and $\boldsymbol{\tau}^{(\mathrm{r})}$ are the fields of the residual stresses satisfiying the periodicity conditions and residual traction forces, resp., f is the yield function and g the inelastic gap potential defined by

$$g(\boldsymbol{\tau}^{(\mathrm{s})}, \mathbf{d}, \mathbf{y}) = \left[\left(\frac{\tau_{\mathrm{n}}^{(\mathrm{s})}}{1-d_{\mathrm{n}}}\right)^2 + \frac{1}{\beta^2}\left(\frac{\tau_{\mathrm{t}}^{(\mathrm{s})}}{1-d_{\mathrm{t}}}\right)^2\right]^{1/2} - \sigma_{\max} \le 0,\ \ \forall\mathbf{y} \in \Omega_{\delta} \tag{8}$$

Here, $\sigma_{\max}$ is a measure of bond strength of the cohesive zone and β is the interface shear-to-normal strength ratio. The variables d_{n} and d_{t} are respectively the normal and the tangential damage variables.

CONCLUSIONS

The presented methodology shows how to apply direct method more realistically to composites by including the process of decohesion between fibres and matrix. The addressed failure mechanism is taken into account by using the concept of a cohesive zone between fibre and matrix. Also, failure due to an unlimited accumulation of the inelastic deformation in the matrix is accounted for. The developed method is applied practically by using finite element analysis and mathematical programming. Illustrative examples will be presented.

Acknowledgement
The authors gratefully acknowledge the support provided for this research by the Deutsche Forschungsgemeinschaft (DFG grant no. WE 736/22).

References

[1] Weichert D., Hachemi A.: Shakedown- and limit analysis of periodic composites. *J. Theo. Appl. Mech.* **40**: 273-289, 2002.
[2] Carrère N., Kruch S., Vassel A., Chaboche J.-L.: Damage mechanisms in unidirectional Sic/Ti composites under transverse creep loading: Experiments and modeling. *Int. J. Damage Mech.* **11**: 41-63, 2002.
[3] Suquet P.: Plasticité et Homogénéisation. *PhD. Thesis*, Université Pierre et Marie Curie, Paris 6, 1982.
[4] Döbert C., Mahnken R., Stein E.: Numerical simulation of interface debonding with a combined damage/friction constitutive model. *Comput. Mech.* **25**: 456-467, 2000.
[5] Hill R.: Elastic properties of reinforced solids: some theoretical principles. *J. Mech. Phys. Solids* **11**, 357-372, 1963.
[6] Weichert D., Hachemi A., Schwabe F.: Shakedown analysis of composites. *Mech. Res. Comm.* **26**: 309-318, 1999.

A CONSTITUTIVE LAW FOR GLASSY POLYMERS AND BLENDS

F. Zaïri*, K. Woznica**, M. Naït Abdelaziz*, J.-M. Gloaguen*
*Polytech'Lille, Avenue P. Langevin, 59655 Villeneuve d'Ascq Cedex, France
**ENSI of Bourges, 10 boulevard Lahitolle, 18020 Bourges Cedex, France

Summary This work deals with modified constitutive equations for the viscoplastic behaviour of homogeneous glassy polymers at isothermal loading. A procedure for determining model parameters is proposed. The modified model is next coupled with a micromechanic formulation to investigate the macroscopic mechanical response of RT-PMMA.

VISCOPLASTIC MODEL

The glassy polymers behaviour is known to be highly nonlinear and sensitive to many parameters like strain rate and temperature. Traditionally, viscoplastic behaviour of glassy polymers is studied by testing under constant strain rates. This behaviour is generally characterized by intrinsic strain softening immediately after yield, followed by progressive strain hardening. Since the viscoplastic deformation mechanisms are not very well understood, certain authors have introduced an approach based on phenomenological considerations by using for example models developed for metals. Indeed, although the deformation mechanisms of polymers and metals are different, on a phenomenologic point of view, such viscoplastic constitutive equations can be used to model the nonlinear and strain rate dependent behaviour of polymers. Particularly, by considering macroscopic formulations, constitutive models based upon internal state variables can be used to simulate flow molecular resistance.
The effects of temperature are not considered in order to simplify constitutive equations and the phenomena such as relaxation and recovery are not accounted for in these. The strain rate is decomposed into an elastic and a viscoplastic part. In this study, the Bodner and Partom state variable constitutive equations [1] has been used to describe the highly nonlinear behaviour and strain rate sensitivity of glassy polymers. Such a model is based upon a thermodynamics formalism of irreversible processes and has been originally developed for metals viscoplasticity. The cumulated viscoplastic strain rate expression used in this investigation is a simplified form of that proposed by Frank and Brockman [2]. To account for the effect of strain softening a new internal state variable has been also introduced.
A method for the determination of the seven independent strain rate material parameters is developed, using tension or compression simple tests across a variety of strain rates. The yield stress allows to determine two parameters, the others are determined from the work hardening rate [1].
The nonlinear differential equations, of the viscoplastic modified model, are integrated using an explicit integration scheme. The trapezoidal method is employed in this study. The parameters of the modified model are determined, in a first step, from isothermal uniaxial experimental data extracted from the literature of two representative glassy polymers (amorphous PET and PMMA). A good agreement is observed between experimental data and the predictions of the modified model.

VISCOPLASTIC MODEL INCLUDING DAMAGE

The addition of low modulus rubber particles into brittle glassy polymers is commonly employed to increase their toughness. If the toughening of modified glassy polymers is understood in a qualitative manner, very few quantitative data have been published.

The rubber-toughened material selected in this work consists of a polybutadiene core-shell particles (30% in volume fraction) dispersed in polymethyl methacrylate (RT-PMMA). This blend is known to have favorable properties and significant volumic growth. Tensile test program was conducted on an hydraulic Instron device to determine the effects of strain and strain rate on the global mechanical behaviour and on void volume fraction. Notched specimen have been produced and deformed under uniaxial tension, under constant true strain rate during the test, for a range of strain rates and at room temperature. The true stress-true strain curves and the volume variation have been determined at the same time using video measurements. Data are determined in the region where the deformation is localized and permits evaluation of the mechanisms and their sequence in RT-PMMA.

The viscoplastic constitutive equation, describing the mechanical behaviour of the polymeric matrix, is coupled with internal damage including both cavitation and growth of voids as introduced in [3-4]. The cavitation is here controlled by the hydrostatic stress [5]. The material parameters appearing in the new micromechanical model are determined from this set of uniaxial test. The predictions of the modified model including damage are generated and compared with experimental data at each strain rate and permit to verify the ability of the model to correctly predict qualitatively and quantitatively the nonlinearity, strain rate dependence and growth of voids at the same time.

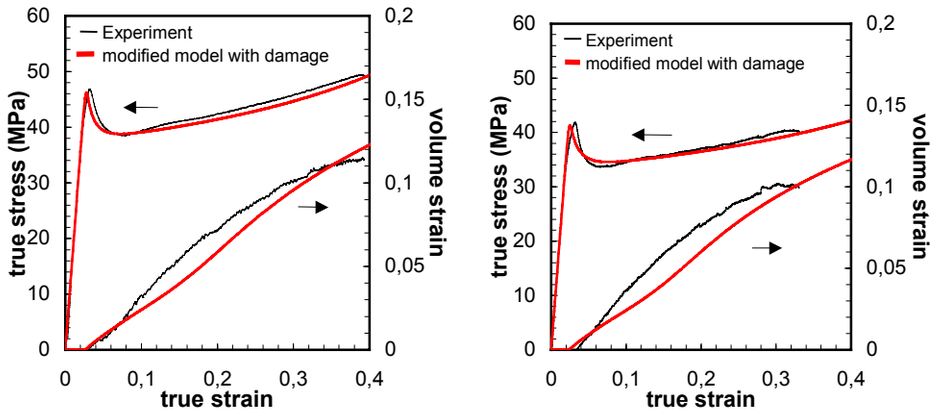


Fig.-True stress-true strain curve and volume strain-true strain curve for RT-PMMA at $10^{-3}s^{-1}$ (left) and at $10^{-4}s^{-1}$ (right).

References

[1] Chan K.S., Bodner S.R., Lindholm U.S.: Phenomenological modelling of hardening and thermal recovery in metals, ASME, J. Eng. Mater. Technol. ***110*** *1-8, 1988*.

[2] Frank G.J., Brockman R.A.: A viscoelastic-viscoplastic constitutive model for glassy polymers, Int. J. Solids Struct. ***38*** *5149-5164, 2001*.

[3] Gurson A.L.: Continuum theory of ductile rupture by void nucleation and growth. PartI: Yield criteria and flow rules for porous ductile media, Trans. A.S.M.E. J. Engng. Mat. Tech. ***99*** *2-15, 1977*.

[4] Tvergaard V.: Influence of voids on shear band instabilities under plane strain conditions, Int. J. Fract. ***17*** *389-407, 1981*.

[5] Jeong H.Y.: A new yield function and a hydrostatic stress-controlled void nucleation model for porous solids with pressure-sensitive matrices, Int. J. Solids Struct. ***39*** *1385-1403, 2001*.

DEVELOPMENT AND IDENTIFICATION OF A PROBABILISTIC TWO-SCALE MODEL FOR HIGH CYCLE FATIGUE PREDICTION

Cédric DOUDARD*, Sylvain CALLOCH*, Philippe CUGY**, André GALTIER** and François HILD*

* Laboratoire de Mécanique et Technologie
61, Avenue du Président WILSON
94235 CACHAN CEDEX - FRANCE

** IRSID
Voie romaine
BP 30320 – 57283 MAIZIÈRES-LÈS-METZ - FRANCE

INTRODUCTION

The present paper is concerned with the development of a probabilistic two-scale model for HCF that accounts for the failure of sample but also for the thermal effects during cyclic loadings. We assume that HCF damage is localized at the microscopic scale. So the microplasticity appears without affecting the behaviour of the material at the macroscopic scale. The development of the model is presented in three successive stages. In the first one, the model is deterministic and we show how to interpret the thermal effects by integrating the conduction heat equation. So we justify the empirical method proposed to estimate quickly the mean fatigue limit. We improve then the model by introducing a probabilistic characteristic at the microscopic scale. We assume that the number of active sites, i.e. a site whose the microplasticity appears, follows a Poisson process. We show that the new model represents better the thermal effects than the first model. With this approach the scatter can be determined but not the mean fatigue limit of a fatigue sample. A method of identification is also proposed. It is based on the analysis of the thermal effects for the scatter and is applied on a dual-phase steel. A first validation of the model is effected by predicting the scatter of the S/N curve. And a second validation is proposed by showing a good agreement between the experimental result and the predicted model for bending fatigue test.

BEHAVIOUR OF A DUAL-PHASE STEEL UNDER CYCLIC LOADINGS

The material studied is here in a ferrite-martensite dual-phase steel grade (around 15% of martensite). This steel offers a better combination of strength and ductility than other conventional steels.

To evaluate the fatigue properties of dual-phase steel, temperature measurements are used. It consists in applying successive series of 3000 cyclic loadings (Fig 1) for different increasing stress amplitudes Σ_0 (Fig 2). For each load amplitude, the change of the temperature $\Delta = T\text{-}T_0$ (T, the temperature of the sample during the test obtained by a thermocouple and T_0 the initial temperature) is recorded (Fig 3). The mean temperature becomes stable after some cycles and equals $\bar{\Delta}(\Sigma_0)$. Figure 4 shows the change of the steady state mean temperature $\bar{\Delta}(\Sigma_0)$ with the load amplitude for a dual-phase steel for two different tests. We can see that the test is reproducible. This result is obtained by different authors [1, 2]. We observes that $\bar{\Delta}(\Sigma_0)$ suddenly increases as the load level is close to the fatigue limit of the material. This evolution can be explained by the occurrence of the first slip bands on the surface [1].

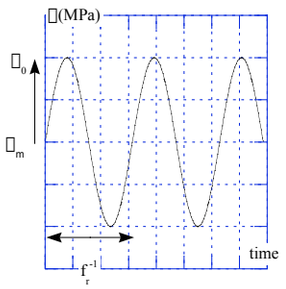


Figure 1. Cyclic loadings

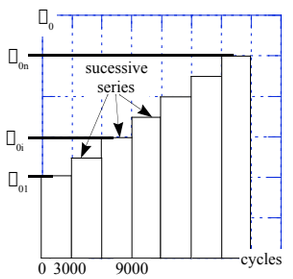


Figure 2. Loadings for different increasing stress amplitudes Σ_0

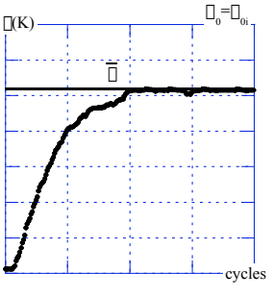


Figure 3. Change of the temperature during 3000 cyclic loadings

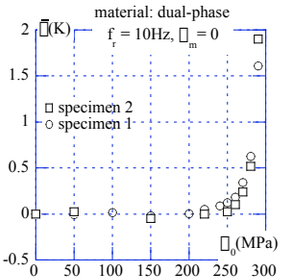


Figure 4. Steady state mean temperature versus load amplitude

A DETERMINISTIC TWO-SCALE MODEL

The two-scale model has been developed by Lemaitre and Doghri [4] in a deterministic way. It is based on the hypothesis that HCF damage is localized at the microscopic scale, whose dimensions are smaller than those of the

representative volume element (RVE) associated to the mesoscopic scale. Consequently, two phases are considered in the model. The first one is an inclusion standing for grains where local plasticity is developed; the second one is the matrix describing the other grains whose behaviour remains elastic. We assume that the two phases have got the same elastic behaviour and that the yield stress of the elasto-plastic inclusion σ_y is less than that of the surrounding material. The constitutive equations of the model are resumed by the following relations:

Strain decomposition in the inclusion: $\underline{\varepsilon} = \underline{\varepsilon}^e + \underline{\varepsilon}^p$ Yield surface in the inclusion: $f = J_2(\underline{\sigma} - \underline{X}) - \sigma_y \leq 0$

Normality rule: $\dot{\underline{\varepsilon}}^p = \dot{\lambda}\frac{\partial f}{\partial \underline{\sigma}}$ Kinematic hardening: $\dot{\underline{X}} = \frac{2}{3}C\dot{\underline{\varepsilon}}^p$

Law of localization: $\underline{\varepsilon} = \underline{E} : \underline{\sigma} + 2\varepsilon_0(1-\beta)\underline{\varepsilon}^p$ Dissipated energy for a loading cycle: $D = \frac{4 f_v \sigma_y}{h}\langle \varepsilon_0 - \varepsilon_y \rangle$

The previous model is now used to analyse the heat transfer induced by the intrinsic dissipation D. The heat equation is deduced from the two first principles of thermodynamics. Let us assume that the convective terms of the material time derivative and the coupling between temperature and hardening variable are negligible and that the external heat supply r is time independent, the local heat conduction equation is given by [5]:

$$\rho c \dot{T} - k\Delta T = D + T\frac{\partial \sigma_{eq}}{\partial T}\Big|^{\varepsilon} : \dot{\varepsilon}^p$$

and the mean steady state temperature is given by the following equation obtained by the resolution of local heat conduction equation:

$$\bar{\theta} = \frac{4 f_v f_r \sigma_{eq} \sigma_y}{h\rho c}\langle \varepsilon_0 - \varepsilon_y \rangle$$

Figure 5 shows the result of the identification of the model. The following section deals with an improvement of the present approach by considering that the microscopic yield stress are scattered.

A PROBABILISTIC TWO-SCALE MODEL

Let us assume that the microscopic yield stress is a probabilistic variable. An active site (in terms of fatigue mechanism) is defined as a site whose the applied stress is greater than the microscopic yield stress. These sites are assumed to be described by a Poisson point process. In this context, it can be shown that the mean state temperature is given by the following relation:

$$\bar{\theta} = \theta V_0 \frac{m}{(m+1)(m+2)} \frac{\sigma_0^{m+2}}{V_0 \sigma_0^m}$$

Figure 6 shows the result of the identification of the probabilistic two-scale model. We can see that the thermal effects are accurately reproduced by the model. The validation of the probabilistic two-scale model is based on the prediction of the scatter of the experimental fatigue result (Fig.7).

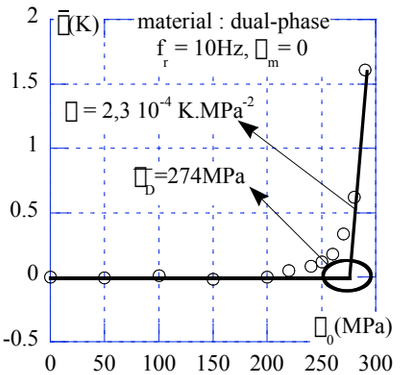


Figure 5. Identification of DTSM

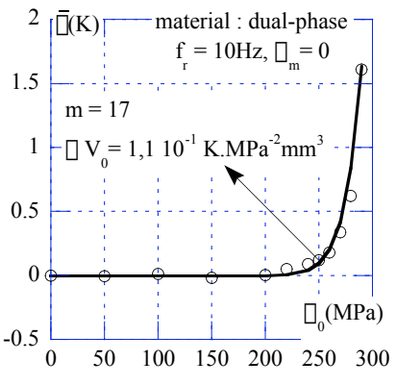


Figure 6. Identification of PTSM

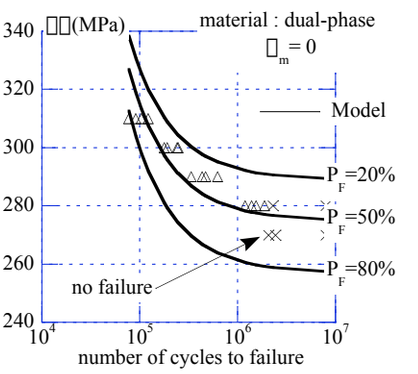


Figure 7. Validation of PTSM

References

[1] Galtier A., Bouaziz O. and Lambert A.: Influence de la microstructure des aciers sur leurs propriétés mécaniques. Méc. Ind., 457-462, 2002.

[2] Mabru C., Chrysochoos A.: Dissipation et couplages accompagnant la fatigue de matériaux métalliques. Photo-méca, 375-382, 2001.

[3] Lemaitre J., and Doghri F.: Damage 90: a post processor for crack initiation. Comput. Methods Appl. Mech. Engrg., **115**:197-232, 1994.

[4] Chrysochoos A., Louche H.: An infrared image processing to analyse the calorific effects accompanying strain localisation. Int. J. of Eng. Sc., **38**:1759-1788, 2000.

XXI ICTAM, 15–21 August 2004, Warsaw, Poland

MODELING THE CRYSTALLOGRAPHIC TEXTURE EVOLUTION BASED ON THE MAXIMUM ENTROPY METHOD

Thomas Böhlke, Albrecht Bertram
Institute of Mechanics, Otto-von-Guericke-University Magdeburg, PO box 4120, D-39016 Magdeburg, Germany

Summary We present a new approach for modeling the texture induced anisotropy that is based on a tensorial Fourier expansion of the crystallite orientation distribution function (CODF). The general evolution equations for the Fourier coefficients are derived. By this approach the texture evolution can be described by modeling some low order Fourier coefficients and by estimating the higher order coefficients based on the maximum entropy method. It is shown that such a low dimensional approach of the CODF yields a reasonable description of the texture evolution and represents a versatile alternative to classical mixture theories (Taylor, Sachs).

INTRODUCTION

The distribution of crystal orientations is an important microstructural feature which affects the overall properties of polycrystalline metals. If this distribution is inhomogeneous, the material has a crystallographic texture. Such a texture influences the overall elastic and the overall viscoplastic behavior as well as the non-mechanical properties of a polycrystal. The distribution of crystal orientations can be described by correlation functions. In texture analysis, the one-point correlation function is called crystallite orientation distribution function. It specifies the volume fraction of crystals having a specific orientation. A crystal orientation can be identified by a proper orthogonal tensor.
Phenomenological models seem to be generally unable to adequately represent the evolution of the crystallite orientation distribution. Therefore, if the evolving texture has to be taken into account in the context of finite element simulations, e.g. of deep drawing processes, in most cases mixture theories (Taylor, Sachs) are applied. In these cases, the texture evolution is described by a system of (algebro-) differential equations. The dimension of such a system is in between 300 - 10000. Hence, at each integration point of the finite element mesh, large systems of differential equations have to be integrated. This fact considerably limits the number of degrees of freedom that can be handled by standard finite element codes. Therefore, there is a need for homogenization strategies which allow to condense the number of degrees of freedom and nevertheless accurately describe the crystallite orientation distribution function.

ELEMENTARY BOUNDS

In the present work, the viscoplastic properties of a textured aggregate of face-centered cubic (fcc) crystals are considered. The advantage of a viscoplastic modeling is that on both scales, the grain scale as well as on the macro scale, the constitutive equations are given by potential relations. Furthermore, the methods of statistical continuum mechanics allow to bound the macroscopic potentials. In the most simple case, the one-point correlation function of crystal orientations is taken into account, which contains only the volume fraction information of the microstructural features. The corresponding bounds are called elementary bounds.

COORDINATE-FREE REPRESENTATION OF A CRYSTALLOGRAPHIC TEXTURE

There exist different approaches for the representation of the CODF. The classical representation by generalized harmonic functions was introduced by Bunge (1965) and Roe (1965). Later on, Adams et al. (1992) introduced a tensorial Fourier expansion of the CODF (see also, Zheng and Fu, 2001). Both representations are principally equivalent. The advantage of the tensorial representation is that it is coordinate-free. Therefore, the texture coefficients that occur in the tensorial representation can be used as micro-mechanically defined and measurable internal variables in continuum mechanics (Böhlke and Bertram, 2003). The general evolution equations for the Fourier coefficients are derived. The evolution equations contain only microscopic parameters and depend on the current CODF. If only a limited number of texture coefficients is taken into account, then the CODF has to be estimated based on these coefficients in order to specify the evolution equation.

MAXIMUM ENTROPY METHOD

How to estimate the CODF, if a fixed number of leading tensorial Fourier coefficients is known? The estimate has to be consistent in the way that it is nonnegative and normalized. Such a type of a problem is usually called moment problem. Moment problems are well known in statistical mechanics and other areas of science. The estimate of a distribution function based on incomplete data is not unique. One way to single out a solution of the aforementioned problem is to maximize the (information-theoretic) entropy of the CODF. In this contribution the moment problem is stated in terms of tensorial texture coefficients. It is shown that the so called crystallographic exponential family, here introduced with tensorial coefficients, solves the moment problem. The tensor-valued functions, which have to be solved in order to specify the exponential form have been formulated for all tensor ranks that occur in the tensorial Fourier expansion (Böhlke, 2004).

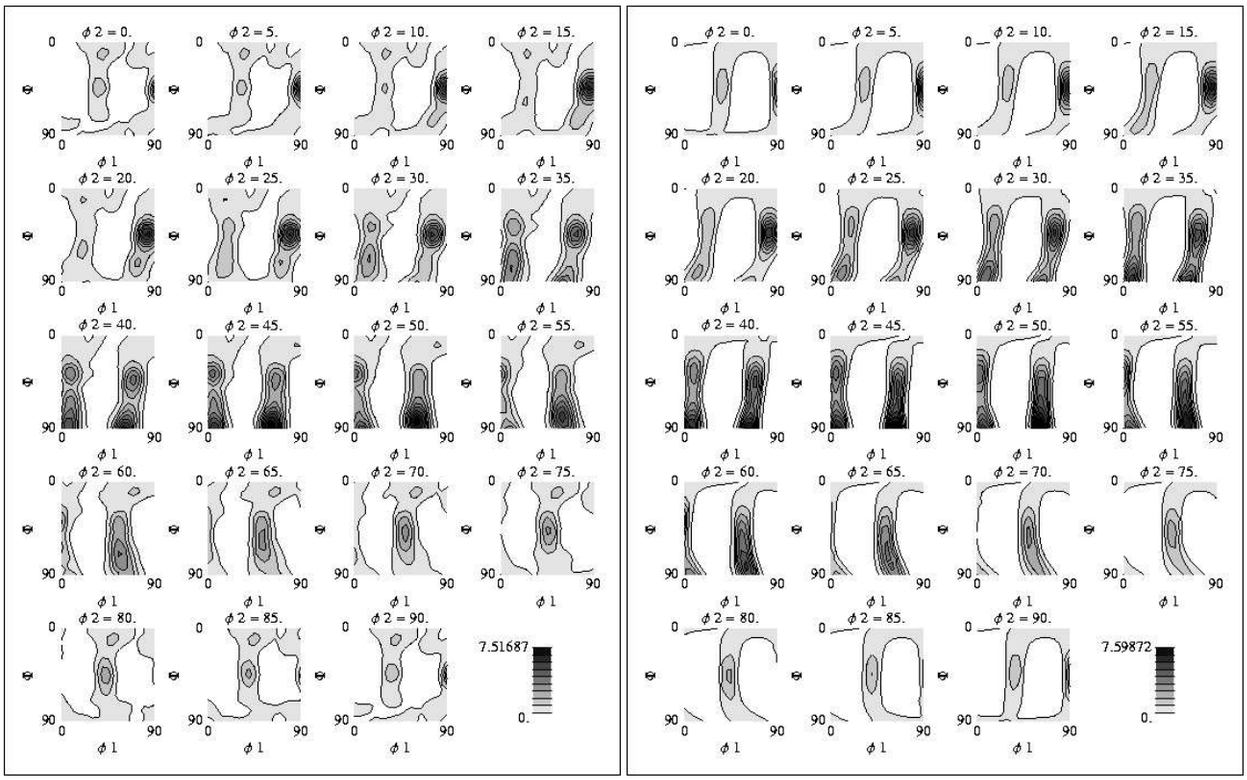


Figure 1. Left: Prediction of the classical formulation of the Taylor model with 1000 discrete crystal orientations. Right: Suggested model based on 22 internal variables (texture coefficients).

The numerical solution of the governing equations is obtained by a combination of an adaptive integration scheme on the orientation space and Newton's method.

If the evolution equations for the texture coefficients are combined with the maximum entropy estimate of the CODF, then it is possible to model the time evolution of the CODF. In this case a much smaller number of internal variables is needed compared to the classical formulation of the Taylor model. Fig. 1 shows a representation of the CODF in the Euler angle space for a simple shear deformation of an initially uniform orientation distribution. The left figure shows the CODF predicted by the Taylor model based on 1000 discrete crystal orientations, i.e. 3000 internal variables describing the orientation distribution. The right figure shows the predicted final CODF based on the 4th- and 6th-order texture coefficients and the maximum entropy method. The 4th-order tensorial coefficient contains 9 independent components and the 6th-order coefficient has 13 independent components.

References

Adams, B., Boehler, J., Guidi, M., Onat, E., 1992. Group theory and representation of microstructure and mechanical behavior of polycrystals. J. Mech. Phys. Solids 40 (4), 723–737.

Böhlke, T., 2004. Application of the maximum entropy method in texture analysis. To appear in: Computational Materials Science .

Böhlke, T., Bertram, A., 2003. Modeling of deformation induced anisotropy in free-end torsion. Int. J. Plast. 19, 1867–1884.

Bunge, H.-J., 1965. Zur Darstellung allgemeiner Texturen. Z. Metallkde. 56, 872–874.

Roe, R., 1965. Description of crystalline orientation of polycrystalline materials. III. General solution to pole figure inversion. J. Appl. Phys. 36, 2024–2031.

Zheng, Q.-S., Fu, Y.-B., 2001. Orientation distribution functions for microstructures of heterogeneous materials: II Crystal Distribution functions and irreducible tensors restricted by various material symmetries. Appl. Math. Mech. 22 (8), 885–903.

AN ELASTOPLASTIC MODEL FOR PREDICTION OF PERMANENT DEFORMATIONS OF UNBOUND GRANULAR PAVEMENT LAYERS

Absamad Elabd*,**, Pierre Hornych*, Denys Breysse**, Alain Denis**, Cyril Chazallon***

*Laboratoire Central des Ponts et Chaussées, Centre de Nantes, France
**Centre de Développement des Géosciences Appliquées, Université de Bordeaux 1, France
***Laboratoire de Modélisation Mécanique des Matériaux et des Structures de Génie Civil, Université de Limoges, Egletons, France

Summary This paper presents a simplified method for modelling of permanent deformations in order to estimate the rutting of low traffic flexible pavements. The method is based on an elastoplastic model of prediction of permanent deformations recently developed and consists in integrating the permanent strains along the vertical direction in order to obtain the vertical displacements in the structure (i.e. rutting of the layer).

CONTEXT

Rutting is one of the main causes of damage in low traffic flexible pavements and recent studies, dealing with the improvement of design methods for flexible pavements, have pointed out the key role of permanent deformations in the unbound granular layers. In spite of this, adequate methods for predicting permanent deformations in unbound pavement material are lacking.

The objective of this study is the prediction of the rutting of several experimental low traffic pavement structures tested on the LCPC accelerated pavement testing facility. A simplified method using an elastoplastic model for permanent deformations of unbound granular layers allow to estimate the vertical displacement of the structure.

This method is based on three steps :

. The material is characterised using repeated load triaxial tests, with different stress levels.
. The tests results are analysed using a model of prediction of permanent deformations. The model selected is an elastoplastic model developed by C. Chazallon [1]. A finite element analysis, with the program CESAR-LCPC, is used to determine the stress distribution in the pavement, and subsequently the permanent deformations.
. The permanent strains are integrated along the vertical direction to obtain the vertical displacements in the structure (i.e. rutting of the layer).

TRIAXIAL TESTS ON UNBOUND GRANULAR MATERIAL

The repeated load triaxial tests were performed with a triaxial apparatus for subgrade soils, designed for 76 mm diameter specimens. A new approach proposed by G. Gidel [2] was adopted for cyclic triaxial tests. It consists in applying cyclic loadings where the axial stress and the confining pressure vary in phase (different stress paths with constant stress ratios q/p).

MODELLING OF PERMANENT DEFORMATIONS

The elastoplastic model for permanent deformations recently developed by C. Chazallon (2000) is based on the yield function and plastic potential of the non associated model of Hujeux [3] in its simplest formulation.
The yield function is given by :

$$f = \sqrt{\frac{27}{2}}\,\frac{S_{II}(\underline{\underline{s}} - \underline{\underline{X}})}{M I_I(\underline{\underline{s}} - \underline{\underline{X}})} + rb\ln\left(\frac{I_I(\underline{\underline{s}} - \underline{\underline{X}})}{3p_c}\right)$$

where I_I is the trace operator, S_{II} is the deviatoric stress operator, b is a parameter which controls the shape of the yield surface in the (p, q) plane. M is the slope of the critical state line in the (p, q) plane and p_c is the critical pressure corresponding to the actual void ratio.

This equation is completed by the definition of a non associated plastic potential g and the following kinetic :

$$d\boldsymbol{e}_p = d\boldsymbol{l}\frac{\partial g(\underline{\boldsymbol{s}},\boldsymbol{a})}{\partial \underline{\boldsymbol{s}}}$$

where

$$g = \sqrt{\frac{27}{2}}\frac{S_{II}(\underline{\boldsymbol{s}}-\underline{X})}{MI_I(\underline{\boldsymbol{s}}-\underline{X})} + \ln\left(\frac{I_I(\underline{\boldsymbol{s}}-\underline{X})}{3p_c}\right)$$

The model includes both isotropic and kinematic hardening, and allows to simulate cyclic loadings with large numbers of load cycles. Three hardening variables are used :

- the hardening variable associated to the volumetric plastic strain is given by :

$$p_c = p_{c0}\exp(\boldsymbol{b}\boldsymbol{e}_v^{\,p})$$

where ε_v^p is the volumetric plastic strain. p_{c0} and $\boldsymbol{b}$ are parameters of the model.

- r is the hardening variable associated to the deviatoric plastic strain :

$$r = r_0^{\,el} + \frac{\boldsymbol{e}_d^{\,p}}{a+\boldsymbol{e}_d^{\,p}}$$

where ε_d^p is the deviatoric plastic strain. r_0^{el} represents the initial elastic domain and a controls the evolution of r.

- $\underline{X}$ is the tensorial kinematic hardening variable. Except at the first loading, X describes the origin of the charge surface.

$$\underline{X} = \underline{\boldsymbol{s}} + P\underline{I}$$
$$\underline{dX} = m\underline{d\boldsymbol{s}}$$

The elastic part of the model is described by the non linear elastic Boyce model.

Three types of tests are performed to determine the parameters model :

- Monotonic triaxial tests are performed till failure at different confining pressures,
- Cyclic triaxial tests with low number of cycles to determine the non linear elastic Boyce model parameters,
- Cyclic triaxial tests with different q/p ratios and 80000 cycles per stress level to determine the cyclic plasticity parameters.

The effect of the different model parameters on the modelling predictions is analysed and discussed.

FINITE ELEMENT CALCULATIONS

A finite element analysis (in 3D), with the program CESAR-LCPC, is used to determine the stress distribution in the pavement. The calculation is performed with the module CVCR, dedicated to pavement structure calculations, and which includes non linear elastic models for unbound granular materials, and visco-elastic models for bituminous materials. The model is applied to calculate the rutting of pavements structures, using the following approach :

- Choice of points (y, z) in the plane perpendicular to the direction displacement,
- Determination at each point of the stress path $\underline{\boldsymbol{s}}(t)$,
- Utilisation of $\underline{\boldsymbol{s}}(t)$ to calculate $\underline{\underline{\boldsymbol{e}}}^{\,p}$ at each point, with a fixed number of cycles,
- In a first time (using the simplified method), the permanent strains are integrated along the vertical direction to obtain the vertical displacements in the structure (i.e. rutting of the layer).

The method is illustrated in an example.

Références

[1] Chazallon C.: Elastoplasticity framework for incremental or simplified methods for unbound granular materials for roads. BCRA, 2002.
[2] Gidel G.: Comportement et valorisation des graves non traitées calcaires utilisées pour les assises de chaussées souples. PhD Thesis, Université Bordeaux 1, 2001.
[3] Hujeux J.C.: Une loi de comportement pour le chargement cyclique des sols, in Génie Parasismique, Presse des Ponts et Chaussées, Paris pp316-331. 1985.

INTRAGRANULAR KINEMATIC HARDENING MODELLING AND VALIDATION

Maxime Sauzay
*CEA Saclay, Service de Recherche en Métallurgie Appliquée, Bât. 455, 91191 Gif-sur-Yvette cedex, France

Summary Various deformation induced dislocation microstructures can appear in metals and alloys. Each is composed of a soft phase (cell interiors, channels) and a hard phase (dense walls). They induce backstresses, which gives kinematic hardening on the specimen scale. The Berveiller-Zaoui localization rule is applied for computing these intragranular backstresses. It is validated using experimental results on the single crystal scale. Polycrystal intragranular and intergranular backstress magnitudes are then compared.

BACKSTRESSES

Experimental studies of polycrystal deformation showed the existence of backstresses. At least three experimental techniques permit the evaluation of these long-range stresses at different scales. First, the study of the hysteresis loops gives the kinematic stress (centre of the elasticity unloading domain) on the specimen scale [1]. Second, TEM observations permit the measure of dislocation radii, the computation of the corresponding line tension stresses and of the backstresses (dislocation equilibrium) [2]. Third, X-ray line broadening measurements give backstress measures in single crystals or polycrystals [3].

INTER- AND INTRAGRANULAR BACKSTRESSES

The kinematic stress obtained for a deformed polycrystal is the macroscopic result of both inter- and intragranular backstresses. Numerous experimental studies on single crystals demonstrated the existence of backstresses, particularly after the appearance of deformation induced dislocation microstructures (cell, wall/channel microstructures which included both hard and soft phases). Other experiments of neutron diffraction showed that backstresses on the grain scale could be measured even if no dislocation microstructure had appeared in the grains studied [4]. Both these inter- and intragranular backstresses are due to plastic heterogeneities which involve residual stresses either between the hard wall and soft channel phases inside a grain (intragranular) or between neighbouring grains in a polycrystal (intergranular). According to the experimental results, the relative magnitude of the intragranular backstress initialy seems to increase with the applied strain level and finally both the relative intra- and intergranular backstresses seem to stabilize [4].

Two approaches of the modelling of intragranular backstresses have been used in the past. The first of these is based on on inclusion problems. The soft phase is considered to be surrounded by the matrix or by an elastic wall and by the matrix. Hypotheses concerning the localization rule, which links the macroscopic scale to the cell or wall/channel scale, are used. Pedersen's model uses Eshelby's transition rule [5] and the Lemoine et al. model considers a cell interior surrounded by a wall and embedded in a matrix [6]. The Lemoine et al. model permits us to take into account the geometry and the wall volume fraction which characterize the dislocation microstructure. Generally, the walls are assumed to be elastic, the soft phase is elastoplastic and the matrix is elastic or elastoplastic. The soft phase backstress depends on the soft phase plastic slip. Using Eshelby's coefficients, it is possible to compute the 3D backstress tensor induced by a given microstructure geometry and by given plastic slips on several slip systems. However, these models are thermoelastic, suppose a pure elastic interaction between phases and use no plastic accommodation factor. That is why the computed backstresses are too high as soon as the plastic strain is higher than a few 10^{-4} [7], except for the specific case of Persistent Slip Bands [5].

The second approach, suggested by Mughrabi, proposed a well-known composite model based on the hypothesis that both the hard and soft phase are plastically deformed at maximal load [2]. In this model, the soft phase backstress depends on the dislocation densities in the two phases but not on the plastic slip. This has been developed more recently by Feaugas in order to evaluate both intra- and intergranular backstress for deformed polycrystals [8]. According to his calculations, the intergranular component of the backstress decreases to zero at high strain. This disagrees with neutron diffraction measurements. Therefore, there is at present no agreement between experiment and modelling of intragranular backstresses [4].

Improved modelling of the intragranular backstress is needed, which could be validated on the single crystal scale. Such work is important for understanding and predicting the polycrystal behaviour with a small number of material parameters and for varied loading conditions. This could help to evaluate the type II and III stresses (grain scale and cell scale) and to better understand the propagation of short fatigue cracks which greatly depends on the local backstresses (cyclic loading).

HYPOTHESES AND COMPUTATIONS

An inclusion approach has been used in order to take into account the dislocation microstructure geometry (except the enrobed character) [9,10]. For the sake of simplicity, a single crystal is considered in this part. The soft and hard phases are assumed to be embedded in the matrix. Crystalline plasticity is assumed in both the matrix and soft phase. The average plastic strain tensor is decomposed as a sum of plastic shear tensors. The average plastic slip slip is denoted as γ^p_i and n_i, m_i are respectively the slip normal and the slip direction of the i^{th} slip system. There are N slip systems (N=12 for CFC and N=24 for CC). Because of their high dislocation densities, the walls are assumed to be purely elastic. Following the Berveiller-Zaoui approach [11], a two-phase model is applied, using the macroscopic secant modulus and the Berveiller-Zaoui accommodation factor. This permits the calculation of backstresses with a physical order of magnitude even for large strains. For a spherical cell, the following soft phase backstress is obtained:

$$\underline{\underline{x_c}} = \frac{f_w}{1-f_w}\mu(1-\beta)\frac{1}{1+\frac{3}{2}\mu\frac{\varepsilon^p_{eq}}{\sigma_{eq}}}\sum_{i=1}^{N}\gamma_i^p\frac{1}{2}\left(\underline{n_i}\,\underline{m_i^T}+\underline{m_i}\,\underline{n_i^T}\right)$$

with μ the elastic shear modulus, $\beta=2(4-5\nu)/15(1-\nu)$ (Eshelby's analysis for a spherical elastoplastic inclusion), ν the Poisson ratio and f_w the wall volume fraction. In this equation, all mechanical values are defined on the single crystal scale (matrix). The single crystal kinematic stress is denoted as x_c which is equal to the soft phase backstress.

Spherical cells have been observed for large cyclic or monotonic strains. Other formulae have been obtained for infinite hard cylinders embedded in soft phase (veins/channels microstructures observed for small cyclic strains).

RESULTS

This model is validated by comparison with many backstress measurements on single crystals for which the backstresses are only intragranular. Even for large strains, the computations agree rather well with the experiment measures, except for very small plastic strains. Microstructure parameter and mechanical values are taken from the literature (hard phase volume fraction, geometry, aspect ratios). These parameters allow the calculation of backstresses on single crystals tested using cyclic or monotonic loadings (pure copper, aluminium, AISI 316 stainless steel…) for comparison with experiment. It should be noticed that no adjustable parameter is used.

The backstress model presented here has been used to compute the division of the backstress into inter- and intragranular parts for deformed polycrystals. The ratios between these two kinds of backstresses have been computed on both grain and polycrystal scales. The two macroscopic polycrystal backstress components are assumed to be equal to those of well-oriented grains because these grains seem to glide first during unloading; this corresponds to the definition of the macroscopic backstress. The evolution of the computed backstresses is now described. Once deformation induced dislocation microstructures appear, the intragranular part increases more rapidly than the intergranular part. However, for large strains, both inter- and intragranular backstresses stabilize. These results agree once more with experimental measurements on the grain scale in polycrystals.

Work is in progress concerning improved modelling considering enrobed inclusions (three phase model [12]).

References

[1] Kuhlmann-Wilsdorf, D., Laird, C.: Dislocation behavior in fatigue II. Friction stress and back stress as inferred from an analysis of hysteresis loops. *Mat. Sci. Eng*. **37**, 111-120, 1979.

[2] Mughrabi, H.: The long-range internal stress field in the dislocation wall structure of persistent slip bands. *Phys. Stat. Sol. (a)* **104**, 107-120, 1987.

[3] Mughrabi, H., Ungar, T., Kienle, W., Wilkens, M.: Long-range internal stresses and asymmetric X-ray line-broadening in tensile-deformed [001]-oriented copper single crystals. *Phil. Mag. A* **53** (6), 793-813, 1986.

[4] Holden T. M., Holt R. A., Clarke A. P.: Intergranular strains in Inconel-600 and the impact on interpreting stress fields in bent steam-generator tubing. *Mat. Sci. Eng.* **A246** 180-198, 1998.

[5] Pedersen O. B.: Mechanim maps for cyclic plasticity and fatigue of single phase materials. *Acta Metall. Mater.* **38** (7) 1221-1239, 1990.

[6] Lemoine X., Muller, D. Berveiller M.: Texture of microstructure in BCC metals for various loading paths. *Mat. Science Forum* **157-162** 1821-1826, 1994.

[7] Langlois L., Berveiller M.: Overall softening and anisotropy related with the formation and evolution of dislocation cell structures. *Int. J. Plasticity* **19** 599-624, 2003.

[8] Feaugas, X., Gaudin, C.: Different levels of plastic strain incompatibility during cyclic loading: in terms of dislocation density and distribution . *Mat. Sci. Eng.* **A309-310** 382-385, 2001.

[9] Sauzay M., Héripré E.: Evaluation of intragranular kinematic hardening, 9th International Conference on the mechanical behaviour of Materials, Geneva, Switzerland, 2003.

[10] Sauzay M. : Modelling of intragranular backstresses due to deformation microstructures, Int. J. Plast., submitted.

[11] Berveiller M, Zaoui A., An extension of the self-consistent scheme to plastically-flowing polycrystals, J. Mech. Phys. Solids 26 (1979) 325-344.

[12] Hervé E., Zaoui A.: Modelling the effective behavior of non-linear matrix-inclusion composites. *Eur. J. Mech., A/Solids* **9** (6) 505-515, 1990.

MEAN-FIELD HOMOGENIZATION OF ELASTO-(VISCO)PLASTIC COMPOSITES: FORMULATIONS FOR TIME-DEPENDENT AND INDEPENDENT BEHAVIORS

Issam Doghri*, Olivier Pierard*
*CESAME, Université Catholique de Louvain,
4 Avenue G. Lemaître, B1348 Louvain-la-Neuve, Belgium

Summary Different formulations for the homogenization of elasto-(visco)plastic composites are examined. In the rate-independent case, a robust and generic incremental formulation using algorithmic tangent operators and implicit time-discretization has been developed. For rate-dependent elasto-plasticity, an affine formulation is adopted which transforms the constitutive law into a fictitious thermo-elastic one on which the homogenization is performed.

INTRODUCTION

In this paper, our latest work on the prediction of the macroscopic behavior of two-phase rate-dependent and independent elasto-plastic composites is presented. For this purpose, a two-scale approach is achieved in order to show the influence of the microscopic properties (material characteristics of each phase, shape, volume fraction and orientation of the reinforcements,…). The transition between the microscopic scale, at which we can see the heterogeneity of the material, and the macroscopic one, that of the body, is performed via a mean-field theory, also known as homogenization method. The development of robust algorithms (in term of accuracy, speed and possibility of cyclic and non-proportional loadings) and the issue of the constitutive laws' formulation will be pointed out.

Micro-macro approach and mean-field homogenization models

The main objective is to relate the macro-strain to the macro-stress at a given point $\bar{\mathbf{x}}$. In a micro-macro approach, each macro-point $\bar{\mathbf{x}}$ can be viewed as the center of a representative volume element (RVE). At this scale, the heterogeneity of the material can be observed. Furthermore, it can be shown that if linear boundary conditions are applied to the RVE, then the macroscopic problem is equivalent to that of relating average strains and stresses on the RVE.
Let's consider now a two-phase composite made of inclusions embedded in a matrix. One can define a strain concentration tensor relating the strain averages per phase. Fixing this strain concentration tensor defines a homogenization model. Most of these are based on the fundamental solution of the Eshelby's problem which introduces Eshelby's tensor.
Some well-known homogenization schemes based on Eshelby's result are the Mori-Tanaka scheme, the self-consistent one and interpolative ones. In linear elasticity, once a homogenization scheme is defined with its strain concentration tensor, the macro stiffness can be computed. In the remainder of this paper, we will make use of the Mori-Tanaka model, which is very appropriate for predictions of polymer matrix composites (PMC's) and metal matrix composites (MMC's) with small volume fraction of inclusions.

RATE-INDEPENDENT ELASTO-PLASTIC COMPOSITE MATERIALS

In the case of rate-independent elasto-plastic composites, we can predict the overall behavior either with a *secant operator* ($C^{\sec}$) or a *tangent operator*. The latter can be a *continuum* one (C^{cont}) or an *algorithmic* one ($C^{a\lg}$ - based on a linearization of the return-mapping algorithm):

$$\sigma(x) = C^{\sec}(x) : \varepsilon(x) \,, \quad \dot{\sigma}(x) = C^{cont}(x) : \dot{\varepsilon}(x) \,, \quad \delta\sigma(x) = C^{a\lg}(x) : \delta\varepsilon(x)$$

The Hill-type incremental formulation (which makes use of the tangent operator) has been criticized in the literature for giving too stiff macro responses. However, the secant formulation presents a major disadvantage: no unloading or cyclic loadings are allowed since it assumes a one-to-one correspondence between stress and strain. Keeping this in mind, we tried to improve the predictions of the incremental formulation. Firstly, the use of the continuum operator or the algorithmic one gives significantly different results (the continuum operator gives the stiffest response - proved in [1]). Secondly, numerical experience has shown that good predictions are obtained only when Eshelby's tensor is computed with the isotropic part of the tangent operator. However, in elasto-plasticity, the tangent operator is no longer isotropic and there are several methods for extracting an isotropic part of a fourth-rank tensor. All the other computations are performed with the anisotropic algorithmic modulus. With the incremental method, we have implemented two plasticity models: classical J2 plasticity and Chaboche's model with non-linear kinematic and isotropic hardening. A wide range of experimental confrontations (or with FE if unavailable) can be found in [1] (for spherical reinforcements), and in [2] (for spheroidal inclusions with various but fixed orientations). A very interesting example is the stabilized cyclic tension/compression test illustrated on Figure 1 for aluminum alloy reinforced by SiC short fibers. Recent and yet unpublished results concern distributed-orientation fibers in an elasto-plastic matrix.

RATE-DEPENDENT ELASTO-PLASTIC COMPOSITE MATERIALS

For rate-dependent elasto-plasticity, Hooke's law is still given by: $\dot{\sigma} = E : (\dot{\varepsilon} - \dot{\varepsilon}^{in})$, in which E is Hooke's operator and $\dot{\varepsilon}^{in}$ (inelastic strain rate) is governed by a plastic flow rule. One major difference with rate independent elasto-plasticity is that there is no continuum tangent operator linking stress and strain rates anymore: the homogenization using an *incremental formulation* becomes then impossible, and using it nevertheless with an algorithmic tangent operator leads to predictions which are too stiff. As Masson *et al.* [3] suggested, an alternative is to use a so-called *affine formulation* (basic ideas can be

found in [4]). We have investigated the development of such a formulation for elasto-viscoplastic composites and its implementation with a Mori-Tanaka homogenization scheme. Guidelines of this formulation are given hereafter.
For an homogeneous material (e.g.: one of the phases of the composite), constitutive laws can be written such that the inelastic strain rate is governed by a function depending on the stress state and internal parameters, reduced in this case to the accumulated plasticity p, also described by a governing equation:

$$\dot{\varepsilon}^{in}(t) = g(\sigma, p)\,, \quad \dot{p}(t) = h(\sigma, p)$$

Once these equations are defined, we can perform a linearization around time $t = \tau$, at which we are looking for the macroscopic response:

$$\dot{\varepsilon}(t) = \underbrace{S : \dot{\sigma}(t)}_{\dot{\varepsilon}^{el}(t)} + \underbrace{g(\tau) + m(\tau) : [\sigma(t) - \sigma(\tau)] + n(\tau) : [p(t) - p(\tau)]}_{\dot{\varepsilon}^{in}(\tau,t)}$$

$$\dot{p}(t) = h(\tau) + l(\tau) : [\sigma(t) - \sigma(\tau)] + q(\tau)[p(t) - p(\tau)]$$

in which $m(\tau)$, $n(\tau)$ and $l(\tau)$, $q(\tau)$ are the derivatives of g and h w.r.t. σ and p respectively. These derivatives can be evaluated analytically from the governing equations. Solving the equation in p and rearranging terms to introduce the Stieljes-type convolution product (noted $\bullet$), we are left with:

$$\dot{\varepsilon}(t) = [S_\tau \bullet \dot{\sigma}]_{(\tau,t)} + \dot{\varepsilon}^0(\tau, t)$$

in which expressions of $S_\tau(\tau, t)$ and $\dot{\varepsilon}^0(\tau, t)$ can be derived analytically. At this stage, we can note that we are in front of a linear viscoelastic problem with an eigenstrain rate. The macroscopic relation can also be written similarly. Classically, this relation is transformed into the Laplace-Carson domain, in which the Stieljes-type convolution product is reduced to a tensorial contraction:

$$\varepsilon^*(s) = S^*_\tau(\tau, s) : \sigma^*(s) + \varepsilon^{0*}(\tau, s)$$

The relation becomes a fictitious linear thermo-elastic one, valid for each phase, on which the classical homogenization of linear thermo-elastic composites can be applied, as described in [5]. This procedure gives the homogenized (noted with an upper bar) functions $\overline{S}^*_\tau(\tau, s)$ and $\overline{\varepsilon}^{0*}(\tau, s)$, defined in the Laplace domain. A numerical inversion is then achieved to get the equivalent temporal functions. Finally, evaluation of the convolution product appearing in the macroscopic relation of linear viscoelasticity gives the macroscopic solution at time $t = \tau$.

From the algorithmic point of view, an iterative method is used on each time interval $[t_n, \tau]$ because $S_\tau(\tau, t)$ and $\varepsilon^0(\tau, t)$ are functions of the past history of the corresponding phase. Finally, for each time step, an iterative loop is necessary in order to find the right strain increment in each phase, similarly as in the proposed algorithm for elasto-plasticity [2]. Another global iterative loop has to be involved if we are performing a uniaxial tension test given the strain rate in order to get a compatible macro stress tensor.

References

[1] Doghri I., Ouaar A.: Homogenization of two-phase elasto-plastic composite materials and structures. Study of tangent operators, cyclic plasticity and numerical algorithms. *Int. J. Solids and Structures* **40** (2003) 1681-1712.

[2] Doghri I., Friebel C.: Effective elasto-plastic properties of inclusion-reinforced composites. Study of shape, orientation and cyclic response. *Mechanics of Materials,* in press, 2004.

[3] Masson R., Zaoui A.: Self-consistent estimates for the rate-dependent elasto-plastic behavior of polycrystalline materials. *J.M.P.S.* **47** (1999) 1543-1568.

[4] Molinari A., Canova G.R. and Ahzi S.: A self-consistent approach of the large deformation polycrystals viscoplasticity. *Acta Metallurgica et Materialia* **35(12)** (1987) 2983-2994.

[5] Pierard O., Friebel C. and Doghri I.: Mean-field homogenization of multi-phase thermo-elastic composites: a general framework and its validation. *Composites Science and Technology*, in press, 2004.

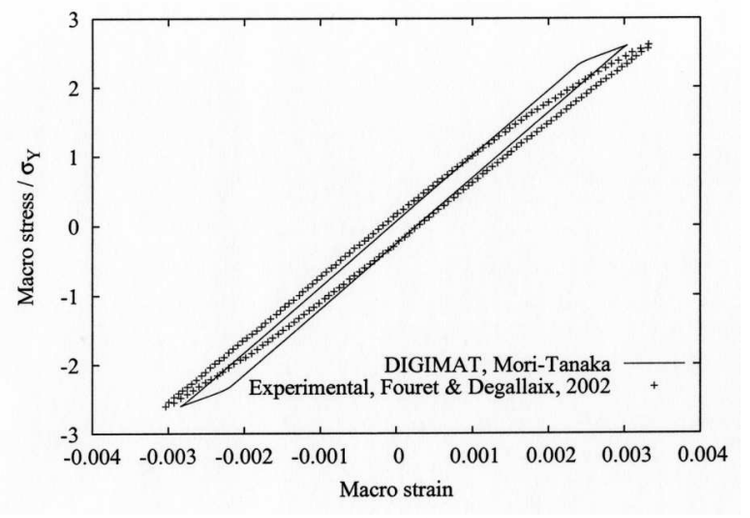


Figure 1

XXI ICTAM, 15–21 August 2004, Warsaw, Poland

A COHESIVE APPROACH TO THIN-SHELL FRACTURE AND FRAGMENTATION

Fehmi Cirak*, Michael Ortiz**, Anna Pandolfi***
*CACR, Caltech, Pasadena, CA 91125, U.S.A.
**GALCIT, Caltech, Pasadena, CA 91125, U.S.A.
**DIS, Politecnico di Milano, 20133 Milano, Italy

Summary We develop a finite-element method for the simulation of dynamic shell fracture and fragmentation based on cohesive models of fracture. We assume the shells to be thin and to obey the Kirchhoff-Love theory. The shell is spatially discretized by means of subdivision shell elements. Fracture is allowed only along element edges and is assumed to be governed by a cohesive law. When coupled to the shell kinematics, the cohesive model accounts both for in-plane or tearing, shearing, and bending or hinge modes of fracture. In order to follow the propagation and branching of cracks, subdivision shell elements are pre-fractured *ab initio*. Prior to crack nucleation, crack opening is constrained by means of a penalty method in implicit calculations, or by a projection or displacement averaging method in explicit calculations.

OVERVIEW

The experimental and analytical investigation of fracture and fragmentation of thin-plates and shells has elicited considerable interest in the past. The analytic models proposed to date often introduce ad-hoc approximations regarding the likely failure modes and are restricted to a few regular geometries, loading conditions, and constitutive models. By contrast, numerical simulation of fracture and fragmentations of shells and plates has received comparatively less attention. A notable exception is furnished by the finite element analysis of "surface-cracked" plates and shells [2]. In [1], Rice and Levy introduced the concept of a line-spring with stretching and bending resistance for the analytical treatment of plates with a surface crack, and computed its compliance from fracture mechanics and energetic considerations. In the finite element context the line-spring is inserted at the location of the surface-crack in the plate or shell in order to compute quantities relevant for fracture mechanics [2].

In the present work, fracture initiation and propagation is considered as a progressive failure phenomenon in which the separation of the crack flanks is resisted by cohesive tractions. The relationship between the crack opening displacements and the tractions is given by a cohesive model. An appealing feature of the cohesive model is that it provides a complete theory of fracture without presuming a particular bulk material behavior or geometry of the specimen and the extend of the crack growth.

For three-dimensional solids, cohesive laws may conveniently be encoded into cohesive elements in the form of double surfaces (e. g., [5, 7, 6, 8] and references therein). The opening of the cohesive elements is compatible with the deformation of the adjacent volume elements and is subject to a unilateral closure constraint. Cohesive elements may be inserted adaptively upon the attainment of a critical stress condition on the interelement boundary [7, 8]. The insertion of cohesive elements introduces new surfaces into the mesh, which undergoes complex topological transitions as a result. For three-dimensional solids these transitions can be classified exhaustively [8], and appropriate actions may be taken in order to update the representation of the mesh in each case.

Certain aspects of the mechanics of shells greatly compound the integration of cohesive theories of fracture. Thus, within the framework of Kirchhoff-Love theory the strain energy density of thin-shells is expressed in terms of the first and second fundamental forms of the shell middle surface. Therefore, a conforming finite element discretization requires smooth shape functions belonging to the Sobolev space H^2. Cirak, Ortiz, and Schröder [3, 4] proposed a new type of discretization based on the concept of subdivision surfaces which delivers smooth H^2 shape functions on unstructured meshes in a particularly natural and efficient way. In addition to several other advantages, an appealing feature of the subdivision elements is that the sole unknowns in the finite element solution are the nodal displacements. However, this comes at a certain cost, namely, that the subdivision shape functions are non-local in the sense that the displacement field within one element depends on the displacements of the nodes attached to the element and the immediately adjacent ring of nodes in the mesh.

The natural extension of the cohesive element concept to shells consists of inserting cohesive elements at interelement edges, and constraining the opening of the cohesive elements to conform to the deformation of the middle surface of the shell and its normal. This approach allows for fracture both in an in-plane or tearing mode, a shearing mode, or a bending of hinge mode. However, within a subdivision-element framework the essential difficulty resides in making the scheme adaptive, in the sense of inserting cohesive elements in an otherwise conforming mesh upon the attainment of some appropriate critical condition. Thus, the non-locality of the displacement interpolation renders the tracking of the topological transitions induced by the insertion of cohesive elements unmanageably complex. In order to sidestep this difficulty we simply fragment *ab initio* all the element edges by duplication of common nodes. In implicit calculations, element conformity prior to fracture is enforced by the addition of a penalty term to the energy. Alternatively, in explicit dynamics calculations conformity is readily enforced by a displacement averaging technique.

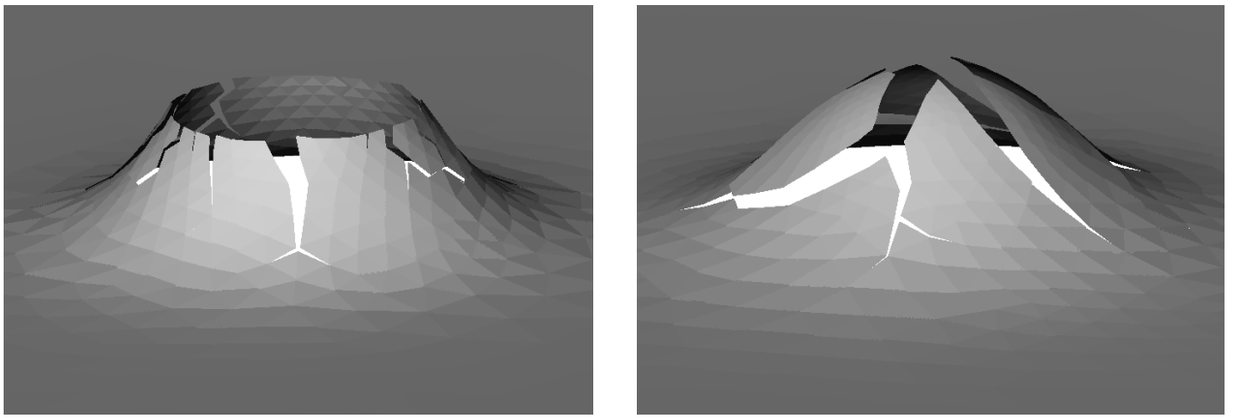


Figure 1. (a) Detail of the petalling formation in a perforated plate. (b) Star-shaped crack formation in a solid plate.

APPLICATIONS

The present framework can be applied to a variety of thin plate and shell fracture and fragmentation problems, such as the perforation of thin-plates impacted by fast moving projectiles. As an example of application, we simulate the experiments of Landkof and Goldsmith [9] concerned with the petalling failure of circular aluminum (Al 2024-0) plates with and without initial holes struck by hard-steel conical projectiles.

In computations we consider a solid and a perforated plate with a 6.35 mm diameter hole. The plate thickness is 3.175 mm in both cases. The striking velocity is $v = 320$ m/s. The bulk material response of the aluminum plates is assumed to obey a rate dependent J2-plasticity model. To simulate the effect of the projectile impact, we apply a pressure history over the impact area corresponding to the force exerted by the conical tip of the projectile. The impact force has been computed from the deceleration Δv of the projectile, as measured in the experiments.

The results of the dynamical analysis of the solid and perforated plate are collected in Fig. 1. For the perforated plate, in keeping with theory and experiment [9], the early states of penetration are characterized by an enlargement of the hole, followed by crack propagation, and final bending of trapezoidal petals. A detail of the central part of the perforated plate at the end of the calculation is shown in Figure 1a. Of course, the fine details of the fracture patterns are to some extend stochastic and are likely to exhibit considerable scatter. For present purposes it suffices to point out that the numerical method allows for complex fracture patterns including branching and fragmentation. As observed in [9], for solid plates petalling starts with the formation of a star-shaped crack at the impact point, and the subsequent propagation of radial cracks. The resulting triangular petals rotate about a continuously shifting circular plastic hinge in order to allow the passage of the projectile. A detail of the central part of the plate after the formation of the star shaped crack is shown in Fig. 1b. The branching events in some of the radial cracks are particularly noteworthy.

References

[1] J.R. Rice and Levy N. The part-through surface crack in an elastic plate. *Journal of Applied Mechanics*, 39(1):185–194, 1972.

[2] D.M. Parks and White C.S. Elastic-plastic line-spring finite elements for surface-cracked plates and shells. *Journal of Pressure Vessel Technology*, 104(4):287–292, 1982.

[3] F. Cirak, M. Ortiz, and P. Schröder. Subdivision surfaces: A new paradigm for thin-shell finite-element analysis. *International Journal for Numerical Methods in Engineering*, 47(12):2039–2072, 2000.

[4] F. Cirak and M. Ortiz. Fully C^1-conforming subdivision elements for finite deformation thin-shell analysis. *International Journal for Numerical Methods in Engineering*, 51:813–833, 2001.

[5] X.-P. Xu and A. Needleman. Numerical simulations of fast crack growth in brittle solids. *Journal of the Mechanics and Physics of Solids*, 42(9):1397–1434, 1994.

[6] M. Ortiz and A. Pandolfi. A class of cohesive elements for the simulation of three-dimensional crack propagation. *International Journal for Numerical Methods in Engineering*, 44:1267–1282, 1999.

[7] G. T. Camacho and M. Ortiz. Computational modelling of impact damage in brittle materials. *International Journal of Solids and Structures*, 33(20–22):2899–2938, 1996.

[8] A. Pandolfi and M. Ortiz. An efficient adaptive procedure for three-dimensional fragmentation simulations. *Engineering with Computers*, 18(2):148–159, 2002.

[9] B. Landkof and W. Goldsmith. Petalling of thin, metallic plates during penetration by cylindro-conical projectiles. *International Journal of Solids and Structures*, 21(3):245–266, 1985.

THE STRESS ANALYSIS OF THE MULTILAYERED PLATES AND SHELLS WITH DEFECTS OF THE STRUCTURE

Lvov G.I., Vereshchaka S.M.

Kharkov National Technical University "KPI"
Frunze str. 21, 61002, Kharkov, Ukraine.

Summary The laminated composite shells have high strength properties. However technological processes of their manufacture are difficultly automated, that causes the increased probability of manufacturing of thin-walled elements of structures with local defects. The local imperfections can produce essential influence on the strength of the total shell. This paper is devoted to such problems.

The theory of laminated anisotropic plates and shells is offered for the analysis of such situations The high order kinematics model reflects nonlinear character of distribution of displacements on thickness of rigid layers. These layers are connected by the thin glue layer It is supposed, that on some local area of the shell glue layer is absent, therefore in this area the unilateral contact between rigid layers is taken into account.

The contact problem of the mechanics of the non-uniform plates and shells with defects such as a local area of the non-glued layer are given in [1-3], where on the basis of the discrete approach the systems of the equations of the problem under condition of the non ideal contact of layers are formulated. In this work the theory multilayered anisotropic shell is offered on the base of the geometrically nonlinear theory of shells in a view of deformations of transverse shear.

The contact problem with aid of the mathematical theory [4] of variational inequalities is offered. The value of the Reissners energy functional of multilayered shell has view

$$R = \sum_{k=1}^{n}(\Pi_{(k)} + \mathrm{A}_{(k)}) + \sum_{k=1}^{n-1}(\Pi_{[k]} + \mathrm{A}_{[k]}), \qquad (1)$$

Where $\Pi_{(k)}$, $\Pi_{[k]}$ – potential energy of deformation k of a rigid layer and k the glue layer accordingly; $\mathrm{A}_{(k)}$, $\mathrm{A}_{[k]}$ – the work of external forces enclosed to k - rigid layer and k - soft layer of the shell.

The main variational inequalities on the base of functional energy (1) in which independent displacements and stresses are varied, allows [5] to receive system of the equations of the equilibrium of the multilayered shells, physical relations, boundary conditions. If between k and $k+1$ - layers of the shell the glue layer is absent, than contact pressure $\vec{q}_{(k)}$, $\vec{q}_{(k+1)}$. acts on the surface of interaction $S_z^{(k,k+1)}$ of these layers.

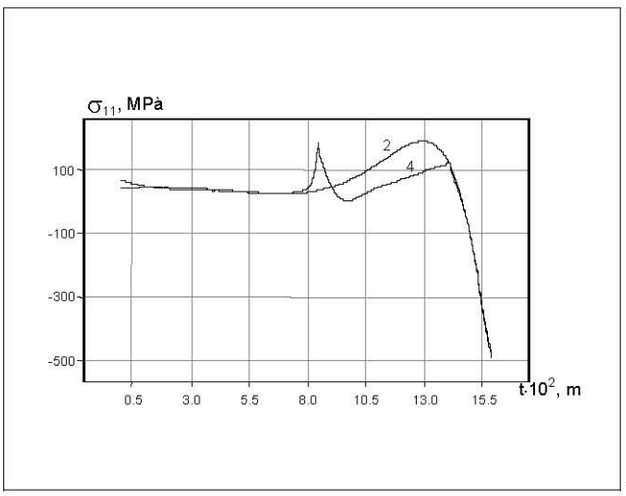
The contact pressure $\vec{q}_{(k)} = q^i_{(k)}\vec{r}^{(k)}_i + q^3_{(k)}\vec{m}^{(k)}$ is absent if the condition

$$(\vec{u}_z^{(k)} - \vec{u}_z^{(k+1)}) \geq 0 \qquad (2)$$

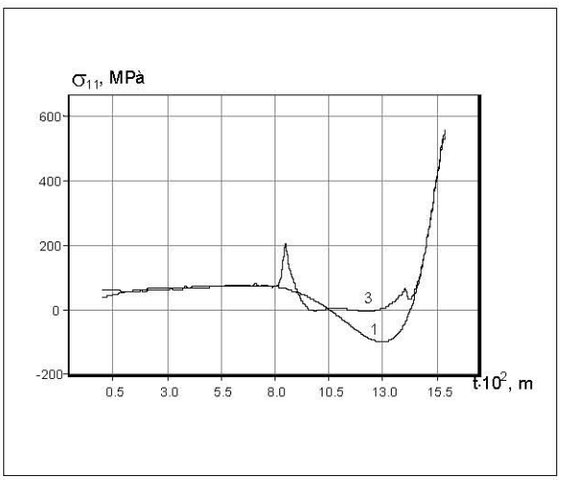
is satisfied in area of interaction of rigid layers.

As an example the stress analysis is considered for anisotropic toroidal shell loaded by internal pressure. The initial surface of shell is formed by rotation of a circle of radius $r = 0.1$m around an axis of rotation. The distance from the axis of rotation up to the circuit center R=0.4m. The shell is made from two of the reinforced layers by thickness h=5 mm and angles of the reinforcement on equator $\varphi^{(1)} = -60°, \varphi^{(2)} = 60°$. It is considered, that on equator the conditions of symmetry are carried out, and the cross-section of the shell with coordinate $t_k = \pi r/2$ is rigidly jammed. The layers are

made from boron-epoxy tape of a composite material. The physical characteristics of boron filaments $E_v=4{,}2\cdot10^5$ MPa, $\nu_v = 0{,}21$, and epoxy binder $E_m=3{,}5\cdot10^3$ MPa, $\nu_m = 0{,}33$.
The stress analysis of the shell was calculated by the Godunov's method. The nonlinear boundary problem was reduced to the decision of a sequence of linear problems by the generalized Newton method.
The distribution of normal stresses σ_{11} in a direction of longitudinal coordinate t are shown on fig. 1à,b for internal pressure q=3 MPa. (3" - internal surface, "4" - outside surface).



a)



b)

Fig. 1.

On length of the shell at 0,085 m<t<0,14 m there is the non-glued area . Thus between rigid layers of the shell there is a unilateral contact. For comparison the distributions of normal stresses σ_{11} without defect area are shown ("1" - internal surface, "2" - outside surface). The analysis of curves 3, 4 proves presence of boundary effect in the non-glued area. The accepted mathematical model of anisotropic shell essentially defines results of numerical analysis.

References

[1] Bolotin V.V., Novichkov U. N. The mechanics multilayered of designs. M.: Mechanical Engineering, 1980. p. 375.
[2] Herakovich C.T. Influence of layer thickness on the strength of angle laminates//*J. Composite Materials,* 1982, 16, p. 216-227.
[3] Herakovich C.T., Nagarkar A., O'Brien D.H. Modern Developments in Composite Materials and Structures/J.R. Vinson, ed., ASME, 1979, p.53-66.
[4] Lions J.L., Stampacchia G. Variational Inequalities. *Comm. Pure Appl. Math.,* **20** (1967), 493-519.
[5] Lvov G., Kostenko E. Physically non-linear contact problems of the shell theory. *XIX International Congress of Theoretical and Applied Mechanics .Abstracts*, Kyoto, 1996, p.628.

SOME NEW THOUGHTS ON THE BUCKLING OF THIN CYLINDRICAL SHELLS

Parthasarathi Mandal*
*Manchester Centre for Civil & Construction Engineering,
UMIST, P.O. Box 88, Manchester, M60 1QD, U.K

Summary The classical theory of buckling of axially loaded thin cylindrical shells predicts that the buckling stress is directly proportional to the ratio of thickness to diameter (t/R), other things being equal. But the empirical data show that the buckling stress is proportional to $(t/R)^{1.5}$, other things being equal. Also there is wide scatter in the buckling stress data. The "imperfection-sensitive", "non-linear" behaviour is thought to be the cause of the above. In this article, it is argued that the boundary conditions, from the "statical determinacy" point of view could explain the shell-buckling paradoxes.

INTRODUCTION

The classical theory, developed in the beginning of the twentieth century, predicts that cylindrical shells will buckle under uniform axial compressive stress σ_{cr}, given by

$$\sigma_{cr} = \frac{E}{\sqrt{3(1-\nu^2)}}\left(\frac{t}{R}\right) \approx 0.6E\left(\frac{t}{R}\right) \qquad (1)$$

where E is the Young's modulus of elasticity and ν the Poisson's ratio of the isotropic material, t is the thickness and R is the radius of the shell.

However, in the 1930s it was discovered that the experimental buckling loads of cylindrical shells are often small compared to the predictions of the classical theory. Since then there have been extensive research to explain: (i) these lower experimental buckling loads; (ii) the large scatter of the experimental data; and (iii) the catastrophic nature of the failure.

The concepts of "non-linearity" and "imperfection-sensitivity" are widely accepted as explanations for the paradox associated with shell-buckling. However, extensive studies based on precise measurements of geometrical imperfection in physical shells, manufactured in various ways, have had limited success in predicting the buckling load. Therefore, it is reasonable to claim that there must be some crucial factors involved in the mechanisms of shell buckling which are missing from existing analytical studies. This article discusses some interesting features of experiments on the self-weight buckling of small-scale, thin, silicone rubber shells.

SELF-WEIGHT BUCKLING EXPERIMENTS

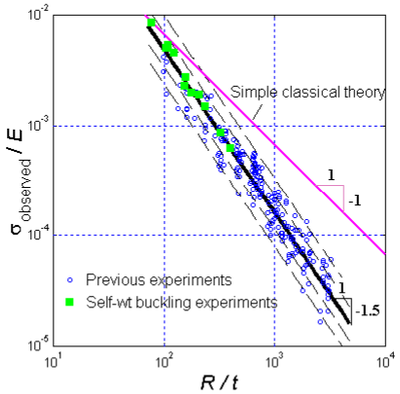


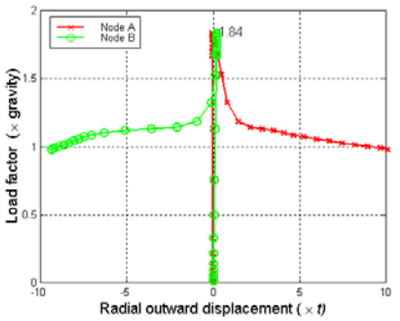
Fig. 1 Log-log plot of experimental data of thin cylindrical shells. The data referred as "previous experiments" have been taken from Brush & Almroth[4]. The heavy best-fit line has a slope of –1.5; and broken lines at 1 and 2 standard deviations from the mean are also shown.

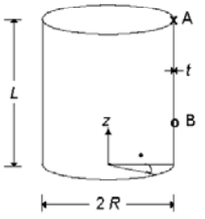
Consider a large-scale, open-topped cylindrical shell. There is a tendency for the structure to collapse under its own weight; and collapse may be precipitated by a disturbance such as an earthquake or wind loading. In order to understand this phenomenon, Calladine and Barber [1] conducted some simple experiments by making long, open-topped, fixed-base thin cylindrical shells in silicone rubber and cutting them down, little by little, until they just stood upright on a flat table without buckling under their own weight. These heights were regarded as the *buckling heights* (L_{cr}) under self-weight. All of the cylinders had the same outside diameter (nominally 172 mm) and ranged in thickness from 0.23 mm to 1.12 mm. The results are shown in Fig. 1, as a log-log plot of dimensionless critical heights against R/t. The ordinate represents the self-weight stress at the base if the shell ($=L_{cr}\ \rho\ g$, where $\rho\ g$ is the unit weight of the silicone rubber material), normalized with respect to E. More recently, some more experiments have been conducted with a larger mould, of diameter 241 mm: see Refs.[2] and [3]. These results are also plotted in Fig. 1, and they agree very well with [1]. There are two distinguishing features of these results. First, in general the buckling clearly does not take place according to the "simple classical theory" (Eqn 1). Second, there is very little scatter in the data, compared to almost all buckling tests on thin cylinders that have been reported in the literature. To assess the situation, the data of experimental buckling strength of cylindrical shells under axial compression that was collected and presented by Brush and Almroth [4], are re-plotted here in Fig 1, on log-log scales of σ_{cr}/E and R/t. It is immediately clear that the experimental data lie on a band which is steeper than the "classical line"; and indeed the best-fitting line through the data points has a slope of –1.5, to two significant figures. Specifically, we find

$$\sigma_{mean} = 5\,E\left(\frac{t}{R}\right)^{1.5} \qquad (2)$$

Non-linear finite element analyses

In order to understand the paradoxical self-weight buckling, non-linear finite element analyses of several experimental shells were conducted using ABAQUS [5]. The result of a typical computation is shown in Fig. 2. The figure shows that the shell does not buckle until a load of 1.84*g* has been reached: this is near to the classical buckling load level for the shell as revealed by a linear-eigenvalue buckling analysis. The load then falls to around 1.3*g*, with very little radial displacement. After this, a dimple starts to appear at Node B, with significant inward displacement, and Node A at the top starts to move outwards. The shell above the dimple deforms inextensionally henceforth, leading to a post-buckling "plateau" corresponding to the experimental critical heights. The "plateau" remains virtually similar if the amplitudes of the initial imperfection were increased by a factor of four.





Imperfection used in the ABAQUS computation:

$$-0.25\, t\,(z/L)\cos(7\theta)\, e^{-6.9\theta^2}$$

Fig. 2 Plot of numerical gravity load factor against radial deflection at two points of an open-topped, fixed base shell ($R/t \approx 210$) from the self-weight buckling experiments. An ordinate of value 1.0 corresponds to the physical shell under gravity at its measured critical height. The geometrical imperfection was deliberately included, primarily as a requirement for the non-linear analysis to be performed smoothly; and the shape of the imperfection was chosen so as to encourage buckling to begin at a desired location.

DISCUSSION AND CONCLUSIONS

The self-weight buckling experiments along with the non-linear finite-element analyses highlight that the critical stress of cylindrical shells under axial compression is proportional to $(t/R)^{1.5}$, compared to $(t/R)^{1.0}$ as in classical theory. This fits well with the large amount of previous experimental data. However, the experiments on self-weight buckling showed negligible scatter compared to the earlier experiments in the literature. We suggest that the explanation lies in the fact that the two sets of shells have a different status in terms of *static determinacy*: thus the open-topped shells in the self-weight buckling experiments are *statically determinate*, whereas almost all the shells used in standard buckling tests in the past had closed ends, hence they are *statically indeterminate* from the membrane stresses point-of-view. The static indeterminacy in a system may be held responsible for any locked-in stresses due to lack-of-fit resulting from the manufacturing process. Such unaccounted, random locked-in-stresses may cause a shell to buckle at a premature load, after reaching the critical stress in a localised area; or in general they may produce a big statistical variation in buckling loads of notionally similar shells.

To verify the above hypothesis of *static determinacy,* another set of non-linear finite element analyses were conducted by Vossos [6]. Three fixed-base cylindrical shells were considered. The boundary conditions at the top were: (i) open, (ii) constrained to be both circular and plane, and (iii) attached to a ring beam. The self-weight buckling analyses of these three shells were carried out in two steps. In the first step a preload was applied to mimic the "residual stresses" in practice, and in the second step gravity load was applied by *modified RIKS* method in ABAQUS [5]. The preload was applied in one of the following ways: (i) a concentrated load in the radial inward direction, applied near Node B (see Fig. 2); (ii) a temperature increase at a small region near Node B; and (iii) uplift of the base at a small portion of the perimeter of the shell. The comparative buckling load factors are shown in Table 1. The buckling load, of course, depends on the amount of preload and their positions. Hence the values given in Table 1 should be read column-wise. They do not have any meaning along a row.

It is clear that the statically determinate shells perform better in buckling than their statically indeterminate counterparts. For example, an increase in temperature in a small region of a statically indeterminate shell will cause higher initial stresses. As a result, when the shells are tested for buckling, the statically indeterminate shells will carry lower loads.

	Boundary Conditions		Statical	Buckling load factor		
	Top	Base	Determinacy	Radial load	Temperature	Uplift
Shell 1	Open	Fixed	Determinate	1.00	1.00	1.00
Shell 2	Circular & Plane	Fixed	Indeterminate	0.90	0.66	0.41
Shell 3	Ring beam	Fixed	Indeterminate	0.94	0.57	0.49

Table 1

References

[1] Calladine C.R., Barber J.N.: Simple experiments on self-weight buckling of open cylindrical shells. *J. App. Mech, Trans ASME*: 1150-1151, 1970.

[2] Mandal P., Calladine C.R.: Buckling of thin cylindrical shells under axial compression. *Int. J. Solids and Structures*: **37**:4509-4525, 2000.

[3] Zhu E., Mandal P., Calladine C.R.: Buckling of thin cylindrical shells: an attempt to resolve a paradox. *Int. J. Mech. Sci.*: **44**:1583-1601, 2002.

[4] Brush D.O., Almroth B.O.: Buckling of bars, plates and shells. McGraw-Hill, NY 1975.

[5] Hibbit, Karlsson, Sorensen Inc: ABAQUS, Version 5.8, web site http://www.hks.com/home.html

[6] Vossos, P.: Buckling of thin cylindrical shells under axial compression. *MSc Thesis*, Civil Engineering, UMIST, UK, 2003.

CONTINUITY CONDITIONS IN ELASTIC SHELLS WITH PHASE TRANSFORMATION

Victor A. Eremeyev[*], Wojciech Pietraszkiewicz[**]
[*]*Rostov State University, Zorge str. 5, 344 090 Rostov-on-Don, Russia*
[**]*Polish Academy of Sciences, Institute of Fluid-Flow Machinery, Fiszera 14, 80-952 Gdańsk, Poland*

Summary The six-field non-linear theory of elastic shells with the phase transformation of the material is developed. Equilibrium conditions are found from the variational principle of stationary total potential energy. New dynamic continuity conditions are derived at the movable singular surface curve modelling the phase interface. Particular forms of the continuity conditions at coherent and incoherent interface curves are given. The results are illustrated by an example of the phase transition in an infinite plate with a circular hole.

INTRODUCTION

Thin films made of shape-memory alloys like NiTi, NiMnGa, NiTiCu, or NiAl can considerably alter their shapes under appropriate external environmental changes. To model the mechanical behaviour of such thin films one can apply two-dimensional (2D) shell models consisting of a base surface endowed with appropriate fields modelling an additional microstructure. Then the notion of a movable surface curve separating the shell regions with different material phases is an appropriate tool for describing the interface of phase transition in the shell material.
A 2D model for single crystal thin films of martensitic materials based on the Cosserat membrane with one director field was proposed in [1]. However, kinematics of such a shell model is incomplete, for it does not contain the rotation about the director (the drilling rotation). The dynamic continuity conditions at the curvilinear phase interface of the shell are not available in the literature as well. The aim of this paper is to develop the complete non-linear theory of elastic shells with an account of occurrence of the phase transformation in the shell material.

WEAK FORMULATION OF THE BOUNDARY VALUE PROBLEM

Within the general non-linear theory of shells [2,3] the 2D local vector equilibrium equations and corresponding dynamic boundary conditions are formulated on the undeformed shell base surface M by an *exact* integration through the shell thickness of the corresponding 3D balance laws of continuum mechanics. The shell kinematics is then established through *energetically exact* dual fields in the 2D virtual work identity. In such a dynamically and kinematically exact shell theory the work-averaged translation vector $\boldsymbol{u}(\boldsymbol{x}) \in E$ and rotation tensor $\boldsymbol{Q}(\boldsymbol{x}) \in SO(3)$, $\boldsymbol{x} \in M$, are the only independent field variables of the boundary value problem (BVP).
In a two-phase elastic shell different material phases may appear on closed complementary subregions N_A and N_B of the deformed base surface $N = \chi(M)$ separated by the curvilinear phase interface D. For a continuous deformation χ we can introduce on M a singular curve $C = \chi^{-1}(D)$ separating $M_A = \chi^{-1}(N_A)$ and $M_B = \chi^{-1}(N_B)$. The position vectors of C and D are related by $\boldsymbol{x}_c(s) = \chi^{-1}(\boldsymbol{y}_c(s))$, respectively, where s is the arc length parameter along C.
The equilibrium BVP for shells with the phase transformation can be formulated in the weak form: Given the external force and couple vector fields $\boldsymbol{f}(\boldsymbol{x}), \boldsymbol{c}(\boldsymbol{x})$ on M and $\boldsymbol{n}^*(s)$, $\boldsymbol{m}^*(s)$ prescribed along ∂M_f find a solution $(\boldsymbol{u}, \boldsymbol{Q}, \boldsymbol{x}_c)$ on the configurational space $C(M; E \times SO(3) \times E)$ satisfying the kinematic boundary conditions $\boldsymbol{u} - \boldsymbol{u}^* = \boldsymbol{0}$, $\boldsymbol{Q} - \boldsymbol{Q}^* = \boldsymbol{0}$ along $\partial M_d = \partial M \setminus \partial M_f$, such that for any kinematically admissible virtual vector fields $\delta\boldsymbol{u}$, $\boldsymbol{w} = ax(\delta\boldsymbol{Q}\boldsymbol{Q}^{\boldsymbol{T}})$, $\delta\boldsymbol{x}_c$ the following variational principle of stationary total potential energy is satisfied:

$$\delta I(\boldsymbol{u}, \boldsymbol{Q}, \boldsymbol{x}_c; \delta\boldsymbol{u}, \boldsymbol{w}, \delta\boldsymbol{x}_c) = 0\,, \quad I(\boldsymbol{u}, \boldsymbol{Q}, \boldsymbol{x}_c) = \iint_{M_A} W(\boldsymbol{u}, \boldsymbol{Q})\, da + \iint_{M_B} W(\boldsymbol{u}, \boldsymbol{Q})\, da - A(\boldsymbol{u}, \boldsymbol{Q})\,. \tag{1}$$

Here W is the 2D elastic strain energy density, and A is the potential of external loads such that $\delta A = \iint_M (\boldsymbol{f} \bullet \delta\boldsymbol{u} + \boldsymbol{c} \bullet \boldsymbol{w})\, da + \int_{\partial M_f} (\boldsymbol{n}^* \bullet \delta\boldsymbol{u} + \boldsymbol{m}^* \bullet \boldsymbol{w})\, ds$. As the stationarity conditions of I we obtain the known local equilibrium equations in M and the dynamic boundary conditions along ∂M_f, see [2,3].

DYNAMIC CONTINUITY CONDITIONS AT THE PHASE INTERFACE

Due to the phase transition of the shell material at the interface C, the principle (1) also requires that the following local dynamic continuity condition be satisfied (for details see [4]):

$$V[W] + [(\boldsymbol{N}\boldsymbol{\nu}) \bullet \delta\boldsymbol{u}] + [(\boldsymbol{M}\boldsymbol{\nu}) \bullet \boldsymbol{w}] = 0 \quad \text{along } C\,. \tag{2}$$

Here $V = \delta\boldsymbol{x}_c \bullet \boldsymbol{\nu}$, $\boldsymbol{N} = \partial W / \partial \boldsymbol{E}$, $\boldsymbol{M} = \partial W / \partial \boldsymbol{K}$ are the resultant stress and couple tensors, $\boldsymbol{E}, \boldsymbol{K}$ are the shell strain and bending tensors, and $\boldsymbol{\nu}$ is the external unit normal to ∂M_A provided that the orientation of C coincides with that of ∂M_A. Besides, $[W] = W^+ - W^-$ is the jump of W at C with W^- and W^+ to be one-sided limits of W when the

respective boundaries ∂M_A and ∂M_B of C are approached. Not all of the virtual fields V, $\delta\boldsymbol{u}^{\pm}$, and $\boldsymbol{w}^{\pm}$ in (2) are independent, in general.

At the *coherent* phase interface C both $\boldsymbol{y}(\boldsymbol{x}) = \boldsymbol{x} + \boldsymbol{u}(\boldsymbol{x})$ and $\boldsymbol{Q}(\boldsymbol{x})$ are supposed to be continuous. In this case we have $[\boldsymbol{y}] = \boldsymbol{0}$, $[\boldsymbol{y}'] = \boldsymbol{0}$, $[\boldsymbol{Q}] = \boldsymbol{0}$, and $[\boldsymbol{Q}'] = \boldsymbol{0}$, where $(.)' \equiv d(.)/ds$. Then from the Maxwell theorem one can find the kinematic compatibility conditions $[\delta\boldsymbol{u}] + V[\boldsymbol{F}\boldsymbol{v}] = \boldsymbol{0}$ and $[\delta\boldsymbol{Q}] + V[(Grad_s\boldsymbol{Q})\boldsymbol{v}] = \boldsymbol{0}$ along C, with $\boldsymbol{F} = Grad_s\boldsymbol{y}$. This allows one to read off from (2) the following set of independent dynamic continuity conditions:

$$[\boldsymbol{N}]\boldsymbol{v} = \boldsymbol{0}, \quad [\boldsymbol{M}]\boldsymbol{v} = \boldsymbol{0}, \quad \boldsymbol{v} \bullet [\boldsymbol{C}_c]\boldsymbol{v} = 0 \quad \text{along } C. \tag{3}$$

Here $\boldsymbol{C}_c = W\boldsymbol{A} - \boldsymbol{N}^T\boldsymbol{F} - \boldsymbol{M}^T\boldsymbol{K}$, with $\boldsymbol{A}$ the surface metric tensor of M. The surface tensor $\boldsymbol{C}_c$ is an analog in shell theory of the Eshelby tensor used in continuum mechanics.

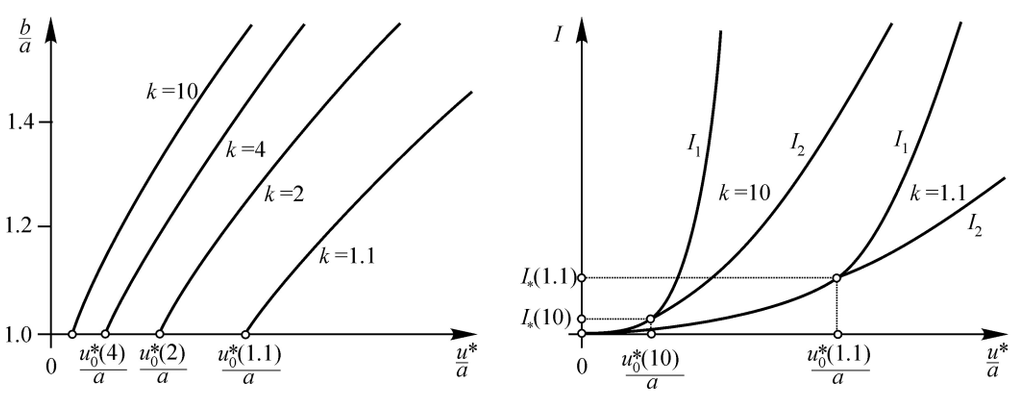
At the *incoherent* phase interface C, $\boldsymbol{y}(\boldsymbol{x})$ is still assumed to be continuous, but the continuity of $\boldsymbol{Q}(\boldsymbol{x})$ is allowed to be violated. It can then be shown that in this case $[\boldsymbol{Q}] \neq \boldsymbol{0}$ and $[\delta\boldsymbol{Q}] + V[(Grad_s\boldsymbol{Q})\boldsymbol{v}] \neq \boldsymbol{0}$. As a result, the condition (2) leads here to the following set of independent dynamic continuity conditions:

$$[\boldsymbol{N}]\boldsymbol{v} = \boldsymbol{0}, \quad \boldsymbol{M}^{\pm}\boldsymbol{v} = \boldsymbol{0}, \quad \boldsymbol{v} \bullet [\boldsymbol{C}_i]\boldsymbol{v} = 0, \text{ with } \boldsymbol{C}_i = W\boldsymbol{A} - \boldsymbol{N}^T\boldsymbol{F} \quad \text{along } C. \tag{4}$$

The conditions $(3)_{1,2}$ and $(4)_{1,2}$ express the balance of forces and couples at the phase interface C. The conditions $(3)_3$ and $(4)_3$ express the thermodynamic equilibrium of the material phases in the two-phase elastic shells. The latter conditions are necessary and sufficient for establishing the position vector $\boldsymbol{x}_c$ of C. The variational principle (1) and the dynamic continuity conditions (2)-(4) for elastic shells with phase transformation seem to be new in the literature.

EXAMPLE

The infinite plate with a central hole of radius a initially consisting of one material phase "B" is subjected to the uniform radial translation u^* of the hole boundary. Under the simple one-constants material laws of the phases defined by $W_{A,B} = C_{A,B}(E_{rr}^2 + \frac{1}{r^2}E_{\varphi\varphi})$ the transition to a new softer material phase "A" develops between the interface circle of radius b and the hole boundary. The solution exists only if $u^* > u_0^* = 2a/k$, with $k = C_B/C_A$. The left-hand Figure indicates the phase diagram for the values of b, and the right-hand Figure shows the values of the functional I of total potential energy calculated for the one-phase I_1 and two-phase I_2 solutions. I_2 is shown to be always lower than I_1.



Additional solutions of the phase transformation in a simply supported circular plate loaded by the surface pressure and in a semi-infinite circular cylinder loaded by the end couples were presented at the ICTAM2004.

Acknowledgements. The first author was partly supported by the Józef Mianowski Fund in Warsaw and The Competition Center of Natural Sciences in Saint-Petersburg State University (grant No E02-4.0-91), the second author was partly supported by the Polish Committee for Scientific Research (grant KBN No 5 T07A 008 25).

References

[1] Bhattacharya K., James R.D.: A theory of thin films of martensitic materials with application to microactuators. *J. Mech. Phys. Solids* **36**:531-576, 1999.

[2] Libai A., Simmonds J.G.: The Nonlinear Theory of Elastic Shells, 2nd ed. Cambridge Univ. Press, Cambridge 1998.

[3] Chróścielewski J., Makowski J., Pietraszkiewicz W.: Statics and Dynamics of Multifold Shells, Non-linear Theory and Finite Element Method (in Polish). Wyd. IPPT PAN, Warszawa 2004.

[4] Eremeyev V..A., Pietraszkiewicz W.: The non-linear theory of elastic shells with phase transitions. *J. Elasticity* **74**:67-86, 2004.

XXI ICTAM, 15–21 August 2004, Warsaw, Poland

ANALYTICAL SOLUTION FOR BENDING OF A CLAMPED ELLIPTICAL PLATE UNDER LATERAL LOAD AND IN-PLANE FORCE

Kenzo Sato*
*AKITA UNIVERSITY, Department of Engineerings and Information Science, Faculty of Education and Human Studies, Akita 010-8502, Japan

Summary On the basis of the ordinary thin plate theory, the analytical solution for the deflection by the bending of a clamped elliptical plate subjected to the uniform lateral load and in-plane force simultaneously is derived by the use of the elliptical cylinder coordinates. The solution is expressed in the form of an infinite series of Mathieu functions. The expressions for the bending moments are also derived analytically. Numerical calculation results are presented.

INTRODUCTION

Plane plates used as the elements of mechanical structures are commonly undergoing the action of various types of external forces in practical uses and therefore many studies on the bending of those plates have been reported during past years. About the bendings of rectangular plates and circular ones, which are subjected to the combined action of lateral load and in-plane force, the analytical solutions can be seen in the reference[1]. Also the studies on the bending of elliptical plates subjected to the action of external forces have been continued up to date[2]-[4]. An attempt to acquire the analytical solution for the bending of a clamped elliptical plate under the combined action of lateral load and in-plane force was made by Basuli[2]. However, his final solution is an approximation made by taking only a single Mathieu function of zero order[5]; besides, he gave no numerical information. Therefore, it cannot be regrettably stated that he had perfectly performed the theoretical analysis of the problem posed in his paper. The research on the purely analytical solutions for the bendings of plates contributes to the advance of the mathematical theory of elasticity; besides, the analytical solutions obtained successfully are very useful for confirming the validity of the other approximate numerical techniques. From the viewpoint of the usefulness of an elliptical plate as structural element and the importance of the research on the analytical solution for its bending, it is the purpose of this report to present the exact analytical solution for the bending of a clamped elliptical plate under the combined action of lateral load and in-plane force. Upon applying the orthogonality of Mathieu functions[6], the final deflection solution is expressed in the form of an infinite series of Mathieu functions. Moreover the expressions for bending moment distributions are also presented in this report. Some numerical calculation results are shown in a table and figures.

BASIC EQUATION AND ITS SOLUTION

The present problem is analyzed exactly in terms of the elliptical cylinder coordinates (ξ, η, z) which are related to the rectangular coordinates (x, y, z) by the relations $x = c\cosh\xi\cos\eta,\ y = c\sinh\xi\sin\eta,\ z = z$ with the semi focal length c. It is noted that c is denoted as $c = \sqrt{a^2 - b^2}$ in terms of the semi major axial-length a and the semi minor axial-length b. The differential equation for the deflection w of a clamped elliptical plate under uniform lateral load p and uniform in-plane compressive force T is given, by using the flexural rigidity D, as

$$\left\{\frac{2}{c^2(\cosh 2\xi - \cos 2\eta)}\left(\frac{\partial^2}{\partial\xi^2} + \frac{\partial^2}{\partial\eta^2}\right)\right\}\left\{\frac{2D}{c^2(\cosh 2\xi - \cos 2\eta)}\left(\frac{\partial^2}{\partial\xi^2} + \frac{\partial^2}{\partial\eta^2}\right) + T\right\} w = p. \tag{1}$$

The boundary conditions of an elliptical plate clamped along its periphery ξ_o are

$$w = 0\,|_{\xi=\xi_o}, \quad \partial w/\partial\xi\,|_{\xi=\xi_o} = 0. \tag{2}$$

The solution w satisfying the boundary conditions (2) is, by using the Mathieu functions ce_{2m}, the modified Mathieu functions Ce_{2m} and the Fourier coefficients $A_{2u}^{(2m)}$ of Mathieu function[5],

$$w = \frac{pc^2}{8T}\sum_{m=0}^{\infty}\left[2A_0^{(2m)}\cosh 2\xi + A_2^{(2m)} - \frac{\mathrm{Ce}_{2m}(\xi,q)}{\mathrm{Ce}_{2m}(\xi_o,q)}\left\{2A_0^{(2m)}\cosh 2\xi_o + A_2^{(2m)}\right\}\right.$$
$$\left. + \sum_{u=0}^{\infty} f_{2u}(\xi_o,q)A_{2u}^{(2m)}\delta_u\left\{\cosh 2u\xi - \frac{\mathrm{Ce}_{2m}(\xi,q)}{\mathrm{Ce}_{2m}(\xi_o,q)}\cosh 2u\xi_o\right\}\right]\mathrm{ce}_{2m}(\eta,q),\ \ \delta_u = 2\,(u=0), 1\,(u\neq 0), \tag{3}$$

where $q = Tc^2/4D$, ν denotes the Poisson's ratio and f_{2u} consist of the hyperbolic functions and the modified Mathieu functions. The bending moments M_ξ and M_η per unit length of sections of an elliptical plate perpendicular to ξ and η axes are, respectively,

$$M_\xi = -\left[pD/\left\{4T(\cosh 2\xi - \cos 2\eta)^2\right\}\right]\sum_{m=0}^{\infty}\left[\left\{H_{2m}^{(3)}(\xi,q) - \nu H_{2m}^{(1)}(\xi,q)(a_{2m} - 2q\cos 2\eta)\right\}(\cosh 2\xi\right.$$
$$\left. - \cos\eta)\mathrm{ce}_{2m}(\eta,q) - (1-\nu)H_{2m}^{(2)}(\xi,q)\sinh 2\xi\,\mathrm{ce}_{2m}(\eta,q) + (1-\nu)H_{2m}^{(1)}(\xi,q)\sin 2\eta\,\mathrm{ce}'_{2m}(\eta,q)\right] \tag{4}$$

$$M_\eta = -\big[pD/\{4T(\cosh 2\xi - \cos 2\eta)^2\}\big] \sum_{m=0}^{\infty} \big[\{-H_{2m}^{(1)}(\xi,q)(a_{2m} - 2q\cos 2\eta) + \nu H_{2m}^{(3)}(\xi,q)\}(\cosh 2\xi$$
$$- \cos\eta)\,\mathrm{ce}_{2m}(\eta,q) + (1-\nu)H_{2m}^{(2)}(\xi,q)\sinh 2\xi\,\mathrm{ce}_{2m}(\eta,q) - (1-\nu)H_{2m}^{(1)}(\xi,q)\sin 2\eta\,\mathrm{ce}'_{2m}(\eta,q)\big], \quad (5)$$

where $H_{2m}^{(1)}, H_{2m}^{(2)}$ and $H_{2m}^{(3)}$ consist of the hyperbolic functions and the modified Mathieu functions, and a_{2m} are the characteristic numbers of Mathieu functions[5].

NUMERICAL RESULTS

In numerical calculations for the elliptical plates having various aspect ratios a_o/b_o, the deflection and the moments were nondimensionalized as

$$\delta(\xi,\eta) = w(\xi,\eta)/(pb_o^4/D), \quad \alpha(\xi,\eta) = M_\xi(\xi,\eta)/(pb_o^2), \quad \beta(\xi,\eta) = M_\eta(\xi,\eta)/(pb_o^2). \quad (6)$$

It is noted that δ, α and β are directly proportional to w, M_ξ and M_η, respectively, and inversely proportional to p. Calculated results for various in-plane compressive force parameters λb_o^2 in the case of $a_o/b_o = 2$ are given in a table and figures. Poisson's ratio ν is 0.3. The numerical results are satisfactory as a whole and the detailed discussion will be presented at the conference.

Table 1. Convergence study of dimensionless deflection $\delta_c = \delta(0,\pi/2)$ at the plate center. $\lambda b_o^2 = 2$.

$m = u$	δ_c
0	0.028272
1	0.040965
2	0.042215
3	0.042126
4	0.042127
5	0.042127

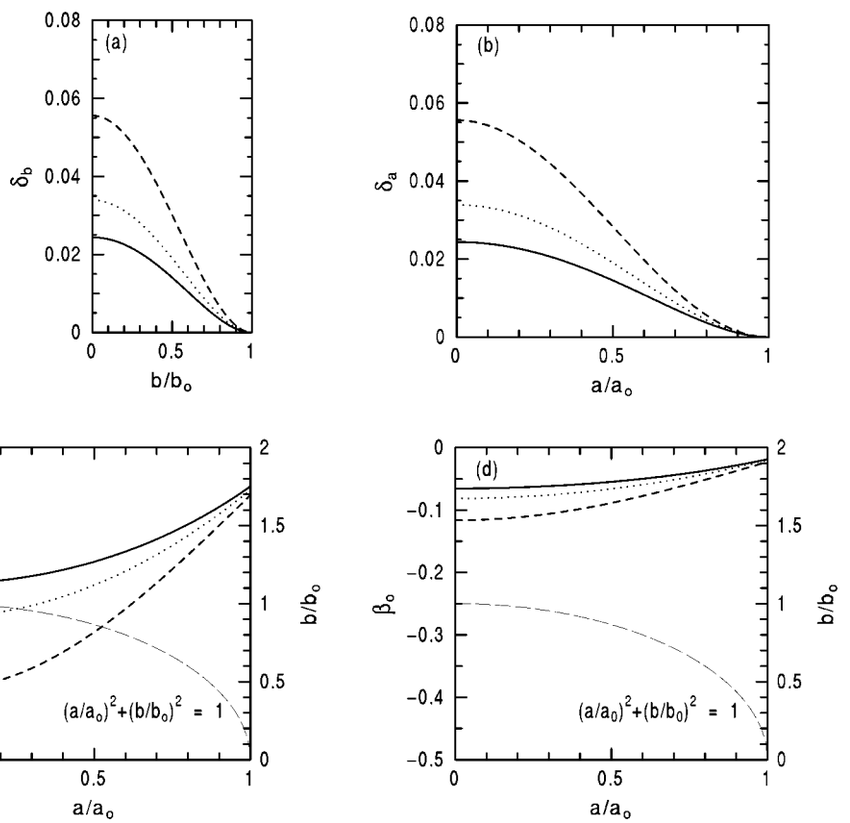


Figure 1. Dimensionless deflection δ and bending moments α, β : (a) $\delta_b = \delta(\xi,\pi/2)$ along the minor axis ; (b) $\delta_a = \delta(0,\eta)(a \le c), \delta(\xi,0)(a \ge c)$ along the major axis ; (c) $\alpha_o = \alpha(\xi_o,\eta)$ along the periphery ; (d) $\beta_o = \beta(\xi_o,\eta)$ along the periphery. ——, $\lambda b_o^2 = -4$; ·····, $\lambda b_o^2 = 0$; - - - - -, $\lambda b_o^2 = 4$; ———, the periphery depicted by taking the dimensionless coordinate axes a/a_o and b/b_o scaled differently for representing the ellipticity 1/2.

References

[1] Timoshenko S. : Theory of Plates and Shells, 2nd ed., 311,378-395 McGraw-Hill, NY 1959.

[2] Basuli S. : Bending of Elliptical Plates under Simultaneous Action of Lateral Load and Force in the Middle Plane of the Plate. Bull. Calcutta Math. Soc. 54, 203-209, 1962.

[3] Vasilenko A.T. : Bending of an Anisotropic Elliptical Plate on an Elastic Plate on an Elastic Foundation. Int. Appl. Mech., 38-3 351-355, 1996.

[4] Laura P.A.A. and Rossit C.A. : Thermal Bending of Thin, Anisotropic, Clamped Elliptic Plates. Ocean Eng., 29, 485-488, 1999.

[5] McLachlan N.W. : Theory and Application of Mathieu Function, Dover, NY 1964.

[6] Sato K. : Vibration and Buckling of a Clamped Elliptical Plate on Elastic Foundation and under Uniform In-plane Force. Theor. and Appl. Mech., 51 49-62, 2001.

XXI ICTAM, 15–21 August 2004, Warsaw, Poland

SENSITIVITY ANALYSIS CONCERNING THE INITIAL POSTBUCKLING BEHAVIOR OF ELASTIC STRUCTURES

Herbert A. Mang* and Christian Schranz*
*Institute for Strength of Materials, Vienna University of Technology, Karlsplatz 13, A 1040 Vienna, Austria

Summary Many engineering structures are imperfection-sensitive. A conversion to an imperfection-insensitive structure may be achieved by specific modes of stiffening. In this paper mathematical relations describing the sensitivity of the initial postbuckling behavior to such modes of stiffening is presented. Koiter's initial postbuckling analysis is applied in the context of the Finite Element Method to deduce these relations. They permit to determine whether or not a specific mode will result in a transition from imperfection sensitivity to insensitivity. Two relatively simple numerical examples serve as the vehicle to corroborate the theoretical findings.

INTRODUCTION

In order to improve the mechanical behavior of imperfection-sensitive structures, it is not sufficient to understand the influence of a specific mode of stiffening of a structure on the prebuckling behavior and the stability limit. What is equally important is knowledge about the corresponding influence on the postbuckling response. This was recognized, e.g., by Bochenek and Krużelecki [1] who have dealt with the challenging research topic of optimization of the postbuckling behavior of elastic structures. In case of loss of stability by means of symmetric bifurcation, the improvement of the (initial) postbuckling response by suitable stiffening may result in a conversion from an originally imperfection-sensitive to an imperfection-insensitive structure. Designation of a structure as either imperfection-sensitive or insensitive depends on the initial postbuckling behavior [2] which may (but need not) be relevant for the entire postbuckling response. In case of symmetric bifurcation, the mechanical consequence of these characteristics is loss of stability of an imperfect structure by snap-through at a load level that may be significantly lower than the one of the first bifurcation point on the primary path of the perfect structure. Hence, a conversion from an originally imperfection-sensitive to an imperfection-insensitive structure is desirable. This has been the motivation for sensitivity analyses concerning the initial postbuckling behavior of elastic structures with respect to specific modes of stiffening.

Conclusions of the present work will be drawn from the sensitivities of the parameters a_1, λ_2, and λ_4, where a_1 is the so-called nonlinearity coefficient, which is trivially zero for linear prebuckling paths, and λ_2 and λ_4 are the first two (generally) non-vanishing parameters in the asymptotic expansion of a load increment in terms of a path parameter for the secondary paths [2]. These quantities depend on a design parameter κ such as, e.g., the thickness of the structure or the stiffness of a suitably attached spring.

THEORETICAL INVESTIGATION

In Mang et al [3] details of Koiter's initial postbuckling analysis [2] in the context of the FEM [4] can be found. It is employed to derive a relationship between the three aforementioned parameters – λ_2, λ_4, a_1 – playing a central role in case of symmetric bifurcation from nonlinear primary paths [3]. The parameter λ_2 is related to the initial slope, whereas the parameters λ_2 and λ_4 are related to the initial curvature of secondary paths at the bifurcation point. The third parameter, a_1, is closely related to the curvature of the so-called "eigenvalue curve" at the stability limit, based on the consistently linearized eigenvalue problem [5].

Using Koiter's initial postbuckling analysis in the context of the FEM, the following relations can be derived:

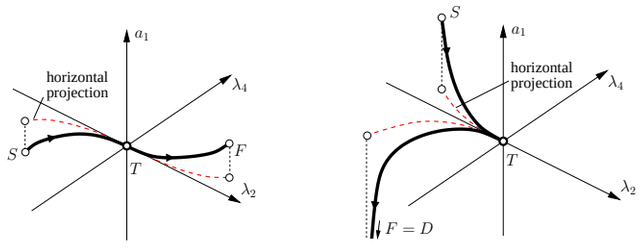
$$a_1\,\lambda_2^2 - d_3 + \lambda_4 = 0 \quad \text{and} \quad 2\,a_1\,\lambda_4 + b_4 = 0\,, \tag{1}$$

where d_3 and b_4 are additional parameters obtained from Koiter's initial postbuckling analysis. These two relations are the basis for assessing whether or not an increase of κ at $\lambda_2 = 0$ results in a transition from imperfection sensitivity to insensitivity. It is shown that the case of interest, i.e., $\lambda_2 = 0$, is characterized either by $a_1 = 0$ or $1/a_1 = 0$ and by special mathematical properties of the eigenvalue curve and the corresponding eigenvector curve, both depending on the load parameter. The common feature of the eigenvector curves at $\lambda_2 = 0$ is the existence of a singular point of the vector function $\mathbf{u}_1^*(\lambda)$ at the stability limit, indicating a fundamental change of the mechanical behavior of the structure. In case of nonlinear prebuckling paths, $a_1 = 0$ is a necessary condition for the aforementioned transition. Performing a sensitivity analysis on Equation (1.1) and specializing the result for this case, i.e., for $a_1 = 0$ and $\lambda_2 = 0$, yields the following relation for the rates of change of a_1 and λ_2 with respect to κ:

$$a_{1,\kappa}\;\lambda_{2,\kappa} = 0\,. \tag{2}$$

Six different sensitivity modes containing the combination of interest, i.e., $\lambda_2 = 0$, $a_1 = 0$, are shown to exist for structures with nonlinear prebuckling paths. However, only three of them lead to a transition from imperfection sensitivity to imperfection insensitivity. These modes are presented in form of λ_2-λ_4-a_1 diagrams which reflect the change of these parameters in the course of varying the design parameter κ, e.g., the stiffness of a suitably attached elastic spring, the thickness of the structure, or the rise of the undeformed structure.

Figure 1 shows λ_2-λ_4-a_1 diagrams of two of the six modes. The arrows on the curves indicate the direction of increase of the design parameter κ. The starting point is denoted as S and the final point as F. Point T is characterized by $\lambda_2 = 0$ and, hence, indicates a candidate point for a transition from imperfection sensitivity to insensitivity. Point D, characterized by $a_1 = -\infty$, indicates loss of stability by means of snap-through. Figure 1(a) illustrates a mode of stiffening for which a transition from imperfection sensitivity ($\lambda_2 < 0$) to insensitivity ($\lambda_2 > 0$) takes place. In contrast, the mode of stiffening illustrated in Figure 1(b) reaches point T, but does not lead to a transition to imperfection insensitivity.



(a) (b)

Figure 1: Qualitative plots of curves $\lambda_2 = \lambda_2(\kappa)$, $\lambda_4 = \lambda_4(\kappa)$, $a_1 = a_1(\kappa)$, with one point $T(\lambda_2 = 0, \lambda_4 = 0, a_1 = 0)$ each

NUMERICAL INVESTIGATION

The numerical investigation [6] involves two different structures which are both imperfection-sensitive. Hence, λ_2, which is related to the initial slope of the postbuckling path [3], is negative.

The first structure is a *von Mises* truss. As a first attempt to improve the initial postbuckling behavior, a spring is applied at the load point. Increasing the stiffness of the spring leads to an increase of λ_2. Eventually, the *von Mises* truss becomes imperfection-insensitive. The corresponding λ_2-λ_4-a_1 diagram is shown in Figure 1(a).

The second structure is a shallow cylindrical shell with a point load at the center. Attempting to improve the initial postbuckling behavior, the thickness of the shell is increased. At first, λ_2 increases and becomes zero for a specific value of the thickness (see point T in Figure 1(b)). However, if the thickness is further increased, λ_2 becomes negative again, and the structure stays imperfection-sensitive.

Next, an elastic spring is attached at the load point for different thicknesses of the shell. Increasing the stiffness of a spring for a thick shell leads to a transition from imperfection sensitivity to insensitivity. Hence, λ_2 becomes positive. For a thin shell, however, λ_2 stays negative and reaches zero only for the asymptotic limiting value of an infinite spring stiffness. Hence, if the thickness of the shell is smaller than a problem-dependent limiting value, a transition from $\lambda_2 < 0$ to $\lambda_2 > 0$ and, consequently, a conversion from imperfection sensitivity to insensitivity, is impossible.

Choosing the rise of the undeformed structure as the design parameter κ, it depends on the initial configuration of the two structures whether the decrease of the rise will result in a transition to snap-through or to no loss of stability.

CONCLUSIONS

Depending on the mode of stiffening, in case of symmetric bifurcation a transition from imperfection sensitivity to insensitivity is possible. Two simple structures were chosen as a vehicle for verification of the theoretical findings. Increasing the stiffness of a suitably attached spring leads to a conversion of the imperfection-sensitive *von Mises* truss to an imperfection-insensitive structure. In case of the shallow cylindrical shell, a minimum thickness is required for such a conversion to occur. Changing the rise of a structure has no influence on the parameter λ_2. Hence, it will not result in a transition from imperfection sensitivity to insensitivity. Increasing the stiffness through a uniform increase of the thickness of the structure does also not result in such a transition.

References

[1] Bochenek B., Krużelecki J.: A new concept of optimization for postbuckling behavior. *Engineering Optimization* **33**:503–522, 2001.

[2] Koiter W.: On the stability of elastic equilibrium. *Translation of* Over de Stabiliteit van het Elastisch Evenwicht, (1945). NASA TT F-10, Polytechnic Institute Delft, H.J. Paris Publisher Amsterdam, 1967.

[3] Mang H.A., Schranz C., and Mackenzie-Helnwein P.: Conversion from Imperfection-Sensitive into Imperfection-Insensitive Elastic Structures I: Theory. Prepared for submission to *IJNME*, 2004.

[4] Reitinger R.: Stabilität und Optimierung imperfektionsempfindlicher Tragwerke. *PhD Thesis*, Institut für Baustatik, Universität Stuttgart, 1983. In German.

[5] Helnwein P.: Zur initialen Abschätzbarkeit von Stabilitätsgrenzen auf nichtlinearen Last-Verschiebungspfaden elastischer Strukturen mittels der Methode der Finiten Elemente. Vol. 79 of Dissertationen an der Technischen Universität Wien. Österreichischer Kunst- und Kulturverlag, Wien, 1998. In German.

[6] Schranz C., Mang H.A., and Mackenzie-Helnwein P.: Conversion from Imperfection-Sensitive into Imperfection-Insensitive Elastic Structures II: Numerical Investigation. Prepared for submission to *IJNME*, 2004.

MESHLESS LBIE FORMULATIONS FOR VISCOELASTIC THIN PLATES

Jan Sladek, Vladimir Sladek
Institute of Construction and Architecture, Slovak Academy of Sciences, 84503 Bratislava, Slovakia

Summary In this paper, simply supported and clamped thin viscoelastic plates are analyzed. Linear viscoelasticity has been considered for which the correspondence principle is applied. The biharmonic differential equation for Laplace transform of deflections is decomposed into two Poisson equations. Local boundary integral equations are derived for this system of equations. The meshless approximation based on the moving least-squares is employed for the implementation.

1. INTRODUCTION

A viscoelastic problem can be solved either in the time domain directly or in the Laplace-transformed domain with the inversion being carried out later for a given time. The direct approach is leading to integro-differential field equations. In the approach based on the Laplace transform technique the correspondence principle [1] is utilized. The later approach is simpler and computationally more efficient if an accurate Laplace inversion technique is available. This method has been successfully applied to viscoelastic plate analyses by the boundary element method (BEM) [2].
If the correspondence principle is applied the governing partial differential equation is of the forth order. In case of plates with clamped edges and/or simply supported straight edges, it is possible to decompose the governing equation into a system of two Poisson equations [3] for Laplace transforms of deflection and its Laplacian, respectively. The meshless approach based on local boundary integral equations (LBIE) is applied to elastic plates [3]. In this paper the idea is extended to viscoelastic plates. Nodes are randomly spread on the middle plane of the plate. Each node is surrounded by a circle for which LBIE can be formulated.

2. LOCAL BOUNDARY INTEGRAL EQUATIONS

In accordance with Boltzmann´s principle the linear viscoelastic model take the form

$$\sigma_{ij}(\mathbf{x},t) = c_{ijkl}(t)\varepsilon_{kl}(\mathbf{x},t) + \int_0^t J_{ijkl}(t-\tau)\varepsilon_{kl}(\mathbf{x},\tau)d\tau \quad , \tag{1}$$

where σ_{ij} , ε_{ij} are the stress and small strain tensors, respectively, and J_{ijkl} the relaxation moduli. The first term in (1) corresponds to the elastic deformations. Viscoelastic materials are often simulated by a rheological model. In such a case the constitutive equations for a linear isotropic viscoelastic material is given as

$$\hat{\mathbf{D}}_1 s_{ij} = \hat{\mathbf{F}}_1 e_{ij} \quad , \qquad \hat{\mathbf{D}}_2 \sigma_{kk} = \hat{\mathbf{F}}_2 \varepsilon_{kk} \quad , \tag{2}$$

where $\hat{\mathbf{D}}_a$ and $\hat{\mathbf{F}}_a$ are the linear differential operators, s_{ij} and e_{ij} are deviators of stress and strain, respectively.
The Laplace transform of the convolution product is given by a simple product of Laplace transforms. Then, one can write

$$\bar{\sigma}_{ij} = 2\bar{\mu}\,\bar{\varepsilon}_{ij} + \bar{\lambda}\delta_{ij}\,\bar{\varepsilon}_{kk} \tag{3}$$

or

$$\bar{s}_{ij} = 2\bar{\mu}\,\bar{e}_{ij}$$
$$\bar{\sigma}_{kk} = 3\bar{K}\,\bar{\varepsilon}_{kk} \quad , \qquad \bar{K} = \left(2\bar{\mu} + 3\bar{\lambda}\right)/3 \quad , \tag{4}$$

where $\bar{\mu}$, $\bar{\lambda}$ and $\bar{K}$ are Laplace transforms of Lame moduli and bulk modulus, respectively.
In the case of quasi-static viscoelasticity the governing equation for bending of thin elastic plates in terms of the Laplace transforms become

$$\nabla^2\nabla^2\,\bar{w}(\mathbf{x},p) = \frac{\bar{q}(\mathbf{x},p)}{\bar{D}(p)} \quad , \tag{5}$$

where $\bar{D}(p)$ is the plate rigidity in the transformed domain given by

$$\bar{D}(p) = \frac{\bar{E}\,h^3}{12\left(1-\bar{\nu}^2\right)} \quad ,$$

with plate thickness *h*, Young modulus $\bar{E}(p)$ and Poisson ratio $\bar{\nu}(p)$. Laplace transform parameter is denoted by *p* and $\bar{q}$ is a load intensity in Laplace transform domain.
The governing equation (5) is decomposed into two Poisson equations:

$$-\bar{D}\,\nabla^2\bar{w}(\mathbf{x},p) = \bar{m}(\mathbf{x},p) \tag{6}$$

$$\nabla^2 \bar{m}(\mathbf{x}, p) = -\bar{q}(\mathbf{x}, p) \quad . \tag{7}$$

The Laplacian of deflection, $\nabla^2 \bar{w}(\mathbf{x}, p)$, has no physical meaning inside the plate. On a clamped edge, however $\bar{m}(\mathbf{x}, p)$ is equal to the bending moment. On a simply supported edge this is only the case if the edge is straight.
The solutions for the Poisson equations (6) and (7) can be expressed in integral form as

$$\bar{m}(\mathbf{y}, p) = \int_{\Omega} \bar{q}(\mathbf{x}, p) U(\mathbf{x}-\mathbf{y}) d\Omega + \int_{\Gamma} \left[\frac{\partial \bar{m}}{\partial n}(\mathbf{x}, p) U(\mathbf{x}-\mathbf{y}) - \bar{m}(\mathbf{x}, p) \frac{\partial U}{\partial n}(\mathbf{x}, \mathbf{y}) \right] d\Gamma \tag{8}$$

$$\bar{w}(\mathbf{y}, p) = \frac{1}{\bar{D}(p)} \int_{\Omega} \bar{m}(\mathbf{x}, p) U(\mathbf{x}-\mathbf{y}) d\Omega + \int_{\Gamma} \left[\frac{\partial \bar{w}}{\partial n}(\mathbf{x}, p) U(\mathbf{x}-\mathbf{y}) - \bar{w}(\mathbf{x}, p) \frac{\partial U}{\partial n}(\mathbf{x}, \mathbf{y}) \right] d\Gamma \quad , \tag{9}$$

where $\mathbf{y} \in \Omega$ and the kernel $U = (1/2\pi) \ln 1/r$ is the fundamental solution of the Laplace equation for an infinite plane.
The global integral equations (8) and (9) are coupled. Thus, they cannot be solved separately. Domain discretization of the coupled system and integration over the entire domain is not convenient for practical implementation. The approach based on a domain decomposition seems to be more convenient. The analyzed domain can be covered by a set of simple, regular subdomains. Integral equations (8) and (9) can be directly applied to each subdomain. Because of regular shape of the subdomains, all integrals can be evaluated easily. Nodal points are distributed not only on the boundary but also inside the investigated domain. No mesh is generated for the approximation of the field variables. The integral equations are considered for small subdomains Ω_s . Hence, no boundary densities (Laplace transforms) are prescribed on local boundary $\partial\Omega_s$ as long as it lies entirely inside Ω . To reduce number of unknowns on $\partial\Omega_s$ the modified fundamental solution [3]

$$U^*(r) = \frac{1}{2\pi} \ln \frac{r_0}{r} \tag{10}$$

is used in local boundary integral equations (LBIEs) for circular subdomains with radius r_0 . The modified fundamental solution is the Green function (for the Laplace equation) vanishing on the boundary of the circular subdomain ($r = |\mathbf{x}-\mathbf{y}| = r_0$) .
This leads to the following simplifications of LBIEs:

$$\bar{m}(\mathbf{y}, p) = \int_{\Omega_s} \bar{q}(\mathbf{x}, p) U^*(\mathbf{x}-\mathbf{y}) d\Omega - \int_{\partial\Omega_s} \bar{m}(\mathbf{x}, p) \frac{\partial U^*}{\partial n}(\mathbf{x}, \mathbf{y}) d\Gamma \tag{11}$$

$$\bar{w}(\mathbf{y}, p) = \frac{1}{\bar{D}(p)} \int_{\Omega} \bar{m}(\mathbf{x}, p) U^*(\mathbf{x}-\mathbf{y}) d\Omega - \int_{\partial\Omega_s} \bar{w}(\mathbf{x}, p) \frac{\partial U^*}{\partial n}(\mathbf{x}, \mathbf{y}) d\Gamma \quad . \tag{12}$$

The moving least-square (MLS) method is considered as the domain type approximation of the Laplace transforms in the LBIEs (11)-(12). The approximated function can be written as [4]

$$u^h(\mathbf{x}) = \sum_{a=1}^{n} \phi^a(\mathbf{x}) \hat{u}^a \quad . \tag{13}$$

Making use of the MLS approximation (13) for $\bar{m}(\mathbf{x}, p)$ and $\bar{w}(\mathbf{x}, p)$, the LBIEs yield the set of algebraic equations for $\hat{m}^a$ and $\hat{w}^a$. The time-dependent values of any of the transformed variables are obtained by an inverse transform. We have used Stehfest´s inversion technique.

References

[1] Lee E.H.: Stress analysis in viscoelastic bodies. *Quart. Appl. Math.* **13**:183-190, 1955.
[2] Ding R., Zhu Z.Y., Cheng C.J.: Boundary element method for solving dynamical response of viscoelastic thin plate. *Appl. Math.Mech.* **18**: 229-235, 1997.
[3] Sladek J., Sladek V., Mang H.A.: Meshless formulations for simply supported and clamped plate problems. *Int. J. Num. Meth. Engn.* **55**: 359-375, 2002.
[4] Belytschko T., Krongauz Y., Organ D., Fleming M., Krysl P.: Meshless methods, an overview and recent developments. *Comput. Meth. Appl. Mech. Eng.* **139**: 3-47, 1996.

EFFECT OF A "STATIC" RESONANCE IN ELASTIC THIN-WALLED CYLINDERS

Vasiliy L. Krasovsky, Maryna A. Varyanychko

Prydniprovs'ka State Academy of Civil Engineering and Architecture, Department of Strength of Materials and Civil Engineering Mechanics
49600, Dniepropetrovsk, Ukraine

Summary. Basing on the experiments the conclusion is drawn about existence of "static" resonance phenomena for shells at presence of periodic non-homogeneity of stress-strain state. The essence of resonance can be explained as a development, at static loading of thin-walled compressed cylinder of large bending deformations in case of variability of non-homogeneity, which is close to variability of first mode of eigen lateral oscillations of a structure.

The experiments data are considered in which deformation and buckling of longitudinally compressed circular cylindrical shells under periodically non-homogeneous in circular direction pre-buckling stress-strain state (SSS) are studied. The estimations have been performed on elastic, smooth, longitudinally reinforced (stringer type) thin-walled cylinders. The non-homogeneity of pre-buckling SSS of smooth shells was caused either by non-uniformity of loading or by non-uniformity of initial imperfections in the middle surface shape. For stringer modules the non-uniformity was caused by change of sign of eccentricity of ribs allocation. All experiments have been performed on high-quality small-sized samples using the same methods. These samples have been made produced from steel strip X18H9n (*conventional yield strength* σ_{02} *= 800 MPa)* using similar technology of spot weld. Given loading scheme and boundary conditions of simple support have been provided with special edge testing devices.

1. Non-uniform compression of smooth shells. One learnt the double-sided (on both edges of a shell) piece-wise-uniform kinematic (the equal displacements were applied) longitudinal compression on segments along the guiding circle. The compression is uniformly distributed along the perimeter. The dimensions of the loaded and unloaded segments were taken equal, and their allocation on the edges was accepted symmetric with respect to the cross-section of the cylinder. The number of segments of the loading (p), corresponding to the variability of the load in circumference direction, varied in a wide range: p = 2-48. The samples with the following relative geometrical characteristics were tested: L/R = 0.3-3.5; R/h = 150 - 300 (L, h are the length and thickness of the shell).

At prebuckling stage under uniform axisymmetric compression of shells the bending deformations were observed, which were caused by Poisson's effect together with the initial deflection development. The loss of stability occurred as a continuous process with one, snap creating 2-4 belts of rhomb shaped dimples. At non-uniform compression, alongside with a non-homogeneity of membrane stresses field the essential periodic in a circumferential direction bending deformation were observed. The character and intensity of these deformations were determined by changing the loading p and the geometry of a shell. The prebuckling radial displacements (w) appeared to be periodic and high stable. For example, for shells with geometry L/R = 2.0; R/h = 300 for all types of prebuckling deformation (excluding the case p = 2) the variability of displacements in a circumference direction corresponds with variability of the loading p. In the loaded zones the displacements develop inside the shell and in the unloaded zones– outside the shell. At $5<p<18$ these displacements can be well described by dependence $w=W\cos(py/R)$. The most intensive bending takes place at p = 6. The maximum curvature of generating line in this case is observed in a middle part of the shell. The increase of p leads to the movements of a zone with maximum curvature to the edges. At $p>$ 24 the non-uniformity of the loading does not cause any peculiarities to the prebuckling behaviour of the shells. In case of small variability of the loading (at $p<$ 5) the bend of generating line occurs along the whole length of a shell, however its intensity is much lower, than at p = 6. Note that at p = 2 the harmonics with a number of waves n= 6 was the basic components of the prebuckling bend in a circumference direction. The load-bearing capacity for non-uniformly compressed shells was reached because of the loss of stability in elastic stage of deformation. The values of N^{cr}, as well as prebuckling deformations, were determined varying the load p. The increase of a critical load (N^{cr}) at increase δ has appeared non-monotone, and the minimum value of N^{cr} in all range δ is marked at maximum prebuckling deformations (δ=6).

The peculiarities of the waveformation at buckling are determined by the type of prebuckling deformation**.** In case p = 6 the buckling mode was similar to mode of the first tone of lateral oscillations of a shell: the half-wave of dimples, spread along the whole length of the cylinder.

Similar results were obtained on the samples with other geometrical characteristics. The most considerable decrease of the critical stresses and loads at the most essential prebuckling deformations is observed. The deformations are characterized by the bending of generating lines on all length of the shell, and by the waveformation, similar mode of the first tone of lateral oscillations of a shell (n – the number of waves in circumference direction). The analysis of results, obtained on samples of the different geometry, showed, that they can be generalized if the variability of the loading in circumference direction connect with variability of the mode the first tone of oscillations n of a shell the shell. According to it the "resonance" variability of the loading, at which one the minimum critical stresses and loads is realized, can be evaluated as $p^*=n$. The generalized dependence "N^{cr}/N^{c}-p/n" (N^{c} is the classical value of critical load at homogeneous compression) is presented in fig. 1.

2. **Smooth shells with imperfections.** The experiments were performed on samples with the following geometry: L/R=2, R/h=360. The initial imperfections of a middle surface, in a form local flat dimples with depth W_0=(1.5-2.0) h, were made on shells artificially – by indenting of the spherical segment in the cylinder from its external surface (since

the natural sag was negligible, it was suppressed by the artificial sag). These dimples were applied in the middle (by length) cross-section, uniformly along the circumference. The number of dimples (variability of periodic imperfections in a circumference direction -n^0) varied from 2 up to 17. The samples without artificial dimples lost their stability with one snap at average values of N^{cr}=0.61N^c. The variability of the postbuckling mode – n^{cr}=9-10 (the calculated number of waves corresponding to N^c is n^c =17). The local buckling preceded to the general loss of stability of shells with artificial imperfections in all cases. The relative loads of transfer to the postbuckling configurations, depending on n^0, are represented in fig. 2. The light circles correspond to the loads of local buckling, the light quadrates ones to bifurcation modification of the local postbuckling configuration, and the dark circles correspond to the general loss of stability.

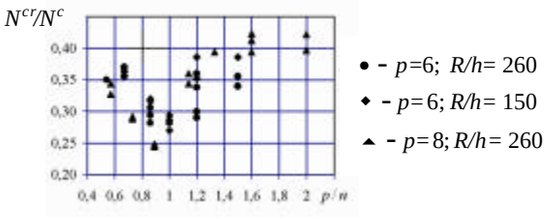


Fig.1

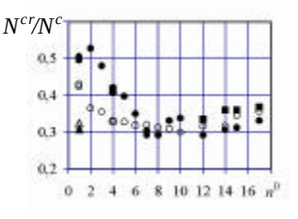


Fig.2

The analysis of dependence "$N^{cr}/N^{\tilde{n}} - n^0$" shows, that there is a selectivity of longitudinally compressed of the shell to the variability of the considered imperfections n^0. The highest influence of imperfections on N^{cr} appears at n^0=7-8. This variability of imperfections corresponds to the variability of the mode of the first tone of lateral oscillations of shell of buckling of the cylinder at external radial pressure, the designed value by which one compounds n = 7. In this case the buckling occurred with creation of the large dimples, similar of the mode of lateral oscillations. It should be noted that the presence of the essentially localized in a longitudinal direction of the initial dimple on a shell lead to the local postbuckling mode. The initial dimple was close to axisymmetric and differs by significant amplitude ($W_0 \geq 0.6h$). The light triangle corresponds to load of transfer to the local postbuckling mode, the dark triangle – to the general postbuckling mode.

3. Stringer shell with an eccentric versatile reinforcement. The series of 9 high-quality shells of equal geometry were tested. Each shell was equipped with 36 stringers, equidistant from each other: two samples with one-sided external and internal ribs and 7 samples - with versatile allocation of ribs periodically located in a circumference direction. The dimensions of panels with external and internal equipment were equal. The stiffeners allocation is shown in the table, where k_+, k_- are the numbers of panels on a sample with internal and external allocation of ribs respectively; t- number of ribs placed on each panel. It should be noted that the sign of an eccentricity of ribs in a circumference direction periodically varied for shells with a versatile reinforcement with frequency k=k_+. The geometry of shells: 2R=172 *mm*; (L/R=1); (R/h=465). The stringers of ⌊-profile with dimensions of cross-sections (3.2×3.9×0.345) *mm* were connected to the skin along the wide side of angle profile.

The local buckling of the skin between the ribs foreran to the overall loss of stability of shells. Such local buckling occurred with creation of large dimples with one half-wave along the length. The levels of the loads for which the intensive local waveformation (N^m) started, are presented in the Table 1.

Table 1

№ of sample	1	2	3	4	5	6	7	8	9
k_+/k_-	1/0	0/1	18/18	9/9	9/9	6/6	4/5	3/3	2/2
t	36	36	1	2	2	3	4	6	9
N^m, *kN*	36.5	32.3	22.3	12.1	13.3	22.0	21.9	22.4	22.2
N^{cr}, *kN*	41.4	59.1	31.9	24.6	26.2	40.8	30.1	46.7	31.9
N^*, *kN*	45.9	59.1	51.7	47.7	48.9	48.1	52.2	54.5	54.4

The collapse of the shells occurred during the process of their sequential loading. At first, the dimples were created "softly" without reduction of the load in zones with internal ribs. The corresponding load in the table is marked as N^{cr}. The limit of local-bearing capacity was reached in all cases with a destruction of external ribs. Such destruction was followed by sharp increase of intensity of buckling due to appearance of zones with plastic deformations. It should be noted that the ultimate loads (N^*) are insignificantly dependent on k. At the same time the value of N^{cr} sharply responds to change k and achieves of minimum value (twice less of N^*) at the most intensive buckling. The value of k is close to variability of general mode of the first tone of lateral oscillations of a shell (n = 11).

Conclusion. The reduced three examples indicate onto essential increase of static lateral deformations of a shell, at the variability of non-homogeneity close to the variability to the first mode of eigen oscillations. Such effect can be called a “static” resonance. It is possible to suppose, that the effect of a static resonance is inherent, to some extent, to all two-dimensional thin-walled structures. It is obvious, that the presence of such negative effect, as a static resonance, should be taken into account at the design of structures.

ENERGY–CONSERVING SCHEME FOR NONLINEAR DYNAMICS OF SHELLS – NUMERICAL EXAMPLES

Jacek Chróścielewski, Izabela Lubowiecka, Wojciech Witkowski[1]
Gdańsk University of Technology, Narutowicza 11/12, PL 80-952 Gdańsk, Poland

Summary We propose an energy-conserving algorithm for dynamics of shell structures. The dynamic analysis is performed using the six-field non-linear shell model, with three independent translations and three rotation parameters. The spatial approximation is based on FEM. Our temporal integration procedure is based on mid-point approximation of the rate equations expressed in state variables. Numerical simulation of non-linear dynamics of the branched shell undergoing multiple turns and large relative deformations is presented.

INTRODUCTION

The objective of the paper is to design an energy-conserving time-integration algorithm for the Hamiltonian dynamics of non-linear shell structures. Using such integration schemes plays the crucial role in the dynamic analysis of trusses, rods and shells as well as of multibody systems and more complex spatial structures. An efficient simulation of the overall motion of shell structures requires the use of relatively long time steps, and consequently the application of rather implicit time-stepping schemes. The FEM solution of flexible irregular shell structures leads to the large set of stiff equations. It can reveal a wide spectrum of vibration frequencies. In such cases some standard time-integration schemes loose their stability. This manifests itself, among others, by the sudden increase of the total energy, see [1,2], and simulations cannot be continued without reduction of the time step size. One of the ways to overcome this problem is to apply energy-conserving time-integration schemes. A number of algorithms capable of enforcing the energy conservation are proposed, e.g. [3–10].

ENERGY–CONSERVING INTEGRATION SCHEME

In this paper we propose an energy-conserving algorithm for shell dynamics based on the six-field shell model [11,14], that is with six engineering degrees of freedom in each FE node [12]. Motion of the irregular shell structure is described by the displacement vector field $\boldsymbol{u}=\boldsymbol{y}-\boldsymbol{x}$, where $\boldsymbol{x}$ and $\boldsymbol{y}$ are position vectors of the undeformed M and deformed shell base surface, and by the proper orthogonal tensor field $\boldsymbol{Q}\in SO(3)$. As a result, the rotation group enters the definition of the configuration space. In such problems of structural mechanics finite-dimensional approximations, like the finite element method and the temporal approximation, require non-standard approaches (see e.g. [1,12–14]). Kinetic constitutive relations for the translational and rotational momentum vectors are $\boldsymbol{p}=m_0\boldsymbol{v}$ and $\boldsymbol{\pi}=I_0\boldsymbol{\omega}$ (see [11]), where $\boldsymbol{v}=\dot{\boldsymbol{y}}$ and $\boldsymbol{\omega}$ are the linear and angular velocity vectors in the spatial representation, with $\mathrm{ad}\boldsymbol{\omega}=\dot{\boldsymbol{Q}}\boldsymbol{Q}^T$, $\mathrm{ad}: E^3\to so(3)$. The initial-boundary value problem in the weak form for the general dynamics of branched shell structures was formulated in [1,2,13]. For hyperelastic shells there exists a 2D strain energy density $W(\boldsymbol{\varepsilon}_\beta,\boldsymbol{\kappa}_\beta;\boldsymbol{x})$, with the shell strain vectors $\boldsymbol{\varepsilon}_\beta=\boldsymbol{y}_{,\beta}-\boldsymbol{Q}\boldsymbol{x}_{,\beta}$ and $\boldsymbol{\kappa}_\beta=\mathrm{ad}^{-1}(\boldsymbol{Q}_{,\beta}\boldsymbol{Q}^{\mathrm{T}})$, which implies the constitutive relations $\boldsymbol{n}^\beta=\partial W/\partial\boldsymbol{\varepsilon}_\beta$, $\boldsymbol{m}^\beta=\partial W/\partial\boldsymbol{\kappa}_\beta$, where $\boldsymbol{n}^\beta$ and $\boldsymbol{m}^\beta$ are the internal stress and couple resultant vectors, respectively.

The energy-conserving integration scheme of Simo and Tarnow [3] was applied to dynamics of shells e.g. in [4–7]. However, in dynamics of the six-field shell structures more adequate seems to be the algorithm proposed for rods in [8] and extended e.g. in [9,10]. The algorithmic energy-conserving approximation in the weak form is written here not in terms of acceleration, but in terms of difference of the momenta at t_{n+1} and t_n instants:

$$\frac{1}{\Delta t}\iint_{M\setminus\Gamma}[(\boldsymbol{p}_{n+1}-\boldsymbol{p}_n)\bullet\boldsymbol{v}+(\boldsymbol{\pi}_{n+1}-\boldsymbol{\pi}_n)\bullet\boldsymbol{w}]\,da+\iint_{M\setminus\Gamma}[\boldsymbol{n}^\beta\bullet(\boldsymbol{v}_{,\beta}+\boldsymbol{y}_{n+1/2,\beta}\times\boldsymbol{w})+\boldsymbol{m}^\beta\bullet\boldsymbol{w}_{,\beta}]\,da=G_{\mathrm{ext}}[\boldsymbol{u},\boldsymbol{Q};\boldsymbol{v},\boldsymbol{w}]\,, \tag{1}$$

where $\boldsymbol{y}_{n+1/2}=\frac{1}{2}(\boldsymbol{y}_{n+1}+\boldsymbol{y}_n)$, and $\boldsymbol{v}$, $\boldsymbol{w}$ are the virtual vector fields. In this algorithm the Cayley transformation $\Delta\mathbf{Q}=\mathrm{cay}(\Delta\mathbf{C})=\boldsymbol{I}+(1+\frac{1}{4}\Delta\mathbf{c}\bullet\Delta\mathbf{c})^{-1}(\Delta\mathbf{C}+\frac{1}{2}\Delta\mathbf{C}^2)=(\boldsymbol{I}+\frac{1}{2}\Delta\mathbf{C})(\boldsymbol{I}-\frac{1}{2}\Delta\mathbf{C})^{-1}$, $\boldsymbol{Q}_{n+1}=\boldsymbol{Q}_n\Delta\mathbf{Q}$, $\Delta\mathbf{C}=\mathrm{ad}(\Delta\mathbf{c})$, plays the crucial role. It allows one to formulate the mid-point approximation of the rate equations expressed in state variables as follows:

$$\boldsymbol{y}_{n+1}-\boldsymbol{y}_n=\boldsymbol{u}_{n+1}-\boldsymbol{u}_n=\Delta\boldsymbol{u}\,,\qquad \boldsymbol{Q}_{n+1}-\boldsymbol{Q}_n=\tfrac{1}{2}(\boldsymbol{Q}_{n+1}+\boldsymbol{Q}_n)\,\Delta\mathbf{C}=\mathbf{Y}_{n+1/2}\Delta\mathbf{C}\,, \tag{2}$$

where $\Delta\boldsymbol{u}=\frac{1}{2}\Delta t(\boldsymbol{v}_{n+1}+\boldsymbol{v}_n)$, $\Delta\mathbf{c}=\frac{1}{2}\Delta t(\boldsymbol{\omega}_{n+1}+\boldsymbol{\omega}_n)$, $\boldsymbol{\omega}=\boldsymbol{Q}^{\mathrm{T}}\boldsymbol{\omega}$, $\mathbf{Y}_{n+1/2}=\frac{1}{2}(\boldsymbol{Q}_{n+1}+\boldsymbol{Q}_n)$. Moreover, the tensor $\mathbf{Y}_{n+1/2}\notin SO(3)$ and the so-called algorithmic constitutive equations in the material representation are the key points of the formulation. The linearised equations of shell dynamics of the type (1) are written in the spatial representation, while the rotation,

[1] The author is awarded by Foundation for Polish Science

angular velocity and acceleration fields are computed in the material representation. Such an algorithm possesses the energy conservation property while retaining the convenience and efficiency of conventional time-stepping schemes.

NUMERICAL EXAMPLES

Large overall motion of the flexible cylindrical panel with change of the curvature sign, reinforced by a plate rib (see Fig. 1), is analysed. The pair of forces, described by the ramp time function, is initially applied to the structure during a short time period. After two seconds the shell is free from external loading and moves freely in space.

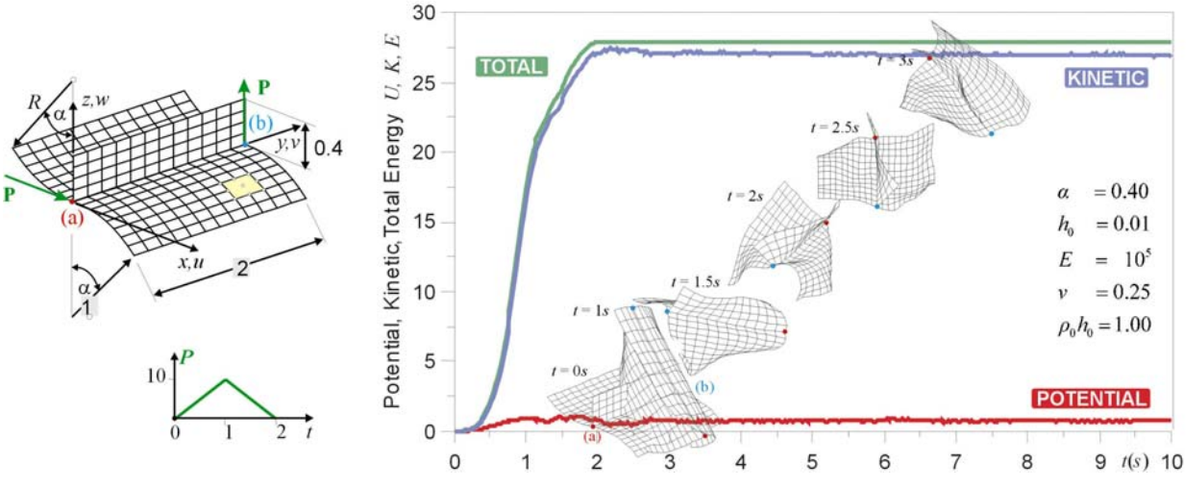


Fig. 1 Cylindrical panel. Geometry, energy functions and shell deformations

The example has been chosen for two reasons. Firstly, the geometry of the structure sharply verifies accuracy and capability of the shell theory applied, like e.g. good description of orthogonal connection of the shell branches. It is also a demanding test for importance of the sixth degree of freedom. Secondly, the overall motion of the shell is also an adequate test verifying the time-stepping scheme. The integration was done with the time step $\Delta t = 0.02\ s$. In the spatial discretization we used 9- and 16-node finite element (FI) with six degrees of freedom in each node. In both cases the energy levels were close to each other. The structure moves freely in space undergoing multiple turns and large relative deformations. Several stages of the motion and the energy histories are shown in Fig. 1.

Following the papers [15] and [16], in the next example, we consider the dynamics of three intersecting plates. The ramping load is applied to the system as in the example above. The shell geometry and resultant forces of the load uniformly distributed along the shell edges are depicted in Fig. 2. Several stages of the motion with shell deformations are shown in Fig. 3.

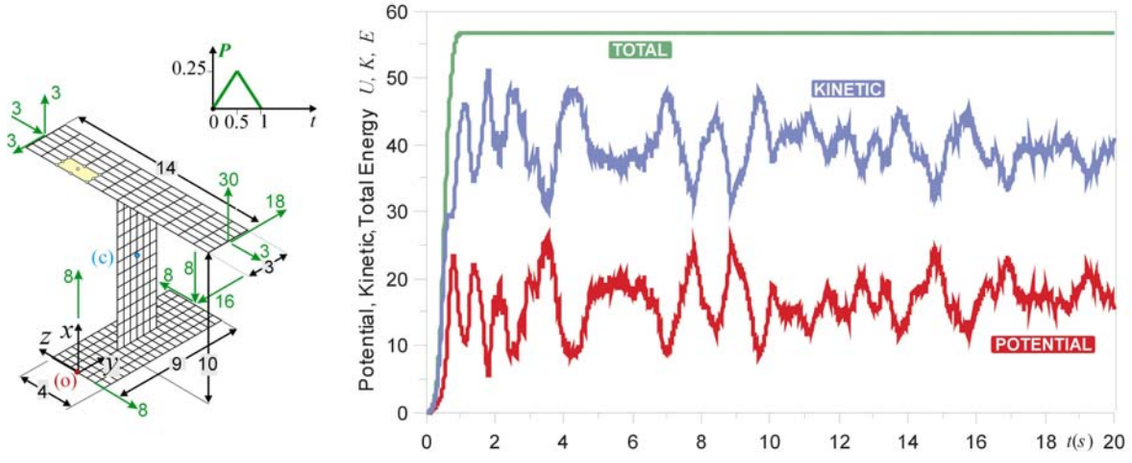
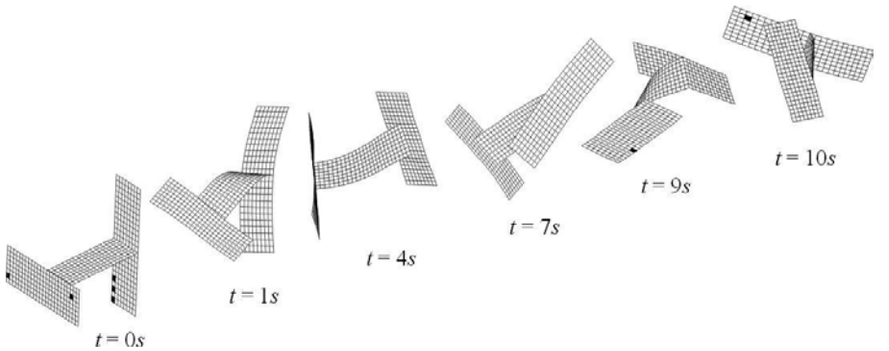


Fig. 2 Three intersecting plates. Geometry and energy functions

In the analysis the time step $\Delta t = 0.002\ s$ was used. Fig. 2 presents the results obtained with 9-node finite elements (FI) with mesh 4×12 elements for each plate. The computed total energy (~56), presented in the figure above, is different than that reported in references [15] and [16]: ~70 and ~20 respectively. This may be attributed, probably, to different

material data, which are not clearly depicted in both papers, and/or some problems with the convergence (mesh and locking phenomenon) of the finite element approximation. This issue has been already addressed in [17].



$$E = 2\times10^{7}$$
$$\nu = 0.25$$
$$h_0 = 0.02$$
$$J_{\rho_0} = 3.333\times10^{-5}$$
$$m_{\rho_0} = 0.02$$

Fig. 3 Three intersecting plates. Data and shell deformations

In this example, the use of 16-node finite elements (FI) with the same mesh yields an increase of the total energy (~60). This may stem from the second fact mentioned above.

CONCLUSIONS

The analysis presented in [1,12,13], based on the classical extended Newmark scheme, after some time leads to unjustified increase of the total energy of the system, which finally leads to numerical instability. However, application of our energy-conserving integration scheme gives in the first example the same results as those in [1,2,13] in the stable range and does not reveal instabilities. The second example shows that the energy-conserving scheme assures the stability of the solution within the entire range (of 20*s*) under investigation (Fig. 2). The comparable results from [15] and [16] are presented in a 10*s* and 15*s* period respectively.

Acknowledgements. This work was supported by the Polish State Committee for Scientific Research under grant No 5 T07A 008 25.

References

[1] Lubowiecka I.: Integration of non-linear equations of motion in structural mechanics. Dynamics of elastic shell structures (in Polish). *PhD Thesis*, Gdańsk University of Technology, 2001.

[2] Lubowiecka I., Chróścielewski J.: On dynamics of flexible branched shell structures undergoing large overall motion using finite elements. *Comput. Struct*. **80**:891-898, 2002.

[3] Simo J.C., Tarnow N.: The discrete energy-momentum method. Conserving algorithms for nonlinear elastodynamics. *J. Appl. Math.Phys.* **43**:757-792, 1992.

[4] Kuhl D., Ramm E.: Constraint energy momentum algorithm and its application to nonlinear dynamics of shells. *Comput. Methods Appl. Mech. Engrg.* **136**:293-315, 1996.

[5] Kuhl D., Ramm E.: Generalized energy-momentum method for non-linear adaptive shell dynamics. *Comput. Methods Appl. Mech. Engrg.* **178**:343-366, 1999.

[6] Simo J.C., Tarnow N.: A new energy and momentum conserving algorithm for the non-linear dynamics of shells. *Int. J. Num. Meth. Engng.* **37**:2527-2549, 1994.

[7] Romero I., Armero F.: Numerical integration of the stiff dynamics of geometrically exact shells: an energy-dissipative momentum-conserving scheme. *Int. J. Num. Meth. Engng.* **54**:1043-1086, 2002.

[8] Simo J.C., Tarnow N., Doblare M.: Non-linear dynamics of three-dimensional rods: exact energy and momentum conserving algorithms. *Int. J. Num. Meth. Engng.* **38**:1431-1473, 1995.

[9] Ibrahimbegović A., Mamouri S., Taylor R.L., Chen A.J.: Finite element method in dynamics of flexible multibody systems: modeling of holonomic constraints and energy conserving integration schemes. *Mult. Sys. Dyn.* **4**:195-223, 2000

[10] Armero F., Romero I.: Energy-dissipative momentum-conserving time-stepping algorithms for the dynamics of nonlinear Cosserat rods. *Comput. Mech.* **31**:3-26, 2003.

[11] Libai A., Simmonds J.G.: The Nonlinear Theory of Elastic Shells, 2nd ed. Cambridge University Press, Cambridge 1998.

[12] Chróścielewski J., Makowski J., Stumpf H.: Finite element analysis of smooth, folded and multi-shell structures. *Comput. Methods Appl. Mech. Engrg*. **141**:1-46, 1997.

[13] Chróścielewski J., Makowski J., Pietraszkiewicz W.: Non-linear dynamics of flexible shell structures. *Comp. Assisted Mech. Engng. Sci.* **9**:341-357, 2002.

[14] Chróścielewski J., Makowski J., Pietraszkiewicz W.: Statics and Dynamics of Multifold Shells, Non-linear Theory and Finite Element Method (in Polish). IPPT PAN, Warszawa 2004.

[15] Simo J.C., Tarnow N.: A new energy and momentum conserving algorithm for non-linear dynamics of shells. *Int. J. Num. Meth. Engng.* **37**:2527-2549, 1994.

[16] Miehe C., Shroeder J.: Energy and momentum conserving elastodynamics of non-linear brick-type mixed finite shell element. *Int. J. Num. Meth. Engng.* **50**:1801-1823, 2001.

[17] Chróścielewski J., Lubowiecka I., Pietraszkiewicz W.: FEM and time stepping procedures in non-linear dynamics of flexible branched shell structures, *Theories of Plates and Shells. Critical Review and New Applications* in *Lecture Notes in Applied and Computational Mechanics*, eds.: R. Kienzler, H. Altenbach, I. Ott, vol. **16**:21-28, 2004.

MINDLIN CYLINDRICAL PANELS WITH TWIST AND DOUBLE CURVATURE

T. Sakiyama[a], C. W. Lim[b], X. X. Hu[b,c], H. Matsuda[a], C. Morita[a]
[a] *Nagasaki University,1-14 Bunkyomachi, Nagasaki 852-8521, Japan*
[b] *City University of Hong Kong, Tat Chee Avenue, Kowloon, Hong Kong*
[c] *Zhejiang University of Technology, Hangzhou, Zhejiang 310032, PRC*

Summary An open cylindrical panel, which has a twist around the lengthways direction and double curvature in the radial and lengthways directions, is a better shell model of some turbine blades. For the sake of high accuracy of a vibration analysis method, a precise relationship between strains and displacement components of the shell model is derived on the general shell theory and the first order shear deformation theory. By using the principle of virtual work and the Rayleigh-Ritz method, the governing equation for free vibration of the model is presented. The effects of parameters such as curvature and twist on vibration are studied.

INTRODUCTION

Several comprehensive surveys of the research work on vibration of blades have been done by Rao [1-3] and Leissa [4,5], respectively. It is known that three models such as beam, plate and shell were adopted for studying the dynamics of blades, among of them the beam was the most common model and is also used for the research of blades now. Although the plate and the shell models were more approximate to the geometric configurations of blades, and there was a little related work reported. Since 80s more complicated and precise shell models have been presented. For example, Leissa, Lee *et al.* used twisted plate, shallow cylindrical shell and doubly curved shallow shell for models of turbo machinery blades and studied their vibration performance by the Ritz method [6-9]. Introducing a *pb*-2 Ritz method, Lim *et al.* studied the problem using several models such as the trapezoidal plate, the shallow cylindrical shell and the shallow conical shell [10-13]. Based on an exact strain-displacement relationship on the general shell theory, Tsuiji *et al.* presented a pretwisted thin plate and thin cylindrical models [14,15], and Hu *et al.* presented a curved and twisted thin cylindrical model [16] for the problem. Recently, Sakiyama *et al.* studied further the vibration characteristics of the twisted cylindrical panel with non-uniform thickness and the parametric effects [17].

The purpose of this work is to extend the research of thin shell model and to introduce an accurate strain-displacement relationship of the model under considering the influence of shear deformation. By the use of the principle of virtual work the energy equation of the panel for vibration is given out, and then the governing equation is achieved by the Rayleigh-Ritz method with orthonormal polynomials as admissible displacement components. The vibration characteristics and the effects on it are investigated briefly.

THEORETICAL FORMULATION

A profile, geometric parameters and the coordinate system of a new blade model is shown in Figure 1 where the cylindrical panel twists around the curvilinear *x*-axis at an constant twist rate *k*, and has two curvature (1/*R* and 1/*r*). Based on the accurate relation between strains and displacement components for the 3D panel [16] and the first order shear deformation theory, an exact strain formulae for the Mindlin cylindrical panel are obtained as follows:

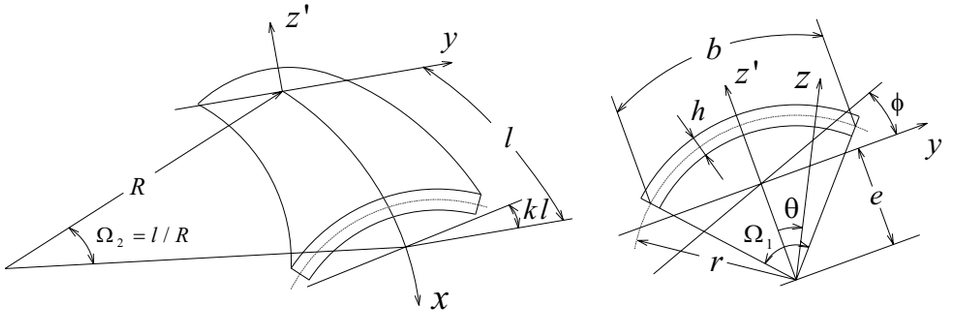


Figure 1. A schematic diagram of a Mindlin cylindrical panel

$$\left\{ \varepsilon_{\xi\xi} \quad \varepsilon_{\eta\eta} \quad \gamma_{\xi\eta} \quad \gamma_{\xi\zeta} \quad \gamma_{\eta\zeta} \right\}^T = \boldsymbol{\mathcal{Z}}_1 \boldsymbol{\mathcal{G}}^{(1)} \boldsymbol{\mathcal{R}}_1 + \boldsymbol{\mathcal{Z}}_2 \boldsymbol{\mathcal{G}}^{(2)} \boldsymbol{\mathcal{R}}_2, \tag{1}$$

$$\boldsymbol{\mathcal{R}}_1^T = \left\{ \frac{\partial u}{\partial x} \quad \frac{\partial u}{\partial y} \quad u \quad \frac{\partial v}{\partial x} \quad \frac{\partial v}{\partial y} \quad v \quad \frac{\partial w}{\partial x} \quad \frac{\partial w}{\partial y} \quad w \right\}, \qquad \boldsymbol{\mathcal{R}}_2^T = \left\{ \frac{\partial \psi_x}{\partial x} \quad \frac{\partial \psi_x}{\partial y} \quad \psi_x \quad \frac{\partial \psi_y}{\partial x} \quad \frac{\partial \psi_y}{\partial y} \quad \psi_y \right\}, \tag{2}$$

where $\boldsymbol{\mathcal{G}}^{(1)}$ and $\boldsymbol{\mathcal{G}}^{(2)}$ are matrices relative to the geometric parameters, matrices $\boldsymbol{\mathcal{Z}}^{(1)}$ and $\boldsymbol{\mathcal{Z}}^{(2)}$ are related to the thickness of panel only, and *u, v, w* are linear and ψ_x, ψ_y are angular displacement components.
The energy equation of motion is given out by the principle of virtual work,

$$\delta\Pi = \iiint_{vol} \varepsilon^T \delta\sigma \, dV_{ol} - \iiint_{vol} \rho\,\omega^2 \boldsymbol{U}\delta\boldsymbol{U} \, dV_{ol}, \tag{3}$$

Considering the Rayleigh-Ritz method, a set of orthonormal polynomials is chosen as admissible functions shown in the following,

$$u = \sum_{i=1}^{N_u}\sum_{j=1}^{M_u} a_{ij}^{u}\,\Phi_i^u(x)\,\Psi_j^u(y), \quad v = \sum_{k=1}^{N_v}\sum_{l=1}^{M_v} a_{kl}^{v}\,\Phi_k^v(x)\,\Psi_l^v(y), \quad w = \sum_{m=1}^{N_w}\sum_{n=1}^{M_w} a_{mn}^{w}\,\Phi_m^w(x)\,\Psi_n^w(y),$$
$$\psi_x = \sum_{p=1}^{N_{\psi x}}\sum_{q=1}^{M_{\psi x}} a_{pq}^{\psi_x}\,\Phi_p^{\psi_x}(x)\,\Psi_q^{\psi_x}(y), \quad \psi_y = \sum_{r=1}^{N_{\psi y}}\sum_{s=1}^{M_{\psi y}} a_{rs}^{\psi_y}\,\Phi_r^{\psi_y}(x)\,\Psi_s^{\psi_y}(y), \tag{4}$$

where $\Phi_P^S(x)$ and $\Psi_Q^S(y)$ $(S = u,\, v,\, w,\, \psi_x,\, \psi_y;\;\; P, Q = 1,\, 2,\, 3, \cdots)$ are orthonormal polynomials generated by the Gram-Schmidt process but their first polynomials $\Phi_1^S(x)$ and $\Psi_1^S(y)$ are defined according to the geometric boundary conditions of panel. Substituting equations (4) into equation (3) and the independent property of the coefficients in equation (4) yield the following governing equation,

$$\left|\boldsymbol{K} - \lambda^2 \boldsymbol{M}\right| = \boldsymbol{0}, \tag{5}$$

and then the eigenproblem of the vibration of blades can be solved.

CONCLUSIONS

Using the general shell theory and the first order shear deformation theory, an accurate relationship between strains and displacement components for the Mindlin cylindrical panel with twist and two curvature is derived. The governing equation for free vibration is formulated by the principle of virtual work and the Rayleigh-Ritz method with a set of orthonormal polynomials. Vibration frequencies and modes are achieved for Mindlin cylindrical panels with different geometric parameters such as the twist, the curvature and the aspect ratio, and then the characteristics of the model is revealed.

Acknowledgement

The work described in this paper was fully supported by a grant from the Research Grant Council of the Hong Kong Special Administrative Region [Project No. 7001534 (BC)]

References

[1] RAO J.S.:Natural frequencies of turbine blades–A survey. *Shock Vib. Digest* **5**,3-16,1973.
[2] RAO J.S.:Turbine blading excitation and vibration. *Shock Vib. Digest* **9**,15-22,1977.
[3] RAO J.S.:Turbomachine blade vibration. *Shock Vib. Digest* **12**,19-26,1980.
[4] LEISSA A.W.:Vibration of turbine engine blades by shell analysis. *Shock Vib. Digest* **12**,3-10,1980.
[5] LEISSA A.W.:Vibrational aspects of rotating turbomachinary blades. *Appl. Mech. Rev.* **34**,629-635,1981.
[6] LEISSA A.W.,LEE J.K.,WANG A.J.:Rotating blade vibration analysis using shells. *J. Eng. Power, ASME* **104**,296-302,1982.
[7] LEISSA A.W.,EWING M.S.:Comparing of beam and shell theories for the vibrations of thin turbomachineary blades. *J. Eng. Power, ASME.* **105**,383-392,1983.
[8] LEISSA A.W.,LEE J.K.,WANG A.J.:Vibrations of cantilevered doubly-curved shallow shells. *Int. J. Solids Struct.* **19**,411-424,1983.
[9] LEE J.K.,LEISSA A.W.,WANG A.J.:Vibration of blades with variable thickness and curvature by shell theory. *J. Eng. Gas Turb. Power.* **106**,11-16,1984.
[10] LIM C.W.,LIEW K.M.:Vibration of pretwisted cantilever trapezoidal symmetric laminates. *Acta Mech.* **111**,193-208,1995.
[11] LIM C.W.,LIEW K.M.:The vibration behaviour of shallow conical shells by a global formulation. *Eng. Strucut.* **17**,63-70,1995.
[12] LIM C.W.:Investigating the limit of turbomachinery blade modeling with linear pretwist. In: Ewing, M.S., Leissa, A.W.(Eds.), 2nd Int. Symp. Vib. Continuous Sys.,33-35. Switzerland,12-16 July,1999.
[13] LIM C.W.:Vibration of turbomachinery blades with non-linear twisting curvature. In: Wang, C.M., Lee, K.H., Ang, K.K. (Eds.), APCOM'99,493-498. Singapore, 15-17 December,1999.
[14] TSUIJI T.,TAKAGI K.,YAMASHITA T.:Free vibrations of curved and twisted cantilevered thin plates (Analytical and experimental results). *JSME* **60**(C),4079-4084,1994.
[15] TSUIJI T.,SUEOKA T.:Vibration analysis of twisted thin cylindrical panels by using the Rayleigh-Ritz method. *JSME* **61**(C),4575-4586,1995.
[16] HU X.X.,TSUIJI T.:Free vibration analysis of curved and twisted cylindrical thin panels. *J. Sound Vib.* **219**,63-88,1999.
[17] SAKIYAMA T.,HU X.X.,MATSUDA H.,MORITA C.:Vibration of twisted and curved cylindrical panels with variable thickness. *J. Sound Vib.* **254**,481-502,2002.

XXI ICTAM, 15–21 August 2004, Warsaw, Poland

APPLICATION OF THE RETURN MAPPING ALGORITHM TO PERZYNA VISCOPLASTICITY FOR PLANE STRESS

Zdzislaw Nowak*, Krzysztof Wisniewski*
*Polish Academy of Sciences, IPPT PAN, Swietokrzyska 21, PL 00-049 Warszawa, Poland

Summary In the paper the elastic-viscoplastic constitutive relations of the Perzyna-type are investigated for plane stress problems. A fully implicit integration algorithm is adopted and the relevant expression for the consistent tangent operator for the von Mises yield criterion and flow functions of arbitrary type is derived. It is shown how the elasto-plastic rate equations of standard plasticity can be generalized to overstress-type models of viscoplasticity, where the stress point can be located outside the loading surface. Numerical example is given to reveal the differences and the similarities between the plastic and the viscoplastic overstress models.

PROBLEM FORMULATION

This paper presents a version of the return-mapping algorithm for plane stress problems. Three-dimensional radial return algorithm can be easily modified for the plane strain problem, but not for problems with additional constraints on stresses. Two such constraints are of interest for plates and shells: (a) the zero normal stress condition, $\sigma_{33} = 0$, and (b) the plane stress condition, $\sigma_{\alpha 3} = \sigma_{33} = 0$. With the latter constraints the radial return algorithm and an explicit expression for viscoplastic multiplier cannot be used (cf. Simo and Taylor [2], Alfano at al.[5]).

In literature, various viscoplastic material models have been proposed for the analysis of time-dependent deformations of materials. A widely-used viscoplastic formulation is the Perzyna model [1]. The main feature of this model is that the rate-independent yield function used for describing the viscoplastic strain can be larger than zero, the effect known as the 'overstress'. The characteristics of the Perzyna model as well as the numerical discretization have been addressed by various authors (e.g. Simo and Hughes[3], Ju [6], Klee and Paulun [7]).

PERZYNA VISCOPLASTICITY

The main idea of the viscoplastic flow mechanism is to accomplish in one model the description of behaviour of material valid for the entire range of strain rate changes. To achieve this aim the empirical overstress function Φ has been introduced and the strain rate is postulated in the form as follows (cf. Perzyna [1])

$$\dot{\epsilon}_{ij}^{vp} = \gamma \ \langle \ \Phi(\frac{\sigma_{eq}}{\sigma_Y(\epsilon_{eq}^{vp})} - 1) \ \rangle \ \frac{\sigma_{ij}^{'}}{\sigma_{eq}} \quad , \tag{1}$$

where σ_{eq} is effective stress, ϵ_{eq}^{vp} is effective strain, σ_Y is a yield stress and the overstress function is defined as

$$\Phi(\cdot) \ = \ (\frac{\sigma_{eq}}{\sigma_Y(\epsilon_{eq}^{vp})} - 1)^m \quad . \tag{2}$$

In equation(1) and (2) the material constants are $\gamma \in [0, +\infty]$ and $m \geq 1$. The symbol $\langle \ \rangle$ means $\langle \Phi \rangle = F$ for F>0 and $\langle \Phi \rangle = 0$ for $F \leq 0$.

NUMERICAL EXAMPLE

We analyze a thin rectangular strip with a circular hole in its axial direction, subjected to increasing extension in a direction perpendicular to the axis of the strip and parallel to the long side of the rectangular section. For symmetry reasons the analysis is performed for one quarter of the section with appropriate boundary conditions. The adopted mesh consists of 230 nodes and 198 elements. The material used was an aluminium $57S$ with elastic modulus $E = 7000$ MPa, Poisson's ratio $\nu = 0.3$, a yield stress $\sigma_y^0 = 243$ MPa. The strain hardening of the aluminium is idealized by a linear hardening function with the plastic tangent modulus $H = 220$ MPa, like in Theocaris and Marketos [4].

The ratio of the diameter d of the hole to the width w of the strip was taken equal to one half. The thickness, t, of the strip was taken equal to 1/56 of the width, w, which is much less than the radius of perforation d. In each analysis, the velocity $\dot{U}$, was fixed. Different velocities $\dot{U} = \Delta u/\Delta t$ are obtained by changing the time increment Δt and keeping Δu constant.

The return mapping algorithm for the Perzyna viscoplasticity model was implemented in ABAQUS via a user-defined material subroutine UMAT. We used a 4-node element with reduced Gauss integration $(CPS4R)$.

The obtained strain and stress distributions are compared with the numerical results of Klee and Paulun [7] and with the experimental data published by Theocaris and Marketos [4]. The following results of the numerical calculations are presented.

1. The isochromatic patterns in normal incidence for the ratio of the diameter of the hole to the width of the strip $d/w = 0.5$ (after Theocaris and Marketos[4] (Steps I-III-V-VI)) is compared with the distribution of the equivalent plastic stress obtained by our numerical method.

2. The evolution of elastic-plastic boundary for $d/w = 0.5$ is presented. The final plastic zones for the loads IV ($\bar{t} = 0.4\sigma_y^0$) and VI ($\bar{t} = 0.53\sigma_y^0$) obtained numerically by our method and Klee and Paulun [7] based on the FEM are compared with the experimental ones.

3. The distribution of stress σ_{22} in the minimum section of strip in dependence of time is given. The steady state can be compared with the measured values of Theocaris and Marketos [4].

A good agreement of the numerical results with the experimental ones is observed.

CONCLUSIONS

A non-linear solution procedure based on the backward-Euler operator for the rate dependent Perzyna-type models is presented. The plane stress return-mapping formulation for a general overstress viscoplasticity models is described, and it has following features:

- the stresses are updated in an efficient and reliable way;
- in one algorithm we can efficiently handle the viscoplastic and plastic plane stress cases;
- the derived consistent tangent operator gives the appropriate convergence rate in the Newton-Raphson solution procedure. For other viscoplastic models (e.g. Duvaut-Lions), results can be readily obtained by specializing the relevant flow and overstress function. In the absence of viscous effects, i.e. when $\gamma\Delta t \longrightarrow \infty$ the consistent plastic tangent operator for plane stress is recovered;

Numerical computations carried out for the typical benchmark problem and comparison with the experimental data of Theocaris and Marketos [4] confirmed the accuracy and robustness of the proposed algorithm.

Acknowledgements

This research was supported by the Polish Committee for Scientific Research (KBN) Grant 7T11F 01921.

References

[1] Perzyna, P.: Fundamental problems in viscoplasticity, Advances in Applied Mechanics, **9**, 343–377, 1966.
[2] Simo J.C., Taylor R.L., A return mapping algorithm for plane stress elastoplasticity, Int. J. Num. Meth. Engng., **22**, 649-670, 1986.
[3] Simo J.C., Hughes T.J.R., Computational inelasticity, Springer, New York, 1998.
[4] Theocaris P., Marketos E.: Elastic-plastic analysis of perforated thin strip of a strain-hardening material, J. Mech. Phys. Solids, **12**, 377-390, 1964.
[5] Alfano G., De Angelis F., Rosati L., General solution procedures in elasto/viscoplasticity, Comput. Methods Appl. Mechy. Engrg., **190**, 5123-5147, 2001.
[6] Ju J.W., Consistent tangent moduli for a class of viscoplasticity, J. Engrg. Mech., **116**, No. 8, 1764-1779, 1990.
[7] Klee K.D., Paulun J., On numerical treatment of large elastic-viscoplastic deformations, Arch. Mech., **32**, 333-345, 1980.

XXI ICTAM, 15–21 August 2004, Warsaw, Poland

A PERTURBATION METHOD FOR NONLINEAR VIBRATIONS OF STRUCTURES

E.L. Jansen
Delft University of Technology, Faculty of Aerospace Engineering, Kluyverweg 1, 2629 HS Delft, The Netherlands

Summary A perturbation theory for the large amplitude vibration analysis of general, statically loaded imperfect structures is used to investigate the dependence of the natural frequencies of structures on finite vibration amplitudes, initial geometric imperfections, and a nonlinear static deformation. An extension to a multi-mode analysis is presented. Characteristic results of the buckling and nonlinear vibration analysis of isotropic and composite shells illustrate the capabilities of the computational modules developed.

INTRODUCTION

A perturbation theory for the large amplitude vibration analysis of general, statically loaded imperfect structures is presented. The method is based on a perturbation expansion for both the frequency parameter and the dependent variables. The theory developed forms an extension of earlier work in [4] and [5], and makes it possible to investigate the dependence of the natural frequencies of structures on finite vibration amplitudes, initial geometric imperfections, and a nonlinear static deformation (orthogonal to the axisymmetric fundamental state).

STATIC AND DYNAMIC ANALYSIS

Using D'Alembert's principle to introduce inertial loading, the variational equation of motion (dynamic equilibrium) can be formulated as follows,

$$M(\ddot{\mathbf{u}}) \cdot \delta\mathbf{u} + \sigma \cdot \delta\varepsilon = \mathbf{q} \cdot \delta\mathbf{u} \tag{1}$$

where $\mathbf{u}$, ε, and σ denote the generalized displacement, strain, and stress, respectively. These field variables can be interpreted as vector functions with variables appropriate to the problem. Further, M is the generalized mass operator, $\mathbf{q}$ is the applied load, and $\ddot{(\,)} = \partial^2(\,)/\partial t^2$, where t denotes time. In Eq. (1) $\mathbf{a} \cdot \mathbf{b}$ is the virtual work of stresses or loads $\mathbf{a}$ acting through strains or displacements $\mathbf{b}$, integrated over the entire structure for kinematically admissible variations $\delta\mathbf{u}$. In addition, we have the strain-displacement relation

$$\varepsilon = L_1(\mathbf{u}) + \frac{1}{2}L_2(\mathbf{u}) + L_{11}(\bar{\mathbf{u}}, \mathbf{u}) \tag{2}$$

where $\bar{\mathbf{u}}$ is an initial geometric imperfection, and where L_1 and L_2 are homogeneous linear and quadratic functionals, respectively, and L_{11} is a homogeneous bilinear functional [4, 5].

The situation of a dynamic state on a nonlinear static state is analysed for the case that a natural frequency corresponds to a single vibration mode. Assuming that the structure is vibrating in a deformed configuration due to a static loading (the 'static' state), the variables can be written as a superposition of two states. The static state response in turn is assumed to consist of a (nonlinear) fundamental ('trivial') state and a nonlinear buckling ('nontrivial' or 'orthogonal') state. The nonlinearity of the buckling state is taken into account via a perturbation expansion of the buckling variables. The equations governing the equilibrium of the fundamental static state, the (nonlinear) buckling state, and the dynamic state, respectively, can be derived systematically.

The first-order state equation forms an eigenvalue problem for the unknown natural square frequency ω_0^2. The relation of the frequency squared to the vibration amplitude and the effective imperfection amplitude is derived via a contraction procedure, i.e., the first-order equilibrium equation at the critical point (which can be seen as an orthogonalization condition for the higher modes with respect to the critical mode) is used as a constraint to eliminate the third-order variables.

DYNAMIC MULTI-MODE ANALYSIS

If a natural frequency corresponds to more than one vibration mode, a multi-mode analysis can be performed, analogous to the analysis in [2] for buckling mode interaction. Supposing that there are M vibration modes, denoted as $\mathbf{u}_{d_i}$, with corresponding natural frequency squared $\omega^2 = \omega_{0_i}^2$ and amplitude ξ_i ($i = 1, 2, \ldots, M$), the dynamic state displacement field for a 'perfect' unloaded structure can be written as

$$\mathbf{u}_d = \xi_i \mathbf{u}_{d_i} + \xi_i \xi_j \mathbf{u}_{d_{ij}} + \ldots \tag{3}$$

with corresponding expressions for the stress and strain fields,

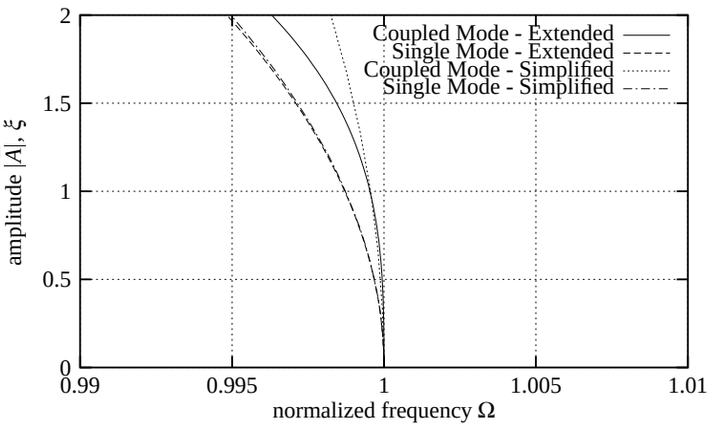


Figure 1. *Amplitude-frequency curves for Single Mode and Coupled Mode nonlinear vibrations of isotropic shell. Comparison between Simplified Analysis (vibration mode amplitude $|\bar{A}|$) and present Extended Analysis (vibration mode amplitude ξ); $\Omega = \omega/\omega_{0_1}$.*

$$\sigma_d = \xi_i \sigma_{d_i} + \xi_i \xi_j \sigma_{d_{ij}} + \dots \tag{4}$$

$$\varepsilon_d = \xi_i \varepsilon_{d_i} + \xi_i \xi_j \varepsilon_{d_{ij}} + \dots \tag{5}$$

In this case nonlinear amplitude-frequency relations are obtained of the following form,

$$\xi_I [1 - \frac{\omega^2}{\omega_{0_I}^2}] + A_{ijI} \xi_i \xi_j + B_{ijkI} \xi_i \xi_j \xi_k = 0, \quad I = 1, 2, \dots, M \tag{6}$$

where the coefficients A_{ijI} and B_{ijkI} depend on the first-order and second-order stress and strain fields, respectively.
The perturbation theory developed is applied to the nonlinear (large amplitude) vibration problem of anisotropic cylindrical shells including edge effects. The starting point of the analysis are the Donnell-type differential equations of an anisotropic circular cylindrical shell. An axisymmetric fundamental state is included in the formulation. The first-order state problem constitutes an eigenvalue problem for the unknown eigenfrequencies and vibration modes. The associated higher-order state problems are response problems with coefficients that depend on the solution of the first-order state problem.
Koiter's initial post-buckling and imperfection sensitivity theory deals with the dependence of the load parameter on the deflection and imperfection amplitudes in the case of static buckling problems. In [1], Koiter's theory has been applied to the buckling of composite cylindrical shells. The theory developed in the present paper is related to the work described in [1]. The perturbation approach has been applied to the single mode nonlinear vibrations of composite shells in [3].

RESULTS

Characteristic results of the buckling and nonlinear vibration analysis of isotropic and composite shells are presented, in order to illustrate the capabilities of the computational modules developed. In Figure 1 the amplitude - frequency curves of the coupled mode nonlinear vibrations of an isotropic shell are compared with the single mode results, for different levels of analysis complexity. In the present analysis (denoted as 'Extended Analysis') the specified ('simply supported') boundary conditions are taken into account accurately, while in the 'Simplified Analysis' these boundary conditions are satisfied only approximately.

References

[1] J. Arbocz and J.M.A.M. Hol. Koiter's stability theory in a computer-aided engineering (CAE) environment. *Int. J. Solids Structures*, 26(9/10):945–975, 1990.
[2] E. Byskov and J.W. Hutchinson. Mode Interaction in Axially Stiffened Cylindrical Shells. *AIAA Journal*, 15(7):941–948, 1977.
[3] E.L. Jansen. Nonlinear vibration analysis of composite cylindrical shells using a semi-analytical formulation. In *Proceedings of the 42nd Structures, Structural Dynamics and Materials Conference*, Seattle, WA, 2001. AIAA Paper 2001-1314.
[4] L.W. Rehfield. Nonlinear free vibrations of elastic structures. *Int. J. Solids Structures*, 9:581–590, 1973.
[5] J. Wedel-Heinen. Vibrations of Geometrically Imperfect Beam and Shell Structures. *Int. J. Solids Structures*, 27(1):29–47, 1991.

NONLINEAR VIBRATIONS OF SHALLOW SHELLS AND THIN PLATES OF ARBITRARY SHAPE

Lidija V. Kurpa, Galina V. Pilgun
Department of Applied Mathematics, National Technical University "Kharkov Polytechnic Institute", *21 Frunze str., 61002 Kharkov, Ukraine*

Summary Large amplitude flexural vibrations of thin plates and shallow shells with the complex plans are studied by the R-function method (RFM). The algorithm is based on the reducing the given problem to research of the nonlinear differential equation of Duffing type. Its factors are determined as a result of solving the boundary value problem by variational Ritz method. The sequences of coordinate functions were constructed by the R-function theory. Obtained results are compared with well-known from other works.

PROBLEM STATEMENT

For research of geometrically nonlinear free vibrations of isotropic shallow shells (neglecting tangential inertia) the equations [1] are used.

$$\rho\frac{12(1-\mu^2)}{Eh^2}\frac{\partial^2 w}{\partial t^2}+\nabla^4 w+\frac{12}{h^2}\left\{(k_x+\mu k_y)\frac{\partial u}{\partial x}+(\mu k_x+k_y)\frac{\partial u}{\partial y}+(k_x^2+k_y^2+2\mu k_x k_y)w+\frac{k_x+\mu k_y}{2}\left(\frac{\partial w}{\partial x}\right)^2+\frac{k_y+\mu k_x}{2}\left(\frac{\partial w}{\partial y}\right)^2-\right.$$

$$\left.-\frac{\partial^2 w}{\partial x^2}\left[\frac{\partial u}{\partial x}+\mu\frac{\partial v}{\partial y}+(k_x+\mu k_y)w+\frac{1}{2}\left(\frac{\partial w}{\partial x}+\mu\frac{\partial w}{\partial y}\right)^2\right]-(1-\mu)\frac{\partial^2 w}{\partial x\partial y}\left(\frac{\partial u}{\partial y}+\frac{\partial v}{\partial x}+\frac{\partial w}{\partial x}\frac{\partial w}{\partial y}\right)-\frac{\partial w}{\partial y}\left[\mu\frac{\partial u}{\partial x}+\frac{\partial v}{\partial y}+(\mu k_x+k_y)w+\frac{1}{2}\left(\frac{\partial w}{\partial y}+\mu\frac{\partial w}{\partial x}\right)^2\right]\right\}=0, \quad (1)$$

$$A\vec{U}=L_k(w)+L(w), \quad (2)$$

where $A\vec{U}=\begin{bmatrix}\frac{\partial^2}{\partial x^2}+\frac{1-\mu}{2}\frac{\partial^2}{\partial y^2} & \frac{1+\mu}{2}\frac{\partial^2}{\partial x\partial y}\\ \frac{1+\mu}{2}\frac{\partial^2}{\partial x\partial y} & \frac{\partial^2}{\partial y^2}+\frac{1-\mu}{2}\frac{\partial^2}{\partial x^2}\end{bmatrix}\begin{bmatrix}u\\ v\end{bmatrix}$, $L_k(w)=-\begin{bmatrix}(k_x+\mu k_y)\frac{\partial w}{\partial x}\\ (k_y+\mu k_x)\frac{\partial w}{\partial y}\end{bmatrix}$, $L(w)=-\begin{bmatrix}\frac{1}{2}\left(w_{,1}^2+\mu w_{,2}^2\right)_{,1}+\frac{1-\mu}{2}\left(w_{,1}w_{,2}\right)_{,2}\\ \frac{1-\mu}{2}\left(w_{,1}w_{,2}\right)_{,1}+\frac{1}{2}\left(w_{,2}^2+\mu w_{,1}^2\right)_{,2}\end{bmatrix}$.

Here $\vec{U}=(u,v)$, w are displacements of a shallow shell median surface in directions x,y,z; k_x,k_y are curvatures of the shallow shell element, E, h, ρ, μ are the modulus of elasticity, thickness of shell element, density of a material and Poisson's ratio, respectively. The equations (1-2) should be jointed with appropriate boundary and initial conditions.

THE METHOD OF SOLUTION

The deflection $w(x,y,t)$ is presented as

$$w(x,y,t)=y_1(t)W_1(x,y), \quad (3)$$

where $W_1(x,y)$ is the eigenfunction, appropriate to the basic linear frequency ω_L. Substituting (3) into (2), one can receive the system of equations. Its solution may be considered as

$$\vec{U}(x,y,t)=y_1(t)\vec{U}_1(x,y)+y_1^2(t)\vec{U}_2(x,y). \quad (4)$$

Here $\vec{U}_1=(u_1,v_1)$ is the solution of system $A\vec{U}_1=L_k(W_1)$, and $\vec{U}_2=(u_2,v_2)$ is the solution of system $A\vec{U}_2=L(W_1)$.

After substituting the known functions u_1,v_1,u_2,v_2,W_1 in (1) and using the Galerkin procedure, one will receive the nonlinear differential equation on time

$$y_{1t}''(t)+\omega_L^2\left(y_1(t)+\gamma y_1^2(t)+\beta y_1^3(t)\right)=0, \quad (5)$$

where factors are double integrals from vector functions $\vec{U}_1,\vec{U}_2,W_1$.

Integrating the given equation by Lindshtedt method [2] or Galerkin procedure [1] (here the orthogonalization is carried out only on a quarter of the period of vibrations), it is possible to receive the period of nonlinear vibrations in the first case, and obvious dependence between nonlinear and linear natural frequencies in the second case, i.e.

$$\upsilon=\frac{\omega}{\omega_L}=\sqrt{1+\frac{8}{3\pi}\gamma A+\frac{3}{4}\beta A^2} \quad \text{(for plates } \gamma=0\text{)}. \quad (6)$$

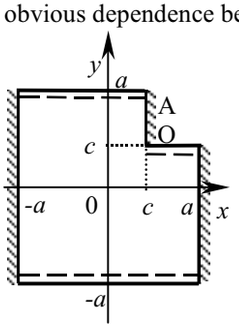


Fig. 1

For shallow shells and plates of arbitrary shape there is a problem to define natural frequencies and the appropriate eigenfunctions, and also displacements vector $\vec{U}_2$. In the present work this problem is carried out by the R-function method (RFM) [3] coupled with variational Ritz method.

NUMERICAL RESULTS

Let's consider a problem about free nonlinear vibrations of a plate (fig.1) with the following boundary conditions: the plate is clamped along $x=\pm a, x=c$ and simply supported along

$y=\pm b, y=c$. The natural frequency and the natural mode of vibrations can be found as a result of solving of the problem considering the minimum of the Lagrangian [4] on set of the functions, which are the linear combination of coordinate sequences $\{u_i\},\{v_i\},\{W_{1i}\}$, satisfying given boundary conditions. The technique of construction of the sequences of coordinate functions is described by V.L. Rvachev in [3] in detail enough. Then the solution of linear vibration problem of shallow shell can be as follows

$$u \approx \sum_{i=1}^{N_1} a_i u_i(x,y),\ v \approx \sum_{i=N_1+1}^{N_2} a_i v_i(x,y),\ W_1 \approx \sum_{i=N_2+1}^{N_3} a_i W_{1i}(x,y).$$

For given example the sequences of coordinate functions are $u_i=\omega\varphi_{1i}, v_i=\omega\varphi_{2i}, W_{1i}=\omega\omega_1\varphi_{3i}$, where $\{\varphi_{ji}\}(j=1,2,3; i=1,...N_3)$ are any complete sequences of functions, for example, power polynomials, $\omega=0$ is the equation of the whole area's boundary and $\omega_1=0$ is the equation of the clamped part of the boundary. Knowing the natural vector appropriate to the basic frequency ω_L and solving system $A\vec{U}_2=L(W_1)$, functions u_2, v_2 are determined. The last system is solved also by Ritz method. The calculation was carried out at total number of coordinate functions 75, that corresponds to 4-th degrees power polynomials approximating u and v, and 8-th degrees polynomial approximating W_1. Testing of the suggested method and the appropriate software was executed for a plate shown in fig.1 if $c=0$. The obtained results are presented on fig.2. The numerical results for square simply supported plate are shown on fig.3*a* and for square clamped one are at fig.3*b*. For the complex shape plate (fig.1) the influence of cut out depth c/a upon frequencies ratio υ were investigated. Obtained results are presented on fig.2. Whenever possible numerical results are compared with similar of other works. It allows to confirm the reliability of suggested method.

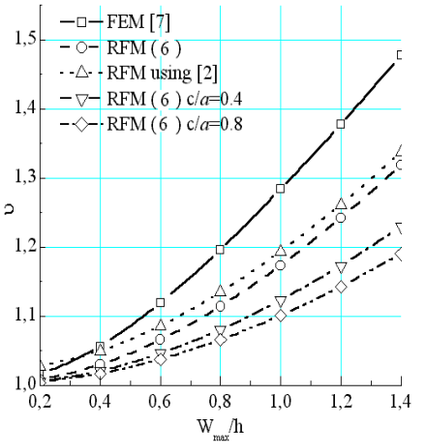
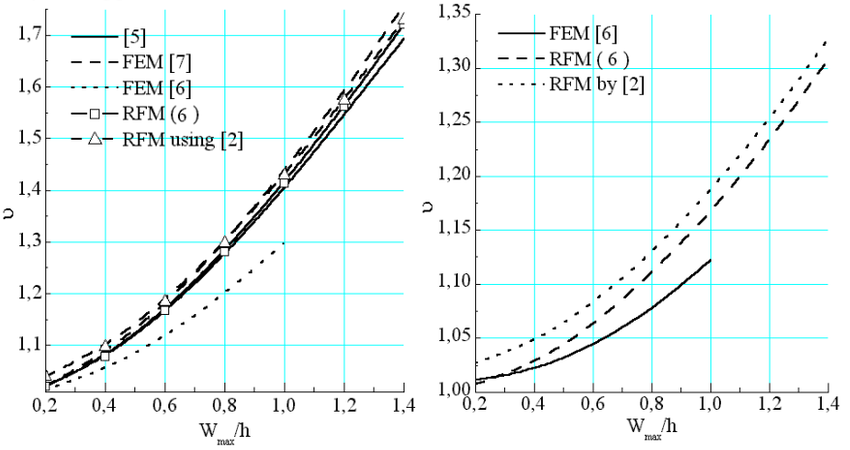


Fig.2. Effect of amplitude upon frequency for plate fig.1



a). simply supported *b*). clamped

Fig. 3(*a,b*). Effect of amplitude upon frequency for square plate with various types of boundary conditions

CONCLUSIONS

The suggested method for an investigation of large amplitude free vibration of shallow shells and thin plates and corresponding software are effective due to the R-function theory. They can be used for shallow shells of arbitrary shape and various types of boundary conditions research.

References

[1] A.S. Volmir, Nonlinear dynamics of plates and shells, Nauka, Moscow, Russia, 1972 (in Russian).
[2] E.I. Grigolyuk, About the vibrations of circular cylindrical panels at finite amplitudes, Applied Mathematics and Mechanics, **19**, 376-382, 1955 (in Russian).
[3] V.L. Rvachev, Theory of R – functions and some of its applications, Nauka Dumka, Kiev, Ukraine 1982 (in Russian).
[4] L.V. Kurpa, G.V. Pilgun, O.G. Onuphrienko, An application of R-functions method for free vibrations of cantilevered orthotropic shallow sheels with given planform, The bulletin of NTU "KhPI" **8**, 125-131, 2002 (in Russian).
[5] H.N. Chu and G. Hermann, Influence of large amplitudes on free flexural vibrations of rectangular elastic plates. J. Appl. Mech. **23**, 532-540, 1956.
[6] Mei Chuh and Kamolphan Decha-Umphai, A finite element method for nonlinear forced vibrations of rectangular plates, J. AIAA **23,** 1104-1110, 1984.
[7] Y. Shi Y, C. Mei , A finite element time domain modal formulation for large amplitude free vibrations of beams and plates, Journal of Sound and Vibration **193**, 453-464, 1996.

PARALLEL MULTILEVEL SOLUTION OF LARGE SCALE NONLINEAR SHELL PROBLEMS

Ekkehard Ramm*, Michael Gee* and Wolfgang A. Wall**

*Institute of Structural Mechanics, University of Stuttgart, Pfaffenwaldring 7, D–70550 Stuttgart, Germany
email: {eramm | gee}@statik.uni–stuttgart.de
**Chair for Computational Mechanics, Technical University of Munich, Boltzmannstrasse 15,
D–85748 Garching b. München, Germany, email: wall@lnm.mw.tum.de

Summary The conditioning problem of thin–walled structures like plates and shells is still a major obstacle for iterative solvers. In the present contribution two procedures to remedy this difficulty are discussed. The first one is a mechanically oriented preconditioner, used for a three–dimensional shell formulation called Scaled Director Conditioning. The second procedure utilizes a parallel multilevel approach which is based on an aggregation concept.

INTRODUCTION

The analysis of large–scale nonlinear shell problems asks for parallel simulation approaches. One crucial part of efficient and well scalable parallel FE–simulations is the solver for the system of equations. Due to the inherent suitability for parallelization one is very much directed towards preconditioned iterative solvers. However thin–walled structures like plates and shells suffer from severe ill–conditioning due to the extreme stiffness differences attributed to membrane, shear and bending action. This is even worse when thickness change effects are included in a sense of a three–dimensional shell formulation. This of course becomes a severe handicap when large scale nonlinear problems ought to be handled by iterative solvers. A preconditioner for this challenging class of problems is presented combining two approaches in a parallel framework.

SCALED DIRECTOR CONDITIONING

The first approach is a mechanically motivated improvement called Scaled Director Conditioning (SDC) [4],[5] and is able to remove the extra – ill conditioning that appears with three dimensional shell formulations [1], compared to formulations that neglect thickness changes of the shell. It is based on the scaling of the director so that the conditioning reaches that of classical Reissner–Mindlin type of formulations. It is introduced at the element level, acts as an almost no–cost pre–preconditioner and harmonizes well with the second approach.

AGGREGATION MULTIGRID CONCEPT

The second approach which essentially remedies the remaining ill–conditioning is a parallel multilevel approach. A hierarchy of coarse grids is generated in a semi–algebraic sense using an aggregation multigrid concept [2],[3]. On each grid level mutually disconnected patches (aggregates) are constructed from the system of equations and from some geometric information taken from the next finer grid. No coarse grid triangulations have to be supplied. The intergrid transfer operators $\mathbf{P}_{(j)}^{(j+1)}$ (j = 1 to n–1 levels) are built such, that the rigid body modes of each aggregate are represented exactly. Except for the coarsest level, each level supplies smoothers based on an overlapping domain decomposition with inexact solves on subdomains. On the coarsest grid, the correction is obtained via a direct exact solve.

EXAMPLES

Both preconditioning approaches are combined and the performance of iterative solvers is demonstrated via some numerical examples. Figure 1 describes the bending of a tube and the iteration performance during the course of solver calls for a one and a four level preconditioning.

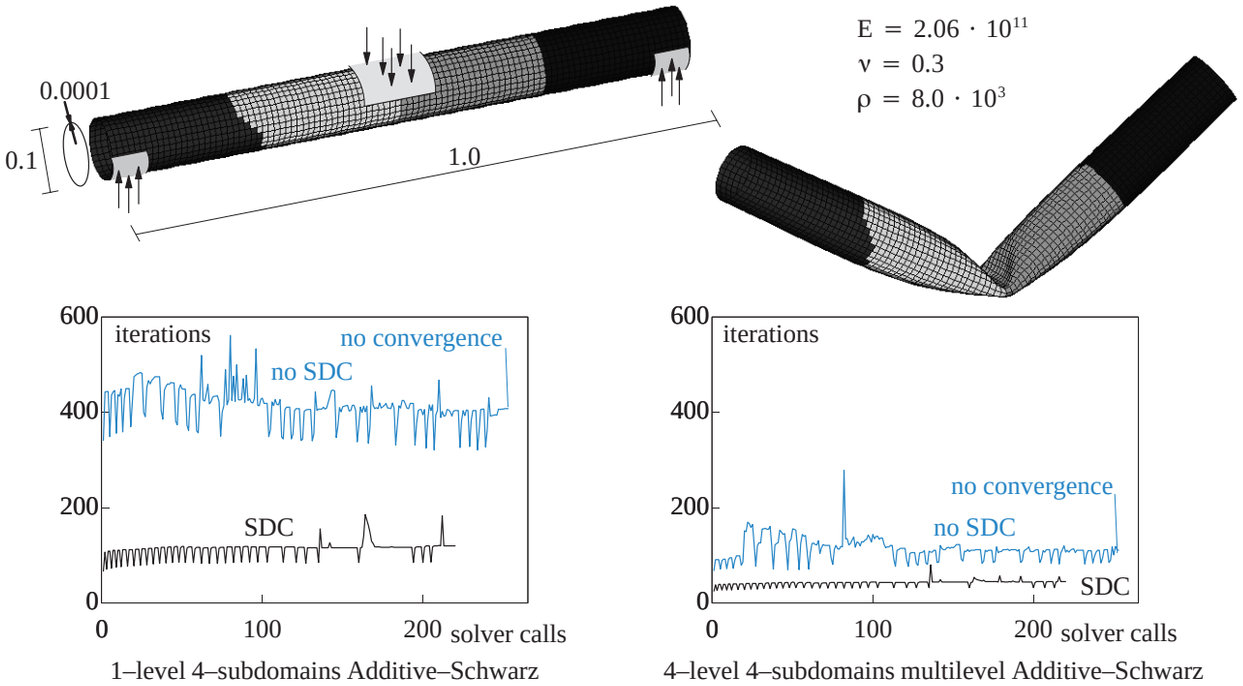


Fig. 1: Tube Bending

For the tube intersection the convergence and number of iterations for different numbers of levels within the aggregation multigrid are shown in figure 2.

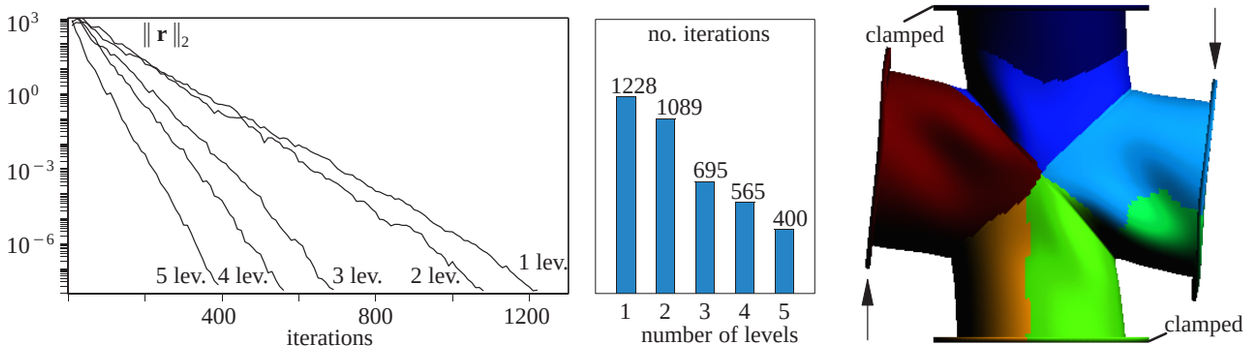


Fig. 2: steel tube intersection, 131.388 dofs , AMG–preconditioned CG, (exact solve on coarsest grid only with 5–level preconditioner)

In addition implementation issues concerning performance and parallelity of the algorithms for distributed memory machines will be discussed.

References

[1] N. Büchter and E. Ramm, "3d–Extension of Nonlinear Shell Equations Based on the Enhanced Assumed Strain Concept", *Computational Mechanics in Applied Sciences*, Elsevier, C. Hirsch (ed.), pp. 55–62, 1992.

[2] R.S. Tuminaro and C. Tong, "Parallel Smoothed Aggregation Multigrid: Aggregation Strategies on Massively Parallel Machines", *Proceedings of SuperComputing 2000*, J. Donnelley (ed.), 2000.

[3] P. Vanek, J. Mandel and M. Brezina, "Algebraic Multigrid Based on Smoothed Aggregation for Second and Fourth Order Elliptic Problems", *Computing*, v. 56, pp. 179–196, 1996.

[4] W.A. Wall, M. Gee and E. Ramm, "The Challenge of a Three–Dimensional Shell Formulation – The Conditioning Problem –", *Proceedings of IASS–IACM 2000, Crete, Greece*, 2000.

[5] M. Gee, E. Ramm, W.A. Wall, "Parallel Multilevel Solution of Nonlinear Shell Structures", to appear in Comp. Meth. Appl. Mech. Engrg.

THE MATERIAL POINT METHOD IN SOIL MECHANICS PROBLEMS

Zdzisław Więckowski*
*TU Łódź, Chair of Mechanics of Materials, Politechniki 6, PL 93-590 Łódź, Poland

Summary The material point method – the finite element method formulated in an arbitrary Lagrangian–Eulerian description of motion – is applied to large strain problems of soil mechanics. Two-dimensional, dynamic problems of pile driving (axisymmetry) and retaining wall failure (plane strain) are analysed. The case of non-cohesive models of the soil is analysed – the elastic–plastic and elastic–viscoplastic material models are applied.

INTRODUCTION

The problems of large strains are still hard to analyse despite of existence of many well-developed computational techniques. This statement refers to some problems of soil mechanics, e.g., the pile driving or landslide problems. For example, the finite element method, the tool used most frequently in engineering analyses, is not sufficiently robust in the case of such problems when formulated in the Lagrangian description of motion. The excessive distortions of an element mesh deforming together with an analysed body lead to inaccuracies in the solution approximation or even to failure of a calculation process due to negative values of Jacobian determinants at points of numerical integration. The use of re-meshing techniques is not a sufficient measure because it is time-consuming and introduces additional errors due to the projection of the solution from a deformed mesh to a regenerated one.
Recently, two groups of computational methods handling the problems of large strains have been developed intensely: the – so called – point based or meshless methods and the methods formulated in an arbitrary Lagrangian–Eulerian description of motion. The material point method (MPM), used as a tool of analysis in the present paper, can be classified to both the groups due to its features. The method, well-known in fluid mechanics as a particle-in-cell method, was introduced by Harlow [1] in 1964 and adapted to problems of solid mechanics by Burgess *et al.* [2] and Sulsky *et al.* [3, 4] about ten years ago. Application of the method to problems of granular flow in a silo has been described in [5].
In the present paper, two-dimensional problems of pile driving and failure of a retaining wall are investigated.

SETTING OF THE PROBLEM

Let $\Omega \subset \mathbb{R}^3$ denote a region occupied by the granular body at instant $t \in I \equiv [0,T]$, where $T > 0$. Let us assume that the boundary of the body consists of two parts Γ_u and Γ_σ such that $\overline{\Gamma_u} \cup \overline{\Gamma_\sigma} = \partial\Omega$ and $\Gamma_u \cap \Gamma_\sigma = \emptyset$.
The solution of the dynamic problem satisfies the equation of virtual work:

$$\int_\Omega (\varrho\, a_i\, w_i + \sigma_{ij} w_{i,j})\,\mathrm{d}x = \int_\Omega \varrho\, b_i\, w_i\,\mathrm{d}x + \int_{\Gamma_\sigma} t_i\, w_i\,\mathrm{d}s \quad \forall \boldsymbol{w} \in V_0, \tag{1}$$

where V_0 denotes the space of kinematically admissible fields of displacements, σ_{ij} the Cauchy stress tensor, ϱ mass density, b_i and a_i are the vectors of mass forces and acceleration, respectively, t_i denotes the Cauchy stress vector given on Γ_σ.
The displacement, velocity and stress fields satisfy the following initial conditions: $u_i(0) = u_i^0$, $\dot{u}_i(0) = 0$, $\sigma_{ij}(0) = \sigma_{ij}^0$, where u_i^0 and σ_{ij}^0 are the initial fields of displacements and stresses, respectively.
The case of non-cohesive soil is investigated in the paper. Two constitutive models of the soil are considered: the elastic–perfectly plastic and elastic–viscoplastic ones. In both the models, the Drucker–Prager yield condition and a non-associative flow rule are involved.
Let f denote the yield function, $f(\sigma_{ij}) = q - mp$, where $m = 18\sin\varphi/(9 - \sin^2\varphi)$ is a function of the angle of internal friction, φ, p and q are invariants of the stress tensor, $p = -\sigma_{ii}/3$, $q = \sqrt{3/2\, s_{ij} s_{ij}}$, where $s_{ij} = \sigma_{ij} + p\,\delta_{ij}$ denotes the deviatoric part of the stress tensor. The constitutive relations for the elastic–perfectly plastic material model are as follows:

$$\dot{p} = K\, d_{kk}, \qquad e_{ij} = e_{ij}^{\mathrm{e}} + e_{ij}^{\mathrm{p}}, \qquad e_{ij}^{\mathrm{e}} = \frac{1}{2\,G}\,\overset{\nabla}{s}_{ij}, \qquad e_{ij}^{\mathrm{p}} = \begin{cases} \dot{\lambda}\,\dfrac{\partial g}{\partial s_{ij}} & \text{if } f(\sigma_{ij}) = 0, \\ 0 & \text{if } f(\sigma_{ij}) < 0, \end{cases} \tag{2}$$

where $\dot{\lambda} \geq 0$, g denotes the plastic potential defined by the relation $g = q$. The following notation is used above: $d_{ij} = (v_{i,j} + v_{j,i})/2$ is the rate-of-deformation tensor, e_{ij}^{e} and e_{ij}^{p} are parts of its deviator, $e_{ij} = d_{ij} - d_{kk}\,\delta_{ij}/3$, the elastic and plastic ones, respectively, $\overset{\nabla}{\sigma}_{ij} = \dot{\sigma}_{ij} - \sigma_{ik}\,\omega_{kj} - \sigma_{jk}\,\omega_{ki}$ is the Jaumann rate of the stress tensor, $\omega_{ij} = (v_{j,i} - v_{i,j})/2$ the spin, K and G are the bulk and shear moduli, respectively.
The second material model is a viscoplastic regularisation of the model described above. The same yield condition and plastic potential are employed. To define the viscoplastic constitutive relations, the second and fourth equations in (2) are

replaced by

$$e_{ij} = e_{ij}^{\mathrm{e}} + e_{ij}^{\mathrm{vp}}, \quad e_{ij}^{\mathrm{vp}} = \gamma \left\langle \Phi(f) \right\rangle \frac{\partial g}{\partial \sigma_{ij}} \quad \text{with} \quad \Phi\left(f(\sigma_{ij})\right) = \left(\frac{q - m\,p}{m\,p} \right)^N, \quad \left\langle \Phi(f) \right\rangle = \begin{cases} \Phi(f) & \text{if } f > 0 \\ 0 & \text{if } f \leq 0 \end{cases}, \quad N > 0.$$

THE MATERIAL POINT METHOD

Two kinds of space discretisation are utilised in the material point method. The Lagrangian discretisation is done by dividing the region occupied initially by the analysed body into a set of subregions – each of them represented by one its points called a material point. The mass density field is expressed as follows: $\varrho(\boldsymbol{x}) = \sum_{P=1}^{N} M_P\, \delta(\boldsymbol{x} - \boldsymbol{X}_P)$, where M_P and $\boldsymbol{X}_P$ denote the mass and the position of the P-th material point, $\delta(\boldsymbol{x})$ is the Dirac δ-function. Another kind of space discretisation is related to an Eulerian finite element mesh, called a computational mesh, covering the virtual position of the analysed body. This mesh can be changed arbitrarily during calculations or remain constant. After substituting the δ-function representation of the mass density field to the equation of virtual work (1) and expressing the field of acceleration, a_i, and the weight functions, w_i, by the shape functions and nodal parameters, defined on the computational mesh as in the finite element method, we obtain the following system of dynamic equations:

$$\mathbf{M}\,\mathbf{a} = \mathbf{F} - \mathbf{R}, \tag{3}$$

where $\mathbf{M}$ is the mass matrix, $\mathbf{a}$ the vector of nodal accelerations, $\mathbf{F}$ and $\mathbf{R}$ are the vectors of external and internal nodal forces, respectively. The main difference between the finite element (FEM) and material point (MPM) methods is based on the fact that the state variables are traced at the material points, defined independently of the computational mesh in MPM, and at integration points connected with elements in FEM.

EXAMPLES

Two examples of application of MPM to soil mechanics are presented: the plane problem of failure of a retaining wall in Fig. 1 and the axisymmetric problem of pile driving with constant velocity in Fig. 2. Several stages of deformation processes are shown in the figures. The viscoplastic and elastic material models have been used in the calculations for soil (sand) and walls and pile, respectively. The dynamic equations (3) have been solved by the use of the explicit time integration scheme.

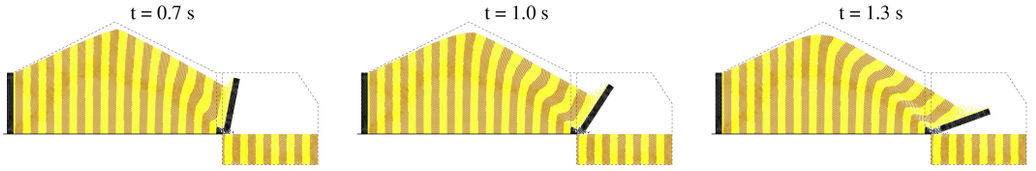


Figure 1: Problem of retaining wall failure

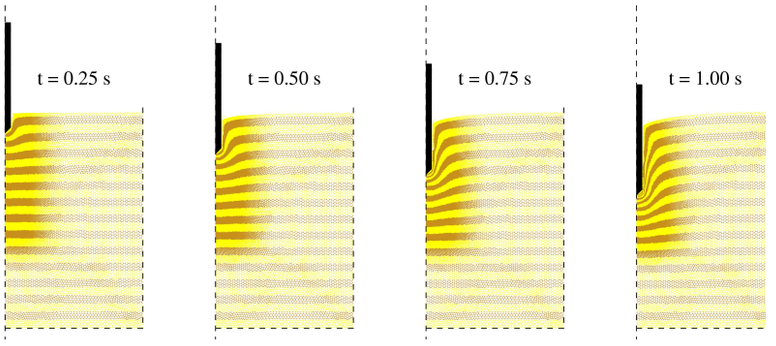


Figure 2: Problem of pile driving

References

[1] Harlow F.H.: The particle-in-cell computing method for fluid dynamics. In Adler B., Fernbach S., Rotenberg M., eds., Methods for Computational Physics, **Vol. 3**:319–343, Academic Press, NY 1964.

[2] Burgess D., Sulsky D., Brackbill J.U.: Mass matrix formulation of the FLIP particle-in-cell method. *J. Computat. Phys.* **103**:1–15, 1992.

[3] Sulsky D., Chen Z., Schreyer H.L.: A particle method for history-dependent materials. *Comput. Meth. Appl. Mech. Engrg.* **118**:179–196, 1994.

[4] Sulsky D., Schreyer H.L.: Axisymmetric form of the material point method with applications to upsetting and Taylor impact problems. *Comput. Meth. Appl. Mech. Engrg.* **139**:409–429, 1996.

[5] Więckowski Z., Youn S.K., Yeon J.H.: A particle-in-cell solution to the silo discharging problem. *Int. J. Numer. Meth. Eng.* **45**:1203–1225, 1999.

DYNAMIC BEHAVIOURS OF SOILS AND ROCKS IN A WIDE PRESSURE RANGE

Anatoly M. Bragov*, Andrey K. Lomunov*, Ivan V. Sergeichev*, Leopold Kruszka**
*Research Institute of Mechanics, Gagarin 23/6, RUS 603950 Nizhny Novgorod, Russia
**Military University of Technology, Kaliski 2, PL 00-908 Warszawa, Poland

Summary Investigations of dynamic compressibility of soils were performed by two various experimental methods: the modified Kolsky method was used at strain rates about $10^3 s^{-1}$ and pressure up to 300 MPa, and the plane-wave shock testing was at higher strain rates and pressure up to 2GPa. As in these above methods deformation state is the same, then it is able to construct total stress-strain curves of dynamic deformation of soft soils in uniaxial strain condition in a wide range of pressure. Besides above testing, there are presented experimental analysis for two rocks' materials, i. e. the gabbro-diabas granite and two kinds of marble tested in compression as well as in tension (splitting tests) by SHPB at high strain rate about 10^3 s^{-1}.

EXPERIMENTAL SET-UPS

Modified SHPB set-ups

Investigation of dynamic compressibility of non-cohesive building soils was performed by two various experimental techniques. The first of them was modified split Hopkinson pressure bar, where soils' specimens were placed in a rigid steel jacket, equipped by strain gauges (Fig. 1) to measure circumferential strain ε_θ. This method was used at high strain rate $\dot{\varepsilon}$ up to 10^3 s^{-1} and pressure P_i up to 300 MPa. In the modified Kolsky method by measuring signals from strain

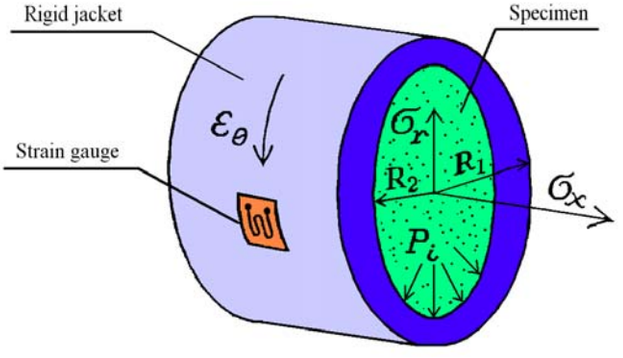


Fig. 1. Soil specimen confined in steel jacket, which was equipped by strain gauges; R_1, R_2 are external and internal jacket's radiuses

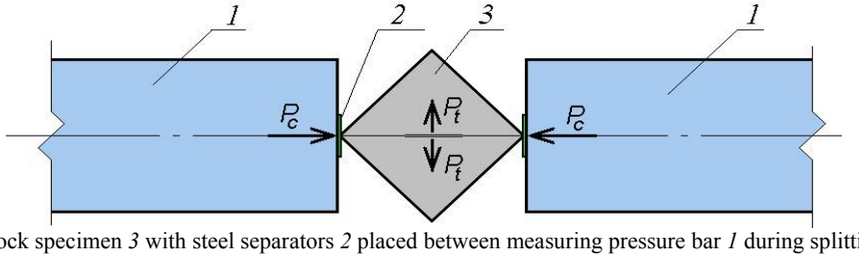


Fig. 2. Rock specimen *3* with steel separators *2* placed between measuring pressure bar *1* during splitting tests

gauges mounted on measuring bars and the jacket, it is possible to determine axial σ_x and radial σ_r components of stress and further to calculate dependence: pressure P_i – volumetric strain θ. The SHPB set-up was also used to determine dynamic behaviors of two rocks' specimens *3*, i. e. the gabbro-diabase granite and two kinds of marble placed between measuring bars *1*, and tested in compression (compressive forces P_c) as well as in tension (splitting forces P_t – see Fig. 2) at high strain rate about 10^3 s^{-1}.

Shock wave tests

Plane-shock wave testing of following soft soils: sand of various grain structures and humidity, loams (dry and at humidity 25 %) and clay of natural humidity and original structure, was used to study their compressibility at higher strain rates and pressure up to 2GPa. Soils' specimens confined in steel jackets and placed between screening and thrust plates, were impacted by a plate-striker – Fig. 3.

EXPERIMENTAL RESULTS

The first example of strain rate effects on tensile strength of rocks from Koelga and PervoUralsy Regions in Russia obtained from static and dynamic splitting tests is showed in Fig. 4. Next examples of dynamic compressibility of a dry and wet sand in ranges of small stresses, determined with the help of the SHPB technique, and in ranges of high stresses - by the

plane-wave experiments, are also presented in Fig. 5. Between these results, there is a small site, experimentally uncertain. It is visible, that the results obtained with the help of various methods satisfactorily correlate.

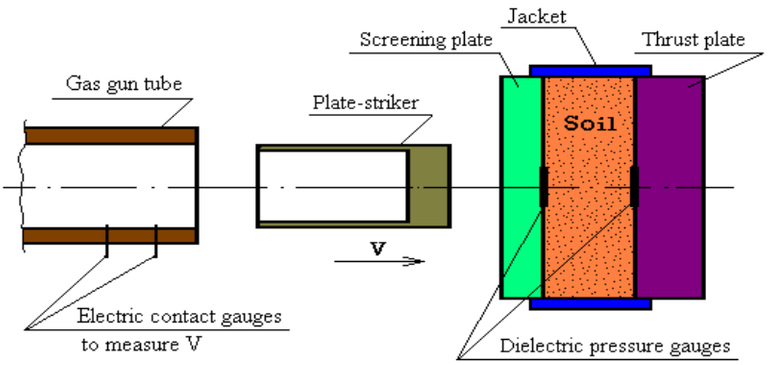


Fig. 3. Scheme of shock-wave test

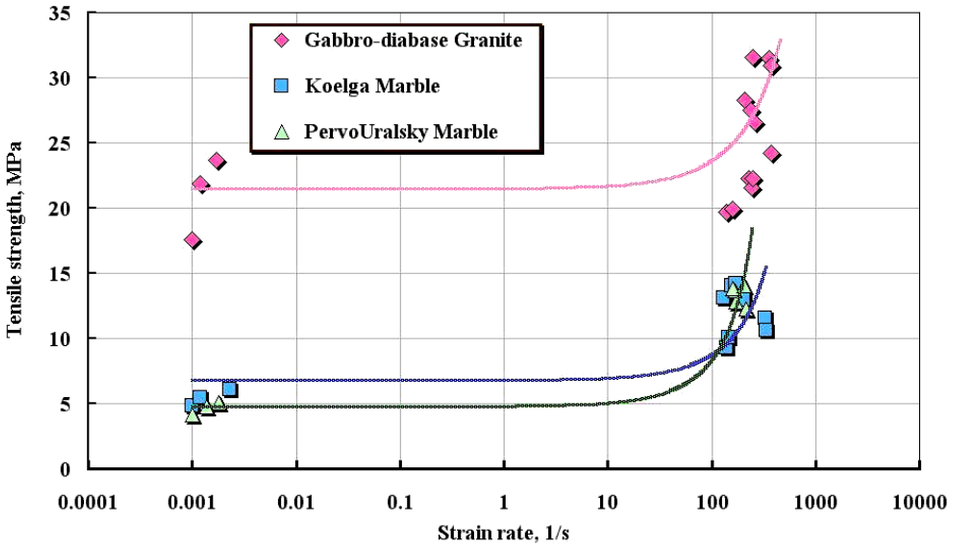


Fig. 4. Strain rate effects on tensile strength of rocks from static and dynamic splitting tests

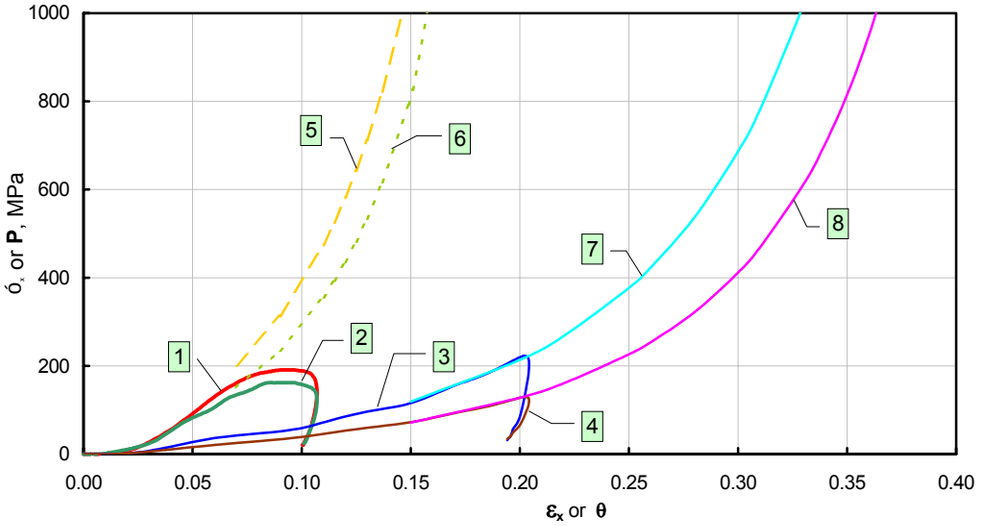


Fig. 5. Examples of "stress σ - strain ε_x" curves for wet (1 & 2) and dry (3 & 4) sand obtained from SHPB tests, and "pressure P_i - volumetric strain θ" curves for wet (5 & 6) and dry (7 & 8) sand from plane-shock wave tests

CONCLUSIONS

Thus, as a result of the carried out experiments the effect of humidity as well as grain structure on both dynamic and shock compressibility of soils is discussed. The possibility of use of complementary experimental techniques for research of a dynamic behavior of soil and rock materials, in a wide ranges of strain rates and pressures is presented.

MICROMECHANICAL STUDY OF MACROSCOPIC FRICTION AND DISSIPATION IN IDEALISED GRANULAR MATERIALS: THE EFFECT OF INTERPARTICLE FRICTION

N.P. Kruyt[*], L. Rothenburg[**]

[*]*Department of Mechanical Engineering, University of Twente, Enschede, The Netherlands*

[**]*Department of Civil Engineering, University of Waterloo, Waterloo, Ontario, Canada*

Summary A micromechanical study is made of the relationship between interparticle friction coefficient μ and macroscopic continuum friction and dissipation in idealised granular materials, using Discrete Element Method simulations with varying μ. As expected, macroscopic friction and dilatancy increase with μ. Surprisingly, dissipation is present even when $\mu \to 0$ or when $\mu \to \infty$. Hence, dissipation in idealised granular materials is not exclusively the result of interparticle friction. The dependence of the dissipation-rate function on plastic strains is also investigated.

INTRODUCTION

Granular materials exhibit macroscopic frictional and dissipative behaviour, which usually is modelled by the theory of plasticity. Currently, there is considerable interest in thermodynamic formulations of plasticity theories for geomaterials, e.g. [2]. In these formulations, knowledge of the (Helmholtz) free-energy function and the dissipation-rate function is sufficient for determining the constitutive behaviour, such as elastic behaviour, yield function, flow rule and hardening rule. The macroscopic frictional and dissipative nature of granular materials seems to be readily explained by the frictional interaction between particles at the microscopic contact level. However, experimental evidence [8] and computational evidence [1] suggests that the macroscopic frictional behaviour is only weakly dependent on interparticle friction coefficient μ (except for very low μ).

The objective of this study is to investigate further the micromechanical origin of macroscopic friction and dissipation in granular materials, and the role of interparticle friction herein. The method used is that of Discrete Element Method (*DEM* for short) simulations on idealised two-dimensional granular assemblies consisting of disks. A great advantage of DEM simulations for micromechanical studies is that detailed information is available, such as that on interparticle forces. Thus it is possible to compute for each state the internal energy associated with the springs that are active between particles in contact.

In particular, the following cases are considered: (i) $\mu \to 0$, (ii) 'normal' interparticle friction coefficients and (iii) $\mu \to \infty$. The first case corresponds to frictionless particles with central interactions for disks (no tangential forces), while in the third case the Coulomb friction limit is never attained. In the first and third cases the behaviour at the contact is elastic (as long as the contact is not disrupted) and hence there is no microscopic frictional dissipation mechanism.

DISCRETE ELEMENT SIMULATIONS

Two-dimensional DEM simulations were performed in a manner similar to that of [3]. A linear elastic relationship between forces and interparticle displacements at contacts has been employed, i.e. $f_n^c = k_n \Delta_n^c$ and $f_t^c = k_t \Delta_t^c$, where f_n^c, f_t^c are normal and tangential contact forces, Δ_n^c, Δ_t^c are corresponding interparticle displacements and k_n, k_t are respective stiffnesses. Only compressive normal forces are allowed: if the normal force were to become tensile, the contact is considered to be broken for cohesionless materials. The tangential forces are limited by Coulomb friction, i.e. $|f_t^c| \le \mu f_n^c$.

Simulated biaxial tests employing periodical boundary conditions were performed on assemblies of 50,000 disks. By simulating additional unloading paths, plastic strains were determined.

EFFECT OF INTERPARTICLE FRICTION COEFFICIENT ON MACROSCOPIC BEHAVIOUR

The results for the macroscopic shear strength and the volumetric strain are shown in Figure 1 for various values of μ. In all cases the shear strength shows behaviour typical for a dense granular material with an initial increase of shear strength until the peak strength is obtained after which softening occurs. In all cases, shear-induced dilation is observed. The volumetric strain and the shear strength (at peak and at large strain) increase with μ. As noted in [1], the effect of μ is fairly small in the range $0.2 - 0.4$. Thus, the qualitative behaviour for $\mu \to 0$ and $\mu \to \infty$ is the same as that for the cases with a normal friction coefficient. This means that the macroscopic behaviour is frictional in nature, even when friction is effectively absent at the microscopic contact level.

DISSIPATION

The dissipation-rate function, $\hat{\Phi}$, is related to the rate at which work is done on the assembly, $\sigma_{ij}\dot{\varepsilon}_{ij}$, and the rate of change of the free-energy function, $\dot{F}$, by $\hat{\Phi} = \sigma_{ij}\dot{\varepsilon}_{ij} - \dot{F}$ for isothermal systems [2]. Contrary to the internal energy u, the free energy can not be determined from the DEM simulations. Here we make the assumption $u \cong F$, as was also done in an experimental study of dissipation in metals [6]. Then the dissipation-rate $\hat{\Phi}$ can be determined.

Surprisingly, dissipation is even present when $\mu \to 0$ or when $\mu \to \infty$. Thus there is macroscopic dissipation in the absence

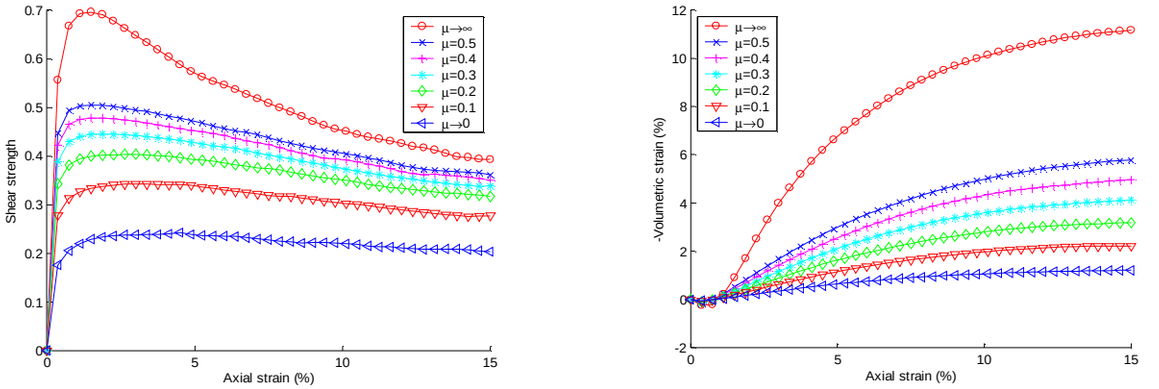


Figure 1. Macroscopic behaviour as a function of imposed axial strain for various interparticle friction coefficients μ .

of a microscopic frictional dissipation mechanism. Ultimately, another microscopic mechanism is always present in DEM simulations as viscous or numerical dissipation. The first is often modelled by a coefficient of restitution. Some dissipation mechanism is necessary to dampen out (uninteresting) transient phenomena associated with elastic vibrational modes.
In [2] a distinction is made between recoverable plastic work and dissipated plastic work. For a 'purely frictional material' all plastic work is dissipated. Since simulations of unloading paths have been performed, plastic strains ε_{ij}^{p} are known. Hence the rate of plastic work, $\sigma_{ij}\dot{\varepsilon}_{ij}^{p}$, can be determined and compared with the dissipation-rate $\hat{\Phi}$. It is found that for axial strains larger than 3% (5% for $\mu \to \infty$) these are practically the same. Thus the present, idealised granular material is a 'purely frictional material' where none of the plastic work is recoverable.
The dependence of the dissipation-rate function on plastic strains was also investigated. A form proposed in [7] is: $\hat{\Phi} = N(\mu) p a_c \dot{\varepsilon}_S^{p}$, where p is the pressure, a_c is the anisotropy of the fabric tensor (or contact distribution function), $\dot{\varepsilon}_S^{p}$ is the rate of change of the magnitude of the deviator of the plastic shear strain and $N(\mu)$ depends solely on μ . The actual and the theoretical dissipation-rate functions are compared in Figure 2, with $N(\mu)$ determined from steady-state considerations. The theoretical relation underestimates the dissipation as observed in the DEM simulations.

DISCUSSION

It has been shown that, even in the effective absence of microscopic friction ($\mu \to 0$ or $\mu \to \infty$), the macroscopic behaviour is frictional and dissipative. The role of microscopic interparticle friction in influencing the macroscopic behaviour is more indirect by giving stability to assemblies, thus leading to increased shear strength and dilatancy with increasing μ .
Further attention must be given to ways in which: (i) the free energy and (ii) the recoverable plastic work can be extracted from the results of DEM simulations. According to [5], for metals this recoverable plastic work is associated with microscopic heterogeneity. Granular materials are very heterogeneous at the microscopic level of contacts, e.g. [4]. Yet, the present results indicate that the recoverable plastic work is small.

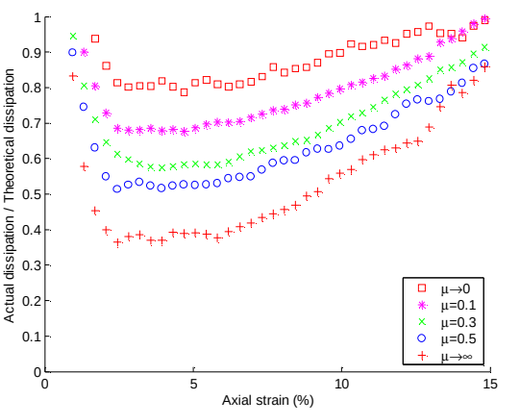


Figure 2. Comparison of dissipation-rate functions.

References

[1] Cambou, B.: From global to local variables in granular materials. In: *Powders & Grains 93* (ed. C. Thornton), pp.73-86, Balkema, Rotterdam, The Netherlands, 1993.
[2] Collins, I.F., Muhunthan, B.: On the relationship between stress-dilatancy, anisotropy, and plastic dissipation for granular materials. *Géotechnique* **53**:611-618, 2003.
[3] Cundall, P.A., Strack, O.D.L.: A discrete numerical model for granular assemblies. *Géotechnique* **9**:47-65, 1979.
[4] Kruyt, N.P., Rothenburg, L.: Kinematic and static assumptions for homogenization in micromechanics of granular materials. *Mechanics of Materials*, in press, 2004.
[5] Mróz, Z.: Non-associated flow laws in plasticity. *Journal de Mécanique* **2**:21-42, 1963.
[6] Mróz, Z., Oliferuk, W.: Energy balance and identification of hardening moduli in plastic deformation processes. *International Journal of Plasticity* **18**:379-397, 2002.
[7] Rothenburg, L., Bathurst, R.J., Matyas, E.L.: Mechanisms of fabric evolution in granular media. In: *Proceedings of the 12th International Conference on Soil Mechanics and Foundation Engineering*, pp.753-756, Rotterdam, The Netherlands, 1989.
[8] Skinner, A.E.: A note on the influence of interparticle friction on the shearing strength of a random assembly of spherical particles. *Géotechnique* **1**:150-157, 1969.

Influence of contact phenomena on structure-subsoil interaction: finite elements method analysis

Marcin Maździarz

Polish Academy of Sciences, IPPT PAN, Swietokrzyska 21, PL 00-049 Warszawa, Poland

Summary.The analysis of deformation of geotechnical structures is formulated by using 3D elasto-viscoplastic relationships incorporating pore pressure. Finite element implementation is then performed for both, contact and structure. Solid isoparametric elements are developed. Contacts elements with zero thickness are also carefully developed, allowing for pore pressure in slip and stick range. The novelty of the contribution consists of using elasto-viscoplastic model incorporating pore pressure for 3D contact. Using implemented spatial elements in the program HYDRO-GEO elasto-viscoplastic analysis of interaction between structure and subsoil was carried out. Earth dam alongside with concrete weir and excursion trough in one of Polish earth dams (Dobczyce) was analyzed. Simulation of deformation of structure and slide of soil on surface of the retaining wall was studied.

Introduction

Phenomenon of contact is very important in variety of engineering problems. In cases where significant differences of material properties of structure and subsoil occur serious problems in theoretical and numerical modeling of interaction between the structure and subsoil exist. In geomechanics very often we meet such problems, e.g. piles, geo-fibers reinforcement of soil, links of weak soil layer, retaining walls, etc. Some group of structure-subsoil interaction problems can be successfully modeled as 2D phenomenon. There are these for which appropriate modeling simplification can be assumed. However there is a group of problems, which requires full 3D modeling e.g. slip on a corner of structure, lack of domination of one of dimension of the structure, etc.

To be able to model the response to loading of spatial object taking into account contact, there is a necessity to use finite element method and introduce special elements called contact elements. The last describe the contact zone between solid elements and allow modeling various effects in this zone.

Aim of investigation

The goal of this study was to examine both from theoretical and numerical point of view the influence of contact phenomena on structure-subsoil interaction. The numerical analysis was carried out by using finite element methods including spatial contact elements with zero thickness. 3D formulation of the interacting structure with subsoil was developed. The program HYDRO-GEO enables to perform numerical calculations of the considered complex contact problem in the 3D case. The paper can be divided into two essential parts.

Discretization

The first part is concerned with discretized 3D description of basic relationships by using the finite element method. To do this 3D solid isoparametric elements were introduced. Pore pressure was taken into account. Spatial contact finite elements were developed and incorporated into the program. These elements cover elasto-viscoplastic contact behavior and take into account pore pressure, slip and stick range.

Numerical part

In this part of the paper the developed discrete model was implemented into the computer program HYDRO-GEO. Then the elasto-viscoplastic interaction between structure and subsoil can be analyzed. A complex system consisting of the earth dam and concrete weir was studied (one of Polish earth dams in Dobczyce). Geometrical model of this system is presented on Figs. 1-2

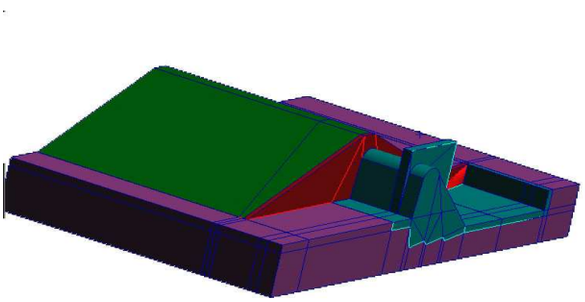


Figure 1 View of the dam from upper water

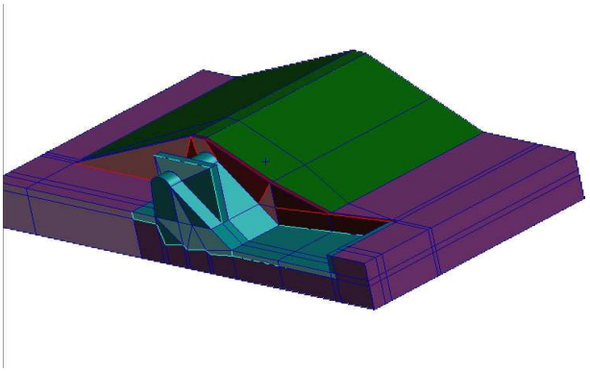


Figure 2 View of the dam from bottom water

On this engineering example the simulation of deformation of the structure and slide of soil on the surface of retaining wall was presented. The obtained results are depicted below on figure from post-processor.

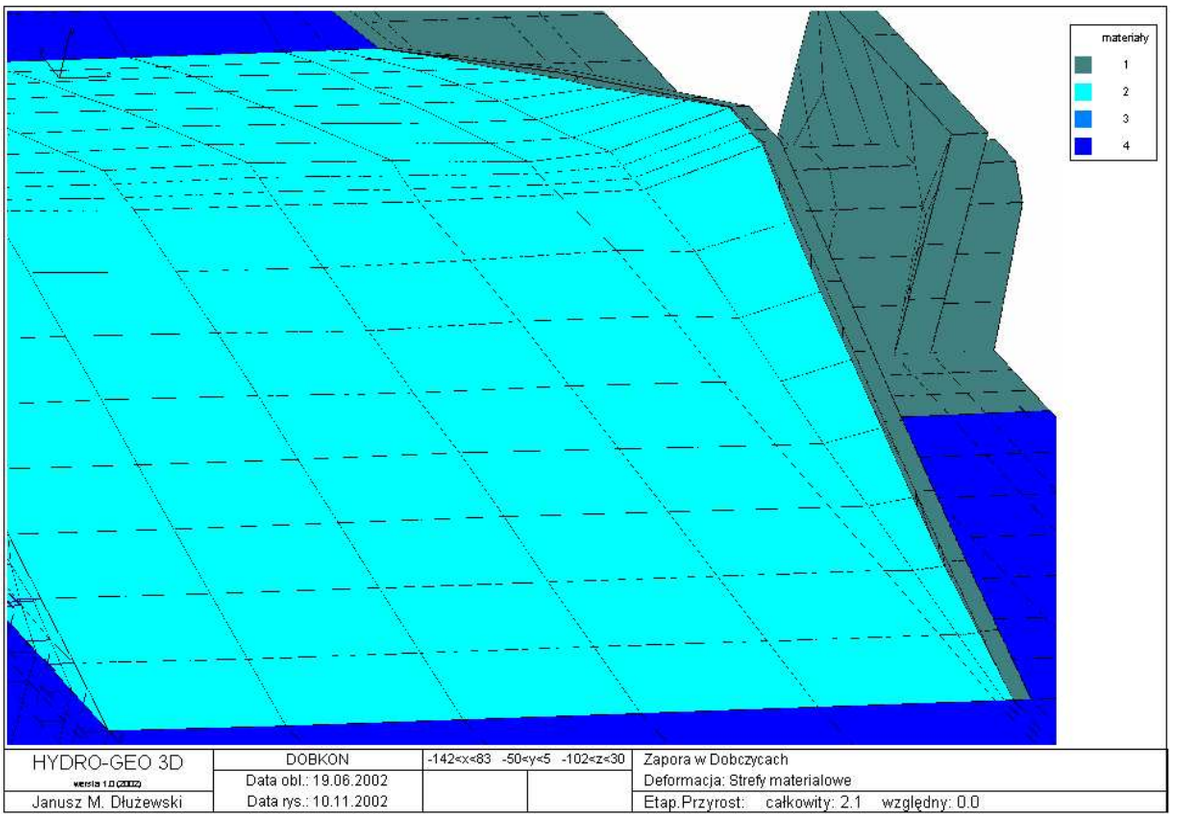


Figure 3 Slide on the surface of contact between the retaining wall and earth dam

Final remarks

Using elasto-viscoplastic model incorporating pore pressure for 3D contact gives new possibilities in comparison to classical elasto-plastic models. Taking into account pore pressure can significantly change the results. A nice feature of this model is that even for nonassociative flow rule we get symmetric stiffness matrix.

References

[1] Crisfield M.A. (1997): *Non-linear Finite Element Analysis of Solids and Structures*, John Wiley&Sons Ltd, England

[2]Desai C. S., Zhang D. (1987): *Viscoplastic model for geologic materials with generalized flow rule*, J. Numerical Methods in Geomechanics Vol. 11

[3]Dłużewski J. M. (1996): *Contact 3D problems*. Zeszyt Naukowy IL Politechnika Warszawska, Warszawa (in Polish)

[4]Dłużewski J. M. (1993): *Numerical modeling of soil-structure interactions in consolidation problems*, Prace naukowe Budownictwo z. 123, Politechnika Warszawska, Warszawa (in Polish)

[5]Kanchi M., Zienkiewicz O. C. (1978): *The viscoplastic approach to problems of plasticity and creep involving geometric nonlinear effects*, Int. J. Numerical Methods in Engineering Vol. 12

[6] Maździarz M. (2003): "*Influence of contact phenomena on structure-subsoil interaction: finite elements method analysis"*, PhD thesis, Politechnika Warszawska, Warszawa (in Polish)

[7]Perzyna P. (1966): *Fundamental problems in viscoplasticty*, Advances in Applied Mechanics, Vol. 9

[8]Swoboda G. (1994): *Simulation of arch dam-foundation interaction with a new friction interface element,* Int. J. Numerical and Analytical Methods in Geomechanics Vol. 17

[9]Zienkiewicz O. C., Taylor R. L. (2000): *The Finite Element Method. Vol 1-3*, Oxford: Butterworth-Heinemann

MODELING OF STATIC LIQUEFACTION AND EVOLVING FAILURE MODES

Nathalie Boukpeti*, Andrew Drescher **
*University of Liege, Chemin des Chevreuils 1, B-4000 Liege 1, Belgium
**University of Minnesota, 500 Pillsbury Dr SE, Minneapolis, MN55455, U.S.A.,

Summary Considered are the elasto-plastic and elasto-viscoplastic versions of the Superior sand model for describing static liquefaction of granular deposits. Limit points and instability in stress-controlled undrained loading are analyzed. Examples of the effect of loading rate on shear band formation and growth of accelerated deformation in an inertial process in biaxial compression numerical simulations also are given.

Refined Superior sand model

Loosely-packed, water-saturated granular deposits (sands, mine tailings) are prone to spontaneous loss of strength and accelerated deformation process when subject to increasing stress-controlled loading (static liquefaction). Due to increase in pore-water pressure the ensuing process transforms a solid-like material into a liquid-like medium. The process may grow unlimitedly, or terminate when the pore-water pressure drops and the material regains its strength. This behavior is described by the elasto-plastic refined Superior sand model formulated within the framework of critical state concept in [3], and subsequently analyzed and generalized in [1, 2, 5]. The elastic deformations are governed by a pressure-dependent elasticity. The evolution of plastic deformations is defined by a closed and smooth yield surface with configuration hardening parameter, and a non-associated flow rule. In terms of triaxial compression invariants p', q, ε_p, and ε_q, the yield condition, plastic potential, and hardening rule are given by

$$F = q^2 - L^2 p'^2 \left[\frac{1+s}{s} \left(1 - \frac{p'}{p'_F} \right) \right]^{2s} = 0, \qquad G = q^2 - M^2 p'^2 \left[\left(\frac{p'_G}{p'} \right)^{\frac{1}{2r}} - 1 \right]^{2r} = 0 \tag{1}$$

$$\dot{p}'_F = p'_F \frac{v}{\lambda - \kappa} \dot{\varepsilon}_p^{vp} + p'_F \sqrt{(\alpha \dot{\varepsilon}_q^{vp})^2 + (\dot{\varepsilon}_p^{vp})^2} \left\langle m \left(\frac{p'_F{}^*}{p'_F} - 1 \right) \right\rangle \tag{2}$$

where v is the specific volume, L, M, m, r, s, α, κ, and λ are constants, and $p'_F{}^*$ is a parameter of the reference surface. Examples of the stress-strain curves and stress paths obtained in undrained loading are depicted in Fig. 1.

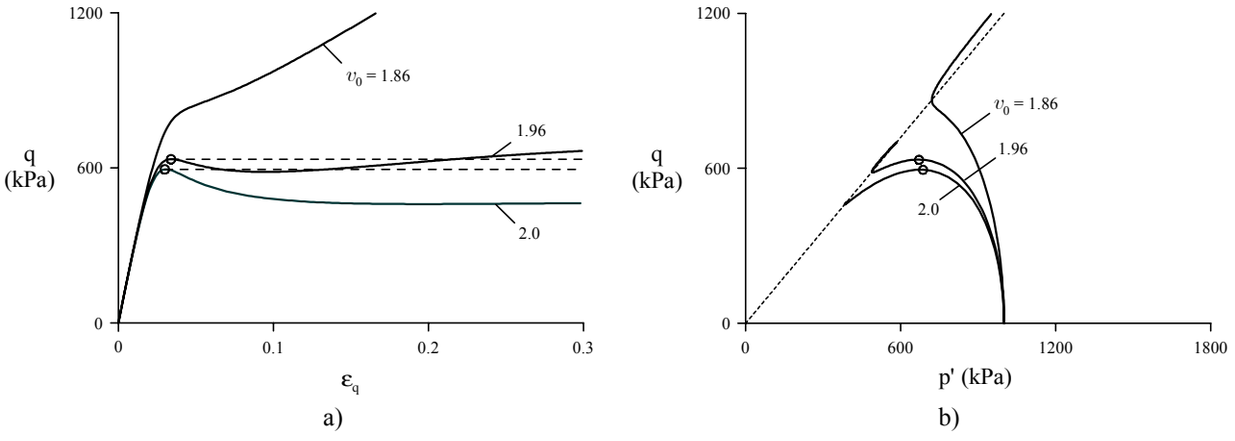


Fig.1 Elasto-plastic response and instability points; a) strain- and stress-control, b) stress paths

The response of the model can be characterized by its limiting and instability points. These depend on the process control variable – stress or strain. In stress-controlled loading, the instability occurs at the first limit point where

$$W_2 = \dot{q}\dot{\varepsilon}_q = 0 \tag{3}$$

as indicated in Fig. 1 by circles. The severity (energy) of liquefaction can be assessed from the excess of applied load over the reduced strength, and in ideal conditions amounts to the area between the applied stress and material stress-strain curve.

To account for the observed experimentally delayed liquefaction under constant load (creep), and the dependence of the stress-strain curves on the rate of strain-controlled loading [4], the refined Superior sand model was modified within the framework of viscoplasticity of Perzyna (1963). The resulting stress-strain curves in strain-controlled loading $\dot{\varepsilon}_q = \dot{\varepsilon}_{q0}$, and in stress-controlled loading $\dot{q} = \dot{q}_0$, are governed, respectively, by

$$\frac{\dot{q}}{\dot{\varepsilon}_q} = 3\mu - \frac{\dfrac{6q\mu}{\tau\dot{\varepsilon}_{q0}}\left\langle \dfrac{p'_d}{p'_F} - 1 \right\rangle^n}{\sqrt{\left\{ p'\eta^2 \left[\left(\dfrac{M}{\eta} \right)^{1/r} - 1 \right] \right\}^2 + 4q^2}}, \qquad \frac{\dot{q}}{\dot{\varepsilon}_q} = \frac{\tau\dot{q}_0 \sqrt{\left\{ p'\eta^2 \left[\left(\dfrac{M}{\eta} \right)^{1/r} - 1 \right] \right\}^2 + 4q^2}}{\dfrac{\tau q_0}{3\mu} \sqrt{\left\{ p'\eta^2 \left[\left(\dfrac{M}{\eta} \right)^{1/r} - 1 \right] \right\}^2 + 4q^2} + 2q \left\langle \dfrac{p'_d}{p'_F} - 1 \right\rangle^n} \tag{4}$$

where τ is the coefficient of viscosity, $\eta = q/p'$, μ and n are constants, and p'_d is a parameter of the dynamic yield surface. The rate-dependence of the model affects the limiting states at which an accelerated process (instability) may commence. In fact, condition (3) no longer applies, because, in contrast to strain-controlled loading, in stress-controlled loading no apparent softening occurs. The onset of accelerated process takes place when

$$W_3 = q\ddot{\varepsilon}_q = 0 \tag{5}$$

and this is demonstrated in Fig. 2

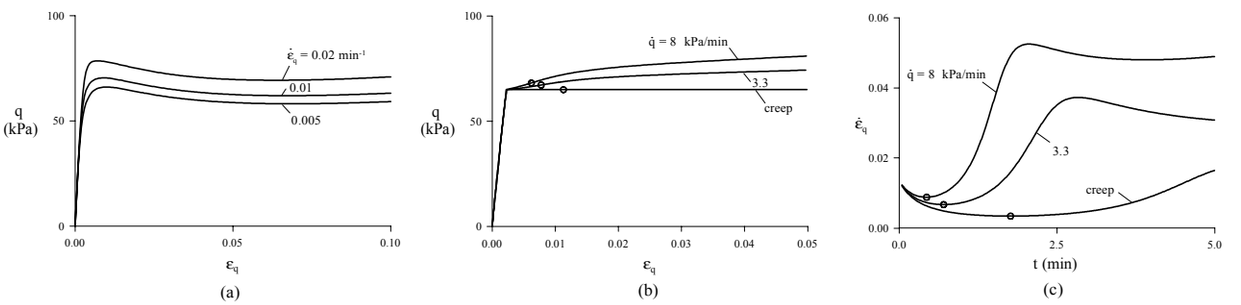


Fig. 2 Elasto-viscoplastic response and instability points; a) strain-control, b) stress-control ,c) evolution of strain-rate

Numerical simulations

To illustrate the model predictions further, two types of numerical simulations (FLAC) of the undrained, plane-strain, biaxial compression test were performed. In the first, the elasto-plastic model was used to demonstrate the effect of hydro-mechanical coupling on the formation of shear bands in a specimen subjected to strain-controlled loading. The results confirm the theoretical findings in [7] that low hydraulic conductivity and high loading rates support the occurrence of shear bands in the case of contractant material; in essence, the process is controlled by a characteristic dimensionless parameter. In the second type of simulation, the specimen made of the elasto-viscoplastic material was subjected to load-controlled loading in a fully inertial system that allows for spontaneous growth of accelerated deformation of the specimen in the post-stable regime. Demonstrated is the resulting difference in stress measurements at the various locations in the specimen. The results of both simulations have direct implications in designing and conducting physical tests on water-saturated granular deposits, and in their data interpretation.

References

[1] Boukpeti, N., Drescher, A.: Triaxial behavior of refined Superior sand model. *Comp. Geotech* **26**: 65-81, 2000.

[2] Boukpeti, N., Mróz, Z., Drescher, A.: A model for static liquefaction in triaxial compression and extension. *Canadian Geotech. J.* **39**: 1243-1253, 2002.

[3] Drescher, A., Mróz, Z.: A refined Superior sand model. *Num. Models Geomech, NUMOG VI*, G. N. Pande and S. Pietruszczak. eds., A.A. Balkema, 21-26, 1997.

[4] Lade, P.V., Yamamuro, J., Bopp. P.: Influence of time effects on instability of granular materials. *Comp. Geotechnics* **20**: 179-193, 1997.

[5] Mróz, Z., Boukpeti, N., Drescher, A.: Constitutive model for static liquefaction. *Int. J. Geomech* **3**: 133-144, 2003.

[6] Perzyna, P.: The constitutive equations for rate sensitive plastic materials. *Quart. Appl. Math* **20**: 321-332, 1963.

[7] Vardoulakis, I.: Deformation of water-saturated sand: I. Uniform undrained deformation and shear banding, II. Effect of pore water flow and shear banding, *Géotechnique* **46**: 441-456, 1996.

DEVELOPMENT OF SHEAR BANDING IN SANDSTONE

Jeffery J. Riedel*, Joseph F. Labuz**
*Geological Sciences, Pennsylvania State University, University Park, PA USA
**Civil Engineering, University of Minnesota, Minneapolis, MN USA

Summary Closed-loop, servo-controlled compression tests were conducted to investigate the development of shear banding in Berea sandstone. The experiments were performed with a Vardoulakis-Goldscheider type plane-strain apparatus, designed to allow the shear band to develop in an unrestricted manner. Dilatancy and friction were evaluated at three confining pressures, and several tests were halted in the strain-softening regime. Thin section microscopy and digital image analysis provided direct observations of the shear band. Porosity increase within the shear band was 4-8 grain diameters wide and associated with intragranular microcracks; increased porosity did not extend beyond the tip of the shear band.

PLANE-STRAIN EXPERIMENTS

From laboratory compression tests on geomaterials, it is observed that a uniform deformation pattern changes and further deformation is localized in a narrow region called a shear band. This localized feature is typically observed in earth materials such as dense sand and overconslidated clay, as a zone of high shear strain relative to the surrounding material. In dense sands, shear banding is associated with motion of individual particles and may be described by equilibrium bifurcation theory [1]. In brittle earth materials such as sandstone, shear banding may be related to intragranular microcracks, phenomenon that has been inferred from other experiments [2,3,4]. A few studies have shown the complexity between porosity and mean stress in the localization process [3,4]. Understanding the mechanisms involved in the development of a shear band in sandstone is of primary interest in this research.

Constitutive behavior

Plane-strain compression [5] experiments were performed and data from three tests (5, 10, 20 MPa confinement) are shown in Figures 1 and 2. The dilatancy angle ψ, where $\sin\psi=-\Delta\varepsilon_p/\Delta\gamma_p$ and $\Delta\varepsilon_p$=incremental plastic volume strain and $\Delta\gamma_p$=incremental plastic shear strain, was calculated from the onset of plastic deformation to near peak stress (Fig. 1). Dilatancy showed strong pressure dependence. The degree of compactive behavior at the onset of plastic deformation, observed as a negative dilatancy angle, was larger for tests with higher confining pressure. The dilatant response of each specimen seemed to approach a limiting value; higher confinement resulted in a smaller value of peak dilatancy.

Using the stress parameters $s=(\sigma_1+\sigma_3)/2$ and $t=(\sigma_1-\sigma_3)/2$, the linear Mohr-Coulomb yield condition can be written as $t=s\cdot\sin\phi+c\cdot\cos\phi$ and the friction angle ϕ can be estimated from $\sin\phi=t/s[1/(1-Q/s)]$. The parameter Q is the intercept at t=0; for Berea sandstone, Q=-9.25 MPa. The linear yield function showed sensitivity to pressure (Fig. 2), while a nonlinear yield function could reasonably represent the response. Note that the sandstone displayed non-normality.

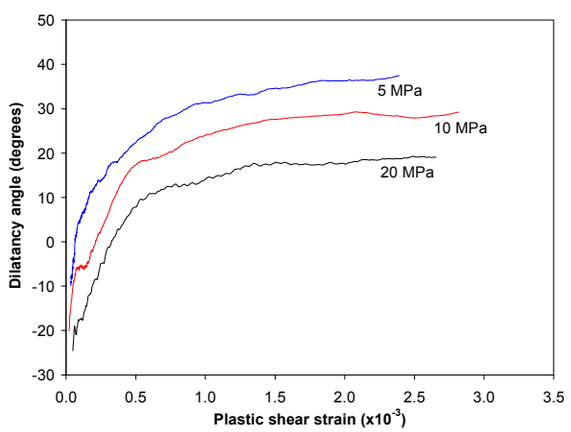


Figure 1. Dilatancy of Berea sandstone.

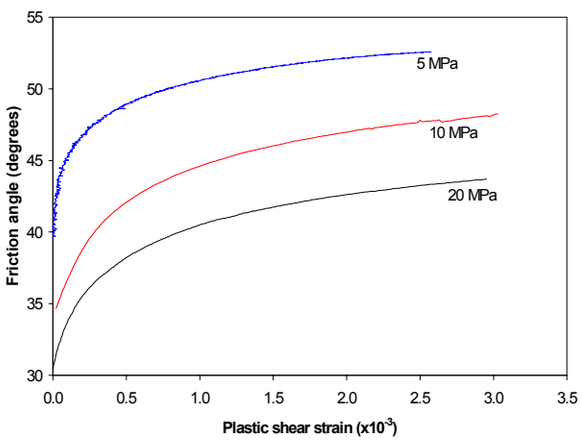


Figure 2. Friction of Berea sandstone.

Post-failure observations

Thin sections for optical microscopy were prepared from specimens where deformation localized and softening occurred, but the shear band was not fully developed; the specimens remained intact and the shear band was well preserved. Care was taken in handling the specimens by potting them in hydrostone to facilitate cutting the specimens in half; then the blocks were quenched in low viscosity, blue epoxy to increase the visibility of porosity and to preserve the structure of the material during slide preparation. The thin-sections were examined under reflected and transmitted light at magnifications ranging from 4x to 52x. Photographs were taken with a digital camera mounted on the microscope.

The shear band seemed to initiate at a stress concentration, either the corner of the specimen (Fig. 3) or, when present, an imperfection (a 3-mm diameter hole) introduced in the specimen. From displacement measurements and acoustic emission locations, it was concluded that the shear band initiated around peak stress and then propagated in the softening regime until the test was stopped. All the specimens showed similar deformation mechanisms along the shear band, although only one experiment at 5 MPa confinement will be presented.

Progressive failure

Microcracking among individual grains was the dominant failure mechanism. For example, areas with high microcrack densities were outlined in black (Figs. 3a,b,c). The intensity of grain cracking within the shear band was greatest near the corner of the specimen and decreased as the surface was traced towards the center of the specimen. Areas of high crack density also appeared to have the greatest amount of grain size reduction and there seemed to be a larger amount of pore space (Figs. 3a,b). The shear band also propagated through regions where grain fracturing was not observed; in these locations the shear band transected grain contacts. Although the path of the shear band was not completely straight, the overall orientation was about 76° from the minor principal stress direction.

A numerical code was written to provide an efficient means for analyzing the relative porosity of epoxy-impregnated thin-sections. The code was set up to receive a digital image (*.bmp). The colors of most concern were blue, the color of the epoxy filling the pore spaces, and white, the color of individual grains which compose the matrix of the sandstone. The bitmap image used three parameters, R, B, and G, to define the color of each pixel, with a value between 0 and 255. The intensity of the R channel consistently defined the boundary of grain and pore space and was the channel used to differentiate blue pore space from the white grains composing the matrix.

The areas of increased porosity, 4-8 grain diameters wide, did not extend beyond the tip, which was determined by the last observable intragranular microcrack. An absence of notable porosity change in the immediate vicinity of the tip suggested that a porosity increase was not detected prior to microcracking. The porosity change that corresponded to the shear band was observed in areas with high densities of intragranular microcracks. Therefore, it seemed that the localized porosity increase was related to the evolution of microcracks after the initial inception of the shear band.

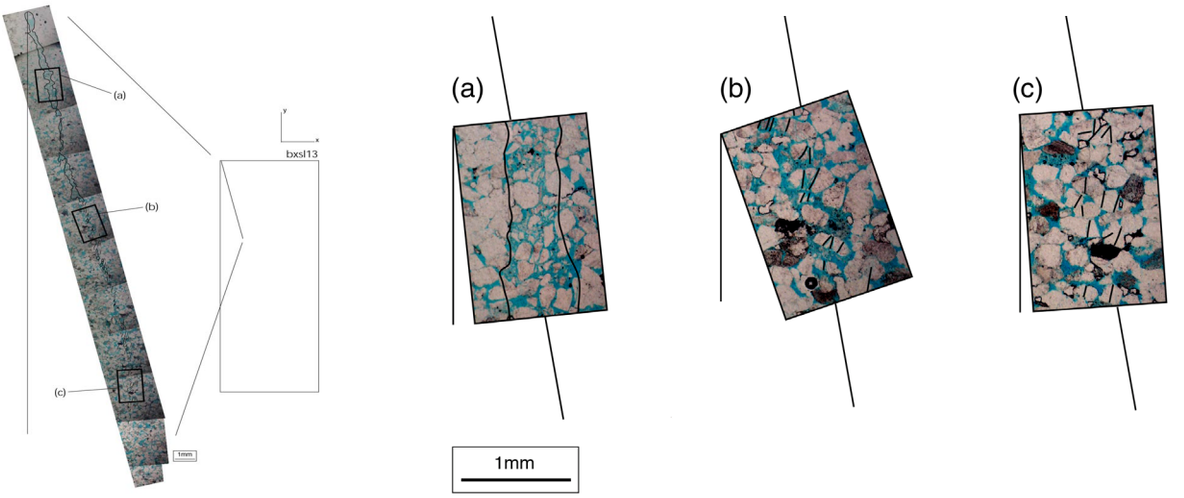


Figure 3. Shear band in Berea sandstone at 5 MPa confinement.

CONCLUDING REMARKS

A suite of plane-strain compression tests were performed on Berea sandstone with the University of Minnesota Plane-Strain Apparatus, which allowed shear banding to develop and propagate in an unrestricted manner. Thin-section microscopy was performed on deformed specimens and the shear band showed a progression of deformation from the inception point, where the deformation was characterized by a high density of intragranular microcracks with broken grains, to the tip, where the intragranular microcracks were significantly less dense and separated by intact grains.

References

[1] Vardoulakis I., Sulem J.: Bifurcation Analysis in Geomechanics. Blackie Academic and Professional, Glasgow 1995.

[2] Bernabe Y., Brace W.F.: Deformation and fracture of Berea sandstone. *Am. Geophys. Un. Geophys. Monogr*. **56**:91-101, 1996.

[3] Besuelle P., Desrues J., Raynaud S.: Experiemental characterization of the localization phenomenon inside a Vosges sandstone in a triaxial cell. *Int. J. Rock Mech. Min. Sci.* **37**:1223-1237, 2000.

[4] El Bied A., Sulem J., Martineau F.: Microstructure of shear zones in Fontainbleau sandstone. *Int. J. Rock Mech. Min. Sci.* **39**:917-932, 2002.

[5] Labuz J.F., Dai S.T., Papamichos E.: Plane-strain compression of rock-like materials. *Int. J. Rock Mech. Min. Sci.* **33**:573-584, 1996.

XXI ICTAM, 15–21 August 2004, Warsaw, Poland

ON THE USE OF SECOND-ORDER TOPOLOGICAL INFORMATION FOR SUBSURFACE IMAGING BY ELASTIC WAVES

Bojan Guzina*, Ivan Chikichev*
* *Department of Civil Engineering, University of Minnesota, Minneapolis, MN 55455, U.S.A.*

Summary
This paper is concerned with the generalization of topological derivative, rooted in structural shape optimization, as it pertains to 3D inverse scattering involving elastic-wave identification of subsurface obstacles. Recently, elastodynamic expressions for topological sensitivity have been proposed for the imaging of both semi-infinite and finite solid bodies. Despite their utility, however, these developments are limited in the sense that they are restricted to the identification of subsurface cavities and that they do not provide an explicit link between the nucleated (infinitesimal) cavity and the finite size of a void being sought. To deal with these impediments, the proposed generalization is two-fold and involves: i) development of a formula for the nucleation of a solid inclusion, and ii) rigorous analysis of the second-order topological information that permits direct estimation of the obstacle size through the solution of a canonic least-squares problem, established on the basis of (first-order) topological sensitivity. Numerical examples are included to illustrate the proposed developments.

BACKGROUND

Solutions to inverse scattering problems in elastodynamics, which have a wade range of applications including geophysics, medical imaging, and nondestructive material testing, are derived from either of the three computational platforms that include i) ray-theory approximation [1], ii) finite-difference methods [2], and iii) boundary integral formulations [3]. In the context of three-dimensional subterranean imaging, however, the former two solution methodologies necessitate an extensive computational effort which precludes their full 3D application in all but major land and marine surveys [2]. To mitigate such limitation, boundary-only imaging algorithms have been proposed as a computationally-tractable alternative for solving inverse scattering problems, especially when coupled with the use of gradient-based minimization and analytical shape-sensitivity estimates [4]. Unfortunately, the latter class of solutions necessitate a reliable prior information about the location, topology and geometry of an obstacle for adequate performance.

Motivated by the foregoing considerations, this study deals with the advancement a robust, yet computationally efficient approach for preliminary subsurface imaging by elastic waves based on the concept of topological sensitivity. With reference to a cost functional $\mathcal{J}$ of the body shape, its topological derivative, $\mathcal{T}(\boldsymbol{x}^{\circ})$, synthesizes the first-order sensitivity of $\mathcal{J}$ with respect to the creation of an infinitesimal cavity at a prescribed location $\boldsymbol{x}^{\circ}$ inside the reference, i.e. void-free counterpart of the probed body. The concept of topological derivative first appeared in [5] and [6] in the context of shape optimization of mechanical structures wherein the spatial distribution of $\mathcal{T}(\boldsymbol{x}^{\circ})$ was used as a criterion for the removal of "excess" material through regions where $\mathcal{T}<0$. Recently, elastodynamic generalizations of the topological sensitivity have been proposed in the context of inverse elastic scattering pertaining to semi-infinite [7] and finite [8] domains.

NUCLEATION OF INHOMOGENEITIES

By building on the approach originally proposed in structural shape optimization, developments in [7] and [8] revolve around the process of *cavity* nucleation. As such, their application is limited to inverse scattering problems where subsurface obstacles are in the form of voids. To establish a more general analytical and computational framework that would permit elastic-wave identification of material heterogeneities, the first part of this study deals with the development of an expression $\mathcal{T}(\boldsymbol{x}^{\circ};\mu^*,\nu^*,\rho^*)$ for topological derivative, explicit in terms of the elastodynamic fundamental solution, obtained by an asymptotic expansion of the misfit-type cost functional with respect to the creation of an infinitesimal *inclusion* (with shear modulus μ^*, Poisson's ratio ν^* and mass density ρ^*) in an otherwise homogeneous (reference) solid. Valid for an arbitrary shape of the infinitesimal domain, the formula revolves around the elastostatic solution to six canonical exterior problems, and becomes fully explicit when the vanishing inclusion is spherical. On the basis of the foregoing result, a computational platform is developed for approximate, yet efficient 3D imaging of heterogeneous solids. In contrast to existing solutions which are restricted to the geometric identification of cavities, the proposed approach permits point-wise identification of "optimal" material properties (e.g. μ^*) which minimize the topological sensitivity at a sampling point, $\boldsymbol{x}^{\circ}$. This in turn enables the approach to differentiate between cavities and inclusions, which is a major step toward providing a reliable initial "guess" for more refined, albeit computationally intensive minimization-based imaging algorithms.

SECOND-ORDER TOPOLOGICAL INFORMATION

Numerical experiments show that the topological derivative approach, when applied to inverse scattering, performs best when used in conjunction with wave lengths exceeding the cavity diameter (so-called resonance region). This is perhaps not surprising since the assumption of an *infinitesimal* cavity, implicit to the formulas for topological derivative, is better conformed with by finite cavities that are '*small*' relative to the probing wavelength. Accordingly, the spatial

distribution of topological derivative does not furnish direct information about the size of the hidden scatterer, although it may effectively point to its approximate location and shape. As a result, estimation of the obstacle size using first-order topological sensitivity is in practical applications critically dependent on a user-defined threshold parameter. To bridge the gap between the infinitesimal size of a trial "bubble" (inherent to $\mathcal{T}(\boldsymbol{x}^{\circ})$) and the finite size of a hidden scatterer, the second part of this investigation is concerned with the rigorous, *second-order* topological expansion of a given cost functional with with respect to obstacle nucleation. It is shown that the explicit knowledge of second-order terms in such elastodynamic expansion, herein obtained by means of a boundary integral analysis, permits direct estimation of the *obstacle size* (whose location is estimated beforehand using the first-order information, $\mathcal{T}(\boldsymbol{x}^{\circ})$) through the solution of a canonical least-squares problem that requires only a minimal increase of computational effort. Although herein presented for the case of cavity nucleation only, the proposed second-order analysis is equally applicable to elastic-wave imaging of material heterogeneities by means of the inclusion-type topological sensitivity $\mathcal{T}(\boldsymbol{x}^{\circ}; \mu^{*}, \nu^{*}, \rho^{*})$. A set of numerical examples is included to illustrate the analytical and computational developments.

References

[1] Aki K., Richards P.G.: Quantitative Seismology. Univ. Science Books, CA 2002.
[2] Sheriff R.E. and Geldart L.P.: Exploration Seismology. Cambridge University Press, UK 1995.
[3] Bonnet M.: Boundary Integral Equation Methods for Solids and Fluids. John Wiley & Sons, NY 1999.
[4] Guzina, B.B., Nintcheu Fata, S., Bonnet, M.: On the stress-wave imaging of cavities in a semi-infinite solid. *Int. J. Solids Struct.* **40**:1505–1523, 2003.
[5] Eschenauer, H.A., Kobelev, V.V., Schumacher, A.: The topological asymptotic for PDE systems: the elasticity case. *Structural Optimization*, **8**:42–51, 1994.
[6] Schumacher, A.: Topologieoptimierung von Bauteilstrukturen unter Verwendung von Kopchpositionierungkrieterien. *Ph.D. thesis*, Univ. of Siegen, Germany, 1995.
[7] Guzina, B.B., Bonnet, M.: Topological derivative for the inverse scattering of elastic waves. *Quart. J. Mech. Appl. Math.*, **57**(1), in press, 2004.
[8] Bonnet, M., Guzina, B.B.: Sounding of finite solid bodies by way of topological derivative. *Int. J. Num. Meth. Eng.*, in review.

XXI ICTAM, 15–21 August 2004, Warsaw, Poland

INCREMENTAL NONLINEARITY IN CONSTITUTIVE RELATION FOR GRANULAR MEDIA

Yuji Kishino*,
*Tohoku University, Department of Civil Engineering, Aoba 06, Sendai 980-8579, Japan

Summary In this paper, the 3D Granular Element Method was utilized to conduct stress probe tests. It was found from these tests that, as far as the conventional tri-axial state concerns, the incremental plastic response is approximated by the non-associated flow rule, and that, for general true tri-axial stress probes, the direction of incremental plastic strain is apparently dependent on the direction of incremental stress. The latter suggests the existence of multiple shear mechanisms in plastic deformation of granular media.

INTRODUCTION

Recently, incrementally nonlinear models have been proposed for constitutive relations of geomaterials[1], [2]. In these theories the direction of incremental plastic strain is generally dependent on the direction of incremental stress. The dependency of the direction of incremental plastic strain on the direction of incremental stress was experimentally demonstrated in a series of torsional shear tests on hollow cylindrical specimens of sand [3]. As the principal directions of stress in these tests were not fixed, it was concluded that the incremental nonlinearity emerged from the rotation of principal axes of stress. For general discussion, we need to develop a sophisticated testing apparatus which enables us to carry out arbitrary probe tests in six dimensional stress or strain space and conduct a huge series of tests of numerous specimens regarded as identical. On the other hand, numerical tests with a suitable discrete element method enable us to extract general information on irrecoverable behaviors of an identical granular specimen. The paper [4] tried to clarify the 3D incremental responses numerically, using the Granular Element Method (GEM) proposed by the author. However, it dealt with only tri-axial stress probes and the incremental nonlinearity was not remarkable. This paper, based on the GEM numerical tests under the true tri-axial state, discusses the incremental nonlinearity in the plastic flow of granular media.

METHODS

The discussions in this paper are based upon numerical element tests of a spherically packed assembly of spherical particles. The numerical experiments are a triaxial compression test and two series of stress probe tests. A stress probe test is a set of incremental loading and reversal loading along a specified stress probe direction, which gives the incremental elastic strain as the recoverable part and the incremental plastic strain as the irrecoverable part. All the loadings are controlled by the stress which can be determined from contact forces between peripheral and inner particles. The Granular Element Method(GEM), which is basically a stiffness method, makes it easy for boundaries to be controlled in arbitrary ways. The movement of each inner particle (parallel displacement and rigid rotation) has six degrees of freedom, while the non-rotational movement of a boundary particle follows a linear transformation determined by the bulk deformation. The relationship between contact force and relative displacement at each contact point is characterized as in DEM by spring coefficients in normal and tangential directions and Coulomb's friction law and the no-tension rule are assumed. The algorithm in GEM utilizes an implicit iterative procedure to secure accurate equilibrium states. Each step-by-step particle movement for unbalanced force and moment is determined by an individual stiffness matrix with 6 x 6 components assembled under the assumption that the neighboring particles do not move. The latter idea has stemmed from a relaxation analysis for elastic frames. However, in non-elastic analyses, the history of relaxation in an iterative process affects the results. Hence, in GEM, all of the particle movements in an iteration step take place at the same time after determining individual particle movements by stiffness matrices. If a particle does not have three contact points, the stiffness matrix of this particle becomes singular. In the GEM algorithm, a singular stiffness matrix is replaced with a diagonal matrix whose components have small values. To avoid excess overlapping between particles, the particle movements calculated by the individual stiffness matrices are modified such that the maximum movement does not exceed a limit.

RESULTS

The numerical specimen used in this research is a random assemblage of 360 spherical particles whose radii range from 1.3 mm to 2.6 mm and 166 particles among them are peripheral particles. Spring constants for normal and tangential directions are 2.0 and 1.4 MN/m, respectively and the friction angle is 15^o. As shown in **Figure 1.**, the tri-axial test starts from a state with isotropic pressure of 0.1 MPa and this value is maintained in the horizontal directions throughout the tri-axial compression test. The tolerance in the boundary stress control is 1.7×10^{-7} MPa. Such small value is required to determine both of the elastic and plastic strains with sufficient accuracy. Stress probe tests are carried out starting from an intermediate state of tri-axial test whose stress ratio is 0.4. All of the stress probe directions lie in the principal stress space, and a series of stress probe tests are a set of 72 probes in a plane of stress space. The magnitude of each stress probe was 0.001 MPa which is one hundredth of the initial confining pressure. To specify probe directions, we define three characteristic directions based on a yield surface (**Figure 1.**). We assume that the yield surface is a cone whose vertex is at the origin of the principal stress space. The validity of this assumption will be demonstrated later by the results for tri-axial loading. We will also find later that we cannot assume a unique yield surface for general incremental

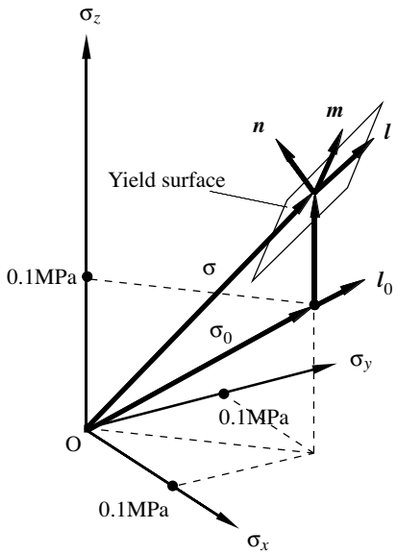


FIgure 1. Loading path

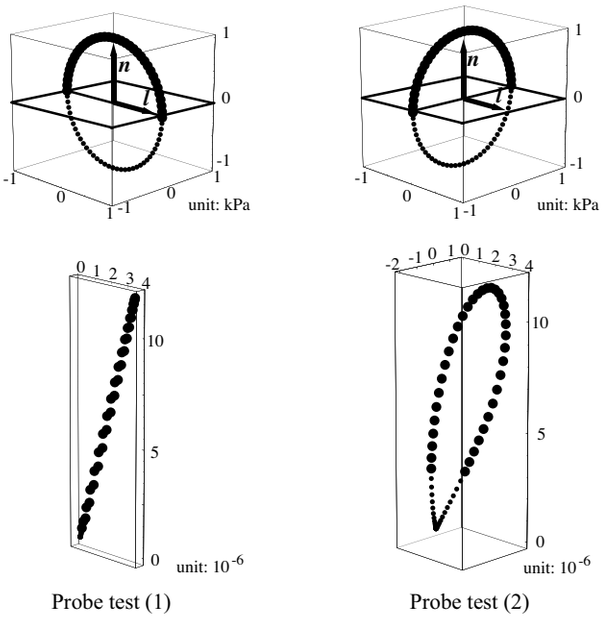


Figure 2. Plastic strain increment

stresses. However, we define characteristic directions by assuming that the yield surface is the cone explained above. The first characteristic direction ***n*** is the outward normal of the yield surface. The second direction ***l*** is the direction of current stress vector which is a generator of the current yield surface. The last direction ***m*** is perpendicular to these two directions. Two types of stress probe tests are carried out. As shown in **Figure 2.**, the probe planes for these probe tests are (***n***, ***l***) and (***n***, ***m***) planes. The stress state in Probe test 1 always remains in the so-called tri-axial state, while, in Probe Test 2, the stress state is generally in the so-called true tri-axial state. **Figure 2.** shows the results obtained in the stress probe tests. Stress probes and incremental strains are plotted in the stress and strain spaces. The incremental response for a stress probe that has downward normal component with respect to the yield surface is usually assumed to be elastic, and in fact the incremental plastic strains in Probe test 1 are almost zero as shown by the smaller dots. The result is also in accord with the previous assumption that the yield surface is given by a cone whose vertex is at the origin of the principal stress space. Further, in Probe test 1, it is observed that the incremental plastic strain vectors are almost on a unique straight line. As this line is not coaxial with the outward normal of yield surface, the plastic flow is non-associative. On the other hand, the incremental plastic response in Probe test 2 is totally different from the above result. The incremental plastic strain vectors are not on a common line and the direction of incremental plastic strain is apparently dependent on the direction of incremental stress. Further, the smaller dots represent incremental plastic strains for stress probes whose directions are inward of the assumed yield surface, which indicate that we can not assume the existence of a unique yield surface generally. From these results, we may conclude that the plastic deformation is generally accompanied by multiple shear mechanisms. One of the definite mechanisms is that of tri-axial shearing which has been developing during the tri-axial compression. Another mechanism begins to develop when the shearing between two horizontal stress components is applied to the specimen for the first time in Probe test 2.

CONCLUSIONS

In this paper, the numerical tests were carried out to verify the incremental nonlinearity in constitutive relationship for granular media. The method used was the 3D Granular Element Method, and the simulation of true tri-axial probe tests led to the following results: 1) As far as the conventional tri-axial state concerns, the incremental plastic response is approximated by the non-associated flow rule. 2) For general true tri-axial stress probes, the direction of incremental plastic strain is apparently dependent on the direction of incremental stress. 3) The latter suggests the existence of multiple shear mechanisms in plastic deformation of granular media.

References

[1] Darve F.: An Incrementally Non-Linear Constitutive Law: Assumptions and Predictions. *Constitutive Relations for Soils*(Eds., G. Gudehus, F. Darve & I. Vardoulakis), A.A. Balkema:385–403, 1984.
[2] Kolymbas D. (Editor): Constitutive Modelling of Granular Materials. Springer, Berlin 2000.
[3] Pradel D., Ishihara K., Gutierrez M.: Yielding and Flow of Sand under Principal Stress Axes Rotation. *Soils and Foundations* **30**(1):87–99, 1990.
[4] Kishino Y., Akaizawa H., Kaneko K.: On the Plastic Flow of Granular Materials. *Powders & Grains 2001*(Ed., Y. Kishino), A.A. Balkema:199–202, 2001.

A High-Pressure High Strain Rate Elastic-Viscoplastic Model for Cementitious Materials

Martin J. Schmidt[*], Oana Cazacu[**], Mark L. Green[*], Nicolaie D. Cristescu[***]

[*] *Air Force Research Laboratory, Eglin AFB FL, USA*

[**] *Graduate Engineering and Research Center, University of Florida, Shalimar FL, USA*

[***] *Mechanical and Aerospace Engineering, University of Florida, Gainesville FL, USA*

Summary A comprehensive experimental study aimed at characterization of the combined effects of high confinement and high strain rate on the deformation and strength of cementitious materials was conducted. Quasi-static triaxial compression tests for confining pressures ranging from 0 to 500 MPa were performed. Dynamic tests for strain rates in the range 60/s to 160/s under both unconfined and confined conditions were conducted using a split Hopkinson pressure bar. A new elastic/viscoplastic model was developed.

The combined effects of high confinement and high strain rate on the mechanical response of two cementitious materials, mortar and concrete, have been investigated. Mortar is defined as simply a mixture of cement, fine-grained sand, water and binders, whereas concrete is defined as a mixture of the same materials plus coarse aggregate. For this study, a nominally 52.5 MPa unconfined compressive strength mortar, and 60 MPa unconfined compressive strength concrete with a 9.5 mm chert aggregate were selected.

The effects of confining pressure on cementitious materials tested at quasi-static strain rates have been extensively studied. Effects of strain rate on the compressive and tensile properties of cementitious materials have also been reported (e.g. Ross et al. [1] and, Malvar and Ross [2] respectively). A very limited set of data on strain rate effects on dynamic shear strength of cementitious materials is given by Schmidt and Ross [3].

Data on the combined effects of confining pressure and strain rate are rather limited due to the necessity of complicated test equipment and the complexity of test procedures. Some of the earliest dynamic confined tests were performed by Malvern et al. [4] using a 7.62 cm diameter Split Hopkinson Pressure Bar (SHPB) and a pressure cell for applying confining pressure in the range 0-6.9 MPa. Using the same device as Malvern et al. [4], confined dynamic tests were performed on strain gage instrumented mortar and concrete test specimens at strain rates ranging from 60/s to about 160/s under both unconfined and confined conditions. Quasi-static triaxial compression tests at a strain rate of 10^{-6}/s were also conducted on the concrete material for confining pressures ranging from 0 to 500 MPa.

For mortar, dilatancy has been observed at high levels of the principal stress difference for both dynamic and quasi-static conditions. The unconfined dynamic compressive strengths are approximately double those of the quasi-static compressive strengths. Most of the confined SHPB mortar specimens showed very little damage post-test. For concrete, the unconfined dynamic strength is as high as 1.5 times the quasi-static strength, the material generally exhibiting far more cracking under similar loading conditions than was observed in mortar. The confined dynamic tests showed similar stress-strain response as the quasi-static tests conducted at the same level of confinement. For both materials, a decrease in strain rate sensitivity with increasing confining pressure was observed. Figure 1 illustrates this phenomenon for concrete. In the figure, results are given in terms of a Dynamic Increase Factor (DIF), or the ratio of the quasi-static to dynamic strength.

For the concrete, quasi-static hydrostatic tests conducted up to a pressure of 0.5 GPa allowed for the accurate determination of the dependence of the bulk modulus on pressure and the correct estimation of the material's compaction properties when subjected to pressures in the range encountered in dynamic events. For confined quasi-static conditions, the material exhibited hardening behavior up to failure. Both compressibility and dilatancy regimes of the volumetric behavior were observed, the dilatancy threshold being highly dependent on the level of confinement. A new elastic/viscoplastic model that captures compressibility and dilatancy, as well as strain rate effects has been developed for concrete. As a general framework, the elastic-viscoplastic formulation of Cristescu [5] was chosen due to its apparent capability to capture the behavior of interest and the fact that there are no a priori limitations or restrictions regarding the specific expressions of the yield function and viscoplastic potential. However, it was found that in order to capture the peculiarities of the volumetric response, namely the reduced dilatancy at very high pressure, the hypothesis of existence of a viscoplastic potential has to be abandoned. The formulation does not assume a decoupling between shear and volumetric effects, and does not require a separate equation of state in order to handle the pressure volume relationship. A new flow rule was proposed using general representation theorems for tensor functions (Cazacu et al. [6]). The general form of the constitutive equation is shown below, where ε is strain, σ stress, G the shear modulus, K the bulk modulus, p the mean normal stress, δ_{ij} the Kronecker delta function, k_T a viscosity parameter, W irreversible stress work, H the yield function, t is time, and N the strain rate orientation tensor function. In the equation, the over dot is used to indicate differentiation with respect to time, while the symbols, $\langle\ \rangle$, represent

$$\dot{\varepsilon}_{ij} = \frac{\dot{\sigma}_{ij}}{2G} + \left(\frac{1}{3K} - \frac{1}{2G}\right)\dot{p}\delta_{ij} + k_T\left\langle 1 - \frac{W(t)}{H(\sigma_{mn})}\right\rangle N(\sigma_{ij})$$

the so-called Macaulay bracket, used to denote the positive part of a function (i.e. $\langle A \rangle = \frac{1}{2}(A + |A|)$). Detailed procedures for determination of the constitutive functions were developed (Schmidt [7]). Figures 2 through 4 present comparisons between the model predictions and experimental data. The results show that the proposed model describes with very good accuracy the behavior of concrete over a broad range of pressures.

References

[1] Ross C.A., Jerome D.M., Tedesco J.W., Hughes M.L.: Moisture and Strain Rate Effects on Concrete. *ACI Materials J.* **93**: 293-300, 1996.
[2] Schmidt M.J., Ross C. A.: Shear Strength of Concrete Under Dynamic Loads. In *Proceedings of the 1999 Structures Under Extreme Loading Conditions Symposium. PVP-Vol. 394* (Jerome D.M., ed.), Boston, MA, pp. 121-126, ASME, August 1-5, 1999.
[3] Malvar L.J., Ross C.A.: Review of Strain Rate Effects for Concrete in Tension. *ACI Materials J.*, 1998.
[4] Malvern L. E., Jenkins D. A., Tang T., McClure S.: Dynamic Testing of Laterally Confined Concrete. *Micromechanics of Failure of Quasi-Brittle Materials.* Elsevier Applied Science, 1990.
[5] Cristescu N.D., *Rock Rheology*, Kluwer Academic Publishers, Dordrecht, The Netherlands, 1989.
[6] Cazacu O., Jin J., Cristescu N.D.: A new constitutive model for alumina powder compaction, *KONA Powder and Particle 15*, pp. 103-112, 1997.
[7] Schmidt M.J.: High Pressure and High Strain Rate Behavior of Cementitious Materials: Experiments and Elastic/Viscoplastic Modeling. *PhD Thesis*, University of Florida, Gainesville, FL, 2003.

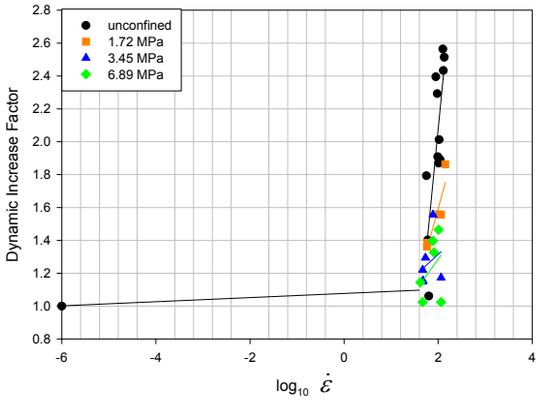


Figure 1: Effect of confinement on Dynamic Increase Factor (DIF) for concrete

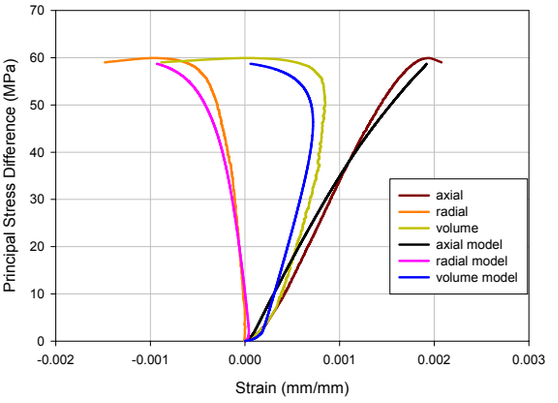


Figure 2: Experimental/Theoretical comparison of uniaxial compression test for concrete

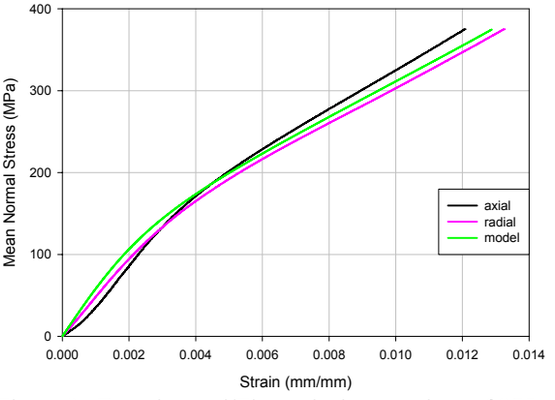


Figure 3: Experimental/Theoretical comparison of 375 MPa hydrostatic compression test

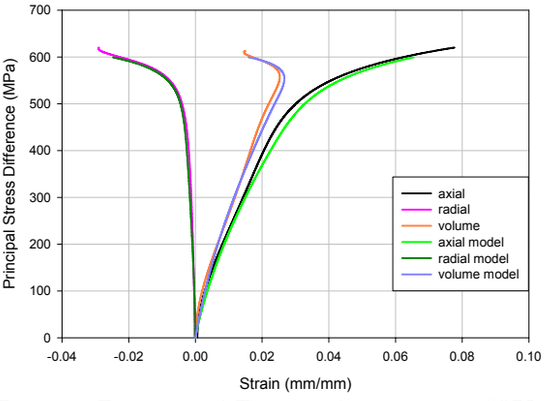


Figure 4: Experimental/Theoretical comparison of 375 MPa deviatoric compression test

THE INFLUENCE OF TEETH ON THE EARTH-WORKING PROCESSES

Jan Maciejewski*, Andrzej Jarzębowski*
* *IPPT PAN, Swietokrzyska 21, PL 00-049 Warszawa, Poland*

Summary The new experimental program of laboratory tests was presented, performed in a soil bin on cohesive soil. Model tools in a shape of an excavator's bucket equipped with teeth of different geometry were used in that study. The change in geometry simulated different subsequent stages of material wear. The experimental verification of the influence of teeth (number of teeth, and the position of teeth on the bucket's inside lip) on the efficiency of the digging cycle is discussed. Three different types of soil samples (dense, medium dense and loose) were used.

EXPERIMENTAL RESULTS

An experimental program was executed on the specialized laboratory stand equipped with a soil bin. The bin, the stand and sample preparation were precisely described in [1]. The bin dimensions were 2 m long x 0,6 m wide x 1,2 m deep. A mixture of 50% cement, 20% bentonite, 18% sand and 12% white vaseline was used to imitate a clayey soil. No water was added. Three different densities of the soil sample were used: loose, medium dense and dense sample. The loose soil sample used could be described by the Coulomb model with the following initial parameters: γ=16.2 kN/m^3, ϕ=27° and c=~15 kPa. For the medium dense soil sample the corresponding values were: γ=16.8 kN/m^3, ϕ=27° and c=~30 kPa, and for the dense soil sample: γ=17,2 kN/m^3, ϕ=27° and c=~45 kPa.

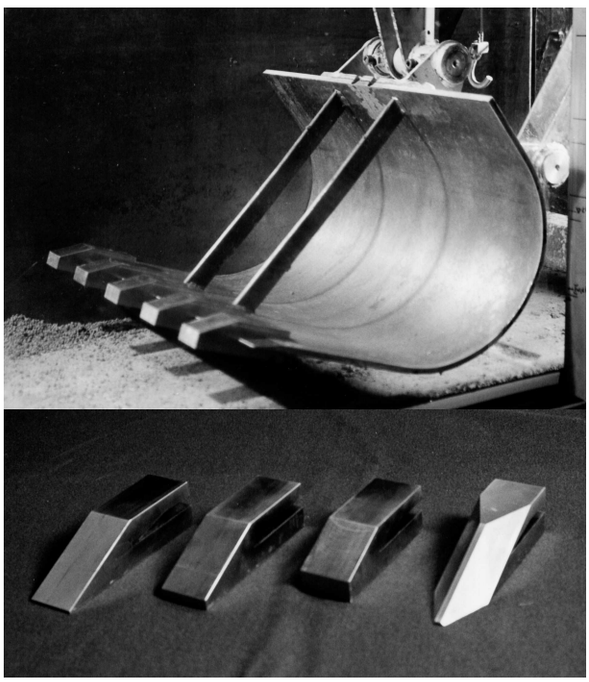


Figure 1. View of the excavator bucket and a set of teeth.

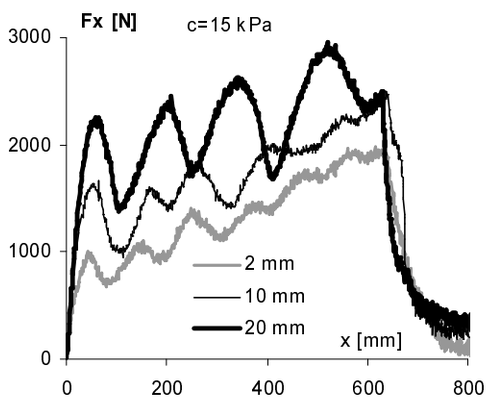


Figure 2. Horizontal force variations for the tools with 5 teeth and three different stages of the teeth wear.

In the experiments the model of an excavator's bucket of the width equal to that of the soil bin was used. The bucket was equipped with teeth. The shape and size of each tooth corresponded to that which is produced for the small bucket excavator K-111 by Waryński Company. Their width was w=46 mm and they stand out 95 mm in front of the inside lip. The model with 1, 2, 3, 4, 5 and 6 symmetrically situated teeth was used, as well, as the model without any teeth and one wide tooth obeying width equal to the width of the soil bin (0,6 m). Several different shapes of teeth were used: "sharp tooth" (2 mm worn-out), 10 mm worn-out, 20 mm worn-out and the tooth with 3-dimensional shape (Figure 1). All tests were executed on the soil samples obeying horizontal free surface. The same trajectory consisting of two linear stages was used. During the first stage, the bucket moved horizontally with the cutting depth 175 mm until it was filled up with the soil. The bucket inclination was 5°. During this stage of the earth-working process subsequent shear bands are generated and within those shear bands material softening is observed. As a result, the observed earth-working force obeyed oscillatory character of peaks followed by drops of the force value. In the second stage of the trajectory the bucket was lifted and withdrawn out of the soil bin. In Figure 2 variation of horizontal force acting on the tool for the number of teeth equal 5 and the loose soil sample are presented for three different stages of the teeth wear. With progressing development of the teeth wear the horizontal component of the force is significantly increasing.

In Figure 3 the variation of horizontal force for the tool equipped with various number of teeth (1, 3 and 5 teeth) is presented and compared with results for the wide tooth (0,6 m wide). In case of these tests the "sharp teeth" (2 mm worn-out) were used and tests were executed on the loose sample. As it was shown in

the previous paper by Maciejewski *et al.*[2] for the buckets with the number of teeth greater or equal to 4, the first and subsequent shear bands were not generated from the inside lip but from the line connecting the tips of the teeth (the range of the teeth spacing l was less then 3.26 w, where the w is the width of the single tooth). For the number of teeth exceeding 3 the line connecting the tips of the teeth played the role of the inside lip. It should be noticed, that the character of this test and the one performed for very wide tooth were similar, but the peak values of horizontal force were smaller. In the zone prior to the teeth the deformation pattern was identical like for the wide tooth, suggesting the existence of a plane strain condition within it. However, in the area surrounding the teeth the three-dimensional deformation pattern was observed. As a result some material was left behind the tool resulting in smaller peak values of the horizontal force component.

Thus, the deformation pattern in front of such an assembly of teeth was again the plane strain deformation pattern, which was observed by the authors for tools of the width equal to the width of the soil bin.

In Figure 4 the variation of horizontal force for the tool equipped with 5 sharp teeth is presented for three different densities of the soil sample.

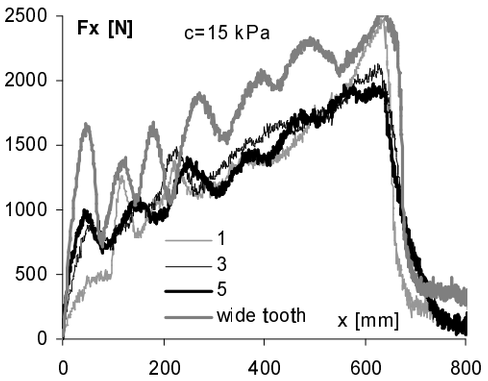


Fig. 3. Horizontal force variations for the tools with different number of teeth.

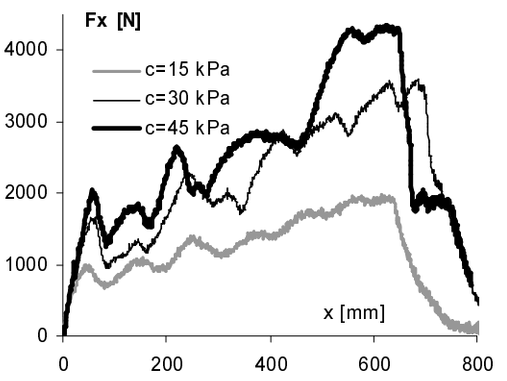


Fig. 4. Horizontal force variations for the tools with 5 teeth and different soil densities.

Conclusion

Periodic character of the digging process (observed for the cohesive soil with softening) manifested in the oscillatory character of force components and generation of the subsequent shear bands is independent of the shape of the tool, number of teeth and the degree of tool wear.

It was found, that for particular cohesive soil, corresponding to sandy clay for the teeth spacing l/w less then 3.26, the line connecting the tips of the teeth played the role of the inside lip. The teeth did not act as separate three-dimensional objects but as one wide tool built up from several modules. Thus, the deformation pattern in front of such an assembly of teeth was similar to the plane strain deformation pattern.

The wear of teeth, approximated to by the simple change of their geometry, has significant influence on the peak values of earth-working force. For wide teeth the influence of teeth wear on the earth-working force is observed for the whole range of the digging process not only for the peak values of force. The observed phenomena are independent from the soil density. However, for higher densities (higher cohesions) the differences between the peak and the minimum force values are more significant.

Acknowledgements

This study is supported by a grant from the Ministry of Scientific Research KBN nr 8 T07C02920 “Analysis of the influence of the tool wear and the tool shape on the efficiency of digging processes”.

References

[1]. Maciejewski, J.and Jarzębowski, A., Optimisation of tool trajectory in soil digging processes – laboratory tests. *J. Terramechanics* **39**, 3, 161-179, 2002

[2] Maciejewski, J., Jarzębowski, A., and Trąmpczyński, W., Study on the efficiency of the digging process using the model of excavator bucket. Proc. 14-th Int. Conf. ISTVS (CD), Vicksburg, MI, USA., 2002.

SHALLOW SPHERICAL CAPS UNDER EXTERNAL PRESSURE

J. Blachut
The University of Liverpool, Department of Engineering, Liverpool L69 3GH, UK

Summary This contribution details buckling tests and corresponding numerical results for shallow spherical caps subjected to static and uniform external pressure. Six mild steel caps were carefully CNC-machined from a solid billet of 245 mm diameter. Shallowness parameter, λ, varied from 3.5 to 5.5.

BACKGROUND

Buckling of spherical caps subjected to uniform and static external pressure has been researched for decades. Reference [1] lists most of the relevant work spanning a century or so. When reviewing the experimental work on buckling of spherical caps it becomes transparent that only small number of tests was carried out on metallic caps. One specific set of tests is reported in Ref. [2]. They were small diameter, 50mm – 70mm, aluminium models. A drop in the buckling strength was confirmed in these tests for small magnitude of caps' slenderness parameter lambda, i.e. for $\lambda \approx 4.0$.
A number of subsequent tests did not follow the same trend. Various reasons were given in order to explain this scatter of results around lambda = 4.0. By-and-large there appears to be no definitive answer to this dilemma.
This limited experimental/numerical study aims at exploring spherical caps' static stability around $\lambda = 4.0$. This is to be achieved through careful manufacturing of caps with well defined boundary conditions. Experiments have already been carried out and results of initial numerical runs are given here.

SUMMARY OF EXPERIMENTAL AND NUMERICAL RESULTS

A series of six cups, designated here as D1, …, D6, were CNC-machined from 245mm diameter mild steel billet. Shells had a heavy edge ring (integral with the wall). Its role was to model the fully clamped boundary conditions. The shallowness parameter, λ, was chosen to be between 3.5 and 5.5. The sequence of manufacturing for these caps was the same as in Ref. [3]. After final machining caps were stress-relieved in a vacuum furnace. Next, shape and wall thickness were measured. Shape was measured using an (XYZ)-co-ordinate measuring table. Measurements were taken along 14 equally spaced meridians and at 10 mm arc-length intervals. Table 1 contains average values for geometry (columns 2 – 5). It is seen from Table 1 that the height-to-wall thickness ratio varied approximately from 2.5 to 4.0 and the radius-to-thickness ratio varied from 300 to 1800. Examining the scatter of wall thickness, and radial deviations from perfect geometry it can be concluded that they all were, geometrically, nearly-perfect. Further details are to be published separately.
Mechanical properties of mild steel were the same as reported in Ref. [3]. That paper should be consulted for further details. Average mechanical properties of the mild steel were found to be: Young's modulus, E = 207.0 GPa, Yield point of material, $\sigma_{yp} = 303.5$ MPa; and Poisson's ratio, $\nu = 0.28$.
The above models were buckled through the application of quasi-static external pressure in a small pressure vessel opened to atmosphere (again, further details are to be published separately). All caps failed suddenly through a snap-through mechanism. Values of experimental buckling pressures are given in Table 1 (column 6). The initial numerical predictions of buckling loads were carried out using axisymmetric modelling of geometry and elastic perfectly-plastic modelling of the stress-strain curve. The latter corresponded well to steel which was used for manufacturing models D1, …, D6. Table 2 contains comparison of experimental and numerical results. Comparison of experimental failure pressures with numerical predictions is found to be good (with the ratio of, p_{expt}/p_{num}, varying from 0.92 to 1.04). Also, the trend of experimental data on load versus the slenderness parameter, λ, confirms a sudden dip in the load carrying capacity around $\lambda = 4.0$.

Model	D_i (mm)	H (mm)	t (mm)	R (mm)	p_{expt} (MPa)
D1	166.12	1.90	1.0	1816.5	0.0458
D2	166.13	2.15	1.02	1605.7	0.0523
D3	166.10	3.93	1.03	878.6	0.211
D4	166.12	2.96	1.76	1166.7	0.330
D5	166.10	4.56	1.76	759.3	0.650
D6	166.18	6.20	1.76	563.4	1.172

Table 1. Average experimental dimensions (mid-surface where appropriate). Also, experimental buckling pressures.

Model	λ	p_{cl}	p_{expt}/p_{cl}	p_{num}/p_{cl}	p_{expt}/p_{num}
D1	3.56	0.0755	0.61	0.59	1.04
D2	3.74	0.101	0.52	0.57	0.92
D3	5.04	0.342	0.62	0.61	1.01
D4	3.35	0.567	0.58	0.59	0.98
D5	4.11	1.338	0.49	0.450	0.98
D6	4.8	2.430	0.48	0.49	0.99

Table 2. Comparison of experimental buckling pressure, p_{expt}, with classical, p_{cl}, and numerical, p_{num}, predictions.

References

[1] J. Singer, J. Arbocz, T. Weller, "Buckling experiments – Experimental Methods in Buckling on Thin-Walled Structures – Volume 2", John Wiley & Sons, NY, Chapter 9, 2002.

[2] M.A. Krenzke, T.J. Kiernan, "Elastic stability of near-perfect shallow spherical shells", AIAA J., vol. 1, 2855-2857, 1963.

[3] J. Blachut, G.D. Galletly, D.N. Moreton, "Buckling of near-perfect steel torispherical and hemispherical shells subjected to external pressure", AIAA J., vol. 28, 1971-1975, 1990.

Notation

t – uniform wall thickness

p_{cl} – linear classical buckling pressure ($p_{cl} \equiv 2\left[3\left(1-\nu^2\right)\right]^{-1/2} E\left(t/R\right)^2$)

D_i - base diameter of spherical cap

H – rise of spherical cap

R - radius of spherical cap

λ - geometric parameter ($\lambda \equiv 2\left[3\left(1-\nu^2\right)\right]^{\frac{1}{4}} \left(H/t\right)^{1/2}$)

ν - Poisson's ratio

ELASTOPLASTIC MICROSCOPIC BIFURCATION AND POST-BIFURCATION BEHAVIOR OF PERIODIC CELLULAR SOLIDS

N. Ohno*, D. Okumura*, H. Noguchi**
*Department of Mechanical Engineering, Nagoya University, Chikusa-ku, Nagoya 464-8603, Japan
**Department of System Design Engineering, Keio University, Kohoku-ku, Yokohama 223-8522, Japan

Summary A general framework to analyze microscopic bifurcation and post-bifurcation behavior of elastoplastic, periodic cellular solids is developed on the basis of a two-scale theory of the updated Lagrangian type. We thus derive the eigenmode problem of microscopic bifurcation and the orthogonality to be satisfied by the eigenmodes. By use of the framework, then, bifurcation and post-bifurcation analysis are performed for cell aggregates of an elastoplastic honeycomb subject to in-plane compression. Thus, demonstrating a long-wave eigenmode of microscopic bifurcation under uniaxial compression, it is shown that the eigenmode causes microscopic buckling to localize in a cell row perpendicular to the loading axis. It is also shown that under equi-biaxial compression, the flower-like buckling mode having occurred in a macroscopically stable state changes into an asymmetric, long-wave mode due to the sextuple bifurcation in a macroscopically unstable state, leading to the localization of microscopic buckling in deltaic areas.

INTRODUCTION

When cellular solids are subject to compression, buckling may occur in cell walls and edges. This kind of buckling, which is called microscopic buckling, is of interest from a mechanics point of view because of two features: The first is the complexity of buckling modes, which has been typically observed in hexagonal honeycombs [1, 2]. The second is the macroscopic localization of microscopic buckling. When metallic and polymer honeycombs were transversely compressed, microscopic buckling was likely to localize *in a cell row* and then propagate to the neighboring cell rows, yet *it localized rather broadly under equi-biaxial compression* [2]. Such macroscopic localization may be enhanced by microscopic plastic deformation, since it generally greatly reduces macroscopic stiffness.

In this study, a general framework to analyze microscopic bifurcation and post-bifurcation behavior of elastoplastic, periodic cellular solids is built on the basis of the updated Lagrangian type of two-scale theory developed in [3]. By use of the framework, bifurcation and post-bifurcation analysis are performed for cell aggregates of an elastoplastic honeycomb subject to in-plane compression.

THEORY

We consider an infinite, periodic body $\mathcal{B}$ that has a unit cell Y and is subject to macroscopically uniform stress or strain. A general framework is then established by employing a two-scale theory of the updated Lagrangian type and by taking into account the kY-periodicity of microscopic deformation as well as the multiplicity of microscopic bifurcation. Here, kY indicates a cell aggregate consisting of k unit cells. The framework is generally built without recourse to the symmetry of microscopic bifurcation in contrast to the previous framework [3]. We thus derive the eigenmode problem of microscopic bifurcation, Eq. (1), and the orthogonality to be satisfied by the eingenmodes, Eq. (2):

$$\left\langle l_{ijkl}\phi_{k,l}^{(r)}\delta\dot{u}_{i,j}^{*}\right\rangle = 0\ ,\ r=1,2,\ldots,m\ , \tag{1}$$

$$\left\langle l_{ijkl}\phi_{k,l}^{(r)}\right\rangle = 0\ , r=1,2,\ldots,m\ , \tag{2}$$

where $\langle\ \rangle$ indicates the volume average in kY, l_{ijkl} expresses microscopic stiffness, $\phi_i^{(r)}$ ($r = 1, 2, \ldots, m$) denote eigenmodes, $\delta\dot{u}_i^*$ is any kY-periodic velocity field, $(\ )_{,i}$ represents the differentiation with respect to Cartesian coordinate x_i, and m signifies the degree of multiplicity.

We can show that at the onset of microscopic bifurcation, orthogonality (2) allows the macroscopic increments to be determined independently of the eigenmodes, resulting in a simple procedure of the elastoplastic post-bifurcation analysis based on the notion of comparison solids.

ANALYSIS OF HONEYCOMBS

The theory mentioned above was applied to the in-plane buckling analysis of an elastoplastic honeycomb. The honeycomb was subject to in-plane either uniaxial or equi-biaxial compression. We employed the periodic unit kY that consisted of $M\times N$ subunits, each of which was the aggregate of 2×2 cells illustrated in Fig. 1. This type of periodic units are denoted as $Y_{2M\times 2N}$.

Uniaxial compression

The analysis of uniaxial compression was done by use of the $Y_{2\times 2N}$ type of periodic units. Then, subsequent to a simple bifurcation with no dependence on the periodic cell number $2N$, a long-wave bifurcation depending on the periodic cell number $2N$ occurred in macroscopically unstable states (Fig. 2). The long-wave bifurcation, which occurred earlier with the increase of $2N$, was double, i.e., $m = 2$, because of the freedom of a phase shift. The post-bifurcation

procedure based on Eq. (2), then, allowed steering into a bifurcated path on which microscopic buckling localized in a cell row perpendicular to the loading axis.

Equi-biaxial compression

The buckling behavior under equi-biaxial compression was analyzed by use of the $Y_{2N\times 2N}$ type of periodic units. Then, as was demonstrated in [3, 4], a triple bifurcation appeared to cause the flower-like buckling mode, which was first found in [2]. Subsequently, a long-wave, sextuple bifurcation occurred soon after initial yielding, if such large periodic units as $Y_{14\times 14}$, $Y_{16\times 16}$, and so on were assumed (Fig. 3). This second bifurcation, which turned out to be asymmetric, induced the localization of microscopic buckling in deltaic areas (Fig. 4 (b)). The localization in such unnarrow regions was likely to occur experimentally [2].

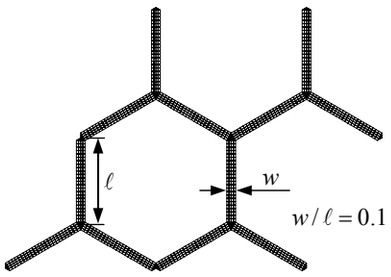


Fig. 1. Subunit of hexagonal honeycomb.

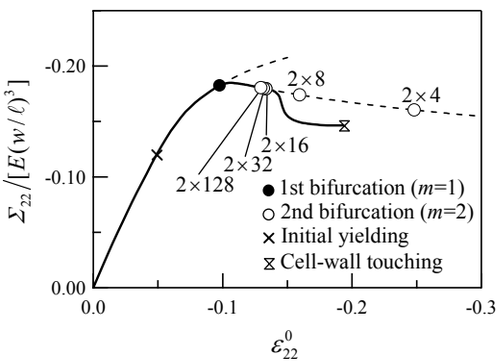


Fig. 2. Macroscopic stress-strain relation under uniaxial compression.

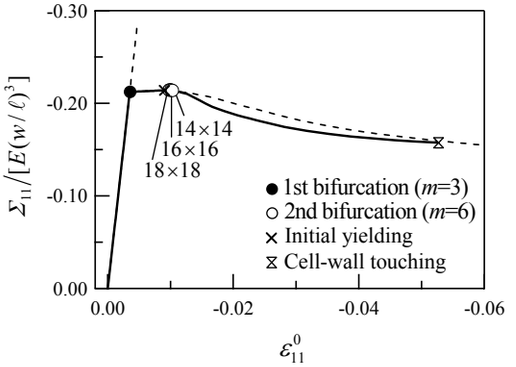
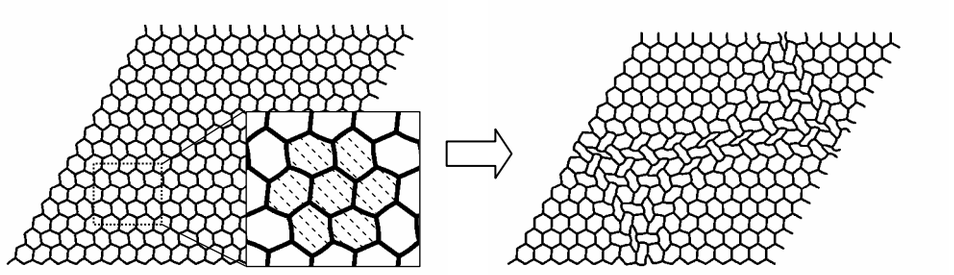


Fig. 3. Macroscopic stress-strain relation under equi-biaxial compression.



(a) $\varepsilon_{11}^0 = \varepsilon_{22}^0 = -0.01$ (b) $\varepsilon_{11}^0 = \varepsilon_{22}^0 = -0.04$

Fig. 4. Change in deformation of $Y_{16\times 16}$ due to the second bifurcation under equi-biaxial compression.

CONCLUSIONS

On the basis of a two-scale theory of the up-dated Lagrangian type, a general framework was developed to analyze microscopic bifurcation and post-bifurcation behavior of elastoplastic, periodic cellular solids. The framework was applied to the in-plane buckling analysis of honeycombs. We thus had the following findings: Subsequent to the microscopic bifurcation with no dependence on periodic length, the long-wave microscopic bifurcation depending on periodic length occurred in macroscopically unstable states. In the case of equi-biaxial compression, the flower-like buckling mode having occurred in a macroscopically stable state changed into an asymmetric, long-wave mode due to the sextuple bifurcation in a macroscopically unstable state, leading to the localization of microscopic buckling in deltaic areas.

References

[1] Gibson, L.J., Ashby, M.F.: Cellular Solids, Structure and Properties, 2nd Edition. Cambridge University Press, Cambridge, 1997.

[2] Papka, S.D., Kyriakides, S.: Biaxial crushing of honeycombs – Part I: experiments. *Int. J. Solids Struct.* **36**:4367-4396, 1999.

[3] Ohno, N., Okumura, D., Noguchi, H.: Microscopic symmetric bifurcation condition of cellular solids based on a homogenization theory of finite deformation. *J. Mech. Phys. Solids* **50**:1125-1153, 2002.

[4] Okumura, D., Ohno, N., Noguchi, H.: Post-buckling analysis of elastic honeycombs subject to in-plane biaxial compression. *Int. J. Solids Struct.* **39**:3487-3503, 2002.

STATICAL MODELS TO ILLUSTRATE SPECIAL INSTABILITIES

Zsolt Gaspar
Budapest University of Technology and Economics, Department of Structural Mechanics, H-1521 Budapest Hungary
Hungarian Academy of Sciences, Research Group for Computational Structural Mechanics, H-1521 Budapest Hungary

Summary The paper shows models to illustrate some special instability. Three models belong to the cusp catastrophe. They have point-like instability, stable-X or unstable-X point of bifurcation, respectively. Two models illustrate classes of the double cusp catastrophes, where the homogeneous quartic parts of the potential energy functions have two distinct or two coincident real roots. The equilibrium paths of the perfect and some imperfect structures and several imperfection-sensitivity curves will be presented.

Classification of instabilities

Elastic structures carrying one-parameter conservative loads will be analyzed. Following the primary equilibrium path the structure loses its stability when its total potential energy function has a degenerate critical point. Catastrophe theory classifies the degenerate critical points ([1]). Thom's theorem has given canonical forms of the typical catastrophes when the number of the parameters is less than six. The potential energy functions depend on the load parameter and the imperfections. The load parameter has a special role which is different from the role of the imperfection parameters, so they cannot be mixed by the necessary transformations to achieve the canonical forms. This is why a subclassification is needed for the stability theory of structures. Changing the load parameter we will have a route in the parameter space. These routes may cross the bifurcation set qualitatively different ways ([2]), i.e. they belong to different classes according to the stability theory.

In the case of the (standard and dual) cusp catastrophe we have the stable-symmetric and unstable-symmetric point of bifurcations, respectively, when the route cross the bifurcation set, and typically there is a cut-off point when the route remains outside of the cusped region. But special cases of these routes result in lip singularity ([2], p. 85) where the equilibrium path has a point-like instability. If the routes remain inside of the cusped region we have a beak-to-beak singularity which will be called as a stable-X or an unstable-X bifurcation in the case of the standard and dual cusp, respectively.

If the smallest critical value of the load parameter is a double eigenvalue of the Hessian matrix of the potential energy function, and the function is symmetric in both buckling modes, then the perfect system must exhibit on of the double cusp catastrophes, which are not included in Thom's theorem (because they need more than five control parameters). Double cusp catastrophes are classified according to the root structure of the homogeneous quartic parts of the (potential energy) functions ([3]). In the case of the Augusti model ([2], p. 144) there are four real roots (and four secondary paths cross the primary equilibrium path). If a guyed cantilever was supported by more than four springs ([4]) then there were no real roots, and the number of the secondary paths was equal to the number of the springs. Here we show models to which two real roots belong, and they are distinct or coincident.

Model for the point-like instability

The model shown in Figure a) consists of two linear, two rotational springs and two telescopic elements. In the case of the perfect structure both linear springs have unit length and their stiffness are c=1. The stiffness of the rotational springs are 3, and they are free of stress when the telescopic members are horizontal. The vertical dead load acts on the middle hinge. We introduce two imperfections: the length of the linear springs are $l = 1 + \varepsilon_1$, and there is also a horizontal load with magnitude ε_2. The critical load of the perfect structure is $\Lambda^{cr} = 0$. The potential energy function can be split into an active and a passive part. The active part has the form:

$$V_a = 0{,}5x^4 + \left(0.125\Lambda^2 - \varepsilon_1\right)x^2 - \varepsilon_2 x ,$$

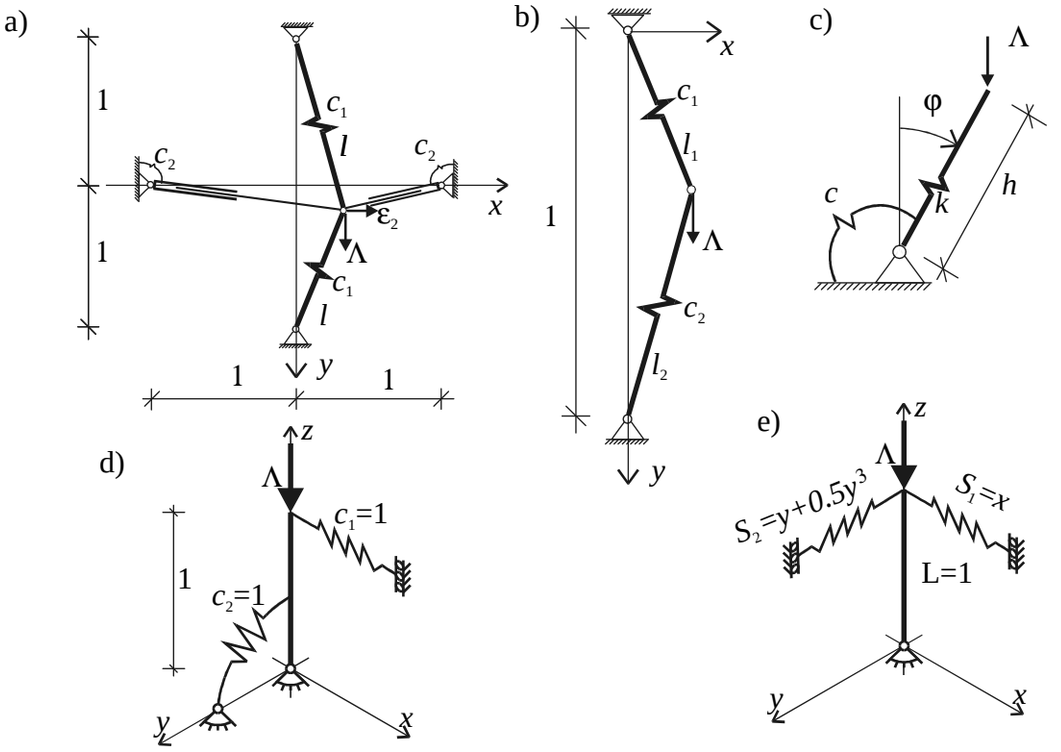
so equilibrium path of the perfect structure is a straight line and every point of it belongs to stable states. The structure is not sensitive to imperfections. For some imperfections the equilibrium path separates into a stable and a close curve.

Model for the stable-X point of bifurcation

The model (Figure b) consists of two linear springs. c_i denotes the stiffness in both tension and compression, and l_i is the stress free length of the ith spring. Let $c_1 = 1.985177808, c_2 = 1, l_1 = 0.4, l_2 = 0.7$. In the critical state: $x^{cr} = 0$, $y^{cr} = 0.5157563683, \Lambda^{cr} = 0.4455533422$. The active part of the potential energy can be transformed to the form:

$$V_a = 1{,}494072598x^4 - 0.6706428261\lambda^2 ,$$

where $\lambda = \Lambda - \Lambda^{cr}$. There are three straight equilibrium paths: the vertical one is unstable while the other two are stable. The structure is not sensitive to imperfections, imperfect structures do not lose their stability when the load increases.



Model for the unstable-X point of bifurcation

The model is a (vertical) hinged cantilever (Figure c) comprising a link with normal rigidity k=4, pinned to a rigid foundation and supported by a linear rotational spring of stiffness c=1. In the critical state: $\varphi^{cr}=0, h^{cr}=0.5, \Lambda^{cr}=2$. The active part of the potential energy can be transformed to the form:

$$V_a=-\frac{1}{12}\varphi^4+\frac{1}{8}\lambda^2\varphi^2-\varepsilon\varphi,$$

where $\lambda=\Lambda-\Lambda^{cr}$ and $\varphi=\varepsilon$ for the unloaded imperfect structure. There are three straight equilibrium paths: the vertical one is stable while the other two are unstable. The structure is very sensitive to imperfections: $\lambda^{cr}=\pm(12\varepsilon)^{1/3}$.

Models for double cusp catastrophes

The model (shown in Figure d) comprising a rigid link, pinned to a rigid foundation and supported by two springs. The linear spring is always parallel with axis x. The trivial equilibrium path is given by $x=y=0$. The critical load is $\Lambda^{cr}=1$. The truncated Taylor expansion of the energy function is:

$$V=-\frac{1}{8}\left(x^4+2x^2y^2-\frac{1}{3}y^4\right)-\lambda\left(\frac{x^2+y^2}{2}+\frac{x^4+2x^2y^2+y^4}{8}\right).$$

There are two secondary paths: one of them belongs to positive values of λ, and is unstable, the other belongs to negative values of λ, and its points are critical. These equilibrium states falls into three paths for a region of the imperfections.

The model (shown in Figure e) consists of two springs, they are always parallel with a coordinate axis. The force in the second spring depends nonlinearly on the elongation. The critical load is $\Lambda^{cr}=1$. The truncated Taylor expansion of the energy function is:

$$V=-\frac{1}{16}y^6-\frac{1}{8}x^4-\frac{1}{4}x^2y^2-\frac{\lambda}{2}\left(x^2+y^2\right).$$

There are two equilibrium paths, both belongs to negative values of λ. One of them is unstable, the points of the other are critical. These equilibrium states fall into three paths for a region of the imperfections.

References

[1] Poston T., Stewart I. N.: Catastrophe Theory and its Applications. Pitman, London 1978.
[2] Thompson J. M. T., Hunt G. W.: Elastic Instability Phenomena. Wiley, Chichester 1984.
[3] Poston T., Stewart I. N.: Taylor expansions and Catastrophes. Research notes in Mathematics, 7. Pitman, London 1976.
[4] Gaspar Z.: Buckling models for higher catastrophes. *J. Struct. Mech.* **5**:357-368, 1977.

XXI ICTAM, 15–21 August 2004, Warsaw, Poland

WRINKLES IN SQUARE MEMBRANES

Yew Wei Wong and Sergio Pellegrino
Department of Engineering, University of Cambridge, Trumpington Street, Cambridge CB2 1PZ, UK

Summary This paper investigates the wrinkling of square isotropic membranes subject to coplanar pairs of equal and opposite corner forces. Two wrinkling regimes are observed experimentally and then reproduced by means of finite-element simulations. A general methodology is presented for making preliminary analytical estimates of wrinkle patterns and average wrinkle amplitudes and wavelengths, while also gaining physical insight into the wrinkling of membranes.

INTRODUCTION

Thin, prestressed membranes will be required for the next generation of spacecraft, to provide deployable mirror surfaces, solar collectors, sunshields, solar sails, etc. Some applications require membranes that are perfectly smooth in their operational configuration; other applications can tolerate membranes that are wrinkled with a known, small deviation from the nominal shape. Because the design of membrane structures with biaxial pretension, which would have a smooth surface, significantly increases the overall complexity of the structure, for those applications in which sufficiently small wrinkles are acceptable, engineers need to estimate the extent, wavelength and amplitude of the wrinkles.

The wrinkling of membranes has attracted much interest in the past, starting from the development of the tension field theory [1]. Simpler formulations and extensions of this theory were later proposed [2-7]. All of these formulations, with accompanying numerical solutions [8,9], model the membrane as a *no-compression, two-dimensional continuum with negligible bending stiffness*. However, the bending stiffness of the membrane cannot be neglected in the present case.

The problem considered in this paper is finding the characteristics of the wrinkles in a uniform elastic square membrane (which is a simple model of a square solar sail) of side length L and thickness t that is prestressed by two pairs of equal and opposite concentrated forces, T_1 and T_2. These forces are uniformly distributed over a small length d at the corners. This membrane is isotropic with Young's Modulus E and Poisson's ratio ν; it is also initially stress free and perfectly flat (before the application of the corner forces).

EXPERIMENTAL OBSERVATIONS

Figure 1 shows photographs of the wrinkle patterns in a Kapton membrane with $L = 500$ mm, $t = 0.025$ mm, and $d = 25$ mm. For symmetric loading ($T_1 = T_2$), Figure 1(a), the wrinkle pattern is fairly symmetric, with wrinkles radiating from each corner; the central region is free of wrinkles. For $T_1/T_2 = 2$ the wrinkles grow in amplitude but remain concentrated at the corners. Then, for $T_1/T_2 = 3$ a large diagonal wrinkle becomes visible, whose amplitude grows further for $T_1/T_2 = 4$.

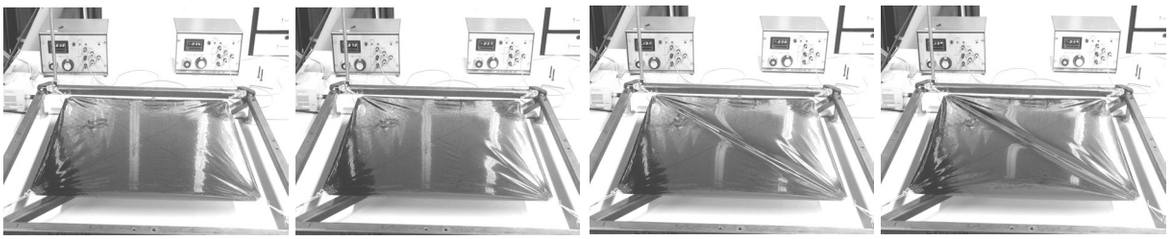


Figure 1. Wrinkled shapes for T_1 equal to (a) 5 N, (b) 10 N, (c) 15 N, and (d) 20 N; $T_2 = 5$ N in all cases.

ANALYTICAL APPROACH

Our analytical approach is in four parts, as follows. First, we propose a two-dimensional stress field that involves no compression anywhere in the membrane; the regions where the minor principal stress is zero are then assumed to be wrinkled, and the wrinkles are assumed to be along the major principal stress directions. Ideally, both equilibrium and compatibility should be satisfied everywhere by the proposed stress field, but analytical solutions in closed-form —obtained by tension field theory— exist only for very simple boundary conditions. We have recently shown [10] that a carefully chosen, simple stress field that satisfies only equilibrium can provide quick solutions that are useful for preliminary design. More accurate stress fields can be obtained from a two-dimensional stress analysis with membrane finite elements.

Second, we note that the bending stiffness of the membrane is finite, although small, and hence a compressive stress will exist in the direction perpendicular to the wrinkles. Because of its small magnitude, this stress was neglected in our previous analysis of the stress field. We assume that this compressive stress varies only with the wavelength of the wrinkles

and set it equal to the critical buckling stress of a thin plate in uniaxial compression. Thus, the stress across the wrinkles is a known function of the wrinkle wavelength.
Third, we enforce equilibrium in the out-of-plane direction. Since the stress distribution is known, except for the wrinkle wavelength, a single equation of equilibrium will determine the wrinkle wavelength.
Fourth, the wrinkle amplitudes are estimated by considering the total strain in the membrane as the sum of two components, a material strain and a wrinkling strain.

RESULTS

We consider two kinds of simple equilibrium stress fields, one for symmetric loading and asymmetric loading with $T_1/T_2 \leq 1/(\sqrt{2}-1)$, and one for $T_1/T_2 \geq 1/(\sqrt{2}-1)$. The first field corresponds to fan-shaped corner wrinkles, which are represented in terms of sine functions. Analytical expressions are then derived for the number of corner wrinkles and their average maximum amplitude. The second field provides, in addition, a large diagonal wrinkle.
For example, we have obtained the following expressions for the wavelength and amplitude of this central wrinkle

$$\lambda = \sqrt[4]{\frac{2\pi^2 R_1 (R_1 - r_1)^2 E t^3 \sin\theta_1}{3(1-\nu^2)T_1}} \tag{1}$$

$$A = \frac{2\sqrt{\lambda(\delta_1 + \delta_2)}}{\pi} \tag{2}$$

Here δ_1 and δ_2 are the radial displacements of the corners loaded by T_1 and T_2, respectively. They can be estimated from

$$\delta_i \approx \frac{T_i}{2Et\sin^2\theta_i}\left[\theta_i \ln\left|\frac{R_i}{r_1}\right| + (1-\nu)\left(\frac{A}{R_i^2} + \theta_i - \frac{1}{2}\tan\theta_i\right)\right] \quad i = 1, 2 \tag{3}$$

More refined estimates can be obtained from two-dimensional finite-element analysis.

DISCUSSION

For the load case $T_1/T_2 = 4$, Table 1 compares the analytical predictions for the large diagonal wrinkle at the centre of the membrane, for two different membrane thicknesses, with predictions from ABAQUS and experimental measurements. The wavelength predictions are very close. The wrinkle amplitudes have been estimated first using only analytical solutions, Equation 2 with δ_1 and δ_2 from Equation 3, and second using Equation 2 but with corner deflections from a 2-D analysis. We can see that the fully analytical estimates are up to 88% higher than those measured experimentally, but if corner displacements from a 2D finite-element analysis are used, the estimates are only 48% and 16% higher than the measurements.
Finite element analysis using thin shell elements is able to replicate real physical experimentation with an accuracy typically better than 10% on amplitude. However, a very fine mesh had to be used to resolve the small corner wrinkles.

References

[1] H. Wagner. Flat sheet metal girder with very thin metal web, *Zeitschrift für Flugtechnik Motorlurftschiffahrt*. **20**, 200–207, 227–233, 256–262, 279-284 (1929).
[2] E. Reissner. On tension field theory. *Proc. 5th Int. Cong. Appl. Mech.*, 88–92 (1938).
[3] M. Stein and J.M. Hedgepeth. *Analysis of Partly Wrinkled Membranes*. NASA Langley Research Center, NASA TN D-813 (1961).
[4] E.H. Mansfield. Tension field theory a new approach which shows its duality with inextensional theory. *Proc. 12th Int. Cong. Appl. Mech.*, 305–320 (1969).
[5] A.C. Pipkin. The relaxed energy density for isotropic elastic membranes. *IMA J. Appl. Math.*, **36** 85–99 (1986).
[6] M. Epstein and M.A. Forcinito. Anisotropic membrane wrinkling: theory and analysis. *Int. J. Solids Structures*. **38**, 5253-5272 (2001).
[7] C. Jenkins and J.W. Leonard. Nonlinear dynamic response of membranes: State of the art. *ASME Appl. Mech. Reviews*, **44**, 319–328 (1991).
[8] A. Adler. *Finite Element Approaches for Static and Dynamic Analysis of Partially Wrinkled Membrane Structures*. Ph.D. Dissertation, University of Colorado at Boulder (2000).
[9] Y.W. Wong and S. Pellegrino. Amplitude of wrinkles in thin membranes. In: *New Approaches to Structural Mechanics, Shells and Biological Structures*, edited by H.R. Drew and S. Pellegrino. Kluwer Academic Publishers, 257-270 (2002).

t	λ (mm)			A (mm)			
(mm)	Eq. 1	Exp.	FE	Eqs 2, 3	Eq. 2+FE	Exp.	FE
0.025	24.6	23.8	22.3	3.5	2.8	1.9	2.0
0.050	41.3	33.9	35.6	3.2	2.1	1.8	1.6

Table 1. Diagonal wrinkle half-wavelengths and amplitudes for $T_1/T_2 = 4$, at centre of membrane

Nonlinear Dynamic Stability of Multi-Suspended Roof Systems

by
Ioannis G. Raftoyiannis[1] and George T. Michaltsos[2]

Introduction

Suspended roof systems are extensively used in many structural applications such as commercial halls, sport centers, airport halls, trade and exhibition centers, etc. Inspired engineers as L. Mies van der Rohe, K. Tange, P. L. Nervi, and others have designed and build numerous great buildings with suspended roofs as their main structural component. The last 10 to 15 years, the development of powerful computers and sophisticated nonlinear FEM software (ADINA, ABAQUS, etc.) has enabled engineers to utilise suspension roofs in complicated large scale structures, some of which can be classified among unique examples of engineering excellence.

A large number of recent studies are concerned with the investigation of the dynamic buckling and stability of simple 2-DOF and 3-DOF initially imperfect models with damping under step loading, that simulate single and double suspension roofs and important findings have been reported. The present work deals with the fully nonlinear static and dynamic stability analysis of a simplified multi-DOF initially imperfect dissipative model, upon which a constant directional (conservative) vertical step loading of infinite duration is applied.

Mathematical formulation

Let us consider the dissipative, initially imperfect multi-DOF system shown in Fig. 1.

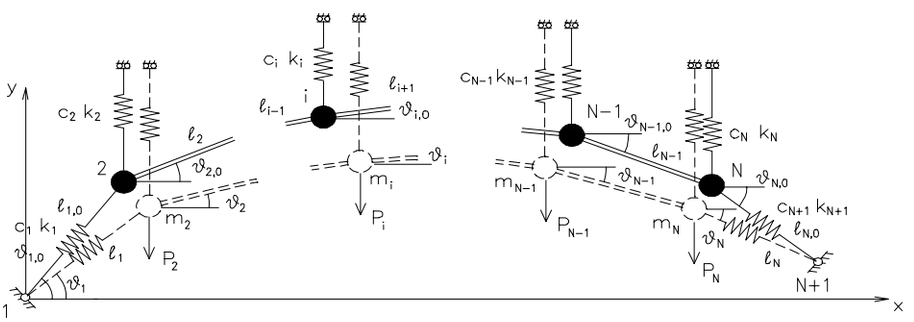


Fig. 1. A N-DOF *autonomous dissipative system under step loading, simulating a multiple suspension roof.*

The system is initially at rest in a configuration described as follows

$$x_{i,0} = \ell_{1,0}\cos\theta_{1,0} + \sum_{j=2}^{i} \ell_j \cos\theta_{j,0} \qquad y_{i,0} = \ell_{1,0}\sin\theta_{1,0} + \sum_{j=1}^{i} \ell_j \sin\theta_{j,0} \tag{1}$$

where $x_{i,0}$ and $y_{i,0}$ are the initial coordinates of joint i, and ℓ_j and $\theta_{j,0}$ are the length and the initial direction of bar j, respectively. After applying the external forces P_i at the joints (i=1,...,N), the deformed configuration of the system is described as follows

$$x_i = \ell_1\cos\theta_1 + \sum_{j=2}^{i} \ell_j \cos\theta_j \qquad y_i = \ell_1\sin\theta_1 + \sum_{j=2}^{i} \ell_j \sin\theta_j \tag{2}$$

where x_i and y_i are the coordinates of joint i, and θ_j is the direction of bar j in the deformed position. The strain energy U of the system is

[1] Lecturer, Lab of Metal Structures, Dept of Civil Engng, National Technical University of Athens, Greece 17580
[2] Professor, Lab of Metal Structures, Dept of Civil Engng, National Technical University of Athens, Greece 17580

$$U = \tfrac{1}{2}k_1(\ell_1 - \ell_{1,0})^2 + \tfrac{1}{2}\sum_{i=2}^{N} k_i(\ell_1 \sin\theta_1 + \sum_{j=2}^{i-1}\ell_j \sin\theta_j - \ell_{1,0}\sin\theta_{1,0} - \sum_{j=2}^{i-1}\ell_j \sin\theta_{j,0})^2 +$$
$$+ \tfrac{1}{2}k_{N+1}\{[(\ell_{1,0}\cos\theta_{1,0} + \sum_{j=2}^{N-1}\ell_j \cos\theta_{j,0} + \ell_{N,0}\cos\theta_{N,0} - \sum_{j=1}^{N-1}\ell_j \cos\theta_j)^2 + \quad (3)$$
$$+ (\ell_{1,0}\sin\theta_{1,0} + \sum_{j=2}^{N-1}\ell_j \sin\theta_{j,0} + \ell_{N,0}\sin\theta_{N,0} - \sum_{j=1}^{N-1}\ell_j \sin\theta_j)^2]^{\frac{1}{2}} - \ell_{N,0}\}$$

The work Ω done by the external forces is

$$\Omega = -\sum_{i=2}^{N} P_i(\ell_1 \sin\theta_1 + \sum_{j=2}^{i-1}\ell_j \sin\theta_j - \ell_{1,0}\sin\theta_{1,0} - \sum_{j=2}^{i-1}\ell_j \sin\theta_{j,0}) \quad (4)$$

The kinetic energy K of the system is

$$K = \tfrac{1}{2}\sum_{i=2}^{N} m_i[(\dot{\ell}_1\cos\theta_1 - \ell_1\dot{\theta}_1\sin\theta_1 - \sum_{j=2}^{i-1}\ell_j\dot{\theta}_j\sin\theta_j)^2 + (\dot{\ell}_1\sin\theta_1 + \ell_1\dot{\theta}_1\cos\theta_1 + \sum_{j=2}^{i-1}\ell_j\dot{\theta}_j\cos\theta_j)^2] \quad (5)$$

and the dissipation energy F is

$$F = \tfrac{1}{2}c_1(\dot{\ell}_1^2 + \ell_1^2\dot{\theta}_1^2) + \tfrac{1}{2}\sum_{i=2}^{N} c_i(\dot{\ell}_1\sin\theta_1 + \sum_{j=1}^{i-1}\ell_j\dot{\theta}_j\cos\theta_j)^2 + \tfrac{1}{2}c_{N+1}[(\dot{\ell}_1\cos\theta_1 - \sum_{j=1}^{N-1}\ell_j\dot{\theta}_j\sin\theta_j)^2 + (\dot{\ell}_1\sin\theta_1 + \sum_{j=1}^{N-1}\ell_j\dot{\theta}_j\cos\theta_j)^2] \quad (6)$$

The equations of motion of the system are derived using the Lagrange equation

$$\frac{\partial}{\partial t}\left(\frac{\partial K}{\partial \dot{\ell}_1}\right) - \frac{\partial K}{\partial \ell_1} + \frac{\partial F}{\partial \dot{\ell}_1} + \frac{\partial V}{\partial \ell_1} = 0, \quad \frac{\partial}{\partial t}\left(\frac{\partial K}{\partial \dot{\theta}_i}\right) - \frac{\partial K}{\partial \theta_i} + \frac{\partial F}{\partial \dot{\theta}_i} + \frac{\partial V}{\partial \theta_i} = 0, \quad i = 1,2,...,(N-1) \quad (7)$$

Numerical results and discussion

In the numerical examples that follow, a 4-DOF system is employed (i.e. N=4) with the following characteristics: $\theta_{1,0}=\theta_{4,0}=30^o$, $\theta_{2,0}=-\theta_{3,0}=10^o$, $k_1=k_i=k_5=1$, $c_1=c_i=c_5=0.1$, $\theta_{2,0}^*=-5^o$, $\theta_{3,0}^*=7^o$, P=0.5, producing the following plots:

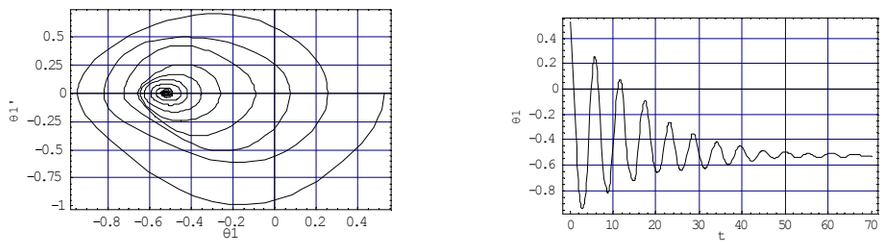


Fig.2 Phase-plane portrait $\dot{\theta}_1 - \theta_1$, and (d) time series θ_1 vs. t

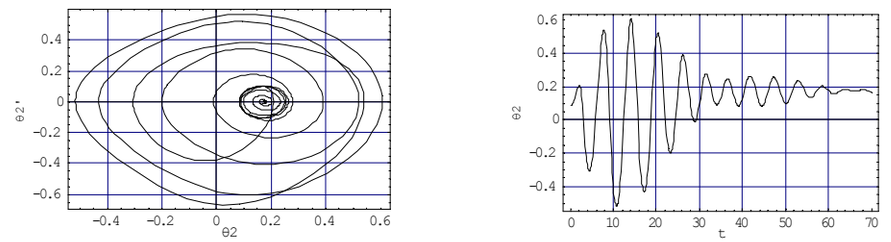


Fig.3 Phase-plane portrait $\dot{\theta}_2 - \theta_2$, and (f) time series θ_2 vs. t

From these plots it is directly concluded that for all model cases dealt with the global dynamic response is stable, which is the primary advantage of multi-suspension roofs, successfully captured by the proposed simulation.

References

[1] Blaser W, Stucky M. Drawings of great buildings. Boston: Birkhauser Verlag, 1983.

[2] Michaltsos G.T., and Sophianopoulos D. S., Nonlinear stability of a simplified model for the simulation of double suspension roofs, *Engineering Structures*, **23**, 705-14, 2001.

COUPLING OF AXISYMMETRIC AND 3D SHELLS MODELS FOR NON LINEAR ELASTOPLASTIC BUCKLING PREDICTION OF MAINLY AXISYMMETRIC SHELLS

A Combescure*, J C Bauruelle,C Baillis

*LaMCoS Insa - Lyon

18-20 allée des sciences 69621 Villeurbanne cedex France

e–mail: alain.combescure@insa-lyon.fr

Summary TheThis paper describes a method which enables to couple 3D shell simulation with axisymmetric models in order to predict the non linear buckling for shells which have localised non axisymmetric geometries, or loadings.

The axisymmetric models are very efficient and powerful for prediction of non linear buckling of axisymmetric shells with non localised imperfections or loadings. The idea is simply to develop the response on a Fourier basis and to use a finite number of Fourier modes to approximate the solution. This strategy has been extensively developed and successfully used for the analysis of axisymmetric perfect or imperfect shells [1], [2], [3] subjected to any load which is slowly spatially varying. When there is a local geometrical imperfection (say a hole) or a local quickly varying load or local support condition the axisymmetric models are not really efficient. The usual way to study the problem is to use a 3D shell model. This method leads to very heavy meshes if one wants to get precise predictions. The idea developed in the paper is to propose a method to combine a 3D analysis for the region where a local strong discontinuity is present and an axisymmetric coupled Fourier analysis for the rest of the structure. The idea was first introduced by Gould [4] and some results were shown for linear elastic response. We have basically to couple two subdomains each having its own discretisation. We shall use the "mortar" method [5] to couple the two subdomains. Subdomain 1 has an axisymmetric representation whereas sub domain 2 has a 3D shell representation. We have used and augmented Lagrangian formulation to expressed the energy of the coupled problem:

$$W^{tot} = W^{3D} + W^{axis} + W^{\text{int}erface} \qquad (1)$$

In equation (1) the energy is split in a 3D part an axisymmetric part and an interface one. On the interface we have two different displacement approximations and a third Lagrange multiplier approximation. As in [5] the interface energy can be expressed by:

$$W^{\text{int}erface} = \int_{\text{int}erface} \underline{\Lambda}^t \left(\underline{U^{axi}} - \underline{U^{3D}} \right) ds \qquad (2)$$

in this equation $\underline{\Lambda}$ is the Lagrange multiplier vector, $\underline{U}$ are the axisymmetric or 3D displacement vectors at the interface. As usual in mortar method the discretisation of Lagrange multiplier (number of Lagrange multipliers and shape functions) are chosen on either with the 3D support or with the axisymmetric one. The Babuska Brezzi condition is used to choose the best representation of Lagrange multiplier on the interface. It is shown that the 3D choice leads to locking of the interface, and that it is best to choose axisymmetric representation of Lagrange multipliers. The method can also be applied introducing interface compliance. Equation (2) can then be replaced by:

$$W^{\text{int}erface} = \frac{1}{2} \int_{\text{int}erface} w^{def} \left(\underline{U^{axi}} - \underline{U^{3D}} \right) ds \qquad (3)$$

in equation (3) w^{def} is the strain energy density of the interface. The interface is supposed to behave elastically and is a small ring having the current thickness t of the shell and a very small height h. Here again the interface energy can be discretised either with a 3D model or with an axisymmetric one. As in the previous one it is shown that 3D representation leads to locking of the interface because of an over-constrained problem.

The method has been applied to basic examples as the torsional buckling of a cylinder one half (the left part on figure 1) of it being meshed with 3D DKT Shell elements and the other part being meshed in axisymmetric. (only two Fourier modes (n symmetric and n anti symmetric) are sufficient to represent the buckling mode). The computed torsion load is 0.5% higher than the theoretical one.

The computed mode is displayed on figure 1

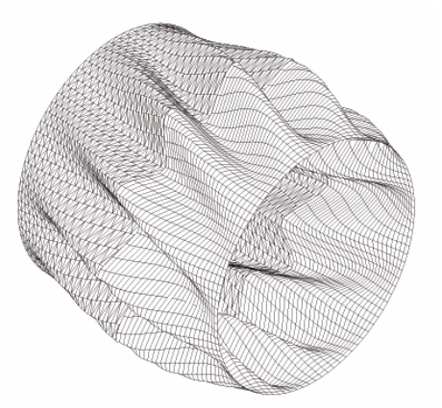


Figure 1: torsion buckling mode

The second example is devoted to the prediction of non linear buckling of a chimney with a square hole at its basis under bending load. The non linear buckling mode is displayed on figure 2, and it compares well with a full 3D analysis.

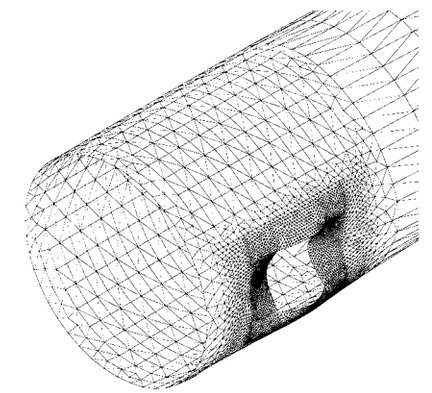


Figure 2: chimney with hole under bending with 3D-2D coupled analysis

References

[1] A Combescure: Static and dynamic buckling of large thin shells.
Nuclear Engineering and Design, 1986, 92, pp 339-354
[2] A Combescure, G Gusic: Non linear buckling of cylinders under external pressure with non axisymmetric thickness imperfection using the COMI finite element
International Journal of Solids and Structures, 2001, 38, pp 6207-6226
[3] Wunderlich H. Cramer and H. Obrecht :Application of ring elements in the nonlinear analysis of shells of revolution under nonaxisymmetric loading
Computer Methods in Applied Mechanics and Engineering, 1985,51,pp 259-275
[4] P L Gould R Ravichandran, S Sridharan: A local global FE model for the non linear analysis of column supported shells of revolution..
Thin walled structures, 1998, 31, pp 25-37
[5] B Herry, L Di Valentin, A Combescure: An approach to the connection between subdomains with non matching meshes for transient mechanical analysis
International Journal for Numerical Methods in Engineering, 2002,55, pp 973-1003

DYNAMIC ARREST OF PROPAGATING BUCKLES IN OFFSHORE PIPELINES

Theodoro A. Netto*, Stelios Kyriakides**
*Universidade Federal do Rio de Janeiro, Prog. de Engenharia Oceânica, Caixa Postal 68508, Rio de Janeiro RJ 21945-970, Brazil
**Center for Mechanics of Solids, Structures & Materials, The University of Texas at Austin, WRW 110 Austin, TX 78712, USA

Summary Buckle arrestors are devices which locally strengthen an offshore pipeline and safeguard it against the catastrophic effects of a potential propagating buckle. They are usually designed based on quasi-static experiments and analyses. This paper discusses how such devices perform under the more realistic dynamic propagation conditions encountered in the sea. It will be shown that dynamics enhance the arresting performance of all arrestors considered.

Offshore pipelines are susceptible to local damage and collapse. Because of the ambient external pressure, such a weakened section can initiate propagation of collapse up and down the line. Buckle propagation usually occurs at high velocity and can quickly catastrophically collapse large sections of the pipeline. An effective way to ensure that collapse, should it occur, affects only a small length of the pipeline, is the periodic placement of buckle arrestors along the line. Buckle arrestors are devices which locally increase the circumferential bending rigidity of the pipe and thus provide an obstacle in the path of a propagating buckle. They are usually thick-walled rings that are grouted onto the pipe (*slip-on* arrestors), welded between two sections of pipe (*integral* arrestors) or slip-fit into the outer pipe in pipe-in-pipe systems (*internal ring* arrestors). The design of such devices has been traditionally based on quasi-static buckle propagation and arrest experiments and analyses, primarily because dynamic experiments are much more difficult and costly to conduct.

The effectiveness of each of these three types of arrestors has been studied first under quasi-static and subsequently under dynamic buckle propagation conditions using combinations of experiments and analyses. In all cases, inertial effects were found to enhance the arrestor performance; in other words, the pressure at which a given arrestor is crossed dynamically is higher than the quasi-static crossover pressure. This presentation will outline the reasons for this dynamic enhancement in performance for each arrestor.

An extensive parametric study of the quasi-static arresting efficiency has been conducted experimentally for each of the arrestors. Each process was also modeled numerically using large scale FE models. The experimental crossover pressure values enriched with numerical ones were used to develop empirical design formulae (e.g., [1,2]). Arrestors designed in accordance with these quasi-static criteria were then tested under the more realistic dynamic buckle propagation conditions. This was achieved by initiating a buckle in a pipe with an arrestor under (nearly) constant pressure conditions. The buckle then propagates and engages the arrestor at velocities ranging from 60-300 m/s. For all arrestors considered, the dynamic crossover pressure was found to exceed the corresponding quasi-static value.

To better understand the reasons behind the dynamic enhancement in the performance of buckle arrestors, the dynamic initiation, propagation and crossing/arrest of buckles were simulated with FEs for both single pipe and pipe-in-pipe systems. The models account for the inertia of the pipe and the nonlinearity introduced by contact between its collapsing walls, while the material is modeled as a finitely deforming elastic-viscoplastic solid (a sequence of deformed configurations from a propagating buckle engaging and crossing an internal ring arrestor in pipe-in-pipe system is shown in Fig. 1). The simulations confirmed the dynamic enhancement of arrestor performance seen in the experiments. They also provided details of the engagement of a running buckle with the arrestor [3-5]. For example, the profile of dynamic buckles is considerably sharper than the quasi-static profile. This produces a zone of reverse ovality downstream of the buckle [6]. In the case of integral and internal ring arrestors, reverse ovality interacts with the arrestor and the pipe downstream of it, and increases its local collapse pressure and, as a consequence, the crossover pressure. For the slip-on arrestor, the prevalent mode of crossover is penetration of the ring by the pipe folding up into a U-shape as shown in Fig. 2a [1]. A running buckle engages the arrestor with a doubly symmetric dogbone-like cross section and penetrates it to some degree as shown in Fig. 2b. It thus takes a higher pressure to switch it to the singly symmetric U-mode than in the quasi-static case where no symmetric mode penetration of the arrestor takes place [7].

References

[1] Lee, L.-H., Kyriakides, S.: On the arresting efficiency of slip-on buckle arrestors for offshore pipelines. *Int'l J. Mechanical Sciences* (submitted) 2003.
[2] Olso, E., Kyriakides, S.: Internal ring buckle arrestors for pipe-in-pipe systems. *Int'l J. Nonlinear Mechanics* **38**:1267-284, 2003.
[3] Netto, T.A., Kyriakides, S.: Dynamic performance of integral buckle arrestors for offshore pipelines. Part I Experiments. *Int'l J. Mechanical Sciences* **42**:1405-1423, 2000a.

[4] Netto, T.A., Kyriakides, S.: Dynamic performance of integral buckle arrestors for offshore pipelines. Part II Analysis. *Int'l J. Mechanical Sciences* **42**:1425-1452, 2000b.
[5] Netto, T.A., Kyriakides, S.: On the dynamic propagation and arrest of buckles in pipe-in-pipe systems. *Int'l J. Mechanical Sciences* (submitted) 2004.
[6] Kyriakides, S., Netto, T.A.: On the dynamics of propagating buckles in pipelines. *Int'l J. Solids & Structures* **37**:6843-6867, 2000.
[7] Netto, T.A., Kyriakides, S., Lee, L.-H.: Dynamic arrest of propagating buckles in pipelines by slip-on arrestors. (In preparation) 2004.

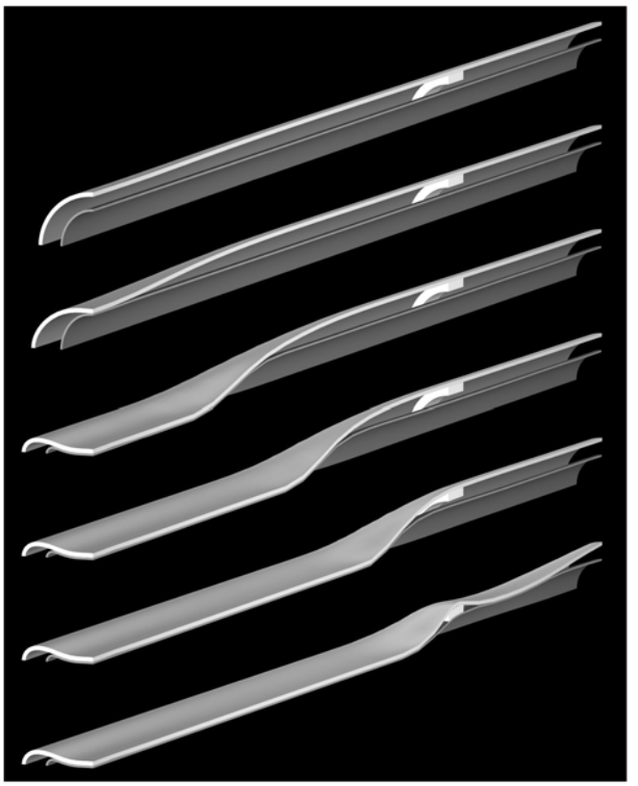


Fig. 1 Sequence of calculated pipe-in-pipe deformed configurations showing dynamic buckle propagation and crossing of internal ring arrestor



(a)



(b)

Fig. 2 Slip-on arrestor crossover modes. (a) Quasi-static case (b) dynamic case

BIFURCATION BUCKLING OF SANDWICH PLATES AND SHELLS IN PLASTIC RANGE

S. C. Shrivastava
Department of Civil Engineering and Applied Mechanics, McGill University, Montreal, Quebec, Canada

Summary Bifurcation buckling of complete circular sandwich plates and complete spherical sandwich shells subjected to uniform equi-biaxial compression is investigated when faces undergo plastic straining and core remains elastic. The presented theory accounts for transverse shear strains. Both J_2 incremental and J_2 deformation theories of plasticity are used. The results generalize the classical formulas for elastic and plastic buckling by adding shear correction terms.

INTRODUCTION

Plastic buckling has a long history of paradoxes starting with the well-known column paradox [1]. It was resolved by Shanley by showing that bifurcation in plastic range occurs with increasing load. A new paradox arose in connection with the plastic buckling of axially compressed rectangular plates. The Mises or J_2 incremental theory of plasticity, accepted as a correct phenomenological theory, predicts bifurcation loads for such plates much higher than experiments. Paradoxically, the incorrect, J_2 deformation theory of plasticity yields good results. This paradox was explained by Onat and Drucker by demonstrating the extreme sensitivity of the incremental theory to geometric imperfections. For axially compressed cylindrical shells, the paradox was found by Batterman to be not as dramatic.

Bijlaard [2] was among the first investigators to conduct rational analyses of plastic buckling of plates and shells, including sandwich plates. However, he argued that the deformation theory was the correct theory. The author has tackled plastic bifurcation problems [3,4,5] by employing both plasticity theories and by including transverse shear strains. The contention is that the two theories need not give widely differing bifurcation loads for all cases.

As interesting examples, the paper presents general non-axisymmetric buckling of complete circular plates and complete spherical shells of sandwich type with equal face thicknesses, subjected to uniform equi-biaxial compression. The loading consists of peripheral radial pressure for plates, and external pressure for shells. Transverse shear strains are included by introducing rotations of normals as additional kinematic variables. Only faces are allowed to undergo plastic straining; core remains elastic. Results generalize previous formulas [2,6,7] by supplying shear correction terms.

OUTLINE OF THE ANALYSIS AND SOME RESULTS

General constitutive relations

Thin shell assumption is used. Pre-buckling strains are considered constant, though stresses are different in core and faces due to differences in moduli. The constitutive relations below are in a form applicable to elastic (core) or plastic (faces) behaviour. Let $\mathring{\sigma}$ be the pre-buckling equi-biaxial compressive stresses in faces due to the applied pressure. The Mises yield condition for such a stress-state is $\sigma_{\text{eff}} = \sqrt{3J_2} = \mathring{\sigma} = \sigma_Y$ where σ_Y is in strain-hardening range of a uniaxial $\sigma - \epsilon$ curve of the face material. Bifurcation induces stress and strain increments, σ_{ij} and ϵ_{ij}, related by the applicable constitutive relations. For the usual small strain plasticity, these relations for J_2 deformation theory [2-5] are

$\sigma_{11} = B'\epsilon_{11} + C'\epsilon_{22}$, $\sigma_{22} = C'\epsilon_{11} + B'\epsilon_{22}, \sigma_{33} = 0$, $\sigma_{ij} = 2F'\epsilon_{ij}\,(i \neq j)$, where

$$B' = A'(3E/E_s + E/E_t), C' = A'(3E/E_s - E/E_t - 2 + 4\nu), F' = \frac{E}{(3E/E_s - 1 + 2\nu)}$$

$$A' = \frac{E}{(E/E_t + 1 - 2\nu)(3E/E_s - 1 + 2\nu)}.$$

Note that $C' = B' - 2F'$. Subscripts 1, 2, 3 refer to radial (or meridional), circumferential, and thickness directions. E and ν are elastic moduli. $E_t = d\sigma/d\epsilon$ and $E_s = \sigma/\epsilon$ are the tangent and secant moduli at stress level $\sigma = \mathring{\sigma}$ on the $\sigma - \epsilon$ curve. For incremental theory $E_s = E$. For elastic cases $E_s = E_t = E$. Unloading is precluded at plastic bifurcation.

Kinematic assumptions and governing equations

The radial (or meridional), circumferential, and normal displacements arising due to buckling are taken respectively as $u - z\alpha$, $v - z\beta$, w, where z is the thickness coordinate. u and v are the 'inplane' middle surface displacements, w is the 'out-of-plane' displacement, and α, β are the rotation components of the middle surface normals. Thus, there are five kinematic variables which are functions of the two surface coordinates. For plates, $u = v = 0$, only three variables are present. Buckling strains ϵ_{ij} in polar or spherical coordinate system follow from these displacements. Principle of virtual work for initially stressed bodies yields equations of equilibrium and boundary conditions in terms of stress resultants consistent with the kinematic assumptions. The stress resultants are expressed in terms of the kinematic variables by using the constitutive relations and integrating through core and face thicknesses. Substitution of the stress resultants thus expressed yields the governing equations and boundary conditions in terms of the kinematic variables.

Some results

Solutions are obtained in Bessel functions for the plate buckling, and in associated Legendre functions for the shell buckling. Space limitation prevents giving details, except some for spherical shell. The minimum buckling pressure is

$$q_{cr}(\text{min}) = \frac{4hB_2}{R^2}\sqrt{\frac{4F_1(B_1-F_1)}{B_1B_2}}\{1-(\frac{h}{R})\sqrt{\frac{4F_1(B_1-F_1)}{B_1B_2}}\times\frac{B_2}{2G}\}$$

where $R=$ middle surface radius, $h=$ core thickness, $t=$ face thickness, $f(t)=6(t/h)+12(t/h)^2+8(t/h)^3$,

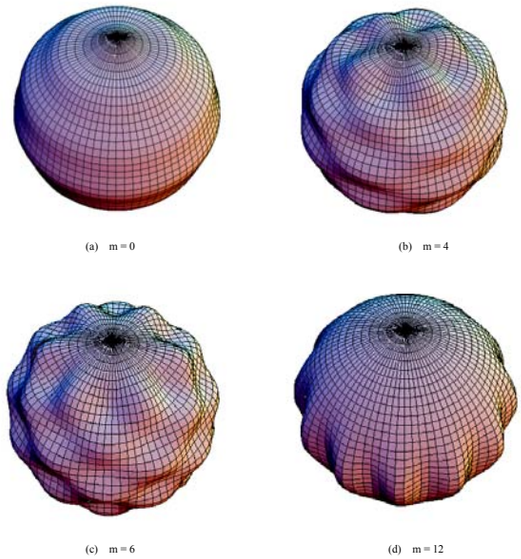
$$B_1=B_c'h\,\{1+\frac{tB_f'}{hB_c'}\},\ F_1=F_c'h\,\{1+\frac{tB_f'}{hB_c'}\},\ B_2=\frac{B_c'h}{12}\{1+\frac{B_f'}{B_c'}f(t)\},\ F_2=\frac{F_c'h}{12}\{1+\frac{F_f'}{F_c'}f(t)\},\ G=kF_c'h.$$

Subscripts f and c refer to face and core moduli. k is shear correction factor. The integer n corresponding to $q_{cr}(\text{min})$ is

$$n(n+1)\approx\frac{2F_1}{B_1}+(R/h)\sqrt{\frac{4F_1(B_1-F_1)}{B_1B_2}}\{1+(\frac{h}{R})\sqrt{\frac{4F_1(B_1-F_1)}{B_1B_2}}\times\frac{B_2}{G}\}.$$

n is related to meridional buckles as explained below. Terms containing G in expressions for $q_{cr}(\text{min})$ and n are shear correction terms. Known formulas for homogeneous shell buckling [2,6,7] are obtained by appropriate specialization and $G\to\infty$. Numerical results show that, as usual, the buckling pressure given by the deformation theory is lower than that from the incremental theory. However, the differences remain within 10% for realistic material properties and geometry. Surprisingly, for simply supported circular sandwich plates, such differences are found almost negligible.

A mode shape of the radial displacements is $w=\cos(m\theta)\,P_n^m(\cos\phi)$ where θ and ϕ are circumferntial and meridional coordinates, $P_n^m(\cos\phi)$ are associated Legendre functions, $2m=$ circumferential buckles, $n-m+1=$ meridional buckles. Although n is uniquely determined from the above formula, m is allowed to be any integer from 0 to n, where $m=0$ signifies an axisymmetric mode. Thus, there is a multiplicity of eigenmodes for the same eigenvalue, a familiar phenomenon in shell buckling. Here, the multiplicity has been determined unambiguously by the analysis. The figure below shows four $(m=0,\ 4,\ 6,\ 12)$ of the thirteen modes for a buckling pressure for which $n=12$.



References

[1] Bleich, F. and H. (1952). Buckling Strength of Metal Structures, McGraw Hill, New York.

[2] Bijlaard, P.P. (1949). Theory and Tests on the Plastic Stability of Plates and Shells. *J. Aero. Sc.,*16:9, 529-541.

[3] Shrivastava, S.C. (1995). Inelastic Buckling of Rectangular Sandwich Plates. *Int. J. Solids Structures,* 32, 1099-1120.

[4] Shrivastava, S.C. (2002). Bifurcation Buckling of Spherical Sandwich Shells under External Pressure in Plastic Range, *New Approaches to Structural Mechanics, Shells and Biological Structures*, H.R. Drew and S. Pellegrino (Eds.), Kluwer, pp. 379-391.

[5] Shrivastava, S.C. (2000). Plastic Buckling of Circular Sandwich Plates, *Proceedings of Seventh International Symposium on Structural Failure and Plasticity*, Melbourne, Australia, X.L. Zhao and R.H. Grzebieta (Eds.), Pergamon, pp 533-538.

[6] Van der Neut, A. (1932). De Elastische Stabiliteit van den Dunwandigen Bol, *Dissertation,* H.J. Paris, Amsterdam.

[7] Zoelly, R. (1915). Über ein Knickungsproblem am der Kugelschale, *Dissertation*, Zürich.

XXI ICTAM, 15–21 August 2004, Warsaw, Poland

ON THE STABILITY OF THE SKY-HOOK

Alois Steindl and Hans Troger
Institute of Mechanics, Vienna University of Technology,
Wiedner Hauptstrasse 8-10, A-1040 Vienna, Austria

Summary The sky-hook, that is a string forming a connection from the surface of the Earth to a satellite in geostationary orbit, which may be used as track for an Earth to space elevator, is an old dream of mankind, originating about 100 years ago in Russia. Besides the question of feasibility from a technological point of view also the question concerning the stability of such a configuration has not yet been completely solved. Under the assumption that a proper material (carbon nanotubes) is available, making the connection possible from the technological point of view, we address the question of stability of the radial relative equilibrium of a very long tapered string, which rotates synchronously with the Earth and reaches from the surface of the Earth up into the sky. The solution of the stability problem for different string materials is given by application of the Reduced Energy Momentum Method. Since the string is orbitally unstable, we connect it to a satellite in geostationary height and give the minimum mass of the satellite to stabilize the whole configuration.

MOTIVATION AND HISTORY OF THE PROBLEM

One of the main problems of modern space exploration and space technology is the high cost of sending a payload from the surface of the Earth into space. Depending on the destination in space these costs were about $10^4 - 10^6$ US Dollars for one kilogram of payload in the year 2000.
Hence for a long time there have been other ideas around for a cheaper way of transporting payloads into space orbit. In 1960 the Russian scientist Yu. Artsutanov ([1]) proposed the very interesting idea to build a celestial elevator from the surface of the Earth to a satellite in geostationary orbit. In order to compensate for the weight of the string, the string must be extended beyond the geostationary radius (35863 km altitude above the Earth). The part of the string extending beyond the geostationary orbit must have a length, which is several times the length to the geostationary orbit ([3]) if it is designed for minimum weight (see also Fig. 2).

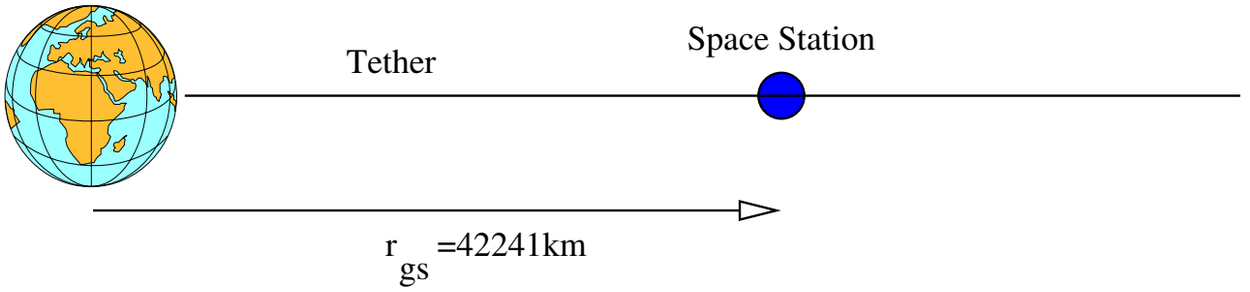


Figure 1. String connecting a satellite in geostationary orbit with the surface of the Earth. As counterweight another string must be deployed outside the geostationary height. For a minimum weight design its length and its shape are given in Fig. 2.

Artsutanov's idea makes use of the fact that a massive string moving on a circular orbit around the Earth, under the action of gravitational and centrifugal forces, finally will reach a relative equilibrium position, which is its radial position. It can be shown that in this equilibrium position the string is under tension ([2]). In order to obtain a minimum weight design the shape of the string must be tapered such that it is thickest at the point of highest tension which is at the geosynchronous radius and thinnest where the tension is lowest (at its ends) (Fig. 2). Such a string configuration could be used as track for a space elevator to provide easy transportation of payloads to the geosynchronous orbit and beyond ([6]).

REALISATION AND STABILITY ANALYSIS

Until 1991 these ideas were purely academic, since no material was available to realize such a project. However, at that time so-called "carbon nanotubes" ([7]) were discovered, which are cylindrical macromolecules composed of carbon atoms, which are formed from a flat periodical hexagonal latice with the thickness of the size of an atom. Single walled nanotubes have been produced with a diameter of a few nanometers ($1[nm] = 10^{-9}[m]$) and a length of the order of Centimeters. Hence sofar an aspect ratio of order 10^7 has been reached. Single walled nanotubes form the building block of multi-walled nanotubes. Moreover, it is conceived to have bundels of nanotubes. Forming nanoropes from nanotubes a theoretical strength of 100 times higher than steel can be expected but with only one-sixth of the weight of steel. Moreover, besides their extreme strength they also allow large strains, up to 16-24 % ([7]).
The ratio between tensile strength and density is crucial for the taper ratio of the string, that is, the ratio between the

calculations performed in [3] and our calculations (Fig. 2) the taper ratio required for steel would be 1.7×10^{33}, for Kevlar 2.6×10^{8} and for carbon nanotubes (theoretical strength) only 1.5 .

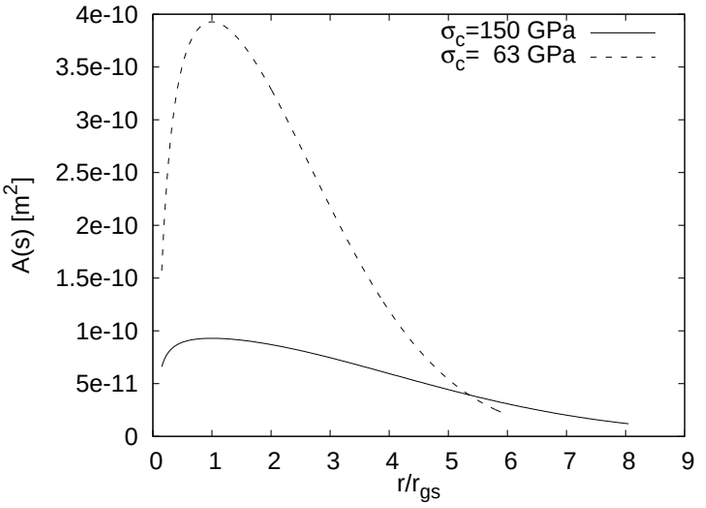


Figure 2. For two strings in the radial relative equilibrium configuration on the geostationary orbit around the Earth the areas of their cross-sections for carbon nanotubes with different admissible tensile stresses σ_c are given. The curve denoted by $\sigma_c = 150$ GPa corresponds to nanotubes of theoretical maximum strength resulting in a strain of $\epsilon = 0.238$, whereas the curve denoted by $\sigma_c = 63$ GPa corresponds to nanotubes of the strength measured experimentally in [7]. The corresponding strain is $\epsilon = 0.1$. For both strings the calculations habe been performed with endmasses of 1 kg. Moreover the ratio between the cross-sectional area at the geostationary hight to the area at the surface of the Earth follows from the figure to 1.41 for $\sigma_c = 150$ GPa and 2.50 for $\sigma_c = 63$ GPa.

A careful, practically relevant investigation of the stability of the system's relative equilibrium would have to take into account various perturbations such as the gravitational attraction of the moon, atmospheric drag and payloads moving up and down the string ([3], [6]). However, even the simpler question of stability of a long unperturbed tapered string in the spherical symmetric Newtonian gravitational field is still an open problem, because in [2] and [4] it is shown that a dumbell satellite, which is a system of two point masses connected by a massless rigid rod, possesses a stable radial relative equilibrium position on a circular orbit around the Earth only if the distance between the two masses is not too large. Here by large we understand a distance of the order of the radius of the orbit.
Hence the purpose of this paper is to investigate whether a continuous massive string, necessary for the realization of the skyhook, has a stable radial relative equilibrium. Since it will turn out that the radial relative equilibrium position of the tapered string is unstable we include at the geostationary height a satellite and ask the question, whether it has a stabilizing effect. Since this is the case we give the answer to the next question what is its minimum necessary mass. The proper theory to answer these questions is the Reduced Energy Momentum Method ([4], [8], [5], [10]). For details see [9].

CONCLUSIONS

Our main result is that the radial relative equilibrium position of a massive tapered string moving in geostationary orbit around the Earth, made of the new material called "carbon nano tubes", reaching from the surface of the Earth beyond the geostationary radius, is orbitally unstable. However, if the string is connected to a massive satellite moving in geostationary height the whole system can be stabilized. The minimum value of the mass of the satellite to achieve this stabilizing effect for the radial configuration is given in [9].

ACKNOWLEDGEMENT

This work has been supported by the Austrian Science Foundation (FWF) and by INTAS

References

[1] Artsutanov, Yu., 'Into Space on an Electric Locomotive', Komsomolskaya Pravda, 31 July 1960.
[2] Beletsky, V. V., Levin, E. M., 'Dynamics of Space Tether Systems', Advances of the Astronautical Sciences, 83, 1993.
[3] Edwards B.C., 'Design and Deployment of a Space Elevator', Acta Astronautica, 47, 2000, 735-744.
[4] Krupa, M., Steindl A., Troger, H., 'Stability of Relative Equilibria. Part II: Dumbell Satellites', Meccanica 35:353–371, 2001.
[5] Marsden, J. E. and Ratiu, T. S., *An Introduction to Mechanics and Symmetry,* A Basic Exposition of Classical Mechanical Systems, Springer-Verlag, New York – Heidelberg – Berlin, 1994.
[6] Pearson, J., 'The orbital tower: a spacecraft launcher using the Earth's rotational energy', Acta Astronautica, 2, 1975,
[7] Ruoff, R. S., Quian, D., Liu, W. K. 'Mechanical properties of carbon nanotubes: Theoretical predictions and experimental measurements', C.R.Physique 4 (2003) 993–1008. 785-799.
[8] Simo, J. C., Lewis, D., and Marsden, J. E., *Stability of Relative Equilibria. Part I: The Reduced Energy-Momentum Method,* Arch. Rat. Mech. Anal. 115, pp. 15–59, 1991.
[9] Steindl A., Troger, H., 'Is the sky-hook configuration stable?', Int.J.Nonlinear Dynamics, 2005, accepted for publication.
[10] Wang, L.-S., Chern, S.-J., Shih, C.-W., 'On the dynamics of a tethered satellite system', *Archives for Rational Mechanics and Analysis*, 127; 1994, 297-318.

STABILITY OF PARAMETRICALLY EXCITED STRUCTURES: NEW RESULTS

Alexander P. Seyranian
Institute of Mechanics, Moscow State Lomonosov University,
Michurynski pr.1, Moscow 119192, Russia

Summary Linear dynamical systems with many degrees of freedom with periodic coefficients also depending on constant parameters are considered. Stability of the trivial solution is studied with the use of the Floquet theory. First and second order derivatives of the Floquet matrix with respect to parameters are derived in terms of matriciants of the main and adjoint problems and derivatives of the system matrix. It is shown how to use this information in gradient procedures for stabilization or destabilization of the system. Then, linear vibrational systems with periodic coefficients depending on three independent parameters: frequency and amplitude of periodic excitation, and damping parameter are considered with the assumption that the last two quantities are small. For arbitrary matrix of periodic excitation and positive definite damping matrix general expressions for regions of the main (simple) and combination resonances are derived. Two important specific cases of excitation matrix are studied: a symmetric matrix and a stationary matrix multiplied by a scalar periodic function. It is shown that in both cases the resonance regions are halves of cones in the three-dimensional parameter space with the boundary surface coefficients depending only on the eigenfrequencies, eigenmodes of the conservative system and system matrices. As an example of the developed theory Bolotin's problem on dynamic stability of a beam loaded by periodic bending moments is solved.

DERIVATIVES OF THE FLOQUET MATRIX WITH RESPECT TO PARAMETERS

We consider a system of linear differential equations

$$\dot{\mathbf{x}} = \mathbf{G}\mathbf{x}, \tag{1}$$

where $\mathbf{G} = \mathbf{G}(t, \mathbf{p})$ is a real square matrix of dimension m, which is smoothly depending on a vector of real parameters $\mathbf{p} = (p_1, p_2, \ldots p_n)$ and is a continuous periodic function of the time $\mathbf{G}(t, \mathbf{p}) = \mathbf{G}(t + T, \mathbf{p})$, T being a period. We denote linear independent solutions of system (1) as $\mathbf{x_1}(t), \mathbf{x_2}(t), \ldots, \mathbf{x_m}(t)$ and form out of them a fundamental matrix $\mathbf{X}(t) = [\mathbf{x_1}(t), \mathbf{x_2}(t), \ldots, \mathbf{x_m}(t)]$. The $\mathbf{X}(t)$ matrix satisfying the equations

$$\dot{\mathbf{X}} = \mathbf{G}\mathbf{X}, \quad \mathbf{X}(0) = \mathbf{I}, \tag{2}$$

where $\mathbf{I}$ is the identity matrix of dimension m, is called a matriciant, and the matrix $\mathbf{F} = \mathbf{X}(T)$ is called a monodromy matrix.

According to the Floquet theory, see Nayfeh and Mook [1], stability of system (1) is determined by multipliers (eigenvalues of the monodromy matrix): if all the multipliers for their absolute value are less than one, the system is asymptotically stable, and if at least one of them is greater than one, the system becomes unstable.

Now we assume that the vector of parameters takes a variation $\mathbf{p} = \mathbf{p_0} + \Delta\mathbf{p}$. Hence, the $\mathbf{G}$ matrix, and therefore the matriciant $\mathbf{X}(t)$ obtain variations. This accordingly leads to a change of the monodromy matrix $\mathbf{F}$. The formulas for the first and second derivatives of a monodromy matrix with respect to parameters are derived in the form of integrals over the period

$$\frac{\partial \mathbf{F}}{\partial p_k} = \mathbf{F_0} \int_0^T \mathbf{X_0^{-1}} \frac{\partial \mathbf{G}}{\partial p_k} \mathbf{X_0}\, dt, \quad k = 1, \ldots, n, \tag{3}$$

$$\frac{\partial^2 \mathbf{F}}{\partial p_i \partial p_j} = \mathbf{F_0} \Big\{ \int_0^T \mathbf{X_0^{-1}} \frac{\partial^2 \mathbf{G}}{\partial p_i \partial p_j} \mathbf{X_0}\, dt + \int_0^T \mathbf{X_0^{-1}} \frac{\partial \mathbf{G}}{\partial p_i} \mathbf{X_0} \left(\int_0^\tau \mathbf{X_0^{-1}} \frac{\partial \mathbf{G}}{\partial p_j} \mathbf{X_0}\, d\zeta \right) d\tau + \int_0^T \mathbf{X_0^{-1}} \frac{\partial \mathbf{G}}{\partial p_j} \mathbf{X_0} \left(\int_0^\tau \mathbf{X_0^{-1}} \frac{\partial \mathbf{G}}{\partial p_i} \mathbf{X_0}\, d\zeta \right) d\tau \Big\}, \quad i, j = 1, \ldots, n, \tag{4}$$

where the zero subscript means that the corresponding value is taken at $\mathbf{p} = \mathbf{p_0}$. Note that to find derivatives (3) and (4) it is necessary to know only the matriciants $\mathbf{X_0}(t)$ and the derivatives of the $\mathbf{G}$ matrix with respect to the parameters taken at $\mathbf{p} = \mathbf{p_0}$. Using derivatives (3) and (4) a variation of the monodromy matrix can be given in the form

$$\mathbf{F}(\mathbf{p_0} + \Delta\mathbf{p}) = \mathbf{F_0} + \sum_{k=1}^{n} \frac{\partial \mathbf{F}}{\partial p_k} \Delta p_k + \frac{1}{2} \sum_{i,j=1}^{n} \frac{\partial^2 \mathbf{F}}{\partial p_i \partial p_j} \Delta p_i \Delta p_j + \cdots. \tag{5}$$

Knowing the derivatives of the monodromy matrix we can calculate the value of this matrix in the vicinity of the initial point $\mathbf{p_0}$, and therefore estimate behavior of the multipliers responsible for the stability of system (1) when the problem

parameters are changed. This is what we call sensitivity analysis of multipliers. Analysis of multipliers provides information for determining stability and instability regions in the parameter space.

MECHANICAL EXAMPLE

As an example of the developed theory, we consider Bolotin's problem on dynamic stability of the trivial solution (plane position) of a beam, see Bolotin [2]. The elastic beam is assumed to be simply supported at its ends and loaded by the periodic bending moments $M(\Omega t) = \delta\varphi(\Omega t)$ in the plane of its maximum stiffness, where $\varphi(t)$ is a 2π-periodic function, Fig. 1. Bending-torsional vibrations off this plane are described by the equations

$$\begin{aligned} m\frac{\partial^2 w}{\partial t^2} + \gamma m d_1 \frac{\partial w}{\partial t} + EJ\frac{\partial^4 w}{\partial x^4} + \delta\varphi(\Omega t)\frac{\partial^2 \theta}{\partial x^2} = 0 \\ mr^2\frac{\partial^2 \theta}{\partial t^2} + \gamma m r^2 d_2 \frac{\partial \theta}{\partial t} + \delta\varphi(\Omega t)\frac{\partial^2 w}{\partial x^2} - GI\frac{\partial^2 \theta}{\partial x^2} = 0 \end{aligned} \tag{6}$$

Here, $w(x,t)$ is the transverse deflection of the beam; $\theta(x,t)$ and r are the torsion angle and the radius of inertia for the beam's cross section, respectively; EJ and GI are the bending and torsion stiffnesses of the beam, respectively; m is the mass per unit length of the beam; γ is the parameter of dissipative force (viscous friction coefficient); and d_1 and d_2 are fixed constants defining the bending and torsional viscous friction forces.

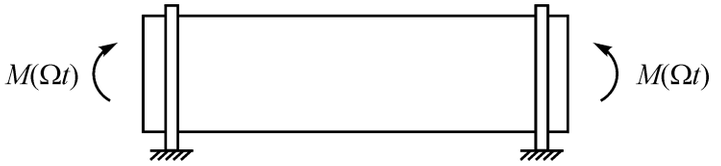


Figure 1. An elastic beam loaded by periodic bending moments.

The boundary conditions take the form

$$x = 0,\ l: \quad w = \frac{\partial^2 w}{\partial x^2} = \theta = 0 \tag{7}$$

where l is the beam length. The problem consists in finding parametric resonance domains in the three-dimensional parameter space δ, Ω, and γ. It turns out that the regions of the difference-type combination resonance are empty, and only summation-type resonance takes place. The regions of the summation-type combination resonance at frequencies close to $\Omega_0 = (\omega_{n1} + \omega_{n2})/k$, k=1,2,… are determined by the formula

$$d_1 d_2 \gamma^2 - \frac{\pi^4 n^4}{l^4 r^2 m^2}\frac{(a_k^2 + b_k^2)}{4\omega_{n1}\omega_{n2}}\delta^2 + 4k^2\frac{d_1 d_2}{(d_1 + d_2)^2}\Delta\Omega^2 \le 0 \tag{8}$$

where a_k and b_k are the Fourier coefficients of the periodic function $\varphi(t)$, and ω_{n1}, ω_{n2} are the eigenfrequencies of the conservative (undamped) system. Other mechanical examples including determination of the parametric resonance regions of elastic columns of non-uniform cross-section loaded by longitudinal periodic forces, and column optimization problems are presented in Seyranian, Solem and Pedersen [3], Seyranian [4], and Mailybaev and Seyranian [5]. Extended discussion of periodically excited structures and mechanical systems is given in a recent book by Seyranian and Mailybaev [6].

References

[1] Nayfeh A.H., Mook D.T.: Nonlinear Oscillations. John Wiley and Sons, NY 1979.
[2] Bolotin V.V.: Dynamic Stability of Structures. In: Non-linear Stability of Structures. Theory and Computational Techniques. Springer Wien, NY 1995.
[3] Seyranian A.P., Solem F. and Pedersen P. : Multi-parameter Linear Periodic Systems: Sensitivity Analysis and Applications. *Journal of Sound and Vibration* **229**: 89-111, 2000.
[4] Seyranian A.P. : Resonance Domains for the Hill Equation with Damping. *Physics-Doklady* **46**(1): 41-44, 2001.
[5] Mailybaev A.A., Seyranian A.P.: Parametric Resonance in Systems with Small Dissipation. *J. Appl. Maths Mechs* **65**(5): 755-767, 2001.
[6] Seyranian A.P., Mailybaev A.A.: Multiparameter Stability Theory with Mechanical Applications. World Scientific, Singapore (to appear).

A UNIFIED TREATMENT FOR THE ELASTOPLASTIC BIFURCATION OF STRUCTURAL ELEMENTS

Philippe Le Grognec*, Anh Le van**

*Ecole des Mines de Douai, Département Mécanique et Comportement des Matériaux, 941 rue Charles Bourseul BP 838, 59508 Douai Cedex, France

**Université de Nantes, Laboratoire de Génie Civil de Nantes-Saint Nazaire, 2 rue de la Houssinière BP 92208, 44322 Nantes Cedex 3, France

Summary This work is devoted to a unified method for the analysis of the elastoplastic bifurcation and post-bifurcation of structural elements such as beams, plates and shells. In each case, the same bifurcation equation is solved, giving rise to analytical relations for the critical load, the eigenmode as well as the initial slope of the bifurcating branch which is essential for the stability analysis.

THE FRAMEWORK

The bifurcation analysis is carried out using the three-dimensional total Lagrangian formulation, where the Green strain is decomposed additively and the elastic strains are assumed small so that the constitutive law for the elastic behavior can be represented by the Saint-Venant-Kirchhoff relation. The plasticity is described within the frame of generalized standard materials, obeying the von Mises yield criterion and a linear isotropic hardening.
It is assumed that a fundamental equilibrium path $\lambda \mapsto \vec{u}_f(\lambda)$ is known, which is the displacement solution of the elastoplastic problem under increasing load λ. Moreover, at a critical instant t_c, it is assumed that there exists a bifurcating solution denoted $\vec{u}$, which is described by the asymptotic expansion :

$$\lambda = \lambda_c + \lambda_m \xi + o(\xi) \qquad\qquad \vec{u} = \vec{u}_f(\lambda) + \xi \vec{X} + o(\xi)$$

where the perturbation parameter ξ corresponds to the projection of the solution onto the buckling eigenmode.
Assuming the so-called tangent modulus hypothesis and uniqueness of the eigenmode, the critical load λ_c and the eigenmode $\vec{X}$ are solutions of the bifurcation equation [1],[2] :

$$\forall\, \delta\vec{u}, \qquad \int_\Omega \nabla^T \delta\vec{u} : \mathbf{K}^i(\vec{u}_f(\lambda_c)) : \nabla\vec{X} d\Omega = 0$$

where Ω is the region occupied by the body, $\mathbf{K}^i$ is either one of the following expressions, depending on the point belongs to the elastic or plastic region :

$$\mathbf{K}^e = \mathbf{F}.\mathbf{D}.\mathbf{F}^T + (\mathbf{I}.\Sigma)^T \qquad \text{or} \qquad \mathbf{K}^p = \mathbf{K}^e - \mathbf{M}^T \otimes \mathbf{M}, \quad \mathbf{M} = \frac{\mathbf{D} : \frac{\partial f}{\partial \Sigma}}{\sqrt{h + \frac{\partial f}{\partial \Sigma} : \mathbf{D} : \frac{\partial f}{\partial \Sigma}}}.\mathbf{F}^T$$

In the above, **F** denotes the gradient of the deformation, **D** the elasticity tensor, Σ the second Piola-Kirchhoff stress tensor (symmetric), **I** the fourth-order unit tensor, f the yield function and h the hardening modulus.
In the case where the elastic unloading zone at bifurcation is reduced to a single point, the initial slope λ_m of the bifurcating branch is given by :

$$\lambda_m = \min\{\lambda \mid \forall\, x \in \Omega,\ \lambda \mathbf{M}_c : \nabla\vec{u}_{f,\lambda}(\lambda_c) + \mathbf{M}_c : \nabla\vec{X} \geq 0\} = \max_{x\in\Omega}\left(-\frac{\mathbf{M}_c : \nabla\vec{X}}{\mathbf{M}_c : \nabla\vec{u}_{f,\lambda}(\lambda_c)}\right)$$

TIMOSHENKO BEAM UNDER AXIAL COMPRESSION

Throughout the sequel, we assume that the stress state in the body is uniaxial, directed in the x axis, and that the yield stress σ_0 is small enough for the buckling to occur when the body is wholly plastic.
Consider a straight cantilever beam with length L, constant cross-section area S, area moment of inertia I and tangent modulus E_T. The beam is subjected to a compressive load λ and its kinematics is described by the Timoshenko model. The fundamental solution writes, when the beam is wholly plastic ($\lambda \geq \sigma_0 S$) :

$$\vec{u}_f = -\frac{x}{S}\left(\frac{\lambda - \sigma_0 S}{E_T} + \frac{\sigma_0 S}{E}\right)\vec{x}$$

Assuming small pre-critical strains, the gradient tensor **F** can be replaced with the identity tensor. The components ($\mathcal{U}$,$\mathcal{V}$,Θ) defining the eigenmode are obtained from the bifurcation equation which simplifies as follows : $\forall\, \delta U, \delta V, \delta\theta$,

$$\int_\Omega \Big[E_T(\mathcal{U}_{,x} - y\Theta_{,x})(\delta U_{,x} - y\delta\theta_{,x}) + \mu(\Theta - \mathcal{V}_{,x})(\delta\theta - \delta V_{,x}) - \frac{\lambda_c}{S}(\mathcal{U}_{,x} - y\Theta_{,x})(\delta U_{,x} - y\delta\theta_{,x}) - \frac{\lambda_c}{S}\mathcal{V}_{,x}\delta V_{,x} \Big] d\Omega = 0$$

It yields three scalar equations :

$$E_T S\mathcal{U}_{,x} = 0 \qquad \mu S\Theta - \mu S\mathcal{V}_{,x} + \lambda_c \mathcal{V}_{,x} = 0 \qquad E_T I\Theta_{,xx} + \mu S\mathcal{V}_{,x} - \mu S\Theta = 0$$

Taking into account the boundary conditions gives the critical load and the eigenmode :

$$\lambda_c = \frac{\frac{\pi^2 E_T I}{4L^2}}{1 + \frac{\pi^2 E_T I}{4L^2 \mu S}} \qquad \mathcal{U} = 0 \qquad \mathcal{V} = \left(1 + \frac{\pi^2 E_T I}{4L^2 \mu S}\right) \frac{2L}{\pi} \left(1 - \cos\frac{\pi x}{2L}\right) \qquad \Theta = \sin\frac{\pi x}{2L}$$

The well-known critical load for a Bernoulli beam is readily obtained from the above result. Moreover, one can get the initial slope of the bifurcating branch : $\lambda_m = 3\lambda_c$.

PLATE UNDER UNIAXIAL COMPRESSION

Consider a rectangular plate with dimensions a along $\vec{x}$, b along $\vec{y}$ ($a > b$ or $a < b$) and thickness h. The plate is subjected to a compressive stress Σ normal to sides of length b and its kinematics is described by the Love-Kirchhoff model. Denoting $\lambda = -\Sigma > 0$, the fundamental solution writes :

$$\vec{u}_f = -\left(\frac{\lambda}{E} + \frac{\lambda - \sigma_0}{h}\right) x\vec{x} + \left(\frac{\nu\lambda}{E} + \frac{\lambda - \sigma_0}{2h}\right) y\vec{y}$$

Solving the bifurcation equation shows that the out-of-plane component $\mathcal{W}$ of the eigenmode satisfies :

$$t^2(\alpha\mathcal{W}_{,xxxx} + \gamma\mathcal{W}_{,yyyy} + (2\beta + 4\mu)\mathcal{W}_{,xxyy}) + 12\lambda_c\mathcal{W}_{,xx} = 0$$

where $\alpha = \frac{2\mu}{D}(E + 4h) \quad \beta = \frac{4\mu}{D}(E + 2\nu h) \quad \gamma = \frac{8\mu}{D}(E + h) \quad$ with $D = 2\mu(5 - 4\nu) + 4h(1 - \nu)$

By assuming a sinusoidal mode along $\vec{x}$ and $\vec{y}$, one gets the critical load and the eigenmode :

$$\lambda_c = \frac{t^2\pi^2}{12}\left(\frac{p^2\alpha}{a^2} + \frac{q^4\gamma a^2}{p^2 b^4} + \frac{q^2(2\beta + 4\mu)}{b^2}\right) \qquad \mathcal{U} = 0 \qquad \mathcal{V} = 0 \qquad \mathcal{W} = \sin\frac{p\pi x}{a}\sin\frac{q\pi y}{b}$$

The wave numbers corresponding to the smallest critical load are $p = \sqrt[4]{\frac{\gamma}{\alpha}}\frac{a}{b}$ along the load direction and $q = 1$. In particular, when $a = b = 1$ the above result leads to the value given in [3] : $\lambda_c = \frac{Et^2\pi^2}{12}\left(\frac{2}{1+\nu} + \frac{9 + \frac{E_T}{E}(8\nu - 1)}{(5 - 4\nu) - \frac{E_T}{E}(1 - 2\nu)^2}\right)$.

As in the beam case, one can also obtain the initial slope of the bifurcating branch : $\lambda_m = \frac{t\pi^2\left(\frac{2p^2}{a^2} - \frac{q^2}{b^2}\right) E E_T}{5E + E_T(2\nu - 1)}$.

TUBE UNDER AXIAL COMPRESSION

Let us now consider a circular tube with length l along axis $\vec{x}$, radius R and thickness t, subjected to a compressive axial stress Σ. Denoting $\lambda = -\Sigma > 0$, the fundamental solution reads in the cylindrical basis :

$$\vec{u}_f = -\left(\frac{\lambda}{E} + \frac{\lambda - \sigma_0}{h}\right) x\vec{x} + R\left(\frac{\nu\lambda}{E} + \frac{\lambda - \sigma_0}{2h}\right)\vec{e}_r$$

Solving the bifurcation equation in the axisymmetric case yields the coupled equations :

$$\alpha t\mathcal{U}_{,x} + \frac{\beta}{R} t\mathcal{W} = 0 \qquad \alpha\frac{t^3}{12}\mathcal{W}_{,xxxx} + \lambda_c t\mathcal{W}_{,xx} + \frac{\gamma}{R^2} t\mathcal{W} + \frac{\beta}{R} t\mathcal{U}_{,x} = 0$$

In the case of simply supported edges, the critical load can be computed by considering a sinusoidal eigenmode. After optimizing the wave number, one obtains $\lambda_c = \frac{Et}{R}\sqrt{\frac{4h}{3[(5-4\nu)E + 4h(1-\nu^2)]}}$ as well as the eigenmode :

$$\mathcal{U} = \frac{l}{n\pi R}\frac{2(E + 2\nu h)}{E + 4h}\left(\cos\frac{n\pi x}{l} - 1\right) \qquad \mathcal{V} = 0 \qquad \mathcal{W} = \sin\frac{n\pi x}{l} \quad \text{with } n = \frac{l}{\pi}\sqrt[4]{\frac{48h[(5 - 4\nu)E + 4h(1 - \nu^2)]}{R^2 t^2 (E + 4h)^2}}$$

The initial slope of the bifurcating branch is $\lambda_m = \frac{2Eh[5E + 4h + 8\nu h + \sqrt{48h[(5-4\nu)E + 4h(1-\nu^2)]}]}{R(E+4h)(5E+4h+2\nu h)}$.

References

[1] Hutchinson J.W.: Plastic buckling. *Advances in Applied Mechanics* **14**:67–144, 1974.
[2] Nguyen Q.S.: Stability and Nonlinear Solid Mechanics, Wiley, 2000.
[3] Cimetière, A. : Sur la modélisation et le flambage des plaques élastoplastiques. *PhD Thesis*, Université de Poitiers, France, 1987.

BUCKLING AND IMPERFECTION-SENSITIVITY OF AXIALLY COMPRESSED CYLINDRICAL SHELLS WITH COMPLIANT CORES

H. Obrecht, B. Rosenthal, P. Fuchs

Baumechanik-Statik, Universitaet Dortmund, D-44221 Dortmund, Germany
msobr@busch.bauwesen.uni-dortmund.de

Summary The extent to which the mechanical properties and dimensions of compliant cores influence the load-carrying capacity and imperfection-sensitivity of axially compressed cylindrical shells is analyzed numerically for a wide range of configuration parameters. It is found that a comparatively thin layer of core material is sufficient to achieve substantial increases in the buckling loads while at the same time the imperfection-sensitivity is significantly smaller than for the unfilled shell.

Recently, the production of high porosity metal foams and integrally filled metal-foam sandwich panels have received considerable attention, and it is estimated that foam-filled structural components of this type will have decisive advantages over more established thin-walled constructions relying on honeycomb cores or discrete stiffener arrangements to achieve the required weight-strength ratios.

Unfortunately, little comparative data exist to verify the high weight-saving expectations often associated with components filled with metal foams. An exception are the results obtained in [1] which suggest that for practical purposes foam core sandwich constructions may have a - comparatively modest - weight-strength advantage over optimized skin-stringer configurations only under fairly exceptional - and largely impractical - design conditions. This conclusion was reached on the basis of idealized model analyses following the classical concepts of structural index and minimum-weight design and therefore may be somewhat conservative.

In fact, the results reported in [2] suggest that for sandwich shells and curved sandwich panels there may indeed be a practically significant loading range for which optimized sandwich constructions employing metal foam cores do have a distinct weight advantage over metal stringer constructions. However, these results also indicate that the imperfection sensitivity is essentially as severe as for the corresponding monocoque cylinder. Thus, in this case, too, there seems to be an "unhappy coexistence of efficient shell design and the curse of imperfection-sensitivity (B. Budiansky)".

On the other hand - even though not directly concerned with weight-strength optimized configurations and imperfection-sensitivity - the work on comparatively thick-walled foam-filled cylindrical shells reported in [3,4] indicates - on the basis of simplified analytical model analyses and experiments on rubber cylinders filled with rubber foam - that compliant foam cores having fairly high porosities and low moduli may not only lead to remarkable increases in the load-carrying capacity of cylindrical shells but also to a reduction in their notorious imperfection-sensitivity. If this conclusion could be shown to be true for other material combinations and configurations as well, it would have far-reaching consequences because it could lead to substantially reduced knockdown factors and to considerably higher design loads for this type of structural component.

To shed more light on this question, the presentation explores the extent to which the mechanical properties and dimensions of compliant core materials may influence the load-carrying capacity and imperfection-sensitivity of axially compressed cylindrical shells in detail (Fig. 1). It starts from the fundamental imperfection-sensitivity analyses presented in [5,6] which treated the buckling and initial postbuckling behavior of long axially compressed circular cylindrical shells containing an initial geometric imperfection in the shape of the classical axisymmetric bifurcation mode. As is well known, these analyses quantitatively established the severe imperfection-sensitivity of this shell configuration and thus provided a theoretical basis for the empirical knockdown factors widely used in the design of thin-walled structures (e.g. [7]).

To validate the computational model employed in the subsequent analyses, the first part of the presentation is concerned with a detailed comparison of the numerical results with those of the well-known (semi-) analytical buckling and imperfection-sensitivity analyses for monocoque cylindrical shells presented in [5,6]. Based on a comparatively high mesh-density and taking into account a significant number of close or nearly coincident buckling modes, excellent agreement with the classical bifurcation and imperfection-sensitivity results were obtained for a wide range of radius-to-thickness ratios and imperfection amplitudes (Fig. 2).

Subsequently we explore the buckling behavior and imperfection-sensitivity of axially compressed circular cylindrical shells completely or partially filled with compliant core material along the lines of the work presented in [3,4]. Comprehensive numerical results - based on computational models using dense meshes for the two-dimensional shell elements as well as the three-dimensional volume elements for the compliant core material - are presented for a wide range of configuration parameters, such as the shell and core thicknesses, the respective material moduli, the

imperfection amplitudes, etc.. They permit the conclusion that a comparatively thin layer of compliant core material may be doubly beneficial because it leads not only to a substantial increase in the bifurcation stress of the partially or completely filled perfect shell compared to that of the perfect unfilled one but also - and somewhat unexpectedly - to a significant reduction in imperfection-sensitivity, as can be seen from Figs. 3 and 4, where results are plotted for a radius-to-thickness ratio of 100 and a ratio of the core to shell moduli of 1/100. Analogous results are obtained for other parameter combinations, and the relative load-carrying increases are found to be most pronounced for large values of R/t.

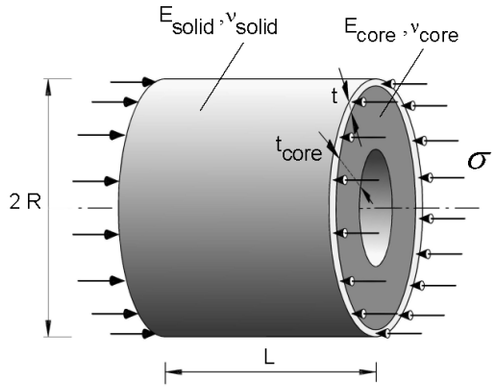


Fig. 1 Shell and load configuration

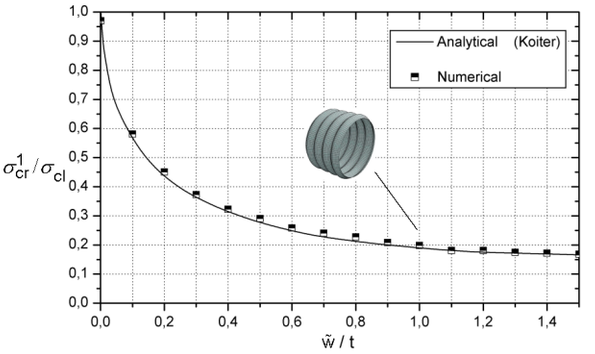


Fig. 2 Imperfection sensitivity of the unfilled shell. Analytical vs. numerical results

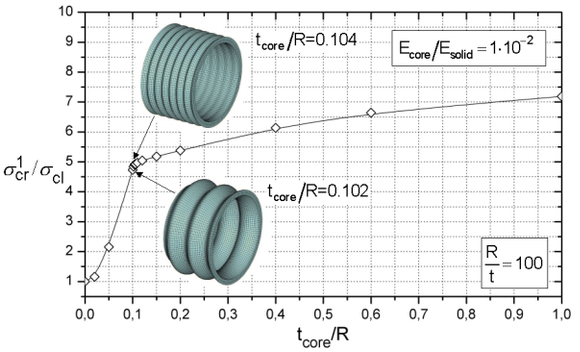


Fig. 3 Influence of the core-thickness on the bifurcation stress of the perfect configuration (relative to the classical buckling stress of the unfilled cylindrical shell)

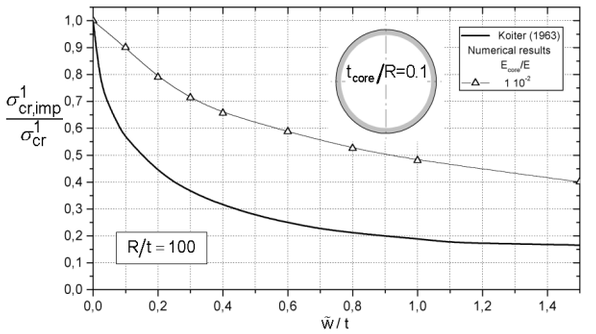


Fig. 4 Imperfection-sensitivity of the imperfect partially filled shell compared to the imperfection-sensitivity of the unfilled shell

References

[1] B. Budiansky: On the minimum weight of compression structures. Int. J. Solids Structures, Vol 36, 1999, pp.3677-3708
[2] J.W. Hutchinson, M.Y. He: Buckling of cylindrical sandwich shells with metal foam cores. Int. J. Solids Structures, Vol 37, 2000, pp.6777-6794
[3] G.N. Karam, L.J. Gibson: Elastic buckling of cylindrical shells with elastic cores I. Analysis. Int. J. Solids Structures, Vol 32, No. 8/9, 1995, pp.1259-1283.
[4] G.N. Karam, L.J. Gibson: Elastic buckling of cylindrical shells with elastic cores - II. Experiments. Int. J. Solids Structures, Vol. 32, No. 8/9, 1995, pp. 1285-1306.
[5] W.T. Koiter: The effect of axisymmetric imperfections on the buckling of cylindrical shells under axial compression. Proc. Kon. Ned. Akad. Wet., B, Vol. 66, 1963, pp. 265-279.
[6] B. Budiansky, J.W. Hutchinson: Buckling of circular cylindrical shells under axial compression. In: Contributions to the Theory of Aircraft Structures (A. van der Neut Anniversary Volume), Delft University Press, Delft, 1972, pp. 239-259.
[7] Anon.: Buckling of thin-walled circular cylinders. NASA Space Vehicle Design Criteria, NASA SP-8007, 1965 (revised 1968).

STABILITY OF SHEAR-FLEXIBLE FRAMES

Esben Byskov, Ronni Dam, Thomas Frost and Lars Hulsbæk
Department of Building Technology and Structural Engineering, Sohngaardsholmsvej 57, Aalborg University, DK-9000 Aalborg, Denmark

Summary

INTRODUCTION

Most studies of postbuckling and imperfection sensitivity of frame structures have assumed shear-inflexibility. Here, we present theoretical, numerical and experimental results for a shear flexible realization of a particular frame, the so-called "Roorda Frame," see Fig. 1. The frame consists of two sandwich beams of length 916 mm



(a) The Roorda Frame. (b) Joint and loading device.

Figur 1. Shear-flexible Roorda Frame with loading device.

connected through a very stiff joint, see Figs. 1(a) and 1(b), which also show the loading device. The core is made of a foam (Divinycell H130) and the face plate material is a high-strength aluminum (2024-T3). The depth of the members is 43.2 mm and the thickness of the face plates is 1.6 mm. All deformations occur only in the plane of the frame.

By moving the loading device, different levels of load imperfection can be introduced.

When dealing with sandwich beams and frames it is very important noticing that the idea of a stiff joint must be reconsidered simply because it is the rotation of the *cross-section*, not the rotation of *beam axis*, which is continuous over the joint. This means that the horizontal member, the beam, does not support the vertical one, the column, as well as in the Bernoulli-Euler case.

POSTBUCKLING AND IMPERFECTION SENSITIVITY

Let u be the axial and w the transverse displacement, respectively, and let ω denote the rotation of the beam cross-section. Then, the generalized strains of a moderately nonlinear Timoshenko beam theory are:

$$\text{Axial strain}: \quad \varepsilon = u' + \tfrac{1}{2}\left(w'\right)^2, \quad \text{Shear strain}: \quad \gamma = w' - \omega, \quad \text{Curvature strain}: \quad \kappa = \omega' \tag{1}$$

Thus, we may apply the asymptotic theory of postbuckling and imperfection theory first developed by Koiter, see e.g. [1] or [2]. Koiter has solved the problem of postbuckling and imperfection sensitivity of the same kind of frame using Bernoulli-Euler beam theory and assuming inextensibility, see [3]. The latter assumption is also approximately valid for frames such as the present one. According to Koiter [1], for an unsymmetric structure the the load-carrying capacity λ_S of a geometrically imperfect realization of the frame may be determined as the maximum of λ on the relation:

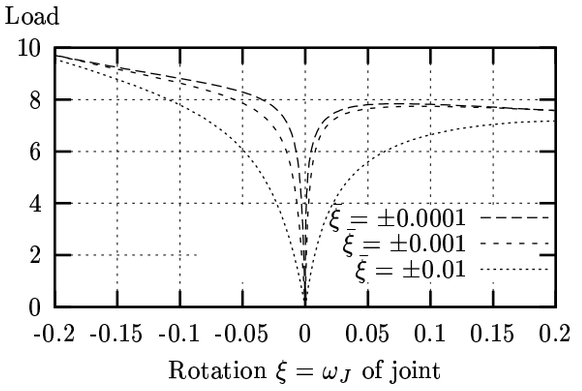
$$\left(1 - \frac{\lambda}{\lambda_C}\right)\xi + a\xi^2 = \frac{\lambda}{\lambda_C}\bar{\xi} \tag{2}$$

where λ denotes a scalar load parameter, λ_C the classic critical load of the perfect structure, ξ the amplitude of the buckling mode, a the (first-order) postbuckling constant, and $\bar{\xi}$ designates the amplitude of the geometric

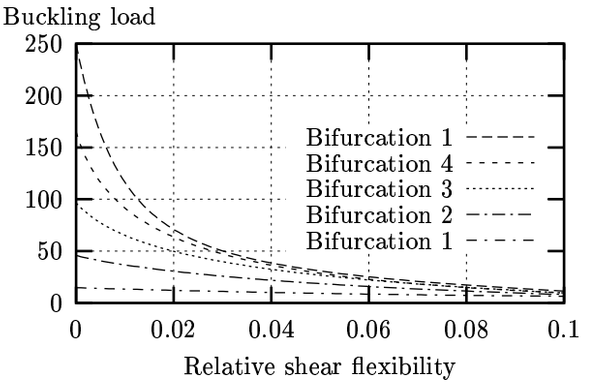
imperfection, which is assumed to be affine with the buckling mode. Once the prebuckling and buckling fields have been determined, the value of a is easily computed. For the original Roorda Frame the buckling mode amplitude is usually chosen as the rotation ω_J of the joint. This is also done here. Below, finite element results, which agree asymptotically with the analytic solutions, but cover a larger range of amplitudes, are compared with experimental results.

FINITE ELEMENT STUDY AND EXPERIMENTAL RESULTS

Unless special elements are utilized the phenomenon of "locking" occurs because the beam theory accounts for shear flexibility. Since the applied beam theory accounts for shear flexibility, usual beam finite elements display "locking" with the consequence that the results become unreliable. Application of special elements handles this problem. Equilibrium paths for various levels of geometric imperfections in the shape of the first buckling mode are shown in Fig. 2(a).



(a) Equilibrium paths of geometrically imperfect sandwich frames. Rotation of joint in radian, positive counter-clockwise. Imperfection levels are given by $\bar{\xi}$.



(b) Variation of bifurcation load with increased shear flexibility.

Figur 2. Finite element results

If the frame consists of a shear-inflexible material the buckling loads are well separated, see Fig. 2(b). The figure also shows that this separation decreases for increasing (relative) shear flexibility. This effect must be accounted for in the numerical procedures in order to avoid inaccuracies.

Comparison between experimental and finite element results shows fair agreement. An important reason for the discrepancies stems from the applied beam theory in that the assumption of cross-sections remaining plane after deformation is too crude to model sandwich beams correctly. In addition to, and associated with this, determination of the beam cross-sectional properties, i.e. the bending and shear stiffness, is not a straightforward issue. The foam, although of very high quality, is neither homogeneous nor isotropic on the global scale.

CONCLUDING REMARKS

Determination, both experimentally and numerically, of postbuckling behavior and imperfection sensitivity of frames of sandwich materials presents serious difficulties in comparison with the equivalent problem for frames made of materials that display little shear-flexibility. Modeling of the cross-sectional properties must be given special attention. Special finite elements must be used in order to avoid shear locking.

References

[1] W.T. Koiter. *On the Stability of Elastic Equilibrium.* H.J. Paris, Amsterdam, 1945. In Dutch, also *NASA TT-F10,833*, (1967); also Air Force Flight Dynamics Laboratory, *AFFDL-TR-70-25*, (1970).

[2] B. Budiansky. Theory of buckling and post-buckling behavior of elastic structures. *Advances in Applied Mechanics*, 14:1–65, 1974.

[3] W.T. Koiter. Post-buckling analysis of a simple two-bar frame. In *Recent Progress in Applied Mechanics.* Almquist and Wiksell, 1966.

INSTABILITIES OF INITIALLY STRESSED HYPERELASTIC CYLINDRICAL MEMBRANE AND SHELL UNDER INTERNAL PRESSURE

Djenane Pamplona, Paulo B. Gonçalves, Stefane R. X. Lopes
Catholic University - PUC-Rio, Civil Engineering Department, Rio de Janeiro, Brazil

Summary This paper investigates the static non-linear behaviour and possible instabilities of cylindrical membranes and shells. A detailed experimental analysis was carried out. The structure was analysed using appropriate membrane or shell finite elements and the resulting non-linear equilibrium equations solved using the FE software ABAQUS. A detailed parametric numerical analysis was carried out and the influence of different types of local imperfections was also studied in detail.

INTRODUCTION

The pioneering work of Green & Adkins [1] on non-linear elasticity set up the basis for the analysis of membranes under large deformations. Since then, many important papers have been published in this field, most of which studies the equilibrium and stability of thin cylindrical and spherical membranes under uniform pressure loading or loads acting along the boundaries (Alexander [2]; Ratner [3]; Chen [4]; Haughton [5]; Pamplona et al. [6]). The analysis of large deformations of shell is not so popular, nevertheless there are some important publications such as the ones by Tang et al [7] and Haussy and Ganghoffer [8], where the theory of thick hyperelastic shells was used for the modelling of carotid arteries and aneurysms, respectively. This paper investigates the large deformations of hyperelastic membranes and shells. The static non-linear behaviour and possible instabilities of these structures are both analysed. A detailed experimental analysis was carried out involving cylindrical membranes and shells and the influence of the axial force and the internal pressure were investigated. An apparatus was developed to support vertically the extended structure while it is filled with air. The membranes and shells used in the experiments are composed of an isotropic, homogeneous and hyperelastic rubber, which is numerically modelled as Neo-Hookean, Mooney-Rivlin or Ogden incompressible material. The constants of these formulations were obtained by comparing the experimental and numerical solutions for the structure under traction. The structure was analysed using appropriate membrane or shell finite elements and the resulting non-linear equilibrium equations solved using the FE software ABAQUS. A detailed parametric analysis was also carried out to study the influence of the initial traction and geometric parameters on the non-linear behaviour and load carrying capacity of the structure. The influence of different types of local imperfections was also studied in detail.

STATEMENT OF THE PROBLEM

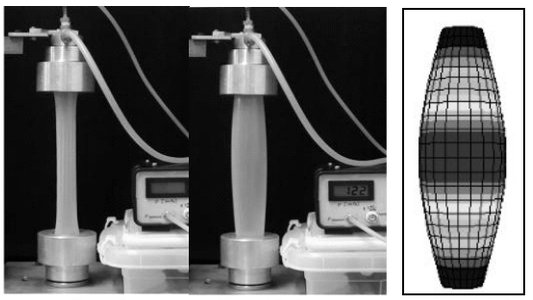
Isotropic elastomeric materials can be conveniently represented in terms of a strain energy density function w [1]. Assuming complete recoverability after deformation, the strain energy density depends on the final state of strain and not on the loading history. Thus, given an undeformed reference state, the final stressed state is characterized by the principal stretches λ_1, λ_2 and λ_3 or equivalently by the strain invariants I_1, I_2 and I_3. A rubber-like material can be considered to behave as an incompressible material as long as stresses do not become too large. This simplifying assumption of incompressibility leads to the constraint I_3=1. Three material constitutive laws were chosen to analyse the problem: Mooney-Rivlin law, $w=C_1(I_1-3)+ C_2(I_2-3)$, Neo-Hookean, $w=C_1(I_1-3)$ and Ogden $w = \sum_{i=1}^{N} \frac{2\mu_i}{\alpha_i^2}\left(\lambda_1^{\alpha i} + \lambda_2^{\alpha i} + \lambda_3^{\alpha i} - 3\right)$, where C_i, α_i, and μ_i, are the material constants. The analysis of the non-linear behaviour and stability for the thick-walled shell and thin membrane, both under traction and increasing air pressure, were performed using ABAQUS. Different finite elements and the three constitutive laws presented above were used to compare the numerical results with the experimental ones, obtaining the critical loads and imperfection sensitivity for different types of imperfection.

NUMERICAL AND EXPERIMENTAL RESULTS

To establish the material constitutive law, each membrane and shell were subjected to increasing traction forces and the material constants were obtained using ABAQUS. Figure 1 illustrates a typical experiment of membrane under traction and increasing air pressure. For the stressed membrane the internal pressure increases with injected air. However, for a specific critical pressure although the volume still increases, there was a gradual decrease of the internal pressure, giving two or more stable equilibrium configurations for different volumes. For an unstressed shell, as the pressure increases the shell deflects laterally as a long column until a critical pressure is reached and a bubble is formed near the middle of the specimen, Figure 2. At this critical point, there was a sudden drop in pressure indicating the existence of limit point instability. When the shell is initially stressed, the global buckling mode is no longer observed and the shell remains in a vertical position until the critical pressure is reached. Typical non-linear equilibrium paths are shown in Figures 3 and 4 for cylindrical membranes and shells respectively where the internal pressure is plotted as a function of the maximum radial displacement for increasing values of the structure thickness. Initially the load-displacement relation is almost linear. As the pressure increases the shell stiffness decreases and a limit point is reached after which

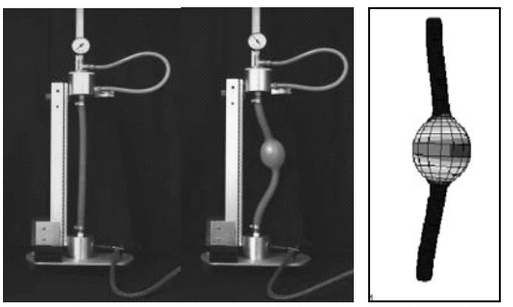
the load decreases as the maximum displacement increases. This behaviour is typical of a softening, imperfection sensitive system. As the thickness increases, the stiffness of the shell increases, increasing the critical load. Similar parametric analysis was carried out both experimentally and numerically. The influence of the structure's geometry, several types of imperfections and load history on the non-linear behaviour and stability of the tube was investigated. Results show that the localization, number of bubbles and critical load may vary depending on the system parameters and imperfections.

Cylindrical membrane and shell



$P = 0$ $P = 12.2$ $P = 11.8$

Figure 1 – Sequence of equilibrium configurations. Membrane under constant traction (ΔL/L=1) and increasing air pressure and FE results. *P(10^{-4} MPa).*



$P = 0$ $P = 7.0$ $P = 7.2$

Figure 2 – Sequence of equilibrium configurations. Unstressed shell under increasing air pressure and FE results. *P(10^{-2} MPa).*

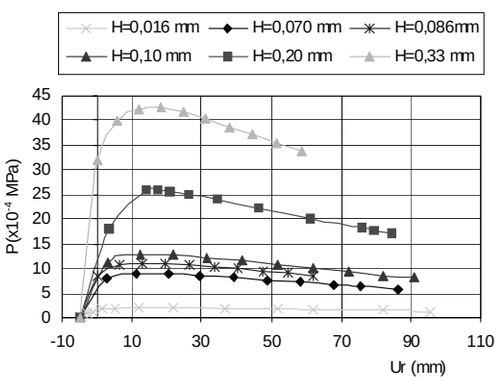


Figure 3 –Influence of the membrane thickness on the load-displacement response. Limit point instability

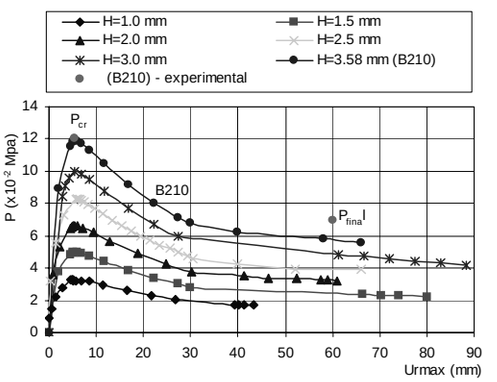


Figure 4 –Influence of the shell thickness on the load-displacement response. Limit point instability

CONCLUSIONS

Finite deformations of isotropic circular cylindrical shell and membrane subjected to a finite extension and gradually filled with air were investigated theoretically and experimentally. When the extended structure was filled with air, it was observed that the pressure increased initially as the volume increased until a critical value was reached, after which a bubble was suddenly formed along the structure (local buckling) and the internal pressure decreased markedly with increasing volume. The experimental results are, as shown in this paper, in satisfactory agreement with the theory.

References

[1] Green A. E., Adkins, J. E.: Large Elastic Deformations and Non-linear Continuum Mechanics. Oxford University Press, 1960.

[2] Alexander H.: Tensile instability of initially spherical balloons. *I. J. Engineering Sciences* **9**:152-162, 1971.

[3] Ratner A.: M.: Tensile Stability of Cylindrical Membranes. *I. J. Non Linear Mechanics* ***18***:133-147, 1971.

[4] Chen Y.: Stability and bifurcation of inflated cylindrical elastic membranes. *Applied mechanics in the Americas* ***1***: 404-409, 1995.

[5] Haughton D. M.: Axially elastic membranes subjected to fluid loads. *IMA Journal of Applied Mathematics* ***56***: 303-320, 1996.

[6] Pamplona D., Gonçalves P. B., Dacidovich M., Weber H. I. Finite axisymmetric deformations of an initially stressed fluid-filled cylindrical membrane. *I. J. Solids and Structures* ***38***, 2033-2047.

[7] Tang D, Chung Y, Huang Y, Ku D. N.: Wall stress and strain analysis using a three-dimensional thick-wall model with fluid-structure interactions for blood flow in carotid arteries with stenoses. *Computers and Structures.* ***72***: 341-356, 1999

[8] Haussy B, Ganghoffer J: An arthotropic hyperelastic model of cylindrical thick shells under pressure: application to the modelling of aneurysm. *15th ASCE Engineering Mechanics Conference*, New York, 2002.

GENERALISED BEAM THEORY FORMULATION TO ANALYSE THE POST-BUCKLING BEHAVIOUR OF ORTHOTROPIC LAMINATED PLATE THIN-WALLED MEMBERS

Nuno Silvestre
Ph.D. Student

Dinar Camotim
Associate Professor

Civil Eng. Department, ICIST/IST, Technical University of Lisbon, Av. Rovisco Pais, 1049-001 Lisboa, Portugal

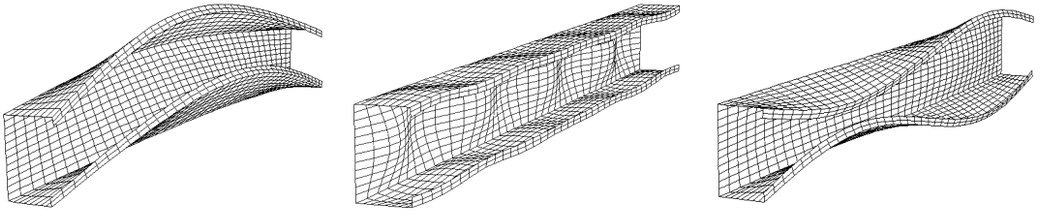
ABSTRACT

This paper presents the derivation and illustrates the application of a non-linear orthotropic GBT formulation, which is intended to perform post-buckling analyses of laminated plate FRP open-section thin-walled members. Different types of loading and end support conditions can be dealt with and the theory can handle the presence of arbitrary initial geometrical imperfections. One is able to determine "exact" and "approximate" (only a few modes) post-buckling equilibrium paths and the evolution, along those paths, of (i) displacements and stresses and, using the GBT unique mode decomposition feature, also of (ii) the deformation mode participation in the member deformed configuration. To validate and illustrate the application and capabilities of the formulated GBT, numerical results, concerning the post-buckling behaviour of laminated plate FRP lipped channel members exhibiting different orthotropic behaviours, are presented and discussed. Some of them are compared with values obtained from finite element analyses, performed in the code ABAQUS and adopting shell element meshes to discretise the member.

INTRODUCTION

The structural use of *composite materials* started in the 1950's and has steadily progressed since then, mainly due to developments taking place in the aeronautical industry, which have led to a wide range of products extensively and routinely employed at present. However, the picture has been quite different in civil engineering, as composite material applications became significant only in the last few years, when their well known (i) structural efficiency (low weight/strength and weight/stiffness ratios) and (ii) excellent behaviour under aggressive environmental conditions were matched by (iii) sufficiently low fabrication costs. In particular, the combination of these three features is responsible for the growing demand for *thin-walled* composite structural members recently observed in the construction industry, namely related to off-shore structures and chemical plants.

As it would seem logical to expect, the heterogeneity and orthotropic constitutive relations of the composite materials render their mechanical behaviour considerably more complex than the one displayed by metals such as steel or aluminium, thus introducing additional difficulties to the analysis of thin-walled structural members. In particular, most composite materials exhibit often (i) linear elastic stress-strain relationships (with relatively low moduli), (ii) no ductility (*i.e.*, an elastic behaviour up to collapse) and (iii) different types of orthotropy (depending on the material constituents and fabrication procedure), leading to mechanical properties that clearly indicate a high susceptibility to (i) local and/or global *instability phenomena* (see figure 1) and (ii) brittle collapse modes. Since mastering these two aspects is of paramount importance to achieve safe and economical (competitive) designs, engineers must be equipped with analytical/numerical tools that are able to model accurately their influence on the structural behaviour and load-carrying capacity of thin-walled composite members. This requires not only the access to specific and sophisticated methods of analysis but also an "unbiased mind", in the sense that is necessary to be suspicious of intuition-based reasonings developed in the context of isotropic materials.



(a) (b) (c)

Fig. 1. Thin-walled member flexural-torsional, local-plate and distortional buckling

A few years ago, a rather elegant and quite powerful theory to analyse the structural behaviour of isotropic elastic prismatic thin-walled members was developed by Schardt [1] and designated as *Generalised Beam Theory* (GBT). This theory incorporates both local (cross-section) and global (member) modes of deformation and could be applied to perform either (i) geometrically linear (first-order GBT) or (ii) linear stability (second-order GBT) analyses, thus providing a general and unified approach to obtain accurate and clarifying solutions for a wide range of structural problems. In the last decade, Davies and his collaborators [2] have applied extensively GBT to investigate the buckling behaviour of thin-walled cold-formed steel members and their work provided a strong contribution towards establishing this theory as a valid and often advantageous alternative to fully numerical finite element or finite strip analyses. Indeed, since the GBT d.o.f. are *modal* (instead of *nodal*) displacements, all the member deformed configuration or buckling mode "ingredients" are revealed by the analysis, which still retains the accuracy of the above "conventional" numerical methods.

RECENT GBT FORMULATIONS

In the last few years, the authors developed two major extensions of the GBT formulation originally derived by Schardt, making it possible to perform (i) first-order and linear stability analyses of *arbitrarily orthotropic* thin-walled members, namely laminated plate members made of fibre-reinforced plastic (FRP) layers [3, 4], and (ii) *post-buckling* analyses of cold-formed steel (isotropic) members [5]. Concerning the orthotropic GBT formulation, it was found that, in general, six stiffness matrices (instead of four) are required to describe the cross-section mechanical behaviour. Moreover, due to the orthotropy induced by the laminated plate layer nature and/or configuration, (i) all these matrices (even the "geometric" stiffness matrix) combine both material properties and geometrical characteristics and, unlike in isotropic materials, (ii) both the first and second-order equilibrium equations are strongly coupled. As for the (isotropic) non-linear GBT formulation, it involves significant developments and extensions, with respect to Schardt's "conventional" GBT. Indeed, besides having to deal with the establishment and numerical solution (by means of a standard incremental-iterative procedure) of the non-linear equilibrium equations governing the member large-displacement geometrically non linear behaviour (the conventional GBT equations are only valid for small deformations and moderate rotations), one also needs to account for two additional sets of deformation modes, namely (i) shear and (ii) transverse extension modes (see figure 2). One very interesting feature of the non-linear GBT analyses is the possibility of performing "approximate analyses", including just a selected sub-set of deformation modes, which yield rather accurate results with much less computational effort than the one required to perform "exact" (all-mode) analyses. The traditional finite element or finite strip analyses do not offer such a possibility.

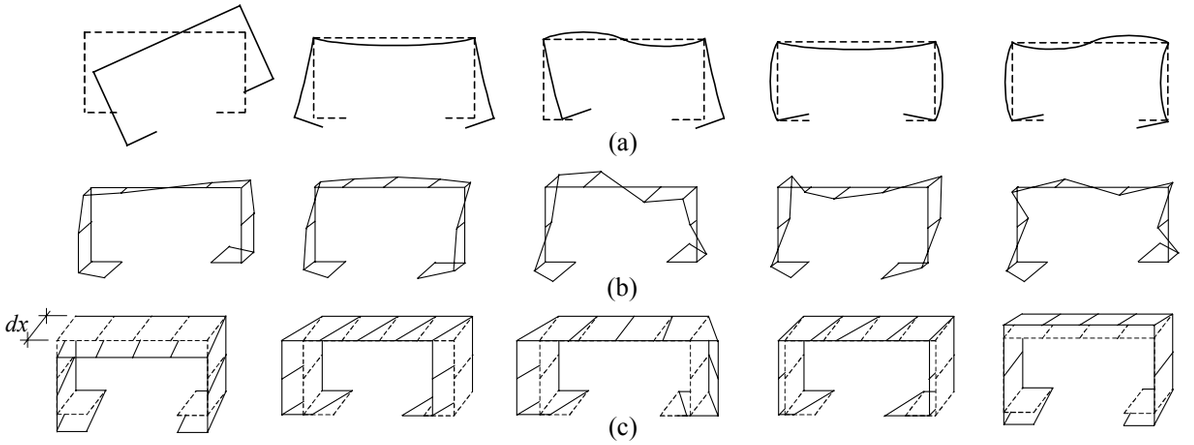


Fig. 2. Sample of (a) conventional, (b) shear and (c) transverse extension GBT deformation modes.

NON-LINEAR ORTHOTROPIC GBT FORMULATION

This paper aims at presenting the derivation and illustrating the application of a non-linear orthotropic GBT formulation, which combines the features of the two formulations briefly described in the previous paragraph, thus making it possible to perform geometrically non linear analyses of laminated plate FRP open-section thin-walled members. Different types of loading and end support conditions can be considered and the theory can handle the presence of initial geometrical imperfections with an arbitrary shape. One is able to determine, with great accuracy, "exact" and "approximate" (*i.e.*, including just a few deformation modes) member post-buckling equilibrium paths, as well as the evolution, along those paths, of (i) the most relevant displacements and stresses and, taking advantage of the GBT unique mode decomposition feature, also of (ii) the deformation mode participation in the member overall deformed configuration. It is worth noting that the deformation mode participation graphs provide a very illuminating insight on the member post-buckling behaviour.

Finally, in order to validate and illustrate the application and capabilities of the formulated non linear orthotropic GBT, several numerical results, concerning the geometrically non linear (post-buckling) behaviour of either pultruded or laminated plate FRP lipped channel columns, beams and beam-columns exhibiting different (orthotropic) material behaviours, are presented and discussed in detail. Some of these results are compared with values obtained from finite element analyses, performed by means of the commercial code ABAQUS and adopting fine shell element meshes to discretise the member.

REFERENCES

[1] Schardt R. – *Verallgemeinerte Technische Biegetheorie*, Springer Verlag, Berlin, 1989. (in German)

[2] Davies J.M. – Generalised Beam Theory for Coupled Instability Problems, *Coupled Instability in Metal Structures: Theoretical and Design Aspects*, Ed. J. Rondal, CISM Course nº379, 151-223, Springer Verlag, Wien, 1998.

[3] Silvestre N. & Camotim D. – First Order GBT for Arbitrary Orthotropic Materials, *Thin-Walled Structures*, **40**(9), 755-789, 2002.

[4] Silvestre N. & Camotim D. – Second Order GBT for Arbitrary Orthotropic Materials, *Thin-Walled Structures*, **40**(9), 791-820, 2002.

[5] Silvestre N. & Camotim D. – Non-Linear Generalised Beam Theory for Cold-Formed Steel Members, *International Journal of Structural Stability and Dynamics*, **3**(4), 461-490, 2003.

XXI ICTAM, 15–21 August 2004, Warsaw, Poland

THE STIFFNESS OF PRESTRESSED FRAMEWORKS: A UNIFYING APPROACH

Simon D. Guest
Department of Engineering, University of Cambridge, Trumpington Street, Cambridge CB2 1PZ, UK

Summary Three different methods are commonly used to analyse the stiffness of prestressed frameworks that consist of bars and spherical joints. This paper will show that in fact the correct tangent stiffness matrix for a prestressed structure, as used in the computational literature, can be written as the sum of two terms. The first is a minor modification of a conventional stiffness matrix, that is best understood in terms of the equilibrium matrix that has been widely studied in the engineering literature. The second term is the stress matrix, that has been widely studied in the mathematical rigidity theory literature.

INTRODUCTION

There are many types of structure where stress stiffening plays a key role in determining structural response. Two obvious engineering examples are tensegrity structures and cable-roof structures; it has also recently been suggested that prestress may have a critical role to play in the stiffness of biological cells [1]. In each of these cases, understanding of the effect of prestress on the stiffness of the structure is critical to understanding how the structure works.

This paper will consider the stiffness of *framework* structures, spherically jointed structures where the structure carries loads by tension or compression of its members, and not in bending. The literature contains three different approaches to calculating the stiffness of these structures; in their own context, each is correct, but it is not clear from the literature how they are related to one another. Making clear the connections between these methods is the aim of this paper.

PREVIOUS APPROACHES

There are essentially three different methods that have previously been applied to finding the stiffness of prestressed frameworks: each will be described briefly here. I will refer to them as the 'computational' approach, the 'equilibrium' approach, and the 'stress' approach.

Papers describing the 'computational' approach (e.g. [2, 3]) show how to correctly set up the local tangent-stiffness matrix $\mathbf{K}$ for a prestressed framework. Generally these papers describe $\mathbf{K}$ in terms of two components

$$\mathbf{K} = \mathbf{K}_{\text{conv}} + \mathbf{K}_{\text{geom}} \tag{1}$$

where $\mathbf{K}_{\text{conv}}$ is a conventional stiffness matrix of the same geometrically identical, but unstressed, structure, and $\mathbf{K}_{\text{geom}}$ is the change to this stiffness that comes about because of prestress. This approach has proved to be highly successful in calculating the response of various structures. However, the approach itself, as distinct from the results, gives little insight into the behaviour of the structures. The remaining two approaches try to give a more intuitive understanding of the behaviour.

The 'equilibrium' approach (e.g. [4, 5]) does not directly define a stiffness matrix, but instead considers *equilibrium* and *compatibility* relationships, written as an equilibrium matrix $\mathbf{A}$ and a compatibility matrix $\mathbf{A}^{\mathrm{T}}$. This approach allows the calculation, for instance, of all possible states of self-stress and mechanisms of the structure. The response of the structure is described in terms of *extensional* modes, that correspond to the stiffness given by $\mathbf{K}_{\text{conv}}$, and *inextensional* modes that correspond to mechanisms of the unstressed structure; the effect of the states of self-stress on the stiffness of these inextensional modes is then calculated.

The 'stress' approach (e.g. [6, 7]) makes no attempt to find the actual stiffness of a prestressed framework. Rather, the stiffness given by a *stress* matrix $\mathbf{S}$ is explored. The stress matrix has the same form as the stiffness matrix, i.e. it relates displacement and forces, and in general has the following form:

- The submatrix (of size 3×3 in 3D) of $\mathbf{S}$ relating two nodes i and j that are connected by a member contains $-(t_{ij}/l_{ij})\mathbf{I} = -\hat{t}_{ij}\mathbf{I}$, where $\mathbf{I}$ is the identity matrix, t_{ij} is the tension in the member, l_{ij} is its length, and $\hat{t}_{ij} = (t_{ij}/l_{ij})$ is the *tension coefficient* of the member;
- The diagonal submatrix of $\mathbf{S}$ corresponding to node i contains $\sum_k \hat{t}_{ik}\mathbf{I}$, where the summation is over the nodes that are connected to node i by members of the structure;
- The rest of $\mathbf{S}$ is empty.

Note that the stress matrix takes no account of the elastic properties of the element. This approach is widely used by mathematicians in *rigidity theory*, and has proved highly useful in exploring whether structures will be stiffened by prestress, or not. The stress matrix is highly structured, and this has, for instance, allowed catalogues of symmetric tensegrities to be automatically generated, many of which were previously unknown [8]. However, it has not previously been explored how this approach is related to the other engineering approaches that have been described.

TANGENT STIFFNESS CALCULATION

The relationship between the different approaches to finding stiffness is most easily illustrated by examining the stiffness of a single bar in a 3-dimensional structure. Consider a bar of length l with axial stiffness g (for an elastic bar $g = AE/l$, where A is the cross-sectional area, and E is the Young's Modulus of the material), that is currently carrying a tension t, giving a tension coefficient $\hat{t} = t/l$. A unit vector along the bar from node 1 to 2 is given by the 3×1 unit vector $\mathbf{n}$. Differentiating the equilibrium relationship at each node allows the tangent stiffness $\mathbf{K}$ to be calculated. For the single bar (denoted by a subscript s), this tangent stiffness is given by

$$\mathbf{K}_s = \begin{bmatrix} \mathbf{n} \\ -\mathbf{n} \end{bmatrix} \begin{bmatrix} g \end{bmatrix} \begin{bmatrix} \mathbf{n}^{\mathrm{T}} & -\mathbf{n}^{\mathrm{T}} \end{bmatrix} - \begin{bmatrix} \mathbf{n} \\ -\mathbf{n} \end{bmatrix} \begin{bmatrix} \hat{t} \end{bmatrix} \begin{bmatrix} \mathbf{n} & -\mathbf{n} \end{bmatrix} + \begin{bmatrix} \hat{t}\mathbf{I}_3 & -\hat{t}\mathbf{I}_3 \\ -\hat{t}\mathbf{I}_3 & \hat{t}\mathbf{I}_3 \end{bmatrix} \tag{2}$$

where $\mathbf{I}_3$ is a 3×3 identity matrix.

Equation 2 can be rewritten using the equilibrium matrix and the stress matrix. For the single bar, the equilibrium matrix is $\mathbf{A}_s = \begin{bmatrix} \mathbf{n}^{\mathrm{T}} & -\mathbf{n}^{\mathrm{T}} \end{bmatrix}^{\mathrm{T}}$, and the compatibility matrix is $\mathbf{A}_s^{\mathrm{T}}$. The final term in (2) is, for a single bar, exactly the stress matrix described earlier, $\mathbf{S}_s$. Thus,

$$\mathbf{K}_s = \mathbf{A}_s \begin{bmatrix} g \end{bmatrix} \mathbf{A}_s^{\mathrm{T}} - \mathbf{A}_s \begin{bmatrix} \hat{t} \end{bmatrix} \mathbf{A}_s^{\mathrm{T}} + \mathbf{S}_s \tag{3}$$

For a structure made up of multiple bars, standard summation techniques allow the assembly of the complete stiffness matrix, which can be written, following the form of (3) as

$$\mathbf{K} = \mathbf{A}\mathbf{G}\mathbf{A}^{\mathrm{T}} - \mathbf{A}\hat{\mathbf{T}}\mathbf{A}^{\mathrm{T}} + \mathbf{S} \tag{4}$$

where $\mathbf{G}$ is a diagonal matrix of the axial stiffness of members and $\hat{\mathbf{T}}$ is a diagonal matrix of the tension coefficients of the members.

Comparing (1) and (4), the conventional stiffness and geometrical stiffness matrices can be written as $\mathbf{K}_{\text{conv}} = \mathbf{A}\mathbf{G}\mathbf{A}^{\mathrm{T}}$, and $\mathbf{K}_{\text{geom}} = -\mathbf{A}\hat{\mathbf{T}}\mathbf{A}^{\mathrm{T}} + \mathbf{S}$, but it is also clear that doing so does not make best use of the structure inherent in these matrices. Rather, it is better to write

$$\mathbf{K} = \mathbf{A}\mathbf{G}'\mathbf{A}^{\mathrm{T}} + \mathbf{S} \tag{5}$$

where $\mathbf{G}' = \mathbf{G} - \hat{\mathbf{T}}$ is a diagonal matrix of *modified* axial stiffness of the members, where each entry is $g' = g - \hat{t}$. For practical structures $\hat{t} \ll g$, and the stiffness given by $\mathbf{K}_{\text{mod}} = \mathbf{A}\mathbf{G}'\mathbf{A}^{\mathrm{T}}$ will be little different from the stiffness $\mathbf{K}_{\text{conv}}$. More importantly, the interesting mechanics associated with $\mathbf{K}_{\text{mod}}$, e.g. zero stiffness modes, are best understood in terms of the equilibrium matrix $\mathbf{A}$.

Thus (5) shows that the correct tangent stiffness, as given by the 'computational' approach, can be written as two terms. The first of these terms is best understood using the 'equilibrium' approach, while the second is exactly the stress matrix used in the 'stress' approach.

CONCLUSIONS

The paper has shown that the correct tangent stiffness matrix for a prestressed structure is best understood in terms of two terms. The first is a minor modification of a conventional stiffness matrix, that is best understood in terms of the equilibrium matrix that has been widely studied in the engineering literature. The second term is the stress matrix, that has been widely studied in the mathematical rigidity theory literature.

References

[1] Ingber D.E.: Tensegrity I. Cell structure and hierarchical systems biology. *Journal of Cell Science* **116**(7): 1157–1173, 2003.

[2] Argyris J.H., Scharpf, D.W.: Large deflection analysis of prestressed networks. *Journal of the Structural Division, Proceedings of the American Society of Civil Engineers* **98**(ST3): 633–654, 1973.

[3] Kebiche K., Kazi-Aoual M.N., Motro R.: Geometrical non-linear analysis of tensegrity systems. *Engineering Structures* **21**: 864–676, 1999.

[4] Pellegrino S., Calladine C.R.: Matrix analysis of statically and kinematically indeterminate frameworks. *International Journal of Solids and Structures* **22**(4): 409–428, 1986.

[5] Pellegrino S.: Analysis of prestressed mechanisms. *International Journal of Solids and Structures* **26**(12): 1329–1350, 1990.

[6] Connelly R.: Rigidity and Energy. *Inventiones Mathematicae* **66**: 11–33, 1982.

[7] Connelly R., Terrell, M.: Globally rigid symmetric tensegrities. *Structural Topology* **21**: 59–78, 1995.

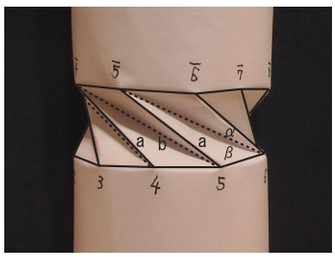
[8] Connelly R., Back A.: Mathematics and tensegrity. *American Scientist* **86**: 142–151, 1998.

XXI ICTAM, 15–21 August 2004, Warsaw, Poland

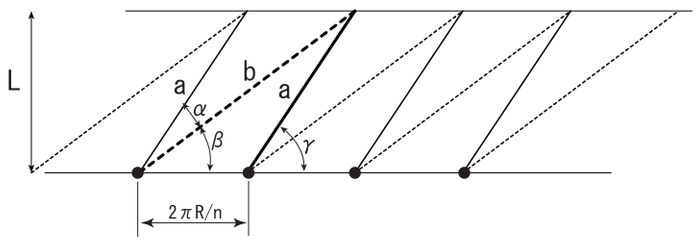
TWIST BUCKLING AND THE FOLDABLE CYLINDER: AN EXERCISE IN ORIGAMI

Giles W. Hunt* Ichiro Ario **
*Centre for Nonlinear Mechanics, University of Bath, Bath BA2 7AY, UK
**Department Civil and Environmental Engineering, Hiroshima University, Higashi-Hiroshima, 739-8527, Japan

Summary When a tube of paper is twisted between two rigid plastic mandrels (see Fig.1), a mechanism familiar from the Japanese art of origami develops, involving bending but little stretching. But the initial buckling problem of a cylindrical shell under torsion (see Fig.2) involves bending and stretching energies in about equal parts. The talk will trace the consequent adjustment of the modeshape though first-order post-buckling, to the final folded pattern, as seen from the viewpoint of a triangulated truss formulation.

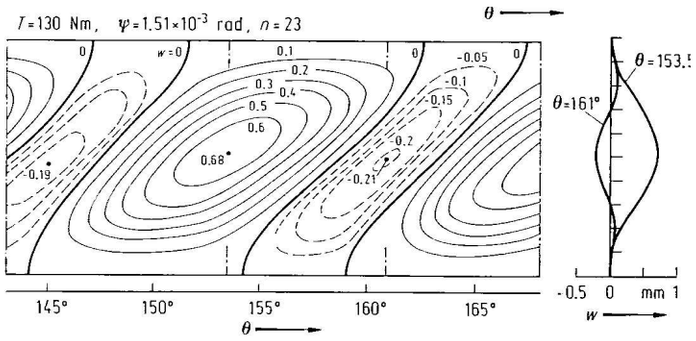


(a) Fold lines and angles of the folding mechanism

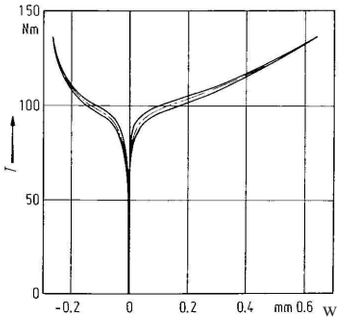


(b) Truss Geometry

Figure 1. The foldable cylinder based on twist buckling of a paper roll. Large deflections involve work being done primarily against bending, with very little stretching energy included; such behaviour is of interest for example, in the field of deployable structures.



(a) Contour of deformation



(b) Relationship between torque and $w(L/2, y)$

Figure 2. Yamaki's shortest cylindrical shell buckling in torsion [1]. Length L = 22.9 mm, Radius $R = 100$ mm, thickness t = 0.247 mm, Young's modulus $E = 5.55$ GPa, Poisson's ratio $\nu = 0.3$.

FORMULATION AND LINEAR EIGENVALUE ANALYSIS

Critical buckling and first-order post buckling analyses are based on the total potential function

$$\begin{aligned} V &= \frac{Et^3}{24(1-\nu^2)} \int_0^L \int_0^{2\pi R} \left\{ \left(\nabla^2 w\right)^2 + 2(1-\nu)\left[(w_{xy})^2 - w_{xx}w_{yy}\right] \right\} \mathrm{d}y\mathrm{d}x \\ &+ \frac{Et}{2} \int_0^L \int_0^{2\pi R} \left\{ \left(\nabla^2 \phi\right)^2 + 2(1+\nu)\left[(\phi_{xy})^2 - \phi_{xx}\phi_{yy}\right] \right\} \mathrm{d}y\mathrm{d}x \\ &- \tau t \int_0^L \int_0^{2\pi R} w_x w_y \, \mathrm{d}y\mathrm{d}x - Et \int_0^L \int_0^{2\pi R} \phi \left[\nabla^4 \phi + \rho w_{xx} - (w_{xy})^2 + w_{xx}w_{yy}\right] \mathrm{d}y\mathrm{d}x. \end{aligned} \tag{1}$$

where $w(x, y)$ is the radial deflection and $\phi(x, y)$ is a stress function. The first term is the bending energy, the second is the membrane energy, the third is the work done by the externally applied torque $T = 2\pi R^2 \tau t$, and the fourth is an extra energy term resulting from the constraint condition familiar from the von Kármán–Donnell equations, linking the stress

function ϕ to the change in Gaussian curvature of the w-surface. In a Rayleigh-Ritz or Galerkin formulation, modeshapes,

$$\begin{aligned} w(x,y) &= A_1 \sin^m\left(\frac{\pi x}{L}\right) \sin\left(\frac{\lambda x}{L} - \frac{ny}{R}\right) + A_2 \sin^2\left(\frac{\pi x}{L}\right), \\ \phi(x,y) &= B_1 \sin^m\left(\frac{\pi x}{L}\right) \sin\left(\frac{\lambda x}{L} - \frac{ny}{R}\right) + B_2 \sin^2\left(\frac{\pi x}{L}\right), \end{aligned} \tag{2}$$

are assumed, where A_i and B_i are unknown amplitudes. The power $m = 1, 2$ accommodates both simply-supported and clamped boundary conditions at the ends of the twisted length. Linear eigenvalue analysis for the critical torque T^C sets A_2 and B_2 to zero and minimises with respect to A_1, B_1, n and λ. Comparisons with experiments are given in Table 1.

Table 1. Comparisons between experiments of Yamaki [1], and linear eigenvalue results for which $\gamma = \arctan(nL/\lambda R)$.

	length L [mm]	22.9	35.9	51.0	71.2	113.8	160.8
Experiment	crit. torque T^C [Nm]	99	64	51	41	33	28
	w/number n	23	21	19	17	15	13
	obliqueness γ [deg.]	44	56	59	67	73 or 69	70
Simple	T^C [Nm]	93.2	62.2	48.1	38.8	29.4	24.3
Supports	n	22	20	18	16	13	11
$(m = 1)$	γ [deg.]	59	63	67	70	75	77
Clamped	T^C [Nm]	115.7	71.3	53.6	42.6	32.0	26.3
Supports	n	23	21	19	17	14	12
$(m = 2)$	γ [deg.]	56	61	65	69	73	76

FIRST-ORDER POST-BUCKLING ANALYSIS

If the full waveshape of equation (2) is adopted, A_1 and B_1 interact with A_2 and B_2 in a symmetry-breaking manner such that inwards deflection can be greater than outwards, as seen in Figs.1 and 2. Results of such a post-buckling analysis for a typical paper specimen are given in Table 2. Minimization is carried out at each stage with respect to the obliqueness

Table 2. Change of orientation γ in the post-buckling range ($R = 21.5$ mm, $L = 19$ mm, $t = 0.106$ mm, $n = 9$).

A_1	0.0	0.1	0.2	0.3	0.4	0.5	0.6	0.7
T/T^C	1.000	0.945	0.791	0.573	0.360	0.216	0.135	0.087
γ[deg.]	53.3	53.7	54.4	55.3	55.2	53.1	49.7	46.4

measure, γ. The reduction in γ as the post-buckling develops shows that the crest and valley lines become more oblique as the system adjusts to accommodate the folding mechanism. This same rotation of fold and valley lines is apparent in the comparisons of Table 1, where the experimental values of γ are always less than those for the linear eigenvalue problem applicable at the first stage of buckling only. To accommodate the mechanism fully, crest and valley lines should rotate by different amounts, although this facility is not available within the limitations of the Rayleigh-Ritz approximation.

TRUSS ANALYSIS

For the apex of each elemental triangle of Fig.1 to fold to a point on the circumference, geometry dictates that $\alpha = \pi/n$. A simple triangulated truss formulation based on this constraint (see Fig.3) shows that, after the initial instability, the applied torque decreases rapidly to almost zero in the final folded state. Comparative results will be presented at the time of the conference.

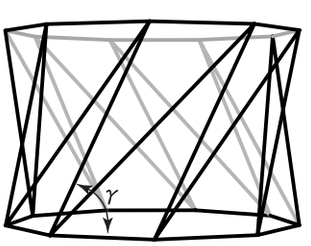


Figure 3. Truss model related to geometry of Table 2 ($R = 21.5$ mm, $L = 19$ mm, $n = 9$).

References

[1] Yamaki, N. 1976. Experiments on the post-buckling behaviour of circular cylindrical shells under torsion. *In:* Budiansky, B. (ed), *Buckling of Structures, IUTAM Symposium, June 1974, Cambridge, USA.* Applied Mathematics and Mechanics. Springer-Verlag.

ON STABILITY OF SYSTEMS SUBJECT TO GENERALIZED FOLLOWER FORCE

Roman Bogacz[*], Szymon Imiełowski[*], Włodzimierz Kurnik[**]

[*]*Polish Academy of Sciences, IPPT PAN, Swietokrzyska 21, PL 00-049 Warszawa, Poland*
[**]*Warsaw University of Technology, Institute of Machine Design Fundamentals, Narbutta 84, PL02-524 Warszawa, Poland*

Summary. Stability and dynamics of columns and whirling shafts subject to a generalized follower force is considered in the paper. The generalized follower force is defined as one, that moves with the body on which it acts, and that always preserves the same attitude to the body as it moves. The both linear and nonlinear analysis are included. The first one relates to the influence of system parameters on the system response whereas the second one is focus on the near critical behaviour of the system under both tension and compression loads including analysis of the corresponding limit cycle.

DESCRIPTION OF THE MODEL

The paper relates to stability and dynamics of slender self-excited structures. The considered structures, columns and whirling shafts, are subject to a generalized follower force that is defined as ones that moves with the body on which it acts, and that always preserves the same attitude to the body as it moves. The model of loading is defined in Fig.1 on example of column structure for which the force inclination χ and eccentricity e, depend on the actual inclination α and displacements f of the structure at the point of the force application.

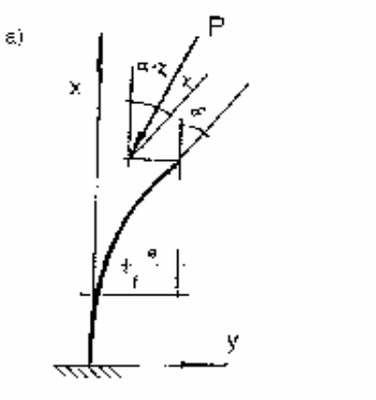


Fig.1. Model of generalized force

$$e = \rho l\alpha + \vartheta f, \qquad \chi = \mu\alpha + \gamma f / l, \tag{1}$$

where $\rho, \vartheta, \mu, \gamma$ are the non-dimensional parameters and l is the length of the characteristic dimension of the element to which the force is applied. An interaction between two surfaces in relative motion like the contact force of the rail and the wheel; a force attached to the structure through any connector that moves due to structural deformation like the bearing of a bridge span; the support force of rotating shafts subject to vapour pressure, like in Laval rotor or loading of the fluid conveying pipes are examples of the considered forces. The tangential concentrated loading is the case of force defined by Eq.(1). Herein, the models of the elastic and viscoelastic columns and whirling shafts are treated in details. The analysed boundary value problem is formulated as following

$$\mu\ddot{w}(x,t) + F_x[P, w(x,t)] + \beta\dot{w}(x,t) = 0, \tag{2}$$

plus homogeneus boundary conditions

where $w=w(x,t)$ is the transverse displacement, μ is the mass density, P is the compressing force (control parameter), β is the damping coefficient and $\ddot{w}$ is the acceleration, $\dot{w}$ is the velocity of the variation of w. The precise equation written for column or whirling shaft are in the class of Eq.(2). Notice that the conservation of the system energy depends on the differential operator F_x, that relates to the internal and the external forces. The selfadjointness of the operator F_x in with respect to the boundary conditions ensures the conservation of the system energy. The condition of

$$\int_0^l w(x,t)F_x[P, v(x,t)]dx = \int_0^l v(x,t)F_x[P, w(x,t)]dx, \tag{3}$$

where w and v are two sufficiently smooth function, which satisfy the boundary conditions is fulfill for conservative system. Also, the condition (3) ensures that the system becomes unstable by divergence.

The next feature of the system, namely existence of the potential, results from the condition of the rotation equal to zero, rot$\boldsymbol{v}=0$, from which one gets

$$\frac{\partial M}{\partial f} = \frac{\partial H}{\partial \alpha}, \tag{4}$$

where $M = Pe$ and $M = P(\alpha - \chi)$.

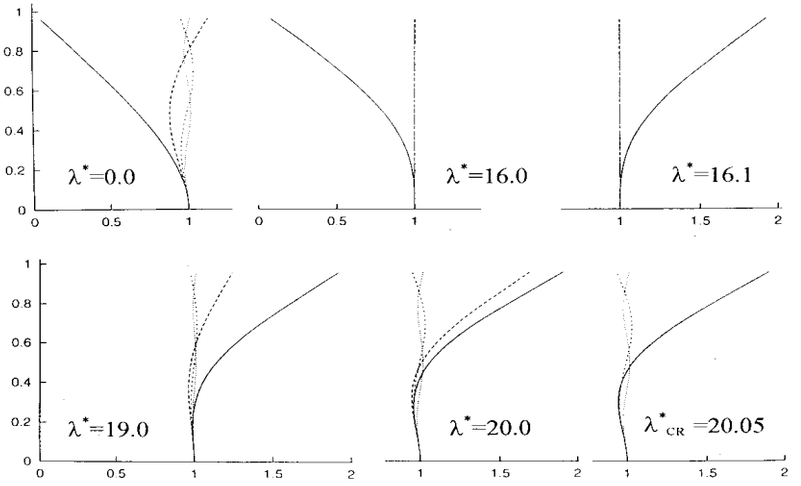


Fig.2. Eigenmodes of column subject to tangential loading, for different values of loading λ^*

RESULTS OF ANALYSIS

The study is divided into two parts, relating to linear and nonlinear analysis respectively. The influence of system parameters on the response of the system is consider for the linear model. It occurs that the shape of the eigenmodes depends of the value of loading, namely the first mode can alter into the second one for high enough value of force. In that case the second eigenmode occurs at the critical point with the fundamental frequency. The phenomenon is explained Fig.2, where λ^* is the nondimensional force. Notice that at the point of eigenmode change, for λ^*= 16, the displacements which relates to higher eigenmodes diminishes whereas the sign of displacements of the first eigenmode switches. On force-frequency plane the point of eigenmode change is observed as the point of intersection of eigencurves that relates to different values of system parameters creating so called fixed point, for which the frequency of natural vibration occurs independent on a variety of the system parameters [1].
The described phenomenon is observed in different types of structures: columns, slender whirling shafts etc., subject to follower type of loading
The variation of the load inclination χ and eccentricity e, described by expression (1) may follow the special design of the supporting condition or can be forced by an additional source of energy, for conservative and nonconservative systems repectively. However the phenomenon of eigenmode change is independent on the system conservativeness or nonconservativeness and come across both types of systems. Notice, that the high value of the critical force observed for structures subject to follower type of loading, that can be 8-10 times higher than for Euler column, can be explained by the higher eigenmode which occur at critical state. Due to the Euler formula the shorter buckle length relates to higher value of critical force. Moreover, in nonconservative systems the flutter point occurs at the double eigenvalue for which the shape of respective eigenforms is exactly the same. Some examples from literature shows that the problem is often not properly touched by researches.

The linear analysis is completed by nonlinear one where an interesting effect is related to the double Hopf bifurcation which consists in simultaneous loss of stability by two eigevalues. On example of the model of whirling shafts supported by fluid film bearings it is shown as the two critical eigevalues enter the instability domain at generally different rotation speeds. It corresponds to a sequence of Hopf bifurcation initiating self-exited vibration induced either by the shaft or by the bearing [1]. The consideration is completed by an additional feature relating to the considered class of structures. On example of Leipholz column, loaded by distributed compressive follower forces, it is shown that flutter can occur either as a supercritical bifurcation into a stable limit cycle when an model of slight internal damping is considered or a subcritical bifurcation into an orbitrary unstable limit cycle existing in the stable region of equilibrium in the case of intensive internal damping [2].

References

[1] W.Kurnik, Stability of a Viscoelastic Shaft in Fluid-Film Bearings, Machine Dynamics Problem, 1999.v.23,no.4, 39-52
[2] W.Kurnik, M.Pekalak, Stability And Bifurcation Analysis Of The Non-Linear Damped Leipholz Column, Journal of Sound and Vibration, 1992, 152(2,285-294)
[3] W.Kurnik, Divergent and oscillatory bifurcations, WNT, Warszawa, 1997
[4] R.Bogacz, Sz.Imielowski, On Eigenmodes of Columns Subject to Generalized Follower Force, 2003, AIAA Journal /in print/

DYNAMIC INSTABILITY OF A HIGH-SPEED FLEXIBLE SHAFT WITH A MASSIVE DISC AND FOLLOWER LOAD

W. Kurnik, J. Weronko
Warsaw University of Technology
Narbutta 84, 02-524 Warsaw, Poland
e-mail: wku@rekt.pw.edu.pl

Extended Summary

The paper is motivated by design and maintenance problems of rotating machinery like turbines, compressors, fans, etc. A dynamic analysis is presented concerned with transverse flutter instability and vibration of a flexible rotating shaft supported like a cantilever beam, carrying a thin massive end-disc and subject to concentrated follower load exerted on the disc. The follower load is a consequence of fluid-structure interaction in real turbomachinery. A working medium flow can produce either compressive or a tensile loads, therefore unlike in Beck's problem, the follower load is considered both positive and negative.

Internal dissipation in the rotating shaft and follower load can cause dynamic flutter-type instability and bifurcation of the considered system. Both instability mechanisms are different in physical nature but mathematically modelled they interact to produce complicated stability domains in the space of rotation speed and follower load. [1].

The main question addressed in the present paper is the gyroscopic effect in the stability and flutter problem of the considered discrete-continuous system. It has been already shown that the gyroscopic effect can considerably change the scenario of bifurcation even in slender shafts. [2]. In case of massive disc mounted at the free end of a shaft the gyroscopic effect can change bifurcation dramatically.

The shaft carrying disc can be a composite structure. Laminated shafts are torsionally stiff and strong being simultaneously much lighter than similar structures made of conventional materials such as steel. Such a system can easily meet requirements concerning torsional strength and stiffness but are more flexible to bending and show high level of internal friction. In consequence, high-speed laminated shafts can be especially endangered by dynamic instability and large-amplitude self-excited whirling.

In the considered discrete-continuous model coupling between cantilever beam and massive disc is realised through boundary conditions.

The shaft is assumed to be slender, transversely unloaded, of circular cross-section, rotating with a constant angular speed. Transverse shear is neglected but rotational inertia is included. External damping is assumed as linear. Internal damping in a generally anisotropic shaft material corresponds to the Kelvin-Voigt model when average using Kirchhoff's deformation hypothesis.

Transverse shaft vibration of the system can be described by the partial equations [2]

$$\begin{aligned}
\rho A\left(\frac{\partial^2 u}{\partial t^2} + h^* \frac{\partial u}{\partial t}\right) &= \frac{\partial}{\partial x}\left[T_Y\left(\sqrt{1+\left(\frac{\partial u}{\partial x}\right)^2}\right)^{-1}\right] - P\frac{\partial^2 u}{\partial x^2} \\
\rho A\left(\frac{\partial^2 v}{\partial t^2} + h^* \frac{\partial v}{\partial t}\right) &= \frac{\partial}{\partial x}\left[T_Z\left(\sqrt{1+\left(\frac{\partial v}{\partial x}\right)^2}\right)^{-1}\right] - P\frac{\partial^2 v}{\partial x^2}
\end{aligned} \tag{1}$$

where, T_Y, T_Z denote shear resultants determined as follows:

$$T_Y = -\frac{\partial M_Z}{\partial x} + \rho I_Z \frac{\partial^3 u}{\partial x \partial t^2} + \rho I_X \Omega \frac{\partial^2 v}{\partial x \partial t};$$

$$T_Z = -\frac{\partial M_Y}{\partial x} + \rho I_Y \frac{\partial^3 v}{\partial x \partial t^2} - \rho I_X \Omega \frac{\partial^2 u}{\partial x \partial t};$$

where in turn u, v denote transverse displacements in perpendicular directions, ρA is shaft mass per unit length, h^* - viscous external damping coeffcient, Ω - angular speed of the rotor, M_Y, M_Z - bending moments: $M_Y = \int \sigma Z dA$, $M_Z = \int \sigma Y dA$, while σ denotes normal stress in the shaft cross-section.

We shall assume stress-strain relation in the global form of the Kelvin-Voigt model, i.e.

$$\sigma = E_0 (1 + \beta_0 \frac{\partial}{\partial t}) \varepsilon \tag{2}$$

Discretisation of partial equations is performed using two cantilever beam functions satisfying mass-dependent boundary conditions. Two boundary eigen-values problem has been solved numerically by means of FEM.

Liapunov criterion of stability applied to discretised system leads to the stability region in the space of active parameters.

$$\Psi = \{(\mu, \omega) : Re\, r_i \le 0 \ (i = 1,...,8)\} \tag{3}$$

where r_i denotes eigenvalues of the linearised system matrix, ω is demensionless rotation speed and μ demensionless follower load.

The non-linear flutter analysis of the system is made using Iooss's approach to determine bifurcation diagrams in terms of rotation speed and flutter amplitude under fixed but changeable follower load.

It is shown that the gyroscopic effect can influence the stability domain of the rotor, especially in highly loaded, weakly internally dissipative systems.

In some regions of the system parameter space the gyroscopic effect can considerable change the near-critical rotation speed can be increased, but simultaneously bifurcation can be changed from super- to subcritical, producing unstable limit cycles in the stable domain of equilitium, as shown in Fig. 1.

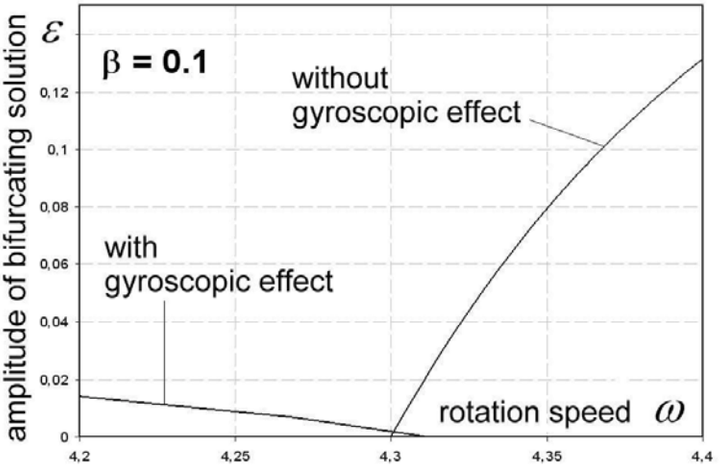


Fig. 1. Bifurcation diagram of the system with gyroscopic effect neglected and included

References:

[1] Kurnik, W., 1994, Stability and Bifurcation Analysis of a Non-linear Transversally Loaded Rotating Shaft, *Nonlinear Dynamics,* 5, No. 1, 39-52.

[2] Kurnik, W., Weronko, J., 2003, Optimisation of a flexible cantilever rotor with intermediate support, *5th EUROMECH Solid Mechanics Conference, Thessaloniki GREECE,* Book Of Abstract, p. 155.

XXI ICTAM, 15–21 August 2004, Warsaw, Poland

SECONDARY BIFURCATIONS AND LOCALISATION OF BUCKLE PATTERNS

Ciprian D. Coman*
*Centre for Mathematical Modelling, University of Leicester,
University Road, Leicester LE1 7RH, England.

Summary The phenomenon of localisation is reasonably well understood in quantum physics and fluid mechanics [1], but less so in the area of structural mechanics. In this contribution we revisit the effect of secondary bifurcations on the post-buckling response of a 3D system of elastically restrained beams. Our objective is to construct a uniform asymptotic expansions for the localised buckling patterns experienced by this model by using a mixture of asymptotics (WKB techniques [2]) and numerics.

INTRODUCTION AND THEORETICAL STUDY

Many buckling problems for structures with large aspect ratio can be cast as

$$\varepsilon \frac{\mathrm{d}\mathbf{u}}{\mathrm{d}x} = \mathbf{A}(x,\, \lambda;\, \varepsilon)\mathbf{u}, \tag{1}$$

where $\mathbf{u} = \mathbf{u}(x) \in \mathbb{R}^n$, $\lambda \in \mathbb{R}$ represents the bifurcation parameter, and $\mathbf{A}(x,\, \lambda;\, \varepsilon)$ is an $n \times n$ matrix, i.e., $\mathbf{A}(x,\, \lambda;\, \varepsilon) \in M_{n\times n}(\mathbb{R})$; here $0 < \varepsilon \ll 1$ is a small parameter. The dependence of $\mathbf{A}$ on x is usually associated with variable mechanical/geometrical properties, or non-homogeneous pre-bifurcation states; certain secondary bifurcations usually fall into this latter category, as we shall shortly see. The presence of inhomogeneities in equation (1) enriches the spectral properties of the problem and calls for a special attention to certain transition points (also known as *turning points*). Such points mark the transition between oscillatory and exponentially decaying regions in the solutions of (1), and in particular they are responsible for the presence of localisation in these functions.

The model

The model adopted in this work is that discussed by Luongo in [3] (see also [4] for a related problem) and which we briefly review next. Roughly speaking, we have in mind a simply supported planar truss consisting of two identical horizontal beams connected by bars. The two beams are restrained against out-of-plane displacements by linear elastic springs; the linking bars are assumed rigid in the xy–plane and infinitely flexible out-of-plane (see Figure 1). To a certain extent, the model mimics the behaviour of thin-walled beams in compression in the sense that the system can buckle either in an overall mode (a “long-wave" in the xy–plane) or in a local mode (a “short-wave" out-of-plane). It has been known for a long time that the extreme imperfection-sensitivity of shell structures is mostly due to an interaction between linearly independent simultaneous, or nearly simultaneous, such global and local buckling modes.

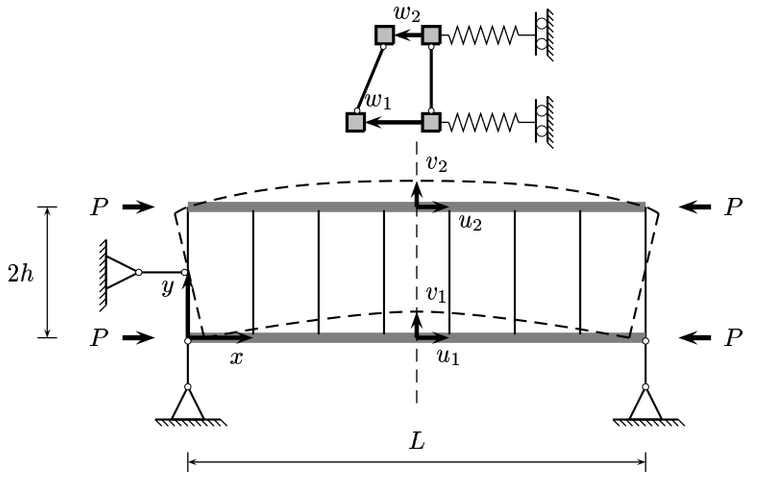


Figure 1. A system of two elastically restrained beams: lateral view (bottom) and axial perspective (top).

Governing equation and asymptotic analysis

By taking into account the long-wave buckling mode and assuming that the overall and local buckling modes correspond to closely spaced load values, one finds that the local instability is described by the (rescaled) boundary-value problem

$$\varepsilon^4 \frac{d^4 w}{dx^4} + 2\varepsilon^2 \left[(1-\gamma)\frac{d^2 w}{dx^2} + \lambda \frac{d}{dx}\left(\sin(x)\frac{dw}{dx}\right)\right] + w = 0, \qquad x \in (0,\, \pi), \tag{2a}$$

$$w = \frac{d^2 w}{dx^2} = 0, \qquad \text{for} \quad x = 0,\, \pi, \tag{2b}$$

where w is the out-of-plane displacement associated with the bottom beam. Here ε is a parameter depending on the geometrical and mechanical properties of the truss, λ corresponds to a rescaled loading parameter, while γ accounts for the closeness of the critical loads corresponding to the two modes of instability. It can be shown that the turning points for (2) are the two solutions x_1 and x_2 in $(0,\,\pi)$ of the equation $\sin(x) = \gamma/\lambda$. A solution of (2) is sought in the form

$$w(x,\,\varepsilon) = W(x) \exp\left\{ i \left(\varepsilon^{-1/2} \eta_0 \zeta + \frac{1}{2} a \zeta^2 \right) \right\}, \tag{3}$$

where $W(x) = W_0(x) + \varepsilon^{1/2}\, W_1(x) + \varepsilon\, W_2(x) + \ldots$, $\lambda = \lambda_0 + \varepsilon\, \lambda_1 + \varepsilon^2\, \lambda_2 + \ldots$, and $\zeta = \varepsilon^{-1/2}(x - x_0)$. Above $x_0 \in (0,\,\pi)$ is supposed to be the centre of localisation, the point where most of the energy is concentrated. Parameter η_0 is meant to characterise the oscillation frequency of the spatial eigenmode, while $\mathcal{I}(a)$, the imaginary part of $a \in \mathbb{C}$, gives the decay rate of the solution amplitude. Thus, localisation requires η_0 to be real and $\mathcal{I}(a) > 0$; also, we assume tacitly that x_1 and x_2 are close to each other, precisely $|x_1 - x_2| \sim \varepsilon^{1/2}$. Standard calculations carried out in [5], lead to the determination of all unknowns in (3).

NUMERICAL EXPERIMENTS

It is found that the eigenvalues of (2) are given by $\lambda^{(m)} = \gamma + \varepsilon\sqrt{\gamma}\,(1 + 2m) + \mathcal{O}(\varepsilon^2)$, where the lowest eigenvalue corresponds to $m = 0$. These eigenvalues are asymptotically double and to each of them there correspond two eigenmodes

$$u^{(0,j)}(x,\,\varepsilon) = \left[\cos\left(\frac{2x - \pi}{2\varepsilon} + \Psi_{0j} \right) + \mathcal{O}(\varepsilon^{1/2}) \right] \exp\left\{ -\frac{\sqrt{\gamma}\,(2x - \pi)^2}{16\varepsilon} \right\}, \tag{4}$$

where $j = 1,\,2$; the phase-angles Ψ_{0j} are found by symmetry considerations as $\Psi_{00} = \pi$ (symmetric mode) and $\Psi_{01} = \pi/2$ (antisymmetric mode). Two typical comparisons between this formula and our numerical runs of (2) are included below. The core of the buckling patterns is described quite satisfactorily by (4), although the tails of the solution in (b)

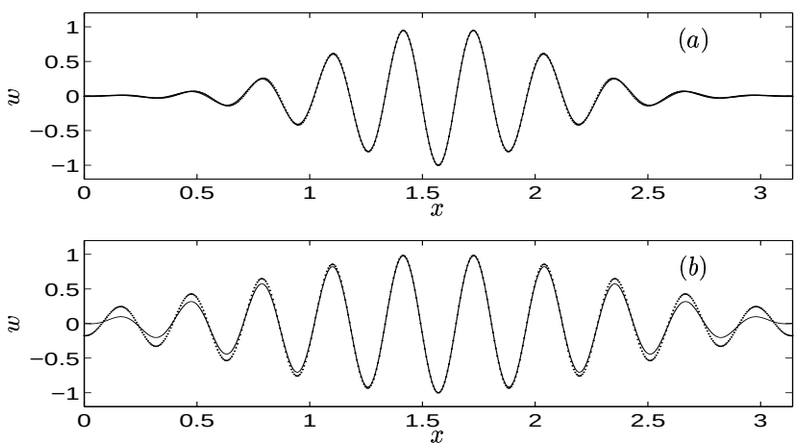


Figure 2. Comparisons between numerical solutions (solid line) and the asymptotic predictions (dotted line) for the first symmetric eigenmodes given by (4); (a) corresponds to $\gamma = 0.2$, while (b) is obtained for $\gamma = 0.02$. In both pictures $\varepsilon = 0.05$.

are poorly approximated. It turns out that this is due to the fact that the scaling assumption for the distance between the two turning points of (2) is violated in Figure $2(b)$; details on this subtle point are provided in [5].

CONCLUSIONS

In contrast to other works on similar topics [3, 4], the approach taken here succeeds in producing a compact uniform asymptotic expansion for the buckling patterns, valid over the entire span of the truss. We believe that more complex solid mechanics problems involving secondary bifurcations are susceptible to a similar analysis, and this is currently under investigation.

References

[1] Maslov V.P., Fedoryuk M.V.: Semi-classical Approximations in Quantum Mechanics. Reidel, Dordrecht 1981.
[2] Tovstik P.E., Smirnov A.L.: Asymptotic Methods in the Buckling Theory of Elastic Shells. World Scientific, Singapore 2001.
[3] Luongo A.: Mode localisation in dynamics and buckling of linear imperfect continuous systems. *Nonl. Dyn.* **25**:133-156, 2001.
[4] Hunt G.W. and Wadee M.A.: Localisation and mode interaction in sandwich structures. *Proc. R. Soc. Lond.* **A 454**:1197-1216, 1998.
[5] Coman C.D.: Secondary bifurcations and localisation in a three-dimensional buckling model. *Preprint* University of Leicester, 2003.

CREEP RUPTURE AND FIBER BREAKS ACCUMULATION IN UNIDIRECTIONAL COMPOSITE

Andrejs Krasnikovs* and Scott Case**
*Institute of Mechanics, Riga Technical University, LV 1058, Riga, LATVIA
**Virginia Polytechnic Institute and State University, Blacksburg, VA 24061, USA

Summary In this work we consider a model, based on Markov's-type stochastic kinetic equations for concentrations growth of adjacent fibers breaks in material under creep rupture conditions. Different from previous investigations, precise variety of all possible clusters geometrical configurations were discussed and form-dependent cluster distributions were obtained. Simultaneously, Monte Carlo simulations were performed.

MATERIAL MODELING

Interest in precise damage accumulation modeling, for fiber composites subjected to long-term (creep-rupture) loading conditions, grown up last years with a new area of composite materials application. High corrosion resistance and competitive market price are making composites (especially polymer matrix composites) very promising in civil engineering application. We consider unidirectional composite material with parallel continuous fibers embedded in matrix. C*hain of bundles* material model is accepted.

Kinetic equations. Modeling of damage accumulation in composite material, under an arbitrary external tensile load is based on the assumption, that failure is a complex stochastic process, starting with scattered, isolated fiber brakes (at fiber's internal flow or structure heterogeneity) overstress redistribution on adjacent to broken fibers, failure of overstressed neighbors, forming breaks clusters and the breaks clusters growth and coalescence in the range of each bundle, orthogonally to the fiber direction. This process starting relatively slowly will transforms to catastrophic ultimate cluster growth, when overstress distributed on closest unbroken neighbors will immediately initiate one of the next fiber break. We can introduce two random variables $I(\sigma,t)$ and $J(\sigma,t)$ with joint probability function: $P\{I(\sigma,t)=i, J(\sigma,t)=j\}=H_i^j(\sigma,t)$, $\sigma \geq 0, t \geq 0$, to find cluster which was born and after that was stayed conservative till time moment *t*, as the cluster consisting of i adjacent fiber breaks and having a form number *j*. $W(\sigma,t)$ is a probability of fiber failure. For example (see Fig.1.), one and two fiber breaks have only one geometrical configuration, three adjacent breaks, in material with hexagonal fiber array, may form three different geometrical configurations (two different configurations for square array).

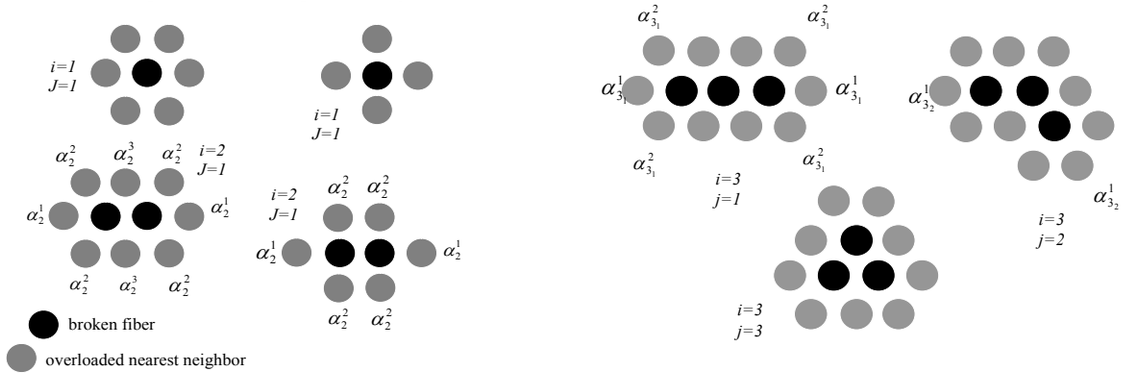


Figure1. Configurations of $i=1,2,3$ adjacent broken fibers. $\alpha_{i_k}^j$ - overloaded nearest fiber.

For hexagonal packing, if the geometrical configuration of three adjacent breaks is forming line, we are designating it like cluster number one (form number $j=1$). Cluster with geometrical configuration forming curved line will have number two ($j=2$) and cluster with compact configuration - number three ($j=3$). For square packing we have $j=1,2$. Chance for double break cluster to grow and form tree break cluster with form index equal to number one, is the chance to fail one of two overstressed fibers belonging to the set of closest neighbors around two broken fibers (designated as α_2^1 in Fig.1). Here we must to note that overstress distributed on adjacent fibers α_2^k, $k=1,2,3$ coming from two breaks is different for fibers around broken and depends on k. Two break cluster growth to three breaks cluster's set with different geometry, will happen by fiber element failure under different overstresses. Probability to obtain cluster, consists of r adjacent fiber breaks and have form number j, is:

$$H_r^j(\sigma,t) = \sum_{l:(r-1)_l+\alpha^k_{(r-1)_l}\to r_j} \int_0^t \frac{dH^l_{r-1}(\sigma,t^*)}{dt^*} m^k_{(r-1)_l} W\left(k^k_{(r-1)_l}\sigma, t-t^*\right)\left(1-W\left(k^k_{(r-1)_l}\sigma, t-t^*\right)\right)^{m^k_{(r-1)_l}-1} dt^* \quad . \qquad (1)$$

These are kinetic equations, in recurrent form, for stable states integral probabilities. Equations are explaining the stochastic process of damage accumulation in loaded unidirectional composite material. Applying constant tensile stress $\sigma = const \neq \sigma(t)$ to composite material, according to statistics of extremes we appropriate Weibull type integral probability function for an element failure. Fiber breakage leads to local stress redistribution in vicinity of failure place. Overstresses on adjacent to broken fibers was calculated using Hedgepeth-Van-Dyke shear lag model and discrete Fourier transform [1].

Lower tail analysis. Using non-effective length δ_0 like the governing parameter for material partition we obtain a large number of fiber elements in any real mechanically loaded composite volume. That's mean we are interesting in a small clusters probabilities or in a lower tail for probabilities distributions. Looking on obtained formulae (1) we can conclude that all clusters probabilities $H_r^j(\sigma,t)$ can be represented multiplying function dependant only on stress and geometry by function dependent on time $H_r^j(\sigma,t) = H_r^j(\sigma)\cdot H_r(t)$. Time dependant integrals $H_r(t)$ can be transformed to incomplete Beta – functions and be written in a form convenient for easy numerical analysis.

NUMERICAL RESULTS

A numerical example of damage accumulation was performed for Kevlar 49/Epoxy. When we calculate the probabilities for clusters with different configurations, some of these configurations are more probable then others. These configurations called dominant. Calculations shown, the probabilistic modeling is sensitive to overstress coefficient (the load concentration factor). Using the dominant cluster approach (a technique widely used by different authors), instead of precise calculations for all configurations, results may be grossly inaccurate. An isolated single broken fiber has six overloaded neighbors with overstress on them taking into account by the same overloading coefficient. Surrounding two broken fibers, we have eight overloaded neighbors: two of them loaded with overstress k_2^1, four have coefficient k_2^2, and another two k_2^3. For three adjacent breaks, there are eleven neighboring overloaded fibers, each having an overstress factor and multiplicity. For four adjacent breaks, we have 46 differently overloaded fibers (for small clusters $r = 1 \div 7$ number of their geometrical configurations was calculated in [2]). It is apparent that the variety of clusters grows rapidly as the number of adjacent broken fibers increases (10 break clusters have a little more than 30000 different configurations, and 11 break clusters have more than 140000 configurations; every particular geometrical configuration has differently overloaded fibers around it), increasing the number of mathematical calculations. We performed precise analysis until the cluster consists of 11 broken fibers. Further, analytical approximation was used. Comprehensive damage accumulation picture was obtained. Parametric analysis was made. Bundle stiffness degradation was appreciated.

Model validation. In order to evaluate model capability, Monte Carlo simulations for fiber break accumulation in composites under creep-rupture loading were conducted. Both methods predict the same small, different configuration, cluster accumulation. In the vicinity of the unstable growth, the situation changes. Clusters with slower growing speed cannot realize all their possible configurations. Predicted in model ultimate cluster appearance lifetime usually would be shorter then in reality (and obtained in Monte-Carlo simulations), if we will look on summarized probabilities curves. That mean, on the stage of formation of ultimate cluster, for its appearance time evaluation, we must to go from the summarized probabilities curves to one dominant cluster growth (this cluster size we designate as ultimate).

CONCLUSIONS

Fiber break accumulation in unidirectional composite material under creep-rupture loading conditions was investigated using kinetic theory and Monte-Carlo simulations. Detailed damage accumulation picture of all varieties of geometrical configurations for fiber break clusters were obtained and analyzed. Material stiffness degradation and volume lifetime prediction was made and compared with experiment. Parametric analysis was made.

References

[1] Bandorawalla, T. Micromechanics-based strength and lifetime prediction of polymer composites, Ph.D. dissertation, Virginia Polytechnic Institute and State University, (2002), http://scholar.lib.vt.edu/theses/available/etd-03172002-151608/

[2] Smith, R. L., Phoenix, S.L., Greenfield, M.R., Henstenburg, R.B. and Pitt, R.E. Lower-tail approximation for the probability of failure of three-dimensional fibrous composites with hexagonal geometry. Proc. Roy. Soc. London., A388 (1983) 353- 391.

XXI ICTAM, 15–21 August 2004, Warsaw, Poland

HOMOGENIZATION OF PLAIN WEAVE COMPOSITES WITH IMPERFECT MICROSTRUCTURE

Jan Zeman*, Michal Šejnoha*
*Department of Structural Mechanics, Faculty of Civil Engineering, Czech Technical University in Prague, Thákurova 7, 166 29, Prague, Czech Republic

Summary A comprehensive computational framework is presented for the determination of a representative volume element (RVE) of plain weave fabric composites with reinforcement imperfections. The presented approach is characterized by quantification of the analyzed material system by appropriate statistical descriptors that are subsequently used to derive the parameters on an idealized geometrical model by minimizing the difference between the original and the idealized unit cell.

INTRODUCTION

The doubtless benefits offered by composite materials such as a high strength, light weight, corrosion resistance and design flexibility resulted in an extensive use of these materials in diverse applications in various areas of engineering. In particular, the popularity of the woven fabric reinforced composites is under continuous rise due to advantageous strength/weight ratio, easiness of manipulation and low production costs.

The complex three-dimensional structure of woven fabric composites, however, makes the analysis and prediction of the overall properties of these material systems a relatively difficult task. Moreover, it is an experimentally confirmed fact that an overall response of such structures is highly influenced by both the material behavior and *geometrical imperfections* of distinct phases of the composite system. A comprehensive discussion of this subject can be found, e.g., in [1] where detailed image analysis of composite micrographs was used to get the frequency spectrum to describe the yarn shape of both woven and braided fabrics. Moreover, it has been recognized that the crimp wavefront is subject to deformation when pressed during the manufacturing process and that the frequency spectrum is therefore disordered compared to that of the free fabric.

In the present contribution, an alternative strategy is adopted to incorporate, at least to some extent, the reinforcement imperfections into the geometrical model of the unit cell. In particular, we follow the path set in papers by [4] and by [6]. In these works, the idealized geometrical model of the analyzed composite is defined in terms of a certain periodic unit cell with geometrical parameters derived by matching microstructural statistics of a real microstructure and the searched PUC. Using the model of plain weave geometry [2] in combination with binary images of real composites, this modeling strategy can be extended to the modeling of woven composites in a rather straightforward way.

MICROSTRUCTURE DESCRIPTION

In the present study, two different statistical descriptors – the two-point probability function S_{rs} and the lineal path function L_r are used to quantify the morphology of random media. Recall that the two-point probability function $S_{rs}(\mathbf{x})$ gives the probability that both endpoints of the vector $\mathbf{x}$, randomly thrown into material, will be located in phases r and s[1], respectively. The lineal path function $L_r(\mathbf{x})$ simply gives the probability that the segment $\mathbf{x}$ will be fully contained in the phase r. Note that the two-point probability function was evaluated by the Fast Fourier transform-based algorithm while the sampling template approach was used for the lineal path functions; see recent monograph [5] for more details.

GEOMETRICAL MODEL

In this work, the model of fabric weave composite proposed in [2] is used since it is reasonably simple to implement and directly incorporates typical features of real composites. For the purpose of the present study, the most important fact is that the the model is fully determined by four parameters a, b, g and h, see Fig. 1; detailed description of the model geometry can be found in [2].

OPTIMIZATION PROBLEM

To determine "statistically" optimal parameters of the periodic unit cell, the parameters a, b, g and h are found by minimizing certain objective functions. In particular, objective functions incorporating the two-point matrix probability function S_{mm}, matrix lineal path function L_m or their combination are considered,

$$F_S(\mathbf{x}) = \sum_{i=-i_{\max}}^{i_{\max}} \sum_{j=-j_{\max}}^{j_{\max}} \left(\overline{S}_{mm}(i,j) - S_{mm}(i,j)\right)^2, \qquad F_L(\mathbf{x}) = \sum_{i=0}^{N_d-1} \sum_{j=0}^{N_\ell(i)-1} \left(\overline{L}_m(i,j) - L_m(i,j)\right)^2 \tag{1}$$

[1] Note that a binary medium is considered in the text with symbol m standing for matrix and f denoting the bundle; i.e., $r \in \{m, f\}$.

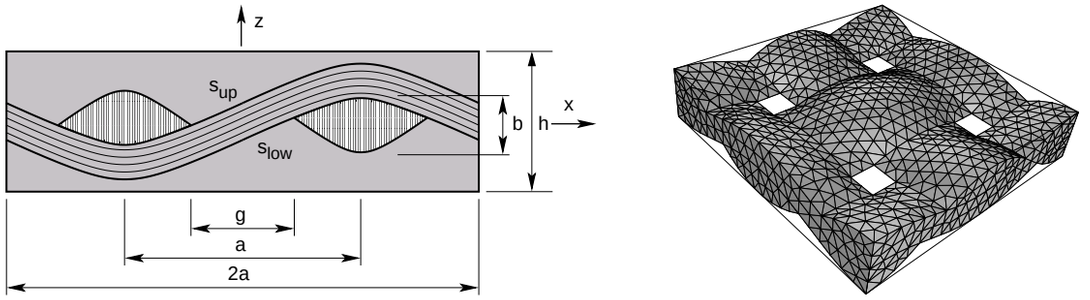


Figure 1. Idealized Periodic Unit Cell, (a) Geometrical model, (b) Example of finite element mesh

where $\overline{S}_{mm}$ and $\overline{L}_m$ are the values of L_m and S_{mm} functions corresponding to the target microstructure. A closer inspection reveals that the objective functions (1) are discontinuous with a large number of local plateaus. This is a direct consequence of working with binary images of a limited resolution. Based on our previous works [3], the *Real-encoded Augmented Simulated Annealing* method is employed to solve the present problem.

NUMERICAL EXPERIMENTS

As a representative of digitized images of real-world multilayered plain weave composites, a set of three artificial bitmaps exhibiting different imperfections was generated. In particular, the "samples" formed by two unit cells with different layer and bundle heights (see Fig. 2a), two identical unit cells shifted by a (see Fig. 2b) and by $a/2$, Fig. 2c were considered.



(a) (b) (c)

Figure 2. Artificial bitmaps of mesoscale geometry with typical tow misalignments, (a) different layer heights (PUC #1), (b) layers shifted by a (PUC #2), (c) layers shifted by $a/2$ (PUC #3)

Finally, we present the comparison of effective elastic properties for the target bitmaps and corresponding statistically optimized unit cells obtained for different objective functions. The material parameters of the matrix phase and the bundle were taken from [6].

PUC #1				***PUC #2***				***PUC #3***			
S_{mm}	L_m	$S+L$	Target	S_{mm}	L_m	$S+L$	Target	S_{mm}	L_m	$S+L$	Target
21.100	22.698	23.334	23.324	25.341	26.309	25.121	24.786	27.629	27.464	27.095	24.694

Table 1. Coefficient $\mathsf{L}^{\mathsf{fem}}{}_{11}$ of the homogenized stiffness matrix [GPa].

The obtained results allow us to conclude that the proposed procedure can be efficiently used for multilayered composites with possibly varying layer heights (PUC #1) provided that the relative shift of individual layers is not very large or approximately equal to the unit cell half-width (PUC #2). In the opposite case, however, it appears to be necessary to formulate the optimized unit cell in terms of at least two-layered composite.

Acknowledgement.
The financial support of this work by grants GAČR 103/04/P254 and GAČR 106/03/0180 is gratefully acknowledged.

References

[1] Košková, B., Vopička, S.: Determination of yarn waviness parameters for C/C woven composites. In: *Proceedings of International Conference CARBON '01*. Lexington (KY,USA), pp. 1–6, 2001.
[2] Kuhn, J. L., Charalambides, P. G.: Modeling of plain weave fabric composite geometry. *Journal of Composite Materials* **33**:188–220.
[3] Matouš, K., Lepš, M., Zeman, J., Šejnoha, M.: Applying genetic algorithms to selected topics commonly encountered in engineering practice. *Computer Methods in Applied Mechanics and Engineering* **190**, 1629–1650, 2000.
[4] Povirk, G. L.: Incorporation of microstructural information into models of two-phase materials. *Acta metallurgica et materialia* **43**: 3199–3206, 1995.
[5] Torquato, S. : Random heterogeneous materials: Microstucture and macroscopic properties. Springer-Verlag, 2002
[6] Zeman, J., Šejnoha, M.: Numerical evaluation of effective properties of graphite fiber tow impregnated by polymer matrix. *Journal of the*

COLLECTIVE PRISMATIC DISLOCATION LOOPS MECHANISM

Yoji Shibutani*, Tomohito Tsuru*
*Osaka University, Department of Mechanical Engineering & Systems, 565-0871 Suita, Japan

Summary Unstable displacement burst observed in the indent load and depth curve of nanoindentation is much possible to be related to the collective dislocation behavior. We have recently reported [1] that the first critical indent load at the first burst is almost linear to the first burst width. To resolve the reason of this experimentally obtained linearity, we must understand the collective prismatic dislocation loops mechanism. In the present research, the dislocation emission and the subsequent prismatic dislocation loop formation of a single crystalline aluminum under nanoindentation are simulated by the molecular dynamics. Also, the collective prismatic loops emitted due to the internal pressure by a rigid sphere embedded into the Al matrix are studied, qualitatively and quantitatively comparing with the micromechanics considerations.

INTRODUCTION

Indentation technique has been put to a wide use in order to obtain the hardness and the elastic properties of materials even at the nanoscale. Recently, it is worthy of notice that indent load and depth curves provide an opportunity to investigate the early events of plasticity (nano-plasticity). The distinctive displacement burst of indent depth observed in nanoindentation [2] is thought to be linked to the dislocation emission, being caused when the maximum shear stress generated under the indenter is of the order of the theoretical shear strength. Moreover, the experimentally obtained linear relation on the burst phenomena has recently been reported [1]. It is a fact that the first critical indent load at the first burst is almost linear to the first burst width. To resolve the reason of this linearity, we must understand the collective prismatic dislocation loops mechanism. In the present research, dislocation emission and the subsequent prismatic dislocation loop formation of a single crystalline aluminum under nanoindentation are simulated by the molecular dynamics (MD). Also, the collective prismatic dislocation loops emitted due to the internal pressure by a rigid sphere embedded into the Al matrix are studied as a reference, because the stress field is more predictable than that of the indentation. On the mechanism of the prismatic dislocation loop, the simple model with the misfitting particle in a ductile matrix has been acknowledged from the micromechanics view point [3]. Therefore, the latter atomistic stress states are compared with the elastic solution, discussing the nucleation mechanism of the collective dislocation loops.

PRISMATIC DISLOCATION LOOP

Nucleation due to Indentation

A prismatic dislocation loop due to the indentation is assembled by the shear loops emitted from the surface and then the cross-slip mechanism. It penetrates on the side surface of the spatially limited atomic model, leaving the rhombic steps. An example of the formation of prismatic dislocation loop emitted from the (111) surface of Al under the spherical punch with 5nm radius using the Finnis-Sinclair type many body potential is depicted in Fig.1.

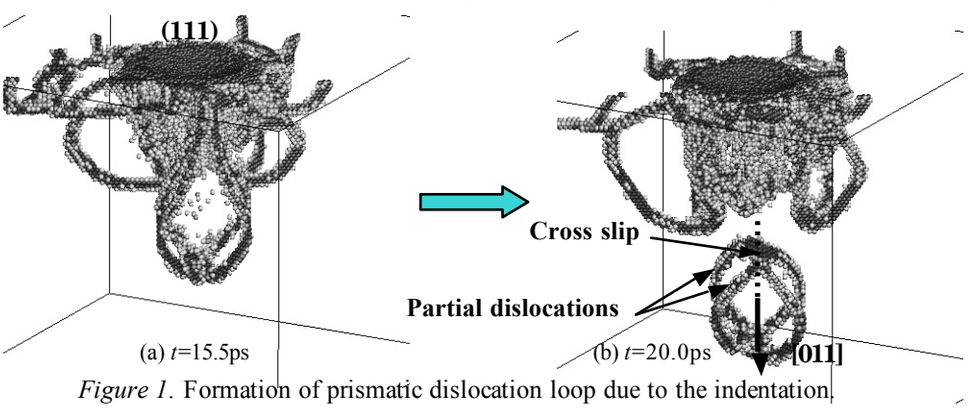


Figure 1. Formation of prismatic dislocation loop due to the indentation.

Nucleation due to internal pressure by a rigid sphere in Al matrix

Studies concerned to the formation of prismatic dislocation loops have been performed experimentally in the past about fifty years. Many of those remarked about the presence of a spherical or a non-spherical precipitate inside a given crystalline matrix. Several quantitative analyses for the spherical particle geometry and a few studies for the non-spherical geometry exist. The nucleation of a shear dislocation loop from the interface of a misfitting spherical particle in a deformable matrix has been discussed in the Ref. [3], as shown in Fig.2. An initial shear loop emits on the slip plane at the maximum shearing stress at $z = a/\sqrt{2}$, where a is radius of the particle ((a) in Fig.2). The screw segments

on both sides of that dislocation move to each highly stressed cross-slip plane that is parallel to each other ((b) and (c) in Fig.2). Finally, the dislocation loop on the cross-slip plane moves to the next cross-slip plane that is parallel to the initial slip plane ((d) in Fig.2).

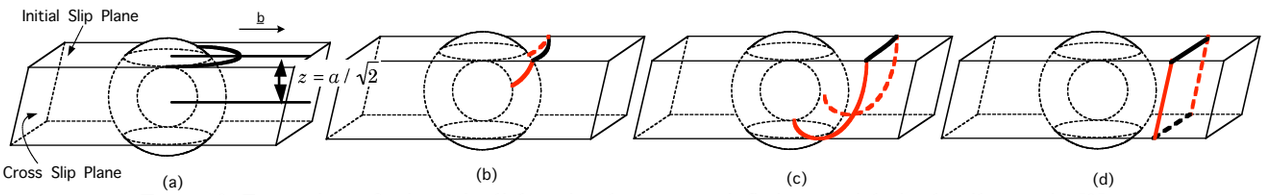


Figure 2. Formation of prismatic dislocation loop at a misfitting particle in ductile matrix [3].

The corresponding stress field to Fig.2 is atomistically realized in the MD simulations, as shown in Fig.3. Due to the increment of the internal pressure by the rigid sphere embedded into the Al matrix, a few shear loops are emitted at the interface whose the critical shear stress is 2.51GPa, one third of the critical pressure and one thirteenth of the shear modulus. Four different shear loops are simultaneously emitted from the same position ($z = a / \sqrt{2}$) from the center on the different family of slip planes {111}. And then they form a prismatic loop under the high-energy reactions between two shear loops.

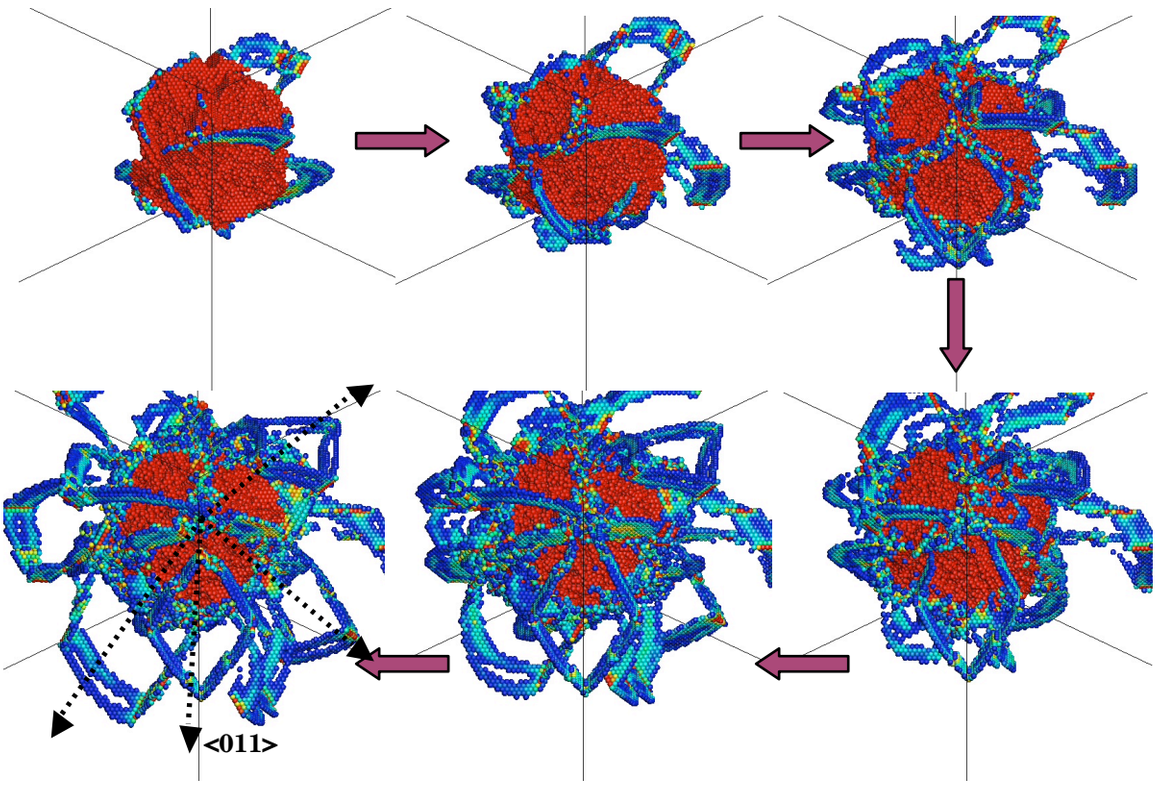


Figure 3. Formation process of the collective prismatic dislocation loops due to internal pressure in the Al matrix.

CONCLUSIONS

We discussed the dislocation emission and the subsequent formation of the prismatic dislocation loop under nanoindentation and also due to the internal pressure in Al matrix by the molecular dynamics simulations. The latter atomic level stress states are in good agreement with the elastic solution and the collective mechanism was discussed.

Acknowledgements
This work was supported by the JSPS Grant-in-Aid for Scientific Research ((B)(2)15360054) and the Handai Frontier Research Center (FRC).

References

[1] Shibutani Y., Koyama A.: Surface roughness effects on the displacement bursts observed in nanoindentation. *J. Mater. Res*., **19**:183-188, 2004.
[2] Suresh S., Nieh T.-G, Choi B.W.: Nanoindentation of copper thin film on silicon substrates. *Scripta Mater*., **41**: 951-957, 1999.
[3] Ashby M.F., Johnson L.: On the generation of dislocation at misfitting particle in a ductile matrix. *Phil. Mag*., **20**: 1009-1022, 1969.

SHAPE SENSITIVITY ANALYSIS FOR FIXED-GRID ANALYSIS BASED ON OBLIQUE BOUNDARY CURVE APPROXIMATION

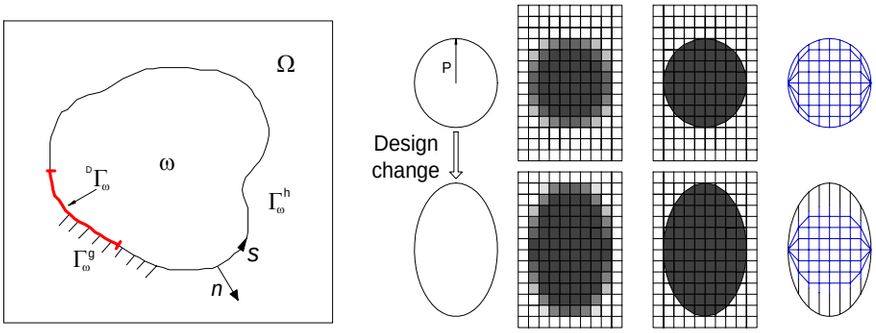
Yoon Young Kim, Gang-Won Jang

School of Mechanical and Aerospace Engineering and National Creative Research Initiatives Center for Multiscale Design, Seoul National University, Seoul 151-742, Korea

Summary Fixed-grid analyses equipped with a fictitious domain method can avoid remeshing for shape optimization, but stresses on domain boundaries cannot be calculated accurately if the boundaries are improperly represented. For improved stress evaluation, we consider the direct boundary curve approximation by piecewise oblique lines which can cross boundary elements. In this approach, the intersection points between the fixed girds and the approximated boundary do not necessarily coincide with the analysis nodes unlike in existing fixed-grid analyses. The objective of this investigation is to derive the analytic shape sensitivity of stresses for the direct piecewise oblique boundary approximation. Since the force term in the sensitivity equation is associated only with the elements crossed by the design boundary curve, only the design velocities of the intersection points between the curve and the fixed mesh are needed for sensitivity analysis.

INTRODUCTION

By the standard shape optimization based on the finite element approach, remeshing cannot be avoided during the optimization process if accurate analysis is required, especially for design problems requiring large shape changes [1]. To overcome such a difficulty, Eulerian-type methods employing a fictitious domain approach (see Fig. 1 (a)) with fixed grids have recently emerged as an alternative analysis tool for shape optimization.



(a) (b) (c) (d) (e)

Fig. 1. A fictitious domain and various Eulerian-type methods

Fig. 1 (c) shows a typical popular fixed-grid modeling with which an element stiffness is evaluated by the area fraction concept [2]. The concept is to evaluate the boundary element stiffness proportionally to the area fraction of the real domain ω within the boundary element. However, the boundary curve in this method needs to be approximated by zigzags that consist only of vertical and horizontal lines, so this area-fraction-based approach is not effective for curved boundaries. The only way to obtain accurate solutions near the boundary is to employ highly-dense grid distributions.

In order to obtain accurate solutions near the curved boundary without excessive grid densities, Jang *et al.* [3] have recently proposed a more direct approach: a curved boundary is approximated by piecewise oblique lines formed by the connections of the points between the curved boundary and the fixed grid lines. In this case, the piecewise oblique line, the approximated boundary curve, does not usually pass through the analysis nodes.

In this paper, we derive the analytic sensitivity analysis for the fixed-grid shape optimization based on the oblique boundary curve approximation [4]. Some results obtained by Hansen *et al.* [5] are used for the present analysis since the analysis grids not interacting with the boundary curves are stationary or fixed during the whole design process as in the method by Hansen *et al.* [5].

SENSITIVITY ANALYSIS

The total potential energy for a problem involving kinematic constraint is

$$\Phi = \int_{\omega} \left\{ \frac{1}{2}\mathbf{e}^T\mathbf{C}\mathbf{e} - \mathbf{f}^T\mathbf{u} \right\} d\omega + \int_{\Omega\setminus\omega} \varepsilon \frac{1}{2}\mathbf{e}^T\mathbf{C}\mathbf{e}\, d\omega \quad \text{with} \quad \mathbf{u} = \mathbf{0} \ \text{ on } \ \Gamma_{\omega}^{g} \tag{1}$$

where $\mathbf{e}$ is the strain vector, $\mathbf{f}$ is the force vector, and $\mathbf{u}$ is the displacement vector. In the above expression, ε denotes a small positive value.

The design derivative of the first variation of equation (1) is given as

$$\delta\bar{\Phi} = \left[\int_{\omega} \delta\mathbf{e}^T\mathbf{C}\bar{\mathbf{e}}d\omega + \int_{\Omega\setminus\omega} \varepsilon\delta\mathbf{e}^T\mathbf{C}\bar{\mathbf{e}}\, d\omega\right] + \left[\int_{\omega}\left\{\delta\bar{\mathbf{e}}^T\mathbf{C}\mathbf{e} - \mathbf{f}^T\delta\bar{\mathbf{u}}\right\}d\omega + \int_{\Omega\setminus\omega} \varepsilon\delta\bar{\mathbf{e}}^T\mathbf{C}\mathbf{e}\, d\omega\right]$$
$$+ \int_{^D\Gamma_\omega}\left\{\delta\mathbf{e}^T\mathbf{C}\mathbf{e} - \mathbf{f}^T\delta\mathbf{u}\right\}\mathbf{V}^T\mathbf{n}d\Gamma - \int_{^D\Gamma_\omega}\left\{\varepsilon\delta\mathbf{e}^T\mathbf{C}\mathbf{e}\right\}\mathbf{V}^T\mathbf{n}\, d\Gamma = 0 \tag{2}$$

where $\mathbf{V}$ and $\mathbf{n}$ are the design velocity and the outward normal vector of the design boundary $^D\Gamma_\omega$, respectively.

Unless the kinematic constraint is imposed on the design boundary, $\delta\mathbf{u}$ and $\delta\bar{\mathbf{u}}$ are in the same vector space, so that the terms in the second bracket in equation (2) vanish and the stiffness matrix for the sensitivity equation is exactly the same as that of the reference problem.

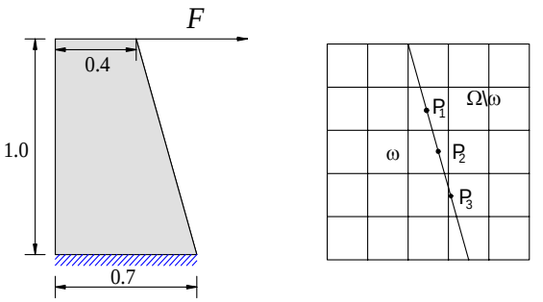
The last two terms in equation (2) form the force vector of the sensitivity equation after numerical formulation:

$$\underline{\tilde{\mathbf{f}}}^e = -\int_{-1}^{1}\left\{\mathbf{B}^T\mathbf{C}\mathbf{B}\underline{\mathbf{U}}^e - \underline{\mathbf{N}}^T\mathbf{f}\right\}\mathbf{V}^T\mathbf{n}\,\tilde{J}d\zeta + \int_{-1}^{1}\varepsilon\left\{\mathbf{B}^T\mathbf{C}\mathbf{B}\underline{\mathbf{U}}^e\right\}\mathbf{V}^T\mathbf{n}\,\tilde{J}d\zeta \tag{3}$$

where $\underline{\mathbf{U}}^e$ is the nodal displacement vector of the element and $\underline{\mathbf{N}}$ is the matrix with bilinear shape functions.

NUMERICAL EXAMPLE

A structure in Fig. 2 (a) is considered as a numerical example. The bottom edge of the structure is fixed and a horizontal force $F = 1.0\times10^5$ is imposed on the upper right corner. The material has Young's modulus $E = 2.0\times10^8$ and Poisson's ratio $\nu = 0.3$. The fixed mesh in Fig. 2 (b) is used for this problem. The design sensitivities of the Von Mises stresses at the points of interest are listed in Table 1. The present analytic sensitivities agree well with the numerical results by the finite difference method (FDM).



(a) (b)

Fig. 2. A cantilever example and its fixed grids on the fictitious domain

Table 1. Sensitivities of the Von Mises stresses and their comparison with the finite difference results.

	Present	FDM
P_1	4.3407e6	4.3405e6
P_2	-4.3989e6	-4.3987e6
P_3	-9.8340e6	-9.8337e6

References

[1] Bennett J. A., Botkin M. E.: Structural shape optimization with geometric description and adaptive mesh refinement, *AIAA Journal* **23**(3):458-464, 1985.

[2] Kim N. H., Chang Y.: Eulerian shape optimization with fixed grid. *44th AIAA/ASME/ASCE/ AHS/ASC Structures, Structural Dynamics, and Materials Conference*, Norfolk, Virginia, 2003.

[3] Jang G. W., Kim Y. Y., Choi K. K.: Remesh-free shape optimization using the wavelet-Galerkin method and its applications to MEMS actuator design. *WCSMO-5 Lido de Jesolo*, 121-122, 2003.

[4] Hansen J. S., Liu Z. S., Olhoff N.: Shape sensitivity analysis using a fixed basis function finite element approach. *Struct. Multidisc. Optim*. **21:**177-195, 2001.

[5] Jang G. W., Kim Y. Y., Sensitivity analysis for fixed-grid shape optimization by using oblique boundary curve approximation, *International Journal of Solids and Structures*, submitted.

PERTURBATION OF THE COMPLIANCE FUNCTIONAL DUE TO THE APPEARANCE OF A SMALL CAVITY IN AN ELASTIC BODY

Tomasz Lewiński*, Jan Sokołowski**
*Warsaw University of Technology, Al.Armii Ludowej 16, PL 00-637 Warszawa, Poland
**Systems Research Institute of the Polish Academy of Sciences, Newelska 6, PL 01-447 Warszawa, Poland

Summary The paper proves that the known methods of assessing an increment of strain energy due to the appearance of small cavities in elastic solids lead to one equivalent result. The following approaches are discussed: the compound asymptotic method by Mazja, Nazarov and Plamenevskii, the topological derivative method by Sokolowski and Zochowski and the method of Eshelby. The result derived determines the characteristic function of the bubble method.

CHANGE OF ENERGY ACCORDING TO MAZJA-NAZAROV-PLAMIENIEVSKII AND ESHELBY

The present paper refers to the problem of assessing a change of a shape functional due to the appearance of a small cavity within the domain. The formulae expressing such changes play a crucial role in the evolutionary methods of topology optimization, see [1]. Finding the stiffest layouts needs assessing the change of the compliance or, equivalently, change of the elastic energy stored in the body. Let us start with the plane elasticity problem. Assume that a plane body is subjected to self-equilibrated tractions of intensity $\mathbf{p}$ on $\partial\Omega$. The elastic energy stored in the body equals

$$\mathcal{E}(\Omega) = \frac{1}{2}\int_{\Omega} \sigma^{\alpha\beta}(\mathbf{v})\epsilon_{\alpha\beta}(\mathbf{v})dx \tag{1}$$

where $\mathbf{v} = (v_1, v_2)$ represents the displacement field caused by $\mathbf{p}$. The stress field $\boldsymbol{\sigma}$ is linked with the deformations by $\boldsymbol{\sigma} = \boldsymbol{A}\boldsymbol{\epsilon}$ and $\boldsymbol{\epsilon}(\mathbf{v})$ represents a symmetric part of $\nabla\mathbf{v}$. Let us consider now the domain $\Omega_\varepsilon = \Omega \setminus \overline{\omega}_\varepsilon$, where $\omega_\varepsilon = \{x \mid x/\varepsilon \in \omega\}$. We assume that $0 \in \omega$, ω being a rescaled domain of the opening; ε is a small parameter. The tractions $\mathbf{p}$ cause the displacement field $\mathbf{u}^\varepsilon$. The elastic energy

$$\mathcal{E}(\Omega_\varepsilon) = \frac{1}{2}\int_{\Omega_\varepsilon} \sigma^{\alpha\beta}(\mathbf{u}^\varepsilon)\epsilon_{\alpha\beta}(\mathbf{u}^\varepsilon)dx \tag{2}$$

should be greater than $\mathcal{E}(\Omega)$ irrespective of the shape of the cavity ω_ε. Note that the origin 0 lies within ω_ε for each $\varepsilon > 0$. We shall say that a hole ω_ε nucleates at 0. The case of $\varepsilon = 0$ refers to the case without any hole within Ω. Let us denote : $\boldsymbol{\epsilon}^0 = \boldsymbol{\epsilon}(\mathbf{v})(0)$ for the deformation state at point 0 caused by the loading $\mathbf{p}$.
The compound asymptotic method, exposed recently in Mazja et al.[4] leads to the following result

$$\mathcal{E}(\Omega_\varepsilon) = \mathcal{E}(\Omega) - \frac{1}{2}\varepsilon^n \varepsilon^0_{\alpha\beta} M^{\alpha\beta\lambda\mu}\varepsilon^0_{\lambda\mu} + o(\varepsilon^n)\ , \tag{3}$$

where $n = 2$ and $\boldsymbol{M} = \left(M^{\alpha\beta\lambda\mu}\right)$ will be called the Polya-Szegö tensor. The above result is reported without proof in Movchan and Movchan [5]; the details of the derivation are given in Lewinski and Sokolowski [3]. Tensor $\boldsymbol{M}$ characterizes the outer problem for ω

$\left(P_\omega^{(\lambda\mu)}\right)$

find $\boldsymbol{\chi}^{(\lambda\mu)}$ defined in $\mathbb{R}^2\setminus\overline{\omega}$ such that

$$A^{\alpha\beta\gamma\delta}\frac{\partial}{\partial y_\beta}\epsilon^y_{\gamma\delta}(\boldsymbol{\chi}^{(\lambda\mu)}) = 0 \quad \text{in } \mathbb{R}^2\setminus\overline{\omega}\ , \tag{4}$$

$$A^{\alpha\beta\gamma\delta}\epsilon^y_{\gamma\delta}(\boldsymbol{\chi}^{(\lambda\mu)})\nu_\beta = -A^{\alpha\beta\lambda\mu}\nu_\beta \qquad \text{on } \partial\omega\ , \tag{5}$$

$$\boldsymbol{\chi}^{(\lambda\mu)} \to \mathbf{0} \qquad \text{if } ||y|| \to \infty \tag{6}$$

Here $y = (y_1, y_2)$ parametrize the domain $\mathbb{R}^2\setminus\overline{\omega}$; $\epsilon^y_{\gamma\delta}(\mathbf{v})$ represents the symmetric part of $\nabla\mathbf{v}$ with respect to the Cartesian system (y_1, y_2); the Cartesian base vectors are denoted by $\boldsymbol{e}_1, \boldsymbol{e}_2$. The vector fields $\boldsymbol{\chi}^{(\lambda\mu)}$ are uniquely determined. The components of $\boldsymbol{M}$ are given by

$$M^{\kappa\delta\sigma\gamma} = -A^{\kappa\delta\sigma\gamma}|\omega| - \mathcal{M}^{\kappa\delta\sigma\gamma} \tag{7}$$

$$\mathcal{M}^{\kappa\delta\sigma\gamma} = A^{\alpha\beta\kappa\delta}\int_{\partial\omega} \chi^{(\sigma\gamma)}_\alpha \nu_\beta\, ds\ , \tag{8}$$

where $\boldsymbol{\nu} = (\nu_1, \nu_2)$ is a unit vector outward normal to $\partial\omega$ and $|\omega|$ represents the area of ω. The tensor $\boldsymbol{M}$ is negative definite under very weak assumptions of regularity of ω, see Ref.[3].

The results (4)-(6) and (7)-(8) can be generalized to the $3D$ case. Then the exponent $n = 3$, see Eq.(3), the contour integral in (8) is replaced by the surface integral; $|\omega|$ stands for the volume of ω. Moreover, one can show that the known Eshelby formulae for the energy change are equivalent to the result .

CHANGE OF ENERGY FOUND BY THE TOPOLOGY DERIVATIVE METHOD

The topological derivative has been introduced by Sokolowski and Zochowski [9] in order to formulate necessary conditions of optimality for optimum shape design problems. The topological derivative measures a change of a functional caused by removing a small ball from the given domain. A method of computing the topology derivative relevant to weakening the domain by a small cavity (or hole) of arbitrary shape is proposed e.g., in Lewinski and Sokolowski [3]. The method is based on the velocity method of shape optimisation. The speed vector field is chosen as a linear function in the space variable. This method can be applied for confirming the formula (3) by a new manner. The final result has the form (3) with tensor $\boldsymbol{M}$ replaced by $\boldsymbol{G}$ given by

$$G^{\gamma\delta\iota\varrho} = -\frac{1}{2}A^{\alpha\beta\lambda\mu}\int\limits_{\partial\omega}\epsilon^{y}_{\alpha\beta}(\boldsymbol{\psi}^{(\iota\varrho)})\epsilon^{y}_{\lambda\mu}(\boldsymbol{\psi}^{(\gamma\delta)})\boldsymbol{y}\cdot\boldsymbol{\nu}\,ds \tag{9}$$

for the $2D$ case. Here

$$\boldsymbol{\psi}^{(\alpha\beta)}(y) = \boldsymbol{\chi}^{(\alpha\beta)}(y) + \boldsymbol{E}^{(\alpha\beta)}(y)\ , \tag{10}$$

where

$$\boldsymbol{E}^{(\lambda\mu)}(y) = \frac{1}{2}(y_\lambda \boldsymbol{e}_\mu + y_\mu \boldsymbol{e}_\lambda)\ , \qquad \lambda,\mu \in \{1,2\} \tag{11}$$

Thus we have arrived at two seemingly different estimates of change of energy, since it is not easily seen why $\boldsymbol{G}$ should be equal to $\boldsymbol{M}$. It is, however, the case. The proof of the equality$\boldsymbol{G} = \boldsymbol{M}$ has been recently reported in Ref.[6].

APPLICATIONS

Topological derivatives are used in numerical methods of topology and shape optimization [1], [2]. Modelling of topological derivatives can be performed [6] by the selfadjoint extensions of elliptic operators with singular potentials [8]. The latter replace the geometrical singularities with the prescribed precision, confirmed by the error estimates. Moreover, new tools for the topology optimisation are provided by the exterior topology derivatives [7] relevant to the case of adding new material to a feasible domain. Some examples of applications are provided.

References

[1] Eschenauer H.A., Kobelev,V.V., Schumacher,A. *Bubble method for topology and shape optimization of structures* Struct.Optimiz. **8** : 42-51, 1994.

[2] Eschenauer H.A., Olhoff N. *Topology optimization of continuum structures: A review.* AMR 54(4) : 331-390, 2001.

[3] Lewiński T., Sokołowski, J. *Energy change due to the appearance of cavities in elastic solids* Int. J. Solids. Structures. **40** : 1765-1803, 2003.

[4] Mazja V.G. , Nazarov S.A., Plamenevskii B.A. *Asymptotic theory of elliptic boundary value problems in singularly perturbated domains* Vol.**1**,**2**. Birkhauser, Basel 2000.

[5] Movchan A.B., Movchan N.V. *Mathematical modeling of solids with nonregular boundaries* CRC Press, Boca Raton 1995.

[6] S. A. Nazarov, J. Sokołowski *Asymptotic analysis of shape functionals*, Journal de Mathématiques pures et appliquées, **82-2** : 125-196, 2003.

[7] S. A. Nazarov, J. Sokołowski *Techniques of asymptotic analysis in shape optimization* TRANSACTIONS of the French–Russian A.M. Liapunov Institute for Applied Mathematics and Computer Science **4**(2003) pp. 49-57.

[8] S. A. Nazarov, J. Sokołowski *Self adjoint extensions of differential operators in application to shape optimization* Comptes Rendus Mecanique, **331**(2003) pp. 667-672.

[9] J. Sokołowski, A. Żochowski *On topological derivative in shape optimization*, SIAM Journal on Control and Optimization. **37** : 1251–1272, 1999.

TOPOLOGY OPTIMIZATION OF VIBRATING STRUCTURES WITH HYDRODYNAMIC SURFACE PRESSURE LOADING

Niels Olhoff and Jianbin Du
Institute of Mechanical Engineering, Aalborg University, DK-9220, Aalborg East, Denmark

Summary This paper deals with the problem of topology optimization of continuum structures subjected to time-harmonic hydrodynamic surface pressure loading. This problem is an extension relative to traditional topology optimization, as both the locations and directions of the loading change as the structural topology changes. Maximization of the integral dynamic structural stiffness for a given value of the frequency of the hydrodynamic pressure loading is the design objective, and the total structural volume is prescribed.

INTRODUCTION

In the design of structures and machines against vibration and noise, many problems are concerned with structures subjected to surface pressure loading like hydrodynamic pressure loading that varies harmonically in time. An important feature of this class of problems is that the surface loads are not only dynamic, but also depend on the design itself, i.e. both the locations and directions of the loads will change with changes of the structural topology and shape. As a few examples we may mention hydrodynamic pressure loading in pump housings and pressure containers, and loading due to fluctuating internal fluid flow in ducts, diffusers and turbomachinery.
In this paper, maximum integral dynamic structural stiffness is chosen as the design objective for prescribed hydrodynamic pressure amplitude and frequency. The boundary conditions, the material, and the total volume of material within the admissible design domain are also given. The volumetric densities of material in the finite elements in the design domain are the design variables. The SIMP material model [1] is used. The design dependence of the loading implies two principal extensions relative to usual topology design problems. Firstly, the sensitivity analysis of the objective function also involves the sensitivities of the loads with respect to the design variables. Secondly, an enhanced design model must be considered, that encounters one or more parameterized, smooth surface domains associated with a prescribed iso-volumetric density of the material. These surface domains serve to define the action of the design dependent loading on the structure, and are determined by the design variables. This was first described by Hammer and Olhoff [2]. In their method, the design dependent loads are assumed to be applied on the surface of the potential structural domain, which is generated by iso-volumetric points of material density during the topology evolution. This method was developed further by Du and Olhoff [3] to automatically handle possible problems of "separate isolines" and "isoline islands" that may appear in the generation of the loading curve (for 2D problems), and the method was extended to 3D problems.

FORMULATION OF THE TOPOLOGY OPTIMIZATION PROBLEM

The problem of optimizing the topology of a structure for maximum value of the integral dynamics structural stiffness is equivalent to minimizing the integral dynamic compliance, which can be formulated as follows:

$$\begin{aligned} &\min_{\rho_e} \{C_d = \mathbf{P}^{\mathrm{T}}\mathbf{U}\} \\ &\textit{Subject to}: \\ &\quad (-\overline{\omega}^2\mathbf{M} + \mathbf{K})\mathbf{U} = \mathbf{P}\ , \\ &\quad \sum_{e=1}^{N_E} \rho_e V_e - V^* \le 0\ , \quad (V^* = \alpha V_0)\ , \\ &\quad 0 < \underline{\rho} \le \rho_e \le 1\ , \quad (e = 1, \cdots, N_e)\ . \end{aligned} \tag{1}$$

The dynamic compliance is equal to the work done by the external dynamic forces against corresponding displacements, and is proportional to the expression given for C_d in (1), where **U** denotes the displacement amplitude vector of the steady-state vibration, and **P** denotes the design-dependent load magnitude vector of the external surface loading. The harmonic external loading vector $\mathbf{p}(t)$ with the given excitation frequency $\overline{\omega}$ can then be expressed as $\mathbf{p}(t) = \mathbf{P}e^{i\overline{\omega}t}$ and the displacement response vector as $\mathbf{a}(t) = \mathbf{U}e^{i\overline{\omega}t}$. The symbols **K** and **M** represent the N dimensional structural stiffness and mass matrices, where N is the number of DOFs. The symbol ρ_e is the volumetric material density of element e and is the design variable in the problem. The symbol α denotes the volume fraction of available material and is given by V^*/V_0, where V_0 is the volume of the admissible design domain and V^* is the prescribed total volume of available material. The symbol N_e represents the total number of finite elements.

Sensitivity analysis

The sensitivity of the objective function C_d with respect to the design variables ρ_e is given by

$$C_d' = (\mathbf{P}^{\mathrm{T}}\mathbf{U})' = \mathbf{P}'^{\mathrm{T}}\mathbf{U} + \mathbf{P}^{\mathrm{T}}\mathbf{U}'\ , \tag{2}$$

where prime denotes partial derivative with respect to ρ_e. The sensitivity $\mathbf{P}'$ of the design-dependent load can be calculated by finite differences. The sensitivity $\mathbf{U}'$ of the displacement is given by

$$(\mathbf{K}-\bar{\omega}^2\mathbf{M})\,\mathbf{U}' = \mathbf{f} \equiv \mathbf{P}'-(\mathbf{K}'-\bar{\omega}^2\mathbf{M}')\,\mathbf{U}\,, \tag{3}$$

where the sensitivities of the stiffness matrix and the mass matrix can be directly obtained from the SIMP material model. Optimization problem (1) can be solved by using the well-known MMA method or an optimality criteria method.
During the design process, the method presented in Pedersen [4] is used to suppress the influence of localized eigenmodes on the global structural response.

RESULTS AND DISCUSSION

Not surprisingly, maximization of the integral dynamic stiffness normally yields a structure whose eigenfrequencies are far from the prescribed excitation frequency $\bar{\omega}$ of the hydrodynamic load; this structural behaviour implies efficient avoidance of resonance phenomena with large displacement amplitudes and low dynamic stiffness. As is well known from other problems of dynamic design of engineering structures, a difficulty that may need to be considered, is how to maintain the *static* stiffness (corresponds to $\bar{\omega}=0$) of the structure when optimizing its *dynamic* properties. In the present topology optimization problem, the initial design, which is normally represented by a uniform distribution of material with intermediate density over the admissible design domain, may have a low fundamental eigenfrequency Ω in comparison with the given loading frequency $\bar{\omega}$. In this case, an increase of the dynamic stiffness corresponding to $\bar{\omega}$ normally implies a decrease of the static stiffness due to a decrease of the fundamental eigenfrequency Ω (thereby avoiding resonance). As a result of this, the structure may become very weak at the (local) optimum of the dynamic stiffness that is obtained. In order to prevent this, one may introduce a lower bound constraint on the static stiffness. However, this will delimit the gain of the optimization of the dynamic stiffness. In fact, much larger values of the dynamic stiffness can be obtained if we can start out the optimization procedure using a value of $\bar{\omega}$ that is lower than the value of Ω for the current design, and then sequentially increase $\bar{\omega}$ up to its originally prescribed value. This procedure has the desirable effect of generating a series of topologies with increasing values of both Ω and the static and dynamic stiffnesses for the sequence of structures produced. Finally, the procedure delivers the optimum dynamic stiffness topology solution subject to the originally prescribed loading frequency $\bar{\omega}$. The procedure automatically avoids resonance, and works very well as long as the prescribed loading frequency $\bar{\omega}$ is lower than the optimum value Ω_{opt} of the fundamental eigenfrequency, i.e. $\bar{\omega}<\Omega_{opt}$.

Now, if the prescribed value of $\bar{\omega}$ is such that $\bar{\omega}>\Omega_{opt}$, the optimization of the dynamic stiffness will drive the fundamental eigenfrequency Ω towards zero. At the same time, the static displacements of the structure become very large, which means that the static stiffness tends to zero. The physical reason for this behaviour is that, in the limit, a disintegration is created in the structure. In this limit, the zero value of the fundamental eigenfrequency is associated with a rigid body vibration mode, and the static displacements of the disintegrated part of the structure become infinite, as the structure cannot sustain the static load.
A straight-forward way of avoiding this unwanted structural behaviour is to include a lower bound constraint on the static stiffness in the mathematical formulation of the problem of maximizing the dynamic stiffness. We have found that such a constraint is extremely effective and well-chosen when optimizing the dynamic stiffness for a value of $\bar{\omega}>\Omega_{opt}$.

NUMERICAL EXAMPLE

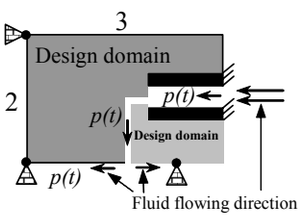


Fig. 1. Initial design

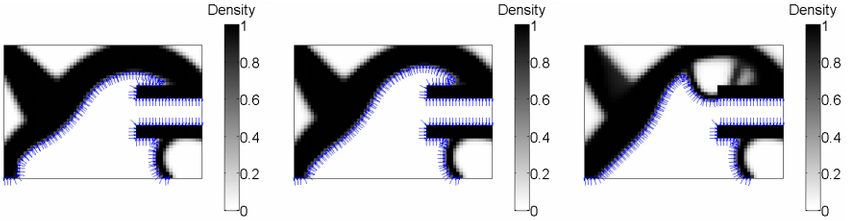


Fig. 2. (a) $\bar{\omega}=0$ (b) $\bar{\omega}=800$ (c) $\bar{\omega}=1000$

This example shows optimum topology designs of an inlet. The fluid flows in the channel of the inlet as shown in Fig. 1, and exerts a hydrodynamic pressure loading on the inner wall of the inlet. Figs. 2(a-c) show the optimized topologies (volume fraction 40%) for the three loading frequencies $\bar{\omega}=0$ (static loading), $\bar{\omega}=800$ and $\bar{\omega}=1000$.

References

[1] Bendsøe, M.P., Sigmund, O.: Topology Optimization: Theory, Methods and Applications, Springer 2003.
[2] Hammer, V.B.; Olhoff N.: Topology Optimization of Continuum Structures Subjected to Pressure Loading. *Struct. Multidisc. Optim*., **19**, 2, 85-92, 2000.
[3] Du, J., Olhoff, N.: Topological Optimization of Continuum Structures with Design-dependent Surface Loading - Part I: New Computational Approach for 2D Problems; Part II: Algorithm and Examples for 3D Problems, *Struct. Multidisc. Optim.* (in print).
[4] Pedersen, N.L.: Maximization of Eigenvalues Using Topology Optimization. *Struct. Multidisc. Optim*., **20**, 2-11, 2000.

A TECHNIQUE FOR NONSMOOTH OPTIMIZATION BASED ON THE INTERIOR POINT FEASIBLE DIRECTIONS ALGORITHM

José Herskovits*, Wilhelm Passarella**, Susana Scheimberg***, Regina Burachik***
* *COPPE/Federal University of Rio de Janeiro, Mechanical Engineering Program, Caixa Postal 68503, 21945 970 Rio de Janeiro, Brazil*
** *Federal University of Juiz de Fora, Department of Mathematics, Juiz de Fora, Brazil*
*** **COPPE/Federal University of Rio de Janeiro, Systems Engineering Program, Rio de Janeiro, Brazil*

Summary A new method for the minimization of nonsmooth convex functions is presented. This approach defines a constrained optimization Equivalent Problem and a sequence of Approximate Problems, where the constraints are substituted by tangent planes. At each iteration a Feasible Direction for the Equivalent Problem is obtained by computing Feasible Descent Directions for the Approximate Problems. The present approach is based on FD_IPA, a Feasible Directions Interior Point Algorithm for constrained smooth optimization. We prove global convergence and solve very efficiently several test problems.

INTRODUCTION

Nonsmooth functions are frequently present in Structural Optimization. This is the case with applications involving eigenvalues of matrices depending of the design variables. Smooth optimization algorithms cannot be applied to this problems because they usually stop at non optimal solutions.

We consider the the optimization problem:

$$(OP) \quad \min_x F(x)$$

where $x \in R^n$ and F is convex and not necessarily differentiable. We call $\partial F(x)$ the Subdifferential of F at x. Any vector $s \in \partial F(x)$, $s \in R^n$, is a Subgradient, [2]. In general, nonsmooth optimization methods assume that there is an available tool that, for a given x, computes $F(x)$ and one subgradient $s(x) \in \partial F(x)$.

Let us define the auxiliary variable $z \in R$ and the constrained Equivalent Problem:

$$(EP) \begin{cases} \min_{x,z} z \\ \text{s. t. } F(x) \leq z \end{cases} \tag{1}$$

The present algorithm builds a sequence (x^k, z^k) at the epigraph of $F(x)$ such that $z^{k+1} < z^k$. At each iterate (x^k, z^k), a sequence of Approximate Problems is constructed, with the constraints of (EP) substituted by tangent planes. A Search Direction for the equivalent problem is obtained by computing a Feasible Descent Direction for the current approximate problem. If the step length is "short", the approximate problem is updated by adding a new tangent plane and a new search direction is computed. This procedure is repeated until a "good" step is obtained. When this happens, the search direction is a Feasible Descent Direction of the equivalent problem. We employ the Feasible Directions Interior Point Algorithm for constrained smooth optimization to compute the search directions, [1].

We prove global convergence and describe the numerical results with a set of test problems. The present method behaves very well when compared to other techniques and is very strong, being all test problems solved with the same set of parameters.

ABOUT FD_IPA, THE FEASIBLE DIRECTIONS INTERIOR POINT ALGORITHM

Some aspects of the numerical implementation of the Feasible Directions Interior Point Algorithm which are of interest in the present paper, are described now. A complete description of FD_IPA and the corresponding theoretical and numerical results can be found in [1].

Let be the smooth inequality constrained optimization problem:

$$\begin{cases} \min_x f(x) \\ \text{s. t. } g(x) \leq 0 \end{cases} \tag{2}$$

where $x \in R^n$ and $g \in R^m$. To get a Feasible Descent Direction of the problem at a point x, FD_IPA solves two linear systems with the same matrix:

$$\begin{bmatrix} B & \nabla g(x) \\ \Lambda \nabla g^T(x) & G(x) \end{bmatrix} \begin{bmatrix} d_0 & d_1 \\ \lambda_0 & \lambda_1 \end{bmatrix} = - \begin{bmatrix} \nabla f(x) & 0 \\ 0 & \lambda \end{bmatrix} \tag{3}$$

where $G(x) \equiv diag[g(x)]$ and $\Lambda \equiv diag(\lambda)$ and $B \in R^{n \times n}$ is a symmetric and positive definite matrix. In particular B can be taken equal to the second derivative of the Lagrangian function or to a quasi-Newton approximation.

In [1], it was proved that the vector $d_0 \in R^n$ is a descent direction of the objective function, that is, $d_0^t \nabla f(x) < 0$. However, d_0 is not always a feasible direction of the problem. We also have that $d_1 \in R^n$, called restoring direction, points to the interior of the feasible set. FD_IPA obtaines a Feasible Descent Direction by computing $d = d_0 + \rho d_1$ for $\rho > 0$ and $\rho > (\alpha - 1) d_0^t \nabla f(x) / d_0^t \nabla f(x)$, $\alpha \in (0, 1)$. Since $d_0^t \nabla f(x) < 0$ it is easy to prove that $d^t \nabla f(x) < 0$.
Finally, FD_IPA carries out a line search on d looking for a new interior point with a lower objective.

AN ALGORITHM FOR NONSMOOTH OPTIMIZATION

The iterative process for present algorithm for nonsmooth optimization is presented now.

Data: Define an initial iterate (x^0, z^0) such that $z^0 > F(x^0)$ and set $k = 0$.
Step 1. Define, for the iteration k, the initial sub-iterate $x_0^k \equiv x^k$ and set $l = 0$.
Step 2. Define the Approximated Problem:

$$(AP_l^k) \begin{cases} \min\limits_{x,z} z \\ \text{s. t. } F(x_0^k) + s(x_0^k)(x - x_0^k) \le z \\ \qquad F(x_1^k) + s(x_1^k)(x - x_1^k) \le z \\ \qquad \ldots\ldots\ldots\ldots \\ \qquad F(x_l^k) + s(x_l^k)(x - x_l^k) \le z \end{cases} \tag{4}$$

where $s(x_l^k) \in \partial F(x_l^k)$. The constraints are linear and tangent to $z = F(x)$ at $x_0^k, x_1^k, ..., x_l^k$ respectively.
Step 3. Search Direction:
Compute $d_l^k \equiv (d_{lx}^k, d_{lz}^k)$, a Feasible Descent Direction given by FD_IPA at (x^k, z^k) when solving (AP_l^k).
Step 4. Line Search:
Find $t_l^k = sup(t;$ such that $g(x + t d_x, z + t d_z) \le 0)$
If $t_l^k > 1$ set $t_l^k = 1$
Step 5. Stopping test for sub-iterations
If

$$F(x^k + \mu t_l^k d_{lx}^k) \le z^k + \mu t_l^k d_{lz}^k$$

the search direction is good. Then, set

$$(x^{k+1}, z^{k+1}) = (x^k + \mu t_l^k d_{lx}^k, z^k + \mu t_l^k d_{lz}^k)$$

Increase iterations counter: $k = k + 1$ and Return to **Step 1.**
Step 6. Define a new sub-iterate:

$$x_{l+1}^k = x^k + \mu t_l^k d_{lx}^k$$

Increase sub-iterations counter: $l = l + 1$ and Return to **Step 2.** □

The present method consists on a two-levels iterative process. For each iterate (x^k, z^k) the sequence of sub-iterates $\{(x_l^k, z_l^k)\}$ is finite. The constraints of (AP_l^k) are taken tangent to $F(x)$ at $\{x_l^k\}$. The sub-iterations stop when the new point $(x^k + \mu t_l^k d_{lx}^k, z^k + \mu t_l^k d_{lz}^k)$ is feasible.

CONCLUSIONS

The present algorithm is simple to code and includes a few number of parameters. The numerical results show that it is very strong, since all the test problems were solved efficiently with the same set of parameters. Complete theoretical results support the present technique.

References

[1] Herskovits J.: Feasible Directions Interior Point Technique For Nonlinear Optimization. *JOTA, Journal for Optimization Theory and Applicationa* **v99-1**, pp. 121-146, 1998.
[2] Hirriart-Urruty, J. B. and Lemarechal, C.: *Convex Analysis and Minimization Algorithms.* Springer Verlag, Heidelberg, 1993.

NASH EQUILIBRIUM IN BICRITERIA STRUCTURAL OPTIMIZATION

Timo Saksala

Institute of Applied Mechanics and Optimization, Tampere University of Technology, P.O.Box 589, FIN-33101 Tampere, Finland

Summary Nash equilibrium, a game theoretic concept, has lately been introduced in multicriteria optimization of structures as a computationally cheap alternative to Pareto optima. In this paper we formulate a bicriteria optimization problem game theoretically and present a class of problems for which there exists a Pareto optimal Nash equilibrium. We illustrate the theory with a static truss optimization example.

INTRODUCTION

Pareto optimality is the key concept of multicriteria optimization. The set of Pareto optima is, however, usually expensive to compute. For this reason some researchers [1] have lately introduced the Nash equilibrium as a computationally cheap alternative to the Pareto optima. The Nash equilibrium is a non-cooperative game theoretic solution concept whereas the multicriteria optimization problem is like a cooperative game. Thus, a Nash equilibrium point as a solution to a multicriteria optimization problem can be dominated, that is, it is not necessarily Pareto optimal. In addition, a Nash equilibrium point, in contrast to a Pareto optimal point, need not exist even in problems with continuous criteria. In this paper we formulate a bicriteria structural optimization problem game theoretically and present a class of problems where a Pareto optimal Nash equilibrium exists.

BICRITERIA OPTIMIZATION PROBLEM AND PARETO OPTIMALITY

We define the bicriteria optimization problem as follows

$$\min_{\mathbf{x}\in\Omega} \mathbf{f}(\mathbf{x}) = \left[f_1(\mathbf{x}),\ f_2(\mathbf{x}) \right]^{\mathrm{T}} \tag{1}$$

where $\mathbf{f} : \Omega \to \mathbf{R}^2$ is a vector objective function whose components are functions from Ω to $\mathbf{R}$ to be minimized simultaneously (criteria). Here Ω is a feasible set which we assume to be of form $\Omega = \{\mathbf{x} \in \mathbf{R}^n \mid \mathbf{g}(\mathbf{x}) \le \mathbf{0}\}$, where $\mathbf{g} : \mathbf{R}^n \to \mathbf{R}^k$ is constraint vector function. Finally, the image of Ω under $\mathbf{f}$ is called an attainable set denoted as $\Lambda = \mathbf{f}(\Omega)$. Next, we define the key solution concept, the Pareto optimality for problem (1).

Definition 1 A vector $\mathbf{x}^* \in \Omega$ is Pareto optimal if and only if there exist no other vector $\mathbf{x} \in \Omega$ such that $f_i(\mathbf{x}) \le f_i(\mathbf{x}^*)$ for i = 1,2 with strict inequality for at least one i. We call $\mathbf{f}(\mathbf{x}^*) \in \Lambda$ a minimal point.

Problem (1) has at least one Pareto optimum if the criteria are smooth and Ω is compact [2].

GAME THEORETIC FORMULATION AND NASH EQUILIBRIUM

When formulating (1) as a non-cooperative two-player game, we assign each player i one objective function f_i, a payoff. Player i wants to minimize his payoff f_i as a function of his strategy $\mathbf{x}_i \in \mathbf{R}^{n_i}$. We denote by $\mathbf{x} = (\mathbf{x}_1, \mathbf{x}_2) \in \mathbf{R}^n$ a strategy profile ($n = n_1 + n_2$). Then the set of feasible strategy profiles is the feasible set of optimization problem (1), $\Omega \subset \mathbf{R}^n$. Now the game formulation of (1) is as follows.

$$\text{player } i\ (i = 1,2): \ \min_{\mathbf{x}_i} f_i(\mathbf{x}) \quad \text{subject to } \mathbf{x} \in \Omega \tag{2}$$

This formulation is not unique but can be done in different ways depending on the dimensions of Ω. In case $\mathbf{x} = (x_1, x_2) \in \Omega \subset \mathbf{R}^2$ these formulations are

$$\text{I}: \text{ player } 1: \min_{x_1} f_1(x_1, x_2) \ \&\ \text{player } 2: \min_{x_2} f_2(x_1, x_2), \quad \text{II}: \text{ player } 1: \min_{x_2} f_1(x_1, x_2) \ \&\ \text{player } 2: \min_{x_1} f_2(x_1, x_2) \tag{3}$$

These formulations represent different games in the sense they may (and usually) have different non-cooperative game solutions, e.g. Nash equilibrium points which we define next.

Definition 2 A strategy profile $\mathbf{x}^* = (\mathbf{x}_1^*, \mathbf{x}_2^*) \in \Omega$ is a Nash equilibrium for game (2) if and only if for all $\mathbf{x} = (\mathbf{x}_1, \mathbf{x}_2) \in \Omega$ it holds that $f_1(\mathbf{x}_1^*, \mathbf{x}_2^*) \le f_1(\mathbf{x}_1, \mathbf{x}_2^*)$ and $f_2(\mathbf{x}_1^*, \mathbf{x}_2^*) \le f_2(\mathbf{x}_1^*, \mathbf{x}_2)$.

As well known, the existence of Nash equilibrium is more complicated issue than that of Pareto optimality. Moreover, the Nash equilibrium tends to be Pareto inefficient [3]. However, there is a class of problems for which there exists a Pareto optimal Nash equilibrium.

Theorem 1 Let $\Omega = [a,b]\times[c,d] \in \mathbf{R}^2$. Let $f_1, f_2 \in C^0(\Omega)$ be such that functions $x_i \mapsto f_j(x_1, x_2)$ $(i, j = 1,2)$ are strictly monotonous for all $\mathbf{x} = (x_1, x_2) \in \Omega$. Finally, let $\mathbf{f} = [f_1, f_2]^{\mathrm{T}}$ be bijection. Then either for game I or game II there exists a Pareto optimal Nash equilibrium point which is one of the corner points of Ω..

Proof. Straightforward and needs too much space to be included.

A STATIC TRUSS EXAMPLE

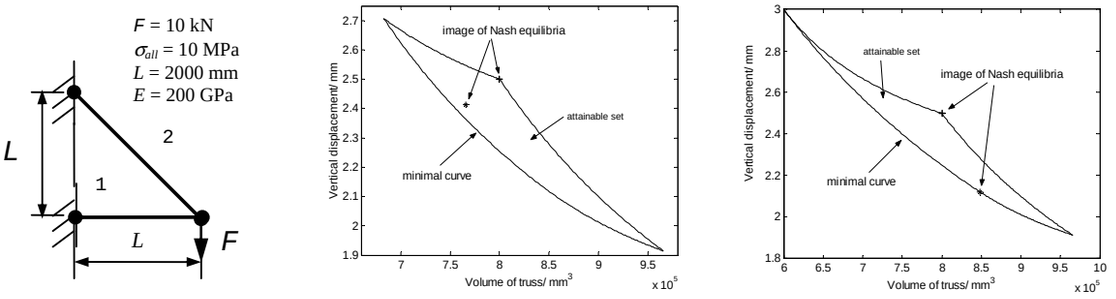
Consider a two-bar isostatic truss under a static vertical loading illustrated below (Fig. 1). Our bicriteria optimization problem is

$$\begin{aligned} &\min\,[V(\mathbf{x}), \Delta(\mathbf{x})]^{\mathrm{T}} \\ &\text{s.t.:}\quad F/\sigma_{sall} \le x_1 \le \bar{x}_1\,, \quad \sqrt{2}F/\sigma_{sall} \le x_2 \le \bar{x}_2 \end{aligned} \tag{4}$$

where $\mathbf{x} = (x_1, x_2)$ is the design vector consisting of areas of the truss members, V is the volume of the truss, and Δ is the vertical displacement of the joint of the truss members. The objective functions are $V(\mathbf{x}) = L\left(x_1 + \sqrt{2}x_2\right)$ and $\Delta(\mathbf{x}) = \frac{FL}{E}\left(\frac{1}{x_1} + \frac{2\sqrt{2}}{x_2}\right)$. These functions are strictly monotonous in the sense of theorem 1 when variables are non-zero. First, let the upper limit for both of the bars of the truss be 200 mm^2. Then the feasible set for this problem is $\Omega_1 = [100, 200]\times[\sqrt{2}\cdot 100, 200]\,\mathrm{mm}^2$. The Nash equilibria in games I and II are $\mathbf{x}_{\mathrm{I}} = (100, 200)$ and $\mathbf{x}_{\mathrm{II}} = (200, \sqrt{2}\cdot 100)$, respectively, and both of them are Pareto inefficient (see Fig. 1). The reason for the Pareto inefficiency of $\mathbf{x}_{\mathrm{I}}$ is that $\mathbf{f}$ is not bijection on Ω_1. The determinant of $\nabla\mathbf{f}$ vanishes on the line $x_2 = \sqrt{2}x_1$ and there are points on this line that dominate $\mathbf{x}_{\mathrm{I}}$. Thus we have to assume bijectivity for theorem 1 to hold generally.

Second, let the feasible set be $\Omega_2 = [\sqrt{2}\cdot 100, 200]\times[\sqrt{2}\cdot 100, 200]$. Now the Nash equilibria of games I and II are $\mathbf{x}_{\mathrm{I}} = (\sqrt{2}\cdot 100, 200)$ and $\mathbf{x}_{\mathrm{II}} = (200, \sqrt{2}\cdot 100)$, respectively. But this time $\mathbf{x}_{\mathrm{I}}$ is Pareto optimal even though it is the only point in Ω_2 where $\nabla\mathbf{f}$ has no inverse.

We see from figure 1 that in both cases the point $\mathbf{x}_{\mathrm{II}}$ is the worst point on Ω in the sense of Pareto optimality.



(a) (b) (c)

Figure 1 Idealized structure and design data of static truss example (a), attainable sets, image of Nash equilibria and minimal curves of the two-bar static truss example for Ω_1 (b) and Ω_2 (c), characters * and + indicate $\mathbf{f}(\mathbf{x}_{\mathrm{I}})$ and $\mathbf{f}(\mathbf{x}_{\mathrm{II}})$

CONCLUSIONS

The game formulation of bicriteria optimization problem can be done in number of ways depending on the dimension of the feasible set. These formulations may have different Nash equilibrium points and some of these points can be the worst in the sense of Pareto efficiency. However, if the conditions of theorem 1 are met then at least one of the Nash equilibrium points is Pareto optimal. Moreover, since all the Nash equilibrium points under the conditions of theorem 1 are corner points of the feasible set they can be determined without computer methods.

References

[1] Habbal, et al.: A Nash game approach for multidisciplinary topology design. In: Short Papers of WCSMO5. Lido di Jesolo, Italy, May 19-23, 2003. pp. 99-100.

[2] Koski, J.: Truss Optimization with Vector Criterion. Tampere University of Technology, Publications 6, 1979.

[3] Dubey, P.: Inefficiency of Nash equilibria. *Mathematics of Operations Research*, 11:1-8, 1986.

ON SHAPE OPTIMIZATION FOR EIGENVALUE PROBLEMS

Pauli Pedersen*, Niels L. Pedersen**
*Department of Mechanical Engineering, Solid Mechanics, Technical University of Denmark,
Nils Koppels Allè, Building 404, DK-2800 Kgs.Lyngby, Denmark
**Institute of Mechanical Engineering, Aalborg University,
Pontoppidanstræde 101, DK-9220 Aalborg East, Denmark

Summary For a broad class of static problems an optimality criterion of constant energy density along the designed boundary is proved earlier. In the present paper we prove a similar criterion for eigenvalue problems. This optimality criterion serve as the tool for more basic understanding and for idealized reference cases also as the basis for recursive procedures. Eigenfrequencies for in-plane vibrations as well as for out-of-plane vibrations of plates are optimized.

INTRODUCTION

In size optimization for minimum compliance with only a volume constraint, the necessary optimality criterion is uniform energy density. This criterion also holds for non-linear power-law, anisotropic elasticity, see [1] and [4].
For eigenfrequency optimization with size parameters a similar criterion specifies constant difference between amplitudes of elastic energy density and kinetic energy density, see [3] which describes the necessary modifications when Timoshenko beam theory is applied.
In shape optimization with prescribed size, say the thickness of a plate, we cannot expect constant energy density everywhere. For compliance minimization with only a single constraint on given volume the necessary optimality criterion will be constant energy density along the boundary to be designed, see [5] for extensions to non-linear power-law, anisotropic elasticity. and for the relations to strength optimization (stress constraints).
In the present paper we study shape optimization for eigenfrequency maximization and prove necessary optimality criteria, which expresses constant difference between amplitudes of elastic energy density and kinetic energy density along the boundary to be designed. The boundary may be internal (holes) as well as external. Numerical results for out-of-plane plate vibrations are recently published in [2]. In the present paper we concentrate on the theoretical aspects and also show results for in-plane plate vibrations.

THEORETICAL ASPECTS

A short version of the proof for the optimality criterion is here attempted. Let the shape of the boundary be described by localized design variables and choose two of these h_i and h_j. Each of these variables are related to areas A_i and A_j at the boundary, The differential dh_i implies the area differential dA_i and the differential dh_j implies the area differential dA_j. The constraint of unchanged total area (total volume) gives $dA_j = -dA_i$.
For a certain squared eigenfrequency ω^2, let the elastic energy amplitude related to the area A_i be U_i and let let the kinetic energy amplitude related to the area A_i be T_i. For the design variable h_j we have the corresponding quantities U_j and T_j. From general sensitivity analysis for eigenvalue problems we have, as a result of changing both design variables h_i and h_j, the differential

$$d(\omega^2) = (dU_i - dT_i)_{\text{fixed displacement mode}} + (dU_j - dT_j)_{\text{fixed displacement mode}} \tag{1}$$

assuming a normalization of displacement mode to give $T/\omega^2 = 1$. With fixed displacement mode we have (assuming homogeneous, explicit dependence on area) $dU_i = \frac{U_i}{A_i} dA_i$ and similar for dU_i, dT_i and dT_j. Inserting these relations in (1) and using the constraint condition $dA_j = -dA_i$ we get

$$d(\omega^2) = \left(\frac{U_i - T_i}{A_i} - \frac{U_j - T_j}{A_j} \right) dA_i \tag{2}$$

Then, a necessary condition for $d(\omega^2) = 0$ (stationarity of eigenvalue) for $dA_i \neq 0$ is

$$\frac{U_i - T_i}{A_i} = \frac{U_j - T_j}{A_j} \tag{3}$$

or in words: Constant difference between mean potential energy U_i/A_i and mean kinetic energy T_i/A_i for all design variables, i.e. with localized design variables: constant difference of energy densities along the boundary to be designed.

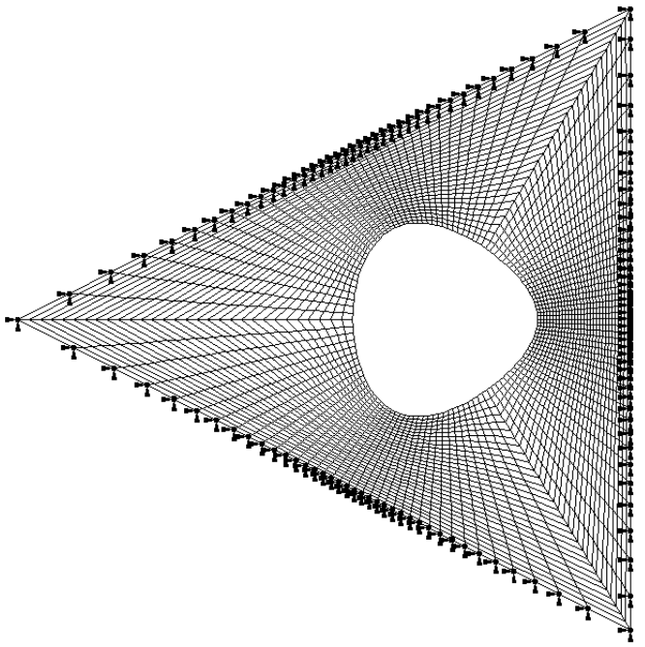


Figure 1. Finite element mesh of optimized plate showing the shape of the optimized hole for maximum first eigenfrequency of triangular plate.

NUMERICAL ASPECTS

Numerical solutions are based on the finite element modeling with extensive use of calculation on the element level. Multiplicity of eigenvalues are often encountered, especially when optimal design is attempted. Thus the method of analysis must be apple to deal with this. Therefore, the method of subspace iteration is applied.

Also the necessary sensitivity analysis must be apple to account for multiplicity. The solution is to locate the eigenmodes that also exist when the design is changed infinitesimal. This involves solving an eigenvalue-problem formulated in terms of mutual sensitivities, and the practical problem is merely to decide when multiplicity is present.

The numerical determination of optimal design parameters is iterative. For idealized problems simple recursive iterations can be based on the actual optimality criterion or a Newton-Raphson procedure can be setup to satisfy the criterion. With several constraints we used methods from mathematical programming.

NUMERICAL EXAMPLES

A number of numerical examples are presented in [2]. Figure 1 shows the optimal shape for a hole of given area in a triangular plate, where the frequency for the fundamental out-of plane free vibrations are maximized. For the present paper we also show a number of cases with in-plane vibrations, where part of the external boundary is subjected to design. Geometrical constraints, including the constraints from the chosen parametrization, can make it impossible to satisfy the optimality criterion completely, and we discuss this aspect in detail.

References

[1] Dems, K., and Mroz, Z.: Multiparameter structural shape optimization by finite element method. *Int. J. Num. Meth. Eng.* **13**:247–263,1978

[2] Pedersen, N. L., and Pedersen, P.: Shape, position and orientational design of holes for plates with optimized eigenfrequencies. *In Cartmell, M., ed.: Modern practice in stress and vibration analysis*, Uetikon-Zurich, Switzerland: Trans Tech Publications: 321–328,2003

[3] Pedersen, P.: Design with several eigenvalue constraints by finite elements and linear programming. *J. Structural Mechanics* **10(3)**:243–271, 1982 83

[4] Pedersen, P.: Some general optimal design results using anisotropic power law non-linear elasticity. *Structural Optimization* **15**:73–80, 1998

[5] Pedersen, P.: On optimal shapes in materials and structures. *Structural and Multidisciplinary Optimization* **19**:169–182, 2000

SHAPE OPTIMISATION OF RAILWAY WHEEL PROFILE

V.L. Markine, I.Y. Shevtsov, C. Esveld
Section of Road and Railway Engineering
Faculty of Civil Engineering and Geosciences
Delft University of Technology
Stevinweg 1, NL-2628, CN Delft, The Netherlands

Summary The paper presents a procedure for optimal design of a wheel profile based on geometrical wheel/rail contact characteristics. An optimized wheel profile is obtained as a solution of inverse (minimization) problem. A number of new wheel profiles are obtained. Their advantage compared with old one is shown.
Keywords: Inverse problems, shape optimisation, wheel-rail contact, multipoint approximations

INTRODUCTION

A rolling radii difference is one of the main characteristics that describes a contact between wheelset and railway track, which in turn defines the dynamic behaviour of a wheelset [[1], [2]]. Generally, it is a non-linear function of the lateral displacement y of wheelset. Due to the wear of wheels the wheel profile and consequently Δr are changing as shown in Figure 1. Determination of '$y-\Delta r$' curve for given wheel and rail profiles is a well-known problem, which is out of scope of this paper. A more interesting problem is solution of the inverse problem, i.e. determination of a wheel profile for a given rail, which has an a priori defined rolling radii difference Δr (Figure 3).

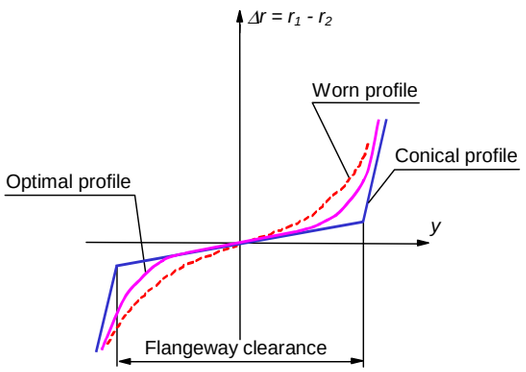


Figure 1 Rolling radii difference vs. lateral displacement of wheelset curve ('$y-\Delta r$'curve)

PROBLEM FORMULATION

Solution of such inverse problem is formulated here as a minimization problem. A shape of a wheel profile is varied in order to minimize the difference between the calculated and given rolling radii difference of a wheelset. The shape of the wheel profile is approximated by a Piecewise Cubic Hermite Interpolating Polynomial. The shape of the wheel profile has been varied by changing position of some points of the profile as shown in Figure 2. The minimization is performed subject to geometrical constrains in order to prevent unrealistic profiles. A solution of the minimization problem is taken as a new wheel profile. Wheels with such a profile have a given contact characteristics, which results in improved wheelset dynamics and in reduction of wheel flange wear.

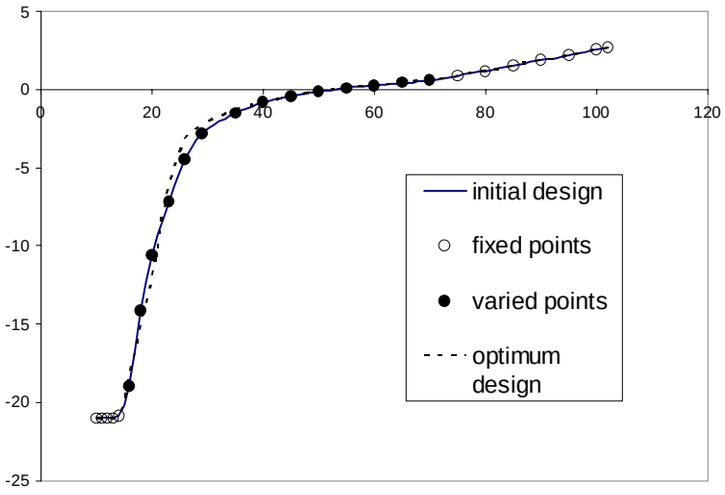


Figure 2 Design variables, initial and optimum shape of a wheel

RESULTS

The problem has been solved using the MARS method (Multipoint Approximation based on Response Surface fitting) [[3]], [[4]]. The method has been specifically developed for problems where multiple response analyses and (time consuming) simulations are involved.

Using the presented procedure a new wheel profile for a tram has been obtained. The dynamic behavior of vehicles with new and original wheel profiles has been analyzed and compared using ADAMS/Rail. The results of optimisation (Figure 2 and Figure 3) are presented and discussed in the full paper.

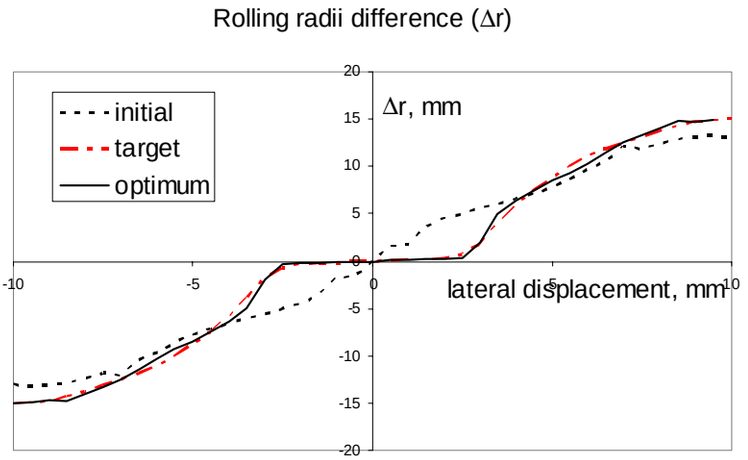


Figure 3 Results of optimisation: target rolling radii difference and the ones for initial and obtained wheel profiles

References

[1] Dukkipati, R.V. (2000) Vehicle Dynamics. Boca Raton: CRC Press. ISBN 0-8493-0976-X

[2] Esveld, C. (1989) Modern Railway Track. MRT-Productions, Duisburg. ISBN 90-800324-1-7

[3] Markine, V.L. (1999) *Optimisation of the Dynamic Behaviour of Mechanical Systems.* PhD Thesis, TU Delft. Shaker Publishing BV. ISBN 90-423-0069-8.

[4] Toropov, V.V. (1989) Simulation Approach to Structural Optimisation. Structural Optimisation, 1, 37-46.

SHAPE OPTIMIZATION OF THERMOMECHANICAL STRUCTURES IN THE PRESENCE OF CONVECTION AND RADIATION USING PARALLEL EVOLUTIONARY COMPUTATION

Ryszard A. Białecki[*], Tadeusz S. Burczyński[**],
Adam Długosz[**], Wacław Kuś[**], Ziemowit Ostrowski[*]
[*]*Institute of Thermal Technology,* [**]*Department for Strength of Materials and Computational Mechanics, Silesian University of Technology, Konarskiego 18a, PL 44-100 Gliwice, Poland*

Summary Shape optimization of heat conducting, elastic bodies subjected to thermal and mechanical loads is considered. Interaction of stress and temperature fields is modeled using the boundary element formulation of steady state thermoelasticity. The presence of heat radiation with mutual irradiation of the boundaries and the presence of shadow zones is taken into account. A parallel evolutionary algorithm is used to evaluate the optimal shape.

INTRODUCTION

The physical problem addressed in the paper is evolutionary shape optimization of thermoelastic bodies whose boundaries exchange heat by convection and radiation and mechanical loads. The novel aspect in the study is the presence of mutual irradiation of concave portions of the boundary. Such model contains strongly nonlinear behavior due to the fourth power Stefan Boltzmann law. Another difficulty is caused by the presence of the shadow zones. The presence of heat radiation in the mathematical models of heat transfer is often neglected. Inclusion of radiation in the model becomes crucial at elevated temperatures, where this heat transfer mode dominates and may be responsible for more that 90% of the total energy transport.
In the shape optimization problems the domains and their boundaries are changing during the iteration process. Every evaluation of the objective function requires a solution of a discretized boundary value problem preceded by a generation of a new numerical grid. Because the boundary element method (BEM) is typically limited only to the boundary its application in shape optimization arises in a natural way.
Evolutionary algorithms (EA) mimic the evolution of subsequent generations of living systems. This class of algorithms does not require evaluation of sensitivity coefficients and is treated as the global optimization technique. The main and very serious drawback of these techniques is their high computational cost. This is partially mitigated by invoking the parallel computations.

FORMULATION OF THE BOUNDARY VALUE PROBLEM

An elastic body occupying a domain Ω bounded by a boundary Γ is considered. The physical problem is considered in the terms of the BEM approach.

Conduction

The heat conduction equation converted into an equivalent integral equation takes the form

$$c(\mathbf{r})T(\mathbf{r}) = \int_{\Gamma}\left[T^*(\mathbf{r},\mathbf{p})q(\mathbf{p}) - q^*(\mathbf{r},\mathbf{p})T(\mathbf{p})\right]d\Gamma(\mathbf{p}) \tag{1}$$

where T and q are the temperature and the heat flux fields on the boundary, respectively, T^* and q^* are temperature and heat flux fundamental solutions, respectively, at points $\mathbf{r}$ generated by a unit pointwise heat sources located at point $\mathbf{p}$ of an infinite medium

Radiation

Radiation is governed by an integral equation linking the radiative heat flux q^r and the blackbody emissive power $e_b=\sigma T^4$, where σ is the Stefan Boltzmann constant. For an enclosure bounded by a closed surface Γ_c the equation takes the form

$$q^r(\mathbf{r}) + \varepsilon(\mathbf{r})e_b(\mathbf{r}) = \varepsilon(\mathbf{r})\int_{\Gamma_c}\left[e_b(\mathbf{p}) + \frac{1-\varepsilon(\mathbf{p})}{\varepsilon(\mathbf{p})}q^r(\mathbf{p})\right]\frac{\cos\phi_r\,\cos\phi_p}{2|\mathbf{r}-\mathbf{p}|}\beta(\mathbf{r},\mathbf{p})d\Gamma_c(\mathbf{p}) \tag{2}$$

where ε is the emissivity, ϕ_r and ϕ_p are angles defined by line connecting points $\mathbf{r}$ and $\mathbf{p}$ and normal at these points, β is the Boolean function.

Thermoelasticity

Boundary integral equations for thermoelasticity are given in the form

$$c_{ij}(\mathbf{r})u_j(\mathbf{r}) + \int_{\Gamma}\left[p_{ij}^*(\mathbf{r},\mathbf{p})u_j(\mathbf{p}) - u_{ij}^*(\mathbf{r},\mathbf{p})p_j(\mathbf{p})\right]d\Gamma(\mathbf{p}) + \int_{\Gamma}\left[P_i(\mathbf{r},\mathbf{p})T(\mathbf{p}) - Q_i(\mathbf{r},\mathbf{p})q(\mathbf{p})\right]d\Gamma(\mathbf{p}) \tag{3}$$

where u_{ij}^* and p_{ij}^* are fundamental solutions of elastostatics, P_i and Q_i are known functions.

Eqs (1), (2) and (3) are completed by suitable boundary conditions. For every geometrical configuration the conjugate problem of heat and stress analysis is solved using BEM. The strongly nonlinear heat transfer problem modeled by equation of conduction (1) and radiation (2) is solved with respect to the boundary temperatures, conductive $\mathbf{q}^c$ and radiative $\mathbf{q}^r$ heat fluxes. The coupling between these equations is due to the continuity of temperature and the total heat balance on the radiating surface $\mathbf{q}=\mathbf{q}^c + \mathbf{q}^r$. Heaving boundary temperatures and fluxes the displacement and traction fields are evaluated solving (3).

EVOLUTIONARY OPTIMIZATION

There are many possible objective functions that may be defined for shape optimization of the considered problem. In the paper two types of optimization criteria were examined: (Case I) minimum volume of the structure (Eq. 4) and (Case II) maximum amount of heat dissipated from a portion of the boundary Γ_d (Eq. 5)

$$\min_{ch} ff_I; \quad where \quad ff_I = \int_\Omega d\Omega \qquad (4) \qquad \text{and} \qquad \max_{ch} ff_{II}; \quad where \quad ff_{II} = \int_{\Gamma_d} q d\Gamma_d \qquad (5)$$

with constraints imposed on admissible temperature and equivalent stress fields (Case I) and on the admissible volume of the structure (Case II)

A chromosome *ch* contains genes that are represented by real numbers and play the role of design variables describing the shape of the structure. The parallel EA performs evolutionary process in the same manner as their sequential counterparts. The difference is in the fitness evaluation. While for the sequential process all members of the population are processed by the same CPU, the values of the fitness function are computed concurrently by M processors. The approach used in this study was to allot to one processor the task of computing the fitness function corresponding to one chromosome. The parallel AE has a master-slave architecture. Using a random process the *master* unit generates the initial population consisting of chromosomes whose genes assume admissible values. These chromosomes are transferred to the *slave* units. In the next step slaves transmit the values of the fitness function to the master. Communication between master and slaves is accomplished invoking the socket mechanism. The generation of a new population of chromosomes is carried out by the master by executing appropriate evolutionary operators (rank selection, cloning, simple crossover and Gauss mutation). The resulting set of new chromosomes is transmitted to the slaves where the fitness function is evaluated. The process of generation of new populations is terminated when the stop criterion is fulfilled.

NUMERICAL EXAMPLES

Numerical tests were performed for shape optimization of a heat radiator used to dissipate heat from electrical devices (Fig. 1). The problem was solved for both criteria (4) and (5) aking into account the symmetry of the structure. In both cases 14 design variables described the shape. The parameters of AE used in this study were: 20 chromosomes, 14 genes and 200 generations. The best radiator optimal shapes are shown in Fig. 2a (Case I) and in Fig. 2b (Case II).

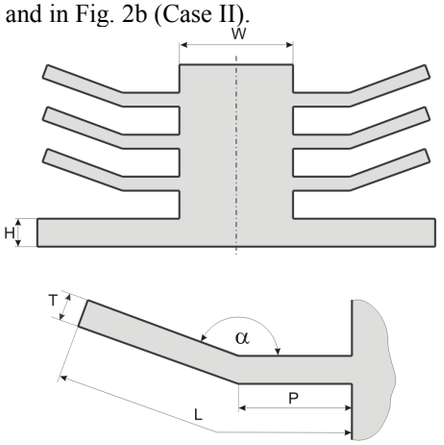


Figure 1: Geometry of the radiator and design variables

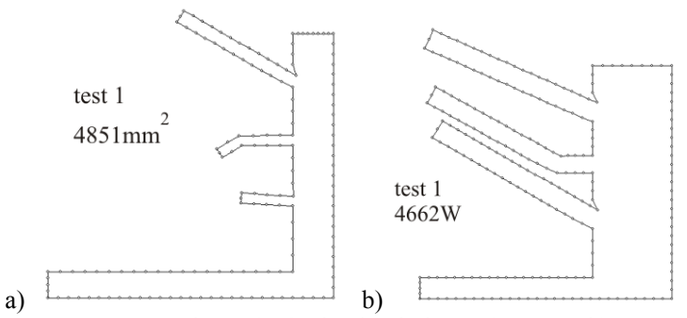


Figure 2: Optimal solutions, a) case I, b) case II

Acknowledgement
The research has been financed by the Polish Committee of Scientific Research within the grant 4T1100822.

EFFICIENT OPTIMIZATION OF TRANSIENT DYNAMIC PROBLEMS FOR A MICRO ACCELEROMETER USING MODEL ORDER REDUCTION

Jeong Sam Han, Evgenii B. Rudnyi, Jan G. Korvink
IMTEK-Institute for Microsystem Technology, University of Freiburg
Georges Köhler Allee 103, D-79110 Freiburg, Germany
Tel. +49 761 203 7387, Fax. +49 761 203 7382, E-mail: han@imtek.uni-freiburg.de

Summary One of the main obstacles to including transient dynamic effects into the performance functions of a structural optimization is the high computational cost of each time-dependent simulation. The focus of this paper is on the application of model order reduction techniques to reduce the transient analysis time for the attainable optimization process. The software mor4ansys developed at IMTEK performs model reduction via the Arnoldi algorithm directly to ANSYS finite element models. We adopt a micro accelerometer as an example to demonstrate the advantages of this approach. The harmonic and transient results of a reduced model of the accelerometer yield very good agreement with those from the original high dimensional ANSYS model. The use of model reduction within the optimization iterations produces almost the same results as without order reduction and speeds up the total computation by about an order of magnitude.

INTRODUCTION

Transient dynamic problems with very large numbers of degrees of freedom are solvable in feasible computational time nowadays due to the tremendous improvement of computers. When a design optimization, however, includes the time-dependent performance functions, the optimization often does not fit within a reasonable design process time because of the repeated simulations. In order to alleviate this difficulty, we utilize techniques of model order reduction for efficient time-dependent simulations during the design optimization. In this paper, we introduce fully automatic software for model order reduction to generate a reduced model of a second-order linear system and to achieve its integration into structural optimizations, and provide an example of successful application to optimization of a micro accelerometer.

METHODS

Model order reduction for second order systems

A structural mechanics problem, after the discretization in space, is described by a system of ordinary differential equations (ODEs) of the second order in time

$$\mathbf{M}\ddot{\mathbf{x}}(t) + \mathbf{C}\dot{\mathbf{x}}(t) + \mathbf{K}\mathbf{x}(t) = \mathbf{B}\mathbf{u}(t) \tag{1}$$

where **M**, **C**, and **K** are the structural mass, damping, and stiffness matrices, **B** is the scattering matrix to distribute the inputs **u**(t) on the domain and **x** is a state vector. It happens that in most cases the trajectory of the state vector can be well approximated by a low-dimensional subspace **V**, and projecting of ODEs on that subspace yields quite and accurate reduced models [1]. The goal of model order reduction is to find a new system of equations

$$\mathbf{M}_r\ddot{\mathbf{z}}(t) + \mathbf{C}_r\dot{\mathbf{z}}(t) + \mathbf{K}_r\mathbf{z}(t) = \mathbf{B}_r\mathbf{u}(t), \quad \mathbf{x} = \mathbf{V}\mathbf{z} + \varepsilon \tag{2}$$

with a lower number of equations and a lower dimensional state vector **z** such that its transfer function matches that of the original system. Our method to find an appropriate low-dimensional subspace is based on moment-matching via the Arnoldi process. The software mor4ansys applies this procedure directly to ANSYS finite element models [2].

Integration of optimization and model order reduction

The optimization process integrates several heterogeneous programs, and their communication is implemented via file transfers. First, a parametric finite element model is developed as an ANSYS script. The DOT optimizer [4] changes the design parameters to reach the optimal value of the objective function by satisfying all the constraints. The latter is summarized by three steps: 1) ANSYS is called to mesh the model for given design variables and to produce an element matrix (EMAT file), a FULL file, lists for the displacement boundary conditions and output degrees of freedom; 2) The software mor4ansys uses these files as input and generates a reduced model by means of the Arnoldi algorithm; 3) The postprocessing, that is, the solution of a reduced ODE system, as well as computing its transfer function, is performed in Mathematica. Finally, the objective and constraint functions for DOT are calculated from the postprocessed data. The optimization stops or continues according to convergence criteria. During the optimization, the gradients are estimated by central differencing. A modified feasible direction algorithm, available in DOT, is used to obtain solutions.

A PIEZORESISTIVE MICRO ACCELEROMETER

A piezoresistive cantilever beam micro accelerometer for automotive airbag applications [3] is studied to demonstrate this approach. The micro accelerometer has a symmetrically bonded silicon proof-mass, a self-diagnostic resistor, and a sensing part (see Fig. 1b). The design objective is to make the output sensitivity (S) as close as possible to a target value (M_S) subject to a set of constraints on the resonant frequency, beam deflection, and impact endurance of the structure.

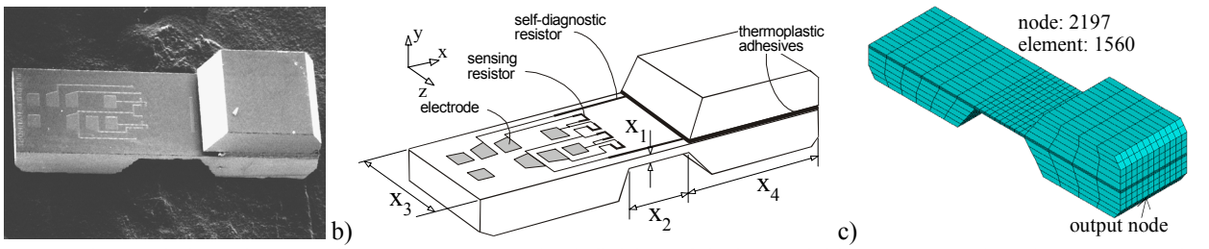


Figure 1: Piezoresistive micro accelerometer. a) SEM; b) definition of design variables; c) FE mesh and an output node.

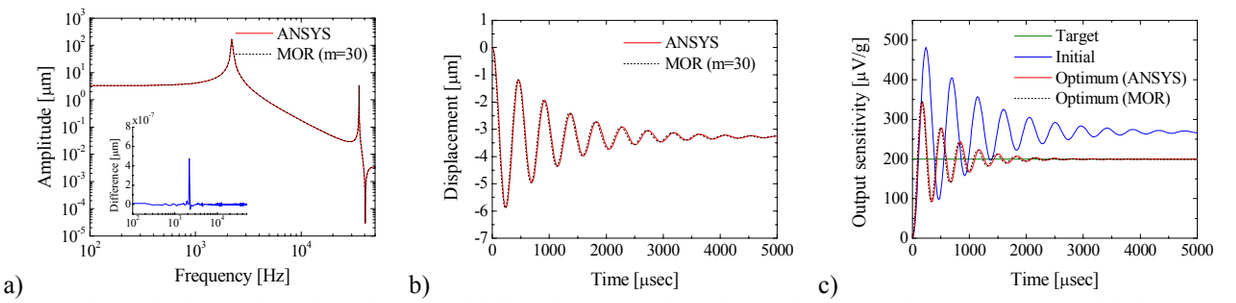


Figure 2: Comparison for reduced and full ANSYS models. a) harmonic; b) transient; c) output sensitivity.

$$\begin{aligned} &\text{Minimize} && \int_0^{t_a} \left| S - M_s \right| dt \\ &\text{subject to} && f_1 \geq f_{req}, \quad \delta_{50g}^t \leq 0.3 d_{gap}, \quad \sigma_{2000g} \leq \sigma_{yield} \end{aligned} \tag{3}$$

where f_1, δ^t_{50g}, d_{gap}, and δ_{2000g} denote the first natural frequency, the beam deflection under an acceleration of 50 g (gravity), a gap of 10 μm, and the von Mises stress under an impact loading of 2000 g, respectively. The output sensitivity is calculated from $S=0.5K\varepsilon V_a/a_y$, where K and ε mean a gage factor of the piezoresistive material and strain on the sensing resistor. An applied voltage of 5 volts and y-directional acceleration of 50 g are taken as an actual case. A target output sensitivity of 200 μV/g is assumed. The four design variables for the optimization are illustrated in Fig. 1b).

Harmonic and transient simulation

Harmonic responses at the output node to a y-directional harmonic excitation for an original ANSYS and a reduced model of order 30 perfectly match to a high frequency (Fig. 2a). It is remarkable that even a reduced model of order 5 shows almost perfect agreement. Figure 2b) illustrates transient responses with a Rayleigh damping of $\alpha=0$ and $\beta=10$ μsec at the output node to a step load for the ANSYS and reduced model. Again, the reduced model catches the transient behaviour almost perfectly.

Structural optimization

Design optimization of (3) has been performed using the time-dependent information from ANSYS and the model order reduction. The two optimizations take almost the same number of design iterations and produces nearly identical optimal shapes. The time-varying output sensitivity of the micro accelerometer before and after optimization is shown in Fig. 2c). The output sensitivity of the optimums oscillates less and converges faster into the target value than the initial design. The total computational cost for the optimization using the reduced model decreases to approximately 1/5 of that by using the original ANSYS model alone.

CONCLUSIONS

We have applied model order reduction techniques to reduce the time for transient simulations in the design optimization process. The use of model reduction within the optimization iterations produces almost the same results and reduces the total computational cost by about an order of magnitude. This approach, although only illustrated for a structural problem, can be easily applied to other linear physical problems as well, where transient information is important but the computational cost needs to be reduced for reasonable design times.

References

[1] Rudnyi E.B., Korvink J.G.: Automatic Model Reduction for Transient Simulation of MEMS-based Devices. *Sensors Update* **11**:3-33, 2002.

[2] Rudnyi E.B., Lienemann J., Greiner A., Korvink J.G.: mor4ansys: Generating Compact Models Directly form ANSYS Models. 2004 NSTI Nanotechnology Conference and Trade Show, Boston, USA, March 7-11, 2004.

[3] Ko J.S., Cho Y.H., Kwak B.M., Park K.: Design and fabrication of piezoresistive cantilever microaccelerometer arrays with a symmetrically bonded proof-mass. IMECE '98, ASME, Anaheim, California, USA, 353-356, 1998.

[4] DOT Users manual version 4.20. VR&D, 1995.

XXI ICTAM, 15-21 August 2004, Warsaw, Poland

DAMAGE IDENTIFICATION IN STRUCTURES BY MEANS OF THERMOGRAPHIC METHODS

K. Dems [1] and Z. Mróz [2]

[1] *Department of Technical Mechanics, Lodz Technical University, Zeromskiego 116, PL 90-944 Lodz, Poland.*

[2] *Polish Academy of Sciences IPPT PAN, Swietokrzyska 21, PL 00-049 Warszawa, Poland.*

Summary The detection of cracks, inclusions or voids as well as their location, orientation and size is performed using measurements of surface temperature caused by steady state or transient thermal loading. On the basis of measurement results, an inverse steady state or transient heat transfer problem is formulated and next solved. The inverse solution is constructed by minimizing the properly defined distance norm of measured and model temperatures. In this stage of research the real measurements are numerically simulated. The model temperature distribution is calculated using the finite element model of a structure, while in minimizing of distance norm functional the gradient-oriented methods are used. The proper sensitivities of introduced identification functional are derived. For particular domain transformation these sensitivities are calculated using a class of path-independent sensitivity integrals. Some numerical examples are presented in order to justify the presented approach.

INTRODUCTION

The prediction of location and degree of damage in existing engineering structures is of great importance from the point of view of their serviceability and safety. Visual inspection and extensive testing can be employed to locate and measure the degradation of structure by a wide class of non-destructive techniques. In the present paper, we shall study damage or fault detection by the analysis of transient of steady state thermal response of structures. The detection of surface, subsurface or internal cracks, inclusions or voids as well as their location, orientation and size can be performed using infrared measurements of surface temperature caused by applied thermal loading. In order to increase the number of available measurement data, the thermal multi-loading case is considered.. The inverse solution is constructed by minimizing the properly defined distance norm of measured and model temperatures at specified surface points or along specified surface lines. In this stage of research the infrared measurements will be numerically simulated. To make the simulation more realistic, some random error will be introduced into simulated measurements in order to model the unavoidable tolerance of real measurement. The influence of magnitude of this error on accuracy of defect estimation will also be inspected.

PROBLEM FORMULATION

Let us consider a transient heat transfer problem within non-homogeneous two-dimensional domain, Fig. 1, described by the conduction equation supplemented with proper set of boundary and initial conditions. The defect in a structure is modeled by introducing two subdomains Ω_1 and Ω_2, so that $\Omega=\Omega_1\cup\Omega_2$ and Ω_1 is a structure domain with conductivity matrix $\mathbf{A}_1$ while subdomain Ω_2 with conductivity matrix $\mathbf{A}_2$ models the crack, inclusion or void within structure domain. The detailed analysis associated with shape modification and optimal design for problem described by Eq.(1) was performed in [3], whereas the steady state problem was discussed in [2]. In this paper the identification problem associated with structural shape will be considered. To identify the structural shape (within the assumed in advance shape class) or location of defect, the identification functional in the form of proper distance norm between temperature fields within the model and real structure should be introduced. In particular, the size, position and orientation of defect can be identified using this procedure. In general, the identification functional can be assumed in the form of time and space integral, given in the form:

$$I(T,T^r,\mathbf{b},t)=\int_{t_0}^{t_f}\int_{\Gamma(\mathbf{b})}\Phi[T(t_k),T^r(t_k)]d\Gamma_r dt \;=\; I(T,T^r,\mathbf{b},t)=\sum_{k=1}^{n}\xi_k\int_{\Gamma(\mathbf{b})}\Phi[T(t_k),T^r(t_k)]d\Gamma_r \tag{1}$$

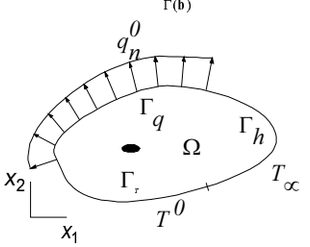


Figure 1: 2D body with internal defect.

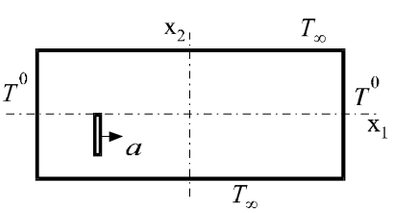


Figure 2: Rectangular disk with translated internal hole

where Φ is an arbitrary function depending on the predicted and measured temperatures T and T^r within assumed time period (t_0, t_f) and Γ_r denotes the boundary portion on which the measurement is performed. The parameters **b** specify the defect properties, and in particular they can specify the position, orientation and scale change of identified defect. Thus, we use the time window of bandwidth $t_f - t_0$ in order to gather the experimental data required to identification procedure.

Both the initial and final times t_0 and t_f of identification procedure can be different from the initial and final times of transient heat transfer problem. Instead of time integral, also the summation of space integral over Γ_r at some selected time instant t_k can be used in formulation of the identification norm, as shown in expression (1). In this case, the summation is expanded on assumed number of time instances and ξ_k denote some weighting factors. Let us note that both expressions in (1) are equivalent, when the Gauss quadrature method is used in numerical integration of time integral in (1). Two particular forms of functional (1) can be considered, namely:

$$I(T,T^r,t,\mathbf{b}) = \int_{t_0}^{t_f} \sqrt{\int_{\Gamma_m} \alpha(\mathbf{x})[T(\mathbf{x},t_k,\mathbf{b}) - T^r(\mathbf{x},t_k)]^2 d\Gamma_r}\, dt = \sum_{k=1}^{n} \xi_k \sqrt{\int_{\Gamma_m} \alpha(\mathbf{x})[T(\mathbf{x},t_k,\mathbf{b}) - T^r(\mathbf{x},t_k)]^2 d\Gamma_r} \tag{2}$$

where $\alpha(\mathbf{x})$ is a weighting function, which can magnify or weaken the difference between the model and measured temperature on some portion of structural boundary. The other form of identification functional can be also used, basing on measurement of temperature differences for structure or its model at initial and actual conditions.

The identification problem can be now formulated as follows

$$\text{min. } I(T, t, \mathbf{b}) \text{ subjected to equality constraints describing heat transfer problem} \tag{3}$$

Since in minimizing of the assumed form of identification functional the gradient-oriented methods will be used, thus there will be a need to calculate the proper sensitivities of introduced identification functional. This procedure will be performed using the adjoint approach to sensitivity analysis.

PATH-INDEPENDENT SENSITIVITY ANALYSIS

In performing the calculations of sensitivity expressions of identification functional (1) the general adjoint or direct method approaches can be used. For particular case of sensitivity analysis with respect to translation and rotation of defect a class of path-independent sensitivity integrals derived by Dems and Mroz [1,4] will be used. This class of sensitivity integrals will allow for integration of desired sensitivity expressions along paths situated far from singular points or areas of rapid changes of temperature gradient. The sensitivity analysis of identification problem will be performed using the material derivative concept and adjoint approach. The application of path independent sensitivity integrals will also require the specification of primary and adjoint fields depending on the form of applied identification functional, as well as the closed contours containing inside the analyzed defect.

In deriving the sensitivity expressions, both the transient and steady state heat transfer cases are considered. In this last case we omit the time dependence of state fields of heat transfer problem as well as in identification functional (1). Therefore, the obtained path-independent sensitivity expressions are also time independent.

The method presented in the paper can be also extended to the case of other physical field (i.e. electric, magnetic) described by the harmonic equation.

EXAMPLES

In order to justify the presented approach, the identification of location of rectangular hole in disk shown in Fig. 2 was performed using the steady state thermal loading. The internal hole within a model disk domain was allowed to translate along x_1 axis in order to identify its location in real structure. The prescribed temperature was applied along boundaries x_1 = const. and convection conditions were assumed along boundary portions x_2 = const. The measured temperature along boundaries x_2 = const. was numerically simulated and some random error of magnitude 1% and 2% was introduced into simulation. In the case of error free identification the location of hole along x_1 direction was exact, while introducing the random error of magnitude 1% and 2% respectively, results in error of location identification equal to 1.09% and 1.54%, respectively.

ACKNOWLEDGMENT

This research work was supported through Scientific Research Committee (KBN) Grant No. 8 T07A 022 20.

References

[1] Dems, K. and Mróz, Z., Shape sensitivity in mixed Dirichlet-Neumann boundary-value problems and associated class of path-independent integrals, Eur. J. Mech., A/Solids, 14,2,169-203,1995

[2] Dems, K., Korycki, R., Rousselet, B., Application of first- and second-order sensitivities in domain optimization for steady conduction problem, J. Thermal Stresses, vol. 20, p. 697-728,1997

[3] Dems, K. and Mróz, Z., Sensitivity analysis and optimal design of external boundaries and interfaces for heat conduction systems, J. Thermal Stresses, vol. 21, p. 461-488,1998

[4] Dems, K and Mróz, Z, Application of thermographic methods in identification of structure properties, Proceedings of WCSMO5 (in print)

TOPOLOGICAL OPTIMIZATION FOR CONTACT PROBLEMS

Jan Sokołowski*, Antoni Żochowski**
*Institut Elie Cartan, Laboratoire de Mathématiques, Université Henri Poincaré Nancy I, B.P. 239, 54506 Vandoeuvre lès Nancy Cedex, France and Systems Research Institute of the Polish Academy of Sciences, Newelska 6, 01-447 Warszawa, Poland
**Systems Research Institute of the Polish Academy of Sciences, Newelska 6, 01-447 Warszawa, Poland

Summary The problem of topology optimization is considered elastic contact problems. The formulae for the first term of asymptotics for energy functionals are derived and verified numerically. The topological differentiability of solutions to variational inequalities is established using the so-called *outer asymptotic expansion* for solutions of contact problems in elasticity with respect to singular perturbation of geometrical domain by nucleation of small holes.

Introduction. In the engineering literature there are many results concerning the shape optimization of contact problems in elasticity. The boundary variations technique for such problems is described in [4] in the framework of nonsmooth analysis combined with the speed method. Nonsmooth analysis is necessary since the shape differentiability of solutions to contact problems is obtained only in the framework of Hadamard differentiability of metric projections onto polyhedric sets in the appropriate Sobolev spaces. However, to our best knowledge, there is no general method for simultaneous shape and topology optimization [6] of contact problems. The main difficulty in analysis of contact problems is associated with the nonlinearity of the *non-penetration condition* over the contact zone which makes the boundary value problem nonsmooth. In the paper we propose a method for numerical evaluation of topological derivatives for such problems.
The main idea we use to derive the topological derivatives for contact problems is the modification of the energy functional by an appropriate correction term and subsequent minimization of the resulting energy functional over the cone of admissible displacements. Such an approach leads to the *outer* approximations of solutions to variational inequalities. The following step in asymptotic approximation of solutions is an application of self adjoint extensions of elliptic operators [3] with asymptotic point conditions for the contact problems which results in the asymptotically exact approximations. We point out that in the framework of self adjoint extensions studied in [3] for linear problems, the approximate solutions with asymptotic point conditions at the center of the hole $\mathcal{O}$ are critical points of the appropriate energy functional. We restrict ourselves to the case of outer approximations of solutions. Such an approach is justified, by applications to numerical methods of topology optimization. For linear problems, outer approximations are used e.g., in [1] for derivation of topological derivatives for isotropic elasticity. However, the complete asymptotic analysis necessary to justify the derivation of topological derivatives for general linear boundary value problems is performed in [2].

Contact problem in elasticity. The asymptotic analysis of 2D contact problems is performed in the framework of linear elasticity. Such a contact problem in the domain Ωreads: Find $\mathbf{u} = \mathbf{u}(\Omega) = (u_1, u_2)$ and $\sigma = (\sigma)_{ij}$, $i, j = 1, 2$, such that

$$-\mathbf{div}\,\sigma = \mathbf{f} \quad \text{in } \Omega\,, \quad C\sigma - \epsilon(\mathbf{u}) = 0 \quad \text{in } \Omega\,, \quad \mathbf{u} = 0 \quad \text{on } \Gamma_0\,,$$
$$\mathbf{u}\nu \geq 0, \quad \sigma_\nu \leq 0, \qquad \sigma_\nu \mathbf{u}\nu = 0 \qquad \sigma_\tau = 0 \quad \text{on } \Gamma_c\,.$$

The compliance functional for the contact problem is given by

$$J(\Omega) = \frac{1}{2}\int_\Omega \sigma(\mathbf{u}) : \epsilon(\mathbf{u})\,dx - \int_\Omega \mathbf{f}\mathbf{u}\,dx = -\frac{1}{2}\int_\Omega \mathbf{f}\mathbf{u}\,dx$$

where $\Omega \subset \mathbb{R}^2$ is a given domain with the boundary $\partial\Omega = \Gamma_0 \cup \Gamma_c$. We obtain the expansion of this functional

$$J(\Omega_\rho) = J(\Omega) + \rho^2 \mathcal{T}_\Omega(\mathcal{O}) + o(\rho^2)$$

for $\rho^2 \to 0$, where $\Omega_\rho = \Omega \setminus \overline{B_\rho(\mathcal{O})}$, $B_\rho(\mathcal{O}) = \{\|\mathbf{x}\| < \rho\}$, and $\mathcal{T}_\Omega(\mathcal{O})$ is the topological derivative of $J(\Omega)$ at Ω for the nucleation of a small hole $B_\rho(\mathcal{O})$ with the center $\mathcal{O} \in \Omega$. To this end the contact problem in Ω_ρ is considered: Find $\mathbf{u} = \mathbf{u}(\Omega_\rho) = (u_1, u_2)$ and $\sigma = (\sigma)_{ij}$, $i, j = 1, 2$, such that

$$-\mathbf{div}\,\sigma = \mathbf{f} \quad \text{in } \Omega_\rho\,, \quad C\sigma - \epsilon(\mathbf{u}) = 0 \quad \text{in } \Omega_\rho\,, \quad \mathbf{u} = 0 \quad \text{on } \Gamma_0\,, \quad \sigma\nu = 0 \quad \text{on } \Gamma_\rho\,, \tag{1}$$
$$\mathbf{u}\nu \geq 0, \quad \sigma_\nu \leq 0, \quad \sigma_\nu \mathbf{u}\nu = 0 \qquad \sigma_\tau = 0 \quad \text{on } \Gamma_c\,. \tag{2}$$

We show that the solution to (1)–(2), denoted $\mathbf{u}_\rho$, is conically differentiable with respect to the small parameter $\rho^2 \to 0$, i.e.

$$\mathbf{u}_\rho = \mathbf{u} + \rho^2 \mathbf{q} + o(\rho^2) \quad \text{in} \quad \Omega \setminus \overline{B(\rho)}$$

for small ρ^2, where $\mathbf{u}$ is a solution to the problem in Ω. The conical differential $\mathbf{q}$ is given by the unique solution of the auxiliary variational inequality: Find $\mathbf{q} \in S(\mathbf{u})$ such that

$$\int_\Omega \sigma(\mathbf{q}) : \epsilon(\mathbf{v} - \mathbf{q})\, dx + b(\mathbf{q}, \mathbf{v} - \mathbf{q}) \geq 0$$

for all $\mathbf{v} \in S(\mathbf{u})$, where $b(\cdot, \cdot)$ is a bilinear form and $S(\mathbf{u})$ is a cone, associated with the initial contact problem in Ω. Our results are based on a conical differentiability of solutions to variational inequalities defined over polyhedral convex sets [4]. These results are combined with an appropriate approximation procedure for the energy functionals, which leads to the bilinear form $b(\cdot, \cdot)$.

Approximation of energy. We determine the modified bilinear form as a sum of two terms, as it is for the energy functional, the first term $a(\mathbf{v}, \mathbf{v})$ defines the elastic energy in the domain Ω, the second term $b(\mathbf{v}, \mathbf{v})$ is a correction term. The correction term is quite complicated to evaluate, and we do not provide its explicit form. The values of the symmetric bilinear form $a(\rho; \cdot, \cdot)$ in Ω_ρ are given by the expression

$$a(\rho; \mathbf{v}, \mathbf{v}) = a(\mathbf{u}, \mathbf{u}) + \rho^2 b(\mathbf{v}, \mathbf{v})\ . \tag{3}$$

The derivative $b(\mathbf{v}, \mathbf{v})$ of the bilinear form $a(\rho; \mathbf{v}, \mathbf{v})$ with respect to ρ^2 at $\rho = 0+$ is given by the expression

$$b(\mathbf{v}, \mathbf{v}) = -2\pi e_{\mathbf{v}}(0) - \frac{2\pi\mu}{\lambda + 3\mu}\big(\sigma_{II}\delta_1 - \sigma_{12}\delta_2\big)\ , \tag{4}$$

where all the quantities are evaluated for the displacement field $\mathbf{v}$. The form of the first term in (4), new to our best knowledge, is given in terms of line integrals over the circle Γ_R. This circle of fixed radius surrounds the hole $B(\rho)$.

$$\begin{aligned} 2\pi e_{\mathbf{v}}(0) = \frac{\pi(\lambda+\mu)}{\pi^2 R^6}\left(\int_{\Gamma_R}(v_1 x_1 + v_2 x_2)\, ds\right)^2 + \\ + \frac{\mu}{\pi^2 R^6}\left(\int_{\Gamma_R}\left((1-9k)(v_1 x_1 - v_2 x_2) + \frac{12k}{R^2}(v_1 x_1^3 - v_2 x_2^3)\right] ds\right)^2 + \\ + \frac{\mu}{\pi^2 R^6}\left(\int_{\Gamma_R}\left[(1+9k)(v_1 x_2 + v_2 x_1) - \frac{12k}{R^2}(v_1 x_2^3 + v_2 x_1^3)\right] ds\right)^2\ , \end{aligned} \tag{5}$$

The values of $\sigma_{II}, \sigma_{12}, \delta_1, \delta_2$ are calculated by means of similar integrals and $k = (\lambda + \mu)/(\lambda + 3\mu)$. Such expressions lead to very efficient numerical methods for the problem under consideration. Numerical results confirm this conclusion.

Acknowledgement. This work was partially supported by the grant 4 T11A 01524 of the State Committee for the Scientific Research of the Republic of Poland.

References

[1] S. Garreau, Ph. Guillaume, M. Masmoudi, *The topological asymptotic for PDE systems: the elasticity case* SIAM Journal on Control and Optimization. **39**(6)(2001) 1756–1778.

[2] S. A. Nazarov, J. Sokołowski *Asymptotic analysis of shape functionals*, Journal de Mathématiques pures et appliquées, 82-2(2003), 125-196.

[3] S. A. Nazarov, J. Sokolowski *Self adjoint extensions for the Neumann Laplacian in application to shape optimization* Les prépublications de l'Institut Élie Cartan 9/2003.

[4] J. Sokołowski, J-P. Zolesio *Introduction to Shape Optimization. Shape Sensitivity Analysis*, Springer Verlag, 1992.

[5] J. Sokołowski, A. Żochowski *On topological derivative in shape optimization*, SIAM Journal on Control and Optimization. **37**, Number 4 (1999), pp. 1251–1272.

[6] J. Sokołowski, A. Żochowski *Optimality conditions for simultaneous topology and shape optimization*, SIAM Journal on Control and Optimization. **42**, Number 4 (2003), pp. 1198–1221.

Coupled sensitivity analysis and design optimization for thermo-structural systems*

Yuanxian Gu, Biaosong Chen, Tao Liu
State Key Laboratory of Structural Analysis for Industrial Equipment,
Department of Engineering Mechanics, Dalian University of Technology, Dalian 116024, China

Summary Thermo-structural systems coupled disciplines of heat conduction and structural mechanics are widely used in engineering. The paper presents a systematical methodology for the design optimization of such systems using the coupled sensitivity analysis and mathematical programming methods on structural behaviors of thermal stresses and thermal buckling.

INTRODUCTION

Thermo-structural systems abound in many industrial engineering such as aerospace and aeronautical engineering, thermodynamic machinery, electronic devices and material engineering. The thermal responses of such system[1], e.g. thermal displacements, stresses, and buckling are commonly the predominant factors in the design phase. Therefore a comprehensive design of thermo-structural system should take the heat conduction and the structural mechanics into account simultaneously. However in some former researches, the designers had to adopt some simplified methods when conducting the optimal design of such system in order to reduce the problem difficulties. For example, the common way was to neglect the coupled effects of the two disciplines in the phases of sensitivity analysis and design optimization. In fact, the rationality of the simplified methods is questionable.

Over the past two decades, the sensitivity analysis and design optimization for structural system have gained fruitful achievements[2], which also placed a solid foundation and offered possible ways for design optimization of thermo-structural system. This investigation makes an attempt to extend the mature techniques to the design optimization of thermo-structural systems, based on which, further attentions may be paid to the design optimization for other kinds of structural multidisciplinary systems such as electro-structural, magneto-structural, acoustic-structural systems.

Two kinds of sensitivity analysis problems are considered in the present research using the direct and the adjoint methods. One is the coupled sensitivity analysis and design optimization of thermal stresses problem. In this respect, many contributions, Ref[3] and references therein, have been published. But most of their attentions were paid to the deduction of sensitivity equations by employing the continuum model (based on the partial differential equations) and neglected the discussions of solution methods. This paper present a set of clearer and more concise deductions for the sensitivity analysis based on the finite element equations, which are suitable for the computer implementations. The other is the coupled sensitivity analysis of thermal buckling problem. There are limited references in this field. Ref[4] discussed the uncoupled thermal buckling problem for the laminated composites. Ref[5] considered the coupled effects but didn't offer procedures on the sensitivity analysis. We present the coupled sensitivity equations in detail for the thermal buckling problem.

Based on the results of sensitivity analysis, the mathematical optimization model is constructed and solved by SLP/SQP algorithms. The computer implementations are performed on the software platform-JIFEX[6], which incorporates size design variables, shape design variables, the technique of semi-analytical sensitivity analysis and the geometrical modeling techniques. The implemented software system can be applied to the general purposes design optimization for the plane, axi-symmetric, and complex thin-walled thermo-structural problems. Numerical examples are employed to validate the present methods and reveal the necessity of coupled sensitivity analysis.

COUPLED SENSITIVITY ANALYSIS OF THERMAL STRESS

Static problem

In the static problem, the finite element equations of heat conduction and structural mechanics are expressed as

$$\boldsymbol{K}\boldsymbol{T} = \boldsymbol{R} \tag{1}$$

$$\boldsymbol{K}^{\mathrm{m}}\boldsymbol{u} = \boldsymbol{f} \tag{2}$$

Where $\boldsymbol{K},\boldsymbol{T},\boldsymbol{R}$ are the heat conductance matrix, the nodal temperature vector and the heat load vector, respectively. And $\boldsymbol{K}^{\mathrm{m}}$, $\boldsymbol{u}$, $\boldsymbol{f}$ are the structural stiffness matrix, the nodal displacement vector, and the external load vector. Suppose that in the optimal model, the index function (objective or constraint function) is $g(x, \boldsymbol{T}, \boldsymbol{u})$ in which x is the design variable. Here just one design variable is considered for simplicity, the same formulations can be extended to multiple design variables problems. Then the sensitivity of g is

$$\mathrm{d}g/\mathrm{d}x = \partial g/\partial x + \left(\partial g/\partial \boldsymbol{T}\right)\left(\mathrm{d}\boldsymbol{T}/\mathrm{d}x\right) + \left(\partial g/\partial \boldsymbol{u}\right)\left(\mathrm{d}\boldsymbol{u}/\mathrm{d}x\right) \tag{3}$$

In sensitivity analysis, the direct method is to derive the Eqn(1) and (2) with respect to x and to apply the results into Eqn(3) to compute the sensitivity of index function. The adjoint method needs to introduce two adjoin vectors $\boldsymbol{\Lambda}_{\mathrm{h}}$ and $\boldsymbol{\Lambda}_{\mathrm{m}}$ which satisfy the following aojoint equations:

$$\boldsymbol{K}^{\mathrm{m}}\boldsymbol{\Lambda}_{\mathrm{m}} = \left(\partial g/\partial \boldsymbol{u}\right)^{\mathrm{T}} \text{ and } \boldsymbol{K}\boldsymbol{\Lambda}_{\mathrm{h}} = \left(\partial g/\partial \boldsymbol{T}\right)^{\mathrm{T}} + \left(\mathrm{d}\boldsymbol{f}/\mathrm{d}\boldsymbol{T}\right)^{\mathrm{T}}\boldsymbol{\Lambda}_{\mathrm{m}} \tag{4}$$

Then the sensitivity of the index function g is

$$\mathrm{d}g/\mathrm{d}x = \partial g/\partial x + \boldsymbol{\Lambda}_{\mathrm{h}}^{\mathrm{T}}\left(\mathrm{d}\boldsymbol{R}/\mathrm{d}x - \left(\mathrm{d}\boldsymbol{K}/\mathrm{d}x\right)\boldsymbol{T}\right) + \boldsymbol{\Lambda}_{\mathrm{m}}^{\mathrm{T}}\left(\partial \boldsymbol{f}/\partial x - \left(\mathrm{d}\boldsymbol{K}^{\mathrm{m}}/\mathrm{d}x\right)\boldsymbol{u}\right) \tag{5}$$

* The project supported by the NSFC (10032030) and Special Funds for National Key Basic Research of China (No. G1999032805)

Quasi-static problem

In the quasi-static problem, the structural mechanics equations are Eqn(2) and the heat conduction is time dependent.

$$\boldsymbol{M}\dot{\boldsymbol{T}} + \boldsymbol{K}\boldsymbol{T} = \boldsymbol{R} \tag{6}$$

Where $\boldsymbol{M}$ is the heat capacity matrix. The index function is defined as

$$g(x,\boldsymbol{T},\boldsymbol{u}) = \int_0^{t_f} p(x,\boldsymbol{T},\boldsymbol{u},t)\mathrm{d}t \text{ and } \mathrm{d}g/\mathrm{d}x = \int_0^{t_f} \left(\partial p/\partial x + (\partial p/\partial \boldsymbol{T})(\mathrm{d}\boldsymbol{T}/\mathrm{d}x) + (\partial p/\partial \boldsymbol{u})(\mathrm{d}\boldsymbol{u}/\mathrm{d}x)\right)\mathrm{d}t \tag{7}$$

Then the direct method is to derive Eqn(6) and (7) with respect to x and to apply the results into Eqn(7) to get dg/dx. With the introducing the adjoint vectors $\boldsymbol{\Lambda}_{\mathrm{h}}$ and $\boldsymbol{\Lambda}_{\mathrm{m}}$ which satisfy

$$\boldsymbol{K}^{\mathrm{m}}\boldsymbol{\Lambda}_{\mathrm{m}} = (\partial p/\partial \boldsymbol{u})^{\mathrm{T}} \text{ and } -\boldsymbol{M}\dot{\boldsymbol{\Lambda}}_{\mathrm{h}} + \boldsymbol{K}\boldsymbol{\Lambda}_{\mathrm{h}} = (\partial p/\partial \boldsymbol{T})^{\mathrm{T}} + (\partial \boldsymbol{f}/\partial \boldsymbol{T})^{\mathrm{T}}\boldsymbol{\Lambda}_{\mathrm{m}} \tag{8}$$

The adjoint method gives

$$\mathrm{d}g/\mathrm{d}x = \int_0^{t_f} \left(\partial p/\partial x + \boldsymbol{\Lambda}_{\mathrm{h}}^{\mathrm{T}}\left(\mathrm{d}\boldsymbol{R}/\mathrm{d}x - (\mathrm{d}\boldsymbol{M}/\mathrm{d}x)\dot{\boldsymbol{T}} - (\mathrm{d}\boldsymbol{K}/\mathrm{d}x)\boldsymbol{T}\right) + \boldsymbol{\Lambda}_{\mathrm{m}}^{\mathrm{T}}\left(\partial \boldsymbol{f}/\partial x - (\mathrm{d}\boldsymbol{K}^{\mathrm{m}}/\mathrm{d}x)\boldsymbol{u}\right)\right)\mathrm{d}t \tag{9}$$

Obviously, the above formulations are clearer and more concise than those based on continuum model[3].

COUPLED SENSITIVITY ANALYSIS OF THERMAL BUCKLING

Based on the results of heat conduction Eqn(1) and structural analysis Eqn(2), the stuctural buckling equations are

$$\left(\boldsymbol{K}^{\mathrm{m}} + \lambda\boldsymbol{K}_{\sigma}^{\mathrm{m}}\right)\boldsymbol{\varphi} = 0 \tag{10}$$

Where $\boldsymbol{K}_{\sigma}^{\mathrm{m}}$, $\boldsymbol{\varphi}$, and λ are the geometrical stiffness matrix, the buckling mode vector and the critical load coefficient, respectively. Then in the sensitivity analysis, the direct method gives

$$\mathrm{d}\lambda/\mathrm{d}x = -\boldsymbol{\varphi}^{\mathrm{T}}\left(\mathrm{d}\boldsymbol{K}^{\mathrm{m}}/\mathrm{d}x + \lambda(\mathrm{d}\boldsymbol{K}_{\sigma}^{\mathrm{m}}/\mathrm{d}x)\right)\boldsymbol{\varphi} \tag{11}$$

Prior to the solution of Eqn(11), the sensitivities of Eqn(1) and (2) should be obtained to compute the sensitivity for $\boldsymbol{K}_{\sigma}^{\mathrm{m}}$ because it is a function of $\boldsymbol{x}$, $\boldsymbol{T}$ and $\boldsymbol{u}$. After some manipulations, the adjoint method gives

$$\frac{\mathrm{d}\lambda}{\mathrm{d}x} = -\boldsymbol{\varphi}^{\mathrm{T}}\left(\partial \boldsymbol{K}^{\mathrm{m}}/\partial x - \lambda(\partial \boldsymbol{K}_{\sigma}^{\mathrm{m}}/\partial x)\right)\boldsymbol{\varphi} - \boldsymbol{\Lambda}_{\mathrm{m}}^{\mathrm{T}}\left(\partial \boldsymbol{f}/\partial x - (\mathrm{d}\boldsymbol{K}^{\mathrm{m}}/\mathrm{d}x)\boldsymbol{u}\right) - \boldsymbol{\Lambda}_{\mathrm{h}}^{\mathrm{T}}\left(\mathrm{d}\boldsymbol{R}/\mathrm{d}x - (\mathrm{d}\boldsymbol{K}/\mathrm{d}x)\boldsymbol{T}\right) \tag{12}$$

Where the adjoint vectors $\boldsymbol{\Lambda}_{\mathrm{h}}$ and $\boldsymbol{\Lambda}_{\mathrm{m}}$ satisfy the adjoint equations

$$\boldsymbol{K}^{\mathrm{m}}\boldsymbol{\Lambda}_{\mathrm{m}} = \boldsymbol{w}^{\mathrm{T}}, (\,w_i = \lambda\boldsymbol{\varphi}^{\mathrm{T}}\left(\partial \boldsymbol{K}_{\sigma}^{\mathrm{m}}/\partial u_i\right)\boldsymbol{\varphi}\,) \text{ and } \boldsymbol{K}\boldsymbol{\Lambda}_{\mathrm{h}} = (\partial \boldsymbol{f}/\partial \boldsymbol{T})^{\mathrm{T}}\boldsymbol{\Lambda}_{\mathrm{m}} \tag{13}$$

DESIGN OPTIMIZATION AND SOFTWARE IMPLEMENTATION

Based on the sensitivity results, the optimal model can be solved by mathematical programming methods: SLP/SQP. The above sensitivity analysis methods are implemented in the software JIFEX[6] of structural design optimization which incorporates semi-analytical method and geometrical modeling technique for all kinds of size and shape design variables. Hence this work can be applied directly to industrial thermo-structural problems with general purposes.

CONCLUSIONS

The main attentions are paid to the systematically coupled sensitivity analysis of thermo-structural system, including the thermal stress and thermal buckling problems. The work reveals the necessity of coupled sensitivity analysis in this respect, and places a solid foundation for the future work on other similar coupled design optimization of structural systems.

References

[1] Thornton E.A.: Thermal Structures for Aerospace Applications. American Institure of Aeronautics and Astronautics, Inc., Virginia, 1996.

[2] Hafka R.T., Gurdal Z.: Element of Structrural Design Optimization, 3rd ed. Kluwer Academic Publishers, Netherland, 1992.

[3] Michaleris P., Tortorelli D.A., Vidal C.A.: Analysis and Optimization of Weakly Coupled Thermoelastoplastic Systems with Applications to Weldment Design. International Journal for Numerical Methods in Engineering, 38: 1259-1285, 1995.

[4] Foldager J. P., Hansen J. S., Olhoff N.: Optimization of Buckling Load for composite structures taking thermal effectes into account. Structural and multidisciplnary optimization 21: 14-31, 2001.

[5] Autio M.: Optimization of Coupled Thermal Structural Problems of Laminated Plates with Lamination Parameters. Structural and multidisciplnary optimization 21: 40-51, 2001.

[6] Gu Y.X., Zhang, H.W. et al: New Generation Software of Structural Analysis and Design Dptimization—JIFEX. Structural Engineering and Mechanics, 7(6): 589-599, 1999.

NEW CLASSES OF ANALYTICALLY DERIVED OPTIMAL TOPOLOGIES AND THEIR NUMERICAL CONFIRMATION

George I.N. Rozvany, János Lógó*, Osvaldo M. Querin***
**Department of Structural Mechanics, Budapest University of Technology and Economics, Mûegyetem Rpt. 3, Kmf. 35, H-1521 Budapest, Hungary*
***School of Mechanical Engineering, University of Leeds, Leeds LS2 9JT, UK*

Summary New classes of exact, analytically derived structural topologies are outlined, their underlying theory summarised, illustrative examples given and their numerical, FE-based confirmation by the DCOC/SIMP method presented..

INTRODUCTION

Topology optimization in real world problems requires highly efficient, numerical (FE-based) methods, which can easily lead to grossly erroneous solutions due to discretization errors (e.g. checkerboard patterns, diagonal element chains, and hinges in plates), singularity of the topology, local minima and other factors. Closed form, exact analytical representation of the optimal topology is therefore very useful in checking on the validity, accuracy and convergence of numerical methods. Analytical solutions are also essential in understanding the true nature and fundamental properties of optimal topologies. It is rather unfortunate that in our time very few researchers carry out research into the theory of exact optimal topologies.
In this paper, the theory of several new classes of optimal topologies is briefly outlined, their application to particular problems illustrated with examples and the analytical solutions confirmed by numerical, FE-based computations.

OVERVIEW OF NEW CLASSES OF ANALYTICALLY DERIVED TOPOLOGIES

It is well known that optimization of perforated plates in in-plane stress leads to the same topology as that of plane trusses, if the volume fraction of the former tends to zero. Exact analytical solutions for optimal truss topologies are therefore used regularly for verifying numerical solutions for perforated plates in plane stress.

(a) Exact optimal topology of new classes of trusses with a stress constraint
In this section, the classical Michell theory [1] is applied to new classes of boundary conditions.
It was already mentioned at ICTAM 2000 by the first author that the exact Michell solution is not yet known for even quite simple boundary and support conditions, particularly for point supports. Michell's *optimality conditions* require that the „adjoint" strain has a constant (say k) absolute value in all truss members and it does not exceed this value in any direction at any point of the design domain for the truss. For zero reaction cost, the adjoint displacements at supports are zero. The Michell problem is convex and even selfadjoint (the real and adjoint strains are proportional). Exact optimal topologies for point-supported cantilevers (including a half „MBB-beam") were given earlier [2] by the first author's research group. New solutions are presented in this paper.

(b) Different permissible stresses in tension and compression
For these problems the adjoint strains are equal to the reciprocal values of the permissible stresses along members (compression is negative) and can take on any value in between the above limits anywhere else within the design domain. This problem is convex but nonselfadjoint. It was explained earlier by the first author [3], that Michell [1] made certain mistakes in deriving his (incorrect) optimality conditions for unequal permissible stresses in tension and compression. The consequences of this error can be quite severe in terms of truss weight [3]. Solutions for this class of problems consist of orthogonal Hencky nets, but the optimal member directions are in general not at 45 degrees to the supporting lines.

(c) Variable external forces (including reactions) of non-zero cost
This problem class has application in support and ballast optimization and in passive control. For these problems the above optimality conditions apply, but at supports (or variable external forces) the adjoint displacement is the subgradient of the support cost function with respect to the reaction force (variable force). If the support cost is r-times the absolute value of the support force (uplift is negative), then the adjoint displacement is r for positive and –r for negative reaction. For zero reaction (variable force) the adjoint displacement may take on any value in between –r and r. This problem class can be made convex and selfadjoint.

(d) Optimization for one or several active displacement constraints
In this case the adjoint strains are proportional to the sum of the products of Lagrange multipliers and virtual strains and the optimal cross sectional areas are proportional to the square root of the sum of the products of the real and adjoint

strains. The problem is in general nonconvex and nonselfadjoint. The topology for this class of problems consists of „generalized" Hencky nets, in which the lines representing optimal member centre lines are in general non-orthogonal.

(e) Optimal topologies for external load plus self weight
It was shown by the first author ([7], see also [8], pp. 72-73 and 206-218) that the adjoint strain for the above structures is the usual adjoint strain multiplied by (1+u), where u is the adjoint displacement in the direction of the gravitational forces (in usual terrestrial structures the vertical direction). This problem class is nonconvex and nonselfadjoint.

Problem class (a) as a special case of problem classes (b), (c), d) and (e).
If under (b) the two permissible stresses are equal, under (c) the reaction costs are zero, under (d) the displacement constraint is a compliance constraint, and under (e) the specific truss weight tends to zero, then the latter four reduce to problem class (a). This can be used for checking on the validity of more advanced solutions.

EXAMPLES OF EXACT SOLUTIONS

At least two examples for non-elementary boundary and support conditions will be derived analytically for each of the above classes of problems, giving the full details of the derivation. The examples will include line and point supports.

NUMERICAL CONFIRMATION OF THE ANALYTICAL RESULTS

The analytical solutions will be confirmed by FE-based numerical computations using the now universally employed SIMP algorithm [4, see also derivation in 5], and its extensions using DCOC [6]. It is to be mentioned that SIMP was first implemented by the first author's research group in the late eighties, when most others were strongly debating the validity and usefulness of this method

Acknowledgement
The present study was conducted in the research group of Computational Structural Mechanics of the Hungarian Acad. Sci. and was supported by The Hungarian National Scientific and Research Foundation (OTKA) (grant T 037922).

References
[1] Michell A.G.M.: The limits of economy of material in frame structures. Phil. Mag. 8, 589-597, 1904.
[2] Lewinski T., Zhou M., Rozvany G.I.N.: Extended exact solutions for least-weight truss layouts. Parts I and II. Int. J. Mech. Sci. 36, 375-398, 399-419, 1994.
[3] Rozvany G.I.N.: Some shortcomings in Michell's truss theory. Structural and Multidisciplinary Optimization, 12, 244-250, 1996.
[4] Rozvany G.I.N., Zhou M.: Applications of COC method in layout optimization. In Eschenauer H, Matteck C, Olhoff N (eds) Eng. Optim. in Design Processes, 1990.
[5] Gáspár Zs, Lógó J., Rozvany G.I.N.: Addenda and Corrigenda to (1) "Aims, Scope, Methods, History and Unified Terminology of Computer-Aided Topology Optimization in Structural Mechanics" and (2) " On Design-Dependent Constraints and Singular Topologies" (21, 2, 2001, 90-108; 164-172) Structural and Multidisciplinary Optimization, Vol.24., No.4., pp. 338-342, 2002.
[6] Zhou M., Rozvany G.I.N.: DCOC: an optimality criterion method for large systems. Part I: Theory, Part II: algorithm. Structural and Multidisciplinary Optimization, 5, 12-25; 6, 250-262, 1992/93.
[7] Rozvany G.I.N: Optimal plastic design: allowance for self-weight. J. Engin. Mech. Div. ASCE 103, 1165-1170, 1977.
[8] Rozvany G.I.N: Structural design via optimality criteria. Kluwer Academic Publishers, Dordrecht, 1989.

OPTIMAL STRUCTURES FOR BUCKLING FORCES AND BUCKLING DISPLACEMENTS

Jacek Krużelecki, Paweł Smaś
Institute of Applied Mechanics, Cracow University of Technology, Jana Pawła II 37, 31-864 Kraków, Poland

Summary In the present paper the problems of optimal design of elastic columns and annular plates, against buckling are investigated. The optimal solutions for loadings controlled by forces and by displacements are presented and compared in the paper. The unimodal and bimodal problems are considered. The results are obtained using the numerical optimization methods, namely the Method of Moving Asymptotes and the Simulated Annealing Method

INTRODUCTION

The optimal design of structures under stability constraints concerns mainly loadings controlled by a system of forces. However, in some practical engineering applications, the loadings, which are controlled by displacements, can also occur. This type of problems is, for example, connected with structures under thermal loadings in the case of immovable supports or in the case of assembly loadings, which are due to initial imperfections of overall dimensions of a structure. Then, the compressive forces, which occur due to assembly displacements or due to an elevated temperature, depend on geometry of the structure, whereas in the classical optimization problem the forces are independent of the structure. Hence, the results of shape optimization can be qualitatively and quantitatively different for both types of loading control.
Relatively many papers deal with optimal design of structures under stability constraints, taking into account loadings controlled by forces. On the other hand, the problem of optimization of structures against buckling under loadings controlled by displacements was investigated, for example, in the papers by Albul, Banichuk, Barsuk [1], Krużelecki, Smaś [2, 3].
The present paper shows a comparison of the optimal shapes of columns and annular plates obtained for loadings controlled by displacements and by forces. The unimodal and multiodal formulations of the optimization problem are applied.

FORMULATION OF THE OPTIMIZATION PROBLEM

We consider an elastic structure on an elastic foundation of the Winkler type with a modulus β. A compressive force or a displacement of the edge loads the structure. It is assumed that both, the force resulting from the displacement of the edge and the compressive force are conservative ones. We look for such a distribution of the material of a structure, which leads to the maximal critical loading (force or displacement), before the structure buckles.
The optimization problem is stated under equality and inequality constraints. It is assumed that the optimal structure has the same volume of material V as a reference structure volume V_0 with a uniform distribution of material. Additionally, the minimal and maximal values of the design variables are constrained. In a case of a multimodal optimization problem, the condition of equality of the lowest (two or more) critical forces is also imposed.

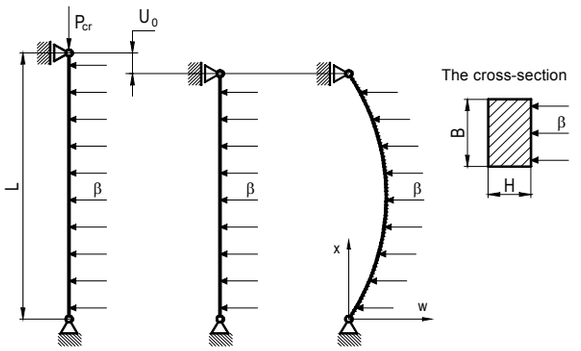


Figure 1. Column with chosen supports, under loadings controlled by displacement U_0 or force P_{cr}

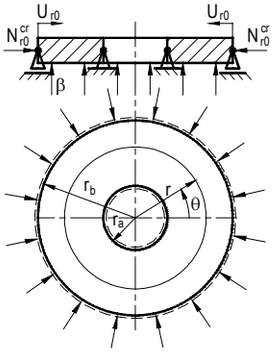


Figure 2. Annular plate with chosen supports, under loadings controlled by displacement U_{r0} or force N_{r0}^{cr}

Optimization of a column of length L with a rectangular cross section of width B and depth H, on the Winkler foundation, supported by a general system of supports and loaded by a compressive force P_{cr} or axial displacement U_0 is considered as one-dimensional problem. A chosen case of supports is shown in Fig.1. The cross-sectional area $A(x)$,

varying along the axis of the column is a design variable. Furthermore, the relation between the cross-sectional area A and moment of inertia I is taken in the following form: $I = cA^n$, where c is a certain constant and $n=1$ is for the cross-sections of constant depth and variable width, $n=2$ for geometrically similar cross-sections or $n=3$ for cross-sections of constant width and variable depth.
However, two-dimensional problem is represented by the optimization of annular plate. A thickness $H(r)$ of the plate that is design variable, is assumed as circularly symmetric and it can vary only in radial direction. The outer or inner edge of the plate can be loaded by radial force N_{r0}^{cr} or radial displacement U_{r0}. The annular plate loaded at the outer edge with a chosen support is shown in Fig.2.

NUMERICAL RESULTS

For the numerical formulations of the optimzation problems stated above two different optimization methods, namely the Method of Moving Asymptotes (MMA) and the Simulated Annealing Method (SAM) were applied. These optimization methods were used for one- and two-dimensional problems. Both methods, allowing for the equality and inequality constraints, were used either separately or alternately, depending on the investigated problem.
The optimal distributions of the cross-sectional area for simply supported column of constant depth (n=1) on an elastic foundation with dimensionless modulus $\overline{\beta} = 100$ are shown in Fig.3. The results are obtained for different types of loading, namely loading controlled by displacement (solid line) and by force (dashed line). The profit measured by increasing of critical loadings, related to prismatic column equals about 78 per cent for loading controlled by displacement and 20 per cent for loading controlled by force.
The optimal shapes of annular plate for both case of loading are presented in Fig.4. The shape plotted by thick line corresponds to loading controlled by displacement whereas the thin line relates to loading controlled by force. The elastic foundation is not active. The optimization was carried out using SAM method, 48 design variables were applied. The obtained results (Fig.4) are unimodal for both types of loading. The increase of critical loadings, in relation to plate of constant thickness, amount about 67 per cent for critical displacement of the edge and 47 per cent for critical force.

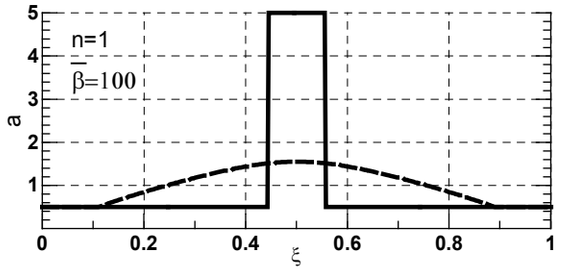


Figure 3. Distribution of dimensionless cross-sectional area $a(\xi)$ of simply supported column on an elastic foundation

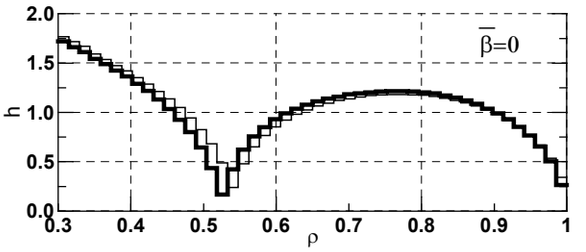


Figure 4. Distribution of dimensionless thickness $h(\rho)$ of annular plate with immovably clumped inner edge, movably simply supported and loaded outer edge.

CONCLUSIONS

The results presented in the Fig.3 show that shapes of columns for both types of ladings are completely different. The differences depend on values of geometrical constraints and value of coefficient $\overline{\beta}$ of an elastic foundation. The lower bound imposed on cross-sectional area of the column has to be necessary in a case of loading controlled by displacements whereas the upper bound constraint seems to be necessary only for a certain group of optimization problems.
The results obtained for annular plates (Fig.4) show very small differences in the optimal shapes and critical loadings for both types of loadings.

References

[1] Albul, A. B., Banichuk, N. W. and Barsuk, A.A.: Optimal design of elastic columns under thermal loadings. *Mekh. Tverdogo Tela*, 15(3), 127-133, 1980 (in Russian).
[2] Krużelecki, J., Smaś, P.: Optimal design of columns for buckling under loadings controlled by displacements and forces. In: Cheng, G., Gu, Y., Liu, S. and Wang, Y. (Eds.), *Proceedings of the Fourth World Congress of Structural and Multidisciplinary Optimization. Liaoning Electronic Press.* Dalian, China, 2001.
[3] Krużelecki, J., Smaś, P.: Optimal design of annular plates against buckling under loadings controlled by displacements. *Proceedings of the Fifth World Congress of Structural and Multidisciplinary Optimization.*, Lido di Jesolo, Italy (in print), 2003.

OPTIMIZATION OF BEAM PROPERTIES WITH RESPECT TO MAXIMUM BAND-GAP

Søren Halkjær, Ole Sigmund
Department of Mechanical Engineering, Section for Solid Mechanics
Technical University of Denmark
Nils Koppels Allé, Building 404, 2800 Kgs. Lyngby, Denmark

Summary We study numerically the frequency band-gap phenomenon for bending waves in an infinite periodic beam. The outcome of the analysis is then subjected to an optimization problem in order to maximize these band-gaps. The band-gap maximization may be performed with respect to material parameters and cross-sectional geometry.

INTRODUCTION

The study of frequency band-gaps in certain material structures subjected to wave propagation has received a lot of attention during the last years. Such materials hinder wave propagation with frequencies in certain intervals (band-gaps). The phenomenon occurs for both acoustic, elastic and electromagnetic waves. Examples among numerous work include [1] which analyzes band-gaps for electromagnetic waves in infinite 2D structures, [2] carries out both an analysis and optimization for the elastic 2D structural problem (infinite and finite), [3] considers infinite periodic plates and cylindrical shells with and without loading. Such studies are relevant in structural design regarding e. g. vibration damping and filters.

In this article, we first perform a numerical analysis of frequency band-gaps for time-harmonic bending waves in an infinite periodic beam. We then formulate an optimization problem for maximizing these band-gaps.

THEORY

Analysis

Bending waves in an infinite periodic beam has been analyzed theoretically using Floquet theory in [4]. Here we adopt the finite element method based on Floquet theory described in [1] to derive the eigenvalue problem for studying the frequency band-gaps.

Bending waves in a beam are described by the fourth order beam equation. We restrict our attention to waves with a time-harmonic behavior $\mathrm{e}^{\mathrm{i}\omega t}$. The differential equation describing the transverse displacement $w(x)$ then becomes

$$\frac{d^2}{dx^2}(E(x)I(x)\frac{d^2w(x)}{dx^2}) = \omega^2\rho(x)A(x)w(x) \tag{1}$$

where E, I, ρ and A are Young's modulus, moment of inertia, mass density and cross-sectional area respectively. Here we consider a periodically segmented beam of infinite length as shown in Fig. 1. The beam consists of an infinite number of identical base cells of length d. Each cell is made up of two different materials with possibly varying cross-section as indicated. Thus, $E(x) = E(x+d)$ and analogously for ρ, I, and A. In order to study the problem, we assume that the

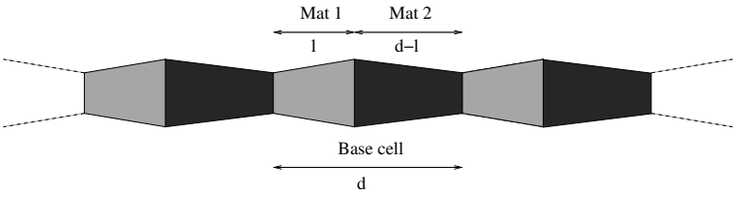


Figure 1. Periodic infinite beam with identical base cells consisting of two materials (Mat 1 and Mat 2) with possibly varying cross-sections.

transverse displacement can be written in terms of Bloch functions

$$w(x) = \mathrm{e}^{ikx}u(x) \tag{2}$$

where k is the wave number and $u(x) = u(x+d)$. Inserting this assumption and integrating over the length of the base cell we obtain

$$-\int_0^d E(x)I(x)(\frac{d}{dx}+\mathrm{i}k)^2u(x)\overline{(\frac{d}{dx}+\mathrm{i}k)^2v(x)}\,\mathrm{d}x = \omega^2\int_0^d \rho(x)A(x)u(x)\overline{v(x)}\,\mathrm{d}x$$

where $v(x)$ is an arbitrary periodic function on the base cell. We use a standard shape function assumption based on a third order polynomial $\phi_i(x)$ on each element, such that $u(x) = \sum_i u_i\phi_i(x)$. We then arrive at the following complex eigenvalue problem

$$\mathbf{K}(k)\mathbf{u} = \lambda\mathbf{M}\mathbf{u}, \qquad \lambda = \omega^2. \tag{3}$$

where

$$K_{ij} = -\int_0^d E(x)I(x)(\frac{d}{dx} + \mathrm{i}k)^2\phi_i(x)\overline{(\frac{d}{dx} + \mathrm{i}k)^2\phi_j(x)}\,\mathrm{d}x, \qquad M_{ij} = \int_0^d \rho(x)A(x)\phi_i(x)\overline{\phi_j(x)}\,\mathrm{d}x$$

The solution to this problem results in the dispersion relation

$$\omega_j = \omega_j(k), \qquad j = 1, \ldots, \text{d.o.f} \tag{4}$$

where ω_i denotes the i'th frequency band and d.o.f. denotes the number of independent variables.

Optimization

The optimization problem for the band-gaps can now be written as a max-min objective using the dispersion relation [2]

$$\max_{\rho,E,A} : c(\rho, E, A) = \frac{\Delta\omega^2(\rho, E, A)}{\omega_0^2(\rho, E, A)} = 2\frac{\min_k \omega_{j+1}^2(k, \rho, E, A) - \max_k \omega_j^2(k, \rho, E, A)}{\min_k \omega_{j+1}^2(k, \rho, E, A) + \max_k \omega_j^2(k, \rho, E, A)} \tag{5}$$

RESULTS

Here we present results for an infinite beam with constant cross-section area $A = 7.74 \times 10^{-4}\,\mathrm{m}^2$, $I = 4.16 \times 10^{-8}\,\mathrm{m}^4$, $d = 0.254\,\mathrm{m}$ and $l = d/2 = 0.127\,\mathrm{m}$. Dispersion plots including the first five frequency bands are shown in Fig. 2 for two material combinations shown in Table 1 (row 1 and 2 respectively). In both cases Mat 1 is Zinc, while Mat 2 is chosen to

Mat 1	E_1 (GPa)	ρ_1 (kg/m^3)	Mat 2	E_2 (GPa)	ρ_2 (kg/m^3)
Zinc	98	7130	Silicon	100	2330
Zinc	98	7130	Chromium	25	7200

Table 1. Material parameters (rows) for two different base cells .

obtain differences in either E or ρ. It is seen that both material combinations result in relative band-gaps approximately the same size but at different frequencies. This is to be studied more thoroughly using (5).

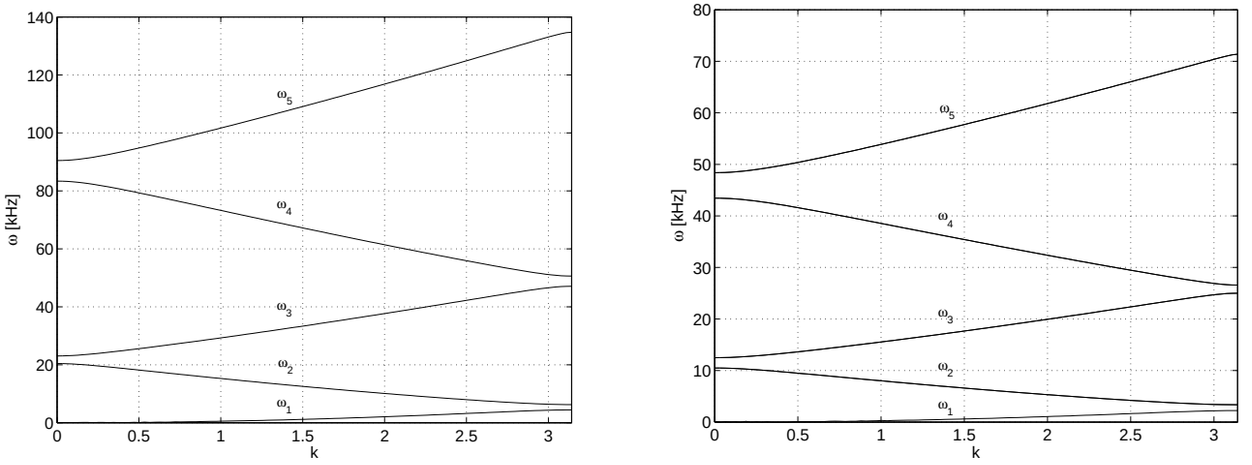


Figure 2. Dispersion plots including the first five frequency bands showing the band-gaps for two base cells with different material combinations. Left: Base cell consisting of Zinc-Silicon. Right: Base cell consisting of Zinc-Chromium.

ACKNOWLEDGMENTS

This work was supported by Denmark's Technical Research Council (the "Phonon project").

References

[1] Axmann W., Kuchment P.: An Efficient Finite Element Method for Computing Spectra of Photonic and Acoustic Band-Gap Materials. *J. Comp. Physics* **150**:468–481, 1999.

[2] Sigmund O., Jensen J. S.: Systematic design for phononic band-gap materials and structures by topology optimization. *Phil. Trans. R. Soc. Lond. A* **361**:1001–1019, 2003.

[3] Sorokin S. V., Ershova O. A.: Frequency band gaps in periodic plates and cylindrical shells. To appear in *Journal of Sound and Vibration*.

[4] Lee S. L., Ke H. Y, Kao M. J.: Flexural Waves in a Periodic Beam. *Journal of Applied Mechanics* **57**:779–783, 1990.

OPTIMAL LAYOUT OF TWO MATERIALS WITHIN THE CORE LAYER OF A SANDWICH PLATE. RELAXED FORMULATION AND ITS COMPUTATIONAL ALGORITHM

Sławomir Czarnecki, Michał Kursa, Tomasz Lewiński

Warsaw University of Technology, Al. Armii Ludowej 16, PL 00-637 Warszawa, Poland

Summary The paper deals with the minimum compliance problem of a sandwich plate with soft core. The aim is to find an optimal layout of two isotropic materials within the core layer. In the relaxed formulation the core is modelled by a 1st rank laminated composite.

Deformation of a sandwich plate of a soft core, see Fig.1, transversely loaded, will be modelled by the Reissner model of 1947, see Sec. 6.3 of Ref.[5]. The bending stiffnesses $\left(D^{\alpha\beta\lambda\mu}\right)$, $\alpha,\beta,\lambda,\mu=1,2$, depend on the properties of the faces and on the distance $2c$. The aim is to optimize the core the transverse shear moduli of which determine the effective stiffnesses $\left(H^{\alpha\beta}\right)$. The moments $\left(M^{\alpha\beta}\right)$ and the transverse forces $\left(Q^{\alpha}\right)$ are interrelated with the deformation measures by

$$M^{\alpha\beta}=D^{\alpha\beta\lambda\mu}\varepsilon_{\lambda\mu}(\boldsymbol{\varphi}),\quad Q^{\alpha}=H^{\alpha\beta}\gamma_{\beta}(w,\boldsymbol{\varphi}) \tag{1}$$

where $\boldsymbol{\varphi}=(\varphi_1,\varphi_2)$ is a vector of the angles of rotation of the transverse cross sections and w represents the plate deflection; the deformations $\varepsilon_{\lambda\mu}(\boldsymbol{\varphi})$ are defined as symmetric part of the gradient of $\boldsymbol{\varphi}$ and $\gamma_{\beta}(w,\boldsymbol{\varphi})=w_{,\beta}+\varphi_{\beta}$. Here comma means differentiation with respect to x_1 or x_2.

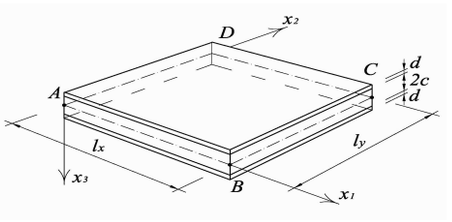


Fig.1 Sandwich plate

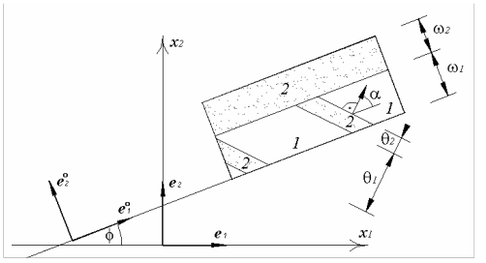


Fig.2 General 2nd rank microstructure of the core layer

The variational equilibrium equation of the plate has the form

$$\int_{\Omega}\left[\ M^{\alpha\beta}\varepsilon_{\alpha\beta}(\overline{\boldsymbol{\varphi}})+Q^{\alpha}\gamma_{\alpha}(\overline{w},\overline{\boldsymbol{\varphi}})\ \right]dx=f(\overline{w})\qquad\forall(\overline{w},\overline{\boldsymbol{\varphi}})\in V\qquad f(\overline{w})=\int_{\Omega}q(x)\overline{w}(x)dx \tag{2}$$

where q represents the transverse loading, Ω is a plate middle plane and V represents the space of kinematically admissible displacement fields. Assume that the core is formed transverse homogeneously of two kinds of isotropic core materials labelled by $\gamma=1,2$. Assume that these materials occupy the domains Ω_{γ} within Ω; the characteristic functions of the domains being denoted by χ_{γ}. Let the areas $\left|\Omega_{\gamma}\right|=C_{\gamma}$ be prescribed. The problem of minimizing the compliance of the plate is put in the form

$$\min\left\{f(w)\middle|w\quad\text{solves (1), (2) and}\ \left|\Omega_2\right|=C_2\right\} \tag{3}$$

The relaxation of the above problem means admitting the characteristic functions χ_{γ} to tend to their weak limits $m_{\gamma}\in L^{\infty}(\Omega;[0,1])$, see Díaz et al.[4] and Lewiński and Telega [5]. Let $G^{per}_{m_2}$ be a set of tensors $\mathbf{H}^{*}$ determining the transverse shear stiffness of the composite material of the core, of two-phase periodic structure, according to the formulae of the homogenization theory, under the assumption of the area fraction of the material 2 being given as m_2. Let us define the effective potential for the transverse forces

$$2W_s(\boldsymbol{\gamma},m_2)=\max\left\{\boldsymbol{\gamma}:(\mathbf{H}\boldsymbol{\gamma})\middle|\mathbf{H}\in G^{per}_{m_2}\right\} \tag{4}$$

and note that its complete characterization is known by analogy with the conductivity problem. Thus the effective constitutive relationships read

$$\mathbf{M}=\mathbf{D}\boldsymbol{\varepsilon}(\boldsymbol{\varphi})\ ,\qquad\mathbf{Q}=\frac{\partial W_s(\boldsymbol{\gamma},m_2)}{\partial\boldsymbol{\gamma}} \tag{5}$$

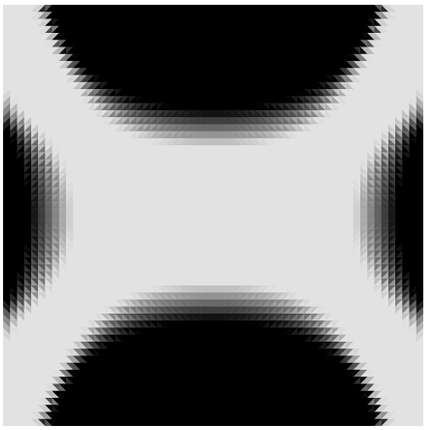


Fig.3 Optimal distribution of the area fraction m_2

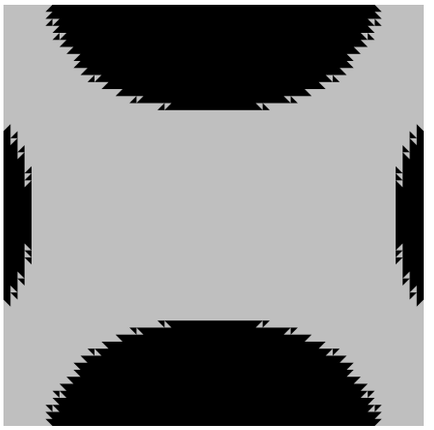


Fig. 4 Types of microstructures:
1st rank laminate is grey; stronger isotropic material is black

The relaxed problem assumes the form

$$\min\left\{ f(w) \middle| w \quad \text{solves}\,(2),(4),(5), m_2 \in L^\infty(\Omega;[0,1]), \int_\Omega m_2 dx = C_2 \right\} \tag{6}$$

The theory of the problem of minimal compliance of two-material plates teaches us that the 2nd rank microstructures, as shown in Fig.2, suffice to achieve the exact result. However, it can be proved that in the case considered one can confine the design to the 1st rank laminated microstructure of the core. Thus the set $G^{per}_{m_2}$ refers to 1st rank laminates, characterized by the design variables ω_2, ϕ, with $\theta_2 = 0$. The effective moduli $\left(H^{\alpha\beta}\right)$ are determined by the formula of Tartar, see Sec. 5.6.4 in Lewiński and Telega [5], applied iteratively. The equilibrium problem is solved with using the DSG finite element, see Bletzinger et al.[2], free of shear locking and satisfying the convergence consistency criteria of Strang. The optimization has been performed with using the COC method and the updating schemes reported in Bendsøe [1]. A similar algorithm has been previously applied to thin plates in Czarnecki and Lewiński [3]. The optimal inclination of ribs is given by the formula

$$\hat{\phi} = \chi - \chi_0, \quad \chi_0 = \frac{1}{2}\arctan\left(\frac{2H_0^{12}}{H_0^{11} - H_0^{22}}\right) \tag{7}$$

where $\chi = \angle(\mathbf{e}_1, \boldsymbol{\gamma})$ and $\left(H_0^{\alpha\beta}\right)$ refer to the basis $\left(\mathbf{e}_1^0, \mathbf{e}_2^0\right)$, see Fig.2. Thus we find the optimal distributions of m_2 in the core layer, see Fig.3. The optimal layout of the core is composed of the weaker material, of the stronger material and of laminates of 1st rank.

The layouts in Figs.3,4 refer to the square plate (AB=5.0 m., c = 16 cm, d = 0.3 cm,) clamped along the sides AB, CD and supported along BC, DA such that there $w = 0, \varphi_2 = 0$. The plate is subjected to a uniform transverse loading. The data are specifically chosen. The faces are made of an isotropic material of moduli E=210.0 GPa, ν=0.21. The core layer is made of two kinds of regular honeycombs of effective transverse shear moduli assessed here by the known formula $\mu_\gamma = 0.577\, t G_\gamma / l$; t = 0.02 cm represents the thickness of the honeycomb wall, while l = 1.00 cm is a length of the side of a honeycomb cell and G_1 = 15.22 GPa, G_2 =26.58 GPa are shear moduli of two materials of the honeycomb. The shear stiffnesses of the plate are computed by $H_\gamma^{\lambda\mu} = H_\gamma \delta^{\lambda\mu}$, $H_\gamma = (2b^2/c)\mu_\gamma$, b=c+d/2, see Sec.6.3 of [5], where the details of computing the bending stiffnesses can be found. The stronger material occupies 0.51 part of the domain Ω. The computations have been performed with using the updating scheme, see [1], with the damping factor $\eta = 0.75$ and the move limit $\zeta = 0.015$. The optimal layouts of the area fraction of both the materials compare favorably with 3D layouts found within the relevant relaxed formulation by homogenization, for various boundary conditions.

References

[1] M. P. Bendsøe .: Optimization of Structural Topology, Shape, and Material. Springer. New York 1995.
[2] K.U. Bletzinger, M. Bischoff, E. Ramm .: A Unified Approach for Shear-Locking-Free Triangular and Rectangular Shell Finite Elements. *Computers and Structures* **75**: 321–334, 2000.
[3] S. Czarnecki, T. Lewiński .: Optimal Layouts of a Two-Phase Isotropic Material in Thin Elastic Plates. European Conference on Computational Mechanics, June 26-29, Cracow, Poland, 2001.
[4] A.R. Díaz, R. Lipton, C.A. Soto.: A new formulation of the problem of optimum reinforcement of Reissner-Mindlin plates. *Comp.Meth.Appl.Mech.Engrg*. **123**: 121-139, 1995.
[5] T. Lewiński, J.J. Telega .: Plates, Laminates and Shells. Asymptotic Analysis and Homogenization. World Scientific. Singapore, New Jersey, London, Hong Kong, 2000.

Material cloud method for topology optimization

Su-Young Chang*, Sung-Kie Youn *

*KAIST, Department of Mechanical Engineering, Daejeon, Republic of Korea

Summary A newly developed material cloud method (MCM) for topology optimization is presented to overcome some difficulties in traditional density distribution method and improve a numerical efficiency in topology optimization procedure. In MCM, an optimal structure can be found out through modifying sizes and positions of material clouds, which are lumps of material having specified properties. A design concept of MCM is presented and results obtained by MCM are compared with those of density distribution method.

INTRODUCTION

Topology optimization method has been a powerful design tool since first numerical implementation by Bendsoe and Kikuchi [1], due to its capability to find out a wonderful design under no restriction of topology change. Even though topology optimization method has been successfully applied into industrial design so far, it still has some difficulties to efficiently obtain better results. It is thought that these difficulties are mainly caused by its optimization concept. In widely used traditional density distribution method for topology optimization, optimal material distribution is found out through search of material densities in all elements in design domain. It can be computationally inefficient due to inclusion of not few elements having low importance and a capability to find out better design, having material out of initial design domain, may be limited. So far there have been many researches to overcome these difficulties [2-3].But most of these have some inefficiency due to still use of density concept. To overcome some difficulties in traditional density-based method, a material cloud method (MCM) for topology optimization is devised in this paper.

MATERIAL CLOUD METHOD

The material cloud is a lump of material having specified properties with a square shape (Ref. Fig. 1).
In material cloud method (MCM), optimal material distribution can be found out through optimizing central positions and sizes of material clouds (Ref. Fig. 2). Methodologies to apply this MCM into topology optimization are categorized as three. One is to optimize only sizes of material clouds (MCMS). Another is to optimize only positions of material clouds (MCMP). And the third is to sequentially optimize positions and sizes of material clouds (MCMPS).
A numerical analysis for a specific distribution of material clouds is carried out using fixed background finite element mesh (Ref. Fig. 2).
Through applying MCM into topology optimization, several advantages can be obtained against traditional density distribution method (MCM). The first is natural and efficient realization of expansion-reduction procedure of design space, which is needed to increase the possibility to find out better optimal solution. The second is that convergence of material distribution can be faster than that of density-based method. The third is a facility to control a minimum-member size in the final material distribution.

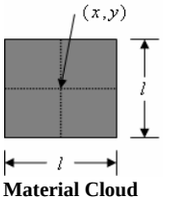


Fig. 1 Material Cloud

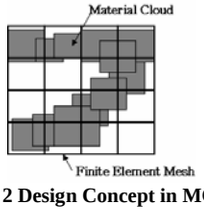


Fig. 2 Design Concept in MCM

NUMERICAL EXAMPLE 1 (MCMS)

A compliance of a structure under one concentrated load is to be minimized under an inequality constraint of total area of material. Topology optimization results of DDM and MCM are compared under same allowable amount of material and same mesh. In this example, MCMS is applied, in which only lengths of material clouds are adopted as design variables. Initially, one material cloud in each element is arranged at the center of the element. During the optimization procedure, sizes of material clouds with fixed center positions can be changed in a range of very small to size of mesh. A function, H like eqn. (1) is introduced to quantitatively measure a closeness of material distribution to 0-1 discrete one.

$$H = \int_{\Omega} \left(\rho^{ub} - \rho\right)\left(\rho - \rho^{lb}\right) d\Omega = \sum_{i=1}^{Nelem} \left(\rho_i^{ub} - \rho_i\right)\left(\rho_i - \rho_i^{lb}\right) A_i \quad (1)$$

Optimal material distribution obtained by MCMS (Fig. 5) is much simpler than that of DDM (Fig. 4). In addition, it has somewhat lower value of objective function. In Fig. 6 and Fig. 7, convergences of both objective function and H-function of MCMS are much faster than those of DDM. Due to approximation of total amount of material into linear

form about design variables in MCMS, a total amount of material is somewhat more than a specified value during first several iteration steps, but this constraint is correctly satisfied after being converged in H-function. The computational cost (time and memory requirement) of MCMS per iteration is very similar to that of DDM. So a total cost to complete optimization procedure can be smaller than that of DDM, because of its excellent convergence.



Fig. 3 Example 1



Fig.4 Optimal Result (DDM, Example1)

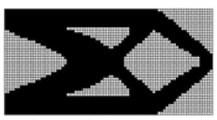


Fig. 5 Optimal Result (MCMS, Example1)

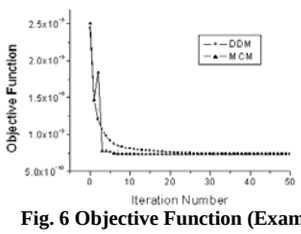


Fig. 6 Objective Function (Example1)

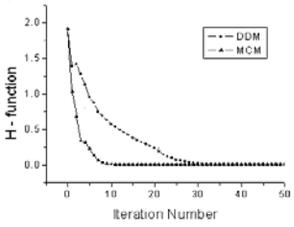


Fig. 7 H-Function (Example 1)

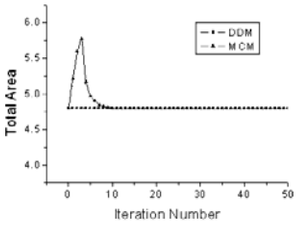
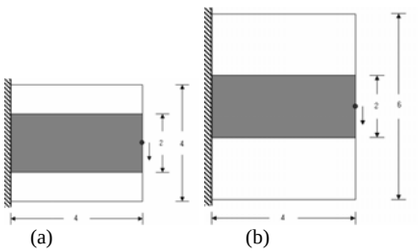


Fig. 8 Total Area (Example 1)

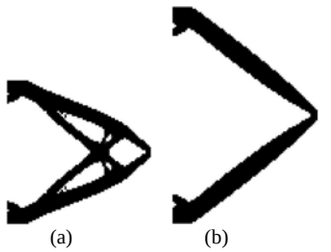
NUMERICAL EXAMPLE 2 (MCMPS)

In this example, MCMPS is applied for 2 different setting up of potential design domain, in which material may be moved to improve a performance of the structure. In MCMPS, firstly central positions of material clouds are optimized (MCMP), and then sizes of material clouds are additionally optimized (MCMS) to compensate clearness of material distribution obtained after MCMP. Through movements of material clouds, an expansion-reduction procedure of design domain can be naturally realized without any additional computations. At this procedure, only active elements, in which any portion of material clouds are contained, are included in analysis. In MCMS, initially, material clouds are arranged at center positions of active elements and have different sizes, which are defined considering amount of material in each active element from results of MCMP. In MCMP, initially material clouds are arranged in shadow region of Fig.9. At Fig. 9, potential design domains are sufficiently largely defined. Fig. 10 shows optimal material distributions through traditional DDM, in which potential domains are identical to fixed design domains. Fig. 11 shows optimal material distributions through MCMPS. Objective function value of Fig. 11(a) and (b) is somewhat less than that of Fig. 10(a) and (b) respectively. Total computational cost of MCMPS is much less than that of traditional DDM, because the number of active elements in optimization procedure is much less than that of DDM.



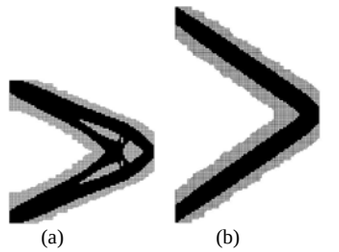
(a) (b)

Fig. 9 Example 2



(a) (b)

Fig. 10 Optimal Result (DDM, Example2)



(a) (b)

Fig. 11 Optimal Result (MCMPS, Example2)

CONCLUSIONS

A newly developed material cloud method (MCM) for topology optimization is presented. In MCM, an optimal structure can be found out through modifying sizes and positions of material clouds, which are lumps of material having specified properties. A numerical analysis for a specific distribution of material clouds is carried out using fixed background finite element meshes. In a case of optimizing only sizes of material clouds, convergences of objective function and H-function are much faster than those of DDM respectively. And in a case of sequential optimizing positions and sizes of material clouds, computational cost in each iteration is much less than that of DDM, because the number of active elements in optimization procedure is much less than that of DDM.

References

[1] M. P. Bendsoe, N. Kikuchi : Generating optimal topologies in structural design using a homogenization method. Computer Methods in applied Mechanics and Engineering 71: 197-224, 1988.

[2] O. M. Querin, Y. M. Xie, G. P. Steven : Evolutionary structural optimization (ESO) using a bidirectional algorithm. Engineering Computations 15 : 1031-1048, 1998.

[3] I. Y. Kim, B. M. Kwak : Design space optimization using a numerical design continuation method. International Journal for Numerical Methods in Engineering 53 : 1979-2002, 2002.

OPTIMAL DESIGN OF UNCONSTRAINED DAMPING LAYER ON BEAMS

Doo-Ho Lee*, Woo-Seok Hwang**
*Department of Mechanical Engineering, Dongeui University, 614-714, Busan, Korea
**School of Automotive/Industrial and Mechanical Engineering, Daegu University, Korea

Summary The optimum layout of unconstrained damping layer on beams is obtained using an equivalent stiffness approach and finite element formulation. The Ross, Ungar and Kerwin(RUK)'s formula is introduced to represent the equivalent complex modulus of the damping layer and beam. The fractional derivative model describes the dynamic characteristics of viscoelastic materials in order to include the non-linearities of real materials with respect to frequency and temperature. Using the equivalent stiffness, a finite beam element is developed and a nonlinear eigenvalue problem is solved for a beam with the unconstrained damping layer on it. The objective of optimization problem is to maximize the product of loss factor and eigenfrequency of a specified mode. Optimum coverage is obtained by combining an analytic design sensitivity analysis and a gradient-based numerical search algorithm.

INTRODUCTION

The damping of structures is one of the most important factors in order to reduce the vibrations of structures. Authors suggested a layout optimization formulation of unconstrained damping layer in Ref [1] that gives maximum loss factor for a specified mode. However, it is noticed that the resonance frequency at the optimal damping layout could be fallen considerably due to mass effect of the damping materials. In this study, optimum layout of unconstrained damping layer on beams that maximizes both the loss factor and the eigenfrequency of a vibration mode will be identified using a numerical search method.

ANALYSIS OF UNCONSTRAINED VISCOELASTIC DAMPING LAYER

Dynamic characteristics of the viscoelastic materials in frequency domain can be represented using the complex modulus such as $\bar{\sigma} = E^*\bar{\varepsilon} = E(1+i\eta)\bar{\varepsilon}$ where $i=\sqrt{-1}$, and $\bar{\sigma}$ and $\bar{\varepsilon}$ are the Fourier transforms of stress and strain, respectively. E^*,E and η are the complex modulus, the storage modulus and the loss factor, respectively. Many environmental factors affect to the dynamic characteristics of the viscoelastic materials. Particularly, the complex modulus of the viscoelastic material is strongly dependent on temperature and frequency. In order to consider the effects of temperature on damping behavior, there is a well-known temperature-frequency superposition principle that says the temperature effects can be converted to those of frequency using a shift factor, $\alpha(T)$ where T is temperature. The shift factor and temperature can be related by the Arrhenius equation such as $\log(\alpha(T)) = d_1(1/T - 1/T_0)$. The fractional derivative model represents the damping elements as a time derivative of order smaller than unity. The constitutive equation of the fractional derivative model of order one can be written as:

$$\sigma(t) + c_1 D^\beta \sigma(t) = a_0\varepsilon(t) + a_1 D^\beta \varepsilon(t) \quad \text{where } D^\beta\sigma(t) = \frac{1}{\Gamma(1-\beta)}\frac{d}{dt}\int_0^t \frac{\sigma(\tau)}{(t-\tau)^\beta}d\tau \tag{1}$$

and $0<\beta<1$, and a_0,a_1,c_1 and β are material parameters. Then, the complex modulus of viscoelastic materials obtained by the Fourier transforms of equations (1) are expressed as:

$$E^* = E(1+i\eta) = \{a_0 + a_1(i2\pi f\alpha(T))^\beta\}/\{1+c_1(i2\pi f\alpha(T))^\beta\} \tag{2}$$

Consider an unconstrained damping layer beam as shown in Fig. 1. The storage modulus and the loss factor of the viscoelastic damping layer are E_2 and η_2, respectively. The storage modulus, the loss factor and the second area moment of the base beam are E_1,η_1 and I_1, respectively. The equivalent complex flexural rigidity, E^*I, of the unconstrained beams by RUK's equivalent rigidity method is written in the form:

$$E^*I/E_1^*I_1 = 1 + e^*h^3 + 3(1+h)^3 e^*h/(1+e^*h) \tag{3}$$

where $h = H_2/H_1$, and $e^* = E_2^*/E_1^*$. The unconstrained damping layer beams can be modeled using a finite beam element formulation with the equivalent flexural rigidity. Following standard finite element formulation procedure with the equivalent flexural rigidity, one can define the corresponding eigenvalue problem as follows.

$$[K]\{y\} = \varsigma[M]\{y\} \tag{4}$$

where $[K] = [K_{Re}] + i[K_{Im}] = [K_{Re}](1+i\eta)$ and $[M]$ and $[K]$ are the global mass and stiffness matrices, respectively. Subscripts *Re* and *Im* mean the real and imaginary parts, respectively, and, the vector, $\{y\}$, is the eigenvector and $\varsigma(=\omega^2=(2\pi f)^2)$ is the eigenvalue. The eigenvalue

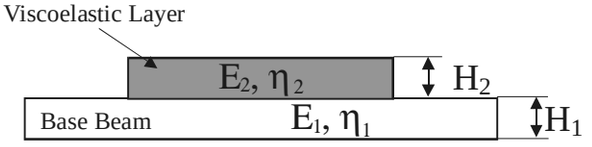


Fig. 1. Unconstrained damping layer beam

problem of Eq. (4) is nonlinear equations because the stiffness matrix is a function of frequency due to the viscoelastic damping layer. In order to solve the nonlinear eigenvalue problem of Eq. (4), an iteration procedure is necessary[1]. The loss factor of a structure for a vibration mode is defined as:

$$\eta^k = \sum_{j=1}^{p} \eta_j \boldsymbol{U}_{ej} \Big/ \sum_{j=1}^{p} \boldsymbol{U}_{ej} = \sum_{j=1}^{p} \eta_j \boldsymbol{U}_{ej} \Big/ \boldsymbol{U} \tag{5}$$

where η^k is the loss factor of the k-th mode, p is the number of finite elements, η_j is a loss factor of the j-th element, and $\boldsymbol{U}_{ej}$ is the strain energy of the j-th finite element.

SENSITIVITY ANALYSIS AND LAYOUT OPTIMIZATION OF DAMPING LAYER

Assuming a uniformly-coated damping layer for a practical consideration, the optimal design problem of the unconstrained damping layout for a specified k-th mode on beams can be defined as follows.

$$\begin{aligned} &\textit{Find the design variables } \boldsymbol{b} \textit{ such that} \\ &\textit{maximize } \eta^k(\boldsymbol{b}; f,T) \times \varsigma^k \textit{ subject to } \boldsymbol{b}_L \le \boldsymbol{b} \le \boldsymbol{b}_U \end{aligned} \tag{6}$$

where $\boldsymbol{b}$ is the design variables and $\boldsymbol{b}_L$ and $\boldsymbol{b}_U$ are the lower and upper bounds of the design variables. Design sensitivity of the loss factor can be obtained from Eqs. (2), (3) and (5) using the chain rule as follows.

$$d\eta^k / db = \{ \sum_{i=1}^{m} \{ d\eta_i(b, f, T)/db \cdot U_{ei} + \eta_i \cdot dU_{ei}/db \} - \eta^k \cdot dU/db \} / U \tag{7}$$

$$d\eta_i(b, f)/db = \partial\eta_i/\partial b + \partial\eta_i/\partial f \cdot df/db \text{ where } \partial\eta_i/\partial f = (Im(\partial \boldsymbol{E}^*/\partial f) \cdot Re(\boldsymbol{E}^*) - Im(\boldsymbol{E}^*) \cdot Re(\partial \boldsymbol{E}^*/\partial f)) / (Re(\boldsymbol{E}^*))^2 \tag{8}$$

Eqs. (7) and (8) can be calculated using the following i-th eigenvalue and eigenvector sensitivity formulae.

$$\dot{\varsigma}^i = \{\boldsymbol{y}^i\}^T [\partial \boldsymbol{K}/\partial b] \{\boldsymbol{y}^i\} - \varsigma^i \{\boldsymbol{y}^i\}^T [\partial \boldsymbol{M}/\partial b] \{\boldsymbol{y}^i\} \tag{9}$$

$$\{\partial \boldsymbol{y}^i/\partial b\} = \sum_{j=1, j\neq i}^{r} -\{\boldsymbol{y}^j\}^T ([\partial \boldsymbol{K}/\partial b] - \varsigma^i [\partial \boldsymbol{M}/\partial b]) \{\boldsymbol{y}^i\} / (\varsigma^j - \varsigma^i) \{\boldsymbol{y}^j\} - 0.5 (\{\boldsymbol{y}^i\}^T [\partial \boldsymbol{M}/\partial b] \{\boldsymbol{y}^i\}) \{\boldsymbol{y}^i\} \tag{10}$$

Therefore, in order to obtain the loss factor sensitivity information, it is necessary to solve one eigenvalue problem, one eigenvalue sensitivity analysis and one eigenvector sensitivity analysis. To validate the optimization formulation of the unconstrained damping layer beams, a numerical example is introduced as shown in Fig. 2. In Fig. 2 a viscoelastic damping material, LD-400[2], is bonded on an aluminum beam. The damping-treated beam is modeled with 20 beam elements. Fig. 3 shows variation of the loss factor and the first resonant frequency. As shown in Fig. 3, the resonant frequency goes down before the loss factor reaches to the maximum. Optimal lengths of the unconstrained damping layer that gives maximum product of the loss factor and eigenfrequency for the first mode are determined using a gradient-based search algorithm. The design variable is the length of the damping layer. Fig. 4 shows the optimal coverage does not vary considerably contrary to the case of maximum loss factor only in Ref. [1].

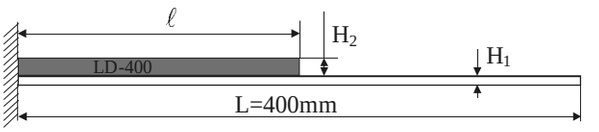


Fig. 2. A clamped-free beam

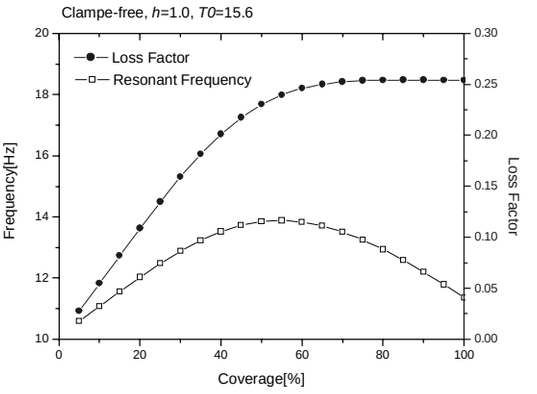


Fig. 3. Variation of loss factor and resonant frequency with respect to coverage of damping layer (h=1)

CONCLUSIONS

Optimal damping treatment layouts on the unconstrained beams are identified according to the thickness ratios and the environmental temperatures. The optimization results show that the proposed formulation is effective for real viscoelastic damping materials.

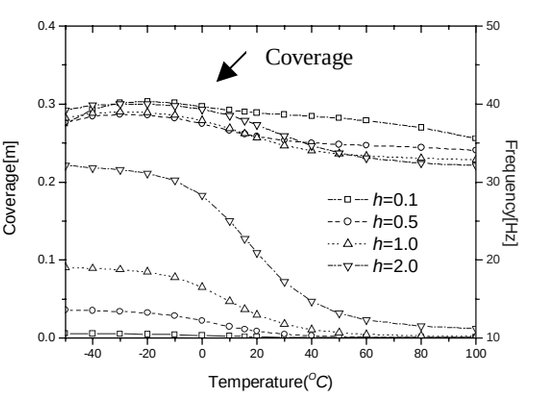


Fig. 4. The optimum coverage of damping layer and the corresponding resonant frequency for the first mode

References

[1] Lee D.-H., Hwang W.-S.: Layout Optimization of Unconstrained Viscoelastic Layer on Beams Using Fractional Derivative Model, *AIAA J.(Submitted for publication)*, 2004.

[2] Jones D.G: Handbook of Viscoelastic Vibration Damping. John Willy & Sons, NY 2001.

ON SEPARATION OF EIGENFREQUENCIES IN TWO-MATERIAL STRUCTURES

Niels L. Pedersen
Institute of Mechanical Engineering, Aalborg University, Pontoppidanstræde 101, DK-9220 Aalborg East, Denmark

Summary We present a method to maximize the separation of two adjacent eigenfrequencies in structures with two material components. The method is based on finite element analysis and topology optimization where an iterative algorithm is used to find the optimal distribution of the materials. Results are presented for vibration problems governed by the 2D scalar wave equations.

INTRODUCTION

One strategy for passive vibration control of mechanical structures is to design the structures so that eigenfrequencies lie as far away as possible from the excitation frequencies. This paper exploits the possibility for using the method of topology optimization to maximize the separation of two adjacent eigenfrequencies in structures with two material components. This study is restricted to 2D structures where the vibrations are governed by the scalar wave equation.

THE 2D SCALAR CASE

Here we show results related to the 2D scalar case. Results also including the 1D scalar case can be found in [1].

Model

The 2D scalar time-reduced wave equation (Helmholtz equation) is given by:

$$\boldsymbol{\nabla}^T(A(x,y)\boldsymbol{\nabla}w) + \omega^2 B(x,y)w = 0, \tag{1}$$

where the problem dependent material coefficients A and B can vary in the 2D plane (x,y). By changing the two coefficients A and B we study different structural vibration problems. Letting $A = 1$ and $B = \rho/T$ enable us to analyze the membrane problem where $\rho(x)$ is the density and T is the uniform tension (force per area). Alternatively with $A = E/(2(1+\nu))$, where $E(x)$ is Young's modulus and $\nu(x)$ is Poisson's ratio, and with $B = \rho(x)$ being the density, (1) governs out-of-plane shear vibrations of a thick elastic body.
To solve the wave equation with in-homogeneous coefficients we apply a standard Galerkin finite element discretization of equation (1) and the boundary conditions, which leads to the discrete eigenvalue problem:

$$\mathbf{K}\boldsymbol{\phi} = \omega^2\mathbf{M}\boldsymbol{\phi}, \tag{2}$$

that has $(\omega_i, \boldsymbol{\phi}_i)$ as the i'th eigensolution (frequency and vector), and $\mathbf{M}$, $\mathbf{K}$ are system matrices given as:

$$\mathbf{K} = \sum_{e=1}^{N} A_e\mathbf{k}_e, \qquad \mathbf{M} = \sum_{e=1}^{N} B_e\mathbf{m}_e, \tag{3}$$

where the summations should be understood in the normal finite element sense, with $\mathbf{k}_e$ and $\mathbf{m}_e$ being element matrices.

OPTIMIZATION

When we optimize a 2D domain with respect to maximizing the gap between eigenfrequencies there are a number of extra difficulties we must deal with. The primary source of the difficulties is the possibility of multiple eigenfrequencies. The multiple eigenfrequencies can be calculated without difficulty using e.g. the subspace iteration method [2]. The objective for the optimization is given by

$$\text{maximize} \quad J = \omega_{n+1} - \omega_n, \tag{4}$$

where the gap between the eigenfrequency of order $n+1$ and n is maximized. If the eigenfrequencies of order $n+1$ and n are both distinct eigenpairs, with squared eigenfrequencies ω_{n+1}^2 and ω_n^2 and corresponding eigenvectors $\boldsymbol{\phi}_{n+1}$ and $\boldsymbol{\phi}_n$, no problems arise and we use the objective (4) directly since the sensitivities of the squared eigenfrequency with respect to a design parameter t_e are then given by:

$$\frac{d\omega^2}{dt_e} = \boldsymbol{\phi}^T\left(\frac{d\mathbf{K}}{dt_e} - \omega^2\frac{d\mathbf{M}}{dt_e}\right)\boldsymbol{\phi}, \tag{5}$$

assumed that the eigenvector have been normalized so that $\boldsymbol{\phi}^T\mathbf{M}\boldsymbol{\phi} = 1$. In the case of multiple eigenvalues we cannot use (5) to find the sensitivities. The extended method is presented in [3] and used more recently in [4], and with this

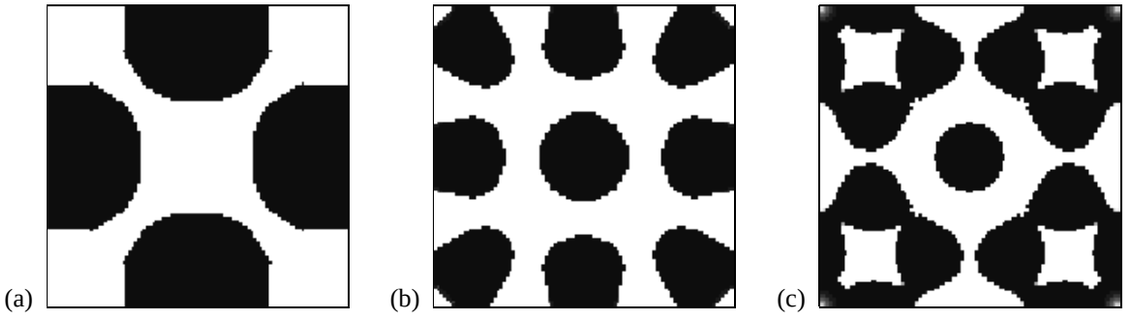


Figure 1. Eigenfrequency optimization of a 2D domain with two different materials, the design domain is a square that have no supports (free boundary conditions); (a) the result when maximizing the gap between 2nd and 3rd eigenfrequency, (b) 8th and 9th eigenfrequency, (c) 12th and 13th eigenfrequency.

method it is now possible to find the sensitivities of multiple eigenfrequencies. There is however still a problem because the sensitivities are given for specific eigenvectors that vary for each design parameter. It is therefore difficult to solve the optimization problem as formulated in (4). As an alternative formulation we propose to use a double bound formulation. The standard bound formulation is used to reformulate a min-max problem. Instead of minimizing the maximum value of a given quantity, a new variable is introduced which is minimized subject to the constraint that the value of the given quantity should be less than this variable. The present optimization problem of maximizing the gap between two eigenfrequencies is reformulated as:

$$\begin{array}{rll} \max_{t_e} & J = C_1 - C_2 & \\ \text{subject to:} & \omega_{n+i} \geq C_1 & i \in [1, n_u] \\ & \omega_{n+1-j} \leq C_2 & j \in [1, n_l] \end{array} \tag{6}$$

Penalization

The basis of topology optimization with a material interpolation scheme is to assign constant material properties to each element in the finite element model and then to associate these material properties with continuous design variables. The simplest interpolation of the material coefficients A and B when using two materials is done using a linear approach:

$$A_e(t_e) = A_1 + t_e(A_2 - A_1), \qquad B_e(t_e) = B_1 + t_e(B_2 - B_1), \tag{7}$$

where t_e is the element design parameter which takes values between 0 and 1. This is however not appropriate when optimizing eigenfrequencies. In [5] it was noted that the important aspect is not the interpolation of the stiffness (here coefficient A) or the interpolation of the mass (here coefficient B) but the interpolation of the eigenfrequency. The squared eigenfrequency ω^2 is by the Rayleigh quotient given as "stiffness divided by mass". A first choice would then be to make an interpolation of the squared eigenfrequency which is a linear function of the design parameter t_e. This will however still not give a 0-1 design i.e. a design with no intermediate material. We must therefore make a penalization that will drive the design to a final 0-1 result. It is possible to make an interpolation/penalization function that will work for an objective where we want to maximize an eigenfrequency but this will not work for a minimization of an eigenfrequency. In the objective of (6) we both have to maximize one eigenfrequency and at the same time minimize a second eigenfrequency this cannot be achieved by one penalization function. To overcome this problem we apply a method where the sensitivities related to the constraints with C_1 in (6) are calculated using one penalization function and the sensitivities related to the constraints with C_2 are calculated using a second penalization function.

EXAMPLES

In figure 1 we show the results of maximizing the gap between three different sets of eigenfrequencies of a square domain, black and white corresponds to the two different materials.

References

[1] Jensen, J.S. and Pedersen N.L. : On separation of eigenfrequencies in two-material structures using topology optimization: the 1D and 2D cases (Submitted), 2003.

[2] Bathe, K.J.: Finite Element Procedures, 2nd Ed. Prentice-Hall, 1996.

[3] Seyranian, A.P., Lund, E. and Olhoff, N.: Multiple eigenvalues in structural optimization problems *Structural Optimization* **8**(4):207-227, 1994.

[4] Pedersen , N.L. and Nielsen, A.K.: Optimization of practical trusses with constraints on eigenfrequencies, displacement, stresses and buckling *Structural and Multidisciplinary Optimization* **25**(5-6):436-445, 2003.

[5] Pedersen N.L.: Maximization of eigenvalues using topology optimization *Structural and Multidisciplinary Optimization* **20**(5-6):2-11, 2000.

XXI ICTAM, 15–21 August 2004, Warsaw, Poland

DENSITY GRADIENT BASED REGULARIZATION OF TOPOLOGY OPTIMIZATION PROBLEMS

Gregor Kotucha*, Klaus Hackl*
*University of Bochum, Institute of Mechanics, D-44780 Bochum, Germany

Summary The numerical solution of topology design problems often results in optimal designs containing microstructures characterized by oscillating material density fields such as the well-known "checkerboard-patterns", whose realization turns out to be difficult from the engineering point of view. In this context we introduce a density gradient based regularization approach including a global penalty functional, which prevents the formation of oscillating density distributions. Furthermore we discuss numerical aspects of the proposed regularization and present solutions of the regularized topology optimization problem for exemplary design problems.

FORMULATION & REGULARIZATION OF THE TOPOLOGY OPTIMIZATION PROBLEM

The formulation of topology design problems requires in general the introduction of a discrete material-indicator function $\rho : \mathbf{x} \rightarrow \{0, 1\}$ as design variable [1], which divides the design domain Ω into a solid region $\Omega^s = \{\mathbf{x} \in \Omega \mid \rho(\mathbf{x}) = 1\}$ and an empty region $\Omega^e = \{\mathbf{x} \in \Omega \mid \rho(\mathbf{x}) = 0\}$. To obtain a continuous optimization problem, instead of a large-scale combinatorial problem, the indicator function is usually identified as the material density and intermediate values between 0 and 1 are admitted. In addition special penalty methods such as the SIMP-approach [1] are used to reduce the set of admissible solutions to so-called "black&white" designs free of "gray" regions characterized by intermediate density values, whose realization turns out to be difficult from the engineering point of view. In the case of linear-elastic maximum-stiffness-design the corresponding optimization problem can be formulated in the following form [1]

$$\min_{\rho} \left\{ \int_{\Omega} \mathbf{f}_v^T \mathbf{u} \, d\Omega + \int_{\Gamma_t} \mathbf{f}_t^T \mathbf{u} \, d\Gamma_t \right\}$$

$$\text{subject to :} \tag{1}$$

$$\int_{\Omega} \boldsymbol{\varepsilon}^T(\mathbf{u}) \, \mathbf{C}(E) \, \boldsymbol{\varepsilon}(\delta\mathbf{u}) \, d\Omega = \int_{\Omega} \mathbf{f}_v^T \delta\mathbf{u} \, d\Omega + \int_{\Gamma_t} \mathbf{f}_t^T \delta\mathbf{u} \, d\Gamma_t \quad , \quad E = \rho^p E_0 \quad , \quad p > 1$$

$$\int_{\Omega} \rho \, d\Omega \leq M_0 \quad , \quad 0 \leq \rho \leq 1.$$

The displacement field $\mathbf{u}$ caused by body forces $\mathbf{f}_v$ and traction forces $\mathbf{f}_t$, acting on the boundary Γ_t of the design domain, is determined by the variational form of the equilibrium condition, which can be handled as a constraint to the optimization problem. In this context $\mathbf{C}$ denotes the material rigidity tensor and E corresponds to the Young's modulus of the material. Nevertheless the implementation of the SIMP-approach or equivalent penalty methods results in discontinuities in the global density distribution and often leads to designs containing unfavourable microstructures such as the well-known "checkerboard patterns" [3] characterized by oscillations of the density function between the discrete values 0 and 1.
To obtain "black&white" designs free of microstructures the optimization problem (1) can be regularized by the so-called X-SIMP-approach [2]

$$E = \rho^p E_0 e^{-\gamma\lambda} \quad , \quad p > 1 \quad , \quad \gamma > 0 \quad , \quad \lambda = \int_{\Omega} (\nabla\rho)^T \nabla\rho \, d\Omega, \tag{2}$$

where γ corresponds to an additional penalty parameter and λ represents a global penalty functional based on the gradient of the density function, which prevents the formation of oscillating density distributions characterized by high density gradients. In consideration of the above penalty-approach the topology optimization problem (1) has to be modified as follows

$$\min_{\rho} \left\{ \int_{\Omega} \mathbf{f}_v^T \mathbf{u}\, d\Omega + \int_{\Gamma_t} \mathbf{f}_t^T \mathbf{u}\, d\Gamma_t \right\}$$

subject to : (3)

$$\int_{\Omega} \boldsymbol{\varepsilon}^T(\mathbf{u})\, \mathbf{C}(E)\, \boldsymbol{\varepsilon}(\delta\mathbf{u})\, d\Omega = \int_{\Omega} \mathbf{f}_v^T \delta\mathbf{u}\, d\Omega + \int_{\Gamma_t} \mathbf{f}_t^T \delta\mathbf{u}\, d\Gamma_t$$

$$E = \rho^p E_0 e^{-\gamma\lambda} \quad , \quad p > 1 \quad , \quad \gamma > 1 \quad , \quad \lambda = \int_{\Omega} (\nabla\rho)^T (\nabla\rho)\, d\Omega$$

$$\int_{\Omega} \rho\, d\Omega \leq M_0 \quad , \quad 0 \leq \rho \leq 1.$$

In this context we present results of numerical studies of different maximum-stiffness-design problems, such as the examples stated below (figure 1), and we compare optimal designs obtained on the basis of the SIMP-approach and the X-SIMP-regularization. Furthermore we discuss numerical aspects of the proposed regularization approach such as the finite-element-discretization of the regularized problem, the formulation of an appropriate finite-element-type and the corresponding stiffness-matrix, the sensitivity analysis and the numerical solution of the discretized optimization problem.

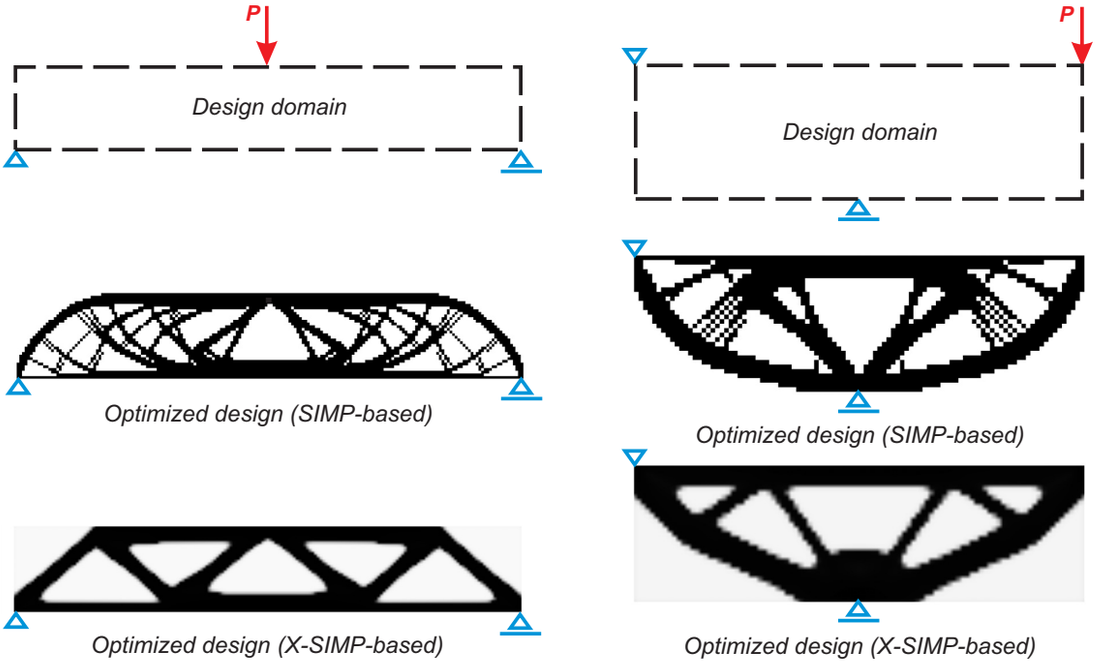


Figure 1. Topology design based on the SIMP-approach and the X-SIMP-regularization

References

[1] Bendsøe, M.P.: Optimal shape design as a material distribution problem. Struct. Optim. **1**, 193-202, 1989
[2] Kotucha, G., Hackl. K.: Density gradient enhanced topology optimization of continuum structures. Proc. Appl. Math. Mech. **3**, 292-293, 2003
[3] Sigmund, O.; Petersson, J.: Numerical instabilities in topology optimization: a survey on procedures dealing with checkerboards, mesh-dependencies and local minima. Struct. Optim. **1**6, 68-75, 1998

XXI ICTAM, 15–21 August 2004, Warsaw, Poland

NEW RESULTS OF STRUCTURAL OPTIMIZATION FOR POST-BUCKLING BEHAVIOUR

Bogdan Bochenek, Michał Życzkowski
Institute of Applied Mechanics, Cracow University of Technology, Jana Pawła II 37, 31-864 Kraków, Poland

Summary Recently the new concept of structural optimization against instability has been proposed. The post-buckling analysis is included directly in the optimization problem and the so-called modified design is formulated. As a result, the optimal structure with stable behaviour after buckling is obtained. Many modified design problems for structures exposed to elastic instability have been already formulated and solved. The paper presents general approach and new results.

INTRODUCTORY REMARKS

Maximization of instability load for a prescribed volume of a designed element is the standard problem of optimization under stability constraints. The analysis of nonlinear post-buckling behaviour and the influence of imperfections are, in general, not included in such a standard formulation and therefore the important information about behaviour of a designed element after buckling is not provided. Very often the standard optimal structure represents unstable post-buckling behaviour. This phenomenon is dangerous in engineering practice since the applicability of such an unstable optimal structure may be questionable. It indicates that a modification of such a standard optimization is necessary especially from practical point of view. The concept of modified optimization including constraints imposed on stability of post-buckling behaviour has been proposed by Bochenek [1]. A broad classification of the modified design problems is given in [2]. Among various proposals of new design problems is optimization against instability in the large. It refers to the case when critical state does not exist and instability occurs only at finite displacements. The standard optimization problem cannot be formulated, but modified design against this form of instability can be performed. This case is discussed in the present paper. In several previous papers Bochenek considered many variants of the modified optimization and obtained effective results using purely numerical approach based on discretization and non-linear programming. Parallelly, Życzkowski [3] derived analytical formulae determining post-buckling path for columns under general behaviour of loading, including active and reactive forces. Making use of both these directions of research alows to develop analytical approach to optimization for post-buckling behaviour. We give here some details concerning that approach. It occurs that modified designs are sensitive to geometry changes in pre-buckling state. This interesting and important problem is demonstrated in this paper on selected examples: optimization of a column loaded by an attached vessel containing liquid and design of a helical spring.

NUMERICAL OPTIMIZATION AGAINST INSTABILITY IN THE LARGE

This paper undertakes the problem of modified optimization against instability in the large providing formulations and numerical solutions for selected elements. The typical deformation path of the structure that suffers from instability in the large is a curve that decreases from infinity, passes its minimum and then increases. The structure instability can be characterized by the minimum value of the deformation curve which refers to lower critical load. In what follows the optimization problem can be formulated either as maximization of lower critical loading or minimization of generalized displacement for lower critical load or maximization of generalized displacement for which unstable equilibrium begins. These formulations are presented in the Fig.1.

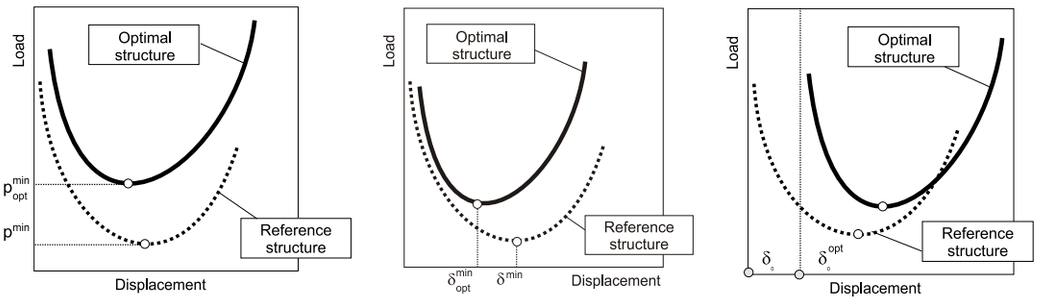


Figure 1. Maximization of lower critical loading when upper critical load is absent (left). Minimization of generalized displacement for lower critical load (middle). Maximization of generalized displacement for which unstable equilibrium begins (right).

Example of compressed and transversally loaded beam placed on the rigid foundation

To illustrate the discussion of this section a cantilever beam placed on the rigid foundation, loaded by an uniform transverse loading and compressed by an axial force, has been chosen. If the value of the transverse load is greater than zero critical state of the beam does not exist, and only for finite values of vertical displacement unstable equilibrium may be observed. Therefore the nonlinear analysis is needed to provide the system response and, what is important from optimization point of view, the design against instability in the large has to be performed.

ANALYTICAL OPTIMIZATION OF COLUMNS UNDER GENERAL BEHAVIOUR OF LOADING

Until now the modified optimal solutions have been obtained using purely numerical approach based on discretization and non-linear programming. Recently Życzkowski [3] derived analytical formulae determining post-buckling path under general behaviour of loading, including active and reactive forces. Based on that analytical approach to optimization of columns for post-buckling behaviour has been developed. Perturbation method combined with Croll's manoeuvre makes it possible to derive general formulae for the subsequent corrections of the force, and hence to analyze stability in the post-buckling range. Based on that the analytical formulae of the postbuckling constraints can be obtained. The constraint imposed on the second correction of the force allows to obtain stable post-critical behaviour of the designed structure locally that is in the vicinity of critical point. The relevant optimization problem is then expressed as an isoperimetric problem of the calculus of variations. In many cases of loading behaviour three ranges for structural parameters may be distinguished: 1) post-buckling stability both for prismatic columns and optimal columns designed for only buckling constraints, 2) post-buckling instability for optimal columns which may be changed into stability by using modified optimization, 3) post-buckling instability in any case. Analytical approach makes it possible to evaluate boundaries of these ranges. The proposed approach is illustrated by the example described in the following section.

INFLUENCE OF GEOMETRY CHANGES IN PRE-BUCKLING STATE ON MODIFIED OPTIMAL DESIGNS

Analytical optimization of a column loaded by an attached vessel containing liquid

Consider a column loaded by an attached vessel filled with a heavy liquid with specific weight γ. The vessel has the form of a symmetric triangular parallellepiped characterized by the dihedral central angle 2β and depth b. The column is loaded by the concentrated axial force.

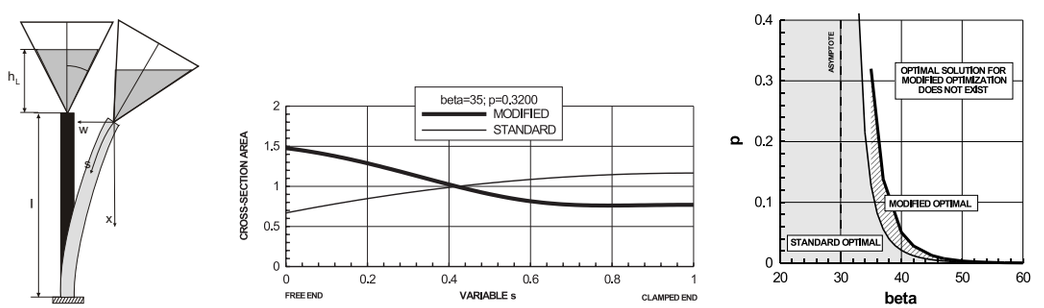


Figure 2. A column loaded by an attached vessel containing liquid (left). Standard and modified optimal column (middle). The three ranges for structural parameters (right).

Loading of the column may be controlled by any of two parameters: specific weight γ or by the volume of liquid V_l. In the first case (rather theoretical, but apparently possible e.g. if a charged liquid is subjected to an electromagnetic field with increasing intensity) we have no pre-buckling geometry changes. In the case of loading controlled by V_l pre-critical geometry changes occur and the differences in shape of standard and modified optimization are more visible.

Numerical optimization of helical springs

A helical spring is an example of a structural element, for which large displacements and changes of geometry should be taken into consideration in a precritical state. It influences the buckling load and the post-critical behaviour of a structure. While a helical spring with a constant radius and constant helix angle has usually a locally stable postcritical path, on the contrary the optimal spring with varying helix angle can show unstable behaviour after buckling. Then the standard formulation of the optimization problem should be modified and post-buckling constraints should be taken into consideration.

CONCLUSIONS

Some structures, in particular columns, optimized for minimal volume under prescribed critical loading (standard optimization) show unstable post-buckling path. Such cases, if possible, should be avoided from engineering point of view. The present paper gives both numerical and analytical treatment of the so-called modified optimization ensuring at least locally stable post-buckling path. General behaviour of loading after buckling is considered (path-dependent loading).

References

[1] Bochenek B.: Selected problems of numerical optimization with respect to stability constraints, *Proceedings of the World Congress on Optimal Design of Structural Systems, Rio de Janeiro 1993, (Ed. Herskovits J.)*, 3–10, 1993.
[2] Bochenek B.: Problems of structural optimization for post-buckling behaviour, *Struct. Multidisc. Opt.*, **25**, 423-435, 2003.
[3] Życzkowski M.: Post-buckling analysis of non-prismatic columns under general behaviour of loading, *Int. J. Non-Linear Mech.* (submitted).

COMPLIANT MECHANISM DESIGN FOR ADAPTIVE TRAILING EDGE FLAPS

Thomas Buhl
Risø National Laboratory, Wind Energy Department
Building VEA-118, P.O. Box 49, Frederiksborgvej 399, DK-4000 Roskilde, Denmark
email: thomas.buhl@risoe.dk, tel: (+45) 46 77 54 67
ICTAM04 ID: 12079

Summery Using a trailing edge flap actively on a wind turbine wing can eliminate the fluctuation in the wind field and thereby reduce the overall load response of the turbine. This work aims at finding the optimal compliant mechanism that controls the flap. Topology optimization is used with a geometrically nonlinear finite element formulation. The optimization problem is formulated as a minimization of the summed error between the desired point and the actual points.

INTRODUCTION

It has been wind turbine developers dream for a long time to be able to eliminate the fast fluctuations in the wind fields that the turbines experiences. This can lead to lower overall loads and less fluctuating loads on the turbine components and thereby longer life time expectancy. This work is a part of a project that aims to uncover the potential of reducing fluctuating loads by actively using a trailing edge flap on the wind turbine wings.

The goal of this work is to find the optimal compliant mechanism that can provide the shape of the flap that is proscribed by the aerodynamic and aeroelastic calculations. This is done by using the topology optimization method (for an overview of the method see M. P. Bendsøe and O. Sigmund) with a geometrically nonlinear finite element method (FEM) as used in Buhl *et al.* and Pedersen *et al.*

The topology optimization method has been used in a wide range of applications from MicroEletricMechanicalSystems to designing satellites (see M. P. Bendsøe and O. Sigmund). However, it is mostly used as a ”first step starting guess” in the design phase since the outer perimeter can be coarse. Experience with designing compliant mechanisms using topology optimization show that the resulting topology often consists of rigid beams connected by hinge type areas (see Pedersen *et al.*). Within this project the found optimized compliant mechanism will be ”translated” into a rigid body mechanism and thereafter tested and optimized using multibody mechanism design. The present paper will, however, concentrate on the topology optimization of the actuating mechanism for the flap.

THE OPTIMIZATION PROBLEM

The optimal topology should in the final configuration consist of only solid and void elements which ensured by the SIMP-model (again look in M. P. Bendsøe and O. Sigmund for further details). To remove the checkerboard problem the standard filter technique discussed in M. P. Bendsøe and O. Sigmund is used. A continuation approach is used on the filter radius such that the possibility of ending in a local minimum is less likely.

A set of points describing the outer shape of the flap in actuated configuration is given from the aerodynamic and aeroelastic calculations. Another set of point on the actual outer perimeter must coincide with the given set of points. This is done by formulating the optimization problem as a minimization of the summed squared error between the two sets of points in the deformed configuration.

The optimization problem has like most standard topology optimization problems with mechanism design constraint on the input displacement and a volume constraint.

The objective function for this optimization problem can be written as

$$\left.\begin{array}{rcl} \min\limits_{\boldsymbol{\rho}} & : & \Phi = \sum_{m=1}^{M} \left(u_{out,m} - u^*_{out,m}\right)^2 \\ \text{subject to} : & & \boldsymbol{v}^T\,\boldsymbol{\rho} \leq V^*, \\ & : & u_{in} \leq U^*_{in}, \\ & : & \mathbf{0} < \boldsymbol{\rho}_{min} \leq \boldsymbol{\rho} \leq \mathbf{1} \end{array}\right\} \tag{1}$$

where $u_{out,m}$ is the actual position of the m^{th} point on the perimeter, $u^*_{out,m}$ is the m^{th} desired point, M is the number of point in total, v is the volume of an element, V^* is the volume constraint, ρ is the density of an element, u_{in} is the actual displacement in input point and U^*_{in} is the constraint of the input point. The design variable has the upper bound of one while the lower bound for ρ is $\rho_{\min}$.

EXAMPLE

In Figure 1 the design domain is shown for the following example. The design domain is supported on the lower and upper fourths of the right edge. The actuator is placed in the middle of the right edge. The flap contour is set to be fixed solid material while the material outside the flap is set to be fixed void.

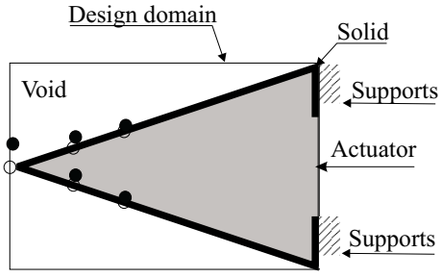


Figure 1. A conceptual layout of the design domain.

The gray color in Figure 1 represents the area where the mechanism can be formed. The flap should follow 5 given point marked with solid circles in Figure 1. The points on the flap (marked with hollow circles) should in the deformed configuration coincide with the solid circles.



Figure 2. The optimized flap mechanism in undeformed configuration.

The optimization problem was solved in 712 iterations and error is less than 10^{-6}. The internal mechanism is a simple rod delivering all its actuation to the out corner of wedge.

CONCLUSIONS

The topology optimization problem of finding the optimal mechanism, to make the trailing edge of a blade follow a given shape, has been solved. The optimization problem was written as an error function where a number of points on the flap should go through the same number of given points. The error between the two sets of points are minimized. The optimization problem was solved with an acceptable error in 712 iterations.

FURTHER WORK

The work presented here is a small part of the steps in finding the optimal mechanism for the trailing edge flap. More work is done with more advanced optimization problems. The optimal mechanism has gone through a postprocessing and the actual mechanism will be built.

REFERENCES

M. P. Bendsøe and O. Sigmund, (2003) "Topology Optimization - Theory, Methods and Applications", *Springer* ISBN 3-540-42992-1

T. Buhl, C.B.W. Pedersen and O. Sigmund (2000) "Stiffness design of geometrically non–linear structures using topology optimization", *Structural and Multi–disciplinary Optimization*, **19**(2): 93–104.

C.B.W. Pedersen, T. Buhl and O. Sigmund (2001) "Topology synthesis of large displacement compliant mechanisms", *International Journal of Numerical Methods in Engineering*, **50**(12): 2683–2705.

XXI ICTAM, 15–21 August 2004, Warsaw, Poland

STRUCTURAL OPTIMIZATION OF COMPOSITE SHELL STRUCTURES USING A DISCRETE CONSTITUTIVE PARAMETERIZATION

Erik Lund, Jan Stegmann
Institute of Mechanical Engineering, Aalborg University,
Pontoppidanstraede 101, DK-9220 Aalborg East, Denmark

Summary In this paper a novel parameterization method for structural optimization of composite laminate shell structures is presented. The method is based on ideas from multi-phase topology optimization where the material stiffness (or density) is computed as a weighted sum of candidate materials. Examples illustrate the potential of the method to solve the problem of proper choice of material, stacking sequence and fiber orientation simultaneously for maximum stiffness or lowest eigenfrequency design.

INTRODUCTION

The use of fiber reinforced polymers in structural design has gained an ever increasing popularity due to their superior mechanical properties and this work focuses on optimal design of composite laminate shell structures. These structures consist of fiber reinforced polymers stacked in a number of layers and bonded together by a resin, and the design problem is to determine the stacking sequence by proper choice of material and fiber orientation of each layer in order to obtain the desired structural performance. For complicated geometries this is a very challenging design problem that calls for use of sophisticated structural optimization tools.

The major problem when solving such design optimization problems is the non-convexity of the design space, i.e. the risk of ending up with a local optimum solution is high. Several different approaches have been proposed to circumvent this difficulty, and the remedy has typically been to either formulate an optimality criteria method [1, 2], to formulate an equivalent convex problem by introducing lamination parameters [3, 4], or to use gradient based methods, e.g. [5], for example by smoothing the non-convex design space by customizing the optimizer [6]. However, for general shell problems the optimality criteria approaches or the lamination parameter approach have not yet been successfully applied and the customization approach is a highly specialized one, which does not impose convexity.

THE DISCRETE MATERIAL OPTIMIZATION APPROACH

The design parameterization method suggested in this work is denoted Discrete Material Optimization (DMO), and it is a gradient based technique that can be used for efficient design of general composite laminate shell structures, see [7, 8]. The approach developed is to formulate the optimization problem using a parameterization that allows us to do gradient based optimization on real-life problems while reducing the risk of obtaining a local optimum solution. To this end we will use the mixed materials strategy suggested by Sigmund and co-workers [9, 10] for multi-phase topology optimization, where the total material stiffness is computed as a weighted sum of candidate materials.

In the present context this means that the stiffness of each layer of the composite will be computed from a weighted sum of a finite number of "plausible" constitutive matrices, each representing a given lay-up of the layer. Consequently, the design variables are no longer the fiber angles or layer thicknesses but the scaling factors (or weighting functions) on each constitutive matrix in the weighted sum. For example, we could choose a stiff orthotropic material oriented at three angles θ_1 = 0°, θ_2 = 45° and θ_3 = 90° and a soft isotropic material, thereby obtaining a problem having four design variables per layer. The objective of the optimization is then to drive the influence of all but one of these constitutive matrices to zero for each ply by driving all but one weight function to zero. As such, the methodology is very similar to that used in topology optimization. This is further emphasized by the fact that penalization is used on the design variables to make intermediate values un-economical. As in topology optimization the parameterization of the DMO formulation is invoked at the finite element level. The element constitutive matrix, $\mathbf{C}^e$, in general may be expressed as a sum over the element number of plausible material configurations, n^e:

$$\mathbf{C}^e = \sum_{i=1}^{n^e} w_i \mathbf{C}_i \;=\; w_1\mathbf{C}_1 + w_2\mathbf{C}_2 + \;\cdots\; + w_{n^e}\mathbf{C}_{n^e}, \quad 0 \le w_i \le 1 \tag{1}$$

where each "plausible" material is characterized by a constitutive matrix $\mathbf{C}_i$. Several new parameterization schemes have been developed, and an example of weighting functions w_i is given by

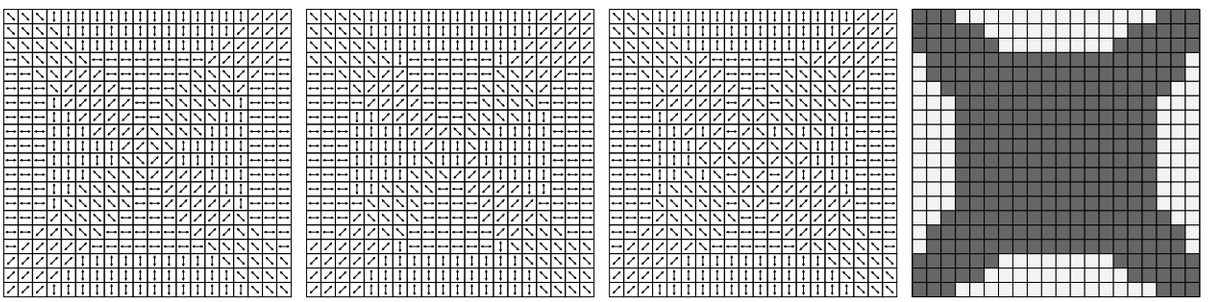
$$\mathbf{C}^e = \sum_{i=1}^{n^e} \underbrace{\prod_{j=1}^{n^e} (x_i^e)^p \left[1 - (x_{j\neq i}^e)^p\right]}_{w_i} \mathbf{C}_i \tag{2}$$

Here x_i^e represents the element design variables, $0 \le x_i^e \le 1$, and p is a penalization power. In case of a mass constraint or eigenfrequency optimization, it is necessary that the sum of the weighting functions equals one. This is not the case for the weighting functions given by Eq. 2, but it can be obtained by normalizing each w_i by $\sum_{i=1}^{n^e} w_i$.

In the examples considered here the design objective is chosen to be a global quantity such as maximum stiffness or lowest eigenfrequency with constraints on the total mass. However, the method is currently being extended to local criteria and geometrically nonlinear structural behavior. Analytical design sensitivity analysis is used and the optimization problem is solved using the Method of Moving Asymptotes [11].

The parameterization is aimed at obtaining practically applicable solutions by choosing the candidate fiber angles to standard integer values (e.g. 0, 45, 90, etc.). The design variables may be associated with each finite element of the model or the number of design variables may be reduced by introducing patches, covering larger areas of the structure. This is a valid approach for practical design problems since laminates are typically made using fiber mats covering larger areas.

Several design optimization results are presented in Figs. 1 and 2.



a) b) c) d)

Figure 1. Results from material design of clamped square plate. a) Material directions in minimum compliance design of 1-layer plate with uniform pressure and 4 DMO design variables per element associated with an orthotropic material oriented at 0°, $\pm 45^\circ$, and 90°, respectively. b) Material directions in maximum lowest eigenfrequency design of 1-layer plate with the same parameterization as in a). c) Material directions in top layer in minimum compliance design of 4-layer plate with uniform pressure and 5 DMO design variables per layer in each element associated with an orthotropic stiff material oriented at 0°, $\pm 45^\circ$, and 90°, respectively, and a soft isotropic core material, thereby allowing the formation of areas with sandwich structures. The mass constraint allows for $2/3$ of the stiff material. After the optimization there is no soft material in the top and bottom layers. d) Distribution of core material in layer 2 and 3 in the example described under c).

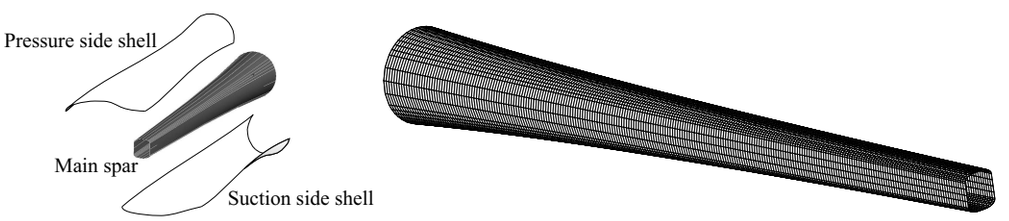


Figure 2. Model for maximum stiffness design of the load carrying main spar from a wind turbine blade. Optimization is performed using 9600 shell finite elements, and the total number of DMO variables varies from 4312 to 153600 for the test cases studied. Results will be presented at the ICTAM 2004 conference.

References

[1] Masur E.F.: Optimum Stiffness And Strength of Elastic Structures. *Journal of the Engineering Mechanics Division, ASCE*, **96**:621–640, 1970.

[2] Pedersen P.: On Thickness and Orientational Design with Orthotropic Materials. *Structural Optimization*, **3**:69–78, 1991.

[3] Tsai S.W., Pagano N.J.: Invariant Properties of Composite Materials. *Composite Materials Workshop*, Stamfort, Connecticut, US, Technomic Publishing Co, 233–253, 1968.

[4] Miki M., Sugiyama Y.: Optimum Design of Laminated Composite Plates Using Lamination Parameters. *AIAA Journal*, **31**:921–922, 1993.

[5] Moita J.S., Infante Barbosa J., Mota Soares C.M., Mota Soares C.A.: Sensitivity Analysis and Optimal Design of Geometrically Non-Linear Laminated Plates and Shells. *Computers and Structures*, **79**:407–420, 2000.

[6] Bruyneel M., Fleury C.: Composite Structures Optimization Using Sequential Convex Programming. *Advances in Engineering Software*, **33**:697–711, 2002.

[7] Stegmann J., Lund E.: Discrete Fiber Angle Optimization of General Shell Structures using a Multi-Phase Material Analogy. In: *Proc. of the 5th World Congress on Structural and Multidisciplinary Optimization, WCSMO 5*, Venice, Italy, 19-23 May 2003, CDROM, 6 pages, to appear.

[8] Stegmann J., Lund E.: Optimizing General Shell Structures Using a Discrete Constitutive Parameterization. In: *Proc. of the American Society for Composites 18th Technical Conference, ASC 18*, Gainesville, FL, USA, 19-22 October 2003, CDROM, 10 pages.

[9] Sigmund O., Torquato S.: Design of Materials With Extreme Thermal Expansion Using a Three-Phase Topology Optimization Method. *Journal of the Mechanics and Physics of Solids*, **45**:1037–1067, 1997.

[10] Gibiansky L.V., Sigmund O.: Multiphase Composites With Extremal Bulk Modulus. *Journal of the Mechanics and Physics of Solids*, **48**:461–498, 2000.

[11] Svanberg K.: The Method of Moving Asymptotes - A New Method for Structural Optimization. *International Journal for Numerical Methods in Engineering*, **24**:359–373, 1987.

Why Parameterizing Element Connectivity for Topology Optimization?

Gil Ho Yoon and Yoon Young Kim
School of Mechanical and Aerospace Engineering
Seoul National University

Summary Recently, a new topology optimization formulation, called the element connectivity parameterization (ECP), has been proposed. The objective of this work is to present the motivation for the development of ECP, the idea behind it and its applications to some topology optimization problems which are otherwise difficult to solve. We begin with the issue of unstable elements for topology design problems involving nonlinear analysis and ascribe the source of the numerical problem to the intermediate density element of the conventional topology optimization formulation. To overcome the numerical problem, the degree of element connectivity is used to describe structural layouts while finite elements remain solid during whole topology optimization iterations. A few numerical problems are considered to show the usefulness of ECP.

1. Element Instability in Nonlinear Problems

Topology optimization formulation using the element density as the design variable has been very successful in a wide class of design problems [1]. However, it suffers from a numerical instability problem resulting from the so-called unstable element in topology optimization involving nonlinear analysis. The application of the element density-based formulation may yield physically incorrect design as indicated in Fig. 1. Fig. 1 shows a typical result for an end-compliance minimization problem considering geometrically nonlinear deformations.

The result in Fig. 1 may be obtained by the direct application of the convergence relaxation method [2]. As shown in Fig. 1, the low-density elements, especially near the loaded end, experience excessively large deformations causing numerically negative element areas, so they become unstable elements. The appearance of the unstable elements causes solution oscillations and poor convergence in the Newton-Raphson iteration. The low-density related problem has motivated the development of a new stable method.

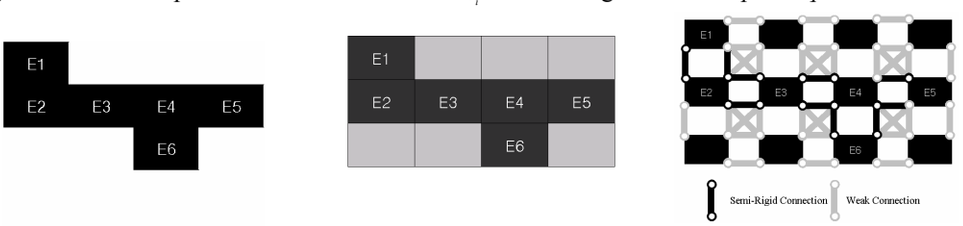


(a) Optimal Layout (b) Deformed Shape

Fig. 1 An optimized result by a direct application of the element-density based topology optimization formulation for an end-compliance topology optimization considering geometrically nonlinear deformations.

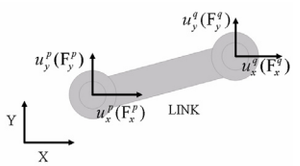
2. Element Connectivity Parameterization

To resolve the problem discussed above, a so-called element connectivity parameterization method [3] has been propose. The best way to describe is, perhaps, to compare how a structural layout in Fig.2 (a) is modeled by the standard element-density method and the element connectivity parameterization (ECP) method. To define the structural topology in Fig. 2(a), the element-density method uses low-density elements while the ECP method introduces semi-rigid zero-length links connecting elements. As in the SIMP method, the stiffness of the link in the ECP method is treated as the function of the link density and is appropriately penalized. Since the element connectivity is used to define structural layouts, all finite elements discretizing the design domain can remain solid during whole design optimization iterations and the appearance of the unstable elements can be prohibited. Fig. 3 illustrates the element connection by a link i and the penalization of its stiffness k_i^{pq} connecting local nodes p and q.



(a) (b) (c)

Fig. 2 Structural layout modeling. (a) A typical structural layout, (b) modeling by the standard element density method (Grey: Weak elastic elements, Black : Solid elements), (c) the modeling by the ECP method (Black Line : Semi-Rigid Connection: Grey Line : Weak Connection).



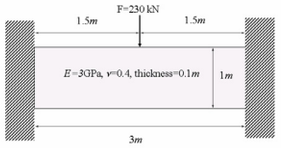
$$k_i^{link} = l_0(\gamma_i^{pq})^n k_{link}$$

$$\gamma_{i,LOW}^{pq} \le \gamma_i^{pq} \le \gamma_{i,UPPER}^{pq} = 1$$

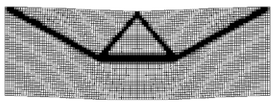
Fig. 3 Link element connecting nodes *p* and *q* at connection *i*. It has the design variable γ_i^{pq}.

3. Numerical Examples

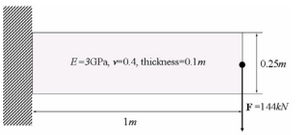
To illustrate the effectiveness of the ECP method, two topology design optimization problems described in Fig. 4 and Fig. 5 are considered. Fig. 4 shows a well-known compliance minimization problem while Fig. 5 shows the topology design problem of a micro electro-thermal-compliant actuator. In both problems, geometrically nonlinear deformations are considered. Though not sated in details here, numerical problems such as solution oscillations, convergence difficulty due to the unstable elements were not observed during the optimization iterations with the ECP method. The skeleton images in the figures denote the images representing the distribution of the density of the artificial link; the density varies from 0 to 1 where the value of 1 corresponds to the rigid connection. In plotting the deformed shapes, the value of the link density has been properly translated as the equivalent value of the finite element density; the translation is done after the design optimization is completed.



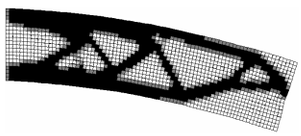




(a)
Skeleton image Deformed shape (Compliance=12,549J)







(b)
Skeleton image Deformed shape (Compliance=26,510J)

Fig. 4 A compliance minimization of geometrically nonlinear structures. (a) Mass constraint ratio=10%, 120×40 4-node bilinear finite elements used, (b) mass constraint ratio=50%, 80×20 4-node bilinear finite elements used.

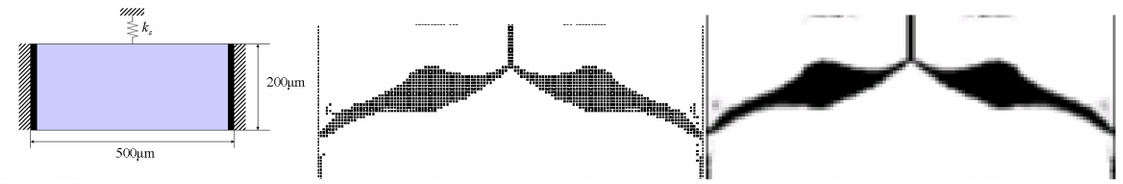


Fig. 5 Design of an electro-thermal-compliant actuator. Output displacement: 6.96 μm (k_s =100N/m, Mass constraint = 30%, Young's Modulus = 200 GPa, Poisson ratio = 0.31, thickness=15 μm , the electric conductivity= $6.4 \times 10^6 K\,(\Omega m)^{-1}$, the thermal conductivity=90.7 W/(Km), the convection coefficient=18.7×10^3W/(m^{2}K), thermal expansion coefficient=15×10^{-6}K^{-1}, applied voltage = 0.3 volt).

4. Conclusions

The element connectivity parameterization method was investigated with specific applications in a nonlinear compliance minimization problem and a nonlinear electro-thermal-compliant actuator design problem. By defining a structural layout inside a design domain through the degree of the element connectivity, low-density unstable finite elements were avoided. In this approach, the discretizing finite element remained solid during the whole design iterations. The element connectivity was parameterized by artificial zero-length one-dimensional links and their stiffnesses were penalized for clear layouts. Work is in progress to extend ECP for stress-constrained design problems.

5. REFERENCES

[1] Bendsøe, M.P., and Sigmund, Optimization of Structural Topology, Shape, and Material, Springer-Verlag, New York. 2003.

[2] Buhl T, Petersen CBW, Sigmund O. Stiffness design of geometrically nonlinear structures using topology optimization. *Structural and Multidisciplinary Optimization* 2000; **19**(2):93-104.

[3] Yoon Gil Ho, Kim Yoon Young. Inter-element connectivity parameterization for topology optimization of geometrically nonlinear structures. Submitted, 2003.

Topology Optimization of the Geometrically Nonlinear Structures Made of Rubberlike Material

Sami Holopainen*
*Tampere University of Technology, P.O. Box 589, FIN-33101 Tampere, Finland

Summary. In this paper a brief review of the topology optimization of the geometrically nonlinear plate composed of a rubberlike material is presented. Thus the material is assumed to be incompressible hyperelastic subjected to the plane stress. A demonstrative example is presented after the topics of the theory of nonlinear continuum mechanics and optimization are introduced.

INTRODUCTION

Typically most structural topology optimization cases are based on the linear elastic assumption. But investigating initially linear structures the optimized structure may be nonlinear as well the structures subjected to the large deformations. So the topics of the nonlinear continuum mechanics, aspects of FEM discretization and solving procedure of the topology optimization are presented and applied to the 2D-plate made of highly nonlinear elastic rubber.

BASIC THEORY OF NONLINEAR COMPUTATIONAL MECHANICS

Linearization and Newton-Raphson process

The basis for FEM is the spatial total virtual work of a deformable body expressed in equilibrium state as,

$$\delta W = \int_v \sigma : \delta\mathbf{d}\, dv - \int_v \mathbf{f}_b \cdot \delta\mathbf{v}\, dv - \int_{\partial v} \mathbf{t} \cdot \delta\mathbf{v}\, da = 0 \qquad (1)$$

Above $\boldsymbol{\sigma}$ is *Cauchy* stress, $\delta\mathbf{d}$ is rate of deformation tensor corresponds to the virtual velocity field $\delta\mathbf{v}$. $\mathbf{f}_b$ are body forces per unit volume v and $\mathbf{t}$ tractions per unit surface area. The rubberlike material is typically incompressible hyperelactic and usually *Ogden, Mooney-Rivlin* or *neo-Hookean* material. Thus the homogenous elastic function may be postulated e.g. to last one as [3] , $\psi(\mathbf{C}) = \mu(\mathrm{I}_\mathbf{C} - 3)$, where $\mathbf{C}$ is the right Cauchy-Green strain tensor defined with deformation gradient $\mathbf{F}$ as $\mathbf{F}^T\mathbf{F}$ depended of the displacement field $\mathbf{u}$. $\mathrm{I}_\mathbf{c}$ is its first principal invariant or tr$\mathbf{C}$ and μ the material parameters determined experimental. The solution of the virtual equilibrium system (1) is achieved using N-R iterative procedure. For that the virtual work equation has to be linearized. Splitting the total virtual work into the internal and external part and further the internal part into the constitutive and initial stress components one can derive the linearized formula for internal part as follows [2]:

$D\delta W_{\mathrm{int}}[\mathbf{u}] = \int_v \delta\mathbf{d} : \mathbf{c} : \varepsilon\, dv + \int_v \sigma : [(\nabla\mathbf{u})^T \nabla\delta\mathbf{v}]\, dv$ where $\mathbf{c}$ is spatial elasticity and ε small strain tensor. The discretized formula for the constitutive component of element e with the standard shape functions N_k connected to node $k = a, b$ is as,

$D\delta W^e_{\mathrm{int}}[N_b\mathbf{u}_b] = \int_v \tfrac{1}{2}\left(\delta\mathbf{v}_a \otimes \nabla N_a + \nabla N_a \otimes \delta\mathbf{v}_a\right) : c : \tfrac{1}{2}\left(\mathbf{u}_b \otimes \nabla N_b + \nabla N_b \otimes \mathbf{u}_b\right) dv$ or rearranged in matrix form as,

$D\delta W^e_{\mathrm{int}}[N_b\mathbf{u}_b] = \delta\mathbf{v}_a \bullet \mathbf{K}^{(e)}_c \bullet \mathbf{u}_b$, where $\mathbf{K}^{(e)}_c$ is the constitutive part of elements tangent stiffness matrix whose components in familiar ortogonal *Cartesian* coordinate system are as, $[\mathbf{K}^{(e)}_{c,ab}]_{ij} = \int_{v^{(e)}} \sum_{k,l=1}^{2} \frac{\partial N_a}{\partial x_k} c_{ikjl} \frac{\partial N_b}{\partial x_l} dv, \quad i, j = 1,2. \qquad (2)$

Further, in general the elasticity tensor can be split into the deviatoric and pressure component and another variational approach has to be used to avoid so-called *locking* phenomenon (*multi-field variational principle*s). But now in-plane stress situation e.g. the neo-Hookean elastic function takes the form [2], $\psi(\bar{\mathbf{C}}) = \tfrac{1}{2}\mu(\mathrm{I}_{\bar{\mathbf{C}}} + \mathrm{III}_{\bar{\mathbf{C}}}^{-1} - 3)$. $\bar{\mathbf{C}}$ is the in - plane part of $\mathbf{C}$ By relation $\mathbf{c} = 4\frac{\partial^2\psi}{\partial\bar{\mathbf{C}}\partial\bar{\mathbf{C}}}$, the components of $\mathbf{c}$ are given in terms of the Kroneker delta as, $c_{ijkl} = 2\mu\mathrm{III}_{\bar{\mathbf{C}}}^{-1}\left(\delta_{ij}\delta_{kl} + \delta_{ik}\delta_{jl}\right)$ (3)
Above $\mathrm{III}_\mathbf{c}$ is the third principal invariant of $\bar{\mathbf{C}}$ or $\det\bar{\mathbf{C}}$. This material model is convenient for vulcanized and natural rubber. For other materials (e.g. Mooney-Rivlin) the elasticity tensor, see [3]. Now only the constitutive part namely the elasticity tensor $\mathbf{c}$ includes explicitly the topology design parameter μ. This linearized virtual work in the spatial description is often called *updated-Lagrangian* formulation. For further detail of nonlinear FEM, see [2],[3].

TOPOLOGY OPTIMIZATION

Problem formulation

We set the optimization problem such that only the end-compliance is minimized, so the FEM-discretized formula is as,

$$\min_{u,\rho_e} \mathbf{f}^T\mathbf{u}$$

$$s.t.: \left(\sum_{e=1}^{N} \rho_e^p \mathbf{K}^{(e)}\right)\mathbf{u} = \mathbf{f} \text{ or } \mathbf{R}(\mathbf{u}) = \left(\sum_{e=1}^{N} \rho_e^p \mathbf{K}^{(e)}\right)\mathbf{u} - \mathbf{f} = \mathbf{0}, \quad \sum_{e=1}^{N} \rho_e v_e \le V, \quad 0 < \rho_{\min} \le \rho_e \le 1, e = 1, \ldots, N. \qquad (4)$$

I.e. the end-compliance is minimized as to the element's (e) material 'density' ρ_e under prescribed loading conditions subject to an upper bound on the effective volume. The elements in their lower bound are considered as void and others as solid. The penalization parameter p forces the densities to the lower or upper bound so that the optimized structure is so 'white and black' as possible. For incompressible material p is large, and to avoid the local minima or dependency of the resulting topology of the initial structure and optimization parameters, p should be slowly raised throughout the optimization (e.g. 1…>4). For further detail of setting the topology optimization problem, see [1]. $\mathbf{R}(\mathbf{u}) = \mathbf{0}$ represents the nonlinear governing equations of the model and $\mathbf{u}$ the vector of displacemets considered as state variables. The optimization problem above is solved using the interior penalty parameter or *augmented Lagrangian method* (ALM). The structural response is solved using the nonlinear quasi-static FEM based on N-R iteration and arc length method. Because of large deformations the line search method instead of straight application of N-R has to be used to improve convergence rate. The convergence criterion can be relaxed if oscillation occurs in nodes surrounded by void elements.

Sensitivity analysis

In gradient based optimization algorithms the sensitivities have to be determined for the objective and constraint functions. Assume the design independent loads and employ the adjoint method. In the equilibrium state for the objective the sensitivity is determined as follows:

$c(\rho,\mathbf{u}) = \mathbf{f}^T\mathbf{u}(\rho) - \lambda^T\mathbf{R}$ and $\dfrac{\partial c(\rho,\mathbf{u})}{\partial \rho_e} = \mathbf{f}^T\dfrac{d\mathbf{u}}{d\rho_e} - \lambda^T\left(\dfrac{\partial \mathbf{R}}{\partial \mathbf{u}}\dfrac{\partial \mathbf{u}}{\partial \rho_e} + \dfrac{\partial \mathbf{R}}{\partial \rho_e}\right)$. By requiring that all values of $\mathrm{d}\mathbf{u}/\mathrm{d}\rho_e$ must be satisfied: $\left(\mathbf{f}^T - \lambda^T\dfrac{\partial \mathbf{R}}{\partial \mathbf{u}}\right)\dfrac{\partial \mathbf{u}}{\partial \rho_e} = 0$, the Lagrangian multipliers λ, can be solved from the system $\left(\mathbf{f}^T - \lambda^T\dfrac{\partial \mathbf{R}}{\partial \mathbf{u}}\right) = \mathbf{0}$ or $\mathbf{K}_T\lambda = \mathbf{f}$. This provides an explicit expression for the objective function sensitivities (noting (2) and (3)):

$$\frac{\partial c}{\partial \rho_e} = -\lambda^T\frac{\partial \mathbf{R}}{\partial \rho_e} = -\lambda^T\frac{\partial \mathbf{K}_T}{\partial \rho_e}\mathbf{u} = -p\lambda^T\frac{\mathbf{K}_c^{(e)}}{\rho_e}\mathbf{u}. \tag{5}$$

The sensitivity of volume constraint is straightforward because of incompressibility. Filtering the sensitivities are used to ensure mesh-independency and to checkerboardcontrol. The filter is general used heuristic method based on modifying the design sensitivity of a spesific element as a weighted average over the element itself and its neighbours.

Numerical example: topology design for the slender plate

The aim is to determine the optimal distribution of the homogenous incompressible neo-Hookean material with μ equals to 600 kPa. Solving the structural response the simple four-noded bilinear quadrilateral elements are used. The plate is clamped on both sides, and three concentrated forces are acted on its top edge with values 1, 2 and 1 N. The dimension of the plate is 520×130×10 mm^3. Suppose 30 % of design domain volume material is available. The design topology using linear analysis is shown in Fig. 1(a) and from nonlinear analysis in Fig. 1(b). The optimum topology is such like that the exhibit snap-through behaviour may be occur [4], but not in this example, Fig. 1(c).

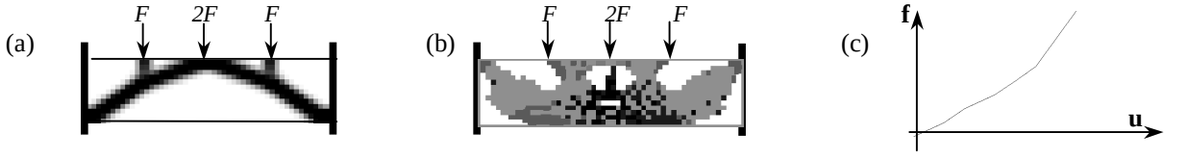


Figure 1. Compliance optimization problem. (a) The design domain, loads, boundary conditions and optimal topology using linear analysis. (b) Optimal topology from nonlinear analysis. (c) Load-disp.-curve of the optimum structure.

CONCLUSIONS

In this paper the topology optimization problem of fully nonlinear structure is studied. The mean compliance is chosen as an objective and the sensitivity analysis is derived using the adjoint method which is rather straightforward despite specially the material nonlinearity. The problem is solved iteratively by a sequential convex approximation method. Numerical examples indicate that for fully nonlinear structures the optimal result differs relatively much from the optimum of linear equivalent ones. For imcompressible nonlinear material achievement of the 'black-and-white' structure is hard and the convergence rate is slow . So the robust optimization solution methods should be used.

References

[1] Bendsoe M. P., Sigmund O.: Topology Optimization. Theory, Methods and Applications. Springer, Lungby 2002.
[2] Bonet J., Wood R.D.: Nonlinear continuum mechanic for finite element analysis. Cambridge University press, 1997.
[3] Crisfield M.A.: Non-linear Finite Element Analysis of Solids and Structures, Essentials,Vol. 1. Wiley, NY 1991 and Advanced Topics, Vol 2, NY 1997.
[4] Bruns T.E., Sigmund O., Tortorelli A.: Numerical method for topology opt. of structures that exhibit snap-through. *Int. J. Numer Meth Engng* **55**:1215-1237, 2002.

XXI ICTAM, 15–21 August 2004, Warsaw, Poland

OPTIMAL DESIGN OF LOSSY BANDGAP STRUCTURES

Jakob S. Jensen
Department of Mechanical Engineering, Technical University of Denmark, DK 2800 Kgs. Lyngby, Denmark

Summary The method of topology optimization is used to design structures for wave propagation with one lossy material component. Optimized designs for scalar elastic waves are presented for mininimum wave transmission as well as for maximum wave energy dissipation. The structures that are obtained are of the 1D or 2D bandgap type depending on the objective and the material parameters.

INTRODUCTION

Elastic and acoustic (commonly referred to as phononic) bandgap structures [1] may find application for vibration suppression and for noise insulation purposes [2]. The periodic arrangement of two materials with different properties may inhibit the propagation of waves at certain frequencies and for the infinite medium total reflection of the wave occurs. So far focus has almost entirely been devoted to the wave-reflecting properties and not to the effects, possibly beneficial for applications, of dissipation in the bandgap structures. This work presents a systematic method for creating optimized designs of bandgap structures for two objectives: 1) minimum wave transmission through the structure and 2) maximum dissipation of wave energy in the structure. The structures are obtained as optimized distributions of two materials where one is lossy, and the design methodology is based on the method of topology optimization. Recently the method was used to design loss-free bandgap structures for optimized wave reflection [3].

MODEL

Wave propagation with frequency Ω is considered. The wave may be elastic or acoustic and the problem is discretized using a standard FEM formulation. The resulting field equation governing the complex wave amplitude $\mathbf{u}$ is:

$$\Big(-\Omega^2\mathbf{M} + i\Omega(\mathbf{C}_{rad} + \mathbf{C}_{loss}) + \mathbf{K}\Big)\mathbf{u} = \mathbf{f}, \tag{1}$$

where $\mathbf{M}$, $\mathbf{K}$ are standard mass- and stiffness-type matrices, and $\mathbf{f}$ is a forcing vector stemming from the wave excitation. The damping matrix generally comprises two terms with $\mathbf{C}_{rad}$ originating in the finite domain termination of the wave propagation, either by a simple radiation condition (Sommerfeld condition) or by extra Perfectly Matching Layers (PMLs). The matrix $\mathbf{C}_{loss}$ represents the contribution to the damping matrix from a lossy material component.

Scalar case: out-of-plane shear waves

As a special case, a 2D problem of an elastic wave propagating in the plane is investigated. By considering the out-of-plane displacement component (out-of-plane shear) the problem is reduced to a scalar one (Helmholtz equation). Two materials are defined with the relevant material properties:

$$\rho_1,\ E_1,\ \nu_1 \qquad\qquad \rho_2,\ E_2(1+i\alpha),\ \nu_2 \tag{2}$$

where ρ is the density, E Young's modulus and ν Poisson's ratio, and where α is the loss factor for the lossy material component.

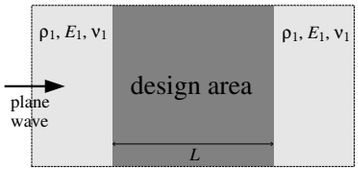


Figure 1. 2D computational domain with a scalar elastic shear wave propagating from left to right.

As an illustrative example, calculations are carried out for the 2D domain in Figure 1. A plane wave propagates from left to right through the structure containing a square design area. Unwanted reflections from the left and the right boundaries are eliminated by using PMLs to terminate the domain. Traction-free boundaries are specified on the upper and lower boundaries.

OPTIMIZATION

The goal of the optimization is to find the distribution of the two material components that minimizes (or maximizes) our objective function J. The following two objectives are considered:

$$\min J_1 = \frac{1}{nn}\sum_{n=1}^{nn}|\mathbf{u}_n|^2, \qquad \max J_2 = \frac{1}{2}\Omega^2\sum_{e=1}^{nel}\Re(\mathbf{u}_e^T\mathbf{c}_{loss}\bar{\mathbf{u}}_e) \tag{3}$$

where J_1 is the average squared amplitude of the wave transmitted through the structure and J_2 is the wave energy dissipated in the design area per unit time. In (3), nn is the number of nodal points along the right boundary where the objective is evaluated and nel is the number of elements in the design area. The element loss damping matrix is $\mathbf{c}_{loss}$, $\Re()$ denotes the real part, and $\bar{\mathbf{u}}$ is the complex conjugate field.

The optimization is performed using the method of topology optimization (see e.g. [3] for details). In the present standard FEM implementation a single design variable is introduced for each finite element in the design domain $x_e,\ e = 1, nel$. The material properties are now specified in each element as a linear function of this variable:

$$E_e = E_1 + x_e(E_2 - E_1), \qquad \rho_e = \rho_1 + x_e(\rho_2 - \rho_1), \qquad \alpha_e = x_e\alpha \tag{4}$$

so that for $x_e = 0$ the properties are those of material 1 and for $x_e = 1$ those of material 2 (the lossy material). Poisson's ratio is assumed to be constant ($\nu_1 = \nu_2 = \nu$).

The optimized material distribution is found using an iterative algorithm where the design change in each iteration is based on analytical design sensitivities and the use of a mathematical programming tool [4].

RESULTS

Figure 2a-c) show optimized designs for the minimization problem (objective J_1). The designs in a) and b) are for different loss factors ($\alpha = 0$ and $\alpha = 0.2$) and show only a small quantitative difference in the designs which are of the 2D bandgap type. The objective values show a 12.6 dB reduction in wave amplitude for a) and 14.6 dB for b). For c) the same parameters are used as in b), but a different initial guess is used in the optimization leading to a different local minimum. The design is a 1D bandgap structure (Bragg grating) with an amplitude reduction of 17.2 dB, thus making it the most efficient design obtained. Figure 2d-f) show designs for three wave frequencies for the maximization problem (objective J_2). The optimized design in d) resembles a 1D Bragg grating whereas the designs in e) and f) are more intriguing 2D structures. In all three cases the dissipation of wave energy is superior to the extreme case where the whole design area is filled with lossy material, i.e. the dissipation is increased by a factor 1.12, 1.87 and 1.50 in d), e), and f), respectively.

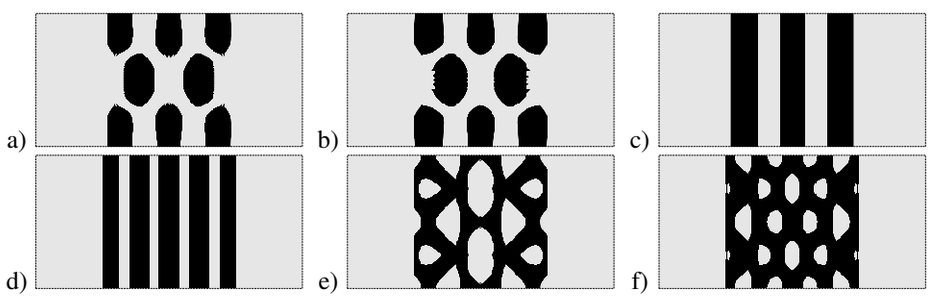


Figure 2. a-c): Minimization of wave transmission, material parameters: $E_2/E_1 = 2.5$, $\rho_2/\rho_1 = 2$, $\tilde{\Omega} = 1.5$, a) $\alpha = 0.0$, b) $\alpha = 0.2$, c) $\alpha = 0.2$ (different initial guess). d-f) Maximization of dissipation, material parameters: $E_2/E_1 = 0.5$, $\rho_2/\rho_1 = 0.8$, $\alpha = 0.05$, d) $\tilde{\Omega} = 1.5$, d) $\tilde{\Omega} = 1.75$, f) $\tilde{\Omega} = 2$. Non-dimensional frequency $\tilde{\Omega} = \Omega L/(2\pi c)$, $c = \sqrt{E_1/(2\rho_1(1+\nu))}$.

CONCLUSIONS

Optimal design of structures for wave propagation was considered. The optimized distribution of two material components, one lossy, was been obtained for two objectives: 1) minimizing the wave transmission, and 2) maximizing the dissipation of wave energy. Results were presented for elastic out-of-plane shear waves. The designs obtained are intriguing 1D and 2D bandgap type structures with good performance for both objectives. Further results will be for the cases of in-plane elastic waves, as well as optimization for a range of frequencies simultaneously.

This work was supported by the Danish Technical Research Council (STVF).

References

[1] Sigalas M.M., Economou E.N.: Elastic and acoustic wave band structure. *J. Sound Vib.* **158**:377–382, 1992.

[2] Goffaux C., Maseri F., Vasseur J.O., Djafari-Rouhani B., Lambin Ph.: Measurements and calculations of the sound attenuation by a phononic band gap structure suitable for an insulating partition application. *Appl. Phys. Lett.* **83**:281–283, 2003.

[3] Sigmund O., Jensen J.S.: Systematic design of phononic band-gap materials and structures by topology optimization. *Phil. Trans. R. Soc. Lond. A* **361**:1001–1019, 2003.

[4] Svanberg K.: The method of moving asymptotes - a new method for structural optimization. *Int. J. Numer. Meth. Engng* **24**:359-373, 1987.

NON-GAP DESIGN METHOD AND TEST FOR POST-TENSIONED PRESTRESSED R.C. STRUCTURE

Li Lijuan[1,2], Liu Feng[1], Fu Ganqing[1], Lu Weiwen[1]
[1]Faculty of Construction Engineering, Guangdong University of Technology, 510643, China
[2]Department of Civil Engineering, The University of Liverpool, Liverpool, L69 3GQ, UK

Summary: A non-gap design method is introduced, which includes using post-poured concrete strips, cold-rolled ribbed welded steel grids and post-tensioned pre-stressed concrete beams. The purpose of the method is to resist cracking in the slabs of the Shenzhen Tian Digital Mansion (in Shenzhen, China), a long span new building. The method was used despite the general requirement for setting gaps in slabs exceeding 40m long in the Chinese code of practice. The design is based on maintaining the concrete slab strain within the specified limits required by the Chinese code at all stages in its life. One purpose of the test is to confirm that the concrete strain is within the desired limits and the other is to see if the stress can be transferred to slabs evenly from beams, as expected. The stresses in the slabs have been tested for one year to determining the stress distribution and the corresponding strains. The test was carried out before the pre-stress was applied and lasted for one year after pre-stress construction finished. The stresses and their variations on different slabs and at different locations were measured. Test results showed that the strains met the requirements of the code of practice and the new design technique used in this new building is effective and can be extended to the design of similar structures.

INTRODUCTION

With the application of pumping-concrete and high strength concrete in super long reinforced concrete structures, it is easy to cause temperature cracks [1,2]. In order to control the flexural, thermal and shrinking cracks, a new design and construction method has been introduced. Cold-rolled ribbed welded steel grids with high strength than mild steel are used in the slabs of the structures. Post-tensioned pre-stressed strands are employed in the longitudinal beams, so that the floor slabs can obtain pre-stress from them. Furthermore, for reasons of economics, pre-stressed tendons are used only in some floors of the structure. The test lasted 12 months to confirm the efficiency of the design method. Stress test readings were recorded from the 22nd to the 26th storey as well as at the roof, with pre-stress tendons used only from the 24th to the 26th storey and at the roof. Stress and temperature, as well as their variations at the different testing points, are given in this paper. The stress variations at different testing points on the different floors are compared. The effects of the temperature variations on the stresses in the slabs are also investigated. Strains in the different floors were also obtained during the test. The strain results show that the design method adopted in this project is feasible and efficient and can be extended to the design of similar structures.

METHOD OF RESISTING CRACKING IN SUPER LONG SLAB

Post-poured strips

Two post-poured strips are set symmetrically in the floor construction, which divides the floor slab plane into three parts. Each part is about 40m long. Concrete with slightly expansive property was used in the post-poured strips to decrease shrinkage and creep deformation.

Cold-rolled ribbed welded steel grids

The excellent crack-resisting ability of welded steel grids has been demonstrated in roads and bridges. For this reason, cold-rolled ribbed welded steel grids with higher strength (f_y=360N/mm^2) than mild steel (f_y=210/ mm^2) were used in the slabs of the structure. This arrangement not only resulted in savings in steel quantity, but also the effects of shrinkage and creep were reduced. The steel grids were ideally suited for factory production, where large numbers of identical units could be economically made under controlled conditions and were easily installed on site. Conventional reinforcements were still used along the lengths of the slabs, which reduced the deformation of the slabs. The arrangement provided a very convenient, efficient, and economical design.

Pre-stressed tendons

Since large temperature differences can exist between the two surfaces of the roof, which will cause and accumulate temperature stress, un-bonded pre-stressed tendons were used to control structural cracking. The pre-stressed floors are shown in Figure 1. Post-tensioned tendons were located in the beams of the floors from the 24th to 26th storeys as well as in the roof. They are in the longitudinal direction. The tensioning sequence was as follows: tension the tendons that are in the beams of left and right parts of the floor slab first and then tension those spanning the post-poured strips.

TEST METHOD AND ARRANGEMENT OF TEST POINTS

In site test, model GGH-10 (with diameter 10 bar) stress sensors and model GSJ-2A digital monitor are used as in [5,6]. Considering the structural symmetry, all 8 of test points were arranged in one half of the floor. The test

points labeled 'S' in Figure 2 sum to 48 (6 levels with 8 points each). All the steel stress sensors were embedded along the longitudinal axis of the floor. Temperature sensors were also embedded to test temperature variations in the slabs. 4 temperature sensors (labeled 'T' in Figure 2) were embedded in the 26th floor and 3 in the roof.

ANALYSIS OF THE TEST RESULTS

Stress variations in different floors

The stress values at the different test points, both before (11/09/2002) and after the tendons were tensioned, are presented in Figure 4. The stress changes along the length of the two different sections are given in Figure5.
It can be seen from Figure 4 that the stress variations at the different test points on the same floor are similar, as are those for similar points on different floors. The maximum stress difference is 70MPa, which happened on 26th floor. The maximum on other floors is about 40MPa. The test results show that most of the concrete stresses are compressive. Tensile stress occurs only in the tensioning period of pre-stress and the maximum tensile stress obtained is 13.8MPa. We can conclude from Figure 5 that, in the same section, the magnitude of the stress level and the stress changes in the floor with pre-stress are similar to those of the floor without pre-stress. The stress level in the longitudinal direction of different floors is even.

Effect of the pre-stressed beams on slabs

The compressive stresses in the floor change periodically for the different test points, which agree with the condition that pre-stressing occurs periodically. The compressive stresses in the floor do not change periodically after all the tensioning is finished but increase slowly with time. The reason is that there exists a time lag between the pre-stress in the beams and in the slabs. Pre-stresses are transferred from beams to floors slowly.
Although it is difficult to have a separate quantitative analysis of the effects that influence thermal stresses in the floors, the comprehensive stress variations from the test readings show that the mean stress difference in the floor reinforcement is about 40MPa, which is acceptable for steel grids. The maximum tensile stress of steel in the slabs is 13.8MPa and the corresponding tensile strain is 69μs.Thus the tensile strain in the concrete is also 69μs, with the steel and concrete stresses being related by the compatibility of strain across the section. This value is less than the ultimate tensile strain value for concrete, being 80μs.

Temperature variation of ambient and floors

The temperature variations at the bottom, the middle and the upper surface of the 26^{th} floor and at the roof, as well as the ambient temperature, are shown in Figure 6. During the 12-month testing, the maximum temperature difference was 20.2^{o}C outdoors and 17.4 ^{o}C indoors; the corresponding mean temperature difference was 4.7 ^{o}C and 3.4 ^{o}C, respectively. As expected, the temperature variation indoors was smaller than that outdoors, showing that the thermal insulating layer used in the roof worked efficiently and decreased the stress in the concrete, and helping to control cracks in the floors.

CONCLUDING REMARKS

(1) Steady and even pre-stresses in concrete floors can be obtained by tensioning tendons in beams. Thus, concrete floors can be maintained in a state of compression throughout, providing resistance to thermal cracking.
(2) The maximum test stress variation in un-pre-stressed steel is about 40Mpa, which is acceptable for conventional reinforcement.
(3) In a high building, the roof and upper floors (4 floors near to top) are the locations most sensitive to temperature variations and needing appropriate reinforcement methods.
(4) Cold-rolled ribbed welded steel grids can reduce concrete deformation, the chance of cracking, and the amount of steel used in floors. It proved to be a very convenient, efficient and economical material for buildings.
(5) Tensioned tendons used properly in some important parts of a building can produce good enough results even if it is not so good as that of the whole building is used.

References

[1] Wu Zhaohui, Sun Bolin. The Effect of Temperature on very Long Structures. Architecture and Structures (in Chinese). 32(8), 28-30, 2002
[2] Jin Jianmin. Design Advice to Avoid and Alleviate Contraction Cracks in very Long Structures Caused by Temperature. Industrial Buildings (in Chinese). 32(6), 57-59, 2002
[3] Song Wei, Yuan Yong. Stress Development Analysis of High and Long in-site Basement. Space Structures (in Chinese). 19(1), 20-23, 2002
[4] Li Shengyong, Long Guobing. Design for Structure of Shenzhen Tian Digital Mansion, Academic Paper of Seventeenth National High Building Conference (in Chinese). 2002. 12. Hangzhou.
[5] Song Yu, Li Lijuan, Zhang Guiwen. Experiment for Structures (in Chinese). Published by Congqing University Press. 2001. 10.
[6] Gu Weijian. Test Analysis of Thermal Stress on High and Long Roof of a Building, Academic Paper of Sixteenth National High Building Conference (in Chinese). 402-409, 2000.

XXI ICTAM, 15–21 August 2004, Warsaw, Poland

DESIGN OF ARTICULATED MECHANISMS WITH A DEGREE OF FREEDOM CONSTRAINT USING GLOBAL OPTIMIZATION

Atsushi Kawamoto, Mathias Stolpe
Department of Mathematics, DTU, DK-2800, Kgs. Lyngby, Denmark

Summary This paper deals with design of articulated mechanisms using a truss ground structure representation. The considered mechanism design problem is to maximize the output displacement for a given input force by choosing a prescribed number of truss elements out of all the available elements, so that the resultant mechanism has one mechanical degree of freedom when supported in a statically determinate manner. The mechanical degree of freedom constraint is included since it is essential for obtaining a proper articulated mechanism design. The Green-Lagrange strain measure is used to accommodate for large displacements. The problem is formulated as a non-convex mixed integer problem and solved using a convergent deterministic global optimization method based on branch and bound with convex relaxations.

INTRODUCTION

Research on design of compliant mechanisms using topology optimization techniques in continuum structures[1] suggests that it should also be possible to obtain results for articulated[1] mechanisms by applying topology optimization. For design of articulated mechanisms the concept of *mechanical* degrees of freedom (DOF)[2] becomes critical for obtaining a proper mechanism design, while it is an insignificant feature for compliant mechanism design as such mechanisms do not have real joints.

It seems natural and advantageous to represent articulated mechanisms by truss elements and pin joints. Firstly, one can directly interpret the truss topology from the kinematic diagram. Also, it is possible to accommodate large displacements (geometrical non-linearity) without element distortion problems. Finally, with this interpretation one can formulate an optimization problem in terms of the so-called ground structure approach for truss topology design.

The idea of the truss ground structure approach is to first give a large set of potential elements in a design domain, then eliminate unnecessary elements, or equivalently chose the necessary elements, by solving an optimization problem. Finally, the optimal solution defines the resultant mechanism design. One truss ground structure is shown in Fig. 1.

The following general assumptions on the geometrical non-linearity are made. Large displacements are allowed but the strains are assumed to be small. The strain is given by the Green-Lagrange strain measure and the material properties are assumed to be linear elastic.

Based on the combinatorial truss ground structure approach with the geometrical non-linearity and the mechanical DOF constraint taken into account an optimization problem with objective to maximize the displacement at a certain point of the structure is stated. The problem is formulated as a non-convex mixed integer optimization problem. One can tackle this problem, for instance, in a nested formulation using gradient-based optimization techniques together with a penalization of non-integer values of the design variables. However, one cannot expect to find a global optimal solution because of the non-convexity. Furthermore, it may be very difficult even to find a feasible solution in many situations.

In this paper we therefore propose to solve the difficult non-convex combinatorial problem using a deterministic global optimization technique based on branch and bound[4]. The proposed branch and bound method can implicitly examine all possible topologies. This allows for identifying the global optimal solution for the first time in this area of application.

PROBLEM FORMULATION

One relevant mechanism design problem is to maximize the output displacement for a given input force by picking N truss elements out of the n possible elements, so that the resultant mechanism has $f_{\mathrm{DOF}}(x) = 1$ degree of freedom when supported in a statically determinate manner. The problem can be formulated as a non-convex mixed integer optimization problem in the variables $(x, f, \epsilon, u) \in \mathbb{B}^n \times \mathbb{R}^n \times \mathbb{R}^n \times \mathbb{R}^d$, where x is the truss connectivity vector; f is the normal force vector; ϵ is the strain vector; u is the nodal displacement vector; n is the number of design variables; d is the number of displacement variables. The problem format is thus:

$$
\begin{array}{lll}
\underset{x,f,\epsilon,u}{\text{maximize}} & q^\top u (= D_{\mathrm{out}}) & \text{(Output displacement)} \\
\text{subject to} & R(f,u) = 0, & \text{(Equilibrium equations)} \\
& f_j = x_j E_j \epsilon_j, & \text{(Force-strain relationship)} \\
& \epsilon_j = b_j^\top u + \dfrac{1}{2} u^\top B_j u, & \text{(Green-Lagrange strain measure)} \\
& f_{DOF}(x) = 1, & \text{(Mechanical degree of freedom)} \\
& e^\top x = N, & \text{(Element number constraint)} \\
& u^{\min} \le u \le u^{\max}, & \text{(Displacement bounds)} \\
& x \in \{0,1\}^n, & \text{(Binary design variables)}
\end{array}
$$

[1] From Oxford Advanced Learner's Dictionary: Articulate (*technical*), to be joined to something else by a joint, so that movement is possible.

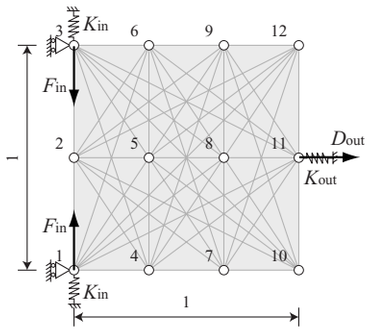


Figure 1. Truss ground structure.

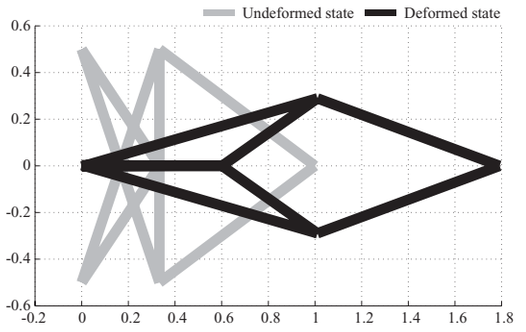


Figure 2. Optimal eight-bar scissors-like mechanism.

where $j = 1, \ldots, n$; $q \in \mathbb{R}^d$ is a given vector defining the displacement of the output port; $N > 0$ is a given integer limiting the number of bars in the optimal structure; $f_{\mathrm{DOF}}(x)$ denotes the mechanical degrees of freedom; $e \in \mathbb{R}^n$ is a vector of all ones; $b_j \in \mathbb{R}^d$ contains the direction cosines divided by the length of the j-th bar; the symmetric positive semidefinite matrix $B_j \in \mathbb{R}^{d\times d}$ defines the nonlinear part of the strain measure; $u^{\min} \in \mathbb{R}^d$ and $u^{\max} \in \mathbb{R}^d$ are given lower and upper bounds on the displacements. The reason for including force variables is that they decrease the nonlinearity in the equilibrium equations. Furthermore, the introduction of the force variables gives the opportunity to enforce stress constraints in a straight-forward way. This problem may also be extended to multiple loads and path-generation problems.

OUTLINE OF THE BRANCH AND BOUND METHOD

In order to perform global optimization on the above problem we have to overcome several obstacles in order to define a convex relaxation. Firstly, the design variables are binary; secondly, the forces f_j are defined with bilinear equality constraints; thirdly, the strains ϵ_j are defined with quadratic equality constraints; fourthly, the equilibrium equations $R(f, u) = 0$ are bilinear; finally, the constraint on the mechanical degree of freedom is non-convex and only well-defined for designs with binary values ($x \in \{0, 1\}^n$).

In the proposed branch and bound method the binary constraints on the design variables and the mechanical degrees of freedom constraint are relaxed and subsequently dealt with in the branch and bound tree. The bilinear equality constraints defining the forces are equivalently written as a set of linear constraints utilizing the fact that the bilinear term contains binary design variables. The remaining bilinear and non-convex quadratic constraints are relaxed using convex envelopes. The relaxation becomes a convex problem with a linear objective function and linear and convex quadratic constraints which can be efficiently solved using sequential quadratic programming. Branching is first performed on the design variables and then on the displacement variables.

NUMERICAL EXAMPLE

To illustrate the capabilities of the method a 66-bar test example is solved. The test example that we employ is shown in Fig. 1. The figure shows the truss ground structure of possible nodes and connections as well as all necessary boundary conditions, load cases and other related parameters. The springs and forces at the input ports model a strain based input actuator (e.g., shape memory alloy or piezoelectric device) and the output spring models a resistance to the movement.

We have applied the proposed global optimization method to the above problem in the case of $V = 8$ bars. The global optimal solution is known for this case from a graph-theoretical enumeration method[3]. This provides a validation of the method proposed in this paper. We have successfully obtained the optimal design which is shown in Fig. 2. Other examples have also been treated successfully.

References

[1] Bendsøe M.P., Sigmund O.: Topology Optimization – Theory, Methods, and Applications. Springer Verlag: Berlin Heidelberg, 2003.

[2] Calladine C.R.: Buckminster Fuller's Tensegrity Structures and Clerk Maxwell's Rules for the Construction of Stiff Frame. *International Journal of Solid and Structures* **14**:161–172, 1978.

[3] Kawamoto A., Bendsøe M.P., Sigmund, O.: Planar Articulated Mechanism Design by Graph Theoretical Enumeration. *Structural and Multidisciplinary Optimization* 2004; *To appear.*

[4] Horst R., Tuy H.: Global Optimization: Deterministic Approaches. Springer-Verlag, 1993.

SIMULATION OF TRABECULAR BONE ADAPTATION – CREATING THE OPTIMAL BIOLOGICAL STRUCTURE

Michał Nowak*, Marek Morzyński*
*Poznań University of Technology, Division of Machine Design Methods, Piotrowo 3, PL 60-965 Poznań, Poland

Summary In the paper the simulation of trabecular bone adaptation based on the micro-structure of the trabecular net is discussed. The assumption to the algorithm of bone remodeling stimulated by mechanical loading is presented. The basics of the own adaptive mesh generator are described. The results of computations, using specialized software, including parallel Finite Element Analysis are presented.

INTRODUTION

The Wolff's law, which has been stated in 19th century tells, that the bone is able to adapt to the mechanical stimulation. After many experiments it is clear, that the amount and organisation of the beams in trabecular bone tend to mechanical optimum. The research of the remodeling of trabecular bone is in the main area of many medical research centers, but the phenomena of bone mass losing is also very important during the space exploration. The mechanical stimulation is one of the most important factors of the normal bone functionality. There are many models of bone remodeling based on the strain energy density [1,2] and used for the adaptation simulations of the bone, treated as a continuum material. The main idea behind that is to prepare the model of the bone adaptation as a material of specific, changing properties depending on the loading history. The progress in computer hardware technology and parallel computations enable now modeling of the bone adaptation process using the real topology of the trabecular bone with use of a linear model of the trabecula. The latter is justified by experimental investigations stating that on the trabecular level the bone can be treated as an linear material [3].



Fig.1. Graphically rebuilt micro-CT slices – an input for the adaptive mesh generator

REMODELING SIMULATION

In the paper the assumption to the algorithm of bone remodeling stimulated by mechanical loading is presented. The beams of trabecular bone are assumed to be an isotropic linear material, where the marrow space is treated as voids. The simulation of the remodeling process needs both finite element mesh generation and evolution, and structural stress and strain analysis. To prepare an appropriate solid mesh an own adaptive mesh generator has been designed and is presented. The micro-CT slices are the input information about the bone topology, but the algorithm needs some graphical operations (Fig.1.).

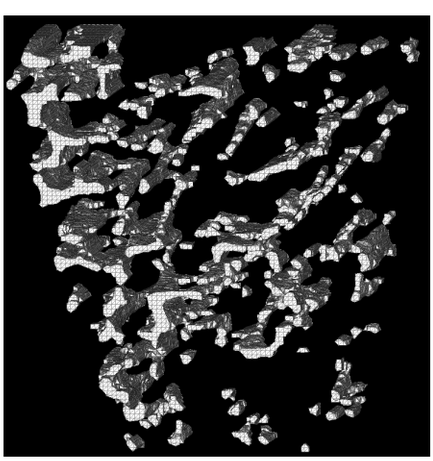


Fig.2. The solid mesh of the trabecular bone structure created by adaptive mesh generator

In contrary to other mesh generator of this type it works very robust. CT slices are converted to the specified format and the solid mesh is build layer by layer according to the topology of the trabecular bone (Fig.2.). The mesh generator enables generation of solid mesh, which can be adapted according the scenario of bone adaptation. It is possible to merge or split regions preserving proper finite elements shape. After applying constrains and loads the FEM computations are performed. The mesh is adapted according to the obtained from FEM strain rate. In the algorithm, exactly as in real trabecular bone the material in regions of low stress intensity is removed. In the healthy bone and in the algorithm this process is balanced by creation of new bone (finite elements in the computations) in the direction of dominant compression. In the algorithm there are two steps of mesh evolution. First the graphical information of each layer, corresponding to the CT-slice is changed. Then the new mesh is generated according to the element building rules. The sequence is repeated until there are no reason for the further adaptation, thus the structure is adapted to the load (Fig.3.a) and optimal. In Fig.3a it can be clearly seen that the structure follows the maximum principal stress trajectory and rebuilds adequately. While Fig.3a illustrates only the principle of the evolution in Fig. 3b the trabecular bone having 5x5x5mm dimension and subjected to compression is modeled. The computational model consists of 650000 elements.

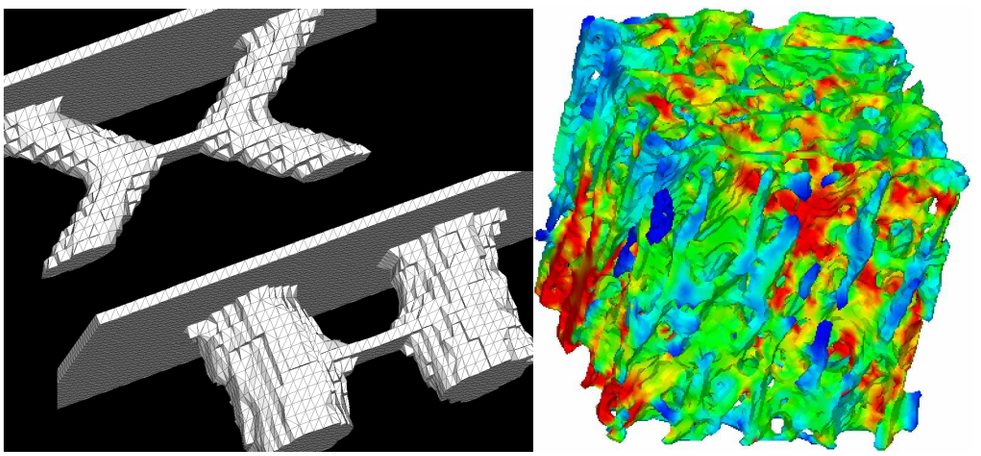


Fig.3. a) The adaptation of the simple test structure under compression – rebuild in the principal stress direction
b) Trabecular bone 5x5x5mm subjected to compression – equivalent stress Von Mises

CONCLUSIONS

The algorithm of building of optimal structure basing on biological principle of trabecular bone is presented. It consists of CT-data processing interface, robust 3D mesh generation tool, mesh evolution tool, remodeling scenario, and parallel FEM software and environment. With this program the trabecular bone remodeling is simulated and reproduced. The optimal structure following principal stresses is the result of the evolution. The used algorithm appeared to be very flexible. It is possible to test different scenarios of the bone remodeling. It is shown that linear material model combined with topological structure evolution is satisfactory for bone modeling and strictly follow the biological behavior. It will yield similar results as the nonlinear models based on the bone homogenization but is simpler and closer to the real trabecular bone properties.

Future investigations will include different scenarios including the ones appropriate for materials found in mechanical applications. The homogenization of bone properties based on microFEM model of the trabecula is considered. The parallel environment is being developed.

References

[1] Huiskes H.W.J. et al.: Effects of mechanical forces on maintenance and adaptation of form in trabecular bone, Nature 404, 704-706, 2000.
[2] Ruimerman R. et al.: A 3-dimensional computer model to simulate trabecular bone metabolism, Biorheology , 40, 315-320, 2003.
[3] Kowalczyk P.: Review of constitutive models for living tissues, Mechanika Techniczna i Stosowana, 29, 333-353, 1991.

SM24 - Structural optimization

OPTIMAL DESIGN OF ELASTO-PLASTIC STRUCTURES SUBJECTED TO NORMAL LOADS AND EARTHQUAKE

Sándor Kaliszky, János Lógó
Department of Structural Mechanics, Budapest University of Technology and Economics, Mûegyetem Rpt. 3, Kmf. 35, H-1521 Budapest, Hungary

Summary The optimal design of elasto-plastic structures subjected to multiparameter (normal) loads and earthquake is presented. It is assumed that under normal loads the structure remains in elastic stage. In case of earthquake, different approximate methods are used in which the plastic reserve of the structure and viscous effects are also taken into account. Introducing bounds for the elastic and permanent deflections a unified optimal design method is elaborated in which both the normal loads and the earthquake are simultaneously taken into consideration. The proposed method is based on the finite element method and on the concept of porous material where the material distribution is described by the densities of the finite elements, which are considered design variables. Numerical test examples are presented.

INTRODUCTION

An important practical application of dynamic plasticity is the investigation of structures subjected to extreme loads as explosion, impact and earthquake [1,2]. In these accidental situations plastic deformations can not be avoided but the structure must be able to absorb the kinetic energy corresponding to the extreme loads without excessive residual displacements and collapse. At the same time, under normal working conditions the structure has to carry the service loads in elastic stage with limited deflections.

The paper presents the optimal layout design of elasto-plastic structures subjected to multiparameter service loads and earthquake. In the solution both the normal and the extreme loads are simultaneously taken into consideration. Considering the normal loads, limits are introduced for the elastic deflections. The investigation of the earthquake is based on approximate methods. The simplest approximation is that the dynamic analysis is reduced to a static analysis where the corresponding loads are determined on the basis of the natural frequency and the stiffness properties of the structure. In case of the pushover method suggested by several Building Codes, the original structure is replaced by a fictitious one-degree-of-freedom elasto-plastic system. Here the properties of this system are calculated also from the natural frequency and from the results of a load history analysis of the original structure and from the diagrams obtained on the basis of the detailed analysis of the El Centro earthquake [3,4].

The mathematical formulation is based on the finite element method and on the concept of porous material where the material distribution is described by the densities of the finite elements, which are the design variables.

The formulation of the problem leads to two nonlinear mathematical programming problems and a natural frequency analysis coupled by the design variables. The solution can be based on iterative procedure.

The application of the proposed method is illustrated by test examples.

PROBLEM FORMULATION

The aim of the proposed approximate method to design a structure which

- -has satisfactory strength to carry the normal loads in elastic stage and the earthquake in plastic stage without collapse,
- -has limited elastic deformations under the action of the normal loads and satisfactory ductility to prevent excessive plastic deformation and fracture during earthquake,
- -has minimum volume.

The standard finite element formulation of the problem is as below. Beside the optimality condition

$$V = \rho_0 h_0 \sum_{i=1}^{n} \Delta_i x_i = \min!$$

in case of the normal loads the equilibrium equation $\mathbf{Q}^{eh} = \mathbf{F}^{-1}(x_i)\mathbf{G}\mathbf{K}^{-1}(x_i)\mathbf{P}_h,\ (h = 1,2,...,s)$;

the stress limits $-Q_i^{e0} \le Q_i^{eh} \le Q_i^{e0},\ (h = 1,2,...,s),\ (i = 1,2,...,n)$;

and the constraints for deflections $\sum_{i=1}^{n} \frac{Q_i^{eh}}{EI} Q_{ji}^{s} \Delta_i - u_{j0} \le 0$;

$$\mathbf{G}^{*}\mathbf{Q}_{\mathbf{j}}^{\mathbf{s}} + \mathbf{S}_{\mathbf{j}} = \mathbf{0};$$

$$\left|\mathbf{S}_{\mathbf{j}}\right| = 1,\ \ (h = 1,2,...,s),\ \ (j = 1,2,...,t);$$

have to be satisfied.

In case of earthquake first the fundamental natural frequency ω_0 has to be calculated and the optimal plastic design of the structure has to be formulated:

$$\left|\mathbf{K}-\omega^2\mathbf{M}\right| = \mathbf{0}$$

and

$$V = \rho_0 h_0 \sum_{i=1}^{n} \Delta_i x_i = \min!$$

$$\mathbf{G}^*\mathbf{Q}^{\mathbf{p}} + \mathbf{R} = \mathbf{0}\,,$$

$$-Q_i^{0p} \le Q_i^p \le Q_i^{0p}, \quad (i = 1,2,...,n);$$

Then following the guidelines of the codes and the pushover method presented in [4] in terms of ω_0 and the results of an elasto-plastic load history analysis the fictitious one-degree –of-freedom system can be constructed which provides the target displacement d_t of the original structure. Introducing an allowable displacement d_{ta} the behaviour constraint is expressed as :

$$d_t - d_{ta} \le 0.$$

In the above equations the following notations are used: $\mathbf{P}_h$, (h=1,2,...,s) multiparameter loading, $\mathbf{Q}_\mathbf{h}^\mathbf{e}$, $\mathbf{Q}^\mathbf{p}$ internal forces in elastic and plastic stage, Q_j^s internal forces due to the dummy forces S_j acting at the points (j=1,2,…,t), $\mathbf{R}$ external loads corresponding to earthquake, Q_i^{e0} and Q_i^{p0} elastic and plastic limit moments of the elements (i=1,2,…,n), $x_i = \frac{\rho_i}{\rho_0}$ dimensionless variables, ρ_0 density of the material, Δ_i length of the finite elements, h_0 a constant, $\mathbf{G}^*$, $\mathbf{F}$, $\mathbf{K}$, $\mathbf{M}$ equilibrium, flexibility, stiffness and mass matrices.

The unified treatment of the two loading cases is defined by two nonlinear mathematical programming problems and a natural frequency analysis coupled by the design variables x_i. For the solution, an iterative procedure or multicriteria optimization method [1,2] can be used. The proposed method can be applied to the approximate optimal design of frames and wall structures. The application is illustrated by examples. The method has been already extended to other structural problems [1,2].

Acknowledgement

The present study was conducted in the research group of Computational Structural Mechanics of the Hungarian Acad. Sci. and was supported by The Hungarian National Scientific and Research Foundation (OTKA) (grant T 042993) and Janos Bolyai Scholarship.

References

[1] Kaliszky, S., Lógó, J.: Layout Optimization of Rigid-Plastic Structures under High Intensity Short Time Dynamic Pressure. Mechanics Based Design of Structures and Machines.31(2), 131-149, 2003.

[2] Kaliszky, S., Lógó, J.: A Unified Model for the Elasto-Plastic Optimal Design of Structures Subjected to Multiparameter Loads and Impact, Proc. of 5th World Congress of Structural and Multidisciplinary Optimization, May 19-23, 2003, Lido di Jesolo, Venice, Italy. 181-182.

[3] Eurocode 8, Structures in Seismic Regions, Commission of the European Communities, 2002.

[4] Chopra A.K. : Dynamics of Structures, Theory and Applications to Earthquake Engineering, Prentice Hall. Englewood Cliffs, New Jersey, 1995.

OPTIMAL FORCE ACTION AND REACTION IN STRUCTURAL DESIGN AND IDENTIFICATION

A. Garstecki, Z. Pozorski, K. Ziopaja
Poznan University of Technology, ul. Piotrowo 5, PL 60-965 Poznań, Poland

Summary. Two classes of optimization problems are discussed in the paper: optimal loading distribution providing maximal or minimal structural response and optimal loading for structural identification providing maximum of the distance measure between the computed response of a model and the response of the actual structure measured in an experiment. Various measures of structural response are discussed, namely the total potential energy which represents the global stiffness of a structure, quadratic norm of displacement vector or arbitrary functional expressed in displacements. Derived optimality conditions for the optimal loading have the form of the coaxiality rule between forces and displacements and/or follow from the solution of the respective eigenvalue problems. The theory is illustrated by examples of optimal loading in structural problems and identification.

OPTIMAL FORCE ACTION

Problems of optimal reaction forces were first formulated in the form of maximization of global stiffness expressed by the total potential energy Π or maximization of limit load [1]. This approach was used in [2] for optimization of loading. Opposite formulation was proposed in [3], where the optimal loading provided minimum Π. Thus obtained the "worst" loading was used for optimal design of composites. The idea was further developed in [7], where it was shown that the formulation leads to Stekloff eigenvalue problem. The present paper is concerned with a generalized class of problems, where the optimal loading distribution provides maximal or minimal structural response measured by various response functions. Discrete formulation will be used.

Let us consider the general case when a structure is subjected to a constant load $\mathbf{f}_0$ and then the load $\Delta\mathbf{f}$ is superposed on it. The designer's concern is to find the best or the worst superposed load $\Delta\mathbf{f} = \mathbf{f} - \mathbf{f}_0$, which is associated with extremal structural response to the total load **f**. Let us introduce the structure response measure in the form of the general function of displacements **u**, namely I = I(**u**) and the constraint on $\mathbf{f} - \mathbf{f}_0$ in the form of the quadratic norm. The problem can be formulated in the form: find optimal load **f**, which provides extremum I and satisfies respective constraints, namely

$$\mathrm{I}(\mathbf{u}) \rightarrow \text{extremum}, \text{ subject to } \quad \mathbf{K}\mathbf{u} = \mathbf{f}\,, \quad (\mathbf{f}-\mathbf{f}_0)^{\mathrm{T}}(\mathbf{f}-\mathbf{f}_0) - \rho_0^2 = 0\,, \tag{1}$$

where **K** denotes the global stiffness matrix. The Lagrange function has the form

$$\mathrm{I}^{\mathrm{L}}(\mathbf{u},\mathbf{f},\mathbf{u}^{\mathrm{a}},\eta) = \mathrm{I}(\mathbf{u}) - (\mathbf{u}^{\mathrm{a}})^{\mathrm{T}}(\mathbf{K}\mathbf{u}-\mathbf{f}) - \frac{1}{2}\eta\left[(\mathbf{f}-\mathbf{f}_0)^{\mathrm{T}}(\mathbf{f}-\mathbf{f}_0) - \rho_0^2\right] \tag{2}$$

and the stationarity condition can be expressed as follows

$$\delta\mathrm{I}^{\mathrm{L}} = \delta\mathbf{u}^{\mathrm{T}}\left(\frac{\partial \mathrm{I}}{\partial \mathbf{u}} - \mathbf{K}\mathbf{u}^{\mathrm{a}}\right) + \delta\mathbf{f}^{\mathrm{T}}\left(\mathbf{u}^{\mathrm{a}} - \eta(\mathbf{f}-\mathbf{f}_0)\right) = 0\,. \tag{3}$$

Assuming $\delta\mathbf{u}$ and $\delta\mathbf{f}$ as independent vectors, the necessary stationarity conditions are

$$\mathbf{K}\mathbf{u}^{\mathrm{a}} = \frac{\partial \mathrm{I}}{\partial \mathbf{u}} = \mathbf{f}^{\mathrm{a}}(\mathbf{f}), \quad \mathbf{u}^{\mathrm{a}} = \eta(\mathbf{f}-\mathbf{f}_0)\,. \tag{4}$$

The first condition (4) specifies the adjoint problem and the second provides the *coaxiality rule* between the adjoint displacement $\mathbf{u}^{\mathrm{a}}$ and the primary load vector $\mathbf{f} - \mathbf{f}_0$. Introducing $\mathbf{u}^{\mathrm{a}} = \mathbf{K}^{-1}\mathbf{f}^{\mathrm{a}} = \mathbf{D}\mathbf{f}^{\mathrm{a}}$ into $(4)^2$ the coaxiality condition can be expressed in explicit form, which may in general be nonlinear as

$$\mathbf{D}\mathbf{f}^{\mathrm{a}}(\mathbf{f}) = \eta(\mathbf{f}-\mathbf{f}_0), \text{ or } \quad \mathbf{K}(\mathbf{u}-\mathbf{u}_0) = \frac{1}{\eta}\mathbf{u}^{\mathrm{a}}(\mathbf{u}) \quad . \tag{5}$$

Let I(**u**) be a quadratic function with a symmetric positive definite weighting matrix **A**, thus

$$\mathrm{I}(\mathbf{u}) = \frac{1}{2}\mathbf{u}^{\mathrm{T}}\mathbf{A}\mathbf{u}\ , \qquad \mathbf{f}^{\mathrm{a}} = \frac{\partial \mathrm{I}}{\partial \mathbf{u}} = \mathbf{A}\mathbf{u} = \mathbf{A}\mathbf{D}\mathbf{f} \tag{6}$$

and the equation (5) becomes linear

$$\mathbf{D}^{\mathrm{T}}\mathbf{A}\mathbf{D}\mathbf{f} = \eta(\mathbf{f}-\mathbf{f}_0) \quad \text{or} \quad \mathbf{B}\mathbf{f} = \eta(\mathbf{f}-\mathbf{f}_0)\,, \quad \mathbf{B} = \mathbf{D}^{\mathrm{T}}\mathbf{A}\mathbf{D}\ . \tag{7}$$

In a special case we may assume **A** = **1**, then $\mathbf{f}^{\mathrm{a}} = \mathbf{D}\mathbf{f} = \mathbf{u}$ in (6) and $\mathbf{B} = \mathbf{D}^{\mathrm{T}}\mathbf{D}$ in (7). Assumption **A** = **K** is equivalent to the energy control which provides minimum or maximum of the global complementary energy C = 0.5 $\mathbf{u}^{\mathrm{T}}\mathbf{K}\mathbf{u}$. In the latter case we arrive at optimal loading conditions $(4)^2$, $(5)^1$ and $(7)^1$ in the form $\mathbf{D}\mathbf{f} = \mathbf{u} = \eta(\mathbf{f}-\mathbf{f}_0)$.

Now, let us assume that initial loading does not appear and the total load **f** can be optimally controlled. Setting $\mathbf{f}_0 = \mathbf{0}$ in the derived stationarity conditions we arrive at coaxiality rules between total force vectors **f** and adjoint displacements $\mathbf{u}^{\mathrm{a}}$ (or **u**) in $(4)^2$ and (7). Moreover, the stationarity conditions $(5)^1$ and (7) take the form of eigenvalue problems. The optimal load action can be illustrated in the form of ellipsoids in the space of load parameters. The principal axes of the ellipsoids coincide with the extremal load vectors. This will be illustrated by a series of examples.

OPTIMAL LOADING IN STRUCTURAL IDENTIFICATION

Assume that the actual structure is described by the stiffness matrix $\mathbf{K}_1$, which is specified from experimental data, whereas $\mathbf{K}_2$ refers to an assumed structure model. Our aim is to find the optimal loading **f,** which maximizes the distance norm $\mathrm{I} = \Psi(\mathbf{u}_2 - \mathbf{u}_1)$

$$\mathrm{I} = \Psi(\mathbf{u}_2 - \mathbf{u}_1) \to \max , \quad \text{subject to} \quad \mathbf{K}_1\mathbf{u}_1 = \mathbf{f} , \ \mathbf{K}_2\mathbf{u}_2 = \mathbf{f} , \ \mathbf{f}^{\mathrm{T}}\mathbf{f} - \rho_0^2 = 0 . \tag{8}$$

The associated Lagrangian and its variation take the form

$$\mathrm{I}^{\mathrm{L}} = \mathrm{I} - (\mathbf{u}_1^{\mathrm{a}})^{\mathrm{T}}(\mathbf{K}_1\mathbf{u}_1 - \mathbf{f}) + (\mathbf{u}_2^{\mathrm{a}})^{\mathrm{T}}(\mathbf{K}_2\mathbf{u}_2 - \mathbf{f}) - \frac{1}{2}\mu(\mathbf{f}^{\mathrm{T}}\mathbf{f} - \rho_0^2) \tag{9}$$

$$\delta \mathrm{I}^{\mathrm{L}} = \left(\frac{\partial \psi}{\partial \mathbf{u}_2}\right)^{\mathrm{T}} \delta\mathbf{u}_2 + \left(\frac{\partial \psi}{\partial \mathbf{u}_1}\right)^{\mathrm{T}} \delta\mathbf{u}_1 - (\mathbf{u}_1^{\mathrm{a}})^{\mathrm{T}}\mathbf{K}_1\delta\mathbf{u}_1 + (\mathbf{u}_2^{\mathrm{a}})^{\mathrm{T}}\mathbf{K}_2\delta\mathbf{u}_2 + \delta\mathbf{f}^{\mathrm{T}}(\mathbf{u}_2^{\mathrm{a}} - \mathbf{u}_1^{\mathrm{a}} - \mu\mathbf{f}) = 0 \ . \tag{10}$$

Here $\mathbf{u}_1^{\mathrm{a}}$, $\mathbf{u}_2^{\mathrm{a}}$ and μ are the Lagrange multipliers. Introduce the adjoint systems specified by

$$\mathbf{K}_1\mathbf{u}_1^{\mathrm{a}} = \frac{\partial \psi}{\partial \mathbf{u}_1} = \mathbf{f}^{\mathrm{a}} , \qquad \mathbf{K}_2\mathbf{u}_2^{\mathrm{a}} = -\frac{\partial \psi}{\partial \mathbf{u}_2} = +\frac{\partial \psi}{\partial \mathbf{u}_1} = \mathbf{f}^{\mathrm{a}} . \tag{11}$$

The optimality condition for load distribution now takes the form

$$\delta\mathbf{f}^{\mathrm{T}}(\mathbf{u}_2^{\mathrm{a}} - \mathbf{u}_1^{\mathrm{a}} - \mu\mathbf{f}) = 0 , \quad \text{hence} \quad \mathbf{u}_2^{\mathrm{a}} - \mathbf{u}_1^{\mathrm{a}} = \mu\mathbf{f} , \quad \text{or} \quad (\mathbf{D}_2 - \mathbf{D}_1)\mathbf{f}^{\mathrm{a}} = \mu\mathbf{f} . \tag{12}$$

Here the optimal load is coaxial to the difference of adjoint displacements of the actual structure and the model. In the case when the energy norm $\mathrm{I} = \mathrm{I}_2 = 0.5\mathbf{f}^{\mathrm{T}}(\mathbf{D_2} - \mathbf{D}_1)\mathbf{f}$ is used as the measure of the distance between responses of the real structure and a model [3], then in (12) the adjoint displacements and forces $\mathbf{u}_1^{\mathrm{a}}$, $\mathbf{u}_2^{\mathrm{a}}$ and $\mathbf{f}^{\mathrm{a}}$ are substituted by primary vectors $\mathbf{u}_1$, $\mathbf{u}_2$ and **f**, respectively. Then, the optimal load follows from eigenvalues of $\mathbf{D}_2$ - $\mathbf{D}_1$. Now, assume **A** to be a quadratic positive definite matrix. Thus, another distance measure $\mathrm{I}=\mathrm{I}_3$ and optimality condition can appear

$$\mathrm{I} = \mathrm{I}_3 = \frac{1}{2}(\mathbf{u}_2 - \mathbf{u}_1)^{\mathrm{T}}\mathbf{A}(\mathbf{u}_2 - \mathbf{u}_1), \quad \text{hence} \ (\mathbf{D}_2 - \mathbf{D}_1)^{\mathrm{T}}\mathbf{A}(\mathbf{D}_2 - \mathbf{D}_1)\mathbf{f} = \mu\mathbf{f} , \quad \text{or} \quad \mathbf{L}\mathbf{f} = \mu\mathbf{f} . \tag{13}$$

The optimal loading follows from the eigenvalue problem $(13)^2$. In simple but practical case when **A** = **1**, the optimal loading can be computed as eigenvectors of the square of $\mathbf{D}_2$ - $\mathbf{D}_1$. Various distance measures were discussed in [5].

Examples of the identification will be presented, where the distance measures I_2 , I_3 and the Euclidean norm of the matrix $\mathbf{D}_2$ - $\mathbf{D}_1$ will be used. Three Euclidean vector spaces are used: R^{n} for FEM, R^{m} for the searched design parameters, and R^{k} for the load control. A step-by-step procedure is proposed, where at each identification step the optimal load is used. Bimodal solutions were encountered in the examples. At the final stage of the identification procedure the wavelet representation of design parameters is used, too.

CONCLUDING REMARKS

Using various response functions the sensitivity derivatives with respect to load parameters and the optimality conditions were derived. The optimal load conditions have the form of the generalized coaxiality rule of loads and adjoint displacements and/or follow from the eigenvalue problems. Numerical examples of structural identification proved the usefulness of the derived optimality conditions.

Acknowledgement. Participation of Prof. Z. Mróz from IFTR Warsaw in the study is kindly acknowledged. The study was supported by State Committee for Scientific Research in Poland, grant 5 T07E 045 22.

References

[1] Mróz Z., Rozvany G.I.N., Optimal design of structures with variable support conditions, J. of Optim. Theory Applications, **15**, 1, 85-101, 1975.

[2] Mróz Z., Garstecki A., Optimal design of structures with unspecified loading distribution, J. of Optim. Theory Applic., **20**, 3, 359-380, 1976.

[3] Gangadharan S., Nikolaidis E., Lee K. Haftka R.T., The use of antioptimization to compare alternative structural models, Proc. 34th AIAA/ASME/ASCE/AHS/ASC Structures, Struct. Dynamics and Material Conference, Part 1, La Jolla, 534-543, 1993.

[4] Lombardi M., Cinquini C., Contro R., Haftka R.T., Anti-optimization Technique for designing composite structures, Proc. 1st WCSMO Congress, Goslar 1995, ed.:N.Olhoff, G.I.N. Rozvany, Pergamon Press, 251-258, 1995.

[5] Lee J., Haftka R.T., Griffin O.H. Jr., Watson L.T., Sensmeier M.D, Detecting delaminations in a composite beam using anti-optimization. *Struct. Optim.*, **8**, 93-100, 1994.

[6] Cherkaeva E., Cherkaev A., Optimal design for uncertain loading conditions, in Homogenization ed. Berdichevsky V., Jikov V., Papanicolaou, World Scientific, 193-213, 1999.

DSA FOR ELASTIC-PLASTIC FINITE ROTATION SHELLS UNDER DYNAMIC LOADS

K.Wisniewski*, Piotr Kowalczyk*, Ewa Turska *
* *IFTR, Polish Academy of Sciences, Swietokrzyska 21, PL 00-049 Warszawa, Poland*

Summary The paper describes a constitutive DSA algorithm for elastic-plastic finite rotation shells and explicit dynamics, by which design derivatives are calculated w.r.t. material parameters. The paper shows that despite a great complexity of the solution algorithm for the finite-rotation elastic-plastic shells, it is feasible to compute analytical design derivative of this algorithm, and the yielded sensitivities are of very good accuracy.

CONSTITUTIVE DSA FOR HUBER-MISES PLASTICITY

Derivative w.r.t. material parameters.

In the paper we consider the constitutive model consisting of Hooke's elasticity and Huber-Mises plasticity with nonlinear isotropic hardening of the saturation type, $\kappa(\bar{e}^p) = \sigma_{y0} + \kappa_1' \bar{e}^p + (\sigma_{y1} - \sigma_{y0})(1 - e^{-a\bar{e}^p})$, and a linear kinematic hardening function $H_\alpha(\bar{e}^p) = H_0 + H' \bar{e}^p$. Hence, the set of material parameters is $\mathbf{m} \doteq \{E,\, \nu,\, \sigma_{y0},\, \kappa_1',\, \sigma_{y1}, a\}$. For a design parameter h and material parameters $\mathbf{m}$ depending on h, i.e. $\mathbf{m} = \mathbf{m}(h)$, we have $\mathrm{D}_h(\,\cdot\,) = \mathrm{D}_{\mathbf{m}}(\,\cdot\,)\,\mathrm{D}_h\mathbf{m}$, where $\mathrm{D}_h\mathbf{m}$ is specified additionally, and it suffices to consider derivatives w.r.t. $\mathbf{m}$, only. For some $A(\mathbf{m}, B(\mathbf{m}))$, the total design derivative of A with respect to $\mathbf{m}$ is written as $\mathrm{D}_{\mathbf{m}}A = \partial_{\mathbf{m}}A + A_{,B}\,\mathrm{D}_{\mathbf{m}}B$, where $\partial_{\mathbf{m}}(\cdot)$ is the explicit derivative.

Update of design derivatives of state variables.

Let us denote by $\mathbf{s}$ the state variables which are updated incrementally, stored and retrieved as constitutive history data, $\mathbf{s} = \{\boldsymbol{\Sigma},\, \bar{e}^{\mathrm{p}},\, \boldsymbol{\alpha}_R^p,\, \boldsymbol{\varepsilon}^p,\, \varepsilon_{33},\, \boldsymbol{\psi}_{\mathbf{R}}\}$, where $\boldsymbol{\psi}_{\mathbf{R}}$ are rotational parameters of the constitutive algorithm. The algorithm for $\mathbf{s}_{n+1}$ can be written as $\mathbf{s}_{n+1} = \mathbf{s}_{n+1}(\mathbf{m},\, \mathbf{s}_n(\mathbf{m}),\, \mathbf{q}_{n+1}(\mathbf{m}),\, \mathbf{q}_n(\mathbf{m}))$, and upon differentiation w.r.t. $\mathbf{m}$ we obtain the update formula

$$\mathrm{D}_{\mathbf{m}}\mathbf{s}_{n+1} = \frac{\partial \mathbf{s}_{n+1}}{\partial \mathbf{m}} + \frac{\partial \mathbf{s}_{n+1}}{\partial \mathbf{s}_n}\,\mathrm{D}_{\mathbf{m}}\mathbf{s}_n + \frac{\partial \mathbf{s}_{n+1}}{\partial \mathbf{q}_{n+1}}\,\mathrm{D}_{\mathbf{m}}\mathbf{q}_{n+1} + \frac{\partial \mathbf{s}_{n+1}}{\partial \mathbf{q}_n}\,\mathrm{D}_{\mathbf{m}}\mathbf{q}_n. \tag{1}$$

The derivatives, $\mathrm{D}_{\mathbf{m}}\mathbf{s}_n$ and $\mathrm{D}_{\mathbf{m}}\mathbf{q}_n$ are known as they are history variables, and $\mathrm{D}_{\mathbf{m}}\mathbf{q}_{n+1}$ in explicit dynamics is predicted. The derivatives, $\partial\mathbf{s}_{n+1}/\partial\mathbf{m}$, $\partial\mathbf{s}_{n+1}/\partial\mathbf{z}_n$, $\partial\mathbf{s}_{n+1}/\partial\mathbf{q}_{n+1}$, $\partial\mathbf{s}_{n+1}/\partial\mathbf{q}_n$, must be explicitly calculated. This update includes the design derivative of back-rotated Kirchhoff stress $\boldsymbol{\Sigma}$ which belongs to $\mathbf{s}$.

Design derivative of stress update algorithm for finite rotation shells.

The algorithmic approach to plasticity for finite-rotation shells follows this of [1], i.e. the constitutive equations are written for the back-rotated Kirchhoff stress $\boldsymbol{\Sigma}$, and equations analogous to those for the small deformation case are used. The constitutive model is the 3D Huber-Mises material with nonlinear isotropic/linear kinematic hardening. The plane stress constraints are directly incorporated into constitutive equations, as in [3] or [2], i.e. the deviatoric stress is parameterized by the plane stress components. The resulting yield surface is ellipsoidal, and not a radial return algorithm but a return map algorithm, with a constitutive Newton loop, must be used. This model is applied to shell laminas.

The algorithm to calculate the 2nd Piola-Kirchhoff stress $\mathbf{S}$ can be written as $\mathbf{S}_{n+1} = \mathbf{S}_{n+1}(\mathbf{m},\, \mathbf{s}_n(\mathbf{m}),\, \mathbf{q}_{n+1}(\mathbf{m}),\, \mathbf{q}_n(\mathbf{m}))$ and upon differentiation w.r.t. $\mathbf{m}$ we obtain

$$\mathrm{D}_{\mathbf{m}}\mathbf{S}_{n+1} = \frac{\partial \mathbf{S}_{n+1}}{\partial \mathbf{m}} + \frac{\partial \mathbf{S}_{n+1}}{\partial \mathbf{s}_n}\,\mathrm{D}_{\mathbf{m}}\mathbf{s}_n + \frac{\partial \mathbf{S}_{n+1}}{\partial \mathbf{q}_{n+1}}\,\mathrm{D}_{\mathbf{m}}\mathbf{q}_{n+1} + \frac{\partial \mathbf{S}_{n+1}}{\partial \mathbf{q}_n}\,\mathrm{D}_{\mathbf{m}}\mathbf{q}_n, \tag{2}$$

where $\{\mathrm{D}_{\mathbf{m}}\mathbf{s}_n,\, \mathrm{D}_{\mathbf{m}}\mathbf{q}_{n+1},\, \mathrm{D}_{\mathbf{m}}\mathbf{q}_n\}$ are known, and the derivatives, $\{\partial\mathbf{S}_{n+1}/\partial\mathbf{m}, \partial\mathbf{S}_{n+1}/\partial\mathbf{s}_n, \partial\mathbf{S}_{n+1}/\partial\mathbf{q}_{n+1}, \partial\mathbf{S}_{n+1}/\partial\mathbf{q}_n\}$ can be explicitly calculated.

DESIGN DERIVATIVE OF EXPLICIT DYNAMICS ALGORITHM

The equations of dynamics for shells are complicated due to rotational inertia terms and parametrization of rotations (we use the canonical rotation vector). The design differentiation of the explicit dynamics algorithm yields, among others, the following equation

$$\mathrm{D}_{\mathbf{m}}\ddot{\mathbf{q}}_{n+1} = \mathbf{M}^{-1}[-\mathrm{D}_{\mathbf{m}}\mathbf{f}_{n+1} - \mathrm{D}_{\mathbf{m}}\mathbf{c}(\boldsymbol{\omega}) - \mathbf{C}\,\mathrm{D}_{\mathbf{m}}\dot{\mathbf{q}}_{n+1/2}], \tag{3}$$

where $\mathbf{q} = \{\mathbf{x}_{0I},\, \boldsymbol{\psi}_I\}$ and $\boldsymbol{\psi}_I$ is a canonical rotation vector. The design derivative of the internal force $\mathbf{f}$ is as follows

$$\mathrm{D}_{\mathbf{m}}\mathbf{f} \doteq \frac{\partial}{\partial \mathbf{m}} \int_V \mathbf{B}^T\mathbf{S}\, dV = \int_V \left(\mathrm{D}_{\mathbf{m}}\mathbf{B}^T\,\mathbf{S} \;+\; \mathbf{B}^T\,\mathrm{D}_{\mathbf{m}}\mathbf{S}\right)\, dV, \tag{4}$$

where $\mathbf{S}$ is the 2nd Piola-Kirchhoff stress, $\mathbf{E}$ is the Green strain. The kinematical operator $\mathbf{B} \doteq \partial \mathbf{E}/\partial \mathbf{q}$ depends on $\mathbf{q}$ for finite rotation shells, hence its design derivative is

$$\mathrm{D}_{\mathbf{m}}\mathbf{B} = \frac{d\mathbf{B}}{d\mathbf{q}}\frac{d\mathbf{q}}{d\mathbf{m}} = \mathbf{B}_{,\mathbf{q}}\,\mathrm{D}_{\mathbf{m}}\mathbf{q}, \tag{5}$$

where $\mathbf{B}_{,\mathbf{q}} = \partial^2 \mathbf{E}/\partial \mathbf{q}^2$ is a $(n_s \times n_{dof} \times n_{dof})$ matrix, and n_s is a number of strain components.

Design derivative of inertial term.

The inertial term $\mathbf{c}(\boldsymbol{\omega}) = I_\rho \boldsymbol{\omega} \times (\boldsymbol{\Pi}\boldsymbol{\omega})$ depends on $\boldsymbol{\psi}_{n+1}$ and $\dot{\boldsymbol{\psi}}_{n+1/2}$, because $\boldsymbol{\omega} \approx \mathbf{T}(\boldsymbol{\psi}_{n+1})\,\dot{\boldsymbol{\psi}}_{n+1/2}$. Hence, the design derivative of it is computed as follows

$$\mathrm{D}_h\mathbf{c}(\boldsymbol{\omega}) = \frac{\partial \mathbf{c}}{\partial \boldsymbol{\psi}_{n+1}}\,\mathrm{D}_h\boldsymbol{\psi}_{n+1} + \frac{\partial \mathbf{c}}{\partial \dot{\boldsymbol{\psi}}_{n+1/2}}\,\mathrm{D}_h\dot{\boldsymbol{\psi}}_{n+1/2}. \tag{6}$$

NUMERICAL EXAMPLE: ELASTIC-PLASTIC COMPRESSION OF RECTANGULAR RAIL

This example tests the DSA procedure in a realistic example of compression of a steel thin-walled rail, a quarter of which is shown in Fig. 1. To avoid contact modelling and enable clear conclusions regarding accuracy of the DSA, computations are performed for first few milliseconds only.

The load is a 270 kg mass with the initial velocity $v_3 = -7.7778$ m/s, applied at the rail end $x_3 = 370$ mm. The material data $E = 210000$, $\nu = 0.3$, $\sigma_{y1} = 250$, $\sigma_{y0} = 250$, $H^{'} = 2000$, $a = 1$, $H^{'}_{kin} = 0$, thickness $h = 1.47$.

The shell element is a 4-node bilinear with 6 dofs/node, based on Reissner's kinematics. The drilling rotation is included on use of the drilling RC-equation by the penalty method. The rotations are parameterized by a canonical rotation vector. The Green strain and 2nd Piola-Kirchhoff stress are used as a work-conjugate pair. For the transverse shear the ANS (Bathe, Dvorkin) approximation is used. A numerical integration with 2x2 Gauss points in lamina, and 5-point Simpson rule over thickness is used.

Design derivatives are computed analytically and by FD method; the derivatives of rotation at point P w.r.t. yield stress σ_{y0} is given in Fig. 1b. As it can be seen, the finite-difference DSA results coincide with the analytical DSA results, which proves that, despite a substantial complexity of the algorithms, the analytical DSA equations are correct.

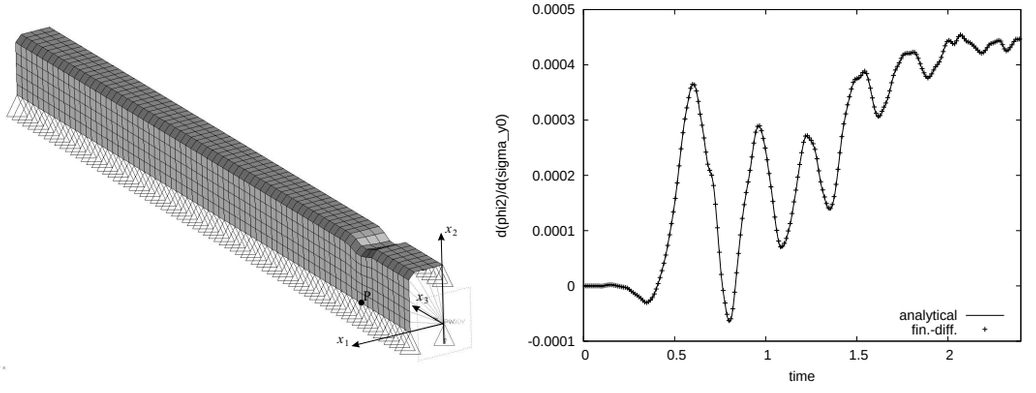


Figure 1. Elastic-plastic compression of rail: (a) geometry, (b) design derivatives of rotation at point P w.r.t. yield stress σ_{y0}.

Acknowledgement. This research was partially supported by: EC Growth Project G3RD-CT-2000-00276, and the Polish Committee for Scientific Research (KBN) Grant 7T11F01921.

References

[1] Hughes T.J.R.: Numerical implementation of constitutive models: rate independent deviatoric plasticity. In S. Nemat-Nasser *et al.*, ed., *Theoretical Foundations for Large-Scale Computing for Nonlinear Material Behaviour*, 29–57. Nijhoff 1984.

[2] Jetteur, P.: Implicit integration algorithm for plane stress elastoplasticity in plane stress analysis. *EC*, **3**:251–253, 1986.

[3] Simo J.C., Taylor R.L.: A return mapping algorithm for plane stress elstoplasticity. *IJNME*, **22**:649–670, 1986

[4] Wisniewski K., Kowalczyk P., Turska E.: On computation of design derivatives for Huber-Mises plasticity with non-linear hardening, *IJNME*, **57**: 271–300, 2003.

[5] Wisniewski K., Kowalczyk P. Turska E.: Design Sensitivity Analysis for elasic-plastic shells and explicit dynamics. *in preparation*, 2004.

OPTIMIZATION OF FUNCTIONALLY GRADED MATERIALS WITH TEMPERATURE DEPENDENT PROPERTIES. A MESHFREE SOLUTION

Florin Bobaru*, Han Jiang*
*University of Nebraska-Lincoln, Department of Engineering Mechanics,Lincoln, NE 68588-0526, USA

Summary We find optimal material composition for FGM by selecting points on a spline-interpolated volume fraction curve as material design variables. For the local effective properties of the FGM we use the rule of mixtures and the Mori-Tanaka model. We minimize the mass while stresses are used as constraints. The nonlinear thermo-elastic problems are solved using a meshfree method. The design space of material configurations is unrestricted and we study convergence properties when the number of design variables increases.

INTRODUCTION

Inspired by some naturally occurring material systems such as bamboo, bone, sea-shells, teeth, functionally graded materials (FGMs) are heterogenous materials featuring a smooth gradation for achieving a specific function. Most commonly, metal-ceramic FGMs are used to make the transition from a metal part which is strong but cannot operate at high temperatures and a ceramic part that is efficient in shielding against high temperatures but has low tensile strength. Some current and potential applications include thermal protective shields of high reliability, thin films and coatings for cutting tools, dental and prosthetic implants, to name just a few.

The function of the smooth gradation characteristic to FGMs is to reduce or eliminate stress concentrations and/or jumps in bimaterial systems, minimize damage due to thermal shock or mechanical impact, etc. Some of the previous theoretical results have analyzed the behavior of FGMs when the function that defines volume fraction variation is given by a monotonic, power-law type function (x^p, $p \in \mathbb{R}$). The monotonic power-law is selected only as a matter of convenience, analytical results are difficult, if not impossible, to obtain otherwise. The finite element method and meshfree methods have also been employed in the study of FGMs (see e.g. [1], [2]). Determining the optimal volume fraction variation for extremizing a specific objective function has been discussed in, for example, [3]. In [3], the function describing the volume fraction is limited to piecewise quadratic. In addition, the temperature dependence of the material properties is ignored.

In this paper we analyze optimal configurations for FGMs in a more general setting: the material variation we use is a shape-preserving spline that interpolates points which are the material design variables. By changing the shape of the volume fraction function we modify the material composition of the FGM. We take into account the temperature dependence of material properties and use a meshfree solution for the thermoelastic problem for possible extensions to combined shape-material optimization of FGMs. The meshfree methods offer considerable benefits when applied to shape optimization problems as recently shown in [4], [5].

PROBLEM FORMULATION

We consider a domain Ω that is occupied by the FGM under thermomechanical loading. The nonlinear heat-transfer equations and the equations of the thermoelastic equilibrium can be written as:

$$\begin{cases} \kappa(\boldsymbol{x},\theta)\Delta\theta + Q(\boldsymbol{x},\theta) = 0 & \text{in} \quad \Omega \\ \theta = \theta_0 & \text{on} \quad \Gamma_\theta^0 \\ \kappa(\boldsymbol{x},\theta)\nabla\theta\cdot\boldsymbol{n} = \overline{q} & \text{on} \quad \Gamma_\theta^1 \\ \kappa(\boldsymbol{x},\theta)\nabla\theta\cdot\boldsymbol{n} + h(\boldsymbol{x},\theta)\,(\theta-\theta_\infty) = 0 & \text{on} \quad \Gamma_\theta^2 \end{cases}, \quad \text{nonlinear heat-transfer} \tag{1}$$

$$\begin{cases} \nabla\cdot\boldsymbol{\sigma}(\boldsymbol{x},\theta) + \boldsymbol{b}(\boldsymbol{x},\theta) = \boldsymbol{0} & \text{in} \quad \Omega \\ \boldsymbol{\sigma}(\boldsymbol{x},\theta)\,\boldsymbol{n} = \overline{\boldsymbol{t}}(\boldsymbol{x},\theta) & \text{on} \quad \Gamma_{\boldsymbol{t}} \\ \boldsymbol{u}(\boldsymbol{x},\theta) = \overline{\boldsymbol{u}}(\boldsymbol{x},\theta) & \text{on} \quad \Gamma_{\boldsymbol{u}} \end{cases}, \text{ where} \boldsymbol{\sigma} = \mathcal{C}(\boldsymbol{x},\theta) : [\boldsymbol{\varepsilon}(\boldsymbol{x},\theta) - \alpha(\boldsymbol{x},\theta)\,\theta(\boldsymbol{x})\mathbf{I}] \tag{2}$$

The corresponding weak-forms for these equations are obtained using the element-free Galerkin (EFG) meshfree method. The variation of the material is captured at the level of the Gauss integration points which are *independent* of the discretization nodes. This is one advantage of the meshfree solution when compared to a FEM solution.

The material parameters of the FGM depend not only on the volume fraction of the two components, but also on the temperatures. The temperature dependence of the thermal expansion coefficients for the materials uses in this paper (ZrO_2 and Ti-6Al-4V) is shown in Figure 1. The critical tensile strength variation is given in Figure 2. The compressive critical strength, thermal conductivity, and Young's modulus, also vary with the temperature.

At a location where the volume fraction of metal is $v(x)$, we evaluate the "composite" material parameters via a rule-of-mixture (ROM) scheme. Other schemes can be selected and easily implemented. We use the ROM for lack of experimental data. The same ROM scheme is used for estimating the critical tensile and compressive stresses. For example, let $S^{metal}(\theta)$ and $S^{ceramic}(\theta)$ be the critical tensile strengths for the metal and the ceramic materials at a given temperature θ. The estimated critical tensile strength at a location where the volume fraction of the metal is $v(x)$ will then be given by:$S(x,\theta) = S^{metal}(\theta)\cdot v(x) + S^{ceramic}(\theta)\cdot[1-v(x)]$.

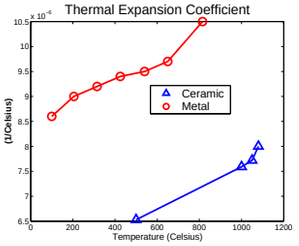


Figure 1. Temperature variation of the thermal expansion coeff.

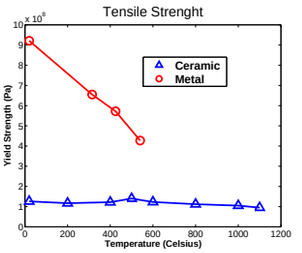
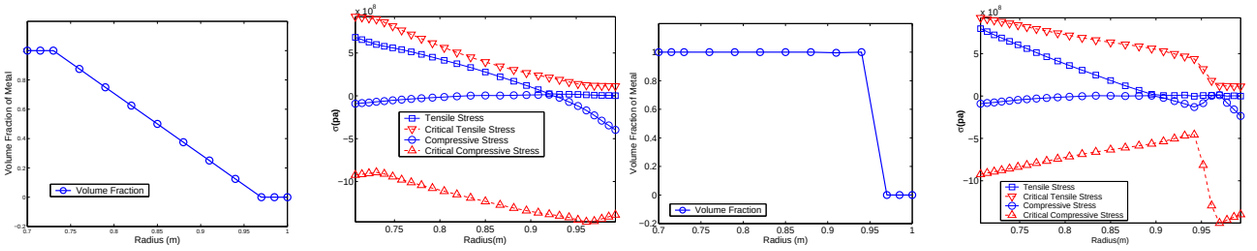


Figure 2. Temperature dependence of the tensile strength

OPTIMIZATION AND NUMERICAL RESULTS

Using the EFG method, we discretize the weak forms of the thermal and thermomechanical response. The heat-transfer problem is *nonlinear*, but the nonlinearity is weak. We use a fixed-point iteration and obtain convergence in just a couple of iterations. With temperature field obtained in this fashion, we calculate the displacements, strains, and stresses. The solution of the thermoelastic problem is repeated at every iteration of the optimization algorithm. We consider a *quarter of a hollow cylinder* with an inner radius of 0.7m and outer radius of 1m. After a convergence analysis, we use 2349 discretization points and 2240 integration cells. Each cell uses 5by5 Gaussian integration. We impose inner pressure 100MPa and the inner temperature is 20 C° while the outer temperature reaches 800C°.

The results for one example are given below. We *minimize the mass* while a constraint is defined in terms of violating the critical tensile and compressive stresses. This leads to a constrained *nonlinear optimization problem* that we solve using SQP. We start with a configuration that has thin coatings of pure metal and pure ceramic at the exterior with a thick FGM layer in-between. We use nine design. We converge to a profile that has a thin FGM layer. The metal (ZrO_2) is lighter than the ceramic (Ti-6Al-4V) and the resulting FGM is metal rich.



(a) Initial vol. frac. (b) Initial stress profile (c) Optimal vol. frac. (d) Final stress profile

Figure 3. The initial and final volume fraction functions and the corresponding critical stress profiles.

CONCLUSIONS

Optimal profiles in minimizing mass under stress constraints for temperature dependent FGMs have been obtained. The points on the material variation function are the design variables. The meshfree solution leads to fast convergence of the SQP optimization algorithm used here. Future plans include combining shape and material optimization for non-symmetrical loading.

References

[1] Reiter T., Dvorak G.J.: Micromechanical models for graded composite materials: II. Thermomechanical loading. *J. Mech. Phys. Solids* **46**(9): 1655-1673, 1998.

[2] Rao B.N., Rahman S.: Mesh-free analysis of cracks in isotropic functionally graded materials. *Engrg. Fract. Mech.* **70**(1): 1-27, 2003.

[3] Tanaka K, Watanabe H., Sugano Y. Poterasu V.F.: A multicriterial material tailoring of a hollow cylinder in functionally graded materials. *Comput. Methods Appl. Mech. Engrg.* **135**:369-380, 1996.

[4] Bobaru F., Mukherjee S.: Meshless approach to shape optimization of linear thermoelastic solids. *Int. J. Num. Meth. Engrg.* **53**(4): 765-796, 2002.

[5] Bobaru F., Rachakonda S.: Boundary Layer in Shape Optimization of Convective Fins using a Meshfree Approach. *Int. J. Num. Meth. Engrg.*, to appear (2004).

OPTIMUM BLANK DESIGN FOR DEEP DRAWING USING INTERACTION OF HIGH AND LOW FIDELITY SIMULATION

Ryutaro Hino*, Fusahito Yoshida*, Vassili V. Toropov**
*Dept. of Mechanical System Engineering, Hiroshima Univ., 1-4-1, Kagamiyama, Higashi-Hiroshima, 739-8527, Japan / Hiroshima Pref. Inst. of Ind. Sci. & Tech., 3-10-32, Kagamiyama, Higashi-Hiroshima, 739-0046, Japan
**Altair Engineering Ltd., Vanguard Centre, Sir William Lyons Road, Coventry, CV4 7EZ, UK

Summary The design optimization system is developed using the interaction of high- and low-fidelity finite element simulations of a deep drawing process, and the multipoint approximation technique based on the iterative response surface building. The system has been applied to the optimum blank design for deep drawing process of a rectangular box to determine the optimum initial blank design that minimizes the waste of material. The blank design was optimized successfully in remarkably short computational time.

INTRODUCTION

One of the major drawbacks of numerical optimization for sheet metal forming process is its too long computational time. Our target is quick and effective optimization system for process design of sheet metal forming. In this work, the optimization system is developed using the interaction of high- and low-fidelity finite element simulations of a deep drawing process, and the multipoint approximation technique [1, 2] based on the iterative response surface building. Approximation functions and a weighting scheme are introduced in order to correct the low-fidelity responses so they can be treated as high quality approximations. The approximated problem is then solved by the multipoint approximation technique, hence there are two levels of approximation in the optimization process to reduce the computational time. The system has been applied to the optimum blank design for deep drawing process of a rectangular box. The optimization problem is to determine the optimum initial blank design that minimizes the waste of material. The validity of the developed optimization technique is discussed based on the obtained results.

OPTIMIZATION BASED ON THE INTERACTION OF HIGH AND LOW FIDELITY SIMULATION

An iterative optimization procedure requires a large number of high-fidelity process simulations (e.g. FE simulations using fine mesh) to obtain accurate responses of the objective and constraint functions, and it takes quite a long time. Therefore, in the present optimization procedure, the low-fidelity simulation (e.g. FE simulation using coarser mesh), which is computationally less expensive, is used as substitution of the original high-fidelity one. The approximation functions:

$$\tilde{F}(\mathbf{x},\mathbf{a}) = \tilde{F}(f(\mathbf{x}),\mathbf{x},\mathbf{a}) \tag{1}$$

are built based on numerical experiments and used to correct the low-fidelity responses. Here, **a** is the set of tuning parameters, **x** the vector of design variables and $f(\mathbf{x})$ the low-fidelity responses, respectively. Several types of simple functions [2] are available as the approximation functions (1). The high-fidelity simulation is used only for the numerical experiments to build the approximation functions (1) prior to optimization and validation of the solution.
The optimization procedure based on the interaction of high and low fidelity simulation is described as follows:

1. Both of the high- and low-fidelity simulations are carried out according to a selected plan of experiments.
2. The approximation functions (1) are built based on the results of the above numerical experiments.
3. The optimization problem is solved using the low-fidelity responses corrected by the approximation functions (1), and the optimum design of the present step, **x***, is obtained. Multipoint approximation method [1, 2] is employed to solve the optimization problem. In this optimization process, the original high-fidelity simulation is never used.
4. The high- and low-fidelity simulations are carried out for the obtained optimum design **x***.
5. The obtained optimum design **x*** is validated.
6. If the solution **x*** is not acceptable, the plan of experiments is modified using the obtained design **x*** and the approximation functions are rebuilt. Weight coefficients are introduced into the least square fitting to rebuild the approximation functions so that the contribution of design points around the solution **x*** becomes comparatively higher. Then the optimization for the next step is carried out.
7. If the solution **x*** is acceptable, it is the final solution and the optimization procedure is completed.

OPTIMUM BLANK DESIGN FOR DEEP DRAWING PROCESS OF A RECTANGULAR BOX

The developed optimization technique is applied to the optimum blank design for deep drawing process of a rectangular box. In deep drawing process, the flange of the product is often trimmed after the drawing process to obtain the desired product shape (see Fig. 1), and the trimmed material is wasted. Since the flange shape of the product is strongly affected by the initial blank design, the optimization problem is to determine the optimum initial blank design that minimizes the waste of material, as shown in Fig. 2. Therefore, the initial blank shape is treated as design variables, and

the objective function is the amount of wasted material, i.e. area α shown in Fig. 2. Two types of blank design, i.e. corner-cut type and B-Spline type are used. They are defined by four design variables. It is well known that too large a blank induces excessive local thinning or fracture of the sheet. On the other hand, when a blank is too small, the contour of the flange penetrates the trimming line. To avoid these defects, two constraints, i.e. the thickness constraint and the contour constraint are introduced. Dynamic-explicit finite element code (PAM-STAMP) and Simplified static-implicit finite element code (PAM-QUIKSTAMP) are used for the high- and low-fidelity simulations, respectively. Besides, the low-fidelity model has only about 120 elements and needs about 10 seconds for one simulation, while the high-fidelity model has about 1100 elements and requires about 150 seconds.
Fig. 3, Fig. 4, Table 1 and Table 2 show the optimum solution in comparison with the solution obtained by using only high-fidelity simulation. The 1st step solution based on the interaction of high and low fidelity simulation is not acceptable since the quality of the approximation function is not good enough. In the 2nd step optimization using weighting scheme, the quality of the approximation function is improved and a successful blank design, which is almost the same as the original high-fidelity solution, is obtained. In terms of computational time, the developed optimization technique has the great advantage over the original high-fidelity optimization as shown in Tables 1 and 2.

CONCLUSION

The presented optimization system using high and low fidelity simulation is found to be effective for the quick determination of the optimum blank design for deep drawing process. Optimum solution is obtained in remarkably short computational time. This is an encouraging result for the construction of optimization system for various sheet metal forming processes.

References

[1] Toropov V.V.: Simulation Approach to Structural Optimization. *Structural Optimization* **1**:37-46, 1989.

[2] Toropov V.V., van Keulen F., Markine V.L., Alvarez L.F.: Multipoint Approximations Based on Response Surface Fitting: A Summary of Recent Developments. *Proc. of 1st ASMO UK/ISSMO conference*:371-380, 1999.

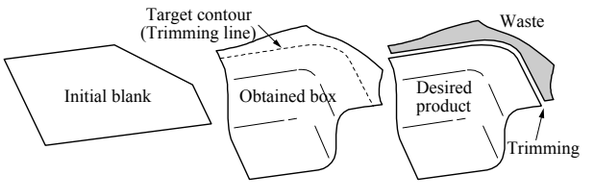


Figure 1. Deep drawing process of a rectangular box

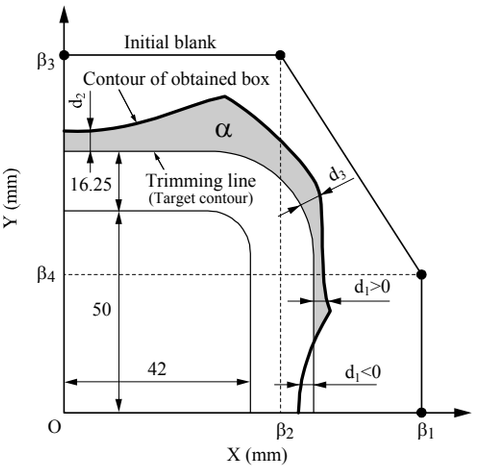


Figure 2. Optimization problem of deep drawing process

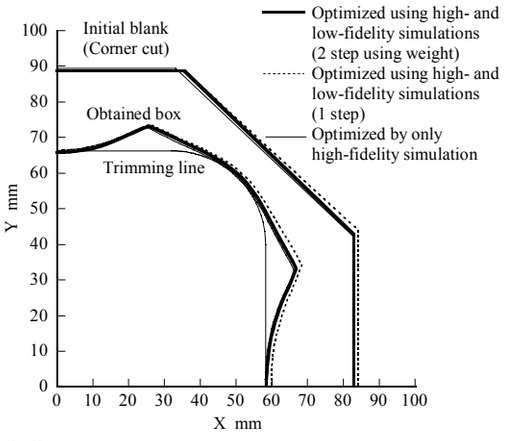


Figure 3. Optimum blank design and drawn box (corner-cut type)

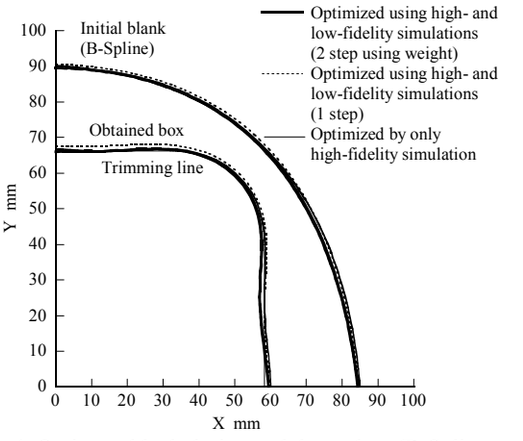


Figure 4. Optimum blank design and drawn box (B-Spline type)

Table 1. Results of optimization (corner-cut type)

	Optimized using high- and low-fidelity simulations (2 step, weighted)	Optimized using high- and low-fidelity simulations (1 step)	Optimized by only high-fidelity simulation
x_1	83.00	84.02	83.10
x_2	42.86	42.75	42.78
x_3	88.60	88.61	89.47
x_4	48.24	49.88	43.45
Objective	307.9	422.6	264.6
Time(min.)	113(22+26+65)	48(22+26)	1040

Table 2. Results of optimization (B-Spline type)

	Optimized using high- and low-fidelity simulations (2 step, weighted)	Optimized using high- and low-fidelity simulations (1 step)	Optimized by only high-fidelity simulation
x_1	84.44	84.65	84.93
x_2	89.54	90.58	90.27
x_3	87.90	90.11	91.48
x_4	98.72	97.91	94.44
Objective	12.0	83.4	29.3
Time(min.)	135(16+57+62)	73(16+57)	533

XXI ICTAM, 15–21 August 2004, Warsaw, Poland

COMPUTATIONAL TRICKS FOR EFFICIENT DESIGN SENSITIVITY ANALYSIS

Henrik T. Møller and Erik Lund
Institute of Mechanical Engineering, Aalborg University,
Pontoppidanstræde 101, DK-9220 Aalborg East, Denmark

Summary When applying gradient based optimization tools on complex coupled problems it is of vital importance that the design sensitivity analysis phase does not take up to much of the time required in the optimization run. However, in the analysis of coupled problems the exact Jacobian is often not available and one is faced with the problem of solving a linear system with an unknown coefficient matrix. In the paper we present two iterative methods to accomplish this task efficiently. The key advantages of the two methods compared to an overall finite difference approach are better efficiency because information obtained during analysis can be reused, and a better or at least a known accuracy, because the sensitivity equations are solved to a specified tolerance. These key points are illustrated with an example.

Keywords: Sensitivity analysis; Implementation; Nonlinear problems; Fluid-structure interaction

SENSITIVITY ANALYSIS

When applying the direct differentiation method to perform sensitivity analysis, one ultimately ends up with the task of solving the following sequence of linear systems for each of the I design variables a_i in the computation of the state variable sensitivities $\frac{d\mathbf{u}}{da_i}$.

$$\frac{\partial \mathbf{R}(\mathbf{u})}{\partial \mathbf{u}} \frac{d\mathbf{u}}{da_i} = -\frac{\partial \mathbf{R}(\mathbf{u}, a_i)}{\partial a_i} \tag{1}$$

Here $\mathbf{R}(\mathbf{u})$ denotes the equations of state for the problem under consideration. The right hand side can be computed analytically or by using finite differences. The Jacobian $\frac{\partial \mathbf{R}}{\partial \mathbf{u}}$ is the same as the one used for the analysis if the analysis problem is based on some variant of Newton's method. Therefore the computation of the state sensitivities can be performed very efficiently when the solution for state is based on Newton's method and a direct solver is used together with an exact Jacobian. If an exact Jacobian is not used in the analysis, then the methodology can not be directly used, and instead an iterative method must be used. In the paper we focus on what kind of efficiency and accuracy that can be obtained in the sensitivity analysis with two types of modified methods which avoids the use of an exact Jacobian.

The base ingredient in both types of methods is the realization that the product of the system Jacobian and an arbitrary vector $\mathbf{z}$ can be computed by using forward differences by means of the definition of the directional derivative of $\mathbf{R}$, i.e.

$$\frac{\partial \mathbf{R}(\mathbf{u})}{\partial \mathbf{u}} \mathbf{z} \approx \frac{\mathbf{R}(\mathbf{u} + \alpha \mathbf{z}) - \mathbf{R}(\mathbf{u})}{\alpha}, \quad \text{with} \quad \alpha \sim \frac{\|\mathbf{u}\|_\infty}{\|\mathbf{z}\|_\infty} \sqrt{10\varepsilon_m} \tag{2}$$

This way to evaluate the matrix-vector product is relatively cost efficient, provided that the computation of the residuals for the solution of the underlying nonlinear equations is efficient. Implementing the matrix product requires little effort. What is needed is to find a good perturbation α and a routine which can update the state variables according to a specified increment. The updating routine is the same as one would use in a Newton method for the analysis problem. The reason for putting 10 in front of the machine precision as indicated in (2) is an assumption that the residual computation is not accurate in the last significant digit. With this selection of the perturbation the implied accuracy in the matrix-vector product is such that approximately half the significant digits contained in the result are accurate provided that the problem is reasonably well scaled. Knowing a way to compute the product of the exact Jacobian with a vector the sensitivity equation can be rewritten in a form which makes use of the finite difference matrix-vector product as

$$\tilde{\mathbf{J}} \left(\Delta \frac{d\mathbf{u}}{da_i} \right)^k = -\frac{\partial \mathbf{R}}{\partial a_i} - \mathbf{J} \frac{d\mathbf{u}}{da_i}^k, \quad \text{with} \quad \frac{\partial \mathbf{R}(\mathbf{u})}{\partial \mathbf{u}} = \mathbf{J} = \tilde{\mathbf{J}} + \mathbf{J}^d \tag{3}$$

where the Jacobian is split into the part used in the analysis as iteration matrix $\tilde{\mathbf{J}}$ and the part discarded in the analysis $\mathbf{J}^d$. This iteration is a stationary iterative method, i.e. the iteration matrix is constant throughout iterations.

The iterative DSA method of (3) can be improved by using a non-stationary method. The benefits are improved robustness and faster convergence. Since many iterative methods for linear systems only require matrix-vector products and preconditioning operations, the sensitivity system can be solved by using the finite difference evaluation of the matrix-vector product within the iterative method. This is a well-known approach for solving nonlinear equations and is often referred to as a matrix-free implementation or as an inexact Newton-Krylov method. The process of obtaining the design sensitivities is efficient because the preconditioner used for the analysis can be reused for the sensitivity analysis. If available, the iteration matrix $\tilde{\mathbf{J}}$ from the analysis phase is often a good preconditioner.

The second method uses Quasi Newton methods to solve the linear system. The initial iteration matrix is chosen as $\tilde{\mathbf{J}}$, and the iteration matrix is then updated during iterations using secant information. When $\tilde{\mathbf{J}}$ is a good approximation to the system Jacobian the methods are effective. The non-stationary method converges at a faster rate to a solution than the stationary method described by (3). For some of the examples studied the non-stationary method can converge to a much tighter convergence tolerance on the sensitivity system.

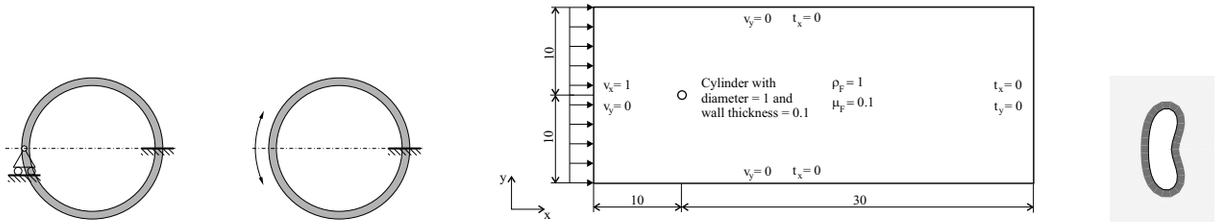


Figure 1. Flexible cylinder example. Note the different boundary conditions in the two different cases.

Table 1. Number of matrix-vector products required for convergence in DSA example on mesh 1. The leftmost column shows boundary conditions. BGM is "Broyden's Good Method", GMRES is Generalized Minimum RESidual, BiCGSTAB is Bi-Conjugate Gradient STABilized, and CGS is Conjugate Gradient Squared.

Load case	DVNo	Stationary	BGM	GMRES	BiCGSTAB	CGS
	1	9	5	3	4	4
	2	9	5	3	4	4
	3	8	5	4	6	4
	4	8	6	4	6	4
	1	NC	6	4	6	6
	2	NC	7	4	6	6
	3	NC	7	5	8	8
	4	NC	7	5	8	12

EXAMPLE

The example is a nonlinear steady state fluid-structure problem and is illustrated in Fig. 1. The analysis problem is to find the flow around the flexible cylinder, which is very flexible, such that it deforms significantly due to the flow induced forcing on the interface between the solid domain and the fluid domain. The design variables we are investigating are two shape design variables (thickness of cylinder dv1 and dv2), and two material parameters, namely the stiffness of the cylinder material (dv3) and the fluid viscosity (dv4). Note that the example has been run with two sets of boundary conditions denoted by "a" and "b" in the table. The difference is that the cylinder is fixed vertically upstream in "a" and it is free to move in "b", see Fig. 1. This does not influence the obtained results, but it changes the spectral radius of the Jacobian, since fixing the cylinder in the front changes the smallest eigenvalue of the solid.

The results of the experiment are shown in Table 1. The basis for comparison is the number of matrix-vector multiplications needed for convergence. The convergence criterion was 10^{-5} on both error and solution update. As preconditioner in the Krylov methods and as the initial iteration matrix in BGM a full factorization of the approximate Jacobian is used. From the results it can be concluded that the stationary method always performs the worst of the methods, and for the case "b" boundary condition it does not converge. Therefore this method is not recommended for general use. The additional work involved in implementing BGM seems well worth the effort. Both the iterative Krylov solvers perform as well as BGM, however the effort required to implement the Krylov methods are substantially larger than what is required for BGM, assuming that the Krylov solvers are not already implemented for other purposes. Also note that the convergence criterion used for BGM is slightly tougher to fulfil than the one used for the Krylov methods. For the same residual norm the number of iterations differs with only one iteration. Of the two Krylov solvers the GMRES method gives the fastest convergence which will often be the case when a small number of iterations is used. The reason is that GMRES does not need to restart for the small number of iterations thus maintaining its minimization property.

The amount of time spent for the complete sensitivity analysis is around 2% of the analysis time for each design variable when a central difference is used in the matrix-vector product. This includes calculating the pseudo load with central differences. If forward differences are used the time would be approximately halved. The time complexity of the sensitivity analysis scales better than the analysis in terms of number of unknowns, where the most time consuming task for the sensitivity analysis is back substitution/preconditioning operations compared to matrix factorizations for the analysis. This has been verified numerically by using a sequence of successively refined discretizations.

CONCLUDING REMARKS

The two improved methods for performing iterative DSA on complex systems both perform better than the simple iterative method, both in terms of efficiency and robustness. The methods have also been successfully used on problems involving turbulence models on top of the coupled analysis, and they are easily extendible to other types of problems, as long as the underlying method for analysis is residual based. The resulting efficiency of the methods is as good as the efficiency of the residual evaluation.

THE CONCURRENT DESIGN OF MATERIALS AND STRUCTURES FOR CELLULAR MATERIALS ON EFFICIENCY OF HEAT DISSIPATION

Wang Bo, Cheng G.D.

Research Institute of Engineering Mechanics, Dalian University of Technology, Dalian 116023, PR China

Summary This paper describes an analytical model for heat transfer of cellular materials and presents a topology optimization method for optimal design of increasing its efficiency of heat dissipation per unit pumping power. Two classes of design variables, volume density and local aperture, are applied not only to optimize macro material distribution as well as the local material topology, so-called concurrent design, but also to avoid confused interpretation for the checkerboard patterns.

INTRODUCTION

It is expected that the function of materials would be applied as efficiently as possibly. However, how to define the so-called efficiency? As a rule, there are two methods. One is to reduce the volume of material as well as gain the indispensable function of structure; the other is to increase the expectation of function while the volume of material is given. All the mentioned above is referred to as light-efficiency. Two groups of researchers, material and mechanical, attain the aim of the game in different pathway that the former is a material design and the latter is a structural design. For example, the team of ultralight metal structures that leaded by Prof. A.G. Evans of Harvard, Prof. M.F. Ashby of Cambridge and Prof. L.J. Gibson of MIT presents several processes of investigation of truss-like materials[1] [2], which are typical material design. In these processes, a discretional local of structure is chose to investigate, which is means that every part of the structure is the same like the local, thus, the contribution of the structural topology for the function is neglected obviously. Topology optimization of two-dimension continuum structures was introduced in the literature by a very significant paper by Bendsøe and Kikuchi[3]. Over the last decade, the researchers have been mainly occupied with two different kinds of topology design processes: the Material or Microstructure Technique and the Geometrical or Macrostructure Technique, which discussed by Eschenauer and Olhoff[4]. The former is a material design because its design domain is a discretional cell just like the material researchers do (Sigmund, Torquato[5]), whereas the latter is a structural design, for the design domain is the structure, which would reduce the weight of structure obviously (Beckers[6], Diaz[7]). It is well known that all the formulations of topology optimization technique are based on the assumption of the material models, such as Hole-in-cell microstructure model and SIMP model. Moreover, the interpretation of intermediate "grey" density of material is often questioned for such models. So suspicion for these models crept into our minds, although Bendsøe and Sigmund can interpret black-white designs in many cases via micro mechanical model[8]. After all, any type of present topology optimization technique does not apply a kind of true models, and too refined micro mechanical models are unpractical for manufacture. In this paper, a true cellular material model based on the efficiency of heat dissipation is applied in the formulation of topology optimization. Since 1980, the cellular material, as a kind of lightweight materials, has been studied for the combinations of mechanical, thermal, acoustic and impact-absorb properties by more and more researchers. Lu.T.J. investigated a sandwich panels with two-dimensional metal cores that be used to carry structural load as well as dissipate heat trough solid conduction and forced convection[9] [10]. As the conclusion, regular hexagonal cores are found to provide the highest levels of heat dissipation. But it is impossible that to obtain the most optimal design by Lu.T.J's method just because the method is a material design mentioned above. In this work we employ numerical techniques for heat dissipation optimization design for two-dimensional cellular structures, which is a concurrent design of materials and structures.

PROBLEM DESCRIPTION

The prototype problem considered is shown in Fig. 1, where the cooling of structure is enhanced by forced convective flow across the honeycomb medium constrained by cylindrical surface Γ of length L. Each element i is all arranged such regular hexagonal cells which axial direction are parallel to the axial direction of cylindrical surface Γ and the direction of cooling fluid passes along. In this paper, our goal is to provide a numerical process (FEM) to discover arrangements of cells for the cross-section of the structure, a 2-dimisional design domain, that optimize the heat dissipate performance at minimum weight. For each element, cell wall length l_i and thickness t_i are showed in Fig. 1. The material topology of each element could be described by two indispensable variables, volume density ρ_i and local aperture a_i.

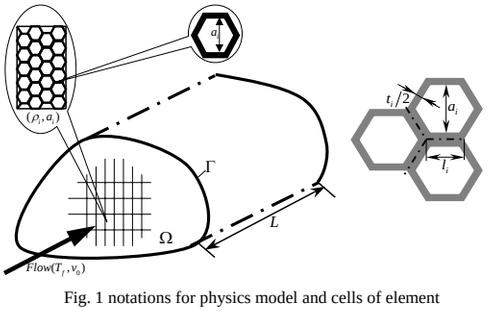


Fig. 1 notations for physics model and cells of element

where $l_i = (a_i + t_i)/\sqrt{3}$ and $\rho_i = \dfrac{l_i^2 - a_i^2/3}{l_i^2} = 1 - \left(\dfrac{a_i}{a_i + t_i}\right)^2$.

OPTIMIZATION MODEL

Objective function

The heat dissipation performance of the structure is commonly gauged by the ratio of total heat dissipated from the structure Q to the pumping power needed to force the fluid through ΔP. In this work, the objective function, the ratio is referred to as $-\Psi$, the higher this ratio, the better the structure performance.

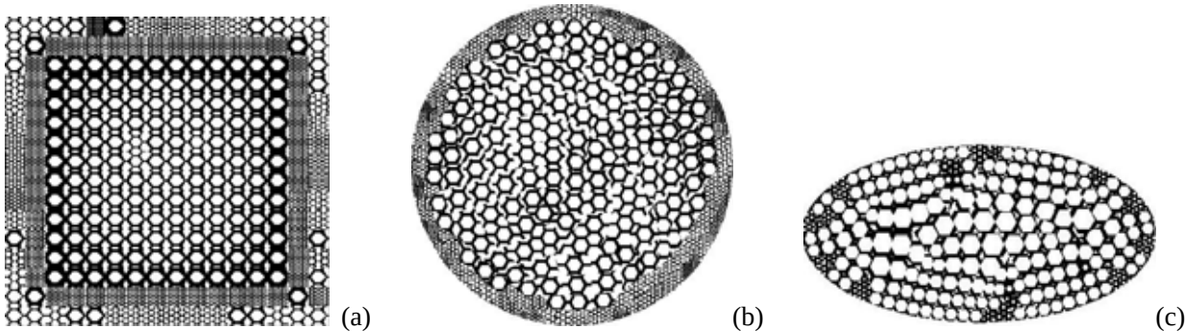
Constraints

A typical constraint in structure optimization problems is a volume constraint. The allowable volume is denoted by V. The design variable ρ_i has upper bound of one while the lower bound is $\underline{\rho}$ determined by manufacturing criteria of cellular material, which values is 0.03 in this paper. Similarly, the other design variable a_i also has upper bound, $\bar{a}$, and lower bound, $\underline{a}$, with $\underline{a} = 0.5mm$ and $\bar{a} = 15mm$ in this work. Banhart John[11] described in detail these manufacturing parameters mentioned above. The parameter of t_i denotes the thickness of cell by Fig.2. Obviously, there should be a lower bound $\underline{t}$ to be applied for it, and $\underline{t} = 0.5mm$ in this work. Otherwise, there should be indispensable number of cells in one element in order to ensure the validity and stability of algorithm. The number is referred to as H, with $\mathrm{H} = 1 \sim 4$ in this work, and in the model, s_i is an area of each element. The constraint equation, $K_T(\rho_i, a_i)T = R(\rho_i, a_i)$, denotes the thermal analysis.

$$\begin{aligned} \underset{\rho, a \in V}{Min} \quad & \Psi = -Q/\Delta P \\ S.t \quad & K_T(\rho_i, a_i)T = R(\rho_i, a_i) \\ & \int_\Omega \rho_i d\Omega = V \\ & a_i\left(1/\sqrt{1-\rho_i} - 1\right) \geq \underline{t} \\ & a_i \leq \frac{1}{\sqrt{\mathrm{H}}}\sqrt{\frac{2}{\sqrt{3}}}\sqrt{s_i(1-\rho_i)} \\ & 0 < \underline{\rho} \leq \rho_i \leq 1; \quad \underline{a} \leq a_i \leq \bar{a} \end{aligned}$$

NUMERICAL EXAMPLES

In order to improve the effective of heat dissipation of cellular material, it has tendency that the bigger density and smaller aperture foam are arranged in the domain of big temperature grads, while the smaller density and bigger aperture foam are arranged in the others. The smallest average temperature grads for the temperature field are gained for the final optimized material distribution.



(a) (b) (c)

Fig.2 the materials distribution for three kinds of cross-sections: the uniform properties of each example are given to be $v_0 = 10m/s$, $T_f = 283K(10^\circ C)$, $\rho_f = 1.247kg/m^3$, $L = 1m$ and $\mu_f = 14.16E-6m^2/s$. The thermal conductivity are given, $k_s = 200W/m \cdot K$ and $k_f = 0.02W/m \cdot K$. All the boundaries are maintained at constant temperature of $800K$ $(527^\circ C)$. The volumes of material are all 0.4.SLP (Sequential Linear Programming) scheme is applied for all examples: (a) a quadrate cross-section $0.4m \times 0.4m$ in size; (b) a circle cross-section as the diameter is $0.4m$; (c) a ellipse cross-section as the length of major axis is $0.2m$ and length of minor axis is $0.1m$

Reference

[1] A.G.Evans, J.W.Hutchinson, M.F.Ashby: Multifunctionality of cellular metal systems. Progress in Materials Science 43:171-221,1999.
[2] A.G.Evans: Lightweight Materials and Structures. MRS BULLETIN 790~797,2001.
[3] Bendsøe M.P., Kikuchi N.: Generating optimal topologies in structural design using homogenization method. Comp Meth Appl Mech Engng 71:197-224, 1988.
[4] H.A.Eschenauer, N.Olhoff: Topology optimization of continuum structures. Applied Mechanics Reviews 54:331-390,2001.
[5] O.Sigmund, S.Torquato:Design of materials with extreme thermal expansion using a three-phase topology optimization method. J. Mech. Phys. Solid 45:1037-1067,1997.
[6] M Beckers: Topology optimization using a dual method with discrete variables. Struct. Optim 17:14-24,1999.
[7] A Diaz, R Lipton :Optimal material layout for 3D elastic structures. Struct. Optim. 13:60-64,1997
[8] Bendsøe MP , Sigmund O: Material interpolation schemes in topology optimization, Arch. Appl. Mech. 69:635-645,1999.
[9] T.J.Lu: Heat transfer efficiency of metal honeycombs. Inter.J.of Heat and mass transfer 42:2031-2040, 1999.
[10] S.Gu, T.J.Lu, A.G.Evans: On the design of two-dimensional cellular metals for combined heat dissipation and structural load capacity. Inter.J.of Heat and mass transfer 44:2163-2175, 2001.
[11] Banhart John: Manufacture, characterisation and application of cellular metals and metal foams. Progress in Materials Science 46: 559-632,2001

EXTREME VALUE DISTRIBUTION AND RELIABILITY OF STOCHASTIC STRUCTURES

Jianbing Chen, Jie Li
Department of Building Engineering, Tongji University 200092 Shanghai, P R China

Summary An original method to compute the extreme value distribution and dynamic reliability of stochastic structures is presented. A virtual stochastic process, related to the extreme value of the dynamic responses of stochastic structures, is constructed firstly, such that the extreme value is the sectioned random variable. A joint probability density equation is then deduced with the probability density evolution method (PDEM), which has been developed in the recent years and can give the instantaneous probability density function (PDF) of the dynamic responses, and numerically solved to give the PDF of the extreme value. The dynamic reliability is then easily computed by a simple integration over the safe domain. The comparison with the Monte Carlo simulation shows that the proposed method is of accuracy and efficiency.

INTRODUCTION

In the past 3 decades, many endeavours have been devoted to analysis of stochastic structures involving random structural parameters. The developed approaches, including the statistical and non-statistical methods, say, the random perturbation method and the orthogonal polynomial expansion method, are mostly aiming at probability characteristics such as second order statistics. On the other hand, in dynamic reliability assessment of stochastic structures, the level-crossing process theory, based on the Rice formula and the assumptions of out-crossing events, is widely used. Nonetheless, the joint PDF needed in the Rice formula is usually unavailable by the aforementioned methods dealing with stochastic structures. Moreover, the assumptions of out-crossing events will lead to additional errors.

As is well known that the extreme value distribution (EVD) is of paramount importance [2]. However, there have been so far few, if any, reports on the EVD of the dynamic responses of stochastic structures. In the present paper, a virtual stochastic process is constructed related to the extreme value of the responses of stochastic structures. With the recent developed probability density evolution method [3, 4], a joint probability density evolution equation is deduced and solved to give the EVD. The dynamic reliability is then easily obtained by the integration over the safe domain.

THE PROBABILITY DENSITY EVOLUTION METHOD FOR DYNAMIC RESPONSE ANALYSIS

For a general multi-degree-of-freedom system

$$\boldsymbol{M}(\boldsymbol{\Theta})\ddot{\boldsymbol{X}}+\boldsymbol{C}(\boldsymbol{\Theta})\dot{\boldsymbol{X}}+\boldsymbol{K}(\boldsymbol{\Theta})\boldsymbol{X}=\boldsymbol{F}(\boldsymbol{\Theta},t) \tag{1}$$

where $\boldsymbol{M}$, $\boldsymbol{C}$, $\boldsymbol{K}$ are the n by n mass, damping and stiffness matrices, respectively, $\boldsymbol{F}$ is the n by 1 excitation vector, $\boldsymbol{\Theta}$ is the $n_{\boldsymbol{\Theta}}$ by 1 random parameters vector, involved in the structure and excitation, with the joint PDF $p_{\boldsymbol{\Theta}}(\boldsymbol{\theta})$.

If the structural dynamics problem in (1) is well posed, the responses, under the deterministic initial condition $\dot{\boldsymbol{X}}(0)=\dot{\boldsymbol{x}}_0$, $\boldsymbol{X}(0)=\boldsymbol{x}_0$, of the stochastic structure are existent, unique and dependent on $\boldsymbol{\Theta}$, namely, $\boldsymbol{X}=\boldsymbol{G}(\boldsymbol{\Theta},t)$. Its component form is $X_l=G_l(\boldsymbol{\Theta},t)$, where X_l is the l-th component of $\boldsymbol{X}$, G_l is the l-th component of $\boldsymbol{G}$.

Denote the joint PDF of $(X_l,\boldsymbol{\Theta})$ as $p_{X_l\boldsymbol{\Theta}}(x,\boldsymbol{\theta},t)$, then there is $p_{X_l\boldsymbol{\Theta}}(x,\boldsymbol{\theta},t)=p_{X_l|\boldsymbol{\Theta}}(x,t\,|\,\boldsymbol{\theta})p_{\boldsymbol{\Theta}}(\boldsymbol{\theta})=\delta(x-G_l(\boldsymbol{\theta},t))p_{\boldsymbol{\Theta}}(\boldsymbol{\theta})$, where $p_{X_l|\boldsymbol{\Theta}}(x,t\,|\,\boldsymbol{\theta})=\delta(x-G_l(\boldsymbol{\theta},t))$, is the conditional PDF, $\delta(\cdot)$ is the Dirac's function. Differentiate Eq.(2) in terms of t on both sides and rearrange it will lead to [3]

$$\partial p_{X_l\boldsymbol{\Theta}}(x,\boldsymbol{\theta},t)/\partial t+H_l(\boldsymbol{\theta},t)\cdot\partial p_{X_l\boldsymbol{\Theta}}(x,\boldsymbol{\theta},t)/\partial x=0 \tag{2}$$

where $H_l(\boldsymbol{\theta},t)=\partial G_l(\boldsymbol{\theta},t)/\partial t=\dot{X}_l$. The initial condition for Eq.(2) reads $p_{X_l\boldsymbol{\Theta}}(x,\boldsymbol{\theta},t)|_{t=0}=p_{\boldsymbol{\Theta}}(\boldsymbol{\theta})\delta(x-x_{l,0})$, where $x_{l,0}$ is the l-th component of $\boldsymbol{x}_0$.

Eq.(2) can be numerically solved combining the deterministic time-integration of Eq.(1) and the finite difference method with a TVD schemes, for the detail, see [4]. Then the PDF of $X_l(t)$, denoted as $p_{X_l}(x,t)$, can be obtained by $p_{X_l}(x,t)=\int_{\Omega_{\boldsymbol{\Theta}}}p_{X_l\boldsymbol{\Theta}}(x,\boldsymbol{\theta},t)\mathrm{d}\boldsymbol{\theta}$, where $\Omega_{\boldsymbol{\Theta}}$ is the distribution domain of $\boldsymbol{\Theta}$.

THE EXTREME VALUE DISTRIBUTION OF STOCHASTIC STRUCTURAL RESPONSES

With the analogous idea, the EVD of the stochastic structural responses can be obtained. For the well-posed problem (1), the extreme value of the response is existent, unique and dependent on $\boldsymbol{\Theta}$, i.e.,

$$Z_l=\sup_{\tau\in[0,T]}X_l(\tau)=W_l(\boldsymbol{\Theta},T) \tag{3}$$

Construct a virtual stochastic process $Q_l(\tau)$, $Q_l(\tau)=Z_l\cdot\tau=W_l(\boldsymbol{\Theta},T)\cdot\tau$.

It is obvious that Z_l is the sectioned random variable of $Q_l(\tau)$, i.e., $Z_l = Q_l(\tau)|_{\tau=1}$.
Similar to Eq.(2), denote the joint PDF of $(Q_l, \boldsymbol{\Theta})$ as $p_{Q_l\boldsymbol{\Theta}}(q,\boldsymbol{\theta},\tau)$, we have

$$\partial p_{Q_l\boldsymbol{\Theta}}(q,\boldsymbol{\theta},\tau)/\partial\tau + W_l(\boldsymbol{\theta},T)\cdot\partial p_{Q_l\boldsymbol{\Theta}}(q,\boldsymbol{\theta},\tau)/\partial q = 0 \tag{4}$$

with the initial condition $p_{Q_l\boldsymbol{\Theta}}(q,\boldsymbol{\theta},\tau)|_{\tau=0} = \delta(q)p_{\boldsymbol{\Theta}}(\boldsymbol{\theta})$. Numerically solving Eq.(4) and integration will give the PDF of $Q_l(\tau)$, i.e., $p_{Q_l}(q,\tau) = \int_{\Omega_{\boldsymbol{\Theta}}} p_{Q_l\boldsymbol{\Theta}}(q,\boldsymbol{\theta},\tau)\mathrm{d}\boldsymbol{\theta}$.

THE DYNAMIC RELIABILITY ASSESSEMENT

For the first passage problem, the dynamic reliability defined given by $R = P\{X_l(\tau)\in\Omega_s, \tau\in[0,T]\}$, where $P\{\cdot\}$ is the probability of the random event, Ω_s is the safe domain. It is equivalent to

$$R = P\{\sup_{\tau\in[0,T]} X_l(\tau)\in\Omega_s\} = P\{Z_l\in\Omega_s\} = \int_{\Omega_s} p_{Q_l}(x,\tau=1)\mathrm{d}x \tag{5}$$

When the boundary is random, the dynamic reliability is $R = \int_{\Omega_{x_B}}\left(\int_{\Omega_s(x_B)} p_{Q_l}(x,\tau=1)\mathrm{d}x\right)p_{x_B}(y)\mathrm{d}y$, in which $p_{x_B}(\cdot)$ is the PDF of x_B, Ω_{x_B} is the distribution domain of x_B, $\Omega_s(x_B)$ means the safe domain is related to x_B.

NUMERICAL EXAMPLES

An 8-story shear-story frame (shown in Fig.1) with random stiffness, subject to El Centro earthquake with random peak ground acceleration (PGA) is studied. The masses of each story are 0.5, 1.1, 1.1, 1.0, 1.1, 1.1, 1.3, 1.2×10^5kg with the height h_1=4.0m, h=3.0m, the sections of the columns 500×500mm^2. The elastic modulus of the column is random with the mean 3.0×10^{10}Pa. $\boldsymbol{C}=a\boldsymbol{M}+b\boldsymbol{K}$, a=0.01Hz, b=0.005sec. The random parameters obey the truncated normal distribution with the coefficient of variation (COV) 0.2 for stiffness and 0.25 for PGA. The mean of the PGA=2.0m/s^2.
The dynamic reliability is defined by the top displacement. Part of the results are listed in Table 1, Table 2 and shown in Fig.2 and Fig.3. In Table 2 the threshold is assumed to be lognormal distributed with the mean 0.15 m and different COV, the EVD in Fig.2 and Fig.3 is the maximum absolute value of the top displacement, Fig.2 shows the computed EVD and the normal and lognormal distribution with the same second statistics and the Rayleigh distribution with the distribution parameter equal to the mean of the EVD. The comparison between the proposed method (PDEM) and the Monte Carlo simulation (MCM) shows that the proposed method is of accuracy. On the other hand, the proposed method is much time saving. Only 174 sec is needed with the proposed method while 13267 sec is needed with MCM.

Table 1 The dynamic reliability for different thresholds

Threshold	0.02 m	0.05 m	0.08 m	0.12 m	0.15 m
MCM	0.00391	0.24629	0.76743	0.97338	0.99033
PDEM	0.00456	0.25292	0.76761	0.97334	0.99010

Table 2 The dynamic reliability when the threshold is random

COV	5%	10%	20%	30%
MCM	0.98961	0.98871	0.98129	0.96652
PDEM	0.98979	0.98893	0.98319	0.96748

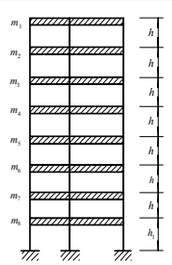


Fig.1 The 8-story frame

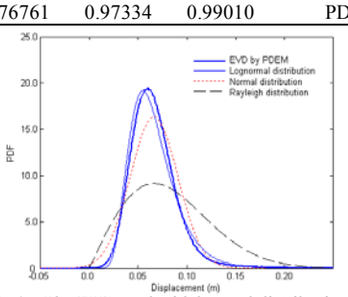


Fig.2 The EVD and widely used distributions

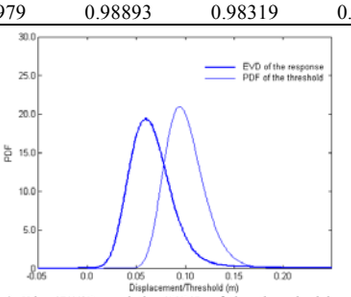


Fig.3 The EVD and the PDF of the threshold

CONCLUSIONS

An original method, based on the probability density evolution method, is proposed to compute the EVD. Naturally, the dynamic reliability is then easily obtained by the integration over the safe domain. The comparison with the Monte Carlo simulation demonstrates that the proposed method is of accuracy and efficiency.

References

[1] Schueller, G. I. (ed.): A state-of-the-art report on computational stochastic mechanics. *Probabilistic Engineering Mechanics* 12(**4**):198-321,1997
[2] Ang, A. H-S., Tang, W. H.: Probability concepts in engineering planning and design (Vol.2). John Wiley & Sons, 1984
[3] Li, J., Chen, J. B.: Probability density evolution method for dynamic response analysis of stochastic structures. Zhu WQ, Cai GQ & Zhang RC (ed.): Advances in Stochastic Structural Dynamics-SSD03, 309-316, May 26-28th, Hangzhou, China. Boca Raton: CRC Press, 2003
[4] Chen, J. B., Li, J.: Dynamic reliability analysis of stochastic structures. Wu ZS, Abe M (ed.) Proceedings of First International Conference on Structural Health Monitoring and Intelligent Infrastructure, 771-776, Nov.13-15th, Tokyo, Japan. A.A.Balkema Publishers, Tokyo, 2003

EXPERIMENTAL STUDY OF NONLINEAR ENERGY PUMPING

D.Michael McFarland[*], Lawrence Bergman [*], Alexander F. Vakakis [**]
[*]*University of Illinois, Dept. of Aerospace Engineering, 104 S. Wright Str., Urbana, IL 61801, U.S.A.*
[**]*National Technical University of Athens, P.O.Box 64042, GR-157 10 Zografos, Athens, Greece and University of Illinois (adjunct)*

Summary Experimental verification of passive nonlinear energy pumping in a system of coupled oscillators with an essentially nonlinear end attachment is carried out. It is shown that passive transfer of energy (energy pumping) from the linear oscillators to the nonlinear attachment can take place. Agreement between simulated and experimental results was observed, in spite of the strongly nonlinear and transient dynamics of the system considered. The experiments bear out earlier predictions that a significant fraction of the energy introduced directly to a linear structure by an external impulsive (broadband) load can be transferred (pumped) to an essentially nonlinear attachment, and dissipated there locally without spreading back to the system. In addition, the reported experimental results confirm that (a) nonlinear energy pumping occurs above a threshold of the input energy, and (b) resonance capture cascades occur where the nonlinear attachment resonates in sequence with a number of linear modes.

INTRODUCTION

This work provides the first experimental verification of the nonlinear energy pumping phenomenon in a system of two coupled oscillators. The system comprises a damped linear oscillator coupled to a damped nonlinear energy sink (NES) with essential (nonlinearizable) cubic stiffness nonlinearity. Transient (broadband) responses of the system are considered, caused by impulsive excitations. It was shown in earlier works [1,2] that one can separate the dynamics of this system into 'fast' and 'slow' components; in particular, the 'slow' dynamics governs the slowly-varying envelopes (modulation) of the oscillator responses, whereas the 'fast' dynamics describes the fast oscillations that take place inside the envelopes. The fact that the NES interacts with a single linear mode, and that energy pumping takes place in the neighborhood of a 1:1 resonant manifold (i.e.., when the instantaneous frequency of the NES is in the neighborhood of the eigenfrequency of the linear mode), implies that in the experiments considered herein the energy pumping will be dominated by a single fast frequency, namely, one close to the eigenfrequency of the linear subsystem.

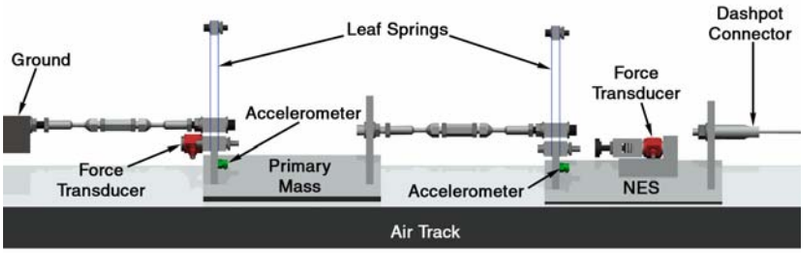


Figure 1. Experimental fixture for nonlinear energy pumping.

EXPERIMENTAL FIXTURE

The experimental fixture of Figure 1 consists of two single-degree-of-freedom oscillators (the 'subsystems') connected by means of a linear stiffness. The left oscillator (the linear subsystem) is grounded by means of a linear spring, whereas the right one (the nonlinear energy sink) is grounded by means of a nonlinear spring with essential cubic nonlinearity. To dissipate the pumped energy, a grounded damper exists in the NES. Transient (shock) excitation of the system is provided by means of a rod that impacts elastically with the left mass. The equations of motion are:

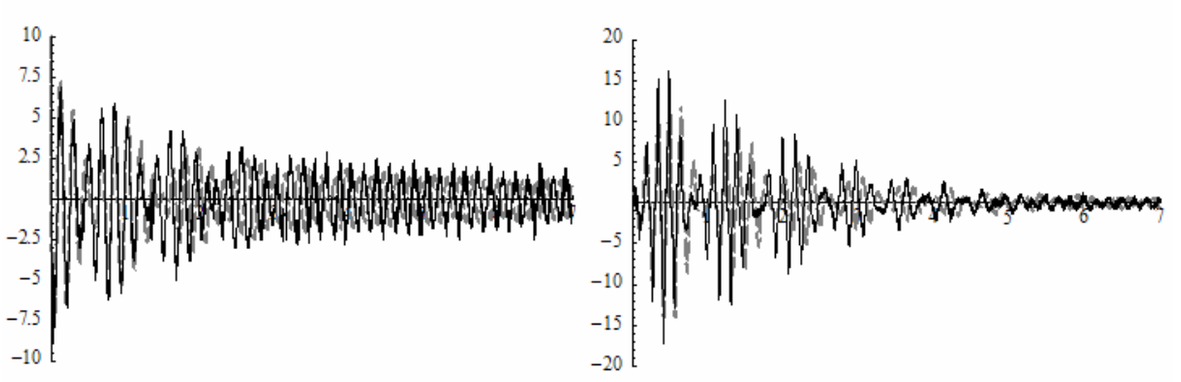
$$\begin{aligned} M\ddot{y} + Ky + \varepsilon\lambda\dot{y} + \varepsilon(y - v) &= F(t) \\ m\ddot{v} + \varepsilon c\dot{v} + Cv^3 - \varepsilon(y - v) &= 0 \end{aligned} \tag{1}$$

with zero initial conditions. Assuming that $F(t)$ is an impulsive (broadband) excitation of finite duration, it is of interest to study the transient (damped and essentially nonlinear) dynamics. Hence, the aim of the experimental work is to show that broadband energy initially imparted to the linear subsystem is passively 'pumped' to the NES where it is confined and dissipates without 'spreading' back to the linear subsystem. Since the essential cubic nonlinearity plays an important role in the realization of the nonlinear energy pumping phenomenon, a discussion of its construction is appropriate. Essential (nonlinearizable) cubic nonlinearity can be achieved by different structural configurations. In this

particular experimental fixture, the essential stiffness nonlinearity was realized by adopting the configuration of a thin rod (piano wire) with no pretension clamped at both of its ends, performing transverse vibrations at its center. The geometric nonlinearity of the system considered produces, to the leading order of approximation, an essential cubic stiffness nonlinearity; moreover, the corrective terms as the displacement increases are of higher order and do not produce a linear term in the stiffness characteristic. If, however, the thin wire is preloaded, a highly undesirable linear term, proportional to the initial preload tension, appears, and the resulting stiffness becomes linearizable. Hence, special care is given to minimize pretension in the wire.

RESULTS AND COMPARISONS TO SIMULATIONS

In Figure 2 we present experimental results for a case when an impulsive force of approximately 6.25msec in duration is applied to the linear subsystem with the entire system initially at rest. This forcing level is typical of the strong excitation that is required to induce nonlinear energy pumping in the system under consideration. A comparison between the experimental and theoretical acceleration time series of the two subsystems is depicted, from which very good agreement is noted. Such agreement is typical of what was observed for all the experimental trials. Nonlinear energy pumping is noted, especially at early times of the response (in the period 0 – 4 sec) when the energy of the system is relatively high and the nonlinear effects are more profound. One notes that, in the energy pumping regime 0 – 4 sec, the NES oscillates with a dominant 'fast' frequency, which is approximately equal to the eigenfrequency of the linear subsystem. This is a manifestation of resonance capture of the dynamics in the neighborhood of a 1:1 resonance manifold of the system. A quantitative measure of energy pumping in the system is performed by computing the percentage of total input energy that is dissipated at the dashpot of the NES. In this case, eventually, 88.5% of the total input energy is absorbed and dissipated at the NES, a result that demonstrates that the NES is an effective mechanism for passively absorbing and dissipating a significant portion of input energy.



(a) (b)

Figure 2. Nonlinear energy pumping: Experimental ——— and numerical — — — acceleration time series of (a) the linear (directly excited) subsystem and (b) the NES.

CONCLUSIONS

The experiments bear out earlier predictions that a significant fraction of the energy introduced directly to the linear substructure by an external impulsive load can be pumped to the NES and dissipated there locally without spreading back to the linear system. Further trials, for which data are not shown herein, proved passive nonlinear energy pumping in this system to be robust, repeatable, and fully predictable.

Acknowledgments

This work was supported in part by AFOSR Contract 00-AF-B/V-0813 (Dr. Dean Mook, Grant Monitor), and ONR Contract N00014-00-1-0187 (Dr. Louise Couchman, Grant Monitor). Mr. Jeff Kowtko, assisted with the experiments.

References

[1] Vakakis, A.F., and Gendelman, O., 2001, "Energy 'Pumping' in Nonlinear Mechanical Oscillators II: Resonance Capture," Journal of Applied Mechanics, Vol. 68, No. 1, pp. 42-48.

[2] Vakakis, A.F., Manevitch, L.I., Gendelman, O., and Bergman L., 2003, "Dynamics of Linear Discrete Systems Connected to Local Essentially Nonlinear Attachments," Journal of Sound and Vibration, Vol. 264, pp. 559-577.

NONLINEAR VIBRATIONS OF JEFFCOTT ROTOR WITH PRELOADED SNUBBER RING

Evgueni V. Karpenko, Marian Wiercigroch, and Ekaterina E. Pavlovskaia
Centre for Applied Dynamics Research School of Engineering and Physical Sciences, University of Aberdeen King's College, Aberdeen AB24 3UE, UK

Summary Nonlinear vibrations of a Jeffcott rotor system with a preloaded snubber ring subjected to out of balance excitation are investigated theoretically and experimentally. The details of the design, experimental set-up and mathematical modelling of the system will be presented. The rotor makes intermittent contacts with the preloaded snubber ring and it can produce five different contact regimes which are determined using the principle of the minimum elastic energy in the springs supporting the snubber ring. As a result this rotor system is modelled as a nonlinear piecewise smooth dynamical system, for which a suite of approximate methods has been devised [1]. Chaotic behaviour and co-existence of attractors have been found [2]. A comparison between the theoretical and experimental results made by using bifurcation diagrams, phase portraits and Poincaré maps shows a good correlation between theory and experiments.

JEFFCOTT ROTOR WITH PRELOADED SNUBBER RING

Dynamics of the rotor system with a preloaded snubber ring shown in Figure 1(a) is considered. The experimental rig comprises essentially two main parts, a rigid rotor, which is visco-elastically supported by four flexural rods, and excited by the out-of-balance mass, and a snubber ring, which is also elastically supporting using four compression springs. The rotor assembly consists of a mild steel rotor, running in two angular bearings. Holes are drilled and tapped in both inner sleeves for the addition of imbalance weights. A pair of dampers is attached to the rotor, one in each direction, to provide the system with heavier damping. Four flexural rods are symmetrically clamped at one end to the outer bearing housing and at the other to a large support block. The discontinuous stiffness is provided by a ring to which four compression springs, of much greater stiffness than that of the flexural rods, are symmetrically secured. The rotor runs inside the ring, with a radial clearance between the ring and the outer bearing housing.

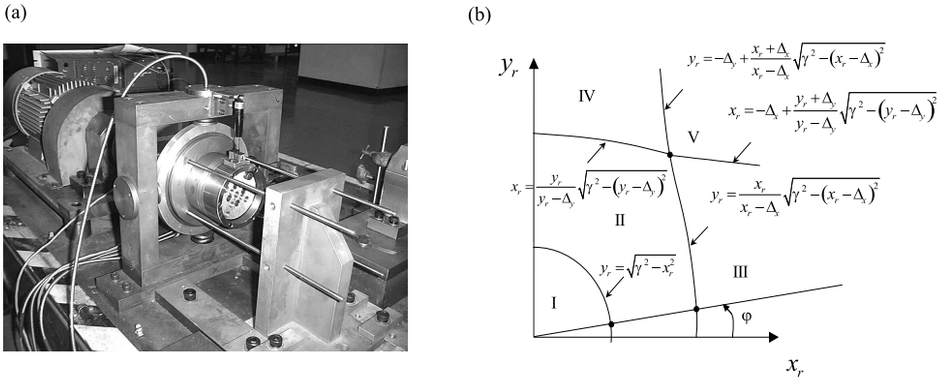


Figure 1. (a) Experimental rig of the investigated rotor system; (b) regions of operation and their boundaries for the first quadrant of (x_r, y_r) plane.

The excitation is provided by an out-of-balance rotating mass $m\rho$. During operation the rotor of mass M makes intermittent contact with the snubber ring. It is assumed that contact is non-impulsive and that the friction between the snubber ring and the rotor is neglected. Also it is assumed that the snubber ring itself is massless. The stiffness and the viscous damping of the snubber ring are equal to k_s and c_s. The stiffness and the damping of the rotor are respectively k_r and c_r. The springs supporting the snubber ring are preloaded by Δ_x in horizontal and Δ_y in vertical directions respectively. There is a gap γ between the rotor and the snubber ring. Also in the initial position, the centre of the rotor is displaced from the centre of the snubber ring by the eccentricity vector $\boldsymbol{\varepsilon}$.

The system can operate in one of two following regimes: (a) no contact and (b) contact between the rotor and the snubber ring [3]. In the latter case, existence of the preloading makes the dynamics of the system more complicated as the force acting from the snubber ring on the rotor depends on whether the displacement of the snubber ring exceeds the preloadings (in one or both directions) or not. Thus the following unique regimes of the system motion can be distinguished: (I) No contact between rotor and snubber ring; (II) Contact between the rotor and the snubber ring, where the both displacements of the snubber ring are smaller than the preloadings, i.e. $|x_s| \leq \Delta_x$ and $|y_s| \leq \Delta_y$; (III) Contact between the rotor and the snubber ring, where the displacement of the snubber ring in the horizontal direction is larger than the preloading, $|x_s| > \Delta_x$, and in the vertical direction is smaller than preloading, $|y_s| \leq \Delta_y$; (IV) Contact between the rotor and the snubber ring, where the displacement of the snubber ring in the horizontal direction is smaller than the preloading, $|x_s| \leq \Delta_x$, and in the vertical direction is larger than preloading, $|y_s| > \Delta_y$; (V) Contact between the rotor and the snubber ring, where the displacements of the snubber ring are larger than the preloadings, i.e. $|x_s| > \Delta_x$ and $|y_s| > \Delta_y$.

MATHEMATICAL MODELLING AND EXPERIMENTAL VERIFICATION

For no contact situation the distance between the centres of the rotor and the snubber ring, $D = \sqrt{(x_r - x_s)^2 + (y_r - y_s)^2}$ is smaller than the gap, γ, that is $D \leq \gamma$. Therefore equations of motion for the rotor and the snubber ring are

$$\begin{aligned} &M\ddot{x}_r + c_r\dot{x}_r + k_r(x_r - \varepsilon_x) = m\rho\Omega^2\cos(\varphi_0 + \Omega t), \\ &M\ddot{y}_r + c_r\dot{y}_r + k_r(y_r - \varepsilon_y) = m\rho\Omega^2\sin(\varphi_0 + \Omega t), \\ &c_s\dot{x}_s + k_s x_s = 0, \quad c_s\dot{y}_s + k_s y_s = 0, \end{aligned} \tag{1}$$

where φ_0 is the initial phase shift and Ω is shaft angular velocity.

Once $D = \gamma$, the rotor hits the snubber ring and one or more of the contact regimes may occur, for which the equations of motion can be written as

$$\begin{aligned} &M\ddot{x}_r + c_r\dot{x}_r + k_r(x_r - \varepsilon_x) + F_{s_x} = m\rho\Omega^2\cos(\varphi_0 + \Omega t), \\ &M\ddot{y}_r + c_r\dot{y}_r + k_r(y_r - \varepsilon_y) + F_{s_y} = m\rho\Omega^2\sin(\varphi_0 + \Omega t), \\ &x_s = x_s(x_r, y_r), \quad y_s = y_s(x_r, y_r). \end{aligned} \tag{2}$$

Here the force in the snubber ring $\mathbf{F}_s = (F_{s_x}, F_{s_y})$ varies for different contact regimes. The unknown $x_s(x_r, y_r)$ and $y_s(x_r, y_r)$ give the current location of the snubber ring as a function of the current location of the rotor.

When the rotor and the snubber ring are in contact, the distance between their centres remains constant and equal to the gap, so $(x_r - x_s)^2 + (y_r - y_s)^2 = \gamma^2$. In order to find the location of the snubber ring centre when it moves being in contact with the rotor, the following approach has been adopted.

The problem of finding the current location of the snubber ring has been reduced to finding the minimum of the energy E with the constraint condition $D = \gamma$. This can be done using the Lagrange multipliers method by constructing the Lagrange function $L = E + \lambda\delta$, where λ is Lagrange multiplier, E is the elastic energy of the snubber ring, δ is the constraint function $\delta = (x_r - x_s)^2 + (y_r - y_s)^2 - \gamma^2$. As E and δ are the continuous and differentiable functions, the current position of the snubber ring (x_s and y_s) as a function of the of the current rotor position (x_r and y_r) can be determined from the conditions of the existence of extremum [3]. This allows to analytically describe the location of the snubber ring and to find the borders between different regimes of operation as shown in Figure 1(b).

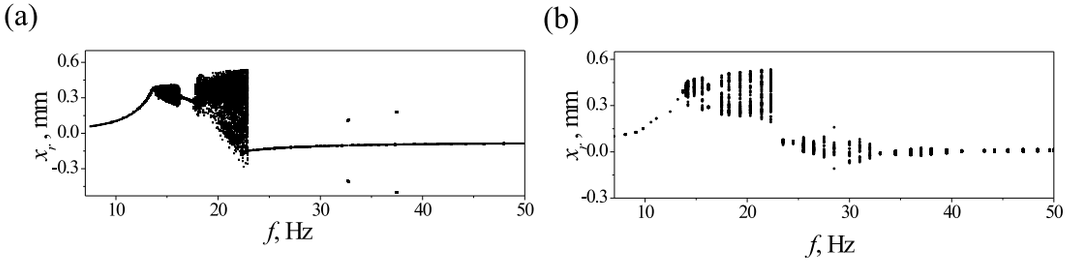


Figure 2. A comparison between (a) theoretical and (b) experimental bifurcation diagrams constructed for varying frequency keeping viscous damping of the snubber ring at $c_s = 3.5\ kg/sec$.

During experiments the response of the rotor system was monitored by noncontacting eddy probes. Two probes were used for the rotor and another two for the snubber ring. Subsequently, the displacement and forcing frequency signals were collected by a data acquisition system LabView, with a purpose-written program controlling rate of sampling, number of samples, calibration and computation of the rotational frequency. The relative velocities of the rotor and the snubber ring $\dot{x}_r$, $\dot{y}_r$, $\dot{x}_s$ and $\dot{y}_s$ were calculated using the LabView digital differentiation facility applied to the output signals from eddy current probes. The data was collated on the computer, where it was scaled, plotted and analysed in the form of Poincaré maps and bifurcation diagrams. A comparison between theoretical and experimental bifurcation diagrams depicted in Figure 2 shows a good correlation [4].

References

[1] E.V. Karpenko, M. Wiercigroch, E.E. Pavlovskaia and M.P. Cartmell: Piecewise approximate analytical solutions for a Jeffcott rotor with a snubber ring, *International Journal of Mechanical Sciences* **44**(3): 475-488, 2002.

[2] E.V. Karpenko, M. Wiercigroch and M.P. Cartmell: Regular and chaotic dynamics of a discontinuously nonlinear rotor system, *Chaos, Solitons and Fractals* **13**(6): 1231-1242, 2002.

[3] E.E. Pavlovskaia, E.V. Karpenko and M. Wiercigroch: Nonlinear dynamic interactions of Jeffcott rotor with preloaded snubber ring, *Journal of Sound and Vibration*, in press, 2004.

[4] E.V. Karpenko, M. Wiercigroch, and R.D. Neilson: Experimental verification of piecewise nonlinear Jeffcott rotor model with preloaded snubber ring, *International Journal of Rotating Machinary*, accepted, 2004.

NON-LINEAR STOCHASTIC VIBRATION PROBLEMS FOR THE PLATES WITH TIME-DEPENDENT PARAMETERS

Victor Z. Gristchak*, Valentin V. Lysenko*
*ZSU, Department of Applied Mathematics, Zhukovskogo 66, UA 69-600, Zaporizhzhja, Ukraine, ID 10656, grk@zsu.zp.ua

Extended Summary

The correlation analysis of behaviour of non-linear systems with time-depended parameters at random loading deals with the significant difficulties in comparison with an analysis of linear systems with constant parameters.

In this paper the new hybrid asymptotic technique that combines the perturbation, WKBJ methods and Hamilton variational principle for the solution of non-linear stochastic problem for the plates with time-dependent parameters is presented. In order to describe the hybrid technique in detail, let us consider non-linear differential equation of second order with time-dependent coefficients, which contains perturbation parameters (usually large or small) and which is used while solving a number of applied problems:

$$f''(t)+\omega_0^2\cdot\varphi(t)f(t)+\alpha\cdot\left(P(t)f^2(t)+Q(t)f^3(t)\right)=\gamma(t), \qquad (1)$$

where ω_0, α – are parameters of frequency of linear system and degree of non-linearity. If the plate is compressed along one direction by static loads and as external force a time-dependent distributed cross loading is enclosed to a plate, then in the equation (1)

$$\omega_0^2=\frac{\pi^4m^4\left[1+\left(\frac{n\lambda}{m}\right)^2\right]^2}{12\lambda^2(1-\mu^2)}\left(\frac{vh_0}{ab}\right)^2,\quad \alpha=\frac{h_0}{a},$$

where: $v=\sqrt{E_0/\rho}$ – is a speed of longitudinal wave propagation in a material of a plate; *f* – is a function of a displacement; $\lambda=\frac{a}{b}$. Let's search for the analytical solution of the initial equation (1) on finite interval of time $[t_0,T]$. The function *f* is subjected to some initial conditions.

At step one (external asymptotic), we use the perturbation method to find an approximate solution for *f* in the form

$$f(t)=\sum_{j=0}^{\infty}\alpha^j f_j(t), \qquad (2)$$

where $f_j(t)$ (*j* = 0, 1, ...) – unknown functions of time. We have to substitute the expansion (2) into equation (1) and equate the coefficients of the same powers of α in the resulting equations:

$$\begin{aligned} &L_0 f_0(t)=\gamma(t),\\ &L_0 f_1(t)=-\left(P(t)f_0^2(t)+Q(t)f_0^3(t)\right),\\ &\ldots, \end{aligned} \qquad (3)$$

where $L_0=\frac{\partial^2}{\partial t^2}+\omega_0^2\varphi(t)$ – is a linear differential operator.

At step two (internal asymptotic), we have to find the approached solution of the linear homogeneous differential equation like

$$L_0 f_{0\,Hom}(t)=0 \qquad (4)$$

with the help of WKBJ method. By replacement $f_{0\,Hom}(t)=\exp\left(\int_{t_0}^{t}\psi(\theta)d\theta\right)$, we shall receive the differential equation concerning unknown function of time $\psi(t)$:

$$\varepsilon^2(\psi'(t)+\psi^2(t))=-\varphi(t), \qquad (5)$$

where $\varepsilon = 1/\omega_0$. According to a WKBJ method the approached solution of the equation (5) we shall present as

$$\psi(t) = \sum_{k=0}^{\infty} \varepsilon^{k-1} \psi_k(t), \tag{6}$$

where $\psi_k(t)$ – is an unknown function of time (k = 0, 1, ...). We have to substitute the expansion (6) into equation (5), equate the coefficients with the same order of ε in the resulting equation and solve a sequence of equations for each of the unknown $\psi_k(t)$ (k = 0, 1, ...).

At step three (internal hybrid solution) of the hybrid method, we use a subset of functions $\psi_k(t)$ (k = 0, 1, ...) of WKBJ-expansion (6), determined at step two, in a WKBJ type expansion, named as hybrid:

$$\psi_H(t) = \sum_{k=0}^{M-1} \lambda_k \psi_k(t). \tag{7}$$

Here the M – is the order of internal approach; λ_k (k = 0, ... , M – 1) represents new unknown "amplitudes" of known functions $\psi_k(t)$ (k = 0, ..., M – 1). Then, it is possible to obtain the hybrid solution of the linear homogeneous differential equation (4) and hybrid solutions of each equation of system (3).

At step four (external hybrid solution) we use a subset of hybrid functions $f_{j_H}(t)$ (j = 0, 1, ...) of perturbation-expansion (2), in a perturbation type expansion, named as hybrid too:

$$f_H(t) = f_{0_H}(t) + \sum_{j=1}^{N-1} \delta_j f_{j_H}(t). \tag{8}$$

Here the N – is the order of external approach; δ_j (j = 1, ... , N – 1) represent unknown parameters. The principle of "optimal" determining of the λ_k (k = 0, ..., M – 1) and δ_j (j = 0, ..., N – 1) is based on the Hamilton variational principle

$$\int_{t_0}^{T} (P + K - A)dt \to 0, \tag{9}$$

where P – is a potential energy, K – is a kinematical energy of the plate and A – is a work of internal and external forces.

For the solution of non-linear stochastic vibration of plates the moment functions of output process are determined by averaging a perturbation-expansion (8). So, for second-order moment function we obtain:

$$\left\langle f_H(t_1) f_H(t_2) \right\rangle = \left\langle f_{0_H}(t_1) f_{0_H}(t_2) \right\rangle + \delta_1 \left\langle f_{0_H}(t_1) f_{1_H}(t_2) + f_{0_H}(t_2) f_{1_H}(t_1) \right\rangle + \ldots \tag{10}$$

In order to reduce higher order moment function of the zero-order approximation $f_{0_H}(t_1)$ we shall use expressions binding higher order moment functions with lower ones, which are correct for normal processes (input and output processes are assumed to be centralized). And then, it is possible to obtain a hybrid correlation function of a displacement of the plate.

It is shown, that hybrid results are more accurate than the classical asymptotic perturbation-WKBJ-solution.

References

[1] Noor A.K., Peters J.M.: Reduced basis technique for nonlinear analysis of structures. *Proc. of the AIAA-ASME-ASCE-AHS 20th Structures*, Structural Dynamics and Materials conference, St. Louis, USA, 1979. – P. 116 – 126.

[2] Geer J.F., Andersen C.M.: A hybrid peturbation-Galerkin technique for differential equations containing a parameter. *Applied Mechanics Reviews*. – 1989. – ¹42(11). – P. S69-S77.

[3] Gristchak, V.Z., Dmitrijeva, Ye.M.: A hybrid WKB-Galerkin method and its application. *Technishe Mechanik*, 1995. – ¹3. – Ð. 281-294.

[4] Gerasimov T.S., Lysenko V.V.: A hybrid approximate solution technique and modal expansion approach with application to forced vibrations of non-homogeneous shells and plates. *Proc of the 7th Conference "Shells structures, theory and applications"*, Gdansk-Jurata, Poland, 2002. – P. 85-86.

A MULTI-STEP TRANSVERSAL LINEARIZATION METHOD IN NONLINEAR DYNAMICS

D. Roy
Associate Professor, Structures Lab, Department of Civil Engineering, Indian Institute of Science, Bangalore 560012, INDIA; E-mail: royd@civil.iisc.ernet.in

THE EXTENDED SUMMARY

An implicit family of semi-analytical integration methods, referred to as multi-step transversal linearization (MTL), is proposed for accurate, efficient and numerically stable integration of non-linear oscillators of interest in structural dynamics. The presently developed method is a multi-step extension and further generalization of the locally transversal linearization (LTL) method proposed earlier by the author (Roy 2001). The MTL-based linearization is achieved through a non-unique replacement of the nonlinear part of the vector field by a conditionally linear interpolating expansion of known accuracy, whose coefficients contain the discretized state variables defined at a set of grid points. For further illustration, consider the following system of *n* second order non-linear ordinary differential equations (ODE-s):

$$\{\ddot{X}\}+[C]\{\dot{X}\}+[K]\{X\}=\{Q(\{X\},\{\dot{X}\},t)\}+\{F(t)\} \quad (1)$$

In the above equations, $[C]$ and $[K]$ are the damping and stiffness matrices respectively, $Q(X,\dot{X},t)=\{Q^{(j)}(X,\dot{X},t)\mid j=1,...,n\}$ is a non-linear vector function of the first two arguments, $\{F(t)\}$ is the externally applied force vector and $\{X\}$, $\{\dot{X}\}\in\Re^n$ are respectively the displacement and velocity vectors. Let the initial condition vector be denoted as $\{X(t_0)\}\underline{\underline{\Delta}}\{X_0\}$ and $\{\dot{X}(t_0)\}\underline{\underline{\Delta}}\{\dot{X}_0\}$. Now, let $I_1=[t_0,T_1\mid T_1>t_0)$ be a sub-interval of the time axis and let it be ordered into p smaller intervals as $t_0<t_1<\ldots<t_p=T_1$. The time step size $h_i=t_{i+1}-t_i=h$ is presently taken to be constant for convenience of further discussion. It is intended to derive the linearized ODE-s such that the linearized and non-linear vector fields remain identical at all the $(p+1)$ grid points, viz. $t_0,t_1,.....,t_p$. Let the non-linear and linearized flows, as parameterized by time t, be denoted by ϕ_t and $\bar{\phi}_t$ respectively. The non-linear flow, ϕ_t may be topologically viewed as a $C^k(k\geq 0)$ diffeomorphism on the associated (compact) manifold M: $\phi_t(\{X\}):M\times R\rightarrow M$ and $\phi_{t_0}\underline{\underline{\Delta}}\phi_0=id_M$, $\phi_{t_0}\ {}^0\phi_{h_1}\ {}^0\phi_{h_2}.....{}^0\phi_{h_p}=\phi_{t_p}$ provided that the vector field is autonomous (an *n*-dimensional non-autonomous field is equivalent to an *n*+1-dimensional autonomous field). The set of all such C^k diffeomorphisms $\phi_t(X)$, under the operation of composition '$\circ$' form a group, G_ϕ. Such compositions may be interpreted via *R*- and *Z*-group actions, defined as:

$$R\rightarrow G_\phi: t\rightarrow\phi_t,\quad Z\rightarrow G_\phi: j\rightarrow\phi_{t_j}\ (R \text{ is the real line and } Z \text{ is the set of integers}) \quad (2)$$

Now, the MTL method attempts to derive a system of linearized ODE-s with solutions having identical Z-action for any t_j, $j\in Z$, and very similar *R*-action $\forall t\in R$ as the solutions of the nonlinear ODE-s. Towards this, the *j*-the component of the non-linear vector term $Q(X,\dot{X},t)$ is approximated as:

$$Q^{(j)}(X,\dot{X},t)\cong Q_M^{(j)}(t)=\sum_{k=0}^{p}Q^{(j)}(X_k,\dot{X}_k,t)\phi_k(t) \quad (3)$$

where the basis set $\{\phi_k\mid k=0,...,p\}$, indexed on I_1, must satisfy $\phi_k(t_l)=\delta_{kl}$ (δ is the Kronecker delta), $\int_0^{ph}\phi_k(t)dt=1$ and $X_k=X(t_k),\dot{X}_k=\dot{X}(t_k)$. Interpolating Lagrange polynomials (ILP-s), distributed approximating functionals (DAF-s) (Wei *et al* 1998) and interpolating wavelets or interpolets (Saito and Beylkin 1993) are a few possible choices for $\{\phi_k\}$. An appropriate choice of the basis set may be dictated by the physics of the problem. Thus the MTL-based linearized form of equation (1) valid over I_1 is:

$$\{\ddot{Y}\}+[C]\{\dot{Y}\}+[K]\{Y\}=\{Q_M^{(j)}(X_k,\dot{X}_k,t\,|k=0,1,...,p)\}+\{F(t)\} \quad (4)$$

where the first term on the RHS may be interpreted as a conditionally known forcing function. Since an exact solution of the above-linearized system is available, the formal accuracy of the MTL method as a function of the time step-size depends only the error of replacement of $Q^{(j)}(X,\dot{X},t)$ with $Q_M^{(j)}(t)$ as in equation (3). Now, by setting up the variational equations corresponding to equations (1) and (4), it may be shown that the tangent spaces of the non-linear and linearized systems are transversal almost everywhere in the associated phase space, and, in particular, at the grid points. Thus the discretized solution vector $\{X_k, \dot{X}_k \mid k = 1,...p\}$ may be interpreted as points of transversal intersections between the solutions of equations (1) and (4) at the grid points. Figure 1 provides a 1-dimensional schematic representation of the concept for $p = 4$. It may be shown that such intersections are indeed possible if the solution vector of equation (4) satisfies:

$$X_l = Y_l(X_k, \dot{X}_k),\ \dot{X}_l = \dot{Y}_l(X_k, \dot{X}_k),\ k = 0,1,..., p;\ l = 1,..., p \qquad (5)$$

where $\{Y_l = Y(X_k, \dot{X}_k, t_l), \dot{Y}_l = \dot{Y}(X_k, \dot{X}_k, t_l) \mid k = 0,1,..., p\}$ denotes the linearized solution vector (which is an explicitly known function of $\{X_k, \dot{X}_k\}$) at $t = t_l$. Equation (5) constitutes a set of $2p$ algebraic equations in as many unknowns $\{X_l, \dot{X}_l \mid l = 1,..., p\}$ and may be solved using a Newton-Raphson or a non-linear iterative solver.

Presently, a limited numerical illustration of the method is provided for a few single- and two-degree-of-freedom nonlinear oscillators in their periodic and chaotic regimes. Figure 2 shows simulated periodic trajectories of a sinusoidally driven hardening Duffing oscillator (with a cubic non-linear term) obtained via MTL and Runge-Kutta (sixth order) schemes under different time step-sizes. The relatively superior numerical stability and convergence of the MTL method even under higher time-step sizes is amply clear. In particular, it is also observed that the Runge-Kutta method leads to overflows for $h = 0.21$. The MTL method used in this figure has been implemented via ILP-s with $p = 3$. It is interesting to note that a non-linear Hamiltonian system remains Hamiltonian under the MTL-based transformation. In fact, the non-uniqueness of the MTL method should be exploitable to tailor it to preserve any other invariants of motion (if they exist). Efforts are also underway to adapt the MTL principle for homogenization of ill-conditioned non-linear operators (e.g., dynamic wrinkling of membranes) of relevance in structural dynamics.

References:

Roy, D., 2001, "A numeric-analytic technique for nonlinear deterministic and stochastic dynamical systems", Proc. A Royal Soc. (Lond.), Vol. 457, pp. 539-566.

Saito, N. and Beylkin, G., 1993, "Multi-scale representations using autocorrelation functions of compactly supported wavelets", IEEE Trans. Signal Process., Vol. 41, pp. 3584-3590.

Wei, G.W., Zhang, D.S., Kouri, D.J., and Hoffman, D.K., 1998, "A robust and reliable approach to nonlinear dynamical problems", Comp. Phy. Comm., Vol. 111, pp. 87-92.

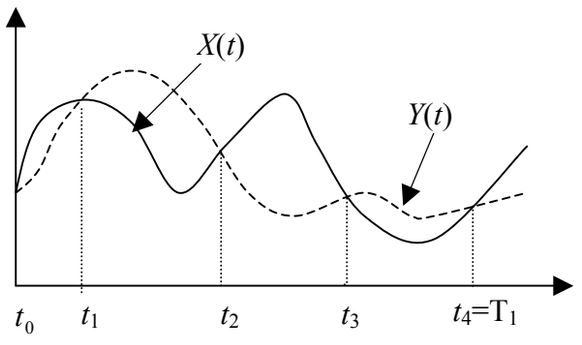


Fig. 1 A schematic representation of the MTL concept

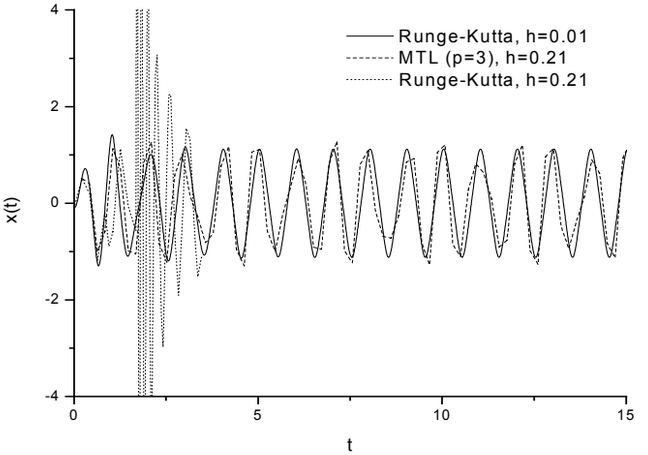


Fig. 2. Relative numerical stability of MTL vis-à-vis the sixth order Runge-Kutta method

Equivalent Stochastic Linearization as an Alternative to Solving the Fokker-Planck Equation

Stephen H. Crandall
Massachusetts Institute of Technology
Cambridge, MA 02139, U.S.A.
crandall@mit.edu

Statistical, or equivalent stochastic, linearization was originally introduced [1, 2, 3] as an *approximate* procedure for estimating the mean and variance of the stationary response of a nonlinear dynamic system. The procedure has been widely applied to a variety of problems [4], but for the sake of simplicity of exposition, the discussion here is limited to an oscillating mass m with linear damping and odd, nonlinear, restoring force $g(x)$, excited by a stationary zero-mean random force $f(t)$, described by the equation

$$m\ddot{x} + c\dot{x} + g(x) = f(t) \tag{1}$$

For this special case the displacement respone has zero mean, and the statistic of interest is just the mean square $E[x^2]$. The basic idea of stochastic linearization is to replace the nonlinear restoring force $g(x)$ by an equivalent linear force kx. One criterion for selecting k, proposed by all three of the pioneers [1,2,3], is that the expectation of the mean square of the equation deficiency should be a minimum; *i.e.*,

$$\frac{d}{dk}E[\{kx - g(x)\}^2] = 0 \tag{2}$$

According to the pioneers, the expectations in (2) should ideally be evaluated on the basis of the true probability distribution of the nonlinear response. Since the actual distribution of the nonlinear response was then unknown, the pioneers made the additional approximation of assuming a Gaussian distribution in their illustrative examples. Caughey [3] did however note that if the correct nonlinear distribution could have been employed, then the linearization procedure would have produced the correct response statistics for the case where $f(t)$ was Gaussian white noise. Subsequently most authors have adopted the Gaussian assumption in their applications of equivalent linearization, There has, however, been some confusion as to whether the Gaussian distribution involved is an approximation for the true nonlinear distribution, as originally proposed, or is the particular Gaussian distribution which describes the response of the equivalent linear system to Gaussian white noise. In [5] it is shown that these two assumptions lead to two distint procedures, but that the second procedure is more labor intensive and generally less accurate than the first.

A few authors have investigated stochastic linearization based on non-Gaussian probability distributions. In [6] the linearization procedure is re-interpreted as a technique for selecting the optimum distribution out of a one-parameter family of possible probability distributions. The novel contribution of the present paper is the recognition that the Maxwell-Boltzmann equation provides a one-parameter family of distributions which includes the the true probability distribution of the stationary solution to the nonlinear equation (1) when the excitation

is Gaussian white noise. In the classical approach [7], the Fokker-Planck equation is solved to select the true distribution. Here it is shown that the same result is obtained by applying dimensional analysis and equivalent stochastic linearization. This means that for any odd restoring force $g(x)$ for which the potential energy

$$G(x) = \int_0^x g(\xi)d\xi \tag{3}$$

is known, the true probability density function for the white-noise response is

$$p(x) = \frac{\exp\{-G(x)/G_0\}}{\int_{-\infty}^{\infty} \exp\{-G(x)/G_0\}dx} \tag{4}$$

where the magnitude of the reference energy G_0 is readily fixed by equivalent stochastic linearization. In this application the linearization procedure is a tool for obtaining a *true* solution. The procedure is illustrated for an array of particular examples, including power-law oscillators, Duffing's system, the double-well oscillator, and oscillators with trancendental restoring forces.

REFERENCES

1. Booton, R.C., Jr., The analysis of nonlinear control systems with random inputs, pp. 369-397 in *Proc. Symposium on Nonlinear Circuit Analysis*, Polytechnic Institute of Brooklyn, 1953.

2. Caughey, T.K., Equivalent Linearization Techniques, *J. Acoust. Soc. Am.* **35**, 1706-1711(1963). Reference is made to presentations of the procedure in Cal Tech lectures in 1953.

3. Kazakov, I.E., Approximate probabilistic analysis of the accuracy of operation of essentially nonlinear systems, (in Russian) *Avtomatika I Telemekhanika* **17**, 385-409(1956). Available in English translation: *Automation and Remote Control* **17**, 423-450(1956).

4. Proppe, C.,Pradlwarter, H.J., & Schuëller, G.I., Equivalent linearization and Monte Carlo simulation in stochastic dynamics, *Probabilistic Engineering Mechanics* **18**, 1-16(2003).

5. Crandall, S.H., Is stochastic equivalent linearization a subtly flawed process?, *Probabilistic Engineering Mechanics* **16**, 169-176(2001).

6. Crandall, S.H., On using non-Gaussian distributions to perform statistical linearization, pp. 49-62, in Advances in Stochastic Structural Dynamics, Proceedings of the Fifth Internatioinal Conference on Stochastic Structural Dynamics-SSD03, Hangzhou, China, May 2003 (re-scheduled to Auigust 11-13, 2003 due to severe acute respiratory syndrome (SARS) alert.

7. Lin, Y.K., Probabilistic Theory of Structrural Dynamics, McGraw-Hill Book Co., New York, 1967, p.265.

NONLINEAR EFFECTS, OBSERVED IN THE PROCESS OF THE LIQUID FLOWING OUT OF THE VIBRATING VESSELS: THEORY, EXPERIMENT AND APPLICATIONS

I.I. Blekhman, L.I. Blekhman, L.A. Vaisberg, V.B. Vasilkov, K.S. Yakimova
Institute for Problems of Mechanical Engineering and "Mekhanobr-Tekhnika" Corp., Saint Petersburg, Russia

Summary A general physical explanation and theoretical description of two nonlinear phenomena observed in the process of the liquid flowing out of the vibrating vessels are proposed. The results of the experimental investigations and of possible applications to the processes of screening flotation are presented.

EXTENDED SUMMARY

The presentation is devoted to two peculiar nonlinear phenomena. The first of them, called vibro-jet effect, has been known for a comparatively long time [1]. It consists in the fact that when a plate with conic holes vibrates in a fluid slow flows of fluid appear in the direction of the narrowing of the holes. The vibro-jet effect is successfully used in a number of technical devices [1-3]. Along with that, this phenomenon was a possible cause of some aviation catastrophes when due to vibration, the fuel stopped coming from the tanks; i.e., there was a vibration closing of the holes. In this case the pressure, facilitating the discharge of the fuel, was balanced by the counter-pressure, appearing due to vibration. The second phenomenon - the vibrational injection of a gas into the fluid - has been discovered quite recently [4]. It consists in the fact that gas is being sucked into the vessel with the fluid through the hole in the lower part of the vessel, vibrating in the gas. Though injection will also take place in the case when the vessel vibrates in the fluid; i.e., we may speak here about a phenomenon of vibrational injection of fluid into fluid.
The theory of vibro-jet effect was considered in [3] and in the book [1]. Here we propose a general explanation comprising, the theory of both phenomena; and also give the results of the experiments.

THE MAIN THEORETICAL RESULTS

The vessel (Fig.1) contains fluid 1, and outside there is either fluid or gas 2. The vessel can be either open or closed, and performs vertical oscillations according to the law $y = -A\sin\omega t$, where A is the oscillation amplitude and ω is the oscillation frequency. The hole is at the bottom of the vessel.

We assume that the well-known formula for hydraulics $Q = \mu F\sqrt{2\Delta P/\rho}$ for discharge is also valid for the instantaneous discharge under the action of pressure difference $|\Delta P|$, variable in time (μ is the coefficient of discharge, ρ is the density of the medium, F is the area of the hole). As a result we obtain the following expressions for the period $T = 2\pi/\omega$ the volume discharge per second of the medium flowing out (Q_+^T, positive) and flowing into the vessel (Q_-^T, negative).

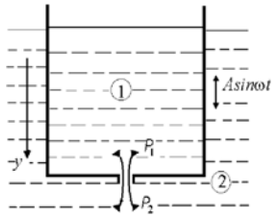


Fig. 1 General scheme of the system

$$Q_\pm^T = \pm\frac{1}{2\pi}\mu_\pm F\sqrt{2\Delta P/\rho_\pm}\,J_\pm(w), \tag{1}$$

where

$$J_\pm(w) = 4\sqrt{2w}\left[\mathbf{E}(k_\pm) - (1-k_\pm^2)\mathbf{K}(k_\pm)\right], \qquad (w \ge 1),$$
$$J_+(w) = 4\sqrt{1+w}\,\mathbf{E}(1/k_+), \qquad J_-(w) = 0, \qquad (0 \le w \le 1), \tag{2}$$

$k_\pm = \sqrt{(w\pm1)/(2w)}$, $\mathbf{K}$ and $\mathbf{E}$ are the complete elliptic integrals of the first and the second type respectively, $w = \rho_1 hA\omega^2/\Delta P$ is the so-called overload parameter, h is the height of the column of water in the vessel, $\rho_1 = \rho_+$, $\rho_2 = \rho_-$ are the densities of the media 1 and 2 respectively (Fig. 1), $\Delta P = P_1 - P_2$ is the static pressure difference at the hole.

In the case of *vibro-jet effect* the fluids inside and outside of the vessel are the same, so that $\rho_+ = \rho_- = \rho$, $w > 1$, and the total average discharge is

$$Q^T = Q_+^T + Q_-^T = \frac{1}{2\pi}F\sqrt{2\Delta P/\rho}\left[\mu_+ J_+(w) - \mu_- J_-(w)\right]. \tag{3}$$

When the inequality $\mu_+/\mu_- < J_-(w)/J_+(w)$ is satisfied, then in spite of the positive static pressure difference $\Delta P = P_1 - P_2 > 0$, the fluid flows into the vessel (for the period more fluid flowing in than flowing out), and when $\mu_+/\mu_- = J_-(w)/J_+(w)$ then the *effect of vibro-closing the vessel*, described above, takes place. At $w > 5$ the condition of the appearance of the inverse flow can be presented approximately as $\mu_+/\mu_- < 1 - 2.27/w$, and the condition of the vibrational closing as $\mu_+/\mu_- = 1 - 2.27/w$.

In the case of the *vibrational injection of gas into the fluid* the vessel is believed to be open and the pressure of gas on the surface of the fluid and at the outlet from the hole is believed to be the same. Then $\Delta P = \rho_1 g h$ and formula (1) for the average for the period T gas and liquid discharges $Q_+^T = Q_f^T$ and $Q_-^T = Q_g^T$ will be presented in the form

$$Q_+^T = Q_f^T = \frac{1}{2\pi}\mu_f F\sqrt{2gh}J_+(w), \quad Q_-^T = Q_g^T = -\frac{1}{2\pi}\mu_g F\sqrt{2gh\rho_f/\rho_g}\,J_-(w) \tag{4}$$

Here, unlike (1) the values referring to the fluid are marked with symbol " f ", while those referring to the gas are marked with the symbol " g " and $w = A\omega^2/g$.

THE RESULTS OF THE EXPERIMENT

The experiments on studying the vibrational injection were made on a special vibrational stand 157 A-YC elaborated at the "Mekhanobr" Institute. On the counter of that stand an open glass cylindrical vessel was fixed, it was 300 mm high with the inner diameter 58 mm. In the center of the bottom of the vessel there was a round hole. A certain level of water was kept in the vessel. The vessel was endowed with vertical vibration whose frequency and amplitude might be changed. The process of vibrational injection was observed in the stroboscopic light. That helped to establish that during every oscillation period one bubble of air was being sucked into the vessel and one drop of water was flowing out. Fig. 2 shows a photo of a vibrating vessel with the air being intensively sucked into it.

In the process of the experiment they measured the dependence of average volume discharge of water $Q_{f\,\exp}^T$, flowing out of the hole on the parameter w with the fixed oscillation amplitude $A = 2.5$ mm , of the height of the column of water in the vessel $h = 200$ mm and the diameter of the hole $d = 2{,}6$ mm .



Fig. 2. Vibrational injection of gas into fluid

The experiments have shown that a sufficiently intensive sucking-in of the air into a vessel, observed in the conditions of the experiment, begins at the value $w \approx 2.5$, while, according to the above-presented theory, it must begin at w somewhat more than 1. This can be explained by the effect of the surface tension when bubbles are being formed.

According to the results obtained, we performed the comparison of the coefficient $\mu_f^{T_+}$ with the value μ for the case of the stationary flow of the fluid through the hole. In this case $\mu_f^{T_+}$ implies the value of the coefficient μ_f , calculated from the experimental average discharge $Q_f^{T_+} = Q_f^T T/T_+$ for that part T_+ of the period T when the fluid is flowing out of the vessel. It was found that the values $\mu_f^{T_+}$ at $w > 4$ do not differ much more from the value μ which, it seems, speaks in favor of the elements of the theory stated above.

To apply the phenomenon of the vibrational injection to the processes of screening and flotation a series of experiments were carried out with the vessel, which had in its bottom a system of holes (round or slot-shaped) instead of a single hole. It was established that even at the area of the holes about 50% of the area of the bottom the process runs with the same intensity as with a single hole if the intensity of vibration is increased by about 10%.

CONCLUSION

It seems that the phenomena considered, as well as many other remarkable effects, appearing under the action of vibration on the gas-fluid and similar systems, are worthy of the attention of specialists. They may find important applications in technique, in particular, in chemical industry and in mineral processing.

The work is carried out with the support of the Russian Foundation of the Fundamental Researches (Grant SSC 1521.2003.8) and the Saint Petersburg Scientific Center.

REFERENCES

[1] Vibration in technology in 6 volumes: Handbook, **4**, Mashinostroenie, Moscow, 1978-1981 (in Russian).
[2] Blekhman I.I. :Vibrational Mechanic – Nonlinear Dynamic Effects, General Approach, Applications. World Scientific 2000. 509 p.
[3] Blekhman I. I., Vaisberg L. A., Korovnikov A. N. Investigations of the processes, machines and apparatus for classifying the material according to size. *Interdepartmental Proceedings, Mekhanobr, Leningrad.* 1988. p. 35-46 (in Russian).
[4] Blekhman I.I., Blekhman L.I., Vaisberg L.A., Vasilkov V.B., Yakimova K.S. In collection *Scientific discoveries, Moscow, Russian Academy of Natural Sciences.* 2002. p. 60-61 (in Russian).
[5] Blekhman I.I., Blekhman L.I., Vaisberg L.A., Vasilkov V.B., Yakimova K.S. Nonlinear effects, observed in the process of the liquid flowing out of the vibrating vessels. *Doklady Acad. of Sc., Russia.* 2003. **391**(2). p. 185-188.

PROPAGATION ANALYSIS OF FLEXURAL WAVES BY WAVELET TRANSFORM

Akihiko Higashi, Fumihiro Mizuguchi
Japan Coast Guard Academy, 5-1, Wakaba-cho, Kure, Hiroshima, 737-8512, JAPAN

The purpose of this study is to investigate the possibility of structural health monitoring by using the propagation of flexural waves. Then, we investigate the velocity of the propagation of flexural waves. In this paper, the rectangular aluminum thin plate is used in the experiment, which is basic element of structures. The specimen, that is the rectangular thin plate, is excited at one point by the exciter, and, the displacement of vibration is measured by using two non-contact displacement sensors. The velocities of the propagation of flexural waves are analyzed by wavelet transform. As a result, the velocities of the propagation of flexural waves could be measured exactly by wavelet analysis. Therefore, it is found that the structural health monitoring by using the flexural waves is possible.

INTRODUCTION

Recently, a lot of structure such as a ship become large-sized and complicated. It is very difficult that the health of structure is always understood. When the damage is occurred to these structures, it does not cause a fall of strength of the structure and may be connected to an important reason. Thus the development of the health monitoring system for these structures is very important problem. However, there are a few studies about identification of the damage for the thin plate [1]-[2]. Furthermore, there are few studies about identification of the damage that took advantage of propagation of the wave motion. The wave motion is possible the wide inspection is possible. Then, we pay attention to wave motion of vibration in order to identify the damage. The purpose of this study, the method of analysis is developed to understand the damage of the structure by propagation of flexural waves. Thus at first, in this study, we examine by experimental analysis, in order to elucidate the propagation of flexural waves in the structure.

EXPERIMENT AND ANALYSIS

Summary of experiment

The specimen and the equipment of experiment are shown in Figure 1. The specimen made by aluminum is fixed one side edge. The specimen is excited by the exciter with the signal of the signal processor within of FFT analyzer. The method of excitation is that it is the change to a sine wave signal of another frequency from a sine wave signal of a certain frequency instantly. In order to investigate the propagation phenomenon of flexural waves, the displacements of vibration at the exciting point and measurement points are measured by Non-contact displacement sensor, respectively. The measurement results are analyzed by personal computer.

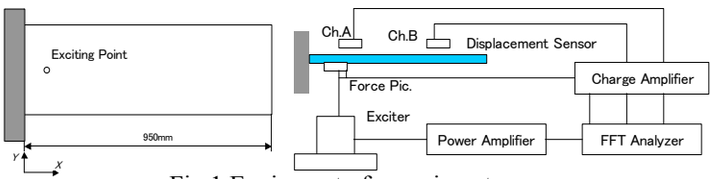


Fig.1 Equipment of experiment

Analysis and results

The used input signal in this experiment is shown in Figure 2. When this input signal is given to the specimen, the displacements such as a vibration response of the specimen are measured at the exciting point and measurement points. In this study, we analyze by using the wavelet transform [3]. In addition, the wavelet analysis and the treatment of experimental results are performed by MATLAB. We detect the time, which is the change frequency of measured signal, by using the wavelet analysis.

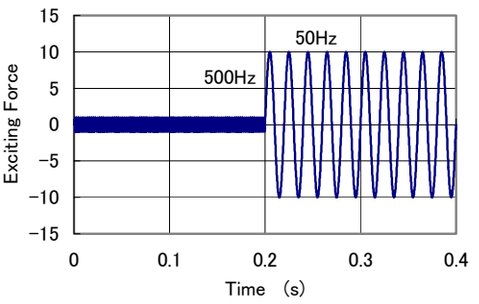
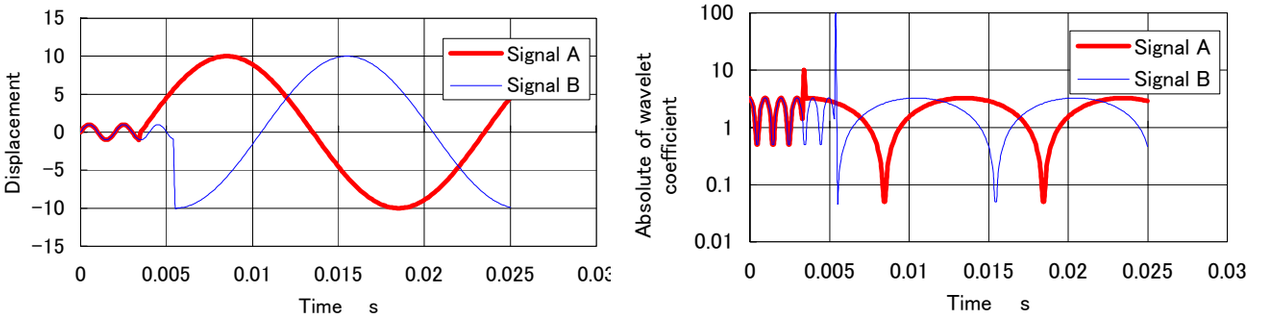


Fig.2 Input signal

These results, which are performed wavelet analysis for signals of various patterns, are shown in Figure 3. Figure 3 (a) shows an original signal before performing wavelet analysis. Figure 3 (b) shows the results, which are preformed wavelet analysis. In addition, the time of change frequency of signal A and B are each moved by 2.0ms. As Figure 3(a) is shown, it is found that it is difficult to detect the time of change frequency. However, as Figure 3(b) is shown, it is found that it is possible to detect the delay time. The delay time of change of frequency is the difference between the signal A and the signal B. Thus the delay time is detected by the wavelet analysis for the measurement result.

In this study, at first, these measurement results at the exciting point and measurement points are analyzed by performing the wavelet analysis. The difference, which is the time of changed frequency, between exciting point and measurement point is decided by cross-correlation function of the wavelet coefficient. And the velocities of the propagation of flexural waves are detected by obtained results and distance form exciting point to measurement point. These analyzed results are shown in Figures 4, 5 and 6. Figure 4 shows the measurement results by the experiment. Figure 5 shows the results of the wavelet analysis performed. Figure 6 shows the results of the velocities of the propagation of flexural waves. In this experiment, the measurement points are 30,60,90,120,150,210,300,450,600mm

distant from the exciting point. As these results are shown, it is found that the appropriate result is obtained by performing the wavelet analysis. And the dispersion by distance of the obtained results is very small. The maximum deviation, which is a gap from the mean of the analyzed results, is around 5%. However, The almost deviation is less than 1%. It is found that the analysis of the velocity of the propagation of flexural wave is possible by using proposed method. As the above-mentioned result, it is found that the appropriate velocities of the propagation of flexural waves by using the proposed method, which is the technique with the wavelet analysis, could be acquire. Thus, the health of structures could be investigated by the propagation of flexural waves. In other words, it is found that the propagation of flexural waves could be the effective parameter for the structural health monitoring.



(a) Before wavelet analysis (b) After wavelet analysis

Fig.3 Results of wavelet analysis for sample signal

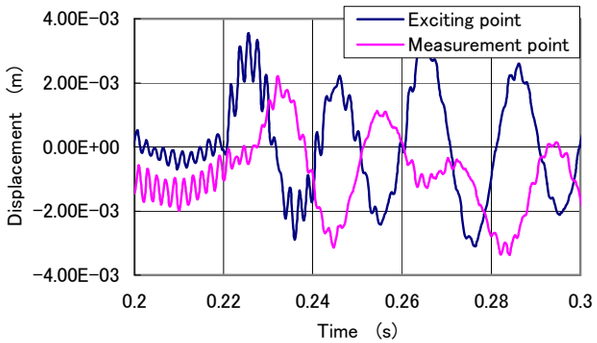


Fig.4 Measurement results

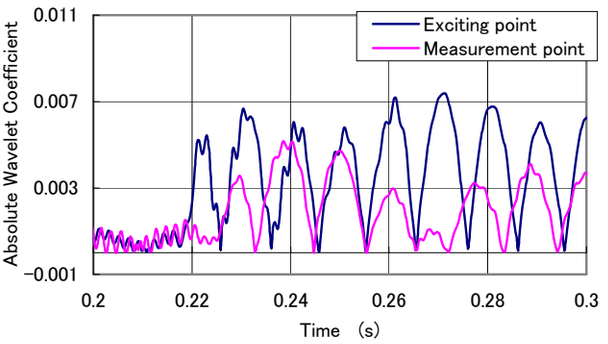


Fig.5 Results after wavelet analysis

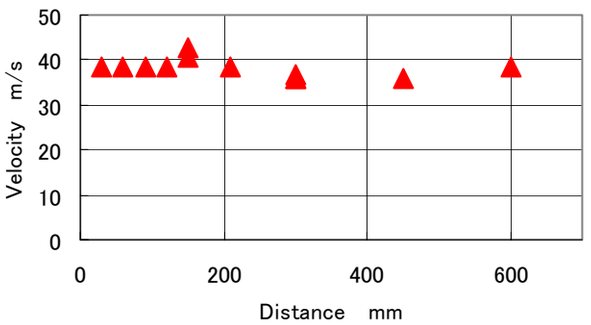


Fig.6 Analyzed results of the velocity of flexural waves propagation

Table 1 Analyzed results of the deviation of the velocity

Distance mm	Velocity m/s	Deviation %
30	38.400	0.893
60	38.400	0.893
90	38.400	0.893
120	38.400	0.893
150	40.421	6.203
210	38.400	0.893
300	35.721	6.146
450	36.000	5.413
600	38.400	0.893

CONCLUSIONS

In this study, we analyzed the propagation phenomenon of wave motion of vibration in the thin plate by using wavelet analysis. The obtained results are as follows. (1) A change of a signal is analyzed almost precisely by using wavelet analysis. (2) The wavelet analysis performs to the measurement results of the exciting point and measurement points. Then, we propose the method, which is investigated the propagation of flexural waves by using correlation of both. In addition, it is found that the investigated results are almost appropriate.

References

[1] B.Stahl, L.M.Keer, Vibration and Stability of Cracked Rectangular Plates, *Int. J. Solids Structures*, 8(1972), 69.
[2] P.Cawley, R.D.Adams, The Location of Defects in Structures from Measurements of Natural Frequencies, *Journal of Strain Analysis*, Vol.14, No.2 (1979), 49-57.
[3] D.E.Newland, Wavelet Analysis of Vibration, *Trans. ASME, J. of Vibration and Acoustics*, 116(1994), 409-417.

BIFURCATIONS OF NONLINEAR NORMAL MODES OF LINEAR OSCILLATOR WITH STRONGLY NONLINEAD DAMPED ATTACHMENT.

Oleg V. Gendelman*
Faculty of Mechanical Engineering, Technion, Haifa, 32000, Israel
** - Horev Fellow – Supported by the Taub and Shalom Foundations*

Summary Damped nonlinear normal modes in a linear oscillator coupled to small damped strongly nonlinear attachment are considered by combining the invariant manifold approach and multiple scales expansion. Three distinct time scales correspond to fast vibrations, evolution of the system towards the nonlinear normal mode (NNM) and time evolution of the invariant manifold. Cusp catastrophe scenario is proved to be the only possible for the invariant manifold in time – amplitude – damping domain.

Introduction

Recently it has been demonstrated that various systems comprised of linear substructures and strongly nonlinear attachments demonstrate localization and irreversible transient transfer (pumping) of energy to prescribed fragments of structure dependent on initial conditions and external forcing [1-4]. Addition of relatively small and spatially localized attachment leads to essential changes in the properties of the whole system. Unlike common linear and weakly nonlinear systems, systems with strongly nonlinear elements are able to react efficiently on the amplitude characteristics of the external forcing in a wide range of frequencies [1,3,4].

The systems under consideration give rise to a new concept of nonlinear energy sink (NES). It was demonstrated [2,4] that the possibility of the energy pumping/resonance capture phenomenon in non-conservative systems can be understood and explained by studying the energy dependence of the non- linear undamped free periodic solutions (non-linear normal modes (NNM,[5-7])) of the corresponding conservative system that is obtained when all damping forces are eliminated. However, that any practical implementation of the energy pumping mechanism requires more detailed understanding of the dynamics of real damped system. Time dependence is crucial feature of the invariant manifolds if the damping is present. Moreover, it will be demonstrated that the topological structure of the invariant manifold is strongly time-dependent and can undergo bifurcations depending on the value of the damping coefficients.

Description of the model and its analysis

Let us consider the following system, which consists of linear oscillator and small strongly nonlinear attachment , described by the set of equations:

$$\ddot{y}_1+\varepsilon(\dot{y}_1-\dot{y}_2)P(y_1-y_2)+y_1+\varepsilon Q(y_1-y_2)=0;\quad \varepsilon\ddot{y}_2+\varepsilon(\dot{y}_2-\dot{y}_1)P(y_2-y_1)+\varepsilon Q(y_2-y_1)=0 \tag{1}$$

where ε<<1 is a small parameter which establishes the order of magnitude for coupling, damping and mass of the nonlinear attachment. Coupling terms are considered to be symmetric and therefore functions P and Q are presented in a form of even and odd polynomials respectively:

$$P(\xi)=\sum_{j=0}^{n}\lambda_j\xi^{2j},\ Q(\xi)=\sum_{j=0}^{m}q_j\xi^{2j+1},\lambda_j,q_j\ge 0 \tag{2}$$

with at least one of λ_j and q_j is nonzero. Changes of variables $v=(y_1+\varepsilon y_2)/(1+\varepsilon)$, $w=y_1-y_2$, $\delta=1/\chi$ $\chi=\varepsilon^{1/3}$, $V=\chi^{-1}v$, $W=w$, $\varphi_1\exp(it)=\dot{V}+iV$, $\varphi_2\exp(it)=\dot{W}+iW$ reduce system (1) to the following form:

$$\dot{\varphi}_1-\frac{i\chi^2}{2}(\varphi_2-\varphi_2^*\exp(-2it))=0$$

$$\dot{\varphi}_2+\chi(\delta[\frac{i}{2}(\varphi_2-\varphi_2^*\exp(-2it))+\frac{1}{2}(\varphi_2+\varphi_2^*\exp(-2it))P(-\frac{i}{2}(\varphi_2\exp(it)-\varphi_2^*\exp(-it)))+ \tag{3}$$

$$+\exp(-it)Q(-\frac{i}{2}(\varphi_2\exp(it)-\varphi_2^*\exp(-it)))]-\frac{i}{2}(\varphi_1-\varphi_1^*\exp(-2it)))=0$$

Standard multiple scales expansion with respect to parameter χ demonstrates that in the conditions of 1:1 resonance the dynamical flow is attracted to nonlinear normal mode. The second-order approximation leads to exactly solvable equation for time evolution of the invariant manifold of this NNM ($\tau_2=\chi^2 t$, $\varphi_{10}=R_1\exp(i\gamma_1)$; $\tilde{\varphi}_{20}=R_2\exp(i\gamma_2)$; $\gamma=\gamma_1-\gamma_2$, $Z=R_2^2$) :

$$\frac{\partial Z}{\partial\tau_2}[\{1-2\sum_{j=0}^{m}\frac{q_j}{2^{2j+1}}C_{2j+1}^{j}Z^j\}\{1-2\sum_{j=0}^{m}\frac{q_j}{2^{2j+1}}C_{2j+1}^{j}Z^j-4Z\sum_{j=0}^{m-1}\frac{(j+1)q_{j+1}}{2^{2j+3}}C_{2j+3}^{j+1}Z^j\}+\{\sum_{j=0}^{n}\frac{\lambda_j}{2^{2j}}\frac{(2j)!}{(j!)^2(j+1)}Z^j\}x$$
$$x\{\sum_{j=0}^{n}\frac{\lambda_j}{2^{2j}}\frac{(2j)!}{(j!)^2(j+1)}Z^j+2Z\sum_{j=0}^{n-1}\frac{\lambda_{j+1}}{2^{2j+2}}\frac{(2j+2)!}{((j+1)!)^2(j+2)}Z^j\}]=-\frac{1}{\delta}Z\sum_{j=0}^{n}\frac{\lambda_j}{2^{2j}}\frac{(2j)!}{(j!)^2(j+1)}Z^j \tag{4}$$

It may be proved that, despite large number of coefficients and complicated structure of (4), the topology of the invariant manifold is surprisingly simple:

1) if $q_0>1$, then $Z(\tau_2)$ decreases monotonously;
2) if $q_0<1$ and at least one of q_j, $j>0$, is positive, then for sufficiently small λ_j there exist two points with divergent derivative $\partial Z/\partial\tau_2$, giving rise to three branches of $Z(\tau_2)$). It is easy to conclude that two of these branches will be stable and one – unstable. As any of λ_j grows, these zeros will eventually disappear by mechanism of trivial cusp catastrophe.

As the topology of the invariant manifold is similar for all possible choices of the coefficients q_j and λ_j (with restrictions formulated above), it is possible to restrict the investigation by the simplest example. Namely, we take $q_1=8$, $q_j=0$ for all $j\neq1$ and $\lambda_0=\lambda$, $\lambda_j=0$ for all $j\neq0$. The shape of the surface $Z(\tau_2,\lambda)$ for $\delta=2.5$ is presented at Fig. 1. In order to illustrate the effect of the bifurcations of the invariant manifold on the dynamics of the system under consideration direct numerical simulation of (1) is performed for the following parameters: $\varepsilon=0.064$, $q_1=8$, $\lambda_0=0.2$ (Fig.2).

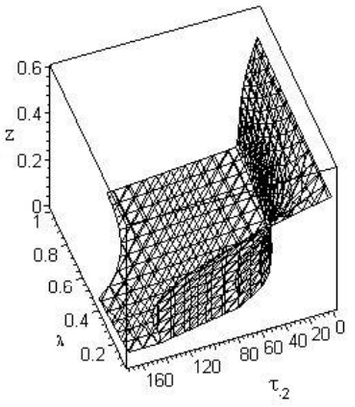


Fig. 1. *Shape of the invariant manifold for the set of parameters $q_1=8$, $\delta=2.5$, $0<\lambda<1$.*

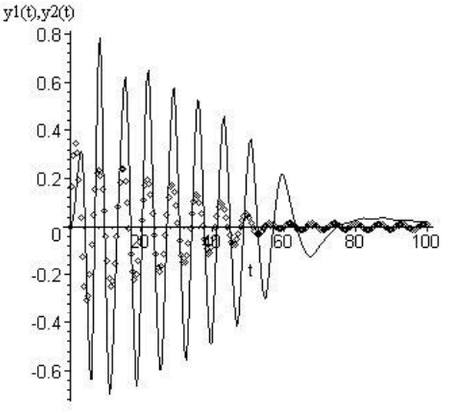


Fig. 2. *Simulation of System (1) for the set of parameters mentioned above, $\lambda=0.2$, $y_1(0)=0$ $dy_1/dt(0)=0.35$, $y_2(0)=0$, $dy_2/dt(0)=0$ (◊◊◊◊◊◊◊ - $y_1(t)$, ——— - $y_2(t)$).*

The picture clearly demonstrates that at about t=20 the trajectory of the system attains the regime of nonlinear normal mode, characterized by simultaneous behavior of $y_1(t)$ and $y_2(t)$. However at about t=50-60 this regime is broken down with rather abrupt decrease of both amplitudes. The phase trajectory of the coupled system completely leaves ("jumps out" from) the resonance manifold and the nonlinear normal mode is totally destroyed as a result of passage through the bifurcation.

Conclusive remarks

We have considered the dynamics of linear oscillator with strongly nonlinear attachment. The above results demonstrate that in the conditions of 1:1 resonance the system under consideration evolutes according to three distinct time scales:

- scale τ_0 corresponds to the fast vibrations of the system with frequency close to unity;
- scale τ_1 corresponds to evolution of the slow variables towards the regime of nonlinear normal mode;
- scale τ_2 corresponds to evolution of the invariant manifold of the NNM.

Time evolution of the invariant manifold may be accompanied by two bifurcations, if the linear frequency of coupling spring is small enough. In this case the bifurcations disappear with increase of the damping coefficient via cusp catastrophe.

Presence of bifurcations of the invariant manifold has rather essential effect on the dynamics of the system. Namely, passage through the bifurcation is able to destroy the regime of nonlinear normal mode and facilitate the energy dissipation. The latter observation leads to certain clue for practical design of the nonlinear energy sinks – the damping coefficient should be chosen in order to ensure the possibility for bifurcations of the NNM invariant manifold. Failure to do so will result in a loss of NES ability to dissipate the energy of vibrations.

References

[1]. O.V.Gendelman Transition of Energy to Nonlinear Localized Mode in Highly Asymmetric System of Nonlinear Oscillators, *Nonlinear Dynamics*, **25**, 2001, 237-253.
[2]. O.V.Gendelman, A.F.Vakakis, L.I.Manevitch and R. McCloskey, Energy Pumping in Nonlinear Mechanical Oscillators I: Dynamics of the Underlying Hamiltonian System, *Journal of Applied Mechanics*, **68**, n.1, 2001, 34-41.
[3]. A.F.Vakakis and O.V.Gendelman, Energy Pumping in Nonlinear Mechanical Oscillators II: Resonance Capture, *Journal of Applied Mechanics*, **68**, n.1, 2001, 42-48.
[4]. A.F. Vakakis, L.I. Manevitch, O. Gendelman, L. Bergman. Dynamics of Linear Discrete Systems Connected to Local Essentially Nonlinear Attachments. *Journal of Sound and Vibration*, **264**, 2003, 559-577.
[5]. Vakakis A. F., Manevitch L. I., Mikhlin Yu. V., Pilipchuk V. N., and Zevin A. A., Normal Modes and Localization in Nonlinear Systems, Wiley Interscience, New York, 1996.
[6]. S.W.Shaw and C. Pierre, Normal modes for Nonlinear Vibratory Systems, *Journal of Sound and Vibration*, **164**, 1993, 85-124.
[7]. Nayfeh A.H. and Nayfeh S.A., On Nonlinear Modes of Continuous Systems, *Journal of Vibration and Acoustics*, **116**, 1994, 129-136.

EFFECT OF ROOT FLEXIBILITY ON THE AEROELASTIC ANALYSIS OF A COMPOSITE WING BOX

Gamal M. Ashawesh[*], Ali M. Elmabrok[**], Tarek A. Abdunabi[***], Alakrami A. Nakas[****]
[*]*Engineering College, Aeronautical Department, Tripoli, Libya*
[**]*Alfatah University, Aeronautical Department, Tripoli, Libya*
[***]*Engineering College, Aeronautical Department, Tripoli, Libya*
[****]*Alfatah University, Computer Department, Tripoli, Libya*

Summary This paper discusses the effect of fibre orientations, composite skin lay-up, bending-torsion material coupling, and the root flexibility or stiffness of a composite rectangular wing box model for different fibre orientations on the dynamic and aeroelastic analysis (flutter and divergence speeds) for the Circumferentially Uniform Stiffness (CUS) and Circumferentially Asymmetric Stiffness (CAS) configurations.

INTRODUCTION

The main objective of this research is to establish the aeroelastic effects of variation of composite fibre orientations, bending-torsion coupling, root flexibility, and stacking sequence of the upper and lower skins for a rectangular closed thin-walled wing box. Although many of these features are already analyzed, usually they are treated individually and not considered collectively. A sensitivity analysis is carried out for the fibre orientation, stacking sequence and root flexibility in order to visualize their influence on the modal behaviour, flutter and divergence speeds. For flutter analysis, it is necessary to study and find the dynamic characteristics of the composite wing box, which are in the form of eigenvalues and associated eigenvectors. The finite element codes used are FEMAP version 8 and MSC/NASTRAN version 70.5 as pre-processor, post-processor and analyzer respectively. The ply-stacking and fibre orientation are studied systematically in the past [1-4] without considering the CAS and CUS configurations in a more realistic manner. The effects of bending-torsion material coupling stiffness on the dynamic and aeroelastic behaviors of both configurations using one laminate for all walls of the wing box is considered by [5-6]. The objective of this research not only entailed these three characteristics but also including root flexibility to determine the response and flutter and divergence speeds of a composite wing box. The first two variables, fibre orientation and ply stacking sequence, are modelled with finite elements. The last variable, the root flexibility, is not usually modelled. Therefore an innovative way is found to quickly and efficiently model the root flexibility. The boundary condition of the composite wing box is modelled with two springs to simulate translation and rotation degree of freedom which is very important to the static and dynamic aeroelastic analysis of aircraft wing structures. The eigenvalues versus root stiffness of the first laminate for different fibre orientations are compared with the change in physical properties, which for composite are essentially the effective bending stiffness, EI, effective torsional stiffness, GJ, and bending-torsion material coupling, K.

FINITE ELEMENT MODELS

Stiffness of the composite wing box

The equations for calculation of the effective bending stiffness, EI, torsional stiffness, GJ, and bending-torsion material coupling stiffness, K are derived using the mathematical equations presented in [7]. The structural stiffness is then calculated for different fibre angles, stacking sequence of both composite wing box configurations.

Wing box description and models

A simple wing box is employed instead of a beam or plate to give a great semblance to a real wing structure. The reason of retaining a simplified structure is to yield workable results without the adding complication of a complex finite element model. The dimensions of the wing box are 762 mm, 24.21 mm and 13.46 mm length, width and depth respectively. The composite wing box is modelled using a structural idealization program FEMAP v8 and analyzed using MSC/NASTRAN v70.5 based on the finite element approach. All sides of the wing box are modelled with QUAD4 plate element with four grids. The root stiffness is modelled using rigid beam elements (REB2) and degree of freedom springs. The grid points at the root of the wing box are all attached to one grid point located at the centre of the wing box root using RBE2 element. This element made the displacements of all the root grids dependent on the displacement of the centre grid. The centre grid is attached to two springs whose translation and rotation stiffness properties could be changed. One end of the springs is attached to the centre grid with the independent degree of freedom. The other end of the springs is attached to a ground point. The additional structure, which the rigid element, RBE2 and springs, (CELAS2 element) are did not interfere with the results. This is checked by making the springs very stiff and comparing the results to the cantilevered boundary condition. The natural frequencies and associated mode shapes are exactly similar to the case where the wing root is fully clamped. Two wing model configurations are selected in the modeling of the composite wing box, namely,

uniform or balanced (CUS) and asymmetric or unbalanced (CAS). In the CAS configuration, the ply lay-ups on the opposite sides are mirror with respect to the mid axis, where as in the case of CUS, the opposite sides are in opposite sign of fibre angle. Bending-twist material coupling stiffness is produced in the case of CAS, where as extension-twist coupling in the case of CUS.

Laminates considered

Symmetric and anti-symmetric laminates are used in the modeling of the composite wing box throughout the research. Symmetric laminate is used for the upper and lower skin and anti-symmetric laminate for the spar webs (side walls). This is done to investigate the effect bending-twist coupling generated only by the upper and lower skin on the eigenvalues and associated eigenvectors of the wing model. Laminate for the spar webs is $[\pm 45]_3$ and unchanged for both configurations throughout the research. The first symmetric laminate for the upper and lower skin is in the form of $[\theta_2/0]_s$ ply stacking sequence, where as the second laminate is in the form of $[0/\theta_2]_s$.

RESULTS

The composite wing box model is validated with [8] for both configurations with a ply stacking sequence of the $[\theta_6]$ for all sides at fibre angle of 30 degree simulating cantilevered case. This is done by using three methods; the first method is with clamping the grids at the root section. The second and third methods are by fixing the centre grid which is attached to the root grids, and with using both REB2 and springs at higher stiffness of 10^9 respectively. Normal mode and aeroelastic analysis are then carried out on the CAS and CUS configuration for both laminates of the composite wing box using Lanczos and PK methods respectively. The variation of the natural frequencies versus the root stiffness is shown in figure 1 of the first laminate at fibre angle of 0^o for illustration. The rest of the figures of both dynamic and aeroelastic analysis will be shown in the full paper. The research showed that the root stiffness has a significant influence on the natural frequencies and associated mode shapes and on the flutter and divergence speeds of the composite wing models especially at root stiffness lower than 10^3.

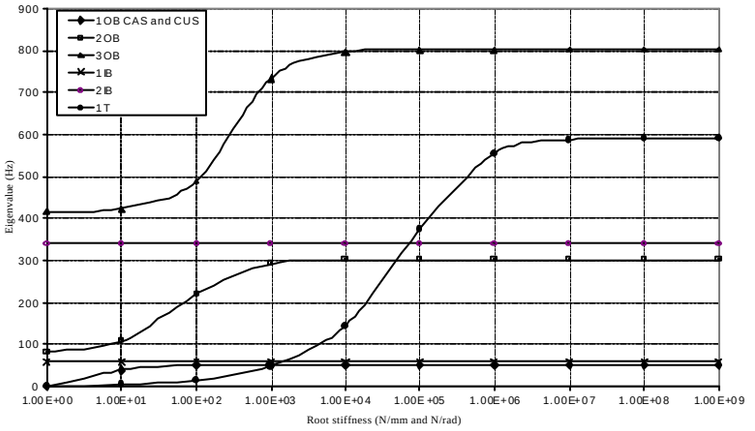


Figure 1. Eigenvalues versus root stiffness for the first laminate at 0^o fibre orientation.

References

[1] C.E. Cesnik, D.H., Hodges and M. J. Patil : Aeroelastic analysis of a composite wings. Proceedings of the 37th AIAA, ASME, ASCE, and AHS, Structures, Structural Dynamics, and Materials Conference and Exhibit, Salt Lake city, UT, TP, pt 2, 1996.

[2] R.V. Doggett and D.L.: Low speed flutter characteristics of some simple low aspect ratio Delta wing models. Proceedings of the 30th AIAA, ASME, ASCE, and AHS, Structures, Structural Dynamics, and Materials Conference, Mobile, AL, T.P. PP. 1442-1450, 1989.

[3] G.A. Georghiades and J.R. Banerjee :Flutter prediction for composite wings using parametric studies. Proceedings of the 37th AIAA, ASME, ASCE, and AHS, Structures, Structural Dynamics, and Materials Conference and Exhibit, Salt Lake city, UT, TP, pt 1, pp. 300-310, April, 1996.

[4] T.A. Weisshaar and R.J. Ryan : Control of aeroelastic instabilities through stiffness cross-coupling. Proceedings of the 25th AIAA, ASME, ASCE, and AHS, Structures, Structural Dynamics, and Materials Conference, Plam springs, CA, T.P., pt 2, pp. 226-235, 1984.

[5] G.M. Ashawesh : Effect of wash-in and wash-out on the flutter characteristics of composite aircraft wings. Proceeding of 10th International Conference on Aerospace Science and Aviation Technology, Cairo, Egypt, May 13-15 2003, in press.

[6] L.L. Librescu, O.L. Meirovitch and O. Song : Refined structural modeling for enhancing vibration and aeroelastic characteristics of composite aircraft wings. La recherché Aerospatiale, no. 1, PP. 23-35, 1996.

[7] S.C. Edward and I. Chopra : Formulation and evaluation of an analytical model for composite box-beams. Journal of the American helicopter society, PP. 23-35, 1991.

[8] E.A. Armanios and A.M. Badir.: Free vibration analysis of antistropic thin-walled closed section beams. AIAA journal Vol. 33, 1905-1910, 1995.

REANALYSIS OF AN SEA HIGH-FREQUENCY VIBRATION CALCULATION BASED ON THE VTCR

Hervé Riou*, Pierre Ladevèze*
*LMT Cachan (ENS Cachan / CNRS / Paris 6 University)
61 Avenue du Président Wilson 94235 Cachan Cedex, France

INTRODUCTION

The analysis of the vibration behavior of structures in the high-frequency range has become a key issue for engineers involved in structural design. In order to control and reduce displacements and stresses, the dynamic response must be properly and accurately predicted.
The finite element method (FEM [1]) is frequently used to analyze the structural response of complex structures. However, the analysis of the response of a system becomes more difficult as the excitation frequency increases, and this method is limited to the low frequency range ([2]). The difficulty resides in the length of variation of the phenomena being studied, which diminishes as the frequency increases. In the contest of the FEM, one often considers that about eight elements must be used to represent each structural wavelength adequately ([3]); thus, high-frequency calculations would require an unreasonably large number of degrees of freedom.
Because of the difficulties involved in developing a detailed model for high-frequency vibrations, considerable research effort has been devoted to the development of more appropriate techniques. One of the most commonly used techniques for high-frequency vibrations is Statistical Energy Analysis (SEA [4]). This procedure consists in modeling the system as a set of subsystems, each of which is assigned a single response variable corresponding to its vibrational energy. Using a description of the energy exchanged among the subsystems, this method yields the dynamic response of each subsystem averaged in time and in space. However, the SEA cannot provide local information on the response in each subsystem, since this response is characterized only by a single energy level. Therefore, an improvement of the SEA model would be welcome. This is the aim of this presentation.
The method of calculation of the vibrations of slightly damped elastic structures in the high-frequency range which is presented here is based on the reanalysis of global information to derive more local information. The global information is given by the SEA. The local information is obtained by reanalyzing the SEA data using the Variational Theory of Complex Rays (VTCR [5]). This method can be viewed as a refined calculation (VTCR analysis) of a large-scale analysis (SEA). It is based on a "Saint Venant" energy principle which gives the spatial distribution of energy density at high frequency, thus yielding a description of the system's behavior which is more accurate than the average constant value given by SEA. Initial applications dealing with simple rod and plate systems are presented and show that the method produces good effective local results under high-frequency exctitation.

THE VTCR

The VTCR is a method dealing with medium-frequency vibrations. The first feature which characterizes the VTCR is the use of a new variational formulation of the problem to be solved, which was developed in order to allow within the substructures approximations which are *a priori* independent, which means that they are not required to verify *a priori* the transmission conditions at the interfaces between substructures, whether in terms of displacements or stresses. Instead, these conditions are included in the variational formulation. The second feature defining the VTCR is the introduction of two-scale approximations with a strong mechanical meaning: the solution is assumed to be properly described as the superposition of an infinite number of local propagative and evanescent waves. These basic waves (which can be interior propagative waves, edge evanescent waves or corner evanescent waves) verify the laws of dynamics. All wave directions are taken into account. The unknowns are the amplitudes of these waves, whose wavelengths are relatively large. The discretization of these amplitudes leads to the resolution of a matrix system whose size is small compared to that of an FEM model, since only large-wavelength quantities are being used.
The example of Figure 1 shows the comparison between the solutions given by the VTCR (left) and by NASTRAN (right) for a missile's structure. The two results are similar. The NASTRAN solution (FEM calculation) was obtained using 10 nodes per wavelength, which leads to 28,800 degrees of freedom (dofs). The VTCR solution was obtained with 672 dofs.

THE REANALYSIS STRATEGY

The reanalysis strategy proposed is based on the calculation of the local energy density distribution in two steps: first, a large-scale calculation, then a refined calculation. The large-scale resolution consists in an SEA calculation over the whole structure divided into many substructures, which yields the average density of vibration energy for each substructure. The refined solution consists in a VTCR calculation over each substructure, which yields the distribution of the average energy density over the substructure.

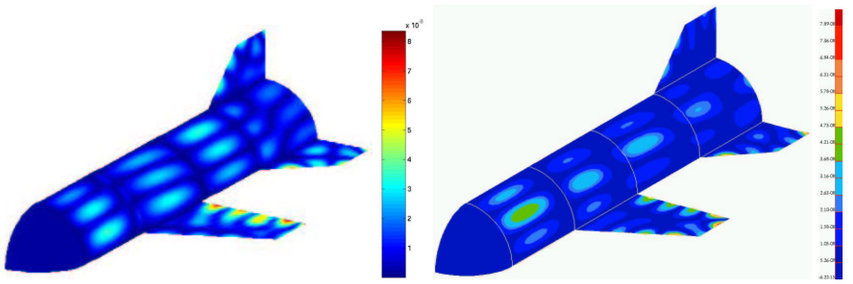


Figure 1: Comparison between the VTCR (left, 672 dofs) and NASTRAN (right, 28, 800 dofs). The scales are the same

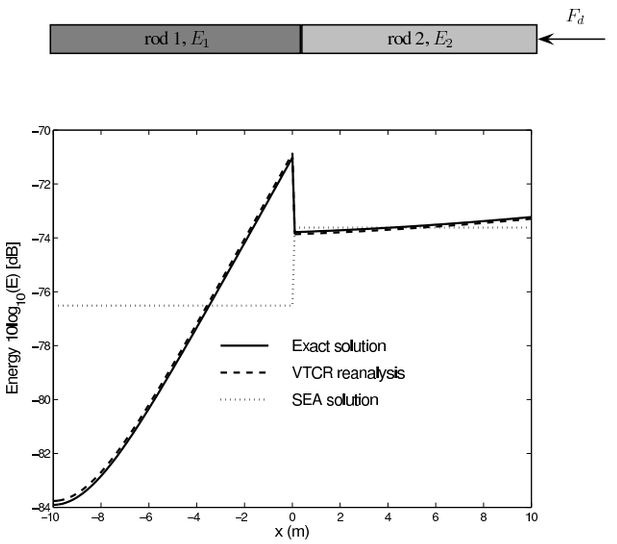


Figure 2: Reanalysis method applied to a rod problem

The large-scale resolution by the SEA requires a knowledge of the injected power and of the coupling loss factors, which can be evaluated using standard methods ([6]). This first calculation provides the power that flows from one substructure to another. This power is assumed to be correct.
The refined solution in each substructure calculated using the VTCR is based on the variational formulation of the vibration problem defined in each substructure of the whole structure. The substructure's boundary conditions are prescribed forces or displacements such that the power injected along each edge is that calculated by the SEA. The local displacements of this substructure subjected to these prescribed conditions are calculated using the VTCR; from this calculated solution, one retains only the total average (in time and space) energy density distribution, which is a quantity whose distribution does not depend on the way the power is injected, but only on the magnitude of the power injected along each edge. This last property, which can be viewed as a "Saint Venant" energy principle, has been proven for rod, the beam and plate structures.
An example of this approach is given in Figure 2, which represents a structure composed of two rods with different Young's moduli. Three curves are shown: the exact calculation (continuous line), the SEA solution (step function per rod) and the SEA/VCTR reanalysis solution (dashed line). The reanalysis solution is very close to the exact solution.

References

[1] Zienkiewicz O.C., Taylor R. L.: The finite element method: basic concepts and linear application. Mc Growhill, London, 1989.
[2] Ihlenburg F., Babušhka I.: Dispersion analysis and error of Galerkin finite element methods for the Helmoltz equation. *International Journal in Numerical Methods Engineering* 38, 3745-3774, 1995.
[3] Barbone P.E., Montgomery J.M., Michael O., Harari I.: Scattering by a hybrid asymptotic/finite element method. *Computer Methods in Applied Mechanics and Engineering* 164, 141-156, 1998.
[4] Lyon R.H., Richard H., Richard G.: Statistical Energy Analysis. Butterworth Heinemann 1995.
[5] Ladeveze P.: A new computational approach for structure vibrations in the medium frequency range (in french). *Comptes Rendus de l'Academie des Sciences Paris*, 322 (IIb 12), 849-856, 1996.
[6] Cremer L., Heckl M.: Structure borne sound: structural vibration and sound radiation at audio frequencies. Springler-Verlag, Berlin, 1973.

ACTIVE CONTROL OF DISK BRAKE SQUEAL

Utz von Wagner, Daniel Hochlenert, Peter Hagedorn
Department for Applied Mechanics, Technische Universität Darmstadt, 64289 Darmstadt, Germany

Summary Considerable effort is spent in the design and testing of disk brakes of modern passenger cars. This effort can be reduced if refined mathematical-mechanical models are used for studying the dynamics of these brakes before prototypes are available. The present paper is devoted to the modeling of a floating caliper disk brake, special regard being given to the suppression of squeal. The model developed includes the brake rotor, modeled as a flexible rotating plate, housing, piston, yoke, and friction pads. In this nonlinear model all the prominent features of squeal are reproduced, such as e.g. independence of the frequency on the speed, etc. In a test rig built in Darmstadt, the model is validated. In addition, the set-up also permits active control by using "smart pads". Those pads, which include piezoceramic actuators are successfully used for the suppression of squeal.

Introduction

Automotive brakes have greatly developed during the last decades. Engine power has increased considerably during this period and since the power to be dissipated in a brake can be several times than that of the engine, so did the forces acting at the brake. The geometric space available for the brakes in a car is however rather limited and constrained by the dimensions of the wheel, so that new forms of brake design had to be developed and some of these new designs were more susceptible to generate unwanted noises.

A typical modern floating caliper disk brake is shown in Fig. 1 in an artist's view, together with a mechanical model to be discussed in more detail later. The brake consists of a brake rotor (the *disk*), housing, piston, yoke and friction pads. The braking force is generated by friction between pads and disk. Not only the power but also the expectation for comfort have greatly increased over the last decades. This means that noise levels, and in particular brake noise, which were acceptable 20 or 30 years ago are no longer tolerated by the modern customer.

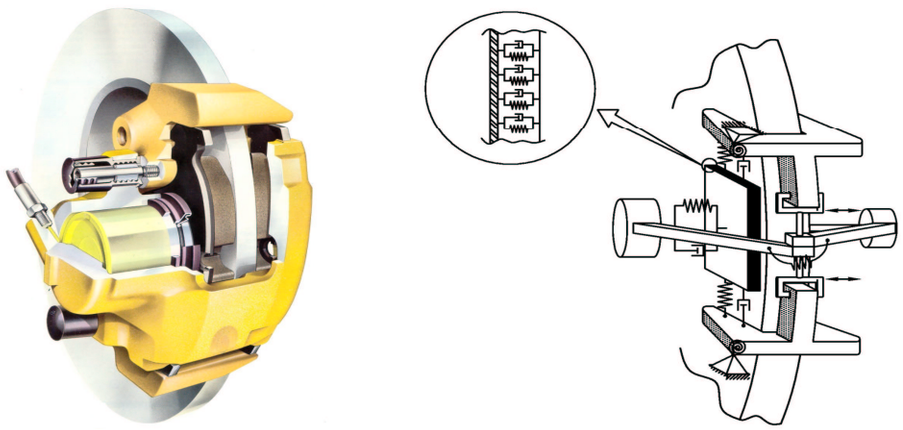


Fig. 1: A typical floating caliper disk brake, a) artist's view, b) dynamic model (schematic).

It should be noted that brake noise in general is exclusively a comfort problem, not affecting the brake function. Although there are some radical developments under way in brakes ('brake by wire'), the noise problem is not affected, as long as the brakes work with energy dissipation by dry friction. The different types of brake noise can be classified with respect to their frequencies and generating mechanisms. Brake noises in the frequency range of 100–1000 Hz are normally known as grind, grunt, moan and groan, etc. and can have different causes. The higher frequency noise in the frequency range between 1-12 kHz is normally termed squeal; it typically occurs at low speeds (0-10 km/h), e.g. during stopping at a traffic light. This paper is exclusively devoted to the modeling of disk brake squeal and the investigation of its suppression.

Modeling

It is commonly accepted by engineers and scientists working in the field, that brake squeal in the disk brake is initiated by an instability due to the friction forces leading to self-excited vibrations. The self-excited brake system then oscillates, reaching a limit cycle. Friction forces are non-conservative restoring forces or follower forces. They result in asymmetric stiffness-matrices, which can produce flutter-type instabilities. This explanation for squeal can be found in the literature (e.g. [1]) and it was used in earlier publications of the authors (e.g. [2]) for several models containing between 4 and 14 degrees of freedom.

The disk is considered as a Kirchhoff plate and discretized using the Galerkin method. Each pad can perform in-plane and out-of-plane motions and is modeled by a rigid plate and a nonlinear deformable layer of negligible inertia. Taking

into consideration corresponding vibration modes from experiments, the yoke and the caliper are discretized by multi-degree of freedom models. The models thus obtained exhibit the main properties of the experimentally observed squeal (Darmstadt test rig Fig. 2), e.g. independence of the squealing frequency from the vehicle speed. For the purpose of active control, a simplified 4-dof model is established (Fig. 3) containing also the active piezoceramic elements.

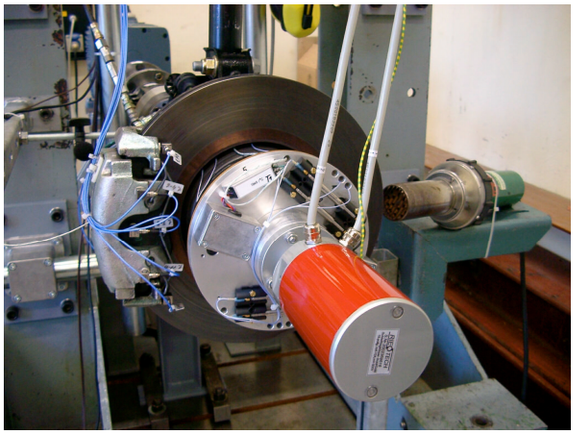


Fig. 2: Darmstadt brake test rig

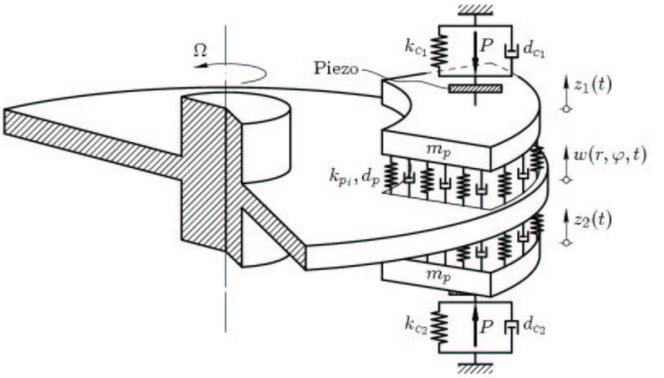


Fig. 3: Simplified model for brake squeal control

Active control

To suppress actively brake squeal, “smart pads” (Fig.4) were designed and manufactured. Those pads contain piezoceramic staple actuators, which can be independently driven at both pads and within the pads. Based on the model shown in Fig. 3, the method of optimal control is established. An observer is used to calculate the state vector from accelerometer measurements. This method was successfully applied in experiments for the active suppression of squeal.

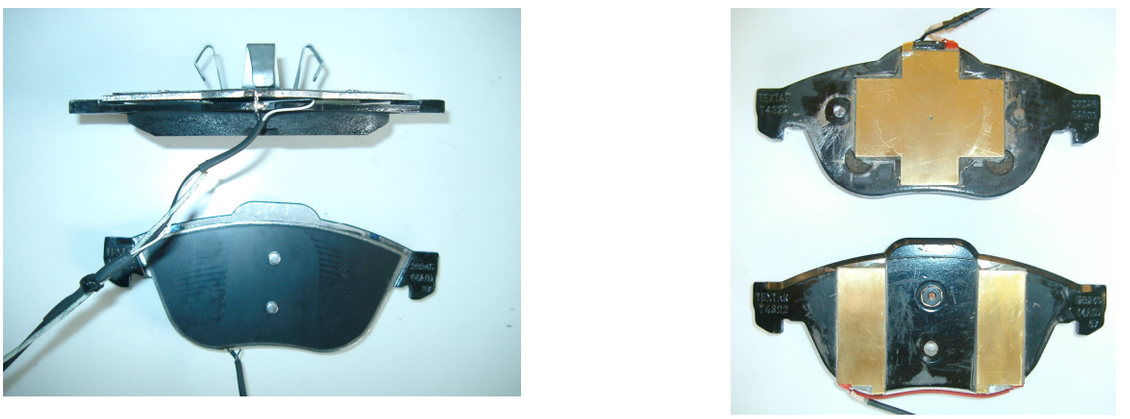


Fig. 4: Prototypes of “smart pads”

Conclusions

A model was developed for a floating caliper disk brake, with particular attention being paid to modeling the self-excitation leading to brake squeal. Suppression of the self-excitation via active control has been studied.

Active control of squeal presently is not envisaged as a technique to suppress squeal in the brake of a passenger car, but rather as a possible tool to be used in industrial laboratories to shorten the time for optimizing new brake designs, with high potential saving benefits. The development and laboratory implementation of the active squeal control goes along with a more profound understanding of brake squeal and a better modeling of the phenomena, ultimately leading to improvements in the design of disk brakes.

References

[1] Popp K., Rudolph, M.: Brake Squeal. In “Detection, Utilization and Avoidance of Nonlinear Dynamical Effects in Engineering Applications”, Shaker-Verlag, 197-225, 2001.

[2] von Wagner U., Jearsiripongkul T., Vomstein T., Chakraborty G., Hagedorn P.: Brake Squeal: Modeling and Experiments. VDI-Report 1749, 173-186, 2003.

Experimental And Theoretical Modal Analysis Of Three Support Rotor Test Rig Using LMS CADA-X and ABAQUS

Marcin Luczak*
*Polish Academy of Sciences IFFM PAN, Fiszera 14, PL 80-952 Gdañsk, Poland

Summary In the paper presented are the preliminary activities for the test, its course and the results of conducted investigations. The comparison of results obtained by means of impact test and numerical simulation and expected further scope of research have been presented.

Introduction

Numerical models find a wide application in diagnostics of turbines of large power. Such models are tuned based on the results of experimental investigations and measurements conducted both on real objects and laboratory apparatus. The objective of tuning a numerical model is a more precise mapping of the real object. In the research conducted at the Division for Rotor Dynamics and Slide Bearings utilized are codes simulating the dynamic states of the turboset. Tuning of such codes is based, amongst the others, on the results of experimental investigations performed on the large-scale laboratory stand for investigations of a three-support rotor fixed in slide bearings. One of the methods of acquisition of data regarding dynamic properties of laboratory rotor and the support structure is experimental method of modal analysis. The present work presents the results of investigations of the support structure and the rotor obtained by means of impact test. The impact test is relatively fast and easy to perform, but the obtained results are approximate. These, however enable planning of a more accurate test using the electro-dynamic shaker, which will be a subsequent part of conducted research. The objective of the presented investigations are preliminary determination of the modal model of supporting structure with the rotor founded at a standstill in the supports together with determination of the further progress of investigations. Also the results of numerical simulation was performed. The results of test and simulation were compared. The paper includes 4 main parts – description of an investigated object, FEM based simulation, modal test and comparison of results.

OBJECT OF INVESTIGATIONS

The object of investigations is a steel frame (6), which is a part of a support structure, bearing's mounts (2) and rotor (1). In the bearings fitted in the bearings stands there is a rotor, which during the tests remained at standstill. In the course of investigated configuration the rotor was founded in three supports. Investigated setup has been presented in Fig. 1

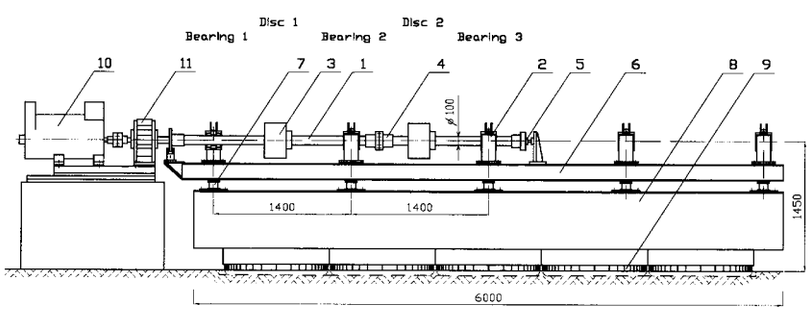


Fig. 1. Rig for investigations of rotor and bearings dynamics.
1 - shaft, 2 – bearings stand, 3 – bearings loading disc, 4 – coupling, 5 – resistance bearing, 6 – frame, 7 – frame supports, 8 - foundation block, 9 – pneumatic absorbers, 10 – propelling engine, 11- gear box

NUMERICAL SIMULATION (ABAQUS)

This part of investigation was performed in three stages: calculation of natural frequencies of rotor, calculation of natural frequencies of steel frame and calculations of eigenvalues of combined structure incorporating rotor and frame - Fig. 2

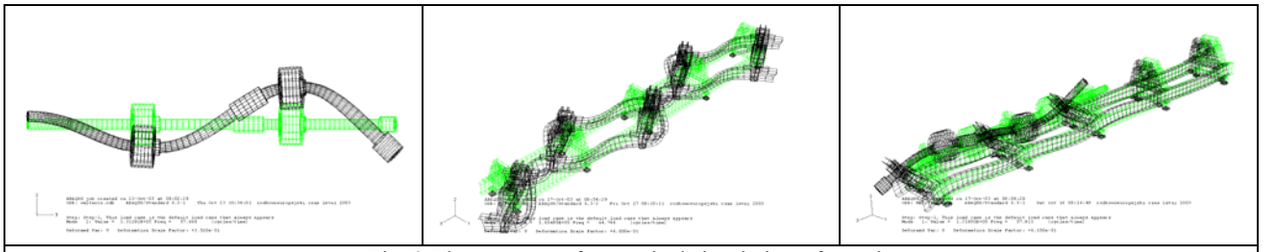


Fig. 2 Three stages of numerical simulation of test rig

EXPERIMENTAL MODAL ANALYSIS

The test has been performed in two excitation and measurement planes – horizontal and vertical in 30 measurement points. Values of spectral transition function, ordinary coherence and spectral function of power density have been measured. Estimation of modal model parameters has been performed by means of the Time Domain MDOF module for both series separately. Estimated were the poles of spectral transition function, constructed has been the stabilisation diagram, selected have been the poles, determined have been the forms of the object free vibrations, compared have been measured and determined during analysis distributions of spectral transition functions, conducted has been the assessment of identified modal model by means of the MAC criterion, enabling orthogonality testing of identified forms of free vibrations, constructed have been distributions of determined forms

COMPARISON

Results of both methods were compared. Two criteria of comparison were established: the accordance of value of natural frequency and corresponding forms – Fig. 3

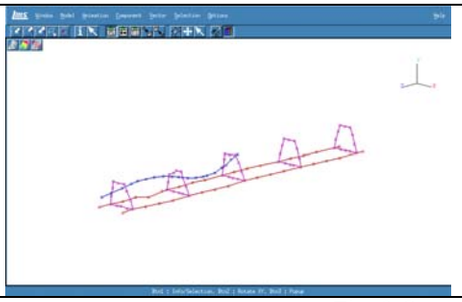
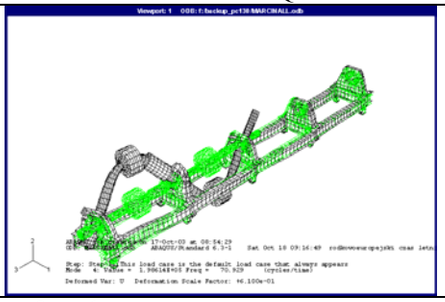
Measurement SCADAS III+PC CADA-X	Numerical simulation - ABAQUS
	

Fig. 3 Comparison of results

CONCLUSIONS

As a result of investigation two modal models of the object have been estimated. The comparison of results of numerical simulation and test is a proper point to continue investigation by means of both methods. FEM model has to be adjusted in order to bring its modal properties closer into line with the measured results. As far as experimental part is concerned, the use of electro-dynamic shaker in test will excite more modes, which could be observed in numerical results, and cannot be excited with relatively small modal hammer.The more precise results of test will enable more precise adjustment of numerical model.

References

[1] Uhl T: Komputerowo wspomagana identyfikacja modeli konstrukcji mechanicznych , WNT, Warszawa, 1997
[2] Uhl T, Lisowski W: Praktyczne problemy analizy modalnej konstrukcji, AGH, Kraków, 1996
[3] Ewins D. J.: Modal testing: Theory and practice, Research Studies Press Ltd, England, 1984
[4] CADA-X Manuals Rev 3.5.D, LMS, Leuven, 2000
[5] Kiciński J. Identyfikacja modeli konstrukcji podpierających maszyn wirnikowych. Oprac. wewn. IMP PAN, nr arch. 655/2000, Gdańsk 2000
[6] Chong-Won Lee, Kye-Si Won, Si-Kyoung Kim: Modal testing of rotors with rotating asymmetry, Proceedings of VETOMAC-1 Conference, Bangalore, INDIA, 2000, (na CD, poz. IP 13)
[7] Rybczyński J. Doświadczalne charakterystyki podatnościowe jako dane do wyznaczania parametrów modalnych korpusu maszyny. Materiały VI Szkoły analizy modalnej AGH, Kraków 2001
[8] S. Banaszek, „Model modalny wielopodporowej konstrukcji podpierającej wirnika laboratoryjnego”, 70-lecie urodzin i 45-lecie pracy naukowej Prof. dr hab. inż. Józefa Giergiela oraz V Szkoła Analizy Modalnej, Kraków 12-14.12.2001

STABILITY OF A ROTOR WITH PERIODICALLY VARYING ANGULAR VELOCITY

J. P. Meijaard
School of Mechanical, Materials, Manufacturing Engineering and Management,
The University of Nottingham, University Park, Nottingham NG7 2RD, U.K.

Summary The stability of a rotor with periodically varying angular velocity is investigated. The stability region in the parameter space is determined, which appears to be remarkably large. Parametric resonances are not found in this case.

INTRODUCTION

In the past, the dynamics of rotors that spin at a nominally constant rate have been studied and their stability has been investigated. An overview has been given by Crandall [1]. The influence of want of balance, asymmetry in stiffness and mass distribution, and viscoelastic material behaviour has been studied. Furthermore, the processes of starting and stopping of a rotor and the transition through critical speeds have been included in the analysis [2]. Less attention has been paid to the case in which the angular velocity is varied periodically, the case of parametric excitation. In the present study, in particular, the case in which the variations of angular velocities are large and the frequency of the excitation is low in comparison with the frequency of rotation will be considered.

As the simplest system, a massless simply supported shaft with equal bending stiffness in all directions and with a disk in its centre is studied; this system is usually called a Jeffcott rotor [3]. The shaft is rotated at a rate Ω that is a prescribed function of time. The dimensionless equations of motion, written in complex variables, with $z = x + iy$, where x and y are the lateral displacements of the centre of the disk, are

$$\ddot{z} + 2(c_\mathrm{e} + c_\mathrm{i})\dot{z} + (1 - 2i\Omega c_\mathrm{i})z = z_0(\Omega^2 - i\dot{\Omega})e^{i\theta}. \tag{1}$$

Here, c_e and c_i are the external and internal relative damping respectively, $z_0 = x_0 + iy_0$ is the mass eccentricity, and θ is the rotation angle. Extended models can include more general kinds of viscoelastic material behaviour for the shaft and different bending stiffnesses in two directions. For a stability analysis, only the homogeneous equations need be studied.

STABILITY ANALYSIS OF THE ROTOR

The stability analysis leads to the transformed equation

$$\ddot{z} + [1 - (c_\mathrm{e} + c_\mathrm{i})^2 - 2i\Omega c_\mathrm{i}]z = 0. \tag{2}$$

The stability condition is now that the real parts of the characteristic exponents must be smaller than $c_\mathrm{e} + c_\mathrm{i}$.

First the results for a rotor that spins at a constant angular velocity are recalled to mind. As has been found experimentally and theoretically by Newkirk and Kimball [4, 5], the internal damping makes the rotor unstable above a limit speed. For the system in Eq. (1), this speed is $\Omega_\mathrm{l} = 1 + c_\mathrm{e}/c_\mathrm{i}$.

For piecewise constant Ω, we are led to an equation studied by Meissner [6], but in the complex domain with complex parameters. The equations for the stability boundaries based on Floquet's theory [7] can be explicitly calculated. In the case that $\Omega = \Omega_0$ during half of the period and $\Omega = -\Omega_0$ during the other half, the expressions remain manageable. For small damping and large rotation rates, these yield equations for the stability boundaries of the form

$$T_\mathrm{p}\sqrt{\Omega_0 c_\mathrm{i}} = O(1). \tag{3}$$

where T_p is the period of the parametric excitation.

It is seen that if the internal damping is small, which is usually the case, the rotor remains stable for quite large values of the angular velocity or large periods of the parametric excitation. In particular, the equations with frozen coefficients can be unstable for all times, while the frequency of the variation of the angular velocity is relatively low.

For the more important case of a harmonically varying angular velocity, $\Omega = \Omega_0 \cos(2\pi t/T_\mathrm{p})$, Mathieu's equation [8] with complex coefficients is obtained. Although the stability conditions cannot be found in closed form, the stability boundaries in the parameter space can be determined either from tabulated values of the characteristic exponents or from numerical calculations. Qualitatively, the behaviour is the same as for the case with piecewise constant angular velocity.

INFLUENCE OF VISCOELASTICITY AND UNEQUAL BENDING STIFFNESSES

If the viscous internal damping is replaced by viscoelastic damping of the Maxwell type with a small relaxation time, which gives the so-called standard linear solid for the shaft [9], the limit speed increases a little and, more importantly, stability is regained at high constant angular velocities. This has as a consequence that for a fixed period of the parametric excitation, the rotor may be stable for any amplitude. In general, the region of stability is increased.

Small differences in the bending stiffness in two perpendicular directions have little influence on the results, although large differences may lead to instability.

CONCLUSIONS

It has been found that a rotor that undergoes a periodic variation of its velocity of rotation shows a remarkably large region of stability, even if the system with a corresponding fixed velocity of rotation is unstable for most of the time. Regions of parametric resonance are not found, which contrasts to most other examples of parametric excitation. For a viscoelastic material behaviour, the region of stability is even further enlarged. These results might be of some importance for rotors for which a constant angular velocity is not needed.

References

[1] S. H. Crandall, 'Rotordynamics', In W. Kliemann and N. Sri Namachchivaya (eds), *Nonlinear Dynamics and Stochastic Mechanics*, CRC Press, Boca Raton, FL, 1995, pp. 3–44.

[2] C. B. Biezeno and R. Grammel, *Technische Dynamik* (2. Auflage), Springer-Verlag, Berlin, 1953.

[3] H. H. Jeffcott, 'The lateral vibration of loaded shafts in the neighbourhood of a whirling speed.—The effect of want of balance', *The London, Edinburgh, and Dublin Philosophical Magazine and Journal of Science* (6) **37** (1919), 304–314.

[4] B. L. Newkirk, 'Shaft whipping', *General Electric Review* **27** (1924), 169–178.

[5] A. L. Kimball, Jr, 'Internal friction theory of shaft whirling', *General Electric Review* **27** (1924), 244–251.

[6] E. Meissner, 'Ueber Schüttelerscheinungen in Systemen mit periodisch veränderlicher Elastizität', *Schweizerische Bauzeitung* **72** (1918), 95–98.

[7] G. Floquet, 'Sur les équations différentielles linéaires à coefficients périodiques', *Annales Scientifiques de l'École Normale Supérieure* (2) **12** (1883), 47–88.

[8] E. Mathieu, 'Mémoire sur le mouvement vibratoire d'une membrane de forme elliptique', *Journal de Mathématiques Pures et Appliquées* (2) **13** (1868), 137–203.

[9] Y. C. Fung, *Foundations of Solid Mechanics*, Prentice-Hall, Englewood Cliffs, NJ, 1965.

PARADOXICAL BEHAVIOUR OF VIBRATING SYSTEMS CHALLENGING RAYLEIGH'S THEOREM

Tibor Tarnai
Budapest University of Technology and Economics, Budapest, Müegyetem rkp. 3., H-1521 Hungary

Summary Rayleigh has proved a theorem that an additional constraint cannot reduce any of the natural frequencies of an elastic vibration system. Since linear free vibration and linear stability problems are analogous to each other mathematically, both lead to eigenvalue problems involving linear operators, the question arises, whether there exist a counterexample to Rayleigh's theorem, because to a similar theorem on the critical loads, there are counterexamples. In this paper, examples of vibrating systems will be shown that contradict Rayleigh's theorem. So the known form of Rayleigh's theorem might need correction.

PROBLEM DESCRIPTION

There is a widely-held opinion in engineering that the reinforcement of an elastic structure, either by an increase of the stiffness or by the provision of additional constraints increases both its critical loads and natural frequencies. This view, however, has not proved to be correct in all aspects.
The general validity of this opinion was contravened first in the case of the effect of stiffening and additional restraints on the buckling load [4]. The effect of additional restraint on the natural frequencies of a conservative vibration system was investigated by Rayleigh [2]. He proved a theorem that an additional constraint or an increase in the stiffness cannot reduce any of the natural frequencies. This theorem is generally accepted and incorporated in all the most important textbooks on the subject.
In this paper, it will be shown that Rayleigh's theorem on the natural frequency increasing effect of constraints or stiffening might need correction. Examples of vibrating systems will be presented in which, paradoxically, an additional restraint decreases the corresponding natural frequencies that contradicts Rayleigh's more than hundred-year-old theorem.

EFFECT OF ADDITIONAL RESTRAINT UPON THE ELASTIC CRITICAL LOAD

Let us assume (a) the system has a potential; (b) only bifurcation problems are considered so that the critical load factor means the load factor associated with the point of bifurcation; (c) the material of the structure is linearly elastic; (d) the displacements are small. Under these conditions, the following theorems hold [4].
THEOREM 1. *Additional restraint on any component of displacement, which is found in the eigenvalue problem of buckling of a structure, cannot decrease the minimum positive critical load factor.*
THEOREM 2. *Additional restraint on any component of displacement, which is not found in the eigenvalue problem of buckling of a structure, can decrease the minimum positive critical load factor.*

Example
To illustrate Theorem 2, consider the structure in Fig. 1, composed of weightless rigid members of length l and weightless elastic springs with rigidities c_1, c_2, c, loaded by a vertical force P at its upper joint, but mass m is not taken into consideration. The critical load of this structure is

$$P_{cr} = \frac{cl}{2}\left(1 + \frac{c_1}{c_2}\right). \tag{1}$$

Expression (1) shows that with an increase of the spring rigidity c_2, the critical load decreases.

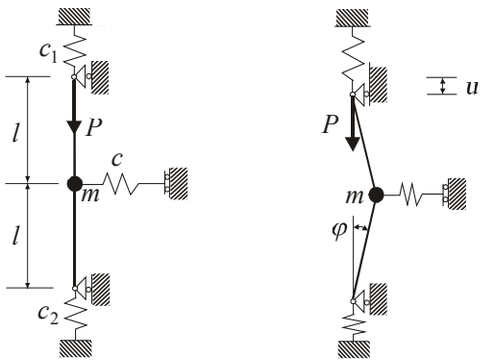


Fig. 1. The structure prior to and after displacements

EFFECT OF ADDITIONAL RESTRAINT UPON THE NATURAL FREQUENCIES

Consider a version of Rayleigh's theorem on constrained vibration as formulated by Renton [3]:
THEOREM 3. *"Suppose that the natural frequencies of a structure are* $\omega_1 \le \omega_2 \le \ldots \le \omega_r \le \ldots \le \omega_n$. *If one constraint is imposed on the structure, then the new natural frequencies of the structure, also arranged in order, will be such that the rth,* ω_r', *will lie between the rth and the* $(r+1)$*th original frequencies, or* $\omega_r \le \omega_r' \le \omega_{r+1}$."
Rayleigh's theorem on stiffening can be stated as follows.
THEOREM 4. *If the system stiffens, every natural frequency increases (or remains the same).*
Here, the term 'constraint' refers to an inhibition of one of the degrees of freedom of the structure; that is, the constraint removes that degree of freedom altogether. Stiffening does not mean simply an increase in the rigidity of one or more springs. According to Courant and Hilbert [1]: "Stiffening of the system means change to a system whose kinetic energy is the same but whose potential energy is greater for the same values of the coordinates." Thus, if a spring rigidity is increased, but as a consequence, the potential energy decreases, and so some of the natural frequencies decrease, then this fact does not contradict Theorem 4. However, if at least one natural frequency decreases by introducing an additional constraint, then Theorem 3 in the present form is not right.
These theorems are obviously valid if the potential energy means strain energy. However, there are vibration problems where static external forces are in the system, so these forces also contribute to the potential. Such a problem is, for instance, where an axial compression force P is on a vibrating beam, which combines two problems: (a) buckling of a beam with no vibration, (b) vibration of an unloaded beam. If the rth vibration and buckling modes are identical, then

$$\omega_r^2 = \omega_{r0}^2\left(1-\frac{P}{P_{r,cr}}\right) \tag{2}$$

where $P_{r,cr}$ is the rth critical force, ω_r is the rth natural frequency of the beam loaded by P, ω_{r0} is the rth natural frequency of the beam not loaded by P [5]. Thus, if additional restraint reduces the critical load then at the same time reduces the corresponding natural frequency.

Example
In Fig. 1, the structure with a mass m at its middle joint forms a two-degree-of-freedom vibration system. Let us suppose that $P < P_{cr}$ is a constant compression force, and $c_1 > c$. The critical force P_{cr} is given by (1).
(a) *An increase in the stiffness of an already existing restraint.* The system has two natural frequencies:

$$\omega_1^2 = \frac{c}{m}\left(1-P\left[\frac{cl}{2}\left(1+\frac{c_1}{c_2}\right)\right]^{-1}\right), \qquad \omega_2^2 = \frac{c_1+c_2}{m}. \tag{3a, b}$$

Relationship (3a) has the same form as (2). If the spring rigidity c_2 is increased then ω_2 increases, but ω_1 decreases, that is, $\omega_1' < \omega_1 < \omega_2 < \omega_2'$, that seemingly contradicts Theorem 4. In fact, however, there is no contradiction because there are displacement coordinates for which the potential energy can decrease with an increase in c_2.
(b) *An addition of a constraint to the structure.* First, let $c_2 = 0$. This case means that we have a two-degree-of-freedom vibration system where the external force P does not play any role even it is present. In this case we have:

$$\omega_1^2 = \frac{c}{m}, \qquad \omega_2^2 = \frac{c_1}{m}. \tag{4a, b}$$

Then, let $c_2 = \infty$. The modified system obtained is a one-degree-of-freedom system where the vertical vibration mode ceases to exist. From (3a), we obtain for the modified system:

$$\omega_1'^2 = \frac{c}{m}\left(1-\frac{2P}{cl}\right), \tag{5}$$

that is, $\omega_1' < \omega_1 < \omega_2$, that contradicts Theorem 3.

CONCLUSIONS

From the results presented here we can conclude that Rayleigh's theorem is valid if additional restraints have no effect on pre-vibration displacements, or there are no pre-vibration displacements, but additional restraints on pre-vibration displacements can decrease the natural frequencies. The latter case can happen if external static forces are in the system.

References

[1] Courant R., Hilbert D.: Methods of Mathematical Physics, Vol. I. Wiley-Interscience, New York 1989.
[2] Rayleigh J.W.S.: The Theory of Sound, Vol. 2, 2nd edn. Dover, New York 1945.
[3] Renton J.D.: Elastic Beams and Frames. Camford, Oxford 2000.
[4] Tarnai T.: Destabilizing Effect of Additional Restraint on Elastic Bar Structures. *Int.J.Mech.Sci.* **22**: 379-390, 1980.
[5] Timoshenko S., Young D.H., Weaver W.: Vibration Problems in Engineering, 4th edn. Wiley, New York 1974.

IMPERFECTION SENSITIVITY OF CIRCULAR ARCH'S NON-LINEAR MODES

Carlos E.N. Mazzilli, Odulpho G.P. Baracho Neto
Mário E.S. Soares, César T. Sanches

Laboratório de Mecânica Computacional
Escola Politécnica da Universidade de São Paulo
Caixa Postal 61548, São Paulo 05508-940, Brazil

Summary The paper addresses the imperfection sensitivity of non-linear vibration modes of moderately low *and* slender circular arches. Such structures may undergo unstable symmetric bifurcation prior to snap-through, under static uniform radial loading. Such instability corresponds to a buckling load that happens to be imperfection sensitive. A small imperfection may drastically cause the reduction of the arch's critical load and, consequently, of its stiffness and vibration properties.

INTRODUCTION

The non-linear static and dynamic behaviour of circular arches is strongly dependent of the slenderness ratio $\left(\lambda = \alpha^2 R / h\right)$, where α, R and h stand for the arch's semi-central angle, radius and thickness, respectively. It is well known that very low arches may experience limit-point instability followed by snap-through. It is also known that arches that are moderately low and slender ($\lambda > 2.65$), under static uniform radial loading, may experience unstable symmetric bifurcation prior to snap-through. Such instability corresponds to a buckling load that happens to be imperfection sensitive. In other words, a small imperfection (such as deviation in geometry, load offset, initial stresses, etc) may drastically cause the reduction of the arch's critical load and, consequently, of its stiffness and vibration properties. The present investigation addresses the issue of imperfection sensitivity of non-linear vibration modes of moderately low and slender circular arches.

NON-LINEAR MODES OF VIBRATION

With regard to non-linear modes, it is mandatory to refer to the recent and relevant work of Shaw and co-workers [1], which set the foundations for evaluating non-linear modes of systems with few degrees of freedom by the invariant manifold technique. The authors have broadened this technique to encompass the analysis of finite-element models of plane frames [2]. Further, they have developed another technique, based upon the method of multiple scales [3], which proved to be capable of handling this problem and, even more, the one of evaluating the so-called non-linear multimodes, which come into play when the system is under internal resonance due to strong modal coupling. It is believed that both techniques, within the frame of finite-element modelling, are state-of-the-art.

PARAMETRIC ANALYSIS AND ASSESSMENT OF IMPERFECTION SENSITIVITY

An extensive parametric survey is under way to consider different slenderness ratios, as well as varied static load levels and equivalent imperfection parameters, so as to supply a sharp picture of non-linear free vibrations in circular arches. Planar frame finite-element models are proposed to represent circular arches, so that it is possible to make use of the computational codes already developed at the Escola Politécnica's Computational Mechanics Laboratory. Of course, prior to any non-linear analysis, a usual linear undamped modal analysis is performed for reference. Next, non-linear normal modes are evaluated following the two approaches afore mentioned, namely the invariant manifold and the multiple-scale techniques, taking into account viscous damping, if so wished, yet still considering the vibrations about the undeformed configuration, and results are carefully compared with each other. Then, for a range of the static loading and the equivalent imperfection parameter, a non-linear static analysis is performed, so as to render the deformed equilibrium configuration. Finally, the non-linear vibration modes about the deformed equilibrium configuration are searched by the multiple-scale technique and the imperfection sensitivity is established.

RESULTS

At present, the authors have already been able to draw results for all types of proposed analyses, yet for only one set of parameters (slenderness ratio, static uniform radial loading, vibration amplitude and imperfection parameter). These first results confirm the authors' expectation with respect to the importance of considering non-linear analyses to establish the vibration properties of moderately low and slender arches. More results will be available at short notice, as an extensive parametric survey continues to be carried out according to the same methodology, thus allowing for a broader view of the problem. Just for the sake of presenting a case study, a pinned-pinned arch (Young's modulus $E = 73.3$ GPa; semi-central angle $\alpha = 0.894$ rad; radius $R = 1$ m; section height $h = 0.002$ m; section depth

$b = 0.02$ m) has been considered. It has been discretised with 14 Bernoulli-Euler beam-elements and its first non-linear mode has been evaluated by both techniques (invariant manifold and the method of multiple scales). Only undamped analyses have been considered — although the developed procedures can also handle systems with viscous-damping —, so that the free vibration responses will last longer and the comparison between the different analyses can be assessed along an extended time range. The unloaded structure without imperfection has been analysed in the first simulation. The rotation at the left-hand side support p_1 has been taken as modal variable. Figure 1 presents the comparison between the linear and non-linear responses. The non-linear responses were obtained by the multiple scale method (ms) and the invariant manifold technique (im). As it is seen in Figure 1, there is a perfect fitting between both non-linear solutions, yet a clear distinction between them and the linear solution as time progresses, due to small frequency differences. Next, the structure without imperfection has been subjected to a static uniform radial loading of $p = 9$ N/m (approximately 75% of the critical load [4], $p_{cr} = 12.1$ N/m), prior to be forced to vibrate freely. Figure 2 shows the time-evolution of p_1 (about the equilibrium configuration) for this situation. Then, an imperfection has been introduced into the system, in the form of an anti-symmetric loading superimposed to the static uniform radial loading. An equivalent imperfection parameter ε can be conveniently introduced to give a measure of the anti-symmetric loading with respect to the symmetric one. In the numerical essay it has been considered $\varepsilon = 8.8\%$. Again, the first non-linear mode about the new deformed configuration has been evaluated and the time-evolution of p_1 for this new situation is also depicted in Figure 2. A comprehensive parametric survey must also take into account that the non-linear modes are characterised by a non-linear relationship between frequency and amplitude. For the imperfect system, it is necessary to keep the amplitudes small; otherwise strong cubic non-linearities will spoil the solution. The linear theory first natural frequency is found to be 4.84 Hz; the first non-linear mode frequency about the undeformed equilibrium configuration is 4.76 Hz, as evaluated by both the invariant manifold and the multiple scales techniques; the first non-linear mode frequency about the deformed equilibrium configuration of the perfect system, under a static uniform radial loading of 75% of the critical one, is 2.38 Hz, as evaluated by the multiple-scale technique; the first non-linear mode frequency about the deformed equilibrium configuration of the imperfect system, under a static uniform radial loading of 75% of the critical one plus an anti-symmetric loading of 8.8% of the symmetric one, is 2.31 Hz, as evaluated by the multiple-scale technique. For the ensemble of control parameters considered here, it is seen that the static uniform radial loading represents a major influence upon the free-vibration characteristics of moderately low and slender circular arches (51% decrease in the frequency with respect to the linear theory). Imperfection sensitivity is only apparently mild here, responding for a "modest" 3% additional reduction with respect to the non-linear mode of the perfect system (yet for extremely small vibration amplitudes 10^{-5} rad!). Nevertheless, the system becomes extremely sensitive to the initial conditions. Larger vibration amplitudes would produce severe change in the vibration properties, which cannot be properly foreseen by the technique. As pointed out before, a complete picture on imperfection sensitivity will only be available after completion of an exhaustive parametric survey, considering a full range of slenderness ratios, static loading levels with respect to the critical one, equivalent imperfection parameters and vibration amplitudes.

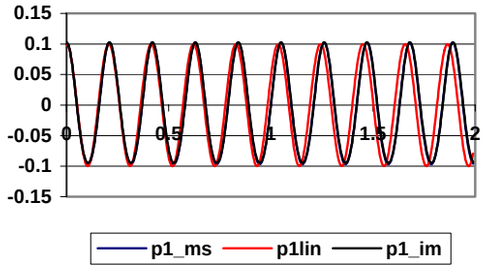


Figure 1: Time evolution of rotation p_1 with respect to the undeformed configuration

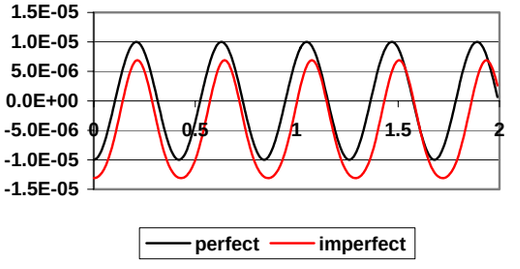


Figure 2: Time evolution of rotation difference Δp_1 with respect to the equilibrium configuration

References

[1] Shaw S.W., Pierre C.: Normal modes for non-linear vibratory systems. *J. Sound and Vibration* **164(1)**, 85-124, 1993.

[2] Soares M.E.S., Mazzilli C.E.N.: Nonlinear normal modes of planar frames discretised by the finite-element method. *Computers & Structures* **77**, 485-493, 2000.

[3] Mazzilli C.E.N., Baracho Neto O.G.P.: Evaluation of non-linear normal modes for finite-element models. *Computers & Structures* **80 (11)**, 957-966, 2002.

[4] Dym C.L.: Stability theory and its application to structural mechanics, Noordhoff, Leiden, The Netherlands, 1974.

OPTIMAL SHAPES OF PARAMETRICALLY EXCITED BEAMS

Alexei A. Mailybaev[*], Hiroshi Yabuno[**], and Hiroyuki Kaneko[**]
[*]*Institute of Mechanics, Moscow State University, Michurinskii pr. 1, 119192 Moscow, Russia*
[**]*Institute of Engineering Mechanics, University of Tsukuba, Tsukuba City 305-8573, Japan*

Summary Straight elastically supported beams of variable width under the action of a periodic axial force are considered. Two shape optimization problems for reducing parametric resonance zones are studied. In the first problem, the range of resonant frequencies is minimized for a given parametric resonance zone and a fixed amplitude of excitation. In the second problem, the minimal (critical) amplitude of the excitation force is maximized. These two optimization problems are proved to be equivalent in case of small external damping and small excitation force amplitude. It is shown that optimal designs have strong universal character, i.e., they depend only on the natural modes involved in the parametric resonance and boundary conditions. Efficient numerical method of optimization is developed. Optimal beam shapes are found for different boundary conditions and resonant modes. Experiments for uniform and optimal simply supported beams are conducted, which show a very good agreement with theoretical prediction.

INTRODUCTION

Shape optimization of beams under different loading conditions is an interesting and important topic both from theoretical and practical point of view. On one hand, this problem requires sophisticated analytical and numerical methods for sensitivity analysis and knowledge from bifurcation and singularity theories. On the other hand, the correct formulation of the problem, including minimal width constraints and analysis of nonlinear behavior, may strongly influence the practical use of optimal designs. We refer the reader to the surveys on optimal beam problems [1] for the case of static loads and [2] for the case of follower loads. In [3], beams were optimized under several natural frequency constraints. The optimal shape of a pipe conveying fluid was investigated in [4]. Optimal shapes of a beam, minimizing the critical excitation amplitudes of primary parametric resonance zones, were analyzed numerically in [5]. Very few experimental works on optimal beams are available; see [4, 6].

OPTIMIZATION PROBLEMS

In this contribution, we consider beams of rectangular cross-section with constant thickness and variable width. The length and total volume of the beam are fixed. Elastic supports at both ends are considered, which, in particular, include the cases of simply supported and clamped boundary conditions. Parametric resonance of the beam under a periodic axial force is studied. Two optimization problems are considered. In the first problem, the range of resonant excitation frequencies is minimized for a given parametric resonance zone and a fixed amplitude of excitation. In the second problem, the minimal (critical) amplitude of the excitation force is maximized.

UNIVERSAL CHARACTER OF OPTIMAL DESIGNS

We prove that the two optimization problems under consideration are equivalent in case of small external damping and a small excitation force amplitude. Moreover, we show that the optimal designs do not depend on the damping coefficient, on the value of the excitation amplitude in the first problem, and on the resonance number. All these properties reveal strong universal character of optimal beam shapes, which depend only on the natural modes involved in parametric resonance and on the boundary conditions. This universality is of great importance for practical use of optimal designs. Numerical computations show that the optimal shape changes weakly if the parametric excitation is applied to a prestressed beam (with a static axial force lower than the critical Euler force).

NUMERICAL METHOD AND RESULTS

In the analysis, we use explicit formulae obtained recently in [7] (see also [8]), which describe the parametric resonance zones as half-cones in the three-parameter space (frequency and amplitude of parametric excitation and damping coefficient). As a result, the optimization problem is reduced to the minimization of an objective functional depending only on natural frequencies and modes involved in parametric resonance. This approach allows avoiding time-consuming multiple integrations of equations of motion required for stability analysis in the Floquet theory, see [8]. Optimal beam shapes are found numerically for different boundary conditions and resonant modes.

EXPERIMENTS

Experiments on simple parametric resonance of the first mode are conducted for the uniform and optimal simply supported beams. The reduction of the resonance zone for the optimal beam is shown to be in very good agreement with theoretical prediction. Nonlinear response of the uniform and optimal beams is analyzed experimentally.

COMPARISON WITH PREVIOUS WORKS

Compared to the previous work [5], where the beam of circular cross-section was optimized, the present study has the following advantages. First, we use a more realistic model of external damping taking into account the beam width variation. We consider two different optimization problems and prove universality properties of our optimal designs. Finally, the gain in optimization attained in our study is about 17–22% (depending on the boundary conditions and width constraints), which is higher than 4–9% obtained in [5].

References

[1] Seyranian A.P., Privalova O.G.: The Lagrange problem on an optimal column: old and new results. *Structural and Multidisciplinary Optimization* **25**:393-410, 2003.

[2] Langthjem M.A., Sugiyama Y.: Dynamic stability of columns subjected to follower loads: a survey. *J. Sound Vibration* **238**:809-851, 2000.

[3] Pedersen P.: Design with several eigenvalue constraints by finite elements and linear programming. *J. Structural Mechanics* **10**:243-271, 1982-83.

[4] Langthjem M.A.: Dynamics, stability and optimal design of structures with fluid interaction. DCAMM Report no. S71, Technical University of Denmark, Lyngby, 1996.

[5] Seyranian A.P., Solem F., Pedersen P.: Multi-parameter linear periodic systems: sensitivity analysis and applications. *J. Sound Vibration* **229**:89-111, 2000.

[6] Langthjem M.A.: Optimum design of cantilevered columns subjected to non-conservative loading by rocket thrust. *Doctoral Thesis*, Osaka Prefecture University, Osaka, 2002.

[7] Mailybaev A.A., Seyranian A.P.: Parametric resonance in systems with small dissipation. *J. Appl. Math. Mech.* **65**:755-767, 2001.

[8] Mailybaev A.A., Seyranian A.P.: Multiparameter Stability Theory with Mechanical Applications. World Scientific, Singapore 2003.

NON TRIVIAL EFFECT OF STRONG HIGH-FREQUENCY EXCITATION ON A NONLINEAR CONTROLLED SYSTEM

Alexander Fidlin*, Jon J. Thomsen**
** LuK GmbH & Co. oHG, Industriestr. 3, D-77815, Buehl, Germany*
*** TU Denmark, MEK – Solid Mechanics, Building 404, DK-2800, Kgs. Lyngby, Denmark*

Summary. Nontrivial biasing effect of high-frequency excitation on a standard nonlinear system with a standard optimal controller is investigated. The interaction between fast excitation and strong damping terms in the control system is identified to be the cause of the permanent control error. A "slow observer" ignoring fast motions is shown to be the simplest way to avoid the undesired bias. All the results are obtained both analytically and numerically.

INVESTIGATED PROBLEM AND OBSERVED EFFECT

Nontrivial effects of high-frequency (HF) excitation on mechanical systems have been investigated intensively in the last decade [1 – 3]. Some of these effects are usually used in controlled systems in form of additional dither signals for example to smoothen out the undesired friction and or to reduce the effective hysteresis. However other effects like stiffening and first of all biasing are normally undesired.
A standard optimal controller for a standard nonlinear system (a movable cart used to balance an inverted pendulum vertically against the acceleration of gravity) is considered in this study. The only difference to the classical control problem [4] is that the system's base is subjected to synchronized HF-excitation in both vertical and horizontal directions.

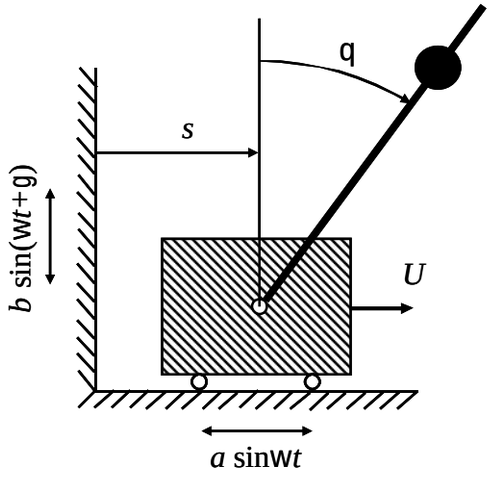


Fig. 1. Inverted pendulum controlled through the moving cart.

This excitation has turned out to affect the behaviour of the considered system dramatically. Both the cart and the pendulum are stabilized on the average by the control system, but the stable position is far away from the desired one even for relative small excitation intensity. Even though the used LQR control is not limited in power and it applies force directly to the cart it is not able to push it in the desired position. The permanent (on the average) control error depends obviously on the intensity of the excitation, but it also depends on the phase difference between vertical and horizontal excitations. The resulting averaged equilibrium can be controlled by the phase difference between the two external HF-excitations. It seems to be even more paradox, that the seemingly obvious idea to increase the control coefficients worsens the situation. On the other hand the whole effect disappears if one of the excitations fails or if their frequencies are different (which would be the case for a standard random noise.

ANALYTICAL PREDICTIONS FOR QUASI-EQUILIBRIUM

The main difference between pure and controlled mechanical systems with respect to HF-vibrations is the damping level. Whereas damping in pure mechanical systems is normally small, its level in the controlled systems is usually high, because usual control strategies try to avoid overshooting. This obstacle makes on the one hand the system unsuitable for the standard averaging; on the other hand it causes the strong interaction between the control system and the external excitation. However a modified averaging procedure suitable for the case of non-critical fast variables [5] can be established and applied in this case. It enables to obtain quite simple approximate expressions for the bias, being quite accurate for the large values of the excitation frequency and sufficiently small values of the average pendulum angle. The approximate solution is given by (1), where $k_1,\ldots,k_4$ are the coefficients of the control system:

$$\varphi_\infty = \frac{\frac{k_2}{\omega} ab\left(\sin\gamma - \frac{k_2 - k_4}{\omega}\cos\gamma\right)}{2\left(1+\left(\frac{k_2-k_4}{\omega}\right)^2\right) - b^2\left(1+\frac{k_2(k_2-k_4)}{\omega^2}\right)}; \qquad \xi_\infty = -\frac{k_3}{k_1}\varphi_\infty \tag{1}$$

$$U = -k_1\xi - k_2\dot{\xi} - k_3\varphi - k_4\dot{\varphi}$$

This solution shows all the important properties of the effect obtained in numerical simulations:

- The bias exists only in presence of both horizontal and vertical vibrations
- Its average level increases with the excitation intensity, but it also increases with the increased control coefficients (first of all with the coefficient k_2 .
- The bias level depends on and can be controlled by the phase difference between the horizontal and vertical excitations

Analytic prediction for the bias shows, the interaction between fast excitation and strong damping terms in the control system to be the cause of the permanent control error.
From the physical point of view the bias is caused by the asymmetric excitation, leading to an asymmetric averaged stiffness. It moves the initially symmetric equilibrium away from zero, and the pendulum leans slightly, on the average. As a consequence the controller has to stabilize the cart in a position located in the opposite direction to the pendulum lean.

CONCLUSIONS

The described effect does not depend on the specific form of the control algorithm. It seems to be a quite general effect, typical for any kind of system with both external and parametric excitation and sufficiently high damping level. It is also possible to avoid it using quite simple means. The simplest way is to keep the HF-excitation away from the control system. A “slow observer” inserted as a filter between the mechanical system and the signal entrance of the control algorithm accomplishes this task perfectly. The only price, which has to be paid for this solution is the fact, that the “brain” of our system will always see the world through the “slow spectacles”.

References

[1] Blekhman I.I.: Vibrational Mechanics - Nonlinear Dynamic Effects, General Approach, Applications, World Scientific, Singapore, 2000.

[2] Thomsen J.J.: Some General Effects of Strong High-frequency Excitation: Stiffening, Biasing, and Smoothening. *J. Sound and Vibration* **253** (4) 807 – 831, 2002.

[3] Fidlin A.: On Asymptotic Properties of Systems With Strong and Very Strong High-frequency Excitation. . *J. Sound and Vibration* **235** (2) 219 – 233, 2000.

[4] Kwakernaak H. , Sivan R.: Linear Optimal Control Systems, Wiley, NY, 1972.

[5] Volosov V.M., Morgunov B.I.: Methods of Averaging in the Theory of Nonlinear Oscillatory Systems (in Russian), Publishers of the Moscow State University, Moscow, 1971.

AN APPROACH TO WORM-LIKE MOTION

Klaus Zimmermann*, Igor Zeidis*, Joachim Steigenberger**, Mikhail Pivovarov*
*TUI, Faculty of Mechanical Engineering, PF 10 05 65, 98684 Ilmenau, Germany
**TUI, Faculty of Mathematics and Natural Sciences, PF 10 05 65, 98684 Ilmenau, Germany

Summary A worm-like motion system in form of material points, connected by a spring is considered. It is shown that at presence of internal excitation and non-symmetric Coulomb dry friction a motion of the system with a constant "on the average" velocity is possible and this motion is stable. The expression for the velocity is obtained. A worm prototype applying the principles outlined above has been constructed.

MATHEMATICAL MODEL

Observing the locomotion of worms one recognizes a conversion of (mostly periodic) internally driven motions into change of external position (undulatory locomotion). In [1] the motion of three material points in a common straight line with the method of direct separation of motion [2] is considered. Left and right points are equipped with scales contacting the ground, and middle point is under action of harmonic external force. In this paper the motion of a system of two material points x_1 and x_2 with the masses m, connected by a spring of stiffness c along an axis x is considered (Fig.1).

It is supposed that the points are under the action of a small non-symmetric Coulomb dry frictional force $\varepsilon m F(\dot{x})$, $\varepsilon << 1$, depending on velocities $\dot{x} = \dot{x}_i\,(i = 1,2)$, where $F(\dot{x}) = F_+$ if $\dot{x} > 0$, $F(\dot{x}) = -F_-$ if $\dot{x} < 0$, $F(\dot{x}) = F_0$ if $\dot{x} = 0$; $-F_- < F_0 < F_+$, $F_- \geq F_+ \geq 0$. Excitation is carried out due to action of small internal forces $G(t) = \varepsilon m(b_0 + b\cos\psi)$, $\psi = \nu t$. Such forces arise, for example, if the spring is a magnetizable elastic material by influence of an external magnetic field [2]. The equations of the motion are:

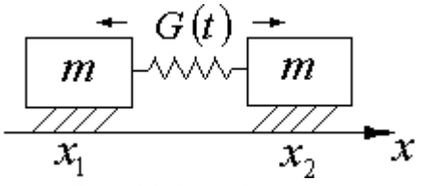


Fig.1. Model of the system

$$\begin{aligned} m\ddot{x}_1 + c(x_1 - x_2 + l_0) + \varepsilon m(b_0 + b\cos\psi) + \varepsilon m F(\dot{x}_1) = 0, \\ m\ddot{x}_2 + c(x_2 - x_1 - l_0) - \varepsilon m(b_0 + b\cos\psi) + \varepsilon m F(\dot{x}_2) = 0. \end{aligned} \tag{1}$$

The system (1) is integrable on intervals where $F(\dot{x})$ is constant. However such approach does not give an opportunity of a qualitative description of motion as whole because the solutions "stick together" on intervals. Designating $\omega^2 = c/m$, and replacing $x_2 \to x_2 - l_0 - \varepsilon b_0/\omega^2$ we receive a system of equations, holding the old symbols:

$$\begin{aligned} \ddot{x}_1 + \omega^2(x_1 - x_2) = -\varepsilon\left[F(\dot{x}_1) + b\cos\psi\right], \\ \ddot{x}_2 + \omega^2(x_2 - x_1) = -\varepsilon\left[F(\dot{x}_2) - b\cos\psi\right]. \end{aligned} \tag{2}$$

To system (2) we apply procedure of averaging according to [4]. For this purpose we introduce variables: the velocity of the center of mass $V = (\dot{x}_1 + \dot{x}_2)/2$ and a deviation of points relatively to the center of mass $z = (x_2 - x_1)/2$. Non-disturbed system ($\varepsilon = 0$) has two integrals: $V = const$ and the amplitude of oscillations relatively to the center of mass a is constant, $z = a\cos\varphi$, $\varphi = \Omega t + \vartheta$, $\Omega = \sqrt{2}\,\omega$, ϑ - is an arbitrary constant. Replacing $V = (\dot{x}_1 + \dot{x}_2)/2$, $z = a\cos(\Omega t + \vartheta)$, $\dot{z} = -a\Omega\sin(\Omega t + \vartheta)$, where V, a, ϑ - slow variables, we receive system(2) in a standard form[4]:

$$\begin{aligned} \dot{V} &= -\frac{\varepsilon}{2}\left[F(V + a\Omega\sin\varphi) + F(V - a\Omega\sin\varphi)\right], \\ \dot{a} &= -\frac{\varepsilon}{2\Omega}\sin\varphi\left[F(V + a\Omega\sin\varphi) - F(V - a\Omega\sin\varphi) + 2b\cos\psi\right], \\ \dot{\varphi} &= \Omega - \frac{\varepsilon}{2a\Omega}\cos\varphi\left[F(V + a\Omega\sin\varphi) - F(V - a\Omega\sin\varphi) + 2b\cos\psi\right], \\ \dot{\psi} &= \nu. \end{aligned} \tag{3}$$

We investigate the system (3) in a vicinity of the main resonance $\nu = \Omega + \varepsilon\,\Delta$, $\Delta \neq 0$. For this purpose we introduce a new slow variable $\xi = \psi - \varphi$ and we exclude a fast variable ψ. After averaging on a fast variable φ we obtain:

$$\begin{aligned}
\dot{V} &= \begin{cases} -\varepsilon\left(\dfrac{F_- + F_+}{\pi}\arcsin\dfrac{V}{a\Omega} - \dfrac{F_- - F_+}{2}\right) & \text{if } 0 \le V < a\Omega, \\ -\varepsilon\,F_+ \quad \text{if } V \ge a\Omega, \end{cases} \\
\dot{a} &= \begin{cases} -\dfrac{\varepsilon}{\Omega}\left(\dfrac{F_- + F_+}{\pi}\sqrt{1 - \dfrac{V^2}{a^2\Omega^2}} - \dfrac{b}{2}\sin\xi\right) & \text{if } 0 \le V < a\Omega, \\ \varepsilon\,\dfrac{b}{2\Omega}\sin\xi \quad \text{if } V \ge a\Omega, \end{cases} \\
\dot{\xi} &= \varepsilon\left(\frac{b}{2a\Omega}\cos\xi + \Delta\right).
\end{aligned} \tag{4}$$

We are interested in an approximately steady motion as a single whole, therefore we seek for the solution $\dot{V} = 0$. Then from (4) we have $\dot{a} = \dot{\xi} = 0$ and

$$\begin{aligned}
&V = \frac{\sin\Phi}{|\Delta|}\sqrt{\frac{b^2}{4} - \frac{(F_- + F_+)^2\cos^2\Phi}{\pi^2}}, \qquad a = \frac{V}{\Omega\cdot\sin\Phi}, \\
&\xi = \arccos\left[-\frac{\Delta}{|\Delta|}\sqrt{1 - \frac{4(F_- + F_+)^2\cos^2\Phi}{\pi^2 b^2}}\right], \quad \Phi = \frac{\pi}{2}\cdot\frac{F_- - F_+}{F_- + F_+}.
\end{aligned} \tag{5}$$

The result $V(t)$ of the numerical integration of the exact system (1) is given in Fig.2. The following values of parameters were taken: $\varepsilon = 0.01$; $F_+ = 1$; $F_- = 2$; $b = 10$; $\Delta = 10$, $\omega = 1$. The formula (5) gives the value for the velocity of center of mass $V = 0.24$. Steady motion with the constant velocity (5) is physically feasible only in the event that it is stable. The characteristic polynomial of system in the variations, received of system (4), is given by expression (6). According to the Hurwitz criterion, all roots of the characteristic polynomial (6) have the negative real part for all values of parameters.

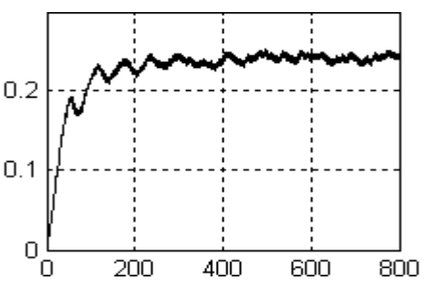


Fig.2. Velocity vs. time

$$P(\lambda) = \lambda^3 + \lambda^2\cdot\varepsilon\,\frac{2(F_- + F_+)}{\pi\,a\Omega}\cdot\frac{1}{\cos\Phi} + \lambda\cdot\varepsilon^2\left[\frac{(F_- + F_+)^2}{\pi^2 a^2\Omega^2}\left(1 + \sin^2\Phi\right) + \Delta^2\right] + \varepsilon^3\,\frac{(F_- + F_+)\Delta^2}{\pi\,a\Omega\cos\Phi}. \tag{6}$$

So, the motion with a velocity V is stable.

CONCLUSIONS

The above fulfilled investigations show: at presence of excitation and non-symmetrical Coulomb dry friction, motion of system with a constant "on the average" velocity $V > 0$ is possible and this motion is stable.
Worm prototype applying the principles outlined above has been constructed and proved positive.

References

[1] Zimmermann K.,Zeidis I.,Steigenberger J.: Mathematical Model of Worm-like Motion Systems with Finite and Infinite Degree of Freedom. *Theory and Practice of Robots and Manipulators. Proc. of 14-th CISM-IFToMM Symposium.* Springer Wien NY 507-516, 2002.

[2] Blekhmann I.I.: Vibrational Mechanics: Nonlinear Dynamic Effects, General Approach, Applications. World Scientific 2000.

[3] Turkov V.A.: Deformation of an elastic composite involving a magnetic fluid. *J. Magnetism and Magnetic Materials*, **252**:156-158, 2002.

[4] Arnold V.I., Kozlov V.V., Neishtadt A.I.: Mathematical Aspects of Classical and Celestial Mechanics. Springer Verlag 1997.

DYNAMICS OF A ROTOR ROLLING ALONG A CIRCULAR SURFACE

Alla D. Firsova

Institute for Problems in Mechanical Engineering RAS, Department of Vibrational Mechanics, Bolshoy pr. V.O., 61, 199178 St. Petersburg, Russia

Summary This work is devoted to investigating the dynamics of centrifugal-vibrational concentrator (CVC) — recently invented device for using in mining industry to separate particles of granular materials according to their densities. Operating process in CVC is based on using both vibration and centrifugal forces. Experience shows that optimal motion of the CVC is a regular precession of the shaft along an inner surface of the hub without sliding. The aim of the presented work is to determine parameters of such motion and to study its stability as well as to consider transient motions at different types of friction.

DYNAMICAL SCHEME OF THE DEVICE

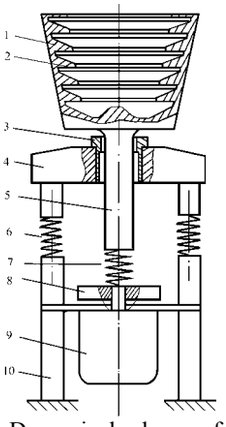


Fig. 1. Dynamical scheme of CVC

Dynamical scheme of CVC is presented in Fig. 1. Here 1 is an operating cup; 2 are fillets, where heavy particles are gathered; 3 is a hub, along which inner surface rolls a shaft 5; 4 is a massive plate; 5 is the shaft rigidly put to the cup 1; 6 are vibration isolators; 7 is elastic element between a shaft of a motor 9 and the shaft 5; 8 is a flyer; 9 is the motor; 10 is a supporting frame.

All parts of the device could be separated into three groups:

- operating cup 1 and details rigidly put to the cup
- plate 4 and details rigidly put to the plate
- frame 10 and details rigidly put to the frame

The details from the first group during operation process rotate together with the shaft of the motor, let us call them “a rotor”. The second group consists of details oscillating during operation process, we will call these details “a stator”. The rest details, “a frame” do not move during operation process.

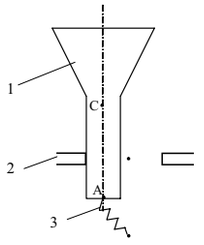


Fig. 2. Considered model.

Let us consider interaction between the rotor and stator according to scheme presented in Fig. 2. Here 1 is the rotor; point C is its centre of mass; 2 is the hub (a detail of stator along which the rotor rolls; 3 is a supporting elastic element; point A is a point, where elastic element is put. We believe that height of a hub surface is negligibly small as compared to rotor size, i.e. even in vertical position the rotor contacts the hub in one point. The second assumption is that mass of the stator is much more that mass of the rotor and when we study motion of the rotor we can take no notice of stator movements.

EQUATIONS OF MOTION

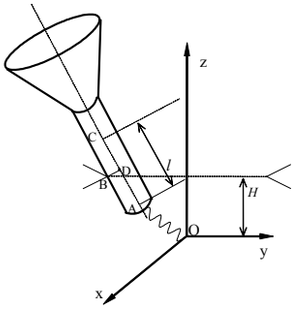


Fig. 3. Calculation scheme.

Let’s denote point of contact between the rotor and the hub B (see Fig. 3) and drop a perpendicular from point B to axis of the rotor. Crossing of these lines we will call point D. It seems reasonably to describe motion of the rotor with respect to fixed coordinate system ($Oxyz$) using coordinates of point D (x_D, y_D), vertical displacement of the rotor from the state of static equilibrium (z) and Euler’s angles ψ, θ, φ (ψ is a precession angle, θ and φ are angles of nutation and proper rotation). We consider nutation angle θ to be small, i.e. $\cos\theta \approx 1$, $\sin\theta \approx 0$.

The peculiarity of the system is the presence of permanent contact between the rotor and the hub. When the rotor moves always staying in contact with the hub the following relationship is valid:

$$x_D^2 + y_D^2 = \varepsilon^2, \qquad (1)$$

where $\varepsilon = R - r$, R and r are radiuses of the hub and the rotor shaft, ε is a small variable. Using (1) we can introduce a new variable α instead of x_D and y_D:

$$x_D = \varepsilon\cos\alpha, \qquad y_D = \varepsilon\sin\alpha\,. \qquad (2)$$

Equations of motion for the rotor could be written in the following form:

$$M\varepsilon\ddot{\alpha} - (Mh\ddot{\theta} - Mh\theta\dot{\psi}^2 - k_1 H\theta)\cos(\psi-\alpha) + Mh(\theta\ddot{\psi} + 2\dot{\theta}\dot{\psi})\sin(\psi-\alpha) = F_{\text{fr}\,y}\cos\alpha - F_{\text{fr}\,x}\sin\alpha,$$

$$M\ddot{z} + k_2 z = F_{\text{fr}\,z},$$

$$A\ddot{\theta} + C\theta\dot{\psi}(\dot{\varphi}+\dot{\psi}) - A\theta\dot{\psi}^2 + h(Mh\ddot{\theta} - Mh\theta\dot{\psi}^2 - k_1 H\theta)\sin^2(\psi-\alpha) - \varepsilon(Mh\dot{\alpha}^2 + k_1 H)\sin(\psi-\alpha) - (Mg - k_1 H)l\theta +$$

$$+ Mh^2(\theta\ddot{\psi} + 2\dot{\theta}\dot{\psi})\sin(\psi-\alpha)\cos(\psi-\alpha) = h[F_{\text{fr}\,x}\cos\alpha + F_{\text{fr}\,y}\sin\alpha]\sin(\psi-\alpha) + m_\xi^{(C)}(F_{\text{fr}})\cos\varphi - m_\eta^{(C)}(F_{\text{fr}})\sin\varphi, \quad (3)$$

$$A\ddot{\psi}\theta - C\dot{\theta}(\dot{\varphi}+\dot{\psi}) + 2A\dot{\theta}\dot{\psi} - \varepsilon(Mh\dot{\alpha}^2 + k_1 H)\cos(\psi-\alpha) + h(Mh\ddot{\theta} - Mh\theta\dot{\psi}^2 - k_1 H\theta)\sin(\psi-\alpha)\cos(\psi-\alpha) +$$

$$+ Mh^2(\theta\ddot{\psi} + 2\dot{\theta}\dot{\psi})\cos^2(\psi-\alpha) = h[F_{\text{fr}\,x}\cos\alpha + F_{\text{fr}\,y}\sin\alpha]\cos(\psi-\alpha) + m_\xi^{(C)}(F_{\text{fr}})\sin\varphi + m_\eta^{(C)}(F_{\text{fr}})\cos\varphi,$$

$$C(\ddot{\varphi}+\ddot{\psi}) = m_\zeta^{(C)}(F_{\text{fr}}).$$

Here M is mass of the rotor; $h = l - H$ (see Fig. 3); k_1 and k_2 are rigidities of supporting elastic elements; A and C are moments of inertia of the rotor; $\boldsymbol{F}_{\text{fr}}$ is a force of friction acting on the rotor; $\boldsymbol{m}^{(C)}(F_{\text{fr}})$ is a moment of this force with respect to the center of mass C. A force of normal reaction N acting in point B is eliminated from these equations, it is determined by the following relationship:

$$N = \varepsilon(M\dot{\alpha}^2 - k_1) - (Mh\ddot{\theta} - Mh\theta\dot{\psi}^2 - k_1 H\theta)\sin(\psi-\alpha) - Mh(\theta\ddot{\psi} + 2\dot{\theta}\dot{\psi})\cos(\psi-\alpha) + F_{\text{fr}\,x}\cos\alpha + F_{\text{fr}\,y}\sin\alpha.. \quad (4)$$

The system of equations (3) has 10th order and is essentially nonlinear even on the assumption that θ is small angle.
In the case when force of friction F_{fr} depends on normal reaction the equations (3) and (4) could be rewritten in a slightly different way.

STATIONARY MOTION OF THE ROTOR AND ITS STABILITY

Equations (3) have the following stationary solution:

$$\begin{aligned} &\alpha = \omega t, && z = 0, \\ &\psi = \omega t + \frac{\pi}{2}, && \theta = \theta_0 = const, \quad \varphi = -\Omega t, \end{aligned} \quad (5)$$

which corresponds to the motion of the rotor without sliding with constant angular velocities of precession (ω) and proper rotation (Ω) and constant nutation angle.
It is shown that such motion does not depend on friction law in the system. It exists in the case of absolutely smooth surface ($\boldsymbol{F}_{\text{fr}} = 0$) as well as in the case of dry and viscous friction in point B. Parameters of the stationary motion θ_0 and N_0 are determined from the equations (3) and (4) when (5) is taken into account. In Fig. 4 transition motion for the case of viscous friction is presented. It can be seen that velocity of point B (curve a) tends to zero, i.e. motion without sliding begins; angle of nutation (curve b) approaches some constant, and difference between angle velocities α'(t) and ψ'(t) (curve c) also tends to zero, so the system approaches the motion (5).

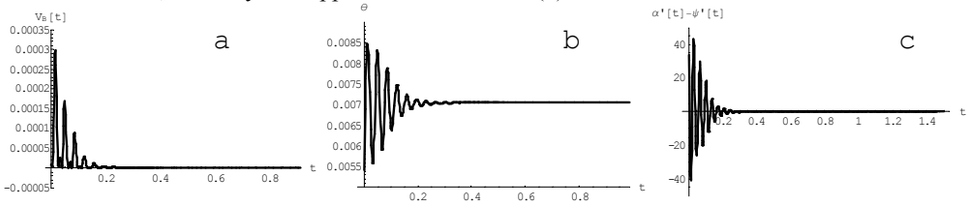


Fig. 4. Transient motion for the case of viscous friction.

Analysis of stability of the motion (5) in a conservative system, when force of friction is not taken into account, allows to obtain conditions which are necessary and sufficient for stability analytically. Together with these rather cumbersome relationships the condition which can be written in a more simple form is obtained:

$$k_1 H^2 > (A + Mh^2)\omega^2 + Mgl. \quad (6)$$

It is proved that this condition is sufficient for stability of the stationary solution. It can be seen that stability of the motion in considered system is not of a gyroscopic type and thus forces of friction could not break stability [1].

CONCLUSIONS

Investigation of stability of stationary motion in considered system rotor–stator shows that together with rather cumbersome conditions of stability the simple condition sufficient for stability could be obtained. Considered motion exists in the system in conservative case as well as in the case when forces of dry and viscous friction are taken into account. It is shown that stability does not have gyroscopic character and thus forces of friction could not break stability.
Author is very grateful to Professor I.I. Blekhman for helpful discussions.

References

[1] Merkin D. R.: Introduction to the theory of stability of motions. M.: Nauka, 1971. 312 p. (In Russian)

THE NEW STATEMENT OF PROBLEM OF UNBALANCE IDENTIFICATION

Yuri L. Menshikov, Nikolaj V. Polyakov
DNU, Department of Differential Equations, st. Nauchnay 13, 49050, Dnenropetrovsk, Ukraine

Summary The algorithms of inverse problem solution of rotor unbalance identification in new statement is offered. This statement of problem permits to obtain the most probable solution. The vibrations of rotor supports in two mutually perpendicular directions during the work for a few rotor rotations as the initial information are used. Tikhonov regularization method is applied for solution of this ill-posed (unstable) problem taking into consideration the error of mathematical model. The numerical calculations of examples are given to illustrate these algorithms.

PROBLEM DEFINITION

Let us consider a deformable rotor rotating on two no region supports [1]. The motion of rotors described by system of ordinary differential equations of 18th order [2,3]. The rotor unbalance is modelling by some external load. The value of this load and the place of its action is it necessary to find. It is assumed that the vibrations of rotor supports in two mutual perpendicular directions are obtained from experiment. Let us suppose that the functions $z_1(t)$, $z_2(t)$, $z_3(t)$ characterize the unbalance of rotor $z_1(t) = m_r r \dot{\varphi}^2 \mathrm{Sin}(\vartheta+\varphi)$, $z_2(t) = m_r r \dot{\varphi}^2 \mathrm{Cos}(\vartheta+\varphi)$, $z_3(t) = hr \dot{\varphi}^2 \mathrm{Sin}(\vartheta+\varphi)$, (r is the radius of rotor, m_r is the mass of unbalance reducing to a surface of rotor, $\dot{\varphi}$ is the angular velocity of rotation, h is unbalance arm, ϑ is angular deviation of the factor of unbalance with respect to correction plane). We suppose that with the help of acceleration transducers the function $\ddot{\xi}_A(t)$, $\ddot{\xi}_B(t)$, $\ddot{\eta}_A(t)$, $\ddot{\eta}_B(t)$ have been recorded ($\ddot{\xi}_A(t)$, $\ddot{\xi}_B(t)$ are the acceleration of supports A and B in horizontal direction, $\ddot{\eta}_A(t)$, $\ddot{\eta}_B(t)$ are the acceleration of supports A and B in vertical direction). Then the problem of unbalance recognition is reduced to the solution of Volltera integral equations of first kind (as an example, we consider the equation for the unknown function $z_1(t)$ only).

$$\int_0^t (t-\tau)\, z_1(\tau)\, d\tau = u_1(t), \quad t \in [0,T] \quad \text{or} \quad A z = B_{\mathbf{p}}\, \mathbf{x}_\delta = u_\delta, \tag{1}$$

where A is a linear operator($A: Z \to U$; Z,U are the functional B- spaces), z is the searched characteristic of unbalance, $B_{\mathbf{p}}$ is a linear irreversible operator ($B_{\mathbf{p}}: X \to U$; X is the functional B- space) depending on parameters vector of MM of "rotor-supports" $\mathbf{p} = (p_1, p_2, \ldots, p_n)^*$ ((.)* is the mark of transposition); $\mathbf{x}_\delta = (\ddot{\xi}_A(t), \ddot{\xi}_B(t), \ddot{\eta}_A(t), \ddot{\eta}_B(t))^*$ is the vector-function of initial data.

Subjective factors influence on the definition of parameters of system "rotor-supports" MM and therefore the parameters are supposed to have their values within certain limits: $p^0_i \le p_i \le \hat{p}_i$, $1 \le i \le N$. In this way the vector $\mathbf{p}$ can be changed inside the known closed region $\mathbf{p} \in \mathbf{D} \subset R^N$.

The equations for required functions $z_2(t)$, $z_3(t)$ will be similar to the equation (1).

The vector-function $\mathbf{x}_\delta$ is obtained using the experimental data (vibrations of supports) where the noise is present. Therefore it is convenient to think that each component of vector-function $\mathbf{x}_\delta$ and function u_δ belong to $L_2[0,T]$. Under this conditions the problem of equation (1) solution is ill-posed problems if the searched functions $z_i(t)$ belong to $C[0,T]$ [4]. The value of function deviation u_δ from the exact function u_T is:

$$\| u_T - u_\delta \|_U = \| B_p\, \mathbf{x}_\delta - B_T\, \mathbf{x}_T \|_U \le \delta_0,$$

where $\delta_0 = \delta\, b_0 + d \| \mathbf{x}_\delta \|_X$, $b_0 = \sup_{\mathbf{p} \in \mathbf{D}} \| B_{\mathbf{p}} \|$, $\| B_T - B_{\mathbf{p}} \|_{X \to U} \le d$, $\| \mathbf{x}_\delta - \mathbf{x}_T \|_X \le \delta$, $\mathbf{x}_T$ is the exact vector- function of initial data; B_T is the exact operator; δ, b_0, d are given values. Let us suppose that such exact solution of equation (1) $\mathbf{z}_T$ ($A\, \mathbf{z}_T = u_T = B_T\, \mathbf{x}_T$) belongs to the function space $W^1_2[0,T]$ [4].

The regularization method of Tikhonov is used for definition of stable approximate solution [4]. This way is based on the search of following problem solution [2,3,5]:

$$\Omega[\tilde{z}] = \inf_{z \in Q_{d;\delta}} \Omega[z], \tag{2}$$

where $Q_{d,\delta}$ is the set of possible solutions of equation (1) with the error of calculation

$$Q_{d,\delta} = \{ z : z \in Z_1 \subset Z, \ \| A z - B_{\mathbf{p}} \mathbf{x}_\delta \|_U \le \delta_o \},$$

$\Omega[z]$ is the stabilizing functional which is defined on Z_1 (Z_1 is the everywhere dense set into Z).

From the practical point of view the function $\tilde{z}$ gives a guaranteed estimation from below sizes of real of a rotor in sense of functional $\Omega[z]$. If $\Omega^0 \le \Omega[\tilde{z}]$ (Ω^0 there is known limiting an allowable value for the given type of rotor machine),

then the rotor works in emergency operation with guarantee. If the inequality $\Omega[\tilde{z}] < \Omega^0$ is carried out, then no objective conclusions can be made.
Let us consider the sets:

$$Q_{\mathbf{p},\delta} = \{ z : z \in Z_1, \ \| A z - B_{\mathbf{p}} x_\delta \|_U \le \delta \| B_{\mathbf{p}} \|, \quad Q^* = \bigcup_{\mathbf{p} \in \mathbf{D}} Q_{\mathbf{p},\delta} \ (\cup \text{ is the union}).$$

In the given work the new statement of a problem of rotor unbalance identification is suggested: to find the function $z_{\mathbf{p}}^r$ among set of the possible solutions of the equation (1) which would give the least maximal deviation from the experimentally measured vibrations of support of a rotor for all operators $B_{\mathbf{p}}$. Such statement is reduced to the solution of the following extreme problem:

$$\| A z_{\mathbf{p}}^r - B_{\mathbf{p}}^r \mathbf{x}_\delta \|_U = \inf_{z_{\mathbf{p}}} \sup_{B_{\mathbf{p}}} \| A z_{\mathbf{p}} - B_{\mathbf{p}} \mathbf{x}_\delta \|_U, \tag{3}$$

where $\Omega[z_{\mathbf{p}}] = \inf_{z \in Q_{\mathbf{p};\delta}} \Omega[z]$.
As all operators $B_{\mathbf{p}}$ it is possible to consider equivalent within the limits of the specified accuracy, it is possible to consider function $z_{\mathbf{p}}^r$ as the most probable solution of a problem of unbalance identification. The function $z_{\mathbf{p}}^r$ will be call the *most probable function of unbalance*. The most probable solution $z_{\mathbf{p}}^r$ will coincide with classical regularizing the solution of an inverse problem of unbalance identification of a rotor if there is the one operator $B_{\mathbf{p}}$ only. The function $z_{\mathbf{p}}^r$ is the best approximation of real unbalance and also is steady to small deviations of the initial data.
For suggested algorithm examination of unbalance characteristics evaluation there was calculated the case when functions $\ddot{\xi}_A(t)$, $\ddot{\xi}_B(t)$, $\ddot{\eta}_A(t)$, $\ddot{\eta}_B(t)$ are the results of mathematical simulation of rotor vibrations with given unbalance. The value of rotor unbalance were chosen as:

$$m_r = 0.5 \text{ kg} \ \text{ by } \ r = 0.25 \text{ м}, h = 0.25 \text{ м}, \vartheta = 0.5 \text{ rad}.$$

The values of initial data inaccuracy were chosen as the following:

$$\| \ddot{\xi}_A(t) - \ddot{\xi}^T{}_A(t) \|_C \le \delta_1 = 0.08 \frac{\text{M}}{\text{sec}^2}, \ \| \ddot{\xi}_B(t) - \ddot{\xi}^T{}_B(t) \|_C \le \delta_2 = 0.1 \frac{\text{M}}{\text{sec}^2}, \ \| \ddot{\eta}_A(t) - \ddot{\eta}^T{}_A(t) \|_C \le \delta_3 = 0.1 \frac{\text{M}}{\text{sec}^2},$$

$$\| \ddot{\eta}_B(t) - \ddot{\eta}^T{}_B(t) \|_C \le \delta_4 = 0.1 \frac{\text{M}}{\text{sec}^2}.$$

The results of identification of most probable function of unbalance are the following: $m_r = 0.42$ kg by $r = 0.23$ м, $h = 0.22$ м, $\vartheta = 0.48$ rad. The discrepancy method defined the parameter of regularization α [4].

CONCLUSIONS

The suggested statement of unbalance identification permits to evaluate all characteristics of rotor unbalance in real time with maximum exactness. It can be used for technical diagnostics of unbalance and for balancing of rotors in their own bearings. The method can be adapted to those cases when measuring velocity or displacement of supports.

References

[1] Dondoshansky B.: The computation of vibrations of elactic systems. Moscow, USSR, 1965.

[2] Menshikov Yu.L.: The operative Evaluation of Rotor Unbalance without Tests. *Proc. of EPMESC VII Int. Conf. on Enhancement and Promotion of Computational Methods in Engineering and Science*, 2-5 August, Macao, Elsevier Science, 149-156, 1999.

[3] Menshikov Yu.L.,Polyakov N.V.: Operative evaluation of unbalance characteristics of a deformable rotor. *Proc. 8th Jnt. Symp. on Technical Diagnostics (IMEKO)*, Sept. 23-25, Dresden, Germany, 399-408 , 1992.

[4] Tikhonov A.N.; Arsenin V.Y.: The methods of solution of the incorrectly formulated problems. Moscow, USSR, 1979.

[5] Menshikov Yu.L.: Recognition of rotor machines unbalance, *J. Differential equations and their applications in Physics*. Univ. of Dnepropetrovsk, USSR, 44-46, 1988.

VIBRORHEOLOGY: MAIN RESULTS, NEW PROBLEMS

Iliya Blekhman[*], Ekaterina Shishkina[**]
[*]*Institute for Problems of Mechanical Engineering and "Mekhanobr-Tekhnika" Corp., Saint Petersburg, Russia, blekhman@vibro.ipme.ru*
[**]*Institute for Problems of Mechanical Engineering, Saint Petersburg, Russia*

Summary A brief review of the results in the field of vibrational rheology developing very intensively is presented. A particular attention has been given to the latest results. Some problems unsolved as yet are also enumerated.

EXTENDED SUMMARY

During the recent years a noticeable interest of the researches is paid to the problems concerning the action of vibration on different nonlinear media such as solid bodies, granular materials, polymeric materials, concrete mixtures, suspensions, pulps, etc. The cases when the behavior of the system is essentially changed under the action of vibration are of the greatest interest both principal and applied.

For the problems stated above P. A. Rebinder suggested the name *vibrorheology*. The authors of this presentation defined vibrorheology as part of nonlinear mechanics and rheology which studies the change (caused by vibration – i.e by fast motions) of rheological properties of bodies with respect to "slow forces" and also the corresponding slow motions of bodies[1]. Vibrorheology is also part of vibrational mechanics [2] – the mechanics for the observer "who does not notice the fast forcers or fast motions" (for the observer "**V**")[2, 3].

Two essential moments should be emphasized: 1) in most cases it is expedient to speak of vibrorheological effects as of the seeming ones, which take place only for the observer "**V**"; 2) as a result of the action of vibration on the nonlinear mechanical systems, in the general case there is not only a change in the rheological characteristics or properties of the body with respect to slow actions, but there also appear either driving or shifting forces or torques.

The approaches of the vibrational mechanics, in particular the method of direct separation of motions, allow to solve the problems of the vibrorheology by the most simple and natural way. In this case it becomes possible to formulate the certain general vibrorheological regularities:

For systems with dry friction and for vibro-shock systems:

Forces of dry friction type, possibility of repetitive shock interactions	+ vibration =	slow vibrational forces of viscous friction type + additional slow vibrational forces + either random or determined vibration

For the nonlinear systems with viscous friction:

Forces of viscous friction	+ vibration =	slow forces of the transformed viscous friction + additional slow vibrational forces + random or determined vibration

The last terms in the right-hand sides of these conventional formulas point to the fact that the resultant oscillations, even under a determined action, are often of a random character, for example, due to the statistic character of the micro-properties of bodies or elements these bodies consist of. Recall that when speaking of the vibrational action, we do not necessarily mean an external effect, but also the effect of either a random or determined vibration, appearing within the autonomous system. These general regularities are clearly displayed when the considering certain problems of vibrorheology. Among such problems the paper considers:

1. Effective friction coefficients during vibration; vibrational conception of sliding friction. 2. Action of vibration on the systems with positional-viscous resistance. Effects of asynchronous suspression and excitation of self-oscillations. 3. Vibrorheology of granular materials. 4. The action of vibration on nonlinear-elastic media. 5. Vibrational hydraulics and hydrodynamics. 6. Vibrational control of rheological properties of bodies. The Indian magic rope effect. The problem of the creation of vibrational dynamic materials.

The paper contains a brief review of the researches in the enumerated directions and a main attention is given to the latest publications. Besides the investigations made by the authors the paper considers the publications by V.M. Chelomey, S.V.Chelomey, V.A.Palmov, G.I.Barenlatt, S.M.Meerkov, M.Zak, K.A.Lurie, D.M.Tolstoy, J.J.Thomsen, S.V.Sorokin, O.A.Ershova, S.V.Grishina, H. Dresig, and other scientists. Specific references to these researches are to be found in the book [3].

The authors mention among the important problems of vibrorheology (either unsolved or solved only partly) the problems of controlling the vibrorheological properties of the media as well as the construction of vibrorheological simulations of vibrational fatigue, vibroflow and vibrocreeping.

The work is carried out with the support of the Russian Foundation of the Fundamental Researches (Grant SSC 1521.2003.8).

References

[1] Blekhman, I. I.: Method of direct separation of motions in problems on the action of vibration on nonlinear dynamic systems. *Izv. AN SSSR, MTT*. 6, 1976. p. 13 – 27.
[2] Blekhman, I. I.: Vibrational Mechanics. Nonlinear Dynamic Effects, General Approach, Applications. World Scientific, Singapore 2000. 509 p.
[3] Selected Topics in Vibrational Mechanics. Edited by I.I.Blekhman. World Scientific, Singapore 2004. p. 370.

XXI ICTAM, 15–21 August 2004, Warsaw, Poland

NONLINEAR VIBRATIONS OF GEAR DRIVES

Vladimír Zeman*, Miroslav Byrtus*, Michal Hajžman*
*Department of Mechanics, Faculty of Applied Sciences, University of West Bohemia in Pilsen, Univerzitní 8, CZ-30614 Plzeň, Czech Republic

Summary The contribution presents the modal synthesis method of the mathematical modelling of the gear drive nonlinear vibrations caused by internal excitation generated in gear meshings. Especially undesirable vibrations characterized by discontinuity of mesh gear can be caused by kinematic transmission errors and time dependent meshing stiffnesses in case of small static load. These gear drive impact motions are explained by direct time–integration method and using time series, phase trajectories and Poincaré map.

INTRODUCTION

The presented original modal synthesis method is based on the system decomposition into subsystems, modelling of linearized uncoupled subsystems by FEM, discretization of linear or nonlinear couplings between subsystems, modelling of gyroscopic effects of the rotating subsystems and a assembling of the condensed mathematical model of the system. The condensed mathematical model of the complex coupled system is created by means of spectral ${}^m\boldsymbol{\Lambda}_j$ and modal ${}^m\boldsymbol{V}_j$ submatrices corresponding to the lower master mode shapes of the mutually uncoupled and undamped subsystems (see [1], [2]). The methodology described in this contribution allows to model very complex systems with complicated structure and nonlinear couplings.

MODELLING OF GEAR DRIVES

Let the gear drive (system) be decomposed into rotating shafts with gears (subsystems $j = 1, \ldots, N-1$) and a housing (subsystem $j = N$). The shafts are joined together by gear couplings $z = 1, 2, \ldots, Z$. The shafts are joined with housing by means the rolling–element bearings. The motion equation of the system, which is decomposed into N subsystems, in the space of their generalized coordinates $\boldsymbol{q}_j(t)$ can be written in the matrix form

$$\boldsymbol{M}_j\ddot{\boldsymbol{q}}_j(t) + (\boldsymbol{B}_j + \omega_j\boldsymbol{G}_j)\dot{\boldsymbol{q}}_j(t) + \boldsymbol{K}_j\boldsymbol{q}_j(t) = \boldsymbol{f}_j^E(t) + \boldsymbol{f}_j^C\,, \quad j = 1, 2, \ldots, N\,, \tag{1}$$

where the mass, damping and stiffness matrices $\boldsymbol{M}_j$, $\boldsymbol{B}_j$, $\boldsymbol{K}_j$ of the mutually uncoupled subsystems are symmetric and gyroscopic matrix $\boldsymbol{G}_j$ of the subsystem rotating by angular velocity ω_j ($\omega_N = 0$) is skew–symmetric. The vector $\boldsymbol{f}_j^E(t)$ describes external forced or kinematic excitation. The interaction between the subsystems in the configuration space $\boldsymbol{q}(t) = [\boldsymbol{q}_j(t)]$ of dimension $n = \sum n_j$ can be expressed by global coupling force vector $\boldsymbol{f}_C = [\boldsymbol{f}_j^C]$ in the form

$$\boldsymbol{f}_C(t, \boldsymbol{q}, \dot{\boldsymbol{q}}) = -\boldsymbol{B}_B\dot{\boldsymbol{q}}(t) - \boldsymbol{K}_B\boldsymbol{q}(t) + \sum_{z=1}^{Z}\boldsymbol{c}_z F_z(t, \boldsymbol{q}, \dot{\boldsymbol{q}})\,, \tag{2}$$

where $\boldsymbol{B}_B$ and $\boldsymbol{K}_B$ are damping and stiffness matrices of linearized bearing couplings. Vectors $\boldsymbol{c}_z$ (see [1]) and forces $F_z(t, \boldsymbol{q}, \dot{\boldsymbol{q}})$ transmitted by gearings correspond to gear coupling z. The elastic parts of these forces are expressed as nonlinear functions of gearing deformations

$$d_z = -\boldsymbol{c}_z^T\boldsymbol{q}(t) + \Delta_z(t)\,, \tag{3}$$

where $\Delta_z(t)$ is the kinematic transmission error on the gear mesh line. In order to make a condensed mathematical model of the system the forces $F_z(t, \boldsymbol{q}, \dot{\boldsymbol{q}})$ will be written in the form

$$F_z(t, \boldsymbol{q}, \dot{\boldsymbol{q}}) = k_z(t)d_z + b_z\dot{d}_z + f_z(d_z, t)\,, \quad z = 1, 2, \ldots, Z\,, \tag{4}$$

where $k_z(t)$ are time dependent meshing stiffnesses, b_z are viscous meshing damping parameters and nonlinear functions $f_z(d_z, t)$ express the influence of an interruption of the mesh gear.

CONDENSED MODEL

The model (1) can be transformed by means of modal submatrices ${}^m\boldsymbol{V}_j \in \mathbb{R}^{n_j, m_j}$ of the uncoupled undamped subsystems into the condensed form using relations $\boldsymbol{q}_j(t) = {}^m\boldsymbol{V}_j\boldsymbol{x}_j(t)$ for $j = 1, 2, \ldots, N$ and $m_j < n_j$

$$\begin{aligned}\ddot{\boldsymbol{x}}(t) + (\boldsymbol{D} + \omega_0\boldsymbol{G} + \boldsymbol{V}^T\boldsymbol{B}_B\boldsymbol{V} + \boldsymbol{V}^T\boldsymbol{B}_G\boldsymbol{V})\dot{\boldsymbol{x}}(t) + (\boldsymbol{\Lambda} + \boldsymbol{V}^T\boldsymbol{K}_B\boldsymbol{V} + \boldsymbol{V}^T\boldsymbol{K}_G(t)\boldsymbol{V})\boldsymbol{x}(t) = \\ = \boldsymbol{V}^T[\boldsymbol{f}_E(t) + \boldsymbol{f}_G(t) + \sum_{z=1}^{Z}\boldsymbol{c}_z f_z(d_z, t)]\,.\end{aligned} \tag{5}$$

The new configuration space of the system is expressed by vector $\boldsymbol{x}(t) = [\boldsymbol{x}_j(t)]$ of relatively small dimension $m = \sum m_j$, $m \ll n$. Matrices $\boldsymbol{D} = \mathrm{diag}({}^m\boldsymbol{V}_j{}^T\boldsymbol{B}_j{}^m\boldsymbol{V}_j)$, $\boldsymbol{G} = \mathrm{diag}(\frac{\omega_j}{\omega_0}{}^m\boldsymbol{V}_j{}^T\boldsymbol{G}_j{}^m\boldsymbol{V}_j)$, $\boldsymbol{V} = \mathrm{diag}({}^m\boldsymbol{V}_j)$ are block diagonal and $\boldsymbol{\Lambda} = \mathrm{diag}({}^m\boldsymbol{\Lambda}_j)$ is diagonal matrix composed from the spectral submatrices ${}^m\boldsymbol{\Lambda}_j \in \mathbb{R}^{m_j,m_j}$ of the subsystems. Matrices ${}^m\boldsymbol{V}_j$, ${}^m\boldsymbol{\Lambda}_j$ satisfy the orthonormality conditions ${}^m\boldsymbol{V}_j\boldsymbol{M}_j{}^m\boldsymbol{V}_j = \boldsymbol{I}_j$, ${}^m\boldsymbol{V}_j\boldsymbol{K}_j{}^m\boldsymbol{V}_j = {}^m\boldsymbol{\Lambda}_j$, $j = 1, 2, \ldots, N$. The interaction between the shafts by means of the gear couplings is expressed by transformed gear coupling matrices $\boldsymbol{K}_G(t) = \sum_{z=1}^{Z} k_z(t)\boldsymbol{c}_z\boldsymbol{c}_z^T$, $\boldsymbol{B}_G = \sum_{z=1}^{Z} b_z\boldsymbol{c}_z\boldsymbol{c}_z^T$, transformed vector of the internal kinematic excitation in gear couplings $\boldsymbol{f}_G(t) = \sum_{z=1}^{Z}[k_z(t)\Delta_z(t) + b_z\dot{\Delta}_z(t)]\boldsymbol{c}_z$ and transformed vector of the nonlinearities in gear couplings $\sum_{z=1}^{Z}\boldsymbol{c}_z f_z(d_z, t)$ in phases of the mesh gear interruption.
The condensed model (5) of order $m = \sum m_j$ can be used for determination of the constant mesh gear regions and simulation of nonlinear system vibration excited by the kinematic transmission errors $\Delta_z(t)$ and time dependent meshing stiffnesses $k_z(t)$, $z = 1, 2, \ldots, Z$. The impact motions are explained using time series, phase trajectories and Poincaré map (see [3]) by direct time–integration of the condensed model. The theory is applied to a simple test–gearbox on Figure 1 (see [4]).

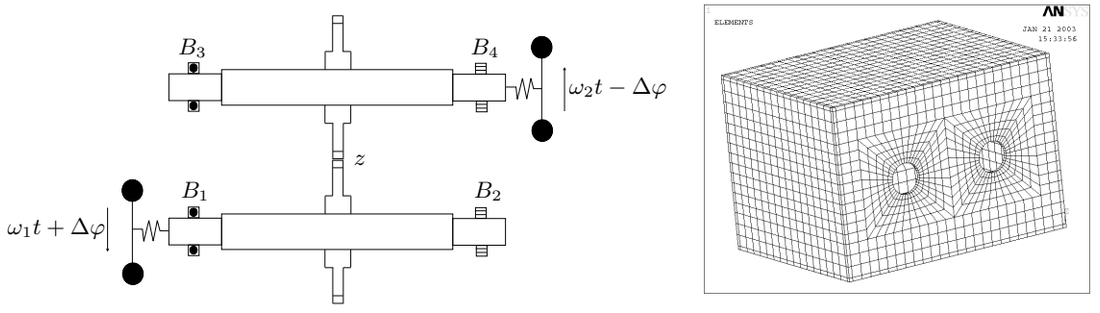


Figure 1. Scheme of the test–gearbox (ω_1 and ω_2 are constant angular speeds)

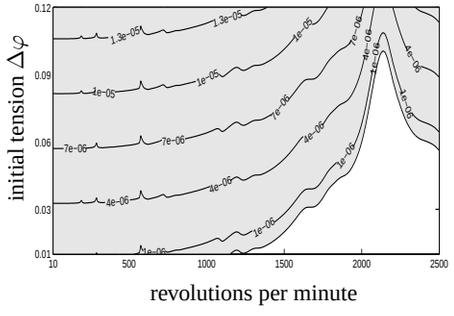


Figure 2. Regions of the constant gear mesh (grey colour) with respect to operating speed of the drive shaft and initial static torsional tension

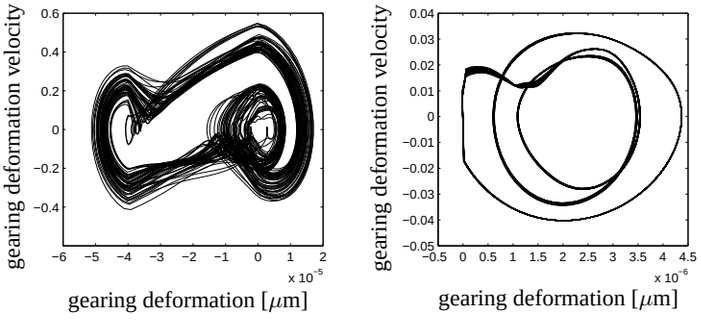


Figure 3. Phase trajectories of the gearing deformation for 1500 rpm of the drive shaft, for two distinct values of the initial tension $\Delta\varphi = 0.015$ rad (left) and $\Delta\varphi = 0.018$ rad (right), and for the tooth backlash $u = 4 \cdot 10^{-5}$ m

CONCLUSIONS

The modal synthesis method for creation of the nonlinear condensed model of gear drives is discussed. This condensed model with small DOF number is constituted by means of the lower undamped vibration mode shapes of the uncoupled subsystems. The maximum and minimum meshing deformations in time and regions of the constant mesh gear are investigated in dependence on the gear drive operating speed and the static load. The condensed model is used for numerical simulation of nonlinear vibration in the phases of the mesh gear interruption caused by the important sources of internal excitation – kinematic transmission errors and time dependent meshing stiffnesses. The impact motions of the gears are explained using time series, phase trajectories and Poincaré map.
The contribution was performed within the framework of research project MSM 235200003 of the Ministry of Education of the Czech Republic.

References

[1] Zeman V., Hlaváč Z.: Mathematical modelling of vibration of gear transmissions by modal synthesis method. *Proceedings of the Ninth World Congres on the Theory of Machines and Mechanisms*, Vol. 1, pp. 397–400, Politechnico di Milano, Italy 1995.
[2] Zeman V., Kovář L.: Dynamical analysis of the large mechanical systems containing subsystems. *ZAMM* 78 (1998), pp. 833–834.
[3] Thompson J. M. T., Stewart H. B.: Nonlinear Dynamics and Chaos. John Wiley & Sons, 2002.
[4] Hajžman M., Zeman V., Byrtus M.: Forced vibrations of gearboxes with time dependent meshing stiffnesses. *PAMM* 3 (2003), pp. 102–103.

PASSIVE VIBRATION CONTROL OF A PIECEWISE LINEAR BEAM SYSTEM

Rob H.B. Fey, Joris H. Bonsel and Henk Nijmeijer
Eindhoven University of Technology, Department of Mechanical Engineering,
P.O. Box 513, 5600 MB Eindhoven, The Netherlands

Summary A linear Dynamic Vibration Absorber (DVA) is applied to suppress the vibrations in a harmonically excited piecewise linear beam system. Both an undamped and a damped DVA are considered. Results of experiments and simulations are presented and show good resemblance. The undamped DVA is able to suppress the first harmonic resonance peak. The damped DVA guarantees vibration reduction over a wider frequency range.

INTRODUCTION

Several reasons can be given for the need to reduce vibrations in a mechanical system: e.g. avoiding damage, increasing the lifetime of the system, increasing comfort for human beings, and decreasing sound radiation. A Dynamic Vibration Absorber (DVA) is a well-known cheap, simple, passive controller for neutralising the vibrations of the structure to which it is attached. It consists of a mass-spring(-damper) system which parameters are tuned to obtain maximal vibration reduction. The application of DVA's to linear systems has been investigated by many authors, see e.g. [5]. In the past piecewise linear systems with one degree of freedom (dof) were studied [6,7] inspired by the fact that in engineering practice many of such systems can be found. Examples are: 1) one-sided springs in folded solar array systems for space applications [4], 2) the periodic slackening of a mooring rope in off-shore applications [8] and 3) elastic stops in a pantograph carbon collector strip suspension [3]. In this paper a linear DVA will be applied to an archetype piecewise linear beam system to investigate if linear DVA's are capable of reducing vibrations in this type of systems, see also [1].

EXPERIMENTAL SET-UP

Figure 1 shows a schematic view of the experimental set-up. A steel beam is supported by two leaf springs at both ends. Below it a shorter clamped-clamped beam acts as a one-sided spring, which only is loaded if the middle of the main beam has downward deflection. Above the middle of the main beam a rotating mass unbalance realizes harmonic excitation. This unbalance is driven by a motor via a shaft with a flexible coupling. Left from the rotating mass unbalance the symmetric DVA is visible. It consists of two mass-leaf spring systems. The damped DVA is realised by addition of two dampers at the ends of the leaf springs.

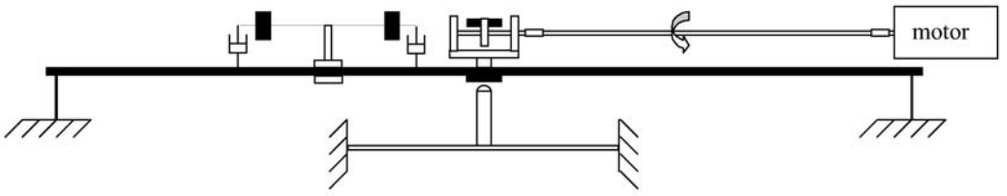


Figure 1 Schematic view of the experimental set-up

NUMERICAL MODEL

The linear part of the model without DVA is modelled using Euler beam elements resulting in a model with 111 dof. In order to decrease computational time while maintaining accuracy for the frequency range of interest a dynamic reduction method [2] based on free-interface eigenmodes and residual flexibility modes is applied to this model. The Ritz approximation of the displacement field consists of a linear combination of 3 free-interface eigenmodes (up to a cut-off frequency of 100 Hz) with corresponding generalised dof p_1, p_2, p_3 and 2 residual flexibility modes. The latter are defined for q_m, the transversal displacement of the middle of the main beam, and q_{ab}, the transversal displacement at the position where the DVA is attached. The equations of motion of the reduced model are given by:

$$M_R \ddot{p} + B_R \dot{p} + K_T p = f_R \qquad \text{where} \qquad K_T = \begin{cases} K_R & if \quad q_m > 0 \\ K_R + K_{nl} & if \quad q_m \le 0 \end{cases}$$

The reduced displacement column is given by $p = [p_1 \quad p_2 \quad p_3 \quad q_m \quad q_{ab} \quad q_{am}]^T$, where q_{am} is the transversal displacement of the DVA (the DVA is modelled as a single dof mass-spring-damper system). Only the 4th element of the

reduced external force column f_R is non-zero. It is a harmonic function with amplitude $mr\omega^2$ (m : mass unbalance, r : radius of mass unbalance, ω : radial rotational frequency) and excitation frequency $f = \omega / 2\pi$. The clamped-clamped beam is modelled as a mass-less one-sided spring causing piecewise linearity and resulting in stiffness matrix K_{nl} (the lowest eigenfrequency of this beam is high enough to justify this approximation). An important system parameter is the quotient of the stiffness of the one-sided spring and the stiffness associated with the first eigenmode, which is a measure for the amount of nonlinearity in the system. In this case this quotient is 4.6.

RESULTS

Figure 2 shows the maximum displacement of q_m for excitation frequencies between 0-60 Hz for 3 system configurations.

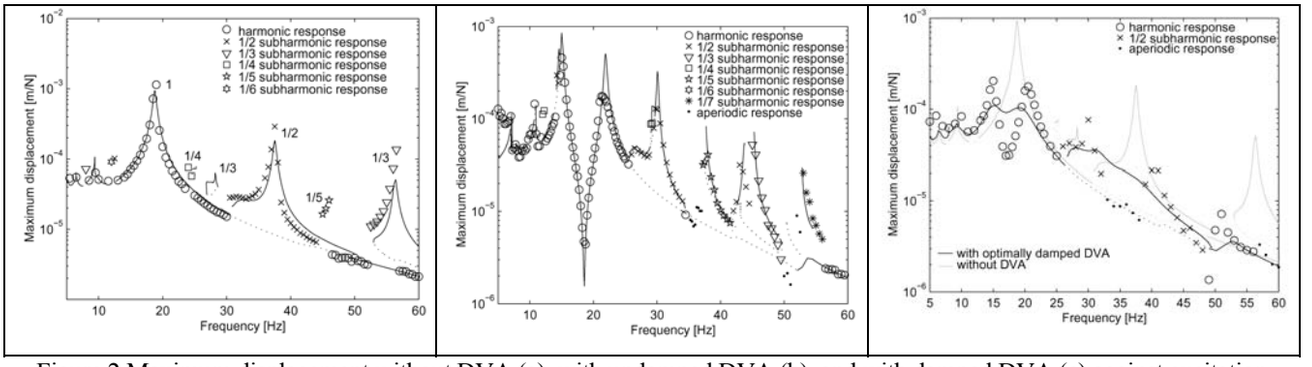


Figure 2 Maximum displacement without DVA (a), with undamped DVA (b), and with damped DVA (c) against excitation frequency. Symbols refer to experimental results, solid and dotted lines to resp. stable and unstable numerical periodic solutions.

Figure 2a: Piecewise linear beam system without DVA
Harmonic resonance occurs near 19 Hz. Related to this resonance ½ and 1/3 subharmonic resonances occur at resp. 38 Hz and 57 Hz and 2nd and 3rd superharmonic resonances at resp. 9.5 Hz and 6.5 Hz. The ¼ subharmonics near 26 Hz are related to the 3rd superharmonic resonance and the 1/3 and 1/5 subharmonics near 28 Hz and 47 Hz resp. to the 2nd superharmonic resonance.

Figure 2b: Piecewise linear beam system with undamped DVA
The eigenfrequency of the undamped DVA is tuned to 19 Hz, enabling the DVA to generate a counteracting force for the excitation force at this frequency. Indeed, at 19 Hz now an anti-resonance occurs. Instead, two new harmonic resonances occur near 15 Hz and 22 Hz. Related to these resonances ½ subharmonic resonances occur near resp. 30 Hz and 44 Hz. The other subharmonic and superharmonic resonances in figure 2b can also be identified. Finally, a quasi-periodic → locked → chaotic sequence is found near 35 Hz.

Figure 2c: Piecewise linear beam system with damped DVA
The optimally damped DVA reduces the vibrations over a wide frequency range. Next to the reduction of the harmonic and ½ subharmonic resonance, the 1/3 subharmonic resonance even completely disappears. Unfortunately, the dampers used in the experiment could not be given the optimal damping values. Nevertheless, the trend in the experiments is correct.

CONCLUSIONS

The undamped linear DVA is able to suppress the first harmonic resonance of the piecewise linear system. The damped DVA guarantees vibration reduction over a wider frequency range. Experimental and numerical solutions corresponded well.

References

[1] Bonsel, J.H., Fey, R.H.B., and Nijmeijer, H., Application of a dynamic vibration absorber to a piecewise linear beam system, subm. to *Nonlinear Dynamics*.
[2] Craig, R.R. Jr., Coupling of substructures for dynamic analyses - An overview, AIAA Paper 2000-1573, 2000.
[3] Drugge, L., Larsson, T., Berghuvud, A., and Stensson, A., The nonlinear behaviour of a pantograph current collector suspension, ASME DETC, Sept. 1999.
[4] Fey, R.H.B. and van Liempt, F.P.H., Int. Conf. on Structural Dynamics Modelling, Eds: Maia, N.M.M. et al., Funchal, Madeira, 201-210, June 2002.
[5] Korenev, B.G. and Reznikov, L.M., Dynamic Vibration Absorbers, John Wiley and Sons, 1993.
[6] Natsiavas, S., On the dynamics of oscillatorswith bi-linar damping and stiffness, *Int. J. Non-Linear Mechanics*, 25(5):535-554,1990.
[7] Shaw, S.W., and Holmes, P.J., A periodically forced piecewise linear oscillator, *J. Sound and Vibration*, 90(1):129-155, 1983.
[8] Thompson, J.M.T., and Stewart, Nonlinear Dynamics and Chaos, 2nd edition, Wiley, Chichester, 2002.

A POWER FLOW MODE THEORY BASED ON INHERENT CHARACTERISTICS OF DAMPING DISTRIBUTIONS IN SYSTEMS AND ITS APPLICATIONS

Y. P. Xiong[1, 2], J. T. Xing[1], W. G. Price[1]
[1]*School of Engineering Sciences, Ship Science, University of Southampton, Southampton, SO17 1BJ, UK*
[2]*Institute of Engineering Mechanics, Shandong University, Jinan* 250061*, People's Republic of China*

POWER FLOW MODE THEORY

Generalised formulation of a dynamical system

For generality, the dynamic equation for a generalized linear system with N degree-of-freedom is represented in the matrix form

$$\mathbf{M}\ \ddot{\tilde{\mathbf{X}}} + \mathbf{C}\dot{\tilde{\mathbf{X}}} + (\mathbf{K} + \mathrm{i}\eta\overline{\mathbf{K}})\tilde{\mathbf{X}} = \tilde{\mathbf{f}}e^{\mathrm{i}\omega t} = \tilde{\mathbf{F}}, \tag{1}$$

where $\tilde{\mathbf{F}}$ denotes excitation force vector, $\mathbf{M}$ is a real, symmetric and semi-positive definite mass matrix, $\mathbf{K}$ represents a symmetric and semi-positive definite stiffness matrix, $\mathbf{C}$ is a damping matrix which may be non-symmetrical and $\overline{\mathbf{K}}$ is a real symmetric stiffness matrix relating to hysteretic damping, **,** where η represents a loss factor. For solution $\dot{\tilde{\mathbf{X}}} = \tilde{\mathbf{V}}e^{\mathrm{i}\omega t}$, Eq. (1) reduces to

$$\tilde{\mathbf{f}} = \tilde{\mathbf{Z}}\tilde{\mathbf{V}}, \qquad \tilde{\mathbf{Z}} = \mathrm{i}\omega\mathbf{M} + \mathbf{C} + (\mathbf{K} + \mathrm{i}\eta\overline{\mathbf{K}})/\mathrm{i}\omega\,. \tag{2a,b}$$

In general, the impedance $\tilde{\mathbf{Z}}$ is non-symmetrical due to the non-symmetric nature of the damping matrix $\mathbf{C}$.

Power flow mode vector and its characteristic factor

Detailed analysis developed in the paper shows the validity of the result

$$\tilde{\mathbf{V}}^{\mathrm{H}}(\mathbf{C} + \mathbf{C}^{\mathrm{T}} + 2\eta\overline{\mathbf{K}}/\omega)\tilde{\mathbf{V}} = \tilde{\mathbf{V}}^{H}\tilde{\mathbf{f}} + \tilde{\mathbf{f}}^{H}\tilde{\mathbf{V}}, \tag{3}$$

where *H* denotes the Hermitian transpose of the matrix. This allows the time-averaged input power to be expressed as

$$P = \frac{1}{2}\mathrm{Re}\{\tilde{\mathbf{V}}^{\mathrm{H}}\overline{\mathbf{C}}\tilde{\mathbf{V}}\}, \tag{4}$$

where, it is proved that, $\overline{\mathbf{C}} = (\mathbf{C} + \mathbf{C}^{\mathrm{T}})/2 + \eta\overline{\mathbf{K}}/\omega$ is a real and symmetric matrix representing the total damping matrix in the system. Based on matrix theory [1], the real symmetric matrix $\overline{\mathbf{C}}$ is decomposed into

$$\overline{\mathbf{C}} = \mathbf{\Phi}\mathbf{\Lambda}\mathbf{\Phi}^{\mathrm{T}}, \tag{5}$$

where $\mathbf{\Lambda}$ is a real diagonal matrix of the eigenvalues λ_j of the matrix $\overline{\mathbf{C}}$ and $\mathbf{\Phi}$ is a corresponding matrix of eigenvectors satisfying $\mathbf{\Phi}^{\mathrm{T}}\mathbf{\Phi} = \mathbf{\Phi}\mathbf{\Phi}^{\mathrm{T}} = \mathbf{I}$ (a unit matrix). We define λ_j as the *j*th *characteristic damping factor* and eigenvector φ_j as the *j*th *power flow mode vector* of the system. These are linearly independent of each other and they are chosen as a set of base vectors spanning the power flow space and therefore allowe a complete description of the power flow of the system. The velocity vector $\tilde{\mathbf{V}}$ in the power flow space can be decomposed into the form

$$\tilde{\mathbf{V}} = \mathbf{\Phi}\tilde{\mathbf{q}}, \qquad \tilde{\mathbf{q}} = \mathbf{\Phi}^{\mathrm{T}}\tilde{\mathbf{V}}, \tag{6a,b}$$

where $\tilde{\mathbf{q}}$ is defined as a complex *characteristic velocity* vector. Therefore, the time-averaged power flow expressed by Eq.(4) is now presented as

$$P = \frac{1}{2}\mathrm{Re}\{\tilde{\mathbf{q}}^{\mathrm{H}}\mathbf{\Lambda}\tilde{\mathbf{q}}\} = \frac{1}{2}\sum_{j=1}^{N}\lambda_j\left|\tilde{q}_j\right|^2. \tag{7}$$

Eq. (6) provides a *damping-based power mode* expression of the power flow, in which $\lambda_j\left|\tilde{q}_j\right|^2/2$ represents the energy dissipated by the *j*th power flow mode. It is demonstrated by Eq.(7) that the total

power can be regarded as the power dissipated by all the N independent power flow modes with each being related to only one characteristic velocity distribution and one characteristic damping factor (i.e., an eigenvalue).

APPLICATIONS OF THE POWER FLOW MODE THEORY

Suspension system with two-degree-of-freedom

Fig.1 illustrates a two mount suspension system which is used to demonstrate application of the generalized power mode theory. Fig. 2 displays the total input power P compared to calculations using other methods [2-4] and the energy dissipated by each power flow mode P_1 and P_2. Fig.3 shows the influence of the system's damping distribution on the total input power spectra.

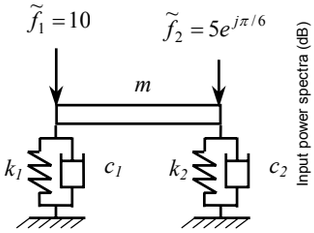


Fig.1 Suspension system

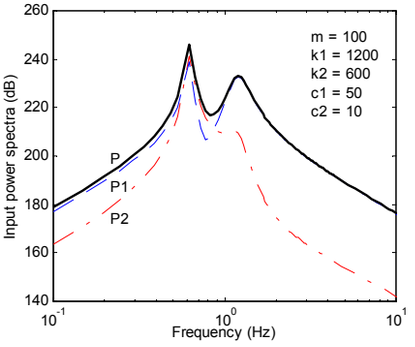


Fig.2 Total power and power flow modes

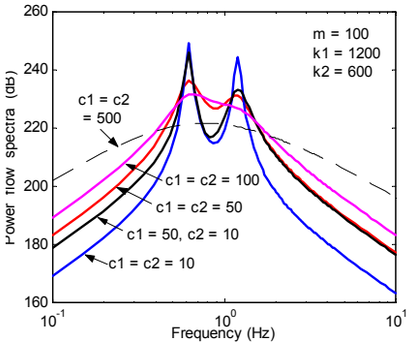


Fig.3 Power affected by system damping

Active vibration control of a human body-seat-boat-wave interaction system

A second example involves a human sitting on a seat mounted by a passive / active suspension system on an elastic vessel travelling in a sinusoidal seaway. In this example, the excitation is a distributed wave load and the system's damping matrix is non-symmetric due to different active damping inputs relating to different control channels [5]. It is demonstrated that the proposed power flow mode approach successfully analyses this complex distributed-lumped system. The effect of feedback control on the input power from waves into the whole coupling system is investigated. More results and detailed analysis are provided in the full paper.

CONCLUSIONS

The developed generalised power flow mode theory demonstrates an effective approach to predict power flow in a dynamical system based on the inherent characteristics of the system's damping distribution. It directly reveals the influence of damping characteristics on energy flow and transmission in the system using its characteristic damping factor and the power flow mode vectors. This power flow mathematical model suggests a design guideline to construct prescribed power flow characteristics through arrangement of the damping distribution in the system.

References

[1] Nering E.D.: Linear Algebra and Matrix Theory. John Wiley&Sons, Inc. NY & London 1963.
[2] Goyder H. G. D., White R. G.: Vibrational power flow from machines into buildup structures, part III: power flow through isolation systems. *Journal of Sound and Vibration* **68**: 97-117, 1980.
[3] Ji L., Mace B. R., Pinnington R. J.: A power mode approach to estimating vibrational power transmitted by multiple sources. *Journal of Sound and Vibration* **265**:387-399, 2003.
[4] Xiong Y.P., Xing J.T., Price W.G.: A general linear mathematical model of power flow analysis and control of integrated structure-control systems, *Journal of Sound and Vibration* **267**:301-334, 2003.
[5] Xiong Y.P., Xing J.T., Price W.G.: Active vibration control of a human body-seat-boat-water dynamic interaction system excited by progressive waves, *CD Proceedings of the 8th International Conference on Recent Advance of Structure Dynamics, SD2003,* Southampton, Paper No.11, 2003.

STABILITY OF A SPINNING DISK UNDER A STATIONARY OSCILLATING UNIT

T. H. Young, C. Y. Lin

Department of Mechanical Engineering, National Taiwan University of Science and Technology, Taipei, 106, Taiwan

Summary This work studies the free vibration and stability of a spinning disk transversely in contact with a stationary oscillating unit. The oscillating unit consists of two parallel combinations of springs and dampers attached above and under a mass such that the displacement of the mass is different from that of the disk at the contact point. The stability analysis is conducted by investigating the eigenvalue problem of the combined system.

Spinning disks are widely used components in mechanical engineering, from circular saw blades, turbine rotors to computer disk memory units. Therefore, the dynamic behaviors of spinning disks have attracted researchers' interest for a long time. For computer disk memory units, the interaction of the read/write head with the surface of the disk demands that the effects of the inertia, stiffness and damping of the head be considered in the analysis. Hence, Iwan and stahl [1] first studied the free vibration and stability of a stationary circular disk excited by a rotating mass-spring-damper load system. The displacement of the mass of the load system is assumed to be equal to the transverse deflection of the disk. Later Iwan and Moeller [2] included the rotational inertia effect of the disk and investigated the free vibration and stability of a spinning disk with a stationary mass-spring-damper load system. They found that the primary effect of the disk rotation was to stiffen the disk and thereby to increase effective natural frequencies over those of a stationary disk with a rotating load system.

In reality, the displacement of the mass of the load system is generally not the same as that of the disk at the contact point. Consider an annular plate that is spinning at an angular speed Ω and is transversely in contact with a stationary oscillating unit at the point $(r_P,0)$, where (r,θ) is a polar coordinate system fixed in space. The plate is clamped at the inner edge and free at the outer edge, and the oscillating unit consists of two parallel combinations of springs and dampers attached above and under a mass. The lower end of the oscillating unit is assumed to contact with the disk closely, and the upper end of it is fastened to a fixed support. With respect to the inertial polar coordinates, the equation of motion of a spinning disk with viscous damping under the action of the stationary oscillating unit can be written as

$$D\nabla^4 w + c\left(\frac{\partial w}{\partial t} + \Omega\frac{\partial w}{\partial \theta}\right) + \rho h\left(\frac{\partial^2 w}{\partial t^2} + 2\Omega\frac{\partial^2 w}{\partial t\partial\theta} + \Omega^2\frac{\partial^2 w}{\partial\theta^2}\right)$$

$$= h\left[\frac{1}{r}\frac{\partial}{\partial r}\left(r\sigma_{rr}\frac{\partial w}{\partial r}\right) + \frac{1}{r^2}\sigma_{\theta\theta}\frac{\partial^2 w}{\partial\theta^2}\right] + \frac{1}{r_P}(c_P\dot{y} + k_P y)\delta(r - r_P)\delta(\theta) \qquad (1)$$

where D and c are the flexural rigidity and the viscous damping coefficient of the disk, respectively; ρ and h are the mass density and the thickness of the disk, respectively. σ_{rr} and $\sigma_{\theta\theta}$ are the initial in-plane stresses induced by rotation. c_P and k_P are the damping coefficient and the spring constant of the lower damper and spring of the oscillating unit, respectively. ∇^4 is a biharmonic operator, and $\delta(\cdot)$ is a Dirac delta function. w is the transverse displacement of the disk. y is the relative displacement of the mass of the oscillating unit, and an overdot denotes a differentiation with respect to time t. The equation of motion of the oscillating unit is given by

$$m_o\ddot{y} + (c_S + c_P)\dot{y} + (k_S + k_P)y = -m_o \frac{\partial^2 w}{\partial t^2}(r_P, 0, t) - c_S \frac{\partial w}{\partial t}(r_P, 0, t) - k_S w(r_P, 0, t) \quad (2)$$

where c_S and k_S are the damping coefficient and the spring constant of the upper damper and spring of the oscillating unit, respectively. m_o is the mass of the oscillating unit.

Assume that the displacement of the spinning disk can be expressed as a linear combination of the eigenfunctions of the corresponding stationary disk. Substituting the assumed displacement into Eq. (1), going through Galerkin's procedure and combining Eq. (2) yields the discretized system equations for the combined system - the spinning disk and the oscillating unit. The discretized system equations of the combined system can be rewritten into a set of the first-order differential equations, and the solution of this set of differential equations has an exponential form. Substituting the solution into the differential equations yields an eigenvalue problem. The eigenvalues and the eigenvectors of the eigenvalue problem appear in complex conjugate pairs. When the real part of an eigenvalue becomes positive, the corresponding mode is unstable. Furthermore, if the imaginary part of this eigenvalue is equal to 0, the corresponding mode experiences a divergence-type instability; if the imaginary part of this eigenvalue is not 0, the corresponding mode experiences a flutter-type instability.

If the inner radius of the disk is assumed to approach zero, and the spring constant and viscous damping coefficient of the lower spring and damper are assumed to approach infinity such that the displacement of the mass is the same as that of the disk at the contact point, the problem considered in this work is reduced to that studied by Iwan and Moeller [2]. The figure of the eigenvalues versus the spin rate reveals that the locations and the widths of the unstable intervals obtained in this study agree excellently with those in Iwan and Moeller's paper. By piling up the unstable intervals with respect to a certain parameter, stability boundaries of the combined system can be obtained. Parametric studies of the system parameters on the stability boundaries of the combined system are conducted numerically.

Numerical results show that inclusion of the spring between the disk and the mass of the oscillating unit will bring about new and larger unstable regions between the oscillating unit and the reflected modes of the disk but repress the original instability by the reflected and backward modes of the disk, of which the unstable regions are much smaller. An increase in the spring constant of either the lower spring or the upper spring of the oscillating unit will enlarge all unstable regions of the combined system. However, the effect of the mass of the oscillating unit is insignificant to all unstable regions of the combined system. Existence of either the lower damper or the upper damper in the oscillating unit will make the combined system unstable once the spin rate exceeds the first critical speed of the disk. The effect of the viscous damping of the disk is favorable to all instability due to the disk modes only but will worsen the flutter-type instability between the oscillating unit and the reflected modes of the disk.

References

[1] Iwan, W. D. and Stahl, K. J.: The response of an elastic disk with a moving mass system. J. Appl. Mech. **40**: 445-451, 1973.

[2] Iwan, W. D. and Moeller, T. L.: The stability of a spinning elastic disk with a transverse load system. J. Appl. Mech. **43**: 485-490, 1976.

High Revolving Speed Spindles Definition Due to Transient Vibration Conditions

Mehdi Sherafati Zangeneh[*], Seyed Saleh Hosseini Yazdi[**]
[*]*Ph.D. in Applied Mechanics-Sharif University of Technology, Tehran, Iran*
[**]*BS. in Mechanical Engineering-Solid Mechanics- University of Tehran, Tehran, Iran*
salehhosseini@yahoo.com

Summary: Spindle is the main part of Machine tools that their products face finishes are influenced by vibrations through cutting process. With consideration of a conventional turret spindle and new production conditions through a Finite Element Transient Analysis (FEA), terms of new spindles, their bearing types and arrangement was defined; Stiffer material for spindle must be used and the bearing sets number must restricted to two sets, Angular trust and Taper roller bearings must be used.

INTRODUCTION

World manufacturers continue to face increased production and quality requirements. Trends towards tighter tolerance specifications further could the picture. In particular, turret products tolerances are becoming smaller and creating new quality challenges. Turret spindle is a very sensitive element which is terribly effective on quality and precision of products. Its role became very important when high revolving speeds which are very common in CNCs are used. Although the spindle precision is important, precision durability which causes steady products is a term of economic production. In manual turrets, the highest revolving speed is around 2400 RPM [1] that is rarely used, whereas in CNCs higher speeds are up to 7500 RPM [2] and they can be reasons for great vibration amplitudes. Vibration can be a sign of imbalance some where inside the machine and that downtime for maintenance and tool changes is probably higher than it need to be, so distribution of mass is important for minimizing the amount of vibration generated by spindle [3].

MODELING

The spindle model was prepared in SolidWorks2003 considering a true prototype turret model TN50 [1]. Mechanical properties were considered isotropic as Possion's ratio $\upsilon = 0.3$, density $\rho = 7850\ kg/m^3$ and Young modules $E = 210 \times 10^9$ Pa. Boundary conditions are result of bearing types and lengths that were used: a) Roller bearings b) Trust ball bearings. (Fig. 1)
In order to calculate force acting on spindle, the following equation was used [4]:

$$F = Cp.t^x.s^y.Ke.K\varphi.K\gamma.Km$$

The definition of above mentioned parameters are; Ke: coolant factor, $K\varphi$: entrance angle factor, $K\gamma$: sweeping angle factor, Km: σ_{ult} factor and Cp, x, y: Machine tool type factor. t: cutting depth (mm) and s: feeding rate (mm/rev).
For this purpose the following analysis must have been done in advance:

- Natural frequency analysis: Ten first natural frequencies and relative mode shapes were obtained using subspace method. The present system has one degree rigid motion around its axis [5-7].
- Harmonic analysis: In resulted frequency range showed which of the natural mode shapes would be excited. In this way the transient time step could be determined ($\Delta t = 1/20 f_{n,i}$). For harmonic analysis full method was used [5-7].

Transient analysis [5-7]:
A) Shock: The mathematical function for shock was as below :(Fig. 2)

$$F(t) = \begin{cases} F & t \le \Delta t \\ 0 & t \ge \Delta t \end{cases}$$

B) Step: The mathematical function for step was as below:

$$F(t) = \begin{cases} F & 0 \le t \le t_1 \\ 0 & t > t_1 \end{cases}$$

As resulted graphs and table show:

- The harmonic resulted graph shows the third, sixth and ninth natural frequencies were excited as the result of entry force [7].
- The results showed that only chuck part is affected. The result has two patterns; a) When the force is acting, only the chuck tip is affected, b) After eliminating force and chuck has free vibration and whole chuck is affected. (Fig. 3)
- As the resulted graphs show, the response is a composition of some harmonics means sixth and ninth mode shapes were excited as well as the third one [7].
- The results showed type, time duration and force amplitudes affect the response amplitude.

CONCLUSION

Bearings are mechanical devices that can strongly influence vibration response of spindle system so; they have to be minimized in number. It means that it is sufficient to use bearings sets in two points, first near chuck position, second next

to driving gear or other spindle end. The first bearing set as it was shown by finite element analysis, prohibits transferring vibration effects, both axial and radial , therefore other bearing set is only used for both leveling and bearing other acting forces [2, 8]. (Fig. 4)

In recent machine tools higher revolving speeds are used so using conventional spindles causes huge energy waste therefore lighter spindles must be used. To prevent great vibrations amplitude due to light weight spindles stiffer materials have to be used [2, 8].

Above mentioned alterations lead us to use different types of bearings. Because of them for the first set, Angular trust bearings and for other set, Taper roller bearing must be used.

In the following some specimens for new spindle generations and their function versus conventional ones are bought [2, 8]. (Fig. 5, Table 1)

Table 1: Vibration amplitude for conventional and modern spindles (FEA)

	Vibration amplitude for conventional spindle(m)				Vibration amplitude for modern spindles (m)			
Force amount	F=300 N	F=400 N	F=500 N	F= 600 N	F=300 N	F=400 N	F=500 N	F= 600 N
Shock	0.396e-6	0.528e-5	0.573e-5	0.791e-5	0.205e-5	0.273e-5	0.341e-5	0.410e-5
Step	0.419e-6	0.559e-5	0.698e-5	0.838e-5	0.205e-5	0.281e-5	0.341e-5	0.371e-5

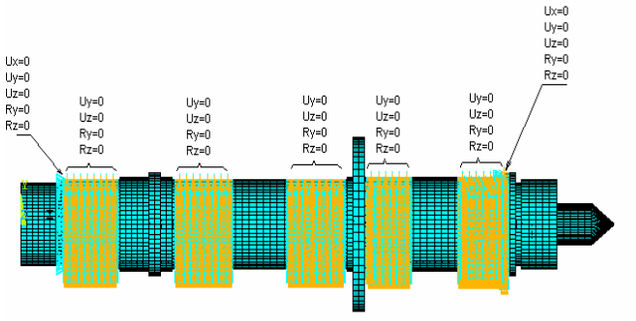


Fig 1: Applied boundary conditions on conventional spindle (Five bearing sets)

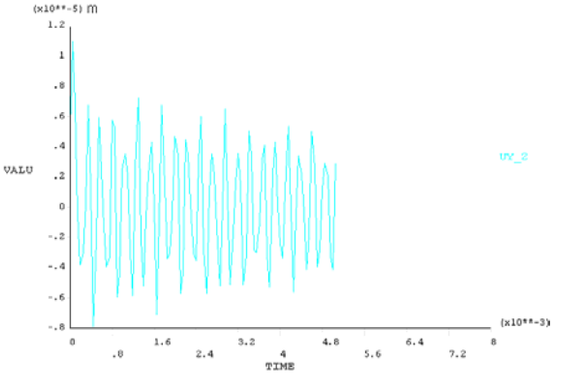
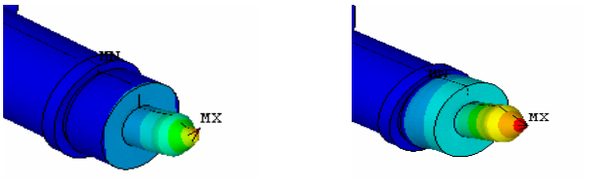


Fig 2: chuck vibration amplitude due to shock force (FEA)



(a) (b)

Fig 3: Displacement contour a) in acting force b) Free vibration

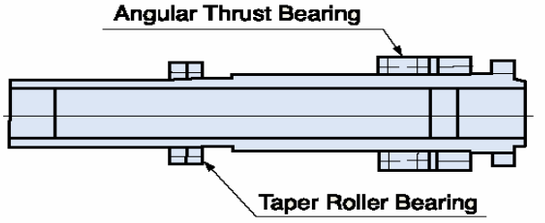


Fig 4: Z340 SM spindle



(a) (b)

Fig 5: a) Modern spindle cutting specimen b) Conventional spindle cutting specimen

REFERENCES:

[1] Data book of TN-50- Machin Sazi Tabriz Co.
[2] Data book of Z340SM-DOSSAN Co.
[3] Machine Shop Guide Magazine December/January 2000
[4] S.K. Basu & D.K. Pal “Design of Machine Tools” Forth edition, Oxford & IBH Publishing Co. PVT, Ltd., 1995
[5] Help of ANSYS 6.1
[6] Zienkiewicz, O.C.,” The finite element method “, McGraw-Hill (UK), London, 1977
[7] William T. Thomson “Theory of vibration with applications” Department of Mechanical and Environmental Engineering-University of California-Santa Barbara California-ALLEN&UNWIN Publisher-Third Edition-1988
[8] Data book of CINCOM FL42-MARBUNI CITIZEN-CINCOM Inc.

XXI ICTAM, 15–21 August 2004, Warsaw, Poland

SUPPRESSING SELF-EXCITED VIBRATIONS IN A COUPLED PENDULUM SYSTEM

Fadi DOHNAL, Horst ECKER
Institute for Machine Dynamics and Measurement, Vienna University of Technology
Wiedner Hauptstrasse 8-10/E303, A-1040 Vienna, Austria
Email: fadi.dohnal@tuwien.ac.at, Fax: +43-1-58801-30399

Summary The main objective of this paper is to show the phenomenon of full vibration suppression of a simple two degree of freedom pendulum system by interaction between self-excitation and parametric excitation. Using the averaging method general conditions for full vibration suppression are derived for the linearized system with harmonic stiffness variation. These analytical results are compared with results obtained from a numerical time integration of the linearized and of the original non-linear system.

MECHANICAL SYSTEM

We investigate a mechanical system consisting of two pendulums in a gravity field. Both pendulums are coupled by a linear spring-element. Self-exciting forces are acting on one pendulum and may destabilize the resting coupled pendulum system upon reaching a certain level. The effect of self-excitation is caused by some kind of mechanism that may be represented by an equivalent negative damping coefficient. Well-known examples for such mechanisms are the constant flow around a body with an aerodynamically unfavourable shape [1], or the contact of sliding surfaces with a velocity-dependent friction coefficient [2]. Both mechanisms are being capable of generating self-sustained vibrations if a characteristic parameter (e.g. flow velocity) reaches a critical value. Without counter measures both pendulums would start swinging with increasing amplitudes until nonlinearities in the system cause the vibrations to enter a limit cycle.

Vibration suppression can be achieved by a periodic excitation of the pendulum's pivot in the direction of gravity. It is well known that a single pendulum can be stabilized in its inverted position by this method, which is based on a periodic "modulation" of the gravity forces by the additional inertia forces acting on the pendulum due to the periodic excitation. The combined effect of gravity and inertia results in a periodically changing restoring force, which appears in the equation of motion as a parametric excitation in the displacement-proportional terms. The basic idea of creating a parametric stiffness excitation by a pivot excitation of a pendulum is adopted for the coupled pendulum system. But since we consider a non-inverted 2-dof system under the effect of self-excitation the stabilization of this system is based on a completely different principle, which is applied for the first time to pendulum systems.

For a coupled pendulum system with harmonic parametric excitation the equations of motion can be written as

$$I_{0,1}\ddot{\varphi}_1 + c_1\dot{\varphi}_1 + m_1 g\, l_1 \sin\varphi_1 + k_{12}(\varphi_1 - \varphi_2) = 0,$$
$$I_{0,2}\ddot{\varphi}_2 + c_2\dot{\varphi}_2 + m_2(\ddot{y}_0 + g)l_2 \sin\varphi_2 + k_{12}(\varphi_2 - \varphi_1) = 0,$$
$$\ddot{y}_0 = -\eta^2 A\cos\eta t,$$

and are hence represented by two coupled non-linear differential equations with a time-dependent periodic coefficient. One pendulum is subject to self-excitation (negative damping coefficient c_1) and the second pendulum is parametrically excited (harmonic function $\ddot{y}_0$) as shown in the following Fig. 1.

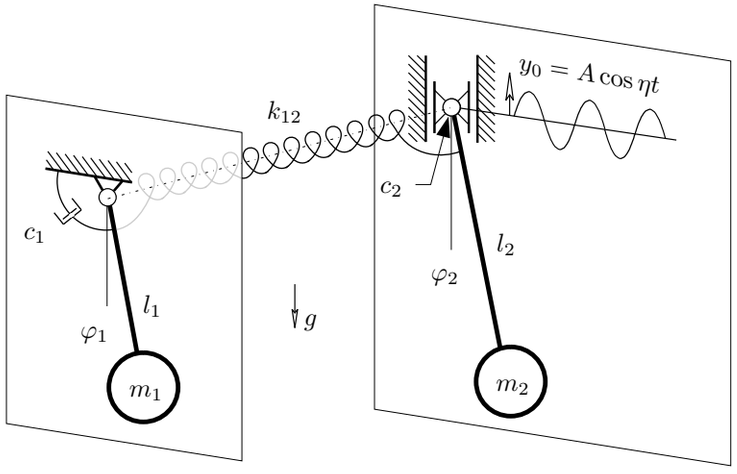


Figure 1. Coupled pendulum system.

AREAS OF VIBRATION SUPPRESSION

To understand the basic behaviour of the original system we first investigate the linearized coupled system for small oscillation amplitudes φ_1, φ_2. The equations of motion remain coupled by the constant stiffness coefficient k_{12}. The first equation of motion simplifies to a differential equation with constant coefficients and the second one is equivalent to the well-known Mathieu-equation.

The equations of motion are still quite complicated to be analyzed analytically. Approximate methods are good instruments for understanding the complex behaviour of mechanical systems. It is convenient if the right-hand side of the set of differential equations contains a small parameter. In a first step the system can be solved analytically if this parameter is set to zero. For nonzero but small values of the parameter, solutions can be obtained by perturbation techniques, e.g. the averaging method [3].

We introduce a small parameter for the damping coefficients and the amplitude of pivot excitation (parametric excitation). Transforming the system to its normal form yields the modal frequencies Ω_1, Ω_2. The method of averaging is used to derivate analytically the necessary conditions for full vibration suppression for the linearized system and small excitation amplitudes. These conditions show that the phenomenon of quenching is only possible near specific excitation frequencies of the pendulums pivot, the so-called secondary parametric resonances $\eta_0 = |\Omega_1 - \Omega_2|/N$, where N is a natural number. It is worth to note that the effect of quenching arises not only at a certain frequency value η_0, as it is the case for a dynamic vibration absorbers, but there exists a whole quenching area.

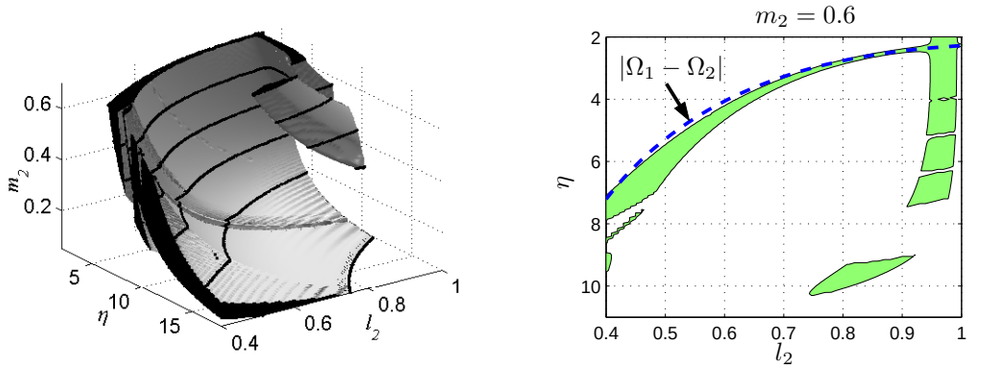


Figure 2. Stability body and chart obtained by numerical integration. Dark area indicates stable system.

The derived analytical conditions for vibration suppression are verified by numerical time integration of the linearized system using Floquet theory. The boundary between stable and unstable motion is investigated for different pivot excitation frequencies η as a function of one or two system parameters and is represented by stability charts and stability bodies, see Fig. 2. The quality of the analytical results for the linearized system are compared numerically with the original non-linear system in the same way.

CONCLUSIONS

In general the self-excited pendulum causes the system to become unstable. Moving the pivot of a second pendulum in the direction of gravity generates a parametric excitation – a harmonic stiffness variation. Coupling both pendulum only by a linear stiffness element can cause the system to become dynamically stable. Although the first pendulum is self-excited which would result in exponentially increasing vibration amplitudes, and also the second pendulum is oscillating due to its pivot motion, the first pendulum is stabilized and gets to rest. This vibration suppression is possible within an area near certain parametric resonance frequencies.

Analytical conditions for vibrations suppression are obtained by applying the averaging method on the linearized system. With these formulas it is possible to predict values of system parameters to achieve the quenching effect.

ACKNOWLEDGEMENT

This contribution was funded by the Austrian Science Fund (FWF) within Project P16248-N02.

References

[1] Tondl A., Ecker H.: Cancelling Of Self-Excited Vibrations By Means Of Parametric Excitation. *Proceeding of the 1999 ASME Design Engineering Technical Conferences (DETC)*, Sept. 12-15, 1999, Las Vegas, Nevada, USA.

[2] Ecker H.: A parametric absorber for friction-induced vibrations. In: Proc. ASME Design Eng. Techn. Conf. DETC2003, (Shabana A.A., ed.), Paper VIB-48474, Chicago, IL, Sept. 2-6, 2003.

[3] Verhulst, F.: Nonlinear Differential Equations and Dynamical Systems. Springer-Verlag, 2000.

THE RUNNING BEHAVIOUR OF AN ELASTIC WHEELSET

Ingo Kaiser*, Karl Popp**
* *German Aerospace Center (DLR), Institute of Robotics and Mechatronics, Postfach 1116, D-82230 Wessling, Germany*
** *University of Hannover, Institute of Mechanics, Appelstrasse 11, D-30167 Hannover, Germany*

Summary The dynamic behaviour of a railway passenger coach running on a straight track is investigated with special respect to the structural elasticities of the wheelsets and the rails. The vehicle and the track are coupled by a nonlinear wheel-rail contact.
The simulations are performed with and without taking into account the structural elasticities of the wheelsets and the rails. Comparisons of these results show a strong influence of the structural elasticities.

FORMULATION OF THE PROBLEM

To simulate the running behaviour of a railway vehicle, the wheelsets are usually considered as rigid bodies; this modelling is regarded to be sufficient for the low frequency-range below about 50 Hz. The wheel-rail contact is however very sensitive to even small relative motions of wheel and rail; so the question arises, whether deformations of the wheelsets can influence the contact and thereby the running behaviour of the entire vehicle.
Beyond a certain travelling speed, the so called critical speed, a limit cycle of the wheelsets occurs; this is called "hunting motion". Since this motion can lead to dangerous operational states, its occurence has to be avoided in regular operation by a proper mechanical design of the vehicle. Because a proper design requires reliable simulations, the influence of structural elasticities of the wheelsets and also of the rails on the simulation results is investigated.

MODELING OF THE SYSTEM

The entire system representing a railway vehicle running on a straight track is split up into three subsystems, as shown in Fig. 1. The characteristics of the subsystems are described in the following.

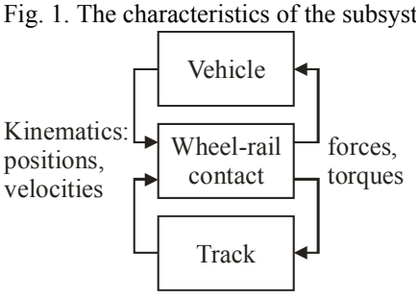


Fig. 1: Structure of the system consisting of subsystems

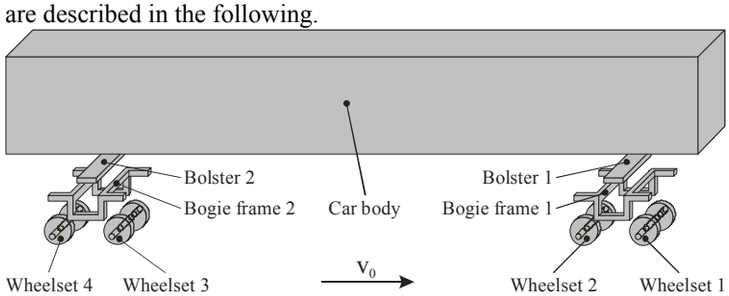


Fig. 2: Multi-body model of the vehicle

Subsystem "Vehicle"
The subsystem "Vehicle" represents a common european railway passenger coach consisting of a car body and two bogies, each equipped with two wheelsets, cp. Fig. 2.
The bodies are connected by linear visco-elastic elements except the pivot between the car body and the bolsters, where a nonlinear force element using dry friction acts. While the car body, the bolsters and the bogie frames are considered as rigid bodies, the four wheelsets are modelled as elastic bodies by superposing the rigid body motions and the deformations, which are described by a modal synthesis. The shape functions required by the modal synthesis are the eigenmodes of the free wheelset obtained by a Finite Element analysis. Fig. 3 shows two flexural eigenmodes.

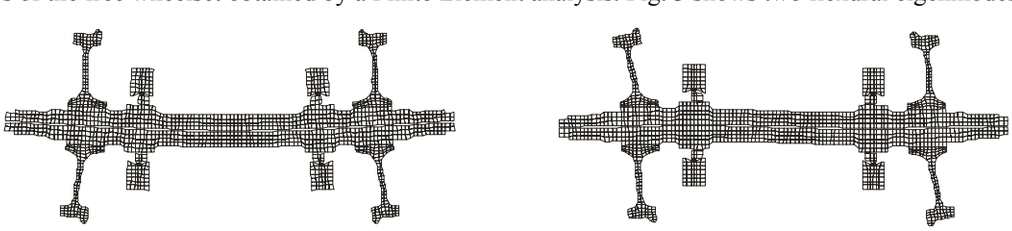


Fig. 3: Eigenmodes of the wheelset.
Left: Symmetric flexural eigenmode (84,2 Hz), right: Antimetric flexural eigenmode (147,2 Hz).

The eigenmodes are calculated for the non-rotating wheelset. Gyroscopic effects resulting from the rolling motion of the wheelsets are taken into account by additional terms. For the description of the rotating wheelsets, an Arbitrary Lagrangian-Eulerian approach is used providing a very simple mathematical structure of the model.

Subsystem "Wheel-rail contact"
The wheel-rail contact is a force element, which is nonlinear in two ways: Firstly, the contact geometry is nonlinear, i.e. the location where the contact forces act depends in a nonlinear way on the relative position of wheel and rail. Secondly, the relations between relative motions and the forces are nonlinear. The coupling of the subsystem "wheel-rail contact" to the other subsystems is performed by an interchange of kinematics and forces at invariant nodes, so that the shifting of the contact area is performed within the subsystem "wheel-rail contact", cp. Fig. 4.

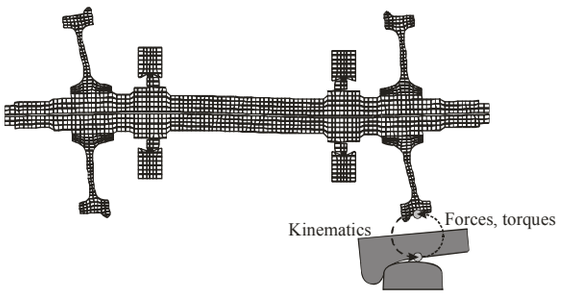


Fig. 4: Coupling of the subsystems

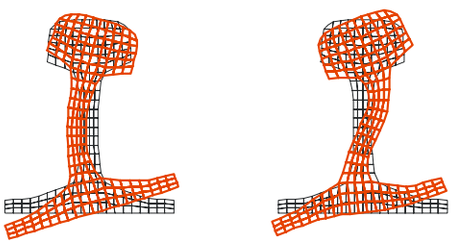


Fig. 5: Deformations of the cross section of the rail

Subsystem "Track"
The subsystem "track" consists of two rails with a continuous support representing the fastenings, the sleepers and the underground. Since the foot of the rail is fastened to the sleeper and the web of the rail is thin compared to the head, deformations of the cross section of the rails are taken into account. Therefore, the cross section is discretized by Finite Elements. This provides further deformations as shown in Fig. 5, additionally to the usual flexural or torsional deformations.

SIMULATION RESULTS

To investigate the influence of the structural flexibility on the running behaviour, different calculations are performed, in which the elasticities of the wheelsets and the track are taken into account or neglected. As an example, the lateral motion of the center of mass of the first wheelset during hunting at $v_0 = 350$ km/h is investigated. Fig. 6 shows the corresponding phase portraits.

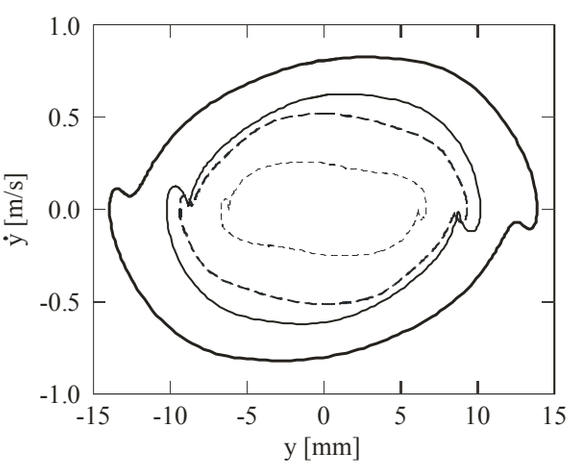


Fig. 6: Lateral motions of the first wheelset.
Thin line: Rigid wheelset, thick line: Elastic wheelset, broken line: Rigid track, full line: Elastic track.

The structural flexibility of the wheelsets and the track leads to distinctly larger amplitudes. Furthermore, the curve for the rigid wheelset on the rigid track is "flattened" at its left and right side; this results from the wheel flange hitting the rail head. Taking into account the structural flexibility leads to smoother curves, because the elastic wheelsets and the elastic track act as springs which are softer than the stiff wheel-rail contact.
Further calculations show, that these elasticities also cause a drop of the critical speed. While the hunting motion of a rigid wheelset on a rigid track starts at $v_0 = 341$ km/h, this motion already occurs at $v_0 = 282$ km/h for an elastic wheelset on an elastic track. This distinct difference may also be of technical interest for the design of a railway vehicle.

XXI ICTAM, 15–21 August 2004, Warsaw, Poland

THERMOELASTIC RELAXATION IN THIN PLATES WITH APPLICATIONS TO MEMS AND NEMS OSCILLATORS

Andrew N. Norris*, Douglas M. Photiadis**
*Mechanical and Aerospace Engineering, Rutgers University, Piscataway NJ 08854-8058, USA
**Naval Research Laboratory, Code 7130, Washington, DC 20375-5350, USA

Summary Equations governing thermoelastic loss in vibrating thin plates are derived, generalizing Zener's theory of thermoelastic loss in beams. The mechanism for the loss of mechanical energy is thermal diffusion caused by inhomogeneous deformation, flexure in thin plates. It is shown that a critical plate thickness, h^*, exists which separates two distinct types of response, which may be called thermally thick and thin. For plates of thickness $h > h^*$ the diffusion, and hence the thermal component of the solution, is restricted to a 1-dimensional heat flux across the plate thickness. If the thickness is less than h^* then in-plane thermal diffusion cannot be ignored, and may in fact dominate. Several general results are obtained for plates with $h > h^*$. Thus, using the Kirchhoff assumption for the elastic deformation, it is shown that the local thermal relaxation loss depends upon the local state of vibrating flexure, specifically, the principal curvatures at a given point on the plate. The thermal loss is zero at points where the principal curvatures are equal and opposite, i.e. saddle shaped deformation. Conversely, thermal loss is maximum at points where the curvatures are equal, or spherical flexure. An effective plate equation is derived that incorporates the thermoelastic loss as a damping term. The general form of the effective damping that is obtained for $h > h^*$ can be generalized to arbitrary thickness, in particular the case of thermally thin plates can be considered. These results are useful in predicting mode widths in MEMS and NEMS oscillators.

INTRODUCTION

High Q resonators are central to the development of new devices and applications that include RF filters, next generation MRI systems, and torque magnetometers. Si-based MEMS/NEMS oscillators are the candidates of choice, and include free standing planar devices, such as double paddle oscillators (DPOs), and micro-cantilevers. As the oscillators shrink in size, it has been found that the Q achieved is orders of magnitude smaller than expected based on classical fundamental loss mechanisms. Many mechanisms have been proposed, including surface loss that increases with the surface to volume ratio. However, under controlled conditions with minimal surface defects and adsorbates, measurements on Silicon DPOs have shown that room temperature losses are adequately described by thermoelastic relaxation, while unexplained mechanisms operate at lower temperatures. Interestingly, the mode of vibration of DPOs is designed to be primarily torsional with very little flexure (and hence no thermoelastic coupling). However, as demonstrated by Photiadis et al. [1] it is precisely the small amount of flexural motion that accounts for loss in these supposedly torsional oscillators. In this talk we describe a consistent theory for predicting intrinsic dissipation arising from thermoelasticity in elastic structures. Particular attention will be given to flexural motion of thin plates. This work is a step towards understanding the fundamental limits of dissipation in small structures such as NEM and MEM devices.

Surprisingly few papers have appeared on the topic of damping of structural vibration via thermal relaxation since Zener published his now-classic theory of anelastic thermoelastic damping, see [2]. Alblas [3] provided a rigorous formulation using continuum thermomechanics and linear elasticity theory for isotropic materials. He derived detailed and explicit solutions for the thermoelastic damping in vibrating beams, including the circular rod and the rectangular beam. The result for the latter was derived separately by Lifshitz and Roukes [4], although Alblas' solution is the more general of the two. Perhaps the most thorough analysis of thermal damping in the context of the coupled equations of thermoelasticity is due to Chadwick [5]. By considering a modal decomposition of the elastic and thermal fields, an exact relation for the complex valued frequency of oscillation of each mode was obtained. This enabled Chadwick to derive a generalization of Zener's expression for the thermoelastic damping of an arbitrary elastic body, and in a far more rigorous way than the original. Chadwick subsequently derived the governing equations of thermoelasticity for thin plates and beams [6]. The equations are in the form of coupled equations, one of which reduces to the classical equations for the structural mode, e.g. flexural waves in thin plates, and the other the temperature diffusion equation, in the limit of zero coupling. The analysis in [6] is restricted to isotropic solids, and no specific structures are considered, only general bodies for which the solution is expressed in terms of the eigenfunctions of Laplace's equation.

THEORY

We are concerned with determining the thermomechanical loss of elastic modes, e.g. the flexural mode of a rectangular thin plate. The key to this approach is the valid assumption (implicit in Zener's work) that there is little relative difference between the isentropic (unrelaxed) and isothermal (relaxed) mechanical responses, and hence the mechanical and thermal problems are essentially decoupled. Since the thermoelasticity is weak, the transition from the instantaneous or unrelaxed system to the relaxed system can be viewed as a quasistatic thermal process, governed by the normal equations for thermal diffusion, although now in the presence of an inhomogeneous deformation.

We employ the general equations of coupled thermoelasticity for anisotropic materials. In addition, we assume the standard form for the heat flux, which makes the dynamic system irreversible and dissipative. The analysis takes advantage of the universally small coupling between the thermal and elastic fields, permitting an asymptotically exact formulation

in the small parameter $\epsilon = E\alpha^2 T/C_p$[1], see Table I. Using the classical Kirchhoff form for the plate deformation, the governing equations are adapted to thin plate configurations. This yields equations for the moments and stresses in terms of the usual elastic deformation plus certain moments of the temperature field θ. The key to obtaining explicit plate equations independent of temperature is to solve the temperature equation, which is in the form of a forced thermal diffusion problem. The forcing depends upon the stress field in the plate, and is greatest in regions of hydrostatic stress, which implies the most significant effects are to be expected from flexural waves.

RESULTS

In deriving effective plate equations for flexural wave motion, we find that there is a characteristic length, h^*(see Table I). This arises from the fact that both the flexural wavenumber and the thermal diffusion wavenumber are proportional to $\omega^{1/2}$, and there is a unique plate thickness when they are commensurate. For plates thicker than this length the thermal diffusion problem can be solved and explicit plate equations found. For instance,

Material	100 ϵ	h^* (μm)
Gold	0.017	5,685
Silicon	0.022	272
SiC	0.059	43
Platinum	0.13	534
Silver	0.22	8028
Nickel	0.27	239
Copper	0.28	2681
GaAs	0.48	16
Beryllium	0.56	141
Lead	0.85	5739
Aluminum	4.7	53

Table I. The thermoelastic coupling parameter ϵ at 300 K, and the length h^* for different materials.

isotropic materials reproduce the classical plate equation $D\nabla^4 u - \rho h\omega^2\, u = 0$ where now the bending stiffness is

$$D = \frac{EI}{1-\nu^2}\big(1 + \epsilon f(kh)\big), \qquad f(\zeta) = \frac{24}{\zeta^3}\left[\frac{\zeta}{2} - \tan\frac{\zeta}{2}\right],$$

where h is the thickness, and k is the complex thermal wavenumber. The dissipation depends on the imaginary part of D. Generalizations to orthotropic plates will be presented.

A general result governing the rate of *local* energy loss in thin plates is also derived. Specifically, it is shown that the relative decay of flexural energy at a point on a plate is of the form (for isotropic plates)

$$\eta = \epsilon\, g(\omega)\, \frac{\big(\kappa_1 + \kappa_2\big)^2}{\big(\kappa_1 + \kappa_2\big)^2 - 2(1-\nu)\kappa_1\kappa_2}$$

where κ_1 and κ_2 are the two principle curvatures at the point, and the function g depends only on frequency and thickness. Thus, thermoelastic damping vanishes at oscillating saddle points, and is maximum for locally "spherical" bending.

For plates of thickness less than h^* the in-plane thermal diffusion can be taken into account, although effective plate equations cannot be obtain. We can however derive dispersion relation for flexural waves, which depend upon the same function f above although in an implicit manner. This permits us to extend the present theory to NEMS rather than just MEMS.

References

[1] Photiadis, D.M. et al.: Thermoelastic Loss Observed in a High Q Mechanical Oscillator. *Physica B.* **316**:408–410, 2002.
[2] Zener, C.: Elasticity and Anelasticity of Metals. University of Chicago Press, Chicago,1948.
[3] Alblas, J.B.: On the General Theory of Thermo-elastic Friction. *Appl. Sc. Res.* **A10**:239–362, 1961.
[4] Lifshitz, R. and Roukes, M.L.: Thermoelastic Damping in Micro- and Nanomechanical Systems. *Phys. Rev. B* **61**: 5600–5609, 2000.
[5] Chadwick, P.: Thermal Damping of a Vibrating Elastic Body. *Mathematika* **9**:38–48, 1962.
[6] Chadwick, P.: On the Propagation of Thermoelastic Disturbances in Thin Plates and Rods. *J. Mech. Phys. Solids* **10**:99–109, 1962.

[1] E, α, T and C_p are respectively Young's modulus, thermal expansion coefficient, absolute temperature and heat capacity

ESTIMATION OF THE VIBRATION ENERGY CHARACTERISTICS FOR JOINTS OF CONSTRUCTIONAL ELEMENTS

Jacek CIESLIK
AGH University of Science and Technology, Faculty of Mechanical Eng. and Robotics, Dept. of Robotics and Machine Dynamics, Al. Mickiewicza 30, 30-059 Krakow, Poland,

Summary Detailed estimation of energy characteristics in vibration structures such as loss factors, potential and kinetic energy, mechanical power flow is important for modeling in many fields of structural acoustics. The paper presents the approach to energy characteristics evaluation for set of constructional element joints based on structural intensity analysis. As the result it is obtained the precise information on vibration energy flow. The analysis of spatial distribution of structural intensity vector fields enables determination and location of paths, sources and sinks of energy of vibrations in application to the mechanical systems. It gives the particular information on the streams of energy flow. The structural intensity method is theoretically based and validated in computer simulations. Some selected results of calculations are discussed in particular.

INTRODUCTION

Structural intensity represents the averaged in time net mechanical energy flow through the unit area perpendicular to the direction of flow [2]. The analysis of spatial distribution of structural intensity vector fields enables determination and location of paths, sources and sinks of energy of vibrations in application to the mechanical systems.
This numerical approach to structural intensity evaluation was based on the modal model [2, 3]. The practical examination on the computational way of vibration energy flow in complex structures consisting of the beam, plates and shells haven't been solved satisfactory till now.

STRUCTURAL INTENSITY FOR SIMPLE CONSTRUCTIONAL ELEMENTS

Instantaneous value of real part of structural intensity $i_k(t)$ is time dependent vector quantity equal to the change of energy density in the infinitively small volume [1]. Its *k-th* component is given by the equation:

$$i_k(t) = -\sigma_{kl}(t) v_l(t), \quad l = 1, 2, 3, \tag{1}$$

where $v_l(t)$ is the *l-th* component of velocity vector and $\sigma_{kl}(t)$ is *kl-th* component of stress tensor.

Structural intensity in beams

Simplest structure which could provide the energy transportation is the unbounded thin rod excited to axial vibrations. The structural intensity is related to the axial line of rod and equal to:

$$I = \sqrt{E\rho}\, \mathrm{v}^2 \tag{2}$$

where E – Young's modulus, ρ – mass density, v – rod axial velocity.
In case of prismatic beam for the single frequency of excitation the particle velocities are found from the complex displacements. The component according main axis of beam is [2]:

$$I_x = -\frac{\omega}{2} \mathrm{Im}\left[\tilde{N}\tilde{u}_0^* + \tilde{Q}_y \tilde{v}_0^* + \tilde{Q}_z \tilde{w}_0^* + \tilde{T}\theta_x^* + \tilde{M}_y \theta_y^* + \tilde{M}_z \theta_z^*\right] \tag{3}$$

where $\tilde{N}$ - tension forces, $\tilde{Q}_y$ i $\tilde{Q}_z$ - shear forces, $\tilde{T}$ - torque, $\tilde{M}_y$ i $\tilde{M}_z$ - bending moments, $\tilde{\theta}_x, \tilde{\theta}_y$, $\tilde{\theta}_z$ - angular displacements, $\tilde{u}_0, \tilde{v}_0, \tilde{w}_0$ - linear displacements of beam neutral line according respectively *x, y, z* axis.

Structural intensity in plates

For the vibration of thin plates dominant are the bending and longitudinal waves. For the longitudinal waves the displacements do not vary with the depth of the plate. In case of bending vibrations there are added up displacements caused by the shear forces, bending and twisting moments. In the numerical calculations by the means of finite element method the structural intensity is related to the neutral not deformed middle plane of plate. There are assumed small deformations which enable the superposition of independent displacements for flat finite element of plate or shell type.

RESULTS OF CALCULATIONS

Modal analysis based on dense grid of finite elements enabled detailed analysis of vibration energy transportation. The results obtained from calculations are presented in graphical form on Fig. 1. The structural intensity vectors distribution

over the flat elements of rectangular frame structure is shown. In region far from connections, external damping or excitation the directions of vectors are ordered, parallel and steady regarding the vector magnitude and direction. There are clear seen the very specific disturbances of vectors distribution in places of element connections. In places close to the connections it can be observed the circulation of a structural intensity vectors. This effect means the circulation and conservation of vibration energy in the mechanical system. In some cases the directions of vectors are focused in small volume. This inclines to the conclusion that is the place of vibration energy dissipation – energy loss caused by the transmission of waves through the connection of elements. The particular analysis leads to conclusion that intensity vectors distribution by its nature enables localization of vibration energy decay in large surface elements.

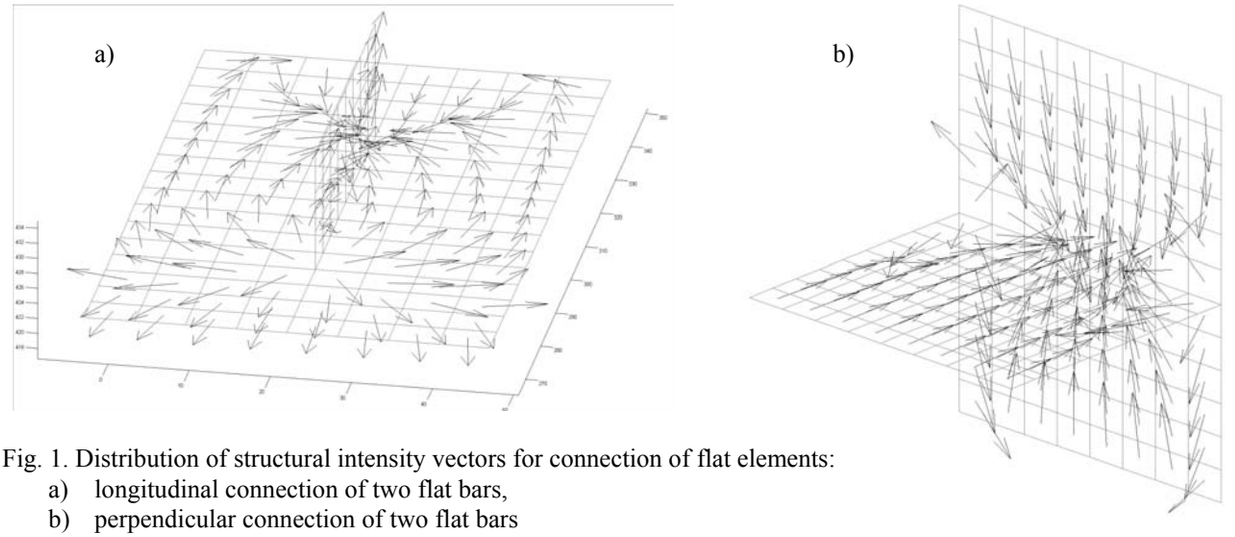


Fig. 1. Distribution of structural intensity vectors for connection of flat elements:
a) longitudinal connection of two flat bars,
b) perpendicular connection of two flat bars

The distribution of structural intensity vectors gives the qualitative characteristic of vibration energy transportation in mechanical systems. Additional measure in form of integral of magnitude structural intensity vector component perpendicular to the certain closed surface e. g. element cross section enables the quantitative assessment of energy transfer paths and its balance in the structure.

CONCLUSIONS

Presented method of structural intensity vector calculation enables its evaluation for chosen frequency range and mode shapes [2]. Structural intensity is the product of stress and velocity for the same point of the structure. Shown dependencies connect the structural intensity with linear and angular displacements, forces and moments exerted to the structures like beams, plates and shells. The method of structural intensity evaluation is based on calculation of displacements in nodes and stresses in inner points i.e. Gauss points of finite elements. The calculations are done on complex modal parameters counted by the use of the numerical modal analysis based on FEM. The disadvantage of the method is its poor convergence. The number of modes which are used in calculation process should be properly chosen. The abrupt changes of stress which occur in regions close to the excitation or discontinuities of structure can not be well described by the limited number of lower modes. This makes the problem of calculation method exactitude. The method of analysis of structural intensity distribution has been applied as a new diagnostic method for assessment of failure which could occur in constructional elements. It enables the investigation in the regions of high concentration of vibration energy flow which consequently are exposed to the risk of damage. It can be considered as the identification of the regions of increased damping of vibrations. Examples of examination of structural intensity distribution in elements of rectangular frame have confirmed the method usability to the investigation of vibration energy transportation paths and places of its concentration in discontinuities. The method enables the qualitative analysis depending on structural intensity vectors distribution. Also there are possible the quantitative analysis based on calculated values of power of vibrations in particular elements of structure.

References

[1] Gavric L.: *Influence of local modifications on energy flow in thin-walled structures.* Ph.D. Thesis 1991, Universite de Technologie de Compiegne, Compiegne.

[2] Gavric L., Pavic G.: *A finite element method for computation of structural intensity by normal mode approach.* Journal of Sound and Vibration, 1993. Vol 164(1), 29-43.

[3] Cieślik J.: *Vector fields of structural intensity in application to analysis of vibrational energy flow.* Archives of Transport, Vol. 15, (1) 2003.

[4] Cieślik J.: *Vibration energy flow in rectangular plates.* Journal of Theoretical and Applied Mechanics. Vol. 41, (4) 2003 r.

[5] Cieślik J.: *Intensity vector fields in application to vibrational energy flow*. Conference Proc. CMM-2003 – Computer Methods in Mechanics, June 3-6, 2003, Gliwice, Poland, s.105-106.

SOUND RADIATION BY THE WHITE NOISE EXCITED VISCOELASTIC SHALLOW SHELLS

Marek S. Kozien, Jozef Niziol
Cracow University of Technology, Institute of Applied Mechanics, PL 31-864 Krakow, Poland

Summary The results of estimation of the sound pressure radiated by structurally vibrating viscoelastic shallow shell are discussed. The shell is loaded by the continuous force, distributed over the middle surface, and randomly varying in time. The white noise type of excitation is assumed.

INTRODUCTION

Shallow shells are commonly used as constructional elements in cages of heavy duty machines. These elements, are sources of structural noise radiated during the machine operation. In the previous authors' papers [2,3,4,5] the analysis of influence of curvature of the shallow shell elements on the level of their structural vibrations for different kinds of excitation (deterministic: harmonic, polyharmonic; random: white and coloured noise) were discussed. In the presented paper the method based on the acoustic power radiated by the shell was applied to estimate the sound radiated by randomly excited shallow shells with different radii of curvatures. The estimations are valid for the acoustic far-field.

MATHEMATICAL MODEL OF VIBRATING SHALLOW SHELL AND SOUND RADIATION

Let us consider the vibrating shallow shell with internal viscoelastic damping. The Voigt-Kelvin model of damping was assumed. The detailed description of the model are given in the paper [5]. Some theoretical background of the applied shell models can be found in [8,9]. The geometry of shallow shell is shown in Fig.1. The inertial components which represents the motion in tangential directions of the middle surface are neglected in the model. Moreover it is assumed that the velocity components in the in-plane equations of motion are neglected, and the only excitation in the Oz direction are taken into account. The excitation has the form of multiplication of the two components: the constant amplitude q_0 and the random function of time $f(t)$. The obtained set of equations of motion have the forms (1a), (1b) and (1c), where the symbols denote: u,v,w – displacements in directions Ox, Oy and Oz respectively, R_x and R_y – radii of main curvatures, h – thickness, E – Young modulus, ν - Poisson ratio, D – bending stiffness, B – in-plane stiffness, ε - viscous damping coefficient, ρ - material density. The lower indexes with apostrophe denotes differentiation with respect to given variables, and the dot symbol above function denotes differentiation with respect to time. The boundary condition of the shell have the following form: the simply supported one for bending vibrations and the free-fixed one for the in-plane vibrations. The mathematical formulation of the boundary conditions are given in [5]. The solution of the excited vibrations problem is proposed in the form of series with unknown functions of time $S_{mn}(t)$ (2), where $w_{mn}(x,y)$ are the shape function for the (m,n)-th mode [4,5].

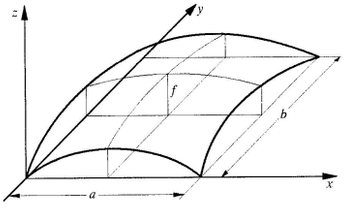


Fig.1: Geometry of the shallow shell.

$$u_{,xx} + 0.5(1-\nu)u_{,yy} + 0.5(1+\nu)v_{,xy} + [w/R_x + (\nu w)/R_y]_{,x} = 0 \tag{1a}$$

$$v_{,yy} + 0.5(1-\nu)v_{,xx} + 0.5(1+\nu)u_{,xy} + [w/R_y + (\nu w)/R_x]_{,y} = 0 \tag{1b}$$

$$\begin{aligned} &w_{,xxxx} + 2w_{,xxyy} + w_{,yyyy} + \varepsilon\dot{w}_{,xxxx} + 2\varepsilon\dot{w}_{,xxyy} + \varepsilon\dot{w}_{,yyyy} + \\ &+ 12[1/R_x + \nu/R_y]/h^2 u_{,x} + 12[1/R_y + \nu/R_x]/h^2 v_{,y} + 12[1/R_x^2 + 1/R_y^2 + 2\nu/R_x/R_y]w + \\ &+ 12\varepsilon[1/R_x + \nu/R_y]/h^2 \dot{u}_{,x} + 12\varepsilon[1/R_y + \nu/R_x]/h^2 \dot{v}_{,y} + 12\varepsilon[1/R_x^2 + 1/R_y^2 + 2\nu/R_x/R_y]\dot{w} + \\ &+ \rho h/D\ddot{w} = q_0 f(t)/D \end{aligned} \tag{1c}$$

$$w(x,y,t) = \sum_{m,n=1}^{+\infty} S_{mn}(t)\sin\left(\frac{m\pi}{a}x\right)\sin\left(\frac{n\pi}{b}y\right) = \sum_{m,n=1}^{+\infty} S_{mn}(t)\,w_{mn}(x,y) \tag{2}$$

The correlation function of the process $w(x,y,t)$ takes the form (3). After suitable averaging over a groups of realizations, and assuming that random function $f(t)$ is the white noise type one, the dispersion of shell displacements can be written in the form (6) [5], where $h_{ij}(t)$ are the transfer functions defined in [5] as a functions of eigenfrequencies and non-dimensional modal damping coefficients. The theoretical background of the random analysis can be found in [7].

$$K_{ww}(t_1,t_2) = \int_{-\infty-\infty}^{+\infty+\infty} w_{mn}(x,y)\, S_{mn}(t_1) \sum_{j,k=1}^{+\infty} w_{jk}(x,y)\, S_{mn}(t_2)\, p(z_1,z_2;t_1,t_2)\, dz_1 dz_2 \tag{3}$$

(4)

$$\sigma_w^2(x,y,t) = 2\frac{256}{\pi^4}\frac{z_0^2}{\rho^2 h^2} \sum_{m,n=1,3,\ldots}^{+\infty} \frac{w_{mn}(x,y)}{mn} \sum_{j,k=1,3,\ldots}^{+\infty} \frac{w_{jk}(x,y)}{jk} \int_0^t h_{mn}(t-\tau_1)\, d\tau_1 \int_0^{\tau} h_{jk}(t-\tau_2)\, \delta(\tau_1-\tau_2)\, d\tau_2$$

Based on the knowledge of the dispersion of displacements in Oz direction, the dispersion of the sound pressure level radiated in chosen control point in acoustic medium is estimated by the analysis of the sound power radiated by vibrating panel. One the one hand the acoustic sound power can be estimated based on the simplified formula (5) [1,6], and on the other one, the pressure for the far-field acoustic analysis can be estimated based on the formula (6) [6]. The applied symbols denote: $<V^2>$ - squared normal velocity averaged over the shell surface, ρ_0 – density of the acoustic medium, c – speed of sound in acoustic medium, S - area of the shell, S^* - area of the hemisphere with radius equal to approximate distance of the control point from the radiating panel, W – sound power radiated by the shell, σ_{rad} – radiation efficiency coefficient, p_{AVG} – averaged sound pressure.

$$W = \sigma_{red}\, \rho\, c\, S <V^2> \tag{5}$$

$$\rho c W = p_{AVG}^2\, S^* \tag{6}$$

NUMERICAL EXAMPLE

Let us consider the shallow shell in the form of elliptical paraboloid made of steel, whose middle surface has the form (7). Their projection on the xy plane has the form of a square a=b=1 m. The thickness is h=0.002 m, and the damping coefficient is equal ε=0.001. The detailed values of geometrical and material parameters are the same like in [4,5]. The amplitude of excitation is equal to q_0=1 N/m^2. The estimated values of the pressure dispersion levels in the control point distanced 3 m over the centre of the middle surface, for different values of deflection f are given in Table 1.

$$z(x,y) = f\left[1 - \frac{(2x-a)^2}{2a^2} - \frac{(2y-b)^2}{2b^2}\right] \tag{7}$$

Table 1: Values of the pressure dispersion level in the control point.

f [m]	0	0.01	0.02	0.05	0.2
σ_p^2 [dB]	70.5	49.0	38.1	24.0	0.9

CONCLUSIONS

The results of analysis show an important influence of the shallow shell radii of middle surface curvatures on dispersion of the pressure in chosen control point in the acoustic surrounding medium.

References

[1] Beranek L. (Ed.), Noise and Vibration Control. Institute of Noise Control Engineering, Washington DC, 1988.

[2] Kozien M., Niziol J.: Analysis of the Value of Normal Surface Velocity for the Vibrating Shallow Shell. *Technical Bulletin of the Cracow University of Technology – Mechanics*, **4-M**: 1-18, 1993 (in Polish).

[3] Kozien M., Niziol J.: Reduction of the Value of Normal Velocity for Vibrations of the Glass of Heavy Duty Machine TD20E – the Theoretical Analysis. *Technical Papers of Rzeszow University of Technology*, **117**, Mechanics, **38**: 71-78, 1993 (in Polish).

[4] Kozien M.S., Niziol J., Random Excitex Vibrations of Viscoelastic Shallow Shells. *Proceedings of the Fifth Workshop: Active Methods of Vibration and Noise Control, Krakow-Krynica, 225-232, 2001 (in Polish).*

[5] Niziol J., Kozien M.S.: White Noise Excited Vibrations of Viscoelastic Shallow Shells. *J.Theoret.Appl.Mech.*, 2, **38**: 351-366, 2000.

[6] Panuszka R.: Research on the Sound Radiated by Circular Plate. *Bulletin of the Academy of Mining and Metallurgy- Mechanics*, 1, **1**: 125-145, 1982 (in Polish).

[7] Piszczek K., Niziol J.: Random Vibration of Mechanical System. PWN Warszawa – Ellis Horwood Ltd. Chichester, 1986.

[8] Waszczyszyn Z.: Mechanics of Buildings. Computer Formulation. Vol.3, Arkady, Warszawa, 1995 (in Polish).

[9] Xia Z.Q., Lukasiewicz S.: On Internal Resonance of Sandwich Cyllindrical Panels Under Periodic Loadings. In: Epstein M. (Ed.): A World of Shells. Festschrift In Honour of Peter G.Glockner on the Occasion of his Retitement from Teaching. The University of Calgary, Calgary, 201-225, 1995.

SELF-EXCITED STICK-SLIP OSCILLATIONS OF DRAG BITS

Thomas Richard[*], Christophe Germay[**], Emmanuel Detournay[***]
[*]*Diamant Drilling Services, Belgium*
[**]*Systèmes et Contrôle, Université de Liège, Belgium*
[***]*Department of Civil Engineering,University of Minnesota, USA*

INTRODUCTION

Rotary drilling systems used to drill deep boreholes for hydrocarbon exploration and production often experience severe torsional vibrations, called stick-slip, characterized by (i) sticking phases where the bit stops, and (ii) slipping phases where the angular velocity of the tool Ω increases up to two times the imposed angular velocity. This problem is particularly acute with drag bits, which consist of fixed blades or cutters mounted on the surface of a bit body. The main attributes of observed stick-slip oscillations are:

Modelling of the stick-slip oscillations of drag bits is typically carried out by considering only the torsional vibration of the drill string and by reducing the bit-rock interface to an equivalent frictional contact with a velocity weakening friction coefficient. In this paper, we propose an alternative approach based on a discrete model of the drilling system and on a rate-independent description of the bit-rock interaction. This model takes into consideration the axial and torsional vibration modes and their coupling through bit-rock interaction laws, which account for both frictional contact and cutting processes at the bit-rock interface. We show that this model experiences self-excited vibrations, which can degenerate into stick-slip oscillations or bit bouncing under certain conditions.

MATHEMATICAL MODEL

A rotary drilling structure consists essentially of a rig, a drill string, and a bit. The principal components of the drill string are the bottom hole assembly (BHA) composed mainly of heavy steel tubes to provide a large downward force on the bit, and a set of drill pipes made of thinner tubes. For the idealized drilling system under consideration, we assume that a constant upward force H_o and a constant angular velocity Ω_o are applied by the rig on the drill string, that the borehole is vertical, and that there are no spurious lateral motions of the bit.

The bit motion as well as the forces acting on the bit can in principle be calculated knowing the prescribed surface boundary conditions, the mechanical properties of the drill string and the bit-rock interaction law. For this analysis, we consider a discrete model of the drill string stripped to its essential elements, i.e., a point mass M and moment of inertia I to represent the BHA and a linear spring of torsional stiffness C to model the drillpipes, see Figure 1.

Given the constant angular velocity Ω_o and constant upward tension H_o imposed to the upper end of the torsional spring, we seek to determine the unknown bit response $\mathcal{R}$. This response, which is generally a function of time t, consists of two sets of conjugated dynamic and kinematic quantities: the weight-on-bit W and the vertical bit velocity V on the one hand, and the torque-on-bit T and the angular bit velocity Ω on the other hand. We introduce the vertical position U and the angular position Φ of the bit. There is a steady-state (trivial) response of the bit, denoted as $\mathcal{R}_o=\{W_o, V_o, T_o, \Omega_o\}$, which is characterized by constant quantities $W_o=W_s-H_o$, $\Omega=\Omega_o$, $\Phi=\Omega_o t-T_o/C$ where W_s is the submerged weight of the drillstring. The non-trivial response $\mathcal{R}$ can be determined in principle from the surface conditions and bit-rock interface laws, together with the following torsional and axial equations of motion

$$I\frac{d^2\Phi}{dt^2}+C\left(\Phi-\Phi_o\right)=T_o-T,\; M\frac{d^2U}{dt^2}=W_o-W$$

We restrict consideration to an idealized drag bit of radius a, consisting of n identical radial blades regularly spaced by an angle equal to $2\pi/n$, see Figure 1. Each blade is characterized by a sub-vertical cutting surface and a wearflat of constant width ℓ_n orthogonal to the bit axis. The depth of cut per blade $d_n(t)$ is constant along the blade and identical for each blade; d_n is given by

$$d_n(t)=U(t)-U\left(t-t_n\right)$$

where $t_n(t)$ is the time required for the bit to rotate by an angle $2\pi/n$ to its current position at time t. The delay $t_n(t)$ is solution of

$$\Phi(t)-\Phi\left(t-t_n\right)=2\pi/n$$

The nature of the bit-rock interaction depends on the bit axial and angular velocity.

Consider first the "normal" case when $V>0$ and $\Omega>0$. The drilling action of a drag bit consists of a pure cutting process in front of each blade and a frictional process along the wear flats. Both the weight-on-bit W and the torque-on-bit T can thus be expressed as $W=W_c+W_f$, $T=T_c+T_f$ where the subscript c denotes the cutting component, and f the frictional component. The forces associated with the cutting process are taken to be proportional to the depth of cut d while the frictional forces mobilized along the wearflats depend on a rate-independent friction coefficient μ. The cutting and frictional components of W and T are explicitly given by (Detournay & Defourny 1992)

$$W_c = a\zeta\varepsilon d,\ \ W_f = a\ell\sigma,\ \ T_c = \frac{a^2}{2}\varepsilon d,\ \ T_f = \frac{a^2}{2}\gamma\mu\ell\sigma$$

where ε is the intrinsic specific energy (the amount of energy required to cut a unit volume of rock), ζ characterizes the inclination of the cutting force on the cutting face (typically, $0.6 \le \zeta \le 0.8$), and σ is the magnitude of the normal stress acting across the wear flat interface (single cutter experiments show that σ ~ ε). The number γ globally characterizes the spatial orientation and distribution of the chamfers/wearflats. When the bit is moving upwards, we assume a complete loss of contact between the wearflat and the rock ($W_f = T_f = 0$).

The case $V = \Omega = 0$ corresponds to the stick phase when the bit remains immobile. Since rotation of the drill pipes continues at the surface, the torque applied by the drillstring on to the BHA builds up until its magnitude is sufficient to overcome the reacting torque; the bit slips.

It is convenient to formulate the model in a dimensionless form via a characteristic length L_* and time t_*. The scaled bit response depends on two sets of parameters: the control parameters $\mathcal{W}_o = W/\zeta\varepsilon a L_*$ and $\omega_o = \Omega_o\, t$; and the problem parameters characterizing the geometry and wear state of the bit, the rock, and the drilling structure, i.e., the number of blades n, and the lumped parameters $\beta = \mu\gamma\zeta$, $\lambda = n\sigma\ell/\zeta\varepsilon L_*$, and $\Psi = \zeta\varepsilon a I/MC$.

SELF-EXCITED OSCILLATIONS

A linear stability analysis indicates that the trivial motion is unstable. Numerical solution of the system of equations confirms that any perturbations to the trivial motion cause the system to evolve towards one regime of self-excited axial and torsional vibrations. Several such regimes exist, with some characterized by stick-slip oscillations or bit bouncing. It appears that most of these regimes of solutions are either periodic characterized by a limit cycle or quasi-periodic, i.e. they evolve extremely slowly compared to the characteristic time of the system. Figure 2 illustrates the evolution of the bit angular velocity ω towards a limit cycle for two cases corresponding to β=0.3 and β=1 (lower and upper plot, repsectively).

The root cause of the self-excitation is the cutting process which introduces, via the delayed axial position of the bit, a feedback into the equations of motion. Growth of the axial oscillations is hindered, however, by an intermittent "high-frequency" loss of contact at the wearflat/rock interface, which is limiting the transfer of energy from the torsional to the axial motion. The coefficient β, which encapsulates the asymmetry between the axial and torsional interface laws, affects the ratio between the energy going into the cutting process and the energy dissipated in frictional contact. In fact, stick-slip oscillations take place only if β<1

The results of an extensive series of numerical experiments can be summarized into the following general observations. In the absence of bit bouncing, the system reaches strictly a limit cycle whenever β>1, or if stick-slip develops when β<1, see Figure 2. If there is no stick-slip and bit bouncing in the case β<1, the response reaches "rapidly" a quasi-periodic regime, with the amplitude of the torsional oscillations increasing extremely slowly, presumably towards a limit cycle with stick-slip oscillations. The susceptibility to stick-slip motion increases with a reduction of the angular velocity ω_o and with an increase of W_o, in accordance with field observations.

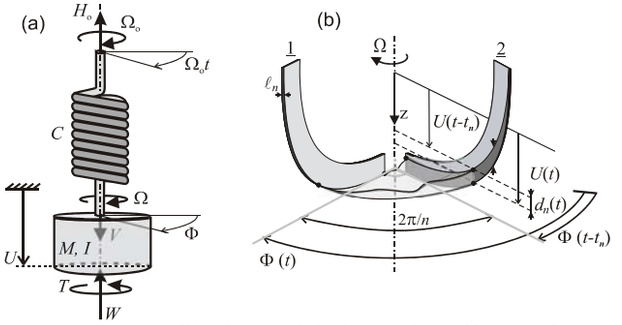


Figure 1: (a) Drillstring model. (b) Section of bottom-hole

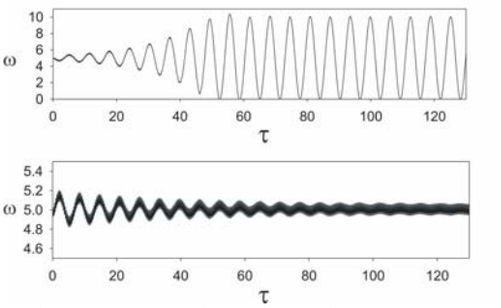


Figure 2: Angular velocity vs time (dimensionless)

CONCLUSIONS

The proposed model differs in significant ways from the standard approach used to analyze stick-slip torsional vibrations. We consider both axial and torsional vibrations of the bit, as well as the coupling between the two vibration modes through the bit-rock interaction laws. Second, the interface laws account both for cutting of the rock and for frictional contact between the cutter wearflats and the rock. Within the framework of the discrete model considered here in this paper, the evolution of the system is governed by two coupled delay differential equations, with the delay being part of the solution, and by discontinuous contact conditions. The proposed model qualitatively reproduces all the field observations (rate dependence of the mean torque, influence of the operating parameters W_o and ω_o on the susceptibility to stick-slip).

References

[1] Detournay, E and P. Defourny (1992) A phenomenological model of the drilling action of drag bits. *Int. J. Rock Mech. Min. Sci & Geomech*. Abstr. 29 (1), 13-23

VIBRATION CHARACTERISTICS OF THE MAIN TOWER, THE BAYON TEMPLE

Yoshikazu Sugiura*, Yuki Fukumoto*, Toshiro Maeda*
*Department of Architecture, Waseda University, 3-4-1 Ookubo, Shinjyuku- ku, Tokyo, JAPAN

Summary In order to capture the structural characteristics of the Main tower, we conducted micro-tremor measurement at the Bayon temple. Soil-coupled vibration natural frequencies of the structure are evaluated by power spectrum density of micro-tremor at the top of the structure and damping ratios are deduced by the random decrement method. Base-fixed natural frequencies of the structure are deduced from the transfer function of the top to the base.

INTRODUCTION

The Bayon temple is one of the main historical monuments in Angkor remains. The masonry temple was built in late 12th century to early 13th century. Since collapse and degradation are advancing, it is anxious for the elucidation of collapse mechanism for the purpose of preservation and restoration. With biased settlement of earth structure and intrusion of plants, there have been pointed out a possibility that micro-tremor excited by strong wind may cause some effects upon the collapse, especially in the rainy season, where strong wind of 20-40 m/s was actually observed. The structures will be analyzed by FEM or DEM to demonstrate the effects of micro-tremor on collapse of the Bayon temple. We measured micro-tremor and studied vibration characteristics of the Bayon temple to provide the reference to this future work. Soil-coupled natural frequencies of the structure are evaluated by power spectrum density of micro-tremor at the top of the structure and damping ratios are deduced by the random decrement method. The base fixed natural frequencies of the structure are deduced from the transfer function of the top to the base.

EXPERIMENTS OF MAIN TOWER AT BAYON TEMPLE

Specification of the main tower

The structure of the main tower consists of a central tower and surrounding eight sub towers as shown in Fig.1.The structure is dry-masonry and made with sandstone. The height of the central tower is 42.2m from the ground level. The main tower stands upon the upper terrace at GL+10m and the diameter of the tower at the bottom is about 25meters.

Seismographs and their arrangements

The portable seismographs GPL-6A3P made by Akashi, which consist of three-component-accelerometer and data logger are used for micro-tremor measurements. Acceleration is acquired from the differentiated over-damped pendulum motion with frequency range of 0.1Hz to 100Hz and sensitivity of 1mV/gal. Sensor outputs are low-pass filterd at 10Hz or 30Hz and amplified by 1000times, then discretised by 20 bit AD converter with 100Hz sampling.

These seismographs were arranged to capture representative motion of top of the central tower and sub towers, the gallery and the bottom of the structure as shown in Fig.1.

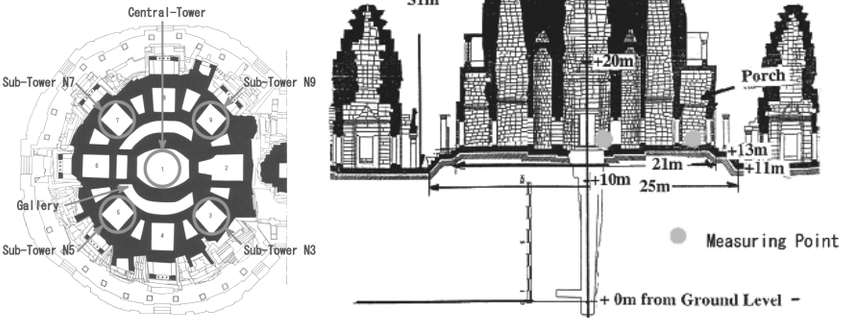


Fig.1 Plan and Section of the Main Tower of the Bayon temple

VIBRATION CHARACTERISTICS OF THE MAIN TOWER

Soil coupled characteristics

Power spectrum densities for horizontal NS, EW motion and vertical motion at the top of the central tower are shown in Fig.2. Soil-coupled 1st predominant frequencies are 2.8 Hz for horizontal motion and 5.9 Hz for vertical motion. Damping ratio of soil-coupled system is evaluated for horizontal motion by the random decrement method (logarithmic

damping factor evaluated by superposition of five thousand 5 sec. waves band passed from 2Hz to 4Hz) as shown in Fig.3. The damping ratios are 2.1% for NS and 2.3% for EW horizontal motion. The same procedure is applied to the surrounding sub towers, except that normal and tangential horizontal components to the central tower are used, since principal analysis reveals predominant horizontal motion are in those directions as shown in Fig.5. The soil-coupled 1st predominant frequencies in tangential direction are higher than in normal direction and they are between 7Hz and 10Hz as shown in Table.1. Damping ratios are estimated between 1.1% and 3.4%.

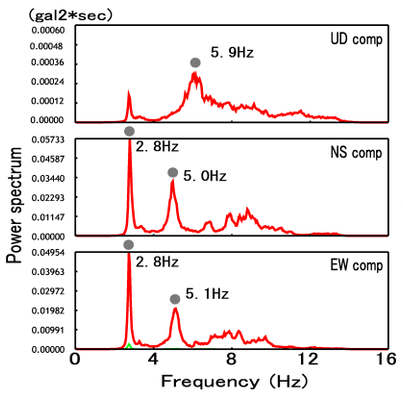


Fig. 2 Power spectra of the central tower

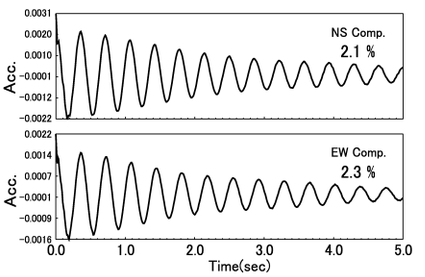


Fig. 3 Free damped waveform by RD method for the central tower

Table 1. 1st Predominant frequencies and damping ratios of Sub-Towers

Tower	normal	tangential
N3	9.0Hz 3.4%	9.7Hz 3.1%
N7	6.8Hz 1.1%	7.8Hz 1.3%
N9	6.8Hz 3.1%	7.9Hz 2.1%

Base fixed characteristics

Transfer functions of horizontal motion at the top to the bottom are computed by H_v evaluation shown in equation (1a), where G_{AA}'s are auto or cross power spectrum densities, G_{AB}'s are cross power spectrum densities, and H_v is obtained for the smallest eigenvalue of ε.

$$\begin{bmatrix} G_{AA} & G_{AB} \\ G_{BA} & G_{BB} \end{bmatrix} \begin{Bmatrix} -H_V \\ 1 \end{Bmatrix} = \varepsilon \begin{Bmatrix} -H_V \\ 1 \end{Bmatrix} \qquad (1a)$$

The natural frequencies of the central tower are evaluated 3.0 Hz and 3.1 Hz in NS and EW directions, respectively as shown in Fig 4.

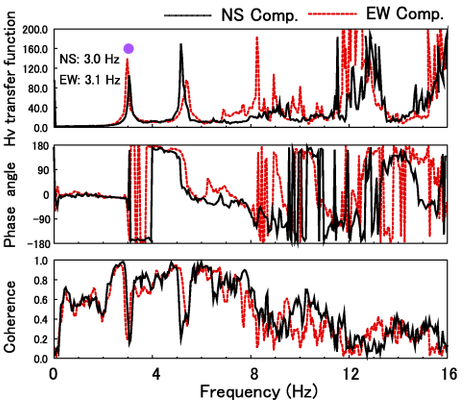


Fig. 4 Transfer functions of horizontal motion

Principal axis of the Vibration

Principal vibration axes of the central tower and sub-towers are computed by principal components analysis on each 1sec data of 1800sec data. Most frequently observed principal axes are shown in Fig.5. It is noted that the principal axis of the central tower is similar to the direction of inclination and those of sub-towers are in normal and tangential to the central tower.

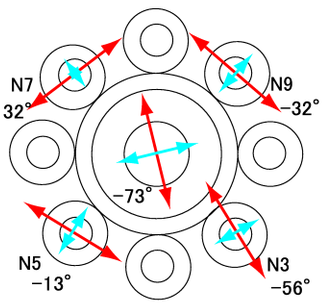


Fig. 5 Principal axis of the Vibration of the central tower and sub-towers

CONCLUSIONS

We conducted micro-tremors measurement at the Bayon temple to show that soil-coupled 1st predominant frequency for horizontal motion of the central tower is 2.8 Hz and the damping ratios is about 2%; Base fixed natural frequency for horizontal motion is about 3Hz.The soil-coupled frequency is much higher than that of general building structures of similar height, e.g. 1Hz. In the future analysis for micro-tremor induced deterioration, additional stiffness provided by thick walls and surrounding sub towers must be included along with detailed material properties.

ACKNOWLEDGMENT

This research is a part of the investigation for Bayon temple preservation master plan creation by JSA (Japanese Government Team for Safeguarding Angkor). We appreciate their kindness and hospitality during this experiment.

XXI ICTAM, 15-21 August 2004, Warsaw, Poland

APPLICATION OF EXTENDED PHASE SPACE TO INVESTIGATION OF FORCED BIHARMONIC OSCILLATIONS

Kazakevitch Michael I., Volkova Viktorija E.
Dniepropetrovsk National University of Railway Transport named after Academician Lazaryan, 2 Lazaryana str, UA-49010 Dniepropetrovsk, Ukraine

Summary The results of investigation of dynamic behaviour of mechanical systems which oscillations are described by a non-linear Duffing-type equation are presented in the paper. The outer periodic biharmonic excitation is applied to the mechanical system.

The development of the qualitative methods of investigation of dynamic systems, suggested by the authors, is the effective means for identification of dynamic systems. The results of the extensive investigations of the behaviour of linear dynamic systems and symmetrical system with double well potential under polyharmonic excitation are given in the paper. The bases of the method of qualitative investigation of oscillations were developed by Poincaré. Application of these methods is most effective for the investigation of oscillations of systems with one degree of freedom. The classical approach to qualitative investigation of oscillations consists in finding out special points on a phase plane $(y, \dot{y})$ and definition of their type (node, saddle, centre or focus). Studying of special points of system explains the picture of trajectories of points on a phase plane (displacement, velocity) in their neighbourhood, however does not allow to study oscillatory processes finally.

Phase space of dynamic systems is multi-dimensional. Each point of this space is characterized by not less than four co-ordinates. In particular: displacement, velocity, acceleration and time. Real space has three dimensions. It is more convenient for the analysis. We consider the phase space as limited to three dimensions, namely displacement, velocity and acceleration. Another choice of parameters of phase planes is also possible [1, 2]. Phase trajectory on a plane $(y, \ddot{y})$ is of the greatest interest. It is known that accelerations of points are more sensitive to deviations of oscillations from harmonic ones.

It is connected with the fact that power criteria on it are interpreted most evidently. Besides, dependence $\ddot{y}(y)$ is back symmetric relative to axis y of the diagram of elastic characteristic. For example, in Figure 1 diagrams of change of the elastic characteristic and acceleration for the system with "backlash" are shown. Only the phase trajectories $\ddot{y}(y)$ allow establishing a type and a level of non-linearity of a system.

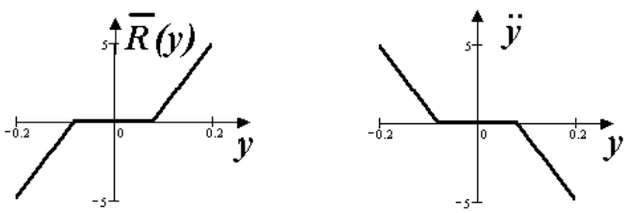


Figure 1. Diagrams of change of elastic properties and acceleration for system with "backlash".

Differential equation of polyharmonic forced oscillations

Let's remark that outer excitation can contain some harmonics for wide range of mechanical dynamic systems. Their amplitudes can be various. The forced oscillations of such systems are described by the non-linear differential equation of the type

$$\begin{aligned} &\ddot{y} + \varepsilon \dot{y} + R(y) = F(t); \\ &F(t) = F_0 + \sum_{i=1}^{n} F_i(t)\cos(\omega_i t) + \sum_{j=1}^{n} F_j(t)\sin(\omega_j t), \quad i = 1, 2, 3\ldots n, \; j = 1, 2, 3\ldots n, \end{aligned} \tag{1}$$

where y is the generalized coordinate; ε is the damping coefficient of the system; $R(y) = -\alpha y + \beta y^3$ is the elastic characteristic of the system; and F_0, F_i, F_j, ω_i are parameters of the outer polyharmonic excitation.

Let's restrict our investigation to symmetrical biharmonic oscillations, then outer polyharmonic excitation has the following form:

$$F(t) = F_1 \cos(\omega_1 t) + F_m \cos(\omega_m t), m = 1,2,3\ldots, \quad (2)$$

The excitation is monoharmonic in a case if $m = 1$. The results of investigation for $m = 2, 3$ are presented in the paper. We compare a linear system with a non-linear symmetric system.

The possibility of occurrence of the non-adjacent stable oscillations at the fixed frequency of excitation is the peculiarity of the investigated systems. The realization of one of the stable regimes of oscillations depends on the initial conditions in a complicated manner. The frequencies of "large" oscillations stall for the cases of monoharmonic and biharmnoic excitation are different. It is important that "skeleton" curves for oscillations on fundamental tone, ultra- and sub-harmonic oscillations have different angles. The amplitude of oscillations within the frequency range of main resonanse is larger then if it was a monoharmonic excitation. As shown in Figure 2 a-b, for all the types of "large" oscillations the phase trajectories are back symmetrical relative to axis y of the diagram of elastic characteristic. It allows to recognise the type of dynamic system.

a) b)

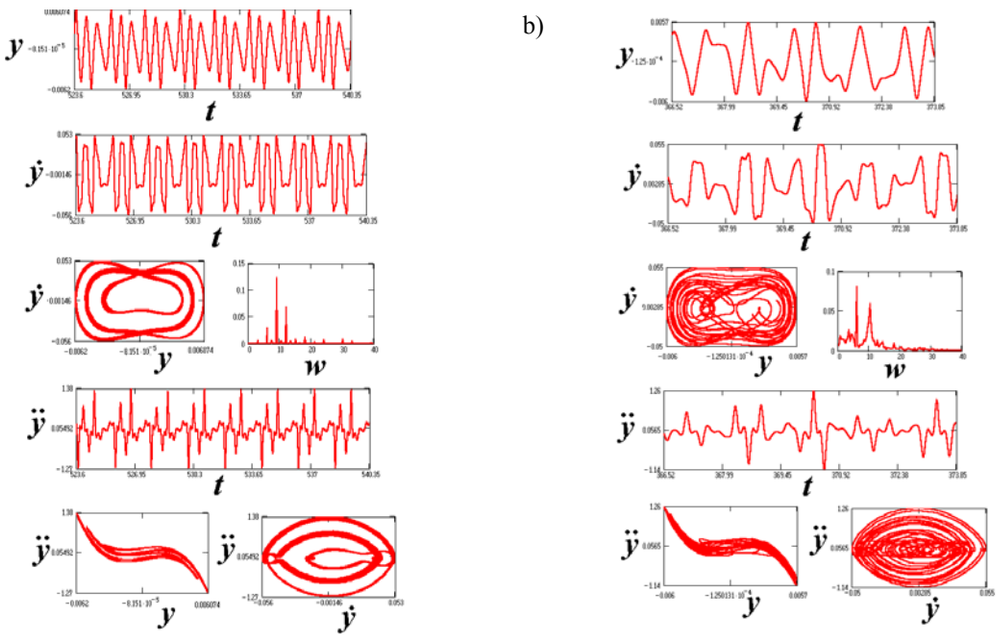


Figure 2. Time characteristics and phase trajectories of the system under consideration ($m = 3$; $\varepsilon = 0.5\ s^{-1}$; $\alpha = 408\ s^{-2}$; $\beta = 7660000\ m^{-2}s^{-2}$; $F_1 = 0.15\ ms^{-2}$; $F_1 = 0.075\ ms^{-2}$): a) combinative oscillations; b) chaotic oscillations.

CONCLUSIONS

The development of qualitative methods of investigation of dynamic systems suggested by the authors is effective means of analysis and identification of dynamic systems. Simultaneous use of all three types of signals registered in time, namely displacement, velocity and acceleration allows to expand considerably the opportunities of traditional methods of investigation. The use of the given phase trajectories enables us to determine with a high degree of reliability the following peculiarities:

- presence or absence of non-linear character of behaviour of a dynamic system;
- type of non-linearity;
- type of dynamic process (oscillations of the basic tone, combinative oscillations, chaotic oscillations.).

Unlike existing asymptotic and stochastic methods of identification of dynamic systems, the use of the suggested technique is not connected with the use of a significant amount of computing procedures, and also it has a number of advantages during investigations of complicated oscillations.

References

[1] Kazakevich, M.I. and Volkova, V.E.: "Dynamics of systems with double well potential". - Dnepropetrovsk: Art-Press. – 2000. - 169 pp. (in Russian)

[2] Kazakevitch, M.I. and Volkova, V.E.: "Identification of non-linear dynamic systems". Proc. 7-th International Conference on Modern Building Materials, Structures and Techniques, vol. 3. - Vilnius: Technika. – 2001. - :P. 145-150.

NON-LINEAR MODELLING OF EARTHQUAKE INDUCED POUNDING OF BUILDINGS

Robert Jankowski*
*Gdańsk University of Technology, Faculty of Civil Engineering,
Centre for Urban Construction and Rehabilitation, Narutowicza 11/12, PL 80-952 Gdańsk, Poland

Summary The aim of the present paper is to analyse earthquake induced pounding between two insufficiently separated buildings with different dynamic characteristics. In the analysis, elastoplastic multi-degree-of-freedom lumped mass models are used to simulate the structural behaviour and non-linear viscoelastic impact elements are applied to model collisions. The results of the study prove that pounding may have considerable influence on behaviour of the structures.

INTRODUCTION

During severe earthquakes, pounding between neighbouring, inadequately separated structures with different dynamic characteristics has been observed repeatedly [1]. It can lead to considerable damage or can be even the reason of structure's total collapse. The phenomenon of structural pounding has been intensively studied recently by applying various structural models and using different models of collisions. The fundamental study on pounding between buildings in series using a linear viscoelastic model of collisions has been conducted by Anagnostopoulos [2]. Jankowski et al. used the same model to study pounding of superstructure segments in bridges [3]. Further analyses were carried out basing on more accurate structural models (discrete multi-degree-of-freedom models [4] and using Finite Elements Method [5]), though, using linear models of collisions. On the other hand, Chau and Wei used a non-linear elastic model of collisions based on Hertz contact law to simulate pounding of structures modelled as single-degree-of-freedom oscillators [6]. In order to simulate collisions more precisely, a non-linear viscoelastic model was introduced by Jankowski [7]. The aim of the present paper is to study pounding of buildings modelled by elastoplastic multi-degree-of-freedom lumped mass systems and using a non-linear viscoelastic model of collisions.

NUMERICAL MODEL

The present paper is focused on the analysis of pounding of two adjacent, three-storey-high buildings with different dynamic characteristics. In order to simulate the response of each structure, a discrete three-degree-of-freedom model, with lumped each storey's mass on the floor level, is applied (Fig.1). The elastic-perfectly plastic approximation of storey shear force-drift relation is ensured. The dynamic equation of motion for a structural model presented in Fig.1, including pounding at each floor level, is formulated as follows:

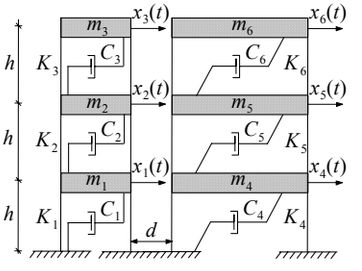


Fig.1. Model of adjacent buildings

$$\mathbf{M}\ddot{\mathbf{x}}(t)+\mathbf{C}\dot{\mathbf{x}}(t)+\mathbf{F}_S(t)+\mathbf{F}(t)=-\mathbf{M}\mathbf{1}\ddot{x}_g(t)\ ; \tag{1a}$$

$$\mathbf{M}=\mathrm{diag}\left[m_1,...,m_6\right];\quad \ddot{\mathbf{x}}(t)=\left[\ddot{x}_1(t),...,\ddot{x}_6(t)\right]^{\mathrm{T}};\quad \dot{\mathbf{x}}(t)=\left[\dot{x}_1(t),...,\dot{x}_6(t)\right]^{\mathrm{T}}; \tag{1b}$$

$$\mathbf{C}=\begin{bmatrix} C_1+C_2 & -C_2 & & & & \\ -C_2 & C_2+C_3 & -C_3 & & & \\ & -C_3 & C_3 & & & \\ & & & C_4+C_5 & -C_5 & \\ & & & -C_5 & C_5+C_6 & -C_6 \\ & & & & -C_6 & C_6 \end{bmatrix};\quad \mathbf{F}_S(t)=\begin{bmatrix} F_{S1}(t)-F_{S2}(t) \\ F_{S2}(t)-F_{S3}(t) \\ F_{S3}(t) \\ F_{S4}(t)-F_{S5}(t) \\ F_{S5}(t)-F_{S6}(t) \\ F_{S6}(t) \end{bmatrix};\quad \mathbf{F}(t)=\begin{bmatrix} F_{14}(t) \\ F_{25}(t) \\ F_{36}(t) \\ -F_{14}(t) \\ -F_{25}(t) \\ -F_{36}(t) \end{bmatrix}, \tag{1c}$$

where: $\ddot{x}_i(t)$, $\dot{x}_i(t)$, $x_i(t)$ (i=1,...,6) are acceleration, velocity and displacement of a storey, respectively; $F_{Si}(t)$ is an inelastic resisting storey shear force: $F_{Si}(t)=K_i\left(x_i(t)-x_{i-1}(t)\right)$ for the elastic range till the storey yield strength F_{yi}, $F_{Si}(t)=\pm F_{yi}$ for the plastic range; K_i, C_i, are elastic stiffness and damping coefficients; $\ddot{x}_g(t)$ is an acceleration input ground motion and $F_{ij}(t)$ (i=1,2,3; j=4,5,6) stands for the pounding force between masses m_i, m_j simulated by a non-linear viscoelastic model according to the formula [7]:

$$\begin{aligned} &F_{ij}(t)=0 && \text{for } \delta_{ij}(t)\le 0 && && \text{(no contact)} \\ &F_{ij}(t)=\bar{\beta}\delta_{ij}^{\frac{3}{2}}(t)+\bar{c}(t)\dot{\delta}_{ij}(t) && \text{for } \delta_{ij}(t)>0 && \text{and} \quad \dot{\delta}_{ij}(t)>0 && \text{(contact-approach period)} \\ &F_{ij}(t)=\bar{\beta}\delta_{ij}^{\frac{3}{2}}(t) && \text{for } \delta_{ij}(t)>0 && \text{and} \quad \dot{\delta}_{ij}(t)\le 0 && \text{(contact-restitution period)} \end{aligned}\ ; \tag{2a}$$

$$\delta_{ij}(t)=x_i(t)-x_j(t)-d;\qquad \bar{c}(t)=2\bar{\xi}\sqrt{\bar{\beta}\sqrt{\delta_{ij}(t)}\frac{m_i m_j}{m_i+m_j}}\ , \tag{2b}$$

where: $\bar{\beta}$ is the impact stiffness parameter depending on material properties and geometry of the colliding elements, d is the initial separation gap and $\bar{\xi}$ denotes a damping ratio which accounts for the energy dissipation during impact.

RESPONSE ANALYSIS

The numerical simulations of pounding-involved response of two adjacent structures have been conducted using the model from Fig.1. In the analysis, the following basic values describing the structural properties have been used: $m_1 = m_2 = m_3 = 25\times10^3$ kg, $C_1 = C_2 = C_3 = 6.609\times10^4$ kg/s, $K_1 = K_2 = K_3 = 3.460\times10^6$ N/m, $F_{y1} = F_{y2} = F_{y3} = 1.369\times10^5$ N, $m_4 = m_5 = m_6 = 10^6$ kg, $C_4 = C_5 = C_6 = 1.058\times10^7$ kg/s, $K_4 = K_5 = K_6 = 2.215\times10^9$ N/m, $F_{y4} = F_{y5} = F_{y6} = 1.442\times10^7$ N, $h = 3$ m, $\overline{\beta} = 80$ kN/mm$^{3/2}$, $\overline{\xi} = 0.35$. A time-stepping integration procedure with constant time step 0.002 s has been applied to solve the equation of motion (1) numerically. In the analysis, various earthquake records have been used. In the present paper, however, the results of the study for the NS component of the El Centro earthquake (18 May 1940) are presented. An example of the displacement time histories for the case when the initial separation gap between structures, *d*, is equal to 0.02 m is shown in Fig.2(a). The corresponding pounding force history is presented in Fig.2(b). The examples of the results of the parametric study conducted for different values of gap size as well as values of mass, elastic stiffness and damping coefficients of a storey of the left-side building are shown in Fig.3-6.

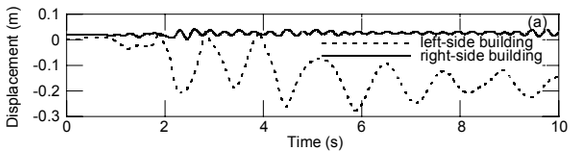


Fig.2. Time histories for 3rd stories of buildings for d = 0.02 m: (a) displacement time histories; (b) pounding force time history

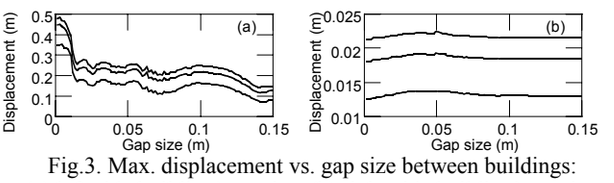


Fig.3. Max. displacement vs. gap size between buildings: (a) left-side building's stories; (b) right-side building's stories

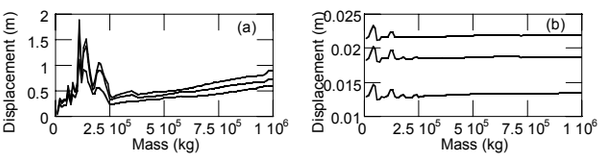


Fig.4. Max. displacement vs. storey mass m_i (i=1,2,3): (a) left-side building's stories; (b) right-side building's stories

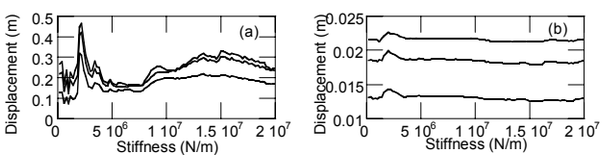


Fig.5. Max. displacement vs. storey elastic stiffness K_i (i=1,2,3): (a) left-side building's stories; (b) right-side building's stories

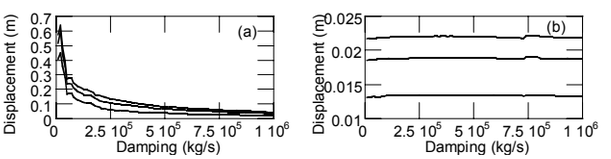


Fig.6. Max. displacement vs. storey damping C_i (i=1,2,3): (a) left-side building's stories; (b) right-side building's stories

CONCLUSIONS

In the present paper, pounding of two inadequately separated buildings with different dynamic characteristics is analysed. The results of the study indicate that pounding has a significant influence on behaviour of a more flexible and lighter structure amplifying its response, which may lead to its permanent deformation. On the other hand, the behaviour of the heavier and stiffer structure is influenced negligibly. Furthermore, the results confirm the effectiveness of the non-linear, viscoelastic model of collisions, which allows to simulate the pounding phenomenon more precisely.

References

[1] Kasai K., Maison B.: Building pounding damage during the 1989 Loma Prieta earthquake. *Engineering Structures* **19**:195-207, 1997.

[2] Anagnostopoulos S.A.: Pounding of buildings in series during earthquakes. *Earthquake Engng. Struct. Dyn.* **16**:443-456, 1988.

[3] Jankowski R., Wilde K., Fujino Y.: Pounding of superstructure segments in isolated elevated bridge during earthquakes. *Earthquake Engng. Struct. Dyn.* **27**:487-502, 1998.

[4] Maison B.F., Kasai K.: Dynamics of pounding when two buildings collide. *Earthquake Engng. Struct. Dyn.* **21**:771-786, 1992.

[5] Jankowski R., Wilde K., Fujino Y.: Reduction of pounding effects in elevated bridges during earthquakes. *Earthquake Engng. Struct. Dyn.* **29**:195-212, 2000.

[6] Chau K.T., Wei X.X.: Pounding of structures modelled as non-linear impacts of two oscillators. *Earthquake Engng. Struct. Dyn.* **30**:633-651, 2001.

[7] Jankowski R.: Non-linear viscoelastic model of structural pounding. *13th World Conf. on Earthquake Engrg.*, Vancouver, Canada, 1-6 August, 2004.

Acknowledgement. The study was supported by the European Community under the FP5 Programme, key-action "City of Tomorrow and Cultural Heritage" (Contract No. EVK4-CT-2002-80005). This support is greatly acknowledged.

DISCONTINUOUS TRANSFORMATIONS AND AVERAGING FOR VIBRO-IMPACT ANALYSIS

Jon Juel Thomsen [*], Alexander Fidlin [**]
[*] *Tech. Univ. of Denmark, MEK / Solid Mechanics, Bldg. 404, DK-2800, Kgs. Lyngby, Denmark*
[**] *LuK GmbH & Co. oHG, Industriestr. 3, D-77815, Buehl, Germany*

Summary Certain vibro-impact problems can be conveniently solved by discontinuous transformations combined with averaging. We outline how this can be accomplished by examples: A self-excited friction oscillator with stop(s), and a particle on a vibrating plane.

INTRODUCTION

Vibro-impact systems are characterized by repeated collisions. Applications include devices to crush, grind, forge, drill, punch, tamp, pile, and cut a variety of objects, and vibrating machinery or structures with slips and stops [1]. The classical approach for solving problems in this area is "stitching", i.e. integrating motions between impacts, and using kinematic impact conditions to switch solution intervals. For numerical simulation this is simple and effective. But for obtaining analytical solutions the method is elaborate, and possible only for the most simple systems [2] – and any additional non-linearity makes it very difficult to apply. For typical applications it is not necessary to obtain solutions at the level of detail provided by exact methods; of more interest may be condensed measures such as oscillation frequencies, stationary amplitudes, and the stability of motions. Thus approximate methods are both necessary and useful. Among these are the methods of *equivalent linearisation* [1], *direct partition of motion* [3], and *averaging* [4,5,6], each with their particular strengths. We demonstrate how special non-smooth transformations and non-standard averaging can be conveniently employed. Compared to classical "stitching", this approach works even in the presence of additional nonlinearities, and provides analytical solutions free of switching conditions. By contrast to equivalent linearisation, it assumes a kinematic rather than kinetic impact formulation. Compared to the averaging approach described in [6] the non-smooth functions need not to eliminate the impacts completely, and are thus much easier to set up.

AVERAGING FOR VIBRO-IMPACT SYSTEMS

Standard averaging applies to systems $d\mathbf{x}/d\varphi = \varepsilon\mathbf{f}(\varphi,\mathbf{x})$, $\varepsilon<<1$, $\mathbf{x}(\varphi)\in D\subset R^n$. According to the averaging theorem [7], if $\mathbf{f}$ is 2π-periodic in φ and bounded and Lipschitz-continuous in $\mathbf{x}$ on D, then $\mathbf{x}$ is asymptotically close to the solution $\mathbf{x}_1$ of the averaged system $d\mathbf{x}_1/d\varphi = \varepsilon\langle\mathbf{f}(\varphi,\mathbf{x}_1)\rangle$ on the scale $\varphi = O(1/\varepsilon)$, where $\langle\ \rangle$ denotes averaging over $\varphi\in[0;2\pi]$. With vibro-impact problems formulated with kinematic impact conditions, the inherent discontinuities in velocity precludes using standard averaging. However, a special form of the averaging theorem has been proven [5], that holds for systems with *small* (i.e. $O(\varepsilon)$) discontinuities in the state variables:

$$\text{(a)}\ \frac{d\mathbf{x}}{d\varphi} = \varepsilon\mathbf{f}(\varphi,\mathbf{x})\ \text{ for }\ \varphi \neq j\pi,\ j = 0,1,\cdots; \qquad \text{(b)}\ \mathbf{x}_+ - \mathbf{x}_- = \varepsilon\mathbf{g}(\mathbf{x}_-)\ \text{ for }\ \varphi = j\pi \tag{1}$$

where $\mathbf{f}$ satisfies the same requirements as stated above, and $\mathbf{x}_-$ and $\mathbf{x}_+$ are the states $\mathbf{x}$ immediately before and after the passage of φ through the value $j\pi$. For that case the averaged system becomes:

$$\frac{d\mathbf{x}_1}{d\varphi} = \varepsilon\left(\langle\mathbf{f}(\varphi,\mathbf{x}_1)\rangle + \pi^{-1}\mathbf{g}(\mathbf{x}_1\right) + \mathrm{O}(\varepsilon^2) \tag{2}$$

To transform vibro-impact problems into the form (1) may not be trivial, not least since for near-elastic vibro-impact the discontinuity in velocity is not small. At least two transforms is required: One for transforming large discontinuities into small ones, and another for transforming the impact-free part of the equations of motion into the form (1)a. Below we outline how this can be accomplished for specific cases.

EXAMPLES

Self-excited friction oscillator with a one-sided stop

Fig. 1 shows the classical "mass on moving belt" model [8], though, with a stop at the right restricting motions to $s<\Delta$ (the left stop is ignored for now). Without stop(s) this system is classical for illustrating friction-induced oscillations; for example, [9] uses averaging to derive stationary amplitudes for pure slip and stick-slip oscillations. With one- or two-sided stops, it models rubbing objects with slipping parts, e.g., loosely mounted brake pads. A typical system is:

$$\begin{aligned} &\ddot{s} + s = -\varepsilon h(\dot{s}) \quad \text{for } s<\Delta, \quad h(\dot{s}) = h_1\dot{s} + h_2\dot{s}^2 + h_3\dot{s}^3, \ \ \dot{s} < v_b \\ &s_+ = s_-, \ \ \dot{s}_+ = -R\dot{s}_- \quad \text{for } s = \Delta \end{aligned} \tag{3}$$

where $h_1 = 2\beta - k_1 + 3k_3v_b^2$, $h_2 = -3k_3v_b$, $h_3 = k_3$, the friction law is $\mu(v_{rel}) = \mu_s\mathrm{sgn}(v_{rel}) - k_1v_{rel} + k_3v_{rel}^3$, R is the coefficient of restitution, and β the viscous damping coefficient. Our main interest here is in the effect of impacts, so $\dot{s} < v_b$ is assumed to avoid unnecessary complications connected with sticking motions ([9] considers stick-slip).

To express (3) in the form (1) we first apply a discontinuous transformation of the dependent variable: $s = \Delta - |z|$, where the new variable $z(t)$ changes sign at every impact, i.e. $z_+ z_- < 0$. In the z-variable every other oscillation of s and $\dot{s}$ will be mirrored, so that if $R = 1$ the velocity-discontinuity at impact is eliminated, while for near-elastic impacts the discontinuity will be small (Fig. 2). Specifically the impact condition becomes $z_+ - z_- = -(R-1)z_-$, which is small for $(R-1) \ll 1$, while the impact-free equation in (3) becomes $\ddot{z} + z = \Delta \operatorname{sgn} z - h_1 \dot{z} + h_2 \dot{z}^2 \operatorname{sgn} z - h_3 \dot{z}^3$ for $\dot{z} \neq 0$.
Next we employ a Van der Pol transformation $z = A\sin\varphi$, $\dot{z} = A\cos\varphi$, where $A = A(t)$ and $\varphi = t + \psi(t)$. Assuming $\Delta, (1-R), h_1, h_2, h_3 = O(\varepsilon) \ll 1$, this yields a system of the form (1). Then it is straightforward to employ (2) for calculating the averaged system, and from that derive stationary values of oscillation amplitude $A_{1\infty}$ and frequency $\omega_{1\infty} = \dot{\varphi}_{1\infty} = 1 + \dot{\psi}_{1\infty}$. The resulting expressions are very simple, and provide good agreement with numerical simulation for even quite large values of $R-1$ (but a small Δ is required). In fact most of the (non-sticking) analytical results derived in [9] for the system without stop also hold for the system with one-sided stop – provided that β is replaced by an effective viscous damping $\beta_{eff} = \beta + (1-R)/\pi$, and the low-speed slope h_1 of the friction curve is replaced by $h_{1eff} = 2\beta_{eff} - k_1 + 3k_3 v_b^2$. For example, periodic motions with stationary amplitude $A_{1\infty} = (-4h_{1eff}/(3h_3))^{1/2}$ exist and are stable for $h_{1eff} < 0$, where the zero-solution is unstable. The frequency of stationary oscillations becomes $\omega_{1\infty} = 1 - 2\Delta/(\pi A_{1\infty}) - 2h_2 A_{1\infty}/(3\pi)$.

... and with a two-sided stop

With both stops (Fig. 1), the impact event in (3) changes to $|s| = \Delta$, and the first equation holds for $|s| < \Delta$. This changes the character of solutions, so that the mirror transformation used with one stop will not reduce the discontinuity in velocity to $O(\varepsilon)$. Instead we employ the transformation $s = 2\Delta\pi^{-1}\Pi(z), \Pi(z) = \int_0^z M(\zeta)d\zeta, M(z) = \operatorname{sgn}\cos z$ (suggested in [5] for $R = 1$; here we use it for $R \approx 1$), which unfolds the sawtooth-like solution s to a polygon-like curve with small discontinuities in velocity (Fig. 3). Using z as a new *in*dependent variable, and the total energy $E(z)$ as the new dependent variable, $E = \frac{1}{2}(\dot{z}^2 + Q(z))$, $Q = \int_0^z M(\zeta)\Pi(\zeta)d\zeta$ – the system attains the form (1), which is applicable for averaging by (2). Note that for motions hitting both stops the oscillation amplitude is fixed, so that with increased energy input only the *frequency* of oscillation can increase. The prediction of this frequency agrees quite well with numerical simulation for parameter values such as, e.g., $R = 0.95$ and $\Delta = 0.5$ (for the two-stop case Δ is *not* assumed to be small).

Particle on a vibrating plane in gravity

Relative motions $y(\tau)$ of a particle bouncing on a vertically vibrating horizontal table are governed by $\ddot{y} = -\gamma + a\sin\tau$ for $y > 0$ and $\dot{y}_+ = -R\dot{y}_-$ for $y = 0$, where $\tau = \Omega t$, $\Omega \gg g/l$, $\gamma = g/l/\Omega^2 \ll 1$ is the gravity to table acceleration ratio, $a \ll 1$ the table amplitude, and l a characteristic plate dimension. We first transform $y = |z|$, $z_+ z_- < 0$, to reduce the discontinuity in velocity, and then apply a Van der Pol like transformation $z(\tau) = A(\tau)N(\varphi)$, $\varphi(\tau) = \omega\tau + \psi(\tau)$ to obtain a system of the form (1). Here N defines the normalized exact solution for a particle bouncing with $R = 1$ on a table at rest, i.e. N is expressed as a second-order polynomial in φ (mod 2π), or as the integral of the sawtooth function $dN/d\varphi = 8\pi^{-2}\arcsin\cos\varphi$. Stationary values of (A, ω, ψ) has been determined as the equilibriums for the averaged system (2). The extension of this procedure to vibro-impact on a vibrating elastic plates or membrane is currently investigated.

CONCLUSION

An extended form of averaging can be used for vibro-impact problems with nearly elastic collisions. This can be accomplished by discontinuous transformations, which converts large discontinuities in state variables into small ones.

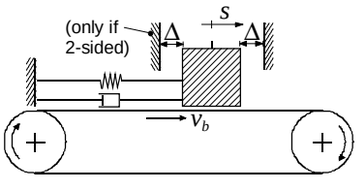


Fig. 1 Self-excited friction-oscillator with stop(s)

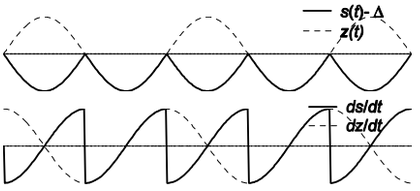


Fig. 2 Motions of friction-oscillator with one-sided stop

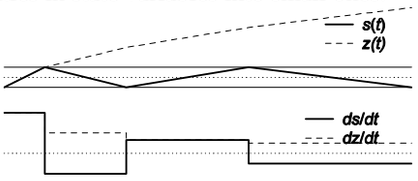


Fig. 3 ... and with a two-sided stop

References

[1] Babitsky, V.I.: Theory of Vibro-Impact Systems and Applications. Springer-Verlag, Berlin, 1998.

[2] Kobrinskii, A. E.: Dynamics of Mechanisms with Elastic Connections and Impact Systems. Iliffe Books, London, 1969.

[3] Blekhman, I.I.: Vibrational Mechanics - Nonlinear Dynamic Effects, General Approach, Applications. World Scientific, Singapore, 2000.

[4] Fidlin, A: On the Oscillations in Discontinuous and Unconventionally Strong Excited Systems: Asymptotic Approaches and Dynamic Effects. Doctoral dissertation, University of Karlsruhe, 2002

[5] Zhuravlev, V.F., Klimov, D.M.: Applied Methods in the Theory of Nonlinear Oscillations (in Russian). Nauka, Moscow, 1988.

[6] Ivanov, A.P.: Dynamics of Systems with Mechanical Collisions (in Russian). International Program of Education, Moscow, 1997.

[7] Sanders, J.A., Verhulst, F.: Averaging Methods in Nonlinear Dynamical Systems. Springer-Verlag, New York, 1985.

[8] Panovko, Y.G., Gubanova, I.I.: Stability and Oscillations of Elastic Systems; Paradoxes, Fallacies and New Concepts. Consultants Bureau, New York, 1965.

[9] Thomsen, J. J., Fidlin, A.: Analytical Approximations for Stick-Slip Vibration Amplitudes. *Int. J. Non-linear Mech.* **38**(3):389-403, 2003.

[10] Thomsen, J. J.: Vibrations and Stability: Advanced Theory, Analysis, and Tools. Springer-Verlag, Berlin Heidelberg, 2003.

EXPERIMENTAL ANALYSIS OF MODAL INTERACTIONS IN THE NON-LINEAR VIBRATIONS OF A PLATE

Pedro Ribeiro
IDMEC/DEMEGI, Fac. de Engenharia, Univ. do Porto, Rua Dr. Roberto Frias, 4200-465 Porto, Portugal

Summary The geometrically non-linear vibrations of a fully clamped plate are experimentally investigated. The plate is excited transversely with harmonic excitations and the amplitudes of the first and higher harmonics of the response are analysed at different points. It is verified that internal resonances occur between the first and higher order modes, that is, that due to the non-linearity of the system, energy is transferred from the first to higher order modes.

INTRODUCTION

Under the action of harmonic excitations, geometrically non-linear plates often experiment periodic, but non-harmonic, vibrations. In this case, the natural frequencies and the mode shapes of vibration usually change with the vibration amplitude, because the stiffness of the system is not constant [1-3]. Therefore, the natural frequencies can easily become commensurable, that is, related by an equation of the form $m_1\omega_1+m_2\omega_2+ \ldots + m_n\omega_n=0$, where m_i are integers. When this happens, and due to the coupling caused by the non-linearity, energy may be interchanged between the different modes of vibration. As a result of this internal resonance phenomenon [2] the structure responds in the two or more coupled modes. Although, the strong effects that modal coupling have on the non-linear response have been predicted in numerical analysis of fully clamped plates [3] and in the experimental analysis of beams [4], there seems to lack in the literature an experimental verification of this interesting phenomenon that includes the actual definition of the mode shapes,.

In this work, the geometrically non-linear vibrations of a fully clamped aluminium plate are experimentally investigated. The main goals are to verify how important the non-fundamental harmonics can be, where fundamental indicates the frequency of excitation and to search for internal resonances. Moderate vibration amplitudes are considered.

EXPERIMENTAL ANALYSIS

Procedure

The dimensions of the aluminium alloy plate analysed are 235×220×1 mm. Approximately fully clamped conditions are implemented by a rigid and heavy fixture, whose natural frequencies are quite higher then the ones of the plate. A grid of 7×7 measuring points was marked on the plate and an electromagnetic exciter was connected to it by a drive rod and a force transducer. In spite of its mass, it was decided to always use the force transducer, because it is necessary to adjust the gain of the amplifying system in order to keep the amplitude of excitation constant for different frequencies. Moreover, the force transducer – often with the help of an accelerometer – allows one to verify that the signal applied in the studies of non-linear vibrations is sinusoidal. The accelerations are measured using two very light weight accelerometers.

The signal sent to the exciter is generated by an analyser, constituted by software, a PC and a front-end. The linear natural frequencies are determined from frequency response functions, after applying low amplitude random excitations. In the non-linear studies, the plate is excited with sinusoidal excitations at frequencies close to its first natural frequency and, at each excitation amplitude, the frequency of excitation is slowly changed upwards and downwards.

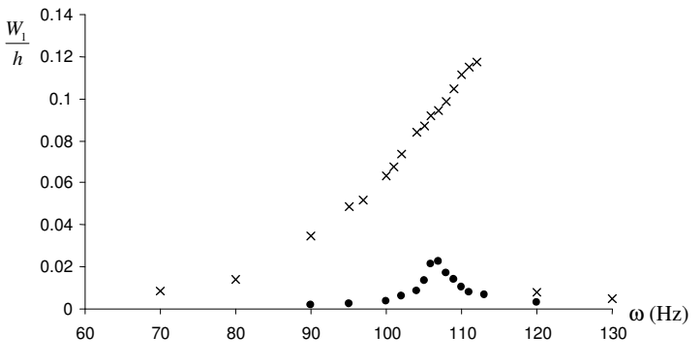


Figure 1. Normalized displacement amplitude, 1º harmonic, excitations with amplitudes: ? 100 mN, × 400 mN.

Resonance curves and coupled modes

Several amplitudes of excitation will be applied, but, in this extended abstract, only the amplitudes of the vibration displacements of the plate's central point for excitations with 0.1 N and 0.4 N are shown (Figure 1). The resonance curve bends towards the right as the amplitude of vibration increases, showing the expected hardening spring behaviour.

Figure 2 represents the autospectra of the accelerations of the central point, when the excitation is harmonic with 113 Hz frequency and two amplitudes: 0.1 N and 0.4 N. One verifies that, due to the non-linearity, the third harmonic is very important at the larger vibration amplitude and negligible at the lower one.

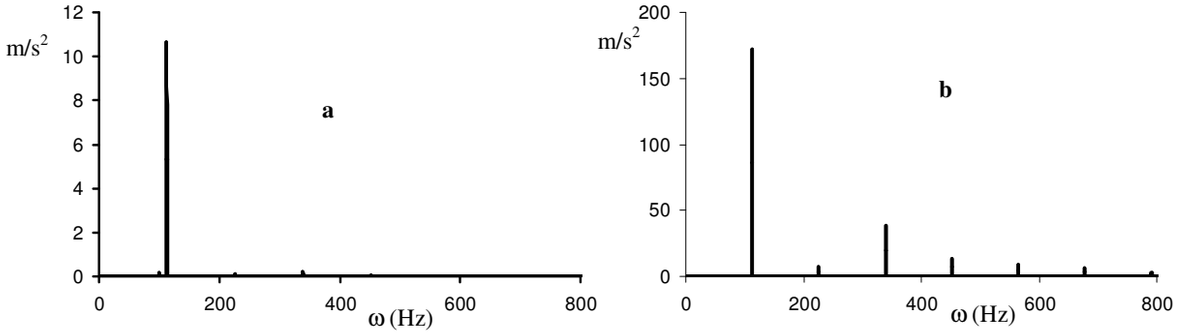


Figure 2. Autospectra of acceleration due to excitations with 113 Hz and (a) 0.1 N, (b) 0.4 N.

The excitation of the third harmonic is particularly strong when the first and fourth modes (Figure 3), whose linear frequencies are related by a factor close to 3, become coupled due to a 1:3 internal resonance. This will be demonstrated by defining the deformations associated with each of the excited harmonics, which form the non-linear mode shapes.

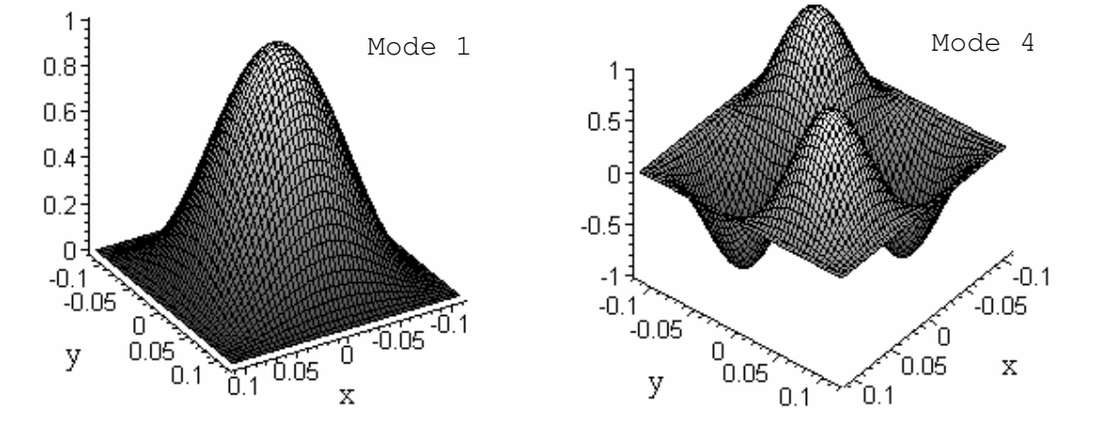


Figure 3. Plate's first and fourth linear modes of vibration.

ACKNOWLEDGMENTS

The support of this work by the Portuguese Science and Technology Foundation, through project POCTI/1999/EME/32641, FEDER, is gratefully acknowledged.

References

[1] Nayfeh A. H., Balachandran, B.: Modal interactions in dynamical and structural systems, *Applied Mechanics Review* **42** S175 - S201, 1989.

[2] Szemplinska-Stupnicka W.: The behaviour of nonlinear vibrating systems. Kluwer Academic Publishers, Dordrecht 1990.

[3] Ribeiro P., Petyt M.: Non-linear free vibration of isotropic plates with internal resonance. *Int. J. of Non-linear Mechanics* **35** 263-278, 2000.

[4] Ribeiro P., Carneiro R.: Experimental detection of modal interaction in the non-linear vibration of a hinged-hinged beam. *J. of Sound and Vibration* **277** 943-954, 2004.

OPTIMUM SELECTION OF DESIGN FEATURES OF ELECTROMECHANICAL DRIVE SYSTEMS INCORPORATING A CONTROL UNIT

Paweł Bachorz, Arkadiusz Mężyk, Eugeniusz Świtoński
Silesian University of Technology, Department of Applied Mechanics, PL 00-049 Gliwice, Poland

Summary Problems relating to modelling, sensitivity analysis and optimization of a high-power electromechanical drive system incorporating a control unit have been dealt with in the paper. A spatial model in which couplings between particular subsystems have been taken into account was employed here. The vibration level has been lowered and the energy consumption of the system has been reduced due to the optimization procedure carried out. Evolutionary algorithms have been used to perform the optimization.

INTRODUCTION

Reducing of excessive vibrations of electromechanical drive systems is a complicated problem that, in general, needs carrying out of numerical simulations with the aid of mathematical models of systems under consideration. The effectiveness of a method used to lower the vibration level depends on the proper selection of parameters of the system and is conditioned by exactitude of the employed mathematical models of electromechanical systems. Thus, there is a tendency to develop the applied models when taking more and more factors determinant of phenomena occurring in kinematic pairs of the system, especially in transient states of the operation of a machine, into account. It seems that a method consisting in incorporation of control units into a coupling loop of electromechanical systems allows the level of vibroacoustic signals, generated by a machine, to be lowered in a simpler way. An active or semiactive control of dynamic phenomena occurring in the drive system involves the necessity of supplying of additional energy to the system. Especially, this is a case when short time-constants of functioning of a vibration reducing system are required. When aiming at obtaining of the system characterized by a low level of vibration, high durability and reliability and by a low energy consumption, it is necessary to tune a mechanical subsystem, an electrical subsystem as well as an electronic subsystem which controls the drive system. The selection of dynamic properties must be aided by optimization-oriented procedures to make the selection effective.
The paper presents problems relating to modelling, sensitivity analysis and optimization of a high-power electromechanical drive system with an induction motor, when considered from the mechatronic point of view. The investigations covered the mining machine`s drive system composed of a squirrel-cage motor, a toothed gear and planetary gear to which a vector control unit is applied.

MODEL OF AN ELECTROMECHANICAL DRIVE SYSTEM

An electromechanical system with a control unit is a system of complicated structure and variable parameters. Therefore, it is difficult to describe exactly the dynamic phenomena occurring in the system. The assumed physical model and the mathematical model serve for describing of an electric subsystem and a mechanical subsystem as well as of a control unit. A model of the electrical part has been considered as a monoharmonic model and as a polyharmonic one with one or several harmonics of the field in the motor`s air-gap being taken into account, respectively. The mechanical gear has been modelled by means of the hybrid finite element method and stiff finite element method. Owing to such an approach to the problem, it was possible to develop a spatial model of transverse torsional vibrations of a gear when taking the flexibility of shaft bearings into account. Numerical calculations were made in the MATLAB/SIMULINK environment.

SENSITIVITY ANALYSIS AND OPTIMIZATION

The sensitivity analysis is suitable for aiding the procedure of selecting of design features of the system and allows exactitude of the applied models to be improved. However, solving of the mathematical model of the system, which depends on the selected decision variables, is a prerequisite. A method of direct differentiation has been employed in the paper, because the algorithm used is relatively simple and the method makes it possible to calculate derivatives and to solve the model at the same time. It is possible to carry out the analysis of sensitivity and optimization, among others, for an objective function described in the time domain, e.g. for time courses of dynamic forces

$$\psi = P^2(\boldsymbol{b}, t)$$

where: P - calculated value of a dynamic force in the selected kinematic pair of the system, $\boldsymbol{b}$ - set of design variables,
t -time
This problem needs solving of differential equations of motion of the system and encounters difficulties involved in the necessary analyzing of a time-varying objective function. Nevertheless, the so formulated problem allows phenomena of energy dissipation, the state of external load and the effect of coupling between the electrical drive and the mechanical part to be taken into consideration during calculations. This method can be applied to minimize vibration amplitudes of electromechanical drive systems in transient states (starting-up, sudden change of load) so that the obtainment of steady state within the minimum time is assured. The objective of investigations has been achieved through minimizing of maximal values of instantaneous dynamic reactions in the selected kinematic pair:

$$Min \ \psi_{max}$$

where: ψ - objective function
The discussed optimization problem, described in the time-domain, is of MinMax type and consists in minimizing of the maximal values of the objective function. Evolutionary algorithms served as a tool for finding the optimum parameters of dynamic systems.

RESULTS OF NUMERICAL CALCULATIONS

The performed numerical calculations embraced simulations of functioning of the system when being started and when operated under steady-state conditions. The obtained time courses of generalized coordinates of a model of the electrical and mechanical part were used to determine dynamic forces in kinematic pairs and the power absorbed from the supply network. Sensitivity of the course of dynamic forces in kinematic pairs of the drive with regard to electromagnetic parameters of the motor was investigated with the aid of the model of torsional vibrations of a gear incorporating a monoharmonic model of an induction motor. It has appeared that parameters of the electric motor have a considerable effect on maximal values of dynamic forces in all kinematic pairs of the gear, especially in transient states. Simulations have also been carried out for a spatial model of transverse torsional vibrations and for a polyharmonic model of the induction motor with a vector control unit. The objective of the optimization problem was to minimize maximal values of the electromagnetic moment of a driving motor.

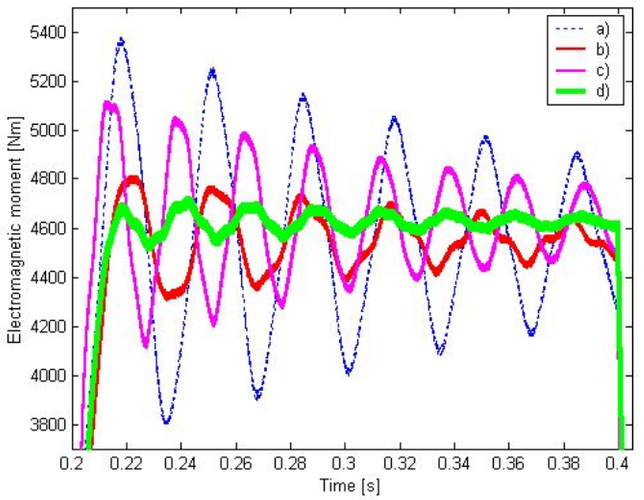


Figure 1. Electromagnetic moment of a driving motor with control unit versus time. Results of calculations for an electromechanical model: a) with preliminary selected settings of a control unit, b) after optimization of settings of a control unit, c) with a control unit before optimization and optimized some parameters of mechanical part, d) optimized control unit and parameters of a mechanical part

According to a variant of calculations, the set of design variables contained separately or jointly parameters describing design features of gear shafts, settings of control units. Numerical simulations have proved that when parameters of the mechanical part and those of the control unit are taken jointly into consideration, the maximal values of dynamic reactions are much lower than the maximal values obtained when a vector control unit of the driving motor is applied (see Figure 1).

CONCLUSIONS

Designing of electromechanical drive systems of machines characterized by the required dynamic properties is a complex problem that needs formulating of developed mathematical models. Results of the performed investigations have indicated that the application of a control unit, that has an active effect on changes of dynamic forces in kinematic pairs of the system, can assure a low level of vibrations. It is evident that when all subsystems are tuned one to another the best results can be obtained in respect of lowering of the vibration level, reducing of energy consumption and improving of durability. However, there is a necessity to aid such investigations by optimization procedures.

References

[1] Mężyk A.: Modelling and optimization of transmission systems with an asynchronous motor. *J. of Theoret and Appl. Mech 1(41):169-198*, 2003.
[2] Bachorz P: Minimization of the vibrations of electromechanical drive systems.*PhD Thesis*, Silesian Technical University, Faculty of Mech. Eng., Gliwice, 2003.

MODE SWITCHING OF RAIN-WIND INDUCED VIBRATIONS

Christian Seidel*, Dieter Dinkler*
*Institut für Statik, Technische Universität Braunschweig, D 38106 Braunschweig, Germany

Summary Rain-wind induced vibrations exist in the range of low wind speed as well as in the range of higher wind speed. The transition from the low speed range to the high speed range results in a mode switching as cable oscillations are regarded. This paper presents a description as well as experimental and numerical investigations concerning this vibration phenomena.

PHENOMENA

Rain-wind induced vibrations are a vibration phenomena that occurs when rain and wind act simultaneously on cables, hangars and ropes. The vibration phenomena may induce oscillations with large amplitudes, thus the fatigue of construction elements is possible. This kind of vibrations are mainly observed at stay cables of cable stayed bridges and hangars of arch bridges. Oscillations could also occur at overhead lines, ropes of pylons and cables of suspension bridges. In the literature, i.e. [1,2], rain-wind induced vibrations are generally described in the range of low wind speeds (8-20 m/s). Continuative experiments in the wind tunnel [3] show that rain-wind induced vibrations exist in the range of higher wind speeds (20-30 m/s), too. These observations indicate that rain-wind induced vibrations are composed of two phenomena. The first phenomena of vibrations is present in the range of low wind speeds and the second phenomena of vibrations is present in the range of higher wind speeds.
Typical for both vibration phenomena is a critical onset velocity and an upper limit of critical velocity. Thus, both kinds of vibrations exist for a special range of wind speed. At first rain-wind induced vibration can be observed in the range of low wind speeds. The vibration in the range of higher wind speeds can only occur when this vibration has finished.
In the majority of cases the vibrations in the range of low wind speeds and also the vibrations in the range of higher wind speeds exhibit dominant but different direction of oscillations. Characteristical vibrations are oscillations perpendicular or parallel to the wind direction. Significant for rain-wind induced vibrations is the mode switching between the vibrations in the range of low wind speeds and the vibrations in the range of higher wind speeds. Therefore, the dominant direction of oscillations may change from parallel to the wind direction in the range of low wind speeds to perpendicular to the wind direction in the range of higher wind speeds or otherwise.
A possible mechanism of excitation of rain-wind induced vibrations is derived in [4]. This mechanism is based on the phenomena of the Prandtl tripwire and considers the rivulets as a movable disturbance. Following this approach the occurrence of the lower and the upper limit of the critical velocity can be explained and all kinds of observable vibrations may be described. Figure 1 shows the effect of the Prandtl trip wire. Herein, a wire, which is attached to a sphere (∅ 300 mm) in the critical point of transition, reduces the drag coefficient significantly. The wire induces a transition from the subcritical to the supercritical flow at considerably lower Reynolds number than for a flow around an undisturbed sphere.

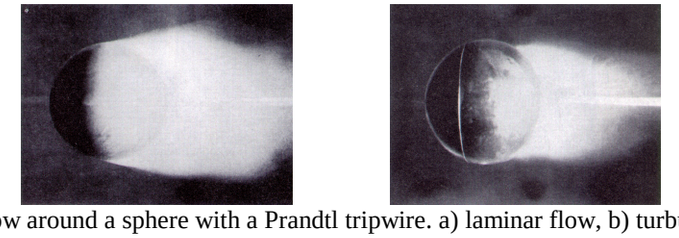


Fig. 1a, b. flow around a sphere with a Prandtl tripwire. a) laminar flow, b) turbulent flow [5]

Similar phenomena can be seen at elongated cylinders. Regarding rain-wind induced vibrations a movable disturbance due to the rivulet exists in contrast to the fixed, immovable disturbance of the Prandtl tripwire. When the oscillations start the rivulets are located near the separation point of the subcritical flow. The Prandtl tripwire is active in the same area. In contrast to the Prandtl tripwire a interaction between the motion of the cable and the rivulets exists in the special case of rain-wind induced vibrations. This interaction is due to the reduction of the drag and stiffness of the cable. For the overall mechanism it is important that rivulets oscillate around the point of transition of the flow with the same frequency as the cable. The result of this motion is a periodical transition of the flow between subcritical and supercritical flow. An energy transfer between the flow around the cable and the elastic structure is induced due to the different pressure distributions of the subcritical and supercritical flow. The interaction between cable, rivulets and flow determines the development of a self-excitation mechanism. This leads to vibrations with large amplitudes parallel or perpendicular to the wind direction depending on the location of rivulets.

MODEL

The equations of motion in two dimensions for cables and rivulets is formulated under consideration of the phenomenology and the assumption that cables are infinitely long cylinders. It is essential to include the influence of the

rivulets and its resulting interaction with the structure in the equations of motion of the cable cross-section and in the quasi-stationary theory. Furthermore, the equations of motion of the rivulets are developed. Therefore the effects of the boundary layer based on the Prandtl boundary layer equations and fundamentals of the physics of drops are considered. The equations of motion of the cables are formulated in an inertial system. Neglecting eigenrotations there are 6 non-linear coupled differential equations. These are required to calculate the unknown translations of cable, the unknown angles of rivulets and the reactive forces for both rivulets.

EXPERIMENTS AND RESULTS

Extensive experimental and numerical investigations confirm the correlation between the Reynolds number and rain-wind induced vibrations, see [4]. It is shown that the excitation mechanism in the range of low wind speeds is different from the mechanism in the range of higher wind speeds. Thus, the observed mode switch can be explained.

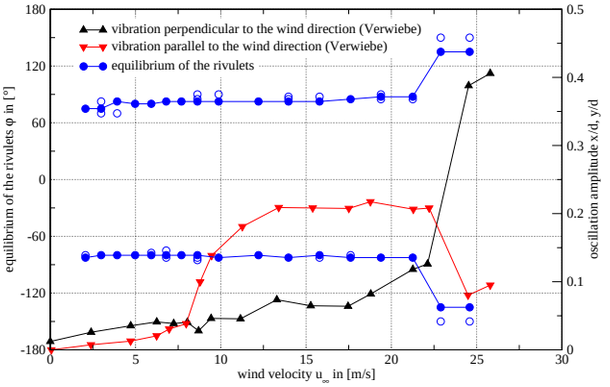


Fig.2. Equilibrium position of rivulets and oscillation amplitudes for a cable (α = 79°, β = -90°, ∅ 110 mm)

Figure 2 shows the response characteristics of the rivulets measured in wind tunnel test. Own experimental investigations illustrate the equilibrium position of the rivulets as function of the wind velocity. Furthermore, the vibration amplitudes measured by Verwiebe are diagrammed in figure 2. When mode switching appears the rivulets move away from the equilibrium position of the subcritical flow to the equilibrium position of the supercritical flow. This phenomena effects a fundamental modification of the drag and lift coefficients. Unless the drag coefficient is dominant in the subcritical flow, the lift coefficient is dominant in the supercritical flow. Due to this effect vibrations parallel to the wind direction decrease when the transition of the flow occurs at a velocity of 21,2 m/s. Then vibrations perpendicular to the wind direction become decisive.

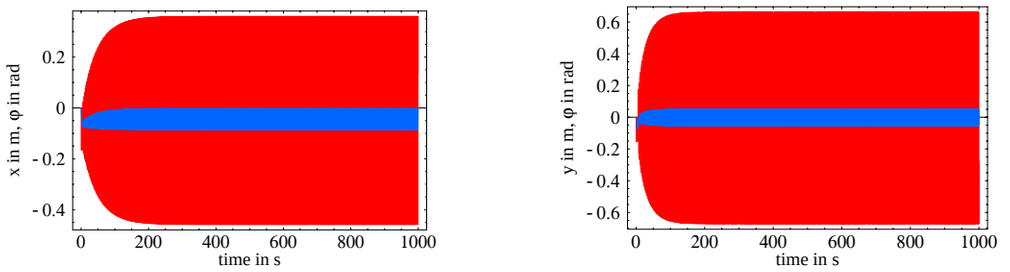


Fig. 3. Vibrations of cable and rivulets parallel (u_∞ = 8 m/s) and perpendicular to the wind direction (u_∞ = 20 m/s)

Numerical investigations based on the mechanical model confirm the experimental results. Figure 3 shows the vibrations of the cable and the rivulets for both cases, the subcritical and supercritical flow. A dominant oscillation exists parallel to the wind direction for a wind speed of 8 m/s (subcritical flow). Though, the wind flow with a speed of 20 m/s leads to a dominant vibration perpendicular to the wind direction.

References

[1] Hikami, Y.; Shiraishi,N.: Rain-Wind Induced Vibrations of Cables in Cable Stayed Bridges. Journal of Wind Engineering and Industrial Aerodynamics. 29 (1988) 409-418.

[2] Matsumoto, M.; Shiraishi, N.; Shirato, H.: Rain-Wind Induced Vibration of Cables of Cable-Stayed Bridges. Journal of Wind Engineering and Industrial Aerodynamics. 41-44 (1992) 2011-2022.

[3] Verwiebe, C.: Erregermechanismen von Regen-Wind induzierten Schwingungen. Baukonstruktionen unter Windeinwirkung (TU Braunschweig 1997). Aachen: Windtechnologische Gesellschaft e.V. 1998.

[4] C. Seidel, D. Dinkler: Phänomenologie und Modellierung Regen-Wind induzierter Schwingungen. Bauingenieur. 2004.

XXI ICTAM, 15–21 August 2004, Warsaw, Poland

REGENERATIVE TOOL CHATTER NEAR A CODIMENSION-2 HOPF POINT

Pankaj Wahi (pankaj@mecheng.iisc.ernet.in)*, Anindya Chatterjee**
*Mechanical Engineering, Indian Institute of Science, Bangalore, 560012, India.
**Mechanical Engineering, Indian Institute of Science, Bangalore, 560012, India.

Summary We study a well known regenerative machine tool vibration model (a delay differential equation) near a codimension-2 Hopf bifurcation point. The method of multiple scales is used directly, bypassing a center-manifold reduction. Both sub- and supercritical bifurcations occur near the reference point, depending on choice of parameters. Analytical approximations are supported by numerics.

INTRODUCTION

The regenerative effect in metal cutting is an important source of undesirable vibrations in machine tools [1]. Mathematical models of the same are delay-differential equations (DDEs). Hopf bifurcations arising in such DDEs have been studied using center-manifold reductions [2, 3] and the method of multiple scales (MMS) [4, 5]. Fofana [3] has also treated double Hopf bifurcation points. We study a double Hopf bifurcation in a tool vibration DDE using MMS, with a definition of the associated small parameter that allows us to *not* treat the vibration amplitude as small. Both sub- and supercritical Hopf bifurcations are observed, depending on how two key parameters vary near the double Hopf point.

MODEL FOR REGENERATIVE TOOL VIBRATION

We consider the non-dimensionalized 1 DOF model for regenerative tool vibrations derived in [2], but with an added stiffening cubic nonlinearity in the restoring force (as in [6]). The governing equation then is:

$$\ddot{x}(t) + 2\,\zeta\,\dot{x}(t) + (1+p)\,x(t) + \alpha_1 x(t)^3 - p\,x(t-\tau) = 3\,p/10\left\{(x(t)-x(t-\tau))^2 - (x(t)-x(t-\tau))^3\right\}\,, \qquad (1)$$

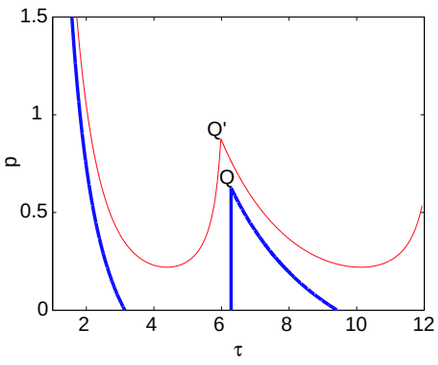


Figure 1. Stability boundary of Eq. (1), thick line: $\zeta = 0$ and thin line: $\zeta = 0.1$.

where $\alpha_1 = \mathcal{O}(\epsilon)$ (where ϵ is defined below), p is a parameter proportional to chip width, and τ, the time-delay, is inversely proportional to the cutting speed. Linear stability analysis of Eq. (1) is given in [2]. The stability boundaries showing the first two lobes in the $p-\tau$ plane for $\zeta = 0$ and $\zeta = 0.1$ are plotted in Fig. 1. $\mathrm{Q} = (2\pi, 5/8) = (6.283, 0.625)$ and $\mathrm{Q}' = (5.980, 0.877)$ represent double Hopf points for $\zeta = 0$ and $\zeta = 0.1$, respectively. Observe that, though the presence of small nonzero damping affects the stability boundary, the local structures (near Q and Q′) are similar.

The damping ratio ζ is often small (e.g., $\zeta = 0.02 - 0.03$ in [4]), so we consider the *unperturbed* linear equation

$$\ddot{x}(t) + (1+p)\,x(t) - p\,x(t-\tau) \;=\; 0\,. \qquad (2)$$

Substituting $x(t) = Ce^{\lambda t}$ in Eq. (2), we get the characteristic equation, $\lambda^2 + (1+p) - p\,e^{-\lambda\tau} = 0$. When $\tau = 2\pi$ and $p = 5/8$ (as noted above), there are two pairs of pure imaginary roots corresponding to $\lambda = \pm i$ and $\lambda = \pm 3i/2$ with all other roots having negative real parts (verified numerically; details not presented here). We will now study small perturbations of Eq. (2) near this double Hopf point.

Scaling: To perform multiple scales analysis, we could scale $x(t)$ as $\epsilon y(t)$, where ϵ is some "small" parameter (as in [4]). However, this restricts $x(t)$ to be small. Instead we take $3\,p/10 = 3/16 = 0.1875$ as ϵ in Eq. (1), allowing $x(t) = \mathcal{O}(1)$.

Detuning: To indirectly account for variations in τ near the double Hopf point, we stretch time as $\bar{t} = (1+\epsilon\,\Delta)t$ (and then drop the overbar for notational simplicity). An increase in Δ now corresponds to a decrease in the delay.

Finally, letting $p = 5/8 + \epsilon p_1$, we obtain

$$\ddot{x}(t) + \frac{13}{8}x(t) - \frac{5}{8}x(t-2\pi) = \epsilon\left(2\,\Delta\left(\frac{13}{8}x(t) - \frac{5}{8}x(t-2\pi)\right) - 2\,\zeta_1\dot{x}(t) - \alpha\,x(t)^3 - p_1\,D + D^2 - D^3\right) + \mathcal{O}(\epsilon^2)\,, \qquad (3)$$

where $D = x(t) - x(t-2\pi)$, $\zeta_1 = \zeta/\epsilon$ and $\alpha = \alpha_1/\epsilon$. Introducing the two time scales t and $T_0 = \epsilon\,t$; writing the solution to Eq. (3) as $x(t) = X(t, T_0) = X_0(t, T_0) + \epsilon X_1(t, T_0) + \cdots$; substituting in Eq. (3); and simplifying, we obtain

$$\frac{\partial^2 X_0}{\partial t^2} + \frac{13}{8}X_0 - \frac{5}{8}X_0(t-2\pi) + \epsilon\left(\frac{\partial^2 X_1}{\partial t^2} + \frac{13}{8}X_1 - \frac{5}{8}X_1(t-2\pi) + 2\frac{\partial^2 X_0}{\partial t\,\partial T_0} + 2\,\zeta_1\frac{\partial X_0}{\partial t} + \frac{5\,\pi}{4}\frac{\partial X_0}{\partial T_0}(t-2\pi) + \alpha X_0^3\right.$$

$$+\frac{5}{4}\,\Delta\,X_0(t-2\pi) - \frac{13}{4}\Delta\,X_0 + p_1\,(X_0 - X_0(t-2\pi)) - (X_0 - X_0(t-2\pi))^2 + (X_0 - X_0(t-2\pi))^3\Big) + \mathcal{O}(\epsilon^2) = 0\,. \tag{4}$$

The solution to the lowest order equation is $X_0 = A_1 \sin t + A_2 \cos t + A_3 \sin(3t/2) + A_4 \cos(3t/2)$, where $A_i = A_i(T_0), i = 1, 2, 3, 4$. Here, we have explicitly dropped infinitely many exponentially decaying components in the solution (see [5]). Substituting this at the next order leads to potentially resonant forcing terms. Eliminating these resonant forcing terms as usual, we obtain $\partial A_i/\partial T_0, i = 1, 2, 3, 4$. Now setting $A_1 = R_1 \cos(\phi_1), A_2 = R_1 \sin(\phi_1), A_3 = R_2 \cos(3\phi_2/2)$ and $A_4 = R_2 \sin(3\phi_2/2)$, we obtain

$$\dot{R}_1 = \epsilon \frac{\left(40\,\pi\,\Delta - 64\,\zeta_1 - 15\,\pi\,\alpha\,R_1^2 - 30\,\pi\,\alpha\,R_2^2\right)\,R_1}{25\,\pi^2 + 64}\,, \tag{5}$$

$$\dot{R}_2 = \epsilon \frac{(40\,\pi\,p_1 - 144\,\zeta_1 - 90\,\pi\,\Delta + 120\,\pi\,R_2^2 + 15\,\pi\,\alpha\,R_2^2 + 30\,\pi\,\alpha\,R_1^2)\,R_2}{25\,\pi^2 + 144}\,, \tag{6}$$

(along with two equations for $\dot{\phi}_1$ and $\dot{\phi}_2$ that are not presented here for space). The bifurcation structure of the above system in the $p_1/\zeta_1 - \Delta/\zeta_1$ plane is shown in Fig. 2. The plane is divided into 5 regions with distinct behaviors.

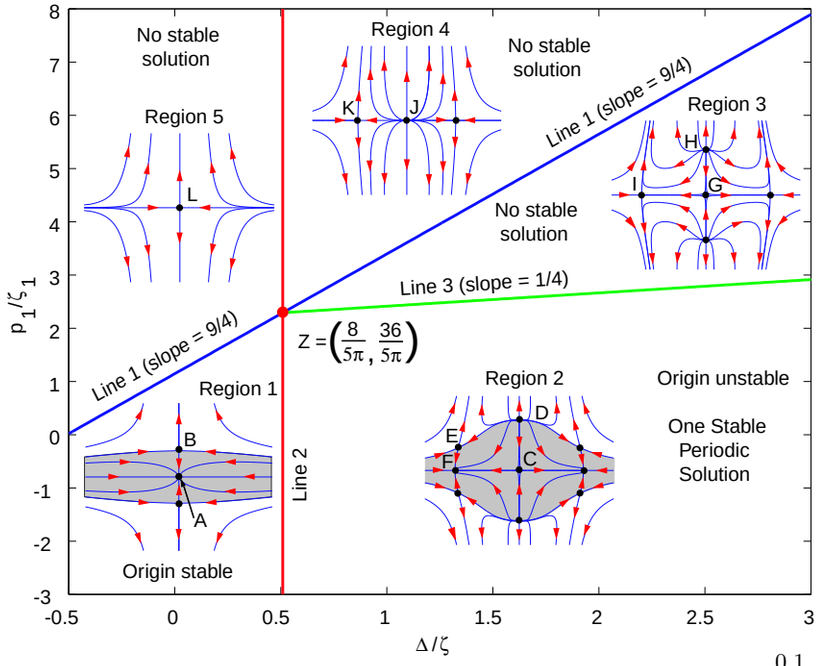


Figure 2. Bifurcation structure of Eqs. (5) and (6). Numerically, for $\zeta = 0.1$ or $\zeta_1 = \frac{0.1}{\epsilon} = \frac{8}{15}$, Z represents $(p, \tau) = (5.979, 0.854)$, agreeing well with numerics. For each of the phase portraits above, the horizontal axis represents R_1 and the vertical axis represents R_2.

In region 1, there are two qualitatively different fixed points (along with reflections of the same) with the origin being stable. In region 2, there are four qualitatively different fixed points marked as C, D, E and F in Fig. 2. F is a stable node, and represents a stable periodic solution of Eq. (3). Numerical simultions of Eq. (3) for $\zeta_1 = 1$, $\alpha = 1$, $\Delta = 8/(5\pi) + 1/4$ and $p_1 = 36/(5\pi)$ (in region 2) verifies this prediction (the steady state amplitude found numerically is 0.75, comparing reasonably well with 0.81 predicted from first order MMS). Hence, in region 2 we have a possibility of supercritical bifurcation. Regions 3, 4 and 5 are qualitatively similar in that there are no stable fixed points in the amplitude equations; in the original equations, no stable solutions remain.

DISCUSSION

The direct use of MMS without center manifold reductions simplified the calculations near the double Hopf point. Our choice of ϵ allowed $x(t) = \mathcal{O}(1)$, giving a glimpse of the dynamics for not-too-small amplitudes. The supercritical bifurcations observed here are important in the context of *control*: a minor excursion into the unstable region causes small amplitudes of vibration, leaving scope for returning to stable operation. In contrast, in the subcritical regime, any excursion into instability leads immediately to large amplitudes from which return to stable operation is problematic.

References

[1] Tobias S.A.: Machine-Tool Vibration. Blackie and Sons Ltd., London 1965.

[2] Kalmár-Nagy, T., Stépán, G., and Moon, F. C.: Subcritical Hopf bifurcation in the delay equation model for machine tool vibrations. *Nonlinear Dynamics* **26**:121–142, 2001.

[3] Fofana, M. S.: Delay dynamical systems and applications to nonlinear machine-tool chatter. *Chaos, Solitons and Fractals* **17**:731–747, 2003.

[4] Pratt, J. R., and Nayfeh, A. H.: Chatter control and stability analysis of a cantilever boring bar under regenerative cutting conditions. *Proc. Royal Society of London-A* **359**:759–792, 2001.

[5] Das, S. L., and Chatterjee, A.: Multiple scales without center manifold reductions for delay differential equations near Hopf bifurcations. *Nonlinear Dynamics* **30**:323–335, 2002.

[6] Hanna, N. H., and Tobias, S.A.: A theory of nonlinear regenerative chatter. *ASME J. Engg. Industry* **96**:247–255, 1974.

AXIAL DECAY OF TIME HARMONIC END PERTURBATIONS IN PRESTRETCHED HYPERELASTIC PLATES

Baruch Karp[*] and David Durban[**]
[*]Dept. of Mechanical Eng., Ben-Gurion Univ. of the Negev, P.O.B. 653, Beer Sheva 84105, Israel
[**]Faculty of Aerospace Engineering, Technion-Israel Institute of Technology, Haifa 32000, Israel

Extended Summary

Existing studies on axial decay rates, of end loads applied to long plates, concentrate almost exclusively on elastostatic response [1], with just a limited number of publications devoted to elastodynamic response. An early paper by Boley [2] showed, for a simple linear elastic model, that the extent of a Saint-Venant zone increases with the rate of applications of end loads. More recent papers have examined axial decay of transient response induced by various non-harmonic [3] and harmonic [4] time histories of end loads, again within the framework of linear elastodynamics.

Here, we present a detailed study of axial decay of time harmonic end perturbations applied to a prestrained plate. The setting is that of a hyperelastic semi-infinite plate, uniformly stretched, under plane strain conditions, in the axial direction. A time harmonic end perturbation is then applied at the edge and we examine axial decay rates of the resulting eigenmodes.

The mathematical formulation is within the framework of continuum elasticity, accounting for large deformations, with various boundary conditions imposed over the long faces of the plate. A separation of variables solution is assumed with due distinction between symmetric and antisymmetric eigenmodes. Our main interest is in axially decaying modes and in propagating (traveling modes).

Compliance with boundary data generates transcendental equations for the wave-numbers at a given frequency, initial stretch, material properties and boundary conditions. We have examined four sets of boundary constraints which include free, clamped, sliding and inextensional boundaries. Material behavior is modeled by hyperelastic strain energy functions, for three different materials (with experimentally determined parameters), over a wide range of initial stretch. Frequency maps are displayed in some detail to assess the various sensitivities of the wave number. We have studied the influence of initial stretch λ, exciting frequency Ω, instantaneous moduli and boundary conditions, with the main findings supported by asymptotic expansions. A rich and complex space of results has been exposed, yet it appears that some observations of general nature can be offered.

Apart from a finite limited number of propagating eigenmodes, all eigenmodes decay with distance from the perturbed end. The number of propagating eigenmodes increases with frequency Ω, yet at low frequencies there are just a few of them. No attempt is made in this study to address the issue of completeness (and orthogonality) of the eigenmodes. Assuming however that any end disturbance can be spectrally decomposed into a linear combination of all eigenmodes, we find that only a limited number of components will not decay in the axial direction. These propagating waves violate of course the principle of Saint Venant. On the other hand, all other eigenmodes, which are infinite in their number, exhibit a clear axial attenuation. That pattern suggests perhaps a restricted validity of Saint-Venant's principle in elastodynamics. In the vicinity of unstable states (necking and buckling) dynamic response of the plate exhibits a strong sensitivity to initial strain. The results of this study are applicable to design of composite laminated structures and to dynamic identification of internal defects.

References

[1] Horgan C.O., Knowles J.K.: Recent Developments Concerning Saint-Venant's Principle. In: Advances in Applied Mechanics, 23, 176-269, 1983.

[2] Boley B.A.: The Application of Saint-Venant's Principle in Dynamical Problems. *J. Appl. Mech* **22**, 204-206, 1955.

[3] Novozhilov V.V., Slepian L.I.: On Saint-Venant's Principle in the Dynamics of Beams. *PMM* **29**, 261-281, 1965.

Grandin H.T., Little R.W.: Dynamic Saint-Venant Region in a Semi Infinite Elastic Strip. *J. Elasticity* **4**, 131-146, 1974.

VIBRATION OF THE TRAIN/TRACK SYSTEM WITH TWO TYPES OF SLEEPERS

Roman Bogacz, Czesław Bajer
Institute of Fundamental Technological Research, Polish Academy of Sciences,
Świętokrzyska 21, 00-049 Warsaw, Poland

Summary The conventional and reinforced railway track is composed of two infinite rails separated from the sleepers by visco-elastic pads. There are numerous assumptions leading to different simplifications in railway track modeling. Two-dimensional periodic model of the track consists of two parallel infinite Timoshenko beams (rails) coupled with the visco-elastic foundation (or equally spaced sleepers). Nowadays the interest of engineers is focused on the Y-shaped sleepers. The fundamental qualitative difference between the track with classic or Y sleepers is related to local longitudinal symmetric or antymetric features of railway track. The sleeper spacing influences the periodicity of elastic foundation coefficient, mass density (rotational inertia) and shear effective rigidity. The track with classical concrete sleepers is influenced stronger by rotational inertia and shear deflections than the track with Y sleepers. The increase of elastic wave velocity in track with Y sleepers and more uniform load distribution will be proved by the analysis and simulations. The analytical and numerical analysis allows us to evaluate the track properties in a range of moderate and high train speed. However, the correct approach is not simple, since the structure of the track interacts with wheels, wheelsets and vehicles, depending on the complexity of the analysis. We can notice the amplitude growth in selected velocity ranges.

The conventional and reinforced railway track is composed of two infinite rails mounted to the sleepers by means of the fastening with pads. There are various assumptions leading to the different simplification in railway track modelling. The two-dimensional periodic model of track consists of two parallel infinite Timoshenko beams (rails) coupled by visco-elastic foundation (or equally spaced sleepers). The qualitative difference in track modelling with classic or "Y sleepers" is related to local longitudinal symmetric or antymetric features of railway track. The dynamic analysis of the above track models as periodic structures can be based on Floquet's theorem. The Timoshenko beam model on an elastic or visco-elastic foundation can also be used to describe the vertical or lateral track motion. In such a case sleeper spacing influences the periodicity of elastic foundation coefficient, mass density (rotational inertia) and shear effective rigidity. The track with classic concrete sleepers is influenced much more by rotational inertia and shear deflections as the track with "Y sleepers". The increase of elastic wave velocity in track with "Y sleepers" and more uniform load distribution will be proved in analysis and simulations.

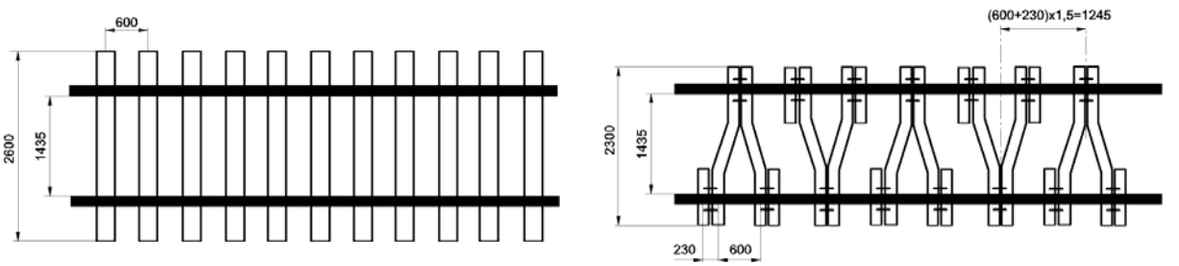


Fig. 1. Classic track (left) and reinforced track with "Y" sleepers (right)

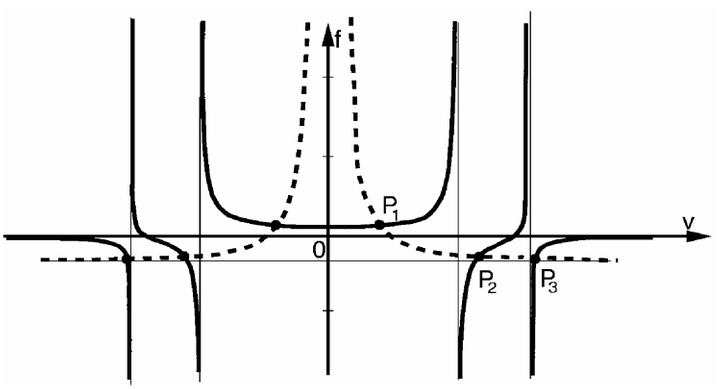


Fig. 2. Wave velocities in conventional track for the case when both rails vibrate "out of phase" and rails – sleepers vibrate "in phase".

In the case shown in Fig. 2 the minimum speed of elastic waves in the track v is determined by point P_1. The value of the speed is smaller as half of share wave velocity. The determination of the velocities of elastic waves (P_1, P_2, P_3) in the track make it possible to estimate maximal speed of the train. The response of the track subjected to moving and oscillating wheelset [1, 2] or boogie is possible in an analytical way by using Floquet's technique similar as in ref. [3]. The numerical analysis of the track response carried out by the space-time finite element method [4, 5] will be presented in the second part of the study.

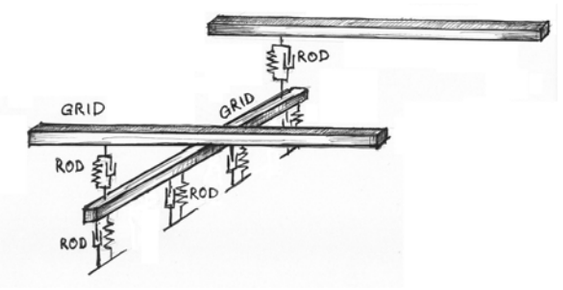


Fig. 3. Model of the track used in computational analysis

Numerical track model was composed of grid and bar finite elements (Fig. 3). Both rails and sleepers were modelled as a grid separated by visco-elastic pads modelled by bar elements. The Winkler type foundation was modelled by visco-elastic springs. The total length of the track was 20 m. Both ends were fixed. Significant damping allowed us to reduce the influence of boundary conditions.

The vehicle was built as a mass and spring 3-dimensional systems combined with frame elements.

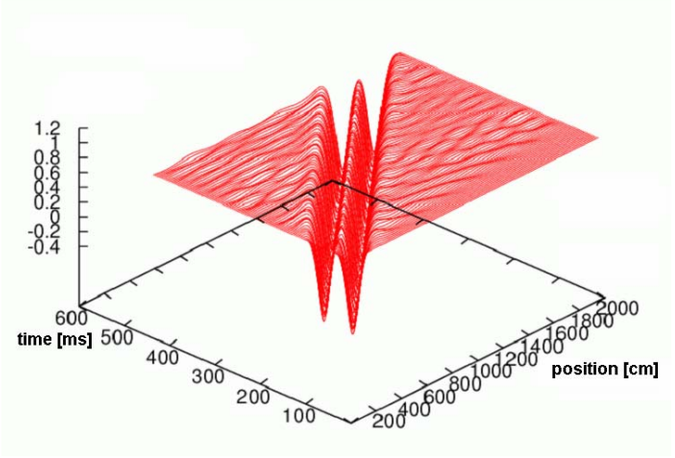


Fig. 4. Vertical displacements of a track obtained in the time-space domain.

The vehicle and the track represented by systems of algebraic equations were solved independently by a direct method. The coupling was ensured by iterations. In practice 3-6 iterations per time step provided sufficient precision. We can say that in spite of simplicity of the approach the results obtained were highly satisfactory.

The selection of parameters of the classic and Y-type sleeper track for various speed ranges enabled us to investigate vibrations of the system and formulate conclusions for proper engineering design.

Advantages of Y-type sleepers are significant for practical use. They are characteristic of lower amplitude level and in the same way lower acoustic emission. The wear (for example corrugations) is decreased since the contact force does not oscillate as much as in the case of the classical track.

REFERENCES

[1] R. Bogacz, S. Dżuła. Dynamics and stability of a Wheelset/Track Interaction Modelled as Nonlinear Continuous System. *Machine Dynamics Problems*, Vol. 20, 1998, 23-24.

[2] R. Bogacz, M. Kocjan, W. Kurnik. Dynamics of wheel-tyre subjected to moving oscillating force, *Machine Dynamics Problems*, 2003 (in press).

[3] R. Bogacz, T. Krzyżyński and K. Popp. Application of Floquet's theorem to high-speed train/track dynamics. *In:* Advance automotive technologies, ASME Congress, 55-61, 1995.

[4] C. Bajer. The space-time approach to rail/wheel contact and corrugations problem. *Comp. Ass. Mech. Eng. Sci.*, 5, 1998, 267-283.

[5] R. Bogacz, C. Bajer. On modelling of contact problems in railway engineering. *In:* Recent Advances in Applied Mechanics, J.T. Katsikadelis, D.E. Beskos and E.E. Gdoutos, Eds., Nat. Techn. Univ. of Athens, Greece, pages 77-86, 2000.

CHARACTERISTICS OF VIBROACOUSTIC SIGNALS IN DIAGNOSING EARLY STAGES OF DEFECTS

Stanisław Radkowski*, Jan Samsonowicz **
* *Warsaw University of Technology, Faculty of Automobile and Heavy Machinery Engineering , PL 02-524 Warszawa, Poland*
** *Warsaw University of Technology , Faculty of Mathematics and Information Science , PL 00-661 Warszawa, Poland*

Summary We are considering certain properties of transformation of time series that register the actual physical process. Our goal is to define these basic features of the data analysis itself that ensure that the "processing" applies to the properties of a phenomenon which generates the signal independently of its numerical representation and could be used for early recognition of arising new type factors and components of the source. It turns out that the information concerning that physical process we may find in some distribution of vector values determined by the time series. This invariant in described here sense characteristics of a vibroacoustic signal, could be used in diagnosing early stages of defects.

INVARIANTS OF NUMERICAL REPRESENTATION OF SIGNAL

When diagnosing the early stages of defects, particularly the initiation phases of fatigue-related cracks, the basic problem is the selection of the diagnostic parameters and methods of detection of diagnostic information. The required digitization of the signal may result in the threat of disregarding or minimizing the diagnostically useful signals. This may result in incorrect identification and location of a defect, and subsequently in formulation of incorrect forecast. Bearing in mind the importance of the problem, in this paper we present the results of analysis related to the possibility of determining the invariants of transformation of certain vibroacoustic signals. We are considering certain properties of transformation of time series that register the actual physical process. Our goal is to define these basic features of the data analysis itself that ensure that the "processing" applies to the properties of a phenomenon which generates the signal independently of its numerical representation. The result of numerical processing of experimental data is intended to be the "deciphering" of the information on quantitative relationships between the physical values of the examined mechanical model, which were constructed earlier in a model. In this paper we deal with the answer to the question concerning the type of information that we can obtain as a result of such an analysis and how to look for such information. We assume that the data available for numerical analysis, collected as a result of an experiment, are recorded in the form of a finite, ordered system of integers $\{x_k\}$. Since a finite sequence of such sets will still render an object of the same kind, thus we can infer that the potential sum (repetition) of experiments will not change the quality of the data available for processing. All the available information (in terms of ability to confirm the information through an experiment) on a physical phenomenon is hidden in $\{x_k\}$ objects, where $x_k \in Z$, $k \in \mathbf{N}$. Numerical processing is a transformation having the form of $x_k \xrightarrow{f} f(x_k)$, whose image, which emerges as a result of registration on a computer disk, is also a finite system of rational numbers. Function f, defined for sequences $\{x_{k_n}\}$, should reflect the feature of the signal while at the same time not being dependent on the randomly selected features of a sample. The fulfillment of this property will be called the invariance of f vis-a-vis random choices made during the experiment.
Due to natural reasons we distinguish three types of invariance depending on: sample length $\{x_{k=1}^{N}\}' = \{x_{k=1}^{N'}\}$, initial moment selection $\{x_k\}' = \{x_{k+m}\}$ and sampling step $\{x_k\}' = \{x_{kn}\}$. The function that fulfills the equation of

$$\lim_{N' \to \infty} f(\{x_k\}') = \lim_{N \to \infty} f(\{x_k\})$$

simultaneously for three such relations will be termed by us, in the same way as in the classical invariance theory, either the invariant function, while taking into account the influence of the affine group, or the globally affine invariant function. The functions that are invariant with regard to small changes of N, n, m parameters will be called by us the locally affine invariant functions.

CHARACTERISTIC RANDOM VARIABLE

In the class of stationary processes a classic example of a locally affine invariant transformation is a module of the Fourier transform $f = |F|$. The examples of affine invariant transformations are also the generalized Hausdorff dimensions. When determining these dimensions the key role is played by the distribution of probability $p(\vec{x_k})$, which is related to the distribution $p(x_k)$ of values $\{x_k\}$. It is precisely its invariance versus the locally affine transformations that implies the same type invariance of the values, which are defined in the terms of this distribution. The information on distribution of probability of value x_k is not sufficient for reconstructing the Hausdorff dimension exactly in the same way as the amplitude spectrum of Fourier transform, and upon neglecting the phase component it s not sufficient for reconstructing the original. In order to analyze these relationships, we narrow our analysis to the class of quasi-periodic signals. By analogy to the periodic signal $x_{k+T} = x_k$, where the phase φ is defined as a parameter from a circle with the length T,

having the form of $\varphi \equiv k \bmod_T$ for d-dimensional quasi-periodic signal being the sum of d periodic signals $x_k^1 + ... + x_k^d$ with incommensurable periods $T_1, ..., T_d$, the phase can be defined as a point $(\varphi_1, ..., \varphi_d)$ on a d-dimensional torus T. The choice of vector $[x_{k+i}, x_{k+2i}, x_{k+3i}, ..., x_{k+mi}] = \vec{x}$ for a sufficiently large m is equivalent to the choice of the signal's phase. It allows for defining the phase space of any signal as a set of points of its Takens' $\mathcal{T}$ space (composed of points $\vec{x}$). In other words, the points of the Takens space contain both the information on the value of the signal (x_k is the first coordinate of point $\mathcal{T}$) as well as on the phase (point $\vec{x_k}$) in which the observed value of the signal is at a given moment. For quasi-periodic signals the full information on the signal is thus contained in the image of mapping of a of a certain d-dimensional torus in the space R^m. This method of reading the dimension d is well known [1] and involves the determination of Hausdorff dimension of a signal [2]. One of the methods of calculating this dimension, based on the observation of the actual signal emitted by an unknown system, involves determination of the set $\mathcal{T}$ through its identification with the probability distribution carrier in the embedding space. Reading the probability distribution $p(\vec{x_k})$ for $\mathcal{T}$ allows one, while relying on well-known methods of calculus of probability, to reconstruct the quasi-periodic signal. The essence of this reconstruction is the assumption that function $k \to \vec{x_k}$ is a random function with constant distribution on $\mathcal{T}$. The map $\{x_k\} \to \{p(\vec{x_k})\}$ is obviously invariant with regard to affine transformations. We also prove the opposite theorem saying that each function $f : N \to Q$, which is invariant with regard to locally affine transformation to N, can be presented as the above assumption $k \to \{x_k\} \to \{(\vec{x_k})\} \to \{p(\vec{x_k})\}$. Thus, the only invariants of affine transformations of signals x_k , and as a result the only values that characterize the quasi-periodic processes, are the functions of parameters of $p(\vec{x_k})$ probability distribution in Takens $\mathcal{T}$ space. Moreover, the changes occurring in a big time-scale in processes modelled by a periodic signal (in a small scale) should be possible to observe in the changes occurring in distribution $p(\vec{x_k})$.

APPLICATIONS

This method applied to vibroacoustic signals allows to detect and trace processes of low energy stages which are unnoticeable or at least unidentifiable by classical Fourier analysis. As we observe in many experiments the structure of histograms approximating the distribution functions of disturbed signal are in many cases more susceptible to changes than Fourier spectrum. Especially the low energy disturbances, poorly visible in Fourier spectrum may be detected as the evolution of the described here random variable and its moments.

References

[1] J.Samsonowicz *Takens space of quasi-periodic signals* Machine Dynamics Problems vol 24
[2] J.Samsonowicz,J.Mączak *Fast algorithm of calculation attractors Hausdorff dimension of time series*, Machine Dynamics Problems vol 24

XXI ICTAM, 15-21 August 2004, Warsaw, Poland

ENTERING THE EXCITATION INTO A MECHANICAL SYSTEM WITH DYNAMIC ELIMINATORS OF VIBRATION

Tadeusz Majewski[*,**], Roza Sokolowska[**], Vadiraja Sudhakar[*]
*Universidad de las Americas-Puebla, 72820 Puebla, Mexico
**Warsaw University of Technology, Mechatronics Faculty, 02-525 Warszawa, Poland

Summary System consists of many objects connected by visco-elastic elements. The objects are equipped with freely rotating vibrators that can eliminate or increase the object's vibration. The paper presents the possibility of elimination the object's vibration. As the result of object's vibration there are vibration forces that push the free elements to a new positions. The authors will discus the relations that describe dynamical properties of the system.

In the earlier papers [1-3] the author showed the possibility of compensation the periodic excitation by dynamic eliminator for one object. Dynamic forces excited the object's vibration. There were a freely rotating vibrators (pendulums, balls or rollers) and they were going to the position for which the vibration of the system vanished. Forces generated by free elements compensated the excitation - the system showed to be balanced.
In the paper we are going to explain the possibility of compensating the excitation that acts on more complex system. The system is showed in Fig.1. There are many objects and each of them has two freely rotating vibrators (pendulums). It is assumed that all object are the same with a mass *M*. Also visco-elastic properties, *c* and *k*, of the elements connecting the objects are the same. A monoharmonic excitation is applied to all objects or only one of them.

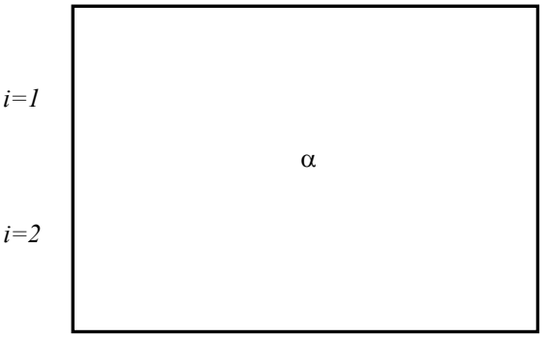


Fig.1. Objects with the pendulums as the vibrators

The motion of the *ijth* object is defined by an equations

$$\begin{aligned} &M\ddot{x}_{ij} + c(2\dot{x}_{ij} - \dot{x}_{i-1,j} - \dot{x}_{i+1,j}) + k(2x_{ij} - x_{j-1,j} - x_{i+1,j}) = P_{oij}\cos(\omega t) + \\ &mR((\omega + \ddot{\alpha}_{ij1})^2 \cos(\omega t + \alpha_{ij1}) + (\omega + \ddot{\alpha}_{ij2})^2 \cos(\omega t + \alpha_{ij2})) \\ &M\ddot{y}_{ij} + c(2\dot{y}_{ij} - \dot{y}_{i,j-1} - \dot{y}_{,i,j+1}) + k(y_{ij} - y_{i,j-1} + y_{i,j+1}) = P_{oij}\sin\omega t + \\ &mR((\omega + \ddot{\alpha}_{ij1})^2 \sin(\omega t + \alpha_{ij1}) + (\omega + \ddot{\alpha}_{ij2})^2 \sin(\omega t + \alpha_{ij2})) \end{aligned} \quad (1)$$

where *i* is a number of the row and *j* is a number of the column of the object's position.
The position of the vibrators are defined by an angles α_1, α_2 with respect to the coordinate system, *0xy*, rotating with the same velocity as the excitation. The motion of the vibrators, *1* and *2*, of the *ijth* object is governed by

$$\begin{aligned} mR\ddot{\alpha}_{ij1} &= m(\ddot{x}_{ij}\sin(\omega t + \alpha_{ij1}) - \ddot{y}_{ij}\cos(\omega t + \alpha_{ij1})) - n\ddot{\alpha}_{ij1}, \\ mR\ddot{\alpha}_{ij2} &= m(\ddot{x}_{ij}\sin(\omega t + \alpha_{ij2}) - \ddot{y}_{ij}\cos(\omega t + \alpha_{ij2})) - n\ddot{\alpha}_{ij2}, \end{aligned} \quad (2)$$

where *m* and *R* are the mass and the radius of the pendulum.
If the pendulums are able to compensate the excitation of the *ith* object then the vibrators should move in synchronous way with the excitation and go to the final positions

$$\alpha_{ij1f} = -\alpha_{ij2f} \qquad \cos\alpha_{ij1f} = \cos\alpha_{ji2f} = -P_{oij}/2mR\omega^2. \quad (3)$$

If the excitation is too large and the vibrators are not able to compensate the *ijth* object`s excitation then they vibrators occupy the position opposed to the excitation ($\alpha_f = \pm\pi$). They only compensate a part of the excitation and the object's vibration does not vanish. The rest of the excitation ΔP goes to the adjacent objects.

$$\Delta P_{oij}(t) = P_{oij} - 2mR\omega^2 . \qquad (4)$$

If the force transmitted to the next objects by the visco-elastic elements is also too large then again a part of it goes to the adjacent objects, etc. In this way the excitation spreads in the system in decreasing way.
To prove this hypothesis the detailed analysis should be done. In Fig.2 there is the results of the simulation of the system from Fig.1. It can be seen that the pendulums behave in the way as it was expected.

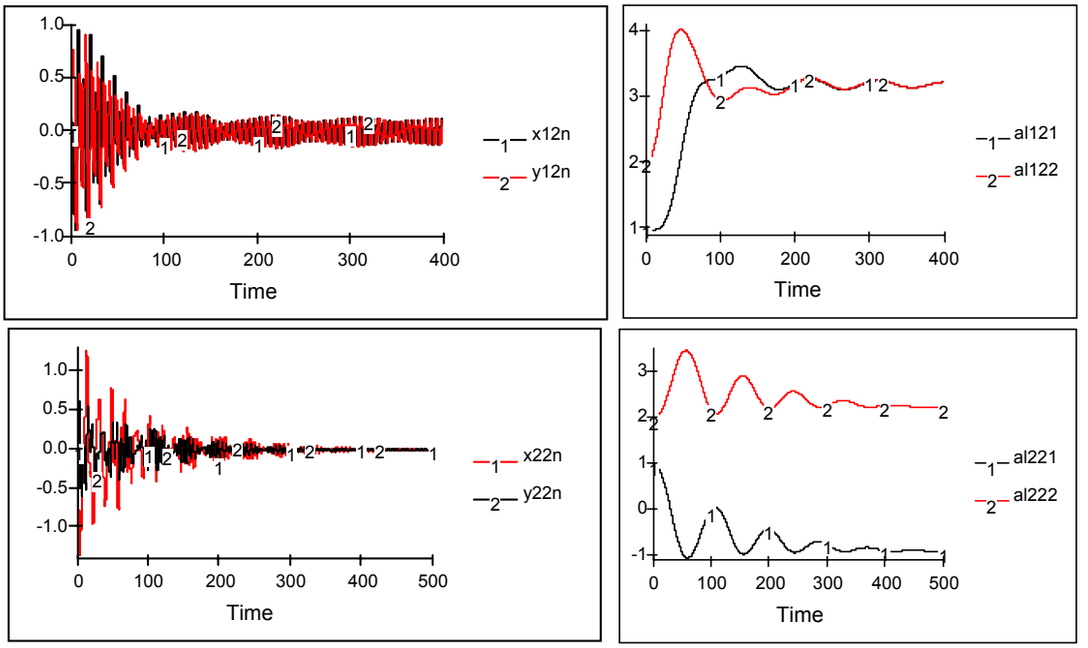


Fig.2. Vibrations of the objects *12, 22* and the positions of the theirs vibrators vs time

The vibrators of the object *12* go to the positions $\alpha_{121} = \alpha_{122} = \pi$ opposed to the excitation P_{o12} but they are not able to compensate object's excitation. The vibration of the object *12* through the visco-elastic element generates vibration of the object *22*. The vibrators of the object *22* change their position in such a way to eliminate the object's vibration. In this way the excitation is restricted to object *12* and its neighbors.
The vibrators will compensate the excitation if its frequency is greater than the natural frequency of the objects. In opposite situation the vibrators will increase the vibrations.
The resistance of the vibrators decreases the efficiency of the system.

References

[1] Majewski T., Synchronous vibration eliminator for an object having one degree of freedom. *Journal of Sound and Vibration,* 112(3), 1987

[2] Majewski T., Synchronous Elimination of Vibrations in the Plane. Analysis of Occurrence of Synchronous Movements, *Journal of Sound and Vibration*, No. 232-2, 2000, pp.555-572

[3] Majewski T., Synchronous Elimination of Vibrations in the Plane. Method Efficiency and its Stability. *Journal of Sound and Vibration*, No. 232-2, 2000, pp.573-586

FRICTIONAL AUTO-OSCILLATIONS UNDER THE ACTION OF ALMOST PERIODIC AND PERIODIC EXCITATIONS

Konstantin V. Avramov*, Jan Awrejcewicz **,Gayane V. Manucharyan*
*National Technical University, Department of Theoretical Mechanics and Department of Applied Mathematics, Frunze St.21, Kharkov 61002, Ukraine
** Technical University of Lodz Polish, Division of Automatics and Biomechanics, 1/15 Stefanowskiego St., 90-924,Lodz, Poland

Summary Frictional auto-oscillations under the action both almost periodic and periodic forces are studied in this paper. The modulation equations are derived to study analytically the bifurcation behavior. The homoclinic Melnikov function is constructed to obtain the region of chaotic solutions of the modulation equations. In the case of the periodical force action and small dissipation a new approach for a construction of homoclinic trajectory of mechanical system is utilized. Also an approach to determine the onset of chaos based on some consequence from the Lyapunov stability definition is suggested for the case when dissipation is not small. Mutual instability of phase trajectories is used as a criterion of chaotic behavior in dynamical systems.

SYSTEM UNDER THE ACTION OF ALMOST PERIODIC FORCE

The mass-spring system interacting with moving belt is considered in this paper. The oscillations excited by both almost periodic and periodic forces are studied here. The multiple scales method is used to study the system under the action of the almost periodic force. The periodic motions and their bifurcations are investigated in the system of modulation equations. The homoclinic Melnikov function is constructed to analyze the chaotic states of the modulation equations. The analytical results are compared with the data of the numerical simulations.

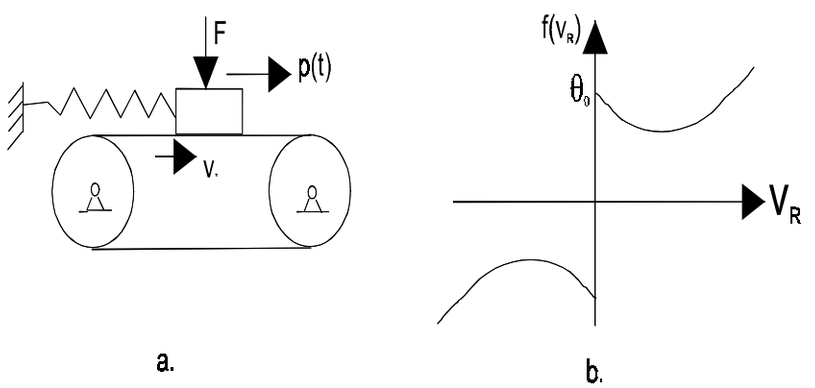


Fig.1. The mechanical system.

Fig.1 shows the system under consideration. The oscillations are described by the generalized coordinate ξ. The differential equation of oscillations is the following:

$$\xi'' + \xi = \varepsilon\left\{-\lambda\xi^3 + \gamma_1\cos\Omega_1\tau + \mu\left[\gamma_2\cos\Omega_2\tau - \tilde{\theta}P(\xi' - v_*)\right]\right\}; \quad (1)$$

where $P(\xi' - v_*) = T_0 sign(\xi' - v_*) - \alpha(\xi' - v_*) + \beta(\xi' - v_*)$ is nonlinear friction characteristics; ε and μ are two small parameters $0 \prec \varepsilon \prec\prec \mu \prec\prec 1$. Let us consider the following resonance: $\Omega_1 = 1 + \varepsilon\sigma; \Omega_2 \approx \Omega_1 + \varepsilon\Delta$. Using the multiple scales method, the following system of nonautonomous modulation equations is obtained

$$\rho' = \sqrt{\rho}\frac{\gamma_1}{\sqrt{2}}\sin\theta + \mu\left\{-\tilde{\theta}\alpha_1\sqrt{2\rho} + \rho\tilde{\theta}(\alpha - 3\beta v_*^2) - \frac{3}{2}\tilde{\theta}\beta\rho^2 + \sqrt{\rho}\frac{\gamma_2}{\sqrt{2}}\sin\theta\cos\Delta T_1 + \sqrt{\rho}\frac{\gamma_2}{\sqrt{2}}\cos\theta\sin\Delta T_1\right\};$$

$$\theta' = \sigma - \frac{3\lambda}{4}\rho + \frac{\gamma_1}{2\sqrt{2\rho}}\cos\theta + \mu\frac{\gamma_2}{2\sqrt{2\rho}}(\cos\theta\cos\Delta T_1 - \sin\theta\sin\Delta T_1). \quad (2)$$

If μ=0 the system is Hamiltonian with heteroclinic orbits. The unperturbated system contains fixed motions. The almost periodic motions close to these fixed points and their bifurcations are studied analytically by the averaging method. The homoclinic Melnikov function is constructed to study the chaotic behavior of the modulation equations.

SYSTEM UNDER THE ACTION OF PERIODIC FORCE

A formation of a homoclinic trajectory (HT) is considered as a criterion of the chaos onset in dynamical systems under the action of periodic force. Mechanical system with a small periodic external excitation, nonlinear friction force and the Duffing type stiffness is governed by the following second order differential equation:

$$y'' - y + y^3 = f\cos(\omega t + \varphi) - P(y' - v_*). \tag{3}$$

Here a new approach for the HT construction in the nonlinear dynamical systems with phase space of dimensions equal to two in the case of small dissipation is proposed. Quasi- Padé approximants (QPA) are used for a representation of the time solution.

Multiplying the equation (3) by $y'(t)$ and integrating within the limits from $t = 0$ to $t = +\infty$ and from $t = 0$ to $t = -\infty$ we obtain the following equations where several integrals containing the small multipliers f, α, β and T_0 are integrated along the zero approximation trajectory ($\theta = 0, f = 0$) $y_0 = \sqrt{2}/ch(t)$:

$$\frac{a_0^2}{2} - \frac{a_0^4}{4} - \left(\alpha v_* - \beta v_*^3 - T_0\right)a_0 - \frac{2\alpha}{3} + \frac{8\beta}{35} + \frac{4\sqrt{2}\beta v_*}{5} + 2\beta v_*^2 + \\ + f\sin\varphi \int_0^{+\infty} \sin\omega t\, y_0'\, dt - f\cos\varphi \int_0^{+\infty} \cos\omega t\, y_0'\, dt = 0; \tag{4}$$

$$\frac{a_0^2}{2} - \frac{a_0^4}{4} - \left(\alpha v_* - \beta v_*^3\right)a_0 + \frac{2\alpha}{3} - \frac{8\beta}{35} + \frac{4\sqrt{2}\beta v_*}{5} - 2\beta v_*^2 - f\sin\varphi \int_0^{+\infty} \sin\omega t\, y_0'\, dt - \\ - f\cos\varphi \int_0^{+\infty} \cos\omega t\, y_0'\, dt - T_0 \int_{-\infty}^{0} sign\left(y_0' - v_*\right) y_0'\, dt = 0. \tag{5}$$

Here $$\int_0^{+\infty} \sin\omega t\, y_0'\, dt = \int_{-\infty}^{0} \sin\omega t\, y_0'\, dt = -\frac{\omega\sqrt{2}\pi}{2} \cdot \frac{1}{ch\dfrac{\omega\pi}{2}};$$

$$\int_0^{+\infty} \cos\omega t\, y_0'\, dt = -\int_{-\infty}^{0} \cos\omega t\, y_0'\, dt = -\sqrt{2} + \omega\sqrt{2}\left(-\frac{\pi}{2} th\frac{\omega\pi}{2} + 4\omega \sum_{k=0}^{\infty} \frac{1}{\omega^2 + (1+4k)^2}\right).$$

For the continuation of the local expansion ad infinitum we rebuild it to QPA:

$$y = a_0 + a_2 t^2 + a_3 t^3 + a_4 t^4 + a_5 t^5 + \ldots \to e^{-t}\frac{\alpha_0 + \alpha_1 e^t + \alpha_2 e^{2t}}{1 + \beta_1 e^t + \beta_2 e^{2t}}. \tag{6}$$

For big values of friction we suggest an approach to determine the onset of chaos based on some consequence from the classical Lyapunov stability definition for a case when initial variations are not arbitrary small and limited below. This approach can be considered as an alternative to the well-known Poincaré map approach. Mutual instability of phase trajectories is used as a criterion of chaotic behavior in dynamical systems. One compares trajectories that are initially very close. The proposed stability test shows the mutual stability or instability of the trajectories. Calculations permit to observe a process of appearance and enlargement of the chaotic behavior regions if some selected parameters of the dynamical system under consideration are changing.

The third author thanks to prof. Yu.V.Mikhlin for the formulation of this problem.

References

[1] Avramov K. V.: Bifurcations of parametric oscillations of beams with three equilibria. *Acta Mechanica* **164**:115-138, 2003.

[2] Avramov K. V.: Non-linear beam oscillations excited by lateral force at combination resonance. *Journal of Sound and Vibration* **257(2)**:337-359, 2002.

[3] Mikhlin Yu.V., Manucharyan G.V. Construction of homoclinic and heteroclinic trajectories in mechanical systems with several equilibrium positions. Chaos, Solitons & Fractals 16, p.299-309, 2003.

[4] Awrejcewicz J, Holicke M.M. Melnikov's method and stick-slip chaotic oscillations in very weakly forced mechanical systems. *Int. J. of Bifurcation and Chaos*, Vol.9, N3, 1999.

OPTIMAL PATH FOLLOWING ROAD VEHICLE STEERING CONTROL

R. S. Sharp, Department of Electrical and Electronic Engineering, Imperial College London, South Kensington Campus, London SW7 2AZ

Summary
Previous work in which the theory of the linear quadratic Gaussian regulator was applied to path following steering control of a car is applied to determine differences between drivers with different priorities and vehicles of different configurations. A new criterion for optimising a vehicle is introduced.

Contents
In a previous paper [1], the theory of the Linear Quadratic Regulator was applied to minimum error path following control of an automobile. The car "driver" was represented as able to preview the path to be followed, in discrete time, and to convert the previewed path data samples, relative to the car, into steering control inputs which cause the car to follow that path with precision. The solution to the optimisation problem accepted was the time invariant steady state one, implying optimality over infinite time if the road disturbance is a Gaussian white noise process. It also implied that the control law is of state feedback form, which means that the control can be determined off-line. It was argued that the preview control was, to some extent, an inverse of the vehicle lateral dynamics. The cost function minimised contains weighted contributions from path error, attitude angle error and steer angle utilisation, such that different driving strategies can be examined and compared. Simulations showed the path following of the optimally controlled neutral steering simplified vehicle to be excellent, over several variations of path type.
Using the same theoretical basis, new results are here generated to show optimal preview controls for cars with different front to rear balance and with different natures (touring and sports). Tight and loose controls are demonstrated by the control laws themselves, Fig. 1, and by path following simulations.

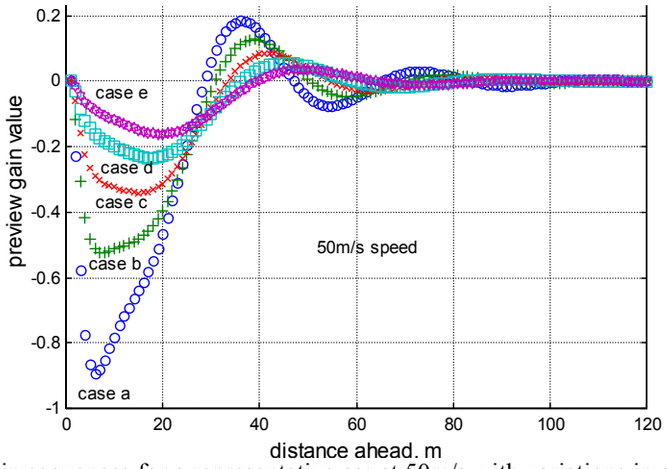


Fig. 1 Preview control gain sequences for a representative car at 50m/s with variations in control authority. Case (a) involves the highest cost on path errors relative to the control power while case (e) involves the lowest.

As can be observed in Fig. 1, the use of the preview data involves diminishing returns. Further away from the car, the path information is of little value. This gives rise to the notion of a required preview distance, which is a function of the vehicle design and the speed, for full path following performance. This notion is quantified and a new car performance criterion is set up, involving the minimisation of the required preview distance. The car is specified by only six basic parameters; the mass, M; the yaw inertia, Izz; the distance from the mass centre to the front axle, a; the corresponding distance to the rear axle, b; the front axle cornering stiffness, Cf and the rear axle cornering stiffness, Cr. The sensitivities of the required preview distance to variations in the car design parameters are calculated, Fig. 2. According to the criterion, it is advantageous to raise b and Cr and to lower Izz and M. The performance, in the current sense, is less sensitive to a and Cf.
The influence on the required preview distance of steering the rear wheels in proportion to the front steering is also shown, Fig. 3. Steer angle ratios up to 0.5 do not have a big influence but from 0.5 to 0.7, the necessary preview distance is reduced substantially and the preview gain sequence is simplified, Fig. 4, suggesting two separate sources of advantage to real drivers. Oscillatory steering control ahead of a uni-directional turn for a rally car at high speed on loose ground, as commonly observed in practice, is demonstrated using the theory. The results yield new insights into driver steering control behaviour and vehicle design optimisation. They lead to some important conclusions about the way ahead for driver modelling from a steering control viewpoint.

[1] Sharp, R. S. and Valtetsiotis, V., Optimal preview car steering control, Supplement to Vehicle System Dynamics, **35** (P. Lugner and K. Hedrick eds), May 2001, 101-117.

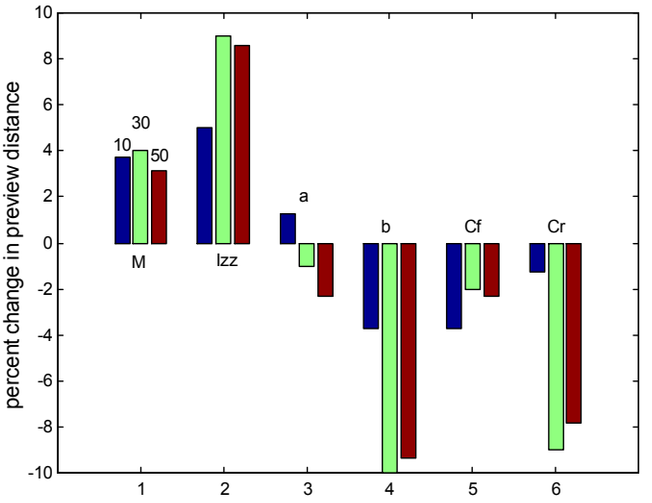


Fig. 2 Sensitivities of required preview distance to design parameter changes for 10, 30 and 50m/s speeds.

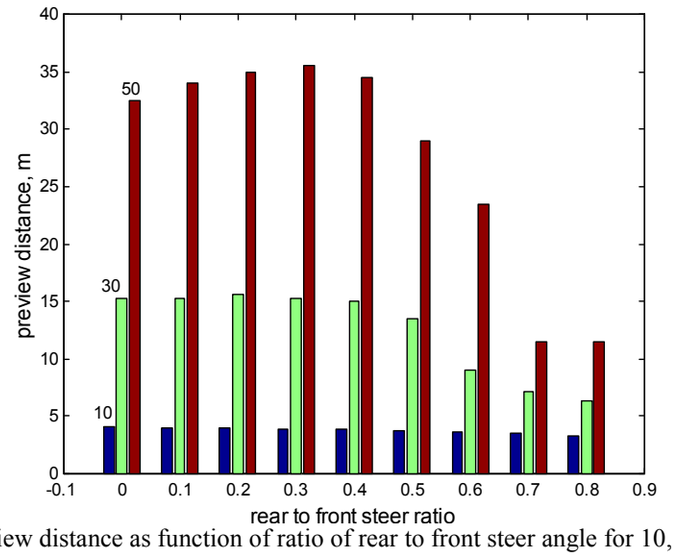


Fig. 3 Required preview distance as function of ratio of rear to front steer angle for 10, 30 and 50m/s speed.

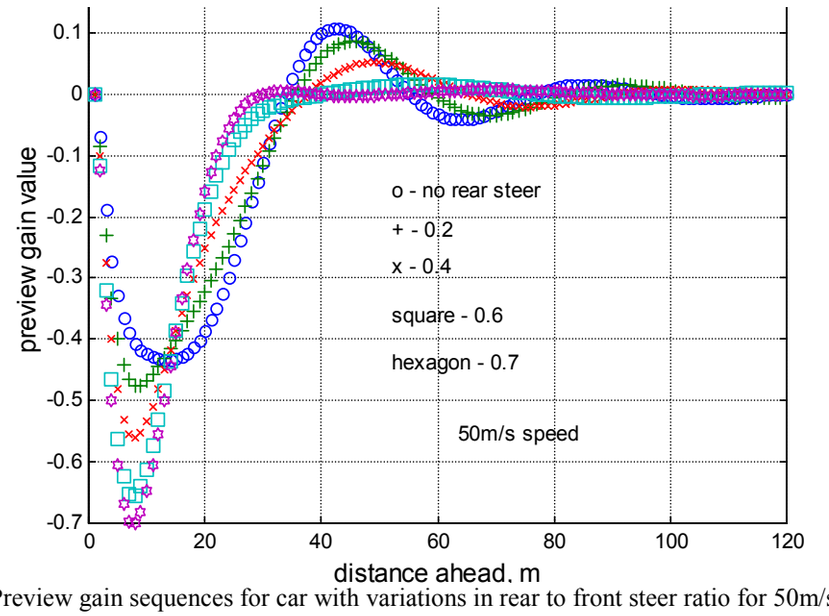


Fig. 4 Preview gain sequences for car with variations in rear to front steer ratio for 50m/s speed.

Simulation and testing of a wheelset with induction motor driven independent wheels

B. Liang, S.D. Iwnicki and F.J. Swift
Department of Engineering and Technology
Manchester Metropolitan University, Manchester M1 5GD, UK
E-mail: b.liang@mmu.ac.uk

Abstract

Independently rotating wheels (IRW) for railway vehicles have been under serious consideration at a theoretical and experimental level for many years. This paper presents dynamic and control simulations of a rail vehicle wheelset with induction motors for independently rotating wheels. Simulation models have been developed for both the mechanical and electrical aspects of the system. The simulation and experimental results have demonstrated that the proposed control strategy has good dynamic performance in term of response time and controllability. A test implementation on a 1/5 scale roller rig has validated the simulation results and shown that good stabilization can be achieved by the proposed wheel motor driven configuration.

1. Introduction

It is well known that railway vehicles with conventional rigid wheelsets can experience problems due to instability at high speed (hunting). The use of IRW has been proposed as a way of eliminating this instability. This paper presents dynamic and control simulations of a railway vehicle wheelset with induction motors driving independently rotating wheels. The mechanical and electrical models for the wheelset and induction motors are presented and the indirect field oriented control for the induction motors is discussed and a comparison between simulation and experiment of the induction motor shown. Simulations of IRW and conventional wheelset are presented and validation of the results with data from a 1/5 scale test rig is carried out.

2. The Wheelset Models and Control Strategy

Fig.1 shows the proposed IRW configuration. It can be seen that the induction motors can either be independently controlled by the inverters or jointly controlled by the inverters and the main computer. Fig. 1 also shows that the yaw rotation of the wheelset is used as an input variable to contol the speed difference between the two wheels. This configuration will give the maximum flexibility and accuracy in controlling the induction motors and yaw movement of the wheelset.

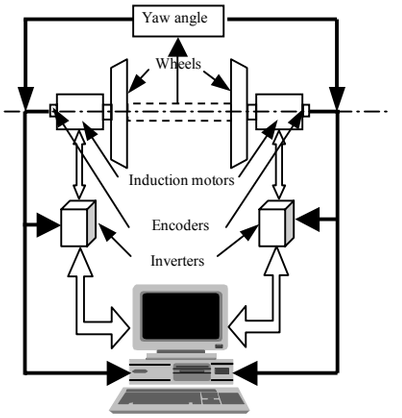


Fig. 1 The configuration of the wheelset

The wheelset is taken as having the two degrees of freedom of lateral translation motion and yaw rotation:
(1) Lateral movement:

$$m\ddot{y} + 2f_{22}(\frac{\dot{y}}{v} - \psi) + f_{23}\frac{\dot{\psi}}{v} + \frac{w\lambda y}{l_0} = 0$$

(2) Yaw movement:

$$J_w\ddot{\psi} - 2f_{23}(\frac{\dot{y}}{v} - \psi) + 2f_{11}(\frac{l_0^2\dot{\psi}}{v} + \frac{l_0\lambda y}{r_0}) + 2f_{11}\frac{l_0 r_0}{v}\dot{\phi} = 0$$

(3) Rotation difference (IRW):

$$I_\phi\ddot{\phi} + f_{11}\frac{r_0^2}{v}\dot{\phi} + f_{11}\lambda y + f_{11}\frac{l_0 r_0}{v}(\dot{\psi} - 1/R) = 0$$

Indirect field oriented control techniques have been used to control the induction motors. Indirect field orientation is based on the slip relation $\omega_e - \omega_r = R_r I_{qs}^e / L_r I_{ds}^e$. If the above condition is satisfied, it ensures that an AC motor can be controlled in the same manner as a DC motor. In order to compensate for the flux disturbance which may slightly alter the electromagnetic torque under transient conditions, a torque controller is introduced into the control loop. Fig.2 shows the comparison between simulation and experimental results for the induction motors.

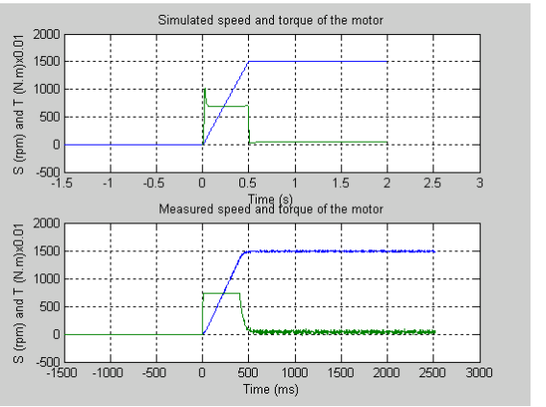


Fig. 2 A comparison between simulated and experimental results of induction motors

3. The simulation and experimental results

The corresponding mechanical and electrical models have been implemented and simulated using Matlab Simulink software. Fig.3 gives the simulation results for a wheelset, without wheel motor driving control, subjected to a 5mm lateral pulse disturbance at speed 30 m/s. It can be seen that the lateral and yaw oscillations of the wheelset after the disturbance increase with time. Fig. 4 shows the corresponding simulation results under the same conditions but with active driving motor control. They clearly show that the lateral ripple and yaw oscillation will die out very quickly after the disturbance. Fig. 5 presents a typical experimental result for the yaw movement of the wheelset. It clearly shows that the speed difference adjustment between left and right wheels by yaw feedback can be used for stabilization. The 1/5 test rig has demonstrated that at a speed of 18 m/s (equivalent to about 88 m/s full scale speed) good stabilization can be achieved.

4. Conclusions

Indirect field orientation control for dynamic control of the induction motors has been shown to be suitable for this application in both its response and its controllability. The simulation of a wheelset with independently rotating wheels and active driving motor control has demonstrated improved stability over a conventional wheelset. These simulation results have been confirmed by a 1/5 scale test rig.

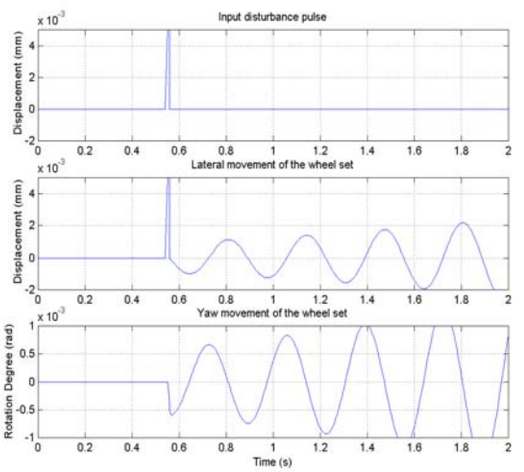


Fig. 3 A wheelset without active motor driving control

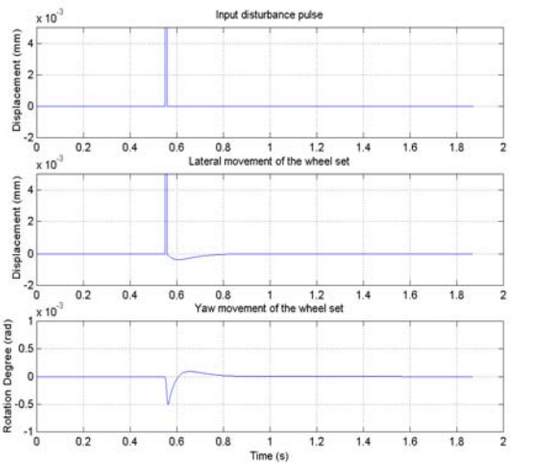


Fig. 4 A wheelset with active motor driving

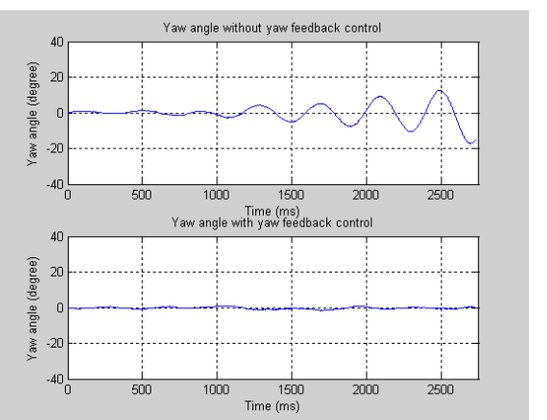


Fig. 5 The measured yaw movement with and without yaw feedback control

RAILWAY VEHICLE SIMULATION USING NON-ELLIPTICAL WHEEL-RAIL CONTACT MODEL

Vladislav Yazykov, Dmitry Pogorelov, Georgy Mikhalchenko
Bryansk State Technical University, bul. 50-letiya Oktyabrya, 7, Bryansk, Russia, well@tu-bryansk.ru

Summary An approximate model of wheel-rail contact, which does not lead to stiff equations of motion and can be used for non-elliptical contact area, is considered. An analytical solution of the tangential contact problem for a slice of contact patch in the formulation of Kalker's simplified theory is used in the model. Results of railway vehicle simulation using an algorithm based on the model are given.

INTRODUCTION

The description of contact between wheel and rail is a necessary condition to obtain reliable results of railway dynamics simulation, prediction of wheel and rail profile wear. The accurate solution of the rolling contact problem is not only a very complex problem even for numerical analysis methods but also a very time-consuming process. Furthermore, mathematical models of the contact forces often lead to stiff equations of motion because of high contact stiffness.
There are numerous methods to solve the contact problem. The choice of them is not easy because it is always a compromise between accuracy and simulation speed for dynamic problems.

NON-ELLIPTICAL WHEEL-RAIL CONTACT MODEL

Taking into account that the contact patch is often far from elliptical it is necessary to develop a non-elliptical wheel-rail contact model. For that we consider the stationary rolling contact of elastic bodies and suppose that material properties of wheel and rail are the same, i.e. the bodies in contact are quasi-identical. In this case the contact problem can be divided into two independent ones: the normal contact problem and the tangential contact problem [1].

Normal contact problem solution

We use the elastic Winkler foundation model to find the contact patch configuration and the distribution of the normal pressure [1]. It means that the normal pressure at a point of the contact patch is proportionate to the interpenetration of the contact bodies at the point [1]. The foundation modulus is determined with the help of the half space method.
In our rail-track model, rail is considered as a massless body on a visco-elastic foundation and the normal force at the contact point is available from the solution of rail equilibrium equations. The interpenetration of the bodies is only used to solve the normal contact problem, and its small value can be neglected in the dynamic equations. Thus the normal force depends on the quite small vertical and lateral stiffness of the rail-track system and this model is not stiff.
Though solving the contact problem is an iterative process, the convergence of solving requires a small number of iterations if initial values of the interpenetration of wheel and rail are taken from the previous step of integration of equations of motion.
Example of the normal contact problem solution is shown in Fig. 1, where the contact of the rail profile R65 and the wheel profile DMetI, which form is similar to a worn profile, is presented. It is clearly shown in the figure that the contact patch computed by the described method is far from the elliptical one.

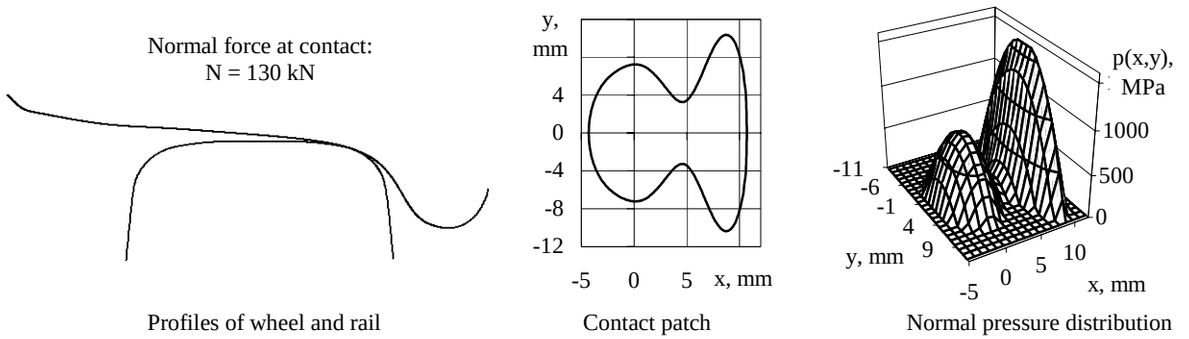


Figure 1. Example of normal contact problem solution.

Tangential contact problem solution

We use the FASTSIM algorithm [1], which was adapted for non-elliptical contact area, to solve the tangential contact problem. To determine the value of flexibility we calculate an equivalent ellipse such that the area of the non-elliptic contact patch is equal to the area of the ellipse [2]. The semi-axis of the ellipse in the rolling direction is set equal to the maximal half-length of the non-elliptical patch.

Though the FASTSIM algorithm is fast, it requires a large number of arithmetical operations. In fact, the algorithm is the numerical solution of a system of ordinary differential and differential-algebraic equations by a method similar to Euler's method, which has low accuracy. We use an analytical calculation of the tangential forces for every slice of the contact patch instead of the numerical computation. This method is exact in an adhesion area and approximate in a sliding area of the contact patch. The diagram of ratio of time required to solve the contact problem using FASTSIM (*Tf*) to solution time for the analytical method (*Ta*) is presented in Fig. 2. The number of slices in the contact patch is taken equal to 10 for both methods while the number of elements (*n*) in a slice is varied for FASTSIM.

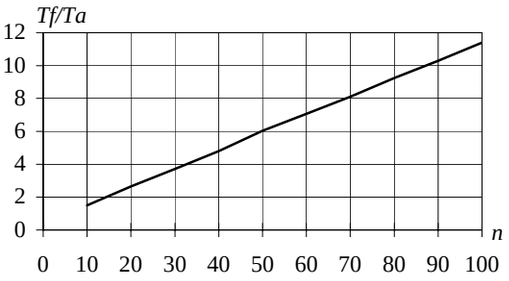


Figure 2. Ratio of required solution time of FASTSIM to time of analytical method.

The detailed description of the wheel-rail contact model can be found in [3].

APPLICATION OF THE DEVELOPED CONTACT MODEL FOR RAILWAY SIMULATION

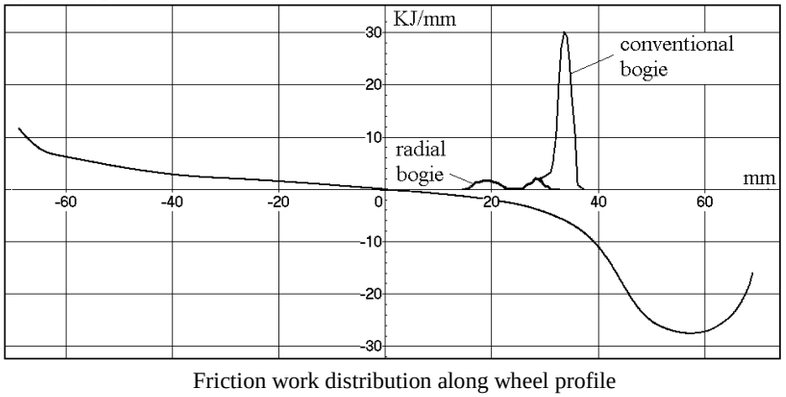
Estimation of effectiveness of radial steering bogie

The effectiveness of the radial steering bogie designed by VNIKTI MPS (Kolomna, Russia) for a six-axle freight diesel locomotive was estimated with the help of the described contact model. The radial steering bogies decrease angle of attack of wheels and correspondingly creep forces that leads to reduction of wheel and rail wear.

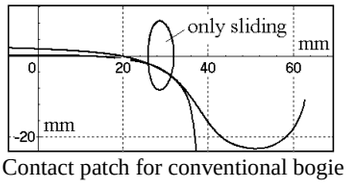
Performances of the vehicle with radial steering bogies and the diesel locomotive TE116 equipped with conventional bogies were compared. Main inertial and geometric parameters of both vehicles are equal. Wheel and rail profiles used for simulation are shown in Fig. 1.

Railway vehicle simulation was performed with the help of the program package "Universal Mechanism" (www.umlab.ru) developed in Bryansk State Technical University.

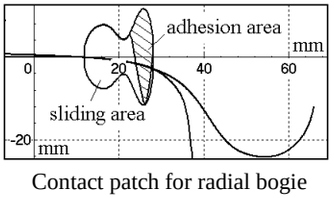
Some results of simulation of both vehicles in even curve R = 300 m are presented in Fig. 3. Contact patches between the first outer wheel and rail are shown on the right part of the figure. It is obvious that the contact patch for the locomotive with conventional bogies is located nearer to the wheel flange because of larger angle of attack. Moreover, as a result of larger values of creep the contact patch has no adhesion area. Curves of the distribution of friction work along wheel profile confirm that wear of wheels of TE116 locomotive will be considerably greater.



Friction work distribution along wheel profile



Contact patch for conventional bogie



Contact patch for radial bogie

Figure 3. Results of railway simulation in even curve.

CONCLUSIONS

The presented algorithm, which computes a non-elliptic wheel-rail contact, can be successfully used for problems of simulation of railway vehicle dynamics and wheel and rail wear prediction. The algorithm is fast enough and does not lead to stiff equations of motion.

The research was supported by Russian Foundation for Basic Research under the grant 02-01-00364 and by the program "Universities of Russia – Basic Research" (UR.04.01.046).

References

[1] Kalker J.J.: Three-Dimensional Elastic Bodies in Rolling Contact. Solid Mechanics and Its Applications, Vol. 2, Kluwer Academic Publishers, Dordrecht, 1990.

[2] Harder R.F., Meekisho L.L., Jones J., and Rhoades V.: Generalized approximation of wheel-rail creep forces and contact patch frictional work using neural network simulation, Proceedings of 2nd mini. conf. Contact Mechanics and Wear of Rail/Wheel Systems, pp. 21-33.

[3] Kovalev R., Yazykov V.N., Mikhalchenko G.S., and Pogorelov D.Yu.: Railway Vehicle Dynamics: Some Aspects of Wheel-Rail Contact Modeling and Optimization of Running Gears. Mechanics Based Design of Structures and Machines, Volume 31, Number 3, 2003, pp. 315-335.

A MODELLING TECHNIQUE FOR FAST COMPUTER SIMULATIONS OF CONFIGURABLE VEHICLE SYSTEMS

Georg Rill, FH Regensburg, University of Applied Sciences, Germany
Cornelius Chucholowski, TESIS DYNAware, Munich, Germany

Summary In this paper the vehicle is modelled by a non perfect multi body system. The specific structure of a vehicle is used to minimize the computational effort. The model is separated into subsystems having a functional skeleton and consisting of several configurable modules. A modified implicit Euler-Algorithm guarantees sufficient accuracy and stability even in combination with third party modules.

MODELLING CONCEPT

The vehicle model is separated into subsystems describing the vehicle framework, the steering system and the drive train, Fig. 1. Each subsystem has a functional skeleton and consists of several configurable modules.

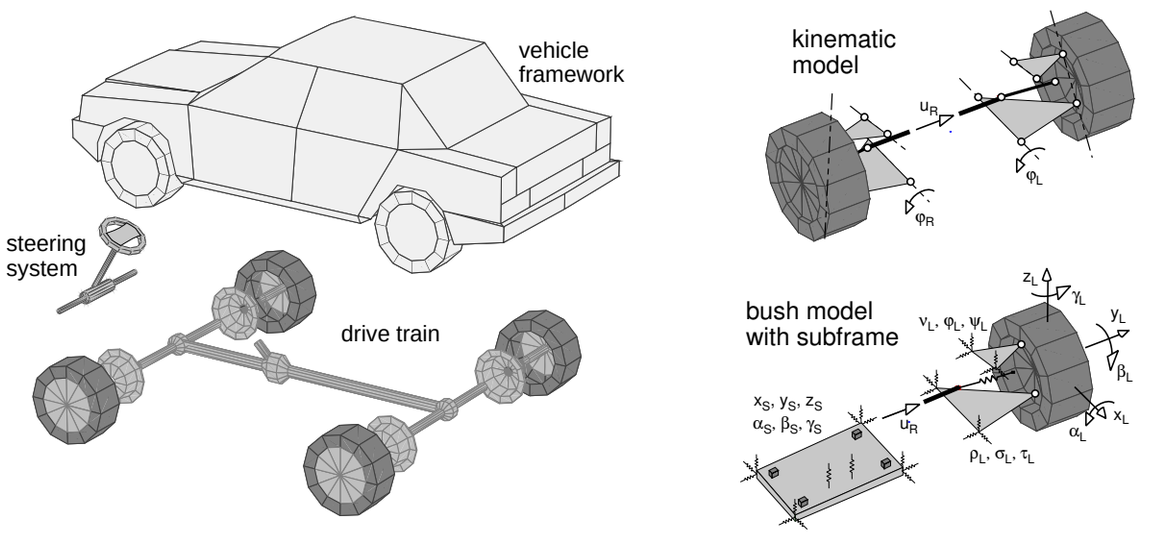


Figure 1: Vehicle Structure and different Axle Modules

The steering system consists at least of the steering wheel, a flexible steering shaft and the steering box which may also be power-assisted. The drive train model is generic. It combines front wheel, rear wheel and all wheel drive. The dynamics of the engine torque may be modelled quit simply by a first order differential equation or by using the enhanced engine torque module en-DYNA developed by the TESIS Company. Tire forces and torques are generated either based on the tire model TMeasy, [3] or by external tire modules, ig. [4]. The vehicle framework consists at least of a rigid or a flexible chassis module and the axle suspension. At present the flexible chassis module takes into account the first torsional mode only. For comfort simulations the vehicle framework can be extended with an elastically suspended engine and passenger models. A lot of different axle suspension modules are available. Pure kinematic axle models overlayed by quasi-static compliancies result in the fastest executables. More enhanced suspension models consider the essential compliances in the bushings and include the subframe. Each suspension model uses simple characteristics or external modules to describe the forces produced by spring damper elements.

EQUATIONS OF MOTION

By neglecting small inertia terms the equations of motion can be derived separately for each subsystem. Via Steering forces and tire forces and torques the subsystems are still coupled to each other. The velocity state of the vehicle chassis and the elastically suspended engine can be described by a specific

set of generalized speeds, cf. [1]. Thus the equations of motion for the vehicle framework can be written as a set of two first order differential equations.

$$\boldsymbol{K_F}(\boldsymbol{y_F})\,\dot{\boldsymbol{y}}_{\boldsymbol{F}} \;=\; \boldsymbol{z_F} \quad \text{and} \quad \boldsymbol{M_F}(\boldsymbol{y_F})\,\dot{\boldsymbol{z}}_{\boldsymbol{F}} \;=\; \boldsymbol{q_F}(\boldsymbol{y_F}, \dot{\boldsymbol{y}}_{\boldsymbol{F}};\, \boldsymbol{y_S}, \dot{\boldsymbol{y}}_{\boldsymbol{S}};\, \boldsymbol{y_D}, \dot{\boldsymbol{y}}_{\boldsymbol{D}})\;, \tag{1}$$

where $\boldsymbol{y_F}$ is the $\boldsymbol{n_F} \times \mathbf{1}$ vector of generalized coordinates, describing the momentary position of the vehicle framework subsystem, $\boldsymbol{K_F}$ is the $\boldsymbol{n_F} \times \boldsymbol{n_F}$ kinematic matrix, $\boldsymbol{M_F}$ is the $\boldsymbol{n_F} \times \boldsymbol{n_F}$ mass matrix, and $\boldsymbol{q_F}$ is a $\boldsymbol{n_F} \times \mathbf{1}$ vector of generalized forces. The number of generalized coordinates depends on the model complexity. An enhanced vehicle model with an elastically suspended engine, four passengers and bush axle models comes up to $\boldsymbol{n_F} \approx \mathbf{80}$. The coupling to the other subsystems is indicated by the generalized coordinates $\boldsymbol{y_S}$, $\boldsymbol{y_D}$ and their time derivatives $\dot{\boldsymbol{y}}_{\boldsymbol{S}}$, $\dot{\boldsymbol{y}}_{\boldsymbol{D}}$ which denote the momentary state of the steering system and the drive train.
As described in [2] the numerical solution is done by a modified implicit Euler-Algorithm where the specific system properties of a vehicle are taken into account. This algorithm guarantees sufficient accuracy and numerical stability even if the vehicle model is combined via co-simulation with third party modules.

APPLICATION

The presented modelling concept is realized with a MATLAB/Simulink® interface in the product ve-DYNA which in the meantime is applied world wide by automotive companies and suppliers.

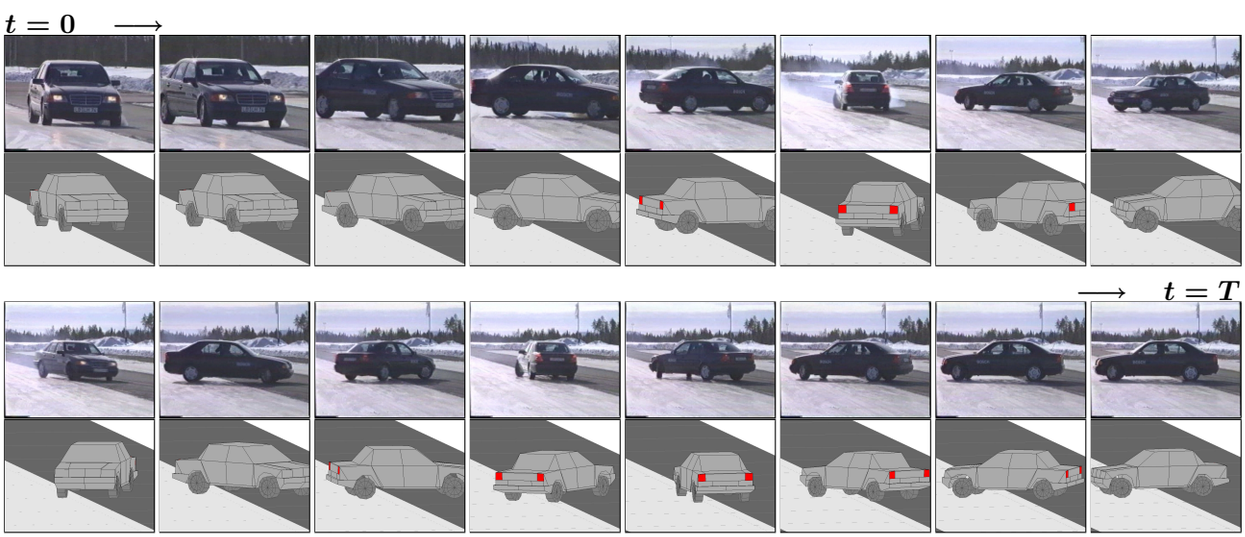


Figure 2: Braking on μ-split: Field Test / ve-DYNA–Simulation

A vehicle without an anti-lock system braked on a μ-split surface shows a strong yaw reaction which causes the vehicle to spin around the vertical axis. In Fig. 2 screen shots of a commercial trailer to the EPS-system from the company Robert Bosch GmbH are compared with the results of a ve-DYNA-simulation. Despite of different vehicles and estimated friction coefficients for the dry ($\mu = 1$) and the icy part ($\mu = 0.05$) of the test track the simulation results are in good conformity to the field test.
Whereas the reproducibility of field tests is not always given a computer simulation can be repeated exactly with the same environmental conditions.

REFERENCES

[1] Rill, G.: Modeling and Dynamic Optimization of Heavy Agricultural Tractors. In: 26th International Symposium on Automotive Technology and Automation (ISATA). Croydon: Automotive Automation Limited 1993.

[2] Rill, G.: Vehicle Modelling for Real Time Applications. RBCM - J. of the Braz. Soc. Mechanical Sciences, Vol. XIX - No. 2 - 1997 - pp. 192-206.

[3] Hirschberg, W; Rill, G. Weinfurter, H.: User-Appropriate Tyre-Modelling for Vehicle Dynamics in Standard and Limit Situations. Vehicle System Dynamics 2002, Vol. 38, No. 2, pp. 103-125. Lisse: Swets & Zeitlinger.

[4] Gipser, M.: Reifenmodelle für Komfort- und Schlechtwegsimulationen. In: Tagungsband zum 7. Aachener Kolloquium Fahrzeug- und Motorentechnik. IKA, RWTH Aachen und VDI 1998.

EXPERIMENTAL AND THEORETICAL ANALYSIS OF FREIGHT WAGON LINK SUSPENSION

Per-Anders Jönsson and Sebastian Stichel
Div. of Railway Technology, Royal Institute of Technology (KTH), SE-100 44 Stockholm, Sweden

Summary In an ongoing study of freight wagons with link suspension, measurement of link and end bearing characteristics are performed. Normal load, amplitude and frequency of excitation are altered. Different maintenance conditions of link and end bearing are tested. The observed behaviour is discussed. A model to describe the observed behaviour is proposed.

INTRODUCTION

In an ongoing project at KTH the running behaviour of freight wagons is studied. The background to the project includes plans to increase axle load, loading gauge and speed of freight trains in Sweden to make freight traffic more competitive. Simulation models for freight wagons with different types of running gear are developed. Prediction of running behaviour for wagons with link suspension is found to bee very difficult. One cause for that is the strongly non-linear characteristic of the link suspension and the fact that the vehicle behaviour is very sensitive to the horizontal suspension characteristics. Another reason is that the characteristics vary with maintenance status of the link suspension and climate conditions [1-3]. The link suspension, shown in Figure 1, is the most common suspension design for freight wagons in Europe today and is used both on two-axle as well as bogie wagons [4]. Even though the design has existed more than 100 years, they are still, in our opinion not fully understood today. The rather simple model used for the link suspension today is not regarded to be sufficient.
The study of the link suspension characteristics is divided into two parts. In the first part a link-bearing system is investigated. Measurements of the characteristics of the link-bearing system are performed and a model based on contact mechanics is developed. In the second part the influence of link suspension characteristics on the running behaviour of a freight wagon is investigated. The present paper covers laboratory measurements and mathematical modelling of a pendulum link.

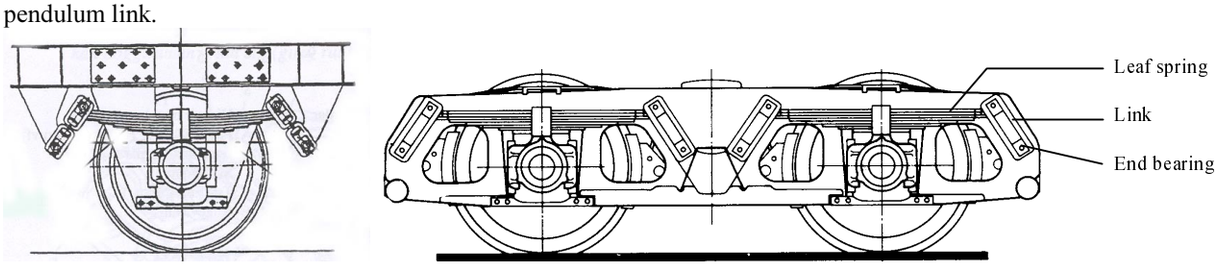


Figure 1: Running gear with link suspension.

LABORATORY MEASUREMENTS

To study the contact between link and end bearing a test rig, shown in Figure 2, is designed. A pendulum mass is hanging in a frame via link and end bearings. The upper end bearing is connected to the frame and the lower to the mass. A hydraulic cylinder applies a horizontal force on the lower part of the link and lateral force-displacement characteristics are measured. The mass is varied between 660, 1380 and 2200 kg. The amplitude and frequency of the applied force is varied. New as well as components worn in service are tested.



Figure 2: Test rig.

Figure 3 shows force-displacement characteristics for different links. The first observation is the significant hysteresis. Another observation is that the hysteresis curves differ from each other.

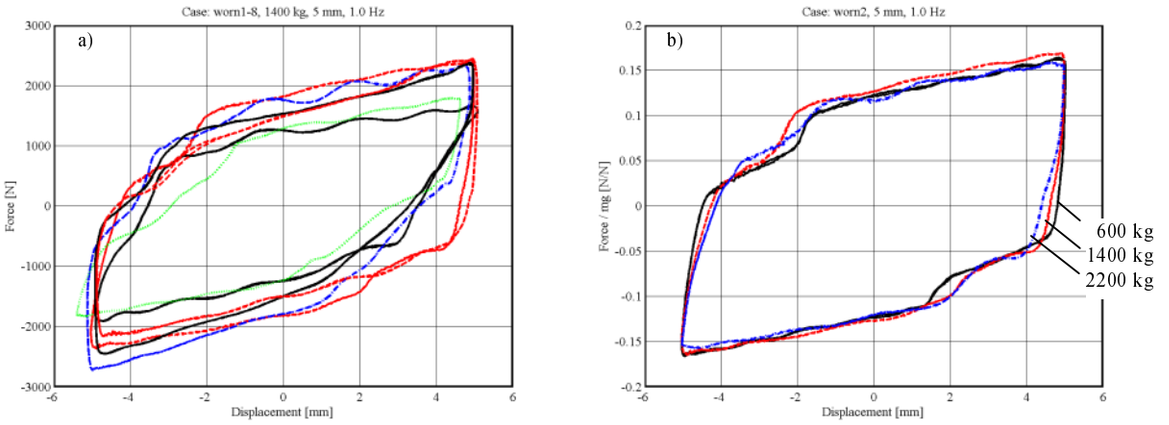


Figure 3: Force-displacement characteristics:
a) Scatter for different worn links.
b) Load dependence.

In Figure 3 b) is the force from the excitation normalized with the normal load. It is observed that in the transition zone between rolling and sliding the behaviour is not proportional to the normal load.

MATHEMATICAL MODELLING

The principle of the link suspension is that of a pendulum. When applying a lateral force on the link, it will start to roll in the bearing. When a certain tangential force is reached between the links and bearing, the link starts to slide. In the rolling case the suspension is stiffer than in the sliding case. The proposed model is using contact mechanics between rolling cylinders [5]. With a given geometry and contact environment the characteristics can be simulated. The motion for centre of gravity of the link pendulum system is described by the vector **q=A+B+C-D-E+F**, as shown in Figure 4. The equation of motion for the link pendulum system is written as **F=M*$\ddot{\mathbf{q}}$**. The tangential force in the contact points between link and end bearings, P_1 and P_2, is given as a function of the creep ratio and normal force in the contact.

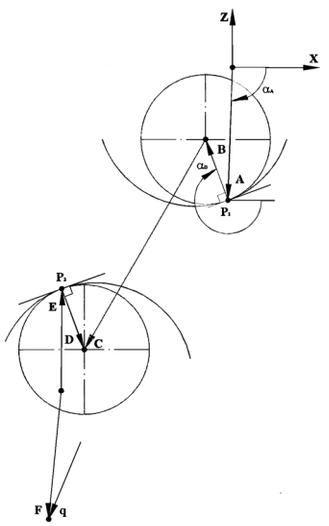


Figure 4: Link model.

CONCLUSIONS

Links worn in service show a significant amount of hysteresis. Links are thus not only providing stiffness but also damping to the vehicle. The characteristics vary with the maintenance status of the components. The results are independent of frequency, in the range 0 – 5 Hz. The rolling stiffness is independent of the amplitude of the displacement. The result is not proportional to the normal load in the transition zone between rolling and sliding.

References

[1] Stichel S.: On freight wagon dynamics and track deterioration, *Proc. Instn. Mech. Engrs.* **213**:243-254, 1999.
[2] Stichel S.: How to Improve the Running behaviour of Freight Wagons with UIC-link Suspension, *Vehicle System Dynamics* **33**:394-405, 1999.
[3] Stichel S.: Limit Cycle Behaviour and Chaotic Motions of Two-Axle Freight Wagons with Friction Damping, *Multibody System Dynamics* **8**:243-255, 2002.
[4] Jönsson P-A.: Freight wagon running gear – a review, *TRITA-FKT Report 2002:35, KTH Railway Technology, Stockholm, Sweden*, 2002.
[5] Johnson K. L.: Contact Mechanics, *Cambridge University Press, Cambridge, United Kingdom, 1985.*

MATHEMATICAL MODELS AND SIMULATION OF STICK-SLIP PROCESSES IN A CAR STEERING SYSTEM

Zbigniew Lozia*, Dariusz Zardecki **
* *Warsaw Univ. of Technology, Faculty of Transport, Koszykowa75, PL 00-662 Warszawa, Poland*
** *Automotive Industry Institute, Jagiellonska 55, PL 03-301 Warszawa, Poland*

Summary. *A method based on piecewise linear luz(...) and tar(...) projections was used for mathematical modelling and digital simulation of stick-slip phenomenon in a car-steering system. Results of simulations refer to typical open-loop tests.*

INTRODUCTION

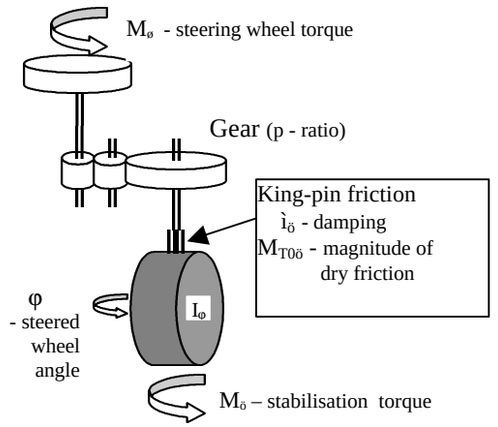
Mathematical modelling of dynamic systems with dry friction and digital simulation of the stick-slip phenomenon have been the subjects of non-linear dynamics presented in numerous research works (see state-of-the-art papers [1], [2], [3]). Surprisingly problems of stick-slip in a car steering system have been rarely taken into account. Dry friction (especially at the king-pin) could be large and it had a significant influence on the car active-safety. The piecewise linear luz(…) and tar(…) projections ([11], [12]) might be useful in studying these rather difficult theoretical problems (see [6]) and developing the complex simulation of car-dynamics with the stick-slip effects taken into consideration ([9], [13]).

CONCEPT OF MATHEMATICAL MODELING

Because of the dynamic properties of a car, its complex dynamic model could be seen as a cascade of two coupled autonomic partial models – a model of steering system dynamics and a model of vehicle motion dynamics.

Model of steering system dynamics

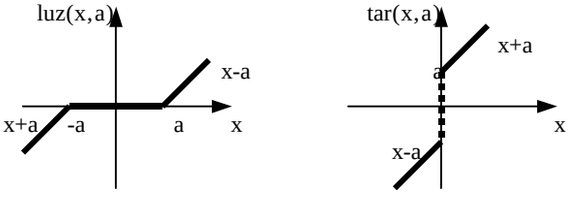
The piecewise-linear non-linear multi-body model of steering system dynamics has been used in the research. It has taken dry (kinetic and static) friction at king-pins as well as a steering box gear freeplay into consideration. This model could be useful for description of the dynamics of car steering system (both manual and power steering system types for 2WS as well as 4WS could be investigated). An idea of application of the luz(...) and tar(...) projections in the steering system mechanism model with dry friction is shown below. The simplest example of a single mass version is presented. (Note: No implicit description of stiction has been made!).



$$I_{\varphi}\cdot\ddot{\varphi}(t)=\begin{cases}-\mu_{\varphi}\cdot\tan\left(\dot{\varphi}(t),\dfrac{M_{T0\varphi}}{\mu_{\varphi}}\right)+pM_{\psi}(t)+M_{\varphi} & \text{when} \quad \dot{\varphi}(t)\neq 0\\ \operatorname{luz}\left(pM_{\psi}(t)+M_{\varphi}(t),M_{T0\varphi}\right) & \text{when} \quad \dot{\varphi}(t)=0\end{cases}$$

where

$$\operatorname{luz}(x,a)=x+\frac{|x-a|-|x+a|}{2} \qquad \operatorname{tar}(x,a)=\operatorname{luz}^{-1}(x,a) \qquad a\geq 0$$



Model of vehicle dynamics

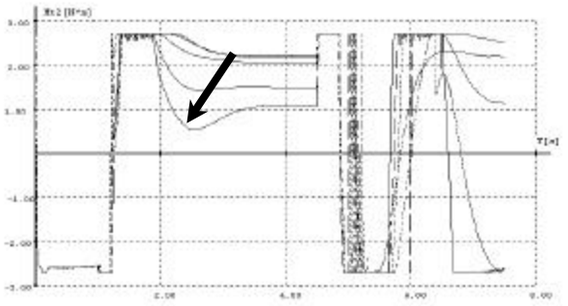
A non-linear multi-body 3D model of 4-wheel passenger car with independent suspension was assumed as the model of vehicle dynamics ([8]). Wheel-road interaction description was based on the extended Dugoff's model (where the transient states of tire according to the von Schlippe-Dietrich relaxation model were accepted). The model of vehicle dynamics had taken also the drive system quasi-dynamics, rolling resistance and aerodynamic drag into account. A simple predictive PD controller was used for programming the steady-state traction conditions.

SIMULATION STUDY

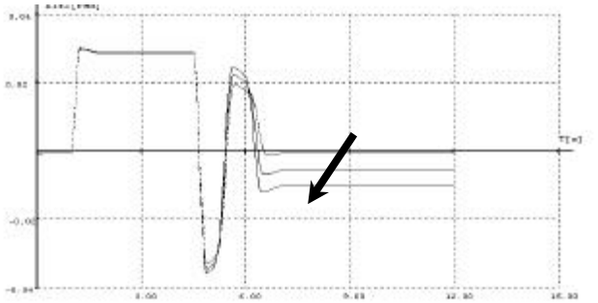
These models were used for simulation research (as well as sensitivity and bifurcation analyses) in stick-slip phenomenon in a steering system and vehicle motion. They related to open-loop tests performed according to the respective ISO regulations. Special modular simulation software (together with 3D graphics and animation) has been worked-out.

The paper presents results of simulation research for a car driven at a constant speed of 80 km/h where the following sequence of manoeuvres have been carried out: a step input to the steering wheel, steady state cornering and sudden release of steering wheel. It has been assumed for the basic version that the vehicle was equipped with a manual

steering system having a damper in its steering box. For the "richer" versions, power elements of steering system as well as the steering of all four wheels have been also investigated. Exemplary results of simulation presented below refer to varying values of the steering king-pin dry friction magnitude and gear freeplay. They refer to a 2WS manual steering system.



Friction torque at the left king-pin for increasing gear freeplay



Left wheel angle for increasing left king-pin dry friction magnitude

The results show a significant influence of both dry friction and freeplay on the stick-slip phenomenon and car's trajectory. The influence of the friction is more visible in steady-states (in the first phase – where the steering wheel has been fixed, and in the second phase – where the turn has been blocked by the stiction). The influence of the freeplay mostly appears in transient states. On the base of investigation, it can be assumed that the friction and freeplay influence on the stick-slip processes and the vehicle motion has been regular. But also some "chaos" referred to levels of steady states was observed for other datasets. On the ground of bifurcation research, it has been ascertained that the freeplay and friction affect the states of blocking in "oscillating fashion" (rises and drops of steady-state values). It could be seen that strong disturbances appear on bifurcation graphs (due to a very large local sensitivity) in certain cases, while in others, horizontal lines occur (due to a local fall in the sensitivity). These have testified to a complicated nature of the modelled processes.

By comparing the results for different structures of the steering system, one could become aware of the fact that the introduction of power steering systems removed the transient processes to a great extent and decreased the sensitivity to the changes of the freeplay and frictions (probably due to increased damping) a little. Similarly, by adding the steering function to the rear wheels the sensitivity has become decreased a little.

CONCLUSIONS

The problems of stick-slip in the steering system lead to more and more complicated (thus, potentially, more and more susceptible to freeplay and friction) mechanisms and control systems in the car.

The method of modelling and simulation of dynamic systems with freeplay and friction taken into account basing on the piecewise linear luz(...) and tar(...) projections appeared very effective.

References

[1] B.Armstrong-Helouvry, P.Dupont, C.Canudas de Wit: A Survey of Models, Analysis Tools and Compensation Methods for the Control of Machines with Friction. *Automatica* **30**, No 7: 1083-1138, 1994.

[2] B.Brogliatto, A.A.T.Dam, L.Paoli, F.Genot, M.Abadie: Numerical simulation of finite dimensional multibody nonsmooth mechanical systems. *Applied Mechanical Review* **55**, No 2: 107-150, 2002.

[3] W.Grzegozek: The Modeling of Vehicle Dynamics with Stabilizing Control of Braking Forces. *Proc. of Cracow University of Technology. Mechanics. Monograph* **275**, 2000 (in Polish).

[4] A.Harlecki: Method of Dynamic Analysis of Multibody Systems with Dry Friction in Joints. *Proc. of Bielsko-Biala University. Monograph*, 2002 (in Polish).

[5] R.A.Ibrahim: Friction-induced vibration, chatter, squeal, and chaos. Part I: Mechanics of contact and friction. Part II: Dynamics and modeling. *Applied Mechanical Review* **47**, No 7: 207-253, 1994.

[6] D.Karnopp: Computer Simulation of Stick-Slip Friction on Mechanical Dynamic Systems. *Transactions of the ASME. J. of Dynamic Systems, Measurement, and Control* **107**: 100-103, 1985.

[7] Z.Lozia: Analysis of Biaxial Car Motion Based upon Dynamic Models. *Proc. of Warsaw University of Technology. Transportation*: **41**, 1998.

[8] Z.Lozia: Vehicle Dynamics and Motion Simulation Versus Experiment. *SAE Paper 980220. SAE Transactions* 1998. *Section 6*, **107**:.344-360, 1998.

[9] Z.Lozia, D.Zardecki: Vehicle Dynamics Simulation with Inclusion of Freeplay and Dry Friction in Steering System. *SAE 2002 Transactions. J. of Passenger Car – Mechanical Systems*: 907-923, 2002.

[10] A.T.Wohnhaas: Simulation von Kraftfahrzeug-Lenkungen unter besonderer Berücksichtigung von Reibung und Spiel. *Dissertation*, IVK Universität Stuttgart, 1994.

[11] D. ardecki: Mathematical model of car steering system dynamics with regard to gearbox backlash and friction. *Proc. of Conf. Autoprogres'98*. PIMOT: T.1, 43-52, 1998 (in Polish).

[12] D.Zardecki: The luz(...) and tar(...) projections – theoretical background and idea of application in modelling of discrete mechanical systems with backlashes or frictions. *Biuletyn WAT*: **L**, Nr 5: 125-160, 2001 (in Polish).

[13] D.Zardecki: Simulation Studies of stick-slip process in Car Steering System. Proc. of III Conf. "Problems of Safety in Road Vehicles". Zeszyty Naukowe Politechniki Swietokrzyskiej. Mechanika: 305-312, 2002 (in Polish).

NONLINEAR OVERALL VISCOELASTIC PROPERTIES OF THE RANDOM MULTICOMPONENT MEDIA

Boris P. Maslov
National Academy of Sciences, S.P. Timoshenko Institute of Mechanics,
Nesterova 3, 03047 Kyiv, Ukraine

Summary This work is concerned with the prediction of the effective or overall response of a random multi-component media with nonlinear visco-elastic constituents. The continuum considered here is suggested to be subjected to finite deformation. Kirchhoff stress tensor and deformation gradients are used as field variables in a fixed reference state. Nonlinear problem is investigated in second order approximation theory when the gradient deformation terms higher than second order are neglected. Five constant elastic potential in elastic problem and five time functionals in visco-elastic one are used to build overall constitutive relations.

Theoretical determination of the overall properties of inhomogeneous media is a problem of a great importance. This work is concerned with the prediction of the effective or overall response of a random multi-component media with nonlinear visco-elastic constituents. The elastic properties of inhomogeneous structures have been studied intensively during last decades. The works of R.M. Christensen, J.R. Willis, Z. Hashin and others represent a comprehensive review of achievements in this area. But there are a lot of questions arise in the case when visco-elastic response is a subject of investigation, nonlinear especially.

Certain representative meso-domain B containing a set of inclusions in reference configuration κ is considered. So the volume v_R of the body may be represented as

$$v_R = v_m \cup v_a, \qquad v_a = \bigcup_{i=1}^{n} v_i;$$

Each volume of v_r, $r \in [1, n+1]$, contains a visco-elastic material, the effective properties of which are determined by the potential of type

$$\hat{W}(\boldsymbol{E},t) = \mu\left[\left(1+\frac{1}{2}\alpha\right)I_1^2 - 2I_2 + \beta_1 I_1^3 + \beta_3 I_1 I_2 + \beta_3 I_3 + \mathrm{O}\left(|\boldsymbol{E}|^4\right)\right], \tag{1}$$

where I_i are the main invariants of Lagrange strain tensors

$$I_1 = tr(\boldsymbol{E}); \qquad I_2 = \frac{1}{2}\left(I_1^2 - tr\boldsymbol{E}^2\right);$$

$$I_3 = \frac{1}{3}\left(tr\boldsymbol{E}^3 - I_1^3 - 3I_1 I_2\right); \qquad \boldsymbol{E} = \frac{1}{2}(\boldsymbol{F}^T\boldsymbol{F} - \boldsymbol{1});$$

$$\boldsymbol{F} = \partial \boldsymbol{x}^A / \partial \boldsymbol{x} = \boldsymbol{1} + \boldsymbol{H}; \qquad \boldsymbol{x}^A = \boldsymbol{x} + \boldsymbol{u}(\boldsymbol{x});$$

$$\boldsymbol{H} = \partial \boldsymbol{u} / \partial \boldsymbol{x} = \nabla \boldsymbol{u}; \qquad \alpha = \lambda / \mu,$$

$\lambda, \mu, \beta_1, \beta_2, \beta_3$ stand for the integral convolution type operators of visco-elasticity or for constants of material in pure elastic case, tr - trace operator of appropriate tensor, $\boldsymbol{F}(t)$ - the strain gradient, $\boldsymbol{H}(t)$ - the gradient of displacement vector $\boldsymbol{u}(\boldsymbol{x},t)$ taken in the coordinate system of the reference configuration, $\boldsymbol{1}$ - unit symmetric tensor of the second order.

So the corresponding Piola-Kirchhoff stress matrices at time t are given by

$$\sigma(t) = \overset{t}{\underset{\tau=t_0}{\Phi}}\{\boldsymbol{H}(\tau)\}, \tag{2}$$

where Φ is linear in time functional of hereditary type. The linear visco-elasticity with finite strain is therefore implemented here. Nonsymmetrical Piola-Kirchhoff first stress tensor σ and the gradient $\boldsymbol{H}$ of displacement vector $\boldsymbol{V}$ after being averaged over unstrained representative volume v_R of a composite B can be well used in terms of conjugated pair of macroscopic variables [1-3,5] as in nonlinear strain theory. Followed, the constitutive equation of non-homogeneous multi-component media may be written in form of

$$\sigma_{ka} = \partial W(\boldsymbol{E}) / \partial H_{ka}. \tag{3}$$

Then for first and second order approximation on deformation gradients there are the expressions

$$\sigma_{ij(1)} = \lambda_{ijkl} e_{kl(1)};$$

$$\sigma_{ij(2)} = \lambda_{ijkl} E_{kl(2)} + H_{im(1)} \lambda_{mjkl} e_{kl(1)} + \nu_{ijklmn} (e_{kl} e_{mn})_{(1)}. \tag{4}$$

Here

$$e_{ij} = \frac{1}{2}(H_{ij} + H_{ji}); \qquad H_{ij} = \nabla_j u_i = u_{i,j};$$

$$E_{ij(2)} = e_{ij(2)} + f_{ij(2)}; \qquad f_{ij(2)} = \frac{1}{2}(H_{mi} H_{mj})_{(1)};$$

$$\lambda_{ijkl} = \mu(\alpha\delta_{ij}\delta_{kl} + 2I_{ijkl}); \qquad I_{ijkl} + \frac{1}{2}(\delta_{ik}\delta_{jl} + \delta_{il}\delta_{jk}); \qquad I_{ijklmn} = \frac{1}{2}(I_{ipkl}I_{jpmn} + I_{jpkl}I_{ipmn}),$$

$$\nu_2 = -\mu(\beta_2 + \beta_3); \qquad \alpha = \lambda/\mu, \tag{5}$$

For an ideally elastic material, the Piola-Kirchhoff stress at time t depends only on the deformation gradient matrix at time t, the functional Φ in (2) becomes a matrix-valued function of $\boldsymbol{H}(\boldsymbol{x},t)$. Correspondingly, the functional Φ becomes a matrix-valued function of $\boldsymbol{H}(\boldsymbol{x})$ only.

Since continuum considered here is suggested to be subjected to finite deformation Kirchhoff stress tensor and deformation gradients are used as field variables in a fixed reference state. Nonlinear problem abovementioned is investigated in second order approximation theory when the gradient deformation terms higher than second order are neglected. Five constant elastic potential in elastic problem and five time integral operator functionals in visco-elastic one are used to build overall constitutive relations for isotropic media. The well known inclusion problem in infinite visco-elastic matrix is a base of investigation. For micro-inhomogeneous media described by linear integro-differential equations with random kernels that are be reduced to linear integral equation by the use of a Green's function for appropriated problem for homogeneous comparison medium [5] in infinite domain.

As it's well known, the essential assumption in the Mori-Tanaka approach states [3.5], that the each inclusion behaves as isolated one in the infinite matrix and subjected to some effective stress field coinciding with the average stress in the matrix. Such an assumption allows uniquely define the effective elastic and visco-elastic properties of multi-component media. A nonlinearly visco-elastic composite medium is considered with stress free strains, which consists of a homogeneous matrix containing a homogeneous and statistically uniform random set of ellipsoidal inclusions having all the same form, orientation and mechanical properties. The main hypothesis of many micromechanical methods is used, according to which each inclusion is located inside a homogeneous stress and method of statistically conditional function and Mori-Tanaka approach can be applied. For a single inclusion such a micromechanical approach based on the Green function technique as well as on the interfacial Hill operators allows investigating the stress and strain concentration on the inter-phase surfaces.

More detailed considerations of the mechanical behavior of visco-elastic non-homogeneous media require the analysis of the interface between the different phases. These interfaces may represent for example weak interfacial layer due to imperfect bonding between the two phases. Therefore, to evaluate more accurately the visco-elastic effective properties of a composite, the behavior and structures of interfaces must be taken into consideration. At first the problem of a single uncoated and coated inclusion is considered inside an infinite matrix and then homogenization scheme proposed is implemented. As the result the overall constitutive equations are obtained.

$$\sigma(\boldsymbol{H}) = J^{-1}\boldsymbol{F}\boldsymbol{S}(\boldsymbol{H})\boldsymbol{F}^T; \qquad J = \det(\boldsymbol{F});$$

$$\boldsymbol{S}(\boldsymbol{H}) = \mu\left[\alpha I_1\boldsymbol{1} + 2\boldsymbol{E} + 3\beta_1 I_1^2\boldsymbol{1} + \beta_2 I_2\boldsymbol{1} + \beta_2 I_1(I_1\boldsymbol{1} - \boldsymbol{E}) + \beta_3(I_2\boldsymbol{1} - I_1\boldsymbol{E}) + \boldsymbol{E}^2\right];$$

$$\lambda = 3\sum_{r=1}^{n+1} c_r\kappa_r\kappa_{Ar} - 2\mu/3; \qquad \mu = 2\sum_{r=1}^{n+1} c_r\mu_r\mu_{Ar}; \qquad \nu_1 = \sum_{r=1}^{n+1} 3c_r\begin{bmatrix} l_A\left[2\lambda\kappa_A(3\kappa+\mu)_A + n_A f_A\right] + 9\nu_1\kappa_A^3 + \\ 6\nu_2 l_A\kappa_A(3\kappa+2\mu)_A + 8\nu_3 l_A^2 n_A \end{bmatrix}_r;$$

$$\nu_2 = \sum_{r=1}^{n+1} c_r\left[4\mu_A^2\left(\frac{1}{2}f_A + 3\nu_2\kappa_A + 4\nu_3 l_A\right) - \frac{1}{2}(3\lambda\kappa_A + 2\mu l_A)\right]_r; \quad \nu_3 = \sum_{r=1}^{n+1} c_r\left[\frac{3}{2}\mu\mu_A(4\mu_A^2 - 1) + 8\nu_3\mu_A^3\right]_r. \tag{6}$$

The dependence of the effective properties from the visco-elastic properties of constituents is numerically investigated. The analysis is carried out by means of two approaches that primarily include investigating local fields of random stress and deformation under the external loading applied. Moreover, the influence of viscous properties of constituents is the subject of problem-solving.

References

[1] Christensen R.: Mechanics of composites. Wiley-Interscience, NY 1979.

[2] Hill R.: On constitutive macro-variables for heterogeneous solids at finite strain. *Proc. R. Soc. London* **A326**:131-147, 1972.

[3] Maslov B.P.: Stress concentration in non-compressible multi-component material. *Int. Appl. Mech.* **36,**N3:108-114, 2000.

[4] Rivlin R.S.: Material Symmetry Revisited *GAMM-Mitteilungen* **25**, Heft 1/2:109-126, 2002.

[5] Willis J.R.: Elasticity Theory of Composites *Mechanics of Solids. The Rodney Hill 60th Anniversary Volume* (eds. H.G. Hopkins, M.J. Sewell), pp.653-686, Pergamon Press, Oxford 1982.

SINTERING SIMULATION OF STAINLESS STEEL POWDER COMPACTS

Rui Zhang, Renata S. Engel
Engineering Science & Mechanics Department, The Pennsylvania State University, University Park, PA 16802

Summary Die compaction of powder metals is a classic discrete component fabrication process that relies on the rearrangement, distortion, and flow of metal particles in a die cavity, where the powders are compressed into a preform that is subsequently sintered. The sintered material has competitive properties, but without the cost associated with additional machining. One of the technological challenges when fabricating parts via powder processing methods is the ability to achieve undistorted, full density parts. For example, density gradients induced from the press motions lead to nonuniform shrinkage during the thermal processing. This research presents a model that predicts the shrinkage during high temperature sintering for powder compacts that have density gradients. The one-dimensional diffusional flow model for pressureless sintering includes an Arrhenius-type viscosity model and allows for the inclusion of grain growth and thermal expansion as functions of temperature.

OVERVIEW OF PAPER

The sintering simulation of metal powder compacts has been a popular topic in powder metallurgy processing for decades. This paper presents a phenomenological model of sintering which has been established to achieve the accurate prediction of sintering shrinkage throughout the sintering cycles. The sintering simulation results are compared and verified using the shrinkage data collected throughout a typical sintering cycle for a stainless steel 316 L cylindrical compact.

SINTERING MODEL DESCRIPTION

Because of the temperature and density variation during sintering, a thermal-visco-elasticity constitutive law has been employed in this model. The strain is comprised of the elastic strain $\boldsymbol{\varepsilon}^e$, thermal strain $\boldsymbol{\varepsilon}^t$, and creep strain $\boldsymbol{\varepsilon}^{cr}$. The portion of elastic strain is assumed to be linear and isotropic. The thermal strain is caused by thermal expansion or shrinkage. The incremental creep strain obeys a linear-viscous law as shown in Riedel (1990) and has the following form,

$$\Delta\boldsymbol{\varepsilon}^{cr} = \left(\frac{\boldsymbol{\sigma}'}{2G} + \frac{tr(\boldsymbol{\sigma}) - 3\sigma_s}{9K}\mathbf{I} \right)\Delta t \tag{1}$$

where $\boldsymbol{\sigma}'$ is the deviatoric stress, G is the shear viscosity modulus, K is the bulk viscosity modulus, $\mathrm{tr}(\boldsymbol{\sigma})$ is the trace of the stress tensor, and σ_s is the sintering stress (the equivalent hydrostatic pressure caused by local capillary stresses in porous structures). It has been shown in Olevsky (1998) that the sintering stress can be written as

$$\sigma_s = \frac{3\omega}{r_0}(1-\theta)^2 \tag{2}$$

where r_0 is assumed to be the mean radius of powder grains and ω is the surface tension energy of the material. The porosity θ is defined as the ratio of the volume of pores V_{pores}, to the total volume V_{total}.

Determining the parameters in equations (1) and (2) requires additional models and assumption. For example, the elastic deformation during sintering is relatively small. Thus an elastic modulus has been calculated (German 1994) and held constant throughout the sintering cycle. For the simulations shown in this work, an average relative density of 82% stainless steel 316L was used to determine the appropriate constant elastic modulus. Observations from initial experiments indicate that below 900°C increases in dimensions due to thermal expansion dominates the response. Therefore, since no sintering densification occurs below that temperature, a linear equation of thermal expansion coefficient was obtained and used to determine the first stage of the sintering shrinkage curve. Olevsky (1998) shows that the viscosity moduli are functions of porosity and apparent viscosity. For this work, the apparent viscosity for 316L type stainless steel powders was calculated with an exponential equation in Brandes (1983). Finally, the sintering driving force is proportional to the reciprocal of grain size, as can be seen in (2). Thus grain growth plays an important role during the sintering of 316L stainless steel. For example, large grain sizes tend to prohibit densification. A widely used empirical grain growth equation (Ashby and Easterling, 1982) for stainless steel 316L has been employed in this research:

$$\frac{dG}{dt} = \frac{A\exp(-Q_G/RT)}{G} \tag{3}$$

where A is a pre-exponent factor, Q_G is the activation energy for grain growth, R is the gas constant, T is the absolute temperature and G is the instantaneous grain size.

SINTERING MODEL VERIFICATION

Figure 1 illustrates a typical temperature cycle and the associated axial shrinkage of a cylindrical stainless steel 316L specimen as measured using a dilatometer and predicted using the finite element (FEM) simulation using the model presented in this paper. Significant features of the model include the description of grain growth by using information from metallographic photos taken of the compacts throughout the sintering cycle. Figure 1 shows two typical metallographs—one at the beginning and another at the end of the sintering cycle. Those images confirm the significant changes in grain size. Analysis of these photos gives material parameters necessary to establish the grain growth equation. For most metals, it is true that no significant shrinkage happens below certain transition temperature; therefore, based on experimental observations, a transition temperature trigger has been set in this model to enforce zero sintering driving force below that temperature. That transition temperature is a function of material and powder size distribution.

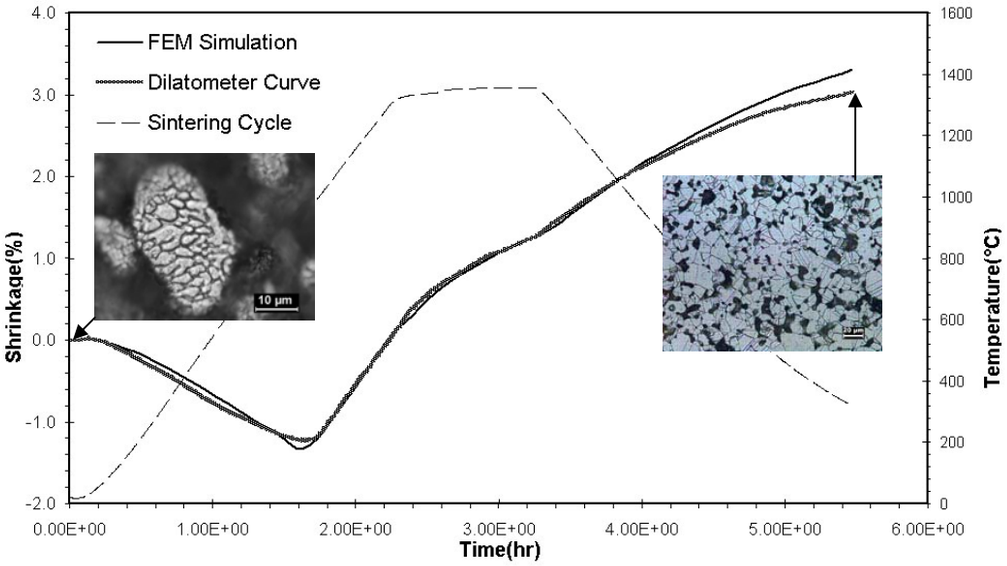


Figure 1. Comparison of the FEM simulation and dilatometry plots on axial shrinkage versus temperature for a stainless steel 316L presintered compact heated at a rate of 10°C/min to 1350°C in hydrogen (powder mean size 52.5μm).

CONCLUSIONS

Density variation in the green compact has been used as the initial condition in the sintering simulation. The distortion is driven by the creep strain which is dependent on the instantaneous grain size. The model presented here incorporates grain size as a function of temperature and knowledge about when particular driving forces dominate, e.g., thermal expansion is critical in the initial stage, whereas grain growth is critical at high temperatures. Axial measurements via a dilatometer throughout the sintering cycle demonstrate that the simulation results accurately describe the shrinkage throughout the cycle, even though the final value of the predicted shrinkage is slightly smaller than the shrinkage recorded experimentally.

ACKNOWLEDGEMENT

This research was supported by the Center of Innovative Sintered Products at The Pennsylvania State University and in part, it is based upon work supported by the National Science Foundation under Grant No. 0200554 and Grant No. 0097610.

References

Ashby, M. F. and Easterling, K. E. 1982. A first report on diagrams for grain growth in welds. *Acta Metall* 30(11-a):1969-1978.
Brandes, E. A. 1983. *Smithells Metals Reference Book*, 6th ed. London: Butterworth and Co.
German, R. M. 1994. *Powder Metallurgy Science*, 2nd ed. Princeton, NJ: Metal Powder Industries Federation.
Olevsky, E. A. 1998. Theory of sintering: from discrete to continuum. *Materials Science and Engineering R, Reports: A Review Journal* R23:41-100.
Riedel, H. 1990. A constitutive model for the finite-element simulation of sintering-distortions and stresses. In *Proceedings of the Third international Conference on Ceramic Powder Science, 1990*, ed. by G. Messing, S. Hirono, and H. Hausner. Westerville, Ohio: American Ceramic Society. pp. 619-630.

CHARACTERISATION OF THE CYCLIC BEHAVIOUR OF ELASTIC-PLASTIC-CREEPING BODIES

Alan R. S. Ponter
Mathematical Modelling Centre, Department of Engineering, University of Leicester, Leicester, LE1 7RH, UK

Abstract The paper describes a systematic theoretical approach to the characterization of the cyclic behaviour of a body that exhibits creep and plasticity. The cyclic state for a particular constitutive equation may be characterized as a minimum theorem in terms of a class of kinematically admissible inelastic strain rate history. The minimum for some particular class of approximating strain rate histories my be determined by means of a new mathematical programming method, the Linear Matching Method, that sequentially reduces the functional through the solution of linear problems. The theory is developed for the standard Mandel thermodynamic model of constitutive behaviour allowing for both plasticity and creep behaviour. Examples are given of applications typical of those occurring in the life assessment of high temperature structures where the load corresponding to a particular failure condition is required.

EXTENDED SUMMARY

INTRODUCTION

Classical plasticity and creep theory was primarily developed to assist in the design of engineering structures. Design codes and life assessment procedures used on a routine basis in industry rely, at their core, on concepts such as limit load, shakedown limit, reference stress and elastic follow-up all derive from basic plasticity theory and its extensions to creep behaviour. Generally these procedures rely upon linear elastic solutions and a sequence of rule based assessment. Over the last 20 years computational methods using advanced constitutive equations have significantly replaced ruled based methods in design. However, unlike rule-based methods, they fail to directly provide answer to the type of question posed by design and life assessment. For example, for the assessment of the strength of a structure, the designer wishes to know the maximum load or load range for which a certain structural phenomenon may occur. Such phenomena may include plastic collapse, excessive growth of creep strain, creep rupture at a particular time, initiation of failure due creep/fatigue interaction all of which may be regarded as related to properties of the inelastic strain rate history.

In recent years there has begun a reassessment of theoretical and computational methods that are capable of providing such direct answers to design related issues. Most of this work has been concerned with shakedown limits [8] but there is a need for methods capable of relating to a wide range of low and high temperature structural phenomenon. For this to be achieved, there is a need for a consistent theoretical approach, combined with appropriate approximation procedures that may be applied to a much wider range of constitutive assumptions than the simpler plasticity models. This forms the subject of this paper. The approach consists of two parts. The first is concerned with the characterization of the cyclic state as a minimum theorem; the second involves strategies for determining the minimum for classes of approximating inelastic strain rate histories. The purpose of the paper is to describe the theoretical basis for these two phases for a class of creep and plasticity constitutive relationships that conform to the Mandel thermodynamic theory, and to present examples of applications.

MINIMUM PRINCIPLES FOR CYCLIC BEHAVIOUR

Consider first the simplest classical case of a body subjected to small deformations, a linear elastic perfectly plastic material and a cyclic history of load $\lambda P_i(x_i,t)$ and temperature $\lambda\theta(x_i,t)$ where λ denotes a load parameter. For certain classes of constitutive relationship, a cyclic state of response exists during a typical cycle, , $0 \le t \le \Delta t$, where the stress history is given by;

$$\sigma_{ij}(x_i,t) = \lambda\hat{\sigma}_{ij} + \overline{\rho}_{ij}(x_i) + \rho^r_{ij} \ , \qquad \hat{\sigma}_{ij} = \hat{\sigma}^p_{ij} + \hat{\sigma}^\theta_{ij} \qquad (1)$$

Here $\hat{\sigma}^p_{ij}$ and $\hat{\sigma}^\theta_{ij}$ denote the linear elastic solutions corresponding to $P_i(x_i,t)$ and $\theta(x_i,t)$ respectively, $\overline{\rho}_{ij}$ denotes a time constant residual stress field, corresponding to the residual stress field at the beginning and the end of the cycle, and $\rho^r_{ij}(x_i,t)$ denotes the change in the residual stress field during the cycle, with $\rho^r_{ij}(x_i,0) = \rho^r_{ij}(x_i,\Delta t) = 0$. For a prescribed load parameter λ the exact cyclic solution may be characterized by the following minimum theorem [1].

A kinematically admissible plastic strain rate history is defined as any history $\dot{\varepsilon}^c_{ij}$ for which the accumulated strain over a cycle $\Delta\varepsilon^c_{ij} = \int_0^{\Delta t} \dot{\varepsilon}^c_{ij} dt$ is compatible with a displacement increment Δu^c_i that satisfies displacement boundary conditions. Then the exact cyclic solution $\dot{\varepsilon}^c_{ij} = \dot{\varepsilon}^p_{ij}$ minimizes the functional,

$$I(\dot{\varepsilon}^c_{ij},\lambda) = \int_0^{\Delta t}\int_v (\sigma^c_{ij} - \lambda\hat{\sigma}_{ij})\dot{\varepsilon}^c_{ij} dV dt \qquad (2)$$

subject to the condition that there exists a constant residual stress field $\overline{\rho}_{ij}$ so that the stress history;

$$\sigma^*_{ij}(x_i,t) = \lambda\hat{\sigma}_{ij} + \overline{\rho}_{ij}(x_i) + \rho^c_{ij} \qquad (3)$$

satisfies the yield condition during the cycle. Here σ^c_{ij} denotes the stress at yield associated with $\dot{\varepsilon}^c_{ij}$ and ρ^c_{ij} denotes the history of residual stress corresponding to $\dot{\varepsilon}^c_{ij}$. Both of the classical shakedown theorems may be derived as special cases when the magnitude of $\dot{\varepsilon}^c_{ij}$ is assumed to be sufficiently small for ρ^c_{ij} to be negligible small in (3). The result is closely related to an earlier result by Gokhfeld and Cherniavsky [2].

For more general constitutive relationships this result may be generalized. For a viscous material, as a model of high temperature creep, the functional I becomes,

$$I(\dot{\varepsilon}^c_{ij},\lambda) = \int_0^{\Delta t}\int_v \Omega(\dot{\varepsilon}^c_{ij}) - \lambda\hat{\sigma}_{ij}\dot{\varepsilon}^c_{ij}\,dV\,dt \qquad (4)$$

where $\Omega(\dot{\varepsilon}^c_{ij})$ is a flow potential [4,5]. A further generalization may be made for constitutive relationships that conform to the Mandel thermodynamic theory [6,7] where the behaviour, for a single state variable A, may be expressed in terms of a Helmholtz free energy $\phi(A)$ and a flow potential $\Omega(\dot{\varepsilon}^c_{ij}, A)$. Such generalizations have been discussed by Pollizzotto [3] for time independent plasticity and may be generalized to creep behaviour. The full paper and the presentation will provide a discussion of these generalizations.

THE LINEAR MATCHING METHOD

Non linear programming methods have been applied to shakedown problems for many years, following early work by Maier and others. A recent summary indicates the diversity of approaches that are now possible [8]. A particularly simple and flexible method has emerged in recent times, based in concept on methods used for many years in engineering design [8,9]. When applied to the minimization of the functionals (2) and (4), the method essentially consists of the solution of a sequence of linear problems where the linear material coefficients are evaluated from two matching conditions. For a known initial kinematically admissible strain rate history $\dot{\varepsilon}^i_{ij}$ the state of stress given by the linear material and the constitutive assumptions are matched. In addition the condition of kinematical admissibility is imposed on the solution of the linear problem. The solution of the linear problem then provides a new kinematically admissible strain rate history that reduces the functional (2) or (4), provided certain convexity conditions are satisfied. During the iterative process, it is then possible to adjust the load parameter λ so that a restriction on some property of the strain rate history is maintained. This methodology has been applied to a range of problems associated with the life assessment of structures [8,9] and has begun to form the basis for methods for use in industry.
The application of such methods to constitutive relationships involving internal state variable requires an extension to the matching of the internal state. This may be done in a number of alternative ways, providing solutions with a range of assumptions concerning the relative magnitude of the timescales involved in changes in the state variable and changes in the residual stress field. This allows a systematic approach to simplification of cyclic loading problems for creep, taking into account known properties of cyclic solutions.

CONCLUSIONS

Previous work on the characterization of the cyclic behaviour of structures for plasticity and creep has identified minimum theorems in terms of kinematically admissible strain rate histories. A new programming method, the Linear Matching Method, has demonstrated that the identification of the minimum for approximating classes of such fields may be achieved for complex problems of the type that occur in the life assessment of structures. The paper gives a systematic account of both the minimum theorems and the Linear Matching Method for plasticity and creep constitutive relationships expressed in terms of the standard Mandel thermodynamic model. Examples of applications show that it is possible to evaluate the loads corresponding to particular failure modes, interpreted as properties of the strain rate history. Such solutions are of particular value for industrial applications.

References

[1] Ponter A. R. S. and Chen H. F., (2001), *European Journal of Mechanics A/Solids*, **20**, 539-554
[2] Gokhfeld D.A. and Cherniavsky, D.F., 1980. Limit Analysis of Structures at Thermal Cycling. , Sijthoff & Noordoff, Alphen aan der Rijn, The Netherlands.
[3] Polizzotto C, 2003, Int. Jn. Of Solids and Structures, **40**, 2673-2697
[4] Ponter A. R. S., " A minimum theorem for the cyclic behaviour of creeping bodies". *Meccanica*, 2001, 36, 37-47.
[5] Ponter A.R.S and Boulbibane M., (2002), *European Journal of Mechanics, A/Solids*, **21**,915-925 .
[6] Lemaitre J. and Chaboche, J.-L., 1990, Mechanics of Solid Materials, Cambridge University Press, Cambridge, UK.
[7] Halphen B. and Nguyen, Q.S., 1975. Sur les matériaux standard généralisées. *J. Méchanique.* **14**, pp. 39–63.
[8] Weichert D and Maier G, (Ed.) , Inelastic Behaviour of Structures under Variable Repeated Loading – Direct Analysis Methods, International Centre for Mechanical Sciences Lecture Series, No 432, Springer-Verlag, May 2002.
[9] Ponter A. R. S. and Chen H. F., (2001), *European Journal of Mechanics A/Solids*, **20**, 555-571

A CREEP CONTINUUM DAMAGE THEORY FOR BEAMS, PLATES AND SHELLS

Holm Altenbach and Konstantin Naumenko

Martin-Luther-University Halle-Wittenberg, Department of Engineering Sciences, D-06099 Halle, Germany

Summary The widely used approach in modelling the creep-damage behavior of structures is the continuum damage mechanics, which is based on constitutive equations for the creep strain rate tensor, and evolution equations for internal state variables. This approach is usually not compatible with those theories of beams, plates and shells which are based on cross-section approximations of displacement and/or stress fields. In this case there is no unique possibility to transform three-dimensional constitutive and evolution equations to the averaged equations for tensors of forces and moments and the corresponding strain or strain rate measures. We discuss an extension of the theory of "simple shells" recently proposed for problems of finite elasticity to the creep-damage analysis. The balance equations are formulated directly without any cross-section approximation. A general structure of creep-damage constitutive equations is discussed considering the symmetries of a shell and within the framework of continuum thermodynamics. Based on simplified examples of rods and plates we compare our approach with the three-dimensional analysis by the finite element method.

In many applications thin-walled structures (beams, plates, pipes, pipe bends, etc.) operate at elevated temperatures. Under such conditions the behavior of metals and alloys is primarily determined by irreversible time-dependent creep and material deterioration processes. In order to estimate the long-term behavior it is important to understand the mechanisms of the time-dependent stress redistribution and damage growth, particularly in the zones of nozzles, pipe connections and welds. The widely used approach in modelling the creep-damage behavior is the continuum damage mechanics, which proposes constitutive equations for the creep strain rate tensor, evolution equations for damage variables, and states nonlinear initial-boundary value problems in order to perform the structural analysis. With the progress in the material science and continuum mechanics, many new constitutive models have been developed which include physically motivated state variables and which are able to consider different effects in material behavior such as the damage induced anisotropy, stress state dependence of damage evolution, etc. These models can be incorporated into a commercial finite-element code in order to analyze time-dependent deformations and stresses in a thin-walled structure under specific mechanical loading. One way is the "three-dimensional approach" which is based on balance equations of the three-dimensional continuum. This approach seems more preferable for creep analysis since the existing constitutive models of creep are developed with respect to the Cauchy stress and strain (rate) tensors, and the proposed measures of damage (scalars or tensors of different rank) are defined in the three-dimensional space. Another way is the use of the structural mechanics of beams, plates and shells, and the balance equations formulated in terms of force and moment tensors. This approach often find application because of simplicity of model creation, smaller effort in solving non-linear initial-boundary value problems of creep, and easily interpretable results. In [1, 2] numerical solutions of the cross-section assumption based equations for shells and the three dimensional equations of creep-damage mechanics are presented. It is found that any theory of beams, plates or shells derived as an approximate version of the three-dimensional equations requires "more accurate" cross-section approximations for the transverse normal and shear stresses if damage processes are taken into account. The type and the order of such approximations cannot be established a priori. Furthermore, there is no unique way to formulate the creep-damage constitutive equations for assumed stress resultants and the corresponding strain measures. In this sense it is more reliable to solve the three-dimensional equations which are "free" from ad hoc assumptions for the displacements and stresses. However, in this case the question about the relevance of "three-dimensional" creep-damage constitutive assumptions for the analysis of thin-walled structural elements is still open.

The aim of this presentation is to recall the governing equations of creep mechanics, to derive a continuum damage shell theory and to compare the long-term predictions based on the standard three-dimensional approaches and the proposed two-dimensional shell model. First, we summarize the basic features of creep behavior in polycrystalline metals and alloys and thin-walled structures. Second, we derive the governing equations of creep damage

mechanics based on the model of "simple shell" [3]. Within this model a shell is assumed to be a two-dimensional continuum in which the neighboring parts interact by means of forces and moments. Based on this assumption the balance equations are formulated by the direct approach without incorporating any cross-section approximation for displacement and/or stress fields. The constitutive equations are formulated with respect to the tensors of forces and moments and to the shell type strain measures, i.e. the membrane strains, changes of curvature and transverse shear strains. The general structure of the rate equations for the description of the creep process is established within the framework of the theory of symmetry and applying the energy balance equation as well as the second law of thermodynamics. Furthermore, we introduce the damage measures suitable for the analysis of thin-walled structures. The tertiary creep behavior is described by the use of the effective stress concept and the strain rate equivalence principle. As a special case we discuss a class of constitutive equations linearized with respect to the strains. The proposed model takes into account the stress state dependence of damage evolution, e.g. the different damage rates in tension and compression.

Another approach of analysis of shells is based on the traditional "three-dimensional" continuum damage mechanics. In this case the shell must be treated as a three-dimensional continuum. We introduce the widely used Kachanov-Rabotnov-Leckie-Hayhurst creep-damage model [4] and demonstrate the description possibilities for stress states which are typical for thin-walled structures.

In order to compare the approaches, we introduce the examples of a transversely loaded beam and of a transversely loaded plate. The material constants are taken for the type 316 stainless steel at 650°C from [5]. The "three-dimensional" solution is performed by ANSYS finite element code by the use of solid type elements. For the comparison a standard "quasi three-dimensional" solution by the use of shell type finite elements is performed. In this case the cross section approximations are applied. The averaged equilibrium conditions formulated for stress resultants are solved step by step. At each time step the creep and damage rates are calculated from three-dimensional stress fields, which are recovered by means of the assumed cross-section approximations. We demonstrate that these two approaches lead in general to quite different long-term predictions. The agreement between the shell and solid type finite element solutions is obtained only in the case that the damage evolution is controlled by the von Mises stress. However, in this case the tertiary creep rates are the same under tension and compression, which in general, contradicts to the known experimental data for steels.

Finally, we present the results obtained by use of the proposed shell theory. From the results follows, that by suitable formulation of creep-damage constitutive and evolution equations for the shell the best agreement of our theory with the three-dimensional solution can be obtained.

References

[1] Altenbach, H., Naumenko, K.: Shear correction factors in creep-damage analysis of beams, plates and shells. JSME International Journal, Series A **45** (1), 77–83 (2002).

[2] Altenbach, H., Kushnevsky, V., Naumenko, K.: On the use of solid and shell type finite elements in creep–damage predictions of thinwalled structures. Arch. Appl. Mech. **71**, 164–181 (2001).

[3] Altenbach, H., Zhilin, P. A.: Osnovnye uravneniya neklassicheskoi teorii uprugikh obolochek (Governing equations of the non-classical theory of elastic shells). Uspekhi Mekhaniki **11**, 107–148 (1988).

[4] Leckie, F. A., Hayhurst, D. R.: Constitutive Equations for Creep Rupture. Acta Metall. **25**, 1059 – 1070 (1977).

[5] Liu, Y., Murakami, S., Kanagawa, Y.: Mesh–dependence and stress singularity in finite element analysis of creep crack growth by continuum damage mechanics approach. Eur. J. Mech., A Solids **13** (3), 395–417 (1994).

MULTISCALE MODELING SCHEMES SPANNING A LARGE RANGE OF SCALES

Fan, J., and He, Y.

Research Center of Materials Mechanics (RCMM)
ChongQing University, ChongQing, P. R. China, 400044

In this work, we present effective multiscale modeling schemes in the interdisciplinary field of solid mechanics and materials science for a large range of scales. The proposed multiscale modeling scheme should be able to carry out analyses spanning micro/meso/macroscopic scales of a continuum and be able to bridge atomistic and continuum scales so that variables such as stress, strain, electric field and electric displacement at different scales can be quantitatively correlated; thereby improving our understanding of the salient features that govern various types of material behavior over a large range of scales.

Though scientists and engineers have realized for a long time that the properties of materials follow from both their atomic and microscopic structures and that failure has its origins at the microscopic and atomistic scales, multiscale analysis remains in its infancy. The efforts so far have been mostly limited to describing relationships of variables at different scales qualitatively rather than quantitatively. The existing quantitative efforts have been limited to analyses that either span only two scales or require extremely intensive calculations due to a lack of effective methodology[1].

The proposed idea of multiscale analysis in the continuum realms is to use the medium of the intermediate scale as a means to connect variables at the lower scale with those at the upper scale through developing equivalent constitutive equations. These equations of the homogenized intermediate medium can be used to connect the variables between the intermediate scale and upper scale through a self-consistent scheme or mean field theory. These equations are developed based on microstructures of the lower scale through making the variables satisfy corresponding physical, chemical and mechanics principles. Therefore, there would be two features of the intermediate medium, with one being a homogenized feature that connects to the upper scale, and the other being a realistic feature, which connects to the lower scale, making quantitative connections of variables between the three scales possible.

Figure 1 shows the comparison between experiments and the simulation results for the size effects on cyclic creep (ratcheting) obtained by the multiscale modeling across micro/meso/macro scales in which specimens with layer thicknesses of 267, 287 and 319 nm of pearlitic high carbon steel were used. The different sizes were obtained by changing the cooling rate of heat-treatment temperature from 860 ^{0}C to room temperature. This success in incorporation of size effects in multiscale modeling has been obtained by introducing a dislocation model for developing size laws of material parameters. The dislocation model used is derived from the solution of Eshelby et al. [2]. From the size laws we found that the Hall-Petch relationship is valid, and most importantly that the kinematic hardening material parameters depend even more on the layer thickness.

In the realm of joint atomisticc and continuum scales, a mixed particle and molecular dynamics (MD) method will be coupled with quantum methods. The particle method is used to lump many atoms together as a molecular particle to reduce degrees of freedom in the low-stress gradient region which has been originally proposed in [3]. This lumped molecular particle can further connect to structure particles that are used in mesh-free finite element analysis to make the transition from the atomic scale to the continuum possible. For ferroelectric materials a polarized quasi-particle pair that forms a particle dipole should be used.

Figure 2 shows the simulated strain-electric field and electric displacement-electric field behavior of a single crystal of PLZT and the composite by the proposed micro/meso/macro/structural modeling schemes. Here micro corresponds to domain scale, meso to single crystal, macro to polycrystal, and structural to layered ferro-plastic composites. For single crystal ferroelectric material, the well-known nonlinear butterfly curve is successfully simulated and, the effect of volume fraction of ferroelectric

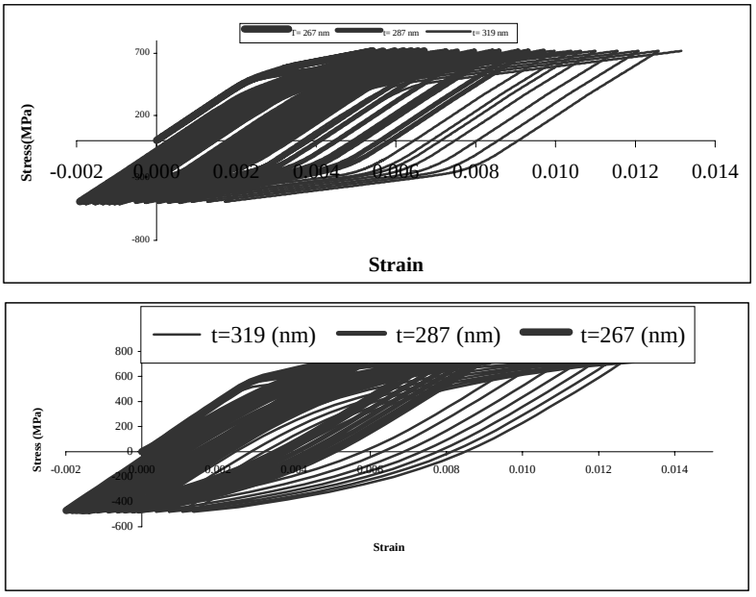


Figure 1: A Comparison between calculated results of three-scale simulation for cyclic creep (ratcheting) of high carbon rail steel specimens of layer thickness t= 319, 287 and 267 nm: (a) Experimental results; (b) Three-scale simulation

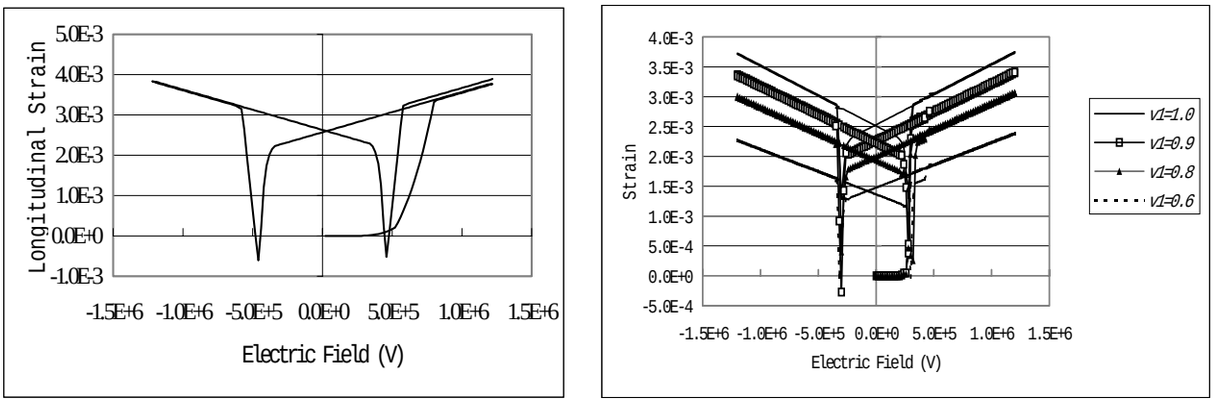


Figure 2: Curves of strain versus electric field: (a) single crystal; (b) ferroelectric-polymer layer composites where v1 indicates the volume fraction of ferroelectric ceramics

ceramics to performance of ferroelectric-polymer layer composites is well described.

Several significant findings resulted. These findings offer additional knowledge to both material behavior and failure mechanisms, proving the value of the proposed methodology and size laws.

Reference

[1]. R. E. Rudd and J. Q. Broughton (2000), Concurrent coupling of length scales in solid state systems, *Phys. Stat. Sol.* (b) **217**, 251-291.

[2].Eshelby, J. D., Frank, F. C. and Nabarro, F. R. N. 1951 The equilibrium of linear arrays of dislocations. *Philosophical Magazine* **42**, 351-364.

[3]. S. Hao, W. K. Liu, G. B. Olson, B. Moran, (2003) " Multi-Scale Constitutive Model and Computational Framework for the Design of Ultra-High Strength, High Toughness Steels", Presented in Plasticity-2003, Quebec; accepted by "Computer Method in Applied Mechanics and Engineering".

CONSTITUTIVE MODELING OF RUBBER COMPONENTS UNDER SMALL VIBRATION SUPERIMPOSED ON LARGE STATIC DEFORMATION CONSIDERING STRAIN-DEPENDENT PROPERTIES

Ji-Hyun Cho* , Sung-Kie Youn* , Wan-Sul Lee* and Bong-Kyu Kim**

*Department of Mechanical Engineering, KAIST, Daejeon, Korea
**Hyundai Motor Company, Korea

Summary A steady-state viscoelastic constitutive equation of filled rubber considering the effects of large static pre-strain and dynamic strain amplitude is proposed. The proposed model is based on the linearization of Simo's finite viscoelastic model and is modified to consider the influence of static pre-deformation and the dynamic strain dependent properties. Various dynamic tests are executed in order to get the model parameters and verify the model. The FEA results using the proposed model are compared with the test results to estimate the performance of the model.

INTRODUCTION

Many rubber components that are used as vibration isolator experience small oscillatory loads superimposed on large static deformation. The widely used Morman's model [1] is derived from the assumption that the time and large pre-strain effects are separable. It is observed in experiments that the separability assumption is restrictively applicable to unfilled rubber and the relaxation function of filled rubber is a function of pre-strain. Therefore it is very important to consider the influences of pre-strain in the constitutive theory of small viscoelastic motion superimposed on large static deformation in many engineering rubber materials. In the author's previous work [2], the K-Y viscoelastic constitutive model including the static deformation influence factor was proposed as a steady-state constitutive equation of filled rubber. Moreover, the dynamic strain amplitude affects the relaxation function of filled rubber and this behaviour is called as Payne's effect [3]. In this work, the viscoelastic constitutive model considering not only the static pre-strain but also the dynamic strain-dependent properties is proposed.

CONSTITUTIVE MODEL

The K-Y viscoelastic constitutive model for small vibration superimposed on large static deformation is derived through the linearization of Simo's finite viscoelastic model [4] and reference configuration transformation. The complex form of linearized model that relate the stress increment ΔS^* and the dynamic strain ε^* is written as follows.

$$\Delta S^* = \left(J\frac{\partial^2 U}{\partial J^2} + P \right)\varepsilon^*_{kk} I - 2P\varepsilon^* - \frac{2}{3}\left[dev(\hat{\sigma}) \otimes I + I \otimes dev(\hat{\sigma}) \right] : \varepsilon^* + \left(1 + i\omega g^*\right)\mathcal{C} : \varepsilon^* \tag{1}$$

In the above equation, $\mathcal{C}$ is the Truesdell elasticity tensor. The relation between g^* and complex shear modulus $G^* = G' + iG''$ is

$$\omega g^* = \frac{G''}{G_\infty} + \left(1 - \frac{G'}{G_\infty}\right) i \cdot \tag{2}$$

It is assumed that g^*, which represents the time effects, is not affected by static deformation. This separability assumption is suitable for the rubber which does not contain filler such as carbon black. However for filled rubber it is known by experiments that g^* depend on the static deformation. A static deformation influence factor, $c^*(B_0)$, is introduced to the constitutive equation in order to describe the non-separability nature of filled rubber. Also the function of strain amplitude and frequency is adapted in order to describe the effects of dynamic strain amplitude and frequency. $\hat{g}^*$,which is the correction of $1 + i\omega g^*$ in eqn. (1), is defined by

$$\hat{g}^* = \tilde{g}^*(\omega, \varepsilon^*) c^*(B_0) \tag{3}$$

where c^* is a complex valued function that depends on the static deformation. Since the value of c^* is unity without the static deformation, following polynomial forms can be served as the static deformation influence factor.

$$c_\gamma^*(\bar{I}_\gamma) = c_\gamma \; e^{i\theta_\gamma}, \; c_\gamma(\bar{I}_\gamma) = 1 + z_{\gamma 1}\bar{I}_\gamma + z_{\gamma 2}\bar{I}_\gamma^{\,2}, \; \theta_\gamma(\bar{I}_\gamma) = {}_\theta z_\gamma \, \bar{I}_\gamma \tag{4}$$

where generalized octahedral shear strain $\bar{I}_\gamma$ is defined as $\bar{I}_\gamma = \frac{1}{6}\left(2\bar{I}_1^2 - 6\bar{I}_2\right)^{1/2}$. $\bar{I}_\gamma$ is an invariant of B_0 and is reduced to octahedral shear strain under infinitesimal deformation.

Where $\tilde{g}^*(\omega,\varepsilon^*)$ is a complex valued function that describes the effects of dynamic strain amplitude and frequency. If it is assumed that the effects of frequency and strain dependent properties are separable, $\tilde{g}^*(\omega,\varepsilon^*)$ can be written by

(5) $$\tilde{g}^*(\omega,\varepsilon^*) = \tilde{g}_\omega{}^*(\omega)\tilde{g}_\varepsilon{}^*(\varepsilon^*)$$

(6) $$\tilde{g}_\omega{}^*(\omega) = f^a$$

(7) $$\tilde{g}_\varepsilon{}^*(\varepsilon^*) = \left(G'_\infty + \frac{\Delta G'}{1+(\|\varepsilon^*\|/\varepsilon_0)^{2m}}\right) + i\left(G''_\infty + \frac{2(G''_m - G''_\infty)(\|\varepsilon^*\|/\varepsilon_0)^m}{1+(\|\varepsilon^*\|/\varepsilon_0)^{2m}}\right)$$

where $\tilde{g}_\varepsilon{}^*(\varepsilon^*)$ is well known by KRAUS model [3]. $\tilde{g}_\omega{}^*(\omega)$ describes the effect of frequency. Eqn. (6) is the simple case of many other candidates. It is not the complete form, so some modifications are needed.

EXPERIMENT AND RESULTS

Dynamic tests for uniaxial tension and complex stress state are carried out in order to verify the proposed constitutive model. The test specimens are made of natural rubber filled with 50phr of carbon black. Fig 1 shows that eqn. (5)~(7) describe the effect of frequency and strain dependent properties well in the case of tension test results. Material parameters are determined from tension test results. Using these parameters, complex stress state test results are compared with the FEA results of the proposed model. Fig 2 shows that the proposed model shows good agreements with the test results of complex stress state in the case of fixed frequency and no pre deformation.

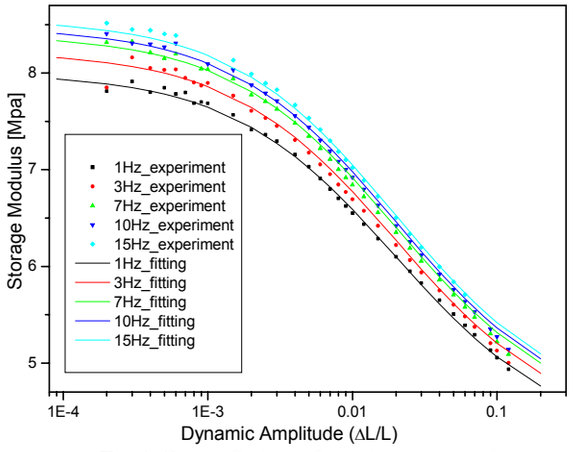


Fig 1 Curve fitting of tension test results

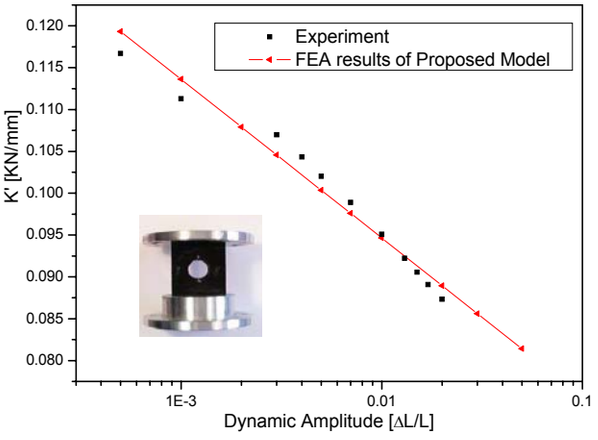


Fig 2 Comparison the experiment results with the FEA results of proposed model for complex shape test

CONCLUSION

A steady-state viscoelastic constitutive equation of filled rubber considering the effects of large static pre-strain and dynamic strain amplitude is proposed. Various dynamic tests are executed in order to get the model parameters and verify the model. The FEA results using the proposed model are compared with the test results to estimate the performance of the model. The proposed model shows good agreements with the test results of complex stress state.

References

[1] J. I. Sulivan, K. N. Morman and R.A. Pett : A Non-linear Viscoelastic Characterization of a Natural Rubber Gum Vulcanizate. Rubber Chemistry and Technology **53** : 805–822, 1980.
[2] B.-K. Kim and S.-K. Youn : A viscoelastic constitutive model of rubber under small oscillatory loads superimposed on large static deformation . Arch. Appl. Mech. **71** : 748–763, 2001.
[3] J.D.Ulmer : Strain dependence of dynamic mechanical properties of carbon black-filled rubber compounds. Rubber Chemistry and Technology **69** : 15-47,1996.
[4] J.C. Simo : Comput. A Fully Three-dimensional Finite-strain Viscoelastic Damage Model:Formulation and Computational Aspects. Method Appl. M. **60** : 153–173, 1987

Acknowledgement This work was supported by grant R01-2001-00393 from the Korea Science & Engineering Foundation.

AN INFLUENCE OF COLD WORK ON CREEP OF ENGINEERING MATERIALS

Zbigniew L. Kowalewski*
*IPPT PAN, Department for Strength of Materials, PL 00-049 Warsaw, Poland

Summary An influence of deformation history on the basic creep parameters of pure copper and PA6 aluminium alloy (notation according to Polish Standards) is analysed for creep due to uniaxial tension at elevated temperatures. Prior plastic deformation up to the several selected levels of strain was realised by means of tension at room temperature. The experimental data achieved are used to verify the assumptions of the recovery creep theory.

INTRODUCTION

During manufacturing and exploitation processes most engineering structures or some their elements are subjected to deformation. Therefore, it is important from engineering point of view to know the influence of this deformation on such different material properties at high temperatures as minimum creep rate, ductility, lifetime, fracture and crack propagation. It has been found that plastic deformation at both room and elevated temperatures prior to creep testing has either beneficial or detrimental effect on the materials. Although the problem has been previously studied experimentally for several materials [1 ÷ 6], only limited amount of available data reflects the influence of plastic predeformation on creep process up to rupture [1, 2, 4, 5]. It is well known that the problem is particularly important during fabrication or assembly processes, where a number of materials used in critical elements of engineering structures may receive such cold work and, as a consequence, it may change significantly their lifetime. Up to now the amount of experimental data is still insufficient to estimate exactly whether the increase or decrease of creep strengthening occurs up to a certain amount of prestrain only, or whether this creep property is in some way proportional to the amount of predeformation. Thus, in order to achieve better understanding of this problem further systematic investigations are required. The aim of this paper is to identify an influence of prior plastic deformation of pure copper and aluminium alloy on the basic creep parameters under uniaxial tension.

EXPERIMENTAL PROCEDURE

Thin-walled tubular specimens were used in all tests. For both materials the experimental programme comprised creep tests under uniaxial tension carried out at two different temperatures (523K and 573 K in case of pure copper, 423K and 473K for aluminium alloy). Creep tests were performed for materials in the as-received state and for the same materials plastically prestrained at the room temperature. In the case of copper the prestrain values of 2.5%, 5.0%, 7.5% and 10.0% were selected in tests at 523 K, whereas tests at 573 K were carried out for testpieces prestrained up to 5% and 10%. The aluminium alloy specimens were prestrained up to 1%, 2%, 6% and 8% for both creep test temperatures taken into account. Experiments were carried out with the use of the Instron 1343 testing machine and standard creep testing stand. The mechanical extensometer connected to the protrusions machined on each testpiece was used for creep strain measurement. These protrusions were applied to transfer the displacement occuring during creep to a location outside of the high temperature furnace where the linear voltage displacement transducers could accurately measure displacement at ambient temperature.

RESULTS

The experimental results for copper and aluminium alloy are presented in Figs. 1 and 2, respectively. It has been shown that the minimum creep rate, and elongation decreases as the amount of the plastic prestrain increases. Such type of response was proportional to the plastic predeformation only up to $\varepsilon = 5\%$ in the case of copper, and up to $\varepsilon = 6\%$ - for aluminium alloy. Higher magnitudes of prior deformation led to increase of the minimum creep rate for both materials. Predeformation also changes the duration of typical creep stages of both materials tested. The duration of the primary creep period decreases, in practice, independently on the amount of prior plastic deformation. In the case of pure copper the duration of secondary creep stage decreases as the magnitude of plastic prestrain increases. An opposite behaviour was observed during creep of prestrained aluminium alloy specimens.

In comparison to the nonprestrained copper a little increase of the time to rupture with the increase of plastic predeformation has been observed for the prestrained specimens tested at higher temperature (573 K). In the case of lower temperature (523 K) the lifetime decreased significantly with the increase of plastic predeformation. The creep data for aluminium alloy exhibit the same tendency of lifetime variation due to prestraining in both temperatures under the question, namely, an extension of lifetime proportional to the magnitude of plastic prestrain. It has to be noted however, that plastic prestrain magnitudes greater than 6% led to the opposite effect, i.e. lifetime reduction.

In the paper the experimental data achieved are discussed in detail and used to verify of the basic assumptions and predictions of the recovery creep theory. It has been found that a good agreement between experimantal data and

predictions of the recovery creep theory can be achieved only for sufficiently low level of predeformation, lower than 5% in the case of copper, and lower than 6% for aluminium alloy.

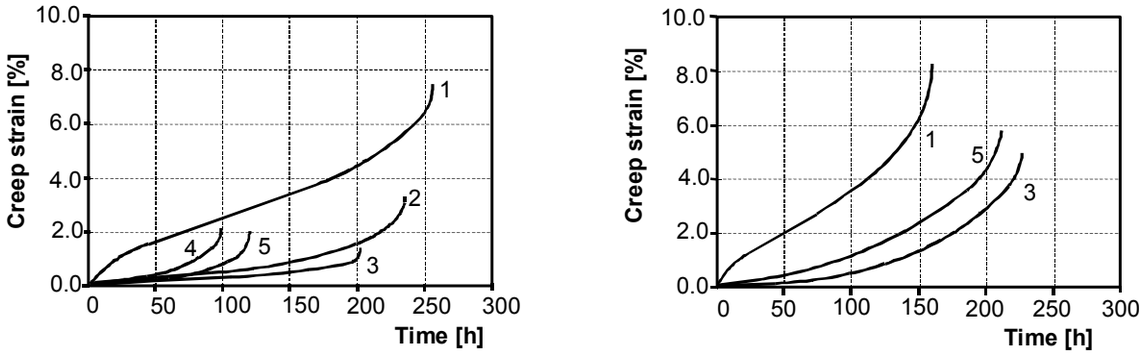


Fig. 1 Creep curves of copper at: (a) σ = 70 MPa and T = 523K: (b) σ = 45 MPa and T = 573K (1 – material in the as-received state; 2, 3, 4, 5 – material prestrained up to 2.5, 5.0, 7.5, 10.0 %, respectively.

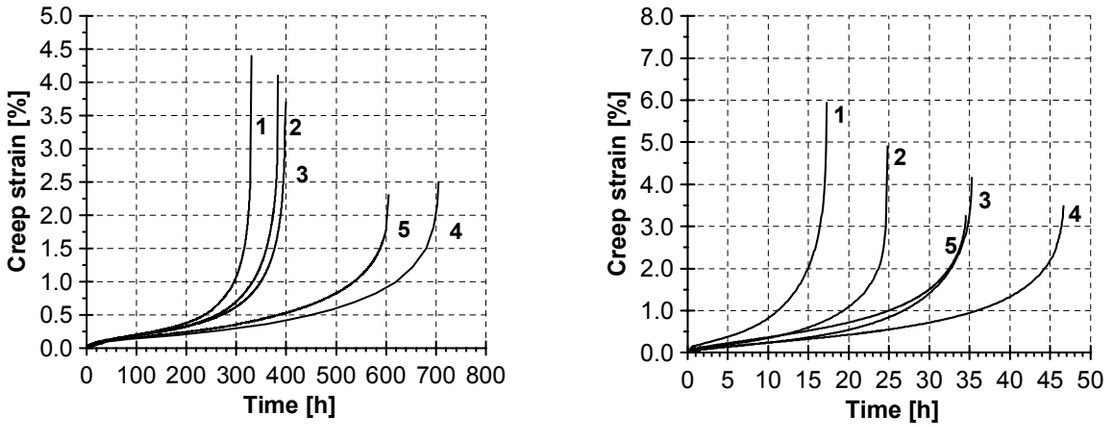


Fig. 2 Creep curves of PA6 aluminium alloy at: (a) σ = 300 MPa and T = 423K: (b) σ = 200 MPa and T = 473K (1 – material in the as-received state; 2, 3, 4, 5 – material prestrained up to 1.0, 2.0, 6.0, 8.0 %, respectively.

CONCLUSIONS

The main remarks stemming from this research can be summarized as follows:

1) The tensile creep resistance was generally enhanced by plastic prestrain, which was expressed by significant decrease of the steady creep rate. However, the amount of this effect, in the case of both tested materials, is not proportional to the increase of predeformation.
2) The results demonstrate that creep fracture process can be modified by prior cold working. In the case of tested copper the creep life dependently on testing temperature may either be increased or decreased to very low levels.
3) The amount of creep deformation for both temperatures considered was markedly reduced by prior tensile plastic strain, yielding very low levels. Elongations of the testpieces were proportionally decreased when the magnitude of plastic prestrain was increased.

References

[1] Dyson B.F., Rodgers M.J., Prestrain, cavitation and creep ductility, *Metal Science*, 8, 261-266, 1974.
[2] Dyson B.F., Loveday M.S., Rodgers M.J., Grain boundary cavitation under various states of applied stress, *Proc. R. Soc. Lond. A*, 349, 245-259, 1976.
[3] Kawai M., Creep and plasticity of austenitic stainless steel under multiaxial non-proportional loadings at elevated temperatures, *Visco-Plastic Behavior of New Materials*, PVP-vol.184, Ed.: D. Hui, and T.J. Kozik, Book No. H00576, 85-93, 1989.
[4] Marlin R.T., Cosandey F., Tien J.K., The effect of predeformation on the creep and stress rupture of an oxide dispersion strengthened mechanical alloy, *Metallurgical Transactions A*, 11A, 1771-1775, 1980.
[5] Pandey M.C., Mukherjee A.K., Taplin D.M.R., Prior deformation effects on creep and fracture in inconel alloy X-750, *Metallurgical Transactions A*, 15A, 1437-1441, 1984.
[6] Xia Z., Ellyin F., An experimental study on the effect of prior plastic straining on creep behavior of 304 stainless steel, *Journal of Engineering Materials and Technology*, 115, 200-203, 1993.

XXI ICTAM, 15–21 August 2004, Warsaw, Poland

MULTI-SCALE MODEL FOR LOW-TEMPERATURE CREEP OF ASPHALT

Roman Lackner, Andreas Jäger, Karl Kappl, Markus Spiegl, Ronald Blab, and Josef Eberhardsteiner
Christian Doppler Laboratory on "Performance-Based Optimization of Flexible Road Pavements"
Vienna University of Technology (TU Wien), Karlsplatz 13/202, 1040 Vienna, Austria

Summary Macroscopic material properties of asphalt are related to finer-scale information by means of a multi-scale model consisting of five observation scales. Having identified the different constituents (material phases) and their assemblages at the scales introduced within the multi-scale model, we present recent results on up-scaling information from the *mastic*-scale to the next higher, i.e., the *mortar*-scale focusing on the influence of the filler (aggregates with diameter smaller than 125 μm) on low-temperature creep. The Mori-Tanaka scheme is chosen to incorporate the effect of aggregates embedded in the viscous bituminous matrix. The good agreement between the material properties obtained via homogenization and the respective experimental results suggests that only the volume content of the filler affects the creep properties of the mastic material, explaining phenomena and problems recently encountered in asphalt pavement engineering.

INTRODUCTION AND MOTIVATION

Asphalt is composed of bitumen, aggregate, and air voids, showing a complex thermo-rheological behavior. E.g., the low viscosity of asphalt at high temperatures ($T > 135$ °C) is a necessary prerequisite during the construction and compaction process of high-quality asphalt layers. When the surface temperature reaches 70 °C during hot summer periods, however, this viscosity should be significantly higher in order to minimize the development of permanent deformations (rutting, see Figure 1). The desirable decrease of viscosity and, hence, increase of stiffness with decreasing temperature at hot and



Figure 1. Damage of flexible pavements by rutting (left) and fatique failure (right)

medium temperatures (0 °C $< T <$ 70 °C) are, on the other hand, disadvantageous at low temperatures ($T <$ 0 °C), causing low-temperature cracking in asphalt pavements. This optimization problem concerning the behavior of asphalt at different temperature regimes is a main objective of the Christian Doppler Laboratory "Performance-Based Optimization of Flexible Road Pavements" (TU Wien), headed by Ronald Blab. For the optimization process of a multi-composed material such as asphalt, three different modes can be distinguished:

1. variation of mixture characteristics (e.g., binder/aggregate-ratio),
2. change of constituents used (e.g. different bitumen or filler type), and
3. allowance of additives (e.g., polymers to modify the bitumen).

MULTI-SCALE MODEL FOR ASPHALT

In order to account for the wide range of asphalt mixtures, resulting from the large number of different bitumen, fillers, and aggregates used in engineering practice, the multiscale concept is chosen for the determination of rheological properties of asphalt. Within the multiscale concept, four additional observation scales are introduced below the macroscale, namely (i) the *bitumen*-scale (asphaltene and maltene morphology), (ii) the *mastic*-scale (bitumen+filler), (iii) the *mortar*-scale (mastic + aggregate with < 2 mm), and (iv) the *asphalt*-scale (mortar + aggregate with > 2 mm), see Figure 2. Within each observation scale, the characteristics (such as structure and material properties) of the constituents present at this scale can be considered.

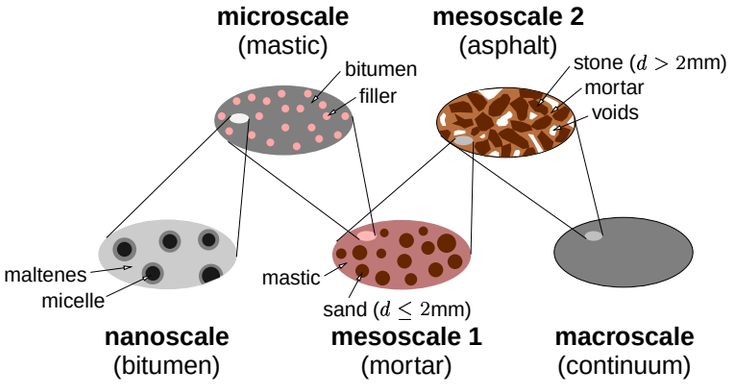


Figure 2. Multi-scale model for asphalt incorporating five scales of observation

LOW-TEMPERATURE CREEP – RESULTS AND CONCLUSIONS

The high viscosity of bitumen at low temperatures and, hence, the reduced capability of stress relaxation cause an increased loading during cold-temperature periods in consequence of both thermal strains and traffic loads. In order to improve the low-temperature behavior of asphalt and, hence, to avoid damage of the infrastructure, a multi-scale model is proposed, allowing to predict low-temperature viscous properties of asphalt at different scales of observation. Bending-beam-rheometer (BBR) experiments [3] were conducted on pure bitumen and mastic material, considering five different types of bitumen (characterized by a penetration depth [1/10 mm] [3] ranging for 10 to 220) and six different types of filler. While the temperature dependence of low-temperature creep is incorporated in the bitumen phase only, employing an Arrhenius-type law, the Mori-Tanaka scheme [2] together with the effective volume fraction for the filler (see, e.g., [1]) is used for consideration of the effect of the filler. Even though fillers characterized by a variation of the air-void content (obtained from Ridgen device) by the factor of two (30 vol-% for the limestone-dust filler and 64 vol-% for the hydrated-lime filler), the creep properties predicted by the multi-scale model are in good agreement with the respective BBR results. This is illustrated in Figure 3, showing selected results for the initial rate of the creep compliance obtained from BBR data of mastic with limestone-dust and hydrated-lime filler. The obtained results suggest that (i) the influence

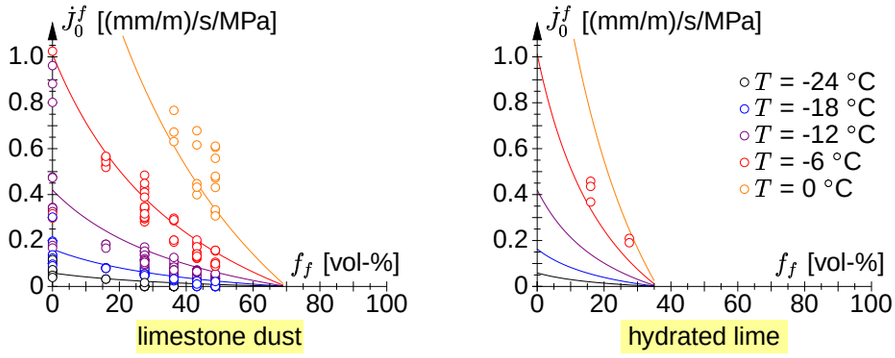


Figure 3. Initial rate of creep compliance for mastic with different filler content (experiments: circles; predicted by multi-scale model: lines)

of the type of bitumen on the viscous behavior of the mastic is marginal and (ii) the filler acts only by the its volume fraction; as a consequence of the good performance of the employed homogenization scheme which uses only the volume content as input, neither shape and grain-size distribution nor chemical composition of the filler affect the overall creep properties of asphalt.

Although the work presented inhere focussed on lower-scale properties, proposing an up-scaling technique from the *mastic*- to the *mortar*-scale, the gained information already allows to explain phenomena and problems recently encountered in asphalt pavement engineering.

References

[1] J.W. Ewers and W. Heukelom. Die Erhöhung der Viskosität von Bitumen durch die Zugabe von Füller. *Straße und Autobahn*, (2):31–39, 1964. In German.

[2] T. Mori and K. Tanaka. Average stress in matrix and average elastic energy of materials with misfitting inclusions. *Acta Metallurgica*, 21:571–574, 1973.

[3] SHRP-A-370. Binder characterization and evaluation. Volume 4: test methods. Technical report, Strategic Highway Research Program, National Research Council, Washington, DC, USA, 1994.

A MODEL OF CYCLIC VISCOPLASTICITY WITH SPECIAL REFERENCE TO YIELD-POINT PHENOMENA

Fusahito Yoshida*
** Hiroshima University, Department of Mechanical System Engineering, 1-4-1, Kagamiyama, Higashi-Hiroshima 739-8527, Japan*

Summary A model of viscoplasticity that describes the yield-point phenomena is presented. This paper describes its modeling and some strong features of this model by comparing the numerical simulations and the corresponding experimental data on fundamental cyclic plasticity, such as rate-dependent cyclic straining and ratcheting. Furthermore, as an example of industrial application of this model, a result of finite element numerical simulation on skin-pass rolling of a sheet metals is presented.

INTRODUCTION

Annealed steels and some bcc metals, as well as some aluminum alloys, exhibit a sharp yield point and the subsequent abrupt yield drop followed by the yield plateau in the stress-strain curves of uniaxial tension. The yield-point phenomena are strongly rate dependent, e.g., the flow stress levels, especially the upper and lower yield strengths, increase with increasing strain rate, and furthermore, the Luders strain becomes larger with the rate. As for cyclic plasticity behavior, the Bauschinger effect is clearly observed even in a cyclic straining at yield plateau region. Constitutive modeling of such rate-dependent yield-point phenomena, as well as the subsequent cyclic plasticity, is of vital importance, since in most of cases of small-scale yielding, plastic deformation occurs in the Luders strain range, but not in the workhardening region. Nevertheless, most of discussions of constitutive modeling so far published scarcely touched this problem.

The present author [1] has recently proposed a constitutive model of cyclic plasticity which takes into account the yield-point phenomena. The first part of this paper presents an extended version of this model, which properly describes the above-mentioned rate-dependent yield-point phenomena and the subsequent cyclic plasticity behavior. The second part of this paper demonstrates how it works in the numerical simulation of cyclic plasticity, such as cyclic straining and ratcheting. Moreover, as an industrial application of this model, a result of FE simulation of skin-pass rolling, which is a process for erasing the yield-point and non-uniformly plastic deformation of sheet metals, is presented.

CONSTITUTIVE MODELING

The framework of viscoplastic constitutive model is constructed based on the overstress theory on the premise that the sharp yield point and the subsequent abrupt yield drop result from rapid dislocation multiplication and the stress dependence of dislocation velocity [2], which is given by the following equations:

$$\dot{\bar{\varepsilon}} = \frac{b\rho_m}{M}\left\langle \frac{\bar{\sigma}-Y}{D} \right\rangle^n, \quad \boldsymbol{\dot{\varepsilon}}^p = \frac{3(\boldsymbol{s}-\boldsymbol{\alpha})}{2\bar{\sigma}}\dot{\bar{\varepsilon}}, \quad \bar{\sigma} = \sqrt{\frac{3}{2}(\boldsymbol{s}-\boldsymbol{\alpha}):(\boldsymbol{s}-\boldsymbol{\alpha})}$$

where $\boldsymbol{\dot{\varepsilon}}^p$ and $\dot{\bar{\varepsilon}}$ are the plastic strain rate and its effective value, and $\boldsymbol{s}$ and $\boldsymbol{\alpha}$ are the stress and back stress deviators, and Y: the radius of yield surface; D: drag stress; b: the Burgers vector; ρ_m: mobile dislocation density; M: Taylor factor. The yield surface kinematically moves within the bounding surface which has isotropic/kinematic hardenings [3]. In addition, workhardening stagnation for the bounding surface, of which rule has been proposed by the present authors [3], is assumed. To describe the rapid multiplication of mobile dislocation density, ρ_m, the rule of evolution equation of the fraction of mobile dislocation density [1] is employed. Furthermore, in the present paper, a new rule to distinguish two regimes, i.e., yield-drop and workhardening regimes, is introduced.

Figure 1 shows an example of stress-strain responses of a material element in uniaxial tension predicted by the present model. It clearly shows the rate dependent stress-strain responses, which consist of two parts: one is yield-drop regime characterized by the sharp yield-point and the subsequent yield drop (softening), and the other workhardening region. It should be noted that this is a stress-strain response for a material element, but not for a stress vs. gage-length strain curve observed in uniaxial tension experiment where non-uniformly plastic deformation occurs in a specimen. If this model is used for FE simulation of uniaxial tension experiment for a real shape of specimen, the calculated result will show almost flat yield plateau as a result of the simulation of the Luders band propagation.

NUMERICAL SIMULATIONS OF VARIOUS ASPECTS OF YIELD-POINT PHENOMENA

Uniaxial Tension and Cyclic Plasticity Deformations

This model has a capability of reproducing realistic stress-strain curves in uniaxial tension, where the rate dependence of flow stress in the yield plateau is much stronger than in workhardening region, and the Luders strain becomes larger with increasing strain rate. This model can also well simulate cyclic plasticity deformations. Figure 2 shows an example of FE numerical simulation of stress-stress response in ratcheting, where the rate of strain accumulation is fast at an

early stage of ratcheting and it tends to shakedown, which are consistent with the experimental observations [1]. Deformation characteristics of cyclic straining and strain-controlled ratcheting are also studied in the present work.

In a specific case of uniaxial tension, extremely high upper yield point, as high as almost twice of the lower yield strength, is found in a center-annealed specimen of a mild steel wire (see its FE simulation in Fig. 3a). However, such a high yield point disappears in a uniformly annealed specimen (see Fig. 3b), because the Luders band propagates from a vicinity of the specimen clamp where plastic deformation zone had been formed by clamping. These phenomena are discussed based on FE simulation.

Modeling of Strain Aging

Strain aging behavior, characterized by the reappearance of the upper yield-point and the increase of flow stress due to aging, is simulated by this model. In the modeling of aging, mobile dislocation density is assumed to be initialized due to dislocation locking, and the isotropic hardening of the bounding surface, caused by the precipitate hardening, is introduced.

FE simulation of Skin-Pass Rolling

Skin-pass rolling, where sheet-thickness reduction is as small as 1-2%, is a popular process conducted at the final stage of sheet metal rolling for the purpose of erasing yield point and non-uniform deformation of sheet metals. To understand the mechanism of erasing of yield point, FE simulation of skin-pass rolling was performed. From the simulation it was found that, after skin-pass rolling, plastic strain covers all over the sheet, therefore, in the subsequent uniaxial tension the upper yield point no longer appears.

CONCLUDING REMARKS

The present model of cyclic viscoplasticity well describes several aspects of rate-dependent yield-point phenomena, and it is a powerful tool for understanding the mechanism of yield-point phenomena, and also for numerical simulations of many industrial applications such as structural analyses and metal forming simulations.

References

[1] Yoshida F.: A model of cyclic plasticity, *Int. J. Plasticity* **16**, 359-380, 2000

[2] Hahn, G. T.: A model for yielding with special reference to the yield-point phenomena of iron and related bcc metals, *Acta Metallurgica* **10**, 727-738, 1962

[3] Yoshida F.: A model of cyclic plasticity, *Int. J. Plasticity* **16**, 359-380, 2000

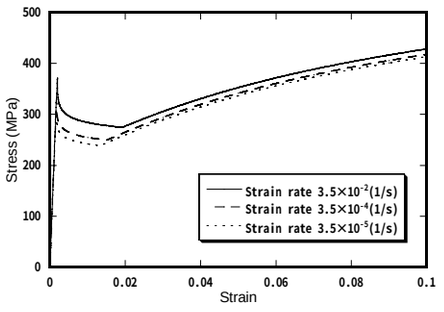


Fig.1 Stress-strain response in uniaxial tension of a material element calculated by the present model.

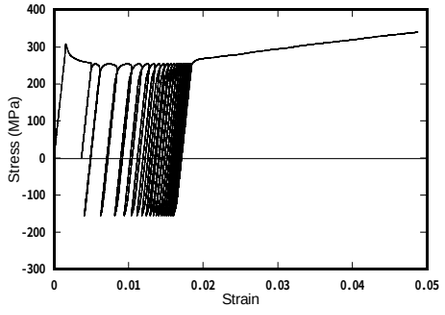
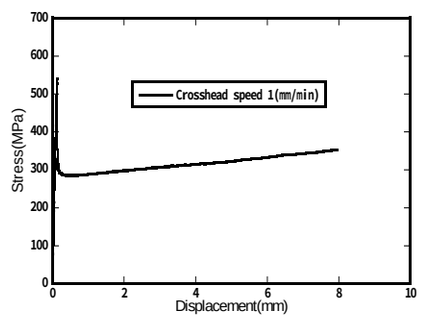
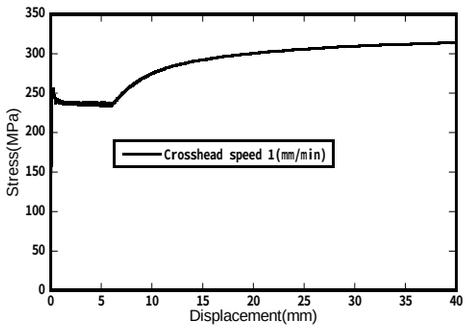


Fig.2 Numerical simulation of ratcheting of a mild steel.



a)



b)

Fig. 3 Calculated results of stress-displacement curves for a) a center-annealed specimen and b) a uniformly annealed specimen of a mild steel wire.